

An aerial, black and white photograph of a coastal city and harbor. The image shows a dense urban area with numerous buildings, a complex highway interchange, and a large harbor area with several piers and ships. The water is dark, and the sky is light. The overall scene is a detailed view of a major coastal city.

VOLUME I

Coastal Engineering

1980 PROCEEDINGS

PROCEEDINGS
OF THE

Seventeenth Coastal Engineering Conference

March 23 to 28, 1980
Sydney, Australia

Volume I

Sponsored by
ASCE Coastal Engineering Research Council
ASCE Waterway, Port, Coastal and Ocean Division
and
The Institution of Engineers, Australia



Published by the American Society of Civil Engineers
345 East 47th Street, New York, N.Y. 10017

Copyright © 1981 by the American Society of Civil Engineers,
All Rights Reserved.
Library of Congress Catalog Card No. 80-69156
ISBN 0-87262-264-9
Manufactured in the United States of America.

FOREWORD

The Seventeenth International Conference on Coastal Engineering was extremely important in many ways to those who attended the conference and to those who will benefit from use of these *Proceedings*. The Seventeenth Conference marked the 30 year point in the history of the coastal engineering conference series and a change in leadership. Since the first conference was held in Long Beach, California in October 1950, Dean Morrough P. O'Brien and Professor Joe W. Johnson have provided the continuity, direction, and motivation that have made the International Coastal Engineering Conferences so successful. For thirty years Dean O'Brien has served as Chairman and Professor Johnson as Secretary of first the Council on Wave Research and now the Coastal Engineering Research Council. Because of the importance of their contributions to the coastal engineering conferences the Council decided that these *Proceedings* will be dedicated to these two leaders. A summary of the accomplishments of each in coastal engineering is presented here.

MORROUGH P. O'BRIEN

His distinguished career in coastal engineering has been much too full to cover adequately in this space; only a sketch of his accomplishments are included here. M. P. O'Brien retired as Dean of the College of Engineering at the University of California, Berkeley, in 1959. His tenure at Berkeley included an impressive record of teaching, research and university administration. During this interval, through his students and research, he established the reputation of "The Father of Coastal Engineering." After leaving his post at Berkeley he has been very active in industrial and governmental research and development projects. At his present age, 78, Dean O'Brien is still an extremely active professional in coastal engineering.

Dean O'Brien graduated from Massachusetts Institute of Technology in 1925 and pursued graduate work at Purdue University. In 1927 he was awarded the ASCE John R. Freeman Scholarship which allowed him to attend the Technische Hochschule, Danzig, and the Royal College of Engineering, Stockholm, to study hydraulic structures and machinery. He has received honorary degrees from Northwestern University, D.Sc.; Purdue University, D.Eng.; and University of California, Berkeley, LL.D.

He joined the Mechanical Engineering Department at the University of California becoming Department Chairman in 1936 and Dean of the College in 1943. During his tenure as Dean he was instrumental in the development of graduate education and research and in the modernization of the undergraduate program.

In 1929, Dean O'Brien organized and initiated a program of research on shoreline processes and coastal engineering for a board appointed by the Chief of Engineers of the Army; subsequently, Congress established this work on a permanent basis under the U.S. Beach Erosion Board. Dean O'Brien has served as a member of this board and its successor, the Coastal Engineering Research Board from 1938 to 1980. He has maintained an active interest in ocean waves and shoreline phenomena. During the war years, this interest led to work on the design of landing craft, on forecasting surf conditions,

and on intelligence studies of landing beaches. Following the war he served as Chairman of the ad hoc committee on Amphibious Operations of the National Research Council which reviewed the plans for modernization of the Marine Corps. Consulting engagements in the field of coastal engineering included restoration of the beach at Santa Barbara, regulation of the estuary of the Columbia River, Dos Bocas Harbor in the Gulf of Campache and other similar coastal projects.

Dean O'Brien's research on hydraulic machinery led to many practical applications by industry. Most of the jet pumps sold in the United States follow the designs of O'Brien and Gosline. Application of the theory of airfoils to the design of propeller pumps and fans by O'Brien and Folsom provided the basis for extensive production of low-head, high-capacity pumps for irrigation and drainage. Consulting engagements on hydraulic machinery during this period included Byron Jackson, Food Machinery, Fairbanks-Morse, Becker Pump, Navy Department, Corps of Engineers, and many other governmental agencies. His experience with turbo-machinery led to his appointment in 1949 as a consulting engineer by the Aircraft Gas Turbine Division of the General Electric Company, an association which has continued to the present. He is now a consultant to the Technical Systems and Materials Sector of General Electric, dealing with both technical and management problems of jet engines, missiles and space vehicles, ordnance, and electronic systems.

During the war years, Dean O'Brien directed the University of California's program of engineers' science and management war training for technical and professional personnel in the aircraft and shipbuilding industries. During the four years of its existence, this program included 1800 instructors and 46,000 students. Concurrently, he served as dean of the college and as consultant in the research section of the Bureau of Ships on problems of submarine propeller noise, and on amphibious operations. In 1946, he participated in Operation Crossroads at Bikini as a consultant on the measurement of waves generated by the bomb tests; most of the photographs of the Baker tests, which appeared in the press, were taken by the tower and aerial cameras which Dean O'Brien and his associates operated for wave measurements.

Twice, he has taken full-time leave from academic duties to engage in engineering practice; once, 1947 to 1949, to serve as director of research and engineering with the Air Reduction Company and, again in 1953, to join General Electric Company's Aircraft Nuclear Propulsion Project. He has held membership on many influential boards and commissions, among them the Coastal Engineering Research Board, formerly the Beach Erosion Board; the National Science Foundation's panel of engineering consultants; the Army Scientific Advisory Panel; the Atomic Energy Commission's personnel security board; the Maritime Research Advisory Committee and the Advisory Board on Education of the National Academy of Sciences, National Research Council; and the board of directors, McGraw-Hill Publishing Company. In 1958 President Eisenhower appointed him a member of the Board of the National Science Foundation. During 1958-1959, he was a visiting institute professor at the Massachusetts Institute of Technology, and a visiting research fellow at Harvard University.

Among awards he has received are the Army-Navy Certificate of Appreciation; the Distinguished Civilian Award, Department of the Army (twice); and the Bliss Medal of the Society of American Military Engineers. In 1968 he received the ASEE's Lamme Award, and in 1969 a building at the University of California's Berkeley Campus was named after Dean O'Brien.

He has written more than 100 published articles on technical subjects and engineering education, and is co-author of "Applied Fluid Mechanics," published by McGraw-Hill in 1937. The bibliography is his own selection of the papers which he most enjoyed

writing. He is a registered professional engineer in the states of California and New York, and a chartered Mechanical Engineer in Great Britain. In 1969 he was elected to the National Academy of Engineering. He is an Honorary Member of both the ASCE and ASME.

Selected Bibliography

- Entrance Area Related to Tidal Prism, *Civil Engineering*, 1931.
- Checks on the Model Law for Hydraulic Structures, *Trans. Amer. Geo. Union*, 1932.
- Review of the Theory of Turbulent Flow and its Relation to Sediment Transportation, *Trans. Amer. Geo. Union*, 1933.
- Model Law for Motion of Salt Water through Fresh (with John Chuno), *ASCE Trans.*, vol. 99, 1934.
- The Transportation of Bed-Load by Streams (with B. B. Rindlaub), *Trans. Amer. Geo. Union*, 1934.
- The Water Jet-Pump (with J. E. Gosline), *Univ. Calif. Publ. in Eng.*, vol. 3, no. 3, 1934.
- A Summary of the Theory of Oscillatory Waves, TR No. 2, Beach Erosion Board, 1941.
- The U.S. Tidal Model Laboratory, *Shore & Beach*, vol. 3, no. 2, 1935.
- Velocity of Large Bubbles in Vertical Tubes (with J. E. Gosline), *Indust. Eng. Chem.*, vol. 27, December 1935.
- Models of Estuaries, *Trans. Amer. Geo. Union*, 1935.
- The Transportation of Sound by Wind (with B. B. Rindlaub), *Trans. Amer. Geo. Union*, 1936.
- The Design of Propeller Pumps and Fans (with R. G. Folsom), *Univ. Calif. Publ. Eng.*, vol. 4, no. 1, 1939.
- Some Problems of Horizontal Steady Flow in Porous Media (with J. A. Putnam), *Am. Inst. Min. & Met. Eng.*, paper 1349, 1941.
- Model Experiments on Impulsive Waves in Shallow Water, *Trans. Amer. Geo. Union*, April 1947.
- Lag and Reduction of Range in Tide-gage Wells, Beach Erosion Board Bulletin, vol. 4, no. 3, 1950.
- The Nature of Engineering, *Jour. Eng. Educ.*, November 1950.
- The Force Exerted by Waves on Objects (with J. R. Morison), *Trans. Amer. Geo. Union*, February 1952.
- The Engineering of Large Systems, *The World of Engineering*, Chapter 9, McGraw-Hill, 1964.
- The Equilibrium Flow Areas of Tidal Inlets on Sandy Coasts, Tenth Int. Conf. on Coastal Eng., ASCE, 1966.
- Hydraulic Coefficients of Tidal Inlets (with R. Clark), Coastal & Oceanographic Engineering Laboratory, Univ. of Florida, 1974.
- Hydraulic and Sedimentary Stability of Tidal Inlets (with R. G. Dean), ASCE, Thirteenth Int. Conf. on Coastal Engineering, 1972.

JOE W. JOHNSON

Professor Johnson has had a long and very distinguished career in coastal engineering. His reputation extends around the world, reaching forth from his consulting, his research and especially his students. In 1975 he retired as Professor of Civil Engineering from the University of California, Berkeley. Professor Johnson is also well known for his excellent handling of the *Proceedings* of all sixteen prior coastal engineering conferences. Since his retirement from the University of California he has been extremely active in his consulting practice and professional duties.

Professor Johnson graduated from the University of California, Berkeley, in 1931 with a B.S. in Civil Engineering and in 1934 with an M.S. degree. Following a brief stay at the Waterways Experiment Station he devoted eight years to studying sediment transport with the Soil Conservation Service. He then returned to the University of California and enjoyed a very fruitful career of teaching, research and public service.

He has been consultant to many international projects involving shoreline development including: an ore port in Vitoria, Brazil; harbor development along the coast of Venezuela; port development in Northwest Australia; port development in Damietta, Egypt; sedimentation at Bahia Blanca, Argentina; Hay Point Coal Port, Australia; and wave action and sedimentation in Brazil. His associations with coastal engineering projects in the United States are equally extensive; a brief list follows of his involvement: Rio Grande Valley, wind tides in Lake Okeechobee, wave analysis of Marina del Rey, San Francisco Bay Area Rapid Transit, Turkey Point Power Plant in Florida and beach erosion at the Zion Atomic Power Plant.

In addition Professor Johnson has been a member, since 1974, of the Shoreline Erosion Advisory Panel created by the U.S. Congress. His expertise in coastal engineering has been quite instrumental in the success of this research and development program. He also has been selected as the chairman of the U.S. Delegation to the U.S.-Japan Cooperative Seminar on Coastal Engineering held in Japan. Professor Johnson has been appointed to numerous other boards and committees. He was the Secretary of the Council on Wave Research during its existence from 1950 to 1964, and then of the subsequent organization, The Coastal Engineering Research Council of the ASCE. He has been very active in the AGU holding key positions and has been a major driving force behind the American Shore and Beach Preservation Association as Vice President and Editor of *Shore and Beach*.

In 1976, Professor Johnson was elected to membership in the National Academy of Engineering and in 1979, he received the distinguished honor of Honorary Member of the ASCE. He is also the recipient of the Guggenheim Fellowship, The Outstanding Civilian Service Medal for his service in the field of coastal engineering and the Berkeley Citation. A selected listing of his over ninety publications are given below. Professor Johnson has been and still is a very active and important part of international coastal engineering.

Selected Bibliography

- The Transportation of Sediment by Streams: Bed Load, *Inter. Union Geod. and Geophys.*, 1939.
- Transportation of Sediment by Flowing Water, *Soil Conserv.*, vol. 6, 1941.

- A Distinction Between Bed Load and Suspended Load in Natural Streams (with Einstein and Anderson), *Trans. Amer. Geo. Union*, 1940.
- "War-time research on waves and surf." *The Military Engineer*, June 1947.
- "Refraction of surface waves by currents." *Trans. Amer. Geo. Union*, 1947.
- "The force exerted by surface waves on piles," (with J. R. Morison, M. P. O'Brien, and S. A. Schaaf), vol. 189, 1950.
- "The Damping Action of Submerged Breakwaters," (with R. A. Fuchs and J. R. Morison), *Trans. Amer. Geo. Union*, vol. 32, 1951.
- "The March 1962 Storm on the Atlantic Coast of the United States," (with M. P. O'Brien), Proc. Eighth Conference on Coastal Engineering, 1963.
- "Ship Waves in Shoaling Water," Proceedings Eleventh Conference on Coastal Engineering, 1968.
- "Lessons in Coastal Engineering," Symposium on Coastal Engineering, Stellenbosch, South Africa, 1970.
- "Closure of Tidal Entrances," Proc. Fourteenth Conference on Coastal Engineering, 1974.
- "Littoral Processes at Some California Shoreline Harbors," *Shore and Beach*, vol. 43, no. 1, April 1975.

The omissions from the accomplishments of Dean O'Brien and Professor Johnson are solely the responsibility of the writer; however, the magnitude of their contributions to coastal engineering has forced the writer to condense their many activities. Indeed a detailed listing of their individual efforts would fill a volume.

While listening to the discussions of the mechanics of sand waves by Professor Arthur Brebner, Professor Longuet-Higgins was able to tie some of Brebner's findings with the theoretical work he (Longuet-Higgins) had done on water waves of maximum steepness. Since Professor Longuet-Higgins' Keynote address begins the *Proceedings*, it was felt proper to end them with a brief summary explaining the application of his limiting wave theory to sand bed-forms. His discussion can be found on page 3107.

Billy L. Edge, Secretary
Coastal Engineering Research Council
American Society of Civil Engineers



Morrough P. O'Brien



Joe W. Johnson



Joe W. Johnson

CONTENTS

FOREWORD	iii
ACKNOWLEDGEMENTS	ix

INVITED LECTURE

THE UNSOLVED PROBLEM OF BREAKING WAVES

by

M. S. Longuet-Higgins
Institute of Oceanographic Sciences
Wormley, Surrey, England

PART I

THEORETICAL AND OBSERVED WAVE CHARACTERISTICS

Chapter 1	
SOME IMPLICATIONS OF RECENT ADVANCES IN WAVE THEORIES	
J. R. Chaplin and K. Anastasiou	31
Chapter 2	
ACCURATE NUMERICAL SOLUTIONS FOR NONLINEAR WAVES	
J. D. Fenton and M. M. Rienecker	50
Chapter 3	
MASS TRANSPORT IN PROGRESSIVE WAVES OF PERMANENT TYPE	
Yoshito Tsuchiya, Takashi Yasuda and Takao Yamashita	70
Chapter 4	
RAY CURVATURE AND REFRACTION OF WAVE PACKETS	
J. Ernest Breeding, Jr.	82
Chapter 5	
VERIFICATION OF A WAVE REFRACTION MODEL	
G. Henderson and N. B. Weber	101
Chapter 6	
WAVE SHOALING CALCULATED FROM COKELET'S THEORY	
T. Sakai and J. A. Battjes	121
Chapter 7	
A SURVEY OF "RANDOM" WAVE GENERATION TECHNIQUES	
J. Ploeg and E. R. Funke	135
Chapter 8	
THE MEASUREMENT OF INCIDENT AND REFLECTED SPECTRA USING A LEAST SQUARES METHOD	
E. P. D. Mansard and E. R. Funke	154
Chapter 9	
ORBITAL VELOCITIES IN IRREGULAR WAVES	
F. C. Vis	173

Chapter 10		
INVESTIGATIONS ON IRREGULAR WAVES IN HYDRAULIC MODELS		
Karl-Friedrich Daemrich, Wolf-Dietrich Eggert and Soren Kohlase	186	
Chapter 11		
METHOD OF ANALYSIS OF RANDOM WAVE EXPERIMENTS WITH REFLECTING COASTAL STRUCTURES		
Pierre Gaillard, Michel Gauthier and Forrest Holly	204	
Chapter 12		
WAVE HEIGHT DISTRIBUTION AROUND PERMEABLE BREAKWATERS		
Shintaro Hotta	221	
Chapter 13		
NON-RESONANT WAVE AGITATION IN SMALL CRAFT HARBOURS		
J. W. Kamphuis and D. A. Y. Smith	241	
Chapter 14		
EXPERIMENTAL INVESTIGATIONS OF PERIODIC WAVES NEAR BREAKING		
J. Buhr Hansen	260	
Chapter 15		
AN HEURISTIC MODEL OF WAVE HEIGHT DISTRIBUTION IN SURF ZONE		
Masaru Mizuguchi	278	
Chapter 16		
RESONANCES OF COASTAL WATERS BETWEEN PERTH AND GERALDTON (WESTERN AUSTRALIA)		
H. Allison, A. Grassia and R. Litchfield	290	
Chapter 17		
A CLOSELY RESPONDING, VERSATILE WAVE TUNNEL		
C. H. Hulsbergen and J. J. Bosman	310	
Chapter 18		
CONDITIONAL SIMULATIONS OF OCEAN WAVE PROPERTIES		
Leon E. Borgman	318	
Chapter 19		
WIND WAVES TRANSMISSION THROUGH POROUS BREAKWATER		
Stanislaw R. Massel and Piotr Butowski	333	
Chapter 20		
FIELD MEASUREMENTS OF WIND WAVE KINEMATICS		
J. A. Battjes and J. van Heteren	347	
Chapter 21		
HF RADAR MAPPING OF EXTENSIVE OCEAN WINDFIELDS		
P. E. Dexter and R. C. Casey	363	
Chapter 22		
SOURCES OF MEASURED WAVE DATA		
Laurence Draper	372	
Chapter 23		
VISUALLY OBSERVED WAVE DATA AT PT. MUGU, CALIF.		
Christine Schneider and Richard Weggel	381	
Chapter 24		
WAVE HINDCASTS AND MEASUREMENTS - BASS STRAIT		
M. N. Silbert, T. P. Barnett, D. J. H. Peters and R. C. Hamilton	395	

Chapter 25	
REALTIME WAVE ANALYSIS, NEWCASTLE, AUSTRALIA	
N. V. Lawson and P. H. Oull	412
Chapter 26	
FLORIDA COASTAL DATA NETWORK	
Gary Howell	421
Chapter 27	
A MEASUREMENT OF SLOPE, CURVATURE, AND DIRECTIONAL SPECTRA OF WIND WAVES IN LAKE MICHIGAN	
Paul C. Liu	432
Chapter 28	
WAVE ATTENUATION AND WAVE SET-UP ON A COASTAL REEF	
Franciscus Gerritsen	444
Chapter 29	
LONGSHORE CURRENT FLOWS IN A WAVE BASIN	
P. J. Visser	462
Chapter 30	
DYNAMIC CHARACTERISTICS IN THE NEAR SHORE AREA	
Kiyoshi Horikawa and Masahiko Isobe	480
Chapter 31	
VELOCITY FIELD IN A STEADY BREAKER	
J. A. Battjes and T. Sakai	499
Chapter 32	
THE FLUID MECHANICS OF WAVES APPROACHING BREAKING	
D. H. Peregrine, E. D. Cokelet and P. McIver	512
Chapter 33	
A SIMILARITY MODEL IN THE SURF ZONE	
Hsiang Wang and Wei-Chong	529
Chapter 34	
VELOCITY AND PRESSURE FIELD IN SPILLING BREAKERS	
M. J. F. Stive	547
Chapter 35	
DIRECTIONAL WAVE SPECTRA AND WAVE KINEMATICS IN HURRICANES CARMEN AND ELOISE	
G. Z. Forristall, E. G. Ward and V. J. Cardone	567
Chapter 36	
PREDICTION OF THE SEVEREST SIGNIFICANT WAVE HEIGHT	
Michel K. Ochi and Joseph E. Whalen	587
Chapter 37	
PREDICTION OF DOMINANT WAVE PROPERTIES AHEAD OF HURRICANES	
Omar H. Shemdin	600
Chapter 38	
LONG PERIOD DISTURBANCES DUE TO WAVE GROUPS	
E. C. Bowers	610
Chapter 39	
TWO-DIMENSIONAL SURF BEAT	
Reinhard E. Flick, Douglas L. Inman and Robert T. Guza	624

Chapter 40	
LONG WAVES GENERATED BY COMPLEX BOTTOM MOTIONS	
J. L. Hammack and F. Raichlen	639
Chapter 41	
TSUNAMIS ALONG WEST COAST OF LUZON, PHILIPPINES	
R. L. Wiegel	652
Chapter 42	
TSUNAMI PRONE FRICTION FACTORS FROM WIND MEASUREMENTS	
Charles L. Bretschneider	672
Chapter 43	
RUN-UP OF TSUNAMIS BY LINEAR AND NONLINEAR THEORIES	
Chiaki Goto and Nobuo Shuto	695
Chapter 44	
ON THE CORRECTION OF LAND-BASED WIND MEASUREMENTS FOR OCEANOGRAPHIC APPLICATIONS	
S. A. Hsu	708
Chapter 45	
NUMERICAL MODELLING OF TROPICAL CYCLONE STORM SURGE	
Rodney J. Sobey, Bruce A. Harper, and George M. Mitchell	725
Chapter 46	
A NUMERICAL MODEL OF STORM WAVES IN SHALLOW WATER	
A. Hauguel	746
Chapter 47	
THE GENERATION OF LONG WAVES IN THE LABORATORY	
Derek Goring and Fredric Raichlen	763
Chapter 48	
CORRECT REPRODUCTION OF LONG GROUP INDUCED WAVES	
N. -E. O. Hansen, S. E. Sand, H. Lundgren, T. Sorensen and H. Gravesen	784
Chapter 49	
AN ELECTROMAGNETIC ANALOGY FOR LONG WATER WAVES	
G. W. Jackson and D. L. Wilkinson	801
Chapter 50	
INTERACTIONS OF WAVES WITH SUBMARINE TRENCHES	
Jiin J. Lee, Robert M. Ayer and Wen L. Chiang	812
Chapter 51	
TRANSIENT FINITE-DIFFERENCE TSUNAMI CALCULATIONS	
Ove Skovgaard and Ivar G. Jonsson	823
Chapter 52	
AN INVESTIGATION OF WAVE SHELTERING BY ISLANDS	
S. V. Hsiao, J. F. Vesecky and O. H. Shemdin	840
Chapter 53	
THE DISSIPATION OF WAVE ENERGY BY TURBULENCE	
Yu Kuang-ming	850

**PART II
COASTAL SEDIMENT PROBLEMS**

Chapter 54	
BEACH CUSPS AT POINT REYES AND DRAKES BAY BEACHES, CALIFORNIA	
Robert G. Dean and E. M. Maurmeyer	863
Chapter 55	
BARRON RIVER DELTA INVESTIGATION	
D. A. Robinson, D. J. Cook and J. G. Barff	885
Chapter 56	
SOFT DESIGNS FOR COASTAL PROTECTION AT SEABROOK ISLAND, S.C.	
Miles O. Hayes, Timothy W. Kana and John H. Barwis	897
Chapter 57	
GEOLOGICAL CONTROLS ON PROCESS-RESPONSE, S.E. AUSTRALIA	
P. S. Roy and A. W. Stephens	913
Chapter 58	
BEACH EROSION-ACCRETION AT TWO TIME SCALES	
B. G. Thom and G. M. Bowman	934
Chapter 59	
PHYSICAL PROCESSES AND SEDIMENT FLUX THROUGH REEF-LAGOON SYSTEMS	
Harry H. Roberts	946
Chapter 60	
INSHORE-NEARSHORE MORPHODYNAMICS- A PREDICTIVE MODEL	
John Chappel	963
Chapter 61	
BEACH CUT IN RELATION TO SURF ZONE MORPHODYNAMICS	
L. D. Wright	978
Chapter 62	
BREAKER TYPE AND PHASE SHIFTS ON NATURAL BEACHES	
Peter J. Cowell	997
Chapter 63	
BEACH RESPONSE TO VARIATIONS IN BREAKER HEIGHT	
A. D. Short	1016
Chapter 64	
THE DYNAMIC SWEPT PRISM	
David M. Chapman	1036
Chapter 65	
A LABORATORY STUDY OF OFFSHORE TRANSPORT OF SEDIMENT AND A MODEL FOR ERODING BEACHES	
Tsuguo Sunamura	1051
Chapter 66	
NEARSHORE CURRENTS ON A PARTIALLY ROCKY SHORE	
T. O. Sasaki, H. Igarashi and S. Harikai	1071

Chapter 67	
TOPOGRAPHIC CONTROL OF RUN-UP VARIABILITY	
Mark P. Bradshaw	1091
Chapter 68	
BEACH PROFILES AND ON-OFFSHORE SEDIMENT TRANSPORT	
Akira Watanabe, Yoshihiko Riho and Kiyoshi Horikawa	1106
Chapter 69	
SECONDARY SAND TRANSPORT MECHANISMS	
A. W. Smith and A. D. Gordon	1122
Chapter 70	
SAND TRANSPORT BY WAVES	
Jan van de Graaff and Wiel M. K. Tilmans	1140
Chapter 71	
NEARSHORE SUSPENDED SEDIMENT LOAD DURING STORM AND POST-STORM CONDITIONS	
Timothy W. Kana and Larry G. Ward	1158
Chapter 72	
ONSHORE-OFFSHORE TRANSPORT AND BEACH PROFILE CHANGE	
Masataro Hattori and Ryoichi Kawamata	1175
Chapter 73	
ON-OFFSHORE SEDIMENT TRANSPORT RATE IN THE SURF ZONE	
Toru Sawaragi and Ichiro Deguchi	1195
Chapter 74	
FIELD MEASUREMENTS OF SAND MOTION IN THE SURF ZONE	
Douglas L. Inman, James A. Zampol, Thomas E. White, B. Walton Waldorf, Daniel M. Hanes and Kim A. Kastens	1215
Chapter 75	
AN APPROACH TO UNDERSTANDING COASTAL PROCESSES	
A. D. Gordon and D. B. Lord	1235
Chapter 76	
RELATIONSHIP BETWEEN ALONGSHORE WAVE ENERGY AND LITTORAL DRIFT IN THE MID-WEST COAST AT TAIWAN	
Ho-shong Hou, Chung-Pan Lee, and Lung-Hui Lin	1255
Chapter 77	
LONGSHORE WATER AND SEDIMENT MOVEMENT	
D. H. Swart and C. A. Fleming	1275
Chapter 78	
CRITERION FOR STABILITY OF SHORELINE PLANFORM	
John D. Wang and Bernard le Mehaute	1295
Chapter 79	
ZETA BAYS, POCKET BEACHES AND HEADLAND CONTROL	
R. Silvester, Y. Tsuchiya, and Y. Shibano	1306
Chapter 80	
BEACHES: PROFILES, PROCESSES AND PERMEABILITY	
Michael R. Gourlay	1320
Chapter 81	
SAND BED-FORM LENGTHS UNDER OSCILLATORY MOTION	
Arthur Brebner	1340

Chapter 82	
SEDIMENT TRANSPORT PROCESSES AND COASTAL VARIABILITY ON THE ALASKAN NORTH SLOPE	
E. H. Owens, J. R. Harper and D. Nummedal	1344
Chapter 83	
SEDIMENT DISPERSAL ON THE N. S. W. CONTINENTAL SHELF	
Ron Boyd	1364
Chapter 84	
FLUID MUD DYNAMICS AND SHORELINE STABILIZATION: LOUISIANA CHENIER PLAIN	
John T. Wells and Harry H. Roberts	1382
Chapter 85	
NEARSHORE SEDIMENT TRANSPORT STUDY EXPERIMENTS	
R. J. Seymour and C. G. Gable	1402
Chapter 86	
A SEDIMENT TRAPPING EXPERIMENT AT SANTA CRUZ, CA.	
R. J. Seymour, G. W. Domurat and D. M. Pirie	1416
Chapter 87	
WAVE FORCING OF BEACH GROUNDWATER	
Evans Waddell	1436
Chapter 88	
LONGSHORE TRANSPORT EVALUATIONS AT A DETACHED BREAKWATER	
R. O. Bruno, R. G. Dean, and C. G. Gable	1453
Chapter 89	
MIGRATION OF LONGSHORE BARS	
Hans H. Dette	1476
Chapter 90	
A PHASED-DREDGING PROGRAM FOR SANTA CRUZ HARBOR	
James R. Walker and Peter J. Williams	1493
Chapter 91	
DESIGN OF ENCLOSED HARBORS TO REDUCE SEDIMENTATION	
Craig H. Everts	1512
Chapter 92	
OPENING AND MAINTAINING TIDAL LAGOONS & ESTUARIES	
Scott A. Jenkins, Douglas L. Inman and James A. Bailard	1528
Chapter 93	
RESEARCH IN SOUTHERN QUEENSLAND INTO THE MANAGEMENT OF COASTAL SAND DUNES	
James B. McKenzie and David A. Barr	1548
Chapter 94	
WIND AND SEDIMENT MOVEMENT IN COASTAL DUNE AREAS	
John R. Hails and John Bennett	1565
Chapter 95	
SAND TRANSPORT UNDER THE ACTION OF WIND	
Ulrich Zanke	1576
Chapter 96	
A NUMERICAL MODEL FOR DUNE DYNAMICS	
J. Sundermann, H. -J. Vollmers and W. Puls	1584

Chapter 97	
ESTUARINE RESPONSE TO DREDGING IN THE TWEED RIVER, AUSTRALIA	
Bruce M. Druery	1599
Chapter 98	
NOOSA BEACH RESTORATION SCHEME	
R. J. Lloyd	1619
Chapter 99	
BEACH NOURISHMENT AS A MANAGEMENT TECHNIQUE	
David M. Chapman	1636
Chapter 100	
CAPRICORN COAST BEACHES	
D. C. Patterson and L. R. Ford	1649
Chapter 101	
THE BEACH IMPROVEMENT PROGRAMME: NEW SOUTH WALES	
Heale A. Philip and Philip H. Waite	1669
Chapter 102	
EDDY CURRENTS AND SEDIMENT TRANSPORT OFF THE DAMIETTA NILE	
S. P. Murray, J. M. Coleman, H. H. Roberts and M. Salama	1680
Chapter 103	
A COMPARISON BETWEEN DREDGE INDUCED SEDIMENT RESUSPENSION AND THAT PRODUCED BY NATURAL STORM EVENTS	
W. Frank Bohlen and Marine Sciences Department., Univ. of Conn.	1700
Chapter 104	
SEDIMENTATION IN CHANNELS AND TRENCHES	
E. W. Bijker	1708
Chapter 105	
SEDIMENTATION IN DREDGED NAVIGATION CHANNELS	
Lars Mikkelsen, Preben Mortensen, and Torben Sorensen	1719
Chapter 106	
SOME ASPECTS OF COASTAL ENGINEERING RESEARCH WORKS IN CHINA	
Yen Kai	1735

PART III
COASTAL STRUCTURES AND RELATED PROBLEMS

Chapter 107	
SIMULTANEOUS WAVE AND CURRENT FORCES ON A PIPELINE	
David A. Knoll and John B. Herbich	1742
Chapter 108	
WAVE FORCES ON AN INCLINED CIRCULAR CYLINDRICAL PILE	
Toshiyuki Shigemura	1761
Chapter 109	
WAVE-INDUCED SEEPAGE EFFECTS ON A VERTICAL CYLINDER	
Thomas J. P. Durand and Peter L. Monkmeyer	1781

Chapter 110	
STABILITY ANALYSIS OF SEAFLOOR FOUNDATIONS	
Tokuo Yamamoto and Yasumasa Suzuki	1799
Chapter 111	
WAVE FORCES ON OFFSHORE PIPELINES	
N. Jothishankar and V. Sundar	1819
Chapter 112	
WAVE IMPACT PRESSURES ON COMPOSITE BREAKWATERS	
G. R. Mogridge and W. W. Jamieson	1829
Chapter 113	
CONSTRUCTION AND MODEL INVESTIGATION OF STORMWATER OUTFALL	
K. A. Heathcote and G. W. Britton	1849
Chapter 114	
FULL SCALE NEAR SURFACE WATER PARTICLE VELOCITIES AND PRESSURES ACTING ON AN INCLINED TUBULAR MEMBER	
Fritz Busching and Eckehard Martini	1869
Chapter 115	
ENERGY TRANSMISSION OVER BREAKWATER—A DESIGN CRITERION?	
P. Bade and H. Kaldenhoff	1885
Chapter 116	
THE DESIGN CONCEPT OF DUAL BREAKWATERS AND ITS APPLICATION TO TOWNSVILLE, AUSTRALIA	
W. Bremner, N. N. Foster, C. A. Miller and B. C. Wallace	1898
Chapter 117	
DESIGN OF AN OVER TOPPING BREAKWATER	
P. D. Treloar and B. Nagle	1909
Chapter 118	
FULL SCALE TRIALS OF DOLOSSE TO DESTRUCTION	
Hans F. Burcharth	1928
Chapter 119	
DOLOSSE: PAST, PRESENT, FUTURE?	
J. A. Zwamborn, D. E. Bosman and J. Moes	1948
Chapter 120	
A DETACHED BREAKWATER SYSTEM FOR BEACH PROTECTION	
James R. Walker, Denton Clark, and Joan Pope	1968
Chapter 121	
STABILITY OF RUBBLE MOUND BREAKWATER	
J. Feuillet and M. Sabaton	1988
Chapter 122	
ARTIFICIAL RESORT BEACH PROTECTED BY OFFSHORE BREAKWATERS AND GROINS	
Shoji Sato and Norio Tanaka	2003
Chapter 123	
SEAWALLS IN DEEP SEAS	
Shoshichiro Nagai and Shohachi Kakuno	2023
Chapter 124	
PROBABILISTIC DESIGN OF SEA DEFENCES	
W. T. Bakker and J. K. Vrijling	2040

Chapter 125	
DESIGN OF CAISSON BREAKWATERS	
A. G. F. Eddie, J. D. Lawson, H. R. Graze and B. K. Dean	2060
Chapter 126	
THE DESIGN AND CONSTRUCTION OF THE NEW OIL PORT IN DALIAN, C.P.R.	
Xin Zhu-Zhuang	2080
Chapter 127	
SITING AND DESIGN CRITERIA OF DOCK STRUCTURES IN THE MARSHALL ISLANDS	
R. M. Noble, K. C. Leslie and D. O'Day	2106
Chapter 128	
COASTAL PROTECTION AGAINST THE ACTION OF WAVES AND CURRENTS	
Leren P. Mikhailov and Sergei M. Uspenskii	2120
Chapter 129	
FLOATING BREAKWATER PERFORMANCE COMPARISON	
Volker W. Harms	2137
Chapter 130	
LITTORAL DRIFT OF SAND NEAR PORT OF OARAI	
Kazumasa Mizumura	2159
Chapter 131	
LONG-TERM EXPERIENCE WITH THE USE OF SYNTHETIC FILTER FABRICS IN COASTAL ENGINEERING	
Georg Heerten	2174
Chapter 132	
BREAKWATER WITH SAND BITUMEN CORE	
E. Loewy, K. G. Witthaus, R. J. Maddrell and J. P. Wood	2194
Chapter 133	
HARBOUR DESIGN INCLUDING SEDIMENTOLOGICAL PROBLEMS USING MAINLY NUMERICAL TECHNIQS	
B. Latteux	2213
Chapter 134	
NEW JETTIES FOR TUNG-KANG FISHING HARBOUR, TAIWAN	
Chi-Fu Su	2230
Chapter 135	
MAJOR RECLAMATION SCHEME FOR MARINA CITY, SINGAPORE	
S. Y. Chew and J. Wei	2245
Chapter 136	
SHIP-BRIDGE-PIER PROTECTIVE SYSTEMS	
Akira Iwai, Hitoshi Nagasawa, Kazuki Oda and Kuniaki Shoji	2261
Chapter 137	
WAVE-WAVE INTERACTIONS, CURRENT-WAVE INTERACTIONS AND RESULTING EXTREME WAVES AND BREAKING WAVES	
Soren Peter Kjeldsen and Dag Myrhaug	2277
Chapter 138	
CAN WE DEVELOP NEW BREAKWATER ARMOUR FORMULAE?	
John Dorrington Mettam	2304

**PART IV
COASTAL, ESTUARINE, AND ENVIRONMENTAL PROBLEMS**

Chapter 139	
SEPARATION OF CLIMATIC FLUCTUATIONS AND IMPACTS OF ENGINEERING ACTIVITIES IN ESTUARIES	
G. Krause	2325
Chapter 140	
WAVE ENERGY DISTRIBUTION IN AN ESTUARY	
Volker Barthel	2340
Chapter 141	
HYDRAULIC RESEARCH IN THE OOSTERSCHELDE ESTUARY	
Anton W. Walther	2360
Chapter 142	
PORT OF BRISBANE SILTATION STUDY	
N. V. M. Odd and T. Baxter	2377
Chapter 143	
A 3-D MODEL FOR PENOBSCOT BAY, MAINE	
Bryan R. Pearce, Bruce R. Fidler and Adrian C. Humphreys	2397
Chapter 144	
THE USE OF ARRAY PROCESSORS FOR NUMERICAL MODELLING OF TIDAL ESTUARY DYNAMICS	
D. Prandle, E. R. Funke, N. L. Crookshank and R. Renner	2413
Chapter 145	
PARAMETER IDENTIFICATION IN ESTUARINE MODELING	
Wen-Sen Chu and William -G. Yeh	2433
Chapter 146	
AUTOMATIC CALIBRATION OF NUMERICAL TIDAL MODELS	
K. -P. Holz and U. Januszewski	2450
Chapter 147	
TIDAL INLET BEHAVIORAL ANALYSIS	
A. F. Nielsen and A. D. Gordon	2461
Chapter 148	
SEDIMENTATION PROCESSES IN TIDAL CHANNELS AND TIDAL BASINS CAUSED BY ARTIFICIAL CONSTRUCTIONS	
E. Renger and H. W. Partensky	2481
Chapter 149	
ARTIFICIAL ROUGHNESS IN PHYSICAL MODELS OF ESTUARIES FOR STORM SURGE INVESTIGATIONS	
D. Berndt, E. Giese, H. Schwarze, and H. -J. Vollmers	2495
Chapter 150	
COMMENTS ON TIDAL ENTRANCES ON SANDY COASTS	
Morrough P. O'Brien	2504
Chapter 151	
TIDAL PRISM-INLET AREA RELATIONS FOR SMALL TIDAL INLETS	
R. J. Bryne, R. A. Gammisch and G. R. Thomas	2517
Chapter 152	
A COASTAL INLET WITH FIXED BED AND MOBILE SIDES	
R. C. Nelson and A. J. Keats	2534

Chapter 153	
INLETS/ESTUARIES DISCHARGING INTO SHELTERED WATERS	
H. P. Riedel and M. R. Gourlay	2550
Chapter 154	
THE CORPS OF ENGINEER'S GENERAL INVESTIGATION OF	
TIDAL INLETS	
Robert M. Sorensen	2565
Chapter 155	
SATELLITE APPLICATIONS ON A COASTAL INLET STABILITY	
STUDY	
Yu-Hwa Wang	2581
Chapter 156	
BOUNDARY CONDITIONS FOR ANALYSIS OF FLOW IN TIDAL	
INLETS	
T. C. Gopalakrishnan and J. L. Machemehl	2595
Chapter 157	
MÉCHANISMS OPERATING AT A JETTIED RIVER ENTRANCE	
Bruce M. Druery and Alexander F. Nielsen	2607
Chapter 158	
STABILITY OF ESTUARY MOUTHS IN THE RHINE-MEUSE DELTA	
J. van de Kreeke and J. Haring	2627
Chapter 159	
BARDEN INLET, N.C.: A CASE STUDY OF INLET MIGRATION	
Limberios Vallianos	2640
Chapter 160	
STUDY ON VORTEX CURRENT IN STRAIT WITH REMOTE-SENSING	
Sotoaki Onishi and Tsukasa Nishimura	2655
Chapter 161	
DYNAMIC SIMILARITY OF TRANSPORT PHENOMENA	
M. S. Yafin and F. Gerritsen	2671
Chapter 162	
MOORING FORCES INDUCED BY PASSING SHIPS—MEASUREMENTS	
IN PROTOTYPE	
K. Haffke	2691
Chapter 163	
NUMERICAL MODELLING OF NEARSHORE CIRCULATION	
Bruce A. Ebersole and Robert A. Dalrymple	2710
Chapter 164	
MODELLING OF PLANFORM INFLUENCE ON CIRCULATION IN	
HARBOURS	
Roger A. Falconer	2726
Chapter 165	
HYDRAULIC CIRCULATION PERFORMANCE OF A CURVILINEAR	
MARINA	
Jeffrey A. Layton	2745
Chapter 166	
THE EFFECT OF BREAKING WAVES ON THE MIXING OF LIQUID	
POLLUTANTS INTO THE SEA	
Arvid Naess	2760

Chapter 167	
ON A ROLE OF THE INTERFACIAL FROUDE NUMBER	
Masakazu Kashiwamura	2780
Chapter 168	
DISPERSION OF COOLING WATER FROM A COASTAL LNG PLANT	
P. Ackers, J. D. Pitt, G. Thompson and K. G. Rippin	2796
Chapter 169	
EXPERIMENTAL STUDY OF THE BUOYANT SURFACE JET WITH THE PRESENCE OF BOTTOM BOUNDARY AND CROSS CURRENT	
B. Safaie	2816
Chapter 170	
DESIGN OF AN INTERMITTENTLY OPERATED OUTFALL	
Roger W. Lindquist and George J. Murphy	2837
Chapter 171	
EXPERIMENTAL EVALUATION OF HEAT EXCHANGE BETWEEN WATER SURFACE AND ATMOSPHERE	
Gunther Barg, Horst Schwarze, and Gerhard Visscher	2851
Chapter 172	
DYNAMICS OF SILT IN ESTUARY, RESIDUAL CURRENT OR FLOCCULATION WHICH PREVAILS?	
J. P. Lepetit and M. Davesne	2861
Chapter 173	
FOR DISPOSAL: 10 m cu m OF CALCIUM CARBONATE SLURRY	
L. Summers and C. A. Fleming	2874
Chapter 174	
AN EXPERIMENT ON CLAY SUSPENSION UNDER WATER WAVES	
Prida Thimakorn	2894
Chapter 175	
CONSIDERATIONS IN THE DESIGN OF AN OFFSHORE DATA COLLECTION PROGRAM	
Cortis Cooper and German Febres	2907
Chapter 176	
THE GERMAN "MORAN" PROJECT	
Winfried Siefert and Volker Barthel	2927
Chapter 177	
ENVIRONMENTAL ASPECTS OF OIL AND GAS PIPELINE LANDFALLS IN NORTHEAST SCOTLAND	
William Ritchie	2938
Chapter 178	
STATISTICAL PROPERTIES OF RANDOM WAVE GROUPS	
Akira Kimura	2955
Chapter 179	
ON THE SYNTHESIS OF REALISTIC SEA STATES	
E. R. Funke and E. P. D. Mansard	2974
Chapter 180	
A COMPARISON OF NATURE WAVES AND MODEL WAVES WITH SPECIAL REFERENCE TO WAVE GROUPING	
Hans F. Burcharth	2992

Chapter 181	
WATER MOVEMENT STUDIES REQUIRED FOR PORT PLANNING	
Graeme C. Dandy, Desmond A. Mills and Jon B. Hinwood	3010
Chapter 182	
INTEGRATION AND COMPUTATION IN AN EXPERIMENTAL STUDY	
J. B. Hinwood, J. E. Watson and D. M. Burrage	3027
Chapter 183	
SOME RECENT RESULTS FOR WAVE INDUCED MOTIONS OF A SHIP IN SHALLOW WATER	
P. A. Madsen, I. A. Svendsen and C. Michaelsen	3043
Chapter 184	
REPORT ON THE DAMAGES TO THE SINES BREAKWATER, PORTUGAL	
William F. Baird, Joseph M. Caldwell, Billey L. Edge, Orville T. Magoon and Donald D. Treadwell	3063
Chapter 185	
DISCRETE-TIME MODELLING OF DISPERSION IN ESTUARIES	
T. Wood	3078
Chapter 186	
MEASUREMENTS OF OSCILLATORY DRAG ON SAND RIPPLES	
Karl E. B. Lofquist	3087
Contribution to the Discussion During Session C, Coastal Processes, Friday, March 28, 2:00 p.m., M. S. Longuet-Higgins, Institute of Oceanographic Sciences, Wormley, Surrey, England	
SUBJECT INDEX	3109
AUTHOR INDEX	3163



Morrough P. O'Brien



Joe W. Johnson



Morrrough P. O'Brien



Joe W. Johnson

THE UNSOLVED PROBLEM OF BREAKING WAVES[†]

by M.S. Longuet-Higgins^{*}

I. INTRODUCTION

"There is nothing so practical as a good theory"

One of the outstanding features of coastal waters is the breaking of swell and wind waves within the surf zone. A sound knowledge of the velocity and pressure fields in breaking waves is clearly of basic importance for coastal engineering, not only because of the need to calculate forces on jetties, breakwaters and other structures, but also because of the dominant role played by wave breaking in the dissipation of wave energy, in the transfer of momentum to longshore currents, and in the erosion and transport of sand and sediment.

The astonishing fact remains that our quantitative knowledge of the velocity field in breaking waves is very meagre. Despite praiseworthy attempts (some reported at previous Coastal Engineering Conferences) to measure velocities both in the field and in laboratory wave channels, the present state of knowledge compares very unfavourably with, say, our knowledge of the dynamics of swell in deep water.

Why is this? After all, we know the basic physical laws of fluid motion. The equations for an incompressible fluid with a free surface (but without suspended sediment) can be written down at will. Our trouble is that even in the simplest case, that of a homogeneous, inviscid fluid in two-dimensional, irrotational motion, we have been unable to find either suitable exact solutions, or useful approximations with which to compare and correlate our hard-won experimental results. Thus we do not know the answer to the question: What is the flow, or more generally the possible class of flows, in an overturning wave? The main reason for our ignorance is not that the observations are difficult in themselves; both the surf zone and breaking waves in the laboratory do indeed present formidable difficulties. It is not that we do not understand the physics.

[†]Keynote address: 17th International Conference on Coastal Engineering. Sydney, Australia, 23-29 March 1980.

^{*}Royal Society Research Professor at Cambridge - Department of Applied Mathematics and Theoretical Physics, University of Cambridge, England, and Institute of Oceanographic Sciences, Wormley, Godalming, Surrey.

It is, that we do not have to hand any simple but valid mathematical solutions as the basis for a physical model.

In this situation it is the applied mathematician who must take the lead and find suitable answers, working always closely with experimenter.

It has been said that there is nothing so practical as a good theory. But what do we mean by "good"? A theory should have two desirable quantities: it should be accurate and it should be simple. Often we can achieve accuracy at the expense of simplicity. Only on rare occasions do we get both.

More often the historical sequence is as follows: First we find a rough but very inaccurate model (for example, shallow-water waves as sine-waves). Then we improve the model, perhaps by a second or higher-order approximation. Next we may achieve a highly accurate model, but it is forbiddingly complicated and difficult to apply. Finally we find a simple but reasonably accurate approximation which is both usable and essentially correct.

This sequence will be illustrated in the case of breaking waves.

It is convenient to divide our problem into four sub-problems.

A. The limiting form of steep, symmetric waves. This problem is well-studied, and the solutions will be seen to have passed through all the four stages mentioned above.

B. The form of steep, steady, but not limiting, waves. In this, substantial progress has been made only quite recently, with some surprising and unexpected results.

C. Steep, time-dependent waves; overturning. This is more difficult than either A or B, since it involves a new dimension - time. Some new theoretical approaches will be reported.

D. Waves after breaking.

Whereas A, B and C are problems in pure fluid dynamics, involving mainly one physical parameter g , Problem D involves also turbulence and mixing, and hence is inevitably more empirical. Problems A, B and C represent challenges primarily to the mathematician, in increasing order of complexity.

2. PROBLEM A: LIMITING FORMS OF STEEP, STEADY WAVES.

First consider waves in deep water. Accurate computations of the steepest, symmetric wave go back as far as Michell (1893) who incorporated Stokes's 120° corner-flow for the wave crest into a series expansion for the whole wave. More recent calculations by Yamada (1957a) and others, using widely different methods, are essentially in agreement to four significant figures (see Table 1).

Table 1. The height and speed of the steepest gravity waves in deep water.

Author	H/L	c^2/c_0
Michell (1893)	0.142	1.20
Yamada (1957a)	0.1412	1.1932
Schwartz (1974)	0.1412	1.1930
Longuet-Higgins (1975)	0.1411	1.1931
Cokelet (1977)	0.1411	1.1928
L-H and Fox (1978)	0.14107	1.1931

The above calculations all involve infinite series. On the other hand a very simple approximation has recently been proposed (Longuet-Higgins 1978b, 1979a) in which the surface profile is approximated by the arc of a circle (see Figure 1) whose radius is equal to the wavelength L . This makes the crest-to-trough height to be $0.1340L$, which differs from the accurate value by only $0.0072L$. The motion of a particle at the free surface can now be seen as that of the bob of a light pendulum of length L , swinging through a 60° arc, on which is superposed a horizontal speed equal to the phase speed. This gives the orbit shown in Figure 2. The mean speed of advance of the particle is then easily found to be $U = 0.282c$, compared to the accurate value

$$U = 0.274c \quad (2.1)$$

based on Yamada's profile (see Longuet-Higgins 1979c).

To obtain the orbital motion of particles below the surface we may adopt the almost equally simple approximation in which the free surface is transformed from one side of a

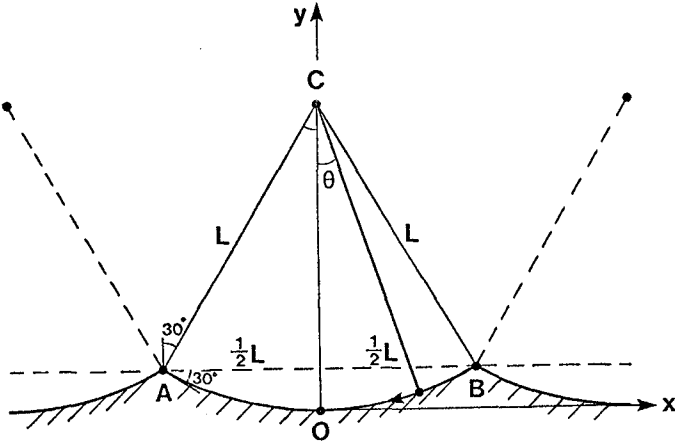


Figure 1. Approximating the profile of a deep-water gravity by the arc of a circle.

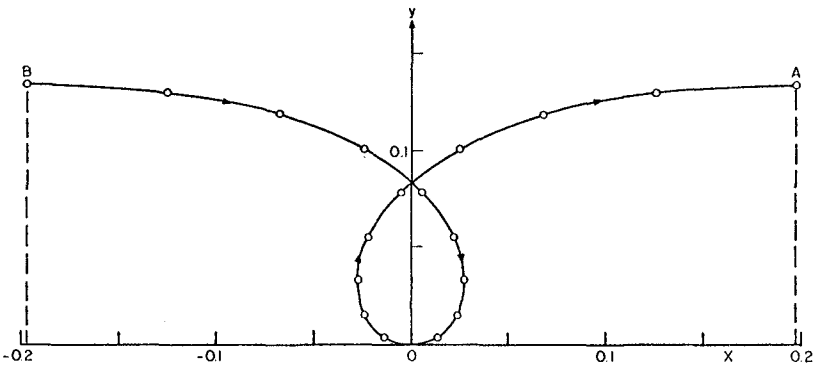


Figure 2. The trajectory of a particle at the surface of a gravity wave in deep water, as given by the approximation of Figure 1.

hexagon (Longuet-Higgins 1973) giving as equation for the profile

$$y = \ln \sec x \quad (2.2)$$

(in units where the wavelength equals $\frac{1}{3}\pi$). The corresponding wave height is now $0.1374L$, in error of only $0.0037L$. But (2.2) has the advantage that the corresponding velocity potential is now easily determined, and from these we get the orbital motions shown in Figure 3 (taken from Longuet-Higgins 1979c). It is easy to see how rapidly the mean displacement falls off as one goes deeper.

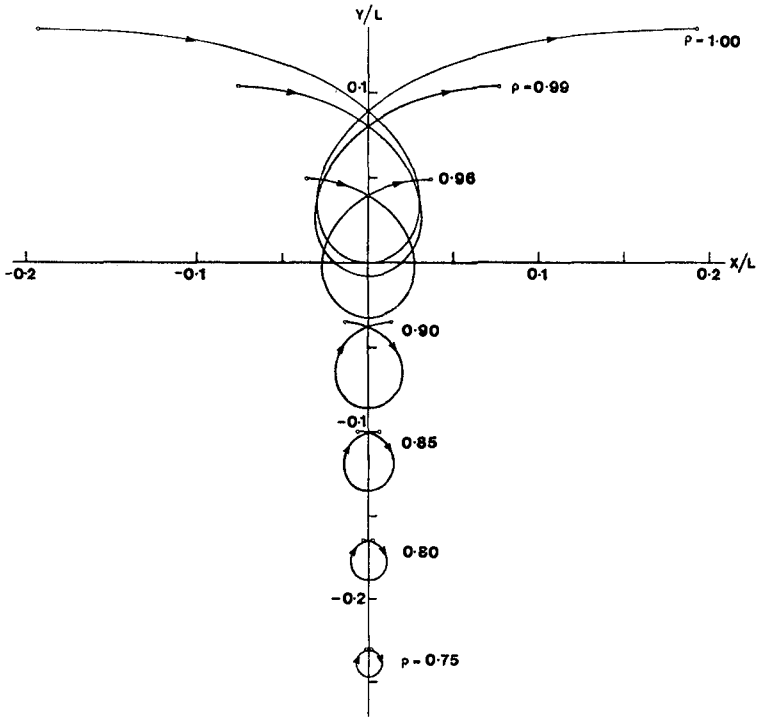


Figure 3. Orbits of subsurface particles in a deep-water wave of maximum steepness, calculated from the "hexagon approximation", equation (2.2).

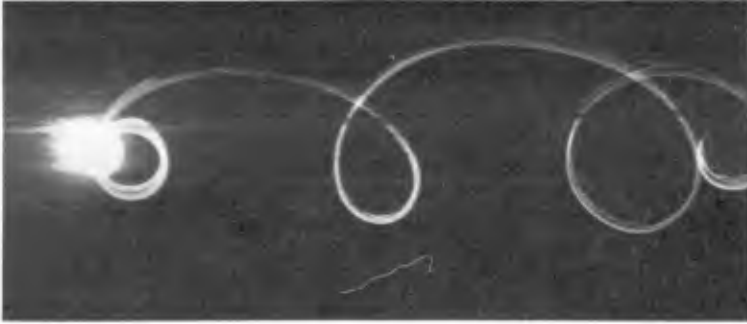


Figure 4. Time exposure of the track of a luminous float disturbed by an advancing wave train.

For comparison, Figure 4 shows the track of a small, luminous float, placed ahead of an advancing wave train (period 1.0 sec) in the 180-ft channel at Wormley. Viewing is through a window in the side. Before the waves arrive, the float is almost stationary and burns a hole in the negative. On arrival of the wave front, the track unwinds like a watch-spring. The steepest wave, which has an amplitude somewhat greater than the waves behind, is just breaking.

We turn now to the steepest symmetric waves in shallow water, beginning with the extreme case of the solitary wave.

Some recent determinations of the height and speed of limiting solitary waves are shown in Table 2. The values of a/h are necessarily half those of the corresponding c^2/gh . It is perhaps not fortuitous that the two most recent calculations are in agreement to four significant figures. Though the details of Witting's calculations are not available, it is believed that like Fox (1977) his method requires some extrapolation. In fact these figures cannot be considered quite so reliable as those for deep water.

Table 2. Accurate determinations of the height and speed of the steepest solitary wave.

	a/h	c ² /gh
Yamada (1957b)	0.828	1.656
Lenau (1966)	0.827	1.654
L-H and Fenton (1974)	0.827	1.653
Witting (1975)	0.8332	1.6664
Fox (1977)	0.8332	1.6664

On the other hand a remarkably simple approximation to the surface profile has been derived recently (Longuet-Higgins 1974a, 1976a) namely

$$y = A e^{-\lambda|x|} + B e^{-\mu|x|} \quad (2.3)$$

(in units where the undisturbed depth equals 1). The values of the constants are

$$\left. \begin{aligned} A &= 1.5389, & \lambda &= 1.0495 \\ B &= -0.7093, & \mu &= 1.4630 \end{aligned} \right\} \quad (2.4)$$

giving

$$F^2 = 2(A+B) = 1.659 \quad (2.5)$$

(compare Table 2). The profile is graphically indistinguishable from that calculated by Yamada (1957b). From (2.3) we may easily calculate the trajectory of a particle at the free surface by the method given in Longuet-Higgins (1979a). The result is shown in Figure 5, assuming there is no backwards drift between successive "solitary waves".

In Figure 6 we show the height and width of surface particle orbits in solitary waves of various steepnesses, measured in a shallow-water wave tank (Longuet-Higgins 1980d).

Lastly, for limiting waves at intermediate ratios of wavelength to mean depth, some properties are given in Table 3, deduced from the accurate computations of Cokelet (1977). For such waves, however, no approximate expressions comparable in simplicity to equations (2.2) or (2.3) have yet been given.

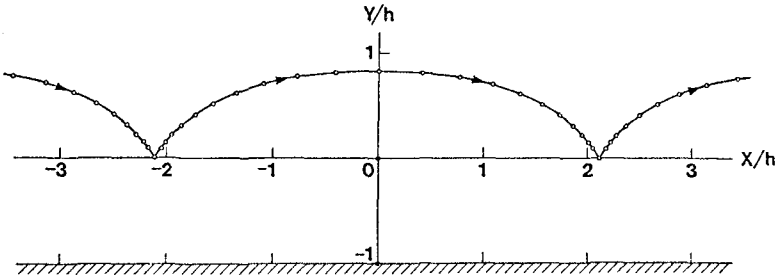


Figure 5. Trajectory of a particle at the surface of a solitary wave of maximum steepness.

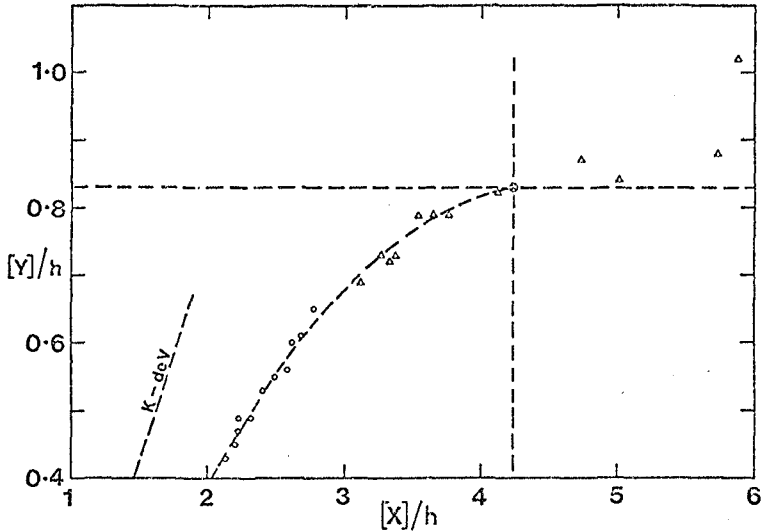


Figure 6. The overall horizontal displacement X and vertical displacement Y of particles at the surface of steep, solitary waves. Δ and o denote observations at distances 3.5m and 6.1m from wavemaker. The depth of water $h = 10\text{cm}$. Plots in upper right-hand quadrant were for spilling breakers. Δ denotes theory for limiting waves, from Figure 5.

3. PROBLEM B. STEEP, STEADY, BUT NOT LIMITING WAVES

This is clearly more general than Problem A, and more difficult. It is also both surprising and interesting.

Let us begin with waves in deep water. Until recently it was customary to use the small-amplitude expansion of Stokes:

$$(x+iy) = (\phi+i\psi)/c + \sum_n a_n e^{n\psi/c} \cos n\phi/c \quad (3.1)$$

carried to second, third or higher orders, in order to calculate the properties of quite steep waves. Following Stokes (1880), the expansion parameter was assumed proportional to a_1 , the coefficient of the first harmonic. It was Schwartz (1974) who showed that the resulting series fails to converge when the wave steepness exceeds a certain value, namely $H/L = 0.131$, short of the highest. The reason is very simple. In steep waves the surface profile becomes markedly non-sinusoidal, being narrow at the crests and broad in the wave troughs. So for the very highest waves the first Fourier coefficient a_1 , which measures the amplitude of the first harmonic, can be less than for waves that are not as steep but are more rounded at the crests. Consequently the coefficient a_1 , considered as a function of a maximum and then turns down again. For some values of a_1 there can be two different waves; convergence to both waves simultaneously is impossible.

However, even before the critical lower value of the wave steepness is reached, convergence of the series becomes exceedingly slow, and so any computations which use it become inefficient and unreliable. Just as it is useless to base mathematical calculations on unsound physics, so it is useless, or worse, to base physical calculations on unsound mathematics.

The remedy, as Schwartz showed, is to choose a different expansion parameter, one which increases steadily throughout the range of waves we are considering. The simplest such parameter is the wave steepness itself. Thus when h , or $2a/L$ is used as expansion parameter, the series all converge up to the steepest wave.

Not long afterwards it was discovered by Longuet-Higgins (1975) that not only a_1 , a_2 ---- but also the phase speed c (whose inverse can be considered as the lowest Fourier coefficient) also has a maximum before the highest wave is reached (see Figure 7). Hence at large wave steepness there may be two different waves with the same speed

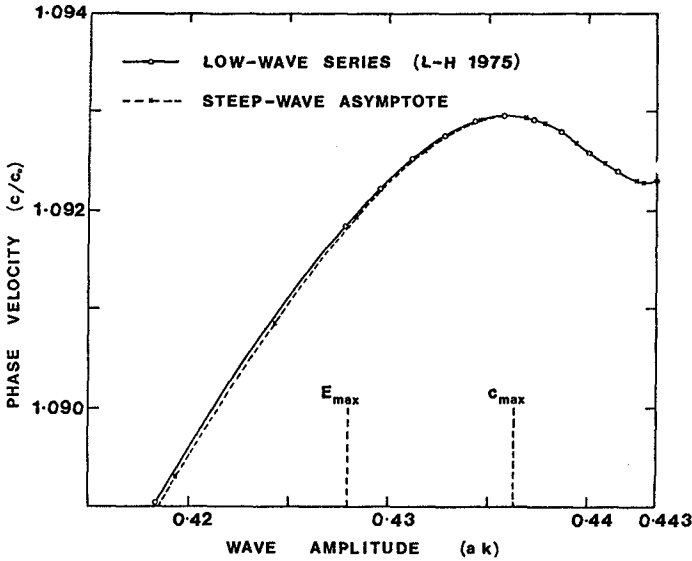


Figure 7. The phase-speed of waves in deep water, at high values of the wave steepnesses ($ak = \pi H/L$). Full curve represents the 80-term series (Padé summed). Broken curve: asymptotic expressions (3.6) and (3.7)

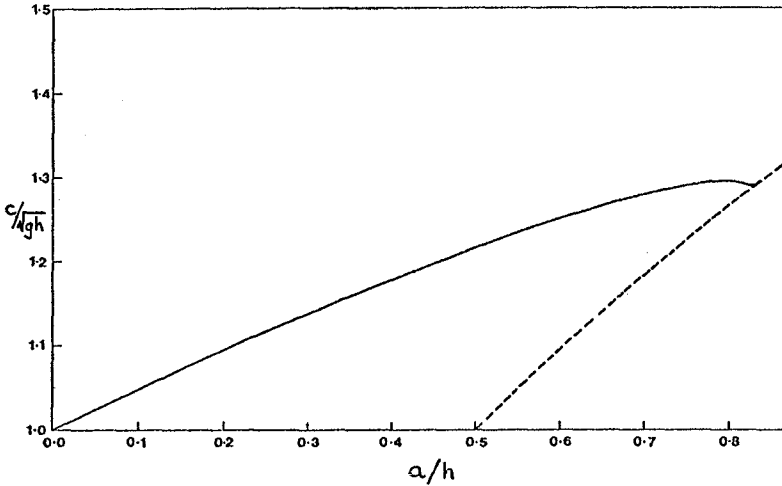


Figure 8. The phase-speed of solitary waves.

and wavelength. This has interesting and unexpected implications for the existence of non-uniform trains of waves (see below).

Meanwhile, similar discoveries had been made for solitary waves. Thus Longuet-Higgins and Fenton (1974) showed by the use of series expansions, that the speed of solitary waves, as a function of their amplitude at fixed depth, increases to a maximum and then decreases again (Figure 8). This was directly related to the profile of the waves. For in a solitary wave, as the wave height increases the crest becomes narrower, and this tendency continues right up to the highest wave (see Byatt-Smith and Longuet-Higgins, 1976). Moreover, the profiles intersect near the crest, so that the highest waves actually lie below the "lower" waves over most of their width. In other words as the highest wave is approached, the "mean elevation"

$$\bar{y} = \int y^2 dx / \int y dx \quad (3.2)$$

tends to diminish. Now (3.2) can be written

$$\bar{y} = 2V/Mg \quad (3.3)$$

where M and V denote the excess mass and potential energy in the wave. But an exact relation for solitary waves due to Starr (1947) is that

$$c^2 = gh + 3V/M \quad (3.4)$$

(A direct proof is given by Longuet-Higgins, 1974). Therefore as \bar{y} diminishes, so must the phase-speed c .

Not only the phase speed but also other quantities such as the mass, momentum and total energy of solitary waves were found to have maxima within the possible range of wave steepness. As pointed out by Longuet-Higgins and Fenton (1974) this implies that steady waves of maximum steepness cannot be attained without some dissipation of energy perhaps by breaking or bottom friction. The maximum may also help to account for the intermittent character of whitecaps in the surf zone as a kind of hysteresis effect.

Waves at intermediate depths between deep and shallow water have been studied by Cokelet (1977) and shown to possess similar characteristics: the speed, energy and other integral properties all take maxima within the possible range of steepness.

These somewhat unexpected results of Longuet-Higgins and Fenton (1974) for solitary waves, of Longuet-Higgins (1975) for deep-water waves and of Cokelet (1977) for waves in water of intermediate depth were all obtained by applying techniques for accelerating the convergence of infinite series, particularly "Padé sums". These are essentially a direct generalisation of the ordinary partial sum. Given a finite number of terms in a power series, the function is approximated not by a polynomial (the partial sum) but by a rational function which has the same power series expansion up to that point. Surprising though they may seem, the results have since been verified in detail by quite different methods of calculation based on integral equations: for solitary waves by Byatt-Smith and Longuet-Higgins (1976), for deep-water waves by Chen and Saffman (1978, Section 5) and Olfe and Rottman (1979) and for waves at intermediate depths by Vanden-Broeck and Schwartz (1979). The stream-function method of Dean, when suitably modified (Chaplin 1979) also gives results consistent with the above.

All such methods, however, are complicated. A radical simplification was introduced by Longuet-Higgins and Fox (1977, 1978) who proposed starting from known solutions for the highest wave and working downwards. First (1977) the rounded form of the wave crest was calculated for a wave approaching (but not quite attaining) the Stokes 120° corner-flow. This is shown in Figure 9. The length-scale ℓ is equal to $q^2/2$, where q is the speed of a particle at the crest, seen in a reference frame moving with the wave. As the highest wave is approached, so q/c and ℓ both tend to zero. Then (1978) this local flow was "matched" asymptotically to the flow in the rest of the wave, assuming that the "matching parameter"

$$\epsilon \propto q/c \quad (3.5)$$

was small. The result is essentially a two-term expression for the total flow. Thus for the height and speed of deep-water waves, for example, Longuet-Higgins and Fox (1978) found that

$$2a/L = 0.14107 - 0.50\pi^{-1}\epsilon^2 + 0.160 \epsilon^3 \cos(2.143 \ln \epsilon - 1.54) \quad (3.6)$$

and

$$c^2/c_0^2 = 1.1931 - 1.18 \epsilon^3 \cos(2.143 \ln \epsilon + 2.22) \quad (3.7)$$

Figure 8 shows a graph of c/c_0 versus $ak = 2 a/L$ for the steepest waves, and it can be seen how closely the two-term asymptotic expansion agrees with the 80-term small-amplitude series.

A further simplification of the theory of the almost-highest wave was introduced by Longuet-Higgins (1979) who showed that the flow near the crest (the "inner solution") is quite accurately described by the simple expression

$$x+iy = \frac{\alpha+\gamma i\chi}{(\beta+i\chi)^{1/3}} \quad (3.8)$$

where $\chi = \phi+i\psi$ and α, β, γ are constants:

$$\begin{aligned} \alpha &= 1.6876 \\ \beta &= 4.8065 \\ \gamma &= 1.3104 \end{aligned} \quad (3.9)$$

A comparison between the profile given by equation (3.8) and the exact inner solution is shown in Figure 9.

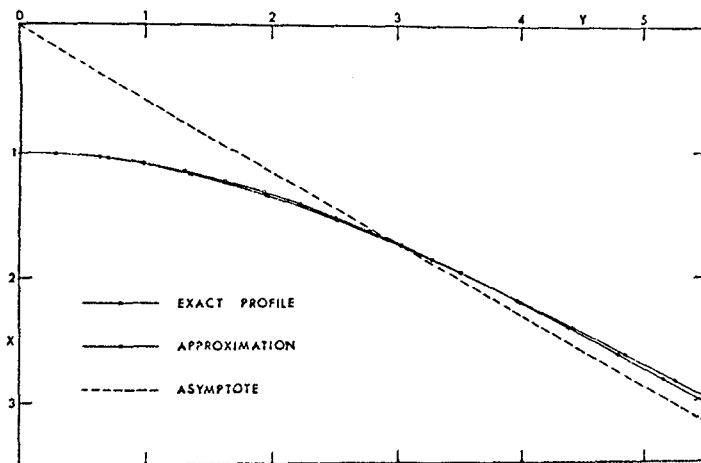


Figure 9. Profile of the almost-highest wave near the wave crest. x = exact computation (Longuet-Higgins and Fox 1977). \circ = approximation (3.8).

Before leaving the subject of steady waves, it will be interesting to mention the recent discovery by Chen and Saffman (1978) of steady but non-uniform trains of waves. Although their approach was different, we can show by the following argument that the existence of such wave trains is not unreasonable. We have seen that at very high steepness it is possible for two uniform trains of waves to exist with the same speed and wavelength. Let us then pick one wave alternately from each wave train, and place them side-by-side to form a new train of waves with alternately high and low amplitudes. Is it possible to join the waves up smoothly so that a continuous motion results? For solitary waves in shallow water, where each wave tails off exponentially in the horizontal direction, the answer is convincingly, yes. Does it remain possible, as we increase the ratio of depth to wavelength? The calculations of Chen and Saffman shows in effect that it is indeed possible even when the depth becomes infinite, provided the waves are sufficiently steep.

Similar arguments apply to the case when every third, fourth or in general every n th, wave is higher than the others, and to more complicated cases.

Normally, we expect the envelope of a non-uniform wave train to move with the group-velocity c_g . For low waves in deep water c_g is only about one-half the phase velocity c . But here the c_g waves are so non-linear that the group-velocity has grown to equal the phase-velocity; the envelope moves with speed c .

Table 3. Parameters of waves of limiting steepness, from computations by Cokelet (1977)

e^{-d}	$(d+\bar{y})/L$	H/L	c^2/c_0^2
0.0	∞	.1411	1.193
0.1	.3763	.1378	1.194
0.2	.2650	.1285	1.200
0.3	.1991	.1144	1.214
0.4	.1516	.0974	1.239
0.5	.1145	.0791	1.127
0.6	.0840	.0609	1.328
0.7	.0583	.0437	1.391
0.8	.0362	.0279	1.460
0.9	.0170	.0153	1.53

4. PROBLEM C. TIME-DEPENDENT WAVES: OVERTURNING

We come now to the central part of our main problem. In spite of excellent laboratory investigations, notably by Pazan and van Dorn (1975) and by Killen and Horning (1976) the theoretical analysis has been largely lacking. No doubt this is because of the highly time-dependent and non-linear character of the fluid motion. The accelerations can no longer be assumed small compared to g , and the free surface, on which two nonlinear conditions must be satisfied, is no longer a streamline, as in steady motions.

Some progress with a numerical method of computation was made by Longuet-Higgins and Cokelet (1976; see also Longuet-Higgins 1976a), in which it was shown how the equation for a two-dimensional motion, periodic in space but not time, could be integrated step-by-step by solving at each step an integral equation involving only the values of x, y and ϕ at the free surface. By this method it was shown how a periodic wave, raised to an energy level greater than the maximum for its particular wavelength, could overturn before the formation of a sharp crest.

In the above example, the wave was initially forced, by the application of pressure to the rear face of the wave (though this was withdrawn before the wave overturned). Some examples where breaking occurred after no pressure was applied were given in a second paper (Longuet-Higgins and Cokelet 1978). It had already been shown by Longuet-Higgins (1978a and b) that the normal instabilities of free gravity waves were of two distinct kinds: the subharmonic instabilities of Benjamin and Feir (1967) which tend to produce a "bunching" of the waves into groups of high and low waves, at least initially; and secondly a local type of instability confined mainly to the wave crests and with a relatively high rate of growth. By following perturbations of the second type by their time-stepping technique (see Figures 10 and 11) Longuet-Higgins and Cokelet (1978) were able to show that the second type of instability led rapidly to overturning of the wave crest.

Moreover, by following the more slowly growing instabilities of the first type for a longer period of time, they showed that these led to a modulation of the wave train so severe that ultimately the steeper waves developed local instabilities of the second kind at their crests, and also overturned. All this occurred without the addition of any energy by surface pressures,

The above calculations were for deep-water gravity waves. The stability calculations for deep-water waves by Longuet-Higgins (1978a and b) have recently been extended to water of finite (but uniform) depth by Cleaver (1980). These show that as the ratio of mean depth to wavelength

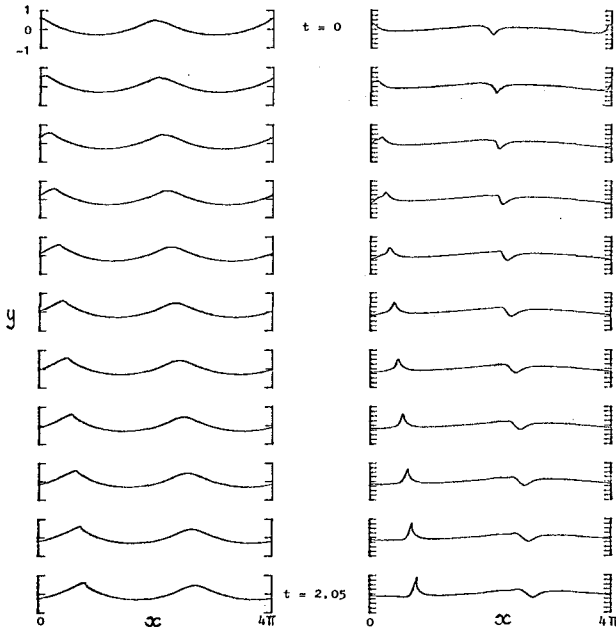


Figure 10. (from Longuet-Higgins and Cokelet, (1978). Development of the highly unstable mode $n = (\frac{3}{2})^+$ when $ak = 0.41$. The vertical scale on the right is magnified 5 times.

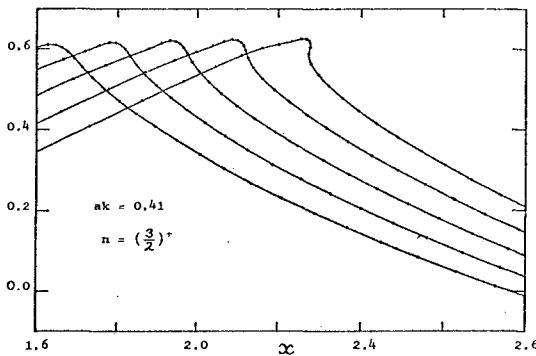


Figure 11. Enlargement of the wave crest in Figure 10 at times near overturning. The time-interval between profiles is $2\pi/50$.

diminishes, so the subharmonic instabilities (those of the first kind) tend to be suppressed. Nevertheless it seems likely the local instabilities (those of the second kind) will be little affected, and may even be enhanced. The corresponding time-stepping test for finite depth has still to be carried out.

One of the most interesting aspects of these results is the close similarity between the overturning of the local instabilities, despite the differences in their initial conditions. This leads us to hope that an overturning progressive wave may assume some typical form asymptotically, largely independent of the initial conditions, save for a local length-scale λ and a time-scale τ related by

$$\lambda/g\tau^2 = O(1) \quad (4.1)$$

Starting from different initial conditions (a progressive sine-wave of large amplitude) Cokelet (1977) has carried the numerical time-stepping well beyond overturning (see Figure 12). The form of the jet is convincing, although the accuracy of the computations near the tip of the jet is questionable.

The same time-stepping technique has also been applied to standing waves in deep water by Saffman and Yuen (1979).

Successful as they may seem, such numerical techniques leave important questions unanswered. For example, what is the appropriate form for the tip of the jet? Is there a sharp cusp? And how are the characteristics of the jet, its total volume, energy and momentum, for example, related to the initial conditions from which the breaking wave begins?

To help answer these questions we need a much simpler, if approximate, analytical model of the overturning wave to complement the numerical results.

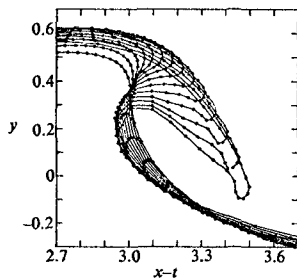


Figure 12. (from Cokelet 1977). Later stages of an overturning jet, as given by the numerical time-stepping method.

5. PROBLEM C (continued). ANALYTICAL APPROACHES

An attempt to obtain a simple analytical model for the crest of an overturning wave, was recently begun by the present author (Longuet-Higgins 1980a, b and c). Our problem is to find an expression for the velocity potential χ which shall be an analytic function of the space coordinate $z = x+iy$ and of the time t , and such that on the free surface the two boundary conditions

$$p = 0 \quad \text{and} \quad Dp/Dt = 0 \quad (5.1)$$

are both satisfied simultaneously. Here D/Dt denotes differentiation following a particle. It can be shown (Longuet-Higgins 1980a) that if as coordinates we use not x, y and t , but z, z^* and t , where $z^* = x-iy$, then the boundary conditions (4.1) can be expressed very compactly in terms of the velocity potential χ and its derivatives.

We can distinguish two aspects of the flow: the formation of a sharp corner at the crest of the wave or the tip of the jet, and on the other hand the overturning of the body of the wave as a whole. That the two problems are quite distinct is indicated by the fact that we sometimes observe upwards-pointing crests or jets, and also (as just mentioned) that overturning can occur before the formation of a sharp corner.

A model for the tip of the wave is proposed in Longuet-Higgins (1980b). In this we imagine the pressure field in the fluid to be extended smoothly beyond the free surface, so that the pressure has a saddle-point at some point O , as shown in Figure 13. At O the pressure gradient vanishes, so that the "fluid" has downwards acceleration g . Assuming O moves with the fluid, we can, by taking a frame of reference attached to O , eliminate g from our equations locally. We can then show that in this free-fall frame of reference there are solutions of the simple form

$$\chi = \frac{1}{2}Az^2 \quad (5.2)$$

where A is a function of the time t only. In fact

$$A = \alpha e^{i\sigma} \quad (5.3)$$

where α and σ are real functions of t given by

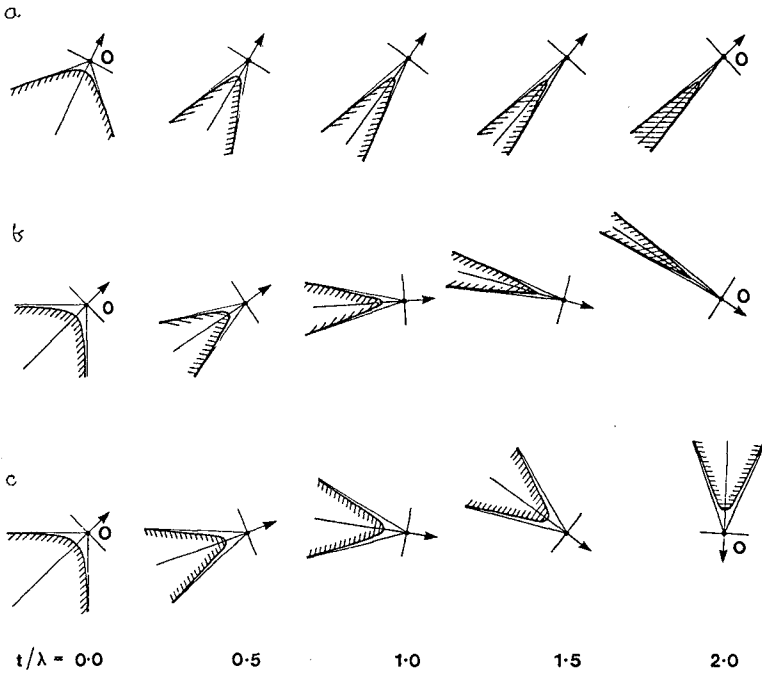


Figure 13. Examples of solutions of type (4.2) for the flow near the tip of the wave (a) when $P/\lambda^4 = 5.0$, (b) when $P/\lambda^4 = 0.30$ (c) when $P/\lambda^4 = 0.25$.

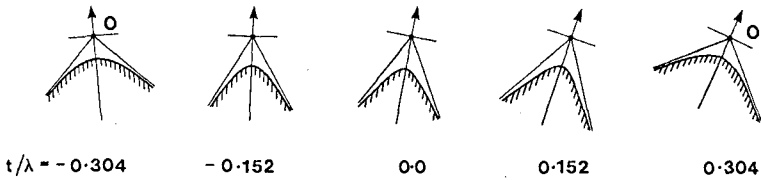


Figure 14. Example of a solution in class (2), when $P/\lambda^4 = 0.20$.

$$\left. \begin{aligned} \sigma &= \int \lambda \alpha^2 dt \\ t &= \int \frac{\lambda d\alpha}{(1-\lambda^2 \alpha^2 + P\alpha^4)^{\frac{1}{2}}} \end{aligned} \right\} \quad (5.4)$$

λ and P being arbitrary constants. The free surface takes the form of a hyperbola, such that the angle γ between the asymptotes varies with time. The principle axes of the hyperbola also rotate, in general, with angular velocity δ , also a function of t .

The solutions to (5.4) fall into two classes:

(1) When $P/\lambda^4 > 1/4$ the angle γ between the asymptotes diminishes monotonically in time, as shown for example in Figure 13. The axes meanwhile rotate through a finite angle, in general. However if $P/\lambda^4 = 1/4$ (Figure 13c) the rate of rotation tends to become a constant.

(2) When $P/\lambda^4 < 1/4$ (Figure 14) the angle γ between the asymptotes can begin at 90° , decrease to a smaller value and then return again to 90° after rotation through a finite angle, as in Figure 14. These solutions resemble the crests of waves partially reflected from a beach or obstacle.

(3) When $P/\lambda^4 < 1/4$ there is a third class of solutions in which the angle γ starts from zero as $t \rightarrow -\infty$, then increases to a maximum less than 45° and falls again to zero as $t \rightarrow +\infty$. These could have applications to falling jets.

These exact solutions are generalisations of the "Dirichlet hyperbolae" studied earlier by Longuet-Higgins (1976b), in which the orientation of the axes was fixed.

Now the origin O is in a free-fall trajectory, that is to say a parabola. When the motion of O is added to the motion just described, we obtain successive configurations such as shown in Figure 15. These are beginning to resemble the flow in the "jet" of a plunging breaker.

The local solution has now to be joined or "matched" mathematically to the flow in the rest of the wave. When we proceed to higher approximations by assuming, in place of (5.2), that

$$\chi = \frac{1}{2}Az^2 + \frac{1}{3}Bz^3 + \dots \quad (5.5)$$

then for certain choices of B the cubic terms are found to dominate and the free surface takes the form of a cusp.

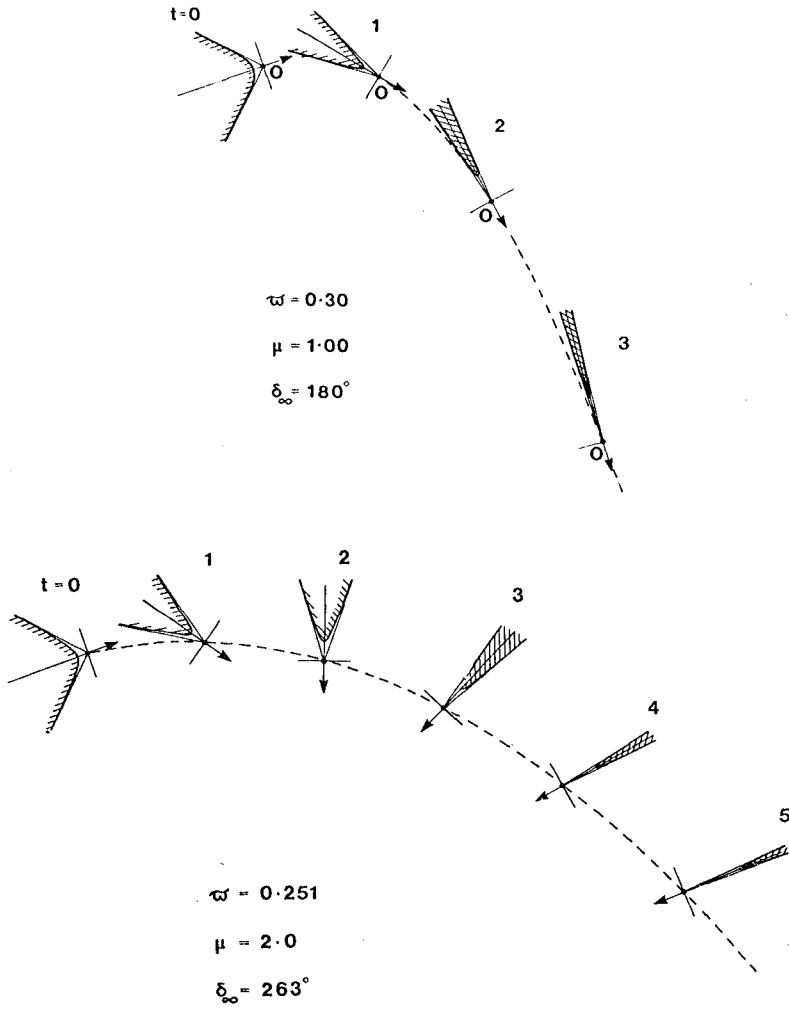


Figure 15. Solutions for the tip of the wave after adding the free-fall motion of the origin 0 .

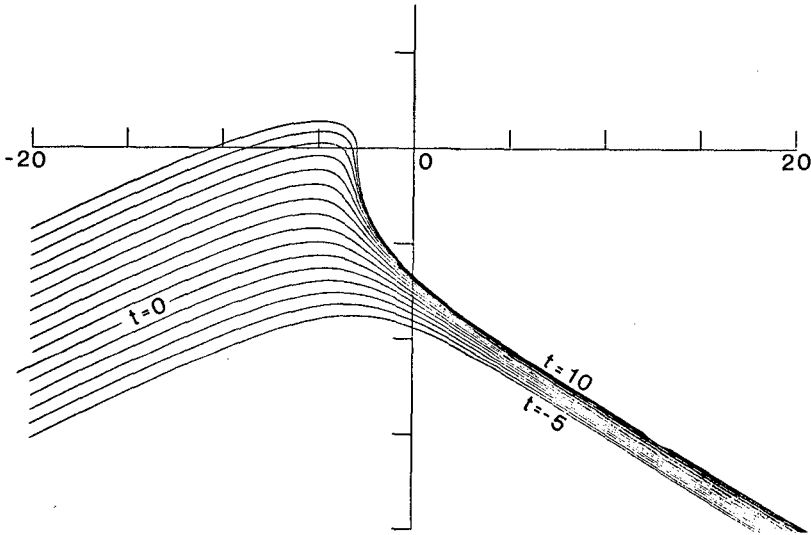


Figure 16. Successive positions of the free surface corresponding to equation (5.6) when $g = 1$, $U = (-1, 0.5)$ and A is chosen to minimise $\int (Dp/Dt)^2 ds$ along the free surface.

Now to solve the second part of the problem, that is to find an analytic expression for the body of overturning fluid, we may begin by observing that the flow in an overturning wave is essentially multivalued: where the "jet" hits the forward face of the wave, the fluid crosses over onto another sheet of the complex plane. Therefore in the cavity or "tube" of the breaker there must be a singularity of the velocity potential χ . The simplest such singularity is a branch-point of order $\frac{1}{2}$, and it is therefore natural to try an expression of the form

$$\chi = \frac{2}{3}ig^{\frac{1}{2}}z^{3/2} + Uz + 2Az^{\frac{1}{2}} \quad (5.6)$$

U being constant and A some function of the time t . The first term on the right of (5.6) represents the Stokes 120° corner-flow (the real axis of z points downward); the third term represents a parabolic flow which dominates near the origin but is relatively small at large distances $|z|$. The second term represents an arbitrary uniform flow past the branch-point at 0. In Longuet-Higgins (1980c) it is shown that

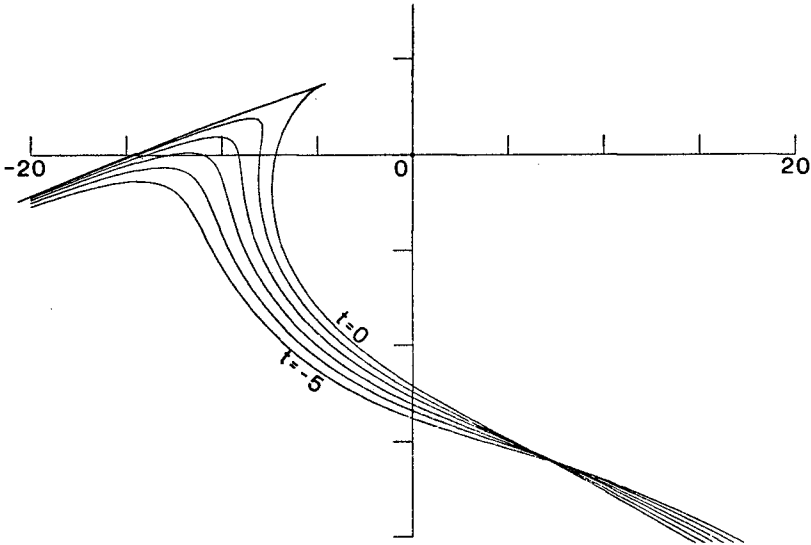


Figure 17. Successive positions of the free surface corresponding to (5.6) when $g = 1$, $U = (-1, 0)$ and \dot{A} is chosen so as to produce a sharp cusp at which $Dp/Dt = 0$.

we can satisfy both free surface conditions (5.1) asymptotically for large values of z provided that $\dot{A} = dA/dt$ is a constant, with

$$\operatorname{Re}(\dot{A}) = \operatorname{Im}(\frac{1}{2}U) \quad (5.7)$$

This leaves $\operatorname{Im}(\dot{A})$ at our disposal, which may be chosen so as to satisfy the boundary condition $Dp/Dt = 0$ at particular points, or in a least-squares sense, along the "free surface" $p = 0$.

An example of the flow (5.6) when $(Dp/Dt)^2$ is minimised along the free surface at time $t = 0$ (when A is real) is shown in Figure 16. At earlier times $t < 0$ the surface is more rounded; at later times the forward face becomes steeper and eventually overturns.

We can however find parameters in (5.6) such that not only is the boundary condition satisfied for large $|z|$ but also the free surface develops a sharp corner, at which point we can make $Dp/Dt = 0$. An example is shown in Figure 17.

To approximate solutions of the type shown in Figures 17 and 18 we may be able to join the solutions for the wave tip described earlier by asymptotic "matching".

For other forms of breaking waves expressions quite different from (5.6) may be appropriate. For example in a wave breaking against a vertical wall we may expect branch-points at two image-points on opposite sides of the wall.

6. PROBLEM D: WAVES AFTER BREAKING

The quasi-steady flow in a spilling breaker is probably the simplest with which to begin a study of post-breaking waves. It seems likely that at least the initial stages of spilling breakers, overturning near the crest of steep waves, differ only in local scale from those of the more violent and time-dependent plunging type.

After the tip of the jet collides with the forward face of the wave, violent turbulence ensues, often with the entrainment of air. This more complicated situation requires a different type of analysis, akin to the modelling of jets and wakes. A tentative model of a spilling breaker as a turbulent jet riding over a laminar fluid of higher density was proposed by Longuet-Higgins and Turner (1974) and seemed to model the initial stages of whitecaps on solitary waves. However, most reliance must be placed on experimental observations. Longuet-Higgins (1974b) reported laboratory measurements of the turbulence in a breaking bow-wave. Duncan (1979) has made extensive measurements of the spilling breaker induced by a submerged aerofoil towed through the water. One significant observation was the existence of a persistent oscillation of about 4.2 times the period of waves having a phase-speed equal to the towing speed. This is not far from the period of the fastest-growing instability of a uniform train of waves, as reported by Longuet-Higgins (1978a).

In an interesting study of plunging breakers, Miller (1976) has observed the formation of a succession of vortices at the free surface. As many as five may occur in one break. Each vortex tends to produce a pocket of air, forced downwards into the water, which then collapses in a cloud of bubbles.

Although aerial observations have been made of the percentage of the ocean surface covered by white water under various wind conditions (e.g. Monahan 1971), these do not easily give the mean energy or momentum lost to the waves through breaking. A new device which detects and measures the heights of sudden "jumps" or discontinuities in the sea surface has been developed by the present author and N.D. Smith. From observations in the North Sea during the MARSEN

program in September to November 1979 it was found that the number of "jumps" of a given magnitude increases sharply between wind-speeds of 6 to 8 m/s. Further analysis of these observations is in progress.

7. CONCLUSION

Out of the many and varied aspects of coastal engineering, I have chosen to speak about only one topic, but one that is central to an understanding of the surf zone. For want of space several aspects even of this topic, particularly the role played by shoaling depth of water, have had to be omitted.

Nevertheless it will be clear that this is a subject to which mathematical analysis can make a substantial, indeed a leading, contribution. I would emphasize that a satisfactory solution requires and deserves the best efforts of applied mathematicians, working in close collaboration with field observers. Some of our best workers have already taken up the challenge. I look forward to hearing some of their contributions, as well as many others, at this Conference.

REFERENCES

- Benjamin, T.B. and Feir. 1967 The disintegration of wave trains on deep water. 1. Theory.
J. Fluid Mech. 28, 417-430.
- Byatt-Smith, J.G.B. and Longuet-Higgins, M.S. 1976 On the speed and profile of steep solitary waves.
Proc. R. Soc. Lond. A. 350, 175-189.
- Chaplin, J.R. 1979 Developments of stream function wave theory.
Coastal Engineering (in press).
- Chen, B. and Saffman, P.G. 1978 Numerical evidence for the existence of new types of gravity wave of permanent form on deep water.
(preprint, to appear).
- Cleaver, R.P. 1980 The instabilities of gravity waves of finite amplitude.
Phil. Trans. R. Soc. Lond. A (in press).
- Cokelet, E.D. 1977a Steep gravity waves in water of arbitrary uniform depth.
Phil. Trans. R. Soc. Lond. A 286, 183-230.
- Cokelet, E.D. 1977b Breaking waves.
Nature, Lond. 267, 769-774.

- Duncan, J.H. 1979 The dynamics of breaking surface waves. Report, Johns Hopkins Univ., Dept. of Earth and Planetary Sciences.
- Fox, M.J.H. 1977 Nonlinear effects in surface gravity waves on water. Cambridge Univ. Ph.D. Thesis.
- Killen, P. and Hornung, H.G. 1976 A stationary oblique wave for laboratory testing of surfboards. J. Fluid Mech. 78, 459-480.
- Lenau, C.W. 1966 The solitary wave of maximum amplitude. J. Fluid Mech. 26, 309-320.
- Longuet-Higgins, M.S. 1972 A class of exact, time-dependent free-surface flows. J. Fluid Mech. 55, 529-543.
- Longuet-Higgins, M.S. 1973 On the form of the highest progressive and standing waves in deep water. Proc. R. Soc. Lond. A 331, 445-456.
- Longuet-Higgins, M.S. 1974a On the mass, momentum, energy and circulation of a solitary wave. Proc. R. Soc. Lond. A 337, 1-13.
- Longuet-Higgins, M.S. 1974b Breaking waves — in deep and shallow water. Proc. 10th Conf. on Naval Hydrodynamics, Cambridge, Mass. pp.597-605. Washington, U.S. Govt. Printing Office.
- Longuet-Higgins, M.S. 1975 Integral properties of periodic gravity waves of finite amplitude. Proc. R. Soc. Lond. A 342, 157-174.
- Longuet-Higgins, M.S. 1976a Recent developments in the study of breaking waves. Proc. 15th Conf. on Coastal Eng. Honolulu pp.441-460.
- Longuet-Higgins, M.S. 1976b Self-similar, time-dependent flows with a free surface. J. Fluid Mech. 73, 603-620.
- Longuet-Higgins, M.S. 1978a The instabilities of gravity waves of finite amplitude in deep water. Proc. R. Soc. Lond. A 360, 471-505.
- Longuet-Higgins, M.S. 1978b The orbital motion in steep water waves. (Appendix to: J.H. Nath, "Drift speed of buoys in waves"). Proc. 16th Conf. on Coastal Eng., Hamburg, pp.874-876.

- Longuet-Higgins, M.S. 1979a Why is a water wave like a grandfather clock?
Phys. Fluids 22, 1828-1829.
- Longuet-Higgins, M.S. 1979b The almost-highest wave: a simple approximation.
J. Fluid Mech. 94, 269-273.
- Longuet-Higgins, M.S. 1979c The trajectories of particles in steep, symmetric gravity waves.
J. Fluid Mech. 94, 497-517.
- Longuet-Higgins, M.S. 1980a A technique for time-dependent free-surface flows.
Proc. R. Soc. Lond. A 371, 441-451.
- Longuet-Higgins, M.S. 1980b On the forming of sharp corners at a free surface.
Proc. R. Soc. Lond. A 371, 453-478.
- Longuet-Higgins, M.S. 1980c A branch-point model of a breaking wave.
(in preparation).
- Longuet-Higgins, M.S. 1980d On the trajectories of particles in steep solitary waves.
(in preparation).
- Longuet-Higgins, M.S. and Cokelet, E.D. 1976 The deformation of steep surface waves on water I. A numerical method of computation.
Proc. R. Soc. Lond. A 350, 175-189.
- Longuet-Higgins, M.S. and Cokelet, E.D. 1978 The deformation of steep surface waves on water II. Growth of normal-mode instabilities.
Proc. R. Soc. Lond. A 364, 1-28.
- Longuet-Higgins, M.S. and Fenton, J.D. 1974 On the mass, momentum, energy and circulation of a solitary wave. II.
Proc. R. Soc. Lond. A 340, 471-493.
- Longuet-Higgins, M.S. and Fox, M.J.H. 1977 Theory of the almost-highest wave: the inner solution.
J. Fluid Mech. 80, 721-741.
- Longuet-Higgins, M.S. and Fox, M.J.H. 1978 Theory of the almost-highest wave II. Matching and analytic extension.
J. Fluid Mech. 85, 769-786.
- Longuet-Higgins, M.S. and Turner, S.J. 1974 An "entraining plume" model of a spilling breaker.
J. Fluid Mech. 63, 1-20.

- Michell, J.H. 1893 The highest waves in water.
Phil. Mag. (5) 36, 430-437.
- Miller, R.L. 1976 Role of vortices in surf zone prediction: sedimentation and wave forces.
Beach and Nearshore Sedimentation, ed. R. A. Davis and R. L. Ethington. Tulsa, Oklahoma. Soc. of Economic Palaeontologists and Mineralogists, pp.92-114.
- Monahan, E.C. 1971 Oceanic whitecaps.
J. Phys. Oceanogr. 1, 139-144.
- Olfe, D.B. and Rottman, J.W. 1979 Numerical calculations of steady gravity-capillary waves using an integro-differential formulation.
J. Fluid Mech. 94, 777-793.
- Saffman, P.G. and Yuen, H.C. 1979 A note on numerical computations of large standing waves.
J. Fluid Mech. 95, 707-715.
- Schwartz, L.W. 1974 Computer extension and analytic continuation of Stokes' expansion for gravity waves.
J. Fluid Mech. 62, 553-578.
- Starr, V.T. 1947 Momentum and energy integrals for gravity waves of finite height.
J. Mar. Res. 6, 175-193.
- Stokes, G.G. 1880 Supplement to a paper on the theory of oscillatory waves.
Mathematical and Physical Papers, Vol.1, pp. 314-326. Cambridge Univ. Press.
- Vanden-Broeck, J.-M. and Schwartz, L.W. 1979 Numerical computation of steep gravity waves in shallow water.
Phys. Fluids 22, 1868-1871.
- Van Dorn, W.G. and Pazan, S.E. 1975 Laboratory investigation of wave breaking.
Scripps Inst. of Oceanogr. Report 75-21, 105 pp.
- Witting, J. 1975 On the highest and other solitary waves.
S.I.A.M. J. Appl. Math. 28, 700-719.
- Yamada, H. 1957a Highest waves of permanent type on the surface of deep water.
Rep. Res. Inst. Appl. Mech. Kyushu Univ. 5, 37-52.
- Yamada, H. 1957b On the highest solitary wave.
Rep. Res. Inst. Appl. Mech. Kyushu Univ. 5, 53-67.



Beach Renourishment, North Cronulla, New South Wales

PART I

THEORETICAL AND OBSERVED WAVE CHARACTERISTICS

Beach Erosion at Floreat Beach after Cyclone "Alby", Perth, Western Australia



CHAPTER 1

SOME IMPLICATIONS OF RECENT ADVANCES IN WAVE THEORIES

by

J. R. Chaplin, Lecturer
and
K. Anastasiou, Research Assistant

Department of Civil Engineering
University of Liverpool
P.O. Box 147
Liverpool, L69 3BX
U.K

1. INTRODUCTION

Calculations using the 'Design Wave' approach in coastal and offshore engineering begin with the specification of wave conditions usually in terms of a wave height, wave period and mean water depth. These three dimensional parameters are sufficient to define all the wave characteristics uniquely if a number of assumptions are adopted, including those of periodicity in space and time, absence of viscosity, and two-dimensional flow. Although these assumptions result in an enormous simplification of waves in the ocean, the ultimate idealised conditions hold some attraction in providing a standard description of wave mechanics for design purposes. Once the design wave approach has been adopted, it follows that the engineer needs to ensure that the theory which he uses to analyse waves generates results equivalent to those of the most accurate theory currently available.

There are in engineering use several wave theories (e.g., Airy, Stokes 5th order, Cnoidal, Stream Function) by means of which required wave properties can be computed from an initial wave specification on the basis of ideal conditions. Unfortunately, none of these theories is exact and in general they disagree, most significantly in conditions of shallow water or high wave steepnesses. The differences between them have stimulated comparative studies based on boundary condition errors (Dean, 1970) and experimental data (Le Méhauté et al, 1968), leading to recommendations on the use of specific theories for given conditions. However, the value of these comparisons has been somewhat limited by the absence of an accurate solution to the problem valid over the whole range of interest.

Such a solution has now been brought nearer by the work of Cokelet (1977), and it is the purpose of this paper to study the implementation of Cokelet's theory and other recent theories in an engineering context. The paper does not make any contribution to the analysis itself but is concerned with applications, and the question whether such developments should influence current engineering practice.

Previously, the wave theory offering greatest analytical accuracy and widest range of application was the Stream Function Theory of Dean (1965).

Tables of functions (Dean, 1974) have facilitated the application of this wave theory, but some results for steep waves given in the tables disagree with Cokelet's results.

The use of Cokelet's theory in an engineering context is discussed in Section 2, and other relevant recent developments introduced in Section 3. In Section 4 numerical results are presented for comparison between different methods.

2. ENGINEERING APPLICATIONS OF THE EXTENDED STOKES THEORY

As Cokelet (1977) presented it, the extended Stokes theory is not in a very convenient form for engineering application. The two dimensionless independent parameters¹ d_* and ϵ_* are not written explicitly in terms of wave height H , period T and mean water depth d . The expansion parameter ϵ_* lies in the range zero (for zero wave height) to unity (for waves of limiting height), and $d_*L/2\pi$ (where L is the wave length) is slightly less than the mean water depth d , and differs from it by 4% at most. In order to relate d_* and ϵ_* to H , T and d , it is necessary to compute some of the series expansions given by Cokelet using Padé approximants. In particular:

$$d/L_0 = \frac{c_*^2}{2\pi} (d_* + \bar{\eta}_*) \quad (1)$$

and

$$H/L_0 = \frac{c_*^2}{\pi} a_* \quad (2)$$

$$\text{where } L_0 = gT^2/2\pi$$

The problem of going in the opposite direction, i.e., finding from given d/L_0 and H/L_0 the corresponding d_* and ϵ_* , and thereby a complete solution for given wave conditions, is a more demanding one. Possibly the extended Stokes solution could be re-formulated with different independent parameters, but in the present work we adopt a more pragmatic approach which provides a satisfactory entry to Cokelet's theory from conditions specified in terms of d/L_0 and H/L_0 . The corresponding values of d_* and ϵ_* are interpolated from Cokelet's (1977) tabulated results as described below.

At points on the d/L_0 , H/L_0 plane corresponding to the intersections of lines at constant d_* and ϵ_* , some of which are shown in Fig. 1, Cokelet provided numerical results of a range of integral wave properties, including c_*^2 , $\bar{\eta}_*$ and a_* . The co-ordinates of the intersections may easily be calculated from Eqs. (1) and (2). In order to interpolate d_* at a specified point in the plane, the procedure adopted in the present work was as follows.

¹ Where Cokelet's parameters are introduced, they appear with a subscripted asterisk.

Conditions of limiting wave height H_B were identified on the axes of Fig. 1 by cubic splines fitted (Ahlberg et al, 1967) through the points at which $\epsilon_* = 1$, to approximate the function H_B/L_0 (d/L_0). The co-ordinates of the intersections at which the data is tabulated could then be transferred to the $d/L_0, H/H_B$ plane, in which lines of constant ϵ_* are predominantly in line with the d/L_0 axis. Cubic splines were then used, along each line of constant ϵ_* in turn, to approximate the functions H/H_B ($d/L_0, \epsilon_*$ =constant) and $d_*(d/L_0, \epsilon_*$ =constant). From each pair of splines H/H_B and d_* were interpolated at the required value of d/L_0 to give a series of (unequally spaced) points on the curve approximating $d_*(H/H_B, d/L_0$ =constant). The final interpolation at the required H/H_B was again performed by means of cubic splines. Linear scales were used throughout, except for d/L_0 and H/L_0 , which were represented in the curve fitting by their logarithms. Various end conditions for the splines were tested and the most accurate results were generally obtained by setting second derivatives equal over the first pair and last pair of data points. Any other of the parameters tabulated in Cokelet's tables (or functions of them) can be interpolated in the same way. Alternative end conditions were used for the limit $H/H_B = 0$ when the behaviour of the required parameter was known from Stokes wave theory.

The accuracy of this method was tested by computing with Padé approximants the parameters $c_*^2, \bar{\eta}_*$ and a_* , for values of d_* and ϵ_* generated by interpolation from Cokelet's data with specified d/L_0 and H/L_0 . The errors in the final d/L_0 and H/L_0 calculated by Eqs. (1) and (2) were always much less than 1%, except in the shallow water conditions $d/L_0 < 0.008$ where some of the integral wave properties converge at best to only one or two significant figures.

Other wave properties which can be computed directly from Cokelet's data by the above method of interpolation (i.e., without the use of Padé approximants) include the wavelength:

$$L/L_0 = c_*^2 \quad (3)$$

the elevation of the crest above mean water level:

$$\frac{\eta_{\text{crest}}}{H} = \frac{K_*}{4a_*} = \frac{2\bar{\eta}_*}{4a_*} \quad (4)$$

the dimensionless particle velocity at the crest $q_{\text{crest}*}$ on a frame of reference moving at the wave celerity:

$$q_{\text{crest}*} = -2a_* + \sqrt{4a_*^2 - c_*^4(\epsilon_*^2 - 1)} \quad (5)$$

and the horizontal particle velocity at the crest on a stationary frame of reference:

$$\frac{u_{\text{crest}}}{H/T} = \frac{\pi(c_* - q_{\text{crest}*})}{c_* a_*} \quad (6)$$

besides the energies and energy flux and other terms presented in the tables.

Unfortunately, no information is available by this means on the profile of the free surface or on particle velocities other than at the crest and the trough. To obtain the free surface profile or general particle velocities and accelerations, it is necessary to solve, (Cokelet, 1977), the series expansions for the coefficients of the Fourier series of the complex potential, from independent parameters d_* and ϵ_* . Since the complex spatial co-ordinate Z_* is expressed in the final solution as a function of the complex potential W_* , rather than vice-versa, it is ultimately necessary to interpolate for Z_* , for instance by complex Newton-Raphson iterations, to obtain conditions at a given location within the wave. A greater handicap, however, is the failure of the series expressions for the high order Fourier coefficients to converge adequately for strongly non-linear cases. Cokelet discussed this problem and showed how the degree of convergence could be determined by comparing values of parameters derived from the surface profile and alternatively directly from a series by Padé approximants.

To define the conditions for which the velocity potential Fourier series would converge we computed a number of cases and compared results for crest elevation and crest particle velocity derived by the two methods. The maximum wave heights for which errors in crest elevation and particle velocity derived from the Fourier series did not exceed 2% are shown as the broken line in Fig. 1. For the most shallow water conditions tested, this occurs at about one half the limiting wave height. In deeper water, with $d/L_0 > 0.1$, satisfactory results were obtained up to within 1% of the limiting height. These computations were carried out in double precision (approximately 28 significant places) on a CDC 7600 to a maximum order of 120. Convergence limits were almost exactly the same for both elevation and particle velocity at the crest. In view of the series formulation of the velocity potential, it might be expected that particle velocity would fail to converge before the profile itself, since the differentiation involved causes the truncated higher spatial frequency components to have a greater relative contribution to the total. This is not the case, however, owing to the inverse formulation of the Stokes series. It is, nevertheless, reasonable to expect that the region of convergence for particle accelerations will be rather more restricted than these, although no numerical comparisons have been carried out.

We conclude that the extended Stokes theory can be used in the same framework as engineering wave theories by means of cubic spline interpolation for the independent parameters d_* and ϵ_* . The velocity potential and its derivatives do not converge in all cases, but much useful information can be computed by interpolation from Cokelet's tables. Comparison of some results with those of other methods follows in Section 4.

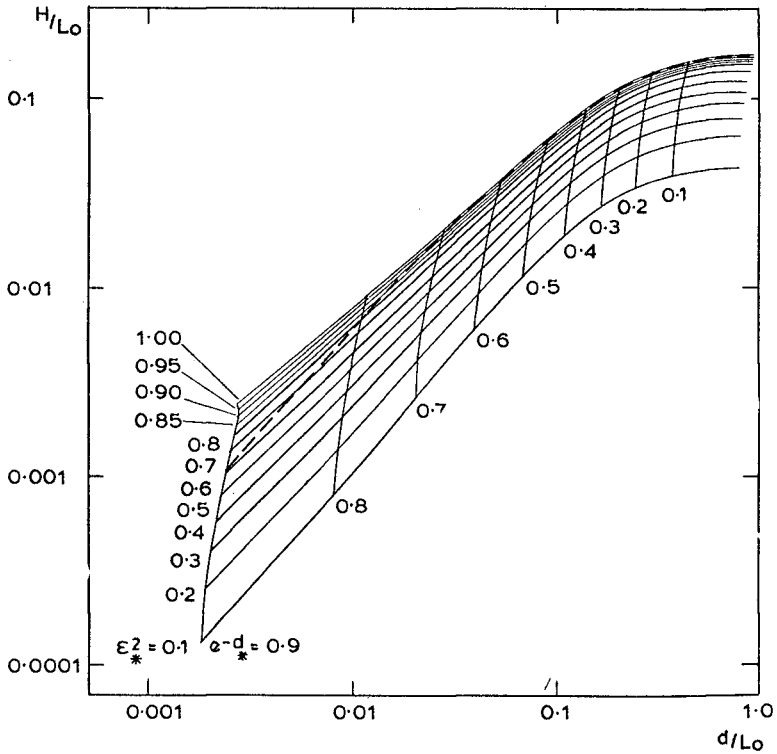


FIG. 1. LINES OF CONSTANT DIMENSIONLESS
UNDISTURBED DEPTH j_* AND EXPANSION
PARAMETER ϵ_* CALCULATED IN TERMS
OF WAVE HEIGHT H AND MEAN WATER
DEPTH d FROM Cokerlet's TABLES.
 L_0 = SMALL AMPLITUDE DEEP WATER
WAVELENGTH

3. FURTHER RECENT METHODS

Properties of steep waves can also be computed accurately by the stream function wave theory (Chaplin, 1980). While this method is more cumbersome than Cokelet's, and does not have in-built checks for convergence, it has the advantage of being formulated in conventional terms, and seems to converge better for steep waves in shallow water. The re-formulation necessary to achieve these results was carried out in an attempt to eliminate errors apparent in data for the steepest waves presented in stream function tables by Dean (1974). Some further comparisons using modified stream function results are presented in the next Section.

The analysis of steep waves by either extended Stokes theory or stream function theory demands much costly computer storage and time. Consequently, simple yet accurate approximations for the crest of the almost-highest wave and for the wave of limiting height in deep water by Longuet-Higgins (1979a and 1973) have great appeal. Results of both methods are presented in the next Section.

The almost-highest wave (AHW) approximation (Longuet-Higgins, 1979a) is expressed in terms of a velocity scale which must be derived by other means from given wave conditions. In the present work this has been achieved by means of interpolation by cubic splines, as described above, from Cokelet's (1977) data as follows. The required unit of velocity is $q/\sqrt{2}$, where q is the crest particle velocity in a reference frame moving with the wave. In terms of Cokelet's parameters:

$$\frac{q}{\sqrt{2}} = \frac{q_{\text{crest}*} c_* C_0}{\sqrt{2}} \quad (7)$$

where C_0 is the small amplitude deep water celerity. The associated unit of length is:

$$\frac{q_{\text{crest}*}^2 c_*^2 C_0^2}{2g}$$

and in order to fix the origin it is necessary also to compute in advance the elevation of the crest.

As shown in Eqs. (4) and (5) these parameters can be related to those presented in Cokelet's tables, and thus obtained for any specified wave conditions by interpolation. The computing effort necessary for the interpolation, followed by application of the AHW approximation is a small fraction of 1% of that required for a full solution by series methods. Furthermore, it applies to the crest where conditions for many purposes are likely to be most severe, and where conventional wave theories are at their weakest owing to poor convergence associated with the original Stokes type series formulation. The almost-highest wave approximation is related to more accurate solutions derived by Longuet-Higgins and Fox (1977, 1978). In the second of these papers the solution for the crest is matched to the rest of the wave for deep water

conditions. Particle trajectories near the crest derived from the AHW approximation, the hexagon transformation and other methods are given in Longuet-Higgins (1979b).

4. COMPARISON OF NUMERICAL RESULTS

In comparing results from different wave theories, particular attention is paid to particle velocities in the region close to the crest for the reasons stated above. Also, we concentrate on steep waves since the earlier stream function tables (Dean, 1974) are accurate to within 5% for almost all cases up to 90% of limiting wave height (Chaplin, 1980). While integral parameters can be derived from any of the theories mentioned, they are now more easily and accurately computed from Cokelet's tables.

Fig. 2 shows the percentage errors in crest elevation above mean water level η as a proportion of wave height H for waves of limiting height. The results for cnoidal theory (for which U denotes the Ursell number L^2H/d^3) were computed in accordance with Keulegan and Patterson (1940) and those for Stokes 5th order theory with Skjelbreia and Hendrickson (1960). Clearly the stream function tables (in which nominally breaking waves are denoted as case D) are the most accurate, although they refer to slightly different wave heights.

Similarly, Fig. 3 shows crest particle velocities in a stationary reference frame u_{crest} as a proportion of the celerity for waves of limiting height. Again the stream function tables are the most accurate, giving results closest to unity for most water depths. In both comparisons, cnoidal theory is seriously in error, either at low Ursell numbers for crest elevations, or at high Ursell numbers for crest particle velocities. Since particle velocities vary only gradually through the water depth in shallow water conditions, it is reasonable to expect that the errors in cnoidal theory demonstrated in Fig. 3 are not confined to the region near the surface. Conversely in deep water conditions, the most significant errors in Stokes 5th order theory occur only close to the surface and predominantly at the crest. A comparison of horizontal particle velocities and vertical particle accelerations on a vertical line through the crest of the wave of limiting height in deep water is given in Fig. 4, in which y is measured upwards from mean water level. Since the velocity potential series in the extended Stokes theory does not converge for this case, we adopt the hexagon transformation (Longuet-Higgins, 1973) as an easily computed and accurate alternative. It gives inevitably the crest particle velocity u equal to the celerity and the upward vertical acceleration dv/dt at the crest level equal to $-1/2 g$. Stokes 5th order theory and the stream function tables seriously underestimate both, but their errors diminish rapidly away from the surface.

The surface profile for the wave of limiting height in deep water is plotted without distortion in Fig. 5 for comparison with Stokes 5th order and stream function tables (case 10D) results. Although the latter is only a third order solution, this refers to the number of terms in the stream function series rather than in the Fourier series for the surface profile as in Stokes 5th order theory. The surface

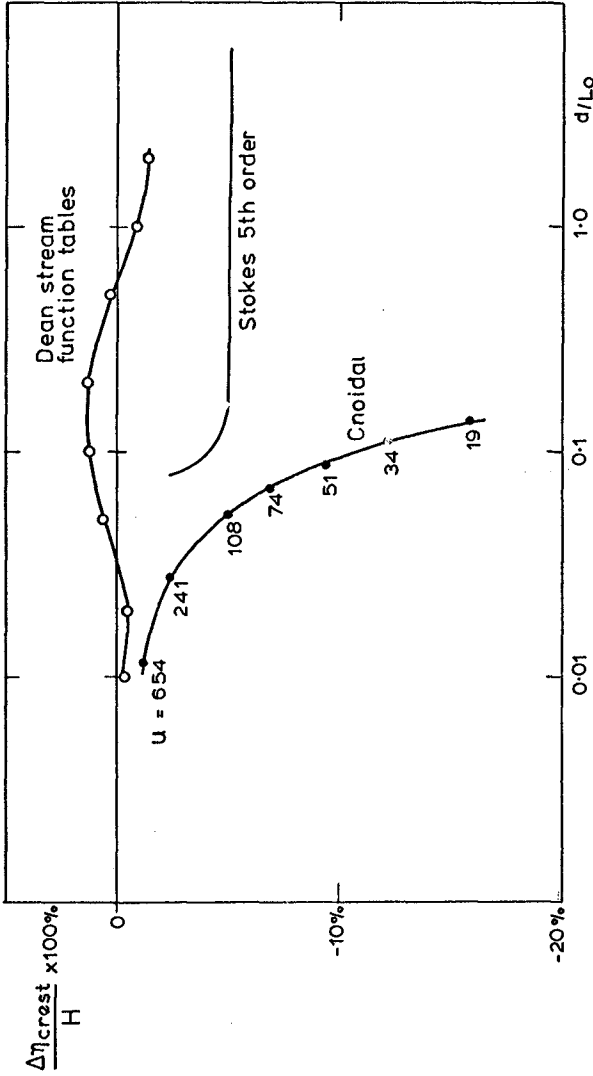


FIG. 2. CREST ELEVATIONS ABOVE MEAN WATER LEVEL IN WAVES OF LIMITING HEIGHT: ERRORS IN CNOIDAL, Stokes 5th ORDER THEORIES AND Dean STREAM FUNCTION TABLES AS A PERCENTAGE OF WAVE HEIGHT

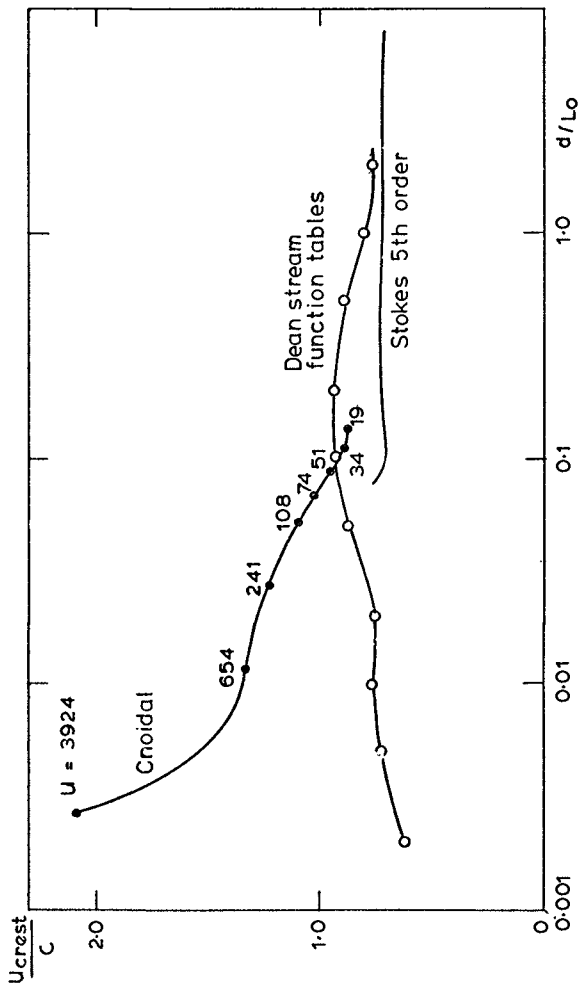


FIG. 3. CREST PARTICLE VELOCITIES OF WAVES OF LIMITING HEIGHT CALCULATED FROM Keulegan and Patterson's CNOIDAL WAVE THEORY, Stokes 5th ORDER WAVE THEORY AND Dean STREAM FUNCTION TABLES

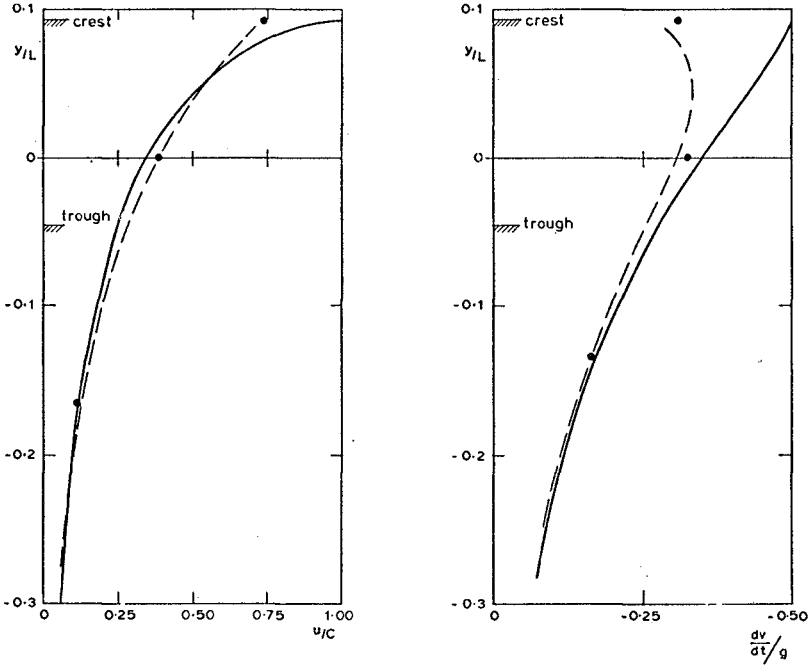


FIG. 4. PROPERTIES OF WAVES OF LIMITING HEIGHT IN DEEP WATER. PARTICLE VELOCITIES AND ACCELERATIONS ON A VERTICAL LINE THROUGH THE CREST PREDICTED BY THE HEXAGON TRANSFORMATION (Longuet-Higgins, —) Stokes 5th ORDER WAVE THEORY (---) AND Dean STREAM FUNCTION TABLES (●)

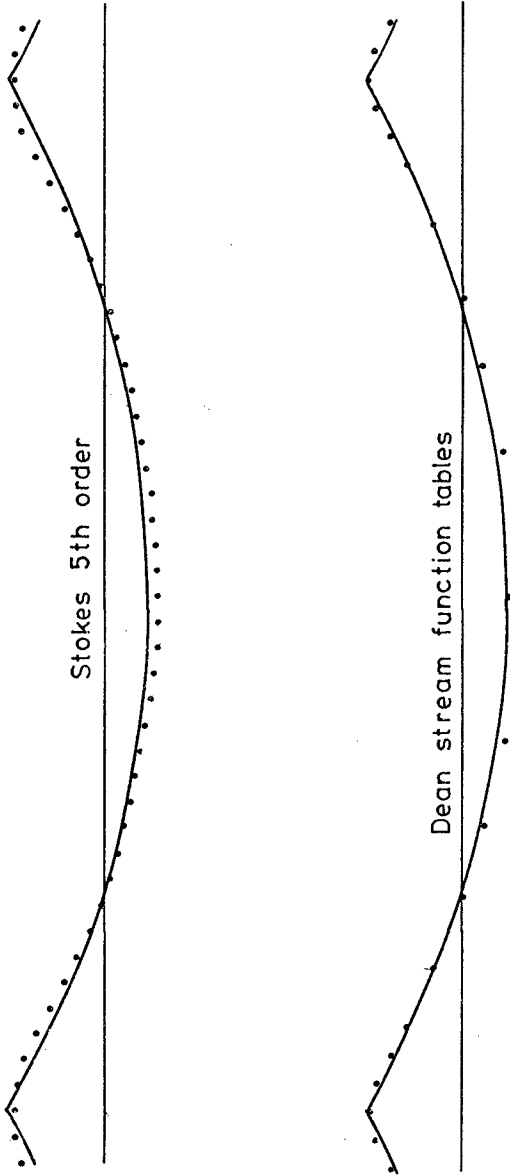


FIG. 5. THE WAVE OF MAXIMUM HEIGHT IN DEEP WATER. COMPARISON OF PROFILES WITH THE HEXAGON TRANSFORMATION (Longuet-Higgins)

profile in the stream function theory is derived from the stream function series, has therefore higher frequency terms and approaches more closely the discontinuity of surface slope at the crest.

The surface particle velocities predicted by the same three methods for the wave of limiting height in deep water are shown in Fig. 6 over the half wave length ahead of the crest. The errors in u at the crest in Stokes 5th order and stream function theories are again not representative of errors elsewhere.

It must be noted that the above comparison of results for limiting deep water waves serves only to demonstrate the performance of Stokes and stream function theories generally in deeper water. For this particular case the hexagon transformation is both more accurate and more convenient to compute than either of them.

If a full solution is needed for very steep waves in transitional water depth, the modified stream function theory (Chaplin, 1980) can provide converged results for cases which are beyond the limits we have found in the extended Stokes theory, and which are shown in Fig. 1. As noted above, the elevation and particle velocity at the crest can be found for all cases from Cokelet's tables by interpolation, and in Fig. 7 are plotted these results for very steep waves for two water depths. The agreement with results taken from full modified stream function solutions is within the accuracy of the interpolation procedure and of Cokelet's tables. Since conditions at the crest are more sensitive than those elsewhere to truncation errors this is taken as some confirmation of the overall accuracy of the full stream function solutions for the profiles and particle velocities of these steep waves.

The flow in a small region near the crest can also be computed, as described in the previous section, by the AHW approximation. For the two water depths referred to in Fig. 7, Figs. 8 and 9, in which x is measured horizontally forwards from the crest, compare elevations and velocity components of surface particles near the crests of steep waves computed by this method and by the modified stream function theory. The extent of agreement between the two methods naturally increases with increasing wave height as the upper part of the surface profile resembles more and more closely the Stokes corner flow which is the asymptote of the AHW approximation away from the crest. Also the two methods agree, not surprisingly, over a greater proportion of the wavelength in the deeper water case because the crest itself is relatively longer. Discrepancies at $x = 0$ are associated with differences between stream function results and those interpolated from Cokelet's tables to provide the scale and the origin of the AHW approximation. Away from the crest the latter tends towards a uniform surface slope and thus increasingly underestimates the actual surface profile elevation. Nevertheless, surface particle horizontal velocity components are accurately predicted by the approximation as far out as $x/L = 0.1$ for the steepest wave with $d/L_0 = 0.2$.

Sub-surface particle velocities are compared in Fig. 10 along a vertical line through the crest. Reasonable agreement is found over a region of similar dimensions as for surface elevations, namely about $L/80$ and $L/20$

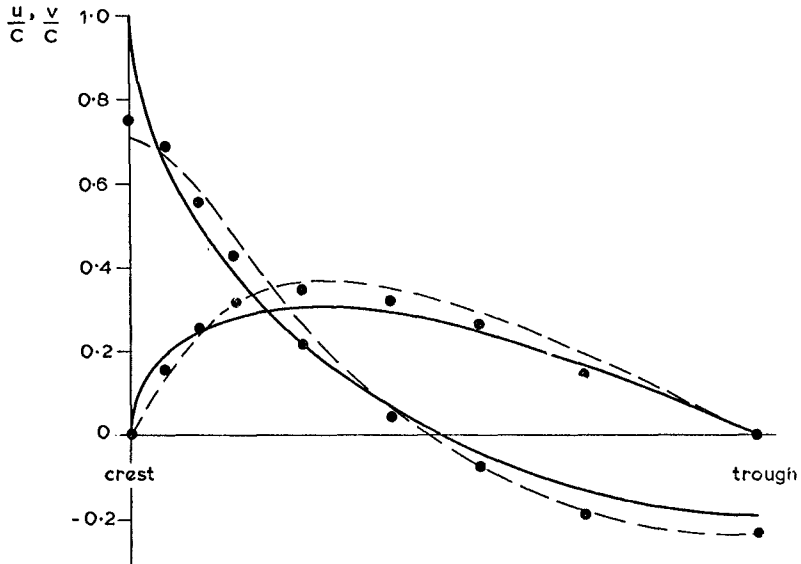


FIG. 6. THE WAVE OF MAXIMUM HEIGHT IN DEEP WATER.
 COMPARISON OF VELOCITY COMPONENTS OF
 SURFACE PARTICLES WITH RESULTS OF THE
 HEXAGON TRANSFORMATION (Longuet-Higgins)
 — — — Stokes 5th ORDER, ● Dean STREAM
 FUNCTION TABLES, CASE 10D

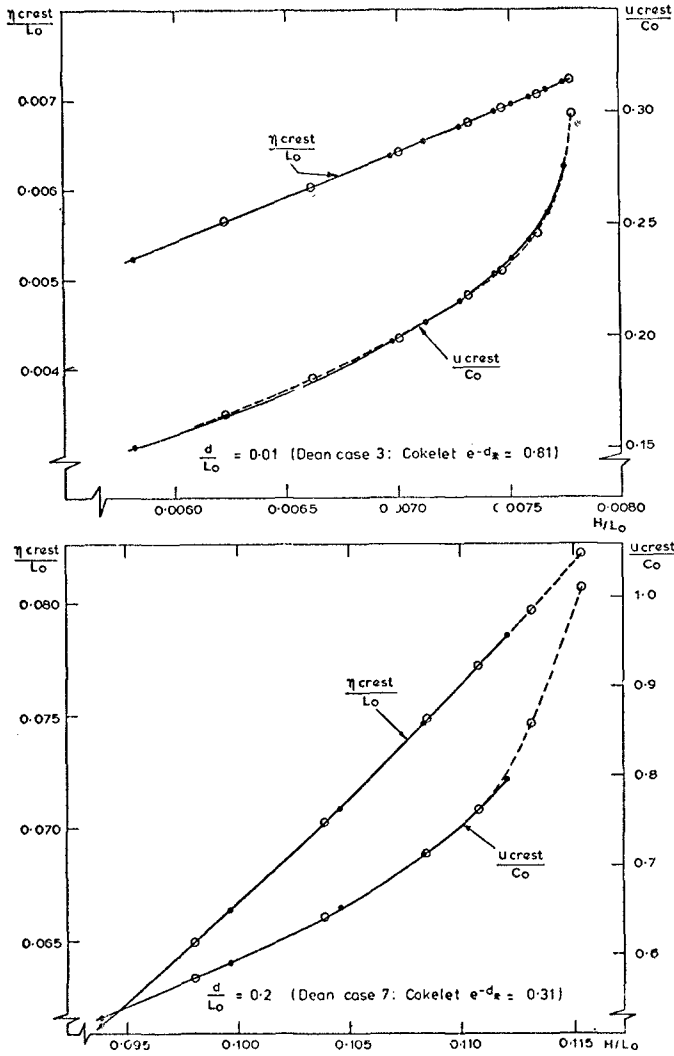


FIG. 7. CREST ELEVATION AND PARTICLE VELOCITY AT THE CREST FOR STEEP WAVES WITH CONSTANT PERIOD AND MEAN WATER DEPTH:
 ● - MODIFIED STREAM FUNCTION WAVE THEORY. ○ - INTERPOLATED BY SPLINES FROM INTEGRAL PROPERTIES TABULATED BY COKELE:

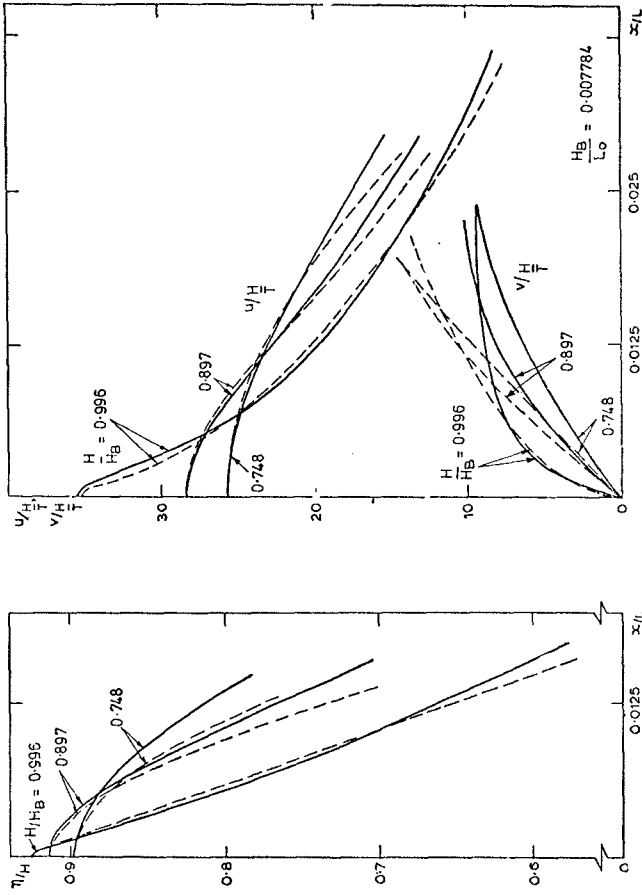


FIG. 8. ELEVATIONS ABOVE MEAN WATER LEVEL (η) AND HORIZONTAL AND VERTICAL VELOCITY COMPONENTS OF SURFACE PARTICLES NEAR THE CREST OF STEEP WAVES WITH $\eta/L_0 = 0.01$. COMPARISON OF RESULTS FROM STREAM FUNCTION THEORY ———, AND THE ALMOST HIGHEST WAVE APPROXIMATION - - - -

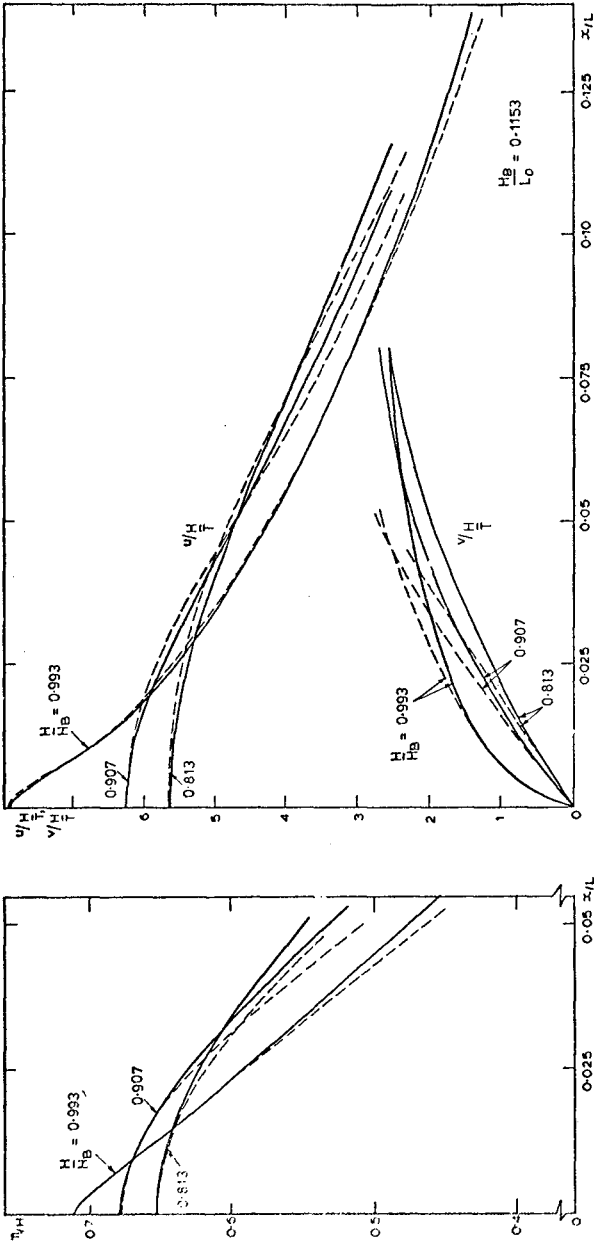


FIG. 9. ELEVATION ABOVE MEAN WATER LEVEL (η) AND HORIZONTAL AND VERTICAL VELOCITY COMPONENTS (u, v) OF SURFACE PARTICLES NEAR THE CREST OF STEEP WAVES WITH $d/L_0 = 0.2$. COMPARISON OF RESULTS FROM STREAM FUNCTION THEORY ———, AND THE ALMOST HIGHEST WAVE APPROXIMATION - - - - -

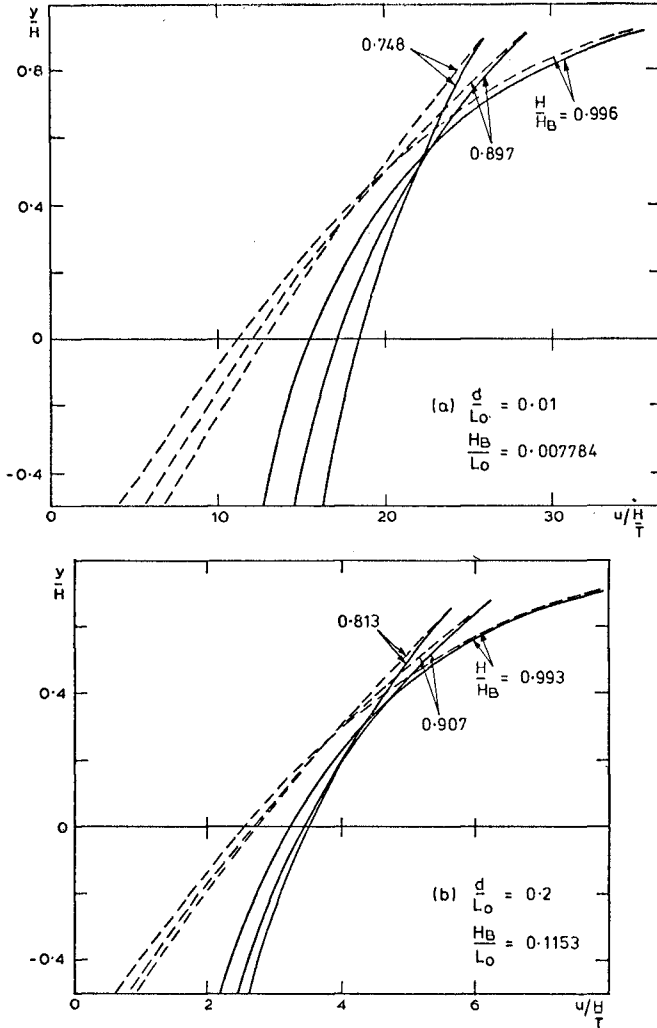


FIG. 10. HORIZONTAL PARTICLE VELOCITIES ON A VERTICAL LINE THROUGH THE CREST COMPUTED FOR STEEP WAVES BY MODIFIED STREAM FUNCTION THEORY ——— AND THE ALMOST HIGHEST WAVE APPROXIMATION - - - - : (a) $d/L_0 = 0.01$, (b) $d/L_0 = 0.2$

for $d/L_0 = 0.01$ and 0.2 , respectively. For deep water conditions the approximation may be extended beyond this region by the method of Longuet-Higgins and Fox (1978).

5. CONCLUSIONS

The extended Stokes theory (Cokelet, 1977) may be used in an engineering context in the same framework as conventional wave theories. From the data which Cokelet tabulated suitable input parameters can be interpolated from known water depth, wave height and period. Integral wave parameters can then be computed for any conditions specified in this way, but the velocity potential series, from which surface profiles and particle velocities and accelerations are derived, does not converge adequately in the region above the broken line in Fig. 1. Full solutions in this region have, however, been obtained for wave heights up to within 1% of limiting wave height by the modified stream function theory (Chaplin, 1980).

Surface elevations and particle velocities near the crest, computed by these methods differ significantly from those calculated by conventional wave theories. However, accurate partial solutions can also be computed much more rapidly by approximations for limiting and near-limiting wave heights (Longuet-Higgins, 1973, 1979a). The almost highest wave approximation (Longuet-Higgins, 1979a) can be applied to specified conditions on the basis of data derived by interpolation from Cokelet's tables. A method for interpolation is described above, and it has been found to yield accurate results with very little computational effort. A subsequent paper will present results for shoaling and refraction computed in this way from Cokelet's tables.

6. ACKNOWLEDGEMENT

This work is supported by the Science Research Council through the North West Universities Consortium for Marine Technology.

7. REFERENCES

- Ahlberg, J. H., Nilson, E. N. and Walsh, J. L., 1967. 'The theory of splines and their applications', Academic Press, New York.
- Chaplin, J. R., 1980. 'Developments of Stream Function Wave Theory', Coastal Engineering, 3, 179-205.
- Cokelet, E. D., 1977. 'Steep gravity waves in water of uniform arbitrary depth', Phil. Trans. Roy. Soc., A286, 183-230.
- Dean, R. G., 1965. 'Stream function representation of non-linear ocean waves', J. Geophys. Res., 70, 4561-4572.
- Dean, R. G., 1970. 'Relative velocities of water wave theories', Proc: A.S.C.E., 96, WW1, 105-119.

- Dean, R. G., 1974. 'Evolution and development of water wave theories for engineering application', Special Report No. 1, U.S. Army Coastal Eng. Res. Center, Fort Belvoir, Virginia.
- Keulegan, G. H. and Patterson, G. W., 1940. 'Mathematical theory of irrotational translation waves', J. Res. Nat. Bur. Standards, 24, 47-101.
- Le Méhauté, B., Divorky, D. and Lin, A., 1968. 'Shallow water waves: a comparison of theory and experiment', Proc. 11th Int. Conf. on Coastal Engineering, Ch.7, 86-107.
- Longuet-Higgins, M. S., 1973. 'On the form of the highest progressive and standing waves in deep water', Proc. Roy. Soc. A331, 445-456.
- Longuet-Higgins, M. S., 1979a. 'The almost-highest wave: a simple approximation', J. Fluid Mech. 94, 269-274.
- Longuet-Higgins, M. S., 1979b. 'The trajectories of particles in steep symmetric gravity waves', J. Fluid Mech. 94, 497-517.
- Longuet-Higgins, M. S. and Fox, M. J. H., 1977. 'Theory of the almost-highest wave: the inner solution', J. Fluid Mech. 80, 721-741.
- Longuet-Higgins, M. S. and Fox, M. J. H., 1978. 'Theory of the almost-highest wave. Part 2. Matching and analytic extension', J. Fluid Mech. 85, 769-786.
- Skjelbreia, L. and Hendrickson, J. A., 1960. 'Fifth order gravity wave theory', Proc. 7th Int. Conf. on Coastal Engineering, Ch.10, 184-196.

CHAPTER 2

ACCURATE NUMERICAL SOLUTIONS FOR NONLINEAR WAVES

by

J.D. Fenton and M.M. Rienecker
School of Mathematics
University of New South Wales
Kensington, N.S.W., Australia 2033

This paper describes numerical methods for the accurate solution of the nonlinear equations for water waves propagating on irrotational flow over a horizontal bed. Fourier approximation is used throughout. Firstly, the problem of waves propagating without change is considered, giving a set of nonlinear equations which may be conveniently solved by Newton's method. It is emphasized that the usual specification of water depth, wave height and wave period is not enough to solve the problem - an assumption as to wave speed or mean current or mass flux must be included. Comparing results with previous theoretical and experimental results, good agreement was obtained. In the second part unsteady wave motion is examined, and a numerical method proposed for studying the evolution of unsteady disturbances. This is applied to the case of a solitary wave being reflected by a vertical wall. Close agreement with experimental results is obtained. In addition, design criteria for force and moment on the wall are suggested.

1. INTRODUCTION

In water wave problems where viscous forces may be assumed to be negligible and the fluid initially irrotational, fluid motion is governed by Laplace's equation for a velocity potential, and for two-dimensional flow, a stream function as well. This equation is linear, but for water wave problems must be solved subject to nonlinear boundary conditions on the free surface, which is also an unknown of the problem, in addition to the relatively simple linear boundary conditions on solid boundaries. It is the nonlinear dynamic and kinematic conditions which make solution difficult.

Approximate solutions of the equations have generally been found either by assuming that the waves are of small amplitude and nonlinearities ignored, or by assuming that the water depth is small relative to the wavelength, giving the long wave equations, or by a combination of both. These approximations can describe most phenomena associated with the propagation of waves to a first level of approximation. However, in some engineering and experimental applications it is necessary to have more accurate solutions of the complete set of nonlinear equations; for example, the design of maritime structures necessitates an accurate knowledge of the fluid velocity and pressure fields acting on them in the presence of waves.

This paper describes the development of numerical methods for the solution of the exact nonlinear equations for waves on fluid in which the flow is irrotational. In §2 the problem of waves propagating without change over water of constant depth is considered. The two best known analytical approximations to this problem are (i) Stokes' solution, in which series are essentially obtained in terms of powers of wave steepness (height/wavelength) and (ii) the cnoidal solution, using series in terms of shallowness (water depth/wavelength) which may be recast to include wave height. Each of these approaches breaks down for opposite extremes of depth - Stokes wave solutions are not valid for shallow water while cnoidal wave solutions are not valid for deep water. For high waves, neither is particularly accurate without the inclusion of many terms and the use of series enhancement techniques (see Cokelet (1977) for Stokes, and Fenton (1979) for cnoidal wave solutions). A method which has the potential for describing even very high waves in water of almost all depths is that which is known as the "stream function" method (Dean, 1965), but which does not depend on the stream function as such; rather it is a method of Fourier approximation of the stream function, and it is the Fourier approach wherein its power lies. The original technique has been modified by other workers, however, it still seems rather more complicated to use than need be the case. An alternative Fourier approximation method is presented in §2.

The rather more general problem of the complete unsteady equations for arbitrary disturbances is tackled in §3. This problem has received little attention except for the marker and cell method of Chan & Street (1970), the nonlinear integral equation of Byatt-Smith (1971) and the integro-differential equations of Longuet-Higgins and Cokelet (1976) for waves on infinitely deep water. Here, a new method to follow the time evolution of an initial disturbance is proposed wherein all dependent variables are accurately approximated by finite Fourier series. The only approximation is the truncation of the series. This method is applicable to water of any (variable) depth, however all motions and depth variation must be horizontally periodic. The method is applied to the problem of a long, but finite, wave approximating a solitary wave moving over a horizontal bottom and being reflected by a vertical wall. In previous approaches to this problem (for example Chan & Street (1970)) values for the force and moment on the wall due to the wave impact have not been given even though these are two very important engineering quantities. The maximum values for the force and moment are obtained from the impact of a solitary wave, hence any results for these quantities should provide the design criteria for a vertical wall subject to wave impact. In §3 results are given for these and also for the wave run-up which is found to agree closely with experimental results.

2. STEADY WAVES

2.1 Formulation of equations

The problem considered is that of two-dimensional periodic waves propagating without change of form over a layer of fluid on a horizontal

bed. With horizontal co-ordinate x and vertical co-ordinate y , the origin is on the bed, and moves in the x direction with the same speed as the waves so that all motion is steady in this frame of reference. If the fluid is incompressible a stream function $\psi(x,y)$ exists such that the velocity components (u,v) are given by

$$u = \frac{\partial \psi}{\partial y} \text{ and } v = - \frac{\partial \psi}{\partial x},$$

and if the motion is irrotational, ψ satisfies Laplace's equation throughout the fluid:

$$\frac{\partial^2 \psi}{\partial x^2} + \frac{\partial^2 \psi}{\partial y^2} = 0. \quad (2.1)$$

The boundary conditions to be satisfied are

$$\psi(x,0) = 0 \quad (2.2)$$

$$\psi(x,\eta(x)) = -Q \quad (2.3)$$

where $y = \eta(x)$ on the free surface and Q is a positive constant denoting the total volume rate of flow underneath the steady wave per unit length in a direction normal to the (x,y) plane. With this sign convention the apparent flow under the stationary wave is from right to left, in the negative x -direction. On the free surface, the pressure is constant so that Bernoulli's equation gives

$$\frac{1}{2} \left[\left(\frac{\partial \psi}{\partial x} \right)^2 + \left(\frac{\partial \psi}{\partial y} \right)^2 \right] + \eta = R, \quad (2.4)$$

where R is the Bernoulli constant. In these equations all variables have been non-dimensionalised with respect to the average depth $\bar{\eta}$ and gravitational acceleration g : that is, x is used for $x/\bar{\eta}$, y for $y/\bar{\eta}$, η for $\eta/\bar{\eta}$, ψ for $\psi/(g\bar{\eta}^3)^{1/2}$, Q for $Q/(g\bar{\eta}^3)^{1/2}$ and R for $R/g\bar{\eta}$. Other dimensionless variables to be introduced are - wave speed: c for $c/(g\bar{\eta})^{1/2}$, wavenumber: k for $k\bar{\eta} = 2\pi\bar{\eta}/\lambda$ where λ is the wavelength, wave period: τ for $\tau/(g\bar{\eta})^{1/2}$, and an arbitrary reference level: D for $D/\bar{\eta}$.

If the symmetry of the wave about the crest is exploited, a series for $\psi(x,y)$ can be written

$$\psi(x,y) = B_0 y + \sum_{j=1}^N B_j \frac{\sinh jky}{\cosh jkD} \cos jkx, \quad (2.5)$$

satisfying (2.1) and (2.2). The B_0, \dots, B_N are constant for a particular wave. The assumption that N is finite, for computational purposes, is the only approximation made in this method of solution. This assumed form is similar to Dean's (1965) series. The two differences are:

(i) the leading coefficient B_0 is not necessarily the wave speed, which will be discussed below, and (ii) the inclusion of $\cosh jkD$ in the denominator so that waves in deep water can be studied. Without this factor the B_j need to become exponentially small for convergence since the $\sinh jky$ go exponentially large. In subsequent iterative solution methods for the equations this cannot be guaranteed and the method may be rather unstable. However, $\sinh jky / \cosh jkD \sim \exp(|j|k(y-D))$ near the surface, so if D is greater than the crest height this ratio is always less than 1 and no problems of exponential magnification arise.

From here, the present method and the "stream function" method have very few similarities. In the latter, equations are obtained by requiring the mean-square error in one free surface boundary condition to be a minimum. Here (2.5) is used to satisfy both nonlinear boundary conditions (2.3) and (2.4) at a finite number of equally-spaced points, giving a number of nonlinear equations which can be directly solved using standard techniques.

To solve the problem numerically the equations produced by the substitution of (2.5) into (2.3) and (2.4), that is

$$B_0 \eta + \sum_{j=1}^N B_j \frac{\sinh jk\eta}{\cosh jkD} \cos jkx = -Q, \quad (2.6)$$

and

$$\frac{1}{2} \{ B_0 + k \sum_{j=1}^N j B_j \frac{\cosh jk\eta}{\cosh jkD} \cos jkx \}^2 + \frac{1}{2} \{ k \sum_{j=1}^N j B_j \frac{\sinh jk\eta}{\cosh jkD} \sin jkx \}^2 + \eta = R, \quad (2.7)$$

which are valid for all x , are to be satisfied at $2N$ points equally spaced over one wavelength, though by symmetry only $N+1$ points, from the wave crest to the trough, need to be considered. In the development of this method, tests were run where the computational points were clustered near the crest and sparsely spaced in the long flat trough, however it was found that there was very little gain in accuracy, and it is recommended that equi-spaced points be used in applications.

Let $\eta_m = \eta(x_m)$, where $x_m = m\lambda/2N$, $m = 0, 1, \dots, N$, and $kx_m = m\pi/N$, so that (2.6) and (2.7) become

$$B_0 \eta_m + \sum_{j=1}^N B_j \frac{\sinh jk\eta_m}{\cosh jkD} \cos(jm\pi/N) + Q = 0, \quad (2.8)$$

$$\frac{1}{2} u_m^2 + \frac{1}{2} v_m^2 + \eta_m - R = 0, \quad (2.9)$$

also for $m = 0, 1, \dots, N$, where

$$u_m = u(x_m, \eta_m) = B_0 + k \sum_{j=1}^N j B_j \frac{\cosh jk\eta_m}{\cosh jkD} \cos(jm\pi/N)$$

$$\text{and } v_m = v(x_m, \eta_m) = k \sum_{j=1}^N j B_j \frac{\sinh j k \eta_m}{\cosh j k D} \sin(j m \pi / N).$$

These $2N + 2$ nonlinear equations involve the $2N + 5$ unknowns η_m ($m = 0, \dots, N$), B_j ($j = 0, \dots, N$), k , Q and R . To obtain a solution 3 more equations must be specified. Since variables have been non-dimensionalised with respect to $\bar{\eta}$, the mean depth is 1. The simple trapezoidal rule can be used to give one more equation:

$$\frac{1}{2N} [\eta_0 + \eta_N + 2 \sum_{j=1}^{N-1} \eta_j] - 1 = 0, \quad (2.10)$$

where this can be shown to have an error proportional to the $(N+1)$ th term of a Fourier series for η . This is the same level of approximation as the Fourier expansion for ψ which was truncated after the N th term.

Now, numerical values for any two of the variables can be specified and the equations solved. However, for practical problems it is usually values of H (for $H/\bar{\eta}$), the wave height and τ (for $\tau(g/\bar{\eta})^{1/2}$) the wave period which define the problem. Two additional equations which specify these physical parameters are (i) the definition of H as being the elevation difference between crest and trough:

$$\eta_0 - \eta_N - H = 0, \quad (2.11)$$

where η_0 is the surface elevation at the crest and η_N that at the trough, and (ii) the statement that wave period is equal to the wave length divided by the wave speed, or

$$kc\tau - 2\pi = 0, \quad (2.12)$$

where the introduction of the wave speed c has added one more variable. It is possible to solve the problem in a frame relative to which motion is steady, without having to define the wave speed, by specifying the wavelength $\lambda (= 2\pi/k)$ instead of wave period. However, in most situations the waves are viewed from a different frame of reference in which they are not stationary and the wave period in this frame is measured. Hence an assumption as to the speed at which the waves travel must be included. The waves could travel at any speed, in a given frame, without change of form, so that the specification of the usual three quantities, water depth, wave height and period is not sufficient to define the problem. Either the wave speed must be specified or a value given (measured or assumed) for a quantity which determines the wave speed; for example, the mean current C_E (the mean Eulerian velocity through-out the fluid), or the mean Stokes drift C_S (the mass transport velocity) may be specified. In the steady frame, the mean velocity on any level over one wavelength is B_0 , so that in a frame through which the

waves pass at speed c , the time mean velocity at all points always within the fluid $C_E = c + B_O$ and so the appropriate equation to use if C_E is specified is

$$c + B_O - C_E = 0. \quad (2.13a)$$

Some previous works have allowed for the specification of C_E , for example Dean (1965), however many papers concerned with the application of wave theory have implicitly assumed $C_E = 0$, for example Skjelbreia & Hendrickson (1961) and Fenton (1979). In many situations however, the mean current is not as fundamental a quantity in determining the wave speed as is the rate of mass transport: for example, wave tank experiments with a closed end must have no net flux over any section. In the steady wave, a volume rate per unit span of Q is passing under the surface, but from right to left with the convention chosen above, so that the mean velocity of all the fluid particles is $-Q/\bar{\eta} = -Q$, because $\bar{\eta}$ is unity in the present non-dimensionalisation. Thus, if C_S is the mass-transport velocity in the stationary frame $C_S = c - Q$, giving the appropriate equation to use if C_S is specified:

$$c - Q - C_S = 0. \quad (2.13b)$$

2.2. Solution of nonlinear equations by Newton's method

The system of nonlinear equations (2.8 --13) may be written

$$f_i(\eta_j, B_j (j = 0, \dots, N), c, k, Q, R) = 0, \quad (2.14)$$

$i = 1, \dots, 2N + 6$, where for $i = 1$ to $(N+1)$ the f_i represent (2.8), for $i = (N+2)$ to $(2N+2)$ the f_i represent (2.9), f_{2N+3} is (2.10), f_{2N+4} is (2.11), f_{2N+5} is (2.12) and f_{2N+6} is either (2.13a) or (2.13b). This set of equations can be solved by Newton's method which iterates with quadratic convergence to a solution from an initial approximation. If the system of equations (2.14) is represented by

$$f_i(Z_\ell; \ell = 1, \dots, 2N+6) = 0, \quad i = 1, \dots, 2N+6 \quad (2.15)$$

where the Z_ℓ are the arguments of f_i as in (2.14), and if the approximate solution after the n th iteration is Z_ℓ^n , $\ell = 1, \dots, (2N+6)$ the error in each equation is $f_i(Z_\ell^n; \ell = 1, \dots, 2N+6) = f_i^n$. From a multivariable Taylor series expansion the error at the next iteration is

$$f_i^{n+1} = f_i^n + \sum_{\ell=1}^{2N+6} \left(\frac{\partial f_i}{\partial Z_\ell} \right)^n (Z_\ell^{n+1} - Z_\ell^n) + \dots, \quad i = 1, \dots, 2N+6,$$

where
$$\left(\frac{\partial f_i}{\partial Z_\ell}\right)^n = \frac{\partial f_i}{\partial Z_\ell} (Z_j^n, j = 1, \dots, 2N+6).$$

However, the desired result is $f_i^{n+1} = 0$ for each $i = 1, \dots, 2N+6$, and the solution Z_ℓ^{n+1} , $\ell = 1, \dots, 2N+6$ which approximately yields this result is found by truncating the series after the terms shown and solving the resulting system of linear simultaneous equations written as a matrix equation:

$$\left[\left(\frac{\partial f_i}{\partial Z_\ell} \right)^n \right] [Z_\ell^{n+1} - Z_\ell^n] = - [f_i^n].$$

The derivatives $\frac{\partial f_i}{\partial Z_\ell}$ have convenient analytical expressions obtained by differentiation of the equations (2.8 -.13). For example, from (2.8), $\partial f_1 / \partial B_0 = \eta_m$, and so on. Expressions for all these derivatives are simply obtained and are given in Rienecker and Fenton (1980).

The initial approximation to the solution is assumed to be a linear sinusoidal wave, that is, $\eta_m = 1 + \frac{1}{2} H \cos m\pi/N$, $m = 0, \dots, N$; $B_0 = -c$; $B_1 = -\frac{1}{2} H/c/k$; $B_j = 0$, $j = 2, \dots, N$; $R = 1 + \frac{1}{2} c^2$; $Q = c$, where c and k are found recursively from

$$k = 2\pi/\tau c$$

$$c = (\tanh k/k)^{1/2},$$

with an initial guess $c = 1$ corresponding to a long wave approximation.

2.3. Results

The method was run on a CDC Cyber 171 computer; convergence of the iteration was extremely rapid so that 5 iterations were usually sufficient to obtain convergence to 12 decimal places. For very high waves it was found that the linear approximation was not a sufficiently accurate initial estimate of the solution and the method did not converge. In this situation it was necessary to extrapolate the initial estimate from converged solutions for lower waves.

With this solution for the elevation of points on the free surface η_m , for the Fourier coefficients B_j , and for c, k, Q and R , it is possible to obtain results for other quantities which may be of interest, in particular the fluid velocities and pressure at any point. All physical variables considered so far have been in a co-ordinate system which moves with the wave so that all motion is steady in that frame. The steady velocities at any point are from differentiation of (2.5):

$$u(x,y) = B_0 + k \sum_{j=1}^N u_j(x,y), \text{ and}$$

$$v(x,y) = k \sum_{j=1}^N v_j(x,y),$$

$$\text{where } u_j(x,y) = jB_j \frac{\cosh jky}{\cosh jkD} \cos jkx, \text{ and} \quad (2.16a)$$

$$v_j(x,y) = jB_j \frac{\sinh jky}{\cosh jkD} \sin jkx. \quad (2.16b)$$

The pressure at any point, $p(x,y)$, representing $p(x,y)/\rho g\bar{\eta}$ where ρ is fluid density, is given by

$$p(x,y) = R - y - \frac{1}{2}[u^2(x,y) + v^2(x,y)].$$

Now consider a stationary co-ordinate system (X,Y) on the bed in which motion is unsteady as the waves move from left to right with speed c . If the wave crest is at $X = X_0$ when $t = 0$, the unsteady fluid velocities

$U(X,Y,t)$ and $V(X,Y,t)$ become

$$U(X,Y,t) = c + B_0 + k \sum_{j=1}^N u_j(X-X_0-ct,Y)$$

$$V(X,Y,t) = k \sum_{j=1}^N v_j(X-X_0-ct,Y),$$

where the (u_j, v_j) are defined in (2.16a,b). Unsteady pressure is given by

$$p(X,Y,t) = R - Y - \frac{1}{2}[u^2(X-X_0-ct,Y) + v^2(X-X_0-ct,Y)].$$

In addition to the above local quantities, gross integral quantities of the wave train such as potential energy may be calculated from the converged solution. Expressions for these are given in Rienecker and Fenton (1980).

2.4. Accuracy

Cokelet (1977) presented a number of accurate results for integral quantities of the wave train. The wave speed c , for the case $C_E = 0$, was used to test the accuracy of the present method. For each of four different values of kQ/c , which is a measure of the ratio of wavelength to depth of fluid, the variation of c^2 with H is shown on Fig. 1. The results indicate close agreement with Cokelet. Only for the very highest and longest wave with relatively coarse numerical approximation (small N) were significant errors obtained. In these cases it was not the height of the wave which caused the lack of accuracy as the method makes no approximation as to height. Instead, for higher waves the crest becomes increasingly sharp and the Fourier approximation becomes less accurate. Also, for longer waves where the wave is more like an isolated hump on otherwise undisturbed fluid, larger values of N are required to describe the wave accurately.

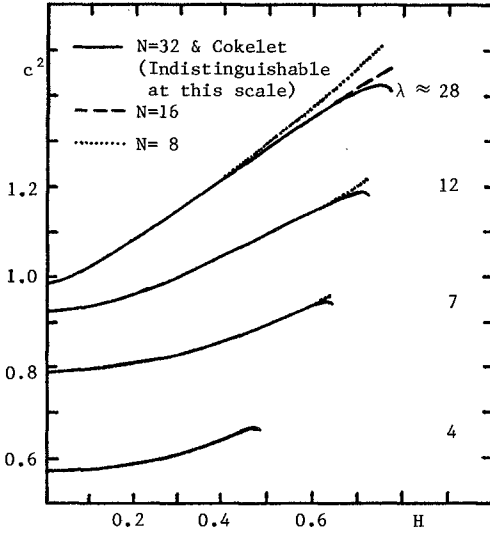


Figure 1. Comparison between the present method and the results of Cokelet (1977) for wave speed squared, c^2 , as a function of wave height H . Each curve is drawn for a constant value of kQ/c taken from Cokelet's tables A2, A4, A6, A8, giving the almost constant values of wavelength shown.

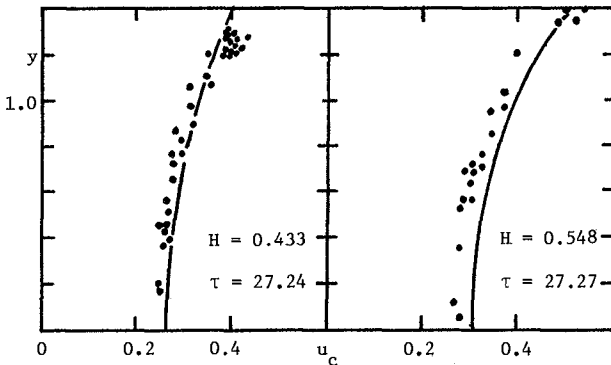


Figure 2. Horizontal fluid velocity under the wave crest, u_c , plotted against height y above the bottom: comparison between present method (—) and the experimental results of Le Méhauté et al (1968). Dimensionless wave heights and periods are shown.

To compare the predictions of the Fourier method for fluid velocities with experiment, the results of Le Méhauté, Divoky and Lin (1968) were used. As the experiments were performed in a closed wave-tank, the condition (2.13b) was used to determine the wave speed $c = Q$. This condition does not seem to have been used in previous comparisons with these experiments, where the incorrect assumption $C_E = 0$ has been used. Also, it should be pointed out that the experimental velocities measured were particle velocities averaged over a finite time and not the instantaneous velocities given by all wave theories. It can be shown that these experimental velocities should be less than those predicted. In Fig. 2, two sets of experimental results are shown for the two longest waves generated, with a wavelength of about 30 times the depth in each case. These longest waves should provide a severe test for the Fourier approximation method, as described above. It can be seen that agreement between theory and experiment was quite close.

3. UNSTEADY WAVES

3.1. Equations

A solution is sought to the equations governing the evolution of waves travelling over a layer of fluid on a horizontal bed. If the fluid is irrotational a velocity potential $\phi(x,y,t)$ exists such that velocity components $u(x,y,t)$ and $v(x,y,t)$ parallel to the x and y co-ordinates respectively are given by

$$u = \partial\phi/\partial x \text{ and } v = \partial\phi/\partial y.$$

If the motion is incompressible, ϕ satisfies Laplace's equation throughout the fluid:

$$\frac{\partial^2\phi}{\partial x^2} + \frac{\partial^2\phi}{\partial y^2} = 0. \quad (3.1)$$

Since the velocity normal to the bed is zero,

$$\frac{\partial\phi}{\partial y}(x,0,t) = 0, \quad (3.2)$$

where the co-ordinate origin has been placed on the horizontal bed. The case where the bed is not horizontal can be treated by the methods of this section, and is described in Fenton & Rienecker (Manuscript in preparation).

On the free surface $y = \eta(x,t)$, the kinematic and dynamic boundary conditions must be satisfied:

$$\frac{\partial\eta}{\partial t} + \frac{\partial\phi}{\partial x} \frac{\partial\eta}{\partial x} - \frac{\partial\phi}{\partial y} = 0 \quad (3.3)$$

$$\frac{\partial\phi}{\partial t} + \frac{1}{2} \left[\left(\frac{\partial\phi}{\partial x} \right)^2 + \left(\frac{\partial\phi}{\partial y} \right)^2 \right] + \eta = C, \quad (3.4)$$

where C is a constant. In these equations all variables have been non-

dimensionalized with respect to the mean depth $\bar{\eta}$, and gravitational acceleration g . If a simple method can be found for solving the linear equations (3.1) and (3.2), and if a convenient and accurate method can be found for approximating all the space derivatives in (3.3) and (3.4), then subject to known initial conditions, (3.3) and (3.4) can be used to advance the solution in time, so that the evolution of disturbances can be followed.

3.2. Numerical approximation and solution of equations

The Fourier methods of §2 are capable of great accuracy, and similar approximations will be used here for $\phi(x,y,t)$ and also for $\eta(x,t)$ so that term by term differentiation can be used for derivatives of each. It is assumed that the dependent variables ϕ and η can be represented by Fourier series in x throughout the region of interest, implying that all motion is periodic in x with some finite period L , referred to as the wavelength.

An expansion for $\phi(x,y,t)$ may be written

$$\phi(x,y,t) = \alpha x + \frac{1}{N} \sum_{j=-\frac{N}{2}+1}^{N/2} A_j(t) \frac{\cosh jky}{\cosh jkD} \exp(-ijkx) \quad (3.5)$$

for some finite value of N , where $k = 2\pi/L$. In general, ϕ is not periodic but will change by a finite amount over the region of interest. The leading term αx has been introduced to allow for the discontinuity in ϕ over one wavelength where $\alpha = (\phi(L,y,t) - \phi(0,y,t))/L$. Now, the finite complex Fourier series shown has to approximate the function $\phi(x,y,t) - \alpha x$ which is continuous. In this case the Fourier series converges absolutely and can be differentiated term by term. The Fourier coefficients $A_j(t)$ are complex, while the $\cosh jkD$ in the denominator (D is an arbitrary depth scale, conveniently chosen to be the mean) has been introduced so that the method may also be used for deep water, as for the steady wave expansion in §2.

A finite complex Fourier series can also be written for $\eta(x,t)$:

$$\eta(x,t) = \frac{1}{N} \sum_{j=-\frac{N}{2}+1}^{N/2} Y_j(t) \exp(-ijkx). \quad (3.6)$$

If η is known at the N discrete points $x_m = mL/N, m = 0 \dots N-1$, such that

$$\eta_m = \eta(x_m, t) = \frac{1}{N} \sum_{j=-\frac{N}{2}+1}^{N/2} Y_j(t) \exp(-i2\pi mj/N), \quad (3.7)$$

then it can be shown that the Y_j can be simply obtained from the η_m :

$$Y_j = \sum_{m=0}^{N-1} \eta_m \exp(i2\pi mj/N), \quad j = -\frac{N}{2} + 1, \dots, \frac{N}{2}.$$

In this form the Y_j are said to be obtained from the η_m by a Discrete Fourier Transform,

$$Y_j = \mathcal{D}[\eta_m],$$

and (3.7) is termed an Inverse Discrete Fourier Transform,

$$\eta_m = \mathcal{D}^{-1}[Y_j].$$

Similarly,
$$\phi(x_m, y, t) = \alpha x_m + \mathcal{D}^{-1}[A_j(t) \frac{\cosh jky}{\cosh jkD}]$$

and
$$A_j(t) \frac{\cosh jky}{\cosh jkD} = \mathcal{D}[\phi(x_m, y, t) - \alpha x_m].$$

Now, the series (3.5) and (3.6) can be differentiated term by term, and substituting $x = x_m$ series (3.8) and (3.9) are obtained, where a subscript x, y or t denotes partial differentiation with respect to that variable. These expressions should be very accurate, provided the coefficients A_j and Y_j decay sufficiently quickly as $|j| \rightarrow N/2$, where the series are truncated.

$$\phi_x(x_m, y, t) = \alpha - ik\mathcal{D}^{-1}[jA_j(t) \frac{\cosh jky}{\cosh jkD}] \tag{3.8}$$

$$\phi_y(x_m, y, t) = k\mathcal{D}^{-1}[jA_j(t) \frac{\sinh jky}{\cosh jkD}]. \tag{3.9}$$

Further differentiation of (3.5) shows that Laplace's equation (3.1) is identically satisfied by (3.5), as is the bottom boundary condition (3.2). Also,

$$\eta_x(x_m, t) = -ik\mathcal{D}^{-1}[jY_j(t)] = -ik\mathcal{D}^{-1}[j\mathcal{D}[\eta_n]].$$

The remaining equations, the nonlinear free surface conditions (3.3-4) become:

$$\begin{aligned} \frac{\partial \phi}{\partial t}(x_m, \eta_m, t) = C - \eta_m - \frac{1}{2}\{\alpha - ik\mathcal{D}^{-1}[jA_j(t) \frac{\cosh jk\eta_m}{\cosh jkD}]\}^2 \\ - \frac{1}{2}k^2\{\mathcal{D}^{-1}[jA_j(t) \frac{\sinh jk\eta_m}{\cosh jkD}]\}^2, \text{ and} \end{aligned} \tag{3.10}$$

$$\begin{aligned} \frac{\partial \eta}{\partial t}(x_m, \eta_m, t) = k\mathcal{D}^{-1}[jA_j(t) \frac{\sinh jk\eta_m}{\cosh jkD}] \\ + ik[\alpha - ik\mathcal{D}^{-1}[jA_j(t) \frac{\cosh jk\eta_m}{\cosh jkD}]]\mathcal{D}^{-1}[j\mathcal{D}[\eta_n]], \end{aligned} \tag{3.11}$$

each for $m = 0, \dots, N-1$. Clearly, if F and G represent the right sides

of these equations, then (3.10) and (3.11) may be written for given k , α , C and D :

$$\frac{\partial \phi}{\partial t}(x_m, \eta_m, t) = F\{A_j(t), j = -\frac{N}{2} + 1, \dots, \frac{N}{2}; \eta(x_n, t), n=0, \dots, N-1\},$$

$$\text{and } \frac{\partial \eta}{\partial t}(x_m, t) = G\{A_j(t), j = -\frac{N}{2} + 1, \dots, \frac{N}{2}; \eta(x_n, t), n = 0, \dots, N-1\},$$

for $m = 0, \dots, N-1$. If all values of $A_j(t)$ and $\eta(x_n, t)$ are known at any time t , then $\partial \phi / \partial t$ and $\partial \eta / \partial t$ may be evaluated, and by discretizing the time domain, the solution may be stepped forward in time. Defining time $t_\ell = \ell \Delta t$, and using centred finite differences to approximate the time derivative, the value of η at the next time step can be written

$$\eta(x_m, t_{\ell+1}) = \eta(x_m, t_{\ell-1}) + 2\Delta t \frac{\partial \eta}{\partial t}(x_m, t_\ell) + O(\Delta t^3),$$

that is,

$$\eta(x_m, t_{\ell+1}) \approx \eta(x_m, t_{\ell-1}) + 2\Delta t G\{A_j(t_\ell), j = -\frac{N}{2} + 1, \dots, \frac{N}{2}; \eta(x_n, t_\ell), n = 0, \dots, N-1\}. \quad (3.12)$$

In the same manner,

$$A_j(t_{\ell+1}) \approx A_j(t_{\ell-1}) + 2\Delta t \frac{\partial A_j}{\partial t}(t_\ell), \quad (3.13)$$

where $\partial A_j / \partial t$ is found from the solution of the N simultaneous linear equations in N unknowns obtained from differentiation of (3.5) with respect to time:

$$\frac{\partial \phi}{\partial t}(x_m, \eta_m, t_\ell) = \frac{1}{N} \sum_{j=-\frac{N}{2}+1}^{\frac{N}{2}} \frac{\partial A_j}{\partial t}(t_\ell) \frac{\cosh jk \eta_m(t_\ell)}{\cosh jk D} \exp(-i2\pi m j / N) \quad (3.14)$$

for $m = 0, \dots, N-1$. Unfortunately these equations cannot be simply inverted by Fourier means to give $\partial A_j / \partial t$ since the $\eta_m(t_\ell) = \eta(x_m, t_\ell)$ vary with m .

To commence solution, initial values of $\eta(x_m, t_\ell)$ at $\ell = 0$ and 1 must be known, as well as values of $A_j(t_\ell)$ $\ell = 0, 1$. The Fourier coefficients are simply found if the values of ϕ are known on some line of constant elevation d :

$$A_j(t_\ell) \frac{\cosh jk d}{\cosh jk D} = \mathcal{D}[\phi(x_m, d, t_\ell) - \alpha x_m], \quad \ell = 0, 1.$$

With these initial values known, $\partial \phi / \partial t$ and $\partial \eta / \partial t$ on the surface can be found from (3.10) and (3.11), $\partial A_j / \partial t$ found from (3.14), and η and A_j found at

the next timestep from (3.12) and (3.13). In this way, the evolution of some known initial disturbance can be followed.

This method of time stepping is susceptible to instability in some finite difference schemes, hence it is necessary to determine if and when the method can be unstable here. To do this, the equations (3.3 & .4) were linearized, and a solution assumed. It was found that for waves of wavelength L/ν , where ν is an integer which can take any value between 1 and $N/2$, on a stream of velocity U , that the stability criterion is

$$\sigma(\nu)\Delta t \leq 1,$$

where $\sigma(\nu)$ is the apparent radian frequency of waves of length L/ν :

$$\sigma(\nu) = \nu k U \pm (\nu k \tanh \nu k)^{1/2}, \quad \nu = 1, \dots, N/2.$$

in which the second part is the frequency of the waves travelling on otherwise undisturbed fluid, while the term $\nu k U$ is the Doppler contribution to the apparent frequency by the waves being carried along on a current U . The criterion $\sigma(\nu)\Delta t \leq 1$ means that time steps must be taken sufficiently small so that a minimum number of time computational points are taken in any one cycle of every frequency component. The most demanding case is the highest frequency component $\nu = N/2$. For $\nu k = Nk/2 = N\pi/L = \pi/\Delta x$ sufficiently large, the criterion is approximately

$$\Delta t \leq (\Delta x/\pi)^{1/2} / (1 + U(\pi/\Delta x)^{1/2}).$$

The most severe case is obtained when U is finite and the waves are convected along with the flow giving a higher apparent frequency at a point. If the fluid is quiescent, $U = 0$, the criterion becomes

$$\Delta t \leq (\Delta x/\pi)^{1/2},$$

which is a relatively weak restriction, when compared with those obtained from diffusion and other equations.

3.3. Reflection of solitary waves by a vertical wall

Here, the method developed in §3.2 is applied to the particular problem of a solitary wave propagating over water of constant depth and being reflected by a vertical wall, a situation studied by Chan and Street (1970) who developed a numerical method for free surface flows based on a marker and cell technique, using finite differences. This problem is of some importance, for the solitary wave is the fastest, highest, largest, and most energetic of all steady waves, comparing the results of Longuet-Higgins & Fenton (1974) and those of Cokelet (1977). In addition, the effects on a wall of an incident solitary wave are greater than those due to a standing wave system even of long wavelength, because the solitary wave can be of full breaking height even before it

strikes the wall, and at the wall will rise to a height about twice that, exerting considerable force. The standing waves, being periodic in time, can never rise greater than their breaking height at the wall, and since this height is lower than the breaking height of the solitary wave, the latter should exert the greatest forces possible and its effects should be used as the design criteria for wall forces and moments. Unfortunately, previous studies have not reported on the forces and moments caused.

Since the horizontal fluid velocity at the wall is zero, it can be seen that the problem of a solitary wave on a wall is precisely one half of the equivalent problem of two equal waves propagating in opposite directions, provided that the effects of viscosity are negligible. Both problems have been studied experimentally by Maxworthy (1976), who reported some unusual aspects of the time lag at the wall of the wave crest.

The method described in §3.2 above was tested on the problem of two equal waves propagating in opposite directions described more fully in Fenton & Rienecker (in preparation). In the following discussion only one half of the problem will be considered and will be referred to as the reflection of a single wave by a vertical wall. As none of the methods developed in this work can handle an infinitely long region, a finite length only was considered for computational purposes. To obtain the initial conditions, where the incoming wave does not yet sense appreciably the presence of the wall, a steady wave solution of specified height and period was calculated, using the method of §2. From trial runs it was found that the resulting body of the wave was independent of wave length, if this exceeded some 20 times the water depth for low waves (height 0.1 of the depth), this limit smoothly decreasing to 10 depths for waves of height 0.4 and above. Each of these waves was considered to be a very close approximation to the solitary wave of the same height, this being verified when quantities such as the propagation speed and potential energy were compared with results for the solitary wave from Longuet-Higgins & Fenton (1974). With the steady wave solution so obtained, two such numerical waves were placed together, so that their velocities of propagation were in opposite directions and of a magnitude such that horizontal fluid velocity under the long flat trough was zero, corresponding to two solitary waves coming together over otherwise undisturbed water. Then each wave was shifted forward slightly by an amount equal to the distance travelled in one computational time step, as if the other wave did not exist (an excellent approximation to motion in this first stage in view of the flatness of the trough, zero velocity under it and the small time step used). With these first two positions of each wave, two complete sets of initial conditions were calculated, so that the leap-frog timestepping procedure described in §3.2 could be initiated.

At first the wave propagated towards the wall, with imperceptible

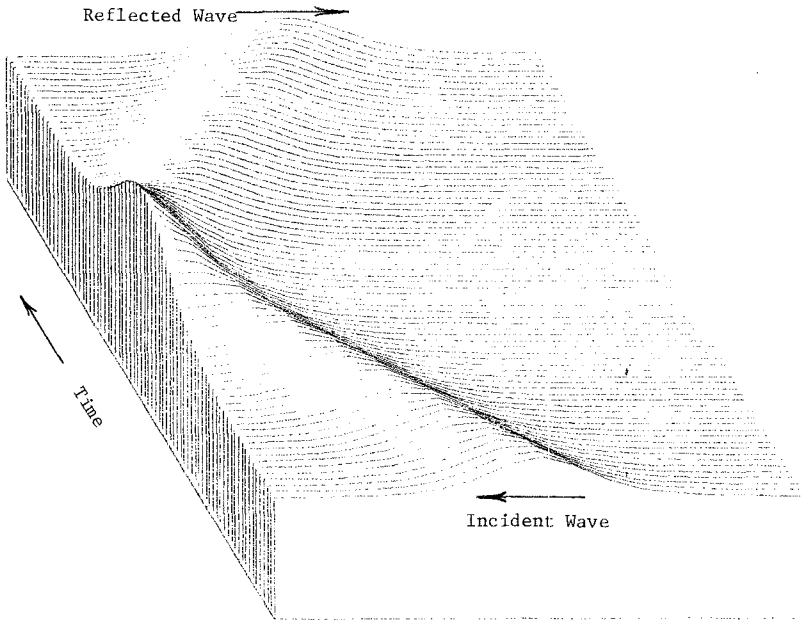


Figure 3. Surface elevation for a long wave of height 0.3 of the mean depth (approximating a solitary wave of height 0.325 above the trough), being reflected by a vertical wall at the left. Profiles are shown for successive times. Vertical exaggeration $\approx 4:1$.

effect on the main body of the wave, as can be seen in Fig. 3, justifying the finite computational length taken. At the wall, the water level slowly rose until it was almost as high as the crest. After this stage, events happened very quickly, the crest "snapped through" to the wall and quickly reared up to more than twice the height of the incident wave. Far away from the wall, all the fluid was sensibly undisturbed. At its highest elevation, the crest at the wall became rather more curved, and for the highest waves became quite sharp. It is in this limit, at this stage, that the use of the Fourier method becomes questionable. The sharp crest of the breaking wave of limiting height cannot be described by the present method which depends on functions and derivatives having no discontinuities. Whereas a real wave may exhibit breaking at the crest for very high waves the numerical wave showed no such behaviour and can provide no breaking criterion. However, up until this point, the solutions were considered to be very accurate since total mass and energy of the fluid were conserved to at least four significant figures. In addition, when compared with experimental results and previous computational results for the maximum runup at the wall on Fig. 4, it can be seen that the present method gave results which agreed very closely, perhaps surprisingly in view of the fact that runup depends critically on whether the waves break or not.

The maximum force and moment exerted on the wall were calculated by obtaining the pressure on the wall at 21 equally-spaced points between the bottom and the crest and integrating using Simpson's rule. These quantities depend on the whole flow field and should be much less dependent on breaking at the crest than might be expected for the runup. Results from the numerical experiments are shown in Fig. 5, on which least-square parabolas have been fitted to each set of points, but with the condition that each pass through the zero amplitude hydrostatic results in which Force on wall = $\frac{1}{2}\rho gh^2$, where h is the undisturbed depth of water, and Moment about the toe of the wall = $\frac{1}{6}\rho gh^3$.

If H is the height of the incident wave crest above the undisturbed fluid, these results are:

Maximum Force on Wall F:

$$\frac{F}{\rho gh^2} = \frac{1}{2} + 2.25\left(\frac{H}{h}\right) - 0.42\left(\frac{H}{h}\right)^2$$

Maximum Moment on Wall about Toe:

$$\frac{M}{\rho gh^3} = \frac{1}{6} + 1.23\left(\frac{H}{h}\right) + 0.80\left(\frac{H}{h}\right)^2.$$

From the figure it can be seen that these empirical curves agree closely with all numerical results and should provide convenient criteria for design purposes.

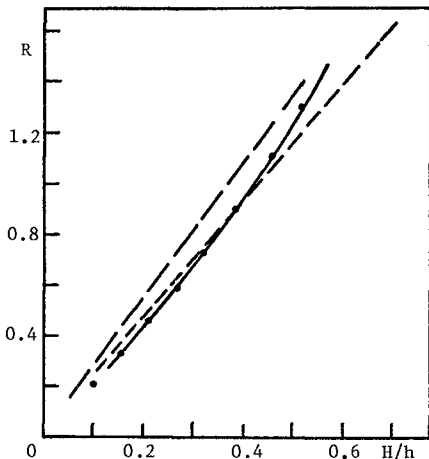


Figure 4. Maximum run-up at the wall $R = (\eta_{max}/h) - 1$, where h is undisturbed depth, plotted against incident wave height H/h . Points (\bullet): numerical results from present method. (—): mean of experimental results reported by Chan & Street. (---): mean of experimental results from wave-wall reflection, and (- · -): wave-wave interaction, both from Maxworthy (1976).

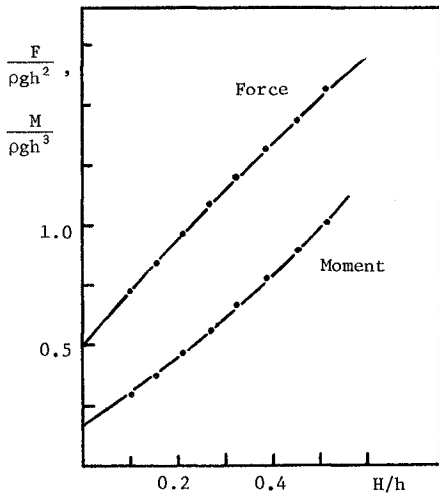


Figure 5. Maximum force and moment on the wall, plotted against incident wave height. The points (\bullet) are numerical results from the present method to which curves have been fitted, as described in the text, shown by solid lines.

As the water flowed back down the wall, the process described above was qualitatively reversed, until the wave was totally reflected and was travelling in the opposite direction. Chan and Street (1970) reported that at this stage "the wave had exactly the same surface profile as its corresponding incident wave". However, in the present work, the reflected wave was not the same as the incident wave. This is not clear from the space-time plot on Fig. 3, as differences are relatively small. Fig. 6 shows rather more clearly the differences that were observed - the reflected wave has a depression behind it, it has a slightly steeper front face, it is lower, and in apparent contradiction of this last fact, it is travelling faster! These differences are not numerical errors: the accuracy of the method is shown by the fact that mass and energy of the water were conserved to within 10^{-4} , even for the highest waves reported. Rather, some differences between the waves is to be expected, for all the governing equations are highly nonlinear and it would be remarkable if two solitary waves of height 33% of the depth should collide, the combined crest grow to a height of 73%, and then each wave pass out through the other, without some nonlinear interaction changing the form of each. A number of details such as the time lag experienced in the interaction, the change in wave height and speed and other details of the nonlinear interaction are of little engineering importance and are being written up for publication elsewhere.

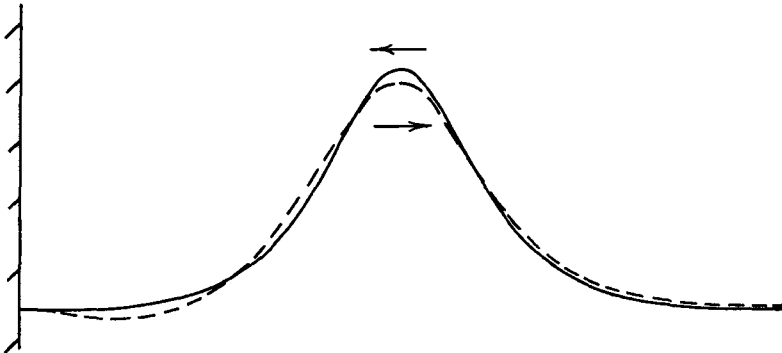


Figure 6. Comparison of surface profiles for an incident wave (—) of height 0.3 of the mean depth travelling towards the wall, and the wave after reflection (---). Vertical exaggeration 16:1.

References

- Byatt-Smith, J.C.B. 1971 An integral equation for unsteady surface waves and a comment on the Boussinesq equation, *J. Fluid Mech.* 49, 625-633.
- Chan, R.K-C. & Street, R.L. 1970 A computer study of finite-amplitude water waves, *J. Comp. Phys.* 6, 68-94.
- Cokelet, E.D. 1977 Steep gravity waves in water of arbitrary uniform depth, *Phil. Trans. Roy. Soc. Lond. A* 286, 183-230.
- Dean, R.G. 1965 Stream function representation of nonlinear ocean waves, *J. Geophys. Res.* 70, 4561-4572.
- Fenton, J.D. 1979 A high-order cnoidal wave theory, *J. Fluid Mech.* 94, 129-161.
- Le Méhauté, B., Divoky, D., & Lin, A. 1968 Shallow water waves : a comparison of theories and experiments, *Proc. 11th Conf. Coastal Engng.*
- Longuet-Higgins, M.S. & Cokelet, E.D. 1976 The deformation of steep surface waves on water I. A numerical method of computation, *Proc. R. Soc. Lond. A* 350, 1-26.
- Longuet-Higgins, M.S. & Fenton, J.D. 1974 On the mass, momentum, energy and circulation of a solitary wave II. *Proc. R. Soc. Lond. A* 340 471-493.
- Maxworthy, T. 1976 Experiments on collisions between solitary waves, *J. Fluid Mech.* 76, 177-185.
- Rienecker, M.M. & Fenton, J.D. 1980 A Fourier approximation method for steady water waves, *J. Fluid Mech.* (In Press).
- Skjelbreia, L. & Hendrickson, J. 1961 Fifth order gravity wave theory, *Proc. 7th Conf. Coastal Engng.*

CHAPTER 3

MASS TRANSPORT IN PROGRESSIVE WAVES OF PERMANENT TYPE

Yoshito Tsuchiya
Professor, Disaster Prevention Research Institute
Kyoto University, Kyoto, Japan

Takashi Yasuda
Associate Professor, Faculty of Engineering
Gifu University, Kagamihara, Japan

and

Takao Yamashita
Instructor, Disaster Prevention Research Institute
Kyoto University

INTRODUCTION

Mass transport phenomenon was first recognized by Stokes in 1847 using a Lagrangian description. Later, a basic theory for the mass transport in water waves in viscous fluid and of finite depth was derived by Longuet-Higgins in 1953. Theoretical solutions of mass transport in progressive waves of permanent type are subjected to the definitions of wave celerity in deriving the various finite amplitude wave theories. As it has been generally acknowledged that the Stokes wave theory can not yield a correct prediction of mass transport in the shallow depths, some new theories have been developed. Recently the authors(1974 & 1977) have derived a new finite amplitude wave theory in shallow water for quasi-Stokes and cnoidal waves by the so-called reductive perturbation method, in which the mass transport is formulated both in Lagrangian and Eulerian descriptions.

On the experimental verification, Russell and Osorio(1957) investigated and compared Longuet-Higgins' solution with experimental data of Lagrangian mass transport velocity obtained in a normal closed wave tank of finite length. Since then, many investigations, and nearly all of them, have employed the finite length of wave tank in carrying out their experiments. However, no experiment has yet been attempted at verifying the Stokes drift in progressive waves of permanent type in a wave tank of infinite length. It is not realistic nor economical in constructing such an infinitely long flume to investigate experimentally the mass transport velocity in progressive waves. Instead of using such an ideal wave tank, a new one incorporated with natural water re-circulation was equipped to carry out experiments by the authors(1978). It was confirmed from these experiments that mass transport in progressive waves of permanent type exists in the same direction of wave propagation throughout the depth, and agrees with both the Stokes drift and the authors' new formulations, within the test range of experiments.

THEORETICAL SOLUTIONS OF MASS TRANSPORT

1. Conventional Expressions

The theoretical solutions of mass transport in progressive waves of permanent type can be grouped into two main categories. The first one is derived for the perfect fluid from using a finite amplitude wave theory, whilst the other is resulted from considering viscous effects at the bottom and near the free surface.

In the first category the theoretical expressions of mass transport velocity in Stokes waves have been formulated in Lagrangian description for two different definitions of wave celerity in deriving the wave theory. The first is so-call the Stokes drift in Lagrangian description which is subjected to the definition of wave celerity and then is given for the first and second Stokes definitions respectively as

$$U_M = \frac{H^2 \sigma k \cosh 2kz}{8 \sinh^2 kh} \dots\dots\dots (1)$$

and

$$U_M = \frac{H^2 \sigma k \cosh 2kz}{8 \sinh^2 kh} - \frac{H^2 \sigma \coth kh}{8h} \dots\dots\dots (2)$$

in which U_M is the mass transport velocity formulated in Lagrangian description, H is the wave height of progressive waves of permanent, h the water depth at the still water level, $\sigma = 2\pi/T$ the angular frequency of waves, T the wave period, $k = 2\pi/L$ the wave number and L the wave length as shown in Fig. 1. The mass transport velocity in Eulerian description may be given as

$$\bar{u} = \frac{H^2 \sigma \coth kh}{8h}; \quad -\frac{H}{2h} < \frac{z}{h} + 1 < \frac{H}{2h} \dots\dots\dots (3)$$

in which u is the mass transport velocity in Eulerian description which is defined to be the horizontal water particle velocity averaged for one wave period. In 1968 Le Méhauté derived the mass transport velocity by means of Laitone's second approximation of cnoidal waves. This seems questionable because the limitation of solution corresponding to solitary wave has a finite value of mass flux.

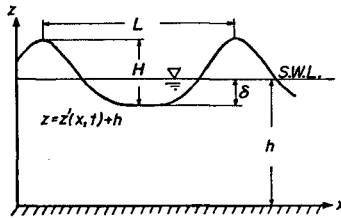


Fig. 1 Co-ordinate system used

On the other hand, Longuet-Higgins' solution represents the second category, and so followed by Huang(1970), Li and Davis(1977) etc. Longuet-Higgins' expression is given as

$$U_M = \frac{H^2 \sigma k}{4 \sinh^2 kh} \left[3 + 2 \cosh 2kz + 3kh \left\{ 3 \left(\frac{z}{h} - 1 \right)^2 + 4 \left(\frac{z}{h} - 1 \right) + 1 \right\} \sinh 2kh + 3 \left\{ \left(\frac{z}{h} - 1 \right)^2 - 1 \right\} \left(\frac{\sinh 2kh}{2kh} + \frac{3}{2} \right) \right] \dots\dots\dots (4)$$

These four kinds of vertical distribution of mass transport velocity are schematically shown in Fig. 2, these are the Stokes drifts of the first and second definitions of wave celerity, and that of Longuet-Higgins. This figure shows the distinctive nature of mass transport when the Eulerian description is considered. In the figure, $U_M/H^2\sigma k$ is the dimensionless mass transport velocity and z/h the dimensionless vertical level from the bottom. It is clear that as well-known relatively strong forward velocity is expected near both boundaries as derived by Longuet-Higgins when viscosity is taken into account.

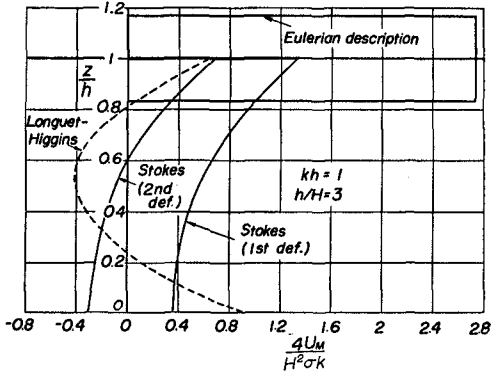


Fig. 2 Vertical distribution of mass transport velocity by conventional expressions

According to the usual expression of mass transport velocity, there is a quite different vertical distribution in Lagrangian and Eulerian descriptions, as a result from the definition of wave celerity in deriving the finite amplitude wave theory. Bagnold's experimental results in 1947 was used to confirm Longuet-Higgins' solution, in which he noted that the mass transport velocities near both boundaries have stronger forward component in the direction of wave propagation, but with reverse flow in the mid-layer between these two viscous boundaries. Ūniuata and Mei(1970) pointed out that Longuet-Higgins' solution corresponded to that would be derived from assuming a constant pressure gradient along the direction of wave propagation thus that no net transport occurs.

2. New Expressions

The new wave theories of quasi-Stokes(1978) and cnoidal waves(1974 & 1977) have recently been derived by the authors from using the so-called reductive perturbation method by Taniuti(1968). From these, the mass transport velocities are then derived.

a) Mass transport in quasi-Stokes waves The mass transport velocity in Lagrangian description is given as

$$U_M/\sqrt{gh} = (\lambda_0^2/16)\{1 - (1/2)(2\pi h/L)^2\} + (\lambda_0^2/8)(\sqrt{gh}/c) [1 + (2/3)(2\pi h/L)^2\{3(z/h - 1)^2 - 1\}] \dots (5)$$

And the mass transport velocity in Eulerian description is given as

$$\bar{u}/\sqrt{gh} = (\lambda_0^2/16)\{1 - (1/2)(2\pi h/L)^2\} \dots (6)$$

in which λ_0 and the wave celerity c are given respectively as

$$\frac{H}{h} = \lambda_0 + \frac{1}{8\pi^2\epsilon} \left(\frac{27}{512\pi^2\epsilon} + \frac{45}{128} \right) \lambda_0^3, \quad \epsilon = \left(\frac{h}{L} \right)^2 \dots\dots\dots (7)$$

and

$$\frac{c}{\sqrt{gh}} = 1 - \frac{1}{6} \left(\frac{2\pi h}{L} \right)^2 + \frac{19}{360} \left(\frac{2\pi h}{L} \right)^4 - \frac{55}{3024} \left(\frac{2\pi h}{L} \right)^6 + \frac{9\lambda_0}{64} \left(\frac{2\pi h}{L} \right)^{-2} \dots\dots\dots (8)$$

b) Mass transport in cnoidal waves The mass transport velocity in Lagrangian description is given as

$$\begin{aligned} \frac{U_M}{\sqrt{gh}} = & \frac{\lambda^2}{6\kappa^4} \left\{ 1 + 2 \left(\frac{\sqrt{gh}}{c} \right) \right\} \left[- \left(\frac{E}{K} \right) \left\{ 3 \left(\frac{E}{K} \right) + 2\kappa^2 - 4 \right\} + \kappa^2 - 1 \right] + \frac{2\lambda^3}{5\kappa^6} \left(\frac{\sqrt{gh}}{c} \right) \left(\frac{z}{h} - 1 \right)^2 \left\{ 2 \left(\frac{E}{K} \right) (\kappa^4 - \kappa^2 + 1) - \kappa^4 + 3\kappa^2 - 2 \right\} \\ & + \frac{\lambda^3}{10\kappa^6} \left(\frac{\sqrt{gh}}{c} \right) \left[5 \left(\frac{E}{K} \right)^2 \left\{ 9 \left(\frac{E}{K} \right) + 10\kappa^2 - 17 \right\} + \left(\frac{E}{K} \right) (12\kappa^4 - 57\kappa^2 + 47) - 6\kappa^4 + 13\kappa^2 - 7 \right] \\ & + \frac{\lambda^3}{15\kappa^6} \left(\frac{\sqrt{gh}}{c} \right)^3 \left[15 \left(\frac{E}{K} \right)^2 \left\{ \left(\frac{E}{K} \right) + \kappa^2 - 2 \right\} + \left(\frac{E}{K} \right) (4\kappa^4 - 19\kappa^2 + 19) - 2(\kappa^4 - 3\kappa^2 + 2) \right] \dots\dots (9) \end{aligned}$$

and that in Eulerian is also given as

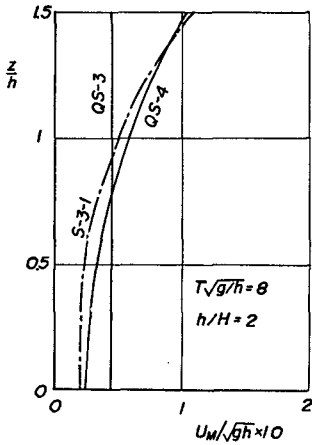
$$\frac{\bar{u}}{\sqrt{gh}} = - \frac{\lambda^2}{6\kappa^4} \left[- \left(\frac{E}{K} \right) \left\{ 3 \left(\frac{E}{K} \right) + 2\kappa^2 - 4 \right\} + \kappa^2 - 1 \right] + \frac{\lambda^3}{20\kappa^6} \left[35 \left(\frac{E}{K} \right)^2 \left(\frac{E}{K} + \kappa^2 - 2 \right) + \left(\frac{E}{K} \right) (6\kappa^4 - 41\kappa^2 + 41) - 3(\kappa^4 - 3\kappa^2 + 2) \right] \dots\dots\dots (10)$$

in which

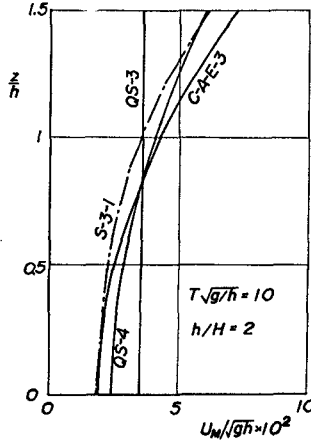
$$\frac{c}{\sqrt{gh}} = 1 - \frac{\lambda}{2\kappa^2} \left\{ 3 \left(\frac{E}{K} \right) + \kappa^2 - 2 \right\} + \frac{\lambda^2}{40\kappa^4} \left[45 \left(\frac{E}{K} \right) \left\{ 3 \left(\frac{E}{K} \right) + 2\kappa^2 - 4 \right\} + 19\kappa^4 - 64(\kappa^2 - 1) \right] \dots\dots (11)$$

E and K are the complete elliptic integrals of the first and second kinds, κ their modulus, and λ is approximately given as

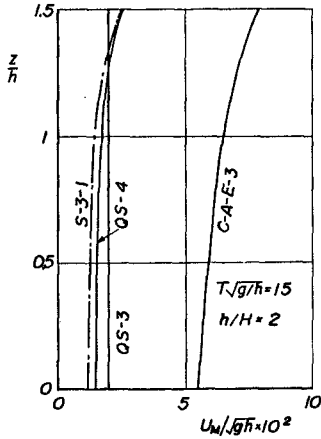
$$\frac{H}{h} = \lambda + \frac{27}{4096\pi^4\epsilon} \lambda^3 \dots\dots\dots (12)$$



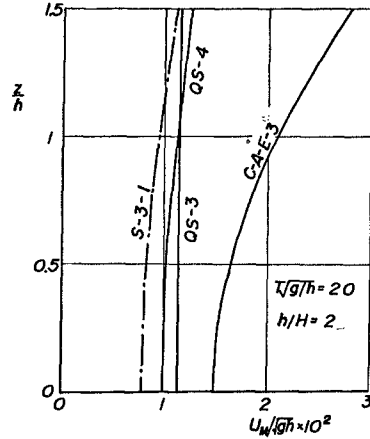
(a)



(b)

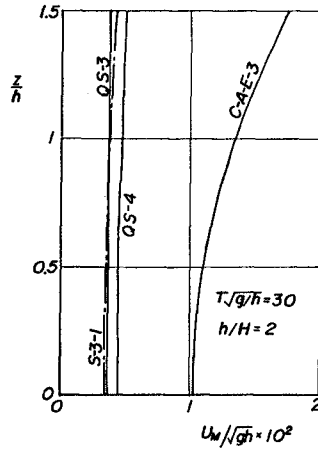


(c)



(d)

It is noted in these expressions that the mass transport exists both in Eulerian and Lagrangian descriptions, and the vertical distribution of Eulerian mass transport is uniform at this order of approximation. Vertical distributions of mass transport velocity in Lagrangian description are shown in Fig. 3. In this figure, the symbol S-3-1 stands for the solution of the usual Stokes wave theory to a third-order approximation and by the first Stokes definition of wave celerity, QS-3 and QS-4 indicate that of the quasi-Stokes wave theory to a third- and fourth-order approximation respectively, whilst C-A-E-3 represents the mass transport velocity predicted by the cnoidal wave theory to a third-order derived by the authors (the letter E for exact). The variation in the dimensionless wave period $T\sqrt{g/h}$ for a constant depth h infers the influence of wave period, or implying the shoaling of a wave with constant wave period T . It is seen that these vertical distributions of mass transport velocity are essentially the same within the range of small dimensionless wave period, and are in the same direction as of wave propagation, but the curve of C-A-E-3 is re-



(e)

Fig. 3 Vertical distributions of mass transport velocity in Lagrangian description

markably higher than that of others when a larger dimensionless wave period is considered.

EXPERIMENTAL VERIFICATION

1. A New Wave Flume

In a wave flume test it is highly desired that the uniformity of wave profile, wave celerity and mass transport are achieved to the progressive waves of permanent type produced over a uniform finite depth of water. As the normal wave tank of finite length constrains wave motion by the side walls, sloping end wall, and the wave generator plate, unavoidable forced re-circulation of water mass would eventually be resulted for within the interior of the fluid in the wave tank. This creates the problem of reflecting waves and the secondary flow and so on. This forced recirculation exerts a great influence on the exactness of the wave motion to be measured, especially mass transport and wave celerity.

A new wave flume incorporated with four rectangular orifices at sides as shown in Fig. 4, has been constructed, such that the desired wave conditions in the flume can steadily be maintained. As shown in this figure

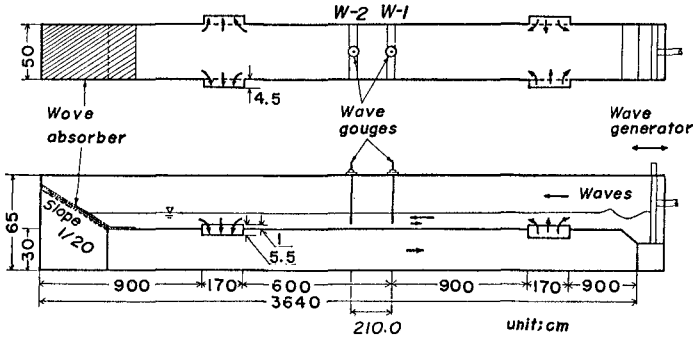


Fig. 4 New wave flume used

the water mass accompanied by the waves can flow into the inlet orifices at sides near the bottom, passing the conduit beneath the wave flume, and finally returns to the upstream part of the flume through the outlet orifices. Punched metal plates were randomly arranged at the end of the flume on a very gentle slope, acting as wave absorber. This enabled to keep the wave reflection coefficient within and below 5% during all experimental operations.

2. Experimental Method

Wave profile, wave height, and wave celerity were carefully measured by using two wave gauges of capacitance type, W-1 and W-2 as shown in Fig.

4, which were placed at 2.10 m apart. For measuring the mass transport velocity in Lagrangian description, a visualization method was employed wherein the orbital motions of the neutral buoyant particles, made by mixing xilen and nitrobenzen at a ratio of 0.72 to 1 and with colouring, were recorded by a still camera for over 10 wave cycles continuously. An example of the recorded orbital motions is shown in Photo. 1. From

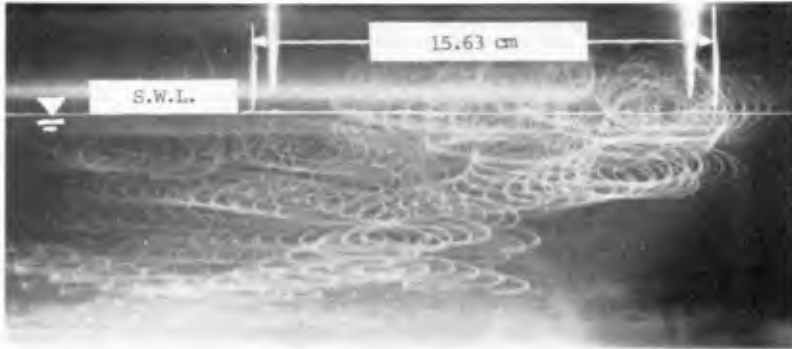


Photo. 1 An example of recorded orbital motions of neutral buoyant particles in the case of $T/g/h = 12.7$ and $h/H = 3.85$

this picture, the mass transport velocity can be accessed for particles introduced at various levels throughout the depth.

In addition, a series of the experiment of mass transport in progressive waves of permanent type has been carried out by a normal wave tank to confirm the forced re-circulation of water mass in the tank. It was already published by the authors(1978).

3. Comparison of Data with Theoretical Prediction

The uniformity of wave height and wave celerity produced in the wave flume was very carefully checked as function of time, as given in Fig. 5, in which H/h is the ratio of wave height to water depth and c/\sqrt{gh} the dimensionless wave celerity. The repeatability of mass transport velocity in Lagrangian description was also confirmed, besides the measurement of wave celerity. It was thus concluded that the wave height, wave celerity, and mass transport velocity reached the steady and uniform state after approximately 80 to 100 waves, i.e. reached its permanent type. Effect of viscosity may however appear near the bottom and free surface after a longer wave cycles.

Wave profiles in the steady state are shown in Fig. 6, in which comparison is made with the theoretical curves of quasi-Stokes(QS-4) and cnoidal waves(C-A-E-3), proven good agreement between them. Similarly, due comparisons on wave celerity and mass transport velocity can also be deduced for under the stable wave condition.

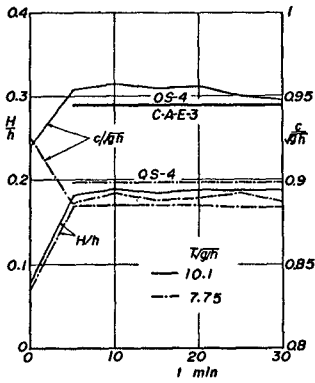


Fig. 5 An example of changes of wave height and wave celerity with time

Fig. 7 compares the experimental values of wave celerity with the theoretical solutions for the quasi-Stokes (QS-4) and cnoidal waves (C-A-E-3), for the value of dimensionless wave period $T/\sqrt{g/h}$ being 10 and slightly under. Fairly good agreement can again be observed for within the range tested.

Similar comparisons on mass transport velocity in Lagrangian description are presented in Fig. 8, in which the theoretical curves were obtained from using the usual Stokes wave theory, the authors' quasi-Stokes and cnoidal wave theories, and that of Longuet-Higgins'. It can be concluded from the figure that the mass transport velocity in progressive waves of permanent type is in the same direction as of wave propagation, and its vertical distribution follows closely the theoretical curves of Stokes waves, particularly to the first Stokes definition of wave celerity, as well as the quasi-Stokes (QS-4) and cnoidal wave (C-A-E-3) theories, within the ranges of $T/\sqrt{g/h}$ and H/h presented.

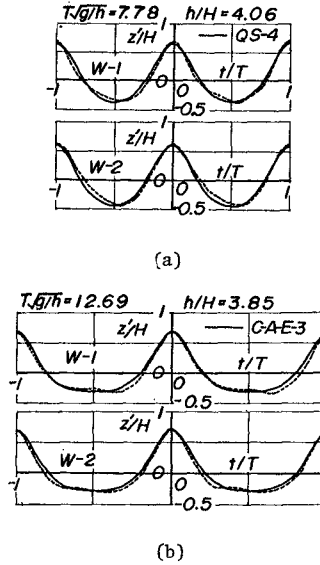


Fig. 6 Comparison of wave profile with theoretical curves

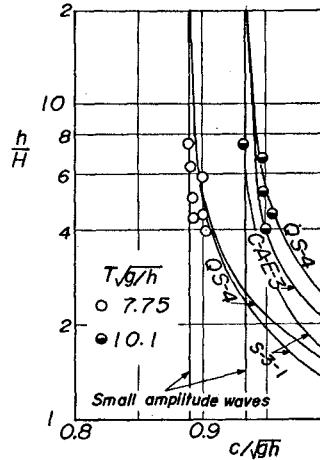


Fig. 7 Comparison of wave celerity with theoretical curves

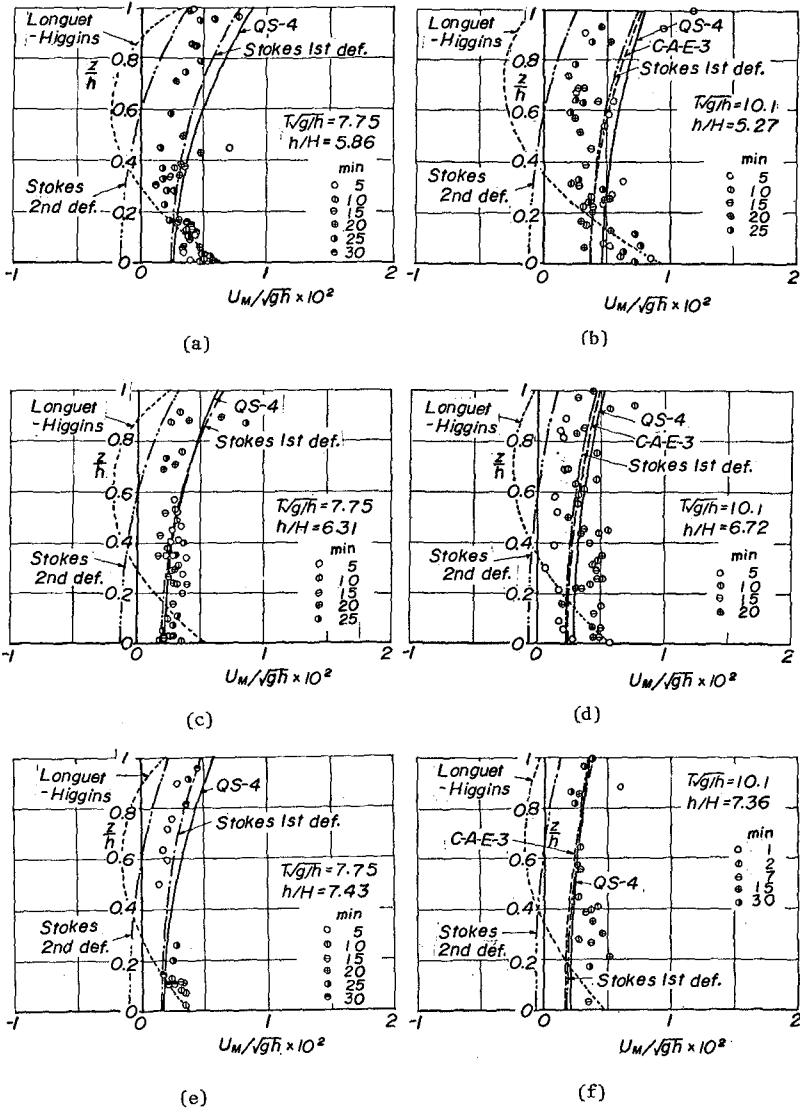


Fig. 8 Comparisons of mass transport velocity with theoretical curves (1)

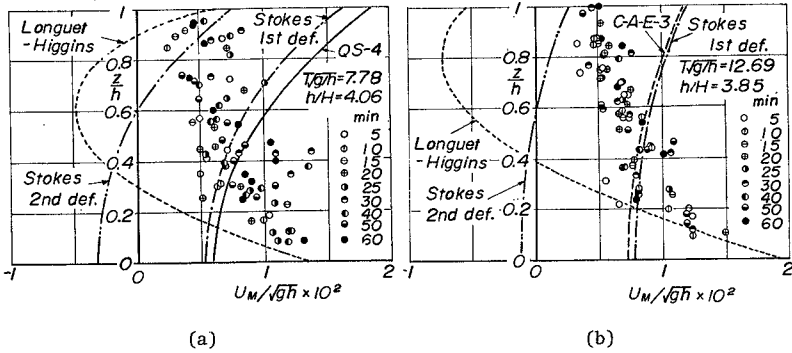
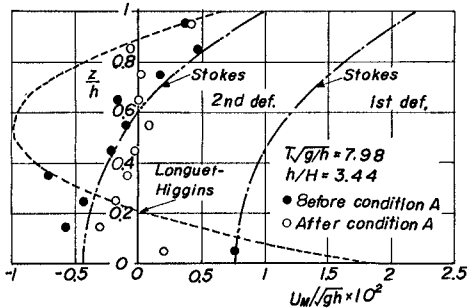


Fig. 9 Comparisons of mass transport velocity with theoretical curves(2)

Notable scattering occurs as wave height increases, i.e. h/H decreases for a constant depth h . However, slightly smaller in magnitude of the experimental data are generally seen as compared with the theoretical curves. This may well be caused from the back drift appeared in the upper part of the flume. This influence can roughly be estimated from assuming a uniform flow of back drift as follows. As the water depth in the upper part of the flume at the orifices was about 10 cm and that in the conduit below was 30 cm, it was therefore estimated that a 25% reduction will be resulted in the mass transport velocity so measured.

For even higher wave height than that presented in Fig. 8, as seen in Fig. 9, the mass transport velocity is still in the same direction as of wave propagation, but the vertical distribution is likely to differ further from the theoretical curves. This might be attributed to the limitation of the inlet and outlet orifices so equipped and even from the undesired reflection.



Finally, an example of the vertical distributions of mass transport velocity in a normal wave tank is shown in Fig. 10 for comparison with Fig. 8. In the figure, the condition A stands for the state at which the steadiness and uniformity of wave profile and wave celerity were made after about 200 to 250 waves. It can be concluded that the vertical distribution of mass transport velocity in a normal wave tank is quite different from those in Fig. 8, and agrees with the theoretical curve of

Fig. 10 Comparison of mass transport velocity in normal wave tank with theoretical curves

the Stokes waves to the second Stokes definition of wave celerity. It may however be expected that experimental data approach to Longuet-Higgins' curve, as Russell and Osorio(1957) confirmed, when the viscosity effect is considered after very long wave cycles.

CONCLUSIONS

Theoretical formulations of mass transport velocity have been derived for progressive waves of permanent type, both in Lagrangian and Eulerian descriptions, for the quasi-Stokes and cnoidal wave theories by the authors. A new wave flume, equipped with orifices for the natural return of water flow, was constructed for the verification of mass transport velocity, since it is submitted that wave reflection occurs at the end of the normal wave tank which is generally of finite length. It can be concluded that the observed direction of mass transport is the same as that of waves propagating on the water surface, and the vertical distribution agrees with the theoretical curves calculated by the usual Stokes wave theory under the first Stokes definition of wave celerity, and that of quasi-Stokes and cnoidal wave theories derived by the authors.

ACKNOWLEDGEMENTS

The authors wish to express their great appreciation to Dr. J.R.C. Hsu, Visiting Scholar, Disaster Prevention Research Institute, Kyoto University, on leave from the Department of Civil Engineering, University of Western Australia. Part of this investigation was accomplished with the support of the Grant-in-Aid for Scientific Research(No. 155190), Ministry of Education.

REFERENCES

- Huang, N.E.: Mass transport induced by wave motion, Jour. Marine Res., Vol.28, No. 1, pp. 35-50, 1970.
- Li, A. and S.H. Davis: Viscous attenuation of mean drift in water waves, Jour. Fluid Mech., Vol. 81, Part 1, pp. 63-84, 1977.
- Longuet-Higgins, M.S.: Mass transport in water waves, Phill. Trans. Roy. Soc. London, Series A, Vol. 245, No. 903, pp. 535-581, 1953.
- Russell, R.C.H. and J.D.C. Osorio: An experimental investigation of drift profiles in a closed channel, Proc. 6th Conf. Coastal Eng., pp. 171-193, 1957.
- Taniuti, T. and C.C. Wei: Reductive perturbation method in nonlinear wave propagation, I, Jour. Phys. Soc. Japan, Vol. 24, No. 4, pp. 941-946, 1968.
- Tsuchiya, Y. and T. Yasuda: A new approach to cnoidal wave theory, Proc. 21st Conf. Coastal Eng., JSCE, pp. 65-71, 1974.
- Tsuchiya, Y. and T. Yasuda: A cnoidal wave theory and its verification, Proc. 3rd Australian Conf. Coastal & Ocean Eng., Supplement paper, 7p, 1977.

- Tsuchiya, Y. and T. Yasuda: Quasi-Stokes wave theory by reductive perturbation method, Proc. 25th Conf. Coastal Eng., JSCE, pp. 6-9, 1978.
- Tsuchiya, Y., T. Yasuda and T. Yamashita: A new wave flume, Proc. 25th Conf. Coastal Eng., JSCE, pp. 51-54, 1978.
- Unluata, U. and C.C. Mei: Mass transport in water waves, Jour. Geophy. Res., Vol. 75, No. 36, pp. 7611-7618, 1970.

RAY CURVATURE AND REFRACTION OF WAVE PACKETS

by

J. Ernest Breeding, Jr.

Department of Oceanography and Ocean Engineering
 Florida Institute of Technology
 Melbourne, Florida 32901

ABSTRACT

Directional wave data obtained simultaneously at two measurement sites is used to confirm the constancy, and therefore the validity, of Snell's laws for wave packets. It is found that the wave packets refract according to Snell's law with the geometric group velocity whereas the wavelets within a packet refract according to Snell's law with phase velocity.

An expression for the ray curvature of a wave packet is derived which is suitable for use in wave prediction programs. The ray curvature of the wave packet is found to vanish if the packet direction becomes either perpendicular or parallel to the wave speed contours, assuming the wavelet direction is not parallel to the contours. This means that as a hydron (wave packet) moves into shoaling water refraction tends eventually to turn the hydron so that it is directed either perpendicular or parallel to the shoreline. The first case is similar to monochromatic waves. For parallel water depth contours, it is the result for hydrons which begin in deep water if the angle of incidence is between 0° and 74.8° with respect to the contour normal. However, for deep water angles of incidence equal to or greater than 74.8° the hydrons are turned and move parallel to shore in water of intermediate depth. The packet ray curvature approaches infinity as the wavelet direction, but not the hydron direction, becomes parallel to the wave speed contours. The result is total reflection of the waves. Total reflection occurs if a hydron is moving into deeper water and its initial direction exceeds a critical angle. At the reflection point the hydron direction becomes perpendicular to the water depth contours. Further, the hydron velocity goes to zero, which is consistent with a particle concept. As in quantum mechanics, the wave-particle duality is encountered.

1 INTRODUCTION

The conventional definition of group speed U has been defined as

$$U = d\omega/dk \quad (1)$$

where ω is the angular frequency and k is the wave number. This equation defines the speed of the group in the direction of the wavelet velocity. The geometric group speed G was defined by Breeding (1978a) as

$$G = U \cos \phi \quad (2)$$

where

$$\phi = \theta - \gamma \quad (3)$$

The direction of movement of the wave packet is represented by θ , and the direction the wavelets move within the packet is specified by γ .

Breeding (1978a) and Black (1979) have found that the trajectories of wave packets are not determined by a monochromatic refraction law, i.e., by simply using Snell's law with phase velocity. Based on a comparison of computed backtracks from the measurement site with the known source of the waves, Breeding (1978a) has shown that wave packets refract according to Snell's law with the geometric group velocity. This refraction law determines the wave path of constructive interference. At each point of the wave packet trajectory the wavelet direction is determined by Snell's law with phase velocity.

One objective of this paper is to investigate more directly the validity of the refraction laws by testing the constancy of Snell's laws for the wave packets and wavelets using directional wave data obtained simultaneously at two measurement sites. A further purpose of the paper is to derive an expression for the ray curvature of a wave packet which is suitable for use in wave prediction programs. Properties of the packet ray curvature are described, and the important features of wave packet refraction are demonstrated using examples of gravity water waves.

2 TEST OF WAVE PACKET REFRACTION LAWS

2.1 Theory

Snell's law for a wave packet can be stated

$$(\sin \theta)/G = C_G \quad (4)$$

where C_G is a constant for a given frequency. The direction of γ is determined by

$$(\sin \gamma)/v = C_v \quad (5)$$

which is Snell's law with phase velocity where $v = \omega/k$ is the phase speed and C_v is a constant for a given frequency. To use (4) and (5) the y-axis is taken parallel with the wave speed contours. By virtue of Snell's law with phase velocity, γ is a function of k . The water depth h is assumed to vary slowly over the distance of a wavelength so that k is given by the classical dispersion relation

$$\omega^2 = gk \tanh kh \quad (6)$$

where g is the acceleration due to gravity. By considering the variation of (5) with respect to frequency it is found that (Breeding, 1978a)

$$\tan \phi = k(d\gamma/dk) \quad (7)$$

which is a useful relation for determining θ from a set of wave measurements.

2.2 Field Observations

2.2.1 Directional wave data

Hurricane Betsy passed over the southern tip of Florida and entered the Gulf of Mexico at about 1500 UT on September 8, 1965. After making a curved path the hurricane entered land at the Mississippi Delta at about 0400 UT on September 10. The storm had winds in excess of 100 knots.

Waves due to Hurricane Betsy were measured (Breeding, 1972) using two independent arrays of six pressure transducers which were placed on the sea floor at the sites of two offshore platforms (stages) near Panama City, Florida. The location and configuration of the arrays are shown in Figure 1. In each array a pressure sensor is located at each corner of a pentagon of side 35.8 m (117.6 ft) and these sensors are located 30.5 m (100.0 ft) from a sensor at the center of the array. Stage 1 is located in 31.7 m (104 ft) of water 17.7 km (11 mi) from shore. Stage 2 is located in 19.2 m (63 ft) of water 2.8 km (1.7 mi) from shore. Directional power spectra with 60 d.f. were computed for time series records about 30 min in length by Bennett (1972) based on the method of Munk et al. (1963).

The results of the wave directional analysis for successive measurement times of 1712 - 1743 and 1744 - 1815 UT on September 9, 1965 at Stage 1 are shown in Figure 2. In the array pressure sensors 1, 2, 4, and 5 were operational. The wavelet directions shown are the bearings from which the waves come relative to true north. It is apparent that the findings for the two measurement periods are consistent. The wave directional results for measurements made independently at Stage 2 for the same times as presented for Stage 1 are shown in Figure 3. For this array all the sensors were working but sensors 2 and 4.

2.2.2 Test of Snell's laws

For the observations presented in Figures 2 and 3 the wavelet direction γ and an estimate of the slope $d\gamma/dk$ were obtained by fitting a quadratic polynomial to the data by the method of least squares. The resulting quadratic curves are shown with the data in the figures. The polynomial obtained for the Stage 1 data is given by

$$\gamma_1 = 3.724 - 17.26 k_1 + 68.32 k_1^2 \quad (8)$$

The similar finding for the Stage 2 data is

$$\gamma_2 = 3.984 - 18.74 k_2 + 92.06 k_2^2 \quad (9)$$

Once γ and $d\gamma/dk$ are determined for a given wavelet period from (8) and (9), the wave packet bearings can be determined for each measurement site, respectively, using (7) and (3). For example, for a wavelet period

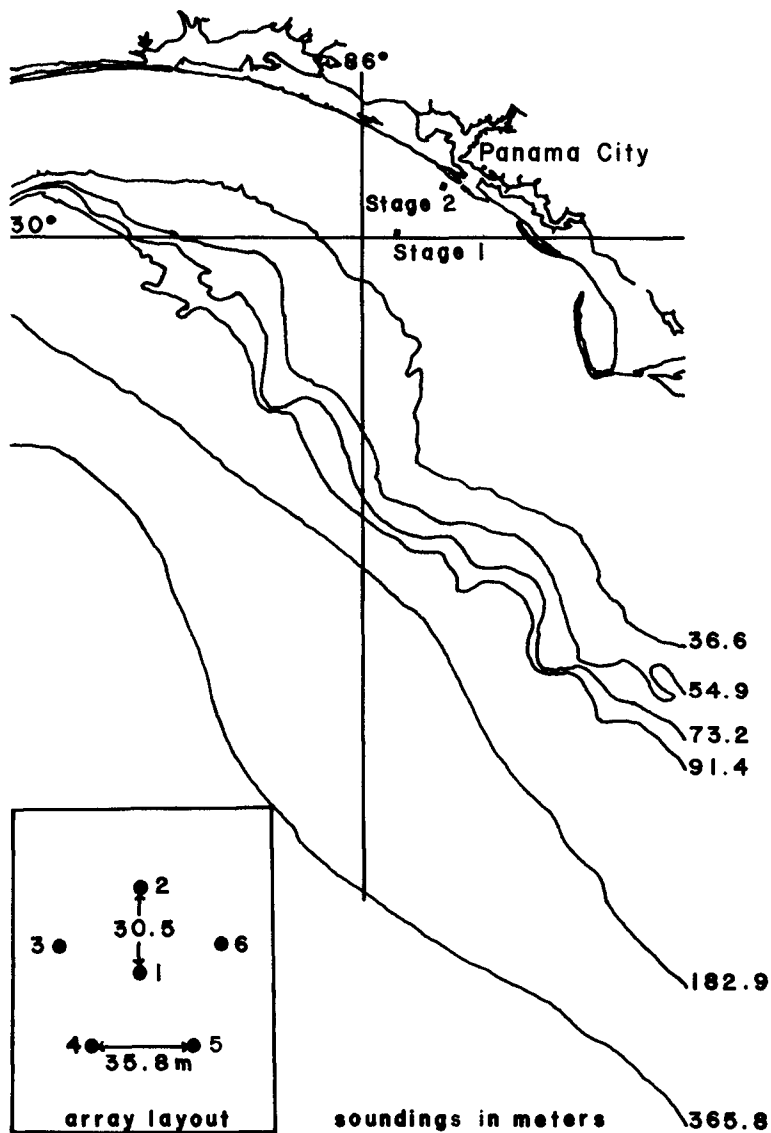


Figure 1. Bottom topography and array configuration near Panama City, Florida.

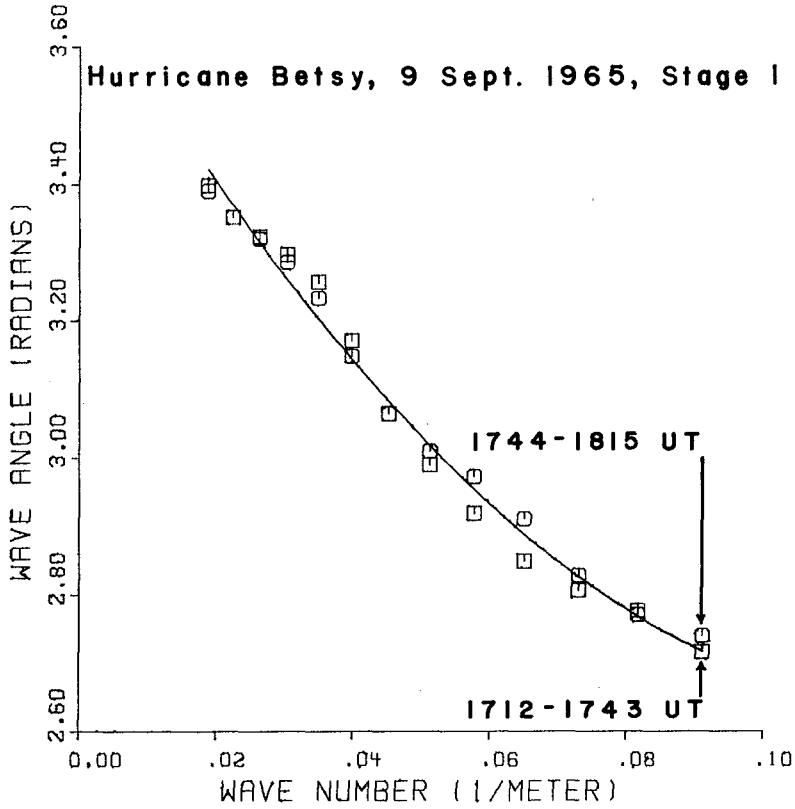


Figure 2. Wavelet directions as a function of wave number at Stage I.

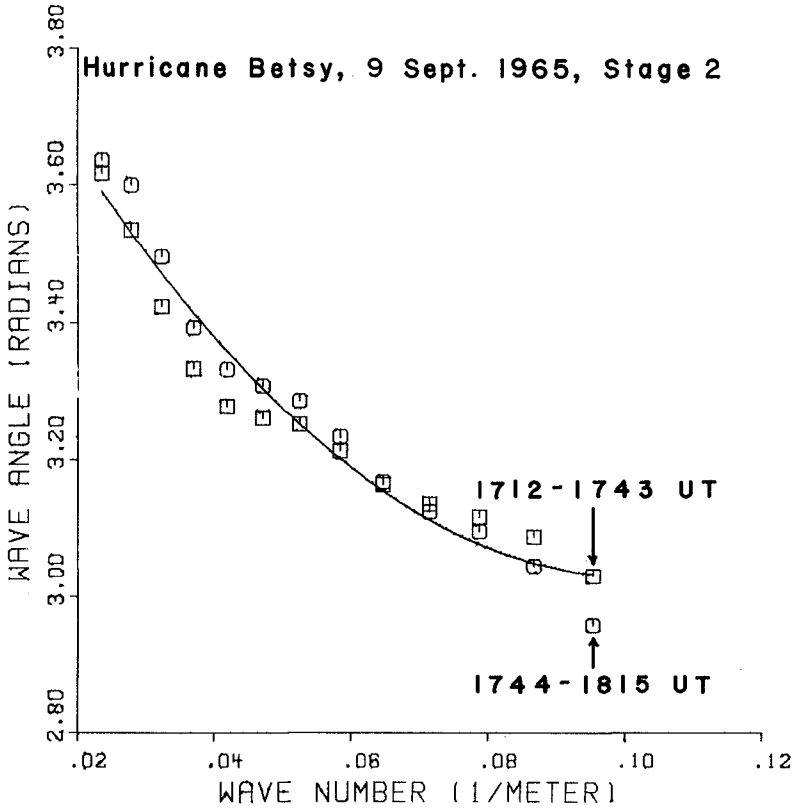


Figure 3. Wavelet directions as a function of wave number at Stage 2.

of 10.9 s, at Stage 1 $v_1 = 14.48$ m/s, $\gamma_1 = 180.19^\circ$, $G_1 = 9.23$ m/s, and $\theta_1 = 154.97^\circ$. The corresponding values at Stage 2 are $v_2 = 12.23$ m/s, $\gamma_2 = 189.37^\circ$, $G_2 = 8.89$ m/s, and $\theta_2 = 164.01^\circ$.

To evaluate the constants in Snell's laws the wave packet and wavelet directions are defined with respect to the normal to the water depth contours. The water depth contours between the stages are approximately parallel with a bearing of 131° with respect to true north. For the data summarized by (8) and (9) the Snell's law constants for both the wave packets and wavelets were evaluated for each wavelet period. The percentage differences of the constants at Stage 2 from the corresponding values at Stage 1 are shown in Figure 4. In the same figure the surface extrapolations of the energy density for the first of the two measurement periods used to determine (8) and (9) are presented for both stages.

2.2.3 Discussion of the results

The difference in the energy density for Stage 1 and Stage 2 shown in Figure 4 is a manifestation of the wave modification occurring between the stages. Over most of the frequency range considered, the Snell's law constants at Stage 2 differ by less than $\pm 10\%$ from the corresponding constants at Stage 1 for both the wave packets and the wavelets. The difference in the constants increases as the waves become less energetic. However, the difference in the constants is less than 5% for both the wave packets and the wavelets at the wave period where the energy density peaks. These findings are significant. Although the validity of Snell's law with phase velocity is well established, the results presented here indicate that Snell's law with the geometric group velocity is equally valid.

There are a number of reasons why different constants are found for Snell's laws for the wave packets and wavelets at the offshore stages. For example, a measurement error of a few degrees for each array is possible from inaccuracies in locating the positions of the pressure sensors. The water depth contours are not exactly parallel as was assumed in the computations. Further, the accuracy in determining the Snell's law constants for the wave packets depends upon the method used in evaluating the slope dy/dk from the data. Higher accuracy could be achieved by the use of higher order polynomials to better fit the data.

3 RAY CURVATURE FOR WAVE PACKETS

It is more convenient to determine ray trajectories using the ray curvature than it is to use Snell's law. The ray curvature κ_v of a ray moving with phase speed v was derived by Munk and Arthur (1952) and Arthur, et al (1952) as

$$\kappa_v = \frac{dy}{ds_v} = \frac{1}{v} \left(\sin \gamma \frac{\partial v}{\partial x} - \cos \gamma \frac{\partial v}{\partial y} \right) \quad (10)$$

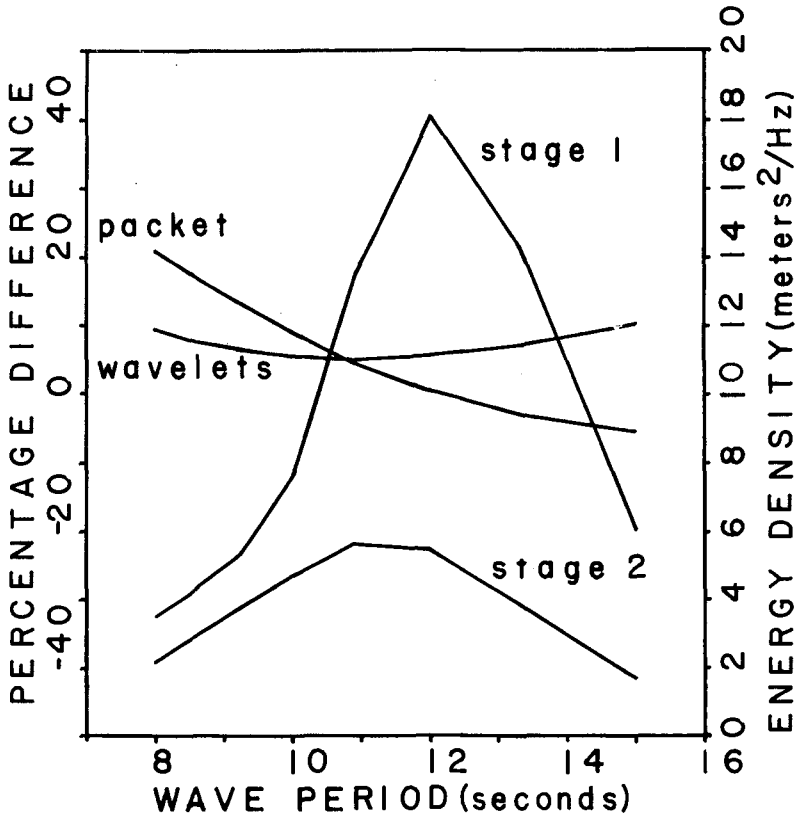


Figure 4. Comparison of Snell's law constants for wave packets and wavelets at Stage 1 and Stage 2 for Hurricane Betsy for measurement times of 1712-1743 and 1744-1815 UT on September 9, 1965. The percentage differences of the constants at Stage 2 from the corresponding values at Stage 1 are shown versus wave period. The energy density is presented for both stages for the time period 1712-1743 UT.

where x, y are the Cartesian coordinates, γ is the direction of the ray with respect to the positive x -axis, and s_γ is the arc length along the ray. The ray curvature κ_G for the trajectory of a wave packet is given by

$$\kappa_G = \frac{d\theta}{ds_G} = \frac{1}{G} \left(\sin \theta \frac{\partial G}{\partial x} - \cos \theta \frac{\partial G}{\partial y} \right) \quad (11)$$

where θ is the direction of the packet ray with respect to the positive x -axis and s_G is the arc length along the ray.

3.1 Packet Ray Curvature

The derivation of the packet ray curvature is greatly simplified by using a x', y' -coordinate system which is chosen so that at each ray point the positive x' -axis is in the direction of the gradient of the water depth. As a result, the first partial derivatives of the water depth and the wave speeds with respect to y' vanish. From (2) the spacederivative of G is then

$$\frac{\partial G}{\partial x'} = \frac{\partial U}{\partial x'} \cos \phi - U \sin \phi \left(\frac{\partial \theta'}{\partial x'} - \frac{\partial \gamma'}{\partial x'} \right) \quad (12)$$

Also

$$\partial \theta' / \partial x' = [(\partial G / \partial x') / G] \tan \theta' \quad (13)$$

$$\partial \gamma' / \partial x' = [(\partial v / \partial x') / v] \tan \gamma' \quad (14)$$

After (13), (14), and (12) are substituted into (11) and the result is simplified, the packet ray curvature is found to be

$$\kappa_G = \frac{[(\partial U / \partial x') / U] + [(\partial v / \partial x') / v] \tan \phi \tan \gamma'}{\csc \theta' + \tan \phi \sec \theta'} \quad (15)$$

This expression is used by Breeding (1978b) in a wave prediction program.

3.2 Properties of the Packet Ray Curvature

The ray curvature of a wave packet defined by (15) exhibits some very remarkable properties. To determine the important properties the discussion is simplified by taking the wave speed contours parallel to the y -axis. It is assumed that v, U , and their derivatives are continuous and finite. However, under various conditions the trigonometric terms of the equation can become infinite or have indeterminate forms. The value of κ_G approaches zero as the wave packet direction θ becomes either parallel or perpendicular to the wave speed contours, provided the wavelet direction γ is not parallel to the contours. This means that given a sufficiently long path, refraction tends to turn the wave packet so that it is directed either parallel or perpendicular to the wave speed contours. If θ is neither parallel nor perpendicular to the wave speed contours, then κ_G approaches infinity as γ becomes

parallel to the wave speed contours. In this case, due to the value of γ , the wave packet undergoes total reflection.

To determine the value of κ_G when there are indeterminate forms it is necessary to consider the variations of θ and γ as the indeterminate forms are approached. For example, (15) contains an indeterminate form when θ becomes perpendicular to the wave speed contours while γ becomes parallel to the contours. If γ approaches parallelism to the contours faster than θ approaches the perpendicular to the contours the value of κ_G becomes infinite.

The relationship between θ and γ due to refraction is clearly seen by integrating the ray curvature expressions (10) and (11). The y -derivatives being zero, integration of (11) leads to (4) which can be stated

$$(\sin \theta) / [U \cos (\theta - \gamma)] = C \quad (16)$$

which is Snell's law for a wave packet. Snell's law with phase velocity, which determines γ , is obtained by integrating (10). The cosine term in (16) can be replaced by the identity for the difference of two angles and the terms rearranged to yield

$$\tan \theta = (UC \cos \gamma) / (1 - UC \sin \gamma) \quad (17)$$

where the variation of θ appears only on the left side of the equation.

It is interesting to note that θ becomes zero if $\gamma = (2m+1)(\pi/2)$ where m is an integer. Thus if the wavelet direction becomes parallel to the wave speed contours the wave packet direction becomes perpendicular to the contours. Further, note that $\theta = (2m+1)(\pi/2)$ if $UC \sin \gamma = 1$. For this case the wave packet direction is parallel to the wave speed contours.

Snell's law can be used to derive an expression for $\cos (\theta - \gamma)$. Eq. (17) is substituted into the identity for $\tan (\theta - \gamma)$ and the result is simplified to obtain

$$\tan (\theta - \gamma) = (UC - \sin \gamma) / \cos \gamma \quad (18)$$

In terms of initial values, Snell's law with phase velocity can be written

$$\sin \gamma = v_r \sin \gamma_i \quad (19)$$

where $v_r = (v/v_i)$ and the subscript i denotes an initial value. Before refraction it is assumed that $\theta_i = \gamma_i$. Then

$$C = (\sin \gamma_i) / U_i \quad (20)$$

When (19) and (20) are substituted into (18), it is found that

$$\tan(\theta - \gamma) = \frac{(U_r - v_r) \sin \gamma_i}{(1 - v_r^2 \sin^2 \gamma_i)^{\frac{1}{2}}} \quad (21)$$

where $U_r = (U/U_i)$. This result can be transformed by the use of an identity to

$$\cos(\theta - \gamma) = \left[1 + \frac{(U_r - v_r)^2 \sin^2 \gamma_i}{1 - v_r^2 \sin^2 \gamma_i} \right]^{-\frac{1}{2}} \quad (22)$$

Eqs. (1), (2), and (22) provide a useful means of computing the geometric group speed.

4 HYDRON EXAMPLES OF WAVE PACKET REFRACTION

To demonstrate the properties of wave packet refraction, examples of gravity water waves will be considered. Gravity water waves are particularly suited as examples because of their highly dispersive nature. The term 'hydon,' suggested by Purser and Synge (1962) and Synge (1962), will be used to denote the wave packet of water waves.

4.1 Waves Starting in Deep Water

In Figure 5 hydon trajectories are shown for waves beginning in deep water (water depth greater than one half the wavelength). The water depth contours are parallel. Initially $\theta_i = \gamma_i$ where each initial direction indicated on the figure is the angle between the hydon velocity vector and the normal to the depth contours. Regardless of the wave period, for deep water angles of incidence between 0° and 74.8° the hydrons follow paths such that the angles increase to the depth of the geometric group speed maximum (see Figure 7), then undergo a point of inflection, and then decrease shoreward. As a hydon approaches shore its direction becomes perpendicular to the wave speed contours and the packet ray curvature approaches zero. For deep water angles of incidence equal to or greater than 74.8° the hydon trajectories turn and move parallel to shore in water of intermediate depth. As the hydon direction becomes parallel to shore the packet ray curvature tends to vanish; this is apparent in ray number 5.

For comparison, monochromatic rays are shown in Figure 6 for the same conditions considered in Figure 5. For large incident angles there is a striking difference between hydon and monochromatic trajectories. Whereas all the hydon rays do not reach shore all the monochromatic rays do. Note that the wavelet direction at each point along a hydon path in Figure 5 is the same as the direction of the corresponding monochromatic ray at the corresponding water depth.

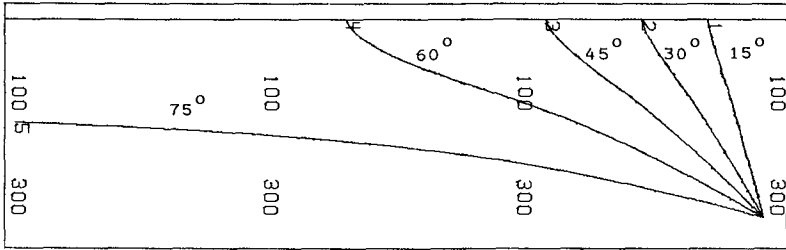


Figure 5. Hydron trajectories for a 20 s wave period for waves beginning in deep water. The water depth contours are parallel, the scale of the plot is 1 cm = 4.87 km, and the sounding depths are in meters. The initial hydron direction is shown for each ray and is the angle between the hydron velocity vector and the normal to the depth contours.

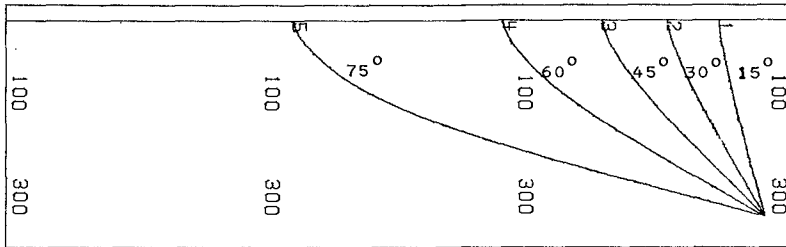


Figure 6. Monochromatic rays for comparison with the hydron rays in Figure 5.

It is interesting to compare the values of G and U when they differ due to refraction. As an example, for gravity water waves which begin in deep water it is found that

$$v_r = \tanh kh \quad (23)$$

$$U_r = \left(1 + \frac{2kh}{\sinh 2kh}\right) v_r \quad (24)$$

where h is the water depth. When (23) and (24) are substituted into (22) and the result is substituted into (2) it is found that

$$G = U \left[\frac{1 + \frac{(kh \sin \gamma_i \operatorname{sech}^2 kh)^2}{1 - (\sin \gamma_i \tanh kh)^2}}{1 - (\sin \gamma_i \tanh kh)^2} \right]^{-\frac{1}{2}} \quad (25)$$

The ratio of the geometric group speed to its initial deep water value is presented for several incident angles in Figure 7. The initial hydron directions are defined as in Figure 5. The curve for $\gamma_i = 0^\circ$ is the same as obtained for the ratio of U to the value of U in deep water. The amount by which the other curves differ from it is a measure of the difference between G and U .

Inspection of Figure 7 shows for a given γ_i that the maximum of G/G_i occurs at a greater value of kh than does the minimum of G/U . An increase in γ_i causes a shift in both the minimum of G/U and the maximum of G/G_i to larger values of kh . Further, the maximum peak tends to get flattened out. The curve for $\gamma_i = 74.8^\circ$ is seen to stop abruptly at the maximum value of G/G_i .

When $\gamma_i = 30^\circ$ the maximum percentage difference of G from U is 2.70%. When $\gamma_i = 45^\circ$ the value is 5.91%, for $\gamma_i = 60^\circ$ it is 10.03%, and for $\gamma_i = 74.79^\circ$ the value is 14.27%.

4.2 Reflection Points

To obtain a reflection point it is necessary that the waves propagate into deeper water and that the initial direction of the hydron ($\theta_i = \gamma_i$) exceed a critical angle. The reflection point occurs at an intermediate water depth when, through refraction, the wavelets are turned parallel to the wave speed contours.

In Figure 8 two rays are shown in which the wave period is 20 sec and the initial water depth is 15 m. For this case a reflection point occurs if $\theta_i \geq 22.2^\circ$. Ray number 1 reaches deep water since $\theta_i = 15^\circ$. For ray number 2, $\theta_i = 23^\circ$, and a reflection point occurs at a water depth of 200 m. The variation of the hydron and wavelet directions with water depth for this ray are shown in Figure 9. The wavelet angle increases continuously with water depth and becomes parallel to the water depth contours at the reflection point. The hydron angle first increases, goes through a maximum, and then becomes perpendicular to

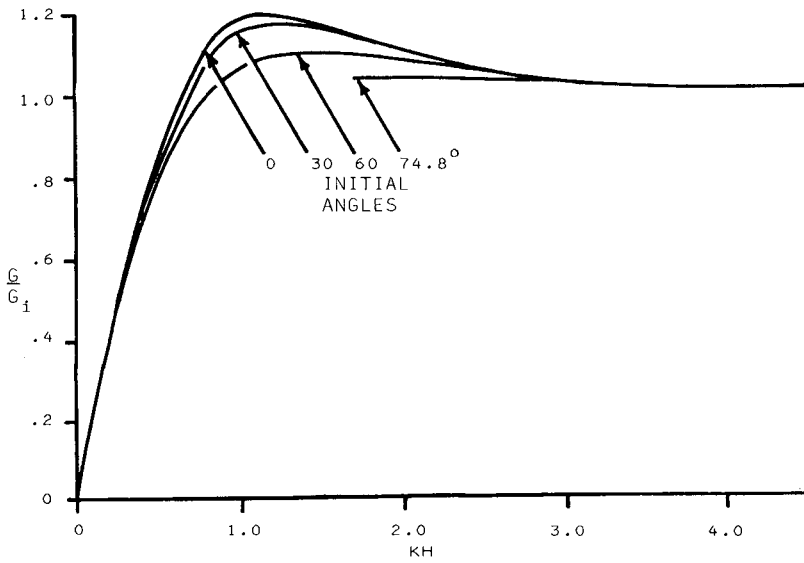


Figure 7. The variation of the geometric group speed with kh for hydrons beginning in deep water. The initial value of the geometric group speed is G_i . The hydron directions are defined as in Figure 5.

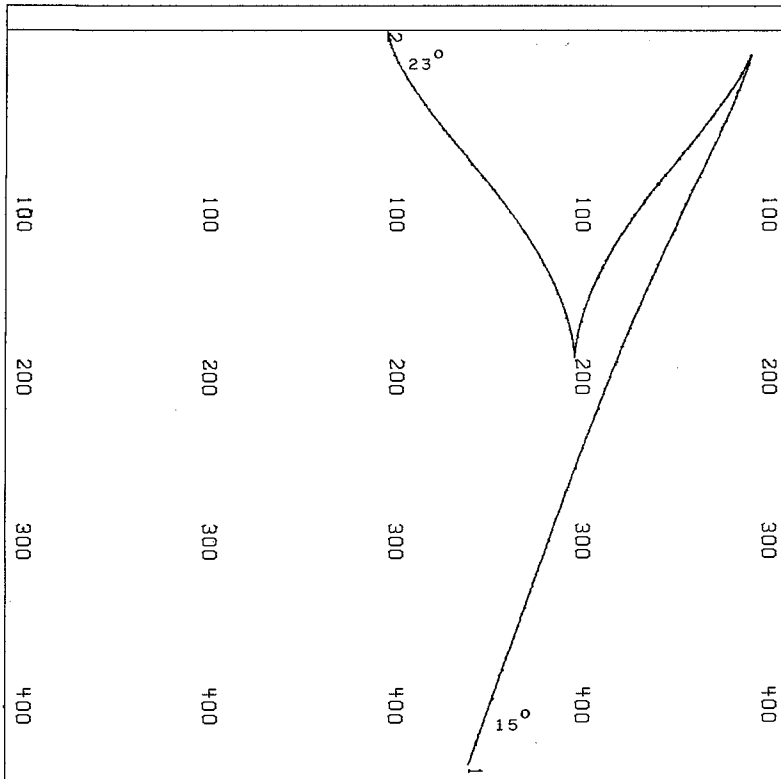


Figure 8. Hydron trajectories for a 20 s wave period for waves which begin at an intermediate water depth. The scale of the plot is 1 cm = 3.10 km and the sounding depths are in meters. The initial hydron direction is shown for each ray and is defined as in Figure 5.

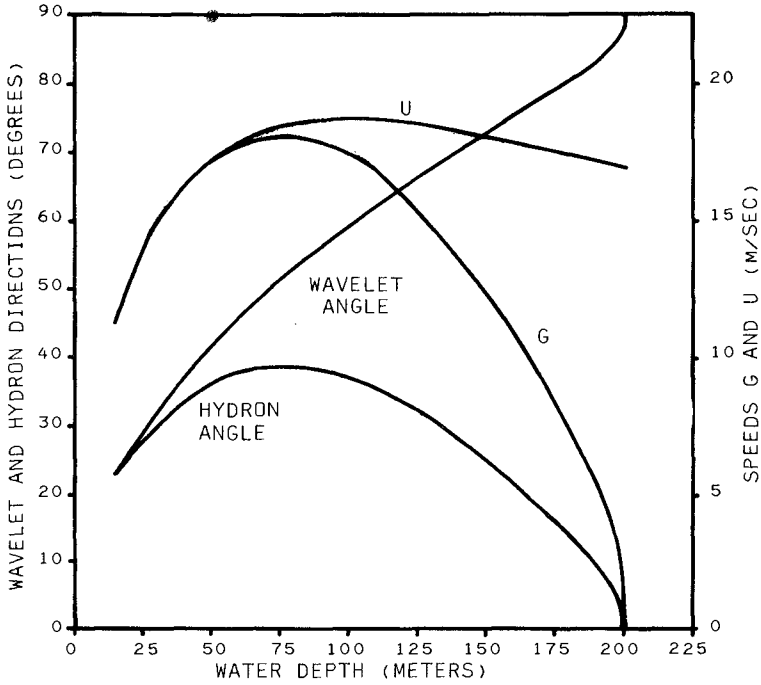


Figure 9. Variations of the wavelet direction γ , hydron direction θ , the speed $U = d\omega/dk$, and the geometric group speed $G = U \cos(\theta - \gamma)$ up to the reflection point for ray number 2 in Figure 8.

the water depth contours at the reflection point. This is clearly seen in Figure 8.

Plots of how G and U vary with water depth in approaching the reflection point are shown in Figure 9. Both speeds have a maximum value. However, there is a marked contrast between G and U at the reflection point where the geometric group speed is zero.

In Figure 10 the ratio of the packet ray curvature to its initial value is sketched as a function of the wavelet direction for ray number 2 in Figure 8. The most striking feature of this curve is that within about 2° of the reflection point the packet ray curvature suddenly goes to infinity.

It is interesting to observe that the velocity of the wave packet goes to zero at the reflection point. This is exactly what the velocity of a particle should do when there is reflection. Therefore, in water waves, as in quantum mechanics, the wave-particle duality is encountered.

5 CONCLUSIONS

Directional gravity water wave data obtained simultaneously at two field stations were used to test the refraction laws for the wave packets (hydrons) and wavelets. It is found that the constancy of Snell's laws is established with equal precision for both the wave packets and wavelets. From the results it is concluded that the wave packets refract according to Snell's law with the geometric group velocity while the wavelets within a packet refract according to Snell's law with phase velocity.

Refraction causes a hydron trajectory to become directed either parallel or perpendicular to the water depth contours. In either case the packet ray curvature will vanish. For hydrons propagating toward deep water, if the initial direction exceeds a critical angle total reflection occurs. At the reflection point the wavelet direction becomes parallel to the wave speed contours, the hydron direction becomes perpendicular to the contours, the geometric group velocity goes to zero, and the packet ray curvature becomes infinite.

6 ACKNOWLEDGMENTS

The data were collected and the spectral analysis obtained at the Naval Coastal Systems Center, Panama City, Florida, by George B. Austin and Carl M. Bennett, respectively. I thank them for their cooperation and suggestions.

Further, I thank Franklyn C. W. Olson, Kenneth C. Matson, and Kimberly Crane Oppenheimer for their help in preparing this paper. The research was supported by the Geography Programs, Earth Sciences Division, Office of Naval Research (USA) under Contract No. N00014-77-C-0329.

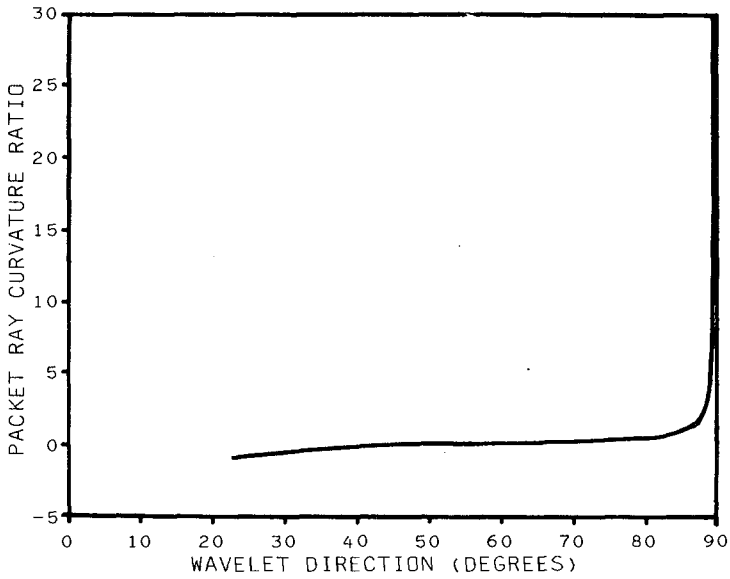


Figure 10. The ratio of the hydron ray curvature to its absolute initial value as a function of the wavelet direction up to the reflection point for ray number 2 in Figure 8.

- Arthur, R.S., Munk, W.H., and Isaacs, J.D. (1952). The direct construction of wave rays. Trans. Am. Geophys. Union, Vol. 33, No. 6, pp. 855-865.
- Bennett, C.M. (1972). The directional analysis of ocean waves: an introductory discussion, 2nd ed. Naval Coastal Systems Center Report No. 144-72. Unpublished.
- Black, J.L. (1979). Hurricane Eloise directional wave energy spectra. Proc. 11th Annual Offshore Tech. Conf., Houston, paper OTC 3594.
- Breeding, J.E., Jr. (1972). Refraction of gravity water waves. Thesis (Ph.D.), Columbia Univ.
- Breeding, J.E., Jr. (1978a). Velocities and refraction laws of wave groups: a verification. J. Geophys. Res., Vol. 83, No. C6, pp. 2970-2976.
- Breeding, J.E., Jr. (1978b). A method for calculating wave packet trajectories and wave heights: part 2. Dep. of Oceanogr., Florida State Univ. Report No. JEB-4. Unpublished.
- Munk, W.H. and Arthur, R.S. (1952). Wave intensity along a refracted ray. Gravity waves, National Bureau of Standards Circular 521. pp. 95-108.
- Munk, W.H., Miller, G.R., Snodgrass, F.E., and Barber, N.F. (1963). Directional recording of swell from distant storms. Phil. Trans. Roy. Soc. London, Ser. A, Vol. 255, No. 1062, pp. 505-584.
- Purser, W.F.C. and Synge, J.L. (1962). Water waves and Hamilton's method. Nature, Vol. 194, No. 4825, p. 268.
- Synge, J.L. (1962). Water waves and hydrons. Science, Vol. 138, No. 3536, pp. 13-15.

VERIFICATION OF A WAVE REFRACTION MODEL UTILISING
RECORDED AND OBSERVED WAVE DATA

BY G HENDERSON¹ and N B WEBBER²

SUMMARY

There are few references in the published literature to the verification of wave refraction models utilising field data. More often, such models have been compared to the results of analytical solutions or using laboratory models.

This paper reviews the present state of knowledge of such verifications and describes a method which has been successfully employed at a coastal site in the central English Channel. The procedure involves hindcasting recorded Waverider Buoy wave information from a nearshore region to deep water. A comprehensive coverage of wind data has been utilised to provide the offshore wave approach direction.

Wave orthogonals have then been tracked inshore and the breaking wave heights and directions compared with observed data.

The results show reasonable comparison where the waves are free from diffraction. However, for oblique wave attack, diffraction around headlands produces evident anomalies.

1 INTRODUCTION

In many coastal or marine engineering problems wave refraction models are employed to determine the wave pattern throughout the nearshore region for a range of offshore wave conditions. But they are by no means precise tools and if the wave refraction model is to play an important role, then some critical assessment of its validity is needed. In many cases small variations of predicted wave height and direction from those actually occurring can produce quite different results. In the present case, the wave refraction model was to be used to make estimates of longshore drift but similar applications are made for design and site selection of harbours, breakwaters and offshore structures (Skovgaard and Bertelsen, 1974).

There are few references to the verification of a wave refraction model utilising field data. In the majority of cases the computed height and direction of orthogonals are compared with known analytical results or correlated with laboratory data. However, an important question is how well a real sea spectrum of wave frequencies, heights

-
1. Post-doctoral Researcher, Department of Civil Engineering, University of Southampton, UK.
 2. Senior Lecturer, Department of Civil Engineering, University of Southampton, UK.

and directions can be approximated by a single selected frequency and direction in a wave refraction model.

More recently, the direction of wave trains has been observed from radar stations and related to computed wave patterns. Such an instrument was not available in the present instance and, in any case, this would not provide information regarding wave heights. Wave directions may also be examined on aerial photographs, but such flights are seldom made in high wind and hence wave conditions when they would be of most value. Three sets of aerial photographs have been obtained for the region concerned and these were compared with wave patterns from the wave refraction model. However, they do not verify the model and in fact result in more questions than answers.

Having reviewed some of the methods described above, it was decided that a new technique using actual field data was required. This was achieved utilising the wave recordings obtained from a Waverider Buoy stationed near the centre of the modelled area and daily beach observations of breaking wave height and direction. The results of this study also provided useful information regarding the relative accuracy of computed wave directions and heights for waves with varying shoreline approach angles.

2 WAVE REFRACTION DIAGRAMS

The plotting of wave refraction diagrams is fairly commonplace in most countries of the world. Early procedures were to employ graphical techniques (Johnson et al, 1948), although, today, computers are almost invariably employed.

The method of wave refraction has been considered in detail by Henderson and Webber (1979(a)). Briefly wave refraction is analogous to the refraction of other types of wave such as light and sound. In these circumstances for a parallel contoured seabed Snell's Law is applicable where

$$\frac{c_1}{c_2} = \frac{\sin \alpha_1}{\sin \alpha_2} \quad (1)$$

where c_1 , c_2 are wave celerities at locations 1 and 2, and α_1 , α_2 are the corresponding angles made by the wave crest with the bed contour.

With a knowledge of seabed depths the refraction behaviour may be analysed and plotted in the form of a diagram.

Wave heights may be obtained by considering that the rate of transmission of energy remains constant between adjacent orthogonals. Thus, by equating wave power at the two locations, it follows that:

$$\frac{\rho g}{8} H_1^2 b_1 c_{g1} = \frac{\rho g}{8} H_2^2 b_2 c_{g2} \quad (2)$$

$$\text{or} \quad \frac{H_1}{H_2} = \left[\frac{b_1}{b_2} \right]^{\frac{1}{2}} \left[\frac{c_{g1}}{c_{g2}} \right]^{\frac{1}{2}} \quad (3)$$

$$\text{or} \quad \frac{H_1}{H_2} = K_R K_S \quad (4)$$

where K_R , the coefficient of refraction is $(b_1/b_2)^{\frac{1}{2}}$
and K_S , the coefficient of shoaling is $(c_{g1}/c_{g2})^{\frac{1}{2}}$

Thus, it is possible to evaluate all the wave characteristics at any point in the refraction diagram, which may, if desired, be related to the incident wave height H in deep water. But in this procedure certain assumptions are made:

- (i) waves are of constant period, small amplitude and monochromatic, so that linear wave theory is applicable.
- (ii) direction of wave advance is perpendicular to the wave crest.
- (iii) changes in the bed topography are gradual.
- (iv) effects of currents, local wind and reflection from bed or shoreline are negligible.
- (v) wave energy is confined between orthogonals and remains constant; thus there is no viscous dissipation of energy.

Consequently, the refraction analysis is more appropriate to long period swell than it is to short crested storm waves. On the other hand, the refraction diagram occupies a relatively greater area with consequently more scope for minor divergencies.

3 METHODS OF VERIFICATION

3.1 Analytical

The direction and height of wave orthogonals passing over regular known bed forms can be derived from the governing equation. A commonly used cross-section is a uniformly sloping bed with parallel contours as shown in Fig. 1 with the resulting orthogonal propagation. For orthogonals impinging at right angles to the bed contours no refraction takes place, while for the oblique path the orthogonals refract to impinge at right angles to the shoreline.

A more severe test for wave refraction is shown in Fig. 2 for movement towards a circular island. In this case the wave orthogonals are again refracted to impinge at right angles to the island surround. The island can be reduced to the extreme of an isolated point of land shown in Fig. 3.

Fig. 4 shows the orthogonal propagation over a circular shoal and the formation of caustics or crossed wave orthogonals in the lee.

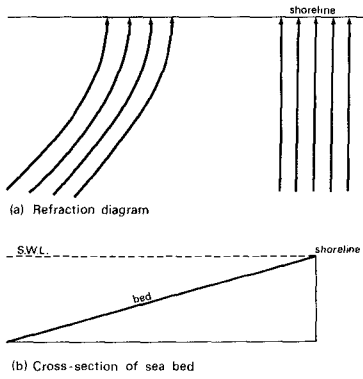


Fig. 1 Wave refraction over a sloping bed with parallel contours

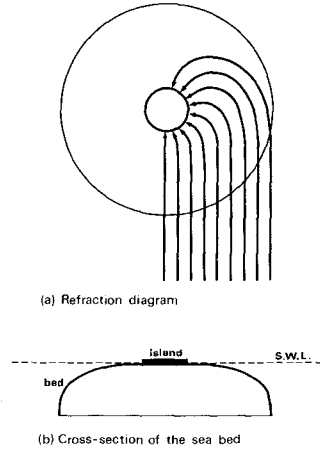


Fig. 2 Wave refraction at a circular island

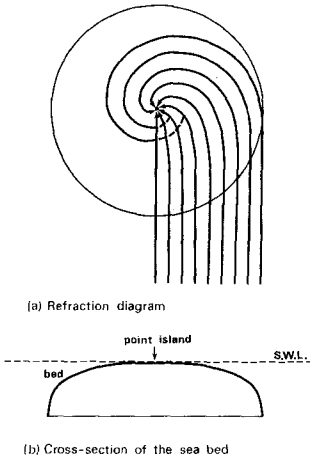


Fig. 3 Wave refraction at a point island

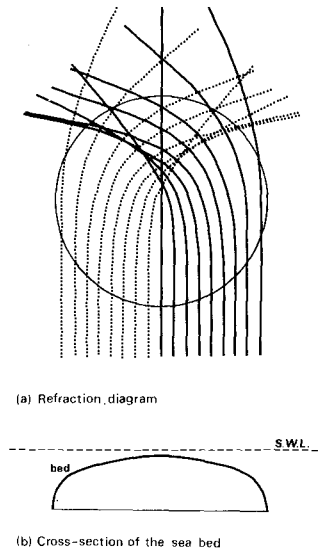


Fig. 4 Wave refraction over a circular shoal

The application of analytical verification was first applied by Arthur (1946) for the direction of wave orthogonals propagating over a number of bed forms. This has since been extended to include wave heights as described by Vastano and Reid (1967), Berkhoff (1972 and 1976), Smith and Sprinks (1975) and Radder (1979).

3.2 Laboratory Models

Laboratory models can be used to simulate wave refraction and enable the recording of directions and heights of wave orthogonals. They have been used to check the analytical solutions described above and computer derived wave refraction diagrams. The most commonly used model is that of a circular shoal first investigated by Pierson (1951). Subsequent studies have included that of Chao and Pierson (1970), Ito and Tanimoto (1972), Whalin (1972) and Berkhoff (1976).

3.3 Radar Observations

Radar observations can be used to identify wave patterns and hence verify the directions of wave orthogonals produced in a refraction diagram. However, radar images cannot be used to estimate wave height.

The use of radar to observe wave trains was described by Oudshoorn (1960), Ijima et al (1964), Loewy et al (1976) and Mattie and Harris (1978).

3.4 Aerial Photography

If the modelled region has been surveyed by aerial photography then it is often possible to determine the direction of incident waves and compare these with a wave refraction diagram. However, as with radar observations the wave height cannot be derived from aerial photographs.

The seaward limit of the photography is limited by the requirement of a recognisable section of land on the photograph. Flying at greater heights will increase the sea coverage but the wave crests become more difficult to distinguish. A major problem when photographing wind waves is that flights are often postponed in high wind which is when waves are most pronounced. This limits the applicability of this method for wind wave verification. Swell waves can more readily be photographed in lower wind speeds, but often the sea surface disturbances are so small that they cannot be easily recognised.

Bryant (1974) has shown reasonable agreement between aerial photographs and wave refraction diagrams for a wind wave and a swell wave case. With this exception no other such comparisons between aerial photography of real sea waves and wave refraction diagrams could be found in the published literature.

3.5 Observed and Measured Wave Data

Although radar observations and aerial photographs can be used

to validate the directions of computed wave orthogonals, the verification of wave heights cannot be made for the case of real sea data. Few references to this topic exist but it appears to be a problem which is undergoing current investigation.

Bryant (1979) has shown a reasonable correlation between breaker wave heights for long period, unidirectional swell waves in Broken Bay, Australia. Offshore wave height was recorded by a Waverider Buoy 30 km from the shoreline, while deep water wave direction was measured at the Buoy. Data for wind waves was not analysed in their study.

King and Hardcastle (1980) refracted a Pierson-Moskowitz wind wave spectrum from deep water and compared this to measured wave heights at three shoreline target areas in Start Bay, UK. Offshore wave height was obtained from a Waverider Buoy located 6 km from the coastline and deep water direction was provided by radar observations. The comparisons between computed and measured nearshore wave heights were reasonable, although the method is undergoing further refinement.

4 WAVE RECORDING IN POOLE BAY

From June 1974 to March 1979 waves were recorded by a Waverider Buoy at a coastal location in Poole Bay, central south coast of England. The Buoy was located (Fig. 5) in a water depth of 14 m below chart datum and was approximately 800 m offshore from Southbourne. Wave information was transmitted from the Buoy to a receiver unit at Boscombe Pier approximately 3 km distant, and waves were recorded for 20 minutes every 3 hours. The wave data was analysed by the Tucker-Draper method (Tucker, 1961 and Draper, 1963) to record parameters such as H_s , H_{max} , T_z etc.

Throughout the operation of the Waverider Buoy two or three observations of the breaking wave height and direction were made at the beach each day. The wave height was estimated to the nearest 10 cm by observing the average peak to trough breaking wave height against a groyne with planks spaced 30 cm apart. Due consideration was given to the tidal height at the time of recording such that the breaking waves were observed. Wave direction was recorded to the nearest 1° using a prismatic compass, the angle between the wave crests and shoreline being recorded. The coastline at this location faces almost due south.

5 THE WAVE REFRACTION METHOD

There are a number of wave refraction methods designed for computer application and many of these have been reviewed by Skovgaard et al (1975). In the present case, the Hydraulics Research Station method was employed which computes the direction of wave orthogonals over a grid of water depths covering the region of interest (Brampton, 1977). This method has been extended to include the calculation of refraction and shoaling coefficients at any position along a wave orthogonal.

Two grids of water depths were used in the present analysis as shown in Fig. 6. The coarser offshore grid extended 50 km south of the Bay shorelines to a depth contour of about 60 m. This was the location

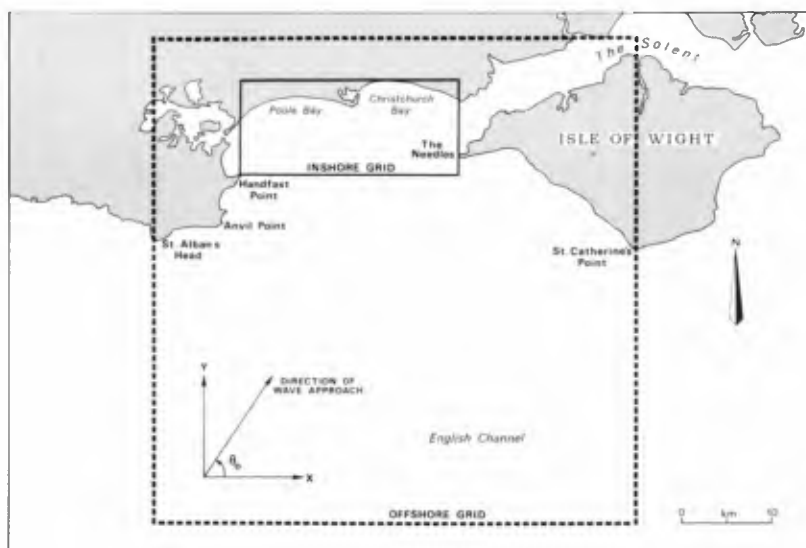


Fig. 6 The two grids of water depths

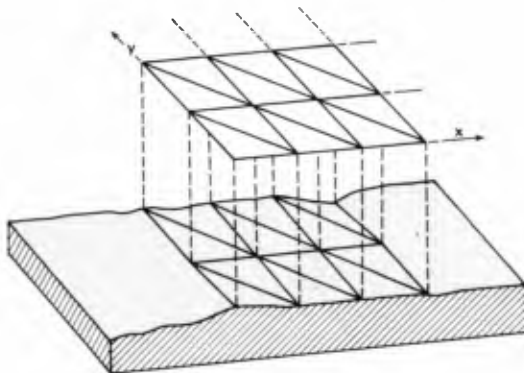


Fig. 7 Schematic representation of sea bed

of deep water for all waves up to 9 seconds period. At approximately the position of the 20 m depth contour, some 10 km from the shoreline, a finer inshore grid was used. Wave orthogonals travelling from deep water over the offshore grid were transferred to the inshore grid over which they moved to the shoreline.

The grids were aligned in the north-south, west-east direction. The bathymetry in the region of interest generally changes more rapidly in a north-south direction and so a rectangular shaped grid element was chosen with greater dimensions in the west-east direction. The offshore grid element size was 1 km west-east by 250 m north-south. For the inshore grid the element size was reduced to 125 m west-east by 31.25 m north-south. The grid of depth values was expressed relative to mean sea level, but a facility was introduced to add or subtract any value to reduce the depths to any tidal condition.

A wave orthogonal originating in deep water with a known period was propagated towards the shoreline. The direction of wave approach was expressed as the anticlockwise angle in degrees made by the wave orthogonal and a positive x-axis as shown in Fig. 6.

Assuming a constant wave period the wave orthogonals having traversed the offshore grid were transferred to the inshore grid before impinging on the shoreline. A new wave orthogonal was then originated in deep water.

The wave orthogonal moved in a series of steps through a set of right-angled triangular elements having vertices at the grid points as shown in Fig. 7. At each step the refraction and shoaling coefficients were computed which permitted the wave height to be calculated using Equation (4) where location 2 is in deep water, thus

$$H_s = K_R K_S H_{so} \quad (5)$$

The wave orthogonals were stopped at the shoreline when the wave height H was related to the water depth, d , by the breaking condition (Munk, 1949)

$$H_s = H_{sb} = 0.78d \quad (6)$$

The breaking wave height H_{sb} , and direction of wave orthogonal approach relative to a positive x-axis, θ_b , were stored. The final wave orthogonal co-ordinates could be adjusted by changing the co-ordinates of the orthogonal at its point of origin in deep water.

It was a simple procedure to change the method of forward progression of wave orthogonals to a back-tracking process. A series of wave orthogonals radiating from a particular point could be transferred in a "fan" to deep water. This enabled wave heights recorded at the Waverider Buoy site to be hindcast using refraction and shoaling coefficients to a deep water wave height for a particular offshore approach angle.

6 COMPARISON WITH AERIAL PHOTOGRAPHS

A number of organisations were approached with regard to obtaining aerial photographs of the region under study. The only available photographs were the property of the Ministry of Defence and, after inspection, it was apparent that only three flights had yielded recognisable wave patterns from a reasonable portion of the Bays. These had been flown on the 7th July 1959, 6th July 1960 and 20th November 1962. Specimen photographs for 7th July 1959 are shown in Figs. 8 and 9.

The offshore wave approach direction and period were required to simulate the wave patterns on the computer. Since no directional wave data was available it was necessary to estimate this value from wind data, assuming that wind waves would follow the path of the wind.

The mean hourly speed and direction during the day of the flights was available from the Meteorological Office wind station at Calshot, located as shown in Fig. 5. As an example, on 7th July 1959 winds were approximately 12 knots (6 m/s) from a direction of 150° from a positive x-axis for seven hours centred about mid-day. The wave approach angle in deep water was assumed to be from this direction. The significant wave height was estimated using an expression relating U to H_s as described by Henderson and Webber (1979(b)) for this particular site and given by:

$$H_s = 8.26 \times 10^{-3} U^{1.627} \quad (7)$$

for onshore winds greater than 9 knots (4.5 m/s) where U is the wind speed in knots and H_s is in metres.

A scatter diagram (Henderson and Webber 1979(c)) was used to show that the estimated value of H_s of 0.5 m, in this case, was associated with an upward zero crossing wave period, T_z , of 4.5 s.

Fig. 10 shows the computer simulated wave orthogonals for a wave period of 4.5 s and an offshore approach angle of 150° from a positive x-axis.

When Figs. 8 and 9 are compared with Fig. 10 reasonable comparability can be seen at locations where wave crests can be identified on the aerial photographs. The wave direction throughout the modelled area and at the shoreline are well depicted by the refraction diagram with the exception of the "shadow region" in Christchurch Bay. In this area, wave diffraction has occurred at the Needles bringing more energy into the Bay than is shown on the refraction diagram which ignores the effects of diffraction. Regions of crossed wave orthogonals can be identified from the aerial photographs in approximately the same positions as those in the refraction diagram.

A comparison of the results of 6th July 1960 and 20th November 1962 for approach angles from the south-west give similar results. Fig. 11 shows the refraction diagram modelling conditions on 6th July 1960 and it is evident that, without diffraction, no disturbances in



Fig. 8 Aerial photograph for 7th. July 1959 (British Crown Copyright Reserved / D.O.E. Photograph)



Fig. 9 Aerial photograph for 7th. July 1959 (British Crown Copyright Reserved / D.O.E. Photograph)

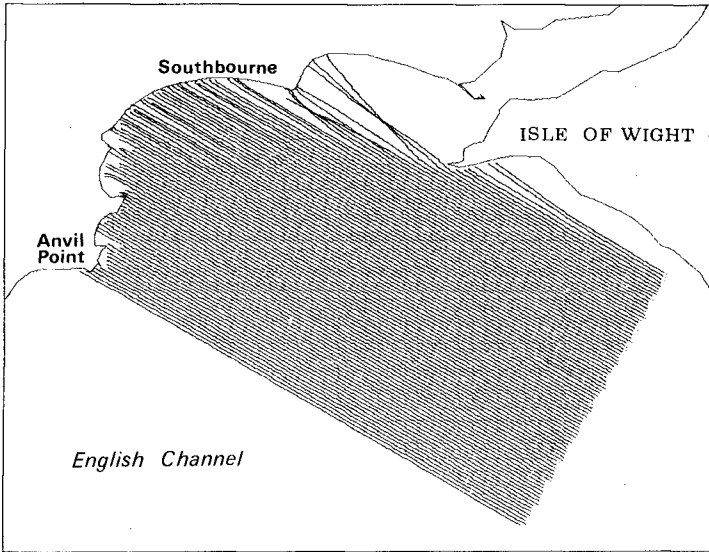


Fig. 10 Computer simulated wave orthogonals for 7th. July 1959

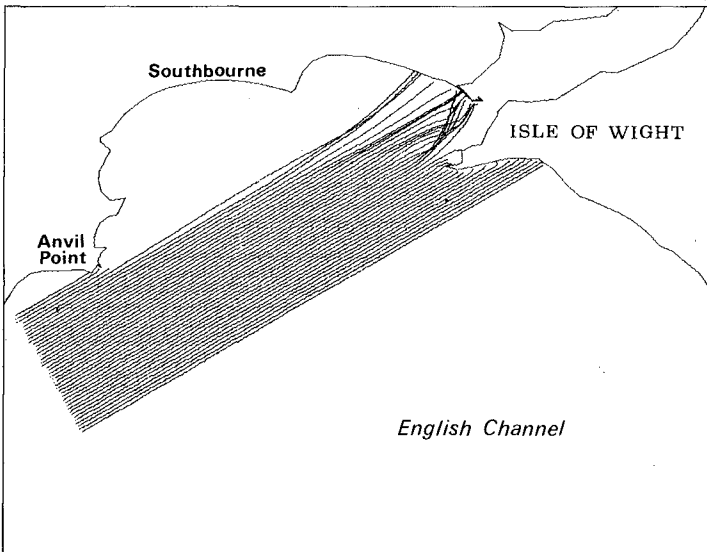


Fig. 11 Computer simulated wave orthogonals for 6th. July 1960

the lee of the headland at Anvil Point are predicted - a feature contrary to actual conditions shown in the aerial photographs.

Although the general conclusions noted above are useful, no detailed analysis has been possible. The aerial photographs are difficult to interpret because the sea surface is reasonably calm and no information is given concerning the variation of the angle at the shoreline as compared with those predicted in the model. In addition, as noted above, no indication of the comparison of wave height values is given. The aerial photographs have, therefore, provided little confidence in the refraction diagram especially in the important region at the shoreline.

7 VERIFICATION UTILISING RECORDED AND OBSERVED WAVE DATA

The aerial photographs having provided only some general indications as to the applicability of the wave refraction model and with no radar observations available, it was necessary to verify the refraction model using some alternative procedure. The method adopted made use of the recorded Waverider Buoy data, the observed breaking wave data and wind information from local Meteorological Office Stations as well as observed winds from coastguards and other personnel.

Listed tables of recorded wave parameters from the Waverider Buoy were inspected on a daily time basis. To avoid the difficulties of simulating swell waves with regard to offshore direction and in an attempt to select unidirectional wind wave trains only, limitations were placed on data that was considered of use in the present analysis. These were:

- (1) Consecutive values of H_s must be rising from a sea state with H_s less than 0.5 m. Values of H_s must return to below 0.5 m before data is considered.
- (2) The values of H_s must exceed 1 m.
- (3) It was evident that the maximum available water depth at the beach site, taking into account tidal variation, was 2.5 m. Hence the value of H_s should be less than 2.0 m.
- (4) A beach observation of breaking waves must have been made at approximately the same time as the data recording from the Waverider Buoy.

A total of 76 records were classified as having satisfied these conditions. The data available for each record for a known day and time consisted of the values of H_s and T_z at the Waverider Buoy site and the observed breaking wave height, H_{bo} and breaking wave angle, θ_{bo} .

At the particular time of each of these records, wind data from six sources was considered in detail as shown in Fig. 5. Portland Bill, Hurn and Calshot Spit are authoritative Meteorological stations recording mean hourly wind speeds and directions. Anvil Point wind data, recorded at the Lighthouse Station, consisted of direction estimated by compass and speed measured by an anemometer at three hourly intervals corresponding to the recording of wave data by the Waverider Buoy. The Bournemouth Pier data consisted of an estimated direction and speed at

approximately mid-day. The Southbourne data was recorded by the wave observer and comprised wind direction and speed.

Utilising this wind data a fairly comprehensive picture of the wind field was available. With consideration given to the fluctuation of wind direction over the preceding six hours, it was possible to estimate the offshore approach angle of the wind to the nearest 10° . With the conditions listed above, the waves were assumed to follow the wind thus providing the vital offshore wave approach direction, θ_o .

For a particular comparison, the recorded H_s was hindcast to deep water using values of K_R and K_S , and to correspond to the correct angle θ_o . The wave period was assumed constant and equal to T_z . This yielded the deep water significant wave height H_{s0} . The grid depths were adjusted to be equivalent to the tidal level at the time of the comparison. For some of the more acute angles (e.g. $\theta_o = 30^\circ$) it was impossible to track the wave orthogonals towards the shoreline from deep water and obtain sufficient refraction for the waves to impinge at the correct location. In such cases the wave orthogonals were started within the Bays and so the resulting waves would be more locally generated.

With values of H_{s0} , T_z and θ_o wave orthogonals were run at an offshore spacing of 50 m until they were stopped at the breaking condition. Provided they had reached the correct location at the shoreline, a region of 250 m width at the Southbourne beach observer site, the values of H_{sb} and θ_b were stored and averaged.

These wave parameters were compared with the observed values of breaking wave height, H_{b0} (equivalent to the significant wave height at breaking) and the breaking wave approach angle θ_{b0} .

8 COMPARISON OF BREAKING ANGLES

The observed (θ_{b0}) and computed (θ_b) breaking angles made by the wave orthogonals with a positive x-axis at the shoreline have been plotted in Fig. 12.

There are three interesting portions to the graph:

- (1) For angles of θ_{b0} between 76° and 100° there is reasonable agreement between the two values with differences of 3° at the most.
- (2) For angles of θ_b less than 90° the value of θ_b is less than θ_{b0} by an average of 3.6° , although variations of up to 14° are illustrated. This suggests that the real sea waves undergo greater deviation than is predicted in the model, such that the wave crests are more parallel to the shoreline at breaking.
- (3) For angles of θ_b greater than, or equal to 90° , the value of θ_b is greater than θ_{b0} by an average of 7.2° although individual points differ by as much as 20° . A similar implication to that in (2) can be made in that the modelled orthogonals are more perpendicular to the coastline at breaking.

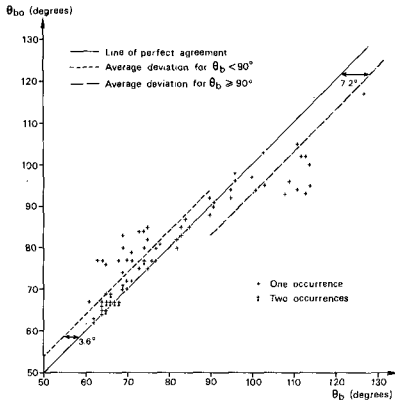


Fig. 12 A Comparison of observed and predicted breaking approach angle

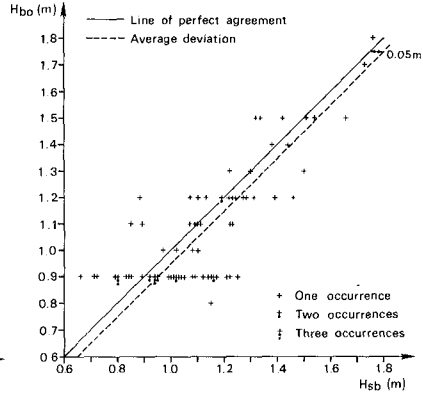


Fig. 13 A Comparison of observed and predicted breaking wave height

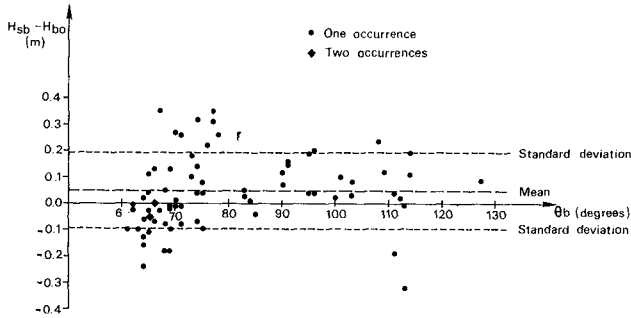


Fig. 14 The difference between predicted and observed breaking wave height as a function of predicted breaking approach angle

These results may indicate that the omission of diffraction effects produce modelled wave orthogonals which undergo less movement than is recorded in the field. This is most apparent when wave orthogonals enter the Bay area at oblique angles, there being only minor deviations for approach angles close to due south. It appears that wave orthogonals are modelled more accurately with westerly than easterly components, probably because of the more complex bed topography and greater occurrence of shoals for waves from easterly directions.

It should, of course, be noted that the method of verification is subject to certain inaccuracies, especially with regard to the prediction of the offshore approach angle θ_0 which was approximated to the nearest 10° .

9 COMPARISON OF BREAKING WAVE HEIGHTS

Fig. 13 shows a plot of the observed (H_{b0}) and computed (H_{sb}) breaking wave heights. There is a fair degree of scatter of the points but, on average, values of H_{sb} are 0.05 m greater than H_{b0} .

In Fig. 14 variations between H_{sb} and H_{b0} have been plotted against θ_b . Also shown is the mean of the wave height difference and the standard deviation. The graph shows that for values of θ_b close to due south the wave height values are more comparable but that greater deviations occur as the approach angles become more oblique. This confirms the comments already made in that for approach angles close to due south when diffraction effects are least, the model reasonably predicts conditions at the shoreline. However, for orthogonal approach directions with westerly or easterly components there is a lateral shedding of wave energy, resulting in a smaller wave height at the shoreline than is predicted by the model.

10 DISCUSSION

Already a number of possible inaccuracies have been suggested but it is considered that the model input data was expressed as precisely as was possible without additional instrumentation. One of the major sources of error was in obtaining an offshore approach angle. The method described using incident wind direction appears to have provided a reasonably good value but there are no data to confirm this.

A further study was undertaken to give an indication of the effect of grid size on the angle of approach of the breaking waves. The inshore grid was made sixteen times coarser by increasing the element size from 125 m by 31.25 m to 1000 m by 250 m. The effect for a variety of offshore approach angles and wave periods was that the breaking wave orthogonal approach angle was increased by less than one degree using the coarser grid. In addition, the same angle showed much smaller differences for a grid four times coarser than the one employed for the analysis. Thus, it seems that the wave refraction model is not unduly affected by changes in grid size for the region considered.

The verification has been undertaken for only a small portion of

the modelled area at a relatively exposed position. An indication has been given of possible correction factors to breaking wave direction and height to bring the model more in line with real wave conditions. However, it would be very difficult to predict similar correction factors for other locations in the modelled region. Certainly the situation in Christchurch Bay would be more complex because water depths are less and a number of shoals exist offshore.

It is, however, evident that wave heights and approach angle parameters could be obtained more accurately which would be of benefit to calculations such as those for longshore drift using the C.E.R.C. formula.

In the present analysis, care has been taken to select recorded and observed data pertaining to unidirectional wave trains. For the more complex situation of superimposed waves from varying directions, no conclusions can be drawn concerning the breaking wave height and direction - apart from the fact that the wave refraction model itself cannot reproduce such conditions.

Although swell waves were not considered in the present analysis it would be possible to undertake a similar comparison provided an offshore approach angle can be assumed or recorded. This is often a fairly simple task since swell waves are unidirectional and, in addition, would be modelled more realistically by the refraction analysis.

Finally, the major criticism of the present model is the omission of diffraction. This is because other phenomena which would change wave height and direction in shallow water are considered to be relatively unimportant in the present case. Friction and percolation effects are probably small and currents, which rarely exceed 0.5 m/s, would cause only minor modifications.

11 CONCLUSIONS

There are few references to the verification of wave refraction models using field data in the published literature, despite the fact that such models are widely used in engineering practice.

A study of aerial photographs show that some general comparisons of wave patterns with refraction diagrams can be made, but that specific details cannot be examined.

A method of verification of such wave refraction models has been described in this paper. It utilises recorded and observed wind and wave data, and could be readily applied in other regions of the world.

At the site it is evident that for unidirectional southerly waves, the observed and computed breaking height and angle are reasonably comparable. For waves approaching with westerly or easterly components, the effects of diffraction are such that the actual wave crests impinge more parallel to the shoreline than is predicted in the model and with slightly lower wave heights. The mean variation in wave breaking angle

is 3.6° and 7.2° for westerly and easterly waves, respectively and a breaking wave height difference of 0.5 m is suggested.

The authors would like to stress the importance of such verifications if wave refraction models are to be used with confidence. There is also a need to verify such models using field data in areas of shoals and complex bed topography where caustics may be formed.

ACKNOWLEDGEMENTS

The authors are indebted to Dr. A.H. Brampton of the Hydraulics Research Station for kindly making available the refraction program and for his subsequent advice. The helpful guidance of Mrs. G. Jewell of the DATS 11 computer section in the Institute of Sound and Vibration Research at Southampton University is gratefully acknowledged.

The Ministry of Defence kindly made available a number of aerial photographs of the region. The Department of the Environment, the consulting engineers, Sir William Halcrow and Partners and Bournemouth Corporation are thanked for permission to utilise data obtained in wave recording and shoreline observation.

There is grateful acknowledgement of the financial support received from the British Council and the Royal Society enabling this paper to be presented.

REFERENCES

- Arthur, R.S. 1946. Refraction of water waves by islands and shoals with circular bottom contours. Trans. Am. Geophys. Union. Vol. 27, No. 2. pp 168-177.
- Berkhoff, J.C.W. 1972. Computation of combined refraction-diffraction. Proc. 13th Conf. on Coastal Eng., Vancouver, Canada. pp 471-490.
- Berkhoff, J.C.W. 1976. Mathematical models for simple harmonic linear water waves: wave diffraction and refraction. Delft Hydraulics Lab. Pub. No. 163. 111 pp.
- Brampton, A.H. 1977. A computer method for wave refraction. Hydraulics Research Station, Wallingford, U.K. Rep. No. INT 172. 48 pp.
- Bryant, E.A. 1974. A comparison of air photograph and computer simulated wave refraction patterns in the nearshore area, Richibucto, Canada and Jervis Bay, Australia. Maritime Sediments. Vol. 10, No. 3. pp 85-95.
- Bryant, E.A. 1979. Comparison of computed and observed breaker wave heights. Coastal Engineering. Vol. 3. pp 39-50.
- Chao, Y.Y. and Pierson, W.J. 1972. Experimental studies of the refraction of uniform wave trains and transient wave groups near a straight caustic. Jour. Geophys. Research. Vol. 77, No. 24. pp 4545-4554.
- Draper, L. 1963. Derivation of a "Design Wave" from instrumental records of sea waves. Proc. Inst. Civ. Eng. Vol. 26. pp 291-304.
- Henderson, G. and Webber, N.B. 1979(a) The application of wave refraction diagrams to shoreline protection problems: with particular reference to Poole and Christchurch Bays. Q. Jour. Engng. Geol. Vol. 12. pp 319-327.
- Henderson, G. and Webber, N.B. 1979(b) Wind-wave relationships for a coastal site in the central English Channel. Estuarine and Coastal Marine Science. Vol. 9. pp 29-39.
- Henderson, G. and Webber, N.B. 1979(c) Summary of wave conditions in Poole Bay, 1975-78. Internal Report of Dept. of Civil Eng., Univ. of Southampton, Southampton, U.K. 38 pp.
- Ijima, J. Takahashi, T. and Sasaki, H. 1964. Application of radars to wave observations. Proc. 11th Japanese Conf. on Coastal Eng. pp 81-88.
- Ito, Y. and Tanimoto, K. 1972. A method of numerical analysis of wave propagation - application to wave diffraction and refraction. Proc. 13th Conf. on Coastal Eng., Vancouver, Canada. pp 503-522.
- Johnson, J.W., O'Brien, M.P. and Isaacs, J.D. 1948. Graphical construction of wave refraction diagrams. U.S. Naval Oceanographic Office, Washington, D.D., U.S.A. H.O. No. 605, TR-2. 45 pp.

- King, H.L. and Hardcastle, P.J. 1980. The evaluation of wave refraction calculations using observed wave data. Draft report of Institute of Oceanographic Sciences, Taunton, Somerset, U.K.
- Loewy, E., Witthaus, K.G., Summers, I. and Maddrell, R.J. 1976. Data collection and analysis for coastal projects. Proc. 15th Conf. on Coastal Eng., Honolulu, Hawaii. pp 43-59.
- Mattie, M.G. and Harris, D.L. 1978. The use of imaging radar in studying oceanwaves. Proc. 16th Conf. on Coastal Eng., Hamburg, Germany. pp 174-189.
- Munk, W.H. 1949. The solitary wave theory and its application to surf problems. Annals of the New York Academy of Sciences. Vol. 51. pp 376-462.
- Oudshoorn, H.M. 1960. The use of radar in hydrodynamic surveying. Proc. 7th Conf. on Coastal Eng., The Hague, The Netherlands pp 59-76.
- Pierson, W.J. 1951. The interpretation of crossed orthogonals in wave refraction phenomena. U.S. Army Corps. of Engineers, Beach Erosion Board. Tech. Mem. No. 21. 83 pp.
- Raddar, A.C. 1979. On the parabolic equation method for water-wave propagation. Jour. Fluid Mech. Vol. 95. pp 159-176.
- Skovgaard, O. and Bertelsen, J.A. 1974. Refraction computation for practical applications. Proc. Int. Sym. on Ocean Wave Measurement and Analysis, New Orleans, U.S.A. 1974. pp 761-733.
- Skovgaard, O., Jonsson, I.G. and Bertelsen, J.A. 1975. Computation of wave heights due to refraction and friction. Jour. of the Waterways, Harbors and Coastal Eng. Div. A.S.C.E. Vol. 101, No. WW1. pp 15-32.
- Smith, R. and Sprinks, T. 1975. Scattering of surface waves by a conical island. Jour. Fluid Mech. Vol. 72. pp 373-384.
- Tucker, M.J. 1961. Simple measurement of wave records. The Dock and Harbour Authority Vol. 42. p 231.
- Vastano, A.C. and Reid, R.O. 1967. Tsunami response for islands; a verification of a numerical procedure. Jour. of Marine Research. Vol. 25, No. 2. pp 129-139.

CHAPTER 6

WAVE SHOALING CALCULATED FROM COKELET'S THEORY.

T. Sakai¹⁾ and J.A. Battjes²⁾

ABSTRACT

Cokelet's numerical non-linear theory for progressive, periodic gravity waves is applied to the two-dimensional shoaling of finite amplitude waves on a beach up to breaking. The shoaling curves so obtained are compared with existing shoaling curves calculated from different finite amplitude wave theories, and with existing experimental data. It was found that the shoaling curves calculated from Cokelet's theory predict higher wave height ratios than other curves. The agreement between the present curves and the experimental results is good except near the breakpoint, where the wave height of the present curves is larger than the experimental wave height.

INTRODUCTION

In recent years, significant developments have taken place in the field of non-linear theories for progressive, periodic gravity waves of constant form.

Schwartz (1974) derived recurrence relations between successive coefficients in a Stokes-type power series, which made it possible to find computer-generated solutions of very high order.

Cokeket (1977) modified the procedure developed by Schwartz. He calculated the wave parameters with great precision, for arbitrary depth-length ratio and arbitrary wave steepness up to the highest wave of permanent form.

For all practical purposes, Cokelet's work can be seen as giving an exact solution to the classical nonlinear irrotational gravity wave problem addressed first by Stokes. It is worthwhile to apply it in situations involving highly nonlinear waves. One such application is given in the present paper, in which Cokeket's results are being used to calculate the two-dimensional shoaling of finite-amplitude waves on a beach, up to breaking.

Shoaling calculations have been made previously by several authors, using one or another approximate non-linear theory of the Stokes type or the cnoidal type, or a semi-numerical theory. The majority of these theories is for periodic waves of permanent form in water of uniform depth.

-
- 1). Associate Professor, Dept. of Civil Engineering, Kyoto University, Sakyo-Ku, 606 Kyoto, Japan (previously, Research Fellow, Dept. of Civil Engineering, Delft University of Technology, The Netherlands)
 - 2) Professor, Dept. of Civil Engineering, Delft University of Technology, Stevinweg 1, Delft, The Netherlands

They are applied locally in water of gradually varying depth on the assumption that the rate of change of the wave parameters is sufficiently small so that its effect on the local wave behaviour is negligible.

While it is difficult to make an a priori assessment of the errors resulting from this assumption, it is reasonable to expect that the approximation improves with decreasing value of the relative depth change within an interval of one wavelength. Thus, provided that the bed slope is sufficiently small, depending on the depth-to-wavelength ratio, it seems reasonable to expect also that the calculated wave height variation in the shoaling process is more nearly exact when it is based on a more nearly exact theory for waves of permanent form in water of constant depth.

The paper is made up as follows. Some relevant points of Cokelet's theory are summarized first. This is followed by an outline of the shoaling calculations, and by a presentation of the results. Finally, a comparison is made with previously published shoaling curves and with experimental data.

The presentation in this proceedings paper is kept rather brief. The reader is referred to Sakai and Battjes (1980) for more details and quantitative formulations.

COKELET'S THEORY

Cokelet (1977) deals with the classical problem of two-dimensional irrotational periodic gravity waves of constant form in a fluid of constant density (ρ) and uniform mean depth (h) and with a stress-free upper surface. The equations describing these conditions are well known and will not be repeated here. Neither shall we describe in detail the method of solution employed by Cokelet.

For given values of ρ and g , the motion is specified entirely by the wave length λ (or, equivalently, the wave number $k = 2\pi/\lambda$), the wave height H (or, equivalently, the semi-wave height $a = H/2$), and the mean depth h . Cokelet makes all quantities dimensionless in terms of k , ρ and g .

An orthogonal system of rectilinear axes is used, with Ox horizontal, positive in the direction of wave advance, and with Oy vertical, positive upward. The reference plane $y = 0$ is chosen near but not in the mean water level. The elevation of the free surface is given by $y = \eta(x,t)$, and that of the sea bed by $y = -d$, so that $d + \bar{\eta} = h$, the mean depth (an overbar denotes a time average).

The Oxy frame of reference is chosen such that the Eulerian mean velocity is zero in all points below the level of the wave troughs. A consequence of this choice is that the mean mass transport in this reference frame is not zero.

A Fourier series development was assumed for the complex velocity potential as a function of the complex coordinate. The Laplace equation and the kinematic boundary conditions at the bottom and the free surface can be made to be satisfied exactly. Satisfaction of the condition of constancy of pressure at the free surface leads to a set of nonlinear algebraic equations which determine the Fourier coefficients completely.

The values of these could be computed on a digital computer up to very high order (>100) and with great accuracy (4 to 6 significant figures). In his calculations, Cokelet used a perturbation parameter ε , whose value ranges from zero for waves of vanishing steepness to 1 for waves of limiting height.

Cokelet has tabulated numerical values of several dimensionless dependent wave parameters as function of ε^2 and the relative depth kd . These parameters include the semi-wave height (a), the square of the phase speed (c^2), and a number of integral properties, such as the mean densities and fluxes of mass, momentum and energy.

For constant relative depth (kd), the wave steepness ka was found to be a monotonic function of ε^2 , but the phase speed and the integral properties appeared to have a maximum for some value of ε^2 a little less than 1, that is, for waves slightly less high than the highest wave possible for the given value of kd . This had been discovered earlier for the solitary wave by Longuet-Higgins and Fenton (1974), and for deep-water waves by Longuet-Higgins (1975).

CALCULATION OF WAVE SHOALING

Assumptions

We consider the classical, idealised wave shoaling problem: a purely periodic, two-dimensional wave motion, an impermeable, rigid sea bed of gentle slope and ending in a dry beach, zero reflection, and zero dissipation. As stated in the introduction, the bed slope is supposed to be sufficiently gentle for the local applicability of a theory for progressive waves of constant form in uniform depth.

The preceding assumptions imply a zero mean mass transport, and constancy of wave frequency and of onshore energy flux.

Adaptations of Cokelet's results

The conditions stated above required an adaptation of Cokelet's results in two ways.

First, we have transformed the results to a new reference frame by adding a vertically uniform mean counter-current, such that the mean mass flux would be zero. The transformed variables are indicated by a prime (e.g. σ' , the wave frequency, and F' , the mean onshore energy flux per unit span).

Secondly, we have non-dimensionalised the results with respect to ρ , g and σ' , instead of ρ , g and k , which had been used by Cokelet. The latter set is less suitable since k varies in the shoaling process, while σ' does not. Variables which have been made non-dimensional in terms of ρ , g and σ' are indicated by an asterisk.

Procedure of shoaling calculation

The onshore energy flux F' , suitably normalized for our purposes, is expressed entirely in terms of dimensionless quantities tabulated by Cokelet as functions of ε^2 and kd . We can write therefore

$$\bar{F}' = \bar{F}'(\epsilon^2, kd) . \quad (1)$$

Since the (dimensional) frequency σ' and energy flux F' are constant in the shoaling process, so is \bar{F}' . It is everywhere equal to its value in deep water, designated with a subscript "o":

$$\bar{F}'(\epsilon^2, kd) = \text{constant} = \bar{F}'_o . \quad (2)$$

The procedure of the shoaling calculation is broadly as follows. A deep-water steepness $H/\lambda = \pi^{-1}ka$ is chosen; this determines the deep-water value ϵ_o^2 , and subsequently all other dimensionless parameters of the motion in deep water, including \bar{F}'_o . For a chosen value of kd , Eq. 2 can be solved for ϵ^2 , as illustrated in Fig. 1. The local values of ϵ^2 and kd in turn determine the local values of all other dimensionless parameters, including ka , $k\bar{\eta}$, and k/k_o , so that the wave height ratio $H/H_o = a/a_o$ is known as a function of relative depth $h/\lambda_o = (d+\bar{\eta})/\lambda_o$, with the chosen value of H_o/λ_o as a parameter.

The variation of \bar{F}' with ϵ^2 and kd was found to be qualitatively similar to that of F of Cokelet's theory itself, in the sense that for each relative depth (kd) it has a maximum (\bar{F}'_m , say) for some value of ϵ^2 less than 1 (see Fig. 1). Eq. 2 has (one) real root(s) for sufficiently large kd -values only, such that the associated maximum of \bar{F}' is at least as large as the given deep-water value \bar{F}'_o (see Fig. 1). In smaller relative depths, where $\bar{F}'(kd) < \bar{F}'_o$, the waves cannot deliver the required energy flux. The point where $\bar{F}'_m(kd) = \bar{F}'_o$ (whose position is determined entirely by \bar{F}'_o , or by the deep-water wave steepness H/λ_o) is provisionally called the breakpoint. The shoaling calculations have been performed only up to that point. In the range of kd where Eq. 2 has two distinct roots in ϵ^2 , the smallest one was taken for reasons of continuity (see Fig. 1).

The numerical values of the functions referred to above were read from Cokelet's tables. In each of these, kd is constant, and ϵ^2 is varied, from 0 to 0.8 with increments of 0.1, and from 0.8 to 1 with increments of 0.01. The tables are given for ten values of e^{-kd} , ranging from 0 (deep water) to 0.9, with increments of 0.1. This grid proved to be too coarse for our shoaling calculations. Using cubic splines (Ahlberg et al, 1967), interpolated values were calculated first with respect to ϵ^2 , with a constant increment of 0.01, subsequently with respect to kd , with a constant increment of 0.02. This was necessary (and sufficient) to obtain a well-defined curve through the calculated points. However, near the breakpoint still greater accuracy with respect to kd is required because of the rapid variation of the wave parameters in that region. To locate the breakpoint, the equation $\bar{F}'_m(kd) = \bar{F}'_o$ was solved for kd to an accuracy of 10^{-4} , using cubic spline interpolations, after which a conventional shoaling calculation yielded the wave height at the breakpoint.

RESULTS

The calculations were performed for different values of the deep-water steepness H/λ_o , ranging from 0.001 to 0.1. The calculated values of H/H_o were plotted versus h/λ_o and a smooth curve was drawn through the points.

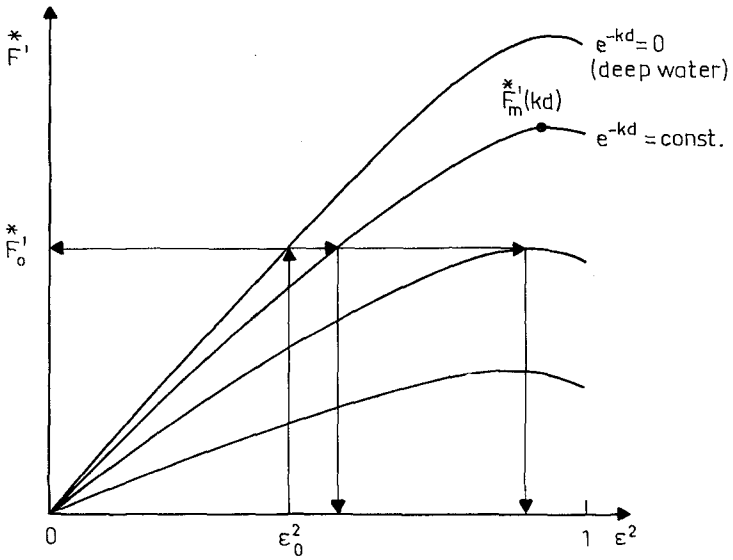


Fig. 1 Sketch illustrating procedure of shoaling calculation

The results are presented in Fig. 2 with a full line. The curve for $H_o/\lambda_o = 0$ is for the linear wave theory. The breakpoints of the non-linear shoaling curves have been connected by a smooth curve. Dashed lines indicate extrapolations.

It should be noted that the quantity λ_o is defined as the wave length in deep water, including non-linear effects. It must be distinguished from the deep-water wave length L_o in the linear approximation. Values of the ratio between the two as calculated by Cokelet (1977), are presented in Table 1, for those values of H_o/λ_o for which the shoaling curves were calculated.

Table 1 Non-linear effect on deep-water wavelength

H_o/λ_o	$0 \leq H_o/\lambda_o \leq 0.02$	0.04	0.06	0.08	0.10
λ_o/L_o	$1 \leq \lambda_o/L_o \leq 1.01$	1.02	1.04	1.07	1.10

DISCUSSIONS

The behaviour of the shoaling curves near the breakpoint deserves a special comment. The curves are seen to have a very steep gradient there. This is a consequence of the fact that (by definition) the energy flux has a maximum (in ϵ^2) at the breakpoint (see Fig. 1). This implies that an infinitesimal variation of ϵ^2 from its value at the breakpoint, at constant value of the energy flux \bar{F} , gives zero variation of kd . Since for constant kd the wave steepness is a monotonically increasing function of ϵ^2 , it follows that the gradient of the shoaling curve becomes infinite at the breakpoint.

The foregoing conclusion contrasts with the assumption of very gradual variation of the wave parameters, which was the justification for the use of a theory for waves of constant form in the calculation of wave shoaling. Notice also that it holds regardless of how small the bed slope is. The use of Cokelet's theory for wave shoaling calculation therefore leads to an internal inconsistency as the breakpoint is approached. Consequently, the behaviour of the waves near that point cannot be inferred from that theory, no matter how small the bed slope may be.

Comparisons with existing shoaling curves

There are several theoretical shoaling curves, calculated by using different finite amplitude wave theories.

Le Méhauté and Webb (1964) calculated shoaling curves of Stokes waves of the third order. Their curves are limited to rather large deep-water wave steepness due to the limitation of applicability of Stokes waves. Iwagaki and Sakai (1967) calculated shoaling curves for rather small deep-water wave steepness and small depth-length ratio. They used an approximate expression of Laitone's cnoidal wave theory of the second approximation which is called "hyperbolic waves". Fig. 2 shows the comparison of the shoaling curves calculated from Cokelet's theory with the above mentioned two kinds of shoaling curves. It is clear that the wave height ratio H/H_o of the present curves increases more rapidly with decreasing relative

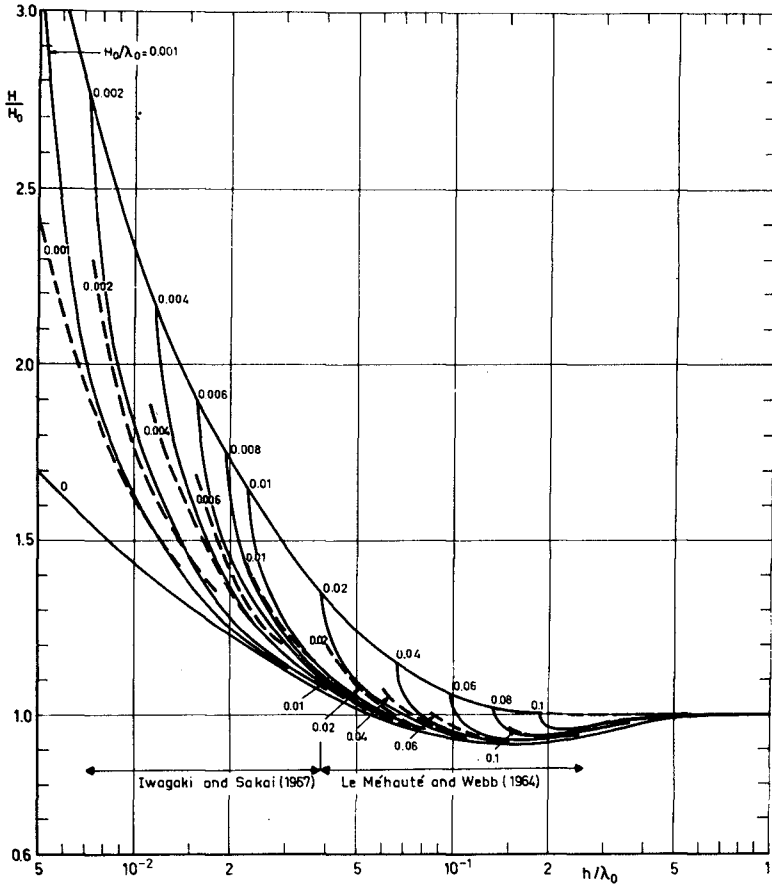


Fig. 2 Full lines: shoaling curves based on Cokelet's theory; values of H/λ_0 are shown.
 Dashed lines, $h/\lambda_0 > 0.04$: shoaling curves after Le Méhauté and Webb (1964); values of H/λ_0 are shown.
 $h/\lambda_0 < 0.04$: shoaling curves after Iwagaki and Sakai (1967); values of H_0/λ_0 are shown.

depth than that of the other two kinds of curves. In general, the difference between the values of the present and other curves becomes large with decreasing water depth. The breaking wave height of the present curves is much larger than that of the other two kinds of curves.

Svendsen and Brink-Kjaer (1972) presented shoaling curves of cnoidal waves. They used Laitone's cnoidal waves of the first approximation (1963). Fig. 3 shows the comparison with their shoaling curves. (The values were read from a table in Skovgaard, Svendsen, Jonsson and Brink-Kjaer, 1974.) In their shoaling curves, the small-amplitude deep-water wave length (L_0) was used, for which reason we have replotted our curves as H/H_0 vs. h/L_0 ; however, we have not found it worthwhile to re-calculate a set of curves so as to obtain slightly different values of the deep-water steepness. The H/H_0 -values given by Svendsen and Brink-Kjaer are considerably smaller than those of the present paper. It must be pointed out in this respect that the former were obtained by matching the calculated energy flux values of the cnoidal theory and the linear theory at $h/L_0 = 0.1$, which gives a discontinuity in wave height. If the wave heights are matched instead, then the calculated H/H_0 -values increase significantly (Svendsen and Buhr-Hansen, 1976).

Shuto (1974) derived several practically useful formulae for wave shoaling from an equation of non-linear long waves including effects of dispersion and variable depth. The trend of Shuto's curves is found to be nearly the same as that of Iwagaki and Sakai's curves. The values of H/H_0 of Shuto's curves (not shown here) are smaller than those of the present shoaling curves.

Yamaguchi and Tsuchiya (1976) calculated shoaling curves from several kinds of finite amplitude wave theories. Their shoaling curves, calculated from Chappellear's (1962) cnoidal wave theory of the second approximation, which predict the highest wave height among their calculated curves, were compared with those of the present paper. The trend of these shoaling curves (not shown here) is also found to be nearly the same as that given by Iwagaki and Sakai.

All of the curves based on approximate shallow-water theories display a smaller rate of wave amplification as the breakpoint is approached, than the curves based on Cokelet's theory. But, as has been pointed out, the application of Cokelet's theory gives an inconsistency near the breakpoint. Therefore, although it may be an exact theory for waves of constant form, its use for the calculation of wave shoaling does not necessarily give more reliable results near the breakpoint than does the use of an approximate theory. Ironically, the inconsistency noted above has not appeared in the existing shoaling calculations, based on more approximate theories for waves of constant form, because in all of these theories the energy flux is an increasing function of wave height, up to the highest wave.

Comparison with experimental data

The theoretical shoaling curves calculated from Cokelet's theory are compared with experimental data. We have selected data published by Svendsen and Buhr-Hansen (1976), since these were obtained in waves which were relatively free from undesired disturbances. Svendsen and Buhr-Hansen's experiments were carried out on a plane beach of 1:35 slope. Six cases of

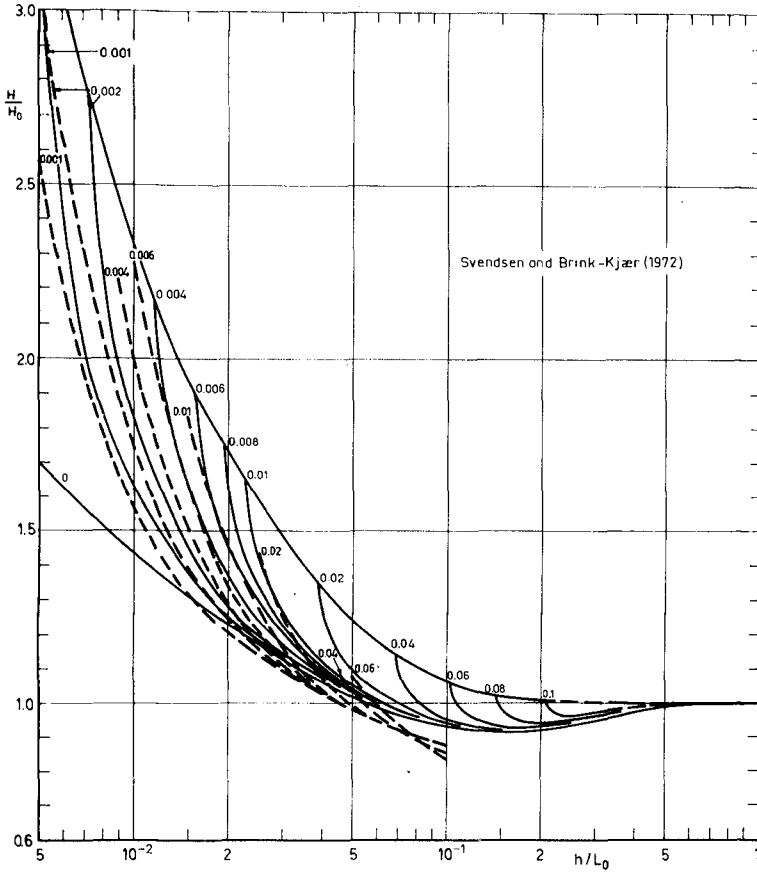


Fig. 3 Full lines: shoaling curves based on Coker's theory; values of H_0/λ_0 are shown.
 Dashed lines: shoaling curves after Svendsen and Brink-Kjaer (1972); values of H_0/L_0 are shown.

variation of wave height were discussed in their paper. These were used for the present comparison. The data were read from data tables which were kindly provided to the present authors.

From the experimental values of wave period, wave height and mean water depth at the toe of the slope, a deep-water steepness (H_0/L_0) was calculated on the basis of the shoaling theory of the present paper.

To estimate the damping due to boundary layers on the bed and the sidewalls, we used Hunt's theory (1952). Although this theory is based on the assumptions of small amplitude and laminar boundary layers, it is thought to be sufficient for an estimate of the damping, which is relatively small anyway. A damping factor C_d (ratio of local damped wave amplitude to local undamped amplitude) was calculated at several points on the slope up to the breakpoint. Its value was found to range from 2% to 7%. The theoretical wave height H was then calculated as

$$H = C_d \cdot H_0 \cdot (H/H_0)_t,$$

where $(H/H_0)_t$ is the wave height ratio of the present theoretical curves, and H_0 is the deep-water wave height determined in the calculation of H_0/L_0 . The still water depth was corrected for wave set-down.

Fig. 4 shows the comparisons between the theoretical wave height variation and experimental results obtained by Svendsen and Buhr-Hansen. The theoretical curve ends at its breakpoint. It is clear that in all cases the agreement with the experimental results is good except near the breakpoint. The theoretical wave height increases more rapidly near the breakpoint than the experimental wave height. The reason for this rapid increase has already been explained.

For completeness' sake, it is noted that Svendsen and Buhr-Hansen (1976) have compared Svendsen and Brink-Kjaer's shoaling curves (1972) to their data. The agreement was found to be very good even near the breakpoint, but only after the original curves were shifted upwards so as to have continuity in wave height at the point of matching with the (linear) theory for deeper water, at the expense of continuity in calculated energy flux.

CONCLUSIONS

Wave shoaling curves were calculated by using Cokelet's (1977) non-linear theory for progressive, periodic gravity waves of constant form in arbitrary uniform depth.

It was found that the shoaling curves calculated from Cokelet's theory show a rapid amplification as the theoretical breakpoint is approached, and that they have an infinite slope at their breakpoints. The reason for this is that the wave energy flux in Cokelet's theory has an intermediate maximum before the highest wave is reached. The rapid variation of wave height is inconsistent with the basic assumption of gradually varying wave parameters. In this meaning, the accuracy of the present curves near the breakpoint is poor.

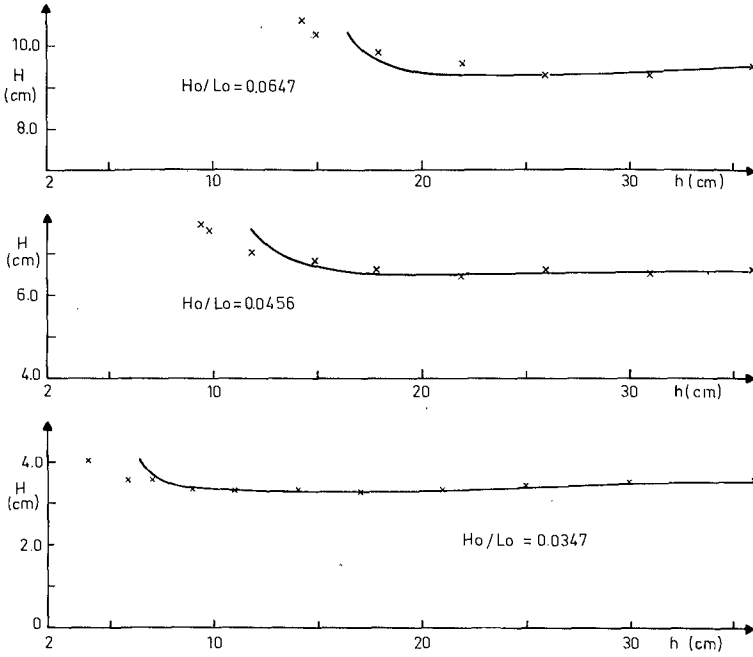


Fig. 4, (1) Comparison of shoaling curves based on Cokelet's theory (corrected for viscous damping) with experimental results of Svendsen and Buhr-Hansen (1976)

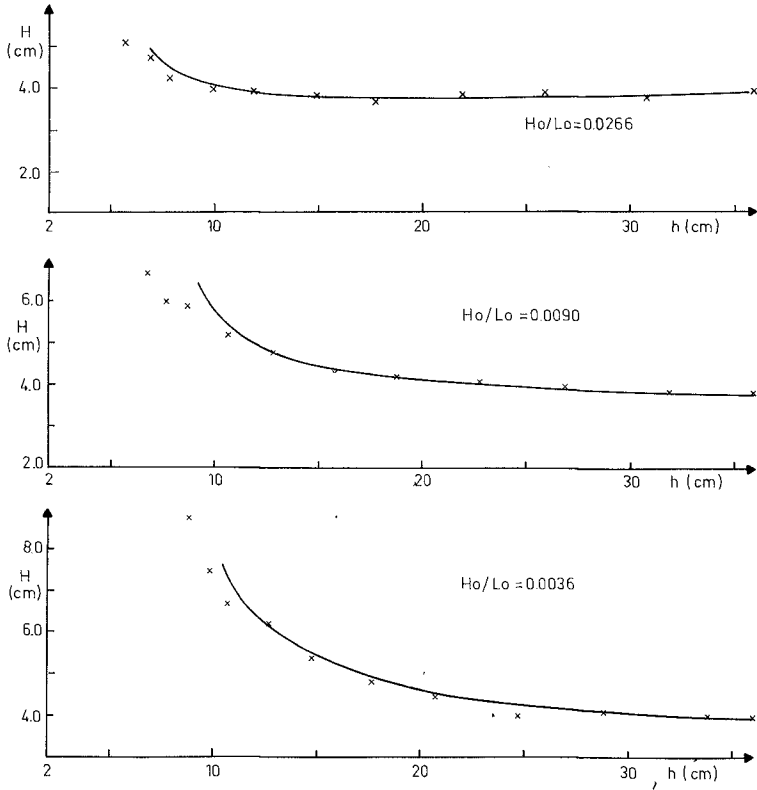


Fig. 4,(2) Comparison of shoaling curves based on Cokelet's theory (corrected for viscous damping) with experimental results of Svendsen and Buhr-Hansen (1976)

The shoaling curves calculated from Cokelet's theory were compared with five kinds of existing shoaling curves calculated from different finite amplitude wave theories: Le Méhauté and Webb (1964), Iwagaki and Sakai (1967), Svendsen and Brink-Kjaer (1972), Shuto (1974), and Yamaguchi and Tsuchiya (1976). The curves of the present paper showed the largest amplification for all initial steepnesses and relative depths. However, except for the region near the breakpoint, the differences between most of the existing curves used in the comparison, and those from the present paper, are relatively minor.

ACKNOWLEDGEMENTS

The authors wish to express their gratitude to Dr. E.D. Cokelet, who kindly provided tables of interpolated values of quantities of his theory, which were useful in the first stage of this study, and to Dr. Ib.A. Svendsen, who gave unpublished tables of experimental data. Acknowledgement is also due to Mr. S. de Boer of the Department of Civil Engineering, Delft University of Technology, who assisted in the computer work. Finally, the first author wishes to thank the Delft University of Technology for granting him a Research Fellowship.

REFERENCES

- Ahlberg, J.H., Nilson, E.N. and Walsh, J.L. (1967) *The Theory of Splines and Their Applications*. New York, Academic Press.
- Chappelear, J.E. (1962) Shallow-water waves. *J. Geophys. Res.*, 67, 12, pp. 4693-4704.
- Cokelet, E.D. (1977) Steep gravity waves in water of arbitrary uniform depth. *Trans. R. Soc. Lond.* 286, A1335, pp.183-230.
- Hunt, J.N. (1952) Viscous damping of waves over an inclined bed in a channel of finite width. *La Houille Blanche*, pp.836-842.
- Iwagaki, Y. and Sakai, T. (1967) On the shoaling of finite amplitude waves. *Proc. 14th Conf. Coastal Eng. Japan*, pp.1-7 (in Japanese).
- Laitone, E.V. (1963) Higher approximation to non-linear water waves and the limiting heights of cnoidal, solitary, and Stokes' waves. *Tech. Memo. Beach Erosion Board*, 133.
- Le Méhauté, B. and Webb, L.M. (1964) Periodic gravity waves over a gentle slope at a third order approximation. *Proc. 9th Conf. Coastal Eng.*, pp.23-40.
- Longuet-Higgins, M.S. and Fenton, J.D. (1974) On the mass, momentum, energy and circulation of a solitary wave, II. *Proc. R. Soc. Lond.* A340, pp. 471-493.
- Longuet-Higgins, M.S. (1975) Integral properties of periodic gravity waves of finite amplitude. *Proc. R. Soc. Lond.* A342, pp.157-174.

- Sakai, T. and Battjes, J.A. (1980) Wave shoaling calculated from Cokelet's theory, to appear in Coastal Engineering, 4, 1, Aug. 1980.
- Schwartz, L.W. (1974) Computer extension and analytic continuation of Stokes expansion for gravity waves. J. Fluid Mech., 62, pp.553-578.
- Shuto, N. (1974) Non-linear long waves in a channel of variable section. Coastal Eng. in Japan, 17, pp.1-12.
- Skovgaard, O., Svendsen, I.A., Jonsson, I.C. and Brink-Kjaer, O. (1974) Sinusoidal and cnoidal gravity waves. Formula and tables. Inst. Hydrodyn. and Hydraulic Eng., Tech. Univ. of Denmark.
- Svendsen, I.A. and Brink-Kjaer, O. (1972) Shoaling of cnoidal waves. Proc. 13th Conf. Coastal Eng., pp.365-383.
- Svendsen, I.A. and Buhr-Hansen, K. (1976) Deformation up to breaking of periodic waves on a beach. Proc. 15th Conf. Coastal Eng., pp.477-496.
- Yamaguchi, M. and Tsuchiya, Y. (1976) Wave shoaling of finite amplitude waves. Proc. 15th Conf. Coastal Eng., pp.497-506.

CHAPTER 7

A SURVEY OF "RANDOM" WAVE GENERATION TECHNIQUES

by J. Ploeg* and E.R. Funke**

Techniques of producing waves in hydraulic models and laboratory flumes have evolved from the simple electrical-mechanical technique of some 15 years ago, to the present sophisticated hydraulic-electric servo systems, controlled by on-line computers and capable of producing a large number of different types of sea states. An accurate definition of the required sea state has become very important, since it has been shown that different types of wave trains, although all having the same significant wave heights and periods, can produce large differences in the results of model tests. Even a specification of the input spectrum, including all relevant spectral parameters, is not sufficient. The occurrence of wave groups, for instance, has to be defined separately. Table 1 illustrates which sea state parameters (A-E) need to be defined and controlled in the laboratory for different types of model studies (1-9). This is just shown as an example, and does not pretend to be a definitive statement.

There exists presently a great variety of different techniques and methods to produce irregular waves and there is no assurance that testing the same model in different laboratories will give similar results. As a first step to address this problem, it was thought to be useful to determine the variety (or perhaps similarity) of all laboratory wave generation systems presently used. A discussion with representatives of a number of hydraulics laboratories and ship towing tanks in the spring of 1979 led to the organisation of a survey of wave generation and analysis systems. The results of the survey are shown in the same format as the questionnaire. A list of all institutes which participated is also included.

Summarizing the results of the survey is impossible within the text of this paper. A general conclusion to be drawn is, that there is a surprisingly large uniformity in the equipment and facilities used for modelling waves. Also, for the suggested definition of sea state, it would not be difficult to list the generally accepted parameters:

$$(S_I(f), S_R(f), f_p, H_{m0}, \epsilon_s, Q_p \text{ and } H_{z,max}, T_{H_{z,max}}, H_{1/3}, \bar{T}_z)$$

Many laboratories mention wave grouping, but only three institutes suggest a definition of the grouping parameter.

It appears that the next logical step has to be a draft proposal of a standard set of methods of wave generation techniques and data analysis methods, based on the results of this survey. The discussion of this presentation at the conference seemed to suggest to involve an existing international organisation, such as the IAHR, to produce such a draft. Other laboratories will hopefully perceive the need for an agreement on standard wave generation techniques and analysis methods, and actively cooperate with this project.

*Head and **Senior Research Officer, Hydraulics Laboratory, National Research Council of Canada, Ottawa, Canada.

SEA STATE PARAMETERS IN COASTAL AND MARINE ENGINEERING STUDIES

TYPES OF STUDIES	SEA STATE PARAMETERS				
	A	B	C	D	E
1. STABILITY OF RUBBLE MOUND BREAKWATERS	X	X	X	X	X
2. FORCES AND PRESSURES ON OFFSHORE STRUCTURES	X	X	X	X	X
3. HARBOUR RESPONSE	X	X		X	
4. STABILITY OF FLOATING STRUCTURES	X		X	X	X
5. RESPONSE OF FLOATING STRUCTURES	X	X		X	X
6. STRESSES IN SHIP HULLS	X	X	X	X	X
7. MOORING FORCES FOR MOORED VESSELS	X	X	X	X	X
8. BEACH PROCESSES	X	X		X	
9. WAVE ENERGY EXTRACTION	X	X	X	X	X
A. TOTAL SPECTRUM, $S(f)$; PEAK FREQUENCY, f_p ; PEAK PERIOD, $T_p = 1/f_p$; RMS = $\sqrt{m_0}$; BROADNESS FACTOR					
B. INCIDENT AND REFLECTED SPECTRA, $S_I(f)$ AND $S_R(f)$; COEFFICIENT OF REFLECTION $C_R(f)$					
C. WAVE HEIGHT DISTRIBUTION PARAMETERS, H_s, H_{MAX} ; PERIODS, $T_{H_s}, T_{H_{MAX}}$					
D. SIWEH, $E(t)$; AVERAGE WAVE ENERGY, \bar{E} ; SIWEH SPECTRAL DENSITY, $e(f)$; PEAK FREQUENCY OF e , f_{pe} ; GROUPINESS FACTOR, GF					
E. WAVE SLOPE DISTRIBUTION, $D(S)$; MAXIMUM WAVE SLOPE, S_{MAX}					

TABLE 1

DATA REPORT OF QUESTIONNAIRES ON
WAVE GENERATION AND ANALYSIS SYSTEMS

GENERAL

Total number of questionnaires sent out to Hydraulics Lab: 184
 Total number of replies received from Hydraulics Labs: 98 (53%)
 Total number of questionnaires sent out to Ship Towing Tanks: 74
 Total number of replies received from Ship Towing Tanks: 44 (59%)
 Number of institutes included in replies which reported
 not having wave making facilities: Hydraulics Labs: 15
 Ship Towing Tanks: 9

The 83 Hydraulics Labs with wave making facilities reported a total of:

176 flumes equipped for regular waves
 79 flumes equipped for irregular waves
 15 flumes equipped for transient waves
 112 basins equipped for regular waves
 39 basins equipped for irregular waves
 7 basins equipped for transient waves.

The 35 Towing Tanks with wave making facilities reported a total of:

51 flumes equipped for regular waves
 31 flumes equipped for irregular waves
 13 flumes equipped for transient waves
 22 basins equipped for regular waves
 18 basins equipped for irregular waves
 6 basins equipped for transient waves.

A. TANKS AND WAVE MACHINES

Note: A distinction was made between wave flumes and wave basins in analyzing the questionnaires. When the length of a tank is larger than 5X the width it was classified as a "Flume"; when the length of a tank is smaller than 5X the width, it was classified as a "Basin". Also, the ranges of tank dimension were set at different limits for Hydraulics Laboratories and Ship Towing Tanks.

HYDRAULICS LABORATORIESFlumes:

Width		Length		Depth	
Range (m)	Number	Range (m)	Number	Range (m)	Number
<0.99	85	<24.9	47	<0.49	18
1.0-2.99	58	25.0-49.9	79	0.5-0.99	78
3.0-4.99	29	50.0-99.9	40	1.0-1.99	75
>5.0	13	>100.0	21	>2.0	16

Type of Wave Machines in Flumes (see Fig. 1):

Types	A	B	C	D	E	F	G	H	K	L	M	N	O	P	Q	R	S	T
Number	33	61	5	4	6	0	28	1	3	5	13	7	4	0	7	4	3	2

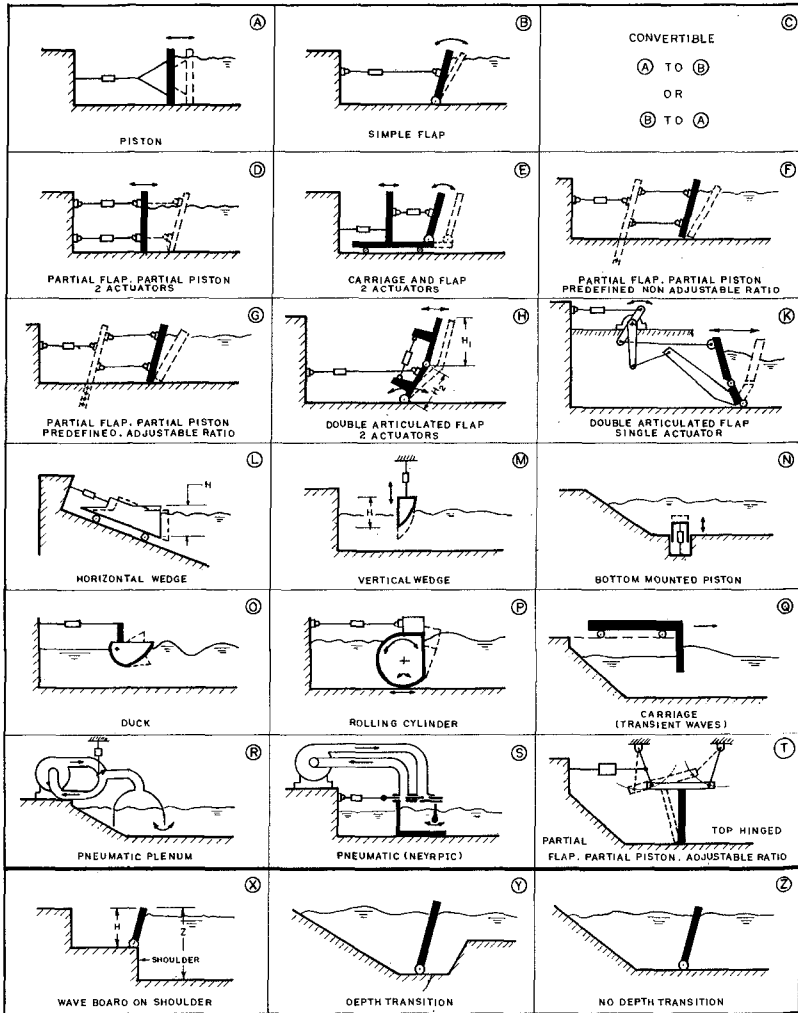


FIG. 1

NATIONAL RESEARCH COUNCIL
HYDRAULICS LABORATORY
OTTAWA, CANADA
JULY 7, 1979

Other Features of Wave Machines in Flumes:

	Fixed	Movable	X	Y	Z	Air	Water
Number	165	20	6	48	128	18	162

Drive	Electric Motor & Gears	Electronic/Electric Servo	Hydraulic/Electric Servo
Number	109	20	57

Features of Flumes:

	Recirculation in tank		Short-Crested Wave Capability		Wind Capability	
	Yes	No	Yes	No	Yes	No
Number	69	118	26	154	50	136

Basins:

Length + Width		Depth	
Range (m)	Number	Range (m)	Number
≤29.9	27	≤0.49	33
30.0-49.9	34	0.5 - 0.74	36
50.0-99.9	50	0.75-0.99	29
≥100.0	8	≥1.0	22

Type of Wave Machines in Basins: (see Fig. 1)

Types	A	B	C	D	E	F	G	H	K	L	M	N	O	P	Q	R	S	T
Number	34	44	4	2	0	1	8	0	3	2	9	4	1	0	2	2	1	3

Other Features of Wave Machines in Basins:

	Fixed	Movable	X	Y	Z	Air	Water
Number	51	71	10	28	83	1	115

Drive	Electric Motor & Gears	Electronic/Electric Servo	Hydraulic/Electric Servo
Number	77	10	35

Features of Basins:

	Recirculation in tank		Short-Crested Wave Capability		Wind Capability	
	Yes	No	Yes	No	Yes	No
Number	46	73	33	85	11	108

SHIP TOWING TANKS:

Flumes:

Width		Length		Depth	
Range (m)	Number	Range (m)	Number	Range (m)	Number
≤4.9	15	≤99.9	20	≤2.9	21
5.0-9.9	21	100.0-199.9	18	3.0-4.9	18
10.0-14.9	13	200.0-299.9	13	5.0-6.9	12
≥15.0	6	≥300.0	4	≥7.0	4

Type of Wave Machines in Flumes: (see Fig. 1)

Types	A	B	C	D	E	F	G	H	K	L	M	N	O	P	Q	R	S	T
Number	1	21	0	2	0	0	2	5	0	0	16	0	0	0	0	7	1	0

Other Features of Wave Machines in Flumes:

	Fixed	Movable	X	Y	Z	Air	Water
Number	48	8	18	1	28	7	39

Drive	Electric Motor	Electronic/Electric Servo	Hydraulic/Electric Servo
Number	23	6	27

Features of Flumes:

	Recirculation in tank		Short-Crested Wave Capability		Wind Capability	
	Yes	No	Yes	No	Yes	No
Number	11	43	7	47	14	40

Basins:

Length + Width		Depth	
Range (m)	Number	Range (m)	Number
≤99.0	12	≤0.99	3
100.0-199.9	10	1.0-1.99	4
200.0-299.9	1	2.0-2.99	6
≥300.0	0	≥3.0	10

Type of Wave Machines in Basins: (see Fig. 1)

Types	A	B	C	D	E	F	G	H	K	L	M	N	O	P	Q	R	S	T
Number	2	10	0	1	0	0	2	1	0	0	5	0	0	0	0	5	0	0

Other Features of Wave Machines in Basins:

	Fixed	Movable	X	Y	Z	Air	Water
Number	19	6	6	1	17	4	16

Drive	Electric Motor & Gears	Electronic/Electric Servo	Hydraulic/Electric Servo
Number	13	3	9

Features of Basins:

	Recirculation in tank		Short-Crested Wave Capability		Wind Capability	
	Yes	No	Yes	No	Yes	No
Number	4	19	5	20	4	19

Hydraulics Laboratories

B. IRREGULAR WAVE GENERATION SYSTEMS

B.1 The following information describes which method of irregular wave generation you employ. Please check one or more of the following systems, adding a W if wind is added to the basic method. Please indicate present practice and/or anticipated practice in future, where applicable. (*78 Laboratories responded in some way.*)

	Now	Future
(a) Harmonic Synthesis:		
(i) by mechanical gear system	15	4
(ii) by special purpose electronic device	8	6
(iii) by computer (other than Fourier transform)	8	12
(b) True Random White Noise (e.g. Thermal or Cosmic) and analog shaping filters	8	7
(c) Pseudo Random Noise:		
(i) by on-line computer	7	14
(ii) by special purpose electronic device	12	10
(d) Reproduction of Prototype Wave Train:		
(i) by punched paper tape	10	7
(ii) by analog magnetic tape	15	9
(iii) by digital magnetic tape	4	5
(iv) by on-line computer	9	22
(e) Synthesis by Fourier Transform Technique:		
(i) by on-line computer	8	18
(ii) by off-line computer	18	15
(f) Frequency Sweep by varying the speed of the actuator drive motor	7	5
(g) Wind Alone	12	5
(h) Other (please specify)		

B.2 The following information defines some of the details of the systems described in B.1. Please check or give details where applicable.

- (a) For harmonic synthesis, give number of discrete frequencies which participate. *Varies from 2 to 1024; mode at (20)*
- (b) Are these frequencies integer multiples of a fundamental component? (+ or -) *14-; 5+*
- (c) Give range of repetition periods of the irregular wave train
 (i) minimum *(40) sec; 0.5 - 3600*
 (ii) typical *(300) sec; 5 - 10800*
 (iii) maximum *(1000) sec; 2 - ∞*
- (d) Is the test period an integer multiple of the repetition period
 (i) always ? (ii) sometimes *19* (iii) never ?

Hydraulics Laboratories

- (e) Do you use compensation techniques for
- (i) the wave board dynamic transfer function (+ or -) 28+; 12-
 - (ii) the servo dynamic transfer function (+ or -) 22+; 17-
 - (iii) the analog low-pass filter (+ or -) 16+; 20-
- (f) If you use time discrete driving signals (i.e. involving digital to analog converters), what is the typical time step rate? 0.01 - 0.2; node at (0.1) sec
- (g) For (f) above, what smoothing do you use?
- (i) analog low-pass filter 20 now; 14 future
 - (ii) straight line interpolator 4 now; 3 future
 - (iii) none 11 now; 2 future
- (h) Do you attempt to control wave steepness by phase control?
- (i) always 1 now; 1 future
 - (ii) sometimes 7 now; 12 future
 - (iii) never 29 now; 5 future

C. DATA ACQUISITION SYSTEM

The following information describes your data acquisition system. Please check or give details where applicable. Please check to indicate present practice and/or anticipated practice in future, where applicable.

- | | Never | | Sometimes | | Every Test | |
|--|------------------------------|--------|-----------|--------|------------|--------|
| | Now | Future | Now | Future | Now | Future |
| (a) What methods of data recording do you employ? | | | | | | |
| (i) Strip-chart recorder | 5 | 1 | 30 | 25 | 26 | 13 |
| (ii) Analog magnetic tape recorder | 6 | 5 | 30 | 22 | 3 | 5 |
| (iii) Digital data logger for off-line analysis | 12 | 8 | 10 | 14 | 4 | 8 |
| (iv) On-line digital computer (please give computer model no.) | 7 | 2 | 24 | 21 | 9 | 13 |
| 10 H.P.; 9 PDP | | | | | | |
| (b) How many wave probes do you employ for: | | | | | | |
| (i) Harbour studies? | Varies from 1-120; node (12) | | | | | |
| (ii) Breakwater studies? | Varies from 1-20; node (3) | | | | | |
| (iii) Beach process studies? | Varies from 1-20; node (6) | | | | | |
| (iv) Offshore fixed structures? | Varies from 1-20; node (5) | | | | | |
| (v) Floating structure studies? | Varies from 2-20; node (5) | | | | | |
| (vi) Others? | | | | | | |

D. DATA ANALYSIS SYSTEM

The following information defines details of the analysis system you use for simulated sea states, as measured in your laboratory tanks. Please indicate present practice and/or anticipated practice in future, where applicable. All notations follow the PIANC report of the International Commission for the Study of Waves.

- | | Never | | Sometimes | | Every Test | |
|--|-------|--------|-----------|--------|------------|--------|
| | Now | Future | Now | Future | Now | Future |
| (a) How frequently do you perform wave analysis? | 3 | 0 | 23 | 14 | 34 | 29 |

Hydraulics Laboratories

	Never		Sometimes		Every Test	
	Now	Future	Now	Future	Now	Future
(b) Do you carry out the analysis by the following techniques						
(i) Visual inspection of graphic records?	5	6	27	19	18	7
(ii) Off-line computer?	8	5	25	20	15	10
(iii) On-line computer?	4	1	20	22	10	16
(c) Which time domain analysis do you normally perform:						
(i) Zero-up crossing?	4	2	21	18	21	19
(ii) Zero-down crossing?	8	6	11	10	5	3
(iii) Other (please specify)						
(d) Which time domain parameters do you derive?						
(i) $H_{Z,1/3}$	4	2	26	15	24	28
(ii) $H_{Z,max}$	5	2	28	18	18	20
(iii) \bar{T}_Z	7	3	22	15	23	21
(iv) $T_{H_Z,1/3}$	10	3	14	12	14	14
(v) $T_{H_Z,max}$	8	3	18	16	9	9
(vi) $c_T^2 = 1 - (\bar{T}_C/\bar{T}_Z)^2$	18	10	9	10	5	8
(vii) Others (please specify)						
(e) Which frequency domain functions and parameters do you derive:						
(i) Fourier transform (periodogram)	9	2	24	22	4	6
(ii) Power spectral density	2	0	27	19	21	18
(iii) F_P (peak frequency)	5	0	22	19	18	17
(iv) $T_P (= 1/F_P)$	5	0	23	18	16	17
(v) $\sigma = \sqrt{JS(f) \cdot df}$	5	0	19	14	21	18
(vi) $H_{m_0} = 4\sigma$	7	0	14	15	16	17
(vii) $T_{m_01} = m_0/m_1$	11	5	18	14	7	7
(viii) $T_{m_02} = \sqrt{m_0/m_2}$	12	4	21	17	5	6
(ix) $\epsilon_S = \sqrt{1 - m_2^2/m_0 m_4}$	12	5	18	18	7	8
(x) Others (please specify) $Q_P = 2/m_0^2 \int_0^\infty f S^2(f) df$						
			Never	Sometimes	Every Test	
(f) Do you describe groupiness? (please specify)	Now	Future	Now	Future	Now	Future
	29	2	15	22	0	4
(g) Do you describe particular wave sequences? (please specify)	26	2	17	26	0	3
(h) Do you derive wave steepness by						
(i) Calculation?	16	0	24	26	6	4
(ii) Measurement?	17	2	18	25	3	3

Hydraulics Laboratories

	Never		Sometimes		Every Test	
	Now	Future	Now	Future	Now	Future
(j) Do you measure structural or beach reflections in the presence of irregular waves?	21	1	24	30	4	9

E. Please comment below on how to define the essential parameters of a sea state.

Ship Towing Tanks

B. IRREGULAR WAVE GENERATION SYSTEMS

B.1 The following information describes which method of irregular wave generation you employ. Please check one or more of the following systems, adding a W if wind is added to the basic method. Please indicate present practice and/or anticipated practice in future, where applicable. (32 Institutes responded in some way.)

		Now	Future
(a) Harmonic Synthesis:	(i) by mechanical gear system	3	1
	(ii) by special purpose electronic device	11	4
	(iii) by computer (other than Fourier transform)	7	11
(b) True Random White Noise (e.g. Thermal or Cosmic) and analog shaping filters		4	1
(c) Pseudo Random Noise:	(i) by on-line computer	3	13
	(ii) by special purpose electronic device	7	7
(d) Reproduction of Prototype Wave Train:			
	(i) by punched paper tape	3	0
	(ii) by analog magnetic tape	16	6
	(iii) by digital magnetic tape	2	2
	(iv) by on-line computer	1	14
(e) Synthesis by Fourier Transform Technique:			
	(i) by on-line computer	3	10
	(ii) by off-line computer	13	4
(f) Frequency Sweep by varying the speed of the actuator drive motor		8	4
(g) Wind Alone		2	2
(h) Other (please specify)			

Ship Towing Tanks

- B.2 The following information defines some of the details of the systems described in B.1. Please check or give details where applicable.
- (a) For harmonic synthesis, give number of discrete frequencies which participate *Varies from 6 to 256; none at (20)*
- (b) Are these frequencies integer multiples of a fundamental component? (+ or -) *6+; 14-*
- (c) Give range of repetition periods of the irregular wave train
 (i) minimum *(40) sec; 2 - 300*
 (ii) typical *(300) sec; 20 - ∞*
 (iii) maximum *sec; 90 - ∞*
- (d) Is the test period an integer multiple of the repetition period
 (i) always *4* (ii) sometimes *11* (iii) never *8*
- (e) Do you use compensation techniques for
 (i) the wave board dynamic transfer function (+ or -) *17+; 5-*
 (ii) the servo dynamic transfer function (+ or -) *16+; 7-*
 (iii) the analog low-pass filter (+ or -) *10+; 6-*
- (f) If you use time discrete driving signals (i.e. involving digital to analog converters), what is the typical step rate? *0.39-1.0; none at (0.1) sec*
- (g) For (f) above, what smoothing do you use?
 (i) analog low-pass filter *7 now; 5 future*
 (ii) straight line interpolator *2 now; 2 future*
 (iii) none *3 now; 0 future*
- (h) Do you attempt to control wave steepness by phase control?
 (i) always *0 now; 1 future*
 (ii) sometimes *6 now; 10 future*
 (iii) never *14 now; 0 future*

C. DATA ACQUISITION SYSTEM

The following information describes your data acquisition system. Please check or give details where applicable. Please indicate present practice and/or anticipated practice in future, where applicable.

	Never		Sometimes		Every Test	
	Now	Future	Now	Future	Now	Future
(a) What methods of data recording do you employ?						
(i) Strip-chart recorder	1	1	10	12	14	5
(ii) Analog magnetic tape recorder	2	1	15	12	10	4
(iii) Digital data logger for off-line analysis	7	4	4	8	4	2
(iv) On-line digital computer (please give computer model no.)	6	3	7	9	10	12

Ship Towing Tanks

- (b) How many wave probes do you employ for:
- (i) Ship motion studies? *Varies from 1-10; none at (2)*
 - (ii) Floating structures studies? *Varies from 1-6; none at (2)*
 - (iii) Fixed structure studies? *Varies from 1-10; none at (2)*
 - (iv) Others?

D. DATA ANALYSIS SYSTEM

The following information defines details of the analysis system you use for simulated sea states, as measured in your laboratory tanks. Please indicate present practice and/or anticipated practice in future, where applicable. All notations follow the PIANC report of the International Commission for the Study of Waves,

	Never		Sometimes		Every Test	
	Now	Future	Now	Future	Now	Future
(a) How frequently do you perform wave analysis?	0	0	5	2	24	20
(b) Do you carry out the analysis by the following techniques						
(i) Visual inspection of graphic records?	0	0	11	7	12	8
(ii) Off-line computer?	1	1	11	10	12	6
(iii) On-line computer?	2	0	4	5	11	16
(c) Which time domain analysis do you normally perform:						
(i) Zero-up crossing?	3	1	9	11	8	2
(ii) Zero-down crossing?	4	1	5	4	1	1
(iii) Other (please specify)						
(d) Which time domain parameters do you derive?						
(i) $H_{z,1/3}$	1	0	9	11	15	7
(ii) $H_{z,max}$	1	0	11	10	11	4
(iii) \bar{T}_z	2	0	11	4	8	3
(iv) $T_{H_z,1/3}$	5	2	4	7	4	2
(v) $T_{H_z,max}$	3	1	7	8	2	1
(vi) $\epsilon_T^2 = 1 - (\bar{T}_c/\bar{T}_z)^2$	5	1	6	8	5	1
(vii) Others (please specify)						
(e) Which frequency domain functions and parameters do you derive:						
(i) Fourier transform (periodogram)	3	1	12	11	5	4
(ii) Power spectral density	0	0	8	5	21	14
(iii) F_p (peak frequency)	2	0	6	6	13	8
(iv) $T_p (= 1/F_p)$	2	0	6	5	14	8

Ship Towing Tanks

	Never		Sometimes		Every Test	
	Now	Future	Now	Future	Now	Future
(v) $\sigma = \sqrt{S(f) \cdot df}$	0	0	8	4	18	12
(vi) $H_m = 4 \cdot \sigma$	1	0	6	4	17	13
(vii) $T_{m01} = m_0/m_1$	2	0	13	8	7	6
(viii) $T_{m02} = \sqrt{m_0/m_2}$	2	0	16	9	6	4
(ix) $\epsilon_s = \sqrt{1 - m_2^2/m_0 \cdot m_4}$	2	0	12	8	9	6
(x) Others (please specify)						
(f) Do you describe groupiness? (please specify)	21	1	1	13	0	4
(g) Do you describe particular wave sequences? (please specify)	14	1	5	13	0	1
(h) Do you derive wave steepness by						
(i) Calculation?	6	0	13	12	4	2
(ii) Measurement?	9	1	8	9	0	1
(j) Do you measure structural or beach reflections in the presence of irregular waves?	19	5	6	9	0	0
E. Please comment below on how to define the essential parameters of a sea state.						

LIST OF INSTITUTES WHICH PARTICIPATED IN
THE SURVEY OF WAVE GENERATION AND ANALYSIS SYSTEMS

Hydraulics Laboratories

Monash University Victoria, Australia	National Research Council of Canada Ottawa, Canada
University of Adelaide Adelaide, Australia	National Water Research Institute Burlington, Canada
State Rivers and Water Supply Commission Victoria, Australia	Université Laval Ste. Foy, Canada
University of New South Wales Manly Vale, Australia	Arctec Canada Ltd, Kanata, Canada
Department of Public Works N.S.W. Manly Vale, Australia	University of Saskatchewan Saskatoon, Canada
Snowy Mountains Engineering Corp. Cooma, Australia	Ontario Hydro Toronto, Canada
University of Tasmania Tasmania, Australia	Universität Hamburg Hamburg, West Germany
University of Melbourne Parkville, Victoria, Australia	Technical University of Berlin Berlin, Germany
University of Western Australia Nedlands, W- Australia	Technischen Universität Braunschweig Braunschweig, Germany
Universiteit te Gent Gent, Belgium	Technical University of Hannover Hannover, Germany
University of Liege Liege, Belgium	Technical University München München, Germany
COPPE/UFRJ - PENO Rio de Janeiro, Brasil	Universität Stuttgart Stuttgart, Germany
HIDROESB - Saturnino de Brito Hydraulic Laboratory Rio de Janeiro, Brasil	Aalborg Universitetscenter Aalborg, Denmark
National Institute for Waterways Research Rio de Janeiro, Brasil	Danish Hydraulic Institute Horsholm, Denmark
Queens University Kingston, Canada	Technical University of Denmark Lyngby, Denmark
Ecole Polytechnique Montreal, Canada	Suez Canal Research Centre Ismailia, Arab Republic of Egypt
	Laboratoire National d'Hydraulique Chatou, France

British Hovercraft Isle of Wight, U.K.	Karnataka Regional Engineering College Surathkal Karnataka State, India
University of Bristol Bristol, England	Motilal Nehru Regional Engineering College Allahabad, India
Wimpey Laboratories Ltd. London, Great Britain	Land Reclamation, Irrigation and Power Research Institute Punjab, Amritsar, India
British Transport Docks Board Middlesex, England	Jawaharlalnearu Technological University Pradesh, India
Hydraulics Research Station Wallingford, England	Maulana Azad College of Technology Bhopal, India
British Hydromechanic Research Association Cranfield, England	Indian Institute of Technology, Kanpur Kanpur, India
Research Centre for Water Resources Development Budapest, Hungary	Indian Institute of Technology Madras India
Hydraulic and Hydraulic Structures Institute Genova, Italia	U.P. Irrigation Research Institute Roorkee, India
Politecnico di Torino Torino, Italia	Regional Engineering College Kashmir, India
Coastal and Marine Engineering Research Institute Haifa, Israel	Port and Harbour Research Institute Ministry of Transport Yokosuka, Japan
Indian Institute of Technology, Bombay Bombay, India	First District Port Construction Bureau Ministry of Transport Niigata, Japan
Maharashtra Engineering Research Institute Maharashtra State, India	Central Research Institute of Electric Power Industry Abiko City, Japan
Central Water and Power Research Station Poona, India	Kyoto University Kyoto, Japan
Irrigation Research Station Tamil Nadu, India	Disaster Prevention Research Institute Kyoto, Japan
Karnataka Engineering Research Station Krishnarajsagara Karnatka State, India	Osaka City University Osaka, Japan

Tohoku University Sendai, Japan	Asian Institute of Technology Bangkok, Thailand
University of Tokyo Tokyo, Japan	Middle East Technical University Ankara, Turkey
Public Works Research Institute Ibaraki-Ken, Japan	University of California Berkeley, U.S.A.
River and Harbour Laboratory Trondheim, Norway	U.S. Army Engineer Waterways Experiment Station Vicksburg, U.S.A.
Delft University of Technology Delft, The Netherlands	Civil Engineering Laboratory Naval Construction Battalion Centre Port Hueneme, U.S.A.
Delft Hydraulics Laboratory Delft, The Netherlands	University of Florida Gainesville, U.S.A.
Ministry of Works and Development Lower Hutt, New Zealand	University of Iowa Iowa, U.S.A.
National Laboratory of Civil Engineering Lisbon, Portugal	University of Illinois Urbana, U.S.A.
Institute of Hydroengineering Polisy Academy of Sciences Gdańsk, Poland	Massachusetts Institute of Technology Cambridge, U.S.A.
Hydraulic Engineering Research Institute Bucuresti, Romania	U.S. Dept. of the Interior Bureau of Reclamation Denver, U.S.A.
Hydraulics Laboratory "Cuillermo C. Céspedes" La Plata, Argentina	Water Conservation Structures Laboratory U.S. Department of Agriculture Stillwater, U.S.A.
Institute of Hydraulic Engineering Ministry of Public Works Bandung, Indonesia	Hydraulics Laboratory Ann Arbor, U.S.A.
Chalmers University of Technology Cöteborg, Sweden	Saint Anthony Falls Hydraulic Laboratory Minneapolis, U.S.A.
Dept. of Water Resources Engineering Lunds Universitet Lund, Sweden	Webb Institute of Naval Architecture Clen Cove, U.S.A.
Royal Institute of Technology Stockholm, Sweden	Oregon State University Corvallis, U.S.A.
IVO Hydraulic Laboratory Helsinki, Finland	University of Texas Austin, U.S.A.

Texas A and M University Texas, U.S.A.	University of Witwatersrand Johannesburg, South Africa
University of Washington Seattle, U.S.A.	National Research Institute for Oceanology Stellenbosch, South Africa
Coastal Engineering Research Center Fort Belvoir, U.S.A.	University of Stellenbosch Stellenbosch, South Africa
Chicago Bridge and Iron Co. Illinois, U.S.A.	

Ship Towing Tanks

Bulgarian Ship Hydrodynamics Centre Varna, Bulgaria	Versuchsanstalt für Wasserbau und Schiffbau Berlin, Germany
Shanghai Chiao-Tung University Shanghai, China	Bassin d'Essais des Carenes Paris, France
Shanghai Ship Design and Research Institute Shanghai, China	Institut de Recherches de la Construction Navale Paris, France
China Ship Scientific Research Centre Kiangsu Province, China	Indian Institute of Technology Kharagpur, India
Helsinki University of Technology Espoo, Finland	Universita deliga Studi di Napoli Napoli, Italy
Wartsila Icebreaking Model Basin Helsinki, Finland	Universita di Genova Genova, Italy
Hiroshima University Hiroshima, Japan	Technical Research and Development Institute Japan Defence Agency Tokyo, Japan
Korea Research Institute of Ship Daejeon, Korea	University of Tokyo Tokyo, Japan
National Research Council Ottawa, Canada	University of Osaka Osaka, Japan
Ship Research Laboratory Lyngby, Denmark	Heavy Industries Ltd. Yokohama, Japan
Versuchsanst für Binnenschiffbau Duisburg, Germany	Mitsubishi Heavy Industries Ltd. Nagasaki, Japan
Hamburg Shipmodel Basin (HSVA) Hamburg, Germany	

Akashi Ship Model Basin Co., Ltd.
Akashi City, Japan

Shipbuilding Research Centre of Japan
Tokyo, Japan

Seoul National University
Seoul, Korea

Technological University
Delft, The Netherlands

Norwegian Hydrodynamic Laboratories
Trondheim, Norway

Ship Design and Research Centre
Gdanski, Poland

Ministerio de Defensa Marina
Madrid, Spain

Statens Skeppsprovvningsanstalt
Goteborg, Sweden

University of Newcastle
Newcastle-upon-Tyne, U.K.

British Ship Research Association
Wallsend, United Kingdom

Admiralty Marine Technology
Establishment
Gosport, United Kingdom

National Maritime Institute of
Technology
Cambridge, U.S.A.

Offshore Technology Corporation
Escondido, U.S.A.

Stevens Institute of Technology
Hoboken, U.S.A.

United States Naval Academy
Annapolis, U.S.A.

University of Michigan
Ann Arbor, U.S.A.

David Taylor Naval Ship Research
and Development Center
Bethesda, U.S.A.

Pennsylvania State University
Pennsylvania, U.S.A.

Hydronautics, Incorporated
Laurel, Maryland, U.S.A.

The Measurement of Incident and Reflected Spectra
Using a Least Squares Method

by

E.P.D. Mansard* and E.R. Funke**

ABSTRACT

A least squares method to separate the incident and reflected spectra from the measured co-existing spectra is presented. This method requires a simultaneous measurement of the waves at three positions in the flume which are in reasonable proximity to each other and are on a line parallel to the direction of wave propagation.

Experimental investigations have shown that there is good agreement between the incident spectra calculated by the least squares method and the incident spectra measured concurrently in a side channel.

1.0 INTRODUCTION

As a large number of hydraulic laboratories now have the capability of generating irregular sea states for their experimental investigations, the necessity for computing reflections in an irregular sea state has become urgent. The presently available technique for this purpose is a 2-point method advanced by Thornton and Calhoun (1972), Goda and Suzuki (1976), and Morden et al (1976), which consists of measuring simultaneously the co-existing wave spectra at two known positions on a line parallel to the direction of wave propagation and deriving from this the incident and reflected spectra. This method has, however, certain limitations.

This paper presents a 3-point method which uses a least square analysis for decomposing the measured spectra into incident and reflected spectra with greater accuracy and range. This method originally derived by Marcou (1969) was used extensively for reflections with periodic waves (Mansard, 1976) and yielded reliable results.†

Assistant* and Senior** Research Officers, Hydraulics Laboratory, National Research Council of Canada, Ottawa.

† A recently proposed method by Gaillard et al (1980) also employs a 3-point measurement and contains some similarity to the method described here.

This paper describes the extension of this method to irregular waves and presents some experimental results obtained with a rubble mound breakwater.

2.0 REFLECTION MEASUREMENTS FOR IRREGULAR WAVES

The main assumption underlying the analysis of reflections in an irregular sea state is that the irregular waves can be described as a linear superposition of an infinite number of discrete components each with their own frequency, amplitude and phase. Another assumption, which is also of importance, is that these components travel at their own individual phase velocities described by the dispersion relationship. The first assumption is a widely accepted axiom in irregular wave studies while the second one has been found, through experimental investigations, to be a good approximation for finite and infinite depths of water (Funke and Mansard, 1980).

2.1 The 2-point Method

This method consists of measuring simultaneously the co-existing waves (two progressive wave trains moving in opposite direction) at two known positions in the flume, in a line parallel to the direction of wave propagation. Fourier analysis of these two signals will then produce the amplitudes and phases of the wave components at these two positions, by means of which the standing wave can be resolved into incident and reflected waves. This method described in detail by Thornton et al (1972) and Goda et al (1976) was developed by applying linear wave theory to monochromatic waves.

The above 2-point method has, however, certain limitations:

1. Limited Frequency Range
 - a) If the spacing between the probes is too great, the coherency factor which estimates the relative phase stability in each spectral frequency band decreases as the frequency increases, thus making the calculations of reflections less reliable.
 - b) If the spacing is too short, then there is a loss of contrast in cross spectral analysis.
2. Critical Probe Spacing

If the probe spacing "x" is such that $x/L = n/2$ ($n=0,1,2 \dots$, $L =$ wave length), the values of reflections become indeterminate because the proposed equa-

tions have singularities at these values.

3. High sensitivity to errors in the measurement of waves due to:
 - a) Transversal waves in the flume,
 - b) Non-linear wave interactions,
 - c) Harmonics due to non-linearities,
 - d) Signal noise, measurement errors, etc.

In order to overcome the above limitations, a 3-point method using a least squares method was developed.

2.2.1 The Least Squares Method

A definition sketch for this analysis is presented in Fig. 1.

Let us assume that waves are travelling in a channel in a longitudinal direction and reflections from some arbitrary structure or beach are travelling in the opposite direction. Assume also that it is possible to measure simultaneously the linear superpositions of these waves at m points $p = 1, 2, 3$ to m , which are in reasonable proximity to each other and are on a line parallel to the direction of wave propagation.

The wave profile observed at any one of these probe positions may be given as a summation of discrete, harmonically related Fourier components, i.e.

$$\eta_p(t) = \sum_{k=1}^N A_{p,k} \cdot \sin\left(\frac{2\pi \cdot k \cdot t}{T} + \alpha_{p,k}\right) \quad (1)$$

where $A_{p,k}$ is the Fourier coefficient for frequency k/T ,
 T is the length of the wave profile which is being observed; thus the fundamental frequency is $f_0 = 1/T$,
 $\alpha_{p,k}$ is the phase relative to the time origin of the record,
 N is an upper limit of summation which depends on the maximum significant frequency component in the series.

The Fourier coefficients and their phases are obtained from a Fourier transform of the function

$$\eta_p(t), \quad 0 \leq t \leq T \quad (2)$$

and are given in polar form as:

$$B_{p,k} = A_{p,k} \cdot e^{i\alpha_{p,k}} \quad (3)$$

or in rectangular form as:

$$B_{p,k} = [A_{p,k} \cdot \cos(\alpha_{p,k}) + i \cdot A_{p,k} \cdot \sin(\alpha_{p,k})] \quad (4)$$

Since the spacing between the various probes is known and since it is established that (except for locked harmonics) individual frequency components in a composite wave train travel at their own celerity (Funke and Mansard, 1980; Goda and Suzuki, 1976), it is possible to calculate the phase relationships between the wave trains as observed by each of the three probes. The general equation for a progressive wave is:

$$\eta_x(t) = \sum_{k=1}^N C_k \cdot \sin \left(-\frac{2\pi \cdot k \cdot t}{T} + \frac{2\pi x}{L_k} + \theta_k \right) \quad (5)$$

where θ_k is some arbitrary phase related to the space and time origin of the function,
 x is a space variable measured from the space origin of the function in a direction of wave propagation,
 L_k is the wave length of frequency k/T .

The observation of wave activity made at point p can now be stated in terms of a summation of

- a) an incident wave $C_{I,k}$
- b) a reflected wave $C_{R,k}$
- c) a noise signal which may be caused due to
 - cross-nodal activity
 - locked harmonics
 - non-linear interactions
 - measurement errors.

Let the distance from the wave source to the probe at $p=1$ be $X1$ and let the distance from the probe at $p=1$ to the reflecting structure be $XR1$, then the wave profile as observed at the probe may be written as:

$$\begin{aligned} \eta_{p=1}(t) = & \sum_{k=1}^N C_{Ik} \cdot \sin \left(-\frac{2\pi \cdot k \cdot t}{T} + \frac{2\pi \cdot X1}{L_k} + \theta_k \right) \\ & + \sum_{k=1}^N C_{Rk} \cdot \sin \left(-\frac{2\pi \cdot k \cdot t}{T} + \frac{2\pi \cdot (X1+2 \cdot XR1)}{L_k} + \theta_k + \phi_k \right) \quad (6) \\ & + \Omega_1(t) \end{aligned}$$

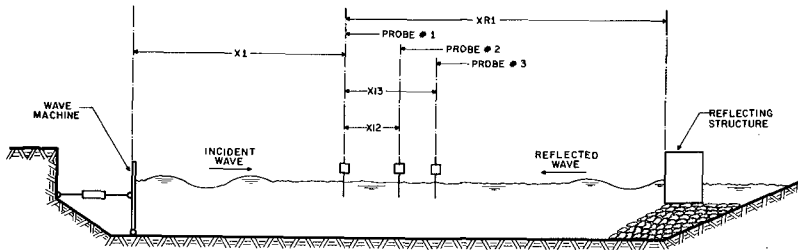


FIG. 1
SET-UP FOR WAVE REFLECTION MEASUREMENT

where $\Omega_1(t)$ is the cumulative effect of all the corrupting signals at probe $p=1$ and ϕ_k is a phase change due to the reflecting structure. The second probe at $p=2$, which is displaced by a distance X_{12} from the probe at $p=1$ in the direction of incident wave propagation (see Fig. 1), will record a similar wave profile as Eq. 6 except the phase angles will now be

$$\left(-\frac{2\pi \cdot k \cdot t}{T} + \frac{2\pi \cdot (X_1 + X_{12})}{L_k} + \theta_k \right) \quad (7)$$

for the incident wave and

$$\left(-\frac{2\pi \cdot k \cdot t}{T} + \frac{2\pi \cdot (X_1 + 2 \cdot X_{r1} - X_{12})}{L_k} + \theta_k + \phi_k \right) \quad (8)$$

for the reflected wave. A similar argument will define the wave angles for other probe positions which are displaced by distances X_{1p} from the first probe.

Fourier transformation of the composite signal, as

described by Eq. 6, over the interval $0 < t < T$ yields:

$$\begin{aligned}
 F[\eta_{p=1}(t)] = B_{1,k} = & C_{I,k} \cdot \exp\left\{i \cdot \frac{2\pi \cdot X1}{L_k} + i \cdot \theta_k\right\} \\
 & + C_{R,k} \cdot \exp\left\{i \cdot \frac{2\pi \cdot (X1+2 \cdot XR1)}{L_k} + i(\theta_k + \phi_k)\right\} \\
 & + Y_{1,k} \cdot \exp \cdot i(\rho_{1,k})
 \end{aligned} \quad (9)$$

where $\exp(\alpha) = e^\alpha$.

Similarly the observed signal for the other probes can be given in terms of their Fourier transforms as:

$$\begin{aligned}
 F[\eta_p(t)] = B_{p,k} = & C_{I,k} \cdot \exp\left\{i \cdot \frac{2\pi \cdot (X1+X1P)}{L_k} + i \cdot \theta_k\right\} \\
 & + C_{R,k} \cdot \exp\left\{i \cdot \frac{2\pi \cdot (X1+2 \cdot XR1-X1P)}{L_k} + i(\theta_k + \phi_k)\right\} \\
 & + Y_{p,k} \cdot \exp \cdot i(\rho_{p,k})
 \end{aligned} \quad (10)$$

Since one is only interested in the phase differences between the various probes, Eqs. 9 and 10 may be simplified in such a manner that the relevant phase differences are revealed. Therefore, let:

$$\begin{aligned}
 Z_{I,k} &= C_{I,k} \cdot \exp\left\{i \cdot \frac{2\pi \cdot X1}{L_k} + i \cdot \theta_k\right\} \\
 Z_{R,k} &= C_{R,k} \cdot \exp\left\{i \cdot \frac{2\pi \cdot (X1+2 \cdot XR1)}{L_k} + i(\theta_k + \phi_k)\right\} \\
 Z_{N,p,k} &= Y_{p,k} \cdot \exp \cdot i(\rho_{p,k})
 \end{aligned} \quad (11)$$

Consequently one obtains for the first three probes:

$$B_{1,k} = Z_{I,k} + Z_{R,k} + Z_{N,1,k} \quad (12)$$

$$B_{2,k} = Z_{I,k} \cdot \exp\left\{i \cdot \frac{2\pi \cdot X12}{L_k}\right\} + Z_{R,k} \cdot \exp\left\{-i \cdot \frac{2\pi \cdot X12}{L_k}\right\} + Z_{N,2,k} \quad (13)$$

$$B_{3,k} = Z_{I,k} \cdot \exp\left\{i \cdot \frac{2\pi \cdot X13}{L_k}\right\} + Z_{R,k} \cdot \exp\left\{-i \cdot \frac{2\pi \cdot X13}{L_k}\right\} + Z_{N,3,k} \quad (14)$$

The Z_N terms cannot be measured, but for the purpose of solving for Eqs. 12, 13 and 14, a least squared error method may be employed as follows:

For convenience define

$$\psi_{p,k} = \frac{2\pi \cdot X1P}{L_k} \quad (15)$$

where $X1P$ is the distance between probe 1 and probe 'p'.

In particular let

$$\begin{aligned} \beta_k &= \psi_{2,k} = \frac{2\pi \cdot X12}{L_k} \\ \gamma_k &= \psi_{3,k} = \frac{2\pi \cdot X13}{L_k} \end{aligned} \quad (16)$$

Eqs. 12 to 14 may now be restated thus:

$$\begin{aligned} Z_{I,k} + Z_{R,k} - B_{1,k} &= \epsilon_{1,k} \\ Z_{I,k} \cdot e^{i\beta_k} + Z_{R,k} \cdot e^{-i\beta_k} &= B_{2,k} = \epsilon_{2,k} \\ Z_{I,k} \cdot e^{i\gamma_k} + Z_{R,k} \cdot e^{-i\gamma_k} - B_{3,k} &= \epsilon_{3,k} \end{aligned} \quad (17)$$

where

$$\epsilon_{p,k} = -Z_{N,p,k} + f_e(Z_{I,k}, Z_{R,k}) \quad (18)$$

By applying a least squares method one may find those values of Z_I and Z_R for which the sum of squares of $\epsilon_{p,k}$ for all 'p' is minimum. This should correspond to those values of $Z_{I,k}$ and $Z_{R,k}$ for which

$$f_e(Z_{I,k}, Z_{R,k}) = 0.$$

It is therefore required that

$$\sum_{p=1}^3 (\epsilon_{p,k})^2 = \sum_{p=1}^3 \left(Z_{I,k} \cdot e^{i\psi_{p,k}} + Z_{R,k} \cdot e^{-i\psi_{p,k}} - B_{p,k} \right)^2 \quad (19)$$

= a minimum.

It is assumed that this minimum is reached when both partial derivatives are zero, i.e.

$$\frac{d \left(\sum_{p=1}^3 (\epsilon_{p,k})^2 \right)}{d Z_{I,k}} = \frac{d \left(\sum_{p=1}^3 (\epsilon_{p,k})^2 \right)}{d Z_{R,k}} = 0 \quad (20)$$

Differentiating Eq. 19, one therefore obtains:

$$\sum_{p=1}^3 \left(Z_{I,k} \cdot e^{i\psi_{p,k}} + Z_{R,k} \cdot e^{-i\psi_{p,k}} - B_{p,k} \right) \cdot e^{i\psi_{p,k}} = 0 \quad (21)$$

and

$$\sum_{p=1}^3 \left(Z_{I,k} \cdot e^{i\psi_{p,k}} + Z_{R,k} \cdot e^{-i\psi_{p,k}} - B_{p,k} \right) \cdot e^{-i\psi_{p,k}} = 0 \quad (22)$$

Eqs. 21 and 22 may now be written as follows:

$$Z_{I,k} \cdot \left(1 + e^{i \cdot 2 \cdot \beta_k} + e^{i \cdot 2 \cdot \gamma_k} \right) + 3 Z_{R,k} = B_{1,k} + B_{2,k} \cdot e^{i\beta_k} + B_{3,k} \cdot e^{i\gamma_k} \quad (23)$$

$$Z_{R,k} \cdot \left(1 + e^{-i \cdot 2 \cdot \beta_k} + e^{-i \cdot 2 \cdot \gamma_k} \right) + 3 Z_{I,k} = B_{1,k} + B_{2,k} \cdot e^{-i\beta_k} + B_{3,k} \cdot e^{-i\gamma_k} \quad (24)$$

where β and γ were defined by Eq. 16. From these, the solu-

tions for Z_I and Z_R may be derived, namely:

$$Z_{I,k} = \frac{1}{D_k} \cdot \left[B_{1,k} \cdot (R1 + i \cdot Q1) + B_{2,k} \cdot (R2 + i \cdot Q2) + B_{3,k} \cdot (R3 + i \cdot Q3) \right] \quad (25)$$

and

$$Z_{R,k} = \frac{1}{D_k} \cdot \left[B_{1,k} \cdot (R1 - i \cdot Q1) + B_{2,k} \cdot (R2 - i \cdot Q2) + B_{3,k} \cdot (R3 - i \cdot Q3) \right] \quad (26)$$

where:

$$\begin{aligned} D_k &= 2 \cdot (\sin^2 \beta_k + \sin^2 \gamma_k + \sin^2 (\gamma_k - \beta_k)) \\ R1_k &= \sin^2 \beta_k + \sin^2 \gamma_k \\ Q1_k &= \sin \beta_k \cdot \cos \beta_k + \sin \gamma_k \cdot \cos \gamma_k \\ R2_k &= \sin \gamma_k \sin (\gamma_k - \beta_k) \\ Q2_k &= \sin \gamma_k \cdot \cos (\gamma_k - \beta_k) - 2 \cdot \sin \beta_k \\ R3_k &= -\sin \beta_k \sin (\gamma_k - \beta_k) \\ Q3_k &= \sin \beta_k \cdot \cos (\gamma_k - \beta_k) - 2 \cdot \sin \gamma_k \end{aligned} \quad (27)$$

2.2.2 Analysis Technique

The two equations (25 and 26) are solved independently for each frequency component (using the Fourier transform technique) or for each frequency band (using the technique of spectral analysis by the method of averaged periodogram) and then squared and scaled to give the incident and reflected spectra.

The parameters D_k , $R1_k$, $R2_k$, $R3_k$, $Q1_k$, $Q2_k$ and $Q3_k$ can be obtained easily from the trigonometric relations of the probe spacings. The characteristics of the co-existing wave profiles $B_{p,k}$ which can be expressed as:

$$B_{p,k} = [A_{p,k} \cdot \cos(\alpha_{p,k}) + i \cdot A_{p,k} \cdot \sin(\alpha_{p,k})] \quad (28)$$

are given by one of the above two techniques. The values of $A_{p,k}$ and $\alpha_{p,k}$ can be calculated directly from the Fourier transform, while in the case of spectral analysis they are

obtained by auto and cross spectral density analysis respectively.

By applying a suitable averaging window for spectral density analysis, a representative value of $B_{D,k}$ for each frequency band rather than for every frequency component is obtained. This technique significantly reduces the erratic variations of the reflection coefficient spectrum and, at the same time, reduces the computational task.

The different steps involved in calculating the solutions for the above Eqs. 25 and 26 are described below:

1. The outputs from the three probes are denoted as $\eta_1(t)$, $\eta_2(t)$ and $\eta_3(t)$. Execute auto-spectral density analysis on each record, yielding:

$$S1(k \cdot \Delta f), S2(k \cdot \Delta f) \text{ and } S3(k \cdot \Delta f)$$

Apply band-limiting, if required and provide spectral smoothing to obtain reliable estimates for each frequency bandwidth.

2. From the auto-spectra compute the amplitude spectra as follows:

$$A1(k \cdot \Delta f) = \sqrt{2 \cdot S1(k \cdot \Delta f) \cdot \Delta f} \quad (29)$$

and similarly for A2 and A3.

3. Obtain the cross-spectral density in polar form for $\eta_1(t)$ with $\eta_2(t)$ and $\eta_1(t)$ with $\eta_3(t)$. Apply band-limiting and smoothing identical to that applied under (1).
4. From the cross-spectra, extract the phase spectra

$$PH12(k \cdot \Delta f) \text{ and } PH13(k \cdot \Delta f)$$

Also set $PH11(k \cdot \Delta f) = 0$ for all k .

5. Pair up the amplitude and the phase spectra in polar form as follows:

$$\begin{aligned} A1(k \cdot \Delta f) & \text{ with } PH11(k \cdot \Delta f) \\ A2(k \cdot \Delta f) & \text{ with } PH12(k \cdot \Delta f) \\ A3(k \cdot \Delta f) & \text{ with } PH13(k \cdot \Delta f) \end{aligned}$$

6. Convert from polar to rectangular form so that

$$B1(k \cdot \Delta f) = \text{REC}\{A1(k \cdot \Delta f) \cdot \exp(PH11(k \cdot \Delta f))\}$$

etc.

7. For all k evaluate the angles $\beta(k \cdot \Delta f)$ and $\gamma(k \cdot \Delta f)$ as per Eq. 16. The wave length L_k must be evaluated in terms of the depth of water which may be considered average for the region in which the probes are located.
8. For all k evaluate all the terms of the set of Eq. 27.
9. Evaluate $Z_I(k \cdot \Delta f)$ and $Z_R(k \cdot \Delta f)$ according to Eqs. 25 and 26.
10. From Z_I and Z_R compute the spectral densities S_I and S_R by

$$S_I(k \cdot \Delta f) = |Z_I(k \cdot \Delta f)|^2 / (2 \cdot \Delta f)$$

and

$$S_R(k \cdot \Delta f) = |Z_R(k \cdot \Delta f)|^2 / (2 \cdot \Delta f)$$

11. The reflection coefficient is then evaluated from

$$R(k \cdot \Delta f) = |Z_R(k \cdot \Delta f)| / |Z_I(k \cdot \Delta f)|$$

12. The coherency factor should also be computed in order to evaluate the degree of significance of the incident and the reflected spectrum. Thus

$$CF_{12}(k \cdot \Delta f) = |S_{12}(k \cdot \Delta f)| / (S_1(k \cdot \Delta f) \cdot S_2(k \cdot \Delta f))^{1/2}$$

and

$$CF_{13}(k \cdot \Delta f) = |S_{13}(k \cdot \Delta f)| / (S_1(k \cdot \Delta f) \cdot S_3(k \cdot \Delta f))^{1/2}$$

3.0 EXPERIMENTAL SET-UP AND TEST RESULTS

Experimental investigations were carried out to determine the reflective characteristics of a rubble mound breakwater subject to irregular wave action. The set-up used for this purpose (Fig. 2) consists of a flume of dimensions 67 m x 1.8 m x 1.25 m, equipped with a hydraulically driven random wave generator. This wave generator, controlled by an on-line computer, can reproduce a variety of simulated natural sea states in the flume (Funke et al, 1980; Funke and Mansard, 1979).

As shown in Fig. 2, the width of the flume was subdivided into three sections: a centre channel of 0.9 m wide and two side channels of 0.45 m wide. The breakwater was placed in the centre channel while beaches with a mild slope of 1:20 ensured a good dissipation of the incident wave energy in the side channels. This particular set-up reduced the secondary reflections from the wave board since half of the secondary reflections were dissipated in the side channels.

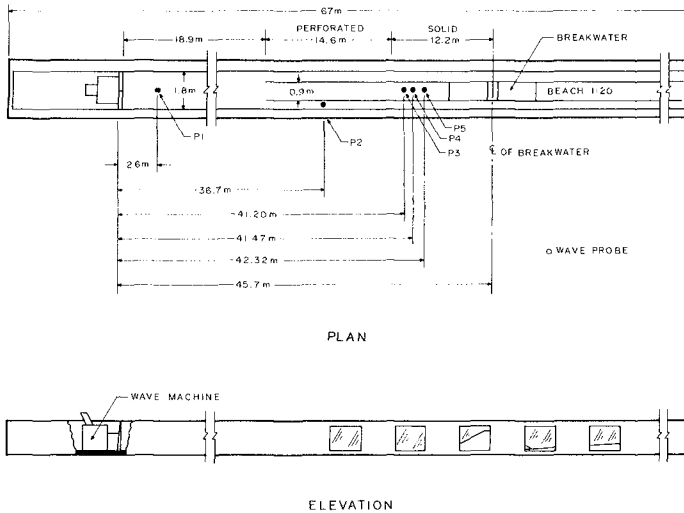


FIG. 2 WAVE FLUME WITH PROBE LOCATIONS

The primary reflections in the side channels being very small (lower than 5% for long waves), the waves therein were considered more or less as pure incident waves. This allowed a direct comparison between the calculated and the actual incident wave spectra.

The waves were sampled simultaneously by the on-line computer at four probe positions (three in the central channel and one in the side channel). The probes used for this purpose are a variation of the Robertshaw capacitance probe which has proved to be quite reliable. The sampling of data, which was initiated only after the reflections had stabilized, was carried out for at least one cycle length of the time series (about 200 s in the model).

Tests were carried out using JONSWAP spectra and the results corresponding to two different peak frequencies are presented below in Figs. 3 and 4. Additional examples can be found in Mansard and Funke (1980).

These results show that the co-existing spectra measured at the three probe positions differ to a certain extent; the values of their characteristic wave height (H_{m0}) and their maximum wave height ($H_{z,max}$) vary. These variations, which could be attributed to the standing wave pat-

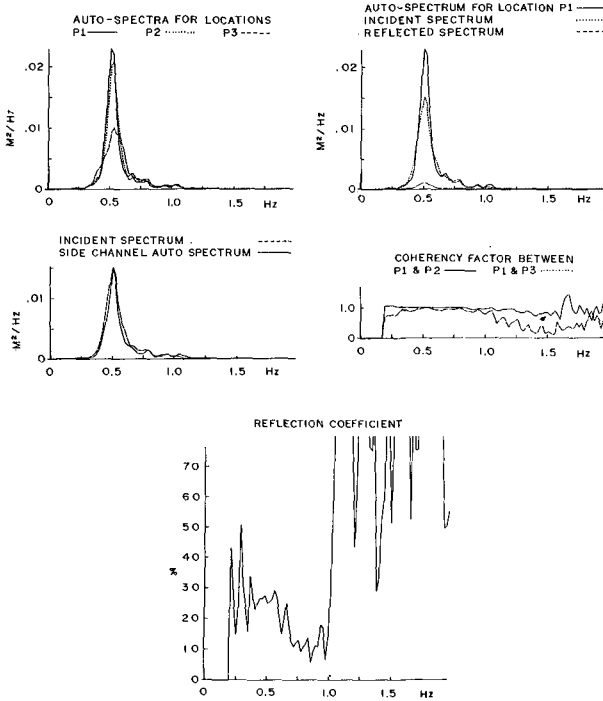


FIG.3 SEPARATION OF INCIDENT AND REFLECTED SPECTRA
FOR A RUBBLE MOUND BREAKWATER
($F_p = 0.51$ Hz)

tern, are found to be higher than 10% for many cases of the rubble mound breakwater study.

The incident spectra calculated by the least squares method are found to agree reasonably well with the spectra measured in the side channel thereby validating this technique as a useful tool in the decomposition of the co-existing spectra.

The reflection coefficients in each band of the spectrum are presented in terms of percentage of the corresponding incident wave height. Their variations do not exhibit any specific trend with respect to frequency. It can be shown, however, that their scatter is partly due averaging applied during spectral analysis.

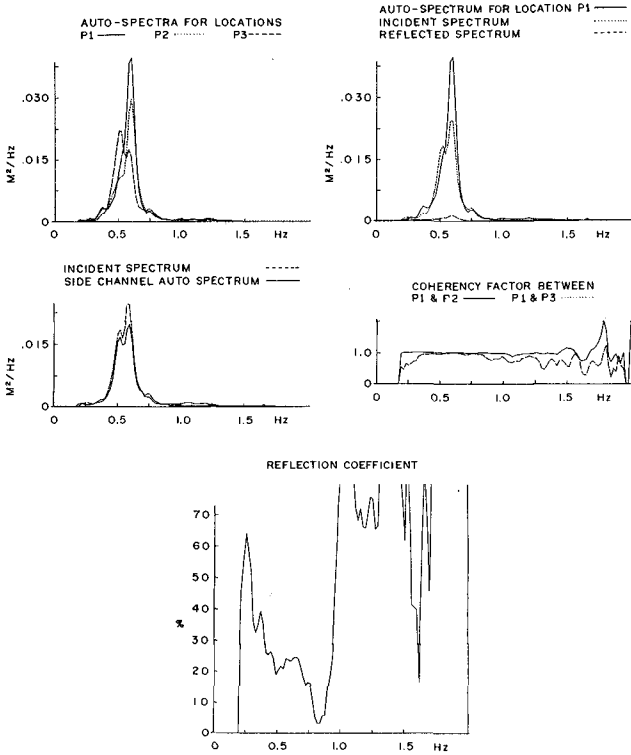


FIG.4 SEPARATION OF INCIDENT AND REFLECTED SPECTRA
FOR A RUBBLE MOUND BREAKWATER
($F_p = 0.60$ Hz)

Another important factor worth noting is the dependency of the reflection phenomenon on wave steepness. Therefore, the reflection coefficient spectrum is highly dependent on the incident spectrum and can only be considered an average value of reflection for each frequency band over the duration of the sample record.

It must also be considered quite likely that the reflection phenomenon leads to a transfer of energy between different frequency bands and not just to its attenuation. Some incident energy at frequency f_a may therefore be radiated back at frequency f_b and appear consequently as an amplification of reflected energy at f_b .

In the range of frequencies where the incident spectrum is very low, the signal to noise ratio is very low. As a result the estimation of reflection coefficients is subject to errors and therefore produces spurious variations.

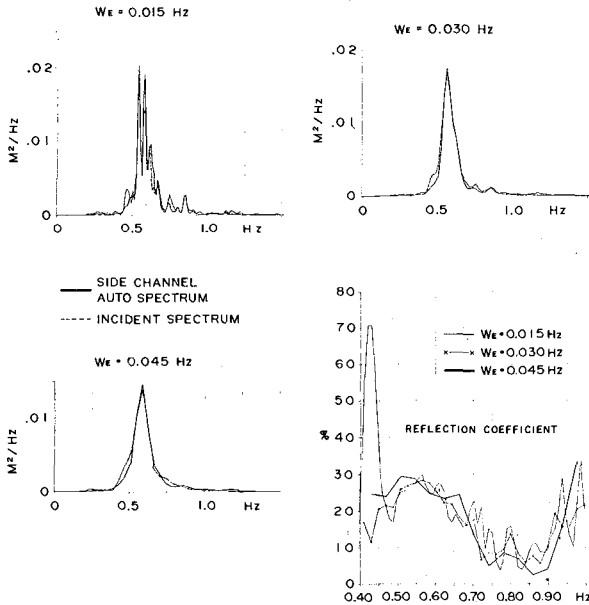


FIG. 5 EFFECT ON THE CALCULATION OF REFLECTIONS
DUE TO SMOOTHING WINDOW SIZE
($F_p = 0.57$ Hz)

The coherency factor $CF(f)$, presented in these figures, gives an indication of the relative phase stability in each frequency band between cross-correlated records. This is therefore a direct measure of the degree of confidence which could be attributed to the reflection coefficient in each band. When $CF(f)$ is close to unity, the records are said to be well correlated and the opposite applies when it approaches zero. Results show that $CF(f)$ decreases with an increase in frequency or with an increase in probe spacings. Where the spectrum has almost zero energy, $CF(f)$ appears to exceed 1. This is clearly incorrect and can be attributed to low signal to noise ratios.

3.1 Effect of Smoothing Spectra

The smoothing of spectra in the analysis of prototype wave data is generally performed in order to improve the reliability of estimating power within a certain band of frequencies. This operation may be performed implicitly, by applying so-called "data windows" in the time domain, or explicitly, by using various frequency windows or filters in the frequency domain. In either case, the net effect is the averaging of several weighted power estimates within a frequency bandwidth defined by the particular window function chosen.

The price to be paid for improved reliability is a loss of resolution or fidelity of analysis (Jenkins and Watts, 1968). Fidelity is the ability of an analysis to reveal the true characteristics or details of a process. A low fidelity analysis would lead to a blurring or smearing of those details which may or may not be a true characteristic of the process under investigation.

The statistical techniques for the choice of window bandwidth in the analysis of prototype wave data are based on the assumption that each individual contributing component within the width of the window is a member of a stochastic process. It is important to realize that this situation does not generally apply to the analysis of wave data under laboratory conditions. If, as is usually the case, the waves were generated by some deterministic process, then the process is also deterministic in the frequency domain and the question of statistical reliability must only be answered in relation to the noise which is added to the wave data by the various mechanisms which were identified in section 2.1.

As the mixture of noise and deterministic signal is not known at this time, the question of a best choice of window bandwidth cannot be answered. Instead it may be better to experiment with different windows and compare the results. A more formal procedure along this line is known as "window closing" and is described by Jenkins and Watts (1968).

For the purpose of this report three separate explicit Hanning windows (Blackman and Tuckey, 1958) were used on laboratory generated wave data with bandwidth of 0.015, 0.03 and 0.045 Hz respectively. The results are shown in Fig. 5. The relatively small differences in results suggest that the solution is fairly stable.

3.2 Effect of Probe Spacings

Past studies using monochromatic waves (Marcou, 1969) have shown that the estimation of the incident and reflected waves are not influenced by the choice of probe spacings. However, there is one critical combination of the probe spacing for which the reflection analysis will be invalid.

The main expression used for the estimation of incident and reflected waves (Eqs. 25 and 26) will become indeterminate if its denominator D_k is equal to zero (one of these equations is given below for easy reference).

$$Z_{I,k} = \frac{1}{D_k} \cdot \left(B_{1,k} \cdot (R1+i \cdot Q1) + B_{2,k} \cdot (R2+i \cdot Q2) + B_{3,k} \cdot (R3+i \cdot Q3) \right)$$

where $D_k = 2 \cdot (\sin^2 \beta_k + \sin^2 \gamma_k + \sin^2 (\gamma_k - \beta_k))$

D_k is equal to zero if

$$\sin \beta_k = \sin \gamma_k = \sin (\gamma_k - \beta_k) = 0$$

$$\text{or } \sin \beta_k = \sin \gamma_k = 0$$

$$\text{or } \sin \left(\frac{2\pi \cdot X12}{L_k} \right) = \sin \left(\frac{2\pi \cdot X13}{L_k} \right) = 0$$

This occurs when

$$X12 = \frac{jL_k}{2} \text{ and } X13 = \frac{m}{n} \cdot X12$$

where j , m , n and m/n are integers and L_k is the wave length for the frequency components ($k \cdot \Delta f$) under consideration. In other words the reflection calculations become indeterminate when:

1. the distance $X12$ is equal to half wave length of the frequency component under consideration or even multiples of half wave length .AND.
2. the distance $X13$ is an integer multiple of the distance $X12$.

More research may be carried out to determine the optimum probe spacing for greatest accuracy and widest bandwidth. The coherency function and, perhaps the spectrum of residues as given by equation 19 could probably be used as a criterion.

On the basis of experience gained at the Hydraulics Laboratory at the National Research Council, and experiments carried out by Marcou (1969) using monochromatic waves, the following range of probe spacings are recommended:

$$X_{12} = L_p/10$$

$$L_p/6 < X_{13} < L_p/3 \quad \text{and} \quad X_{13} \neq L_p/5 \quad \text{and} \quad X_{13} \neq 3L_p/10$$

Another parameter which is of similar importance is the distance of probes from the reflective structure (test structure and wave paddle). It has been shown by Ishida (1972) and Goda et al (1976) that the co-existing wave height fluctuates to a certain extent near the reflective structures. However, these fluctuations become negligible beyond a distance of one wave length. Hence it is suggested that the probes be located at least one wave length (wave length corresponding to peak frequency) away from the reflective structures.

4.0 CONCLUSIONS

A satisfactory technique based on least squares analysis is described whereby the incident and reflected spectra are resolved from the measured co-existing spectra.

There is good agreement between the incident spectrum calculated by the least squares method and the corresponding spectrum measured concurrently in the side channel.

This method can be considered as superior to the 2-point method since it has:

- a) wider frequency range,
- b) reduced sensitivity to noise and deviations from the linear theory and,
- c) lesser sensitivity to critical probe spacing.

The effect of varying the size of smoothing window in the calculation of the incident spectrum has been found to be relatively small. However a relationship between the best smoothing window and the general properties of the wave spectrum is still a subject of continuing research.

Suitable locations of probes are recommended. Probe spacings which must be avoided to eliminate singularities are also defined.

6.0 REFERENCES

1. Blackman and Tukey (1959), "The Measurement of Power Spectra from the Point of View of Communications Engineering", Dover Publications.
2. Funke, E.R. and E.P.D. Mansard (1979), "Synthesis of Realistic Sea States in a Laboratory Flume", Hydraulics Laboratory Technical Report LTR-HY-66, National Research Council, Ottawa.
3. Funke, E.R., N.L. Crookshank and M. Wingham (1980), "An Introduction to GEDAP - An Integrated Software System for Experiment Control, Data Acquisitions and Data Analysis", Proc. XXVI International Instrumentation Symposium, Seattle. (Also available as NRC Hydraulics Lab. Tech. Report LTR-HY-75.)
4. Funke, E.R. and E.P.D. Mansard (1980), "Reproduction of Prototype Random Wave Trains in a Laboratory Flume", Hydraulics Laboratory Technical Report no. LTR-HY-64, National Research Council, Ottawa (to be published).
5. Gaillard, P., M. Gauthier and F. Holly (1980), "Method of Analysis of Random Wave Experiments with Reflecting Coastal Structures", 17th International Coastal Engineering Conference, Sydney, Australia.
6. Goda, Y. and Y. Abe (1968), "Apparent Coefficient of Partial Reflection of Finite Amplitude Waves", Rep. Port and Harbour Res. Inst., Vol. 7, No. 3, pp. 3-58.
7. Goda, Y. and Y. Suzuki (1976), "Estimation of Incident and Reflected Waves in Random Wave Experiments", 15th Coastal Engineering Conference, Hawaii.
8. Ishida, A. (1972), "Transformation of Power Spectra of Wind Generated Waves Caused by Reflection", Coastal Engineering in Japan, Vol. 15, JSCE, pp. 25-33.
9. Jenkins and Watts (1968), "Spectral Analysis and Its Applications", Holden-Day.
10. Mansard, E.P.D. (1976), "Contribution à l'étude expérimentale de la propagation de la houle à travers des obstacles en forme de diaphragme", Thèse Grenoble.
11. Mansard, E.P.D. and E.R. Funke (1980), "The Measurement of Incident and Reflected Spectra Using a Least Squares Method", Hydraulics Laboratory Technical Report LTR-HY-72, National Research Council.
12. Marcou, C. (1969), "Contribution expérimentale à l'étude de la houle complexe du laboratoire", Thèse, Grenoble.
13. Morden, D.B. et al (1976), "Decomposition of Co-existing Random Wave Energy", 15th Coastal Engineering Conference, Hawaii.
14. Tadjbaksh et al (1960), "Standing Surface Waves of Finite Amplitudes", Journal of Fluid Mechanics, Vol. 8, pp. 442-451.
15. Thornton, E.B. and R.J. Calhoun (1972), "Spectral Resolution of Breakwater Reflected Waves", Journal ASCE Waterways Harbour and Coastal Engineering, WW4.

CHAPTER 9 .

ORBITAL VELOCITIES IN IRREGULAR WAVES

by

F.C. VIS

Project Engineer

Delft Hydraulics Laboratory

The Netherlands

1 ABSTRACT

Experimental and theoretical study to determine the applicability of linear wave theory for the description of the velocity field in irregular waves. A comparison between theory and measurement was executed both in frequency and in time domain. In frequency domain by means of the experimentally and theoretically determined frequency response functions of wave motion to orbital velocity, and in time domain by means of the measured and computed time records of the velocities. The time records for the velocities were computed from the measured waterlevel fluctuations by using the impuls response function method. The orbital velocities were measured contactless with laser-doppler equipment.

2 INTRODUCTION

In order to determine the applicability of linear wave theory for conversion of irregular wave motion to wave induced orbital velocities near the bottom, the Delft Hydraulics Laboratory has carried out in the past experimental investigation where the velocities were measured by means of a propeller-type flowmeter. The results of this study were used for the computation of wave forces on submarine pipelines. Although in general a reasonable agreement was found between theory and measurement, also significant discrepancies were observed. However, these discrepancies had to be ascribed to the distortion of the flow by the flowmeter.

The development of the laser-doppler velocity meter made it possible to measure accurately the orbital velocities in an extremely small area, without influence of the meter. With this accurate instrument new experiments in irregular waves were carried out, where apart from the bottom velocity also the horizontal and vertical orbital velocities at half water depth and just beneath the deepest trough were measured. The program

comprised waves of moderate steepness at intermediate depth/wavelength ratios ($0.008 < h/g T_p^2 < 0.069$, $0.0009 < H_s/g T_p^2 < 0.0064$). It appeared that the discrepancies mentioned above were indeed due to inaccuracies of the flowmeter and that the agreement with linear wave theory was even better than was found in the first set of experiments.

3 NOTATION

a	distance from the bottom where the velocities were measured
a_{cs}	significant crest of the waves
a_{c1}	crest exceeded by 1% of all the crests of the wave record
a_{ts}	significant trough of the waves
a_{t1}	trough exceeded by 1% of all the troughs of the wave record
g	acceleration of gravity
h	water depth
$H(\omega)$	computed frequency response function
$\hat{H}(\omega)$	"measured" frequency response function
$h(\tau)$	impuls response function
H_s	significant wave height
H_1	wave height exceeded by 1% of all the heights of the wave record
i	$\sqrt{-1}$
k	wave number
$S_{xy}(\omega)$	cross-spectrum
$S_{xx}(\omega)$	auto-spectrum
u_{cs}	significant crest velocity of the horizontal velocity component u
u_{c1}	crest velocity exceeded by 1% of all the crest velocities of the record of the horizontal velocity component u
u_{ts}	significant trough velocity of the horizontal velocity component u
u_{t1}	trough velocity exceeded by 1% of all the trough velocities of the record of the horizontal velocity component u
v_{cs}	significant crest velocity of the vertical velocity component v
v_{c1}	crest velocity exceeded by 1% of all the crest velocities of the record of the vertical velocity component v
v_{ts}	significant trough velocity of the vertical velocity component v
v_{t1}	trough velocity exceeded by 1% of all the trough velocities of the record of the vertical velocity component v
ϵ	relative error

4 THEORETICAL APPROACH

In Appendix A it is shown that according to the linear wave theory the water level fluctuations $\eta(t)$ and the horizontal and vertical orbital velocity components $u(t)$ and $v(t)$ at distance a from the bottom are mutually related by

$$u(t) = \int_0^{\infty} h_u(\tau) \{ \eta(t-\tau) + \eta(t+\tau) \} d\tau \quad (1)$$

$$v(t) = \int_0^{\infty} h_v(\tau) \{ \eta(t-\tau) - \eta(t+\tau) \} d\tau, \quad (2)$$

where $h_u(\tau)$ and $h_v(\tau)$ are impuls response functions. The corresponding frequency response functions are given by

$$H_u(\omega) = \frac{\omega \cosh ka}{\sinh kh} \quad (3)$$

$$H_v(\omega) = i \frac{\omega \sinh ka}{\sinh kh} . \quad (4)$$

The "measured" frequency response functions $\hat{H}_u(\omega)$ and $\hat{H}_v(\omega)$ can be obtained from the measured data by using the relation

$$\hat{H}(\omega) = \frac{S_{xy}(\omega)}{S_{xx}(\omega)}, \quad (5)$$

where $S_{xy}(\omega)$ is the cross-spectrum of input (wave motion) and output (orbital velocity component) and $S_{xx}(\omega)$ is the auto-spectrum of input (see e.g. Bendat and Piersol, 1971).

5 MEASUREMENTS

5.1 Experimental Set-up

The tests were carried out in the 2 meter wide windwave flume of the Delft Hydraulics Laboratory. In this flume irregular waves can be generated up to a height of 30 cm by means of wind and/or a hydraulically driven wave generator. A detailed description of the wave generator is given in (DHL, 1976). For the actual tests no wind was applied. The water level fluctuations were measured by means of a resistance type wave height meter, consisting of two vertical metal rods, and the orbital velocities were measured by means of a laser-doppler equipment which could simultaneously measure horizontal and vertical component. A description of the laser-doppler velocity meter is given in (Godefroy, 1978). In order to measure the undisturbed velocities with this instrument, the walls of the flume had to be translucent for transmitting the laser beams. As this was not the case, the flume was partially provided with an inner flume with perspex walls (see Figure 1). For absorption of the waves, beaches were used with a slope of 1:10 for minimal reflection.

Wave motion and orbital velocities were simultaneously measured in the same cross-section of the flume at a mutual distance of 20 cm. This distance proved to be sufficient for avoiding disturbance of the velocity measurement by the wave height meter. As the waves were long-crested this solution could be used.

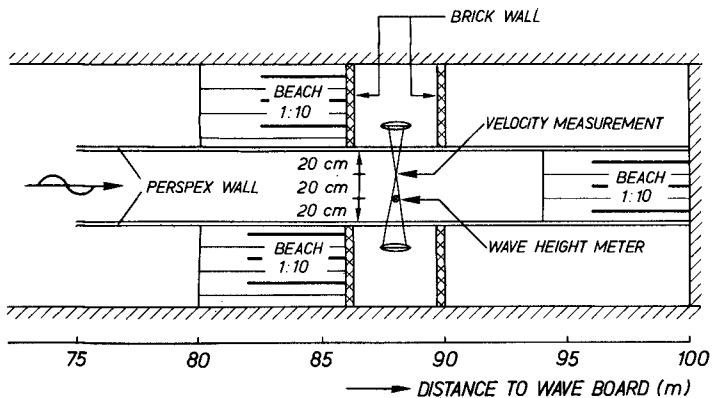
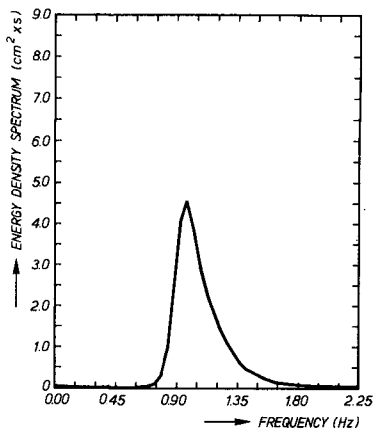
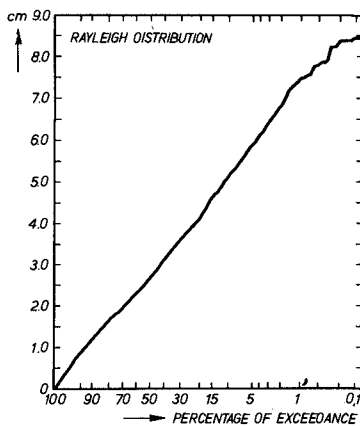


Fig. 1 Lay-out of the 2 m wide wind wave flume



$M_{0\eta} = 1.43 \text{ cm}^2$
 $4\sqrt{M_{0\eta}} = 4.78 \text{ cm}$
 $T_p = 1.02 \text{ s}$

Fig. 2 Wave spectrum at test 16



$H_s = 4.73 \text{ cm}$
 $H_{z,max} = 8.83 \text{ cm}$

Fig. 3 Wave height distribution at test 16

For elaboration with the computer the measured signals were digitized with sample frequency of 25 Hz.

5.2 Test Program

The test program comprised irregular waves of moderate steepness at intermediate depth/wave length ratios, which are the normal working conditions for offshore structures. The wave parameters are given in Tables I and II. The wave heights, defined as the maximum difference of the record between two succeeding zero-down crossings, appeared to be nearly Rayleigh distributed. As an example the energy density spectrum of a wave record and the corresponding cumulative frequency distribution of the wave heights at test 16 are presented in Figures 2 and 3. Velocities were measured at three locations along the vertical: the horizontal bottom velocity just outside the boundary layer, and the horizontal and vertical components at mid-depth and just beneath the deepest trough (see Tables I and II).

TABLE I TEST PROGRAM FOR BOTTOM VELOCITIES

TEST	$\frac{1000 h}{g T_p^2}$	$\frac{1000 H_s}{g T_p^2}$	ϵ_u %
1	7.8	0.89	1.4
2	11.8	0.88	5.2
3	19.2	1.75	2.1
4	19.2	2.49	2.3
5	24.4	2.02	1.7
6	24.4	2.81	2.2
7	26.3	3.13	4.8
8	26.3	3.12	2.8
9	33.5	2.69	1.2
10	33.5	3.94	2.6
11	43.6	3.85	5.8
12	43.6	5.62	2.9

TABLE II TEST PROGRAM FOR VELOCITIES AT DISTANCE a FROM THE BOTTOM

TEST	$\frac{1000 h}{g T_p^2}$	$\frac{1000 H_s}{g T_p^2}$	$\frac{a}{h}$	ϵ_u %	ϵ_v %
13	13.3	1.3	0.500	2.0	4.4
14	13.3	1.3	0.873	2.9	2.1
15	16.3	2.0	0.500	4.7	7.6
16	16.3	2.0	0.825	1.4	3.5
17	17.0	1.5	0.500	3.5	3.1
18	20.6	1.6	0.850	3.0	2.6
19	39.2	4.8	0.500	3.2	7.1
20	39.2	4.6	0.825	1.4	3.4
21	53.9	5.2	0.500	5.2	5.4
22	53.9	5.0	0.873	0.6	2.1
23	68.6	5.2	0.500	4.6	2.8
24	68.6	5.3	0.850	1.0	1.7
25	35.9	6.4	0.810	1.0	1.2

6 COMPARISON OF THEORY AND MEASUREMENT

The comparison of the measured velocities in irregular waves with the linear wave theory has been carried out in frequency domain and, except for the bottom velocities, also in time domain.

In frequency domain theory and measurement were compared by defining a relative error ϵ by

$$\epsilon = \frac{1}{N} \sum_{i=1}^N \left| \frac{|\hat{H}(\omega_i)| - |H(\omega_i)|}{|H(\omega_i)|} \right|,$$

where the "measured" frequency response functions $\hat{H}(\omega_i)$ were determined by (5), and $H(\omega_i)$ by means of (3) or (4). The notation $|\cdot|$ denotes the

amplitude of the (complex) number. The relative errors ϵ have been evaluated only for those frequencies ω_i for which both the spectral density functions of input and output were greater than 10% of their peak value, as for smaller values the spectral densities are relatively inaccurate. All spectra were computed using a Fast Fourier Transform method. The relative errors are given in Tables I and II. The indices u and v have been attached for distinction between horizontal and vertical velocity.

Figure 4 presents most amplitudes of the "measured" and computed frequency response functions.

A comparison in time domain was executed for the velocities above the bottom by computing the time records of the orbital velocity components, for which either (1) or (2) was used, and by comparing them with the measured ones. The significant and the 1% crest and trough velocities are presented in Tables III and IV. Crest and trough velocities are defined in accordance with crests and troughs of the wave motion by the maximum positive and maximum negative velocity between two succeeding zero-down crossings. A positive velocity means for the horizontal velocity a velocity in direction of propagation of the waves, and for the vertical velocity a velocity in upwards direction.

An example of measured and computed time record is presented in Figure 5 and in more detail in Figure 6.

TABLE III WAVE MOTION AND MEASURED AND COMPUTED HORIZONTAL ORBITAL VELOCITY

TEST	WAVE MOTION MEASURED				HORIZONTAL ORBITAL VELOCITY							
	a_{cs} cm	a_{cl} cm	a_{ts} cm	a_{tl} cm	MEASURED				COMPUTED			
					u_{cs} cm/s	u_{cl} cm/s	u_{ts} cm/s	u_{tl} cm/s	u_{cs} cm/s	u_{cl} cm/s	u_{ts} cm/s	u_{tl} cm/s
13	2.5	3.9	2.4	3.5	9.0	12.6	9.4	14.2	9.0	12.7	9.9	14.9
14	2.4	3.6	2.7	3.5	11.7	16.5	12.0	18.3	11.6	16.8	12.2	18.4
15	2.6	3.9	2.4	3.6	7.6	11.5	7.7	13.1	6.8	10.6	8.1	13.0
16	2.5	4.0	2.3	3.6	12.0	17.8	12.4	20.8	12.0	18.6	12.2	18.6
17	2.8	4.0	2.6	4.0	9.6	13.2	9.5	16.0	9.5	13.3	9.6	16.1
18	2.8	3.8	2.7	4.1	12.6	17.0	11.5	17.2	12.6	17.0	12.0	17.2
19	2.9	4.8	2.5	4.0	5.9	9.1	5.9	10.0	5.6	9.4	5.9	9.3
20	2.7	4.5	2.5	3.8	12.0	19.1	12.9	20.4	12.7	21.0	12.3	18.8
21	3.5	5.2	3.2	4.6	10.1	14.6	10.1	16.2	9.6	14.9	9.8	14.5
22	3.0	4.5	2.8	4.0	10.8	16.1	11.5	16.9	11.8	17.4	11.0	16.0
23	2.7	4.6	2.7	4.1	4.2	6.1	4.1	6.8	4.1	6.5	4.3	6.7
24	2.9	4.5	2.6	3.8	10.6	15.3	11.8	18.4	11.2	17.0	11.1	16.4
25	7.3	13.1	6.2	9.6	22.0	34.0	25.1	41.2	23.1	36.2	24.6	40.5

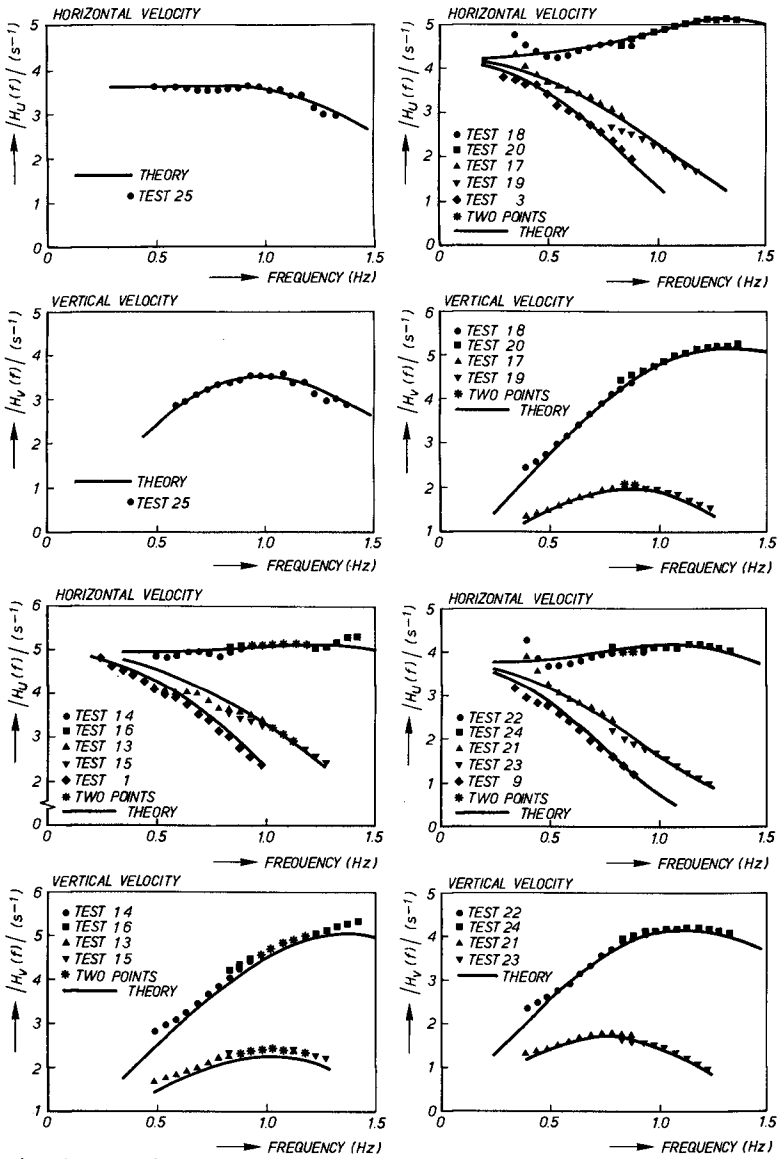


Fig. 4 Comparison of measured and computed frequency response function

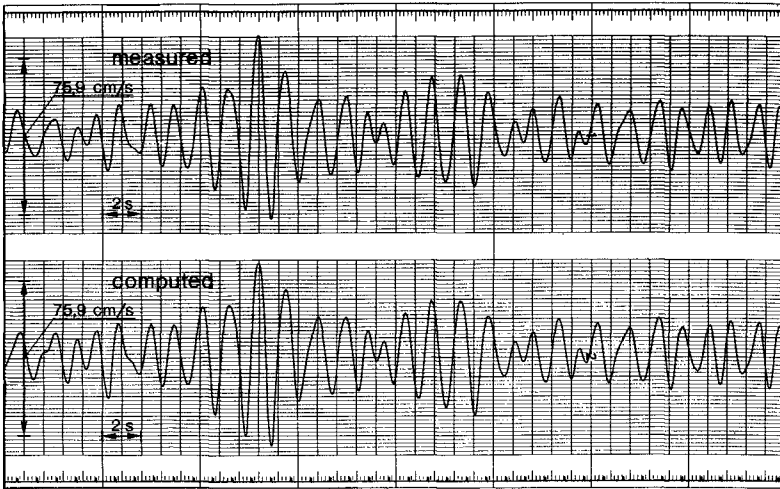


Fig. 5 Time records of measured and computed horizontal orbital velocity component at test 25

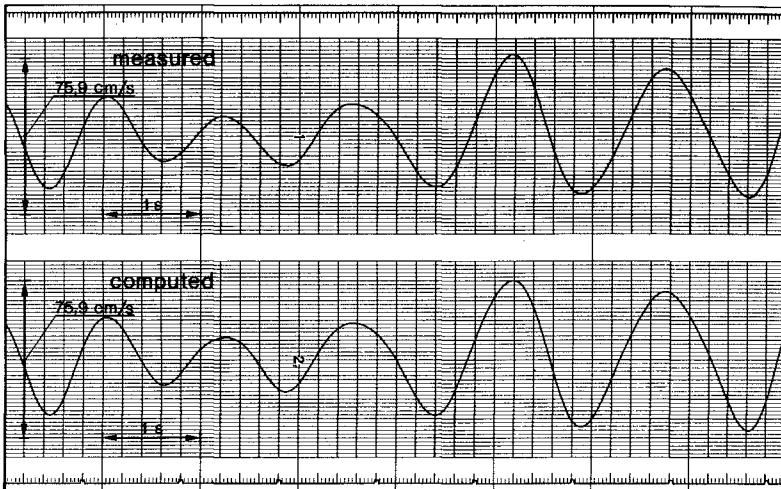


Fig. 6 Time records of measured and computed horizontal orbital velocity component at test 25 in more detail

TABLE IV MEASURED AND COMPUTED VERTICAL ORBITAL VELOCITY

TEST	VERTICAL ORBITAL VELOCITY							
	MEASURED				COMPUTED			
	v_{cs} cm/s	v_{cl} cm/s	v_{ts} cm/s	v_{tl} cm/s	v_{cs} cm/s	v_{cl} cm/s	v_{ts} cm/s	v_{tl} cm/s
13	5.2	7.8	5.2	7.5	4.9	7.0	4.8	7.0
14	9.2	14.2	9.0	13.3	9.0	13.2	8.7	12.9
15	5.7	9.0	5.8	8.9	5.3	8.3	5.3	8.1
16	11.2	18.3	11.4	17.8	11.0	17.7	11.1	17.9
17	4.4	6.3	4.6	6.6	4.2	6.1	4.3	6.4
18	8.7	12.9	8.4	12.6	8.6	12.6	8.8	12.4
19	4.7	8.0	4.9	7.9	4.6	7.5	4.6	7.3
20	12.2	19.9	12.3	19.4	12.1	19.9	12.1	19.2
21	4.9	7.6	5.6	7.8	5.0	7.6	5.0	7.3
22	9.1	14.5	9.0	13.9	9.0	14.3	8.9	13.4
23	3.7	5.7	3.7	5.8	3.6	5.7	3.6	5.8
24	11.0	16.4	11.0	17.0	10.8	16.5	10.8	16.8
25	21.0	34.7	20.9	32.8	20.8	35.6	21.2	33.0

7 DISCUSSION OF THE RESULTS

It is remarkable to see from the comparison in frequency domain that the velocities near the free surface match linear wave theory better than the velocities at mid-depth, whereas in view of test results in regular waves (see e.g. Le Méhauté, Divoky and Lin, 1968) just the opposite would be expected. This phenomenon was observed for both the orbital velocity components. The bottom velocities were indeed in more agreement with linear wave theory than the velocities at mid-depth. However, from the comparison in time domain, as far as executed, these tendencies could not be observed.

From Table III it appears that for the horizontal velocities the trough velocities are greater in magnitude than the crest velocities, contrary to the wave motion where the crests are higher than the troughs. The vertical velocities appeared to be distributed more symmetrically. It is important to note that these tendencies are followed by linear wave theory in most cases. However, when a higher order wave theory, such as the fifth order Stokes' method of De (1954), would be used for description of the velocity field in the individual waves of the irregular sea (the so-called deterministic approach) just the opposite would be found, apart from the fact that with respect to the crests of the waves only a "symmetrical" velocity distribution would be found. Also when linear wave theory is used in the random phase model, these tendencies will not be found, just as a consequence of the random phases by which equal crest and trough velocities will be found.

8 CONCLUSIONS AND RECOMMENDATIONS

In the present study low to moderately steep irregular waves have been

investigated, and it appeared that linear wave theory gives a reasonable description of the velocity field, in particular for the velocities near the free surface just beneath the deepest trough.

In view of these results it is advised to carry out further investigation of the applicability of linear wave theory to more severe wave conditions and to the velocities in the crests of the waves.

It will also be interesting to check linear wave theory for a spatial description of the velocity field. As for long-crested waves the correlation between water level fluctuations and orbital velocities in the same vertical has now been shown, this investigation can then be restricted to a check of the correlation in space of the wave motion at different locations. This was already investigated by Lundgren and Sand (1978), who found that the dispersion of the waves over limited distance is well described by linear wave theory, but that deviations increase with increasing distance. For directional seas research of the velocity field is necessary.

9 REFERENCES

- BENDAT, J.S. and PIERSOL, A.G. (1971).
Random data: Analysis and measurement procedures.
New York, Wiley.
- DE, S.C. (1955).
Contributions to the study of Stokes waves.
Proc. Camb. Phil. Soc.
- DELFT HYDRAULICS LABORATORY (1976).
Random wave generation of research on immersed marine vehicles.
Publication no. 167.
- GODEFROY, H.W.H.E. (1978).
Application of the Laser-Doppler velocity measurement in open and closed conduits.
Proc. of Flomeko 1978, Groningen, The Netherlands.
- LE MEHAUTE, B., DIVOKY, D. and LIN, A. (1968).
Shallow water waves. A comparison of theory and experiment.
Proc. Eleventh International Conference on Coastal Engineering.
- LUNDGREN, H. and SAND, S.E. (1978).
Natural wave trains: Description and reproduction.
Proc. Sixteenth International Conference on Coastal Engineering.

APPENDIX A. THEORY OF LINEAR SYSTEMS

Suppose that $x(t)$ is the input and $y(t)$ the output or response of a linear system and that $X(\omega)$ and $Y(\omega)$ are the corresponding Fourier transforms. Put $H(\omega)$ equal to the ratio $Y(\omega)/X(\omega)$; thus

$$Y(\omega) = H(\omega) \cdot X(\omega) \quad (A.1)$$

Inverse Fouriertransform of this relation yields the well-known convolution expression

$$y(t) = \int_{-\infty}^{+\infty} h(\tau) x(t-\tau) d\tau, \quad (\text{A.2})$$

where $h(t)$ is the inverse Fouriertransform of $H(\omega)$, given by

$$h(t) = \frac{1}{2\pi} \int_{-\infty}^{+\infty} H(\omega) e^{i\omega t} d\omega \quad (\text{A.3})$$

Often $h(t)$ is denoted by impuls response function, as

$$h(t) = \int_{-\infty}^{+\infty} h(\tau) \delta(t-\tau) d\tau,$$

and $H(\omega)$ by frequency response function.

Expression (A.1) yields the relation between input and output of the linear system in frequency domain and (A.2) in time domain. Thus if the frequency response function $H(\omega)$ of the linear system is known, then the response $y(t)$ on any arbitrary input can be computed, either by using (A.3) followed by (A.2), or by using (A.1), in which case first the input has to be Fouriertransformed, resulting in $X(\omega)$, and the output $Y(\omega)$ has to be Fourier inverted in order to obtain $y(t)$.

The frequency response function between wave motion and orbital velocity component at distance a from the bottom (both in the same cross-section of the flume) can be found with linear wave theory by putting as input of the linear system the wave motion in frequency domain

$$X(\omega) = e^{i\omega t} = \cos\omega t + i \sin\omega t. \quad (\text{A.4})$$

(Note that $e^{i\omega t}$ is the Fouriertransform of the impulse on time $-t$; t has to be considered as a parameter.)

According to linear wave theory the response $Y(\omega)$ is then given by

$$Y(\omega) = \frac{\omega \cosh ka}{\sinh kh} e^{i\omega t} \quad (\text{A.5})$$

for the horizontal orbital velocity component, which is defined positive in wave direction, and by

$$Y(\omega) = i \frac{\omega \sinh ka}{\sinh kh} e^{i\omega t} \quad (\text{A.6})$$

for the vertical orbital velocity component, which is defined positive in upwards direction.

Then by using (A.1) the frequency response functions can be determined to be

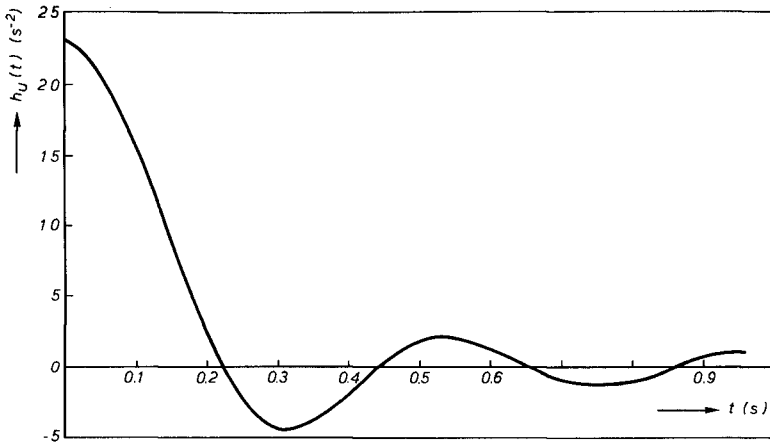


Fig. 7 Impuls response function for the horizontal orbital velocity component at test 14 and 16.
 $\omega_0 = 15 \text{ rad/s}$, $t_0 = 4.0 \text{ s}$

$$H_u(\omega) = \frac{\omega \cosh ka}{\sinh kh} \tag{A.7}$$

$$H_v(\omega) = i \frac{\omega \sinh ka}{\sinh kh}, \tag{A.8}$$

where indices u and v have been attached for distinction. With the aid of (A.3) it follows that

$$h_u(t) = \frac{1}{\pi} \int_0^\infty \left\{ \frac{\omega \cosh ka}{\sinh kh} \cos \omega t \right\} d\omega, \tag{A.9}$$

$$h_v(t) = \frac{1}{\pi} \int_0^\infty \left\{ \frac{\omega \sinh ka}{\sinh kh} \sin \omega t \right\} d\omega, \tag{A.10}$$

where also use was made of the property that the impuls response of a physical system is real. From these expressions it can be seen that $h_u(t)$ is an even and $h_v(t)$ an odd function of t. With these properties it follows from (A.2) that the horizontal and vertical orbital velocity components u and v at distance a from the bottom are respectively given by

$$u(t) = \int_0^\infty h_u(\tau) \{ \eta(t-\tau) + \eta(t+\tau) \} d\tau \tag{A.11}$$

$$v(t) = \int_0^\infty h_v(\tau) \{ \eta(t-\tau) - \eta(t+\tau) \} d\tau \tag{A.12}$$

It is remarkable to see from these relations that the response on time t depends on the wave motion $\eta(t)$ before and after t. Thus, not only the past but also the future of $\eta(t)$ determines the velocities at time t. Physically seen this is rather strange. However, it has to be realized that these relations are based on linear wave theory where it is assumed that the sinusoidal wave motion is present from $t = -\infty$ to $t = +\infty$. In view of this basic assumption, the results (A.11) and (A.12) could be expected.

In order to achieve existing integrals in (A.9) and (A.10), the constituent functions $H_u(\omega)$ and $H_v(\omega)$ have been put equal to zero for $\omega > \omega_0$, which implies that the response on input in this frequency range is zero. However, this interference is no limitation if ω_0 is chosen such that for higher frequencies the input signal does not contain energy.

For numerical computation of the integrals in (A.11) and (A.12), the functions $h_u(t)$ and $h_v(t)$, which approach to zero for $t \rightarrow \infty$, have been put equal to zero for $t > t_0$, where t_0 is chosen such that for $t > t_0$

$$|h(t)| < \epsilon \cdot \max_p |h(p)|$$

(e.g. is 0.01). An example of $h_u(t)$ is presented in Figure 7.

CHAPTER 10

INVESTIGATIONS ON IRREGULAR WAVES IN HYDRAULIC MODELS

by

Karl-Friedrich Daemrich, Wolf-Dietrich Eggert

Sören Kohlhasse

Franzius-Institut, University of Hannover, Germany

ABSTRACT

The first part of the paper deals with some aspects of wave generation by mechanical wave-generators, especially with hydraulic transfer functions for pusher movement of the paddle, and the influences of signal characteristics and analysis methods. In the second part, results of measurements of orbital velocities and pressures in irregular waves are presented, together with some results from theoretical simulation methods in the frequency and time domain, based on linear wave theory.

SCOPE OF INVESTIGATIONS AND INSTRUMENTATION

The possibility of the generation of predictable and reproducible irregular waves with servo-controlled wave-machines extends considerably the validity of hydraulic models and also allows an effective basic research for the improvement of dimensioning methods.

To get an impression of the transformation process of paddle-generated waves, hydraulic transfer functions between pusher movement of the board and generated wave trains are measured in different water depths, using as well noise spectra as natural wave trains as a basis for control signal calculations.

The investigations on orbital velocities and pressures in irregular waves are presented mainly under the aspect of the applicability of special analysis and simulation methods within investigations with irregular waves.

The investigations were performed in a wave basin of the "SONDERFORSCHUNGSBEREICH 79" and in a wave channel at the FRANZIUS-INSTITUTE of the University of Hannover (Table 1).

	wave basin	wave channel
length	45 m	118 m
width	18 m	2.2 m
max. water depth	0.6 m	1.5 m
max. wave height	0.4 m	0.5 m

Table 1: Dimensions of the hydraulic models

Both facilities are equipped with servo-controlled hydraulically driven wave generators and allow predefined partial flap/partial piston motions of the wave board.

Control signals were generated with a "WAVE SYNTHESIZER" as developed at the "HYDRAULIC RESEARCH STATION WALLINGFORD" and with a "WAVE SIGNAL GENERATOR" consisting of a tape-reader, a Digital to Analog Converter and some more electronic equipment, as produced by the "DANISH HYDRAULIC INSTITUTE".

The "WAVE SYNTHESIZER" generates pseudo-random signals with selectable power spectra and different sequenth lengths. However, the generated signals do not consider special wave characteristics like flat troughs and peaked crests or a definite wave grouping. The "WAVE SIGNAL GENERATOR" reads digitized data from punchtape and converts them to analog signals. With this instrument it is possible to generate control signals with arbitrary characteristics. The input signal may be converted with a built in approximate transfer function for pushertype motion. This allows to generate wavetrains - which are numerically described by the punch tape - at the wave board without any further calculations.

INVESTIGATIONS ON WAVE GENERATION

To generate a suitable spectrum in a basin or a channel the following transfer functions have to be considered:

- the mechanical transfer function of the wave-generator
- the hydraulic transfer function between paddle movement and generated wave at the paddle or near the paddle
- the transfer function for the transformation of the waves with increasing distance from the wave-generator.

The characteristics of the mechanical transfer function of the wave generator depend on the type of the generator and the settings of the servo-amplifiers and shall not be discussed here.

To prove the validity of the theoretical hydraulic transfer functions, several test series were performed. Fig. 1 shows a comparison of measured and theoretical transfer functions for a deepwater wave spectrum with noise characteristics.

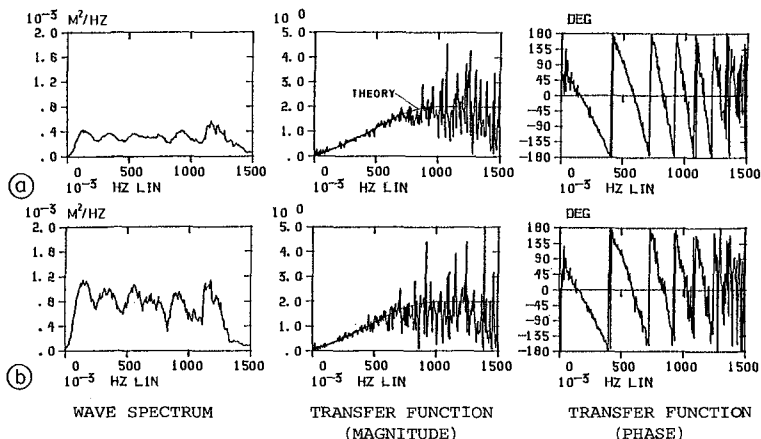


Fig. 1 Measured and theoretical hydraulic transfer functions for different wave steepnesses in deepwater ($d/(g \cdot T_m^2) = 0.058$)

a) $H_{1/3}/(g \cdot T_m^2) = 0.0051$ (nonbreaking waves)

b) $H_{1/3}/(g \cdot T_m^2) = 0.0077$ (slight breaking of high waves)

The wave probe was located in a distance of 5 m from the wave board. The transfer function was calculated from one sequence length of the pseudo-random signal (1024 data) without any averaging in this case, while the spectrum was smoothed by a moving average (11 data) in the frequency domain.

There is a rather good agreement between theory and measured values, even for slight breaking conditions, and it can be seen that it may be possible, to measure transfer functions very effective also with such an unrealistic wave spectrum.

As a next example results from waves in more transitional water are used to demonstrate the influence of the control signal characteristics.

From former tests in smaller water depths it could be expected, that transformation processes influence the quality of the hydraulic transfer functions.

Transformation process is called the changing of the wave train from a simple irregular water level fluctuation without any typical characteristics - for instance generated by a band-limited noise signal - to a wave train with distinct characteristics (peaked crests and flat troughs) depending on the relative water depth. We therefore selected a natural wave train as a basis for control signal generation of this example (Fig. 2).

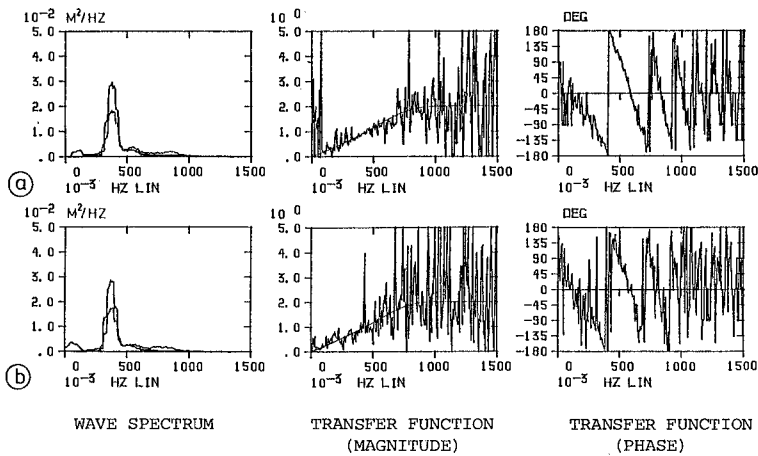


Fig. 2 Measured and theoretical hydraulic transfer functions for different signal characteristics in transitional water depths ($H_{1/3}/(g \cdot T_m^2) = 0.0056$); $d/(g \cdot T_m^2) = 0.025$)

- a) natural wave train
- b) random wave train with same amplitude spectrum, but random phase spectrum

Fig. 2a shows the measured transfer function using a wave train which was generated according to the natural wave train. This wave train includes all characteristics typical for the water depth and the period-range.

Contrarily, Fig. 2b shows the transfer function measured with an artificial wave train with the amplitude spectrum corresponding to the natural wave train, but with random

phase values of the frequency components.

The distinct minor scatter of the first transfer function may be seen as an indicator for the optimization of the control signal i.e., the transformation of the wave train from random-noise characteristics to the suitable and necessary characteristics for this waterdepth is indicated clearly by an increased scatter in the transfer function.

The next example shows hydraulic transfer functions in different water depths for wave spectra, generated with pseudo random control signals (Fig. 3).

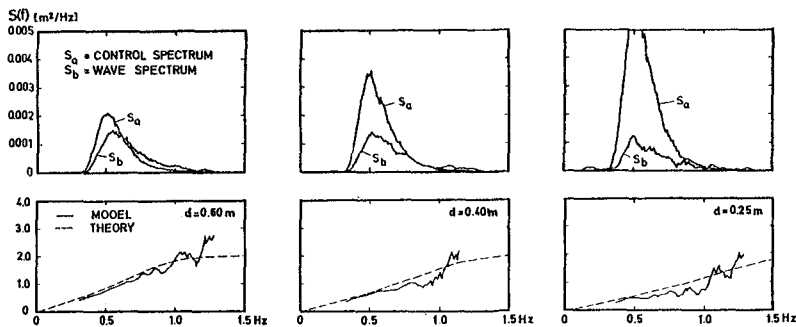


Fig. 3 Measured and theoretical hydraulic transfer functions for different water depths d (pseudo random control signals)

To make clearer the increasing losses, the transfer functions were smoothed in the frequency domain for this example.

The differences between measured and theoretical transfer functions are increasing with decreasing water depths. This may be explained by the stronger transformation processes.

These examples lead to the conclusion that for deepwater and to some extent also for transitional water depths the theoretical transfer functions are sufficient to calculate control signals for spectrum generation, but that corrections are necessary in small relative water depths, especially if bandlimited random noise signals are used as control signals.

Finally, the problem of generating special wave trains in a definite distance from the wave board shall be mentioned.

Some tests were performed, simulating a self-correcting system with the DHI-WAVE SIGNAL GENERATOR. The desired wave train was used as an input signal and corrected with the measured transfer function. This correction was repeated several times. It was found that with a well characterized wave train as a first input signal the first correction leads to rather good results (Fig. 4). However, this work is only at the beginning and demands more experience.

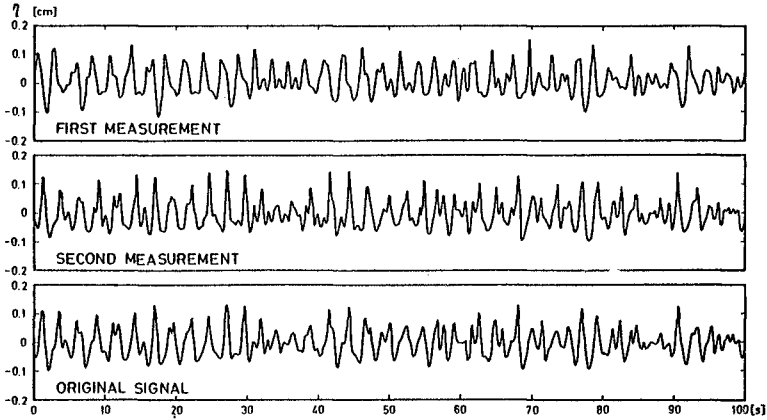


Fig. 4 Simulation of a self-correcting system with the DHI-WAVE SIGNAL GENERATOR

SOME REMARKS ON THE CALCULATION OF TRANSFER FUNCTIONS

As shown for demonstration before, the transfer functions were generally calculated from wave trains with pre-defined repetition periods and always the complete sequenth-length was analyzed as one data block. Sometimes a frequency smoothing was performed.

Calculation in that way was done, because the distance between the wave board and the wave probe leads to unrealistic values of the measured transfer functions, if the time series is shared into small time cycles, and the final results were calculated from the averaged auto-power and cross-power spectra. The following example may demonstrate this (Fig. 5).

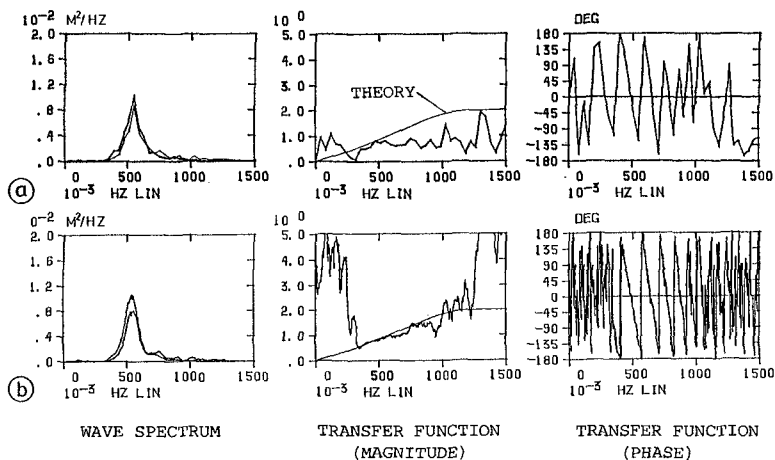


Fig. 5 Influence of the calculation method on the magnitude and phase of a transfer function

- a) averaged auto- and cross-spectrum
- b) without averaging but with equivalent frequency smoothing of the magnitude

Fig. 5a shows a transfer function calculated from eight parts of the time series using the averaged auto- and cross-power spectra; Fig. 5b shows the transfer function calculated from the same time series without averaging, but with an equivalent frequency-smoothing.

The tendency can be seen clearly. The averaged transfer function (Fig. 5a) does not describe the change in the wave spectrum sufficiently.

DEVELOPMENT OF THE WAVE SPECTRUM WITH INCREASING DISTANCE

Fig. 6 shows two examples of measured transfer functions between 5 and 12.5 m from the wave board (Fig. 6a) and between 15 and 22.5 m (Fig. 6b).

The change in the spectrum, expressed by the magnitude of these transfer functions, is not very important.

In addition, the development of some wave parameters from 2.5 to 30 m from the wave board in intervals of 2.5 m was calculated for this example (Table 2).

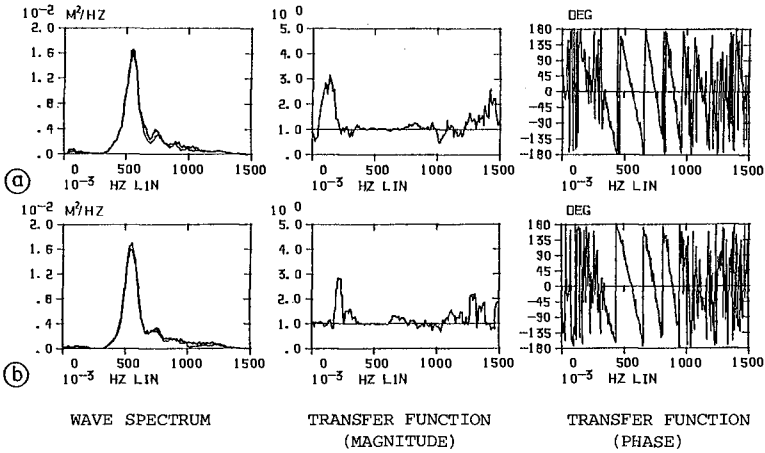


Fig. 6 Changes of the wave spectra with increasing distance and transfer functions

- a) 5.0 m to 12.5 m from the wave board
- b) 15.0 m to 22.5 m from the wave board

distance [m]	H_s [cm]	$H_{1/3}$ [cm]	$H_{1/10}$ [cm]	H_{max} [cm]	$T_{m0,1}$ [sec]	T_m [sec]	Q_p -
2.50	16.1	14.9	18.3	23.3	1.59	1.50	3.46
5.00	15.7	15.3	19.1	22.8	1.53	1.51	3.43
7.50	15.9	15.3	18.4	23.8	1.57	1.60	3.58
10.00	15.7	15.5	18.6	22.0	1.57	1.58	3.44
12.50	16.1	15.8	19.3	24.6	1.57	1.60	3.47
15.00	15.9	15.3	18.2	22.3	1.55	1.49	3.59
17.50	15.7	15.0	18.2	22.0	1.58	1.52	3.54
20.00	15.6	15.2	17.9	23.2	1.55	1.57	3.65
22.50	15.8	14.9	17.5	20.7	1.59	1.62	3.77
25.00	16.0	15.4	18.1	22.9	1.56	1.53	3.90
27.50	16.1	15.5	19.1	22.0	1.56	1.59	3.95
30.00	15.7	15.2	18.3	21.6	1.57	1.61	3.91

Table 2: Wave parameters in different distances from the wave board

It can be seen that characteristic wave parameters, e. g. significant wave heights or mean periods, derived from the spectrum or from the time series did not change with a clear tendency over this distance.

Only the peakedness factors Q_p show a slight trend from about 3.4 at the first wave gauge^B to 3.9 in a distance of 30 m.

ORBITAL VELOCITIES IN IRREGULAR WAVES

Velocities and pressures, the actual values causing the load of a structure, are used as an input for many dimensioning methods dealing with wave forces on structures.

It was the purpose of the investigations to check simulation methods with respect to the prediction of velocities and pressures, especially the maximum positive and negative values in every single irregular wave.

Inductive type and impeller type probes were used to measure horizontal and vertical velocity components. However, transfer functions were only calculated from signals of the inductive type probe.

The spectra were mostly JONSWAP-spectra, generated with the "WAVE SYNTHESIZER", but additionally a natural wave train and a random noise spectrum were investigated for comparison.

The significant wave heights ranged from 10 to 25 cm, the water depth was 1.0 m in most of the tests; the velocities were measured in different depths (- 0.25 m, - 0.50 m, - 0.85 m).

The first step of the analysis was the calculation of the transfer function between wave spectrum and velocity spectrum and the comparison with the theoretical transfer function according to linear wave theory.

Fig. 7 shows exemplarily some typical results for velocity components measured in a depth of 25 cm below "still water level".

It can be stated, that there are no significant differences between the transfer functions of the different wave spectra, and even or just the spectrum in Fig. 7b yields to a good agreement with the theory.

However, it was the purpose of the investigation, to predict maximum positive and negative velocities in every wave of a given wave train. Therefore, three simulation methods on the

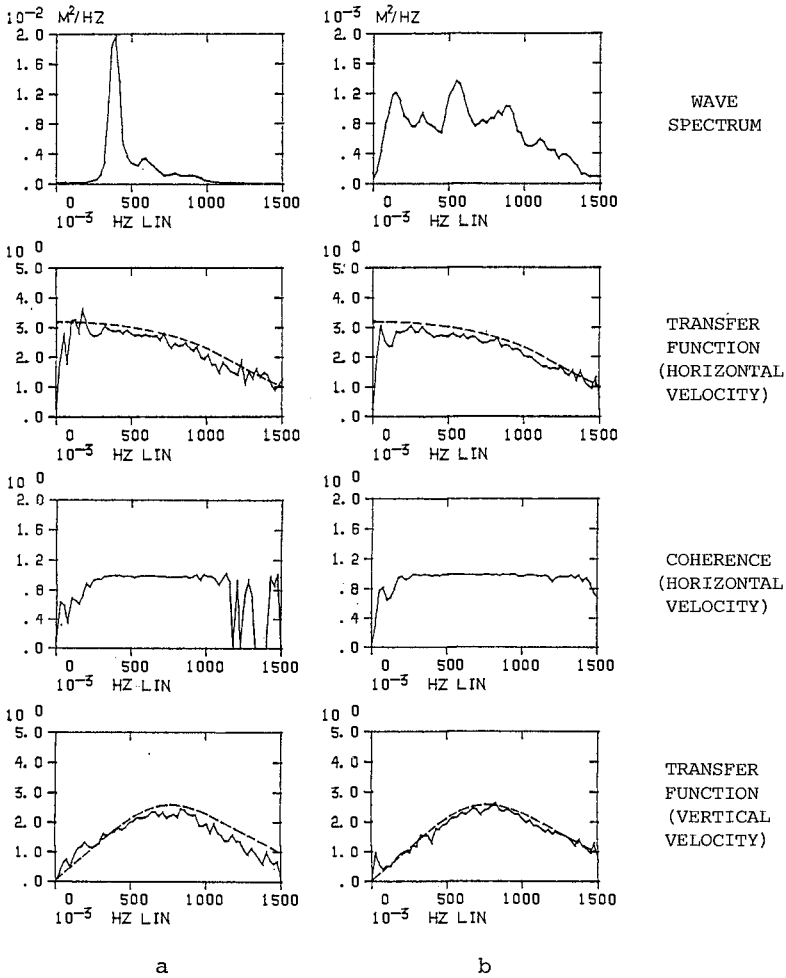


Fig. 7 Transfer functions and coherence functions of orbital velocities
 a) natural wave train
 b) random noise control signal

basis of linear wave theory were applied, one in the frequency domain and two in the time domain.

For the superposition method with theoretical transfer functions the FOURIER-transformation of the measured wave train was calculated, each frequency component was multiplied with the pertinent value of the theoretical transfer function according to linear wave theory. The time series of the velocities was then recalculated or superimposed from this FOURIER-components. The maxima of the measured velocity time series were now compared with the maxima of the simulated velocities (Fig. 8).

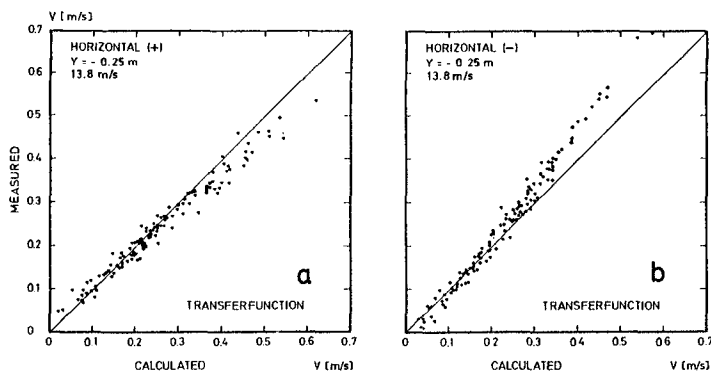


Fig. 8 Comparison of measured and with the theoretical transfer function predicted horizontal velocities (JONSWAP spectrum, $\gamma = 3.3$, $U = 13.8$ m/sec, scale 1 : 20)

- a) positive maxima
- b) negative maxima

The scatter of the data is relatively small, but the tendency is generally, that the measured horizontal velocities are lower than the predicted ones under a wave crest, and higher than the predicted ones under a wave trough.

The next two simulation methods are based on analysis methods in the time domain. Such methods have to be used, because it is not always possible to calculate a FOURIER-transformation, for instance when measurements are available only on recording chart, when signals are distorted or if there is no suitable computer equipment available. For these methods regular wave parameters must be defined for every irregular wave of the wave train.

A common method to define a wave parameter in the time domain is the zero-crossing method. For these examples the zero-down-crossing parameters were used to calculate velocities with the linear wave theory.

A typical result from the same test as Fig. 8 is shown by Fig. 9.

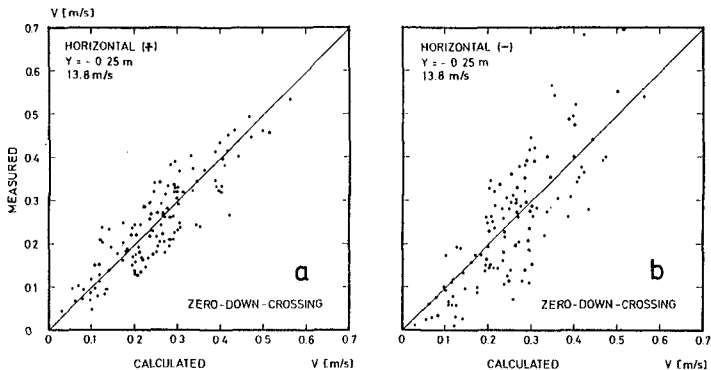


Fig. 9 Comparison of measured and predicted horizontal velocities according to zero-down crossing definition

- a) positive maxima
- b) negative maxima

The scatter of the data is remarkably wider in comparison to the superposition method.

A better definition for the physical efficient part of the wave was found by comparing the measured wave train and the pertinent velocity time series visually (Fig. 10).

The similarity of the both time series is evident. It seems that, for instance the velocity in the positive region has the same trend as the positive part of the wave. This effect, which is independent on the shape of the preceding wave trough leads to the following definition of the wave parameters for this special problem.

It was proved to take no longer the wave height and period of the whole wave, according to zero-crossing-definition, but to take the height and period of the pertinent halve wave to calculate the maximum velocities with linear wave theory.

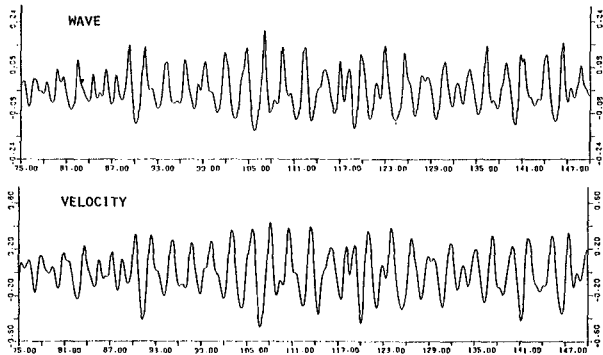


Fig. 10 Example of time series of waves and pertinent measured horizontal velocities

Fig. 11 shows a sketch of this definition, which is called "complementary method" in the following.

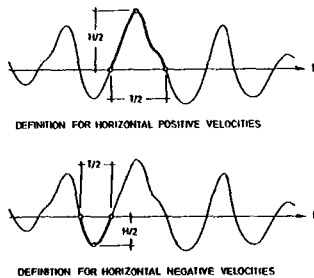


Fig. 11

Definition sketch for determination of wave parameters according to complementary method (horizontal velocities)

This - in the physical sense - efficient part of the wave was completed to a full sine wave for calculation.

Comparative results from the simulation of horizontal velocities with the complementary method are shown in Fig. 12, again for the same test as shown by Fig. 8 and 9.

The scatter of the results is of the same order as the scatter of the results from the much more comprehensive superposition method and remarkably smaller than the results according to zero-crossing method.

In the following, two more examples of measurements of positive horizontal velocities are given.

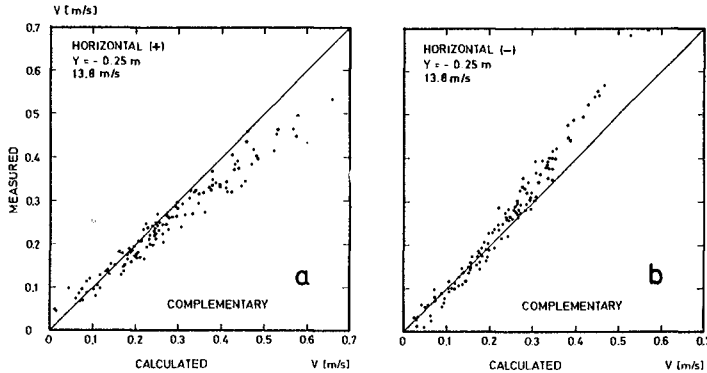


Fig. 12 Comparison of measured and predicted horizontal velocities according to complementary method

- a) positive maxima
- b) negative maxima

Fig. 13 shows results derived from measurements in a natural wave train with wave heights and periods similar to the preceding example.

For all simulation methods the scatter is of the same order as in the example before.

Finally, Fig. 14 shows results from a test with a wave time-series similar to the first example, but with amplitudes of only 50 %.

The scatter is very small in comparison to the examples before, but still the same tendency can be seen.

The velocities under the wave crest are generally smaller than the predicted values and, under the wave trough, they tend to be higher or equal to the predicted values.

The three simulation methods were also used to determine vertical velocities theoretically. For the complementary method it was proved to take the pertinent wave height as sketched in Fig. 15.

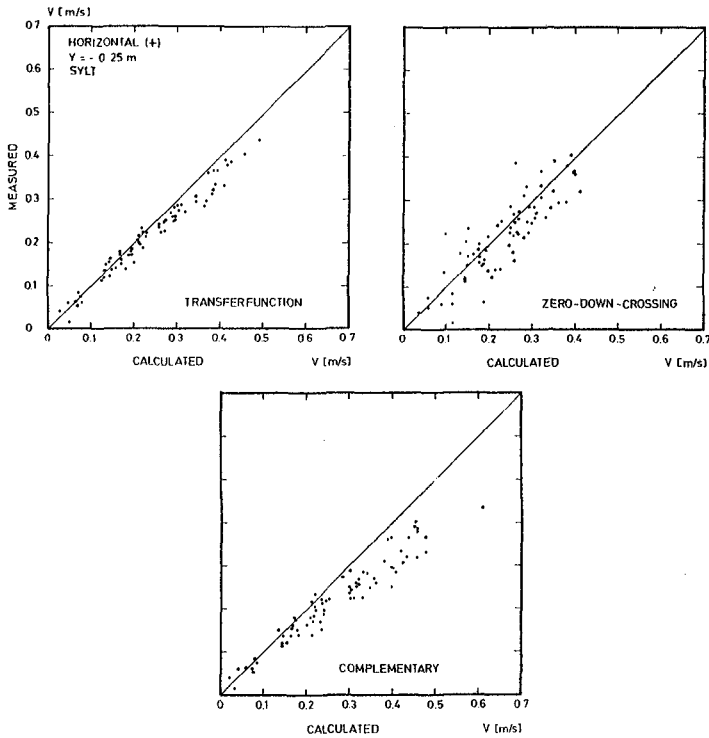


Fig. 13 Comparison of measured and predicted positive horizontal velocities according to different simulation methods (natural wave train)

For calculations of the positive maximum of the vertical velocity the wave height between the preceding trough and the crest was used and the wave height between the crest and the following trough for the calculation of the negative maximum of the vertical velocity respectively. The corresponding wave periods were defined as shown in Fig. 15.

Some results from the measurements of vertical positive and negative velocities are presented in Fig. 16.

The scattering of the data using the complementary method and superposition method (with theoretical transfer function) is of the same order but, contrarily to the results from horizontal velocity components, there is no remarkable difference between the positive and negative velocities.

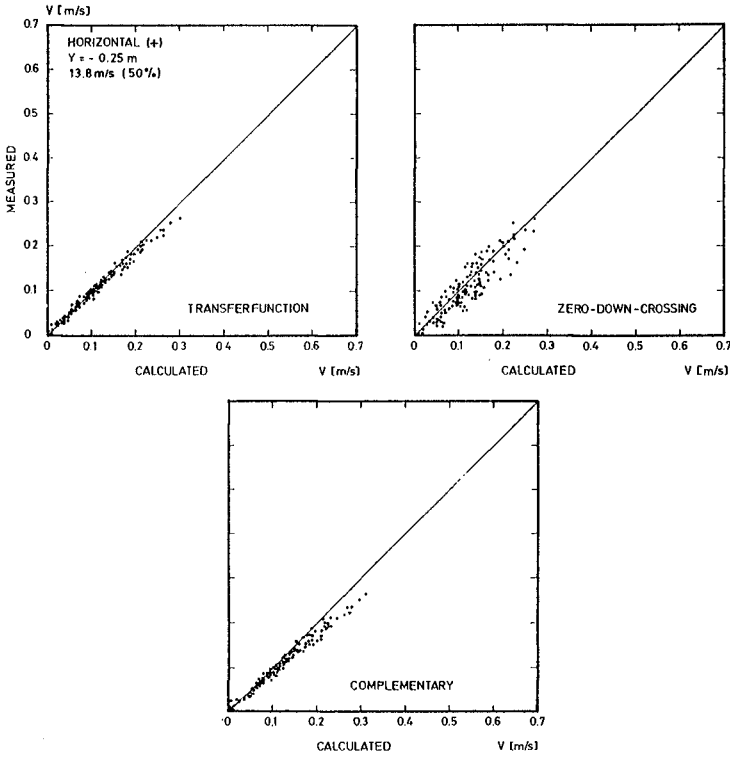


Fig. 14 Comparison of measured and predicted positive horizontal velocities according to different simulation methods (JONSWAP spectrum, $\gamma = 3.3$, $U = 13.8$ m/s, scale 1 : 20, halved amplitude)

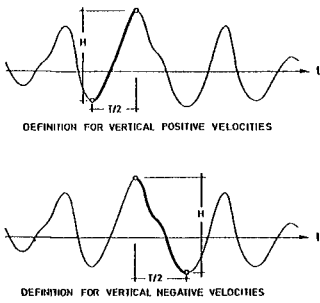


Fig. 15

Definition sketch for determination of wave parameters according to complementary method (vertical velocities)

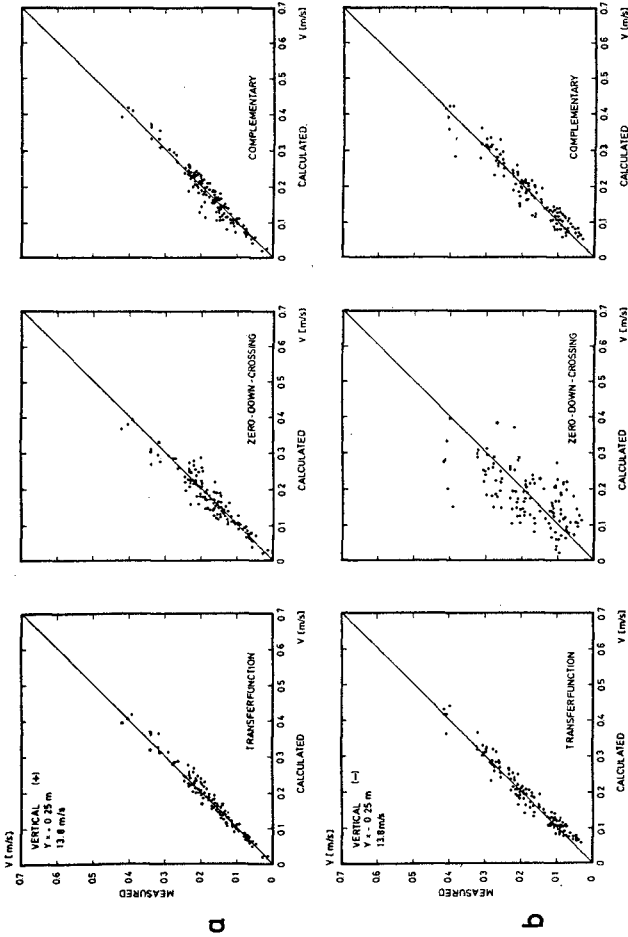


Fig. 16 Comparison of measured and predicted vertical velocities according to different simulation methods (JONSWAP spectrum, $\gamma = 3.3$, $U = 13.8$ m/sec, scale 1 : 20)

- a) positive maxima
- b) negative maxima

In this case the zero-down crossing method leads to good results for the positive values too, because nearly the same part of the wave is used to calculate the velocity components. However, for the negative velocities the scatter is remarkably wide.

The investigations on the pressure in irregular waves can only be mentioned in the scope of this paper. Theoretical simulations were done similarly to the simulations of the velocities. Results from the superposition method with theoretical transfer functions were still better than for the velocities. The scatter of the results simulated by the complementary method was less than the scatter from zero-crossing simulation. There is the same tendency too, that the predicted pressure under the wave crest is higher than the measured pressure and the predicted negative pressure is lower than the measured pressure in the wave trough.

ACKNOWLEDGEMENTS

This investigation was carried out as a part of the research programme of the Sonderforschungsbereich 79 at the Franzius-Institut für Wasserbau und Küsteningenieurwesen, Technical University of Hannover and was financed by the Deutsche Forschungsgemeinschaft. The authors gratefully acknowledge for having provided the facilities to conduct the investigations presented in this paper.

CHAPTER 11

METHOD OF ANALYSIS OF RANDOM WAVE EXPERIMENTS WITH REFLECTING COASTAL STRUCTURES

by

Pierre Gaillard, Michel Gauthier and Forrest Holly
Sogreah, Grenoble, France

ABSTRACT

A method of evaluation of the incident and reflected wave spectra in laboratory experiments or field investigations, based on the analysis of wave records obtained with a three-gauge array, is presented.

Results of a laboratory investigation with a rubble-mound breakwater and with a special type of sea-wall (ARC system) are given to illustrate the applications of the method.

INTRODUCTION

Random wave experiments performed with reflecting coastal structures require calibration of the wave generator movement in order to obtain incident waves conforming to specified characteristics. This calibration raises a problem because of multiple wave reflections from the structure and the wave paddle.

A technique often used in such cases, as well as in field investigations, consists in measuring the water level variation in front of the structure and in applying a method of analysis which estimates the incident and reflected waves.

Several methods of analysis based on measurements with two wave-gauges have formerly been published by Kajima (3), Thornton and Calhoun (5), Goda and Suzuki (2), Morden, Richey and Christensen (4). In these methods, however, the incident wave spectral density cannot be estimated correctly in the vicinity of a discrete number of critical frequencies, for which the distance between the two wave-gauges is a multiple of half the corresponding wave-length.

In this paper a different method, based on the analysis of wave records obtained with a three gauge array is presented. With this method, it is possible to estimate the incident and reflected wave spectra for the whole range of frequencies of interest.

BASIC ASSUMPTIONS

The incident waves are considered as a stationary, ergodic random process with gaussian properties. The water surface level variations related to waves propagating along the positive x axis are accordingly represented by:

$$\eta_I(x, t) = \text{Re} \left\{ 2 \int_0^{\infty} e^{i(2\pi ft - mx + \phi)} \sqrt{S_I(f)} df \right\} \quad (1)$$

with:

$$4\pi^2 f^2 = mg \tanh(mh) \quad (2)$$

f = wave frequency
 m = wave number
 h = Water depth at rest
 ϕ = random phase with constant probability density
 S_I = two-sided power spectral density of the incident waves

We shall consider a coastal structure in the wave tank, with its longitudinal axis parallel to the wave fronts. The structure section is assumed uniform so that diffraction effects are negligible. The reflected waves can thus be represented by:

$$\eta_I(x, t) = \text{Re} \left\{ 2 \int_0^{\infty} T(x, f) e^{i(2\pi ft - mx + \phi)} \sqrt{S_I(f)} df \right\} \quad (3)$$

The transfer function $T(x, f)$ related to the wave reflection, is a function of the location of the point of observation, and of frequency. In the following, we consider as reference the abscissa x_s of the seaward face of the structure, where the transfer function takes the value:

$$T_s = T(x_s, f) = C_R(f) e^{i\phi_s(f)} \quad (4)$$

$C_R(f)$: reflection coefficient of the structure

$\phi_s(f)$: phase lag due to wave reflection.

Provided that there is no wave damping or breaking along the wave flume, the transfer function T_k associated with any abscissa x_k is related to T_s by:

$$\begin{aligned} T_k &= T(x_k, f) = T_s \cdot e^{i2\theta_k} \\ \theta_k &= m(x_k - x_s) \end{aligned} \quad (5)$$

The objective of the analysis is to estimate from records of water level variations three unknown functions of frequency: the incident wave power spectral density S_I , the reflection coefficient $C_R(f)$ and the phase lag $\phi_s(f)$ due to this reflection.

Let us now consider the relationship between the incident waves and the partially or totally standing waves observed in front of the structure. Since the observed water level variations are simply a linear superposition of the incident and reflected waves given by (1) and (3), the relationship between incident waves and observed waves is defined by the transfer function:

$$T\eta_K\eta_I = 1 + T(x_k, t) \quad (6)$$

and the relationship between the spectrum of the observed waves $S_K(f)$ and the spectrum of the incident waves $S_I(f)$ is:

$$S_K(f) = S_I(f) \cdot T\eta_K\eta_I \cdot T\eta_K\eta_I^* \quad (7)$$

Where T^* stands for the complex conjugate of T .

From equations (4) to (7), the following expressions result:

$$S_K(f) = S_I(f) \cdot (1 + 2\text{Re}(T_s) \cos 2\theta_K - 2\text{Im}(T_s) \sin 2\theta_K + |T_s|^2) \quad (8)$$

$$S_K(f) = S_I(f) \cdot (1 + 2C_R(f) \cdot \cos(2\theta_K + \phi_s) + C_R^2(f)) \quad (9)$$

ANALYSIS WITH TWO WAVE GAUGES

From measurements of water level variations η_j, η_k at two locations x_j, x_k , it is possible to estimate the spectra $S_j(f)$ and $S_k(f)$, which are related to the unknown functions S_I, C_R and ϕ_s by equations similar to (8) and (9). It is also possible to obtain the cross-spectrum:

$$S_{jk}(f) = C_{jk}(f) - i Q_{jk}(f) = \int_{-\infty}^{+\infty} R_{jk}(t) e^{-i2\pi ft} dt \quad (10)$$

$$R_{jk}(\tau) = E(\eta(x_j, t) \cdot \eta(x_k, t - \tau))$$

The following relationship holds between the cross-spectrum $S_{jk}(f)$ and the incident wave spectrum $S_I(f)$:

$$S_{jk} = S_I(f) T\eta_j\eta_I \cdot T\eta_k\eta_I^*$$

$$S_{jk} = S_I(f) \cdot (1+T_j) \cdot (1+T_k^*)$$

$$S_{jk} = S_I(f) \cdot (1+T_s e^{i2\theta_j}) \cdot (1+T_s^* e^{-i2\theta_k}) \quad (11)$$

By separating the real and imaginary parts of (11), we obtain the co-spectrum and quad-spectrum:

$$C_{jk}(f) = S_I(f) \{ (1+|T_s|^2) \cdot \cos(\theta_j - \theta_k) + 2 \text{Re}(T_s) \cos(\theta_j + \theta_k) - 2 \text{Im}(T_s) \sin(\theta_j + \theta_k) \} \quad (12)$$

$$Q_{jk}(f) = S_I(f) (1 - |T_s|^2) \cdot \sin(\theta_j - \theta_k) \quad (13)$$

For simplicity, we shall write hereafter:

$$\theta_{jk} = \theta_j - \theta_k = m(x_j - x_k) \quad (14)$$

With the expressions of $S_j(f)$, $S_k(f)$ given by (8) and the expressions of the co and quad-spectra given by (12) (13), we have a set of four linear equations with three unknown functions of frequency $\text{Re}(T_s)$, $\text{Im}(T_s)$ and $|T_s|^2$. A necessary and sufficient condition for having a non zero solution of this set of equations is:

$$\begin{vmatrix} 2 \cos 2\theta_j & -2 \sin 2\theta_j & 1 & S_j/S_I - 1 \\ 2 \cos 2\theta_k & -2 \sin 2\theta_k & 1 & S_k/S_I - 1 \\ 2 \cos(\theta_j + \theta_k) & -2 \sin(\theta_j + \theta_k) & \cos \theta_{jk} & C_{jk}/S_I - \cos \theta_{jk} \\ 0 & 0 & -\sin \theta_{jk} & Q_{jk}/S_I - \sin \theta_{jk} \end{vmatrix} = 0 \quad (15)$$

This condition gives the following expression of the incident wave spectrum:

$$S_{Ijk}(f) = \frac{S_j + S_k - 2(C_{jk} \cos \theta_{jk} - Q_{jk} \sin \theta_{jk})}{4 \sin^2 \theta_{jk}} \quad (16)$$

The subscript jk is added to indicate that this is an estimate of $S_I(f)$ derived from the wave records at abscissas x_j and x_k .

The spectra of the incident and reflected waves are related by:

$$S_R(f) = C_R^2(f) \cdot S_I(f) = |T_s|^2 \cdot S_I(f) \quad (17)$$

From (16) and (17) we get the following expression of the reflected wave spectrum:

$$S_{Rjk}(f) = \frac{S_j + S_k - 2(C_{jk} \cos \theta_{jk} + Q_{jk} \sin \theta_{jk})}{4 \sin^2 \theta_{jk}} \quad (18)$$

Expressions (16) and (18) are similar to those used by Kajima (3). Differences come only from the orientation of the positive x axis in opposite directions. From the preceding set of equations we can also derive the following expression for the transfer function:

$$T_{Sjk}(f) = \frac{-S_j e^{-2i\theta_k} - S_k e^{-2i\theta_j} + 2C_{jk} e^{-i(\theta_j + \theta_k)}}{4S_I(f) \cdot \sin^2 \theta_{jk}} \quad (19)$$

which can also be written as:

$$T_{Sjk}(f) = \frac{-S_j e^{-2i\theta_k} - S_k e^{-2i\theta_j} + 2C_{jk} e^{-i(\theta_j + \theta_k)}}{S_j + S_k - 2(C_{jk} \cos \theta_{jk} - Q_{jk} \sin \theta_{jk})} \quad (20)$$

CRITICAL FREQUENCIES

Formula (9) shows that the power spectral density of the actually observed waves is a periodic function of space, for a given frequency, with a period equal to one half of the wave length associated with this frequency.

For a given pair of wave gauges, there is a discrete number of frequencies f_{cjk} , for which the distance between the wave gauges is a multiple of half the corresponding wave length $L(f_{cjk})$.

$$x_j - x_k = \pm p \frac{L}{2} (f_{cjk}) \quad p = 1, 2, 3... \quad (21)$$

For those critical frequencies, the following properties should hold:

$$\left. \begin{aligned} S_j(f) &= S_k(f) \\ C_{jk}(f) &= \pm S_k(f) \\ Q_{jk}(f) &= 0 \\ \sin(\theta_j - \theta_k) &= 0 \end{aligned} \right\} C_{jk} \cos(\theta_j - \theta_k) > 0 \quad f = f_{cjk} \quad (22)$$

As a result the numerator and denominator of (16) and (18) tend towards zero and the incident and reflected wave spectra cannot be evaluated with these formulae for these specific frequencies.

Because of round-off errors and background noise the numerator does not actually vanish, and it is observed in numerical computations that the absolute value of S_I and S_R increases considerably in the vicinity of the critical frequencies. This behaviour has been observed with all the methods of analysis based on measurements with two-gauge arrays.

Because of this difficulty, the distance between the wavegauges must be chosen carefully, with due consideration to the frequency range (f_{min} , f_{max}) over which the wave spectrum extends. Goda and Suzuki (2) suggest the following rule for this choice.

$$x_j - x_k = 0.05 L(f_{min}) = 0.45 L(f_{max}) \quad (23)$$

ANALYSIS WITH THREE WAVE GAUGES

From simultaneous measurements of water level variations with a three-gauge array, nine functions of frequency are derived i.e. the three spectra S_1, S_2, S_3 corresponding to the observed partially standing waves at the gauge locations, the three co-spectra C_{21}, C_{31}, C_{32} and quad-spectra Q_{21}, Q_{31}, Q_{32} associated with the different couples of gauges.

With each of these functions, is associated an equation such as (8), (12) or (13). We thus have a set of nine equations for three unknown functions only. Since there are more data available than unknown parameters many different formulae can be derived for evaluating the incident wave spectrum and the transfer function representing the wave reflection from the structure. Many of these formulae are inappropriate because they cannot be applied for critical frequencies associated with some or all of the gauge intervals.

A theoretical analysis developed in (1) led us to the following formulae for evaluating the incident and reflected wave spectra:

$$\begin{aligned} S_I(f) &= \alpha_{21} S_{I21}(f) + \alpha_{31} S_{I31}(f) + \alpha_{32} S_{I32}(f) \\ S_R(f) &= \alpha_{21} S_{R21}(f) + \alpha_{31} S_{R31}(f) + \alpha_{32} S_{R32}(f) \end{aligned} \quad (24)$$

$$\alpha_{21} + \alpha_{31} + \alpha_{32} = 1 \quad \alpha_{jk} \geq 0 \quad (25)$$

S_{Ijk} and S_{Rjk} are estimates of the incident and reflected wave spectra obtained from (16) and (18) for the different possible associations of gauges by pairs.

The weighting factors α_{jk} are positive functions of frequency, defined in such a way that (24) be valid for all frequencies, of interest, including for the critical values associated with the different gauge intervals. For this to be true, the gauge locations must be chosen so as to avoid any coincidence of the critical frequencies associated with the different gauge spacings; otherwise, effects similar to those observed with a two-gauge array would be encountered for these frequencies.

For critical frequencies f_{c12} , S_{I12} cannot be computed from (16) as shown in the preceding section, so α_{21} should vanish for this frequency. By an analysis of equations (8), (12), (13), it can be shown that solutions given by (16) for S_{I32} , S_{I31} and by (18) for S_{R32} , S_{R31} are theoretically equivalent for these critical frequencies. However, since slight differences may result from background noise $S_I(f)$ and $S_R(f)$ are estimated by:

$$\begin{aligned} S_I(f_{C12}) &= 0.5 (S_{I31} + S_{I32}) \\ S_R(f_{C12}) &= 0.5 (S_{R31} + S_{R32}) \end{aligned} \quad (26)$$

Similar formulae are used for the critical frequencies f_{C31} , f_{C32} associated with the other gauge intervals. The weighting functions are thus subject to the conditions:

$$\begin{aligned} \alpha_{jk}(f) &\rightarrow 0 \\ \alpha_{j1}(f) &\rightarrow 1/2 \quad \text{for } f \rightarrow f_{cjk} \\ \alpha_{k1}(f) &\rightarrow 1/2 \end{aligned} \quad (27)$$

We use the following functions, which satisfy conditions (25) and (27):

$$\begin{aligned} \alpha_{jk}(f) &= \frac{\sin^{2n}\theta_{jk}}{S_\alpha^{(n)}} \quad n = 1, 2, 3 \dots \\ S_\alpha^{(n)} &= \sin^{2n}\theta_{21} + \sin^{2n}\theta_{31} + \sin^{2n}\theta_{32} \end{aligned} \quad (28)$$

Insertion of these functions in (24), for $n = 1$ and 2 , leads to:

$$\begin{aligned} S_I(f) &= \frac{\bar{S}^{(n)} - \bar{C}^{(n)} + \bar{Q}^{(n)}}{2 S_\alpha^{(n)}} \\ S_R(f) &= \end{aligned} \quad (29)$$

$$\bar{S}^{(1)} = S_1 + S_2 + S_3$$

$$\bar{C}^{(1)} = C_{21} \cos \theta_{21} + C_{31} \cos \theta_{31} + C_{32} \cos \theta_{32} \quad (30)$$

$$\bar{Q}^{(1)} = Q_{21} \sin \theta_{21} + Q_{31} \sin \theta_{31} + Q_{32} \sin \theta_{32}$$

$$\bar{S}^{(2)} = 0.5(S_1+S_2)\sin^2\theta_{21}+0.5(S_1+S_3)\sin^2\theta_{31}+0.5(S_2+S_3)\sin^2\theta_{32}$$

$$\bar{C}^{(2)} = C_{21}\cos\theta_{21}\sin^2\theta_{21}+C_{31}\cos\theta_{31}\sin^2\theta_{31}+C_{32}\cos\theta_{32}\sin^2\theta_{32} \quad (31)$$

$$\bar{Q}^{(2)} = Q_{21}\sin^3\theta_{21}+Q_{31}\sin^3\theta_{31}+Q_{32}\sin^3\theta_{32}$$

The transfer function associated with the wave reflection on the coastal structure is estimated by means of:

$$T_S(f) = \frac{N_{21}\sin^2\theta_{21}+N_{31}\sin^2\theta_{31}+N_{32}\sin^2\theta_{32}}{D_{21}\sin^2\theta_{21}+D_{31}\sin^2\theta_{31}+D_{32}\sin^2\theta_{32}} \quad (32)$$

with:

$$\begin{aligned} N_{jk} &= -S_j e^{-i2\theta_k} - S_k e^{-i2\theta_j} + 2 C_{jk} e^{-i(\theta_j+\theta_k)} \\ D_{jk} &= S_j + S_k - 2 (C_{jk} \cos \theta_{jk} - Q_{jk} \sin \theta_{jk}) \end{aligned} \quad (33)$$

N_{jk} and D_{jk} are the terms involved in (20) when estimating the transfer function from each pair of gauges.

The reflection coefficient of the structure can be estimated by two possible methods:

- the first is by the use of (17) with the expressions of S_I and S_R given by (24), i.e. by (29) (30) (31) for the two lowest orders of the weighting functions.
- the second is by the use of (4) with the transfer function given by (32) and (33).

In the following we refer to these two estimates as $C_R(f)$ and $C'_R(f)$ respectively.

APPLICATION TO LABORATORY EXPERIMENTS

Examples of application of the present method to random-wave experiments conducted at Sogreah's laboratory will now be given.

EXPERIMENTAL SET-UP

The experiments were performed in a wave tank of 39 m length, 1.40 m depth and 0.60 m width, with the set-up indicated in figure 1. The bottom profile conforms to an actual situation for which breakwater stability tests were required. Two kinds of structures were considered at a scale of 1/50:

- a) a rubble mound breakwater with a two layer tetrapod covering on a seaward slope of 4/3.
- b) a vertical sea-wall with an anti-reflection chamber (ARC system), as described in (6)

Though a three-gauge array is generally sufficient for applying the present method, a four-gauge array was used in these particular experiments, in order to compare the results provided by the four different combinations of gauges by triplets. Water level variations were measured with capacitance-type wave gauges.

Figure 1 shows one of the wave-gauge arrangements used. In this case, gauges 1 and 4 are located respectively at the third anti-node and third node of the partially standing waves corresponding to the spectral peak frequency.

Data retrieval and digitization of water level measurements were performed on a General Automation GA220 minicomputer of 16 Kwords capacity. A Fortran computer code based on the previously described method, is implemented on this computer for current experiments.

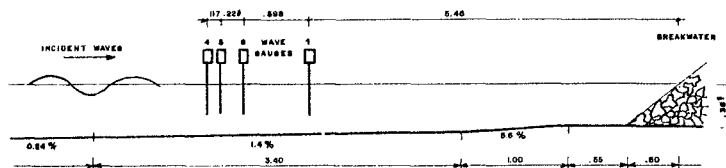
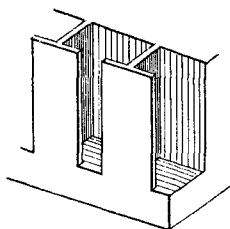


Fig.1 EXPERIMENTAL SET-UP



Model 1: BREAKWATER WITH TETRAPODS



Model 2: SEA-WALL WITH ARC SYSTEM

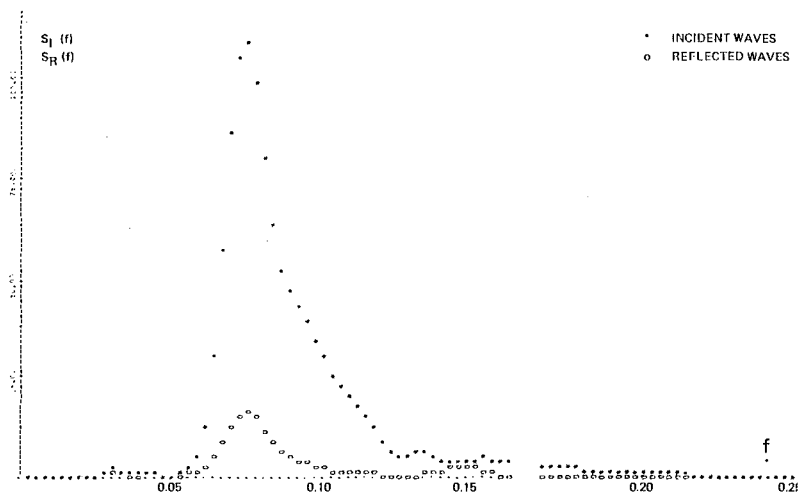


Fig. 2 Incident and reflected wave spectra obtained with model 1

For processing the data of the four-gauge array and for comparing the results of the four different triplets, a special code was implemented on an ITEL AS 6 computer.

Wave records were analysed over a period of 160 s, with a time step of 0.1 s. Auto and cross-covariance functions were computed with a maximum lag of + 10 s. This analysis provided values of the 16 following functions with a frequency interval of 0.02 Hz at model scale, i.e. of 0.0028 Hz at prototype scale:

- the spectra of waves observed at the gauge locations S_1, S_2, S_3, S_4
- the six co-spectra $C_{21}, C_{31}, C_{41}, C_{32}, C_{42}, C_{43}$
- the six quad-spectra $Q_{21}, Q_{32}, Q_{41}, Q_{32}, Q_{42}, Q_{43}$

The number of degrees of freedom associated with the preceding parameters is approximately 40, with a Hamming spectral window. From the Chi-square law it is concluded that the 80% confidence interval lies between 73% and 130% of the estimated power spectral density.

INCIDENT AND REFLECTED WAVE SPECTRA

Figure 2 shows the incident and reflected wave spectra derived from the wave records of gauges 2, 3, 4 of figure 1, with the first type of structure, by application of formulae (29) and (31).

Figure 3 gives a simultaneous plot of the incident wave spectra obtained by analysis of the four different combinations of wave gauges (O stands for gauges 1, 2, 3; v for gauges 1, 2, 4; x for gauges 1, 3, 4 and * for gauges 2, 3, 4). As this graph results from a printer output, coincident values of the power spectral densities are plotted by a single symbol. The four estimates of the incident wave spectrum are in excellent agreement.

Figure 4 gives a simultaneous plot of the incident wave spectra obtained by analysis of the four gauges with the two lowest orders of weighting functions (28) (* stands for $n=1$ and O for $n=2$). No significant difference appears here between the two procedures of estimation of the incident wave spectrum.

The same conclusions were drawn from tests with the second type of structure.

With this technique, the gauge locations should be chosen so as to avoid too proximate values of the critical frequencies associated with the different intervals. Figure 5 refers to a particular wave gauge arrangement, 1, 2, 4, where critical frequencies associated with the gauge intervals are very nearly coincident, so that $S_{\alpha}^{(n)}$, defined by (28), drops to a very low value for frequencies near $f=1.55$ Hz at model scale and $f=0.22$ Hz at prototype scale. This situation leads to undesirable effects shown in figures 6 and 7.

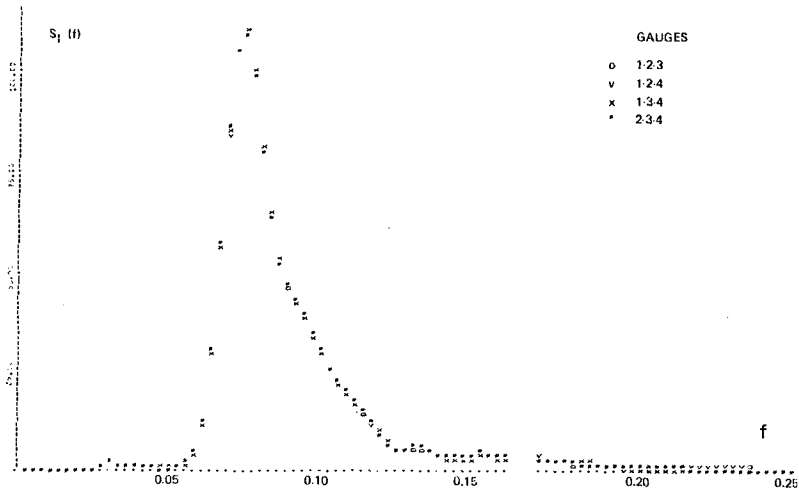


Fig. 3 Incident wave spectrum resulting from 4 different 3 - gauge arrays with $n = 2$

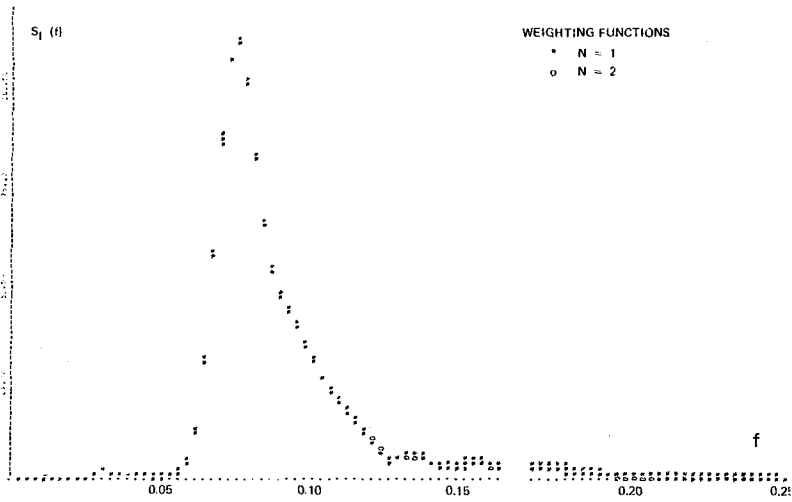


Fig. 4 Incident wave spectrum obtained with weighting functions of order $n = 1$ & 2

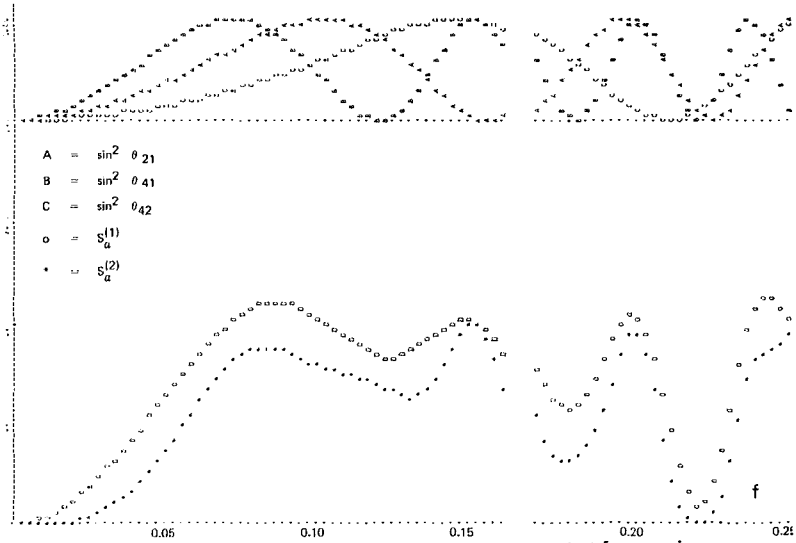


Fig. 5 Weighting functions with nearly coincident critical frequencies

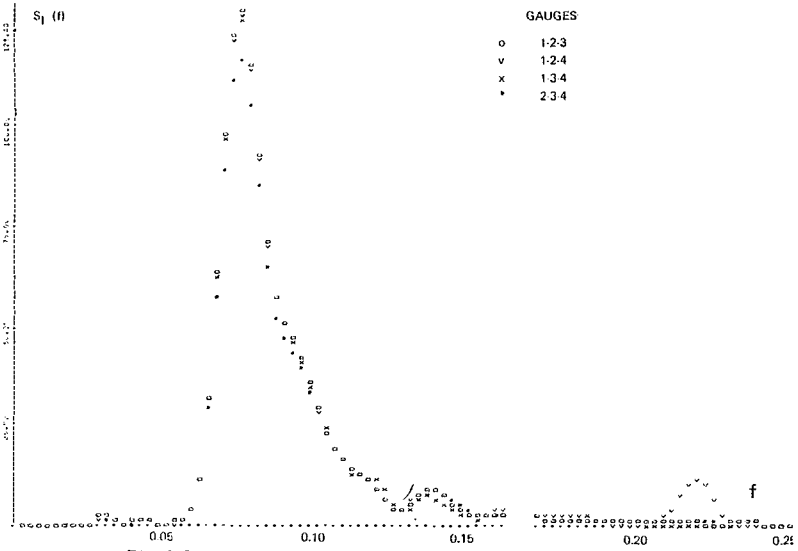


Fig. 6 Comparison of results in the situation of Fig. 5, for gauges 1-2-4

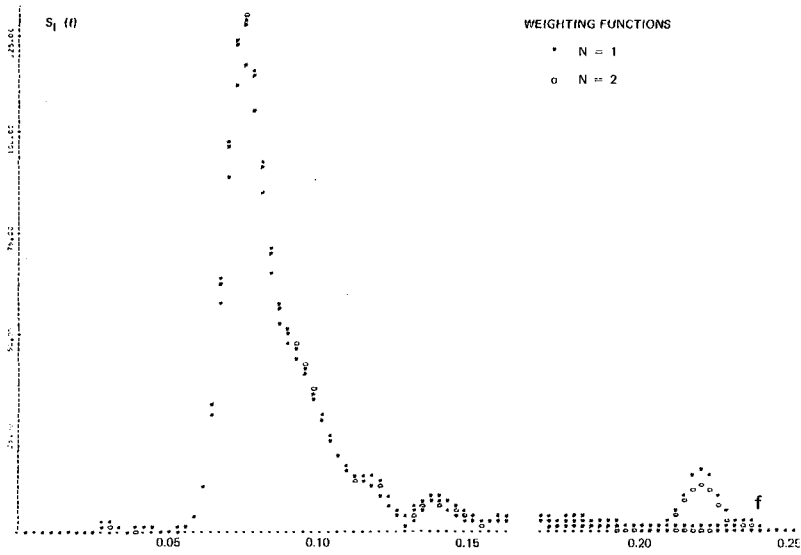


Fig. 7 Effect of weighting parameter n in the situation of fig. 5

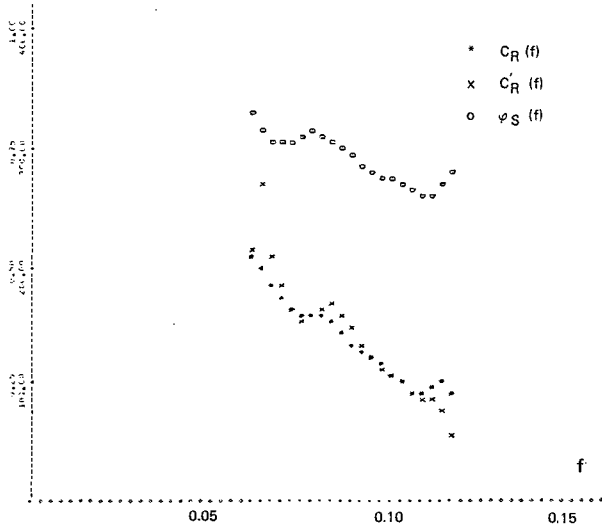


Fig. 8 Reflection coefficients and phase lag for model 1

In figure 6, it is seen that the incident wave spectrum estimated from gauges 1, 2, 4 exhibits a small hump in the vicinity of the previously mentioned frequency, while this is not observed with the spectra estimated from the three other gauge associations.

Figure 7 is a graph similar to figure 4. It shows that the weighting functions of order 1 gives a hump of greater magnitude than those of order 2, in the frequency interval where critical frequencies are nearly coincident, while results are almost the same for other frequencies. Because of this, preference should be given to (31) for evaluating the incident and reflected wave spectra.

Another point should be stressed about the presentation of wave spectra derived through this analysis. The frequency $f=0$ is a critical frequency whatever the choice of the gauge intervals, since $\sin \theta_{jk}$ vanishes for this value. For this reason, a sharp rise in the absolute value of $S_I(f)$ and $S_R(f)$ is observed at very low frequencies, with a three-gauge array as well as with a two-gauge array. This effect was illustrated in (1) with numerically simulated random waves, for which it was clear that no energy was actually present in the low frequency range. This spurious effect affects a frequency interval equal to the width of the specific spectral window used for smoothing wave spectra. A cut-off frequency equal to this bandwidth is introduced in the computations.

REFLECTION COEFFICIENTS

Figures 8 and 9 show the variation with frequency of the reflection coefficients $C_R(f)$, $C'_R(f)$ for the two structures previously mentioned, together with the phase lag $\phi_S(f)$. $C_R(f)$ is derived here by means of the weighting functions of order 2.

It was shown in (1), with numerically simulated water waves, that a good estimate of the reflection coefficients cannot be obtained for frequencies where the power spectral density is very low. A threshold value dependent on the peak spectral density, was accordingly chosen for selecting the frequency range over which these parameters are computed. Results are presented here for a threshold value of 10%.

The two procedures described for evaluating the reflection coefficient of the structure versus frequency, though theoretically equivalent, give slightly different estimates of this parameter. Both procedures give the same general trend which is typical of the structures considered. The rubble-mound breakwater exhibits a progressive decrease in reflection as frequency increases, due to higher dissipation as waves impinge on the artificial blocks. The ARC system on the other hand exhibits a U-shaped curve, with minimum reflection for a frequency dependent on the dimensions of the anti-reflection chamber, which acts as a resonator.

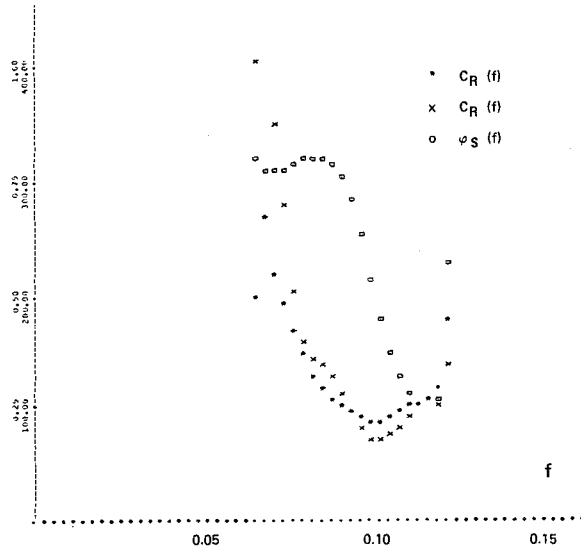


Fig. 9 Reflection coefficients and phase lag for model 2

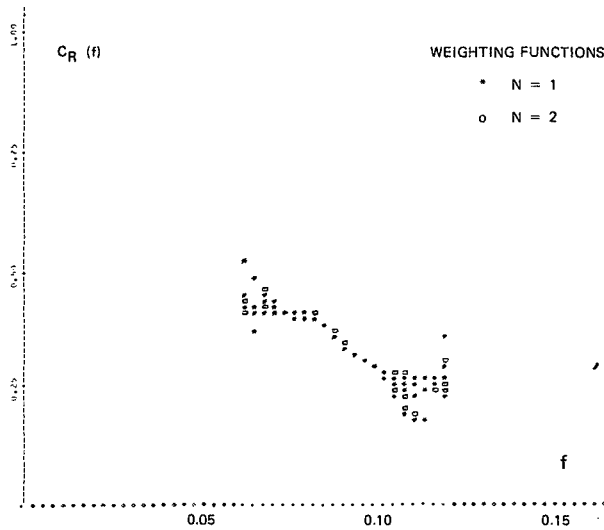


Fig. 10 Reflection coefficients $C_R(f)$ resulting from different gauge arrays with $n = 1$ & 2

As shown on figures 8 and 9 $C_R(f)$ has generally a more regular variation as a function of frequency than $C'_R(f)$. The reason for this behaviour has not yet been fully understood. From our experiments, the differences between $C_R(f)$ and $C'_R(f)$, did not seem to be connected with non-linear effects, as they did not increase with the significant wave height of the waves considered.

Figure 10 compares the reflection coefficients $C_R(f)$, associated with the first and second order weighting functions (28): * stands for $n=1$, 0 for $n=2$. As this graph results from a printer output, coincident values of $C_R(f)$ by both methods are plotted by a single symbol. Results shown here come from the analysis of the four combinations of gauges. A generally good agreement is observed between results of different triplets, and between the two methods of estimations of $C_R(f)$ for frequencies where wave energy is high. The scatter of experimental points increases on the boundaries of the wave spectrum.

CONCLUSION

In conclusion, the method of analysis just described has proven to be a valuable tool for estimating incident and reflected wave spectra in instances where wave reflection on structures has to be accounted for. Examples of application of the method to flume experiments have been given here. The method should also be applicable to field investigations, provided that the incoming waves are directed normally to the reflecting structure.

The numerical and experimental tests have shown that the incident wave spectrum is estimated accurately, provided that the gauge spacings are properly selected, so as to avoid too small a frequency interval between critical frequencies. The incident wave spectrum is practically insensitive to the order of the weighting functions used, except when critical frequencies are nearly coincident.

The method also proves to be an interesting means of studying the reflection coefficient (and the associated phase lag) of coastal structures as a function of frequency. It enables a better assessment of the efficiency of wave absorbing devices, such as the ARC system.

Two procedures of evaluation of the reflection coefficient have been investigated, one directly connected with the incident and reflected wave spectral densities by equations (17) and (29), the other derived from the theoretical transfer function (32). The first one is considered preferable since it showed a more regular variation of the reflection coefficient versus frequency.

REFERENCES

- (1) P. Caillard
Méthode d'analyse de la houle irrégulière produite en canal en présence d'un ouvrage réfléchissant - SOGREAH, NT 1834, Décembre 1976
- (2) Y. Goda & Y. Suzuki
Estimation of incident and reflected waves in random wave experiments. Proc. 15th Coastal Eng. Conf. Honolulu, Hawaii, July 1976, p. 828-845
- (3) R. Kajima
Estimation of an incident wave spectrum under the influence of reflection - Proc. 13th Congress of IAHR, Kyoto Japan 1969, Vol. 5.1 (Seminars), p. 285-288
- (4) D.B. Morden, E.P. Richey & D.R. Christensen
Decomposition of coexisting random wave energy. Proc. 15th Coastal Eng. Conf. Honolulu, Hawaii, July 1976, p. 846-865
- (5) E.B. Thornton & R.J. Calhoun
Spectral resolution of breakwater reflected waves. J. Waterways, harbors and coastal Eng. Proc. ASCE WW4 November 1972, p. 443-460
- (6) L. Tourmen, J.P. Montaz, L. Doublet
Un nouveau dispositif amortissant la reflexion des vagues sur les parois verticales : la chambre anti-reflexion (ARC), 17e Congrès AIRH Baden-Baden, RFA, août 1977, Sujet C6, p. 41-48.

CHAPTER 12

WAVE HEIGHT DISTRIBUTION AROUND PERMEABLE BREAKWATERS

BY

Shintaro Hotta*

ABSTRACT

A phase lag phenomenon in which waves are delayed in transmission through a permeable breakwater⁸ was considered in an approximate calculation method using the superposition principle of Sommerfeld. Experimental verifications were carried out for a semi-infinite permeable breakwater. In addition, a field observation of wave height distribution around a small detached breakwater is reported.

PART 1

APPROXIMATE CALCULATION METHOD FOR WAVE HEIGHT DISTRIBUTION AROUND A PERMEABLE BREAKWATER WITH A PHASE LAG

INTRODUCTION

At the 16th International Conference on Coastal Engineering at Hamburg, 1978, the author reported a calculation method for the wave height distribution around permeable breakwater using the superposition method of Sommerfeld. The cases dealt with were a semi-infinite breakwater, a single relatively large gap in a long breakwater and an insular breakwater (or a single detached breakwater). As discussed in the last paper (Chapter 39, Proc. 16th ICCE, pp 695-714, hereafter referred to as I), the weak point of this method is that it is not strictly correct theoretically, that is, the boundary conditions are not completely satisfied, and the wave height becomes discontinuous on the x and y axis and on the lines which divide the calculation region considered. However, this method has some advantages, that is, the wave height distribution can be calculated very easily by addition and subtraction, if we have the Fresnel Integrals. Another advantage is that if the waves have a phase lag due to a time lag upon transmission through a permeable breakwater, the influence of this time lag can easily be taken into consideration in the equations, without any complication. That is, we can replace y with $(y \pm \Delta L)$ in the term which represents the transmitted waves. Here ΔL is related to the phase lag between the transmitted and free waves. In this paper, the equations with the phase lag are given,

* Research Associate, Dept. of Civil Engineering, Tokyo Metropolitan University, Setagaya-ku, Tokyo, JAPAN

and the experimental verification of this method for semi-infinite permeable breakwaters are shown together with the case of no phase lag.

NUMERICAL CALCULATION OF WAVE HEIGHT DISTRIBUTION IN TRANSMISSION THROUGH THE PERMEABLE BREAKWATERS WITH PHASE LAG

As mentioned before, if waves are delayed in transmission through a breakwaters, the phase lag on the shoreside of the breakwaters can be expressed by replacing y with $(y \pm \Delta L)$ in the terms which represent the transmitted waves, namely

$$\alpha \{ e^{-ik(y + \Delta L)} f(u) + e^{-ik(y - \Delta L)} g(u) \} \text{-----} \quad (1)$$

Calculations will be done using the same figures, symbols and coordinate systems described in reference I.

(1) A semi-infinite permeable breakwater

By replacing y with $(y \pm \Delta L)$ in the terms which represent the transmitted waves (See Fig. 5 - (3) in reference I) we have the final forms of these equations, with a phase lag accounted for in regions A and B1, as follows:

Region A $x > 0, y > 0$

$$\begin{aligned} F_{2t}^A &= F_0^A + \alpha F_{1t}^A \\ &= e^{-iky} f(u_1) + e^{iky} g(-u_2) + \alpha \{ e^{-ik(y+\Delta L)} f(-u_1) + e^{ik(y-\Delta L)} g(-u_2) \} \\ &= (S_1 + S_2) \cos ky + (W_1 - W_2) \sin ky \\ &\quad + \alpha \{ (1 - S_1) \cos(k(y+\Delta L)) + S_2 \cos(k(y-\Delta L)) \\ &\quad \quad + (-W_1) \sin(k(y+\Delta L)) + (-W_2) \sin(k(y-\Delta L)) \} \\ &+ i \{ (W_1 + W_2) \cos ky + (-S_1 + S_2) \sin ky \\ &\quad + \alpha \{ (-W_1) \cos(k(y+\Delta L)) + W_2 \cos(k(y-\Delta L)) \\ &\quad \quad + (-1 + S_1) \sin(k(y+\Delta L)) + S_2 \sin(k(y-\Delta L)) \} \} \text{-----} \quad (2) \end{aligned}$$

Region B₁ $x < 0$, $y > 0$

$$\begin{aligned}
 F_{2t}^{B1} &= F_0^{B1} + \alpha F_{2t}^{B1} \\
 &= e^{-iky} f_r(u_1) + e^{iky} g_r(-u_2) + \alpha \{ e^{-ik(y+\Delta L)} f_r(-u_1) + e^{ik(y-\Delta L)} g_r(-u_2) \} \\
 &= (1-S_1+S_2) \cos ky + (-W_1-W_2) \sin ky \\
 &\quad + \alpha \{ S_1 \cos(k(y+\Delta L)) + S_2 \cos(k(y-\Delta L)) \\
 &\quad \quad + W_1 \sin(k(y+\Delta L)) + (-W_2) \sin(k(y-\Delta L)) \} \\
 &\quad + i [(-W_1+W_2) \cos ky + (-1+S_1+S_2) \sin ky \\
 &\quad \quad + \alpha \{ W_1 \cos(k(y+\Delta L)) + W_2 \cos(k(y-\Delta L)) \\
 &\quad \quad \quad + (-S_1) \sin(k(y+\Delta L)) + S_2 \sin(k(y-\Delta L)) \}] \quad \text{-----} \quad (3)
 \end{aligned}$$

To indicate the cases with a phase lag, a suffix t is added to the equivalent equations for no phase lag.

If we put $\Delta L = 0$ in Eqs. (2) and (3), they become Eqs. (23) and (24) in reference I, respectively.

(2) A single relatively large gap in a long permeable breakwater

As in section (1), replacing y with $(y \pm \Delta L)$ in the transmitted wave terms (See Fig. 6-(4) in reference I) the final forms of the equations in regions A1 and A2 for an opening in a breakwater become:

Region A₁ $0 < x < b/2$, $y > 0$

$$\begin{aligned}
 F_{3pt}^{A1} &= F_3^{A1} + \alpha [F_{1t}^{B1} + F_{0t}^A] \\
 &= e^{-iky} f_r(u_1) + e^{iky} g_r(-u_2) + e^{-iky} f_l(u_1) + e^{iky} g_l(-u_2) - e^{-iky} \\
 &\quad + \alpha [e^{-ik(y+\Delta L)} f_l(-u_1) + e^{ik(y-\Delta L)} g_l(-u_2) \\
 &\quad \quad + e^{-ik(y+\Delta L)} f_r(-u_1) + e^{ik(y+\Delta L)} g_r(-u_2)] \\
 &= (1-S_{r1}-S_{l1}+S_{r2}+S_{l2}) \cos ky + (-W_{r1}-W_{l1}-W_{r2}-W_{l2}) \sin ky \\
 &\quad + \alpha \{ (S_{r1}+S_{l1}) \cos(k(y+\Delta L)) + (W_{r1}+W_{l1}) \sin(k(y+\Delta L)) \\
 &\quad \quad + (S_{r2}+S_{l2}) \cos(k(y-\Delta L)) + (-W_{r2}-W_{l2}) \sin(k(y-\Delta L)) \} \\
 &\quad + i [(-W_{r1}-W_{l1}+W_{r2}+W_{l2}) \cos ky + (-1+S_{r1}+S_{l1}+S_{r2}+S_{l2}) \sin ky \\
 &\quad \quad + \alpha \{ (W_{r1}+W_{l1}) \cos(k(y+\Delta L)) + (-S_{r1}-S_{l1}) \sin(k(y+\Delta L)) \\
 &\quad \quad \quad + (W_{r2}+W_{l2}) \cos(k(y-\Delta L)) + (S_{r2}+S_{l2}) \sin(k(y-\Delta L)) \}] \quad \text{-----} \quad (4)
 \end{aligned}$$

Region A2 $x > b/2, y > 0$

$$\begin{aligned}
 F_{3t}^{A2} &= F_3^{A2} + \alpha [F_{1t}^A + F_{2t}^A] \\
 &= e^{-iky} f_r(-u_1) + e^{iky} g_r(-u_2) + e^{-ky} f_l(u_1) + e^{iky} g_l(-u_2) - e^{-iky} \\
 &\quad + \alpha [e^{-ik(y+\Delta L)} f_l(u_1) + e^{ik(y-\Delta L)} g_l(-u_2) \\
 &\quad + e^{-ik(y+\Delta L)} f_r(-u_1) + e^{ik(y-\Delta L)} g_r(-u_2)] \\
 &= (S_{r1} - S_{l1} + S_{r2} + S_{l2}) \cos ky + (W_{r1} - W_{l1} - W_{r2} - W_{l2}) \sin ky \\
 &\quad + \alpha \{ (1 - S_{r1} + S_{l1}) \cos(k(y+\Delta L)) + (-W_{r1} + W_{l1}) \sin(k(y+\Delta L)) \\
 &\quad + (S_{r2} + S_{l2}) \cos(k(y-\Delta L)) + (-W_{r2} - W_{l2}) \sin(k(y-\Delta L)) \} \\
 &\quad + i [(W_{r1} - W_{l1} + W_{r2} + W_{l2}) \cos ky + (-S_{r1} + S_{l1} + S_{r2} + S_{l2}) \sin ky \\
 &\quad + \alpha \{ (-W_{r1} + W_{l1}) \cos(k(y+\Delta L)) + (-1 + S_{r1} - S_{l1}) \sin(k(y+\Delta L)) \\
 &\quad + (W_{r2} + W_{l2}) \cos(k(y-\Delta L)) + (S_{r2} + S_{l2}) \sin(k(y-\Delta L)) \}] \quad \text{-----} \quad (5)
 \end{aligned}$$

Letting $\Delta L = 0$, Eqs. (4) and (5) become Eqs. (32) and (33) in reference I.

(3) A single insular permeable breakwater

Similar to the above, replacing y with $(y \pm \Delta L)$ in the transmitted wave terms (See Fig. 8 in reference I) the equations for regions A1 and A2 become:

Region A1 $0 < x < b/2, y > 0$

$$\begin{aligned}
 F_{1t}^{A1} &= (S_{r1} + S_{l1} + S_{r2} + S_{l2}) \cos ky + (W_{r1} + W_{l1} - W_{r2} - W_{l2}) \sin ky \\
 &\quad + \alpha \{ (1 - S_{r1} - S_{l1}) \cos(k(y+\Delta L)) + (-W_{r1} - W_{l1}) \sin(k(y+\Delta L)) \\
 &\quad + (S_{r2} + S_{l2}) \cos(k(y-\Delta L)) + (-W_{r2} - W_{l2}) \sin(k(y-\Delta L)) \} \\
 &\quad + i [(W_{r1} + W_{l1} + W_{r2} + W_{l2}) \cos ky + (-S_{r1} - S_{l1} + S_{r2} + S_{l2}) \sin ky \\
 &\quad + \alpha \{ (-W_{r1} - W_{l1}) \cos(k(y+\Delta L)) + (-1 + S_{r1} + S_{l1}) \sin(k(y+\Delta L)) \\
 &\quad + (W_{r2} + W_{l2}) \cos(k(y-\Delta L)) + (S_{r2} + S_{l2}) \sin(k(y-\Delta L)) \}] \quad \text{-----} \quad (6)
 \end{aligned}$$

Region A2 $x > b/2, y > 0$

$$\begin{aligned}
 F_{2t}^{A2} &= (1 + S_{r1} - S_{l1} + S_{r2} + S_{l2}) \cos ky + (W_{r1} - W_{l1} - W_{r2} - W_{l2}) \sin ky \\
 &\quad + \alpha \{ (-S_{r1} + S_{l1}) \cos(k(y+\Delta L)) + (-W_{r1} + W_{l1}) \sin(k(y+\Delta L)) \\
 &\quad + (S_{r2} + S_{l2}) \cos(k(y-\Delta L)) + (-W_{r2} - W_{l2}) \sin(k(y-\Delta L)) \} \\
 &\quad + i [(W_{r1} - W_{l1} + W_{r2} + W_{l2}) \cos ky + (-1 - S_{r1} + S_{l1} + S_{r2} + S_{l2}) \sin ky \\
 &\quad + \alpha \{ (-W_{r1} + W_{l1}) \cos(k(y+\Delta L)) + (S_{r1} - S_{l1}) \sin(k(y+\Delta L)) \\
 &\quad + (W_{r2} + W_{l2}) \cos(k(y-\Delta L)) + (S_{r2} + S_{l2}) \sin(k(y-\Delta L)) \}] \quad \text{-----} \quad (7)
 \end{aligned}$$

With $\Delta L = 0$, Eqs. (6) and (7) become Eqs. (39) and (40) in reference I.

EXPERIMENTAL FACILITIES AND PROCEDURES

Experiments were carried out using a small wave basin which was 2.4 meters in width, 6.0 meters in length and 0.5 meters in depth. The dimensions and the arrangement of the experimental facilities are shown in Fig. 1. Because of the limited wave basin width, only the case of a semi-infinite breakwater was treated.

As a model of a breakwater, a vertical homogeneous crib-style wall of 8 cm thickness, filled with 17 mm diameter glass balls, was used. Wave heights were measured with 18 capacitance-type wave gauges. Three of these were placed on a line extending from the breakwater axis ($x < 0$, $y = 0$) to measure the incoming waves and to synchronize three 6-channel paper oscillographs. The remaining 15 gauges were mounted on an arm having wheels at both ends, and which moved on rails fixed to both side walls of the basin. Using these wave gauges, wave heights at 15 locations could be simultaneously measured across the basin. To avoid wave interactions between the incoming waves and the waves reflected from the basin walls (of course a wave absorber was placed along the basin walls; See Fig. 1), the third wave height of each wave train generated was adopted as the height for comparison with the calculations. So, waves were generated from the still water state for each measurement on different transects parallel to the x-axis.

First, the experiments with no phase lag were carried out using wave periods of 0.7 and 1.2 seconds, and a water depth of 0.2 meters. Similar to the above, the experiments where the transmitted waves suffered a phase lag, due to the breakwater, were carried out using only one wave period (0.7 second) and the same water depth. In these experiments, it was difficult to obtain transmitted waves under the conditions of a phase lag. Instead of this, the waves generated in the region of the gap were forced to propagate ahead of the waves arriving at the breakwater by increasing the thickness of the wave generator flap in the former region. Then, to avoid the wave interaction between the two regions, the partition was placed as shown in Fig. 1.

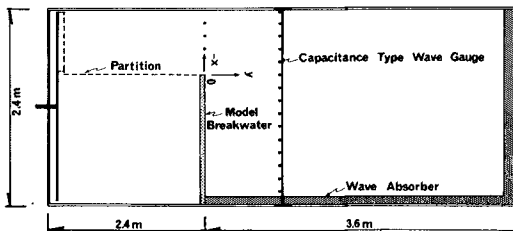


Fig. 1 Experimental facilities

EXPERIMENTAL RESULTS AND DISCUSSION

Figure 2 shows the experimental results for no phase lag. The transmission coefficient was about 0.25. The water depth was 0.2 meters. In Fig. 2, the solid lines are the calculated values from equations (23) and (24) in reference I, and the solid and empty triangles show the experimental values for wave periods of 0.7 and 1.2 seconds, respectively. These figures show that the calculations agree with the experiments qualitatively. The experimental wave heights at the antinodes of the superimposed waves were a little smaller than the those in the calculations, and the experimental wave heights at the nodes became larger than those in the calculations. It is inferred that this is due to the interaction between the two waves, the transmitted and diffracted waves. Deviation of the experimental results from the calculations becomes larger according to the progress of the waves, especially in the case of the 0.7 second period. Perhaps this effect is due to an energy loss, since it is considered that the energy loss is greater for shorter waves.

Figure 3 shows the experimental results when the transmitted waves suffered a phase lag due to the breakwater. The wave period was 0.7 seconds and the water depth was 0.2 meters. In this experiment, the phase lag was 0.2 wave length, about 15 cm. In Fig. 3, the solid, dotted and broken lines show the calculated values from equations (2) and (3) for phase lags of $\Delta L = 0.1L$ and $\Delta L = 0.2L$, respectively. Here ΔL is the phase lag and L is the wave length. Solid rectangles show the experimental results for no phase lag and solid circles show the experimental results for a phase lag of $\Delta L = 0.2L$. From these figures, you can see a similarity with the experimental results for the case of no phase lag previously discussed. That is, first of all, the calculation agrees with the experiments qualitatively. Second, at the antinode the calculated wave heights are smaller than those in the experiments, and at the nodes we find the contrary. Thirdly with continued propagation, the wave interaction becomes larger, and the wave heights become constant.

From these results, we feel this method may be acceptable to roughly predict the wave heights distribution around permeable breakwaters. Furthermore, if we accept this method, then we have the possibility of expressing the wave height distribution around permeable breakwaters for irregular waves, by superimposing waves which have different incident wave angles and heights.

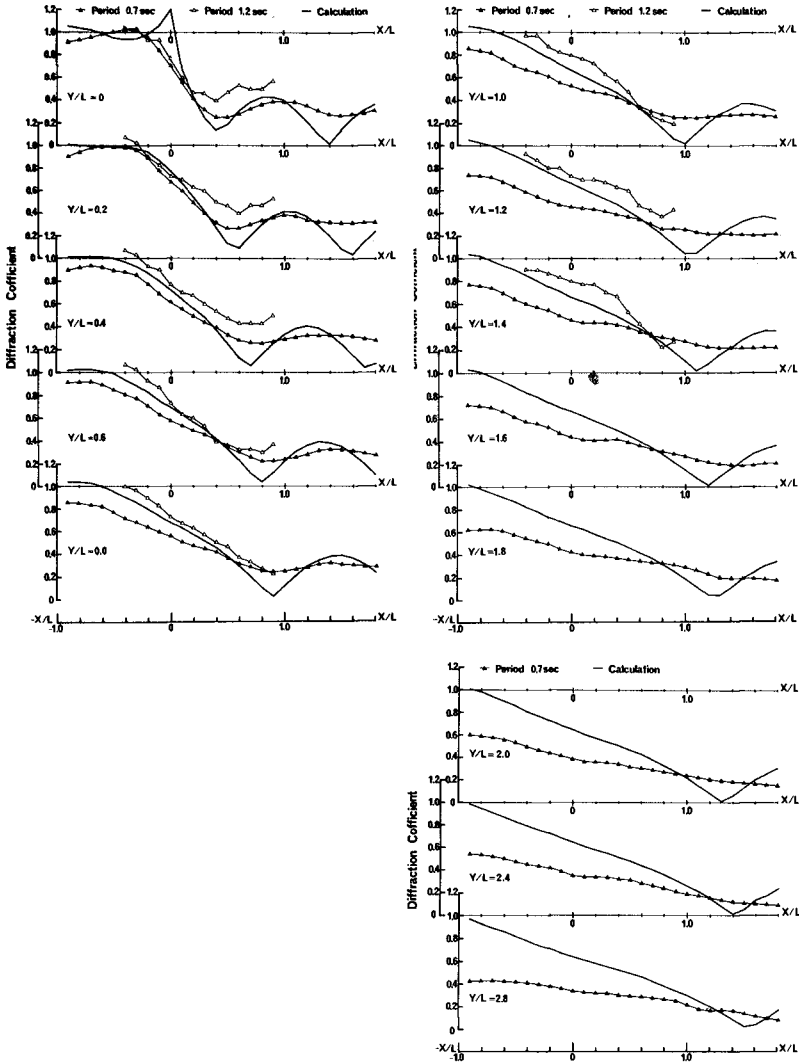


Fig. 2 Comparison of experimental results and calculations with no phase lag for semi-infinite breakwater

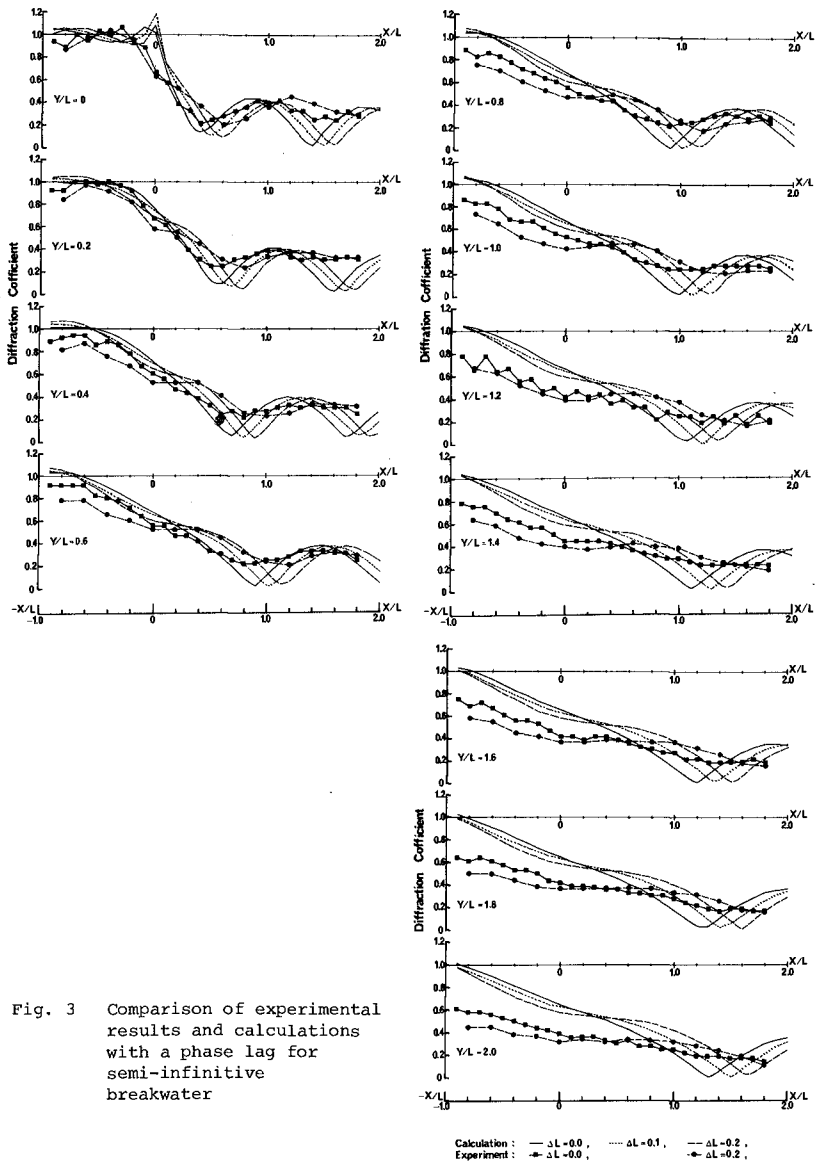


Fig. 3 Comparison of experimental results and calculations with a phase lag for semi-infinite breakwater

• PART II

A FIELD STUDY OF WAVE HEIGHT DISTRIBUTION
AROUND A SMALL DETACHED PERMEABLE BREAKWATER

FORWARD

The field observation was carried out on September 4, 1979 at Oharai beach (See Fig. 4). Data are presently still under analysis. However, a part of the results are described and discussed here because of their interest which still remains to be expanded upon in a more detailed analysis and discussion. In the preceding section, the calculation and experiments were dealt with assuming regular waves, no breaking waves and a constant water depth. The field observation which will be described here was under the conditions that waves were irregular, had already broken and were on a sloping sea bottom. Because of these idealized constraints, this field observation is not considered as a verification of the calculation or experiments in the preceding section. However, it is expected that field wave data will give important information about the applicability of these calculations, or suggest an improvement of these calculation methods or development of new calculation methods in the future.

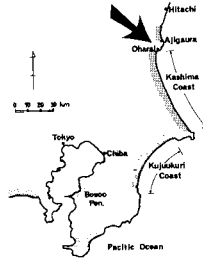


Fig. 4 Location of field observation site

FIELD OBSERVATION SITE AND INSTRUMENTATION

Field observation was carried out at Oharai beach where eleven small detached breakwaters had been constructed of hexalegs on the front of the seawall for defense from beach erosion. The detached breakwaters are about 20 m in length and situated with a 30 m spacing between each other, parallel to and 50 m from the seawall. Observation of wave height was done around the 5th detached breakwater counting from the North.

The wave height distribution at the shoreside of the detached breakwater was observed using a pole array and a 16 mm memo-motion camera system. This system is a photographic method of measuring waves on the sea water surface at poles placed in the sea, using several synchronized cameras. In this observation, 5 cameras were used and 25 poles were photographed. The arrangement of poles (station Nos.) shown in Fig. 5.

The tidal range of this beach was 1.1 m at the time, and at low tide the water depth of the breakwater site was about 0.2 - 0.3 m. At low tide, poles were erected in the sandy bottom using water jets, and wave heights were observed at high tide.

The data from 16 mm photographs of the water surface variations were transferred to paper tapes by using a 16 mm film analyzer and sonic digitizer graf pen system. Data on paper tapes were again transferred to magnetic tapes for convenient analysis by computer. Data station Nos. 12, 31, 32 and 63 were not recorded because it happened that these stations were out of the field of view. Three electromagnetic current meters were used to measure the current. However, the author has no intention of describing the current data in the present study.

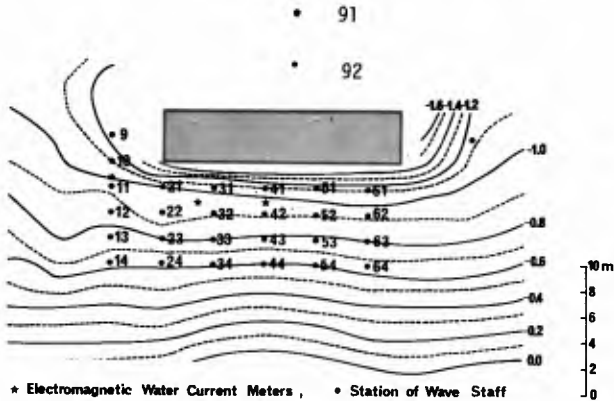


Fig. 5 Sea bottom topography and position of poles

DEFINITION OF WAVES

How are waves defined? The zero-up or zero-down crossing methods are one of the ways generally accepted at present. The field studies of waves in the surf zone being carried out by the author and coworkers (Hotta, Mizuguchi, and Isobe (1978, 1979, 1980)), using the same pole array and a 16 mm memo-motion camera system, have shown that many small amplitude waves could be defined by the zero-up or zero-down crossing methods for the waves in the surf zone. As a result, these small amplitude waves had small values of the representative wave statistics, for example, the one-tenth wave height and period ($H_{1/10}, T_{1/10}$) or the significant wave height and period ($H_{1/3}, T_{1/3}$). The same thing was found in this field observation. In studying the characteristics of the waves in the field it does not appear reasonable to take into consideration small amplitude waves. However, we have no evidence that smaller waves should be ignored. We have still not reached a conclusion yet, though we have extensively scrutinized and investigated this problem. One of the guidelines which the author wants to state, at least, is that the waves which have heights smaller than 3 times the minimum scale unit in reading water surface variations, should be ignored. This is concluded from checking the accuracy of our data (Hotta et al.(1980)). In this study the minimum scale unit was 2 cm, and time interval of photographing was 0.2 second. Then, the minimum wave which could be defined in this study was 6 cm in height and had a 0.6 second period.

We have other problem in the definition of waves. That is, as just mentioned above, we have ignored waves which were smaller than 6 cm and had period of less than 0.6 second. The problem is in choosing which way is more reasonable to add the small wave which we have ignored, to the main wave: to the previous main wave or to the next main wave? (See Fig. 6) This does not influence the height of the main wave, but influences the wave period. We have no idea which choice should be made. It seems that the zero-down crossing method might be good for defining waves in the surf zone, because it is considered that the elevation between the top of the propagating wave crest and the sea surface in front of the crest would characterized waves in the surf zone. Then, profiles of the waves defined by the zero-down crossing method would look good if the small waves ignored could be added to the trailing part of the main wave.

In this study waves were defined using the zero-down or zero-up crossing methods with W as shown in Fig. 6.

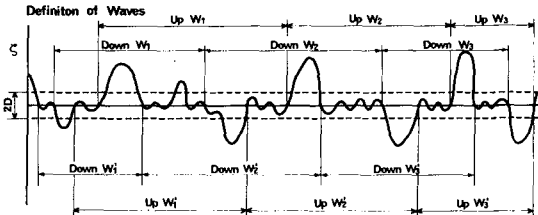


Fig. 6 Definition of waves

FIELD OBSERVATION RESULTS AND DISCUSSION

(1) Wave height distribution at the shoreside of the breakwater.

Figure 7A shows the significant wave height and period around a small detached breakwater. Fig. 7B shows a graph the same values along the section A-A, B-B and two other sections parallel to the former ones. From Fig. 7 we can point out the following. The significant wave height along section A-A, near the leeside of the breakwater, becomes smaller from the tip of the breakwater towards the center of the breakwater and at the center the wave height decreases by about 75% of that at the tip. Contrarywise, wave heights along section B-B, about 10 m from the breakwater, are getting large towards the center of the breakwater. This might depend on the superposition or convergence of waves, i.e. transmitted waves and waves diffracted from both sides of the breakwater.

Figure 8 shows part of the experimental results for wave height distribution around a permeable breakwater carried out by Horikawa, Isobe and Shiozaki (1980). Wave heights are shown in cm units. Experiments were carried out on a 1/20 sea bottom slope and the water depth at the site of the breakwater was 5.8 cm. The wave length at the site of breakwater and the length of the breakwater were about 72 cm and 90 cm, respectively. Noticing that this experiment and the field conditions were almost the same, we find the following fact. That is, we can see wave heights of 1.4 and 1.9 cm at the leeside of the breakwater and at positions about one-fourth of the breakwater length from both ends of the breakwater. These positions might be considered as nodes of three dimensional partial standing waves which were formed by the transmitted and diffracted waves. In the experiments described in part I, it was shown that the wave height at nodes of the partial standing waves became larger than the calculated values and it was imagined that this depended on energy transfer from antinodes to nodes by interaction of the two waves: transmitted and diffracted waves.

The same thing might have occurred the experiments of Horikawa et al. Comparing Fig. 7 and Fig. 8, we recognize that the energy transfer from the antinodes to the nodes of the partial standing waves in an irregular wave in the field becomes larger than that in regular waves in laboratory experiments. That is, to wave height averages at the leeside of the breakwater for regular waves is smaller than that for irregular waves. This is natural.

The significant wave period (See Fig. 7B) shows a tendency to become smaller at the leeside of the breakwater.

(2) Waves at the offshoreside of the breakwater.

Significant wave heights and periods at stations 91 and 92 were 113 cm and 8.7 sec. and 70 cm and 5.0 sec using the zero-up crossing method; and 119 cm and 9.4 sec, and 79 cm and 6.4 sec using the zero-down crossing method, respectively. The number of waves defined were 123 and 166. From the big difference between these two stations, we can predict that at the offshoreside of the breakwater, the partial

standing waves were formed by incoming waves and reflected waves. At the node the number of waves defined becomes larger than that at the anti-node, and the wave period becomes smaller. (See Fig. 9)

(3) Wave height distribution at one location as a function of time.

Figure 10 shows the wave height and period distribution as a function of time at stations on the leeside of the breakwater. Fig. 10A shows the wave heights and period distribution at section C-C in Fig. 7. It is considered that waves on this section suffer little influence from the breakwater, and are almost the same as on a natural beach. Fig. 10B, 10C and 10D show the wave height distribution at each station on sections B-B, C-C and D-D, respectively.

In these Figures, histograms show the nondimensional wave heights, the ratio of wave heights and average wave height, H/\bar{H} . Solid circles show the nondimensional period, the ratio of wave periods and average period, T/\bar{T} . The distribution graph to the left side is that derived from the zero-up crossing method, and that to the right side is the one derived from the zero-down crossing method. These are distinguished by UP and DOWN, respectively.

Glancing at these figures, you can readily see that the nondimensional wave height distributions completely differ with the definitions of waves. Distributions defined by the zero-up crossing method become unimodal distributions, and those defined by the zero-down crossing method result in bi-modal distributions, except at stations 21, 41 and 51. This tendency is especially evident on section C-C. As mentioned before, waves on this section are not influenced by the existing breakwater so much, and we may consider that waves in this section are almost the same as on beaches with no structures. This phenomenon has often been observed by the author and his coworkers (1979 and 1980) on natural beaches.

The facts that the wave height distribution become uni-modal with its peak in the neighborhood of $H/\bar{H} = 1.0$, if we define the waves by the zero-up crossing method, and that the wave height distribution becomes bi-modal with two peaks located to the right and left side of $H/\bar{H} = 1.0$, if we define the waves by the zero-down crossing method, can be interpreted as follows. We shall consider defining waves for a case in which a relatively small wave follows a big wave, as shown in Fig. 11. Clearly, a large and a small wave are defined by the zero-down crossing method and two waves of almost the same height are defined by the zero-up crossing method. In addition to this, the average wave height and number of waves defined are the same in spite of the two different methods of definition. It is probable that these facts take place in the distributions shown in Fig. 10. No doubt, waves as shown in Fig. 11 exist very much in the surf zone on natural beaches. We can guess that the distribution for stations on the leeside of the breakwater change due to their dependence on the different positions of the waves.

Another thing to be pointed out from Fig. 10 is that the distribution of nondimensional wave periods roughly agrees with the wave height distribution. This means that the wave periods are roughly proportional to the wave heights. This is not inconsistent with the general concept.

- (4) Difference of representative waves statistics due to wave definitions.

Table-1 shows the wave heights and periods of the one-tenth and significant waves, and the number of waves defined. Wave heights show no difference between the zero-up and down crossing methods. However, wave periods defined using the zero-up crossing method become less large than those defined using the zero-down crossing method. This means that waves defined using the zero-down crossing method become steeper than those from the zero-up crossing method. There are relatively large differences in the numbers of waves defined. This relates to the differences of wave positions of the transmitted and diffracted waves, but this is not all. We can not offer exact answers or interpretations for the above results. Many things remain to be discussed in the future.

ACKNOWLEDGEMENTS

The experiment was carried out with the wave basin belonging to Dr. M. Mizuguchi, Associate Professor, University of Chuo. The author gratefully acknowledges the help of Dr. Mizuguchi. The author acknowledges the permissions given by Drs. K. Horikawa, M. Isobe and Mr. M. Shiozaki for reproduction of their data and figures. The author also thanks staffs of Nearshore Environment Research Center for their assistance in the field observations and analysis.

A part of this study was supported by The Grant in Aid for Co-operative Research A 435026, (1979) "Study of Dynamics in the Surf Zone" given to Dr. Kiyoshi Horikawa, Professor, Dept. of Civil Eng., University of Tokyo. The Grant is offered by the Ministry of Education, Science and Culture.

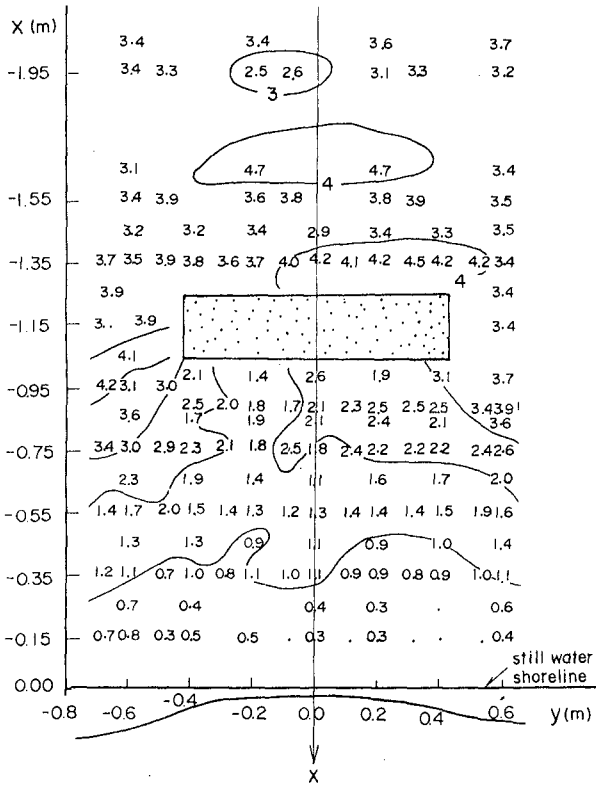


Fig. 8 Experimental wave height distribution around a permeable breakwater (after Horikawa, Isobe and Shiozaki)

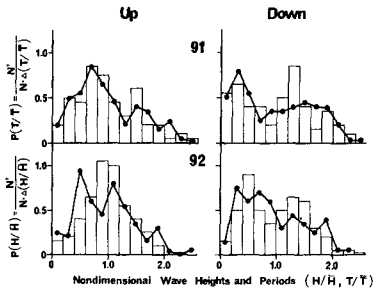


Fig. 9 Wave height distribution as a function of time at Station 91 and 92

Fig. 10A

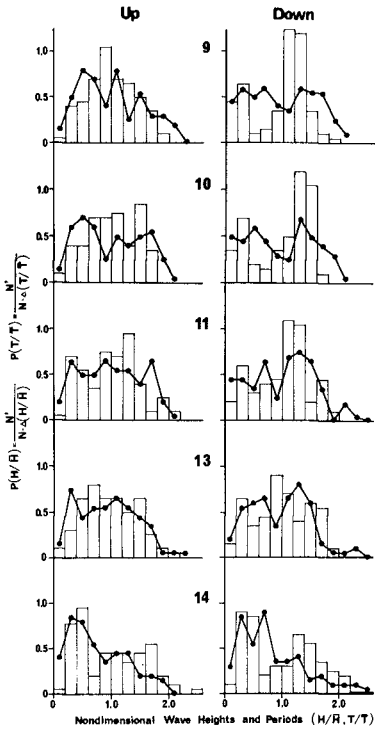


Fig. 10D

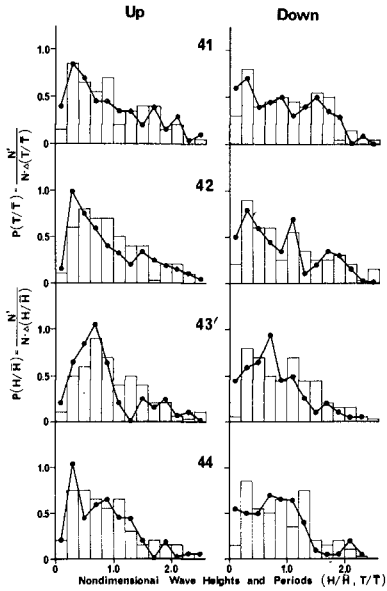


Fig. 10 Wave height distribution as a function of time at the leeside stations

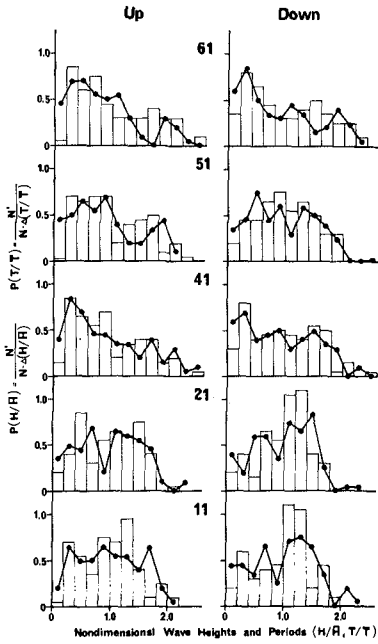


Fig. 10C

Fig. 10B

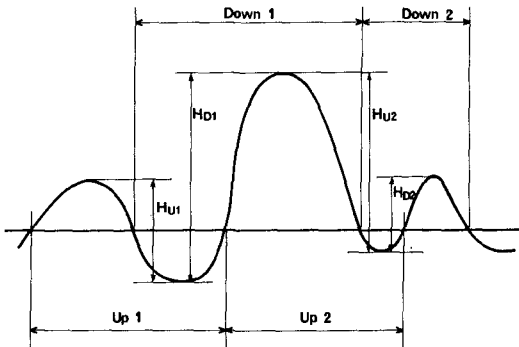
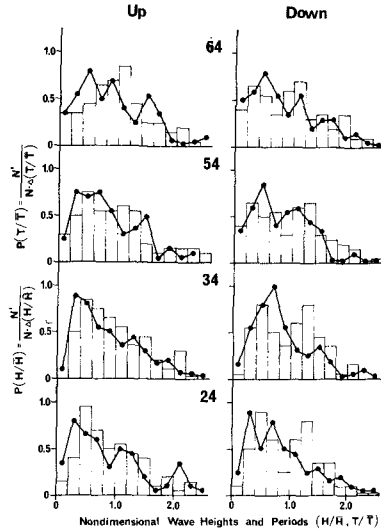


Fig. 11 Difference of wave heights due to methods of defining wave heights

Table - 1 Significant waves

St. No.	K	Height		Period	
		DOWN	UP	DOWN	UP
9	100	75	75	11.1	11.7
10	102	72	72	11.1	10.9
11	97	76	77	11.4	11.1
13	96	7	70	10.4	10.4
14	123	57	57	9.9	10.1
21	90	70	72	11.7	12.1
22	102	72	73	11.0	11.5
23	111	69	70	9.8	10.2
24	119	56	57	9.3	9.5
33	112	62	61	9.2	10.6
34	104	59	60	10.5	11.0
41	112	58	59	10.7	11.8
42	127	54	52	10.0	10.0
43	104	56	59	9.3	10.5
44	128	63	64	9.8	10.0
51	107	64	66	10.5	11.2
52	105	64	65	11.0	11.4
53	128	65	65	9.1	9.1
54	116	64	61	9.9	9.7
61	130	62	62	9.4	9.5
63	132	79	75	9.6	9.6
64	128	62	58	9.3	8.5

K: Number of waves defined

Wave Height (cm)

Wave Period (second)

REFERENCES

- Hotta, S..(1979): Wave height distribution around permeable breakwater, Proc. 16th ICCE, pp 695-714, A.S.C.E.
- Hotta, S. and M. Mizuguchi(1978): A field study of waves after breaking waves, Proc. 25th Conf. on Coastal Eng. in Japan, pp 151-154, J.S.C.E. (in Japanese).
- Hotta, S. and M. Mizuguchi(1979): A field study of waves in the surf zone, Proc. 26th Conf. on Coastal Eng. in Japan, pp J.S.C.E. (in Japanese).
- Hotta, S., M. Mizuguchi and M. Isobe(1980): A field study of wave characteristics in the surf zone, Proc. 27th Conf. on Coastal Eng. in Japan (in printing and Japanese).
- Horikawa, K., M. Isobe and M. Shiozaki (1980): Laboratory investigation on the wave and current system induced by coastal structures, Annual Report of the Engineering Research Institute, Faculty of Technology, University of Tokyo. (in printing and Japanese)

CHAPTER 13

NON-RESONANT WAVE AGITATION IN SMALL CRAFT HARBOURS

by

J.W. Kamphuis ¹⁾ and D.A.Y. Smith ²⁾

ABSTRACT

A model study of wave agitation in small craft harbours was performed using a square and a rectangular marina basin subjected to monochromatic waves. Wave agitation was measured in up to 273 points within the marina basin and overall wave energy levels were calculated from these measurements for 4 different wave periods, 6 different entrances and 5 different lengths of energy absorbing sections along the perimeter walls. These values were compared and found to correspond well with a rather simple theoretical expression.

INTRODUCTION

Ancient harbours were small craft harbours and their design was already very sophisticated (2,9)³. The development of harbour design from the early Minoans, Phoenicians and Romans, however, has not been a linear process. First, the same mistakes were often repeated throughout history (and indeed are repeated today). Secondly, with increase in the size of ships, design was mainly concerned with harbours for large vessels. Around 1900, a parting of the ways is evidenced and two distinct types of harbour designs are found — the large harbour for large vessels and the smaller craft harbour, mainly for fishing vessels. Not until the 1960's can the concept of "small craft harbour" or "marina" be found regularly in the literature and the design of these small craft harbours is very often simply a scaled down version of design for large commercial harbours.

Two examples of scaled down design may suffice.

It makes good sense when designing a harbour for large vessels, not to obstruct navigation unnecessarily and hence to design a relatively straight, open entrance, directed away from the predominant wave direction. Only "small waves", which do not unduly affect the stability of the large vessels, are permitted to enter the harbour. But this design criterion is anathema for small craft which are terribly disturbed by these so-called "small waves".

-
1. Professor of Civil Engineering, Queen's University, Kingston, Canada.
 2. Engineer, Jamaica Bauxite, Kingston, Jamaica.
 3. Numbers in brackets refer to the Reference section.

Applying the same entrance design criterion to both types of harbours is therefore ludicrous, especially in view of the fact that small craft are very easily maneuverable and can negotiate more complicated entrance configurations quite easily. An additional entrance design criterion for small craft harbours is that the entrance prevent penetration of waves generated by other small craft passing the entrance.

Vertical perimeter walls around a harbour also constitute sensible design for harbours with large vessels. The vessels can easily come alongside. Vertical sheetpile walls are inexpensive compared to the alternatives. Loading and unloading platforms can be constructed immediately adjacent to the vessels. The fact that wave energy is reflected by these walls, resulting in ever-present chop within the harbour and along the docks is of no concern to the large vessels. But in a small craft harbour reflected and re-reflected waves present an unacceptable level of motion. Hence vertical, reflecting perimeter walls constitute very poor design for small craft harbours.

It is possible to quote many examples of small craft harbours with open entrances and vertical, reflecting perimeters. Portsmouth Olympic Harbour, reconstructed for the 1976 Olympic games, is shown as one such example in Figure 1. The unacceptable energy levels in this marina basin prompted the Queen's University Coastal Engineering Laboratory to begin investigation of agitation in small craft harbours.

A literature search indicated very little work directly applicable to small craft harbour design — especially with respect to non-resonant agitation (as opposed to studies on resonance — so important for larger harbours containing large vessels). Hence a series of very basic research tests was initiated. So far, one earlier paper was published (5). The work discussed in this paper may be found in detail in the junior author's Ph.D. thesis (8). It consists of

- a. Obtaining some basic data with respect to wave penetration, diffraction, reflection, etc.
- b. Testing a simple theory to explain (overall average) energy levels in simple harbour configurations.

The program has been continued to investigate

- c. Local wave energy levels in sections of the harbour
- d. Energy absorber location design
- e. Entrance design,

and will in the future also focus on

- f. Arrangement of "furniture" (docks, piers, boats, etc.) within the harbour
- g. Effects of irregular waves
- h. Construction of a Finite Element Model based on the above experimental data.

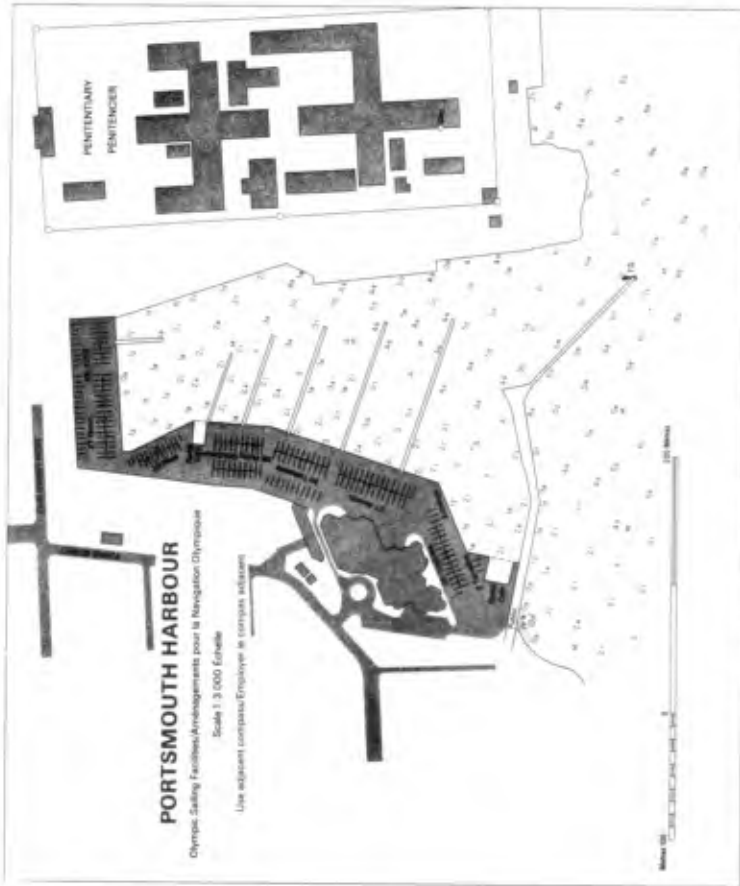


FIGURE 1: EXAMPLE OF SMALL CRAFT HARBOUR DESIGN BY SCALING DOWN LARGE HARBOUR DESIGN CONCEPTS.

Some work on marina and harbour agitation has been published by others such as the Danish Hydraulics Institute and their System 21 (1), Daenrich and Kohlhase (6) and others. Their work consists of rather sophisticated mathematical and theoretical analysis, but is based on very limited data. The purpose of the work discussed in this paper is:

- a. to provide an experimental data base on which to construct mathematical models,
- b. to provide some simple relationships that can be used in preliminary engineering design.

The last point is very important since many small craft harbours are never really designed, but are evolved from committee meetings, etc. using available space and money as the basic design criterion, while hard technical study is only of secondary importance. A simple expression and indications of trends give the harassed engineer something in hand to plead his case.

THE EXPERIMENTS

The experimental facility is shown in Figure 2. Regular waves were generated in a 3-dimensional wave basin and two harbour models, a 6.1 m square and a 4.25 x 6.1 m rectangular one, were tested. Heavy wave filters were used and energy absorbing material was placed along the front face of the model to prevent coupling and secondary reflections between the model and the wave generator.

The testing procedure was as follows: after the generator was started, a period of approximately 20 minutes was found to be sufficient to damp long waves resulting from generator start-up. The square harbour was tested with fully reflecting vertical walls all around the perimeter for six different entrance widths ($b = 0.61, 1.07, 1.60, 2.13, 2.67$ and 3.23 m). These tests were repeated using a horsehair, beach type absorber¹, first along the back wall, then along the back and one side, the back and both sides and all around the perimeter — each time testing for six entrance widths. Such complete series of tests were run for each of four wave periods ($T = .985, 1.152, .858$ and $.69$ seconds) and the whole program was completely repeated for the rectangular harbour. Wave measurements were taken by a bank of seven capacitance wave gauges, which moved to locations outside the harbour and to locations spaced at .15 m inside the harbour resulting in 189 to 273 individual wave height measurements within the harbour per test.

Because of the monochromatic nature of the incident wave, it was entirely possible to choose wave periods which caused very large agitations in the models without energy absorbing perimeters. A deliberate attempt was made to de-tune the model, i.e. to adjust the wave period slightly to cause agitation to be a minimum for the harbours without absorber. This method yields conservative results when

¹ The absorber exhibited reflection coefficients between 7 and 18%, depending on the incident wave period and would be comparable to prototype sloping rubble walls, launching ramps, etc.

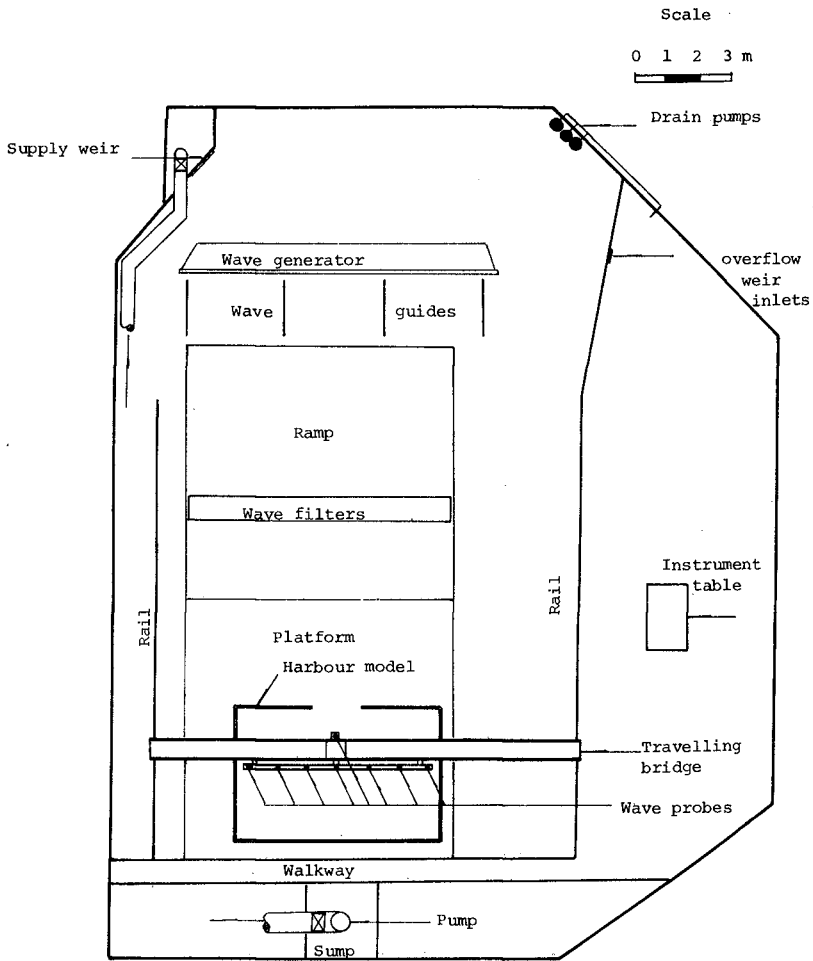


FIGURE 2: EXPERIMENTAL FACILITY.

discussing reduction in wave agitation by perimeter absorbers. Changes in wave period of 1/100 of a second showed remarkable impact on the wave action. This is frightening since the prototype waves contain all sorts of wave frequencies and could respond to any one of these frequencies rather violently.

EXPERIMENTAL RESULTS

The readings from the wave gauges were reduced in the first analysis to normalized wave height plots, of the variety shown in Fig. 3. Normalized wave height is defined as the ratio of local wave height (H) to the incident wave height (H_i). Figure 3(a) with the vertical, reflecting walls shows pronounced reflection patterns in spite of all efforts to de-tune the model. Comparison with Fig. 3(b) shows the influence of an absorbing perimeter. A decrease in overall energy level may be noted, but also a very marked decrease in local agitation, i.e. the internal reflection pattern is gone and the energy is more evenly distributed throughout the harbour. The latter is a particularly important consideration which is not studied in this paper but will be studied in future work. Also in Fig. 3(b), the measured wave agitation is compared with the output of a diffraction program, indicating that wave heights may essentially be determined from diffraction analysis if reflection from the perimeter is minimum. Figures 3(c) and 3(d) show the effect of increased entrance width.

It was also seen from the tests that the absorber was much more efficient when placed along the back wall than when placed along the sides and Fig. 4 shows some examples of overall energy level reduction, clearly indicating that absorber along the back wall only and absorber all around are almost equally effective at decreasing the overall energy level, while the former costs only 30% of the latter. This optimisation of absorber location is under further investigation and the topic of another paper.

THEORY

Assuming conservation of energy, it is possible to state:

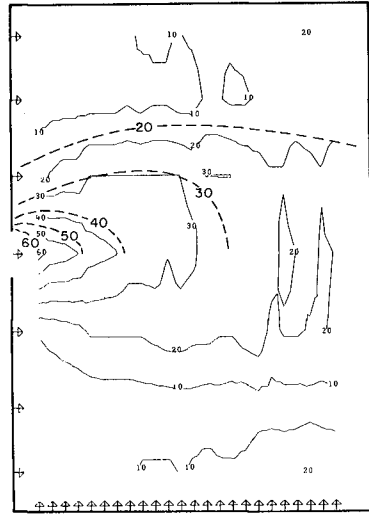
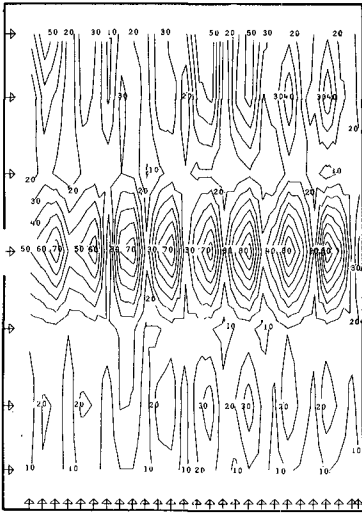
$$A \frac{dE(t)}{dt} = P_i - P_o - P_a - P_f - P_d \quad (1)$$

where A is the harbour area,

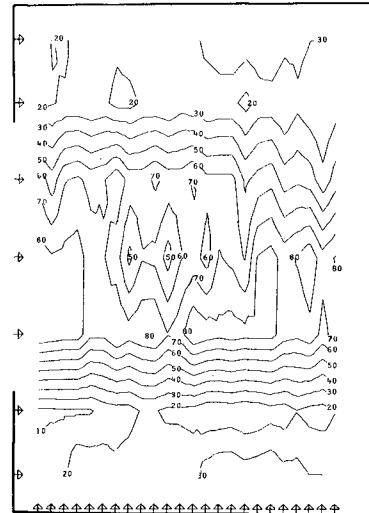
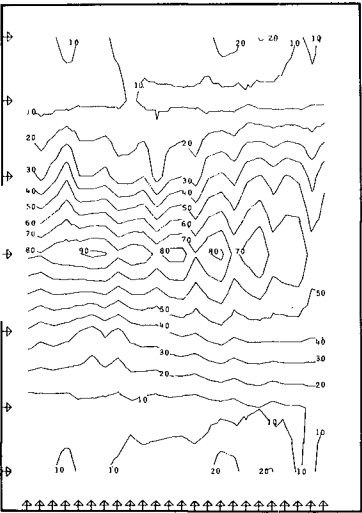
E(t) is the energy density in the harbour as a function of time,

P_i is the rate of energy input (Power in) through the harbour entrance,

P_o is the rate at which energy radiates out (Power out) through the harbour entrance,

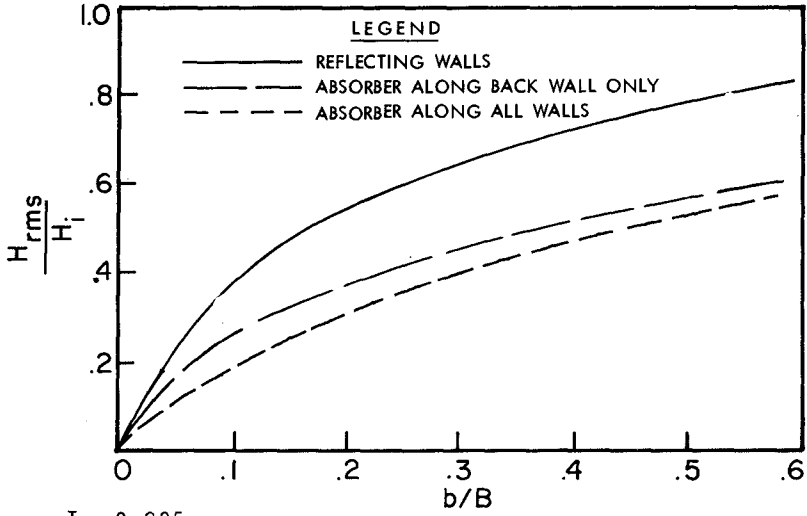


a. VERTICAL REFLECTING WALLS. ($b = 0.61$ m) b. ABSORBER ON ALL WALLS.

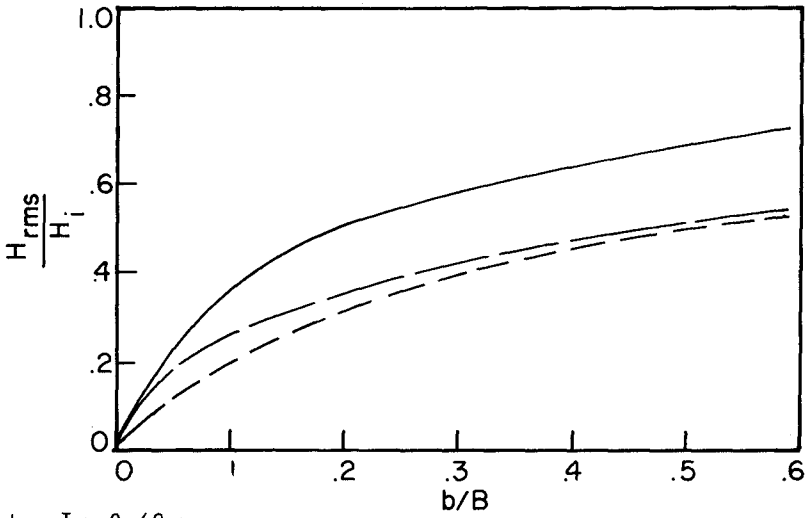


c. $b = 1.60$ m d. $b = 3.23$ m
 ABSORBER ALL AROUND.

FIGURE 3: NORMALIZED WAVE HEIGHT PLOTS.



a. $T = 0.985$ s.



b. $T = 0.69$ s.

FIGURE 4: REDUCTION IN OVERALL ENERGY LEVEL BY ABSORBERS.

P_a is the rate at which energy is absorbed
(Power absorbed) by the perimeter,

P_f is the rate of energy dissipation by bottom friction,

P_d is the rate of energy dissipation by internal friction.

There are additional terms such as energy dissipated by the docks, boats, etc. which will be included at a later stage of the work.

The term $E(t)$ in Eq. 1 describes the overall average energy density for the complete harbour in this particular study. In subsequent studies, the harbour will be divided to study energy buildup in particular sections individually. In either case, it is possible to define an RMS wave height for the harbour or particular section as:

$$E(t) = \frac{1}{8} \rho g \{ H_{\text{rms}}(t) \}^2 \quad (2)$$

for ease of comparison with the experimental results. Experimentally H_{rms} is simply the RMS value of all the wave heights measured by the probes within the harbour or within a particular section and this value of course corresponds to $t = \infty$.

The rate at which energy enters the harbour may be expressed as

$$P_i = bnC \frac{\rho g H_1^2}{8} \quad (3)$$

where b is the entrance width,

C is the phase velocity of the waves,

ρ is the density of the water,

g is the gravitational acceleration,

n is the ratio of group velocity to phase velocity

$$n = \frac{1}{2} \left\{ 1 + \frac{2kd}{\sinh 2kd} \right\}$$

where k is the wave number ($2\pi/L$),

L is the wave length,

d is the depth of water.

In actual fact, Eq. 2 should use H_1^1 , the incident wave height immediately inside the harbour entrance since the entrance causes energy losses. Work by Unluata and Mei (10) and Murakami and

Noguchi (7) states:

$$H'_i = H_i - K_e \frac{\hat{u}_e |\hat{u}_e|}{2g} \quad (4)$$

where K_e is an entrance loss coefficient
 \hat{u}_e is the maximum velocity in the entrance.

The value used for K_e was 1.5 and this will be verified in some later research. Equation 3 must therefore be rewritten as:

$$P'_i = bnC \frac{\rho g H_i'^2}{8} = bnCR^2 \frac{\rho g H_i^2}{8} = R^2 P_i \quad (5)$$

where

$$R = \frac{H'_i}{H_i}$$

If complete and even diffusion of wave energy is assumed, it is possible to write:

$$P_a = \left(k_a^2 \frac{\epsilon}{S} \right) P'_i \quad (6)$$

where k_a is the absorption coefficient for the perimeter absorbers,
 ϵ is the length of absorber,
 S is the length of harbour perimeter.

In actual fact diffraction takes place and Eq. 6 needs to be modified as:

$$P_a = \left\{ \sum_{j=1}^J k_{a_j}^2 k_{D_j}^2 \frac{\Delta S_j}{b} \right\} P'_i \quad (7)$$

Here the perimeter, S , has been divided into J incremental lengths ΔS_j ,

k_{a_j} is the absorption coefficient for incremental perimeter length ΔS_j ,

k_{D_j} is the diffraction coefficient for the waves reaching section ΔS_j .

Finally, the waves that are incident on the absorber have been modified by bottom friction and hence to be totally correct, Eq. 7 should be rewritten as:

$$P_a = \left\{ \sum_{j=1}^J k_{a_j}^2 k_{D_j}^2 \frac{\Delta S_j}{b} \right\} (P'_i - P_f) \quad (8)$$

where it is assumed that energy dissipation by friction occurs evenly throughout the harbour.

The weakest link in this rather simple analysis is the expression for radiation of energy outward through the entrance. It is assumed that the waves reflected from the face directly opposite the entrance radiate outward through the entrance completely. Any other reflected waves are assumed to re-reflect and remain in the harbour. Essentially a balance in error is assumed between ignoring dispersion of the waves involved in the outward radiation and ignoring the portion of wave energy escaping after secondary reflection. Thus

$$P_o = \left(\sum_{m=1}^M k_r^2 k_{D_m}^2 \frac{\Delta S_m}{b} \right) (P'_i - P_f) \quad (9)$$

where k_r is the reflection coefficient of perimeter length ΔS_m and the summation is only over a width of perimeter b , directly across the harbour entrance consisting of M incremental lengths of perimeter ΔS_m . Energy dissipation by friction for the return journey of the waves from the backwall to the entrance is also ignored in Eq. 9.

The rate of energy dissipation is based on work done earlier at Queen's and summarized in Ref. 4.

$$P_f = \frac{0.18 \rho \omega^2 H_{rms}^3}{8n \sinh^3 kd} f_w \quad (10)$$

where ω is the wave frequency ($2\pi/T$),

T is the wave period,

f_w is the wave friction factor defined in Refs. 3 and 4.

The dissipation by internal friction, P_d , was found to be insignificant.

Introducing P'_i instead of P_i into Eq. 1 and integrating yields:

$$E = \frac{t}{A} (P'_i - P_o - P_a - P_f) \quad (11)$$

where the expression has been averaged over several wave periods.

Substitution of Eqs. 2 to 10 now yields:

$$\frac{H_{rms}}{H_i} = \sqrt{\frac{t}{A} \left[bnCR^2 - \frac{0.18 \omega^2 H_{rms}^3}{ngH_i^2 \sinh^3 kd} \right] \left[1 - \sum_{j=1}^J k_{a_j}^2 k_{D_j}^2 \frac{\Delta S_j}{b} - \sum_{m=1}^M k_r^2 k_{D_m}^2 \frac{\Delta S_m}{b} \right]} \quad (12)$$

Note that to solve Eq. 12 requires both diffraction analysis and iteration.

Figure 5, based on calculations using the above equations, shows the influence of the individual terms in Eq. 11 as well as the development of the ratio H_{rms}/H_i . It may be seen that when the perimeter consists of reflecting walls, P_o is the important energy sink, as expected, while P_a is the dominant energy sink when absorbing perimeter walls are present. It may also be seen that the harbour takes a relatively short time to build up its wave energy to an asymptotic value. The dimensionless time scale used simply means time divided by the time it takes the wave to reach the back wall of the harbour (D is the depth of the harbour).

COMPARISON OF THEORY WITH EXPERIMENT

The relatively simple theoretical development of the previous section was compared with the experimental results and sample plots are shown in Figs. 6,7,8 and 9 (B is the width of the harbour). These figures indicate very good agreement except when the perimeter walls are reflecting. There are two possible reasons for this discrepancy:

- a. Local values of H deviate very far from H_{rms} but on a rather regular reflection pattern (Fig. 3(a)). The seven wave probes shown in Fig. 2 can therefore consistently measure values of H which result in substantially high or low values of H_{rms} depending on the reflection pattern present in the harbour.
- b. In the case of reflecting walls, the dominant energy sink in Eq. 11 is P_o , which is defined in the least reliable fashion.

CONCLUSIONS

1. The average, overall energy level in a harbour may be adequately calculated using a relatively simple theoretical expression such as Eq. 1 or Eq. 11. For the simple square or rectangular harbour used in this paper, the expressions reduce to Eq. 12.
2. The fit of the theoretical expression improves with the absorption qualities of the perimeter.
3. It was further seen from the tests that:
 - a. absorbing perimeter sections are valuable for reducing overall energy levels in a small craft harbour (Fig. 4).
 - b. absorbing perimeter sections reduce local wave energy peaks or locally large wave heights drastically, spreading the energy more evenly throughout the harbour (Fig. 3(a) and (b)).

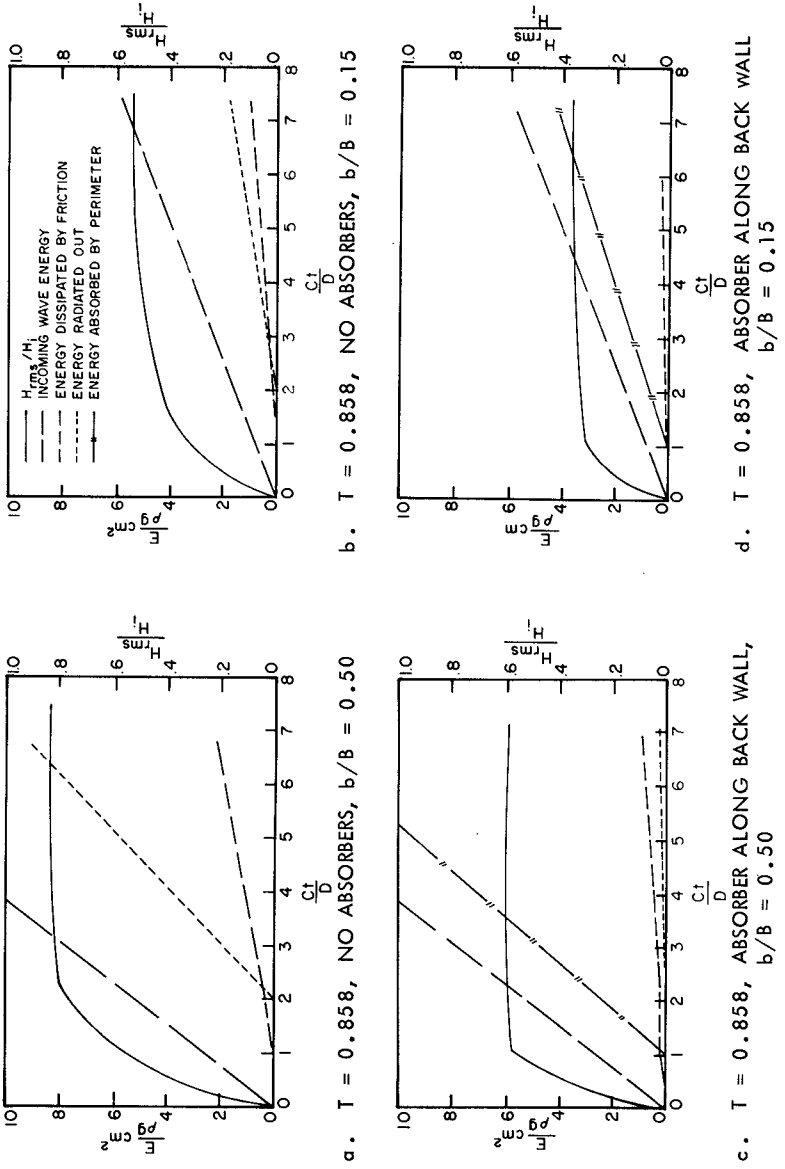
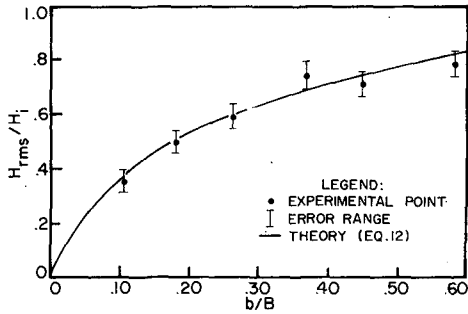
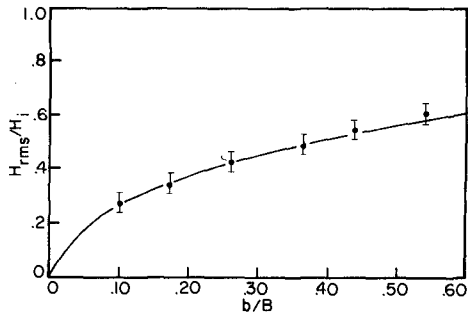


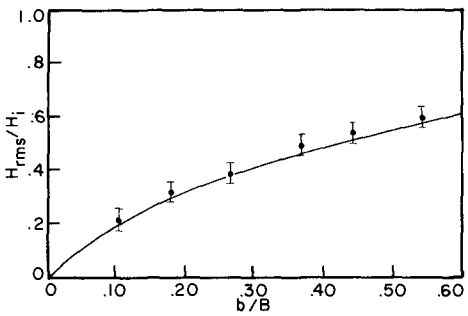
FIGURE 5: HISTORY OF INDIVIDUAL TERMS OF EQUATIONS 1 AND 12.



a. REFLECTING WALLS.

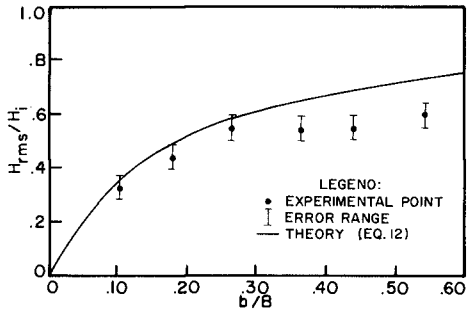


b. ABSORBER ON BACK WALL ONLY.

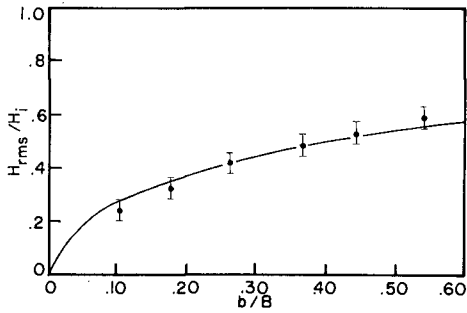


c. ABSORBER ON ALL WALLS.

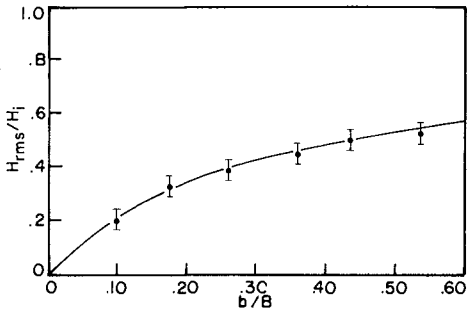
FIGURE 6: NORMALIZED RMS WAVE HEIGHT COMPARISON WITH THEORY $T = 0.985$ s RECTANGULAR HARBOUR.



a. REFLECTING WALLS.

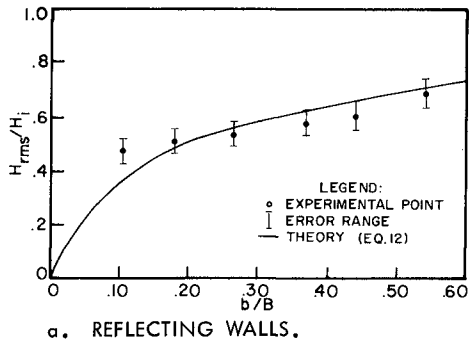


b. ABSORBER ON BACK WALL ONLY.

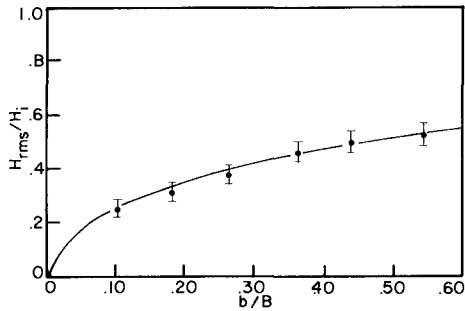


c. ABSORBER ON ALL WALLS.

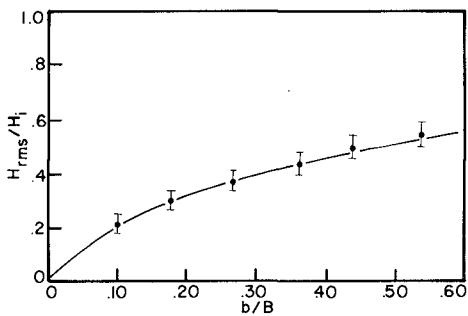
FIGURE 7: NORMALIZED RMS WAVE HEIGHT COMPARISON WITH THEORY
 $T = 0.858$ s RECTANGULAR HARBOUR.



a. REFLECTING WALLS.

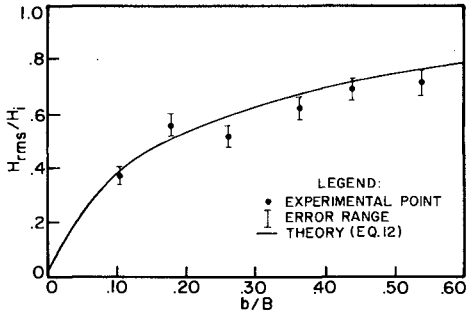


b. ABSORBER ON BACK WALL ONLY.

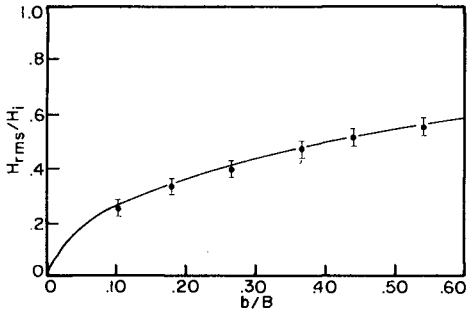


c. ABSORBER ON ALL WALLS.

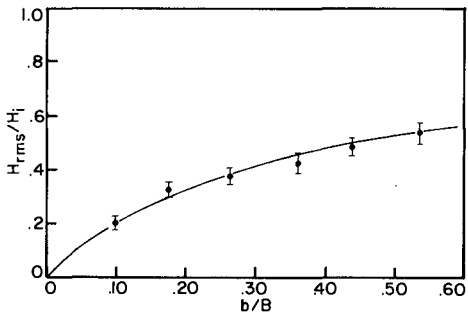
FIGURE 8: NORMALIZED RMS WAVE HEIGHT COMPARISON WITH THEORY
 $T = 0.69$ s RECTANGULAR HARBOUR.



a. REFLECTING WALLS.



b. ABSORBER ON BACK WALL ONLY.



c. ABSORBER ON ALL WALLS.

FIGURE 9: NORMALIZED RMS WAVE HEIGHT COMPARISON WITH THEORY
 $T = 0.985$ s SQUARE HARBOUR.

- c. absorbing perimeter sections can be located judiciously in order to bring about maximum attenuation of wave action per unit length of absorber, (Fig. 4).
- d. Energy levels in the harbour build up rapidly until the main energy sinks begin to function. In any case, response of a marina to outside agitation is rapid — of the order of the time taken for a wave to cross the marina and reflect back to the entrance, (Fig. 5).

Much more work needs to be done. This is only one building block which is useful in solving a rather pressing problem.

REFERENCES

1. Abbott, M.B., Petersen, H.M. and Skovgaard, O., (1978) "Computations of Short Waves in Shallow Water", *Proceedings, 16th Conference on Coastal Engineering*, Hamburg, pp 414-433.
2. Inman, D.L., (1974) "Ancient and Modern Harbours: a Repeating Phylogeny", *Proceedings 14th Conference on Coastal Engineering*, Copenhagen, pp 2049-2067.
3. Kamphuis, J.W., (1975) "Friction Factor Under Oscillatory Waves", *Waterways, Harbours and Coastal Engineering Journal*, A.S.C.E., Vol. 101, WW2, May 1975, pp 135-144.
4. Kamphuis, J.W., (1978) "Attenuation of Gravity Waves by Bottom Friction", *Coastal Engineering*, Vol 2, No 2, Oct 1978, pp 111-118.
5. Kamphuis, J.W., (1979) "Hydraulic Design of Small Craft Harbours", *Proceedings Canadian Society for Civil Engineering Conference on Coastal Engineering*, Kingston, April 1979, pp 133-152.
6. Kohlase, S., Daemrich, K.F. and Berger, U., (1978) "A Numerical Approach for the Determination of the Wave Height Distribution in a Harbour", *Proceedings 16th Conference on Coastal Engineering*, Hamburg, pp 664-676.
7. Murakami, H., and Noguchi, E., (1977) "Effects of Entrance Loss on Wave Induced Oscillations in Rectangular Harbours", *Coastal Engineering in Japan*, Vol. 20, pp 27-42.
8. Smith, D.A.Y., (1980) On the Damping of Non-Resonant Wave Agitation in Small Craft Harbours. *Ph.D. Thesis*, Queen's University.
9. Townson, J.M., (1973) "History of Coastal Engineering", *Dock and Harbour Authority*, Vol 54, pp 16-19.
10. Unluata, U. and Mei, C.C., (1975) "Effects of Entrance Loss on Harbor Oscillations", *Waterways, Harbours and Coastal Engineering Journal*, A.S.C.E. Vol 101, WW2, pp 161-180.

ACKNOWLEDGEMENTS

The financial research support of the Natural Sciences and Engineering Research Council of Canada for this project is gratefully acknowledged. The junior author extends his appreciation for the MacLaughlin Fellowship he held throughout his studies.

CHAPTER 14

EXPERIMENTAL INVESTIGATIONS OF PERIODIC WAVES NEAR BREAKING

J. Buhr Hansen*

ABSTRACT

The results presented are from a series of experiments of periodic waves approaching breaking on a gently sloping beach.

The recorded surface profiles are compared with a cnoidal theory taking into account the effect of the bottom slope. In both theory and experiments a skewness of the profile is observed. A fair agreement is found within certain limits of the wave height to water depth ratio and when the slope is sufficiently gentle. The change in water depth over a wave length must be sufficiently small.

The detailed analysis of the surface profiles including the skewness element shows good agreement with the cnoidal theory in cases where the wave height variation is as predicted by cnoidal wave shoaling.

The recorded surface profiles together with the recorded phase velocities are further used in computing the wave energy flux based on the theoretical relations from linear and cnoidal theories. Reasonable constancy is observed over the whole length covered by the experiments.

Finally the recorded wave set-down is compared with the results of linear and cnoidal theories. When approaching breaking neither of the theories can apparently predict the recorded water level changes.

1. INTRODUCTION

An extensive series of experiments with periodic waves approaching breaking on a 1:34.26 plane sloping beach were carried out from 1975 through 1978.

In these experiments were studied the wave transformation on a gentle slope up to the point of breaking, and the measurements supplied information about height, speed of propagation, and variation of mean water level, as well as the shape and deformation of the surface profiles. In particular the wave profiles differ significantly from those reported in literature because the waves generated were nearly free of free second harmonic components, which so seriously have hampered other investigations.

Much of the raw data from 17 different wave conditions is published in Buhr Hansen and Svendsen (1979). This report further contains a detailed description of the experimental set-up and data acquisition system.

*Assoc. Prof., Inst. Hydrodyn. and Hydraulic Engrg. (ISVA),
Technical University of Denmark, Building 115, DK-2800 Lyngby.

Some of the results extracted from the measurements have already been published in journals and at conferences:

Svendsen and Buhr Hansen (1977 and 1976 a) compared the observed wave height variation over the sloping bottom with the theoretical shoaling of the waves as predicted by sinusoidal and cnoidal wave theories. A good agreement between experiments and theory was observed for waves of relatively small deep water steepnesses (Svendsen and Buhr Hansen, 1976 a, Fig. 4).

In case of rather steep waves, deviations between experiments and theory become pronounced (Svendsen and Buhr Hansen, 1976 a, Fig. 5). However, the shoaling assumption requires that the relative change in water depth, h , over a wave length, L , is small. This indicates that, in case of very long waves, other deviations between experiments and theory might be observed. This is in Svendsen and Buhr Hansen (1977) expressed in terms of a bottom slope parameter $S \equiv h_x L/h$, where h_x is the bottom slope. To fulfill the shoaling assumption, linear theory requires that S is of the same order of magnitude (or smaller) as the wave steepness, H/L , and Svendsen (1974) showed that for (first order) cnoidal waves S must be small compared to $(h/L)^2$. Further, H/h must be sufficiently small ($\ll 1$).

In this paper a detailed analysis of wave surface profiles will be presented, and the results will be compared with a cnoidal theory covering cases from very long waves with low steepness to shorter waves with a considerable steepness.

The analysis of the surface profiles includes a comparison with a cnoidal theory taking into account the distortion (skewness) of the profile due to the sloping bottom as given in Svendsen and Buhr Hansen (1978). A preliminary comparison between some measured wave profiles and the above mentioned theory is included in Svendsen and Buhr Hansen (1976 a, 1978).

Further, the wave energy flux, as calculated from the experimental data, will be analysed for the influence of profile skewness and phase velocity. Svendsen and Buhr Hansen (1976 a) contains some preliminary comparison between the measured and the theoretical phase velocities.

Finally this paper will include a comparison of wave set-down near breaking between the experiments and different theoretical approaches. Svendsen and Buhr Hansen (1976 b) contains some cnoidal wave approximations for the wave set-down and a comparison with two experiments.

2. THE EXPERIMENTAL SET-UP

The waves are generated by a piston type wave generator in a flume 32 m long, 60 cm wide, with a plane beach sloping 1:34.26 (see Fig. 1). The motion of the wave generator is controlled by a PDP 8 mini-computer, which generates a command signal of the form

$$\xi = e_1 \sin \omega t + e_2 \sin(2\omega t + \beta) \quad (1)$$

(Buhr Hansen and Svendsen, 1974). The recording system is described in details in Buhr Hansen and Svendsen (1979).

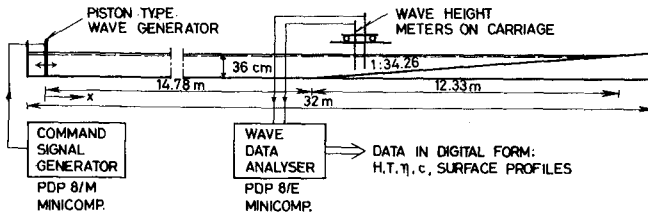


Fig. 1 Experimental facility

The resulting wave profiles on the horizontal bottom are in Svendsen and Buhr Hansen (1977, 1978) compared with a Stokes' second order wave for rather short waves ($U = HL^2/h^3$ is about 2 and 7, respectively), indicating the generation of waves with almost no free second harmonic components.

It appears that even for waves with U as large as 40 (which is far up in the cnoidal region), the waves generated remain of clean and constant form. In Fig. 2 the recorded surface profiles of three wave conditions are compared with theoretical cnoidal profiles, and a good agreement is observed.

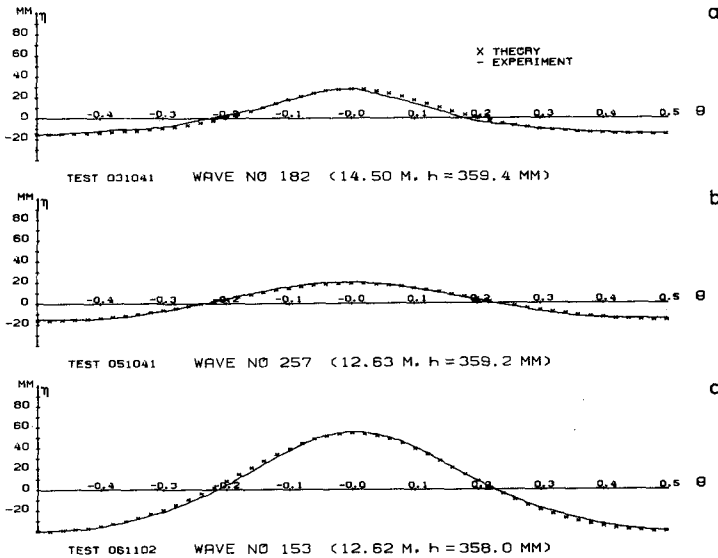


Fig. 2 Surface profiles on horizontal bottom. Measurements compared with first order cnoidal theory. a) $T = 1/3$ s, $U = 32.2$; b) $T = 1/5$ s, $U = 10.7$; c) $T = 1/6$ s, $U = 17.5$

For the longest of these waves the wave height variation over the sloping bottom is clearly not predicted by theoretical cnoidal wave shoaling (see Fig. 3), indicating that the bottom is not 'sufficiently gently sloping' in this case.

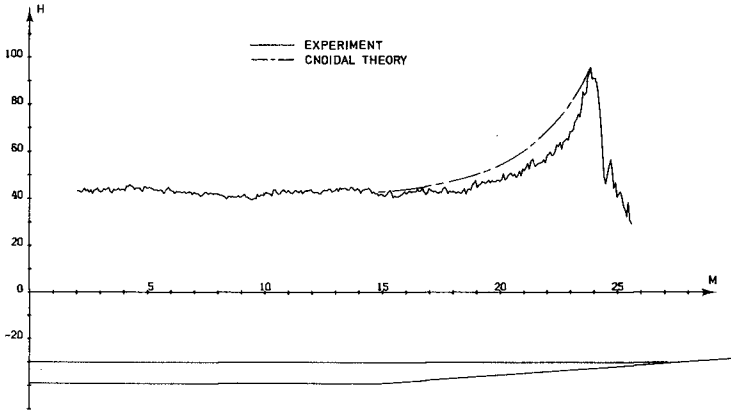


Fig. 3 Variation of wave height for 'long' waves with low steepness $T = 1/.3 s, H_0/L_0 = .0019$

Table 1 includes the basic dimensionless parameters for the wave conditions analysed in this paper. In the following the waves will be characterized by their period, T, and deep water steepness H_0/L_0 .

Period T(s)	H_0/L_0	Gener- ated height H(mm)	At $h \approx 360$ mm			At breaking ($\lambda (H/h)_{max}$)			
			U	S	$T\sqrt{g/h}$	h(mm)	U	S	$T\sqrt{g/h}$
1/.3	.0019	40	32.2	.50	17.4	89	1800	1.30	35.0
1/.4	.0038	40	17.5	.37	13.1	85	1000	.93	26.9
1/.4	.0064	71	30.6	.37	13.1	129	650	.74	21.8
1/.5	.0060	38	10.7	.28	10.4	69	890	.92	23.8
1/.5	.0102	67	18.7	.28	10.4	112	520	.66	18.7
1/.6	.0093	38	7.0	.22	8.7	64	630	.73	20.6
1/.6	.0167	69	12.3	.23	8.7	107	300	.54	16.0
1/.6	.0241	99	17.5	.23	8.7	149	220	.45	13.5
1	.0279	40	1.8	.12	5.2	56	205	.45	13.2

Table 1 Basic data for analysed waves

3. SURFACE PROFILES ON SLOPING BOTTOM

The deformation of waves passing over a sloping bottom is evaluated theoretically by Svendsen and Buhr Hansen (1978). Their theoretical result is based on a two-scale expansion of the cnoidal theory in which

it is essential that the bottom slope is so small that the shoaling condition is fulfilled, $S \ll (h/L)^2$, but still so steep that the deformation (skewness) due to the slope is an order of magnitude greater than the second order terms of the constant depth solution, $S \gg (h/L)^4$. Simultaneously H/h must be sufficiently small. Under these assumptions the surface profile is given by

$$\eta = \eta^{(0)} + \eta^{(1)} \tag{2}$$

where $\eta^{(0)}$ is the constant depth, first order cnoidal solution

$$\eta^{(0)} = \eta_{\min} + H \operatorname{cn}^2(\theta, m) \tag{3}$$

and $\eta^{(1)}$ is the skewness term given by

$$\eta^{(1)}/H = 3 (L/h)^2 h_x T \sqrt{g/h} G(\theta, U) \tag{4}$$

where g is the acceleration of gravity, and the function $G(\theta, U)$ is given in Fig. 4.

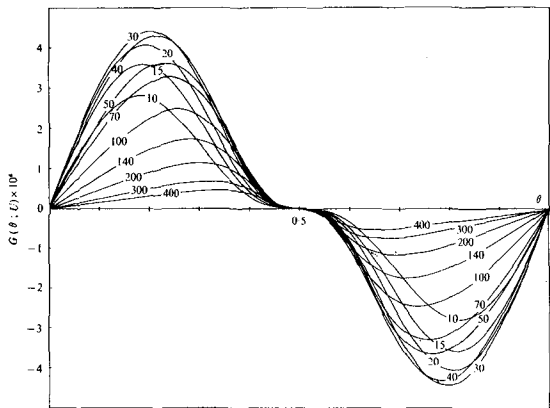


Fig. 4
 $G(\theta, U)$ as function
of phase angle.
Each curve marked
with the value of
 $U = HL^2/h^3$
(From Svendsen and
Buhr Hansen, 1978)

Recorded surface profiles: In analysing the experimental re-sults, the total recorded η is assumed to be a sum of two contributions as given by (2). Knowing the basic features of each of the two terms, $\eta^{(0)}$ and $\eta^{(1)}$ may be separated through

$$\eta_{\theta}^{(0)} = \frac{1}{2} (\eta_{\theta} + \eta_{-\theta}) \quad \text{and} \quad \eta_{\theta}^{(1)} = \frac{1}{2} (\eta_{\theta} - \eta_{-\theta}) \tag{5 and (6)}$$

with $\theta = 0$ at the wave crest.

A direct comparison between the measured and the theoretical profiles as well as the $\eta^{(0)}$ and $\eta^{(1)}$ are given in Fig. 5. The theoretical profiles are computed using the recorded horizontal-bottom-wave height $H^{(0)}$, determined from the $\eta^{(0)}$ profile, and the actual h as input values to the computations.

The four profiles in Fig. 5 are for two different wave conditions, and for each of these are shown the recorded profiles halfway between the toe of the slope and the point of breaking and the last profile recorded before the point of breaking. The recorded $\eta^{(0)}$ -profiles are

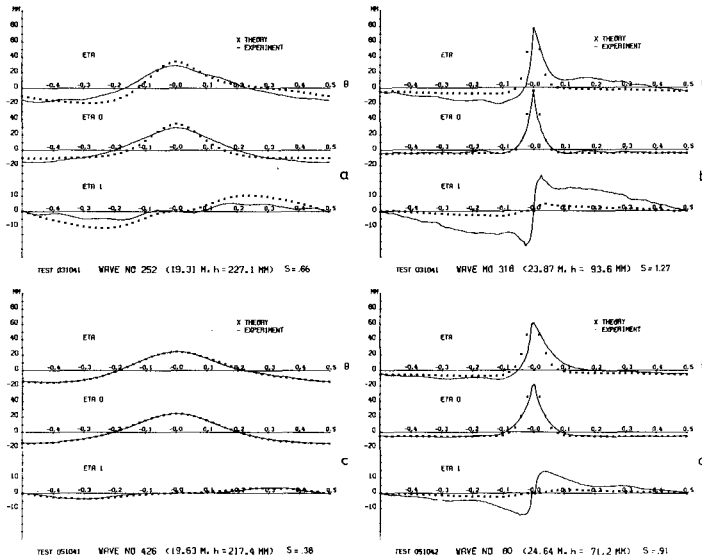


Fig. 5 Surface profiles on sloping bottom. Measurements compared with cnoidal theory. a) and b) $T = 1/3 s$, $H_0/L_0 = .0019$; c) and d) $T = 1/5 s$, $H_0/L_0 = .0060$

seen to agree fairly well with the theoretical profiles even for relatively high H/h values. On the other hand, the observed skewness of the profiles close to breaking is obviously not predicted by the theory. This might, of course, be expected since neither the slope parameter S nor the H/h ratio are within the limits of the theoretical approximation.

Analysis of observed wave skewness: The figures 6 through 9 show the variation of the maximum relative skewness $\eta_{max}^{(1)}/H^{(0)}$ (abbreviated to MRS) with $H^{(0)}/h$ for six different wave conditions. The characteristic feature of the theoretical variation with H/h showing a maximum MRS is clearly reproduced in the tests with waves of low deep water steepness, Figs. 6, 7, 8 and 9 a. Only in case of the shortest of the waves (Fig. 9 a) is the maximum MRS observed at the same H/h as predicted by the theory. When the wave period is increased (Figs. 8, 7 and 6) the maximum MRS should according to the theory be found at decreasing H/h ratios, but this is not observed in the experiments.

Inspection of the figures further shows that the development of the skewness from the toe of the slope is as predicted by the theory in Fig. 8, and with a reasonable accuracy in Figs. 7 and 9 a. In Fig. 6 the skewness is obviously developing gradually over a considerable range of $H^{(0)}/h$ from the toe of the slope, indicating - presumably - that the slope is too steep for this long wave to adjust itself to the local water depth instantaneously as assumed in the theory. This further supports the observation in Fig. 3 indicating that the wave height

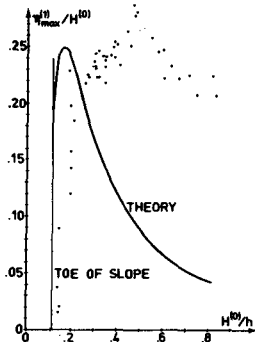


Fig. 6 Max. relative skewness $T = 1/3.3$ s, $H_0/L_0 = .0019$

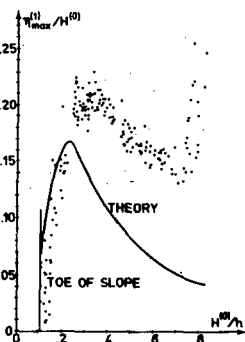


Fig. 7 Max. relative skewness $T = 1/4.5$ s, $H_0/L_0 = .0038$

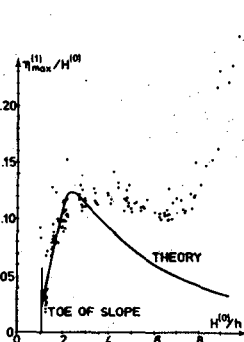


Fig. 8 Max. relative skewness $T = 1/5.5$ s, $H_0/L_0 = .0060$

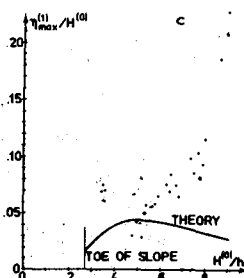
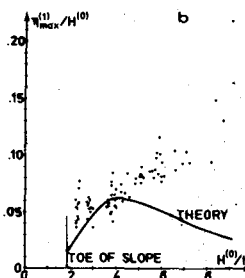
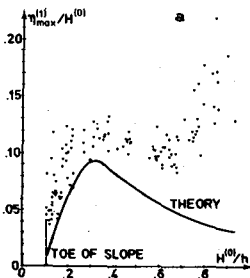


Fig. 9 Maximum relative skewness for waves with $T = 1/6$ s
a) $H_0/L_0 = .0093$, b) $H_0/L_0 = .0167$, c) $H_0/L_0 = .0241$

does not vary as predicted by cnoidal wave shoaling. In the case of relatively short waves with greater steepness, Fig. 9 b and c, the characteristic feature of the theoretical MRS variation with a maximum and subsequent decrease of MRS for increasing $H^{(0)}/h$ is not observed in the tests. However, if not only the maximum recorded $\eta^{(1)}$ - which may obviously be greatly influenced by small disturbances of the waves recorded - but the entire $\eta^{(1)}$ profile is included in this analysis, the maximum and subsequent decrease of relative skewness is hardly observed in any of the tests. In Fig. 10 is shown the variations of $\text{RMS}\{\eta^{(1)}\}/\text{RMS}\{\eta^{(0)}\}$ for the same tests as reported in Figs. 6, 8 and 9 a. For the not too long waves the skewness development up to the theoretical maximum is still seen to be reproduced in the experiments, but the subsequent decrease is hardly noticeable. This may indicate that the shape of the recorded $\eta^{(1)}$ profile deviates more from the theoretical shape than the observed maximum value alone, which may be due to the presence of small reflected waves and parasitic waves. For two tests one measure of the shape of the $\eta^{(1)}$ profile is compared with the theory. In Fig. 11 is plotted $\text{MS}\{\eta^{(1)}/\eta_{\text{max}}^{(1)}\}$ versus $U = (H^{(0)}/h)^2 L^2/h^3$.

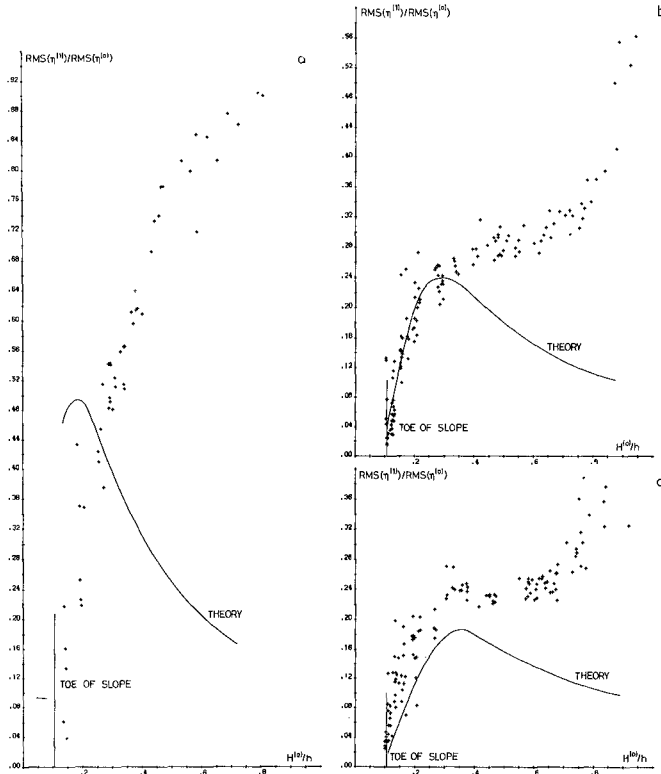


Fig. 10 Relative skewness in terms of $\left\{ \frac{\overline{\eta^{(1)2}}}{\overline{\eta^{(2)2}}} \right\}^{1/2}$
 a) $T = 1/3$, $H_0/L_0 = .0019$; b) $T = 1/5$, $H_0/L_0 = .0060$
 c) $T = 1/6$, $H_0/L_0 = .0093$

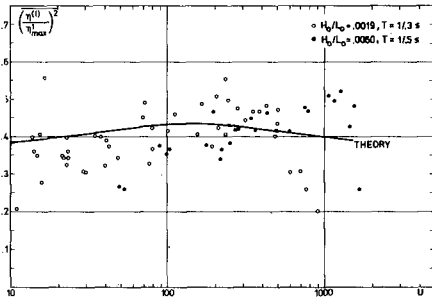


Fig. 11
 Shape of $\eta^{(1)}$ profile
 compared with theory

The measurements show a considerable scatter around the theoretical curve calculated from the $G(U, \theta)$ function given in Fig. 4, but the general trend of the theory is reproduced in the tests.

Having determined the $\eta^{(1)}$ profile from the experiments, it is from eq. (4) possible to compare an experimentally determined G function with the theoretical function. In Fig. 12 this comparison is shown in terms of RMS (G), indicating that the general trend is the same in theory and experiments, but also that for $U > 100$ all experiments show an experimental value above the theoretical one, and with a constantly increasing ratio between the measured and the theoretical values for increasing U . It is further observed that for $U > 100$ the experiments yield higher values for higher deep water wave steepness. Both these observations indicate the increasing importance of $H^{(0)}/h$, which in this region cannot really be regarded as small.

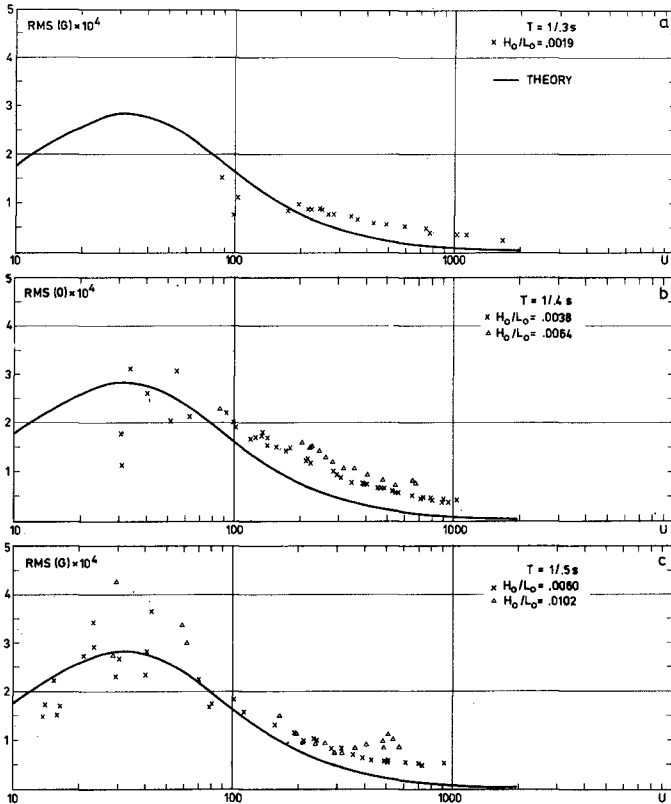


Fig. 12 Skewness function G . Comparison between theory and experiments

It is interesting to observe that the experimental G-values continue to decrease when the waves approach breaking, indicating the possibility of establishing a higher order theory valid for $H < h$ rather than the present theory requiring $H \ll h$.

Waves close to breaking: The skewness is seen to increase rapidly just prior to breaking (see Figs. 6 through 9). This might indicate the commencement of the irreversible deformation of the waves eventually leading to the actual breaking. For those tests, where the MRS shows a clear maximum and subsequent minimum for increasing $H^{(0)}/h$ (e.g. Figs. 6, 7, 8 and 9 a), the minimum MRS is observed at an $H^{(0)}/h$ which is very close to the theoretical H/h for the highest stable wave at horizontal bottom according to Ridler (1979), see Fig. 13. This may be taken as support of the idea that this indicates the commencement of the breaking process. Fig. 13 also includes the total wave height to water depth ratio, H/h , at the observed minimum MRS and the $(H/h)_D$ at the breaking point defined as $\max(H/h)$. Close to the breaking point

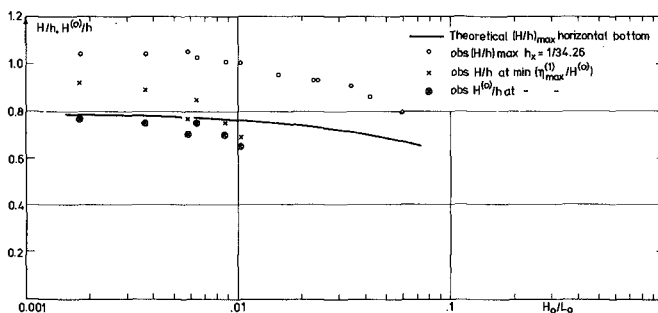


Fig. 13 Theoretical and observed $(H/h)_{\max}$

the skewness yields a significant change in the wave height recorded, which is not accounted for in the theory. For waves with very low deep water steepness - which in the tests are at the same time 'long' waves - the total wave height may be more than 20% higher than the horizontal bottom wave height, $H^{(0)}$. For the 'shorter' waves with higher deep water steepness the total wave height is only 5 - 10% higher than $H^{(0)}$. This may again support the previous observations indicating incomplete shoaling conditions for the long waves of periods 1/.3 and 1/.4 s, since the $H^{(0)}$ variation if plotted in Fig. 3 would indicate greater discrepancy from the theory than the plotted H variation.

4. ENERGY FLUX FOR WAVES ON SLOPING BOTTOM

One of the basic assumption in wave shoaling is that the wave energy flux through a vertical section remains constant when the water depth is changing.

The basic expression for the energy flux, E_f , as function of time, t , is

$$E_f(t) = \int_{-h}^{\eta} \left(p^+ + \frac{1}{2} \rho (u^2 + w^2) \right) u \, dz \tag{7}$$

where p^+ is the excess pressure due to the wave motion, u and w are the horizontal and vertical particle velocities, and ρ the density of the water.

When (7) is evaluated to the second order in η/h and averaged over a wave period, it reduces to

$$E_f = \rho g h^2 c \left\{ \overline{\left(\frac{\eta}{h}\right)^2} + \frac{1}{2} \overline{\left(\frac{\eta}{h}\right) \left(\frac{\eta}{h+\eta}\right)^2} + \frac{1}{3} \overline{\eta \eta_{xx}} \right\} \quad (8)$$

Using the KdV equation, the last term may be expressed in terms of η

$$\frac{1}{3} \overline{\eta \eta_{xx}} = 2 \left(\frac{c}{c_0} - 1 \right) \overline{\left(\frac{\eta}{h}\right)^2} - \frac{3}{2} \overline{\left(\frac{\eta}{h}\right)^3} \quad (9)$$

where $c_0 = \sqrt{gh}$, and c is the cnoidal approximation to the phase velocity

$$c = c_0 \sqrt{1 + A H/h} \quad (10)$$

$A = A(U)$ is given by the cnoidal theory, see e.g. Skovgaard et al. (1974). When further η is assumed to be a sum of the horizontal bottom profile, $\eta^{(0)}$, and a small skewness component, $\eta^{(1)}$, (8) may be written

$$E_f = \rho g H^2 c B \quad (11)$$

with

$$B = \overline{\left(\frac{\eta^{(0)}}{H}\right)^2} + \overline{\left(\frac{\eta^{(1)}}{H}\right)^2} + 2 \left(\frac{c}{c_0} - 1 \right) \overline{\left(\frac{\eta^{(0)}}{H}\right)^2} - \overline{\left(\frac{\eta^{(0)}}{H}\right)^3} \frac{H}{h} \quad (12)$$

In B the first term is the first order horizontal bottom component

$$B_{01} = \overline{\left(\frac{\eta^{(0)}}{H}\right)^2} \quad (13)$$

which is a function of U only. Of the remaining three terms the first one is the skewness term, while the last two terms are the second order horizontal bottom terms. The direct influence of the skewness on the B value can be seen in Fig. 10 which shows directly the square root of the skewness term relative to the B_{01} term.

While the skewness term is obviously positive, the second order terms of the horizontal bottom profile will be negative for $U < \sim 390$. This is seen when (10) is introduced in the last two terms in (12) yielding an overall negative result for

$$A < \frac{\overline{\eta^{(0)^3}}}{\eta^{(0)^2 H} \quad (14)$$

(A is positive for $U > 47$ and a negligible influence of the second order horizontal bottom terms is observed for $U > \sim 250$).

Experimental results for B_{01} : In Fig. 14 is shown the comparison between the theoretical B_{01} and the value obtained from the recorded $\eta^{(0)}$ profiles. (The theoretical wave length is used in computing U).

While the experiments with not too long waves and a low deep water steepness plotted in Fig. 14b and one test in Fig. 14c show a good agreement with theory up to $U \sim 700$ (corresponding to $H^{(0)}/h \gtrsim .75$) the same agreement is not found neither in Fig. 14a nor in the other two

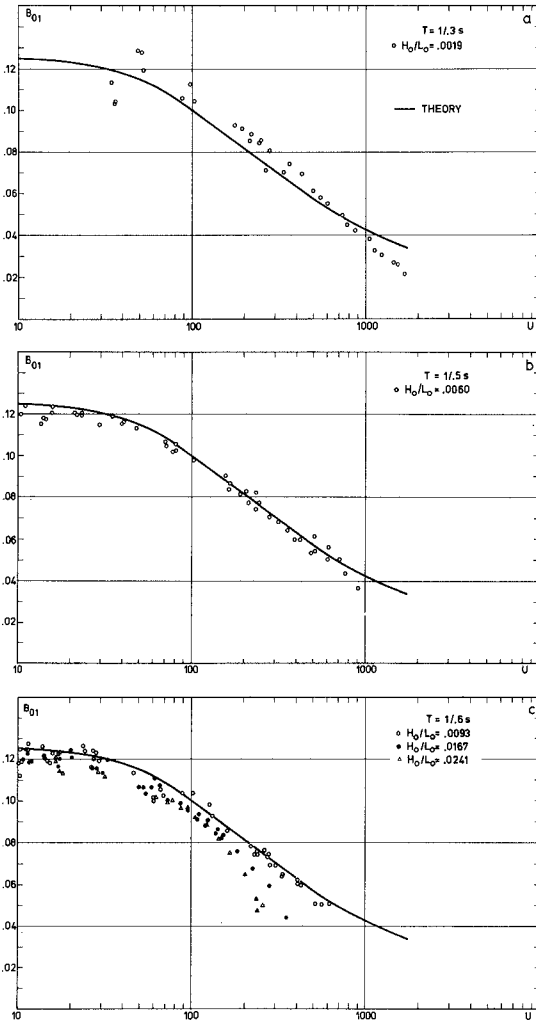


Fig. 14 Experimental values of $B_{01} = \overline{\eta(0)^2}/H(0)^2$ compared with cnoidal theory

tests included in Fig. 14 c. Fig. 14 a shows experimental values greater than the theoretical values, which is yet another indication of the incomplete shoaling of these long waves. Within $50 < U < 300$ the experimental values would agree with the theory if they had been recorded at a 15% greater water depth, indicating that the shape of the profile corresponds to a greater - earlier - water depth.

For waves with greater deep water steepness (Fig. 14 c) the experimental values are all below the theoretical curves. In this case only the change in wave height can explain the deviation from theory, indicating the importance of the $H^{(0)}/h$ ratio when this is not really small. For increasing wave steepness, a constant U will reflect increasing H/h ratios seen in Fig. 14 c to cause increasing discrepancy between theory and experiments.

Experimental results for B : The combined influence of the skewness and the second order horizontal bottom terms on the energy flux may be analysed through analysis of B given by (12) compared with B_{01} given by (13).

The theoretical B is from (12), (3) and (4) seen to be a function of U , but at the same time dependent on $h_x T \sqrt{gh}$. Theoretically this causes B to be generally greater than B_{01} for long waves of low steepness, and smaller than B_{01} for shorter waves of considerable steepness.

In Fig. 15 is compared the experimental values for B with the theory for three experiments. For all experimental values are plotted two different B values based on both the theoretical and the recorded phase velocities.

The general trend of all three tests is that the combined skewness and second order influence on B is more pronounced in the experiments than predicted by the theory. This is especially pronounced in Fig. 15 a for the long waves with low steepness, and in this case the difference between measured and theoretical phase velocities is seen to be of minor importance.

As seen in previous comparisons, the test in Fig. 15 b shows a very close agreement with theory over the whole range of U values with measured and theoretical phase velocities plotting on either side of the theoretical curve. For the short, steep waves plotted in Fig. 15 c the trend is the same as in the comparison of B_{01} term in Fig. 14 c.

A comparison between measured and theoretical phase velocities is included in Svendsen and Buhr Hansen (1976 a) indicating a fair agreement with cnoidal theory. However, a closer analysis shows that for high values of H/h , the measured phase velocities are in general 5-10% below the theoretical values.

Energy flux: Having determined B , the total energy flux may be computed from (11), now taking into account the combined effect of wave height, phase velocity and the shape of the surface profile. It should be noticed that (11) is valid in linear wave theory as well with

$$B = \frac{1}{16} (1 + G) \quad (15)$$

and

$$G = \frac{2 kh}{\sinh 2kh} \quad (16)$$

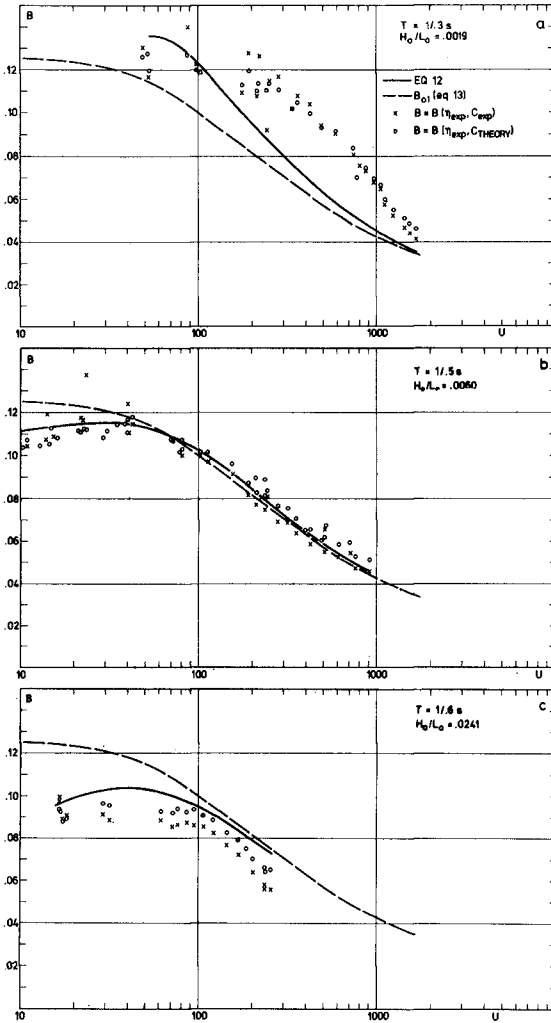


Fig. 15 Experimental values of B compared with cnoidal theory

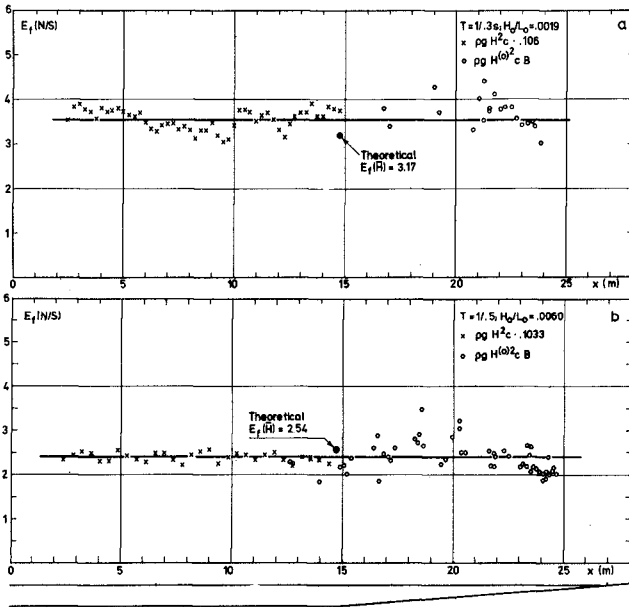


Fig. 16 E_f calculated from experimental results

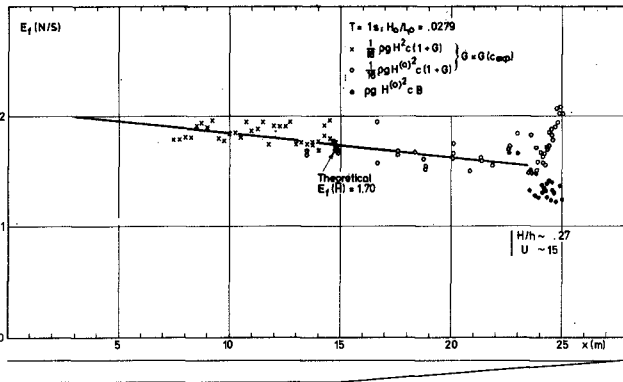


Fig. 17 E_f for short waves calculated from experimental results

The figures 16 and 17 show for three tests the energy flux determined from (11) using recorded data.

In front of the sloping bottom the recorded H and c values are applied together with an average B determined from the profile recordings available in this region. For the tests in Fig. 16 with rather long waves, B is determined from (12) with no skewness component. For the short waves dealt with in Fig. 17, B is determined from the linear theory (eqs. (15) and (16)).

Over the sloping bottom, on the other hand, $H^{(0)}$, the height of the horizontal bottom part of the profiles is used in determining E_f both in case of a cnoidal computation, Fig. 16, and in case of linear theory computations, Fig. 17.

The scatter about the - by eye placed - regression line is in both figures considerable, mainly due to variation in the recorded phase velocities. However, the two tests in Fig. 16 show some evidence of the presence of a small reflected wave, but with an overall constant energy flux. In Fig. 17 both cnoidal and linear computations of E_f are performed for $U > \sim 15$. As expected, the linear theory yields too high E_f values in this region, but the cnoidal theory on the other hand seems to underestimate E_f . The energy flux is in this case clearly decreasing by the distance from the wave generator (at $x = 0$). The rate of decrease corresponds to a rate of decrease in wave height of $\Delta H/H = .0054$ pr. m, which agrees well with the direct measured attenuation of the wave heights, see Fig. 18. The same agreement is obviously not observed for the tests analysed in Fig. 16.

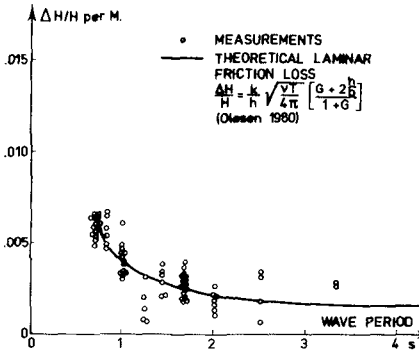


Fig. 18
 Recorded attenuation of wave heights. Water depth 36 cm, flume width 60 cm (Buhr Hansen and Svendsen, 1979)

5. WAVE SET-DOWN NEAR BREAKING

The last topic to be discussed in this paper is a comparison between recorded and theoretical wave set-down.

From linear theory the wave set-down is given by the well-known expression

$$b = -\frac{1}{16} \frac{H^2}{h} \frac{2kh}{\sinh 2kh} \quad (17)$$

Close to breaking, however, the H/h ratio is not small, and usually the L/h is so large that (17) is a poor approximation, as indicated in both examples given in Fig. 19, where (17) is evaluated using the recorded $H^{(0)}$ and $L (= cT)$ values.

The first approximation to b in cnoidal theory is (Svendsen, 1974)

$$b = -\frac{\eta^2}{2h} \quad (18)$$

In Svendsen and Buhr Hansen (1976 b), (18) is shown to be as poor an approximation to the experimental results as the linear theory. This is confirmed in Fig. 19 where (18) is evaluated using the recorded η values.

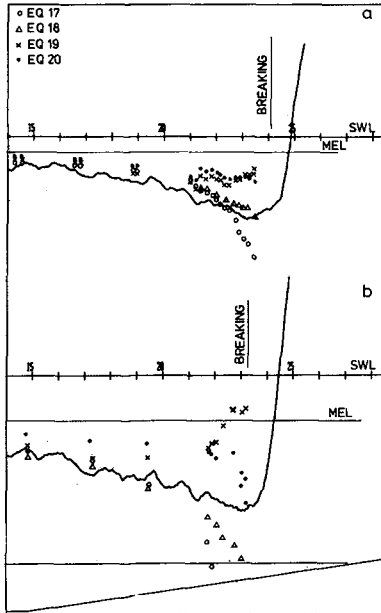


Fig. 19
Wave set-down
a) $T = 1/.4 \text{ s}$, $H_0/L_0 = .0038$
b) $T = 1/.5 \text{ s}$, $H_0/L_0 = .0102$

When taking into account the non-linearity of the bottom particle velocity and the vertical accelerations, Svendsen and Buhr Hansen (1976 b) obtain the following approximation to b in cnoidal theory

$$b = -\frac{c^2}{2g} \left[\left(2 \frac{c}{\sqrt{gh}} - 1 \right) \frac{\eta^2}{h^2} - \frac{\eta}{2} \frac{\eta^3}{h^3} \right] \quad (19)$$

When (19) is evaluated from the recorded η and c values, this is in Fig. 19 seen to underestimate the set-down close to breaking where (17) and (18) overestimate b .

Svendsen and Buhr Hansen (1976 b) develop (19) further through certain approximations. (The approximation op. cit. eq. (11) stated to be 'correct within a few per cent for $0 < \eta/h < 1$ ' is, however, only correct within 7% for $\eta/h > .4$. For $\eta/h = .1$ it is incorrect by 35% yielding a severe underestimate of the wave set-down at the toe of the slope in the present experiments, where (17) and (19) yield almost identical results.) The final equation given by Svendsen and Buhr Hansen (1976 b, eq. (14)) based on the above mentioned approximation is

$$b = -\frac{c^2}{2g} \left[\left(\frac{c^2}{gh} - .35 \right) \frac{\bar{\eta}^2}{h^2} - 1.9 \frac{\bar{\eta}^3}{h^3} \right] \quad (20)$$

In Fig. 19 this is to some extent seen to reflect the shape of the measured set-down but at a different elevation, when (20) is evaluated from recorded η and c values.

Compared to the observations in the previous chapters of this paper it is remarkable to observe that, while the surface profiles and the energy flux seem to be reasonably well predicted by the cnoidal theory, this is certainly not the case for the set-down.

6. REFERENCES

- Buhr Hansen, J. and I.A. Svendsen (1974) 'Laboratory generation of waves of constant form'. Proc. 14th Coastal Engrg. Conf., Copenhagen, Chap. 17, pp. 321-339.
- Buhr Hansen, J. and I.A. Svendsen (1979) 'Regular waves in shoaling water - Experimental data'. Series Paper 21, Inst. Hydrodyn. and Hydraulic Engrg., Tech. Univ. Denmark.
- Olesen, E. (1980) 'Energy dissipation and integrated wave parameters before breaking'. M.Sc. thesis (in Danish) supervised by I.A. Svendsen and J. Buhr Hansen, ISVA, Tech. Univ. Denmark.
- Ridler, S.H. (1979) 'High waves on horizontal bottom'. M.Sc. thesis (in Danish) supervised by I.G. Jonsson and O. Skovgaard, ISVA/LAMF, Tech. Univ. Denmark.
- Skovgaard, O., I.A. Svendsen, I.G. Jonsson, and O. Brink-Kjær (1974) 'Sinusoidal and cnoidal gravity waves - Formulae and tables'. Inst. Hydrodyn. and Hydraulic Engrg., Tech. Univ. Denmark, 8 pp.
- Svendsen, I.A. (1974) 'Cnoidal waves over a gently sloping bottom'. Series Paper 6, Inst. Hydrodyn. and Hydraulic Engrg., Tech. Univ. Denmark.
- Svendsen, I.A. and J. Buhr Hansen (1976 a) 'Deformation up to breaking of periodic waves on a beach'. Proc. 15th Coastal Engrg. Conf., Honolulu, Chap. 27, pp. 477-496.
- Svendsen, I.A. and J. Buhr Hansen (1976 b) 'Wave set-down near breaking'. Prog. Rep. 41, pp. 31-36, Dec. 1976, Inst. Hydrodyn. and Hydraulic Engrg., Tech. Univ. Denmark.
- Svendsen, I.A. and J. Buhr Hansen (1977) 'The wave height variation for regular waves in shoaling water'. Coastal Engrg., 1, pp. 261-284.
- Svendsen, I.A. and J. Buhr Hansen (1978) 'On the deformation of periodic long waves over a gently sloping bottom'. J. Fluid Mech., 87, pp. 433-448.

An Heuristic Model of Wave Height Distribution in Surf Zone

Masaru MIZUGUCHI
 Department of Civil Engineering
 Chuo University
 Kasuga, Bunkyo-ku
 Tokyo, JAPAN

INTRODUCTION

Until now, almost every study on coastal processes has considered the basic type of two-dimensional beach profile as being of constant slope. However, as our knowledge on this problem advances, we realize the importance of the influences of the bottom configuration on the hydrodynamic phenomena in a given area.

Figure 1 shows a recent experimental result on the longshore current profile on a step type beach. (Here the step type beaches are defined as those which have a step in the bottom profile, whether the beaches are of accretion type or not.) The wave height and mean water

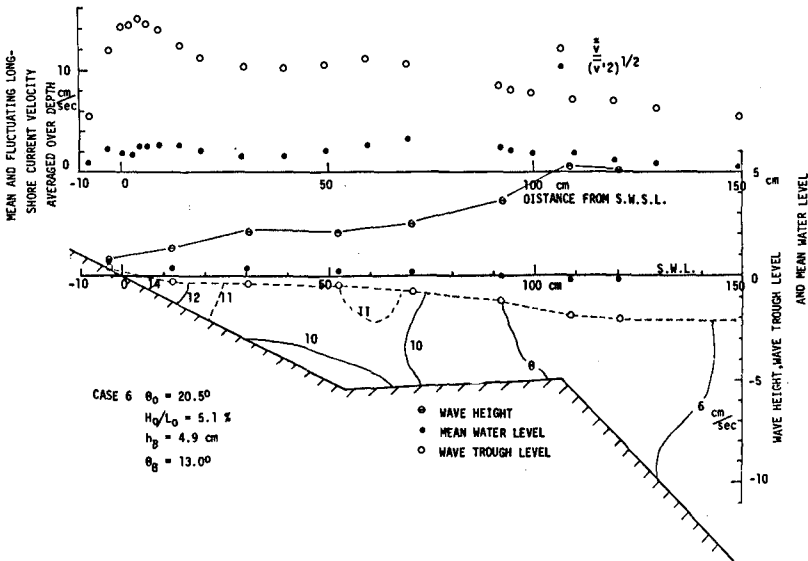


Figure 1 Longshore current on a step type beach [Mizuguchi & Horikawa (1978)]

level distribution are also plotted in this figure. The current velocity profile exhibits a different pattern from the one expected on a uniformly sloping beach. The difference is mainly due to the wave height distribution in the surf zone, which contributes to the radiation stress gradient and to generating the current. On uniformly sloping beaches, the wave height in the surf zone is almost proportional to the water depth, and thus the external force to generate the current is a monotonous function of the onshore or offshore direction. The wave height distribution after breaking at the step in Fig. 1 is not proportional to the local water depth but, rather, is unique to the step type beach, showing exponential-like decay after the first breaking, recovery at the uniform depth area, second breaking on the inner slope and linear decay on the uniformly sloping beach. The long-shore current velocity tends to increase shoreward where the wave height decreases, being modified by the turbulent viscosity. Therefore it is absolutely essential to be able to calculate the wave height distribution in a surf zone with a non-uniform bottom profile. And the beach profile usually observed in field experiments is not a uniformly sloping one, but a much more complex profile.

Outside the surf zone the energy equation, combined with a theory of permanent wave, is capable of giving the wave height change with good approximation, if the beach slope is not very steep. Inside the surf zone, turbulence induced by wave breaking plays an important role. At present, we have both experimental results and semi-empirical theories based on the energy conservation equation to evaluate the wave height (or energy) decay on a constant depth beach [for example, Horikawa & Kuo (1966)]. The most sophisticated but still gross treatment of that problem originates with the work of LeMehaute (1962), where the energy dissipation process is assumed to be similar to that in the hydraulic jump. Following this line, Battjes & Janssen (1978) treated the change of the r.m.s. value of the irregular wave height in the surf zone and succeeded in adjusting their theory to the experimental results, which included the case of a non-uniformly sloping beach.

In the above mentioned theories the energy dissipation depends on the wave height itself. This means that the wave height decays until reaching zero. However, suppose that the water depth after the wave breaking is constant; the broken wave will recover somewhere and start to propagate as a reformed wave in the constant depth area, if the energy dissipation due to the bottom friction is negligible.

In this paper an heuristic model is developed by employing the simplest formulation, that is, an eddy viscosity assumption. In order to construct the model, two limiting conditions were taken into account, namely, 1) wave breaking on a constant depth beach and 2) wave breaking on a uniformly sloping beach. These will be shown to be well described by the model.

DERIVATION OF THE MODEL

Four major assumptions are employed to derive the model as are now listed.

1) The following wave energy equation can be applied in the surf zone.

$$\frac{d}{dx}(Ec_g) = -\epsilon \quad (1)$$

with expressions

$$E = (1/2)\rho ga^2 \quad (2)$$

and

$$c_g = \sqrt{gd} \quad (3)$$

where E: wave energy per unit area, c_g : energy propagation velocity, ρ : fluid density, g : gravity acceleration, a : wave amplitude, ϵ : energy dissipation rate, d : water depth. In a strict sense, these expressions are inadequate to describe wave motion in the surf zone. The validity of Eq. (1) depends on the dissipation rate ϵ . Equation (2) can be used if the ratio of the wave height squared to the wave energy is constant through the surf zone. The unknown constant ratio will be included in the dissipation rate. In the surf zone the wave energy propagation velocity may be the same as the phase velocity, and is well approximated by that of the solitary wave theory [Mizuguchi (1979)].

$$c_g = \sqrt{g(d+2a)} \quad (4)$$

Equation (3) can be considered to be a first approximation to Eq. (4).

2) When applying the idea of turbulent eddy viscosity, ν_e , the rate of energy dissipation is given by

$$\epsilon = 2\rho g\nu_e(ka)^2 \quad (5)$$

where k : wave number. Here the energy dissipation due to the bottom friction is neglected. Equation (5) is obtained by replacing the molecular viscosity ν by the turbulent eddy viscosity ν_e in the final expression of the wave energy dissipation in irrotational flow. Ijima, Takahashi & Nakamura (1956) introduced Eqs. (1) and (5) to treat wave height decay in a surf zone of uniform depth with constant eddy viscosity. It should be noted that the eddy viscosity is not equivalent to that proposed by Battjes (1975), which is introduced through a discussion of energy dissipation due to (isotropic) turbulence induced in wave breaking.

3) Then the eddy viscosity is modeled in the following way. First, when the depth in the surf zone is constant, the broken wave should recover (or reform) as mentioned before. This suggests that the energy dissipation rate or the eddy viscosity should be a function of the difference between the real wave height and the reformed wave height. Secondly, the dissipation rate may also be related to the ratio of the real wave height to the possible maximum wave height at any location. On uniformly sloping beaches the waves are considered to be continuously breaking and the state of the maximum wave height is always realized. Then the possible maximum wave height may be expressed by $\gamma'd$, where

γ' is the constant wave amplitude to water depth ratio in the surf zone on a uniformly sloping beach. These hypotheses result in the following expression for v_e :

$$v_e = v_{eB} [(a-c'd)/\gamma'd]^m \quad (6)$$

where c' is the ratio between the wave amplitude and the water depth in the wave recovery zone on a constant depth beach, and m is a constant to be determined later. The subscript B denotes quantities evaluated at the breaker line.

Then the nondimensional equation describing the wave height distribution in the surf zone is

$$\frac{d}{dX} (A^2 D^{1/2}) = -N_B (AD^{-1} - c_0)^m A^2 D^{-1} \quad (7)$$

where

$$N_B = 4v_{eB} \sigma / (g d_B) \quad (8)$$

and $c_0 = c'/\gamma'$, $A = a/a_B$, $D = d/d_B$, $X = k_B x$ and σ : angular frequency. In Eq. (7) the constant m should be less than 1.0, since the broken wave should recover in a finite distance in a constant depth surf zone. Here we take m as 0.5, for the advantage of easy handling.

4) The nondimensional eddy viscosity N_B can be calculated as follows from the experimental fact that the ratio γ' is constant on uniformly sloping beaches.

$$N_B = 5(1-c_0)^{-1/2} s_B / (2k_B d_B) \quad (9)$$

Here s_B is a representative beach slope (including the expected wave set-up_B) outside the breaker line, so that

$$s_B = s'_B / (1 + 3\gamma'^2/2) \quad (10)$$

where s'_B is a representative beach slope for wave breaking. Actually Eq. (9) is derived by equating the wave height decay ratio at the breaking point with the mean decay ratio a_B/x_B , where x_B is the surf width.

The wave set-up $\bar{\eta}$ in the surf zone is usually given by the following nondimensional equation,

$$\frac{dH}{dX} = -(3/2)\gamma'^2 AD^{-1} \frac{dA}{dX} \quad (11)$$

where the radiation S_{xx} is assumed to be given by $3E/2$ with Eq. (2), and $H = \bar{\eta}/d_B$. Combining Eqs. (7) and (11), we can calculate both the wave height and the wave set-up distribution in the surf zone for arbitrary bottom profile $d(x)$. The flowchart to solve Eqs. (7) and (11) numerically is shown in Fig. 2, for the case of no second wave recovery. The differential equations are solved numerically by the Runge-Kutta-Gill method. The calculation converges within two or three

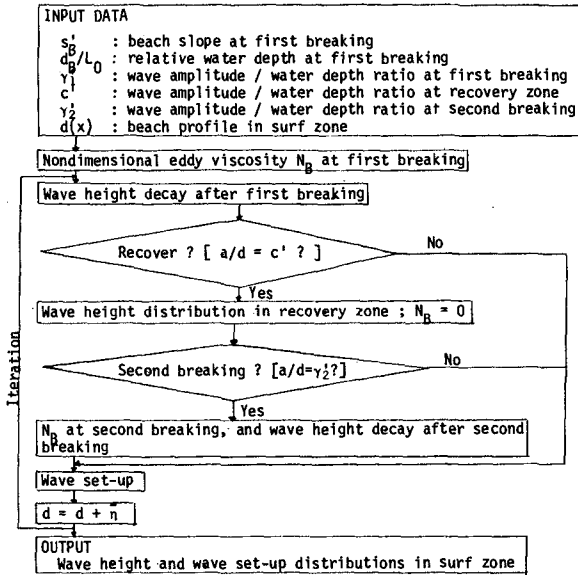


Figure 2 Flowchart to calculate wave height and wave set-up in the surf zone (no second wave recovery)

iterations as described in the flowchart.

As shown in Fig. 2, the unknowns are the breaker depth, the breaker height, the wave amplitude to water depth ratio, c' , in the recovery zone, and the bottom topography $d(x)$. The second wave breaking criterion γ'_2 may be chosen as 0.4, which is an approximate value for breaking solitary wave, because once-broken waves may be better expressed by solitary wave theory. Any kind of breaker index can be used to predict the breaker depth and the breaker height (or the ratio γ'_1) for uniformly sloping beaches [for example Goda (1970)]. The next simple empirical relation was given by Sunamura & Horikawa (1974):

$$a_B/H_0 = 0.5s'_B{}^{0.2}(H_0/L_0)^{-0.25} \quad (12)$$

$$0.01 < s'_B < 0.1$$

$$0.003 < H_0/L_0 < 0.07$$

Equation (12) was obtained by using the collected (and also corrected) data in Goda (1970). The following relation may also be derived from

the same data:

$$a_B/d_B (= \gamma'_1) = 0.75s_B'^{0.3} (d_B/L_0)^{-0.1} \quad (13)$$

$$0.03 < s_B' < 0.1$$

$$0.01 < d_B/L_0 < 0.05$$

In Eqs. (12) and (13), H_0 and L_0 denote deepwater wave height and deepwater wave length respectively. These equations provide full information for a wave to break. The ratio γ'_1 has two limiting conditions. It tends to a constant as the slope s_B' goes to zero when the relative water depth is small, and the wave steepness should be limited when the relative water depth is large. Then Eq. (13) can hold only in the indicated range. The ratio c' is expected to be determined by the intensity of wave breaking. The values obtained in laboratory experiments [Mizuguchi, Tsujioka & Horikawa (1978) and Nagatoh & Ohishi (1979)] centered on the range from 0.21 to 0.28, slightly decreasing with increase of wave steepness.

If wave set-up is neglected, Eq. (7) can be solved in closed form for the case of a constant depth surf zone.

$$A = c_0 \sec^2 \left(-\sqrt{c_0} N_B X/4 + \arctan \sqrt{(1-c_0)/c_0} \right) \quad (14)$$

Figure 3 show calculated curves for various values of N_B . The distance X_R to the recovery point where $A = c_0$ is given by

$$X_R = 4 \arctan \sqrt{(1-c_0)/c_0} / (N_B \sqrt{c_0}). \quad (15)$$

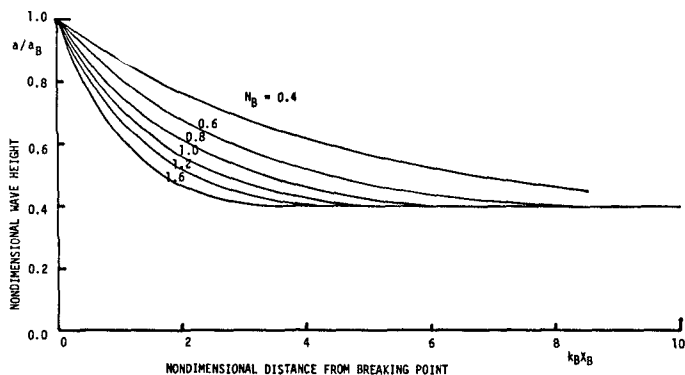


Figure 3 Wave height decay in a constant depth surf zone

COMPARISON WITH EXPERIMENTS

Figures 4 - 7 show the comparisons of the predicted results (solid lines) with the experimental results. The broken lines will be explained later. In the calculation the constant c' is roughly chosen as noted in the figures to give the best fitted curve in the recovery or almost recovery zone. In the case of uniformly sloping beaches as in Fig. 5, the value of c' does not affect the results.

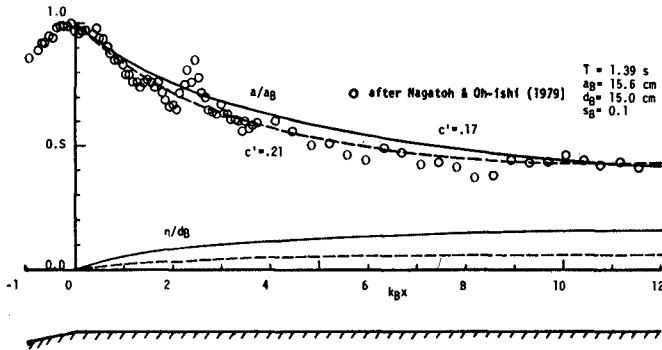


Figure 4 Comparison with experiment (constant depth beach)

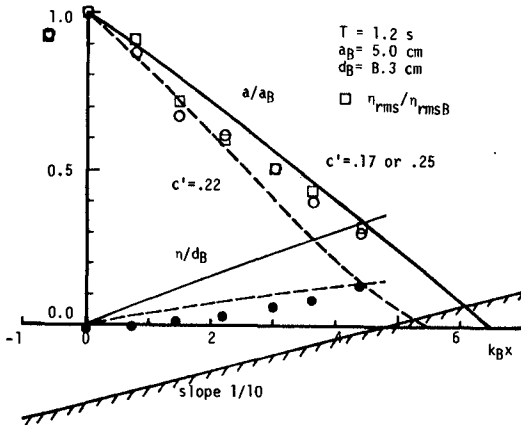


Figure 5 Comparison with experiment (uniformly sloping beach)

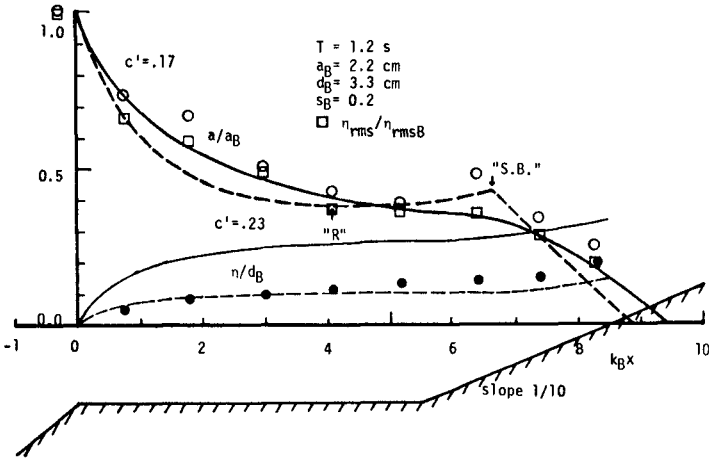


Figure 6 Comparison with experiment (step type beach)

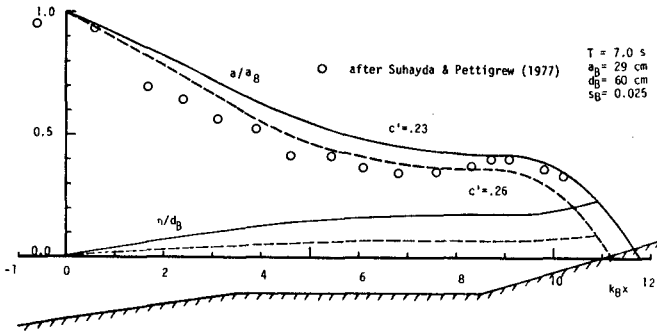


Figure 7 Comparison with field experiment

Generally the agreement is good enough. However, the model shows a tendency to underestimate the wave height decay near the first breaking, except in Fig. 6. In figs. 5 and 6, it is also seen that the wave set-up is also overestimated. The overestimated wave set-up increases the water depth, so that the wave height decay is relaxed. These are mainly caused by the fact that the wave energy is overestimated in the form given by Eq. (2). The delay of the wave set-up starting point from the wave breaking point, which is usually defined by the point of the maximum wave height, is also responsible for the results in Fig. 5.

Figure 8 shows the relation of the wave set-up $\bar{\eta}_R$ in the recovery zone to the wave breaking height on step type beaches. The solid line is from the next relation.

$$H_R (= \bar{\eta}_R/d_B) = 0.75(\gamma'^2 - c'^2) \tag{16}$$

which follows immediately from Eq. (11). The fitted line is

$$H_R = 0.25(\gamma'^2 - c'^2) \tag{17}$$

and indicates that the wave energy (or radiation stress) should be estimated by the following relation:

$$E = (1/6)\rho g a^2 \tag{18}$$

Here it is worth noting that the data plotted in Fig. 8 were obtained by changing the wave height while keeping the water depth fixed in the step region. Figure 8 also suggests that the value of c' is approximately 0.25.

In Figs. 5 and 6, the nondimensional r.m.s. values of the water surface fluctuation η_{rms}/η_{rmsB} are also plotted. Taking the long wave or small amplitude wave assumption, we have the next relation.

$$E = \rho g \eta_{rms}^2 \tag{19}$$

Therefore, in a sense, the ratio of the wave height to η_{rms} denotes the unknown factor mentioned in the derivation of the model. The difference between η_{rms}/η_{rmsB} and a/a_B is within the

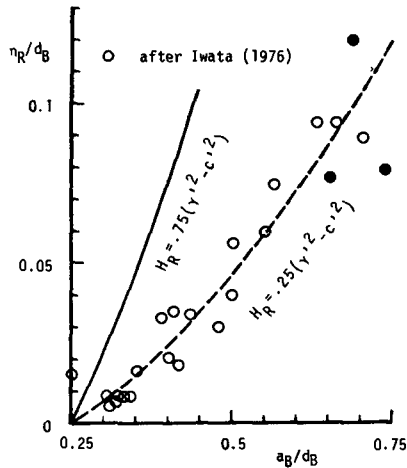


Figure 8 Wave set-up in recovery zone (constant depth or step type beach)

error of the allowance for surf zone phenomena. Then the relation (18) is expected to hold through the surf zone and should be taken into consideration in evaluating the wave energy from the wave height. Actually the ratio of a^2 to n_{rms}^2 is calculated from the experimental data for the cases in Figs. 5 and 6. In and near the surf zone the values are about 3 to 4, which is much larger than the value 2 for small amplitude waves but almost half of that expected from Eq. (18).

The broken lines in Figs. 4 - 7 are the results obtained by using the empirical relation (18). Then Eq. (10) is also modified. They agree better with the experimental results. A typical wave height transformation over a step type beach is shown in Fig. 6; decay after the first breaking, recovery at the uniform depth area (marked by "R"), increase due to the decrease in water depth, second wave breaking ("S.B.") after which the wave height linearly decreases to zero at the mean water shoreline. However, this time, the wave set-up is a little underestimated. It reflects the above-mentioned experimental results that the ratio a^2 to n_{rms}^2 should be smaller than 6. In addition, the broken line shows the overestimation of the wave height decay just after the first breaking in Fig. 6. This is connected with the determination of the representative beach slope for the wave breaking. The step part of the bottom profile in the case of Fig. 6 was made of bent plate, which was placed on the uniformly sloping (1/10) beach. The slope just before the wave breaking was about 1/5, which was used to calculate the predicted curve. The slope might be steeper than the value which really governs the process of the wave breaking and gives too rapid decay of the wave height after breaking.

DISCUSSION

The model developed herein is an expedient, although it predicts rather well the experimental results over a wide range of conditions. There are two points which one should treat carefully when applying this model. The first point is how to choose the representative beach slope s'_B before wave breaking. In laboratory experiments, it should be pointed out that the beach slope s'_B is not equal to a real slope, unless the uniformly sloping beach section extends to a sufficient deep region. When the water is not so deep in the uniform depth region, waves may deform while travelling in that region and easily break. Then the breaking phenomena cannot be considered to depend only on the beach slope just before wave breaking. We suggest that Eq. (13) is to be applied to determine the beach slope s'_B , once the wave amplitude - water depth ratio γ'_1 at the breaking point is given independently. This ratio may be considered to indicate how the wave is deformed before breaking, representing the wave's history. The second point is how to give the value of c' . In this respect our knowledge on wave breaking phenomena is still unsatisfactory. Well-controlled experiments are required to give the proper value of the c' in this model.

Finally it should be pointed out that the eddy viscosity assumption in the energy equation is physically obscure, although it could be more easily modeled as in Eq. (6) than that proposed by Battjes (1975). This model reflects the present state of the study on wave

properties in the surf zone and reveals some problems to be investigated in the future. For example, on uniformly sloping beaches where the waves are considered to be continuously breaking, why is the wave height always proportional to the water depth through the surf zone and why does the wave set-up delay its start from the point of the maximum wave height? How is the turbulence generated and how does it affect the wave height decay? How should the constant c' be determined? What is the best expression for breaking or broken waves in and near the surf zone? The investigation to answer such questions will lead to a more complete modeling of the wave breaking process. The work by Sawaragi & Iwata (1974) and Svendsen, Madsen & Hansen (1978) are along these lines, but still further progress must be made before one can reach a firm understanding of the wave transformation in the surf zone.

ACKNOWLEDGEMENT

I appreciate the assistance of Mr. K. Tsujioka and Prof. K. Horikawa in carrying out this study. A portion of this paper was authored with them and published in Japanese in the Proceedings of 25th Japanese Conference on Coastal Engineering held in November, 1978, [Mizuguchi, Tsujioka & Horikawa (1978)].

REFERENCES

- Battjes, J. A. (1975), Modeling for turbulence in surf zone, Proc. Symp. Modeling Tech., ASCE, p. 1050-1061.
- Battjes, J. A. & J. P. F. M. Janssen (1978), Energy loss and set-up due to breaking of random waves, Proc. 16th Intern. Conf. Coastal Eng., Hamburg, p. 569-587.
- Goda, Y. (1970), A synthesis of breaker indices, Trans. Jap. Soc. Civil Eng., Vol. 180, p. 39-49 (in Japanese).
- Horikawa, K. & C. T. Kuo (1966), A study on wave transformation inside surf zone, Proc. 10th Intern. Conf. Coastal Eng., Tokyo, p. 69-81.
- Ijima, T., T. Takahashi & K. Nakamura (1956), A study of wave properties in the surf zone by using stereo-camera system, Proc. 3rd Jap. Conf. Coastal Eng., p. 99-116 (in Japanese).
- Iwata, K. (1976), A basic study of wave transformation and its control in shallow water region, Doctoral Dissertation, Dept. Civil Eng., Osaka Univ., 262p (in Japanese).
- LeMehaute, B. (1962), On non-saturated breakers and the wave run-up, Proc. 8th Intern. Conf. Coastal Eng., Mexico, p. 77-92.
- Mizuguchi, M. (1979), Experimental study on wave refraction and wave celerity in the surf zone, Trans. Jap. Soc. Civil Eng., Vol. 291, p. 101-105 (in Japanese).
- Mizuguchi, M. & K. Horikawa (1978), Experimental study on longshore current velocity distribution, Bull. Fac. Sci. & Eng., Chuo Univ., Vol. 21, p. 123-150.

Mizuguchi, M., K. Tsujioka & K. Horikawa (1978), On wave height distribution in the surf zone, Proc. 25th Jap. Conf. Coastal Eng., p. 155-159 (in Japanese).

Nagatoh, T. & K. Oh-ishi (1979), Experimental study on wave height distribution in the surf zone, Graduation Thesis, Dept. Civil Eng., Chuo Univ., 57p (in Japanese).

Sawaragi, T. & K. Iwata (1974), On wave deformation after breaking, Proc. 14th Intern. Conf. Coastal Eng., Copenhagen, p. 481-499.

Suhayda, J. H. & N. R. Pettigrew (1977), Observation of wave height and wave celerity in the surf zone, Jour. Geophys. Res., Vol. 82, p. 1419-1424.

Sunamura, T. & K. Horikawa (1974), Two-dimensional beach transformation due to waves, Proc. 14th Intern. Conf. Coastal Eng., Copenhagen, p. 920-938.

Svendsen, I. A., P. A. Madsen & J. B. Hansen (1978), Wave characteristics in the surf zone, Proc. 16th Intern. Conf. Coastal Eng., Hamburg, p. 520-539.

CHAPTER 16

Resonances of Coastal Waters Between Perth and Geraldton (Western Australia)

H. ALLISON, Ph.D. M.Sc., MIE Aust., M.R. Soc (Vic. & W.A.), Senior Research Scientist, CSIRO, Div. of Land Resources Management, Wembley, 6014.

A. GRASSIA, Dr. Math. & Phys., B.A. Principal Research Scientist, CSIRO, Div. of Mathematics and Statistics, Wembley, 6014.

R. LITCHFIELD, CSIRO, Div. of Mathematics and Statistics, Wembley, 6014.

SUMMARY Sea-level oscillations along the Western Australian coast, with periods in the range of 20-40 mins, have considerably greater amplitudes between Perth and Geraldton than at other locations along the coastline. It is shown that amplification of these oscillations is due to resonance in the near shore basin formed by the shore and a submerged reef-chain parallel to and 5 km from the shore.

The rigorous analytical solution for the resonance frequencies is obtained for the two-dimensional hydrodynamic model. Comparison with results from spectral analysis of recorded oscillations indicates a satisfactory agreement with the theory. Statistical estimation of damping of the observed oscillations indicates that the predominant resonance in the first mode is sharp, having the quality factor $Q=10$.

1 Introduction

Nearshore sea-level oscillations, apart from tides, are observed at many locations. The oscillations have periods ranging from several minutes (surf beat, nearshore edge waves, harbour seiches) through several hours (continental shelf waves) to hundreds of days (planetary waves) (Le Blond and Mysak, 1978). Research on continental shelf waves in Western Australia (Hamon, 1966) initiated world-wide theoretical and experimental study of the subject. Later studies by Hamon (1976) indicated that the shelf waves in Australia were generated by wind, supporting the point of view of Gill and Schumann (1974). Recently sea-level oscillations along the Western Australian coastline, with periods in the range 20-40 min, were reported by Allison and Grassia (1979) to be attributed to the presence of a reef-chain parallel and 5 km from the Western Australian shore (Fig. 1).

The new results are reported below, including the spectral analysis of sea-level oscillations, theoretical solutions for the two-dimensional hydrodynamic model, which in particular indicates the presence of oscillating currents near the coastline.

2 Long-term statistics

Western Australian tidal records for the last 15 years were analysed. On many of them, short period (relative to tidal period) oscillations

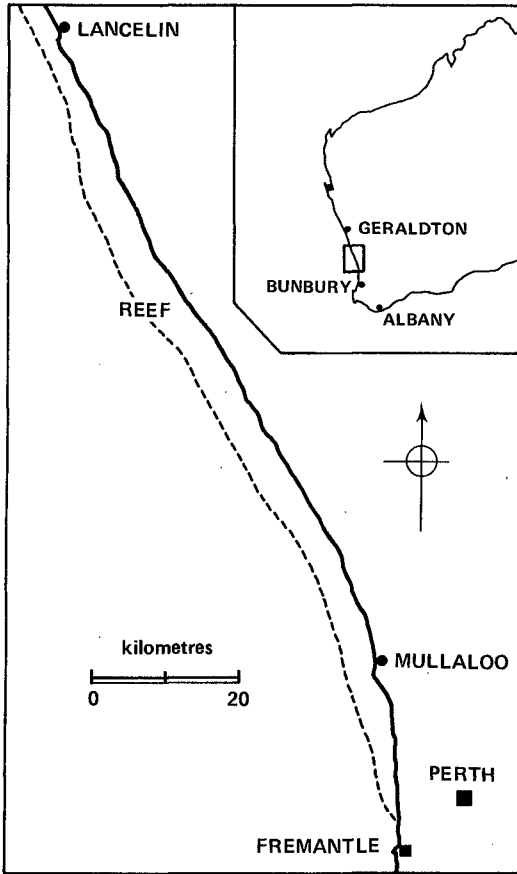


Figure 1. Submerged Reef Chain Off Western Australian Coast

were present. These oscillations usually were of small amplitudes, of the order of several centimetres. However, occasionally large amplitude oscillations occurred and lasted several hours, sometimes persisting for one or two days (with corresponding smaller amplitudes). A typical such sporadic oscillation is presented in Figure 2.

In the following any sea-level oscillation, having its amplitude ≥ 10 cm is called an event. In total, 219 such events were observed between 1963 and 1978.

To characterise the intensity of the event we have used its energy E, which was calculated on the basis of the following formula:

$$E = \frac{\rho g A^2 \tau}{4T} \quad (1)$$

which follows from the familiar expression of a maximum energy of a standing wave per unit surface and per one cycle of oscillations of the period T:

$$E_T = \frac{1}{4} \rho g A^2 \quad (2)$$

Here ρ is the mass density of water, g is a gravity acceleration, A was taken as a maximum amplitude during the sea-level oscillation event, and τ is a duration of the oscillation event, which was taken as a length of time during which amplitudes of oscillations exceeded the threshold value of 10cm.

Estimate of energy obtained by (1) is, of course, exaggerated, because the formula is valid, strictly speaking, only for waves, sinusoidal in time, while the recorded oscillations decay with time (Fig. 2). A justification of its use is however simple: we are interested only in relative variation of the energy of the events in the long term, rather than in the absolute value of the energy.

To characterise the probability of occurrence of large sea-level oscillation events we used their frequency of appearance, meaning number of events occurring during a certain selected interval, such as a month or a year. (Notice that on the following pages we shall also use the word 'frequency' in the physical sense, such as 'resonance frequency', not to be confused with the statistical frequency of occurrence).

The results of calculations of seasonal and yearly variations of event frequencies and energies are shown in Fig. 3 and 4. (In Fig. 4 the yearly averages of Zürich sunspot numbers are shown for comparison).

The monthly averages (Fig. 3) indicate that more events and events with larger energy occur in the Southern Hemisphere winter. This may indicate that observed events are possibly caused by long waves, generated by winter storms in the Indian Ocean, but we do not possess any independent proof of this.

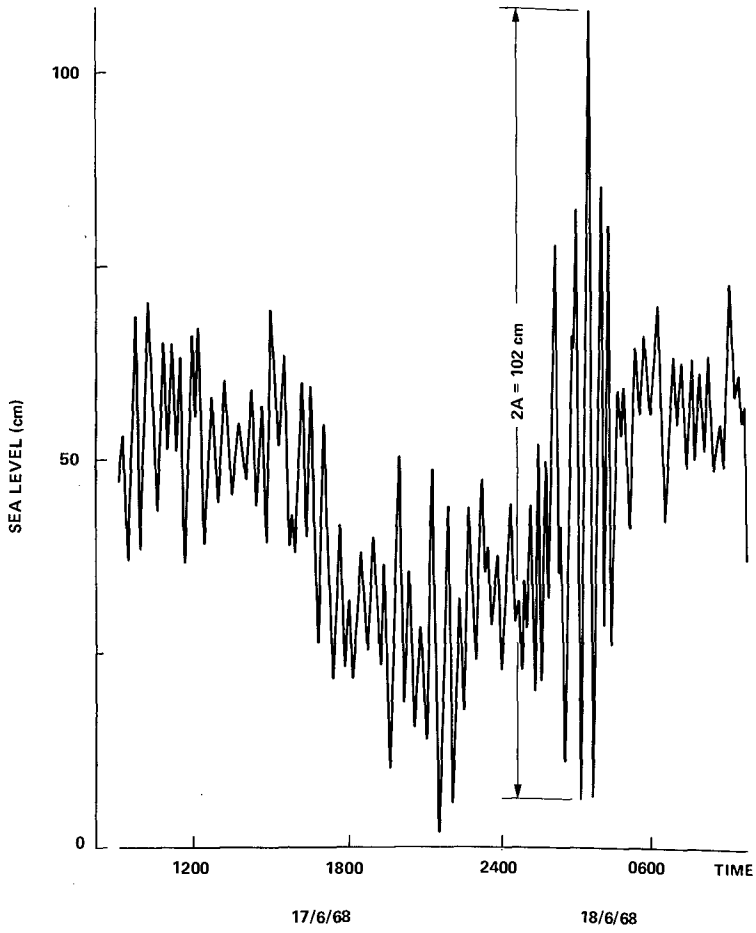


Figure 2. Tidal Record Geraldton, W.A.

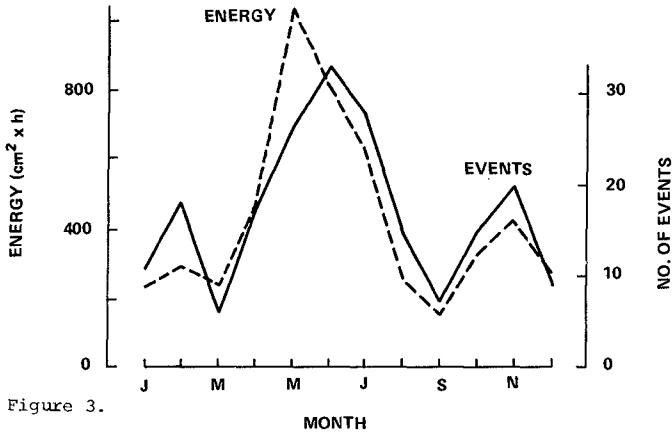


Figure 3.

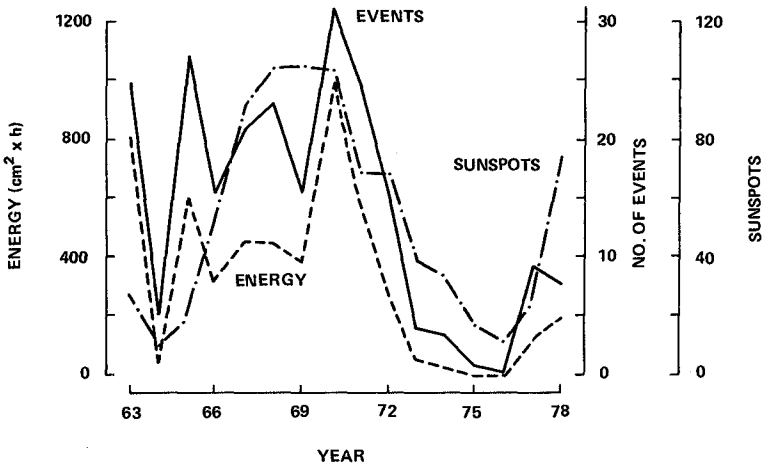


Figure 4. Monthly and Yearly Frequencies of Events

The yearly averages demonstrate a remarkable resemblance to the solar activity pattern (in fact, our calculations had shown a statistically significant correlation of the energies and frequencies of occurrence of events to solar activity). However, in spite of some recent claims about solar-terrestrial relationship (see, for example, Currie, 1976) we are reluctant to speculate here on the subject, leaving room for further study, which might, possibly, indicate the correlation between storms in the Indian Ocean and solar activity.

3 Short-term statistics - spectral analysis

The large sea-level oscillation event, described above, usually occur on the background of small amplitude oscillations. These small oscillations, (with the amplitudes below threshold of 10cm) are persistent practically always, and generate permanently present oscillating currents in the nearshore zone of Western Australia.

An example of such small amplitude oscillations is shown in Fig. 5.

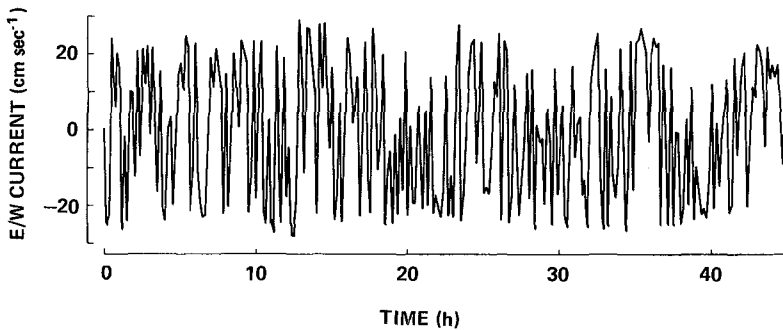


Figure 5 Small Oscillations of East-West Current, Mullaloo, W.A.

While it has been proved (Allison and Grassia, 1979) that large sea-level oscillations events are associated with the standing waves between the shore and the reef-chain, no such proof has been made for small amplitude background oscillations. We present here some evidence in support of the point of view, that these always persistent small amplitude oscillations originate in the same way as the large ones. To this point, let us consider the results of spectral analysis of both large sea-level oscillations and small-amplitude background. These results are presented correspondingly on Fig. 6a,b.

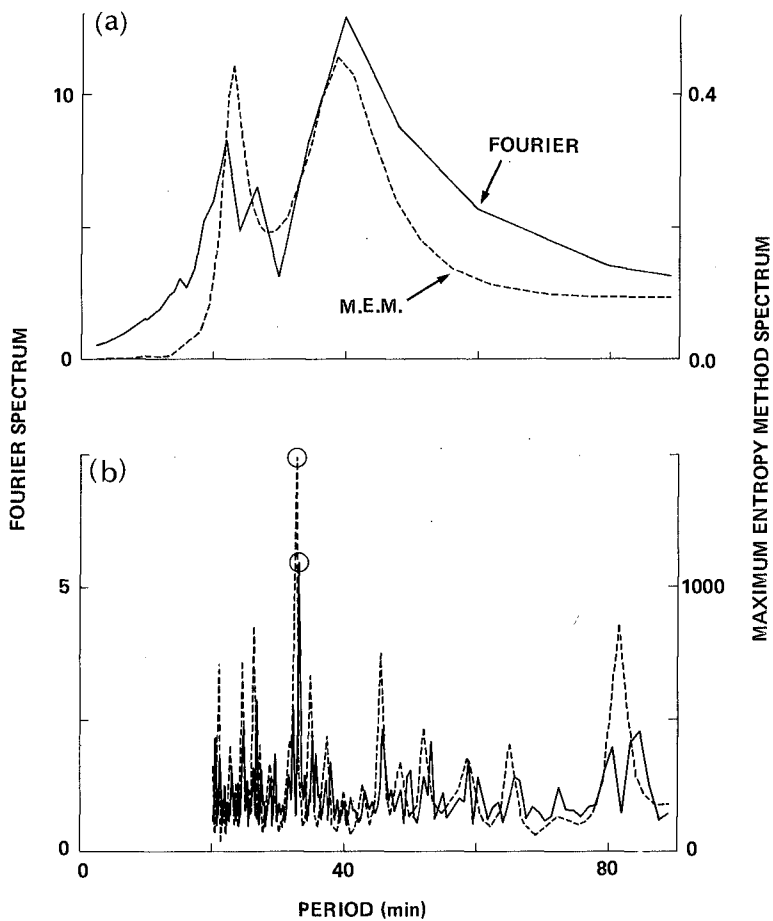


Figure 6. Period Spectrum of:

(a) Large Oscillations (b) Small Oscillations

The solid lines on both parts (a) and (b) of Fig. 6 correspond to the modulus of the Fourier Spectrum of the oscillations, the dashed lines show the Maximum Entropy Method spectra. It is seen, first of all, that the Maximum Entropy Method gives results, closely corresponding to the ordinary Fourier Analysis, although some spurious peaks, given by Fourier Analysis are effectively suppressed by the Maximum Entropy Method. Most important, however, is the presence of considerably sharp resonance peaks on both spectra.

The comparison of computed resonance periods for large sea-level oscillation events and small-amplitude background is given in Table 1.

Table 1

	Distance from reef to shore	Dominant Period	Non-dimensional Frequency
	ℓ (km)	T (mins)	$R = \frac{2\pi}{T} \frac{\ell}{\sqrt{gh}} \dots (18)$
Large oscillations Geraldton, W.A.	5	40	1.32
Small oscillations Mullaloo, W.A.	4.5	33	1.44

As seen from Table 1, the non-dimensional frequencies of large and small oscillations are in reasonable agreement, thus substantiating the point of view, that both types of oscillations are, in essence, resonances in a hydrodynamic system, namely, the basin formed by the shore and nearshore reef chain. We consider now the analytical treatment of the resonances.

4 Analytical Development

The bottom topography of the nearshore basin is represented by the dashed area in Fig. 7. We approximate this profile by the parabolic expression

$$h(x) = h_0 \left[1 - \left(\frac{x}{\ell} \right)^2 \right] (1-\alpha) \quad (3)$$

where h_0 refers to the depth at $x=0$, ℓ being the length of the basin (in our case the width of the channel) and α is a non-dimensional parameter, describing the fact that the reef-chain is submerged. For the values $h_0 = 10\text{m}$; $\alpha = 0.3$ the graph of expression (3), shown by a solid line in Fig. 7, provides an idealised smooth representation of the bottom profile. The chief advantage of using (3) is that it allows us to obtain a rigorous analytical solution of the equation of water motion in the basin partly open to the ocean. One may notice that variation in the parameter α permits also consideration of various cases of submergency of the reef.

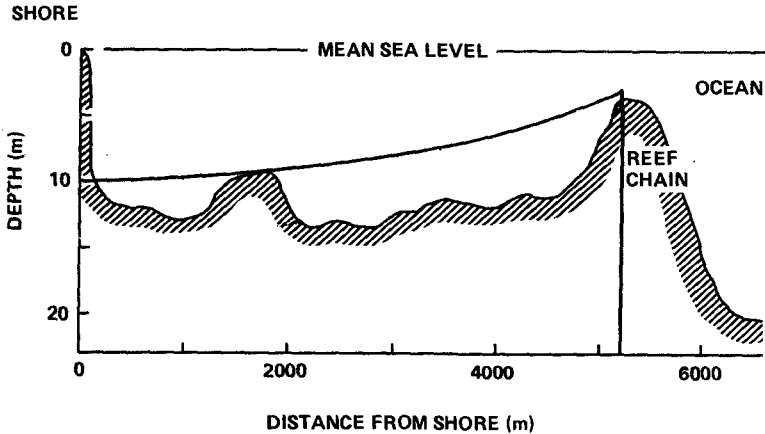


Figure 7 Typical Bottom Topography in W.A. (normal to shore)

When $\alpha = 1$ the basin has a uniform depth with one end ($x=0$) closed and the other end ($x=l$) opened into the deep ocean, being the classical problem, for which the exact solutions are known (Lamb, 1932). When $\alpha = 0$, we have the closed basin with a parabolic bottom profile, being the other classical case (Chrystal, 1904).

We give below the rigorous solution for the intermediate case of a partly open basin with the parabolic bottom for $0 \leq \alpha \leq 1$: the classical problems, considered by Chrystal and Lamb emerging as the limiting cases of the solution that follows. As the depth is in the order of 10m, while length of the basin (width of the channel) is in the range 4-6 km, we accept as a starting point the familiar shallow water equation:

$$g \frac{\partial}{\partial x} [h(x) \frac{\partial \eta}{\partial x}] = \frac{\partial^2 \eta}{\partial t^2} \quad (4)$$

where g is a gravity acceleration and $\eta(x,t)$ represents the elevation of the free surface of water above its undisturbed surface level.

Considering free oscillations with frequency ω , we, as usual, represent $\eta(x,t)$ as a product of two functions, one describing the shape of water motion $\xi(x)$ and the other being a time-dependent term $e^{-i\omega t}$.

$$\eta(x,t) = \xi(x)e^{-i\omega t} \quad (5a)$$

The second time derivative becomes:

$$\frac{\partial^2}{\partial t^2} \eta(x, t) = -\xi(x) e^{-i\omega t} \omega^2. \quad (5b)$$

After the separation of variables, and substitution of $h(x)$ as in (3), eq. (4) takes the form:

$$\frac{d^2 \xi}{dx^2} \left[1 - \left(\frac{x}{\ell} \right)^2 (1-\alpha) \right] - \frac{d\xi}{dx} \left[\frac{2x}{\ell^2} (1-\alpha) \right] + \frac{\omega^2}{gh_0} \xi = 0. \quad (6)$$

Introducing the new variable

$$z^2 = \left(\frac{x}{\ell} \right)^2 (1-\alpha) \quad (7)$$

we obtain the following sequence of simple formulae:

$$z = \left(\frac{x}{\ell} \right) (1-\alpha)^{1/2} ; \quad \frac{dx}{dz} = \ell (1-\alpha)^{-1/2} \quad \} \quad (8a)$$

$$x = z\ell (1-\alpha)^{-1/2} ; \quad \frac{d^2 x}{dz^2} = 0 \quad \}$$

$$\frac{d\xi}{dx} = \left(\frac{dx}{dz} \right)^{-1} \frac{d\xi}{dz} = (1-\alpha)^{1/2} \ell^{-1} \frac{d\xi}{dz} \quad \} \quad (8b)$$

$$\frac{d^2 \xi}{dx^2} = \left(\frac{dx}{dz} \right)^{-2} \frac{d^2 \xi}{dz^2} - \left(\frac{d^2 x}{dz^2} \right) \left(\frac{dx}{dz} \right)^{-3} \frac{d\xi}{dz} = (1-\alpha) \ell^{-2} \frac{d^2 \xi}{dz^2} \}$$

Substitution of (8a), (8b) and (7) in (6) leads to the following equation:

$$(1-z^2) \frac{d^2 \xi}{dz^2} - 2z \frac{d\xi}{dz} + \frac{\omega^2 \ell^2}{gh_0 (1-\alpha)} \xi = 0 \quad (9)$$

which has the familiar form of a Legendre equation, if we put

$$\frac{\omega^2 \ell^2}{gh_0 (1-\alpha)} = n(n+1) \quad (10)$$

where the integer n , being a mode number, takes the values 1, 2, 3, ...

The general solution of (9) with the notation (10) has a form:

$$\xi(z) = AP_n(z) + BQ_n(z) \quad (11)$$

where A and B are arbitrary constants and $P_n(z)$ and $Q_n(z)$ are the Legendre functions, of which $P_n(z)$ is always a polynomial, but $Q_n(z)$ is not. Let us consider initially the boundary condition at the shore side of the basin, where no current is possible. This can be written as a condition on the first derivative of the vertical displacement ξ , at the point $x = z = 0$:

$$\left. \frac{d\xi}{dz} \right|_{z=0} = 0 \quad (12)$$

which, after substitution of (11) into (12) becomes:

$$\left. \frac{d\xi}{dz} \right|_{z=0} = AP_n'(0) + BQ_n'(0) = 0 \quad (13)$$

We can utilize now the useful properties of the Legendre functions, given in the Table 2.

Table 2

For even n	For odd n
$P_n'(0) = Q_n'(0) = 0$	$P_n'(0) = Q_n'(0) = 0$
$P_n(0) \neq 0 ; Q_n(0) \neq 0$	$P_n(0) \neq 0 ; Q_n(0) \neq 0$

Substituting the values from Table 2 into eq. (11) we obtain that the solutions, satisfying the boundary condition (12) are:

$$\xi = AP_n(z) \quad (n \text{ even}) \quad (14a)$$

$$\xi = BQ_n(z) \quad (n \text{ odd}) \quad (14b)$$

Explicit expressions for the first six solutions are given below:

$$\begin{aligned} P_0(z) &= 1 \\ Q_1(z) &= \frac{z}{2} \ln \frac{1+z}{1-z} - 1 \end{aligned} \quad (15)$$

$$P_2(z) = \frac{1}{2} (2z^2 - 1) \tag{15 cont.}$$

$$Q_3(z) = \left(\frac{5z^3}{4} - \frac{3z}{4}\right) \ln \frac{1+z}{1-z} - \frac{5}{2} z^2 + \frac{2}{3}$$

$$P_4(z) = \frac{1}{8} (35z^4 - 30z^2 + 3)$$

$$Q_5(z) = \left(\frac{63}{16} z^5 - \frac{70}{16} z^3 + \frac{15}{16} z\right) \ln \frac{1+z}{1-z} - \frac{63}{8} z^4 + \frac{49}{8} z^2 - \frac{8}{15}$$

$$P_6(z) = \frac{1}{16} (231z^6 - 315z^4 + 105z^2 - 5)$$

These solutions and also the solutions of any desirable higher orders can be obtained by use of the recurrence relations (Abramowitz and Stegun, 1975).

$$(n+1)P_{n+1}(z) = (2n+1)zP_n(z) - nP_{n-1}(z) \tag{16a}$$

$$(n+1)Q_{n+1}(z) = (2n+1)zQ_n(z) - nQ_{n-1}(z) \tag{16b}$$

by starting from $P_0(z)$, $Q_1(z)$ as in (13) and using:

$$P_1(z) = z; \quad Q_0(z) = \frac{1}{2} \ln \frac{1+z}{1-z} \tag{17}$$

The domain of definition of the functions (15) in our problem is within $0 \leq z \leq (1-\alpha)^{1/2}$, as it follows from eq. (8). The solutions (15) within the mentioned domain of definition give for any selected n the shape of possible modes of oscillations of water in the basin, the corresponding angular frequencies being determined from (10) depending once again on the integer n .

It is convenient to introduce the non-dimensional frequency parameter R , which, as follows from (10), is equal:

$$R = \frac{\omega \ell}{(gh_0)^{1/2}} = [(1-\alpha)n(n+1)]^{1/2} \tag{18}$$

If the basin would be of constant depth h_0 , the parameter R will take the following values:

$$R_0 = \{ \pi/2; 3\pi/2; 5\pi/2 \dots (2k-1) \pi/2 \} \tag{19a}$$

$$R_c = \{ \pi; 2\pi; 4\pi; \dots 2k\pi \} \tag{19b}$$

Here R_0 refers to the basin open to the ocean ($\alpha = 1$); R_c refers to the closed basin ($\alpha = 0$).

In our case of a parabolic bottom the parameter R can be calculated by the use of (18). The results, giving R as a function of α and various values of n , are plotted in Fig. 8, where the values of R , as in (19), for constant water depth are shown by horizontal dashed lines. Open dots on the graphs $R_n(\alpha)$ indicate the positions of the first and second zeroes of the Legendre P_{2j}, Q_{2j-1} ($j=1,2,3$) functions, the solid lines marked Z_1 and Z_2 , joining the zeroes, show the tendency of the zeroes to approach the limiting values of $R = \pi/2; 3\pi/2$ for $\alpha \rightarrow 1$, as from (19a), for $n \rightarrow \infty$. This indeed must be the case, because when $\alpha = 1$, our basin in Fig. 7 is becoming a constant depth basin, fully open to a deep ocean. Hence, one of limiting cases, that of a fully opened basin, appears naturally as a limiting case of the present theory. The values of R for the other limiting cases, a closed basin ($\alpha = 0$), with parabolic bottom, discussed by Chrystal (1905), can be seen in Fig. 8. There are no zeroes of the Legendre functions for $\alpha = 0$, due to the fact that in the closed basin there is a vertical displacement of water at the end $x = l$.

The shapes of the modes of oscillations corresponding to $\alpha = 0$ are presented as the top graphs in Fig. 9. It is seen that the solutions, corresponding to Q_2 and Q_4 are finite, while the solutions given by Q_1 and Q_3 tend to infinity at $x = l$. The last two solutions were described by Chrystal (1904) as "paradoxical seiches" and, indeed, they can not be present in any real situation, because they involve the infinite water displacement at the right end of the basin.

However, these "paradoxical seiches" become finite in amplitude and, hence, very real when the basin is not fully closed. For example, when $\alpha = 0.06$ the modal shape given by Q_3 has a zero vertical displacement at $x = l$, and Q_1 does not tend to infinity because for $\alpha = 0.06$ our domain is $[0, \sqrt{1-0.06}]^{1/2}$ where all values for Q_1 are finite.

We assign a particular significance to the modal shapes, giving zero (or nearly zero) vertical displacement at the sea side end ($x = l$ in Figure 7) when $\alpha > 0$ for the following reason.

In the outer region ($x > l$ in Fig. 7) there must exist the outgoing wave, propagating into the ocean, away from the basin, and carrying some energy of oscillations within the basin with the wave. The amplitude of this outgoing wave has to be matched to the amplitude of water oscillations in the basin at the point $x = l$. The higher is the amplitude of the modal shape at $x = l$, the larger will be the amount of seiche energy radiated to the ocean, hence, the more severe will be the damping of oscillation within the basin. The energy radiated towards the ocean will be minimal when amplitudes of modes at $x = l$ equal zero, hence the resonances within the basin will be the sharpest. Obviously, as the parameter α is approaching unity, the modal shapes of strong resonances are becoming very close to those for the fully open basin with constant depth. (Compare the cases of $\alpha = 0.8$ and $\alpha = 1$ on Fig. 9).

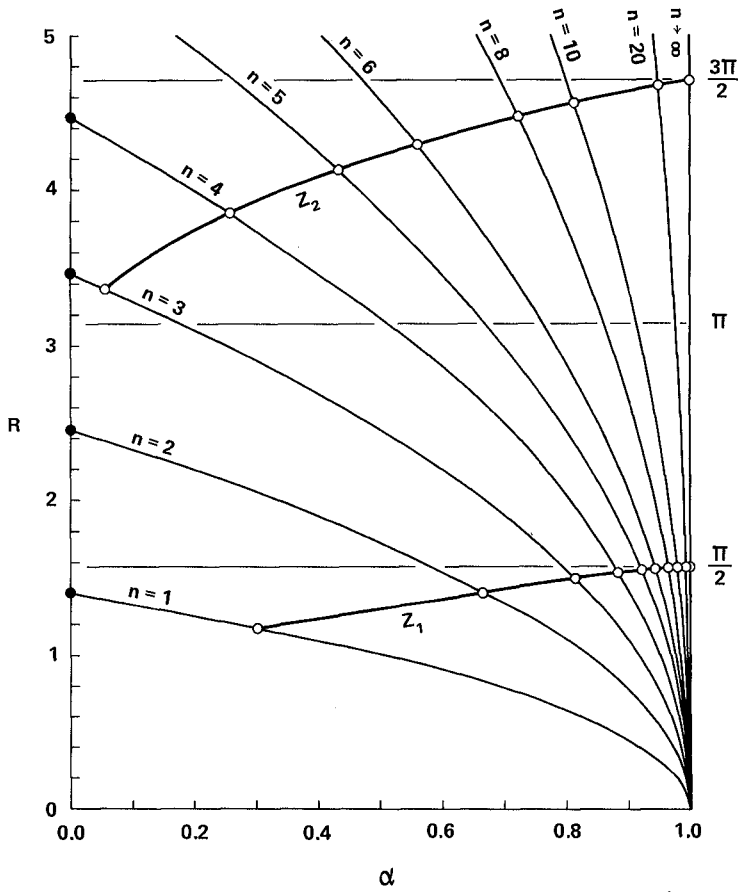


Figure 8. Non-dimensional Frequency of Oscillations R vs Relative Opening α

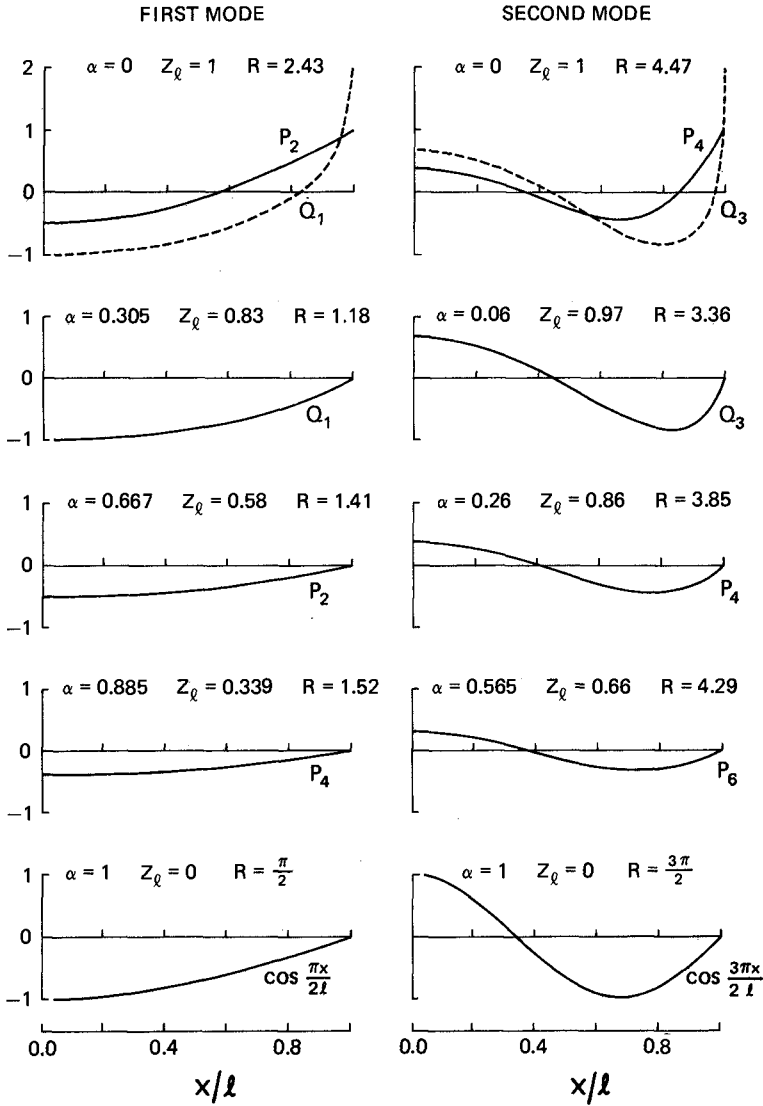


Figure 9. Modes of Water Oscillations in the Basin for Various Values of the Relative Opening α .

Returning back to Fig. 8, one can see, that the point $\alpha = 1$ is the point of condensation for zeroes of Legendre functions, hence for any $\alpha \approx 1$ there exist a strong resonance plus an infinitely increasing number of weak resonances, also condensing near $\alpha = 1$.

It is clear now, that the second boundary condition, which we deliberately avoided to discuss so far, is:

$$\xi = 0 \quad \text{at } x = l \quad (z = \sqrt{1-\alpha}) \quad (20a)$$

for strong resonances and

$$\xi < \infty \quad \text{at } x = l \quad (z = \sqrt{1-\alpha}) \quad (20b)$$

for weak resonances.

In the Figure 9 the frequencies of strong resonances (in terms of non-dimensional values of R) together with the corresponding modal shapes are given. The case of a completely closed basin is also classified as a strong resonance, because there is no radiation of energy to the ocean when $\alpha = 0$.

Consulting again Fig. 8, we can see, that solid lines joining the zeroes display the interesting tendency to decrease, when α is decreasing from $\alpha = 1$. This means the frequencies of strong resonances are decreasing while the basin is becoming more closed. This result is in agreement with Tuck, (1980), who predicts a similar tendency for the basin of a constant depth with an infinitely thin barrier of a variable height ($0 < \alpha < 1$) at the point $x = l$. However, the essential difference is that in our case there exists a set of discrete parameters α , for which strong resonance is possible, while for the basin of a constant depth the strong resonances exist for any α within the continuum $0 \leq \alpha \leq 1$, if the outer basin (ocean) is deeper, than the inner basin.

5 Periods and damping of the strong resonances for the Western Australian Coastline

The average value of a reef height for the coastline corresponds to a value $\alpha = 0.3$. It is seen from Fig. 8, that this particular value is near the zeroes of the Legendre functions Q_1 and P_4 , thus being capable of producing the two strong resonances, the modal shapes of which are depicted on Fig. 9.

The values R for $\alpha = 0.3$ are, as taken from Fig. 8, $R_1 = 1.18$; $R_2 = 3.84$, correspondingly for the first and second strong resonances. The average distance from reef chain to the shore can be taken as 5000 m, the periods of resonance oscillations are then, as follows from (18):

$$T = \frac{2\pi}{\omega} = \frac{2\pi l}{R(gh_0)^{1/2}} \quad (21)$$

Taking $h_0 = 10\text{m}$ and substituting the above values for R_1 and R_2 one finds: $T_1 = 2688 \text{ sec} = 44.8 \text{ min}$; $T_2 = 826 \text{ sec} = 13.8 \text{ min}$. In the spectral analysis of the large sea-level oscillations the period prominent was 40 min.

The current measurements were taken in the Mullaloo area, where the average distance of the reef chain from the shore is about 4500 m. Using the same values of R_1 , R_2 as above, we would obtain from (21) the following periods: $T_1 = 40.3 \text{ min}$, $T_2 = 12.4 \text{ min}$. The last value is too small to be verified by our experimental data as the current meter records were sampled at 10 minute intervals. The results of the spectral analysis of currents gave a prominent period of 33 mins.

The difference of about 20% between the theoretical and experimental results is not bad when taking into account the crude estimates of water depth h and distance l and the uneven bottom topography.

Our theoretical analysis gives consequently, reasonable prediction of the periods of sea-level oscillations. However, the damping was not considered in the theory and when the term "strong" resonance is used it does not give a quantitative idea yet of how strong the resonance is.

The quantitative measure, by which the resonance capabilities are usually judged, is the so-called "quality factor", denoted as Q (e.g. Miles and Munk, 1961). Resonances are considered sharp when $Q \gg 3-5$. Sometimes the values Q up to 18 occur (e.g. Gill and Schumann, 1974). We give below an estimate of this factor for the recorded sea-level oscillations.

Considering one of the normal modes with a wave-length λ , we can write the maximum potential energy in this mode as

$$W = \frac{1}{4} \rho g \lambda A^2 \quad (22)$$

Let the amplitude A during one period T of free oscillations decrease by the value ΔA . The new value of maximum potential energy is

$$W - \Delta W = \frac{1}{4} \rho g \lambda [A^2 - 2A \cdot \Delta A + (\Delta A)^2] \quad (23)$$

Neglecting the second-order term $(\Delta A)^2$ and subtracting eq (22) from eq (23) one obtains a loss in potential energy:

$$\Delta W = \frac{1}{2} \rho g \lambda A \cdot \Delta A \quad (24)$$

From eq (24) and eq (22), it follows that the relative energy loss ψ is twice the relative amplitude decrease δ during one cycle of oscillations.

$$\psi = \frac{\Delta W}{W} = \frac{2\Delta A}{A} = 2\delta \quad (25)$$

The values of ψ and δ are independent of λ , and hence independent of the shape and order of the normal modes. This means that damping of water oscillations can be studied without any knowledge of normal modes.

Let us denote by A_T the amplitude of sea-level oscillations after one period T has elapsed and consider the following supplementary relationship, which holds for small values of δ :

$$\ln \frac{A}{A_T} = \frac{\Delta A}{A} = \delta \quad (26)$$

From eq (26) it follows immediately the exponential law for the amplitude decay of free sea-level oscillations in the basin:

$$A_T = A \exp(-\delta) \quad (27)$$

The damping coefficient δ was estimated on the basis of the relationship (27) for the nine largest sea-level oscillation events recorded in Geraldton during the years 1963-1978.

Letting i be the event number and j be the order number of an amplitude with respect to the maximum, we can rewrite (27) as

$$A_{ij} = A_i \exp(-K_{ij} \delta_i) \quad (28)$$

where K_{ij} is the order number of j th amplitude in the event i and has the values 1, 2, 3... Taking the logarithm of (28), one obtains:

$$Y_{ij} = \ln A_{ij} - \ln A_i = -K_{ij} \delta_i \quad (29)$$

Linear regressions through the origin were fitted to individual sea-level oscillation events and estimates of the δ_i 's were obtained from

$$\delta_i = - \frac{\sum_j K_{ij} Y_{ij}}{\sum_j K_{ij}^2} \quad (30)$$

The estimated values of δ_c , ranged from 0.22 to 0.57, with a pooled value δ_c , obtained from combining sums of squares and cross products over events, of 0.29. From eq(25) it follows that the average relative energy loss ψ during one cycle of oscillations equals twice the value of δ_c , i.e. $\psi = 0.58$. The average resonance amplification factor Q can be estimated as:

$$Q = \frac{2\pi}{\psi} = \frac{6.28}{0.58} = 10.8 \quad (31)$$

with a range from 5.5 to 14.3 in the individual sea-level oscillation events. The large value of Q obtained indicates that observed water oscillations are caused by resonance of the coastal waters in the nearshore basin between Perth and Geraldton, and the resonances are sharp indeed.

6 Conclusions

- 1) Sea-level oscillations between Perth and Geraldton, Western Australia, with periods of the order of 10-40 min. are caused by resonance of local waters in a basin between a shore and submerged reef chain.
- 2) The theory presented gives a reasonable agreement between observed and theoretical values of resonance periods.
- 3) Statistical analysis of recorded oscillations gives the average value of $Q = 10.8$, indicating that the resonances are sharp.

7 Acknowledgements

The authors are grateful to Mr. Austin from Public Works Department, Perth, for supplying the tidal records; Mr. T.J. Golding of CSIRO Division of Fisheries and Oceanography, Cronulla, for digitizing the current records and Mr. R. Symes of the Australian Survey Office, Perth for digitizing the tidal records.

8 References

- ABRAMOWITZ, M. and STEGUN, I.A. (1970). Handbook of mathematical Functions. Dover, New York.
- ALLISON, H.A. and GRASSIA, A. (1979). Sporadic sea-level oscillations along the Western Australian Coastline. Aust. J. Mar. Freshwater Res. 30(6), (in press).
- CURRIE, R.G. (1976). The spectrum of sea level from 4 to 40 years. Geophys. J. Roy. Aston. Soc. 46, 513-520.
- CHRYSAL, G. (1904). Some results in the mathematical theory of seiches. Proc. Roy. Soc. Edin. XXV, 328-337.

- GILL, A.E. and SCHUMANN, E.H. (1974). The generation of long shelf waves by the wind. J. Phys. Oceanogr. 4, 83-90.
- HAMON, B.V. (1966). Continental shelf waves and the effect of atmospheric pressure and wind stress on sea-level. J. Geophys. Res. 71, 2883-93.
- HAMON, B.V. (1976). Generation of shelf waves on the East Australian Coast by wind stress. Mémoires Société Royale des Sciences de Liège, 6^e Série, tome X. pp 359-367.
- LAMB, H. (1932). Hydrodynamics. Cambridge Univ. Press, London.
- LE BLOND, P.H. and MYSAK, L.A. (1978). Waves in the ocean. Elsevier, Amsterdam.
- MILES, J. and MUNK, W. (1961). Harbour paradox. J. Waterways and Harbour Div., ASCE, WW3, 111-130.
- TUCK, E.O. (1980). The effect of a submerged barrier on the natural frequencies and radiation damping of a shallow basin connected to open water. J. Aust. Math. Soc. Series B. (in press).

CHAPTER 17

A CLOSELY RESPONDING, VERSATILE WAVE TUNNEL

C.H. Hulsbergen

Project Adviser, Harbours and Coasts Branch,
Delft Hydraulics Laboratory, The Netherlands

and

J.J. Bosman

Project Engineer, Harbours and Coasts Branch,
Delft Hydraulics Laboratory, The Netherlands

ABSTRACT

A new wave tunnel is presented as has been recently built at the Delft Hydraulics Laboratory. Several design aspects of the wave tunnel will be discussed and special attention is drawn to the required force and power diagrams.

1. INTRODUCTION

It is often emphasized that wave asymmetry and the corresponding orbital velocities have a dominating influence on the behaviour of bed material i.e. on the geometry and stability of ripples, on the concentration and on the transport of sand, see e.g. Russell and Dyke (1963) and Kamphuis (1973). Yet hardly any systematic investigation has been reported so far. An important reason for this is the very nature of the wave: the free surface wave form cannot be controlled in detail due to its continuous adaptation to bed geometry changes. As a matter of fact, the near-bed orbital velocity rather than the wave surface history determines the sediment transport.

In order to study the effect of different orbital velocity regimes on onshore-offshore sand transport, preliminary tests were carried out in a simple pulsating water block, affirming the very close systematic dependence of direction and rate of sand transport on slight changes in the asymmetry of the orbital velocity (Hulsbergen, 1974). It has been concluded that fundamental research on sand/water interaction required a facility in which prescribed water motions can be exactly generated. This research will be performed in the here presented wave tunnel.

2. DESIGN CONSIDERATIONS

The water motion to be generated should meet the following requirements:

- i Exact reproduction should be possible of any water motion as occurring in the existing laboratory channels.
- ii The complete range of sand ripple evolution should be covered, including the phenomenon of "sheet flow".
- iii A relatively high amount of high frequency components should be available.

Further some general requirements were formulated:

- iv The facility should serve as a pilot model for possible future tests in a larger facility.
- v Access to the test section should be easy for visual inspection, for measuring devices and for changing the sand bed.
- vi The whole system should be automatized to a high degree in order to facilitate efficient research.

It was decided to construct a tunnel because a "pulsating bottom apparatus" or a "pulsating water block" would not meet all of these requirements. A water tunnel has the important advantage that it can be composed of various sections. These sections can have different shapes, different cross section areas and can even contain different fluids, in order to most properly meet the specific requirements for their function in the system. The only thing which is constant throughout the tunnel is the instantaneous rate of flow. Through this constancy the flow history can be controlled and programmed exactly according to a given signal, provided that the leakage is nihil and the driving power is sufficient. Once the requirements i, ii and iii are specified in terms of amplitudes, velocities and accelerations (Chapter 4), the dimensions of the test section (Chapter 5) and the rest of the apparatus (Chapter 6) can be determined, and thence the required power of the driving mechanism (Chapter 7).

3. LAY-OUT OF THE WAVE TUNNEL

As the tunnel contains both water and oil, and is aiming at simulating certain aspects of wave motion, it is called a "wave tunnel" rather than a "water tunnel". In principle it is a U-shaped tunnel (Fig. 1) with a horizontal test section between large-diameter vertical legs. The test section and one of these tanks contain water, the other tank contains oil. In order to separate both fluids there is a third tank in between, which contains a large-diameter rubber diaphragm. The driving piston, which is forced by a programmable hydro-power unit, moves in oil in a horizontal cylinder section located between the diaphragm tank and the vertical oil tank. Superimposed on the oscillatory mode, a mean flow may be induced by a pump in the by-pass circuit.

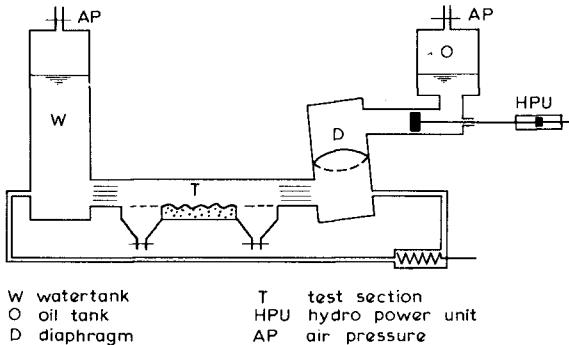


Figure 1 Schematic lay-out of the DHL wave tunnel

4. THE DESIGN WATER MOTION

In order to meet requirement i), viz. the exact reproducibility of any orbital motion as measured in laboratory wave channels (outside the surf zone), the following steps were made:

- determine the maximum near-bed orbital velocity, $(\hat{u}_b)_{\max}$, as a function of the wave period T,
- select the design wave condition in terms of T and $(\hat{u}_b)_{\max}$
- add some fraction of higher harmonic components,
- add some mean flow capacity (see Chapter 8).

The relation between $(\hat{u}_b)_{\max}$ and T has been determined on the basis of first order wave theory and a breaking criterion as follows. The orbital peak velocity near the bed, in a progressive first order gravity wave with period T, height H, length L and in a water depth d is written as

$$\hat{u}_b = \pi H/T \sinh(2\pi d/L) \quad (1)$$

The question is now: what is the maximum value, $(\hat{u}_b)_{\max}$, for a given wave period T? In shoaling waves \hat{u}_b increases until there is a limit, set e.g. by the breaking criterion of Miche (1944):

$$(H/L)_{\max} = 0.142 \tanh(2\pi d/L) \quad (2)$$

from which

$$H_{\max} = 0.142 L \tanh(2\pi d/L) \quad (3)$$

Further,

$$L = 1.56 T^2 \tanh(2\pi d/L) \quad (\text{in metres, secs}) \quad (4)$$

Substituting equations (3) and (4) into (1) yields for $(\hat{u}_b)_{\max}$

$$(\hat{u}_b)_{\max} = \left[0.696 T \tanh^2(2\pi d/L) / \sinh(2\pi d/L) \right]_{\max} \quad (5)$$

The quotient \tanh^2/\sinh has a maximum value of 0.50 for $d/L = 0.141$ or $d/L_0 = 0.10$, so that

$$(\hat{u}_b)_{\max} = 0.348 T \quad (\text{in metres, secs}) \quad (6)$$

Further, at the breaker location as defined above where $d/L_0 = 0.10$, the following relations apply:

$$\left. \begin{aligned} \sinh(2\pi d/L) &= 1.00 \\ d &= 0.156 T^2 \quad (\text{in metres, secs}) \\ H_{\max} &= 0.111 T^2 \quad (\text{in metres, secs}) \\ H_{\max}/d &= 0.71 \\ H_{\max} &= A_b, \text{ where } A_b \text{ is the near-bed water particle} \\ &\quad \text{stroke (= } 2 \times \text{near-bed particle amplitude)} \\ \text{max. acceleration} &= 2.2 \text{ m/s}^2 \end{aligned} \right\} \quad (7)$$

The equations (6) and (7) are tabulated for some values of T in Table 1.

T (seconds)	d (m)	$(\hat{u}_b)_{\max}$ (m/s)	$H_{\max} = A_b$ (m)
0.8	0.10	0.28	0.07
1.4	0.31	0.49	0.22
2.0	0.62	0.70	0.44
3.0	1.40	1.04	1.00
5.0	3.90	1.74	2.77
10.0	15.60	3.48	11.08

Table 1 Conditions at $d/L_o = 0.10$, where $(\hat{u}_b)_{\max}$ occurs.

From this range of periods, strokes and velocities the condition of $T = 2$ seconds was adopted as a design basis. The design water motion has been composed of this sinusoidal motion, with period = 2 seconds and amplitude = 0.22 m, plus a second harmonic motion with an amplitude ratio of 0.333, plus a third harmonic motion with an amplitude ratio of 0.20, all in arbitrary phase relationship to each other. This combines to the following maximum values in the test section for the oscillatory mode:

maximum stroke = 0.69 m
 maximum velocity = 1.60 m/s
 maximum acceleration = 9.1 m/s^2

These maximum values do not appear simultaneously, but they may be reached within the course of a single oscillation. It is noticed that the acceleration rate of 9.1 m/s^2 is more than 4 times the acceleration rate in sinusoidal waves at maximum steepness, as given in equation (7), reflecting the requirement iii of Chapter 2. Also, the maximum velocity of 1.60 m/s should be enough to generate "sheet flow" conditions as was stated in requirement ii of Chapter 2.

5. THE TEST SECTION

The test section accommodates the 0.2 m thick sand bed with sand traps at both ends. The width of the test section was chosen at 0.3 m as a compromise between small side wall effects and small power consumption. The height above the sand bed was chosen at 0.4 m, high enough to accommodate suspended sediment concentrations and ripple formation as expected under the design water motion. The length of the sand bed was taken as 3 times the maximum stroke, or 2.0 m. Each sand trap has a length of 1.5 times the maximum stroke, or 1.0 m. The sand bed can be extended over the sand traps and is then 4.0 m long. Also, the sand may be replaced by dummy bottom plates. The test section consists of a steel framework with glass side panels and steel top hatches. Special attention has been paid to the details of the ceiling in order to facilitate de-aeration. Through the hatches instruments can be inserted via pivoting connections every 0.3 m over the entire test section. On both ends of the test section 1.0 m long tunnel sections are installed with flow straighteners.

6. THE OIL SECTION

The requirement that the water motion in the test section should very closely respond to the programmed signal means that virtually no leak is allowed along the driving piston. Thus absolutely no sediment should reach the piston in order

to prevent wearing of the cylinder. By means of a separating diaphragm, and by having the piston moving in oil, these requirements were met. The position of the diaphragm is continuously monitored, and it is integrated in the automatic control system of the tunnel. Extreme positions of the diaphragm are defined by two perforated steel plates. For practical reasons the piston stroke is limited to 0.50 m, so its cross section area is 1.36 times the area of the test section and its velocity is 0.74 times the velocity in the test section.

7. THE DRIVING MECHANISM

Acceleration/velocity

The combined acceleration and velocity, stemming from the design water motion as defined in Chapter 4, can be easily calculated. However, the analytical form of the maximum acceleration rate as a function of the simultaneous velocity is rather complex. Therefore this relation is shown in graphical form in Fig. 2.

Forces

The forces on the piston stem from different sources which are in general not in phase:

- Inertial forces due to the accelerated mass of the piston and of the fluids. This is by far the dominant force.
- Forces proportional to the squared velocity due to fluid friction.
- Forces proportional to the piston excursion, due to hydrostatic pressure differences and air pressure differences in both vertical legs.
- Other sources such as friction between the piston and the cylinder.

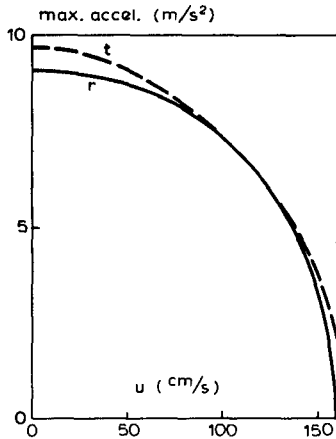


Figure 2 The maximum acceleration rate as a function of the simultaneous velocity in the test section, both as required (r) and as measured in tests (t)

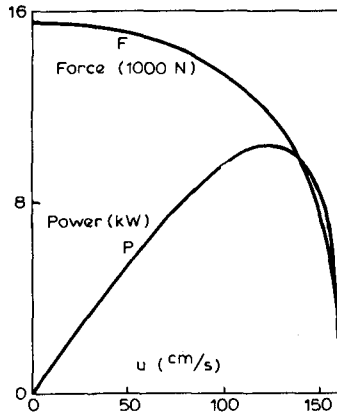


Figure 3 The maximum required force (F) and power (P) as a function of the velocity in the test section.

The maximum total required force is depicted in Fig. 3 as a function of the velocity in the test section.

Power

The required power is found as the product of the force applied by the piston, and the piston velocity. Hence the required power-velocity diagram follows from the force-velocity diagram. In Fig. 3 the power is depicted as a function of the water velocity in the test section. The nett maximum power required at the piston is about 11 kWatt. The gross power of the installed hydro-power unit is 22 kWatt.

8. VARIOUS DESIGN ASPECTS

Apart from the programmable oscillating motion, a nett flow can be induced. A special pump has been chosen with a discharge virtually unaffected by the large fluctuations in head over the test section. The maximum discharge is 20 litres/second, generating an average velocity of 0.17 m/second in the test section of 0.12 m² cross section area. The pump is driven by a 15 kWatt electric engine. The instantaneous discharge is measured with an electromagnetic flow meter.

As can be seen from Fig. 2, quite large acceleration rates may occur in the tunnel. Consequently large pressure drops may result. The low water pressure might cause air intrusion, or even an inward collapse of the windows. In order to prevent this, the whole system is 100 kPa (= 1 bar) overpressurized by controlling the air pressure above the fluids in both vertical tanks.

The tunnel is remotely controlled by a programmable operation panel to perform operations such as quick emptying and filling from a reservoir, air pressure control, definition of piston and diaphragm starting conditions, etc. This panel also includes complete safety-guarding of the whole system while in operation.

9. VARIOUS PERFORMANCE ASPECTS

The full range of acceleration rates in its relation to the simultaneous velocity, as observed during tests in the wave tunnel, is shown by curve (t) in Fig. 2. For purely sinusoidal motion the maximum amplitude of water motion that could be generated within 5% distortion is shown in Fig. 4.

The amplitude upper limit of 0.34 m for frequencies below about 0.8 Hz is imposed by the limits of the piston movement. For these conditions there is enough power at hand to increase the water velocity and the stroke in the test section, by decreasing the cross section area of the test section.

For frequencies over 3 Hz the attainable amplitude is quite small because of the very high inertial forces. A frequency of 2.5 Hz has shown to be a very effective mode to flatten a rippled bed after a sand transport test, so that a whole series of experiments can be done without opening the hatches. One of the design considerations was to create sheat flow conditions, which indeed has been observed during some preliminary tests.

Among other tunnels, the DHL wave tunnel is certainly not outstanding for its size, but for its ability to generate any prescribed motion within quite strict margins of accuracy, e.g. purely sinusoidal motion, regular motion with any prescribed sort of skewness, and irregular motions, with or without a nett

flow. Also, special flow conditions can be generated, e.g. a prescribed fluctuating head over a model of a soil structure, packed in a module box in the test section. In this case a digital driving signal can be calculated, based on the resistance characteristics of the specific structure. These must be determined by correlating the measured pressure head and the simultaneous velocity and acceleration of the piston.

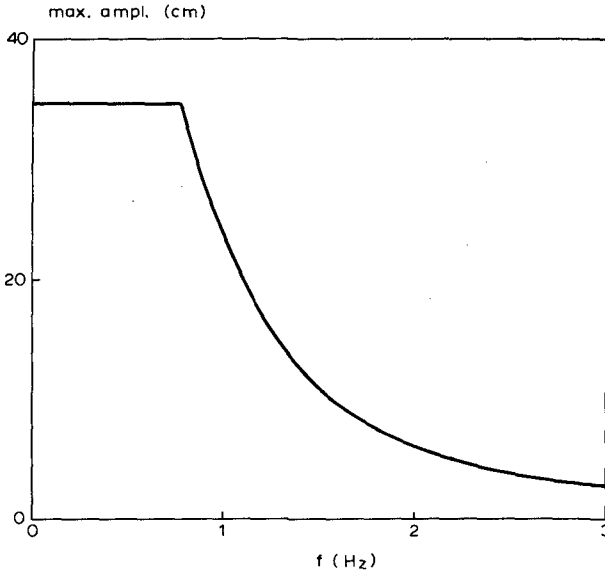


Figure 4 Maximum amplitude of water displacement in pure sinusoidal motion as a function of frequency, as measured in the test section

Measurements may be performed with any probe through the hatch connections (velocity, pressure, sand concentration). As standard velocity measuring system, a laser doppler velocimeter is mounted on a x, y, z frame on rails, covering the entire test section.

10. CONCLUSIONS

The presented wave tunnel has shown to operate quite satisfactorily. Hence it is expected to be a powerful tool for future experiments on the interaction between a well-defined velocity field and movable bed material.

ACKNOWLEDGEMENTS

This work has been performed as part of the Applied Research Program (TOW) of the Dutch Public Works Department (Rijkswaterstaat) under the contract number M 1388.

REFERENCES

- Hulsbergen, C.H. (1974),
Origin, effect and suppression of secondary waves,
Proc. 14th Coastal Eng. Conf., Copenhagen, pp. 392-411.
- Kamphuis, J.W. (1973),
Sediment transport by waves over a flat bed,
Conference on Engineering Dynamics in the Surf Zone, Sydney, pp. 228-233
- Russell, R.C.H. and Dyke, J.R.J. (1963),
The direction of net sediment transport caused by waves passing over a horizontal bed,
Proc. 10th Congress of IAHR, London, pp. 41-46.



The DHL wave tunnel

Conditional Simulations of Ocean Wave Properties.

Leon R. Borgman¹

1. INTRODUCTION

Computer simulation is a convenient procedure to produce artificial data with specified statistical properties. The usual procedure in ocean wave simulations is to take the ensemble or theoretical mean and spectral relations as given by selected formulas and to produce with pseudo-random numbers and various statistical techniques a long Gaussian (multi-variate normal) time series which is one realization of the stochastic population. The simulation may be constructed directly in time, or (usually, more rapidly) in frequency domain with subsequent reversion to time by the fast Fourier transform algorithm (Borgman, 1969, 1980).

A number of such simulated time series are ordinarily generated, and used, as typical realizations of the sea state for vibration or fatigue studies. The sample mean and sample spectra computed for a given realization will differ from the theoretical values initially assigned in accordance with the random structure of the process. Thus, the fatigue or vibrational behavior produced is not that associated with the theoretical spectral density initially assigned but rather with the particular sample spectral density which was, by accident, present in that realization. If one has an actual sequence of sample spectra and mean water levels, and wishes to study the vibration or fatigue behavior which might have been associated with that particular sequence, standard simulation procedures will not suffice. Rather, constrained simulations are necessary, with the randomness being restricted so as to produce the required sample mean and spectra for each time interval. Any simulation, whose randomness is restricted so that the sample function satisfies some specified behavior, will be referred to as a constrained simulation.

The concept of constraints may be extended to sets of statistically interrelated time series. Suppose that the first time series represents the water level elevations as measured by a wave staff at a specified location on a drilling

¹/Professor of Geology and Statistics, University of Wyoming, Laramie, Wyoming.

platform. Let the other time series represent velocity or acceleration time series at loading points down the legs of the platform. Simulations of the velocity and acceleration sequences would be produced by the computer, conditional on the wave profile having the assigned values. Such sequences will be called conditional simulations.

2. FOURIER RELATIONS

Although the development of simulated sequences directly in time is intuitively more obvious and easily understood, it is much slower in terms of computer operations than indirect procedures starting in the frequency domain and later reverting to the time domain. Therefore, it is worthwhile to briefly enumerate the statistical properties which Fourier coefficients must have in order that the time-domain inverse will form a real-valued stationary, Gaussian process (Borgman, 1976). Let $\{X_n, n=0,1,2,\dots,N-1\}$ be the time-domain series and $\{A_m, m=0,1,2,\dots,N-1\}$ be the frequency domain sequence which is related to the X_n by the equations

$$A_m = \Delta t \sum_{n=0}^{N-1} X_n e^{-i2\pi mn/N} = U_m - i V_m \quad (1)$$

$$X_n = \Delta f \sum_{m=0}^{N-1} A_m e^{i2\pi mn/N}, \quad \Delta f = 1/N\Delta t \quad (2)$$

where $i = \sqrt{-1}$, Δt is the increment in time, and Δf is the frequency increment.

The following properties hold. (All sums run from 0 to $N-1$ unless otherwise noted. The asterisk denotes complex conjugation.)

$$A_0 = \Delta t \sum_n X_n \quad (3)$$

$$A_{N-m} = A_m^* = U_m + iV_m \quad (4)$$

$$X_0 = \Delta f \sum_m U_m \quad (5)$$

$$E(U_m) = E(V_m) = 0, \quad 0 \leq m < N, \quad \text{if } E(X_n) = 0 \quad (6)$$

$$\text{Variance}(U_m) = \text{Var}(V_m) = S_m N \Delta t / 2, \quad \text{for } 0 < m < N/2 \quad (7)$$

$$\text{Var}(U_m) = S_m N \Delta t, \quad \text{if } m=0 \text{ or } m=N/2 \quad (8)$$

(U_m, V_m, U_m^i, V_m^i) are independent and normally distributed for $0 < m < m^i < N/2$. In the above,

$$S_m = \Delta t \sum_k C_k e^{-i2\pi km/N} \quad (9)$$

and

$$C_k = \text{Covariance}(X_n, X_{n+k}) \quad (10)$$

where X_n is repeated periodically for n outside $(0, N-1)$.

3. TWO TIME SERIES

All of the Fourier properties reported in Section 2 hold separately for two time series, X_n and Y_n . In addition, the Fourier coefficients are independent for different subscript values, $0 < m < N/2$. However, the Fourier coefficients for the two series at the same m value are multivariate normal with covariance matrix

$$\text{Cov} \begin{bmatrix} U_m \\ V_m \\ U'_m \\ V'_m \end{bmatrix} = \frac{N\Delta t}{2} \begin{bmatrix} S_m & 0 & c_m & q_m \\ 0 & S_m & -q_m & c_m \\ c_m & -q_m & S'_m & 0 \\ q_m & c_m & 0 & S'_m \end{bmatrix} \quad (11)$$

In this formula, c_m and q_m are the co- and quad-spectral densities defined as

$$c_m - iq_m = \Delta t \sum_k C_{XY,k} e^{-i2\pi km/N} \quad (12)$$

where

$$C_{XY,k} = \text{Covariance}(X_n, Y_{n+k}) \quad (13)$$

Also U_m and V_m are the FFT coefficients for X_n while U'_m , V'_m are the corresponding coefficients for Y_n .

The generalization to more than two time series is straightforward. The matrix in (11) is just enlarged to include the additional spectra and cross-spectra.

4. UNCONDITIONAL FREQUENCY-DOMAIN SIMULATIONS

The simulation of j simultaneous time series reduces to the development of $2j$ multivariate normal variates independently for each $0 < m < N/2$. The Fourier coefficients for $m > N/2$ are obtained by complex conjugation (see(4)). Usually the coefficients at $m=0$ are set equal to zero (a constrained simulation producing exactly zero mean water level) and $N\Delta t$

is chosen large enough so that there is no energy left of any consequence for frequencies approaching $N\Delta t/2$. This forces $A_{N/2} = 0$.

Various schemes can be used to produce the multivariate normal random deviates approximating wave properties (Borgman, 1980). One procedure based on multiplication of independent standard normal random deviates is given by Scheuer and Stoller (1962).

5. CONSTRAINED AND CONDITIONAL SIMULATIONS

A constrained simulation is a simulation in which the resulting artificial sample functions are adjusted to have specified sample properties. The simplest example would be a sequence of standard normal independent pseudo-random numbers, $\{Z_0, Z_1, Z_2, \dots, Z_{N-1}\}$ which are adjusted by subtracting the sample average and dividing by the sample standard deviation. The resulting sequence will exactly will exactly have mean zero and variance one. The original sequence $\{Z_n\}$ was a sample from a population with theoretical mean zero variance one, but its sample values will deviate slightly from these theoretical values due to the randomness and finite extent of the sample.

Correlated simulated sequences may be constrained to have other specified sample properties. For example, a specified sample covariance function or sample spectral density can be forced onto the simulated sequence. It is not always clear if the resulting sequence has the same distribution as the original one. In fact, in general it will not. The original example above of a sequence of independent normal random numbers will have a weak correlation between successive values after the sample mean is subtracted from each term. Nevertheless, it is occasionally useful to work with simulated time series which have been constrained.

What type of questions may be answered with constrained time series simulations? Generally such questions are related to behavior which pivotally are concerned with a given sample property. Consider the following two questions:

1. What is the vibrational behavior of an oil-drilling structure which is experiencing ocean waves for one hour whose theoretical spectral density is specified?
2. What is the vibrational history of the same structure when it experiences waves for one hour whose sample spectral density is a specified function?

In a simulation for the first question, the actual sample

spectra for the one hour of data will not equal the theoretical function. In fact, it may differ quite a bit from the theoretical value which holds for the population. A simulation for the second question will force the spectra for the one hour record to equal the specified function. One source of variation, the sample fluctuation, will have been removed. Several simulations will all have exactly the same sample spectral density.

There are many unresolved theoretical questions connected with constrained simulations. The foregoing is intended only to be a brief introduction to the problem. However, it is common engineering practice to introduce constraints on simulations, at least for some types of studies.

Conditional simulations are less theoretically questionable. In a conditional simulation, one or more of the simulated values are assigned numerical values, and the rest are obtained from distribution theory and pseudo-random numbers. For example, suppose $\{X_0, X_1, X_2, \dots, X_{N-1}\}$ are a multivariate Gaussian sequence and it is known, a priori, that X_0 and X_{N-1} are both zero. The sequence $\{X_1, X_2, \dots, X_{N-2}\}$ can be simulated conditionally given $X_0 = X_{N-1} = 0$. If the original sequence was highly positively correlated, the simulated X_1 will not differ appreciably from $X_0 = 0$. That is, the correlation will be preserved between the given and the simulated values. Techniques of conditional simulation have been used in geological problems (Journal, 1974). The concept appears to be very promising for coastal engineering applications.

The concept can be extended to several simultaneous time series. One or more of the time series can have specified values and the remaining time series can be simulated conditionally. Thus the sea surface elevation time series could be set equal to a measured wave record, and the inter-correlated bottom pressure which was occurring simultaneously could be simulated conditionally. This latter type of conditional simulation (one or more time series specified, the remaining ones simulated) will be given the primary attention in the following.

Conditional simulations may be generated either by matrix multiplication or filtered white noise. (At the present time, it is not clear how the random phase procedures could be used.) Only matrix multiplication procedures will be presented here. Two basic theorems for the matrix multiplication technique are as follows:

Let \underline{W} be a normal random (column) vector with n components,

which has mean vector $\underline{\mu}$ and covariance matrix C . Let \underline{W} be partitioned into two vectors \underline{W}_1 and \underline{W}_2 with n_1 and n_2 components respectively. The vector $\underline{\mu}$ and the matrix C are similarly partitioned. Thus

$$n = n_1 + n_2 \quad (14)$$

$$\underline{W} = \begin{bmatrix} \underline{W}_1 \\ \underline{W}_2 \end{bmatrix} \quad (15)$$

$$\underline{\mu} = \begin{bmatrix} \underline{\mu}_1 \\ \underline{\mu}_2 \end{bmatrix} \quad (16)$$

$$C = \begin{bmatrix} C_{11} & C_{12} \\ C_{12}^T & C_{22} \end{bmatrix} \quad (17)$$

where the superscript "T" denotes the matrix transpose.

Theorem A

The conditional probability law for \underline{W}_2 , given $\underline{W}_1 = \underline{w}_1$, is multivariate normal with conditional mean of

$$\underline{W}_2 = \underline{\mu}_2 + C_{12}^T C_{11}^{-1} (\underline{w}_1 - \underline{\mu}_1) \quad , \text{ and} \quad (18)$$

conditional covariance matrix

$$\underline{W}_2 = C_{22} - C_{12}^T C_{11}^{-1} C_{12} \quad (19)$$

Proof. (See Anderson, 1958, pp. 27-29)

Theorem B

Let \underline{W} be an unconditional simulation of the random vector. That is, \underline{W} follows a multivariate normal probability law with mean $\underline{\mu}$ and covariance matrix, C . The vector $\underline{\tilde{W}}_2$ defined by

$$\underline{\tilde{W}}_2 = C_{12}^T C_{11}^{-1} (\underline{w}_1 - \underline{W}_1) + \underline{W}_2 \quad (20)$$

will be a conditional simulation of \underline{W}_2 , given $\underline{W}_1 = \underline{w}_1$.

The mean vector and covariance matrix for \underline{W}_2 are the same as the conditional mean and covariance relations specified in Theorem A and \underline{W}_2 is a multivariate normal random vector.

Proof

Since every linear combination of multivariate normal is also multivariate normal (Anderson, 1958), \underline{W}_2 is a multivariate normal vector. Also

$$E[\underline{\tilde{W}}_2] = C_{12}^T C_{11}^{-1} (\underline{w}_1 - \underline{\mu}_1) + \underline{\mu}_2 \quad (21)$$

$$\begin{aligned} \text{Cov}(\underline{\tilde{W}}_2) &= E[\{\underline{\tilde{W}}_2 - E(\underline{\tilde{W}}_2)\}\{\underline{\tilde{W}}_2 - E(\underline{\tilde{W}}_2)\}^T] \\ &= E[\{(\underline{W}_2 - \underline{\mu}_2) - C_{12}^T C_{11}^{-1} (\underline{W}_1 - \underline{\mu}_1)\}\{(\underline{W}_2 - \underline{\mu}_2) \\ &\quad - C_{12}^T C_{11}^{-1} (\underline{W}_1 - \underline{\mu}_1)\}^T] \\ &= C_{22} - C_{12}^T C_{11}^{-1} C_{12} \quad \text{Q.E.D.} \quad (22) \end{aligned}$$

For a time domain simulation by matrix multiplication, \underline{W}_2^T would contain the given values and \underline{W}_1^T would be simulated as a normal with the mean and covariance matrix listed in the theorem. Either of the previous techniques (triangular matrix or eigenvector) could be used to generate \underline{W}_1^T . A mean zero version of \underline{W}_1^T would be developed first, and then the appropriate mean vector as listed in the theorem would be added on.

It is usually easier to do the conditional simulation in frequency domain by matrix multiplication. The unknown and the given time series each have Fourier coefficients which are uncorrelated from frequency to frequency ($0 < m < N/2$), and have the covariance matrix for each m as previously discussed. The Fourier coefficients for the given time series can be easily developed by a fast Fourier transform computation. The coefficients for the unknown (i.e., to be simulated conditionally) time series are normally distributed with mean vector and covariance matrix as specified by the theorem. The simulation of these unknown coefficients, for each m , can be done by matrix multiplication. At each frequency, only a $2L$ -component vector is involved if L is the number of unknown time series. This is a much smaller operation than the corresponding time-domain simulations.

6. EXAMPLE A

Suppose a wave profile is represented by a time series with 32 values spaced over a wave period of $T=14$ sec. That is,

$$\begin{aligned}\Delta t &= 14/32 \text{ seconds} \\ N &= 32, \quad \Delta f = 1/N\Delta t = 1/14 \text{ Hertz} \quad (23) \\ \eta_n &= \eta(n\Delta t) = \text{water level elevation above mean} \\ &\quad \text{water level.}\end{aligned}$$

Let $\eta_0 = \eta_{16} = \eta_{32} = 0$, $\eta_8 = 18$ ft., and $\eta_{24} = -12$ ft. Then the wave will have a height at least as large as 30 ft. and the crest elevation to height ratio will be around 18/30. What are reasonable simulated values for the other unspecified η_n values assuming the following spectral density and covariance values?

$$S(m\Delta f)\Delta f = (0, 5.446, 6.990, 1.184, .279, .090, .036, .020, .005, 0,0,0,0,0,0,0) \quad (24)$$

$$C(n\Delta t) = (28.1, 26.1, 20.7, 13.3, 5.4, -1.9, -7.7, -11.6, -13.5, -13.5, -12.0, -9.5, -6.5, -3.5, -1.0, .6) \quad (25)$$

The convention used here is that the values in the parenthesis represent the sequences for $m = 0,1,2,\dots,15$ and $n = 0,1,2,\dots,15$ for the two functions.

Theorem B provides the theory for the simulation of the profile passing through the specified points.

$$\underline{w}'_1 = (\eta_0, \eta_8, \eta_{16}, \eta_{24}) = (0, 18, 0, -12) \quad (26)$$

$$\begin{aligned}\underline{w}'_2 &= (\eta_1, \eta_2, \eta_3, \eta_4, \eta_5, \eta_6, \eta_7, \eta_9, \eta_{10}, \eta_{11}, \eta_{12}, \eta_{13}, \\ &\quad \eta_{14}, \eta_{15}, \eta_{17}, \eta_{18}, \eta_{19}, \eta_{20}, \eta_{21}, \eta_{22}, \eta_{23}, \eta_{25}, \\ &\quad \eta_{27}, \eta_{28}, \eta_{29}, \eta_{30}, \eta_{31}) \quad (27)\end{aligned}$$

Since the profile is periodic, $\eta_{32} = \eta_0 = 0$, and it is not necessary to specifically introduce the constraint that $\eta_{32} = 0$. The covariance matrix C_{11} will be the 4x4 array of covariances for $(\eta_0, \eta_8, \eta_{16}, \eta_{24})$. The covariance matrix C_{22} will be the 28x28 matrix of covariances for the other η_n , excluding $n = 0, 8, 16$, and 24.

The application of theorem B proceeds in two steps. First

an unconditional simulation of a wave profile for η_n with the specified theoretical covariance function and spectral density is prepared by any convenient procedure. This simulation is not constrained to pass through the specified η_n values. It is an ordinary unconstrained or unconditional simulation. This simulation produces random values for

$$\underline{W}'_1 = (\eta_0, \eta_8, \eta_{16}, \eta_{24}) \quad (28)$$

and for \underline{W}'_2 . By theorem B, the conditional or constrained simulation of \underline{W}_2 (denoted by \tilde{W}_2) given $\underline{W}_1 = \underline{w}_1$ (the assigned values) is provided by

$$\tilde{W}_2 = C_{12}^T C_{11}^{-1} (\underline{w}_1 - \underline{W}_1) + \underline{W}_2 \quad (29)$$

since $\underline{\mu}_1 = \underline{0}$ and $\underline{\mu}_2 = \underline{0}$. Two graphical examples of such a constrained simulation are given in Fig. 1.

7. EXAMPLE B

Suppose now that the complete wave profile is specified and one wishes to simulate the time series for the horizontal water particle velocity components $v_x(t)$ (in-line) and $v_y(t)$ (transverse) at still water level. Let $T=14$ sec., $H=30$ ft., and $d=100$ ft. For convenience, suppose the period is subdivided into 32 increments as in example A. The same spectra and covariance function used in the first example will be assumed here. However, a spreading function with equivalent standard deviation of 20° will be taken as holding for all frequencies. The wave profile will be taken from Table 1 for the assumed H , d , and T values. This gives the wave profile listed in the second column of Table 2.

It is convenient to perform the conditional simulation in the frequency domain. Let the real and imaginary parts for the Fourier coefficients (FFT coefficients) for η , v_x , and v_y be specified by

$$U_m - iV_m = \text{FFT coeff. for } \eta \quad (30)$$

$$U_{m,vx} - iV_{m,vx} = \text{FFT coeff. for } v_x \quad (31)$$

$$U_{m,vy} - iV_{m,vy} = \text{FFT coeff. for } v_y \quad (32)$$

By properties of the discrete Fourier transform, these six random values for a given m ($0 < m < 16$) are independent of the corresponding values at other $0 < m < 16$. Thus the frequency domain version of the time series can be constructed independently for each frequency between 0 and the Nyquist frequency. For convenience the Fourier coefficients at zero

and at the Nyquist frequency are set to zero (no DC component and the spectra dies to zero before reaching the folding frequency).

At a given frequency, the four random variables U_m, v_x , V_m, v_x , U_m, v_y , and V_m, v_y are to be simulated conditionally on U_m and V_m having the values specified by the discrete Fourier transform of the wave profile at that same frequency. For this example, it is perhaps easiest to use theorem A applied to each frequency. In this case $\underline{w}_1^T = (U_m, V_m)$ and $\underline{w}_2^T = (U_m, v_x, V_m, v_x, U_m, v_y, V_m, v_y)$. C_{11} is the 2x2 covariance matrix for (U_m, V_m) and C_{22} is the 4x4 covariance matrix for \underline{w}_2 . C_{12} is the 2x4 matrix of cross covariances. The three matrices C_{11} , C_{22} , and C_{12} change value from frequency to frequency. The random vector \underline{w}_2 , as conditioned on $\underline{w}_1 = \underline{w}_1$, will have a 4x4 conditional covariance matrix given by $C_{22} - C_{12} C_{11}^{-1} C_{12}$. The mean vector will equal $C_{12}^T C_{11}^{-1} \underline{w}_1$ since it has been assumed that $\underline{\mu}_1 = 0$ and $\underline{\mu}_2 = 0$. Thus, the conditional simulation of the FFT coefficients for v_x and v_y involves producing a 4-component multivariate normal with the specified conditional covariance matrix and mean for each frequency. The FFT coefficients are then inverted back to the time domain by the fast Fourier transform to produce a conditional simulation of v_x and v_y consistent with the assumed wave profile.

The present example is substantially simplified in that it can be shown that the velocity FFT coefficients have the structure

$$U_m, v_x = aRZ_1 + \text{cond. mean} \quad (33)$$

$$V_m, v_x = aRZ_2 + \text{cond. mean} \quad (34)$$

$$U_m, v_y = bRZ_3 + \text{cond. mean} \quad (35)$$

$$V_m, v_y = bRZ_4 + \text{cond. mean} \quad (36)$$

where Z_1 , Z_2 , Z_3 , and Z_4 are standard normal independent random variables. The R value is the appropriate attenuation factor for the distance down in the water where the velocities are taken as occurring. Actually the different Z_i values could be used simultaneously to produce simulations at any number of depth positions vertically. The constant a and b can be selected to provide the proper conditional covariance matrix.

A conditional simulation for v_x and v_y is given in Table 2.

8. CONCLUSIONS

Techniques are outlined for efficient conditional and/or constrained simulations of wave properties in the frequency domain. Through the speed of the fast Fourier transform algorithm and the directness of conditional simulations in producing targeted results, substantial savings in computer time are possible.

9. REFERENCES

- ANDERSON, T. W. (1958). AN INTRODUCTION TO MULTIVARIATE STATISTICAL ANALYSIS, John Wiley, New York.
- BORCMAN, L. E. (1969). Ocean wave simulation for engineering design. Jour. Waterways and Harbors Div., ASCE, Vol. 95, WWS, 6925, pp 557-583.
- BORGMAN, L. E. (1976). Statistical properties of fast Fourier transform coefficients computed from real-valued, covariance-stationary, periodic, random sequences. No.76-9, U.S. Army Coast. Engr. Res. Center, Ft. Belvoir, Va.
- BORCMAN, L. E. (1980). Directional spectra from wave sensors. OCEAN WAVE CLIMATE. Marine Science Series, Vol.8, pp 269-300. Plenum Press, New York.
- BORCMAN, L. E. (1979). Techniques for computer simulation of ocean waves. Submitted for publication to ASCE as part of report by Committee on Reliability for Offshore Structures.
- DEAN, R. C. (1974). Evaluation and development of water wave theories for engineering applications. Spec. Rep. No. 1, U.S. Army Coast. Eng. Res. Center, Ft. Belvoir, Va.
- JOURNEL, A. C. (1974). Geostatistics for conditional simulation of ore bodies. Economic Geology, Vol. 69, pp 673-687.
- SCHEUER, E. and STOLLER, D. S. (1962). On the generation of normal random vectors. Technometrics, Vol.4, pp 278-281.

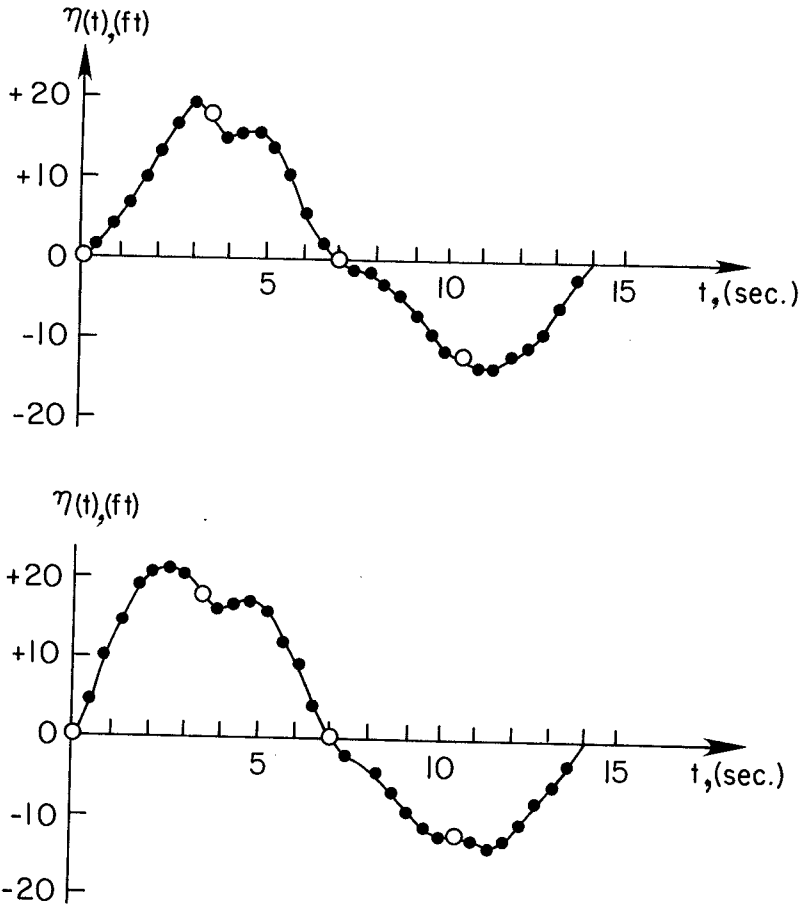


Fig. 1. Example A. Two simulations of the conditional wave profile.

Table 1. Wave profiles from numerical solutions of wave theory.^{1,3} (H = wave height, H_B = breaking wave height, L = wave length, L_0 = deep water wave length, d = water depth, η = elevation above mean water level, θ = phase within wave = $2\pi x/L$, where x = distance from crest horizontally.)

Case	H/H_B	H/L_0	H/d	L/L_0	d/L_0	η/H values									
						θ (degrees)	0	10	20	30	50	75	100	130	180
1-A	.25	.00390	.194829	.119648	.002000	.910	.600	.199	.009	.080	-.090	-.090	-.090	-.090	-.090
1-B	.50	.000779	.389717	.128262	.002000	.938	.413	.049	-.039	-.062	-.061	-.061	-.062	-.062	-.062
1-C	.75	.001169	.584426	.137070	.002000	.951	.287	.002	-.042	-.050	-.048	-.048	-.049	-.049	-.049
1-D	1.00	.001564	.782113	.146465	.002000	.959	.210	-.014	-.039	-.043	-.040	-.040	-.041	-.041	-.041
2-A	.25	.000974	.194887	.186504	.005000	.857	.713	.424	.177	-.060	-.129	-.141	-.143	-.143	-.143
2-B	.50	.001946	.389164	.199023	.005000	.904	.606	.228	.031	-.079	-.095	-.096	-.096	-.096	-.096
2-C	.75	.002925	.585097	.210547	.005000	.927	.470	.116	-.014	-.068	-.072	-.072	-.073	-.073	-.073
2-D	1.00	.003884	.776719	.222852	.005000	.944	.341	.056	-.027	-.055	-.056	-.056	-.056	-.056	-.056
3-A	.25	.001948	.194817	.259570	.010000	.799	.723	.538	.329	.025	-.135	-.183	-.199	-.201	-.201
3-B	.50	.003886	.388630	.276172	.010000	.865	.692	.387	.153	-.061	-.123	-.133	-.135	-.135	-.135
3-C	.75	.005821	.582125	.291992	.010000	.898	.596	.251	.059	-.072	-.099	-.102	-.102	-.102	-.102
3-D	1.00	.007753	.775326	.308203	.010000	.922	.460	.154	.015	-.064	-.077	-.078	-.078	-.078	-.078
4-A	.25	.003902	.195117	.358594	.020000	.722	.682	.575	.431	.146	-.089	-.204	-.266	-.278	-.278
4-B	.50	.007772	.388580	.379687	.020000	.810	.715	.506	.294	.010	-.131	-.174	-.188	-.190	-.190
4-C	.75	.011678	.583909	.401172	.020000	.858	.667	.383	.173	-.041	-.119	-.137	-.141	-.142	-.142
4-D	1.00	.015553	.777657	.422461	.020000	.889	.583	.284	.101	-.055	-.101	-.110	-.112	-.111	-.111
5-A	.25	.009752	.195032	.541016	.050000	.623	.603	.548	.465	.257	.007	-.177	-.334	-.377	-.377
5-B	.50	.019505	.390096	.566016	.050000	.716	.673	.562	.420	.150	-.077	-.196	-.269	-.284	-.284
5-C	.75	.029163	.583254	.597070	.050000	.784	.687	.498	.318	.059	-.106	-.175	-.209	-.216	-.216
5-D	1.00	.038997	.779945	.627344	.050000	.839	.582	.363	.207	.012	-.096	-.137	-.156	-.161	-.161

Table 1 continued.

Case	H/H _B	H/L ₀	H/d	L/L ₀	d/L ₀	η/H values								
						θ	5	10	20	30	50	75	100	130
6-A	.25	.018312	.183115	.718164	.100002	.571	.558	.519	.458	.293	.061	-.144	-.360	-.429
6-B	.50	.036631	.366304	.743750	.100002	.642	.617	.549	.452	.232	-.009	-.178	-.320	-.358
6-C	.75	.054927	.549254	.783203	.100002	.713	.657	.530	.390	.146	-.061	-.180	-.266	-.287
6-D	1.00	.073041	.730398	.824414	.100002	.782	.594	.417	.279	.079	-.071	-.151	-.205	-.218
7-A	.25	.031267	.156335	.899219	.199999	.544	.533	.501	.450	.306	.087	-.124	-.370	-.456
7-B	.50	.062490	.312451	.931055	.199999	.593	.576	.527	.453	.270	.038	-.152	-.345	-.407
7-C	.75	.093785	.468925	.981055	.199999	.653	.616	.528	.420	.207	-.010	-.165	-.305	-.347
7-D	1.00	.124492	.622465	1.035156	.199999	.724	.580	.443	.326	.137	-.033	-.147	-.247	-.276
8-A	.25	.041995	.083990	1.013086	.499998	.534	.524	.494	.447	.310	.097	-.116	-.373	-.466
8-B	.50	.083974	.167949	1.059180	.499998	.570	.555	.514	.450	.285	.061	-.138	-.356	-.430
8-C	.75	.125988	.251977	1.125195	.499998	.611	.586	.521	.434	.243	.025	-.150	-.329	-.389
8-D	1.00	.168087	.336176	1.193750	.499998	.677	.572	.456	.355	.177	-.002	-.140	-.278	-.323
9-A	.25	.042615	.042615	1.017578	.999996	.534	.523	.494	.446	.310	.097	-.116	-.373	-.446
9-B	.50	.085197	.085197	1.065234	.999996	.569	.554	.513	.450	.286	.062	-.137	-.356	-.431
9-C	.75	.128025	.128025	1.132813	.999996	.609	.585	.522	.436	.245	.026	-.149	-.330	-.391
9-D	1.00	.169650	.169650	1.210937	.999996	.661	.595	.483	.375	.187	-.002	-.146	-.291	-.339
10-A	.25	.042602	.021301	1.017773	1.999993	.533	.523	.494	.446	.310	.097	-.116	-.374	-.467
10-B	.50	.085218	.042609	1.065234	1.999993	.569	.554	.513	.450	.286	.062	-.137	-.356	-.413
10-C	.75	.127534	.063767	1.134375	1.999993	.608	.584	.521	.435	.245	.026	-.149	-.331	-.392
10-D	1.00	.170401	.085201	1.222070	1.999993	.657	.603	.496	.385	.189	-.004	-.148	-.284	-.343

Table 2. Conditional simulation for v_x and v_y associated with the specified wave profile and directional spectrum.

<u>n</u>	<u>η</u>	<u>$v_x(Z=0)$</u>	<u>$v_y(Z=0)$</u>
0	18.5	12.1	.11
2	15.5	12.8	.14
4	8.8	8.6	.16
6	2.5	5.0	.17
8	- 3.0	2.7	.13
10	- 5.4	- 1.7	.06
12	- 9.4	- 4.8	-.03
14	-10.9	- 5.0	-.11
16	-11.5	- 5.6	-.19
18	-10.5	- 7.13	-.16
20	- 9.4	- 8.1	-.11
22	- 5.4	- 7.0	-.04
24	- 3.0	- 5.6	.02
26	2.5	- 3.8	.04
28	8.8	2.8	.06
30	15.5	7.2	.08

WIND WAVES TRANSMISSION THROUGH
POROUS BREAKWATER

by

Stanisław R. Massel¹ and Piotr Butowski²

INTRODUCTION

Rubble - mound breakwaters are designed to protect exposed marine areas from excessive wave activity. The resulting interaction of the incident waves with the rubble units is extremely complex due to the variable reflective and frictional properties of the permeable structure. In the past decade considerable effort has been expended to derive rational methods for of such type structure. The theoretical and experimental investigations have been focused especially on the prediction of the reflection and transmission of regular waves incident to breakwater. Sollitt and Cross /1972/ presented the analytical approach to the problem based on the assumption that the original nonlinear governing equation of the wave motion into porous media may be replaced by a linear one so as to give the same average rate of dissipation/Lorentz approximation/. Under the assumption that severe wave conditions for most breakwaters correspond to relatively long waves, the considerably simple solutions were developed by Kondo and Toma /1972/ and in series of papers by Madsen and co-authors /1974, 1977, 1978/. Madsen's solutions follows rather a physical than mathematical rigorous approach to the problem. The momentum equation evaluated him explains the influence of the inertia force associated with the unsteady flow around the solid particles. Very careful analytical examination of this problem for the long waves past the narrow gaps and holes has been presented by Mei et al. /1974/. The study indicate that apparent mass term can be ignored in most practical cases. The number of studies concerning reflection and transmission of waves by breakwaters conducted in the field are

¹Asst. Prof., ² Res. Asst., Institute of Hydroengineering of the Polish Academy of Sciences, Gdańsk, Poland.

very few. Thoratou and Calhoun /1972/ reported the results of the field measurements at the rubble - mound breakwater in Monterey Harbor, California. The incident wave motion was measured at two locations in front of the breakwater in order to resolve the incident and reflected wave components; the transmitted wave was measured at one point behind the breakwater. The incident, reflected and transmitted power spectra were next calculated using the linear wave theory. This model is not truly predictive in that it relies on the knowledge of the wave records at the three locations near the breakwater in any particular case.

For more realistic representation of the interaction between ocean - wind waves and the rubble - mound breakwater, the consideration of the random character of the wave motion is needed.

Thus, the probability theory is the natural frame of reference for the description of such time - varying quantities. For the incident wave the Gaussian model involving superposition of linear waves predicts all the probability properties of the sea surface. Unfortunately, the wave motion into porous media cannot be considered linear.

Massel and Mei /1977/ presented the analytical theory for random waves passing a perforated and porous breakwater. However, these theories are approximate for the shallow coastal zone where the energy of the incident wave is concentrated in the long - wave part of the spectrum. The quadratic damping term is treated by the stochastic equivalent linearization technique. They defined the statistical transmission and reflection coefficients in terms of the standard deviations and the wave spectra.

In this paper an extension of previous work is given. The various aspects of the rectangular porous breakwater - wave interaction are considered under the assumption that the incident wave spectrum is arbitrary. To simplify the analysis the damping terms in the body of breakwater will be replaced by an equivalent linear term. The standard deviations for both wave velocity components are then calculated assuming that they are non - correlated random functions with zero mean values. Results obtained from this analysis are compared with the field measurements of reflection and transmission characteristics of porous breakwater and numerical examples are given.

We consider the motion of an incompressible inviscid fluid and Cartesian axes x, z ; with z increasing vertically upward. The homogeneous, rectangular breakwater is subjected to normally incident wind - induced waves. The depth of the water is constant.

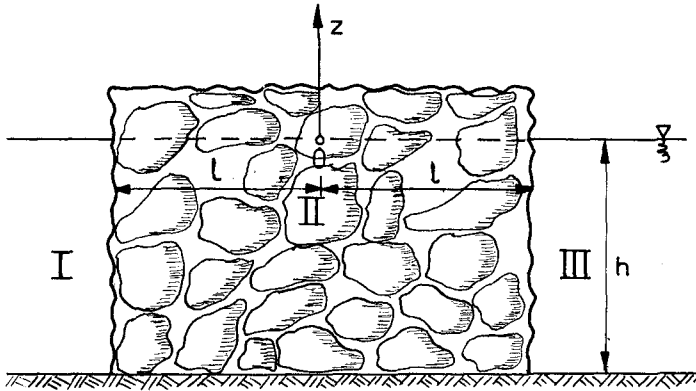
ANALYSISGoverning Equations

Fig. 1: Definition Sketch

Three different computational regions are identified in Fig. 1.

In the region I, the random incident wave is assumed to be Gaussian with zero mean and is represented by the following Fourier - Stjeltjes integral:

$$\zeta_i = \int_{-\infty}^{\infty} dA(\omega) e^{i(kx - \omega t)} \quad /1/$$

where $\omega^2 = gk \cdot \tanh(kh)$

For a stationary and homogeneous process, the amplitude spectrum dA satisfies:

$$E[dA(\omega) \cdot dA^*(\omega')] = \frac{1}{2} \cdot S(\omega) \cdot \delta(\omega - \omega') \cdot d\omega d\omega' \quad /2/$$

The wave motion in region I consists of an incident and a reflected wave. Thus, the resultant velocity potential takes the form

$$\Phi_1(x, z, t) = \operatorname{Re} \int_{-\infty}^{\infty} \frac{-ig}{\omega} \cdot e^{-i\omega t} \cdot \left[e^{ik(x+l)} - e^{-ik(x+l)} \right] \cdot \frac{\cosh k(z+h)}{\cosh kh} + \sum_{\alpha} M_{\alpha}(\omega) \cdot e^{\alpha(x+l)} \cdot \frac{\cos \alpha(z+h)}{\cos \alpha h} \cdot dA(\omega) \quad /3/$$

in which the wave number α must satisfy the following dispersion relation

$$\frac{\omega^2}{g} + \alpha \cdot \operatorname{tg}(\alpha h) = 0 \quad /4/$$

In the region III, the wave motion is simply transmitted wave. The velocity potential may be expressed as

$$\Phi_3(x,z,t) = \operatorname{Re} \int_{-\infty}^{\infty} \frac{ig}{\omega} \cdot e^{-i\omega t} \cdot \sum_{\alpha} \left\{ N_{\alpha}(\omega) \cdot e^{\alpha(l-x)} \cdot \frac{\cos \alpha(z+h)}{\cos \alpha h} \right\} dA(\omega) /5/$$

A complete mathematical description of flow through a coarse granular material in the region II would be a very difficult and tedious task. A more reasonable approach to the problem is to determine the important physical and hydraulic properties of the media and then evaluate the macroscopic flow field in terms of these properties. The analysis yields the velocities and pressures which are averaged over the small but finite pore volumes. Thus, for porous media ($-h \leq z \leq 0, -l \leq x \leq l$), we write the equation of motion in the form

$$\frac{\partial \vec{u}_2}{\partial t} = -\frac{1}{\rho} \cdot \nabla(p_2 + \gamma z) + \text{resistance forces} \quad /6/$$

in which \vec{u}_2 - the "seepage velocity", p_2 - water pressure.

In order to specify the resistance forces, the equation proposed by Forchheimer is adopted in the form

$$\frac{\partial \vec{u}_2}{\partial t} = -\frac{1}{\rho} \nabla(p_2 + \gamma z) - \frac{\nu \cdot n}{K} \cdot \vec{u}_2 - \frac{C_f \cdot n^2}{\sqrt{K}} \cdot |\vec{u}_2| \cdot \vec{u}_2 \quad /7/$$

where ν - kinematic viscosity of fluid, K - intrinsic permeability, n - porosity, C_f - coefficient dependent on properties of porous media.

According to Arbbabhirama and Dinoy /1973/

$$C_f = 100 \left[d_m \left(\frac{n}{K} \right)^{1/2} \right]^{-3/2} \quad /8/$$

in which d_m - particle mean diameter of porous media. Although the damping term in Eq. /7/ is derived from steady state concepts it is assumed that it accounts for the damping due to the instantaneous velocity occurring at all phases of the wave cycle. Thus, the linear term dominates when velocities are low and the turbulent term dominates when velocities are high. The assumptions which limit the application of the expression /7/ are that convective accelerations be and that the motion be periodic with frequency low enough to maintain the validity of the damping term. Thus, Eq./7/ applies when the wave lengths of the particular spectral components are long with respect to wave amplitudes and media grain size.

An analytical solution to Eq.7 is possible after its linearization. It is done using a technique that approximate the turbulent damping condition inside the porous media. The dissipative nonlinear stress term in Eq. 7 is

replaced by an equivalent stress term linear in \vec{u}_2 , i.e.

$$\frac{\nu \cdot n}{K} \vec{u}_2 + \frac{C_f \cdot n^2}{\sqrt{K}} \cdot |\vec{u}_2| \cdot \vec{u}_2 \longrightarrow f_e \cdot \omega_p \cdot n \cdot \vec{u}_2 \quad /9/$$

in which f_e is a dimensionless friction /damping/ coefficient and ω_p is the peak frequency. To evaluate f_e in terms of the known damping law in the deterministic case, we choose f_e such that the total rate of energy dissipation, integrated over the breakwater cross section and averaged over period is unchanged. Alternatively, for random waves one may minimize, the mean square error ϵ^2 when the mean is taken over time in the stochastic sense as well as space. The relation between f_e and the physical parameters of motion is developed in Appendix A. As a motion inside the porous media is a result of the harmonic excitation, it may be written as

$$\vec{u}_2(x, z, t), p_2(x, z, t) = [\vec{u}_2^{\sim}(x, z), \tilde{p}_2(x, z)] \cdot e^{-i\omega t} \quad /10/$$

Combining Eqs. 7 and 10 and taking into account Eq. 9 and the equation of continuity $\nabla \vec{u}_2 = 0$, gives

$$\frac{\partial \Phi_2}{\partial t} + \frac{1}{g} (p_2 + \gamma z) + f_e \cdot \omega_p \cdot n \cdot \Phi_2 = 0 \quad /11/$$

in which Φ_2 - velocity potential in the porous media. Eq. 11 yields the surface displacement in the form

$$\zeta_2 = -\frac{1}{g} \left(\frac{\partial \Phi_2}{\partial t} + f_e \cdot \omega_p \cdot n \cdot \Phi_2 \right)_{z=0} \quad /12/$$

Substituting the above expression into the kinematic free surface condition leads to its final form in the term of potential function

$$g \cdot \frac{\partial \Phi_2}{\partial z} - \omega^2 \left(1 + i \cdot n \cdot f_e \cdot \frac{\omega_p}{\omega} \right) \cdot \Phi_2 = 0 \quad /13/$$

At the bottom ($z = -h$), the foundation is taken to be impervious, i.e.

$$\frac{\partial \Phi_2}{\partial z} = 0 \quad /14/$$

Finally, in the region II we adopte the potential Φ_2 in the form

$$\Phi_2(x, z, t) = \mathcal{A} e \int_{-\infty}^{\infty} \frac{g \cdot e^{-i\omega t}}{\omega (i - n f_e \frac{\omega_p}{\omega})} \cdot \sum_{\psi} \left\{ [P_{\psi} \cdot e^{-\psi(x+l)} + Q_{\psi} \cdot e^{\psi(x-l)}] \cdot \frac{\cos \psi(z+h)}{\cos \psi h} \right\} \cdot dA(\omega) \quad /15/$$

in which γ - complex wave number being a solution of the following dispersion relation

$$\omega^2 \left(1 + i \cdot n \cdot f_e \cdot \frac{\omega_p}{\omega} \right) + g \cdot \gamma \cdot \operatorname{tg}(\gamma h) = 0 \quad /16/$$

Eq. 16 has an infinite number of complex roots.

Matching Conditions

For the moment we assume that porosity n , permeability K and the linearization coefficient f_e are known. The general solutions developed in the proceeding section then contain 4 unknown functions of frequency: M_α , N_α , P_ψ and Q_ψ . To determine the functions the general solutions for the horizontal mass flux and pressure are matched at $x = \pm l$. This yields 4 equations from which the 4 unknowns may be determined.

It is of interest to note that the matching conditions may be expressed in the form of set of two equations with an infinite number of solutions for coefficients M_α and N_α /Massel, Butowski 1980/.

Solving this set by the standard Galerkin's method we obtain the following expressions for coefficients P_ψ and

$$Q_\psi \quad P_\psi + e^{-2\psi l} \cdot Q_\psi = \sum_{\alpha} L_{\psi\alpha} \cdot M_\alpha \quad /17/$$

$$e^{-2\psi l} \cdot P_\psi + Q_\psi = \sum_{\alpha} L_{\psi\alpha} \cdot N_\alpha$$

in which

$$L_{\psi\alpha} = \frac{1 + i \cdot n \cdot f_e \cdot \frac{\omega_p}{\omega} \cdot \cos(\psi h)}{B_\psi^2 \cdot \cos(\alpha h)} \cdot \int_{-h}^0 \cos\psi(z+h) \cdot \cos\alpha(z+h) dz \quad /18/$$

and

$$B_\psi = \left\{ \frac{h}{2} \left[\frac{\sin(2\psi h)}{2\psi h} + 1 \right] \right\}^{1/2} \quad /19/$$

Transmission and reflection coefficients

Taking the analogy to the deterministic waves we adopted the following expressions for the statistical transmission and reflection coefficients

$$K_r = \frac{\sigma_r}{\sigma_i} = \left[\frac{\int_0^\infty S_r(\omega) d\omega}{\int_0^\infty S(\omega) d\omega} \right]^{1/2} \quad /20/$$

$$K_t = \frac{\sigma_t}{\sigma_i} = \left[\frac{\int_0^\infty S_t(\omega) d\omega}{\int_0^\infty S(\omega) d\omega} \right]^{1/2} \quad /21/$$

where $S_r(\omega)$ - spectrum of reflected waves, $S_t(\omega)$ - spectrum of transmitted waves, $S(\omega)$ - incident wave spectrum.

The reflected wave spectrum can be expressed as

$$S_r(\omega) = S_{1r}(\omega) = \left[\hat{M}_k(\omega) \right]^2 \cdot S(\omega); \quad \hat{M}_k(\omega) = \left| M_k(\omega) - 1.0 \right|_{\alpha = -ik/22/}$$

and for the transmitted wave spectrum we have

$$S_t(\omega) = S_3(\omega) = \left[\hat{N}_k(\omega) \right]^2 \cdot S(\omega); \quad \hat{N}_k(\omega) = \left| N_k \right|_{\alpha = -ik} / 23/$$

The spectrum $S_1(\omega)$ for the total wave on the incidence side ($x < -l$) is

$$S_1(\omega, x) = \left\{ \left[1 + \hat{M}_k^2(\omega) \right] + 2 \cdot \hat{M}_k(\omega) \cdot \cos[2k(x+l) - \varphi_k] + \left(M_{\Sigma_1}(\omega, x) \right)^2 + 2 \cdot M_{\Sigma_1}(\omega, x) \cdot \cos[k(x+l) - \varphi_{\Sigma_1}] + 2 \cdot \hat{M}_k(\omega) \cdot M_{\Sigma_1}(\omega, x) \cdot \cos[k(x+l) - \varphi_k + \varphi_{\Sigma_1}] \right\} \cdot S(\omega) \quad /24/$$

in which

$$M_{\Sigma_1}(\omega, x) \cdot e^{i\varphi_{\Sigma_1}} = \sum_{\alpha} e^{\alpha(x+l)} \cdot \hat{M}_{\alpha}(\omega) \cdot e^{i\varphi_{\alpha}}, \quad /25/$$

$\hat{M}_{\alpha}(\omega)$, φ_{α} - absolute value and phase angle of the complex M_{α} , respectively. \sum_{α} denotes summation over all the real values of α ; i.e. $\alpha = -ik$ is omitted from the sum.

It is of special interest to note that the spectrum $S_1(\omega)$ is also the function of distance from front face of the breakwater.

The transmitted waves at the arbitrary distance from the lee face are described by the spectrum in the form

$$S_3(\omega, x) = \left| \sum_{\alpha} N_{\alpha}(\omega) \cdot \exp \alpha(l-x) \right|^2 \cdot S(\omega) \quad /26/$$

When $x \rightarrow \infty$, we obtain $S_3(\omega, x) \rightarrow S_t(\omega)$.

It is easy to demonstrate that when $f_e = 0$ /no break-water/, Eqs. 20 and 21 reduce to

$$K_r = 0 \quad \text{and} \quad K_t = 0 \quad /27/$$

NUMERICAL RESULTS

The application of the semi - empirical theory in the previous section is illustrated first for the porous breakwater of thickness $2l = 15$ m. Let the water depth be $h = 10$ m. Assume that the wind velocity is $U_{10} = 20$ m/sec and the fetch $X = 100$ km. The frequency at the spectral peak is $\omega_p = 0.821$ rad/sec and the mean wave height is $H = 2.23$ m. The incident wave energy distribution let to be represented by the JONSWAP formula /Hasselmann et al., 1973/. For a prototype rubble diameter $d = 1$ m/,

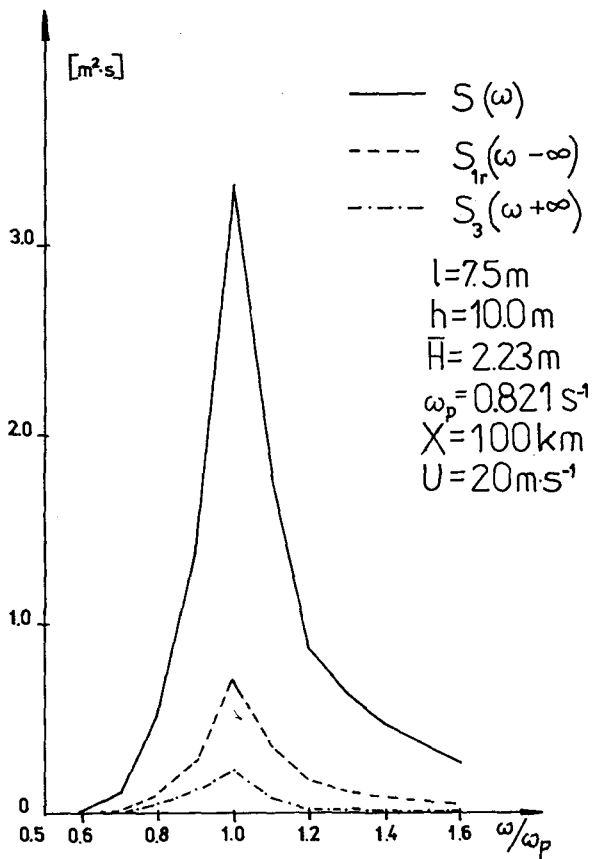


Fig.2 Spectra of the incident $S(\omega)$ and transmitted $S_3(\omega)$ and reflected $S_{1r}(\omega)$ waves.

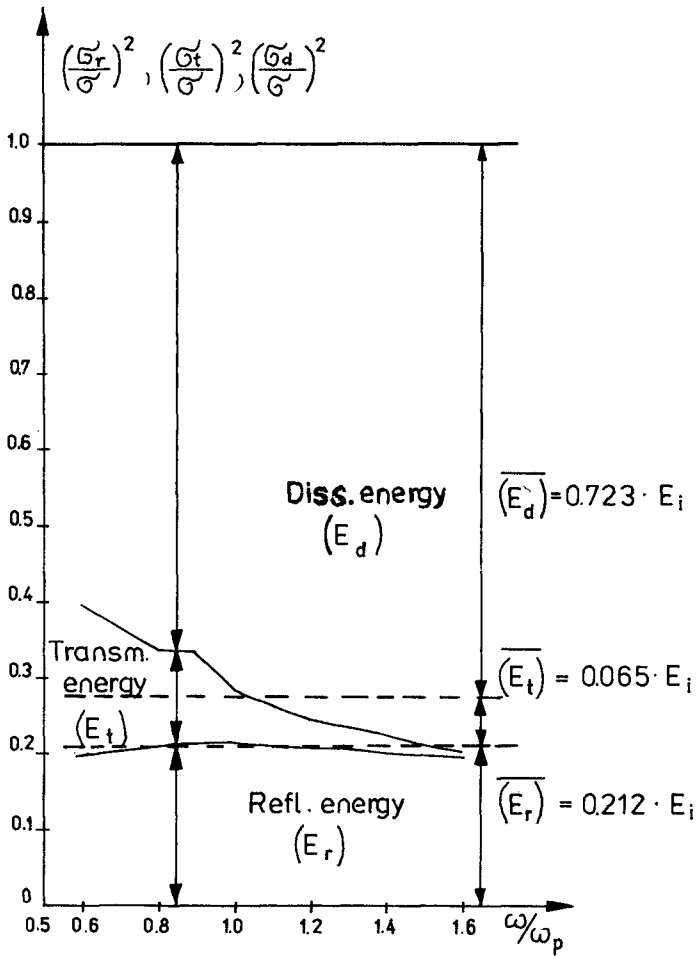


Fig.3 Frequency dependence of the transmission, reflection and dissipation energy.

the permeability and porosity is estimated from the model tests /see Appendix A/ to be

$$K = K_m \left(\frac{d}{d_m} \right)^2 = 5.52 \cdot 10^{-4} \text{ m}^2, \quad n = 0.437, \quad C_f = 0.228 \quad /28/$$

From the Appendix A follows that equivalent linear friction coefficient is $f_e = 4.2654$. Finally by performing the numerical integration in Eqs. 20 and 21 the statistical transmission and reflection coefficients are found, $K_t = 0.255$ and $K_r = 0.460$. In the Fig.2 the spectra of the incident wave, and the reflected and transmitted wave are shown.

Fig.3 shows the frequency dependence on the respected energies. From this Figure it is evident that almost 73 % of the mean value of incident energy is dissipated within the body of breakwater. The transmitted energy varies considerably with frequency from a maximum at low frequency and decreasing with increasing frequency. The reflection part of energy is almost constant in the band of frequency under consideration. Small maximum of reflected energy is observed at the frequency of spectral peak in $S(\omega)$ function. Both energies are decreasing for high frequencies.

The measurements and calculations performed by Thornton and Calhoun /1972/ in California represent of some opportunity to check the developed theory against the prototype data. In the fig. 4 the cross section of the Monterey Breakwater is shown.

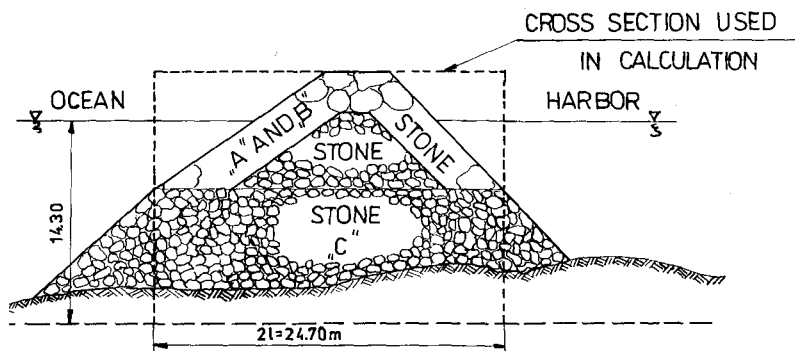


Fig. 4 Monterey Breakwater cross section

As the preceding analysis is limited to permeable structure of rectangular form only, we adopte the equivalent rectangular cross section to the Monterey Breakwater which has approximately the same submerged volume /see Fig.4/. The hydraulic properties of the breakwater /permeability and porosity/ are roughly estimated taking into account that the structure is a mound of stones of different sizes and shapes, mainly of "C" type. The averaged total weight of the stone equal to $\sim 10^4$ N with specific gravity $\gamma \approx 26 \cdot 10^3 \text{ N/m}^3$ is used in the calculation. Then, the mean diameter of the stone is approximately $d_m \approx 0.8$ m.

Assuming that the prototype stone angularity and packing are the same as in the small scale rubble investigated by Sollitt and Cross /1972/ we can calculate the permeability K and the coefficient C_f . The incident wave spectrum is specify as in field investigation for December 1, 1970 at 2330 hr /see Tabl.1 in Thornton and Calhoun paper/.

Performing the numerical calculation of the K_t and K_r coefficients we obtain:

$$K_r = 0.448, K_t = 0.344, K_d = [1 - (K_r^2 + K_t^2)]^{1/2} = 0.825 \quad /29/$$

While the field measurement yields

$$K_r = 0.52, K_t = 0.11, K_d = 0.84 \quad /30/$$

The above numbers suggest that the transmission rate of energy in the field is higher than that predicted by theory. The reflection rate of energy is almost the same in both methods. The coefficient K_d represents the rate of energy which is dissipated in the body of breakwater. A possible explanation for this discrepancy is probably associated with the rectangular shape and value of permeability introduced in the analysis. Especially, the knowledge of the hydraulic properties of the porous material of Monterey Breakwater is rather poor. It is worthwhile to note that the experimental results for the reflection coefficient and dissipation rate are in good agreement with the theoretical values.

CONCLUSIONS

The present analysis was undertaken in order to extend a previous simplified theory for the determination of transmission and reflected characteristics of porous breakwaters subjected to the action of the wind - induced waves. The extension consisted of a more rigorous analysis of wave motion inside the breakwater space

when the incident wave spectrum may be arbitrary. The original nonlinear equation of motion into porous structure was linearized using statistical linearization technique. The computed output consists of the spectral density functions for the reflected and transmitted waves. The statistical transmission and reflection coefficients are introduced in terms of the standard deviations and the wave spectra.

From a comparison with experimental data it appears that the method may be valuable in practical applications. Probably more good quality experimental data is needed for the determination of the applicability range of the method.

APPENDIX A

Equivalent friction coefficient

Let the error between nonlinear and linear resistance forces be

$$e(x, z, t) = \frac{\gamma n}{K} \vec{u}_2 + \frac{C_f \cdot n^2}{\sqrt{K}} |\vec{u}_2| \cdot \vec{u}_2 - \int e \cdot \omega_p \cdot n \cdot \vec{u}_2 \quad /31/$$

Upon minimizing the mean square error

$$\frac{1}{2lh} \int_{-h}^l \int_{-l}^l E[e^2] dx dz \quad /32/$$

one gets

$$f_e = \frac{1}{n \cdot \omega_p} \left[a + b \cdot \frac{\int_{-l}^l \int_{-h}^l E[|\vec{u}_2| \cdot \vec{u}_2^2] dx dz}{\int_{-l}^l \int_{-h}^l E[\vec{u}_2^2] dx dz} \right] \quad /33/$$

in which

$$a = \frac{\gamma n}{K}, \quad b = \frac{C_f \cdot n^2}{\sqrt{K}} \quad /34/$$

The symbol $E[]$ represents the statistical average.

In order to calculate the statistical moments in Eq. 33 we assume that in the breakwater space the both wave velocity components u_2 and v_2 are the independent random values with gaussian probability density. The mean values are zero and the standard deviations are equal to σ_{u_2} and σ_{v_2} , respectively.

Thus, the probability density function for $U = |\vec{u}_2| = (u_2^2 + v_2^2)^{1/2}$ takes the form /Papoulis/

$$p(U) = p(|\vec{u}_2|) = \frac{U}{\sigma_{u_2} \cdot \sigma_{v_2}} \cdot I_0(m_1 \cdot U^2) \cdot \exp(-m_2 \cdot U^2) /35/$$

where I_0 - modified Bessel function and

$$m_1 = \frac{1}{4} \cdot \frac{\sigma_{u_2}^2 - \sigma_{v_2}^2}{\sigma_{u_2}^2 \cdot \sigma_{v_2}^2}, \quad m_2 = \frac{1}{4} \cdot \frac{\sigma_{u_2}^2 + \sigma_{v_2}^2}{\sigma_{u_2}^2 \cdot \sigma_{v_2}^2} \quad /36/$$

It can be easily demonstrated that

$$p_2(u_2) = p_2(\vec{u}_2^2) = \frac{1}{2 \cdot \sigma_{u_2} \cdot \sigma_{v_2}} \cdot I_0(m_1 \cdot u_2) \cdot \exp(-m_2 \cdot u_2) \quad /37/$$

and

$$p_3(u_3) = p_3(\vec{u}_2^2 | \vec{u}_2) = \frac{1}{3 \cdot \sigma_{u_2} \cdot \sigma_{v_2} \cdot u_3^{1/3}} \cdot I_0(m_1 \cdot u_3^{1/3}) \cdot \exp(-m_2 \cdot u_3^{1/3}) \quad /38/$$

By virtue of the definition of the mean of the random value we obtain

$$E[\vec{u}_2^2] = \sigma_{u_2}^2 + \sigma_{v_2}^2$$

$$E[\vec{u}_2^2 | \vec{u}_2] = \frac{12 \cdot \sqrt{\pi} \cdot \sigma_{u_2}^4 \cdot \sigma_{v_2}^4}{(\sigma_{u_2}^2 + \sigma_{v_2}^2)^{5/2}} \cdot \left(\Gamma(5/4) \cdot \Gamma(7/4) \right)^{-1} \quad /39/$$

$$\sum_{n=0}^{\infty} \frac{\Gamma(5/4+n) \cdot \Gamma(7/4+n)}{(n!)^2} \cdot \left(\frac{\sigma_{u_2}^2 - \sigma_{v_2}^2}{\sigma_{u_2}^2 + \sigma_{v_2}^2} \right)^{2n} \quad /40/$$

Substituting Eqs. 39 and 40 into Eq. 33 we are able to calculate the equivalent friction coefficient f_e . To initiate the solution, a value for f_e is assumed / $f_e \approx 1.0$ is suitable/. Then the appropriate potentials are evaluated. The standard deviations of the velocity components are extracted and substituted into linearization condition to compute f_e . If the result is different from the assumed value it is necessary to iterate in order to obtain next value for f_e .

REFERENCES

1. Arbbahhirama, A., and Dinoy, A.A., "Friction Factor and Reynolds Number in Porous Media Flow", Jour. of the Hydr. Div., Vol. 99, HY6, 1973.
2. Hasselmann, K. et al., Measurements of Wind - Wave Growth and Swell Decay during the Joint North Sea Wave Project /JONSWAP/, Dtsch. Hydrogr., Z., 1973.
3. Kondo, H., and Toma, S., "Reflection and Transmission for a Porous Structure", Proc. of the 13th Coastal Eng. Conf., 1972.
4. Madsen, O.S., "Wave Transmission through Porous Struc-

- tures", Jour. of the Waterways, Harb. and Coastal Eng. Div., Vol. 100, WW3, 1974.
5. Madsen, O.S., and White, S.M., "Wave Transmission through Trapezoidal Breakwaters", Proc. of the 15th Coastal Eng. Conf., 1977.
 6. Madsen, O.S., Shusang, P., and Hanson, S.A., "Wave Transmission through Trapezoidal Breakwaters", Proc. of the 16th Coastal Eng. Conf., 1978.
 7. Massel, S.R., and Mei, C.C., "Transmission of Random Wind Waves through Perforated or Porous Breakwaters", Coastal Eng., Vol. 1, No.1, 1977.
 8. Massel, S., and Butowski, P., "Transmission of Wind - Induced Waves through Porous Breakwater", Tech. Report, Inst. of Hydroengineering, Polish Academy of Sciences, 1980 /in Polish/.
 9. Mei, C.C., Liu, P.L.F., and Ippen, A.T., "Quadratic Loss and Scattering of Long Waves, Jour. of the Waterways, Harb. and Coastal Eng. Div., Vol.100, WW3, 1974.
 10. Papoulis., A., Probability, Random Variables, and Stochastic Processes, Mc Graw - Hill., Inc. 1965.
 11. Sollitt, C.K., and Cross, R.H., "Wave Reflection and Transmission at Permeable Breakwaters", Technical Rep. No. 147, R.M.Parsons Lab., Department of Civil Eng., MIT, 1972.
 12. Thornton, E.B., and Calhoun, R.J., "Spectral Resolution of Breakwater Reflected Waves", Jour. of Waterways, Harb. and Coastal Eng. Div., Vol.98, WW4, 1972.

CHAPTER 20

FIELD MEASUREMENTS OF WIND WAVE KINEMATICS

by

J.A. Battjes¹⁾ and J. van Heteren²⁾

ABSTRACT

Measurements of surface elevations and three orthogonal subsurface velocity components have been performed from a platform in the southern North Sea, off the Dutch coast, in order to check linear spectral transfer functions relating subsurface velocities to surface elevations, to obtain information about the directional properties of the waves, and to investigate the velocity statistics. The data obtained as far do not cover a sufficiently wide range of conditions to permit general conclusions. Some preliminary results are presented in the paper.

1. INTRODUCTION

Routine instrumental measurements of wind wave parameters are usually restricted to the free surface fluctuation. However, in applications in offshore and coastal engineering one needs information about the internal wave kinematics. Examples are the calculation of the loads on a structure due to a given wave field, or the calculation of densities and fluxes of energy and momentum, which are needed in problems of wave shoaling and refraction, and the prediction of nearshore currents.

Transforming data on surface elevations into velocity data can be accomplished in different ways. These can broadly be classified into two groups, that of a quasi-deterministic non-linear, individual wave analysis, and that of a random linear spectral approach. The principal advantage of the latter is its superiority in dealing with aspects of randomness in time and space (short-crestedness) of the wind waves. Its main drawback is the restriction to linear problems, but there are developments towards the inclusion of some degree of nonlinearity in the formulations (see for example Sharma and Dean, 1979).

- 1) Professor, Department of Civil Engineering, Delft University of Technology, The Netherlands
- 2) Staff Member, Hydraulic Division, Deltadepartment, Rijkswaterstaat, The Hague, The Netherlands.

Until a few years ago, there have been rather few published experimental verifications of the linear spectral approach, and those were typically in waves of rather low steepness (Thornton and Krapohl, 1974). It was then decided to initiate a research project in The Netherlands, aimed at such verification, to be based on measurements off an available platform in the southern North Sea. More specifically, the aims were to test the validity of linear spectral transfer functions relating internal velocities to surface elevations, to check the applicability of the model of a Gaussian process to the velocities, and, in addition, to obtain data on the short-crestedness of wind waves.

Due to a variety of causes related to equipment and personnel, progress in this work has been below expectations. Meanwhile, a number of studies by others has been published in which aims were pursued similar to those of the present investigation, and in which significant results were obtained (Cavaleri et al, 1977; Forristall et al, 1978; Guza and Thornton, 1980). It was nevertheless deemed useful to continue the present work, inasmuch as it gives independent additional data, obtained in different geographical conditions, with different sensors, and in part analysed differently. However, due to the delays referred to above, the measurements do not yet cover a wide range of conditions, so that no general conclusions can be drawn. For that reason this paper is kept rather brief. It is planned to give a more extensive presentation elsewhere, after additional data have been obtained and analysed.

The contents of this paper are as follows. Section 2 contains a description of the platform used for the measurements, and of its location. In section 3 the sensors, the data logging system and the transmission are described. The data available at the moment of writing are described in section 4. The methods of estimation of the transfer function, wave direction and short-crestedness are dealt with in section 5. Examples and some results of the estimated transfer functions are presented in section 6, those of the wave directions and short-crestedness in section 7, and those of the statistical properties in section 8. Section 9 gives some preliminary conclusions.

2. LOCATION AND DESCRIPTION OF THE PLATFORM

The measurements were made from a platform (MPN) located in the southern North Sea, about 10 km off the Dutch Coast (see figure 1). The local depth is about 17 m below M.S.L., and the local mean tidal range is approximately 1.80 m.

The platform has been built on a jacket construction, made from tubular elements which are up to 0.80 m in diameter. At three of the four corners of the platform, vertical sensor supports have been mounted (figure 2). These supports are space trusses

consisting of tubes with diameters up to 0.15 m. They can be lifted out of the water for attachment, inspection and cleaning of sensors.

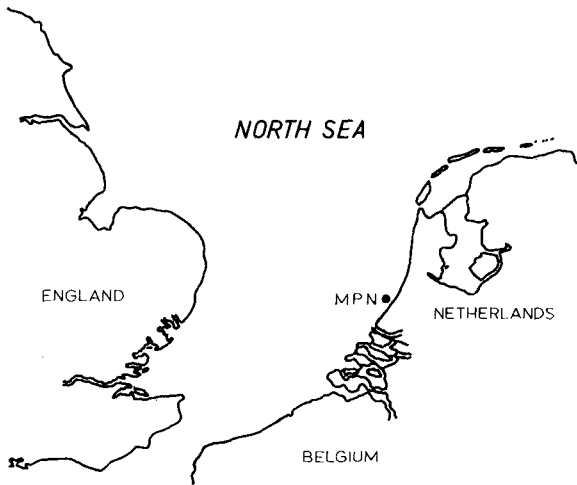


Figure 1: Location of the platform (MPN)

3. INSTRUMENTATION

The velocity meter used for the measurements described in this paper is based on the principle of travel time of acoustic pulses. A meter of this type designed for use in tidal rivers has been described by Botma (1978), who also designed the meters used in the present study.

At first the velocity meter consisted of only one pair of transducers/responders. The distance between this pair of transducers/responders was 1.71 m and they were mounted with the axis in the vertical position so that the vertical velocity component (w) could be measured. The calibration factor of this instrument was calculated using a nominal value of the speed of sound in sea water, and an effective travel distance which was 10 cm less than the actual distance between the sensors, to allow for wake effects.

The wave gauge used for these measurements of the surface elevation, a Baylorgauge, is based on the conductivity of water and it consists of two vertically tensed wires with a length of about 20 m. The distance between the two wires is 22.5 cm. Deviations from linearity and variations in calibration factors were both less than 0.5 %.

Both sensors were fixed to the sensor support situated at the

south west side of the platform, with the wave gauge in the centre of the sensor support and the velocity meter at the west side of the sensor support. The horizontal distance between the two sensors was 1.20 m. The elevation of the velocity meter was 5.70 m below M.S.L.



Figure 2: side-view of MPN (north-side)

Afterwards this velocity meter has been extended in such a way that three mutually orthogonal velocity components (u,v,w) could be measured. To that end three pairs of transducers/responders were mounted in a glued frame, see figure 3. This frame consists of copper pipes (outer diameter 50.4 mm) to minimize marine fouling. It was mounted outside the sensor support with one of its axes in the vertical position. The orientation of the other axes is arbitrary.

The distance from the vertical axis of the velocity meter to the center of the sensor support has been increased from 1.20 m to 1.75 m so as to decrease the influence of the sensor support and platform piles.

In contrast to the one-dimensional meter, the three-dimensional version compensates for variations in the speed of sound due to variations in temperature and salinity of the sea water. The calculated calibration factor was checked experimentally by oscillating the frame rectilinearly in a laboratory basin. It was found to be correct within 5%, except when the meter was oscillated exactly in line with two sensors measuring one component, in which case the

deviation was up to 10%. This phenomenon is ascribed to the wake development. Since in the field the flow is not rectilinear, this deviation in the calibration is not taken into account in the analysis.

The wave gauge used for the measurements with the extended velocity meter is a stiff step gauge with a length of 15 m. It measures the number of wet electrodes of known mutual distance (0.1 m), so that the calibration is trivial.

The horizontal distance between the two sensors is 1.75 m. The elevation of the velocity meter has been 4.91 m below M.S.L. and 7.94 m below M.S.L.

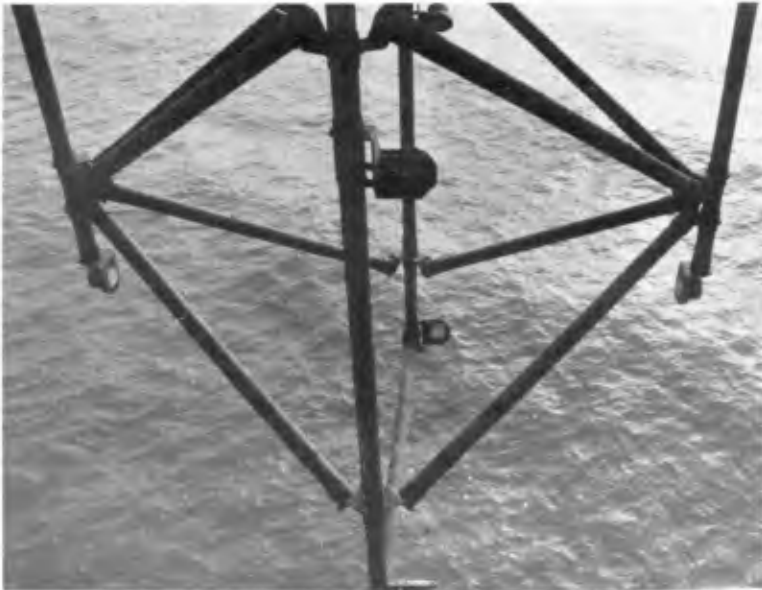


Figure 3: the three-dimensional velocity meter

Through a data logging system the measured quantities can be scanned at intervals of 0.25 s (per quantity). Because the different channels are scanned successively there is a time interval between two successive channels of 0.25 s divided by the number of channels of the data logging system, in this case 32.

The data are transmitted by an F.M. radio-link to a shore station where they are recorded on magnetic tape. At intervals of 5 min. the significant wave height and the total energy of the frequencies lower than .1 Hz are recorded as well (as part of another project).

4. DATA

The time of recording is normally chosen to be near slack water in order to minimize disturbances due to the wake of the platform and sensor piles.

With the original one-dimensional velocity meter 31 measurements have been made, simultaneous with measurements of the surface elevation, distributed over three days with different climatologic conditions.

With the extended velocity meter two sets of measurements have been performed at the time of writing. First, 26 measurements of the three velocity components only were made, distributed over 6 days. The depth of the centre of the frame was 4.91 m below M.S.L. Later, velocity measurements have been made simultaneous with those of the surface elevation. At the moment of writing 32 such measurements have been made, distributed over 6 days with different climatologic conditions. During the second set of measurements the depth of the sensor was larger, namely 7.94 m below M.S.L.

5. CALCULATIONS

The respective transfer functions are calculated by auto- and cross spectral analyses, which also yield phase and coherence information. Standard procedures as described by Bendat and Piersol (1971) and Jenkins and Watts (1968) have been used based on an F.F.T. algorithm. The length of the analyzed records has been taken 1800 s. For the calculations of the spectra the records are divided in 30 segments, each with duration of 60 s. Because no data window has been used the number of degrees of freedom is 60 and the resolution 0.0167 Hz.

The auto- and cross spectra of the vertical velocity w and the surface elevation ζ , written as S_{ww} , $S_{\zeta w}$ and $S_{\zeta\zeta}$, have been used to calculate the transfer function

$$H_{\zeta w} = |S_{\zeta w}|/S_{\zeta\zeta},$$

the phase function

$$\phi_{\zeta w} = (\arg S_{\zeta w})/S_{\zeta\zeta}$$

and the squared coherence function

$$\gamma_{\zeta w}^2 = |S_{\zeta w}|^2 / (S_{\zeta\zeta} S_{ww}).$$

The procedure sketched above cannot be used for the relation between the surface elevation and the horizontal velocity $\vec{u} = (u, v)$, because of the short-crestedness of the waves. Assuming the system to be free of noise, a transfer function can be estimated as

$$H_{\zeta \vec{u}} = \{(S_{uu} + S_{vv})/S_{\zeta\zeta}\}^{1/2}$$

Transfer functions calculated from the measurements as indicated above will in the following be referred to as "measured" transfer functions.

Assuming the water motion and the measurements to be linear and noise-free, the calculated auto- and crossspectra for (u, v, ζ) or (u, v, w) can be used to estimate directional properties of the waves by standard procedures (see Borgman, 1979, for a review). Via the auto spectra and cross spectra the truncated Fourier series and the parameters of the \cos^2 -model of the directional spectrum have been calculated, for different frequencies. From these results, short-crestedness parameters can be calculated, again as a function of frequency.

In addition to the spectrally resolved short-crestedness parameters referred to above, an overall (i.e. non-spectral) measure of the short-crestedness of the waves can be defined.

Generally the mean squares and the mean product of u and v are non-zero. Let (u_x, v_x) denote the values of (u, v) in a reference frame in which $\overline{u_x v_x} = 0$. The axes of this reference frame then define the principal directions, and $(\overline{u_x^2}, \overline{v_x^2})$ represent the principal values of the velocity product tensor. An overall measure of the short-crestedness of the waves can then be defined as:

$$\Gamma = \frac{\overline{v_x^2}}{\overline{u_x^2}},$$

such that by definition $0 \leq \Gamma \leq 1$. Values of this short-crestedness parameter have been calculated from the data.

From the mean squares and the mean product of u and v , an overall principal wave direction can be obtained, e.g. by using the Mohr circle.

In addition to these calculations the statistical properties of the surface elevation and the velocity components are investigated. The distributions of the instantaneous values are compared with the normal distribution.

6. COMPARISON WITH LINEAR THEORY

6.1. The transfer function of the vertical velocity component and the surface elevation.

As indicated in section 4, the first set of measurements (31) was carried out with a one-dimensional velocity meter, which was so aligned that it measured the vertical velocity component. The results will not be presented here, with one exception. The average of the 31 ratios of the measured transfer function ($H_{\zeta w}$) to the theoretical (linear) one, at the peak frequency of $S_{\zeta \zeta}$, was about 0.87. If the effects of possible density variations of the sea water are considered, this ratio is estimated to vary between 0.87 and 0.92, with a standard deviation of 0.04. (Note: in an example given in the Conference preprint of this paper, said ratio was 0.75. However, it later turned out that the calculation procedure con-

tained an error; the corrected values are those mentioned above.)

At the moment of writing a series of simultaneous measurements have been made of (ζ, u, v, w) , using a wave gauge and the three-dimensional velocity meter. They have not yet been analysed fully. Some results of one measurement will be shown here by way of illustration. The data were recorded on Jan. 16, 1980, from 17 h.10 min. GMT to 17 h.40 min.

In figure 4 the wind- and sea conditions prior to and during the time of recording are shown. Figure 5 shows the surface elevation spectrum ($S_{\zeta\zeta}$), and figure 6 the coherence function between surface elevation and vertical velocity. The dashed lines indicate the 90% confidence bands. In the frequency interval which contributes most to ζ^2 , the squared coherence appears to be nearly 1. This indicates that the relation between ζ and w is approximately linear and noise-free in that interval.

In figure 7 the measured transfer function $H_{\zeta w}$ is compared with the corresponding transfer function based on the linear theory. For the range where the coherence is nearly one the calculated transfer function corresponds well with the theoretical one.

Figure 8 shows the ratio of the measured transfer function to the theoretical (linear) one as a function of frequency. This ratio does not vary significantly from the 100% value. A comparison of the measured velocity spectrum (S_{ww}) and the corresponding spectrum calculated from the linear transfer function and the measured elevation spectrum is given in figure 9. As expected from the results contained in the figures 7 and 8, the discrepancies are small in the region where most of the energy is located.

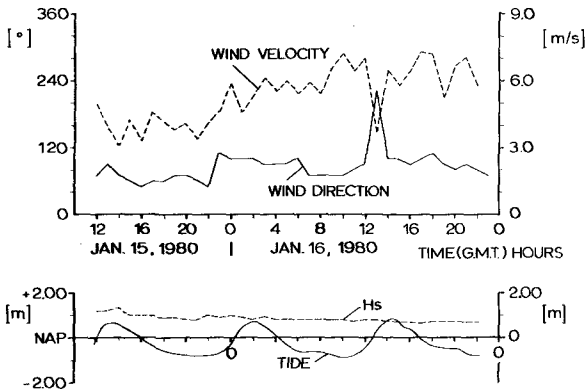


Figure 4: the wind- and sea conditions prior to the time of recording on Jan. 16, 1980, 17.10h - 17.40h.

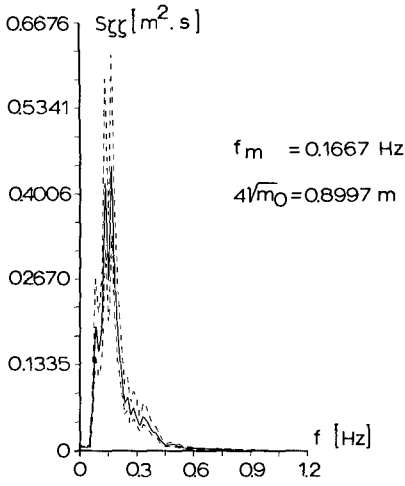


Figure 5: surface elevation spectrum, with peak frequency f_m and area m_0 .

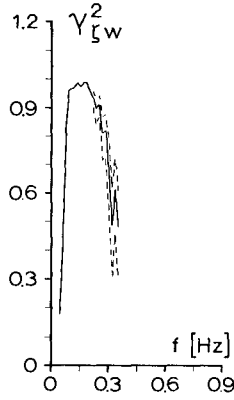


Figure 6: squared coherence function

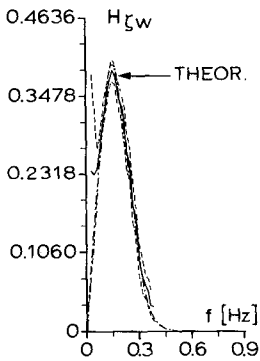


Figure 7: measured (—) and theoretical (---) transfer function

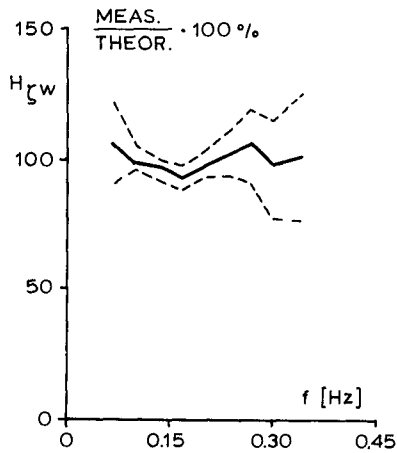


Figure 8: measured transfer function as a percentage of the theoretical transfer function

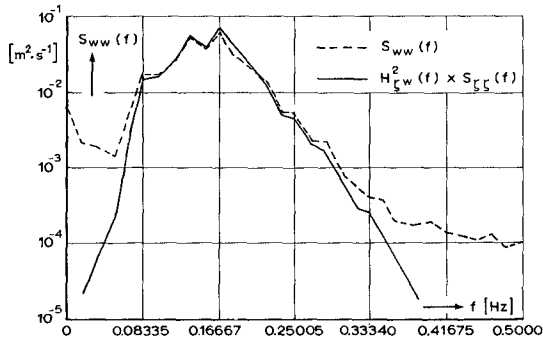


Figure 9: auto spectrum of the vertical velocity; measured (---); calculated via the linear transfer function and the measured surface elevation spectrum (—)

The phase difference between surface elevation and vertical velocity is shown in fig. 10. It is seen to vary approximately linearly with frequency; if extrapolated to $f = 0$ Hz, the phase difference is 90° , as expected in the linear approximation for all frequencies.

The observed phase function indicates a constant (with respect to frequency) time shift (0.83 s in the example of fig. 10) between elevation and vertical velocity, in addition to the predicted 90° phase difference. This seems very unrealistic physically, and it gave rise to suspicions about the system of instrumentation and data handling. However, search efforts in that direction have so far not given evidence of the source of the "observed" shift. Another contributing factor may be the horizontal separation between the two sensors, but the effect of that would be too small to explain the 0.83 s. At the moment of writing the response times of the instruments are being re-investigated. No further results about phase differences will be reported in the present paper.

In the context of observed phase lags which seem to be unrealistic, in the sense that they cannot be explained by known processes, reference is made to Cavaleri et al (1977), who found good agreement in the observed and predicted phase difference between elevation and vertical velocity, but not for the horizontal velocities. The fact that horizontal and vertical velocities in their results were not in quadrature implies a net vertical transfer of horizontal momentum, which however could not be balanced with other physical processes such as wind stress at the water surface.

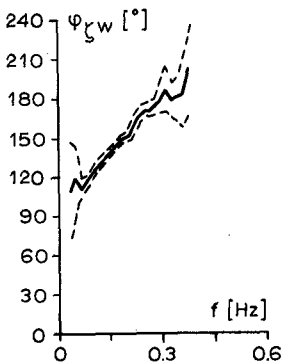


Figure 10: phase lag between surface elevation and vertical velocity component.

6.2. The transfer function of the vertical velocity component and the horizontal velocity component.

Figure 11 shows a comparison of the measured transfer function $H_{w\vec{u}}$, defined as $\{(S_{uu} + S_{vv})/S_{ww}\}^{1/2}$, to the theoretical one. Since this transfer function is estimated via the auto-spectra, possible noise is not eliminated. In the case of the relation between vertical velocity and surface elevation, the noise level was found to be negligible in the frequency band where most of the energy is concentrated (see figures 6 and 9). Assuming the same for the relation between vertical and horizontal velocities, the transfer function $H_{w\vec{u}}$ was calculated in the frequency range in which S_{ww} is at least 5% of its maximum value. In the lower - frequency part of this range there is a good agreement between the measured and predicted transfer functions, but the measured values show irregularities in the higher - frequency part, which suggests the presence of velocities not related to surface waves.

6.3. The transfer function of the surface elevation and the horizontal velocity component.

A comparison of the measured transfer function $H_{\zeta\vec{u}}$ to the theoretical one is shown in figure 12, within the range where $S_{\zeta\zeta}$ is at least 5% of its maximum value. In most of this range there is a good agreement between the calculated transfer function and the theoretical one according to the linear theory.

Figure 13 shows three sequences of ratios of measured transfer functions to the linear prediction, at the peak frequency of the auto-spectrum of the input (ζ in case of $H_{\zeta\vec{u}}$ and $H_{\zeta\vec{w}}$; w in case of $H_{w\vec{u}}$). The sequences were obtained from a series of 30 min. measurements in one day, with mild and almost-constant wind and sea conditions (see figure 4). The

average value of each of the three ratios is very nearly 100%. Additional data, including some taken in more severe conditions, are being analyzed so as to obtain a broader base for conclusions.

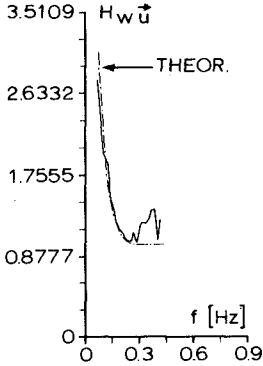


Figure 11: transfer function of the vertical velocity and the horizontal velocity; measured (—), theoretical (---).

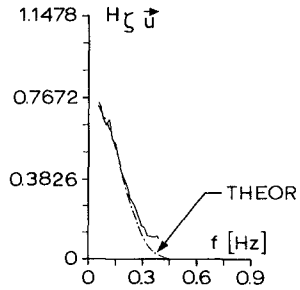
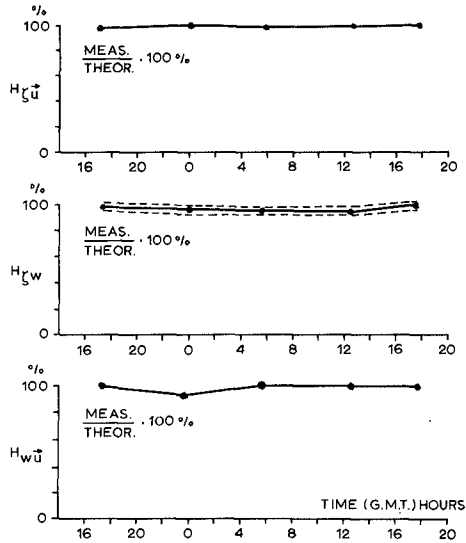


Figure 12: transfer function of the surface elevation and the horizontal velocity; measured (—); theoretical (---).

Figure 13: ratios of measured to theoretical transfer function values near the peak of the auto-spectra, for some successive 30 min. measurements on Jan. 15 and 16, 1980.



7. WAVE DIRECTION AND SHORT-CRESTEDNESS

Via the auto spectra and the cross spectra of the surface elevation and the two horizontal velocity components two components of the truncated Fourier series per frequency and the parameters of the \cos^{2s} -model per frequency can be calculated. This can also be done via the auto spectra and cross spectra of the vertical velocity component and the two horizontal velocity components. Because the resolution of this truncated Fourier series is very low (72° , Longuet Higgins, 1963) and because the \cos^{2s} -model only gives one main direction per frequency, interpretation of the results of these calculations is very difficult. Therefore only an indication of the principal wave directions can be obtained. Some typical results will be given in the following, without going into the details.

For the frequencies round 0.10 Hz the calculated main wave directions are found to be in agreement with the direction of swell coming from the northern part of the North Sea if refraction is taken into account (Holthuysen, 1973). For the frequencies round 0.30 Hz the calculated wave direction is about the same as the direction of the wind. Between these frequencies the direction of the waves changes slowly from the direction of the swell near $f = 0.10$ Hz to the wind direction near $f = 0.30$ Hz. It may be that in this range there are two main directions per frequency of which for the lower frequencies the direction of the swell dominates and for the higher frequencies the direction of the sea.

In figure 14 an example is given of the determination of the overall measure of the main wave direction and of the overall short-crestedness, using the Mohr circle. Measured values of $\overline{u^2}$, \overline{uv} and $\overline{v^2}$ are plotted, from which the principal values ($\overline{u_*^2}$, $\overline{v_*^2}$) and the principal directions ($\theta, \theta + \frac{\pi}{2}$) can be obtained. The angle θ is referred to the direction of the u -component, from which the angle θ' is calculated, which is referred to North.

As can be seen from the example, the overall principal direction calculated from $\overline{u^2}$, \overline{uv} and $\overline{v^2}$ ($\theta' = 277^\circ$) has about the same

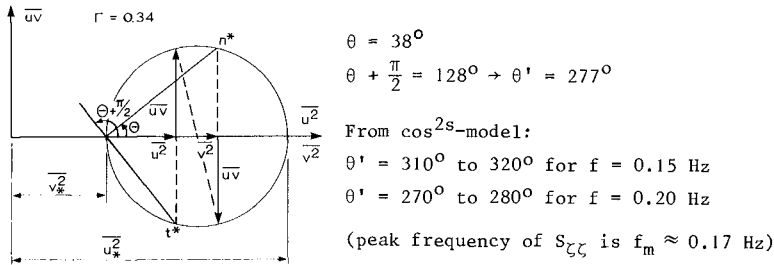


Figure 14: the calculation of the main wave direction and short-crestedness using the Mohr circle.

value as the main directions in the $\cos^{2\alpha}$ -model for frequencies near the spectral peak.

For the example shown the value of the short-crestedness parameter Γ is $\overline{v_x^2}/\overline{u_x^2} \approx 0.34$. The measurements were made in a mild sea state following about 20 hours of almost constant wind direction, so that this value of the short-crestedness parameter is expected to be typical for wind waves in an ideal, steady generation situation. The value of 0.34 is in accordance with an indirect result by Forristall et al (1978), who found that a value of the ratio $\overline{u_x^2}/(\overline{u_x^2} + \overline{v_x^2})$ of about 0.75 gave the best fit of the theoretical distribution of the magnitude of the horizontal velocity to the observations (said ratio is a parameter of this distribution). These measurements were made in a hurricane. Lastly, it is noted that a value $\Gamma = 1/3$ is consistent with a $\cos^2\alpha$ - directional spectrum, which has often been used in the past as a rough approximation.

Although this paper does not deal with applications, it is pointed out that the overall short-crestedness is important in the determination of the radiation shear stresses, which are proportional to $(\overline{u_x^2} - \overline{v_x^2})$, in a wave field of given total energy, which is proportional to $(\overline{u_x^2} + \overline{v_x^2})$ (Battjes, 1972). The radiation shear stress is the driving force for longshore currents.

8. STATISTICAL PROPERTIES

Figure 15 shows a histogram of instantaneous values of a horizontal velocity component and the best fitting Gaussian probability density function. Based on visual observations from results such as shown in figure 15, it appears that for engineering purposes, the three velocity components and the surface elevation are normally distributed. However, it should be borne in mind that the measurements so far have taken place in rather mild to moderate sea conditions.

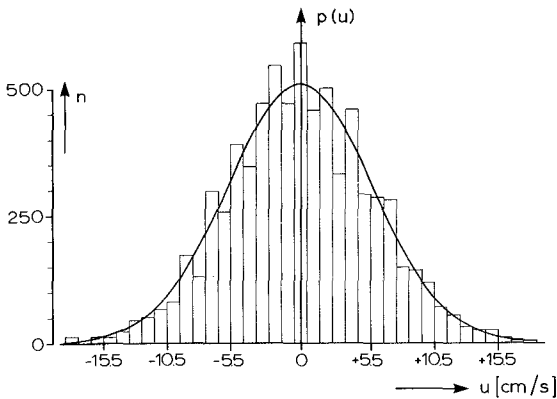


Figure 15: example distribution of instantaneous values of a velocity component

9. CONCLUSIONS

The measurements available at the time of writing do not cover a sufficiently wide range of conditions to permit very general conclusions. The following tendencies have been observed.

In the first series of measurements, in which a one-dimensional (vertical) velocity meter was used together with a Baylor-type surface wave staff, the measured vertical velocities were found to be on the average about 10% below the predictions using linear theory and measured elevation spectra. No significant deviation has been found in the analysis of the simultaneous measurements of the three mutually orthogonal velocity components and the surface elevation. A reason for these different results has not yet been firmly established.

The observed phase spectra for the relations between elevation and velocity show a linear dependence on frequency, which indicates a constant time shift between the two signals. Although it is believed that this shift is not physically realistic, efforts to locate its origin in the system of instrumentation and data handling have so far not been successful.

The principal wave directions calculated via the auto spectra and cross spectra of the surface elevation and the two horizontal velocity components show for the low frequencies a direction which corresponds with the direction of swell coming from the northern part of the North Sea if refraction is taken into account and for the high frequencies a direction which corresponds with the direction of the local wind. Between these two ranges the calculated main wave direction changes slowly.

From the mean squares and the mean product of the two horizontal velocity components an overall (i.e. non-spectral) short-crestedness parameter and an overall main wave direction have been calculated. It appears that there is a good agreement between the direction of the waves calculated in this way and the directions calculated by conventional spectral methods for the frequencies near the spectral peak.

From the investigation of the statistical properties of the three velocity components it appears that for engineering purposes, the distribution of these components can be accepted as being normally distributed.

ACKNOWLEDGEMENTS

The work described in this paper was carried out as part of the Coastal Research Program (TOW-K) of the Department of Public Works of The Netherlands.

REFERENCES

- Battjes, J.A. 1972 - Radiation stresses in short-crested waves. *J. Mar Res.*, 30: 56-64.
- Bendat, J.S. and Piersol, A.G. 1971 - Random data: analysis and measurement procedures, Wiley-Interscience, N.Y.
- Borgman, L.E. 1979 - Directional wave spectra from wave sensors, In: *Marine Science 8*, Plenum Press, N.Y.
- Botma, H.C. 1978 - Acoustic flow meter for use with hydraulic models, In: *Flow measurements of fluids*, North-Holland Publishing Company: 285-390.
- Cavaleri, L. et al 1977 - Measurement of the Pressure and Velocity Field Below Surface Waves. In: *Turbulent fluxes through the sea surface, wave dynamics, and prediction*, Eds.: A. Favre and K. Hasselmann, Plenum Press, N.Y.: 257-270.
- Forristall, G.Z. et al 1978 - The directional spectra and kinematics of surface gravity waves in tropical storm Delia. *J. Phys. Oc.* 8: 888-909.
- Guza, R.T. and Thornton, E.B. 1980 - Local and shoaled comparisons of sea surface elevations, pressures, and velocities. *J. Geoph. Res.*, 85: 1524.
- Holthuysen, L.H. 1973 - Refraction of waves near the Dogger bank. Internal report R/1973/3/L of Department of Civil Engineering, Delft University of Technology.
- Jenkins, G.M. and Watts, D.C. 1968 - Spectral Analysis and its applications, Holden-day, San Francisco.
- Longuet-Higgins, M.S. et al 1963 - Observations of the directional spectrum of sea waves using the motions of a floating buoy. *Proc. Conf. Ocean Wave Spectra*, Prentice-Hall: 111-132.
- Sharma, J. and Dean, R.G. 1979 - Second-Order Directional Seas and Associated Wave Forces. *Proc. OTC*, IV: 2505-2514.
- Thornton, E.B. and Krapohl, R.F. 1974 - Wave particle velocities measured under ocean waves, *J. of Geoph. Res.*, 79: 847-852.

CHAPTER 21

HF-RADAR MAPPING OF EXTENSIVE OCEAN WINDFIELDS

by

P.E. Dexter

Physical Research Section, Bureau of Meteorology,
Melbourne, Australia

and

R.C. Casey

Physics Department, James Cook University,
Townsville, Australia

1 INTRODUCTION

The possibility of deriving parameters of sea wave spectra remotely from characteristics of radio waves at high frequency (HF) scattered from the sea surface was first raised when Crombie (1955) correctly deduced that Doppler frequency shifts in the signal returned from short range in his HF radar resulted uniquely from components of the sea wave spectrum having wavelengths exactly one-half the radio wavelength, and travelling radially with respect to the radar. Since then the technique has been expanded in two directions:

- (a) The use of ionospherically propagated HF radio waves ('Skywave' HF radar) to examine extensive ocean areas out to some 4000 km from the observing site, to obtain oceanographic and meteorological data suitable for input to synoptic observation systems. This approach has been developed through the experimental work of Tveten (1967) and Ward (1969), and the empirical technique proposed by Long and Trizna (1973) to allow the simple extraction of sea surface wind vectors from Doppler spectra of the backscattered radio signals.
- (b) The determination of directional sea wave spectra and sea surface currents at short ranges with HF radars operating in the ground-wave propagation mode, based on theoretical analyses of the scattering process such as those of Barrick (1972).

The HF Skywave radar constructed and operated at Townsville by the Physics Department of James Cook University has been employed for some years now on research into the possibilities for mapping sea states and sea surface winds over ocean areas surrounding Australia (Ward, 1969; Ward and Dexter, 1976; Dexter and Casey, 1978).

While the high spatial resolution necessary for the accurate mapping of such meteorological systems as tropical cyclones with a Skywave radar (Maresca and Carlson, 1979) can be achieved with extensive aerial arrays, these arrays are necessarily fixed, and the spatial coverage which may be obtained is thus limited. The James Cook University radar employs a fully rotatable aerial array, thus enabling a full 360° azimuthal cov-

erage of the sea surface, out to ranges approaching 4000 km from the coastline. The limited physical size of the array in this case in turn limits spatial resolution, although the resolution obtainable is sufficient to delineate most large-scale meteorological systems (Dexter and Casey, 1978).

The present paper will describe briefly the James Cook University radar, and discuss recent results involving the mapping of sea surface wind vectors over extensive ocean areas to the east and south of Australia. It will also examine some of the limitations imposed on data collection and analysis by a moving ionosphere, and will argue that the resolution and coverage of the James Cook University radar are well suited to the input data requirements of numerical meteorological analysis and forecast systems currently in use for the southern hemisphere.

2 RADIO THEORY

The backscatter of HF radio waves from the sea surface is interpreted, to first order, as a Bragg resonant interaction between the incident radio waves and ocean waves of one half the radio wavelength propagating along the radar radial. The backscattered radio wave has a Doppler frequency shift imposed by the moving ocean waves, and its frequency spectrum contains discrete components at

$$\omega = \omega_0 \pm (2gk_0)^{1/2} = \omega_0 \pm \omega_B \quad (1)$$

where k_0 and ω_0 are the wave number and frequency of the incident radiation (wavelength g_0) and g is gravitational acceleration. These components, the Bragg lines, correspond to advancing and receding ocean waves, respectively. The ratio r of the amplitudes of the two Bragg lines is directly related to the relative proportions of advancing to receding waves and, through a directional model of the sea wave spectrum, may be interpreted in terms of surface wind direction. For the James Cook University radar, operating at 21.84 MHz, Bragg scatter occurs from ocean waves of 6.9 m wave length. These waves will be in equilibrium with the local wind for all wind speeds above about 4 m/s.

Unfortunately, this saturation of the resonant ocean wave components means that the Bragg lines can supply no information on state of development of the sea (in simple terms, wave heights or ultimately surface wind speeds). For this information recourse must be made to second and higher order scattering, which produces lower-level sidebands in the frequency spectrum of the backscattered signal. Various empirical and theoretical techniques have been developed to extract relevant information from the second order Doppler spectrum. For a full discussion of radio scatter theory, to both first and second order, see Barrick (1972, 1977, 1978), Johnstone (1975) and Lipa (1977).

3 RADAR FACILITY

The James Cook University HF skywave radar has been described in detail by Ward and Dexter (1976), Dexter and Casey (1978) and Dexter (1979). Some of the characteristics of the facility are summarised in Table 1.

TABLE I

JAMES COOK UNIVERSITY HF SKYWAVE RADAR

Transmitter	
Operating frequency	21.840 MHz
Peak power	20 kW
Pulse repetition frequency	25 Hz
Pulse length	0.5-1.0 ms
Receiver	
Bandwidth	1-4 kHz
Antenna (monostatic)	
Gain	+13 dB over free space dipole
Front/back ratio	+20 dB
Beamwidth	24 ⁰ (-3 dB points)
Sidelobes	-15 dB
Targets	
Range coverage	1000-4000 km
Range resolution	0.5 ms group delay ≅ 75 km
Angle coverage	360 ⁰ of azimuth
Angle resolution	Of the order of ±7 ⁰ (700 km at 3000 km range)
Expected Bragg Doppler	±0.475 Hz
Doppler resolution	0.04 Hz system, 0.14 Hz due to ionosphere
Range accuracy - relative	30-40 km
- absolute	around 50 km
Angle accuracy	±0.5 ⁰

4 OBSERVATIONS, ANALYSIS AND INTERPRETATION

A quasi-operational test of system performance was conducted on 26 October 1978. Observations were made during the 3 hour period 0130Z to 0430Z (the optimum time as determined by Ward (1972) and Heron and Rose (1978(a)) to minimise mean ionospheric Doppler shifts), with 102.4s data blocks being obtained from scattering areas selected at group delays of from 9 ms to 25 ms (ground ranges approximately 1200 to 3700 km) on azimuths from true bearing 050⁰ from Townsville to true bearing 190⁰. Radar coverage was thus fairly uniform over a total sea area of some 2 × 10⁷ km² in the Coral Sea, Tasman Sea and Southern Ocean (Fig 2).

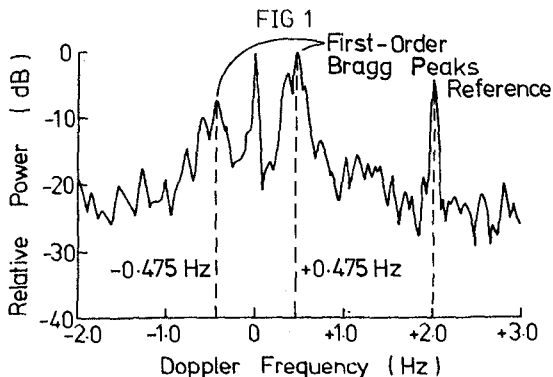


Figure 1 Doppler spectrum from 102.4s of data recorded near 0230Z on 26 October 1978. Scattering area located on true bearing 070° from Townsville, at a ground range of 2800 km. Bragg peaks (exhibiting multipath) occur at ± 0.475 Hz. Peaks at Doppler frequency shifts of 0 Hz and 2 Hz represent transmitter frequency leakage and a reference signal, respectively.

The 102.4s data blocks for each scattering cell were digitised at 10/s. The resulting 1024 data points were divided into four sets of 256 points, spectral analysis performed on each with an FFT, and the resulting raw spectral estimates incoherently averaged to give spectral resolution of 0.04Hz and approximate 90 per cent confidence limits of +2.0 and -3.1 dB (Dexter and Casey, 1978; Dexter 1979).

An example of the resulting Doppler spectrum for a single scattering cell (true bearing 070° , range 2800 km from Townsville) is shown in Fig 1. There was some leakage of transmitter frequency into the processor circuitry during this experiment, and this has resulted in the peak at zero Doppler frequency. The spectral line near +2Hz is a locally injected reference.

The frequency spectrum exhibits both positive and negative first-order lines, with the dominant positive line indicating approaching waves (and winds). Wind direction analyses were performed on this and similar spectra for all scattering cells using the technique of Stewart and Barnum (1975). Briefly, this assumes a wave directional spectrum of the form

$$g(\theta) = \cos^s (\theta/2) \quad (2)$$

where θ is the angle between mean wind and radio propagation direction, and s is a parameter related to wind speed (Tyler et al., 1974). The ratio of advancing to receding waves is thus $\tan^s (\theta/2)$. However, this is also the ratio of the advance to recede Bragg line amplitudes, A^+ and A^- respectively. Thus

$$\theta = 2 \arctan \left\{ \left(\frac{A^+}{A^-} \right)^{\frac{1}{s}} \right\} \quad (3)$$

In practice, for reasons discussed by Dexter and Casey (1978), a uniform wind speed of 10 m/s was adopted in this analysis. Full results of the direction analysis are shown in Fig 2. The fit to the meteorological mean sea level (MSL) pressure analysis for 0300 Z (1300 h local time) on 26 October is obviously good, particularly when allowance is made for cross-isobar flow. A similar direction analysis using the technique of Long and Trizna (1973) was also performed, with inferior results (although this technique has been used with success in the North Atlantic by Shearman et al. (1977)).

Most of the Doppler spectra obtained in this experiment (including that shown in Fig 1), display features characteristic of an unstable ionospheric propagation mode. Of most significance are:

- (a) ionospheric multipath, manifest as a splitting of the Bragg lines into three or more distinct peaks;
- (b) broadening of the Bragg lines due to small scale and random ionospheric movements, imposing a spectral resolution limit of the order of 0.14 Hz (at 21.840 MHz), as found by Heron and Rose (1978(b)).

Neither of these phenomena affects wind direction determinations, but both interfere substantially with wind speed computations. The approach employed in this case was again that of Stewart and Barnum (1975), in which the width (B) of the principal Bragg line, at a level 10 dB below the peak, is related empirically to surface wind speed. The approach can only be applied to spectra which do not exhibit multipath, and the particular empirical relationship employed has been that derived by Dexter and Casey (1978). The few wind speeds which could be computed in this way are also displayed in Fig 2. Comparison with available surface observations is reasonable.

Absolute ground ranges have been computed for all scattering cells using ionospheric data supplied by the Australian Ionospheric Prediction Service for Brisbane, applied to a technique devised by Dexter (1979). These ranges could only be confirmed where identifiable land features occurred in a scattering cell, but errors are unlikely to be greater than system range resolution.

5 DISCUSSION

While the low spatial resolution (average scattering cell for 'almost independent' observations of the order of 150 km × 470 km) of the James Cook University radar makes it unsuitable for the detailed observations of such small-scale atmospheric features as fronts and tropical cyclones as have been attained with the high resolution radar of Barnum et al. (1977) and Maresca et al. (1978), its flexibility of operation and large scanning area do afford other advantages. In particular, a total potential sea area coverage of some 5×10^7 km² makes this radar an attractive possibility for the observation of surface wind vectors over a significant portion of the data sparse southern hemisphere oceans. An illustration of the areal coverage for the radar when sited at Townsville and near Alice Springs is shown in Fig. 3. It remains to be seen whether such data is compatible with required meteorological synoptic analyses.

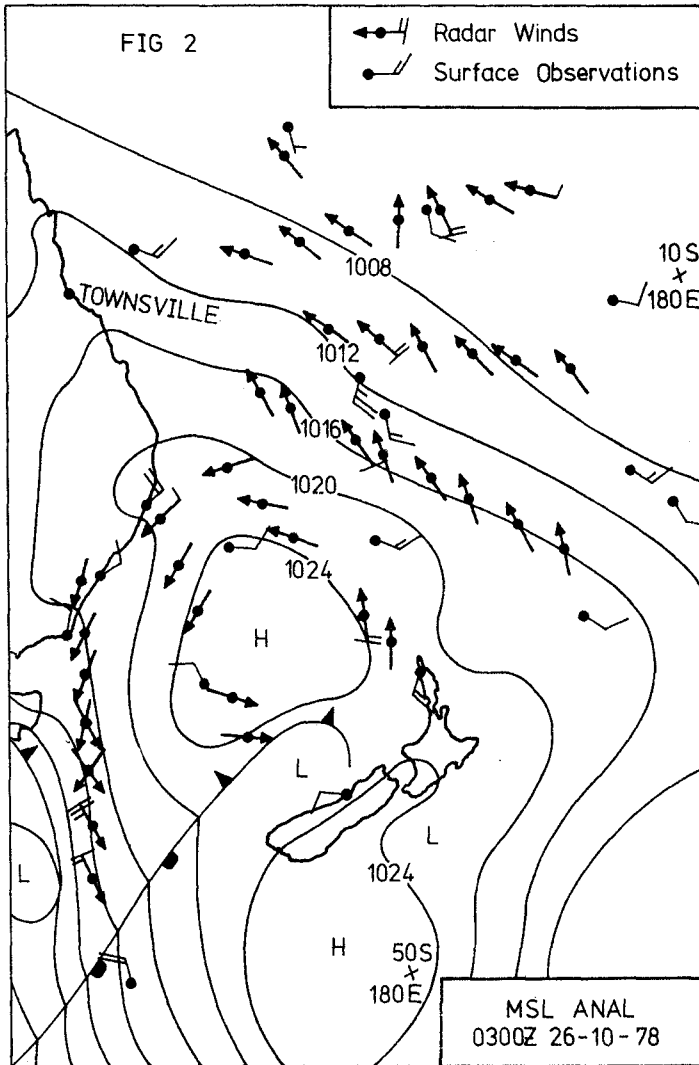


Figure 2 Surface meteorological analysis for 0300Z on 26 October 1978, with radar-derived winds superimposed. Solid arrows are radar wind directions, with feathers in wind speed intervals of 2.5 m/s. Measured surface winds are also shown, where available.

FIG 3

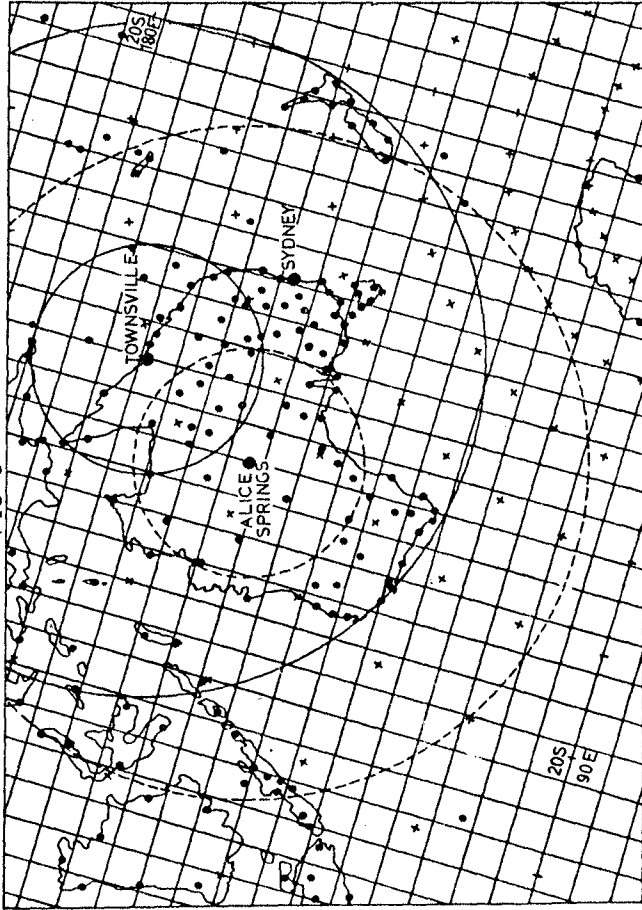


Figure 3 Standard meteorological chart for Australian region, polar stereographic projection (true at 60°S), with relevant portion of 47 x 47 grid superimposed. Also shown is approximate areal coverage of the James Cook University radar in its present site, and when more conveniently sited near Alice Springs. Dots represent meteorological synoptic observing station.

Numerical meteorological analysis and prognosis models currently in use with the Australian Bureau of Meteorology are hemispheric in scope and based on a rectangular grid, either 61×61 (grid spacing approximately 330 km at 60°S), or 47×47 (grid spacing approximately 490 km at 60°S (Fig. 3)). Both grid spacings are comparable with the average spacing between observations for the radar winds, of around 300-400 km. Seaman (1977) has analysed the optimum density of an observational network in terms of such observational parameters as spatial correlation of observational errors, observational error variance, and the scale size of particular meteorological systems required to be observed and forecast. If it is assumed that this latter scale size is approximately twice the numerical grid spacing, this analysis shows that the point of diminishing return for the rms analysis error in the absolute value of a particular meteorological element is reached for an observational network spacing between 1.0 and 1.4 of the grid spacing. Thus the density of 'almost independent' observations attainable by the radar is well matched to the operational numerical grid, and the maximum system resolution.

In addition, a complete Australian region coverage can be made by the radar in a 2 to 3 hour period at least once per day. While this is not ideal, it is at least similar to the observational frequency in the Australian region from orbiting meteorological satellites.

Similar considerations apply to numerical wave forecast models for southern hemisphere oceans with the additional factors: (a) in the absence of extensive sea state observations, initial wave fields must be computed from analysed surface wind fields. Thus direct observations of these wind fields over the ocean assume even greater significance. (b) The low success rate for wind speed extraction (around 15% of all observations) to date could limit utility in this regard. While the problems of multipath and peak broadening are always likely to be present for a skywave radar of this configuration, work is currently underway to develop a more reliable technique for wind speed determination from observed Doppler spectra, and hopefully this will raise the success rate to better than 60%. This work is to be reported on separately at a later date.

6 ACKNOWLEDGMENTS

We thank Professor J.F. Ward for his continued interest in, and support for, the skywave radar project. This paper is published by permission of the Director of Meteorology, Australia.

7 REFERENCES

- BARNUM, J.R., MARESCA, J.W. AND SEREBRENY, S.M. 1977. I.E.E. Trans. Ant. Prop., AP-25(1), 128-132.
- BARRICK, D.E. 1972. Chapter 12 of Remote Sensing of the Troposphere ed. V. Derr, U.S. Govt. Printing Office, Washington, D.C.
- BARRICK, D.E. 1977. Remote Sensing of Environment, 6, 201-227.

- BARRICK, D.E. 1978. Bound.-Lay. Met, 13, 23-43.
- CROMBIE, D.D. 1955. Nature 1975, 681-682.
- DEXTER, P.E. 1979. Radio oceanography : the determination of sea surface wind and wave parameters with an HF radar. PhD Thesis, James Cook University.
- DEXTER, P.E. AND CASEY, R. 1978. Aust. Met. Mag., 26, 35-44.
- HERON, M.L. AND ROSE, R.J. 1978(a). Aust. J. Phys. 31, 333-345.
- HERON, M.L. AND ROSE, R.J. 1978(b). Geophys. Res. Letters, 5, 379-381.
- JOHNSTONE, D.L. 1975. Tech. Rep. 3615-3, Stanford Electronics Labs, Stanford, California.
- LIPA, B. 1977. Radio Sci., 12, 425-434.
- LONG, A.E. AND TRIZNA, D.B. 1973. I.E.E.E. Trans. Ant. Prop, AP-21, 680-685.
- MARESCA, J.W. et al. 1978. Proc. 16th Intnl. Coastal Eng. Conf., Hamburg, Sep 1978.
- MARESCA, J.W. AND CARLSON, T. 1979. Proc. AGARD Conf. Portugal, May 1979.
- SEAMAN, R.S. 1977. Mon. Weath. Rev. 105, 1211-1222.
- SHEARMAN, E.D.R., BAGWELL, D.J. AND SANDHAM, W.A. 1977. I.E.E. Radar 77 I.E.E. Conf. Pub. 155, 41-45.
- STEWART, R.H. AND BARNUM, J.R. 1975. Radio Sci., 10, 853-857.
- TVETEN, L.H. 1967. Science, 157, 1302-1304.
- TYLER, G.L. et al. 1974. Deep Sea Res., 21, 989-1016.
- WARD, J.F. 1969. Nature, 223, 1325-1330.
- WARD, J.F. 1972. Res. Report 23, Phys Dept, James Cook University.
- WARD, J.F. AND DEXTER, P.E. 1976. Aust. J. Phys. 29, 183-194.

SOURCES OF MEASURED WAVE DATA

by

Laurence Draper
Institute of Oceanographic Sciences
Wormley, Godalming, Surrey GU8 5UB, U.K.

ABSTRACT

A Catalogue listing 550 known sources around the world of instrumentally-measured wave data has been prepared by the Marine Information and Advisory Service under the auspices of the Intergovernmental Oceanographic Commission of UNESCO.

A source of good wave data is a prime requirement of the coastal engineer. "Perhaps I exaggerate the importance of the wave climate but from my own experience I rate it as the most frustrating gap in the kit of tools available to the coastal engineers..." so said Dean Morrough P. O'Brien, Chairman, Coastal Engineering Research Council A.S.C.E., in his opening address to the 13th Conference on Coastal Engineering, Vancouver, 1972.

Since that time there have been significant developments in a number of aspects. Existing wave climate measurement programmes have been extended and new ones have been started, so that the world-wide effort has increased considerably. The International Waves Commission of PIANC (Larras 1973) (which was already in operation in 1972) developed its proposals for a wave data inventory, and the Intergovernmental Oceanographic Commission (IOC) of UNESCO accepted an offer by the Marine Information and Advisory Service of the Institute of Oceanographic Sciences to establish what is in effect a wave data centre, a Responsible National Oceanographic Data Centre for Waves (RNODC (Waves)). A world-wide network of Area Representatives has been established; each representative provides the RNODC (Waves) with information on instrumental wave measurements in his area. Data are not transmitted at this stage. The information is in a standard format so that a potential user can assess the value of the data to his own project; negotiations for use of the data then proceed between owner and potential customer.

It is not planned to publish the complete Master Catalogue, because of its bulk, but a condensation entitled Catalogue of Wave Data has been published and is available

from MIAS at the Institute of Oceanographic Sciences. An example of one page of this catalogue, showing two stations, is given in Figure 1. A list of Area Representatives as of April 1980 is given as an Appendix to this paper, and the countries involved are shown in Figure 2, which also gives the number of entries published for each area. The most intensively covered areas are those around the British Isles, and a larger scale map showing actual locations is given in Figure 3. Maps of eastern Australia (Figure 4) and eastern Canada and north eastern USA (Figure 5) are also given to indicate the coverage in these areas.

Although Area Representatives provide reasonable coverage of the world's coastlines, seas and oceans (see Figure 2), additional offers of help would be appreciated at any time. These should be addressed to the author, who is Scientific Co-ordinator RNODC (Waves), at the Institute of Oceanographic Sciences, Wormley.

The establishment of such an organization has been needed for many years. The first two years of its life have shown great promise, both in the number of people eager to help and the enormous effort they have shown in tackling the major task of completing the questionnaire forms for data already in existence. So far, nearly 600 forms have been received and many more have been promised. It looks as though Dean O'Brien will soon need a larger toolbox.

REFERENCES

- LARRAS, M.J. (1973). Report on the International Commission for the study of waves. PIANC Bulletin No. 15, Vol. II.
- DRAPER, L. (1978). A world Wave Data Centre. 16th Conference on Coastal Engineering, Hamburg. Vol. 1, Chapter 1.

APPENDIX

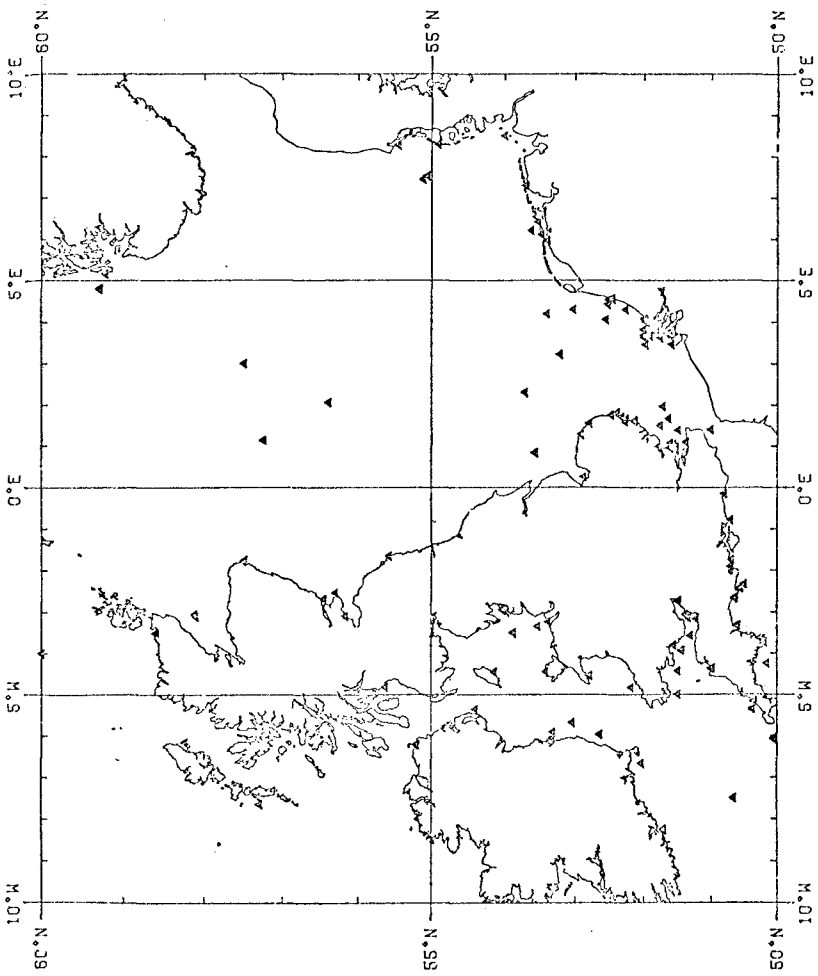
RNODC(Waves) Area Representatives April 1980.

ARGENTINE: Lic. Sergio A. Schmidt, Armada Argentina, Servicio de Hidrografia Naval, Departamento Oceanografia, Av. Montes de Oca 2124, 1271 Buenos Aires.

AUSTRALIA: Mr F.L. Wilkinson, Chief Engineer Maritime Works, Dept of Housing and Construction, Box 111, Dickson 2602, A.C.T.

BRASIL: Mr Jose Antonio dos Santos, Director INPH/PORTOBRAS, Rue General Gurjao 166, Caju ZC-08, 20.000 Rio de Janeiro.

BELGIUM: Mr R. Simeon, Ingenieur de Constructions Civiles, Tarwestraat 70, Ostend 8400.



BRITISH AND ADJACENT WATERS

FIG. 3

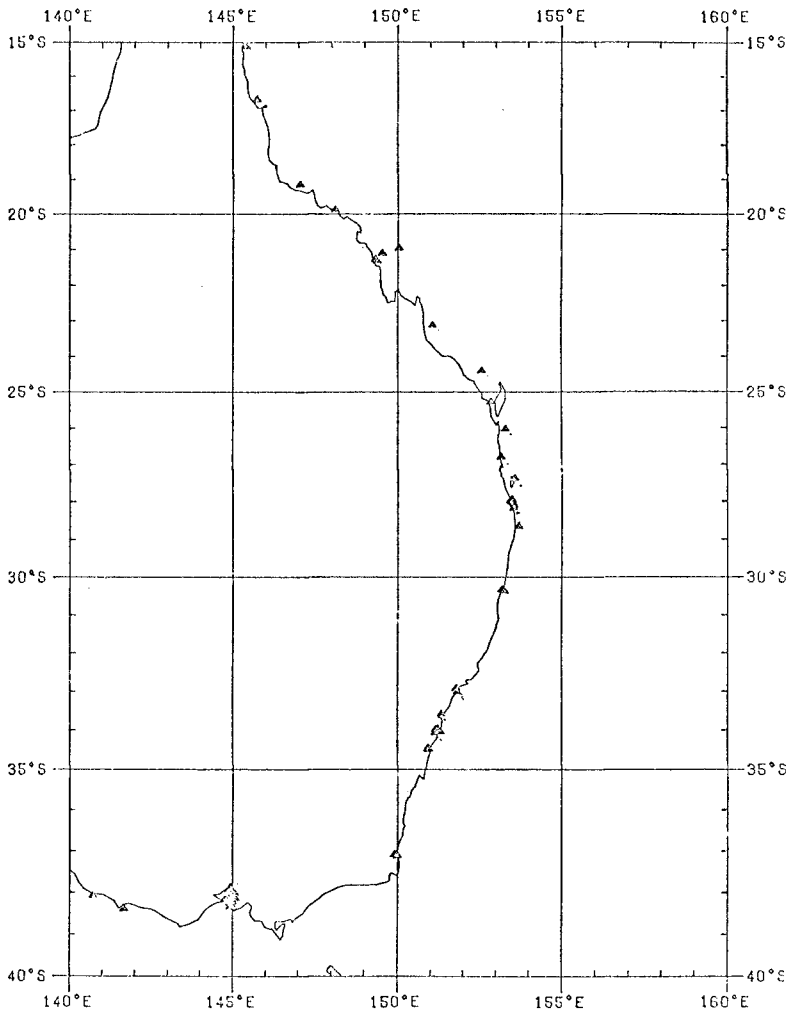


FIG. 4

EASTERN AUSTRALIA

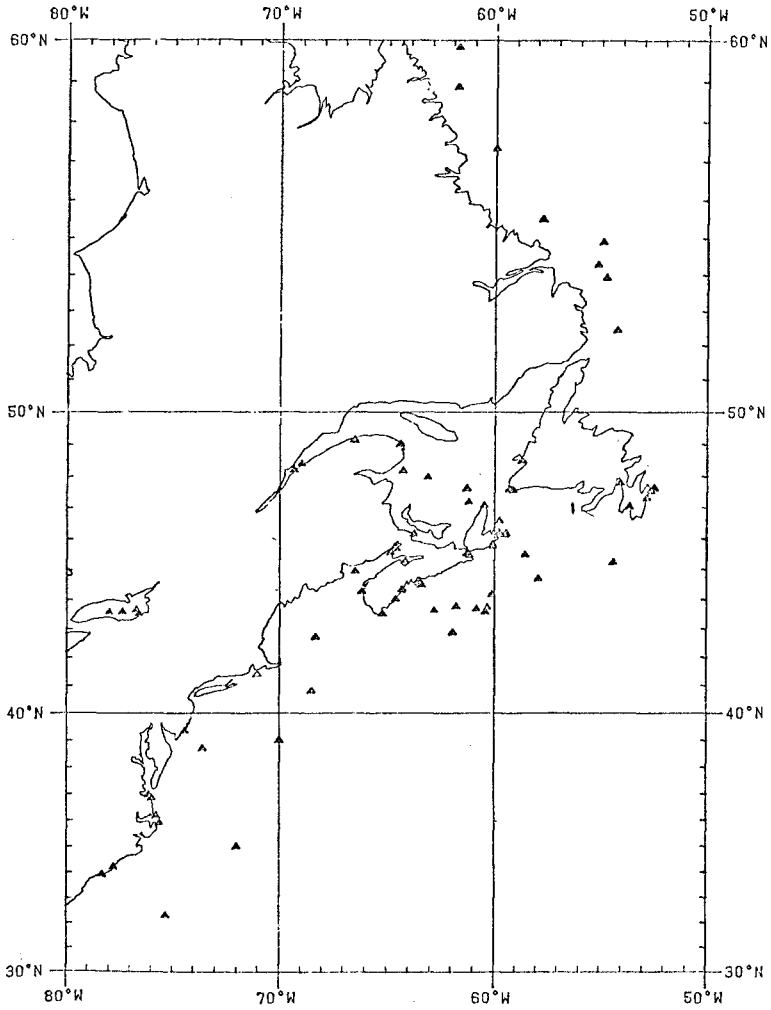


FIG. 5

EASTERN CANADA and NORTH EASTERN USA

CANADA: Dr R. Wilson, MEDS, Environment Canada, Ottawa
K1A 0H3.

DENMARK: Mr Chr. Laustrup, Kystinspektoratet, Højbovej 1,
DK 7620 Lemvig.

Mr Henning Nørgaard, Statshavnsadministrationen, Hulvejen,
Postboks 2, 6700 Esbjerg.

EIRE: Mr Neil Clotworthy, Commissioners of Irish Lights,
16 Lower Pembroke Street, (Box 73), Dublin 2.

FRANCE: Le Chef de BNDO, CNEXO, B.P. 337, 29273 Brest Cedex.

F.R. GERMANY: Dr D. Kohnke, German Oceanographic Data
Centre, Postfach 220, Bernhard-Nocht-Strasse 78, beim
Deutschen Hydrographischen Institut, 2000 Hamburg 4.

F.R. GERMANY (Baltic Coast): Akad Rat. Dr-Ing H.H. Dette,
c/o Lehrstuhl für Hydromechanik und Küstenwasserbau,
Leichtweiss Institut für Wasserbau, Technische Universität
Braunschweig, Beethovenstrasse 51a, Postfach 3329, 3300
Braunschweig.

ICELAND: Dr G. Viggosson, Hafnamalastofnun Ríkisins,
Seljavegi 32, Reykjavík.

INDIA: Dr J.S. Sastry, National Institute of Oceanography,
P.O. Don Paula, Goa Pin 403004.

INDONESIA: Mr Y. Singh, Maunsell Consultants, P.O. Box
2982, Jakarta.

ISRAEL: Hydrographic Services, Israel Ports Authority,
P.O. Box 5, Ashdod.

JAPAN: Dr Y. Goda, Head, Marine Hydrodynamics Division,
Port & Harbour Research Institute, Ministry of Transport,
3-1-1, Nagase, Yokosuka-shi, Kanagawa-ken, 239.

Mr Shiro Kadowaki, Head, Maritime Meteorology Division,
Marine Division, Japan Meteorological Agency, 1-3, 4 Ote-
Machi, Chiyoda-ku, Tokyo 100.

Mr Atsushi Tokuhiko, Director Japan ODC, Hydrographic
Dept., Maritime Safety Agency, No 3-1 Tsukiji 5-Chome,
Chuo-ku, Tokyo 104.

MEXICO: Dr R. Vazquez de la Cerda, address unknown.

NETHERLANDS: ir P. Geerders, Netherlands Centre for
Oceanographic Data, KNMI, Wilhelminalaan 10, Postbus 201,
3730 AE de Bilt.

NEW ZEALAND: Dr R.A. Heath, N.Z. Oceanographic Institute,
P.O. Box 12-346, Wellington North.

NORWAY: J. Borresen, Det Norsk Meteorologiske Institutt,
Postboks 320, Blindern, Oslo 3.

PORTUGAL: Prof. F. Vasco Costa, Rua Joaquin Ant Aguiar 27
8^o E, Lisboa 1.

SOUTH AFRICA: C.C. Stavropoulos, National Research
Institute for Oceanology, P.O. Box 320, Stellenbosch, 7600

SPAIN: Dr F.M. Fernandez, Director, Centro Espanol de Datos
Oceanographicos, Instituto Espanol de Oceanografia, C/Alcala
No. 27-4^o, Madrid 14.

SRI LANKA: Mr S.R. Amarasinghe, Director, Coast Conserva-
tion Division, 69 Horton Place, Colombo 7.

SWEDEN: Mr R. Berggren, Swedish Meteorological and
Hydrological Institute HBF, Fack, S-601 01, Norrkoping.

U.S.A.: Mr Wellington Waters, NODC (D 752), Environmental
Data Service, NOAA, Washington D.C. 20235.

*This work was funded in part by the
Departments of Energy and Industry.*

CHAPTER 23

VISUALLY OBSERVED WAVE DATA AT PT. MUCU, CALIF.

Christine Schneider¹

J. Richard Weggel², M. ASCE

Abstract

A Littoral Environment Observation (LEO) Program was established along the West Coast of the United States in 1968. This program provides for visual observations of waves and surf conditions to be made systematically on a daily basis. The data addressed in this report were collected at three LEO sites (as shown in Figure 1) at Pt. Mugu California, located 50 miles northwest of Los Angeles.

In order to evaluate the reliability of wave heights and periods collected using the LEO techniques, comparisons of visual observations and measured wave gage records were made.

The study revealed that individual visual observations of breaker height can deviate significantly from measured wave heights even when the gage wave heights had been corrected for shoaling effects. On the average the LEO observations gave a fair estimate of prevailing wave heights.

LEO estimates of wave period tended to overpredict the period of maximum energy density. It is presumed that this occurred because observers often fail to count smaller waves when making this measurement. Statistics of the gage measurements of wave height and LEO wave heights are reasonably close.

Introduction

In an effort to provide low-cost coastal information for the planning, operation and maintenance of coastal structures and projects, the U.S. Army Coastal Engineering Research Center (CERC) in cooperation with coastal states and other public entities, established the Littoral Environment Observation (LEO) program. This program has been in operation since 1968, and provides a data bank of wind, wave and current statistics which have been collected on a repetitive and systematic basis by volunteer observers. (BERC, 1968)

Presently fifteen pieces of information are gathered during each observation; included are: the wave period, height, angle and type of breaker; wind speed and direction; foreshore slope; surf zone width; current and direction; and rip current and beach cusp spacings.

-
1. Engineering Technician, Evaluation Branch, U.S. Army Coastal Engineering Research Center.
 2. Chief, Evaluation Branch, U.S. Army Coastal Engineering Research Center, Fort Belvoir, VA.

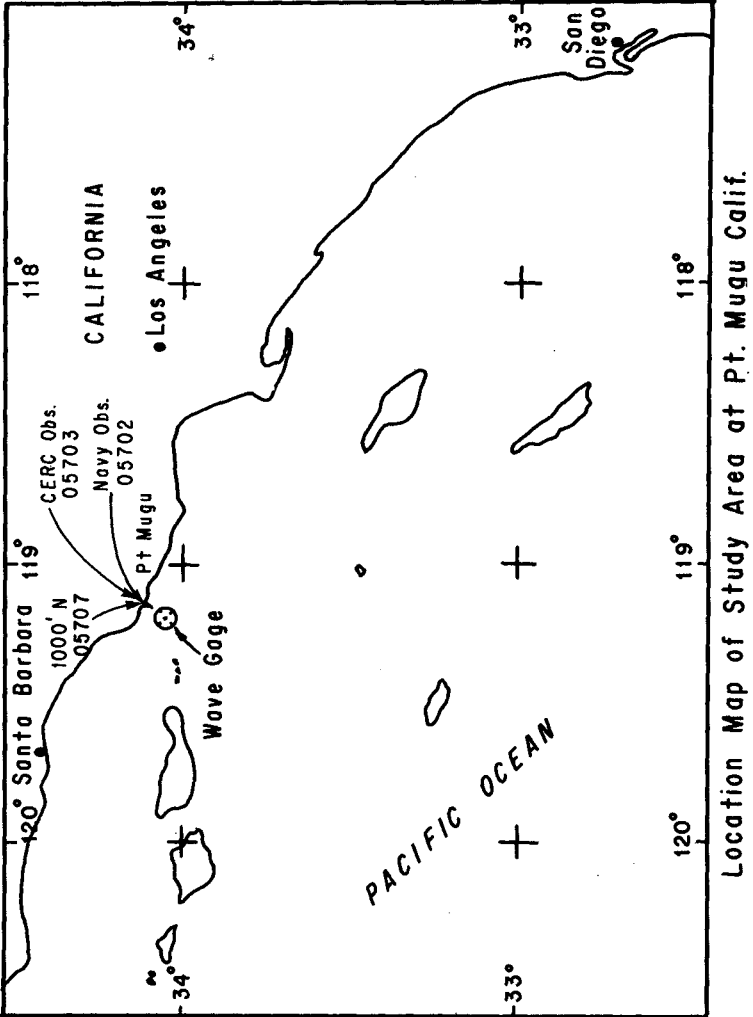


Fig. 1. Location map of study area at Pt. Mugu, California.

LEO data have been collected primarily at sites where little or no wave data existed or where resources are not available for installation of wave recording instruments. This report presents comparisons between LEO observations of wave characteristics and gage measured characteristics made for the period from March to December 1972 at Pt. Mugu, California where a 5-gage array and several LEO Sites were operated simultaneously. At the Pt. Mugu site, LEO observations were obtained by two separate observers, a CERC observer and a Navy observer. In addition, CERC observations were made at two adjacent locations 1000 ft. upcoast (northwest) and 1000 ft. downcoast (southeast) from the primary site. The primary site was located at a pier constructed across the surf zone and thus the observers at this location were not constrained to make observations from the beach. All of the Navy observations were made from the deck of the pier while most of the CERC observations were made from the beach. At the adjacent sites, the CERC observer made estimates of breaker height, surf zone width, breaker period, etc. from the beach. It is thus possible to look at differences between two independent observers at a given site and to look at spatial variations introduced by a single observer making observations at three sites spaced 1000 ft. apart. Only data from the pier site and the upcoast were analysed for this study and thus only results from these two sites are presented herein. For observations made by a single observer at two separated sites, it is not known how much influence the observation at one site has on the same observer's estimate of wave conditions 1000 ft. away. Presumably, the observations are independent and describe real spatial variations; however, it seems reasonable to assume that observations made at one site may have some influence on what the observer reports from an adjacent site.

DATA ANALYSIS

Comparisons were made of wave heights obtained visually at three LEO stations (two sites) with the significant wave heights obtained from a pressure wave gage located in about 30 ft of water. The gage was about 2.5 feet above the bottom and pressure readings were corrected to obtain water surface elevations including the effect of tide. Additionally, comparisons were made of wave periods obtained by timing the passage of 11 breaker crests and the period of maximum energy density obtained from the wave spectrum. The comparison was made for the gage observations taken closest to the time the LEO observation was made. Since gage measurements were taken every six hours the greatest time between gage measurement and corresponding LEO observation was 3 hours.

Figure 2, shows scatter plots of the LEO estimated wave heights for both the Navy observer and CERC observer at the pier and 1000 ft upcoast, respectively, and how they compare with the significant wave heights measured in 30 ft of water.

No corrections for refraction and shoaling between the gage and breaking were applied to the gage data for these plots. The lines shown on the plots are (a) the line of equality, (b) a least-squares best-fit straight line and (c) a least-squares-best-fit straight line constrained to pass through the origin. Comparing this latter line for the three sets of observations, it appears that the Navy observations

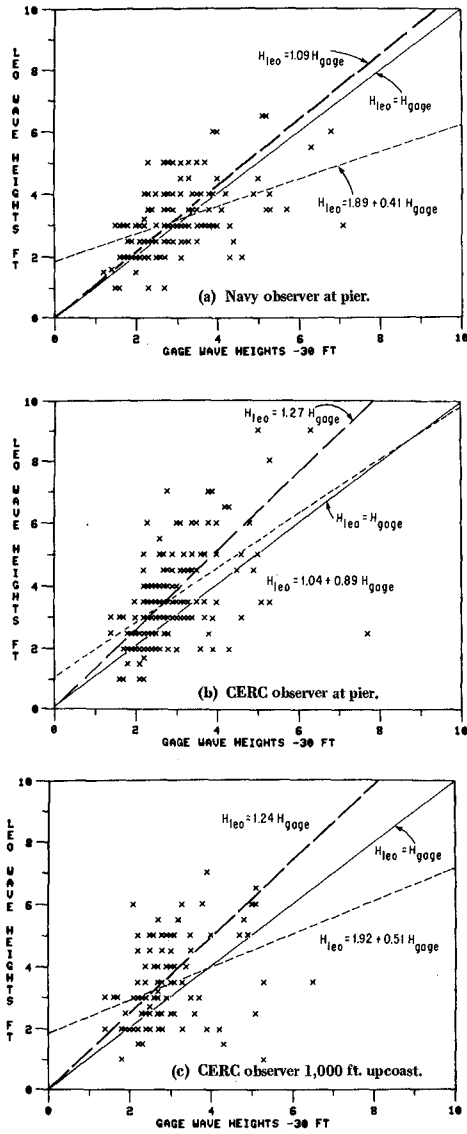


Figure 2. LEO observations of breaker height versus uncorrected wave gage heights, 1972.

of breaker height most closely approximate the gage values while the CERC observations at both the pier and 1000 feet upcoast are generally greater than the significant wave height as recorded at the gage. The least-squares best-fit line suggests that there is a tendency for both observers to overestimate the height of smaller waves and underestimate the height of larger waves. Obviously, the effects of shoaling and refraction between the gage and breaker line need to be considered.

Two shoaling models were applied to the gage data to estimate breaker heights that could be compared with LEO breaker height observations. Recognizing that the transformation of a wave spectrum across the nearshore area is a complex phenomenon, a crude approximation to the shoaling process was made by characterizing the spectrum as monochromatic waves having height and period equal to the significant height and the period of maximum energy density. No correction for refraction was applied. The first shoaling model used linear wave theory with the assumption that the group velocity and phase velocity were the same at breaking. From linear theory,

$$\frac{H_{bl}}{H_{gage}} = \sqrt{\frac{(C_G)_{gage}}{(C_G)_b}} = \sqrt{\frac{(nC)_{gage}}{(C_G)_b}} \quad (1)$$

$$\text{where } (C_G)_b \approx \sqrt{g(d_b + H_{bl})} \quad (2)$$

$$\text{and } d_b = 1.28 H_{bl} \quad (3)$$

where H_{bl} is the breaker height

H_{gage} is the gage wave height in 30 ft of water

$(C_G)_{gage}$ is the wave group velocity at the gage

$(C_G)_b$ is the wave group velocity at breaking, and

n = ratio of wave group velocity to phase velocity

Combining these expressions gives, for H_{bl} as a function of H_{gage} , the explicit relationship

$$H_{bl} = \left\{ H_{gage} \sqrt{n \frac{L_{gage}}{T}} (0.1167) \right\}^{4/5} \quad (4)$$

where L_{gage} is the wave length at the gage of a wave with period T equal to the period of maximum energy density. Applying this shoaling adjustment to the gage data results in the scatter plots of figure 3 for the Navy observer, the CERC observer at the pier and the CERC observer 1000 feet upcoast of the pier, respectively. The approximate shoaling correction results in higher gage wave heights and better comparison with the LEO observations. Comparing the least-squares-best-fit lines passing through the origin, the Navy observations now generally underpredict the corrected gage heights while the CERC

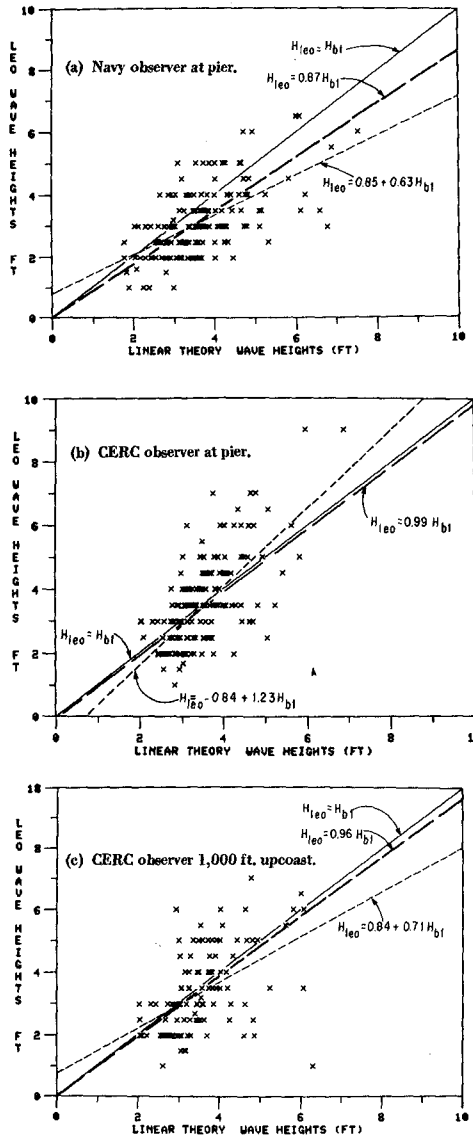


Figure 3. LEO observations of breaker height versus wave gage heights corrected for shoaling (shoaling model 1).

observations at both the pier and 1000 ft. upcoast, on the average, predict the measured values rather well.

The second shoaling model used was an iterative solution to the linear shoaling relationship and the breaker height to water depth ratio (equation 3.) This implicit scheme makes no a priori assumptions about the relationship between the wave group velocity and phase velocity at breaking, nor does it require that the shallow water approximation be made to determine the wave phase velocity. This second shoaling model resulted in higher breaker heights than the first model (figure 4.) As a result, the LEO observations by both the Navy and CERC observer are quite a bit lower than the transformed significant wave height obtained from the gage. If the root-mean-square wave height is used instead of the significant height (assuming that $H_{rms} = 0.71 H_S$) the equations on figure 4 become,

$$H_{leo} = 0.86 (H_{b2})_{rms} \quad (\text{Navy Observer, pier})$$

$$H_{leo} = 0.96 (H_{b2})_{rms} \quad (\text{CERC Observer, pier})$$

$$H_{leo} = 0.92 (H_{b2})_{rms} \quad (\text{CERC Observer, 1000 ft upcoast})$$

where H_{b2} is now the breaker height determined from the second shoaling model using the rms wave height measured at the gage.

The statistical distribution of wave heights was estimated for the LEO observations at the three sites and compared with the distribution of heights obtained from the gage and from the gage as corrected by the two shoaling models. Comparisons between the LEO observations and the wave gage heights are shown on figure 5 plotted on a log-normal probability scale. Probabilities were estimated by ranking the individual observations and using the plotting position formula,

$$P(X \geq x) \approx \frac{m}{N+1} \quad (5)$$

where m is the rank of the observation (m=1 for the largest) and N is the number of observations in the sample. The distribution of gage heights shown on figures 5a, 5b, and 5c are essentially identical; any small differences are due to a slightly different sample size. These differences are most apparent at the extreme ends of the distribution (near the largest and smallest observations.) The Navy observations (5a) compare favorably with the uncorrected gage heights whereas the CERC observations at both sites overestimate the significant wave height at the gage.

Figure 6 shows the probability distribution of the gage wave heights transformed by the two shoaling models. In both cases the curve is shifted upward for shoaling-corrected wave heights. Shoaling model 1 applied to the significant wave height gives the best comparison with the LEO observations. If the H_{rms} wave height is assumed to characterize the wave spectrum at the gage, the second shoaling model and the

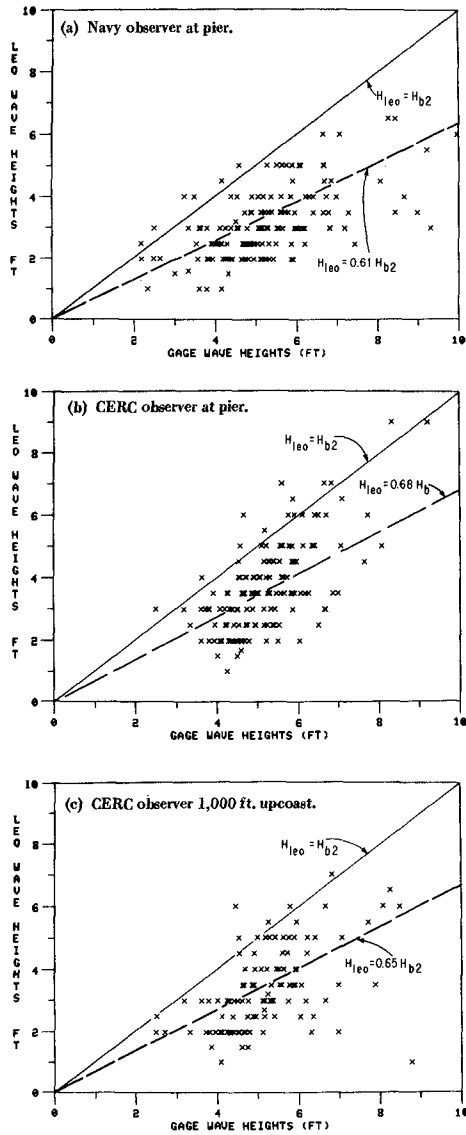


Figure 4. LEO observations of breaker height versus wave gage heights corrected for shoaling (shoaling model 2).

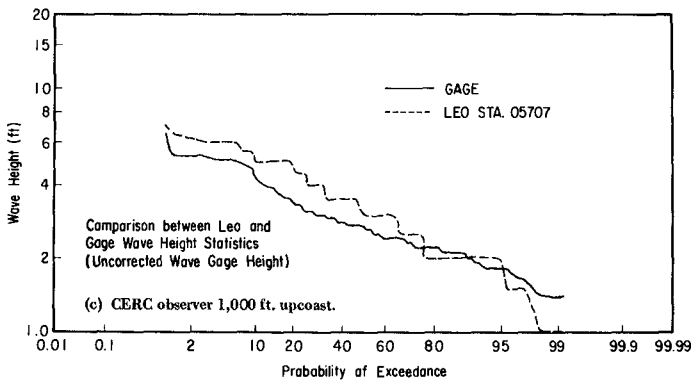
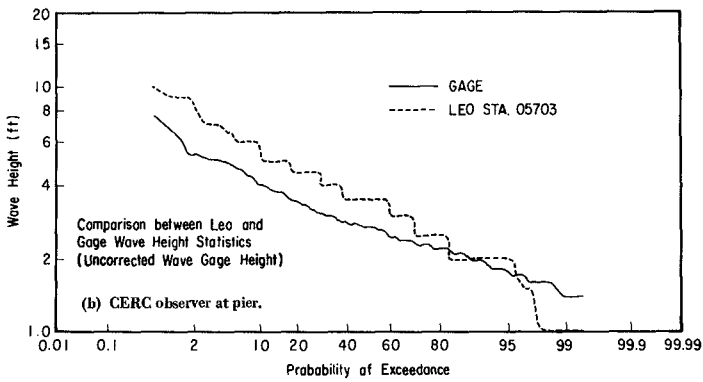
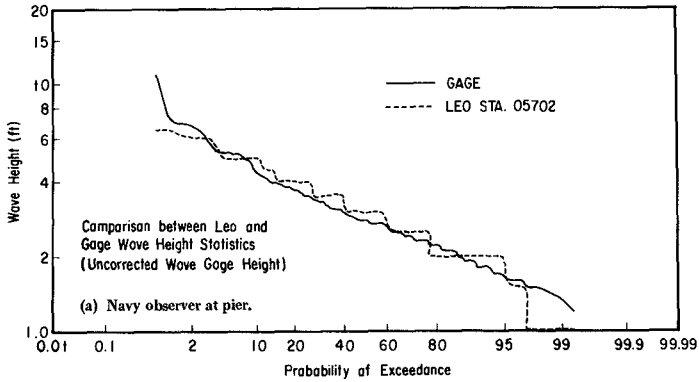


Figure 5. Probability a given wave height is exceeded, LEO breaker heights compared with uncorrected wave gage heights.

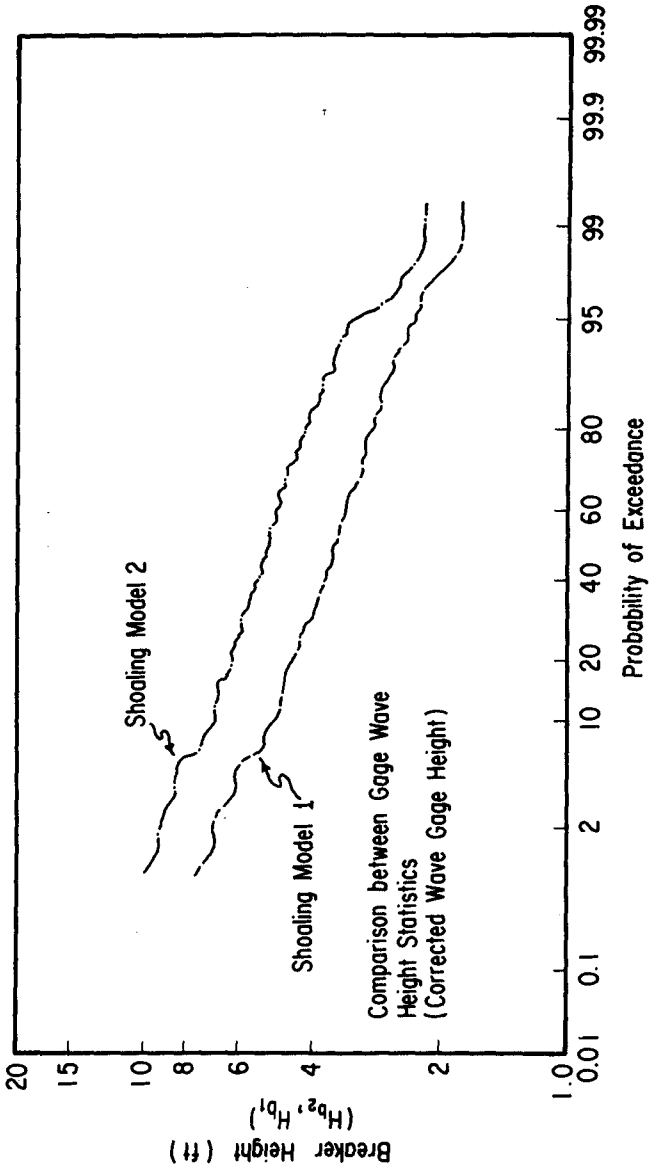


Figure 6. Probability a given wave height is exceeded, wave gage data corrected using shoaling models 1 and 2.

LEO observations are comparable. No firm conclusions can be reached regarding which wave of the spectrum an observer sees when he estimates the breaker height. It appears to be some wave between the root-mean-square height and the significant height; however, the scatter of individual observations about the line of best fit indicates that any individual visual observation may be in significant error. Statistically, however, the data appear to give comparable results. Data on observed wave periods and the measured period of maximum energy density are compared on figure 7 for each of the three data sets. In each case the tendency is for the observer to overestimate the wave period especially for lower wave periods. For larger periods there is some tendency for the LEO observer to underestimate the period. This apparent bias is presumably due to the observer's failure to count the smaller waves that pass a given point when timing the passage of 10 waves. This leads to a bias toward recording longer wave periods. Also, during times when there is a local sea which may dominate the wave energy spectrum, long period waves may continue to dominate in the breaker zone.

Table 1 compares the coefficients (ratio of LEO observation to gage measurement) of the best-fit line through the origin for (a) uncorrected gage heights, (b) the two shoaling models and (c) for wave period. All gage heights are significant heights or transformed significant heights. The gage period is again the period of maximum energy density in the spectrum and the LEO period is the time for 11 wave crests (10 wave lengths) to pass a fixed point in the surf zone.

TABLE 1: COMPARISON OF COEFFICIENTS OF BEST FIT LINE THROUGH ORIGIN

STA	OBSERVER	LOCATION	H_{LEO}/H_{GAGE}	H_{LEO}/H_{b1}	H_{LEO}/H_{b2}	T_{LEO}/T_{GAGE}
05702	(NAVY)	AT PIER	1.09	0.87	0.61	1.38
05703	(CERC)	AT PIER	1.27	0.99	0.68	1.18
05707	(CERC)	1000' N of PIER	1.24	0.96	0.65	1.21

Conclusions

When using the LEO method to collect wave data, the breaker height can deviate from measured heights, even after models had been applied to correct the information for shoaling effects. On the average, the LEO observations are a fair estimate of prevailing breaker heights.

Again the LEO estimates of breaker period tend to overpredict the period of maximum energy density, presumably because of the observer's failure to count smaller waves.

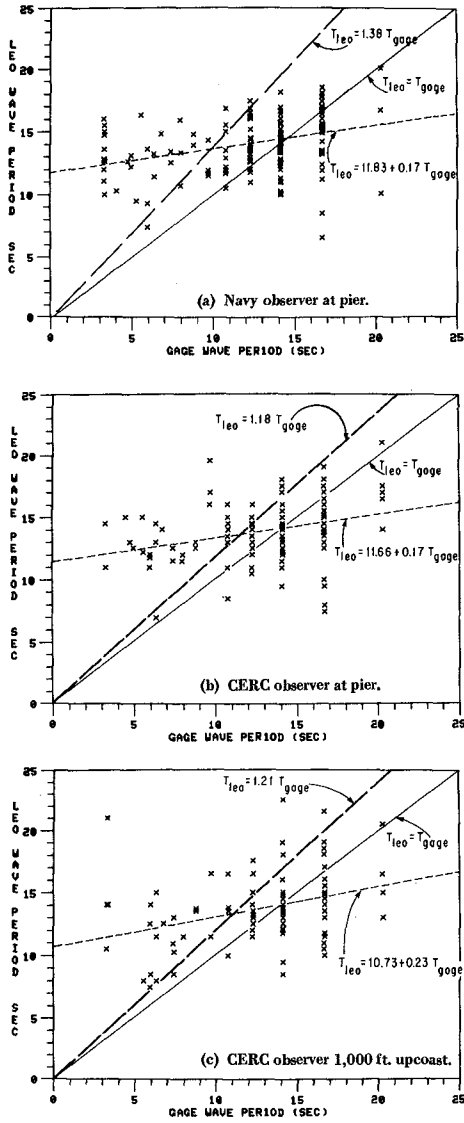


Figure 7. LEO observations of wave period versus period of maximum energy density from wave gage.

These conclusions are not general, as the capability of each observer is a real factor. Periodic visits and checks of observers are needed to insure data are collected conscientiously. Recognizing the shortcomings of visual observations, they still represent a useful and inexpensive source of coastal information, but data that must be used carefully with full recognition of its limitations.

ACKNOWLEDGEMENTS

The authors wishes to extend special thanks to Mr. Mike Leffler and Dr. Todd Walton for their assistance during the data analysis.

The analysis and results presented in this paper, unless otherwise noted, were based on research conducted at the Coastal Engineering Research Center under the Coastal Engineering Research Program of the U.S. Army Corps of Engineers. Permission to publish this information is appreciated.

REFERENCES

BERG, D.W., "Systematic Collection of Beach Data" Proceedings of the 11th Conference on Coastal Engineering, London, September 1968.

WAVE HINOCASTS AND MEASUREMENTS
BASS STRAIT

By

M. N. Silbert*, T. P. Barnett**, O. J. H. Peters† and R. C. Hamilton††

1.0 INTROOUCTION

The Bass Strait of Australia is the location of significant offshore oil and gas production. At the time of this writing eight self-contained drilling and production platforms as well as many miles of submerged pipeline comprise the Esso Australia Ltd. (EAL) and Broken Hill Proprietary Company Ltd. (BHP) operation in the Bass Strait. During the course of the next five years significant additional development and platform construction will take place in this offshore oil and gas area.

Observation of offshore wind and wave conditions are greatly facilitated by the presence of fixed platforms from which to collect data. Visual observations of waves along with measurements of wind speed and direction and barometric pressure from Bass Strait Platforms have been routinely recorded and reported to the Australian Bureau of meteorology for more than ten years. Close cooperation between EAL and the Meteorological Bureau has resulted in continuous weather forecasts for the Bass Strait region.

In March of 1977 EAL decided to upgrade the instrumentation on two of the platforms in the Bass Strait. The purpose of this was to reduce the subjectivity of visual wave observations and to eliminate the uncertainty of such observations at night and during inclement weather. Additionally it was felt that by instrumenting both a deep water (250 feet) and a shallow water (150 feet) platform the data collected would help quantify the observation that the storm waves seemed to be larger in deeper water than in shallow water. It was felt that use of the data along with a computer based wave hindcast model would aid in the development of an understanding of the Bass Strait wave environment.

Two platforms were chosen for instrumentation. The Barracouta (BTA) platform in 150 feet of water, located about 20 miles from shore, was instrumented with a wavestaff. The Kingfish B (KFB) platform in 250 feet of water, located about 50 miles southeast of BTA, was instrumented with a wave staff, electromagnetic current meters, anemometer, barometer and air temperature sensor. Figure 1 shows the location of these platforms in the Bass Strait. The design, fabrication and installation of the data station was performed by Evans-Hamilton Inc. of Houston, Texas.

*Exxon Production Research Company, Houston, Texas

**Scripps Institute of Oceanography, La Jolla, California

†Oceanographic Services, Inc., Santa Barbara, California

††Evans-Hamilton, Inc., Houston, Texas

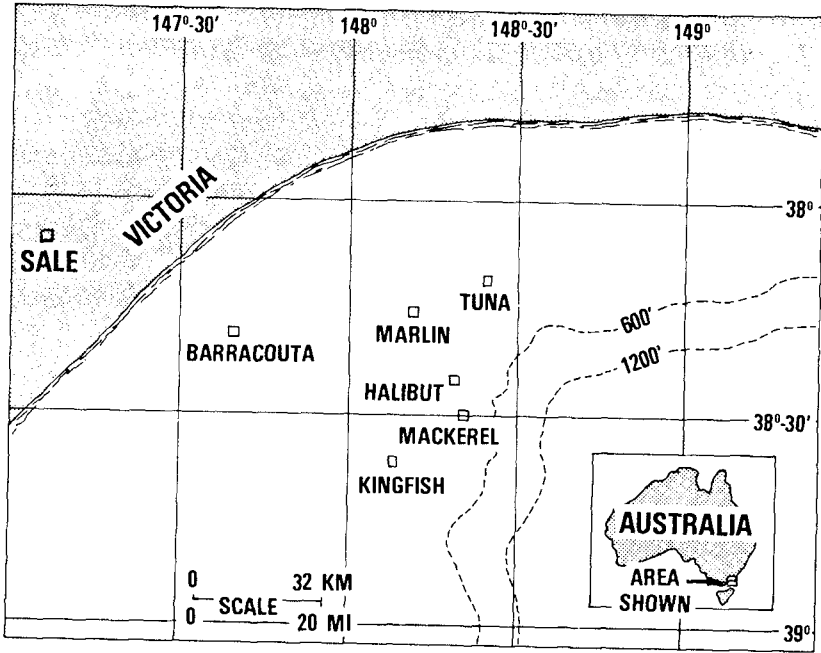


Figure 1. Bass Strait location map

Section 2 of this paper provides an overall summary of the Bass Strait weather. This is followed, in Section 3, by a review of the data acquired in the Bass Strait through the first six months of 1978. The wave hindcast model used is described in Section 4. Comparisons between measured and predicted sea conditions are detailed in Section 5.

2.0 AN OVERVIEW OF BASS STRAIT WEATHER AND WAVE CONDITIONS

During most of the year, the general atmospheric circulation in the region surrounding Tasmania and southeast Australia can be characterized as a steady procession of anticyclones moving from west to east with intervening troughs of low pressure. These troughs are usually accompanied by unsettled weather which often lasts for several days.

Low pressure systems track eastward across the southern Indian Ocean, south of 50° south latitude. Cold or occluded fronts associated with these systems usually extend northwestward from the storm center and track rapidly eastward through the Bass Strait region. Secondary low centers often form along these trailing fronts and move eastward or southeastward toward New Zealand. There are two favored areas for the formation of the secondary low centers: (1) the Great Australian Bight, and (2) the western Tasman Sea. On rare occasions one of these low centers will intensify enough to generate very strong wind (≥ 50 knots) in the Bass Strait. These storm events can be classified in one of three categories: (1) southwest storms, (2) southeast storms, and (3) southeast/southwest storms.

When intense cold fronts approach the Bass Strait, prefrontal winds blow from the northwest. Immediately after frontal passage, the wind direction shifts to the southwest, with strong wind speeds accompanied by high seas. The most intense southwest storms can generate winds as high as 50 to 60 knots.

The second class of severe storms are those that traverse or develop in the Tasman Sea. As these systems move into the central portion of Tasman Sea, they generate strong east to southeast winds (up to 60 knots).

Typical surface synoptic chart representations of these two types of storms are presented in Figures 2a and b. Note the classical closed circulation of the southeast storm (2a) typical of large extra-tropical storms. The southwest storm (2b) on the other hand presents a more complicated synoptic situation.

The final class of severe storms is similar to the southeast type. That is, they develop in or traverse the Tasman Sea. However, at some point near the peak (highest wind speeds) of the storm, a trough forms in the Bass Strait, generating south to southwest winds (waves) throughout most of the Strait. At the same time, very strong southeast winds are present just outside of the Bass Strait, extending well into the

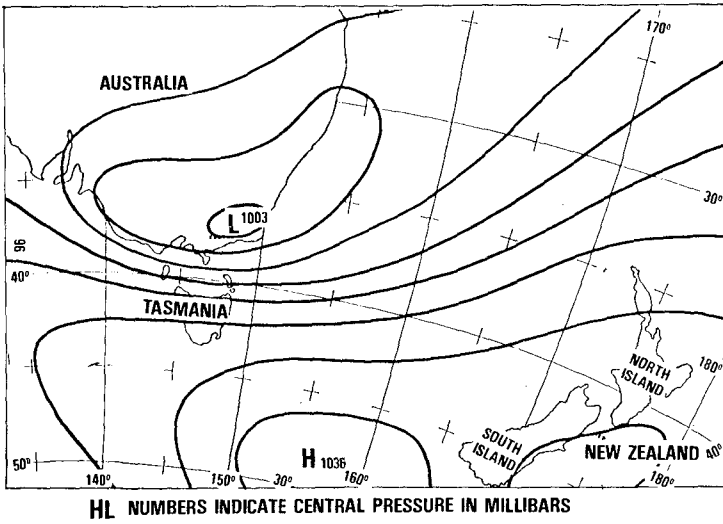


Figure 2a. Typical Southeast Storm

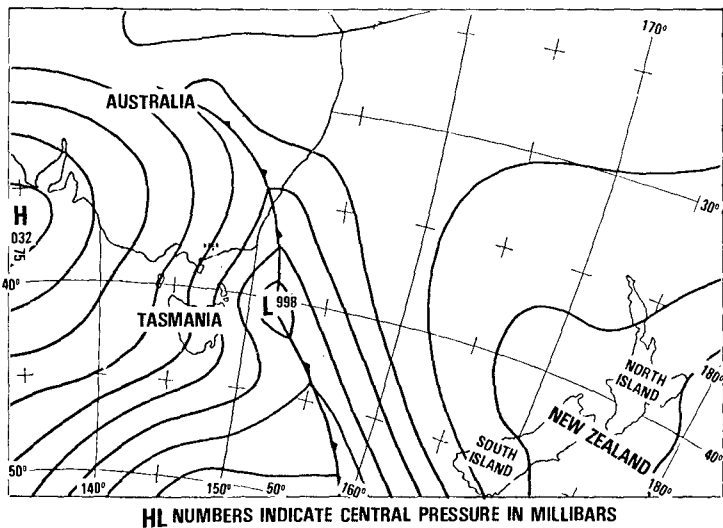


Figure 2b. Typical Southwest Storm

Tasman Sea. These southeast winds generate waves that propagate into the Bass Strait from the southeast.

3.0 SUMMARY OF OATA COLLECTED

Both data stations were made operational in early January of 1978. Since that time a large amount of "operational" (day-to-day normal conditions) data have been gathered. While these data are of great interest, the remainder of this paper will only discuss data collected during storms and the modeling of these storms.

3.1 STORM OATA (WIND AND WAVES)

During the period between January 1978 and June 1978, four storms occurred which were suitable for our analysis. Three of these storms were "southeasters" and one was a "southwester". Maximum significant wave heights ranged between 13.5 feet at BTA during a southwest storm in February to 29 feet at KFB during a June storm. For the sake of brevity we will present details of only two of these storms. However model comparisons have been made, and they will be discussed for all four storms.

3.1.1 SOUTHEAST STORM: Jan. 27-29, 1978

This storm developed on the east coast of Australia near 33°S latitude. The storm tracked to the southwest across Bass Strait and then southeast across the Tasman Sea. Maximum sustained wind speeds of 40 kts and largest significant wave heights of 21 feet were noted.

The measured H_s vs. time during this storm is shown in Figure 3a for the KFB location and in Figure 3b for the BTA location. Plots showing the measured average zero crossing wave period vs. time for KFB and BTA are shown in Figures 4a and b. The measured wind speed vs. time at KFB is shown in Figure 5.

3.1.2 SOUTHEAST STORM: JUNE 1-4, 1978

Initial development occurred over the interior of Australia near 28°S latitude, 147°E longitude. The storm moved off the east coast of Australia and tracked south near Bass Strait. It then moved east across the Tasman Sea. Maximum sustained winds reached 50 kts and significant wave heights as high as 29 feet were measured. A single zero crossing wave in excess of 60 feet was measured at KFB.

Significant wave height (H_s) time history plots for this storm are shown in Figure 6a and b for KFB and BTA respectively. Zero crossing period plots are shown in Figure 7a and b. Measured wind speed and direction vs time are shown in Figure 8a and b for the KFB location.

As shown in Figures 7-8, for some reason the KFB data station was not recording for a 10 hour period during this storm.

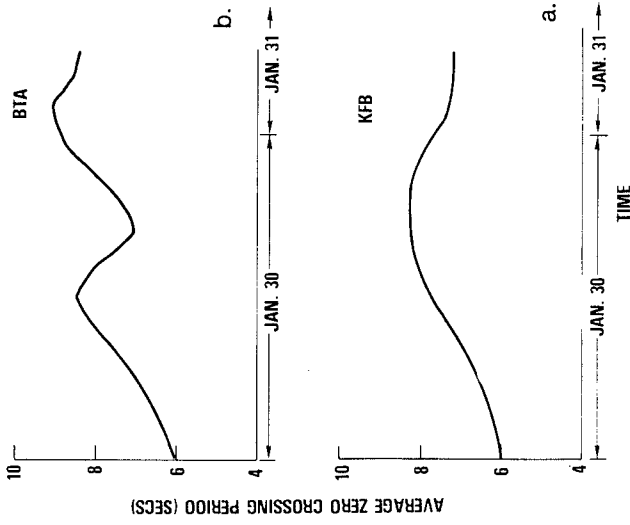


Figure 4. Wave Periods—Jan. 1978

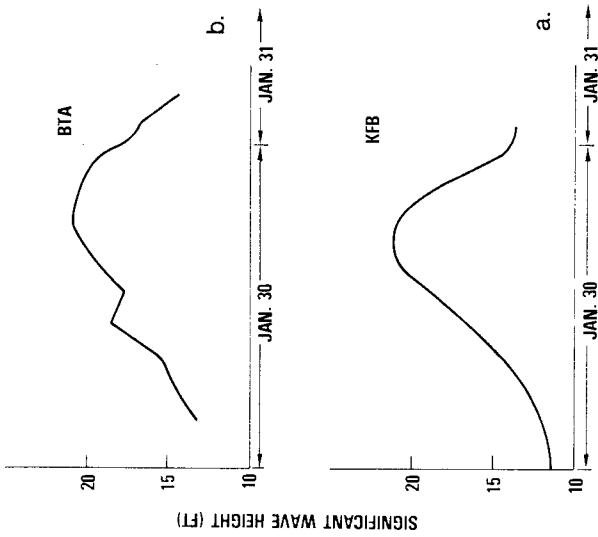


Figure 3. Storm Sea States—Jan. 1978

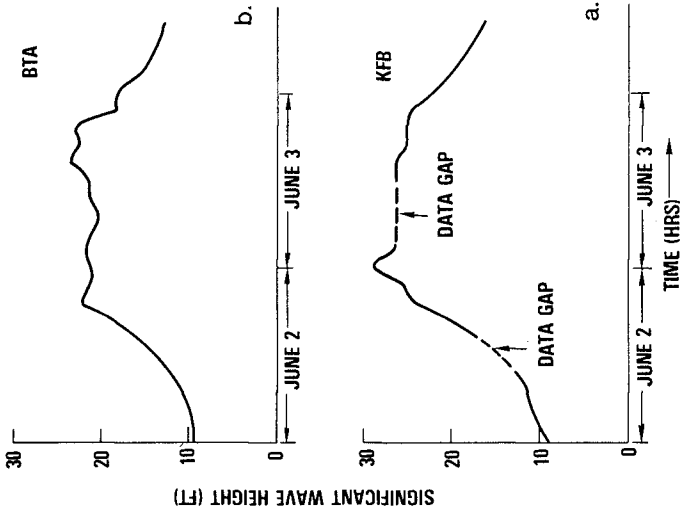


Figure 6. Storm Sea States—June 1978

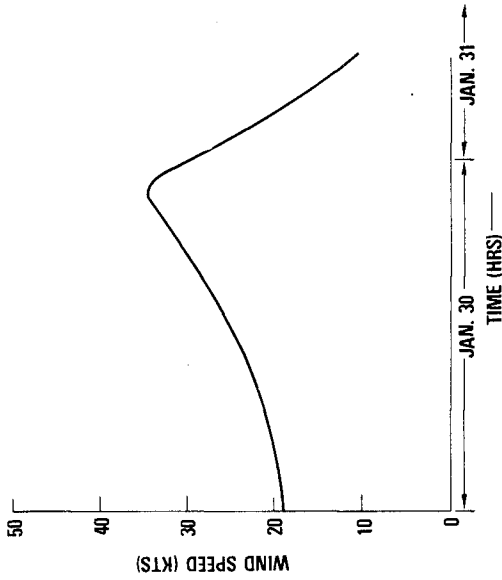


Figure 5. Wind Speed at KFB—Jan. 1978

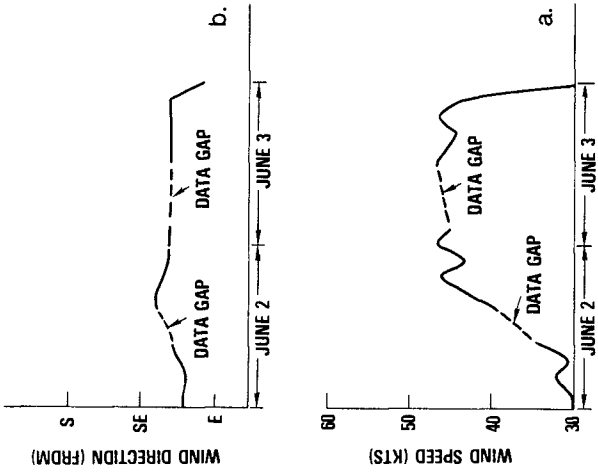


Figure 8. Wind Data—June 1978

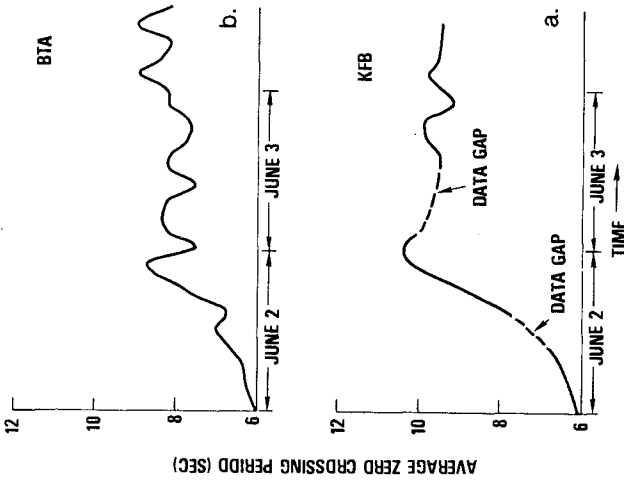


Figure 7. Wave Periods—June 1978

3.2 CURRENT DATA

One of the original goals of the instrumentation installed on KFB was to obtain data from the electromagnetic current meters that would enable determination of a directional wave spectrum. Due to various problems with the current meters and their mountings this goal was not achieved during the storms mentioned above.

4.0 DESCRIPTION OF THE WAVE HINCAST MODEL

We approach hindcasting the storms described above in two steps. First we treat the general problem of the generation of waves by wind in deep water. The wave model used in this part of the study was a spectral model based on the equation of radiative transfer (Barnett, 1968; Barnett, et al, 1969). In this model, propagation of wave energy is accounted for by the method of characteristics and is highly accurate numerically. Wave growth and decay are accounted for by atmospheric source terms that are based on theory (Miles, Phillips) and on empirical fits of observed wave generation cases. The wave-wave interaction terms are parameterized from the theoretical results of Hasselmann. The dissipation in deepwater is partially empirical and partially theoretical, relying on the concept of an equilibrium range in the high frequency portion of the spectrum.

The model is easily adjustable to arbitrary grids in physical space, as well as frequency-direction space. Thus it has been easy to test the model in both open ocean environments (e.g., North Atlantic, North Pacific) and enclosed bodies of water (South China Sea, Lake Superior) against actual observation. In all cases the average significant wave height hindcast error has been less than 3 feet rms. Recently the model has been applied to several storms in the North Sea with notable success in comparison with measured wave data.

The second step in our modeling procedure was to account for effects due to the interaction between the waves and the sea bottom. We have used a model based on the work of Hasselman and Collins (1968) to account for wave energy dissipation due to interaction with the sea bottom. This model does not account for shallow water generation, nor does it consider other forms of dissipation. It does provide an order of magnitude estimate of energy loss. Results of the dissipation calculations along with the difference between the results of the deep-water modeling at both KFB and BTA are used to estimate the wave energy at BTA.

4.1 WIND FIELD SPECIFICATION

Three basic marine wind field analysis methods are available for use in hindcasting severe storms:

- a. parametric wind models
- b. objective analysis schemes
- c. manual wind field analysis

Parametric models have been utilized (with considerable success) in modeling the surface wind field associated with tropical cyclones. However, these models have not been successfully applied to the complex wind fields associated with severe extratropical cyclones (Bretschneider, 1972).

Various objective analysis schemes are available for use in the specification of surface marine wind fields. These schemes range from computer-based routines that utilize surface pressure fields and marine wind observations, to complex planetary boundary layer (PBL) models that relate the surface pressure gradient, air-sea temperature difference and thermal advection to the local wind speed and direction (see Overland and Gemmill, 1977; Mooers and Partagas, 1976; Druyan, 1973, 1972; and Cardone, 1969). Provided a reasonably dense network of marine observations is available, the objective analysis schemes will yield results suitable for use in hindcasting severe extratropical storms.

The third analysis method (c above) is a technique in which experienced meteorologists derive the surface wind field distribution based on manually analyzed surface pressure fields and available marine wind observations. Although this method is very time consuming and therefore costly, a skilled, patient, meteorologist can produce very accurate results. The manual method has obvious advantages in that questionable data can be screened out more effectively, and observations not recorded at synoptic time periods can be easily incorporated into the evaluation.

4.1.1 DATA BASE

The marine areas surrounding Australia, Tasmania and New Zealand (like most marine areas) can be characterized as data sparse regions, where surface pressure analyses are based on a very limited number of ship observations. On the average, there are only 3 or 4 marine observations contained on the Australian Weather Service charts over the entire area of interest both east and west of the Bass Strait. Therefore, it was decided that the manual wind field analysis method would be the most appropriate technique to use in this hindcast, as it would provide the most accurate input data.

The Australian maps were reanalyzed OSI (Oceanographic Services Inc.) meteorologists based on: 1) additional observational data derived in a data search (through the National Climatic Center in Asheville North Carolina), and 2) prior experience in analyzing marine wind fields for the purpose of wave hindcasting in all areas of the world. In many cases existing historical surface pressure analyses can be improved by reanalysis, thereby improving the accuracy of hindcast wind fields.

4.1.2 SELECTION OF WIND SPEEDS AND DIRECTIONS

An appropriate grid system was developed for each storm type analyzed. Grid points were densely spaced within the Bass Strait with spacing increasing outside the Bass Strait. The grid system was

designed so that all regions of potential wave generation could be covered.

Hindcast wind speeds (10-minute average, 10-meter/standard level) and directions were derived at each grid point from horizontal pressure gradients, as reanalyzed from the Australian maps. Wind observations, recorded by ships operating in the basins during the hindcast time periods (acquired from the National Climatic Center) were also used in conjunction with the pressure analyses in selecting wind parameters.

In addition, observations from drilling units, and locally analyzed pressure maps (analyzed by OSI meteorologists in Sale, Australia during forecast projects in the Bass Strait) were used by OSI to augment the wind field analysis. During this earlier work, OSI found good correlation between wind speeds for various Bass Strait locations and pressure gradients between selected Australian and Tasmanian coastal stations. These relations were used as initial guidance in selecting wind parameters at grid points in the Bass Strait. OSI's choice of the wind field analysis method made it easier to incorporate these relations into the hindcasting scheme.

Finally, hindcast wind speeds and directions were compared with wind parameters reported at Australian and Tasmanian coastal stations. Reported coastal winds were adjusted to compensate for differing frictional effects as well as observed topographical effects.

The final wind field analyses were derived using all sources of available data. We believe that these analyses were as accurate as possible, within the limitations of the available data.

4.1.3 TIME INTERPOLATION OF WIND SPEEDS AND DIRECTIONS

It was necessary to provide wind input for each time step (one hour) of the model integration. Therefore, wind data were interpolated between available input map times. A linear interpolation scheme (for both wind speed and direction) was chosen as the best approximation for this hindcast after careful analysis of the wind speed time histories recorded at two marine measurement stations in the Bass Strait during the severe storms under consideration.

5.0 COMPARISON BETWEEN MEASURED AND CALCULATED CONDITIONS

To date we have compared calculated conditions with measurements for four storms at two locations. In general the results of this comparison have been very encouraging. Figure 9 shows a summary of the comparison between maximum measured H_s and maximum hindcast H_s . The discrepancy between model and data was unbiased while the rms deviation was less than 3 feet. Comparisons of this type have been reported elsewhere (Cardone et. al. Ewing et. al.) and allow a gross level of agreement to be established.

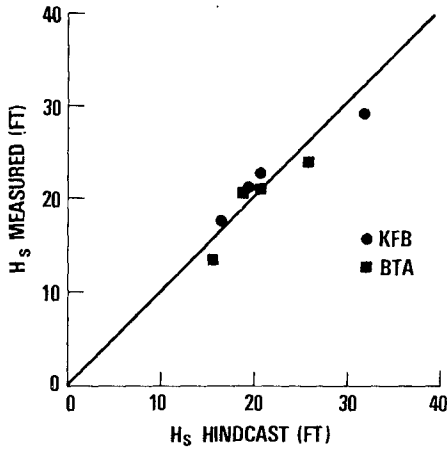


Figure 9. Measured and Calculated Maximum Sea States

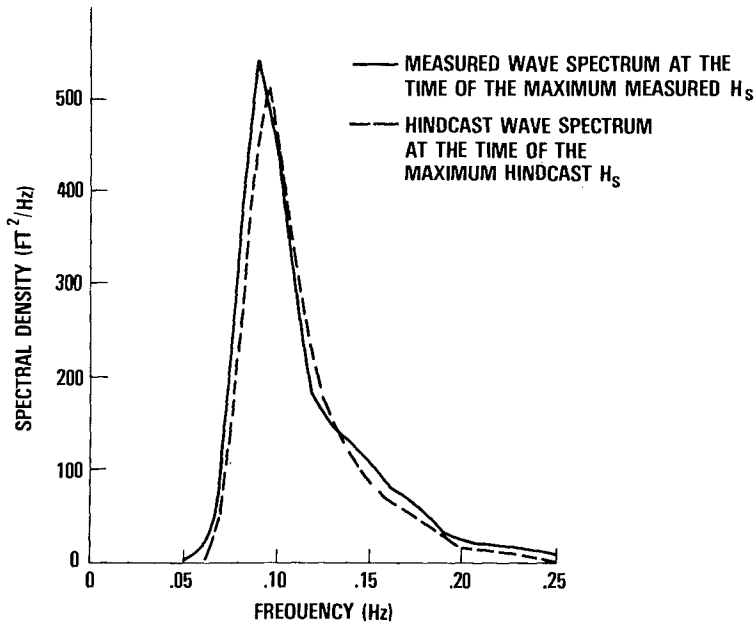


Figure 10. Wave Spectrum Comparison—Jan. 1978

More detailed comparisons between the measured data and the wave model have been made. These comparisons are useful in determining areas in which the modeling process can be improved. A more detailed model comparison for the two storms discussed earlier (January and June 1978) is given below.

5.1 STORM OF JANUARY 1978

During the peak of this storm the maximum measured wind speed at KFB reached 36 kts while the maximum hindcast winds reached 40 kts. The resulting maximum significant wave heights were 21 feet (measured) and 19.5 ft (hindcast) respectively. Figure 10 shows a comparison (for KFB) between the maximum measured and maximum hindcast wave spectra during the peak of this storm. Subjectively this comparison is excellent both in terms of total energy and frequency distribution.

Figure 11 presents a comparison of the sea state intensity (H_s) as the storm passes at KFB. It is clear from this plot that the general character of the storm development has been depicted by the model results. However, Figure 11 also illustrates the fact that there is a several hour shift in the time of occurrence of the peak seas. Given the 6 hour synoptic interval this fact is not surprising. A similar result was obtained at BTA with the agreement between measured and hindcast sea states being even better than it was at KFB. Numerical calculations convinced us that shallow water dissipation would not be evident in a storm of this intensity in these water depths.

5.2 STORM OF JUNE 1978

The results of our comparison of the measured and hindcast storm of June 1978 illustrate several interesting problems that can enter studies such as ours, but which are not usually reported.

5.2.1 DEEP WATER RESULTS

The maximum hindcast significant wave height for this storm at KFB was 32 feet. The maximum measured significant wave height for this storm at KFB was 29 feet (for a 40 minute period). The spectral comparison for this storm is shown in Figure 12. The maximum hindcast windspeed at KFB was 50 kts while the maximum measured wind speed was 46 kts. The wind/wave comparison stated in this way appears extremely good. However, if we look at the overall storm profile of H_s shown in Figure 13, several points become clear:

- o The duration of the storm was underestimated
- o The buildup of the seas was not reproduced
- o The period of sustained high waves for the hindcast storm was substantially different from the measured storm

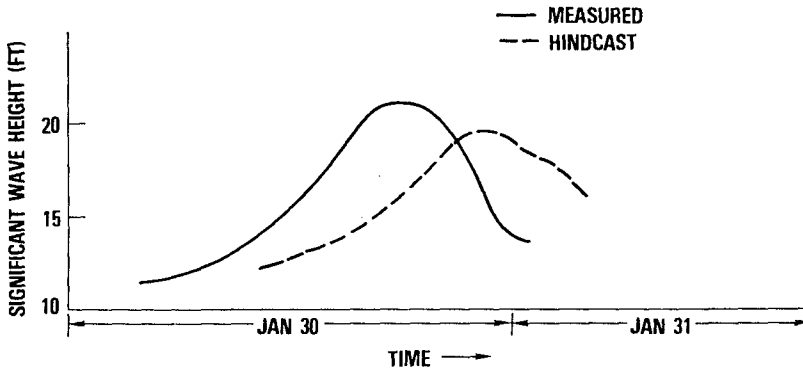


Figure 11. Measured and Hindcast Storm Profiles—Jan. 1978
KFB

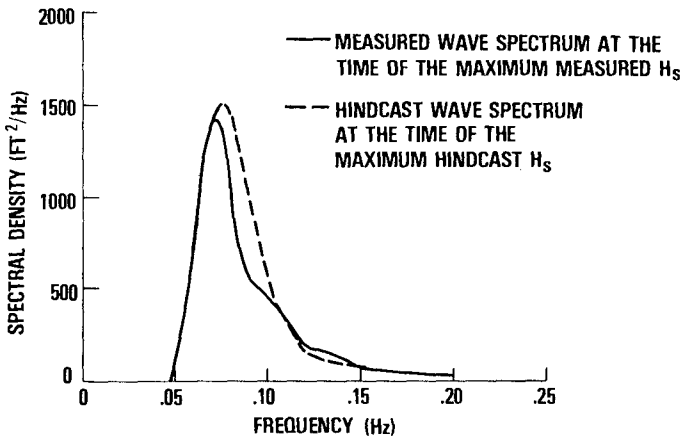


Figure 12. Wave Spectrum Comparison—June 1978

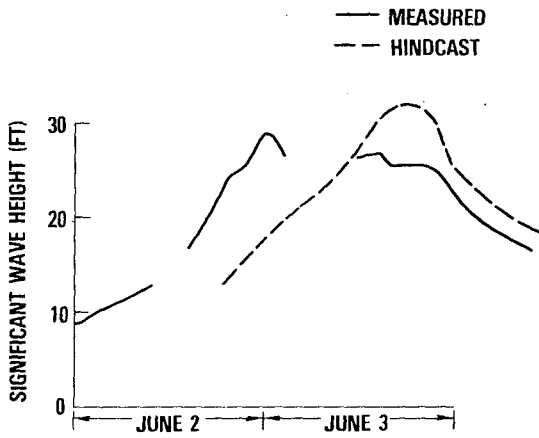


Figure 13. Measured and Calculated Storm Profiles

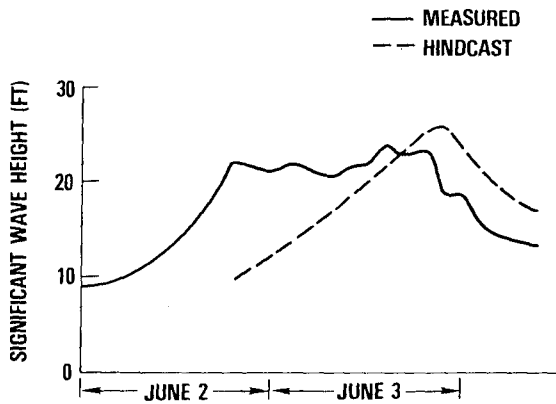


Figure 14. Measured and Calculated Storm Profiles

BTA

The reasons behind the above mentioned shortcomings, in this particular hindcast, can almost certainly be traced to the weather map construction. Due to the fact that the wave hindcast was conducted almost immediately following the construction of the weather charts, there was insufficient time to include any post analysis in this particular hindcast. It is the opinion of the authors that the shortcomings in this case are more indicative of weather forecast limitations than wave model inadequacy.

5.2.2 SHALLOW WATER EFFECTS

As mentioned previously we have used a shallow water computational algorithm to help quantify the reduction in wave intensity between KFB and BTA. The hindcast deepwater spectra at KFB were input to the model and the resulting spectra at BTA were computed. Since the shallow water model did not account for wave energy input from local winds, these computed values were further adjusted (somewhat arbitrarily) by the difference between the "deepwater" values at KFB and BTA. The purpose of this adjustment was to account for the spacial variability in the hindcast wind field in an order-of-magnitude way. In this case the adjustment led to a reduction in the calculated BTA sea intensities of approximately 2 feet. The results of this operation are shown in Figure 14. Once again, the peak sea intensity is reasonably represented by our model but the overall storm characteristics are not well represented. We again believe that the major influence for this storm is the inaccuracy in the weather analysis.

6.0 MODEL COMPARISON CONCLUSIONS

In general we have demonstrated that the numerical hindcast techniques discussed herein can be used to adequately estimate storm sea state characteristics. The model was applied to four storms at two locations yielding estimates of maximum significant wave height that on the average were within 3 feet of the measured values. Detailed comparison of model results with data indicate that the primary limitation in model capability is associated with the windfield description.

Furthermore we have documented the fact that significant differences in sea state intensity can exist between KFB and BTA during large storms with wind and waves from the southeast. Some of this difference can be attributed to bottom dissipation while some can likely be attributed to windfield variations. Additional studies along these lines that quantify the various influences more precisely (Shemdin et al.,) would be worthwhile.

7.0 ACKNOWLEDGEMENTS

The authors would like to thank Henry Gerlach, Ian Edwards and Alan Lunghusen of EAL for their help in this project. We would also like to thank the Royal Australian Navy Research Laboratory for their interest

and help in maintaining the equipment. The Australian Bureau of Meteorology is to be thanked for their cooperation in providing synoptic weather charts. Special thanks are directed to R. E. Haring of Exxon Production Research for his help and encouragement during the almost 2 years that this project spanned.

REFERENCES

1. Barnett, T. P., 1968, "On the Generation, Dissipation, and Prediction of Ocean Wind Waves," *Journal of Geophysical Research*, Vol. 73, pp. 513-530.
2. Barnett, T. P., C. H. Holland, and P. Yager, 1969: "A General Technique for Wind Wave Prediction with Application to the South China Sea," Final Report Contract N62306-68-C-0285, Westinghouse Research Laboratories, 31pp.
3. Bretschneider, C., 1972: "A Non-Dimensional Stationary Hurricane Wave Model," Offshore Technology Conference, Paper OTC 1517, pp. I-51-I-68.
4. Cardone, V., 1969: "Specification of the Wind Distribution in the Marine Boundary Layer for Wave Forecasting," *GSL Report TR-69-1*, Dept. of Meteorology and Oceanography, New York University.
5. Oruyan, L., 1973: "Objective Sea-Level Pressure Analysis for Data-Sparse Areas," *Journal of Applied Meteorology*, Vol. 12, pp. 256-263.
6. Oruyan, L., 1972: "Objective Analysis of Sea-Level Winds and Pressures Derived from Simulated Observations of a Satellite Radar-Radiometer and Actual Conventional Data," *Journal of Applied Meteorology*, Vol. 11, pp. 413-428.
7. Ewing, J. A., Weare, T. J. and Worthington, B. A.: "A Hindcast Study of Wave Climate in the Northern North Sea", EUR 10, European Offshore Petroleum Conference and Exhibition, October 24-27, 1978, London.
8. Hasselman, K. and Collins, J. I. 1968: "Spectral Dissipation of Finite Depth Gravity Waves Due to Turbulent Bottom Friction," *Journal of Marine Research*, Vol. 26, pp 1-12.

9. Miles, J. W., 1957: "On the Generation of Surface Waves by Shear Flows. Part I," *Journal of Fluid Mechanics*, Vol. 3, pp. 185-204.
10. Mooers, C., and J. Partagas, 1975: "Meteorological Forcing Fields in the New York Bight," Technical Report, University of Miami, Roseniel School of Marine and Atmosphere Science, 117 pp.
11. Overland, J., and W. Gemmill, 1977: "Prediction of Marine Winds in the New York Bight," *Monthly Weather Review*, Vol. 105, pp. 1003-1008.
12. Phillips, O. M., 1977: "The Dynamics of the Upper Ocean", Cambridge University Press.
13. Shemdin, O. H., Hasselmann, K., Hsiao, S. V., and Herterich, K., 1977: "Nonlinear and Linear Bottom Interaction Effects in Shallow Water," *Nato Symposium on Turbulent Fluxes Through the Sea Surface, Wave Dynamics and Prediction*, Marseille, France.
14. van Loon, H., J. J. Taljaard, T. Sasamori, J. London, D. V. Hoyt, K. Labitzke, and C. W. Newton, 1972: "Meteorology of the Southern Hemisphere," *Meteorological Monographs*, Vol. 13, No. 5, 263 pp.
15. Ward, E. G., Borgman, L. E. and Cardone, V. J.: "Statistics of Hurricane Waves in the Gulf of Mexico," OCT 3229, 10th Offshore Technology Conference, May 8-11, 1978, Houston, Texas.

REALTIME WAVE ANALYSIS, NEWCASTLE, AUSTRALIA

N.V. Lawson, Director, Lawson and Treloar Pty. Ltd.
P.H. Youll, Planning Engineer, The Maritime
Services Board of N.S.W.

1. INTRODUCTION

The Port of Newcastle, N.S.W., Australia, is being deepened from 11m to 15.2m below chart datum to permit the navigation of 120,000 D.W.T. bulk coal vessels. Part of this project, which is expected to reach a cost of approximately A\$90 million, involves the removal of two million cubic metres of rock, some of which is located outside the breakwaters and exposed to ocean waves (see Fig. 1).

Drilling and blasting of rock in the area subjected to ocean wave activity is being carried out by two self elevating platforms. On completion of drilling and prior to blasting the platform must make a transition from being supported by its legs to floating so it can be removed from the blasting area. While the two self elevating platforms have been built with a very fast jacking rate of 6m/minute, with a sophisticated shock absorbing system connecting the legs to the platform, the rigs cannot be jacked up or down when wave conditions exceed a certain limit. Even though the rigs can survive worse conditions than those allowable for jacking down by remaining on their legs at a sufficient height above the water, this would entail loss of drilling time, and the presence of the rigs in the channel could close the port to shipping.

Thus from an operational point of view it is vital that present wave conditions are reliably described. Estimation of wave height by observation is difficult enough during daylight hours but is virtually impossible in darkness (drilling operations are carried out 24 hours/day). The dredging contractor (WestHam Dredging Co. Pty. Ltd.) therefore decided that a real time wave analysis system should be established and co-operated with The Maritime Services Board of N.S.W. in a joint project for this purpose.

2. THE SYSTEM HARDWARE

A block diagram of the system hardware is shown in Fig. 2. Because of the large investment that the system is designed to protect it has been designed for maximum reliability.

Three Waverider buoys are used as the water surface elevation sensing instrument. The location of these buoys is shown in Figure 1. The offshore buoy and one inshore buoy were part of a traditional type Waverider installation which had been operating since 1975 (Lawson and Youll, 1977). The second inshore buoy (closest to the shore) was installed to add reliability to the system and to ensure that at least two buoys were always operating.

The Waverider buoy signal is received at a shore based station. Each buoy has its own receiver/ phaselock loop/digitiser circuit with an additional spare set of circuits to ensure minimum down time.

Each buoy is continuously monitored and the signal is digitised once every $\frac{1}{2}$ second to indicate the average position of the buoy over the previous $\frac{1}{2}$ second. An arbitrary datum is established 2000cm below mean water level and the position of the buoy in elevation is resolved to 1cm. A multiplexor samples all three channels and sends the 3 x 4 ASCII characters through the leased line, prefaced by a status character which indicates which buoys are not in position.

The characters are collected from the leased line by a PRIME 400 minicomputer running under a real time operating system. The Prime performs the required calculations and interpretations and sends these results back through the leased line to the WestHam site office. Input data is stored in a buffer while the calculations are performed so that no input data is lost, and all raw data and results of analysis is stored on disc, to be dumped to magnetic tape at fortnightly intervals.

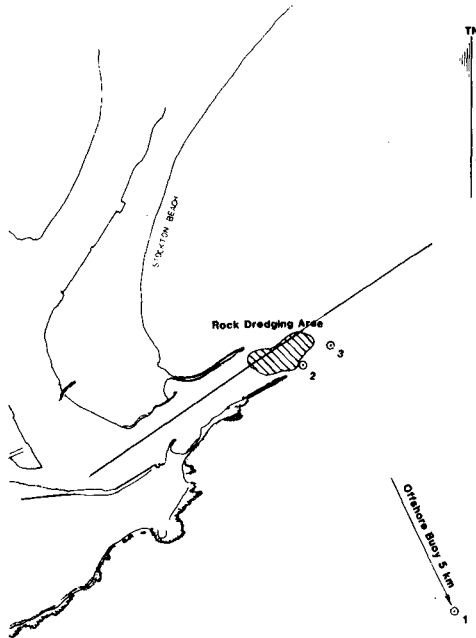


FIG 1 LOCATION PLAN FOR NEWCASTLE HARBOUR

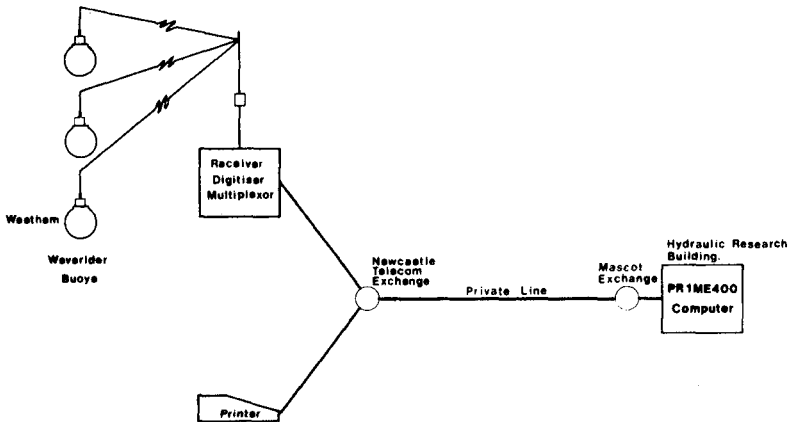


FIG 2 REALTIME WAVE ANALYSIS SYSTEM-NEWCASTLE

3. THE SYSTEM SOFTWARE

The system software performs the following functions :-

- (a) Collects the data from the leased line and checks for errors in line transmission, parity errors and for a Waverider buoy being hit or spun, which is usually indicated by a large displacement.
- (b) If it is recognised that the buoy has been hit or spun, a message is immediately sent to Newcastle with advice as to which buoy has been tampered with, and the appropriate action which should be taken.
- (c) Every 10 minutes, calculates for the previous 20 minutes of data, a wave-by-wave routine analysis and an auto-correlation type spectral analysis yielding the parameters of significant wave height (H_s), maximum wave height in 15 minutes (H_{max}) and peak period in the energy spectrum (T_p) (Abernethy and Lawson, 1973, Lawson and Abernethy 1975).
- (d) Following calculation H_s , H_{max} and T_p values are sent to Newcastle with H_s and T_p also being represented graphically.
- (e) If the value of H_s for any buoy has exceeded 1.75m since the previous computation, a message to that effect is sent to Newcastle with a warning bell to alert WestHam personnel.
- (f) The programme also checks the amount of energy at 0.0 Hertz. If the value is large, a message is sent to Newcastle indicating that a buoy is faulty, either due to interference or a twisted accelerometer suspension.

The system is in continuous operation, producing 144 analyses per day. CPU demand is very low at about 2 minutes/hour for data logging and analysis.

4. RECENT DEVELOPMENTS

While the system has been able to provide the dredging contractor with sufficient warning on most occasions, the provision of information from the waverider system at Botany Bay, 160Km to the south, would give earlier notice of waves arriving from the south. This addition to the system is at present being installed.

5. EXAMPLES

In the examples shown in Figures 3 and 4, the isobar spacing is 4mb. The two examples have been selected to show the two types of wave conditions which can occur off Newcastle :-

- (a) where Newcastle is within the wave generation area (Fig. 3).
- (b) where the swell generation area is some distance away from Newcastle (Fig. 4).

In Figure 3 a reasonably intense high pressure system and associated front formed over south eastern Australia during the early hours of 23rd September, 1979. Prior to its formation, low background type swell conditions existed from a weak high pressure system to the east of Newcastle. The significant wave height was about 1.1m while the peak period about 12 seconds. With the arrival of the locally generated waves from the south the amount of energy in these shorter period waves soon became larger than the underlying swell reducing the peak period from about 12 seconds down to 5 seconds. As the locally generated waves became larger the peak period became longer. In this example the warning that waves were going to get larger would have been accepted at about 1200 hrs. on 23rd September, 1979 providing more than the required 2 hours notice that waves inshore were likely to rise above 1.75m.

Figure 4 illustrates a classic example of swell waves arriving from a distant generation area. In this case the low pressure system is moving south east from Tasmania towards New

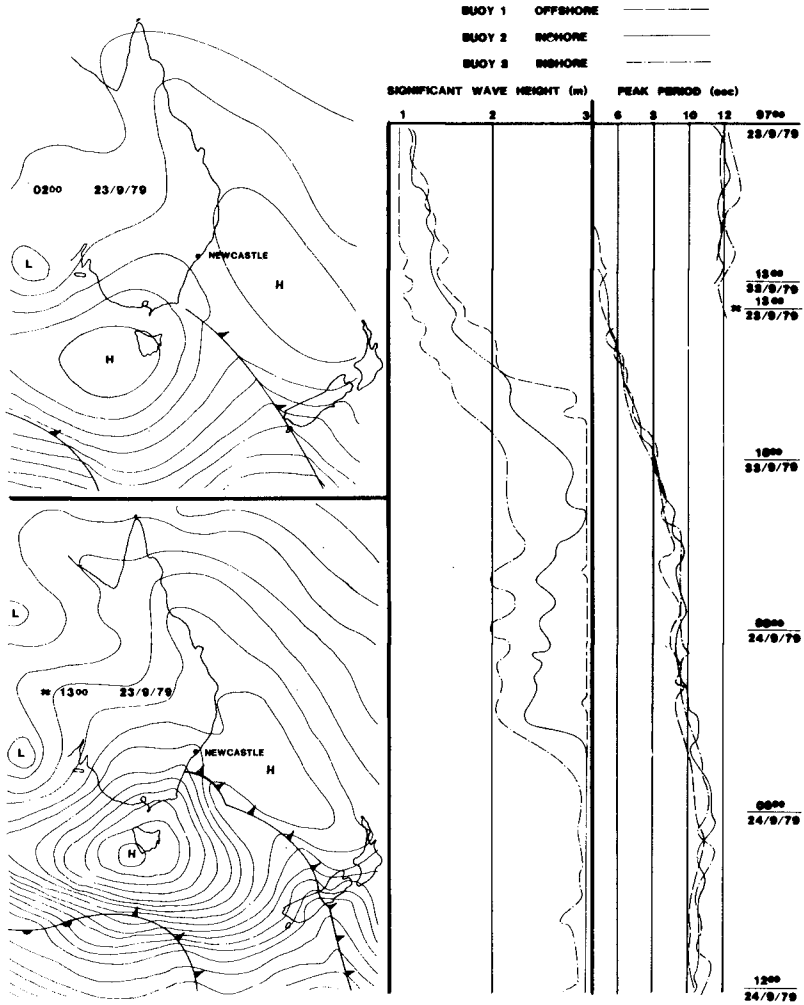


FIG 3 WAVE ANALYSIS OUTPUT

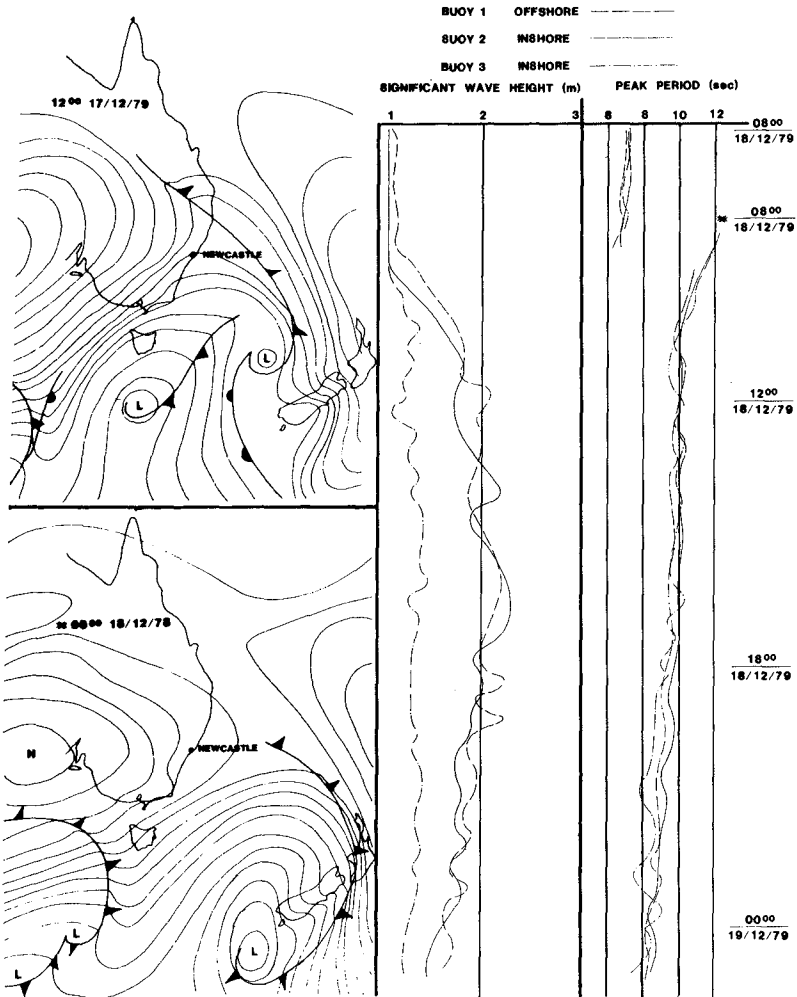


FIG 4 WAVE ANALYSIS OUTPUT

Zealand. The longer period waves of low wave height arrive first resulting in an abrupt change in peak period with no apparent immediate increase in wave height. However, this change is a clear indication that larger waves will follow within the next few hours. In this case the warning of increasing waves would have been accepted just after 0800 hours on 18th December, 1979, again providing at least the required 2 hours notice.

Situations similar to these two examples have been repeated on numerous occasions since the installation of the system during April 1979. The output format was chosen to provide clear results, requiring no interpretation. All the operator has to look for is a sudden change in peak period, either up or down, associate the change with the synoptic situation from a Facsimile (Fax) receiver, and issue a warning. It would be possible to provide more warning if the amount of energy in discrete period bands had been investigated, but this approach was rejected because of the additional interpretation required. With the system chosen all the operator needs to do is look for a change in peak period.

6. CONCLUSIONS

The system has now operated with good reliability for over 12 months. The most unreliable section of the system has proven to be the leased telephone line between Newcastle and Mascot. The system has provided the dredging contractor with a reliable warning system which on the great majority of cases has provided at least 2 hours notice that waves will rise above 1.75m.

This system has real advantages over traditional methods of wave data collection and analysis :-

- (a) There is an increase in reliability of the total system resulting from the early warning of a Waverider being hit or tampered with.

- (b) Data collection and analysis is a one step process rather than 2 or 3 steps resulting in less manhours in wave analysis and data storage.
- (c) There are significant benefits in the description of storm events. This type of recording will eventually allow more reliable and rational methods of describing and predicting return intervals of storms.

7. ACKNOWLEDGEMENTS

The authors wish to thank WestHam Dredging Co. Pty. Ltd. and their electronics sub-contractors Summit Electronic Systems, without whose assistance the system would not have been established, and the Engineer-in-Chief of The Maritime Services Board for permission to publish this paper.

8. REFERENCES

ABERNETHY, C.L. and LAWSON, N.V. (1973). Statistical Distributions of Wave Parameters off Botany Bay. 1st Aust. Conf. on Coastal Engineering. Sydney, pp. 52-58.

LAWSON, N.V. and ABERNETHY, C.L. (1975). Long Term Wave Statistics off Botany Bay. 2nd Aust. Conf. on Coastal and Ocean Engineering. Gold Coast pp. 167-176.

LAWSON, N.V. and YOULL, P.H. (1977). Storm Duration and Return Interval for Waves off the Central N.S.W. Coast. 3rd Aust. Conf. on Coastal and Ocean Engineering. Melbourne, pp. 123-130.

FLORIDA COASTAL DATA NETWORK

Gary Howell
Coastal and Oceanographic Engineering Department
University of Florida, Gainesville, Florida

1. INTRODUCTION

The application of wave and tide data to coastal engineering problems has been demonstrated frequently by university and government research organizations. However, problems faced by practicing coastal engineers are often solved without recourse to such data, since it is frequently not available for the required location. The high cost and low reliability of long term wave measurement is the primary factor limiting the wider application of analysis techniques requiring wave energy and wave direction parameters. In order to improve this situation several organizations, notably the Army Corps of Engineers, Coastal Engineering Research Center (CERC), Peacock (1974), and the California Department of Navigation and Ocean Development, Seymour (1976), have employed advanced electronics and computer techniques to reduce the cost of wave measurement. The Florida Coastal Data Network (CDN) is a similar effort which due to the special problems of Florida wave climate has employed advanced instrumentation not only to reduce cost, but to provide additional capability. Like other tropical and sub-tropical regions, Florida's coastal environment is characterized by relatively infrequent but severe tropical storms. In many coastal engineering applications, the specification of the hurricane-associated storm surge and storm waves will be the major design criteria. The Florida CDN was created in order to provide field measurements of waves and tides year-around as well as during hurricanes.

A measurement program of this nature must respond to both the immediate needs of practicing engineers as well as to research needs. Since it is unrealistic to hope for measurements of hurricane conditions at every location, the long term goal of research is to produce better models of storm waves and surge. Field measurements are required to assist in the formulation and validation of models. In the near term, actual measurements of both normal and severe waves and tides are the most reliable design input for the shallow and intermediate water depths.

Unfortunately, the severity of hurricanes, which makes them of interest to coastal engineers, also creates problems for instruments. Very few standard instrumentation installations have survived hurricanes. Most successful hurricane wave measurements have been made by either large, deep water

buoys or from oil production platforms in intermediate or shallow water depths. Most tide records of storm surge are from sheltered gages in bays or estuaries. Since large, offshore structures such as oil platforms are unavailable in Florida coastal waters, other strategies were investigated. Mounting instruments on existing piers was rejected due to the historically low survivability of such structures. Consistent with the low cost goals, a completely bottom-mounted instrument in a survivable structure was chosen. In order to gain as much benefit as possible from the high cost of installing and maintaining an installation, multiple purposes were defined. Each station was required to transmit wave and tide data over telephone lines to a central location. Additionally a self-contained power and recording capability was required for hurricane conditions.

Measurement sites were chosen at approximately equally spaced intervals around the coast (Figure 1). Specific locations were determined by considerations such as regular bathymetry, absence of nearby obstructions or inlets, and logistics. A target water depth of ten meters was specified in order to guarantee survivability during storm conditions and to provide measurements in the transition region between deep and shallow water. This water depth generally corresponds to distances of about one kilometer offshore on the East coast and over two kilometers on the Gulf coast.

2. INSTRUMENTATION

Absolute reading pressure transducers are bottom mounted on a completely self-contained electronics cylinder. The cylinder contains a microcomputer controlled data acquisition system (Howell, 1978) which can operate according to an internally stored program or upon commands received from shore. The shore connection supplies power to continuously charge internal batteries as well as two-way data communications using a standard computer interface (Figure 2).

A digital cassette recorder controlled by the microcomputer completes the underwater instrumentation.

The instrument cylinder is mounted inside a large steel tripod which is anchored at each apex to steel pipes jettied into the bottom sediment. The cylinder may be easily installed or removed by divers (Figure 3).

Two types of shore boxes are available. The first, a real time shore station, consists of a power supply and a telephone connected modem (Figure 4). Using the shore box, a central computer in Gainesville may interrogate the underwater microcomputer, and record a time series of water pressure in real time. The second type of shore box, the

PRESENT and PROPOSED FIELD STATIONS

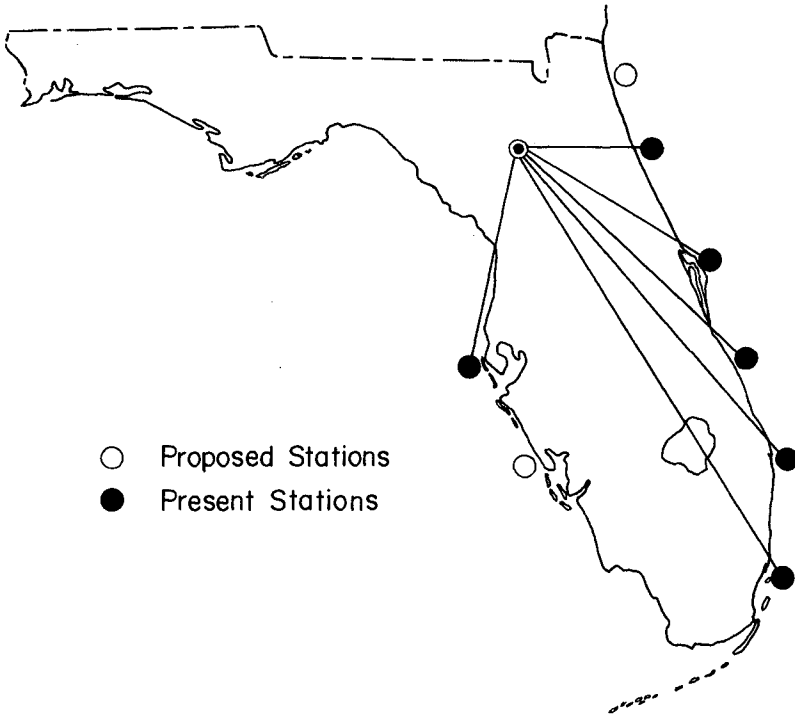


Figure 1

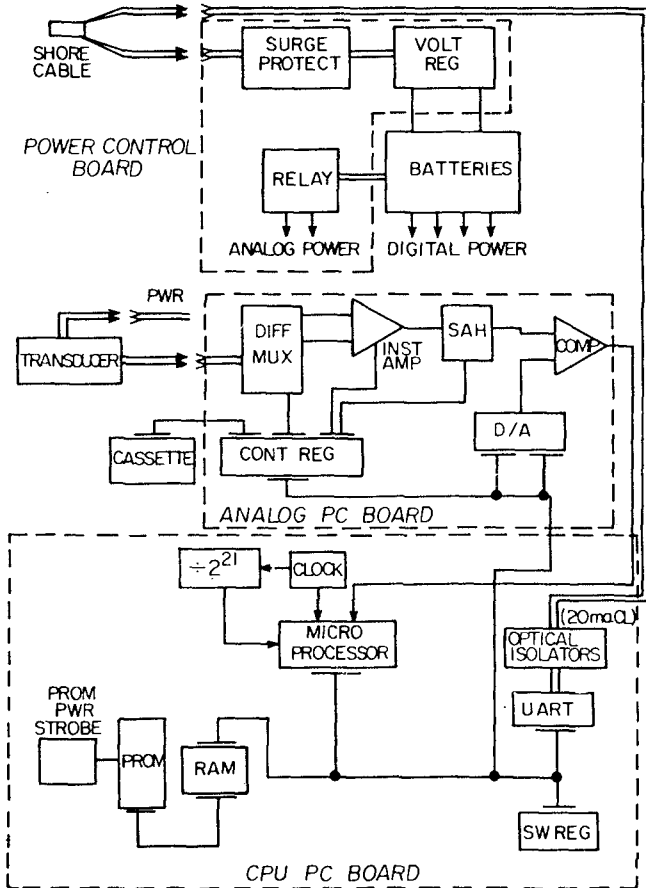


Figure 2
Block Diagram of Underwater Data Acquisition System.



Figure 3
 Dry run of instrument installation in underwater tripod
 mount. Note top retaining plate in foreground and
 anchoring pipes at apexes.

REAL TIME SHORE STATION

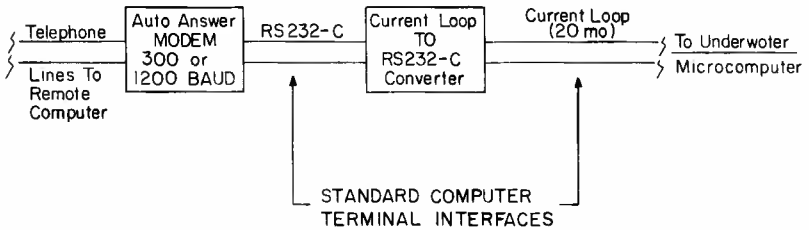


Figure 4

buffered data shore station, consists of a high performance microcomputer with 0.5 megabytes of disc storage, and a high speed modem (Figure 5). This shore station may be programmed to record data internally at scheduled intervals and has a limited analytical capability to record more data when certain parameters exceed a preset threshold. It is primarily employed to reduce long distance telephone charges by as much as a factor of 50 over the real time station.

At present, all CDN stations are programmed to operate in two modes. The first, a field station mode, allows data to be recorded in Gainesville over standard dial-up telephone lines. During these calls, a complete check of the underwater system is carried out by inspecting status indicators and exercising test routines. The second, called storm mode, is entered on command from Gainesville. Once entered, the underwater microcomputer automatically records (on the internal cassette) a seventeen minute data record and a four minute data record every hour for six days. The long and short records are spaced to give equal off-times during the hour. Once storm mode has been entered, data recording will continue even if the shore station and cable are lost.

3. DATA ANALYSIS

Just as important in reducing costs as a wave gage system are the data analysis techniques employed. Spectral analysis by digital computer has made a significant contribution to cost reduction, however most real systems still require significant time from skilled technicians to process all data records. This is due to inevitable errors and artifacts inherent in any instrumentation system. For the CDN a significant effort has been made to automate data analysis, achieving a goal that 90% of all records are analyzed without human intervention, and a minimum amount of effort required for the remainder.

The central computer at Gainesville can generate power spectra statistics of any recorded file immediately after the data has been recorded. This capability is useful for applications requiring real time data for operational purposes or in following the development of storms. A sample report output is shown in figure 6.

Figure 7 shows the routine procedure used for acquiring daily data from each station. Monthly summaries of recorded data are produced regularly and spectrally analyzed data are stored in archival files for long term statistical analysis.

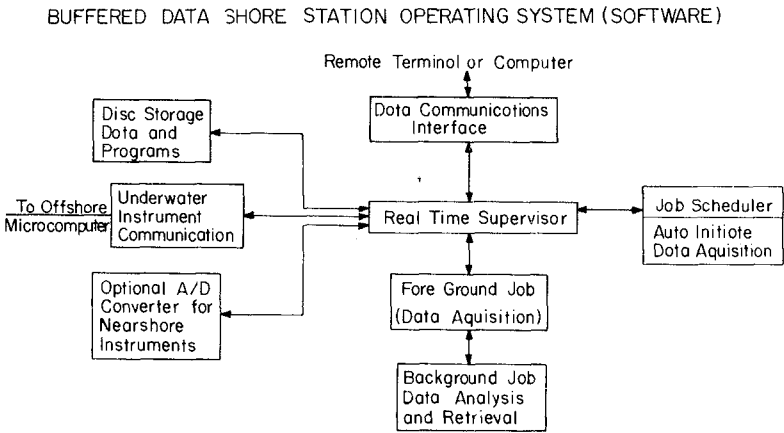
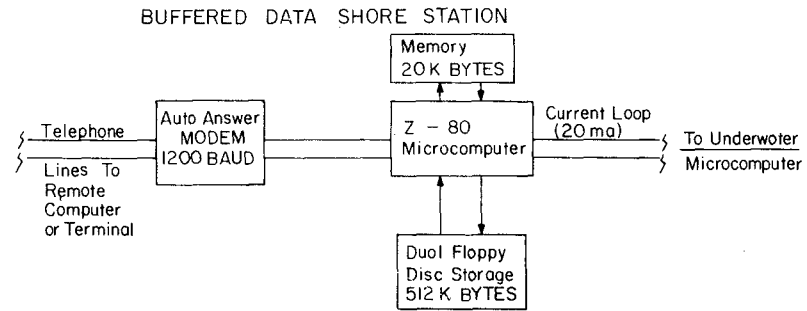


Figure 5

COASTAL DATA NETWORK

UNIVERSITY OF FLORIDA, GAINESVILLE, FL.

25-APR-79

WAVE DATA ANALYSIS REPORT FORMAT B VERSION 1.2
POWER SPECTRUM

FILENAME	STATION	JULIAN DAY	YEAR	LOCAL TIME
M8R31F	MARINELAND	504	1978	6:47

TIME SERIES STATISTICS (CM)

AVG	MIN	MAX	RMS
1079.003	961.339	1135.182	37.518

SPECTRAL STATISTICS CORRECTED TO WATER DEPTH

MEAN (CM)	TOTAL ENERGY (CM-CM)	S.D. (CM)
1079.114	2253.146	47.782

SPECTRAL PEAK (HZ)	SWH (CM)
0.109	131.129

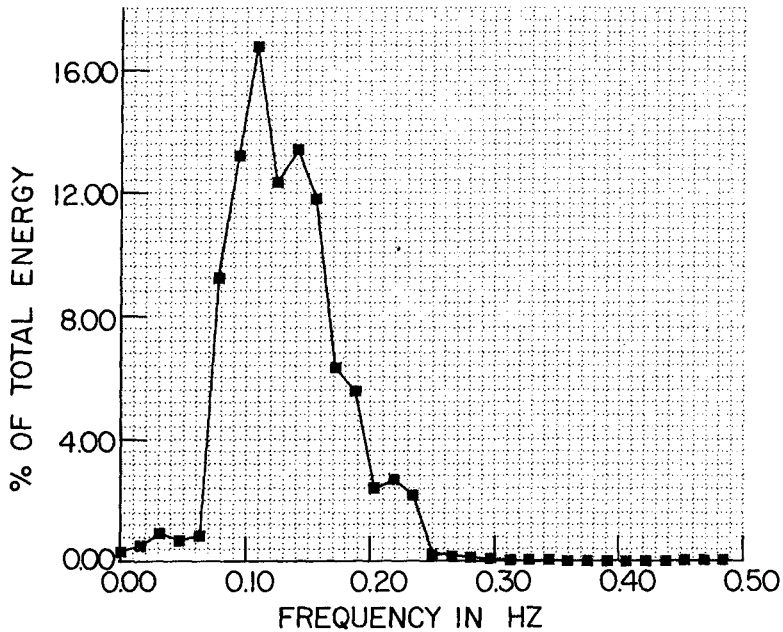


Figure 6

DATA AQUISITION FLOW DIAGRAM

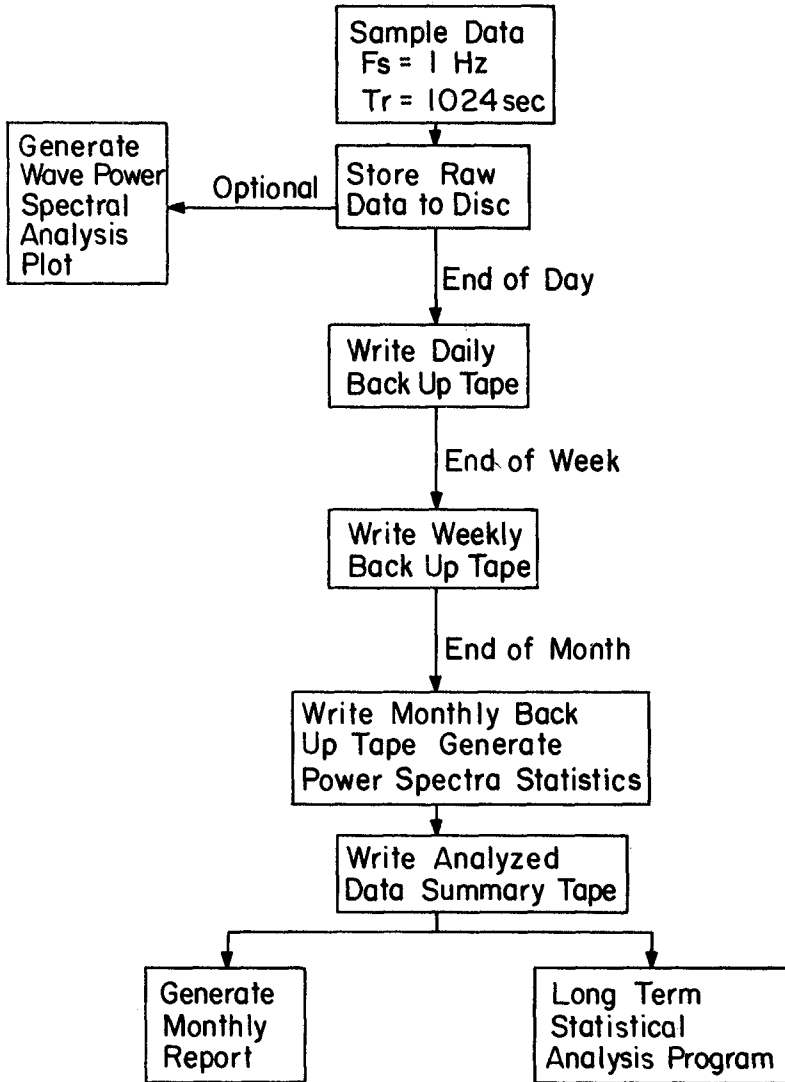


Figure 7

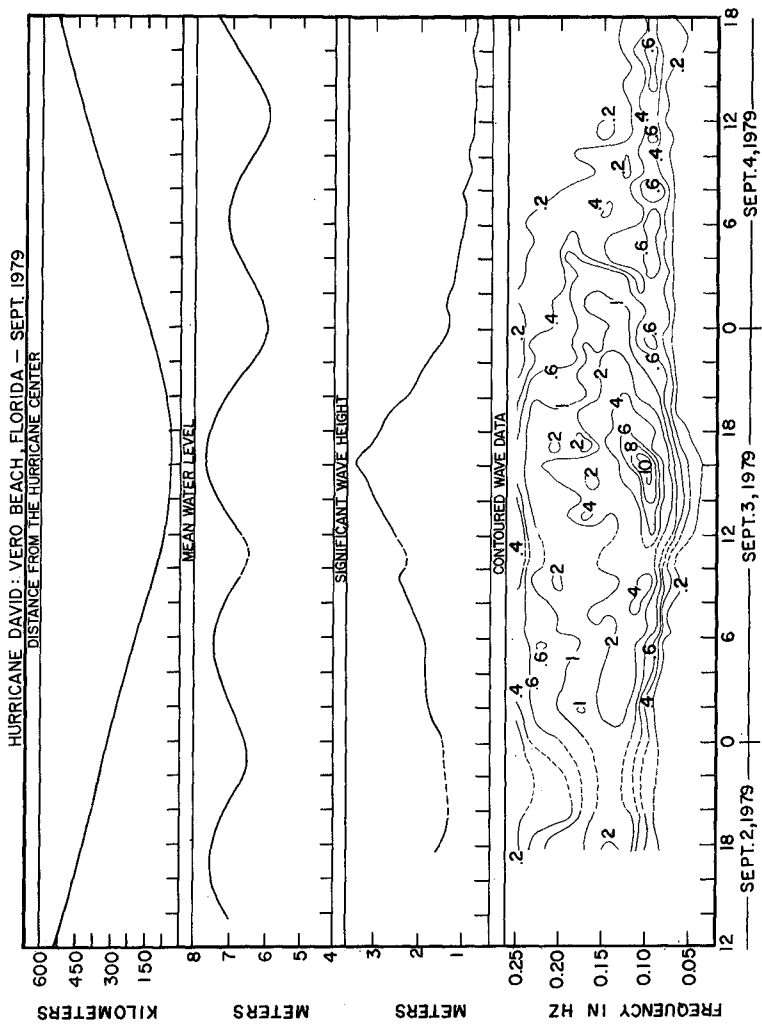


Figure 8

4. RESULTS

CDN has successfully recovered regular wave data from the oldest stations for a period of three years. Data sets are now large enough that a variety of analysis projects are feasible. In addition hurricane David which moved up the Atlantic coast in September 1978 passed directly over two measurement sites. Data from these stations were obtained as planned and are now being analyzed. Figure 8 shows composite plots of tide and significant wave height from one station. A contour plot of constant spectral energy density lines as a function of time is also shown. These data were calculated using spectral analysis techniques and depth attenuation correction by linear wave theory assumptions. Thus, some error can be anticipated in the most severe time periods.

5. CONCLUSIONS AND FUTURE DEVELOPMENTS

A combination of advanced instrumentation with designed in maintenance features and improved data analysis procedures have improved the economy and reliability of single point wave measurements. Progress still needs to be made in the area of wave direction measurements both in the area of instrumentation and data analysis. The tools and techniques developed by the Florida CDN, can readily take advantage of the rapid cost-performance increases of microelectronics. The time is approaching when coastal engineers may have reliable and economical long term measurements of basic parameters for site-specific and problem-specific applications. Finally a new breed of small, intelligent instruments based on the microcomputer is already under development. These instruments will bring analytical capability, decision making, and flexibility to previously passive observers of coastal phenomena.

6. REFERENCES

1974. Peacock, H.G. CERC Field Wave Gaging Program. Int. Symp. Ocean Wave Measurement and Analysis, New Orleans, pp. 170-185.
1976. Seymour, R.J. and Sessions, M.H. Regional Network for Coastal Engineering Data. Proc. Fifteenth Coastal Engineering Conference, Honolulu, pp. 60-71.
1978. Howell, G.L. A Microprocessor Based Underwater Data Acquisition System. TR-038, Coastal & Oceanographic Engineering Dept., Univ. of Fla., Gainesville. (NTIS NUREG/CR-1354).

CHAPTER 27

A MEASUREMENT OF SLOPE, CURVATURE, AND DIRECTIONAL SPECTRA OF WIND WAVES IN LAKE MICHIGAN

Paul C. Liu, M. ASCE¹

1. INTRODUCTION

Wave recording activity among coastal and oceanic engineers has increased rapidly in recent years, and ample wave data covering a large number of gage stations are now available. Directional wave spectra, however, are relatively scarce. The detailed knowledge of directional wave characteristics that correlate with the simultaneously recorded wind field is needed immediately for a proper understanding of the generation, growth, and propagation of a wave field. The data are necessary for engineering design, for verification and improvement of wave prediction models, and for provision of appropriate ground truth for calibrating remote sensing measurements. This paper represents the results of an effort to fulfill this need.

2. MEASUREMENTS

From July to October 1977, the Great Lakes Environmental Research Laboratory (GLERL) installed a light-weight, solar-powered research tower in Lake Michigan to provide a stable platform for supporting wind anemometers, temperature sensors, and an array of four wave staffs to measure meteorological and directional wave variables. The tower was located 2 km offshore from Muskegon, Mich., in 16 m of water (Fig. 1). The wave staffs, 6 m Kelk, Model P116, Zwarts gages (Zwarts, 1974), were placed at the center and vertices of an equilateral triangle of 3.05-m sides. The wave data were recorded digitally at 0.5-s sampling intervals for 30 minutes during each hour. The wind data used in this paper were recorded from an anemometer installed at 10 m above water level. A detailed description of the tower instrumentation data collection and reduction systems are given in Schwab *et al.* (1980).

3. DATA ANALYSIS

Conventional analysis for calculating the directional wave spectrum with a gage array usually yields poor directional resolution unless a large number of wave gages are used (e.g., Borgman, 1978). In order to

¹2939 Renfrew St., Ann Arbor, MI. 48105

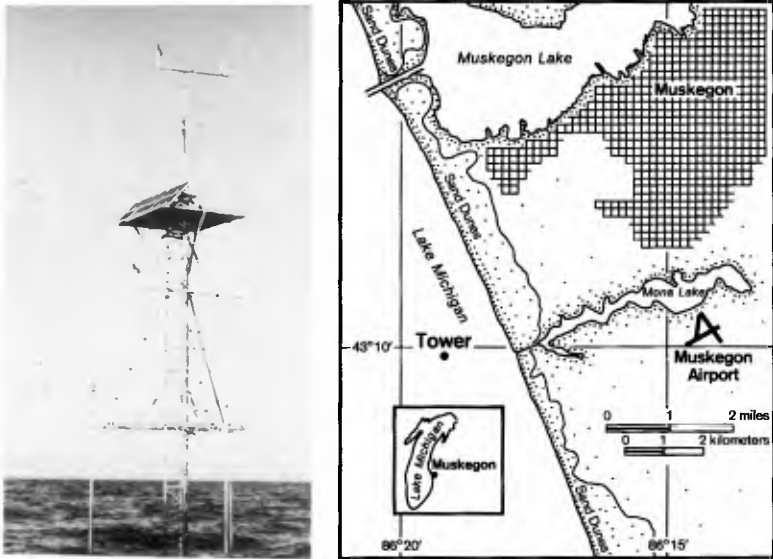


Fig. 1. GLERL research tower and its location.

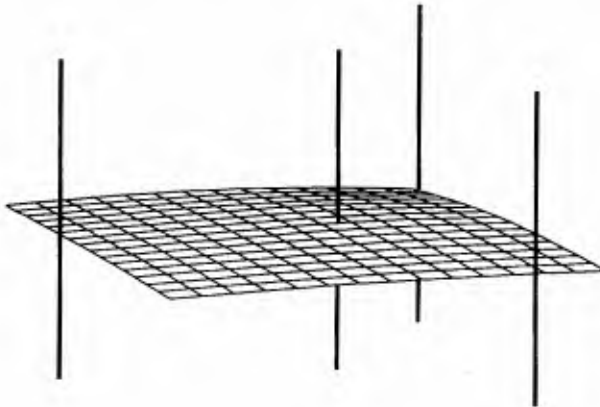


Fig. 2. An example of a fitted wave surface. The wave staffs are 6-m long.

improve the resolution with merely four wave staffs, the present study analyzes the data by fitting a cubic surface through the wave measurements. The fitted surface provides cubic spline approximations to the slopes and curvatures of the waves. Analysis was performed with the six quantities ζ , ζ_x , ζ_y , ζ_{xx} , ζ_{yy} , and ζ_{xy} , where ζ is the surface fluctuation at the center wave staff and the subscripts x,y indicate partial differentiations in the east-west and north-south directions, respectively. In addition to directional spectra, which can be calculated readily using these quantities in the method developed by Longuet-Higgins *et al.* (1963) and extended by Cartwright and Smith (1964), this method also provides an opportunity to examine characteristics and statistical distributions of wave slope and wave curvature. An example of a fitted cubic surface is shown in Fig. 2.

4. WAVE SLOPES

Perhaps because of a lack of practical measuring instruments, there have been very few field measurements of surface wave slope except for those reported by Cox and Munk (1956) and Longuet-Higgins *et al.* (1963). A number of laboratory measurements have been conducted by Schoolley (1954), Cox (1958), Wu (1971, 1977), and Long and Huang (1976), among others. These previous studies have shown that the statistical distribution of the wave slopes is approximately normal and the mean square surface slope increases as a function of wind speed. The data from this study basically agree with these results.

Fig. 3 presents a typical set of histograms for the statistical distribution of the east-west and north-south components of surface wave slope. They show essentially normal distributions. These histograms represent conditions during a southerly, 5 m s^{-1} wind, and skew is not evident. However, under stronger and growing wind speeds, an appreciable skew toward the windward direction indicated by Cox and Munk (1954) can also be found. The correlation of the mean square slope with wind condition is shown in Fig. 4. The data covered a wide range of wind conditions including both growing and decaying winds. The line drawn through the scattered points is representative of the mean square slope as proportional to the square of 10-m-level wind speed. The points away from the line are those under decaying winds. While the magnitude of the mean square slopes is similar to those oceanic cases calculated by Longuet-Higgins *et al.* (1963), it is much smaller than laboratory results. This is because laboratory measurements are for short dominant waves that contribute more toward mean square slopes than the long dominant waves found in the field and the instruments used in the field are not capable of measuring short waves.

5. WAVE CURVATURES

The study of wave curvatures is important in understanding the optical properties of the sea surface. Surprisingly few measurements have been made other than those made in the laboratory studies of Wu (1971, 1972, 1977). Theoretical studies (e.g., Kepr, 1969) have shown

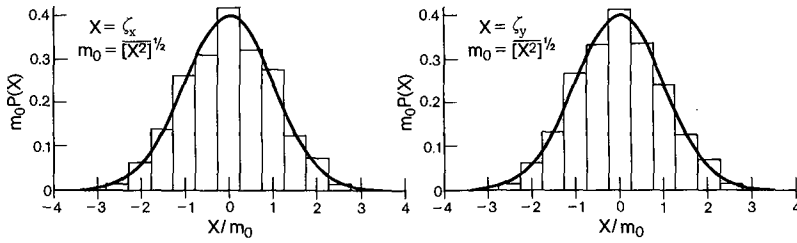


Fig. 3. Typical histograms of the distribution of x- and y-components of surface wave slope.

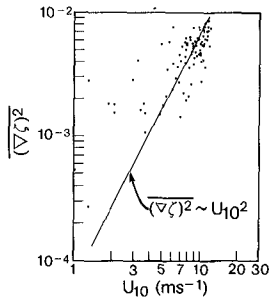


Fig. 4. Mean square surface slopes as a function of wind speed.

that if the surface is represented in the form

$$z = \zeta(x,y) \quad (1)$$

where (x,y) are horizontal coordinates and z is measured vertically upwards, the mean curvature J of the surface is given by

$$J = \frac{(1 + \zeta_y^2)\zeta_{xx} - 2\zeta_x\zeta_y\zeta_{xy} + (1 + \zeta_x^2)\zeta_{yy}}{(1 + \zeta_x^2 + \zeta_y^2)^{3/2}} = \zeta_{xx} + \zeta_{yy} \quad (2)$$

and its total curvature, Ω , is given by

$$\Omega = \frac{\zeta_{xx}\zeta_{yy} - \zeta_{xy}^2}{(1 + \zeta_x^2 + \zeta_y^2)^2} = \zeta_{xx}\zeta_{yy} - \zeta_{xy}^2 \quad (3)$$

The simplified versions in (2) and (3) are obtained by neglecting the squares of the surface slopes since they are much smaller than 1. In general, the statistical distribution of the components ζ_{xx} , ζ_{yy} , and ζ_{xy} are normal, as shown in Fig. 5. Therefore the mean curvature J , being the sum of two normal variates, is also normally distributed (Fig. 6). Longuet-Higgins (1958) derived a strikingly non-normal distribution for the total curvature Ω . This distribution was found to be asymmetrical with positive skewness; its distribution function satisfies a linear differential equation depending on two parameters derived from the moments of the surface energy spectrum. A comparison of Longuet-Higgins' distribution with histograms from the present data is shown in Fig. 6. It is seen that the histogram does exhibit an asymmetrical character with positive skewness. However, its fit with the theoretical distribution is by no means close. Further examination shows that the theoretical distribution has a maximum skewness of 1.15, while the skewness obtained from the data is consistently greater than 1.15 by a factor of 2 or more. One possible explanation is that the statistical characteristics of the variates ζ_{xx} , ζ_{yy} , and ζ_{xy} are assumed to be similar in the theoretical derivations. In the data, however, it has been found that the moments of ζ_{xy} are consistently an order of magnitude smaller than those of ζ_{xx} and ζ_{yy} 's.

The variations of curvature with wind have also been examined. Fig. 7 represents mean square values of J and Ω plotted against wind speed. From the data obtained under varied wind fields, the mean square of total curvature appears to be proportional to U_{10}^2 , while the mean square of mean curvature is proportional to the square root of U_{10} .

6. DIRECTIONAL WAVE SPECTRA

Previous studies of directional wave spectra have been concerned mostly with single instances of time. The continuous measurements available from the GLERL research tower provide an opportunity to study directional characteristics of waves episodically. In the present

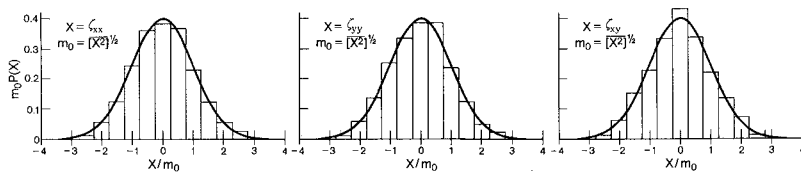


Fig. 5. Typical histograms of the distribution of component curvatures.

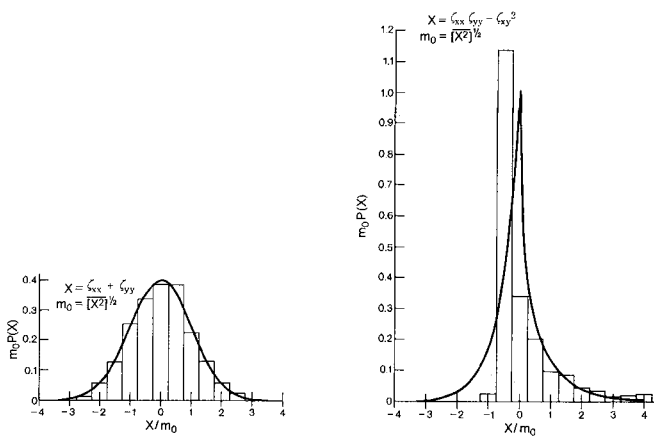


Fig. 6. Typical histograms of the distribution of mean and total curvatures. The non-normal distribution curve represents Longuet-Higgins' theory.

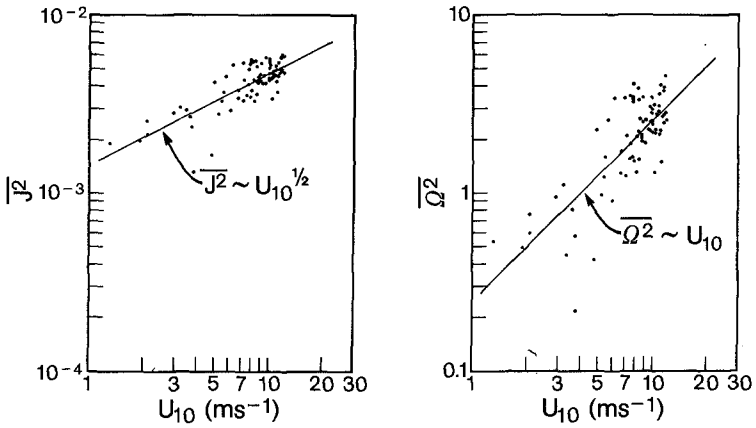


Fig. 7. The mean square values of mean and total curvatures as a function of wind speeds.

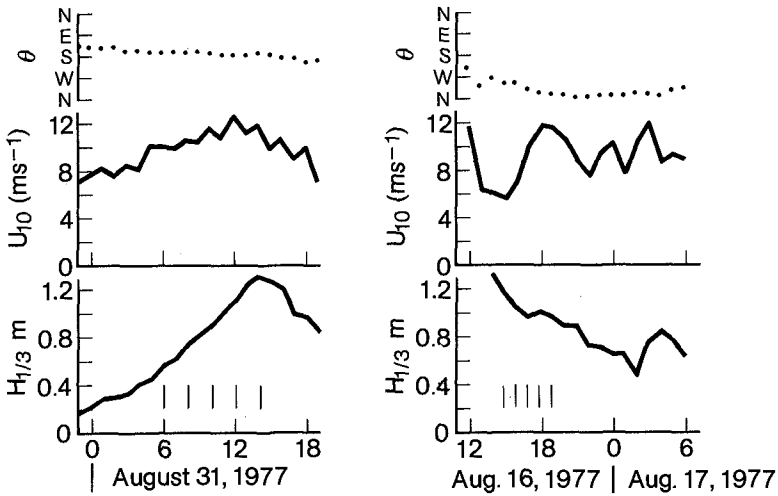


Fig. 8. Two episodes of wind and wind fields for directional spectral study, August 31, 1977, and August 16, 1977.

study two episodes, each with a characteristic wind field, were selected for illustration. Fig. 8 presents the wind and wave fields of the two episodes.

The episode of August 31, 1977, has a constant southerly wind direction with increasing wind speed that generates steadily growing waves. Five sets of single and directional wave spectra at 2-hour intervals between 0600 and 1400 hours, as shown by the tick marks in Fig. 8, are presented in Fig. 9. The directional spectra were plotted on a polar graph with frequency as the radial axis. The contours represent equal spectral energy densities. While contour levels were not indicated, in order to avoid crowding in the figure, it should be noted that the outside contours had the lowest magnitude and remained the same for all the figures. The contour levels increased logarithmically toward the hill, which corresponded to the spectral peak in the single spectrum. It can be seen that as waves grow the contours spread toward lower and higher frequencies and higher spectral density develops around the hill. The directional spectra are unimodal with some skewness toward higher frequency, especially when waves grow higher.

These results also show that the directional spreading tends to be narrow only around the spectral peak and wide for both higher and lower frequencies. This is consistent with the $\cos^2\theta$ model, where a higher s indicates narrower spreading. It has been shown by Mitsuyasu et al. (1975) that s is the highest at the spectral peak and decreases toward both higher and lower frequencies.

The episode of August 16, 1977, on the other hand, shows a wind direction changing from south to northwest, with a somewhat fluctuating wind speed. The five directional spectra shown in Fig. 10 were between 1500 and 1900 hours during periods of increasing wind speed, while waves decayed because of the changing wind direction. At 1500 hours, the spectrum was clearly northward owing to previously southerly wind. At 1600 and 1700 hours the waves decayed, the hill remained northward even though the wind direction had changed. There were indications that the contours at both the higher and lower frequency sides tended to spread toward the new wind direction. At 1800 hours an interesting bimodal picture had developed. A new hill showed up in the new south-southwest wind direction, but an old hill remained northward with diminishing magnitude. It was also interesting to note that with the bimodal directional spectrum, there were corresponding two peaks in the single spectrum. Finally, at 1900 hours, the waves conformed to the direction of the prevailing wind. The actual duration to which the wind switched from a steady south to a steady northwest direction lasted over 8 hours. The directional spectra carried the memory of northward direction during most of this time.

Changing wind direction is a familiar and common phenomenon. Hence the response of waves should also be familiar and common. However, the process of direction is also extremely varied; hence a knowledge of these responses is difficult to assess. The results shown in Fig. 10 represent a first look into one of these interesting and intriguing common occurrences.

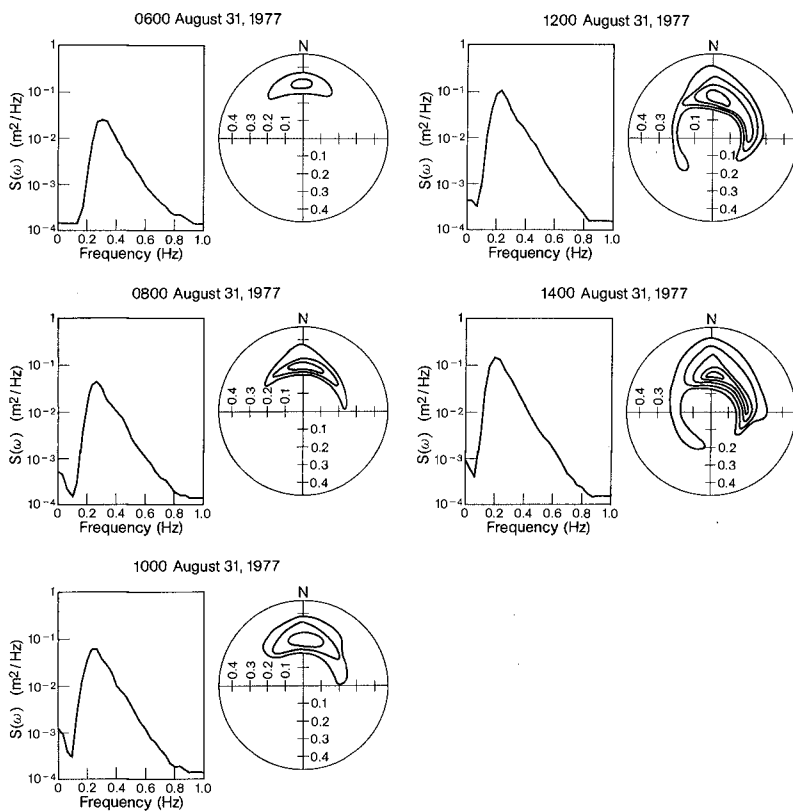


Fig. 9. Single and directional spectra during an episode with constant wind direction, August 31, 1977.

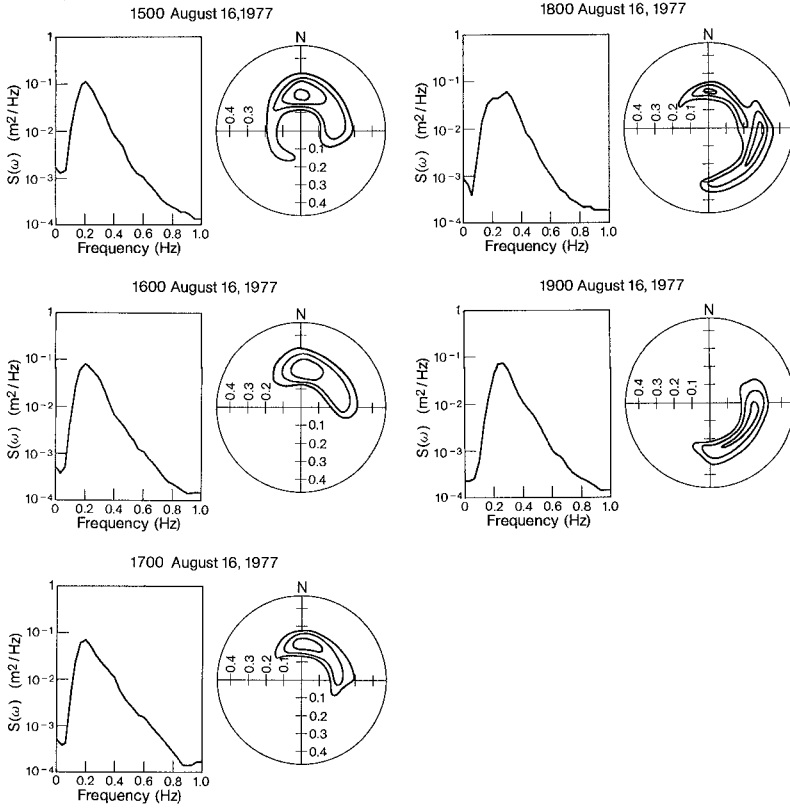


Fig. 10. Single and directional spectra during an episode with changing wind direction, August 16, 1977.

7. CONCLUDING REMARKS

By fitting a cubic surface through the measurements of the four wave staffs, the result of this paper has shown that wave slope, curvature, and directional spectra can be readily calculated with improved resolution over conventional array measurements. Direct measurement of wave slope and curvature in the field has been extremely rare. This study was able to provide these data indirectly and an examination of their statistical characteristics. The results are generally consistent with previous studies. The continuous measurements made from the research tower provided an opportunity for interesting episodic case studies, which is an improvement over previous directional wave analysis that studies mostly single instances in time. This paper represents a first step toward filling the need for definitive directional wave information. Efforts to quantify these results by parameterization, correlation, and modeling are presently under way at GLERL.

8. REFERENCES

- Borgman, L. E. 1978. Directional wave spectra from wave sensors. In Ocean Wave Climate. M. D. Earle and A. Malahoff, ed. Plenum Press, New York, N.Y., 253-267.
- Cox, C. S. 1958. Measurements of slopes of high-frequency wind waves. J. Mar. Res. 16, 199-225.
- Cartwright, D. E., and Smith, N. D. 1964. Buoy techniques for obtaining directional wave spectra. Buoy Technology, Washington, D.C., Marine Tech. Soc., 112-121.
- Kepr, B. 1969. Differential geometry. In Survey of Applicable Mathematics. K. Rektorys, ed. The M.I.T. Press, Cambridge, Mass., 298-373.
- Longuet-Higgins, M. S. 1958. The statistical distribution of the curvature of a random Gaussian surface. Proc. Camb. Phil. Soc. 54, 439-453.
- Mitsuyasu, H., Tasai, F., Suhara, T., Mizuno, S., Ohkusu, M., Honda, T., and Rikiishi, K. 1975. Observations of the directional spectrum of ocean waves using a cloverleaf buoy. J. Phys. Oceanogr. 5, 750-760.
- Schooley, A. H. 1954. A simple optical method for measuring the statistical distribution of water surface slopes. J. Opt. Soc. Am. 44, 37-40.
- Schwab, D. J., Liu, P. C., Soo, H. K., Kistler, R. D., Booker, H. L., and Boyd, J. D. 1980. Wind and wave measurements taken from a tower in Lake Michigan. J. Great Lakes. Res. 6, 76-82.

- Wu, J. 1971. Slope and curvature distributions of wind-disturbed water surface. J. Opt. Soc. Am. 61, 852-858.
- Wu, J. 1972. Surface curvature of wind waves observed from different angles. J. Opt. Soc. Am. 62, 395-400.
- Wu, J. 1977. Directional slope and curvature distributions of wind waves. J. Fluid Mech. 79, 463-480.
- Zwarts, C. M. G. 1974. Transmission line wave height transducer. In Proc. Internat. Symposium on Ocean Wave Measurement and Analysis 1, 605-620.

CHAPTER 28

WAVE ATTENUATION AND WAVE SET-UP ON A COASTAL REEF

by

Franciscus Gerritsen
Professor of Ocean Engineering
University of Hawaii at Manoa
Honolulu, HI 96822

ABSTRACT

In attempting to specify criteria for the design of structures on coastal reefs, it was found that no adequate method existed to derive those criteria from the deep water wave conditions.

In order to fill the gap, a program of measurements and analysis was initiated at the University of Hawaii.

The program consisted of prototype and laboratory measurements. Great emphasis was placed on reliable field data, which were collected on Ala Moana Reef, in Honolulu.

Laboratory investigations on the behavior of waves on shallow reefs are subject to scale effects; verification from field observations is required to obtain reliable results. As a result of this study, a mathematical model was developed for the calculation of wave attenuation and wave set-up on a shallow reef, using the incident waves in the ocean as boundary conditions.

This paper discusses the general behavior of waves approaching a shallow reef and presents some essential characteristics of the mathematical model. The study is limited to waves approaching the shoreline at right angles.

The results of this study can be extended to breakwaters with wide, submerged berms.

1. INTRODUCTION

In Hawaii many coastal areas have a relatively low elevation and require protection against wave attack by storm waves. In some of these areas a shallow coral reef extends between the shoreline and the deeper water. The reef may be biologically alive or dead. Such coastal reef offers significant protection to the coast; the large ocean waves will break on the edge of the reef and the wave that reaches the coastline is of reduced magnitude. Not only is wave energy lost in the breaking process but attenuation of wave height also takes place due to friction along the bottom.

After the breaking of waves on the reef's seaward edge, regeneration of waves may occur over the reef, creating waves of lower height and shorter period. If wind blows over the reef in shoreward direction, wind energy is transferred into wave energy but the growth of wind generated waves over the shallow reef is limited by the depth of the water.

The effect of wave breaking and wave attenuation on a shallow reef, however, also has another aspect: it generates a setup of the mean water level over the reef and near the coastline. The increased water

depth in turn results in greater wave heights near the shoreline. Onshore winds may further increase the depth of water near the shoreline and in this way also contribute to a potentially greater wave height.

The depth over a reef usually varies in the direction parallel to the shoreline, giving rise to differences in setup along the coast. The resulting gradients of the mean water level drive a mean current system. Such currents are of major importance with regard to the transportation of coastal sediments, and also for the onshore-offshore mixing of the water leeward of the reef and the ocean waters. Quantitative knowledge of the setup is required for a prediction of these currents and their effects.

Knowledge of the setup and the wave characteristics leeward of a reef is furthermore necessary in numerous engineering endeavors, such as the assessment of beach stability or the design of coastal structures, as well as the prediction of the dynamic response of ships or the design of marine terminals in waters partly protected by a reef. The existing grave uncertainties with regard to the design parameters mentioned above has led to a widespread practice of producing conservative results, which needless to say, results in unnecessarily high costs.

In view of the preceding discussion it was proposed to carry out a study on the attenuation of ocean waves on a reef and of the associated wave setup.

In addition to a theoretical analysis of the problem the study would consist of a field study and a laboratory study.

It was believed that a scale model study in a wave flume would in itself not be conclusive and that data from the field, properly analyzed, would be required to arrive at reliable answers.

A comparison between field and model data would furthermore provide interesting information regarding possible scale effects.

2. WAVE TRANSFORMATION ON A SHOALING BOTTOM AND A HORIZONTAL OR SLIGHTLY SLOPING REEF

Waves moving from deep into shallow water are subject to transformation, which may take different forms, whether the waves are monochromatic or random and whether they are breaking or not breaking.

The following general characteristics have been documented.

- a. Periodic waves propagating into shallow water are likely to demonstrate cnoidal characteristics (Svendsen and Buhr Hansen, 1976).
- b. A solitary wave progressing over a sloping bottom onto a shelf or reef, with no breaking occurring, demonstrates a remarkable behavior in that the initial wave disintegrates into a train of solitary waves of decreasing amplitude. These are called solitons. (Madsen and Mei, 1969; Johnson, 1972).
- c. For waves approaching a beach or a shallow reef, breaking occurs when the wave height over depth ratio assumes a

critical value. The behavior of breaking waves has been documented by many experimental studies (e.g. Galvin, 1968). Battjes (1974) found that the similarity parameter

$$\xi_o = \frac{\tan \alpha}{\sqrt{\frac{H_o}{L_o}}},$$

in which α represents the slope and H_o and L_o re-

spectively the deep water wave height and wave length is a characteristic parameter useful in describing breaking wave characteristics.

- d. The behavior of random waves after breaking over a sloping bottom or on the edge of a natural reef is not well documented in the literature. These are the type of waves that are particularly relevant to this study. At the study site incident waves usually have a narrow-band spectrum, often showing distinct wave group behavior.

As the waves shoal and break, secondary waves are typically formed and are indicative of a nonlinear wave process. Because of the wave height variation in the (random) waves the zone in which initial breaking occurs extends over a certain width; a consequence of this is that the fraction of breaking or broken waves in a wave record varies over the breaking zone.

Energy dissipation leading to a reduction in wave height is primarily due to bottom friction and breaking. When the bottom is porous, percolation losses may become important. The wave attenuation is primarily at the expense of the energy near the peak frequency of the spectrum. At the same time nonlinear energy transfer takes place from the peak frequencies to higher and lower frequencies.

The lower frequency energy components demonstrate themselves in the surf beat which is induced by the height modulation of the breaking waves and the corresponding variation in shoreward mass transport. The higher frequency waves are generated in the breaking process in the form of secondary waves riding on the crests of the primary waves.

As a result of these transformations, the mean period of the waves inside the reef is considerably lower than the period of the incident waves outside the reef.

The decrease in wave energy is associated with a rise in the mean water level over the reef (wave set-up). Low frequency waterlevel variations may be observed as the dynamic part of the wave set-up.

It has been the objective of this study to quantify the above processes and to provide the design engineer with the tools to calculate the relevant design conditions.

For a mathematical model to adequately describe the behavior of random waves after breaking, the following aspects need consideration:

- energy losses due to wave bottom friction and percolation;
- energy losses due to wave breaking;
- the fraction of breaking waves in a wave record, as a function of location

- exchange of energy from medium to lower and higher frequency components of the wave spectrum;
- wave set-up and wave set-down.

Within the framework of this paper it will not be possible to give adequate coverage to all aspects of these transformations. Most attention will be given to wave energy dissipation and wave set-up.

Empirical coefficients from the mathematical model are verified from the analysis of the field and model observations. The experimental set-up is described in the following section.

3. EXPERIMENTAL SET-UP

3.1 Field Experiments

The field experiments were conducted on a shallow reef at Ala Moana Park, in Honolulu, Hawaii. Site conditions, bathymetry, and measurement stations are shown in Fig. 1. In all stations, except Station 6, waves were measured with a capacitance wave gage (Black, 1978). In Station 6 where heavy breaking occurred, wave heights were obtained by filming the motion of a tethered buoy from a location offshore.

For the determination of wave set-up best results were obtained from visual readings of the mean water level using five separate manometers, fixed to the reef bottom and carefully levelled from a bench mark on shore (Wentland, 1978). At the study site the offshore bottom consists of a stable coral reef, whereby the (dead) coral heads produce a rough surface.

3.2 Model Experiments

The model experiments were conducted in the outdoor wave flume of the J.K.K. Look Laboratory. The flume is 54 m long and 1.22 m wide. Maximum water depth is about 1.0 m. Waves are generated with a parabolically shaped plunger type wave generator; the maximum wave height is about 0.3 m, whereas wave periods range from 0.5-4.0 sec. Only regular waves can be generated. The vertical walls partly consist of glass panels, which allow visual inspection of the wave phenomena from outside.

The size of the tank allowed the construction of a 1:12 scale model of the outdoor reef site, whereby 130 m of the actual reef could be simulated. Waves were measured with capacitance wave gages in positions corresponding to the field stations. The waves were recorded on two channel wave recorders and on magnetic tape.

For the measurement of wave set-up in the tank best results were obtained by visual readings of manometers, attached to the outside of the flume and connected with 3 mm plastic tubes mounted inside to the side-wall of the tank, with their openings close to the bottom.

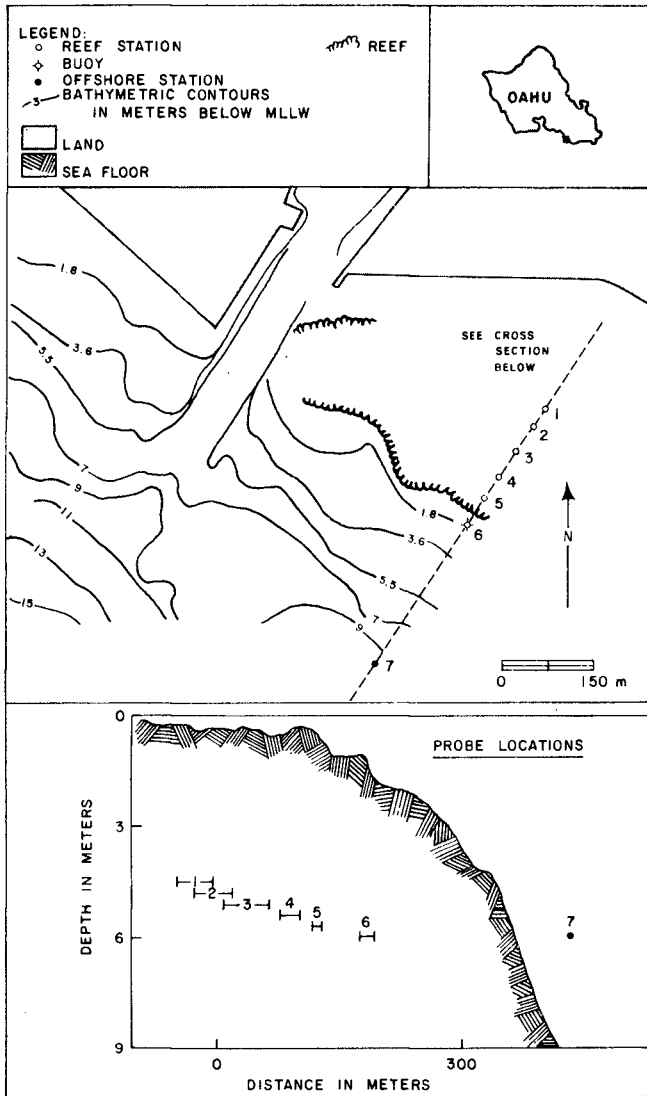


Figure 1 Offshore bathymetry and measurement stations at Ala Moana Reef, Honolulu

4. RESULTS OF INVESTIGATIONS

4.1 Background

Prototype measurements were taken at Ala Moana Reef, Honolulu, at a site where the bottom consists of coral reef. It has been assumed that energy losses due to percolation are negligible at this site and need not be taken into consideration. Energy losses therefore are limited to losses due to bottom friction and to breaking.

Observations at the study site furthermore show that under most conditions waves approach the shoreline at near right angles. The effect of refraction on changes in wave heights can then be ignored. Consequently in all our analysis the waves were treated as a two-dimensional problem.

Because of variations in reef elevation some wave refraction did occur across the reef. Since the experimental set-up did not provide quantitative information on these three-dimensional effects they could not be taken into consideration in the analysis. It was found, however, that at times, certain observations were adversely affected by this aspect of the problem.

For waves moving perpendicular to the coast the process of wave attenuation is governed by the equation:

$$\frac{dF}{dx} = -(\epsilon_f + \epsilon_b) \quad (1)$$

where F is the energy flux per unit of width,
 x is the direction of wave propagation
 (perpendicular to coastline),
 ϵ_f is the rate of energy dissipation per unit of (horizontal)
 area due to friction, and
 ϵ_b is the rate of energy dissipation per unit of (horizontal)
 area due to breaking.

Equation (1) assumes a steady state condition where the variation of the mean energy with time equals zero.

In monochromatic waves (laboratory conditions) variations in wave height can be directly obtained from Eq. (1); however because of strong nonlinearities, values for mean energy and energy flux have to be used as they apply to nonlinear waves. Both the value of the mean energy and of the velocity of propagation of the waves near and after breaking are affected by the nonlinearity of the waves, so that linear expressions need to be modified.

In random waves the situation is even more complicated; besides nonlinearity, the variation in wave heights and wave period pose additional problems to define dissipation parameters. (Gerritsen, 1980).

One of the objectives of the study is to evaluate the numerical values of ϵ_f and ϵ_b so that a mathematical model for wave attenuation can be developed.

The wave set-up on the reef is governed by the equation (Battjes, 1974):

$$\frac{dS_{xx}}{dx} + \rho g (h_0 + \bar{\eta}) \frac{d\bar{\eta}}{dx} + \bar{\tau} = 0 \quad (2)$$

where S_{xx} is the radiation stress component, perpendicular to the shoreline,
 h_0 is the mean depth,
 ρ is the density of the water,
 g is the acceleration of gravity,
 $\bar{\eta}$ is the time-averaged value of the wave set-up, and
 $\bar{\tau}$ is the mean value of the bottom shear stress.

In the above expression for wave set-up it is assumed that the mean mass transport velocity equals zero.

In most previous studies (Battjes, 1974, Van Dorn, 1976) the authors have neglected the contribution of $\bar{\tau}$ to the wave set-up.

From analyzing wave set-up on a reef, there is some evidence that the contribution of $\bar{\tau}$ is not entirely negligible, and needs to be taken into consideration.

In the calculation of S_{xx} , the linear formulation is usually accepted, although the nonlinearity of the waves will also have an effect on the value of the radiation stress.

In this study we have also used the linear expression of S_{xx} for the analysis of data.

4.2 Energy Losses Due to Bottom Friction

In the literature extensive information is available in the bottom friction in low amplitude, harmonic waves. (Jonsson, 1963, 1966; Riedel, et al., 1972; Kajiura, 1964, 1968).

The concepts introduced by these authors have been extended to waves under shoaling and breaking conditions, whereby the assumption was made that even under breaking waves the orbital velocities near the bottom retain oscillatory characteristics (Gerritsen, 1979).

It can be shown, that both the nonlinearity of the waves and the turbulence induced by breaking will affect the numerical value of the bottom friction coefficient, if the latter is based on a linear wave formulation. (Gerritsen, 1979).

The wave bottom shear stress coefficient f_w is here defined by the equation

$$\tau = f_w \frac{1}{2} \rho U_b |U_b| \quad (3)$$

where U_b is the instantaneous value of the orbital velocity near the bottom. Linear assumptions give the following value for the energy dissipation rate ϵ_f :

$$\epsilon_f = \frac{2}{3} f_w \frac{\rho}{\pi} \left(\frac{\pi H}{\bar{\tau} \sinh kh} \right)^3 \quad (4)$$

where k is the wave number. From field and model data, numerical values of the friction coefficient f_w have been obtained.

It appears that the results follow the general trends established by Jonsson and others surprisingly well. (Gerritsen, 1979) The values of the bottom friction coefficient seem to be only slightly larger than for linear waves, possibly with the exception of plunging breakers where turbulence affects the wave boundary layer and higher values of f_w may be expected.

Values of f_w for prototype conditions usually ranged between 0.1 and 0.5, indicating that the role of friction in energy dissipation in the breaking zone is of considerable significance.

4.3 Energy Losses in Breaking and Broken Waves

The problem of energy dissipation in breaking waves is highly complex and so far no completely satisfactory solution has been proposed.

A number of investigators have used the similarity between a breaking wave and a bore as a model for energy dissipation. (e.g. LeMéhauté, 1962, Battjes and Jansen, 1978). Such approach has also been followed in this study. Utilizing an analysis on bore propagation by Schönfeld (1955) the following expression for the rate of energy dissipation can be derived (Gerritsen, 1979)

$$\epsilon_b = \frac{\zeta}{8\pi\sqrt{2}} \rho g \omega H^2 \quad (5)$$

In this expression ω is the angular wave frequency, and ζ is a dimensionless energy dissipation coefficient, which is a function of the Froude number, the ratio between wave height and depth in front of the breaker and of the fraction of energy dissipated by turbulence. The latter is highest for a plunging breaker and lowest for a spilling breaker.

Expected values of the coefficient ζ range between 0.3 and 0.6, which is in agreement with experimental results.

4.4 Energy Losses in Random Breaking Waves

For monochromatic waves a breaking point can be defined using conventional methods. This in turn defines the width of the breaking zone, over which energy dissipation due to breaking occurs. In this analysis,

the similarity parameter $\xi_o = \frac{\tan \alpha}{\sqrt{\frac{H_o}{L_o}}}$ plays an important role. Battjes

(1974) has shown that there is a relationship between the value of ξ_o , the ratio between wave height and depth at the breaking point. The value of ξ_o is also indicative of the type of breaker that can be expected.

In random waves the above analysis is useful for a wave-by-wave analysis of wave dissipation when wave observations are available at successive stations. Such approach has been used to experimentally determine the values of f_w and ζ .

For prediction purposes, however, this approach is less useful because of lack of wave data across the surf zone.

For the calculation of energy dissipation in breaking waves in a predictive manner two methods can be considered:

- (1) Calculation of the transformation of the wave spectrum when waves move into shallow water and across the reef after breaking. Utilizing this method the effects of shoaling, and energy dissipation and of energy shifts in the wave spectrum must be considered. (Gerritsen, 1980)
- (2) A simplified method, which is based on the mean energy of the wave spectrum, appears to give adequate results for engineering purposes. This method is based on the attenuation of the root mean square wave height and does not take into account energy shifts between frequency components.

In this paper the discussion will be limited to the second method. In order to calculate the energy dissipation due to breaking, the fraction of breaking waves at various locations in the breaking zone must be predicted. Battjes and Jansen (1978) developed a method, based on the truncated Rayleigh distribution, to describe the frequency distribution of waves in the surf zone. This model assumes that the wave height at the point of breaking is limited by depth and that the higher waves of the distribution are reduced to the maximum possible wave height corresponding to that depth.

In evaluating Battjes and Jansen's model to describe our experimental data a difficulty emerged in relation to the assumed truncated distribution. In reality wave heights in the breaker zone do not conform to such a distribution. The distribution is continuous rather than truncated and may be described by a two parameter Weibull distribution.

The concept of a maximum wave height for a certain depth has been verified. Indeed the presence of such maximum could be assumed to exist and could be expressed by

$$H_m = \gamma_m h \quad (6)$$

where H_m is the maximum wave height and γ_m a proportionality parameter, depending on ξ_0 . The prototype experiments showed γ_m to vary between 0.46 and 1.11 with mean values for each station (see section 3) varying gradually from $\gamma_m = 0.81$ for station 5 to $\gamma_m = 0.60$ to station 1.

Because of the difference between the actual distribution (Weibull) and the assumed distribution (Truncated Rayleigh) the probability of occurrence of H_m was expectedly much smaller in reality than predicted in Battjes and Jansen's model for the same value of H_m . A correction is therefore required.

For random waves Eq. (5) is modified to:

$$\epsilon_b = Q \frac{\xi^2}{4\sqrt{2}} \rho g \bar{f} H^2 \quad (7)$$

where Q is the fraction of broken waves at a given location and \bar{f} a mean frequency of the waves obtained from the first order moment of the wave spectrum.

The reduction parameter Q is related to the ratio $\frac{H_{rms}}{H_m}$, and may be calculated from Battjes and Jansen's model, if a correction factor is applied. (Gerritsen, 1980)

The modified equation is:

$$\frac{1-Q}{y^2 \ln Q} = - \left(\frac{H_{rms}}{H_m} \right)^2 \tag{8}$$

where y is the correction factor involved; the latter may be obtained from

$$y = 0.71(Q-1)^2 + 1 \tag{9}$$

Equations (8) and (9) are to be seen as being of empirical nature fitted to observed data.

Results of some measurements and calculations are shown in Figs. 2 and 3. The observations were made on August 25, 1976. The location of the measurement stations is shown in Fig. 1.

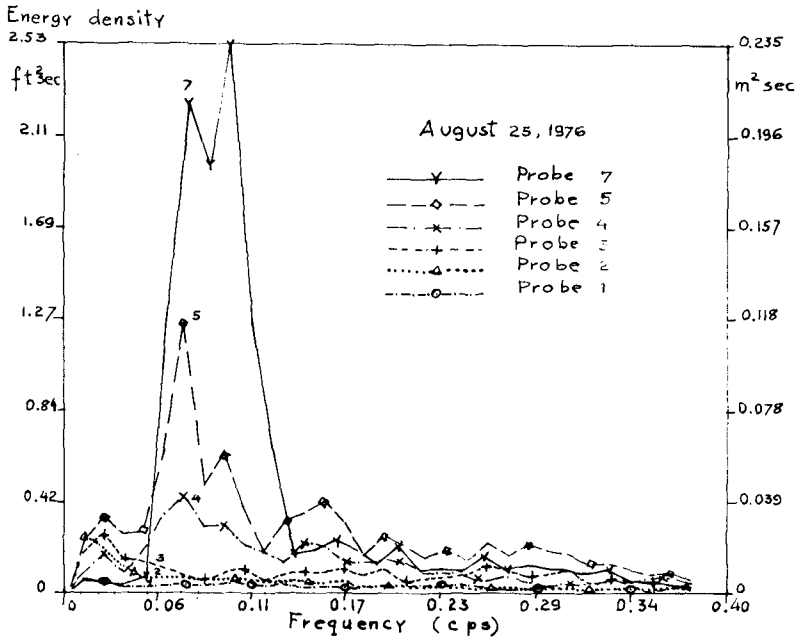


Figure 2 Calculated Wave Spectra for Stations on Ala Moana Reef

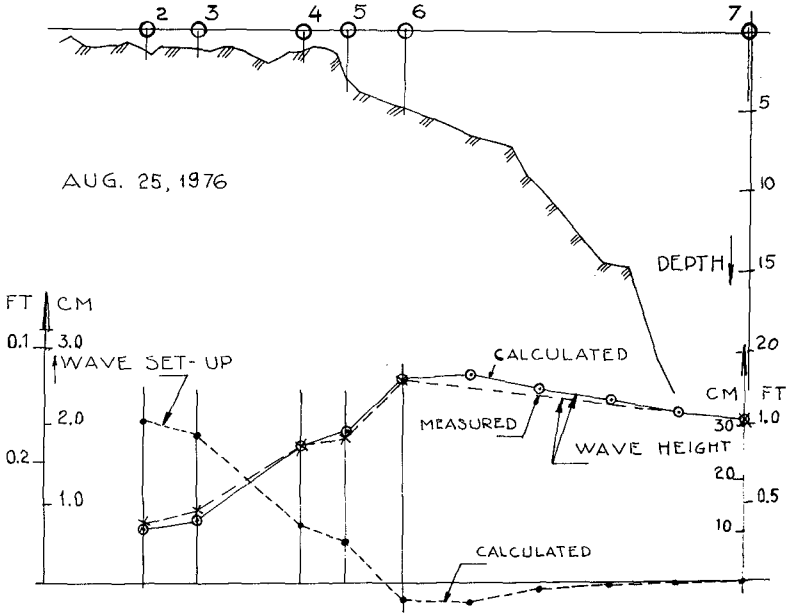


Figure 3 Root Mean Square Wave Heights from Measurements and Calculations

Figure 2 shows calculated wave spectra for the various measurement stations. It shows the sharp decline in energy densities around the peak frequencies, and the shift of energy to low and high frequencies.

Part of the shift is an apparent shift and may not be real; it is due to the Fourier analysis applied to nonlinear wave forms.

The higher frequency components may not represent free harmonics, but they may be bound in phase to the principal wave.

Figure 3 shows the results obtained from the above described dissipation model. Calculated values of H_{rms} , obtained directly from the wave records, and obtained from the dissipation model are both shown. For the latter the root mean square wave height at the offshore station was used as input for the calculations.

Satisfactory agreement between the data from observations and from the model is obtained if the correct values of the dissipation coefficients are introduced into the calculations.

4.5 Wave Set-Up

Analysis of model investigations

Measurements on wave set-up were carried out in the field as well as in a hydraulic model (scale 1:12), allowing a comparison between the two types of measurements. However waves in the laboratory were restricted to the monochromatic type which made the comparison less than ideal.

The range of test conditions in the field measurements was limited, therefore the broader scope of the model data was used as the basis of verification.

An overall view of the test results indicated that both the mean relative waterdepth over the reef $\frac{h_s}{H_1}$ and the wave steepness parameter $\frac{H_1}{gT^2}$ were playing a role in the wave set-up phenomenon. In these parameters H_1 is the incident wave height and T the incident wave period. These values were taken at the offshore station. An attempt was made to define a single parameter (most likely a combination of the two other parameters mentioned), that would function as a governing parameter for the wave set-up on a reef.

A suitable parameter of this kind is:

$$\chi = \frac{gT^2 H_1}{h_s^2}$$

which appears to be a modified Ursell parameter, for shallow water.

In Fig. 4 the dimensionless maximum wave set-up on the reef $\frac{\bar{\eta}_{\max}}{H_1}$ is plotted against χ . Although there is considerable scatter the solid line may represent a unique relationship. Much of the scatter is probably due to inaccuracies in the reading of the manometers, particularly for low values of the wave set-up. As the values of the wave set-up get larger the scatter seems to become smaller.

It may be noted that χ is related to relative reef depth and wave steepness:

$$\chi = \frac{gT^2 H_1}{h_s^2} = \frac{1}{\frac{H_1}{gT^2} \cdot \left(\frac{h_s}{H_1}\right)^2}$$

so that

$$\frac{\bar{\eta}_{\max}}{H_1} = \text{fct} \left[\frac{H_1}{gT^2}, \frac{h_s}{H_1} \right] \quad (10)$$

A graphical representation of (10) can be accomplished in two manners:

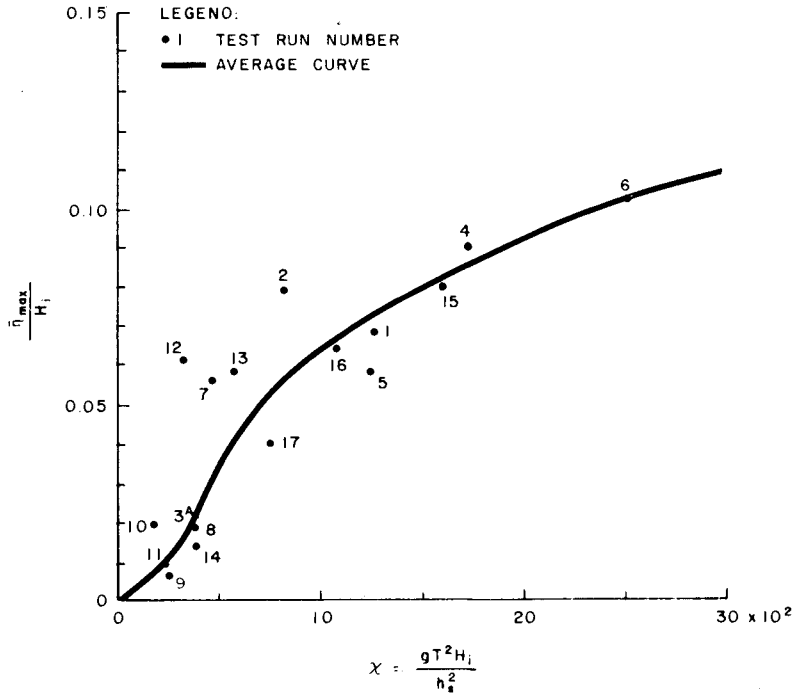


Figure 4 Maximum dimensionless wave set-up on reef versus χ

- (1) $\frac{\bar{\eta}_{max}}{H_1}$ as function of $\frac{h_s}{H_1}$, with $\frac{H_1}{gT^2}$ as a variable parameter;
- (2) $\frac{\bar{\eta}_{max}}{H_1}$ as function of $\frac{H_1}{gT^2}$, with $\frac{h_s}{H_1}$ as a variable parameter.

In view of the space limitations for the paper only the second representation is shown. (Figure 5)

The scatter that was observed in Fig. 4 is visible again in Fig. 5.

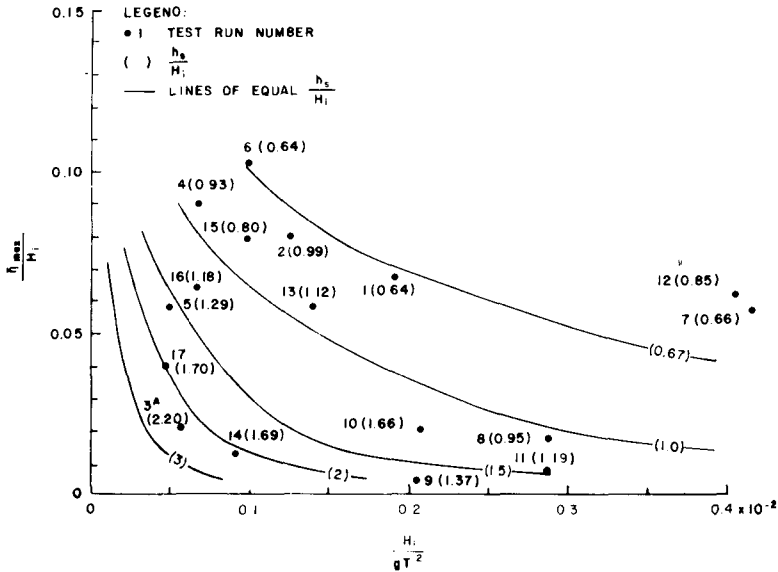


Figure 5 Maximum Dimensionless Wave Set-Up on Reef as a Function of the Wave Steepness Parameter

Verification of hydraulic model with theory

For the verification of the model with theory, a numerical integration of (2) was used. The computations were carried out in two different ways: by letting the mean shearstress $\bar{\tau}$ be equal to zero and by letting it be different from zero. In the latter case its value was adjusted until satisfactory agreement between observation and theory was obtained.

For the numerical integration of Eq. (2) the gradient in mean wave energy must be known in order to determine $\frac{dS_{yx}}{dx}$. For this the dissipation equations developed in the previous sections, were applied.

The results of this analysis indicated that a positive shearstress $\bar{\tau}$ must be introduced to obtain satisfactory agreement between observation and theory. If this positive shearstress is not applied theoretical values are too high and do not agree with observed values.

A positive shearstress is indicative of a resultant watermotion toward the coast in the bottom layers. The nature of this will have to

be investigated in future studies. The analysis further showed that reasonable agreement between observation and theory was usually obtained when a shearstress proportional to the (negative) gradient of the radiationstress

$$\bar{\tau} = -B \frac{dS}{dx} \quad (11)$$

was introduced.

B is a numerical coefficient for the model for which a mean value $B_m = 0.36$ was found.

Comparison between field and model data

It is unfortunate that the extensive 1976 field measurements provided inaccurate information on wave set-up.

Improved measurements were taken in 1978, although without the simultaneous wave data that characterized the measurements in 1976. In 1978 wave measurements were limited to the offshore wave station.

Over a total of about 14 days of measurement the maximum wave set-up on the reef was found to be 10.7 cm.

Wave set-up values were found from the difference in waterlevel elevation on the reef and in the small harbor behind the reef. The latter is connected with the ocean by a 6 m deep channel. (It was assumed that the wave set-up inside the harbor, compared to the instantaneous mean sealevel in the ocean, would be negligible).

Utilizing available field data and comparing measurements with theory, the coefficient B of Eq. (11) for field conditions could be determined. It was found that $B_p = 0.17$ which is less than the value found for the model.

This difference suggests a difference in resultant bottom shear stress between model and prototype possibly related to a difference in circulatory water movement.

In the field surface drift velocity measurements near reef stations showed low and variable currents (between 0.03 and 0.1 m/sec) usually westerly in longshore direction, occasionally directed shoreward. Onshore mass transport, is expected to have been very small. However velocities near the bottom were not measured and consequently no information is available regarding the resultant current conditions near the bottom.

In the model resultant mass transport to the shore must necessarily be zero, but a resultant shoreward bottom current may nevertheless still be present. An imperfection of the model: return ground waterflow through a not completely sealed bottom, and a porous reef may have had some lowering effect on the wave set-up, which consequently may have increased the value of B_m .

The difference in the values of B for the model and prototype may be considered as a scale effect of the model, and may be used to calculate corrections on the model data.

The results are presented in Fig. 6. In this figure the average of four field observations under approximately equal conditions is also shown, which plotting fits the corrected model data well.

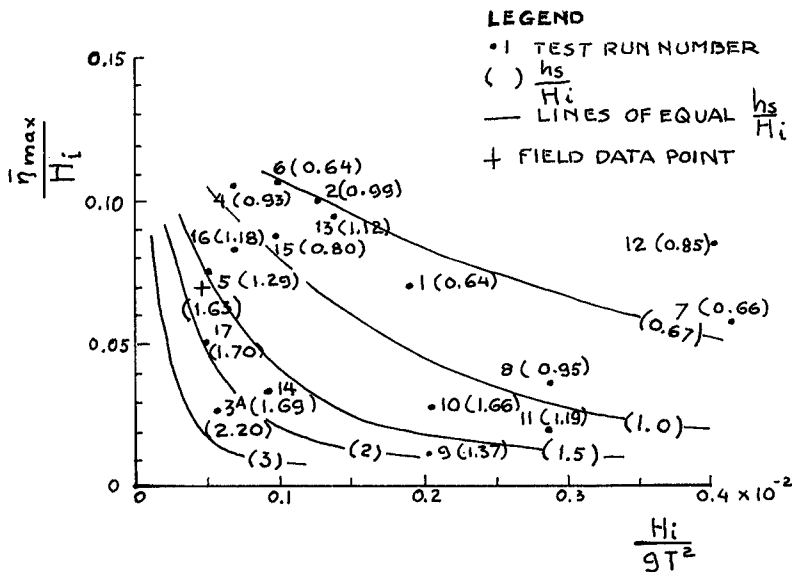


Figure 6 Dimensionless maximum wave set-up on reef versus wave steepness parameter from model, corrected for scale effect

5. CONCLUSIONS AND RECOMMENDATIONS

1. Waves breaking on a coral reef are subject to energy dissipation due to bottom friction losses and breaking losses.
2. The linear wave bottom friction coefficient is affected by the nonlinearity of the waves and by near bottom turbulence.
3. In spilling breakers the wave friction coefficient is of the same order of magnitude as the value of this coefficient in nonbreaking waves.
4. In plunging breakers the overturning jet affects the turbulence of the near bottom fluid motion, and a considerably higher friction coefficient may be expected.
5. Wave friction coefficients in the breaking zone, obtained from the reef measurements are usually between 0.1 and 0.5.

6. The similarity with the bore is utilized to define a breaking loss coefficient ζ . Its value is usually between 0.3 and 0.6 depending on the type of breaker.
7. The randomness of broken waves is an important element in the calculation of wave energy dissipation. A modified Battjes-Jansen model gives adequate results.
8. Wave set-up on a shallow reef is governed by a dimensionless parameter

$$\chi = \frac{gT^2 H_1}{h_s^2}$$

which may be considered as a modified Ursell parameter.

9. Experimental evidence suggests that the resultant shearstress $\bar{\tau}$ cannot be neglected in the calculation of wave set-up.
10. More research is required to obtain a full understanding of the physical phenomena. The study of the resultant shearstress $\bar{\tau}$ in the wave set-up equation is particularly recommended.

6. ACKNOWLEDGMENTS

This work was sponsored by the University of Hawaii Sea Grant College Program under institutional grant nos. 04-6-158-44026 and 04-6-158-44114 from NOAA Office of Sea Grant, U.S. Department of Commerce and the State of Hawaii. Many individuals contributed to the planning, the measurements, and the analysis of the data: T.T. Lee, J.A. Battjes, E. Thornton, K. Black, L. Brower, T.C. Hwang, G. Zee, D.A. Wentland, H.L. Kaul and K.G. Weber. Their contributions and cooperation are gratefully acknowledged.

7. REFERENCES

- Battjes, J.A. (1974), "Computation of set-up, longshore currents, run-up and overtopping due to wind-generated waves," Communications on Hydraulics, Delft University of Technology, The Netherlands, Rept. 74-2.
- Battjes, J.A. and J.P.F.M. Jansen (1978), "Energy loss and set-up due to breaking random waves," Proc. 16th Conf. on Coastal Engineering, A.S.C.E., Hamburg.
- Black, K.P. (1978), "Wave transformations over shallow reef (field measurements and data analysis), Tech. Rept. #42, University of Hawaii, Look Lab, 78-42.
- Brower, L.E. (1978), "Numerical analysis of wave attenuation in a breaking wave regime with special emphasis on friction," Plan B paper, University of Hawaii, Dept. of Ocean Engineering.
- Dorrestein, R. (1961), "Wave set-up on a beach," Proc. 2nd Conference on Hurricanes, Miami.
- Galvin, C.J. (1968), "Breaker type classification on three beaches," J. Geophysical Research 73, 12, June 1968, pp. 3651-3659.

- Gerritsen, F. (1979), "Energy dissipation in breaking waves," Proc. 5th Int. Conference on Port and Ocean Engineering under Arctic Conditions, (POAC), Trondheim, Norway, pp. 607-619.
- Gerritsen, F. (1980), "Wave attenuation and wave set-up on a shallow coastal reef," University of Hawaii Seagrant Tech. Report, in print.
- Johnson, R.S. (1972), "Some numerical solutions of a variable coefficient Korteweg-de-Vries equation with application to soliton wave development on a shelf," Journal of Fluid Mechanics, 54, pp. 81-91.
- Jonsson, I.G. (1963), "Measurements in the turbulent wave boundary layer," Int. Assoc. for Hydr. Res., Proc. 10th Congress, 1, pp. 85-92, London.
- Jonsson, I.G. (1966), "Wave boundary layers and friction forces," Proc. 10th Conf. on Coastal Engineering, Chapter 10, pp. 127-148.
- Longuet-Higgins, M.S. and R.W. Stewart (1964), "Radiation stress in water waves, a physical discussion with applications," Deep-Sea Research II.
- Kajiura, K. (1964), "On the bottom friction in an oscillatory current," Bull. Earthquake Res. Inst., Vol. 42, #1.
- Kajiura, K. (1968), "Model of the bottom boundary layer in water waves," Bull. Earthquake Res. Inst., Vol. 46.
- Lee, T.T. and K.P. Black (1978), "The energy spectra of surf waves on a coral reef," Proc. 16th Conf. on Coastal Eng., ASCE, Hamburg.
- Leméhauté, B. (1962), "On the non-saturated breaker theory and the wave run-up," Proc. 8th Conf. on Coastal Eng., A.S.C.E., pp. 77-92.
- Madsen, O.S., and C.C. Mei (1969), "The transformation of a solitary wave over uneven bottom," J. Fluid Mech., Vol. 39, part 4, pp. 781-791.
- Riedel, H.P., J.W. Kamphuis and A. Brebner (1972), "Measurement of bed shear stress under waves," Proc. 13th Int. Conf. on Coastal Engineering, Copenhagen, pp. 587-603.
- Schönfeld, J.C. (1955), "Theoretical considerations on an experimental bore," Proc. 6th Congress, Int. Assoc. for Hydraulic Res., A15.
- Svendsen, Ib.A and J. Buhr Hansen (1976), "Deformation up to breaking of periodic waves on a beach," Proc. 15th Conf. on Coastal Engineering, ASCE, Honolulu, Chapter 27, pp. 477-496.
- Van Dorn, W.G. (1976), "Set-up and run-up in shoaling breakers," Proc. 15th Conf. on Coastal Engineering, Chapter 42, pp. 738-751.
- Wentland, D.A. (1978), "Field observations and theoretical analysis of wave set-up on Ala Moana Reef," Plan B paper, University of Hawaii, Dept. of Ocean Engineering.
- Whitham, G.R. (1974), "Linear and nonlinear waves," John Wiley and Sons, Inc., New York.

CHAPTER 29

LONGSHORE CURRENT FLOWS IN A WAVE BASIN

by P.J. Visser *)

ABSTRACT

This paper describes the investigation into a method how to adjust the proper longshore current in a wave basin. In this method the basin geometry and the proper recirculation flow (outside wave guides) are determined by minimising the circulation flow (between wave guides). Using one wave field and one uniform beach the length of the downstream wave guide wall, the distribution of the recirculation flow at the upstream wave guide wall and the recirculation flow were varied. The investigation shows that the adjustment of the longshore current has to be done carefully in order to get uniformity along the beach and the correct magnitude and distribution normal to the beach.

1 INTRODUCTION

Since the introduction of the concept of radiation stresses by Longuet-Higgins and Stewart (1964) considerable progress has been made in the understanding of the physics of longshore currents induced by obliquely incident breaking waves on beaches. The investigation of the uniform (along the straight shoreline) longshore current profile has been first undertaken by Bowen (1969), Thornton (1969) and Longuet-Higgins (1970). The investigation has been continued by, among others, Battjes (1974) using irregular waves, Jonsson, Skovgaard and Jacobsen (1975), Liu and Dalrymple (1978) and Skovgaard, Jonsson and Olsen (1978). Although some assumptions done in above mentioned studies are rather crude, the achievements obtained by these authors are considerable and call for an accurate comparison with experimental results. Moreover, most of above mentioned models comprise coefficients which, for the present state of knowledge, have to follow from experiments. Comprehensive experiments, in which the longshore current profile was measured are, however, scarce.

In most of the published laboratory and field experiments of longshore currents, see for instance the reviews of Galvin (1967) and Komar (1975), the "longshore current velocity" was measured. In general this longshore current velocity is defined as the averaged (over the width of the surf zone) current velocity. In fact only Galvin and Eagleson

*) Scientific Officer, Department of Civil Engineering, Delft University of Technology, The Netherlands.

(1965) measured the variation of the longshore current across the surf zone in extensive series of laboratory experiments. Unfortunately the measured currents were not uniform along the beach. Therefore care must be taken in comparing these experiments with theoretical longshore current profiles.

Dalrymple, Eubanks and Birkemeier (1977), see also Kamphuis (1977), measured circulation streamlines and "longshore velocities along surf zone" in the three commonly used wave basin configurations:

- (1) A basin as used by Brebner and Kamphuis (1963) with surf zone openings in both wave guide walls to allow recirculation outside the wave guide walls. The recirculation flow takes place behind the wave generator or through a pipe under the beach.
- (2) The completely enclosed wave basin: used by Putnam, Munk and Traylor (1949) and Saville (1950).
- (3) A basin as used by Galvin and Eagleson (1965) with an opening in the downstream wave guide wall and with an opening under the wave board to allow recirculation.

Dalrymple et al. (1977) concluded in their paper that if a working recirculation procedure could be devised for the type (1) basin that this would reduce the amount of return flow in the offshore region. It has been the objective of the investigation described in this paper to develop such a procedure, resulting in a uniform longshore current, for a basin similar to that of type (1) but equipped with a pump to effect the recirculation and with longshore current openings in the wave guides rather than surf zone openings. This investigation is a first step to a theoretical and laboratory study of longshore current and wave set-up induced by obliquely incident breaking waves on beaches. The longshore current study will probably be followed by a laboratory investigation of sediment transport caused by this current.

2 CRITERION FOR PROPER LONGSHORE CURRENT FLOW

To approximate the longshore current flow generated by a uniform (along the shoreline) wave field on an infinitely long and uniform (along the shoreline) beach, a wave basin configuration was chosen with longshore current openings in both wave guide walls and with a recirculation outside the wave guide walls which is effected completely by a pump (fig. 1). Very likely the choice of such a wave basin is the only way to obtain a uniform longshore current in a wave basin, it also yields, however, the following unknown quantities:

- the width of the longshore current openings in both wave guide walls,
- the recirculation flow rate.

These quantities have to be determined preceding to a longshore current or littoral transport investigation in a basin as shown in fig. 1, preferably in a relatively short period of time.

The criterion for the proper longshore current flow generated by a uniform wave field is that the profile is uniform along the beach, or also that the slope of the mean water in longshore direction is zero.

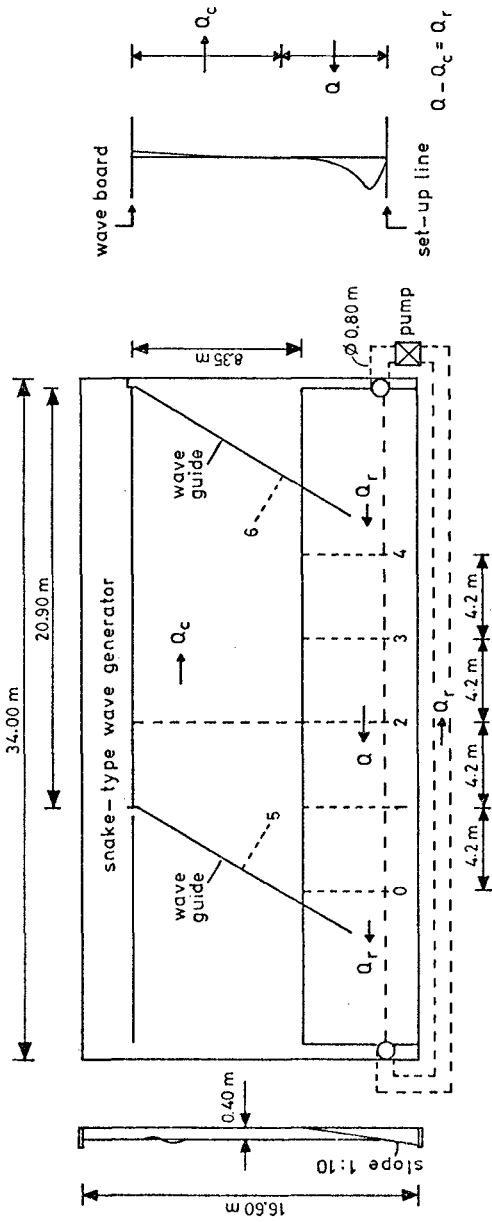


Figure 1 - Wave basin configuration.

It is, however, impossible to optimise the recirculation procedure from measurements of mean water level in longshore direction. This is caused by the inevitable small variation along the shoreline of wave set-up and set-down and the limited length of a wave basin. This paper describes the investigation into an alternative method. In this method the wave basin geometry and the proper recirculation flow (outside wave guides) Q_{ru} are determined such that the circulation flow (inside wave guides) Q_c is minimised (fig. 1). Q_{ru} is the recirculation flow Q_r which yields the uniform longshore current flow Q_u . This method is based on the physical consideration that in an optimised wave basin geometry Q_c is minimal if $Q = Q_u$: because if $Q_r < Q_{ru}$ the shortage returns offshore in Q_c and Q_c will increase and if $Q_r > Q_{ru}$ the surplus generates a circulation flow, also yielding an increase of Q_c .

To verify the method outlined above, experiments were carried out in which the following quantities were varied:

- the width of the longshore current opening in the downstream wave guide wall,
- the distribution of the recirculation flow in the longshore current opening of the upstream wave guide wall,
- the recirculation flow Q_r .

The completely enclosed wave basin and the basin with surf zone openings in both wave guide walls and a recirculation achieved outside the wave guide walls without a pump were also investigated. The wave field quantities and beach slope and beach roughness were not varied as yet.

3 EXPERIMENTAL PROCEDURE

The experiments were done in a $16.60 * 34.00 \text{ m}^2$ wave basin (fig. 1) equipped with a snake-type wave generator. Opposite to the (regular wave) generator a smooth concrete 1 : 10 slope was constructed in the basin. The wave guide walls were composed of concrete elements and installed at an angle of 31 degrees with the normal of the wave board. The recirculation has been effected through a $\varnothing 0.80 \text{ m}$ pipe by means of a pump. The adjustment of the desired recirculation flow Q_r was done with the help of an orifice plate.

Figure 1 shows the position of the 7 sections in which measurements of current velocity were performed. In each experiment the current velocity was measured in section 2, which extends from the wave board to the wave set-up line. In some experiments the velocity was also measured in sections 5 and 6 perpendicular to the wave guide walls and/or in the "longshore current zone" in sections 0, 1, 3 and 4 parallel to section 2. The distance along a section between two measuring points was 0.20 m in and near the surf zone and 0.40-0.60 m in the other region.

In the measuring points the current velocity was measured near the surface, at mid-depth (with exception of sections 5 and 6 and the shallow zone between plunge line and wave set-up line) and near the bottom. The current velocities were measured by timing the travel (along 0.80 m, 0.50 m or 0.30 m, depending on the velocity) of dye (KMnO_4) perpendicular to a measuring section. To this end, near each measuring section strings were stretched parallel to the section and just above the waves. In the surf zone dye was followed over a distance of 0.80 m and not longer because of the rather fast spreading of dye by turbulence in this zone. To serve accuracy, the number of readings giving one measurement result (that is a velocity at a certain depth) was increased and the measurements were conducted by two persons in this zone. Outside the surf zone, the spreading of dye was rather small and there the measured travel time of dye was at least 3 seconds. The number of readings which gave one measurement result are as follows:

- in the surf zone : at least 20,
- near the surf zone: at least 10,
- remaining region : at least 5.

To eliminate the influence of the orbital velocities on the measurement results, the velocities were measured in different phases of the waves. Dye was chosen in accordance with the choice of dye by the Delft Hydraulics Laboratory (1977) after a series of experiments in which the application of floats, dye, the propeller-type miniature current meter and the Ott propeller-type current meter was investigated.

Wave set-up and set-down were measured in sections 1 and 2 with tappings, flush-mounted in the beach. The horizontal distance between 2 tappings was 0.10 m in the surf zone, and 0.20 m outside the surf zone. The tappings were connected with pots, in which the static head was measured.

Measurements of wave heights were performed with resistance wave probes. The distance between two measuring points was 0.10 m in the surf zone and 0.20 m outside this zone. In the constant depth part of the basin wave heights were measured in 5 sections (yielding a number of 100 measuring points). In the slope zone wave heights were measured in sections 1 and 2 and, to measure the position of the breaker line and the mean breaker height, in 3 sections parallel to the wave board at and near the breaker line, each section containing 29 measuring points on a mutual distance of 0.20 m.

Measurements of angles of incidence were done:

- in the constant depth part of the basin with wave probes directly after the start of the wave generator,
- on the breaker line by photograph.

The results of the measurements of wave heights, breaker depths, angles of incidence, wave set-up and set-down are listed in table 1. These wave field quantities were measured in the optimised wave basin geometry with the uniform longshore current flow. The breaker line is defined here as the averaged (along the shoreline) position of the measured breaker points. A breaker point is defined here as the point

wave period	= 2.01 sec	sloping beach with $\text{tga} = 0.101$
still water depth	= 39.9 cm	
mean wave height	= 7.1 cm	} in constant depth part of the wave basin
adjusted angle of incidence	= 31.1°	
measured angle of incidence	= 31.6°	
mean breaker depth	= 10.4 cm	mean breaker height = 10.5 cm
mean maximum set-up	= 4.2 cm	mean max. set-down = 0.32 cm
mean width surf zone (from wave set-up line to breaker line)	= 1.45 m	
angle of incidence on breaker line	= 20.9°	
mean wave run-up	= 7.2 cm	

Table 1 - Measured wave field quantities.

in which the wave height is maximal (in a section normal to the coast) : at the shoreward side of this point the wave height decreases (more or less) continuously.

The velocity measurements which are described in this paper can be summarized as follows:

A. first series of experiments in which

- width opening in upstream wave guide (= 1.90 m) = 1.3 * width surf zone,
- width opening in downstream wave guide varied from 1.0 * width surf zone to 2.0 * width surf zone (ratios of 0.97, 1.17, 1.31, 1.45 and 2.00),
- recirculation flow Q_r varied from 0 l/sec to 59 l/sec.

B. second series of experiments in which

- distribution system in longshore current opening of upstream wave guide wall,
- width opening in downstream wave guide wall varied from 1.0 * width surf zone to 1.6 * width surf zone (ratios of 0.97, 1.17, 1.31, 1.45 and 1.59),
- recirculation flow varied from 25 l/sec to 50 l/sec.

C. measurements in completely enclosed wave basin.

D. measurements in wave basin with surf zone openings in both wave guides rather than longshore current openings and a free recirculation (no pump).

The distribution system in the longshore current opening of the upstream wave guide wall is 1.20 m long (in longshore direction) and 2.40 m wide (in the direction normal to the wave board) and consists of 12 channels each 1.20 m long and 0.20 m wide. With gates, slide-valves, etc., it is possible to vary the rate of flow in each channel.

4 EXPERIMENTAL RESULTS

The mean velocity in a measuring point was calculated from the measured current velocities as follows

$$\bar{v} = \frac{1}{4} (v_{\text{surface}} + 2 v_{\text{mid-depth}} + v_{\text{bottom}}).$$

The rate of flow between two adjacent measuring points followed from the mean velocities and mean water levels measured in these points. The enumeration of these flow rates between adjacent points gave the longshore current flow Q and the circulation flow Q_c , as defined in fig. 1. By comparing the difference $Q - Q_c$ with the adjusted flow rate of the pump Q_r an indication of the accuracy of the experiments was obtained. At the end of this chapter the accuracy of the experiments will be discussed.

In the first series of experiments (A) the width of the longshore

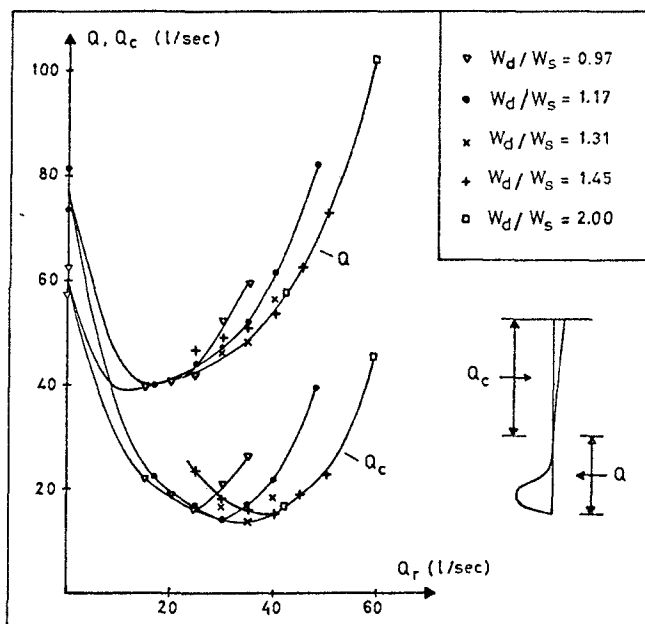


Figure 2 - Longshore current flows Q and circulation flows Q_c measured in section 2' in first (A) series of experiments.

current opening in the upstream wave guide was constant, namely $1.3 * w_s$ (w_s = width surf zone), which after the completion of these experiments turned out to be a fortunate choice. The width w_d of the longshore current opening in the downstream wave guide and the recirculation flow Q_r were varied. Figure 2 gives a graphical representation of the longshore current flows Q and circulation flows Q_c measured in section 2 (25 measurements) in the first series of experiments. From this figure it can be seen that Q_c is more or less a parabolic function of Q_r for a given w_d/w_s -ratio. The locus of the minima of these parabolas gives a graphical relation between w_d/w_s and Q_r (such that Q_c is minimal for a given Q_r or w_d/w_s -ratio). In the first series of experiments the circulation flow Q_c is minimal for $w_d/w_s = 1.31$ and $Q_r = 35$ l/sec : $Q_c = 13.6$ l/sec and $Q = 48.4$ l/sec. In this situation (here labeled as \hat{A} -experiment) also velocity measurements were done in sections 5 and 6 and, to examine the uniformity along the beach, in sections 0, 1, 3 and 4. The results of these measurements and of the measurements in section 2 are shown in fig. 3. From this figure it can be seen that from section 2 to section 0 the longshore current profile is uniform, but that almost half a wave basin length is necessary to establish this uniform longshore current. In order to increase the length of uniformity, a distribution system was installed in the longshore current opening in the upstream wave guide wall after the completion of the first series of experiments.

The distribution of the recirculation flows Q_r in this system was adjusted according to the measured distribution of the longshore current flows Q in the first series of experiments. In the second series of experiments (B) the number of measurements in section 2 was restricted to 11 : 6 with $w_d/w_s = 1.31$ and a Q_r -range from 25 to 50 l/sec, 5 with a varying w_d/w_s -ratio (according to the locus of the minima in fig. 2) and a Q_r also ranging between 25 and 50 l/sec. The longshore current flows Q and circulation flows Q_c measured in this series of experiments are shown in figure 4. Also in the second series of experiments the circulation flow Q_c is minimal for $w_d/w_s = 1.31$ and $Q_r = 35$ l/sec : $Q_c = 19.2$ l/sec and $Q = 52.1$ l/sec. The results of the velocity measurements in section 2 and the results of the measurements in sections 0, 1, 3, 4, 5 and 6, which were also performed in this situation (here labeled as \hat{B} -experiment), are shown in figure 5. This figure shows that the longshore current is uniform from section 3 to section 0: due to the distribution system the distance along which the longshore current is uniform increases substantially.

The smallest Q_c in the second series of experiments is $Q_c = 19.2$ l/sec, in the first series of experiments: $Q_c = 13.6$ l/sec. The influence of

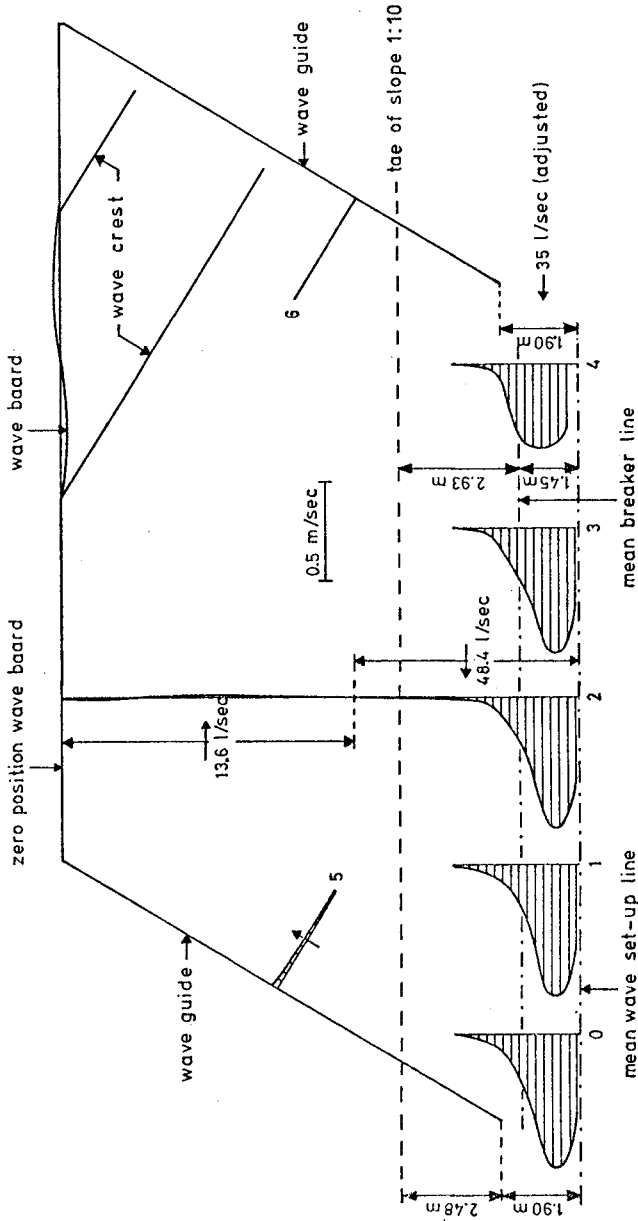


Figure 3 - Depth averaged longshore current and circulation velocities (A-measurements).

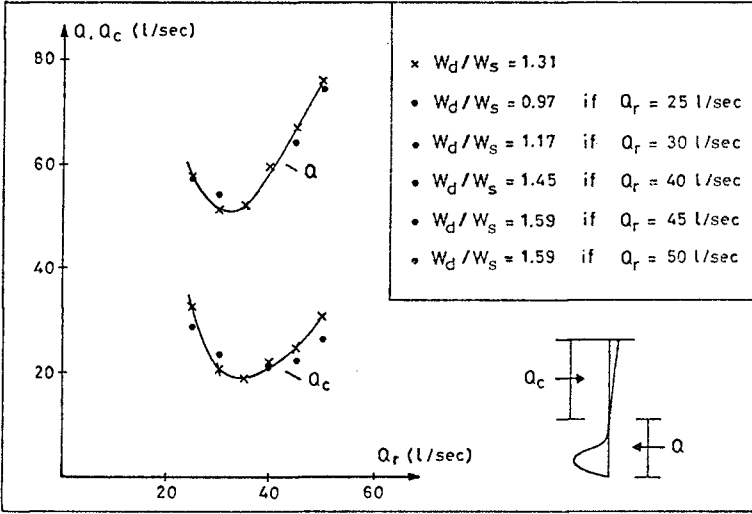


Figure 4 - Longshore current flows Q and circulation flows Q_c measured in section 2 in second series of experiments (B).

the distribution system on the rate of circulation flow Q_c does not follow from a comparison of these circulation flow rates due to the fact that not only a distribution system was installed but also some small (but not unimportant) leaks in the wave guides were closed. To investigate this influence an additional experiment was performed without the distribution system, with $Q_r = 35$ l/sec and with $1.31 * w_s$ wide openings in both wave guides. The result of this experiment: $Q_c = 29.4$ l/sec and $Q = 62.2$ l/sec.

The depth averaged velocities resulting from the measurements in the completely enclosed wave basin are shown in figure 6. The longshore current is clearly non-uniform; the profile is strongly disturbed by the significant large circulation flow ($Q_c \approx 128$ l/sec).

Figure 7 shows the depth averaged velocities which follow from the velocities measured in the type (1) basin, that is a basin with surf zone openings in both wave guides and with a recirculation outside the wave guides without the use of a pump. Also the longshore current measured in this type wave basin is clearly non-uniform. In this experiment the return flow took place directly alongside of the longshore current, yielding an anti-clockwise circulation in the offshore region. The "free recirculation flow" was also measured: $Q_r = 12.4$ l/sec, which is about one third of the proper Q_r .

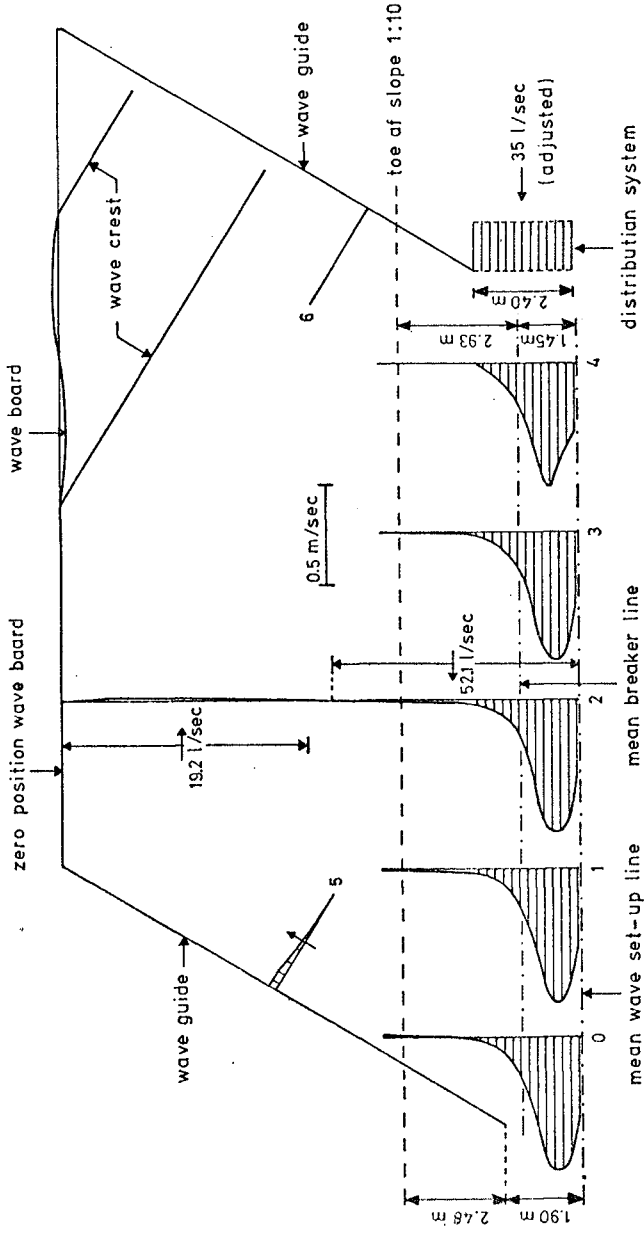


Figure 5 - Depth averaged longshore current and circulation velocities (\bar{B} -measurements).

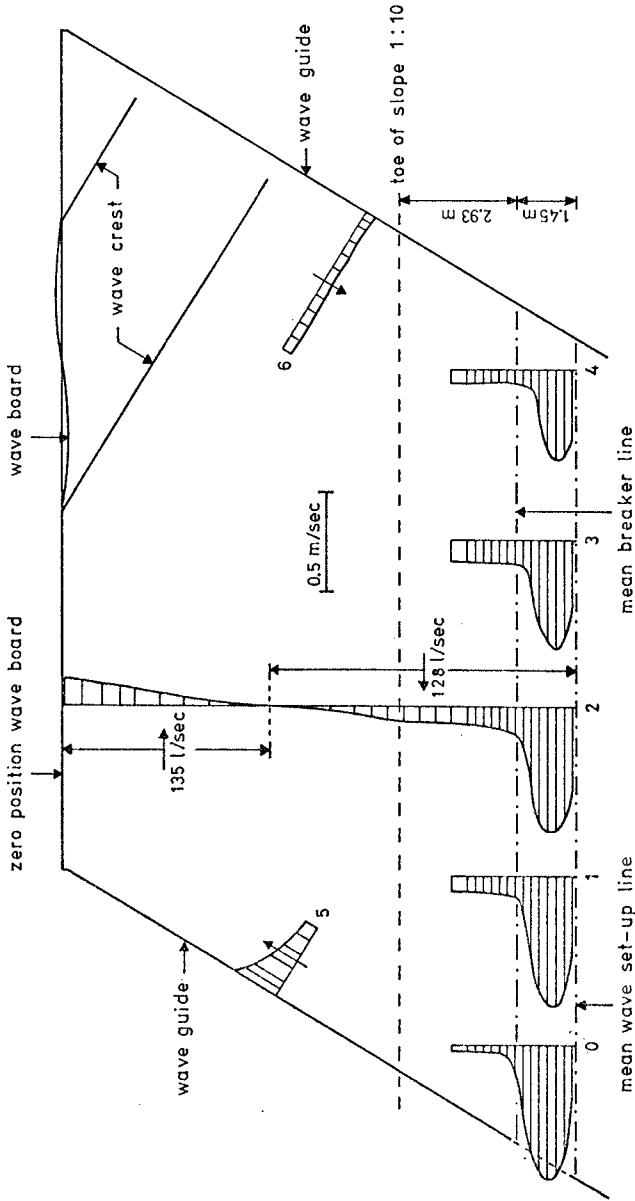


Figure 6 - Depth averaged longshore current and circulation velocities (C-measurements).

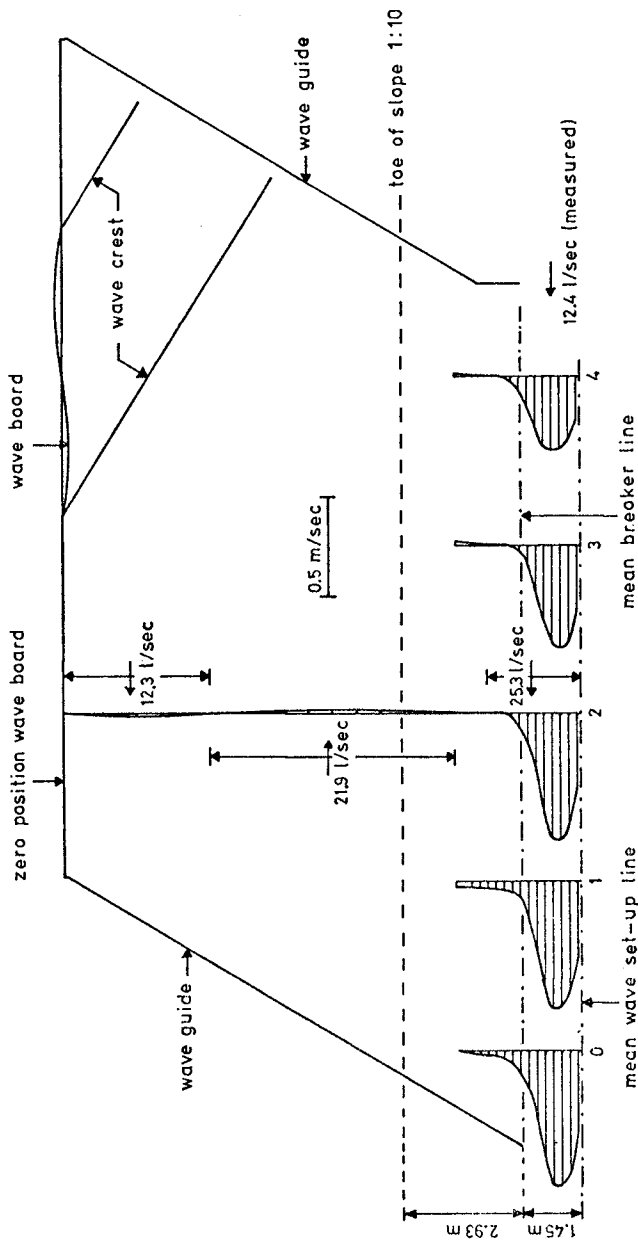


Figure 7 - Depth averaged longshore current and circulation velocities (D-measurements).

	\hat{A} -experiment					\hat{B} -experiment				
section nr	0	1	2	3	4	0	1	2	3	4
Q_s (1/sec)	29.0	27.9	28.4	27.3	24.5	28.3	28.1	28.0	26.8	26.4
Q_{2s} (1/sec)	45.1	43.4	43.6	42.9	39.9	42.5	43.3	42.9	41.2	39.6
v_{\max} (m/sec)	0.67	0.66	0.66	0.61	0.42	0.67	0.67	0.66	0.64	0.62
v_{br} (m/sec)	0.24	0.21	0.22	0.27	0.36	0.23	0.22	0.20	0.20	0.22
	C-experiment					D-experiment				
ray nr	0	1	2	3	4	0	1	2	3	4
Q_s (1/sec)	30.4	25.8	25.5	19.2	12.2	24.9	23.5	22.9	17.5	16.2
Q_{2s} (1/sec)	42.5	48.4	50.9	49.2	29.8	34.6	34.9	25.3	16.6	17.6
v_{\max} (m/sec)	0.67	0.65	0.63	0.55	0.45	0.67	0.63	0.65	0.52	0.39
v_{br} (m/sec)	0.21	0.14	0.15	0.12	0.07	0.14	0.10	0.10	0.06	0.10

Table 2 - Some results of the measurements along the shoreline.

The flows along the coast in the surf zone (Q_s) and in a section with a width of 2 times the width of the surf zone (Q_{2s}) measured in the four experiments \hat{A} , \hat{B} , C and D are given in table 2. The table presents also the depth averaged maximum velocities along the coast and the depth averaged velocities on the breaker line. Table 2 shows again the uniformity and non-uniformity of the measured longshore currents which is already depicted in figures 3 and 5-7. The depth averaged longshore current velocities measured in section 2 in the experiments \hat{A} , \hat{B} (both with practically the same uniform longshore current profile), C and D are shown in figure 8. The differences between the uniform longshore current profiles and the non-uniform longshore current profiles near the middle (in longshore direction) of the sloping beach in the completely enclosed wave basin and the type (1) basin are clear, especially near the breaker line. Deviations from the uniform longshore current profile can become also considerable in the

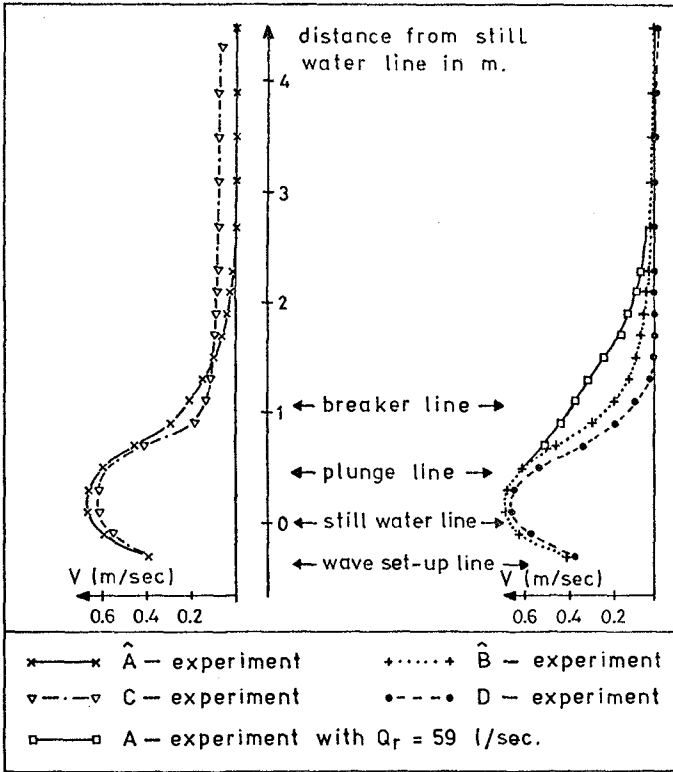


Figure 8 - Depth averaged longshore current velocities.

fig. 1 type basin, especially if the rate of recirculation flow differs substantially from the proper recirculation flow. This is demonstrated in figure 8 with the help of the longshore current profile measured in the first series of experiments with $Q_r = 59$ l/sec and $w_d/w_s = 2.00$.

Adding all recirculation flows Q_r , all longshore current flows Q and all circulation flows Q_c of the experiments described in this paper gives respectively:

$$\sum Q_r = 1253 \text{ l/sec,}$$

$$\sum Q - \sum Q_c = 2320 - 1080 = 1240 \text{ l/sec.}$$

The difference of 13 l/sec is for 70% due to the experiment with the completely enclosed wave basin (with the large circulation flow) and only 1% of $\sum Q_r$. So it can be concluded that the systematic error in the longshore current and circulation velocity measurements is small. The random error of one measurement result was restricted as far as the experimental time this permitted by the number of readings (5, 10 or 20) which gave this measurement result. From the above and from the smooth longshore current profiles reflected in the figures 3, 5, 6, 7 and 8 it can be concluded that rather accurate measurements of longshore currents are possible.

5 DISCUSSION

The investigation described in this paper shows that the adjustment of the correct longshore current flow in a wave basin has to be done conscientiously. Deviations from the uniform longshore current profile can become considerable

- in non-optimised wave basin geometries and/or if
- the adjusted recirculation flow deviates substantially from the proper recirculation flow.

One of the most important aims of this investigation is to set-up a method for the adjustment of the uniform longshore current flow (or profile) in a wave basin and to verify this experimentally. From the previous chapters it can be concluded that this objective has been attained, at least for the wave field/wave basin combination which was used for the experiments described in this paper. From this investigation a "wave basin prescription" will be set-up. With this wave basin prescription it has to be possible to create a uniform longshore current flow in a wave basin for given wave field and beach quantities in a rather short time. To verify this wave basin prescription the experiments will be continued with other wave fields on the same slope.

ACKNOWLEDGEMENTS

The author is greatly indebted to Mr. D.C. Post for his assistance with the velocity measurements in and near the surf zone and for his performance of the remaining measurements. The author also wishes to thank Prof. J.P.Th. Kalkwijk for his critical comments during the investigation.

REFERENCES

- Battjes, J.A., 1974, Computation of set-up, longshore currents, run-up and overtopping due to wind-generated waves, Communications on Hydraulics, Department of Civil Engineering, Delft University of Technology, Report no. 74-2.
- Bowen, A.J., 1969, The generation of longshore currents on a plane beach, *J. Mar. Res.*, vol. 27, pp. 206-215.
- Brebner, A. and Kamphuis, J.W., 1963, Model tests on the relationship between deep-water wave characteristics and longshore currents, C.E. Research report no. 31, Queens University, Kingston, Ontario, Canada.
- Dalrymple, R.A., Eubanks, R.A. and Birkemeier, W.A., 1977, Wave-induced circulation in shallow basins, *Journal of the waterway, port, coastal and ocean division, A.S.C.E.*, vol. 103, pp. 117-135.
- Delft Hydraulics Laboratory, 1977, Water motion in a coastal model with fixed bottom (in Dutch), T.O.W. report M918 part 4.
- Galvin, C.J. and Eagleson, P.S., 1965, Experimental study of longshore currents on a plane beach, U.S. Army Coastal Eng. Res. Center Tech. Mem. 10.
- Galvin, C.J., 1967, Longshore current velocity : a review of theory and data, *Reviews of Geophysics*, vol. 5, pp. 287-304.
- Jonsson, I.G., Skovgaard, O. and Jacobsen, T.S., 1975, Computation of longshore currents, Proc. 14th Conf. Coastal Eng., Copenhagen, 1974, pp. 699-714.
- Kamphuis, J.W., 1977, Wave-induced circulation in shallow basins : discussion, *Journal of the waterway, port, coastal and ocean division, A.S.C.E.*, vol. 103, pp. 570-571.
- Komar, P.D., 1975, Nearshore currents : generation by obliquely incident waves and longshore variations in breaker height, in *Nearshore Sediment Dynamics and Sedimentation*, edited by J. Hails and A. Carr, Wiley, London, pp. 17-45.
- Liu, P.L-F. and Dalrymple, R.A., 1978, Bottom frictional stresses and longshore currents due to waves with large angles of incidence, *J. Mar. Res.*, vol. 36, pp. 357-375.
- Longuet-Higgins, M.S. and Stewart, R.W., 1964, Radiation stresses in water waves : a physical discussion with applications, *Deep-Sea Research*, vol. 11, pp. 529-562.
- Longuet-Higgins, M.S., 1970, Longshore currents generated by obliquely incident sea waves, *J. Geoph. Res.*, vol. 75, pp. 6778-6801.

- Putnam, J.A., Munk, W.H. and Traylor, M.A., 1949, The prediction of longshore currents, Transactions of the American Geophysical Union, vol. 30, pp. 337-345.
- Saville, T., 1950, Model study of sand transport along an infinitely long straight beach, Transactions of the American Geophysical Union, vol. 31, pp. 555-565.
- Skovgaard, O., Jonsson, I.G. and Olsen, G.O., 1978, Calculation of longshore current profiles, Proc. Breaking waves, surf and run-up on beaches, Euromech 102, Bristol, 1978, 4 pp.
- Thornton, E.B., 1969, Longshore current and sediment transport, Technical Report 5, Department of Coastal and Oceanographic Engineering, University of Florida, Gainesville, Florida (see also Proc. 12th Conf. Coastal Eng., Washington D.C., 1970, pp. 291-308).

CHAPTER 30

DYNAMIC CHARACTERISTICS IN THE NEARSHORE AREA

Kiyoshi Horikawa
and
Masahiko Isobe

Department of Civil Engineering
University of Tokyo
Bunkyo-ku, Tokyo, Japan

ABSTRACT

A detailed discussion is made on the dynamic characteristics of waves and wave-induced currents in the nearshore area by using the laboratory and field investigation data collected during the last few years. The main purposes of this paper are to get the insight on the precise mechanism of the nearshore dynamic phenomena and to evaluate critically the applicability of the various assumptions commonly applied by the previous researchers.

INTRODUCTION

During the last several years, the research group supervised by the senior author have carried out the series of field and laboratory investigations on the nearshore dynamic phenomena. The final target of the research works is to understand precisely and more deeply the coastal sediment processes, which must be governed by the nearshore dynamics. However, in the present paper, the authors would like to focus their discussions on the several subjects which are closely related to the detailed mechanism of nearshore dynamics.

Since the radiation stress concept was presented by Longuet-Higgins and Stewart (1960, 1964), various important phenomena in the nearshore area have been analyzed extensively. Wave set-down and wave set-up, longshore current velocity distribution, and nearshore circulation must be typical examples in these phenomena.

Generally speaking, the phenomena in the nearshore area are extremely complex due to the complicated action of breaking waves. Therefore, in the previous treatments, some appropriate assumptions have been introduced to formulate the dynamical equations. These assumptions are that, for example, the small amplitude wave theory is applicable to the wave motion in the nearshore area, the wave height in the surf zone is proportional to the local water depth, and the bottom and lateral frictional terms are expressed in specified forms.

These previous works contributed very much to the advancement of coastal engineering research in the 1970s. On the other hand the instrumentation techniques have been developed extensively during these days. These facts encourage the scientists to carry out the detailed investigations to clarify the fine structures of nearshore phenomena, such as wave characteristics and current fields in the nearshore area.

Reflecting the above fortunate circumstances, the staffs at the Coastal Engineering Laboratory, University of Tokyo, have continued the extensive field and laboratory investigations during the last three years. Based on the data obtained up to the present stage, the authors' concept or understanding on the dynamic characteristics of waves and wave-induced currents in the nearshore area will be introduced in the following sections.

GOVERNING EQUATIONS

Figure 1 indicates the definition sketch. By using these terms, the dynamic equations, such as the total mass conservation equation, and the total momentum conservation equation, can be written down as shown in the following forms after Phillips (1977).

1) Conservation of total mass:

$$\frac{\partial}{\partial t} [\rho(h+\bar{z})] + \frac{\partial}{\partial x_\alpha} \hat{M}_\alpha = 0 \quad (1)$$

2) Conservation of total momentum:

$$\frac{\partial}{\partial t} \hat{M}_\alpha + \frac{\partial}{\partial x_\beta} [\hat{U}_\alpha \hat{M}_\beta + S_{\alpha\beta}] = T_\alpha + R_\alpha \quad (2)$$

where $\hat{U}_\alpha = \hat{M}_\alpha / \rho(h+\bar{z}) = U_\alpha + M_\alpha / \rho(h+\bar{z})$, $S_{\alpha\beta} = \int_{-h}^{\bar{z}} (\rho u_\alpha u_\beta + p \delta_{\alpha\beta}) dz$

$$- \frac{1}{2} \rho g (h+\bar{z})^2 \delta_{\alpha\beta} - M_\alpha M_\beta / \rho(h+\bar{z}), \quad T_\alpha = -\rho g (h+\bar{z}) \frac{\partial}{\partial x_\alpha} \bar{z}, \quad \text{and}$$

$$R_\alpha = \int_{-h}^{\bar{z}} \frac{\partial}{\partial x_\beta} \tau_{\beta\alpha} dz + \bar{\tau}_{z\alpha} - \bar{\tau}_{h\alpha} = -\frac{\partial}{\partial x_\beta} (S'_{\alpha\beta}) + \bar{\tau}_{z\alpha} - \bar{\tau}_{h\alpha}$$

Here t is the time, x_α the horizontal axis, z the vertical axis taken above the still water level, p the pressure intensity, u_α the horizontal component of wave orbital velocity, ρ the fluid density, g the acceleration due to gravity, $\delta_{\alpha\beta}$ the Kronecker delta, $\tau_{\beta\alpha}$ the Reynolds stress and $\bar{\tau}_{z\alpha}$, $\bar{\tau}_{h\alpha}$ are the mean shear stresses at the free surface and at the bottom respectively. The term $S_{\alpha\beta}$ is the so-called radiation stress which corresponds to the excess momentum flux tensor, T_α the horizontal force per unit surface area induced by the free surface gradient, and R_α the frictional term consisting of the lateral and boundary frictional terms. The term $S'_{\alpha\beta}$ introduced here may be expressed by $\int_{-h}^{\bar{z}} \rho u'' v'' dz$, where u'' and v'' are the horizontal components of turbulent velocity.

As stated previously, it is very common to apply the small amplitude wave theory in evaluating the radiation stress tensor $S_{\alpha\beta}$ which is given by

$$S = \bar{E} \begin{pmatrix} \frac{c_g}{c} \cos^2 \theta + \frac{1}{2} \left(\frac{2c_g}{c} - 1 \right) & \frac{1}{2} \frac{c_g}{c} \sin 2\theta \\ \frac{1}{2} \frac{c_g}{c} \sin 2\theta & \frac{c_g}{c} \sin^2 \theta + \frac{1}{2} \left(\frac{2c_g}{c} - 1 \right) \end{pmatrix} \quad (3)$$

where the wave profile ζ is assumed to be expressed by $\zeta = \frac{H}{2} \cos(x_1 k \cos\theta + x_2 k \sin\theta - \sigma t)$, in which H is the wave height, k the wave number, σ the angular frequency, θ the wave direction angle, and $\bar{E} = \frac{1}{8} \rho g H^2$ the average wave energy per unit water surface.

TWO DIMENSIONAL CASE

WAVE SET-DOWN AND WAVE SET-UP

As a first step of the present discussion, the following simple case will be taken. That is to say, the waves are coming perpendicularly to the shoreline, hence the wave direction angle θ is equal to zero. In addition to the above it is assumed that the phenomenon is in the steady state, and the bottom contour lines are parallel to the shoreline. In such a case, the basic equation is simply expressed by

$$\frac{d}{dx} S_{xx} = -g(h + \bar{\zeta}) \frac{d}{dx} \bar{\zeta} + R_x \quad (4)$$

where x is taken in the onshore-offshore direction.

The nearshore area is usually separated into two regions; the first one is the outside of the surf zone, and the other one is the inside of the surf zone. The reason is that there exists a remarkable difference in wave characteristics in these two regions. The treatments given by Eqs. (5) and (6) in the following are the very common ways to evaluate the amount of wave set-down as well as that of wave set-up.

- 1) Outside the surf zone:

$$\bar{\zeta} = -\frac{H^2}{8} \frac{k}{\sinh 2kh} \quad (5)$$

under the conditions of $R_x \approx 0$ and $\bar{\zeta} \ll h$.

- 2) Inside the surf zone:

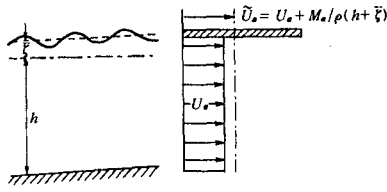
$$\bar{\zeta} = K(h_b - h) + \bar{\zeta}_b$$

$$K = [1 + (8/3\gamma^2)]^{-1} \quad (6)$$

under the conditions of $R_x \approx 0$ and $H \approx \gamma(h + \bar{\zeta})$, where the subscript b indicates the value at the breaking point.

It has been realized that these equations give the curves of mean water level which agree well with the laboratory data except in the vicinity of the breaking point.

Figure 2 demonstrates a result of comparison among the mean water level measured in a wave flume and those calculated by using any one of the small amplitude wave theory, the linear long wave theory, the stream function theory (Dean, 1967), and the radiation stress S_{xx} obtained from the measured velocity field through an approximate expression (Isobe, Fukuda & Horikawa, 1979). Here it should be mentioned that these calculations except the last one were made by using the measured wave profile at each location. That is to say, in the case of the small amplitude wave theory the measured wave height only



$$u_\alpha = U_\alpha + u_\alpha'$$

$$\hat{M}_\alpha = \int_{-h}^{\zeta} \rho u_\alpha dz = \hat{M}_\alpha + M_\alpha$$

$$\hat{M}_\alpha = \int_{-h}^{\zeta} \rho U_\alpha dz = \rho(h + \bar{\zeta}) U_\alpha$$

$$M_\alpha = \int_{-h}^{\zeta} \rho u_\alpha' dz$$

Fig. 1 Definition sketch (adapted from Phillips, 1977).

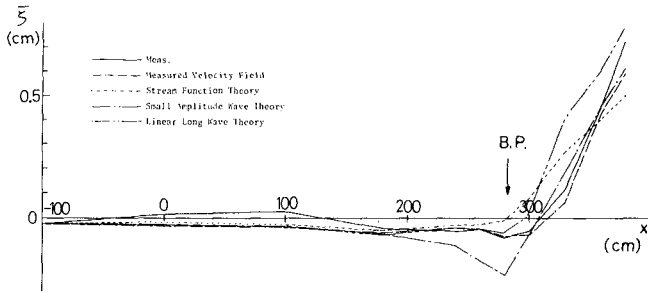


Fig. 2 Comparison between the measured and predicted wave set-down and wave set-up curves.

was used for the computation, while in the case of the linear long wave theory the instant horizontal velocity component was calculated by using the well-known relationship of $u = \sqrt{g/h} \zeta$, where u is the horizontal velocity component and ζ is the surface wave elevation above the mean water level. On the other hand, the stream function theory contains in it the non-linear effect of wave characteristics.

From this diagram, it is realized that the curve calculated by using the values of S_{xx} stated above fits best in the measured mean water level. However the curve based on the small amplitude wave theory deviated extremely from the measured one especially in the vicinity of breaking point.

EVALUATION OF RADIATION STRESS

The fact stated above indicates that the radiation stress S_{xx} outside the surf zone evaluated here on the basis of the small amplitude wave theory seems to be inadequate for the present purpose. Figure 3 demonstrates the above surmise; that is to say, the small amplitude wave theory seems to have a tendency to overestimate the value of $S_{xx}/\rho g$ especially near the breaking point. This conclusion is quite natural, because the non-linearity of waves is normally intensified in the shallow water region. In addition to the above, it should be mentioned that the actual wave height change on the gently sloping beach up to the breaking point differs from the curve calculated by using the small amplitude wave theory as shown in Fig. 4. Here the predicted curve is based on the simple rule of energy flux conservation, and only the wave height in deep water is given in the present computation. Due to the double fault stated above, it is quite possible that the onshore-offshore distribution curve of $S_{xx}/\rho g$ outside the surf zone can be predicted a little more closer to the reference curve from the deep water wave height on the basis of the small amplitude wave theory.

On the other hand, the wave height inside the surf zone, H , is well expressed by the relationship of $H = \gamma (h + \bar{\zeta})$, where h is the still water depth, $(h + \bar{\zeta})$ is the local water depth, and γ is a proportionality constant. However, the field and laboratory data indicate that the above proportional relationship between the wave height and the local water depth holds good only on a uniformly gently sloping beach (Hotta & Mizuguchi, 1978, Mizuguchi, Tsujioka & Horikawa, 1978, and Mizuguchi & Horikawa, 1978).

The wave set-down and wave set-up are closely related to the gradient of radiation stress, while the radiation stress has a close connection with the local wave pattern. That is why the stream function theory predicts well the radiation stress, thus the mean water level, at least outside the surf zone.

WAVE CELERITY

From the above discussion, it is clear that the small amplitude wave theory is not powerful to predict the wave height change on a gently sloping beach. However the wave celerity is in a little different situation from the wave height. Figure 5 show the comparison between the measured wave celerity curve and the theoretical curves based either on the small amplitude wave theory or on the solitary wave theory. From this diagram it is realized that the discrepancy between the measured one and the theoretical one based on the small amp-

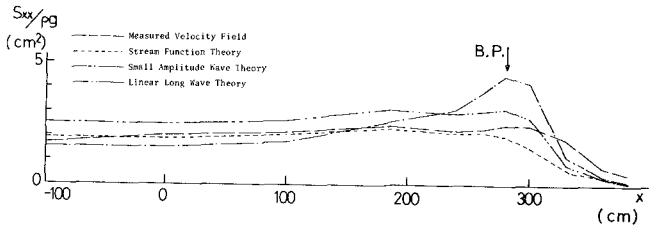


Fig. 3 Radiation stress curves predicted by the various methods.

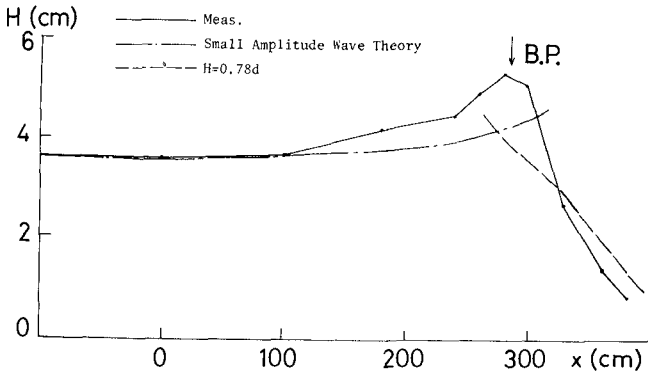


Fig. 4 Comparison between the measured and predicted wave height change.

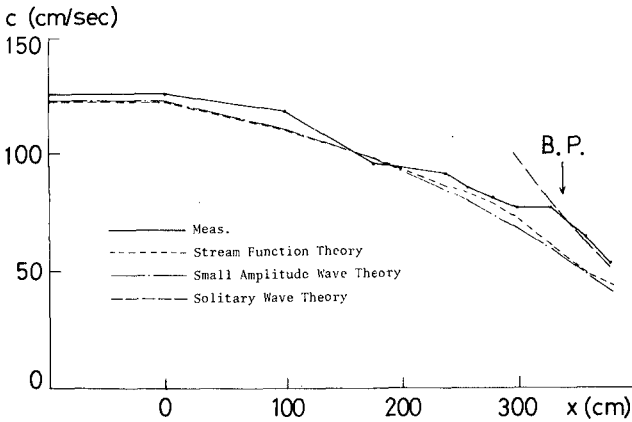


Fig. 5 Comparison between the measured and predicted wave celerity change.

litude wave theory is not large in the offshore region, but becomes large in the nearshore region. However in the surf zone, the wave celerity can be predicted fairly well by the solitary wave theory.

CORRELATION BETWEEN SURFACE PROFILE AND VELOCITY FIELD

In order to investigate the detailed mechanism of wave-induced velocity field, the surface fluctuation and the fluid velocity components were measured at numerous locations in a laboratory flume (Fig. 6). Table 1 gives the conditions of laboratory experiments carried out for the present investigation. Figure 7 shows sample records of wave profile and the horizontal velocity component taken simultaneously. For the comparison, the stream function method and the 5th order Stokes wave theory were applied to the wave profile, and the time history of velocity components were calculated by these methods. In addition to these, the linear filter method was applied to calculate the velocity component from the wave profile. As for the wave profile, it is quite natural that the curves based on the stream function method agree well with the measured ones both outside and inside the surf zone. The 5th order Stokes wave theory gives fairly good results in the offshore region. As for the velocity component, the curves obtained outside the surf zone agree well with those based on either the Stokes wave theory or the stream function method. The linear filter is also applicable to calculate the velocity component near the bottom from the surface profile. On the other hand, the velocity component inside the surf zone has the following remarkable tendency. The velocity near the free surface measured at the location just after breaking differs largely from the predicted one, but the velocity near the bottom agrees well with the one predicted by using the stream function theory.

That is to say, in the region just after the breaking the turbulent fluctuation is very strong, therefore the simple prediction methods stated above are not powerful for our purposes, but the turbulent fluctuation does not penetrate down to the sea bottom. Of course, such situation is strongly dependent on the breaking type and the distance to the questioned point measured shoreward from the breaking point. The above fact indicates that the Reynolds stress of the turbulent fluctuation induced by breaking phenomenon should play an important role in the nearshore dynamics.

In the ordinary treatment on the wave set-up in the surf zone, the frictional term is conventionally neglected as shown in Eqs. (5) and (6). The frictional term consists of the bottom frictional and the lateral frictional terms, in which the latter term is the depth integral of the Reynolds stress. Based on the laboratory investigation data, the authors have the insight that the bottom frictional term averaged over many wave cycles does not contribute significantly to the wave set-up phenomenon due to the time-dependent oscillatory motion, while the lateral frictional term must have an important influence on the stated phenomenon. At the present stage, the data on this subject are extremely scarce, hence the further effort to accumulate laboratory and field data seems to be of essential importance.

FIELD OBSERVATION

In the foregoing discussion, the laboratory data were only used. In order to confirm the stated results, a part of the field observation data will be presented in the following.

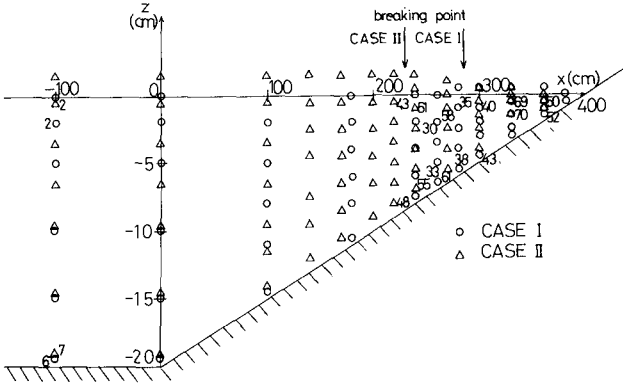


Fig. 6 Location diagram of the measuring points.

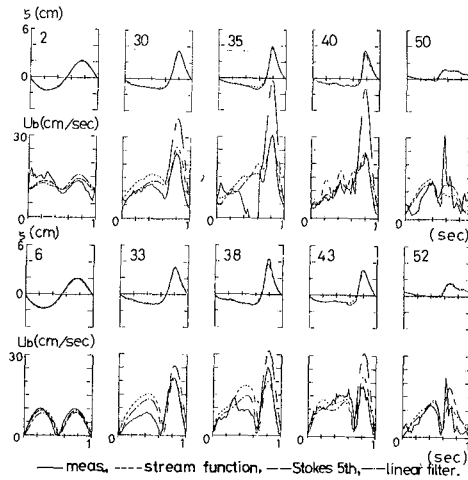


Fig. 7 Comparison of the measured time histories of wave profile and of corresponding absolute velocity with those predicted by the various methods (Case I).

A number of poles were installed closely in a row perpendicular to the shoreline inside the surf zone on Ajigaura coast, Ibaragi Prefecture, Japan, and the data of sea surface fluctuations at these poles were collected by using simultaneously operated 16mm memo-motion cameras. In some cases a frame was set in the surf zone. On this frame a certain number of electromagnetic current meters were attached in order to measure the vertical distribution of wave-induced current velocities. Hence the surface fluctuation and the corresponding velocity fluctuations were measured simultaneously.

Two records of surface fluctuations obtained at two points 2m apart in the direction perpendicular to the shoreline in the surf zone were picked up. The wave direction angle was negligibly small, hence the wave celerity could be calculated by the phase shift between these two records. The abscissa of the diagram shown in Fig. 8 is the frequency in Hz and the ordinate is the phase shift. Therefore the wave celerity is proportional to the slope of the curve. The plotted points fall on the theoretical curve based on the solitary wave theory, and this fact confirms the conclusion obtained in the laboratory investigations.

Figures 9 (a), (b), and (c) show the serial comparison between the time history of measured velocity components and those predicted by the various methods using the corresponding surface profiles. From these figures, it can be said in general that the stream function method is useful in field also for the prediction of velocity components outside the surf zone. However, the predicted velocity curves by the various methods are not always fit to the measured ones inside the surf zone. Especially it is remarkable that there is time lag between the calculated and measured velocity components.

Figures 10 (a) and (b) give the power spectra of water surface fluctuations at two points, one is located outside and the other is inside the surf zone. Figures 11 (a) and (b) indicate the power spectra of wave induced velocity components at the corresponding locations in Figs. 10 (a) and (b), where u_2 and v_2 are the onshore-offshore and alongshore components of velocity measured near the water surface, while u_4 and v_4 are near the sea bed. From these diagrams it can be observed that the turbulent velocity fluctuation is very weak outside the surf zone, but it is strong just after the breaking point especially near the surface. Looking at these data, the authors have tried to construct the following conceptual model of turbulent fluctuation in the nearshore area.

The turbulent fluctuation in the nearshore area is primarily generated by the wave breaking, therefore the turbulence outside the surf zone is negligibly small but that inside the surf zone is remarkably strong especially in the vicinity of the breaking point. The disturbance induced by the breaking waves penetrates into the body of water, and reaches slightly to the bottom. Therefore the distribution of the Reynolds stresses is negligibly small outside the surf zone, but is large enough to be considered inside the surf zone. It is needless to say that the wave-induced turbulence depends upon the breaker type, the running distance of breakers, and the depth below the water surface.

In addition to the above, it should be mentioned that the power spectra of velocity fluctuation inside the surf zone contain tremendously big spectral density in the low frequency part as shown in Fig. 11 (b) comparing with

Table 1 Experimental conditions.

Case	Incid. Wave Height H_i (cm)	Wave Period T (s)	H_o I_o	Breaker Type
I	3.5	1.0	0.025	Plunging
II	5.5	1.0	0.039	Plunging

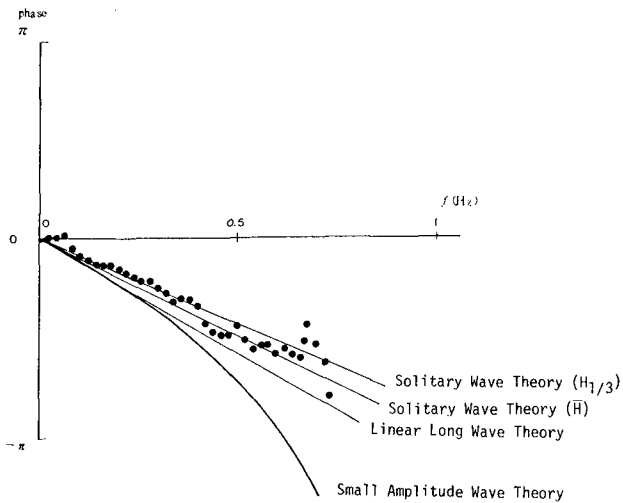


Fig. B Wave celerity in the surf zone observed in field.

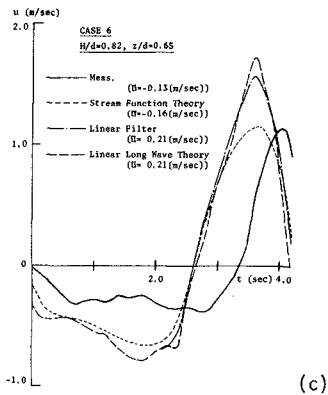
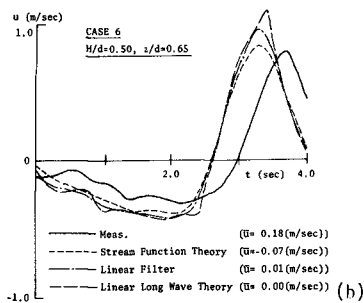
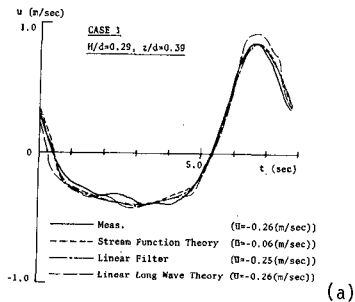
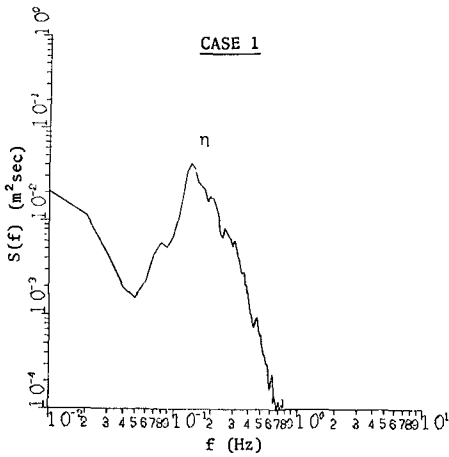
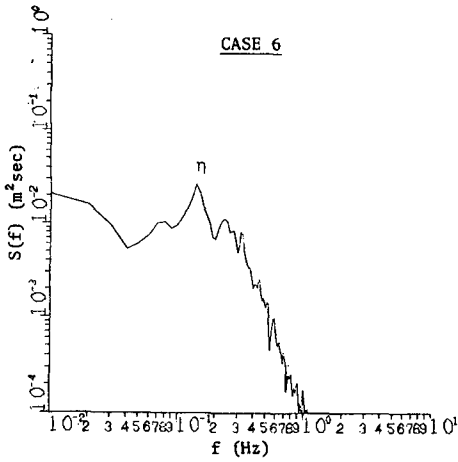


Fig. 9 Time history of horizontal velocity component. Comparison between the measured and predicted curves, where z is taken upward from the sea bottom, d the mean water depth at the measuring site, and \bar{u} the shoreward mean constant velocity. Thus u is the value subtracted the \bar{u} value from the actual velocity.



(a) Outside the surf zone.



(b) Inside the surf zone.

Fig. 10 Spectra of surface fluctuation at the two measuring points, where η is the surface elevation measured upward from the mean sea level.

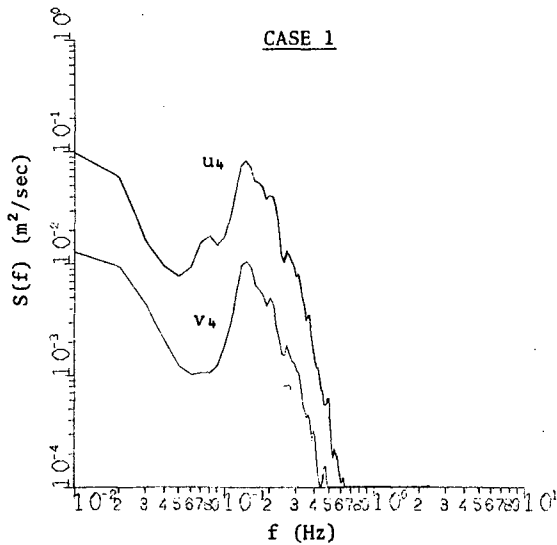
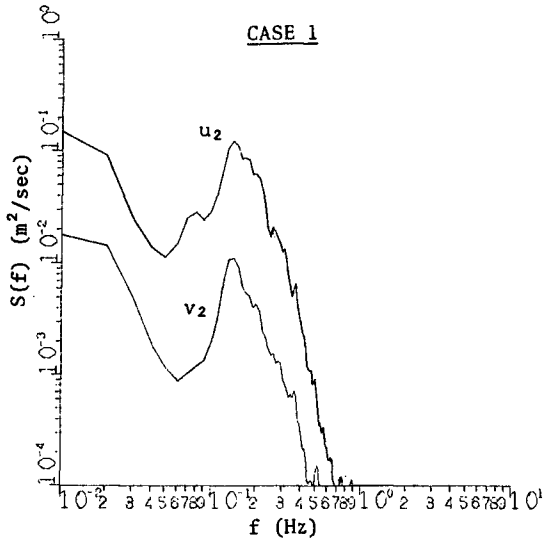


Fig. 11 (a) Spectra of velocity components outside the surf zone.

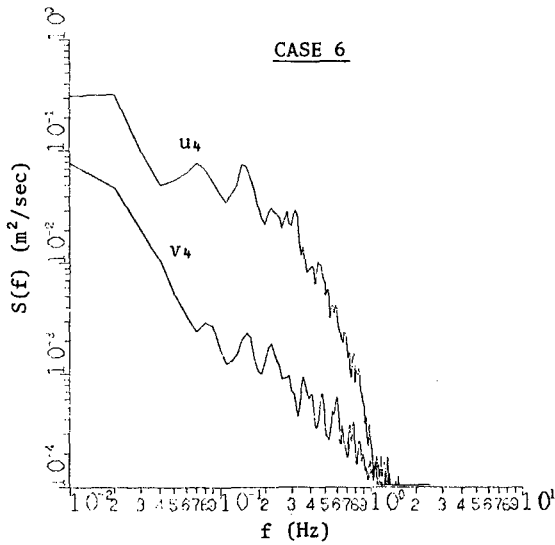
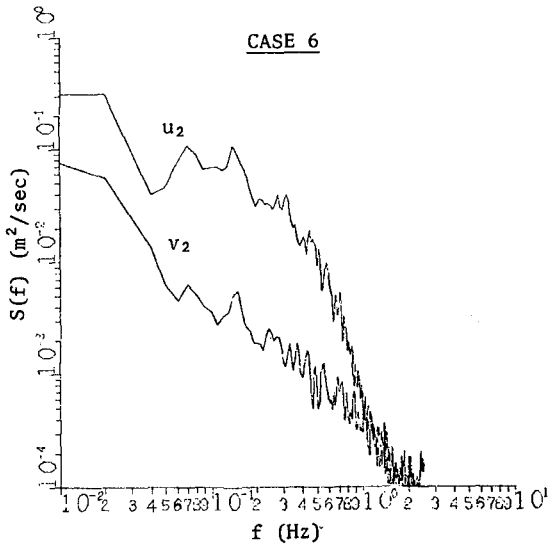


Fig. 11 (b) Spectra of velocity components inside the surf zone.

those for the outside of the surf zone as shown in Fig. 11 (a). This fact indicates that the low frequency (that is, long period) oscillation is predominant inside the surf zone as reported by Sasaki and Horikawa (1978).

THREE DIMENSIONAL CASE

LONGSHORE CURRENT VELOCITY DISTRIBUTION

In order to proceed the present discussion to the three dimensional case, longshore current velocity distribution will be treated. As Longuet-Higgins (1970) pointed out in his paper, the longshore current velocity is used to have its maximum at a certain point located between the shoreline and the breaker line. The velocity distributions in a wave basin have so far been measured under the various conditions of bottom slope, wave approaching angle, and wave characteristics. Through the analysis of these data, it was realized that the shoreward pattern of velocity distribution in the surf zone on a uniformly sloping beach fits very well with the one calculated under an appropriate value of P on the basis of the Longuet-Higgins analytical result. Here P is defined by Longuet-Higgins as a non-dimensional parameter representing the relative importance of horizontal mixing and lateral friction. However, the seaward pattern of the measured velocity distribution curve drops abruptly comparing with the theoretical one. One example is shown in Fig. 12. The above discrepancy is presumably caused by the following two reasons. The first reason is that the value of S_{xy} used for the calculation was derived by using the small amplitude wave theory. The second reason is that the expression for the lateral friction outside the surf zone was estimated to be too large comparing with the actual one. In addition to these, the effect of wave approaching angle can be pointed out as discussed independently by Liu & Darliple (1978) and Kraus & Sasaki (1979).

INTERNAL CHARACTERISTICS OF SURF ZONE

Izumiya, Isobe, Watanabe & Horikawa (1980) reported recently a detailed laboratory measurement of the internal characteristics of waves and wave-induced current in the surf zone. Their measurement was performed under such a simple condition as the longshore current being predominant on a fixed uniform slope of $1/20$ in a wave basin. The characteristic conditions of the waves are as follows: the wave height at the uniform water depth $h=25\text{cm}$ is 4.1cm , the wave period is 0.87s and the wave angle at the breaker line is 15° .

The fluctuation of velocity components were measured directly by using hot-film anemometers. Based on these laboratory data, they tried to evaluate how well the radiation stresses outside and inside the surf zone can be evaluated by using the appropriate theory, and to find out how much the lateral frictional term contributes to the balance in the dynamical equation.

The governing equation of the present case is expressed by

$$\frac{d}{dx} S_{xy} = R_y = -\frac{d}{dx} S_{xy} + \overline{\tau_{xy}} - \overline{\tau_{hy}} \quad (7)$$

where x and y are taken perpendicular and parallel to the shoreline respectively. In order to predict precisely the spatial velocity distribution of

longshore current, the characteristics of the two terms S_{xy} and R_y should be clarified in more detail. Equation (7) can be rewritten in the next form;

$$\frac{d}{dx} (S_{xy} + S_{xy}^{\prime}) = \overline{\tau_{xy}} - \overline{\tau_{hy}} \quad (8)$$

Here the new term $S_{xy}^{\prime} = S_{xy} + S_{xy}^{\prime}$ will be defined for the convenience of the following discussion.

It is quite natural that the record of current velocity components taken inside the surf zone is the superposition of the turbulent fluctuation generated by the breaking wave action on the wave orbital and steady current velocity components. In the forgoing treatment, the vertically uniform steady current is assumed, however the actual current must have a certain vertical distribution which is not yet clearly known. Considering the above fact, it should be noticed that the term S_{xy} in the paper reported by Izumiya, Isobe, Watanabe & Horikawa (1980) is not exactly equal to the radiation stress or the excess momentum flux defined by Longuet-Higgins & Stewart (1964). However, they reported that the calculated term S_{xy} is well expressed by the 5th order Stokes wave theory outside the surf zone.

Figure 13 indicates the variations of S_{xy}^{\prime} and S_{xy} from offshore to onshore. From this diagram, it is clearly seen that the $S_{xy}^{\prime} = S_{xy}^{\prime} - S_{xy}$ is zero outside the surf zone but is large enough to be considered inside the surf zone. In Eq. (8) the shear stress along the water surface $\overline{\tau_{xy}}$ is negligibly small, therefore the gradient of S_{xy}^{\prime} must be balanced with the bottom shear stress $\overline{\tau_{hy}}$.

The lateral frictional stress is used to be expressed simply to be proportional to the gradient of the longshore current velocity. However, it seems to be unreasonable that the proportionality constant becomes negative just after breaking as seeing from Figs. 12 and 13.

Here it should be noticed that the term S_{xy} takes its maximum at the location a little offshoreward from the breaking point. That is to say, the gradient of S_{xy} between that point and the breaking point determines the velocity distribution of longshore current outside the surf zone. The above mechanism is quite important to understand the real longshore current pattern.

Figure 14 demonstrates the spatial distribution of Reynolds stress $-\overline{u''v''}$ from which the statement made in the previous section can be confirmed.

CONCLUSIONS

The main conclusions of the present paper are summarized in the following:

- (1) It is quite naturally true that the small amplitude wave theory is not powerful to take the insight of the detailed mechanism of nearshore dynamics.
- (2) Therefore some appropriate theory or method should be applied to evaluate the dynamic characteristics of waves outside and inside the surf zone.

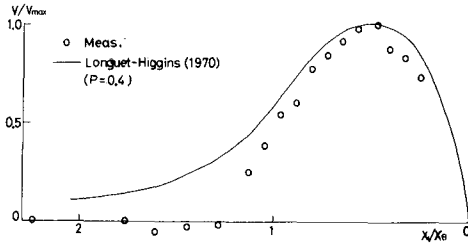


Fig. 12 Longshore current velocity distribution ($\tan\beta = 1/20$) (adapted from Izumiya, Isobe, Watanabe & Horikawa, 1980).

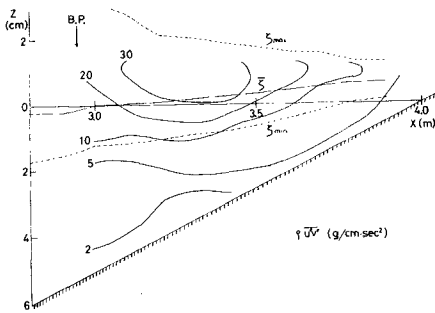


Fig. 13 Distribution curves of \bar{S}_{xy} and S_{xy} (adapted from Izumiya, Isobe, Watanabe & Horikawa, 1980).

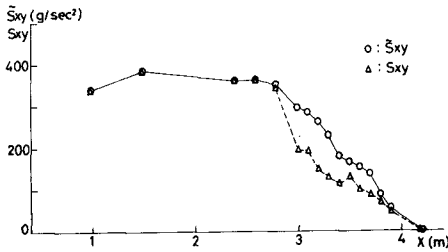


Fig. 14 Distribution pattern of $pu''v''$ (adapted from Izumiya, Isobe, Watanabe & Horikawa, 1980).

- (3) The precise calculation of radiation stresses is of essential importance to predict the phenomena actually happening in the nearshore area,
- (4) The Reynolds stresses are negligibly small outside the surf zone, but is large enough to be taken into consideration inside the surf zone due to the strong breaking wave disturbance. Therefore the evaluation of Reynolds stresses in the surf zone is also needed to understand the various phenomena in the surf zone.
- (5) In order to clarify the detailed mechanism of nearshore phenomena, more data should be accumulated in laboratory as well as in field.

ACKNOWLEDGEMENTS

The authors would like to express their appreciation to the personnel at the Coastal Engineering Laboratory, University of Tokyo, for their effort to carry out the laboratory and field measurements. The present research was supported by the research grant of the Ministry of Education of Japan.

REFERENCE

- Dean R. G. (1965): Stream function representation of nonlinear ocean waves, *J. Geophys. Res.*, Vol. 70. No. 18, pp.4516-4572.
- Hotta, S, and M. Mizuguchi (1978): Field observations of broken wave characteristics, *Proc. 25th Conf. on Coastal Eng. in Japan*, pp.151-154 (in Japanese).
- Isobe, M., N. Fukuda and K Horikawa (1979): Two-dimensional laboratory experiments on the velocity field inside the surf zone, *Proc. 26th Conf. on Coastal Eng. in Japan*, pp.41-45 (in Japanese).
- Izumiya, T., M. Isobe, A. Watanabe and K. Horikawa (1980): Laboratory investigation on the internal velocity and the frictional stress coefficient in the wave and wave induced current field, *Proc. 27th Conf. on Coastal Eng. in Japan* (in Japanese, in press).
- Kraus, N. C. and T. O. Sasaki (1979): Influence of wave angle and lateral mixing, *Comm. of Marine Sci.*, Vol. 5, No. 2, pp.91-126.
- Liu, P. L - F. and R. A. Dalrymple (1978): Bottom frictional stresses and longshore currents due to waves with large angle of incidence, *J. Marine Res.*, Vol. 36, No. 2, pp.357-375.
- Longuet-Higgins, M. S. (1970): Longshore currents generated by obliquely incident sea waves, 1 & 2, *J. Geophys. Res.*, Vol. 75, No. 33, pp.6778-6789 & pp.6790-6801.
- Longuet-Higgins, M. S. and R. W. Stewart (1960): Changes in the form of short gravity waves on long waves and tidal currents, *J. Fluid Mech.*, Vol. 8, pp.565-583.
- Longuet-Higgins, M. S. and R. W. Stewart (1964): Radiation stresses in water waves; a physical discussion, with application, *Deep Sea Res.*, Vol. 11, pp.529-562.

Mizuguchi, M., K. Tsujioka and K. Horikawa (1978); A consideration on wave height variation after breaking, Proc, 25th Con-on Coastal Eng. in Japan, pp.155-159 (in Japanese).

Mizuguchi, M. and K. Horikawa (1978): Experimental study on longshore current velocity distribution, Bull. Faculty of Science and Eng., Chuo Univ., Vol, 21, pp.123-149.

Phillips. O. M. (1977): The Dynamics of the Upper Ocean, Cambridge Univ. Press, 336p.

Sasaki, O. T. and K. Horikawa (1978): Observation of nearshore current and edge waves, Proc 16th Int. Conf. on Coastal Eng., Hamburg, pp.791-809,

VELOCITY FIELD IN A STEADY BREAKER

by

J.A. Battjes¹⁾ and T. Sakai²⁾

ABSTRACT

An experimental investigation is described of the velocity field in a steady, spilling-type breaker, generated on a steady current by a submerged hydrofoil. Velocities have been measured with a laser-doppler system, and analysed with respect to mean and rms-values as well as Reynolds stresses. The results indicate that the turbulent flow field downstream of the initiation of the separation at the surface resembles that in a turbulent wake.

INTRODUCTION

Peregrine and Svendsen (1978) have proposed a model for the flow field in a class of steady and quasi-steady breaking flows such as hydraulic jumps, bores, and spilling breakers. They concluded from visual observations that the turbulent flow, immediately following the breaking, resembles a turbulent mixing layer, which arises because the smooth flow from upstream meets the relatively slowly moving water in the toe of a surface roller. This roller, which is small compared to the region of high-intensity turbulence, is believed not to play an important role in the dynamics of the wave, other than that it triggers the turbulence.

In Peregrine and Svendsen's model, the region of turbulent flow following breaking is supposed to spread downstream and downward as in a mixing layer; at some distance downstream the upper region becomes affected by gravity, and for waves in shallow water the lower region by the bottom. Still further downstream there is a so-called wake or decay region.

The usefulness of a model such as this is that it enables one to describe the main features of the turbulence induced by breaking in terms of better known classes of turbulent flows. However, the model is partly hypothetical. It is based on visual observations, which are largely qualitative. A more quantitative verification is still needed. It is the purpose of the present study to contribute to such verification, through the measurement and analysis of the mean flow, the turbulent intensities, the turbulent shear stresses, and their decay with distance downward and downstream.

-
- 1) Professor, Dept. of Civil Engineering, Delft University of Technology, Stevinweg 1, Delft, The Netherlands
 - 2) Associate Professor, Dept. of Civil Engineering, Kyoto University, Sakyo-Ku, 606 Kyoto, Japan (previously, Research Fellow, Dept. of Civil Engineering, Delft University of Technology, The Netherlands)

The contents of the paper are as follows. The experimental arrangement and procedure are described first. This is followed by a presentation of the main results. These are subsequently discussed and compared with the model of a turbulent mixing layer and a turbulent wake. The conclusion is that the observed flow field appears to be predominantly like a turbulent wake.

This proceedings paper is kept rather brief. A more extensive presentation will be given in a forthcoming paper.

EXPERIMENTAL ARRANGEMENT AND PROCEDURES

Flow conditions

As stated in the introduction, the purpose of the present study is to investigate the turbulence induced by a breaking water surface, with special reference to the model proposed by Peregrine and Svendsen (1978) for the flow field in a class of steady or quasi-steady breakers. A partial check of the validity of that model can be obtained in a breaker in which the mean (non-turbulent) motion is steady. Such type of flow was used in this study, because its investigation is experimentally much simpler than that of non-steady flows, while at the same time it should yield useful information about the flow characteristics in quasi-steady breakers.

We have set out to obtain a steady breaker, which should be relatively unaffected by a bottom boundary layer, and the geometry of which should resemble that of a spilling breaker or a post-breaking bore on a beach. We have created such a flow condition by inserting a hydrofoil below the free surface of a steady flow in a laboratory flume (Fig.1).

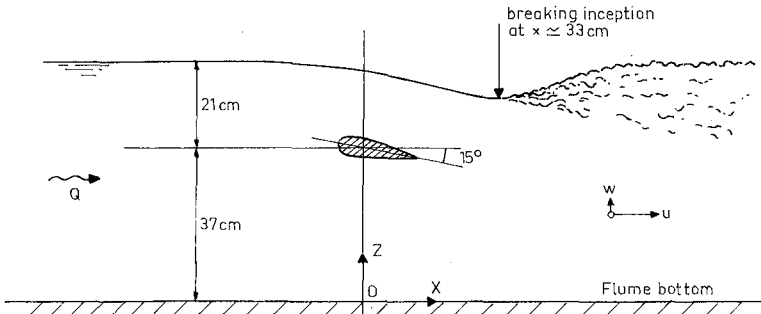


Fig.1 - Sketch indicating flow condition and definition of reference frame

Under these conditions, there is no need for the entire upstream flow to be supercritical, or even to have a Froude number near 1. We could therefore choose a relatively large depth (larger than the critical

depth for the given maximum discharge), so as to obtain an extensive region in which the post-breaking turbulent flow near the free surface would not be affected by the proximity of the bottom. The maximum discharge in the flume is $0.50 \text{ m}^3\text{s}^{-1}$, and the flume width is 0.80 m; the corresponding critical depth is 0.34 m. The experiments were performed with a mean undisturbed flow depth (h) of 0.58 m.

Our ultimate interest is in "full-size" breakers, with high Reynolds numbers and intensive air entrapment. We have therefore chosen for as large dimensions and discharge as could be achieved in the available flume, so as to minimize scale effects. These experiments will be referred to as "full scale". The cross-sectionally averaged undisturbed flow velocity in these runs was 1.08 ms^{-1} . In addition, a few measurements were made in a so-called "half scale" run, which was a Froudian model of the full-scale situation, with a length scale of about 1:2, with the purpose of obtaining insight into possible scale effects. The numbers given in the following refer to the full-scale experiments.

The hydrofoil was chosen to have a relatively full profile. A NACA 6024 profile was used, with a maximum thickness of 4.8cm and a chord of 20.0cm.

In preliminary runs, the depth of the center of the hydrofoil below the undisturbed mean water level (d) and its angle with respect to the horizontal (α) were varied, in order to find conditions which appeared suitable to our purpose (as described above). For the values of mean depth and discharge mentioned above, useable flows were obtained for values of d from about 0.15 m to 0.30 m, and for values of α from about 5° to 20° . The final full-scale experiments were performed with $d = 0.21 \text{ m}$ and $\alpha = 15^\circ$ (see Fig.1).

Velocity measurements

Velocities were measured by means of a laser-doppler velocity (LDV) meter. Such meter works on the principle of measuring the Doppler frequency shift of a laser beam scattered by small particles in a moving fluid. It measures some average velocity value for a volume with a characteristic linear dimension of the order of 1 mm. In what follows these dimensions are ignored, and we shall refer to the measurements as "point" measurements.

The LDV system which was used operates in the reference beam mode. Laser beams were transmitted transversely through the flume (through the glass-panelled side-walls) and the water in it. The components radiating and detecting the signals were mounted in a fairly rigid frame over the flume, to maintain proper alignment. This frame could be moved in its entirety, along the flume as well as vertically.

If no light scattering is detected by the laser-doppler system, the output signal contains no information about the flow velocity. This situation is called "signal drop-out". In this experiment, the signal drop-out is most often induced by air bubble interruption of the laser beam near the breaking surface. The occurrence of drop-outs was accounted for in the data analysis.

The LDV system is capable of measuring two velocity components in one point simultaneously. We have measured the downstream component (u) and the vertical component (w , positive upward).

The outputs of the LDV were recorded simultaneously in an analog magnetic tape recorder (Bell Howell adr 1000). The recording time was 2 minutes per measurement point.

The velocity signals (u, w) were separated in their mean values (\bar{u}, \bar{w}) and the fluctuations about these means, (u', w') = (u, w) - (\bar{u}, \bar{w}). (Here and in the following, an overbar denotes a time average.) Estimates of $\bar{u}, \bar{w}, u'^{\text{rms}} = (\overline{u'^2})^{1/2}, w'^{\text{rms}} = (\overline{w'^2})^{1/2}$ and $\overline{u'w'}$ in all the measurement points were obtained using standard analog equipment. The procedures which were used in the analyses will be described in more detail in a forthcoming paper.

RESULTS

Measurements of (u, w) have been made in a number of points in the central verticals of flume cross-sections, at various distances (x) downstream of the center of the hydrofoil. The minimum distance used was $x = 0.33$ m, in the cross-section of the toe of the breaker (Fig.1). The maximum distance was 4 m. It was believed that beyond that too much bottom influence would occur.

A number of points in each vertical were used, with a height (z) above the flume bottom varying from 0.21 m (the minimum possible with the frame supporting the LDV apparatus) to somewhat below the free surface, where the signal drop-outs were judged to become too severe. Measurements were also made in the undisturbed flow, i.e. in absence of the hydrofoil.

The results have been plotted in two ways, vz , as a sequence of vertical profiles, and as isolines in the x, z -plane. For brevity, only the profiles of \bar{u}, u'^{rms} and $\overline{u'w'}$ are given here (Figs. 2, 3 and 4), as well as isolines of $\overline{u'w'}$ (Fig.5).

Data points of the full-scale experiments are indicated by crosses, and those of the half-scale experiments by open circles. The latter points have been scaled up from the measured values. The lengths have been multiplied with a factor 2. With a strict Froude scaling, the velocities should have been multiplied with a factor $2^{1/2}$. In fact, the ratio of the actually measured upstream mean velocities was used, which was about 1.6. The difference is due to a mal-adjustment of the discharge.

The full-scale data points have been connected by full-drawn straight-line segments for purposes of visualisation.

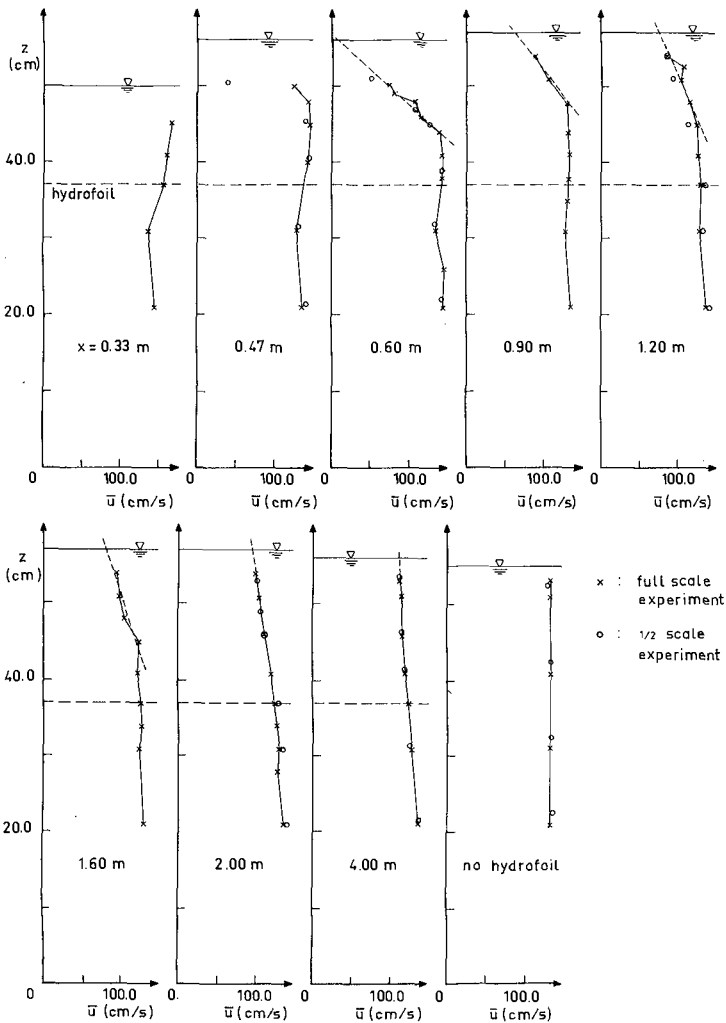


Fig.2 - Vertical profiles of \bar{u} in sections at various distances downstream of the hydrofoil. The dashed lines in the upper part indicate linear extrapolations. The profile in the lower right hand corner is for the flow in absence of a hydrofoil.

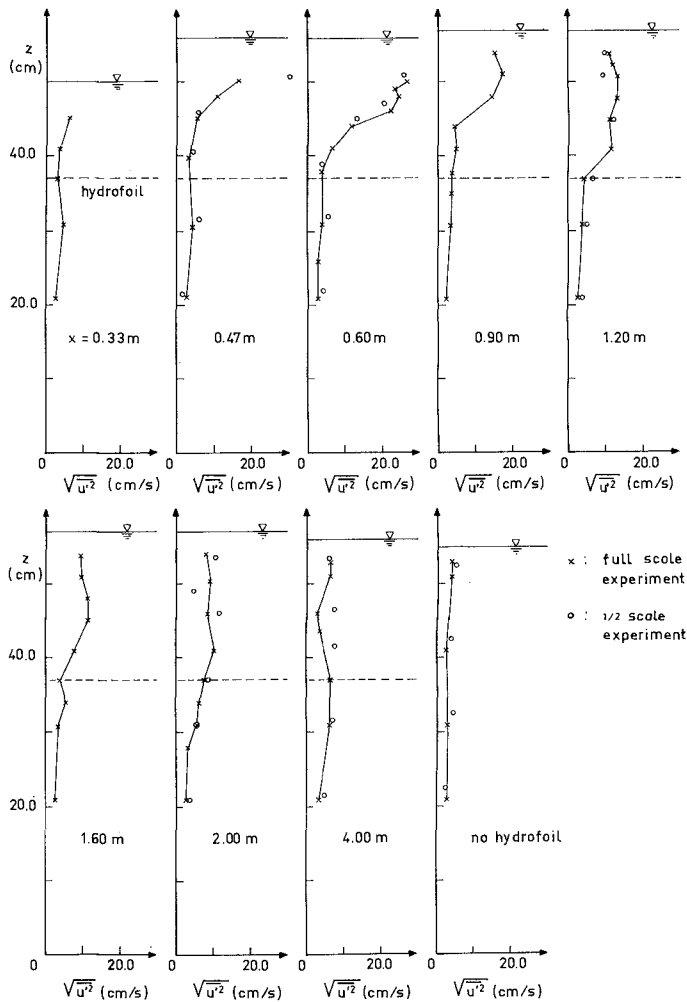


Fig. 3 - Vertical profiles of $\sqrt{u'^2}$ in sections at various distances downstream of the hydrofoil. The profile in the lower right hand corner is for the flow in absence of a hydrofoil.

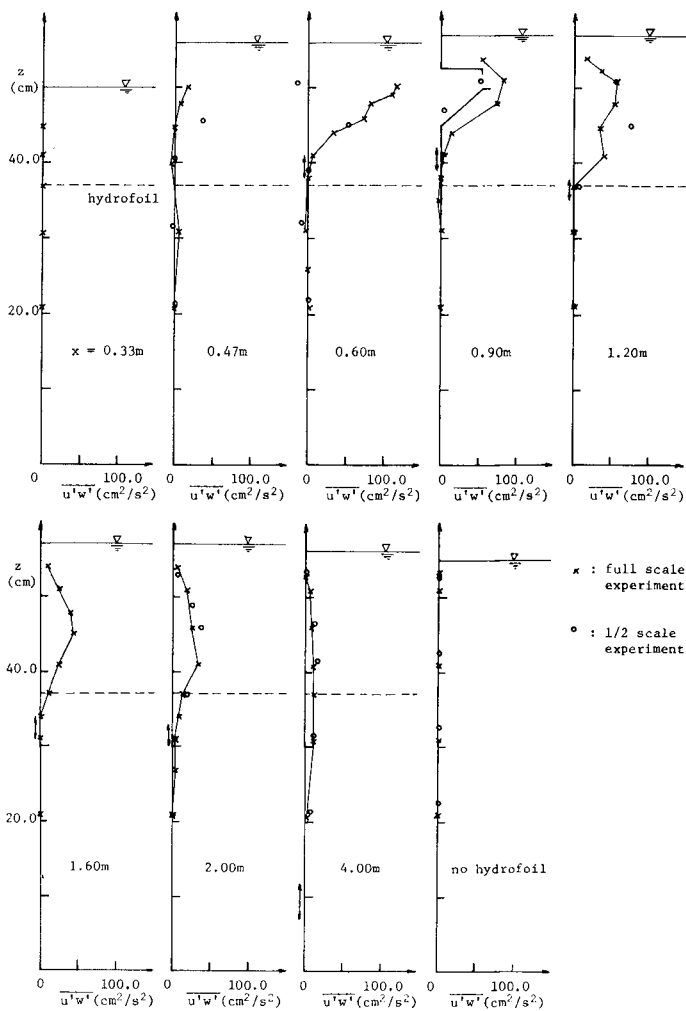


Fig.4 - Vertical profiles of $\overline{u'w'}$ in sections at various distances downstream of the hydrofoil. The profile in the lower right hand corner is for the flow in absence of a hydrofoil.

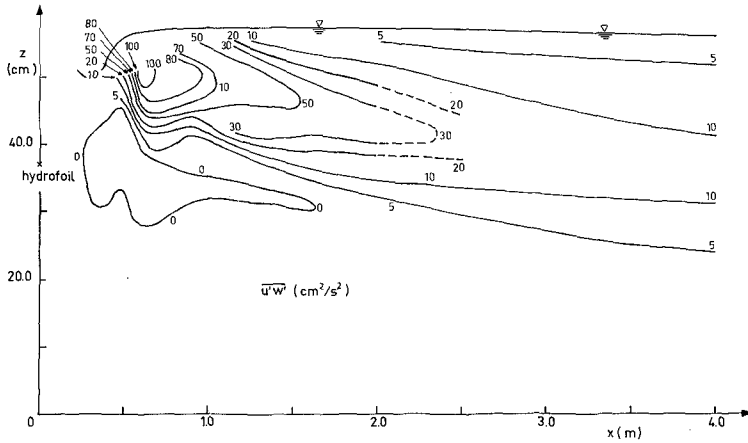


Fig. 5 - Lines of constant $\overline{u'w'}$ values downstream of the hydrofoil

DISCUSSION

General trends

The half-scale results are in general in good agreement with the full-scale results. Significant deviations are present in all three profiles at $x = 0.47$ m, and in the $\overline{u'w'}$ - profile at $x = 0.60$ m as well. This matter has not been pursued in the present study, so that no conclusions concerning scale effects can be drawn other than that these appear to be absent in the region downstream of the cross-sections mentioned above.

The profiles in the lower right-hand corner of the Figs. 2 through 4 refer to the undisturbed flow conditions. It can be seen by inspection that the corresponding mean-velocity profile (Fig. 2) is virtually uniform in the upper part of the flow, while the turbulent shear stresses there do not deviate visibly from zero, when drawn on the same scale as the profiles for the flow with a hydrofoil (Fig. 4). This indicates a virtual absence of any influence of a bottom boundary layer in the upper flow region.

It is clear from Fig. 2 that the profiles of \bar{u} in the presence of the hydrofoil exhibit a strong defect near the breaking surface. This defect penetrates into the deeper region of the flow with increasing distance downstream, while at the same time it diminishes in magnitude. However, even at $x = 4$ m it is still clearly present, as can be seen by

comparing that profile with the one for the flow in absence of the hydrofoil.

At the most upstream cross-section, a slight velocity defect can be discerned at a height $z \approx 0.3$ m, which is an indication of the wake generated behind the hydrofoil.

Fig.3 shows that the turbulence has its greatest intensity near the toe of the breaking surface, from where it decays downward and downstream. At $x = 4$ m, the station farthest downstream, it is still significantly in excess of its value in the undisturbed flow. The wake of the hydrofoil shows up in Fig.3 as a slight excess of u'_{rms} .

The quantity $\overline{u'w'}$, which is proportional to the turbulent shear stress, has significant non-zero values only in a fairly well-defined upper layer downstream of the toe of the breaker. It is virtually zero in the cross-section of this toe ($x \approx 0.33$ m); no evidence of a wake behind the hydrofoil is present in this profile.

Altogether, the results shown in the Figs.2 through 5 clearly indicate the presence of a region of relatively high shear on top of a more or less undisturbed flow. The thickness of the shear layer increases in the downstream direction, while the mean-velocity defect and the turbulent intensity and shear stress decrease.

Comparison with wake and mixing layer

In the classical theory of turbulence a number of freely evolving shear flows has been studied, such as mixing layers, jets and wakes. In this section, the question will be considered to which extent the observed flow is similar to one of these.

A mixing layer forms the transition between two uniform parallel flows of different velocity, while a jet and a wake can be seen as laterally limited regions of velocity surplus and velocity deficit, respectively, relative to the undisturbed flow. In a mixing layer the cross-stream variation in mean flow velocity is constant in the downstream direction (if the two external flows have a sufficient lateral dimension), while this quantity decreases downstream in jets and wakes.

It follows from the above that the flow observed in our experiment, which is characterized by having a velocity deficit with respect to the undisturbed flow, which deficit is decreasing downstream, is qualitatively most nearly like a flow in a wake. This can be checked quantitatively, or at least semi-quantitatively, by estimating the values of some characteristic parameters and their variation downstream, and comparing this with the corresponding results for a typical wake flow. This is done in the following. We have also concluded some theoretical results for a mixing layer, since this was taken by Peregrine and Svendsen as a model for the initial phase of the post-breaking flow.

The quantities to be considered in the comparison are the mean velocity defect (\bar{u}_d), a characteristic value for the turbulent velocity magnitude (\bar{u}'), and a lateral length scale (l).

Asymptotic theoretical relations have previously been derived

between these quantities and their variations downstream, assuming a high Reynolds number (Re) and a nearly parallel, self-preserving flow, away from bounding surfaces. The results are asymptotic in the sense of $Re^{1/2} \gg 1$ and $l \ll L$, in which L is a longitudinal length scale, as well as in the sense that only the far field is considered, sufficiently far downstream from the physical origin of the shear layer, so that the flow has settled down to self-preservation. Some such results, taken from Tennekes and Lumley (1974), have been collected in Table 1, in which the symbol \sim indicates a proportionality, and $x = x - x_0$ is the downstream distance to some reference point $x = x_0$. (This point is near the physical origin of the shear layer. However, a theory for self preserving flow in the far field cannot predict the location of $x = x_0$ in terms of the details of the physical origin of the shear flow, since by definition a self preserving flow has no "memory" of those details.)

Table 1 - Downstream variation of characteristic parameters in free shear layers

	Mixing layer	Plane wake
\bar{u}_d	const.	$\sim x^{-1/2}$
l	$\sim x$	$\sim x^{1/2}$
\hat{u}'	$O\{(l/L)^{1/2}\}\bar{u}_d$ = const.	$O(\bar{u}_d) \sim x^{-1/2}$

Experimental values of \bar{u}_d , \hat{u}' and l were determined as follows. The mean velocity defect was calculated as $\bar{u}_d = \bar{u}_1 - \bar{u}_f$, in which \bar{u}_1 is the value of \bar{u} in the lowest point of measurement ($z = 0.21$ m), and \bar{u}_f the value of \bar{u} at the mean free surface elevation, as estimated by linear extrapolation of the upper part of the measured profile (see Fig.2). For \hat{u}' the maximum value of u'_{rms} in the vertical profile was taken, and l was defined as the depth of the shear layer, from the mean free surface elevation down to the region where there is a fairly abrupt transition between the region of high shear above and the more or less homogeneous flow beneath. The locations of these transition zones were estimated from the vertical distributions of $u'w'$; they have been indicated in Fig.4 by vertical arrows.

The most upstream cross-sections where meaningful estimates could be made were $x = 0.60$ m for \bar{u}_d and l , and $x = 0.90$ m for \hat{u}' (see Figs. 2, 3 and 4).

For a comparison of the observed downstream variations of \bar{u}_d , \hat{u}' and l with the theoretical ones, it is necessary to have an estimate of the location of the reference point for the downstream distance, $x = x_0$. This point is expected to be near the point of initiation of breaking, $x = x_b \approx 0.33$ m (see Fig.1). A more exact estimate is not necessary if one considers points far downstream ($x-x_0 \gg |x_0-x_b|$), but since our measurement points may not fulfill this condition it is worthwhile to

allow x_0 to differ from x_b .

A value of x_0 can be determined so as to optimize the fit of the data points to some theoretical model. We have not done this numerically; we found by visual inspection that $x_0 = 0.5$ m gives results (see Fig.6) which appear to be consistent with the asymptotic theory for a plane wake: u_d and u' both vary approximately as $(x-x_0)^{-1/2}$ and l varies approximately as $(x-x_0)^{1/2}$ (excluding the most upstream measurement of l). Based on these results, we conclude that the flow downstream of the breaking surface is not only like a wake flow in a qualitative sense, but also in a more quantitative sense.

A quantitative comparison of our observations with the theoretical model of a mixing layer was not attempted in view of the observed downstream decrease of u_d and u' , which is absent in the classical mixing layer model.

CONCLUSIONS

Measurements have been made of horizontal and vertical velocities, including turbulent fluctuations, in a steady mean flow with a breaking surface, similar to a so-called spilling breaker in shallow water. These measurements have given rise to the following conclusions:

- (1) A region downstream of the initiation of breaking can be recognized in which the flow evolves as in a free self-preserving turbulent wake. This conclusion rests on the observed downstream variation of mean velocity defect, turbulence intensity, and shear layer thickness.
- (2) The region mentioned in (1) is bounded above by the free surface, which is more or less horizontal because of gravity. The lateral (= vertical) spreading of the shear layer occurs mainly in the downward direction. The flow can therefore be compared to that in one half of a symmetric wake.
- (3) The measurements of the flow in the region mentioned in conclusion (1) appear to be free of scale effects if scaled up according to Froude's law.
- (4) If -as hypothesised by Peregrine and Svendsen (1978)- there exists a region immediately downstream of the initial breakpoint, in which gravity is unimportant, and in which the flow is similar to that in a mixing layer, then such region is small compared to the overall vertical dimensions of the breaker. The model of a mixing layer does not appear to be useful for the prediction of the downward and downstream spreading of the turbulence induced by the breaker, over distances of the order of the breaker height or layer.

ACKNOWLEDGEMENTS

One of us (S.) thanks the Delft University of Technology for granting him a Research Fellowship.

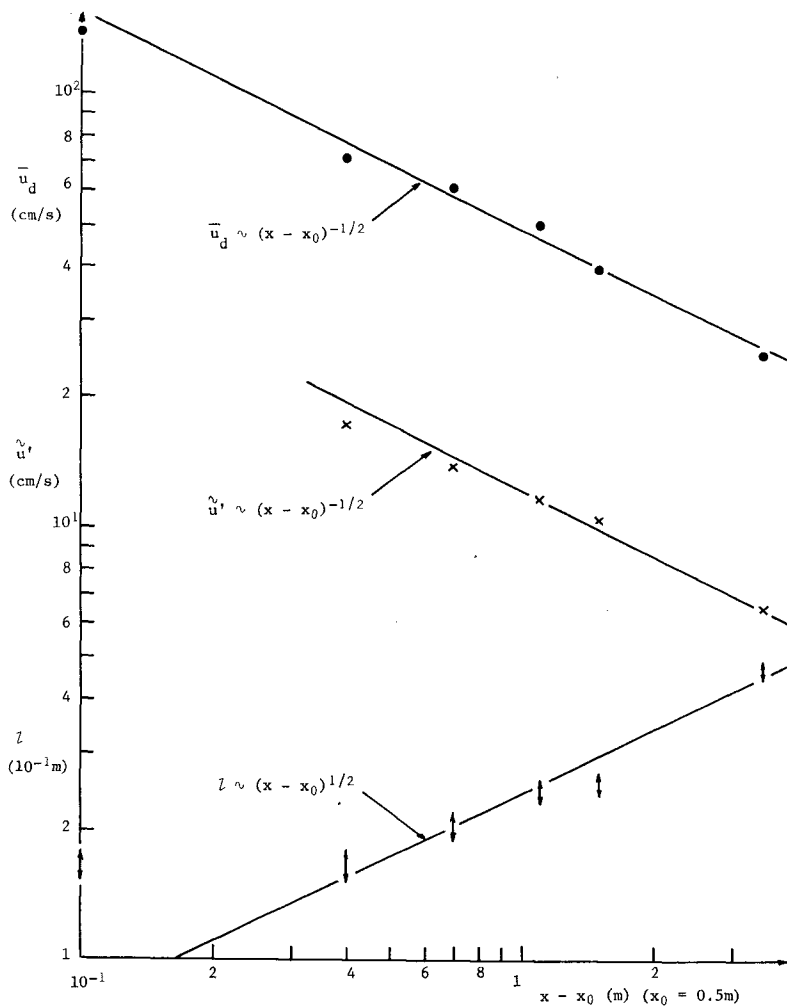


Fig.6 - Variation of flow parameters with distance downstream, for $x_0 = 0.5$ m. Mean velocity defect (\bullet), turbulent intensity (\times) and layer thickness (\updownarrow). The straight lines indicate proportionalities to $(x-x_0)^{\pm 1/2}$.

REFERENCES

- Peregrine, D.H. and Svendsen, I.A. (1978) Spilling breakers, bores, and hydraulic jumps. Proc. 16th Conf. Coastal Eng., pp.540-550.
- Tennekes, H. and Lumley, J.L. (1974) A First Course in Turbulence. The MIT Press.

CHAPTER 32

THE FLUID MECHANICS OF WAVES APPROACHING BREAKING

by

D. H. Peregrine¹

E. D. Cokelet²

P. McIver³

Abstract

Numerical computations of water waves deforming until an overhanging, incipient jet has formed near the crest are studied in detail. Velocity and acceleration plots lead to the identification of three regions in the water which appear to be significant in the approach to breaking. In particular there is a region with particle accelerations greater than the acceleration of gravity.

1. Introduction

The initial stages of a plunging breaker are described from calculations by Longuet-Higgins and Cokelet (1976). They succeeded in computing the motion of particles on the surface of deep-water waves which are periodic in space. Similar computations are the basis of the present work which considers the flow properties in more detail.

The mathematical model is for irrotational flow. The viscosity, the surface tension and the density of the fluid above the free surface are all taken to be zero. The only physical quantities which are present in the flow are the fluid's inertia and gravity. This appears to be quite sufficient since realistic looking results are obtained up to a time when a portion of the surface near the wave crest has been projected forward as an overhanging incipient jet. The numerical scheme then loses accuracy rapidly, apparently because the surface curvature has become too large for the method to resolve without more points along the wave profile.

Waves can be forced to break in several different ways. For these deep-water waves Longuet-Higgins and Cokelet (1978) describe how a small growing, normal-mode perturbation grows until waves break, and Cokelet (1979) shows how sinusoidal waves of sufficient initial amplitude also break, even if their energy density is less than that of the highest wave. Longuet-Higgins and Cokelet (1976) used a pressure distribution

¹Reader in Mathematics, University of Bristol, England

²Oceanographer, Pacific Marine Environmental Laboratory/NOAA, Seattle, Washington, U.S.A.

³Research Assistant, University of Bristol, England

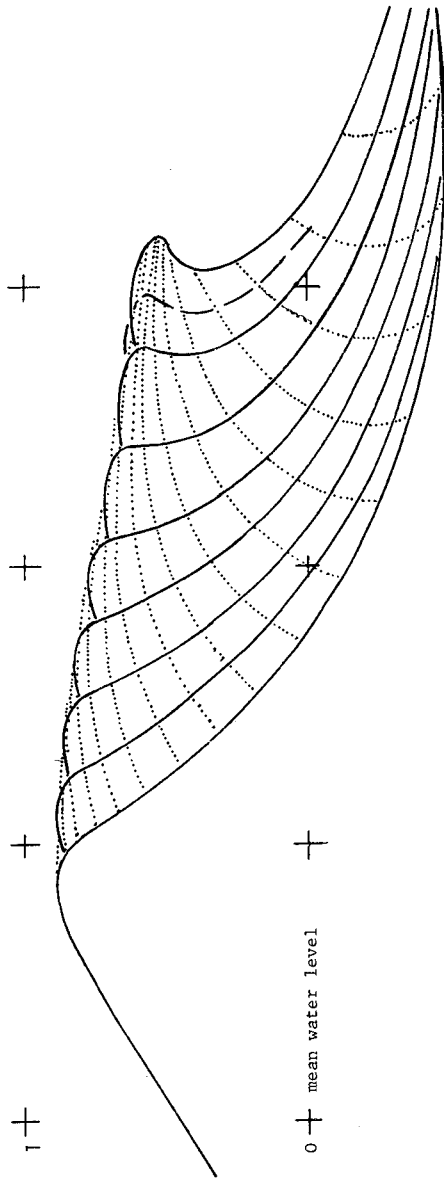


Figure 1. Surface profiles for $\pi \leq t \leq 22\pi/15$, $p_0 = 0.20$.

imposed on the free surface for a limited time to drive the waves to break, and the same set of solutions are considered in more detail here. Full details of the method are to be found in that paper.

Details relevant to this work include the units used and the particular initial and forcing conditions. Units are made dimensionless using the fluid density, the acceleration due to gravity and the wave number of the waves. That means the waves have wavelength, $L = 2\pi$, and the phase velocity and radian frequency of infinitesimal waves of that wavelength are equal to one. The infinitesimal wave period is 2π . The initial conditions are an accurate, steadily-progressing wave of steepness $H/L = 0.13$, or $ak = 0.40$, which may be compared with the values 0.14, or 0.43, for the steepest wave.

The wave forcing is by a sinusoidal pressure pattern travelling at the same speed as the initial wave, in quadrature with the wave profile to give an energy growth and smoothly applied for $0 < t < \pi$. The value, p_0 , of the maximum pressure used is a useful parameter for identifying particular cases.

2. Surface Profiles and the Flow Field

Some profiles of the surface for $p_0 = 0.0729, 0.100, 0.126$ and 0.146 are given by Longuet-Higgins and Cokelet (1976). A sequence of profiles for $p_0 = 0.200$ are shown in Figure 1. This figure shows a succession of wave profiles in the reference frame which has water at depth at rest. The paths of surface particles are indicated by dotted lines. The extra partial profile indicates the last calculations which we consider to be reliable for both particle displacements and velocities (see Sec. 3).

A good way to illustrate the velocity field of an irrotational flow is by the use of equipotentials and streamlines. Cokelet (1979) outlines how to calculate these inside the fluid from surface-evaluated quantities using Cauchy's theorem. Figure 2 shows such isolines for a full wave profile with the fluid at rest at great depth, and Figure 3 gives details near the crest at a slightly later time. These are not as informative as such diagrams for steady flows since the approach to breaking is unsteady. The fluid does not travel along fixed streamlines, but rather the flow is instantaneously tangent to changing streamlines.

Clearly it would be an improvement to consider flow in a reference frame moving with the wave crest. However there is no unique velocity that can be chosen. Any particular feature of the wave could be used to define a velocity, but that velocity would be unsteady. In Figures 4 and 5 we have chosen to view the flow of Figures 2 and 3 in a reference frame moving with the speed of the original steady wave. This gives another, possibly clearer, picture of the motion, and there are some indications that this particular reference frame is of especial relevance. This aspect is being studied further.

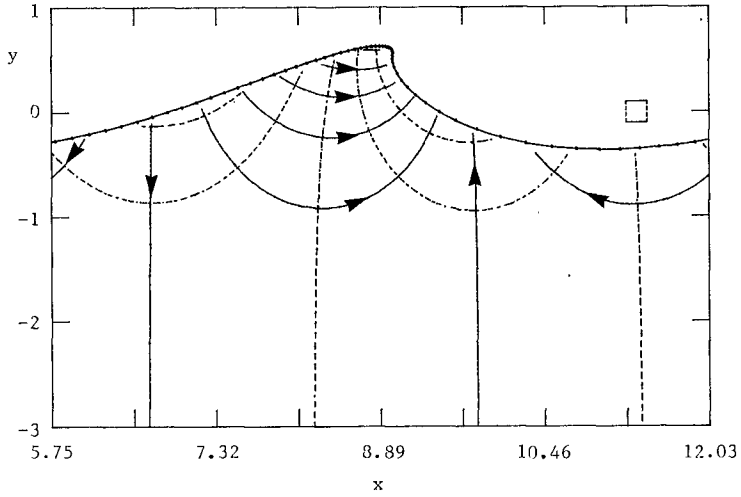


Figure 2. Equipotentials (dashed) and streamlines (solid) at $t = 4.61$ for $p_0 = 0.146$ in a frame of reference with water at great depth at rest. The box at upper right represents contour spacing corresponding to a dimensionless velocity of 1.

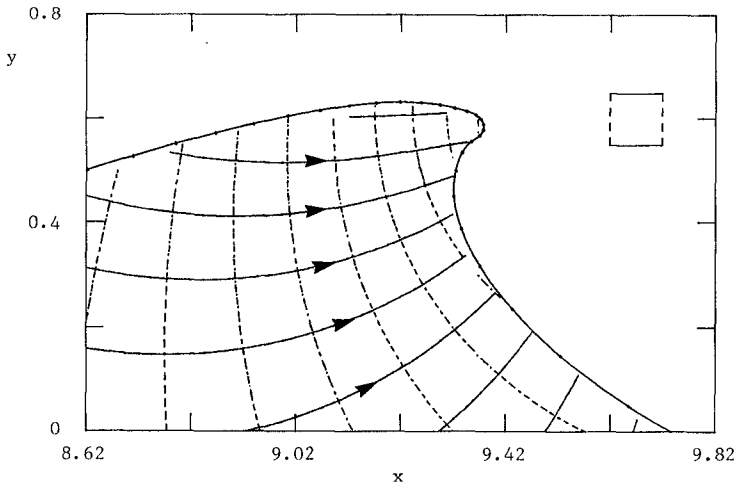


Figure 3. As for Figure 2 but near the crest at $t = 4.82$.

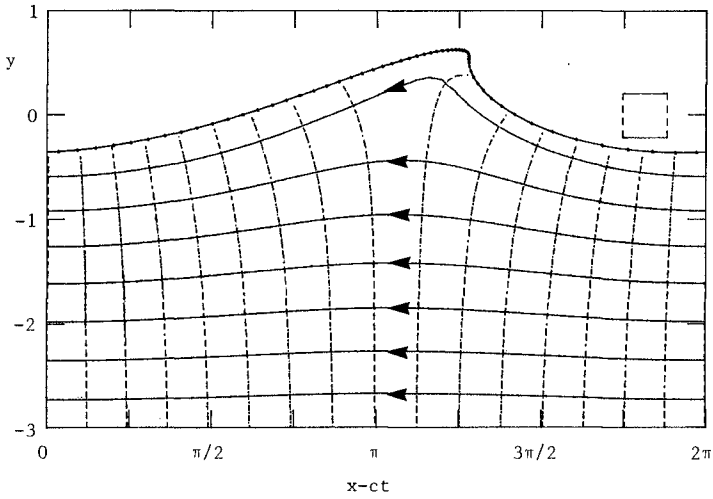


Figure 4. Equipotentials (dashed) and streamlines (solid) at $t = 4.61$ for $p_0 = 0.146$ in a frame of reference moving with speed $c = 1.082$ relative to water at great depth.

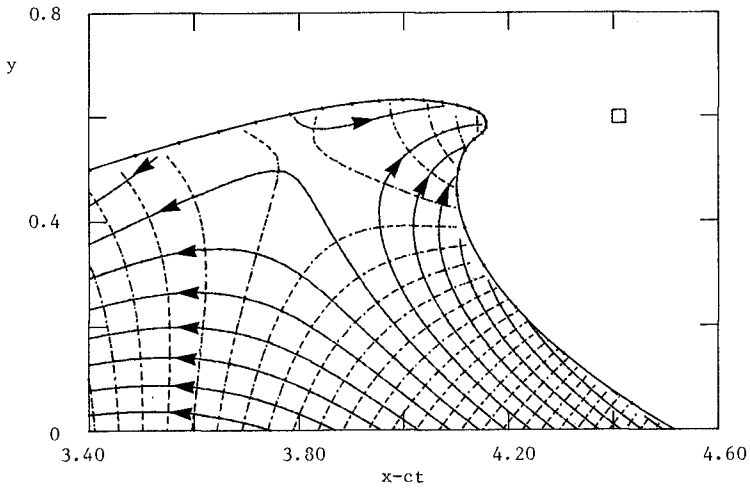


Figure 5. As for Figure 4 but near the crest at $t = 4.82$.

3. The Hodograph Plane

The search for a relevant reference frame leads to consideration of the hodograph plane. That is the (u,v) plane where u and v are, respectively, the horizontal and vertical components of velocity. A change of reference frame by a Galilean transformation (i.e. involving only a uniform constant relative velocity) corresponds only to a change of origin in the (u,v) plane. Thus the character of the (u,v) trajectory for any particle, or of the (u,v) "profile" of surface particles at any instant is unchanged. For a motion which is steady in some Galilean reference frame the trajectory of surface particles is the same as the profile of those particles at any instant. For example, it is a circle for infinitesimal waves on deep water.

To help the reader appreciate the hodograph plane in this context Figure 6 shows the surface particle trajectory/profile for the initial steady wave. The origin in this example corresponds to water at depth. Different portions of the wave are labelled. The crest-trough asymmetry is clear.

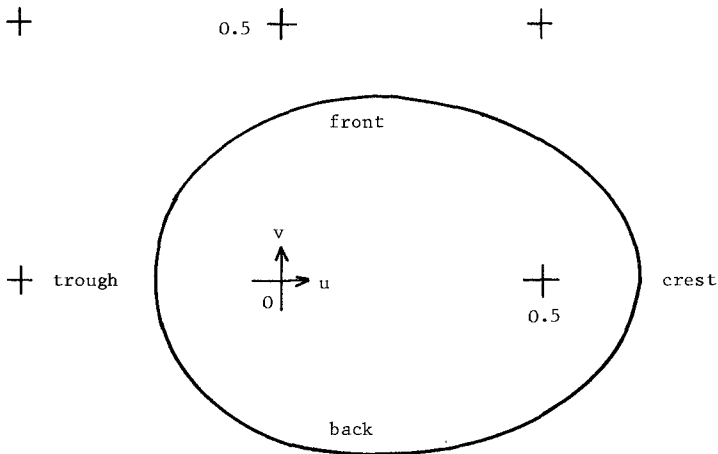


Figure 6. The hodograph plane for surface particles on a steady wave, $H/L = 0.13$, $ak = 0.40$.

The (u,v) profiles of the surface of waves approaching breaking are shown in Figures 7 and 8 together with some of the (u,v) trajectories of surface particles.

There are several features to note in these figures. Firstly each successive profile differs from its predecessor, especially on the front and crest of the wave. Secondly the magnitude of the maximum velocities continually increases. In particular the maximum horizontal velocity component soon exceeds one, the phase velocity of infinitesimal waves, and also 1.093 the maximum phase velocity of waves of this wavelength.

Further, the rate of increase of velocity also increases. That is, the acceleration of some particles increases. These particles are on the front of the wave. The dynamical importance of particle acceleration leads us to draw the corresponding profiles and trajectories in the acceleration plane (see the next section).

The last profile illustrated is not smooth. This indicates that the numerical method becomes inaccurate probably because the surface curvature is too great to be resolved by 60 points along the wave profile. This happens only in the region where a jet is beginning to form. Further development in time can be computed. The particle positions in the (u,v) plane, and eventually in space, become more irregular but do follow a general pattern similar to that which is to be expected for a jet. That is, particles converge towards a free fall trajectory which has a constant horizontal velocity component and a uniformly accelerating downward velocity component.

An envelope of trajectories and profiles is a prominent feature of Figure 8. It cannot be considered as typical since it does not occur in Figure 7. However, one point of that envelope is noteworthy. From the smoothness and continuity of the curves it is easy to deduce that one particle trajectory approaches the envelope and then recedes away from it without any tangential component along the envelope at the instant it touches. This is clear since some particles move to the left and some to the right. At the instant this particular particle is at the envelope it has zero acceleration. As may be seen in the next section there is nothing special about the value zero, but it is representative of a region of water of low acceleration.

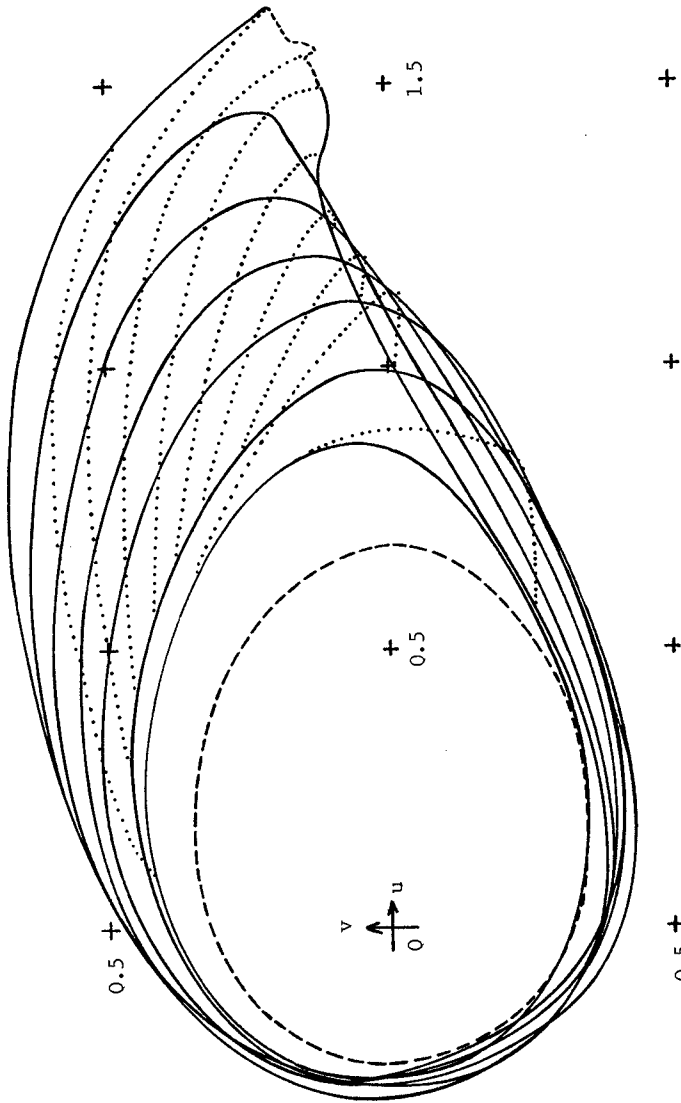


Figure 7. The hodograph plane for $p_0 = 0.10$. The full lines are surface profiles for $\pi \leq t \leq 5\pi/3$, the dotted lines are trajectories of surface particles and the broken line is the initial profile.

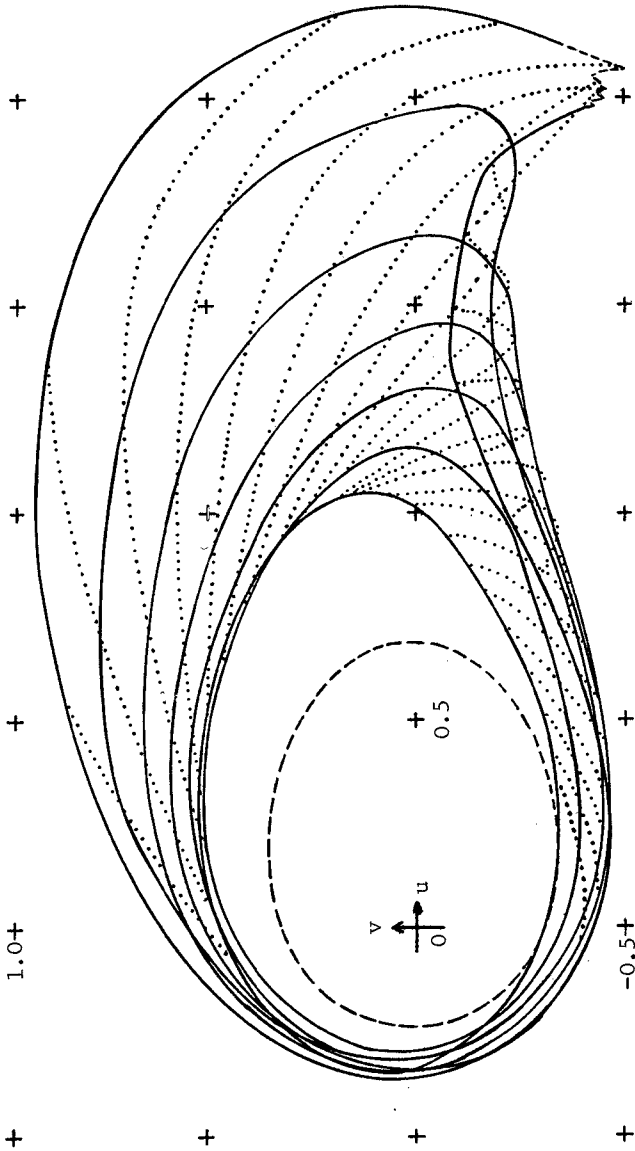


Figure 8. The hodograph plane for $p_0 = 0.20$, $\pi \leq t \leq 3\pi/2$.

4. The Acceleration Plane and Pressure

The hodograph plane indicates both large and small particle accelerations. It is particle accelerations that are important in dynamics and it has proved instructive to draw surface profiles and particle trajectories in the particle acceleration plane (Du/Dt , Dv/Dt). As a guide Figure 9 shows the surface profile and particle trajectories of the initial progressing wave. These are coincident as in the hodograph plane. The crest-trough asymmetry is also clear.

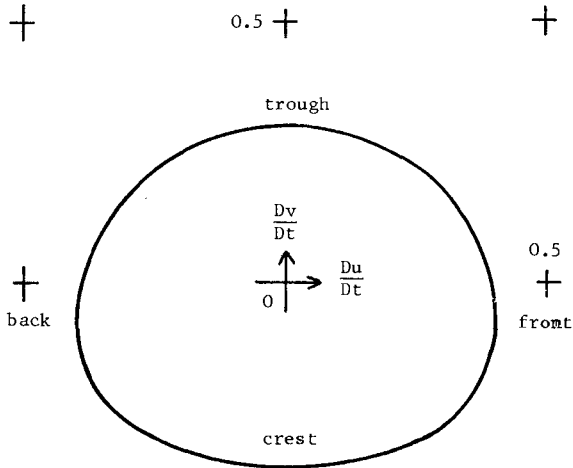


Figure 9. The particle acceleration frame for surface particles on a steady wave, $H/L = 0.13$, $ak = 0.40$.

For the approach to breaking the particle trajectories and surface profiles of acceleration show very large departures from the steady-state, as Figures 10 and 11 show. These are for the same two examples as the hodograph plane of Figures 7 and 8. The greatest reliably computed accelerations are so large, e.g. (4.3, -2.0) for Figure 11 that they have been left beyond the margins of the figures rather than reduce the scale of the more complex region illustrated.

The region of high accelerations, i.e. accelerations greater than gravity, is the dominant first impression from these figures. The region in (x,y) space which has these accelerations is the steep front portion of the wave just below the crest. In that region, water which was originally in the trough travelling towards the crest is accelerated in a relatively short time until it is travelling with or faster than the crest. It is thus not surprising that the largest component of acceleration is in a horizontal direction.

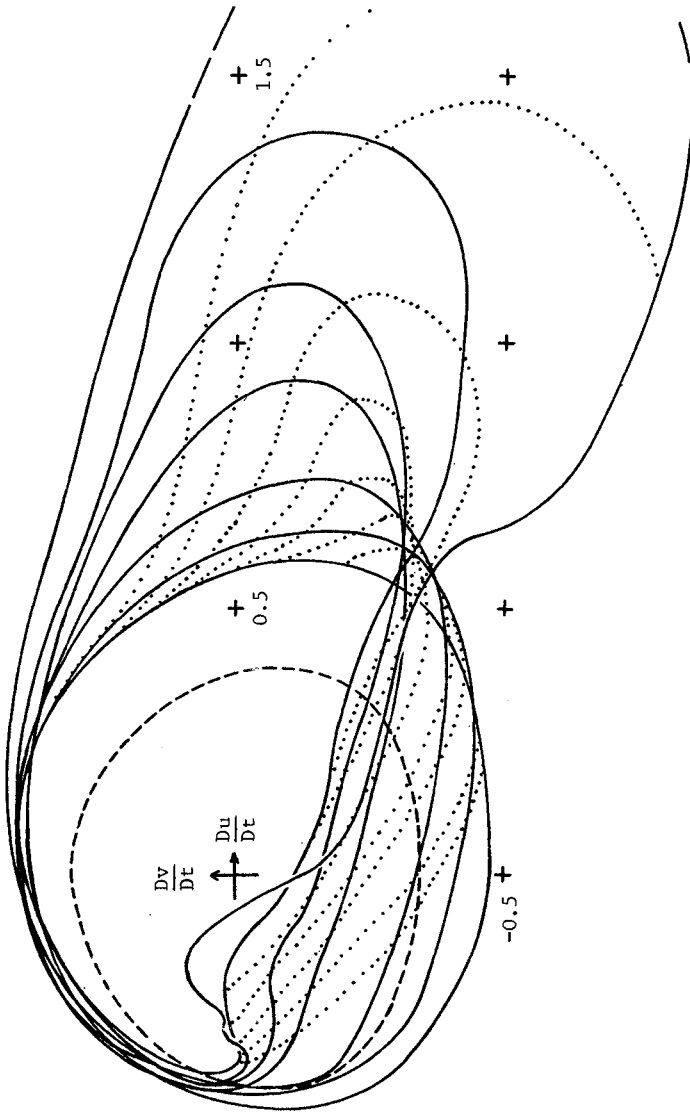


Figure 10. The particle acceleration plane for $p_0 = 0.1$. The full lines are surface profiles at times $\pi \leq t \leq 8\pi/5$. The dotted lines are particle trajectories, the broken line is the initial profile.

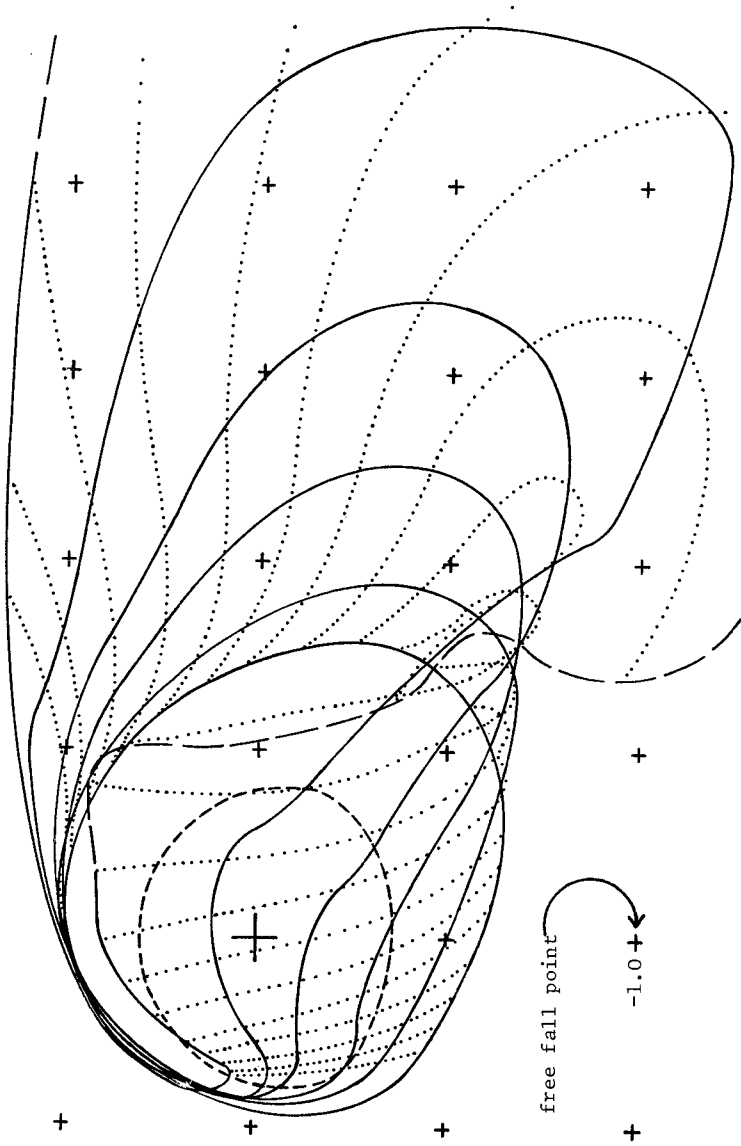


Figure 11. The particle acceleration plane for $p_0 = 0.2$, $\pi \leq t \leq 43\pi/30$.

In all these cases the direction of large accelerations is such that it is directed away from the surface. This implies there is no tendency to a Rayleigh-Taylor instability which occurs if the total acceleration field is directed into the fluid. The downward accelerations which are greater than gravity are for overhanging parts of the free surface so they do not contradict this statement.

For water to receive a large acceleration there must be a corresponding large pressure gradient. At all surface points the pressure gradient is normal to the surface and directed inwards since the pressure is zero at the free surface. Figure 12 is a vector diagram of the equation of motion,

$$\rho \frac{Du}{Dt} = -\nabla p + \rho g$$

to illustrate this.

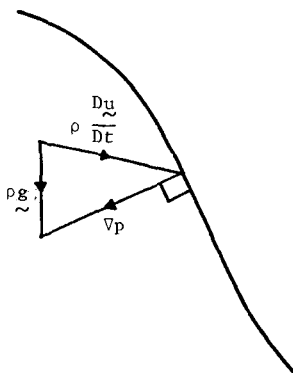


Figure 12. The equation of motion at the free surface.

The quantity $p + \rho gy$ is a good indicator of acceleration since it is a particle-acceleration potential,

$$\rho \frac{Du}{Dt} = -\nabla(p + \rho gy).$$

Figure 13 shows a contour plot of $p + \rho gy$ near the crest of the wave of Figures 2 and 4. The large gradients below the crest are clear. The direction of acceleration is perpendicular to the contours and is directed away from the closed contour. When the jet reaches a state of free-fall the particles must be at $(0, -1)$ in the acceleration plane.

A region of low acceleration shows clearly at the crest and its back in Figure 13 which includes a point of zero acceleration, and the same feature is also clear in Figures 10 and 11. Figure 11 includes the zero-acceleration point passing through the surface profile but also indicates that it has no special place in the acceleration plane.

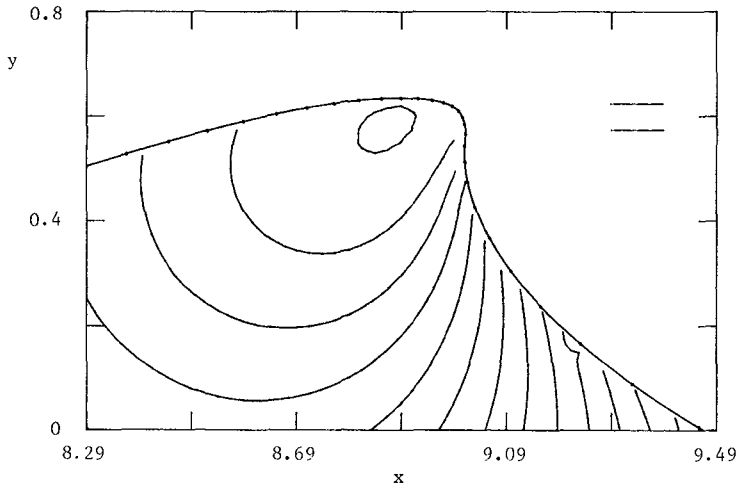


Figure 13. Lines of constant acceleration potential at $t = 4.61$ for $p_0 = 0.146$. The pair of parallel lines at upper right indicate the spacing for an acceleration equal to that of gravity.

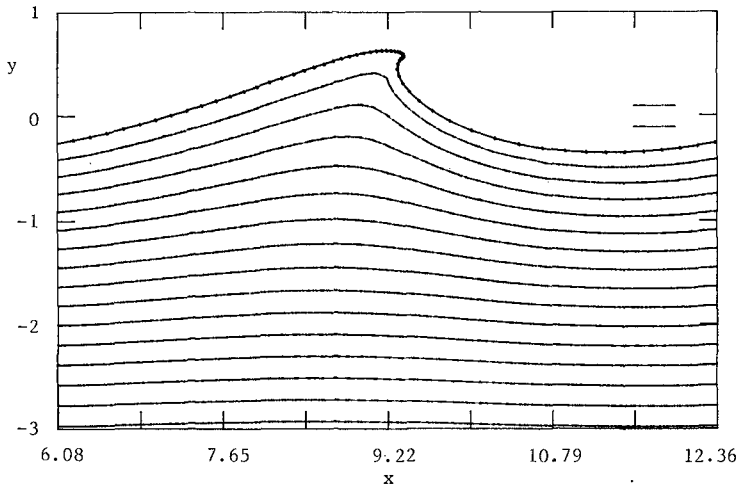


Figure 14. The pressure distribution at $t = 4.82$ for $p_0 = 0.146$.

The low acceleration region has a pressure distribution little different from hydrostatic. This particular region might be thought of as providing a "support" for the strong pressure gradient accelerating the front of the wave.

The pressure distribution for much of the flow at one time is shown in Figure 14. One aspect of it is relevant to the interpretation of pressure measurements beneath waves. The maximum of pressure at any level shows a significant variation of phase with depth. This means that the usual deductions about free-surface shape from pressure measurements are likely to be in serious error for waves at or near breaking.

5. Concluding Discussion

Analysis of the velocities and accelerations of a wave approaching breaking indicates three features that may be important in its dynamics. These are regions with:

- (i) a velocity greater than the maximum phase velocity for that wavelength,
- (ii) water particle accelerations greater than gravity,
- (iii) low particle accelerations.

All these three regions become evident well before breaking is indicated by the presence of a projecting jet. The extent of these regions at the time at which the wave face becomes vertical is indicated in Figure 15. The development of the regions in time is indicated in Figure 16.

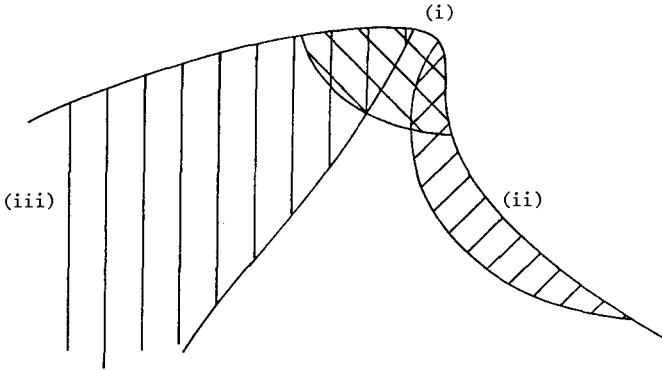


Figure 15. The crest of a wave at $t = 4.61$ for $p_o = 0.146$.
 Region (i) $u > 1.09$, (ii) $|\underline{Du}/Dt| > 1$,
 (iii) $|\underline{Du}/Dt| < 0.33$.

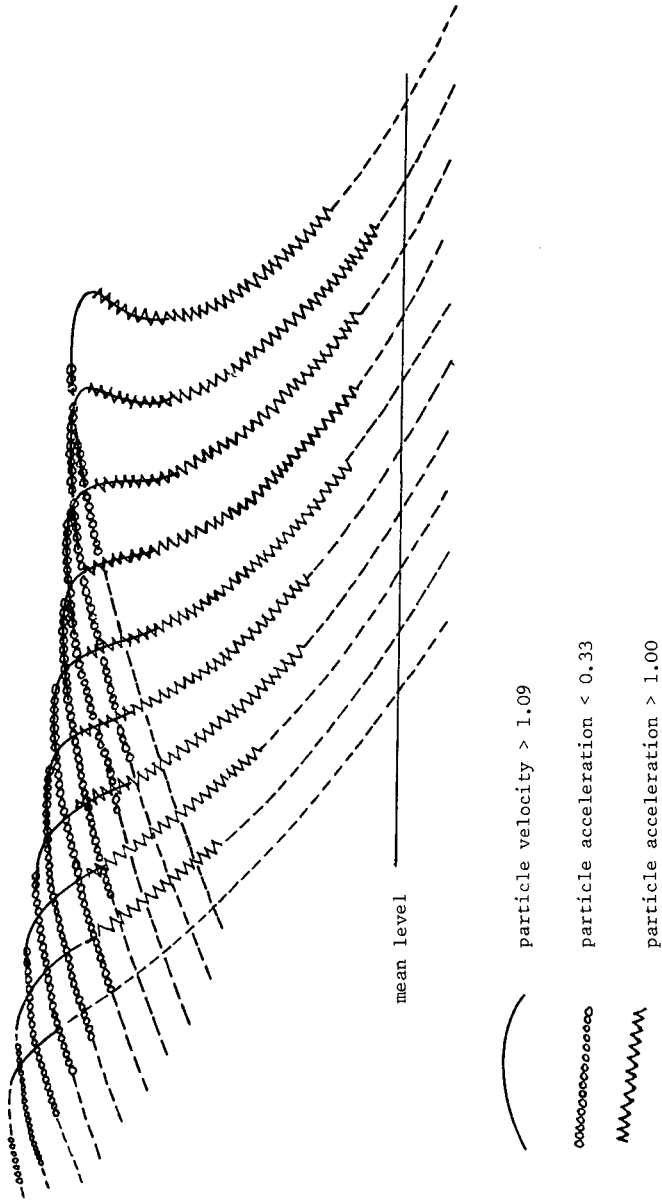


Figure 16. Properties of wave approach to breaking $37\pi/30 \leq t \leq 46\pi/30$, $P_0 = 0.146$.

Each of these regions could be defined slightly differently, and although with a given set of bounding conditions the appearance of one may precede another there is no clear indication that any one appears first. For example, for $p_0 = 0.146$ at $t = 3.87$, the horizontal velocity has just exceeded 1.10, the maximum acceleration has reached 0.98 and the minimum acceleration is 0.30.

Some surprise has been felt at the maximum accelerations calculated, though once the flow is considered carefully they are entirely consistent. It would be interesting to have confirmation from experiments or observations of water waves, but accelerations are difficult quantities to measure in a difficult environment for instruments. A small, freely floating accelerometer may be the best direct approach to measuring them.

The influence of the high accelerations on any fixed object in the path of a breaking wave could also be important. Not only is there a drag force due to the velocity but also an inertial force due to the strong pressure gradient. In addition both these forces act in nearly the same direction, whereas for a steadily progressing wave the accelerations and velocities are more or less perpendicular to each other.

Only a few examples of waves approaching breaking have been examined in detail, and it is certain that the features described here do not occur in all breaking waves. However, for plunging breakers we have examined other examples and found reasonable agreement with the above description.

Acknowledgement

P. McIver acknowledges the support of the Science Research Council.

References

- Cokelet, E. D. (1979) Breaking waves the plunging jet and interior flow-field, Mechanics of Wave-Induced Forces on Cylinders (ed. T. L. Shaw), pp. 287-301. San Francisco: Pitman.
- Longuet-Higgins, M. S., and Cokelet, E. D. (1976) The deformation of steep surface waves on water I. A numerical method of computation. Proc. R. Soc. Lond. A 350, 1-26.
- Longuet-Higgins, M. S., and Cokelet, E. D. (1978) The deformation of steep surface waves on water II. Growth of normal-mode instabilities. Proc. R. Soc. Lond. A 364, 1-28.

CHAPTER 33

A Similarity Model in the Surf Zone

by

Hsiang Wang, Professor
Department of Civil Engineering and College of Marine Studies
University of Delaware
Newark, DE 19711

and

Wei-Chong Yang, Coastal Engineer
PRC Harris, Inc.
3003 New Hyde Park Road
Lake Success, NY 11042

1. INTRODUCTION

In fluid mechanics, a powerful tool known as the similarity model has been applied successfully to describe velocity and pressure fields in steady boundary layer flows, jet flows and wake flows. These flows, with the exception of a few laminar cases, are quite complex and are usually not amenable to theoretical analysis. The similarity analysis offers an alternative and often provides useful engineering information on the mean flow characteristics. The present work explores the possibility of applying the similarity concept to describe the flow field of breaking waves in the surf zone.

Before presenting the similarity solution, a non-dimensional surf zone parameter is examined. This parameter, in addition to its many implications of characterizing surf zone properties, is pertinent to defining the region of validity of the similarity solutions. Solutions on mean flow characteristics are then established based upon a similarity hypothesis which states that the profiles of flow properties such as velocity and wave form preserve geometrical similarity downstream from the source of the disturbance and, therefore, can be defined by a few local characteristic parameters. Conditions required to preserve similarity are examined. Finally, laboratory results from a number of studies (Flick, 1978; Svendsen et al., 1978; Sakai and Iwagaki, 1978) and those from the authors are used to test the validity of the proposed model.

2. SURF PARAMETER

Considering a single long-crested wave breaking on a beach of uniform slope, say $\tan \alpha$, the cyclic breaking process can be approximately divided into three stages as illustrated in Fig. 1. The developing stage covers the period when the wave begins incipient breaking at the crest until it collapses on the beach in the vicinity of the water level unit. During this stage, the shape of the wave evolves from a highly asymmetric curled form to a triangular form with numerous white caps. Its potential energy is converted into kinetic energy which in turn is partially dissipated as the remaining portion preserved to stage the upwash. In the second stage, the flow surges

up to its runup limit similar to a solid element moving up-slope while the kinetic energy is being converted back to potential energy. In the last stage, the flow washes down as a thin sheet to the breaking point to complete the cycle.

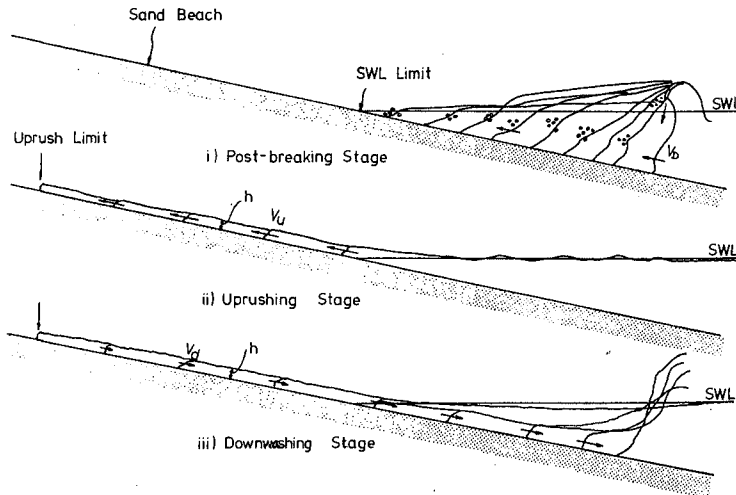


FIGURE 1. ILLUSTRATION OF BREAKING PROCESS.

The time required to complete each respective stage can be estimated based upon a simple energy model shown in Fig. 2. This energy

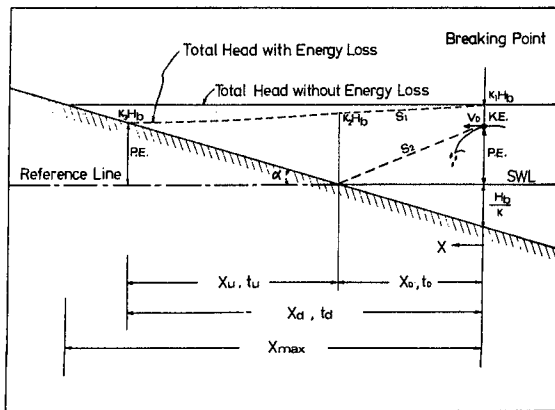


FIGURE 2. ENERGY CONSIDERATION OF BREAKING WAVE.

model is based upon the premise that the fluid element at the crest of the wave during breaking remains at the crest and is the same element that reaches the runup limit. This condition is clearly observed from recorded slow-motion films.

If the kinetic energy of the fluid element at the wave crest at the breaking point is assumed to be proportional to the breaking height, say $k_1 H_b$, then the kinetic energy in the developing stage can be expressed as

$$KE(x) = k_1 H_b + (S_2 - S_1)x \quad (1)$$

where S_2 and S_1 are the slopes of the total energy line and potential energy line, respectively. The velocity of the fluid element is

$$v_D(x) = \sqrt{2g[k_1 H_b + (S_2 - S_1)x]} \quad (2)$$

and the corresponding time required for the element travelling from the breaking point to the water level limit is

$$\begin{aligned} t_D &= \int_0^{x_D} \frac{dx}{v_D(x)} \\ &= \frac{\sqrt{2}(\sqrt{k_2} - \sqrt{k_1})}{k(k_2 - k_1)} \frac{H_b^{1/2}}{g^{1/2} \tan \alpha} \end{aligned} \quad (3)$$

where k_2 and k are constants of proportionality as defined in Fig. 2.

During the uprush and downwash stages, the crest element can be treated as a solid body moving on a sloped plan. In such cases, we have the following relationship on the basis of Newton's second law:

$$\mp Mg \sin \alpha - \rho f A_o \frac{v|v|}{8} = M \frac{dv}{dt} \quad (4)$$

where f is a frictional coefficient and A_o is the contact surface area; the "-" sign corresponds to the uprush condition and the "+" sign the downwash case. If we let $M = \rho t_h A_o$ the above equation simplifies to

$$\mp g \sin \alpha - \rho f \frac{v|v|}{8t_h} = \frac{dv}{dt} \quad (5)$$

where t_h is the thickness of the runup water sheet. Equation (5) can be integrated to obtain the uprush and downwash time which are, respectively,

$$t_u = \left(2\sqrt{\frac{k_2}{\beta}} \tan^{-1} \sqrt{\frac{\beta}{2}}\right) \frac{H_b^{1/2}}{g^{1/2} \tan \alpha} \quad (6)$$

and

$$t_d = 2\sqrt{\frac{k_2}{\beta}} \exp\left(\frac{\beta}{4} \frac{k_3 + \frac{1}{k_2}}{k_2}\right) \frac{H_b^{1/2}}{g^{1/2} \tan \alpha} \quad (7)$$

where

$$\beta = \frac{fV_0^2}{4t_h \sin \alpha}$$

and k_3 is a runup coefficient as shown in Fig. 2.

Based upon Eqs. (3), (6), and (7), the swash period of a single wave can be determined:

$$T_n = K \frac{H_b^{1/2}}{g^{1/2} \tan \alpha} \quad (8)$$

where

$$K = K_1 + K_2 + K_3$$

with

$$K_1 = \frac{\sqrt{2}(\sqrt{k_2} - \sqrt{k_1})}{k(k_2 - k_1)}$$

$$K_2 = 2\sqrt{\frac{k_2}{\beta}} \tan^{-1} \sqrt{\frac{\beta}{2}}$$

$$K_3 = 2\sqrt{\frac{k_2}{\beta}} \exp\left(\frac{\beta}{4} \frac{k_3 + \frac{1}{k_2}}{k_2}\right)$$

Therefore, the natural swash period is found to be a function of

$\frac{H_b^{1/2}}{g^{1/2} \tan \alpha}$. We now define a non-dimensional surf zone parameter as the

ratio of natural swash period to the incoming wave period (T):

$$I_w = \frac{T_n}{KT} = \frac{H_b^{1/2}}{g^{1/2} T \tan \alpha} \quad (9)$$

This non-dimensional parameter has the same form as the one suggested by Iribareu and Nogales (1949) to define breaking criterion. Battjes (1974), through dimensional reasoning, came to a similar non-dimensional parameter, which he amplified its significance to a variety of surf zone phenomena, including breaking type classification, set-up and set-down, etc. In here, we add another physical implication which can be explained as follows:

The I_w is the surf zone interference index. When I_w is small, each individual wave will complete the swash cycle with little or no interference from the successive waves. The flow in the swash zone is mainly oscillating and the breaker is of the plunging type. When I_w increases, the degree of interference from successive waves also increases; a circulatory motion is gradually developing which will result in a return flow in the main water column; the breaking phenomenon gradually transforms from plunging to spilling. This sequence of events is illustrated in Fig. 3.

This surf parameter also seems to play an important role in the similarity model to be presented in the following sections.

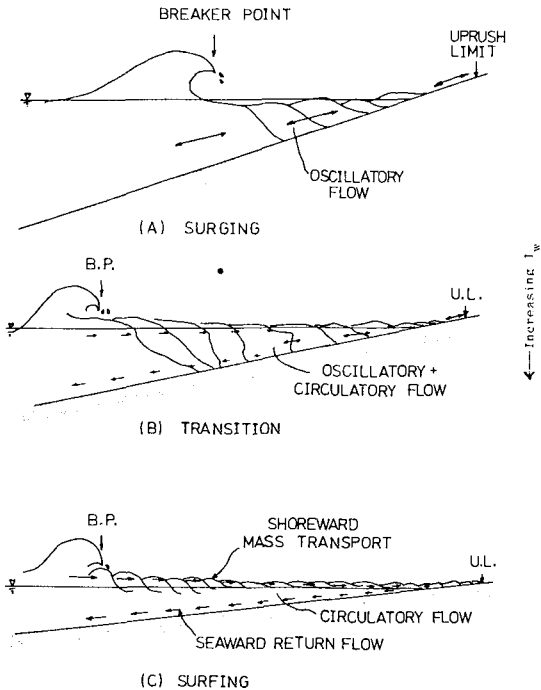


FIGURE 3. BREAKER CLASSIFICATION BASED UPON I_w .

3. BREAKING WAVE SIMILARITY

For a wave train of single frequency shoaling on a beach, a more or less amount of energy is being transferred from the primary wave component to its higher harmonics. The amplitude dispersing among harmonics coupled with phase lags developed due to differential shoaling of each harmonic component results in a highly asymmetric wave form upon breaking.

After breaking, as the wave travels further inshore, the wave form tends to stabilize although it remains asymmetrical. The conventional higher order wave theories are no longer adequate to describe these asymmetrical wave forms. A variation would be the introduction of phase angles among harmonic components such that the water surface fluctuation is expressed as

$$\eta(t) = \sum_{n=1}^{\infty} a_n \sin(n\sigma t + \phi_n') \quad (10)$$

where a_n is the nth harmonic amplitude; ϕ_n' is the nth harmonic phase and σ is the fundamental frequency.

Equation (10) most certainly can be used to prescribe the wave form of any particular set of breaking waves. Yet, it serves little useful engineering purpose if the solution cannot be generalized. If we assume that (1) each harmonic amplitude is limited by the local water depth, and (2) the phase velocity of each harmonic is also depth limited, then, we have

$$a_n = \alpha_n (d + \bar{\eta}) \quad (11)$$

and

$$c_n \propto \sqrt{g(d + \bar{\eta})} \quad (12)$$

where $\bar{\eta}$ is wave setup. Equation (10) can now be expressed as:

$$\frac{\eta(t)}{d + \bar{\eta}} = \sum_{n=1}^{\infty} \alpha_n \sin(n\sigma t + \phi_n) \quad (13)$$

where α_n 's are non-dimensional coefficients and ϕ_n 's are constant phase angles. Thus, the wave profile remains similar and its magnitude is affected only by a local parameter $(d + \bar{\eta})$.

In shallow water, if we express the depth averaged horizontal velocity in terms of η , we have

$$u(t) = \frac{C\eta(t)}{d} + \text{higher order terms of } \eta \quad (14)$$

recognizing that the net contribution of the higher order terms is a

mean return flow in the water column, Eq. (14) becomes

$$u(t) = \frac{C\bar{\eta}(t)}{d} - \bar{U}_R \quad (15)$$

The fact of having a similarity solution of $\eta(t)$, leads to the following similarity solutions for $u(t)$:

$$\frac{u(t) + \bar{U}_R}{C(1 + \frac{\bar{\eta}}{d})} = \sum_{n=1}^{\infty} \beta_n \sin(n\sigma t + \psi_n) \quad (16)$$

where β_n and ψ_n are constant coefficients.

Since C can be approximated by

$$C = \kappa\sqrt{g(d + \bar{\eta})} \quad (17)$$

we have

$$\frac{u(t) + \bar{U}_R}{\kappa\sqrt{g(d + \bar{\eta})} (1 + \frac{\bar{\eta}}{d})} = \sum_{n=1}^{\infty} \beta_n \sin(n\sigma t + \psi_n) \quad (18)$$

The solution $u(t)$ now depends only upon certain local parameters d , $\bar{\eta}$ and \bar{U}_R .

4. LABORATORY EXPERIMENT

To check the validity of the similarity solutions, experiments were conducted in a wave tank shown in Fig. 4. Water surface variations and horizontal particle motions were measured at four stations inside the surf zone on a smooth beach with a slope $m = 0.1$. The waves were measured by motion pictures and the horizontal particle velocity was measured by an air bubble system following the same principle as the hydrogen bubble system for flow visualization (for detailed measurement techniques see Yang, 1980). Since the wave flow field is unsteady, the dynamic response of an air bubble is established as shown in Fig. 5.

A total of ten sets of experiments were conducted. The test conditions are summarized in Table 1.

5. RESULTS

The wave amplitude coefficients, α_n , and wave phase coefficients, ϕ_n , of the first five harmonics are shown in Fig. 6 plotted against the surf parameter, I_w . The phase angles are adjusted so that $\phi_1 = 0$. These data are quite scattered but the trend is clear. Both α and ϕ become constant when I_w becomes large. Since a large I_w corresponds to a spilling breaker, the results seem to indicate a similarity solution,

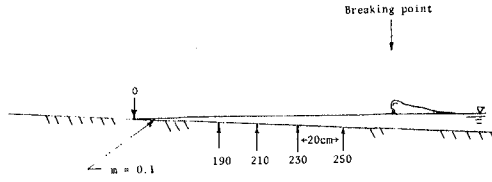
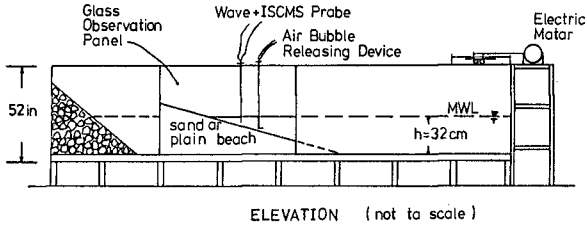


FIGURE 4, LABORATORY SETUP.

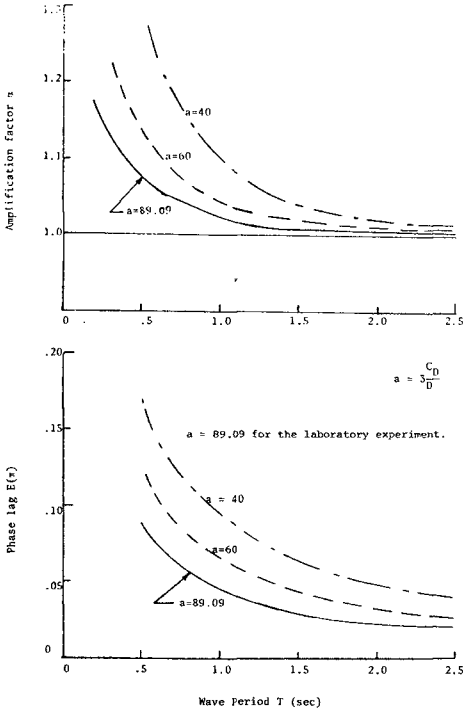
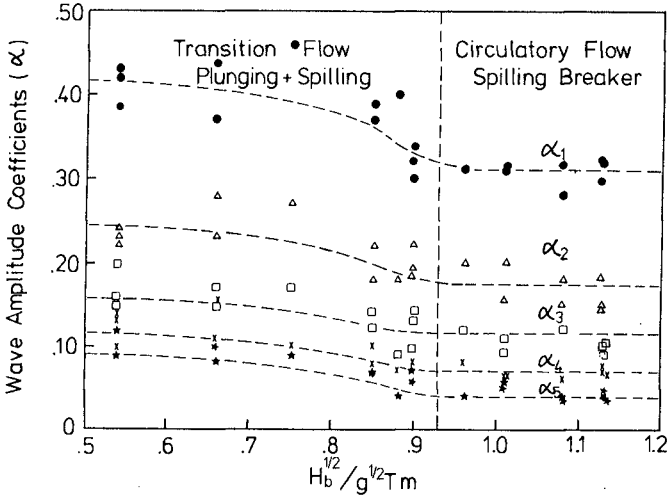


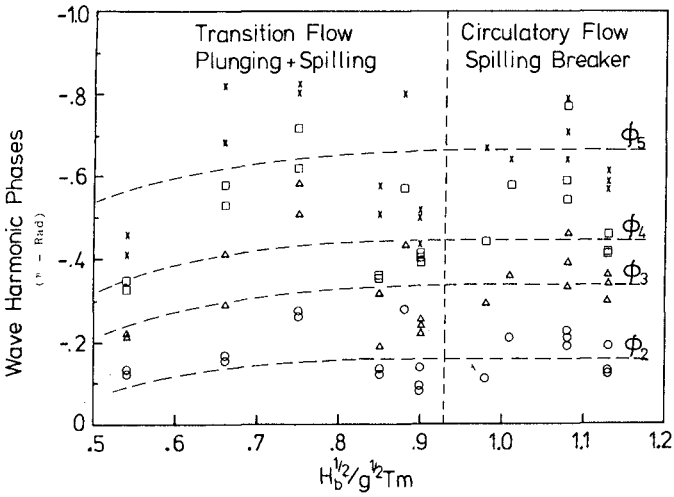
FIGURE 5, DYNAMIC RESPONSE OF AIR BUBBLE IN THE WAVE FIELD.

TABLE 1. EXPERIMENTAL CONDITIONS

LAB CONDITIONS (DELAWARE)				
Run No.	Incident Wave Height H_c (cm)	Breaking Wave Height H_b (cm)	Wave Period T (sec)	$\frac{H_b^{1/2}}{g^{1/2} T M}$
PB-1	9.5	11.5	2.0	.54
PB-2	11.0	14.0	1.8	.66
PB-3	11.0	14.0	1.6	.75
PB-4	13.5	14.0	1.4	.85
PB-5	10.0	11.5	1.2	.90
PB-6	11.0	12.5	1.0	1.13
PB-7	10.5	11.5	1.0	1.08
PB-8	9.0	10.0	1.0	1.01
PB-9	8.0	9.0	1.0	.96
PB-10	6.0	7.5	1.0	.88
LAB CONDITIONS (ISVA) (1978)				
070703		4.12	1.43	1.50
070705		4.43	1.43	1.64
451015		5.25	2.22	1.12
451018		4.95	2.22	1.09
LAB CONDITIONS (SAKAI AND IWAGAKI) (1978)				
2-2-2		9.4	1.24	1.58
3-2-1		11.5	1.24	2.27



a)



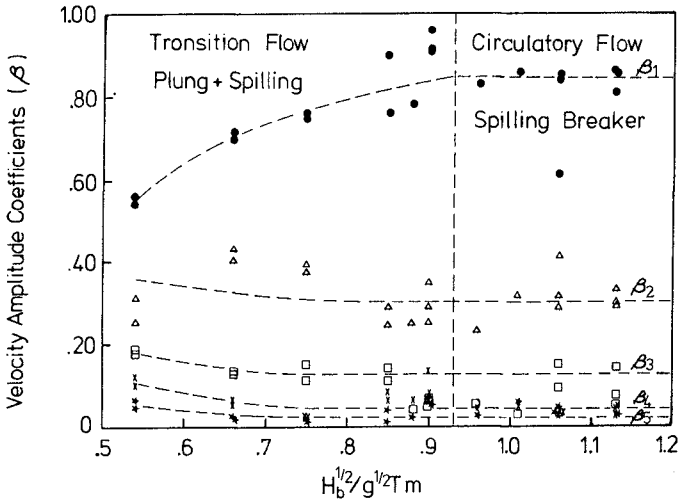
b)

FIGURE 6. WAVE AMPLITUDE COEFFICIENTS AND PHASE COEFFICIENTS VS. I_w .

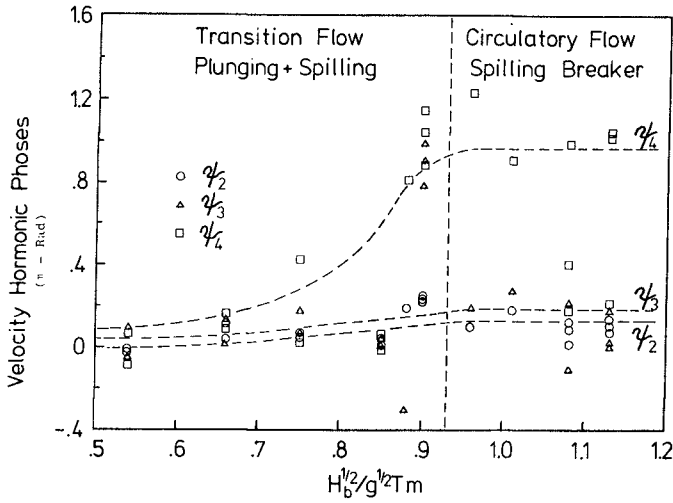
if exists, would be in the spilling breaker region where I_w is larger than 0.9. In the case of horizontal velocity, the amplitude and coefficients are plotted against I_w as shown in Fig. 7. These data reveal that the similarity solution also yields reasonable approximations for large I_w . In fact, the similarity approximations for velocity seems to extend to regions of smaller I_w than the corresponding region where the similarity solution of η becomes valid, i.e. velocity profile approaches similar form as early as the transition flow zone, whereas the surface profile will not become similar until spilling breaker condition is attained.

Figure 8 plots the non-dimensional surface variation for various experiments. In there, data from Svendsen et al. (ISVA, 1978) and Sakai and Iwagaki (1978) are also shown. Both Svendsen's and Sakai's data are well within the spilling breaker region (I_w ranging from 1.12 to 2.27). Their test conditions are listed in Table 1. All the data sets seem to exhibit a gross similarity feature. A closer examination of these profiles reveals that the fine features of similarity vary for data sets obtained by different investigators. These variations can best be explained with the aid of Table 2 where the statistics of the coefficients in the similarity solution are tabulated. First of all, the standard deviations of the amplitude coefficients are all very small (no more than 4% from the mean), which means the similarity solution is good in the region specified. On the other hand, the absolute value of α 's are different. The present laboratory value data and Sakai and Iwagaki's values are very close. They both differ somewhat from ISVA's values. The relative importance of each harmonic component can be assessed from the values listed under $\alpha/\Sigma\alpha$. For instance, the fundamental component has a value of 0.4 to 0.5. The total contribution due to harmonics higher than third is usually less than 20%. In terms of wave height, the effect of these higher harmonics is insignificant because of the phase shift. In terms of energy, their contributions are even less. The relative importance of the first three harmonic components is quite consistent among the three sets of data. The results of phase angle are somewhat unexpected. All the data show that the second harmonic leads the first harmonic and the third harmonic leads both first and second. One would expect the other way around as the higher harmonics should have smaller phase velocities. The values of phase coefficients are very close for the Delaware and ISVA data. They both differ from Sakai and Iwagaki's value. This point is further examined later.

Figure 9 illustrates the non-dimensional velocity profiles. The statistics of velocity harmonics are also tabulated in Table 2. In here, the fundamental component dominates the others. The higher component lags the successive lower component as expected. However, these phase lags are all very small. The combined effects of dominant fundamental components and small phase shift result in a more symmetrical profile than that of wave forms. The same kind of results have been obtained by Flick (1978) and Thornton (1976). A tentative explanation has been offered on the reasoning that bottom and internal frictions tend to dampen the higher wave components at a fast rate. The experimental data also show here that the peak horizontal velocity always lags the peak water surface variation such as illustrated by an example in Fig. 10.



a)



b)

FIGURE 7. VELOCITY AMPLITUDE COEFFICIENTS AND PHASE COEFFICIENTS VS. I_w .

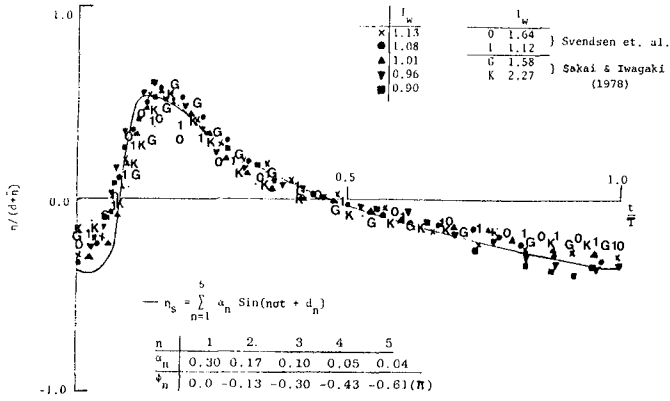


FIGURE 8. NON-DIMENSIONAL SURFACE PROFILES.

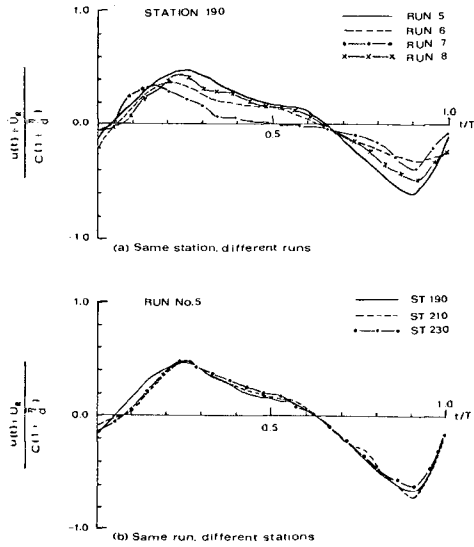


FIGURE 9. NON-DIMENSIONAL VELOCITY PROFILES.

TABLE 2. STATISTICS OF AMPLITUDE COEFFICIENTS AND PHASE COEFFICIENTS.

AMPLITUDE HARMONICS

Source	Amplitude (α)				Phase (ϕ)			No. Exps.
		Mean	σ	$\alpha/\Sigma\alpha$		Mean	σ	
Delaware	α_1	0.30	0.038	0.41	ϕ_1	--	--	9
	α_2	0.17	0.022	0.22	ϕ_2	-0.13π	0.027	
	α_3	0.10	0.011	0.15	ϕ_3	-0.30π	0.22	
ISVA	α_1	0.23	0.035	0.47	ϕ_1	--	--	32
	α_2	0.11	0.016	0.22	ϕ_2	-0.14π	0.08	
	α_3	0.07	0.012	0.14	ϕ_3	-0.28π	0.14	
Sakai	α_1	0.32	--	0.48	ϕ_1	--	--	2
and	α_2	0.15	--	0.23	ϕ_2	-0.25π	--	
Iwagaki	α_3	0.09	--	0.13	ϕ_3	-0.40π	--	

VELOCITY HARMONICS

Source	Amplitude (β)				Phase (ψ)			No. Exps.
		Mean	σ	$\beta/\Sigma\beta$		Mean	σ	
Delaware	β_1	0.81	0.078	0.63	ψ_1	--	--	8
	β_2	0.30	0.054	0.23	ψ_2	0.05π	0.09	
	β_3	0.08	0.043	0.06	ψ_3	0.07π	0.15	

 σ : standard deviation

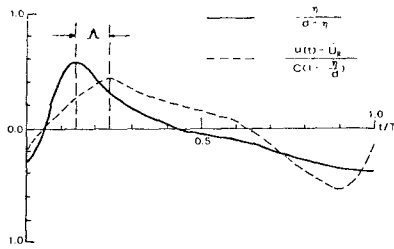


FIGURE 10. COMPARISONS OF SURFACE AND VELOCITY PROFILE.

As the wave breaks on a slope, the motion appears to be quite disorderly. When the breaking wave proceeds up-slope, it gradually regains its regular appearance. The question is how far shoreward from the breaking point beyond which the similarity solution can be considered adequate. For this purpose, the phase angles are plotted against the non-dimensional depth d/d_b and d_b the depth at the breaking point. Four sets of data from different investigators are defined in terms of cosine phase lag, i.e.,

$$\eta = \sum_{n=1}^{\infty} \alpha_n \cos(n\omega t + \zeta_n) \tag{19}$$

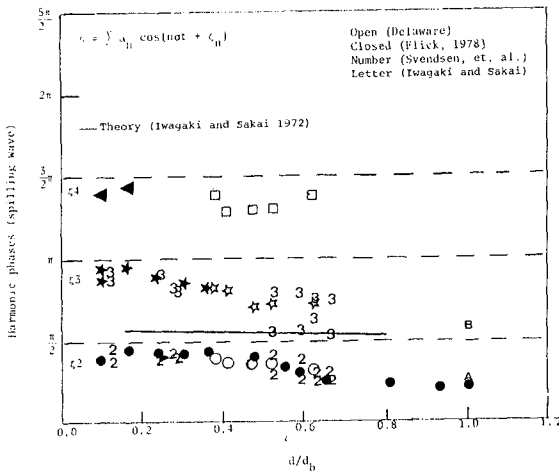


FIGURE 11. VARIATIONS OF PHASE COEFFICIENTS AS A FUNCTION OF d/d_b .

The relationship between ζ_n and ϕ_n , which is defined as the sine phase lag, is

$$\zeta_n = (n - 1) \frac{\pi}{2} + \phi_n \quad (20)$$

These phase coefficients are shown to vary slowly with d/d_b and approach limits at $\pi/2$ intervals when $d/d_b \rightarrow 0$. Since the profiles measured by Sakai and Iwagaki are near the breaking point, the results in this figure explain why they differ from that of the present experiment and that of ISVA; both were carried out in the inner zone where $d/d_b < 0.7$.

To utilize the similarity equations to describe the breaking wave properties one must have knowledge of \bar{U}_R and κ as appeared in Eq. (18). At present, we are unable to predict either. The experimental results of these quantities are, however, shown in Figs. 12 and 13 respectively. It appears that the return flow strength increases with increasing I_w but gradually reaches a constant in the spilling breaking region. The κ value, on the other hand, decreases with increasing I_w . Since κ is actually the ratio of wave celerity and \sqrt{gd} , the results are the consequence that spilling breakers travel slower than plunging breakers.

6. CONCLUSIONS

Assuming both the water surface variations and the depth-averaged horizontal particle velocities in the surf zone can be expressed by the summation of Fourier components, similarity solutions are proposed here. These solutions are based upon a pair of rather restrictive conditions; namely, both the amplitude and the phase velocity of each harmonic component are depth limited. The solutions, however, offer the advantage of being simple and completely defined by a few local flow parameters.

Laboratory data from a number of investigators including those obtained by the authors are used to test the validity of the proposed solutions.

The results seem to suggest that the similarity solution is not universally applicable. However, if the wave is of the spilling type and is far inshore in the inner breaking zone, the similarity solution becomes suitable to describe the mean flow characteristics. These

conditions can be defined in terms of a surf parameter $I_w = \frac{H^{1/2}}{g^{1/2} T \tan \alpha}$

and a relative depth parameter d/d_b . The region of suitability is found to be when $I_w > 0.9$ and $d/d_b < 0.6$. In this region, both surface profile and horizontal velocity can be adequately described by the first three harmonics. The velocity profile is found to be less asymmetric than the surface profile.

For surface profile, the higher harmonics lead the lower ones whereas the contrary is true for the velocity profile.

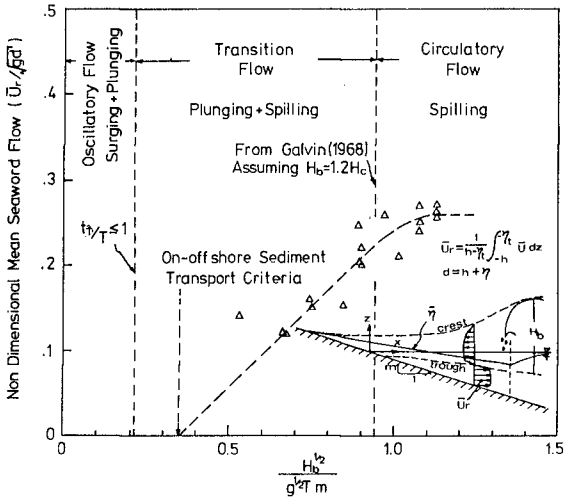


FIGURE 12. RETURN FLOW VS. I_w .

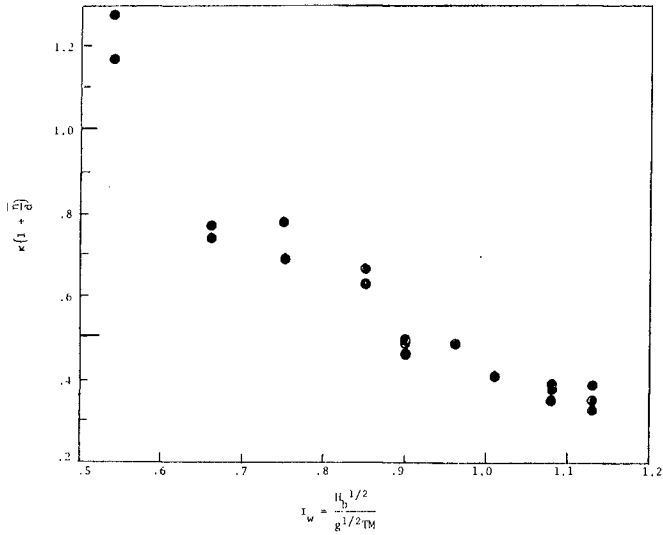


FIGURE 13. κ VS. I_w .

7. ACKNOWLEDGMENT

The work is supported by the Office of Naval Research Geography Branch under Contract No. N00014-76-C-0342. The authors wish to thank Dr. I. A. Svendsen of the Institute of Hydrodynamics and Hydraulic Engineering, Technical University of Denmark, who provided their laboratory data.

8. REFERENCES

- Battjes, J. A. (1974), "Surf Similarity", Proc. 14th Coastal Engineering Conference, Copenhagen, Denmark, p. 466-479.
- Flick, R. F. (1978), "Study of Shoaling Waves in the Laboratory", Ph.D. Dissertation, University of California, San Diego, pp. 159.
- Iribarren, C. R. and Nogales, C. (1949), "Protection Des Ports", Section II, Comm. 4, XVIIth Nav. Congress, Lisbon, p. 31-80.
- Sakai, T. and Iwagaki, Y. (1978), "Estimation of Water Particle Velocity of Breaking Wave", Proc. 16th Coastal Engineering Conference, Hamburg, Germany, p. 551-568.
- Svendsen, I. A., Madsen, P. A., and Hansen, J. B. (1978), "Wave Characteristics in the Surf Zone", Proc. 16th Coastal Engineering Conference, Hamburg, Germany, p. 520-539.
- Thornton, E. B. et al. (1976), "Kinematics of Breaking Waves", Proc. 15th Coastal Engineering Conference, Hawaii, Vol. I, p. 461-476.
- Yang, W. C. (1980), "Surf Zone Properties and Onshore-Offshore Sediment Transport", Ph.D. Dissertation, Dept. of Civil Engineering, University of Delaware (in preparation).

CHAPTER 34

VELOCITY AND PRESSURE FIELD OF SPILLING BREAKERS

M.J.F. Stive¹⁾

ABSTRACT

The internal velocity and pressure fields of quasi-steady spilling breaking waves have been investigated experimentally. The internal flow fields are shown to be in qualitative agreement with a model proposed by Peregrine and Svendsen (1978). Furthermore a quantitative comparison is made with non-breaking wave theories. Measurements of the pressure field are presented, and interpreted semi-quantitatively using the vertical momentum balance. Finally, it is shown how the integral properties can be obtained and analysed.

1. INTRODUCTION

The surfzone water motion is a topic that deserves and receives a lot of theoretical and experimental investigation. However, in experimental studies of the surf zone measurements have generally been restricted to the external characteristics, i.e. the instantaneous and time mean surface elevations. It is conspicuous that the internal kinematics of breaking waves have received little experimental attention. It is also conspicuous that the experimental study of the energy dissipation and the momentum flux variation is literally "superficial". Based on measurements of the internal kinematics and dynamics a more fundamental approach is possible, e.g. gradients in the momentum flux can be related to variations in mean water level, and gradients in the energy flux can provide the local energy dissipation. At the same time it may be possible to relate the turbulence intensity to the energy dissipation (Battjes, 1975).

Along the lines indicated above an experimental study was initiated of the internal velocity and pressure field of waves breaking on a gentle slope. The experimental data from this study are analysed in two consecutive phases. The first phase concentrates on instantaneous values. The second phase concentrates on integral properties, i.e. the densities and fluxes of momentum and energy, and on the energy dissipation in relation to the measured turbulence.

This paper presents an indication of the results obtained so far. A more extensive presentation of the results will follow.

Following Svendsen et al (1978) a characteristic description of the surfzone water motion is given in § 3. The kinematics are described in § 4, in which the model for the flow field of a quasi-steady breaking wave as proposed by Peregrine and Svendsen (1978) is shown to agree with the experimental results. Furthermore the measurements are compared to non-breaking wave theories. A semi-quantitative description of the dynamics is given in § 5. Finally, the planned evaluation of the integral properties is outlined in § 6 and illustrated with a preliminary result.

¹⁾Project Engineer, Harbours and Coasts Branch, Delft Hydraulics Laboratory, The Netherlands.

2. EXPERIMENTS

Arrangements

The experiments were conducted in a wave flume of the Delft Hydraulics Laboratory. The flume is 55 m long, 1 m wide and 1 m high.

Regular waves without free second harmonic components were generated in a water depth of 0.85 m. To obtain a control signal for the wave generator which resulted in a maximum suppression of the free second harmonics a simple trial and error procedure was applied, using Fontanet's theory (see e.g. Hulsbergen, 1974) as a first approximation.

To enable the construction of instruments in the bottom of the horizontal section a false, concrete floor was made, which reduced the water depth of the horizontal section to 0.70 m. The waves broke on a plane, concrete beach of a 1:40 slope (see Fig. 1a).

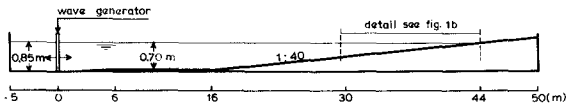


Figure 1a Experimental set-up

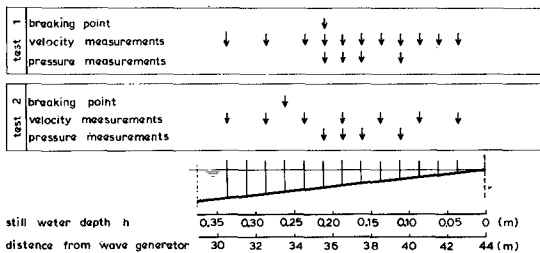


Figure 1b Detail experimental set-up

Measurements

The surface variations, i.e. the time mean and instantaneous vertical elevations of the surface, were measured over the whole length of the flume at positions with an interval of 1 m by means of resistance type wave gauges. Velocities of propagation were determined from the time of propagation of characteristic points of the wave surface between these positions.

It must be noticed, that resistance type wave gauges in principle cannot be used in the aerated region of breaking waves. Awaiting the results of a study of this aspect the conclusions of the study of Svendsen et al (1978) were used, i.e. (1) the wave gauges measure solid water and (2) the actual air content in the most densely entrained laboratory wave is only 2-4 percent. Thus, in view of the required accuracies the measured surface elevations are regarded as the elevation of water with normal density.

The horizontal and vertical component of velocity were measured by means of a laser doppler velocimeter, which is described elsewhere (Godefroy, 1978). The measurements were concentrated on the breaking and the near-breaking zone (see Fig. 1b). They were conducted at different levels between bottom and surface elevation.

It must be noticed, that during measurements the doppler signal may drop out temporarily for several reasons, such as the presence of air bubbles or large opacities. When the doppler signal drops out the last detected doppler frequency is held until the next doppler burst of about the same frequency is detected. Consequently these drop-outs occur when measuring above the level of the wave troughs and in water with entrained air as found in the front of breaking waves. Concerning the latter case it can be remarked that in view of the procedure of signal processing measurements are meaningless if the time scale of the drop-outs exceeds the time scale of the turbulent fluctuations. The time scale of the drop-outs increases with the density of the aeration. As a consequence measurements are only possible up to lightly aerated regions.

Pressures were measured by means of differential pressure transducers (0.8 cm diameter) at only four positions in the breaker zone (see Fig. 1b). In each of these positions the transducers were mounted at different elevations in a transparent, dummy side wall.

Symbol and sign conventions are as follows. The surface elevation is denoted η , the horizontal velocity component u , the vertical velocity component w and the pressure p . The horizontal x -axis is positive in the direction of wave propagation. The vertical z -axis is positive upwards, while the z -origin is chosen at the still water level.

Because of the exploratory nature of the investigation the experiments were restricted to two wave conditions, which are referred to as test 1 and test 2. The wave characteristics are as follows:

	H_o (m)	$H_{hor. section}$ (m)	$T_{wave maker}$ (m)	$H_{breaker}$ (m)	H_o/L_o (-)
test 1	0.159	0.145	1.79	0.178	0.032
test 2	0.142	0.145	3.00	0.226	0.010

The breaking behaviour at the breaking point of test 1 falls in the category "spilling breaking", while that of test 2 falls in the category "plunging breaking".

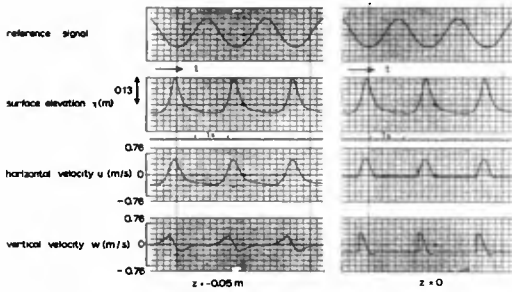


Figure 2a Typical recording near-breaking region (test 1, $x = 34.5$ m)

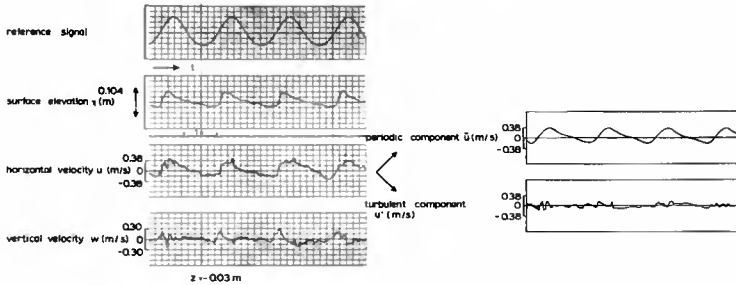


Figure 2b Typical recording breaking region (test 1, $x = 38.5$ m)

Procedures

Typical recordings of the surface elevation and the velocity components in the near-breaking and the breaking region (see Fig. 2a and 2b) show that the non-breaking wave motion is a purely periodic quantity, and that the breaking wave motion is a fluctuating quantity with a quasi-periodic character. To describe the breaking motion it is considered as the sum of a purely periodic component (indicated by a tilde) and a non-periodic residual component (indicated by a dash). The periodic component is obtained by averaging the signals at a fixed phase of the reference signal, i.e. the command signal of the wave generator. This procedure may be described as ensemble averaging. The major part of the residual component is formed by the turbulent fluctuations of the breaking process and is therefore termed the turbulent component. These fluctuations are non-stationary in time. Because of their time-scale a recording over say n waves may be considered as n independent recordings of the turbulent process. From this ensemble an estimate of e.g. the r.m.s.-value at a fixed time may be obtained.

Summarising, the non-breaking wave motion can be fully described just by a periodic component, i.e. $\eta = \tilde{\eta}$, $u = \tilde{u}$, $w = \tilde{w}$ and $p = \tilde{p}$. The breaking wave motion can be described as the sum of a periodic and a "turbulent" component, i.e. $\eta = \tilde{\eta} + \eta'$, $u = \tilde{u} + u'$, $w = \tilde{w} + w'$ and $p = \tilde{p} + p'$.

The periodic components are obtained as the ensemble mean over a minimum of 20 waves. The r.m.s.-value of the turbulent component at a fixed phase is obtained from the ensemble of minimum 20 "recordings" of the turbulent process. The time mean value of the turbulent component is zero by its definition. Consequently, the time mean value of the wave motion is equal to the time mean value of the periodic wave motion, i.e. $\bar{\eta} = \bar{\tilde{\eta}}$, $\bar{u} = \bar{\tilde{u}}$, $\bar{w} = \bar{\tilde{w}}$ and $\bar{p} = \bar{\tilde{p}}$, where an overbar indicates time-averaging over an integral number of wave periods. Furthermore, for points above the level of the wave troughs which are not always submerged, u , w and p are zero by definition when $z > \eta(x,t)$, while their time mean value is the time mean over an integral number of full wave periods.

At each of the indicated positions the velocities and the pressures at the different levels were measured consecutively, i.e. non-simultaneously. Simultaneously with a velocity or pressure measurement at a certain level the command signal of the wave generator and the surface elevation were recorded. Using these signals as a reference it is possible to couple the non-simultaneous measurements in one cross-section. This procedure of composing the velocity and pressure fields introduces inaccuracies due to the determination of the wave motion from an ensemble of a limited number of waves. These inaccuracies are found to be of the order of $\pm 2-3\%$ of the maximum periodic value. They exceed the instrumental inaccuracies, with the exception of inaccuracies due to drift of the laser doppler velocimeter and the pressure transducers, amounting to ± 1 cm/s and ± 0.2 cm (H_2O) respectively.

3. CHARACTERISTIC DESCRIPTION

This study is restricted to the kind of breaking waves that are usually found on gently sloping, sandy beaches with relatively wide breaker zones. A characteristic description of the breaking wave motion on these beaches is given by Svendsen et al (1978). They differentiate between a so-called outer and inner region (see Fig. 3). In the outer region the initial, chaotic breaking (ranging from spilling to plunging) takes place over a relatively short horizontal distance of several times the waterdepth at the breaking point. In the inner region soon a relatively well organized motion develops. The breaking motion is fully turbulent, while the mean motion is quasi-steady. A definition of a quasi-steady wave is given by Peregrine and Svendsen (1978): "one which changes little during the time a water particle takes to pass through it, excluding water particles which may become trapped in a surface roller". At this stage of its breaking motion a breaker on a beach may be described as a spilling breaker or bore. In case the depth continues to decrease the quasi-steady breaking motion is maintained until the shoreline is reached.

Indeed, the remarkable feature of the inner region is that the wave shapes throughout this region are very similar, as a comparison of the dimensionless surface profiles of the inner region shows (see Fig. 6 and 8). This conservation of wave shape is also illustrated by the tendency of the velocities

of propagation of characteristic points of the wave front to coincide as the waves propagate into the inner region (see Fig. 4). Comparison of the wave shapes for test 1 and test 2 shows that the similarity also holds for waves at the same position originating from different deep water conditions.

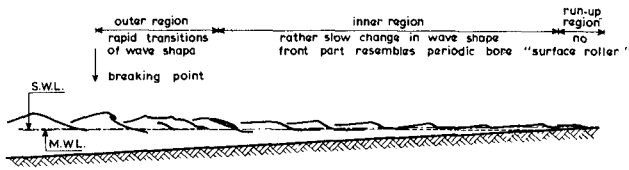


Figure 3 Wave characteristics in the surfzone (after Svendsen et al, 1978)

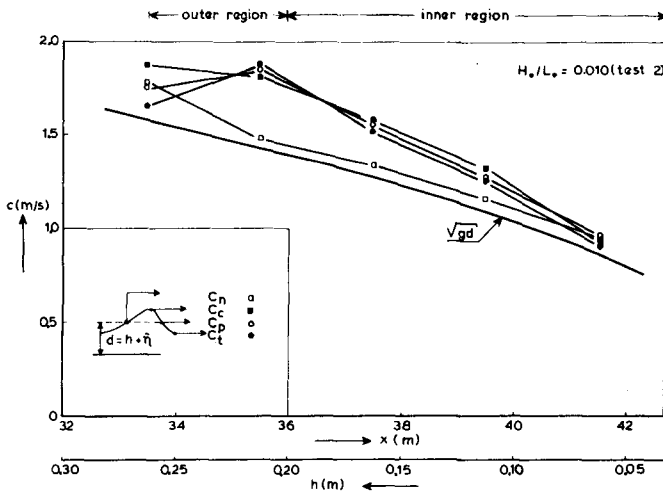


Figure 4 Velocities of propagation

From the surface variations it can be concluded that the water motion at each depth seems to be strongly locally controlled. Local depth and bed slope determine the characteristics of flow and hence the shape of the wave, including the energy flux, the energy dissipation and consequently the decrease in wave height. This hypothesis finds support in the nearly constant ratio of

wave height over mean water depth H/d for both tests (see Fig. 5), which is used to define the extent of the inner region.

In the next paragraph it is shown that the flow fields of the inner breaking region confirm the hypothesis of similarity with regard to the water motions.

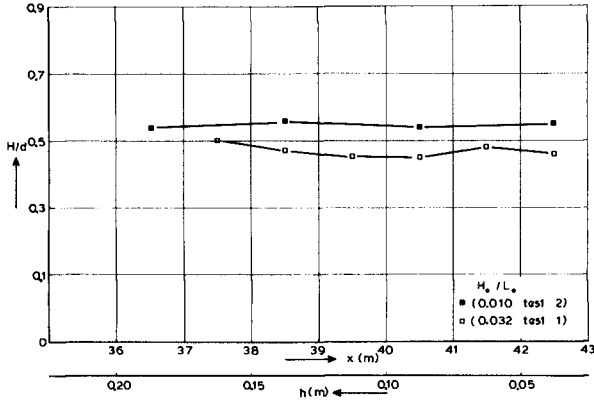


Figure 5 Variation of wave height to water depth ratio

4. HORIZONTAL VELOCITY FIELD

The measured velocity fields presented and analysed in this paragraph belong to the inner breaking region. Because of the quasi-steady motion in this region it is possible to interpret the measured motion as being of waves of constant form. Virtually no velocity measurements were conducted in the relatively small outer region. The violent variation of the water motions in this region prohibits a constant form interpretation, so that for an analysis detailed spatial measurements would be required.

Comparison with non-breaking wave theories

The measured periodic velocity fields are compared to the theoretical fields for non-breaking waves of constant form to check the applicability of these theories, since they are commonly used for lack of breaking wave theories.

The selection of the theories used for the comparison is mainly based on the recommendations of the study of LeMéhauté et al (1968), because the experimental wave characteristics of their study are close to the experimental characteristics at the different measuring positions of both tests of this

study. In the study by LeMéhauté et al (1968) a number of theories were used for comparison with measured horizontal velocities under the wave crest. Dean (1974) extended the comparison with the stream function method. Of the 12 theories included in the comparison the stream function theory provided the best agreement followed in order by Goda's empirical formula, the cnoidal theory of Keulegan and Patterson and linear theory. Since Dean's stream function theory requires interpolation from tables and since Goda's formula is empirical, it was at this stage of the study decided to use the third and fourth best theories, viz. the cnoidal theory of Keulegan and Patterson (Masch and Wiegel, 1964) and the linear theory.

Firstly, the measured horizontal periodic velocity fields for test 1 are compared with the theoretical cnoidal fields (see Fig. 6). Secondly, the measured maximum (shoreward) and minimum (seaward) horizontal periodic velocities for both tests are compared with the extreme velocities following from the cnoidal and linear theory (see Fig. 7). Thirdly, in the same figure the measured time mean horizontal velocities are compared to the cnoidal and linear time mean velocities.

For both tests a number of representative results for the breaking waves in the inner region is presented. For comparison also a near-breaking wave is included. Vertical distances are made dimensionless by the local mean water depth, horizontal distances by the wave length and time by the wave period. It is noticed that the origin of the vertical z-axis is at the still water level. The horizontal lines indicate the levels at which the measurements were conducted. On the basis of these measurements fields with lines of equal velocities are constructed. The positive time axis of the measured velocity fields is directed to the right, so the wave profiles "propagate" to the left. It is stressed that the measured velocities are Eulerian velocities.

For both the cnoidal and linear theory two different formulations are used. The unbracketed values in Figure 6 and the full curves in Figure 7 are for the usual formulation in which the frame of reference is chosen such that the mean horizontal momentum or mass flow under the level of the wave troughs is zero: $-\int_{-h}^{\eta} \rho u \, dz = 0$. The in-phase relation of surface elevation and horizontal velocity introduces a net mass flow or Eulerian mass transport in the region above the level of the wave troughs. Since the measurements were conducted in a closed wave flume in a stationary situation the total mean mass flow is zero: $-\int_{-h}^{\eta} \rho u \, dz = 0$. Therefore a second formulation is chosen, such that the net shoreward mass flow in the region above the wave troughs equals the net seaward mass flow in the region below the troughs. This formulation is simply found by changing the speed of the frame of reference by the amount $-\eta_t$ $\int_{-h}^{\eta} \rho u \, dz / \rho d$. The results are given by the bracketed values in Fig. 6 and the dashed curves in Fig. 7.

It is noticed that for an irrotational wave motion, which is spatially homogeneous (apart from phase differences), the mean mass flow under the wave troughs is essentially constant. The "conduction solution" of Longuet-Higgins (1953) for rotational wave motion in a viscous fluid of finite depth predicts a mean mass flow which is maximum seaward right below the level of the wave troughs but which changes to a shoreward mass flow near the bottom.

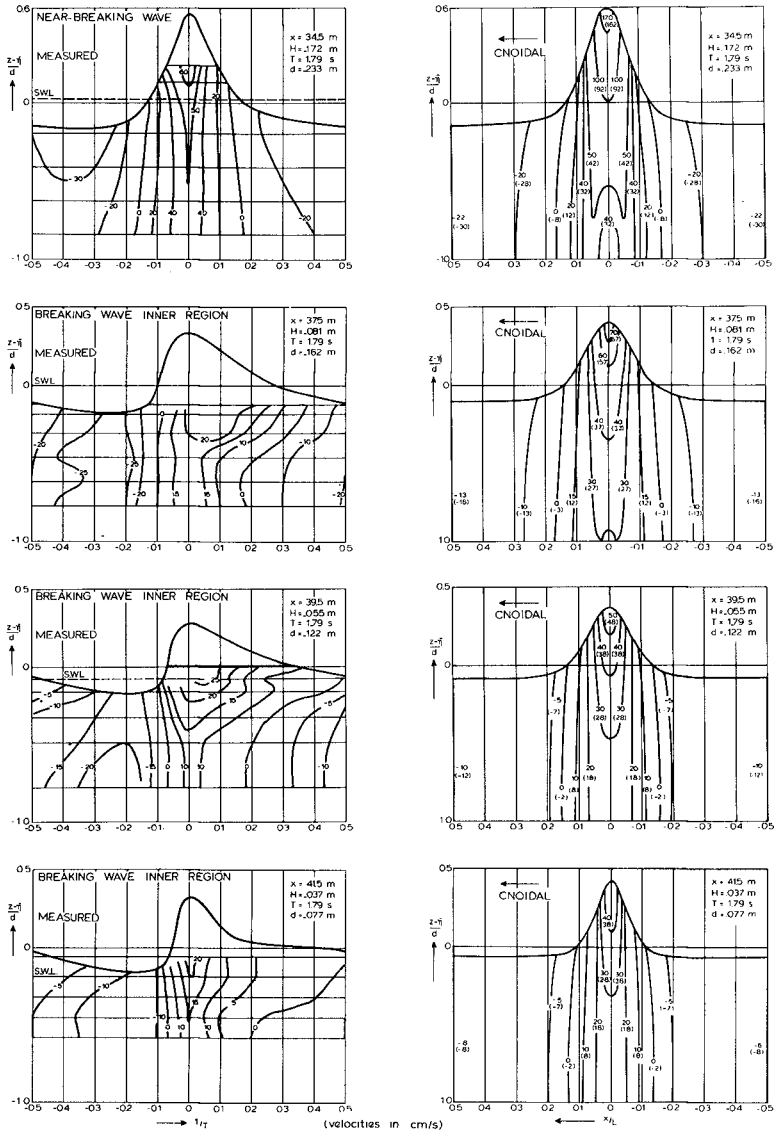


Figure 6 Comparison of measured and theoretical (cnoidal) horizontal periodic velocity fields of test I (see text for explanation)

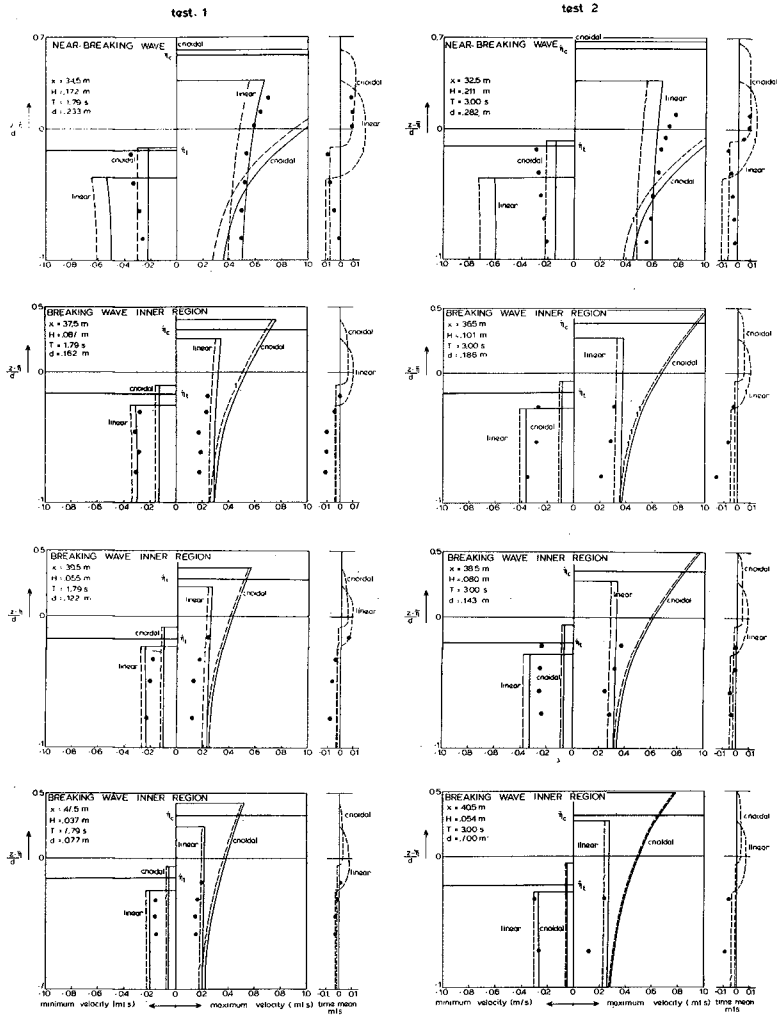


Figure 7 Comparison of measured and theoretical extreme horizontal periodic velocities for both tests (see text for explanation)

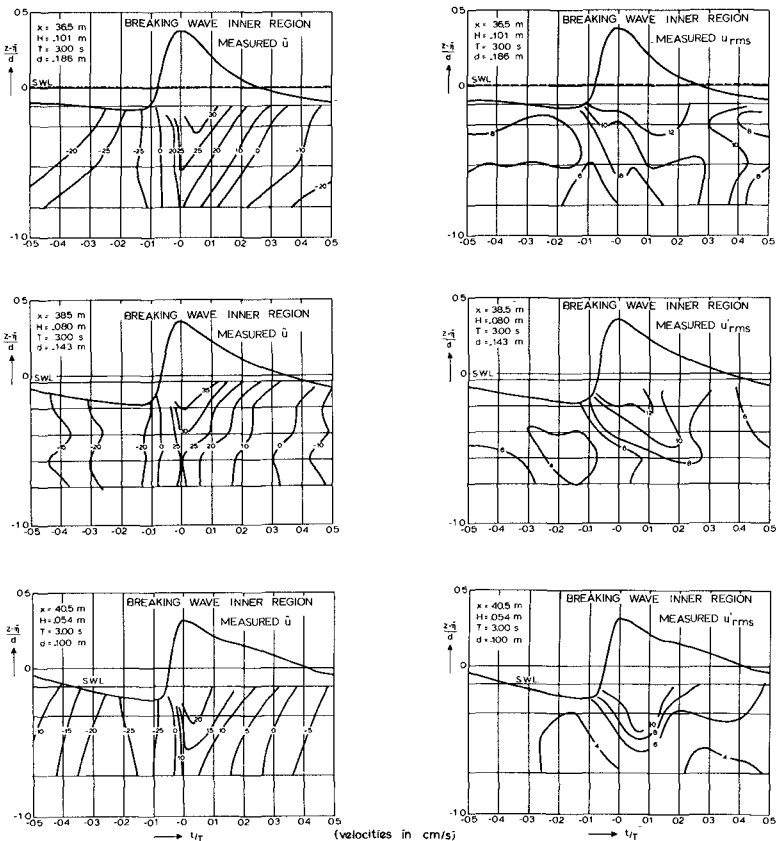


Figure 8 Measured horizontal periodic and turbulent velocities of test 2

Lagrangian measurements of Russell and Osorio (1958) in a closed wave flume confirmed this picture for non-breaking waves and found it to hold even for a sloping bottom.

From the comparison relating to the near-breaking waves (top of Fig. 6 and 7), it can be noted that:

- the surface elevation and the orbital wave motion remain quite symmetric horizontally,

- the surface elevation is well predicted by the cnoidal theory,
- the horizontal velocity is qualitatively and, with the exception of the upper crest region, quantitatively well predicted by the cnoidal theory,
- the discrepancies between the theoretical and measured maximum and minimum velocities are of the same order of magnitude as found by LeMéhauté et al. (1968),
- the time mean horizontal motion shows the tendencies as described by Longuet-Higgins' "conduction solution" (1953).

From the comparison relating to the breaking waves of the inner region (lower part of Fig. 6 and 7) it can be noted that

- the surface elevation and the orbital water motion are quite asymmetric horizontally and vertically,
- the cnoidal theory (for symmetric waves) is not able to predict the horizontal velocity field,
- the linear maximum and minimum horizontal velocities compare favourably to the measured extreme velocities,
- the net seaward flow below the wave troughs does not tend to zero or to shoreward flow near the bottom.

Figures 6 and 8 show that the horizontal periodic velocity fields of the inner breaking region for both tests and for different positions show a similar pattern that can be characterised as follows: in the regions just before the bore front arrives and in the lower regions a vertically homogeneous orbital motion exists which shows a horizontal asymmetry as can be expected from a non-breaking wave theory based on a similar asymmetric wave profile. Just behind the bore front a disturbed region exists, which seems to restore itself to a smooth velocity profile just before the next wave front arrives. The nature of these flow fields is described by the following model.

A model for the flow field

Based on visual observation Peregrine and Svendsen (1978) developed a model of a quasi-steady breaking wave (see Fig. 9a), which is briefly outlined below. The flow fields resulting from this model are compared to the measured flow fields of the inner breaking region.

At the front face of a spilling breaker an aerated surface layer can be observed, which is rapidly mixed into an increasing volume of aerated flow by the strong turbulence. The aerated flow commences at the toe of the aerated surface layer and forms a wedge. Longuet-Higgins and Turner (1974) describe the surface layer as a roller, falling down the front face of the wave. It is doubted, whether the surface layer can be treated as a roller separate from the region of highly turbulent flow. Peregrine and Svendsen (1978) hypothesize that it acts as a trigger to initiate the turbulence and that the initial volume of turbulent flow resembles a turbulent mixing layer.

The influence of gravity limits the development of the mixing layer region strongly, due to the absence of an upper fluid. A substantial part of the aerated, turbulent flow is found behind the mixing region, where the flow is like that in a wake. In this wake region the turbulence spreads and decays.

The horizontal velocity field resulting from this model is sketched in Figure 9b, for a frame of reference moving with the wave. The uniform flow approaching the breaking wave meets the toe of the surface roller, which has a velocity not very different from zero. In the moving reference frame the uniform velocity of the undisturbed flow is of the order of the propagation velocity c to which the oscillatory motion of order of $0.1 - 0.2 c$ is added. The mixing layer region develops in which the uniform velocity of the lower fluid changes to the zero velocity of the surface layer until the influence of gravity becomes dominant. In the wake region the uniform velocity of the undisturbed lower regions is slowly restored over the whole depth.

In figure 9c the velocity field described above is translated to a field with isolines of horizontal velocity for a fixed frame of reference. Comparison of this typical velocity field with the presented measured periodic flow fields (Fig. 6 and 8) shows that the model of the flow field agrees encouragingly well with the measured flow fields. However, the lack of measurements in the most aerated regions restricts this conclusion to the far wake region and the lower boundaries of mixing region and initial wake region.

Turbulent mixing layers grow linearly with distance in a wedge. The growth rate depends primarily on the velocity difference of the meeting flows. Brown and Roshko (1974) present values for the visually observed growth rate for a range of velocity differences including the case where the upper fluid velocity is zero. The measured flow fields (Fig. 6 and 8) give an indication of the lower boundary of the mixing layer. Since the model assumes the surface elevation to be the upper boundary, it is possible to obtain the growth rate of the mixing regions of the flow fields measured at the different positions in the inner breaking region. These growth rates are compared (see Fig. 10) to the values which Brown and Roshko present for their cases $u_2 = 0$, $\rho_2/\rho_1 = 1$ and $u_2 = 0$, $\rho_2/\rho_1 = 1/7$, in which the subscripts 1 and 2 stand for the lower and upper fluid respectively. Although the measurements on which these values are based show a considerable scatter, which is also true for the presented growth rates, it is concluded that there is a fair order of magnitude agreement. The density difference that Brown and Roshko introduced in their experiments appears to create only quantitative differences. Because of the scatter in the measured growth rates presented in Fig. 10 it is not possible to perceive any effects of a lower mean density of the surface layer due to air entrainment.

Finally, it is shown that also the measured horizontal turbulent velocity field ($u_{r.m.s.}$) is in agreement with the model. For positions corresponding to the measured periodic velocity fields of Figure 8 some typical examples are given in the same figure. The lower boundary of the mixing region is indicated by the spreading of the high intensities of the turbulence. In the wake region behind the mixing zone a decay of the turbulent intensities is clearly observed. It is noticed that the velocity fluctuations in the initial wake region are of the same order of magnitude as the mean velocity defect. This is typical for wakes (Tennekes and Lumley, 1974). A clear indication of the wake type flow in the region behind the crest is also found from the measurements of Battjes and Sakai (1980) in a steady breaking wave.

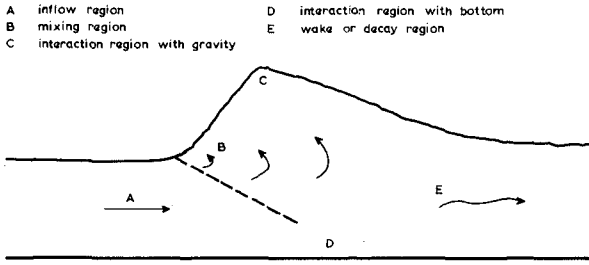


Figure 9a Model of a quasi-steady breaking wave (after Peregrine and Svendsen, 1978) for a reference frame moving with the wave

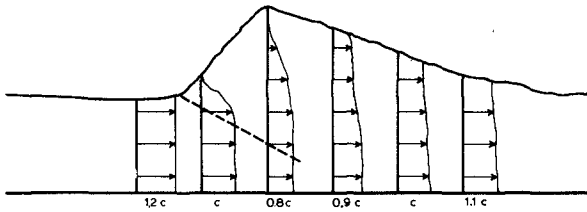


Figure 9b Horizontal velocity field of a quasi-steady breaking wave for a reference frame moving with the wave

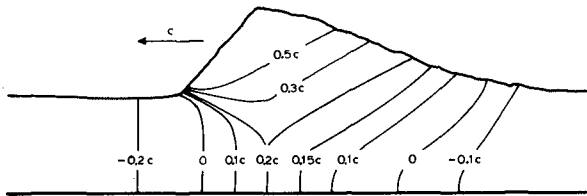


Figure 9c Horizontal velocity field of a quasi-steady breaking wave for a fixed frame of reference

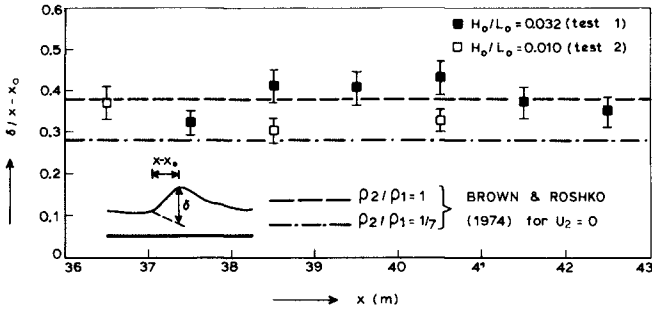


Figure 10 Growth rate of mixing regions

Summarizing, it is concluded that the measured horizontal periodic and turbulent velocity fields are at least in qualitative agreement with the model of a quasi-steady breaking wave as proposed by Peregrine and Svendsen (1978).

5. PRESSURE FIELD

In this paragraph a semi-quantitative description of a typical, measured periodic pressure field of the inner breaking region is presented. As will be shown, the magnitude and gradients of the vertical velocity and the surface elevation control the dynamic pressure field. From the comparison with the theories in §3 it is clear that the cnoidal theory is unable to predict the magnitudes of the velocity field. Linear theory is not able to describe the gradients in the velocity fields and surface elevation. Therefore a quantitative comparison with the cnoidal and linear theory is not considered appropriate at this stage of the study.

In Figure 11a the periodic dynamic pressure $\tilde{p}/\rho g + z$ measured at different levels in the inner region is given, along with the surface elevation or equivalently the dynamic hydrostatic pressure head, i.e. the dynamic pressure head that would result from a hydrostatic pressure distribution. The test conditions differ from the conditions of test 1 only in the presence of the dummy side wall, which is the cause of a surface elevation profile slightly different from test 1. Figure 11b shows the measured periodic vertical velocity at different levels and the surface elevation of test 1. The following description is based on the balance of vertical momentum (Dorrestein, 1961). Consider a fixed control volume of length δx extending between a level $z = z_1$ and the surface $z = \eta$. The dynamic equation reads:

$$\left(\frac{p}{\rho g} + z \right) \Big|_{z=z_1} = \eta - \frac{1}{g} w^2 \Big|_{z=z_1} + \frac{1}{g} \frac{\partial}{\partial t} \int_{z_1}^{\eta} w \, dz + \frac{1}{g} \frac{\partial}{\partial x} \int_{z_1}^{\eta} uw \, dz$$

From the measurements it is concluded that the magnitude of the last term on the right hand side, representing the advective gain of vertical momentum through the side boundaries, is at all times small, i.e. less than 10%, relative to the second and third term. The second term represents the advective gain of vertical momentum through the base of the control volume and the third term represents the gain due to the difference of vertical momentum at time t and $t + \delta t$. These terms are responsible for the deviation of the pressure $\bar{p}/\rho g$ from the hydrostatic pressure $\bar{\eta} - z$. A schematic representation of the magnitude and gradients of these two terms is given in Figure 11c in which 3 zones are distinguished. In zone A \bar{w} and $z \int \bar{\eta} \bar{w} dz$ are small in magnitude and gradients, resulting in a hydrostatic pressure distribution. In zone B at first a strong gradient in $z \int \bar{\eta} \bar{w} dz$ and small \bar{w} result in a pressure higher than the hydrostatic value. The magnitude of w increases strongly and w^2 tends to cancel out $\frac{\delta}{\delta t} z \int \bar{\eta} \bar{w} dz$. In zone C both terms contribute negatively to the right hand side of the equation, so at the crest a pressure lower than the hydrostatic pressure results.

The measured periodic pressure field as presented in Figure 11a appeared to be typical not only for the breaking waves of the inner region but also for the breaking waves in the outer region. Nearer to the breaking point the pressure fields show qualitatively the same deviations though more pronounced. The opposite effects are found nearer to the shoreline.

These findings are in agreement with measurements of crest and trough pressure in breaking waves of van Dorn (1976), who found a hydrostatic pressure under the troughs and a pressure lower than hydrostatic pressure under the crests, increasing substantially nearer to the breaking point.

6. INTEGRAL PROPERTIES

As described in the introduction the integral properties are evaluated in the second phase of this study. The planned approach is outlined hereafter and illustrated with a preliminary result for the mean momentum balance.

Time averaging of the vertically integrated density and flux of horizontal momentum and energy yields the so-called integral properties, which enables the following analyses. Firstly, local values of the integral properties can be compared to accepted theoretical expressions. Secondly, a check is possible on the theoretical and measured relation between gradients in the time and depth integrated momentum flux and gradients in the mean water level. Thirdly, the mean energy dissipation can be obtained from gradients in the time and depth integrated energy flux, so that dissipation models can be checked.

To quantify the integral properties the ensemble mean values of u , p , u^2 , w^2 , u^3 , uw^2 and pu must be integrated over time and depth. Since u and p were not measured simultaneously the term pu is approximated by $\bar{p}\bar{u}$, thus neglecting the turbulent pu -interaction and the joint contribution of waves and turbulence. However, because of the air entrainment velocity measurements were only possible up to lightly aerated regions. For a full time and depth integration it is therefore necessary to make extrapolations in the crest regions of the breaking waves. For the most essential extrapolation of the horizontal velocity u it is

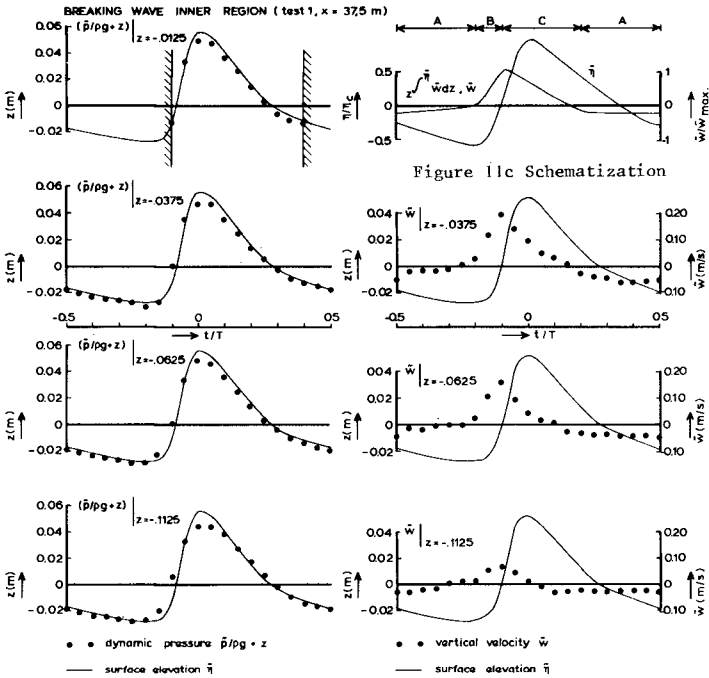


Figure 11a Dynamic pressure distribution

Figure 11b Vertical velocity distribution

possible to use the continuity equation and the constant form assumption - as suggested by the measurements - as follows. For constant form $\frac{\delta}{\delta t} = -c \frac{\delta}{\delta x}$ so the continuity equation can be written:

$$-c \frac{\delta}{\delta x} \int_{-h}^{\eta} \rho dz + \frac{\delta}{\delta x} \int_{-h}^{\eta} \rho u dz = 0$$

Using $\int_{-h}^{\eta} \rho u dz = 0$ it follows: $\int_{-h}^{\eta} \rho u dz = \rho c (\eta - \bar{\eta})$.

From the measurements the velocity of propagation c and the surface elevation $\eta - \bar{\eta}$ are known. The value of the velocity integral so obtained yields a constraint that can be used for the extrapolation. A check on the validity of this expression in the trough regions where $-\int_{-h}^{\eta} \rho u dz$ can be determined, showed it to be a valid relation.

A preliminary result of the analysis of the integral properties is given by the following evaluation of the mean momentum balance.

For a number of stations in the surfzone the time mean horizontal momentum flux $I_{xx} = -h \int_{-h}^{\eta} (\rho + \rho u^2) dz$ is determined using the measured (and extrapolated) p and u . Gradients in the excess time mean horizontal momentum flux due to the presence of waves or radiation stress induce a variation of mean water level, $\bar{\eta}$, as follows from the mean momentum balance (Longuet-Higgins and Stewart, 1962):

$$\frac{dS_{xx}}{dx} + \rho g (h + \bar{\eta}) \frac{d\bar{\eta}}{dx} = 0$$

in which:

$$S_{xx} = I_{xx} - \frac{1}{2} \rho g (h + \bar{\eta})^2$$

The measured mean water level is compared (Fig. 12) with

- the mean water level calculated from the measured I_{xx} using the equation above and
 - the mean water level calculated from the measured wave height, H_{rms} , using the linear approximation of $S_{xx} = (2n - \frac{1}{2})E$ and the equation above.
- The comparison shows that a fair agreement exists between the measured mean water level and the mean water level calculated from the measured momentum flux. This is not unexpected because the derivation of the mean water level from the measured momentum flux using the momentum balance is nearly exact, since only the bottom shear stress is neglected. Use of the linear approximation of the radiation stress gives strong deviations in magnitude and gradients of the calculated mean water level around the breaking point.

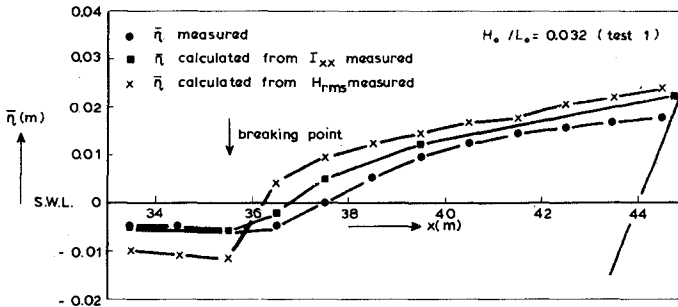


Figure 12 Comparison of measured and calculated mean water level

7. CONCLUSIONS

The internal velocity and pressure fields of quasi-steady spilling breaking waves have been investigated experimentally. So far the following conclusions can be drawn:

- The flow fields in the inner breaking region show a similarity not only from point to point for a particular wave condition, but also at corresponding points for different deep water wave conditions (see Fig. 6 and 8). This is a generalisation of the conclusions made by Svendsen et al (1978) on the basis of the similarity of the surface profiles in the inner region.
- A comparison of the horizontal periodic velocity fields with the non-breaking cnoidal (Keulegan & Patterson) and linear theory shows that:
 - a) the cnoidal theory fails to predict the horizontal velocity field qualitatively and quantitatively;
 - b) linear theory predicts the order of magnitude of the maximum and minimum horizontal velocities quite well, which is probably due to the full wave profiles.
- The model of a quasi-steady breaking wave as proposed by Peregrine and Svendsen (1978) is - at least qualitatively - shown to be in agreement with the measured horizontal periodic and turbulent velocity fields.
- The periodic pressure field deviates from hydrostatic pressure at the breaking wave front and at the wave crest. Shortly behind the wave crest and at the trough region the periodic pressure field is hydrostatic. The deviations can be explained semi-quantitatively from the vertical velocity distribution using the vertical momentum balance.
- The integral properties can in principle be quantified from the measured internal velocity and pressure field. This makes a valuable check possible on known relations, such as the mean momentum balance. It also allows for a fundamental study of the energy dissipation.

8. ACKNOWLEDGEMENT

This study was suggested by dr. J.A. Battjes as a part of the coastal research program (TOW) of the Public Works Department of the Netherlands (Rijkswaterstaat). The author gratefully acknowledges the encouragement and valuable suggestions of dr. Battjes.

9. REFERENCES

- Battjes, J.A. (1975). Modeling of turbulence in the surfzone. Proc. Symp. on Modeling Techniques, San Francisco, p. 1050-1061.
- Battjes, J.A. and Sakai, T. (1980). Velocity field in a breaker. Proc. 17th Coast. Engng. Conf., Sydney.
- Brown, G.L. and Roskko, A. (1974). On density effects and large structure in turbulent mixing layers. J. Fluid Mech., 64, p. 775-816.

- Dean, R.G. (1974). Evaluation and development of water wave theories for engineering application. Special Report No. 1, Coast. Engng. Research Center.
- Dorrestein, R. (1961). On the deviation of the average pressure at a fixed point in a moving fluid from its "hydrostatic" value. Appl. sci. Res., A, 10, p. 384-392.
- Godefroy, H.W.H.E. (1978). Application of the laser doppler velocity measurement method in open and closed conduits. Proc. Flomeko, Groningen.
- Hulsbergen, C.H. (1974). Origin; effect and suppression of secondary waves. Proc. 14th Coast. Engng. Conf. Copenhagen, chap. 22, p. 392-411.
- LeMéhauté, B., Divoky, D. and Lin, A. (1968). Shallow water waves: a comparison of theories and experiments. Proc. 11th Coast. Engng. Conf., London, chap. 7, p. 86-107.
- Longuet-Higgins, M.S. (1953). Mass transport in water waves. Phil. Trans. Roy. Soc. London, A. 903, 245, p. 535-581.
- Longuet-Higgins, M.S. and Stewart, R.W. (1962). Radiation stress and mass transport in gravity waves, with applications to "surf-beats". J. Fluid Mech., 13, p. 481-504.
- Longuet-Higgins, M.S. and Turner, J.S. (1974). An "entraining plume" model of a spilling breaker. J. Fluid Mech., 63, p. 1-20.
- Masch, F.D. and Wiegel, R.L. (1961). Cnoidal waves, tables of functions. Berkely, Calif.: The Engng. Found. Council on Wave Research.
- Peregrine, D.H. and Svendsen, I.A. (1978). Spilling breakers, bores and hydraulic jumps. Proc. 16th Coast. Engng. Conf., Hamburg, chap. 30, p. 540-551.
- Russell, R.C.H. and Osorio, J.D.C. (1958). Proc. 6th Coast. Engng. Conf., USA, Chap. 10, p. 171-183 and appendix by Longuet-Higgins, M.S. The mechanics of the boundary-layer near the bottom in a progressive wave, p. 184-193.
- Svendsen, I.A., Madsen, P.A. and Buhr Hansen, J. (1978). Wave characteristics in the surfzone, Proc. 16th Coast. Engng. Conf., Hamburg, chap. 29, p. 520-539.
- Tennekes, H. and Lumley, J.L. (1972). A first course in turbulence. MIT Press.
- Van Dorn, W.G. (1976). Set-up and run-up in shoaling breakers. Proc. 15th Coast. Engng. Conf., Hawaii, chap. 42, p. 738-751.

CHAPTER 35

DIRECTIONAL WAVE SPECTRA AND WAVE KINEMATICS IN HURRICANES CARMEN AND ELOISE

G. Z. Forristall and E. G. Ward
Shell Development Company
P. O. Box 481
Houston, Texas 77001

and

V. J. Cardone
Oceanweather, Inc.
170 Hamilton Avenue
White Plains, New York 10601

ABSTRACT

A realistic description of the kinematics of hurricane waves requires that the directional spectrum of the sea be known. Models for hindcasting the directional spectrum have existed for some time, but there has been a dearth of data available for checking the directional characteristics of the hindcasts. Hurricane Carmen in 1974 and hurricane Eloise in 1975 passed reasonably close to platforms in the Gulf of Mexico which were instrumented with wave staffs and electromagnetic current meters. The maximum recorded significant wave height was 29 feet. The simultaneous measurements of wave height and water particle velocity permitted estimates of the directional spectra to be made. The estimated directional spectra are complicated and often bimodal in frequency and direction. Swell from the center of the storm can propagate in directions over 90 degrees away from the direction of the shorter waves which are in local equilibrium with the wind. The hindcast model reproduces these directional features remarkably well. The measurements of wave kinematics also permitted tests of the accuracy of wave theories in high and confused storm waves. All of the unidirectional theories tested showed a bias toward overpredicting the velocity under the highest waves. However, the kinetic energy in the velocity components and the velocity probability distribution could be found to within a ten percent scatter using directional spectral concepts and linear wave theory.

INTRODUCTION

Hurricane waves are steep, confused, and short-crested. The directional spectrum provides a concise description of this chaos by giving the most important statistical measures of the motion of the sea surface. Knowledge of the directional spectrum is of obvious practical importance in predicting ship motions. Using wave height and velocity measurements made in tropical storm Delia, Forristall et al. (1978) showed that the details of the directional spectrum can also be important when the subsurface kinematics of the wave motion are needed, as for predicting wave forces on slender members of a structure. For the short-crested waves in that data set, unidirectional wave theories consistently overpredicted the subsurface velocities while linear directional theory came close to matching the observed velocity spectra.

Measurements of directional spectra in the most severe conditions are unlikely to be available, and hindcasts of historical storms are needed to establish design conditions. The hindcast models can be of either a discrete or parametric type, as discussed in the review by Vincent and Resio (1979). At the present state of development, the discrete models such as the one developed specially for hurricanes by Cardone et al. (1976) offer more flexibility in handling variable wind directions. However, parametric models based on the work of Hasselman et al. (1976) are well suited to fetch limited generation cases, and with the addition of discrete swell bands as discussed by Gunther et al. (1979), they may be extended to situations with rapidly changing winds.

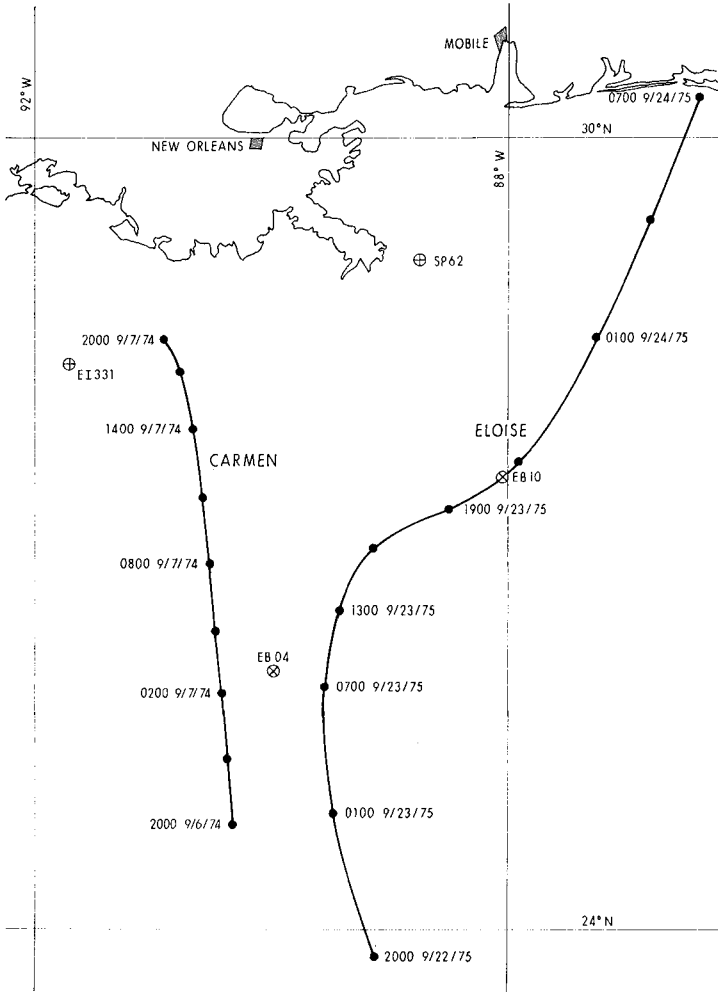
Wave hindcast models have been reasonably well verified with wave height measurements, but there has been little data on the directional characteristics of storm waves available for verification of the hindcast directional spectra. The main purpose of this paper is a description of directional spectra estimated from wave staff and electromagnetic current meter measurements made in hurricanes Carmen in 1974 and Eloise in 1975. The measurements compare reasonably well with hindcasts made using the model of Cardone et al (1976).

The measurements of particle velocities under the waves were compared with the predictions of various wave theories and general confirmation of the results of Forristall et al. (1978) was obtained. That is, all unidirectional theories tested, including irregular and nonlinear theories, overpredicted the measured velocity. In contrast, the kinetic energy spectra and statistical distributions of the velocity were predicted to within a reasonable scatter using linear theory.

DATA AND METHODS OF ANALYSIS

The measurements were made in the northern Gulf of Mexico at the oil and gas production platforms designated EI331 and SP62 in Figure 1. The water depth at EI331 is 246 feet and the depth at SP62 is 315 feet. At both stations, continuous analog recordings were made from a Baylor wave staff and a string of cylindrical electromagnetic current meters manufactured by Marsh-McBirney, Inc. The current meters were hung from pairs of taut wires designed to hold them as rigidly as possible with minimum interference to the flow. Forristall and Hamilton (1978) give a more complete description of the instrumentation and suspension system.

Tank testing has shown that the cylindrical electromagnetic current meters respond linearly to the flow speed but that their response to flow 45° from an electrode axis is down by eight percent. It was easy to correct for this feature during the analysis. The meters included an internal calibration circuit which was switched on automatically once a day to provide a check on the gain of most of the amplifiers in the circuitry, and which was used to give the calibration to engineering units during the analysis. The 0.80 Hz low pass output filter used on the meters was squared off by applying the inverse filter during the spectral analysis.



77-0291-21

Fig. 1 - Storm tracks of hurricanes Carmen and Eloise, with OCMF stations and NOAA data buoy sites.

All the signals were transformed to the frequency domain using an FFT over 2048 samples. Power spectra and co-spectral estimates were formed by multiplying the Fourier transforms together and averaging over ten raw frequency lines. The estimates thus have 20 degrees of freedom and a resolution of 0.0098 Hz.

The information on wave direction available from a wave staff and current meter is equivalent to that from a pitch and roll buoy, and does not provide very sharp directional resolution. However, it is sufficient to determine the mean direction of travel and degree of directional spreading for waves in each frequency band. The co-spectra were thus used to find the best estimates for the parameters in the function

$$H(\theta) = N(s) \cos^{2s}(\theta - \theta_0) \quad (1)$$

where θ_0 is the mean direction of travel, s is a spreading parameter which increases as the directional spread becomes narrower, and $N(s)$ is included to normalize the area to unity. The details of the calculations, including a correction for the Doppler shift caused by steady currents, are given by Forristall et al (1978).

The hindcasts of directional spectra in the storms were made using the discrete model described by Cardone et al (1976). The processes of wave growth, dissipation, and propagation are simulated on a hexagonal grid system which covers the Gulf of Mexico with a grid spacing of 35 kilometers. At each grid point, the directional spectrum is resolved into 13 frequency and 24 directional bands. The growth of spectral components by linear and exponential mechanisms is limited by the Pierson-Moskowitz fully developed spectral form. Propagation of spectral components is accomplished by a simple Lagrangian scheme. For comparison with the measurements, the hindcast results were fit to equation (1) with a nonlinear least squares program.

The quality of a wave hindcast depends to a great extent on the accuracy of the wind field used as input. For hurricanes, it is possible to use a model storm approach since the similarity of hurricane pressure fields allows their description with relatively few parameters. Once the pressure field is specified, the wind speed and direction can be found by solving the equations of motion averaged over the atmospheric boundary layer.

HURRICANE CARMEN

Carmen was a rather severe storm with minimum central pressure of 937 mb and estimated peak gusts of 140 miles/hr. Figure 1 shows her track past EI331 and SP62 on her way to landfall near Vermillion Bay on the Louisiana coast. The NOAA data buoys shown in the figure were not operational during Carmen. Hope (1976) gives a description of the meteorological conditions in the storm.

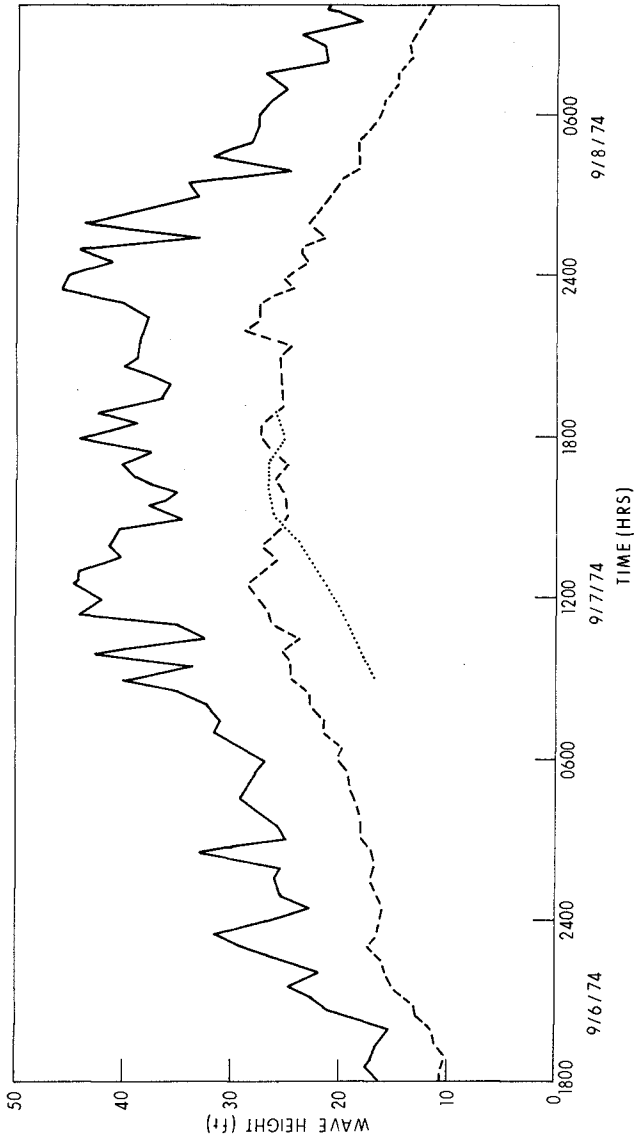
The wave hindcast for Carmen was performed as part of an extensive study of waves generated by historical hurricanes in the Gulf of Mexico (Ward et al., 1978). For consistency, only the type of meteorological information available in the historical records was used in the windfield analysis. This limitation gives an indication of the accuracy of the historical hindcasts, but a better windfield could probably have been constructed using the additional data available for a storm in 1974. In particular, the modeled wind direction early in the storm at EI331 and SP62 was considerably clockwise from the measured directions. This discrepancy is probably due to a poor specification of the large scale pressure field.

Figure 2 shows the comparison between the measured and hindcast significant wave heights at EI331 as estimated from the total variance of the spectra. The solid line shows the half-hour maximum wave height, the dashed line shows the measured significant wave height, and the dotted line shows the hindcast significant wave height. The hindcast results are available for only a rather short stretch of the storm and the hindcast waves are slower in reaching their maxima than the measured waves. However, the eventual fit of the maxima is excellent. The conditions during this storm were the most severe during the measurement program, with the maximum spectral significant wave height equal to 29 feet and a maximum zero downcrossing 46 feet high.

There were several current meter failures at the measurement sites which affected the usefulness of the data for calculating directional spectra. In particular, the boat deck clamps holding the current meter taut wire assembly broke at both stations, making the particle velocity data completely unusable after 0930 at EI331 and after 1300 at SP62. Even before then, only the data from Current Meters 2 and 3 at EI331 and Current Meters 1 and 2 at SP62 could be used.

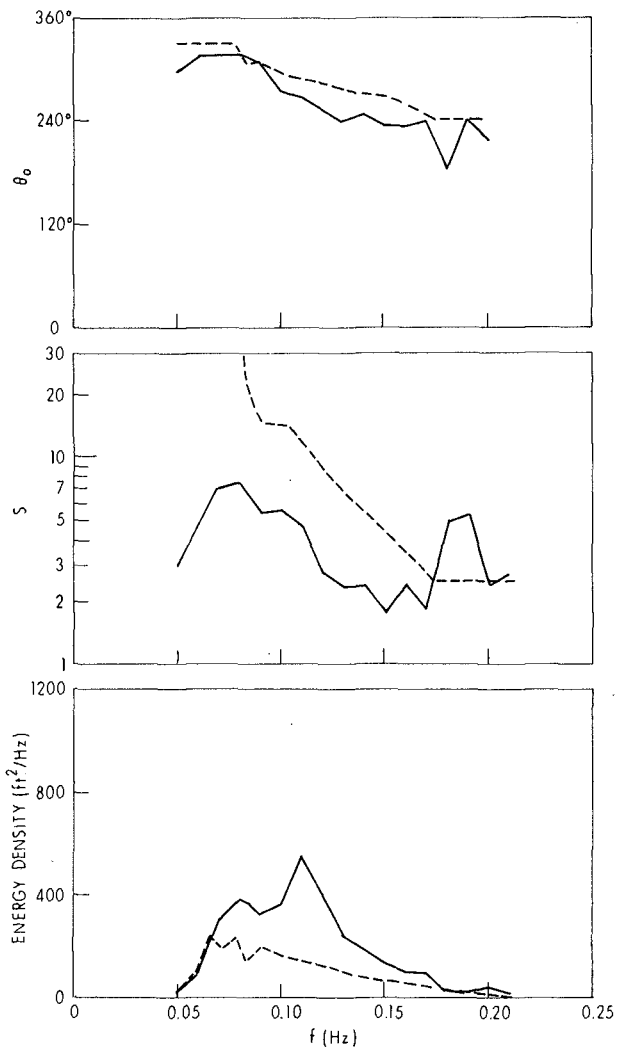
Despite the problems with the instrumentation, some interesting directional spectra are available for comparison with the hindcasts. Figure 3 shows a comparison for EI331 and Figure 4 shows data from SP62. The hindcast for EI331 at 0900 shows too little energy at all frequencies as would be expected from Figure 2. The hindcast energy is not spread as much as the measurements, which may be related to noise in the data. The mean direction of the hindcast energy at the higher frequencies is in error by about 30° in the same sense as the wind direction errors noted above. At later times in the storm, when only the power spectrum was measured, the total hindcast energy was nearly correct, but the peak frequency was considerably lower than that measured.

As shown in Figure 4, the hindcast compares much more favorably with the measurements at SP62. The fit of the power spectrum and the mean direction of travel is very good for all frequencies. The energy is more directionally spread in the measured spectrum, but the difference is slight.



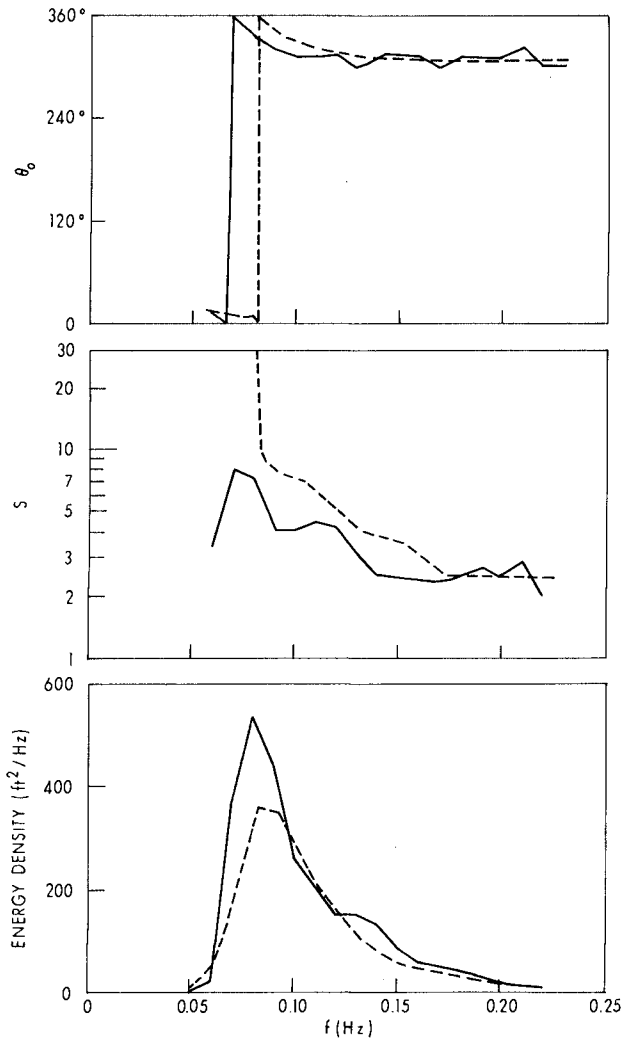
77-0291-24

Fig. 2 - Wave height at EI331 during Carmen. Solid line--maximum. Dashed line--measured significant. Dotted line--hindcast significant.



77-0291-7

Fig. 3 - Directional spectrum at EI331, 0900 CDT, September 7, 1974. Solid line--measurements. Dashed line--hindcast.



77-0291-18

Fig. 4 - Directional spectrum at SP62, 1200 CDT, September 7, 1974. Solid line--measurements. Dashed line--hindcast.

HURRICANE ELOISE

The track taken by hurricane Eloise in September 1975 is shown in Figure 1. After heading northward in the direction of SP62, she was forced eastward by a cold front which had been moving southeast over Texas and Louisiana and made landfall near Fort Walton Beach, Florida. The minimum pressure recorded near landfall was 955 mb and wind gusts to 155 miles/hr were recorded. A review of the storm meteorology is given by Hebert (1976). Withee and Johnson (1975) summarize the measurements made from the data buoys located in Figure 1, and Friese (1977) used that data to discuss the oscillations of the thermocline caused by the storm. The Corps of Engineers (1976) has prepared a report describing the coastal damage caused by the storm.

The large amount of meteorological information available for Eloise permitted a detailed investigation of the windfield. Aircraft and satellite reconnaissance, shore radar, buoy data, and data recorded at EI331 and SP62 were all used in a determination of the storm track and pressure history. The storm winds were unusually asymmetric due to the intruding high pressure ridge, and thus the tangential pressure distribution was fit to a five-term Fourier series. The resulting wind field solution had several unusual features which were corroborated by the available data. There was very sharp inflow in the right rear and left front quadrants, pronounced outflow in the left rear quadrant, and a sharp almost front-like wind shift line extending to the south of the center.

Although the model wind field is very good, it does not perfectly match all the details of the observed winds. The model misses small scale variations due to individual rain bands, and the wind speed is underpredicted early in the storm at EI331 when the wind was dominated by the high pressure ridge intruding before the hurricane.

The underpredicted wind speeds at EI331 led to underpredicted significant wave heights until about midnight on September 22. The hindcast wave heights at SP62, shown in Figure 5, also began a bit low, but they followed the observed buildup quite well and were within a few feet of the observed peak. Some of the most interesting measurements during Eloise were made by National Data Buoy Office at EB-10 which was directly under the storm track. Figure 6 shows a comparison between the peak wave spectrum measured by an accelerometer on the buoy and the spectrum hindcast for the same time. The fit is quite good, and the hindcast would be well within the 90 percent confidence limits for the measured spectrum.

Figures 7 and 8 show measured and hindcast directional spectra at EI331 and SP62, respectively. At 1800 CDT on September 22 at EI331, the measured spectrum is strongly bimodal, with the swell component clearly separated from the locally generated sea. The directions of travel of the two components are over 90° different. The hindcast spectrum shows good qualitative agreement with the measurements, but the amount of energy is too low in every frequency band, in large part

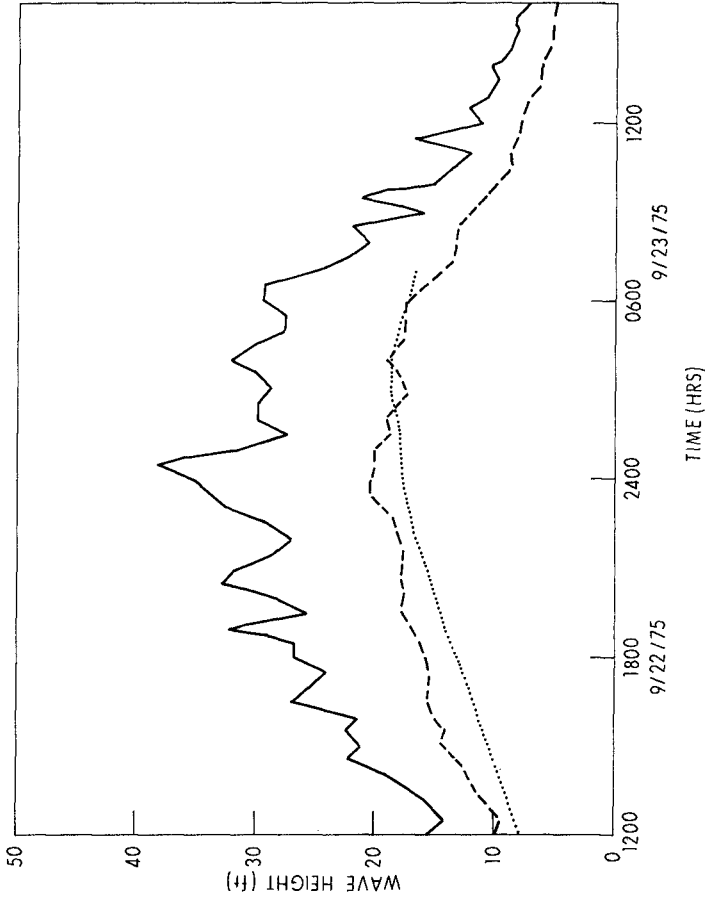
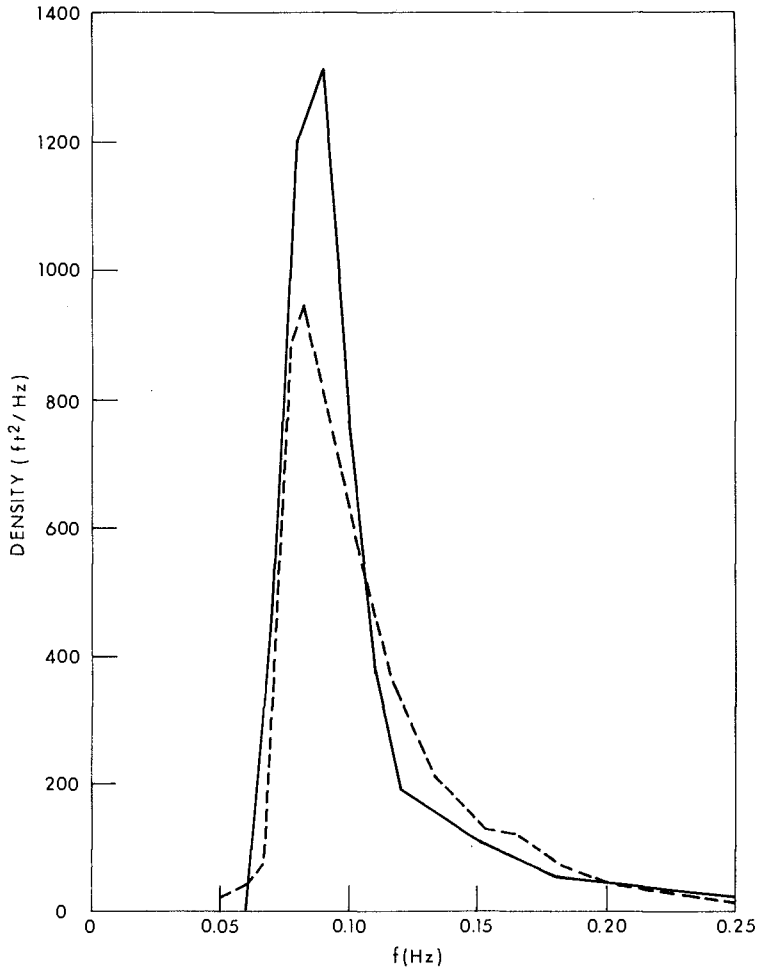


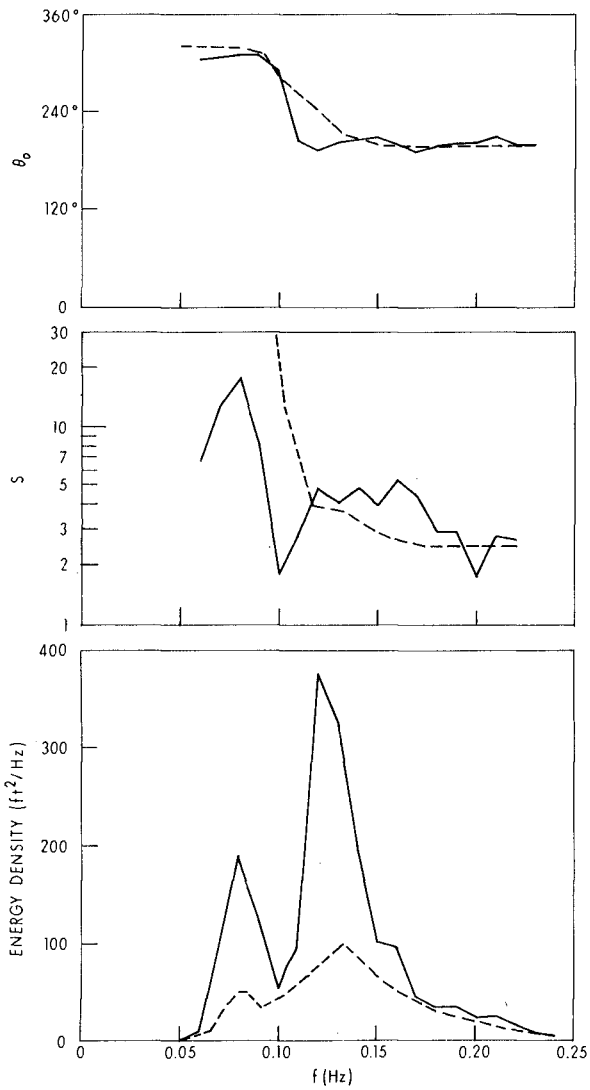
Fig. 5 - Wave heights at SP62 during Eloise. Solid line--maximum. Dashed line--measured significant. Dotted line--hindcast significant.

77-0291-27



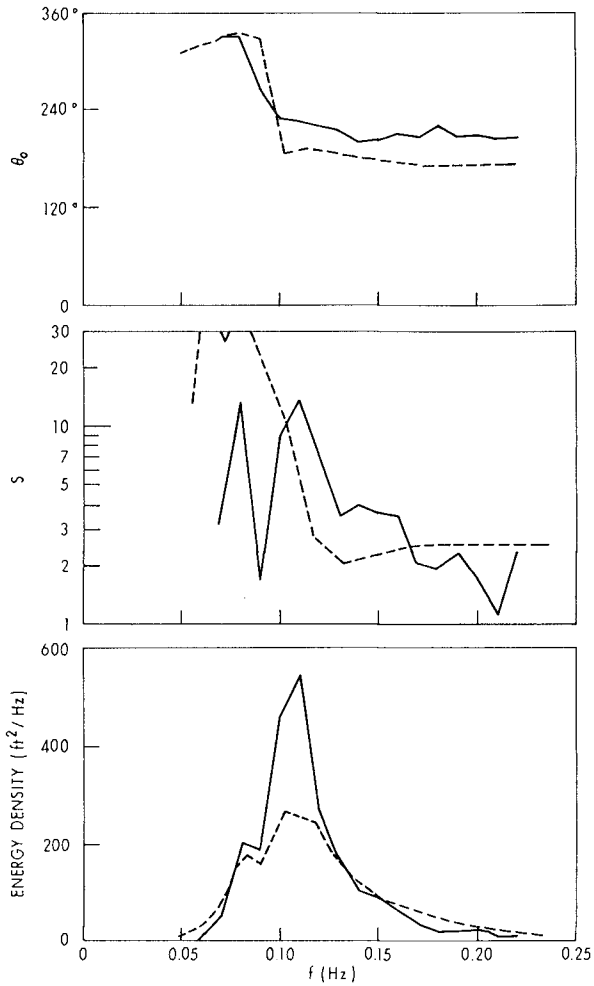
77-0291-35

Fig. 6 - Wave frequency spectrum at EB-10, 2000 CDT, September 22, 1975. Solid line--measurements. Dashed line--hindcast.



77-0291-8

Fig. 7 - Directional spectrum at EI331, 1800 CDT, September 22, 1975. Solid line--measurements. Dashed line--hindcast.



77-0291-14

Fig. 8 - Directional spectrum at SP62, 0100 CDT, September 23, 1975. Solid line--measurements. Dashed line--hindcast.

due to the underspecification of the local wind speed. The transition in wave direction between sea and swell is much sharper in the measurements.

Throughout most of the storm at SP62, the spectra were also bimodal. This bimodality cannot always be recognized from consideration of the frequency spectrum alone, but in both the measurements and hindcasts there is a sharp break in the direction of travel at about 0.10 Hz, as shown in Figure 8. The error in the direction of travel of the high frequency waves is due to a small scale shift in wind direction at SP62 which persisted for a few hours and was not modeled.

Black (1979) used the EI331 and SP62 data sets to determine the wave power spectrum and mean direction of travel of waves in each frequency band. In general, his results are consistent with those presented here. However, at 2400 CDT, September 23 at SP62, he finds high frequency energy propagating upwind while we do not. The discrepancy could be due to the considerable difference in the methods of analysis or to the possibility that a calibration mark on the data tape was inadvertently included in Black's analysis.

The measured directional spectra show that the sea state in a hurricane is typically very complicated. Different frequencies can have greatly different mean directions of travel and directional spreads. The discrete model used for the wave hindcasts is well suited to accounting for the development and propagation of the energy in the various frequency bands, and the hindcasts generally agree well with the measurements. In fact, the directional parameters often seem to be more accurately hindcast than the power spectrum, although this is in part associated with the natural statistical variability in measured power spectra. Many details of the errors in the hindcasts can be ascribed to errors in the details of the local wind specifications, which again emphasizes the importance of the wind field specification to wave hindcasting.

WAVE KINEMATICS

The calculation of wave kinematics in confused seas is of considerable importance in the specification of wave forces on ocean structures. Forristall et al. (1978) showed that unidirectional wave theories consistently overpredicted measured velocities during tropical storm Delia, and this result was confirmed in the data sets considered here. Figure 9 shows a comparison between measured horizontal velocities and those predicted by Stokes' fifth-order theory for SP62 during Eloise. Data from the top current meter 16 feet below mean sea level are given, and each data point represents the highest wave in a half-hour segment of data. The measured velocity is the maximum resultant of the two horizontal measured components during the wave. The wave height and period for the Stokes' calculation were determined by the zero down-crossing method. The scatter in the comparisons and the bias toward overprediction are both quite large and both can be explained by the directional spreading of the confused waves.

COMPARISON OF MEASURED VS PREDICTED VELOCITIES
(EXISTING WAVE THEORIES)

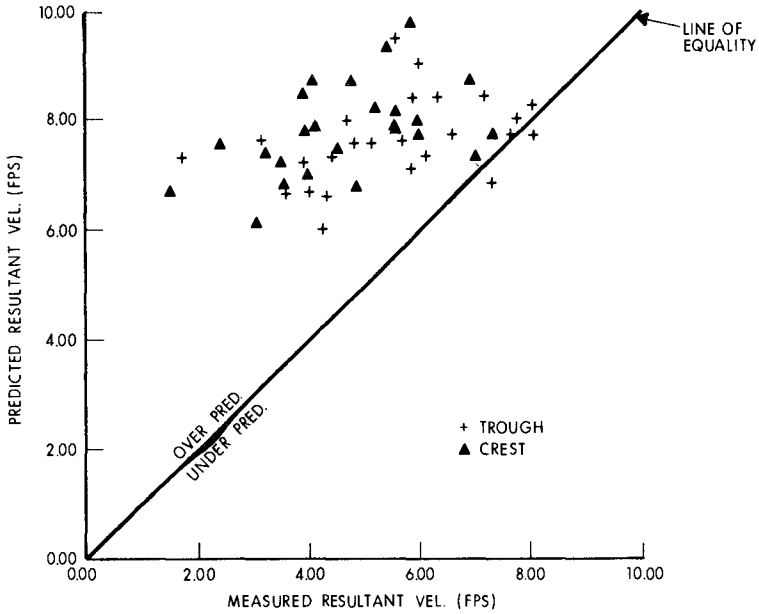


Fig. 9 - Measured compared to Stokes wave kinematics at SP62 during Eloise.

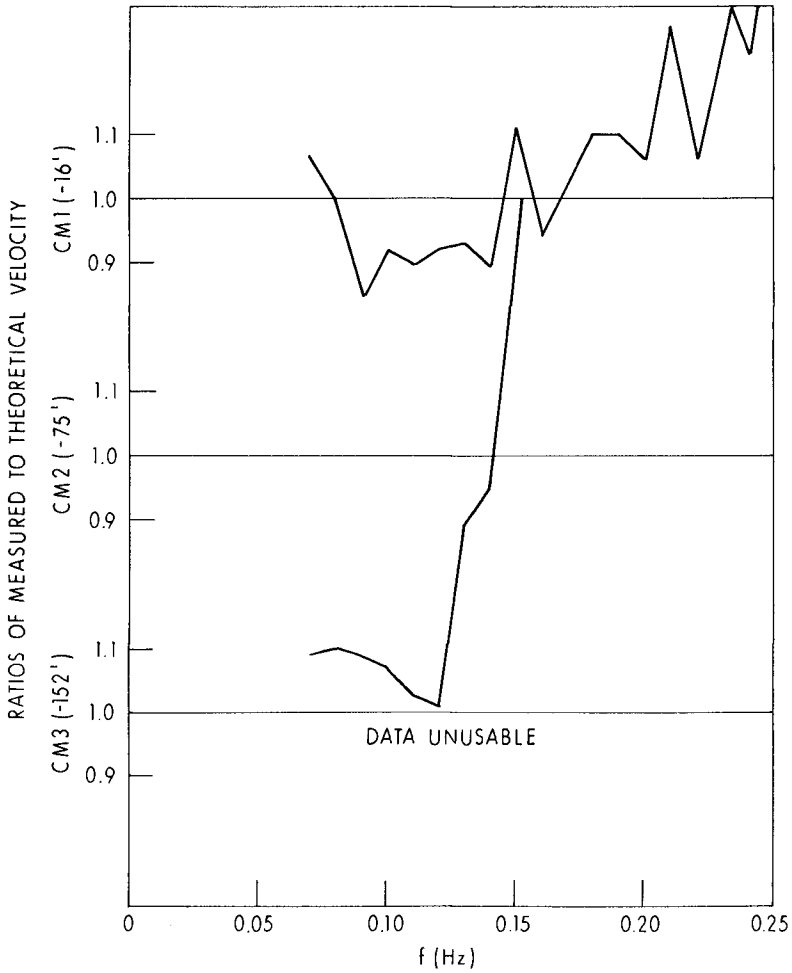
Linear wave theory can be extended to directionally spread seas since linear waves with different frequencies and directions can be combined by superposition. However, the applicability of linear theory is questionable for the high and steep waves of a hurricane. It is possible to check the theory by comparing the measured and theoretical horizontal kinetic energy. The measured kinetic energy is found by adding the spectra from the two horizontal axes of the current meter, and the theoretical energy is found by attenuating the measured wave height spectra by the factor given by linear wave theory. An amplitude ratio of measured-to-theoretical velocity may then be found by taking the square root of the ratios between the spectra. This process is complicated somewhat by the Doppler shift due to steady currents as described by Forristall et al. (1978), but for the moderate currents measured during the storms, the change in the ratios is slight.

The amplitude ratios of measured over theoretical velocity for SP62 during Carmen and EI331 during Eloise are shown in Figures 10 and 11, respectively. The ratio for the top meter at SP62 was about 0.9 at the peak of the wave spectrum, rising to 1.1 at the higher frequencies. In contrast, the ratio at the top meter at EI331 was about 1.1 throughout the energetic part of the spectrum. Note that the rise to a higher ratio at about 0.10 Hz corresponds to a notch in the wave spectrum. The meter at the 47-foot depth at EI331 had a ratio near 1.0 for all frequencies, while the deeper meters at both stations showed wide variations due in part to the very small predicted velocities at these levels. For high frequencies, electronic noise or turbulent fluctuations in the flow can overwhelm the signal from the wave induced oscillations.

Similar amplitude ratios were calculated for many hours of each storm at each station. The results were nearly constant for a given storm and current meter, but varied as noted between storms and meters. The meter at the 47-foot depth at EI331 during Carmen had a ratio of about 0.95 while the meter at the 16-foot depth at SP62 during Eloise had a ratio of only 0.85. There does not seem to be any consistent pattern of change in velocity amplitude ratio with different sea states, and it seems most likely that the observed changes are due to changes in the response of the instrumentation systems.

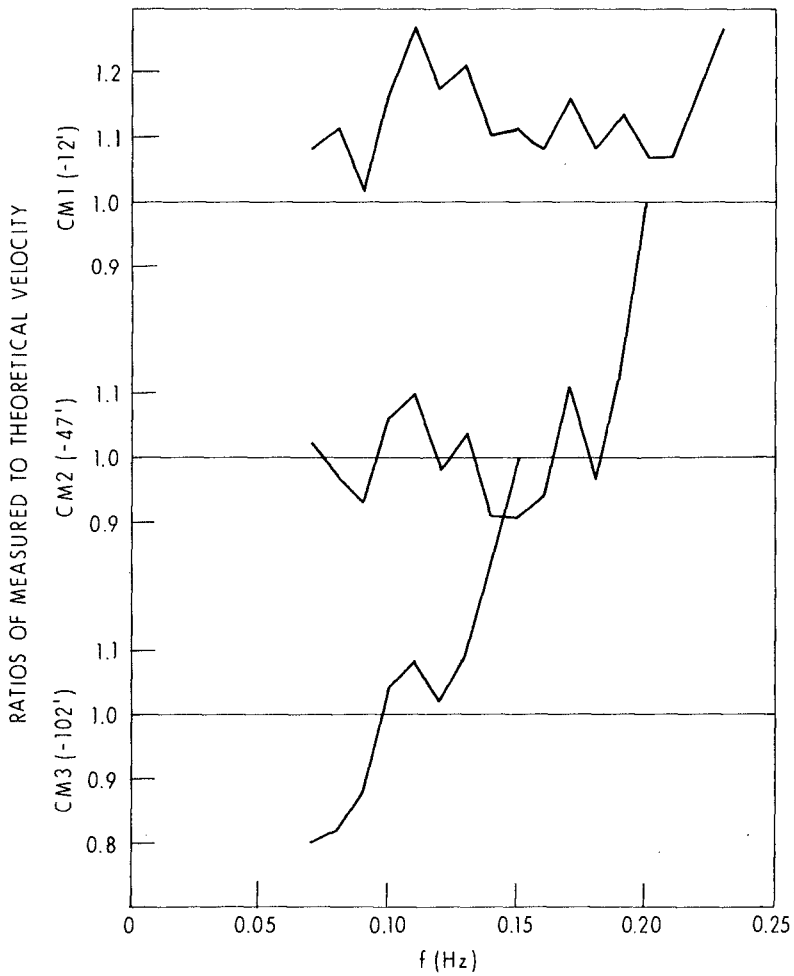
There have been several other field studies of wave kinematics in recent years and it is interesting to compare results. The results were not all presented as amplitude ratios, but they can easily be discussed in that form. Thornton and Krapohl (1974) used electromagnetic meters to measure the kinematics of a moderate swell off the coast of California. The amplitude ratio for the horizontal velocity was 0.94. Cavalieri et al. (1978) made measurements using electromagnetic meters mounted on a tower in the Adriatic Sea and found a ratio of 0.9. Battjes and Heteren (1980) used acoustic travel time meters in the North Sea and found a ratio of only 0.85. Our previously reported measurements during tropical storm Delia (Forristall et al., 1978) showed ratios of 1.1, decreasing to 0.9 at frequencies twice that of the spectral peak.

Our interpretation of the variability of results, both in our work and that of other investigators, is that present instrument



77-0291-32

Fig. 10 - Ratio of measured to theoretical velocity, SP62, 1200 CDT, September 7, 1974.



17-0291-33

Fig. 11 - Ratios between measured and theoretical velocity, EI331, 1800 CDT, September 22, 1975.

technology is capable of making field measurements of wave kinematics with an accuracy of about ten percent. This accuracy is sufficient to determine that unidirectional wave theories perform poorly in confused seas, but it is not sufficient to enable any conclusions to be made about the nonlinearity of storm waves.

The results also indicate that it is appropriate to make engineering calculations of forces on structures using wave kinematics derived from the superposition of directionally spread linear waves. A kinematic field for a given directional spectrum can be generated using a Monte Carlo simulation of wavelet phase angles and the fast Fourier transform, and we are presently developing and testing design programs using this approach.

ACKNOWLEDGEMENTS

R. C. Hamilton and T. E. Long contributed greatly to the success of the measurement program. A. M. Reece and M. E. Thro made helpful comments on an earlier version of the manuscript. The measurements were made by Shell Development Company with financial support from Amoco Production Research, Chevron Oil Field Research, Exxon Production Research, and Mobil Research and Development.

REFERENCES

- Battjes, J. A. and van Heteren, J. (1980), Field Measurements of Wind Wave Kinematics, 17th International Conference on Coastal Engineering, Sydney.
- Black, J. L. (1979), Hurricane Eloise Directional Wave Energy Spectra, Proceedings of the Eleventh Annual Offshore Technology Conference, Houston, OTC Paper 3594.
- Cardone, V. J., Pierson, W. J., and Ward, E. G. (1976), Hindcasting the Directional Spectra of Hurricane Generated Waves, J. Petrol. Tech., 25, 385-394.
- Cavaliere, L., Ewing, J. A., and Smith, N. D. (1978), Measurements of the Pressure and Velocity Field below Surface Waves, in Turbulent Fluxes through the Sea Surface, Wave Dynamics, and Prediction, Edited by A. Favre and K. Hasselmann, Plenum, New York.
- Corps of Engineers, Mobile District (1976), Post Disaster Report Hurricane Eloise, Mobile, Alabama, 89 pp.
- Forristall, G. Z. and Hamilton, R. C. (1978), Current Measurements in Support of Fixed Platform Design and Construction, Proceedings of a Working Conference on Current Measurement, University of Delaware, Newark.
- Forristall, G. Z., Ward, E. G., Cardone, V. J., and Borgman, L. E. (1978), The Directional Spectra and Kinematics of Surface Gravity

- Waves in Tropical Storm Delia, *J. Phys. Oceanog.*, 8, 888-909.
- Friese, L. V. (1977), Response of the Upper Ocean to Hurricane Eloise, Masters Thesis, Naval Postgraduate School, Monterey, California.
- Gunther, H., Rosenthal, W., Weare, T. J., Worthington, B. A., Hasselmann, K., and Ewing, J. A. (1979), A Hybrid Parametrical Wave Prediction Model, *J. Geophys. Res.*, 84, 5727-5738.
- Hasselmann, K., Ross, D. B., Muller, P., and Sell, W. (1976), A Parametrical Wave Prediction Model, *J. Phys. Oceanog.*, 6, 201-228.
- Hebert, P. J. (1976), North Atlantic Tropical Cyclones, 1975, *Mariner's Weather Log*, 20, 63-73.
- Hope, J. R. (1976), Annual Data and Verification Tabulation of Atlantic Tropical Cyclones, 1974, NOAA Technical Memorandum NWS NHC 1, Miami, Florida, 54 pp.
- Thornton, E. B. and Krapohl, R. F. (1974), Water Particle Velocities Measured under Ocean Waves, *J. Geophys. Res.*, 79, 847-852.
- Vincent, C. L. and Resio, D. T. (1979), A Discussion of Wave Prediction in the Northwest Atlantic Ocean, in *Marine Forecasting*, Edited by J. C. J. Nihoul, Elsevier, Amsterdam.
- Ward, E. G., Borgman, L. E., and Cardone, V. J. (1978), Statistics of Hurricane Waves in the Gulf of Mexico, Proceedings of the Tenth Annual Offshore Technology Conference, Houston, OTC Paper 3229.
- Withee, G. W. and Johnson, A. (1975), Buoy Observations during Hurricane Eloise, NOAA Data Buoy Office, Bay St. Louis, Mississippi.

PREDICTION OF THE SEVEREST SIGNIFICANT WAVE HEIGHT

Michel K. Ochi* and Joseph E. Whalen**

ABSTRACT

This paper presents a method to statistically estimate the severest sea state (significant wave height) from the observed data. For the estimation of extreme significant wave height, a precise representation of the data by a certain probability function is highly desirable. Since we do not have any specific technique to meet this requirement, this situation seriously affects the reliability of the current method of predicting the severest sea condition. The author's method is to express asymptotically the cumulative distribution of the significant wave height as a combination of an exponential and power of the significant wave height. The parameters involved are determined numerically by a nonlinear minimization procedure. The method is applied to available significant wave height data measured in the North Sea, the Canadian coast, and the U.S. coast. The results of the analysis show that the data are well represented by the proposed method over the entire range of the cumulative distribution.

INTRODUCTION

For the design of coastal and ocean structures, it is necessary to obtain the severity of sea over a period of time on the order of 50 years, sufficiently long enough to cover the lifetime of the structure. The severity of the sea is most commonly expressed in terms of significant wave height. Therefore, if the probability law which governs the significant wave height is found, then the statistical prediction of the severest sea in the long-term can be achieved.

It should be noted that the probability distribution function of the significant wave height is derived empirically from analysis of data accumulated over a certain period of time, and that there is no way to theoretically derive the probability distribution function, in contrast to the probability function applicable for wave height in a given sea severity. Observations (or measurements) of the significant wave height are usually made several times a day, each for 15 to 20

* Professor, University of Florida

** Senior Scientist, Operations Research, Inc.

minutes duration. Since the observations (or measurements) of the significant wave heights are made intermittently, the information on the sea severity is given as a discrete phenomenon, although in reality the sea severity is continuously changing with time.

The results of analysis made on available data have indicated that statistical properties of the significant wave height appear to follow the log-normal probability law, in general, but not to the extent that this probability law can be used for the estimation of extreme values. On the other hand, when the data are plotted on the Weibull probability paper, it is the general trend that the higher significant wave heights are fit reasonably well to the Weibull distribution, but the representation over the entire range of the significant wave height by the (two-parameter) Weibull distribution is substantially poor.

It should be noted that the data of severe seas (significant wave heights) are always sparse; on the order of one to two percent of the total number of observations are spread over the range of higher significant wave heights. Hence, the question always remains as to how reliable the prediction technique is if we estimate the extreme significant wave height by extending the line plotted on either the log-normal or the Weibull probability paper taking into account the higher significant wave heights which are extremely unreliable data.

For the estimation of extreme significant wave height, a precise representation of the data by a certain probability function is highly desirable. The precise representation implies that the data shall be represented by a probability function over the *entire* range of the cumulative distribution except data points of very high cumulative distribution such as 0.999 or higher due to the reason discussed in the foregoing paragraph.

In order to represent the measured data with sufficient accuracy for estimating extreme values, this paper presents a method to express the cumulative distribution function as a combination of an exponential and power of the significant wave height.

The method is applied to available significant wave height data measured in the North Sea, the Canadian coast, and the U.S. coast. The extreme significant wave heights expected in 50 years estimated by the proposed method are presented.

PROBABILITY DISTRIBUTION FUNCTION FOR THE SIGNIFICANT WAVE HEIGHT

For the probability density function applicable to the significant wave height, the Weibull distribution and the log-normal distribution have often been considered to date. The Weibull probability density function is given by,

$$f(x) = c\lambda^c x^{c-1} e^{-(\lambda x)^c} \quad 0 \leq x < \infty \quad (1)$$

where x is the significant wave height for the present problem, and c and λ are parameter to be determined from observed data. Since the probability density function given in (1) carries two parameters, it may be called the two-parameter Weibull distribution.

It has been claimed that some data of significant wave heights can be represented very well by the three-parameter Weibull distribution which is given by,

$$f(x) = c\lambda^c (x-a)^{c-1} e^{-\{\lambda(x-a)\}^c} \quad a \leq x < \infty \quad (2)$$

It is noted, however, that the three-parameter Weibull distribution carries the minimum non-zero value, a , as one of its parameters. If this is the case, it is not possible to explain the physical meaning of this minimum significant wave height associated with the distribution. The sea state of significant wave height zero, which represents the calm sea, is an important part of the distribution. The sample space of significant wave height has to be chosen between zero and ∞ for the probability distribution of the significant wave height. For this reason, it is not appropriate to use the three-parameter Weibull distribution for the analysis of the significant wave height data.

The log-normal probability function is another distribution that has been used to represent the statistical properties of the significant wave height. The density function is given by,

$$f(x) = \frac{1}{\sqrt{2\pi} \sigma x} e^{-\frac{(\ln x - \mu)^2}{2\sigma^2}} \quad 0 \leq x < \infty \quad (3)$$

where, μ and σ are parameters to be determined from the observed data.

An example of data of significant wave height measured at the location 53.5° N, 4° E in the North Sea is shown in Table 1 (Bouws 1978). A total of 5,412 measurements of significant wave heights were made in three years. This information implies that the significant wave heights were measured at every 5-hour interval, as an average. Hence, the data provide information on the significant wave height at 5-hour intervals, just to cover all severe sea conditions expected to occur at the site. It should be noted here that the observed (or measured) data of significant wave height obtained in a relatively long time interval may not provide sufficient information on severe seas that do not persist for a long period.

Figures 1 and 2 show the cumulative distribution function of the data given in Table 1 plotted on log-normal probability paper and Weibull probability paper, respectively. As can be seen in these figures, the data appear to follow the log-normal distribution for the cumulative distribution up to 0.99, and the data also may be represented by the Weibull probability distribution except for small significant wave heights.

Table 1 Significant wave height data obtained from measurements in the North Sea (from Bouws 1978)

SIGNIFICANT WAVE HEIGHT (M)	NUMBER OF OBSERVATIONS
0 - 0.5	1,280
0.5 - 1.0	1,549
1.0 - 1.5	1,088
1.5 - 2.0	628
2.0 - 2.5	402
2.5 - 3.0	192
3.0 - 3.5	115
3.5 - 4.0	63
4.0 - 4.5	38
4.5 - 5.0	18
5.0 - 5.5	21
5.5 - 6.0	7
6.0 - 6.5	8
6.5 - 7.0	2
7.0 - 7.5	1
TOTAL	5,412 in 3 Years

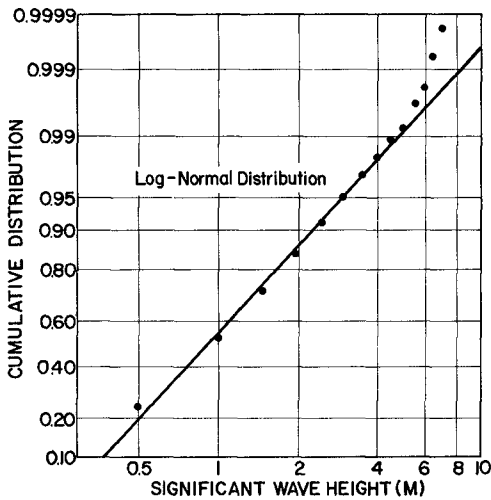


Figure 1 Cumulative distribution function of significant wave height plotted on log-normal probability paper (data from Bouws 1978)

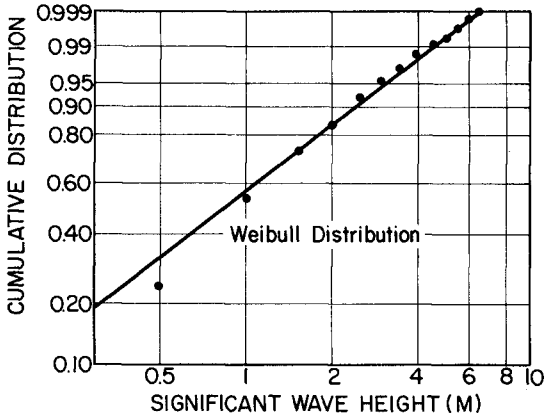


Figure 2 Cumulative distribution function of significant wave height plotted on Weibull paper (data from Bouws 1978)

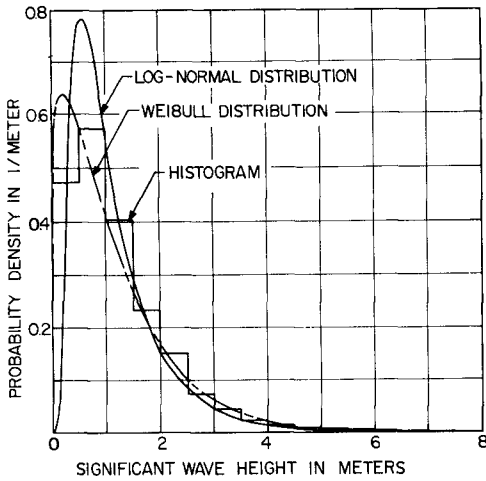


Figure 3 Comparison between histogram of significant wave height and log-normal and Weibull probability distributions (data from Bouws 1978)

In order to see the difference between the histogram constructed from the original data and the two probability functions, Figure 3 is prepared. As seen in this figure, the difference between Weibull probability function and the data is pronounced when the probability density functions and histogram are compared. It is noted that the Weibull probability paper is usually constructed by taking the logarithm of the cumulative distribution function twice. Hence, a small difference between data and the cumulative distribution function drawn on the Weibull probability paper may result in a substantial difference between the histogram and theoretical probability density function.

As another example, Figure 4 shows the comparison between the histogram of significant wave height and Weibull and log-normal probability density functions for the data observed at Tiner Point, Canada (Khanna and Andru 1974). The figure shows that the log-normal probability density function agrees well with the histogram over the entire range of significant wave height. On the other hand, the Weibull probability density function agrees well with the histogram for large significant wave heights, but the agreement is rather poor for small significant wave heights.

Although these examples show that the data are represented satisfactorily by the log-normal distribution, this may not always be the case. Some other significant wave data may be better fitted by the (two-dimensional) Weibull distribution depending on the geographical location, depth of the water, frequency of occurrence of the storm, etc. In principle, as was mentioned earlier, there is no scientific basis for selecting any particular probability distribution to characterize the significant wave height.

It may be noted, however, that the representation of significant wave height by the log-normal probability distribution results in a significant benefit for the derivation of the joint probability distribution of the significant wave height and wave period (Ochi 1978).

Since our goal is to statistically predict the extreme significant wave height from the observed data, a precise representation of the data by a certain probability function is highly desirable. However, we should consider the fact that the data of severe significant wave heights are always sparse, and hence the frequency of occurrence is extremely unreliable. For example, the data given in Table 1 show that the largest significant wave height of 7-7.5 meters was observed once in three years, and that 99 percent of the data are significant wave heights less than 4.5 meters. This implies that, on the order of one percent of the total number of observations are spread over the range of higher significant wave heights, which are most interesting for us from the view point of statistical estimation.

It is appropriate, therefore, to establish a probability function which represents the significant wave height data over the entire range for the cumulative distribution up to about 0.99. Then, the extreme significant wave height will be estimated based on this probability function. For this, let us express the cumulative distribution function

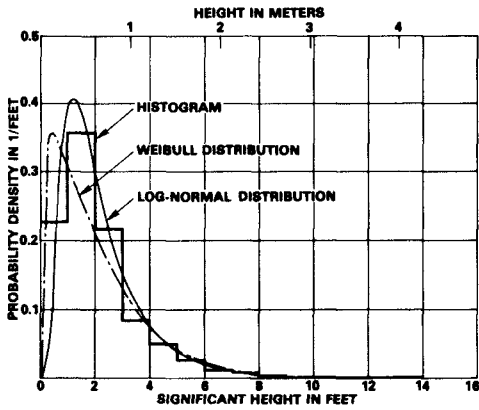


Figure 4 Comparison between histogram of significant wave height and log-normal and Weibull probability density functions (data from Khanna and Andru 1974)

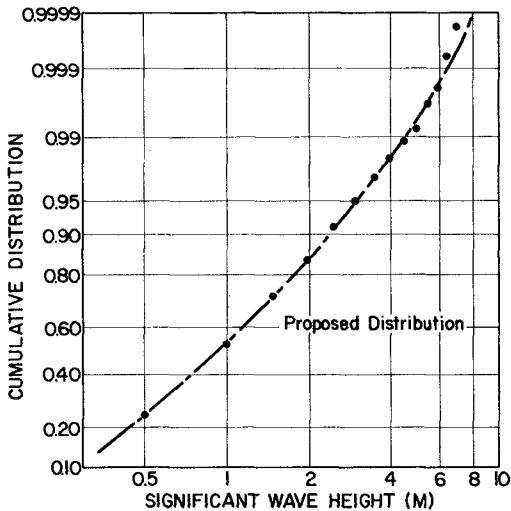


Figure 5 Cumulative distribution function based on Equation (6) plotted on log-normal probability paper (data from Bouws 1978)

in the following form,

$$F(x) = 1 - e^{-q(x)} \quad (4)$$

where, $q(x)$ is a monotonically increasing, real-valued function. Then, it can be proved that, for a large number of observations, the probable extreme value in n -observations, denoted by \bar{Y}_n , is given as the inverse function of $q(x)$. That is,

$$\bar{Y}_n = q^{-1}(\ln n) \quad (5)$$

The probable extreme value can also be obtained graphically by equating the return period, $1/\{1 - F(x)\}$, to the number of waves expected in a specified period of time, 10 years, 50 years, etc.

The authors' method is to express $q(x)$ as a combination of an exponential and power of the significant wave height. That is,

$$q(x) = a x^m \exp\{-px^k\} \quad (6)$$

The parameters involved in $q(x)$ are determined numerically by a nonlinear minimization procedure. The form used in the procedure is given by,

$$G = \ln\{-\ln(1 - F)\} = \ln a + m \ln x - px^k \quad (7)$$

The parameters are optimized such that the sum of the difference between G and the corresponding observed values squared is minimal. The procedure is iterative, and thus requires a single set of priori estimates for the parameters. It was found through results of many numerical examples, the value of each parameter converges to a fixed value, individually, irrespective of the priori estimates, if sufficient many number of iterations, approximately 100 iterations, are carried out.

As an example, the method is applied to significant wave height data observed in the North Sea. For this example, values of the four parameters involved in (6) are obtained as,

$$\begin{aligned} a &= 0.908 \\ m &= 1.101 \\ p &= 0.181 \\ k &= -1.328 \end{aligned}$$

The cumulative distribution function evaluated by using these values are plotted on the log-normal probability paper as shown in Figure 5 together with data points, while Figure 6 shows those plotted on the Weibull paper. As can be seen in these figures, the data are

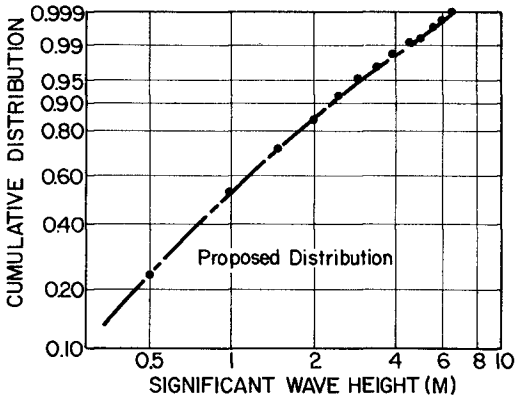


Figure 6 Cumulative distribution function based on Equation (6) plotted on Weibull probability paper (data from Bauws 1978)

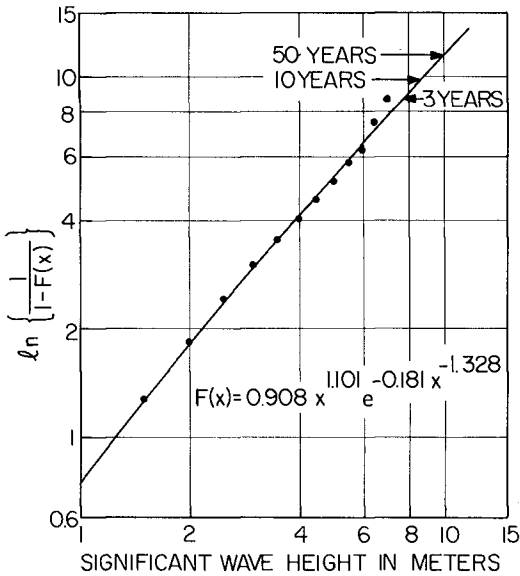


Figure 7 Prediction of extreme significant wave height by using the proposed cumulative distribution function (data from Bauws 1978)

well represented by the proposed probability distribution over the entire range of the cumulative distribution function. It can be seen, from these figures together with the results shown in Figures 1 and 2, that the log-normal distribution substantially overestimates, while the Weibull distribution underestimates the magnitude of the extreme significant wave height for this example.

Figure 7 shows the return period in the logarithmic scale. Given that 5,412 observations are made in 3 years, the magnitude of significant wave height most likely to occur in 10 years and 50 years are estimated from the figure as 8.8 meters and 10.0 meters, respectively.

As another example, presentations similar to those shown in Figures 5 and 6 are made using the significant wave height data observed at Tiner Point, Canada, and results are shown in Figures 8 and 9. Again, the data are well represented by the proposed distribution over the entire range. Given that 2,304 observations were made in one year, the magnitudes of extreme significant wave height expected in 10 years and 50 years are estimated from Figure 10 as 19.0 ft (5.8 meters) and 22.2 ft (6.8 meters), respectively.

Figure 11 shows another example of application using the significant wave height data observed at Port Hueneme, California (Thompson 1977). As can be seen in the figure, the data follow fairly well the log-normal distribution; however, the log-normal distribution appears to underestimate the extreme significant wave height for this example. The data are represented well by the cumulative distribution function obtained by the proposed method. The extreme significant wave heights estimated by the proposed method are shown in Figure 12.

CONCLUSIONS

This paper discusses a method to statistically predict the severest sea state (significant wave height) from the observed data. For the estimation of extreme significant wave height, a precise representation of the data by a certain probability function is highly desirable. For the probability distribution function applicable to the significant wave height, the log-normal distribution and the Weibull distribution have often been considered to date. Although it is a general trend that the data appear to follow the log-normal probability law, but not to the extent that this probability law can be used for the estimation of extreme values. In principle, there is no scientific basis for selecting any particular probability distribution (either the log-normal or the Weibull) to characterize the significant wave height.

The authors' method is to express asymptotically the cumulative distribution function of the significant wave height as a combination of an exponential and power of the significant wave height. The parameters involved are determined numerically by a nonlinear minimization procedure.

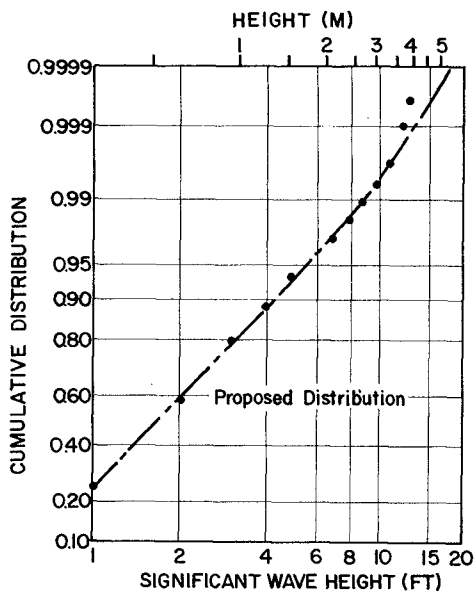


Figure 8 Cumulative distribution function based on Equation (6) plotted on log-normal probability paper (data from Khanna and Andru 1974)

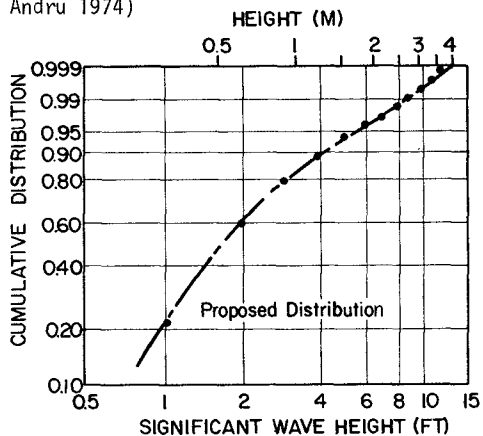


Figure 9 Cumulative distribution function based on Equation (6) plotted on Weibull probability paper (data from Khanna and Andru 1974)

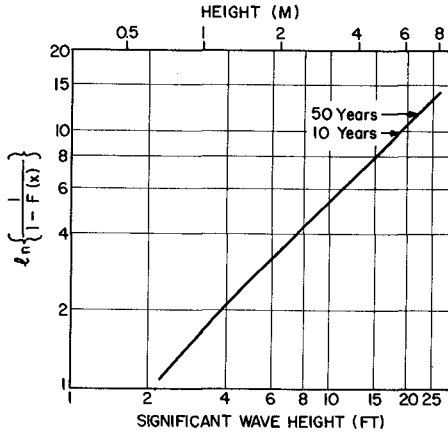


Figure 10 Prediction of extreme significant wave height by using the proposed cumulative distribution function (data from Khanna and Andru 1974)

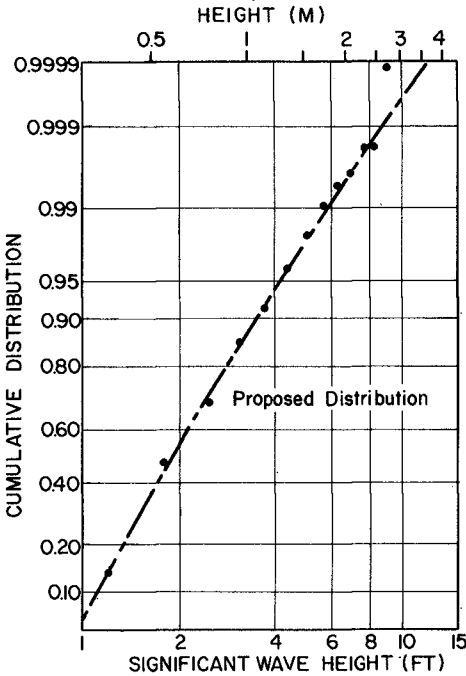


Figure 11 Cumulative distribution function based on Equation (6) plotted on log-normal probability paper (data from Thompson 1977)

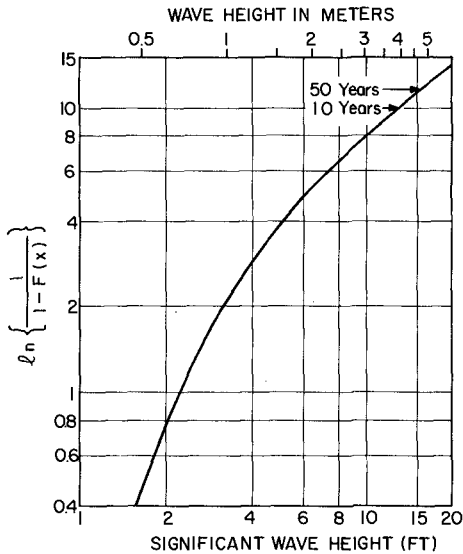


Figure 12 Prediction of extreme significant wave height by using the proposed cumulative distribution function (data from Thompson 1977)

The proposed method is applied to significant wave height data obtained in the North Sea, Tina Point, Canada, and Port Hueneme, California. The results of analysis show that the data are well represented by the proposed method over the entire range of the cumulative distribution. Thus, it is believed that a more accurate estimation of the severest sea state (significant wave height) can be achieved based on the proposed cumulative distribution function.

REFERENCES

- Bouws, E., (1979): Wind and Wave Climate in the Netherlands Sector of the North Sea Between 53° and 54° North Latitude. Koninkrijk Netherlands Meteorologisch Inst., Report 78-9.
- Khanna, J. and Andru, P., (1974): Lifetime Wave Height for Saint John Deep Canada. Proc. Symp. on Ocean Wave Measure. and Analysis, Vol 1, pp 301-319.
- Ochi, M. K., (1978): On Long-Term Statistics for Ocean and Coastal Waves. Proc. 16th Conf. on Coastal Eng., Vol 1, pp 59-75.
- Thompson, E. F., (1977): Wave Climate at Selected Locations Along U.S. Coasts. Tech. Report 77-1, Coastal Eng. Res. Center.

CHAPTER 37

PREDICTION OF DOMINANT WAVE PROPERTIES AHEAD OF HURRICANES

by

Omar H. Shemdin¹

ABSTRACT

A method is proposed for predicting properties of dominant waves in the forward region of hurricanes where the waves are found to propagate predominately in the direction of hurricane forward travel. An extended fetch concept is used in which each wave component is exposed to the action of wind over a fetch length that is determined by wave group speed, hurricane forward speed, and location with respect to eye. Maximum extended fetches are found to the right of the eye (with respect to direction of hurricane travel) in the northern hemisphere. The method correctly predicts dominant wave frequencies and significant wave heights. The prediction method utilizes recently developed concepts in wave generation and energy transfer among wave spectral components; the predicted values are compared favorably with observations

Introduction

There is substantial interest in techniques that can predict properties of waves generated by hurricanes. Considerable damage results in the coastal zone when hurricane-generated waves impact a coast even when the hurricane eye is located far offshore. The damage is most dramatic when the hurricane eye crosses the shoreline (land fall) because of flooding generated by both storm surge and wave-induced set-up. The hurricane windfield is complex but has been successfully described in terms of a translating vortex. For the purpose of this investigation it is assumed that the wind field can be adequately described and that information on the wind field is available as input. This paper outlines a procedure which uses the wind field as input to predict properties of dominant waves which are found ahead of hurricanes (see King and Shemdin, 1978).

Up to 1970 the available hurricane wave measurements were not of sufficient quantity or quality to promote either understanding of the wave generation process or to achieve verification of the empirical predictive techniques available. An organized program was instituted by a consortium of oil companies in the late 60's and early 70's to amend this deficiency (see Ward, 1974). The results were used to develop and verify models that predict the significant wave height (Bea, 1974) and others that provide two-dimensional wave spectral properties (Cardone, Pierson and Ward, 1976).

¹Jet Propulsion Laboratory, California Institute of Technology, Pasadena, California, and University of Florida, Gainesville, Florida.

Additional valuable data sets on several hurricanes were collected by buoys operated by the NOAA-Data Buoy Office and by our airborne Synthetic Aperture Radar (SAR) which was operated by Jet Propulsion Laboratory (JPL). These data sets were reviewed by King and Shemdin (1979); a condensed summary of measured hurricane parameters is given in Table 1.

The numerical wave spectral model of Cardone, Pierson and Ward (1976) has been shown to predict satisfactorily the significant wave height in hurricanes. Because of the dearth of directional wave measurements the model wave direction predictions have not been verified completely by comparison with measurements. Such measurements have only become available recently through the use of airborne synthetic aperture radars such as discussed by King and Shemdin (1978). Empirical models for predicting the significant wave height have also been advanced by Bretschneider (1972) and Ross (see Cardone and Ross, 1979). The Ross model does not recognize the influence of hurricane forward speed in wave generation and for that reason it is limited in application to very slow moving hurricanes. The Bretschneider model does account for the hurricane forward speed; however, the model is strictly empirical and does not incorporate recent advances in wave generation physics and consequently does not provide insight on the wave generation process in hurricanes.

The purpose of this paper is to propose a method that adequately predicts the frequency and significant wave height of dominant waves which are found in the forward region of the hurricane (ahead of the eye in the direction of forward travel). The model is consistent with known mechanisms of wave generation and incorporates the hurricane forward speed as a central factor in our ability to correctly predict dominant wave properties in moving hurricanes.

Wave Prediction Model

King and Shemdin (1978) presented SAR images showing waves in different hurricane sectors for several hurricanes. The wave images contained valuable information on dominant wave lengths and directions. A striking asymmetry was observed in the wave field when the wave images were assembled in location with respect to the hurricane eye. The asymmetric wave generation was attributed to two mechanisms: (1) the cyclonic wind speed is greater on the right hand side of a moving hurricane (in the northern hemisphere), and (2) the waves generated on the right side of the moving storm propagate in the same general direction as the storm and therefore remain in the wind generation zone longer than those generated on the left side of the storm. The residence time of a wave component in the wind generation area to the right of the storm is inversely proportional to the difference between the wave group velocity in the direction of hurricane forward travel and the hurricane forward speed. In a wind generation setting various wave frequencies are generated in various directions. The waves which propagate in the same direction as that of hurricanes forward travel are

Table 1. Measured Hurricane Parameters

Hurricane	1 f_m (Hz)	2 V (m/s)	3 U_m (m/s)	4 r (km)	5 D (hrs)
PT-35 ^a	.067	21	42	16	0
Camille ^{b,c,d}	.072	5	64	20	24
Eloise ^{e,f}	.090	6.8	35	27	0
Belle I ^{f,g}	.075	8.8	31	30	16
Belle II ^g	.075	11.3	27	30	0
Emmy I ^{h,i}	.077	4.2	22	32	0
Emmy II ^{h,i}	.085	7.1	24	35	18
Frances ^{h,i}	.080	5.8	32	40	16
Gloria I ^{h,i}	.106	3.1	23	35	12
Gloria II ^{h,i}	.075	7.6	34	35	12
Anita ^j	.090	4.2	37	20	24

a - Arakawa & Suda (1953)

b - Cardone, Pierson and Ward (1976)

c - Patterson (1974)

d - Unpublished data from U.S. Army Corps of Engineers

e - Withee and Johnson (1975)

f - Cardone and Ross (1979)

g - Johnson and Speer (1978)

h - SAR spectral analysis data

i - Unpublished data from NOAA - NHEML

j - Johnson and Renwick (1978)

1. Dominant wave frequency

2. Speed of hurricane forward travel

3. Maximum hurricane wind speed reduced to 10 m elevation

4. Eye radius

5. Duration of linear travel

expected to grow fastest. Of those the wave spectral components which travel slower or equal to the storm forward speed grow rapidly and saturate in the wave generation zone. Very low frequency waves travel faster than the storm and consequently have small residence duration in the wind generation zone. The intermediate wave frequencies which correspond to wave group velocities slightly larger than the hurricane forward speed remain in the wind generation zone long enough to achieve substantial wave heights. These waves eventually overcome the hurricane intense region and appear as dominant waves ahead of the hurricane as shown in the images presented by King and Shemdin (1978). It was shown that these dominant waves have group velocities 1.3 to 2.5 times greater than the hurricane forward speeds.

The above observations also suggest that the dominant waves ahead of the hurricane are primarily generated by a fetch system to the right of the eye that translates with the speed of the storm. In a stationary fetch situation the duration of a wave component in the fetch area is related to the fetch length by the wave group velocity. When a fetch translates in the direction of wave travel the duration of a wave in the fetch area is determined by the difference between the wave group velocity and the forward speed of the fetch.

In a fetch-limited wave generation setting Hasselmann et al (1973) obtained a relationship for the dominant frequency, f_m , in terms of fetch length, X , and wind speed at 10m above the mean sea level, U_{10} , given below:

$$f_m = 3.5 \left(\frac{g^2}{X U_{10}} \right)^{1/3}, \quad (1)$$

where g is gravitational acceleration. For the same conditions, they found the mean squared surface displacement, ϵ , to be:

$$\epsilon = 1.6 \times 10^{-7} \left(\frac{X U_{10}^2}{g} \right), \quad (2)$$

where ϵ is related to the significant wave height, H_s , by

$$H_s = 4 \sqrt{\epsilon}. \quad (3)$$

In a translating fetch setting such as in a hurricane the following transformation is proposed:

$$X U_{10} = \left(\frac{K U_m}{1 - (V/C_g)} \right), \quad (4)$$

where U_m is the maximum hurricane wind speed reduced to 10m elevation, K is an equivalent fetch which is established empirically, V is the hurricane forward speed and C_g is the wave group velocity in the direction of hurricane forward travel. Substituting Equation (4) into Equation (3) yields:

$$f_m = 3.5 \left(\frac{g^2 - 4\pi f_m g V}{K U_m} \right)^{1/3} \quad (5)$$

King and Shemdin (1979) used the available data, from several hurricanes, on f_m , V and U_m , shown in Table 1, to establish that an equilibrium wave generation condition exists in hurricanes when the hurricane forward travel remains along a linear path over a period specified by time required for waves to propagate through the fetch area. For those hurricanes satisfying the equilibrium condition they empirically determined the equivalent fetch length, K , to be 80 Km. Using this value of K in Equation (5) it was possible to predict f_m from available values of U and U_m . As a test of this procedure, predicted f_m values were compared with observed f_m values as shown in Figure 1. As can be seen the agreement is satisfactory for equilibrium hurricanes and unsatisfactory for non-equilibrium hurricanes.

The wave prediction model is now extended to predict the significant wave height. Substituting Equation (4) into Equation (2) and adopting a scaling factor, α , between U_{10} and U_m ($U_{10} = \alpha U_m$):

$$\epsilon = 1.6 \times 10^{-7} \left(\frac{\alpha U_m^2 K}{g - 4\pi f_m V} \right) \quad (6)$$

Alternatively, ϵ may be expressed in terms of the dominant frequency, f_m ,

$$\epsilon = 6.86 \times 10^{-6} \left(\frac{\alpha U_m^2 K}{f_m^3} \right) \quad (7)$$

Predicted significant wave height, H_s , values derived from Equations (6) and (7) are compared with observed values in the following section.

Comparison with Observations

The comparison between f_m values predicted from the hurricane wind parameters and those observed f_m are shown in Figure 1. The favorable comparison substantiates the relatively simple process with which waves are generated in a translating hurricane wind field. The prediction model extends the usefulness of wave length measurements obtained from airborne SAR images to provide estimates of the significant wave height ahead of the hurricane.

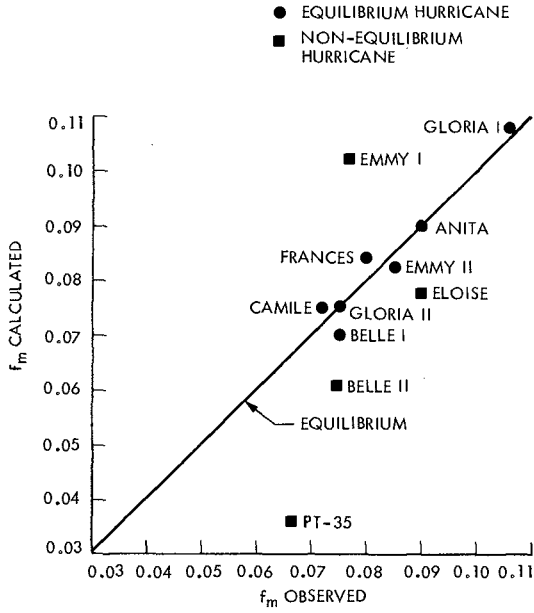


Figure 1. Comparison of observed and predicted f_m values of dominant waves.

The available observations for verifying Equation (7) are summarized in Table 2; only equilibrium hurricanes are included in this table. As shown, significant wave height measurements are available only for three of the seven equilibrium hurricanes listed. The observed wave heights are those measured with NOAA-NDBO buoys. The observed f_m values refer to direct measurements from the buoys or inferred from wave length values in aircraft SAR images. The SAR does not provide wave height measurements. The H_s values predicted with Equation (7) using observed f_m and U_m values are also shown in Table 2. The scaling parameter α was assumed to be one. The H_s comparison is displayed graphically in Figure 2. Because of the limited number of observations no further analysis was pursued to determine the optimum scaling factor α . Clearly, this will become useful as more wave height measurements become available. The favorable comparison shown in Figure 2 provides substantiation for the usefulness of the proposed method for predicting the significant wave height of the dominant waves ahead of the hurricanes.

Summary and Conclusions

The insight gained from the observed asymmetrical distribution of waves in the various hurricane sectors and the proposed model for describing and predicting the dominant wave properties ahead of hurricanes can be summarized in the following:

1. The dominant and most energetic waves generated in a translating hurricane wind field are found immediately ahead of the storm. These waves propagate in the same general direction as that of hurricane forward travel.
2. The dominant waves are generated by a translating fetch system that is of order 80 km in length and located to the right of the hurricane eye (in the northern hemisphere). The fetch translates with the speed of hurricane forward travel.
3. The hurricane forward travel speed plays a central role in determining the properties of the dominant waves. Fast traveling hurricanes are expected to generate longer and more energetic waves ahead of the hurricane compared to stationary hurricanes.
4. The above description of wave generation is substantiated by favorable comparisons between predicted and measured dominant wave frequencies ahead of hurricanes. The comparisons are only favorable in equilibrium hurricanes.
5. The proposed model predicts the significant wave height, H_s , of dominant waves from either the observed or predicted values of the dominant frequency, f_m . The model is considered valid only for equilibrium hurricanes.

TABLE 2

Comparison of predicted and observed H_S values for equilibrium hurricanes.

Hurricane	Observed Values			Predicted H_S (m) from Eq. (7)*
	$f_m(H_z)$	U_m (m/s)	H_S (m)	
Camille	0.072	64	13.8	13.6
Belle I	0.075	31	7.5	8.9
Emmy II	0.085	24		6.5
Frances	0.080	32		8.2
Gloria I	0.106	23		4.6
Gloria II	0.075	34		9.3
Anita	0.090	37	6.7	7.4

* $\alpha = 1$ assumed in these calculations.

6. The proposed model is suitable for statistical studies of dominant wave properties in hurricanes. It can be applied productively when complex and costly numerical procedures are not needed such as in predicting H_s or f_m values of dominant waves. Detailed directional wave properties in various sectors of the hurricane require detailed numerical procedures, however.

ACKNOWLEDGEMENT

The research described in this paper was carried out at the Jet Propulsion Laboratory, California Institute of Technology, under NASA Contract NAS 7-100. The author acknowledges the valuable support of Dr. R. Sheets of the NOAA-National Hurricane and Environmental Meteorological Laboratory.

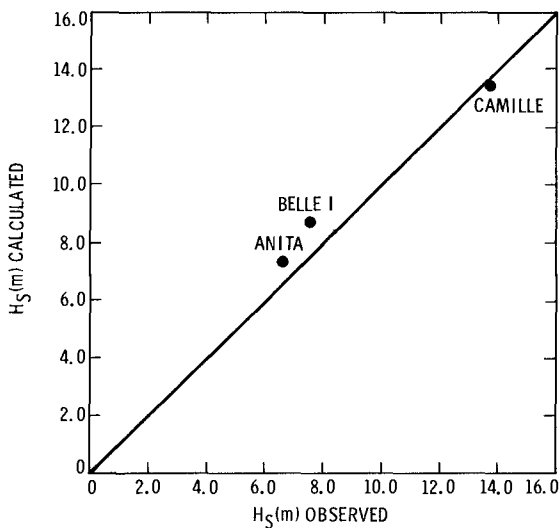


Figure 2. Comparison of observed and predicted H_s values for dominant waves.

REFERENCES

- Arakawa, H. and K. Suda, Analysis of Wind Waves and Swill over the Sea to the East of Japan during the Typhoon of September 16, 1935, Monthly Weather Review, Vol. 81, no. 2, 31-37, 1953.
- Bea, R. G., Gulf of Mexico Hurricane Wave Heights, Proc. of 6th Annual Offshore Technology Conf., Houston, Texas, 1974.
- Bretschneider, C. L., A Non-dimensional Stationary Hurricane Wave Model, Proc. of 4th Annual Offshore Technology Conf., Houston, Texas, 1972.
- Cardone, V. J., W. J. Pierson and E. G. Ward, Hindcasting the Directional Spectra of Hurricane Generated Waves, J. of Petroleum Tech., 28, 385-394, 1976.
- Cardone, V. J. and D. B. Ross, State-of-the-Art Wave Prediction Methods and Data Requirements, Ocean Wave Climate, edited by M. D. Earle and A. Malahoff, Plenum Publishing Corp., 1979.
- Hasselmann, K., T. P. Barnett, E. Bouws, H. Carlson, D. E. Cartwright, K. Enke, J. A. Ewing, H. Gienapp, D. E. Hasselmann, P. Kruseman, A. Meerburg, P. Muller, D. J. Olbers, K. Richter, W. Sell, and H. Walden, Measurements of Wind-Wave Growth and Swell Decay during the Joint North Sea Wave Project (JONSWAP), Deutsche Hydrogr. Zeits., Reihe A (B⁰), Nr. 12, Hamburg, 1973.
- Johnson, A., and G. A. Speer, Data Report: Buoy Observations During Hurricane Belle, August 1976, Report from the NOAA Data Buoy Office, National Space Technology Laboratories, NSTL Station, Mississippi 39529, 1978.
- Johnson, A., and S. M. Renwick, Data Report: Buoy Observations During Hurricanes Anita and Babe, 1977, Report from the NOAA Data Buoy Office, National Space Technology Laboratories, NSTL Station, Mississippi, 39529, 1978.
- King, D. B. and O. H. Shemdin, Radar Observations of Hurricane Wave Directions, Proc. of 16th International Conference on Coastal Engineering, Hamburg, Germany, 1978.
- King, D. B. and O. H. Shemdin, Equilibrium Wave Generation in Hurricanes, submitted to JGR, 1979.
- Patterson, M. M., Oceanographic Data from Hurricane Camille, Proc. of 6th Annual Offshore Technology Conf., Houston, Texas, 1974.
- Ward, E. G., Ocean Data Gathering Program - An Overview, Proc. of 6th Annual Offshore Technology Conf., Houston, Texas, 1974.
- Withee, G. W. and A. Johnson Jr., Data Report: Buoy Observations During Hurricane Eloise (September 19 to October 11, 1975), report from the NOAA Data Buoy Office, Environmental Sciences Division, Bay St. Louis, Mississippi 39520, 1975.

LONG PERIOD DISTURBANCES DUE TO WAVE GROUPS
by
E.C.BOWERS, Ph.D, HYDRAULICS RESEARCH STATION, ENGLAND

SUMMARY

Measurements of long period disturbances associated with wave groups are compared with theoretical predictions. The experiments were carried out in a wave flume with an absorbing beach at one end. Tests were carried out using both regular wave groups (made up of two wave frequencies so that groups occur at a single beat frequency) and a random sea. The theoretical predictions are based on a Stokes expansion of the basic wave equations up to second order. The results are consistent with having three components in the long period disturbance at wave group periods. The first is set-down beneath wave groups, a disturbance that is tied to the wave groups travelling towards the beach. The second is a surf beat, a free long wave propagating back from the beach that is generated by reflection of the set-down from the beach. The third component is a secondary wave, a free long wave propagating towards the beach, that is generated by the wave-maker when it is only programmed to produce the primary wave system without its associated set-down beneath wave groups. The experimental results show that this third component can be minimised for both regular wave groups and a random sea by adding an appropriate long period movement of the wave-maker. Also, results are presented that indicate that long cycles of truly random waves, lasting many hours in model terms, are required to obtain reliable estimates of the effect of wave grouping on marine structures.

1 INTRODUCTION

Long wave disturbances with periods of the order of minutes are of importance to large moored vessels since the natural periods of horizontal oscillation of such vessels on their moorings are typically within the range of 30 seconds to 2 minutes depending on the displacement of the vessel and the stiffness of the moorings. As hydrodynamic damping of these oscillations is low, a significant resonant response of the vessel on its moorings can be produced by relatively small amplitude long period wave motions. Such disturbances with average heights of 0.3m to 0.4m are known to cause moorings to part (Hydraulics Research Station Report, 1976 and Stammers et.al., 1977). The problem can be compounded for vessels moored inside harbours when long period wave motions are amplified through harbour resonance.

One source of long wave energy, described by Longuet-Higgins and Stewart (1964) arises from disturbances generated by wave grouping. A group of large waves will tend to cause a depression in the mean water level with a corresponding rise in level between groups of large waves. This effect, sometimes known as set-down beneath wave groups, has a periodicity that is associated with the groups but it differs from a free long wave because it is tied to the wave groups. Therefore, it propagates at the group velocity which is less than the phase velocity of a free long wave of the same period as the set-down. Even so, it has been shown both theoretically and experimentally by Bowers (1977) that set-down behaves much like an ordinary long wave when it excites the resonant modes of harbours. This result indicates that in situations where wave diffraction occurs, the energy contained in disturbances that are tied to the wave envelope can be released as free long waves. This is similar to the effect described by Biesel (1966) where diffraction of a regular wave around a breakwater is accompanied by the emission of free waves at twice the regular wave frequency. The energy for these free waves, clearly visible in the shelter of the breakwater, comes from the second order disturbances that cause the regular wave to have sharper crests and more shallow troughs than a sine wave, ie disturbances at twice the primary frequency that are tied to the waves incident on the breakwater.

Tucker (1950) reported a correlation, which occurred off a beach in Cornwall, between fluctuations of period of the order of minutes and the envelope of incoming waves. This correlation occurred with a depression in the long wave lagging behind a group of high waves by 4 to 5 minutes. It was suggested by Longuet-Higgins and Stewart (1964) that the time lag in these long waves or surf beats correspond to the time taken for the ordinary waves with their associated set-down beneath wave groups to propagate from the wave recorder position into the breaker zone and for the set-down to be reflected back past the recorder as free long waves. This mechanism of surf beat generation is consistent with the experimental results reported in this paper. It is to be expected that in many situations part of the energy in the incoming set-down will be trapped by the coastline in the form of edge waves (Gallagher, 1971; Bowen and Guza, 1978).

In physical model studies of harbours and moored ships a wave generator which produces a good representation of the primary wave system is used to produce irregular waves. Since this wave system is irregular it naturally contains wave groups and therefore it should also contain set-down beneath wave groups. If the wave generator is not programmed to produce this set-down then it can be appreciated that the expected long period water particle movement will not occur. Experiments carried out as part of the research programme of the Hydraulics Research Station (Bowers, 1976 and 1977) have demonstrated that the result of not programming the wave generator to produce set-down is to introduce long waves with the same period and approximately the same amplitude as set-down. These secondary long waves arise so that their water particle movement near the wave-maker tends to cancel the water particle movement of set-down in such a way that the boundary condition of no long period movement on the face of the wave-maker is satisfied. This mechanism of secondary wave generation is similar to that reported by Fontanet (1961). As the primary wave system propagates away from the generator it carries with it the set-down associated with wave groups and propagating with the system are secondary long waves. As mentioned before, set-down propagates more slowly than the free secondary long waves. As they are exactly out of phase at the wave generator they will gradually come into phase with one another with increasing distance from the generator. As distance increases further the two will again go out of phase with one another, and so on. Thus, in physical models the response of harbours and moored ships sensitive to long period disturbances could depend on their distance from the wave-maker. For this reason a programme of research was started at HRS into methods of adding in the necessary movement of the wave-maker to produce set-down at the generator. By this means it should be possible to minimise secondary long waves from the generator

Summarising, we see that wave diffraction, wave breaking and model wave generation are three mechanisms whereby free long waves are produced in irregular seas. It is a description of an effort to minimise the third kind, free secondary long waves produced by the wave-maker, that forms the main body of this paper.

2 THEORETICAL MODEL

The basic equation describing irrotational motions is

$$\nabla^2 \phi = 0 \quad \text{.....(1)}$$

Here, water particle motion in the vertical x, z plane of a right handed orthogonal co-ordinate system with velocity \underline{v} (horizontal component u and vertical component w) is related to the velocity potential ϕ by

$$\underline{v} = (u, w) = -\nabla\phi$$

The boundary conditions to be satisfied by surface waves are, on the bottom ($z = -d$)

$$w = 0 \quad \text{.....(2)}$$

on the free surface ($z = \eta$)

$$\eta_t + u\eta_x - w = 0 \quad \text{.....(3)}$$

$$\frac{1}{2} v^2 + g\eta - \phi_t = 0 \quad \text{.....(4)}$$

Here, ϕ_t indicates the partial derivative of ϕ with respect to time with corresponding meanings for the other variables with a suffix

The usual assumption made in describing surface waves is that the product terms in (3) and (4) are small in comparison with the other terms in the equations. Thus, the following set of equations is obtained

$$\nabla^2 \phi^{(1)} = 0 \quad \dots(5)$$

where

$$\underline{v}^{(1)} = (u^{(1)}, 0, w^{(1)}) = -\nabla \phi^{(1)}$$

and the boundary conditions are,

on $z = -d$

$$w^{(1)} = 0 \quad \dots(6)$$

on $z = 0$

$$\eta_t^{(1)} - w^{(1)} = 0 \quad \dots(7)$$

$$g\eta^{(1)} - \phi_t^{(1)} = 0 \quad \dots(8)$$

(5) to (8) are the first order set of equations in a Stokes expansion of the basic equations (1) to (4). This is why the variables have been given a super script of one.

To second order we obtain

$$\nabla^2 \phi^{(2)} \approx 0 \quad \dots(9)$$

where the boundary conditions are

on $z = -d$

$$-\phi_z^{(2)} = 0 \quad \dots(10)$$

on $z = 0$

$$\phi_{tt}^{(2)} + g\phi_z^{(2)} = \eta^{(1)} (w_{tt}^{(1)} + gw_z^{(1)}) + 2\underline{v}^{(1)} \cdot \underline{v}_t^{(1)} \quad \dots(11)$$

Here, (11) is obtained by expanding (3) and (4) to second order and eliminating the second order surface elevation

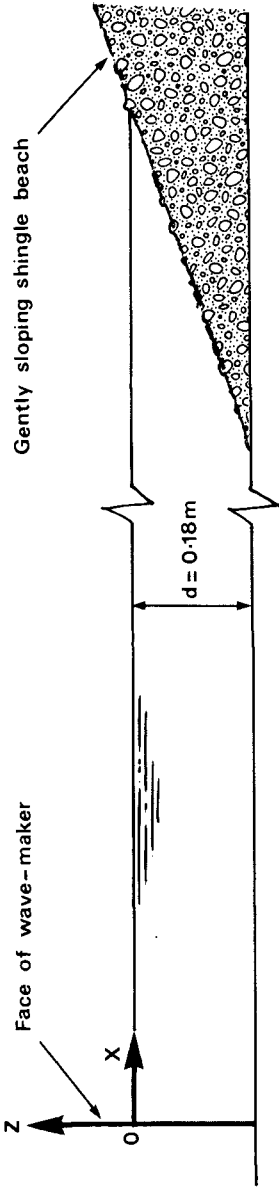


Fig 1 Experimental layout

3 EXPERIMENTAL AND THEORETICAL RESULTS FOR REGULAR WAVE GROUPS

The experimental layout (Fig 1) consisted of a wave flume about 7m long, 0.6m wide and 0.18m deep. To establish the feasibility of generating set-down with the wave-maker it was decided to work with regular wave groups. The primary wave system consisted of two frequencies (f_1 and f_2) so that wave groups occurred at a single beat frequency ($f'' = f_2 - f_1$). Wave heights were measured with twin wire wave probes and the horizontal movement of the face of the piston type wave-maker was measured with a transducer. The data were analysed with a fast Fourier transform (FFT) computer program to give spectra of the waves and the wave-maker. The three peaks of interest in the spectra occur at the difference frequency (f'') and at the primary wave frequencies (f_1 and f_2). The amplitude (a) of each component was obtained from the area (A) under each peak by using

$$\frac{1}{2} a^2 = A$$

It was established that measurements were accurate to within 0.2mm. The beach at the end of the flume resulted in reflection coefficients of less than 10% for the primary wave system so that the assumption that the primary system is purely progressive is a reasonable one. Equations (5) to (8) can be used to give a mathematical representation of the two progressive primary waves.

3.1 Progressive secondary wave system

To second order (9) to (11) can be used to solve for $\phi_s^{(2)}$ say, representing set-down beneath the regular wave groups. From (11) we see that a surface perturbation (the product of first order terms on the right-hand side of (11)) is the forcing term leading to set-down (terms involving $\phi_s^{(2)}$ on the left-hand side of (11)).

It was clear from experiment that although the beach was an efficient absorber of the primary waves it was not such a good absorber of disturbances at the beat frequency. This resulted in secondary long waves travelling back towards the wave generator. It can be appreciated that such waves will tend to reflect from the face of a wave-maker board as though reflecting from a vertical wall. Therefore, long waves travelling back from the beach will give rise to a standing wave system with nodal points at distances of $L/4, 3L/4, 5L/4$ etc from the face of the wave-maker. Here, L is the wavelength of a free long wave at the beat frequency. Thus, a wave probe placed at these nodal points will not register the long wave system caused by reflection from the beach. This allows a comparison to be made between theory and experiment for a progressive secondary wave system.

The second order velocity potential found so far ($\phi_s^{(2)}$) would result in set-down at the wave generator but as explained in the introduction, the predicted long period water particle movement does not occur in the absence of an appropriate movement of the wave-maker at the group period. The boundary condition on the face of the wave-maker is

$$u = \xi_t$$

Primary wave frequencies f_1, f_2 and beat frequency f' (cycles/sec)	Distance of wave probe from wave-maker in terms of wavelength (L) of free wave at the beat frequency	(a) Without secondary paddle movement		(b) With secondary paddle movement		Amplitude of paddle movement at the beat frequency (mm)	
		Amplitude of surface elevation at the beat frequency (mm)		Amplitude of surface elevation at the beat frequency (mm)			
		Experiment	Theory	Experiment	Theory	Experiment	Theory
(1) $f_1 = 1.2$ $f_2 = 1.5$ $f' = 0.3$	L/2	2.6	2.01	1.8	1.3	2.6	2.3
	3L/4	1.5	1.24	1.1	0.92		
	L	0.4	0.2	<u>0.5</u>	<u>0.5</u>		
(2) $f_1 = 1.05$ $f_2 = 1.35$ $f' = 0.3$	5L/4	1.2	0.73	1.0	0.92	2.8	2.84
	L/2	<u>3.3</u>	<u>3.3</u>	2.2	1.6		
	3L/4	2.8	2.86	1.0	1.2		
(3) $f_1 = 0.9$ $f_2 = 1.2$ $f' = 0.3$	L	1.8	2.1	0.7	0.67	2.7	2.5
	5L/4	1.2	1.39	1.1	1.2		
	L/2	1.8	1.2	0.8	0.6		
(4) $f_1 = 1.18$ $f_2 = 1.35$ $f' = 0.17$	3L/4	1.9	1.4	1.2	0.93	5.2	4.32
	L	<u>1.9</u>	<u>1.9</u>	1.1	1.2		
	5L/4	1.5	1.4	1.1	0.93		
(5) $f_1 = 0.63$ $f_2 = 0.8$ $f' = 0.17$	L/4	1.5	1.42	1.0	0.94	6.0	5.87
	3L/8	2.3	2.14	1.3	1.18		
	L/2	<u>1.9</u>	<u>1.9</u>	1.2	1.24		
(6) $f_1 = 0.46$ $f_2 = 0.63$ $f' = 0.17$	5L/8	2.3	1.63	0.8	0.54	5.8	6.22
	3L/4	2.0	2.17	1.0	0.94		
	L/4	0.9	0.51	1.3	1.06		
(6) $f_1 = 0.46$ $f_2 = 0.63$ $f' = 0.17$	3L/8	0.8	0.48	<u>1.0</u>	<u>1.0</u>	5.8	6.22
	L/2	0.7	0.26	0.7	0.55		
	5L/8	1.3	0.98	0.9	0.8		
(6) $f_1 = 0.46$ $f_2 = 0.63$ $f' = 0.17$	3L/4	1.7	1.19	1.4	1.06	5.8	6.22
	L/4	0.6	0.34	0.9	1.04		
	3L/8	0.5	0.65	0.7	1.06		
(6) $f_1 = 0.46$ $f_2 = 0.63$ $f' = 0.17$	L/2	<u>0.5</u>	<u>0.5</u>	0.6	0.7	5.8	6.22
	5L/8	0.9	0.63	0.8	0.75		
	3L/4	1.3	0.74	0.9	1.04		

Table I

where u is the horizontal water particle velocity and ξ is the horizontal deviation of the paddle from its equilibrium position $x = 0$

To second order this boundary condition becomes

$$-\phi_{xx}^{(2)} - \phi_{xx}^{(1)} \xi^{(1)} = \xi_t^{(2)} \quad \text{at } x = 0 \quad \dots(12)$$

In the absence of secondary paddle movement ($\xi^{(2)} = 0$) experiments have shown that secondary free waves are formed in addition to set-down. Denoting the velocity potential of the free waves by $\phi_L^{(2)}$ we obtain from (12) an equation determining the secondary free waves

$$-\phi_{Lx}^{(2)} = \phi_{Sx}^{(2)} + \phi_{xx}^{(1)} \xi^{(1)} \quad \dots(13)$$

Here $\phi_L^{(2)}$ satisfies the usual equations for a surface wave ie (9) (10) and (11) with the right-hand side set to zero.

Experimental values of the amplitude of the surface elevation at the beat frequency are compared with theoretical values, obtained using (9),(10),(11) and (13), in column (a) of Table I. In this table a comparison between theory and experiment for a progressive secondary wave system can only be made at wave probe positions $L/4, 3L/4$ or $5L/4$. This table shows results for six different pairs of primary wave frequencies. The first three pairs each have a difference frequency of 0.3 c/s and the last three each have a difference frequency of 0.17 c/s. As expected, the theoretical results in column (a) predict that the amplitude of the beat frequency disturbance at nodal points should vary with distance from the wave-maker depending on the phase relationship between set-down and secondary wave. Example 2 is a good illustration. Theory predicts that at $3L/4$ the set-down and secondary wave from the wave-maker are in phase, resulting in an enhanced amplitude of 2.8mm. Then, at a greater distance from the wave-maker the two are no longer in phase giving a reduced disturbance of 1.2mm at $5L/4$. In general, qualitative agreement is obtained between theory and experiment at nodal positions in column (a) of Table I in that increasing and decreasing trends measured in the amplitude of the beat frequency disturbance at various distances from the wave-maker are much as predicted by theory

If the secondary free wave from the wave-maker is to be eliminated we see from (12) that a secondary paddle movement $\xi^{(2)}$ is required such that

$$\xi_t^{(2)} = -\phi_{Sx}^{(2)} - \phi_{xx}^{(1)} \xi^{(1)} \quad \dots(14)$$

In the absence of secondary waves only set-down should be present and so the amplitude of the beat frequency disturbance should not vary with distance from the wave-maker. In the experiments an appropriate movement of the wave-maker based on (14) was applied until the beat frequency disturbance became equal at nodal points. The results are given under column (b) of Table I. They show that an appropriate secondary movement of the wave-maker can almost eliminate secondary waves from the generator. The column giving amplitude of secondary paddle movement also shows that the amount of secondary movement required is much as predicted by (14).

To appreciate what these model results represent in prototype terms we can assume that Froude scaling applies at I to 100. Then primary wave periods cover the range 7s to 20s with wave heights up to 5m. The heights of the disturbance at the beat frequency are about 0.2m with periods of about 30s or 60s.

Summarising, we see that the results indicate that secondary long waves from the wave-maker can be minimised for regular wave groups by adding an appropriate movement of the wave-maker at the group period.

3. 2 Surf beats

The presence of a surf beat, ie a reflection of set-down from the beach as a free long wave, is demonstrated by the results in column (b) of Table I. If set-down were dissipated on the shingle beach along with the primary waves, the amplitude of the surface elevation at the beat frequency would be the same at all positions in the flume. But, it is clear from the experimental results in column (b) of Table I that there are considerable variations in this amplitude particularly when the primary waves are of short period (see cases 1,2 and 4). From the description of results in Section 3.1 we know that secondary waves from the wave-maker are not the cause of these variations because such waves have been minimised by an appropriate movement of the wave-maker.

In an effort to explain these variations we can assume that part of the energy in set-down is reflected as a free long wave or surf beat and that this surf beat is perfectly reflected from the face of the wave-maker. One method of proceeding is to estimate the magnitude of the reflection coefficient for set-down. This estimate was obtained in the following way. The coefficient of reflection from the beach (R_L) of a free wave at the beat frequency was measured by carrying out monochromatic long wave tests. If we then assume that R_L is equal to the ratio of horizontal water particle movement in the surf beat to the horizontal water particle movement in set-down, we have

$$R_L = \frac{Ka}{k^2 a^2}$$

Here, K and a are the wave number and amplitude, respectively, of the surf beat and k and \bar{a} are the wave number amplitude of the set-down; all these quantities being evaluated in the depth of water at the toe of the slope. If \bar{a}/a the reflection coefficient of set-down, is denoted by R , then

$$R = \frac{k}{K} R_L = c/cg R_L$$

Here, c is the phase velocity of the surf beat and cg is the group velocity. Since $c > cg$ we see that this relationship produces an enhancement in the reflection coefficient of set-down. The shorter the primary waves, the smaller the group velocity and the larger this enhancement becomes. This trend is illustrated by the experimental results in column (b) of Table I in that variations representative of the presence of a surf beat are larger when the primary waves are short. Having estimated the magnitude of R , the actual point of reflection on the shingle beach was chosen such that theoretical and experimental values of the resultant amplitude at the beat frequency agreed at one position in the flume for each pair of frequencies. This position is indicated in Table I by a line under the experimental and theoretical values. Of course, in obtaining the theoretical values given under column (a) in Table I it was necessary to include a free secondary wave from the wave-maker together with its reflection from the beach.

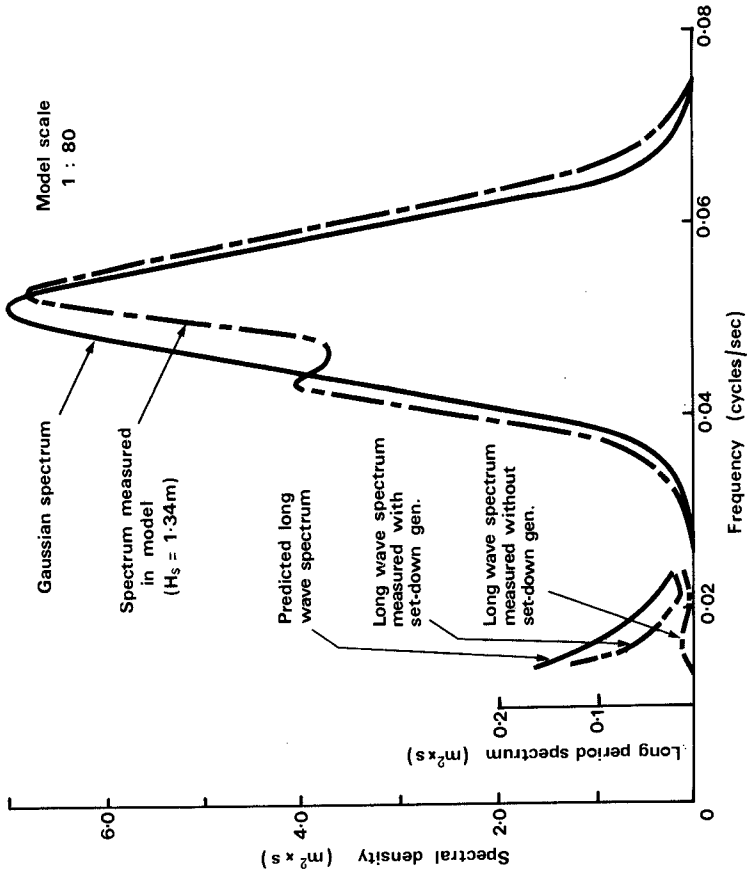


Fig 2 Long wave results for a random sea

Summarising, we see from the results given in Table I for positions in the flume other than nodal points that the somewhat rough and ready theoretical model for surf beat generation does predict the increasing and decreasing trends measured in the amplitude of the beat frequency disturbance at various distances from the wave-maker. These results indicate that the energy in set-down beneath wave groups can be released in the form of free long waves when the primary waves are dissipated

4 EXPERIMENTAL AND THEORETICAL RESULTS FOR A RANDOM SEA

To make theoretical calculations more tractable it was decided to work with a Gaussian shaped wave spectrum. This is shown in Fig.2 which is drawn to a scale of 1 to 80. The spectrum can be considered representative of swell waves. With the same experimental layout as that already described (Fig 1) the primary wave system was essentially progressive. The measuring instruments and the method of data analysis were also the same

Two experimental results for the spectrum of set-down are compared with a theoretical result in Fig 2. We see that theory and experiment are in reasonable agreement only when the set-down generator is used, ie, an appropriate long period movement of the wave-maker is used to produce set-down at the wave generator. The small amount of energy at low frequencies measured without the set-down generator indicates that secondary long waves from the wave-maker were cancelling the set-down at the positions in the flume used for measurement. The long period spectra are only plotted for periods of less than 70 seconds since the time constants in the set-down generator limited its effectiveness to that range for these tests. The theoretical prediction for the spectrum of set-down is in fact Gaussian with its maximum spectral density at zero frequency.

To avoid measuring the effect of surf beats in the flume the following procedure was used. The spectral density for a particular low frequency (f) band was measured at a distance from the wave-maker that was a nodal point for the secondary waves (at frequency f'') caused by reflection from the beach and re-reflection from the wave-maker. This meant that the spectral density for different low frequency bands was obtained from spectral measurements at different positions in the flume. This allowed an experimental estimate of the low frequency spectrum to be obtained for a purely progressive wave system.

A theoretical estimate of the spectrum of set-down associated with a progressive random sea was obtained in the following way. The first order surface elevation ($\eta^{(1)}$) was represented by a sum of sine waves with random phases. The products of first order quantities on the right-hand side of (11) were then evaluated and the equation solved to give the second order velocity potential. Expanding (4) to second order and substituting for the second order velocity potential results in an expression for the second order surface elevation, $\eta^{(2)}$ say.

Denoting the slowly varying part of $\eta^{(2)}$ by $\tilde{\eta}^{(2)}$ we find

$$\tilde{\eta}^{(2)} \cong A \tilde{\eta}^{(1)2} \dots(15)$$

where

$$A = - \frac{\omega^2 n^2}{2k^2 d(1-n^2 \tanh kd)} \left[\frac{\omega^2}{g^2 n \sinh^2 kd} (2 - 2kd \tanh kd - n) + \frac{2k^2}{\omega^2} (1 + \tanh^2 kd) \right] + k \tanh kd - \frac{gk^2 \cosh 2kd}{2\omega^2 \cosh^2 kd}$$

$$n = \frac{cgk}{\omega}$$

Here, it has been assumed that the primary wave spectrum is sufficiently narrow band to approximate A (a function of frequencies in the primary wave spectrum) by its value at the frequency at which the peak occurs in the primary spectrum. It has also been assumed that for the depths of interest the wave group lengths are much greater than the water depth. It can be shown (Bowers 1976) that the spectrum of $(\eta^{(1)})^2$ is given by

$$2 \int S(f) S(f + f^-) df$$

where $S(f)$ is the primary wave spectrum. Hence from (15) we obtain the following estimate of the spectrum of set-down

$$S(f^-) = 2A^2 \int S(f) S(f + f^-) df \quad \dots(16)$$

Using (16) for the Gaussian wave spectrum shown in Fig 2 resulted in the predicted long wave spectrum shown in that figure.

5 REQUIREMENT FOR A GOOD ESTIMATE OF THE EFFECT OF WAVE GROUPS IN PHYSICAL MODELS

Here, it is demonstrated by using an example, that long cycles of truly random waves, lasting many hours in model terms, are required to obtain reliable estimates of the effect of wave groups on marine structures.

Equation (15) shows that set-down and surf beats are related to the slowly varying part of the square of the wave elevation. It is clear that an adequate representation of the spectrum of $(\eta^{(1)})^2$ is required if wave grouping effects are to be well represented. Table II gives values for the area under the spectrum of $(\eta^{(1)})^2$ for ten records of random data each containing about 350 waves. Each record represented a surface elevation with the same wave spectrum $S(f)$. The predicted value for the area under this spectrum was obtained from the following (Bowers, 1976)

$$[\int S(f) df]^2 + 4 \int df^- \int S(f) S(f + f^-) df$$

When the predicted value of 35.83 is compared with the corresponding values obtained from individual records it can be seen that fluctuations of up to +15% and -24% occur. However, the average for the ten records is well within 10% of the predicted value.

These results illustrate the large variability in the response of structures to wave grouping effects found by many observers when short repeating cycles of random data are used in physical model studies. However, the results given here also show that a result closer to the predicted value will be obtained if the cycle of random data used is of long enough duration. This requirement may well result in model tests lasting the equivalent of many times the duration of the design condition of interest. The results of such long tests can be interpreted by considering the following example. Suppose the design condition has a return period of 10 years. If this design condition only lasts 3 hours, say, then the response of a structure sensitive to wave grouping may vary considerably each time the design condition occurs.

Record No.	Area under η^2 spectrum
1	29.12
2	41.29
3	33.9
4	35.15
5	31.36
6	37.75
7	31.35
8	32.34
9	27.01
10	31.76
	Average value = 33.3
	Predicted value = 35.83

However, if a good average estimate of the structure response can be obtained by running a scale model for the equivalent of 30 hours, or 10 times the duration of the design condition, then it appears reasonable to attach a return period of 10 years to that good average estimate of structure response. This technique is particularly appropriate if one is interested in obtaining the standard deviation of the long period response of harbours and moored vessels to wave grouping effects. In such cases long runs are required to obtain reasonable estimates of the standard deviation. Of course, the average maximum response, over the duration of the design condition, can also be obtained from such long model tests.

It is clear from the above that if a structure is sensitive to wave grouping then it is important in physical model tests to carry out sufficiently long tests using random waves. This means that the method of random sea generation used in the laboratory must be capable of producing long cycles of truly random waves lasting many hours in the model.

6 CONCLUSIONS

- (a) Experiments carried out with regular wave groups show that secondary long waves introduced by the wave-maker can be minimised by the addition of a secondary movement of the wave-maker at wave group periods. These experiments also provide evidence for the existence of surf beats, ie reflections of set-down as free seaward going long waves.
- (b) Secondary long waves from the wave-maker can also be minimised for the general case of a random sea.
- (c) Evidence is given to show that in physical model studies long cycles of truly random waves, lasting hours in model terms, are required to obtain reliable estimates of wave grouping effects.

7 ACKNOWLEDGEMENTS

I am grateful to Mr D Fryer who designed the electronic equipment used to generate set-down beneath wave groups. The work is part of the research programme of the Hydraulics Research Station, Wallingford and the paper is published by permission of its Director.

8 REFERENCES

- BIESEL F (1966) Les phenomenes due second ordre rayonnants dans les ondes de gravite. La Houille Blanche No.4
- BOWEN A J and GUZA R T (1978) Edge waves and surf beat. J Geophys Res. Vol 83 No.C4 p 1913.
- BOWERS E C (1976) Long period oscillations of moored ships subject of short wave seas. Trans.Roy.Inst.Naval Archit. Vol 118 p 181.
- BOWERS E C (1977) Harbour resonance due to set-down beneath wave groups. J Fluid Mech. Vol 79 p.71.
- FONTANET P (1961) Theorie de la generation de la houle par un batteur plan. La Houille Blanche No.1.
- GALLAGHER B (1971) Generation of surf beat by nonlinear wave interactions. J Fluid Mech. Vol 49 p.1.

HYDRAULICS RESEARCH STATION REPORT (1976) Port of Acajutla- random wave model study EX 739.

LONGUET-HIGGINS M S and STEWART R W (1964) Radiation stresses in water waves: a physical discussion with applications. Deep Sea Res. Vol 11 p 529.

STAMMERS A J et al (1977) Investigation of vessel mooring subject to wave action. Dock and Harbour Vol LVII No 677.

TUCKER M J (1950) Surf beats: sea waves of 1 to 5 min period. Proc. Roy.Soc. A. Vol 202 p 565.

TWO-DIMENSIONAL SURF BEAT

by

Reinhard E. Flick¹
 Douglas L. Inman²
 Robert T. Guza³

ABSTRACT

Surface elevation and velocity measurements in shallow water on beaches show large fluctuations known as surf beat in the long period range from approximately 20s to 2000s (Munk, 1949; Tucker, 1950). A laboratory study was conducted to determine if two shoaling primary waves of nearly equal frequency would generate two-dimensional surf beat at their difference frequency. The experiments, carried out in the Scripps Institution of Oceanography Hydraulics Laboratory 30 m glass walled wave channel, show that the beat frequency motion in the channel consists of the sum of a forced progressive wave and two free standing waves. The progressive wave is forced by the local nonlinear interaction of the primary waves and grows sharply in shallow water. One of the free standing waves is generated directly by the wavemaker. The data is consistent with the hypotheses that the second, much larger, free wave is generated in shallow water as the reflection of the long, forced progressive wave, leading to the observed standing wave surf beat pattern.

Introduction

Surf beat was first observed by Munk (1949) and by Tucker (1950) who noted from field records of swell in shallow water that the envelope of wave amplitude was correlated with wave energy at the envelope, or beat, period. Longuet-Higgins and Stewart (1962) derived the result that the difference interaction of the incoming swell nonlinearly generated forced waves ("set-down" wave) at the difference frequency and wavenumber with some properties like those observed by Munk and Tucker. However, the nonlinear forcing hypotheses could not explain the observed

¹ Assistant Research Oceanographer/Academic Administrator

² Professor of Oceanography

³ Assistant Professor of Oceanography

Shore Processes Laboratory, Scripps Institution of Oceanography,
 La Jolla, California 92093

lag between the envelope of the swell offshore and the arrival of the difference frequency wave. This discrepancy led to the idea that the nonlinearly forced wave was reflected from the shore line as a free wave (Tucker, 1950; Longuet-Higgins and Stewart, 1962), but a plausible mechanism for this was not proposed.

At about the same time, Munk et al (1964) showed that low frequency energy on the continental shelf was mostly in the form of trapped, three-dimensional edge waves. Furthermore, Gallagher (1971) was able to show that resonant growth of edge waves due to nonlinear difference interaction of incoming waves was theoretically possible and consistent with field data. Inman et al (1976) presented field data suggesting that beat period edge waves can be trapped and grow because of longshore discontinuities in topography such as headlands and submarine canyons. Recently, Bowen and Guza (1978) showed in the laboratory that difference interactions of obliquely incident waves caused resonant edge wave growth according to the Gallagher (1971) hypotheses.

With all the interest in edge waves, however, it still remained to show whether or not two-dimensional free long waves existed as a consequence of reflection or surf zone forcing. It was suggested by Tait and Inman (1969) that special surf zone widths and bars and other slope discontinuities could lead to enhancement effects in the surf zone which would amplify runup at special frequencies. Observations by Inman and Tait (unpublished manuscript) show that large runup amplitudes may be observed at certain frequencies. However, it was found that some of the runup peaks appeared at resonant frequencies of the channel, while some did not, thus still leaving the problem unresolved.

A long wave channel conveniently suppresses three-dimensional motions such as edge waves which have longshore dependence. Thus, on-offshore processes can be measured without interference. For example, the upper panel of Figure 1 shows two superposed spectra taken from two single frequency wave experiments at primary frequencies σ_1 and σ_2 run separately. Only the harmonics of each primary appear as secondary peaks. The lower panel of Figure 1 shows the spectrum resulting from measurements made when the two primary waves appear together. Note the energy present at sum and difference frequencies, particularly $\sigma_2 - \sigma_1$.

Wave channels introduce a completely different set of problems which complicate the interpretation of data, especially long wave measurements. These problems are essentially associated either with the wavemaker or with reflection and dissipation in the flume, or in some cases with both (Ursell, et al, 1960; Fontanet, 1961; Madsen, 1971; Hansen and Svendsen, 1974; Bowers, 1977; Flick and Guza, 1980).

It was the purpose of the experiments outlined in this paper to clarify the role of free, two-dimensional surf beat in light of reflection and wavemaker effects peculiar to wavechannels. The measurements were conducted in the Scripps Institution of Oceanography Hydraulics Laboratory. Figure 2 illustrates schematically the 30 m glass wall wave channel, the high-pressure servo-hydraulic wavemaker system and the high resolution resistance wire wavestaff system (Flick, et al, 1979) used in the study.

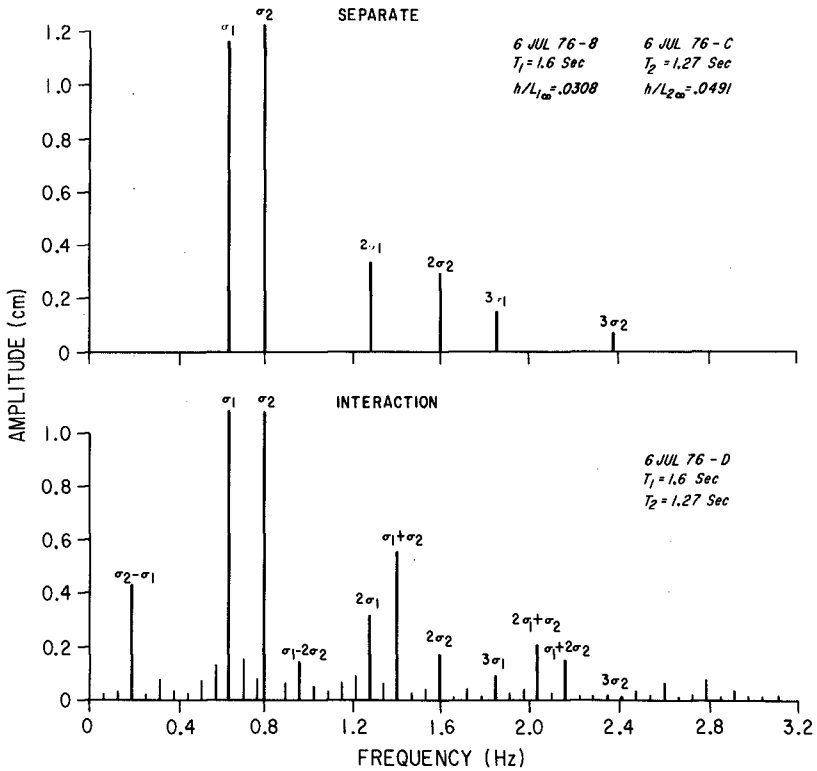


Figure 1. Upper panel shows superposed spectra of single frequency (σ_1 and σ_2) wave experiments. Note harmonics of each primary. Lower panel shows spectrum of run with both primaries present simultaneously. Note sum and difference frequencies, particularly $\sigma_2 - \sigma_1$ peak.

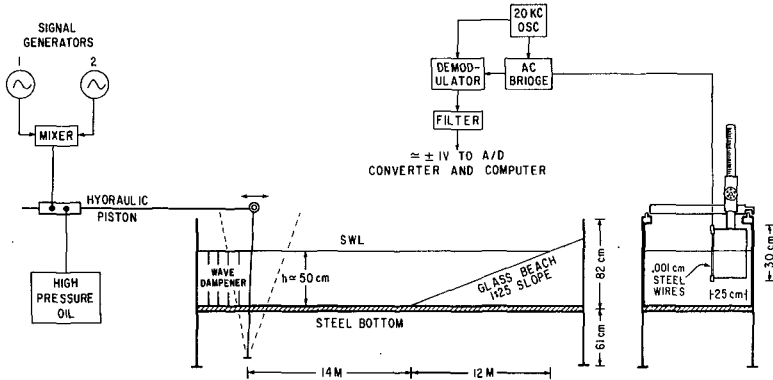


Figure 2. Schematic of Scripps Institution of Oceanography Hydraulic Laboratory 30 m glass wall wave channel, servo-hydraulic wavemaker and resistance wire wave-staff system.

It can be shown (Madsen, 1971) that free difference frequency waves always exist at some amplitude (perhaps small) when a wavemaker is used to generate two primary waves, unless paddle motion corrections are imposed (Bowers, 1977). These free waves were shown by Flick and Guza (1980) to theoretically be of the same order as the forced non-linear "set-down" wave propagating with wave groups (Longuet-Higgins and Stewart, 1962). These free waves are generated at the wavemaker as progressive waves. After several wave periods, reflections produce a standing wave pattern. Assuming free, long waves are also generated in shallow water or in the surf zone, these also soon exist as standing waves. This makes it difficult to distinguish the source of free waves in wave channels.

The effect of dissipation, particularly in shallow water, may also be important. Long standing waves of sufficiently small amplitude usually exhibit downchannel profile changes too small to measure. However, swash dissipation on the beach face can be significant (Guza and Bowen, 1976) and can lead to progressive wave components in the standing wave profile which further complicate long wave data interpretation. On the other hand, strongly enhanced shallow water wave dissipation by means of a wave absorber was used in this study to eliminate the primary waves before the breakpoint without affecting the free long waves.

Results and Discussion

Flick and Guza (1980) have shown that to lowest order, the surface elevation of free standing waves in a channel with a flat section and a sloping beach (Figure 3) can be written

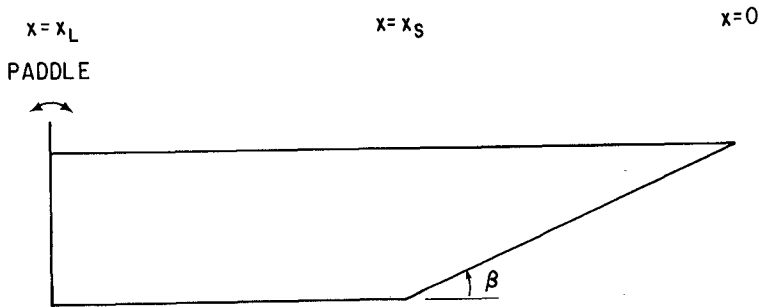
$$\eta = a_p f(x) \cos \left[\int_0^x k dx - \frac{\pi}{4} \right] \cos \sigma t \quad (a)$$

where

$$f(x) = \begin{cases} 1 & , x_S < x < x_L \text{ (flat)} \\ \left(\frac{x_S}{x}\right)^{1/4} & , 0 < x < x_S \text{ (slope)} \end{cases} \quad (b) \quad (1)$$

$$\int_0^x k dx = \begin{cases} \left(\frac{\sigma^2}{g\beta x_S}\right)^{1/2} (x + x_S), & \text{(flat)} \\ \left(\frac{4\sigma^2 x}{g\beta}\right)^{1/2} & , \text{(slope)} \end{cases} \quad (c)$$

WAVE CHANNEL CONFIGURATION



LINEAR LONG WAVES $\eta = a f(x) \cos \left[\int_0^x k dx - \frac{\pi}{4} \right] \cos \sigma t$

Figure 3. Definition sketch of wave channel with a beach showing location of wavemaker and the coordinate system used.

Here σ is the radian wave frequency, k the wavenumber, β the beach slope, g the acceleration of gravity and the coordinate system is defined in Figure 3. This form is valid except very near the shoreline.

The channel resonance frequencies can be computed by assuming that resonant standing waves will have an amplitude antinode at $x = x_L$. The resonance frequencies are

$$\sigma_n = (n + \frac{1}{4})\pi \frac{(g\beta x_S)^{\frac{1}{2}}}{x_L + x_S} \quad n = 1, 2, \dots \quad (2)$$

Relations (1) and (2) follow from the asymptotic form for large arguments of the J_0 Bessel function (Abramowitz and Stegun, 1965) which is the exact linear standing wave solution on a sloping beach, together with the required matching at the beach toe $x = x_S$.

Figure 4 shows the amplitude of surface displacement for two paddle generated standing waves in a channel with a beach. The triangles show wave elevation data taken with a short-wave absorbing barrier at the location indicated. The solid dots indicate data taken in the absence of the barrier. The location of the barrier in both experiments shown in Figure 4 was chosen so as not to change the location of nodes and antinodes of displacement of the paddle generated long waves. The theoretical wave amplitude normalized by the vertical runup amplitude, according to equation (1) is shown as a solid line.

The upper part of Figure 4 shows the displacement of a free wave with frequency between that of two adjacent channel modes (non-resonant). The wave length is determined by the period and depth since the wave is free. The condition that no flow can occur through the beach face means that the wave has an antinode at the beach. Therefore, the location of nodes and antinodes is determined. The phase of the wave at the paddle then depends only on the channel length. This phase for the non-resonant wave is very close to a node, while in the case of the wave at a channel resonance frequency (Figure 4, lower) the phase at the paddle corresponds to an antinode. In fact, the location of the antinode at the paddle is the resonance condition.

Since non-resonant standing waves generated directly by the wave-maker have antinodes of displacement at the beach face, it is a plausible assumption that standing waves generated in shallow water at the other end of the flume have antinodes at the paddle. The existence of antinodes at the paddle for non-resonant modes would therefore constitute evidence for shallow water long wave generation.

The results of eight beat wave experiments are summarized in Table 1. Four runs were at channel resonance frequencies and the other four were non-resonant. Each experiment consisted of driving the wave-maker simultaneously at two primary wave frequencies (periods T_1 and T_2) and measuring the amplitude of the difference frequency oscillation as a function of position in the channel. Each run consisted of two parts: one with the barrier to absorb the short primary waves and one without the barrier. The position of the barrier was chosen in each

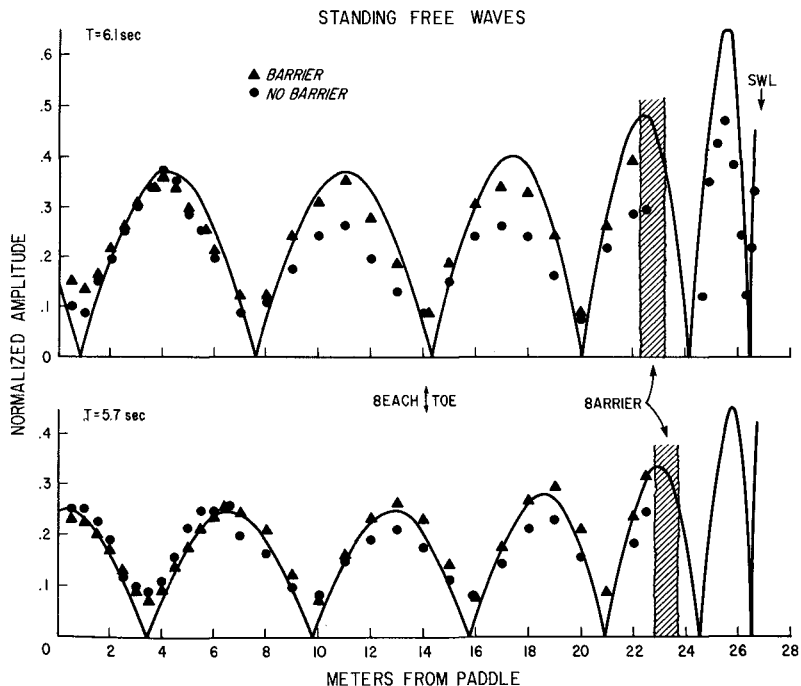


Figure 4. Amplitude of standing waves generated directly by the wavemaker. Location of short wave absorbing barrier shown by cross hatching. Triangles are data taken with the barrier installed, circles were taken without barrier. Solid line is theory from relation (1).

Table 1. Experimental Conditions for Beat Wave Experiments

RUN	BEAT PERIOD (sec)	T_1/T_2 (sec)	TYPE	a_1/a_2 (cm)	a_Δ (cm)	a_B (cm)	a_P (cm)	c_r
1	6.1	1.60	No Barrier	1.2	.037	0.	.15	2.17
	Non res.	1.27	Barrier	1.2	.037	0.	.07	
2	6.1	0.78	No Barrier	4.0	.152	0.	.20	---
	Non res.	0.90	Barrier	4.0	.152	.03	0.	
3	6.1	1.60	No Barrier	2.0	.103	0.	.30	---
	Non res.	1.27	Barrier	2.0	.103	0.	.10	
4	7.47	1.60	No Barrier	1.5	.062	0.	.40	---
	Non res.	1.32	Barrier	1.5	.062	0.	.40	
5	5.7	1.60	No Barrier	1.0	.025	0.	.20	1.04
	Resonant	1.25	Barrier	1.0	.025	0.	.07	
6	5.7	1.60	No Barrier	1./1.	.025	0.	.32	1.86
	Resonant	1.25	Barrier	1.5/1.5	.100	0.	.20	
7	5.7	1.60	No Barrier	2.5/2.5	.156	0.	.20	2.64
	Resonant	1.25	Barrier	3./3.	.225	0.	.60	
8	6.73	1.30	No Barrier	2./2.	.072	0.	.40	---
	Resonant	1.09	Barrier	3./3.	.163	0.	.40	

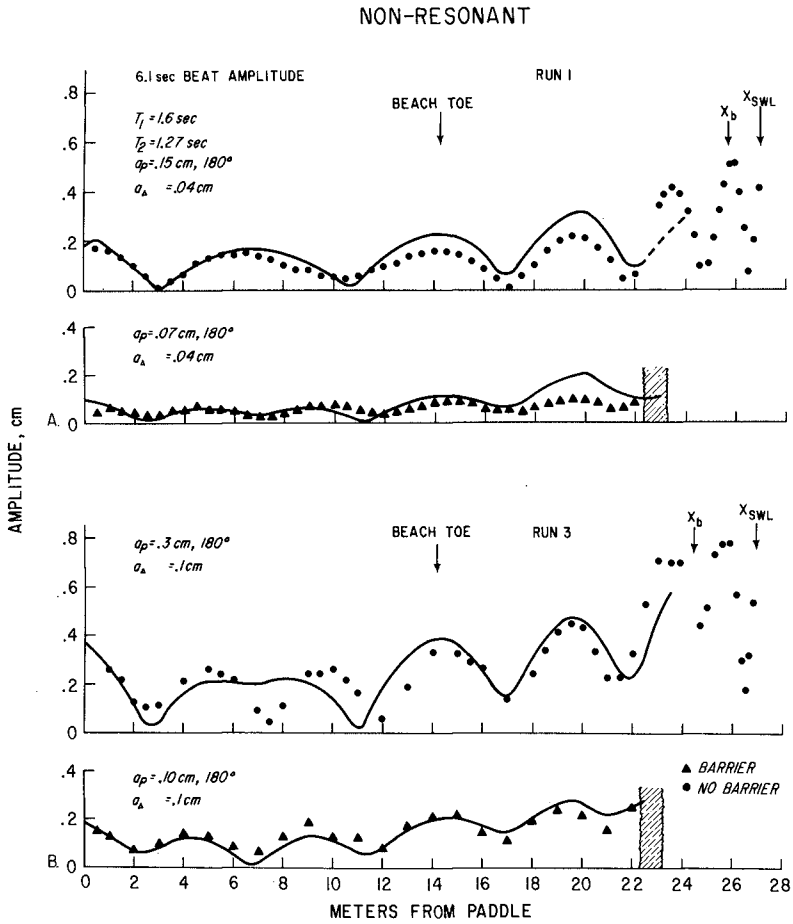


Figure 5. Detailed data of two non-resonant beat wave runs summarized in Table 1. Dots show beat frequency fluctuation without a barrier, triangles are taken with the barrier. Solid line is the best fit of an ad-hoc surf beat theory described in the text.

RESONANT

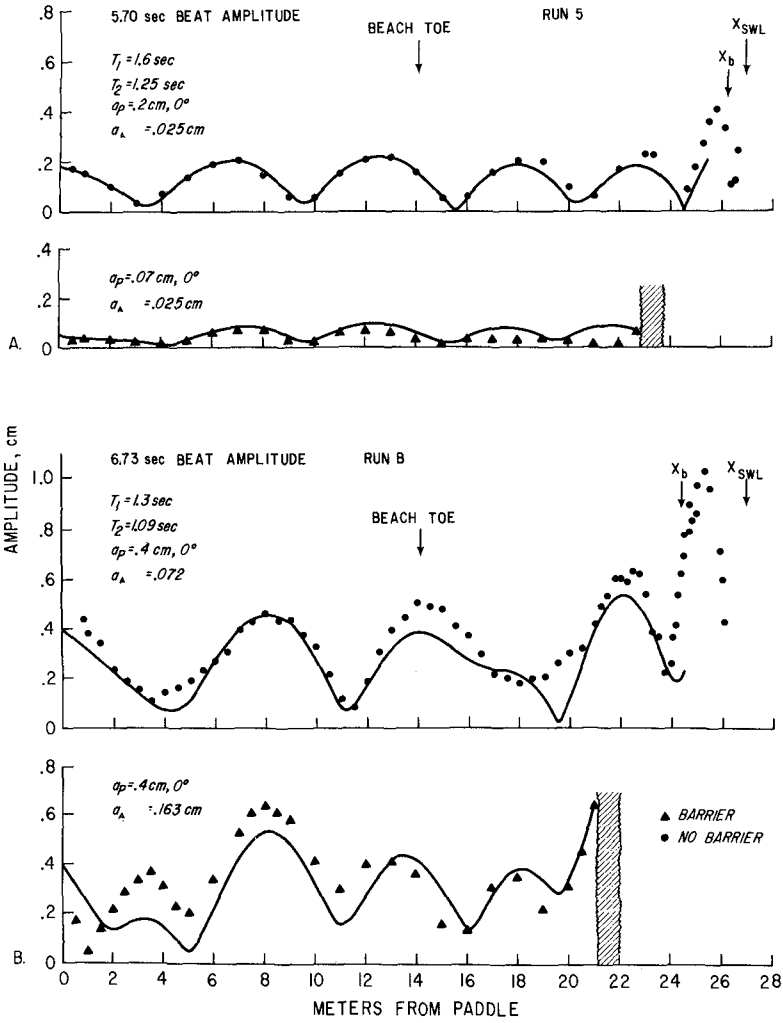


Figure 6. Same as Figure 5 for resonant beat waves.

run to correspond to the position found from earlier long wave measurements (Figure 4) not to affect the paddle generated beat frequency free wave of the same period. The purpose of the barrier was to eliminate the primary wave forcing and the surf zone and any associated long waves generated there. This scheme was supposed to leave only the set-down wave of size a_s and any free waves generated by the paddle. Further discussion of the effect of the barrier is given below.

Figures 5 and 6 show the results of four beat wave experiments in detail. Runs 1 and 3 (Figure 5) are non-resonant examples and 5 and 8 (Figure 6) are resonant. First, it is clear that the phase at the paddle corresponds more closely to an antinode than to a node in the non-resonant data both with and without the barrier. This is also true for the other non-resonant runs not shown in detail, but summarized in Table 1. Of course, there is also an antinode at the paddle for resonant runs, but this is expected and does not help distinguish the source of the free wave component.

The solid lines in Figures 5 and 6 represent the results of an ad-hoc surf beat theory consisting of the sum of two free standing waves and the set-down wave. One standing wave with amplitude a_B is given by equation (1) and has an antinode on the beach face. The second standing wave is similar in form, but has an antinode at the paddle and amplitude denoted a_D . The set-down wave is a forced, progressive correction and is given by Longuet-Higgins and Stewart (1962) in terms of the primary wave parameters. The amplitudes a_s , a_B and a_D have been adjusted to best fit the data and are listed in Table 1. The results show that a_D is negligible compared with a_B for all runs except run 2 where it is small. Therefore, only the progressive set-down wave and the free wave generated or reflected from shallow water seem to be important in the non-resonant runs 1-4.

The data shown are consistent with the hypotheses that the non-linearly generated set-down wave is reflected from the beach when there is no barrier, and from the barrier when it is present. In runs 1, 2, 3, 5 and 6 the standing wave amplitude without the barrier is always larger than with the barrier. For the same primary wave forcing, the amplitude of a_s is doubled by removing the barrier in both runs 1 and 5. In runs 3 and 6 removal of the barrier increased the response by about 50%.

The set-down wave amplitude increases sharply in shallow water. This fact accounts qualitatively for the increased standing wave amplitude in the absence of the barrier, since the beat wave is forced to larger amplitude before being reflected. In the presence of the barrier, the progressive wave is apparently reflected from the barrier, thus reaching relatively smaller amplitude.

The data suggest that the standing wave a_B is merely the result of reflection of the incoming wave a_s . No special enhancement was observed in the conditions tested. The absolute amplitude of the standing wave response depended on whether or not the frequency corresponded to a channel mode. The proportional increase in response caused by removing the barrier was the same for the resonant or non-resonant cases until saturation was reached. The saturation hypothesis advanced by Guza and Bowen (1976) is illustrated by the

standing waves in runs 4, 7 and 8. Removal of the barrier caused no increase in response in runs 4 and 8, and actually decreased response in run 7. In these cases, the reflection parameter c_r exceeds 2,

$$c_r = \frac{a_j \sigma^2}{g \tan^2 \beta}$$

where a_j is the standing wave amplitude at the beach face. This results in increased long wave dissipation in the shallow water region shoreward of the barrier (Guza and Bowen 1976). Run 4 corresponded to a non-resonant case, so that the free wave amplitude could not increase due to resonance with or without the barrier. Run 7, however, corresponded to a resonant case and the amplitude was saturated without the barrier. With the barrier, the dissipative region in shallow water was removed but the resonance condition was unaltered, so that the response was larger. The increase in primary amplitude while other conditions remain the same results in increased standing wave response until saturation is reached (see runs 1, 3, 5, 6 and 7).

In runs 6, 7 and 8 primary amplitudes seem to be larger in the presence of the barrier than without. Without contrary evidence, it seems reasonable to assume that the primary waves were partially reflected from the barrier in these runs and so were able to increase their amplitude. Why the primary waves in the analogous non-resonant experiments, runs 1, 3 and 4 were not so affected is not known.

Finally, Figure 7 shows a plot of the "forcing" a_Δ versus the beat wave response, a_p . The squares denote data with the barrier in place, the triangles are data taken without the barrier. Filled symbols were resonant runs, open symbols were non-resonant. The amplitudes plotted were chosen from the ad-hoc theory described above. When the barrier was in position, a_Δ at the barrier location was used. When the barrier was absent, the value of a_Δ at the breakpoint of the largest wave in the sets was used. The value of a_p is that on the flat portion of the channel. The data plotted in Figure 7 show that a line $a_p = a_\Delta$ separates resonant from non-resonant runs so that resonance occurs for $a_p \geq a_\Delta$.

Conclusion

It has been shown that beat wave data in a 2-dimensional laboratory channel are consistent with the hypotheses that the set-down wave described by Longuet-Higgins and Stewart (1962) is reflected from the shore when the primary waves break. Surf beat experiments in wave channels are severely complicated by the fact that long waves reflect from the beach and from the paddle and thus exist as standing waves. This and the presence of free paddle generated waves make it difficult to distinguish the source of long waves.

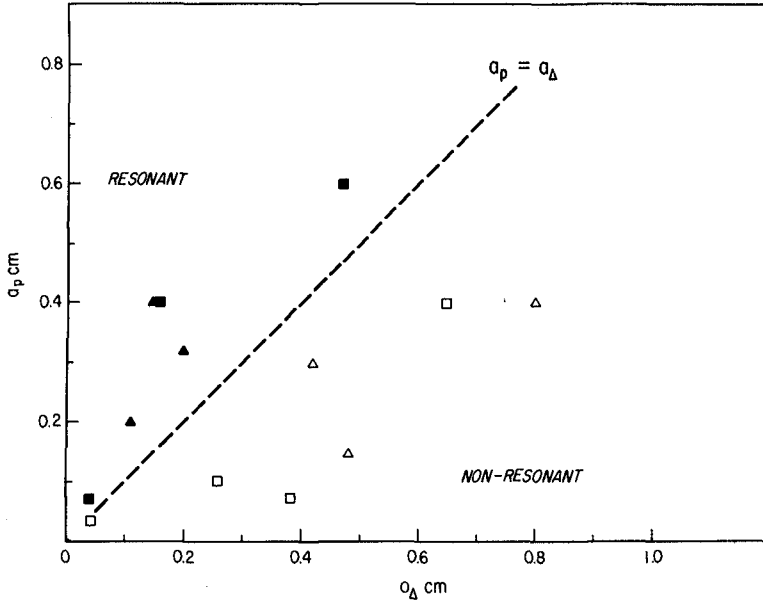


Figure 7. Standing beat wave "response" (a_p) as a function of set-down wave "forcing" (a_Δ). Amplitudes plotted are taken from ad-hoc surf beat theory as described in the text. Line $\bar{a}_p = a_\Delta$ separates resonant from non-resonant runs.

Acknowledgement

The support of the Office of Naval Research Coastal Sciences Program, Code 462 under contract N00014-75-C-0300 with the University of California, San Diego is very gratefully acknowledged.

REFERENCES

- Abromowitz, M. and I. Stegun, 1965, Handbook of Mathematical Functions, Dover Publ., New York, 1946 pp.
- Bowen, A.J. and R.T. Guza, 1978, "Edge waves and surf beat", Jour. of Geophys. Res., vol 83, no C4, p 1913-1920.
- Bowers, E.C., 1977, "Harbor resonance due to set-down beneath wave groups", Jour. Fluid Mech., vol 79, part 1, p 71-92.
- Flick, R.E. and R.T. Guza, 1980, "Paddle generated waves in laboratory channels", Jour. Waterway, Port, Coastal and Ocean Div., Amer. Soc. Civil Eng., vol 106, no WN1, p 79-97.
- Flick, R.E., R.L. Lowe, M.H. Freilich and J.C. Boylls, 1979, "Coastal and laboratory wavestaff system", Oceans 79, Inst. Electrical and Electronic Eng. and Mar. Tech. Soc., p 623-625.
- Fontanet, P., 1961, "Theorie de la generation de la houle cylindrique par un batteur plan", Houille Blanch, vol 16, no 1, p 3.
- Gallagher, B., 1971, "Generation of surf beat by nonlinear wave interaction", Jour. Fluid Mech., vol 49, part 1, p 1-20.
- Guza, R.T. and A.J. Bowen, 1976, "Resonant interactions for waves breaking on a beach", Proc. 15th Int. Conf. Coastal Eng., Amer. Soc. Civil Eng., p 560-79.
- Hansen, J.B. and I.A. Svendsen, 1974, "Laboratory generation of waves of constant form", Proc. 14th Int. Conf. Coastal Eng., Amer. Soc. Civil Eng., p 321-339.
- Inman, D.L., C.E. Nordstrom and R.E. Flick, 1976, "Strong currents in submarine canyons: An air-sea-land interaction", Ann. Rev. Fluid Mech., vol 8, p 275-310.
- Inman, D.L. and R.J. Tait, unpublished manuscript, "Surf beat resonance and runup".
- Longuet-Higgins, M.S. and R.W. Stewart, 1962, "Radiation stress and mass transport in gravity waves, with application to 'surf beats'", Jour. Fluid Mech., vol 13, part 4, p 481-504.
- Madsen, O.S., 1971, "On the generation of long waves", Jour. Geophys. Res., vol 76, no 36, p 8672-83.
- Munk, W.H. 1949, "Surf beats", Trans. Amer. Geophys. Union, vol 30, no 6, p 849-54.

- Munk, W.H. and F. Snodgrass and F. Gilbert, 1964, "Long waves on the continental shelf: an experiment to separate trapped and leaky modes", Jour. Fluid Mech., vol 20, part 4, p 529-554.
- Tait, R.J. and D.L. Inman, 1969, "Low frequency resonance in the surf zone", Trans. Amer. Geophys. Union, vol 50, no 4, p 319.
- Tucker, M.J., 1950, "Surf beats: sea waves of 1 to 5 minute period", Proc. Roy. Soc., Series A, vol 202, p 565-73.
- Ursell, F., R.G. Dean and Y.S. Yu, 1960, "Forced small amplitude water waves: a comparison of theory and experiment", Jour. Fluid Mech., vol 7, part 3, p 32-52.

CHAPTER 40

LONG WAVES GENERATED BY COMPLEX BOTTOM MOTIONS

J. L. Hammack
Associate Professor of Civil Engineering
University of California, Berkeley, U.S.A.

and

F. Raichlen
Professor of Civil Engineering
California Institute of Technology, Pasadena, U.S.A.

1. Introduction

Studies of tsunami generation often employ simple models of the sea floor dislocations to permit tractable analytical solutions. Although these solutions provide basic insight into the generation process, they are incapable of producing explicit results for prototype events where both the spatial and temporal distributions of the sea floor dislocation may be quite complicated. Herein we exploit the apparent linearity of the generation process and demonstrate both the use and validity of the superposition principle to construct solutions for complex bed motions. Analytical and experimental results are presented for a monopolar dislocation (block upthrust or downthrow) with a complex time-displacement history. The time history used in the computations is obtained from an integrated accelerogram recorded at Pacoima Dam, near Los Angeles, during the earthquake of February 9, 1971. A complex spatial deformation is not used in order to enable experimental verification of the analytical results. This is unfortunate since it appears that the details of the time-displacement history are not important for prototype phenomena where the motion may be considered instantaneous. However, it is important to note that the analysis treats both space and time variations in an identical manner; hence, confirmation of this approach for complex time variations strongly suggests analogous behavior for complex spatial variations.

Finally, we examine and compare several alternative time-displacement histories for the mean motion. It is shown that the results for each mean motion can be unified by introducing a velocity as a descriptive parameter which is based on the kinetic energy input of the moving bottom to the overlying fluid.

2. Time-Displacement History

To define a complicated time-displacement history with relevance to earthquake-induced ground motions, we have chosen an accelerogram for the vertical component of motion recorded at Pacoima Dam (near Los Angeles) during the earthquake of February 9, 1971. The accelerogram

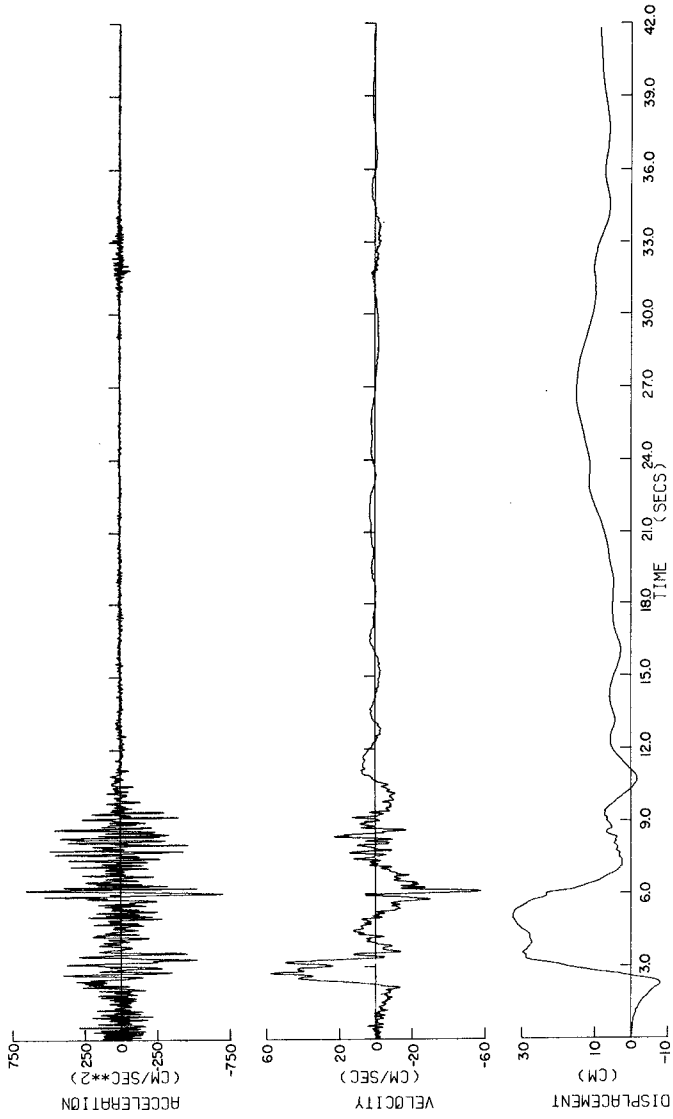


Figure 1. Vertical component of ground acceleration recorded 2/9/71 0600 PST Pacoima Dam, California, with integrated velocity and ground displacement.

shown in Figure 1 may be integrated numerically using appropriate precautions (e.g., see Nigam and Jennings, 1968), to yield a time history of the vertical ground displacement. Results of the integration process for the "smoothed" velocity history and the corresponding ground displacement history are shown below the accelerogram in Figure 1.

An analytical representation of the algebraically complex time-displacement history of Figure 1 over a finite record interval, $0 \leq t \leq T$, may be constructed using a Fourier series of the form:

$$\zeta(t) = C_0 + \sum_{n=1}^N C_n \sin(K_n t + \beta_n). \quad (1)$$

In (1) C_n are the amplitudes of the Fourier components with C_0 representing the mean (permanent) ground displacement, K_n are the component wave frequencies, and β_n are the component phase angles. The accuracy of (1) in representing the integrated displacement of Figure 1 is determined by the number of components N retained in the Fourier sum. Results of computations with $N = 18$ are illustrated in Figure 2; this truncated sum will be adopted in the subsequent analysis.

It should be emphasized that both the instrument characteristics and the numerical integration techniques used to obtain ground displacements from acceleration measurements necessarily distort (filter) information in long period components. In particular, the mean (and permanent) displacement of the integrated motion shown in Figure 1 (and, of course, its Fourier representation in Figure 2) is not expected to accurately model the actual permanent deformation. To compensate for this distortion, we may again exploit the superposition principle and add a nonsinusoidal component to the Fourier series representation of (1). As an example of this approach, consider the ramp motion in time of the form:

$$\zeta_r(t) = \zeta_0 t/T \quad (2)$$

during the time interval $0 \leq t \leq T$; other choices for the mean motion are discussed and compared in section 5. In practice, the sum of the mean component resulting from the Fourier synthesis, C_0 , and the additional component ζ_0 from (2) should be chosen to equal the actual permanent ground offset. Hence, a general representation for a complicated time-displacement history becomes:

$$\zeta(t) = C_0 + \zeta_0 t/T + \sum_{n=1}^N C_n \sin(K_n t + \beta_n). \quad (3)$$

3. Solutions of the Water Wave Problem

Consider a two-dimensional (x,y) and incompressible ocean of uniform depth h initially in equilibrium with the earth's gravitational field g which acts in the negative y direction. At time $t = 0$ a section of the

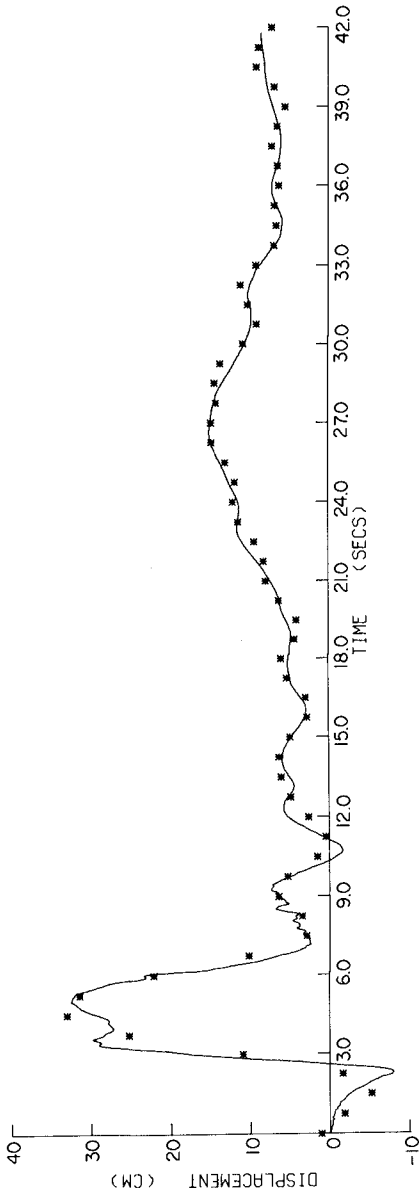


Figure 2. Vertical ground displacement (—) and Fourier synthesis (*) using eighteen components.

sea floor begins to deform vertically with a time and spatial variation given by $\zeta(x,t)$. We seek the inviscid, irrotational, and barotropic deviations $\eta(x,t)$ of the ocean free surface from its equilibrium position. With the coordinate system at the equilibrium position of the free surface, the linearized description of motion in terms of a velocity potential $\phi = \phi(x,y,t)$ is:

$$\phi_{xx}(x,y,t) + \phi_{yy}(x,y,t) = 0 \tag{4}$$

$$\phi_y(x,-h,t) = \zeta_t(x,t) \tag{5}$$

$$\phi_y(x,0,t) = \eta_t(x,t) \tag{6}$$

$$\phi_t(x,0,t) = -g\eta(x,t) \tag{7}$$

where subscripted variables indicate partial differentiation. It is convenient to eliminate $\eta(x,t)$ in (6) and (7) by combining to yield a single condition for the velocity potential:

$$\phi_{tt}(x,0,t) + g\phi_y(x,0,t) = 0 \tag{8}$$

Using the Laplace transform in t and the Fourier transform in x , equations (4), (5) and (8) become:

$$\bar{\phi}_{yy}(k,y,s) - k^2\bar{\phi}(k,y,s) = 0 \tag{9}$$

$$\bar{\phi}_y(k,-h,s) = s\bar{\zeta}(k,s) \tag{10}$$

$$\bar{\phi}_y(k,0,s) + \frac{s^2}{g}\bar{\phi}(k,0,s) = 0 \tag{11}$$

where the overbar of a function $f(x,t)$ indicates:

$$\bar{f}(k,s) = \int_{-\infty}^{\infty} dx \int_{-\infty}^{\infty} e^{ikx} e^{-st} f(x,t) dt. \tag{12}$$

Solving (9), (10), and (11) for $\bar{\phi}(k,y,s)$ and noting from (7) that

$$\bar{\eta}(k,s) = -(s/g)\bar{\phi}(k,0,s) \tag{13}$$

we find:

$$\bar{\eta}(k,s) = s^2 \bar{\zeta}(k,s) / (s^2 + \omega^2) \cosh kh \tag{14}$$

where $\omega^2 = gk \tanh kh$. Inverting the Laplace and Fourier transforms yields:

$$\eta(x,t) = \frac{1}{2\pi} \int_{-\infty}^{\infty} \left\{ \lim_{\Gamma \rightarrow \infty} \frac{1}{2\pi i} \int_{\mu-i\Gamma}^{\mu+i\Gamma} \frac{s^2 e^{-ikx} e^{st}}{(s^2 + \omega^2) \cosh kh} \bar{\zeta}(k,s) ds \right\} dk \tag{15}$$

where the complex inversion integral for the Laplace transform has been used. In (15) ω is the wave frequency ($\omega = is$) and k is the wavenumber. Explicit results for specific deformations of the sea floor $\zeta(x,t)$ will be developed now.

3.1 Solution for a single Fourier component

Consider a block section of the sea floor of length $2b$ whose time-displacement history corresponds to a single Fourier component of (1). With the coordinate system centered above the block section, we have

$$\zeta_n(x,t) = C_n H(b^2 - x^2) [\sin(K_n T + \beta_n) H(T - t) + \sin(K_n t + \beta_n) H(t - T)] \quad (16)$$

where $H(\cdot)$ is the Heaviside step function. Finding the transform of (16), substituting into (15), performing the integration around the Bromwich contour, taking only the real part of the resulting integral, and noting that the integrand is an even function of k , we find:

$$\eta_n(x,t) = \frac{2C_n}{\pi} \int_0^\infty \frac{\cos kx \sin kb}{k \cosh kh} \left\{ A+B - H(t-T) [C+D+E] \right\} dk \quad (17)$$

where

$$A = \sin \beta_n [(\omega^2 \sin \omega t - K_n^2 \sin K_n t)/(\omega^2 - K_n^2)] \quad (18)$$

$$B = K_n \cos \beta_n [(\omega \sin \omega t - K_n \sin K_n t)/(\omega^2 - K_n^2)] \quad (19)$$

$$C = \sin(K_n T + \beta_n) \left\{ [\omega^2 \cos \omega(t-T) - K_n^2 \cos K_n(t-T)]/(\omega^2 - K_n^2) \right\} \quad (20)$$

$$D = K_n \cos(K_n T + \beta_n) \left\{ [\omega \sin \omega(t-T) - K_n \sin K_n(t-T)]/(\omega^2 - K_n^2) \right\} \quad (21)$$

$$E = -\sin(K_n T + \beta_n) \cos \omega(t-T). \quad (22)$$

The final integration over wavenumber k in (17) is obtained by numerical quadratures.

3.2 Solution for ramp mean motion

The ramp time-displacement history of (2) for the block deformation is described by

$$\zeta(x,t) = \zeta_0 H(b^2 - x^2) [tH(T - t)/T + H(t - T)]. \quad (23)$$

Following the same procedure outline in section 3.1, we obtain (again after considerable algebra) the water surface motion η_r due to the ramp

$$\eta_r(x,t) = \frac{2\zeta_0}{\pi} \int_0^\infty \frac{\cos kx \sin kb}{k \cosh kh} \left(\frac{1}{\omega T} \right) [\sin \omega t - H(t - T) \sin \omega(t - T)] dk. \quad (24)$$

Again, the final integration over wavenumber k must be evaluated numerically.

4. Comparison of Theory and Experiment

As noted earlier, the simple block deformation of the sea floor was chosen to enable experimental verification of the analytical model developed for complicated time-displacement histories. The experimental facility used in these tests has been described in detail by Hammack (1972, 1973). Basically, the wave-maker consists of a rectangular piston in the bottom of a wave tank (and spanning its width) whose motion is controlled by an electro-hydraulic-servo system. The servo system converts a time-voltage command signal into a proportional vertical displacement of the piston. For the experiments reported herein, the piston length in the direction of wave motion is $b = 61$ cm while the quiescent water depth above the piston is $h = 10$ cm. Before presenting results of the tests, we describe the motivation for choosing other experimental scales.

A "global" time scale for the forcing of the overlying ocean by the sea floor is the period T . The appropriate time scale for the gravitational response of the long barotropic wave modes is $b/(gh)^{1/2}$ which corresponds to the time required for waves to escape the generation region. For prototypical earthquakes the ratio of the forcing and response time scales, $\tau = T(gh)^{1/2}/b$, termed the time-size ratio, is small so that details of the time-displacement history generally are not important. However, our interests herein require that the details of the temporal motion have a significant impact on the generated wave structure. Hence, the period T for the experimental tests must be scaled so that τ exceeds unity; in fact, for the experiments a period $T = 4$ secs was chosen which yields $\tau = 6.5$. Previous experiments by Hammack (1973) also indicate that the generation process for prototypical tsunamis is linear and that nonlinearity remains insignificant for vertical displacements which do not exceed about 20% of the overlying ocean depth. This criterion is adhered to in the experiments by restricting the instantaneous displacement of the piston to less than 2 cm.

In the first test we examine experimental and theoretical results for the time-displacement history shown in Figure 2 using experimental parameters $T = 4$ secs and a chosen permanent (mean) displacement of $C_0 = 0.38$ cm, with the amplitudes C_n and frequencies K_n of the eighteen Fourier components used in Figure 2 scaled appropriately. (In Figure 2 the corresponding parameters of the actual ground displacement are $T = 40$ secs and $C_0 = 7.63$ cm.) The scaled Fourier components are then summed and the result is converted to an analogue (time-voltage) signal which is used to command the wavemaker. The resulting wave motion at the leading edge of the piston ($x = b$) is measured, and the results are shown in Figure 3. Theoretical results at $x = b$ are evaluated for each of the eighteen (scaled) Fourier components according to (17) and summed to yield

$$\eta(b,t) = C_0 + \sum_{n=1}^{18} \eta_n(b,t); \quad (25)$$

the results also are shown in Figure 3. The excellent agreement between the predicted and measured data is self-evident.

Similar results are shown in Figure 4 where a ramp mean motion with an amplitude of $\zeta_0 = 1.33$ cm is added to the Fourier synthesis of Figure 2. The total permanent displacement of the piston is $\zeta_0' = C_0 + \zeta_0 = 1.71$ cm which has been used to normalize the measured and theoretical wave amplitudes. The theoretical result is equivalent to (25) with an added component for the ramp computed from (24). Again, the agreement between measured and computed data is excellent with the wave structure clearly showing the added volume (mass) resulting from the enhanced mean displacement.

5. A Comment on Mean Motions

In previous studies (Hammack, 1972, 1973) two additional models for the mean displacement of a block section of the sea floor have been examined. These time histories are:

- a. exponential: $\zeta_e(t) = \zeta_0 [1 - \exp(-1.1t/T_e)]$
- b. half-sine: $\zeta_s(t) = \zeta_0 [(1 - \cos \pi t/T_s)H(T_s - t)/2 + H(t - T_s)]$

and we repeat for completeness the mean motion introduced here:

- c. ramp: $\zeta_r(t) = \zeta_0 [tH(T_r - t)/T_r + H(t - T_r)]$.

The three mean motions listed above span a wide range of displacement characteristics. We note that the choice of characteristic time scales T_e , T_s and T_r are, in fact, arbitrary to a certain extent even though "natural" choices are apparent. (This flexibility is most obvious for the exponential motion where T_e was chosen for experimental convenience to represent the time for two-thirds of the displacement to occur.) It has been found that the properties of waves generated by these motions correlated strongly with the time-size ratio τ based on these time scales. For example, the maximum wave amplitude, say η_0 , occurring at $x = b$ when normalized by the permanent displacement ζ_0 exhibits a simple and similar functional dependence on τ for each bed motion. With the size scale b/h of the dislocation fixed and for $\tau \ll 1$, the normalized amplitude, η_0/ζ_0 , reaches a maximum value of one-half for all size scales exceeding unity. Bed motions with $\tau \ll 1$ are termed impulsive. For τ very large, termed creeping generation, η_0/ζ_0 decreases at a rate which is inversely proportional to τ . The constant of proportionality for creeping generation varies with the specific choice of the characteristic time scale for the mean motion. Since it is unlikely that any of these mean motion models is "correct" from a geophysical point of view, there is a need to seek a unification of results by generalizing the concept of characteristic time scale. One generalization which closely

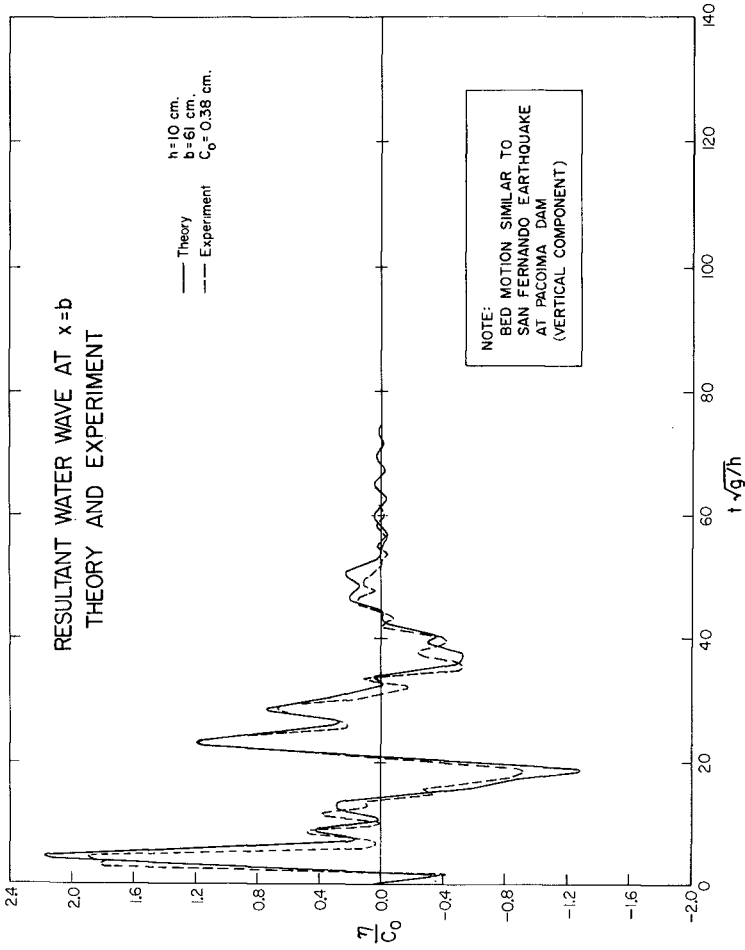


Figure 3. Theoretical (—) and experimental (---) wave records at $x = b$.

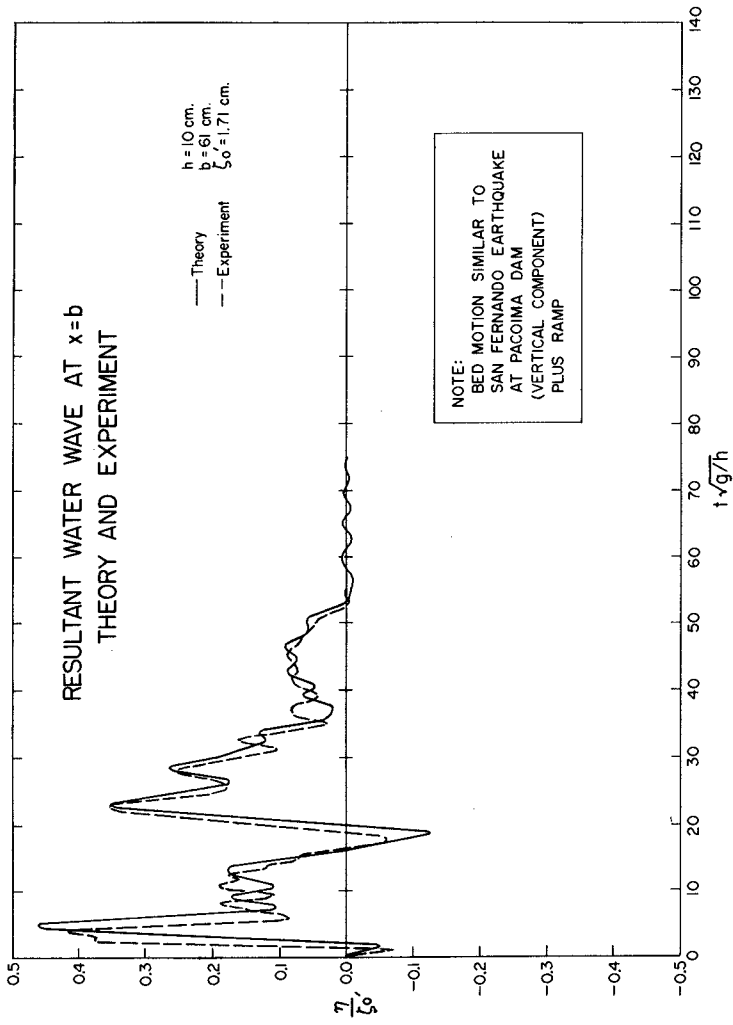


Figure 4. Theoretical (—) and experimental (- - -) wave records at $x = b$ with ramp mean motion.

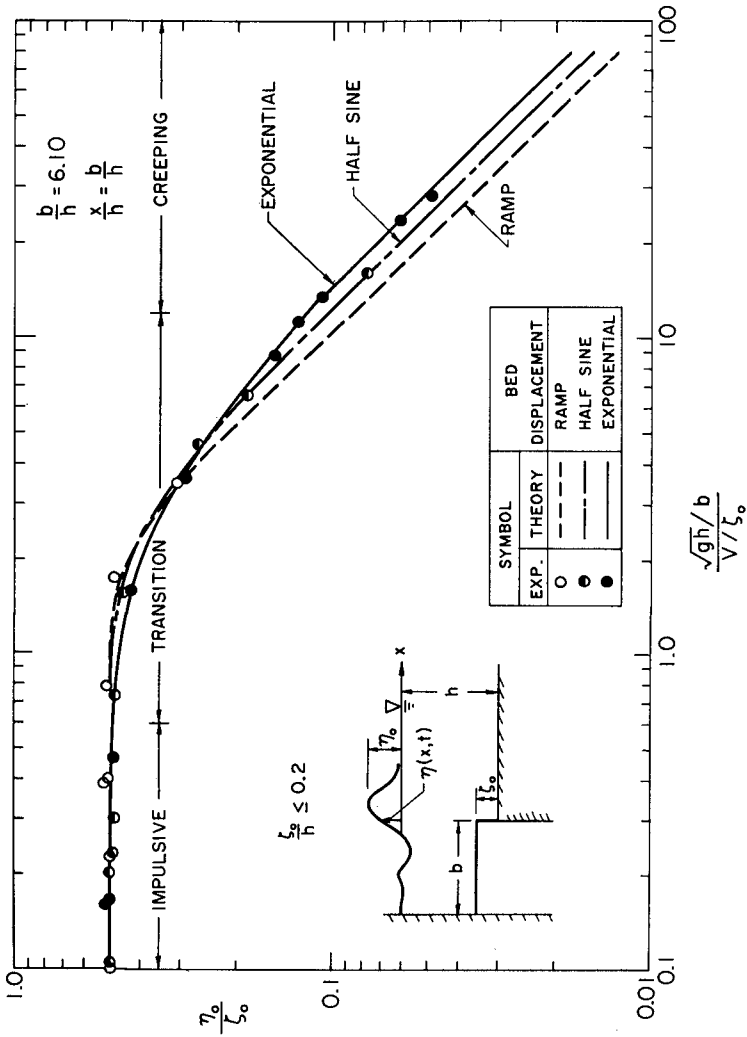


Figure 5. Theoretical and experimental variation of normalized wave amplitude at $x = b$ with generalized time-size ratio for three mean motions.

produces the desired unification is the following. Consider a velocity V , where V^2 is the kinetic energy imparted to the fluid by the sea floor divided by one-half the total mass of fluid displaced during bed motion ($\frac{1}{2} \rho b \zeta_0$); then V is given by:

$$V = \frac{1}{\zeta} \int_0^{\zeta_0} \zeta_t^2 d\zeta \quad (26)$$

and a corresponding time scale $T = \zeta_0/V$. In terms of this time scale the time-size ratio becomes

$$\tau^* = T(gh)^{1/2}/b = \zeta_0(gh)^{1/2}/bV \quad (27)$$

The variation of η_0/ζ_0 at $x = b$ for $b/h = 6.1$ with τ^* is shown in Figure 5 for each of the mean motions; both theoretical and experimental results are presented. For all of the experimental data we have taken $\zeta_0/h < 0.2$ to avoid significant nonlinear effects. The collapse of results for such a wide range of mean motion characteristics shown in Figure 5 is good although a small spread still exists.

6. Conclusions

We have demonstrated both the application and validity of a strategy which employs multiple uses of the superposition principle to develop theoretical solutions for waves generated by sea floor motions with complicated time-displacement histories. Although a more useful test for prototypical phenomena would utilize complicated spatial distributions for the sea floor dislocation, the tests herein were restricted to simple block dislocations due to experimental limitations. However, it is emphasized that the solution method does not distinguish between space and time, and the validity established herein strongly suggests that the methods could be extended to complicated spatial deformations. Finally, we have demonstrated that wave properties (in particular the maximum amplitude of waves escaping the generation region) for a wide range of mean motion characteristics may be (almost) collapsed into a single functional relationship in terms of a time-size ratio based on an average vertical velocity of the sea floor obtained from energy considerations.

7. Acknowledgments

The authors gratefully acknowledge the support of the National Science Foundation under Grant AEN 72-03587-A02 at the California Institute of Technology and the Office of Naval Research under contract N00014-78-C-0889 at the University of California. One author (JLH) would also like to thank the La Jolla Institute, Center for Studies of Nonlinear Dynamics, where portions of this study were completed.

8. References

Hammack, J. L., "Tsunamis: A Model of Their Generation and Propagation," *Report KH-R-28*, W. M. Keck Laboratory of Hydraulics and Water Resources, California Institute of Technology, Pasadena, 1972.

Hammack, J. L., "A Note on Tsunamis: Their Generation and Propagation in an Ocean of Uniform Depth," *Journal of Fluid Mechanics*, Vol. 60, No. 4, 1973, pp. 769-800.

Nigam, N. C., and Jennings, P. C., "Digital Calculation of Response Spectra from Strong-motion Earthquake Records, Earthquake Engineering Research Laboratory Report, California Institute of Technology, Pasadena, 1968.

CHAPTER 41

TSUNAMIS ALONG WEST COAST OF LUZON, PHILIPPINES

by

R. L. Wiegel, F. ASCE*

INTRODUCTION

A detailed engineering study was made by Ebasco Services, Inc., (1977), for a proposed nuclear power plant in the Napot Point region of Bataan, between the entrance to Manila Bay and Subic Bay, Republic of the Philippines (about 14°-37-12'N, 120°-18-3/4'E), Figure 1. As a part of the oceanographic portion of this work, a study was made by the writer of the characteristics of tsunamis that had occurred in the region, and the statistics of occurrence (Wiegel, 1976). The study of tsunamis has been updated to the present time (May, 1980).

The location of the site is such that the large tsunamis generated in some areas of the Pacific Ocean (such as off the coasts of Chile, Alaska, Japan and Kamchatka) are not likely to reach Napot Point with any appreciable amplitude (see, for example, Wiegel, 1976). There is good evidence that this is the case. Owing to the relative stability from the standpoint of earthquakes (aseismic) of Borneo, the Malaya Peninsula, most of Indochina and the intervening China Sea (Gutenberg and Richter, 1949, pp. 82 and 93), there is probably little, if any, chance of tsunamis being generated in this region; this appears to be a fact (Berninghausen, 1969). The great eruption of Krakatoa and the tsunami generated by it was not noticed on tide gages at either Singapore or Hong Kong, so that it would be reasonable that it would not have been detected at Manila (Wharton, 1888). Also, the large tsunamis that have been generated in the Sulu Sea and the Celebes Sea do not seem to reach the site with any appreciable amplitude. Thus, the tsunamis of importance to the site are those which will be generated in the local seas off the west coast of Luzon. In order to establish this fact, information is presented on a number of tsunamis generated in other regions, especially those generated in the seas off the west coast of the Philippine Islands.

HISTORIC RECORD OF TSUNAMIS GENERATED OFF THE WEST COAST OF LUZON

A seismological station, established as a part of the Manila Central Observatory in 1865 (Saderra Masó and Smith, 1913), operated continuously until World War II. It was reestablished after the war. During the interval from about 1900 until the start of World War II, the seismological

* Professor of Civil Engineering, University of California, Berkeley.

station was directed by two scientists: first by the Rev. Miguel Saderra Masó, S.J., and then by the Rev. W. C. Repetti, S.J., both of whom were familiar with tsunamis and their relationship to earthquakes, and who were alert for their occurrence. Owing to this fortunate circumstance, there exist a number of references to historic tsunamis generated in the areas surrounding the Philippine Islands. The sources for finding these references, together with appropriate quotations from the references, are given in the paper. Records of more recent tsunamis are available from several sources. All references to tsunamis in the Philippines found by the writer have been included. In addition, several citations are given in which a statement is made that no tsunami waves were observed, and for which no statement on tsunami waves is given.

The fact that the two scientists mentioned above were familiar with tsunamis and their relationship to earthquakes is shown by the following quotations from three of their reports:

"These facts would appear to afford sufficient foundation for attributing the earthquakes which are confined to the Ilocos Provinces to movements and displacements of the first section or coastal range. The absence of seismic tidal waves and similar phenomena in the case of the two earthquakes mentioned [15 August 1897 and 14 November 1897] may be accounted for, partly by the relative smallness of the portion of the coast disturbed, partly by the fact that it is not the bottom of the sea which is affected, but merely a bordering ledge." -- Saderra Masó (1909)

"As this is one of the few Philippine instances of the waves or tsunamis caused by earthquakes [17 December 1677], it is certainly a pity that the author did not mention the region principally affected. It may be supposed that the waves were raised in the China Sea near the west coast of Cavite, Bataan and Zambeles." -- Saderra Masó (1927)

"Waves were observed at Mambajao, Camiguin Island, and the disturbances of the sea lasted about an hour. The International Summary placed the epicenter at 9.5°N, 128.8°E, but this is scarcely possible, because sea waves from this point could not have passed through the Suriago straits and across the Mindanao Sea without being noticed at other places." -- Repetti (1931), [earthquake of 18 July 1923]

The area to the east of the southern Philippines, bordering the Philippine Trench, and portions of the Celebes Sea, are much more active seismically than is the area off the west coast of central and northern Luzon, in the South China Sea. As commented on by Berninghausen (1969), most of the tsunamis which have been reported from the entire Southeast Asia region have been local in origin and relatively restricted in the extent of the regions affected. This is in agreement with the information contained in the additional references found during the present search, including the 17 August 1976 Moro Gulf tsunami, associated with a shallow local depth earthquake, magnitude determined to be about 7.9 (Badillo and Astilla, 1978).

Thirty-six of the citations included in the paper either mention specifically tsunamis generated in Philippine waters or possible seiches. Details are given in the original report, with a brief citation given

herein. Eleven were generated in the region of direct interest: seven are tsunamis, three are probably seiches, and one is for the case of a hill sinking in a bay. These eleven are marked by an asterisk (*) in the appendix.

The tsunamis that have been observed in the area of interest must have been relatively small; if not, there should be observations to the contrary. Consider two tsunamis generated off the northwest coast of Luzon: 6 May 1924, Agno, Pangasiana. Saderra Masó (1925) states:

"... town of Agno on the west coast of Luzon at 16.1°N and 119.8°E, shortly after an earthquake, was invaded by four big sea waves which flooded its low portions and caused great consternation to the people but without doing considerable material damage nor harm to people.

"A similar occurrence took place in the same town on January 26 of 1872. It is reported that the town was flooded by sea waves shortly after an earthquake....

"In fact, Agno is the only important town existing in the north part of the Zambales coast nearest to the origin of the shocks; moreover its bay and the low alluvial plain where empties the River Balincaguin offered more favorable conditions to the advance of the waves caused by the earthquake than any other place of this west coast of Luzon generally high and cliffy."

There is evidence that the drawdown of the tsunami waves is as important as the runup. The following two tsunamis occurred in the general area of interest: 3 June 1862, water in the bay receded from Manila to Cavite and returned from that direction (Saderra Masó, 1927, p. 95; Repetti, 1935). 14 February 1934, at San Esteban the first movement of the sea was reported to have been a recession, and to such an extent that people hurried out on the exposed shore to gather fish which had been stranded (Repetti, 1934). In these two cases (and perhaps in others; there is no evidence one way or the other) a drawdown occurred first. If the source was a downward vertical tectonic displacement, a drawdown would occur first. The comment of Ludwig, Hayes and Ewing (1967) in their paper on the Manila Trench and Luzon Trough, indicates this to be the case.

In regard to the occurrence of an initial drawdown it is interesting to note that a common observation at widely scattered places was a deep recession of water before the arrival of the first wave during the Moro Gulf tsunami of 17 August 1976 (International Tsunami Information Center, 1976; Badillo and Astilla, 1978).

Essentially, no information was obtained on the "periods" of the tsunami waves generated off the northern and central west coast of Luzon. It is important to obtain this information, as it is useful in determining an estimate of the "width" of the tectonic (or volcanic or landslide) source of the tsunamis. The information obtained of the Moro Gulf tsunami of 17 August 1976 is useful in this respect. Badillo and Astilla (1978) state that the interval between waves was from one to five minutes.

Care must be exercised in obtaining information from the records of tidal gages owing to the natural frequency characteristics of bays (see, for example, Raichlen, 1972); however, very useful information can be obtained from them. Owing to this, the National Ocean Survey (NOAA, U.S. Department of Commerce) was contacted, and it was learned that they have

Philippine Islands tidal data on file in their archives as follows: Cavite, 1921 (3 months); Subic Bay, 1911-1912; Manila, 1901-1940. It was not possible, however, to obtain copies of these.

What can be determined about the heights of the tsunamis? There is good evidence that a large tsunami would be observed and documented. The rationale for this statement is the information available for other areas of the Philippine Islands; information on this follows.

TSUNAMIS IN THE SULU SEA AND THE CELEBES SEA

Devastating tsunamis have been generated in the Sulu Sea and in the Celebes Sea, but were of little importance as far as the vicinity of Manila Bay, Luzon. Three of these are described briefly below.

The epicenter of the subsea earthquake of 21 September 1897 was in the Sulu Sea, about 70 kilometers WNW of Zamboanga, Mindanao, about 70 kilometers NW of Isabela (Basilan Island), about 150 kilometers NNW of Jolo (Sulu Archipelago) and about 380 kilometers SSE of Cuyo Island (Cornoas, 1899; Saderra Masó, June 1909). According to Saderra Masó:

"... immense waves from the west which swept away everything near the shore that was at a less height than 7 meters above mean sea level [Isabela, Basilan Island]... They commenced with an ebb in which the level fell about 5 meters, followed by a series of floods and ebbs, one of the former being extraordinary in height [Zamboanga, Mindanao]... The greatest height reached by the flood was 1 meter [Jolo, Sulu Archipelago]... earthquake was followed by a tidal movement of the sea in which the water rose about 2 meters [Dapitan (NW of Mindanao)]... The port of Cuyo faces towards west. The first ebb was observed an hour and a half after the shock, the water receding during half an hour far beyond the lowest tide; then it returned, reaching within a few minutes the limit of the highest tides. There were alternate ebbs and floods in regular succession during more than one hour [Cuyo Island]."

The tsunami that is described above apparently did not reach Manila, or at least it was so small by then that it was not noticed. It is important for two reasons. It shows that a large tsunami has been observed at a number of locations, and it appears that this may be the largest tsunami that occurred in the Philippines during the past three hundred years, probably larger than the Moro Gulf tsunami of 17 August 1976. The maximum run-up elevation of the tsunami, at a distance of about 70 kilometers from the surface, was about 7 meters above mean sea level.

Another example is the earthquake of 15 August 1918 off southern Mindanao, with a magnitude of 8-1/4 (Gutenberg and Richter, 1949). Its epicenter was located between 5° and 6°N and between 124° and 125°E in the Celebes Sea. This region is active seismically, and many more tsunamis have been generated in the Celebes Sea than off the northern and central west coast of Luzon. Saderra Masó (1918) quotes eyewitness accounts such as:

"... Sarangani Bay ... a tidal wave as high as 24 feet at some points and at the Constabulary station at Glan [Cotabato] to a height of 18 feet ... at Port Lebak, reports that a tidal wave at his place was

between 6 and 8 feet ... south of Port Lebak for some forty miles there was a tidal wave variously estimated at from 20 to 25 feet."

On 17 August (local time; 16 August GMT time), another major earthquake (magnitude 7.9, or 8.0 M_s) occurred in the Celebes Sea (Moro Gulf), at 06.26°N, 124.2°E (International Tsunami Information Center, 1976; Stratta, et al., 1977; Badillo and Astilla, 1978; Pararas-Caryannis and Wigen, 1978; Acharya, 1978), generating a large tsunami. Some comments from the report by The Reverend Victor L. Badillo (Director of Manila Observatory) and Zinnia C. Astilla (1978), follow.

"The Moro Gulf tsunami of 17 August 1976 was the most disastrous tsunami experienced by the Philippines. There have been more severe tsunamis, but areas hit were less populated and had less manmade structures (p. 9)... When the sea had spent its fury and rolled back to its normal cadence, the survivors looked upon scenes of death and destruction. About 8,000 were dead or missing. About 10,000 were injured and about 90,000 were homeless (p. 1)... A common observation at widely scattered places was a deep recession of the water before the arrival of the first wave ... Some persons ran out to the newly exposed sea bottom out of curiosity or to pick up stranded fish (p. 6)... Estimates of wave heights had to be based on qualitative descriptions of the waves being as tall as a coconut tree, a two storey house, twice a man's height, etc., or had to be deduced from photographs of damaged structures ... Places where waves were reported to be higher than five meters are: Linek (Maguindanao), Kalanganan (Cotabato City), Pagadian City, Sacol Island (Zamboanga City), Lebak (Sultan Kudarat). At Lebak waves may have been as high as nine meters (p. 5)*... That there were three or four waves were indicated by the majority of respondents. The largest number was seven, reported by one person. One thing is definite-- there was more than one wave. Majority of respondents estimated the interval between waves to be between one to five minutes. As many considered the first wave to be the most destructive as considered it was the third. At the time of the earthquake the last quarter moon was some 30 degrees above the eastern horizon, so that there was enough light to see."

The International Tsunami Information Center (1976) gives some additional information on the tsunami waves:

"... Based on the survey of the affected area, it was concluded that maximum waves in the entire Moro Gulf area were in the order of 14-15 feet, which were considerably less than what had been reported in the newspapers. Such large waves were experienced at Alicia, Pagadian City, Bongo Island, Resa Bay, Lebak, and the east coasts of Basilan and Jolo islands. Based on the distribution of wave heights along the coastline of Moro Gulf, estimates of travel times of the tsunami to each point, and the directional failure of structures, both by the earthquake and the tsunami, it was concluded that the earthquake and the tsunami generating area was in

* A listing of tsunami wave heights at various localities is given in Table 1 of the report by Badillo and Astilla.

the upper part of Moro Gulf, somewhat south of Baganian Peninsula and having an orientation from southeast to northwest." (p. 6)

In the U. S. Department of Commerce, NOAA publication (1978, p. 71), it is stated that the wave was recorded on the Davao tidegauge with a maximum amplitude of 35 cm.

Additional information on the tsunami, and its effect on shorelines and structures, is given in the report by Stratta, et al. (1977).

For some details on the tectonics of the region, see Hamilton (1977). He believes the earthquake occurred along a subduction zone which is breaking through on the west side of the Sangihe ridge-Halmahera arc collision aggregate. Stewart and Cohn (1977) state that the 1976 event represents the first seismic evidence for a subduction zone in this area.

SEISMIC AND GEOLOGIC INFORMATION

Papers on the seismicity of the region and geological studies of the region are of great use in interpreting the historical information that has been obtained on tsunamis and to estimate future tsunamis. Of great importance are the many papers of the Rev. Miguel Saderra Masó, S.J. (1909; 1927), and the Rev. William C. Repetti, S.J. (1930; 1931a; 1931b; 1946), of the Seismological Station, Manila Central Observatory (Weather Bureau, Philippine Islands). Barazongi and Dorman (1969) plotted the epicenters of 29,553 earthquakes which occurred during the interval 1 January 1961- 31 December 1967. Earthquakes with shallow focal depths are the most important from the standpoint of the generation of tsunamis. Their Plate 3 shows the epicenters for earthquakes with focal depths between 0 and 100 kilometers.

Saderra Maso and Repetti did not assign magnitudes to earthquakes, as the techniques to do so had not yet been developed. The magnitude and focal depth have been shown to be important to the generation of tsunamis (see, for example, Iida, 1970). Gutenberg and Richter (1949) determined the magnitudes for a large number of earthquakes. A list of the earthquake dates, times, locations and magnitudes for Region 22 (Philippine Islands) is not included herein owing to space limitations. For an update on this, see Sevilla, et al. (1965), Damasco (1970), Rowlett and Lelleher (1976), Acharya (1978); also, see NOAA tapes.

Work has been done on the relationship between earthquakes and structure of the Philippines (Willis, 1944), and on the submarine morphology of the Philippines (Irving, 1951). The term "Philippine rift" was used by Irving rather than the term "Philippine fault" as being more descriptive of the situation. Irving shows instrumentally determined epicenters of Philippine earthquakes for the period 1900-1945.

Geophysical studies have been made in recent years of the region in the South China Sea off the coast of Northern and Central Luzon, specifically studies of the Manila Trench and the West Luzon Trough* (Ludwig

*Murphy (1973) refers to the long West Luzon Trough as "graben-like." This paper discusses the relationship of the Manila Trench and the West Luzon Trough with the West Taiwan Foldbelt and the Philippine Trench.

Hayes and Ewing, 1967; Hayes and Ludwig, 1967; Ludwig, 1970). Ludwig, Hayes and Ewing (1967) state:

"The west wall of the trench is a remnant of the original sea floor which has been depressed. The steps in the western wall of the trench are interpreted as normal faulting and are most likely caused by extensional forces introduced in the oceanic crustal plate as it is being further depressed. The steps and perched ledges of transparent sediments, which form the foot of the west wall, attest to the downward movement and recent activity. The perched ledges indicate post-depositional subsidence and (perhaps) extension of the sea floor near the axis of the trench. This is further evidenced by eastward dipping stratified beds beneath the floor of the trench (profiles E-F and L-N), suggesting downward movement with respect to the east wall. The alternative explanation is that the perched ledges were formed by erosion; however, no direct evidence is available at present to support it."

This is in agreement with the observations of several tsunamis in which a substantial drawdown of the water occurred first, that is, a downward vertical tectonic displacement probably was the source of the tsunamis. A similar drawdown seems to occur in the large tsunamis generated in the Celebes Sea (Badillo and Astilla, 1978).

Hayes and Ludwig (1967) present a map of the earthquake hypocenters of central Luzon, the Manila Trench and the West Luzon Trough, Figure 1. In comparing the locations of the plots, one must be aware of the accuracy of the locations. Gutenberg and Richter (1949) state:

"Epicenters have in general not been determined more closely than the nearest quarter degree of latitude and longitude except for unusually favorable shocks. More accurate revision would involve considering the effect of geocentric latitude, which may amount to as much as 0.4 degree in extreme cases...."

Hayes and Ludwig (1967, p. 546) state:

"Accuracies are estimated at several tens of kilometers for good determination to ± 100 km or more for poor ones...."

Salient features of the bathymetry west of Luzon are given by Ludwig, Hayes and Ewing (1967), as are seismic reflection profiles across the Manila Trench and West Luzon Trough. Some conclusions reached by the investigators have been cited earlier in this report, in context with the possible generation of tsunamis.

For additional analyses of the tectonics of this area, see the papers by Murphy (1973) and Rowlett and Kelleher (1976). For details of studies of adjacent regions, such as the Sulu Sea, Celebes Sea, Bareda Sea and Molucca Sea, see Krause (1966) and Hamilton (1977).

REFERENCES

- Acharya, H. K., "Mindanao Earthquake of August 16, 1976: Preliminary Seismological Assessment," *Bulletin of the Seismological Society of America*, Vol. 68, No. 5, October 1978, pp. 1459-1468.
- Adams, Wm. Mansfield, *An Index to Tsunami Literature to 1966*, Data Report No. 8, HIG-67-21, Hawaii Institute of Geophysics, University of Hawaii, November 1967.
- Adams, William Mansfield (editor), *Tsunamis in the Pacific Ocean*, Proceedings of the International Symposium on Tsunamis and Tsunami Research, East-West Center Press, University of Hawaii, Honolulu, Hawaii, 1970, 513 pp.
- Allen, C. R., "Circum-Pacific Faulting in the Philippines-Taiwan Region," *Journal of Geophysical Research*, Vol. 67, No. 12, 1962, pp. 4792-4812.
- Badillo, Victor, and Zinnia C. Astilla, *Moro Gulf Tsunami of 17 August 1976*, Manila Observatory, Quezon City, Republic of the Philippines, prepared for the Special Committee on Tsunami Warning System, National Committee on Marine Sciences, National Science Board, 1978, 37 pp.
- Barazangi, Muawia and James Dorman, "World Seismicity Maps Compiles from ESSA, Coast and Geodetic Survey," *Bulletin of the Seismological Society of America*, Vol. 59, No. 1, February 1969, pp. 369-380.
- Berninghausen, Wm. H., "Tsunamis and Seismic Seiches of Southeast Asia," *Bulletin of the Seismological Society of America*, Vol. 59, No. 1, February 1969, pp. 289-297.
- Centeno Y Garcia, José, "Abstract of a Memoir on the Earthquakes in the Island of Luzon in 1880," (translated by Prof. W. S. Chaplin), *Transactions of the Seismological Society of Japan*, Vol. V, 1882 May-December, Tokyo, 1883, pp. 43-88.
- Coffman, J. L. and W. K. Cloud, *U.S. Earthquakes, 1968*, Coast and Geodetic Survey, U.S. Department of Commerce, 1970, 111 pp.
- Coffman, J. L. and Carl A. von Hake, *United States Earthquakes, 1970*, National Oceanic and Atmospheric Administration, Environmental Data Service, U.S. Department of Commerce, 1972, 81 pp.
- Coronas, Rev. José, S. J., *La Actividad Sísmica en el Archipiélago Filipino durante el Año 1897*, Manila, 1899, pp. 47-92.
- Cox, Doak C. (editor) and Ethel McAfee (associate editor), *Proceedings of the Tsunami Meetings Associated with the Tenth Pacific Science Congress, University of Hawaii, Honolulu, Hawaii, August-September 1961*, International Union of Geodesy and Geophysics, Monograph No. 24, Paris, France, July 1963, 265 pp.
- Damasco, Z., "Seismicity of the Philippines (1897-1967)", *International Institute of Seismology and Earthquake Engineering, Individual Studies*, Vol. 6, 1970, pp. 53-58, and appendix.

- Ebasco Services, Inc., *National Power Corporation, PNPP Unit No. 1- PSAR: Hydrologic Descriptions of PSAR*, 1977.
- Georgetown University, *Seismological Dispatches*, Seismological Observatory, Georgetown University, Washington, D. C., December 1928, I page.
- Gutenberg, B. and C. F. Richter, *Seismicity of the Earth and Associated Phenomenon*, Princeton University Press, 1949, 273 pp.
- Hamilton, Warren, "Subduction in the Indonesian Region," *Island Arcs, Deep Sea Trenches and Back-Arc Basins*, edited by Manik Talwani and Walter C. Pitman, III, Maurice Ewing Series, American Geophysical Union, 1977, pp. 15-31.
- Hayes, Dennis E. and William J. Ludwig, "The Manila Trench and West Luzon Trough- I. Gravity and Magnetics Measurements," *Deep-Sea Research*, Vol. 14, 1967, pp. 545-560.
- Iida, Kumizi, Doak C. Cox and George Pararas-Carayannis, *Preliminary Catalog of Tsunamis Occurring in the Pacific Ocean*, Data Report No. 5, HIG-67-10, Hawaii Institute of Geophysics, University of Hawaii, August 1967.
- Iida, K., "The Generation of Tsunamis and the Focal Mechanism of Earthquakes," *Tsunamis in the Pacific Ocean*, ed. by W. M. Adams, East-West Center Press, University of Hawaii, Honolulu, 1970, pp. 1-18.
- International Tsunami Information Center, *Newsletter*, Vol. II, No. 2, 5 April 1969, 9 pp.
- International Tsunami Information Center, *Newsletter*, Vol. III, No. 2, 25 June 1970, 8 pp.
- International Tsunami Information Center, "Philippine Islands Earthquake," *Newsletter*, P. O. Box 3650, Honolulu, Hawaii 96811, Vol. 8, No. 4, December 1975, p. 15.
- International Tsunami Information Center, "ITIC-PAGASA-USGS Survey of the Earthquake and Tsunami of 16 August 1976 in the Philippines," *Newsletter*, Vol. IX, No. 3, September 1976, pp. 3-6.
- International Tsunami Information Center, *Tsunami Reports*, No. 1978-II, P.O. Box 50027, Honolulu, Hawaii 96850, June 1979, 2 pp.
- Irving, Earl M., "Submarine Morphology of the Philippine Archipelago and Its Geological Significance," *The Philippine Journal of Science*, Vol. 80, No. 1, March 1951, pp. 55-88.
- Krause, Dale C., "Tectonics, Marine Geology, and Bathymetry of the Celebes Sea-Sulu Sea Region," *Geological Society of America Bulletin*, Vol. 77, August 1966, pp. 813-832.
- Ludwig, William J., "The Manila Trench and West Luzon Trough- III. Seismic-refraction Measurements," *Deep-Sea Research*, Vol. 17, 1970, pp. 553-571.

- Ludwig, William J., Dennis E. Hayes and John I. Ewing, "The Manila Trench and West Luzon Trough—1. Bathymetry and Sediment Distribution," *Deep-Sea Research*, Vol. 14, 1967, pp. 533-544.
- Minoza, W. A., A. T. Ocampo, Jr. and S. Bellosillo, Jr., "Significant Philippine Earthquakes (1949-1959)," *Philippine Weather Bureau Scientific Papers*, 101, 1960, 65 pp.
- Murphy, Leonard M. and William K. Cloud, *United States Earthquakes: 1952*, Serial No. 773, Coast and Geodetic Survey, U. S. Department of Commerce, 1954.
- Murphy, Leonard M. and Franklin P. Ulrich, *United States Earthquakes: 1948*, Serial No. 746, Coast and Geodetic Survey, U. S. Department of Commerce, 1951(a).
- Murphy, Leonard M. and Franklin P. Ulrich, *United States Earthquakes: 1949*, Serial No. 748, Coast and Geodetic Survey, U. S. Department of Commerce, 1951(b).
- Murphy, Richard W., "The Manila Trench – West Taiwan Foldbelt: A Flipped Subduction Zone," *Geological Society of Malaysia*, Bulletin 6, July 1973, pp. 27-42.
- Pararis-Carayannis, George and Sydney O. Wigen, "Philippine Earthquake and Tsunami of August 17, 1976," *Tsunami Reports*, No. 1976-26, International Tsunami Information Center, P. O. Box 3830, Honolulu, Hawaii, April 1978, 3 pp.
- Philippine Weather Bureau, *Annual Report of the Philippine Weather Bureau: Fiscal Year 1951/51*, Department of Commerce and Industry, Republic of the Philippines, October 1952.
- Philippine Weather Bureau, *Annual Report of the Philippine Weather Bureau, Fiscal Year 1961/60*, Department of Commerce and Industry, Republic of the Philippines, 1960.
- Philippine Weather Bureau, *1961-1962 Annual Report*, Department of Commerce and Industry, Republic of the Philippines, 1962.
- Raichlen, F. "Discussion of Tsunami-response of San Pedro Bay and Shelf, Calif.," *Journal of the Waterways, Harbors and Coastal Engineering Division, Proc. ASCE*, Vol. 98, No. WW1, 1972, pp. 104-110.
- Repetti, Rev. William C., S. J., "The Hinatuan Earthquake of June 13th, 1929," *Seismological Bulletin for 1930: January-June*, Weather Bureau, Manila Central Observatory, Government of the Philippine Islands, 1930, pp. 28-33.
- Repetti, Rev. W. C., S. J., "Philippine Earthquake Epicenters," *Seismological Bulletin for 1930: July-December*, Weather Bureau, Manila Central Observatory, Government of the Philippine Islands, 1931(a), pp. 71-85. Note: these are for epicenters north of Manila.

- Repetti, Rev. W. C., S. J., "Philippine Earthquake Epicenters South of Manila, 1920-29," *Seismological Bulletin for 1931: January-June*, Weather Bureau, Manila Central Observatory, Dept. of Agriculture and Natural Resources, Government of the Philippine Islands, 1931(b), pp. 37-52.
- Repetti, Rev. W. C., S. J., "The China Sea Earthquake of February 14th, 1934," *Seismological Bulletin for 1934: January-June*, Weather Bureau, Manila Central Observatory, Dept. of Agriculture and Commerce, Government of the Philippine Islands, 1934, pp. 22-26.
- Repetti, Rev. W. C., S. J., "The China Sea Earthquake of November 26th, 1934," *Seismological Bulletin for 1934: July-December*, Weather Bureau, Manila Central Observatory, 1935, p. 55.
- Repetti, Rev. W. C., S. J., "Tectonic Lines of the Philippine Islands," *Seismological Bulletin for 1934: July-December*, Weather Bureau, Manila Central Observatory, Dept. of Agriculture and Commerce, Government of the Philippine Islands, 1935, pp. 57-71.
- Repetti, Rev. W. C., S. J., "The Alabat Earthquake of August 20th, 1937," *Seismological Bulletin for 1937: July-December*, Weather Bureau, Manila Central Observatory, Dept. of Agriculture and Commerce, Commonwealth of the Philippines, 1938, pp. 49-53.
- Repetti, Rev. W. C., S. J., "May, 1938: Macroseismic Record," *Seismological Bulletin for 1938: January-June*, Weather Bureau, Manila Central Observatory, Dept. of Agriculture and Commerce, Commonwealth of the Philippines, 1938, p. 17.
- Repetti, William C., S. J., "Catalogue of Philippine Earthquakes, 1589-1899," *Bulletin of the Seismological Society of America*, Vol. 36, No. 3, July 1946, pp. 133-322.
- Rowlett, Hugh and John Kelleher, "Evolving Seismic and Tectonic Patterns along the Western Margin of the Philippine Sea Plate," *Journal of Geophysical Research*, Vol. 81, No. 20, July 10, 1976, pp. 3518-3524.
- Rudolph, E., "Ueber Submarine Erdbeben und Eruptionen," *Beitrage zur Geophysik*, Stuttgart; Band 1, 1887, pp. 133-365; Band 11, 1895, pp. 537-666.
- Saderra Masó, Rev. M., S. J., "The Strongest Earthquakes Felt in the Philippines During the Last Half Century," *Seismological Bulletin for February, 1909*, Weather Bureau, Manila Central Observatory, Department of the Interior, Philippine Islands, 1909, pp. 61-63.
- Saderra Masó, Rev. M., S. J., "Submarine Seismic Centers Near the Coast of Northern Luzon," *Bulletin for May, 1909*, Manila Central Observatory, Weather Bureau, Department of the Interior, Manila, 1909, pp. 167-169.
- Saderra Masó, Rev. M., S. J., "Seismic Epicenters Near Western Mindanao and Jola," *Seismological Bulletin for June, 1909*, Weather Bureau, Manila Central Observatory, Department of the Interior, Philippine Islands, 1909, pp. 203-207.

- Saderra Masó, Miguel, "Great Earthquake and Tidal Wave in Southern Mindanao, P. 1.," *Bulletin of the Seismological Society of America*, Vol. 8, No. 4, December 1918, pp. 125-126.
- Saderra Masó, Rev. Miguel, S. J., "Mindanao Earthquakes, November 7 and 11, 1921," *Bulletin for November 1921*, Weather Bureau, Manila Central Observatory, Government of the Philippine Islands, 1923, pp. 371-372.
- Saderra Masó, Rev. Miguel, S. J., "The Mati Earthquake, April 14, 1924," *Bulletin for January to April, 1924*, Weather Bureau, Manila Central Observatory, Government of the Philippine Islands, 1925, pp. 123-214.
- Saderra Masó, Rev. Miguel, S. J., "Earthquake and Sea Waves at Agno, Pangasinian, May 6, 1924," *Bulletin for May 1924*, Weather Bureau, Manila Central Observatory, Government of the Philippine Islands, 1925, p. 156.
- Saderra Masó, Rev. Miguel, S. J., "Earthquakes Felt in the Philippines: Seismological Bulletin for May, 1925," *Bulletin for May to August, 1925*, Weather Bureau, Manila Central Observatory, Government of the Philippine Islands, 1926, p. 147.
- Saderra Masó, Rev. Miguel, S. J., "Southern Negros Earthquake, May 5, 1925," *Bulletin for May to August, 1925*, Weather Bureau, Manila Central Observatory, Government of the Philippine Islands, 1926, pp. 152-153.
- Saderra Masó, Rev. Miguel, S. J., "The Samar Earthquake, November 13, 1925," *Bulletin for September to December, 1925*, Weather Bureau, Manila Central Observatory, Government of the Philippine Islands, 1926, p. 353.
- Saderra Masó, Rev. M., S. J., "Destructive and Violent (VII-X R.F.) Philippine Earthquakes and Eruptions 1585-1925," *Seismological Bulletin for 1926*, Weather Bureau, Manila Central Observatory, Government of the Philippine Islands, 1927, pp. 61-64.
- Saderra Masó, Rev. Miguel, S. J., "Ancient Philippine Earthquakes, 1585-1865," *Seismological Bulletin for 1926*, Weather Bureau, Manila Central Observatory, The Government of the Philippine Islands, 1927, pp. 65-103.
- Saderra Masó, Miguel and Warren D. Smith, "The Relation of Seismic Disturbances in the Philippines to the Geologic Structure," *The Philippine Journal of Science: A. Chemical and Geological Sciences and the Industries*, Vol. 8, No. 4, August 1913, pp. 199-233.
- Selga, Miguel, S. J., "The Zamboanga Mareogram of the Coquimbo Earthquake," *Proceedings of the Pan-Pacific Science Congress, Australia, 1923*, Vol. 1, ed. by Gerald Lightfoot, The Australian National Research Council and The Commonwealth and State Governments, 1923, pp. 587-590.
- Sevilla, F. Q., R. G. Valenzuela and S. Bellosillo, Jr., "Seismicity of the Philippines (1907-1964)," *Intern. Inst. Seismology Earthquake Eng. Individual Studies*, Vol. 2, 1965, pp. 34-63.

- Spaeth, Mark G., *Annotated Bibliography on Tsunamis*, Monograph No. 27, International Union on Geodesy and Geophysics, Paris, France, July 1964, 249 pp.
- Stewart, Gordon S. and Stephen N. Cohn, "The August 16, 1976 Mindanao, Philippine Earthquake (MS = 7.8)—Evidence for a Subduction Zone South of Mindanao," *EOS, Transactions, American Geophysical Union*, Vol. 58, No. 12, December 1977, p. 1194. This is an abstract only.
- Stratta, James L., Ted. J. Canon, C. Martin Duke, Lawrence G. Selna, J. Eugene Haas and David J. Leeds, *Reconnaissance Report: Mindanao, Philippines Earthquake, August 17, 1976*, Earthquake Engineering Research Institute, 2620 Telegraph Avenue, Berkeley, California, 94704, U.S.A., August 1977, 106 pp.
- United States Department of Commerce, *United States Earthquakes, 1975*, published jointly by U.S. Department of Commerce, National Oceanic and Atmospheric Administration, and the U. S. Department of Interior, Geological Survey, 1975.
- United States Department of Commerce, *United States Earthquakes, 1976*, published jointly by U. S. Department of Commerce, National Oceanic and Atmospheric Administration, and the U. S. Department of Interior, Geological Survey, 1978, p. 71.
- Wallace, R. E., George Pararas-Carayannis, Rolando Valenzuela and J. N. Taggart, "Earthquake and Tsunamis of August 16, 1976, Mindanao, Philippines," *Abstracts with Programs, South-Central Section, 11th Annual Meeting*, March 17-18, 1977, El Paso, Texas, The Geological Society of America, 1977, p. 523. Note: This is only a half-page abstract.
- Weather Bureau, Geophysical Division, no title, No. 38, Dept. of Commerce and Industry, Republic of the Philippines, February 1952.
- Weather Bureau, *Annual Report of the Weather Bureau, FY 1964-1965*, Weather Bureau, Department of Commerce and Industry, Republic of the Philippines, Manila, 1965, 51 pp.
- Wharton, W.J.L., "On the Seismic Sea Waves Caused by the Eruption of Krakatoa, August 26th and 27th, 1883, Part III," *The Eruption of Krakatoa and Subsequent Phenomena, Report of the Krakatoa Committee of the Royal Society*, ed. G. J. Symons, London: Trübner & Co., 1888, pp. 89-150.
- Wiegel, R. L., "Tsunamis," *Seismic Risk and Engineering Decisions*, ed. C. Lomnitz and E. Rosenblueth, Chapter VII, Elsevier Scientific Publishing Company, Amsterdam, 1976, pp. 225-286.
- Wiegel, R. L., *Possibility of Tsunamis along the Bataan Coast, Between Entrance to Manila Bay and Subic Bay, Republic of the Philippines*, report to Ebasco Services, Inc., 3 June 1976, 63 pp.
- Willis, Bailey, "Philippine Earthquakes and Structure," *Bulletin of the Seismological Society of America*, Vol. 34, No. 2, April 1944, pp. 69-81.

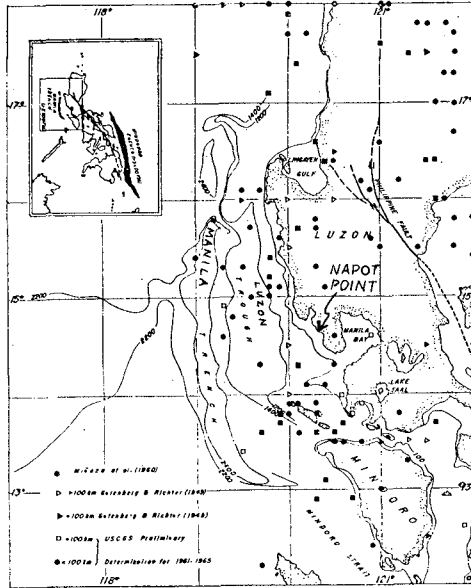


Fig. 1. Earthquake hypocenter map of central Luzon, Manila Trench—
the area outlined on the inset of the regional geography. Location of the Philippine Fault is
taken from ALLEN (1962). Contours in nominal fathoms.
(From Hayes and Ludwig, 1967)

APPENDIX: PHILIPPINE TSUNAMIS

September 1627, northern Luzon (Repetti, 1946).

"... trees were overthrown by the terrific force of the waves of the sea, which invaded the land for a distance of a league, and in that area the land could not be seen."

*30 November 1645, Manila (Saderra Masó, 1927).

"Of this most disastrous earthquake all the writers about the Philippines both ancient and modern give notice ... The disturbance of the Pasig River was so tremendous that its waters invaded parts of the town and even passed over the bridge."

Repetti (1940) believes the earthquake of 14 February 1934 more severe.

*7 December 1677, S and SW Luzon (Saderra Masó, 1927 quotes Fr. Diaz):

"Some people who were navigating related the dangers of foundering that they encountered because of the high waves caused by the earthquakes, which at placed invaded the coast and flooded large inland tracks of land with great damage."

*1744, Northern Luzon (Repetti, 1946)

"In the *Diccionario Ibanag-Español* there is mention of earthquakes under the word ALLUYU, meaning great waves ... 'The sea enters the river with great force....'"

December 1770, Manila (Repetti, 1946). The expression "the sea was agitated" that appears in Berninghausen's (1969) paper was "... a very strong south wind, which agitated the sea ..." in Repetti's paper.

*9 November 1828, Manila (Repetti, 1946, p. 173).

"After the earthquake, the river rose to the same height that it reaches in the rainy season and inundated the lowland near its banks. The next day it fell as much below its ordinary level...."

*18 January 1830, Manila and nearby provinces (Repetti, 1946, quoting an article in the Singapore *Chronicle* of 25 March 1830):

"...having made the best of his way to the river, he was there 'taken aback,' as the water came rushing up the steps several feet ... but the water quickly retreated, and broke upon the opposite bank with a noise resembling thunder, and then gradually subsided."

22 March 1840, Sorsogon Province (Saderra Masó, 1927, p. 91).

"A large tract of the northern shore of the bay where the town of Sorsogon is located sank five feet, the advance of the sea causing considerable material and personal loss."

Saderra Masó quotes a report of 22 February 1843 by the Governor of Albay:

"As a result of the earthquakes felt in the town of Sorsogon in March 1840 ... surely the bottom of the bay underwent a change because today boats of great draft can drop anchor where formerly small craft grounded at low tide, ... the sea submerged a great portion of the shore and the nearer houses of the water front...."

*16 September 1852, Manila and western provinces (Saderra Masó, 1927, p. 93).

"This destructive earthquake made itself felt with violence in west Rizal and Bulacan, SW Nueva Ecija and the provinces of Cavite, Batangas, Bataan, Zambales, Tarlac and Pampanga.... A hill called Ubamba in the Subic Bay sank completely."

*3 June 1862, South Luzon (Saderra Masó, 1927, p. 95).

"It is stated that the water in the bay receded from Manila to Cavite and returned from that direction...."

Repetti (1946), quoting works dating to 1865, states:

"... Earthquake in Manila. J. Winchester, captain of the English frigate *Caribbean* and D. Cobbs, captain of the English frigate *John Banks* describe the action in the Bay of Manila: '3 June, 7^h30^m p.m. we saw a wave coming on us from the SE to NW. It struck us with such force that it came over the deck which it covered completely. The frigate shook and shivered strongly as if it had struck bottom. The water boiled around the ship in strong convulsions...."

16 August 1869, Southeastern Luzon and eastern Visayan (Repetti, 1946).

"... and the sea was disturbed ... A small island, among the many at the north end of Ticao, is said to have disappeared."

*26 January 1872, Agno, Zambales Province (Saderra Masó, 1927). Intensity VII, Rossi-Forel scale, "earthquake and tidal wave." Repetti (1946) states:

"... It is reported that the town was flooded by sea waves shortly after an earthquake and, as it is said, noises like explosions were heard, which excited and terrified the people."

14 July 1880, Luzon (Centeno & Garcia, 1883). Repetti (1946) lists this as 15 July 1880, on the east coast of Luzon, just east of Manila.

"At Quinanliman the depression had a wide extent, but was very irregular in depth: the greatest depth was four metres at the centre line DE of the submerged surface ..." (Centeno & Garcia, p. 78)

26 and 27 August 1883. Eruption of Krakatoa (Wharton, 1888), Sunda Strait between Sumatra and Java. See comments in main body of paper.

23 July 1885, near northwest coast of Mindanao (Saderra Masó, June 1909).

"These facts locate the focus of the disturbance in the sea, opposite the northwestern coast ... no mention is made of any extraordinary commotion of the sea although the observer spoken of lived in a place on the coast and describes—with almost painful attention to detail—everything abnormal which he observed during the earthquake."

5 February 1889, in the Celebes Sea (Saderra Masó, June 1909).

"At the time of this earthquake the steamer *Churruca* was underway from Zamboanga to Cotabato, passing over the very region which, according to our opinion contained the focus ... the water became turbid with mud rising from the bottom of the sea and formed whirls. No great waves could be seen from aboard the vessel, nor are such mentioned in the reports from Zamboanga and Cotabato."

21 September 1897, E and SE part of the Sulu Sea (Saderra Masó, June 1909). Details of this great event given in the main body of present paper.

"The great tsunami ... is of special interest, since it is almost the only one to be found in the seismic annals of the Philippines."

21 August 1902, northern Illana Bay, Mindanao (Saderra Masó, June 1909).

"Great fissures and landslides were caused, both on land and in the sea, the latter being proved by the fact that the cables which connected Cotabato with several military posts in southern Mindanao were broken ... a clear proof of the displacements which must have taken place on the bottom of the bay."

15 August 1918, Mag. 8¼ (G&R*, 1949). Celebes Sea, between 124° and 125°E and 5° and 6°N (Saderra Masó, 1918, also Dec. 1918).

"Captain Malone ... reports that the earthquake ... was later followed by a tidal wave reaching as high as 24 feet at some points and at the Constabulary station at Glan to a height of 18 feet, thereby destroying all of the houses that had been shaken down by the shock and drowning a number of people ... All native vintas were either destroyed or taken out to sea L.B. Kidwell, who has a saw-mill at Port Lebak, reports that the tidal wave at his place was between 6 and 8

*G&R refers to Gutenberg and Richter.

feet, killing six people and carrying a number of logs quite a distance inland.... To the south of Port Lebak for some 40 miles there was a tidal wave variously estimated at from 20 to 25 feet."

11 November 1921, Mag. 7½, epicenter 8N, 127E (G&R, 1949). Off SE coast of Mindanao, in southern part of the Philippi-Deep (Saderra Masó, 1923).

"The most unusual effect of the second earthquake was a tide-wave which invaded the few bays with low lands there existing, Manay being the one which sustained greater loss in structures and crops. ... The tide-wave was also noticed in great Sanguir Island."

10-11 November 1922, Chile, Coquimbo earthquake (Selga, 1923). Although the earthquake epicenter was thousands of miles from the Philippines, the tsunami was recorded by the tide gage in Zamboanga. Selga (1923) states:

"... the mareogram shows that the seismic wave arrived at Zamboanga on 12th November, 1922, at 2 hours 40 min p.m. standard time of the 120th meridian east of Greenwich ... Five crests and five troughs are clearly discernible ... the period of the wave is 100 minutes, if derived from the maximums; 106 minutes if derived from the minimums..."

The tide station at Manila was not operating at the time of this tsunami.

2 March 1923, Mag. 7.2 (G&R, 1949). Berninghausen [incorrectly?] lists as 23 Feb. 1923. Mindanao, epic. 6°45'N, 123°35'E (Repetti, 1931).

"The position given by the International Summary, 6°N, 125°E, can scarcely be admitted because it is inland, and sea waves were reported as making into the Rio Grande River at Cotabato."

18 July 1923, Mambajao, Camiguin, epicenter 9°20'N, 125°E, Repetti (1931).

"Waves were observed at Mambajao, Camiguin Island, and the disturbance of the sea lasted about an hour."

14 April 1924, Mag. 8.3, epicenter 6½N, 126½E (G&R, 1949), off Pacific Coast. SE Mindanao (Saderra Masó, 1925).

"A large tract of the sea shore of Mati, at the head of the small Pujada Bay, separated from the ocean by a narrow peninsula, sunk about half a meter... The disturbance caused by shocks in the sea was not so great as the maremoto which followed the earthquake of November 1921 originated near the same coasts. On board of a steamer at anchor in the Caraga Bay, about 150 kilometers NNW of the epicenter, two sharp shocks followed by ... similar to the effect of the keel striking against a rock. The sea became suddenly and terribly rough causing in the boat such strong jerks that threatened to break the anchor chains; at the same time big waves were seen to break against the cliffs of the near coast."

Repetti (1931) states:

"Sea waves were reported from Mati and Caraga...."

*6 May 1924, Agno, Pangasinan (Saderra Masó, 1925).

"At about midnight of the 6th of May, the town of Agno on the west coast of Luzon at 16.1°N and 119.8°E, shortly after an earthquake, was invaded by four big sea waves which flooded its low portions and caused great consternation to the people but without doing considerable material damage nor harm to persons."

30 August 1924, Mag. 7.3 (G&R, 1949), epic. 9°N, 126°40'E (Repetti, 1931).

"A sea wave was noticed at Bislig Hinatuan situated on bays whose trend is slightly more in the direction of our position."

5 May 1925, Mag. 6.75 (G&R, 1949). Southern Negros (Saderra Masó, 1926).

"Its origin lay under the sea near the south coast of Negros Island not far from 9.3°N and 122.7°E ... Moreover, only the said south coast was invaded by the waves caused by the earthquake."

25 May 1925, Mag. 6.25, epicenter 12.5°N, 122.5°E (G&R, 1949). Tablas and Romblon Islands (Saderra Masó, 1926).

"... A small earthquake wave developed and flooded some small low villages on the SE coast of Tablas. The steamer *Compeador* felt distinctly the shock while navigating SW of Romblon Island."

Repetti (1931) states:

"Sea waves observed at Tugdan in the east coast of Tablas Island."

13 November 1925, Mag. 7.3 (G&R, 1949), Philippine Deep, NE of Samar Island, near 125.5°E and 13.0°N (Saderra Masó, 1926).

"... cracks opened and the low shores were flooded by the waves caused by the earthquake; many fishermen lost their fishing boats and several were drowned. Numerous native houses on this and on Laoang Island were destroyed. On the coast of Samar not only native houses but ... more substantial constructions suffered considerable damage."

Repetti (1931) states:

"Sea waves were observed along the north coast of Samar."

19 December 1928, Cotabato, Mindanao, Mag. 7.3, epic. 7°N, 124°E (G&R, 1949). Seismological Dispatches (Georgetown Univ., Dec. 1928) state:

"MANILA, P.I., Dec. 24, 1928. Rocked by an earthquake, and swept by a tidal wave, Cotabato, capital of Mindanao Province, was practically destroyed on Wednesday night."

28 December 1928, Cotabato, Mindanao, Mag. 6.9; epicenter 7.5°N, 123°E (G&R, 1949). Not listed by Repetti (1931a,b). Berninghausen (1969):

"Destructive earthquake reported ... Wave probably struck the coast near Cotabato which is inland (Georgetown Univ., 1926)."

The reference (1926) must be wrong and is (1928) instead, and no mention of tsunami waves is given in the original reference. The statement of Berninghausen seems to apply to the earthquake of 19 December 1928.

13 June 1929, Mag. 7.2 (G&R, 1949), Hinatuan earthquake, epicenter over western slope of the Mindanao Deep, 8°20'N, 126°53'E (Repetti, 1930).

"Thousands of dead fish of all kinds and all sizes, up to 30 inches, were seen floating in the ocean and case up on shore. They had evidently been killed by the concussion of the shocks.... A small sea-wave came in." (NOTE: Hinatuan, due west of the epicenter.)

*14 February 1934, Mag. 7.6 (G&R, 1949). China Sea off west coast of Luzon, epicenter 17°20'N, 119°20'E (Repetti, 1934).

"At San Esteban the first movement of the sea was reported to have been a recession, and to such a noticeable extent that the people hurried out on the exposed shore to gather fish which had been left stranded. Some persons narrowly escaped drowning when the water returned.... We can not be certain that the entire reported change of depth occurred suddenly. The changes in sea bottom conditions as given in the various reports of the cable ship and the shocks felt while repairing the cable suggest that the cable break of March 2nd was due to slumping set up by the earthquake of February 14th."

Repetti (1940) makes the following very important statement:

"The earthquake of particular interest in this present series is that of February 14, 1934, at 3:59:35 G.M.T. The records of this earthquake obtained throughout the world show that it was the strongest earthquake in the Philippines of which we have definite evidence. The famous Manila earthquakes of 1645, 1658, 1863, and 1880 were far more destructive but we are of the opinion that the destructive was due to a very great extent to the type of weakness of construction and deterioration, thus giving an exaggerated estimate of the severity of the earthquakes."

26 November 1934, Mag. 6.25 (G&R, 1949), China Sea, 50 km off Manila Bay entrance, epicenter $14^{\circ}10'N$, $120^{\circ}10'E$ (Repetti, 1934). An article appeared in the *Philippine Times*, 14 November 1934. This event is listed herein owing to its location and because no sea waves were mentioned. See also: *Annual Report of the Philippine Weather Bureau: Fiscal Year 1951/52*, p. 18.

20 August 1937, Mag. 7.5, epicenter $14.5N$, $121.5E$, (G&R, 1949), Alabat Island earthquake, off east coast of Luzon (Repetti, 1938).

"The water is said to have risen at the town of Queson at the south end of Alabat Island. This town is practically on Calauag Bay at the head of which there was a rise in the sea level. The people of the town of Calauag at the head of the bay reported that the water rose from low to high tide level in the space of ten minutes."

23 May 1938, Luzon; epicenter, China Sea (Repetti, 1938). No mention of waves.

24 January 1948, Iloilo Strait near southwest coast of Panay, $11^{\circ}N$, $122^{\circ}E$, Richter Mag. 8.2 (Murphy and Ulrich, 1951a, p. 29).

"2 killed by tidal wave in Iloilo Strait."

*29 December 1949, N. Luzon, M_s 7.2, epicenter $17^{\circ}30'N$, $121^{\circ}30'E$. (Murphy and Ulrich, 1951b, p. 47).

"Heavy property damage along northwest coast of Isabela Province and minor damage in Manila. One death from sea wave near Mercedes."

19 March 1952, Butuan, epicenter in Mindanao Sea about 50 km NNW of Butuan City (Weather Bureau, Geophysical Division, 1952). Murphy and Cloud (1954) state:

"The earthquake ... created sea waves that were recorded as waves only one-fourth foot at Yap Island and Apra Harbor and Tarague, Guam. A gage on Angaur Island, Palau I., showed a maximum oscillation of 2.2 feet."

24 May 1960, Chile. Although the earthquake epicenter was thousands of miles from the Philippines, tsunamis were experienced in the islands.

"... 'tsunamis' of slight magnitudes struck the eastern Coasts of the Philippines in the early morning (from 6:30 to 8:30 a.m.) of May 24, 1960. These waves, which brought the sea level from 2 to 8 feet higher than normal tide level, caused some damage to some towns situated near open bays along these coasts...."

31 March 1962, Antique earthquake (Philippine Weather Bureau, 1962).

"... generated a freak tidal wave that hit the coast of Dao ... the wave was caused by a vertical displacement at the epicenter region about five kilometers from the coast of Dao along a line of weakness running north to south from Marinduque to Zamboanga."

1 August 1968, Luzon, epicenter 16.5°N, 122.2°E (Coffman and Cloud, 1970).

"... generated a minor tsunami that was reported to have an amplitude of 6 to 8 centimeters in the Ryuku Islands... Honolulu, 0.1 foot; Attu, 0.3 foot; Wake Island, 0.3 foot; and Guam, 0.1 foot."

Also listed in the *Newsletter*, International Tsunami Information Center, (June 1980):

"Thus far in 1970 one tsunami has been reported to ITIC. The 12 07 08.6 GMT 10 January 1970 earthquake, M_s 7.5, in Mindanao [P.I.] generated a weak tsunami that was recorded at the Malakal, Palau I., Caroline Islands Tide Station with a height of 0.06 m."

7 April 1970, Luzon east coast. Mag 7.3; epicenter 15.8°N, 121.7°E, (International Tsunami Information Center, June 1970):

"... The April 9, 1970 issue of the Manila Times Newspaper quoted observers near Dingalan Bay thus: 'Then the bay water line receded as far as 70 meters out into the ocean' ... 'And then the sea came surging inland, swamping huts built on the shore. He described the incoming waves as taller than a man.' ... ITIC has not received any marigraphic records to show that this event was other than local..."

31 October 1975, NE of Samar Island, Mag. 7.4 Richter scale (International Tsunami Information Center, 1975).

"... A tsunami was generated, and registered a maximum wave height of 10 cm at the Okinawa gage, 6 cm at Yap, and 6 cm at Wake Island. ITIC has received no reports to this date of wave heights or impact on the adjacent Philippine Islands coast."

U. S. Department of Commerce, NOAA (1875, p. 116) state:

"Generated a tsunami that killed one person and swept away about 30 houses on the east coast of Samar Island."

17 August 1976, (16 August GMT time), Moro Gulf (06.26°N, 124.02°E, Earthquake Mag. 7.9 or 8.0 M_s). A major local tsunami. Details not presented here, as they have been presented in the body of the paper.

14 January 1978, Panay, Philippines, 8.8°N, 122.4°E, (International Tsunami Information Center, June 1979).

"Slight tsunami activity recorded at Jolo Island, Philippines."

TSUNAMI PRONE FRICTION FACTORS FROM WIND MEASUREMENTS

by

Charles L. Bretschneider
 Chairman and Professor, Department of Ocean Engineering
 University of Hawaii, Honolulu, HI, U.S.A.

SUMMARY

The long wave equations, used for tsunami run-up and flood wave calculations, have an unknown friction term. As an alternative to hydraulically determined friction factors, an adjustable three-level anemometer staff system is used for making wind profile measurements over typical Hawaii terrain. Results from measurements taken during trade wind conditions are given for three types of terrain: (1) golf course, (2) large flat knoll covered with 2 to 2 1/2 feet tall grass thin to medium dense, and (3) a large rock farm covered with several layers of stone 2 1/2 to 3 feet or more in diameter. Average values of Manning's "n" determined approximately from the von Karman friction length, $n \cong .06 z_0^{1/6}$ vary from 0.028 over the golf course, 0.046 over the grass knoll, and 0.051 over the rock farm. The top level anemometer for both systems is at elevation 10.6 meters (35.8 feet) and the remaining anemometers are equally spaced on the log scale, with the bottom level anemometer at 1.3 meters (4.28 feet) above the support base. We are presently repeating the experiments using an adjustable five-level anemometer staff system.

It is pointed out that the results obtained from wind experiments have not yet been correlated with hydraulic experiments, and it is known that the friction factor decreases with increase in the Froude number, given by $F = \bar{V}/\sqrt{gR}$, where \bar{V} is the mean velocity over the vertical distance of the hydraulic radius, R. The question seems to be, what is the equivalent hydraulic radius for the adiabatic atmosphere that would give the same friction factor for the same roughness for the von Karman velocity profile in hydraulic experiments? The wind experiments do show that there is a tendency for the friction factor to decrease with increase of mean wind speed. It would be of scientific interest to determine an equivalent hydraulic radius for wind profile experiments, making it possible to correlate the data with hydraulic experiments. This needs further investigation.

It is important in our wind experiments that we use only wind profiles that are adiabatic or nearly adiabatic in order that the von Karman velocity profile is in similitude with hydraulic water profiles for turbulent flow. It is also important that we do use only wind profiles having ten meter anemometer level wind speeds greater than about 6 to 7 meters per second, in order to assure us that the experiments are well

above the minimum friction velocity Reynolds number, $R_e = \frac{u_* k}{\nu} \gtrsim 70$ or 80, where $k \hat{=} 30 z_0$, and z_0 = the von Karman friction length.

Finally, we have included a re-analysis of the canal experiments of Lane and Carlson (1953) and hope to open the way for further research and experimentation for possible correlation between wind experiments and hydraulic experiments.

1. INTRODUCTION

Two important purposes of the tsunami research are to increase the "State of the Art" - (1) tsunami forecasting for warning and evacuation purposes, and (2) tsunami hindcasting for prediction of future events for zoning and design criteria. In the past, most tsunami research has been directed more-or-less toward four general categories: (1) source area and mechanisms of tsunami generation; (2) propagation of tsunamis from source area to the coastline; (3) harbor surging and beach run-up; and (4) historical data collection and statistical interpretations.

Very little consideration has been given to the nature of the flooding problem as a consequence of tsunami transformation into a flood wave at the top of the beach or the coastline and its propagation over previously dry bed or coastal terrain. All tsunami statistics are based on data that were compiled for the then existing topographical conditions. In case of Hawaii, this covers up to 140 years of tsunami data at Hilo, for example. If the pre-existing topographical conditions are changed as a result of urban and industrial development and, if the same tsunami event occurred, then the consequences of flooding will be entirely different than those which occurred from past history. The U.S. Army Corps of Engineers recommends the use of rip-rap, seawalls, or other construction methods to reduce the hazards of flooding. On the other hand, land developers bulldoze and level the roughness terrain for urban and industrial development. This has a direct bearing on the two important purposes of tsunami research for the purpose of increasing the "State of the Art": (1) tsunami forecasting and warning for evacuation, and (2) tsunami hindcasting for prediction of future events and design criteria.

Since coastal regions are choice locations for urban and industrial development, there is a need to study the effect of bed roughness on potential tsunami flooding, because there is a potentially dangerous risk in loss of life and property if the terrain roughness is decreased, and the proper friction factors are not considered.

The long wave equations are generally used to determine tsunami run-up, flood wave, and inundation of low coastal areas. The two-dimensional computer program, developed by Houston and Butler (1979) of the U.S. Army Corps of Engineers Waterways Experiment Station, is applicable from deep water to beyond the coastline; and the one-dimensional analytical solution given by Bretschneider and Wybro (1976) is applicable only in the final reaches inland from the coastline. The main difference between the two solutions mentioned above is that the first one is

two-dimensional, neglects the convective acceleration terms and retains the local acceleration terms, whereas the second one is one-dimensional and assumes steady state by neglecting the local acceleration terms but retains the convective acceleration terms. Common to both solutions is the retention of the friction term. The friction term is related to bed-roughness, and is usually given by the Chezy coefficient "C" or Manning's "n". Presently, the friction coefficients used in the long wave equations are based on experiences with river, channel and canal flows, or are estimated from wind profile experiments or scaled from hydraulic model tests. The conditions are quite different for a tsunami flood wave over a previously dry bed or rough terrain. There are no measured friction factors determined under these conditions and it is not practical to measure friction factors over previously exposed terrain during a tsunami flood wave.

As an alternative to hydraulically determined friction factors, an adjustable three-level anemometer staff system was used for taking wind profile measurements over typical Hawaii terrain. Presently, a five-level anemometer staff is being used. The scheme of testing is shown in Figure 1. From the wind profile measurements under neutral atmospheric conditions, one can estimate Manning's "n" which is proportional to the sixth root of the von Karman friction length z_0 .

Thus far, of a number of typical Hawaii terrain, three types have been studied: (1) a golf course, (2) a broad grassy knoll, with medium dense grass 2 to 2 1/2 feet tall, and (3) a rock farm, consisting of a large area of stock pile stones 2 to 3 feet average size and more-or-less level conditions as best as can be expected. The results of the data analysis are summarized in Table I, along with the compilation of Ann-Dof, Högstrom and Högstrom (1977). The z_0 scale of Table I was originally given in meters. The left scale of z_0 in meters has been changed to feet, and Manning's "n" $\cong 0.006 z_0^{1/6}$ (in feet) $^{1/6}$ has been added on the right. This gives Manning's "n" to within ± 5 to 10 percent of the types of conditions expected in the present study.

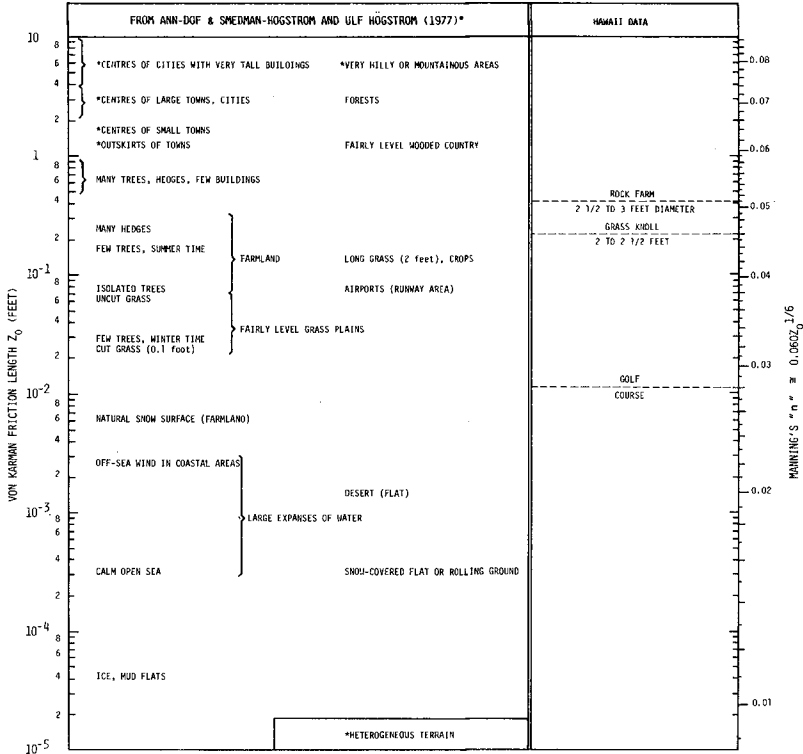
2. BRIEF SUMMARY ON FRICTION FACTOR RELATIONSHIPS

The various forms of the friction factors can be expressed as follows:

$$f_c = \frac{1}{4} f = \frac{2\tau_b}{\rho u^2} = \frac{2g}{C^2} = \frac{2gn^2}{(1.486)^2 R^{1/3}} = 2 \left[\frac{k}{\log_e \frac{R}{ez_0}} \right]^{-2} \quad (1)$$

where f_c and f are the Darcy-Weibach friction factors for open channel flow and full flow in closed conduits, respectively. τ_b is the bottom shear stress; ρ , the density of the fluid; u , the mean velocity of flow; g , the acceleration of gravity; C , the Chezy-Kutter coefficient; n ,

TABLE I
 TERRAIN DESCRIPTION OF AREA WITHIN SEVERAL KILOMETERS UPWIND OF SITE



*NOTE: ORIGINAL Z_0 WAS GIVEN IN METERS, NOW CHANGED TO Z_0 IN FEET (LEFT SCALE) AND MANNING'S "n"

Manning's "n"; R, the hydraulic radius; e, the base of the natural logarithm; z_0 , the von Karman friction length; and $k = 0.4$ von Karman universal constant.

Rouse (1949) has shown that Manning's "n" is proportional to $z_0^{1/6}$ power over a wide range of conditions. Calculations over a wide range of z_0 and hydraulic radius R shows that:

$$n/z_0^{1/6} \cong 0.060 \pm 5 \text{ to } 10\% \quad (2)$$

Figure 1 shows the range of $n/z_0^{1/6}$ versus hydraulic radius R, for the ranges of z_0 expected from the wind profile measurements.

The U.S. Air Force Air Research Development command (1961) summarized typical values of z_0 . These values are given in Table II

together with Manning's "n" based on eq. 2. Bretschneider and Wybro (1976) suggested values of Manning's "n" for various types of terrain and they are repeated in Table III. There is a tendency for reduction in friction factor with increase in velocity. This is similar to what one expects from hydraulic experiments where the friction factor decreases with increase of Froude number, as shown in Figures 2 and 3, based on the reanalysis of the canal data of Lane and Carlson (1953).

Table IV gives additional relations for Manning's "n" based on hydraulic experiments. Equations a, b, c, and d in Table IV can be made universally dimensionless by multiplying the left side by $\sqrt{g}/1.486$, and changing the K values from inches to feet. However, eq. e cannot be made dimensionless in a similar manner, except by introducing either another $R^{1/6}$ or $K^{1/6}$ in the denominator of the left side of eq. e. Using $R^{1/6}$ in the denominator of the left side of eq. e and rearranging terms and $\sqrt{g}/1.486$, one can determine eq. g. Using K instead of R, one can arrive at eq. h. Eliminating K from eq. e, one can arrive at eq. f. Evidently, eq. f is a function of R, eq. g is a function of K_m , eq. h is a function of R and K_m ; but all three equations, f, g and h are functions of the flow as defined by the Froude number.

3. FREE AIR WIND EXPERIMENTS

There is nothing new in using wind experiments to study hydrodynamic problems due to water current forces. This has been done in the past by naval architects and marine engineers for offshore floating and rigid structures. What is unique in this study and approach is the use of prototype wind experiments for the determination of friction factors over typical Hawaii terrain to aid in the solution of the hydraulic problems associated with tsunami run-up, flood wave and inundation.

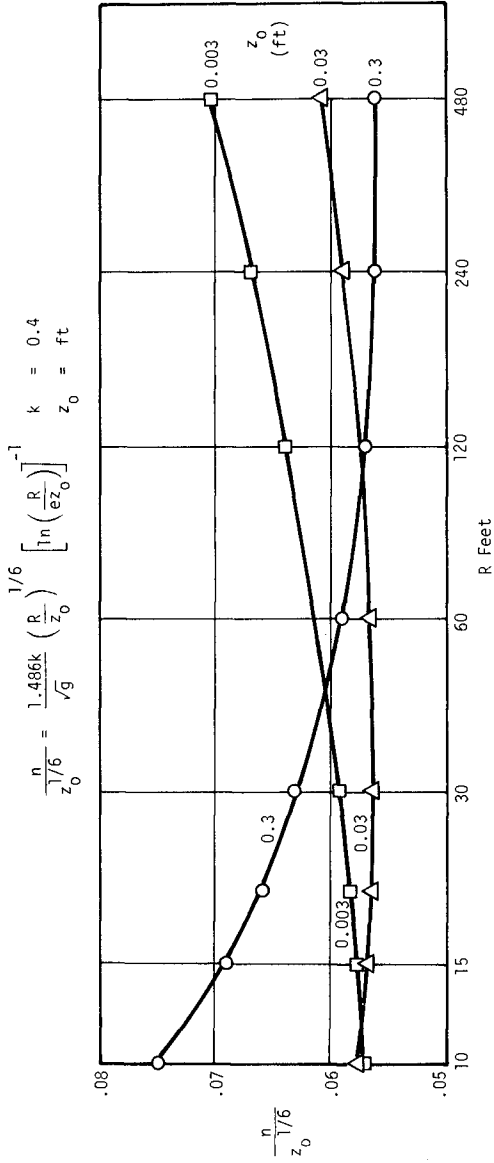


FIG. 1 Variation of $\frac{n}{z_0^{1/6}}$ for various values of z_0 and R

TABLE II
SUMMARY VALUES OF z_0^*

Values of z_0 and Manning's "n"		
Type Surface	z_0 (ft)	$n = .06 z_0^{1/6}$
Very smooth (mud flats, ice)	0.00003	.011
Lawn grass up to 0.4 inches high	0.003	.023
Downland thin grass up to 4 inches high	0.02	.031
Thick grass up to 4 inches high	0.075	.039
Thin grass up to 20 inches high	0.16	.044
Thick grass up to 20 inches high	0.30	.049
*Obtained from U.S. Air Force Research Development Command (1961)		

TABLE III
 SUGGESTED VALUES OF MANNING'S "n" FOR VARIOUS COASTAL TERRAIN CONDITIONS

n	Conditions
0.015 - 0.025	Very smooth (mud flats, ice, well maintained concrete paved ways, beaches of fine sand)
0.025 - 0.030	Smooth (dried earth, coarse sand beaches, badly maintained concrete paved ways, very thin lawn grass up to 1 cm high)
0.030 - 0.035	Average for developed areas (lawn grass up to 5 cm high, gravel, presence of some buildings, houses, and other obstructions)
0.035 - 0.045	Open coast, relatively smooth and open area (grass up to 10 cm, sparse population of trees*, sparse bush, even bottom)
0.045 - 0.055	Moderately rough open coastal areas (thick grass, uneven bottom consisting of large rocks, coral, etc., presence of trees with low foliage, brush, lava rock, etc.)
0.055 - 0.070	Unusually rough coastal areas (dense brush, dense tree population with exposed roots, coarse lava rock formations)

*Trees with high foliage such that only trunks are exposed to flow

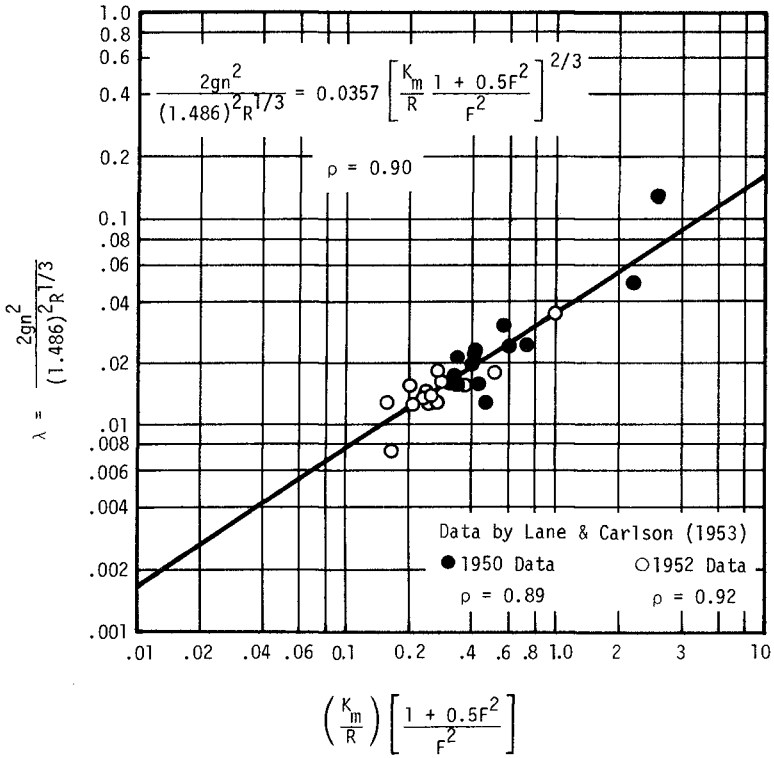


FIG. 2 Non-Dimensional Mannings "n", λ vs $\left(\frac{K_m}{R} \right) \left[\frac{1 + 0.5F^2}{F^2} \right]$
 $F = \bar{V}/\sqrt{gR}$, λ = Kelegan Non-Dimensional Mannings "n"

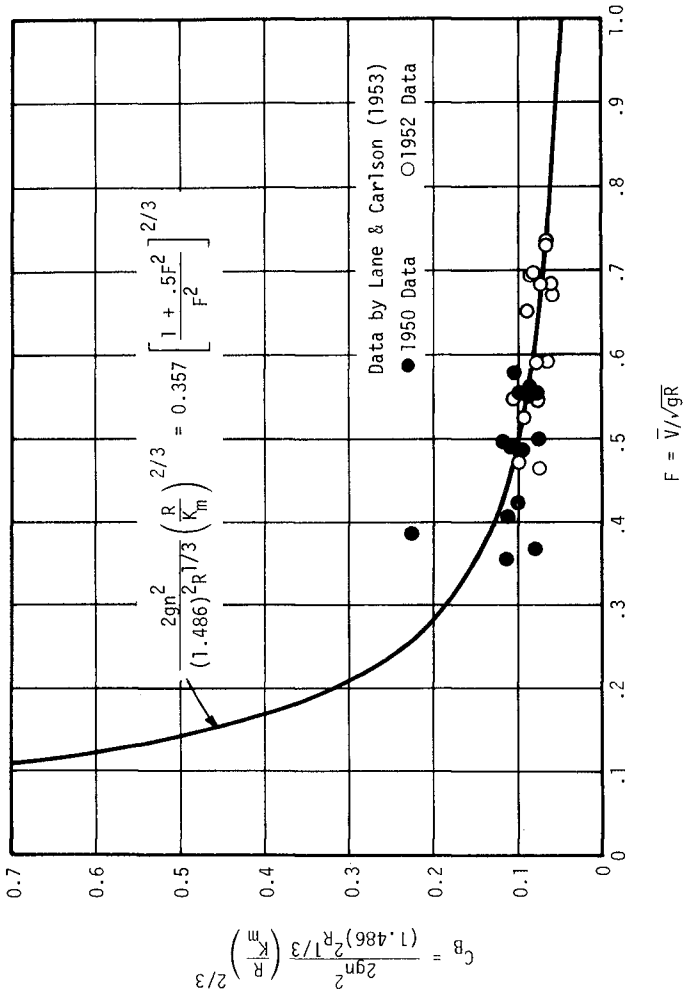


FIG. 3 Non-Dimensional Mannings "n", C_B vs Froude No. $F = \bar{V}/\sqrt{gR}$

$$C_B = \lambda (R/K_m)^{2/3}$$

TABLE IV SUMMARY OF ADDITIONAL RELATIONS FOR MANNINGS "n"

EMPIRICAL EXPRESSIONS FOR MANNINGS "n"		
Expression	Source	
a) $44.4 n = K_{50}^{1/6}$	Strickler (1923)	
b) $46.9 n = K_{50}^{1/6}$	Keulegan (1938)	
c) $39.0 n = K_{25}^{1/6}$	Lane and Carlson (1953)	
d) $49.0 n = K_{10}^{1/6}$	Irmay (1948)	
e) $26.0 n = \left(\frac{K_{35}}{R}\right)^{1/6}$	Lane and Carlson (1953)	
NON-DIMENSIONAL EXPRESSIONS FOR MANNINGS "n"		
f) $\lambda = \frac{2gn^2}{(1.486)^2 R^{1/3}}$	Keulegan (1967)	
g) $C_M^2 = \frac{gn^2}{(1.486)^2 K_m^{1/3}}$	Squarer, Mostafa & McOermid (1971)	
h) $C_B = \frac{2gn^2}{(1.486)^2 R^{1/3}} \left(\frac{R}{K_m}\right)^{2/3}$	Bretschneider (1978) (See Figs. 4 and 5)	}
or		
$C_B = \frac{2gn^2}{(1.486)^2 K_m^{1/3}} \left(\frac{R}{K_m}\right)^{1/3}$		
i) $C_B = \lambda \left(\frac{R}{K_m}\right)^{2/3} = 2C_M^2 \left(\frac{R}{K_m}\right)^{1/3}$	(Relations between Eqs. c, d & e)	

K_{50} , K_{25} , K_{10} bed material size in inches of which 50, 25 and 10 % are larger by weight, respectively k_m = medium size (50%) in feet.

Sutton's (1953) *Micrometeorology* is one of many books on meteorology dealing with lower level atmospheric turbulence and motion. Sutton (1953), as well as all meteorologists, uses the same basic fluid mechanics equations of flow over smooth and rough surfaces that hydraulic engineers use, but the meteorologists also include atmospheric stability criteria. The free air can be treated as incompressible flow. Anticipated winds will not be greater than 30 or 40 knots. The primary interest is to obtain wind profile measurements during neutral atmospheric conditions. There are plenty of tradewinds in Hawaii. Mid-day measurements should be avoided when thermal gradients near the ground would affect the interpretation of the data.

Under absolute neutral atmospheric conditions, only two level anemometer readings are necessary for obtaining z_0 friction length in the logarithmic velocity profile equation. The third level can be considered as a check point. The three points should fall along a straight line on semi-log graph paper. If the deviations are too great, the data should be rejected for the proposed method of analysis. A very sophisticated method of analysis of five-level anemometer wind data over the tops of pine trees in Canada was made by Lo (1977). An eight-level anemometer was used by O'Brien (1965) to study the diabatic wind profile for winter and summer conditions over a hay field near Dallas, Texas. One of the purposes of many previous wind profile experiments was to aid in wind predictions under various atmospheric stability conditions. Since we are only interested in those data for adiabatic conditions, we can be selective, and the data can be analyzed more easily using the von Karman logarithmic profile.

4. INSTRUMENTATION

Figure 4 shows a schematic of the three-level adjustable anemometer staff, which includes sensors for wind speed, wind direction and temperature at each of the three levels. The top of the staff is at 10 meters making the top sensor (No. 1) at 10.9 meters = 35.8 feet. Anemometers No. 2 and No. 3 can be adjusted to various elevations. Anemometer No. 2 was located half way on the log scale between No. 1 and No. 3.

The instrumentation package consists of Weather Measure Corporation's: (3 ea.) W103-DC-3SS, low threshold anemometer, 0.C. generator with stainless steel cups; (3 ea.) W104, lightweight wind direction vane 0-360--540 degrees; (3 ea.) W1034-CAW pre-wired cross arm to mount wind sensors; (1 ea.) SC-710 card file, pre-wired for 10 parameters; (3 ea.) MD103-0C, wind speed translator module 0-540 deg.; (1 ea.) MD910, power supply; (1 ea.) MO-OPM-S, digital panel meter, switch selectable channels; (1 ea.) WM-INT, systems integration and documentation. Air temperature sensors are located at each anemometer position, and can be shifted as necessary.

The analog data are recorded in a digital format by a 16 channel Datal Cassette Recorder. Following field data acquisition, the data cassette is then read by a Datal Cassette Reader into a Hewlett-Packard

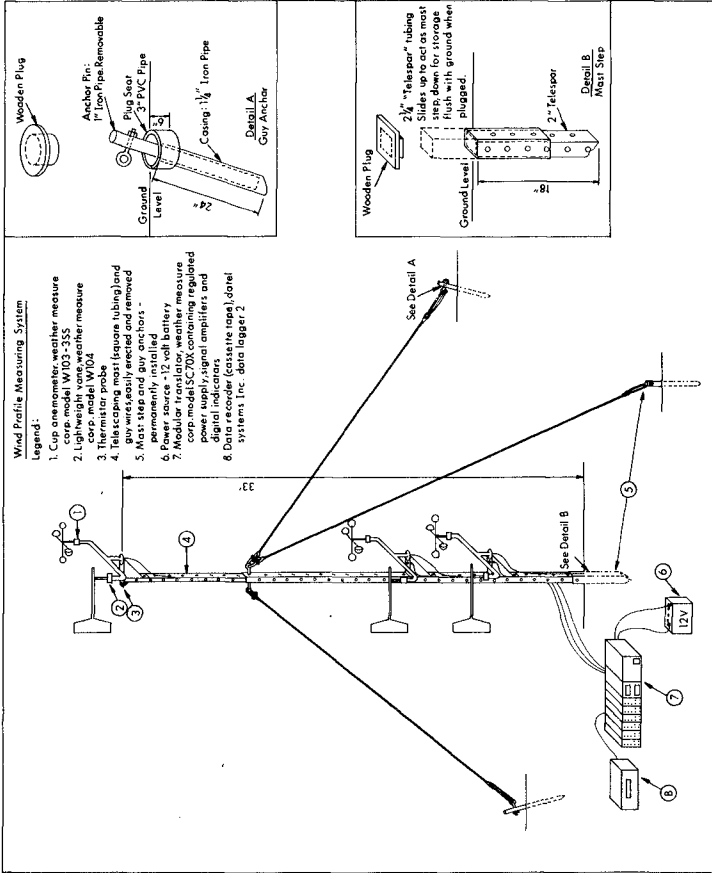


FIG. 4 SCHEMATIC ARRANGEMENT OF ADJUSTABLE THREE LEVEL ANEMOMETER STAFF

HP-9845 Mini-Computer System. The HP-9845 system then performs all data calculation and analysis, and either prints or directly generates computer drawn graphs for visual display of the data.

5. A SIMPLE METHOD OF WIND PROFILE DATA ANALYSIS

The three-level anemometer experiments. There is no proof that eq. 2 is probably a better relationship than eq. 1 between Manning's "n" and von Karman's z_0 . However, it is found that eq. 2 is very useful for the three-level anemometer data analysis, as can be demonstrated.

The von Karman logarithmic velocity profile is:

$$\frac{u}{u_*} = \frac{1}{k} \ln \frac{z + z_0}{z_0} \quad (3)$$

where u is the wind speed at elevation z above the mean reference surface, z_0 is the friction length and $u_* = \sqrt{\tau/\rho}$ the friction velocity. Equation 3 does not include the zero displacement concept such as used by O'Brien (1965) or Lo (1977).

Assuming $z_0 \ll z$ for the lowest anemometer elevation, then by rearranging the terms in eq. 3, multiplying through by $1/6$ and using eq. 2, one obtains

$$n = .06z^{1/6} e^{-\frac{1}{6} \left(\frac{ku}{u_*} \right)} (\text{feet})^{1/6} \pm 10\% \quad (4)$$

Equation 4 is a straight line on semi-log graph paper when $z^{1/6}$ is on the log scale and u is on the linear scale. Anemometer Nos. 1, 2 and 3 are elevations 35.8, 11.48 and 4.26 feet, respectively, which results in the anemometer levels in terms of $0.06z^{1/6}$ equal to 0.109, 0.009 and 0.076 (feet) $^{1/6}$, respectively. At $u = 0$, $n = 0.06z_0^{1/6}$.

The above method was introduced as a matter of convenience in order to give engineers an idea of Manning's "n" determined from wind experiments. There is nothing unique about the method, except that the data can be shown on a one cycle semi-log scale instead of on four to six cycle semi-log log.

Figures 5 and 6 show typical examples of Hawaii terrain and corresponding values of Manning's "n". Values of Manning's "n" by this method are only estimates.

The five-level anemometer experiments. The five-level anemometer staff is shown in Figure 7. The log-linear regression analysis of the

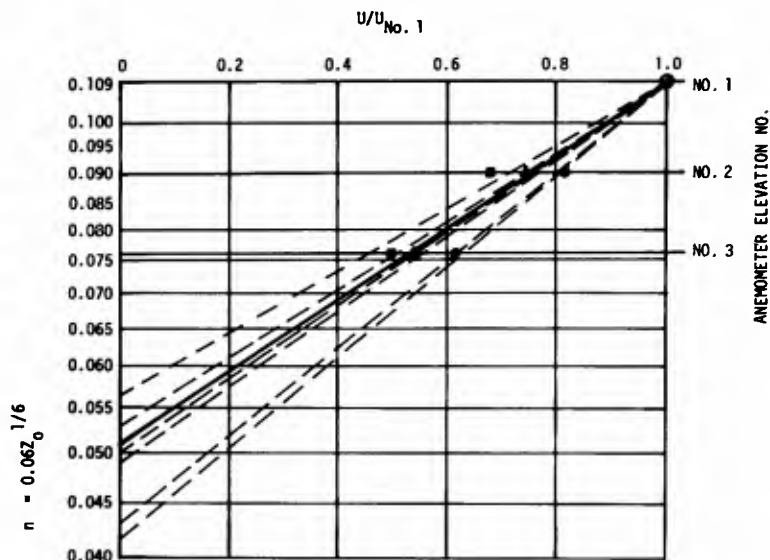


Fig. 5 MANNING'S "n" DETERMINATIONS FOR ROCK FARM
STONE 2 1/2 TO 3 FT. AVE. DIAMETER

■---■ DNE-MINUTE WIND AVERAGES
 ▲---▲ EIGHT-MINUTE WIND AVERAGES
 \bar{U} (NO. 1) = 23 FT/SEC (8-MIN. AVE.)
 DATE 7/24/79 TIME 12:41

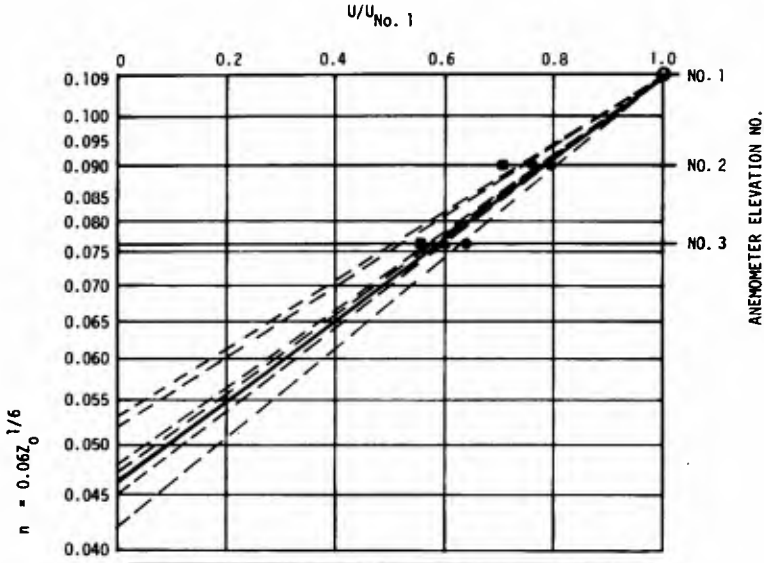


Fig. 6 MANNING'S "n" DETERMINATIONS FOR GRASS KNOLL THIN TO MEDIUM 2 TO 2 1/2 FT. TALL

■ — — — ■ ONE-MINUTE WIND AVERAGES
 ▲ — — — ▲ EIGHT-MINUTE WIND AVERAGES
 \bar{U} (NO. 1) = 32 FT/SEC (8-MIN. AVE.)
 DATE 7/23/79 TIME 13:39



data is used including the zero-plane displacement concept, in which case the data fall more closely along a straight line than that given in the paper. The results of these analyses, however, will be reported at a later date, after the project has been completed.

6. POSSIBLE METHODS OF CORRELATING WIND EXPERIMENTS WITH HYDRAULIC EXPERIMENTS

One of the missing links between the wind experiments and the hydraulic experiments is the determination of the equivalent hydraulic radius R or the slope of the energy grade line for the wind experiments. The hydraulic radius and/or energy slope can be measured for the hydraulic experiments.

The friction velocity method. Beginning with the von Karman velocity profile equation,

$$u_z = \frac{u_*}{k} \ln \frac{z}{z_0} \quad z_0 \ll z, \quad (5)$$

one can obtain a mean velocity \bar{u}_z as follows:

$$\bar{u}_R = \frac{1}{R} \int_0^R u_z dz = \frac{u_*}{k} \ln \frac{R}{ez_0} \quad (6)$$

and

$$u_R = \frac{u_*}{k} \ln \frac{R}{z_0} \quad (7)$$

where u_R is the velocity at elevation $z = R$ and \bar{u}_R is the integrated mean velocity between $z = 0$ and $z = R$. $u_* = \sqrt{\tau/\rho}$ the friction velocities, $k = 0.4$ and $z_0 =$ friction length as given before.

It can then be shown for the von Karman velocity profile that

$$u_* = k(u_R - \bar{u}_R) = \sqrt{gRS} \quad (8)$$

where S is the slope of the energy grade line.

The friction velocity Reynolds number and Froude number (if such is a possibility) are given as follows:

$$R_e^* = \frac{u_* K_m}{\nu} = \frac{k(u_R - \bar{u}_R) K_m}{\nu} \quad (9)$$

where $\nu =$ kinematic viscosity and $K_m =$ mean stone size.

$$F_R^* = \frac{u_*}{\sqrt{gR}} = \frac{k(u_R - \bar{u}_R)}{\sqrt{gR}} \quad (10)$$

The minimum hydraulic radius method. It is quite well established in the literature, for example, Squarer, et al (1971), among many others, and also as shown in Figure 3 based on a re-analysis of the canal data of Lane and Carlson (1953), that the non-dimensional friction factor relationships are a function of the Froude number. The friction factor relationships decrease with increase in the Froude number.

The Froude number is given by

$$F_R = \frac{\bar{u}_R}{\sqrt{gR}} \quad (11)$$

where \bar{u}_R is the mean velocity and is the same as \bar{v} used in Manning's equation and also in Figure 3.

Using \bar{u}_R from equation 6, one obtains

$$F_R = \frac{\frac{u_*}{k} \ln \frac{R}{ez_0}}{\sqrt{gR}} \quad (12)$$

Differentiating equation 12 and setting the expression equal to zero, one obtains an expression for minimum hydraulic radius as follows:

$$R_{\min} = e^3 z_0 \quad (13)$$

It then follows that

$$u_{R_{\min}} = \frac{u_*}{k} \ln e^3 \frac{z_0}{z_0} = 3 \frac{u_*}{k} \quad (14)$$

and

$$\bar{u}_{R_{\min}} = \frac{u_*}{k} \ln \frac{e^3 z_0}{ez_0} = 2 \frac{u_*}{k} \quad (15)$$

whence

$$F_{R_{\min}} = \frac{\bar{u}_{R_{\min}}}{\sqrt{gR_{\min}}} = \frac{2 \frac{u_*}{k}}{\sqrt{ge^3 z_0}} \quad (16)$$

where $u_* = k(u_{R_{\min}} - \bar{u}_{R_{\min}}) = k(u_R - \bar{u}_R) = k(u_z - \bar{u}_z)$.

u_R , \bar{u}_R and z_0 can be obtained from velocity profile measurements, whether in water or air without any knowledge of the actual hydraulic radius, provided the von Karman velocity profile conditions exist over the elevations of measurements.

It can also be shown that

$$z_0 = R e^{-\left(\frac{ku_R}{u_*}\right)} = R e^{-\left(\frac{u_R}{u_R - \bar{u}_R}\right)} \tag{17}$$

Therefore, it might be possible to correlate wind and water experimental results. At least, this is worthy of further investigation.

For example, one might re-define the Keulegan non-dimensional form of Manning's "n" $\lambda = \lambda^*$ as follows:

$$\lambda^* = \frac{2gn^2}{(1.486)^2 R_{min}^{1/3}} \tag{18}$$

A re-analysis of the data by Lane and Carlson (1953) is given in Table V. R_{min} is determined from eq. 13, where z_0 is determined from eq. 1, using values of R and n from the data of Lane and Carlson (1953). It is noticed in the re-analysis of the data that test nos. 8 and 10 can be considered questionable. For example, there is one case (test no. 10 (1950)) where R_{min} is actually greater than the true hydraulic radius, R, and also K_m is very large compared with R_{min} . It is for these reasons that in all previous analysis, Lane and Carlson (1953), Squarer, Mostafa and McDermid (1971), and also in this present paper that the data for test nos. 8 and 10 fall considerably out of the range of the other test data. The analysis of the data in Table V for λ^* and $\sqrt{\lambda^*}$ are given separately for the 1950 and 1952 tests and also for the combined 1950 and 1952 tests. Omitting tests 8 and 10 results in considerable reduction in the variance from the mean values of $\bar{\lambda}^*$ and $\sqrt{\hat{\lambda}^*}$, particularly for the 1950 test data, which were for normal flow. The 1952 data were for peak discharge, which increased the actual hydraulic radius and decreased the minimum hydraulic radius, $R_{min} = e^3 z_0$.

It then follows for the data of Lane and Carlson (1953), excluding test nos. 8 and 10 that

TABLE V

A RE-ANALYSIS OF DATA OF LANE & CARLSON (1953)
USING MINIMUM HYDRAULIC RADIUS

TEST SECTION	K_m (ft.)	R (ft.)	R_{min} (ft.)	λ^* --	R (ft.)	R_{min} (ft.)	λ --
1	0.269	2.93	0.485	.040	3.53	0.403	.038
2	.253	1.92	0.552	.046	2.27	0.196	.037
4	.249	2.15	0.385	.031	2.48	0.140	.035
5	.177	1.74	0.274	.040	2.17	0.163	.036
6	.138	1.29	0.166	.039	1.40	0.067	.035
7	.135	1.01	0.200	.042	1.31	0.066	.035
8	.128	0.44	0.257	.059	0.80	0.088	.038
10	.210	0.48	0.737	.112	0.48	0.178	.049
11	.158	1.29	0.249	.042	1.56	0.126	.036
12	.112	1.25	0.099	.036	1.41	0.084	.035
14	.066	1.26	0.100	.036	1.52	0.068	.035
15	.164	1.65	0.128	.036	2.61	0.170	.036
16	.161	1.39	0.102	.036	No Data	---	---
17	.125	1.39	0.145	.038	2.22	0.112	.035
18	0.069	1.13	0.051	.035	2.03	0.021	.034
(1950, 15 Tests)		$\bar{\lambda}^* = .0445$		(1952, 14 Tests)		$\bar{\lambda}^* = .0367$	
		VAR = 44.3%				VAR = 10.2%	
(1950 and 1952, All 29 Tests)				$\bar{\lambda}^* = .0408$			
				VAR = 36.2%			
FOR ALL TESTS EXCEPT NOS. 8 and 10							
(1950, 13 Tests)		$\bar{\lambda}^* = .0382$		(1952, 12 Tests)		$\bar{\lambda}^* = .0356$	
		VAR = 10.1%				VAR = 3.0%	
(1950 and 1952, 25 Tests)				$\bar{\lambda}^* = .0370$			
				VAR = 8.47%			
(1950, 15 Tests)		$\sqrt{\hat{\lambda}^*} = .2078$		(1952, 14 Tests)		$\sqrt{\hat{\lambda}^*} = .1914$	
		VAR = 18.4%				VAR = 4.8%	
(1950 and 1952, 29 Tests)				$\sqrt{\hat{\lambda}^*} = .1999$			
				VAR = 14.5%			
FOR ALL TESTS EXCEPT NOS. 8 and 10							
(1950, 13 Tests)		$\sqrt{\hat{\lambda}^*} = .1953$		(1952, 12 Tests)		$\sqrt{\hat{\lambda}^*} = .1886$	
		VAR = 5.0%				VAR = 1.5%	
(1950 and 1952, 25 Tests)				$\sqrt{\hat{\lambda}^*} = .1921$			
				VAR = 4.2%			

$$n = .060 z_0^{1/6}, \quad \text{var} = 5.0\% \quad (13 \text{ tests}) \quad 1950 \text{ data}$$

$$n = .058 z_0^{1/6}, \quad \text{var} = 1.5\% \quad (12 \text{ tests}) \quad 1952 \text{ data}$$

and

$$n = .059 z_0^{1/6}, \quad \text{var} = 4.2\% \quad (25 \text{ tests}) \quad 1950 \text{ and } 1952 \text{ data} .$$

7. ACKNOWLEDGEMENTS

"The Effect of Terrain Roughness on Tsunami Run-up and Inundation" is a research project sponsored by the University of Hawaii Sea Grant College Program under Institutional Grant No. OE/R-5 from NOAA, Office of Sea Grant, U.S. Department of Commerce. Acknowledgements are given to Fred Casciano, in charge of field data collection, George Weber, electronics technician; and Eiji Nakazaki, M.S. graduate student working on his Plan B paper, including data analysis and results of both three-level and five-level anemometer field experiments. Appreciation is also given to KACOR Realty and, in particular, Mr. Stanley Fujimoto for obtaining entry permits for the Queens Beach area, where the wind experiments were conducted.

8. REFERENCES

- ANN-DOF and SMEDMAN-HÖGSTROM and ULF HÖGSTROM (1977) "A practical method of determining wind frequency distributions for the lowest 200 meters from routine meteorological data." Report no. 47, Meteorological institutionen, Uppsala, p. 7.
- BRETSCHNEIDER, C.L. and WYBRO, P. (1976) "Tsunami inundation predictions." Proc. 15th Coastal Engr. Conf. (ASCE), Vol. I, Ch. 60, pp. 1006-1D24, Research in partial support under NOAA/Sea Grant Contract No. 04-06-158-44026.
- HOUSTON, J.R. and BUTLER, H. (1979) "A numerical model for tsunami inundation." U.S. Army Waterways Experiment Station, Tech. Rept. H-79-2.
- IRMAI, S. (1949) "On steady flow formulas in pipes and channels." Paper No. III-3, Third Meeting, IAHR, Grenoble, France.
- KEULEGAN, G.H. (1967) "Tidal flow in entrances: Water level fluctuations of basins in communication with the sea." U.S. Army Corps of Engineers Waterways Experiment Station, Vicksburg, Committee on Tidal Hydraulics, Tech. Bulletin No. 4.
- KEULEGAN, G.H. (1938) "Laws of turbulent flow in open channels." United States Department of Commerce, National Bureau of Standards, Res. Paper RP1151.

LANE, E.W. and CARLSON, E.S. (1953) "Some factors affecting the stability of canals constructed in coarse granular materials." In Proceedings, Minnesota International Hydraulic Convention IAHR/ASCE, pp. 37-88.

LO, A.K. (1977) "An analytical-empirical method for determining the roughness length and zero-plane displacement." Boundary-Layer Meteorology 12, pp. 141-151, Reidel Publishing Co., Dordrecht, Holland.

MONIN, A.S. and OBUKHOV, A.M. (1954) "Basic regularity in turbulent mixing in the surface layer of the atmosphere." Akad. Nauk/SSSR Geobiz. Inst. Trudy, No. 24, pp. 163-186.

O'BRIEN, J.J. (1965) "An investigation of the diabatic wind profile of the atmospheric boundary layer." Journal of Geophysics Research, Vol. 70, No. 10, pp. 2277-2290.

RAMSER, C.E. (1929) "Flow of water in drainage channels." U.S. Department of Agriculture, Tech. Bulletin No. 129, p. 102.

ROUSE, H. (1949) "Engineering Hydraulics." In Proceedings of the 4th Hydraulic Conference, Iowa Institute of Hydraulic Research, p. 1039, John Wiley and Sons, Inc.

SQUARER, D.M., MOSTAFA, G. and MC DERMID, R.M. (1971) "Sediment transportation mechanics F. hydraulic relations for alluvial streams." In ASCE Proceedings, Journal of the Hydraulics Division 97 (HY 10): pp. 1775-1780.

STRICKLER, K. "Beitrage zur Frage der Geschwindigkeitsformal und der Rauheitszahlen fur Strom Kanale und geschlossene Leitungen." Mitt. No. 16, des Eidg. Amtes fur Wasserwirtschaft, Bern, 1923.

SUTTON, O.G. (1953) Micrometeorology, 333 pages, McGraw-Hill Book Co., Inc.

U.S. AIR FORCE AIR RESEARCH DEVELOPMENT COMMAND (1961) Handbook of Geophysics, Revised Edition. The MacMillan Co., New York, chapter 9.

CHAPTER 43

Run-up of Tsunamis by Linear and Nonlinear Theories

Chiaki Goto

Instructor of Civil Engineering
Tohoku University, Sendai, Japan

and

Nobuo Shuto

Professor of Civil Engineering
Tohoku University, Sendai, Japan

ABSTRACT

Linear and nonlinear sets of equations of long waves in the Lagrangian description are solved numerically to obtain run-up heights. Numerical results are compared with theoretical ones in case of simple topographies and the agreement is quite satisfactory. As a practical application, the computation is carried out for the Okkirai Bay in Japan. The computed run-up heights agree fairly well with the recorded ones.

1. INTRODUCTION

One of the most difficult problems in the numerical simulation of tsunami run-ups lies in the fact that it is not easy to introduce the boundary condition which should precisely reflect the topography of the land where the tsunami arrives at.

In the present paper, one- and two-dimensional problems are treated numerically by adopting both linear and nonlinear sets of equations described in the Lagrangian coordinates. In this system, the boundary condition can be easily satisfied. The water particles lying on the sea bottom at the beginning of the motion do not leave the bottom during the subsequent motion. The water particle at the wave front is the one which is at the shoreline at the initial instant.

For the analysis, an explicit finite difference method is used. The computation is first carried out for simple topographies, for which the linear equation gives analytical solutions. The numerical results of the linear theory are compared with the theoretical values and agreement is quite satisfactory.

Then, the nonlinear computation is carried out. The difference between linear and nonlinear theories amounts 20% at most.

As an example of practical application, The computation is carried out for the Okkirai Bay on the South Sanriku Coast in Japan, which suffered much by the attacks of tsunamis in the past.

2. BASIC EQUATIONS AND NUMERICAL TECHNIQUES

Let us consider the irrotational, three-dimensional motion of an incompressible fluid. The displacements of the water particle which is at the point (a,b,c) at the initial instant is (a+x,b+y,c+z) at the time t. The still water surface is taken as the a-b plane, and the c-axis is taken vertically positive upward. Linear and nonlinear equations of long waves in the Lagrangian coordinates have been derived by authors (Shuto, 1967; Goto, 1979; Goto and Shuto, 1979).

The linear theory is written:

$$\eta + h(a,b)\{x_a + y_b\} + h(a+x,b+y) - h(a,b) = 0 \text{ -----(1)}$$

$$\begin{bmatrix} x_{tt} \\ y_{tt} \end{bmatrix} + g \begin{bmatrix} \eta_a \\ \eta_b \end{bmatrix} = 0 \text{ -----(2)}$$

And the nonlinear one is

$$(1 + x_a + y_b)\{\eta + h(a+x,b+y) - h(a,b)\} - h(a,b)\{x_a + y_b + \frac{\partial(x,y)}{\partial(a,b)}\} = 0 \text{ -----(3)}$$

$$\begin{bmatrix} 1 + x_a & y_a \\ x_b & 1 + y_b \end{bmatrix} \begin{bmatrix} x_{tt} \\ y_{tt} \end{bmatrix} + g \begin{bmatrix} \eta_a \\ \eta_b \end{bmatrix} = 0 \text{ -----(4)}$$

where g denotes the acceleration of gravity, h(a,b) the still water depth where the water particle existed at the initial instant and h(a+x,b+y) also still water depth where the water particle arrives at. The relationships between these theory is similar to that between linear long wave and shallow water theories in the Eulerian coordinates.

These equations are expressed in terms of the displacements (x,y,\eta) of the free surface from the original position. In the present analysis, the Lagrangian velocities (u=x_t, v=y_t, \eta_t) are introduced in place of them. The bottom friction expressed in Manning's n and proportional to the square of the velocity is also introduced. This change of variables makes the numerical computation more stable and easier.

Therefore, the equations are, for linear waves,

$$(\eta_t + u_{a+x} + v_{b+y}) + h(a,b)(u_a + v_b) = 0 \quad \text{-----(5)}$$

$$\begin{bmatrix} u_t \\ v_t \end{bmatrix} + g \begin{bmatrix} \eta_b \\ \eta_a \end{bmatrix} + \frac{gn^2}{D} \sqrt{u^2 + v^2} \begin{bmatrix} u \\ v \end{bmatrix} = 0 \quad \text{-----(6)}$$

and, for nonlinear waves,

$$(1 + x_a + y_b)^2 (\eta_t + u_{a+x} + v_{b+y})$$

$$h(a,b) \{ u_a + v_b + \frac{\partial(u,y)}{\partial(a,b)} + \frac{\partial(x,v)}{\partial(a,b)} \} = 0, \quad \text{-----(7)}$$

$$\begin{bmatrix} 1 + x_a & y_a \\ x_b & 1 + y_b \end{bmatrix} \begin{bmatrix} u_{tt} \\ v_{tt} \end{bmatrix} + g \begin{bmatrix} \eta_a \\ \eta_b \end{bmatrix} + \frac{gn^2}{D} \sqrt{u^2 + v^2} \begin{bmatrix} u \\ v \end{bmatrix} = 0 \quad \text{-----(8)}$$

Where D denotes the total water depth.

For the water particle at the initial instant, the still water depth h is equal to zero. Therefore, in these equations of continuity of long waves, the value $(\eta_t + u_{a+x} + v_{b+y})$ is equal to zero provides the boundary condition at the wave front.

For the numerical computation, an explicit finite difference method similar to the staggered leap-frog scheme is used. For example, the difference equations of the linear theory are expressed as

$$\eta_{i,j}^{n+1} = \eta_{i,j}^n - h_{i,j} \lambda \{ (u_{i+1/2,j}^{n+1/2} u_{i-1/2,j}^{n+1/2}) + (v_{i,j+1/2}^{n+1/2} - v_{i,j-1/2}^{n+1/2}) \}$$

$$- \Delta t (h_x u_{i,j}^n + h_y v_{i,j}^n) \quad \text{-----(9)}$$

$$u_{i+1/2,j}^{n+1/2} = \frac{1}{1 + \mu_{i+1/2,j}^{n-1/2}} \{ (1 - \mu_{i+1/2,j}^{n-1/2}) u_{i+1/2,j}^{n-1/2} - g \lambda (\eta_{i+1,j}^n + \eta_{i,j}^n) \} \quad \text{-----(10)}$$

$$v_{i,j+1/2}^{n+1/2} = \frac{1}{1 + \mu_{i,j+1/2}^{n-1/2}} \{ (1 - \mu_{i,j+1/2}^{n-1/2}) v_{i,j+1/2}^{n-1/2} - g \lambda (\eta_{i,j+1}^n + \eta_{i,j}^n) \} \quad \text{-----(11)}$$

where $\lambda = \Delta t / \Delta s$; Δs and Δt denote horizontal and time mesh size, respectively, and

$$u_{i,j}^n = \frac{gn^2 \Delta t}{(D_{i,j}^n)^{4/3}} \{ (u_{i,j}^n)^2 + (v_{i,j}^n)^2 \}^{1/2}$$

Notations h_x and h_y denote the local slopes, in the x- and y-direction where the water particle arrives at, so we calculate and store them beforehand.

In Fig. 1, the numerical computation mesh is shown. The velocity are calculated for the point where arrows are shown and vertical displacement at the point where black circles are shown. When we need the velocities for the points of the black circles, we estimate them by a linear interpolation. For the points along the initial shoreline, we estimate the velocities by a linear extrapolation.

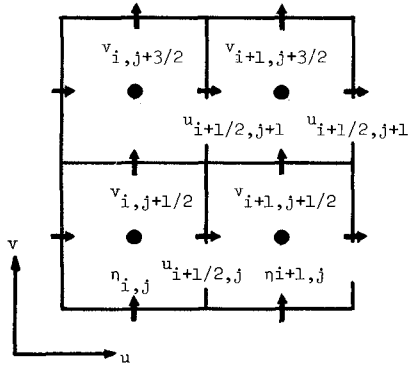


Fig. 1 Numerical mesh.

The same procedure was also adopted in case of nonlinear theory.

3. RESULTS OF COMPUTATION

(1) Comparisons with the analytical solutions.

First, we examine the accuracy of the numerical scheme for one-dimensional cases. A simple topography, a uniform slope connected to the channel of constant depth, is used. In this topography, the maximum run-up height R was theoretically presumed by Keller and Keller (1964) and confirmed by Shuto (1972), by using the linear theory.

$$\frac{R}{H} = \{ J_0^2(4\pi \frac{l}{L}) + J_1^2(4\pi \frac{l}{L}) \}^{-1/2} \tag{12}$$

Where L is the wave length in water of constant depth, H the incident wave height, l the horizontal length between the toe of the slope and the shoreline and J_n the n-th Bessel Function of the first kind.

For the simple topography, we have computed several cases with no friction effect. Figure 2 shows the comparison. The curve is the result given by the analytical solution, while black circles are the numerical

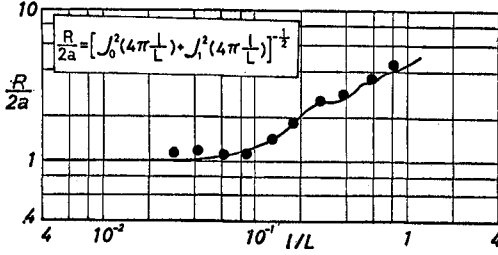


Fig. 2 The comparison between the analytical and the numerical (linear) results.

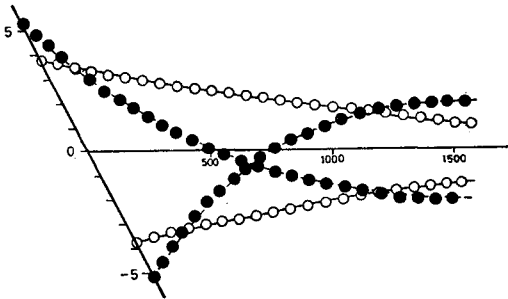


Fig. 3 The comparison of wave profile.

results. Examples of wave profile are shown in Fig. 3. They are for maximum run-up and run-down for wave periods of 300 sec and 600 sec by linear theory. The lines are the analytical solution and the circles the numerical results. We consider the agreement is satisfactory.

Though examination of the numerical results obtained for different conditions, we find that the accuracy of the numerical results depends upon three factors, the spatial mesh size Δs , the slope of topography α and the wave length L . In order to see this, the ratio of the computed maximum run-up height to the analytical one is shown in Fig. 4 as a function of a parameter made of the three factors. With the bigger value of the parameter, the accuracy becomes worse. The reason is considered due

to deterioration of the linear extrapolation used at the wave front, with steeper slopes, longer mesh size and shorter wave length.

Secondly, it is checked how big the effect of nonlinearity is. The computation is carried out for the same topography. The results are compared with analytical results of the linear theory. In nonlinear computations, a particle with the higher vertical displacement moves with the higher velocity. Therefore, in some cases, a particle behind the wave front overtakes the wave front. We consider that this introduces the breaking and it is necessary to make an adjustment. We set a restriction that the particles behind should not get ahead of the particles in front of them. White circles in Fig. 5 show the results of the computation with the adjustment and the black ones those without the adjustment. This phenomenon becomes distinct with the wave of big steepness. In the computation of actual tsunamis, the phenomena is almost negligible, because of their small steepness.

Examples of wave profile with the adjustment are shown in Fig. 6. The wave fronts are similar to a bore. However, due to the small amplitude, difference between the nonlinear results and the linear ones is not large.

Thirdly, the accuracy of our numerical scheme for the two-dimensional cases are examined. We employ the case of a rectangular bay with the bottom of a uniform slope. In this simple topography, an analytical solution of maximum run-up height are obtained by use of the linear theory in the Lagrangian coordinates as follows,

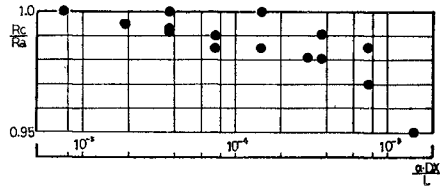


Fig. 4 The accuracy of the numerical computation.

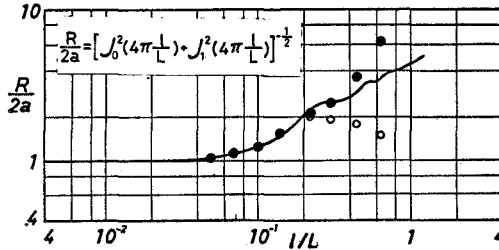


Fig. 5 The comparison between the analytical and the numerical (non-linear) results.

$$\frac{R}{H} = \{ (J_1(4\pi\frac{1}{L})\psi_1)^2 + (J_0(4\pi\frac{1}{L}) - J_1(4\pi\frac{1}{L})\psi_2)^2 \}^{-1/2}, \text{-----(13)}$$

where

$$\psi_1 = \frac{2kd}{\pi} \int_0^{kd} \frac{\sin^2 s}{s^2 \sqrt{(kd)^2 - s^2}} ds,$$

$$\psi_2 = \frac{2kd}{\pi} \int_0^{kd} \frac{\sin^2 s}{s^2 \sqrt{s^2 - (kd)^2}} ds,$$

and where 2d denotes the width of the bay and k the wave number. Tsunami in a bay may increase their heights due to resonance, and then the effects of nonlinearity may become unnegligible. Figure 7 shows the comparison of the analytical results of the linear theory and the numerical results. White circles are of nonlinear theory and black circles are of linear theory.

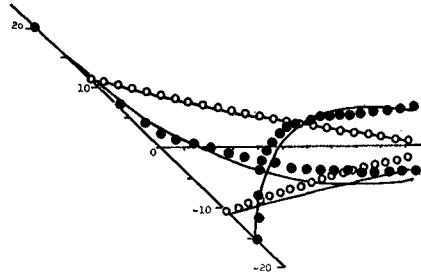


Fig. 6 Examples of wave profile for the nonlinear theory.

As the results of these preliminary examinations, we get the following conclusions.

1. Our numerical scheme is stable and satisfactory with respect to the accuracy of the results, for both one- and two-dimensional cases.

2. The nonlinear effects can increase the linear results by amount of 20% at most.

(2) An application to the Okkirai Bay.

The method with the nonlinear and bottom friction ($n = 0.029$) effects is applied to a bay on the Sanriku Coast, in Japan. This area

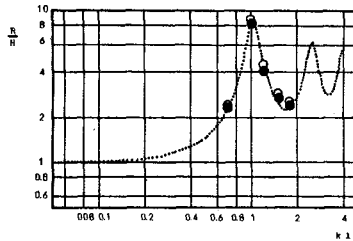


Fig. 7 The comparison between the analytical and the numerical results for a rectangular bay.

has been frequently attacked by tsunamis. In the Okkirai Bay, there are five fishing ports with flats behind them. Along the other part of the coast, we find the almost vertical cliffs and no village. Therefore, the main interests are upon the five places.

The tsunami selected as the input is the Great Meiji Sanriku Tsunami in 1896. Due to this tsunami, more than 27,000 persons were dead and about 10,000 houses were destroyed and lost. The source of the earthquake located at about 100km off the Sanriku Coast. Figure 8 shows the area of the source of the tsunami and the movement of the sea bottom which estimated by Hatori (1976). The number in the figure is the vertical displacement of the sea bottom. We assume that the displacement occurred instantly and the water surface showed the same movements as the sea bottom.

In order to economize the computation time, the whole region is divided into four sub-regions of different mesh size. The minimum mesh size is 1/9km. Figure 9 shows the smallest region in the Okkirai Bay.

The origin of time is taken at the time when the earthquake occurred. At about 17 minutes after the earthquake, the water level begins to recede. Then, it follows a slight ebb of water level. Figure 10 shows the time history of water surface elevation at the entrance of the bay.

An example of the numerical results is given in Figs. 11 to 15. In Figs. 11 and 12, which correspond to the time 2100 s and 2280 s, arrows show the horizontal velocities, lines the contour lines of the water surface and numbers attached the height in meters above still water level. Then, the first maximum run-up occurs at the bottom of the bay. We show the details in Figs. 13 to 15. The solid line is the network connecting the initial positions of water particles when we have no tsunami. The dotted line denotes the deformation of the network at each time. The

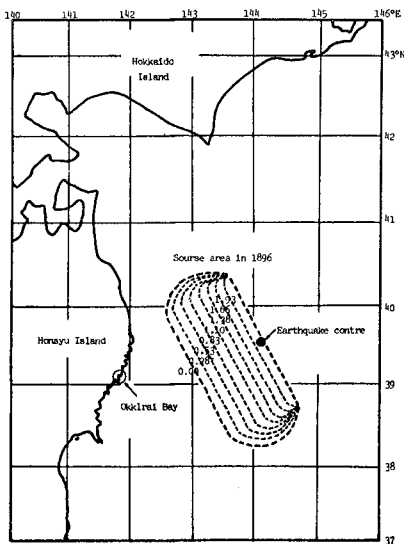


Fig. 8 The area of the source of the Tsunami in 1896.

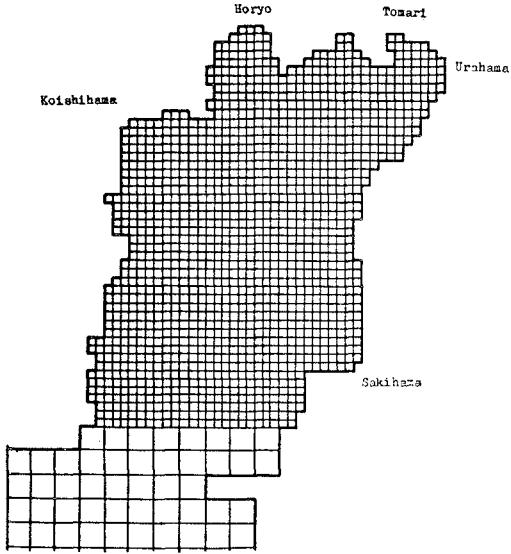


Fig. 9 The region of the smallest mesh in the numerical simulation.

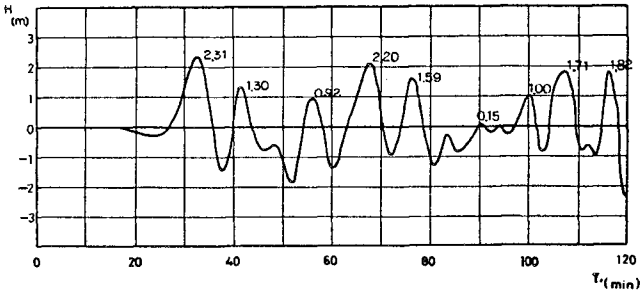


Fig. 10 The water level at the entrance of the bay.

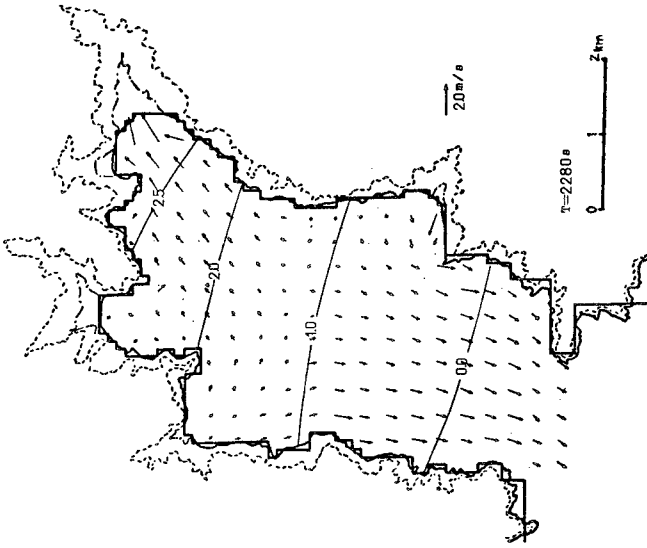


Fig. 12

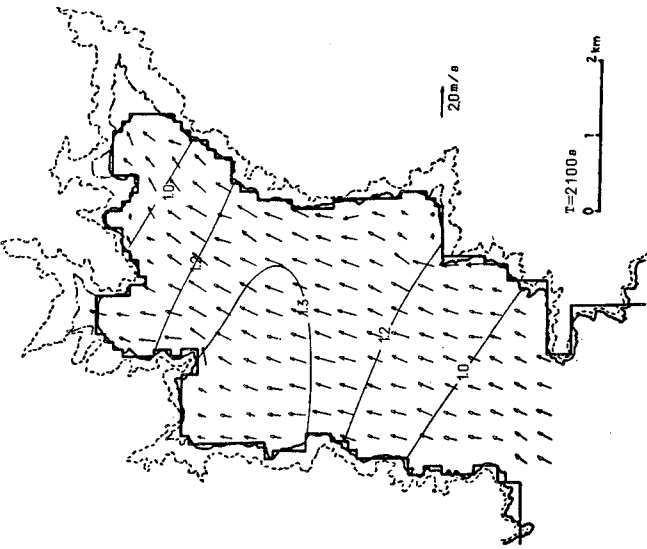


Fig. 11

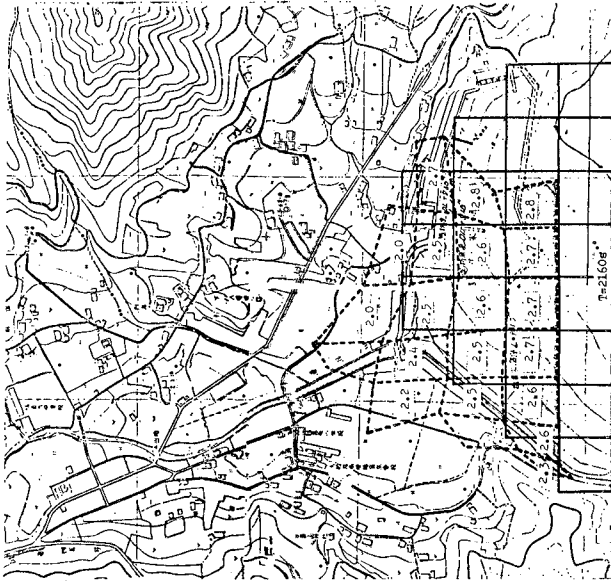


Fig. 14

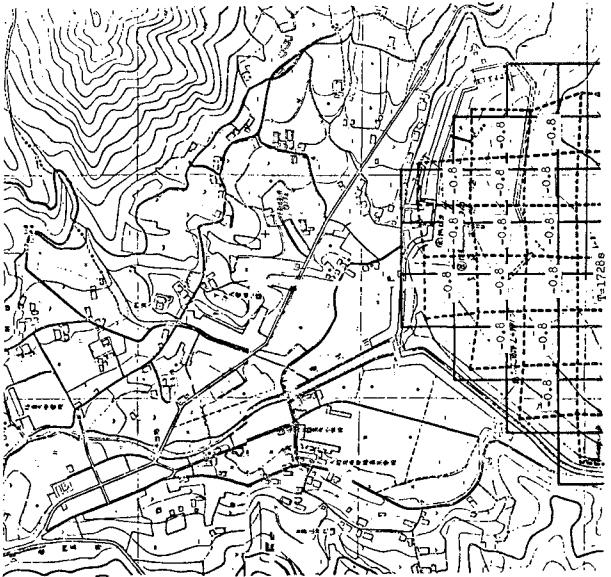


Fig. 13

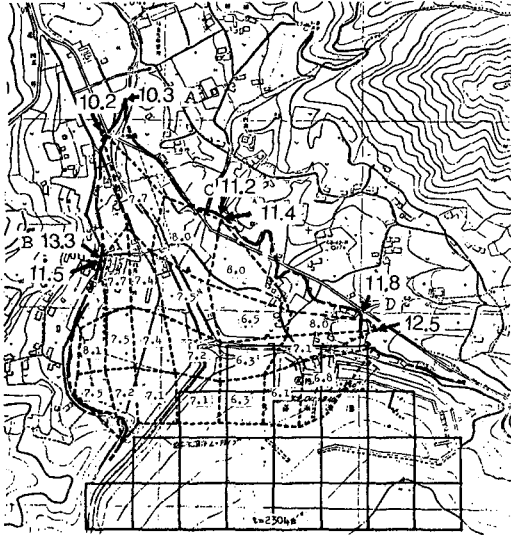


Fig. 15 The comparison between the recorded and the numerical maximum run-up height for the Great Meiji Sanriku Tsunami in 1896.

values shown in the center of the dotted mesh is the mean value of the vertical displacement, averaged from the value at four corners.

Figure 15 corresponds to the maximum run-up. The chain line in this figure shows the recorded inundation heights in 1896. There is a small river in this village. The record shows the run-up height of 10.3 m along the river (point A). The numerical simulation gives 10.2 m. Due to the finite grid cell, the computed point can not exactly coincide with the recorded point. At the point B, the record shows 13.3 m. The numerical ones is 11.5 m. Although the difference is rather big, the inundation lines of the recorded and the numerical ones coincide well, because the land here is almost vertical. At the point C, the record is 11.2 m and the computed one is 11.4 m. At the point D, 11.8 m and 12.5 m, respectively.

As the result, it is considered that the agreement is satisfactory and the method employed here is effective to simulate the run-up of a tsunami.

4. CONCLUSION

Linear and nonlinear long wave theories in the Lagrangian description are proved to be applicable to the analysis of tsunami run-up. Computation schemes are examined and established in both one- and two-dimensional cases. The present method can be also applied without difficulty to the actual topography of complicated geometry.

ACKNOWLEDGEMENT

The authors wished to express their gratitude to Dr. T. Iwasaki and Dr. A. Mano, Professors of Civil Engineering, Tohoku University, for their discussions and co-operation.

A part of the study was supported by a grant from the Ministry of Education.

REFERENCES

- 1) Shuto, N. : Run-up of long waves on a sloping beach, Coastal Engineering in Japan, Vol. 10, pp. 23-38, 1967.
- 2) Goto, C. : Nonlinear equation of long waves in the Lagrangian description, Coastal Engineering in Japan, Vol. 22, pp. 1-9, 1980.
- 3) Goto, C. and N. Shuto : Two-dimensional run-up of tsunami by nonlinear theory, Proc. of the 26th Conf. on Coastal Engineering in Japan, Vol. 26, pp. 56-60, 1979 (In Japanese).
- 4) Keller J. B. and H. B. Keller : Water wave run-up on a beach, Research Report No. NONR-3828(00), Office of Naval Research, Dept. of Navy, 1964.
- 5) Hatori, T. : Tsunami magnitude and wave source regions of historical Sanriku Tsunamis in Northeast Japan, Bull. Earthq. Res. Inst. of Tokyo, University, Vol. 51, pp. 197-207, 1976 (In Japanese).

CHAPTER 44

ON THE CORRECTION OF LAND-BASED WIND MEASUREMENTS FOR OCEANOGRAPHIC APPLICATIONS

S. A. Hsu

Coastal Studies Institute, Louisiana State University
Baton Rouge, LA 70803, U.S.A.

Abstract

Simultaneous offshore and onshore wind measurements were made at stations ranging from Somalia, near the equator, to the Gulf of Alaska. Offshore data obtained from standard U.S. NOAA buoys, research platforms, and merchant ships were compared with data from coastal stations. The results indicated that, under the commonly observed speed of 5-6 m/s, land measurements of mean wind speed are only 63% of the offshore mean speed. Furthermore, it was found that only those stations located in the beach area that measure wind speed above both the internal boundary layer and the nocturnal inversion height represent offshore conditions. In order to correct land-measured wind data, a formula is developed and verified by all existing data sets. A simplified equation, i.e., $U_{\text{sea}} = 3 U_{\text{land}}^{2/3}$ is proposed for offshore applications. Criteria for in situ wind measurements near the coast are outlined. Data reduction procedures for inland stations are also provided.

1. Introduction

For some time, differences in onshore and offshore wind speeds have been known to exist (see, e.g., Davenport, 1965; Yu, 1970; Hsu, 1979; Zimmerman and Burton, 1979). Many studies related to coastal marine sciences and engineering require wind data from offshore regions. Yet, in situ measurements over water are often lacking. Therefore, engineers as well as scientists traditionally rely on wind measurements over land, preferably near coasts. However, because simultaneous onshore and offshore observations do not always exist, systematic studies such as simple comparison between these two environments are also lacking. Only recently the U.S. National Oceanic and Atmospheric Administration (NOAA) deployed several buoys for longer term measurements over the continental shelf as well as farther offshore. It is the purpose of this paper to study the systematic variations in wind speed between offshore and onshore areas by comparing these buoy data with data from coastal and inland stations operated by NOAA.

In order to substantiate the results, four specialized experiments have been selected. The phenomenon of wind variability across the coastal zone is described in section 2. In order to correct onshore measurements a formula is developed in section 3. Experimental results are summarized in section 4. Since existing stations are not necessarily located near the shore, in situ measurements may be required for certain engineering projects. Furthermore, height correction for those data obtained from existing urban stations should be made. All these problems are discussed and correction criteria are outlined in section 5. Finally, conclusions are drawn in section 6.

2. Wind Variability across the Coastal Zone

In this study U.S. NOAA data from six buoys and twelve land stations for a period of 1 year (July 1977 through June 1978) are utilized. Information on these data buoys may be found in Hamilton (1980). Data from each buoy are compared to those of the two nearest land stations: one located on the coast, i.e., keys, capes, and islands, and another a few kilometres inland, preferably less than 20 km. Two buoys are located in the Atlantic Ocean, two are in the Gulf of Mexico, and one each is in the Pacific Ocean and Gulf of Alaska. In order to avoid height variations between wind sensors, only those land stations whose height is within 20 m above sea level are used.

The results are shown in Figure 1. They indicate that, contrary to common practice, even stations such as those located on a small, flat, open area (e.g., Key West, Florida, and Cape Hatteras, North Carolina) cannot represent monthly mean offshore conditions. Furthermore, at stations located in an estuarine environment such as Homer, in Cook Inlet, Alaska, the mean wind speed on the average is less than half that offshore. Figure 1 also shows that the largest difference between onshore and offshore conditions usually occurs in winter, when offshore storms are more frequent because of the more pronounced aerodynamic roughness or drag effect on land. During the warmer part of the year higher speeds may be recorded, at times, for diurnal onshore (sea breeze) winds than for offshore winds (Fig. 1). As expected, the wind speed decreases inland (Fig. 1).

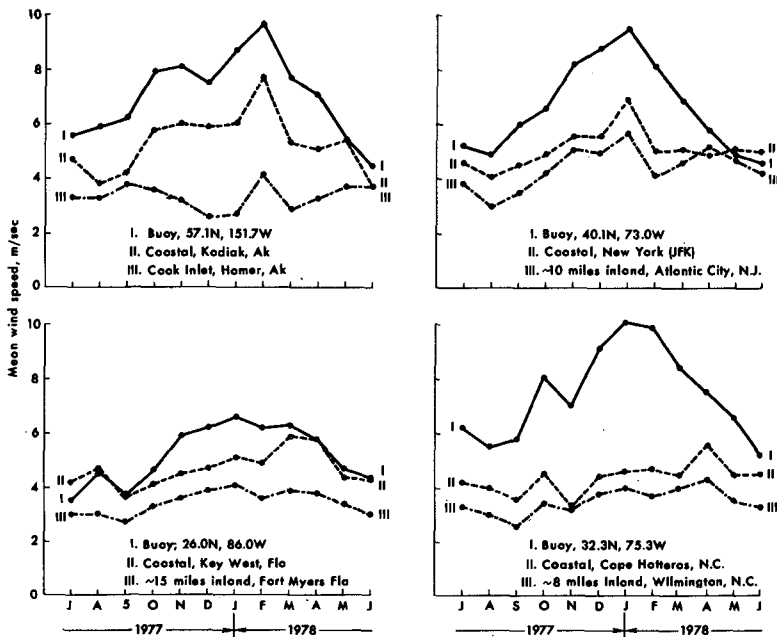


Figure 1. Examples of differences in monthly wind speed (meters per second) at stations ranging from offshore to coastal to inland (from July 1977 through June 1978).

The average of all buoys and land stations indicates that the ratio of buoys to land stations is 1.60 ± 0.28 (mean \pm standard deviation). In other words, the average land-based mean speed is only 63% of that offshore. Two pairs of buoy data not shown in Figure 1 are incorporated in the above statistics. They are a buoy located at 26.0°N , 93.5°W , which was compared to Corpus Christi and Brownsville, Texas, stations, and a buoy at 41.1°N , 137.8°W , which was compared to stations at Astoria, Oregon, and San Francisco, California.

Figures 2 and 3 represent some diurnal variations across the upper Texas coastal zone (Yu, 1970). Nine mechanical weather stations were used to record surface temperature, wind speed, and wind direction. The offshore station was located about 19 km directly offshore (station SOC, shown in Fig. 2). The instrument at that location was mounted on top of an oil drilling platform, which placed it about 20 m above the water surface. The others were located inland at distances of approximately 0.01, 0.09, 1.7, 3.5, 5.2, 8.0, 10.7, and 14.0 km from the coastline. The instruments at these eight inland stations were set up at a height of 2 m above the ground. In order to compare SOC (offshore) data with that from the other

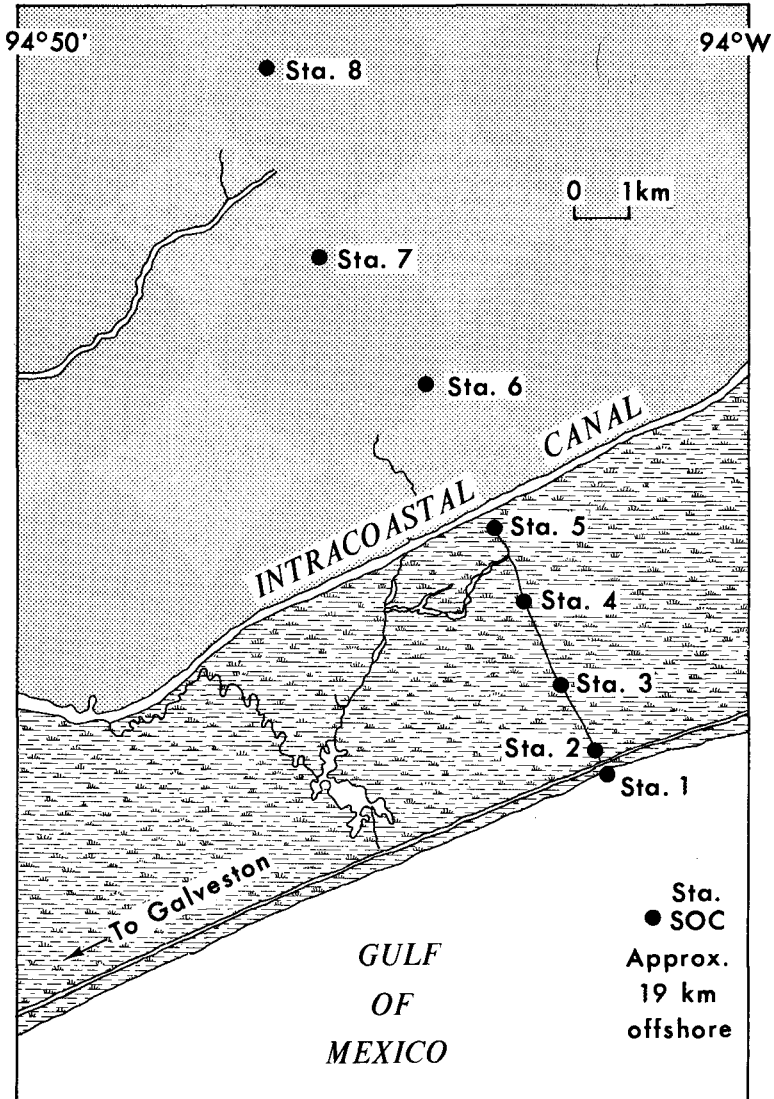


Figure 2. Locations of the nine mechanical weather stations (eight onshore and one about 19 km offshore on a platform). They were located approximately along a line perpendicular to the shoreline. (After Yu, 1970.)

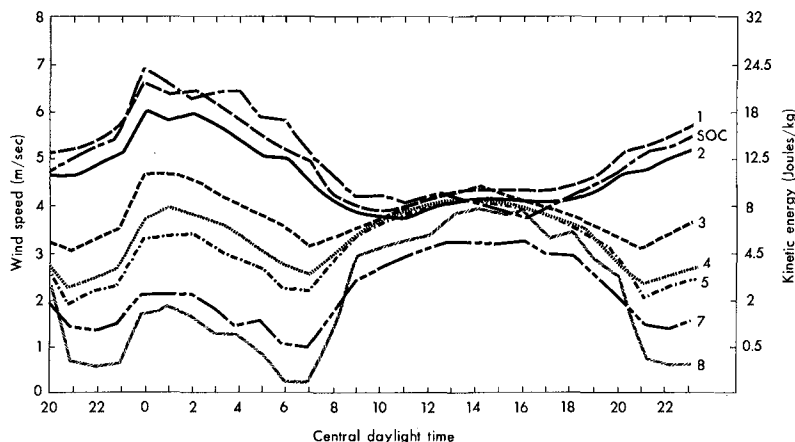


Figure 3. Diurnal variation of wind speed measured from eight stations (cf. Fig. 2 and text) deployed on the upper Texas coast and averaged for the period 9-11 June 1968. (After Yu, 1970.)

stations, the data were all reduced to the 2-m level. As shown in Figure 2, the nine stations were located along a line almost perpendicular to the coast. A 1-hour average time centered on the hour was used, that is, 0830 to 0930 for the 0900 value, etc. Accuracy is limited to the reading accuracy of the record, which is approximately ± 0.1 mi/hr (± 0.045 m/s) (for further details, see Yu, 1970).

The diurnal variation of wind speed at the various stations is shown in Figure 3. Curves are drawn on the basis of a 3-day average, i.e., June 9, 10, and 11 taken together. The most important feature shown in this figure is that there are two different types of curves. The curves for stations SOC, 1, and 2 are similar; we shall call these marine-type stations. Stations 3, 4, 5, 7, and 8 we shall call inland-type stations. Data for station 6 are missing because that instrument did not function properly. At the marine-type stations maximum wind speeds occurred about midnight and minimum wind speeds occurred about noon. More detailed examination of the figure reveals that at the offshore station (SOC) the minimum wind speed occurred at 1600 central daylight time (CDT), while at nearshore stations 1 and 2 minimum speeds occurred at 1000 CDT and 1100 CDT, respectively. At inland stations the primary maximum wind speeds occurred at 1400 CDT, primary minimum wind speeds occurred at 0600 CDT or 0700 CDT, a secondary maximum occurred at 0000-0100 CDT, and a secondary minimum occurred at 2100-2200 CDT.

It is clear from Figure 3 that only those stations (i.e., 1 and 2) that are within about 100 m of the surf zone represent offshore conditions. Since most coastal weather stations worldwide are not located that close to the shoreline, inland wind measurements may not be extended to the offshore

unless proper corrections are made.

Figure 4 shows that on the tropical (trade-wind-dominated) island of Barbados wind speeds were also different along a horizontal grid that extended from the beach to 10 km inland (Aspliden et al., 1977). Note that the station located on the shore (Fig. 4) agrees closely with the 1968 upper Texas coast beach station shown in Figure 3. About 2 km inland nighttime and daytime peaks are about equal, and 10 km inland only a strong daytime maximum is indicated. This also resembles the inland data from the upper Texas coast (compare Figs. 3 and 4) (for explanation of the variability see Yu, 1970, and Aspliden et al., 1977). The prevailing wind

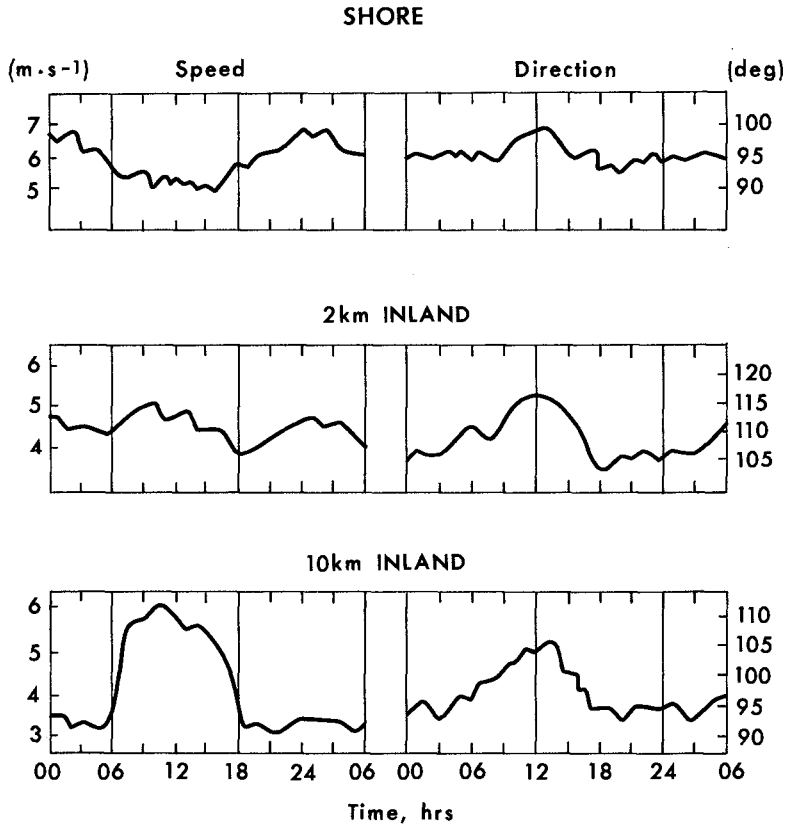


Figure 4. Diurnal variations of wind speed and direction at three locations on the eastern shore of the tropical island Barbados in August 1972. (After Aspliden et al., 1977.)

direction at Barbados was from 90° to 120° at all stations.

3. Development of the Correction Formulas

It has been demonstrated in the preceding section that large differences exist between wind measurements made onshore and those made offshore. Corrections, therefore, should be made to inland station data before they are applied to offshore regions. In order to facilitate such a correction, the following formula, based on the power law wind distribution in the PBL (see, e.g., Davenport, 1965), is proposed (see Fig. 5)

$$\frac{U}{U_H} = \left(\frac{Z}{Z_H} \right)^P \quad (1)$$

where U at height Z and U_H at Z_H are the velocity within and above the atmospheric planetary boundary layer (PBL), respectively. The thickness of the PBL is $Z_H (=H)$, and P is an exponent that depends on atmospheric stability and surface roughness, Z_0 . (For determination of P , see, e.g., Sedefian, 1980.)

The power law, equation (1), has two significant characteristics that make it very useful for work involving the whole of layer H : the law is a good average representation of the velocity profile over the entire PBL, and integral relations based on this easily integrated law are not far from correct (see, e.g., Blackadar, 1960; Plate, 1971).

If we assume that equation (1) is valid both onshore and offshore, we get

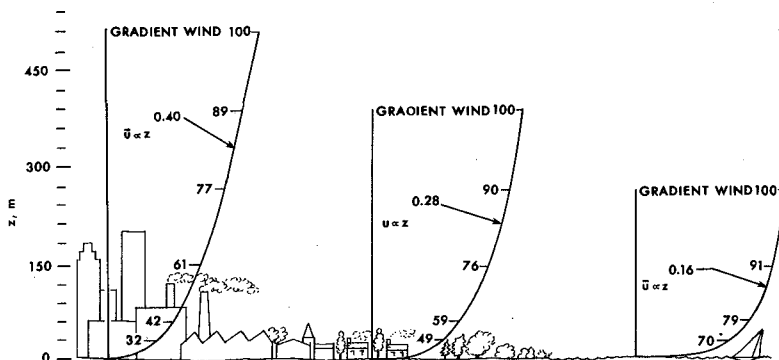


Figure 5. The power law (equation 1) over different terrain. The profile on the left represents the vertical variation of the wind over an urban area; the center profile, over a forest; and the one on the right over flat, open country. (After Davenport, 1965.)

$$\frac{(U/U_H)_{\text{sea}}}{(U/U_H)_{\text{land}}} = \frac{(Z/H)_{\text{sea}}^p}{(Z/H)_{\text{land}}^p} \quad (2)$$

If we assume that U_H on top of the PBL does not change appreciably across the coastal zone and that $Z = 10$ m, equation (2) becomes

$$\frac{U_{\text{sea}}}{U_{\text{land}}} = \frac{10^p_{\text{sea}}}{10^p_{\text{land}}} \cdot \frac{H_{\text{land}}^p}{H_{\text{sea}}^p} \quad (3)$$

According to Hsu (1979a)

$$H_{\text{sea}} = H_{\text{land}} - 123 (T_{\text{land}} - T_{\text{sea}}) \quad (4)$$

where T_{land} ($^{\circ}\text{C}$) and T_{sea} ($^{\circ}\text{C}$) are the temperatures at 2 m over the land and the sea, respectively, and the corresponding H is in metres. Furthermore, according to Hsu (1970)

$$U_{\text{land}} \propto (T_{\text{land}} - T_{\text{sea}}) \quad (5)$$

Since H_{land} is routinely available from twice-daily radiosoundings, it may be considered as a known value. Using this reasoning, and with equation (5), equation (4) may be written as

$$H_{\text{sea}} \propto U_{\text{land}} \quad (6)$$

and, since H_{land} is known, equation (3) becomes

$$\frac{U_{\text{sea}}}{U_{\text{land}}} \propto U_{\text{land}}^{-p} \quad (7)$$

or

$$\frac{U_{\text{sea}}}{U_{\text{land}}} = a U_{\text{land}}^{-b} \quad (8)$$

where a and b are positive numbers.

Equation (8) is our formula for the correction of land-based observations for offshore conditions.

4. Experimental Results

Equation (8) is verified in this section. In addition to the data presented in Figure 1, four more specialized experiments were conducted to substantiate this equation.

Table 1 summarizes all available data pairs measured simultaneously onshore and offshore. Column 3 provides the data obtained from Figure 1, and column 4 shows data from SethuRaman and Raynor (1980). Column 5 was based on field experiments (Hsu, 1979a) from an offshore (stage 1) platform and an existing NOAA weather station at Apalachicola, Florida, during February and again in November-December 1977. Since wind speeds in previous experimental data were low, except those from SethuRaman and Raynor (1980), another special experiment was conducted in Somalia, where a low-level atmospheric jet exists during summer (see Fein and Kuettner, 1980).

Our experiments were conducted in May and June. For comparison, ship data obtained from the National Climate Center were employed. Pairs of Gardo-ship data (8-12°N and 51-55°E) and Mogadishu-ship (0.0-7.9°N and 41-50°E) were collected during June, when the jet is more pronounced between Gardo and the downwind region offshore than at Mogadishu and its offshore area (Fein and Kuettner, 1980). In fact, station Gardo was located very close to the area where the jet core passed. Note that wind measurements from merchant ships are considered reasonable when compared with standard ocean weather ship measurements (see Quayle, 1980). All the available data were analyzed and compiled in Table 1.

Figure 6 shows the result of these comparisons. The constants a and b of equation (8) are determined experimentally to be

$$\begin{aligned} a &= 2.98 \\ b &= 0.34 \end{aligned}$$

with high correlation coefficient,

$$r = 0.95 .$$

We therefore have

$$\frac{U_{\text{sea}}}{U_{\text{land}}} = 2.98 U_{\text{land}}^{-0.34} \quad (9)$$

Table 1. Summary of the Ratio of $U_{\text{sea}}/U_{\text{land}}$ as a Function of U_{land} (in m/s) as Measured at Coastal Stations and Offshore Buoys, Ships, and Research Platforms

U_{land} Class Interval (1)	U_{land} Class Mdpt. (2)	NOAA Buoys vs Coastal Sta. ^a (3)	BNL Buoy vs Onshore Tower ^b (4)	NCS Platform vs Apalachicola ^e (5)	Ship vs Mogadishu ^f (6)	Ship vs Cardo ^g (7)	Avg. by Region ^h (8)
2.0-3.9	3	1.51±0.42 ^b (5) ^c	2.30	1.99±0.70 (102)	2.64±0.94 (5)	2.52±1.52 (7)	2.19±0.45 (8) ⁱ
4.0-5.9	5	1.34±0.32 (39)	2.02	1.42±0.54 (35)	1.72±0.71 (25)	1.72±1.20 (7)	1.64±0.27 (8)
6.0-7.9	7	1.36±0.08 (4)	1.59	1.33±0.43 (8)	1.50±0.62 (39)	2.19±1.26 (14)	1.59±0.35 (8)
8.0-9.9	9		1.35	1.19 (1)	1.38±0.47 (13)	1.52±0.72 (5)	1.35±0.13 (4)
10.0-11.9	11		1.23	1.09 (1)	1.13 (1)	1.31±0.32 (15)	1.19±0.10 (4)
12.0-13.9	13		1.20			1.29±0.21 (7)	1.25±0.06 (2)
14.0-15.9	15		1.20			1.35±0.25 (2)	1.28±0.06 (1)
16.0-17.9	17		1.20				

a. From Figure 1

b. Mean ± standard deviation

c. Total number of observational pairs (onshore and offshore)

d. Averaged data pairs between beach tower at Long Island, New York, and offshore Brookhaven National Laboratory buoy (from Sethuraman and Raynor, 1980)

e. U.S. Naval Coastal Systems Center platform offshore from Panama City, Florida, and NOAA Apalachicola station (see Hsu, 1979a)

f. Merchant ship observations vs. Mogadishu, Somalia (under conditions of general summer monsoon, but away from the Somali jet)

g. Merchant ship observations vs. Gardo, Somalia (under conditions of Somali low-level jetstream)

h. Mean ± standard deviation averaged from five columns between (3) and (7)

i. Total areas studied. Note four areas already included in Figure 1.

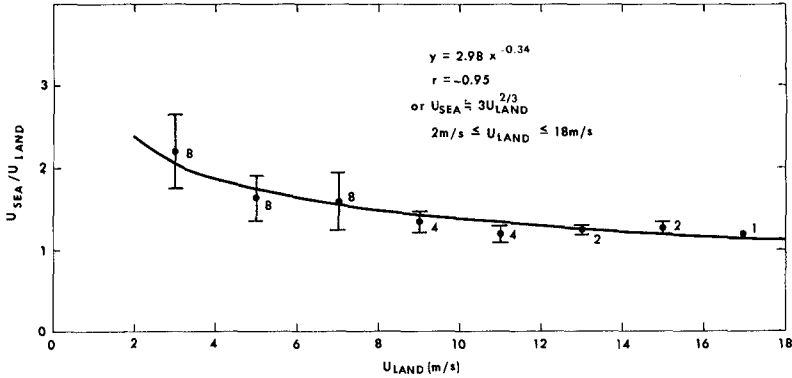


Figure 6. Ratio of U_{sea}/U_{land} as a function of U_{land} . Data were based on Table 1. Vertical bars are the standard deviation, and numbers beside the mean point are the areas incorporated in the computations.

or approximately

$$U_{sea} = 3 U_{land}^{2/3} \quad (10)$$

where $2 \text{ m/s} \leq U_{land} \leq 18 \text{ m/s}$.

Equation (10) is an average that encompasses many geographic regions as well as various climatic conditions. For a specific location the coefficients a and b of equation (9) may vary, but the general relationship will not be altered appreciably. It is therefore recommended that equation (10) be used as an average condition.

5. Criteria for Wind Measurements near the Coast

The preceding discussions presuppose a wind measurement station near the coast. However, in many places such coastal stations are not available. In other cases the station may be located not on flat and open country but on rugged terrain, where local topographic effects are large and measurements there may not represent offshore conditions. For certain engineering projects in situ measurements may be required but because of logistical problems shore stations must be substituted. Under these and similar conditions we suggest a set of criteria which will alleviate the problems or at least reduce them to a minimal and acceptable level. Before we outline these criteria, some theoretical considerations may be helpful.

As air passes from land to sea or vice versa, it must readjust to a new set of boundary conditions. The adjustment is not immediate throughout

the depth of the air layer but is generated at the surface and diffuses upward. The layer of air whose properties have been affected by the new surface is referred to as an internal boundary layer (IBL), and its depth grows with increasing distance, or fetch, downwind from the shoreline (see, e.g., Hsu, 1971). Since a simple but accurate model for the IBL has been formulated by Elliott (1958) (see, e.g., SethuRaman and Raynor, 1980), we adapt Elliott's relationship for the height of the IBL, h , given by

$$\frac{h}{Z_o''} = \left[0.75 + 0.03 \ln \frac{Z_o'}{Z_o''} \right] \left(\frac{x}{Z_o''} \right)^{0.8} \quad (11)$$

where Z_o' and Z_o'' are the upwind and downwind roughness lengths and x is the downwind distance. We require the anemometer to be higher than the IBL, i.e., higher than h . An example is given by SethuRaman and Raynor (1980). If the wind blows from sea to land and the beach is 50 m wide, $Z_o' = 0.05$ cm (offshore condition) and $Z_o'' = 10$ cm (onshore condition), the anemometer should be at least 8 m above the surface in order for the wind to represent the offshore condition.

The average condition for Z_o sea is 0.01 cm (Hsu, 1974), and Z_o land in coastal areas is given in Figure 7. For longer Z_o land values, see, e.g., Sellers (1965). From these roughness parameter values, and if the landward fetch from the surf zone is known, equation (11) may be used to compute the optimum height for the wind sensors. For example, suppose a small dune about 2 m high is located 100 m from the mean water line, i.e., the average beach width is 100 m. If the wind is blowing from sea to land, we set $Z_o' = 0.01$ cm, $Z_o'' = 1$ cm, and $x = 10,000$ cm; the height of the anemometer should be at least 9.7 m above the dune ridge. On the other hand, assuming Z_o is the same but the beach is only 10 m wide, the height of the wind sensor needs to be only 2 m above the dune. Note that all examples given above assume that winds are perpendicular to the shoreline. For certain regions, the mean wind may have some angle to the beach; then the over-beach fetch (length) will be larger. This effect should be used in the computation rather than the simple beach width.

The foregoing discussions are valid for onshore winds, i.e., when the wind blows from sea to land. However, when the wind blows from land to sea the anemometer must be located as close to the water's edge as possible because nocturnal cooling will produce calm winds only a short distance from the beach. This phenomenon has been explained by Hsu (1979b) and is shown in Figure 8. It can be seen that higher wind speeds near the beach and farther offshore are the results of a combination of Venturi and gravity-wind effects. For more detail see Hsu (1979b).

For offshore engineering design extreme winds are usually inferred from long-term onshore measurements. However, the reference station must be located on an open and flat country. Certainly data from rugged places must be corrected. An example is given in Figure 9, which shows that the 100-year return period wind at Guantanamo Bay, Cuba (station 13), is only 71 knots, whereas at San Juan, Puerto Rico (station 14) the 100-year return

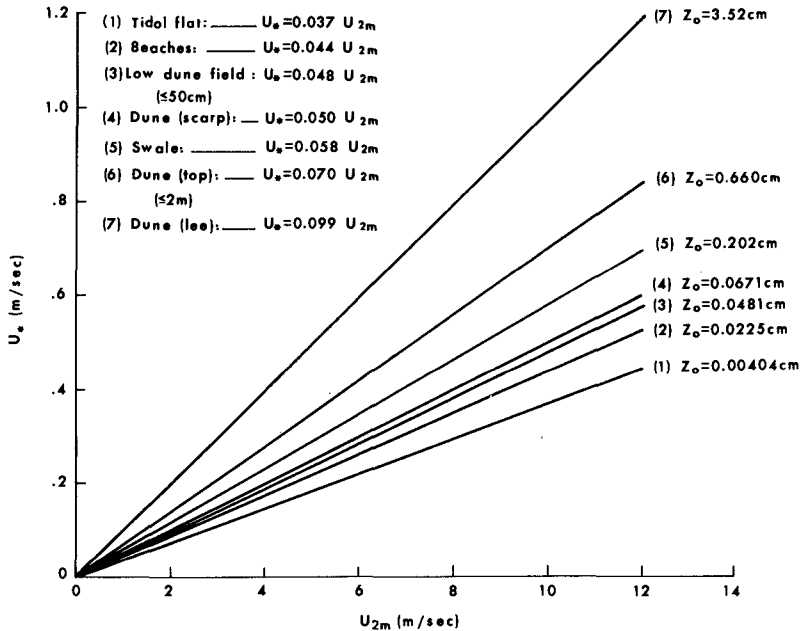


Figure 7. Summary of the aerodynamic roughness length Z_o and the relationship between shear velocity U_s and the wind velocity at 2-m height U_{2m} , measured in various coastal environments. Note that (1) was obtained from Ecuador; (2) is a synthesis of six beaches, Barbados, Ecuador, Texas, Brazil, Florida, and the Alaskan Arctic; (3) is from Texas; and (4) through (7) are all from Brazil. (For more detail, see Hsu, 1977.)

period wind is expected to be 124 knots. The lower value for Guantanamo is probably due to the sheltering effects of the nearby mountains and the island of Hispanola to the sea, whereas San Juan is exposed to the full force of Atlantic hurricanes (Atkinson, 1971).

For completeness, wind variation with height should be taken into account. Some average conditions are already shown in Figure 5. If analysis of wind loading as a function of height for offshore structures is needed, equation (1) may be applied. Values of the exponent P for different terrain are also shown in Figure 5, for example, for open and flat country, $P = 0.16$. Therefore, this condition may be applied to the offshore, or existing measured winds may be extrapolated to the height required and then corrected by applying equation (10).

We now outline the criteria for wind measurements near the coast:

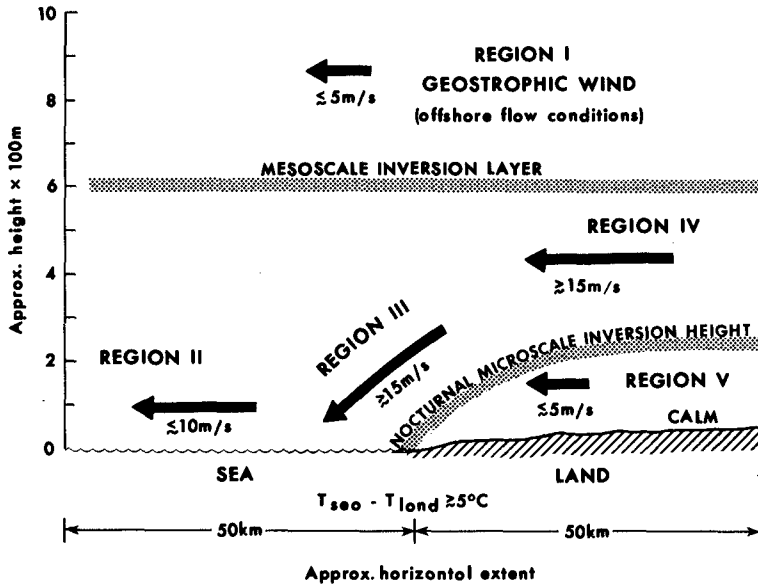


Figure 8. An example of higher wind speed near the shoreline and farther offshore but nearly calm wind inland under the influence of nocturnal cooling over land (for more detail, see Hsu, 1979b).

- (1) The anemometer site must be located on flat, open country, preferably on the ridge of the first dune field next to the beach, to represent both onshore and offshore winds. If a small island, cape, or key is located offshore, it should be used instead of the coastal dune fields.
- (2) The anemometer height may be optimized by applying equation (11). Proper roughness parameter and beach width should be used.
- (3) Existing wind data may be corrected to the proper height by applying equation (1) and Figure 5. Equivalently, one could apply the ratio obtained from the same height above ground level. For example, at the height of 30 m the wind over flat, open country is about 70/32 (from Fig. 5) or 2.19 times higher than that over a large urban area, and about 70/49 or 1.43 times higher than that over a woodland forest.
- (4) After the data have been measured from the nearshore area on the basis of (1) and (2) or have been reduced from existing inland measurements by (3), one then corrects them by applying equation (10). If a certain height above the sea surface is needed, one

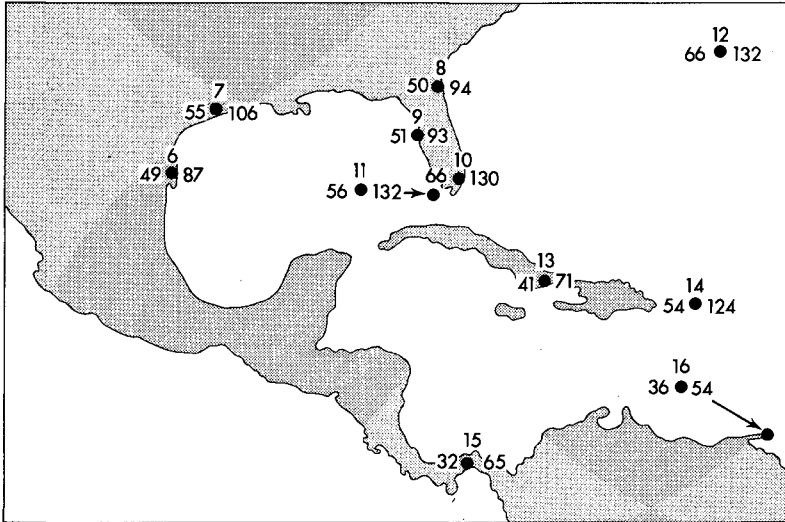


Figure 9. Examples of expected extreme wind gusts (knots) for 2-year and 100-year return periods for selected stations. Station numbers are located on the tops of the dots, 2-year return period on the left, and 100-year on the right. (After Atkinson, 1971.)

may apply equation (1) to the desired height with $P = 1/7$.

6. Conclusions

Several conclusions may be drawn from this study.

- (1) Monthly averages of six standard U.S. NOAA buoys and coastal stations in areas ranging from the Gulf of Mexico to Alaska indicated that the land-based mean wind speed is only 63% of the offshore.
- (2) Simultaneous hourly wind observations based on four more specialized experiments both onshore and offshore in various coastal environments showed that not only were there large differences, as indicated above, but also that only those stations located near the beach area above both the internal boundary layer and the nocturnal inversion height can represent offshore conditions.
- (3) In order to correct land-based wind data, a formula is developed which has been verified by existing data sets. A simplified equation, i.e., $U_{sea} = 3 U_{land}^{2/3}$, is also proposed for offshore applications.

- (4) Criteria for in situ wind measurements near the coast are outlined. It is recommended that the anemometer be deployed on open, flat country and that the optimum height for wind sensors be based on the local roughness parameter and the height of the internal boundary layer. Data reduction procedures for inland stations should begin by correcting the data to the beach environment from the proper speed ratio for the same height because of differences in roughness parameters. Then the beach data may be applied to offshore conditions by employing the simplified equation given above.

Acknowledgments

This study was sponsored by the Coastal Sciences Program, Office of Naval Research, Arlington, Virginia 22217, under a contract with Coastal Studies Institute, Louisiana State University, Baton Rouge. The Somali experiment during the summer 1979 MONEX, as well as travel for presentation of this paper, were supported in part by the Global Atmospheric Research Program, Division of Atmospheric Sciences, National Science Foundation, under Grants ATM 7813388 and 8013644. Appreciation is also expressed to the Somali Government for allowing us to conduct the experiment in order to obtain the essential data to substantiate this study. Buoy information were provided by Captain Glenn Hamilton, of the NOAA Data Buoy Office.

References

- Aspliden, C. I., Lynn, A., Desouza, R. L., and Rudder, G., "Diurnal and Semi-diurnal Low Level Wind Cycles over a Tropical Island," *Boundary-Layer Meteorol.*, Vol. 12, 1977, pp. 187-199.
- Atkinson, G. D., "Forecaster's Guide to Tropical Meteorology," Tech. Rept. 240, Air Weather Service, U. S. Air Force, 1971.
- Blackadar, A. K., "A Survey of Wind Characteristics below 1500 ft," *Meteorol. Monogr.*, Vol. 4, No. 22, 1960, pp. 3-11.
- Davenport, A. G., "The Relationship of Wind Structure to Wind Loading," National Physical Laboratory Symposium No. 16, *Wind Effects on Buildings and Structures*, pp. 54-102, Her Majesty's Stationery Office, London, 1965.
- Elliott, W. P., "The Growth of the Atmospheric Internal Boundary Layer," *Trans. Amer. Geophys. Union*, Vol. 39, 1958, pp. 1048-1054.
- Fein, J. S., and Kuettner, J. P., "Report on the Summer MONEX Field Phase," *Bull. Amer. Meteorol. Soc.*, Vol. 61, 1980, pp. 461-474.
- Hamilton, C. D., "NOAA Data Buoy Office Programs in Coastal Waters," Preprints, Second Conf. Coastal Meteorol., Los Angeles, Calif., Amer. Meteorol. Soc., 1980, pp. 44-47.
- Holzworth, G. C., "Mixing Heights, Wind Speeds, and Potential for Urban Air Pollution throughout the Contiguous United States," Office of Air

- Programs Pub. No. AP-101, Environmental Protection Agency, Research Triangle Park, North Carolina, 1972.
- Hsu, S. A., "Coastal Air-Circulation System: Observations and Empirical Model," *Monthly Weather Review*, Vol. 98, 1970, pp. 487-509.
- Hsu, S. A., "Measurement of Shear Stress and Roughness Length on a Beach," *Jour. Geophys. Res.*, Vol. 76, 1971, pp. 2880-2885.
- Hsu, S. A., "On the Log-Linear Wind Profile and the Relationship between Shear Stress and Stability Characteristics over the Sea," *Boundary-Layer Meteorol.*, Vol. 6, 1974, pp. 509-514.
- Hsu, S. A., "Boundary-Layer Meteorological Research in the Coastal Zone," *Geoscience and Man*, Vol. 18, School of Geoscience, Louisiana State University, Baton Rouge, 1977, pp. 99-111.
- Hsu, S. A., "An Operational Forecasting Model for the Variation of Mean Maximum Mixing Height across the Coastal Zone," *Boundary-Layer Meteorol.*, Vol. 16, 1979a, pp. 93-98.
- Hsu, S. A., "Mesoscale Nocturnal Jetlike Winds within the Planetary Boundary Layer over a Flat, Open Coast," *Boundary-Layer Meteorol.*, Vol. 17, 1979b, pp. 485-494.
- Plate, E. J., "Aerodynamic Characteristics of Atmospheric Boundary Layer," available as TLD-25465, National Technical Information Center, Springfield, Virginia, 1971.
- Quayle, R. G., "Climatic Comparisons of Estimated and Measured Winds from Ships," *Jour. Appl. Meteorol.*, Vol. 19, 1980, pp. 142-156.
- Sedefian, L., "On the Vertical Extrapolation of Mean Wind Power Density," *Jour. Appl. Meteorol.*, Vol. 19, 1980, pp. 488-493.
- Sellers, W. D., *Physical Climatology*, The University of Chicago Press, Chicago, 1965, 272 pp.
- SethuRaman, S., and Raynor, G. S., "Comparison of Mean Wind Speeds and Turbulence at a Coastal Site and Offshore Location," *Jour. Appl. Meteorol.*, Vol. 19, 1980, pp. 15-21.
- Yu, T. W., "Diurnal Variation of Kinetic and Internal Energy in Onshore Winds along the Upper Texas Gulf Coast," Rept. No. 19, Atmospheric Science Group, University of Texas, Austin, 1970.
- Zimmerman, J. R., and Burton, W. D., "Late Summer Gale Winds Offshore Coastal Oregon-Washington," *National Weather Digest*, Vol. 4, 1979, pp. 27-40.

NUMERICAL MODELLING OF TROPICAL CYCLONE STORM SURGE

by

Rodney J. Sobey¹
Bruce A. Harper²
George M. Mitchell³

ABSTRACT

Details are presented of a general numerical hydrodynamic model for the generation and propagation of tropical cyclone or hurricane storm surge. The model, known as SURGE, solves the two-dimensional depth-integrated form of the Long Wave Equations using an explicit finite difference procedure, with tropical cyclone surface wind and pressure forcing estimated from an adaption of available models based on U.S. hurricanes. Variations in tropical cyclone parameters as well as the physical characteristics of a coastal location such as bathymetry and details of capes, bays, reefs and islands are accommodated by the model. The accuracy and stability of the numerical solution have been confirmed by a comprehensive wave deformation analysis including quasi-non-linear effects and the open boundary problem has been overcome by the use of a Bathystrophic Storm Tide approximation to boundary water levels. A detailed sensitivity analysis has identified the principal surge generating parameters and the model has been checked against an historical tropical cyclone storm surge. SURGE has been used extensively in the northern Australian region and examples are presented.

INTRODUCTION

The tropical cyclone or hurricane storm surge is a meteorologically forced long wave motion resulting in a sustained superelevation of the sea surface, at least for a few hours, above that produced by the normal periodic astronomical tide. It is the result of the combined action on the underlying water body of the extreme atmospheric pressure gradients and wind shear stresses generated by a mature tropical cyclone. The region of surge intensification can extend over a substantial length of coastline (of order 200 km) and the development and impact of the surge wave at a particular site is sensitive to a number of meteorological and topographical factors. Briefly these are the intensity and scale of the tropical cyclone, the speed and track of the storm, the underwater and overbank terrain, offshore reefs and islands, local coastal features

-
1. Senior Lecturer, Department of Civil and Systems Engineering, James Cook University, Townsville 4811, Australia.
 2. Engineer, Hydraulics Laboratory, N.S.W. Public Works Department, Manly Vale 2093, Australia.
 3. Research Dynamicist, Atkins Research and Development, Epsom, Surrey KT18 5BW, United Kingdom.

(bays, headlands, estuaries) and the astronomical tide. Historically, storm tides have resulted in considerable damage to exposed coastlines, the flooding of low lying land and loss of life. A potentially critical situation arises when the total sustained water level (surge + tide) exceeds the highest astronomical tide (HAT) level.

In response to the need for reliable storm surge estimates in northern Australia for the design of coastal structures and for the protection of coastal communities, a numerical hydrodynamic model was developed within the Department of Civil and Systems Engineering at James Cook University. The model, known as SURGE, is a general numerical hydrodynamic model for the generation and propagation of tropical cyclone storm surge and can be applied to most coastal regions (12). It includes the effects of undersea bathymetry, offshore islands, reefs and other coastal features, as well as the flooding of low lying land. Tropical cyclone size, intensity and track can be varied continuously throughout a simulation to produce water flow patterns, contours of water level, coastal surge profiles at any time and water level and flow velocity time histories anywhere within the model area. SURGE is a comprehensive software system and is fully documented in the form of a user's guide (3). Particular attention has been given to the quite considerable problems of input data format and especially output data selection and presentation.

While numerical modelling of long wave propagation is not new, there are a number of unique aspects of the storm surge problem. In particular, the complex character and geophysical extent of the meteorological forcing, the specification of suitable open boundary conditions and the satisfactory resolution of the storm structure in discretised form all require special attention (12).

MATHEMATICAL FORMULATION

The response of a homogeneous sea to the meteorological forcing of a tropical cyclone is described by the full Navier-Stokes Equations for a homogeneous, incompressible fluid. Direct numerical solutions of these equations are as yet not feasible and a three-dimensional solution would only appear necessary where fluid density difference and/or the vertical flow structure may be important. An adequate description of long wave propagation (astronomical tides and storm surge) can be had from a two-dimensional vertically integrated form of the Reynolds Equations - the Long Wave Equations (17). These equations represent the conservation of mass and the conservation of momentum in horizontal directions x and y and time t :

$$\frac{\partial \eta}{\partial t} + \frac{\partial U}{\partial x} + \frac{\partial V}{\partial y} = 0 \quad (1)$$

$$\frac{\partial U}{\partial t} + \frac{\partial}{\partial x} \left(\frac{U^2}{\eta-d} \right) + \frac{\partial}{\partial y} \left(\frac{UV}{\eta-d} \right) - fV = -g(\eta-d) \frac{\partial \eta}{\partial x} - \left(\frac{\eta-d}{\rho_w} \right) \frac{\partial p_s}{\partial x} + \frac{1}{\rho_w} (\tau_{sx} - \tau_{bx}) \quad (2)$$

$$\frac{\partial V}{\partial t} + \frac{\partial}{\partial x} \left(\frac{UV}{\eta-d} \right) + \frac{\partial}{\partial y} \left(\frac{V^2}{\eta-d} \right) + fU = -g(\eta-d) \frac{\partial \eta}{\partial y} - \left(\frac{\eta-d}{\rho_w} \right) \frac{\partial p_s}{\partial y} + \frac{1}{\rho_w} (\tau_{sy} - \tau_{by}) \quad (3)$$

The x - y datum plane is located at the mean water level with the z axis directed vertically upwards. The water surface elevation with respect to datum is $\eta(x,y,t)$, the sea bed is $d(x,y)$ with respect to datum,

U and V are depth-integrated flows per unit width, f is the Coriolis parameter and ρ_w is the mass density of sea water. The forcing influence of the tropical cyclone is represented through the surface wind shear stress vector $\tau_s(x,y,t)$, resolved into components τ_{sx} and τ_{sy} , and the x and y gradients of the M.S.L. atmospheric pressure $p_s(x,y,t)$. The effect of bottom stress is represented through the seabed shear stress vector $\tau_b(x,y,t)$, resolved into components τ_{bx} and τ_{by} such that, for example, in blue water regions:

$$\tau_{bx} = \frac{\lambda}{8} \rho_w \frac{|Q|U}{(\eta-d)^2} \quad (4)$$

where $Q = (U^2+V^2)^{1/2}$ and λ is the Darcy-Weisbach friction factor, assumed depth-dependent according to the Colebrook-White formula for a hydraulically rough boundary layer. Modified values of λ are adopted near reefs and for overbank flooding, the details being presented below.

At this stage the equations are sometimes linearised, neglecting the (normally small) convective accelerations. In SURGE all terms have been retained as they present no particular numerical problems and in some cases the commonly neglected terms (such as Coriolis and convective accelerations) can even be relatively important (5,12). A SURGE input option however does allow the convective terms to be omitted (3).

NUMERICAL SOLUTION

The flow field, coastal details, offshore and overbank bathymetry and coral reefs are represented on a square grid of unit dimension Δs and discrete values of the variables are specified on a space (x,y) and time (t) staggered computational grid, whose node points are defined as $(i\Delta x, j\Delta y, n\Delta t)$. Water surface elevation H (or η), bed elevation D (or d) with respect to M.S.L. and barometric head $B = p_s/\rho_w g$ are located at points (i,j,n) , depth-integrated flow U and the surface wind shear stress term $WX = \tau_{sx}/\rho_w$ at $(i+\frac{1}{2}, j, n+\frac{1}{2})$ and the depth-integrated flow V and the surface wind shear stress term $WY = \tau_{sy}/\rho_w$ at $(i, j+\frac{1}{2}, n+\frac{1}{2})$ points.

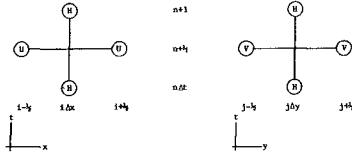
Numerical integration of the partial differential Equations 1,2 and 3 is accomplished by an explicit "leapfrog" procedure similar to that used in the numerical simulation of storm tides in Galveston Bay, Texas, by Reid and Bodine (8). The computational molecules and explicit finite difference equations are listed in Table 1, the continuity equation being centred at $(i,j,n+\frac{1}{2})$, the x momentum equation at $(i+\frac{1}{2}, j, n)$ and the y momentum equation at $(i, j+\frac{1}{2}, n)$. In a number of special cases associated with boundary or internal (reef, weir, island) constraints, the complete finite difference Equations b and c of Table 1 cannot be implemented and suitably reduced forms (12) are adopted in such circumstances. Successive application of the x and y momentum equations and the continuity equation, together with appropriate boundary conditions advance the solution by one simulation time step Δt .

STABILITY AND WAVE DEFORMATION

As SURGE is based on explicit finite difference equations, numerical stability for all wave numbers is ensured only when the Courant number $Cr = (gA/b)^{1/2} \Delta t/\Delta x$ does not exceed unity.

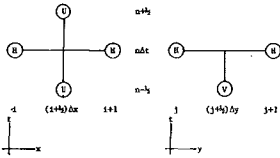
TABLE 1. SURGE COMPUTATIONAL MOLECULES AND FINITE DIFFERENCE EQUATIONS

Mass Conservation Equation -



$$U_{i,j}^{n+1} = U_{i,j}^n - \left[\frac{U_{i+1/2,j}^{n+1/2} - U_{i-1/2,j}^{n+1/2}}{\Delta x} + \frac{V_{i,j+1/2}^{n+1/2} - V_{i,j-1/2}^{n+1/2}}{\Delta y} \right] \Delta t \quad (a)$$

X Momentum Equation -

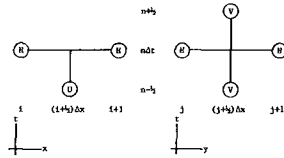


$$U_{i,j}^{n+1/2} = \left[\frac{U_{i,j}^{n-1/2}}{1 + \Delta t \left(\frac{U_{i+1/2,j}^{n+1/2} - U_{i-1/2,j}^{n+1/2}}{\Delta x} + \frac{V_{i,j+1/2}^{n+1/2} - V_{i,j-1/2}^{n+1/2}}{\Delta y} \right)} + \frac{U_{i+1/2,j}^{n-1/2} - U_{i-1/2,j}^{n-1/2}}{\Delta x} + \frac{V_{i,j+1/2}^{n-1/2} - V_{i,j-1/2}^{n-1/2}}{\Delta y} \right] \Delta t \quad (b)$$

where $\overline{U}_{i+1/2,j}^n = \frac{1}{2}(U_{i,j}^n + U_{i+1,j}^n + U_{i+1,j}^n + U_{i+1,j}^n)$

$$U_{i+1/2,j}^{n-1/2} = \frac{1}{2}(U_{i+1/2,j}^{n-1/2} + U_{i+1/2,j}^{n-1/2} + U_{i+1/2,j}^{n-1/2} + U_{i+1/2,j}^{n-1/2})$$

Y Momentum Equation -



$$V_{i,j}^{n+1/2} = \left[\frac{V_{i,j}^{n-1/2}}{1 + \Delta t \left(\frac{U_{i+1/2,j}^{n+1/2} - U_{i-1/2,j}^{n+1/2}}{\Delta x} + \frac{V_{i,j+1/2}^{n+1/2} - V_{i,j-1/2}^{n+1/2}}{\Delta y} \right)} + \frac{U_{i+1/2,j}^{n-1/2} - U_{i-1/2,j}^{n-1/2}}{\Delta x} + \frac{V_{i,j+1/2}^{n-1/2} - V_{i,j-1/2}^{n-1/2}}{\Delta y} \right] \Delta t \quad (c)$$

where $\overline{V}_{i,j+1/2}^n = \frac{1}{2}(V_{i,j}^n + V_{i,j+1}^n + V_{i,j+1}^n + V_{i,j+1}^n)$

$$V_{i,j+1/2}^{n-1/2} = \frac{1}{2}(V_{i,j+1/2}^{n-1/2} + V_{i,j+1/2}^{n-1/2} + V_{i,j+1/2}^{n-1/2} + V_{i,j+1/2}^{n-1/2})$$

Compliance with this equation, however, does not necessarily guarantee the accuracy of the solution and a broader analysis of the model behaviour is necessary to fully examine the numerical distortion of the physical surge wave. Some measure of this distortion can be had from a comparison of the numerical and analytical solutions of the equations in the time domain using the complex propagation factor of Leendertse (6). This method allows evaluation of the wave-number-dependent amplitude and phase distortions introduced by the numerical solution.

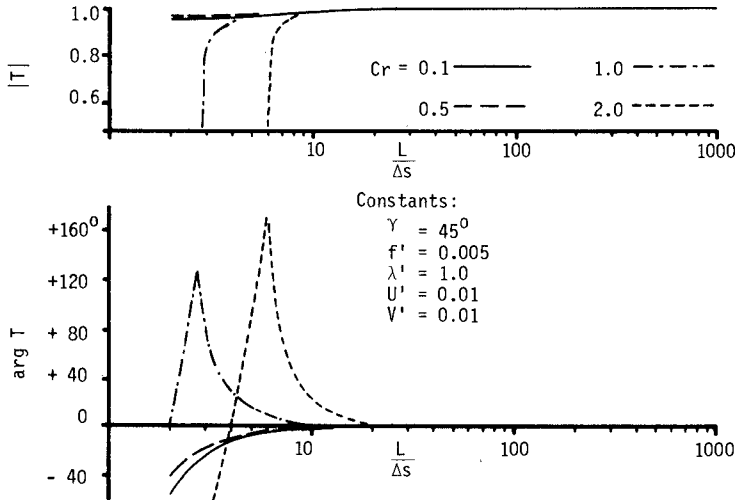


FIGURE 1. COMPLEX PROPAGATION FACTORS FOR COMPLETE QUASILINEAR FORM.

Assuming the non-linear interactions to be weak, as is generally the case for the Long Wave Equations, an evaluation of the wave deformation characteristics of the solution can be obtained from a quasilinear approximation to the finite difference equations (12). The complex propagation factor T is defined (6) as the ratio of the computed wave solution to the physical wave solution after a time interval in which the physical wave propagates over its wavelength L . Figure 1 shows the behaviour of $|T|$ and $\arg T$ for the complete quasilinear form of the Long Wave Equations with a constant wave propagation direction γ of 45° and various values of Cr . Typical values of the non-dimensional parameters of the system,

$$\begin{aligned} U' &= U_* \Delta t / D_* \Delta s & f' &= f \Delta t \\ V' &= V_* \Delta t / D_* \Delta s & \lambda' &= \lambda \Delta s / 8 D_* \end{aligned} \quad (5)$$

have been used to illustrate the solution behaviour. The starred variables U_* , V_* and D_* are constant and representative of the local flow field. The results show that the finite difference equations are appropriate discrete approximations to the partial differential equations

across the complete wave number spectrum. For typical applications with Cr of 1.0 and $L/\Delta s$ of order 25, negligible phase and amplitude distortion can be expected.

BOUNDARY CONDITIONS

The mathematical description of the computational field is completed by the specification of suitable boundary conditions, which for SURGE can be divided into a number of broad categories. Consistent with the staggered finite difference representation of the flow field, boundary conditions for either U or V (i.e. flow) situations take effect at spatial locations midway between nodes. For H (i.e. water level) situations the conditions require some interpretation in terms of the general finite difference equations; two or more conditions could apply at the one location and in many cases the spatial coverage of the general schemes needs to be restricted in the vicinity of a constraint. All this information is supplied to the model by the systematic specification of over fifty different flag conditions (3).

(a) *Coastal Boundaries*. These represent the simplest boundary conditions, stipulating vanishing normal transport across the coast at sea nodes adjacent to land nodes

$$\text{i.e. } U_{i+\frac{1}{2},j}^{n+\frac{1}{2}} = 0 \quad \text{or} \quad V_{i,j+\frac{1}{2}}^{n+\frac{1}{2}} = 0 \quad (6)$$

Various combinations of these component conditions, together with the normal case of uninterrupted flow, allow the representation of any area of coastline.

(b) *Reefs and Low Barriers*. In terms of long wave propagation it is appropriate to represent the presence of reefs or sand banks within the flow field as a submerged broad-crested weir, an overflow broad-crested weir, or a total flow barrier. The exact representation depends upon the crest elevation of the reef z_{crest} with respect to the instantaneous water levels, H_u on the upstream side and H_d on the downstream side of the reef. This is shown schematically in Figure 2 where q is the resulting water discharge (i.e. U or V, depending on reef orientation) across the reef. In the vicinity of reefs it is convenient to omit the smaller convective and Coriolis acceleration terms from the momentum equations. The influence of the reef is then represented by an effective Darcy-Weisbach friction factor (7,13) based on the normal submerged and overflow broad-crested weir equations through an assumption of locally uniform flow:

$$\tau_{bx} = \frac{\lambda}{8} \rho_w \frac{|U|U}{(\eta-d)^2}$$

$$\lambda = \frac{8(\eta-d)^2}{(C_1 \Delta W_1)^2 \Delta s} \quad \text{for submerged weir} \quad (7)$$

$$\lambda = \frac{16(\eta-d)^3}{(C_2 \Delta W_2)^2 \Delta s} \quad \text{for over flow weir}$$

C_1 = submerged weir discharge coefficient ($\sqrt{2}$)
 ΔW_1 = submerged weir head = $\frac{1}{2}(H_u + H_d) - z_{\text{crest}}$
 C_2 = overflow weir discharge coefficient (0.5)
 and ΔW_2 = overflow weir head = $H_u - z_{\text{crest}}$

For the case of $z_{crest} > H_u$ or H_d (total flow barrier), the conventional coastal boundary (a) applies. The continuity equation remains unchanged for all cases. For the representation of offshore reefs, the seabed levels ($D_{i,j}$) need not necessarily represent the selection for z_{crest} in regions where it is the subgrid effect which is being modelled. Such reef conditions have been used extensively for computations in the vicinity of the Great Barrier Reef.

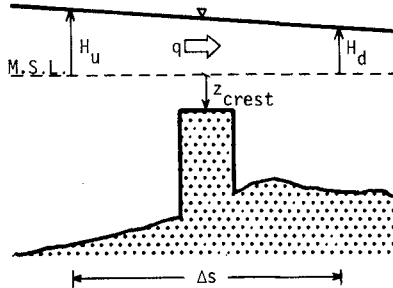
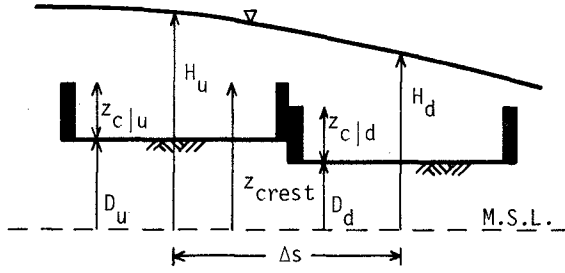


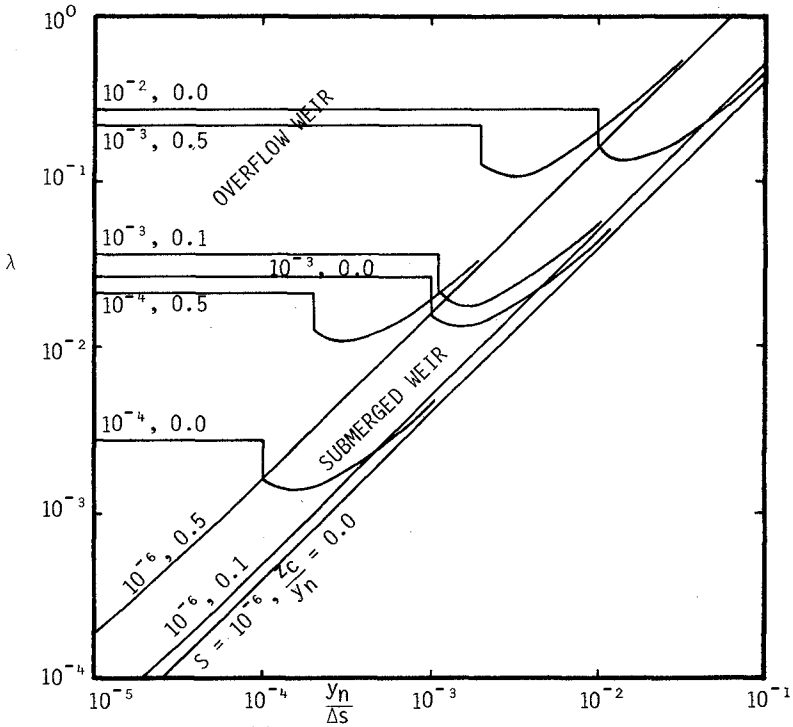
FIGURE 2. SCHEMATIC REPRESENTATION OF REEF BOUNDARY CONDITION.

(c) *Coastal Flooding*. The coastal flooding algorithm in SURGE represents the wetting and drying of low lying land through a two-dimensional cascade of broad-crested weirs and local storages (7,13). It is consistent in spirit with the representation of offshore reefs in (b). Each flood element is considered centred on a grid or H point and has horizontal dimensions Δs by Δs , with sides passing through the U and V locations at half-grid points. Bed elevation $D_{i,j}$ is as usual specified at the H point while broad-crested weirs with elevation $D_{i,j} + z_c|_{i,j}$ along all four sides totally surround each flood element. Adjacent elements have potentially different bed levels and crest elevations and at matching sides the higher of the two crest levels is considered operative in determining element exchange flows across that side, as illustrated in Figure 3a; this procedure was also followed for (b). The continuity equation is again unchanged, except that each element is constrained to empty only to the element crest level to characterise local pondage.

Frictional resistance to overbank flow is represented through the weir height z_c relative to local bed level and through the spacing of these weirs Δs . Given a grid scale, the choice of appropriate z_c , in the absence of calibration data, can reasonably be based on an engineering estimate of the equivalent weir behaviour of say urban housing or mangrove swamps. A non-dimensional weir friction diagram, Figure 3b, has been prepared to assist in the estimation and evaluation of overbank resistance. It is based on the λ estimates of Equation 7 and shows the dependence of the friction factor on the dimensionless relative weir height z_c/y_n , the dimensionless normal depth $y_n/\Delta s$ and the slope of the uniform flow energy grade line S , y_n being the normal depth.



(a) Crest Elevation for Element Exchange Flow.



(b) Broad-Crested Weir Friction Diagram.

FIGURE 3. COASTAL FLOODING BOUNDARY CONDITION.

(d) *Open Sea Boundaries*. While open boundary conditions for *astronomical* tide propagation are quite straightforward and require only the specification of water surface histories at these locations for satisfactory representation, *meteorological* tides are generated by local surface forces. For a tropical cyclone the spatial extent of the forcing approaches 1000 km, although the region of peak positive and negative surges has a spatial scale of the order of the radius of maximum winds (typically 30 km). In such a case meteorological forcing outside the computational field can only be represented by the open boundary condition. Ideally the open boundaries would be insignificant. However, the storage and speed limitations of present time-shared computer systems preclude the adoption of a computational field that has linear dimensions of the order of 1000 km and simultaneously reproduces details on the scale of the radius of maximum winds. A practical compromise to this conflict of scales has been incorporated in SURGE by effectively including the forcing influence outside the computational field in the open boundary conditions.

Three separate forms of open boundary conditions are available in SURGE (11,12):

(i) Pressure Surge Condition ($H = \Delta B$), where open boundary water levels are set equal to the pressure surge, the head of water equivalent to the local atmospheric pressure deficit, i.e.

$$H_{i,j}^n = (p_{\infty} - p_s^n) / \rho_w g \quad (8)$$

This condition is regarded as only a first approximation to the actual water levels along an open boundary as it does not include the effects of the wind tide. The pressure surge condition is the default condition and is used as an initial value in condition (ii) below.

(ii) Bathystrophic Storm Tide (B.S.T.) Approximation, where open boundary water levels are set equal to the local bathystrophic storm tide, i.e. the quasi-steady profile described, for example by

$$0 = -g(\eta-d) \frac{\partial \eta}{\partial x} - \frac{(\eta-d)}{\rho_w} \frac{\partial p_s}{\partial x} + \frac{\tau_{sx}}{\rho_w} \quad (9)$$

when the open boundary is in the x direction and intersects the coastline.

From a physical viewpoint the bathystrophic tide condition provides a reasonably realistic boundary condition. It involves a lowest order momentum balance along the open boundary to include the forcing influence of the tropical cyclone outside the boundary. Water levels along the open boundary can rise and fall in response to the intensity and position of the tropical cyclone as shown in Figure 4. Such a boundary condition enables optimal use of the grid coverage, realistic water levels and flow patterns being obtained in close proximity to the boundaries. Detailed discussions are given elsewhere (11,12).

(iii) Time Dependent Water Level Inputs, where open boundary water levels are set equal to supplied water levels (e.g. tidal input, hydrographs),

$$H_{i,j}^n = h(t) \quad (10)$$

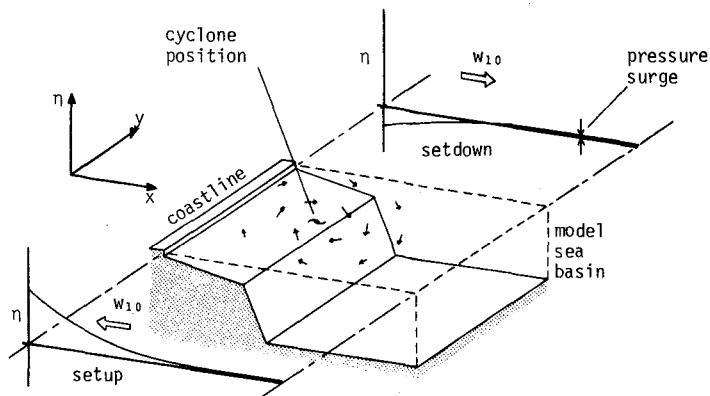


FIGURE 4. CONCEPT OF BATHYSTROPHIC STORM TIDE OPEN BOUNDARY CONDITION.

This form of open boundary condition can also be used in conjunction with (i) and (ii) above, although no interaction between the two inputs (e.g. meteorological and astronomical) is assumed. The appropriate meteorological forcing, pressure surge or B.S.T., is first applied with water levels at M.S.L., and the time dependent water levels are then added. Additionally this condition allows a "dual model" approach, in which water levels derived from a large scale model are used later as open boundary inputs to a smaller scale, detailed model of a particular section of coast.

TROPICAL CYCLONE FORCING

The aerodynamics of the tropical cyclone and the hydrodynamics of the underlying water body are coupled by the atmospheric pressure p_s and wind shear stress τ_s at the air-sea interface. Their estimation throughout the flow field during the passage of a tropical cyclone follows from the adoption of a suitable model of the near-surface meteorological structure of the storm. The model developed initially by Graham and Nunn (2,16) under the National Hurricane Research Project (NHRP) of the former U.S. Weather Bureau forms the basis of the tropical cyclone sub-model in SURGE. No claim is made that this model is entirely satisfactory; in fact our knowledge of tropical cyclone wind fields is far from complete, especially in Australia. It has been adopted in the absence of a more suitable alternative.

Many of the highly empirical aspects of the original NHRP model, such as rate of filling over land and the reduction of over-land wind speeds,

have been omitted in favour of representing the major features of the tropical cyclone. In particular the radial wind and pressure profiles, the variation of the radial inflow angle and the asymmetry of the wind field are included and expressed in terms of the four parameters commonly assumed to characterise a tropical cyclone:

- (i) Central pressure p_0 at M.S.L.
- (ii) Maximum sustained wind V_{10} at a height of 10 m above M.S.L.
- (iii) Radius of maximum winds R .
- (iv) Speed V_{FM} and direction θ_{FM} of storm forward movement.

SURGE allows all four parameters to be varied continuously to represent changes in storm intensity and track. Details may be found in Ref.12. Radial profiles of near-surface wind and M.S.L. atmospheric pressure are sketched in Figure 5a and Figure 5b shows a typical isovel and wind vector pattern for a moving model storm. The over-water wind speed W_{10} at height 10 m above M.S.L. and the resulting shear stress τ_s on the water surface are assumed to be related as

$$\tau_s = C_{10} \rho_a W_{10}^2 \quad (11)$$

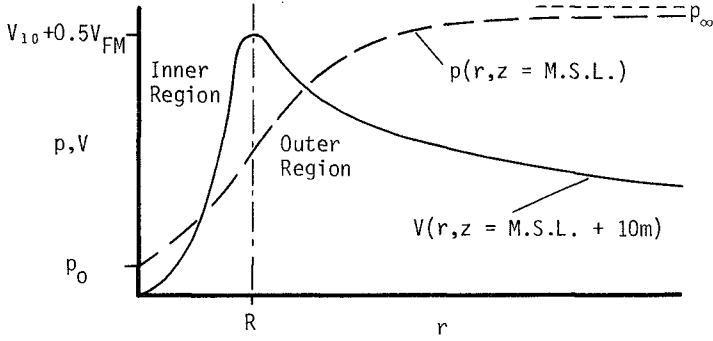
where C_{10} is a non-dimensional surface friction or drag coefficient. Approximate relations for C_{10} over the range of wind speeds for oceanic applications according to W_u (18) are incorporated in SURGE.

MODEL VERIFICATION AND SENSITIVITY TESTING

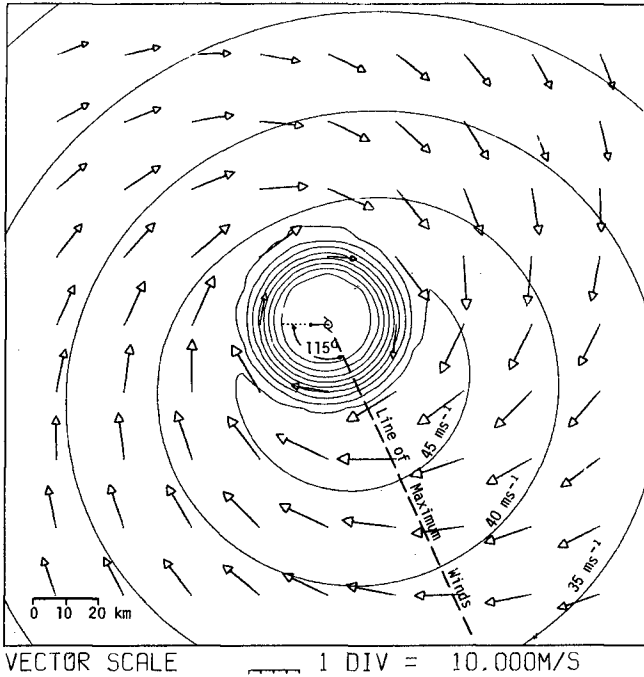
Initial verification of the model hydrodynamics was accomplished by comparison of a numerical prediction with a known analytical solution for wind setup on a rectangular lake under constant wind forcing. The agreement was almost exact. Since analytical solutions more closely related to open coast tropical cyclone storm surge are not available, an alternative approach to detailed verification was adopted involving comparison with a documented record of an historical tropical cyclone storm surge (12).

The tropical cyclone ALTHEA storm surge near Townsville in December 1971 is probably the best documented storm surge to occur in Australia. Water level records from four automatic tide gauges (Mourilyan, Lucinda, Townsville and Bowen) plus post-cyclone debris level surveys enabled an order-of-magnitude reconstruction of the surge profile development along the coast. No flow velocity data was available, nor was there any record of water levels at other than coastal locations. The Bureau of Meteorology (1), with the aid of shore-based radar, traced the path of ALTHEA as it approached and crossed the continental shelf and estimated the meteorological parameters. The central pressure fell to 952 mb and the radius to maximum winds was typically 35 km. The storm crossed the coast approximately 45 km north of Townsville and registered a peak surge of 2.78 m above predicted tide level at Townsville Harbour.

The coastal region from Innisfail in the north to Bowen in the south and up to 260 km offshore was represented on a 5 n mile grid system of 30 by 40 points as shown in Figure 6 which includes the reconstructed path of ALTHEA. The coastline is shown as a series of straightline barriers while the Great Barrier Reef is indicated by a series of broken line barriers that maintain the recognised shipping passages. Due to an almost complete lack of information on the offshore astronomical tide, the simultaneous propagation of tide and surge could not be considered and the



(a) Typical Wind Velocity and Atmospheric Pressure Profiles Along the Line of Maximum Winds.



(b) Typical Isovel and Wind Vector Pattern for a Moving Model Storm

FIGURE 5. STRUCTURE OF TROPICAL CYCLONE FORCING.

hindcast is compared to the deviation of water levels away from predicted astronomical tide (and ignoring nonlinear interactions). Figures 7a and b show the results of the SURGE simulation compared with the storm surge hydrograph recorded at Townsville Harbour and also with less reliable data available on maximum coastal water levels. The results show good agreement with this limited historical record, even at this coarse 5 n mile resolution level. A more thorough evaluation will only be possible when spatially comprehensive time histories of sea surface development of the type promised by the SEASAT satellite programme become available. Figure 8a shows part of the model flow field shortly after the storm has crossed the line of barrier reefs and the strong currents generated along the coastline and through the numerous reef passages. Figure 8b shows contours of water level above M.S.L. at the time of storm landfall.

In addition to the comparison with an historical record, a comprehensive sensitivity analysis was undertaken to evaluate the model performance under various conditions (5,12) and to define the likely envelope of response. In particular, testing of various dynamic open boundary situations was undertaken together with consideration of bed friction specifications, bathymetry effects, coastal forms and initialization. A broad range of tropical cyclone parameters, including track, was also examined and highlighted the need for adequate resolution of the storm wind and pressure structure. An $R/\Delta s$ ratio of at least 4 was shown to be necessary for an accurate representation of the structure of the storm forcing.

MODEL APPLICATIONS

SURGE has been used extensively for the study of the tropical cyclone storm surge hazard in northern Australia. In particular a comprehensive analysis was undertaken for the Beach Protection Authority, Brisbane, at ten separate sites along the Queensland coast and covering over 2000 km of coastline (4,12). At each of the sites three tropical cyclones at each of three approach directions were modelled, based on a statistical analysis of historical tropical cyclone records, and their effect on coastal locations was examined in detail. This extensive study required the modelling of a wide range of coastal features from the shallow waters of the Gulf of Carpentaria, through the Great Barrier Reef dominated Coral Sea coast to the comparatively narrow and plunging continental shelf along Queensland's Gold Coast region. Other study areas in northern Australia include Mermaid Sound in Western Australia (14), an area subject to the most severe tropical cyclones in Australia, and even more detailed investigations of estuarine storm surge penetration at Weipa on Cape York Peninsula (15) and Trinity Inlet at Cairns (13). The latter two studies included the use of a one-dimensional hydrodynamic model ESTFLO (9) which was interfaced with SURGE. Figure 9 shows the Trinity Inlet model structure where a three-pass procedure was adopted, involving two successive grid scale reductions by factors of six and appropriate truncation of the computational field at each pass. This structure was necessary to include the area of significant meteorological forcing and still reproduce overbank flooding within Trinity Inlet and in a loop around Admiralty Island. This formulation was necessary to achieve a realistic representation of the flow pattern between the deeper channels which are the major vehicle for surge penetration, and the extensive mangrove areas. Figure 10 shows a typical time sequence of surge penetration and overbank flooding within the C grid region. Heights are in cm above M.S.L. datum.

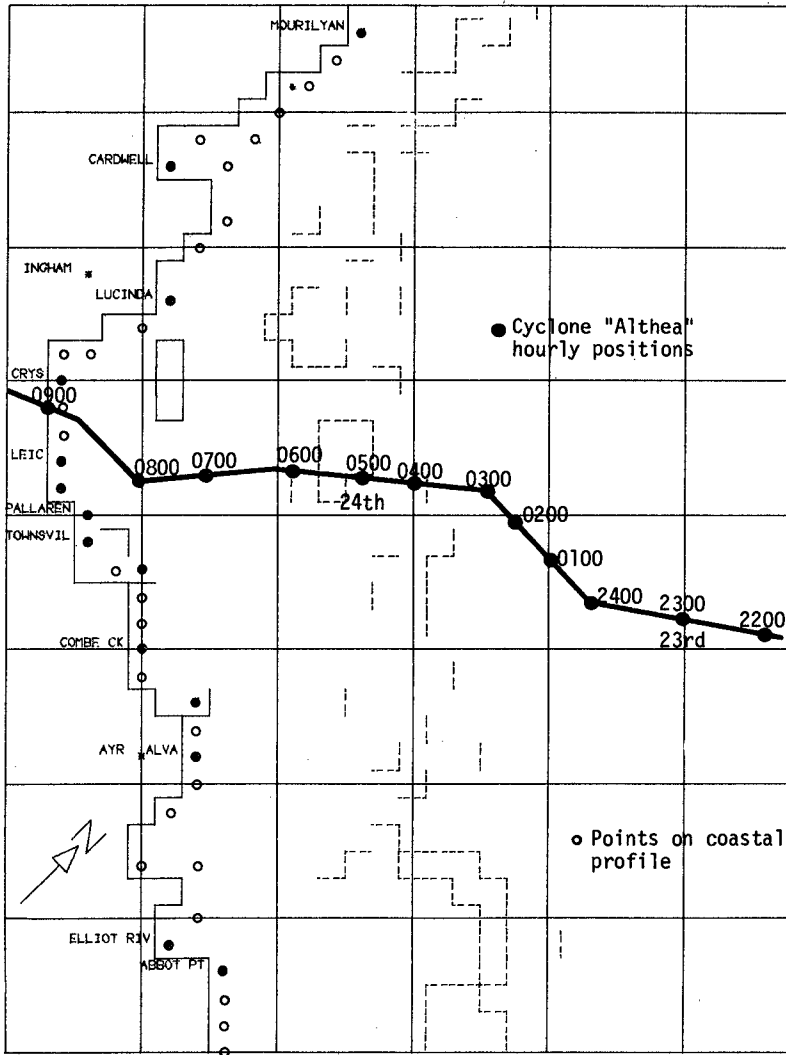
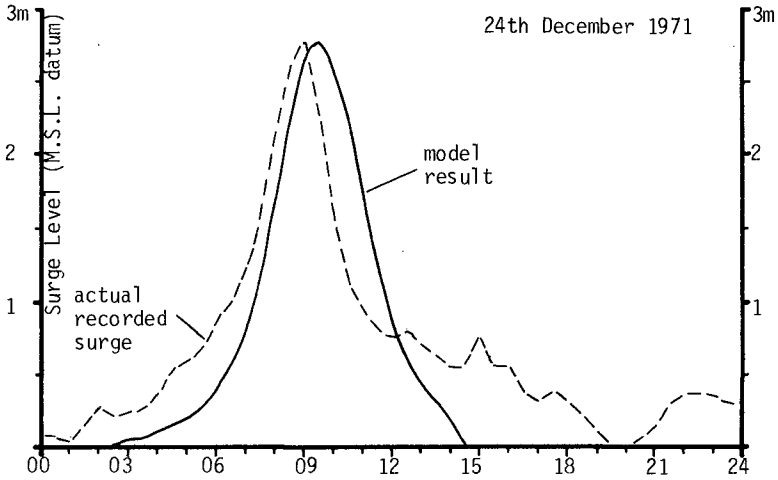
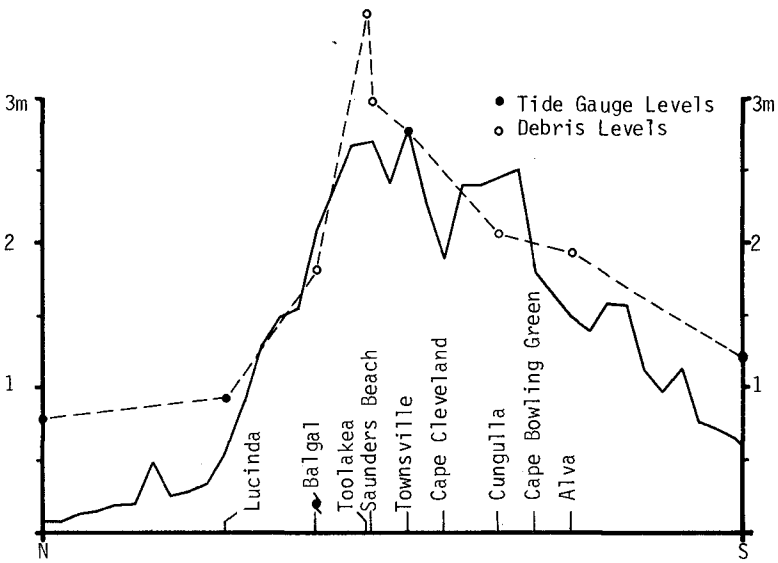


FIGURE 6. MODEL REPRESENTATION OF TOWNSVILLE REGION AND TRACK OF TROPICAL CYCLONE ALTHEA

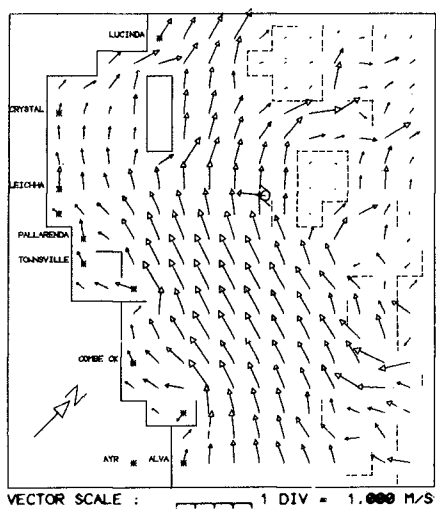


(a) Storm Surge Hydrograph at Townsville.

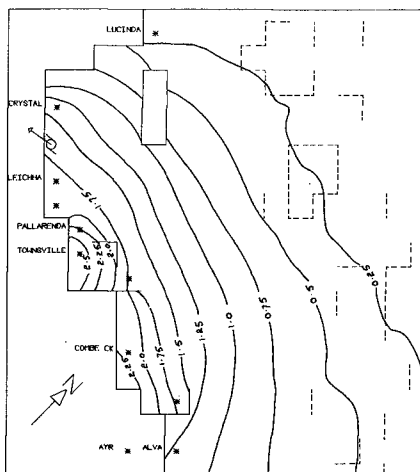


(b) Maximum Water Level Envelope Along Coast.

FIGURE 7. SURGE HINDCAST OF TROPICAL CYCLONE ALTHEA.



(a) Flow Velocity Pattern Three Hours before Storm Landfall.



(b) Water Surface Contour Pattern at Time of Storm Landfall.

FIGURE 8. TYPICAL SURGE OUTPUT FOR ALTHEA HINDCAST.

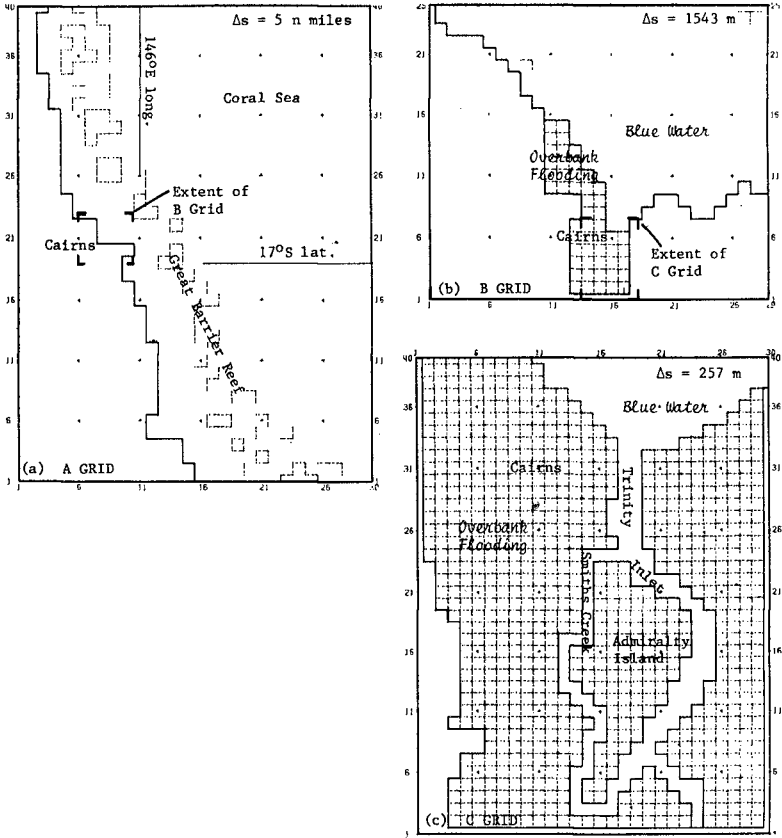
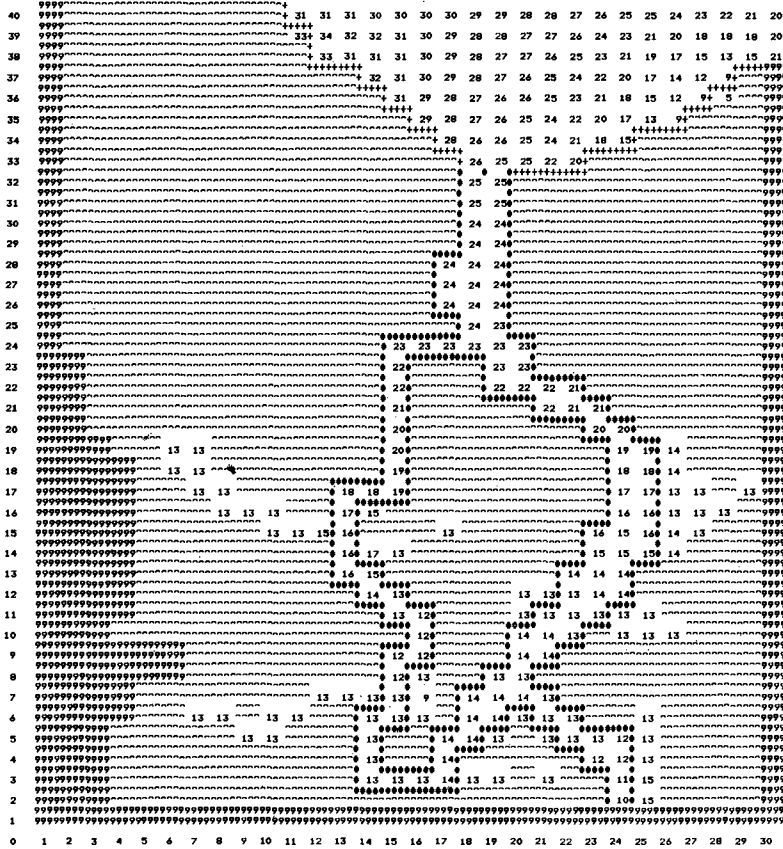
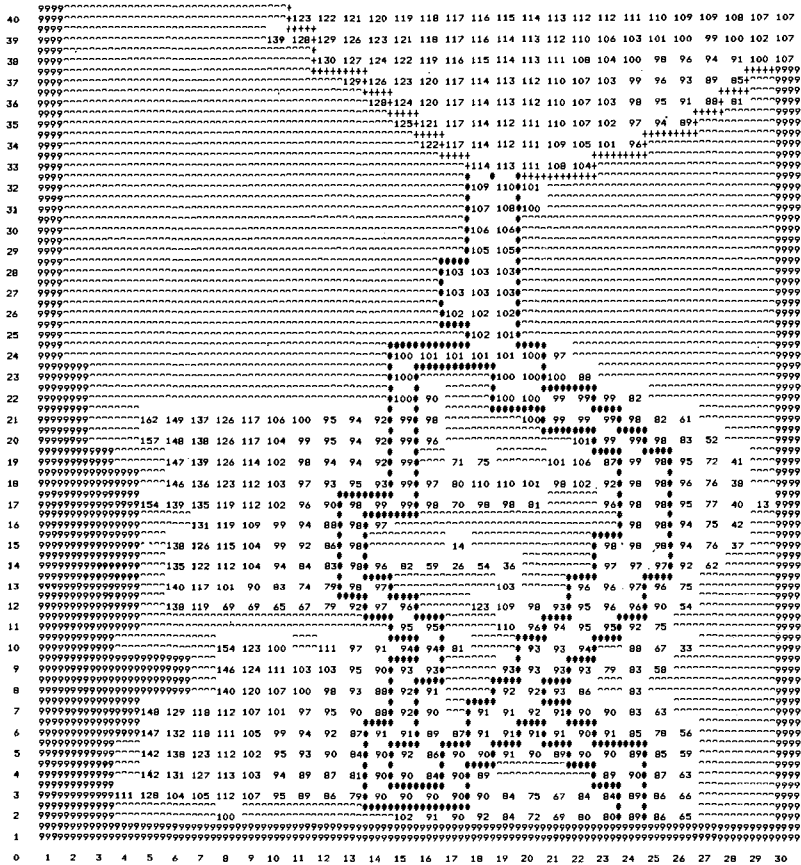


FIGURE 9. TRINITY INLET MODEL STRUCTURE.



(a) Water Levels over C Grid One Hour before Storm Landfall.

FIGURE 10. OVERBANK FLOODING IN TRINITY INLET.



(b) Water Levels over C Grid at Storm Landfall.

FIGURE 10 (Continued). OVBANK FLOODING IN TRINITY INLET.

CONCLUSIONS

The numerical hydrodynamic model SURGE adequately describes the generation and propagation of tropical cyclone storm surge and is sufficiently flexible to represent a wide range of coastal features and storm effects. Apart from applications in coastal engineering investigations, SURGE has a potential role, with improved weather monitoring, in providing real-time forecasting advice to aide in counter-disaster planning.

ACKNOWLEDGEMENTS

The authors wish to thank Professor K.P. Stark for his initiation and continued support of this programme of research. We also acknowledge contributions by colleagues T.S. Adil and A.B. Mills for overall model development. Financial support from the Beach Protection Authority, Brisbane, is gratefully acknowledged together with the kind permission of the Department of Housing and Construction, Canberra, for the use of some illustrations.

REFERENCES

1. Bureau of Meteorology, "Report by Director of Meteorology on Cyclone 'Althea'", July, 1972.
2. Craham, H.E. and Nunn, D.E., "Meteorological Considerations Pertinent to Standard Project Hurricane, Atlantic and Gulf Coasts of the United States", U.S. Weather Bureau, National Hurricane Research Project, Report No.33, 1959.
3. Harper, B.A., Sobey, R.J. and Stark, K.P., "User's Guide to SURGE", Department of Civil and Systems Engineering, James Cook University, November, 1977.
4. Harper, B.A., Sobey, R.J. and Stark, K.P., "Numerical Simulation of Tropical Cyclone Storm Surge along the Queensland Coast, Part I Weipa", Department of Civil and Systems Engineering, James Cook University, November, 1977 (for Beach Protection Authority, Brisbane). (Also Part II Cooktown, Part III Cairns, Part IV Innisfail, Part V Ingham, Part-VI Townsville, Part VII Bowen, Part VIII Mackay, Part IX Rockhampton, Part X Gold Coast.)
5. Harper, B.A., Sobey, R.J. and Stark, K.P., "Sensitivity Analysis of a Tropical Cyclone Surge Model", in Noye B.J. (Editor) "Numerical Simulation of Fluid Motion", North-Holland, 1978, pp 371-381.
6. Leendertse, J.J., "Aspects of a Computational Model for Long Period Water-Wave Propagation", Rand Corporation, Santa Monica, RM-5294-PR, 1967.
7. Mitchell, G.M. and Sobey, R.J., "Coastal Flooding from Hurricane Storm Surge", Manuscript in preparation, 1980.
8. Reid, R.O. and Bodine, B.R., "Numerical Model for Storm Surges in Galveston Bay", Jnl. Waterways and Harbors Div., ASCE, 94, 1968, pp 33-57.
9. Sobey, R.J., Adil, T.S. and Vidler, P.F., "User's Guide to ESTFLO/Version 2B-A Numerical Hydrodynamic Model of Unsteady Gradually Varied Flow in a One-Dimensional, Well-Mixed Estuarine System", Department of Civil and Systems Engineering, James Cook University, February, 1980.
10. Sobey, R.J. and Harper, B.A., "Tropical Cyclone Surge Penetration Across the Great Barrier Reef", Procs., Third Australian Conference on Coastal and Ocean Engineering, I.E.Aust., Melbourne, 1977, pp 58-63.

11. Sobey, R.J. and Harper, B.A., "Open Boundary Conditions for Open Coast Hurricane Storm Surge", Manuscript in preparation, 1980.
12. Sobey, R.J., Harper, B.A. and Stark, K.P., "Numerical Simulation of Tropical Cyclone Storm Surge", Department of Civil and Systems Engineering, James Cook University, Research Bulletin No. CS14, May, 1977.
13. Sobey, R.J., Mitchell, G.M. and Adil, T.S., "Trinity Inlet Storm Surge Study", Department of Civil and Systems Engineering, James Cook University, May, 1979 (for Department of Housing and Construction, Melbourne).
14. Sobey, R.J., Mills, A.B. and Young, I.R., "Mermaid Sound Extreme Water Level Study", Department of Civil and Systems Engineering, James Cook University, May, 1979 (for Woodside Petroleum Development Pty. Ltd., Perth).
15. Sobey, R.J., Stark, K.P. and Adil, T.S., "Weipa Peninsula Extreme Water Level Study", Department of Civil and Systems Engineering, James Cook University, August, 1979 (for Comalco Ltd., Brisbane).
16. U.S. Weather Bureau, "Interim Report - Meteorological Characteristics of the Probable Maximum Hurricane, Atlantic and Gulf Coasts of the United States", Report No. HUR.7-97, 1968.
17. Welander, P., "Numerical Prediction of Storm Surges", *Advances in Geophysics*, 8, 1964, pp 315-379.
18. Wu, J., "Wind Stress and Surface Roughness at Air-Sea Interface", *Jnl. Geophysical Research*, 74, 1969, pp 444-455.

CHAPTER 46

A NUMERICAL MODEL OF STORM WAVES IN SHALLOW WATER

A. HAUGUEL+

ABSTRACT

For studying storm waves in coastal areas, usual waves theories are no more valid. The presented cnoidal theory allows the modelling of these problems. Furthermore, thanks to its non-linear properties, it makes possible the simulation of many phenomena usually neglected.

A numerical model using this theory has been developed. It has been tested against analytical results and certain properties of non-linear waves experimentally observed.

Finally, the practical problems raised by the utilisation of this model for harbour agitation computations, have been solved.

1 INTRODUCTION

Two-dimensional numerical models are now of common use to study tidal propagation and related currents in coastal areas. These models are based upon long waves equations. By assuming that the vertical velocity linearly increases from the bottom to the sea surface, instead of doing the classical hypothesis of hydrostatic pressure distribution, it is possible to simulate non-linear waves in shallow water. This theory (Serre, 1953) belongs to the so called cnoidal waves theories. This assumption leads to new third-order derivatives in the momentum equations, and it is possible to adapt the tidal models to non-linear waves in shallow water problems by taking in account these new terms.

With such a model, it will be possible to compute non-linear waves of any form over any given bathymetry and current field. As this modelling gives quite correct simulation of breaking waves and associated radiation stresses, it seems that it will be possible to compute longshore currents.

The paper presents the modifications made on a tidal numerical model and the problems raised by the new conditions of utilisation.

2 EQUATIONS

By assuming that the vertical velocity linearly increases from the bottom to the sea surface, it is possible to average over the depth the Navier-Stokes equations. So the mass and momentum conservation laws (Serre type equations) can be written as follow :

+ Division Hydraulique Maritime. Laboratoire National d'Hydraulique. Electricité de France. Chatou, France.

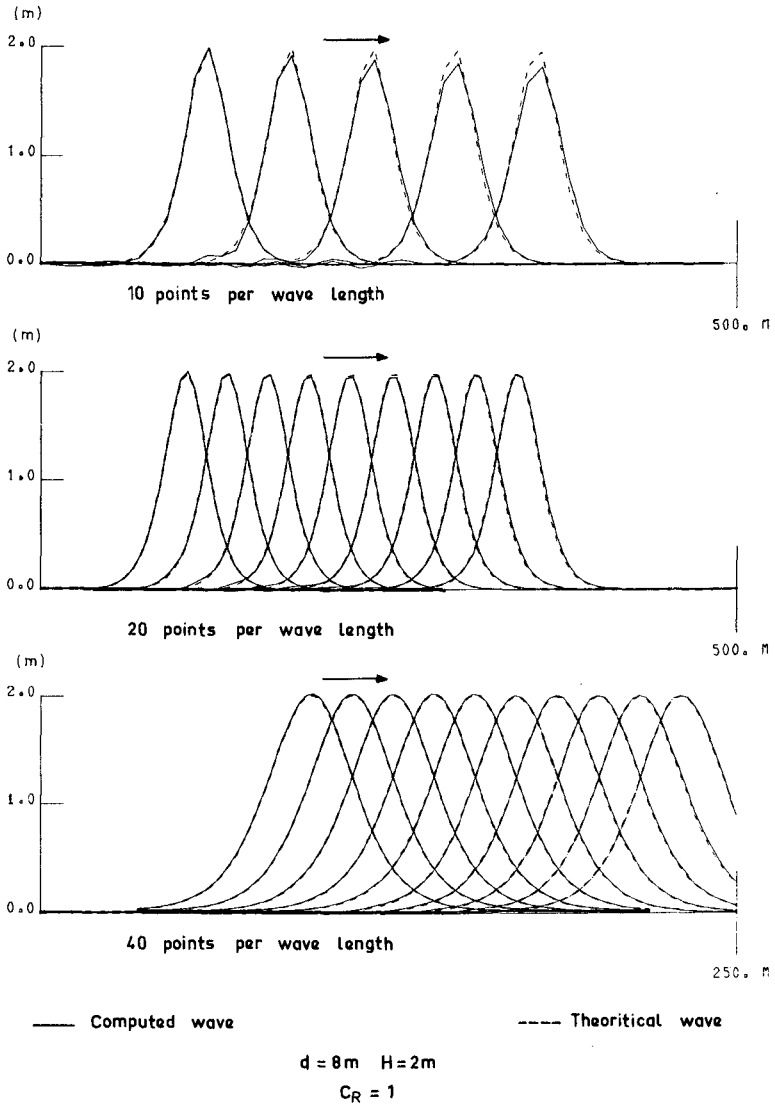


Fig.1- INFLUENCE OF COMPUTED POINTS PER WAVE LENGTH NUMBER

$$\frac{\partial h}{\partial t} + \frac{\partial p}{\partial x} + \frac{\partial q}{\partial y} = 0 \quad (1)$$

$$\begin{aligned} \frac{\partial p}{\partial t} + \frac{\partial}{\partial x} \left(\frac{p^2}{h} + \frac{\partial}{\partial y} (pq) + \frac{\partial}{\partial x} \left(\frac{(g+\beta + \frac{\alpha}{2}) h^2}{3} \right) \right) \\ = - (g + \beta + \frac{\alpha}{2}) h \frac{\partial z}{\partial x} - g \frac{p}{c^2} \frac{\sqrt{p^2 + q^2}}{h^2} \end{aligned} \quad (2)$$

$$\begin{aligned} \frac{\partial q}{\partial t} + \frac{\partial}{\partial x} (pq) + \frac{\partial}{\partial y} \left(\frac{q^2}{h} + \frac{\partial}{\partial y} \left(\frac{(g+\beta + \frac{\alpha}{2}) h^2}{3} \right) \right) \\ = - (g + \beta + \frac{\alpha}{2}) h \frac{\partial z}{\partial y} - g \frac{q}{c^2} \frac{\sqrt{p^2 + q^2}}{h^2} \end{aligned} \quad (3)$$

where h is the water depth, p and q are x - and y - volume fluxes, z is the bed elevations, g the gravitational acceleration. The new terms α and β come from the new assumption, and characterise the vertical accelerations raised by the steepness of the waves and the slope of the bed :

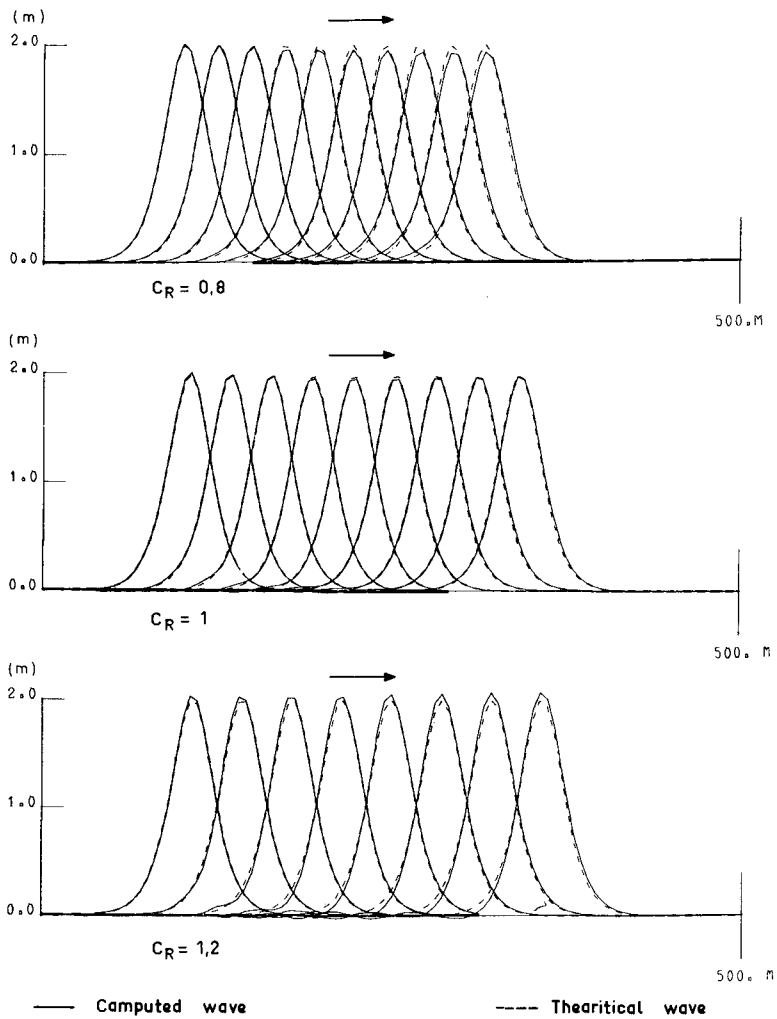
$$\alpha = \frac{d^2 h}{dt^2}, \quad \beta = \frac{d^2 z}{dt^2} \quad (\text{with } \frac{d}{dt} = \frac{\partial}{\partial t} + \frac{p \partial}{h \partial x} + \frac{q \partial}{h \partial y}) \quad (4)$$

3 NUMERICAL MODELS

More than the existence of the new terms α and β (which are introduced both in the same maner in this theory and then will be computed with the same procedure), the increased non-linearity in waves computation compared to tidal problems, and the reduced number of computed points per wave length required to assure the viability of the system in engineering practice, are the main difficulties to solve.

A finite amplitude permanent (cnoidal) wave can be in fact regarded as the superposition of several sinusoidal waves. If the main one is described with a reduced number of points (10 for example), the first harmonic is computed with only 5 points, and the difference scheme must be able to propagate these coarsly described waves without any relative phase error, which would induce changes in shape, amplified then by the marked non-linearity of the problem. This leads to an extreme sensivity of the solutions of the equations to numerical error influence (Abbott, 1978).

The numerical model developed in the Laboratoire National d'Hydraulique uses finite differences approximations built on a single space grid. The fractionnary steps are used to compute each part of the equations.



$d = 8\text{ m}$ $H = 2\text{ m}$

Fig.2 - INFLUENCE OF COURANT NUMBER
(20 points per wave length)

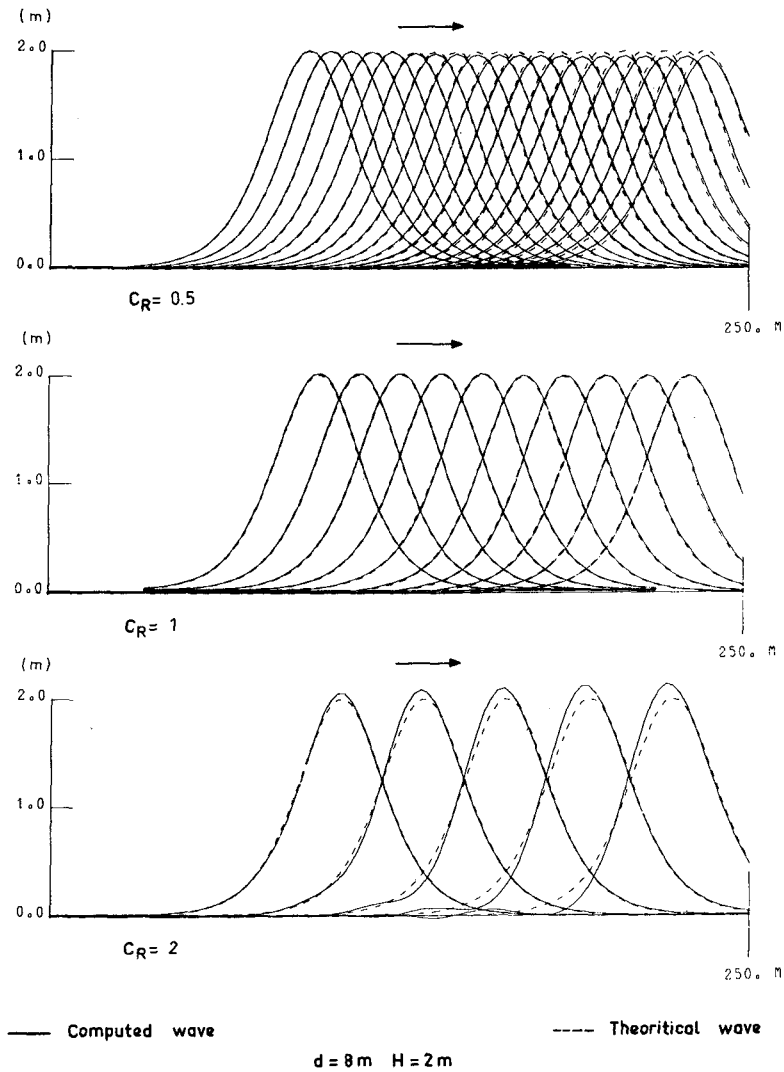


Fig.3-INFLUENCE OF COURANT NUMBER
 (40 points per wave length)

3.1. One dimensional model :

The advective terms of (2) are computed the first, the propagative and friction terms being solved in a second step. A third-order accuracy scheme based upon characteristic method is used for the advective components of (2) ; this one has been fitted to total derivatives computations of (4). The elaboration of a high-accuracy difference approximation of propagative components of (1, 2) including α and β terms, has necessitated the use of an implicit three-stage difference scheme. A Newton discretisation is used to linearize the h^3 term which appears in the pressure gradient of (2). The discretization has been designed to eliminate in the linear case, any damping and phase error for any number of computed points per wave length, at least for a Courant number equal to 1 (Von Neumann stability analysis). These propagative components are solved by a tri-diagonal double sweep algorithm after combination of the discretized form of (1, 2), which decouples the variations of flux and water depth. In spite of the marked non-linearity of the problem, and as for other reasons the Courant number must be as closer as possible to 1, no iterative procedure is necessary to solve the equations.

3.2. Two-dimensional model :

The fractionary steps are also used in the 2.D model. The advective components are solved by the one dimensional characteristic method scheme in the x-direction and then in the y-direction. The α and β terms are computed with the same procedure (characteristics). To solve the left terms of (1, 2, 3) (propagation), a two-dimensional iterative procedure is used. This one is based on splitting with coordination. Usually, a simple splitting induces differences between the resolutions in the x-and the y-directions. In our model, iterations are used to obtain same water depths in the two directions. The method of coordination used is very fast. It suppresses any polarisation due to the grid (see fig. 8, 10, 11), but the advantages of 1-D-computations are preserved.

3.3. Boundary conditions :

In order to simulate entering waves in the model at the seaward boundary, a condition allowing outgoing waves is necessary (see fig. 8, 9). The relation on the outgoing characteristic of the linearised theory has been suited in the following form :

$$f_n - C(h + z) = - 2C W_i \quad (5)$$

where f_n is the outgoing normal flux

W_i is the sea surface elevation of the incident wave

C is the celerity which appears in the discrete form of the propagative components.

The same sort of condition has been imposed on inside breakwaters to model partial reflections :

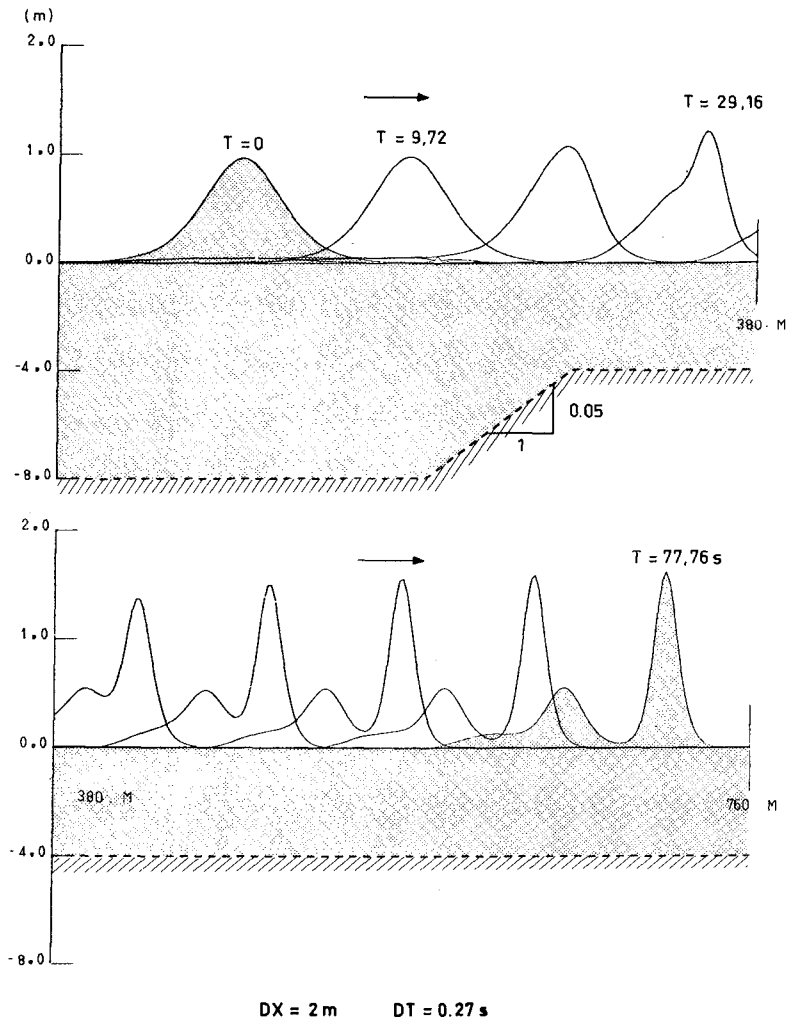


**Fig.4 - TRANSFORMATION OF A SOLITARY WAVE
OVER AN UNEVEN BOTTOM**

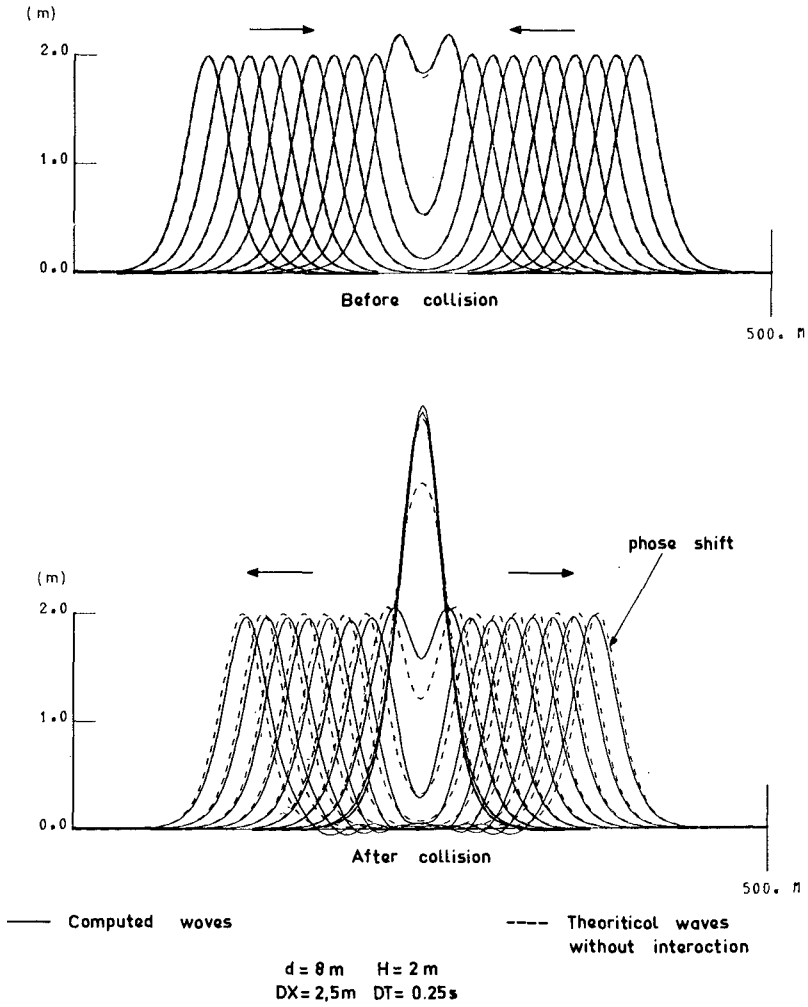


Fig.5 - COLLISION BETWEEN TWO SOLITARY WAVES

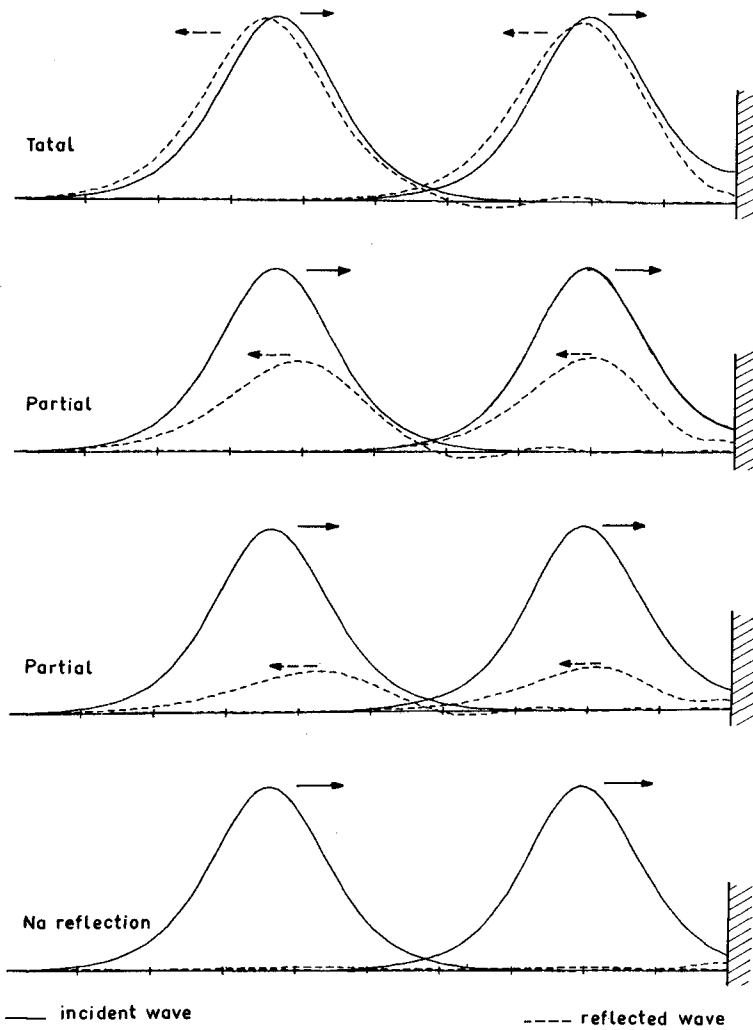
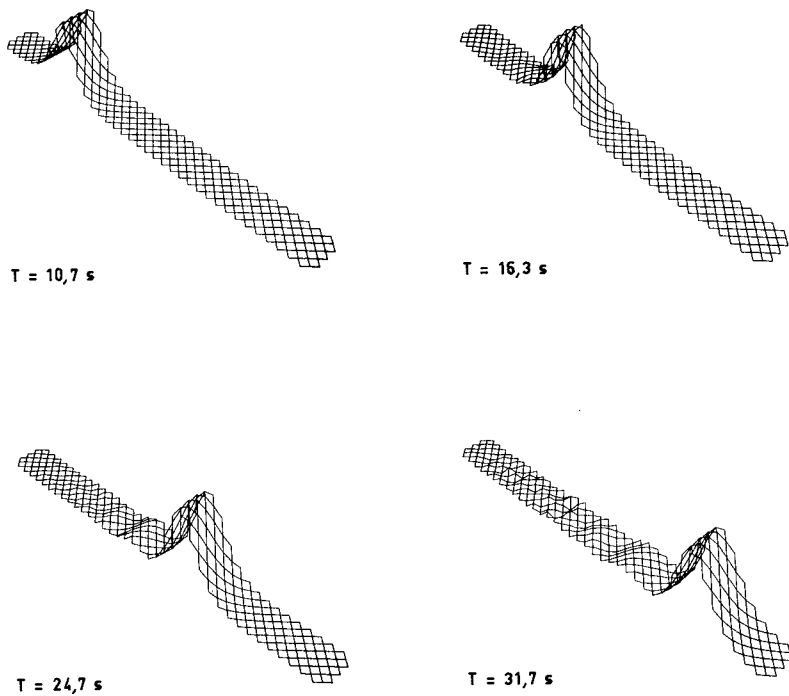


Fig.6 - DIFFERENT CONDITIONS OF REFLECTION
OF A SOLITARY WAVE



$d = 8 \text{ m}$ $H = 2 \text{ m}$
 $DX = 7 \text{ m}$ $DT = 0,7 \text{ s}$

Fig.7 - PROPAGATION OF A SOLITARY WAVE
IN A INCLINED CHANNEL (45°)

$$f_n - C(1 - \gamma)(h + z) = 0 \quad (6)$$

where γ is a coefficient of reflection :
 (if $\gamma = 1$: total reflection, if $\gamma = 0$: no reflection).

In the 2.0 model, when there is an inflow a second boundary condition is required (Daubert, 1967). In that case, the normal derivative of the tangential flux is put equal to zero in the advective step. Thanks to the method of coordination used in the propagative step, the condition (6) can also be imposed on boundaries inclined to the grid, although it couples the two components of the volume flux. This coordination nearly suppresses shear effects on inclined boundaries (see fig. 7, 10).

4 NUMERICAL RESULTS

The modifications have been tested against analytical results in one and two dimensions for various Courant numbers and numbers of points per wave length. The different tests have shown that, for a Courant number equal to 1, a very good accuracy is obtained with values of the number of points per wave length as low as 20, even with a relative wave height equal to 0.4 (see fig. 1). For much smaller relative wave heights, the non-linearity of the governing equations decreases, and the number of points per wave length required can be reduced to 10. On the contrary, this one must be increased to conserve an acceptable accuracy if the Courant number differs from 1 (see fig. 2, 3).

The influence of the bottom shape and the geometry of the area has also been studied. Figure 4 shows the transformation of a solitary wave propagating over a slope onto a shelf of smaller depth. On the shelf, a desintegration of the initial wave into a train of solitary waves of decreasing amplitude is found. The amplitude of the crests is in good agreement with the results obtained by Madsen (1969) in the same case.

Figure 5 presents the phase shift obtained from non-linear effects after collision between two waves. This shift is in good agreement with the one experimentally obtained by Maxworthy (1976).

Figure 6 shows the aptitude of the boundary condition (6) to simulate the whole range of reflections on different breakwaters.

The possibility of propagating a wave in a narrow channel inclined in the grid has also been studied. Figure 7 shows such a computation. Thanks to the coordinator, the condition on the normal flux ($f_n = 0$) can be well imposed. The shear effect numerically induced by the boundary condition nearly disappears in this case.

Figures 8 and 9 show the aptitude of the boundary condition (5) to generate incident waves in the domain (even with an angle of incidence) without presuming anything on outgoing waves. In these

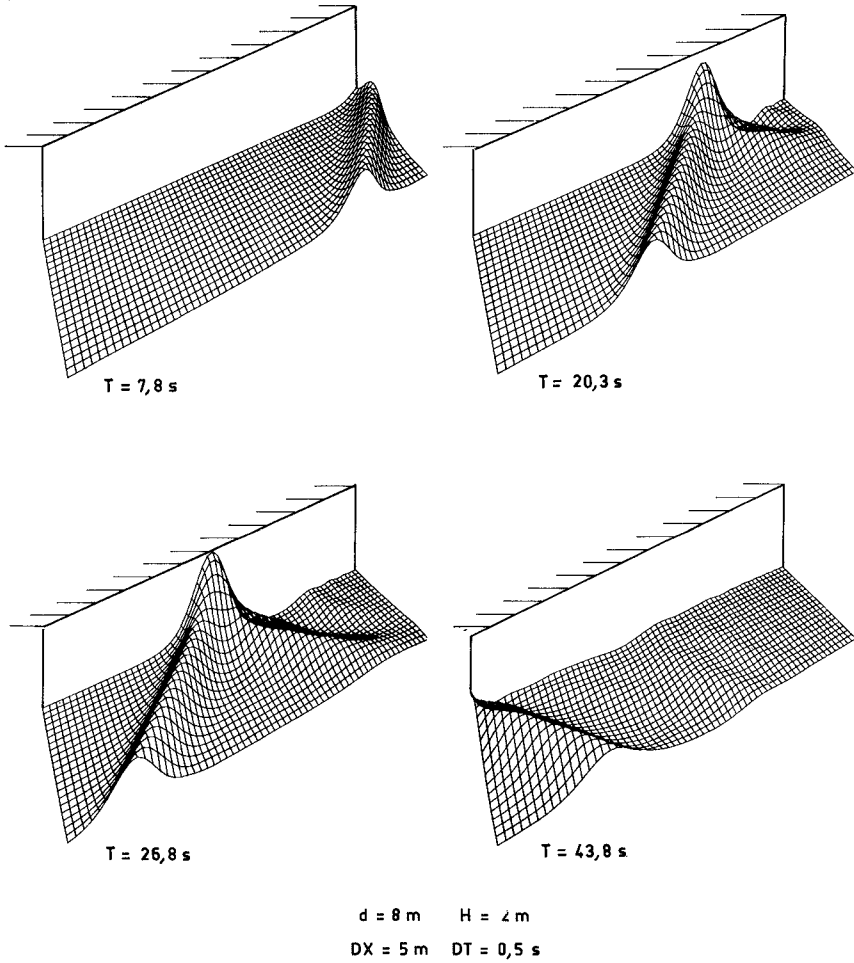
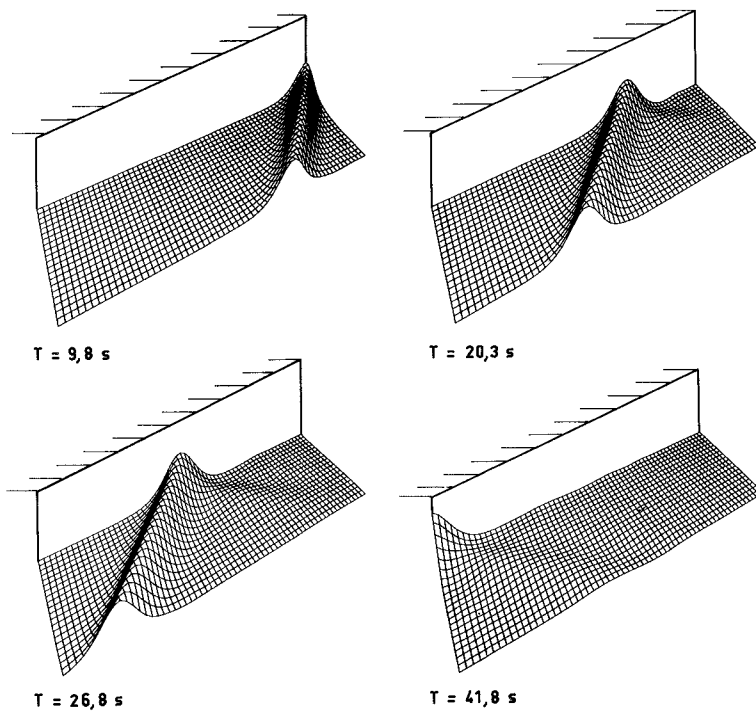
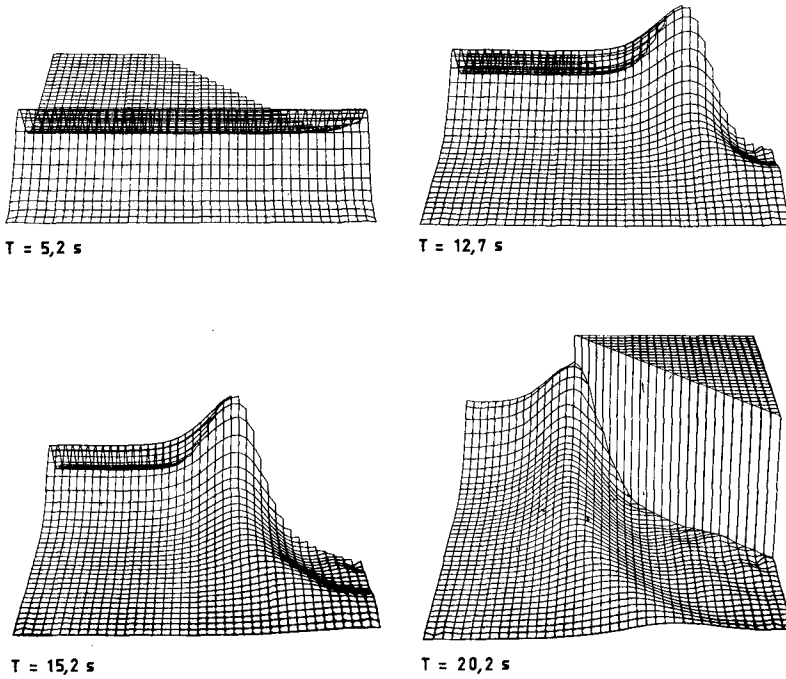


Fig.8 - GENERATION AND TOTAL REFLECTION OF A WAVE ENTERING THE DOMAIN WITH AN ANGLE (45°)



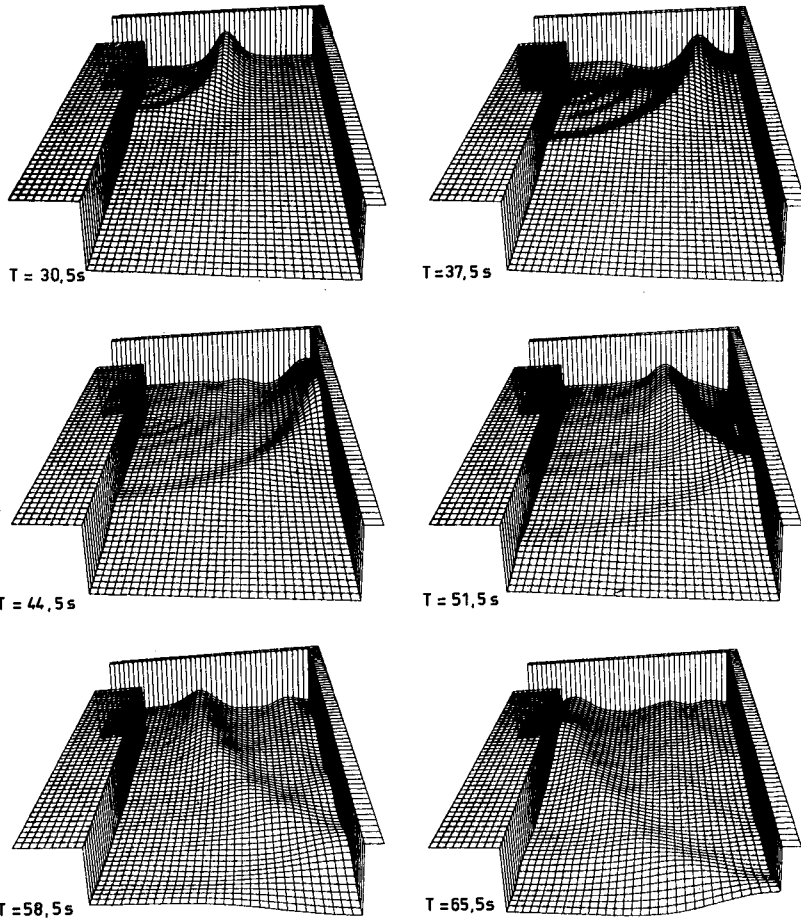
$d = 8 \text{ m}$ $H = 2 \text{ m}$
 $DX = 5 \text{ m}$ $DT = 0,5 \text{ s}$

Fig.9 - GENERATION AND PARTIAL REFLECTION OF A WAVE ENTERING THE DOMAIN WITH AN ANGLE (45°)



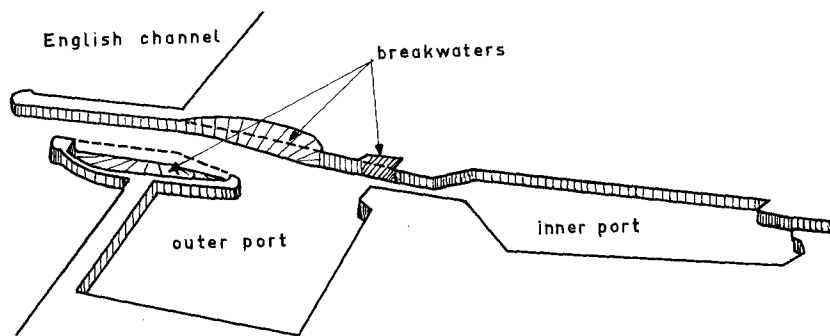
$d = 8 \text{ m}$ $H = 2 \text{ m}$
 $DX = 5 \text{ m}$ $DT = 0,5 \text{ s}$

Fig.10 - REFLECTION OF A WAVE
ON A INCLINED BOUNDARY



$d = 8\text{ m}$, $H = 2\text{ m}$
 $DX = 7\text{ m}$ $DT = 0,7s$

Fig.11 - DIFFRACTION - REFLEXION OF A SOLITARY
 WAVE (BASIN 217 m x 392 m)



PORT OF FECAMP

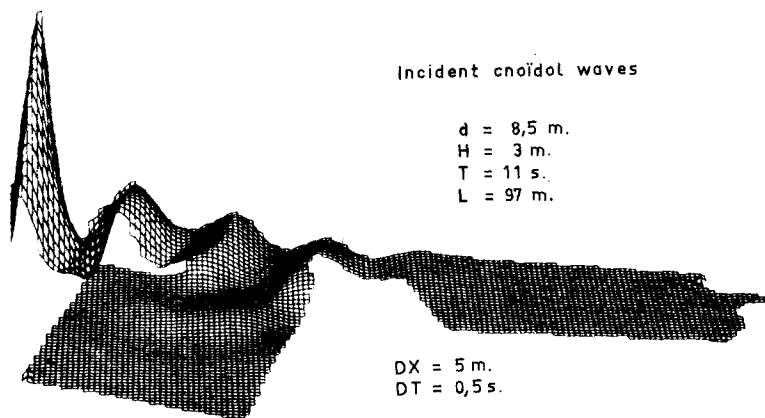


Fig. 12 - WAVE FIELD IN THE PORT OF FECAMP
AFTER 50 sec. SIMULATION

figures two reflection conditions have been imposed on the opposite boundary : total reflection (fig. 8), partial reflection (fig. 9). In the two cases, the reflected wave has to establish itself after a diffraction period, which is best shown in figure 10. This one presents the computation of the reflection on an inclined boundary.

As, any changement in water depth induces harmonics due to non-linear effects, any variation of the geometry of the area (diffraction) desintegrate the initial wave into a train of waves of decreasing amplitude. This is again shown in figure 11, where a wave entering a closed basin of 217 m x 392 m is presented. This example demonstrates that there is no polarisation induced by the grid in the computed wave (coordinator). In this case, the variation of width creates harmonics at the point of diffraction. Then, they propagate into the basin giving circular waves. After reflection on the opposite boundary, this induced a lapping in the basin.

5 CONCLUSION

The model, severly tested over the operational range of wave parameters, and over different physical conditions (all the computational tests presented have been done without any bottom friction, so there were no damping decreasing the computed waves) is now applied in coastal engineering practice. Figure 12 presents the first computations done in the port of Fecamp (French port on the English Channel).

6 REFERENCES

- SERRE, F. (1953). Contribution à l'étude des écoulements permanents et variables dans les canaux. La Houille Blanche, pp 374-388, pp 830-872.
- MADSEN, O.S. and C.C. MEI (1969). The transformation of a solitary wave over an uneven bottom. J. Fluid Mech, vol 39, part 4, pp 781-791.
- ABBOTT M.B., PETERSEN, H.M. and SKOVGAARD, O. (1978). On the numerical modelling of short waves in shallow water. J. Hydr. Research, vol 16, pp 173-203.
- DAUBERT, A. and GRAFFE, O. (1967). Quelques aspects des écoulements presque horizontaux à deux dimensions en plan et non permanents. La Houille Blanche, vol 22, n° 8, pp 847-860.
- VON NEWMANN, J. (1945). Use of variational methods in hydrodynamics. John Von Newmann. Collected works, vol VI, pp 357-359.
- MAXWORTHY, T. (1976). Experiments on collisions between solitary waves. J. Fluid Mech, vol 76, part 1, pp 177-185.

THE GENERATION OF LONG WAVES IN THE LABORATORY

by Derek Goring¹ and Fredric Raichlen²INTRODUCTION

It became evident in the experimental aspects of a recent study of the propagation of nonlinear long waves past a step and up a slope that it was important to be able to generate waves which were initially well defined. The investigation dealt with the reflection and transmission of tsunamis past the continental shelf-break, and as such, two simple waves were used to represent certain characteristics of tsunamis: solitary waves and cnoidal waves. (Both of these permanent waves are solutions to the Korteweg-de Vries equation which to a certain order describe the propagation in two dimensions of nonlinear dispersive shallow water waves (see, e.g. Whitham, 1974).)

The solitary wave actually can be generated in the laboratory in a simple manner if the wave tank is long enough and wave groups trailing the main wave are unimportant to the study. An example of the resulting waves obtained in the laboratory using a crude generation procedure is demonstrated by the oscillograph record presented in Figure 1. Six traces are shown: the one at the bottom of the figure describes the time-displacement history of a vertical bulkhead wave generator which is moved by a hydraulic-servo system, the other five are the time variations of the water surface obtained using resistance wave gages spaced at the indicated number of depths downstream from the generator. (In the example presented, the depth of water was 10 cm and the wave plate was moved linearly with time a distance of 10.33 cm in 0.8 sec.) The wave generated and first shown 10 depths downstream appears to consist of a large wave followed by a series of oscillatory waves (termed the tail). As would be expected, as the waves propagate, due to the frequency content and the amplitude of the waves, the system separates into a leading wave followed some distance behind by the tail. The lead wave has the characteristic shape of a solitary wave. However, if the oscillatory tail is unacceptable for the type of experiments being conducted, and if it cannot be eliminated or the method of elimination is unacceptable, then a means of generation must be sought which eliminates the trailing waves initially.

The method used in this study to produce a nonlinear shallow water wave which is well formed near the generator attempts to match the velocities of the wave plate and the water particles of the desired wave as the plate moves. An example of the result of doing this for a solitary wave is shown in the oscillograph record presented in Figure 2; again the motion of the wave generator is shown at the bottom of the

¹Scientist, Christchurch Science Centre, New Zealand Ministry of Works & Development; formerly Grad. Student, W. M. Keck Lab of Hydr. & Water Res., California Institute of Technology, Pasadena, CA.

²Professor of Civil Engineering, W. M. Keck Lab of Hydr. & Water Res., California Institute of Technology, Pasadena, CA.

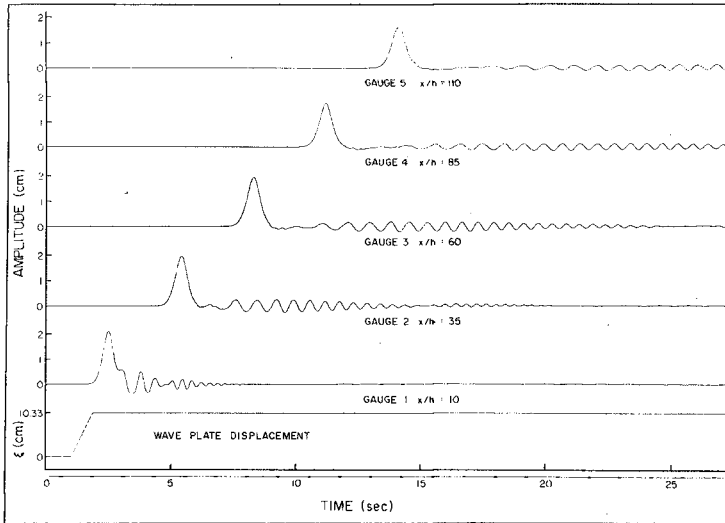


Figure 1 Oscillograph record of the waves generated by a ramp trajectory ($S = 10.33$ cm, $\tau = 0.80$ sec and $h = 10$ cm).

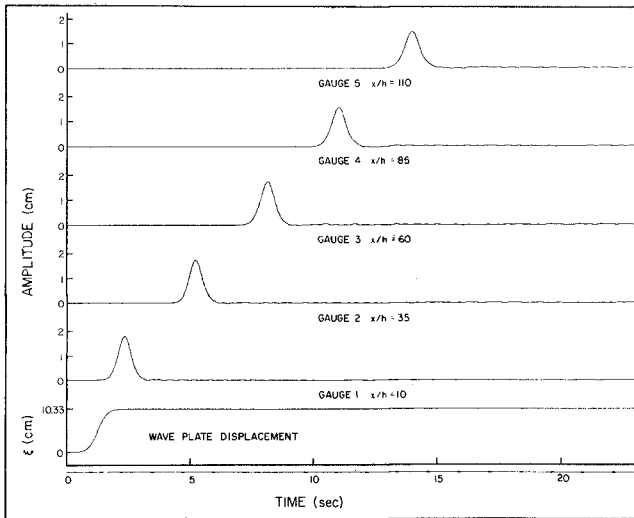


Figure 2 Oscillograph record of the waves generated by the solitary wave trajectory with $H/h = 0.2$ ($S = 10.33$ cm, $\tau = 2.044$ sec and $h = 10$ cm).

figure and five wave profiles are presented above. (The location of the wave gages are the same as in Figure 1.) The motion (or trajectory) of the wave plate is no longer linear and the time of motion is more than twice that for the case shown in Figure 1, i.e., $\tau = 2.044$ sec. A comparison of the time history of the water surface elevation at 110 depths downstream of the generator shows the trailing oscillatory waves essentially have been eliminated.

Similar time histories of water surface and wave generator displacements are presented in Figures 3 and 4 for periodic wave plate motions. (It was desired for this example to produce cnoidal waves which, as mentioned, are the exact periodic solution of the Korteweg-de Vries equation.) Figure 3 shows the wave resulting from an "incorrect" plate motion where the shape changes as it propagates; note the period of the plate motion is $T = 4.28$ sec. When the same trajectory is used but a "correct" period is chosen ($T = 2.90$ sec) a system of waves is generated with the central portion of the train appears relatively unchanged for the nearly 60 depths of propagation shown. The shape of these waves and their method of generation will be discussed more fully later; suffice to say that Figures 2 and 4 demonstrate, at least qualitatively, that the desired system of waves can be generated if adequate attention is given to the method of generation.

ANALYTICAL CONSIDERATIONS

A qualitative description of the generation process is provided by the phase-plane presented in Figure 5. The upper part of the figure (Part c) shows a desired sinusoidal water surface profile; in the lower left the corresponding horizontal water particle velocity time history is given. (For purposes of this discussion it is assumed the water particle

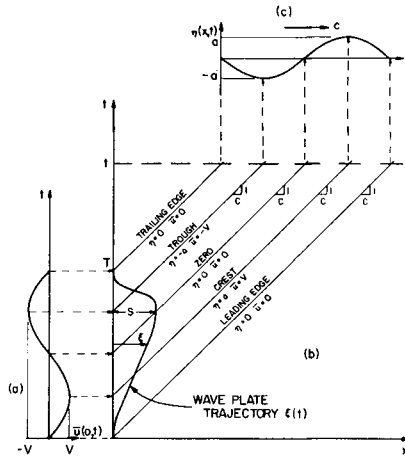


Figure 5 Wave generation phase-plane.

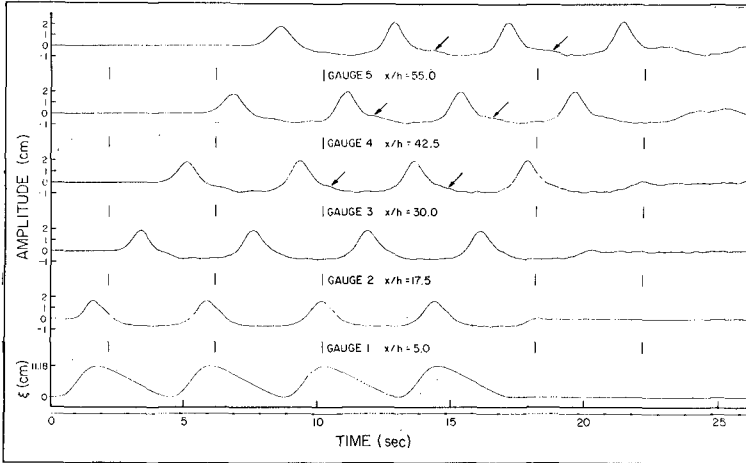


Figure 3 Oscillograph record showing the waves generated by trajectory CN4 with $h = 20$ cm, $S = 11.18$ cm and $T = 4.28$ sec.

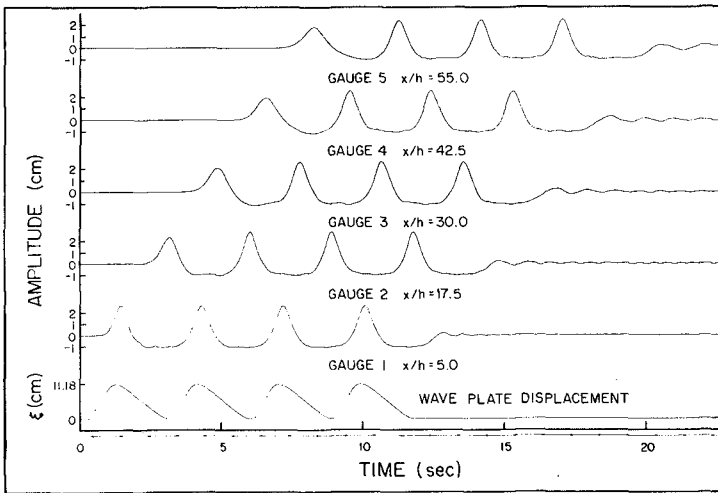


Figure 4 Oscillograph record showing the waves generated by trajectory CN4 with $h = 20$ cm, $S = 11.18$ cm and $T = 2.90$ sec.

velocity distribution is either constant with depth or that represented in Figure 5 a is the depth-averaged velocity.) If in the $x-t$ plane (Part b) the wave propagates unchanging to the right with celerity c , the wave properties such as amplitude and velocity propagate along lines which are straight and parallel and have a slope $dx/dt = c$. The time-history of the motion of the wave plate which generated the wave is represented in Part b by the curve $\xi(t)$ which is termed the "trajectory" in this study.

Referring to Figure 5, for time $t < 0$ the wave plate is at rest and $\xi = 0$. At time $t = 0$ the wave plate begins to move along the trajectory $\xi(t)$. The object of this development is to determine the trajectory $\xi(t)$ which will generate a given long wave $\eta(x,t)$ with permanent shape propagating with celerity c . As mentioned previously, the basic concept is to match the velocity of the wave plate, $d\xi/dt$, at all positions, with the corresponding velocity of the water particles (or the depth-averaged velocity) under the long wave, i.e., $\bar{u}(x,t)$. Thus, on the face of the wave maker:

$$\frac{d\xi}{dt} = \bar{u}(\xi,t) \quad (1)$$

Including the position of the plate, ξ , in the velocity, $\bar{u}(\xi,t)$, takes into account that during the generation process the wave is propagating away from the plate. The effect is to produce a trajectory which is distorted from what it would be if the velocity at the mean position of the plate, $\bar{u}(0,t)$ were used. This can be seen in Figure 5, where if the velocity $\bar{u}(0,t)$ were used in Eq. (1), the trajectory would be sinusoidal and the maximum displacement of the plate, $\xi = S$, would occur at time $\frac{1}{2}T$. However, Figure 5(b) shows that the maximum of the trajectory occurs at $t = \frac{1}{2}T + S/c$. Thus, the time taken for the plate to travel to its maximum position is S/c longer than it would be if a sinusoidal trajectory were assumed, and consequently the time for the plate to travel back to its original position is time S/c shorter than for a sinusoidal trajectory. Therefore, the effect of including the position ξ in the velocity is that when the plate and wave are moving in the same direction, the time coordinate stretches; when the plate and the wave are moving in opposite directions, the time coordinate contracts.

The simple sinusoidal variation of the water particle velocity shown in Figure 5a was presented as an example; for finite amplitude shallow water waves of permanent shape it can be shown from continuity considerations that the velocity averaged over the depth is:

$$\bar{u}(x,t) = \frac{c \eta(x,t)}{h + \eta(x,t)} \quad (2)$$

where h is the depth, and $\eta(x,t)$ and c are defined in Figure 5. Thus, in terms of the plate velocity, from Eq. (1):

$$\frac{d\xi}{dt} = \frac{c \eta(\xi,t)}{h + \eta(\xi,t)} \quad (3)$$

Eq. (3) must be integrated to obtain the trajectory, $\xi(t)$. It is assumed that at the position of the wave plate the wave has the form:

$$\theta = \theta_0 = kct - k\xi$$

$$\xi = ct - \theta_0$$

$$\eta(\xi, t) = H[f(\theta)] \quad (4)$$

where

$$\theta = k(ct - \xi) \quad (5)$$

$$\frac{d\xi}{dt} = c$$

By algebraic manipulation of Eqs. (3), (4) and (5) it can be shown that:

$$\frac{d\xi}{d\theta} = \frac{H[f(\theta)]}{kh} \quad (6) \quad \text{near } \theta \text{ just } H f(\theta) \quad t = \frac{1}{c}\xi + \theta_0$$

and

$$\xi(t) = \frac{H}{kh} \int_0^\theta f(w)dw \quad (7)$$

where w is the dummy variable of integration. Equation (7) is an implicit equation which in general, for a particular time t , must be solved numerically. The most efficient method of solution was found to be Newton's Rule. Using Eq. (5), θ is substituted for the displacement ξ in Eq. (7) to yield:

$$F = \theta - kct + \frac{H}{h} \int_0^\theta f(w)dw = 0 \quad (8)$$

Equation (8) must be solved for θ at a given time t . Differentiating Eq. (8):

$$\frac{\partial F}{\partial \theta} = 1 + \frac{H}{h} f(\theta) \quad (9)$$

Newton's Rule is:

$$\theta^{(i+1)} = \theta^{(i)} - \frac{F(\theta^{(i)})}{F_\theta(\theta^{(i)})} \quad (10)$$

where superscripts denote iteration number and $F_\theta = \partial F / \partial \theta$. Substituting for F and F_θ in Eq. (10) yields:

$$\theta^{(i+1)} = \theta^{(i)} - \frac{\theta^{(i)} - kct + \frac{H}{h} \int_0^{\theta^{(i)}} f(w)dw}{1 + \frac{H}{h} f(\theta^{(i)})} \quad (11)$$

Having found θ for given time t , the displacement ξ is given by:

$$\xi = ct - \theta/k \quad (12)$$

Eqs. (7), or (11) and (12) provide the wave plate displacement as a function of time, $\xi(t)$, for a general wave form $f(\theta)$. These equations will now be applied for specific functions $f(\theta)$ which describe solitary and cnoidal waves. For a solitary wave which satisfies the Korteweg-de Vries equation, the wave function $f(\theta)$ in Eq. (4) is:

$$f(\theta) = \text{sech}^2 \theta \quad (13)$$

where $\theta = \kappa(ct - \xi)$, $\kappa = \sqrt{\frac{3H}{4h^3}}$, $c = \sqrt{g(h+H)}$,

Substituting Eq. (13) into the generation equation, Eq. (7), and performing the integration yields:

$$\xi(t) = \frac{H}{\kappa h} \tanh \kappa(ct - \xi) \quad (14)$$

In Figure 6 a typical trajectory, $\xi(t)$, is presented which was calculated from Eq. (14). The origin of the displacement ξ and of the time t occurs at the wave crest in accordance with the definition of the solitary wave, Eq. (13). In addition, since the function $f(\theta)$ in Eq. (13)

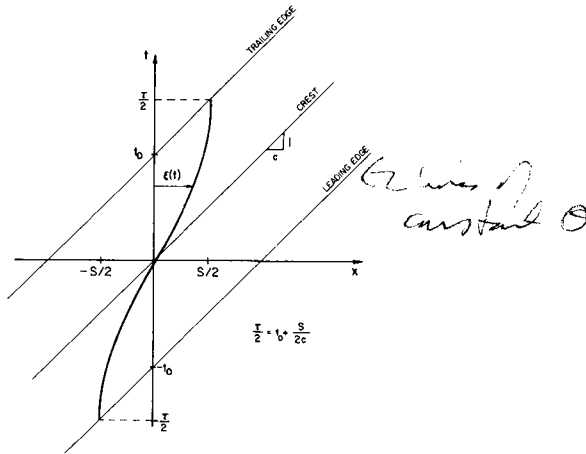


Figure 6 Phase plane showing typical wave plate trajectory for a solitary wave.

tends to zero as θ goes to infinity, the intercepts of the characteristics associated with the leading and trailing edges of the wave with the time axis, $\pm t_0$, occur at $\pm \infty$. However, for practical purposes, to three significant figures, the intercept, t_0 , may be defined as:

$$t_0 = \frac{\tanh^{-1}(0.999)}{\kappa c} = \frac{3.80}{\kappa c} \quad (15)$$

The stroke S is obtained by evaluating Eq. (14) at time $t = +\infty$ and $t = -\infty$ and subtracting to yield:

$$S = \frac{2H}{\kappa h} = \sqrt{\frac{16}{3}} \frac{H}{h} h \quad (16)$$

The duration of motion τ is obtained (see Figure 6) by computing the times at which the leading and trailing edge characteristics intersect the trajectory $\xi(t)$ and subtracting; thus:

$$\tau = 2t_0 + S/c \quad (17)$$

Substituting for the intercept t_0 and stroke S yields for the duration:

$$\tau = \frac{2}{\kappa c} \left(3.80 + \frac{H}{h} \right) \quad (18)$$

(In practice, the origin of the trajectory, $\xi(0)$, is moved to the point $(-\tau/2, -S/2)$ in the $x-t$ plane so that motion starts from rest and proceeds in the forward direction.)

Substituting Eqs. (15), (16) and (18) in Eq. (14) and rearranging gives the following normalized form of the generation equation for solitary waves:

$$\frac{\xi}{S} = \frac{1}{2} \left\{ 1 + \tanh 2 \left[\left(3.80 + \frac{H}{h} \right) \left(\frac{t}{\tau} - \frac{1}{2} \right) - \frac{H}{h} \left(\frac{\xi}{S} - \frac{1}{2} \right) \right] \right\} \quad (19)$$

A family of normalized generation trajectories calculated using Eq. (14) is presented in Figure 7 for wave height-to-depth ratios of $H/h = 0.1$ to 0.7 .

The Korteweg-de Vries equation has a solution which is a permanent form periodic wave usually termed the cnoidal wave. Using the general form shown in Eq. 4 for cnoidal waves the function $f(\theta)$ is:

$$f(\theta) = \frac{y_t - h}{H} + \text{cn}^2(\theta|m) \quad (20)$$

where $\theta = 2K \left(\frac{t}{T} - \frac{\xi}{L} \right)$ and K is the first complete elliptic integral, cn is the Jacobian elliptic function, m is the elliptic parameter, T is the period, L is the wave length, y_t is the distance from the bottom to the trough of the wave, and h is the depth. Substituting Eq. (20) into the generation equation, Eq. (7), and performing the integration yields:

$$\xi(t) = \frac{L}{2Kh} \left\{ (y_t - h)\theta + \frac{H}{m} [E(\theta|m) - m'\theta] \right\} \quad (21)$$

where $E(\theta|m)$ is the second incomplete elliptic integral, and m' is the complementary parameter, $m' = 1 - m$.

In Figure 8 a typical trajectory, $\xi(t)$, is presented which is normalized with respect to the total movement (stroke) of the wave plate, $\xi_{\max} = S/2$, calculated from Eq. (21). Because of the definition of the function $f(\theta)$ in Eq. (20), the origin occurs at a point of maximum velocity. However, it is desirable to start the motion of the wave plate at a position where the velocity of the plate and the amplitude

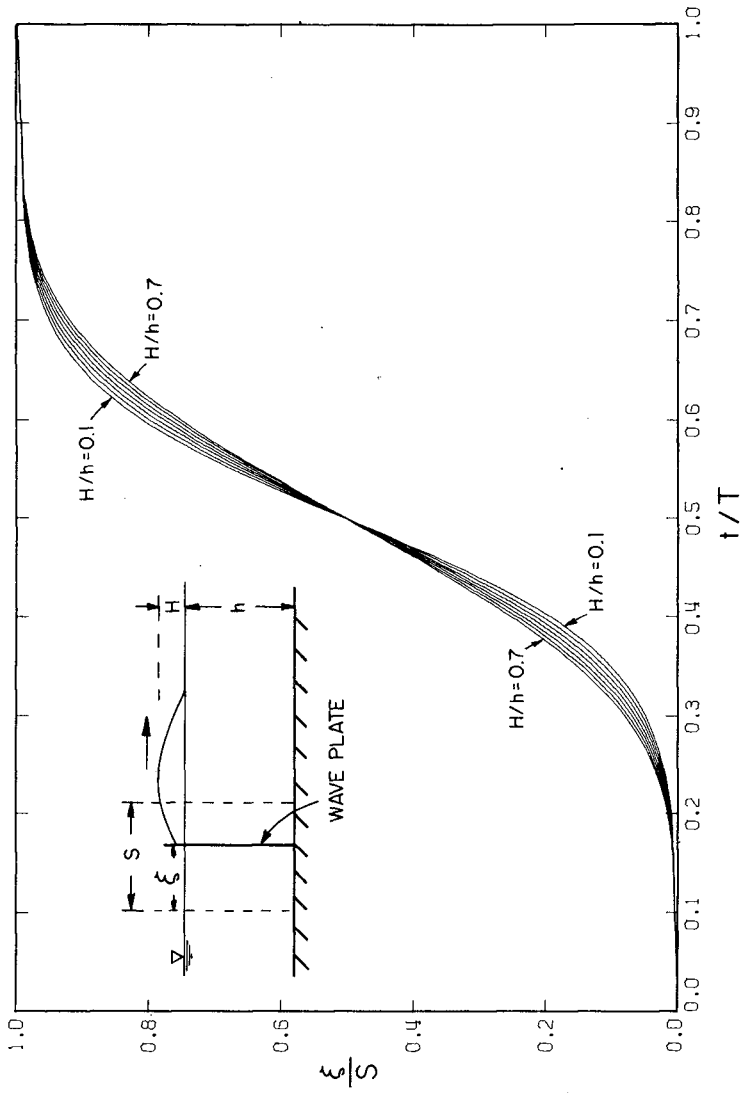


Figure 7 Solitary wave generation trajectories, $H/h = 0.1$ to 0.7 .

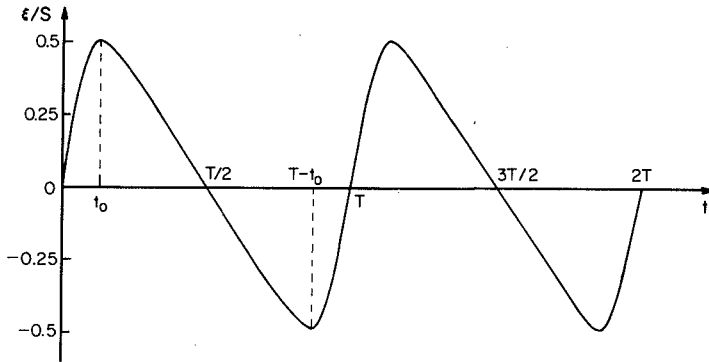


Figure 8 Typical wave plate trajectory for cnoidal wave generation.

of the wave are each zero, i.e., where;

$$\frac{d\xi}{dt} = \bar{u} = 0 \quad , \quad (22)$$

and

$$\eta = y_t - h + H \operatorname{cn}^2(\theta_0|m) = 0 \quad . \quad (23)$$

The parameter θ_0 is the argument of the cnoidal function determined such that the wave amplitude is zero. Eq. (23) can be written as:

$$\theta_0 = \operatorname{cn}^{-1} \left[\frac{h-y_t}{H} \right]^{1/2} \quad . \quad (24)$$

Substituting for θ_0 in Eq. (21) realizing this is the position of maximum plate displacement⁰ gives:

$$\xi_{\max} = -\xi_{\min} = \frac{L}{2Kh} \left\{ (y_t - h)\theta_0 + \frac{H}{m} \left[E(\theta_0|m) - m'\theta_0 \right] \right\} \quad (25)$$

and

$$\frac{t_0}{T} = \frac{\xi_{\max}}{L} + \frac{\theta_0}{2K} \quad . \quad (26)$$

The maximum excursion of the wave plate (or stroke S) is:

$$S = 2\xi_{\max} \quad . \quad (27)$$

Since the leading wave of a group of cnoidal waves would be a transient wave, it was desirable to make this wave a positive wave rather than a negative wave so the train would not overtake it. Thus, the motion is started at a minimum-point in Figure 8, i.e., the origin of the trajectory is at $t = T - t_0$. (The interested reader is referred to Goring

(1978) for details of the numerical procedures involved in defining the cnoidal wave relationships.)

Six trajectories for cnoidal waves which were used in this study are presented in Figure 9 (denoted as CN1 to CN6) along with the corresponding profiles of the waves the theory predicts will be generated. In theory each cnoidal wave is defined by the parameters: H/h and $T\sqrt{g/h}$ which are shown next to each wave in the table to the right in Figure 9. However, for a given value of t_0/T it has been found that reasonably good cnoidal waves can be produced with the appropriate pairs of H/h and $T\sqrt{g/h}$ (see Goring, 1978).

Certain other characteristics of the generation process will be discussed later when the theoretical results are compared to the results of experiments.

EXPERIMENTAL EQUIPMENT AND PROCEDURES

The wave generator used in this study consists of a vertical plate which is moved horizontally in a prescribed manner by means of an electro-hydraulic servo-system which is driven by a programmed input voltage. The displacement-time history of the wave-plate is directly proportional to the time history of the input voltage.

In general, the system is similar to many other hydraulically operated wave machines in use; hence, only one unique aspect will be discussed here. That is the function generator which provides a voltage-time history which is proportional to the desired trajectory of the wave plate (as was shown schematically in Figure 5). The function generator used in this investigation consists of a device which is capable of storing 1000 three digit words. The memory can be filled either manually or through a punched paper tape reader; the data rate and the voltage of the output can be changed over a wide range. In this way, for a given shape of the trajectory, the amplitude and the duration of the motion can be adjusted.

The wave tank in which the piston type wave generator is mounted is 37.7 m long, 61 cm deep, and 39.4 cm wide. The tank is constructed of 13 modules each of which has been leveled accurately. The bottom is composed of sections of structural steel channel and the sidewalls are glass throughout.

All wave profile measurements were made using resistance wave gages whose sensitive elements were two parallel stainless steel wires (0.25 mm dia.) spaced 4 mm apart. The wires were stretched taut in a "C" shaped frame of stainless steel rod. These gages were used in conjunction with a Hewlett Packard (7700 Series) oscillograph for most measurements. Some detailed profiles were obtained with the aid of an analog-to-digital converter so that data reduction and plotting were accomplished using a digital computer.

PRESENTATION AND DISCUSSION OF RESULTS

As noted in Figure 1, if a linear trajectory of the wave machine were used to generate a solitary wave, for the conditions shown an

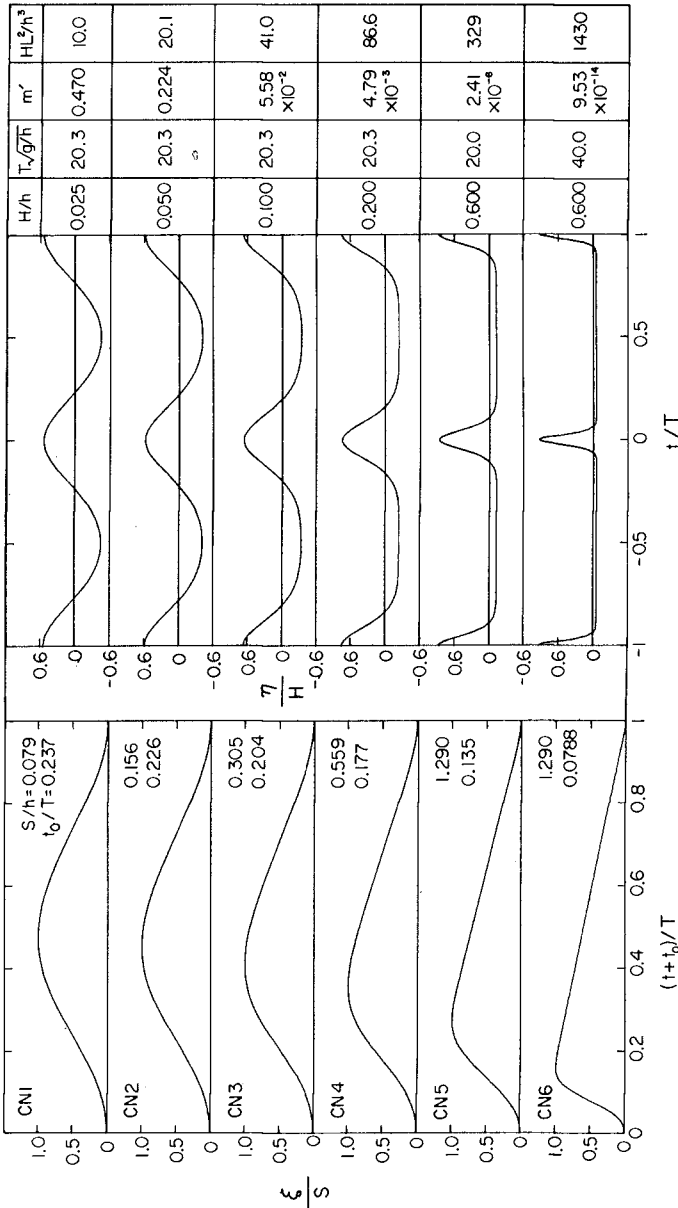


Figure 9 Trajectory shapes, waves, and associated data for cnoidal wave trajectories CN1 to CN6.

oscillatory tail with waves about 25% of the height of the leading wave would be present. As a better approximation, if the generation equations were solved assuming small motions of the generator the height of the waves in the tail could be reduced to about 10% of the first wave. Using the full theory for solitary wave generation (Eq. 19) results in the wave profiles presented in Figure 2, which shows that oscillatory waves nearly can be eliminated by a correct wave generation program. For the waves shown in Figure 2 the duration is $\tau = 2.044$ sec which is 7.4% greater than that predicted by Eq. (18); this difference decreases the magnitude of the trailing waves. That the optimum duration is not the theoretical duration is due in part to the fact that the wave plate velocity is constant with depth whereas there is a variation of horizontal water particle velocity with depth under a solitary wave. Thus, the desired boundary condition is not met precisely at the wave plate for this type of generator.

A comparison of experimentally determined profiles of solitary waves with two theories is presented in Figure 10. The theories chosen for comparison are those developed by Boussinesq (1782) and McCowan (1891) and the appropriate expressions for the profiles are shown in Table 1.

Table 1 Solutions of the solitary wave due to Boussinesq (1782) and McCowan (1891).

	Boussinesq	McCowan
Wave profile $\eta =$	$H \operatorname{sech}^2 \sqrt{\frac{3H}{4h}} \frac{X}{h}$	$\frac{h N \sin M (1+\eta/h)}{M [\cos M (1+\eta/h) + \cosh M \frac{X}{h}]}$
Wave speed $C =$	$\sqrt{gh(1+H/h)}$	$\sqrt{\frac{gh}{M}} \tan M$
Note		<p>N and M are:</p> $N = \frac{2}{3} \sin^2 \left[M \left(1 + \frac{2}{3} \frac{H}{h} \right) \right]$ $\frac{H}{h} = \frac{N}{M} \tan \left[\frac{1}{2} M \left(1 + \frac{H}{h} \right) \right]$

In Figure 10 waves with ratios of height to depth of 0.15 and 0.61 are shown and in both cases the agreement with each of the two theories is reasonable. The smaller wave agrees well with the Boussinesq theory over nearly the full range of the abscissa. The same degree of agreement is not apparent for the larger wave; however, over the major

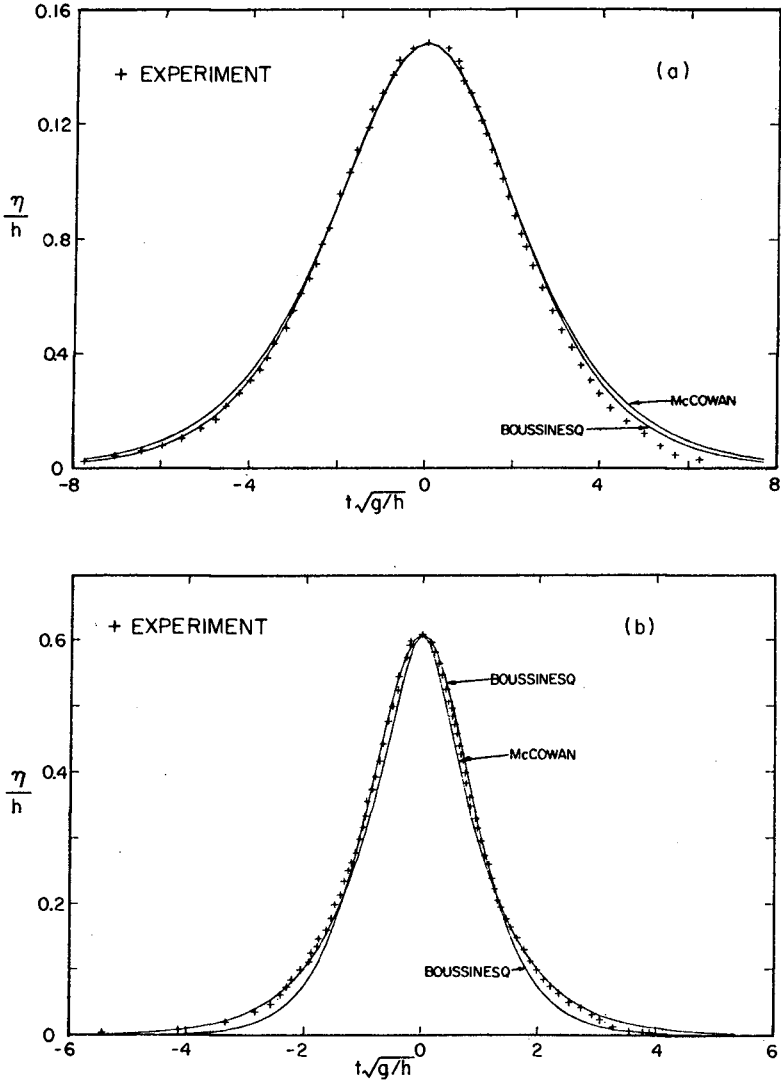


Figure 10 Comparison of the shape of solitary waves with relative heights (a) $H/h = 0.15$ and (b) $H/h = 0.61$ with the theories of Boussinesq and McCowan.

portion of the wave agreement with the Boussinesq theory is fairly good. (Similar results have been found by others, e.g. French (1969).)

Fenton (1972) developed a ninth-order solution for the solitary wave, and Boussinesq profiles were compared to his numerical results for waves with $H/h = 0.492$ and $H/h = 0.716$. The maximum difference in amplitude between the two theories was less than 7%, and for the larger height-to-depth ratio the differences were consistent with the comparison of McCowan's theory with that of Boussinesq; i.e., for x/h (or $t/g/h$) less than unity the Boussinesq results were above those from the ninth-order theory and for $x/h > 1.5$ the converse was true. Considering possible experimental errors and the rather small differences involved, it is felt the comparisons presented in Figure 10 are adequate to describe the capabilities of the long wave generator program developed herein.

An explanation of the differences which must not be forgotten is that the solutions obtained by Boussinesq (1782), McCowan (1891), and Fenton (1972) are approximations to the exact wave. Thus, the fact that agreement with the theories is limited is probably to be expected.

In Figure 11 the relative stroke of the wave machine (H/S) predicted by this approach (see Eq. 16) is compared to experimental results. In general agreement between the experiments and the theory is reasonably good for small relative wave heights, but as H/h increases disagreement increases. It is noted, in all cases the experimental data indicate wave heights which are less than those predicted for a given stroke of the wave machine plate. It appears that friction may be one cause for the observed differences, since measurements were made at two fixed distances from the wave machine; at $x = 8.4$ m for the six largest depths shown and at $x = 1.0$ m for the two smallest depths.

Since the wave gage at which the wave heights shown in Figure 11 were obtained was located less than 50 depths from the wave generator, at first it was considered that it was possible that the propagation distance was too short for a solitary wave to evolve completely. To investigate this, the waves were propagated analytically to infinity using the technique of inverse scattering. (For a review of this method and a comparison to experiments the interested reader is directed to Segur (1973) and to Hammack and Segur (1974), among others.) For a particular initial wave, the inviscid analysis yields the number and heights of solitary waves which emerge at infinity from a given initial disturbance. For a wave which is initially a solitary wave, only one solitary wave with the same height as the initial wave will emerge at infinity. The results of applying this analysis to the data are presented in Figure 12. The abscissa is the ratio of wave height-to-depth and the ordinate is the ratio of the wave height obtained by the analytical technique of inverse scattering compared to the initial measured wave height, H_{inv}/H . Thus, a value of the ordinate of unity indicates there is a good probability that the wave generated is a "solitary wave." Generally the agreement is reasonably good except for the experiments for the two smallest depths ($h = 10.0$ cm and 5.0 cm). The reason for this disagreement may be due to the effects of friction at the smaller depths, which has been mentioned earlier. A detailed discussion of other aspects of the generated wave and changes of the wave as it propagates is presented by Goring (1978).

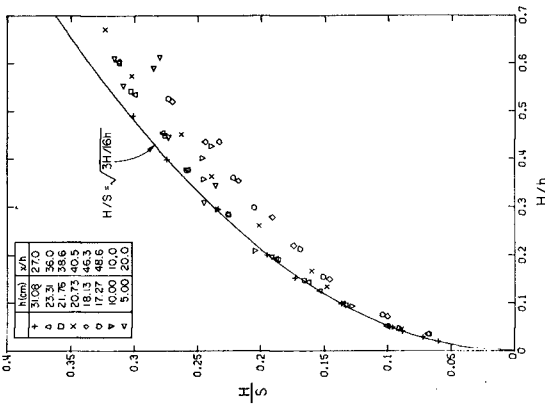


Figure 11 Variation of H/S with the relative wave height, H/h , for solitary wave generation.

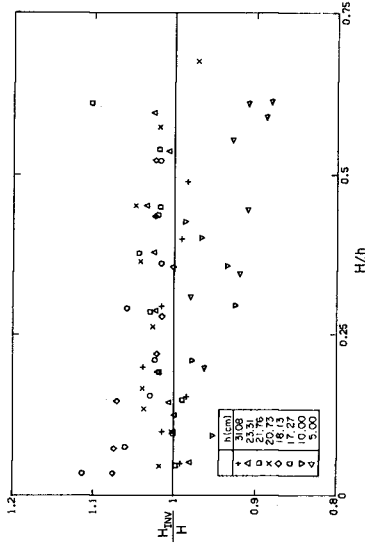


Figure 12 Variation of the inverse scattered wave height ratio, H_{inv}/H , with relative wave height, H/h .

Examples of periodic long waves generated with different trajectories have been presented in Figures 3 and 4. As mentioned previously, the object was to generate waves which formed the periodic solution to the Korteweg-de Vries Equation, namely cnoidal waves (see, e.g., Whitham, 1974). The experiments from which the wave profiles of Figures 3 and 4 were obtained were similar with the only difference being the period of the motion. For the experiment shown in Figure 4 the period of the motion was 2.90 sec compared to a period of 4.28 sec for the case shown in Figure 3; in both examples the depth was 20 cm and the stroke of the wave plate was 11.18 cm. It should be noted that the secondary waves which appear to be forming in the oscillograph traces shown in Figure 3 (as indicated by the arrows) are absent in the wave profiles at corresponding positions in Figure 4. In addition, the waves near the center of the group shown in Figure 4 appear to propagate with relatively constant shape.

Waves generated using the wave plate trajectories shown in Figure 9 are compared to theoretical wave profiles in Figures 13a and 13b. In these figures the corresponding conditions are shown in each portion of the figures; it is noted, the Ursell Number (HL^2/h^3) for these experiments varies by two orders of magnitude from 10 to 1229. The experimental record was obtained from a wave gage located between 5 and 20 depths from the wave plate ($x = 1.0$ m). In an attempt to minimize the effects of both the leading and the trailing part of the wave train, the data shown are for the third cycle in the wave train. The wave height which was measured was used to construct the theoretical profile; thus, reducing the effect of friction during propagation and disagreements with the generation theory as embodied in Equation 16. Therefore, only the shape of the wave is being compared in Figures 13a and 13b. It appears that agreement between the experimental and theoretical results is relatively good with discrepancies apparent primarily in the region of the trough, especially for the cases of large Ursell Number.

In Figure 14 experimental and theoretical results are presented which summarize the generation theory for long waves. The ordinate is the ratio of wave height to stroke, H/S , and the abscissa is a non-dimensional wave period, $(1/T)(\sqrt{h/g})$. Shown in the figure are curves of constant wave height-to-depth, H/h , and of constant nondimensional time, t_0/T , which describe the time to the maximum of the trajectory as shown in Figure 8. Thus, for a desired wave height, wave period, and depth, the stroke of the wave machine and the time to the maximum of the trajectory can be obtained. It is noted that the line which emanates from the origin describes small amplitude shallow water waves and the curve $t_0/T = 0.25$ is tangent to it. The intersection of curves of constant H/h with the ordinate describe the generation of solitary waves. Experimental data are presented for periodic waves in Figure 14 where the symbols correspond to particular values of wave height-to-depth and relative time to the extreme of the trajectory, t_0/T . Thus, the comparison can be made between the data and the curves of constant relative wave height, H/h , and constant relative duration, t_0/T . It is apparent that agreement increases with increasing t_0/T and decreasing H/h . Considering the shape of the trajectories this would be expected.

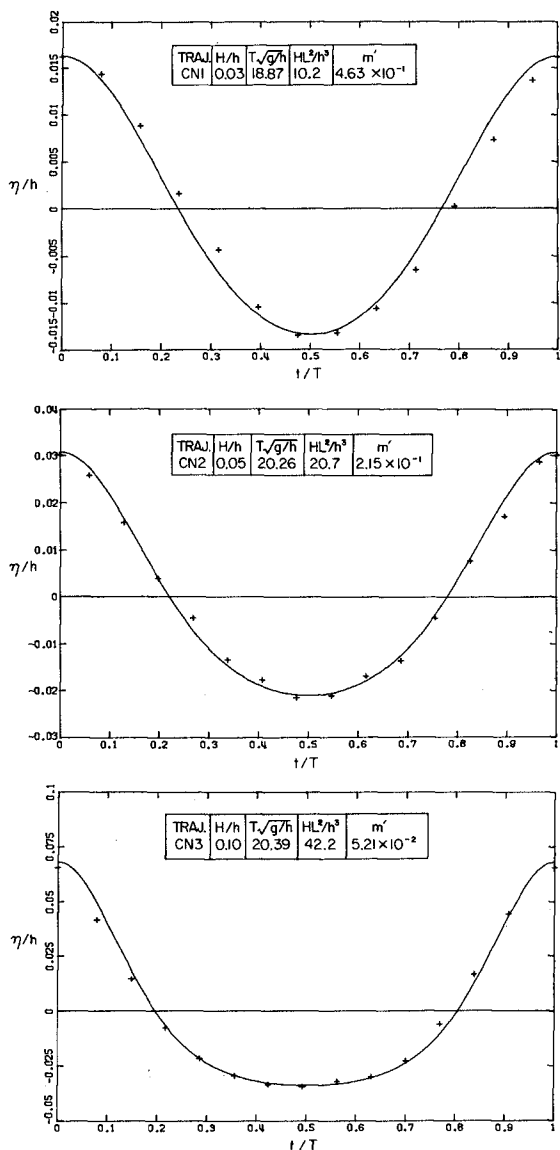


Figure 13a Comparison of the shape of experimental cnoidal waves with theory. (Trajectories CN1, CN2 and CN3)

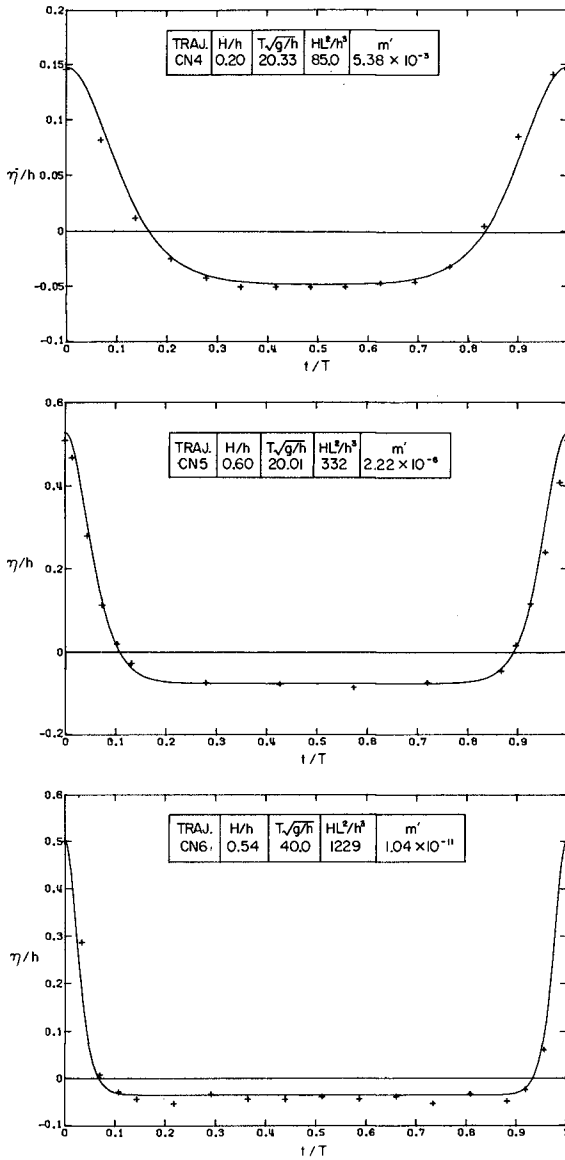


Figure 13b Comparison of the shape of experimental cnoidal waves with theory. (Trajectories CN4, CN5 and CN6)

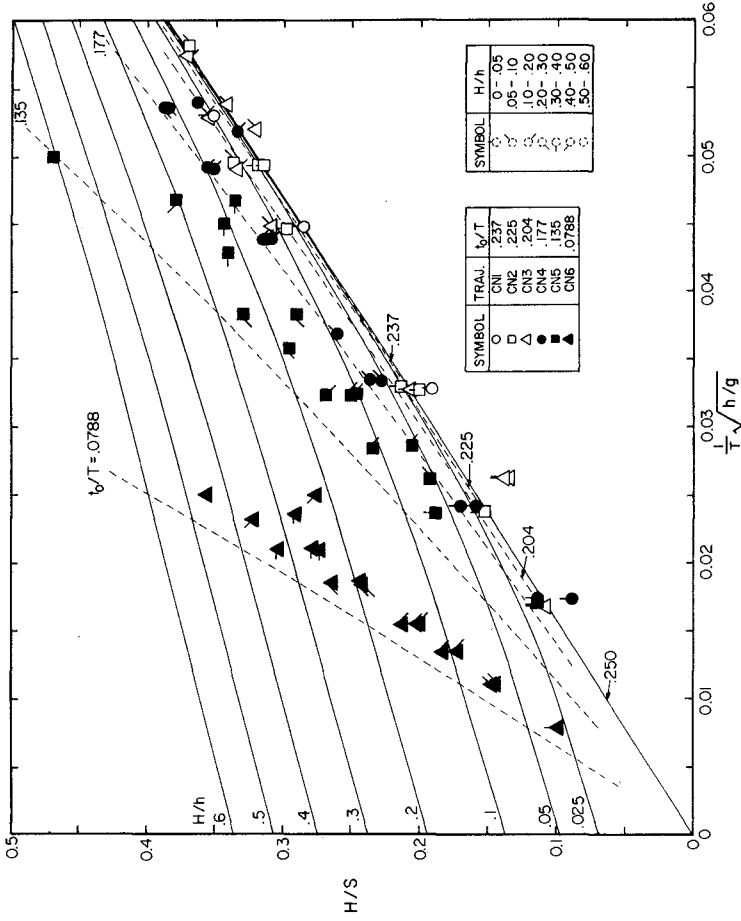


Figure 14 Variation of H/S with the inverse nondimensional period $1/T\sqrt{h/g}$ for cnoidal wave generation.

CONCLUSIONS

This study has shown the importance of considering the position of the wave plate relative to the position of the generated wave in a long wave generation model. If this is done, quite acceptable profiles for solitary and cnoidal waves are possible.

ACKNOWLEDGMENTS

This study was supported by NSF Grant Nos. ENV72-03587 and ENV77-20499 and by the New Zealand Ministry of Works and Development. It was carried out while the junior author was a graduate student at the California Institute of Technology as part of his Ph.D. thesis.

REFERENCES

- Boussinesq, J. (1872), "Théorie des Ondes et des Remous qui se Propagent le Long d'un Canal Rectangulaire Horizontal, en Communiquant au Liquide Contenu dans ce Canal de Vitesses Sensiblement Paralleles de la Surface au Fond," Journal de Mathematiques Pures et Appliquées, 2nd Series, Vol. 17, pp. 55-108.
- Fenton, J. (1972), "A Ninth-Order Solution for the Solitary Wave," Journal of Fluid Mechanics, Vol. 52, Part 2.
- French, J. A. (1969), "Wave Uplift Pressures on Horizontal Platforms," W. M. Keck Laboratory of Hydraulics and Water Resources, Report No. KH-R-19, California Institute of Technology, Pasadena, CA.
- Goring, D. G. (1978), "Tsunamis - The Propagation of Long Waves Onto a Shelf," Report No. KH-R-38, W. M. Keck Laboratory of Hydraulics and Water Resources, California Institute of Technology, Pasadena, CA.
- Hammack, J. L. and Segur, H. (1974), "The KdV Equation and Water Waves. Part 2. Comparison with Experiment," Journal of Fluid Mechanics, Vol. 65, pp. 289-314.
- McCowan, J. (1891), "On the Solitary Wave," London, Edinburgh and Dublin Philosophical Magazine, Vol. 32, pp. 45-58.
- Segur, H. (1973), "The Korteweg-de Vries Equation and Water Waves. Part 1. Solutions of the Equation," Journal of Fluid Mechanics, Vol. 59, pp. 721-736.
- Whitham, G. B. (1974), Linear and Nonlinear Waves, Wiley-Interscience.

CHAPTER 48

CORRECT REPRODUCTION OF GROUP-INDUCED LONG WAVES

N.-E. Ottesen Hansen¹ Stig E. Sand²
H. Lundgren³ Torben Sorensen⁴ H. Gravesen⁵

ABSTRACT

In nature short period storm waves generate longer waves with periods corresponding to the wave group periods. The long waves are generally referred to as the wave set-down of water level. The set-down term is of second order in the height of the short waves. With first-order reproduction of natural storm waves in the laboratory, the set-down bound to the wave groups is not reproduced. As a result, various free waves are generated, propagate towards the model and reflect from the boundaries. These so-called parasitic waves cause an exaggeration of long wave phenomena, such as harbour resonance and slow drift oscillations of moored ships.

The parasitic waves can be eliminated by means of compensating free waves imposed on the system by second-order paddle motion reproducing the natural set-down. The control signal for this motion has been calculated and checked by testing. The agreement between calculated and measured results is found to be good.

Further, an alternative method for reducing the parasitic wave problem is presented. Utilizing the shoaling properties of the various waves, the influence of parasitic waves can be diminished by generating the waves in somewhat deeper water before they propagate into the shallower model area.

INTRODUCTION

Resonance conditions ('seiche') in harbours and bays are experienced all over the world. They can be a nuisance for the operation of ship terminals because, from time to time, they may induce unacceptably large movements of moored ships resulting in breaking of moorings. The periods of interest are usually in the range of 20 seconds to 5 minutes.

¹ Ph.D., Head, Harbour and Marine Structures Department, Danish Hydraulic Institute, Agern Allé 5, DK-2970 Hørsholm.

² Ph.D., Research Engineer, Institute of Hydrodynamics and Hydraulic Engineering, Technical University of Denmark, DK-2800 Lyngby.

³ Professor of Marine Civil Engineering, Institute of Hydrodynamics and Hydraulic Engineering, Technical University of Denmark. Consultant, Danish Hydraulic Institute.

⁴ M.Sc., Director, Danish Hydraulic Institute.

⁵ M.Sc., Manager, Research Section, Danish Hydraulic Institute.

Harbour resonance may be induced by various mechanisms, such as tsunamis, storm surges, land slides or calving glaciers (Greenland). Most frequently, however, the source will be meteorological pressure fluctuations or long period waves from distant storms or wave groups. In this paper long period waves induced by wave groups are considered. This is the most common mechanism of generation.

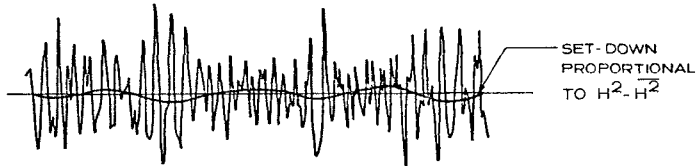


Fig. 1 Long period wave generated by wave groups.

Long waves generated by storm wave groups are generally referred to as the wave set-down, because they are characterized by having their troughs in the regions of the larger waves in the groups. Typically, a group contains from 5 to 20 waves (Fig. 1).

To each wave pertains an internal compressive force, the radiation stress (Longuet-Higgins and Stewart, 1960) or wave thrust (Lundgren, 1963), acting in the direction of wave propagation. For a regular wave this force is proportional to the square of the wave height. To balance this force a set-down in mean water level has to appear within the series of higher waves, and a corresponding set-up is produced within the series of smaller waves. This problem has previously been considered and quantified by Longuet-Higgins and Stewart (1964) and by Ottesen Hansen (1978).

An example of the effect of long waves generated by wave groups is the 'seiche' in the Bay of Telok Plan at Bintulu in Malaysia (Fig. 2a). The 'seiche' in the bay and the incoming waves were recorded simultaneously (Fig. 2b). It appeared that wave groups, approaching from NW produced an edge wave between the head of the bay and the tip of the promontory Tanjong Kidurong with a period of 100 - 180 s. This long period wave normally occurred when the offshore significant wave exceeded 0.9 m.

PROBLEMS IN PHYSICAL MODELS

Mooring forces and ship movements are normally determined by physical model tests, which at present is the simplest and most reliable method. Physical model technique has developed considerably over the past decade. Presumably, the major improvement has been the introduction of natural, irregular waves in the model. The use of natural wave trains secures that important phenomena found in nature are reproduced accurately in the model. This applies particularly to:

- (i) Direct wave action on ships.
- (ii) The effect of wave groups or long waves on harbour resonance and slow drift ship motions.

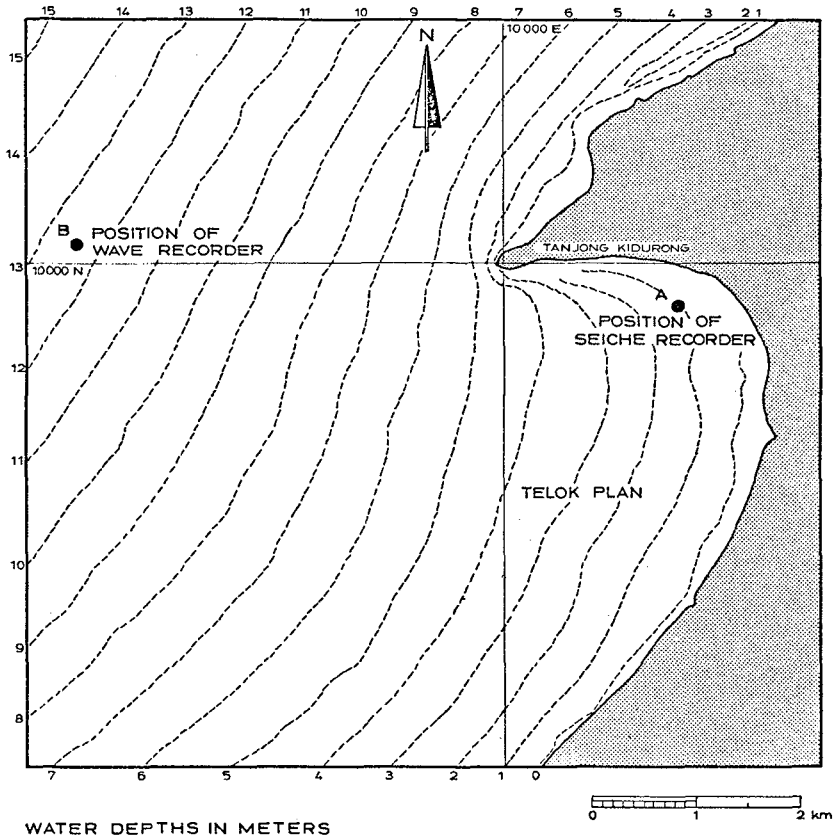


Fig. 2a Topography of the Bay of Telok Plan at Bintulu, Sarawak, Malaysia. A 'seiche' (long wave) recorder is placed in the bay, and a waverider buoy approximately 4 km offshore.

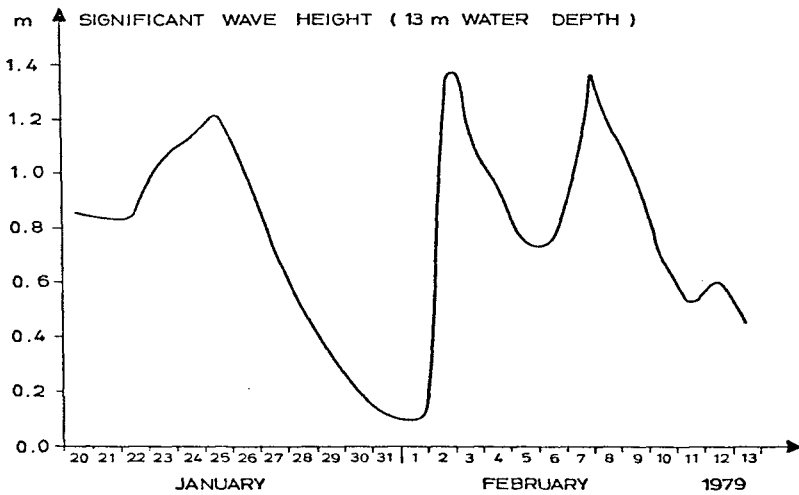
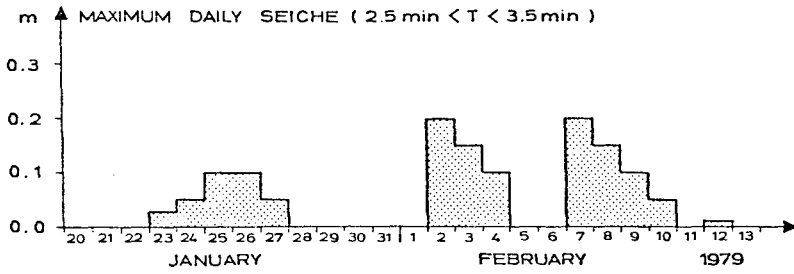


Fig. 2b The results of simultaneously recorded 'seiche' in the Bay of Telok Plan and the significant wave height 4 km offshore.

For problems with ships moored in harbours or movements of large vessels, the effect of long waves is particularly important due to the risk of resonance with the longer natural vessel periods pertaining to surge, sway and yaw.

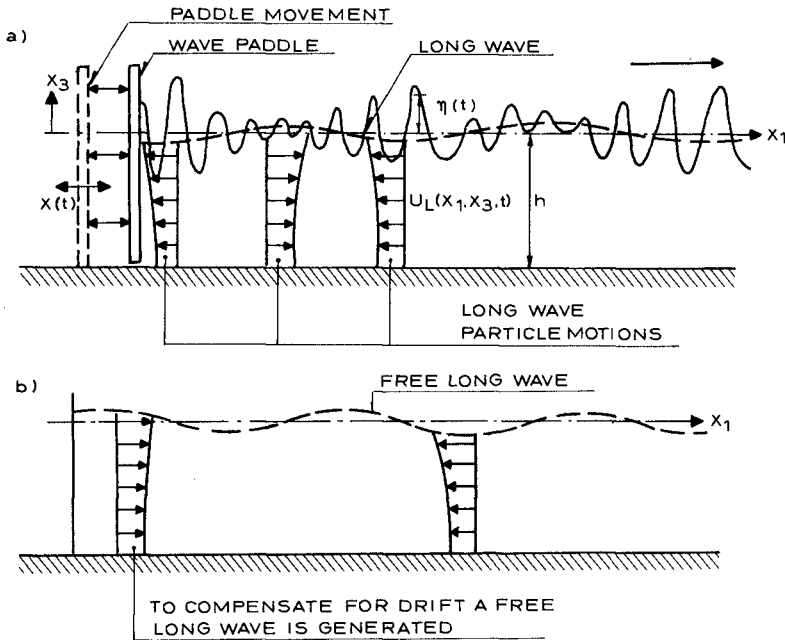


Fig. 3 Origin of parasitic long wave when generating irregular waves in the laboratory.

When natural waves are reproduced in the laboratory, the paddle is normally controlled by a 1st order signal. The wave groups are accompanied by a long wave corresponding to the set-down (Fig. 3a). The set-down behaves as a normal progressive wave with forward orbital velocities underneath the crests and backward orbital velocities under the troughs, also called drift velocities.

At the paddle, however, the desired 2nd order (long period) drift velocities are not produced by the 1st order (short period) signal. With no flow through the paddle the natural drift velocities will be compensated by identical velocities of opposite sign (Fig. 3b). The latter velocities generate a progressive long wave that is free, i.e. not bound to the groups. This phenomenon is called a parasitic long wave, and it results in an exaggeration of the long wave effects mentioned under (ii) above.

In order to eliminate the parasitic long wave, the 1st order signal must be superposed by a 2nd order long period signal that will produce

the drift velocities required by the set-down wave. In principle, these drift velocities must be produced at the mean piston position, $X = 0$. In practice, the long period signal will control the piston velocity, and hence the drift velocity, at the instantaneous piston position X , which is displaced somewhat from $X = 0$. This piston displacement gives a correction to the long period signal, see discussion below.

As will be seen from the formulae below, the long period signal is a sum over differences between each pair of frequencies in the short wave spectrum. Therefore, the long period signal may be designated as a sum of subharmonics.

The control of the paddle by the 1st order short wave signal also gives rise to a displacement. The corresponding 2nd order correction would contain a number of terms, each term corresponding to the sum of a pair of frequencies in the short wave spectrum. Hence, this correction would be a sum of superharmonics, cf. the second harmonic introduced in the generation of regular waves (BuhrHansen et al., 1975). In the present paper the superharmonic correction has not been considered.

METHOD OF SOLUTION

The mathematical description of the long wave and the parasitic wave problem depends on the description used in the wave generation. In all modern laboratories, models are tested with irregular waves. Often a Fourier approach with random or specified phase spectrum is used for the generation, but at present a time-domain generation must be preferred (Lundgren and Sand, 1979).

The direct Fourier approach with specified phases is the simplest one for the problem discussed in this paper and will be used in the following to illustrate the principles.

A regular wave group with water surface elevation η_{nm} and frequency Δf_{nm} consists of two regular waves with water surface elevations η_n, η_m and frequencies f_n, f_m , respectively, where

$$\eta_{nm} = \eta_n + \eta_m \quad \text{and} \quad \Delta f_{nm} = f_n - f_m \quad (1)$$

n and m being indices indicating the numbers of the waves considered.

According to the previous outline of the physical principles, the wave group η_{nm} generates a wave set-down ξ_{nm} . Each pair n, m of components in the wave spectrum contributes to the set-down. This means that the wave set-down ξ in an irregular wave train can be calculated by summing up the contributions from all pairs, i.e.

$$\xi = \sum_{n=m^*}^{\infty} \sum_{m=m^*}^{\infty} \xi_{nm} \quad \text{with} \quad m^* = f^*/f_0 \quad (2)$$

in which f_0 is the interval of discretization of the short wave spectrum, and f^* is the lowest frequency in the short wave spectrum.

Hence, the first step in the problem is to solve the simpler problem of two regular, interacting waves. In this analysis the following assumptions are made:

- (1) The short period waves can be described by first order Stokes' theory.
- (2) The long period waves constitute a second order phenomenon, i.e. of the order $O(H^2/h^2)$.
- (3) The bottom is plane.
- (4) The waves are progressive and propagate in only one direction.
- (5) Frictional effects can be neglected.

With these assumptions the following solution for the wave set-down ξ_{nm} under a regular wave group has previously been found (Ottesen Hansen, 1978)

$$\frac{\xi_{nm}}{h} = G_{nm} h \left(\frac{a_n a_m + b_n b_m}{h^2} \cos(\Delta\omega_{nm} t - \Delta k_{nm} x_1) + \frac{-a_n b_m + b_n a_m}{h^2} \sin(\Delta\omega_{nm} t - \Delta k_{nm} x_1) \right) \quad (3)$$

The notation in this paper is:

- (x_1, x_3) = horizontal/vertical coordinates
- t = time
- n, m = indices indicating numbers of the waves considered
- L_n = length of the n 'th wave
- k_n = $2\pi/L_n$ = wave number of the n 'th wave
- Δk_{nm} = $k_n - k_m$ = long wave number
- σk_{nm} = $k_n + k_m$
- c_n = phase velocity of the n 'th wave
- T_n = period of the n 'th wave
- f_n = $1/T_n$ = frequency of the n 'th wave
- Δf_{nm} = $f_n - f_m$ = long wave frequency
- ω_n = $2\pi f_n$ = cyclic frequency of the n 'th wave
- $\Delta\omega_{nm}$ = $\omega_n - \omega_m$
- h = water depth
- η_n = $a_n \cos(\omega_n t - k_n x_1) + b_n \sin(\omega_n t - k_n x_1)$
= elevation of water surface for the short wave
- ξ = elevation of water surface for the long wave
- ρ = density of water
- U_L = long wave horizontal velocity
- u_s = short wave horizontal velocity
- u = total, instantaneous horizontal velocity
- x = paddle position

The function G_{nm} , which is shown graphically in Fig. 4, is a transfer function given by (Ottesen Hansen, 1978)

$$G_{nm} = \left(\frac{g}{2} \Delta\omega_{nm} \Delta k_{nm} \left(\frac{1}{c_n} + \frac{1}{c_m} \right) \Delta k_{nm} h \coth(\Delta k_{nm} h) - \frac{1}{2} \Delta k_{nm}^2 \Delta\omega_{nm}^2 h + \frac{\omega_n \omega_m \Delta k_{nm}^2 h \cosh(\Delta k_{nm} h)}{\cosh(\sigma k_{nm} h) - \cosh(\Delta k_{nm} h)} \right) / \left(\Delta k_{nm} h \coth(\Delta k_{nm} h) \Delta\omega_{nm}^2 - g h \Delta k_{nm}^2 \right) \quad (4)$$

The asymptotic expressions for the shallow and deep water cases of Eq. (4) are presented in Fig. 4 on the left hand and right hand sides, respectively.

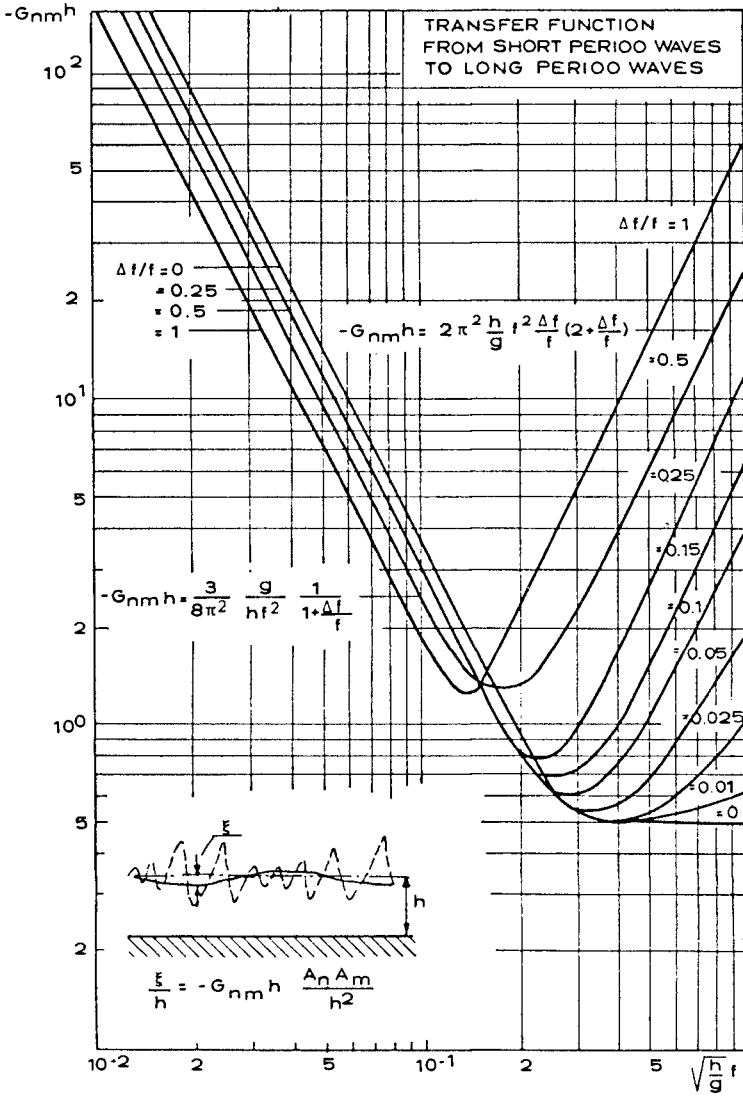


Fig. 4 Transfer function for long waves generated by two regular waves with amplitudes A_n, A_m and frequencies $f_n = f + \Delta f$ and $f_m = f$, respectively.

PRINCIPLE OF SOLUTION

A natural wave train is generated by a piston type wave paddle in a flume of depth h , cf. Fig. 3a. The paddle position as function of time is $X(t)$ with paddle amplitude X_a . The short wave horizontal velocity is $u_S(x_1, x_3, t)$, and the corresponding long wave velocity is $U_L(x_1, x_3, t)$. The total, instantaneous horizontal velocity in the flume is denoted $u(x_1, x_3, t)$. Further, the velocity potential ϕ with $\phi_{x_1} = u(x_1, x_3, t)$ must satisfy Laplace equation.

The general boundary condition at the paddle expresses the equality between paddle velocity and horizontal orbital velocity, i.e.

$$\phi_{x_1} = u(x_1, x_3, t) = \frac{\partial X(t)}{\partial t} = X_t(t) \quad \text{for} \quad \begin{cases} x_1 = X(t) \\ -h \leq x_3 \leq 0 \end{cases} \quad (5)$$

A perturbation method is applied to the problem. This implies that the variables u and X are written

$$\begin{aligned} u &= \epsilon u^{(1)} + \epsilon^2 u^{(2)} + \dots \\ X &= \epsilon X^{(1)} + \epsilon^2 X^{(2)} + \dots \end{aligned} \quad (6)$$

It is not practical to deal with a boundary condition at $x_1 = X(t)$. Therefore it is transferred to $x_1 = 0$ by means of the following Taylor expansions

$$\begin{aligned} u^{(1)}(X, x_3, t) &= u^{(1)}(0, x_3, t) + X u_{x_1}^{(1)}(0, x_3, t) + \dots \\ u^{(2)}(X, x_3, t) &= u^{(2)}(0, x_3, t) + X u_{x_1}^{(2)}(0, x_3, t) + \dots \end{aligned} \quad (7)$$

The 1st and 2nd order boundary conditions now appear to be

$$\begin{aligned} u^{(1)}(0, x_3, t) &= X_t^{(1)} \\ u^{(2)}(0, x_3, t) &= -X^{(1)} u_{x_1}^{(1)} + X_t^{(2)} \quad \text{for} \quad x_1 = 0 \end{aligned} \quad (8)$$

Then the problem is reduced to the following:

- (i) For a given $X^{(1)}(t)$ (with $X^{(2)} = 0$) determine the corresponding $u^{(2)}(0, x_3, t)$ in the flume. This includes contributions from both the real wave set-down and parasitic waves.
- (ii) Determine the signal $X^{(2)}(t)$ so that the progressive long waves correspond to the set-down, i.e. $u^{(2)} = U_L$, and all parasitic waves are eliminated.

In step (i) Laplace equation has to be solved with all the boundary conditions, including Eq. (8) written as

$$\begin{aligned} \phi_{x_1}^{(1)} &= X_t^{(1)} \\ \phi_{x_1}^{(2)} &= -X^{(1)} \phi_{x_1 x_1}^{(1)} \quad \text{for} \quad x_1 = 0 \end{aligned} \quad (9)$$

SHALLOW WATER SOLUTION

In the shallow water case the horizontal velocity distribution matches the paddle profile, and therefore no local disturbances will appear. Thus, Laplace equation will give the usual, well-known solution. Hence, step (ii) above may be solved directly from the 2nd order boundary condition Eq. (8) or through mass transport considerations

at the paddle. This leads to

$$u^{(2)}(0, x_3, t) = U_L(0, x_3, t) = -X^{(1)} u_{x_1}^{(1)} + X_t^{(2)} \quad \text{for } x_1 = 0 \quad (10)$$

i.e.

$$X_t^{(2)} = U_L(0, x_3, t) + X^{(1)} u_{x_1}^{(1)} \quad (11)$$

For a regular wave group, $\eta_{nm}(t)$, produced by two short waves as defined by Eq. (1), the 1st order horizontal velocity, $u_{nm}^{(1)}$, is found from the usual expressions for progressive waves. The paddle movement $X_{nm}^{(1)}$ is calculated by application of the asymptotic transfer function kh , which is easily derived from the 1st order equations (cf. Biésel, 1951). The long wave velocity $U_L(0, x_3, t)$ is calculated from Eq. (3). Hence, the necessary 2nd order piston positions $X_{nm}^{(2)}(t)$ may be found from Eq. (11) as

$$X_{nm}^{(2)}(t) = \frac{k_n^2 + k_m^2 - 3/h^2}{2h^2 k_n k_m (k_n - k_m)} \left[(a_n a_m + b_n b_m) \sin \Delta \omega t + (a_n b_m - a_m b_n) \cos \Delta \omega t \right] \quad (12)$$

In the numerator the term $-3/h^2$ is the dominant one and corresponds to elimination of the parasitic wave. The term $k_n^2 + k_m^2$ originates from the paddle displacement.

For short shallow water waves the transfer function is kh , i.e. the ratio between generated wave amplitude and 1st order paddle amplitude is $A/X_a = kh$. Similarly, a 2nd order transfer function can be defined as the ratio between the amplitude of the generated long waves, ξ_a , and the 2nd order paddle amplitude, $X_a^{(2)}$. These transfer functions are shown in Fig. 5. A good approximation to the 2nd order transfer function is $\xi_a/X_a \approx \Delta k_{nm} h$.

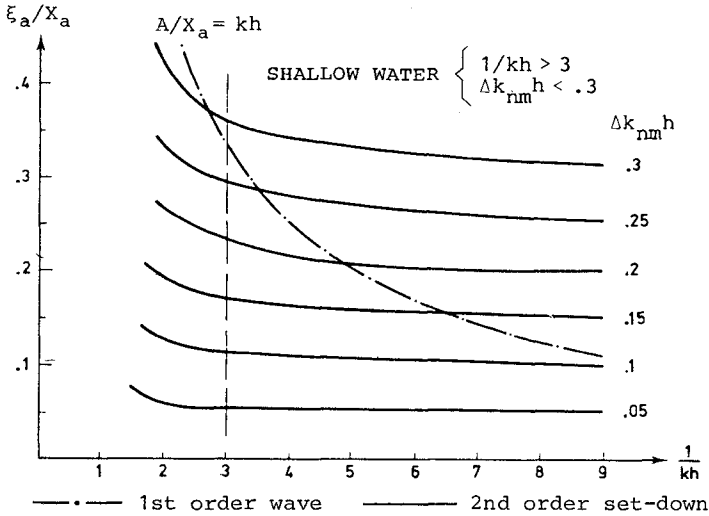


Fig. 5 Shallow water transfer functions.

Assuming $L > 20h$ for shallow water waves, the term $k_n^2 + k_m^2$ in the numerator of Eq. (12) is less than 6% of the term $3/h^2$. If the smaller term is neglected, Eq. (12) becomes

$$X^{(2)}(t) \approx \frac{-3}{2h^3 k_n k_m (k_n - k_m)} Z_{nm}(t) \quad (13)$$

where $Z_{nm}(t)$ is the expression in the brackets.

GENERAL SOLUTION FOR THE PADDLE MOVEMENT

In the general (non-shallow) case the horizontal orbital velocity of the waves diminishes hyperbolically towards the bottom. As this velocity profile is not compatible with that of the paddle, local disturbances, damped as $e^{-k_j x_1}$, arise both in 1st and 2nd order. These disturbances and the general x_3 -dependence make it imperative to solve the Laplace equation with the appropriate boundary conditions. Thus the problem is as follows

$$\phi_{x_1 x_1}^{(2)} + \phi_{x_3 x_3}^{(2)} = 0 \quad (14)$$

$$g \phi_{x_3}^{(2)} + \phi_{tt}^{(2)} = g \eta_{x_1}^{(1)} \phi_{x_1}^{(1)} - g \eta^{(1)} \phi_{x_3 x_3}^{(1)} - \eta_t^{(1)} \phi_{t x_3}^{(1)} - \eta^{(1)} \phi_{t x_3 t}^{(1)} + \phi_{x_1}^{(1)} \phi_{x_1 t}^{(1)} + \phi_{x_3}^{(1)} \phi_{x_3 t}^{(1)} \quad \text{for } x_3 = 0 \quad (15)$$

$$\phi_{x_3}^{(2)} = 0 \quad \text{for } x_3 = -h \quad (16)$$

$$\phi_{x_1}^{(2)} = -X^{(1)} \phi_{x_1 x_1}^{(1)} + X_t^{(2)} \quad \text{for } x_1 = 0 \quad (17)$$

The precise form of the local disturbances pertaining to the 1st order equations is (cf. Biésel)

$$\phi_{x_1, \text{disturbance}} = X_a \sum_{j=1}^{\infty} C_j \omega \cos(k_j (x_3 + h)) e^{-k_j x_1} \cos \omega t \quad (18)$$

where $C_j = \frac{2 \sin k_j h}{\sin k_j h \cos k_j h + k_j h}$ and $\omega^2 = -g k_j \tan k_j h$.

Firstly, step (i) of the preceding section is considered, viz. $X^{(2)} = 0$. A paddle controlled by a 1st order signal will generate in 2nd order

$$\phi_{x_1}^{(2)} = -U_{L, \text{free}} + a_L \cos(\Delta \omega t - \Delta k x_1) + b_L \sin(\Delta \omega t - \Delta k x_1) + \sum_i C_{L,i} e^{-k_i x_1} \quad (19)$$

when the input is the regular wave group given by Eq. (1). The functions $C_{L,i}$ represent the (x_3, t) -dependent local disturbances of 2nd order, which can be accepted in model tests because they are strongly damped away from the paddle. The first three terms in Eq. (19) are illustrated in Fig. 6 together with the short wave groups (full line) and the dash-dotted long wave (set-down) that follows the groups, and which it is desired to reproduce. The latter is characterized by the velocities $U_L(x_1, x_3, t)$. The first term, $-U_{L, \text{free}}$, is the free parasitic long wave shown as a fat dotted line and designated '180° out of phase with U_L ' because it cancels U_L at $x_1 = 0$. The terms with a_L and b_L represent free long waves and contain the contribution from the paddle displace-

ment shown as a thin dotted line and designated 'from the $X_{x_1 x_1}^{(1)}$ term'. These terms also include a complicated 2nd order free-wave effect from the 1st order local disturbances, cf. the formula for $F_{3,n}$ below.

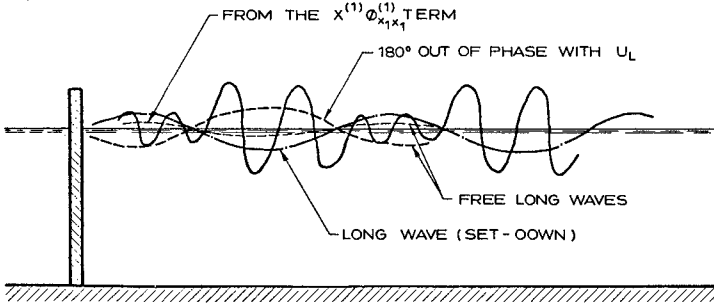


Fig. 6 Long waves for 1st order control signal.

Secondly, the appropriate $X_{nm}^{(2)}(t)$ must be determined as a part of the solution of the 2nd order Laplace equation in such a manner that:

- (a) The long wave following the group is generated.
- (b) All free long waves are eliminated.

The lengthy calculations result in the following solution:

$$X_{nm}^{(2)}(t) = \left((a_n b_m - a_m b_n) F_1 + (a_n a_m - b_n b_m) F_2 (F_{3,m} - F_{3,n}) \right) \cos \Delta \omega t + \left((a_n a_m + b_n b_m) F_1 + (a_m b_n - a_n b_m) F_2 (F_{3,m} - F_{3,n}) \right) \sin \Delta \omega t \quad (20)$$

in which

$$F_1 = \frac{\omega_m \Delta k_{nm} k_m (1 + G_n) \left\{ (k_n - 2k_m) \sinh(k_n h) + k_n \sinh([k_n - 2k_m]h) \right\}}{8(k_n^2 - 2k_n k_m) \Delta \omega_{nm} \sinh(\Delta k_{nm} h) \tanh(k_n h) \sinh(k_m h)} + \frac{\omega_n \Delta k_{nm} k_n (1 + G_m) \left\{ k_m \sinh([2k_n - k_m]h) + (2k_n - k_m) \sinh(k_m h) \right\}}{8(2k_n k_m - k_m^2) \Delta \omega_{nm} \sinh(\Delta k_{nm} h) \tanh(k_m h) \sinh(k_n h)} + \frac{G_{nm}(1 + \Delta G_{nm})}{2 \tanh(\Delta k_{nm} h)} \quad (20a)$$

$$F_2 = \frac{\Delta k_{nm} (1 + G_n) (1 + G_m)}{8 \Delta \omega_{nm} \tanh(k_n h) \tanh(k_m h)} \quad (20b)$$

$$F_{3,n} = \omega_n \sum_{j=1}^{\infty} \frac{2 k_j \sin(k_j h) \left\{ k_j \sin(k_j h) \coth(\Delta k_{nm} h) + \Delta k_{nm} \cos(k_j h) \right\}}{(k_j^2 - \Delta k_{nm}^2) \left\{ \sin(k_j h) \cos(k_j h) + k_j h \right\}} \quad (20c)$$

Here k_j is found as the solution to

$$\omega_n^2 = -g k_j \tanh k_j h \quad \text{with} \quad \left(j - \frac{1}{2} \right) \pi < k_j h < j \pi \quad (20d)$$

Analogously for $F_{3,m}$. Further, G_{nm} is given by Eq. (4) and

$$G_n = \frac{2 k_n h}{\sinh(2 k_n h)} \quad \Delta G_{nm} = \frac{2 \Delta k_{nm} h}{\sinh(2 \Delta k_{nm} h)} \quad (20e)$$

The summation in Eq. (20c) is less troublesome than would appear at first glance because $\sin(k_j h)$ converges rapidly towards zero with increasing j .

REPRODUCTION OF NATURAL LONG WAVES

The 2nd order paddle control signal, $x_{nm}^{(2)}(t)$, given by Eq. (12) for the shallow water case and by Eq. (20) for the general case, is valid for a regular short wave group characterized by the pair of indices nm . For the reproduction of natural long waves (without parasitic, paddle displacement and progressive disturbance waves) it is necessary to carry out a summation over all pairs nm in analogy to Eq. (2) for the natural set-down, i.e.

$$x^{(2)}(t) = \sum_{n-m=1}^{\infty} \sum_{m=m^*}^{\infty} x_{nm}^{(2)}(t) \quad (21)$$

This signal has to be superposed upon the 1st order control signal $x^{(1)}$ that reproduces the natural short wave train.

EXAMPLES OF APPLICATION

Fig. 7 shows a wave record from Angra, Brazil. By means of pressure cells also the set-down was recorded. Eq. (3) was applied for the computation of the long waves (set-down). It is seen that calculated and measured long waves agree reasonably well. The paddle control signal for the correct reproduction of short and long waves was also calculated, applying Eqs. (21) and (20). The resulting signal is seen in Fig. 8. It is apparent that the correct reproduction of the long waves requires a much larger total stroke of the paddle than is the case for the short waves proper.

Another example of measured and calculated set-down is given in Fig. 9. These waves were recorded at Bintulu, Malaysia.

SHOALING PROPERTIES OF LONG WAVES

Alternatively to the direct compensation of the parasitic waves by a 2nd order control of the wave paddle, the model errors can be reduced by deriving advantage from the shoaling properties of the various long waves. The shoaling of the set-down can be calculated from Eq. (4). For simplicity, however, only the shallow water case shall be considered.

The shoaling of a parasitic wave ξ_p when it propagates from a larger depth h_1 to a smaller depth h_2 can be found by expressing that the energy flux is constant, i.e.

$$\frac{1}{2} \rho g \xi_{p,1}^2 c_1 = \frac{1}{2} \rho g \xi_{p,2}^2 c_2 \quad (22)$$

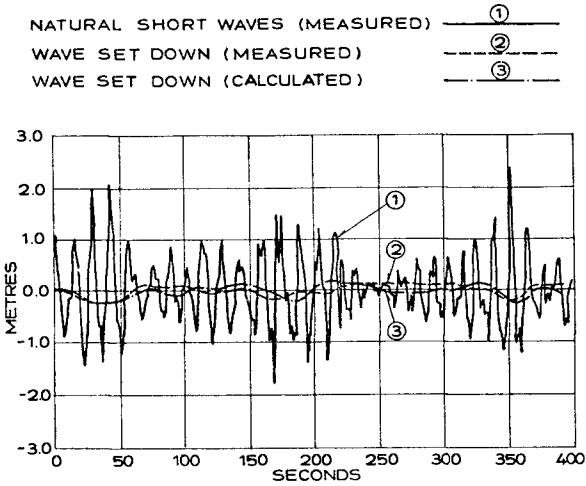


Fig. 7 Wave record from Angra, Brazil.

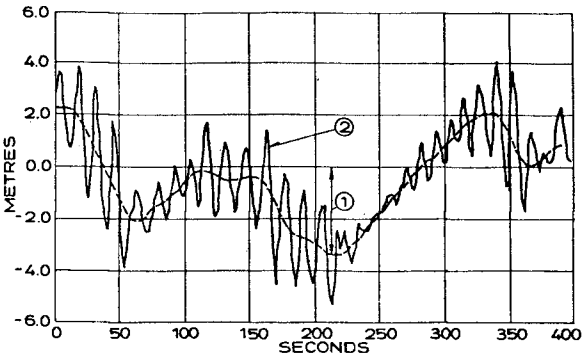
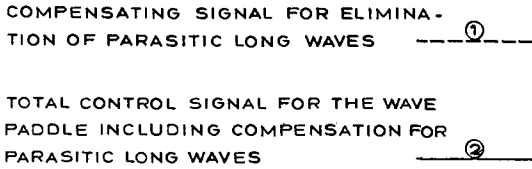


Fig. 8 Paddle control signal (to 2nd order).

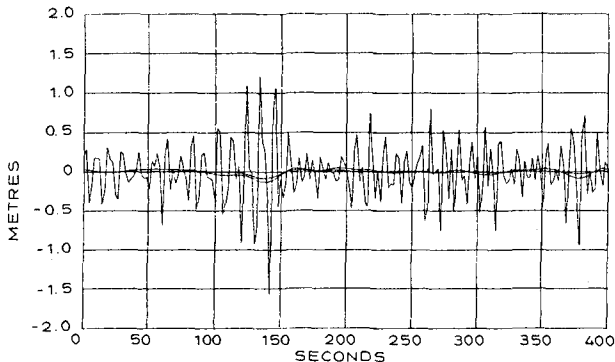


Fig. 9 Wave record from Bintulu, Malaysia.

With the phase velocity $c = \sqrt{gh}$ it appears that

$$\xi_{p,2}/\xi_{p,1} = (h_1/h_2)^{1/4} \quad (23)$$

The corresponding shoaling of the wave set-down can be found by applying an equation similar to Eq. (22) in combination with Fig. 4 and is

$$\xi_2/\xi_1 = (h_1/h_2)^{5/2} \quad (24)$$

Thus, the ratio between the wave set-down and the parasitic wave is

$$\xi_2/\xi_{p,2} = (h_1/h_2)^{9/4} \xi_1/\xi_{p,1} \quad (25)$$

This implies that the relative effect of parasitic waves can be reduced by generating the waves in somewhat deeper water, letting them propagate into the shallower model area (Fig. 10).

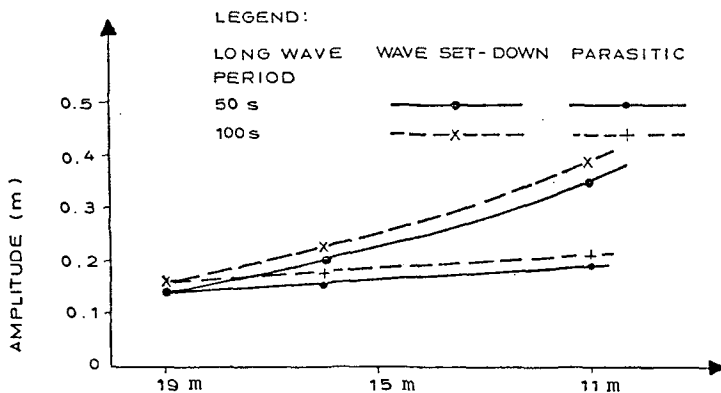


Fig. 10 Shoaling of long waves propagating from 19 m to 11 m depth for short period waves with $H_s = 2.4$ m and peak period $T_p = 13$ s.

In this connection, however, it should be mentioned that the method is not perfect. Thus, although the parasitic waves in Fig. 10 are small, they will build up gradually due to reflections from the boundaries of the model basin, because it is virtually impossible to absorb parasitic long waves. Still the method of shoaling is better than doing nothing.

ABSORPTION OF LONG WAVES

It is generally known that long waves constitute a serious problem in physical model tests because they are reflected from the boundaries, thus increasing the long wave disturbances in the basin.

In tests where basically the long waves are generated by the wave groups and appear as wave set-down, it is possible to avoid these boundary effects because the wave set-down disappears during the breaking of the short period waves (Fig. 11). This breaking, however, has to be gentle and take place over a certain distance, i.e. as spilling breakers. If, instead, the waves break abruptly in front of a steep slope, the wave set-down will be reflected as free long waves, which propagate back into the basin as parasitic waves. Therefore the criterion for absorption of wave set-down is simply that the short wave shall be absorbed as spilling breakers.

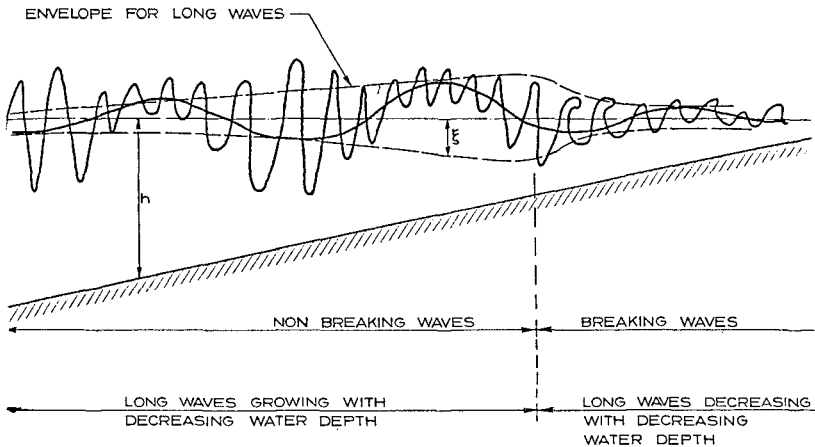


Fig. 11 Wave set-down in breaking waves.

CONCLUSIONS

Long wave phenomena in physical model tests can be correctly reproduced only if the following requirements are met:

- (a) The parasitic long waves generated by the reproduction of natural waves must be eliminated by application of the 2nd order control signal defined by Eq. (21) in connection with Eq. (20) or, in the shallow water case, Eq. (12).
- (b) Along the boundaries of the model basin waves shall be absorbed by spilling breakers.

As an alternative to the direct compensation of the parasitic waves, the model errors can, to a certain extent, be reduced by deriving advantage from the shoaling properties of the wave set-down and the parasitic waves. This requires:

- (c) The wave generator be placed in a depth as large as possible compared with the general depth of the model area.

REFERENCES

- Biéssel, F. (1951) Étude théorique d'un type d'appareil à houle. *La Houille Blanche*, 6^e Ann., N° 2, pp. 152-165.
- Buhr Hansen, J., Schiøltén, P. and Svendsen, I.A. (1975) Laboratory generation of waves of constant form. *Inst. Hydrodyn. and Hydraulic Engrg.*, Tech. Univ. Denmark, Series Paper 9, 56 pp.
- Longuet-Higgins, M.S. and Stewart, R.W. (1960) Changes in the form of short gravity waves on long waves and tidal currents. *Jour. Fluid Mech.*, Vol. 8, pp. 565-583.
- Longuet-Higgins, M.S. and Stewart, R.W. (1964) Radiation stresses in water waves; a physical discussion, with applications. *Deep-Sea Research*, Vol. 11, pp. 529-562.
- Lundgren, H. (1963) Wave thrust and wave energy level. *Proc. 10th Congr. Int. Assoc. Hydraulic Research*, London, Vol. 1, Paper 1.20, pp. 147-151.
- Lundgren, H. and Sand, S.E. (1979) Natural wave trains: Description and reproduction. *Proc. 16th Coastal Engrg. Conf.*, Hamburg, ASCE, Vol. I, pp. 312-319.
- Madsen, O.S. (1971) On the generation of long waves. *Jour. Geophysical Research*, Vol. 76, No. 32, pp. 8672-8683.
- Ottesen Hansen, N.-E. (1978) Long period waves in natural wave trains. *Inst. Hydrodyn. and Hydraulic Engrg.*, Tech. Univ. Denmark, Prog. Rep. 46, pp. 13-24.

AN ELECTROMAGNETIC ANALOGY FOR LONG WATER WAVES

by G.W.Jackson¹ and D.L.Wilkinson²1. Introduction

Seiching must be considered when designing mooring, berthing or navigational facilities in semi enclosed basins and harbours. The considerable oscillatory currents which may be generated along nodal lines of a seiche can result in serious surging of a vessel moored in such areas. Hydraulic modelling of the long gravity waves which form the seiche poses particular problems for the hydraulic modeller. In the prototype situation, a balance is achieved between the long wave energy entering a basin, the energy dissipation within the basin, and the wave energy which is radiated back into the ocean. The presence of the wave generator in the model may result in much of the radiated energy being reflected back into the basin, thereby distorting the seiche observed in the model.

The relatively low Reynolds numbers present in the model leads to exaggerated frictional damping of the waves and possible suppression of certain resonant modes. Scaling of long wave amplitudes in resonance situations cannot be determined from simple Froude laws but must be based on equivalent dissipation rates in the model and the prototype (Ippen, 1966).

Alternative methods of physically reproducing long wave behaviour have been studied, such as acoustic modelling (Nakamura, 1977). However, these models also have their limitations and are largely confined to constant depth situations.

It is suggested that electromagnetic radiation in the microwave range may be used to model long gravity waves and that this method has many advantages over the various techniques which have previously been used. It can be rigorously shown that the laws which govern the propagation, reflection and dissipation of electromagnetic radiation (Maxwell's equations) are identical to the linearised equations describing the motion of long gravity waves, (Jackson and McKee, 1980). The linear wave equation gives an accurate description of long wave oscillation in basins as the wave length is of the same order as the basin dimensions and non-linear effects do not have time to develop.

1. Research Student, Water Res.Lab., Univ. N.S.W., Australia
2. Senior Lecturer, Water Res. Lab., Univ. N.S.W., Australia

The microwave model consists of a flat box or cavity whose plan outline is geometrically similar to the boundaries of the harbour basin under investigation. The entrance to the basin is connected to a source of micro wave energy, a klystron, via a length of wave guide. As the klystron generates microwaves which propagate in all directions, the vertical dimension of the wave guide and the microwave cavity is made less than half a wave length of the microwave. This eliminates the vertical component of the microwave radiation. Microwaves in the frequency range from 1 to 10 G.Hertz are most suitable for these models and the corresponding wave lengths are 30 to 3 cm. Thus the model size is typically 10 to 20 cm in plan by 1 cm deep.

The properties of the wave field are determined by measuring the voltage induced on small antennæ probes which are inserted into measurement ports in the cavity wall.

The unwanted secondary interactions between the seiche and the wave generator, which poses a major problem in hydraulic models, can be eliminated in the microwave model by installing an isolator between the energy source and the microwave cavity. The isolator will pass the incident wave but totally dissipate the reflected wave travelling in the opposite direction. Microwave models are not restricted to constant depth situations as are acoustic models. The parameters equivalent to water depth in the microwave model are the electric and magnetic permeabilities of the cavity interior. The former can be readily varied by using materials with different dielectric constants (air, perspex, teflon etc.) to represent different contour intervals in the model.

Microwaves are potentially a relatively inexpensive, convenient and accurate means of modelling long wave motions in semi enclosed basins and harbours. In this paper the performance of microwave analogue is examined for some simple geometries whose prototype behaviour is well known.

Formulation

It is well known that many similarities of behaviour exist between water waves and electromagnetic radiation. Penny and Price (1953) adopted the equations describing the diffraction of light to describe the diffraction of water waves around breakwaters. Both types of waves are known to obey similar laws of reflection and refraction.

At first sight Maxwell's equations, which describe the propagation and characteristics of electromagnetic radiation, bear little resemblance to the equations describing the motion of long gravity waves (compare columns (i) and (ii) respectively in Table 1). However, if a vector potential \tilde{W} is defined as

$$\tilde{W} = - \hat{i}hv + \hat{j}hu$$

where \hat{i} and \hat{j} are the horizontal unit vectors in the x and y directions

u and v are the x and y velocity components

and h is the local depth

The conventional linearised long wave equations transform to a set which are identical to Maxwell's equations. The transformation is somewhat involved and is described in detail by Jackson and McKee (1980).

For a plane wave the vector potential \tilde{W} has a magnitude which is equal to the instantaneous flow per unit wave front but has a direction which is orthogonal to the direction of wave propagation (i.e. along the crest).

Table 1 gives equivalent expressions for electromagnetic radiation and long gravity waves.

Table 1: Field Equations

(i) Maxwell's Equations for Electromagnetic Waves	(ii) Long Water Waves Conventional Form	(iii) (constant depth) In terms of the Vector Function
Paraday's Law $\nabla \times \tilde{\mathbf{E}} = -\frac{\partial \tilde{\mathbf{B}}}{\partial t}$	Continuity Equation $\frac{1}{h} \frac{\partial \eta}{\partial t} + \frac{\partial u}{\partial x} + \frac{\partial v}{\partial y} = 0$	
$\nabla \times \tilde{\mathbf{B}} = \epsilon \mu_0 \frac{\partial \mathbf{E}}{\partial t}$	Linearised Bernoulli Equation $\frac{\partial u}{\partial t} + g \frac{\partial \eta}{\partial x} = 0$ $\frac{\partial v}{\partial t} + g \frac{\partial \eta}{\partial y} = 0$	
$\nabla \cdot \tilde{\mathbf{E}} = 0$	Irrotational Flow $\frac{\partial v}{\partial x} - \frac{\partial u}{\partial y} = 0$	
$\nabla \cdot \tilde{\mathbf{B}} = 0$	Horizontal Wave Field $\frac{\partial \eta}{\partial z} = 0$	
where $\tilde{\mathbf{E}}$ = electric field vector $\tilde{\mathbf{B}}$ = magnetic flux density vector ϵ = dielectric constant μ_0 = permeability (constant)	where η = local elev- ation of water surface above the mean level h = mean water depth u and v = horizontal components of water part- icle velocity g = gravitational acceleration see Proudman (1953) page 310	
		where $\tilde{\mathbf{W}} = -\hat{i}v + \hat{j}u$ $\tilde{\xi} = (0, 0, \eta)$
		$\nabla \times \tilde{\mathbf{W}} = -\frac{\partial \tilde{\xi}}{\partial t}$ (1)
		$\nabla \times \tilde{\xi} = \frac{1}{gh} \frac{\partial \tilde{\mathbf{W}}}{\partial t}$ (2)
		$\nabla \cdot \tilde{\mathbf{W}} = 0$ (3)
		$\nabla \cdot \tilde{\xi} = 0$ (4)

Boundary Conditions

The tangential component of \vec{E} is continuous	:	The tangential component of \vec{W} is continuous
The normal component of $\epsilon \vec{E}$ is continuous	:	The normal component of $\frac{\vec{W}}{h}$ is continuous
The tangential and normal components of \vec{B} are continuous	:	The tangential and normal components of $\vec{\xi}$ are continuous

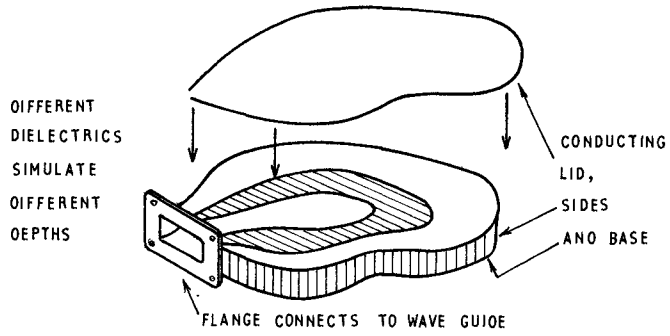
The equivalent parameters in the two systems are

$$\begin{aligned} \vec{E} & \text{ and } \vec{W} \\ \vec{B} & \text{ and } \vec{\xi} \\ \epsilon & \text{ and } \frac{1}{h} \\ \mu_0 & \text{ and } \frac{1}{g} \end{aligned}$$

Furthermore frictional effects can be simulated by having the interior of the microwave cavity partially conducting. It can be shown that this has an effect equivalent to that of introducing a linearised friction term into Bernoulli's equation (Jackson and McKee, 1980)

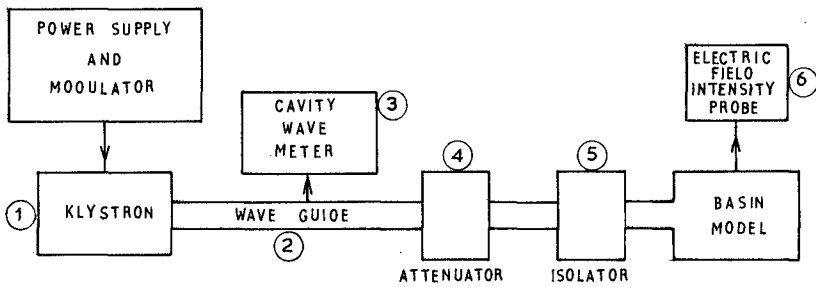
The Microwave Modelling Technique

Although in principle any frequency electromagnetic radiation could be used to model long gravity waves, radiation in the microwave range is of a convenient wave length for model construction. Since vector potential \vec{W} vanishes normal to a reflecting boundary its electromagnetic equivalent the electric field vector \vec{E} must be made to do the same. This is achieved if the boundary is electrically conducting so that the boundaries of the microwave cavity are constructed of highly conductive material such as copper sheet. Various materials such as air, glass and various plastics have dielectric constants which vary over a range of five or more and by using these materials between the various contour intervals, varied bottom topographies can be simulated by a series of step changes in depth as shown in Figure 1.



EXPLODED VIEW OF MICROWAVE CAVITY

FIGURE 1.



SCHEMATIC DIAGRAM OF THE MICROWAVE SET-UP

FIGURE 2.

Figure 2 shows a schematic diagram of typical microwave setup. It might be noted that similar equipment is readily available in most electrical engineering departments of tertiary institutions and the only irregular item would be the cavity model itself. The various items of equipment are briefly described.

1. The Microwave Source generates microwaves with a wavelength of 2.42 to 3.66 cm. Because of the high frequency of these waves (typically 10 GHz) it is impossible to detect them directly, hence they are modulated by a 1 KHz square wave.

2. The wave guide is simply a hollow metal tube of rectangular cross section which conveys the microwaves from the source to the model.

3. The cavity wave meter is a device for accurately determining the wave length of the microwaves using an adjustable resonator cavity. It is a passive device and has negligible effect on the microwave in the wave guide.

4. The attenuator reduces the microwave amplitude to any desired level.

5. The isolator permits microwaves to pass in one direction but dissipates the energy of microwaves travelling in the reverse direction. Therefore microwaves radiating back out the cavity are totally attenuated and do not affect readings within the harbour cavity. The major problem encountered with hydraulic models is thereby eliminated.

6. A probe, consisting of a fine needle approximately 0.3mm diameter and 3mm long, is inserted into the model. A voltage is induced onto the probe which is proportional to the intensity of the electric field at that location. This is equivalent to the instantaneous volume flux of the waves.

The microwave system used for the experiments described in this paper operated in the X band and generated microwaves with a frequency of 9 to 11 G.Hertz and a wave length of approximately 3 cm. This is too small for modelling complex basins but was adequate for the relatively simple geometries examined in the experiments described here. Systems are available for generating microwaves with wave lengths of up to 1m. However, a wave length of 30cm would be adequate for most model studies.

Two further points must be considered when designing a microwave model.

1. The microwave source is an essential point source of radiation; the waves do not propagate down the waveguide as plane waves but rather "bounce" from wall to wall. This has the effect of limiting the wave length that can be used with each size wave guide and the maximum wave length which will propagate down an X band wave guide which is 4.57 cm. (Lance 1964, p.87).

2. It is far simpler to measure the electric field intensity \vec{E} than the magnetic flux density \vec{B} . The hydraulic equivalents are the vector potential \vec{W} and the water surface elevation vector $\vec{\xi}$. However η can easily be calculated once \vec{W} and the wave period are determined.

Experiments

The interactions of long waves with two simple geometries were examined using the microwave analogy and compared with well known theoretical solutions for the same geometries.

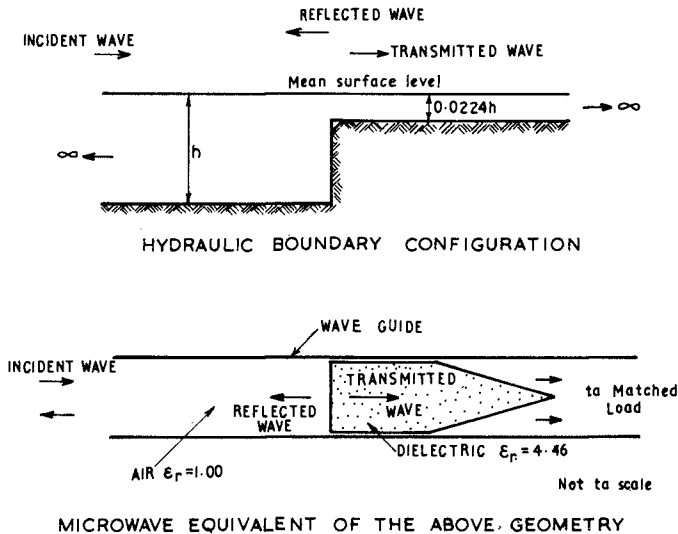


FIGURE 3. - EXPERIMENT 1.

Experiment 1

The reflection and transmission characteristics of a long wave normally incident to a step change in water depth were studied. The physical geometry and its microwave equivalent are shown in Figure 3. The water is assumed to be of infinite extent on either side of the step so that reflected waves are only generated at the step. The depth on the shallow side of the step was taken as 0.224 of the depth on the deeper side. Since this is basically a one dimensional problem it was modelled in a length of wave guide. The shallower region was simulated by inserting an acrylic plastic with a relative permittivity of $(0.224)^{-1} = 4.46$ (at 9.0 G.Hertz) into the wave guide, while air was the dielectric on the deeper side of the step. In order to avoid reflections from the end of the acrylic (which must be of finite length) it was tapered to a knife edge over a distance of several wave lengths.

The reflection coefficient for the reflected wave was found to be 0.357 compared with theoretical value of 0.365 (Lamb, 1932) while the transmission coefficient was found to be 1.34 compared with the theoretical value of 1.35. Wave heights determined from the microwave experiment are in close agreement with the theoretical values for long water waves.

Experiment 2

This experiment was similar to the previous experiment except that the shallow region was truncated at a vertical reflective wall as shown in Figure 4. In this case a resonant condition is possible on the shelf if its length is an odd multiple of the quarter wave length of waves travelling in the shallower depth.

The microwave setup is similar to that shown previously except that the shelf region, which is again simulated by the acrylic dielectric is terminated by a conducting end which is normal to the wave guide. A probe was inserted adjacent to the step on the shallow side, and wave heights at the reflecting end wall were determined from measurements of the field intensity (equivalent to the volume flow) at the step. The wave height at the end wall (H_{max}) expressed as a fraction of the incident wave height (H_0) is shown in Figure 5 for a range of wave lengths (L) normalised with respect to the length of the shelf (X). Resonance occurs when $\frac{X}{L} = \frac{1}{4}$ and again agreement between the theoretical wave heights and those deduced from the microwave experiment are in close agreement. Near resonance dissipative effects become significant both in the prototype and the model and the data points depart from the non-dissipative solution which is graphed in Figure 5.

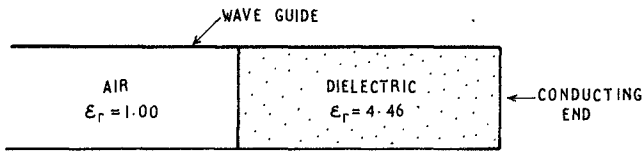
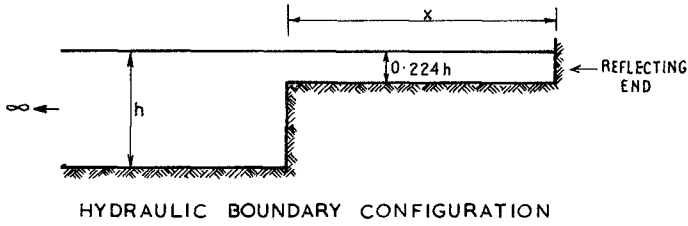
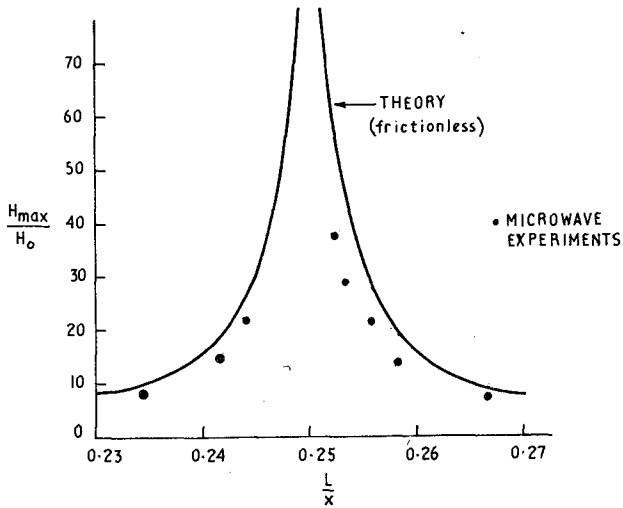


FIGURE 4. - EXPERIMENT 2.



WAVE HEIGHT AS A FUNCTION OF WAVE LENGTH FOR THE GEOMETRY SHOWN IN FIGURE 4

FIGURE 5.

Conclusions

Microwave cavities promise to be a relatively simple and effective means of studying long water waves in semi enclosed basins. Many of the inaccuracies invariably present in conventional hydraulic models can be eliminated in a microwave analogue. The vector potential (the equivalent of the instantaneous wave induced flow) is the most readily measured parameter in a microwave study and in many cases it is this parameter which is of most interest in the prototype. The analogy has been verified for some simple one dimensional geometries, whose behaviour is well known, and the work is being extended to look at more realistic geometries.

If a partially conducting dielectric is used in the model, some microwave energy is dissipated and the effect is exactly equivalent to that of introducing a linear friction term into the equation of motion for the water waves. It should therefore be possible to incorporate frictional effects into the microwave model.

Acknowledgement

The authors would like to thank John Baildon of North Sydney Technical College for his technical assistance with this project.

References

- Jackson, G.W. and McKee, W.D. (1980). Aust. J. Mathematics Series B. (in press).
- Lamb, H., (1932). Hydrodynamics. Camb.Univ.Press. U.K.
- Lance, A.L. (1964). Introduction to Microwave Theory and Measurement. McGraw-Hill.
- Nakamura, S. 1977. On acoustic analogy for oscillations in harbours and bays. La mer, 15, No.3 pp.107-115.
- Penny, W.G. and Price, A.T. (1952). The diffraction theory of sea waves by breakwaters, and the shelter afforded by breakwaters. Phil.Trans. Roy.Soc. (London) ser.A, 244 pp.236-53.
- Proudman, J. (1953). Dynamical Oceanography, London
- Ippen, A.T. (1966). Estuary and Coastline Hydrodynamics. McGraw-Hill.

CHAPTER 50

INTERACTIONS OF WAVES WITH SUBMARINE TRENCHES

by Jiin-Jen Lee,¹ Robert M. Ayer,² Wen-Li Chiang³

ABSTRACT

An analysis is presented for the propagation of water waves past a submarine trench of irregular shape. Two dimensional, linearized potential flow is assumed. The fluid domain is divided into two regions along the mouth of the trench. Solutions in each region are expressed in terms of the unknown normal derivative of the potential function along this common boundary with the final solution obtained by matching. Reflection and transmission coefficients are found for various submarine geometries. The accuracy of the technique employed is demonstrated by comparing with previously published results for a rectangular trench. In addition, results from limited laboratory experiments were included for comparison. The result shows that for a particular flow configuration, there exists an infinite number of discrete wave frequencies at which waves are completely transmitted.

INTRODUCTION

A class of problems involving the propagation of water waves in a fluid of variable depth is one in which the depth is constant except for variations over a finite interval. Interest in these problems is largely due to the phenomena associated with the passage of waves over submarine trenches in the ocean and wave propagation across navigational channels, where changes in water depth are commonly the case. A common method employed in the solution of problems involving changes in water depth is that of matching the solution along a geometrical boundary that separates the regions of different depths. Such an approach is found in the work of Bartholomeusz (1958) and Miles (1967). It has also been found by Newman (1965) and Black, et. al. (1971) that for wave propagation over submarine obstacles there exists an infinite set of wavelengths such that the incident wave is totally transmitted.

Lassiter (1972) solved for the transmission and reflection coefficients in the case of monochromatic plane progressive surface waves over a rectangular submarine trench where the water depths before and after the trench are constant but not necessarily equal. Lassiter formulated the problem in terms of complementary variational integrals and solved for the velocity potential by matching the solution along vertical lines before and after the trench.

In this present study, the problem considered is two-dimensional motion of linear periodic water waves over an arbitrarily shaped sub-

¹Assoc. Prof. of Civil Engrng., Univ. of Southern Calif., Los Angeles, Calif., 90007 USA.

^{2,3}Graduate Research Asst., Dept. of Civil Engrng., Univ. of Southern Calif., Los Angeles, Calif., 90007 USA.

marine trench where the water depths before and after the trench are equal and constant. By drawing a horizontal line, the authors have separated the domain into two subregions, namely an infinite rectangular region of constant depth and a finite region of irregular shape representing the trench itself.

An analytic solution for each region is then found explicitly in terms of an unknown velocity distribution along the trench -- constant depth boundary. By superimposing a linear periodic incident wave of specified frequency in the infinite constant depth region, the final solution is obtained by matching the solutions in each subregion along the common boundary.

THEORETICAL CONSIDERATIONS

Let (x,y) constitute a Cartesian coordinate system with $y = 0$ coinciding with the impermeable boundary of the constant depth region as shown in the definition sketch in Fig. 1. Assuming a steady-state solution for the velocity potential in the form of

$$\Phi(x,y;t) = \phi(x,y)e^{-i\sigma t} \quad (1)$$

the potential function $\phi(x,y)$ must satisfy Laplace's equation throughout the fluid domain and the following boundary conditions:

$$\begin{aligned} \frac{\partial \phi}{\partial y} &= \frac{\sigma^2}{g} \phi & \text{on } y = h, \quad -\infty < x < \infty \\ \frac{\partial \phi}{\partial y} &= 0 & \text{on } y = 0, \quad x < 0 \\ \frac{\partial \phi}{\partial y} &= 0 & \text{on } y = 0, \quad x > \ell \\ \frac{\partial \phi}{\partial n} &= 0 & \text{on solid boundary in the trench} \\ \frac{\partial \phi}{\partial y} &= q(x) & \text{on } y = 0, \quad 0 < x < \ell \end{aligned} \quad (2)$$

(the function $q(x)$ is to be determined by matching)

In Eqs. (1) and (2), σ represents the circular frequency, $2\pi/\text{wave period}$; i is the complex number $\sqrt{-1}$.

In order to solve for $\phi(x,y)$ in an efficient manner, the fluid domain is divided into two regions, Region I and Region II, by the common boundary Γ shown in Fig. 1.

The strategy used herein is to solve for $\phi(x,y)$ in each respective region in terms of the unknown $\partial\phi/\partial y$ along the common boundary Γ . Thus, by matching the solutions in each region at Γ , one is able to obtain the final solution.

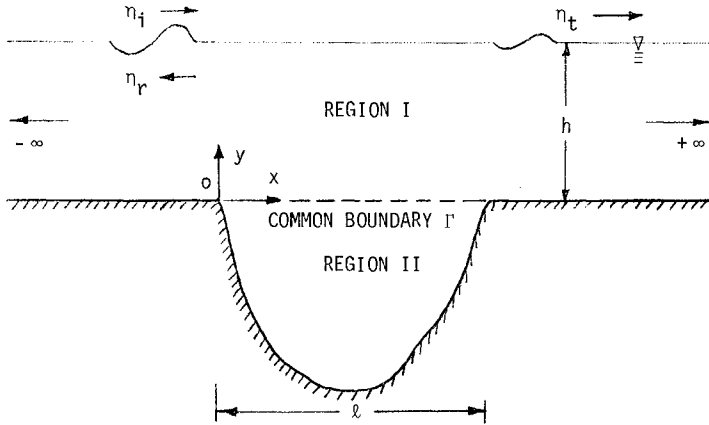


FIGURE 1. Definition sketch of the trench with regions of consideration.

Region I Solution

The solution for the velocity potential in Region I assuming that the unknown normal derivative of the velocity potential $\partial\phi_I/\partial y$ is equal to $q(x)$ (along $y = 0, 0 < x < l$) has been obtained by Lee and Ayer (1980). This solution can be summarized as follows:

- (1) If $x > x_j$ for all j ,

$$\phi_I(x,y) = \sum_{j=1}^N Q_j \left\{ \frac{\left[e^{ik_r(x-x_j)} - e^{ik_r(x-x_{j-1})} \right]}{k_r^2} \cdot S_r(k_r,y) + \sum_{n=1}^{\infty} \frac{\left[e^{-k_n(x-x_{j-1})} - e^{-k_n(x-x_j)} \right]}{k_n^2} \cdot S_n(k_n,y) \right\} \quad (3)$$

- (2) If $x < x_j$ for all j ,

$$\phi_I(x,y) = \sum_{j=1}^N Q_j \left\{ \frac{\left[e^{-ik_r(x-x_{j-1})} - e^{-ik_r(x-x_j)} \right]}{k_r^2} \cdot S_r(k_r,y) + \sum_{n=1}^{\infty} \frac{\left[e^{k_n(x-x_j)} - e^{k_n(x-x_{j-1})} \right]}{k_n^2} \cdot S_n(k_n,y) \right\} \quad (4)$$

(3) If $x > x_{j-1}$ and $x < x_j$ for some j ,

$$\begin{aligned} \phi_I(x,y) = & \sum_{j=1}^{j-1} Q_j \left\{ \left[\frac{e^{ik_r(x-x_j)} - e^{ik_r(x-x_{j-1})}}{k_r} \right] \cdot S_r(k_r,y) \right. \\ & + \left. \sum_{n=1}^{\infty} \left[\frac{e^{-k_n(x-x_{j-1})} - e^{-k_n(x-x_j)}}{k_n} \right] \cdot S_n(k_n,y) \right\} \\ & + Q_j \left[\frac{1 + \frac{\sigma^2}{g}(y-h)}{\sigma^2/g} - \frac{[e^{ik_r(x-x_{j-1})} + e^{-ik_r(x-x_j)}]}{k_r} \right] \cdot S_r(k_r,y) \\ & + \sum_{n=1}^{\infty} \left[\frac{e^{-k_n(x-x_{j-1})} + e^{k_n(x-x_j)}}{k_n} \right] \cdot S_n(k_n,y) \left. \right] \\ & + \sum_{j+1}^N Q_j \left\{ \left[\frac{e^{-ik_r(x-x_{j-1})} - e^{-ik_r(x-x_j)}}{k_r} \right] \cdot S_r(k_r,y) \right. \\ & + \left. \sum_{n=1}^{\infty} \left[\frac{e^{k_n(x-x_j)} - e^{k_n(x-x_{j-1})}}{k_n} \right] \cdot S_n(k_n,y) \right\} \end{aligned} \quad (5)$$

In Eqs. (3) - (5) the functions S_r and S_n are defined by

$$S_r(k_r,y) = \frac{k_r [\cosh k_r(y-h)] + \sigma^2/g \sinh [k_r(y-h)]}{k_r h \operatorname{sech} k_r h + \sinh k_r h}$$

and

$$S_n(k_n,y) = \frac{k_n [\cos k_n(y-h)] + \sigma^2/g \sin [k_n(y-h)]}{k_n h \sec k_n h + \sin k_n h}$$

The value of k_r and the values of k_n are determined by

$$\frac{\sigma^2}{g} = k_r \tanh (k_r \cdot h)$$

$$\frac{\sigma^2}{g} = -k_n \tan (k_n \cdot h) \quad .$$

The value of Q_j is the average value of $q(x)$ in the j^{th} subinterval whose midpoint is defined as $(x_j,0)$ within the common boundary of the trench mouth.

Region II Solution

Again, the solution for the velocity potential in Region II has the steady-state form

$$\phi_{II}(x,y;t) = \phi_{II}(x,y) e^{-i\sigma t} \quad (6)$$

and the potential ϕ_{II} must satisfy Laplace's equation subject to the boundary condition of $\partial\phi_{II}/\partial n = 0$ along the solid boundary of the trench.

As the trench shape is considered arbitrary it can be conveniently solved by boundary integral method. The potential function along the boundary of the trench can be expressed as follows:

$$\phi_{II}(\vec{x}_j) = \frac{1}{\pi} \int \left[\ln\left(\frac{1}{r}\right) \frac{\partial\phi_{II}}{\partial n} - \phi_{II} \frac{\partial}{\partial n} \ln\left(\frac{1}{r}\right) \right] ds \quad (7)$$

The term $\partial\phi_{II}/\partial n$ in Eq. (7) is zero except along the mouth of the trench which is equal to $q(x)$ according to Eq. (2). This integral equation can be approximated by a matrix equation as used in Raichlen and Lee (1978).

Therefore, the value of ϕ_{II} along the trench mouth can be expressed in terms of the unknown vector, Q_j . This unknown vector Q_j can then be solved by matching the value of $\phi_{II}(x_j)$ and $\phi_I(x_j) + \phi_{in}(x_j)$ (where $\phi_{in}(x_j)$ is a specified potential function of an incident wave along the trench mouth with the coordinate of $(x_j, 0)$).

Once the value of Q_j is obtained, the velocity potential at any position in Region I can be computed by Eqs. (3) - (5) along with the superposition of the incident wave potential.

PRESENTATION AND DISCUSSION OF RESULTS

The effect of the trench on the propagation of waves can be demonstrated most easily by the transmission characteristics. In order to ensure that the present analysis for Region II using the boundary integral method can provide a reliable result, the method is applied to a rectangular trench, where in a separate study, the solution has been obtained in terms of an Eigenfunction expansion, therefore providing a basis for comparison. Figure 2 shows the transmission coefficient, K_t , as a function of the relative wave length. The ordinate is the ratio of the transmitted wave amplitude divided by the incident wave amplitude, while the abscissa is the ratio of the water depth, h , in Region I divided by the incident wave length, λ . The wave length λ is computed from the dispersion relationship, $\lambda = (gT^2/2\pi) \tanh(2\pi h/\lambda)$, where T is the incident wave period.

The present theoretical results (as can be seen from Figure 2) come within 3% of the results of Lee and Ayer (1980). The result of

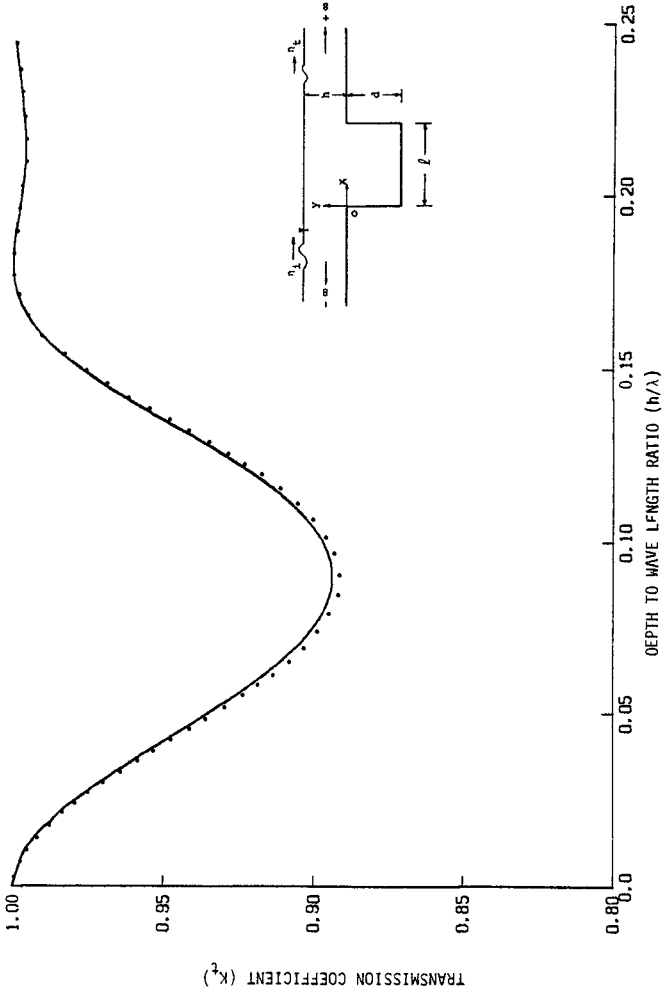


Figure 2 Transmission coefficient as a function of relative wave length ($h = 4''$, $d = 26\frac{1}{2}''$, $\lambda = 21 \frac{1}{8}''$). — theoretical results of Lee & Ayer (1980), present results.

Lee and Ayer (1980) was obtained by using an analytic solution in Region II. The fact that the present solution is so close to the more exact theory demonstrates that the approximate method used can provide a fairly accurate result. It is seen from Figure 2 that for $h/\lambda > 0.18$, the incident waves are almost fully transmitted. At $h/\lambda = 0.09$, the transmission coefficient is approximately 0.89. To understand the trench effect further, one can compute the value of l/λ at these critical points. At $h/\lambda = 0.18$, it corresponds to $l/\lambda = 0.95$ while at $h/\lambda = 0.09$, it corresponds to $l/\lambda = 0.475$. It appears that for a relatively short trench length, the maximum reduction of transmitted wave occurs as l/λ approaches 0.5. As the wave period is decreased to where l/λ approaches 1, the effect on wave transmission due to the trench is negligible.

As the trench length increases, the effect of the trench on the transmission characteristics of the incident waves becomes more interesting. This is shown in Figure 3. The trench length for this case is three times that shown in Figure 2 with other dimensions held constant. Two theoretical curves, one obtained by the present analysis and the other obtained from Lee and Ayer (1980) are shown for comparison. The experimental data obtained by Lee and Ayer (1980) in a laboratory wave tank of 12 inches wide, 48 feet long and 18 inches deep are also included for comparison. Again, it is seen that the two curves agree very well in every peak and trough (the results are within 3% of each other) for the range of h/λ presented. In the range of $0 < h/\lambda < 0.25$, there are six different wave periods at which waves are fully transmitted. The results indicate that the trench does exert a greater influence on wave transmission characteristics in that the transmission coefficient at $h/\lambda = 0.042$ is only about 0.70. It is also seen that the experimental data in general tend to confirm the theoretical prediction. However, due to experimental errors and the unavoidable wave reflections from both ends of the wave tank, the experimental data show considerable scattering as evident in the figure.

An example for wave transmission over an even longer rectangular trench is shown in Figure 4. The length of the rectangular trench is now four times that shown in Figure 2. Again, the present results using the boundary integral method agree well with the result of Lee and Ayer (1980) further confirming that the method designed for an irregular shaped trench can be used for a trench of rectangular shape. The number of wave periods at which waves are fully transmitted is now increased to nine for the same range of h/λ . For each of the troughs in the response curve, the effect of the trench is further dramatized. For example, at the first trough ($h/\lambda = 0.034$), the transmission coefficient is reduced to 0.68, while at the second trough ($h/\lambda = 0.081$), the transmission coefficient is about 0.84. These are clearly smaller values than those shown in Figure 3.

An example of the transmission of waves over an irregularly shaped trench is presented in Figure 5. The dimension of the trench shape is shown in the insert of the figure. The transmission coefficient is very close to one, showing that the trench does not effect the wave transmission drastically. However, it is clear that there are a number of peaks and troughs in the transmission curve (a similar feature as

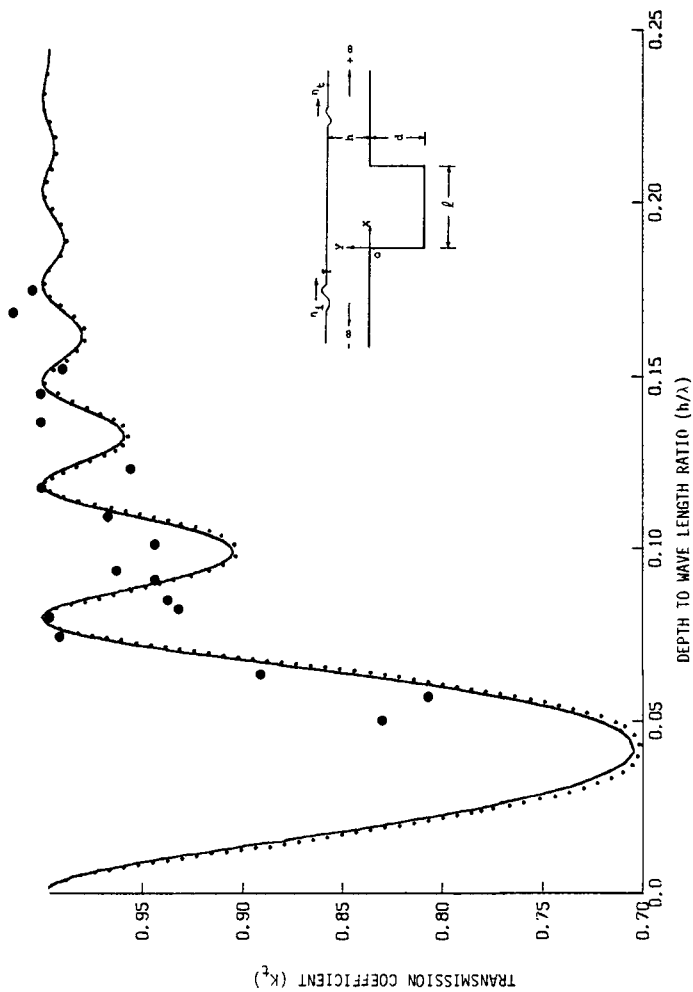


Figure 3 Transmission coefficient as a function of relative wave length ($h = 4''$, $d = 26\frac{1}{2}''$, $\lambda = 63\frac{5}{8}''$, — theoretical results of Lee & Ayer (1980), Experimental results of Lee and Ayer (1980), present results using boundary integral method).

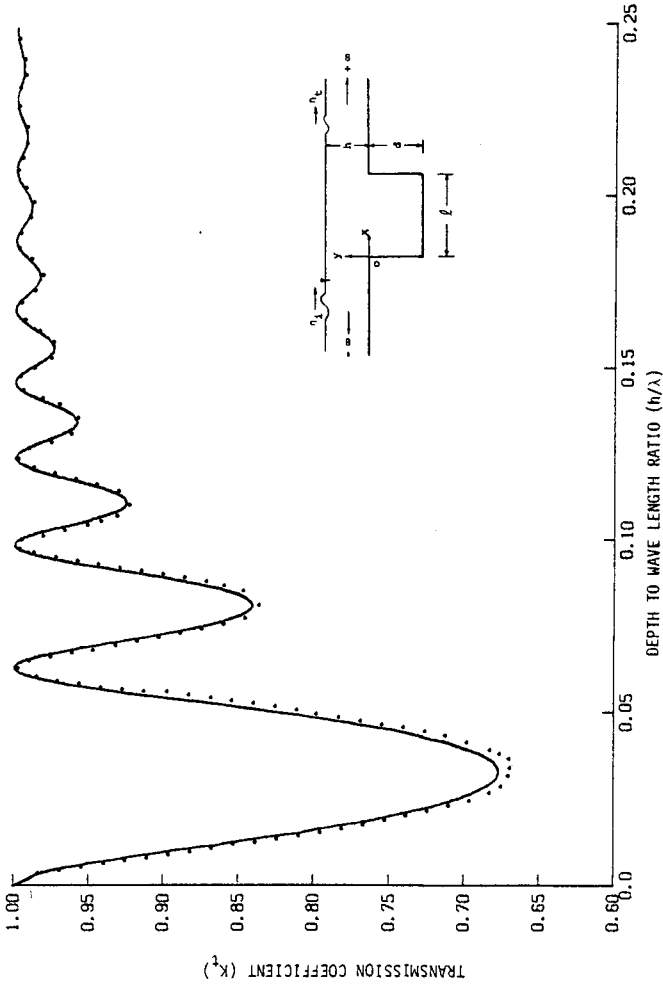


Figure 4 Transmission coefficient as a function of relative wave length ($h = 4''$, $d = 26\frac{1}{2}''$, $\lambda = 85''$, — theoretical results of Lee & Ayer (1980), present results using boundary integral method).

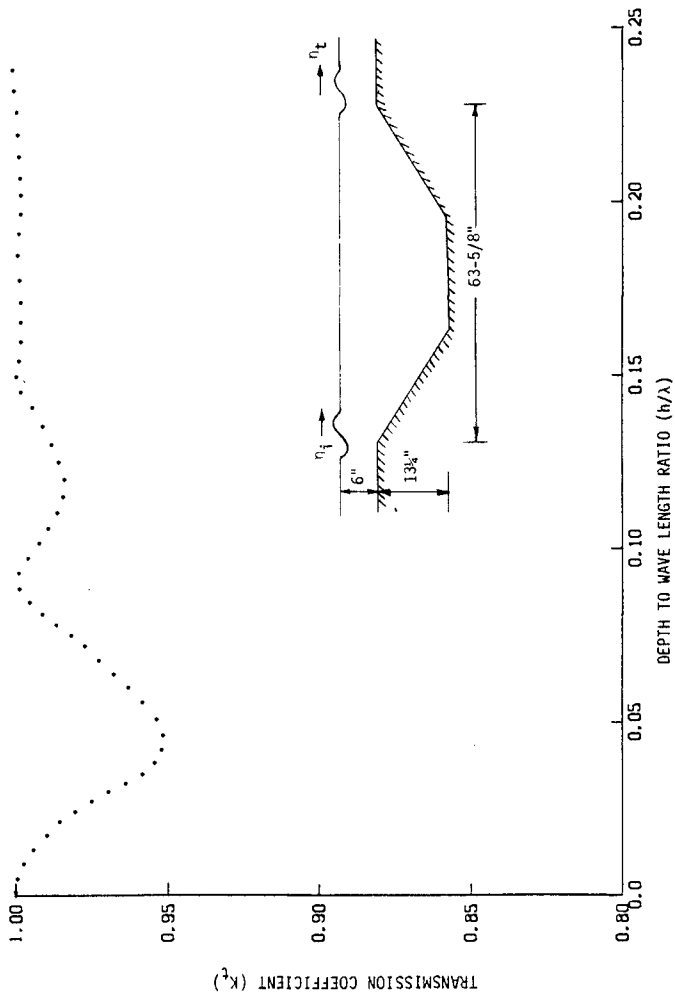


Figure 5 Transmission coefficient as a function of relative wave length

that shown in Figures 2 - 5).

CONCLUDING REMARKS

The methods outlined in this paper for analyzing the effect of an arbitrarily shaped trench on the propagation of periodic incident waves has been shown to be quite effective as illustrated by comparison with the solution techniques for a rectangular trench and with experiments. From the results on wave transmission and reflection, it is seen that there exists an infinite number of wave periods at which waves are fully transmitted, and that the effect of the trench on wave transmission is progressively smaller for higher wave frequencies (the larger values of h/λ).

ACKNOWLEDGEMENT

The work reported herein is supported by the National Science Foundation under Grant No. ENV 77-01599 and by N.O.A.A. Sea Grant under Grant No. 04-80M01-186.

LIST OF REFERENCES

1. Bartholomeusz, E.F., "The Reflection of Long Waves at a Step," Proc. Camb. Phil. Soc., Vol. 54, 1958, p. 106.
2. Black, J.L., Mei, C.C., and Bray, M.C.C., "Radiation and Scattering of Water Waves by Rigid Bodies," Journal of Fluid Mechanics, Vol. 46, 1971, p. 151.
3. Kreisel, H., "Surface Waves," Quarterly Applied Math., Vol. 7, 1949, p. 21.
4. Lassiter, J.B., "The Propagation of Water Waves over Sediment Pockets," Ph.D. Thesis, Mass. Inst. of Tech., July 1972.
5. Lee, J.J., and Ayer, R.M., "Wave Propagation over Rectangular Trench," submitted to Journal of Fluid Mechanics, 1980.
6. Miles, J.W., "Surface-Wave Scattering Matrix for a Shelf," Journal of Fluid Mechanics, Vol. 28, 1967, p. 755.
7. Newman, J.N., "Propagation of Water Waves Past Lone Two-Dimensional Obstacles," Journal of Fluid Mechanics, Vol. 23, 1965, p. 23.
8. Newman, J.N., "Propagation of Water Waves over an Infinite Step," Journal of Fluid Mechanics, Vol. 23, 1965, p. 399.
9. Raichlen, F., and Lee, J.J., "An Inclined-Plate Wave Generator," Proc., 16th Int'l. Coastal Engrng. Conf., Hamburg, Germany, August 1978, pp. 388-399.

TRANSIENT FINITE-DIFFERENCE TSUNAMI CALCULATIONS

Ove Skovgaard¹ and Ivar G. Jonsson²

ABSTRACT

The applicability of a time-stepping approximate finite difference method is tested for the response of a plane incoming tsunami of small amplitude meeting an idealized island (see Fig 1). The resulting amplitudes are compared with the exact solution, which comes out of solving the linear shallow water wave equation for the area in question. Since this wave equation excludes dissipation (bottom friction) and the Coriolis force, these terms are omitted in the Boussinesq equations, formulated as mass and momentum conservation, which are the bases of the finite difference scheme. Grid size is 1×1 km. The incoming wave is time-harmonic with a period of $T = 480$ s; the (test) solution to the wave equation is thus a truly steady-state solution. The finite difference scheme, however, has a so-called "cold start" and so it is transient in principle. During a time corresponding to three periods, in which disturbances from the open boundaries still have only a small effect on the wave field near the island, the time-series of signals in selected points can define a steady response, though. Considering the inevitable shortcomings of a provisional study like the present, satisfactory agreement with the exact solution is met over the shoal in Fig 1. We have thus a promising starting point for more elaborate studies, comprising new filtering algorithms for the boundaries, tests with real transient input signals, and including non-linearity, bottom friction, and the Coriolis force.

The numerical scheme used is the so-called System 21, developed at the Danish Hydraulic Institute and placed at our disposal for the present study.

1. INTRODUCTION

A seismic sea wave, a so-called tsunami (Japanese for "harbour wave"), consists of a series of waves that approaches the coast with periods usually ranging from 5 to 90 min (Murty, 1977, p 2). The length of these waves is of the order of hundreds of kilometres in the deep ocean, while here their amplitude is usually of the order of a metre. They are therefore difficult to detect from the air or from ships. Near land, however, the tsunami will build up in height due to the decrease in water depth.

¹ Associate Professor, Laboratory of Applied Mathematical Physics (LAMF), Bldg 303, Technical University of Denmark, DK-2800 Lyngby.

² Associate Professor, Institute of Hydrodynamics and Hydraulic Engineering (ISVA), Bldg 115, same address.

At the same time the amplitude can be further amplified because of lateral convergence and reflections. The wave length will be reduced in shallower water.

The final run-up of tsunamis is a highly non-linear phenomenon. In this preliminary report of our study, however, we shall investigate the modification of the tsunami wave over that area near the coast, where linear theory can be used, ie excluding the final run-up.

A tsunami can also be generated by non-seismic causes, such as landslides and nuclear explosions. Therefore Murty (1977, p 1) cites the more general definition by van Dorn: "Tsunami is the Japanese name for the gravity wave system formed in the sea following any large-scale, short-duration disturbance of the free surface." Most of the current knowledge about tsunamis is excellently reviewed in the above-mentioned book by T S Murty.

We will calculate the transformation of a small, time-harmonic, and plane incident wave caused by an idealized island of circular cylindrical form, situated on a paraboloidal shoal in an infinite ocean of constant depth, see Fig 1.

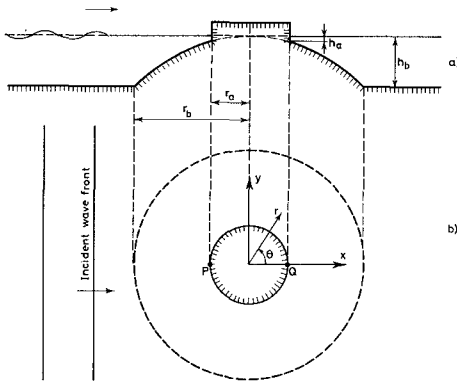


Fig 1. Sketch of the idealized island on a paraboloidal shoal;
a) vertical, b) horizontal.

The water depths h are

$$\begin{aligned} h &= \alpha r^2 & \text{for } r_a \leq r \leq r_b & \text{ and } 0^\circ \leq \theta < 360^\circ \\ h &= h_b (= \alpha r_b^2) & \text{for } r_b \leq r < \infty & \text{ and } 0^\circ \leq \theta < 360^\circ \end{aligned} \quad (1.1)$$

Shoreline radius is $r_a = 10$ km, outer radius of shoal is $r_b = 30$ km, and depth $h_b = 4,000$ m. Thus shoreline depth is $h_a = h_b (r_a/r_b)^2 = 4,000/9 \approx 444$ m. (Generally subscript a denotes a value at the shoreline, and subscript b denotes a value at the outer boundary of the shoal.) The factor of proportionality α in (1.1) becomes $\alpha = 4/9 \times 10^{-5} \text{ m}^{-1}$.

This type of island is seemingly accepted as being representative of a "Pacific island" (Homma, 1950). Experiments have been performed by Williams and Kartha (1969).

The present paper is a sequel to papers by Jonsson et al (1976) (hereafter referred to as paper I), where we restricted the presentation to the wave field at the shoreline, including some shallow water refraction calculations, and by Jonsson and Skovgaard (1979) (hereafter referred to as paper II), where we looked at the wave field over the shoal for wave periods up to 240 s, including a few intermediate depth refraction calculations for the shoreline.

The purpose of the present paper is twofold. Firstly to investigate the exact wave field (amplitudes and phase angles) outside the shoal, ie to study the "disturbance" out in the deep ocean due to the presence of the island. Secondly, we will use a finite difference (FD) method (FD in space and time) to see how accurate such an approximate solution is in a small region around the island and the shoal. For both cases the diffraction contours will be determined corresponding to small, time-harmonic and plane incident waves, and only for one wave period $T = 480$ s. This period is above the shallow water limit for the island, which for $h/L = 1/20$ gives $T \approx 410$ s. Notice that for larger islands $T = 480$ s corresponds to a greater period (fixed ratio between wave length L and radius).

Earlier FD approaches for tsunami wave problems are described by Camfield (1980), and finite-element (FE) methods for such problems are reviewed in Sklarz et al (1979).

Tsunami waves are basically transient, but we have performed this preliminary study with "unphysical" periodic waves in order to assess the feasibility of transient FD models for "small" regions with long open boundaries. Our ultimate goal is to test the FD model for a short transient Gaussian-like pulse, where we can also construct the "exact" test solution, by superposition of time-harmonic exact solutions.

2. ASSUMPTIONS AND DEFINITIONS

The incident surface gravity waves are assumed to be plane, time-harmonic, and of small amplitude. The Coriolis force is neglected, which is justified for the considered higher end of the tsunami frequency range. The island sides are assumed fully reflecting. Non-linear effects (including dissipation) will be neglected, although they can easily be included in the approximate solution, see Sect 4.

The diffraction of simple time-harmonic and very long surface gravity waves (in practice $h/L < 0.05$) over a gently sloping sea bed is governed by the linearized long-wave equation

$$\nabla \cdot (h \nabla \eta) + h k^2 \eta = 0 \quad (2.1)$$

where ∇ is the horizontal gradient operator ($\partial/\partial x$, $\partial/\partial y$) or ($\partial/\partial r$, $r^{-1}\partial/\partial\theta$), $k = 2\pi/L$ is the wave number, $L = cT$ is the wave length, c is the phase speed (2.6), $h = h(r, \theta)$ the water depth, and $\eta = \eta(r, \theta)$ is the (complex) surface wave amplitude. r and θ are defined in Fig 1.

Note that the instantaneous complex surface elevation is $\eta \exp(-i\omega t)$, where i is the imaginary unit, $\omega = 2\pi/T$ is the (constant) angular fre-

quency, and t is time. The instantaneous real surface elevation ζ is thus

$$\zeta = \text{Re} \{ \eta \exp(-i\omega t) \} \quad (2.2)$$

We define the real surface amplitude $A = A(r, \theta)$ and phase angle $\varphi = \varphi(r, \theta)$ (also real) by

$$\eta = A \exp(i\varphi) \quad (2.3)$$

ie we have from (2.2)

$$\zeta = A \cos(\varphi - \omega t) \quad (2.4)$$

Phase angle φ is still determined less an arbitrary constant. This is remedied by demanding that φ be zero in the far field at $\theta = \pm 90^\circ$ for $t = 0$. In other words, φ is the phase angle at that instant, when the undisturbed wave crest passes through the centre of the island.

The real amplitude of the incoming wave is called A_i . In the amplitude graphs we have depicted the relative amplitudes A/A_i .

The incident waves have the surface elevation

$$\zeta_i = A_i \cos(kx - \omega t) \quad (2.5)$$

For very long waves there is no dispersion and the phase and group speeds (c and c_g) are equal and given by

$$c = c_g = \sqrt{gh} \quad (2.6)$$

in which g is the gravity acceleration.

For calculations involving (2.1) we use the acronym SWT which stands for Shallow Water Theory.

Equation (2.1) is correct to first order in both wave amplitude and bed slope, see eg Jonsson and Brink-Kjær (1973).

The diffraction of mildly non-linear surface gravity waves (transient or periodic) over a gently sloping sea bed is governed by the Boussinesq equations, in which the vertical velocity is supposed to increase linearly from zero at the bed to a maximum at the surface, in two horizontal space variables and time. The Boussinesq equations are formulated as mass and momentum conservation laws (integrated over depth). In terms of volume discharge or depth-integrated velocities the governing equations read (see Abbott et al, 1978, p 177, (4) - (6)):

$$\frac{\partial \zeta}{\partial t} + \frac{\partial p}{\partial x} + \frac{\partial q}{\partial y} = 0 \quad (2.7)$$

$$\frac{\partial p}{\partial t} + \frac{\partial}{\partial x} \left(\frac{p^2}{h^*} \right) + \frac{\partial}{\partial y} \left(\frac{pq}{h^*} \right) + gh^* \frac{\partial \zeta}{\partial x} = \frac{1}{2} hh^* \left[\frac{\partial^3}{\partial x^2 \partial t} \left(\frac{hp}{h^*} \right) + \frac{\partial^3}{\partial x \partial y \partial t} \left(\frac{hq}{h^*} \right) \right] \quad (2.8)$$

$$- \frac{1}{6} h^2 h^* \left[\frac{\partial^3}{\partial x^2 \partial t} \left(\frac{p}{h^*} \right) + \frac{\partial^3}{\partial x \partial y \partial t} \left(\frac{q}{h^*} \right) \right]$$

$$\frac{\partial q}{\partial t} + \frac{\partial}{\partial y} \left(\frac{q^2}{h^*} \right) + \frac{\partial}{\partial x} \left(\frac{pq}{h^*} \right) + gh^* \frac{\partial \zeta}{\partial y} = \frac{1}{2} hh^* \left[\frac{\partial^3}{\partial y^2 \partial t} \left(\frac{hq}{h^*} \right) + \frac{\partial^3}{\partial x \partial y \partial t} \left(\frac{hp}{h^*} \right) \right] \quad (2.9)$$

$$- \frac{1}{6} h^2 h^* \left[\frac{\partial^3}{\partial y^2 \partial t} \left(\frac{q}{h^*} \right) + \frac{\partial^3}{\partial x \partial y \partial t} \left(\frac{p}{h^*} \right) \right]$$

where $h^* \equiv h + \zeta$, ie the instantaneous total depth, p is the x -component of the volume discharge, and q is the y -component of the volume discharge. x and y are defined in Fig 1. For the long, small amplitude waves considered in this preliminary study the third derivative terms (the right-hand sides) in (2.8) and (2.9) are almost negligible, as they represent the deviation of the pressure distribution from the hydrostatic pressure.

In (2.8) and (2.9) we have for the time being neglected the Coriolis force and dissipative effects (bottom friction).

3. THE EXACT SHALLOW WATER THEORY (SWT) SOLUTION

In order to calculate the total wave field in any point of the area we must solve the partial differential equation (2.1), the shallow water wave equation. The boundary conditions are full reflection at the island ($r = r_a$) and Sommerfeld's radiation condition at infinity (for the scattered part of the wave field). See paper I for details.

Because of the rotational symmetry of the bathymetry we can apply the method of separation of variables.

Over the shoal ($r_a \leq r \leq r_b$) the solution for the complex amplitude is

$$\eta = \sum_{n=0}^{\infty} R_n(r) \cos(n\theta) \quad 0 \leq \theta < 360^\circ \quad (3.1)$$

where the functions $R_n(r)$, ($n = 0, 1, 2, \dots$), are solutions to linear two-point boundary value problems. These ordinary differential equations were solved by Homma (1950), see paper I, pp 473-476, for details. Angle θ is defined in Fig 1.

Outside the shoal ($r \geq r_b$) the wave field is the sum of an incident and a scattered wave field, ie

$$\eta = \eta_i + \eta_{sc} \quad (3.2)$$

with η_i rewritten as

$$\eta_i = A_i \sum_{n=0}^{\infty} \epsilon_n i^n J_n(k_b r) \cos(n\theta) \quad (3.3)$$

and

$$\eta_{sc} = \sum_{n=0}^{\infty} C_n H_n^{(1)}(k_b r) \cos(n\theta) \quad (3.4)$$

In these equations A_i is the amplitude (real) of the incoming wave, ϵ_n is the Neumann factor (ie $\epsilon_n = 1$ for $n = 0$, and $\epsilon_n = 2$ for $n \neq 0$), i is the imaginary unit, J_n are Bessel functions of n th order and first kind, $k_b = 2\pi/L_b$, the wave number for $r \geq r_b$, C_n are integration constants, and $H_n^{(1)}$ are Hankel functions of the n th order and first kind.

At $r = r_b$ there is continuity in η and in its first derivative with respect to r . Using the former condition we find from (3.1) and (3.2) for the determination of C_n

$$C_n = \frac{1}{H_n(\tau)} \left[(R_n)_{r=r_b} - A_i \epsilon_n i^n J_n(\tau) \right] \quad n = 0, 1, 2, \dots \quad (3.5)$$

where we have dropped the superscript (1) on H , and further $\tau \equiv k_b r_b$. Functions $(R_n)_{r=r_b}$ are determined by Homma's (1950) solution (see (3.19) in paper I). Inserting the results in (3.5) yields

$$C_n = \frac{A_i \epsilon_n i^n}{H_n} \left[\frac{i \left[\rho^{\alpha_n} \frac{\alpha_n - 1}{\alpha_n + 1} \rho^{-\alpha_n} \right] \frac{2}{\pi} \rho^{\alpha_n}}{\rho^{\alpha_n} \left[(1 - \alpha_n) H_n + \tau H_n' \right] \frac{\alpha_n - 1}{\alpha_n + 1} \left[\tau H_n' + (1 + \alpha_n) H_n \right]} - J_n \right] \quad n = 0, 1, 2, \dots \quad (3.6)$$

where $\rho \equiv r_b/r_a$, $\alpha_n \equiv \sqrt{1 + n^2 - \tau^2}$, and we have dropped the argument τ of the Hankel function and its derivative (ie here $H_n^{(1)}(k_b r)/d(k_b r)_{r=r_b}$).

The complete solution outside the shoal hereafter emerges from (3.2) - (3.4) with (3.6) inserted in the latter equation.

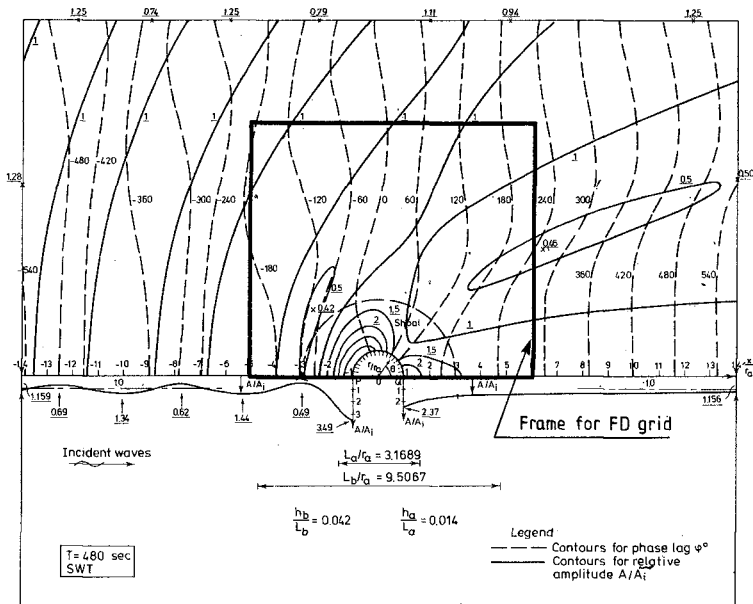


Fig 2. Contours for relative amplitude A/A_1 and phase angle ϕ over the shoal and on constant water depth outside. Solution of (2.1) (ie SWT) for $T = 480$ s. The intervals between A/A_1 -curves are 0.5 and between ϕ -curves they are 60° . Underscored numbers are A/A_1 . The rectangular frame (the very thick line) will be discussed in Sect 4.

A solution for $T = 480$ s is depicted in Fig 2 showing contours for relative amplitude A/A_1 and phase lag φ^0 over the shoal and on constant water depth outside. The solution is presented for $|x/r_a| \leq 14$ and $y/r_a \leq 14$. Maxima and minima are indicated along the boundaries of the depicted area. It appears that even some wave lengths away from the island the incident wave is quite perturbed. A similar figure to Fig 2 has been constructed for a smaller wave period ($T = 240$ s), see Skovgaard and Jonsson (1980), Fig 2.

An important application of the very accurate ("exact") solution in this section is that it can serve as a check for more general numerical schemes (see Sect 4). In order to facilitate such a check a test solution is tabulated in Table 1. In the table relative amplitude A/A_1 and phase angle φ are given for one period ($T = 480$ s), for seven values of azimuth θ ($= 0^\circ, 30^\circ, 60^\circ, 90^\circ, 120^\circ, 150^\circ, \text{ and } 180^\circ$), and for four values of relative distance, r/r_a ($= 1, 3, 9, \text{ and } 27$). The table is an extension of paper I, Table 2a, which stopped at the base of the shoal ($r/r_a = 3$). Also another period is chosen here, $T = 480$ s, instead of $T = 410.47 \dots$ s.

For the practical application of the finite Fourier series for the diffraction solution (3.1) or (3.2) to (3.4) it is useful to know how many terms one needs in order to obtain a given accuracy. This information can be even more important when we discuss whether a certain solution approach at all can be applied in a certain period range or in a certain space region of r and θ .

In paper I (3.24) we introduced the number of terms n_{\max} necessary to obtain a prescribed relative accuracy ϵ s ($0 < \epsilon \ll 1$), which we here define by the relation

$$\left| \sum_{n=0}^{n_{\max}} R_n(r) \cos(n\theta) - \text{exact solution} \right| < \epsilon \times A_1 \tag{3.7}$$

or

$$\left| (A/A_1)_{\text{approximate}} - (A/A_1)_{\text{exact}} \right| < \epsilon \tag{3.8}$$

This simple accuracy criterion, which directly controls the amplitudes and neglects the phases, is selected because of its simplicity. The exact solutions to (3.1) or (3.2) to (3.4) were constructed by continuing the summation until the last term of $|R_n/A_1|$ was less than ϵ s squared.

In Fig 3 for $T = 480$ s (using the shallow water wave equation (2.1) and $\theta = 0^\circ$ (ie along the positive part of the x-axis) n_{\max} vs x/r_a is shown for $1 \leq x/r_a \leq 28$ and for ϵ s = 10^{-2} , 10^{-4} , and 10^{-8} . (ϵ s = 10^{-d} is normally referred to as two times d-places decimal accuracy.)

Similar figures have been constructed for other values of θ , and from these figures we can conclude that Fig 3 is in practice valid for arbitrary θ . For a fixed r/r_a the difference between n_{\max} in Fig 2 and the n_{\max} in figures for other θ was never larger than 2.

The general conclusion is that n_{\max} increases monotonously with x/r_a . For ϵ s constant the variation is nearly linear from the island and outwards. From Fig 3 we can further conclude that for points on the shoal, n_{\max} is only increased by one or two (depending on ϵ s) when we "move"

Table 1. Diffraction solution for the wave field over the shoal, and on constant water depth. The values of phase angle ϕ are chosen in the interval $0^\circ \leq \phi < 360^\circ$. Integers in parentheses indicate powers of 10 by which the following numbers are to be multiplied.

Using SWT, (2.1), $T = 480$ s.

	$\theta = 0^\circ$	$\theta = 30^\circ$	$\theta = 60^\circ$	$\theta = 90^\circ$	$\theta = 120^\circ$	$\theta = 150^\circ$	$\theta = 180^\circ$
$(A/A_i)_{r=r_a}$	2.3692	1.7783	1.5253	2.6996	3.4019	3.5147	3.4886
$(\phi^0)_{r=r_a}$	(+2)1.4971	(+2)1.3245	(+1)5.9653	(+1)1.5667	(+2)3.5518	(+2)3.4112	(+2)3.3548
$(A/A_i)_{r=3r_a}$	1.5321	1.0055	(-1)8.0589	1.3347	(-1)9.9241	(-1)5.1496	(-1)4.9201
$(\phi^0)_{r=3r_a}$	(+2)1.9384	(+2)1.7399	(+1)7.0596	(+1)2.0287	(+2)3.4407	(+2)2.8704	(+2)2.4844
$(A/A_i)_{r=9r_a}$	1.2252	(-1)5.7584	1.0596	(-1)9.6740	1.1041	(-1)7.7372	1.0993
$(\phi^0)_{r=9r_a}$	(+1)2.6548	(+2)3.3426	(+2)1.6076	(+2)3.4795	(+2)2.0800	(+1)4.6236	(-1)2.2356
$(A/A_i)_{r=27r_a}$	1.0872	(-1)8.3750	1.0067	(-1)8.9622	1.1868	1.1405	(-1)7.9512
$(\phi^0)_{r=27r_a}$	(+2)3.2973	(+2)1.4407	(+2)1.4437	(+2)3.5730	(+2)2.1209	(+2)2.0341	(+1)5.2146

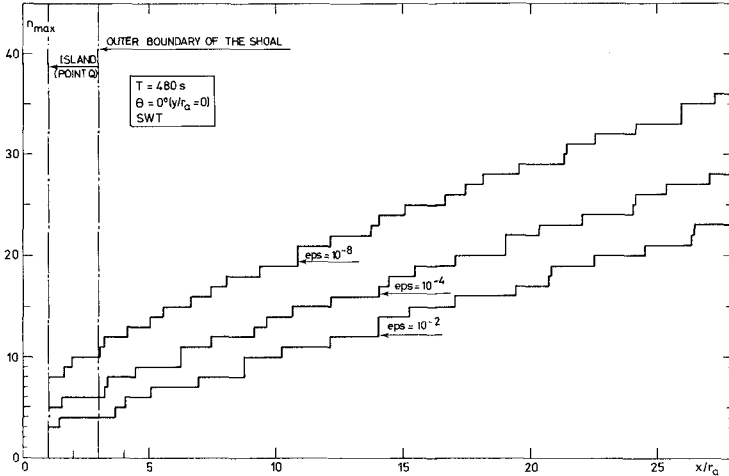


Fig 3. The necessary number of terms n_{max} in the Fourier series (SWT solution) vs x/r_a for $T = 480$ s, $1 \leq x/r_a \leq 28$ (θ of shadow region), and $\epsilon \approx 10^{-2}$, 10^{-4} , and 10^{-8} .

from the island to the outer boundary of the shoal. If ϵ is decreased from 10^{-2} to 10^{-4} only up to five additional terms are needed in the solution series for x/r_a less than 28 and for $T = 480$ s (Fig 3). If ϵ is again squared (ie $\epsilon = 10^{-8}$) only up to seven additional terms are needed. (Notice that for $\theta = 0^\circ$ all the $\cos(n\theta)$ factors in (3.7) are equal to one.)

Similar figures to Fig 3 have been constructed for other values of wave period T and from these figures we have found that if we use x/L (instead of x/r_a) as abscissa, Fig 3 becomes in practice valid for an arbitrary SWT wave period (or wave length L):

Inspection of the calculated phases revealed that the approximation errors for these basically followed the same dependence on wave period T and on the horizontal coordinates r and θ as depicted for A/A_1 in Fig 3.

The conclusion is that n_{max} increases with decreasing period (shorter waves). Far away from the island the increase is rapid. We can further summarize that for all periods in the SWT range, and for all points as far as at a distance of, say $r/r_a \approx 10$, only up to 20 terms of the series solution are needed for $\epsilon \gtrsim 10^{-4}$. As far as at a distance of, say $r/r_a \approx 30$ only up to 40 terms are needed for $\epsilon \gtrsim 10^{-4}$. For solutions in any point on the shoal only up to eight terms are needed in the SWT period range for $\epsilon \gtrsim 10^{-4}$.

4. THE FINITE-DIFFERENCE (FD) SOLUTION

The time-dependent vertically integrated mass and momentum equations (2.7) - (2.9) are approximated by a third order alternating direction implicit (ADI) finite difference (FD) method with space- and time-staggered grids. The program or the modelling system (known as System 21) is described in detail in Abbott et al (1978) and (1979).

The program is designed primarily to cover physical situations with relatively short open boundaries, in contrast to the island cases, where we have radiation out of the computational area along all outer boundaries. For given incident waves the program allows the radiated waves to pass through the open boundaries, assuming that the radiated and the incident waves are of small amplitude and are propagating perpendicularly to the boundary. In the tsunami cases with isolated islands, the open boundaries are normally situated over the deeper part of the oceans where the waves in practice fulfil the first assumption (small amplitude).

The second assumption (waves propagating perpendicularly to the opening) can be well fulfilled in for instance a harbour resonance study. This has been demonstrated in a number of cases, some of which were reported by Abbott et al (1978). In the present case, however, the assumption can at best be approximately fulfilled at some of the boundaries, and the computations will give errors in the computed surface elevations at the open boundaries. These errors will have the appearance of waves reflected from the open boundaries into the region under investigation. If the reflected waves have a large angle of incidence at a physical open boundary the best one can do with the present system is probably to close the boundary in question and put a strong dissipation over a few grid lines along it, thereby simulating that most of the wave energy which enters the boundary region is radiated out. Another - much more expensive - possibility is to make the computational area so large that reflection from "critical" boundaries is delayed sufficiently. It is immediately seen from Fig 2 that the top boundary is the most critical one. See also Sect 6.

The open boundaries mean that we have exposed the system to quite a nasty test, trying to reproduce the solution in Sect 3 using time-stepping calculations. The input wave in the FD system is time-harmonic, but as the calculations are started from a so-called "cold state" they are transient in principle.

The island with the shoal and a fraction of the surrounding ocean (the area within the thick frame in Fig 2) has been covered by a grid, see Fig 4. The grid spacing Δx and Δy is the same in both directions. Δx or Δy denotes the distance between two consecutive grid points for the water level or for the bathymetry; due to the staggered grid the distance between the flux grid points and the elevation grid points is $\frac{1}{2}(\Delta x)$ in the x-direction and $\frac{1}{2}(\Delta y)$ in the y-direction. In this paper we have used only one grid-size ($\Delta x = \Delta y = 1$ km) and only one frame, which covers an area of (109×99) km², or 110 grid points ($J = 0, 1, \dots, 109$) in the x-direction and 100 grid points ($K = 0, 1, \dots, 99$) in the y-direction, see Fig 4. The model is closed along the symmetry line (x-axis), here $K = \frac{1}{2}\Delta y$. The model is open along $J = 0$, where we prescribe a given time-harmonic "incident" surface elevation of small amplitude. Similarly the model is open along $J = 109$, where we prescribe an "incident" wave of

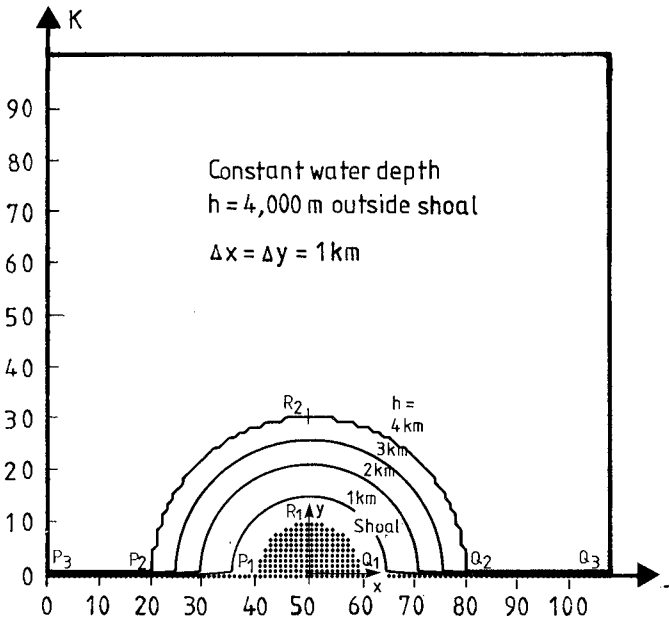


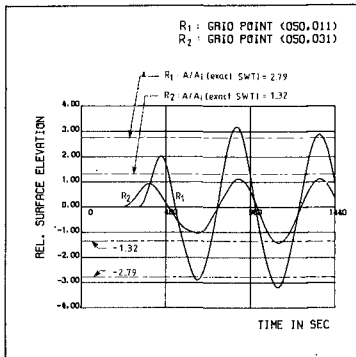
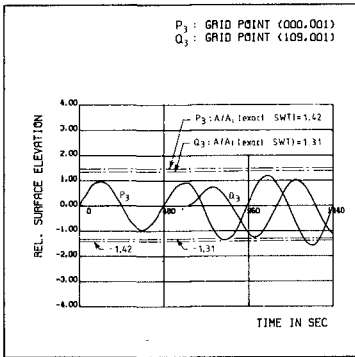
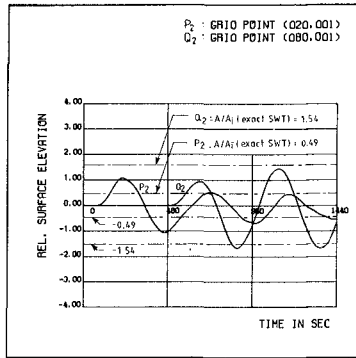
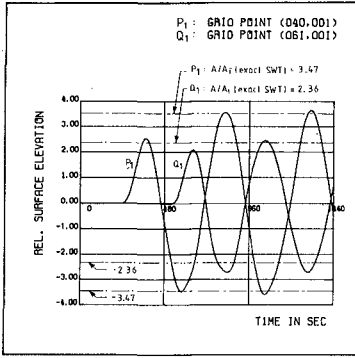
Fig 4. The numerical model bathymetry of the area within the thick frame in Fig 2. The intervals between the depth contours are 1 km. The coordinates for $P_1, P_2, P_3, Q_1, Q_2, Q_3, R_1,$ and R_2 are defined in Table 2.

zero amplitude. Along $K = 99$ (the most critical boundary) we have closed the model and put some dissipation along the boundary. The origin O of the x - y coordinates in Fig 1 (centre of the island) has the coordinates $(J, K) = (50\frac{1}{2}, \frac{1}{2})$.

Due to the simple rectangular discretization of the island (see Fig 4) and to a smaller extent of the shoal we can only get an approximation of the diffraction pattern over the shoal, especially so at the shoreline.

The most direct representation of the solution is time-series plots of relative surface elevations (ie calculated surface elevations divided by A_i , see (2.5)) in characteristic points of the modelled area. We have selected eight such points ($P_1, P_2, P_3, Q_1, Q_2, Q_3, R_1,$ and R_2), see Fig 4 and Table 2. The eight relative surface elevations are given in Figs 5, 6, 7, and 8 for the one incident wave period tested, $T = 480$ s.

In this provisional stage of the project we have run the model only, a rather short time, viz three wave periods or 3×480 s = 1440 s. This integration time was determined by an estimate of the propagation time for a small disturbance entering the model at P_3 (see Fig 4), travelling along the negative x -axis to point P (see Fig 1), continuing along the border of the island to the y -axis, further along the y -axis up to the



Figs 5-6-7-8. Relative surface elevation vs time t ($0 \leq t \leq 1440s = 3 \times 480 s$) for 8 points ($P_1, P_2, P_3, Q_1, Q_2, Q_3, R_1,$ and R_2) within the FD grid, see Fig 4. Period is $T = 480 s$. Exact max/min SWT values of A/A_1 from Sect 3 also shown.

most critical "closed" dissipative boundary and back to the outer boundary of the shoal. Using SWT (2.6) this travel time can be estimated as

$$t_s = \int \frac{ds}{c} = \frac{20,000 + 2 \times 68,000}{\sqrt{9.80665 \times 4000}} + \frac{2 \times \ln 3}{\sqrt{9.80665 \times 4/9 \times 10^{-5}}} + \frac{1/2 \pi \times 10,000}{\sqrt{9.80665 \times 444.4 \dots}} \tag{4.1}$$

$$t_s \approx 788 + 333 + 238 = \underline{1359 s} . \tag{4.2}$$

s being a local coordinate along the travel path for the disturbance. If the disturbance is allowed to travel further from the outer boundary of the shoal to the island (along the y -axis) we have $t_s \approx 1359 + 166 = 1525 s$.

	P_1	P_2	P_3	Q_1	Q_2	Q_3	R_1	R_2
J	40	20	0	61	80	109	50	50
K	1	1	1	1	1	1	11	31
x/r_a	-1.05	-3.05	-5.05	1.05	2.95	5.95	-0.05	-0.05
y/r_a	0.05	0.05	0.05	0.05	0.05	0.05	1.05	3.05

Table 2. Coordinates for the points $P_1, P_2, P_3, Q_1, Q_2, Q_3, R_1,$ and R_2 in Fig 4.

We can conclude that for $t_s = 1440$ s ($= 3 \times 480$ s) the wave field over the shoal cannot be seriously distorted by our "crude" closing of the boundary along $K = 99$. On the other hand we must admit that the complete time-harmonic diffraction pattern over the shoal has not reached an equilibrium state within the three wave periods we have simulated, but it is promising to observe how close we come to the eight exact maximum/minimum SWT values of A/A_1 from Sect 3. (To ensure linearity, which is assumed in the exact solutions, we have used a very small value of A_1 .)

5. COMPARISON BETWEEN EXACT (SWT) AND APPROXIMATE (FD) SOLUTIONS

In the preceding section we compared in Figs 5-8 with the exact SWT values of A/A_1 , for eight characteristic points within the FD frame in Figs 2 and 4. A more convincing approach is to compare the contours for the relative amplitude A/A_1 from the exact (SWT) solution with the FD approximations. Details of the exact SWT wave field over the shoal and in its immediate vicinity are for $T = 480$ s presented in Fig 9 which is an enlarged version of the central part of Fig 2.

The contour lines in Fig 10 were found in the following way. All results from the FD calculations were stored on a file, and for 960 s $\leq t \leq 1440$ s (or $2 \times T \leq t \leq 3 \times T$) the maximum value ζ_{max} was found in each grid point and stored on a second file. For the same time interval the minimum value ζ_{min} was found in each grid point and stored on a third file. The relative amplitude A/A_1 was then calculated in each grid point as $A/A_1 \equiv \frac{1}{2}(\zeta_{max} - \zeta_{min})/A_1$ and stored on a fourth file. From the latter file the contour plot for A/A_1 in Fig 10 was prepared, and A/A_1 in 14 selected points along two half-circles ($r/r_a = 1.05$ and $3, \theta^{\circ} = 0, 30, \dots, 180$) was plotted against the exact SWT solution for $r/r_a = 1.05$ and $3, 0 \leq \theta \leq 180^{\circ}$, see Fig 11.

Remembering that in this provisional stage of the project we are interested only in the diffraction pattern over the shoal we can by comparison of Figs 9 and 10 (which are drawn to the same scale) conclude that the FD approximation is able to model all essential features of the diffraction pattern both in the illuminated region and in the shadow region.

If we look at the comparison in Fig 11 we notice an excellent agreement along the outer boundary of the shoal and a reasonably good agreement along the half-circle very near the island. It is natural that the

crude discretization of the island will give the strongest modification very near the island and can be detected far less at the outer boundary of the shoal.

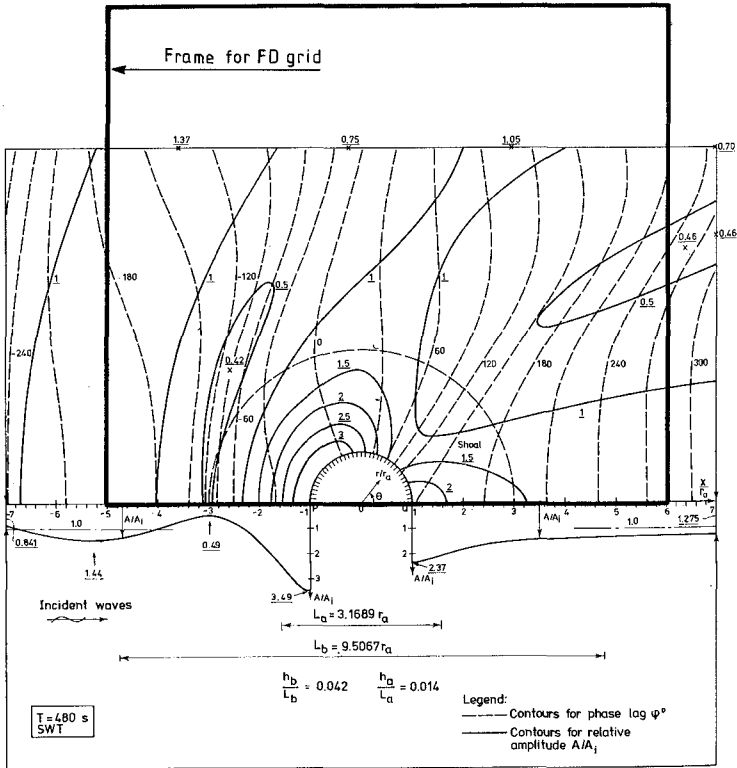


Fig 9. Contours for relative amplitude A/A_1 and phase angle ϕ over the shoal and on constant water depth outside. Solution of (2.1) (ie SWT) for $T = 480$ s. The intervals between A/A_1 -curves are 0.5 and between ϕ -curves they are 30° . Underscored numbers are A/A_1 . The thick frame refers to the FD area covered in Fig 10, see also Fig 2.

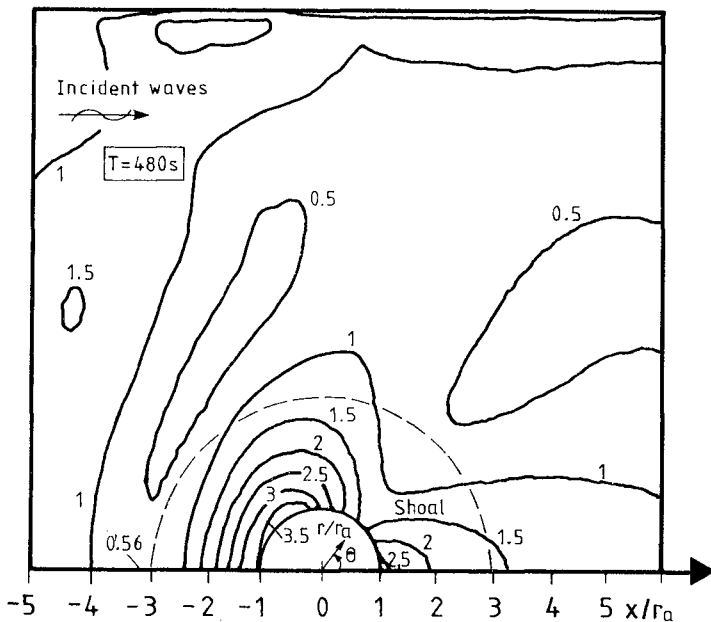


Fig 10. Contours for relative amplitude A/A_i over the shoal and on constant water depth outside. FD solution of (2.7-2.9) for periodic incident waves ($T = 480$ s) of small amplitude. The intervals between A/A_i -curves are 0.5. Same horizontal scale as in Fig 9.

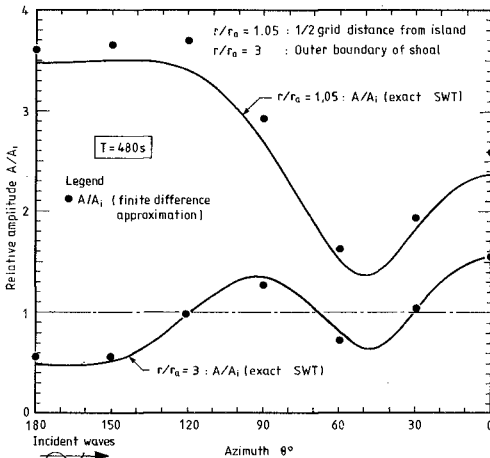


Fig 11. Relative amplitude A/A_i vs azimuth θ° along two half-circles, $r/r_a = 1.05$ and 3. Full curves from exact solution of (2.1) (ie SWT) for $T = 480$ s, and dotted points from FD solution of (2.7 - 2.9) for periodic incident waves ($T = 480$ s) of small amplitude.

6. FUTURE WORK

In this preliminary study we have constructed and used the exact time-harmonic SWT solution (Sect 3) as reference solution for the periodic small amplitude approximate FD solution. In the subsequent more refined work we may construct and use the exact time-harmonic intermediate depth theory (IDT) solution (see Skovgaard and Jonsson (1980), Sect 3.2) as reference solution for the periodic small amplitude FD solution.

The FD model will be improved by construction and analysis of filtering algorithms which take account of the direction of the waves in relation to the boundary and which work for arbitrary Courant numbers $Cr \equiv c\Delta t/\Delta x$, Δt being the full time step in the FD-model.

We are also going to construct a more realistic "exact" test solution corresponding to a transient input (a Gaussian pulse, for instance). With this transient input we will expose the FD model to a more realistic test than the periodic test in this paper.

For this transient FD solution we will construct associated FD solutions which separately will include the Coriolis force and friction forces, thereby being able to show the effects of these two forces.

Finally the FD model will be used on some existing islands in the Pacific Ocean exposed to some "recorded" incident tsunami waves, thereby including the non-linear part of the FD model in the very shallow regions around the islands.

ACKNOWLEDGEMENTS

The Computational Hydraulic Centre, Danish Hydraulic Institute, is acknowledged for letting us use their versatile System 21 for the finite difference computations, including their many service programs.

The Joint Institute for Marine and Atmospheric Research (JIMAR), University of Hawaii, is acknowledged for the stimulating hospitality offered one of the authors (I.G. Jonsson) in the spring 1980 in connection with this study.

REFERENCES

- Abbott, M B, H M Petersen, and O Skovgaard, 'On the numerical modelling of short waves in shallow water', *J Hyd Res*, 16, 3, 173-204, 1978.
- Abbott, M B, H M Petersen, and O Skovgaard, 'Computations of short waves in shallow water', *Proc 16th Coastal Engrg Conf*, Aug-Sept 1978, Hamburg, Am Soc Civ Engrs, N Y, 1, 722-741, 1979.
- Camfield, F E, 'Tsunami engineering', Special Rep No 6, U S Army Coastal Engrg Res Center, U S Government Printing Office, Washington, D C, p 222, 1980.
- Homma, S, 'On the behaviour of seismic sea waves around circular island', *Geophys Mag*, 21, 3, 199-208, 1950.
- Jonsson, I G, and O Brink-Kjær, 'A comparison between two reduced wave equations for gradually varying depth', *Inst of Hydrodyn and Hydr Engrg (ISVA)*, Tech Univ Denmark, Prog Rep No 31, 13-18, 1973.
- Jonsson, I G, and O Skovgaard, 'A mild-slope wave equation and its application to tsunami calculations', *Marine Geodesy*, 2, 1, 41-58, 1979. (Paper II).
- Jonsson, I G, O Skovgaard, and O Brink-Kjær, 'Diffraction and refraction calculations for waves incident on an island', *J Mar Res*, 34, 3, 469-496, 1976. (Paper I).
- Murty, T S, 'Seismic sea waves. Tsunamis', Bull No 198, Dept of Fisheries and Marine Service, Scientific Information and Publications Branch, Ottawa, x + 337 + 41 pp, microfiche, 1977.
- Sklarz, M A, L Q Spiello, and H G Loomis, 'Numerical simulation of the 29 November 1975 Island of Hawaii tsunami by the finite-element method', *J Phys Oceanogr*, 9, 5, 1022-1031, 1979.
- Skovgaard, O, and I G Jonsson, 'Computation of wave fields in the ocean around an island', Danish Cent Appl Math & Mech (DCAMM), Tech Univ Denmark, Rep No 175, 67 pp, 1980.
- Williams, J A, and T D K Kartha, 'Model study of long-wave amplification by circular islands', *Bull Seism Soc America*, 59, 1, 299-316, 1969.

AN INVESTIGATION OF WAVE SHELTERING BY ISLANDS

BY

S. V. Hsiao¹, J. F. Vesecky², and O. H. Shemdin¹

SUMMARY

The West Coast Experiment, a meso-scale oceanographic experiment, was conducted from February to April, 1977, off the coast of Southern California. The wave data measured by an air-borne synthetic aperture radar (SAR) and a shore-based high frequency (HF) radar on March 25, 1977, are used to study the sheltering effect of islands on waves propagating towards shore. The comparisons between wave directional spectra offshore, in the vicinity of islands, and nearshore show that islands play a significant role in determining the near shore wave climate. The data show clearly the "shadow" and "window" effects. An investigation of waves coming out of the "shadow" region indicates that nonlinear wave-wave energy transfer is the likely mechanism responsible for producing such waves.

I. Introduction

The study of waves around islands was one of the objectives of the West Coast Experiment (Shemdin, 1980) conducted from February to April, 1977 off the coast of Southern California. To this objective, waves were measured by synthetic aperture radar (SAR), high frequency (HF) radar, wave rider buoy, and pressure sensor array. The use of radar made it possible to obtain wave measurements over a large area in a short period under various weather conditions. The Jet Propulsion Laboratory (JPL) L-band SAR was flown aboard a NASA CV-990 airplane at 8500m altitude and 240 m/sec speed. The flight paths relevant to this study are shown in Figure 1. The HF radar was operated from the coast south of San Clemente, California. This radar measured the energy of waves at 77m wave length (corresponding to .142 Hz frequency in deep water) moving directly toward or away from the radar site. The extent of HF radar observations is also shown in Figure 1. Wave measurements on March 25, 1977, are used in this study because all the above mentioned sensors were operating on that day and the dominant wave length match the wave-length HF radar observed. The wave spectra measured by pressure sensor array and wave rider buoy show that the primary peak at Torrey Pines and the secondary peak northwest of San Clemente Island are both near the wave frequency (.142 Hz) HF radar observed. The effects of islands on the directional properties of waves at this frequency are examined in this paper. The mechanisms which could generate waves coming out of the shadow of San Clemente Island are then discussed.

¹Jet Propulsion Laboratory, California Institute of Technology

²Stanford Center for Radar Astronomy, Stanford University

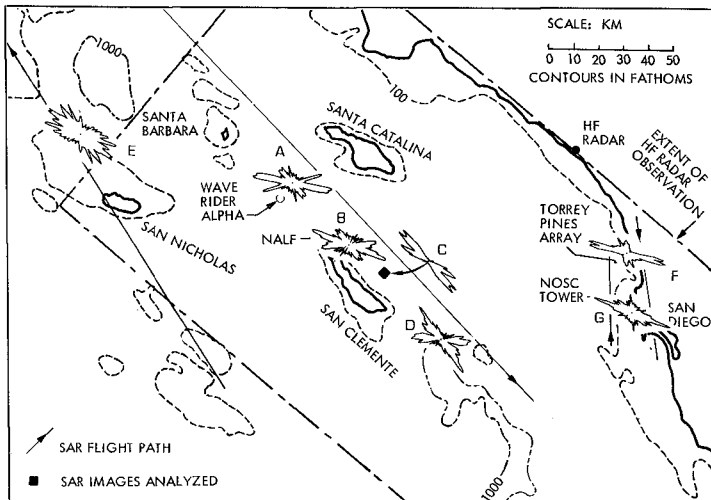


FIGURE 1. The West Coast Experiment area. Also shown are the normalized directional distributions of 80m waves measured by the L-band SAR on March 25, 1977, and the extent of HF radar observation.

II. THE SYNTHETIC APERTURE RADAR OBSERVATIONS

The synthetic aperture radar is an airborne or spaceborne microwave active sensing system. It uses its own power to transmit electromagnetic waves as the illumination. Therefore it has all weather and day/night capability. The SAR takes the advantage of the motion of aircraft or spacecraft to form a long "synthetic" antenna thus increases its azimuth (along track) resolution of the images. For the detail of the SAR system, see Brown and Porcello (1969).

The ability of SAR to image the ocean surface wave patterns have been demonstrated by Brown et al. (1973), Elachi (1976), and others. But the systematic measurements and comparisons of SAR and conventional surface wave instruments were not done until the Marineland Experiment (Shemdin, 1980). The Marineland Experiment was conducted during December, 1975, off the Florida Atlantic coast. The simultaneous wave measurements by SAR, pitch-and-roll buoy, and pressure sensor were compared (Shemdin et al., 1978; Hsiao, 1978; and McLeish et al., 1980). It was found that the dominant wave frequencies and parameterized wave directional distributions can be detected by SAR accurately (see Table 1). The comparisons of wave measurements by SAR, pressure sensor array, CERC coastal radar, and aerial photos during the West Coast Experiment (Mattie et al., 1980) show similar results (see Figure 2). Furthermore, the wave directional measurements obtained during the West Coast Experiment by SAR and a pressure sensor array were compared by Pawka et al. (1980). The results show generally favorable agreement at the primary mode of the normalized directional distribution. A comparison for 6.9 sec waves is shown in Figure 3. Although the SAR imaging mechanism of ocean surface waves is not yet fully understood, these SAR-ground truth comparisons show that the SAR can provide useful information on the dominant wave frequency and the wave directional distributions.

The Jet Propulsion Laboratory (JPL) L-band SAR operates at a frequency of 1.2 GHz corresponding to a wave length of 25 cm (see Brown et al., 1976). The signals returned from the ocean surface were recorded on the signal film by optical recorders on board the airplane. The signal film was then optically processed to form the raw image of the ocean surface. The resolution of this system is estimated to be 25m. The image was further digitized and geometrically corrected for the slant range distortion. Finally two-dimensional fast Fourier transforms were taken at selected locations to obtain two-dimensional wave number spectra. Examples of a geometrically corrected image and its 2-d FFT are shown in Figure 4. This image was taken near Torrey Pines, California at 1154 PST, March 25, 1977.

The directional distributions at 80m wavelength, which is the spectral peak on March 25, 1977, were plotted by tracing along circles centered at the origin with the radius $k=2\pi/80m$ on the 2-d spectra. The normalized directional distributions under this study are shown in Figure 1 for a few carefully selected locations. The 180° ambiguity can be resolved by assuming that all waves were propagating shoreward.

TABLE 1. SAR - SURFACE TRUTH COMPARISONS, MARINELAND EXPERIMENT
(after Hsiao, 1978)

(a) Comparisons of Peak Frequency and Peak Direction

	<u>SAR</u>	<u>P-R BUOY</u>	<u>PRESSURE GAUGE</u>
OBSERVED PEAK WAVE LENGTH (M)	80.4		
WAVE LENGTH CORRECTION (M)	4.6		
PEAK WAVE LENGTH (M)	85.0		
PEAK FREQUENCY (Hz)	0.122	0.125	0.117
OBSERVED PEAK DIRECTION (DEGREES TOWARD)	282		
DIRECTION CORRECTION (SAR)	-6		
DIRECTION CORRECTION (REFRACTION)	-5		
PEAK DIRECTION	271	270	

(b) Comparisons of Directional Distribution Parameters

	<u>SAR</u>	<u>P-R</u>	<u>SAR</u>	<u>P-R</u>	<u>SAR</u>	<u>P-R</u>	
WAVE LENGTH (M)	85.0		62.2		40.2		
FREQUENCY (Hz)	0.122	0.125	0.151	0.156	0.195	0.188	0.203
PEAK DIRECTION (DEGREES TOWARD)	271	270	270	267	266	268	275
P (1ST HARMONIC)	21	21	14	10	12	10	7
P (2ND HARMONIC)	19	28	14	11	13	11	8

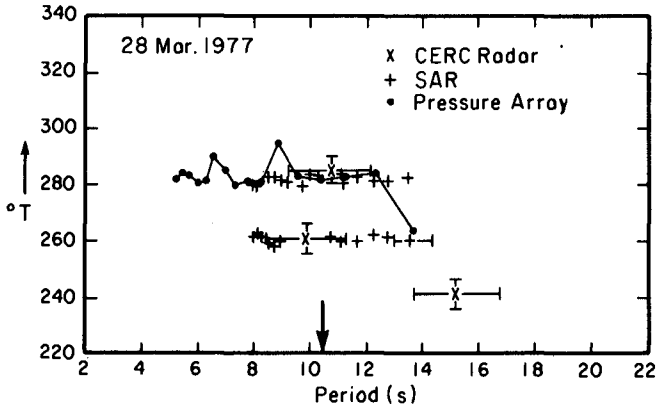


FIGURE 2. Comparisons of wave direction measurements among SAR CERC Coastal radar, and pressure array, (After Mattie et al., 1980)

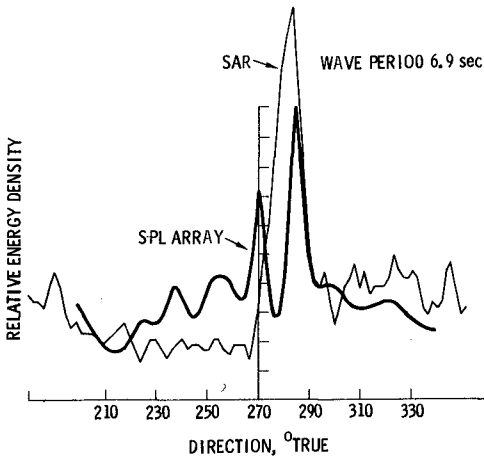
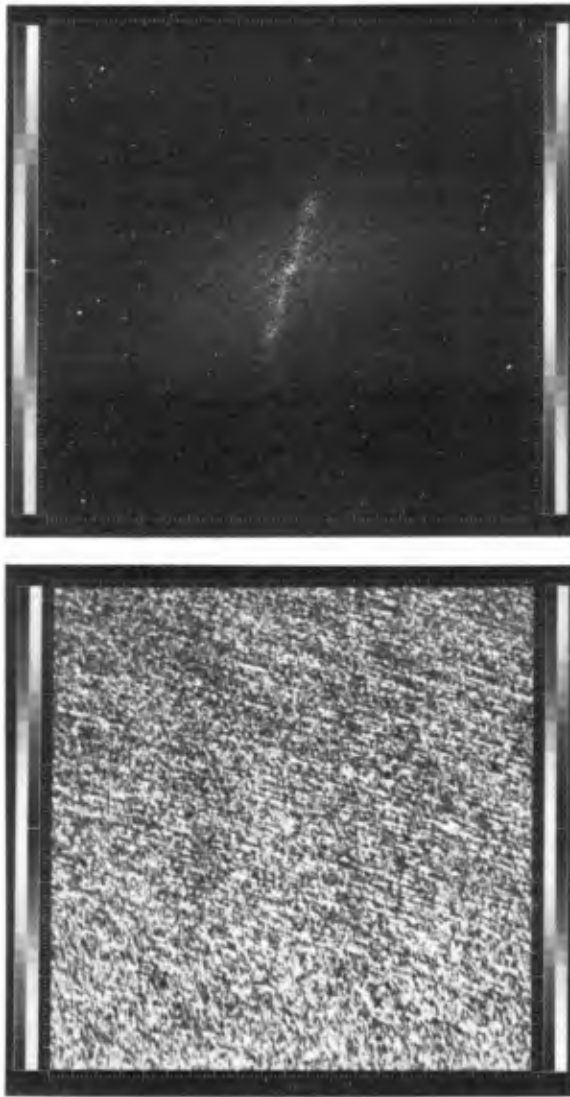


FIGURE 3. Comparison of directional distribution of 6.9 sec waves estimated by SAR and pressure sensor array, March 25, 1977, near Torrey Pines, California (After Pawka et al., 1980)



(a) (b)

FIGURE 4. (a) Geometric corrected SAR image near Torrey Pines, California, March 25, 1977. Each small division is approximately 54m. (b) 2 - d FFT of $f_1(a)$, the wave number scale in each small division is $\frac{1}{54} \approx 0.0057 \text{ m}^{-1}$.

In Figure 1, the directional distribution at E, northwest of San Nicholas Island, is relatively broad. There is no island sheltering effect on this distribution. The directional distributions at A and B show the shadow effects of Santa Barbara and San Nicholas Islands. The directional distributions at C and D show significant shadow effects of San Clemente Islands. Comparing the distributions at C and E, only the waves parallel to San Clemente Island are detected at C, the rest of the waves are blocked by the Island. The distribution at D also shows the wave components detected at C. In addition it shows the wave components passing by the southern tip of San Clemente Island. The gap between the two groups of waves shows the shadow of San Clemente Island clearly. At F and G, the directional peaks both point to the window between San Clemente and Santa Catalina Islands, thus clearly showing the line of penetration of wave energy. These measurements indicate that a broad directional wave distribution offshore can be significantly different behind the islands. The distributions become narrow and multi-peaked because of the shadow effects. The distributions nearshore have peak directions aligned with the window between islands.

III. THE HIGH FREQUENCY RADAR OBSERVATIONS

The HF radar was operated in a synthetic aperture mode with a frequency of 1.9 MHz. This radar measures, by the first-order Bragg resonance, the energy of waves having a wavelength (77m) equal to one half the radar wavelength (154m) moving radially toward or away from the radar (Teague et al., 1975). This ocean wavelength corresponds to the spectral peak of waves measured on March 25, 1977. It has been shown experimentally that the HF radar echo energy is proportional to the resonant ocean wave energy (Teague et al., 1975). During this experiment, the 1 MW peak power LORAN-A transmitter at San Mateo Point, California was used as the signal source. The receiving antenna was synthesized by driving a van at a fixed speed along nearly straight stretches of interstate highway 5. This radar system has an azimuth resolution of 4° and a range resolution of 5 km.

The result of HF radar observation on March 25, 1977, is shown in Figure 5. The 5 dB contours show relative wave energy of 77m wavelength which moves radially toward the radar site. The shadow region of San Clemente Island and the window between Santa Catalina and San Clemente Islands are clearly shown in this Figure.

IV. WAVE TRANSFORMATION MECHANISMS IN THE VICINITY OF ISLANDS

In order to interpret the significance of the results, in Figure 6 the wave energy is plotted versus the distance from radar for two radial lines. One passes through the center of San Clemente Island and the other passes through the center of the window between San Clemente and Santa Catalina Islands. The energy level shown is the average of 10° azimuth angles and 10 km range distances. The steep drop of wave energy at San Clemente Island again shows the shadow effects. After passing San Clemente Island both curves of wave energy show approximately linear increases of the same slope in dB scale, or exponential increase in linear scale.

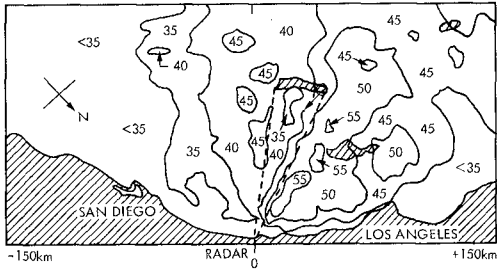


FIGURE 5. HF radar observations of 77m waves approaching the radar site. The contours show relative wave energy on dB scale.

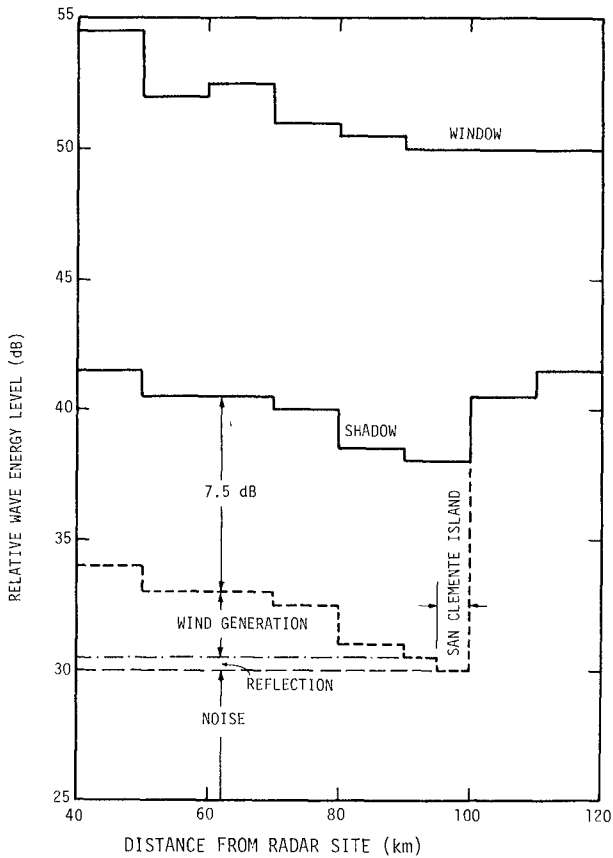


FIGURE 6. Relative wave energy level of 77m waves approaching HF radar site, averaged over 10° azimuth angles and 10 km range distances.

These results suggest that there must be local wave generation. The wind measurements over the West Coast Experiment area show the wind speed to be too small to contribute to the generation of 77m waves during this period. However, no reliable measurement were recorded in the wave generation area.

Despite the reduced level of wave energy behind San Clemente Island, the energy level is still significantly higher than the noise level. The contributions to the measured energy in the shadow of the Island from the waves passing by the northern and southern tips of the Island through the antenna side lobes are considered. The energy average is taken over 10° azimuth along the center of the shadow which is 19° wide. The effect of antenna side lobes is found to be negligible in this average region. The question regarding the mechanism by which waves gain energy in the shadow arises.

Since the water depth increases abruptly near San Clemente Island, the refraction of 77m waves is limited to narrow regions at the northern and southern tips of the Island. The same is true for the diffraction of waves. Thus the waves observed behind the Island in the center of the shadow region cannot be explained by either refraction or diffraction. The HF radar also measures the waves going away from the radar. The energy of such outgoing waves near San Clemente Island was ~ 25 dB. The reflection of these waves by San Clemente Island has some contributions to the observed energy in the shadow region. But even assuming 100% reflection the reflected wave energy is too weak to account for the observed energy, (see Figure 6). By adding the wind generated energy estimated from Figure 6 to the energy level, there is still 7.5 dB difference to be explained.

The SAR data show that behind San Clemente Island there are waves propagating parallel to the direction of the Island. The transfer of energy from these waves to those toward the radar site through nonlinear interaction is suspected to be the source of the observed waves. The computation of the nonlinear energy transfer involves the evaluation of the Boltzmann integral describing by Hasselmann (1963). It is beyond the scope of this paper and is being pursued separately.

V. CONCLUSION

The use of SAR and HF radar made it possible to obtain an overall view of wave conditions off the coast of Southern California. The study of waves at about 80m wavelength on March 25, 1977, gives the following conclusions:

1. The shadow of San Clemente Island and the window between Santa Catalina and San Clemente Islands significantly modify the deep water wave spectrum as it propagates towards the coast.
2. The nonlinear transfer is the most likely source of the observed wave energy moving out of the shadow of San Clemente Island.
3. Remote sensing by SAR and HF radar provides useful information for the study of waves around islands.

ACKNOWLEDGEMENTS

The Jet Propulsion Laboratory contributions were supported by the National Aeronautic and Space Administration under contract NAS 7-100. The Stanford University contribution was supported by the Office of Naval Research under contract N-00017-75-C-0356.

REFERENCES

- Brown, Jr., W. E., C. Elachi, and T. W. Thompson, (1976), Radar imaging of ocean surface patterns, J. Geophys. Res., 81, 2657-2667.
- Brown, W. H. and L. Porcello, (1969) An introduction to synthetic aperture radar, IEEE Spectrum, 52-60.
- Elachi, C., (1976) Wave patterns across the North Atlantic on September 28, 1974 from airborne radar imagery, J. Geophys. Res., 81, 26.
- Hasselmann, K., (1963) On the nonlinear energy transfer in a gravity-wave spectrum. 3: Computation of the energy flux and the swell-sea interaction for a Neumann spectrum, J. Fluid Mech., 15, 385-398.
- Hsiao, S. V., (1978) The comparison between the synthetic aperture radar imageries and the surface truth of ocean waves, Oceans '78, Marine Tech. Soc., Washington, D.C., 385-389.
- Mattie, M. G., D. D. Evans and S. V. Hsiao, (1980) Wave direction measured by four different systems, submitted to Proc. ASCE WW.
- McLeish, W., D. Ross, R. A. Shuchman, P. G. Teleki, S. V. Hsiao, O. H. Shemdin, W. E. Brown, Jr., (1980) Synthetic-aperture radar imaging of ocean waves: Comparison with wave measurements, J. Geophys. Res., in press.
- Pawka, S. S., S. V. Hsiao, O. H. Shemdin, and D. L. Inman, (1980) Comparison between wave directional spectra from SAR and pressure sensor arrays, J. Geophys. Res., in press.
- Shemdin, O. H., (1980) The Marineland Experiment: An Overview, EOS, in press.
- Shemdin, O. H., (1980) The West Coast Experiment: An Overview, EOS, in press.
- Shemdin, O. H., W. E. Brown, Jr., F. G. Staudhammer, R. Shuchman, R. Rawson, J. Zelenka, D. B. Ross, W. McLeish, and R. A. Berles, (1978) Comparison of in-situ and remotely sensed ocean waves off Marineland, Florida, Boundary-Layer Meteorology, 13, 193-202.
- Teague, C. C., G. L. Tyler and R. H. Stewart, (1975) The radar cross-section of the sea at 1.95 MHz; comparison of in-situ and radar determination, Radio Science, 10, 847-852.

The Dissipation of Wave Energy by Turbulence

1

by

Yu Kuang-ming*

I. Abstract

This paper first gives a brief review of the existing research works on the laws governing the dissipation of wave energy by turbulence. Starting from the general theory of turbulent motion and the writer's suggestion in regard to the mixing length of water particles in two-dimensional flow and making use of the principle of dimensional analysis and the trochidal wave theory, a formula has been derived to compute the mean dissipation per unit time and per unit horizontal area of wave energy due to turbulence. The formula takes the horizontal and vertical gradients of both the horizontal and vertical velocity fields into consideration. Coefficient in the formula has been determined through laboratory experiments.

2. A Brief Review of Former Research Works

It is not far since the presentation of the suggestion that fluid turbulence plays an important role also in wave motion. The scientific researches on the laws governing the dissipation of wave energy by turbulence were started in the late forties of this century, but only in and after the fifties of this century had more research works been gradually done.

There are generally three different methods to study the problem of turbulent dissipation of wave energy. The first one bases solely on the principle of dimensional analysis, making use of the π -theorem. The advantages of this method lie in the simplicity of the process of derivation, but the selection of the independent variables and the determination of the formula patterns are to a certain degree arbitrary. The typical example applying this method of analysis can be found in literature (1).

* Hydraulics Engineer, Nanjing Scientific Research Institute of Hydraulic Engineering, 34 Huchukuan, Nanjing 210024, China.

2

The second method utilizes the theoretical relationship of viscous dissipation of wave energy, replacing the coefficient of kinematic viscosity by means of the coefficient of kinematic eddy viscosity and then finds the functional relationship between the latter coefficient and the relevant physical quantities characterizing wave motion, applying the principle of dimensional analysis. The virtues and defects of this method are basically the same as that of the first method. Its typical example of application can be found in literature (2).

The third method makes use of the theory of turbulent flow. This method proceeds from the internal structure of the current, gives a deeper insight into the essence of the phenomenon and therefore has been widely used. Nevertheless, the existing theories take only the vertical gradients of the horizontal velocity field into consideration. But in wave motion, the magnitudes of the horizontal and vertical gradients of both the horizontal and vertical velocity fields are of the same order. They should be considered simultaneously. Literatures (3) and (4) can be referred to as the examples of application of this method.

The discrepancies among the results of the existing research works are very great. For instance, according to ЖУКОВЕЦ (5), the average rate of energy dissipation of wave motion due to turbulence is 108 times as great as that computed by means of the formula suggested by КРЫЛОВ (1). Similarly, if one uses the results of ШУЛЕЙКИН (6) and ДОБРЮКЛОВСКИЙ (3), the calculated values of this quantity will be several times to nearly one hundred times as great as that of КРЫЛОВ for flat waves and steep waves respectively.

3. Theoretical Analysis

For two-dimensional turbulent flow, one may assume (7), (8)

$$\left. \begin{aligned} \tau_{xy} &= \rho \varepsilon \left(\frac{\partial u}{\partial y} + \frac{\partial v}{\partial x} \right) \\ \tau_{xx} &= -\bar{C}_1^2 + 2\rho \varepsilon \frac{\partial u}{\partial x} \\ \tau_{yy} &= -\bar{C}_2^2 + 2\rho \varepsilon \frac{\partial v}{\partial y} \end{aligned} \right\} (1)$$

in which: τ_{xy} --- y component of the turbulent stress acting on a surface element, the outward normal of which is parallel to the X -axis;

τ_{xx} and τ_{yy} have a similar meaning;

ρ --- mass density of liquid;

ε --- coefficient of kinematic eddy viscosity;

U, V ---- component velocities averaged over time in the X and Y directions;

C_1, C_2 ---- constantes;

Referring to Prandtl's suggestion (8), in the case of two-dimensional flow, one may put

$$\varepsilon = l^2 |F| \quad (2)$$

Where

$$F^2 = 2 \left(\frac{\partial U}{\partial X} \right)^2 + 2 \left(\frac{\partial V}{\partial Y} \right)^2 + \left(\frac{\partial V}{\partial X} + \frac{\partial U}{\partial Y} \right)^2 \quad (3)$$

l is the mixing length of fluid particles.

According to the trochoidal wave theory of deep water (7), the Cartesian coordinates of water particles are:

$$\left. \begin{aligned} X &= a + \frac{1}{2} h e^{Kb} \sin \varphi \\ Y &= b - \frac{1}{2} h e^{Kb} \cos \varphi \end{aligned} \right\} \quad (4)$$

where: $\varphi = Ka + \sigma t$ $K = \frac{2\pi}{\lambda}$ $\sigma = \frac{2\pi}{T}$;

λ ---- wave length;

T ---- wave period;

t ---- time;

h ---- wave height;

a, b ---- the Lagrangian coordinates of a water particle, $b=0$ at free surface;

e ---- base of the natural logarithm;

X, Y ---- the horizontal and vertical coordinates of water particle (a, b) at time t ; X -axis coincidea with the central line of water surface and its positive direction is opposite to that of wave propagation; Y -axis is vertical and positive upwards. It passes wave trough at $t=0$.

Differentiating Eq. (4) with respect to t yields

$$\left. \begin{aligned} U &= \frac{\partial X}{\partial t} = \frac{1}{2} h \sigma e^{Kb} \cos \varphi = -\sigma(Y-b) \\ V &= \frac{\partial Y}{\partial t} = \frac{1}{2} h \sigma e^{Kb} \sin \varphi = \sigma(X-a) \end{aligned} \right\} \quad (5)$$

Differentiating Eqs.(4) and (5) with respect to X and Y successaively and simplifying the resulting equations gives

$$\left. \begin{aligned} \frac{\partial U}{\partial X} &= \frac{-\sigma K_1 \sin \varphi}{1 - K_1^2} , & \frac{\partial U}{\partial Y} &= \frac{\sigma K_1 (K_1 + \cos \varphi)}{1 - K_1^2} \\ \frac{\partial V}{\partial X} &= \frac{-\sigma K_1 (K_1 - \cos \varphi)}{1 - K_1^2} , & \frac{\partial V}{\partial Y} &= \frac{\sigma K_1 \sin \varphi}{1 - K_1^2} \end{aligned} \right\} \quad (6)$$

in which

4

Hence
$$\left. \begin{aligned} R_1 &= \frac{\pi h}{\lambda} e^{kb} \\ F^2 &= \frac{4\sigma^2 R_1^2}{(1-R_1^2)^2} \\ |F| &= \frac{2\sigma R_1}{1-R_1^2} \end{aligned} \right\} \quad (7)$$

Substituting Eqs. (2), (6) and (7) into Eq. (1) and rearranging the results, one can obtain

$$\left. \begin{aligned} \tau_{xy} &= \frac{4PR^2\sigma^2 R_1^2 \cos\phi}{(1-R_1^2)^2} \\ \tau_{xx} &= -C_1^2 - \frac{4PR^2\sigma^2 R_1 \sin\phi}{(1-R_1^2)^2} \\ \tau_{yy} &= -C_2^2 + \frac{4PR^2\sigma^2 R_1 \sin\phi}{(1-R_1^2)^2} \end{aligned} \right\} \quad (8)$$

Based on the theory of turbulent flow (9), the energy loss ψ of turbulent motion per unit time and per unit liquid volume is

$$\psi = \tau_{xx} \frac{\partial v}{\partial x} + \tau_{yy} \frac{\partial v}{\partial y} + \tau_{xy} \left(\frac{\partial v}{\partial x} + \frac{\partial v}{\partial y} \right) \quad (9)$$

Substituting Eq. (6) and (8) into Eq. (9) yields

$$\psi = \frac{8P^2\sigma^3 R_1^3}{(1-R_1^2)^3} + (C_1^2 - C_2^2) \frac{\sigma R_1 \sin\phi}{1-R_1^2} \quad (10)$$

If one imagines two vertical planes to be drawn at unit crest width apart, parallel to the direction of wave propagation and extended from water surface to bottom, the total turbulent dissipation E_λ per unit time and per wave length of the fluid between these planes is

$$E_\lambda = \iint \psi dx dy \quad (11)$$

According to the rule of changing of variables (10), it follows immediately that

$$\iint \psi dx dy = \iint \psi \left| \frac{D(x,y)}{D(a,b)} \right| da db \quad (12)$$

in which $\left| \frac{D(x,y)}{D(a,b)} \right|$ is the functional determinant of x, y with respect to a, b .

Differentiating Eq. (4) with respect to a and b successively, substituting the results into the expression of $\left| \frac{D(x,y)}{D(a,b)} \right|$ and simplifying leads to

$$\left| \frac{D(x,y)}{D(a,b)} \right| = 1 - R_1^2 \quad (13)$$

From Eqs. (10)-(13) it may be seen that

$$E_\lambda = 8P^2\sigma^3 \int_{-\infty}^0 \frac{R_1^3}{(1-R_1^2)^2} \left[\int_{a_\lambda=0}^{a_\lambda=\lambda} l^2 da \right] db \quad (14)$$

In two-dimensional flow, the writer suggests that

$$l = l \left(F, \frac{\partial F}{\partial x}, \frac{\partial F}{\partial y} \right) \quad (15)$$

In accordance with the principle of dimensional analysis, putting

$$l = C F^{\beta_1} \left(\frac{\partial F}{\partial x} \right)^{\beta_2} \left(\frac{\partial F}{\partial y} \right)^{\beta_3}$$

where C is a dimensionless constant, one obtains

$$\beta_1 = 1, \quad \beta_2 + \beta_3 = -1$$

Thus

$$l = 2 \left| \frac{\alpha F^2}{\frac{\partial F^2}{\partial Y}} \left[\frac{\frac{\partial F^2}{\partial X}}{\frac{\partial F^2}{\partial Y}} \right] \beta_2 \right| \quad (16)$$

Differentiating Eq. (7) with respect to X and Y respectively and substituting the result into Eq. (16) gives

$$l = \left| \frac{\alpha(1-R_1^2)^2}{K(1+R_1^2)(1+R_1 \cos \phi)} \left[\frac{-R_1 \sin \phi}{1+R_1 \cos \phi} \right] \beta_2 \right| \quad (17)$$

β_2 is determined from the following conditions: at bottom ($R_1=0$), $l=0$; at water surface ($b=0$), $l=h$. Based on these conditions, one may put $\beta_2=1$. Hence,

$$l^2 = \frac{\alpha^2 R_1^2 (1-R_1^2)^4 \sin^2 \phi}{K^2 (1+R_1^2)^2 (1+R_1 \cos \phi)^4} \quad (18)$$

Setting X equal to λ and 0 successively in the first part of Eq. (14) and subtracting yields

$$\lambda = a_{x=\lambda} - a_{x=0} + \frac{1}{2} h e^{Kb} [\sin(Ka_{x=\lambda} + \phi t) - \sin(Ka_{x=0} + \phi t)] \quad (19)$$

Evidently, $a_{x=\lambda} - a_{x=0} = \lambda$ is a solution satisfying Eq. (19). Utilizing this relationship and resolving rational fraction into simpler partial fractions, one gets from Eq. (18) by integration

$$\int_{a_{x=0}}^{a_{x=\lambda}} l^2 da = \frac{\pi \alpha^2 R_1^2 (1-R_1^2)^{3/2}}{K^3 (1+R_1^2)^2} \quad (20)$$

Substituting Eq. (20) into Eq. (14) and then integrating, neglecting the minor terms and applying the relationship $\phi = CK$ (c is wave celerity), one finds the average dissipation E_T of wave energy due to turbulence per unit time and per unit horizontal area as follows:

$$E_T = \frac{E_\lambda}{\lambda} = \frac{4}{5} \rho \alpha^2 C^3 \left(\frac{\pi h}{\lambda} \right)^5 \left[1 - \frac{15}{14} \left(\frac{\pi h}{\lambda} \right)^2 \right] \quad (21)$$

4. Experimental Results

In order to find the value of the constant α in Eq. (21), experiments were conducted in hydraulic laboratory. The ratios of water depths to wave lengths were controlled in these experiments in such a manner that the condition of deep water wave was fulfilled and thus the dissipation due to bottom friction may not enter.

The wave tank is 62.10 m long, 0.80m wide and 1.80m deep and has glass panels on both sides throughout its length. It is provided with an end slag mound of slope 1:10 to avoid wave reflection. Two wave gauges of resistance type were used. They were placed along the center line of the tank in measuring sections I and 2 which were 18.00m apart. The equation of balance of wave energy between sections I and 2 is

$$E_1 - E_2 = L(E_T + E_\mu + E_q + E_w) \quad (22)$$

where

6

E_1, E_2 --- the average quantity of energy transmitted by waves per unit time and per unit crest width in the direction of wave propagation through sections I and 2 respectively;

E_{ν} --- rate of dissipation due to fluid viscosity, negligible in comparison with that of turbulent dissipation;

E_a --- the average dissipation per unit time and per unit horizontal area in the boundary surfaces between air and liquid when wave propagates in calm air;

E_w --- the average dissipation per unit time per unit horizontal area caused by the friction of the side walls of the wave tank;

L --- horizontal distance between sections I and 2, $L=18.00m$;

In accordance with the trochoidal wave theory, it is well known that

$$\left. \begin{aligned} E_1 &= \frac{\rho g h_1^2 C}{16} \left(1 - \frac{\pi^2 h_1^2}{2\lambda^2}\right) \\ E_2 &= \frac{\rho g h_2^2 C}{16} \left(1 - \frac{\pi^2 h_2^2}{2\lambda^2}\right) \end{aligned} \right\} \quad (23)$$

in which h_1 and h_2 are the wave heights in sections I and 2 respectively, and g is the acceleration of gravity. E_a is calculated by means of ШУЛЕЙКИНС formula (6), which was derived on the basis of wind tunnel tests.

$$E_a = \bar{X} \rho' \frac{A \alpha^2}{T} \quad (24)$$

where ρ' is the density of air and \bar{X} is a dimensionless coefficient. As for the value of E_w , Hunt's result (II) is applied.

$$E_w = \frac{\rho g}{4B} \sqrt{\frac{\pi \mu}{\rho T}} h^2 \quad (25)$$

where B is the width of the wave tank and μ is the dynamic viscosity of water.

From Eqs. (21)-(25), the value of α^2 can be computed with the help of the measuring data. The result of computation is shown in Table I.

From Table I, the mean value of α^2 can be calculated to be $\bar{\alpha}^2 = .0376$, its standard deviation $\sigma = \sqrt{\frac{E(\alpha^2 - \bar{\alpha}^2)^2}{B}} = .0209$ and its coefficient of variation $C_v = 55.5\%$

Substituting $\bar{\alpha}^2$ into Eq. (21) yields finally

$$E_T = \frac{3}{100} \rho C^3 \left(\frac{\pi h}{\lambda}\right)^5 \left[1 - \frac{15}{14} \left(\frac{\pi h}{\lambda}\right)^2\right] \quad (26)$$

5. Conclusions

Three methods of studying the problem of energy dissipation of wave motion due to turbulence have been reviewed and their advantages and disadvantages briefly discussed.

Table I

7

Experimental Results of Energy Losses due to Wave Motion

Run No.	Water Depth H (cm)	Wave Period T (sec)	Wave Celerity C (cm/sec)	Wave Length λ (cm)	H/λ	Wave Height (cm)			Water Temperature ($^{\circ}$ C)
						h_1	h_2	$\frac{h_1+h_2}{2}$	
1	90	1.05	170	178	0.50	13.61	12.70	13.17	27.0
2	105	0.96	156	150	0.70	11.60	13.10	13.85	17.0
3	105	1.07	180	193	0.51	15.20	13.80	14.50	17.0
4	120	1.10	163	179	0.67	17.13	15.16	16.14	11.2
5	120	1.23	196	211	0.50	17.90	16.33	17.12	25.0
6	130	1.28	208	266	0.49	19.33	17.49	18.41	11.2
7	140	1.24	201	249	0.56	20.23	18.17	19.35	21.5
8	140	1.36	221	300	0.47	36.14	32.17	34.16	22.0

Run No.	Atmospheric Temperature ($^{\circ}$ C)	Atmospheric Pressure (mm Mercury Column)	Density of Air $\rho' \times 10^2$ (g/cm^3)	Dynamic Viscosity of Water $\mu \times 10^2$ (Poise = dyne-sec/cm 2)	$E_1 \times 10^{-3}$ (g-cm/sec 2)	$E_2 \times 10^{-3}$ (g-cm/sec 2)
1	29.5	751.4	0.115	0.854	1,882	1,638
2	20.0	765.9	0.121	1.08	1,942	1,578
3	20.0	765.9	0.121	1.08	2,170	2,018
4	12.0	759.7	0.124	1.26	2,800	2,215
5	24.5	758.4	0.118	0.891	3,740	3,130
6	12.0	759.7	0.124	1.26	4,615	3,818
7	22.0	759.2	0.120	0.969	4,890	4,090
8	23.0	759.4	0.119	0.958	16,700	13,160

Table I

8

Experimental Results of Energy Losses due to Wave Motion

Run No.	$\frac{E_1 - E_2}{L}$ (g/sec ³)	E_a (g/sec ³)	E_w (g/sec ³)	$E_T = \frac{E_1 - E_2}{L} - E_a - E_w$ (g/sec ³)	α^2	$(\alpha^2 - \bar{\alpha}^2)^2 \times 10^4$
1	135.6	9.9	85.2	40.5	0.0161	1.62
2	202.2	13.2	111.2	77.8	0.0138	5.67
3	234.4	12.8	115.2	106.4	0.0332	0.19
4	325.0	14.5	152.2	158.3	0.0274	1.01
5	339.0	14.2	136.3	188.5	0.0593	4.71
6	459.4	16.7	183.5	259.2	0.0783	16.56
7	444.4	18.8	180.5	245.1	0.0465	0.79
8	1800	59.0	544.5	1196.5	0.0262	1.30

$$\bar{\alpha}^2 = 0.0376$$

It seems more properly to approach the subject by making use of the theory of turbulent flow.

The importance of considering simultaneously the horizontal and vertical gradients of both the horizontal and vertical velocity fields have been pointed out. An analytical formula, i.e., the Eq. (26), has been derived theoretically, with the coefficient in it determined experimentally, which can be used to compute the rate of turbulent dissipation of wave energy.

Acknowledgements

The aid of comrades Chang Chia-chang, Tu Chin-man and Wu Yung-cheng in performing the experiments is greatly appreciated.

Appendix I References

- (1) Крылов, Ю.М., Теория и Расчет Ветровых Волн Глубокого Моря, Тр.ГОИНа, вып. 26(38), 1954.
- (2) Bowden, K. F., The Effect of Eddy Viscosity on Ocean Waves, The Philosophical Magazine, 1950.
- (3) Доброклонский, С. В., Турбулентная Вязкость В Поверхностном Слое Моря и Волнение, Докл. АН СССР, 1947, Т. LVIII, No.7.
- (4) Бровиков, И.С., О Расчете Элементов Ветровых Волн При Переменном Ветре, Тр. ГОИНа, вып. 38, 1957.
- (5) Жуковец, А.М., Определение Потерь Энергии Волн Зыбь, Вызванных Действием Турбулентной и Кинематической Вязкости, Океанология, 1963, No.2
- (6) Пулейкин, В.В., Теория Морских Волн, Тр. Морского Гидрофизического Института, Т.Ж, 1956.
- (7) Кочин, Н.Е., Кибель, И.А. и Розе, Н. В., Теоретическая Гидромеханика, 1963.
- (8) Goldstein, S., Modern Developments in Fluid Dynamics, Vol. I, 1938.

(9) Lamb, H., Hydrodynamics, 6th Edition, 1932.

(10) Омиров, В.И., Курс Высшей Математики, Т. II, 1952.

(II) Hunt, J. N., Viscous Damping of Waves over an Inclined Bed in a Channel of Finite Width, La Houille Blanche, 1952, No. 6.

Appendix 2 Notation

- a, b ---- Lagrangian coordinates of liquid particles, $b = 0$ at free surface
- B ---- width of wave tank
- c ---- wave celerity
- c_1, c_2 ---- constants
- c ---- coefficient of variation
- D ---- symbol, $\left| \frac{D(x, y)}{D(a, b)} \right|$ is the functional determinant of X, Y with respect to a, b
- e ---- base of the natural logarithm
- E_1, E_2 ---- average quantity of energy transmitted by waves per unit time and per unit crest width in the direction of wave propagation through sections I and 2 respectively
- E_a ---- average dissipation per unit time and per unit horizontal area in the boundary surface between air and liquid when wave propagates in calm air
- E_λ ---- turbulent dissipation of energy per unit time, per unit crest width and per wave length of the liquid volume extended from water surface to bottom
- $E_T = E_\lambda / \lambda$
- E_μ ---- rate of dissipation due to fluid viscosity
- E_w ---- average dissipation per unit time and per unit horizontal area caused by the friction of the side walls of a wave tank
- F ---- quantity defined by Eq.(3)
- g ---- acceleration of gravity
- h, h_1, h_2 ---- wave heights
- $K = \frac{2\pi}{\lambda}$ ---- wave number
- $k_0 = \frac{\pi h}{\lambda} e^{kb}$
- l ---- mixing length of fluid particles
- L ---- horizontal distance between wave gauge stations
- t ---- time

- T ---- wave period
 u ---- component velocity in X direction
 v ---- component velocity in Y direction
 X, Y ---- Cartesian coordinates
 \bar{X} ---- dimensionless coefficient
 $\alpha, \beta_1, \beta_2, \beta_3$ ---- dimensionless constants
 ξ ---- coefficient of kinematic eddy viscosity
 λ ---- wave length
 μ ---- coefficient of dynamic viscosity
 $\pi = 3.142$
 ρ ---- mass density of liquid
 ρ' ---- mass density of air
 σ ---- radian frequency ($= \frac{2\pi}{T}$); standard deviation
 τ_{xy} ---- Y component of turbulent stress acting on a surface element, the outward normal of which is parallel to X -axis
 τ_{xx}, τ_{yy} ---- similar in meaning to τ_{xy}
 $\Phi = Ka + \sigma t$, Eq.(4)
 ψ ---- energy loss of turbulent motion per unit time and per unit liquid volume



Entrance to the Hastings River at Port Macquarie, New South Wales

PART II

COASTAL SEDIMENT PROBLEMS

Training Jetties, Narooma, New South Wales



BEACH CUSPS AT POINT REYES AND DRAKES BAY BEACHES, CALIFORNIA

by

R. G. Dean¹ and E. M. Maurmeyer²INTRODUCTION

Beach cusps, fairly common and periodic features along many shorelines have been the focus of numerous investigations. The primary efforts have been directed toward (1) determining a causative mechanism for their formation; (2) describing qualitatively the associated water motions and sediment transport; and (3) developing a predictive relationship for their spacing. As in other problems in nearshore dynamics (e.g. rip currents), it may be that there are various valid explanations for different occurrences of beach cusps. In addition to satisfying scientific curiosity, an improved qualitative and quantitative understanding of beach cusp mechanisms would contribute substantially to swash zone dynamics and to nearshore hydrodynamics and sediment transport in general.

This paper describes a series of measurements of beach cusps and associated parameters carried out at Point Reyes and Drakes Bay beaches in northern California during the summers of 1977-1979. An attempt to idealize the beach cusp topography and the resulting swash hydromechanics led to a possible relationship between beach cusp spacing and swash parameters in which the spacing is linearly related to maximum swash excursion.

PREVIOUS INVESTIGATIONS

Early attempts at establishing causative mechanisms for beach cusp initiation and development focused on erosion and/or deposition by swash and backwash processes (Shaler, 1895; Johnson, 1910; Smith and Dolan, 1960; Otvos, 1964; Russell and McIntire, 1965; Gorycki, 1973). Several investigators (Palmer, 1834; Lane, 1888; Johnson, 1910) noted that conditions conducive for cusp formation include parallel wave approach, although others (Evans, 1938; Otvos, 1964) observed cusps forming by oblique wave approach. Branner (1900) and Dalrymple and Lanan (1976) noted that cusps may form by intersecting wave trains. Cusp formation associated with the escape of ponded water from a ridge or other barrier on the berm or backshore has been observed and documented by Jefferson (1899, 1903), Evans (1938), Dubois (1978), and Sallenger (1979). Following Ursell's (1952) popularization of edge waves, recent investigations (Galvin, 1964; Bowen and Inman, 1969; Komar, 1973; Guza and Inman, 1975; Sallenger, 1979) have attributed both the initiation and spacing of cusps to the action of edge waves.

¹Professor, Department of Civil Engineering and College of Marine Studies, University of Delaware, Newark, DE 19711.

²Assistant Professor, Department of Geology, Franklin and Marshall College, College Avenue, Lancaster, PA 17604.

AREA OF STUDY

The Point Reyes peninsula is located approximately 50 km north of San Francisco, California (Figure 1). The orientations of the two beaches studied and their sediment characteristics result in markedly different beach morphologies.

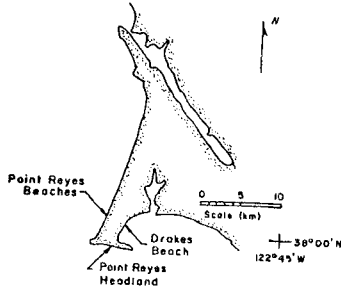


Figure 1. Location Map, Point Reyes and Drakes Bay Beaches, California.

Point Reyes Beach

Point Reyes Beach trends north-northeast and is exposed to the direct action of waves generated in the Pacific Ocean (Figure 2). The

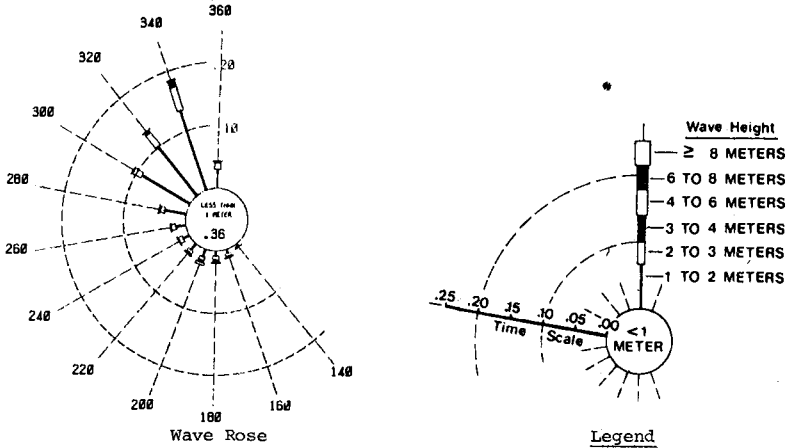


Figure 2. Annual Deep Water Wave Rose, Offshore Point Reyes Area. Combined Sea and Swell, Station 3. (Meteorological International Incorporated, 1977).

beach morphology reflects the highly variable waves through a series of "summer" and "winter" berm terraces, with the uppermost berm approximately 4 m above mean sea level. During the summer of 1977, three terraces each with beach cusps, were present (Figure 3). The beach face is fairly steep with an average slope of 1:10, and beach sediments consist of coarse sand with a mean diameter of approximately 0.8 mm. P. D. Trask and his co-workers (1955a, 1955b, 1956, 1959, 1961) have studied the geological characteristics and cusp formations of the Point Reyes beaches.



Figure 3. Point Reyes Beach, California, August 1977, Showing Three Cusped Berm Terraces.

Drakes Bay Beach

The beach along Drakes Bay is located approximately 6 km southeast of the Point Reyes beach, and is sheltered from the direct attack of high waves from the north and north-northwest. This beach and its southern extension have been studied by Yasso (1965) and identified as a hooked or crenulate bay which is associated with and dependent on sheltering by and diffraction around the Point Reyes headland. As a result of this sheltering, there is only one berm present, with a maximum elevation of approximately 1 m above mean sea level (Figure 4). The average beach face slope is 1:25; and the beach is composed of fine sand having a mean diameter of 0.2 mm.



Figure 4. Drakes Bay Beach, California, July, 1979.

FIELD STUDIES

The observed and measured field data include beach cusp circulation and sediment transport patterns, sediment characteristics, statistics of intercusp spacing, plane table surveys of beach cusps, observations of wave heights and wave periods, and measurements of swash velocities and excursions. Cusp formation on a planar beach was documented during one trip:

Beach Cusp Circulation Patterns

For most of the cases which were observed in the field, beach cusps were already established and thus the observed circulation patterns relate more to the development and maintenance of these features than to their initial formation. In all cases where cusps were present, it was evident that the waves were causing vigorous sediment transport on the beach cusps, with a net circulation landward on the horns (Figure 5a) and seaward in the bays (Figure 5b). This is the same pattern reported by Johnson (1910), Bagnold (1940), O'Brien (1978) and Longuet-Higgins and Parkin (1962), but opposite to that noted by Kuenen (1948). An additional characteristic which to our knowledge has not been reported in the literature (although M. P. O'Brien had recorded this in his field notes on beach cusps in 1930) is that in cases of most effective beach cusp development, the wave and swash period are nearly equal; this equivalence contributes strongly to the net water circulation noted above. This mechanism is illustrated schematically in Figure 6 and described as follows: Waves breaking at the base of the horns cause a strong uprush on these features; however, during the upward excursion, the lateral (longshore) beach gradient causes the trajectories of the water particles to be directed toward the bays. The water accumulates in and flows seaward through the bays. In cases where the swash period is nearly coincident with the wave period, the backrush flow interferes destructively with the succeeding uprush at the embayment positions of the cusps. In some cases, this effect is so complete that following the uprush on the horn, no water will be left on the horn whereas a fairly narrow zone of water (say one-eighth of the cusp spacing in width) will be flowing seaward with a depth on the order of 15-30 cm as shown at Point Reyes Beach in Figure 7. The net result is a dominance of uprush on the horns with the backrush concentrated through the embayments thereby interfering destructively with the next potential uprush. Of substantial relevance to later discussions, is that the swash and wave period do not need to be precisely synchronous since the backrush occurs over a greater time period than the uprush (due to the toll that friction has taken on these velocities) and any dominance of return flow through the embayments will reinforce this net circulation. A "finely tuned" system is thus not required. As discussed in the next paragraphs, this net water circulation pattern is closely related to the maintenance and development of the beach cusp morphology.



(a) Uprush on Cusp Horns.



(b) Backwash in Cusp Bays.

Figure 5. Beach Cusp Circulation Patterns, Drakes Bay Beach, California, July 1978.

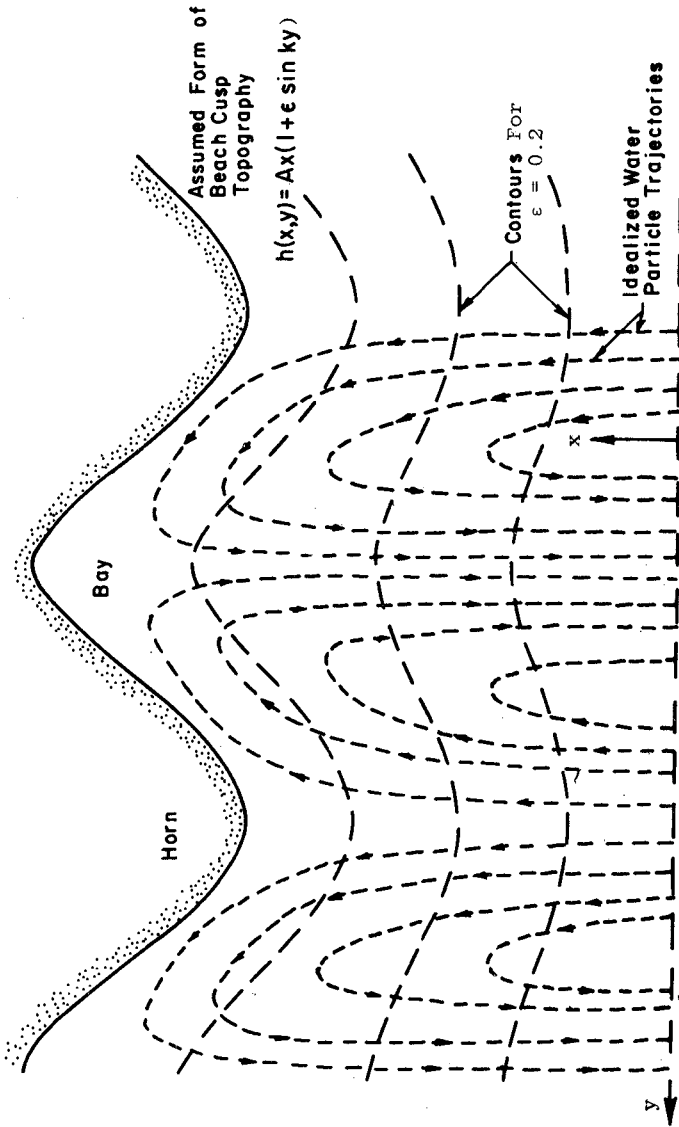


Figure 6. Assumed Beach Cusp Topography and Observed Mean Flow Pattern. Uprush Concentrated on Horns, Seaward Return Flow Concentrated in Bays.



Figure 7. Narrow Zone of Seaward Flow in Cusp Bay, Point Reyes Beach, California, July 1978. Water Depth is on the Order of 15-30 cm.

Sediment Transport Patterns

The sediment transport patterns can be discussed best in the context of the swash characteristics for a planar beach. The swash is two-dimensional with the uprush velocities being higher than the backrush velocities due to friction. Percolation may also play an important role in this inequality on highly permeable beaches. In fact it is these features which result in the positive beach face slope. The uprush transports sediment landward thereby increasing the slope and the backrush transports sediment seaward reducing the beach face slope. The resulting beach face slope is therefore in a state of dynamic equilibrium changing slightly with each uprush and backrush.

As noted previously, the effect of the longshore slopes associated with beach cusps is to concentrate the uprush on the horns and to channel the backrush through the embayments. The result is a steeper slope on the horns since there is little or no destructive backrush to transport sediment seaward. In the embayments, the backrush inequality is greatly augmented by flow from the horns and, as noted, by the reduction of uprush by the local interference with the succeeding wave crest. The results are steeper horn and milder embayment slopes. The equilibrating mechanism that limits the slopes of the horns and bays is the lateral transport of sediment by the water circulation pattern presented in Figure 6. Thus, at equilibrium, the lateral slope from the horns to the embayments and the associated water transport are just sufficient to transport that sediment carried up the horns by the local dominance of uprush. On a smaller scale, the turbulence associated with the uprush plays a role in moderating the "sharpness" of the contours on the horns.

Sediment Characteristics

As noted previously, the mean grain diameter of the sand comprising Point Reyes Beach is approximately 0.8 mm, whereas sand at Drakes Bay

Beach is much finer, with a mean grain size of 0.2 mm. These values are in reasonable accord with those found by Trask and Johnson (1955), Trask, Johnson and Scott (1959) and Trask and Snow (1961). The latter reference found the average diameters at Point Reyes Beach and Drakes Beach to be 0.58 and 0.19 mm, respectively. As shown in Figures 8 and 9, the sand characteristics of cusp horns and bays at each beach did not differ greatly. This is contrary to the findings of several investigators (King, 1972; Komar, 1973; Williams, 1973), who noted that material comprising cusp horns is generally quite coarser than material in the bays. However, in a laboratory study of beach cusps, Flemming (1964) found no significant size sorting between cusp horns and bays. Russell and McIntire (1965) suggest that size variations are most pronounced during the "juvenile" stage but that the contrast diminishes as cusps continue to develop.

Intercusp Spacing

The apparent regularity of spacing between cusps is of particular interest and has been documented by numerous investigators (Shaler, 1895; Kuenen, 1948; King, 1972; and Komar, 1973). Detailed measurements by others (Jefferson, 1903; Evans, 1938) have shown that intercusp spacing often is not so uniform as perceived. Johnson (1919) and Russell and McIntire (1965) suggest that spacing is irregular during the early stages of cusp formation and becomes more uniform as cusps continue to develop.

Intercusp spacings at Point Reyes and Drakes Bay beaches were measured during the summers of 1977 and 1979, and are summarized in Table I. Figures 10 and 11 present sample histograms of spacing between active beach cusps at Point Reyes and Drakes Bay Beaches, respectively.

TABLE I
SPACING CHARACTERISTICS OF BEACH CUSPS AT
POINT REYES AND DRAKES BAY BEACHES

Location	Berm Level	Year	No. of Cusps	Average Spacing (m)	Standard Deviation of Spacing (m)
Point Reyes South Beach	Upper	1977	11	62.0	8.8
	Upper	1979	10	61.6	9.5
	Mid	1977	15	41.4	7.2
	Mid (Active)	1979	21	42.8	7.9
	Lower (Active)	1977	30	27.9	2.5
Drakes Beach	Only One Berm Present	1977	31	29.8	5.2
		1979	26	23.2	4.5

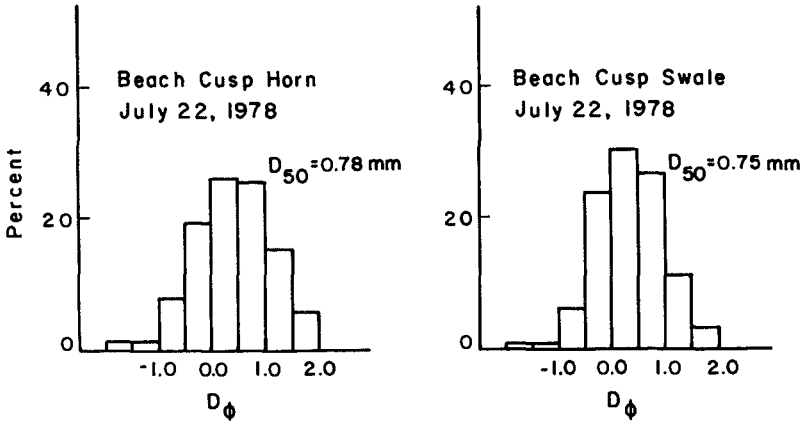


Figure 8. Representative Sediment Size Characteristics on Beach Cusps at Point Reyes Beach, California.

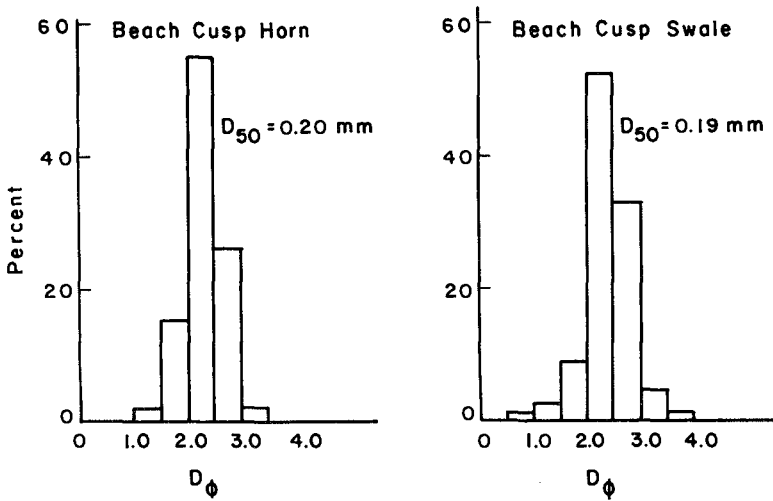


Figure 9. Representative Sediment Size Characteristics on Beach Cusps at Drakes Beach, California.

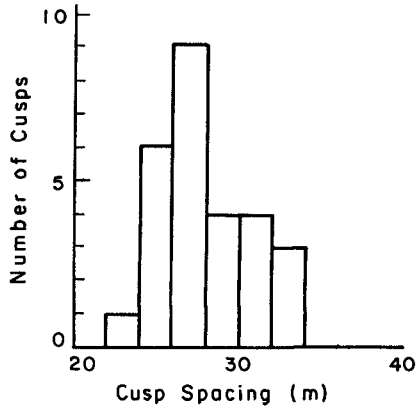


Figure 10. Histogram of Spacing of 30 Beach Cusps. Active Lower Berm, Point Reyes Beach South, California, August 23, 1977.

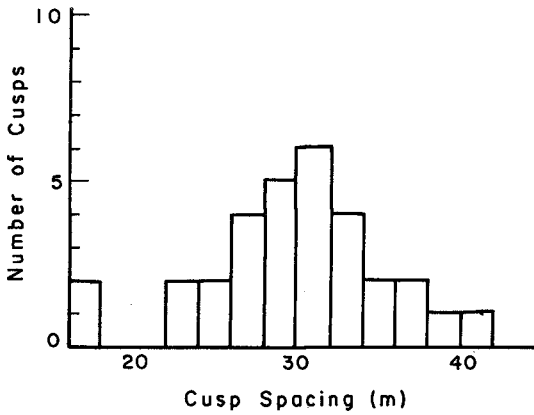


Figure 11. Histogram of Spacing of 31 Active Beach Cusps, Drakes Bay Beach, California, August 23, 1977.

During the 1977 field trip, there were three levels of cusps at Point Reyes beach, with only the lower level active. It is of interest to note that there is a consistent increase in cusp spacing with increasing berm elevation. Also of interest is the consistency of mean cusp spacing in 1977 and 1979. It is possible but unlikely that the beach cusps at the upper berm were not active during the intervening winters. The mean spacings at this level differed for the two summers by only 0.4 m of 61.8 m (0.6%). At the mid-level, which was active during the 1979 trip, the means differ by 1.4 m of 42.1 m (3.3%). At the Drakes Bay beaches, the difference is greater--6.6 m of 25.5 m (25.9%). The ratio of standard deviation of beach cusp spacing to mean varies over a fairly narrow range. For the Point Reyes and Drakes Bay beaches, these ranges are 9.0 to 18.5% and 17.4 to 19.4%, respectively.

Plane Table Surveys

Plane table surveys of beach cusps were conducted at various locations along Point Reyes and Drakes Bay beaches. Each survey included three horns and the two intervening bays. The mapping consisted of lines located approximately along the horns and bays and lines at each quarter point, which provided reasonable definition of cusp topography. Three example surveys are presented in Figures 12 to 14. The characteristics of these beach cusps will be discussed in a later section.

Swash and Wave Observations

During the 1979 field trip, limited observations of swash velocity and excursion were measured. Stakes were driven in the beach at 5 m intervals along lines extending upward along the horns and embayments. Maximum swash excursions were readily estimated to an accuracy of 1 m, and using an electronic stopwatch, swash velocities were calculated based on the time required for a floating object to advance (retreat) from stake to stake on the uprush (backrush). On July 28, 1979, uprush distance and associated beach cusp spacings were measured at both Point Reyes and Drakes Bay beaches. The parameters of interest including the ratio of cusp spacing, λ , to uprush distance, $(\xi_x)_{\max}$, are presented in Table II.

TABLE II

SUMMARY OF UPRUSH EXCURSION AND BEACH CUSP SPACING MEASUREMENTS
JULY 28, 1979

Location	Uprush Excursions		Beach Cusp Spacings		$\lambda/(\xi_x)_{\max}$
	No. Observed	Average Value, $(\xi_x)_{\max}$, (m)	No. Observed	Average Value, λ (m)	
Drakes Bay*	46	12.5	26	23.2	1.9
Point Reyes	11	14.6	4	46.0	3.2

*Cusps in process of formation.

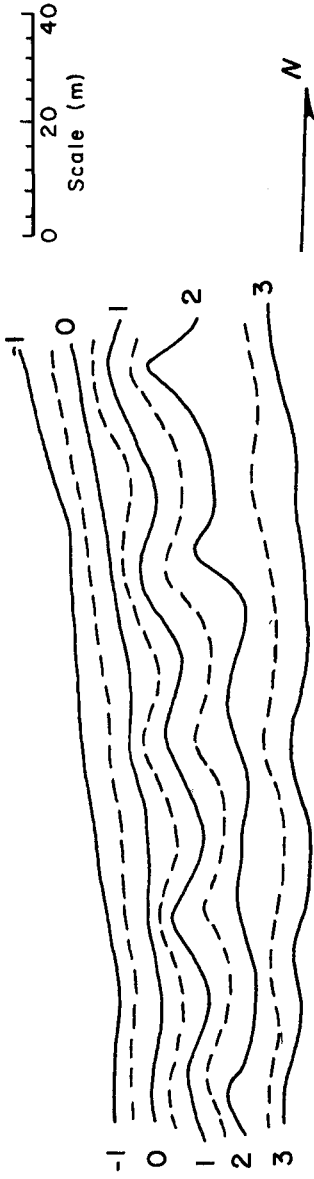


Figure 12. Beach Cusps at Point Reyes Beach North, California, July 22, 1978. Contours are in Meters Relative to an Arbitrary Datum.

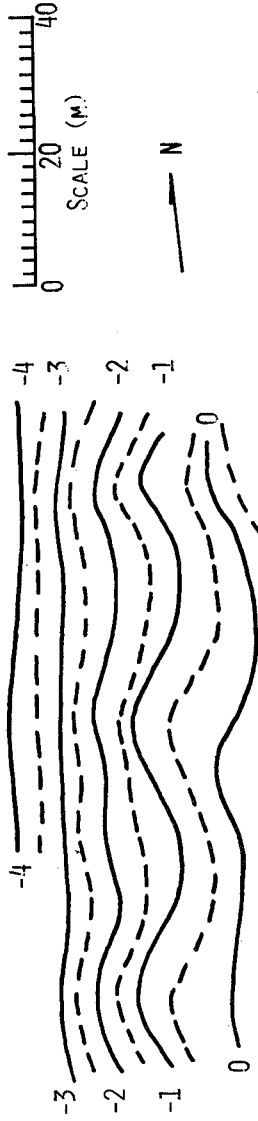


Figure 13. Beach Cusps at Point Reyes Beach South, California, July 23, 1978. Contours are in Meters Relative to an Arbitrary Datum.

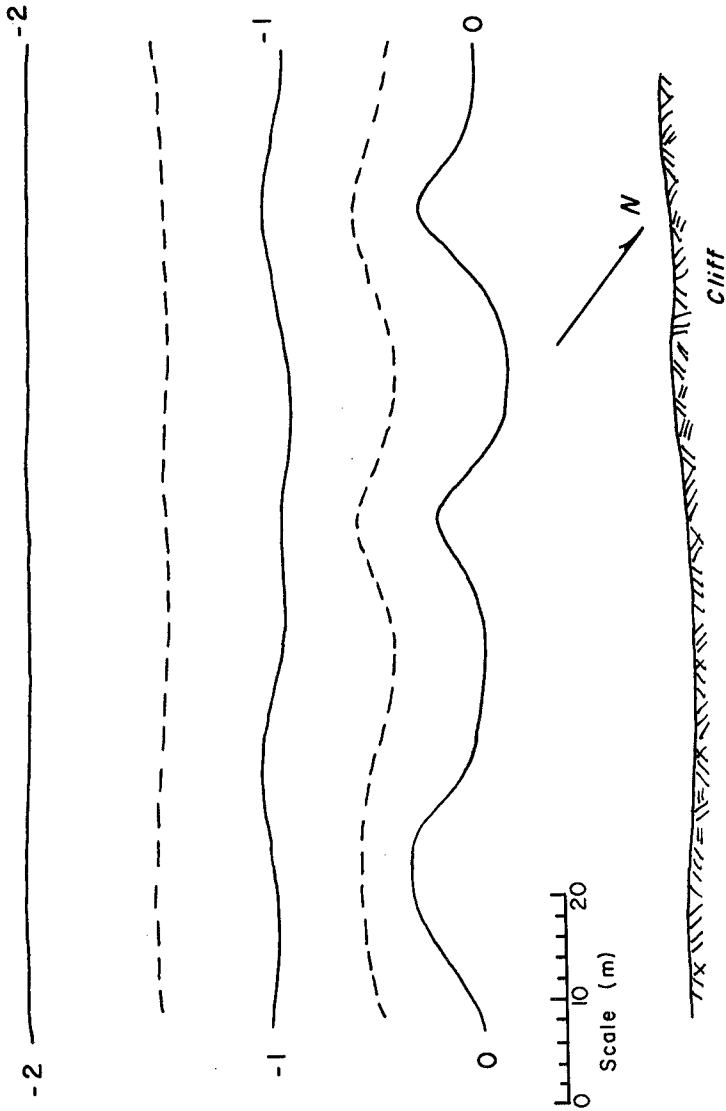


Figure 14. Beach Cusps at Drakes Beach, California, August 25, 1977. Contours are in Meters Relative to an Arbitrary Datum.

The ratio of $\lambda/(\xi_x)_{\max}$ of 1.9 and 3.2 are of interest as will be discussed later.

Observations of Beach Cusp Initiation

During the 1979 field trip, storm waves caused the cusps at Drakes Beach to be essentially eradicated leaving a planar beach. The following day (July 28, 1979), the cusps started to reform and the periods of 100 consecutive waves were measured and the associated breaking heights estimated visually. The range in breaking heights (10 to 70 cm) resulted in breaking at varying locations offshore and caused the observed wave periods at the breaking point to differ from those that would occur at a fixed location; the periods were corrected to a common breaking location considering linear shallow water wave theory for the celerity and a uniform slope of 1:25. The resulting histogram of wave periods is presented in Figure 15; the mean and standard deviation of the wave periods are 15.4 sec. and 5.1 sec., respectively. In addition a series of 46 wave heights and associated uprush excursions were observed. The mean and standard deviation of 46 wave heights (visually observed) were 33.5 cm and 17.0 cm, respectively and those of the 46 uprush excursions were 12.5 m and 4.0 m, respectively. It is interesting that the ratio of standard deviation to mean was determined to be less for the uprush excursions than for the wave heights--0.32 vs. 0.51. The correlation coefficient, r , was calculated between the breaking wave heights, H_b , and the associated uprush excursions, $|\xi_{x_i}|$

$$r = \frac{\sum (H_{b_i} - \bar{H}_b)(|\xi_{x_i}| - \overline{|\xi_x|})}{\sqrt{\sum (H_{b_i} - \bar{H}_b)^2 \sum (|\xi_{x_i}| - \overline{|\xi_x|})^2}} \quad (1)$$

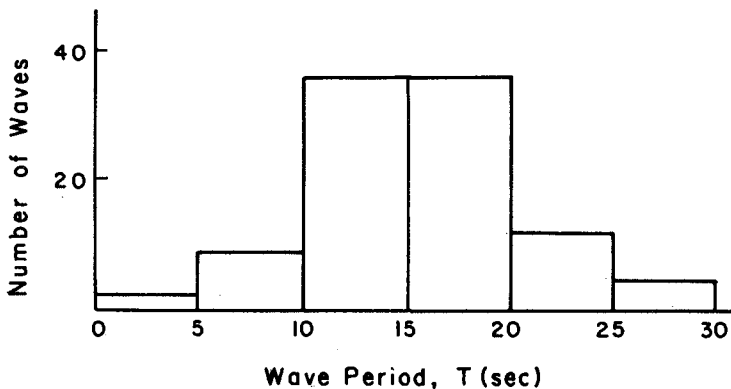


Figure 15. Histogram of the Periods of 100 Consecutive Waves, Measured During Formation of Beach Cusps, Drakes Beach, July 28, 1979.

and a very small negative value ($r = -0.15$) was found. The explanation may be that the mild slope causes the larger waves to break further offshore and in the vicinity of the beach face, the amount of wave energy available for the uprush is nearly independent of the breaking wave height.

THEORY

Introduction

In this section, the interpretation of field observations will form the basis for an attempt to develop a theory representing the swash dynamics on a cusped beach. In addition to the goal of clarifying the mechanisms, a successful theory should yield reliable predictions of beach cusp spacing. The theory presented here commences with an idealization of the beach cusp topography, then proceeds to develop the swash characteristics and finally an equation for the beach cusp spacing is presented in terms of the swash mechanics and the topographic relief of the cusp.

Idealization of Beach Cusp Topography

Based on examination of a number of beach cusps, a reasonable, simple and idealized representation was selected as

$$h(x,y) = Ax(1 + \epsilon \sin ky) \quad (2)$$

in which x and y represent horizontal distances in the shore normal and shore parallel directions, respectively, h represents the elevation of the sand surface above some datum, k is the longshore wave number of the beach cusps, A is the average slope, and ϵ is a small parameter. Figure 6 presents example calculated contours for $\epsilon = 0.2$. The parameter, ϵ , can be shown to be

$$\epsilon = \frac{h_H - h_B}{2Ax} \quad (3)$$

or

$$\epsilon = \frac{h_H - h_B}{(h_H + h_B)} \quad (4)$$

where the subscripts "H" and "B" denote horn and Bay respectively and h_H and h_B are measured at the same x value.

Water Particle Kinematics

The approach will be to consider the water particle motion as that of a discrete particle subject to an initial velocity and gravitational force. The effects of friction will be neglected.

The governing equations for the water particle are

$$\frac{dv_x}{dt} = -g \sin \alpha_x = -g \frac{\partial h}{\partial x} = -gA(1 + \epsilon \sin ky) \quad (5)$$

$$\frac{dv_y}{dt} = -g \sin \alpha_y = -g \frac{\partial h}{\partial y} = -gAx k(\epsilon \cos ky) \quad (6)$$

and the solutions for the water particle excursions can be shown to be

$$\xi_x(t) = v_{x_0} t - \frac{gAt^2}{2} \quad (7)$$

$$\xi_y(t) = -\frac{1}{2} gAxk \epsilon \cos ky t^2 \quad (8)$$

Equations (7) and (8) are approximate since these solutions do not account for variations in slope as the particle moves across the cusp. In utilizing these equations below, the mid-position of the excursion in the x and y directions will be used to approximate this effect.

One use of these equations is in calculating the swash period, i.e. to a first approximation the water particle will return to the initial position in a time T_s , i.e. $\xi_x(T_s) = 0$, or

$$0 = v_{x_0} T_s - \frac{gAT_s^2}{2} \quad (9)$$

or

$$T_s = \frac{2v_{x_0}}{gA} \cong \frac{2v_{x_0}}{g \sin \alpha_x} \quad (10)$$

The maximum uprush occurs at $t = \frac{T_s}{2}$, i.e.

$$(\xi_x)_{\max} = \frac{v_{x_0}^2}{2gA} \quad (11)$$

which simply represents a conversion of the initial kinetic energy of the water particle to potential energy.

The maximum displacement of a water particle in the y-direction should be more-or-less equal to one-half the cusp spacing, λ , and should occur at $t = T_s$. In addition, as noted above, taking values of x and $\cos ky$ in Eq. (8) as

$$x \cong \bar{x} = \frac{(\xi_x)_{\max}}{2} \quad (12)$$

$$\cos ky \approx \cos k\bar{y} \approx 0.6 \tag{13}$$

and noting that $k = \frac{2\pi}{\lambda}$, $(\xi_y)_{\max} = \frac{\lambda}{2}$, and $A \approx \sin \alpha_x$, yields for the cusp spacing, λ

$$\lambda \approx \sqrt{1.2 \pi \epsilon \frac{V_x^2}{gA}} \tag{14}$$

and using Eq. (11), the cusp spacing can be expressed in terms of the maximum swash as

$$\lambda \approx 3.9\sqrt{\epsilon} (\xi_x)_{\max} \tag{15}$$

Six of the sets of observed cusp systems provided enough information to determine ϵ . Three of these systems are presented in Figures 12, 13, and 14. The average ϵ values are presented in Table III and range from 0.07 to 0.29 with the values at Drakes Bay generally smaller than those at Point Reyes Beaches.

TABLE III
SUMMARY OF BEACH CUSP ϵ PARAMETERS

Date and Location of Survey	ϵ
Drakes Bay Beach August 25, 1977	0.13
Point Reyes Beach, North July 22, 1978	0.15
Point Reyes Beach, South July 23, 1978	0.10
Drakes Bay Beach July 23, 1978	0.07
Drakes Bay Beach July 23, 1979	0.09
Point Reyes Beach, South July 24, 1979	0.16
Point Reyes Beach, South July 27, 1979	0.20
Point Reyes Beach, South July 29, 1979	0.29

Selecting a value of 0.15 as reasonably representative and employing Eq. (15),

$$\lambda \approx 1.5 (\xi_x)_{\max} \quad (16)$$

i.e. cusp spacing is linearly related to swash excursion. It is relevant to note that Longuet-Higgins and Parkin (1962) found that their beach cusp data demonstrated a linear relationship between spacing and excursion. Their approximate empirical relationship is

$$\lambda (m) = 2.8 + 0.54 (\xi_x)_{\max} \quad (17)$$

where $(\xi_x)_{\max}$ is in meters. If the empirical relationship to their data is constrained to pass through the origin, the fit is not nearly as good as with the constant in Eq. (17); however, it would be

$$\lambda (m) \approx 1.2 (\xi_x)_{\max} \quad (18)$$

DISCUSSION

"Active" beach cusps as discussed herein refers to a system in which the swash is sufficiently vigorous to transport significant quantities of sediment and which strongly reinforces the beach cusp topography, i.e. a tendency for deposition on the horns and erosion in the bays. In all cases observed "active" beach cusps were characterized by strong and predominant runup on the horns with a seaward flow concentrated through the embayments. This motion was enhanced by a near equality of the wave and swash periods which tended to maintain the cusp topography. The measured ratios $\lambda/(\xi_x)_{\max}$ (1.9 and 3.2) presented in Table III are in order of magnitude agreement with the value (1.5) predicted in Eq. (16). Based on a plane table survey of August 22, 1977, the three berm elevations mapped are approximately 2 m, 3 m and 4 m above mean sea level. Although we did not establish elevations relative to a known datum, (e.g. MSL) these elevations are believed to be accurate to within 0.5 m. Considering the beach face slope, A, to be the same (1:10) during periods when all berms were formed, the Approximate maximum swash excursion would be

$$(\xi_x)_{\max} \approx \frac{B}{A} = 10 B$$

in which B is the berm elevation. For the cusp spacings presented in Table I, the ratios of cusp spacing to maximum swash excursions, $(\lambda/(\xi_x)_{\max})$, are 1.6, 1.4 and 1.4 for the upper, mid and lower sets. These ratios are in remarkably good agreement with the value (1.5) predicted by Eq. (16).

The relationship developed herein between cusp spacing and maximum swash excursion is in qualitative agreement with the effect of sediment size and cusp spacing, other factors being the same. Based on Eq. (11), the swash increases with decreasing beach slope. It is well-known that the beach face slope increases with grain size (Bascom, 1951), thus the swash excursion and cusp spacing would decrease with increasing sediment size. Trask, Johnson and Scott (1956) have documented for the Point

Reyes Beach area, a trend of decreasing cusp spacing with increasing sediment size.

Edge waves provide a possible alternate explanation of beach cusp formation; the associated predicted spacing, λ , is

$$\lambda = \frac{gT^2}{2\pi} \sin(2n+1)\beta \quad (19)$$

in which T is the wave period, β is the beach slope and n is the modal number. For a beach slope of 1:25 and the data presented in Figure 15 (associated with observed formation of cusps), the average wave period of 15.4 seconds yields spacings of 14.8, 44.3 and 29.6 m respectively for the three classes of edge waves noted above. The average observed spacing was 23.2 m which is closest to but differs by approximately 30% from the zeroth mode subharmonic case. Moreover, these subharmonic oscillations entail alternating uprush and backwash in adjacent cusp swales; this was clearly not occurring in any of the cusps observed. A more serious concern in accepting the edge wave explanation is the rather wide range of wave periods presented in Figure 15, and the uncertainty of the use of a single value for the effective beach slope. Additionally, the edge wave theory is linear and thus strictly applies only for small displacements. The swash excursions observed during cusp formation were on the order of 12 m thus raising questions as to the validity of a linear wave theory. Finally it is noted that edge waves would predict an increasing spacing with increasing slope which is contrary to the field observations of Trask, Johnson and Scott (1956) in which beach slope was inferred herein from sediment size.

CONCLUSIONS

There are several results from this study that support the conclusion that swash mechanisms govern beach cusp formation and spacing.

- (1) The water circulation patterns resulting from the swash are such that they cause sediment transport upward and deposition on the horns and a seaward flow and scour in the embayments;
- (2) The simple theory developed herein predicts a linear relationship between cusp spacing, λ , and maximum swash excursion, $(\xi_x)_{\max}$, i.e.

$$\lambda \approx 3.9\sqrt{\epsilon} (\xi_x)_{\max}$$

in which ϵ is a parameter describing the cusp geometry (Eq. (4)). This relationship is in general accord with field results obtained in this study and that of Longuet-Higgins and Parkin (1962).

- (3) The correspondence of large cusp spacing with high berm elevations at Point Reyes (Table I) and inferred maximum swash excursions provide very good quantitative agreement with the simple relationship developed herein.

- (4) Wave periods were measured during beach cusp formation from an approximately planar beach. These periods were quite variable, suggesting that edge waves are probably not the causative mechanism. Additional difficulties in accepting edge waves as the cause are the characteristic non-planar beach geometry and a different trend than inferred from the field data of Trask, Johnson and Scott (1956).

Although swash mechanisms appear to control cusp formation and maintenance at the beaches studied, edge waves or other mechanisms may dominate for cusp features on other beaches and/or under different wave conditions.

REFERENCES

- Bagnold, R. A., 1940, "Beach Formation by Waves: Some Model Experiments in a Wave Tank", Inst. Civil Engineers Jour., v. 15, p. 27-52.
- Bascom, W. N., 1951, "The Relation Between Sand Size and Beach Face Slope", Trans. Amer. Geophys. Union, v. 32, p. 866-874.
- Bowen, A. J. and D. L. Inman, 1969, "Rip Currents, 2: Laboratory and Field Observations", J. Geophys. Res., v. 74, p. 5479-5490.
- Branner, J. C., 1900, "The Origin of Beach Cusps", J. Geol., v. 8, p. 481-483.
- Dalrymple, R. A. and G. A. Lanan, 1976, "Beach Cusps Formed by Intersecting Waves", Geol. Soc. Amer. Bull., v. 87, p. 57-60.
- Dubois, R. N., 1978, "Beach Topography and Beach Cusps", Geol. Soc. Amer. Bull., v. 89, p. 1133-1139.
- Evans, O. F., 1938, "The Classification and Origin of Beach Cusps", J. Geol., v. 46, p. 615-627.
- Flemming, N. C., 1964, "Tank Experiments on the Sorting of Beach Material During Cusp Formation", J. Sed. Petrology, v. 34, p. 112-122.
- Galvin, C. J., Jr., 1964, "Cusps Formed by Standing Edge Waves on a Laboratory Beach", (Abstract) Geol. Soc. Amer., Spec. Paper 82, p. 69-70.
- Gorycki, M. A., 1973, "Sheetflood Structure: Mechanism of Beach Cusp Formation and Related Phenomena", J. Geol., v. 81, p. 109-117.
- Guza, R. T. and D. L. Inman, 1975, "Edge Waves and Beach Cusps", J. Geophys. Res., v. 80, p. 2997-3012.
- Jefferson, M. S. W., 1899, "Beach Cusps", J. Geol., v. 7, p. 242.
- Jefferson, M. S. W., 1903, "Shore Phenomena on Lake Huron", J. Geol., v. 11, p. 123.

- Johnson, D. W., 1910, "Beach Cusps", Geol. Soc. Amer. Bull., v. 21, p. 604-624.
- Johnson, D. W., 1919, Shore Processes and Shoreline Development, J. F. Wiley, New York.
- King, C. A. M., 1972, Beaches and Coasts (2nd ed.), Edward Arnold (Publishers) Ltd., London, 570 p.
- Komar, P. D., 1973, "Observations of Beach Cusps at Mono Lake, California", Geol. Soc. Amer. Bull., v. 84, p. 3593-3600.
- Kuenen, Ph. H., 1948, "The Formation of Beach Cusps", J. Geol., v. 56, p. 34-40.
- Lane, A. C., 1888, "The Geology of Nahant", (Abstract) Bost. Soc. Nat. Hist. Proc., v. 24, p. 91-95.
- Longuet-Higgins, M. S. and D. W. Parkin, 1962, "Sea Waves and Beach Cusps", Geogr. Jour., v. 128, No. 2, p. 194-201.
- Meteorological International, Incorporated, 1977, "Deep-Water Wave Statistics for the California Coast, Station 3", Prepared for the Department of Navigation and Ocean Development, State of California.
- O'Brien, M. P., 1978, Personal Communication.
- Otvos, E. G., 1964, "Observations of Beach Cusps and Pebble Ridge Formation on the Long Island Sound", J. Sed. Petrology, v. 34, p. 554-560.
- Palmer, H. R., 1834, "Observations on the Motion of Shingle Beaches", Phil. Trans. of the Royal Soc., London, v. 124, p. 567-576.
- Russell, R. J. and W. G. McIntire, 1965, "Beach Cusps", Geol. Soc. Amer. Bull., v. 76, p. 307-320.
- Sallenger, A. H., Jr., 1979, "Beach Cusp Formation", Marine Geol., v. 29, p. 23-37.
- Shaler, N. S., 1895, "Beaches and Tidal Marshes of the Atlantic Coast", Natl. Geogr. Monograph I, p. 137-168.
- Smith, D. and R. Dolan, 1960, "Erosional Development of Beach Cusps Along the Outer Banks of North Carolina", (Abstract), Geol. Soc. Amer. Bull., v. 71, p. 1979.
- Trask, P. D., 1956, "Changes in Configuration at Point Reyes Beach, California, 1955-56", B. E. B. Tech. Memo. No. 91, 61 p.
- Trask, P. D., 1958, "Beaches Near San Francisco, California, 1956-57", B.E.B. Tech. Memo No. 110, 89 p.
- Trask, P. D. and C. A. Johnson, 1955, "Sand Variation at Point Reyes Beach, California", B.E.B. Tech. Memo No. 65, 86 p.

Trask, P. D., C. A. Johnson and T. Scott, 1955, "Cut and Fill on Point Reyes Beach, California", Univ. of California Hydraulic Engineering Laboratory, Report No. 14-19, 31 p.

Trask, P. D. and D. T. Snow, 1961, "Beaches Near San Francisco, California, 1957-58", Univ. of California Hydraulic Engineering Laboratory, Report No. 14-23, 90 p.

Ursell, F., 1952, "Edge Waves on a Sloping Beach", Proc. Royal Soc. London, Ser. A, v. 214, p. 79-97.

Williams, A. T., 1973, "The Problem of Beach Cusp Development", J. Sed. Petrology, v. 43, p. 857-866.

Yasso, W. E., 1965, "Plan Geometry of Headland Bay Beaches", J. Geol., v. 73, p. 702-714.

BARRON RIVER DELTA INVESTIGATION

D.A. Robinson*, A.M.ASCE,
D.J. Cook** and J.G. Barff***

1.0 INTRODUCTION

The Barron River flows to sea through a 50 km² alluvial Delta on the narrow coastal plain near Cairns, Queensland in north eastern Australia. The Delta is in the tropics at 17 degrees south latitude. Most of the 2175 km² catchment lies above 450 m above sea level. The coastal portion of the catchment has an average annual rainfall in excess of 2000 mm. River flows are highly variable with peak flood flows of over 4000 m³ s⁻¹, and dry season flows of less than 15 m³ s⁻¹. The Delta is tidal with ocean tides having a range of 1.8 m at Spring Tides. There are three water storages on the catchment, one on the upper catchment having an ungated spillway and a capacity of 407 x 10⁶ m³ for irrigation purposes and the other two just upstream of the Delta, are a small weir of 1.7 x 10⁶ m³ capacity to regulate water supply to the Barron Gorge Hydro-electric Power Station, and Copperlode Falls Dam on Freshwater Creek, a 45 x 10⁶ m³ ungated storage to provide water to Cairns City and the nearby Mulgrave Shire.

The Delta consists of alluvial soils which support 3600 hectares of sugar cane farm land. The beaches in the Delta are being developed as resort towns and dormitory suburbs.

Sand and gravel is regularly dredged from the lower reaches of the main river in the Delta at the rate of 50,000-80,000 m³ per year. Increasing scarcity of sand sources, and the concern that dredging and dam construction is threatening beach sand sources have raised conflicting pressures on the Authority which licences the extraction of sand and gravel from the river.

This, coupled with regular flooding of the Delta and the cutting of major highways, and the continuing erosion of cane farm land has initiated a major data collection programme as a prerequisite to formulating solutions for the flooding and erosion problems.

2.0 IDENTIFICATION OF THE PROBLEM

A Steering Committee consisting of representatives of the local administering bodies and relevant State Government Departments was formed to supervise the data collection programme.

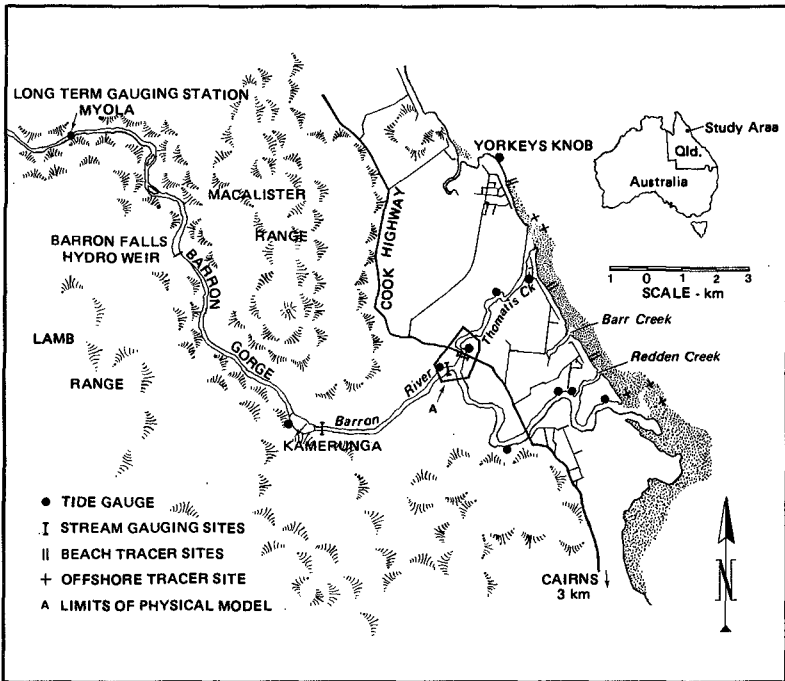
* Engineer, Beach Protection Branch, Department of Harbours and Marine, Queensland.

** Officer in Charge, Hydraulics Laboratory, Department of Harbours and Marine.

*** Engineer, Foreshore Development Branch, Department of Harbours and Marine.

Five major problems relating to the physical processes of the Delta were identified.

- (a) The increasing urban settlement and the increasing value of the sugar crop has brought pressures to mitigate floods in the delta.
- (b) Erosion of the river banks, particularly in Thomatis Creek is resulting in the loss of farm lands.
- (c) Erosion of the ocean beaches is threatening beachfront facilities and degrading the recreational value of the beaches.
- (d) The maximum quantity of sand and gravel, which can be removed from the river without damage to the river banks and adjacent beaches needs to be determined.
- (e) The percentage of flow down each of the two main river channels in the delta needs to be determined, with regard to the conflicting requirements of bank stability, sediment discharge capacity and flood levels for each stream.



LOCALITY PLAN

Figure 1

A three year data collection programme (1975-1979) was initiated to provide the basis for solution of these problems. The data collection and collation was co-ordinated and largely undertaken by the Queensland State Government Department of Harbours and Marine. This paper is a summary of the much larger investigation report prepared by the Department of Harbours and Marine for the Steering Committee. (Reference 1).

3.0 DATA COLLECTION

A large component of this investigation was the data collection programme. This programme, spread over a 3 year period included the following:-

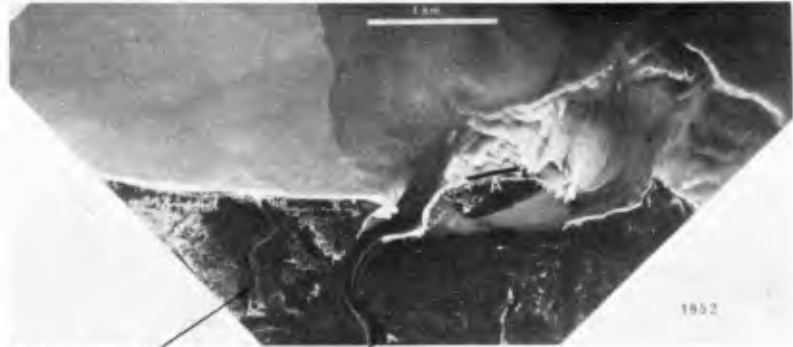
- (a) orthophoto mapping of the Delta at scale 1:2500
- (b) cross-section survey of river and creek channels at 250 m intervals
- (c) water level recording (tide and flood) at 7 locations in the Delta
- (d) bed material sampling for particle size determination in river channels and on the beaches
- (e) stream flow measurement at 5 locations during flood conditions
- (f) tidal flow measurements in the river and creek channels and offshore
- (g) repetitive beach surveys
- (h) wave recording
- (i) radio active tracer studies at the junction of Barron River and Thomatis Creek and on the beaches
- (j) siltation survey of the Tinaroo Falls Dam; and
- (k) geological and geophysical studies of the Delta and immediate offshore area
- (l) historical searches of cadastral surveys and aerial photographs.

During the study period, two of the three largest floods experienced in the Delta since the commencement of streamflow measurement on a systematic basis in 1915, occurred, presenting a remarkable opportunity for stream flow measurement and suspended sediment sampling.

In relation to the specific objectives listed in section 2.0 of this paper, the data collection programme is obviously very extensive. However a second, but equally important aim of the study was to provide a comprehensive data base for the understanding of Delta behaviour and the assessment of management proposals for the area. As a result of the success of this data collection programme, the study report will fulfil this second objective, providing a comprehensive and detailed description of the Delta which will be of immense value in the future.

4.0 RIVER PROCESSES

The Barron River, in creating a delta where it reaches the sea, has created some of the most valuable agricultural land in northern Australia, and, if left undisturbed, would continue to expand the Delta land mass. It would also however, continually change the plan geometry of the river channels and the importance of each of the distributaries would also change from time to time. These processes can be seen at work in the Delta today. Channel meandering has threatened valuable farmland by bank erosion and many examples of this can be found in the Delta. It is however, the question of distributary dominance that is of more interest to this paper, affecting as it does the overall stability of the river/beach system by controlling the distribution of sedimentary materials.



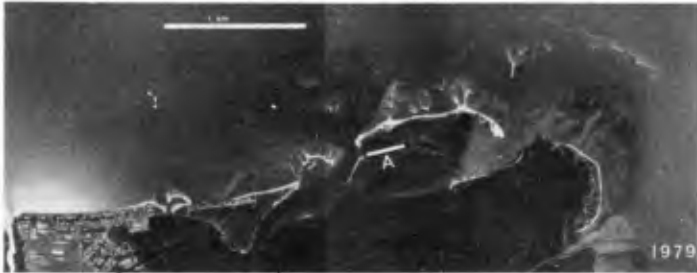
Redden Creek

Barron River



Redden Creek

Barron River



Redden Creek

Barron River

Position of line 'A' common to all photographs.

DEVELOPMENT OF THE BARRON RIVER BAR 1952-1979

Figure 2

The Barron River has three tidally connected outlets to the sea - the main channel, Thomatis Creek and Redden Creek. The relative importance of these three channels has changed over the past fifty years. Until 1932, the Thomatis channel carried Barron River water only in major floods, but surveys dating from about 1900 show clearly the development of Thomatis Creek, until, in the major 1932 flood, the River broke through and Thomatis Creek began to develop as a permanent mouth. There is a gradient advantage along this channel to the sea. The flow path is 6 km compared to 9 km via the Barron and it is reasonable to assume that unless man intervenes, the main Barron Channel will become less important and Thomatis Creek will become the major mouth.

The proportion of flow carried by each channel at high flood is difficult to estimate because of the large overland flows which occur at such times. However, at the bankfull stage, which many authors suggest is most closely associated with the channel forming process, the flow split is about 65% main channel to 35% Thomatis Creek. Hardin (Reference 2) in studies of the distributaries of Mississippi Delta suggested that when the emerging distributary has grown to the size where it can carry 40% of the flow the process is very difficult to reverse.

Whilst there is no reason to suggest that an identical figure will apply to the Barron River, it is clear that Thomatis Creek is increasing in size and that siltation is occurring in the Barron River downstream of the junction, and that the longer an attempt to reverse the process is delayed, the more difficult it will be to effect. To investigate ways of controlling the flow split at the junction, a 100:1 undistorted physical model was constructed at the Queensland Government Hydraulics Laboratory (Reference 3) to examine a variety of control works and to estimate their effect elsewhere in the system. The limits of the model are shown on Figure 1.

An important factor to be considered is the effect of works at the junction on distribution of sediments to the beaches. Suspended sediment measurements and tracer experiments show that the sand size and smaller sediments in the Barron River, in all but the smallest floods, are carried in suspension. At the bankfull condition, it is estimated that only 12% of sediments are carried to the sea via Thomatis Creek, so total closure of that mouth (to bank full level) would have only a very small effect of supply to the beaches, as the great bulk of transport takes place in floods larger than bank full. These would be affected to a much smaller extent.

So even if the junction is closed off to the maximum practicable level, (about bankfull), the study has shown that only a few percent of the sediments carried by Thomatis Creek will be diverted. Closing off the junction will also have only a very minor effect on the tidal flows in the Delta channels. Field measurements have shown that there is only a very small net tidal circulation through the junction which is what one would expect when the history of development of Thomatis Creek, first as a tidal creek and then later as a distributary, is considered.

Redden Creek, whilst only a very minor distributary, has quite an interesting history nonetheless. Prior to 1939, the main Barron River channel entered the sea about 1.5 km further south than at present, and Redden Creek was then considerably more important than at present. Since the new entrance developed, it is not only less favoured hydraulically but its mouth is dominated by the sands of the Barron River bar and is closed for most of the year. Figure 2 illustrates the changes that have taken place over the last 27 years. In the last fifty years the Thomatis Creek mouth has also moved 1.2 km to the North.

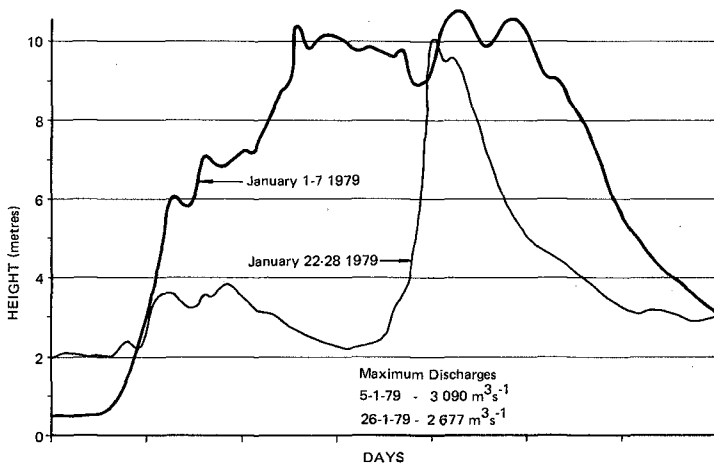
Although these changes are very important to property owners with river and creek frontages, they are far less significant when compared to changes that have taken place over the much longer geological time scale. Geophysical evidence suggests that in the period before the last major sea level change (6000 years ago) the main Barron River channel flowed to the sea close to the modern Thomatis/Richters Creek channel alignment.

5.0 FLOODS

During the summer monsoon period, November to April, tropical cyclones or hurricanes can occur. While rainfall in the Delta is reliable flood rains in the 2175 km² catchment can be quite variable. River flows can range from less than 15 m³s⁻¹ in the dry season to annual peak flows which have been recorded to vary from 80 m³s⁻¹ to 4500 m³s⁻¹ in 63 complete years of record.

Figure 4(a) shows the variation of the annual maximum instantaneous discharges. The major floods are all associated with tropical cyclones crossing the catchment.

During major floods agricultural land on the Delta is inundated to depths of between 1 and 3 metres. In the 1979 flood over 100 houses had to be evacuated. The duration of floods can be quite variable. In 1979 two floods with almost equal peak flows occurred. While the peak discharges are similar Figure 3 shows that the total discharge and hence total sediment discharge will be markedly different.



NOTE: Flood levels shown for Myola Water Level Recorder Station for two 1979 floods.

COMPARISON OF TWO FLOODS

Figure 3

Following the major 1979 floods, flood inundation maps for the Delta have been prepared. The 1979 flood, the second largest on record had a peak discharge of $4600 \text{ m}^3 \text{ s}^{-1}$ on the Delta. The inundation maps reveal that virtually all of the Delta is subject to river flooding. The only areas free from flooding are the coastal sand ridges occupied by residential development. These coastal ridges are only 2 metres above the ocean high water level and are vulnerable to inundation by storm surges associated with tropical cyclones.

Further development of the Delta for residential purposes will require careful planning to ensure adequate escape routes are available in the event of major floods or storm surge inundation.

6.0 RIVER SEDIMENT TRANSPORT

Sediment in the river consists of fine to medium sands up to gravels of 300 mm diameter at the head of the Delta, to medium to fine sands and muds in the lower reaches. River bed samples were collected during the dry season. 268 suspended sediment samples were collected during floods and 240 samples collected during the dry season when river flows in the Delta were tide generated.

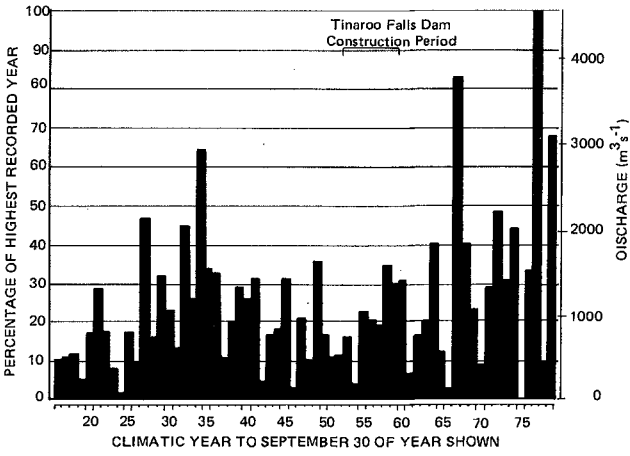
Several approaches for estimating sediment transport in the river were used including estimates from -

- * recent geological evidence
- * regional catchment predictors which use catchment characteristic parameters such as slope area, soil type etc.
- * direct measurements of suspended sediment load
- * sediment transport predictor formulae.

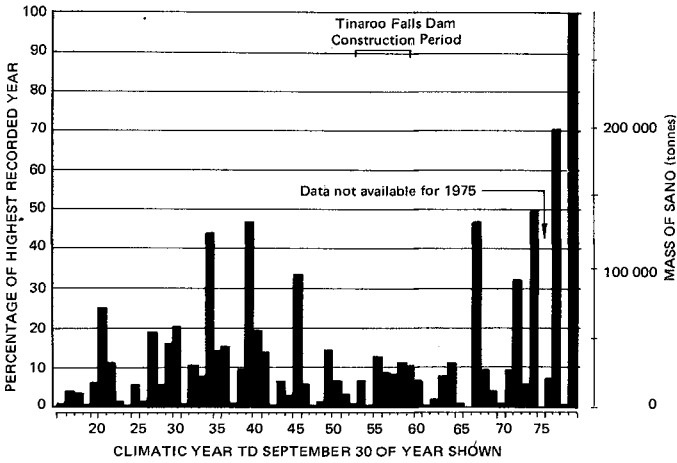
Considering only sand size particles, estimates of sediment transport were made using several theoretical methods, notably those of Engelund and Hansen (Reference 4) and White-Ackers (Reference 5) calibrated against the measured suspended sediment (Figure 5). At high flows sand sized particles are all carried in suspension. Observations during flood conditions confirm this. In sections of the river that could be accessed during major floods the channel bed was found to be composed of gravel or stiff clay indicating that the rivers capacity for transporting sand exceeded the actual transport. During the falling stages of the flood sand was deposited over the river bed.

Several difficulties were encountered in estimating sediment transport using total load predictors. Selection of a suitable gauging site required a compromise between sites at the head of the Delta where multiple channels exist but little overbank flow occurs and downstream sites where well defined channels occur but overbank flow is significant though difficult to quantify.

Based on 63 years of river flows transport of sand was estimated to be of the order of $23,000 \text{ m}^3$ per year. The annual sediment transport rate estimate is shown in Figure 4(b).



a. Annual Maximum Discharge

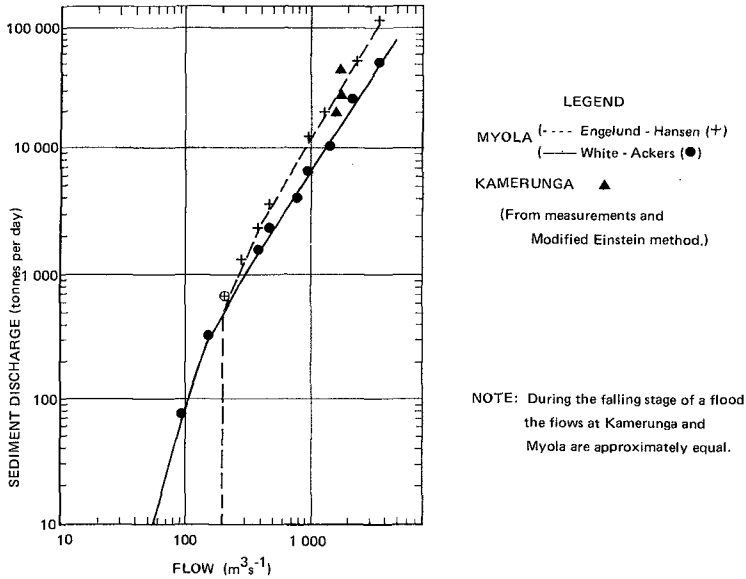


b. Sediment Discharge

NOTES: Plots for discharge past Myola Water Level Recorder each Climatic Year.
 Calculation of Sediment Discharge used the Engelund and Hansen Method.

DISCHARGES AT MYOLA 1916 to 1979

Figure 4



SAND TRANSPORT CAPACITY VS FLOW AT KAMERUNGA AND MYOLA GAUGING STATIONS

Figure 5

The estimates of sand transport gave sediment transport rates ranging from 3500 m³/year based on beach ridge accumulation through 11,000 m³/year from regional catchment characteristics and 23,000 m³/year from sediment transport formulae to 35,000-50,000 m³/year from recent geological evidence. For sand resource management a figure of 23,000 m³/year has been adopted.

7.0 COASTAL PROCESSES

Geological evidence shows that the most of the Delta has formed during the last 6000 years following the last major change in the world's sea level. From geological evidence the Barron River is supplying about 300,000 m³/year of sediment of which 60,000 m³/year is sand and gravel. Written history of the Delta only exists from the 1870s with firm evidence restricted to this century. During the last 50 years the Delta's beaches north of the Barron River have eroded at rates of the order of 30 m in 50 years.

The Beach Protection Authority is currently undertaking a study of beach processes in the Cairns area. The study includes the 8 km of beaches of the Barron Delta. Preliminary results from the Authority's study have been used. The Authority's beach study is similar in approach to a study of the Capricorn Coast Beaches reported elsewhere in these proceedings.

The Delta's beaches are protected from ocean swells by the coral reefs of the Great Barrier Reef, which restricts fetches to 50 km. The beaches of the Barron River Delta exhibit the typical North Queensland beach profile which consists of a steep beach down to Mean Sea Level and extensive, nearly horizontal sand and mud flats extending 1000 m or more offshore. Waves recorded in 18 m of water offshore from the Delta over a three year period, using a Datawell "Waverider" recorder show how sheltered the beaches are under normal weather conditions (Reference 6). A significant wave height (H_s) of 0.5 m was exceeded 50% of this time, while only 3% of the time did H_s exceed 1.0 m. No waves over 2.0 m were recorded over the 3 year period. Using 9 years of available wind data, a hindcast wave climate (wave height, period and direction) was also determined (Table 1).

TABLE 1
WAVE CLIMATE
BARRON RIVER BEACHES

WAVE HEIGHT m	PERCENTAGE OF TIME WAVE HEIGHT EXCEEDED		
	RECORDED	OFFSHORE HINDCAST	BREAKING WAVES - MACHANS BEACH (observed)
0.2	95.	99.6	54.
0.4	63.	67.	18.
0.6	37.	42.	6.
0.8	17.	2.8	1.5
1.0	3.0	0.7	0.15
2.0	--	0.02	--

The Delta region is subject to tropical cyclones (hurricanes). Historically the Delta has not experienced a major cyclone in the last 50 years. Statistically however, it is estimated that 7 cyclones pass within 100 km of the Delta every 66 years. A cyclone of 50 year return period within 200 km radius of the Delta is estimated to have a central pressure of 963 mb.

Beach profiles were measured from the dune crest extending out to 3000 metres offshore along the 8 km of the Delta's beaches. Sixteen profile lines were repeatedly surveyed to assess seasonal variations and to measure any changes in beach shape directly attributable to floods. Surface sediment samples were collected and an explanatory geophysical survey was undertaken of the nearshore marine sediments.

The beaches exhibit a wide range of sediment sizes reflecting the river source of the material and the poor sorting by the low energy wave climate. The beaches between low water mark and the dunes are fine to medium silica sands (0.2 to 0.5 mm median size) while offshore silt and mud fractions become significant as water depth increases.

A radioactive tracer study was undertaken to measure sediment movement on the beaches, and on the bars at the mouths of the Barron River and Thomatis Creek. Active gold - 198 labelled sand was used offshore while an inactive tracer (Indium Nitrate) was used to label the beach sands.

Estimates of longshore transport were made using the method in the Shore Protection Manual, and methods of Bijker, Komar and the Authority's own procedure using observed daily longshore currents and breaking wave data (Reference 1). Annual nett longshore transport capacity was predicted to be in the range of 10,000-30,000 m³/year to the north.

It was the longer term beach changes with 5 to 50 year cycles, and changes related to major flood events which were of interest to this study rather than seasonal onshore-offshore or short term fluctuations.

The Barron River supplies 23,000 m³/year of sand sized sediments. Currently most of these sediments reach the coast via the main Barron River mouth, with minor amounts debouching from the other distributaries. The supply rate is very irregular as can be seen in Fig. 4(b). This contrasts with the longshore transport which tends to be of the same order from year to year.

The Barron River mouth moved 1.5 km with the connection of a meander to the sea 40 years ago. The old mouth closed and a new mouth and bar formed. The growth of the new bar and some reduction in size of the old bar can be seen in Fig. 2 as well as evidence of the strong onshore transport which has produced a new beach ridge south of the present mouth - the only coastal accretion recorded in the last 50 years on the Delta's beaches.

Geologically the coastline has accreted over the last 6000 years, at an "average" rate of 30 metres per 100 years. Historically the coastline has eroded in the order of 30 m in the last 50 years. A possible explanation for this paradox was found in the growth of the new Barron River bar. Empirical relationships between the volume of sand in the bar and the tidal prism of the river estuary (Reference 7), suggest that 500,000 m³ of sand sized sediments are required to form the new bar. The main source of these sediments can only be from the river. Until the bar reaches an equilibrium state then excess sediment will not be readily available for transport away from the river mouth to the northern beaches. Thus until the new bar is fully developed erosion of the adjacent beaches is expected as longshore transport is removing sand from these beaches while little sand is being supplied from the river mouth.

8.0 CONCLUSION

The Barron River Delta Investigation had two clear objectives -

- (a) to compile a data base to assist those Authorities with responsibility for management of the waterways and sedimentary resources of the Delta in the formulation of a management plan for the Delta; and
- (b) to interpret the data as it relates to several important areas of concern at the Delta - the Barron River/Thomatis Creek junction, the Barron River beaches, sand and gravel dredging, and flooding of urban areas, and to suggest ways alleviating problems in these locations.

The first of these objectives has clearly been met, climatic events having provided an unequalled opportunity for data collection. Whether the second objective has been fully met will not be known until a considerable period of time has elapsed and the effects of any remedial works that are undertaken can be assessed.

9.0 ACKNOWLEDGEMENTS

The permission of Mr J. Leech, the Director of the Department of Harbours and Marine, Queensland State Government, and Mr A.H. Britton, the Chairman of the Barron River Delta Investigation Steering Committee, to present this paper is gratefully acknowledged. It is desired to especially thank those members of the several organisations who assisted in the data collection and collation for the study.

10.0 REFERENCES

1. Barron River Delta Investigation Steering Committee, *Report of Barron River Delta Investigation*, Harbours and Marine Department, Brisbane (in preparation).
2. J.R. Hardin, 'Old River - The General Problem', *Journal of the Waterways Division*, Proceedings of the American Society of Civil Engineers, Paper 906, 1956.
3. Department of Harbours and Marine, *Barron River-Thomatis Creek Confluence Model*, Queensland Government Hydraulics Laboratory Report M6, Deagon, June, 1979.
4. F. Engelund & E. Hansen, *A Monograph on Sediment Transport in Alluvial Streams*, Teknisk Forlag, Copenhagen, 1967.
5. P. Ackers & W.R. White, 'Sediment Transport: New Approach and Analysis', *Journal of the Hydraulics Division*, Proceedings of the American Society of Civil Engineers, Vol. 99, No. HY11, November, 1973, pp. 2041-2060.
6. Beach Protection Authority, *Wave Data Recording Programme: Cairns Region*, BPA Report No. W 01.1, Brisbane, November, 1978.
7. T.L. Walton & W.D. Adams, 'Capacity of Inlet Outer Bars to Store Sand', *Proceedings of the Fifteenth Coastal Engineering Conference*, American Society of Civil Engineers, New York, 1976, pp. 1919-1937.

CHAPTER 56

SOFT DESIGNS FOR COASTAL PROTECTION AT SEABROOK ISLAND, S.C.

Miles O. Hayes¹, Timothy W. Kana² and John H. Barwis³

ABSTRACT

To gain a better understanding of the cycles of shoreline changes on Seabrook Island, South Carolina and advise a private developer on how to deal with localized erosion problems, a detailed field survey and historical study were completed. The data base included historical charts dating from 1661, vertical aerial photographs from 1939, field surveys of beach profiles and nearshore bathymetry over a six-month period, and sediment cores through the entire Holocene section. Seabrook Island, less than 6 km in length, is bounded by tidal inlets with extensive seaward shoals. With a 2 m tidal range for the area, changing exposure and orientation of the shoals over time has had a profound effect on the adjacent shoreline of Seabrook Island. Historical evidence points to the importance of offshore shoals which act as natural breakwaters and sediment storage systems. At various times in recent history, these shoals have supplied sediment to Seabrook beaches by means of bypassing mechanisms around tidal inlets. On the other hand, migration of shoals has allowed excess wave energy to strike portions of the shore causing local erosion. Along a portion of the shoreline, short-term erosion is jeopardizing the development. Based on the present study, a set of "soft" engineering designs was proposed which attempt to manipulate offshore sand bodies in a way that will be beneficial to the development and preserve the inherent beauty of the shoreline. Remedial measures recommended for the developer included dredging new inlet channels and construction of a breakwater in the position of a former protective shoal.

INTRODUCTION

Seabrook Island near Charleston, South Carolina, U.S.A. (Fig. 1) is a typical mesotidal (tidal range 2.0 m) barrier island consisting of vegetated beach ridges and low frontal dunes bounded by tidal inlets and a marsh-tidal creek system. Within the past 5 years, it has been developed as a private vacation resort. Due to its proximity to a major tidal inlet and the presence of numerous shifting offshore shoals, the ocean shoreline has tended to change rapidly in response to local variations in wave energy. This has presented significant problems to portions of the existing development. Several homes and the community center are located in erosion zones and have required seawalls or rubble mound rip-rap for protection; whereas, some nearby beaches are presently accretional.

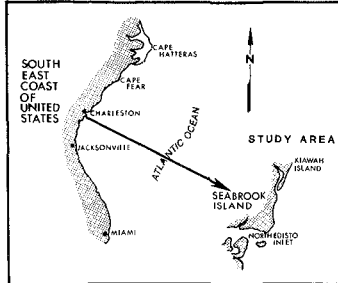
¹Coastal Research Division, Dept. of Geology, University of South Carolina, Columbia, S. C., U.S.A., 29208

²Research Planning Institute, Inc., 806 Pavillion Ave., Columbia, S. C., U.S.A., 29205

³Shell Oil Company, P. O. Box 527, Houston, TX, U.S.A., 77001

While coastal protection works are providing immediate relief to certain highly erosional areas of the development, they are causing long-term adverse effects, including acceleration of erosion in unprotected areas and destruction of the natural character of the island. This latter effect is of great concern since the key attraction of this and other South Carolina coastal developments is their unspoiled beaches.

Figure 1. Location map of Seabrook Island, S. C. (30 km south of Charleston, S. C.).



To gain a better understanding of the cycles of shoreline changes on Seabrook Island and advise the development company on how to deal with localized erosion problems, a detailed field survey and historical study were completed. Solutions were sought which would allow natural sedimentation processes of the adjacent inlet shoals and beaches to work in harmony with proposed engineering modifications. Large volumes of sand are stored in the ebb-tidal deltas (outer shoals) of the inlets at either end of Seabrook Island. It was hypothesized that manipulation of these shoals would modify the distribution of wave energy along the shore and reduce or eliminate the erosion problem. Thus, the approach taken was to utilize geologic and coastal process information and determine appropriate "soft" engineering solutions which would have the aesthetic advantage of preserving the character of the Seabrook beaches.

DATA BASE

A combination of laboratory analysis of historical data and a variety of field observations completed during a six-month period between June and December, 1978 are available. The data base included:

1. Historical charts from 1661, 1853, 1867, 1919, and 1914.
1. Vertical aerial photographs from 1939, 1949, 1954, 1957, 1963, 1973, and 1978.
3. Nine permanent beach profile stations monitored monthly for six months.
4. Monthly wave process data at 8 stations (wave height, breaker angle, longshore currents, and wave period).

5. Monthly surveys of two cross-sectional bathymetric profiles of N. Edisto Inlet (Fig. 1).
6. Preparation of a detailed bathymetric map of the seaward shoals of the inlet.
7. Sediment cores through the entire Holocene section along two transects across Seabrook Island.

COASTAL PROCESSES

Winds

Seabrook Island is influenced by prevailing winds from the SW (36% of the time) and storm winds generally from the NE (28% of the time). In general, the NE winds, though less frequent, are stronger, causing waves and longshore transport directed SE along the island. Hurricane force winds have a return period of approximately one event every 14 years (Myers, 1975). While hurricanes are relatively rare along this portion of the South Carolina coast, they have been known to cause extensive damage to property from high winds and associated storm tides.

Tides and Storm Surges

The mean tidal range at Seabrook Island is approximately 1.7 m (5.2 feet), with spring tides ranging up to 2 m (6.1 feet). These tides generate strong currents in North Edisto Inlet (south end of Seabrook) and Kiawah River Inlet (north end of Seabrook) as well as in major tidal creeks. This moderately large tidal range allows a wide portion of the beach to be exposed to wave action. Storm surges superimposed on normal astronomic tides occur during extratropical and tropical storms and have produced tides up to 12 feet (3.7 m) above normal along the South Carolina coast.

Waves

Wave energy along the Seabrook Island shoreline varies widely due to a combination of factors, including: 1) the direction of wave approach whether from the E or SW, and 2) the position of offshore shoals. The intertidal shoals act to dampen waves, reducing wave heights along the corresponding lee shore. This has an important effect on the distribution of sediment transport along the coast since longshore transport is related to wave energy and the angle of wave approach.

Between June and December 1978, representative monthly wave measurements were obtained at 8 stations on Seabrook Island (Fig. 2). Although these data are not detailed enough to establish a seasonal trend, they allow comparison of relative wave energy at various points along the shore. Variables measured included wave height, breaker angle, longshore current velocity, and wave period.

Average wave heights ranged from a low of 11 cm at P8 in October to a high of 80 cm in July at station 3 located near the development's clubhouse. The bar graph inset in Figure 3 shows the average distribution of wave heights. Note that the highest average waves occur at stations 3 (49 cm) and 6 (42 cm), both of which are presently experiencing the most severe erosion. The wide variance in wave heights along the shoreline results from a combination of factors including: (1) the direction of wave approach, whether from the east or southwest, and (2) the position of offshore shoals. The intertidal shoals act to dampen waves, reducing wave heights along the corresponding lee shore. For example, stations 2, 5, and 8 are relatively protected by offshore shoals, accounting for their reduced average wave height; whereas, stations 3 and 6 are more exposed.

Longshore Transport

The variability in wave heights along the Seabrook Island shoreline produces different rates of longshore sand transport. This has important consequences to shoreline changes because where transport is reduced, as along lee shores protected by offshore shoals, sand accumulates. At Seabrook Island, two wave directions are most common. During summer, waves from the southwest and south produce longshore transport northeast along the beach. Storms, on the other hand, generally cause sand transport to the southwest. When averaged over the entire year, more sand moves southwest under the influence of storm waves. This fact is evident at Kiawah Island, located north of Seabrook, where a large recurved spit at the southwest end of the island continues to grow rapidly toward Seabrook as a result of the influx of sand from the north.

To determine relative transport rates, wave data from the 8 process stations were used to estimate daily longshore transport. These data do not indicate long-term rates, but they offer an explanation for the erosional and depositional trends discussed in succeeding sections.

Figure 3 gives the average daily transport rates at each of the 8 process stations, based on monthly wave observations between June and December. Highest transport rates occur at stations 3 and 6, which are least sheltered by offshore shoals and which have higher than normal erosion rates. The range of equivalent yearly rates are $75-300 \times 10^3 \text{ m}^3/\text{year}$.

Modification of Coastal Processes by Artificial Structures

Coastal structures existing in 1978 at Seabrook Island included: (1) sand bag groins designed to trap sediment moving alongshore, (2) vertical poured-concrete seawalls to protect a clubhouse at station 3 and houses between stations 4 and 5, and (3) rubble mound rip-rap to anchor the shoreline between stations 2 and 3 (Fig. 4).

Sand bag groins. - The groins at Seabrook trapped some of the sand moving alongshore and initially caused minor reorientation of the shoreline as fillet beaches developed on the updrift (northeast) side and erosion on the downdrift side. However, after the reorientation to a new "equilibrium" shoreline, the erosional trend continued at stations 3 and 5 despite the presence of these groins.

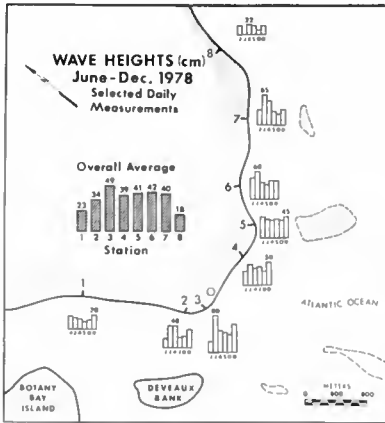


Figure 2. Distribution of wave heights measured monthly from June to December 1978 along Seabrook Island. Highest waves (inset) occur at station 3 at the southwest point of the island.



Figure 3. Net and (gross) long-shore transport rates along Seabrook Island based on wave energy flux. Highest net rates at stations 3 and 6 correspond to erosion zones at the time of the survey.

Figure 4. Oblique aerial photograph taken in 1978 of the southwest point of Seabrook Island. View looking southwest. Note coastal structures, including a groin, seawall, and revetment built to protect a community clubhouse. Erosion of the adjacent shoreline has produced the shoreline offset.



Concrete seawalls. - The vertical seawalls at Seabrook have protected several houses and the clubhouse by retaining sand behind them. However, they have had some adverse effects including an apparently accelerated erosion along adjacent shorelines. Vertical seawalls also reflect wave energy back offshore rather than absorbing or dissipating it. This tends to cause scour and remove sediment from the nearshore area.

Rubble mound rip-rap. - The rip-rap built between stations 2 and 3 has been more successful than the vertical seawalls since it absorbs much of the wave energy and reduces the scouring effect of reflected waves. Its main disadvantage is eliminating a recreational beach if erosion continues. While protecting property, the rip-rap seawall at Seabrook is not solving the long-term problem of continued erosion due to lack of sediment supply from updrift.

SHORELINE CHANGES

Historical Charts and Maps

In order to learn about the more recent short-term shoreline changes on Seabrook Island, all charts and maps available were assembled and studied. Particular attention was placed on the changing location of shoals and inlet channels. Five historical charts were available covering the period 1661 to 1924. One example, from 1867, is shown in Figure 5. Key reference points were located on each chart to establish shoreline and tidal inlet positions. It became apparent that two points warranted attention: 1) the spit at the southwest end of Kiawah Island which periodically overlapped much of the shoreline along Seabrook Island, and 2) an offshore supratidal shoal, referred to as Deveaux Bank, associated with the ebb delta of North Edisto Inlet which borders the southwest end of Seabrook.

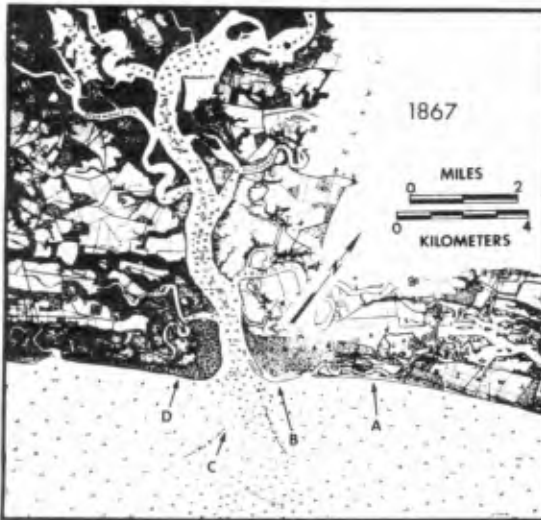


Figure 5. Bathymetric chart for 1867 (USC & GS Chart No. 154, Ed.1). Arrows indicate points of reference for comparison between charts. Note extension of recurved spit of southern end of Kiawah Is. at A.

SEABROOK 1939

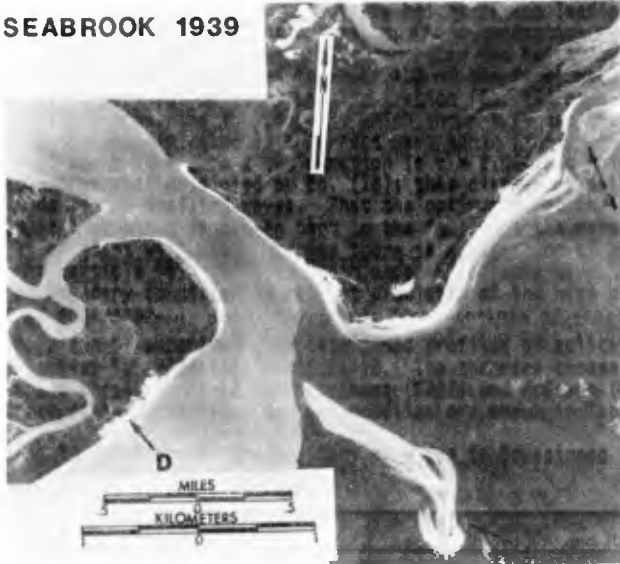
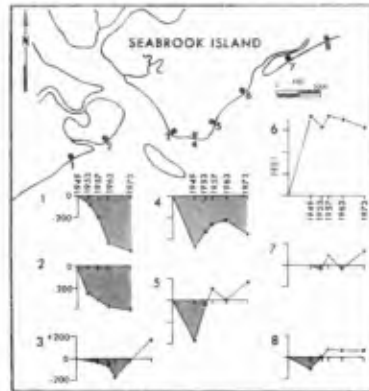


Figure 6. Mosaic of vertical aerial photographs for 1939 (National Archives). Note position of Klawah spit at A and seaward extension of Deveaux Bank at C. Deveaux Bank effectively blocked all deepwater wave energy arriving from the south.

Figure 7. Erosion-deposition graphs for Seabrook Island, covering the period between 1939 and 1973, based on aerial photos (modified from Stephen et al., 1975). Accretion is positive (up) on graphs. Units are in meters. Note considerable shoreline instability at all stations.



Vertical Aerial Photographs

A sequence of vertical aerial photographs was obtained, covering the period 1939 to 1973. These, of course, provide much greater detail of the shoreline changes of the island than the older maps and charts. Unfortunately, no detailed bathymetric surveys were conducted during the interval between 1934 and 1978. An example from 1939 is shown in Figure 6. Based on this sequence of aerial photographs, Stephen *et al.* (1975) constructed graphs of erosion-deposition trends for the island (Fig. 7). Historical shoreline changes dating to 1853 are shown in Figure 8. Note that Seabrook was largely accretional until 1973.

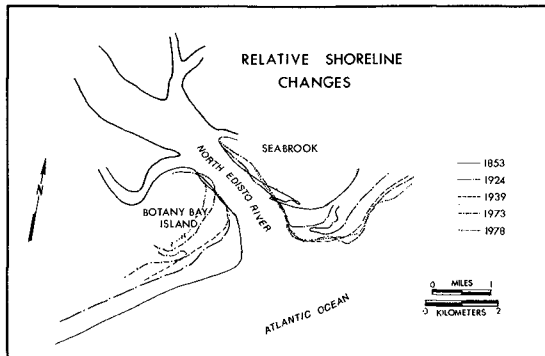


Figure 8. Relative changes of the shorelines of Seabrook and Botany Bay Islands between 1853 and 1978.

Changes of Kiawah River Inlet

The maps, charts, and aerial photographs studied indicate that the recurved spit affiliated with the Kiawah River undergoes a cycle of change that has occurred at least four times since 1661. The cycle (Fig. 9) includes:

- (a) breaching of the spit at the neck (where Kiawah River crosses the island perpendicularly) during a major storm;
- (b) migration of the spit southwestward at the rate of approximately 30.5 m (100 ft.) per year;
- (c) extension of the spit up to as much as the entire distance from the spit neck to the southwest end of Seabrook Island; and
- (d) breaching of the spit by another storm.

As the spit-inlet complex migrates, the affiliated ebb-tidal delta complex migrates with it. As waves refract around the moving ebb-tidal delta, the beach downdrift of the inlet tends to build out.

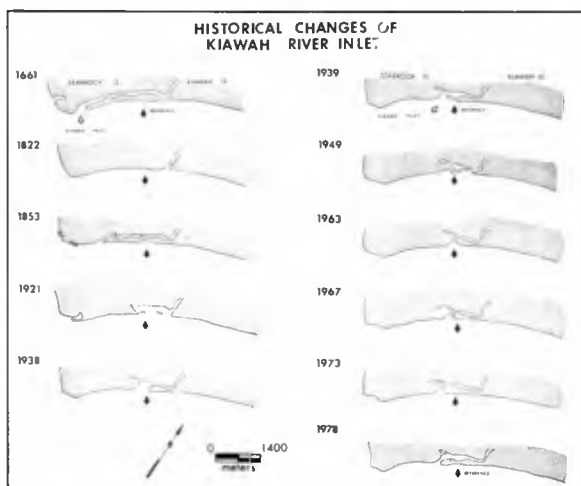


Figure 9. Historical changes of Kiawah River Inlet since 1661. Note cyclic response of spit growth over time (modified after Hayes *et al.*, 1975)

Changes of Deveaux Bank

One of the most important discoveries of the historical analysis was the fact that Deveaux Bank has retreated a phenomenal amount since 1939 (over 1000 m (.030 ft.)). From 1939 to approximately 1970, Deveaux Bank was an effective natural offshore breakwater that sheltered the shoreline in the vicinity of the southwest point from direct wave attack. In recent years, however, the bank is too far landward to provide this protection, a fact which has, no doubt, contributed significantly to the increased rate of erosion of the Seabrook shorefront. In recent years, the rate of erosion appears to have accelerated. Figure 10 shows the changes to Deveaux Bank, and Figure 11 is a photograph of the bank in 1978 at the time of the present study. The supratidal portion of the bank underwent rapid landward migration and erosion. The small intertidal shoal remaining in the former location is relatively ineffective in blocking wave energy at high tide.

Bathymetric Surveys

Since the study area is located adjacent to North Edisto Inlet, one of the largest tidal inlets on the South Carolina coast, bathymetric surveys of the main channel were compared from historical re-

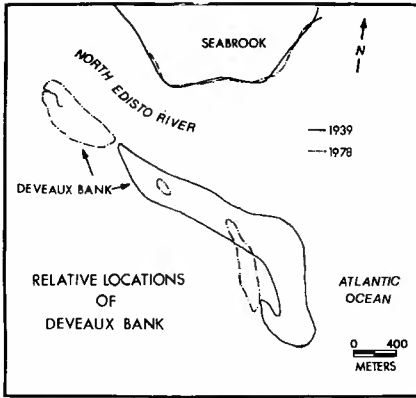


Figure 10. Comparison of aerial extent of Deveaux Bank between 1939 and 1978. The center of the bank retreated 1500 m (4922 ft.), and the bank decreased to roughly one fourth its original size between 1939 and 1978.

Figure 11. Oblique aerial photograph of Seabrook (foreground) and Kiawah Islands, taken on 7 December 1978. Note position of Deveaux Bank (foreground), located 1500 m landward of the 1939 position. View looking northeast.



cords to determine if the channel had migrated north. Such channel migration would undoubtedly contribute to erosion of the adjacent shoreline. However, the surveys found no evidence to suggest channel meandering was occurring in the vicinity of the southwest point. There was evidence, however, that the northern marginal flood channel (a secondary channel dominated by flood currents) which flanks the main channel had shifted slightly landward toward the southwest point. This probably helped cause the observed increase in erosion.

CAUSES OF EROSION

The historical evidence indicates that until 1973, Seabrook Island had undergone long-term accretion. This indication that Seabrook Island is basically a regressive barrier (seaward building) in a geological sense, as well as the fact that tremendous volumes of sand are stored in the North Edisto ebb-tidal delta complex (roughly $\frac{1}{2}$ the volume of the sand stored in the entire Kiawah-Seabrook barrier island complex) (Hayes *et al.*, 1976), suggests that localized erosion problems at Seabrook are reversible. It is primarily a matter of inducing an adequate amount of the sand available in the area to reside on the beach.

The foregoing analysis suggests the following major causes of shoreline change along Seabrook Island:

1. Southerly migration of the updrift (Kiawah River) inlet and inlet-affiliated ebb-tidal delta which causes erosion along the inlet shoreline and accretion in the lee of the delta.
2. Encroachment of the northern marginal flood channel of the downdrift (North Edisto) inlet against the SE point of Seabrook Island.
3. Erosion and landward migration of an offshore supratidal bank (Deveaux) which has allowed increasing amounts of wave energy to reach the shore.

Southwesterly Migration of Kiawah River Inlet

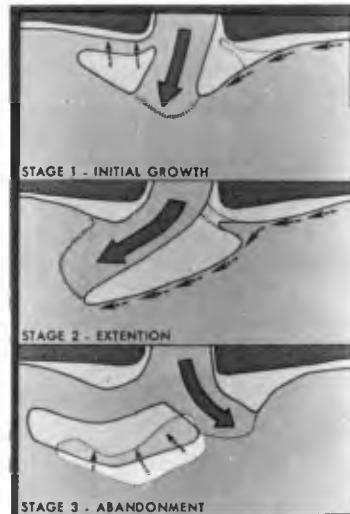
Tidal inlets are the most dynamic feature of barrier island shorelines such as the coast of South Carolina. The two aspects of this dynamic nature that are of greatest importance to coastal landowners are geographic and geomorphic instability. Geographic instability means that entire tidal inlet systems migrate in an alongshore direction. This is generally a long-term process, taking place over a period of years or decades. Geomorphic instability means that, within an inlet system at any given time, shoals, channels, and adjacent beaches are constantly changing their position and orientation. This is generally a relatively shorter-term process, taking place over a period of weeks or months. All inlets display both of these characteristics to varying degrees.

In response to the longshore transport of sand by waves, tidal inlets migrate alongshore in the direction of net longshore transport.

This is accomplished by spit accretion on the updrift side of the inlet, which forces the channel to erode the opposite bank. The history of Kiawah River Inlet is a classic example of this process, as shown by Figure 9. Note that westerly spit growth between 1924 and 1939 was interrupted in 1949 as the Kiawah River breached the neck of the spit. Since 1949, the cycle has repeated itself, and spit accretion has continued to date. Unfortunately, jetty construction to halt this geographic instability would deprive Seabrook Island of its major source of beach sand, which is material transported by waves across the mouth of the Kiawah River. The manner in which this sand bypasses the inlet comprises the geomorphic instability of the system and will be described below.

Figure 12 is a diagrammatic sketch of the short-term instability of inlets like Kiawah River. The three stages describe a process by which the inlet channel oscillates back and forth from its main point between the two islands (like a dog wagging its tail). This oscillation is simultaneous with inlet migration, so that while the inlet moves along shore, the channel, through its outer shoals, is moving back and forth (the dog walking and wagging its tail at the same time). Beach erosion rates on the downdrift side of the inlet (the left side in the diagram -- analogous to Seabrook) are related to which stage of instability happens to be operating at a particular time. In stage two, with the bar extending, sand bypassing the inlet can remain offshore for a considerable distance before being carried up onto the beach, and downdrift beach erosion rates immediately adjacent to the inlet are at a maximum. When a new channel is cut in stage three, the entire bar migrates onto the beach which, in effect, provides a large package of natural beach nourishment material and minimizes beach erosion.

Figure 12. Diagrammatic sketch of the short-term instability of inlets like Kiawah River Inlet. Stage 1 and 2 show initial growth and extension of the ebb delta in the downdrift direction. In stage 3, channel abandonment occurs, allowing by-passing of sand onto downdrift beaches. (Diagram by Dennis K. Hubbard and Duncan M. FitzGerald.)



This process has occurred naturally at Kiawah River Inlet, as shown in Figure 13. These aerial photographs were taken over the eleven month period between March, 1975 and February, 1976. They document the evolution from the bar elongation (Fig. 13, upper) through channel abandonment (Fig. 13, middle) to eventual welding of the bar onto the beach (Fig. 13, lower). In 1978, during the present study, Kiawah River was in stage two (bar elongation).

Encroachment of Marginal Flood Channel

The large shoal system seaward of North Edisto Inlet comprises what is referred to as an ebb-tidal delta. Studies of numerous ebb-tidal deltas on the east coast of the U.S. (e.g., Finley, 1975; Hine, 1975; Hubbard, 1975) and reconnaissance studies on the coasts of Alaska, Baja California, and the Gulf of St. Lawrence by the Coastal Research Division of the University of South Carolina indicate that the morphology of these sand bodies is similar from place to place.

The components of a typical ebb-tidal delta include a main ebb channel, which usually shows a slight-to-strong dominance of ebb-tidal currents over flood-tidal currents. The main ebb channel is flanked on either side by linear bars, which are levee-like deposits built by the interaction of ebb- and flood-tidal currents with wave-generated currents. At the end of the main channel is a relatively steep, seaward-sloping lobe of sand called the terminal lobe. Broad sheets of sand, called swash platforms, flank both sides of the main channel. Usually, isolated swash bars, built by the swash action of waves, occur on the swash platforms. Marginal tidal channels dominated by flood-tidal currents, called marginal flood channels, usually occur between a swash platform and the adjacent updrift and downdrift beaches.

A well-defined marginal flood channel has existed for some time off the south-southeast end of Seabrook Island. By 1978, it had shifted toward the island at the southeast point (see aerial photograph in Fig. 11). Sediment eroded from the beach in that vicinity would be carried offshore into the channel where it is undoubtedly redistributed by the strong flood-tidal currents that exist in the channel. In 1978, it appears that the marginal flood channel was too close to the beach to allow for the natural onshore-offshore transfer of sand that normally occurs on beaches.

The Erosion of Deveaux Bank

As discussed in some detail previously, Deveaux Bank eroded over 1500 m since 1939. As the bank eroded, the area near the southwest point became more and more exposed to open ocean waves. This is probably the single most important factor in the increase of the erosion rate for that locality.



Figure 13. Bar-bypassing at Kiawah River Inlet.

Aerial photograph of Kiawah River Inlet in March, 1975. This is stage two - bar over-extension.

Aerial photograph of Kiawah River Inlet in November, 1975. Note that the channel has breached the updrift end of the bar.



Aerial photograph of Kiawah River Inlet in February, 1976, showing partial welding of the bar onto Seabrook Island. (Photograph by Dennis K. Hubbard.)

PROPOSED SOLUTIONS

Based on the above causes of erosion, a number of "soft" engineering solutions have been proposed to retard or eliminate local erosion problems at Seabrook Island. These include: 1) dredging of a new inlet channel north of Kiawah River Inlet to allow sand in the ebb delta to naturally migrate onshore at Seabrook, 2) dredging of a new northern marginal flood channel further seaward on the North Edisto River ebb-tidal delta to relieve the erosive pressure at the southeast point of Seabrook, and 3) reestablishment of a natural (or artificial) breakwater in the former position of Deveaux Bank. One possibility for the latter would be to construct a floating offshore breakwater. These solutions are outlined in Figure 14.

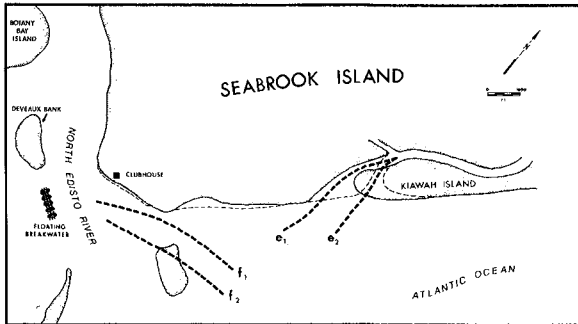


Figure 14. Proposed "soft" engineering solutions for reducing shoreline erosion along Seabrook Island, including: 1) dredging new channels at e_2 and f_2 , allowing existing Kiawah River Inlet channel (e_1) and North Edisto Inlet marginal flood channel (f_1) to infill; and 2) construction of a floating breakwater (or hydraulic filling) in the former position of Deveaux Bank.

Although the proposed solutions do not have the permanence of "hard" engineering coastal protection works, their cost of implementation is at least an order of magnitude less than presently-used structures, and they have the aesthetic advantage of preserving the character of Seabrook beaches. Present plans are to implement at least two of these solutions. If successful, they will demonstrate the relevance of geologic and coastal process information not only for use in "hard" designs, but as a means for determining appropriate "soft" design solutions for coastal protection.

CONCLUSIONS

Erosion problems on Seabrook Island appear to be localized and due to three independent but related processes: (1) the migration of Kiawah River Inlet; (2) the encroachment of a marginal flood channel of North Edisto Inlet on the shoreline in the vicinity

of the southeast point; and (3) increased wave activity caused by the erosion of Deveaux Bank. All of these processes are the direct results of the highly dynamic nature of tidal inlets and are common occurrences in similar environments elsewhere. None of the erosion trends were caused by Seabrook Island construction. Future construction activities on the island would benefit if these natural trends are considered. Several "soft" engineering solutions are available which would considerably retard or reverse present localized erosion trends.

ACKNOWLEDGEMENTS

We would like to thank Drs. Per Bruun and Cyril Galvin for their consultations and helpful advice on several occasions during the project. Dan Domeracki, Jacqueline Michel, Tom Moslow, Mohammed Al-Sarawi, and Kent Taylor assisted in the field. Special thanks to Jerry Sexton who managed much of the field work and data reduction.

REFERENCES

- Finley, R.J., 1975, Hydrodynamics and tidal deltas of North Inlet, South Carolina: in Cronin, L.E. (ed.), Estuarine Research II, p. 277-291.
- Hayes, M. O., FitzGerald, D.M., Hulmes, L.J., and Wilson, S.J., 1976, Geomorphology of Kiawah Island, South Carolina: in Hayes, M. O. and Kana, T. W., (eds.), Terrigenous Clastic Depositional Environments, Tech. Rept. No. 11-CRD, Dept. of Geology, U. of South Carolina, p. II-80 to II-100.
- Hayes, M.O., Wilson, S.J., FitzGerald, D.M., Hulmes, L.J., and Hubbard, D.K., 1975, Coastal processes and geomorphology: in Environmental Inventory of Kiawah Island, Environmental Research Center, Inc., Columbia, S. C., p. G-1 to G-165.
- Hine, A. C., 1975, Bedform distribution and migration patterns on tidal deltas in the Chatham Harbor Estuary, Cape Cod, Massachusetts: in Cronin, L.E., (ed.), Estuarine Research II, New York, Academic Press, p. 235-252.
- Hubbard, D. K., 1975, Morphology and hydrodynamics of the Merrimack River ebb-tidal delta: in Cronin, L.E., (ed.), Estuarine Research II, New York, Academic Press, p. 253-266.
- Myers, V., 1975, Storm tide frequencies on the South Carolina coast: NOAA Tech. Rept. NWS-16, U.S. Dept. of Commerce, 79 p.
- Stephen, M.F., Brown, P.J., FitzGerald, D.M., Hubbard, D.K. and Hayes, M.O., 1975, Beach erosion inventory of Charleston County, South Carolina: A preliminary report: Tech. Rept. No. 4, South Carolina Sea Grant, Charleston, S. C., 79 p.

CHAPTER 57

GEOLOGICAL CONTROLS ON PROCESS-RESPONSE, S.E. AUSTRALIA

by

P.S. Roy* and A.W. Stephens*

ABSTRACT

Results of regional geological studies on the southeastern Australian coast and inner continental shelf suggest that broad relationships between nearshore sediments and morphologies are often the result of factors other than incident waves and wave-induced currents. Five main factors (including wave action) have been identified:

1. degree of compartmentization and sand bypassing,
2. incident wave energy,
3. offshore sand loss to deep water sinks,
4. inherited sediment characteristics,
- and 5. substrate control.

It is thought that these factors have controlled coastal evolution in the past and also influence present-day coastal changes. Identification of the role played by individual factors in specific areas provides valuable information on coastal sediment budgets.

INTRODUCTION

Many coastal engineering problems focus on the interaction of marine processes and sediments. Hydrodynamic processes are usually seen as the dominant control on the coastal sediments and morphologies. Because of this, many studies use measurements of dynamic processes taken over short time periods to predict sediment response. We suggest that geological factors also influence process-response relationships. Past geological events have both a direct impact on processes themselves, and their imprint modifies the way in which sediments and morphologies react to present-day dynamic conditions. Geological interpretation of sediment patterns and seabed morphologies can provide information on the cumulative effects of variable dynamic processes operating over a time span ranging from decades to millenia. These data can be used to test results derived by other techniques such as direct process measurements, sand tracing and theoretical predictions.

* Marine Geology Section,
Geological Survey of New South Wales, Department of Mineral
Resources, Box 5288, G.P.O., Sydney, Australia, 2001.

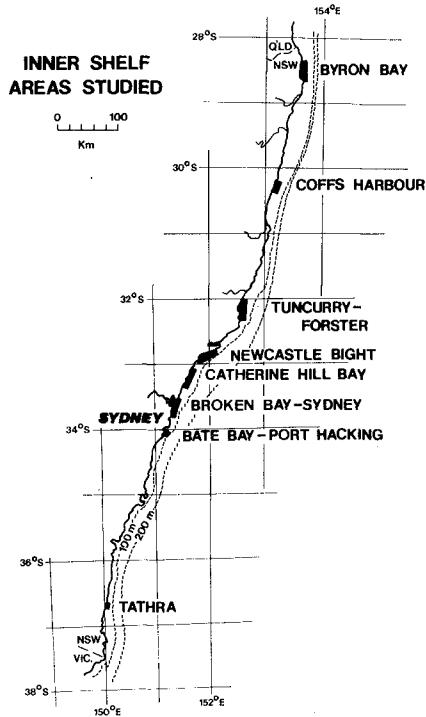


Figure 1. New South Wales coastal zone showing inner shelf areas discussed in text.

Studies in several areas along the New South Wales (N.S.W.) coast (Figure 1) have documented modes of coastal evolution and identified a number of geological controls which affect responses of sediment and morphology to nearshore processes.

COASTAL SETTING

The N.S.W. coast comprises sand barriers between rock headlands in embayed bedrock compartments. It is subject to a moderate to high energy wave climate with dominant waves from the south and south-east. A high degree of compartmentization exists on the south and central coast where rock headlands extend into deep water but in the north, sediment by-passing commonly occurs between embayments as a result of northward littoral drift (Thom and Roy, in press). Rivers do not supply significant quantities of sand to the coast (Roy and

Crawford, 1977). Most barriers on the coast are of Holocene age and lie seawards of a variety of estuarine and alluvial deposits infilling coastal valleys (Roy et al. 1980). In parts of central and northern N.S.W. the Holocene barriers onlap older barriers of Pleistocene age but in some embayments Holocene barriers are absent and Pleistocene sand deposits are exposed at the coast. The barriers formed during the Last Interglacial and Postglacial periods of high sea level (Langford-Smith and Thom, 1969; Marshall and Thom, 1976; Thom et. al., 1978; Thom and Roy, in press).

Sediments

Three main sediment units are recognised on the inner half of the N.S.W. continental shelf: nearshore sand, inner shelf sand and mid-shelf muddy sand (Figure 2). Sedimentation is believed to be presently active in the nearshore and mid-shelf zones but on the inner shelf the sand is palimpsest (Swift et al., 1971).

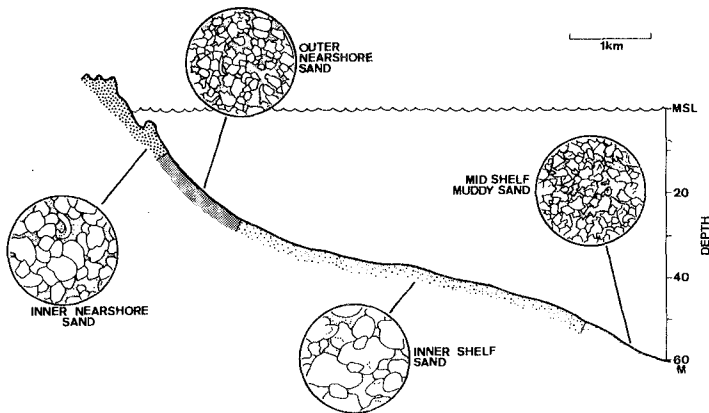


Figure 2. Typical, concave-up sea bed profile showing normal arrangement of sediment types. Lithologies (insets) illustrating grain sizes and shapes are drawn from photomicrographs at the same scale; stippled areas are open spaces.

Nearshore Sand

Nearshore sands comprise inner and outer nearshore sand types although the latter is not found at all embayments. They normally occupy a concave-up nearshore zone that varies greatly in width

(0.7-2.6 km) and depth range (15-30 m). Both inner and outer nearshore sand types occupy a zone of active reworking that corresponds to the seaward face of the coastal barriers.

Inner nearshore sand includes the beach and extends seawards of the longshore bar to depths of 4-12 m. It is fawn, quartzose, medium to coarse grained, moderately to well sorted (unimodal to bimodal) and composed of rounded grains. Usually it contains less than 10% shell fragments and less than 20% of the grains are ironstained although in a few embayments values are much higher. Texture and composition may vary widely between compartmented embayments. Landward of the longshore bar, grainsize changes reflect variations in surf zone processes and morphologies; seaward of the bar, sand size usually decreases with increasing depth. Bedforms vary from small ripples to large symmetrical and asymmetrical sand waves.

Outer nearshore sand lies seaward of the inner nearshore sand unit, often with a relatively sharp boundary and extends to depth of 15-30 m. It is olive grey, quartzose, fine grained, well sorted (unimodal) and composed of sub-angular to rounded grains. Shell content and iron staining are usually similar to the associated inner nearshore sand although outer nearshore sand is texturally more uniform between embayments. Despite decreasing wave turbulence, grainsize usually shows little variation with increasing depth. Small symmetrical wave-formed ripples are the typical bed form.

Inner Shelf Sand

Inner shelf sand occupies the gently sloping inner shelf surface and extends seawards from the zone of nearshore sand to depths of 50-60 m+. It is orange-brown (due to extensive ironstaining), quartzose, medium to coarse grained and, in places, gravelly. It is generally poorly sorted (polymodal) and composed of well rounded grains. Shell content is highly variable but is usually less than 20%. Mud occasionally forms a minor component (<5%), mainly in the outer part of the unit. Inner shelf sands are texturally variable both within and between regions. Symmetrical (wave-formed) megaripples commonly occur in areas of coarse sand and gravel. Algae coatings on pebbles indicate that movement occurs mainly during high energy events.

Inner shelf sands do not conform to a classical "equilibrium" trend of fining seaward. They are essentially relict deposits that are presently being reworked.

Mid-Shelf Muddy Sand

Muddy sediments occur discontinuously over large areas of the mid-shelf seawards of the 50-60 m isobath (Thom and Roy, in press). They comprise dark grey, fine to very fine sand plus mud and support an abundant fauna of foraminifera, polychaetes and bivalves. Sand grains are angular to subangular and non-ironstained. Lithic content in the sand is usually higher than in other sediment on the inner shelf. In places the muddy

unit contains a coarse sand mode that is thought to be related to an underlying relict sand substrate; intermixing is presumably by bioturbation.

From the occurrence of fine sediment in this region we infer a low energy "window" between the wave-dominated inner shelf and the current-dominated outer shelf and upper continental slope (not discussed here).

The normal relationship between sediments and morphology seawards of the surf zone is for nearshore sands to form a moderately steep, concave-up slope (Figure 2); grainsizes generally decrease seawards with increasing depth. This region corresponds to an active zone in dynamic semi-equilibrium with the local wave climate. Further seawards the palimpsest, inner shelf sands form a more gently sloping planar surface. The relatively abrupt change in grainsize between fine outer nearshore sand and coarser inner shelf sand suggests that the latter do not presently contribute significantly to the modern coastal sediment budget.

Barrier sediments on the N.S.W. coast were derived from three sources: (a) the inner continental shelf, (b) coastal sand barriers of Pleistocene age, and (c) modern fluvial supply.

(a) The majority of the barrier and nearshore deposits are formed of sand reworked from the inner shelf and transported onshore during and since the Postglacial Marine Transgression (Roy et al., 1980; Thom and Roy, in press). This sediment type is mainly composed of mature, rounded and partly iron oxidized-coated quartz sand and shell that has been repeatedly reworked, mainly by marine processes during one or more glacial/interglacial cycles. Locally it is termed "marine" sand (Roy and Crawford, 1977).

(b) In areas where Pleistocene barriers are exposed at the coast, marine erosion of these deposits supplies sand to the modern beach and nearshore zones. The parent sand is "marine" in character and, except for leaching of shell and the absence of iron oxide coatings, its erosion product is similar to the sand forming the Holocene barriers.

(c) Rivers supply sand to only a few small embayments in southern N.S.W. (R. Kidd, unpubl. Ph.D. Thesis, 1980). "Fluvial" sand is typically immature (angular) and contains abundant lithic (rock and feldspar) grains. Elsewhere, medium to coarse river sand is deposited in the lower river valleys and in coastal estuaries (Roy and Crawford, 1977). Fine to very fine terrestrial sand and mud that is carried to the sea during floods is transported (diffused) across the inner shelf and deposits in the mid-shelf region (Thom and Roy, in press).

Barrier Formation

Considerable radiocarbon age data on shelly beach and nearshore facies in prograded beach ridge systems (Thom, 1978; Thom et al., 1978) show that most Holocene barriers accreted between about 6000 and 3000 years ago, with a few continuing to grow up to 1000 years ago. Over this time span, sea level on the tectonically stable southeast Australian margin

has remained fairly constant (± 1 m) (Thom et al. 1969, 1972; Cook and Polach, 1973; Thom and Chappell, 1975; Belperio, 1979; Jones et al., 1979).

Thus it is reasonable to assume that barrier building occurred under marine conditions broadly similar to those operating today. The composition of most barrier deposits clearly shows that they are formed of sand reworked from the inner shelf; not from modern fluvial sources. In some areas there was undoubtedly a strong littoral drift supply from upcoast, but in closed compartments the sand feed was essentially in an onshore direction. Figure 3 shows the latter situation for an embayment that is closed in terms of littoral drift inputs and outputs. The original 6000 year profile configuration has been reconstructed by transposing the volume of sand in the existing barrier to the offshore sea bed. A prograded wedge of barrier deposits (stippled) composed of beach and nearshore sand forms the inshore part of the profile. Further seawards are inner shelf sands that have acted as a sand source for barrier building in the past. Thus the inner part of the profile is aggradational while its outer part is erosional. From this reconstruction it is clear that, during barrier formation, sand was transported landwards in water depths considerably deeper and from further seawards than is apparently occurring today as indicated by the present active zone of nearshore sediments. There is virtually no evidence in N.S.W. that barriers are still prograding: in fact the reverse is generally the case. What has stopped them growing?

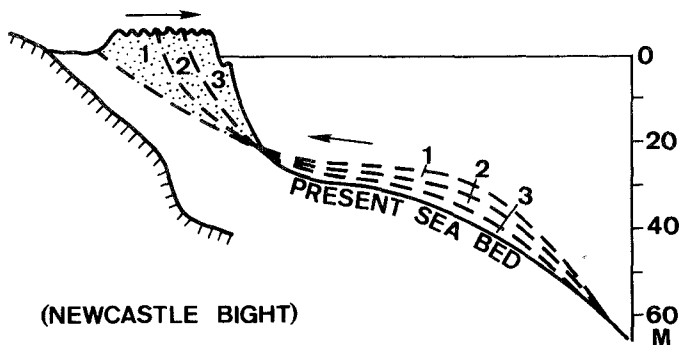


Figure 3. Model of mid Holocene barrier development in a compartmented embayment showing inferred movement of sand from the inner shelf under sea level conditions similar to the present day. Numbers 1-3 represent the chronological sequence of barrier growth and corresponding sea bed erosion. Arrows show directions of beach ridge progradation and associated sand supply from offshore.

One possibility is that the sand supply was cut off once a wave-formed profile of equilibrium was established. Further, from the preceding discussion, we would expect the equilibrium profile to extend to water depths of 50 m or more. In these depths the open ocean wave climate is broadly consistent along the N.S.W. inner shelf although local variations occur in the inshore zone due to refraction and diffraction effects. Thus, if waves were the principal control limiting barrier development, we would anticipate general similarities in profile shape (especially in its outer part) and in sediment patterns between embayments.

Figure 4 shows a selection of shore-normal profiles across the N.S.W. inner continental shelf. General similarities in the inner parts of these profiles suggest that equilibrium conditions may exist in water depths above about 15 m. Below this depth, the wide diversity in gradients and morphologies are difficult to account for in terms of a simple, wave-controlled equilibrium profile of the type proposed by Zenkovitch (1967). Obviously, factors other than wave action are important in producing present-day sea bed patterns. Interest in the morphology and sediments in coastal embayments and on the inner shelf arises from the belief that factors controlling barrier development in the past also influence modern shoreline changes.

CASE STUDIES

Geological investigations have been carried out in a number of areas along the N.S.W. coast in conjunction with coastal engineering studies by the N.S.W. Department of Public Works. These projects were

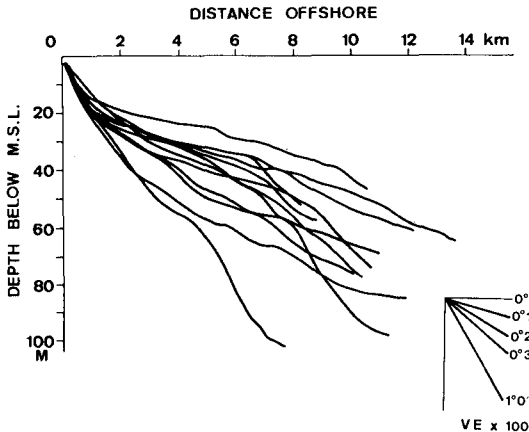


Figure 4. Shore-normal sea bed profiles from open ocean embayments in N.S.W. showing the diversity of shapes.

aimed mainly at providing information on coastal erosion and its management. Results from several areas illustrate the ways in which geological factors have influenced coastal sedimentation. The areas are: Byron Bay and Coffs Harbour in northern N.S.W. and Newcastle Bight in central N.S.W. (figure 1).

Byron Bay

The Byron Bay embayment (figure 5) is an example of an open, zetaform bay in which southeasterly swell waves generate a strong northward littoral drift and ocean currents cause an offshore sediment loss (Roy et al., in press). Uninterrupted sediment bypassing is indicated by the continuity of the nearshore sediment zone around headlands. Despite variations in incident wave energy, inner nearshore sand is of uniform composition and texture throughout the area due to longshore mixing. Progressive deepening and steepening of the shoreface towards the north is related to increasing wave energy in the same direction (see profiles A and B in Figure 5).

Alongshore variations in the energy and obliquity of the incident waves produce higher littoral drift rates in the north than in the south (Figure 6). As a result of this drift differential, the embayment between Cape Byron and Hastings Point is eroding into old Pleistocene sand deposits. Average rates of shoreline recession are 0.6 m/yr based on historical data (40-90 years) and between 0.25 and 0.35 m/yr from radiocarbon evidence spanning the past 400 years.

The present imbalance between drift gains and losses is attributed to three causes: (a) a regional increase in obliquity of the coast to the dominant wave approach; this tends to increase littoral drift rates towards the north.

(b) both regional and long-term tendencies in northern N.S.W. for embayments to become compartmented earlier in the south than in the north thus causing a gradual reduction in sand supply to areas downdrift.

(c) a long-term loss of nearshore sand at Cape Byron at the southern end of the bay to deep water sinks offshore (see below).

It is probable that, in mid Holocene times, onshore transport of sand from the inner shelf resulted in barrier development in Byron Bay as it did in most other embayments in N.S.W. However, eventually the Byron Bay barrier was eroded as a drift imbalance developed and it is likely that recession rates have gradually increased over the Late Holocene, mainly due to (b) above.

Areas of offshore sediment loss are identified by abnormalities in the shape, width and depth range of the nearshore sediment zone. In the north this zone is narrow and extends to depths of about 25 m. Profiles are concave-up and indurated Pleistocene sediments, exposed on the shoreface to depths of 18 m, indicate that the whole nearshore zone is erosional. However in central and southern parts of the area, the nearshore

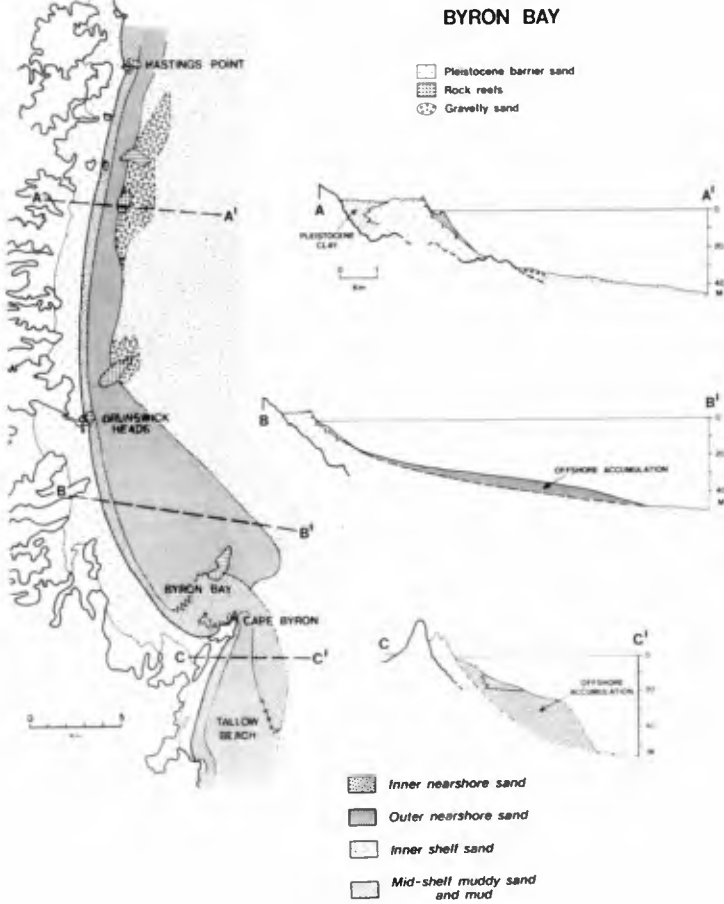


Figure 5. Byron Bay offshore area showing distribution of sediments and inferred Holocene stratigraphy. The inner parts of cross sections A and B show a thin wedge of active nearshore sand above an eroding Pleistocene substrate. Accumulations of nearshore sand lost from the shoreface since mid Holocene times occur in profiles B and C. Bedrock margin onshore indicated by solid, heavy line.

sediment unit widens and extends to depths of 50 m, twice the normal depth, and profiles become convex-up (figure 5, profiles B and C). These trends are attributed to deposition of sand in offshore sinks by southward flowing ocean currents (figure 6). During strong southeasterly swell action, nearshore sand which drifts northwards along Tallow Beach is "jetted" past Cape Byron. At times when the southward flowing East Australian Coast Current impinges on the headland, wave-suspended sand is entrained and transported southwards. In this area low amplitude, current-formed sand waves occur in depths of 20 m +. Deposition occurs in a southward trending lobe (figure 5) where the ocean current diverges from the coast, velocities weaken and eddies form (Figure 6). Accumulation of a smaller volume of finer outer nearshore sand over a broad area to the north of Cape Byron is probably due to a clockwise sediment circulation generated by wave drift inshore and ocean currents offshore.

A regional alongcoast movement of sediment is indicated by the continuing supply of sand to both depositional sites. Northward littoral drift in the surf zone together with deep water wave drift from the south and (possibly) ocean current transport from the north within the outer nearshore zone are probable supply mechanisms (Figure 6). The principal source of beach and nearshore sand in this area is from the erosion of Pleistocene barriers both within the embayment and up coast (i.e. to the south).

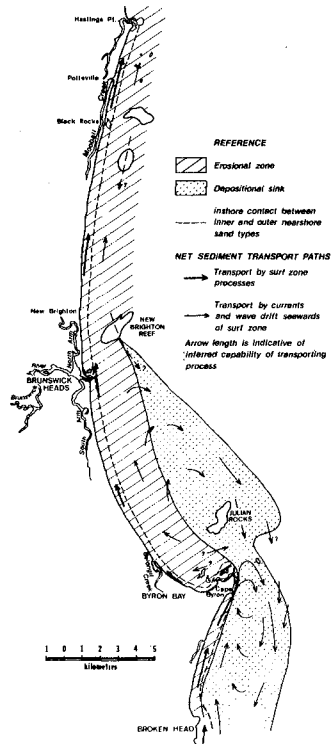


Figure 6. Byron Bay area showing regions of offshore erosion and deposition and inferred sediment transport mechanisms and paths.

The deposit to the south of Cape Byron is up to 20 m thick and has been calculated to contain approximately 160 million m^3 of outer nearshore sand above an initially concave-up substrate. Assuming deposition commenced about 6000 years ago, the average rate of sand loss from the nearshore system has been about 26,000 m^3/yr of inner and 58,000 m^3/yr of outer nearshore sand.

Coffs Harbour

This area lies within a sector of bedrock controlled coast; rock reefs occur extensively offshore (figure 7). Changes in coastal orientation and bedrock embayment size are responsible for contrasting coastal development north and south of Coffs Harbour. Southern embayments are relatively large and contain extensive Pleistocene estuarine deposits that originally accumulated behind sand barriers of the same age. These Pleistocene barriers have subsequently been destroyed by marine erosion, presumably towards the close of the Last Interglacial. Later, they were replaced by Holocene beachridge barriers that prograded in bay mouth positions. The coast north of Coffs Harbour is characterised by small embayments and pocket beaches with narrow Holocene barriers backed, in most areas, by bedrock.

Nearshore and inner shelf sediments form a generally thin veneer above bedrock or a Pleistocene clay substrate. Maximum thicknesses occur beneath the southern barriers (Figure 7, cross section C-C') but elsewhere, nearshore sediments are commonly less than 2 m thick. The continuity of the inner nearshore sand unit is interrupted by Coffs Harbour and by a number of headlands to the north of the harbour. This sediment unit is wider and extends to greater depths (c. 12 m) in the south than in the north (c. 5-8 m). Beach and inner nearshore sand in the south is uniformly medium grained and the beaches have wide surf zones but in the north beaches are coarse, steeply sloping and usually reflective in character. Outer nearshore sand forms a continuous zone alongshore but is interspersed by rock reefs and exposures of coarse inner shelf sand and gravel that form the underlying substrate. Outer nearshore sand forms a thin "mobile carpet" that is completely remobilised under even moderate storm conditions. This unit occurs in depths ranging from 12-25 m in the south and 5-20 m in the north.

Shore-normal profiles in the south are steeper and more concave than in the north where the underlying substrate exerts an over-riding control on sea bed configurations (Figure 7).

Since harbour construction commenced in 1915, northward littoral drift has been interrupted and sand has been trapped in the southern embayment. Historical data spanning the last 40 years indicate that the northern end of this embayment has prograded up to 100 m and about 5 million m^3 of sand has deposited on the beach and in the inner nearshore zone. Over approximately the same period, more than 1.5 million m^3 of mainly fine, outer nearshore sand has accumulated inside the Harbour and off its mouth where the sea bed has developed a marked convexity.

It is reasonable to assume that, prior to harbour construction, northward littoral bypassing operated, albeit at a low rate, throughout the whole region. The northern beaches at this time are reported to have

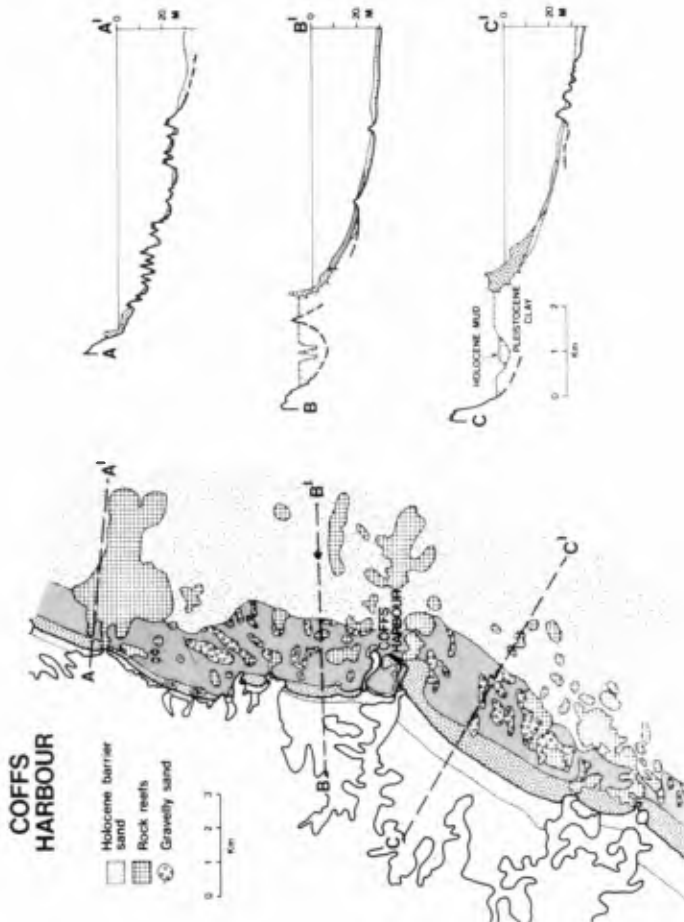


Figure 7. Coffs Harbour area showing surface sediment units and stratigraphic sections. Progressive increase in barrier size towards the south is related to bedrock embayment size. Note change in coastal orientation at Coffs Harbour. (Key to offshore sediments shown in Figure 5).

been fine grained, gently sloping and dissipative in character. The response of these northern beaches to the cessation of updrift sand supply in the period following harbour works has been strongly influenced by the shallow substrate. Coastal retreat has been mitigated not only by the bedrock hinterland but also by the character of the offshore sea bed. Radiocarbon dating on subsurface shell samples from within the zone of fine outer nearshore sand suggests that the underlying, coarse inner shelf sediments are reworked during storms to depths in excess of 1 m below the sea bed. Their periodic exposure has released coarse sand and fine gravel that has migrated onshore. As a result beaches in this area have coarsened and steepened and, in at least one case, have prograded slightly in historical times.

Newcastle Bight

Newcastle Bight (figure 8) is a broad shallow embayment oriented normal to the dominant wave regime. There is a large gross littoral drift but no net drift. It has acted as a sand trap during two periods of interglacial high sea level, and is the best known example of a dual barrier system on the N.S.W. coast (Thom, 1965; Roy, 1980, Thom et al. in press).

The oldest sand deposits on the inner continental shelf of Newcastle Bight form a drowned coastal barrier (proto-barrier) located 3-6 km seawards of the present coastline in water depths of 55-60 m+. An associated sequence of estuarine clay in the subsurface extends shorewards from the proto-barrier and underlies the onshore barriers (Inner and Outer Barriers, Figure 8). The clay unit is up to 60 m thick and is of polycyclic origin. Both the proto-barrier and estuarine deposits predate the Inner Barrier which is of Last Interglacial age (Roy and Crawford, 1980).

Sandy strandline deposits overlie the clay substrate offshore and occupy the inner shelf plain between the proto-barrier and the concave-up nearshore zone. These inner shelf sands contain gravels related to an old drainage system of the Hunter River; they form a basal transgressive unit beneath the Outer Barrier.

The Outer Barrier is Holocene in age and comprises beach ridges transgressed on three separate occasions by dunes. To the rear of the barrier, estuarine backbarrier deposits infill the interbarrier depression. Modern muds and sandy muds blanket the seaward face of the proto-barrier in water depths greater than 60 m.

The Newcastle Bight sediment budget is in deficit due to the loss of beach sand landwards into presently mobile dunes. Present-day inputs of sand to the nearshore zone by littoral drifting, cliff erosion, biogenic production and river supply are small. In historical times the shoreline has receded at rates of 1-2 m/yr (Gordon and Roy, 1977; Roy and Crawford, 1980).

On the seaward face of the Holocene barrier is a zone of nearshore sand which is compartmented by deep water rock reefs at either end of the embayment. The contact between nearshore and inner shelf sand types is abrupt and occurs at depths of between 15 and 30 m. The nearshore zone shows a number of alongshore trends: In the centre of the embayment where sediments are coarse the nearshore profiles are steep, a single bar is

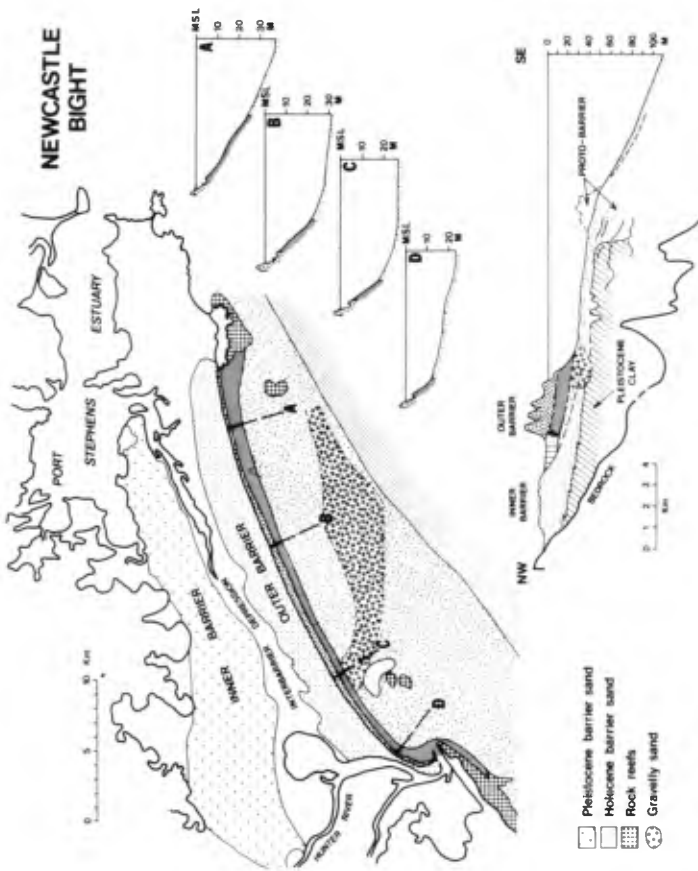


Figure 8. Newcastle Bight showing dual barriers onshore and offshore sediment distribution; gravelly sands are related to an old course of the Hunter River. Stratigraphic section is based on onshore drilling and marine seismic data for the axial part of the embayment. (Key to offshore sediments shown in figure 5).

developed and the nearshore sand zone is narrow. Towards the northeast where sediments are finer, profile slopes are more gentle, multiple bars are developed and the nearshore sand zone is wide. Grain size trends in the inner nearshore sand unit mirror those within the eroding Holocene barrier. This barrier is composed of sand reworked from the inner shelf. Here the sediments are coarse, relict fluvial deposits in the centre of the bay and fine, relict dune sand at its northeastern end (Roy and Crawford 1980). Their onshore transport has produced a similar size grading in the barrier. Subsequent shoreline erosion has thus exposed barrier deposits of different grain sizes on the beach and shoreface with the result that nearshore morphologies vary alongshore. Despite a large gross drift, continuing erosion has allowed inherited grain size characteristics to dominate in controlling the profile shapes.

DISCUSSION

Based on studies of the type described above, at least five main factors can be identified as influencing the relationships between sediments and morphology in coastal embayments of southeastern Australia. These are:

1. Compartmentization
2. Incident Wave Energy
3. Offshore Deposition
4. Inherited Sediment Characteristics
5. Substrate Control.

1. Compartmentization

Varying degrees of compartmentization and sediment bypassing are shown by the plan distribution of nearshore sand types. In the Byron Bay region (Figure 5) the continuity of inner and outer nearshore sand units around headlands at either end of the embayment indicate that this compartment is open to littoral bypassing although drift rates within it vary. The Coffs Harbour area (Figure 7) is compartmented with respect to inner nearshore sand but not outer nearshore sand although subtle differences in grain size within the latter unit suggest that alongshore mixing rates are relatively low. In Newcastle Bight (Figure 8), both inner and outer nearshore sand units terminate against headlands and submarine rock reefs at either end of the embayment. In this case alongshore gains and losses of sand to the sediment budget are negligible.

2. Incident Wave Energy

Local variations in wave energy within an embayment are reflected by relationships between nearshore sediments and morphology. This is best displayed in zetaform bays which are oriented obliquely to the dominant wave climate and, in southeastern Australia, are hooked at their southern ends (e.g., Byron Bay). In areas of low wave energy the sea bed is shallower and shoreface profiles are less steep than in more exposed sites (see trend between south, central and north profiles of the Byron Bay embayment, Figure 9a). These morphological changes may or may not be accompanied by grain size trends in the beach and nearshore sand units. In compartmented bays with negligible littoral bypassing

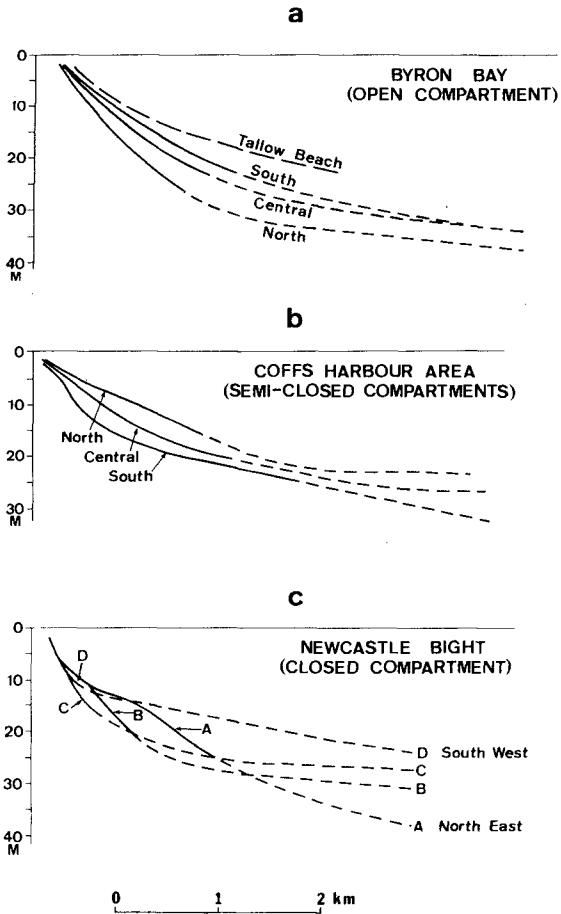


Figure 9. Shore-normal sea bed profiles for three areas each showing progressive variations in shape and distribution of nearshore (solid lines) and inner shelf (dashed lines) sediment units.

grainsizes coarsen in response to increasing wave energy (e.g., Pearl Beach in Broken Bay, Chapman, 1978). However, in compartments open in terms of littoral bypassing (these are almost invariably "zeta" shaped in N.S.W.), sand sizes are uniformly well mixed alongshore (e.g., Byron Bay).

Zetaform bays usually evolve erosionally due to a drift differential within an open littoral drift system. Eventually, shoreline retreat and headland emergence prevents further littoral throughout and, providing no other sand loss mechanisms operate, the bay achieves a stable configuration. The presence or absence of alongshore grainsize trends in such bays is a useful criterion to determine whether a stable planform has been achieved, especially where headland bypassing is difficult to establish by other methods.

3. Offshore Deposition

For sediment budget calculations, permanent sand losses into transgressive dune fields and estuarine tidal deltas are usually easily recognised. Newcastle Bight and Bate Bay (Figure 1) are embayments that have lost sand into transgressive dunes; Broken Bay and Port Hacking are drowned river valleys containing large flood tide deltas composed of "marine" sand. Less obvious are sand losses to relatively deep water offshore. The progressive accumulation of sand offshore in water depths of up to 50 m cause abnormal distributions of nearshore sediment types and sea bed profiles that are convex, rather than concave-up.

In Byron Bay (Figures 5 and 6), loss of nearshore sand by ocean current action to offshore sinks is exacerbating coastal erosion within the embayment. Here volume estimates of the sand contained in the offshore sinks are based on assumptions that the transporting mechanisms have operated since sea level reached its present position about 6000 years ago and that a pre-existing substrate on which deposition has occurred can be recognised in the subsurface.

At Tathra (Figure 1), river sand is jetted seawards during major floods and deposited offshore in water depths of up to 26 m. In this embayment a major flood in 1971 appears to have initiated shoreline recession of up to 40 m as sand was transported alongshore (northwards) to infill the overdeepened river mouth and reform the river mouth bar (Gordon and Lord, unpubl. Public Works Department report., 1980). Onshore transport of excess sand from the bay bed has not yet (i.e., 9 years later) restored the shoreline to its pre-flood configuration. In this case it remains to be determined whether the supply of river sand to the bay during mid and late Holocene times has produced net, long-term shoreline accretion despite short-time erosion following floods. If not, then presumably other mechanisms, as yet unidentified, cause a continuing loss of river supplied sand from the bay (to deep water offshore?) in which case the shoreline may be experiencing long-term retreat.

4. Inherited Sediment Characteristics

The source of Holocene sediments infilling most sandy embayments in N.S.W. was from the inner continental shelf, and was the result of marine reworking during and following the Postglacial Marine Transgression (Thom et al., 1978; Roy et al., 1980). In embayments which are suffering

erosion, the composition of the Holocene barriers may control nearshore sediment-morphology relationships and over-ride dynamic influences. This situation has only been found in compartments with no littoral drift throughput.

In Newcastle Bight (Figure 8), shoreface erosion into coarse grained barrier sands in the centre of the embayment has resulted in steep but relatively shallow nearshore slopes (profiles C in Figure 9c). Towards the northeast, sands become finer and profiles have responded to similar wave conditions by becoming more gently sloping but deeper (profiles A and B in Figure 9 c).

A similar situation appears to exist in Shoalhaven Bight, 120 km south of Sydney. Here the over-riding influence of inherited sediment textures is highlighted by a northward fining of the beach and nearshore sediments despite an increase in wave energy in the same direction (Wright, 1970).

These relationships demonstrate that a number of different nearshore configurations may accommodate a given incident wave regime. The controlling factor is sediment size; the dependent variable is morphology.

Substrate Control

Holocene barriers have accumulated on a gently inclined substrate that includes medium to coarse sands and gravels. Where this substrate had been transgressed and is exposed on the sea bed, it forms the inner shelf sand unit. Under eroding conditions, landward retreat of the seaward face of the coastal barriers intersects the rising surface of the underlying substrate. As a result, nearshore sediment patterns and morphologies are modified: nearshore sediment zones become narrow and occur at shallower than normal depth while profiles flatten and become more planar.

In the Coffs Harbour area these trends are increasingly developed towards the north (Figure 9 b). Reworking and onshore transport of sand from the shallow substrate in the region north of the harbour has presumably been responsible for the relatively coarse nature of the adjacent onshore deposits both during their formation in mid Holocene times and more recently after harbour works interrupted the littoral sand supply.

In the Byron Bay area coastal retreat over an inclined substrate has exposed patches of gravelly, inner shelf sand on the lower shoreface between Brunswick Heads and Hastings Point (Figure 5). In contrast, offshore deposition in the Tallow Beach embayment immediately to the south of Byron Bay (Figure 5) has resulted in a shallower and more gently sloping sea bed than in nearby areas with similar wave exposure (compare the Tallow Beach profile in figure 9a with that from the northern part of the Byron Bay embayment).

In the Forster-Tuncurry area (Figure 1) large embayments either side of Cape Hawke show contrasting offshore morphologies that have influenced barrier development onshore. The sea bed off the southern embayment is deep and steeply sloping; the Holocene barrier here is narrow. The northern embayment has a wide, shallow inner shelf plain that has acted as a large sand source during barrier building in the past. Both Holocene and Pleistocene beachridge barriers are well developed in this embayment.

CONCLUSION

Geological studies of marine deposits along the N.S.W. coast have led to the identification of a number of factors that have played an important role in producing present-day nearshore morphologies and sediment patterns. The geological setting in which these factors operate is a tectonically stable shelf and coast with a very small supply of modern sediment and a moderate to high energy wave climate. Here, coastal barriers in bedrock embayments are mostly composed of sand derived from the inner shelf; many barriers are presently eroding.

Although incident waves are the principal sand transporting mechanism on the open coast, their influence on many coastal sand deposits is modified by the nature of the local bedrock and older sediment surfaces at the coast and on the inner shelf. These modifications are reflected by: the extent to which sand is exchanged between embayments (factor 1); variations in embayment orientation and incident wave energy within the embayment (factor 2); the range of shoreface morphologies produced by different inherited sediment types (factor 4); differing shoreface responses to changes in sediment supply (factor 5). In isolated cases, ocean currents modify wave-induced sand transport patterns and produce atypical nearshore sediment distributions and morphologies (factor 3).

Recognition of factors such as these provide information on how specific coastal sand deposits originally formed and have evolved subsequently. Except possibly for factor 3, they do not directly quantify sediment budgets but rather provide a framework within which the importance of separate budgetary components can be assessed. Undoubtedly additional factors remain to be identified on this coast. Certainly, on coasts which are presently receiving large sediment influxes, have lower energy or are undergoing relative sea level change, other factors will be found to be important.

REFERENCES

- Belperio, A.P., 1979. Negative evidence for a mid-Holocene high sea level along the coastal plain of the Great Barrier Reef Province. *Marine Geology* 32, M1-M9.
- Chapman, D.M., 1978. Zetaform or logarithmic spiral beach. (Australian landform example No. 32). *Aust. Geographer*, 14, 44-45.
- Cook, P.J. and Polach, H.A., 1973. A chenier sequence at Broad Sound, Queensland and evidence against a Holocene high sea level. *Marine Geology*, 14, 253-268.
- Gordon, A.D. and Roy, P.S., 1977. Sand movements in Newcastle Bight. *Third Aust. Conf. Coast and Ocean Eng.*, 77, 64-69. *Instn. Eng., Aust.*
- Jones, B.G., Young, R.W. and Eliot, I.G., 1979. Stratigraphy and chronology of receding barrier-beach deposits on the northern Illawarra coast of New South Wales. *J. geol Soc. Aust.*, 26, 25--264.

- Lanford-Smith, T. and Thom, B.G., 1969. Coastal morphology of New South Wales. *J. geol. Soc. Aust.*, 16, 572-580.
- Marshall, J.F. and Thom, B.G., 1976. The sea level in the last interglacial. *Nature*, 263, 120-121.
- Roy, P.S., 1980. Quarternary depositional environments of the Fullerton Cove region, central New South Wales. *Rec. geol. Surv. N.S.W.*, 19, 189-220.
- Roy, P.S. and Crawford, E.A., 1977. Significance of sediment distribution in major coastal rivers, northern New South Wales. *Third Aust. Conf. Coast and Ocean Eng.*, 77, 177-184. *Inst. Eng., Aust.*
- Roy, P.S. and Crawford, E.A., 1980. Quaternary geology of the Newcastle Bight inner continental shelf, New South Wales, Australia. *Rec. geol. Surv. N.S.W.*, 19, 145-188.
- Roy, P.S., Thom, B.G. and Wright, L.D., 1980. Holocene sequences on an embayed high-energy coast: and evolutionary model. *Sedim. Geol.*, 16, 1-19.
- Roy, P.S., Stephens, A.W. and Gordon, A.D., (in press). Quarternary Geology and sediment budget for the Byron Bay region, eastern Australia. *Rec. geol. Surv. N.S.W.*
- Swift, D.J.P., Stanley, D.J. and Curry, J.R., 1971. Relict sediments, a re-consideration. *J. geol.* 79, 322-346.
- Thom, B.G., 1965. Late Quaternary coastal morphology of the Port Stephens-Miyall Lakes area, N.S.W. *J. Proc. R. Soc. N.S.W.*, 98, 23-36.
- Thom, B.G., 1978. Coastal sand deposition in Southeast Australia during the Holocene. In Davies, J.L. and Williams M.A.J. (Eds.), *Landform Evolution in Australasia*. Australian National University Press, Canberra, Australia.
- Thom, B.G., Hails, J.R. and Martin, J.R.H., 1969. Radiocarbon evidence against higher post-glacial sea levels in eastern Australia. *Marine Geology*, 7, 161-168.
- Thom, B.G., Hails, J.R., Martin, J.R.H., and Phipps, C.V.G., 1972. Post-Glacial sea levels in eastern Australia - in reply. *Marine Geology*, 12, 233-242.
- Thom, B.G., and Chappell, J., 1975. Holocene sea levels relative to Australia. *Search*, 6, 90-3.
- Thom, B.G., Polach, H.A. and Bowman, G.M., 1978. Holocene age structure of coastal sand barriers in New South Wales. Department of Geography, Faculty of Military Studies, University of N.S.W., Duntroon, Canberra, 86 pp. (unpublished).
- Thom, B.G. and Roy, P.S. (in press). Late Quaternary Marine deposition in New South Wales and Southern Queensland - an evolutionary model. *J. geol. Soc. Aust.*

- Thom, B.G., Shepherd, M., Ly, C.K., Roy, P.S. and Bowman, G.M., (in press).
Quaternary geomorphology and geology of the Port Stephens - Myall
Lakes area, N.S.W. Australian National University, Monograph.
- Wright, L.D., 1970. The influence of sediment availability on patterns
of beachridge development in the vicinity of the Shoalhaven River
delta, N.S.W. Aust. Geographer, 11, 336-348.
- Zenkovitch, V.P., 1967. Processes of Coastal Development. Oliver and
Boyd. Edinburgh. 738 pp.

BEACH EROSION-ACCRETION AT TWO TIME SCALES

B. G. THOM

Department of Geography, Faculty of Military Studies,
The University of New South Wales, Duntroon,
A.C.T. Australia
and

C. M. BOWMAN

Department of Geography, Faculty of Military Studies,
The University of New South Wales, Duntroon,
A.C.T. Australia

Introduction

Erosion and accretion on the beachface have been studied at two time scales on the central and south coast of New South Wales, Australia. This research aims at providing a temporal perspective to contemporary problems of beach erosion in areas where the historic map record of changes in shoreline position is poor. Field work has been concentrated at two localities Moruya (lat. 35° 53'S long. 150°09'E) and Newcastle Bight (lat. 32°48'S long. 151°55'E)(Fig. 1).

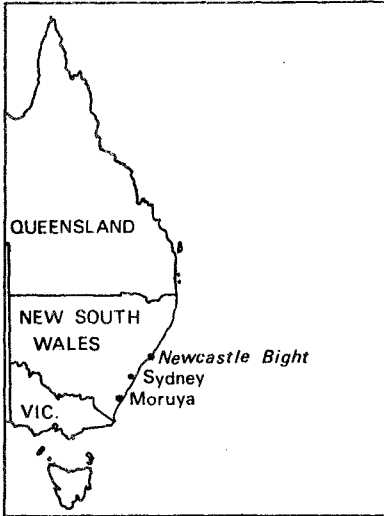


Figure 1. Location map of eastern Australia.

Beach and inshore systems on the N.S.W. coast exhibit pronounced morphologic and dynamic variability with respect to both time and local environment (Wright et al., 1977; Wright, Thom and Chappell, 1979; Chappell and Eliot, 1979; Short, 1978, 1979). Beach systems on this coast are characterized on a regional scale by a steep, narrow inner continental shelf and nearshore zone (Wright, 1976), and by pronounced compartmentalization with alternating rocky headlands and embayed sandy beaches (Davies, 1974; Roy et al., 1980, in press). The compartments are of widely varying dimensions, and often involve the blocking of estuaries, lagoons and swamps by a variety of bay-barrier types (Thom, 1974; Thom et al., 1978).

Open-ocean beaches display highly dynamic foreshore and inshore topographies in response to a relatively high energy, but variable, wave regime (McKenzie, 1958; Thom et al., 1973; McLean and Thom, 1975; Wright et al., 1979). The wave regime is characterized by a variable wind-wave climate, superimposed on a persistent long-period southerly to southeasterly swell. Significant wave heights of 1.5 m are exceeded for 50% of the time, with deepwater storm wave heights being known to exceed 10 m (Lawson and Abernethy, 1975). Southerly and southeasterly waves are the highest. Severe storm waves can occur at any time of the year. The loss of wave power by bottom friction seaward of the breaker zone averages only 3.4% of the incident deepwater wave power along the open coast (Wright, 1976). However, the distribution of wave power within an embayment will vary appreciably with exposure and degree of indentation.

Both localities discussed in this paper are exposed to high energy waves and strong onshore winds (Fig. 1). Moruya (Fig. 2) faces due east whereas Newcastle Bight (Fig. 3) is oriented more towards the south. Since sea level has been at its present position along this coast for the last 6000 to 6500 years (Thom and Chappell, 1975), both localities have experienced sand barrier development. At Moruya, a simple Holocene beach-ridge plain has formed seawards of "drowned" river valleys and an ancient bedrock cliff (Fig. 2). The barrier of similar age at Newcastle Bight is more complex. Figure 3 shows an elongate sand complex blocking an interbarrier depression. A Pleistocene "Inner Barrier" occurs landward of this depression. The Holocene barrier at Newcastle Bight is composed of beach ridges (eastern end), overlain by vegetated and mobile transgressive dunes. The complex morphology of this locality expresses partial eolian reworking of a prograded barrier since sea level has been at its present position.

Geologic Scale of Coastal Erosion-Accretion

One time scale used in the study of shoreline erosion and accretion is termed "geologic" and is measured in radiocarbon years before present (BP, where the "present" is AD1950). All radiocarbon dates on marine shell material used here have been corrected for the "environmental" or "ocean reservoir effect" caused by the lack of equilibrium between ocean and atmospheric ^{14}C . Calibration of radiocarbon years to calendar years, by correcting for secular variations in the radioactive isotope ^{14}C (Clark, 1975), have not been made although more accurate

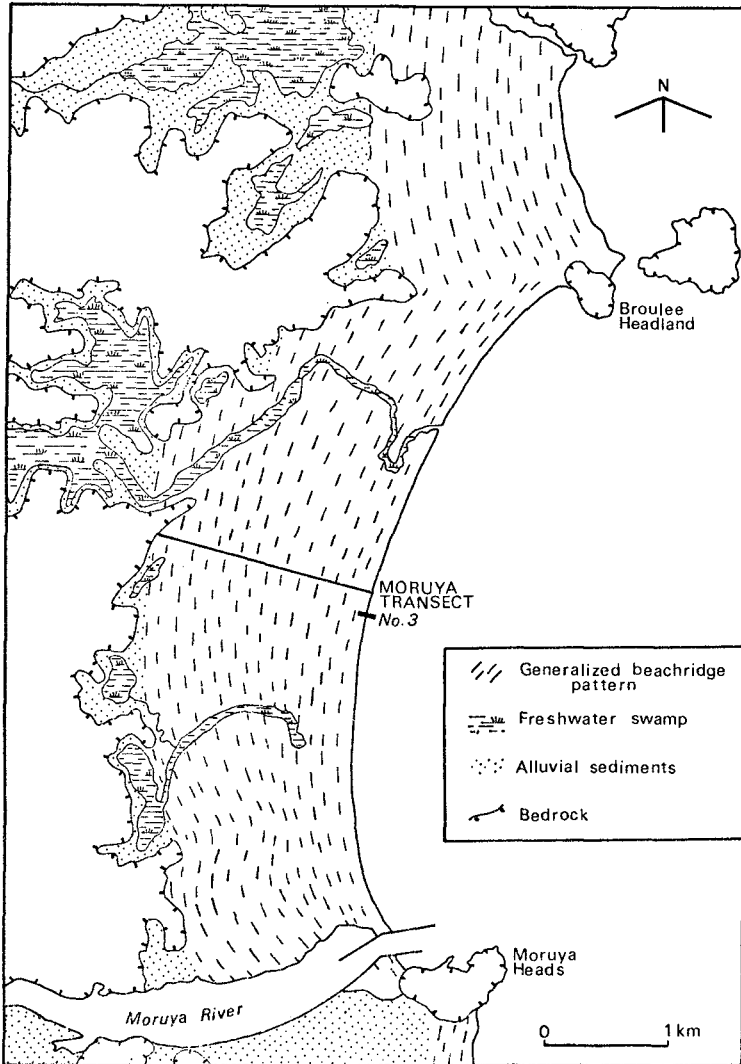


Figure 2. Moruya beach ridge plain, showing drillhole transect and beach profile number 3.

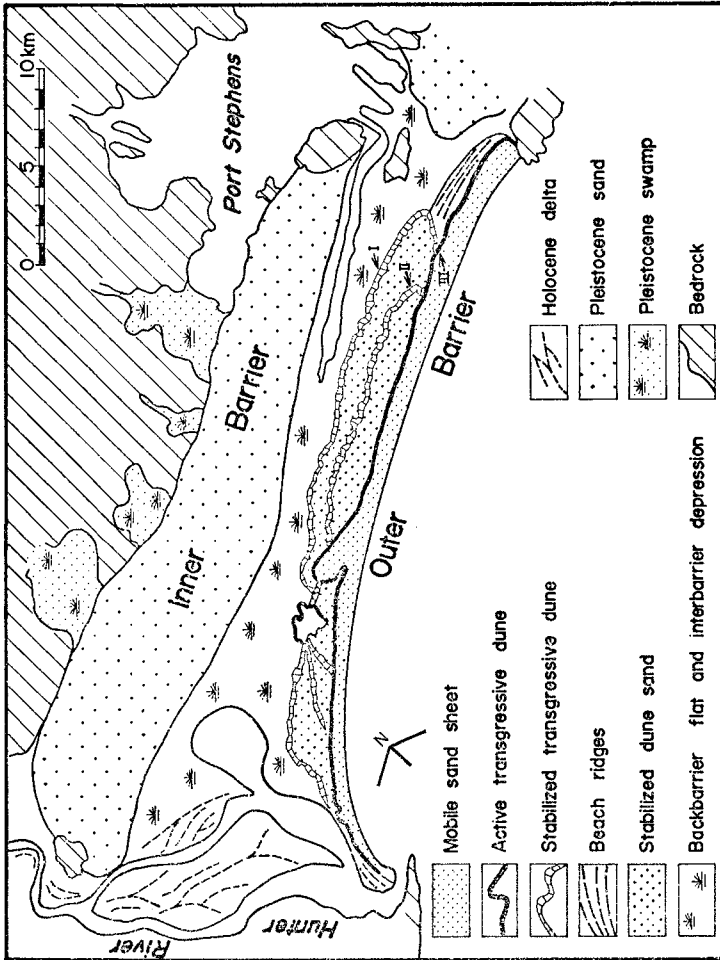


Figure 3. Morphological map of Newcastle Bight. Note beach ridges at eastern end of Outer Barrier and transgressive dune ridges I, II and III.

estimates of rates of shoreline accretion would require calibration. Details of dating techniques used in this study, and the dates themselves, are discussed in Thom et al. (1978).

Sampling of materials for radiocarbon dating involved power auger drilling. Samples of shell were collected from various depths below barrier surfaces. Shells and shell fragments associated with the nearshore environment of deposition (especially the species *Bankiviva fasciata*) were submitted for dating.

The pattern of accretion at Moruya, based on an analysis of 30 ^{14}C dates, is summarised in Figure 4. This figure highlights changes in the rate of shoreline accretion and volumetric addition for a single cross-section in the centre of the embayment. The diagram involves the grouping of ^{14}C dates into episodes. Two points arise from this figure.

(a) The dates show a relatively rapid decline in the rate of accretion with time with little evidence of progradation in the last 2000 years in the vicinity of the section.

(b) In the centre of the embayment the amount of sediment added to the coast has also declined with time.

At Moruya, it is likely that accretion did not decline at a continuous rate. There is evidence at this locality and elsewhere on the N.S.W. coast for the dates to cluster into discrete episodes (Thom, 1978; Thom et al., 1978).

Several factors must be evaluated in any attempt to explain the pattern in Figure 4. Alongshore transport of sand bypassing headlands cannot be regarded as a significant contributor to sand budgets since sea level has been at its present position (Davies, 1974). Furthermore, erosion of bedrock cliffs or supplies of sand from rivers to the beach-face can be shown to be negligible. River sand supplies are typically trapped in estuaries. The barriers are composed of rounded quartz-rich "marine" sands; these are clearly differentiated mineralogically from the angular feldspathic and lithic-rich "fluvial" and cliff-eroded sands. Variations in sea level over the last 6000 to 6500 years along this coast have not been documented, and cannot be used to explain patterns of shoreline movement. Therefore, it appears that the trends shown in Figure 4 relate to equilibration of the inner shelf gradient and profile form to the wave climate since sea level stabilized at its present position. Readjustment of nearshore profiles from a condition of disequilibrium, which existed after the termination of the Postglacial Marine Transgression, to a condition of equilibrium involving no further accretion, is being discussed elsewhere (Chappell and Thom, in prep. based on principles discussed in Chappell, 1980). Superimposed on this adjustment process are fluctuations in rates of accretion in response to changing wave climates in the Holocene (Thom, 1978). At Moruya, these changes are expressed by clusters of ^{14}C dates differentiating periods of marked shoreline accretion from periods of limited or no accretion.

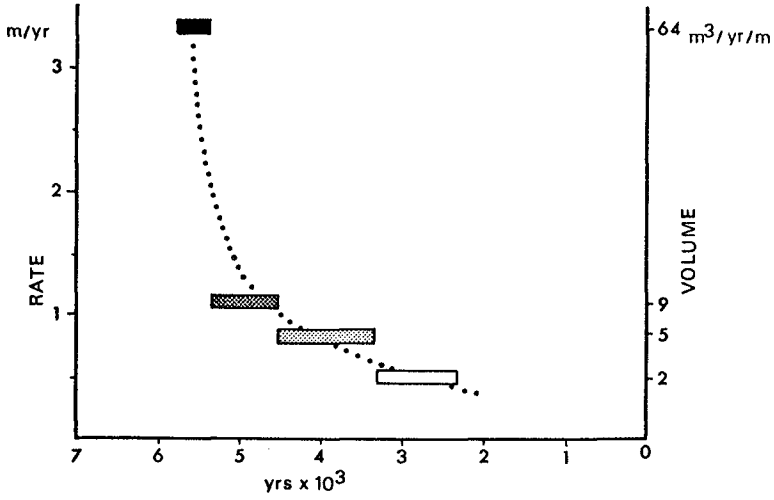


Figure 4. Changes in accretion rates and volumetric addition, Moruya beach ridge plain.

However, the sand barrier at Newcastle Bight, exposed to strong southerly winds, has experienced a different geomorphological history.

The morphological map of the Holocene or Outer Barrier at Newcastle Bight (Fig. 3) depicts a "core" of beach ridges at the eastern end overlain by three discrete, massive dune ridges. Two of these dune ridges (I and II) are vegetated by an *Eucalyptus* woodland and are over 15 km long and 30 m high. The third ridge (III) is unvegetated and is currently transgressing the vegetated dunes and beach ridges from the south. These "waves" or "surges" of sand represent episodes of eolian instability in the backshore, probably following periods of high wave energy (Thom, 1978). The sequence of deposition based again on drilling and radiocarbon dating can be summarized as follows:

- (a) Accretion following termination of the postglacial sea level rise approximately 5500 to 6500 years ago;
- (b) Initiation and landward movement of Ridge I in excess of 4500 years ago;
- (c) Stabilization of Ridge I by vegetation and possible accretion of the shoreline;
- (d) Initiation and landward movement of Ridge II approximately 2000 years ago;
- (e) Stabilization of Ridge II by vegetation involving foredune growth;
- (f) Initiation and landward movement of Ridge III 300 to 500 years ago accentuated by human disturbance in last 100 years.

The sequence at Newcastle Bight can be best explained by long-term equilibration of inner shelf and nearshore profiles to fluctuating wave regimes following sea level "stillstand" (see below). As at Moruya, there is little evidence for supplies of river sand or alongshore sand reaching the beach or mobile dunes over this time period (Roy, 1977; Roy and Crawford, 1977; Ly, 1978).

Synoptic Scale of Coastal Erosion-Accretion

The other time scale applicable to the study of beachface erosion and accretion is termed "synoptic". This involves fortnightly to monthly measurement of beach-nearshore profiles from fixed datum points. At Moruya, six profiles have been monitored since January, 1972. Progress reports on trends revealed by these profiles have been published (Thom et al., 1973; McLean and Thom, 1975), and morphodynamic conditions associated with particular beach configurations have also been reported (Wright et al., 1979; Wright, Thom and Chappell, 1979).

The prime objective of this monitoring is to relate beach-face morphology to seasonal and year-to-year changes in wave and atmospheric climate. It is clear that the beachface responds strongly to year-to-

year variability in wave climate. Periods of one year or more of distinct beachface accretion are separated by years when east and southeast storms predominate and the beachface erodes (e.g. 1974-75). Figure 5 highlights the changes in cross-sectional area expressed by one profile near the centre of the Moruya embayment (comparable data are not available for Newcastle Bight, but similar studies in the Sydney area by Short and others reveal similar trends for the period 1975-76 to the present). Four phases are suggested in Figure 5 for the period 1972 to 1980:

- (a) growth in beach cross-sectional area to mid 1973 compared to the reference profile in January, 1972;
- (b) dramatic erosion of beachface and foredune in 1973 and 1974;
- (c) oscillating erosion and accretion involving fluctuation in sectional area (and beachface volumes) to 1978;
- (d) a steady build-up of beach sand from 1978 to the present, to levels well in excess of the reference cross-sectional area.

Beachface erosional periods of the type witnessed in 1973-74, involved "clusters" of storms over a minimum period of 6 months which are generated off the east coast in the Tasman Sea. Sustained periods of erosion are of irregular incidence with similar events to 1974-75 being recorded in 1912, 1950 and 1967 (Thom, 1974, Table 1). Accretion periods are associated with zonal westerly flow in winter and the absence of the marginal effects (high swell wave) of tropical cyclones in summer. There are also periods of a year or more in duration when the beachface does not significantly accrete or erode (e.g. 1976-78).

Discussion

The two time scales of study are linked by a climatic model of variation in the magnitude and frequency of storminess (Thom, 1978). The synoptic scale provides the "modern analog" for understanding changes of the geologic scale. Short-term wave conditions are associated with processes responsible for short-term climatic variability. Sea surface temperature distribution and changes in sea ice extent are two broad scale forcing mechanisms which influence major cyclonic frequencies in the Tasman Sea region. These forcing mechanisms interact with the general circulation in the atmosphere to create climatic "disturbances". In turn they may be influenced by solar cycles (Stevenson, 1980). Years with frequent extratropical cyclones can be linked to increased atmospheric "blocking" action to the east of New Zealand. In contrast, relatively non-stormy years are dominated by zonal flow, that is, the more-or-less continuous movement of pressure systems across southern Australia. Expanded to a longer time scale, it is postulated that, for periods of several hundred years, the magnitude and frequency of storminess changes.

During more stormy periods, like the Little Ice Age of the 16th and 17th centuries, wave and wind conditions promoted beachface and

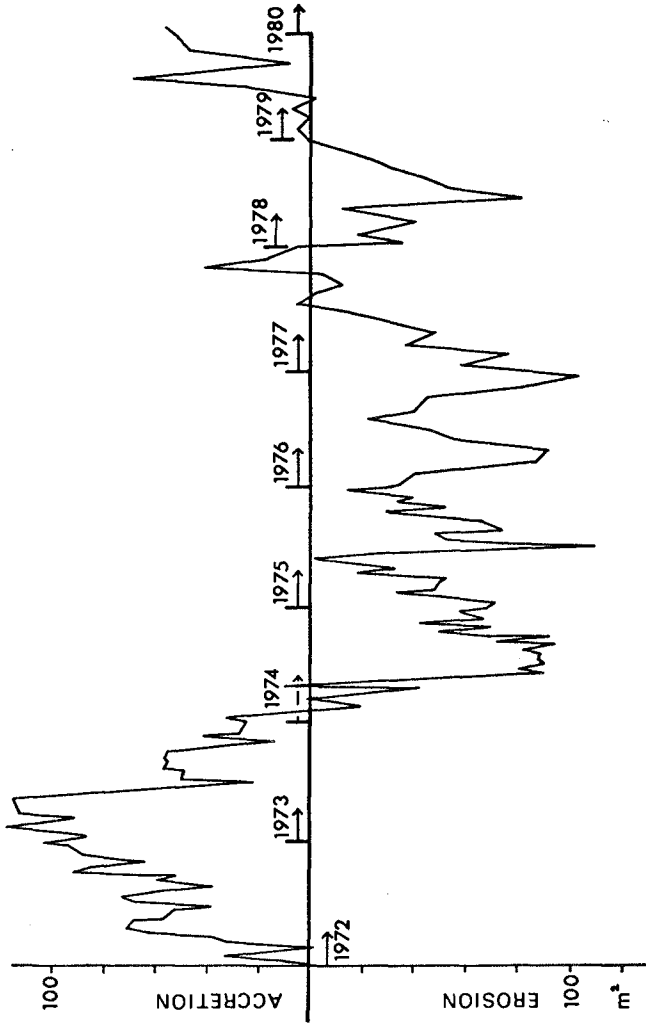


Figure 5. Change in beach cross-sectional area: Moruya profile 3, 1972-1980. Reference zero is cross-sectional area in January 1972.

foredune erosion. Those embayments facing south endured more severe foredune erosion and the initiation of transgressive dunes (e.g. New-castle Bight). In contrast, the more sheltered bays underwent vertical foredune building, or where gradients were less steep, no shoreline accretion. During non-stormy periods, backshore colonization of sand-binding plants became more dominant, encouraging stabilization of blow-outs and mobile sand sheets. Locally, beachface accretion may have occurred where nearshore sand supplies were abundant.

The above discussion highlights the role of one major variable, wave energy, in the erosion-accretion balance within sandy bays of the N.S.W. coast. The other major variable is the changing supply of sand in the nearshore zone as the inner shelf configuration adjusts to a long-term equilibrium condition. We see this equilibration process as a long-term trend upon which is superimposed fluctuation in wave energy. Thus, as barriers grow, the nearshore zone is progressively depleted of sand. Nearshore profiles are steepening during this period as no fresh inputs, or very limited fresh inputs, are available from offshore, alongshore or from river sources on this coast. As a consequence, progressively less material is available for beachface accretion in non-stormy periods.

The net result of these two factors, fluctuations in storminess and dwindling supplies of nearshore sand, is that periods of beachface erosion, at either the long or short term scale, are becoming more severe. It is possible that erosional conditions in the last 1000 years are more severe compared to the previous 5000 years of sea level "still-stand". Any deterioration in global climate involving more storms of high intensity will be manifested in more severe erosion in the future than in the past. Major schemes of artificial beach nourishment may be required in these circumstances on the N.S.W. coast.

REFERENCES

- CHAPPELL, J., 1980: Inshore-nearshore morphodynamics - a predictive model for equilibrium and change. 17th International Conference on Coastal Engineering, Sydney, Institution of Engineers, Australia, 80/1 99-100.
- CHAPPELL, J. & ELIOT, I.G., 1979: Surf-beach dynamics in time and space - an Australian case study, and elements of a predictive model. Marine Geology, 32, 231-250.
- CLARK, R.M., 1975: A calibration curve for radiocarbon dates, Antiquity, 49, 251-266.
- DAVIES, J.L., 1974: The coastal sediment compartment, Australian Geographical Studies, 12, 139-151.
- LAWSON, N.V. & ABERNETHY, C.L., 1975: Long term wave statistics off Botany Bay, 2nd Australian Conference on Coastal and Ocean Engineering, Institution of Engineers, Australia, 75/2, 167-176.

LY, C. K., 1978: Late Quaternary deposits of the Newcastle-Port Stephens area as revealed by grain size analysis and scanning electron microscopy, Journal and Proceedings of the Royal Society of New South Wales, 111, 77-88.

McKENZIE, P., 1958: The development of beach sand ridges, Australian Journal of Science, 20, 213-214.

McLEAN, R.F. & THOM, B.G., 1975: Beach changes at Moruya, 1972-1974, 2nd Australian Conference on Coastal and Ocean Engineering, Institution of Engineers, Australia, 75/2, 177-184.

ROY, P.S., 1977: Does the Hunter River supply sand to the New South Wales coast today? Journal and Proceedings of the Royal Society of New South Wales, 110, 17-24.

ROY, P.S. & CRAWFORD, E.A., 1977: Significance of sediment distribution in major coastal rivers, northern New South Wales, 3rd Australian Conference on Coastal and Ocean Engineering, 77, 177-184, Institution of Engineers, Australia.

ROY, P.S., THOM, B.G. & WRIGHT, L.D., 1980: IN PRESS: Holocene sequences on an embayed high-energy coast: an evolutionary model. Sedimentary Geology.

SHORT, A.D., 1978: Wave power and beach-stages: a global model, Proceedings of 16th Coastal Engineering Conference, Hamburg, 1145-1162.

SHORT, A.D., 1979: Three dimensional beach-stage model, Journal of Geology, 87, 553-571.

STEVENSON, B., 1980: Solar cycles and erosional events on the New South Wales Central and South Coasts, Search, 11, 117-118.

THOM, B.G., 1974: Coastal erosion in eastern Australia, Search, 5, 198-209.

THOM, B.G., 1978: Coastal sand deposition in southeast Australia during the Holocene. In: Landform Studies in Australasia, (editors J. Davies & M. Williams), Australian National University Press, 197-214.

THOM, B.G. & CHAPPELL, J., 1975: Holocene sea level relative to Australia, Search, 6, 90-93.

THOM, B.G., McLEAN, R.F., LANGFORD-SMITH, T. & ELIOT, I., 1973: Seasonal beach change, Central and South Coast, N.S.W., Engineering Dynamics of the Coastal Zone, Institution of Engineers, Australia, 73/1, 35-42.

THOM, B.G., POLACH, H.A. & BOWMAN, G.M., 1978: Holocene Age Structure of Coastal Sand Barriers in New South Wales, Australia, Department of Geography, Faculty of Military Studies, University of New South Wales, Duntroon, 86 pages.

WRIGHT, L.D., 1976: Nearshore wave-power dissipation and the coastal energy regime of the Sydney-Jervis Bay region, New South Wales: a comparison, Australian Journal of Marine and Freshwater Research, 27, 633-640.

WRIGHT, L.D., CHAPPELL, J., THOM, B.G., BRADSHAW, M.P. & COWELL, P., 1979: Morphodynamics of reflective and dissipative beach and inshore systems: Southeastern Australia, Marine Geology, 32, 105-140.

WRIGHT, L.D., THOM, B.G. & CHAPPELL, J., 1979: Morphodynamic variability of high energy beaches, Proceedings of 16th Coastal Engineering Conference, Hamburg, 1180-1194.

CHAPTER 59

PHYSICAL PROCESSES AND SEDIMENT FLUX THROUGH REEF-LAGOON SYSTEMS

Harry H. Roberts
Coastal Studies Institute, Louisiana State University
Baton Rouge, LA 70803

Abstract

Studies of physical processes in reef-lagoon systems continue to emphasize the importance of waves and wave-induced currents at the reef crest as agents of sediment transport to backreef environments. These across-the-reef currents are also largely responsible for driving back-reef lagoon circulation. Rapid energy transformations associated with the process of wave breaking at the reef crest are responsible for strong reef-normal surge currents. Estimates of energy loss, as determined by wave height changes caused by wave breaking, can be as high as 70-80% for discontinuous reefs and >90% for continuous examples. The amount of energy loss is related to depth of water over the reef crest, a function of reef topography and tidal regime. Low-tide conditions promote the greatest incident wave modification and attenuation as a result of increased breaking-wave intensity. Under trade-wind conditions found in the Caribbean, surge currents of 50-80 cm/sec for durations of 2-6 sec are common in a low to moderate wave-energy setting (4-6 sec input waves, 40-50 cm average heights). Sediments through the sand sizes up to pebbles are easily transported lagoonward by these periodic bursts of energy.

Flow in shallow backreef lagoons (generally <3 km wide) is driven largely by across-the-reef currents resulting from breaking waves. Long, unbroken reefs tend to induce axial currents in the backreef lagoon which flow roughly parallel to the reef trend. Side-scan sonographs indicate that large bedforms define a region of bottom sediment migration related to strong currents down the lagoon axis, presumably activated during periods of abnormal wave activity on the reef.

Localized and discontinuous shallow reefs tend to store coarse sediments in the backreef in sand bodies oriented at high angles to the reef trend. Combined effects of wave refraction and tidal exchange around the flanks of these localized reef masses give rise to tombolo-like sediment accumulations in the shallow backreef area. Backreef sand bodies

associated with continuous linear reefs tend to be oriented parallel to the reef trend.

Lagoonal sediments are transported through tidal passes to the forereef shelf, where sediment sinks commonly develop behind actively growing shelf-margin reefs. Side-scan sonar and high-resolution sub-bottom data confirm both sediment sinks and preferential offshelf transport routes on narrow, rough-bottomed forereef shelves. In trade-wind-island systems (e.g., Grand Cayman and St. Croix) sediments are stored in large quantities on the forereef shelf at the downwind flanks of the islands. Forereef shelf morphology indicates that at these same locations routes for offshelf sediment transport are optimized.

Introduction

Investigations of process-response interactions in coral reef and reef-associated environments (Munk and Sargent, 1954; Inman et al., 1963; Roberts, 1974; Roberts et al., 1975; Davies, 1977; Roberts et al, 1977; Suhayda and Roberts, 1977; and others) have demonstrated close relationships between physical processes, reef geometry, and sediment distribution. Sediment transport routes and sinks in lagoon and shelf environments display considerable variability, depending largely on linearity of the reef, closeness of the reef to the shoreline, lagoon geometry, and local physical process setting.

Recent studies conducted on the Caribbean islands of Grand Cayman, Great Corn (Nicaragua), and St. Croix have provided a framework for better interpreting sediment flux through lagoon-reef-shelf systems by integrating results of wave-current investigations with side-scan-sonar surveys and high-resolution seismic profiles. Results of these studies regarding the magnitude and variability of physical processes and the resultant effects on sediment transport are summarized in this paper for continuous linear reefs with narrow backreef lagoons (Grand Cayman and St. Croix) and a discontinuous reef example (Great Corn Island, Nicaragua).

Direct field measurements of waves and wave-driven currents were replicated in contrasting reef geometries and under a variety of tide and incident wave conditions typical of the trade-wind-dominated and microtidal Caribbean region. The data acquisition system for studies near the reef crest consisted of an array of absolute pressure transducers and low-inertia ducted current meters (Fig. 1). Data were cabled back to a central collection center and recorded in an analog format. In situ recording bottom-mounted current meters (Marine Advisers Q-16) and drogue studies were used to determine the characteristics of lagoon and shelf circulation. A Klein 100-kHz side-scan-sonar system equipped with a 3.5-kHz subbottom profiler was used for mapping lagoon and shelf bottom features. Accurate navigational control was provided by a Decca Del Norte locating system.

Reef-Crest Wave/Current Interactions

Shallow linear and quasilinear reefs that are situated close to a land mass generally have profiles similar to the one shown in Figure 1.

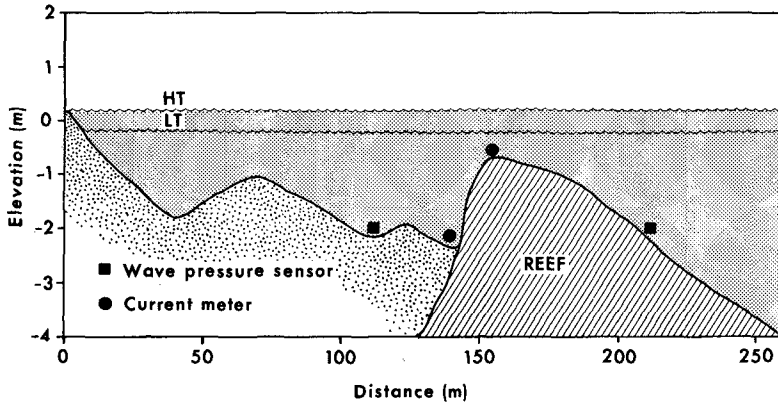


Figure 1. Instrument array for a study of wave/current interaction at the reef crest, Great Corn Island, Nicaragua. A similar instrument array was used for a reef crest study in St. Croix, U.S. Virgin Islands.

In the Caribbean region these reefs tend to be narrow and are commonly associated with a backreef lagoon with water depths generally less than 10 m. Although the shallow zone of living reef is very narrow compared to most backreef lagoons, it functions as a renewable source of abundant sediments to backreef areas. Both biological and mechanical degradation of skeletal components of the reef produces sediments that are available for transport to other environments. The apex or crest of this linear reef is a critical zone for intense wave-related processes. Shallow water depths (commonly about 1 m) induce extreme modification of incoming waves, usually resulting in wave breaking. Because water depth over the crest can strongly influence the intensity of wave-reef interactions, even small tidal variations such as those found in the Caribbean region become important. Waves may break continually as they transit the reef crest, or they may propagate unbroken until secondary wave crests are formed. The degree of wave transformation is highly dependent on water depth at the reef crest and incident wave characteristics.

Reef crest experiments were conducted on a rather discontinuous linear reef approximately 150 m from the northwest shoreline of Great Corn Island, Nicaragua. Wave sensors placed at the same depth (2 m) in the water column seaward and lagoonward of the reef crest (Fig. 1) were used to evaluate wave modification and energy loss as incident waves intersected the reef and propagated across it to the backreef lagoon. Forereef and backreef wave spectra (Fig. 2) derived from 20-min wave records collected at high tide describe a 68% energy loss as a result of wave breaking at the crest. Although the breaking process is not explained well by hydrodynamic theory, the reduction of wave height across the reef crest induced by breaking and wave reformation can be empirically described. Suhayda and Roberts (1977) show that data from Nakamura et al. (1966), as well as the Nicaragua experiments, can be used to establish an

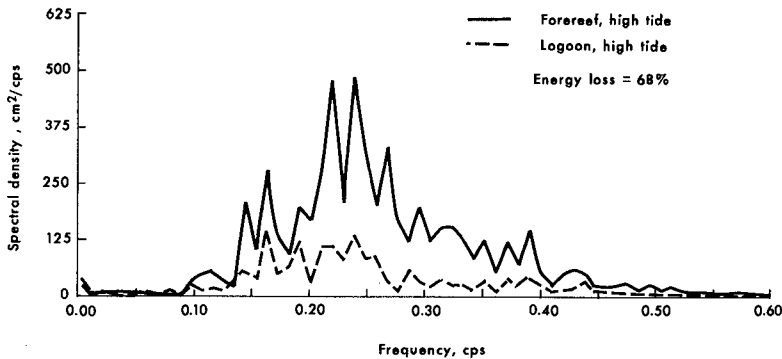


Figure 2. Comparison of forereef and backreef wave spectra derived from data collected at high tide. Interaction between incoming waves and the reef crest results in an energy loss of 68%.

expression for wave height H at the point of reforming. This expression is given by:

$$H = H_0 (1 - 0.8 e^{-0.6 d/H_0}), H_0 > 0$$

where H_0 is the wave height near the breakpoint and d is the mean water depth at the reef crest. The range of water depths for which the formula is valid is d/H_0 from zero to about 5. This expression indicates that when $d/H_0 = 0$ wave heights in the lagoon will be about 20% of the wave heights outside the reef. Actual field measurements show that the heights of lagoon waves are closer to 30% of waves outside the reef. These estimates assume a narrow reef crest, which is generally the case in Caribbean settings.

As water depth over the reef crest declines during falling tide, the process of wave breaking becomes more intense. Energy loss associated with these conditions is accelerated. Forereef and backreef wave spectra derived from low-tide data sets indicate that approximately 10% more energy is lost through reef-crest/wave interactions at low tide than at high tide (Fig. 3). These values, derived from a discontinuous reef, are conservative compared with similar data sets collected from a continuous linear system (St. Croix), where a 92% energy loss was recorded during high tide and 97% at low tide (Fig. 4). Although a 77% energy loss is indicated in the Nicaragua low-tide data, the dominant incoming wave period (about 6 sec) is present as the highest energy peak of the backreef spectrum. Leakage of energy around the flanks of the discontinuous reef may be partially responsible for this relationship, in which case the estimate of energy loss resulting from wave breaking is conservative. In both the continuous and the discontinuous reef-crest data sets, only the

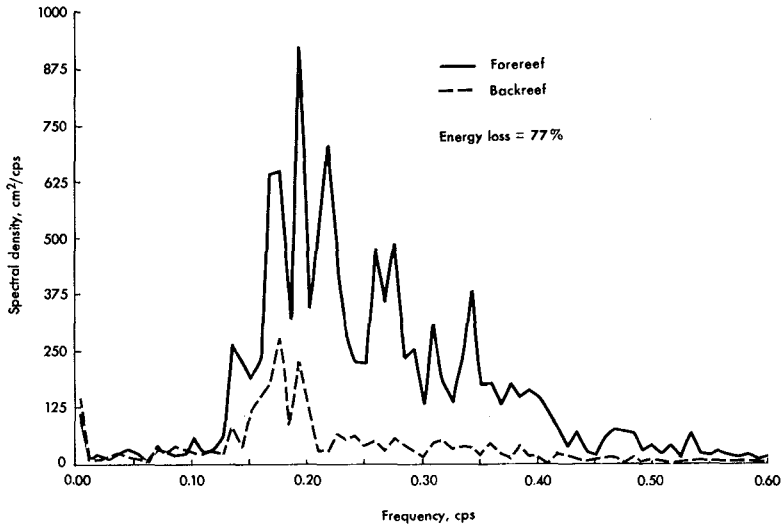


Figure 3. Comparison of forereef and backreef wave spectra derived from data collected at low tide. A 77% energy loss is described due to interaction between the reef crest and incoming waves.

low-frequency peaks of the forereef spectra persist in the backreef records. Shape of the backreef wave spectrum is important because wave steepness (wave height/wavelength) has an important effect on sediment transport and shoreline beach stability (Hayami, 1958). It therefore follows that reef-crest morphology exerts a critical influence on the characteristics of waves impacting the backreef shoreline.

Surprisingly strong but short-lived across-the-reef currents are associated with breaking waves. As waves break on the reef crest, water is driven into the backreef by surge currents. Under typical 4-6-sec input waves with heights of approximately 45 cm, shoreward-directed crest-normal currents displayed average velocities of between 10 and 20 cm/sec. Intensity of energy transformation associated with the wave-breaking process and current velocities that result varies with tide, as can be clearly seen in the wave spectra of Figures 2, 3, and 4 and the averaged reef-crest currents shown in Figure 5. The current data show that variations about the mean speed of up to 50% can occur on time scales of 1-2-min. Although the averaged reef-crest currents seem quite low, actual instantaneous measurements show that the effect of each wave transiting the reef crest produces surge currents with maximum measured speeds as high as 80 cm/sec. These periodic and short-lived currents have durations of only a few seconds (Fig. 6). During times when wave breaking at the reef crest is most intense (low tide), surge currents display the highest range of velocities. This trend was also true of reef-parallel currents monitored in the

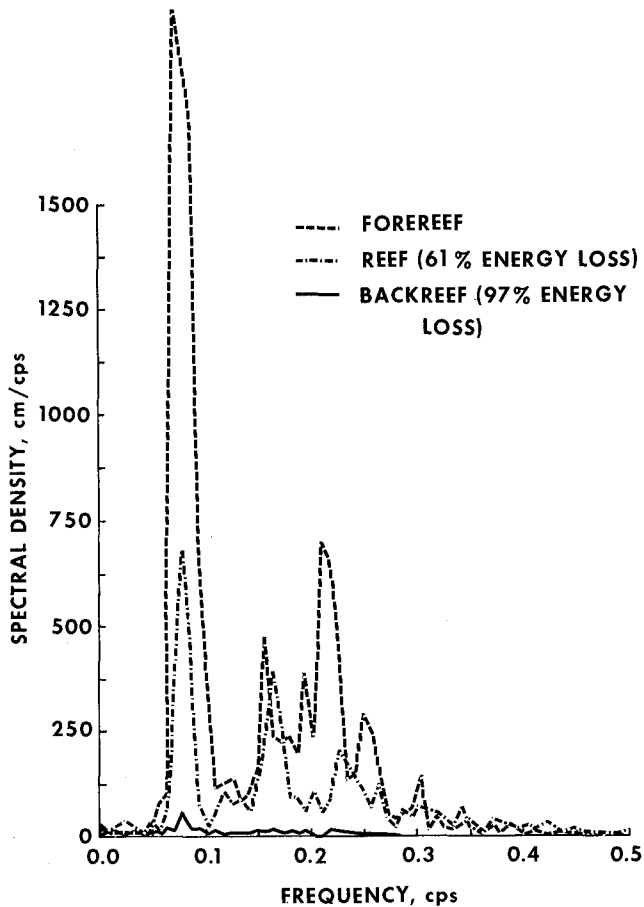


Figure 4. Comparison of forereef, reef crest, and backreef spectra derived from wave data collected at low tide from a continuous linear reef separating Great Pond Bay, along the south coast of St. Croix, from the forereef shelf. The reef crest spectrum is uncorrected for sensor depth and thereby represents a very conservative estimate of the energy loss.

immediate backreef (Fig. 1). Although backreef current speeds averaged 30-40% less than simultaneous reef-crest values, speeds at high tide were about 30% lower than low-tide values in the discontinuous reef example. As

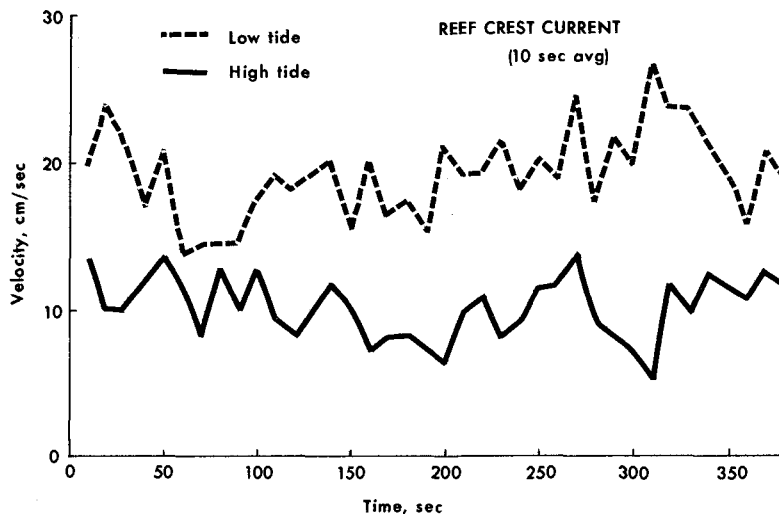


Figure 5. Shoreward-directed reef crest current at high tide and low tide. Current velocities represent values derived from 10-sec averages.

average velocity changed, currents directly behind the reef changed direction. These currents generally described lagoon filling during rising tide and draining of the lagoon as the tide fell.

Lagoon Processes

Shallow backreef lagoons that are fronted by a continuous linear reef are generally very homogeneous water bodies with regard to both density and current structure. Currents near the reef are primarily the results of mass transport of water associated with the previously described process of wave breaking at the reef crest. General lagoon circulation is commonly forced by a combination of momentum provided by the wind and mass transport across the reef. Water input may be associated with the combined effects of waves and tide, but field studies suggest that wave input is the dominant process (von Arx, 1954; Inman et al., 1963; Storr, 1964; Roberts et al., 1975; Suhayda and Roberts, 1977). However, Kjerfve (personal communication) reports that water in the backreef lagoon at Carrie Bow Cay (British Honduras) is primarily wind driven and does not have an obvious tidal signature.

Drifting-drogue studies, current-meter profiles, and in situ recording-current-meter data from Great Pond Bay, along the south coast of St. Croix, suggest that mean flow velocities under typical trade-wind conditions (5-7 m/sec) are in the range of 10-25 cm/sec (Roberts et al., 1980). The Great Pond Bay system is similar in size and shape to other backreef lagoons in the Caribbean reef province, as well as other carbonate

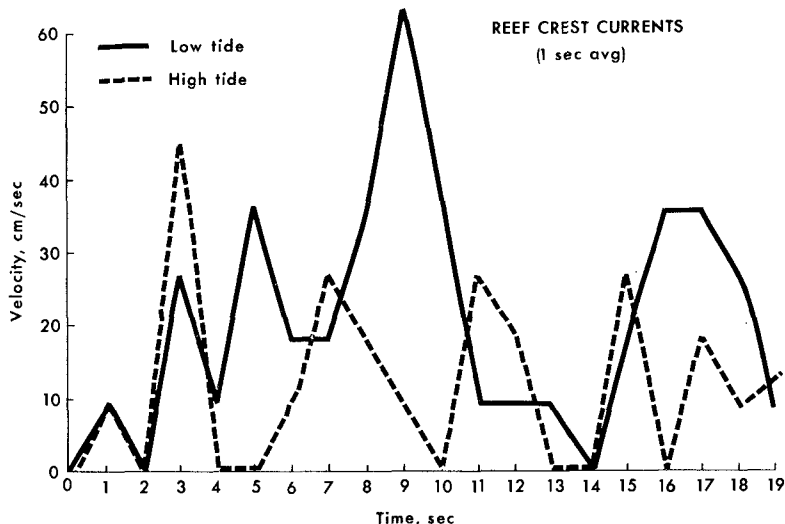


Figure 6. Crest-normal surge currents associated with waves transiting the reef crest. Current velocities represent values derived from 1-sec averages.

coasts of the world. Drogue tracks in Figure 7 illustrate that flow through the lagoon is directed slightly toward the northwest. Near the coast continuity of flow forces currents to become more parallel to the shoreline. As water is forced through the tidal pass at the west end of the lagoon, velocities increase. Water involved in this flow enters Great Pond Bay through a small tidal pass at the east end of the lagoon as well as across the continuous reef that separates the lagoon from the open shelf. During the Great Pond Bay studies it was observed in both the drogue and the current-meter data that the passage of squalls greatly increased flow toward and through the tidal passes, as wave state in the lagoon increased significantly. These events induced greater variability in current velocities than tidal fluctuations. Brief but frequent squalls may be very important in transporting sediment through these shallow environments.

Studies conducted on Grand Cayman Island (Roberts et al., 1975; Suhayda and Roberts, 1977; M. E. C. Giglioli, personal communication) indicate that the long-term lagoon circulation pattern is reflected in sediment thickness and facies relationships. Figure 8 illustrates that the eastern region of the lagoon, which is characterized by low current velocities, collects a thick sequence of relatively fine grained sediments. As current velocities increase to the west, toward the opening to the open shelf, sediments tend to coarsen and accumulations become thinner. In the tidal channel throat strong currents remove sediments, leaving

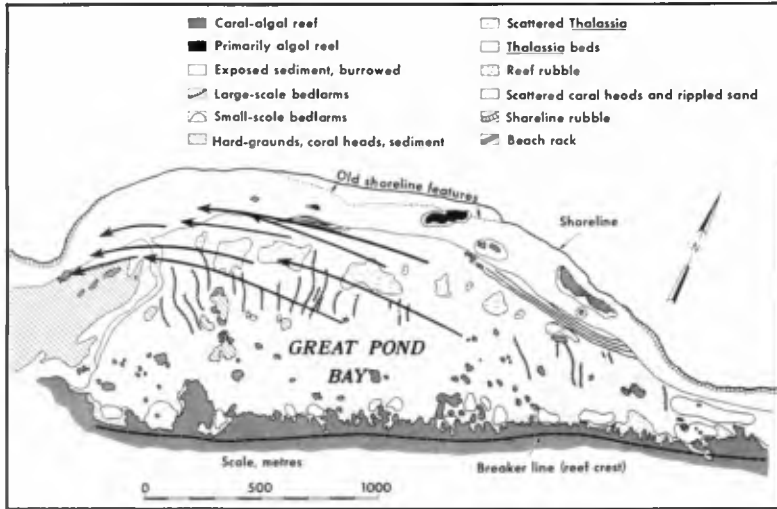


Figure 7. Lagoon circulation under typical easterly wind conditions as determined by drogue tracks (Great Pond Bay, St. Groix). Tracks are superimposed on bottom features. Bottom feature map interpreted from side-scan-sonar data, bottom samples, and diving. Arrows indicate the basic circulation pattern and areas of water input to the system.

the limestone floor of the lagoon exposed. Only beach-related sediments near the coast and coarse sand and rubble directly behind the reef are preserved at the western end of the lagoon.

The geometry of Great Pond Bay (St. Groix) is similar to that of South Sound (Grand Cayman), with the exception of an opening at the upwind end connecting it with an adjacent lagoon. Both systems are characterized by a continuous linear reef which separates a shallow lagoon from the open shelf. Side-scan sonar coverage of Great Pond Bay permitted a detailed bottom-features map to be prepared (Fig. 7). As in the case of South Sound (Grand Cayman), sediments have been generally scoured from the downwind opening tidal pass between the lagoon and the shelf. Because of the connection with an adjacent lagoon, coarse sediments are transported to Great Pond Bay and a well-defined carbonate mud facies, which is commonly present at the upwind end of the system, does not develop. Small-scale bedform distribution indicates active exchange between the adjacent lagoons, as well as preferential sites along the linear reef, where waves and wave-induced currents transit the reef crest to interact actively with lagoon sediments. These areas are obviously key pathways for input of shelf water and sediment into the relatively low energy setting of the backreef. They are also areas where these relatively coarse sediments derived from degradation of the reef are transported toward the lagoon

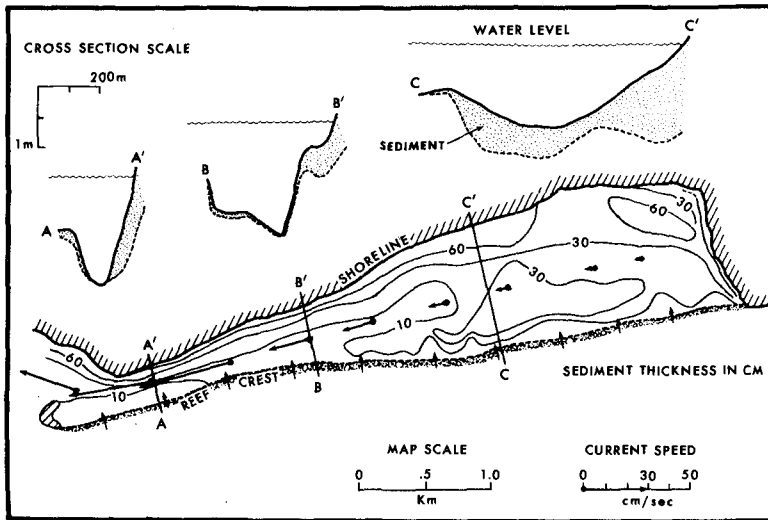


Figure 8. Sediment thickness and facies relationships in South Sound along the southwestern coast of Grand Cayman Island, West Indies. Arrows indicate the direction and relative velocities of the lagoon axis current as determined by Roberts et al. (1972). Note the correspondence of thick sediment accumulation with regions of low speed and sediment-free lagoon floor, where currents are maximized.

interior. Larger, low-amplitude and long-wavelength bedforms were found roughly down the axis of the lagoon (Fig. 7). Since these features were obviously inactive during average conditions, they probably represent remnant bedforms generated by a hurricane that passed near the island several weeks prior to collection of the side-scan data. The presence of such bedforms confirms active sediment transport from east to west nearly down the lagoon axis. Although bioturbation had destroyed much of the bedform morphology, the averaging effect of side-scan sonar data permitted discrimination of these features over higher frequency bottom-roughness elements.

Sediment Transport Routes and Sinks

Sediment storage sites and transport routes for two types of reef-lagoon systems are being considered in this study. One type is composed of linear but discontinuous reef elements (Nicaragua example), while the other has a continuous linear reef between the backreef lagoon and the open shelf (Grand Cayman and St. Croix examples). In both cases the reef functions as a major source of sediments for the backreef lagoon and a low-pass filter for incident waves from the open shelf.

In the discontinuous example numerous large breaks between reef elements allow the transfer of open shelf waves through the lagoon to the backreef shoreline. Refraction and diffraction effects under these conditions generally result in a highly irregular backreef shoreline consisting of numerous cusped coastal features with dimensions related primarily to the width of the lagoon and spacings of openings in the reef trend. Breaks in the general reef trend also function as sites for tidal exchange of lagoon and shelf water. However, mass transport across the reefs, associated with wave breaking, is important as a sediment transport process as well as a source of water to drive backreef circulation. As schematically shown in Figure 9, sand bodies associated with the dis-

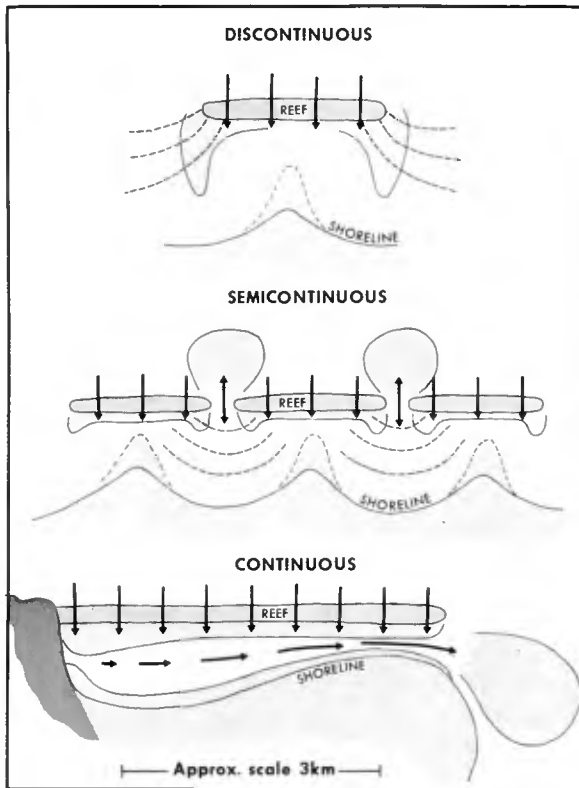


Figure 9. Schematic representation of sediment sinks and transport routes in discontinuous, semicontinuous, and continuous reef-lagoon systems.

continuous reef elements are generally oriented at high angles to the reef trend and tend to form horns attached to the ends of the reef at the tidal channel margins. The combined effects of tidal exchange and wave refraction/diffraction are responsible for shaping these sediment bodies. Sediments are also commonly stored in backreef shoreline cusps, which arise from energy gradients along the coast set up by wave refraction through the major breaks between reef elements. Sediments accumulate in cusped shoreline features, which prograde toward the offshore reef elements. If the distance between reef elements and the shoreline is not great, cusps may prograde toward the reef until attached. Such depositional features commonly form in response to manmade offshore breakwaters.

Continuous reef systems store sand in the backreef lagoon in sediment bodies that tend to parallel the reef trend (Fig. 9). These coarse sediments are composed of debris which originates from the reef and is transported to the lee of this structure by across-the-reef currents previously described. Constituent particles decrease in grain size in a lagoonward direction, but there is generally a very distinct transition between the coarse reef-derived material and the finer lagoonal facies. Lagoon interiors commonly are floored with abundant sediment-producing calcareous green algae. The disintegration products of many members of the algal community are 2-4-micron needles of aragonite, which accumulate to form a carbonate mud. Frequently it is only at the backreef shoreline that there is enough energy to hydraulically sort the sediments so that coarse particles are concentrated. Under these conditions a narrow sandy beach develops. The beach is commonly oriented roughly parallel to the continuous reef trend that separates the lagoon from open-shelf conditions.

As discussed with regard to lagoon circulation, strong currents can develop in the downwave ends of these systems (Fig. 8). Such flow is driven by both the wind and constant input of water to the lagoon by wave overwash at the reef crest. These currents provide the driving force for exporting reef-derived and lagoonal sediments to the adjacent forereef shelf. Actual sediment budgets for systems of this description have never been established. However, geomorphic and sedimentologic evidence suggests that large volumes of sediment are transported, from reef-lagoon systems to deeper sedimentary environments on the shelf. Side-scan sonar data from St. Croix (Fig. 7) suggest that during intense storms large-scale bedform migration can be an active form of sediment transport. During average conditions the intense burrowing activity of shrimp and polychaete worms may be important to the sediment transport process. Sediment mounding, which is typical of the two groups of organisms, requires that both coarse and fine sediments be expelled from a burrow into the water column. These particles may be transported downcurrent by the mean drift in the lagoon. The intensity of burrowing in these backreef environments suggests that significant quantities of sediment can be moved by this mechanism.

Processes responsible for transporting sediments from the lagoon to the open shelf and beyond have not been studied in detail. However, sedimentological evidence (Moore et al., 1976; Land and Moore, 1977; James, 1978) shows that sediments generated in shallow backreef environments are transported to the forereef shelf. A significant proportion of these sediments are conducted across the shelf to adjacent deepwater slope

and basal settings. Figure 10 shows the sediment transport paths and sinks in a lagoon-reef-shelf complex along the southwestern flank of Grand Cayman Island. Both physical process measurements and geological data from several field projects were integrated to produce the sediment transport model described in this figure. Although most sediment produced by the shallow reef is either trapped in the reef matrix or transported toward the lagoon, some sediments produced on the reef front are transported seaward to deeper parts of the shelf. It is common that a sediment sink develops on the lower forereef shelf behind an actively growing shelf-margin reef. As shown by Roberts et al. (1975), the dramatic break in slope at the seaward edge of many reef-dominated shelves is a focal point for strong tidal exchange. Shelf-margin reefs respond to the energy expenditure at this point along the shelf profile by developing into flourishing sill-like structures that impound sediment in their lee. This deep-shelf sediment sink is represented in Figure 10 by a tabular sand body paralleling the shelf edge. High-resolution seismic data suggest that maximum thicknesses of Holocene sediments may be on the order of 20 m in the Grand Cayman example.

Side-scan sonar data indicate that shelf-margin reef morphology is a key to interpreting significant offshelf sediment transport routes. In regions of the shelf where the shelf-margin reef has coalesced to form a coherent ridge, sediments impounded in the lee of this structure can be transported off the shelf only through narrow grooves (Fig. 11A). These grooves are active transport routes (Meaney, 1973), but only limited amounts of sediment can be fluxed to the slope and possibly the adjacent basin by this means. However, around islands there are preferential sites

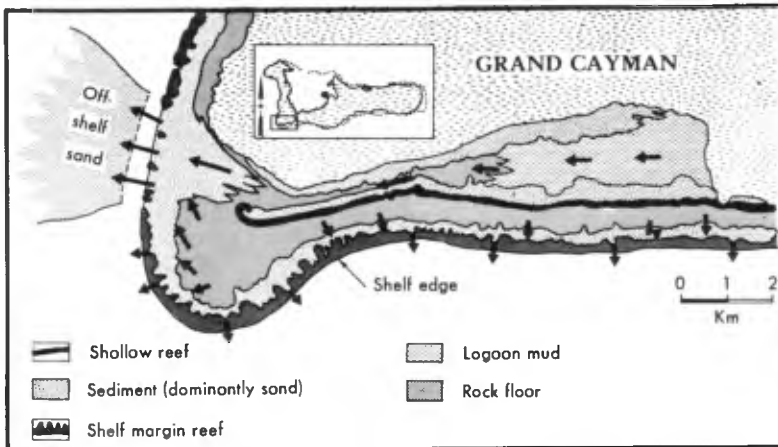


Figure 10. Sediment transport routes and sinks associated with South Sound and the adjacent shelf, Grand Cayman Island. Arrows indicate sediment transport directions.

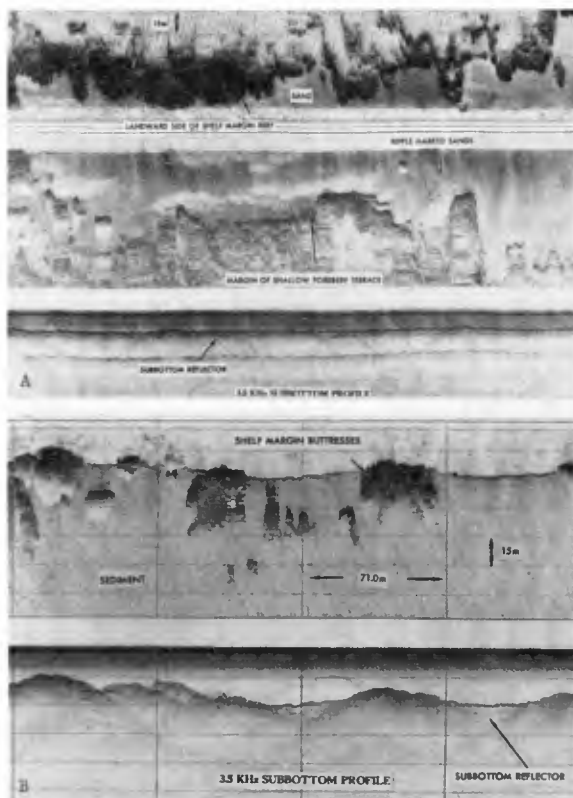


Figure 11. A, side-scan sonograph of lower foreereef shelf, Grand Cayman Island, illustrating a well-developed shelf margin reef with only narrow grooves through it for off-shelf sediment transport. The shelf margin reef has relief of 3-4 m above the adjacent sediment plain. Seismic profile shows a reflection of the sediment plain at a depth of 5 m.

B, side-scan sonograph (only one channel) showing broken shelf-margin reef morphology with wide channels for offshelf transport of sediments. This broad area of sediment accumulation is opposite the downcurrent opening to South Sound (see Fig. 10).

for sediments to accumulate on the shelf (Murray et al., 1977). In the Grand Cayman example, an island in a strong unidirectional drift and trade-wind setting, the major sediment accumulation zones are at the southwest and northwest flanks. The site at the southwest flank, as shown in Figure 10, is also opposite the downcurrent end of the South Sound reef-lagoon system. Shelf-margin reef morphology at this location (Fig. 11B) describes a broken reef trend with wide channels for the offshelf movement of sediments. This type of reef morphology implies that sediments have been supplied in abundance to this site for a long period of time; that is, the substrate for shelf-edge reef building has been partially eliminated by the unstable movement of sediments over the shelf edge to the slope and basin environments. Once sediments reach depositional sites on the lower forereef shelf, they are nonrenewable to the coast.

Conclusions

Field studies conducted on the Caribbean islands of Grand Cayman, Great Corn (Nicaragua), and St. Croix have provided a data base from which the magnitudes and variations of physical processes as well as the flux of sediment through lagoon-reef-shelf systems can be better interpreted. The following conclusions can be made from these studies.

1. Wave breaking on the reef crest creates strong reef-normal surge currents, 50-80 cm/sec, with durations of 2-6 sec under normal trade-wind wave conditions. Sediments larger than the sand sizes are easily transported lagoonward by these periodic current bursts.

2. Estimates of forereef to backreef wave energy loss from the breaking process were in the range of 70-80% for discontinuous reefs and up to 97% for continuous examples. Intensity of the breaking process varied with tide. Wave energy loss between the forereef and backreef was greatest at low tide. Surge current velocities were maximized at this time. Across-the-reef currents were always directed lagoonward and did not change direction with tide.

3. Flow in shallow backreef lagoons is driven largely by water introduced to the system by across-the-reef currents. Long, unbroken (continuous) reefs tend to develop near axial currents that roughly parallel the reef trend.

4. Migratory bedforms in the lagoon environment, as determined by side-scan sonar, indicate sediment transport during storms. It appears that an interaction between bioturbation and the mean lagoon drift may also be a significant process of sediment transport under ambient conditions, even though data specific to this subject have not been collected.

5. Discontinuous reefs store coarse backreef sediments in sand bodies oriented at high angles to the reef trend. These features are shaped by tidal exchange and wave refraction/diffraction through breaks between reef elements. Cuspate shorelines commonly develop in response to the sheltering effects of discontinuous reefs.

6. Backreef sand bodies associated with continuous reefs tend to parallel the reef trend.

7. Lagoon sediments are transported through tidal passes to the forereef shelf, where sediment sinks commonly occur behind an actively growing shelf-margin reef. These sediments are nonrenewable to the coast. Some are transported through shelf-edge grooves and channels to deeper slope and basinal environments. Morphology of the shelf-margin reef is a clue to important avenues for offshelf sediment transport.

Acknowledgments

This work was funded by the Naval Environmental Prediction Research Facility, under Program Element 62759N, Project 9F52551792, "Atmospheric Environmental Support," through ONR Contract N00014-75-C-0192. Dr. Robert Dill, director of the Fairleigh Dickinson West Indies Laboratory on St. Croix, is acknowledged for providing excellent support facilities during our 1979 field project. Sneider and Meckel Associates of Houston, Texas, and Canadian Hunter Exploration Company of Calgary, Canada, supported a side-scan-sonar study of forereef shelf morphology which provided valuable insight into the problem of offshelf sediment transport.

References

- Davies, P. J., "Modern Reef Growth - Great Barrier Reef," Proceedings, Third International Coral Reef Symposium, Rosenstiel School of Marine and Atmospheric Sciences, University of Miami, Vol. 2 (geology), 1977, pp. 326-330.
- Hayami, S., "Types of Breakers, Wave Steepness and Beach Slope," Coastal Engineering in Japan, Vol. 1, 1958, pp. 21-23.
- James, N. P., "Facies Models, 10, Reefs," Geosci. Canada, Vol. 5, 1978, pp. 16-26.
- Inman, D. L., Gayman, W. R., and Cox, D. C., "Littoral Sedimentary Processes on Kauai, A Subtropical High Island," Pacific Sci., Vol. 17, 1963, pp. 106-130.
- Kohn, A. J., and Helfrich, P., "Primary Organic Productivity of a Hawaiian Coral Reef," Limnology and Oceanography, Vol. 1, 1957, pp. 241-251.
- Land, L. S., and Moore, C. H., Jr., "Deep Forereef and Upper Island Slope, North Jamaica," in Reefs and Related Carbonates: Ecology and Sedimentology, S. H. Frost, M. P. Weiss, and J. B. Saunders, eds., Amer. Assoc. Petrol. Geol. Studies in Geology, No. 4, 1977, pp. 53-67.
- Meaney, W. R., "Sediment Transport and Sediment Budget in the Forereef Zone of a Fringing Coral Reef, Discovery Bay, Jamaica," unpublished M.S. thesis, Louisiana State University, Baton Rouge, 1973, 106 pp.
- Moore, C. H., Jr., Graham, E. A., and Land, L. S., "Sediment Transport and Dispersal across the Deep Forereef and Island Slope (-55 m to -305 m), Discovery Bay, Jamaica," Jour. Sed. Petrol., Vol. 46, 1976, pp. 174-187.

- Munk, W. H., and Sargent, M. S., "Adjustment of Bikini Atoll to Ocean Waves," U.S. Geol. Survey Prof. Paper 260-C, 1954, pp. 275-280.
- Murray, S. P., Roberts, H. H., Conlon, D. M., and Rudder, C. M., "Nearshore Current Fields around Coral Islands: Control on Sediment Accumulation and Reef Growth," Proceedings, Third International Coral Reef Symposium, Rosenstiel School of Marine and Atmospheric Sciences, University of Miami, Vol. 2 (geology), 1977, pp. 53-59.
- Nakamura, M., Shiraishi, H., and Sasaki, Y., "Wave Dampening of Submerged Dike," Proceedings, Tenth Conference on Coastal Engineering, Tokyo, Japan, 1966, pp. 254-267.
- Roberts, H. H., "Variability of Reefs with Regard to Changes in Wave Power around an Island," Proceedings, Second International Coral Reef Symposium, Great Barrier Reef Committee, Brisbane, Vol. 2, 1974, pp. 497-512.
- Roberts, H. H., and Suhayda, J. N., "Wave and Current Interactions on a Fringing Coral Reef Crest, Great Corn Island, Nicaragua" (abst.), 8th Caribbean Geological Conference, Curacao, 9-24 July, Abstracts Volume, 1977, pp. 161-162.
- Roberts, H. H., Hsu, S. A., Murray, S. P., Wiseman, Wm. J., Jr., and Coleman, J. M., "Physical Dynamics and Sediment Transport in a Trade-wind Carbonate System--St. Croix," Field trip report to Geography Programs, Office of Naval Research, 1980, 33 pp.
- Roberts, H. H., Murray, S. P., and Suhayda, J. N., "Physical Processes in a Fringing Reef System," Jour. Marine Research, Vol. 33, 1975, pp. 233-260.
- Roberts, H. H., Murray, S. P., and Suhayda, J. N., "Physical Processes in a Forereef Shelf Environment," Proceedings, Third International Coral Reef Symposium, Rosenstiel School of Marine and Atmospheric Sciences, University of Miami, Vol. 2 (geology), 1977, pp. 507-515.
- Storr, J. F., "Ecology and Oceanography of the Coral-reef Tract, Abaco Island, Bahamas," Geol. Soc. Amer. Special Paper 79, 1964, pp. 1-98.
- Suhayda, J. N., and Roberts, H. H., "Wave Action and Sediment Transport on Fringing Reefs," Proceedings, Third International Coral Reef Symposium, Rosenstiel School of Marine and Atmospheric Sciences, University of Miami, Vol. 2 (geology), 1977, pp. 65-70.
- von Arx, W. S., "Circulation Systems of Bikini and Rongelap Lagoons," U.S. Geol. Survey Prof. Paper 260-B, 1954, pp. 265-273.

INSHORE-NEARSHORE MORPHODYNAMICS - A PREDICTIVE MODEL

John Chappell

Dept. of Biogeography and Geomorphology, R.S.Pac.S.,
Australian National University, Canberra, Australia.

ABSTRACT The two-dimensional topography, developed on a sandy sea bed between surf base and the breaker zone, is computed using (i) sediment gain or loss per unit bed area = zero, (ii) simple models of sediment drift in terms of, firstly, simplified saltation under Stokesian waves, and secondly, frictional wave work on the sea bed, (iii) the drift tendency in direction of wave propagation being offset of the local sea bed gradient. An input contour line at surf base is assumed, across which the input wave train is propagated. Using standard wave refraction combined with (i) to (iii), above, an equilibrium topography is generated by iteration. Inshore of the breaker line, longshore currents generated by radiation stress are combined with the gradient effect to balance sediment drift, producing bar - trough topography.

INTRODUCTION

Nearshore bathymetric profiles commonly are modelled by concave power functions of distance from shore (eg., Le Blond, 1979), on empirical grounds (Bruun, 1962). This paper seeks to model 2-dimensional bathymetric topography in terms of shoreward sediment drift induced, in an idealised way, by shoaling waves, in opposition to the effect of a downslope (gradient) factor. In the inshore zone, the effects of longshore currents and of shore-normal rip currents on sediment movement are included, again in a simplified way. The nearshore zone is defined here as extending from the primary breaker line seawards to surf base, which is taken as the maximum depth at which sediment is likely to be moved by wave motion. The inshore zone is taken to be between the primary breaker line and the swash zone, on the beach face.

Sediment movement under shoaling waves is complex, involving both saltating grains and suspension clouds, which move differently at different phases of a wave cycle and at different points above a bed ripple (eg., Neilson, 1978). Furthermore, the type of small scale bed form (ripple, megaripple, etc.) varies with depth (Boyd, this volume). The net drift tendency also varies with wave shape - a function not only of shoaling but also of wind direction relative to wave direction. As a general model of sediment drift under shoaling waves does not yet appear to exist, we commence with a highly idealised picture.

SEDIMENT DRIFT

Sediment movement is initiated when the horizontal component (u_x) of wave orbital velocity at a certain distance from the bed exceeds a critical value, u_t . This threshold value has been shown to be a discontinuous function of sediment particle size (Komar and Miller, 1975). Once movement is initiated, sediment drift generally is argued to be related to the cube of u_x (eg., Bagnold, 1966) on the grounds that mass transport should be proportional to frictional wave work (W) on the bed, where

$$W = \rho u_x^3 \quad \dots \quad (1)$$

(Inman et al., 1966; Kachel and Sternberg, 1971). However, while the magnitude of mass transport may depend on W, the sense of direction is not indicated when u_x is estimated from the maximum of the horizontal orbital velocity component, as is conventional. An approach here is to estimate u_x by integrating instantaneous velocity through a wave cycle, although suggestions along these lines (Wells, 1967; Wright et al., 1980) so far are heuristic rather than analytic or well verified.

Shoaling waves are asymmetrical, and non-zero values of net water transport and of bed shear stress appear when Stokesian and higher order wave equations are integrated through a wave cycle. Although the magnitudes of these resultants are small compared with instantaneous values, they are likely to induce sediment drift at depths shallower than surf base, where instantaneous velocities exceed u_t for a substantial part of the wave cycle. Thus, for Stokes waves, Longuet-Higgins (1953) gives the net shoreward velocity near the bottom as

$$U_0 = \frac{5}{4} \left[\frac{\pi H}{L} \right]^2 C \frac{1}{(\sinh(kh))^2} \quad \dots \quad (2)$$

where H is local wave height, L is wavelength, C is celerity, $k=2\pi/L$, and h is depth to bed. Bed drift data of Russell and Osorio (1958) correlate quite well with U_0 , although as Komar (1976) points out, it is not known whether the relationship is causal. However, setting aside the problematic interaction between small scale bed forms and sediment movement, it seems reasonable that net sediment flux is proportional to the product of the entraining factor (bed shear stress) and net velocity U_0 , ie.,

$$Q_s = U_0 \zeta \tau \quad \dots \quad (3)$$

where ζ is a coupling factor and τ is effective bed shear stress. Whether $\tau \propto u_x^2$, or $\tau \propto (u_x - u_t)^2$ (cf. Wright et al., 1980) is not known; here it is taken as proportional to u_x^2 . It is noted that U_0 is better calculated by using a wave equation more accurate than the Stokes model (eg., that of Fenton and Rienecker, this conference). However, eq.(2) is used in the present paper.

Net sediment drift should be influenced by bed slope. Experimental data seem not to indicate how this factor might be combined with any formulation for flux such as eq.'s (1) - (3), although Taylor and Dyer

(1977) suggest that for bedload flux

$$\vec{Q}_s(\text{bedload}) = \frac{\zeta \vec{W}}{(\tan\phi \pm \tan\beta) \cdot \cos\beta} \dots\dots (4)$$

where ϕ is an angle of intergranular friction and β is slope angle, positive upslope. ζ has the same meaning but different value as in eq.(3). Wave hemicycle vectors (\vec{Q}_s , \vec{Q}_s , etc.) are assessed by integrating through each hemicycle.

The approach in this paper is to assume that grains have average trajectories of pathlengths $\bar{\lambda}$, $\bar{\lambda}$ in each hemicycle, and that saltating grains, on descent, make an angle α with the horizontal. It is assumed that suspended grains have a net displacement of U_0 per wave cycle. From figure 1, net saltation displacement comes to

$$\Lambda \approx 2\bar{\lambda} \frac{\tan\beta}{\tan\alpha} \dots\dots (5)$$

where $\bar{\lambda}$ is the mean of $\bar{\lambda}$, $\bar{\lambda}$ (without sense of sign). Hence, Λ is down-slope, as β is negative in this direction. In the following section, eq's (3) and (5) are used to balance sediment drift, at the equilibrium condition.

An alternative approach is to consider sediment drift as directly proportional to wave frictional work on the bed. Friction per wave cycle per unit area is

$$F = \frac{2}{3\pi} \rho f u_{\max}^3 \dots\dots (6)$$

(Jonsson, 1965) where u_{\max} is maximum instantaneous bottom orbital velocity. Although the friction coefficient, f , usually is taken as constant for a given bed sediment, Jonsson (1965) shows that it changes with horizontal length scale of bottom orbital motion, i.e., is proportional to u_{\max} (in turbulent motion). The frictional loss (K_f) as a function of wave height, based on a similar $F \propto u^3$ relationship, is given by Bretschneider and Reid (1954) as

$$K_f = (1 + \int_0^x \eta \, dx)^{-1} \dots\dots (7)$$

where

$$\eta = H \frac{8f K_s}{3g^2 T} \left\{ \frac{\omega}{\sinh(kh)} \right\}^3 \dots\dots (8)$$

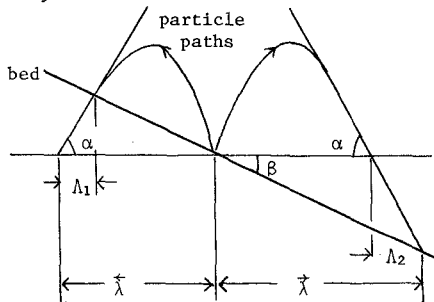
where T is wave period and ω is $2\pi/T$. Again in the next section this is balanced against a slope-dependant drift, although in this case figure 1 and eq.(5) have no direct relevance, and the downslope component is simply

$$\Lambda' = 2\bar{\lambda} \tan\beta \dots\dots (9)$$

EQUILIBRIUM PROFILE

Bed equilibrium occurs when sediment gain or loss per unit area is zero. This occurs when either there is no sediment movement to or

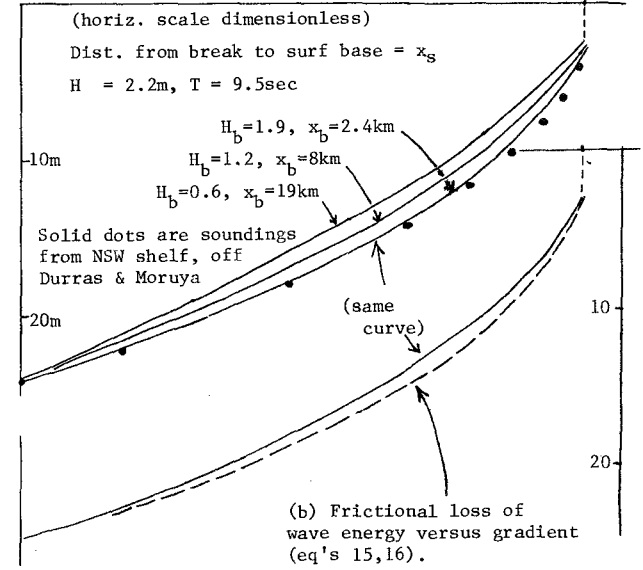
Figure 1: SIMPLIFIED SALTATION DRIFT. Wave hemicycles separated for clarity.



Net displacement $\Lambda = \Lambda_1 + \Lambda_2 \approx 2\bar{\lambda} \frac{\tan\beta}{\tan\alpha}$. ($\bar{\lambda} = 0.5(|\lambda| + |\lambda|)$).

Figure 2: MODEL EQUILIBRIUM BED PROFILES.

(a) Sediment drift versus gradient (eq's 12 - 14)



from a unit area (closed system case), or there is a constant flux along the profile (external sources and sinks case). Either way,

$$\text{grad } Q_s = \text{zero.} \quad \dots\dots (10)$$

In what follows, the nearshore zone is considered as a closed system case, while the inshore zone can locally be regarded as a steady state case where $Q_s \neq 0$ but eq.(10) applies.

We take the nearshore zone first. From the foregoing, at equilibrium the drift Q_s according to eq.(3) is set equal and opposite to the down-slope tendency $\bar{\Lambda}$ in eq.(5). In the results which follow, $\bar{\lambda}$ is taken as equal to mean bed velocity

$$u_b = \frac{\pi H}{T} \frac{1}{\sinh(kh)} \quad \dots\dots (11)$$

It is noted that a better estimate would be achieved by integrating higher order wave equations through a cycle. Similarly, τ , $\bar{\tau}$, are taken as equal and opposite, although a better estimate could also be based on higher order wave equations. In this simple formulation, zero net displacement occurs when

$$U_0 = 2\bar{\lambda} \frac{\tan\beta}{\tan\alpha} \quad \dots\dots (12)$$

Hence, using eq's (2), (11), (12), the bed gradient is a function of local wave height, water depth, and the unknown parameter, α . The latter may depend directly on u_{\max} (in a similar way to friction coefficient, f) but initially it is assumed that α is constant, and the assumption is discussed later.

As we are seeking two dimensional topography for an arbitrary surf-base contour, wave refraction must be taken into account, and local wave height H varies from deepwater wave height H_∞ according to

$$H = H_\infty K_r K_s K_f \quad \dots\dots (13)$$

where K_f is given at eq.(7), K_s (shoaling coefficient, also in eq.(7)) and K_r (refraction coefficient) are as given in standard works (eg., Komar, 1976).

The local profile along a given wave ray, from eq's (11) and (12) can therefore be computed from

$$\frac{dz}{dx} = \frac{5 H \pi \tan\alpha}{8 C \sinh(kh)} \quad \dots\dots (14)$$

To calculate a profile, values must be assumed for f (entering eq.(13) from eq.(8), and for α . The approach used here is to assume that the overall distance from surf base to the breaker line is set by the initial width of the inner shelf (geologically determined), and the profile $z(x)$ then calculated from (14) using $f = 0.02$ and α adjusted to suit. Although arbitrary in this last particular, computed profiles closely accord with actual profiles, as shown in figure 2a.

The trajectory parameter clearly subsumes other factors and, as mentioned, is likely to vary with u_b amongst other things. Although intrinsically unsatisfactory, this parametric approach is useful in that α can be related to objective factors, through comparisons such as in figure 2, as has been the case in the past with coefficient f .

An alternative to using the simple sediment movement model of figure 1 is to equate sediment drift with net bed friction. For example, Q_s may be directly related to W in eq.(1) (cf. Bagnold, 1966) by $Q_s = \zeta W$, and this can be opposed to a gradient force to give

$$\frac{dz}{dx} = \frac{\rho u_*^3}{\Lambda g} \cdot \zeta$$

Using a similar idea, Chappell and Eliot (1979) used the Bretschneider and Reid frictional factor η (eq.8) to offset the gradient force, arguing that frictional loss of wave energy is proportional to the sediment drift tendency, as follows. Wave height change δH over length δx is

$$\delta H = 1 - \left(\frac{\eta \eta \delta x}{T^4 K_s} + 1 \right)^{-1} \quad \dots\dots (15)$$

Wave energy loss, δE , is

$$\delta E = 2H \delta H \cdot \rho g / 8 \quad \dots\dots (16)$$

and setting $dz/dx \propto \delta E$ again gives a computational solution for $z(x)$, using, as before, the wave height equation (13) as appropriate*. Figure 2b compares the result of this model with that of the more explicit sediment drift model in figure 1 and figure 2a. A disadvantage of this model, compared with the previous one, is that it does not explicitly assess frictional drift tendencies for each wave hemisphere because, as it stands, it rests on Airy waves.

Both models illustrated in figure 2 fit quite closely to the curve $z = a x^b$, $b < 1$ (where $z=0$ is the breaker line, and z is +ve with depth), which is quite widely used to fit empirically to real nearshore profiles. However, empirical $z = a x^b$ has no explanatory power, whereas the arguments outlined here explicitly develop bed profile in terms of bed equilibrium assessed by sediment drift models, albeit crude ones. As the first model is the more complete, in the sense that it is based on a conception of sediment movement and that Stokes (or higher order wave equations) can be used, it is employed in the following section, where 2-dimensional topography is developed.

The inshore zone can be more complex, in that the sediment flux locally can be different from zero in the presence of rip current cells, although eq.(10) still holds. Treatment of this area is deferred to a later section.

* Chappell and Eliot (1979), using this type of approach, simplified the problem by assuming that frictional work on the bed is uniformly distributed at equilibrium. Empirical calculations of η (eq.8) for real profiles and waves show that this is not true, and the opportunity is taken here to correct this. Following from this, it would be interesting to discover whether "entropy production" (eg., $\delta E/h_*$, $h_* = h_s - h$ where h_s is surf base depth) is constant on real profiles.

2-DIMENSIONAL NEARSHORE TOPOGRAPHY

The hypothesis here is that the seabed sediment shorewards of surf base is freely redistributed until it comes to equilibrium with an input wave field. It is assumed that the redistribution process occurs essentially in the directions of the wave rays. The profile along any ray is to be calculated according to the methods of the previous section, using eq.(14), and the resulting contour of the breaker zone (approximating to the shoreline) will be therefore dependant on the shape of the surf base contour and the resulting refraction field. The standard ray equation is used, i.e.,

$$\Delta\gamma = \sin^{-1}\left\{ \left(1 + \frac{\Delta C}{C}\right) \sin\gamma \right\} - \gamma \quad \dots\dots (17)$$

(see figure 3a for definitions), where C, ΔC are calculated for the given contour depth and depth change between contours, as normal.

The problem now is as follows. A profile z(x) for any ray path can be calculated by eq.(14), where the local value of H in this equation is subject to eq.(13). The initial direction of the ray is determined by its angle with the assumed surf base contour, and its locus thereafter is modified as it passes each succeeding contour. Inputting a set of parallel rays across an arbitrary surf base contour s(x, z_s) will yield a set of profiles which also define the field of nearshore contours s(x, z), which must be consistent with the set of ray paths themselves. This is approached by iterative calculation, which can be simplified by knowing that locally the contours fall between two relational conditions - either they can locally be parallel in which case the crossing angle γ is altered only by eq.(17), or they can approach a concentric relationship, in which case the crossing angle is modified by an offset ξ, where this is given as shown in figure 3b. For the concentric case (or any case where contours are not locally parallel) there is a similar modification to the refraction coefficient K_r (eq.13). In general, contour relationships will lie between these extremes, and the approach used, to commence iteration, was to assume that the local relationship is such that an offset angle = 0.5ξ applies.

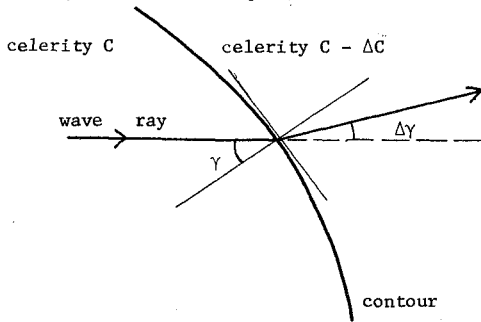
Figure 4 shows a computed example of nearshore topography, for which each ray satisfies eq.(14) subject to eq.(13), and for which the resulting contour positions, on each ray, are consistent between rays and with eq.(17), within the calculation limits (about 5% of each local value, on average). A check on this result can be made by computing the longshore sediment drift, inshore of the breaker line. If the model is correct, longshore sediment drift, resulting from longshore variations of wave height and approach angle (γ_b) at the breaker line, should be zero. This equilibrium condition is given by Komar (1975) as

$$\frac{1}{c_f} \frac{\partial H_b}{\partial y} = \frac{0.6 G^3 \sin\gamma_b \cos\gamma_b}{1 + \frac{3G^2}{8} - \frac{G^2 \cos^2\gamma_b}{4}} \quad \dots\dots (18)$$

where G = H_b/z_b. Although as Komar (1975) notes, this is an approxi-

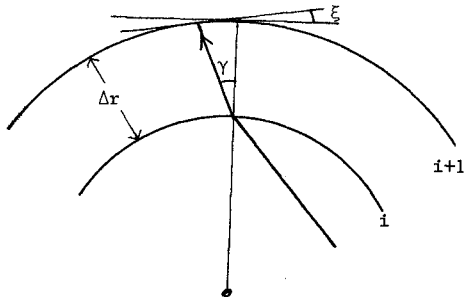
Figure 3: DEFINITIONAL SKETCHES, REFRACTION PROCESS

(a) Refraction (eq.17)



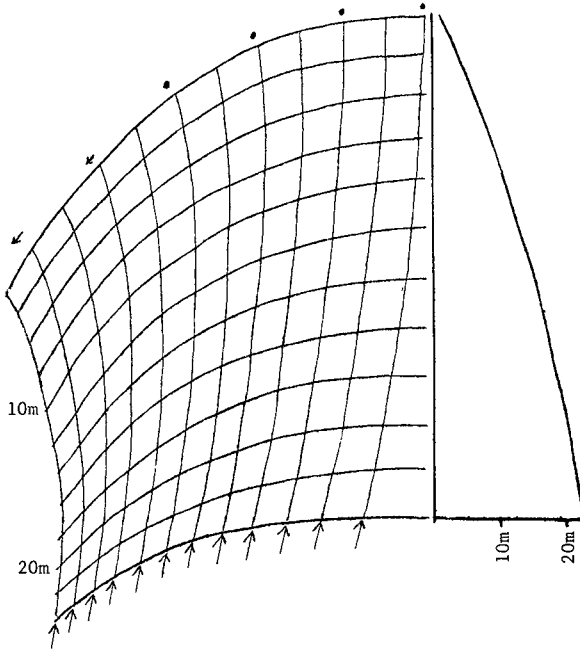
(b) Angular alteration of ray/contour crossing for non-parallel (concentric) contours, used in computing ray paths once a ray passes surf base contour. A bed profile for each ray is computed in similar fashion to figure 2a, and each contour azimuth then is estimated.

$$\xi = \tan^{-1} \left(\frac{\Delta r \tan \gamma}{r + \Delta r} \right)$$



On first iteration it is assumed that crossing angle at contour (i+1) is $\gamma_i - \xi/2$ (see page 7).

FIGURE 4: Self-generated wave-ray and contour field. Input rays ($H_{\infty} = 2.2\text{m}$, $T = 9\text{sec}$) incident at input surf-base contour at bottom. On first iteration no correction is made to wave height for refraction coefficient K_R ; then K_R



calculated from first iteration is used to correct H at all intersection points, providing basis for second iteration. Figure is plotted from printout of second iteration intersections. Depth profile at right applies to right hand ray. Small arrows at top left show residual longshore current, arising because $\partial H_b / \partial y$ effect exceeds effect of wave obliquity at breaker line (ref. eq.18) (Note that input rays are increasingly closely spaced as surf base contour curvature increases towards left).

mation to the complete solution of the problem, it is well supported by measurements (Komar, op. cit.). When applied to the refraction/topography field in figure 4 this equilibrium condition is approximately met along the model shoreline, although there is a deviation which increases towards the left hand (low energy) end, such that the LHS of eq.(18) exceeds the RHS by about 15%, implying net drift towards the left (shown by small arrows in figure 4). This discrepancy probably reflects the assumption, used in the calculation method, that sediment drift occurs in the direction of a wave ray without a drift component perpendicular to the ray, when its contour-crossing angle is other than 90° . The discrepancy is not large in this simple model calculation, however, and it is concluded that the general approach is sound, although refinements of computational strategy are desirable.

This method, in enabling computation of equilibrium nearshore topography, points the way to predicting the changes which occur when the wave field changes, or when the surf base contour is altered (say by offshore dredging). It is noted that the actual 'equilibrium' topography, developed in any real situation, is the statistical product of a wave climate best expressed in terms of probabilities of wave heights, periods, and directions. An actual topography should be compared with model predictions which embody this consideration. Such a calculation would take into account the variation of surf base contour with wave height and period.

INSHORE EQUILIBRIUM

The sediment drift approach used above for the nearshore region cannot be extended to the inshore area, because in this zone of surf and rip current cells the near bed flow approaches or sometimes even exceeds the critical (Froude number = 1) condition, and sediment moves extensively in suspension. Inshore topography can approximate to a steady state under constant incident waves for more than several days (see Wright, et al., 1979; Chappell and Eliot, 1979, for accounts of inshore states and state changes). The existence of quasi-steady states, with active sediment circulation through longshore and rip current cells, suggests that some parameter in the system is constant, to maintain the condition that $\text{grad } Q_s = \text{zero}$ (eq.6). Chappell and Eliot (1979) suggested that

$$\text{grad } W = \text{zero} \quad \dots\dots (19)$$

where W is work done on the bed. As noted above (footnote, page 6) this is incorrect in the nearshore, but may approximately be true inshore where depth variation is small, between the primary breaker and the base of the swash. Alternatively, some entropy-like measure may be constant, such as W/h_* (see footnote, page 6), as suggested for fluvial systems by Leopold and Langbein (1962), although it is not clear why this should be so.

There are two approaches to the problem of inshore equilibrium. One is to oppose the gradient effect (eq.9) an estimate of sediment drift in terms of bed friction, as was done for the nearshore. As noted, this is difficult in the absence of a coherent picture of

sediment entrainment and drift. The other is to use an assumption such as eq.(19) and then to compute the inshore depth field to satisfy this condition. As it turns out, both approaches yield similar but not identical results. In either case, the local wave height will be subject to

$$H = H_b K_r K_s^* K_f^* \dots\dots (20)$$

where K_r^* and K_f^* are shoaling and friction coefficients, respectively, as they apply in the inshore zone (cf. eq.13). Further, as inshore current velocities can be a significant fraction of orbital velocities, work on the bed is

$$W = W_w + W_u \dots\dots (21)$$

where the two RHS terms signify wave and current work, respectively.

Inshore waves generally continue to break, to some degree, as they cross the surf zone, although they may locally reform as steep non-breaking waves where they cross the trough. Measurements taken with composite flowmeter and pressure transducer arrays show that inshore waves, between primary break and swash base, show orbital behaviour although not strictly Airy-wave like in form (see data in Wright, et al., 1979; Chappell and Wright, 1978). Hence, a simple paramter θ is introduced to characterise inshore waves, such that

$$H = H_b \int_{x_b}^x \theta dx \dots\dots (22)$$

where H_b is breaker height and x_b indicates position of the primary breaker line. $\int \theta$ thus is equivalent to K_s^* , and θ itself represents the diminution of effective (orbital) wave motion through the breaking process. In what follows, θ is taken as 0.05/m for spilling waves, 0.1 for plunging waves, and zero for reformed inshore waves. Transition to plunging is taken as G (=wave height/depth) = 1.0, and to spilling when $0.8 < G < 1.0$. These somewhat arbitrary parameters can be better calibrated through field measurements. K_f^* is again given by eq's (7), (8), where $\sinh(kh) \approx kh$.

Total work on the bed, from eq.(21), then becomes

$$W = \delta E + \rho \vec{u}^3 \dots\dots (23)$$

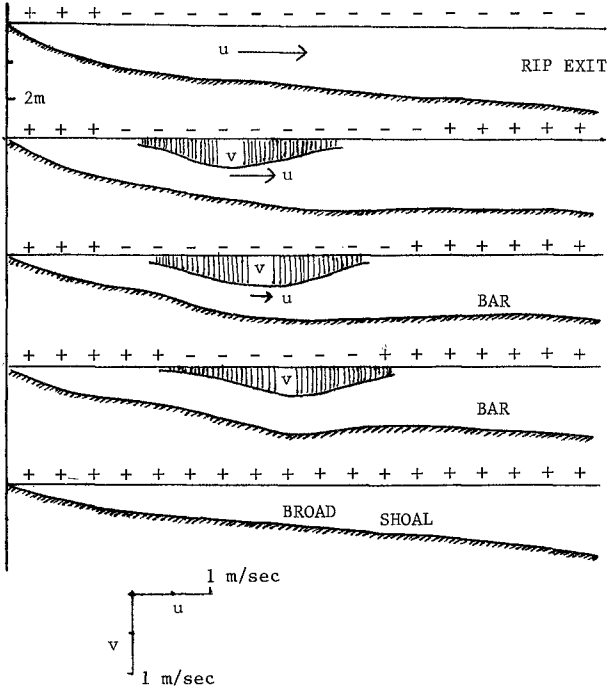
where δE is given by eq.(16) and the work by longshore or other current \vec{u} is shown at the second RHS term (cf. eq.1). If eq.(19) applies, then it follows that the local depth must increase in the presence of a current, as δE is depth dependant and total W is constant. This accords qualitatively with the observation that inshore currents are associated with a trough, between primary breaker zone and the shoreline.

Eq's (19) to (23) now are used to compute an inshore topography field, with a shore-parallel train of incident waves. An inshore current is generated by using the appropriate re-arrangement of eq.(18) (given by Komar, 1975); ie., the current arises from the inshore radiation stress field generated by longshore

Figure 5: SELF-GENERATED INSHORE MORPHOLOGY AND LONGSHORE CURRENT - RIP CURRENT SYSTEM.

Input $H_b = 1.5$ m

Surf type: Plunging break or spilling bore + +
 Reformed inshore wave - -



Note: As wave-current interaction is not considered, model does not generate a primary break at rip exit, with parameters used as in text.

variations of wave height. H_b is assumed to vary sinusoidally as a consequence of interaction between incident waves and an inshore stationary edge wave (Bowen, 1969; Chappell and Wright, 1978). A quarter wavelength segment is examined, with a rip located where resultant H_b is a minimum and no longshore current existing at the point where H_b is maximum. No account is taken of inshore refraction arising from wave-current interaction, although this is an important factor (Noda, 1974). The technique used proceeds in two stages. Firstly, the inshore current is calculated from the longshore variation of H_b , and this current is located midway between primary break and shoreline. Profiles across the inshore zone then are computed at 5 positions between the H_b max and H_{bmin} positions, using eq's (19) to (23). The resulting radiation stress field then is computed (from the standard equations given by Komar, 1975; 1976), and then, as a second stage, the longshore current field is recalculated followed by recomputation of the inshore profiles. This iteration reduces divergence between the current field and topography.

Results of the model are shown in figure 5. The 'self-generated' topography emerges as a shallow bar-trough system, which qualitatively agrees well with real inshore circulation-topography systems described as Types 2 and 3 by Wright, et al., (1979).

CONCLUDING DISCUSSION

The models set out in this paper generate nearshore and inshore topography, on mobile sandy beds, with deep water wave H and T as the only input variables, although there are several calibration factors. The models can be criticised as being amalgamations of a number of approximations, some of which are insufficiently tested. Viewed positively, the models produce topographies which appear highly realistic, and offer a method by which changes associated with either variations of wave field, or human alteration of the nearshore-inshore system, can be estimated. The negative side, that undue parameterisation is employed here, can be assessed by reviewing some of these factors.

The main weakness lies with characterisation of sediment drift. To estimate a topographic profile, either explicitly directional wave-induced transport must offset the gradient effect (as in the nearshore case, above), or a non-directional transport function is made everywhere equal, as in the inshore model. The latter suffers from its not being visualisable in terms of fundamental processes; the former, as set out in this paper, suffers in its usage of a naive sediment simplification of sediment drift. This undoubtedly can be improved and would affect the result but not the strategy of calculation. A second weakness lies with the approximations used in wave models, particularly in the formulation used for waves in the surf zone. However, assembly of all parameterised factors into a single model focusses attention on areas of weakness. Finally, despite the approximations, the sea bed topography generated by these models appears realistic.

References

- Bowen, A.J., 1969. Rip currents. I. Theoretical investigations. Jour. Geophys. Res., 74, 5467-5478.
- Bretschneider, C.L., and Reid, R.O., 1954. Modification of wave height due to bottom friction, percolation, and refraction. U.S. Army Corps of Engineers, Beach Erosion Board Tech. Memo., 45.
- Brunn, P., 1962. Sea level rise as a cause of shore erosion. A.S.C.E. Waterways and Harbours Divn., 88, 117.
- Chappell, J., and Wright, L.D. 1978. Surf zone resonance and coupled morphology. Proc. 16th Coastal Engineering Conf., 1359-1377.
- Chappell, J., and Eliot, I.G. 1978. Surf beach dynamics in time and space - an Australian case study, and elements of a predictive model. Marine Geol., 32, 231-250.
- Fenton, J.D., and Reinecker, M.M., 1980. Numerical solution of exact equations of water waves. Proc. 17th Coastal Engineering Conf. (this series).
- Jonsson, I.G., 1965. Friction Factor Diagrams for Oscillatory Boundary Layers. Basic Res. Rept., 10, Tech. University of Denmark, Copenhagen. 10-21.
- Kachel, N.B., and Sternberg, R.W., 1971. Transport of bedload as ripples during an ebb current. Marine Geol., 19, 229-244.
- Komar, P.D., 1975. Nearshore currents: generation by obliquely breaking waves and longshore variations in breaker height. In Hails, J., and Carr, A. (eds). Nearshore Sediment Dynamics and Sedimentation (Wiley), 17-46.
- Komar, P.D., 1976. Beach Processes and Sedimentation. (Prentice-Hall), 429pp.
- Komar, P.D., and Miller, M.C., 1973. The threshold of sediment movement under oscillatory water waves. Jour. Sed. Petrol., 43, 1101-1110.
- Le Blond, P.H., 1979. An explanation of the logarithmic spiral plan shape of headland-bay beaches. Jour. Sed. Petrol., 49, 1093-1100.
- Leopold, L.B., and Langbein, W.B., 1962. The entropy concept in geomorphology. U.S. Geol. Soc. Prof. Paper 500-C.
- Longuet-Higgins, M.S., 1953. Mass transport in water waves. Trans. Roy. Soc. London, 245, 525-581.
- Nielsen, P., 1979. Some Basic Concepts of Wave Sediment Transport, Inst. Hydrodynamics and Hydraulic Engineering Tech. University of Denmark, Ser.Pap. 20.

- Noda, E.K., 1974. Wave-induced nearshore circulation. Jour. Geophys. Res., 79, 4097-4106.
- Russell, R.C.H., and Osorio, J.D.C., 1958. An experimental investigation of drift profiles in a closed channel. Proc. 6th Coastal Engineering Conf., 171-183.
- Taylor, P.A., and Dyer, K.R., 1977. Theoretical models of flow near the bed and their implications for sediment transport. In Goldberg, E.D., McCave, I.N., O'Brien, J.J., and Steele, J.H. (eds). The Sea: Marine Modelling, v.6.
- Wells, D.R., 1967. Beach equilibrium and second-order wave theory. Jour. Geophys. Res., 72, 497-504.
- Wright, L.D., Chappell, J., Thom, B.G., Bradshaw, M.P., and Cowell, P.J., 1979. Morphodynamics of reflective and dissipative beach and inshore systems, southeast Australia. Marine Geol., 32, 105-140.
- Wright, L.D., Coffey, F.C., and Cowell, P.J., 1980. Nearshore Oceanography and the Morphodynamics of the Broken Bay-Palm Beach Region, N.S.W. Coastal Studies Unit, Dept. Geography, Sydney University, 210pp.

BEACH CUT IN RELATION TO SURF ZONE MORPHODYNAMICS

L.D.Wright

Coastal Studies Unit, Dept of Geography
University of Sydney
Sydney, N.S.W. 2006. Australia

ABSTRACT

Field experiments on the coast of Southeastern Australia, supplemented by systematic observations in a variety of environments in other parts of the world, indicate at least three quasi-discrete modes of subaerial beach cut, each of which is related to a distinct set of mechanisms. For any given set of incident wave conditions, the operation or non-operation of a particular mode of cutting depends on the morphodynamic state of the surf-zone and beach. Steep, reflective beaches are susceptible to cut under moderate swell conditions by accentuated runup and berm overtopping associated with subharmonic resonance. Appreciably more energy is required to cut flat dissipative beaches. Cut of dissipative beaches involves high setup which oscillates at infragravity frequency and allows the bores of broken waves to penetrate to the backshore. Beach states intermediate between the reflective and dissipative extremes are subject to cut by both the modes just described as well as by scour in the embayments of topographically arrested rips which can cause significant localized erosion even when the coast regionally is accreting. Beaches which most commonly exhibit intermediate topographies are the least stable and most mobile.

INTRODUCTION

Most recent studies of beach stability and problems of beach erosion versus accretion have focused either on sediment budget imbalances related to littoral drift or on onshore-offshore sediment migration and associated "cyclic" or seasonal changes in beach/inshore profiles. Prominent examples of the latter include studies of the critical conditions responsible for the shift in beach profile from the accreted "swell" (or "summer") profile to the erosional "storm" (or "winter") profile (e.g. Komar, 1976); Davis and Fox, 1972; Sonu and James, 1973; Winant et al., 1975).

Some valuable successes have been attained in predicting the likelihood of sediment moving offshore versus onshore over simple beach topographies in terms of critical wave steepness, sediment fall velocity, and beach slope (Dean, 1973; Hattori and Kawamata, 1980; Sawaragi and Deguchi, 1980). However, criteria which take account of pre-existing complex three dimensional or bar-trough beach and surf zone topographies, such as prevail in Southeastern Australia, do not yet exist and quantitative predictions of the direction of beach change are far from straightforward. Furthermore, it is impractical to address the problem simply in terms of shifts between extreme "swell" and "storm" profiles since either extreme or intermediate topographies may be arrested by environmental conditions for extended periods and since the "cyclic" alternation between extremes often requires several years to complete (e.g. Thom & Bowman, 1980).

From the point of view of most coastal engineers concerned with beach protection the most immediate threat to beaches is manifest as subaerial beach cut. There appear to be at least three quasi-discrete modes of beach cut, each of which is related to a distinct set of mechanisms. For any given set of incident wave conditions, the operation or non-operation of a particular mode of cutting depends on the morphodynamic state of the surf-zone and beach. The morphodynamic state is in turn, dependent partially on stage in an erosional or accretionary cycle and partially on local environmental conditions. Because the mechanisms controlling each mode are different, identical incident wave conditions may cause erosion in one situation while causing accretion in another. The erosion "hazard" associated with any given beach, as well as beach mobility as expressed by the range or standard deviation of shoreline positions over an average year thus depend on the modal or most prevalent morphodynamic state of the beach and surf zone.

This paper, is aimed at elucidating, qualitatively, three aspects of the beach erosion and beach stability problem: (1) What are the major modes of subaerial beach cut and how do they depend on the morphodynamic state of the beach and surf zone? (2) What surf-zone processes may act to determine the possible seaward transport of the eroded material to the outer surf zone and hence aggravate the severity of erosion? (3) What is the consequent relationship between relative erosion hazard, beach mobility and morphodynamic state?

The concepts and examples presented have been synthesized from an extensive set of direct field observations on the high wave energy, microtidal coast of Southeastern and Southern Australia. Many of the beaches

examined are strongly compartmented and all are dominated by shore-normal rather than longshore sediment exchange. Our experiments have involved beach surveys, repeated and time lapse photography, and direct measurements of surf-zone pressure and current time series. The various methods employed are described by Bradshaw et al. (1978), Wright et al. (1979a & b), and Short (1979, 1980).

MORPHODYNAMIC STATES AND MODES OF CUT

The likelihood of a particular mode of cut occurring on a beach, for example with increasing wave height, depends on the morphodynamic state that the surf zone and beach are in at the time. Wright et al. (1979a & b) recognise at least six different states, each of which is distinguished by a different association of morphology, circulation, surf behaviour, and resonant frequencies. Short (1979a & b) has shown how different morphologic types relate to stages in erosional accretionary sequences or "cycles". The two morphodynamic extremes are : (1) steep reflective beaches with narrow surf zones; and (2) dissipative, flat beaches with wide, barred surf zones. (3) Between the two extremes are several intermediate types of bar-trough and "rhythmic" inshore topographies including alternating transverse bars and rips. The reflective state is characterized by maximum storage of available sediment within the subaerial and intertidal part of the beach and is equivalent to the "swell" (or "summer") profile whereas the dissipative state is equivalent to the "storm" (or "winter") profile with most of the sediment stored subaqueously in the surf zone. As in the "classic" beach cycle models, the reflective and dissipative extremes represent respectively the accretional and erosional end points. However, different sets of environmental conditions can cause one or the other of the extremes to prevail virtually year round as the modal state or may favour the prevalence of intermediate states.

Each beach state presents its own distinctive erosion "hazard" both in terms of the probability of erosion and in terms of the most likely mode of cut. In the immediate time frame the "instantaneous" beach state, which depends in part on antecedent processes, determines the day-to-day sensitivity of the beach to short term increases in wave energy. Over the long term, the modal beach state and range of states determine the annual probability of cut for any given wave climate as well as the mobility of the beach (see Short, 1980 for a discussion of beach mobility). Table 1 summarizes the characteristics and causes of the three primary modes of beach cut together with their relationships to morphodynamic conditions. Figure 1 illustrates the major plan and profile configurations of

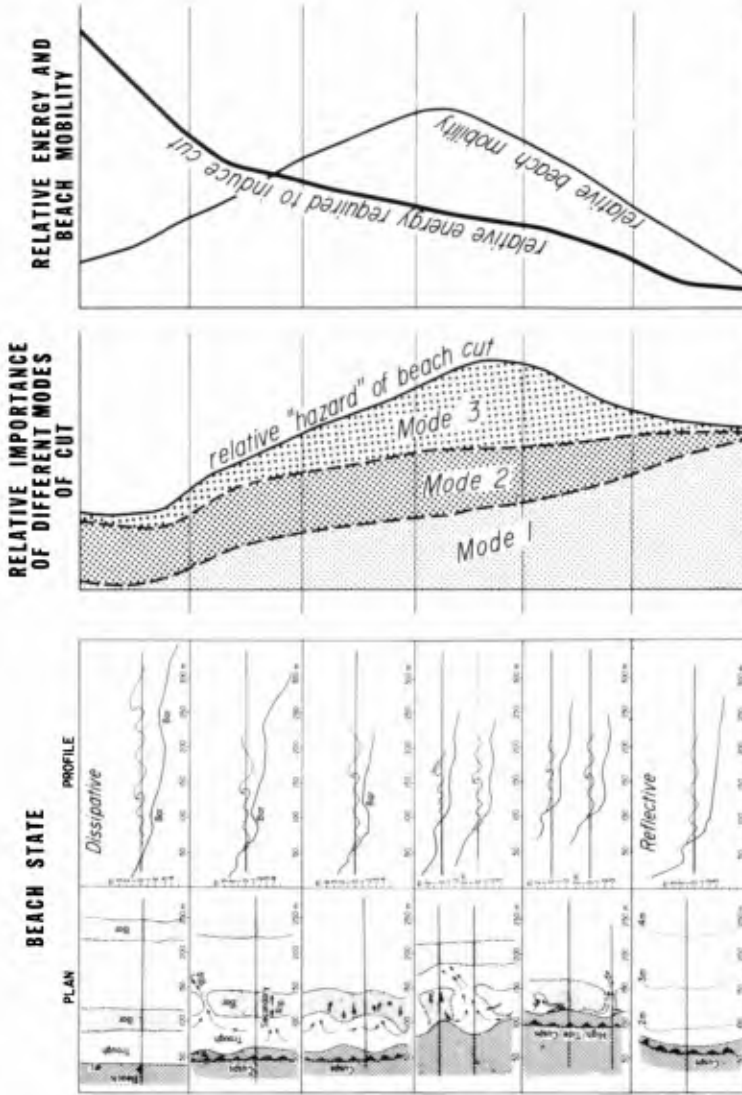


Figure 1: Characteristic Beach States and associated Modes of Beach Cut and Relative Erosion "Hazard".

the extreme and intermediate beach states and indicates the relative erosion hazard and relative importance of each mode of cut corresponding to each state. The relative wave energy required to induce erosion and relative beach mobility for modal states are also indicated. As Figure 1 suggests, Mode 1 cut is probably the most important mode of cut on reflective beaches but is suppressed on extremely dissipative beaches where it is replaced by Mode 2 cut. Beaches in intermediate states are susceptible to cut by both Modes 1 & 2 as well as by Mode 3.

Table 1: Modes of Beach Cut in Relation to Beach State.

<i>MODE OF BEACH CUT</i>	<i>CAUSE</i>	<i>ASSOCIATED BEACH & SURF-ZONE CONDITIONS</i>	<i>RELATIVE ENERGY REQUIRED TO INDUCE BEACH CUT</i>
1 <i>Accentuated runup and berm overtopping, formation of erosional cusps</i>	<i>Strong subharmonic resonance</i>	<i>REFLECTIVE</i>	<i>LOWEST</i>
2 <i>Backshore scarping by bores superimposed on long-period setup oscillations</i>	<i>Strong infragravity oscillations</i>	<i>DISSIPATIVE</i>	<i>HIGHEST</i>
3 <i>Beach scarping in embayments of arrested rip cells</i>	<i>Radiation stress gradients induced by irregular surf zone topography</i>	<i>INTERMEDIATE, RHYTHMIC Surf-zone topography, regions adjacent to shoreline protrusions, inlets or river mouths.</i>	<i>INTERMEDIATE</i>

CUT OF REFLECTIVE BEACHES

The steep reflective beach states tend to prevail in highly indented compartments, in the protected lee of headlands, in the presence of coarse material, or at the "end points" of prolonged accretion. On the New South Wales coast, they are particularly common at the low energy (southern) ends of spiral (or "zeta curved") embayments. Storage of active sand is primarily in the intertidal and subaerial beach rather than in the surf zone or nearshore and relatively deep water reaches to the base of the intertidal beach. The surf-zone is narrow or nonexistent and waves surge up the beach face with maximum runup (relative to incident wave height).

Near the beach, oscillations tend to be standing at a range of frequencies. A prominent feature of the hydrodynamics of reflective beaches is subharmonic resonance. There is now considerable evidence indicating that these subharmonic oscillations are edge waves (Huntley and Bowen, 1975; 1979; Wright et al., 1979a & b). Furthermore, field data (Wright et al., 1979a & b; Wright, in prep) suggest that, so long as the reflective condition is maintained (i.e. steep beach, low-steepness waves), increased wave energy will increase the amplitude near the beach of the subharmonic resonance. Runup maxima under these conditions are strongly dominated by the subharmonic motion with the result that alternate swashes reach extreme elevations on the beach. Typical power spectra of water surface oscillations on a reflective beach (Bracken Beach, south of Sydney, see Wright, et al., 1979b) are shown in Figure 2. These spectra are based on observations made under moderate energy conditions (breaker height, $H=1.5$ metres) and clearly show a pronounced subharmonic peak which exceeds the incident wave peak over the step at the base of the beach (inner station).

The growth of subharmonic resonance on steep beaches under conditions of long-period swell is a major cause of the first mode of beach cut (Table 1). This mode is characterized by accentuated runup and berm overtopping (Fig.3) accompanied by strong seaward pulsing at subharmonic frequencies below the base of the beach. During the early phases, liquifaction and slumping of the beach face takes place in the mid and low swash zone while large erosional cusps develop on the upper beach with maximum scour occurring in the cusp bays.

Since subharmonic resonance is most easily excited on reflective beaches and requires the least energy to excite (Guza and Davis, 1974; Guza and Bowen, 1977) reflective beaches are most sensitive to Mode 1 erosion under the wide range of energy conditions. Probably for this reason it is common, on the New South Wales coast for moderate, long swell to cut reflective beaches while promoting accretion on nearby dissipative beaches. Provided energy conditions are not severe, cut ceases once reflectivity has been sufficiently reduced to reduce resonance and runup. Conversely, accretion normally ceases once maximum reflectivity has been attained. In strongly embayed compartments where the reflective beach represents the modal state, beach mobility thus tends to be low.

Inshore circulation seaward of modal reflective beaches is normally weak or nonexistent (Wright et al., 1979a) and, although subaerial cut may be severe, the eroded sand is not normally transported very far offshore except when the erosive conditions persist long enough to alter the state

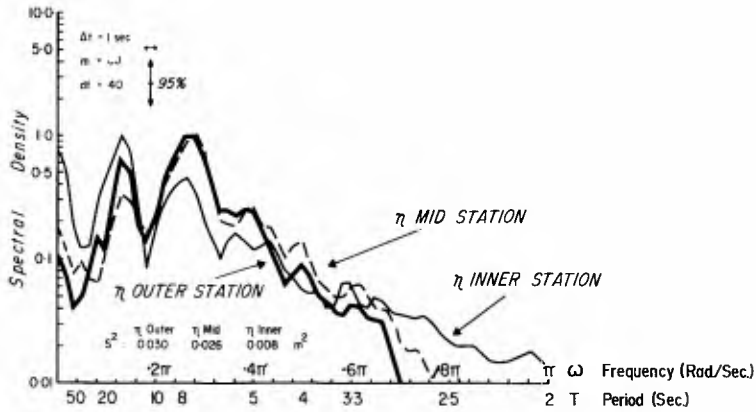


Figure 2: Typical power spectra of surface elevation (η) and shore-normal current (u) from a reflective beach. Note the pronounced subharmonic peak. (Bracken Beach, 10 Dec. 1977).



Figure 3: Accentuated runup, berm overtopping, and the initiation of erosional cusps on a reflective beach under conditions of long-period, moderate energy swell (Bracken Beach).

of the beach significantly. However, an exception exists for reflective beaches which prevail at the protected southern ends of spiral embayments. Large, relatively strong rips frequently develop in these localities under moderate to high energy conditions. Some prominent examples include Cronulla, Dee Why, and Palm beaches near Sydney. These rip systems increase the severity of erosion when it occurs.

CUT OF DISSIPATIVE BEACHES

On exposed time-varying beaches the extreme dissipative state occurs following severe erosion. The dissipative state may also be arrested as the modal state in localities exposed to persistent high-energy waves or when there is an abundance of fine-grained sediment in the inshore. Along deltaic coasts dissipative conditions commonly prevail even with relatively low wave energy.

An example of a perennially dissipative beach in New South Wales is the northern section of Seven Mile Beach, 150 km south of Sydney where fine sand, drifted northwards accumulates in an exposed inshore zone. An even more prominent example is found along the Coorong coast of South Australia where a long straight dissipative beach extends from Goolwa 190 kilometres to the southeast (Fig.4). Goolwa's high energy dissipative state is maintained by long period southwesterly swell with heights which persistently exceed 3 metres combined with a sediment suite consisting of fine carbonate sands. Both Goolwa and Seven Mile Beach exhibit wide surf zones with multiple parallel bars and negligible rip circulation. The Goolwa surf zone is normally 500 metres or more wide.

The flat profiles and high turbulent viscosities of the dissipative extreme preclude Mode 1 cut since subharmonic resonance and standing oscillations at incident wave frequencies are suppressed and runup is very low relative to breaker height. In fact, dissipative beaches generally have a greater probability of accreting than they do of eroding. Nevertheless, dissipative beaches may erode under high energy conditions although this erosion often consists solely of backshore scarping without consequential removal of sand to seaward of the foreshore. Neglecting the effects of non-wave-induced water level rises, (e.g. storm surges, extreme tides), cut of highly dissipative beaches primarily involves the second mode of cutting (Table 1). Pronounced setup on the landward margins of flat dissipative inshore profiles increases the effectiveness of return flows and may, under conditions of high energy or steep waves, allow the bores of broken waves to penetrate to the backshore or to the foredune base where scarping

without consequential removal of sand to seaward of the foreshore. Neglecting the effects of non-wave-induced water level rises, (e.g. storm surges, extreme tides), cut of highly dissipative beaches primarily involves the second mode of cutting (Table 1). Pronounced setup on the landward margins of flat dissipative inshore profiles increases the effectiveness of return flows and may, under conditions of high energy or steep waves, allow the bores of broken waves to penetrate to the backshore or to the foredune base where scarping occurs as illustrated in Figure 5. This mechanism may operate to cause dune recession even where there is an abundance of inshore sediment and without necessarily resulting in a net loss of beach material. The setup normally oscillates at infragravity frequency with maximum bore penetration occurring at "surf-beat" highs.



Figure 4: Highly dissipative, barred surf zone near Goolwa, S.A. (surf zone is 500 metres wide).

Data from Goolwa (Jan-Feb 1980) and Seven Mile Beach (Feb.1979) emphasize the dominance of infragravity oscillations on the subaerial beach processes of dissipative systems. Figure 6 shows simultaneous water surface (η) time series from three different stations across the Goolwa surf zone. Progressive shoreward attenuation of oscillations at incident wave frequency and shoreward growth of infragravity oscillations at periods of 100-150 seconds are apparent. Power spectra of both η and shore normal current, u (Fig.7) from the inner surf zone are strongly dominated by infragravity peaks. Infragravity oscillations near the beach at Goolwa exceeded 1 metre in

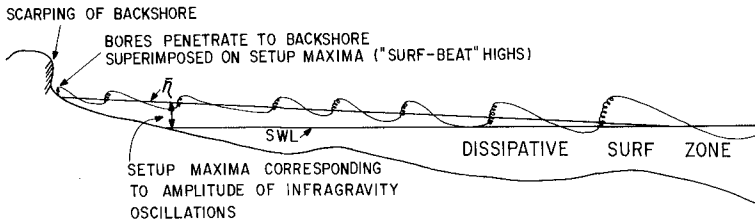


Figure 5: Cut of highly dissipative beaches: bores penetrate to foredune base on highs of infragravity oscillations.

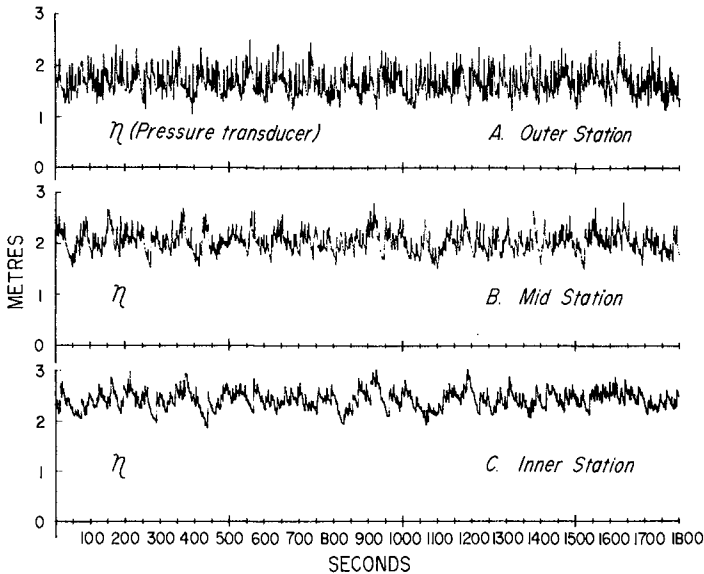


Figure 6: Simultaneous water surface (η) time series from Goolwa Surf Zone (1 Feb.1980) showing progressive shoreward attenuation of incident waves and growth of infragravity oscillation. Outer, mid, and inner stations were located respectively at 160m, 100m, and 60m seaward of the mid swash zone.

height at the time the data were obtained.

Seaward transport of sands within the surf zones of long straight dissipative beaches such as Goolwa Beach is the result of vertical segregation of shoreward versus seaward flows rather than rips. Figure 8 shows the cross-sectional current structure as observed at Goolwa under conditions of comparative beach stability. Strong shoreward flow near the surface is accompanied by weaker seaward flow near the bed. Spectra indicate the seaward flows to be dominated by infragravity pulsing. Although no storm data exist from such a high energy surf zone, it may be tentatively inferred that seaward-directed bottom flows intensify under storm conditions and move sand to the outer surf zone.

Cross spectra of u and v and current statistics from multiple positions across the Goolwa and Seven Mile Beach surf zones demonstrate that the infragravity oscillations are standing in the shore-normal direction and may exist as longshore-progressive edge waves (Wright, in prep). The inferred antinodal regions normal to the shore approximately correspond to regions of sediment accumulation at bars. On long straight dissipative beaches, sediment eroded from the subaerial beach remains within the surf zone as multiple longshore bars from where it may be readily returned to the beach during periods of falling wave height. However when highly dissipative conditions and associated strong infragravity oscillations are superimposed during storms or periods of heavy swell, on crenulate coasts where short embayed beaches are bounded by headlands, erosive effects may be greatly enhanced. This is often the situation for many of the beaches near Sydney. Destructive effects and increased erosion hazards which are related to embayment geometry include: (1) low-frequency resonance at infragravity and seiche frequencies; and (2) giant, powerful storm rips which may transport sediment to over a kilometre offshore. The storm rips have feeder systems which may occupy the whole of an embayment (see Figure 8 of Wright et al., 1979b for an example). In many cases the rips appear to be closely coupled to low-frequency resonant phenomena and pulse strongly at periods of several minutes.

CUT OF INTERMEDIATE BEACHES

Time varying beaches, must in the process of shifting from one extreme state to the other, pass through the intermediate states shown in Figure 1. The period of time that the beach occupies any of these states may, in some cases, be very short as for example during a period of rapid erosion. However, in regions which experience highly variable wave climates like that of Eastern Australia the

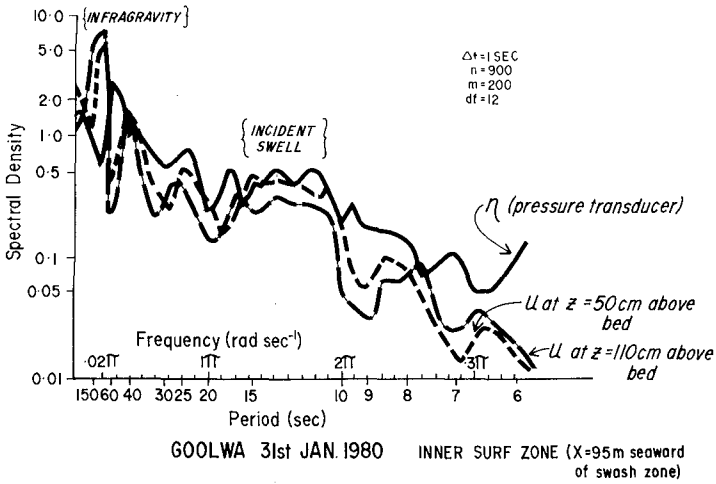


Figure 7: Power spectra of η and u from the inner surf zone at Goolwa (31 Jan. 1980) showing strong dominance of infragravity oscillations.

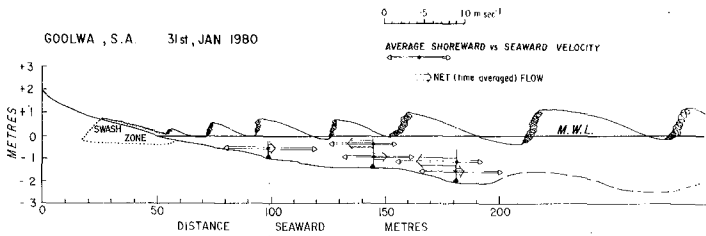


Figure 8: Cross-sectional current structure of the Goolwa surf zone (31 Jan. 1980).

beach may continually oscillate around one or several intermediate states without reaching either extreme. In addition, some intermediate states may persist for several months or even year round on many of the compartmented beaches of New South Wales. Environmental conditions which favour intermediate modal states include moderate energy but temporally variable wave climates and medium to coarse sand.

Intermediate beach states include various types of bar-trough, crescentic bar, and rhythmic transverse-bar-rip topographies which allow part of the beach inshore system to be reflective while another part is dissipative (Wright et al., 1979a). For example steep reflective subaerial beaches can coexist with partially dissipative surf zones when deep pronounced troughs separate the beach from the dissipative parts of the surf zone or where the reflective beach sectors occur in rip embayments adjacent to dissipative transverse bars. Under these conditions the beach is affected by a combination of incident waves, subharmonic resonance, and infragravity oscillations, as well by resonance at intermediate frequencies determined in part by topographic dimensions (Wright, in prep). An example of current spectra from the inner surf zone of Type 3 intermediate topography (as described by Wright et al., 1979a) and exhibiting all of the frequencies just mentioned is shown in Figure 9.

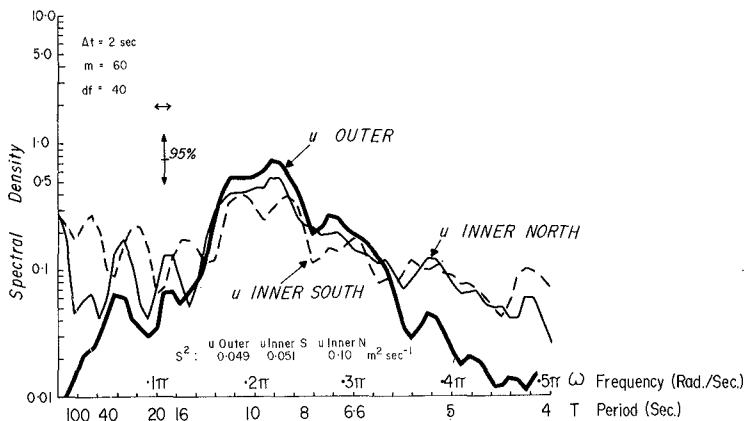


Figure 9: Power spectra of u from intermediate crescentic-bar-trough topography on North Moruya Beach (13 Dec. 1977).

Intermediate states permit both Mode 1 and Mode 2 cut to operate together when seas rise. In addition, it is on the intermediate states that different scales of rip circulation are best developed so that Mode 3 cut also plays an important and often major role. Mode 3 cut is associated with rip circulations which are forced by topographic irregularities (e.g., transverse bars and alternating embayments), particularly irregularities which are persistent in their location. Localized but often severe erosion may occur in the embayments of rips, even when the coast regionally is experiencing accretion, by means of current scour at the base of the beach face. Paradoxically, this form of erosion may be intensified by abnormally rapid accretion in immediately adjacent zones or by the nearby occurrence of arrested shore-line protrusions such as tidal inlets or man-made structures, which produce steep alongshore gradients in radiation stress and setup. Despite its spatial limitations, this mode of erosion may cause chronic local shoreline recession, often endangering beach front properties. Figure 10 shows an example of a large arrested rip system on Wamberal Beach north of Sydney which caused the destruction of three beach-front properties at a time when the flanking shoals were rapidly accreting.

A large-scale analogue to Mode 3 cut occurs adjacent to river mouth bar deposits and deltaic lobes influenced by moderate to high energy waves. This type of erosion is related to large-scale rips which drain water trapped by high dissipative wave breaking over the seaward-protruding river-mouth bar or deltaic bulge deposits. Large erosional bays result along margins of the regions of high deposition rates. This form of erosion is most acute on the downdrift margins of the depositional bulge but also occurs on the updrift margins. An example from the mouth of the Shoalhaven River south of Sydney is shown in Figure 11. The process of delta-margin erosion is also discussed by Wright et al., 1980.

DISCUSSION AND CONCLUSIONS

This paper has emphasized the dependence of beach cut on morphodynamic state. The probability of some form of cut occurring, the possible severity of cut and the mode of cut all vary with morphologic state on the one hand and breaker conditions and sediment size on the other. Quite obviously, the threat to beach front properties depends as much on the absolute width of the subaerial beach as it does on cut probability. However for any given beach width, the relative erosion "hazard" of a beach sector may be readily assessed at a first order with reference to beach state, degree of exposure, and forecast wave



Figure 10:

Topographically arrested rip on Wamberal Beach (north of Sydney) which caused chronic shoreline recession and resulted in the destruction of beach front homes.

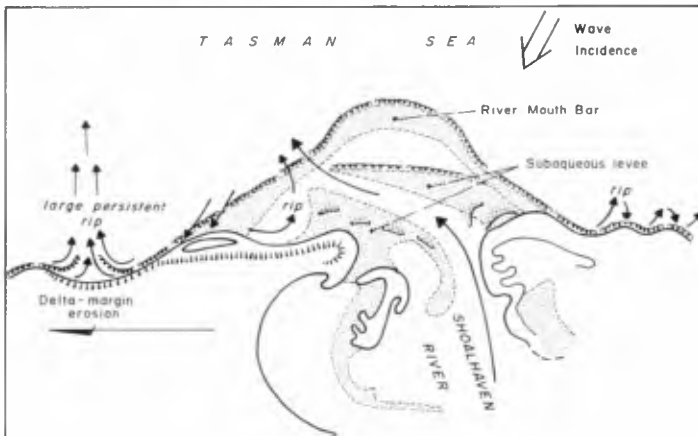


Figure 11: Delta-margin erosion adjacent to river-mouth bar deposits, mouth of Shoalhaven River (south of Sydney).

conditions. Since the physical processes responsible for cut are different, different beach protection strategies may be required for different morphodynamic states. For purposes of long-term advance planning, it is the modal beach states and/or normal range of states that are important. These may be recognized from sets of long-term ground or remotely-sensed observations.

On many New South Wales beaches, particularly those along the crenulate coast in the vicinity of Sydney, modal beach state varies appreciably with degree of exposure to the dominant southeasterly swell and storm waves. Spiral or zeta curved embayments typically are protected and experience low refraction coefficients at their southern ends but are fully exposed at their northern ends. Reflective beaches are the modal state in the southern sectors whereas the accumulation of sands within the surf zone combined with high exposure tends to maintain more dissipative conditions at the northern ends. Intermediate states are most common in the middle sectors. This pattern of longshore variation in beach state together with the associated variations in likely mode of beach cut is illustrated in Figure 12. Typically it is the middle (intermediate) sections of these beaches which are most susceptible to cut and are most mobile. In a more general sense, Table 2 summarizes the relationships between beach state, beach mobility and environmental conditions.

Table 2: Modal Beach State and Beach Mobility in Relation to Environmental Conditions.

<i>'MODAL' BEACH STATE</i>	<i>RELATIVE AMPLITUDE OF CHANGES IN SHORELINE POSITION</i>	<i>ENVIRONMENTAL CONDITIONS</i>
<i>REFLECTIVE</i>	<i>LOW</i>	<i>Low-steepness waves or strongly embayed compartments; coarse or high-density (e.g. volcanic 'black' sands) material</i>
<i>DISSIPATIVE</i>	<i>LOW TO MODERATE</i>	<i>Persistent high energy waves or Abundant fine sands in inshore zone (e.g. deltaic coasts)</i>
<i>INTERMEDIATE-RHYTHMIC</i>	<i>HIGH</i>	<i>Highly variable wave climate; medium sands; best developed where there is also a significant fraction of shell fragments and a meagre sediment supply.</i>

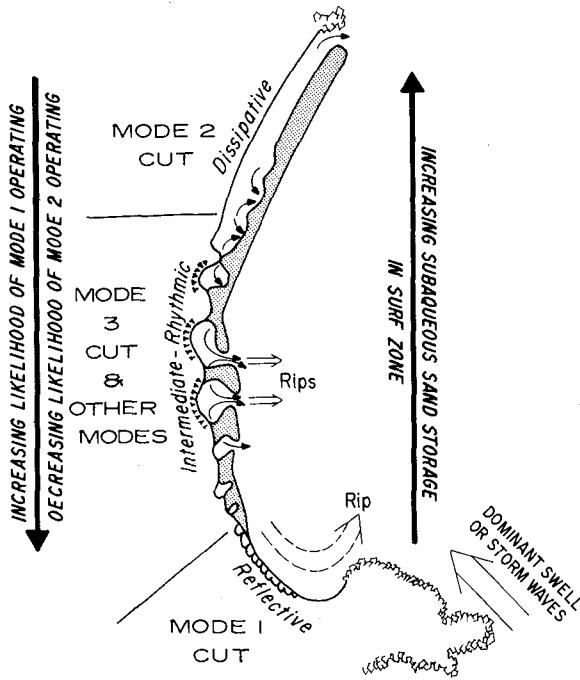


Figure 12: Longshore variation in modal beach state and associated modes of beach cut in a typical New South Wales spiral embayment.

ACKNOWLEDGEMENTS

This study has been supported by the Australian Research Grants Committee and by the U.S. Office of Naval Research, Coastal Sciences Program, Task NR 388-157, Grant N-00014-80-G-0001. I am grateful for assistance provided throughout the study by M.P. Bradshaw, F. Coffey, P.J. Cowell, M. Green, and A.D. Short. Figures were prepared by J. Roberts and M. Rigney.

REFERENCES

- Bradshaw, M.P., Chappell, J., Hales, R.S. and Wright, L.D., 1978, "Field Monitoring and Analysis of Beach and Inshore Hydrodynamics", Proc. 4th Aust. Coastal and Ocean Engineering Conf., (Adelaide), 1978, pp. 171-175.
- Davis, R.A. and Fox, W.T., 1972, "Four-dimensional model for beaches and nearshore sedimentation", J. Geol. 80, 484-493.
- Dean, R.G., 1973, "Heuristic models of sand transport in the surfzone", Proc. of Conf. on Engineering Dynamics in the Surf Zone, Sydney, pp. 208-214.
- Guza, R.T. and Bowen, A.J., 1977, "Resonant interactions from waves breaking on a beach", Proc. 15th Conf. Coastal Eng., 560-579.
- Guza, R.T. and Davis, R.E., 1974, "Excitation of edge waves by waves incident on a beach", J. Geophys. Res., 79(9): 1285-1291.
- Hattori, M. and Kawamata, R., 1980, "Onshore-Offshore Transport and Beach Profile Changes", Abstract, 17th International Conf. Coastal Engineering, Sydney, pp. 254-255.
- Huntley, D.A. and Bowen, A.J., 1975, "Field observations of edge waves and their effect on beach material", J. Geol. Soc. London, 131: 69-81.
- Huntley, D.A. and Bowen, A.J., 1979, "Beach Cusps and Edge Waves", Proc. 16th Coastal Eng. Conf. Hamburg, 1378-1393.
- Komar, P.D., 1976, Beach Processes and Sedimentation, New Jersey, Prentice-Hall, 429 pp.
- Sawaragi, T. and Deguchi, I., 1980, "On- Offshore sediment transport rate in the surf zone", Abstracts, 17th International Conf. Coastal Engineering, Sydney, pp. 256-257.
- Sonu, C.J. and James, W.R., 1973, "A Markov model for beach profile changes", J. Geophys. Res., 78, 1462-1471.
- Short, A.D., 1979a, "Wave power and beach stages: A global model", Proc. 16th International Conf. Coastal Eng., p. 1145-1162.
- Short, A.D., 1979b, "Three dimensional beach-stage model", J. Geol., v.87, p. 553-571.

- Short, A.D., 1980, "Beach response to variations in breaker height", Proc. 17th International Conf. Coastal Engineering, Sydney.
- Thom, B.G. and Bowman, G., 1980, "Beach Erosion and Accretion at two time scales", Proc. 17th International Conf. Coastal Engineering, Sydney.
- Winant, C.D., Inman, D.L. and Nordstrom, C.E., 1975, "Description of Seasonal beach changes using empirical eigenfunctions". J.Geophys. Res. V.80, pp. 1979-86.
- Wright, L.D., in preparation, "Field Observations of Long-Period Surf-Zone Oscillations in Relation to Contrasting Beach Morphologies: Implications for Edge Wave Models". submitted to Austr.J. Marine and Freshwater Res.
- Wright, L.D., Chappell, J., Thom, B.G., Bradshaw, M.P. and P. Cowell, 1979, "Morphodynamics of Reflective and Dissipative Beach and Inshore Systems: Southeastern Australia", Marine Geology, vol. 32, pp. 105-140.
- Wright, L.D., Thom, B.G., Chappell, J., 1979, "Morphodynamic Variability of High Energy Beaches", Proc. 16th International Conf. Coastal Eng. (Hamburg), 1978, Chapt. 68, pp. 1180-1194.
- Wright, L.D., Thom, B.G. and Higgins, R., 1980, "Wave Influences on Sediment Transport and Deposition at River Mouths: Examples from Australia and Papua - New Guinea", Estuarine and Coastal Marine Science, v.10.

BREAKER TYPE AND PHASE SHIFTS ON NATURAL BEACHES

Peter J. Cowell

Coastal Studies Unit, Dept of Geography
University of Sydney
N.S.W. 2006 Australia**ABSTRACT**

The kinematics of incipient breakers were measured on various complex natural beaches. Water velocities were found to consistently lag behind the wave crest. This phase shift appears to be partly inherent in shoaling waves and partly a result of partial wave reflection. Phase shifts vary from 5 degrees through to quadrature. This variation probably depends to a large extent upon beach reflectivity and distance of the break point from the shoreline. Phase shifting also varies vertically beneath the wave crests from uniform distributions to those in which maximum shifts occur near the bed. There is a strong relationship between the nature of phase shifting, the morphodynamic condition and the breaker type. Surging waves were associated with large, and vertically uniform phase shifts. Waves towards the plunging and spilling end of the breaker type continuum occurred where phase shifts were significantly larger at lower depths than near the surface.

INTRODUCTION

The importance of breaker type in differentiating surf-zone morphodynamic regimes is implicit in the delineation of beaches into reflective and dissipative categories (e.g., see Short, 1978 and Wright et.al., 1979). The six morphodynamic states of Wright et.al. (1979) range from the highly dissipative type through intermediate complex and rhythmic forms to the highly reflective extreme. Breaker characteristics have received little direct attention in recent theoretical developments of the surf-zone dynamics associated with these beach states. However, it is obvious that spatial patterns of energy dissipation related to breaker type must be as important to morphodynamic response as incident angle and wave height distribution.

Peregrine and Cokelet (1980) use numerical solutions of water motions in deep water which provide apparently good simulation of the initial breaking process. Unfortunately, there exists at present no theory capable of successfully describing the shallow-water breaking process even under simple circumstances. Accordingly, in order to investigate the process in the context of breaker types occurring with each of the morphodynamic states, the kinematic structure of waves near breaking was investigated in association with each of these beach types. The investigation involved measurement of the vertical distribution of horizontal velocities.

The purpose of this paper is to present some results concerning one of the least considered properties of waves at breaking; the phase relationship between the wave crest and the horizontal velocity components below it. Two aspects of this problem will be considered: (1) the variation in this phase relationship for waves breaking in association with the different morphodynamic beach types; and (2) the influence of this phase relationship on breaker type through the effect on the vertical distribution of horizontal velocity components for waves on the respective beach types.

Both Adeyemo (1970) and Thornton et.al.(1976) report without comment as to cause or implications the occurrence of phase shifting between water surface and horizontal velocities in laboratory and field experiments respectively. Adeyemo employed photographic measurement of hydrogen bubble displacement in waves on both a steep beach (slope 1:9) on which plunging breakers occurred, and on a moderately flat beach (slope 1:18) with spilling breakers. In both cases Adeyemo reports wave crests leading velocity maxima by more than 30 degrees. Further, this phase shift was found to exist throughout the shoaling region seaward of the break point (see Table 1).

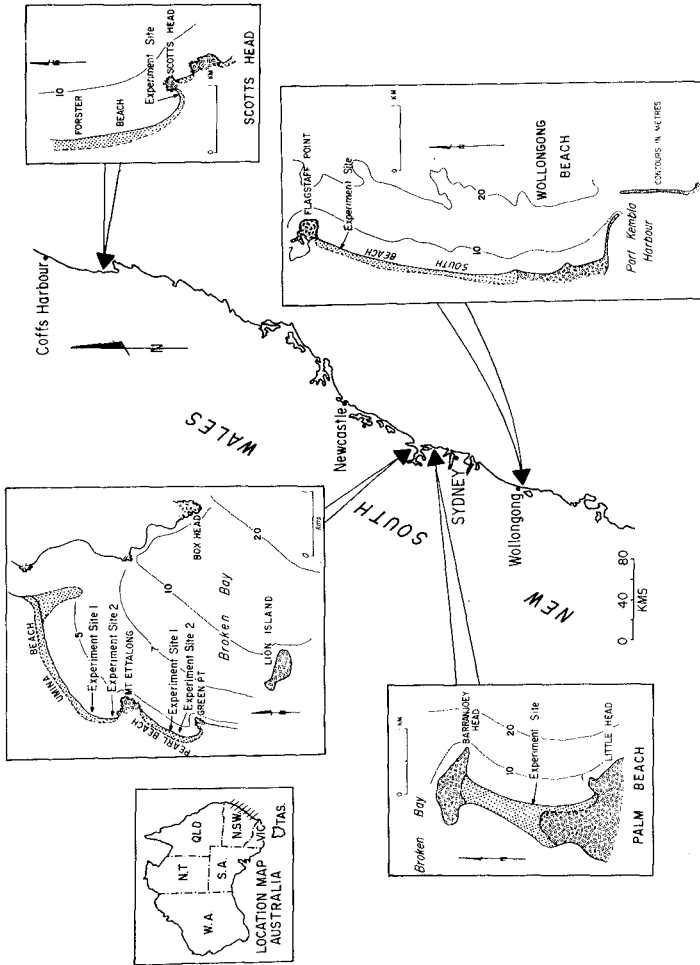
Thornton et.al. used electromagnetic flow metres and capacitance wave staffs to measure waves and currents on field beaches. They report a 15 degree lag of water velocities behind the water surface at peak frequencies for surging breakers on a steep natural beach (average slope, 1:8). They found phase shifts varying from 5 to 30 degrees in the same direction in measurements made on a flat beach (average slope, 1:20) where spilling breakers prevailed (see Table 1).

TABLE 1

Typical Phase Shifts in Lower Half of Water Column

Example	Experiment	r	$\hat{\theta}$ (degrees)	$\hat{\theta}_{max}$ (degrees)	$\hat{\theta}$ (degrees)	$r\hat{\theta}$	$r\hat{\theta}_{max}$	h/L
1	Adeyemo (1970) Curve a (tan $\beta = 1:18$) curve e	.01	-0.1	0.5	32	n.p.	.29	.0823
	curve h	.01	0.5	0.5	32	.29	.29	.0907
		.01	0.0	0.5	32	.91	.29	.1130
2	Adeyemo (1970) curve a (tan $\beta = 1:19$) curve e	.03	1.2	3.2	36	.64	.33	.0800
	curve h	.03	-3.2	3.2	36	n.p.	.33	.0938
		.03	0.3	3.2	36	.86	.33	.1135
3	Del Monte Beach; tan $\beta = 1:20$ (Thornton et al., 1976)	.06	-1.7	7.0	27	n.p.	.24	.0111
4	Carmel River Beach; tan $\beta = 1:8$ (Thornton et al., 1976)	.14	2.3	16.0	15	.6	.13	.0333
5	Offshore Bar, Umira Beach (1) (26-8-78, Run 1)	.00	0.0	0.2	30	.74	.27	.0211
6	Offshore Bar, Scotts Head (3-12-78, Run 2)	.00	-0.2	0.3	23	n.p.	.20	.0314
7	Transverse Bar, Palm Beach (7-4-79, Run 1)	.01	0.0	1.0	14	.71	.12	.0231
8	Rip-head bar, Palm Beach (7-4-79, Run 4)	.01	-0.5	0.5	22	n.p.	.32	.0241
9	Beach face, rip-bay, Palm Beach (7-4-79, Run 5)	.21	21.3	23.7	88	.97	.97	.0149
10	Cusp Horn, Pearl Beach (1) (3-8-78, Run 1)	.32	32.3	35.7	16	.16	.14	.0330
11	Cusp Horn, Pearl Beach (2) (7-8-78, Run 6)	.12	1.0	14.2	56	.96	.53	.0255
12	Cusp bay, Pearl Beach (2) (7-8-78, Run 5)	.11	1.5	12.2	30	.82	.27	.0245

Notation: r = Miche's (2/Ei) reflection coefficient
 $\hat{\theta}$ = phase predicted from r and kx
 $\hat{\theta}_{max}$ = phase predicted from r, kx = $\pi/4$
 $\hat{\theta}$ = measured phase
 $r\hat{\theta}$ = reflection coefficient required for $\hat{\theta} = \hat{\theta}$ at kx
 $r\hat{\theta}_{max}$ = reflection coefficient required for $\hat{\theta} = \hat{\theta}$ at kx = $\pi/4$
 n.p. = not possible



Field Site Locations

FIGURE 1

EXPERIMENTS AND METHODS

Field measurements of vertical distributions of horizontal velocities were made at various sites on the microtidal, New South Wales coast of Australia, shown in Figure 1. These beaches were chosen in each case as being characteristic of a particular morphodynamic type. Of these, experiments from three beaches (Umina, Pearl and Palm) will be used to illustrate the general results concerning phase shifting.

Umina beach provides an example of the dissipative beach type with low bed slopes, parallel bars and generally spilling breakers (Fig. 2). Beach sediments are largely fine sands (2.75 phi). The break point during experiments was located on the outer bar. Pearl Beach (Fig. 3) provided the reflective extreme with waves breaking against the beach face. The beach was heavily cusped during experiments (Fig. 6a). Steep beach slopes are enhanced by the coarse to very coarse sand (1 to -.5 phi). Palm Beach will be used to illustrate wave breaking on an intermediate-rhythmic beach type (Fig.4). Median diameter of sediments is slightly less than 1.5 phi. During experiments type 4 beach morphology of Wright et.al.(1979) prevailed. Three break points with distinctly different breaker type characteristics were distinguished on this beach: On the rip head bars waves were heavily plunging; at the beach face in rip embayments waves were of the surging type after reforming across the rip channel; and on the seaward margins of transverse bars between rip channels breaker types were weakly plunging to spilling.

Wave and current sensors were recorded both digitally on magnetic tape and continuously on strip chart. Photographic records were obtained using a movie camera with single frame exposures synchronised with the digital scanning of wave and current sensors. Pressure and water surface measurements were made using bottom mounted pressure transducers together with the photographic record of surface piercing, visually calibrated staffs attached to each instrument station used. From one to three stations were used in experiments. They are depicted in Figures 2, 3 and 4. At the incipient break point the instrument station also supported a vertical array of up to 7 miniature, bidirectional, ducted impellor-type flow metres. The axes of these flow metres were orientated shore normal in the horizontal plane. The photographic record was also used to determine breaker type geometries of each passing wave. A description of the data acquisition system can be found in Bradshaw et.al. (1978).

Spectra and cross spectra were computed between adjacent

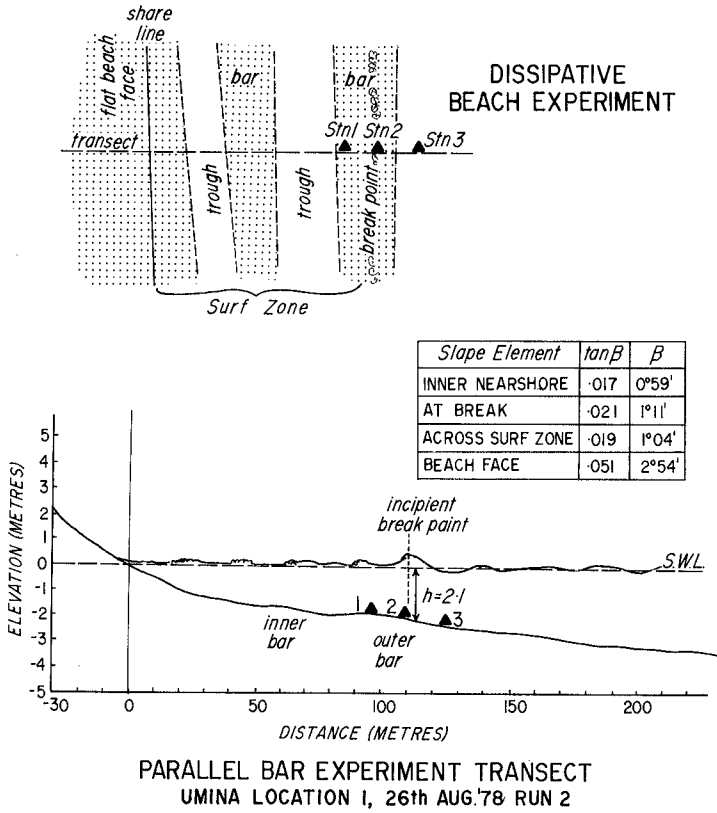


FIGURE 2

Dissipative Beach Experiment

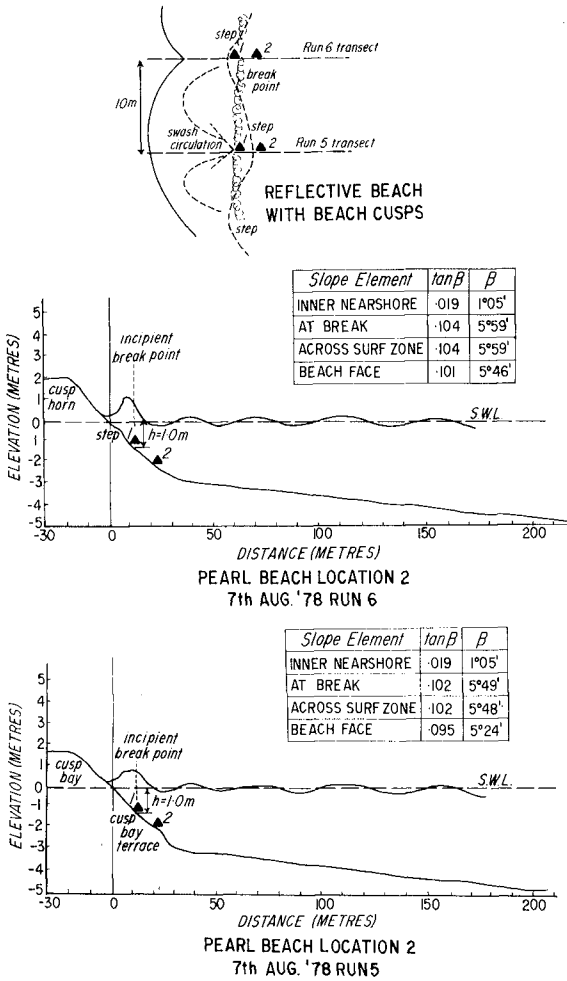


FIGURE 3

Reflective Beach Experiment

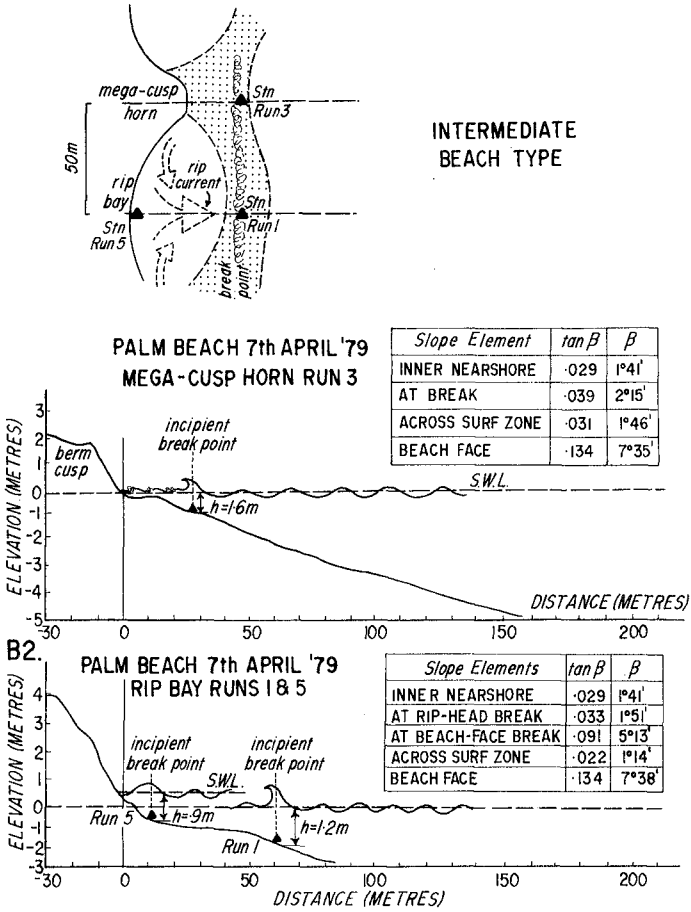


FIGURE 4

Intermediate Beach Type Experiment

current meters in the vertical array, as well as between each current meter and the pressure transducer. These computations were made by Fourier transforming covariance functions calculated from the records and smoothed with a Tukey window. The covariance functions were computed using a maximum lag of 22% of the record length. The resulting spectral estimates contain 24 degrees of freedom.

Phase differences at peak spectral frequencies were used. These are shown in Figure 5 where the horizontal bars indicate 95% confidence intervals. These bars are located at the elevation (z) of each flow meter used. This elevation is shown on the ordinate normalized with respect to mean height of waves above mean water level (η) and the depth (h). Dashed confidence bars indicate phase estimates for sensors which occasionally emerged from the water, giving zero readings. The reliability of these estimates is therefore suspect although comparison of power spectra with those of non-emerging instruments suggests comparable frequency content. Solid phase curves are interpolated between flow meters. Dashed curves are less reliable due to either extrapolation or current records being less reliable due to reasons just given.

The contribution to phase shifting resulting from instrument response characteristics was assessed by comparison of analyses and the variously obtained time series. The phase curves in Figure 5 were therefore determined for both phase between currents and pressure, and between each adjacent current record. Phase shifts and confidence intervals between each successive pair of adjacent current records were summed over the vertical array. This produced good agreement with phase between pressure and each of the current records.

Pressure records were also compared against current and photographic records with respect to frequency content. Close agreement is exhibited. The pressure record also appears to follow the photographically determined water surface time series fairly faithfully, which is important in terms of the coincidence of maximum pressure and the passage of the wave crest.

As explained by Thornton et.al.(1976), interpretation of such spectra requires caution due to nonhomogeneity and nonstationarity resulting from the break point wandering on flat beaches. For this reason cross-spectra phase was checked against wave by wave inspection of phase shifting between individual time series. The comparison revealed reasonable agreement. It also enabled use of reliable segments of records from those instruments which failed to produce a complete time series. These segments were used to estimate the interpolated and extrapolated parts of the

curves in Figure 5.

DISCUSSION OF RESULTS

It is evident from Figure 5 that phase shifting is substantial under each set of morphodynamic conditions. Water velocities generally lag behind the wave crest, particularly in the lower half of the water column. This is consistent with the observations of both Adeyemo (1970) and Thornton et.al.(1976). For spilling breaker types on dissipative beaches (Fig. 2) velocities follow the water surface more closely towards the surface, with a sharp decrease in phase lags above mid depth. High waves heavily plunging on a steep beach (Fig. 3) exhibit a similar phase profile (Fig. 5c), as do waves of the outer break on the intermediate beach type (Fig. 5d). In the former case the phase shift in the cusp bay is smaller than at the break point on the cusp horn. This is probably attributable to the interaction of waves with the intense backwash drainage from the cusp bay illustrated in Figure 6a. Resulting turbulence causes strong vertical mixing, which may produce greater flow homogeneity throughout the water column, and thus reduced phase shifting in the lower half. Breaker type differences are related to this. Whereas heavily plunging breakers occur on the cusp horns, the general form in the bay is collapsing and even surging. In the latter case the wave is injected with turbulence before breaking. Hence the breaker form is described by the general water motion rather than by the water surface alone.

It is also apparent that the vertical distribution of phase is more uniform in situations where surging-collapsing breakers occurred (Figs. 5b and 5d, beach face). Collapsing breakers prevailed in association with the 20 degree phase shift at the break point (Fig. 5b). The standing wave apparent at the beach-face break of the rip embayment on the intermediate beach type occurred in association with surging waves. In this case the break point (and instrument station) was located one quarter wave length from the shore line antinode.

It is interesting to note that both the harmonic (Fig. 5a) and subharmonic (Fig. 5b) have phase shifts of roughly twice the primary wave. In the former case the development of a harmonic in the spectrum is expected on such a flat beach where significant cross-spectral transfer is likely (e.g., Guza and Thornton, 1980). It is expected that the harmonic is phase linked although this cannot be demonstrated from this analysis. On the steep beach it is consistent with expectation that spectra should exhibit a significant peak at subharmonic frequency rather than at harmonic frequencies (e.g., Guza and Bowen, 1975).

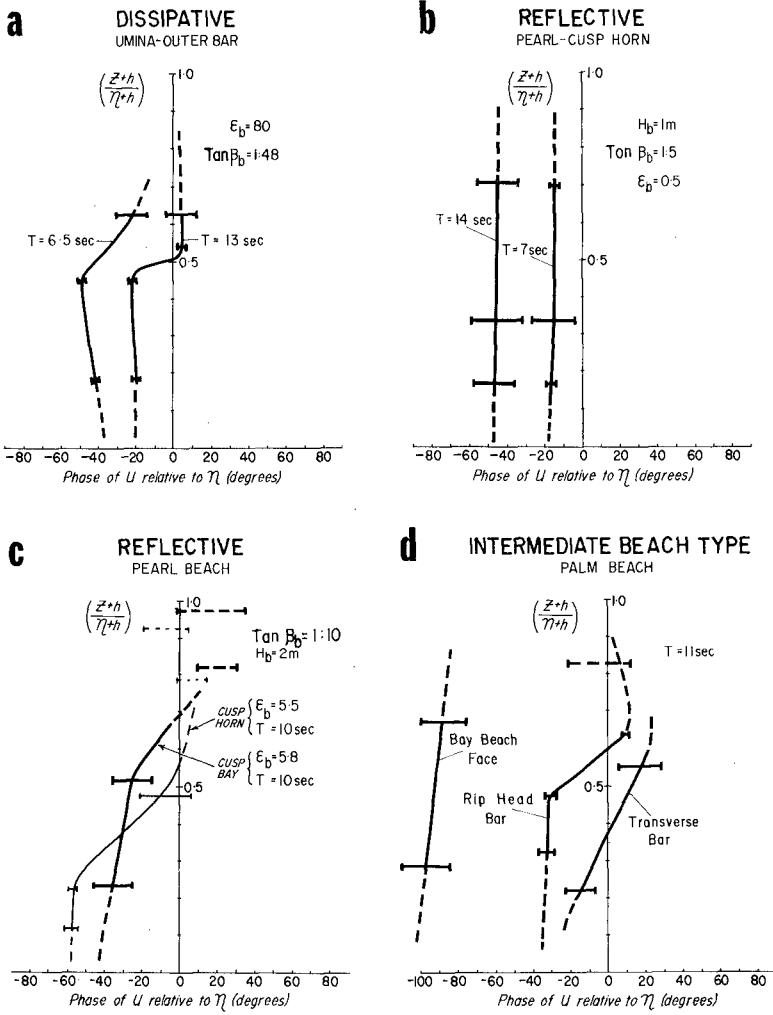


FIGURE 5

Cross-Spectra Phase

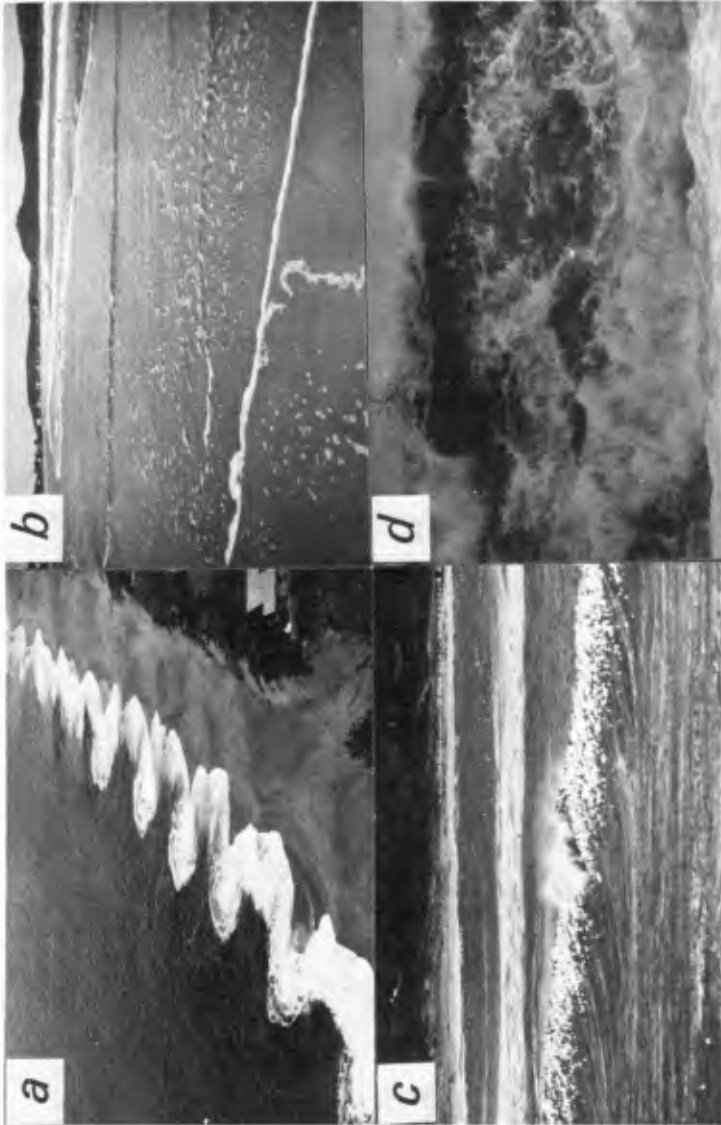


FIGURE 6. A. Beach-Cusp Drainage - Pearl Beach
B. Swash Lense - Umina Beach
C Spilling Breaker
D. Collapsing Breaker

However, the subharmonic might have been expected to be closer to quadrature phase than that actually displayed (Fig. 5b).

Before it becomes possible to account for the phase difference under the various morphodynamic conditions it will be necessary to explain the occurrence of phase shifting in general. Jonsson (1978) showed for oscillatory flows that the phase of water velocities within a laminar boundary layer leads those outside by $\pi/4$. In the fully turbulent case this phase shift is about $\pi/6$. This results from the inertia forces decreasing significantly near the bed whereas the accelerating pressure force the same in both the boundary layer and in the higher velocity free flow. Flow near the boundary therefore follows the phase of pressure more closely. However, the problem with the application of this argument is twofold: (1) phase shifting can only occur near the bed, whereas it has been measured by Adeyemo, Thornton et.al. and this study well away from the bed; and (2) the measured phase shifting occurs in the reverse sense to that predicted within the boundary layer.

Another explanation for phase shifting is provided by partial wave reflection. Using linear theory for partial reflection, the amount by which the surface elevation phase (ψ) leads the velocity phase (ϕ) x is given by

$$\begin{aligned} &= \psi - \phi \\ &= \tan^{-1} \left(\frac{1+r}{1-r} \tan kx \right) - \tan^{-1} \left(\frac{1-r}{1+r} \tan kx \right) \quad (1) \end{aligned}$$

where kx is the distance from an antinode nondimensionalized with respect to the wave number (k), and r is reflection coefficient. The reflection coefficient can be approximated by

$$r = 2/\xi_i \quad (2)$$

$$\text{where, } \xi_i = \frac{a_\infty \sigma^2}{g} (2\pi)^{1/2} \tan^{-5/2} \beta \quad (3)$$

a_∞ is the wave amplitude in deep water, σ is its radial frequency, g is the gravitational acceleration, and β is the bed slope (Guza and Bowen, 1976). Complete reflection occurs for $r \geq 1$. Equation 1 shows that phase shifting varies with reflectivity, the distance from the antinode and the wave length.

The results of Adeyemo (see Table 1) indicate that

reflectivity does not provide a general explanation. It is evident from his results that phase shifting is relatively constant as h/L varies throughout the shoaling region (L being the local wave length). Also the relatively steep laboratory waves provide insufficient reflection to produce the observed phase shift at any location, even on the steeper beach. The very low r shown in Table 1 for the 1:18 beach is totally inadequate for explaining the measured phase shift (θ) even when $kx = \pi/4$, where the phase shift predicted from (1) reaches its maximum (θ_{\max}). Nor is it conceivable that the reflection coefficient ($r_{\hat{\theta}}$) required for $\hat{\theta}$ at respective locations (kx) could be sufficiently large for such steep waves on such a flat beach. Similarly, reflection coefficients ($r_{\hat{\theta}_{\max}}$) at positions of phase shift maxima ($kx = \pi/4$) could not be expected to attain required values.

The same argument can be applied to the results from the dissipative Del Monte Beach of Thornton et.al. and Umina Beach of this study where substantial values of $\hat{\theta}$ were obtained (Table 1). The impossibility of reflection coefficients capable of explaining $\hat{\theta}$ values is demonstrated by the nature the runup at Umina Beach shown in Figure 6b.

Nevertheless, on steep beaches partial reflection theoretically and intuitively must be important in phase shifting. The linear predictions of θ in examples 4 and 9 to 12 (Table 1) for r approximated from (2) generally show fairly poor agreement with $\hat{\theta}$. However, θ is very sensitive to kx and so relies on accurate positioning of the antinode. Local kx at the break point has been used in this paper. It was determined from linear theory and phase measurements between instruments along transects. Better results may be possible using the average of local wave lengths between the break point and the shoreline. It is apparent in Table 1 that θ_{\max} and $r_{\hat{\theta}_{\max}}$ are at least of the right order of magnitude for the steep beach examples (particularly examples 4 and 10).

It is therefore evident from waves on non-reflective, flat beaches that phase shifting is generally inherent in both shoaling and near-breaking waves. It is probable that phase shifts due to reflection will be superimposed upon these inherent shifts. In accounting for phase shifting due to reflection therefore, it will be first necessary to gain some understanding of the inherent phase relationship. Wave-wave interaction and associated cross-spectral transfer may be important in gaining this understanding (e.g., Thornton, 1979; Guza and Thornton, 1980).

IMPLICATIONS FOR BREAKER TYPE

Since phase shifting appears to be a significant factor in the kinematics of waves near breaking it should be an important determinant of the breaking process and resulting breaker type. Iwagaki et.al. (1974) found in laboratory waves that systematic differences exist in velocity profiles below the crests of breakers of different type. Vertical gradients in horizontal velocity components are shown in Figure 7 to be steepest toward the surging end of the breaker type continuum. This is particularly evident near the crest, though also general over the entire profile.

The vertical distribution of horizontal velocities together with rates of decrease in wave phase speed provide a useful concept of kinematic stability. This concept may provide a signature of general form $(\partial u/\partial z) (\partial C/\partial x)^{-1}$ which is the kinematic equivalent of previous breaker type indices (e.g., Galvin, 1968; Battjes, 1974), where u is the horizontal water velocity, $z = -h$, and C is the phase speed. Kinematic stability is related to the kinematic criterion for the initiation of wave breaking ($u_0 \geq C$) extended through all z . Sharp crested waves breaking on gentle slopes (Fig. 6c) have relatively large vertical gradients in horizontal velocity. The significantly higher velocities at the crests of these waves are indicative of their strong non linearity. At the break point, the slow decrease in phase speed results in velocities exceeding the phase speed in the vicinity of the crest only and spilling breakers result. On steep slopes with surging-collapsing waves the vertical gradient in velocity components is smaller. Since the phase speed decreases abruptly velocities tend to exceed the phase speed through much of z almost simultaneously, as illustrated in Figure 6d.

If kinematic stability is significantly effected by phase shifting then the latter will be important in the determination of breaker type. Figure 8 shows for the different field results the distribution of horizontal velocities below the crest expressed as a percentage of horizontal velocity component maxima (u_{zmax}). These profiles are to be expected if the velocity at any point below the crest can be assumed to be a cosine function of u_{zmax} and θ_z .

For surging breakers it is apparent that the near quadrature phase at the break point results in very low horizontal velocities below the wave crest. This produces a stabilizing tendency such that horizontal velocities do not come to exceed the phase speed until the latter is very small. This stability is commonly recognized for surging waves as being the non-breaking, totally reflected case

(e.g., $\xi_i \leq 2$ of Miche; see Guza and Bowen, 1976). Clearly however, since phase shifting can evidently occur by degrees this stability must also vary accordingly.

For the larger (relatively steeper) surging-collapsing waves in Figure 8, reduction of velocities below the crest due to phase shifting is not so great. However, the vertical gradient in velocities resulting from phase shifting is much smaller than in the more dissipative breaker types towards the plunging and spilling end of the continuum. In terms of the kinematic stability of these waves therefore, this phase shift produces no additional steepening of the velocity gradient below the crest.

For the more dissipative plunging and spilling waves in Figure 8 it is clear that vertical differences in phase shifting produce a considerable augmenting of the velocity gradient. This combined with lower gradients in phase speed should tend to confine initial breaking to the crest region.

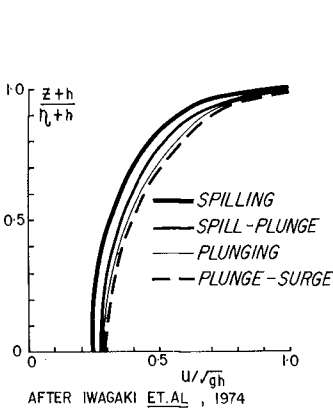


FIGURE 7. Horizontal velocities below crests of different breaker types

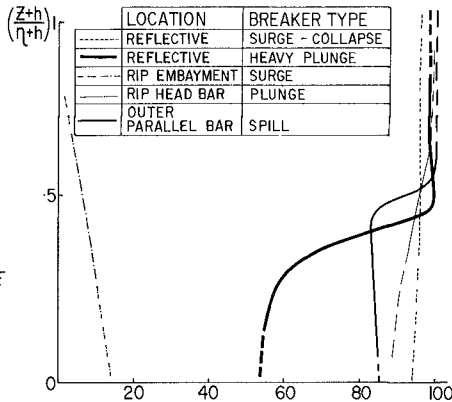


FIGURE 8. Velocity below crest as percentage of U_{max}

CONCLUSIONS

Phase of velocities lag behind the surface elevation under most conditions of waves near breaking. It appears that a certain amount of this phase shift is inherent in the shoaling process. However partial wave reflection must also produce some phase shifting. The contribution of each process to phase shifting has not been determined. It is obvious however that the greatest potential for phase shifting lies on reflective beaches where anything up to near phase quadrature may be obtained. It is also apparent that the vertical distribution of phase is more homogeneous on reflective beaches. On dissipative beaches substantial phase shifting appears to be restricted to depths midway beneath the crest.

Phase shifting must therefore be an important determinant of the kinematics of waves near breaking. It therefore must also be important in determining the breaker type. Large, vertically uniform distribution of phase shifting causes low velocities beneath the wave crest inducing stability with resulting surging waves. Smaller phase shifts uniformly distributed below the wave crest tend to develop with collapsing waves on steep slopes. Where phase shifting increases markedly toward the bed velocities beneath the crest are reduced in that direction. The vertical velocity profile is thus significantly steepened. Breaking then tends to be confined to the crest region of the wave. This is consistent with the development of spilling waves where beach slope is low. It may also help explain the well known development of plunging waves where slope is steep.

Wave-current and wave-wave interactions occur extensively on complex natural topographies. It is likely that these also have significant effects on breaker kinematics both directly and indirectly through the influence on phase shifting. However, these effects are not yet obvious particularly with respect to phase shifting. Nevertheless it will be necessary to account for kinematic effects of phase shifting when considering breaker type response to surf-zone morphodynamics. Similarly, theoretical development of near breaking waves in shallow water will require inclusion of this factor.

ACKNOWLEDGEMENTS

This study has been supported by the Australian Research Grants Committee, Dept. of Science and Environment, Canberra and by the U.S. Office of Naval Research, Coastal Sciences Program, Task NR 388-157, Grant N 00014-80-G-0001. I am grateful for useful advice provided by P. Nielsen. Diagrams were drawn by J. Roberts and M. Rigney.

REFERENCES

- Adeyemo, M.D., 1970, Velocity fields in the wave breaker zone, Proc. 12th Int. Conf. Coastal Eng., pp 435-460.
- Battjes, J.A., 1974, Surf similarity, Proc. 14th Int. Conf. Coastal Eng., pp 466-488.
- Bradshaw, M.P., Chappell, J., Hales, R.S. and Wright, L.D., 1978, Field observations and analysis of beach and inshore hydrodynamics, Proc. 4th Aust. Coastal and Ocean Eng. Conf., pp 171-175.
- Galvin, C.J., 1980, Breaker type classification on three laboratory beaches, J. Geophys. Res., Vol. 73, pp 365-369.
- Guza, R.T. and Bowen, A.J., 1975, The resonant instabilities of long waves obliquely incident on a beach, J. Geophys. Res., Vol. 88 (33), pp 4529-4534.
- Guza, R.T. and Bowen A.J., 1976, Resonant interactions of waves breaking on a beach, Proc. 15th Conf. Coastal Eng., pp560-579.
- Guza, R.T. and Thornton, E.B., 1980, Local and shoaled comparisons of sea surface elevations, pressures, and velocities, J. Geophys. Res., Vol. 85 (C3), pp 1524-1430.
- Iwagaki, Y., Sakai, T., Tsukioka, K. and Sawai, N., 1974, Relationship between vertical distribution of water particle velocity and type of breakers on beaches, Coastal Eng. in Japan, Vol. 17, pp 51-58.
- Jonsson, I.G., 1978, A new approach to oscillatory, rough turbulent boundary layers, Series Paper 17, ISVA, Tech. Univ. Denmark.
- Peregrine, D.H. and Cokelet, E., in press, The fluid mechanics of a breaking wave, Proc. 17th Int. Conf.

Coastal Eng.

- Short, A.D., 1978, Wave power and beach stages: A global model, Proc. 16th Int. Conf. Coastal Eng., pp 1145-1162.
- Stoker, J.J., 1957, Water waves, Interscience Pub. Inc.
- Thornton, E.B., Galvin, J.J., Bub, F.L. and Richardson, D.P., 1976, Kinematics of breaking waves, Proc. 15th Int. Conf. Coastal Eng., pp 461-476.
- Thornton, E.B., 1979, Energetics of breaking waves in the surf zone, J. Geophys. Res., Vol. 84 (C8), pp 4931-4938.
- Wright, L.D., Chappell, J., Thom, B.G., Bradshaw, M.P. and Cowell, P., 1979, Morphodynamics of reflective and dissipative beach and inshore systems: South Eastern Australia, Marine Geol., Vol. 32, pp 105-140.

BEACH RESPONSE TO VARIATIONS IN BREAKER HEIGHT

A.D.Short

Coastal Studies Unit, Dept of Geography
University of Sydney
Sydney, N.S.W. 2006. Australia

ABSTRACT

The breaker wave height required to produce a particular beach-surfzone morphology is examined for micro-tidal, medium to fine sand beaches. Waves $>2.5\text{m}$ produce dissipative beach systems with wide surfzones and shore parallel bar/s and channel/s. Breakers between 1 and 2.5m result in rip circulation and associated rhythmic morphology (crescentic bars, rip channels, megacusps, etc). Low waves ($<1\text{m}$) form steep, barless reflective beaches with characteristic cusps/berm. To gauge the stability/mobility of each of these beach types the range of beach profile changes associated with each is presented, for both the time and space domain. Modally dissipative beaches where breakers consistently exceed 2.5m undergo minor changes in profile and are consequently stable both temporally and spatially. Modally rhythmic beaches have a variable moderate energy wave climate are highly unstable both over time and alongshore. Modally reflective beaches with their low waves are relatively stable. Beaches which experience a highly variable wave climate over time exhibit all three types and are consequently highly unstable. The environmental parameters useful for quantifying these beach types and associated profile changes, and the implications of these results are discussed.

INTRODUCTION

Two dimensional beach response to eroding and accreting wave conditions has been well documented both in the laboratory and in the field. High storm waves or steep waves lead to a lowering of the beach profile resulting in beach cut and seaward transport of beach materials into the surfzone and nearshore. Low swell or long waves result in a steepening of the profile by onshore sediment movement and beach fill. Between these two extremes, systematic mesoscale patterns of beach-surfzone response have been

observed. The nature of the beach morphology and associated surfzone dynamics (i.e. beach morphodynamics) under a range of wave conditions is described by Short 1979 a and b, and Wright, et al., 1979. In particular Short 1979a associates sequences of beach response with rising and falling wave conditions.

In this paper the absolute level of breaker wave height required to achieve a given level or type of beach morphological response is examined. Short's 1979a ten beach-stage classification is used to quantify beach response within three broad categories of beach type: low wave energy - reflective beaches, moderate energy - rhythmic beaches, and high energy - dissipative beaches. This paper is therefore concerned with the actual breaker height required to produce a given level of beach surfzone morphodynamic response; and the characteristic temporal and spatial changes in beach profile and on-offshore sediment transport that are associated with the three beach types. The temporal changes are associated with variations in breaker wave height over time and the resultant movements in on-offshore sand transport and consequent changes in beach profile. For a particular wave-beach environment the most frequently occurring or characteristic beach profile or morphologic configuration is called the modal beach type. The degree of departure from the modal type is dependent on the variation in the breaker wave climate. Spatial changes are concerned with alongshore variation in beach profile at any point in time. The variability within both temporal and spatial suites of beach profiles is used to quantify beach stability/mobility.

DATA BASE

The correlation between breaker height and beach stage is based on 1174 daily observations of both parameters at Narrabeen Beach, N.S.W., a medium to fine sand (mean grain diameter 0.3 to 0.4 mm), single barred beach in a moderate to high energy wave environment (east coast swell, Davies 1980). Modal wave period in the study area ranges from 10 to 12 seconds. The procedure for recording the observations is discussed by Short 1978b. The daily observations are supplemented by field investigations of beaches composed of very fine to coarse sand in wave environments ranging from low to very high energy (west coast swell) around the 6,000 km of the south and east coasts of Australia (Short, 1978) (see Fig.1) and elsewhere (Short, 1979a).

The main field sites are in microtidal environments and in coastal segments where littoral drift is negligible. The prime concern of this paper is the effect of breaker

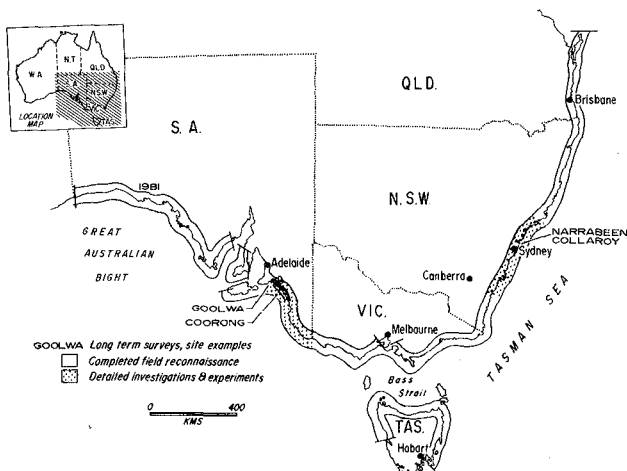


Figure 1: The southeast of Australia showing the main field sites discussed and area of field investigations.

height in influencing on-offshore sediment transport and morphologies in the absence of littoral drift and large tides.

BREAKER WAVE HEIGHT AND BEACH STAGE

The relationship between breaker height and beach response is presented in Figure 2a and 2b. In each figure the probability of occurrence of each beach-stage is plotted for the given level of breaker height (in 0.5m intervals) during falling (Fig. 2a) and rising (Fig. 2b) wave conditions. Falling wave height is associated with onshore sand transport, beach accretion and movement from the dissipative beach-stage 6 through the rhythmic stages 5, 4 and 3 to the reflective stages 2 and 1. Rising wave height on the other hand is associated with offshore sand transport and movement through the erosional beach cycle from the reflective beach stages 1 and 2 through the channel forming and rip dominating stages 3', 4' to the dissipative stages 5' and 6.

Falling Wave Height

Figure 2a illustrates the beach-stage distribution associated with discrete levels of falling wave height

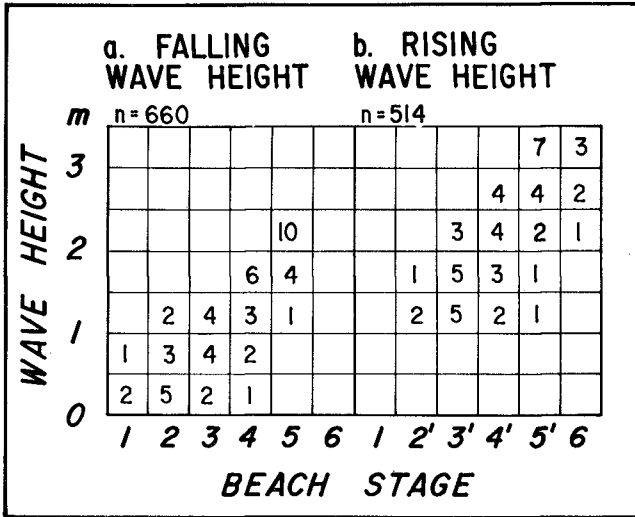


Figure 2: Plot of the probability of occurrence (out of 10) of each beach-stage for a given level of breaker wave height, under falling wave and rising waves.

under falling wave conditions. In an idealised situation as waves decrease from >3.5 m (beach-stage 6) they must drop to 2-2.5m before onshore sand movement combined with low frequency edge waves (Wright et al, 1979) produce the crescentic bars of stage 5. The crescentic bars dominate until waves fall to 1-1.5m. At this level stage 4 dominates with well developed crescentic bars and adjacent shoreline megacusps. The 1-1.5m waves encourage channel infilling and movement to stage 3 which at 0.5-1m completes infilling resulting in bar welding to the beach face. Subaerial deposition of beach cusps on a reflective beach face (beach-stage 2) dominates the lowest wave height (0-0.5m) eventually leading to a formation of a highly reflective beach berm (beach-stage 1).

Rising Wave Height

Figure 2b plots the beach-stage distribution for levels of rising wave height (0-0.5 to >3.5m). Beach erosion begins when breakers exceed 1m with waves 1-1.5m high leading rapidly through beach-stage 2' to 3' (incipient channel formation across the newly formed bar). The channel excavation continues as waves rise to 1.5-2m. Only

when waves reach 2-2.5m do the individual incipient rip channels begin to coalesce alongshore forming beach-stage 4' (continuous channel). Higher waves (2.5-3m and 3-3.5m) and substantially higher wave energy is required to excavate the continuous longshore channel that feeds the rips of beach-stage 5'. Very high waves >3.5m and extreme energy conditions are required to produce the fully dissipative beach-stage 6 with its shore normal low frequency return flow and parallel bar-channel morphology. At Narrabeen Beach the observations of this stage are insufficient to provide a reliable distribution against wave height. However observations on higher energy beaches elsewhere in southeast Australia indicate that waves 3.5 to 4m are required to achieve this most dissipative stage.

The above results are concerned solely with the beach response to levels of breaker height. The spread of the distribution either side of the modal beach response represents a parameter not considered in this summary, that is, the inherent lag in beach morphology as it responds to the more rapid changes in wave height. Whereas substantial changes in wave height may occur on the order of 1 to 10 hours, beach morphology has a lag on the order of 10 to 100 hours. The modal beach stages of Figures 2a and 2b represent the beach stage reached when waves have operated at a particular height for a time period sufficient for the beach morphology to fully respond to the ambient conditions.

The results are further summarised in Figure 3a and which plots the location of the modal beach-stage for rising and falling wave conditions. It illustrates the levels of breaker height required to generate movement to various stages in the erosional (rising) or accretional (falling) wave-beach cycles. Figure 3b illustrates all possible linkages through and between the beach-stage cycle. By comparing figure 3a and 3b a fuller understanding of natural beach response can be extracted. A movement to any beach-stage must be in the direction of the arrows in figure 3b. Therefore, for example, to achieve stage 4, stages 4' or 5 must first be reached. In figure 3a if conditions oscillated between 0-1.5m the corresponding beach stages would be 2' and 3' on the erosional phase and 2, 3 and 1 on accretion, stage 4 could not be produced, because the prerequisite stage 4' or 5 require waves greater than 2m.

Modal Breaker Height and Beach Type

The Narrabeen field site experiences the entire spectrum of beach response from reflective to dissipative beach-stages. This is a consequence of the range in breaker height at the coast and the medium to fine beach

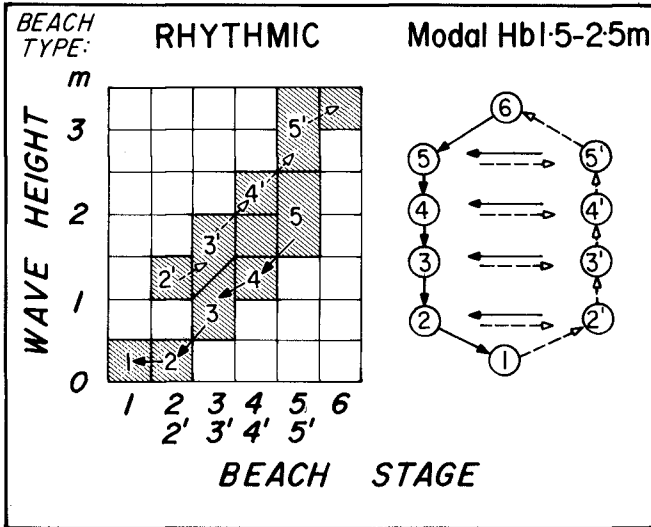


Figure 3: Location of the modal beach-stage (shaded) for levels of breaker wave height under rising and falling wave conditions. On right are the linkages between the ten beach-stages. Solid lines indicate falling wave height and movement to accretionary stages, dashed lines rising wave height and movement to erosional stages. Movement between and amongst the stages can only be in the direction of the arrows.

sand. However, over shorter time periods and in many locations wave height does not vary so considerably and as a consequence the beach oscillates around a modal type. Basically three modes of wave-beach interaction have been described in the literature - reflective, rhythmic and dissipative. Table 1 lists their origin and characteristics. The breaker height required to generate a modal reflective, rhythmic or dissipative beach (on medium to fine sand beaches) can readily be determined from Figure 2b.

Reflective beaches are associated with waves less than 1m in height. They are characterised by beach-stages 1 (berm) and 2 (cusps), with a relatively steep beach face, waves breaking on a coarse grained low tide step and barless surfzone (though 'relic' outer bars may exist further offshore).

Table 1 - MODES OF WAVE - BEACH INTERACTION

Wave Energy (Breaker Height)	Surf Zone Dynamics	Beach-Surfzone Morphology	Reference - terminology
High (>2.5m)	Dissipative	Shore parallel bars, channels mega-rips predominantly shore normal circulation	Sasaki - Ingravity (>2.5m) Short - Beach-stages 6, 5 Wright, et al - Beach Type 1, 2
Moderate (1-2.5m)	Rhythmic	Rips crescentic bars megacusps, etc. rip circulation	Sasaki - Instability Short - Beach-stages 5, 4, 4', 3, 3' Wright, et al. - Beach type 3, 4, 5
Low (<1m)	Reflective	Barless steep beach- face cusps, berm, wave reflection	Sasaki - Edge Wave Short - Beach-stages 2, 2', 1 Wright et al. - Beach type 6

1. Guza and Inman's (1975) terms, dissipative and reflective are used to describe the high and low energy surf dynamics, while Homa-ma and Sonu (1962) term rhythmic is attached to the intermediate moderate energy beaches.

Rhythmic beaches require breakers 1 to 2.5m high to maintain their classic rip circulation. Crescentic/transverse bars, rip feeder and rip channels, and megacusps produce the characteristic 'rhythmic' longshore variation in beach and surfzone morphologies.

Dissipative beaches occur when waves exceed 2.5m resulting in the formation of shore parallel channel/s and bar/s and predominately shore normal circulation (beach-stage 6). Beach-stage 5 characterises the dissipative extreme in shorter embayed beaches where the constraints imposed by headlands, etc. encourage megarips to persist even during very high wave conditions.

Temporal Variation in Beach Morphology

The foregoing is concerned with beach response to the absolute level of breaker height. To illustrate how natural beaches respond to variations in breaker height through time, ten years of daily wave data and four years of daily beach response for the Sydney region are summarised in Figure 4. The annual wave climate varies systematically through the year from periods of high to moderate to low waves with the beaches responding accordingly moving between dissipative, rhythmic and reflective beach types.

In a typical year beginning in December northeast seabreeze waves of moderate height (1-1.5m) cause minor beach scarping and erosion and a series of rips. During February and March, seabreezes persist but their effect is often overshadowed by the arrival of moderate to high 2-3m northeast and east swell generated by tropical cyclones. These waves cause moderate beach erosion, and the development of fewer but larger and more intense rip systems. If high waves persist, longshore channels and offshore bars eventually form. April and early May is a low energy transition period of beach accretion. May and particularly June and July are dominated by cycles of moderate to high (2-3m) southeast swell and storm waves resulting in moderate erosion. The beaches in this period are dissipative with major rip systems (spacing 500m) and in exposed portions longshore bars and channels. This period of erosion is followed by gradually decreasing southeast swell. The low waves (0.5-1.5m) produce onshore sediment transport and beach accretion at times moving the bar onto the beach as a series of cusps or a berm. By November the beaches are often in their most accreted and reflective form.

A further method of illustrating the range of Sydney

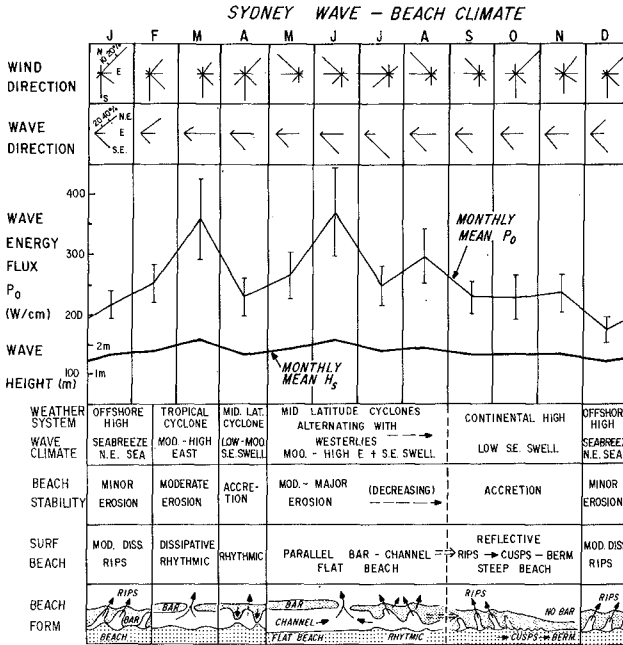


Figure 4: The annual Sydney wave climate and beach form. The wave height and energy is based on a nine years (1971-79) monthly mean of daily wave conditions (M.S.B. data). The straddling line and bars equal \pm one standard deviation. The beach response through the year is reflected in the beach stability, surfzone type and beach form. The plan view of beach form illustrates the beach response typical open beach responding fully to the above conditions (from Short and Wright, in press).

beach types is the beach-stage curve (Short, 1979a) shown in Fig. 5. This plots the percent frequency of occurrence of the accretion and erosion beach-stages, along with the annual (combined) beach-stage curve. The curve identifies the modal rhythmic beach type for the Sydney coast. This is to be expected given Sydney's modal wave characteristics ($H = 1.5-2m$, $T = 10$ sec). Short 1979a presents hypothetical beach-stage curves for other higher and lower energy wave-beach systems.

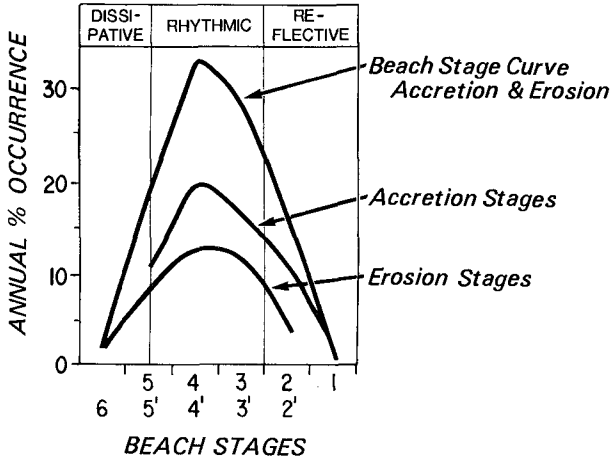


Figure 5: Beach-stage curves for Narrabeen beach plotting the percent frequency of occurrence of accretionary, erosional and combined beach-stages. Based on 950 daily observations.

MODAL BEACH TYPES AND MORPHOLOGIES

Whereas the typical Sydney beach presented in Figures 4 and 5 can experience the entire spectrum of beach types, many beaches tend to remain at the dissipative or reflective extreme or oscillate within the rhythmic range. To examine how such beach morphologies vary over time in reference to modally high, low, or moderate waves three sets of field observations are presented for persistently dissipative, rhythmic and reflective beaches (see Figure 6).

To enable comparisons the data is presented both graphically as two-dimensional beach profiles or cross sections, and numerically using mean beach width (x_b), its standard deviation (σ_x) and coefficient of variation (σ_x/x_b). The standard deviation is a useful indicator of beach mobility and is in fact called the beach mobility index by Dolan et al., (1978). Further, the coefficient of variation is an indicator of backshore mobility and is here termed the backshore mobility index.

The nature of a beach's cross-sectional or profile variation is basically a function of the amount and form of sediment transfer within and between the subaerial beach, surfzone and nearshore. Where wave height is persistently

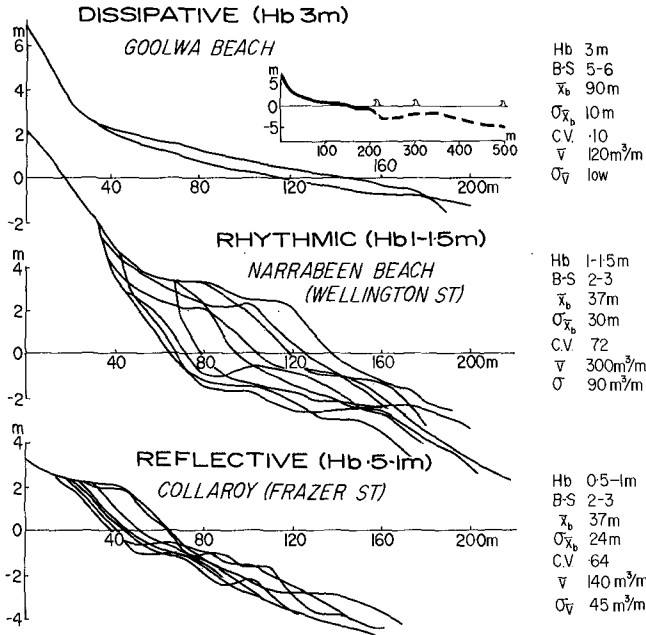


Figure 6: Variation in beach profile and morphometric parameters for a dissipative, rhythmic and reflective beach. Note the relative stability of the dissipative and reflective beach compared to the rhythmic beach. Narrabeen and Collaroy profiles selected from 3 years of monthly beach profiles. Goolwa profiles one year apart.

high (>2.5m) most sediment is carried seaward and stored in the surfzone and nearshore. Because of the time lag in moving sediment onshore from the outer bars bar/s and nearshore the beach face rarely accretes or experiences substantial changes in profile (Fig. 6). The beach is wide with a low gradient. Beach and backshore mobility is low because of the low sediment exchange. While a dissipative beach face represent an 'eroded' beach profile with minimum sand stored on the subaerial beach they are relatively stable features experiencing minor changes in beach profile. Erosion associated with dissipative beaches does not normally result from beach face retreat, rather low frequency wave set up tends to overrun the beach and attack

the backshore directly, (as described by Wright, this vol.).

Rhythmic beaches exposed to waves of moderate height (1-2.5m) have the greatest potential for changes in beach form as a consequence of the variable wave climate and storage of sediment in the highly energetic surfzone. As wave height rises and falls, sediment is transported between the three storage zones. Beach volume is large as is the standard deviation reflecting the active sediment exchange between the beach, surfzone and nearshore (Fig. 6). Over time rhythmic beach form can shift from a flat eroded beach face, deep channel and offshore bar, through all the onshore bar migratory forms to a reflective beach. Beach and backshore mobility are both high, indicating a high potential for beach and backbeach erosion through sand removal particularly in rip embayments (see Short, 1979b and Wright, this vol.).

Low wave (< 1m) reflective beaches have low mobility and are relatively stable. Sediment exchange on reflective beaches (Fig. 6) is between the steep cusped or bermed subaerial beach through a pivot point (~1m depth) to the attached low tide terrace. Because of their proximity the exchange is rapid. Reflective beaches are most susceptible to erosion (see Short 1979b and Wright, this vol.), however erosion is usually followed by rapid beach accretion. As Collaroy beach (Fig. 6) lies at the more energetic end of the reflective beach type ($H = .5-1m$) lower energy beaches will show even less mobility.

Figure 7 illustrates the range of temporal changes in beach profile for dissipative, rhythmic and reflective beaches in southeast Australia. The variation in profile elevation within the beach surfzone and nearshore has further implications for identifying areas of sediment storage and exchange. Table 2 indicates the relative importance of the beach, surfzone and nearshore as zones of active sediment storage.

Dissipative beaches represent an 'eroded' beach profile, and as such the 'eroded' material is stored in and particularly seaward of the surfzone. On the southeast Australian coast the active nearshore zone extends out to depths of at least 20m. Because of the depth and location of the potentially active sediment long periods (several weeks to months) of lower waves are required to move the sediment shoreward. On modally dissipative beaches such as Goolwa this rarely, if ever, occurs however in seasonally dissipative-reflective beaches as in Southern California this exchange is well documented (Aubrey, 1979). On N.S.W. dissipative beaches the inner bar occasionally attaches to the shore in late winter. The outer bar while moving

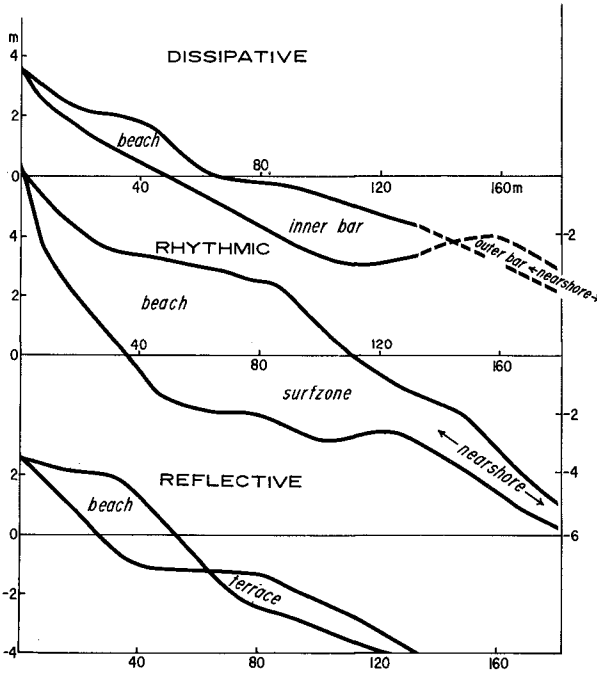


Figure 7: The active sweep zone for a dissipative, rhythmic and reflective beach based on 3 years of monthly beach profiles. Upper from Fens embayment, N.S.W. (data from P. Hesp), lower Narrabeen and Collaroy beaches.

Table 2

ZONES OF SEDIMENT STORAGE (%)

	SUBAERIAL	SURFZONE	NEARSHORE
REFLECTIVE	70	30	—
RHYTHMIC	40	40	20
DISSIPATIVE	10	20	70

inshore has not been observed attaching to the shore.

Rhythmic beaches can potentially store sand throughout the system, particularly in the beach and surfzone, and following high wave events in the nearshore. Sand stored in the energetic surfzone and perched on the subaerial beach can rapidly be moved between the two as wave conditions vary.

Reflective beaches store sand almost exclusively on the steep beach or following erosion in the low tide terrace. Exchange is rapid being accomplished in a matter of hours during erosion and a few days to weeks during accretion.

SPATIAL (ALONGSHORE) VARIATIONS IN BEACH TYPE MORPHOLOGIES

In addition to characteristic changes in beach profile through time, each beach type has a characteristic variation in beach profiles alongshore, at any point in time. Three examples from the same beaches are illustrated in figure 8.

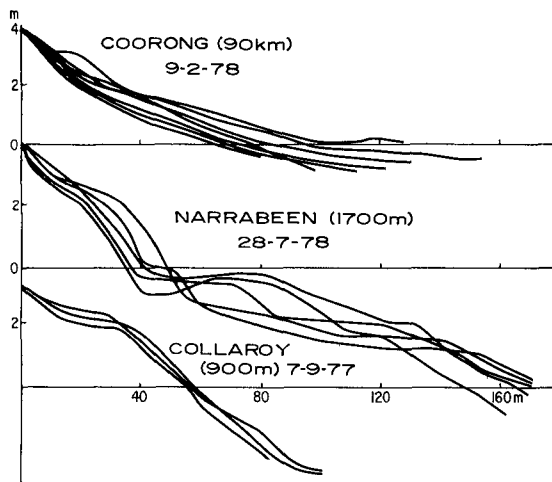


Figure 8: Alongshore changes in beach profiles on a dissipative, rhythmic and reflective beach.

Dissipative beaches are characteristically uniform alongshore having a wide low gradient beach face, fronted by a wide deep channel/s and shore parallel offshore bar/s. Figure 8a shows seven beach face profiles surveyed on the one day at 15 km intervals along 90km of the highly dissipative Coorong beach. All profiles have a concave subaerial beachface morphology. Each is low gradient with slight variations in gradient resulting from minor changes in grain size. Figure 9a illustrates that the shore parallel channels and bars of the surfzone possess the same conformity alongshore. Therefore dissipative beaches exhibit extreme stability and uniformity alongshore.

Rhythmic beaches with their alternating bars and rip channels, megacusps, etc are as unstable spatially as they are temporally. Figures 8b and 9b illustrate this fact. The Narrabeen profiles show the alongshore variation from rip channels, to well developed bars and channels to a welded bar.

Reflective beaches are uniform alongshore except on a microscale when cusps are present. In plan form the continuous cusps or berm and barless surfzone results in the regular beach profiles illustrated in Figure 8c, and plan form as show in Figure 9c.

DISCUSSION

Given the seemingly endless variety of beaches around the globe and their ever-changing response to wave conditions it is essential that a logical genetic classification of natural beaches be developed, one that not only permits identification of beach type, but also contains a characteristic set of morphological response and dynamic interactions associated with each beach type.

The results presented here are an attempt to classify beaches into three basic types based on response to the level of breaker wave height for microtidal, medium to fine sand beaches. The characteristics associated with each beach type are tabulated for breaker wave height (Figure 3), two dimensional beach profile response over time (Figures 6 and 7), zones of sediment storage (Table 2), two dimensional alongshore variation in beach profile (Figure 8) and other morphometric parameters (Figure 6). More detailed discussion of beach-surfzone morphodynamics and modes of beach erosion are contained in Short 1979a and b, Short and Hesp (in press), Wright et al. 1979 and Wright (this vol.).

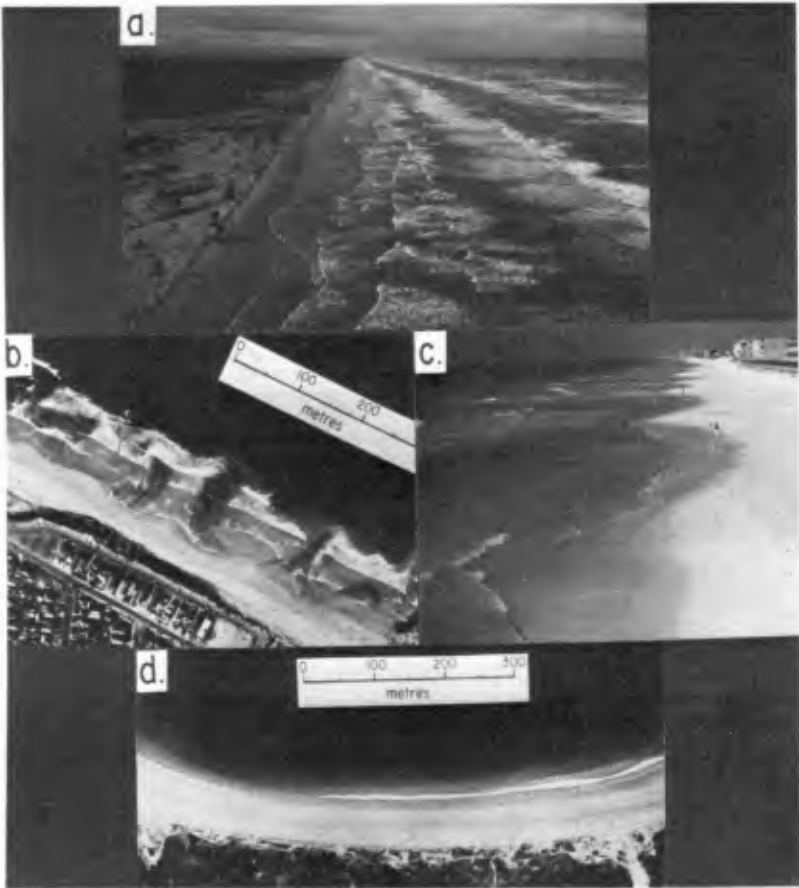


Figure 9: Examples of dissipative, rhythmic and reflective beaches. a. Aracaju, Sergipe (Brazil) note the longshore equilibrium in beach-surfzone form. b. Rhythmic beach-stage 3 at Cronulla Beach, N.S.W.; c. Rhythmic beach-stage 4+3 at Panama City Beach, Florida. d. Reflective beach at North Cronulla, N.S.W.

ENVIRONMENTAL PARAMETERS

In order to explain beach type and beach morphological characteristics, this study has indicated that certain morphometric variables are particularly useful

Breaker wave height, together with period, determine the amount of wave energy available to do work across the nearshore and in the surf-swash zone. As shown in Figure 3 breaker wave height can be used as a simple rule to determine modal beach type, particularly when wave period is relatively constant.

Beach sand size, is equally important in controlling beach response. The foregoing results are based on observations on medium to fine sand beaches (mean diameter 0.2-0.4 mm). However as Short 1979b indicated that coarser sand-gravel beaches will result in more reflective beach types, even in moderate to high wave energy, and fine to very fine sand will lead to a wide shallow surfzone, more dissipative conditions and multiple bars even under moderate to low waves. The foregoing results refer only to high energy dissipative beaches.

The surf scaling parameter is a function of wave characteristics and beach slope and is also a useful measure of the degree of beach reflectivity or dissipativeness (see Wright et al. 1979).

The mean beach width is the basic measure for describing the beach profile and shoreline position. However in terms of application the standard deviation of mean beach width, called the beach mobility index, is an excellent index of the mobility or stability of a shoreline position. The backshore mobility index, is the coefficient of variation of mean beach width, and again is a very useful indicator of likelihood of backshore/foredune erosion.

Finally the mean beach volume and its standard deviation, here called the volume exchange are important indices of sediment location and transport within and across the beach-surfzone-nearshore (see Table 2).

IMPLICATIONS

The foregoing results are based on selected field sites in southeastern Australia. The frequency and duration of the observations have produced some findings that may have implications for beach investigations elsewhere.

1. The modal breaker wave climate (interacting with the local sediment type) will determine the modal beach type.

In medium to fine sand beaches modal waves less than 1m produce reflective beaches, between 1 and 2.5m rhythmic beaches, and greater than 2.5m dissipative beaches. Associated with each beach type is a characteristic beach-surfzone morphology and dynamics, modes of beach erosion (see Wright, this vol.) and zones of sediment storage.

2. In undertaking beach investigations the classification presented here provides a format for locating a particular beach type and planning survey and dynamic investigations based on the characteristics mentioned in (1) above. A program of study on a reflective beach will of necessity, be markedly different from one on a rhythmic or dissipative beach.

3. Beach nourishment programs are concerned primarily with nourishing the subaerial beach. However as Table 2 and Figures 6 and 7 indicate in all beach types a certain amount of this sand must be redistributed seaward. On dissipative beaches most sand placed on the subaerial beach can be expected to be redistributed seaward of the breakpoint. Understanding the beach type is important not only for determining how much sand might be required to nourish the system, but also when and where and at what beach stage would be most suitable to undertake the nourishment.

4. In extrapolating results of beach investigations to other beaches and other coasts it is imperative that the beach type (and grain size) be considered. Findings on a coarse grained reflective beach may have little bearing on a fine grained dissipative beach. Beaches have a predictable range of morphodynamic variation, the spatial and temporal beach variability should be understood before between beach comparisons are made.

5. Beach erosion is of concern to all who investigate, work with and use the beach system. Wright (this vol.) discusses the three separate modes of erosion associated with reflective, rhythmic and dissipative beaches. The results presented here and elsewhere (Short 1979b, Short and Hesp, in press) support Wright's classification. Each mode of erosion possesses different morphological and dynamic characteristics, in turn leading to varying degrees of beach and backshore mobility. Therefore the contribution of each mode must be considered separately where designing a beach erosion program for a particular section of beach or beach type.

6. As stated in the Introduction the field sites investigated in this study experience negligible littoral drift. However in many area littoral drift is a major component of the beach system. Observations on the

northern New South Wales coast where littoral drift is significant show that the beach types and on-offshore characteristics still hold. However downdrift skewing of the mesoscale forms (bars, channels, rips, etc) does occur, as does significant net longshore sediment transport. Therefore in system experiencing littoral drift, the contribution of the mesoscale forms of on-offshore sediment exchange associated with dissipative, rhythmic and reflective beach types must be considered if accurate calculations of total transport are to be made.

ACKNOWLEDGEMENTS

The field investigations reported have been funded by the Australian Research Grants Committee. Since late 1979 additional support has been provided by the U.S. Office of Naval Research, Coastal Science Programs, Task NR 388-157, Grant N-0014-80-G-001. During 1979 support in South Australia was provided by the Coast Protection Board. I thank the numerous people who have assisted with the field surveying. In terms of sorting out some of the ideas and results presented here I also thank L.D.Wright, P.A. Hesp for many useful discussions. J.Roberts and M.Rigney prepared the diagrams.

REFERENCES

- Aubrey, D.G., 1979, Seasonal patterns of onshore/offshore sediment movement. *J.Geophys.Res.*, v. 84, p.6347-6354.
- Davies, J.L., 1980, *Geographical Variation in Coastal Development* (2 ed), Longman, London, 212 pp.
- Dolan, R. and Hayden, B., and Haywood, J., 1978, A new photogrammetric method for determining shoreline erosion. *Coastal Engr.*, v.2, p.21-39.
- Guza, R.T. and Inman, D.L., 1975, Edge waves and beach cusps. *J. Geophys. Res.*, v. 80, p. 2997-3012.
- Hom-ma, M. and Sonu, C.J., 1962, Rhythmic pattern of longshore bars related with sediment characteristics. *Proc. 8th Conf. Coastal Engr., Council on Wave Research*, p. 248-278.
- Sasaki, T., 1975, Simulation of shoreline and nearshore currents. *Proc. Conf. Civil Eng. in Oceans/III*, Newark, Delaware, p.179-196.
- * Short, A.D, 1978, Characteristic beach morphodynamics on the southeast Australian coast. *4th Australian Conf.*

- Coastal Ocean Engineering, Adelaide, The Inst. Engineers, Australia, pp. 148-152.
- Short, A.D., 1979a, Wave power and beach stages: A global model. Proc. 16th Conf. Coastal Engineering, Hamburg, pp. 1145-1162.
- Short, A.D., 1979b, Three dimensional beach stage model. J.Geology, v.87, pp. 1145-1162.
- Short, A.D. and Hesp, P.A. (in press) Wave, beach and dune interactions in southeast Australia, and implications for global wind-wave environments.
- Short A.D. and Wright, L.D. (in press), Sydney's dynamic beaches, in Thom, B.G., (ed), Coastal Environments at Risk, Edward Arnold.
- Wright, L.D., (this volume), Modes of beach cut in relation to surfzone morphodynamics. 17th Int.Conf.Coastal Engr., Sydney.
- Wright, L.D., Chappel, J., Thom, B.G., Bradshaw, M.P., Cowell, P., 1979, Morphodynamics of reflective and dissipative beach and inshore systems: Southeast Australia. Marine Geology, v.32, pp.105-140.

THE DYNAMIC SWEEP PRISM

David M. Chapman,
Coastal Studies Unit,
University of Sydney, Australia.

A.W. (Sam) Smith,
Consulting Civil Engineer,
Gold Coast, Australia.

INTRODUCTION

In the course of an intensive study of beach and inshore morphodynamics associated with a nourishment project on the Lower Gold Coast, Australia (Chapman, 1978), approximately 400 profile lines were surveyed from backshore to the point of zero change in the nearshore zone, to a high degree of accuracy (Chapman & Smith, 1977). Analysis of this data base has led, inter alia, to the development of the concept of the dynamic swept prism, since the maximum and minimum ordinates on a shore-normal profile line, over a specified time period, form the vertices of an irregular polygon which may be regarded as the cross-section of the prism of sand which is worked over by waves during that time period. Representative prism cross-sections from the Lower Gold Coast are displayed in Figure 1. The important limits of the swept prism, viz., the landward and seaward extremities and the lower surface, are probabilistically, not deterministically defined. Prism cross sections as illustrated are not isotropic with respect to the probability of disturbance by waves. Isolines of probability may be conceptually defined, with the zone of maximum probability of disturbance corresponding to that zone which is re-worked during the tidal cycle (cf. Duncan, 1964). Moreover, although the

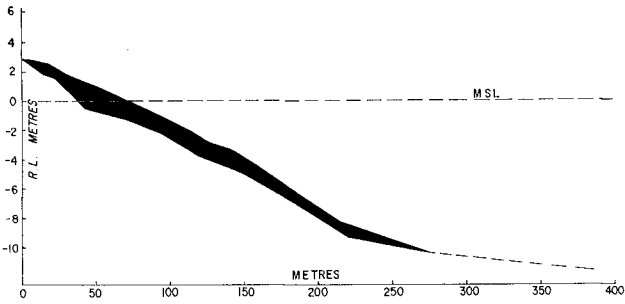
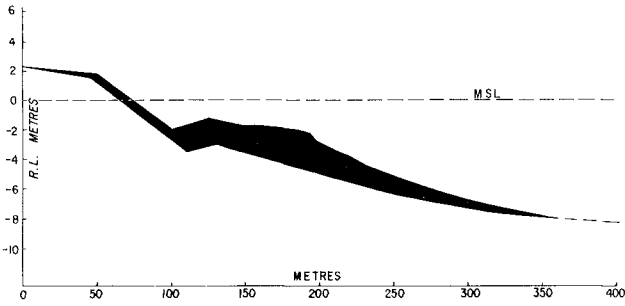
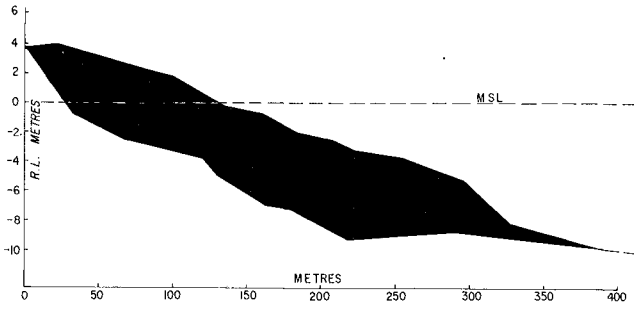


FIGURE 1. Representative Swept Prism Cross-Sections, Lower Gold Coast.

surveyed cross-sections illustrated are closed at the landward and seaward extremities, in probabilistic terms these extremities are undefined, being asymptotic at each end.

The swept prism, especially in its subaqueous zone, may also be recognized as the envelope enclosing the range of beach and inshore morphologies described by workers such as Short (1978) or Wright, et. al. (1979).

It is the purpose of this paper to discuss the behaviour of a swept prism as observed on the lower Gold Coast, and to comment on the implications of the concept for management and planning, since effective planning and design must be cognizant of the probabilistic nature of the prism limits with respect to structures which may be placed therein.

BEHAVIOUR OF THE SWEEPED PRISM, LOWER GOLD COAST

The lower Gold Coast is located in the southern end of a large zetaform embayment, extending from Point Danger to Stradbroke Island (a location map is provided in Chapman, 1980). Environmental characteristics include a relatively narrow and steep continental shelf, reaching 200 metres depth at 40km. offshore, and average deep water wave power of 10kw/m of wave crest. There is no seasonal pattern of cut and fill such as is reported from many North American sites.

Figure 2 illustrates the alongshore variation in the cross-sectional area of the swept prism during the Gold Coast study, when mean breaking wave power was approximately $6.4 \text{ kilowatts m}^{-1}$ over the 5km. of shoreline surveyed. Mean cross-sectional area was 312m^2 ; the large maximum value of 737m^2 at 1617 metres from the arbitrary origin was due to input of beach fill at that point. The mean value of 312m^2 , during normal wave energy conditions, is comparable with $420\text{m}^3/\text{m}$ of sand eroded from the subaerial beach and translated to the inshore zone by cyclone induced storm activity in 1967 (McGrath, 1968), and reveals that considerable re-working of the beach and inshore zone occurs, even under moderate energy conditions.

Examination of the swept prism cross-sections

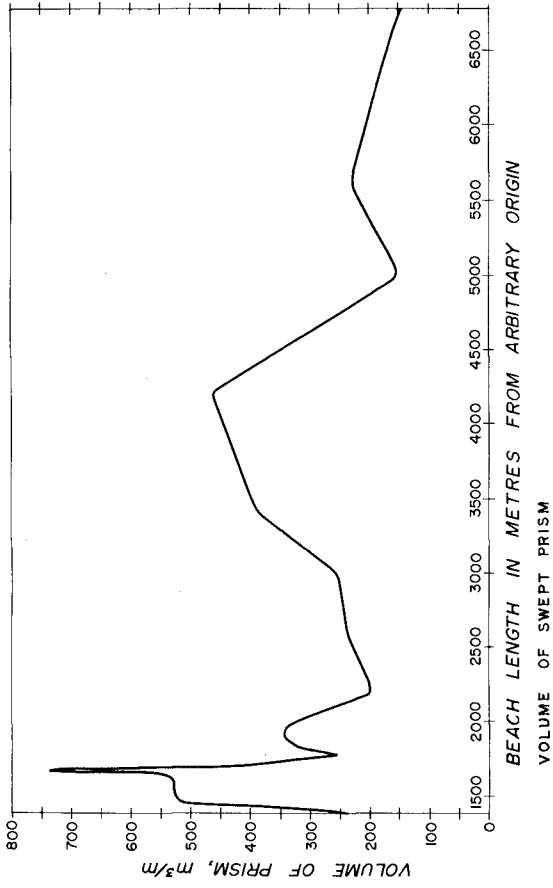


FIGURE 2. Alongshore Variation in Swept Prism Cross-Section Area, Lower Gold Coast.

illustrated in Fig. 1 reveals that the beach as defined by the recreational user (and indeed by most lay people) is merely the residuum of inshore processes. The prism cross sections also illustrate the fact that variability in the prism is principally accommodated within the subaqueous zone; most of this variability would not be apparent to the recreational beach user or resource manager who was merely concerned with evaluating the subaerial beach.

The large proportion of the swept prism in the subaqueous zone is significant in accounting for the re-distribution of beach fills, since re-distribution can involve substantial apparent losses from the subaerial beach without material being lost from the prism. If nourishment material applied is of such a nature that the upper surface of the prism is induced to adopt a lower overall gradient, a large volume of fill material would be absorbed in order for this redistribution to take place, but would result in little gain in beach width.

The lower boundary of the swept prism is a scour surface, activated by vigorous reworking of the prism. The scour surface as derived statistically from over 400 lower Gold Coast profiles is illustrated in Fig. 3 where the mean surface is illustrated together with its standard deviation bounds. Observations on the Gold Coast suggest that the scour surface under high energy storm conditions may be underlain by a fluidised sediment layer. Direct measurement during storm conditions is not possible with presently available techniques, but the existence of a fluidised layer is suggested by events such as the collapse of a boulder wall during high energy conditions and subsequent settlement of the armour to a depth of over 1 metre below the sand surface within a matter of minutes. Observation of the event in progress suggested that the boulders sank through a semi-quick layer rather than having the sand scoured from around them by the waves. The result of this event is illustrated in Fig. 4. We also found that measuring stakes embedded to a depth of 1m. below the sand surface in the inshore zone showed pronounced departures from the vertical after a week or

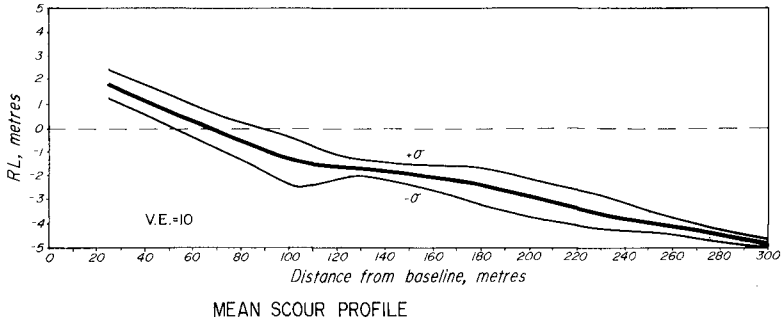


FIGURE 3. Mean Scour Surface, Lower Limit of Swept Prism, Lower Gold Coast.

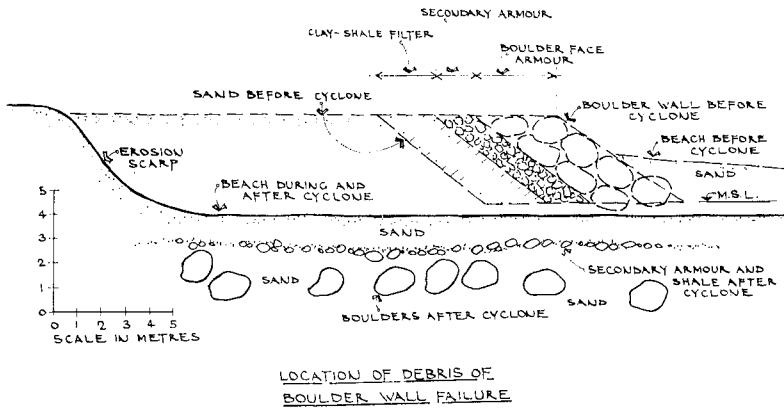


FIGURE 4. Location of Debris of Boulder Wall Failure.

two of moderate energy wave action.

The landward asymptote of the prism would normally include the frontal dune and foredune, as these are mobilized by the highest energy events. In the case of a beach in its natural state the landward extension of the prism under high energy conditions will encounter that part of the cross section which is capped by a dune so that the high energy event which causes the extension of the prism is also responsible for the release of a large volume of stored sand into the active zone.

The modes of cut and recovery are not complementary. During periods of cut (which may involve recession of the dune scarp) rapid removal of sand occurs from the subaerial part of the swept prism; however during periods of recovery the replacement of this sand occurs over a longer period and in addition involves the development of an incipient foredune. Initial stabilization of this foredune requires pioneer dune species which are sensitive to recreational pressure so that the stabilization of the replaced sand by woody vegetation may be extremely slow or non-existent on a recreational beach. In this way a mechanism for cut without replacement exists.

The cut of the subaerial beach, even under cyclone conditions, is normally quite localised with the incidence of the most severe cut along the Gold Coast being fairly random. Therefore, in the three dimensional sense the re-working of the swept prism is also a probabilistic phenomenon.

The seaward asymptote of the prism represents the seaward limit of sediment exchange between bed and beach. It corresponds in broad terms with the limiting depth of erosion as postulated by Hallermeier (1978), or the seaward limit of Swart's (1974) equilibrium profile. It does not correspond to surf base, the seaward limit of incipient sediment motion, which would be reached some considerable distance seaward of the prism limits.

IMPLICATIONS FOR MANAGEMENT

The probability of activation of the swept prism decreases landward, and will be inversely related to the magnitude of the wave power which is applied to it. The well known inverse relationship between magnitude and frequency of geomorphological phenomena (see, e.g., Chorley & Kennedy, 1971) applies. As shown in Fig. 5 a minor storm event is virtually certain to occur in any given year (i.e. probability ≈ 1). Events of moderate magnitude, which may cause significant activation of the subaerial beach but little or no damage to shore front property, fall within the "normal" range at about the point of inflexion of the curve, whilst the high magnitude event which causes damage to shore front property has very low probability of occurrence; e.g. the event of magnitude m has a probability of 5%, or a 1 in 20 year recurrence interval, with the curve becoming asymptotic to the vertical axis for events of very high magnitude. Thus it may be seen that damages incurred as a result of high energy wave events are related to magnitude such that the events of low or moderate magnitude cause no damage at all to man-made structures, with extremely high magnitude events required to cause significant damage. The probability of damage to shore-front property may therefore be expressed as shown in Fig. 6. There is a finite probability of $(100 - x)\%$ that no damage at all will be incurred in any given year and a moderately high probability that the damages incurred will be trivial. The probability of high damages is extremely low and asymptotic to the vertical axis for very large values.

It follows that in a situation where secular sea level rise is not a major causal factor in coastal erosion, losses to shore-front property due to landward extension of the swept prism have some probability less than 1 of occurring and may be related to shore-front property values as shown in Figure 7. Curve (7a) illustrates cumulative property value as a function of distance from the present high water mark. If shoreline retreat is progressive and inevitable this curve also relates losses and time since secular erosion will consume property according to some function relating

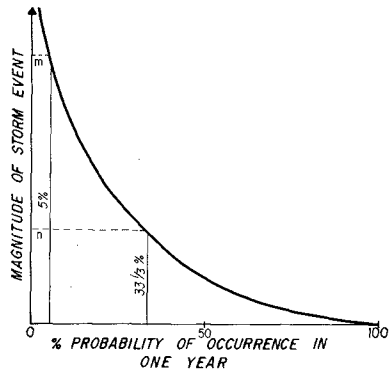


FIGURE 5. Magnitude Vs Frequency of Storm Events.

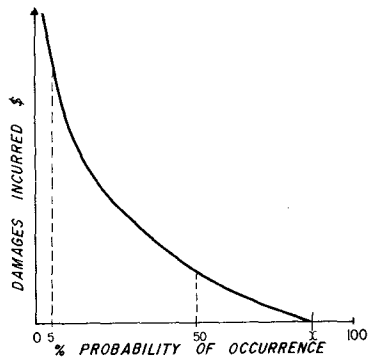


FIGURE 6. Probability of Damage, Storm Events.

distance from the present high water mark to time. However, in the absence of secular sea level rise as a major causal factor, the probability of loss becomes a function of the extension of the swept prism, and is therefore an asymptotic function of distance from the shore line as illustrated by curve (7b). On the one hand some loss of shore-front property is virtually certain to occur, since the maximum storm event has probably not been recorded*, but on the other hand there is some point inland from the present shore-line at which zero loss from coastal erosion is also a certainty.

A realistic appraisal of probable loss from coastal erosion then becomes a function of both cumulative property value and the probability of activation of the landward asymptote of the swept prism, i.e. one should multiply together the ordinates of curves (a) and (b) in order to arrive at the function of probable loss (curve 7c).

Under normal processes of planning and development, a coastal land value gradient decreasing inland from the shore-line applies. The implications of the foregoing analysis are that the appropriate land uses should be arranged so that capital intensive development is not placed in the zone where the probability-cumulative loss function is highest. In other words the application of capital to land would be controlled so that investment would be minimised at the point where probability of loss is highest and allowed to increase inland to some point where the probability of loss is low but shoreline amenity still obtains.

* A familiar concept in civil engineering practice which has been given legal recognition in doctrine derived from Rylands & Fletcher, e.g. in Ruck Vs Williams, 1868, Bramwell (B) stated "in truth it is not an extraordinary storm which happens once in a century or once in fifty or twenty years; on the contrary, it would be extraordinary if it did not happen."

Management of land use thus becomes part of a strategy of shoreline protection. A variety of shoreline protection options is available to the resource manager as displayed in Table 1. These have been subdivided into structural and nonstructural categories. The resource manager charged with the responsibility of planning for the protection of the shore-front community from coastal erosion must choose an appropriate strategy (which may involve one or a mix of management options) in order that the total benefit to the community is maximised.

The optimum management strategy will not necessarily provide maximum protection or minimise expenditure, but will be that point where the sum of losses incurred by the community and costs to the community of protective measures is minimised, as illustrated in Figure 8. The vertical axis is one of dollar values, either the value of losses incurred by the community or the costs of management strategies, whilst the horizontal axis plots either the degree of protection afforded by management strategies or the amount of physical damage incurred as a result of coastal erosion. The loss curve (AA') is (ideally) inversely related to the degree of protection afforded by the management strategy (curve BB'), although it will be observed that the loss curve (AA') does not reach the zero point on the vertical axis. At the point where losses are minimised the cost of protective strategies is likely to be exceedingly high, therefore the optimum point for management is neither that point where losses alone are minimised, or costs alone minimised, but the minimum point on the curve CC', which shows the sum, added vertically, of costs and losses. Expressed in the language of conventional land management economics, this would be the point where marginal benefit equals marginal cost.

CONCLUSION

The active zone of a beach may be conceptually defined as a prism of sand within which the probability of disturbance by waves varies greatly. Recognition of the three-dimensional nature of the swept prism, and of its varying probability of excitation is required for effective planning and design.

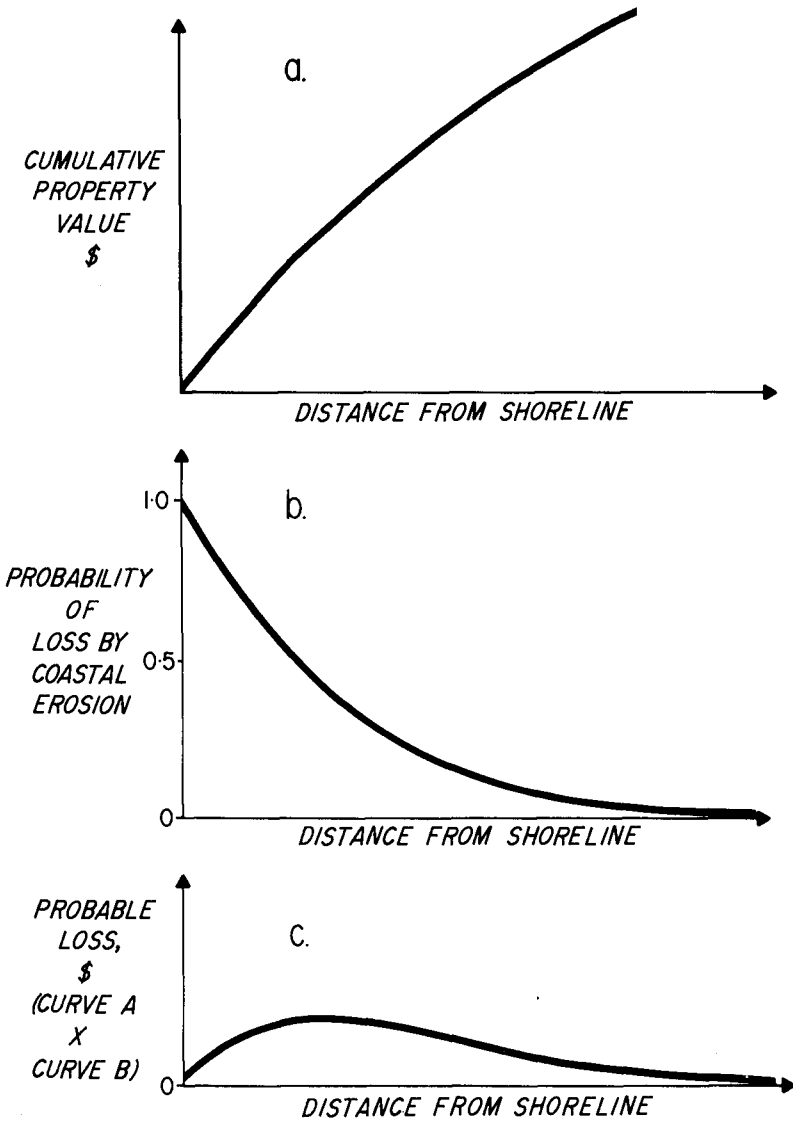


FIGURE 7.

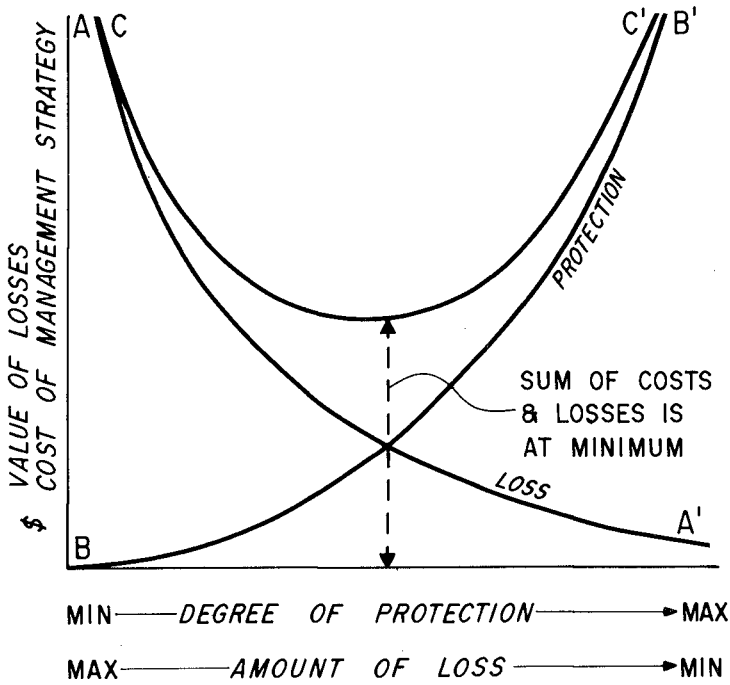


FIGURE 8.

TABLE 1. COASTAL EROSION - MANAGEMENT OPTIONS

NON-STRUCTURAL	<p>Dedicate land to remain in natural state e.g. National Park.</p> <p>Regulations against removal of sand from system.</p> <p>Regulations against destruction of dune vegetation.</p> <p>Regulations against destruction of structures in hazard zone.</p>	<p>Storm prediction/warning/evacuation systems.</p> <p>Civil Defence.</p> <p>Land Use Zoning (incl. Buffer zones).</p> <p>Relocation Schemes.</p> <p>Building Codes.</p> <p>Public ownership of hazard zone and/or structures thereon.</p> <p>Regulations against re-building of severely damaged structures.</p>	<p>Loss Bearing.</p> <p>Loss Sharing:</p> <p>a) Insurance schemes</p> <p>b) Compensation of loss bearers from community funds - appeals, government assistance etc.</p>
STRUCTURAL	<p>Movement of endangered structures;</p> <p>a) moving "permanent" structures.</p> <p>b) use of portable structures only in hazard zone.</p>	<p>Protective structures, a) "hard": Seawalls, revetments, breakwaters, groins, etc.</p> <p>b) "soft": Beach nourishment, emergency fill, sand fences, dune planting, construction of dunes and stabilization thereof.</p> <p>Deep Piling.</p> <p>Landfill.</p> <p>Use of Expendable structures in hazard zone.</p>	<p>Rebuilding.</p>

REFERENCES

- CHAPMAN, D.M. (1978). Beach behaviour following nourishment, Lower Gold Coast, Queensland. Search, 9: 460-462.
- CHAPMAN, D.M. (1980). Beach nourishment as a management technique. Proc. 17th. Coastal Eng. Conf., ASCE, Sydney.
- CHAPMAN, D.M., SMITH, A.W. (1977). Methodology of a large scale tracer experiment. pp. 185-189 in Proc. 3rd. Aust. Conf. on Coastal and Ocean Engineering, The Institution of Engineers, Australia.
- CHORLEY, R.J., KENNEDY, Barbara A. (1971). Physical Geography - A Systems Approach. London, Prentice-Hall.
- DUNCAN, J.R. (1964). The effects of water table and tidal cycle on swash-backwash sediment distribution and beach profile development. Mar. Geol., 2: 186-197.
- HALLERMEIER, Robert J. (1978). Uses for a calculated limit depth to beach erosion. Proc. 16th Coastal Eng. Conf., ASCE, Hamburg, pp. 1493-1512.
- McGRATH, B.L. (1968). Erosion of Gold Coast Beaches, 1967. J. Inst. Engrs. Aust., 40: 7,8,155,156.
- SHORT, A.D. (1978). Wave power and beach stages: A global model. Proc. 16th. Coastal Eng. Conf., ASCE, Hamburg, pp. 1145-1162.
- SWART, D.H. (1974). Offshore sediment transport and equilibrium beach profiles. Delft Hyd. Lab., Pub. 131, 302 pp.
- WRIGHT, L.D., CHAPPELL, J., THOM, B.G., BRADSHAW, M.P., and COWELL, P. (1979). Morphodynamics of reflective and dissipative beach and inshore systems: southeastern Australia. Mar. Geol., 32: 105-140.

PROCEEDINGS
OF THE

Seventeenth Coastal Engineering Conference

March 23 to 28, 1980
Sydney, Australia

Volume II

Sponsored by
ASCE Coastal Engineering Research Council
ASCE Waterway, Port, Coastal and Ocean Division
and
The Institution of Engineers, Australia



Published by the American Society of Civil Engineers
345 East 47th Street, New York, N.Y. 10017

Copyright © 1981 by the American Society of Civil Engineers.
All Rights Reserved.
Library of Congress Catalog Card No. 80-69156
ISBN 0-87262-264-9
Manufactured in the United States of America.

FOREWORD

The Seventeenth International Conference on Coastal Engineering was extremely important in many ways to those who attended the conference and to those who will benefit from use of these *Proceedings*. The Seventeenth Conference marked the 30 year point in the history of the coastal engineering conference series and a change in leadership. Since the first conference was held in Long Beach, California in October 1950, Dean Morrough P. O'Brien and Professor Joe W. Johnson have provided the continuity, direction, and motivation that have made the International Coastal Engineering Conferences so successful. For thirty years Dean O'Brien has served as Chairman and Professor Johnson as Secretary of first the Council on Wave Research and now the Coastal Engineering Research Council. Because of the importance of their contributions to the coastal engineering conferences the Council decided that these *Proceedings* will be dedicated to these two leaders. A summary of the accomplishments of each in coastal engineering is presented here.

MORROUGH P. O'BRIEN

His distinguished career in coastal engineering has been much too full to cover adequately in this space; only a sketch of his accomplishments are included here. M. P. O'Brien retired as Dean of the College of Engineering at the University of California, Berkeley, in 1959. His tenure at Berkeley included an impressive record of teaching, research and university administration. During this interval, through his students and research, he established the reputation of "The Father of Coastal Engineering." After leaving his post at Berkeley he has been very active in industrial and governmental research and development projects. At his present age, 78, Dean O'Brien is still an extremely active professional in coastal engineering.

Dean O'Brien graduated from Massachusetts Institute of Technology in 1925 and pursued graduate work at Purdue University. In 1927 he was awarded the ASCE John R. Freeman Scholarship which allowed him to attend the Technische Hochschule, Danzig, and the Royal College of Engineering, Stockholm, to study hydraulic structures and machinery. He has received honorary degrees from Northwestern University, D.Sc.; Purdue University, D.Eng.; and University of California, Berkeley, LL.D.

He joined the Mechanical Engineering Department at the University of California becoming Department Chairman in 1936 and Dean of the College in 1943. During his tenure as Dean he was instrumental in the development of graduate education and research and in the modernization of the undergraduate program.

In 1929, Dean O'Brien organized and initiated a program of research on shoreline processes and coastal engineering for a board appointed by the Chief of Engineers of the Army; subsequently, Congress established this work on a permanent basis under the U.S. Beach Erosion Board. Dean O'Brien has served as a member of this board and its successor, the Coastal Engineering Research Board from 1938 to 1980. He has maintained an active interest in ocean waves and shoreline phenomena. During the war years, this interest led to work on the design of landing craft, on forecasting surf conditions,

and on intelligence studies of landing beaches. Following the war he served as Chairman of the ad hoc committee on Amphibious Operations of the National Research Council which reviewed the plans for modernization of the Marine Corps. Consulting engagements in the field of coastal engineering included restoration of the beach at Santa Barbara, regulation of the estuary of the Columbia River, Dos Bocas Harbor in the Gulf of Campache and other similar coastal projects.

Dean O'Brien's research on hydraulic machinery led to many practical applications by industry. Most of the jet pumps sold in the United States follow the designs of O'Brien and Gosline. Application of the theory of airfoils to the design of propeller pumps and fans by O'Brien and Folsom provided the basis for extensive production of low-head, high-capacity pumps for irrigation and drainage. Consulting engagements on hydraulic machinery during this period included Byron Jackson, Food Machinery, Fairbanks-Morse, Becker Pump, Navy Department, Corps of Engineers, and many other governmental agencies. His experience with turbo-machinery led to his appointment in 1949 as a consulting engineer by the Aircraft Gas Turbine Division of the General Electric Company, an association which has continued to the present. He is now a consultant to the Technical Systems and Materials Sector of General Electric, dealing with both technical and management problems of jet engines, missiles and space vehicles, ordnance, and electronic systems.

During the war years, Dean O'Brien directed the University of California's program of engineers' science and management war training for technical and professional personnel in the aircraft and shipbuilding industries. During the four years of its existence, this program included 1800 instructors and 46,000 students. Concurrently, he served as dean of the college and as consultant in the research section of the Bureau of Ships on problems of submarine propeller noise, and on amphibious operations. In 1946, he participated in Operation Crossroads at Bikini as a consultant on the measurement of waves generated by the bomb tests; most of the photographs of the Baker tests, which appeared in the press, were taken by the tower and aerial cameras which Dean O'Brien and his associates operated for wave measurements.

Twice, he has taken full-time leave from academic duties to engage in engineering practice; once, 1947 to 1949, to serve as director of research and engineering with the Air Reduction Company and, again in 1953, to join General Electric Company's Aircraft Nuclear Propulsion Project. He has held membership on many influential boards and commissions, among them the Coastal Engineering Research Board, formerly the Beach Erosion Board; the National Science Foundation's panel of engineering consultants; the Army Scientific Advisory Panel; the Atomic Energy Commission's personnel security board; the Maritime Research Advisory Committee and the Advisory Board on Education of the National Academy of Sciences, National Research Council; and the board of directors, McGraw-Hill Publishing Company. In 1958 President Eisenhower appointed him a member of the Board of the National Science Foundation. During 1958-1959, he was a visiting institute professor at the Massachusetts Institute of Technology, and a visiting research fellow at Harvard University.

Among awards he has received are the Army-Navy Certificate of Appreciation; the Distinguished Civilian Award, Department of the Army (twice); and the Bliss Medal of the Society of American Military Engineers. In 1968 he received the ASEE's Lamme Award, and in 1969 a building at the University of California's Berkeley Campus was named after Dean O'Brien.

He has written more than 100 published articles on technical subjects and engineering education, and is co-author of "Applied Fluid Mechanics," published by McGraw-Hill in 1937. The bibliography is his own selection of the papers which he most enjoyed

writing. He is a registered professional engineer in the states of California and New York, and a chartered Mechanical Engineer in Great Britain. In 1969 he was elected to the National Academy of Engineering. He is an Honorary Member of both the ASCE and ASME.

Selected Bibliography

- Entrance Area Related to Tidal Prism, *Civil Engineering*, 1931.
- Checks on the Model Law for Hydraulic Structures, *Trans. Amer. Geo. Union*, 1932.
- Review of the Theory of Turbulent Flow and its Relation to Sediment Transportation, *Trans. Amer. Geo. Union*, 1933.
- Model Law for Motion of Salt Water through Fresh (with John Chuno), *ASCE Trans.*, vol. 99, 1934.
- The Transportation of Bed-Load by Streams (with B. B. Rindlaub), *Trans. Amer. Geo. Union*, 1934.
- The Water Jet-Pump (with J. E. Gosline), *Univ. Calif. Publ. in Eng.*, vol. 3, no. 3, 1934.
- A Summary of the Theory of Oscillatory Waves, TR No. 2, Beach Erosion Board, 1941.
- The U.S. Tidal Model Laboratory, *Shore & Beach*, vol. 3, no. 2, 1935.
- Velocity of Large Bubbles in Vertical Tubes (with J. E. Gosline), *Indust. Eng. Chem.*, vol. 27, December 1935.
- Models of Estuaries, *Trans. Amer. Geo. Union*, 1935.
- The Transportation of Sound by Wind (with B. B. Rindlaub), *Trans. Amer. Geo. Union*, 1936.
- The Design of Propeller Pumps and Fans (with R. G. Folsom), *Univ. Calif. Publ. Eng.*, vol. 4, no. 1, 1939.
- Some Problems of Horizontal Steady Flow in Porous Media (with J. A. Putnam), *Am. Inst. Min. & Met. Eng.*, paper 1349, 1941.
- Model Experiments on Impulsive Waves in Shallow Water, *Trans. Amer. Geo. Union*, April 1947.
- Lag and Reduction of Range in Tide-gage Wells, Beach Erosion Board Bulletin, vol. 4, no. 3, 1950.
- The Nature of Engineering, *Jour. Eng. Educ.*, November 1950.
- The Force Exerted by Waves on Objects (with J. R. Morison), *Trans. Amer. Geo. Union*, February 1952.
- The Engineering of Large Systems, *The World of Engineering*, Chapter 9, McGraw-Hill, 1964.
- The Equilibrium Flow Areas of Tidal Inlets on Sandy Coasts, Tenth Int. Conf. on Coastal Eng., ASCE, 1966.
- Hydraulic Coefficients of Tidal Inlets (with R. Clark), Coastal & Oceanographic Engineering Laboratory, Univ. of Florida, 1974.
- Hydraulic and Sedimentary Stability of Tidal Inlets (with R. G. Dean), ASCE, Thirteenth Int. Conf. on Coastal Engineering, 1972.

JOE W. JOHNSON

Professor Johnson has had a long and very distinguished career in coastal engineering. His reputation extends around the world, reaching forth from his consulting, his research and especially his students. In 1975 he retired as Professor of Civil Engineering from the University of California, Berkeley. Professor Johnson is also well known for his excellent handling of the *Proceedings* of all sixteen prior coastal engineering conferences. Since his retirement from the University of California he has been extremely active in his consulting practice and professional duties.

Professor Johnson graduated from the University of California, Berkeley, in 1931 with a B.S. in Civil Engineering and in 1934 with an M.S. degree. Following a brief stay at the Waterways Experiment Station he devoted eight years to studying sediment transport with the Soil Conservation Service. He then returned to the University of California and enjoyed a very fruitful career of teaching, research and public service.

He has been consultant to many international projects involving shoreline development including: an ore port in Vitoria, Brazil; harbor development along the coast of Venezuela; port development in Northwest Australia; port development in Damietta, Egypt; sedimentation at Bahia Blanca, Argentina; Hay Point Coal Port, Australia; and wave action and sedimentation in Brazil. His associations with coastal engineering projects in the United States are equally extensive; a brief list follows of his involvement: Rio Grande Valley, wind tides in Lake Okeechobee, wave analysis of Marina del Rey, San Francisco Bay Area Rapid Transit, Turkey Point Power Plant in Florida and beach erosion at the Zion Atomic Power Plant.

In addition Professor Johnson has been a member, since 1974, of the Shoreline Erosion Advisory Panel created by the U.S. Congress. His expertise in coastal engineering has been quite instrumental in the success of this research and development program. He also has been selected as the chairman of the U.S. Delegation to the U.S.-Japan Cooperative Seminar on Coastal Engineering held in Japan. Professor Johnson has been appointed to numerous other boards and committees. He was the Secretary of the Council on Wave Research during its existence from 1950 to 1964, and then of the subsequent organization, The Coastal Engineering Research Council of the ASCE. He has been very active in the AGU holding key positions and has been a major driving force behind the American Shore and Beach Preservation Association as Vice President and Editor of *Shore and Beach*.

In 1976, Professor Johnson was elected to membership in the National Academy of Engineering and in 1979, he received the distinguished honor of Honorary Member of the ASCE. He is also the recipient of the Guggenheim Fellowship, The Outstanding Civilian Service Medal for his service in the field of coastal engineering and the Berkeley Citation. A selected listing of his over ninety publications are given below. Professor Johnson has been and still is a very active and important part of international coastal engineering.

Selected Bibliography

- The Transportation of Sediment by Streams: Bed Load, *Inter. Union Geod. and Geophys.*, 1939.
- Transportation of Sediment by Flowing Water, *Soil Conserv.*, vol. 6, 1941.

- A Distinction Between Bed Load and Suspended Load in Natural Streams (with Einstein and Anderson), *Trans. Amer. Geo. Union*, 1940.
- "War-time research on waves and surf." *The Military Engineer*, June 1947.
- "Refraction of surface waves by currents." *Trans. Amer. Geo. Union*, 1947.
- "The force exerted by surface waves on piles," (with J. R. Morison, M. P. O'Brien, and S. A. Schaaf), vol. 189, 1950.
- "The Damping Action of Submerged Breakwaters," (with R. A. Fuchs and J. R. Morison), *Trans. Amer. Geo. Union*, vol. 32, 1951.
- "The March 1962 Storm on the Atlantic Coast of the United States," (with M. P. O'Brien), Proc. Eighth Conference on Coastal Engineering, 1963.
- "Ship Waves in Shoaling Water," Proceedings Eleventh Conference on Coastal Engineering, 1968.
- "Lessons in Coastal Engineering," Symposium on Coastal Engineering, Stellenbosch, South Africa, 1970.
- "Closure of Tidal Entrances," Proc. Fourteenth Conference on Coastal Engineering, 1974.
- "Littoral Processes at Some California Shoreline Harbors," *Shore and Beach*, vol. 43, no. 1, April 1975.

The omissions from the accomplishments of Dean O'Brien and Professor Johnson are solely the responsibility of the writer; however, the magnitude of their contributions to coastal engineering has forced the writer to condense their many activities. Indeed a detailed listing of their individual efforts would fill a volume.

While listening to the discussions of the mechanics of sand waves by Professor Arthur Brebner, Professor Longuet-Higgins was able to tie some of Brebner's findings with the theoretical work he (Longuet-Higgins) had done on water waves of maximum steepness. Since Professor Longuet-Higgins' Keynote address begins the *Proceedings*, it was felt proper to end them with a brief summary explaining the application of his limiting wave theory to sand bed-forms. His discussion can be found on page 3107.

Billy L. Edge, Secretary
 Coastal Engineering Research Council
 American Society of Civil Engineers

ACKNOWLEDGMENTS

ORGANIZING COMMITTEE

Mr. J. G. Betty, Chairman,
Macdonald Wagner & Priddle Pty. Ltd.
Mr. G. Evans,
Department of Public Works of N.S.W.
Professor D. N. Foster,
The University of New South Wales.
Mr. W. J. Kerle,
Department of Public Works of N.S.W.
Mr. N. Lawson,
Maritime Services Board of New South Wales.
Mr. W. M. Lewis,
Esso Australia Ltd.

LADIES COMMITTEE

Mrs. D. E. Betty,
Wahroonga, N.S.W.
Miss K. Winter,
Maritime Services Board of New South Wales.
Miss J. Shaw,
The University of New South Wales.

SUPPORT

The Institution of Engineers, Australia, in collaboration with the Coastal Engineering Research Council of the American Society of Civil Engineers, acknowledges the support and encouragement given by the following organizations:

Department of Public Works, N.S.W.
Esso Australia Ltd.
Macdonald, Wagner & Priddle Pty. Ltd.
Maritime Services Board of New South Wales
New South Wales State Government
The Sydney County Council
The Exhibiting Companies
The University of New South Wales.

INTERSTATE CORRESPONDING COMMITTEE MEMBERS

Mr. R. Culver, Dept. of Mechanical Engineering, The University of Adelaide,
South Australia 5000.
Dr. J. Hinwood, Dept. of Mechanical Engineering, Monash University, Clayton,
Melbourne, Victoria, 3168.
Mr. B. McGrath, Dept. of Harbours and Marine, G.P.O. Box 2195, Brisbane,
Queensland, 4001.
Professor R. Silvester, Dept. of Civil Engineering, University of Western Australia,
Perth, 6009.



Morrough P. O'Brien



Joe W. Johnson

CONTENTS

FOREWORD	iii
ACKNOWLEDGEMENTS	ix

INVITED LECTURE

THE UNSOLVED PROBLEM OF BREAKING WAVES

by

M. S. Longuet-Higgins
Institute of Oceanographic Sciences
Wormley, Surrey, England

PART I

THEORETICAL AND OBSERVED WAVE CHARACTERISTICS

Chapter 1	
SOME IMPLICATIONS OF RECENT ADVANCES IN WAVE THEORIES	
J. R. Chaplin and K. Anastasiou	31
Chapter 2	
ACCURATE NUMERICAL SOLUTIONS FOR NONLINEAR WAVES	
J. D. Fenton and M. M. Rienecker	50
Chapter 3	
MASS TRANSPORT IN PROGRESSIVE WAVES OF PERMANENT TYPE	
Yoshito Tsuchiya, Takashi Yasuda and Takao Yamashita	70
Chapter 4	
RAY CURVATURE AND REFRACTION OF WAVE PACKETS	
J. Ernest Breeding, Jr.	82
Chapter 5	
VERIFICATION OF A WAVE REFRACTION MODEL	
G. Henderson and N. B. Weber	101
Chapter 6	
WAVE SHOALING CALCULATED FROM COKELET'S THEORY	
T. Sakai and J. A. Battjes	121
Chapter 7	
A SURVEY OF "RANDOM" WAVE GENERATION TECHNIQUES	
J. Ploeg and E. R. Funke	135
Chapter 8	
THE MEASUREMENT OF INCIDENT AND REFLECTED SPECTRA USING A LEAST SQUARES METHOD	
E. P. D. Mansard and E. R. Funke	154
Chapter 9	
ORBITAL VELOCITIES IN IRREGULAR WAVES	
F. C. Vis	173

Chapter 10	
INVESTIGATIONS ON IRREGULAR WAVES IN HYDRAULIC MODELS	
Karl-Friedrich Daemrich, Wolf-Dietrich Eggert and Soren Kohlhase	186
Chapter 11	
METHOD OF ANALYSIS OF RANDOM WAVE EXPERIMENTS WITH REFLECTING COASTAL STRUCTURES	
Pierre Gaillard, Michel Gauthier and Forrest Holly	204
Chapter 12	
WAVE HEIGHT DISTRIBUTION AROUND PERMEABLE BREAKWATERS	
Shintaro Hotta	221
Chapter 13	
NON-RESONANT WAVE AGITATION IN SMALL CRAFT HARBOURS	
J. W. Kamphuis and D. A. Y. Smith	241
Chapter 14	
EXPERIMENTAL INVESTIGATIONS OF PERIODIC WAVES NEAR BREAKING	
J. Buhr Hansen	260
Chapter 15	
AN HEURISTIC MODEL OF WAVE HEIGHT DISTRIBUTION IN SURF ZONE	
Masaru Mizuguchi	278
Chapter 16	
RESONANCES OF COASTAL WATERS BETWEEN PERTH AND GERALDTON (WESTERN AUSTRALIA)	
H. Allison, A. Grassia and R. Litchfield	290
Chapter 17	
A CLOSELY RESPONDING, VERSATILE WAVE TUNNEL	
C. H. Hulsbergen and J. J. Bosman	310
Chapter 18	
CONDITIONAL SIMULATIONS OF OCEAN WAVE PROPERTIES	
Leon E. Borgman	318
Chapter 19	
WIND WAVES TRANSMISSION THROUGH POROUS BREAKWATER	
Stanislaw R. Massel and Piotr Butowski	333
Chapter 20	
FIELD MEASUREMENTS OF WIND WAVE KINEMATICS	
J. A. Battjes and J. van Heteren	347
Chapter 21	
HF RADAR MAPPING OF EXTENSIVE OCEAN WINDFIELDS	
P. E. Dexter and R. C. Casey	363
Chapter 22	
SOURCES OF MEASURED WAVE DATA	
Laurence Draper	372
Chapter 23	
VISUALLY OBSERVED WAVE DATA AT PT. MUGU, CALIF.	
Christine Schneider and Richard Weggel	381
Chapter 24	
WAVE HINDCASTS AND MEASUREMENTS - BASS STRAIT	
M. N. Silbert, T. P. Barnett, D. J. H. Peters and R. C. Hamilton	395

Chapter 25	
REALTIME WAVE ANALYSIS, NEWCASTLE, AUSTRALIA	
N. V. Lawson and P. H. Oull	412
Chapter 26	
FLORIDA COASTAL DATA NETWORK	
Gary Howell	421
Chapter 27	
A MEASUREMENT OF SLOPE, CURVATURE, AND DIRECTIONAL SPECTRA OF WIND WAVES IN LAKE MICHIGAN	
Paul C. Liu	432
Chapter 28	
WAVE ATTENUATION AND WAVE SET-UP ON A COASTAL REEF	
Franciscus Gerritsen	444
Chapter 29	
LONGSHORE CURRENT FLOWS IN A WAVE BASIN	
P. J. Visser	462
Chapter 30	
DYNAMIC CHARACTERISTICS IN THE NEAR SHORE AREA	
Kiyoshi Horikawa and Masahiko Isobe	480
Chapter 31	
VELOCITY FIELD IN A STEADY BREAKER	
J. A. Battjes and T. Sakai	499
Chapter 32	
THE FLUID MECHANICS OF WAVES APPROACHING BREAKING	
D. H. Peregrine, E. D. Cokelet and P. McIver	512
Chapter 33	
A SIMILARITY MODEL IN THE SURF ZONE	
Hsiang Wang and Wei-Chong	529
Chapter 34	
VELOCITY AND PRESSURE FIELD IN SPILLING BREAKERS	
M. J. F. Stive	547
Chapter 35	
DIRECTIONAL WAVE SPECTRA AND WAVE KINEMATICS IN HURRICANES CARMEN AND ELOISE	
G. Z. Forristall, E. G. Ward and V. J. Cardone	567
Chapter 36	
PREDICTION OF THE SEVEREST SIGNIFICANT WAVE HEIGHT	
Michel K. Ochi and Joseph E. Whalen	587
Chapter 37	
PREDICTION OF DOMINANT WAVE PROPERTIES AHEAD OF HURRICANES	
Omar H. Shemdin	600
Chapter 38	
LONG PERIOD DISTURBANCES DUE TO WAVE GROUPS	
E. C. Bowers	610
Chapter 39	
TWO-DIMENSIONAL SURF BEAT	
Reinhard E. Flick, Douglas L. Inman and Robert T. Guza	624

Chapter 40		
LONG WAVES GENERATED BY COMPLEX BOTTOM MOTIONS		
J. L. Hammack and F. Raichlen		639
Chapter 41		
TSUNAMIS ALONG WEST COAST OF LUZON, PHILIPPINES		
R. L. Wiegel		652
Chapter 42		
TSUNAMI PRONE FRICTION FACTORS FROM WIND MEASUREMENTS		
Charles L. Bretschneider		672
Chapter 43		
RUN-UP OF TSUNAMIS BY LINEAR AND NONLINEAR THEORIES		
Chiaki Goto and Nobuo Shuto		695
Chapter 44		
ON THE CORRECTION OF LAND-BASED WIND MEASUREMENTS FOR OCEANOGRAPHIC APPLICATIONS		
S. A. Hsu		708
Chapter 45		
NUMERICAL MODELLING OF TROPICAL CYCLONE STORM SURGE		
Rodney J. Sobey, Bruce A. Harper, and George M. Mitchell		725
Chapter 46		
A NUMERICAL MODEL OF STORM WAVES IN SHALLOW WATER		
A. Hauguel		746
Chapter 47		
THE GENERATION OF LONG WAVES IN THE LABORATORY		
Derek Goring and Fredric Raichlen		763
Chapter 48		
CORRECT REPRODUCTION OF LONG GROUP INDUCED WAVES		
N. -E. O. Hansen, S. E. Sand, H. Lundgren, T. Sorensen and H. Gravesen		784
Chapter 49		
AN ELECTROMAGNETIC ANALOGY FOR LONG WATER WAVES		
G. W. Jackson and D. L. Wilkinson		801
Chapter 50		
INTERACTIONS OF WAVES WITH SUBMARINE TRENCHES		
Jiin J. Lee, Robert M. Ayer and Wen L. Chiang		812
Chapter 51		
TRANSIENT FINITE-DIFFERENCE TSUNAMI CALCULATIONS		
Ove Skovgaard and Ivar G. Jonsson		823
Chapter 52		
AN INVESTIGATION OF WAVE SHELTERING BY ISLANDS		
S. V. Hsiao, J. F. Vesecky and O. H. Shemdin		840
Chapter 53		
THE DISSIPATION OF WAVE ENERGY BY TURBULENCE		
Yu Kuang-ming		850

**PART II
COASTAL SEDIMENT PROBLEMS**

Chapter 54	
BEACH CUSPS AT POINT REYES AND DRAKES BAY BEACHES, CALIFORNIA	
Robert G. Dean and E. M. Maurmeyer	863
Chapter 55	
BARRON RIVER DELTA INVESTIGATION	
D. A. Robinson, D. J. Cook and J. G. Barff	885
Chapter 56	
SOFT DESIGNS FOR COASTAL PROTECTION AT SEABROOK ISLAND, S.C.	
Miles O. Hayes, Timothy W. Kana and John H. Barwis	897
Chapter 57	
GEOLOGICAL CONTROLS ON PROCESS-RESPONSE, S.E. AUSTRALIA	
P. S. Roy and A. W. Stephens	913
Chapter 58	
BEACH EROSION-ACCRETION AT TWO TIME SCALES	
B. G. Thom and G. M. Bowman	934
Chapter 59	
PHYSICAL PROCESSES AND SEDIMENT FLUX THROUGH REEF-LAGOON SYSTEMS	
Harry H. Roberts	946
Chapter 60	
INSHORE-NEARSHORE MORPHODYNAMICS-A PREDICTIVE MODEL	
John Chappell	963
Chapter 61	
BEACH CUT IN RELATION TO SURF ZONE MORPHODYNAMICS	
L. D. Wright	978
Chapter 62	
BREAKER TYPE AND PHASE SHIFTS ON NATURAL BEACHES	
Peter J. Cowell	997
Chapter 63	
BEACH RESPONSE TO VARIATIONS IN BREAKER HEIGHT	
A. D. Short	1016
Chapter 64	
THE DYNAMIC SWEEP PRISM	
David M. Chapman	1036
Chapter 65	
A LABORATORY STUDY OF OFFSHORE TRANSPORT OF SEDIMENT AND A MODEL FOR ERODING BEACHES	
Tsuguo Sunamura	1051
Chapter 66	
NEARSHORE CURRENTS ON A PARTIALLY ROCKY SHORE	
T. O. Sasaki, H. Igarashi and S. Harikai	1071

Chapter 67	
TOPOGRAPHIC CONTROL OF RUN-UP VARIABILITY	
Mark P. Bradshaw	1091
Chapter 68	
BEACH PROFILES AND ON-OFFSHORE SEDIMENT TRANSPORT	
Akira Watanabe, Yoshihiko Riho and Kiyoshi Horikawa	1106
Chapter 69	
SECONDARY SAND TRANSPORT MECHANISMS	
A. W. Smith and A. D. Gordon	1122
Chapter 70	
SAND TRANSPORT BY WAVES	
Jan van de Graaff and Wiel M. K. Tilmans	1140
Chapter 71	
NEARSHORE SUSPENDED SEDIMENT LOAD DURING STORM AND POST-STORM CONDITIONS	
Timothy W. Kana and Larry G. Ward	1158
Chapter 72	
ONSHORE-OFFSHORE TRANSPORT AND BEACH PROFILE CHANGE	
Masataro Hattori and Ryoichi Kawamata	1175
Chapter 73	
ON-OFFSHORE SEDIMENT TRANSPORT RATE IN THE SURF ZONE	
Toru Sawaragi and Ichiro Deguchi	1195
Chapter 74	
FIELD MEASUREMENTS OF SAND MOTION IN THE SURF ZONE	
Douglas L. Inman, James A. Zampol, Thomas E. White, B. Walton Waldorf, Daniel M. Hanes and Kim A. Kastens	1215
Chapter 75	
AN APPROACH TO UNDERSTANDING COASTAL PROCESSES	
A. D. Gordon and D. B. Lord	1235
Chapter 76	
RELATIONSHIP BETWEEN ALONGSHORE WAVE ENERGY AND LITTORAL DRIFT IN THE MID-WEST COAST AT TAIWAN	
Ho-shong Hou, Chung-Pan Lee, and Lung-Hui Lin	1255
Chapter 77	
LONGSHORE WATER AND SEDIMENT MOVEMENT	
D. H. Swart and C. A. Fleming	1275
Chapter 78	
CRITERION FOR STABILITY OF SHORELINE PLANFORM	
John D. Wang and Bernard le Mehaute	1295
Chapter 79	
ZETA BAYS, POCKET BEACHES AND HEADLAND CONTROL	
R. Silvester, Y. Tsuchiya, and Y. Shibano	1306
Chapter 80	
BEACHES: PROFILES, PROCESSES AND PERMEABILITY	
Michael R. Gourlay	1320
Chapter 81	
SAND BED-FORM LENGTHS UNDER OSCILLATORY MOTION	
Arthur Brebner	1340

Chapter 82	
SEDIMENT TRANSPORT PROCESSES AND COASTAL VARIABILITY ON THE ALASKAN NORTH SLOPE	
E. H. Owens, J. R. Harper and D. Nummedal	1344
Chapter 83	
SEDIMENT DISPERSAL ON THE N. S. W. CONTINENTAL SHELF	
Ron Boyd	1364
Chapter 84	
FLUID MUD DYNAMICS AND SHORELINE STABILIZATION: LOUISIANA CHENIER PLAIN	
John T. Wells and Harry H. Roberts	1382
Chapter 85	
NEARSHORE SEDIMENT TRANSPORT STUDY EXPERIMENTS	
R. J. Seymour and C. G. Gable	1402
Chapter 86	
A SEDIMENT TRAPPING EXPERIMENT AT SANTA CRUZ, CA.	
R. J. Seymour, G. W. Domurat and D. M. Pirie	1416
Chapter 87	
WAVE FORCING OF BEACH GROUNDWATER	
Evans Waddell	1436
Chapter 88	
LONGSHORE TRANSPORT EVALUATIONS AT A DETACHED BREAKWATER	
R. O. Bruno, R. G. Dean, and C. G. Gable	1453
Chapter 89	
MIGRATION OF LONGSHORE BARS	
Hans H. Dette	1476
Chapter 90	
A PHASED-DREDGING PROGRAM FOR SANTA CRUZ HARBOR	
James R. Walker and Peter J. Williams	1493
Chapter 91	
DESIGN OF ENCLOSED HARBORS TO REDUCE SEDIMENTATION	
Craig H. Everts	1512
Chapter 92	
OPENING AND MAINTAINING TIDAL LAGOONS & ESTUARIES	
Scott A. Jenkins, Douglas L. Inman and James A. Bailard	1528
Chapter 93	
RESEARCH IN SOUTHERN QUEENSLAND INTO THE MANAGEMENT OF COASTAL SAND DUNES	
James B. McKenzie and David A. Barr	1548
Chapter 94	
WIND AND SEDIMENT MOVEMENT IN COASTAL DUNE AREAS	
John R. Hails and John Bennett	1565
Chapter 95	
SAND TRANSPORT UNDER THE ACTION OF WIND	
Ulrich Zanke	1576
Chapter 96	
A NUMERICAL MODEL FOR DUNE DYNAMICS	
J. Sundermann, H. -J. Vollmers and W. Puls	1584

Chapter 97	
ESTUARINE RESPONSE TO DREDGING IN THE TWEED RIVER, AUSTRALIA	
Bruce M. Druery	1599
Chapter 98	
NOOSA BEACH RESTORATION SCHEME	
R. J. Lloyd	1619
Chapter 99	
BEACH NOURISHMENT AS A MANAGEMENT TECHNIQUE	
David M. Chapman	1636
Chapter 100	
CAPRICORN COAST BEACHES	
D. C. Patterson and L. R. Ford	1649
Chapter 101	
THE BEACH IMPROVEMENT PROGRAMME: NEW SOUTH WALES	
Heale A. Philip and Philip H. Waite	1669
Chapter 102	
EDDY CURRENTS AND SEDIMENT TRANSPORT OFF THE DAMIETTA NILE	
S. P. Murray, J. M. Coleman, H. H. Roberts and M. Salama	1680
Chapter 103	
A COMPARISON BETWEEN DREDGE INDUCED SEDIMENT RESUSPENSION AND THAT PRODUCED BY NATURAL STORM EVENTS	
W. Frank Bohlen and Marine Sciences Department., Univ. of Conn.	1700
Chapter 104	
SEDIMENTATION IN CHANNELS AND TRENCHES	
E. W. Bijker	1708
Chapter 105	
SEDIMENTATION IN DREDGED NAVIGATION CHANNELS	
Lars Mikkelsen, Preben Mortensen, and Torben Sorensen	1719
Chapter 106	
SOME ASPECTS OF COASTAL ENGINEERING RESEARCH WORKS IN CHINA	
Yen Kai	1735

PART III
COASTAL STRUCTURES AND RELATED PROBLEMS

Chapter 107	
SIMULTANEOUS WAVE AND CURRENT FORCES ON A PIPELINE	
David A. Knoll and John B. Herbich	1742
Chapter 108	
WAVE FORCES ON AN INCLINED CIRCULAR CYLINDRICAL PILE	
Toshiyuki Shigemura	1761
Chapter 109	
WAVE-INDUCED SEEPAGE EFFECTS ON A VERTICAL CYLINDER	
Thomas J. P. Durand and Peter L. Monkmeier	1781

Chapter 110	
STABILITY ANALYSIS OF SEAFLOOR FOUNDATIONS	
Tokuo Yamamoto and Yasumasa Suzuki	1799
Chapter 111	
WAVE FORCES ON OFFSHORE PIPELINES	
N. Jothishankar and V. Sundar	1819
Chapter 112	
WAVE IMPACT PRESSURES ON COMPOSITE BREAKWATERS	
G. R. Mogridge and W. W. Jamieson	1829
Chapter 113	
CONSTRUCTION AND MODEL INVESTIGATION OF STORMWATER OUTFALL	
K. A. Heathcote and G. W. Britton	1849
Chapter 114	
FULL SCALE NEAR SURFACE WATER PARTICLE VELOCITIES AND PRESSURES ACTING ON AN INCLINED TUBULAR MEMBER	
Fritz Busching and Eckehard Martini	1869
Chapter 115	
ENERGY TRANSMISSION OVER BREAKWATER—A DESIGN CRITERION?	
P. Bade and H. Kaldenhoff	1885
Chapter 116	
THE DESIGN CONCEPT OF DUAL BREAKWATERS AND ITS APPLICATION TO TOWNSVILLE, AUSTRALIA	
W. Bremner, N. N. Foster, C. A. Miller and B. C. Wallace	1898
Chapter 117	
DESIGN OF AN OVERTOPPING BREAKWATER	
P. D. Treloar and B. Nagle	1909
Chapter 118	
FULL SCALE TRIALS OF DOLOSSE TO DESTRUCTION	
Hans F. Burcharth	1928
Chapter 119	
DOLOSSE: PAST, PRESENT, FUTURE?	
J. A. Zwamborn, D. E. Bosman and J. Moes	1948
Chapter 120	
A DETACHED BREAKWATER SYSTEM FOR BEACH PROTECTION	
James R. Walker, Denton Clark, and Joan Pope	1968
Chapter 121	
STABILITY OF RUBBLE MOUND BREAKWATER	
J. Feuillet and M. Sabaton	1988
Chapter 122	
ARTIFICIAL RESORT BEACH PROTECTED BY OFFSHORE BREAKWATERS AND GROINS	
Shoji Sato and Norio Tanaka	2003
Chapter 123	
SEAWALLS IN DEEP SEAS	
Shoshichiro Nagai and Shohachi Kakuno	2023
Chapter 124	
PROBABILISTIC DESIGN OF SEA DEFENCES	
W. T. Bakker and J. K. Vrijling	2040

Chapter 125	
DESIGN OF CAISSON BREAKWATERS	
A. G. F. Eddie, J. D. Lawson, H. R. Graze and B. K. Dean	2060
Chapter 126	
THE DESIGN AND CONSTRUCTION OF THE NEW OIL PORT IN DALIAN, C.P.R.	
Xin Zhu-Zhuang	2080
Chapter 127	
SITING AND DESIGN CRITERIA OF DOCK STRUCTURES IN THE MARSHALL ISLANDS	
R. M. Noble, K. C. Leslie and D. O'Day	2106
Chapter 128	
COASTAL PROTECTION AGAINST THE ACTION OF WAVES AND CURRENTS	
Leren P. Mikhailov and Sergei M. Uspenskii	2120
Chapter 129	
FLOATING BREAKWATER PERFORMANCE COMPARISON	
Volker W. Harms	2137
Chapter 130	
LITTORAL DRIFT OF SAND NEAR PORT OF OARAI	
Kazumasa Mizumura	2159
Chapter 131	
LONG-TERM EXPERIENCE WITH THE USE OF SYNTHETIC FILTER FABRICS IN COASTAL ENGINEERING	
Georg Heerten	2174
Chapter 132	
BREAKWATER WITH SAND BITUMEN CORE	
E. Loewy, K. G. Witthaus, R. J. Maddrell and J. P. Wood	2194
Chapter 133	
HARBOUR DESIGN INCLUDING SEDIMENTOLOGICAL PROBLEMS USING MAINLY NUMERICAL TECHNIQS	
B. Latteux	2213
Chapter 134	
NEW JETTIES FOR TUNG-KANG FISHING HARBOUR, TAIWAN	
Chi-Fu Su	2230
Chapter 135	
MAJOR RECLAMATION SCHEME FOR MARINA CITY, SINGAPORE	
S. Y. Chew and J. Wei	2245
Chapter 136	
SHIP-BRIDGE-PIER PROTECTIVE SYSTEMS	
Akira Iwai, Hitoshi Nagasawa, Kazuki Oda and Kuniaki Shoji	2261
Chapter 137	
WAVE-WAVE INTERACTIONS, CURRENT-WAVE INTERACTIONS AND RESULTING EXTREME WAVES AND BREAKING WAVES	
Soren Peter Kjeldsen and Dag Myrhaug	2277
Chapter 138	
CAN WE DEVELOP NEW BREAKWATER ARMOUR FORMULAE?	
John Dorrington Mettam	2304

**PART IV
COASTAL, ESTUARINE, AND ENVIRONMENTAL PROBLEMS**

Chapter 139	
SEPARATION OF CLIMATIC FLUCTUATIONS AND IMPACTS OF ENGINEERING ACTIVITIES IN ESTUARIES	
G. Krause	2325
Chapter 140	
WAVE ENERGY DISTRIBUTION IN AN ESTUARY	
Volker Barthel	2340
Chapter 141	
HYDRAULIC RESEARCH IN THE OOSTERSCHELDE ESTUARY	
Anton W. Walther	2360
Chapter 142	
PORT OF BRISBANE SILTATION STUDY	
N. V. M. Odd and T. Baxter	2377
Chapter 143	
A 3-D MODEL FOR PENOBSCOT BAY, MAINE	
Bryan R. Pearce, Bruce R. Fidler and Adrian C. Humphreys	2397
Chapter 144	
THE USE OF ARRAY PROCESSORS FOR NUMERICAL MODELLING OF TIDAL ESTUARY DYNAMICS	
D. Prandle, E. R. Funke, N. L. Crookshank and R. Renner	2413
Chapter 145	
PARAMETER IDENTIFICATION IN ESTUARINE MODELING	
Wen-Sen Chu and William -G. Yeh	2433
Chapter 146	
AUTOMATIC CALIBRATION OF NUMERICAL TIDAL MODELS	
K. -P. Holz and U. Januszewski	2450
Chapter 147	
TIDAL INLET BEHAVIORAL ANALYSIS	
A. F. Nielsen and A. D. Gordon	2461
Chapter 148	
SEDIMENTATION PROCESSES IN TIDAL CHANNELS AND TIDAL BASINS CAUSED BY ARTIFICIAL CONSTRUCTIONS	
E. Renger and H. W. Partensky	2481
Chapter 149	
ARTIFICIAL ROUGHNESS IN PHYSICAL MODELS OF ESTUARIES FOR STORM SURGE INVESTIGATIONS	
D. Berndt, E. Giese, H. Schwarze, and H. -J. Vollmers	2495
Chapter 150	
COMMENTS ON TIDAL ENTRANCES ON SANDY COASTS	
Morrough P. O'Brien	2504
Chapter 151	
TIDAL PRISM-INLET AREA RELATIONS FOR SMALL TIDAL INLETS	
R. J. Bryne, R. A. Gammisch and G. R. Thomas	2517
Chapter 152	
A COASTAL INLET WITH FIXED BED AND MOBILE SIDES	
R. C. Nelson and A. J. Keats	2534

Chapter 153	
INLETS/ESTUARIES DISCHARGING INTO SHELTERED WATERS	
H. P. Riedel and M. R. Gourlay	2550
Chapter 154	
THE CORPS OF ENGINEER'S GENERAL INVESTIGATION OF	
TIDAL INLETS	
Robert M. Sorensen	2565
Chapter 155	
SATELLITE APPLICATIONS ON A COASTAL INLET STABILITY	
STUDY	
Yu-Hwa Wang	2581
Chapter 156	
BOUNDARY CONDITIONS FOR ANALYSIS OF FLOW IN TIDAL	
INLETS	
T. C. Gopalakrishnan and J. L. Machemehl	2595
Chapter 157	
MECHANISMS OPERATING AT A JETTIED RIVER ENTRANCE	
Bruce M. Druery and Alexander F. Nielsen	2607
Chapter 158	
STABILITY OF ESTUARY MOUTHS IN THE RHINE-MEUSE DELTA	
J. van de Kreeke and J. Haring	2627
Chapter 159	
BARDEN INLET, N.C.: A CASE STUDY OF INLET MIGRATION	
Limberios Vallianos	2640
Chapter 160	
STUDY ON VORTEX CURRENT IN STRAIT WITH REMOTE-SENSING	
Sotoaki Onishi and Tsukasa Nishimura	2655
Chapter 161	
DYNAMIC SIMILARITY OF TRANSPORT PHENOMENA	
M. S. Yalin and F. Gerritsen	2671
Chapter 162	
MOORING FORCES INDUCED BY PASSING SHIPS--MEASUREMENTS	
IN PROTOTYPE	
K. Haffke	2691
Chapter 163	
NUMERICAL MODELLING OF NEARSHORE CIRCULATION	
Bruce A. Ebersole and Robert A. Dalrymple	2710
Chapter 164	
MODELLING OF PLANFORM INFLUENCE ON CIRCULATION IN	
HARBOURS	
Roger A. Falconer	2726
Chapter 165	
HYDRAULIC CIRCULATION PERFORMANCE OF A CURVILINEAR	
MARINA	
Jeffrey A. Layton	2745
Chapter 166	
THE EFFECT OF BREAKING WAVES ON THE MIXING OF LIQUID	
POLLUTANTS INTO THE SEA	
Arvid Naess	2760

Chapter 167	
ON A ROLE OF THE INTERFACIAL FROUDE NUMBER	
Masakazu Kashiwamura	2780
Chapter 168	
DISPERSION OF COOLING WATER FROM A COASTAL LNG PLANT	
P. Ackers, J. D. Pitt, G. Thompson and K. G. Rippin	2796
Chapter 169	
EXPERIMENTAL STUDY OF THE BUOYANT SURFACE JET WITH THE PRESENCE OF BOTTOM BOUNDARY AND CROSS CURRENT	
B. Safaie	2816
Chapter 170	
DESIGN OF AN INTERMITTENTLY OPERATED OUTFALL	
Roger W. Lindquist and George J. Murphy	2837
Chapter 171	
EXPERIMENTAL EVALUATION OF HEAT EXCHANGE BETWEEN WATER SURFACE AND ATMOSPHERE	
Gunther Barg, Horst Schwarze, and Gerhard Visscher	2851
Chapter 172	
DYNAMICS OF SILT IN ESTUARY, RESIDUAL CURRENT OR FLOCCULATION WHICH PREVAILS?	
J. P. Lepetit and M. Davesne	2861
Chapter 173	
FOR DISPOSAL: 10 m cu m OF CALCIUM CARBONATE SLURRY	
L. Summers and C. A. Fleming	2874
Chapter 174	
AN EXPERIMENT ON CLAY SUSPENSION UNDER WATER WAVES	
Prida Thimakorn	2894
Chapter 175	
CONSIDERATIONS IN THE DESIGN OF AN OFFSHORE DATA COLLECTION PROGRAM	
Cortis Cooper and German Febres	2907
Chapter 176	
THE GERMAN "MORAN" PROJECT	
Winfried Siefert and Volker Barthel	2927
Chapter 177	
ENVIRONMENTAL ASPECTS OF OIL AND GAS PIPELINE LANDFALLS IN NORTHEAST SCOTLAND	
William Ritchie	2938
Chapter 178	
STATISTICAL PROPERTIES OF RANDOM WAVE GROUPS	
Akira Kimura	2955
Chapter 179	
ON THE SYNTHESIS OF REALISTIC SEA STATES	
E. R. Funke and E. P. D. Mansard	2974
Chapter 180	
A COMPARISON OF NATURE WAVES AND MODEL WAVES WITH SPECIAL REFERENCE TO WAVE GROUPING	
Hans F. Burcharth	2992

Chapter 181	
WATER MOVEMENT STUDIES REQUIRED FOR PORT PLANNING	
Graeme C. Dandy, Desmond A. Mills and Jon B. Hinwood	3010
Chapter 182	
INTEGRATION AND COMPUTATION IN AN EXPERIMENTAL STUDY	
J. B. Hinwood, J. E. Watson and D. M. Burrage	3027
Chapter 183	
SOME RECENT RESULTS FOR WAVE INDUCED MOTIONS OF A SHIP IN SHALLOW WATER	
P. A. Madsen, I. A. Svendsen and C. Michaelsen	3043
Chapter 184	
REPORT ON THE DAMAGES TO THE SINES BREAKWATER, PORTUGAL	
William F. Baird, Joseph M. Caldwell, Billey L. Edge, Orville T. Magoon and Donald D. Treadwell	3063
Chapter 185	
DISCRETE-TIME MODELLING OF DISPERSION IN ESTUARIES	
T. Wood	3078
Chapter 186	
MEASUREMENTS OF OSCILLATORY DRAG ON SAND RIPPLES	
Karl E. B. Lofquist	3087
Contribution to the Discussion During Session C, Coastal Processes, Friday, March 28, 2:00 p.m., M. S. Longuet-Higgins, Institute of Oceanographic Sciences, Wormley, Surrey, England	
SUBJECT INDEX	3109
AUTHOR INDEX	3163

A LABORATORY STUDY OF OFFSHORE TRANSPORT OF SEDIMENT AND A MODEL FOR ERODING BEACHES

Tsuguo Sunamura *Institute of Geoscience, University of Tsukuba,
Ibaraki 305, Japan*

ABSTRACT

A two-dimensional laboratory investigation of sediment transport, induced by shallow-water waves, showed that the sediment motion over suspension-dominant asymmetric ripples is closely related to the development of eroding beaches. High-speed motion picture analysis revealed that vortices, formed over this type of ripple, play a crucial role in transporting the sediment to the offshore region. A relation for net offshore sediment flux was formulated for sand 0.02 cm in diameter. A simple model for eroding beaches was proposed and its validity was checked by using two existing data sets for 0.02-cm sand beaches; the model could predict fairly well profile and shoreline changes in the early stages.

INTRODUCTION

Shallow-water waves produce a net sediment transport on a beach. Since beach changes do occur only when a spatial difference of net sediment transport rate exists, an explicit understanding of sediment motion under shallow-water wave action is necessary for beach change studies. Although much research on sediment motion has been conducted in the laboratory (e.g., Davies and Wilkinson, 1977), few have focussed attention on this point.

Beach erosion is clearly caused by the net offshore movement of sand. However, the mechanisms of the offshore movement have not yet been fully clarified even in a laboratory environment; so that no models for predicting erosional beaches have been developed on the basis of sediment dynamics.

The present two-dimensional laboratory study attempts to (1) investigate sediment motion by shallow-water waves and relate this to the beach profile change, (2) elucidate the processes of net offshore transport of sand and estimate the transport rate, and (3) develop a simple model for eroding beaches.

SEDIMENT MOVEMENT CAUSED BY SHALLOW-WATER WAVES AND ITS RELATION TO BEACH PROFILE CHANGE

Komar and Millar (1973; 1974) gave the following relation for the sediment threshold, which was a dimensionally corrected Bagnold's (1946) empirical relation:

$$\rho u_m^2 / (\rho_s - \rho) g D = a (d_o/D)^{1/2} , \quad (1)$$

where u_m = maximum orbital velocity of the water near the bottom, d_o = maximum orbital diameter near the bottom, D = sediment size, ρ_s = sediment density, ρ = water density, g = gravitational acceleration, and a = dimensionless constant. Equation (1) reduces to

$$H_o/L_o = a' (D/L_o)^{1/3} (H_o/H) \sinh(2\pi h/L) , \quad (2)$$

where $a' = [(2a/\pi) (\rho_s/\rho - 1)]^{2/3} = \text{const.}$, using the following relations based on the Airy wave theory:

$$u_m = \pi H / T \sinh(2\pi h/L) , \quad (3)$$

$$d_o = H / \sinh(2\pi h/L) , \quad (4)$$

$$L_o = g T^2 / 2\pi , \quad (5)$$

where H and L = wave height and length at a water depth of h , respectively, H_o and L_o = wave height and length in deep water, respectively, and T = wave period. Equation (2) is basically the same relation that Sato et al. (1962) introduced for the description of sediment motion. A theoretical study by Horikawa and Watanabe (1967) indicated that Eq. (2) is valid only for the onset of sediment movement under conditions of a hydraulically rough bottom and turbulent boundary layer flow. However, Eq. (1) is in good agreement with Bagnold's (1946) and Manohar's (1955) data obtained under laminar boundary layer flow conditions, although the values of a differ slightly from each other (Komar and Miller, 1973; 1974). A further investigation by Komar and Miller (1975) showed that Eq. (1) can also specify the initiation of ripple formation, which amounts to a change in the value of a . A review of these existing studies suggests that the form of Eq. (1) may be applicable to sediment movement under various flow conditions and also to ripple initiation, although this application is theoretically restricted. A useful dimensionless parameter describing sediment motion and bedform would be

$$F = \rho u_m^2 / (\rho_s - \rho) g D^{1/2} d_o^{1/2} , \quad (6)$$

which is an algebraic rearrangement of Eq. (1).

Shallow-water waves create a near-bottom velocity field which is characterized by a larger onshore velocity of shorter duration under wave crests, and a smaller offshore velocity of longer duration under wave troughs, as compared to a purely sinusoidal orbital velocity field. A dimensionless parameter on which the deviation from the sinusoidal velocity field depends, is the Ursell number (Ursell, 1953):

$$U = H L^2 / h^3 \tag{7}$$

With increasing U , the degree of deviation becomes greater.

A relationship between F and U (Eqs. (6) and (7)) was investigated on the basis of a laboratory experiment performed using a large (25 m long, 1.5 m deep, and 0.8 m wide) and a small wave tank (6 m long, 0.3 m deep, and 0.2 m wide). Both tanks were equipped with flap-type wave makers at one end of the tank, and wave absorbers were placed at the other end. Four kinds of well-sorted bed material with Trask's (1930) sorting coefficients of 1.05~1.10 were used. Three kinds of sand with the same density, $\rho_s = 2.65 \text{ g/cm}^3$, and different diameters, $D = 0.02, 0.07, \text{ and } 0.156 \text{ cm}$, and plastic beads with $\rho_s = 1.33 \text{ g/cm}^3$ and $D = 0.055 \text{ cm}$ were used. A flat horizontal bed was set up in the central portion of the wave tank. Water depth over the horizontal bed was 30~40 cm for the large tank test, and 10~15 cm for the small tank test. Wave period ranged from 1.0~3.4 sec for the former, and 0.69~1.7 sec for the latter. A series of tests was performed by gradually increasing wave height with wave period being kept constant. The mode of sediment motion and bedform were observed visually.

The results are shown in Fig. 1. Different values of k in the following equation gave a fairly good demarcation of the different regions of bedforms:

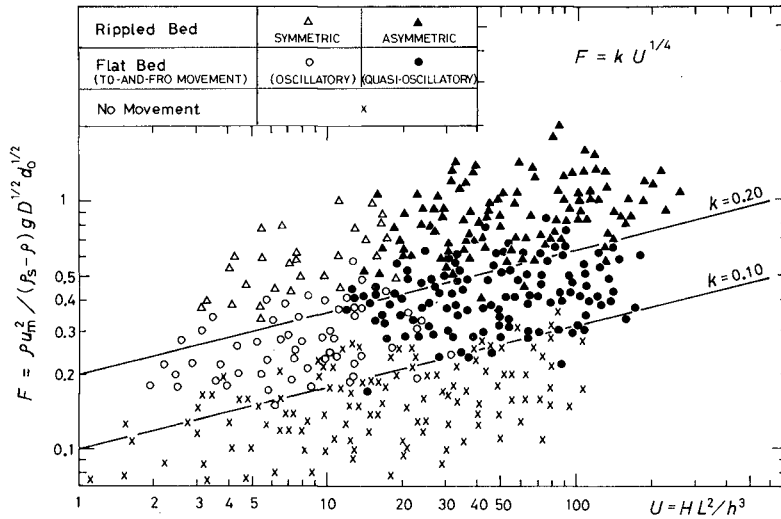


Figure 1. Relationship between F and U for bedform demarcation.

$$F = k U^{1/4} . \quad (8)$$

With increasing the Ursell number, either non-sinusoidal sediment movement or asymmetric bedform occurs becoming noticeable for $U \geq 10 \sim 20$. The region occupied by solid circles ($0.10 \lesssim k \lesssim 0.20$) denotes the occurrence of a quasi-oscillatory bedload producing a net onshore transport. Above this region, lies a region of asymmetric ripples, shown by a cluster of solid triangles ($k \gtrsim 0.20$). When ripples are formed, there always exists suspended sediment, which is defined here as the sediment moved not only in pure suspension but also in saltation.

To study sediment motion over asymmetric ripples, Sato and Tanaka (1962) and Sato et al. (1962) have performed radioactive-tagged sand tracer experiments. They replaced the sand forming one asymmetric ripple by radioactive sand and traced its movement. The results demonstrated the occurrence of two different types of sediment motion: one is bedload dominant movement producing a net onshore transport (Fig. 2), while the other is suspended-load dominant movement producing a net offshore transport (Fig. 3). Note that Fig. 3 shows no onshore dispersion of the tracer.

Figure 4 is a plot of selected data showing the directions of net sediment transport over asymmetric ripples; solid symbols denote offshore transport, while open symbols onshore transport. Although there are not a sufficient number of the data points, a boundary between onshore and offshore regions could be expressed by the dashed line:

$$F \begin{array}{l} > \\ < \end{array} 0.28 U^{1/4} \quad \begin{array}{l} \text{Net offshore transport} \\ \text{Net onshore transport.} \end{array} \quad (9)$$

If this relation is applicable at the wave breaking point of a sloping beach, then the following relation can be written:

$$F_b \begin{array}{l} > \\ < \end{array} 0.28 U_b^{1/4} . \quad (10)$$

The subscript "b" denotes quantities at the wave breaking point. If the left-hand side of this equation is greater than the right-hand side, then net offshore transport of sediment takes place through the wave breaking point; this leads to the development of an eroding beach as shown in the inset of Fig. 5. For the reverse case, an accreting beach develops. If the preceding assumption is valid, then a boundary between eroding and accreting beaches should be given by

$$F_b = 0.28 U_b^{1/4} , \quad (11)$$

where

$$F_b = \rho (u_m)_b^2 / (\rho_s - \rho) g D^{1/2} (d_o)_b^{1/2} ,$$

$$U_b = H_b L_b^2 / h_b^3 ,$$

$$(u_m)_b = \pi H_b / T \sinh(2\pi h_b / L_b) ,$$

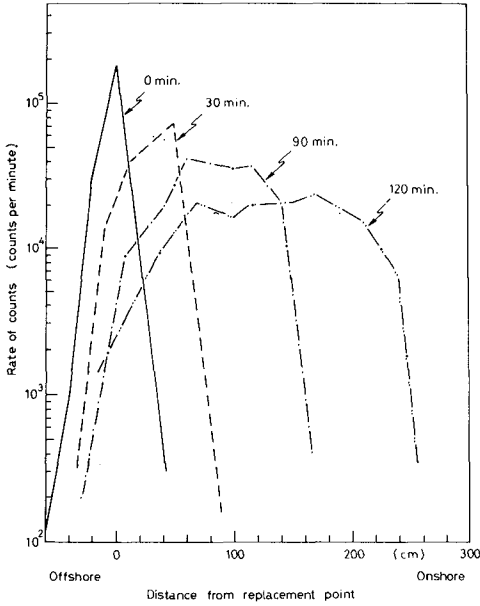


Figure 2.

Temporal change of radioactive sand distribution, showing net onshore transport. (Sato et al., 1962)

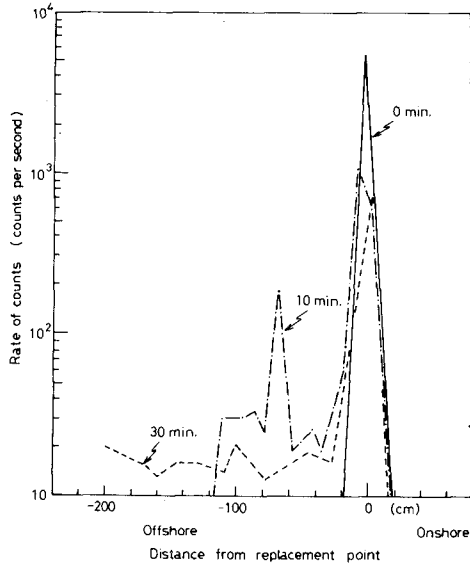


Figure 3.

Temporal change of radioactive sand distribution, showing net offshore transport. (Sato et al., 1962)

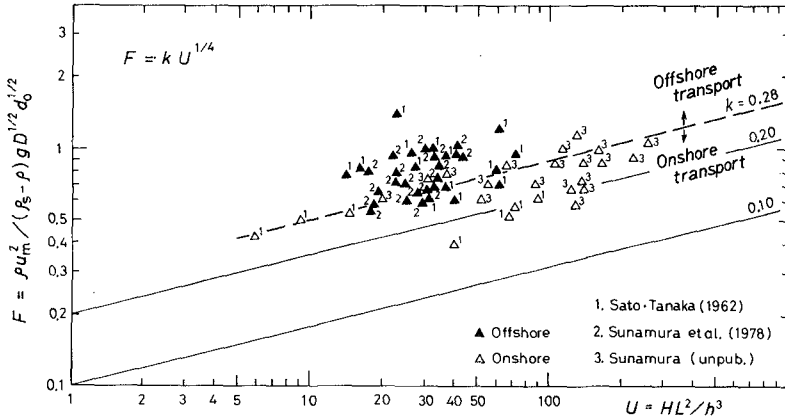


Figure 4. Directions of net sediment-transport over ripples.

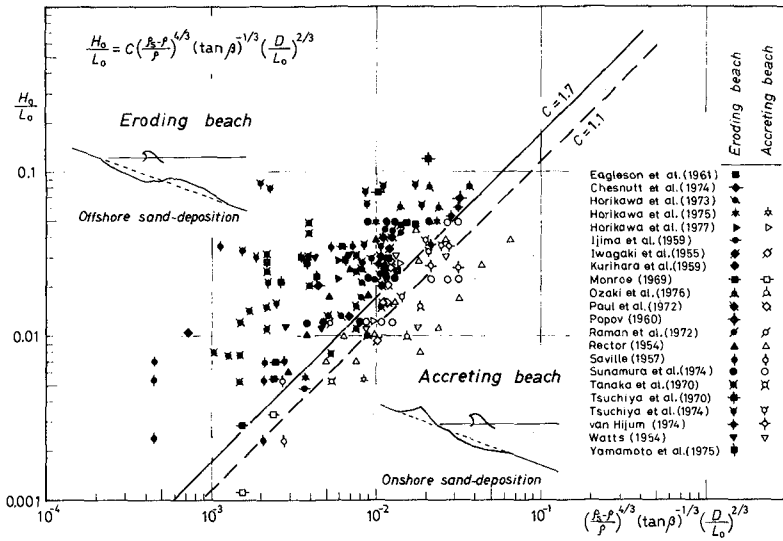


Figure 5. Demarcation of eroding and accreting beaches.

Table 1. Data sets used for the validity check of Eq. (12).

No.	Researcher(s)	δ_0 (cm)	ρ_s (g/cm^3)	$\tan \beta$	H_0 (cm)	T (sec)	t (hr)	Remarks*
1.	Eagleson et al. (1961)	0.037	2.65	1/20-1/45	9.1-10.8	1.15-1.53	121-222	S, M
2.	Chesnut et al. (1974)	0.02	2.65	1/10	11.8	1.9	375	S, M
3.	Horikawa et al. (1973)	0.02	2.65	1/24	5.3-7.3	1.4-1.7	48-240	S, M
4.	Horikawa et al. (1975)	0.02-0.07	2.65	1/10	3.4-7.6	1.0-2.0	178-266	S, M
5.	Horikawa et al. (1977)	0.02-0.07	2.65	1/10	7.5-10	1.5-2.0	1-20	S, M
6.	Ijima et al. (1959)	0.028	2.65	1/20	6.8-7.7	1.5-3.0	20-23.3	S, M
7.	Iwagaki et al. (1955)	0.03	2.63	1/10	2.09-5.88	1.07-1.21	4-12	S, M
8.	Kurthara et al. (1959)	{ 0.02 0.03	{ 2.65 1.30	{ 1/10 1/10	{ 3.84 4.30	{ 1.39 1.64	{ 5-7 5-7	{ S, M C, M
9.	Monroe (1969)	0.027	2.65	1/15	4.33-17.1	1.19-5.06	16-47	S, M
10.	Ozaki et al. (1976)	0.022-0.049	2.65	1/50	4.4-14.4	0.86-1.69	60-128	S, M
11.	Paul et al. (1972)	0.0357-0.063	2.67-2.71	1/10	4.15-78.2	1.29-1.71	≥ 36	S, M
12.	Popov (1960)	0.6	2.65	1/3	31.3	1.73	16.8	S, M
13.	Raman et al. (1972)	0.03	2.65	1/8-1/15	6.49-7.54	1.0-2.0	40-45	S, M
14.	Rector (1954)	0.022-0.344	2.65	1/30	10.1-13.1	1.3-3.3	70-200	S, M
15.	Saville (1957)	0.022	2.65	1/16	3.05-168	1.77-11.3	40	S, M
16.	Sunamura et al. (1974)	0.02-0.07	2.65	1/10-1/30	3.4-7.6	1.0-2.0	160	S, M
17.	Tanaka et al. (1970)	{ 0.02 0.023	{ 2.65 1.60	{ 1/20 1/10-1/20	{ 3.2-10.8 2.5-10.8	{ 0.95-1.98 0.95-2.2	{ 10-15 10-15	{ S, M C, M
18.	Tsuchiya et al. (1970)	0.02	2.65	1/15	7.2	0.62	130	S, W
19.	Tsuchiya et al. (1974)	{ 0.022-0.073 0.032	{ 2.59-2.65 1.36	{ 1/15 1/15	{ 2.08-18.7 1.90-14.8	{ 0.76-1.34 0.69-1.27	{ 15-60 7-15	{ S, M C, W
20.	van Huijsum (1974)	0.13-0.61	2.65	1/5-1/10	16.2-38.0	1.6-2	0.5-4	S, M
21.	Watts (1954)	0.022-3.44	2.65	1/20	12.7-18.7	2.0-2.68	40	S, M
22.	Yamanoto et al. (1975)	{ 0.018 0.021	{ 2.65 1.45	{ 1/10-1/50 1/10-1/50	{ 11.4-18.8 2.06-3.59	{ 1.8-2.0 0.8-0.9	{ 10-31.5 4-17	{ S, M C, M

* S = Sand; C = Coal powder; M = Monochromatic waves; W = Wind waves

$$(d_o)_b = H_b / \sinh(2\pi h_b/L_b) .$$

Equation (11) was transformed using the approximations: $\sinh(2\pi h_b/L_b) \approx 2\pi h_b/L_b$, $\tanh(2\pi h_b/L_b) \approx 2\pi h_b/L_b$, $29/30 \approx 1$, and $35/12 \approx 3$; and two empirical relations on breaker characteristics:

$$H_b/h_b = 1.1 (\tan \beta)^{1/6} (H_o/L_o)^{-1/12} , \quad (\text{see Appendix}) \quad (12a)$$

$$H_b/H_o = (\tan \beta)^{1/5} (H_o/L_o)^{-1/4} , \quad (12b)$$

where $\tan \beta =$ beach slope and Eq. (12b) was given by Sunamura and Horikawa (1974). This results in

$$H_o/L_o = C (\rho_s/\rho - 1)^{4/3} (\tan \beta)^{-1/3} (D/L_o)^{2/3} \quad (13)$$

with the constant, C , being equal to 1.1. The parameters, H_o/L_o and $(\tan \beta)^{-1/3} (D/L_o)^{2/3}$, are very similar to the parameters used for beach profile classification, which were semi-empirically obtained on the basis of surf-zone hydraulics, i.e., H_o/L_o and $(\tan \beta)^{-0.27} (D/L_o)^{0.67}$ (Sunamura and Horikawa, 1974). The validity of Eq. (13) was checked using the existing beach profile data with various wave durations, t (Table 1). The results are plotted in Fig. 5; $C = 1.1$ gives a good demarcation between eroding and accreting beaches, although $C = 1.7$ provides the best. This suggests that the sediment transport mode at the wave breaking point is closely related to beach profile change.

MECHANICS OF OFFSHORE TRANSPORT OF SEDIMENT AND QUANTIFICATION OF TRANSPORT RATE

For the development of a model for eroding beaches, knowledge of net offshore sediment flux, associated with the wave and sediment parameters, is required. Sediment motion producing a net offshore transport is very rapid and complex. This quickness and complexity have hampered this sort of study.

In order to overcome these difficulties, a 16-mm high-speed movie camera was adopted for a laboratory test, in which the small wave tank was used (Sunamura et al., 1978). The movement of the well-sorted 0.02-cm sand, which formed asymmetric ripples with suspension-dominant transport on a horizontal bed, was photographed at a film speed of 200 500 frames/sec. Neutral-buoyant polystyrene beads, 1.5 mm in diameter, were used for tracing the water orbital motion.

Figure 6 shows one characteristic example of sediment movement, taken from the high-speed motion picture films via a film analyzer. The ellipses indicate the orbital motion of the water and the multiple arrows denote sand particle velocity vectors. Note that the sand particles are entrapped in a vortex formed at the onshore side of the R_2 ripple in stage (1); the particles are represented by open circles. Immediately after the onset of offshore flow, these sand particles are

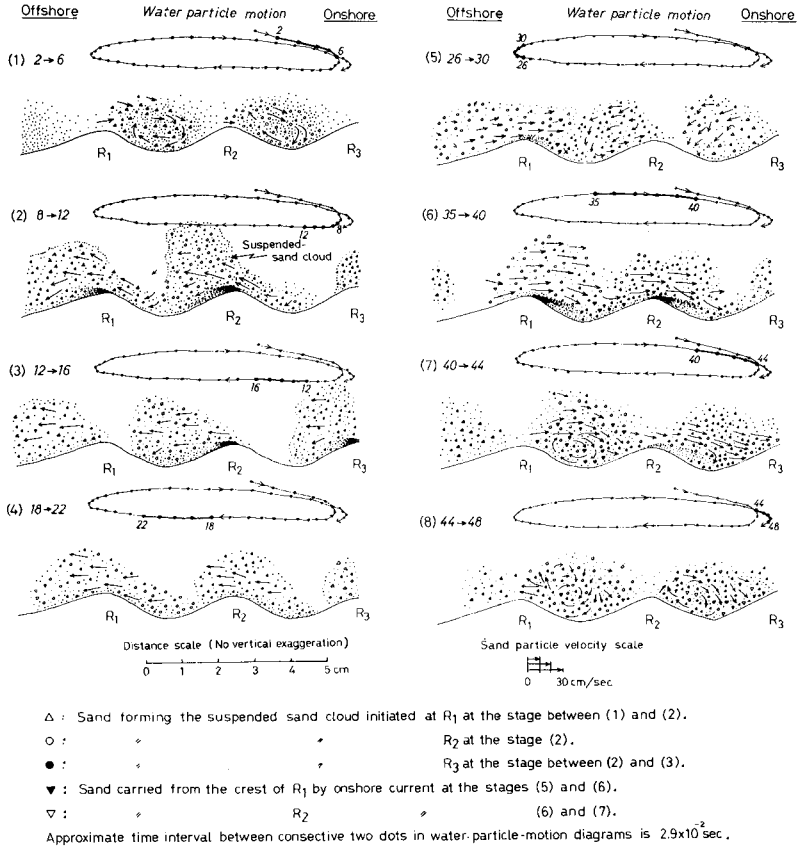


Figure 6. Sediment movement over asymmetric ripples with suspension-dominant transport. (Sunamura et al., 1978)

thrown up obliquely in an offshore direction to form a suspended-sand cloud, which is shown in stage (2). The following two stages, (3) and (4), show that the offshore flow carries this sand cloud offshore, partially depositing the sand particles. As shown in stages (5) and (6), the onshore flow returns these offshore-transported sand particles to the place where they were initially entrapped in the vortex, that is, to the onshore side of the R_2 ripple. During this return travel, however, the sediment once transported offshore beyond a certain limit cannot return to the onshore side of the R_2 ripple, due to being captured in a vortex formed at the onshore flank of the R_1 ripple, as shown in stage (7). This unreturned sediment constitutes the net offshore-transported load. It should be emphasized that strong vortices, formed over the onshore flank of asymmetric ripples, play a vital role in continuing the net offshore sediment transport in this mode of suspension. These vortices are formed with an approximate phase lag of $\pi/6$ after the onshore orbital motion attains its maximum speed.

The film analysis indicated that the offshore limit, beyond which offshore-transported sediment never returns to the initial position, is located at 1.5λ , where λ is the ripple length (Fig. 7). Sediment in the hatched portion constitutes the net offshore-transported load. In this figure, ℓ is the maximum offshore extension of the sand cloud. Precise measurement of this transported load is extremely difficult, because the measurement must be done without disturbing ripple configuration or the velocity field. However, an estimation is possible if we assume a triangular distribution of sediment particles over the ripples at the stage of maximum offshore extension of the sand cloud (Fig. 8). The following relation can be written:

$$Q_{\text{off}} = \delta Q, \quad (14)$$

where Q_{off} = net offshore transport volume of sediment, Q = volume of sediment included in a sand cloud, and

$$\delta = \begin{cases} 0, & \ell \leq 1.5 \lambda \\ (1 - 1.5 \lambda / \ell)^2, & \ell > 1.5 \lambda. \end{cases}$$

The direct measurement of Q is difficult due to the variability of shape and size of the sand cloud. Since the sand cloud originates from the sand vortex, Q is considered to be approximately equal to the volume of sand forming the vortex. During the vortex formation, (1) the area of the vortex only changes a little and (2) the sand distribution within the vortex seems to be uniform. Then, Q can be expressed by

$$Q = A S / T, \quad (15)$$

where A = area of the vortex, S = volumetric sand concentration in the vortex, and T = wave period. In order to relate Q to the parameters associated with the velocity field and sediment characteristics, the following dimensionless quantities are introduced:

$$\Omega = Q / \sqrt{(\rho_s / \rho - 1) g D D} \quad \} \quad (16)$$

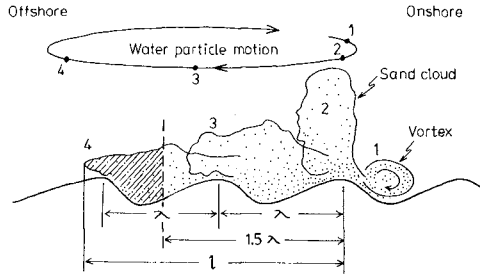


Figure 7.
Definition sketch.

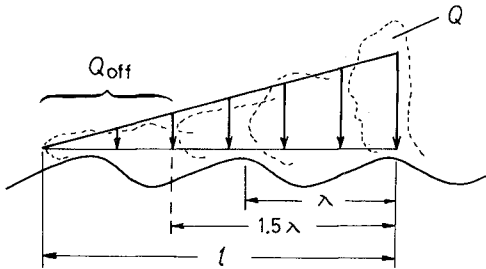


Figure 8.
Definition sketch.

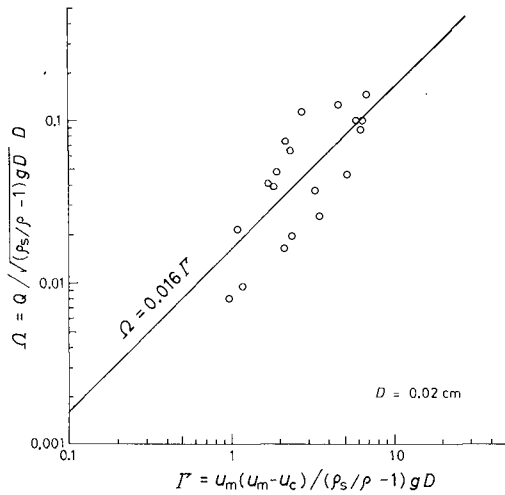


Figure 9.
Relationship between Ω and Γ for 0.02-cm sand.

$$\Gamma = u_m (u_m - u_c) / (\rho_s/\rho - 1) g D \quad] ,$$

where u_c = critical velocity for asymmetric ripple formation = $0.02^{1/2} (\rho_s/\rho - 1)^{1/2} g^{1/2} D^{1/4} d_o^{1/4} (HL^2/h^3)^{1/8}$; this was obtained by substituting $k = 0.20$ and $u_m = u_c$ into Eq. (8) (see Fig. 1).

To find a connection between Ω and Γ , a laboratory experiment was performed on a horizontal bed, in the small wave tank, made of the well-sorted 0.02-cm sand. The high-speed movie camera was used for the measurement of A . An Iowa-type sediment concentration meter (Locher et al., 1974) was employed to measure S . The measurement, made in the vicinity of the vortex center, was completed within four or five waves, because longer installation of the sensor skewed the ripples so that a change of sand volume in the vortex occurred. For the computation of Q , using Eq. (15), the mean values of A and S were used; the former was averaged over several waves and the latter was a time-averaged value, over three consecutive waves, of the record during the period of vortex formation. Figure 9 shows the relationship between Ω and Γ . Although some scatter of data points is seen, a linear relation is present:

$$\Omega = 0.016 \Gamma. \quad (17)$$

Using Eqs. (14), (16), and (17), a net offshore sediment flux equation is finally obtained:

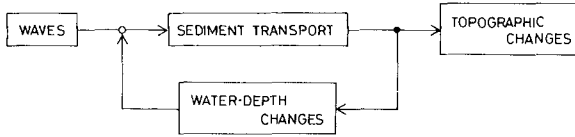
$$Q_{off} = 0.016 \left(\frac{\ell - 1.5 \lambda}{\ell} \right)^2 \frac{u_m (u_m - u_c) \sqrt{D}}{\sqrt{(\rho_s/\rho - 1) g}}, \quad (18)$$

which gives volumetric transport rate per unit width. This equation is valid only for $\ell > 1.5 \lambda$. It should be noted that this is not a general relation for different sediment sizes, but a relation for only 0.02-cm sand. A generalization must await future studies.

A MODEL FOR ERODING BEACHES

In the two-dimensional laboratory beach changes, a feedback relationship between input waves and the resultant topography usually exists (Fig. 10(a)). Especially, on an eroding beach which is characterized by the sediment accumulation in the offshore region, the wave breaking point shifts offshore in time due to the decrease in water depth accompanying the changes of breaker type and height. This was investigated by Chesnutt and Galvin (1974). Since the formulation of the feedback system seems complicated, the present study attempts to develop a simpler model for eroding beaches, based on an open-loop system (Fig. 10(b)), i.e., the system in which no wave-topography interaction exists. Accordingly, no temporal changes occur in the breaker parameters. We further assume that the sand elevation at the wave breaking point does not change with time. Hence, this model has a time-independent breaking point.

(a) CLOSED-LOOP SYSTEM



(b) OPEN-LOOP SYSTEM



Figure 10. Closed-loop and open-loop systems in beach changes.

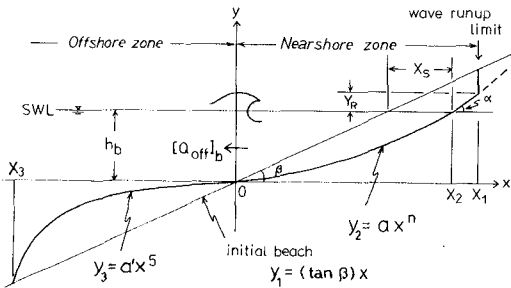


Figure 11.
Definition sketch.

Figure 11 shows the co-ordinate system in which the origin is chosen at the wave breaking point on the initial beach which is expressed by

$$y_1 = (\tan \beta) x , \tag{19}$$

where $\tan \beta$ = initial beach slope. In the nearshore zone, from the wave breaking point to the wave uprush limit, the eroding beach profile is assumed to be described by

$$y_2 = \alpha x^n , \tag{20}$$

where both α and n are time-dependent variables. At the wave runup limit, $x = x_1$, the beach profile is expressed by a vertical line or scarp:

$$x_1 = [(h_a + Y_R) / \alpha]^{1/n} , \tag{21}$$

where h_b = breaker depth and Y_R = maximum height of wave runup. At the shoreline position, $x = x_2$,

$$\left(\frac{dy_2}{dx} \right)_{x=x_2} = \tan \alpha, \quad (22)$$

where $\tan \alpha$ = local beach slope or beach gradient at the shoreline, and

$$x_2 = (h_b / a)^{1/n}. \quad (23)$$

Equations (20), (22), and (23) lead to

$$a = (\tan \alpha)^n / n^n h_b^{n-1}. \quad (24)$$

Since

$$(Q_{\text{off}})_b = (1/t) \int_0^{x_1} (y_1 - y_2) dx, \quad (25)$$

where $(Q_{\text{off}})_b$ = net offshore sediment transport rate at the wave breaking point, substitution of Eqs. (19), (20), and (21) into Eq. (25) gives

$$\frac{\tan \beta}{2} \left(\frac{h_b + Y_R}{a} \right)^{2/n} - \frac{a}{n+1} \left(\frac{h_b + Y_R}{a} \right)^{(n+1)/n} = (Q_{\text{off}})_b \cdot t. \quad (26)$$

From Eqs. (24) and (26), both a and n are respectively obtainable as a function of time. Thus, the nearshore beach profile changes can be described by Eq. (20). The shoreline displacement, X_S (see Fig. 11), is given as

$$X_S = \begin{cases} 0, & (h_b / a)^{1/n} \leq (h_b / \tan \beta) \\ (h_b / a)^{1/n} - (h_b / \tan \beta), & (h_b / a)^{1/n} > (h_b / \tan \beta). \end{cases} \quad (27)$$

In the offshore zone beyond the wave breaking point, $x < 0$ (see Fig. 11), the depositional topography is assumed to be simply given by

$$y_3 = a' x^5, \quad (28)$$

where a' is a time-dependent variable. Since

$$(Q_{\text{off}})_b = (1/t) \int_{x_3}^0 (y_3 - y_1) dx, \quad (29)$$

where $x_3 = -[(\tan \beta)/a']^{1/4}$, Eqs. (19), (28), and (29) give the offshore beach profile as

$$y_3 = (\tan \beta)^3 x^5 / 9 (Q_{\text{off}})_b^2 t^2. \quad (30)$$

If the direct application of Eq. (18) is possible to the wave

breaking point on a sloping beach made of 0.02-cm sand, then

$$(Q_{\text{off}})_b = 0.016 \left(\frac{\ell_b - 1.5 \lambda_b}{\ell_b} \right)^2 \frac{(u_m)_b [(u_m)_b - (u_c)_b] \sqrt{D}}{\sqrt{(\rho_s/\rho - 1)g}}, \quad (31)$$

where ℓ_b = maximum offshore extension of suspended sand cloud at the wave breaking point, λ_b = length of sand ripples formed at the wave breaking point, and

$$(u_c)_b = 0.20^{1/2} \left(\frac{\rho_s - \rho}{\rho} \right)^{1/2} g^{1/2} D^{1/4} (d_o)_b^{1/4} \left(\frac{H_b \ell_b^2}{h_b^3} \right)^{1/8}.$$

Knowing the four quantities, $\tan \alpha$, Y_R , ℓ_b , and λ_b , it is possible to calculate beach profile changes and shoreline displacements. However, these quantities must be experimentally determined at present.

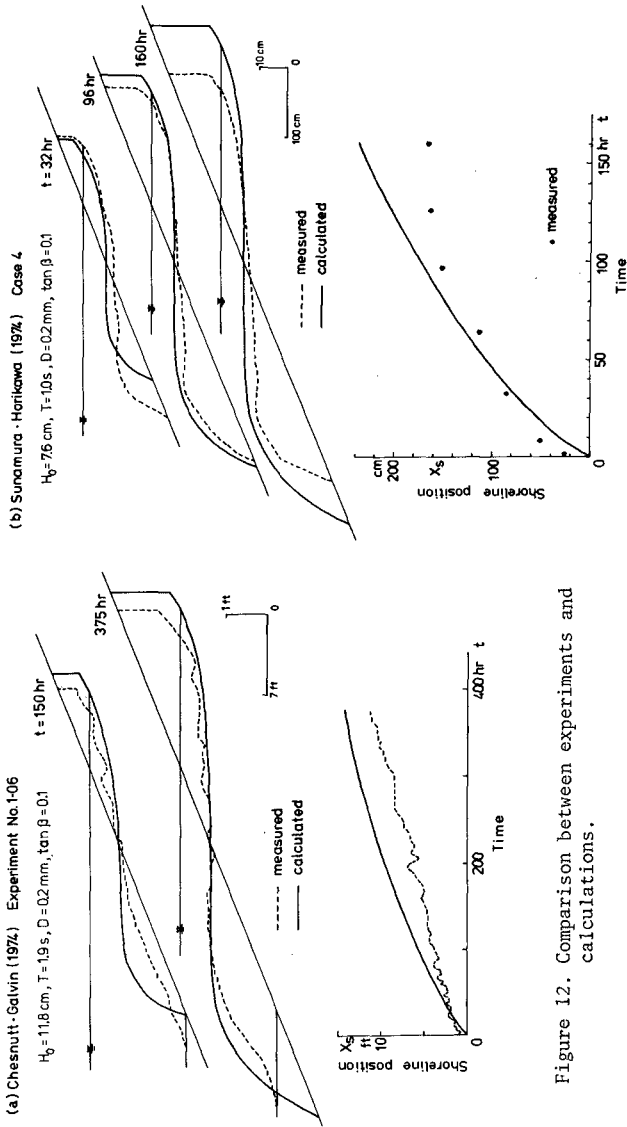
Table 2 shows the data for two selected experiments with eroding beaches, which was used for a check of the validity of this model. The selection was based on the following three criteria: (1) the grain size of sand used should be 0.02 cm, because the sediment flux equation is available for only 0.02-cm sand; (2) the duration of wave action should be more than 100 hours, because the longer the duration, the better is the check of the characteristics of this model; and (3) data of temporal changes of the beach profile and shoreline position should be available.

A similar experiment on a sloping beach was carried out under the same conditions as listed in the upper rows of Table 2, for only first hour. A flap-type wave maker-equipped tank 16 m long, 0.7 m high, and 0.5 m wide, was used. The four quantities were measured immediately

Table 2. Data sets used for the validity check of the model.

	Chesnutt-Galvin (1974) Experiment No.1-06	Sunamura-Horikawa (1974) Case 4
D	0.02 cm	0.02 cm
$\tan \beta$	0.1	0.1
H_o	11.8 cm	7.6 cm
T	1.9 sec	1.0 sec
t	375 hr	160 hr
λ_b^*	11 cm	5 cm
ℓ_b^*	$\approx 2.3 \lambda_b$	$\approx 2.3 \lambda_b$
Y_R^*	8 cm	4 cm
$\tan \alpha^*$	0.12	0.12

* Measured immediately after 30-minute wave action



after 30 minutes of wave action; the results are listed in the lower rows of Table 2. Assuming these quantities are all independent of time, a calculation was done with breaker characteristics obtained from Eqs. (12a) and (12b).

Figure 12(a) shows that the calculation overestimates the nearshore zone profile, and that the calculation and the experiment are in fairly good agreement only in the early stages. A noticeable disagreement is evident in the mid-late stage. Both the nearshore beach profile and the shoreline changes in Fig. 12(b) show that the calculation and the experiment are in good agreement during the early stages. However, the disagreement becomes marked after these stages, like the result of the former case. One of the reasons for this would probably be the neglect of the effect of wave-topography interaction. Some modification of this model is therefore needed.

CONCLUSIONS

Vortices formed over asymmetric ripples with suspension-dominant transport play a vital role in continuing a net offshore sand transport in this mode of suspension. A validity check using two existing data sets indicates that the eroding-beach model worked fairly well in predicting the erosional features in the early stages.

ACKNOWLEDGMENTS

The horizontal-bed experiments were performed while the author was at the Coastal Engineering Laboratory, University of Tokyo; the supplementary experiment on a sloping beach was conducted using the facilities of the Environmental Research Center, University of Tsukuba. This study was partly supported through the Science Research Fund of the Ministry of Education.

REFERENCES

- Bagnold, R. A. (1946): Motion of waves in shallow water; interaction between waves and sand bottoms. Proc. Royal Soc. London, v.187, Series A, p.1-15.
- Battjes, J. A. (1974): Surf similarity. Proc. 14th Conf. Coastal Eng., p.466-480.
- Chesnutt, C. B. and Galvin, C. J., Jr. (1974): Lab profile and reflection changes for $H_0/L_0 = 0.02$. Proc. 14th Conf. Coastal Eng., p. 958-977.
- Davies, A. G. and Wilkinson, R. H. (1977): The movement of non-cohesive sediment by surface water waves, Part I: Literature survey. Inst. Oceanogr. Sci., Report 45, 73 p. (unpub. manuscript).

- Eagleson, P. S., Glennie, B. and Dracup, J. A. (1961): Equilibrium characteristics of sand beaches in the offshore zone. U.S. Army Beach Erosion Board, Tech. Memo. 126, 66p.
- Horikawa, K. and Watanabe, A. (1967): A study on sand movement due to wave action. Coastal Eng. Japan, v.10, p.39-57.
- Horikawa, K., Sunamura, T. and Kitoh, H. (1973): A study of beach deformation by wave action. Proc. 20th Japan. Conf. Coastal Eng., p. 357-363 (in Japanese).
- Horikawa, K., Sunamura, T. and Shibayama, T. (1977): Experimental study of two-dimensional shore transformation — Methods for measurement of sand transport rate in offshore region —. Proc. 24th Japan. Conf. Coastal Eng., p.170-174 (in Japanese).
- Horikawa, K., Sunamura, T., Kondo, K. and Okada, S. (1975): Experimental study of two-dimensional shoreline change due to waves. Proc. 22nd Japan. Conf. Coastal Eng., p.329-334 (in Japanese).
- Ijima, T. and Aono, M. (1959): The effect of sediment size on beach profile change. Proc. 6th Japan. Conf. Coastal Eng., p.49-56 (in Japanese).
- Iwagaki, Y. and Sawaragi, T. (1955): An experiment of equilibrium beach profile and sand movement by waves. Proc. 2nd Japan. Conf. Coastal Eng., p.99-105 (in Japanese).
- Komar, P. D. and Miller, M. C. (1973): The threshold of sediment movement under oscillatory water waves. Jour. Sed. Petrology, v.43, p.1101-1110.
- Komar, P. D. and Miller, M. C. (1974): Sediment threshold under oscillatory waves. Proc. 14th Conf. Coastal Eng., p.756-775.
- Komar, P. D. and Miller, M. C. (1975): The initiation of oscillatory ripple marks and the development of plane-bed at high shear stress under waves. Jour. Sed. Petrology, v.45, p.697-703.
- Kurihara, M., Shinohara, K., Tsubaki, T. and Yoshioka, M. (1956): Beach sediment movement by waves. Proc. 3rd Japan. Conf. Coastal Eng., p.151-158 (in Japanese).
- Locher, F. A., Glover, J. R. and Nakato, T. (1974): Investigation of the operating characteristics of the Iowa sediment concentration measuring system. Iowa Inst. Hydraulic Res.; Univ. Iowa, Report 170, 99p.
- Manohar, M. (1955): Mechanics of bottom sediment movement due to wave action. U.S. Army Beach Erosion Board, Tech. Memo. 75, 121p.
- Monroe, F. F. (1969): Oolitic aragonite and quartz sand: laboratory comparison under wave action. U.S. Army Coastal Eng. Res. Center, Misc. Paper 1-69, 22p.
- Ozaki, A. and Watanabe, H. (1976): Scale effect in the experiment of two-dimensional beach profile changes. Proc. 23rd Japan. Conf. Coastal Eng., p.200-205 (in Japanese).
- Paul, M. J., Kamphuis, J. W. and Brebner, A. (1972): Similarity of equilibrium beach profiles. Proc. 13th Conf. Coastal Eng., p. 1217-1236.
- Popov, I. J. (1960): Experimental research in formation by waves of stable profiles of upstream faces of earth dams and reservoir shores. Proc. 7th Conf. Coastal Eng., p.282-293.
- Raman, H. and Earattupuzha, J. J. (1972): Equilibrium conditions in beach wave interaction. Proc. 13th Conf. Coastal Eng., p.1237-1256.

- Rector, R. L. (1954): Laboratory study of equilibrium profiles of beaches. U.S. Army Beach Erosion Board, Tech. Memo. 41, 38 p.
- Sato, Sh. and Tanaka, N. (1962): Wave induced sand movement on a horizontal bed. Proc. 9th Japan. Conf. Coastal Eng., p.95-100 (in Japanese).
- Sato, Sh., Ijima, T. and Tanaka, N. (1962): A study of critical depth and mode of sand movement using radioactive glass sand. Proc. 8th Conf. Coastal Eng., p.304-323.
- Saville, T., Jr. (1957): Scale effects in two dimensional beach studies. Proc. 7th Meeting Int. Assoc. Hydraulic Res., p.(A3)1-8.
- Sunamura, T. and Horikawa, K. (1974): Two-dimensional beach transformation due to waves. Proc. 14th Conf. Coastal Eng., p.920-938.
- Sunamura, T., Bando, K., and Horikawa, K. (1978): An experimental study of sand transport mechanisms and transport rate over asymmetric sand ripples. Proc. 25th Japan. Conf. Coastal Eng., p.250-254 (in Japanese).
- Tanaka, N. and Sinbo, O. (1973): Properties of coal grains as bed material in the model experiment on littoral drift. Port and Harbour Res. Inst., Report 12, p.3-57 (in Japanese).
- Trask, P. D. (1930): Mechanical analysis of sediments by centrifuge. Econ. Geol., v.25, p.581-599.
- Tsuchiya, Y. and Yoshioka, S. (1970): Experimental study of beach deformation by wind waves (1). Memoir 25th Annual Conv., Japan. Soc. Civil Eng., p.97-98 (in Japanese).
- Tsuchiya, Y. and Inada, K. (1974): Laboratory experiment of beach changes due to wind waves. Proc. 21st Japan. Conf. Coastal Eng., p.219-224 (in Japanese).
- Ursell, F. (1953): The long-wave paradox in the theory of gravity waves. Proc. Cambridge Phil. Soc., v.49, p.685-694.
- Van Hijum, E. (1974): Equilibrium profiles of coarse material under wave attack. Proc. 14th Conf. Coastal Eng., p.939-957.
- Watts, G. M. (1954): Laboratory study of effect of varying wave period on beach profiles. U.S. Army Beach Erosion Board, Tech. Memo. 53, 19p.
- Yamamoto, K. and Nozumi, M. (1975): A study of similarity law in beach changes. Public Works Res. Inst., Tech. Memo. 975, 131p. (in Japanese).

APPENDIX

Figure A-1 is taken from Battjes (1974), in which γ_b = ratio of breaker height to depth = H_b/h_b , and ξ_0 = surf similarity parameter = $\tan \beta / (H_0/L_0)^{1/2}$. He stated that $\gamma_b \approx 0.8$ for $\xi_0 \leq 0.2$ and that γ_b increases slightly with increasing ξ_0 for $\xi_0 > 0.2$. However, such a general tendency as indicated by the dashed line (drawn by the present author) is clearly seen in spite of the considerable scatter of the data points. This line is expressed by

$$\gamma_b = 1.1 \xi_0^{1/6}$$

or

$$H_b/h_b = 1.1 (\tan \beta)^{1/6} (H_0/L_0)^{-1/12} .$$

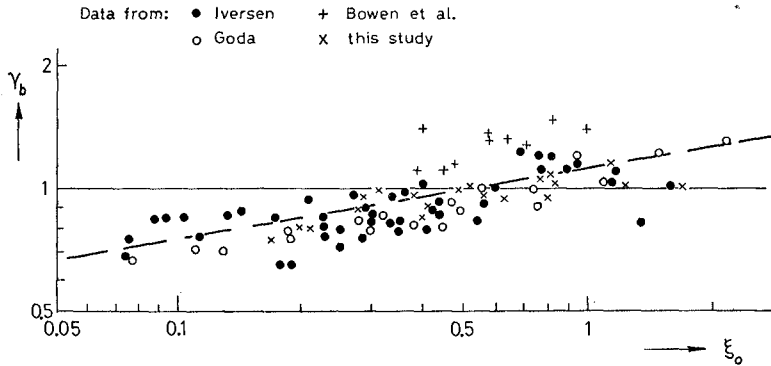


Figure A-1. Breaker height-depth ratio vs. surf similarity parameter (Battjes, 1974).

CHAPTER 66

NEARSHORE CURRENTS ON A PARTIALLY ROCKY SHORE

BY

T. O. Sasaki*, H. Igarashi** and S. Harikai**

ABSTRACT

Nearshore circulation on a partially rocky shore at Haranomachi Beach, Fukushima Prefecture, Japan has been studied in terms of field observations and numerical experiments for a low energy wave regime and with a physical experiment for a high energy wave regime. No significant distinctions were found in current velocity and rip current spacing between rocky and sandy beaches for the low energy wave regime, however the positions of rip currents were affected by wave refraction from the offshore exposed rocky bottom. On the other hand, since the surf zone bed is largely occupied by an exposed rocky floor for the high energy wave regime, the circulation exhibited fairly irregular patterns, so that a rip current becomes difficult to define, however the positions of inflow across the breaker line were found to be coincident with wave convergence zone.

INTRODUCTION

Japanese coasts have been classified as "island arc collision coasts" according to the global classification of Inman and Nordstrom (1973) based on recent plate tectonics. Since the major morphological feature of these coasts are mountains, rocky coastlines claim a large share of the Japanese Islands.

Because major national parks occupy the most scenic segments associated with rocky shores, recent nuclear and conventional power stations have been and are being placed on the remaining rocky shores.

The term "partially rocky shore" is defined as a rocky shore that has a portion of its beach on an upper part of a rocky bottom profile. Geologically, it consists of less consolidated Tertiary and/or Quaternary sedimentary rocks, such as sandstone and/or mudstone.

* Chief Engineer, Nearshore Environment Research Center, 1202 Familie Hongo Bldg., 1-20-6 Mukohgaoka, Bunkyo-ku, Tokyo, 113 Japan.

** Research Engineer, Nearshore Environment Research Center, Tokyo 113, Japan.

When attempting to assess environmental impacts, such as power stations on rocky shores, coastal engineers face a general lack of information regarding nearshore processes on such shores in comparison with ordinary sandy beaches.

Since 1975, the authors have been making field observations of nearshore currents and the resulting sediment transport on such rocky shores. The study sites are on the Fukushima Coast, which is about an 80 km long rocky coast running north to south, and located about 200 km north of Tokyo, and fronting on the Pacific Ocean (Figure 1).

One nuclear power station is already operating on this 80 km stretch; one nuclear and one conventional power station are under construction; and another two power stations have been proposed. A portion of the results on nearshore circulation for one of the two proposed sites is presented here.

GEOLOGY AND MORPHOLOGY OF THE SITE

Mogi and Iwabuchi (1961) have given a general description and origin of continental shelf topographies off the Fukushima Coast. Figure 1 shows the northern part of Fukushima Coast and also gives the location of the study site, Haranomachi Beach which is about an 8 km long, somewhat embayed, shore.

The general shape of the shoreline of the Fukushima Coast is convex seaward. Roughly parallel contour-lines are found in the areas shallower than 20 m and deeper than 50 m. The remaining area, whose depths lie between 20 m and 50 m, exhibits very complicated configurations, showing relics of valleys eroded during the past glacial age. The ranges of depths here is important, because it just corresponds to the wave refraction zone. The dotted lines indicate relics of valleys traced from submarine topographic charts [Mogi and Iwabuchi (1961)]. These relics can easily be connected with present day streams on land.

The dot appearing at the center bottom indicates the location of a wave gage, whose data will be given later. The cross-sectional profiles along the "A" and "B" lines are shown in Figure 2. The profiles of neighboring drowned valleys are indicated by dotted lines.

The bottom slope of the flat terrace extending up to 40 - 50 m is about 1/500, whereas the shallowest part of the profiles up to 5 - 10 m is filled with recent sediment supplied from small streams and erosion of sea cliffs, producing beach slopes of about 1/70.

An aerial photograph in Figure 3 shows the southern half of Haranomachi Beach taken in 1979. Low lying hills and coastal plains alternately extend east and west from about 10 km inland. Small streams flow into the sea on this coastal plain at intervals of 5 to 10 km alongshore. Between them, low sea cliffs run up to 40 m in height, composed on sandstone and mudstone. The cliff at this site, seen in the center of Figure 3, extends about 1.3 km. The jetty appearing on the lower-right is Mano River Inlet, which supplies sediment to the area, about 20,000 to 30,000 m³ annually.

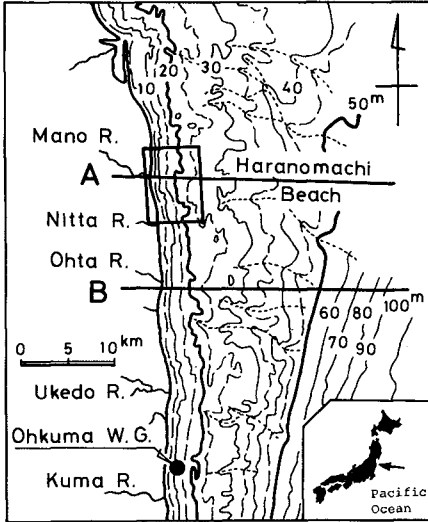


Figure 1 Continental shelf topography off north part of Fukushima Coast. Haranomachi Beach is indicated with a rectangle and dotted lines show inferred drowned valleys traced by Mogi and Iwabuchi (1961).

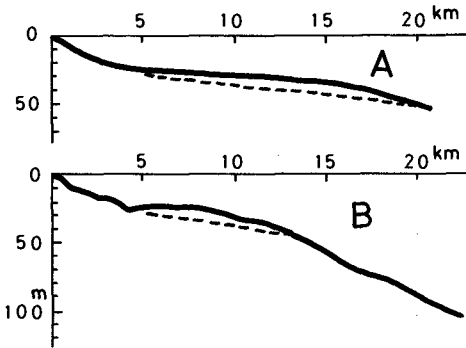


Figure 2 Typical profiles off Fukushima Coasts, after Mogi and Iwabuchi (1961). Range lines are shown in Fig. 1, and dotted lines indicate bottoms of drowned valleys.



Figure 3 Overview of Haranomachi Beach. Mano River Inlet jetty is seen on the lower-right.

A front view of the active sea cliff at this site shown in Figure 3 is given in Figure 4. An indicator of its activity is the existence of fallen materials at the foot of the cliff. In the middle of the cliff, a dark mudstone layer is seen, the upper part of which is composed of sand and sandstone. In front of the cliff, there is a beach about 50 m wide.

A sounding chart for the region off Haranomachi Beach, which covers the nearshore topography up to about 25 m in depth and 6 km alongshore, is given in Figure 5. The cliff seen at the center bottom corresponds to the one in Figure 4. In front of this cliff, there is a beach down to a depth of 4 to 5 m. Beyond it, an exposed mudstone floor appears which is clearly seen by its irregular contour-lines. Parallel contour-lines seen at the left, indicate that the bottom there is composed of loose sediment. The coastal structure seen at the lower-left is the Mano River entrance jetty. Accretion and erosion occur on both sides of the jetty, indicating the dominant direction of longshore drift.

The geological cross-section of the range line at the left side of the mudstone bedrock is given in Figure 6. At the top, there are sandstone, mudstone, and fine and medium sand layers. At the bottom, mudstone is the base rock comprising the sea floor.



Figure 4 Front view of active sea cliff. Fallen materials are seen at the foot of the cliff.

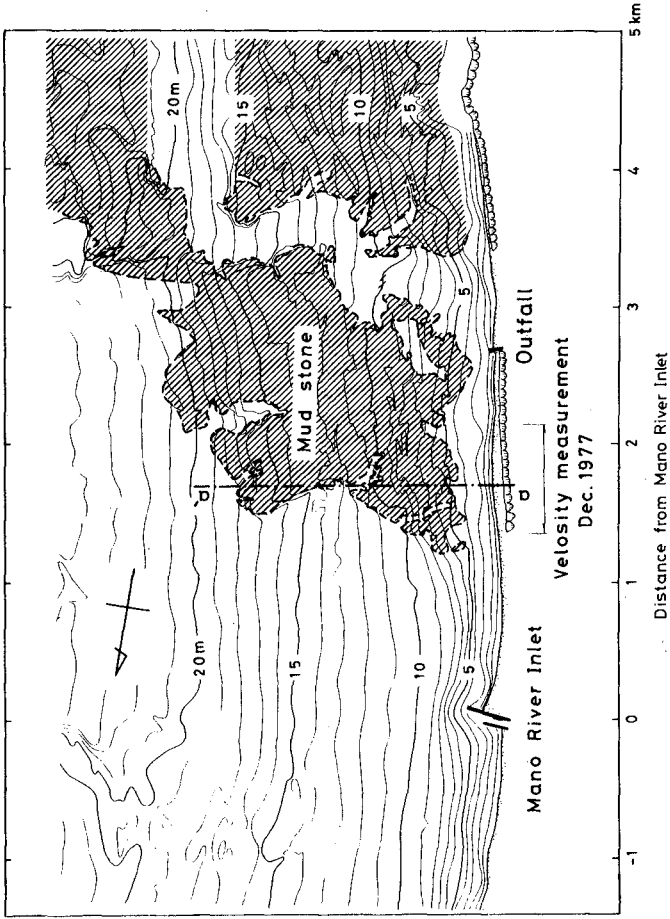


Figure 5 Nearshore topography of Haranomachi Beach. Beach sand covers the upper portion of the rocky profile (a-a' range; Geological cross-section is given in Figure 6). Location of velocity measurement is shown in the center bottom.

a-a' Profile

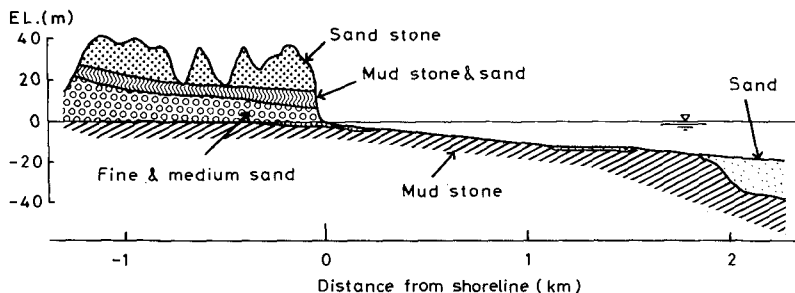


Figure 6 Typical geological cross-section of the site. Location of the a-a' range line is given in Figure 5.

WAVE CLIMATE OF THE AREA

Wave climate data are available from the Ohkuma wave gage as shown in Figure 1. The gage depth is 12 m. Using refraction diagrams, Ohkuma wave gage data over a 5 year period from 1966 to 1971 were converted to wave heights off Haranomachi Beach and allowed us to fill in the lack of records, by wave hindcasting. The resulting combined plot of frequency of wave heights and periods is shown in Figure 7. The typical wave height range is less than 4 m, and the wave periods range from 8 s to 14 s. The maximum significant wave height during this period was 8.3 m in November, 1970.

Wave directions were obtained by visual observation twice daily with a transit at Ohkuma observatory at the Fukushima 1st Nuclear Power Station, Tokyo Electric Power Co., Inc. As shown in Figure 8 the most dominant direction is obviously normal to the shore, that is, from the east.

The preponderance of normally incident waves is evidently caused by the fairly gentle continental shelf profile as shown in Figure 2, and is important in view of wave refraction, which in turn may produce a certain wave height distribution alongshore.

Figure 9 is a typical refraction diagram [Wilson (1966)] for 10 sec waves incident normally onto the northern Fukushima Coast from the east. Wave convergence and divergence caused by the diversified offshore submarine topography as shown in Figure 2 are clearly seen.

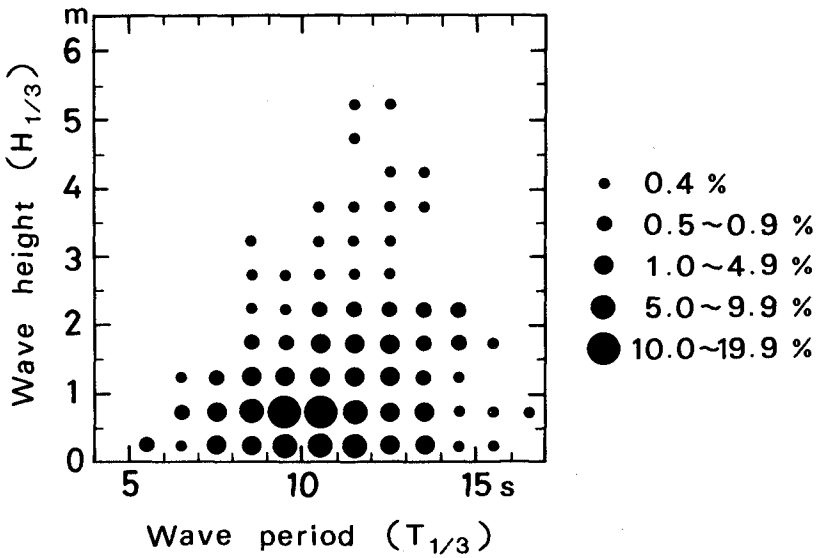


Figure 7 Combined plot of frequency of wave heights and periods over a 5 year from 1966 to 1971 off Haranomachi Beach.

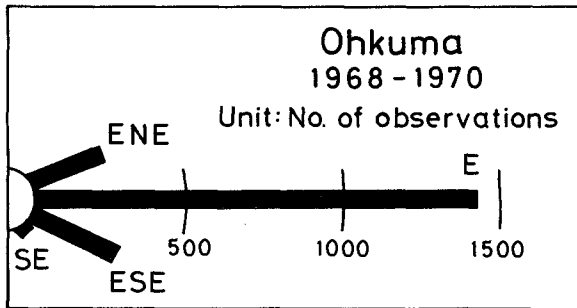


Figure 8 Wave rose at Ohkuma wave Observatory at the center of Fukushima Coast, modified after Toyoshima et al.(1973).

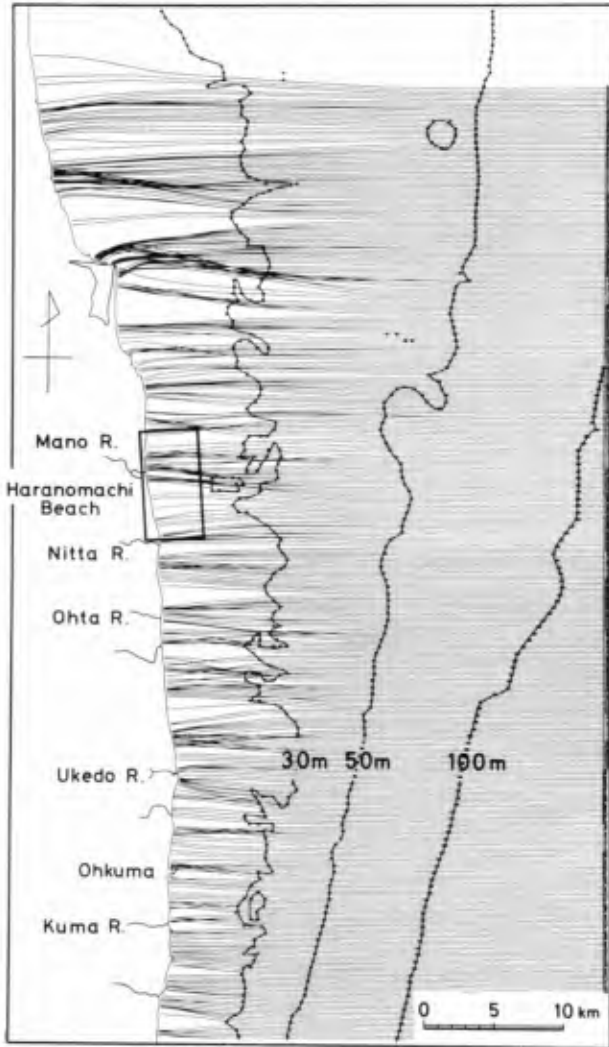


Figure 9 Refraction diagram of 10 s waves incident normally to the northern Fukushima Coast.

NEARSHORE CURRENT OBSERVATION ON HARANOMACHI BEACH
UNDER LOW ENERGY WAVE CONDITIONS

Measurements of rip current spacings were made by the tethered float technique[Sasaki et al. (1978)], seven times between December 1977 and August 1978 on a beach section about 8 km long, south of the Mano River Inlet. The southern end of this beach section is bounded by a small groin shaped irrigation drain. Also, velocity field measurements using a balloon[Sasaki and Horikawa (1975)] were carried out in December 1977 in front of the cliff, as shown at the center bottom in Figure 5.

Results from three of the seven measurements are shown in Figure 10. The CASE numbers appearing at the top also give a rough indication of wave height, and they correspond to about 1 m (1.0 m), 2 m (2.4 m), and 3 m (3.1 m), respectively. The wave periods were 11 s - 12 s, and the widths of the surf zone, X_b , were 60 m, 120 m, and 150 m, respectively. Wave directions outside of the breaker line were measured by transit.

In CASE-1, a pure southward longshore current system extending about 2 km long due to northerly incident waves is apparent, except near the Mano River Inlet. Such a typical longshore current has rarely been seen on such a gentle beach like this. On the other hand, several rip currents developed in CASE-2 and 3, resulting in the formation of an asymmetrical cellular circulation[Harris (1969)].

The circulation patterns do not exhibit large differences from those on ordinary sandy beaches under a similar wave climate, because beach sediments cover the surf zone or nearshore zone sea floor down to a depth of 4 to 5 meters as was seen on the sounding chart.

However, comparing the positions of rip currents with refraction diagrams, it is found that the positions of rip currents coincide with regions of wave divergence, particularly in CASE-3. The ratio of rip current spacing to the surf zone width also shows no significant differences from those on a sandy beach.

Additional evidence for the similarity of this rocky beach to a sandy beach was obtained from computing the bottom roughness length from velocity measurements. On the day following CASE-3 in Figure 10, velocity measurements in front of the northern end of the cliff (Figure 11) were made by aerial photography from a tethered balloon. The breaker height and period were 1.7 m and 12.5 sec, respectively. The wave incidence was somewhat shifted to the north. And it was almost windless.

Figure 12 shows comparisons of the observed velocity field with computed ones using Sasaki's(1975) numerical model, which applies Jonsson's(1966) wave friction factor on Noda's(1974) circulation model. The southward longshore current is dominant in the observed velocity field and its velocity ranges around 50 cm/s. Computations of the velocity field were made with roughness lengths of 2 cm, 5 cm, and 10 cm. Comparison of the computed velocity fields with the observed one shows that the 5 cm roughness length gave the most reasonable estimate of the current velocity.

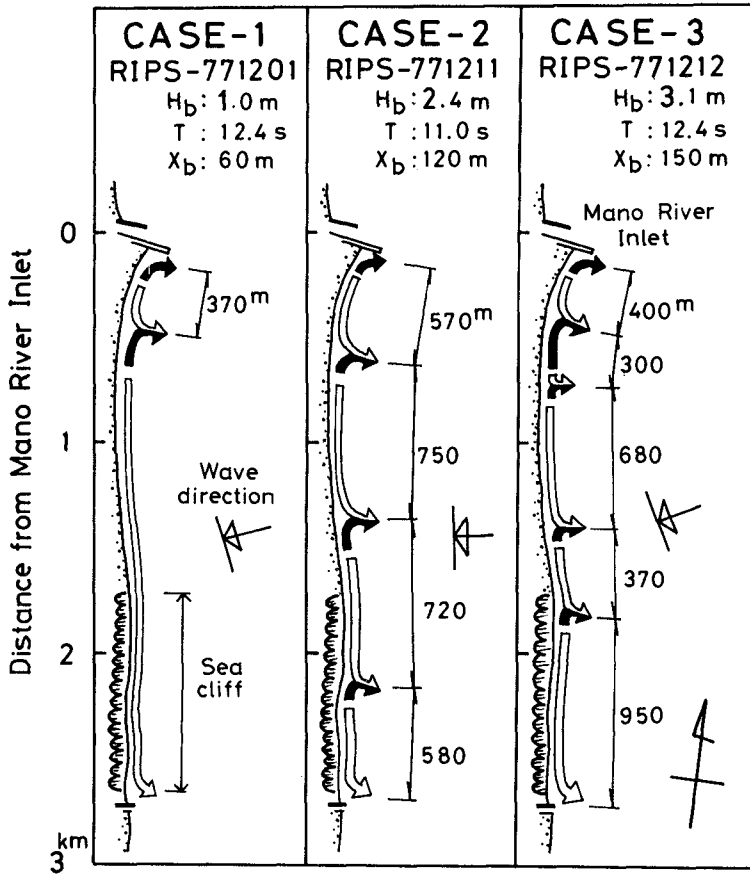


Figure 10 Selected observed nearshore current patterns under low energy wave conditions on Haranomachi Beach.

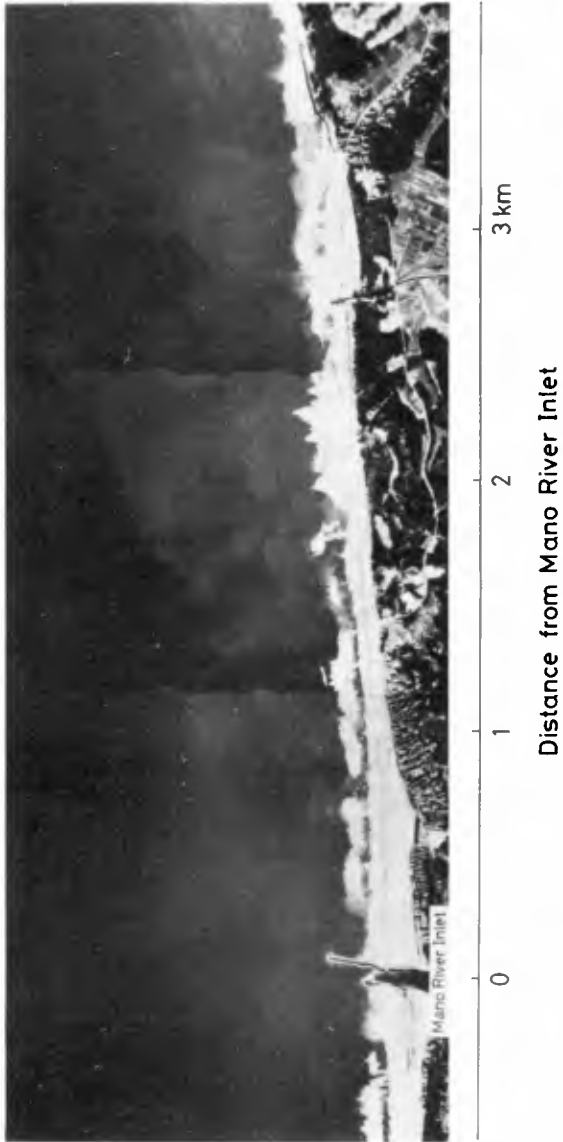


Figure 11 Aerial photograph of a part of Haranomachi Beach where the velocity measurements was made.

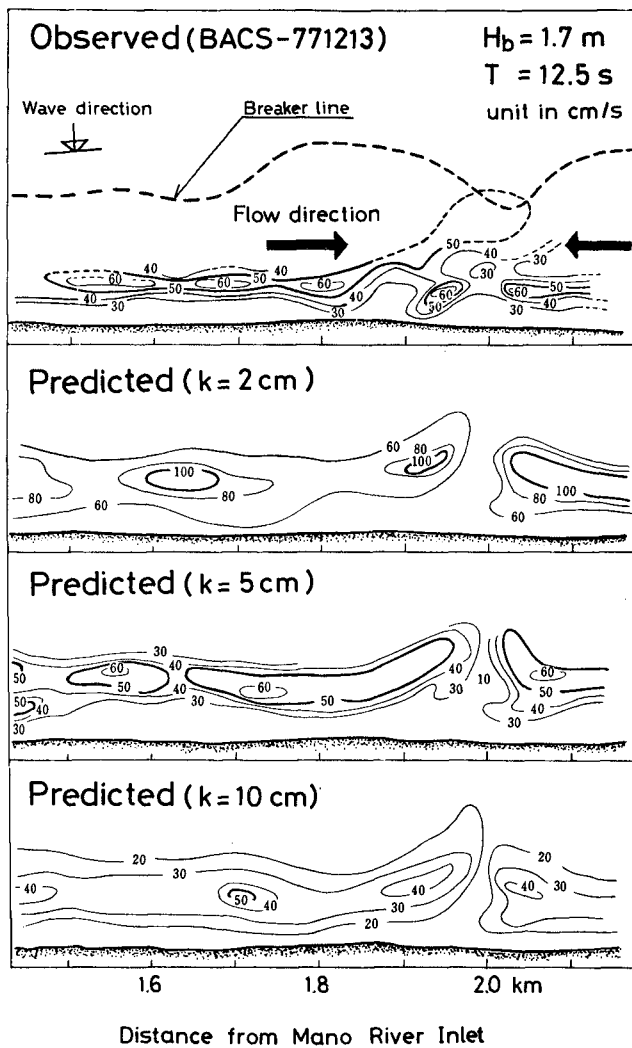


Figure 12 Comparison of observed and predicted current speeds. Reasonable estimate of the current speed is given when roughness length for the bottom, k is 5 cm.

This value falls within a representative value for a sandy floor [Jonsson et al.(1974), Skovgaard et al.(1975)], and provides strong evidence of the similarity of this partially rocky shore to a sandy beach in a low energy wave regime. In contrast, for a primarily rocky floor, the authors have found that the values of the bottom roughness should be greater than 20 cm.

PREDICTED NEARSHORE CIRCULATION PATTERN UNDER STORM WAVE CONDITION IN A LABORATORY WAVE BASIN

To simulate currents in a high energy wave regime, laboratory experiments were performed on a fixed bed in a 70 m wide by 40 m long wave basin at the University of Tokyo. Figure 13 shows the laboratory set-up of the fixed beach model scaled to 1/125. No distortion of the vertical scale was made. About 8 km of the somewhat indented shore bounded by promontories was modeled down to a depth of about 25 m. Seven 10-m long regular wave generators were arranged as seen in the top of Figure 13. About half of the sea floor area to be tested was covered by exposed base rock.

Under high seas, the surf zone bed, particularly the breaker zone bed, is largely occupied by an exposed rocky bed similar to a laboratory fixed bed. High energy wave regimes for deep water wave heights of 4 m and 6 m were simulated. The corresponding model wave heights were 3.2 cm and 4.8 cm, respectively. The wave incidence was normal to the shore as frequently occurs in the field.

Wave heights were measured by a capacitance type on-offshore direction wave gage array placed successively alongshore and consisting of 11 sensors. Nearshore current fields were measured with an array of 5 motor-driven cameras, tracing dye patches and small floats released in the nearshore zone. Current directions were also measured with 15 cm long yarns attached at one end to each 1-m reference grid spacing on the floor.

Figure 14 shows the resulting current patterns for both cases, indicating very irregular circulation patterns. The thick black and white arrows denote northerly and southerly currents, respectively, and the thick broken lines indicate the breaker line. Widths of the surf zone averaged 500 m and 1000 m, respectively.

Due to their complex circulation pattern, it is not as easy to define rip currents as on a sandy beach, but the location of the inflow of water into the surf zone can be identified without much difficulty. Comparing these nearshore circulation patterns with refraction diagrams, keeping in mind the above facts on the characteristics of irregular current patterns, it is found that the positions of the onshore currents entering the surf zone at the breaker line are significantly controlled by the location of wave convergence due to refraction over irregular offshore submarine topographies. However, coincidence between positions of rip currents and wave divergence was less significant than for the onshore current.

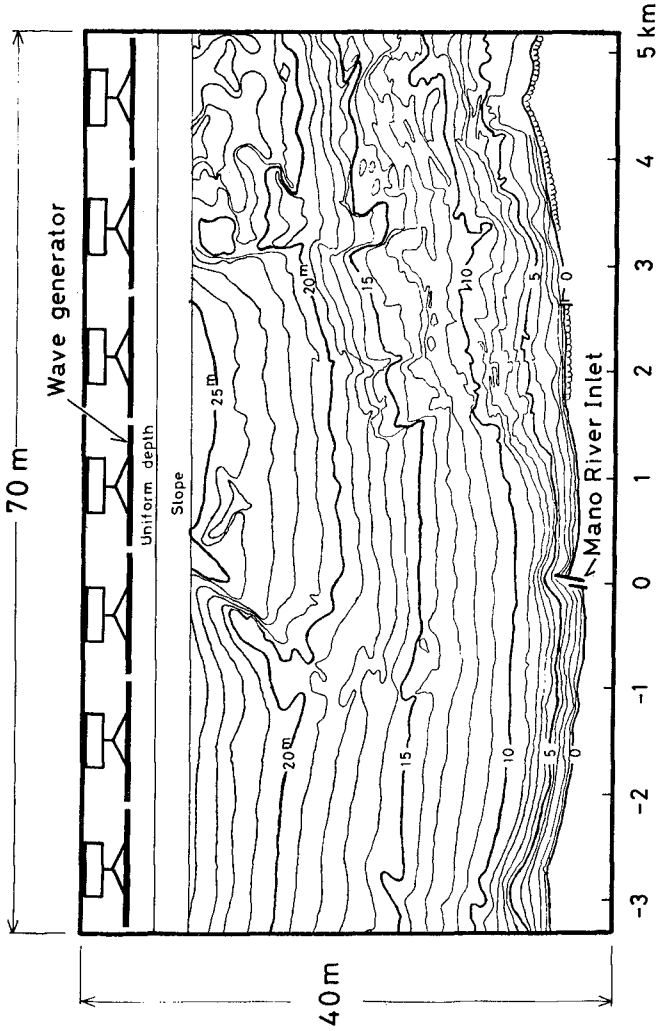


Figure 13 Laboratory set-up of 1/125 scaled fixed bed model in a 70 m x 40 m wave basin at the University of Tokyo.

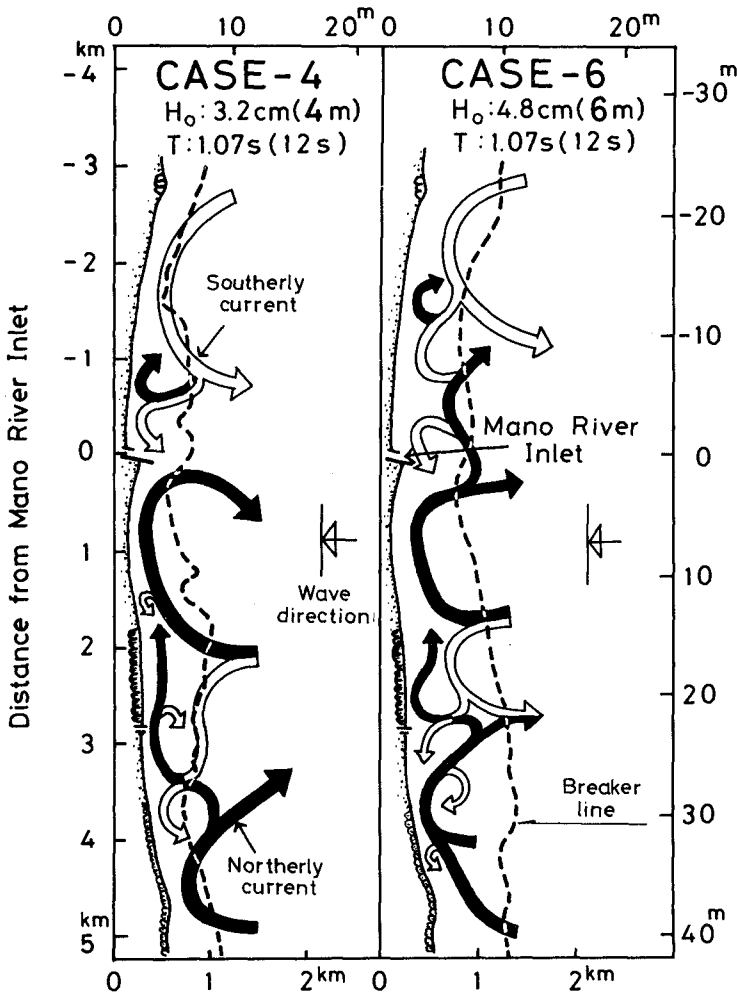


Figure 14 Predicted nearshore circulation pattern under high energy wave conditions for 4 m and 6 m waves in the laboratory wave basin.

DISCUSSION

A plot of the positions of water inflow, measured in the laboratory, and of rip currents, measured in the field, on a 12 s period wave refraction diagram for normally incident waves is shown in Figure 15. Good correlations can be seen between the positions of wave convergence and water inflow (larger open arrows), and between the positions of wave divergence and rip currents (smaller arrows) as stated above. Because a detailed sounding chart necessary to provide a finer wave ray separation, as seen in Figure 15, was not available in the offshore region beyond a depth of about 25 m, the effects of refraction due to the drowned valley (Figure 1, 2) have not been included in Figure 15. However, the increase of refraction due to inclusion of drowned valleys would not change the major conclusions, since its extent is not so large compared with refraction on nearshore zone (Figure 9).

A very similar and comprehensive study has been made by Shepard and Inman(1950) in the early stage of coastal engineering. However, the La Jolla and Scripps Canyons, where they did their study has a much more pronounced topography and is located nearer (approx. 300 m) to the shore than those here. Thus we expect that the effects on wave refraction should be much larger in their study.

CONCLUSIONS

- 1) In the low energy wave regime, no significant differences were found in the current velocity, rip current spacing and bottom roughness for a sandy beach. However, the positions of rip currents were coincident with wave divergence points due to refraction over an offshore exposed rocky bed.
- 2) In the high energy wave regime, currents exhibited a fairly irregular circulation pattern. However, the positions of inflow across the breaker line were found to be coincident with the wave convergence points.

To quantify nearshore currents on a rocky shore, nearshore current velocity measurements in the high energy wave regime would be necessary to evaluate bottom frictional forces.

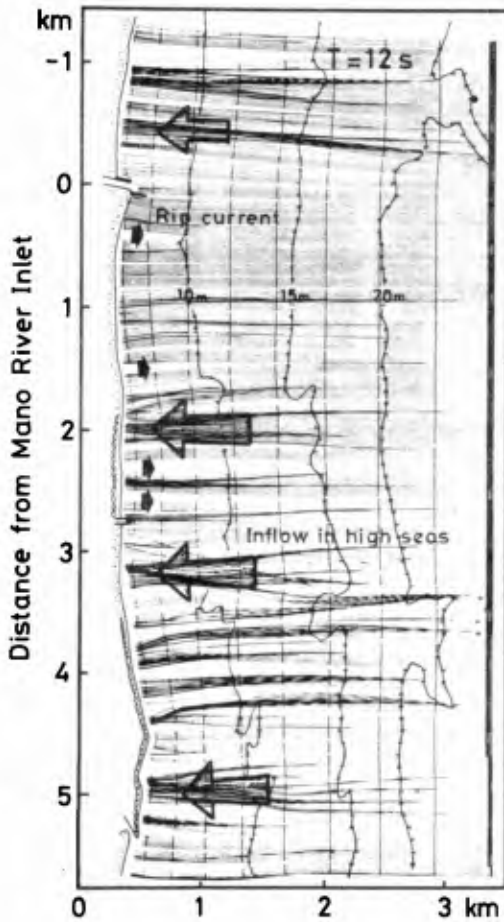


Figure 15 Comparison of positions of rip currents and inflows with positions of wave divergence and convergence on a 12 s refraction diagram incident normally to the shore. Larger open arrows and smaller arrows indicate the points of inflow in high seas and rip currents in low energy waves, respectively.

ACKNOWLEDGEMENT

The present research includes partly the work performed under the general direction of the Soso Coast Beach Erosion Review Committee chaired by Professor T. Iwasaki, Tohoku University, under the auspices of Technology Center for National Land Development under contract with INA Civil Engineering Consulting Co., Ltd., Tokyo.

Without kind and constructive directions of Professor K. Horikawa, University of Tokyo and Dr. S. Sato, Port and Harbor Research Institute, Ministry of Transport, such a large scale laboratory experiment could not be made. The permissions given by the Tohoku Electric Power Co., Ltd., Sendai, and the Technology Center for National Land Development, Tokyo, for the reproduction of data and figures of the field observations and laboratory measurements are gratefully acknowledged.

Also thanks are due to proofreading by Dr. R. S. Farinato, drawing by Mr. S. Kubota, and typing by Mrs. H. Yokoi.

The findings in the present paper are not to be construed as an official Soso Coast Beach Erosion Review Committee position.

REFERENCES

- Harris, T.F.W.(1969): *Nearshore circulation, Field observations and experimental investigations of an underlying cause in wave tanks, Symposium on Coastal Engineering, South Africa.*
- Horikawa, K., M.C. Lin, and T.O. Sasaki(1978): *Mixing of heated water discharged in the surf zone, Proc. 16th Coastal Eng. Conf., ASCE, Hamburg, 2563-2583.*
- Inman, D.L. and C.E. Nordstrom(1971): *On the tectonic and morphologic classification of coasts, Jour. Geol., 79, 1-21.*
- Jonsson, I.G.(1966): *Wave boundary layers and friction factors, Proc. 10th Coastal Eng. Conf., ASCE, Tokyo, 127-148.*
- Jonsson, E.G., O. Skovgaard and T.S. Jacobsen(1974): *Computation of longshore currents, Proc. 14th Coastal Eng. Conf., ASCE, Copenhagen, 699-714.*
- Mogi, A. and Y. Iwabuchi(1961): *Submarine topography and sediments on the continental shelves along the coasts of Johban and Kashimanada, Geographical Review, 34(3), 159-177. (in Japanese).*
- Noda, E.K.(1974): *Wave-induced nearshore circulation, Jour. Geophys. Res., 79(27), 4097-4106.*

- Sasaki, T.O. and K. Horikawa(1975): Nearshore current system on a gently sloping bottom, Coastal Eng. in Japan, 18, 123-142.
- Sasaki, T.O.(1975): Simulation of shoreline and nearshore current, Proc. Civil Engineering in the Oceans/III, ASCE, Newark, Del, 179-196.
- Sasaki, T.O., K. Horikawa, and S. Hotta(1976): Nearshore current system on a gently sloping beach, Proc. 15th Coastal Eng. Conf., ASCE, Honolulu, 626-644.
- Sasaki, T.O. and K. Horikawa(1978): Observation of nearshore current and edge waves, Proc. 16th Coastal Eng. Conf., ASCE, Hamburg, 791-809.
- Shepard, F.P. and D.L. Inman(1950): Nearshore water circulation related to bottom topography and wave refraction, Trans. AGU, 31(2), 196-212.
- Skovgaard, O., I.G. Jonsson and J.A. Bertelsen(1975): Computation of wave heights due to refraction and friction, Proc. ASCE, 101(WW1), 15-32.
- Sunamura, T.(1973): Coastal cliff erosion due to waves - Field investigations and laboratory experiments - Jour. Fac. Eng., University of Tokyo, 32, 1-86.
- Toyoshima, O., H. Okuda, and T. Mutoh(1973): On the beach erosion and beach characteristics on Fukushima Pref. Coast, Proc. 20th Coastal Engineering Conf. in Japan, 507-511. (in Japanese).
- Wilson, W.S.(1966): A method for calculation and plotting surface wave rays, TM-17, Coastal Engineering Research Center, Corps. of Engineers.

TOPOGRAPHIC CONTROL OF RUN-UP VARIABILITY

Mark P. Bradshaw

Coastal Studies Unit, Dept of Geography
University of Sydney
N.S.W. 2006 Australia

ABSTRACT

This paper presents observations of currents recorded in the swash zones of a number of morphologically different types of beaches in order to demonstrate the large variability in run-up patterns that exists primarily because of variability in beach face and surf zone configuration. Run-up spectra are shown for steep and flat beaches under low (<0.5m) and moderate (0.5-2.0m) wave energy. The longshore variability of run-up patterns on rhythmic beaches is also discussed. On reflective beaches run-up occurs only at incident wave frequency under low energy conditions and at both incident frequency and its first subharmonic under moderate energy. Low energy dissipative beaches exhibit a range of frequencies across the swash zone from incident through low frequency infragravity. As wave height increases on flat beaches, high frequency oscillations vanish leaving a concentration of energy at low infragravity frequencies. On more complex inshore rhythmic topographies under low to moderate energy conditions, alternating transverse bars and troughs give rise to a close spatial co-existence of zones of surging, reflective run-up and zones of over-running progressive bores of the type observed on flat profiles.

INTRODUCTION

In the recent literature on nearshore and surf zone processes several papers have placed considerable emphasis on the interdependence of morphologic features and hydrodynamic regimes. Of particular note are those by Chappell and Wright (1979), Chappell and Eliot (1979), Short (1979), Wright et.al. (1979) and Short (1980).

These papers point out either explicitly or implicitly that the morphologic and hydrodynamic characteristics exhibited by a beach at any one time are the result of mutual interaction between process and beach form and that

many feedback loops, both positive and negative, are involved. Some (eg. Wright et.al, 1979) demonstrate quite clearly that the nature of nearshore hydrodynamics is not uniform across the range of beach types that we commonly find in nature. Others (Chappell & Eliot, 1979; Short, 1979 & 1980) discuss beach changes over time and consider how existing morphologic and hydrodynamic conditions are, to a large extent, a function of antecedent conditions.

All, however, have in common the consideration of process/form interaction and because of this they complement a large body of literature which describes various hydrodynamic and sedimentologic characteristics of sandy beaches but does not (except in a few cases) explicitly link these to beach morphology.

The reports cited above mainly confine their attention to the nearshore/inshore zone and treat it essentially as a single unit. However, smaller sub-systems can be studied in the same way and it is the intention of this paper to focus more closely on the swash zone.

Most workers addressing problems related to swash zone processes have done so either with the view of (i) extending and refining hydrodynamic theory as applied to run-up on steep beaches of uniform slope and simple morphology (see Meyer and Taylor, 1972, for a review of these studies), or of (ii) describing and explaining the nature of swash/backwash processes on real beaches (eg. Sonu et.al., 1974; Waddell, 1973). There have been few comments from either group on the relationship between beach face morphology and run-up characteristics such as swash/backwash velocity fields, swash frequency domains and sediment transport mechanisms. Huntley and Bowen's (1975) discussion of steep and shallow beaches is a notable exception.

This paper focuses on the frequency characteristics of the swash zone and presents field data which relates run-up frequencies to beach face morphology over a range of beach configurations. The aim, however, is not only to present relevant field data but, more importantly, to demonstrate the great variability of swash zone processes which hitherto, have been treated as being similar across the range of beach face types.

FIELD SITES AND METHODOLOGY

Swash zone data and observations used in this paper were collected as part of a larger study of the nearshore processes operating on the beaches of the Southeastern Australian coast. Beaches of all kinds were observed

ranging from the flat dissipative extreme to the steep reflective extreme and including a number of examples with more complex types of inshore morphology (Wright et.al.,1979). Experiments were carried out under wave energy conditions ranging from low (<0.5 metre primary break) to moderate (0.5 to 2.0 metres). It is important to note that in all cases incident waves were dominated by moderate to long period swell ($T > 10$ seconds). This contrasts with reports of nearshore experiments in other parts of the world where short period wind wave conditions predominate (eg. US Atlantic and Gulf Coasts).

Current data were collected using miniature bi-directional ducted flow meters and water surface oscillations were obtained from bottom mounted pressure transducers. Details of these instruments are discussed by Bradshaw et.al. (1978). Spectra were computed using the auto-correlation method (Bendat and Piersol, 1971) and raw spectral estimates were smoothed with a Tukey filter. Since this paper is concerned only with run-up frequencies observed on natural beaches all spectral estimates are non-dimensionalized relative to the maximum for the series.

THE OBSERVATIONS

Field observations are considered for each different type of beach morphology in turn. Data are presented for these beaches under low and moderate wave energy conditions and the effects on run-up of tidal fluctuations in water level are noted.

1. Steep Beaches

This type of beach is common on sections of the Southeast Australian coast that exhibit a high degree of compartmentization. It tends to be sheltered and coarse grained and has the morphologic characteristics of a steep linear beach face (slope > 0.12), a prominent step at the breakpoint and relatively deep water immediately seaward of the step (Figure 1). Waves surge up the beach face under low energy conditions but change abruptly to plunging or collapsing as wave heights rise above about 0.5 m.

The only rhythmic features observable on this type of beach are cusps. These are regularly spaced and are of small scale but are not always present. When cusps are absent, the beach, because of its simple configuration closely resembles an artificial laboratory beach and run-up patterns, especially under low energy, are simple and uniform along shore.

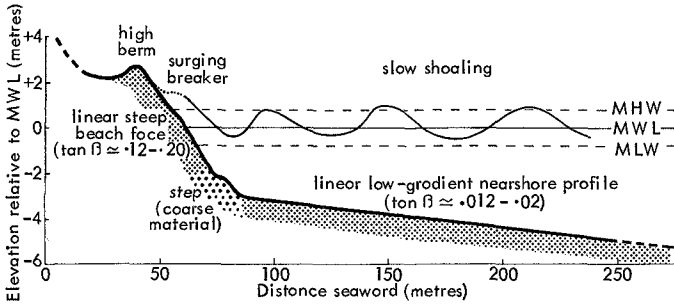


Figure 1: Typical cross section of a reflective beach (after Wright et.al., 1979)

When cusps are present however, run-up patterns generated by the longshore rhythmic undulations of the beach face are far more complex especially under high energy conditions. Data are discussed here only for non-cusped or very weakly cusped reflective beaches.

An example of a low energy reflective beach is shown in Figure 2. For most of the time waves surge up the beach face for a short distance and return completely before the onset of the next surge. Collisions at the base of the beach face between the backwash from one wave and the runup from the following wave are rare.

The spectrum of water motions on the beach face and slightly seaward of the step is shown in Figure 3. Of note is the fact that all energy on the beach face is confined solely to incident frequency oscillations with no evidence of subharmonic or infragravity peaks. This is in accordance with the suggestion by many (eg. Huntley & Bowen, 1975) that the collision process at the base of the step is largely responsible for the generation of oscillations at frequencies below that of the incoming waves.

Figure 4 shows a moderate energy reflective beach. Waves now collapse or plunge on the step sending swash high up the beach face, often resulting in over-topping of the berm. The backwash almost inevitably ends in a turbulent collision at the base of the step. Under these conditions

we note the emergence of water motions at twice the period of the incident waves both on the beach face and seaward of it. Figure 5 is an example of the spectrum which we consistently observe on reflective beaches under moderate energy wave attack.

The importance of tides is minimal on purely reflective beaches particularly when waves are small. Even at low tide water depth seaward of the step remains deep relative to wave height.

It should be noted that the profile shown in Figure 5 is not that of a purely reflective beach (as defined by figure 1) because of the existence of the bar seaward of the step. It is used here for two reasons: (i) the depth of water at high tide was such that no energy was dissipated in breaking over the bar and the profile was reflective, and (ii) the example illustrates the behaviour of sections of a more complex type of beach topography at high tide, a point which is discussed later in the paper.

2. Flat Beaches

Flat beaches with gradients of less than 0.02 occur mainly in high energy exposed environments or in areas where there is an abundant supply of fine grained sediments. They have a wide surf zone often exhibiting one or more linear bars (Figure 6). Waves plunge on the bar under low to moderate energy conditions with an increasing incidence of spilling breakers as the energy rises. Under all energy conditions the result is a shoreward progression of over-running, dissipative bores. Set-up is large on these beaches compared to steep profiles and has been shown to oscillate at surf beat frequencies (Sasaki et.al., 1977).

Figure 7 shows a low energy dissipative situation where a single plunging break results in a bore which travels inshore retaining its initial shape and velocity through most of the traverse. Only in the vicinity of the limit of uprush do successive bores begin to overrun each other.

Compared to the higher energy situations, turbulence is relatively low in the zone between the breaker line and the limit of uprush. Individual bores can often be followed across the surf zone from their originating wave to their landward limit.

Shore normal current spectra for two stations landward of the breaker line on a low energy dissipative profile are shown in Figure 8 (U-swash and U-mid surfzone). The current meters were located 5-6 metres landward of the



Figure 2: Low energy reflective beach.

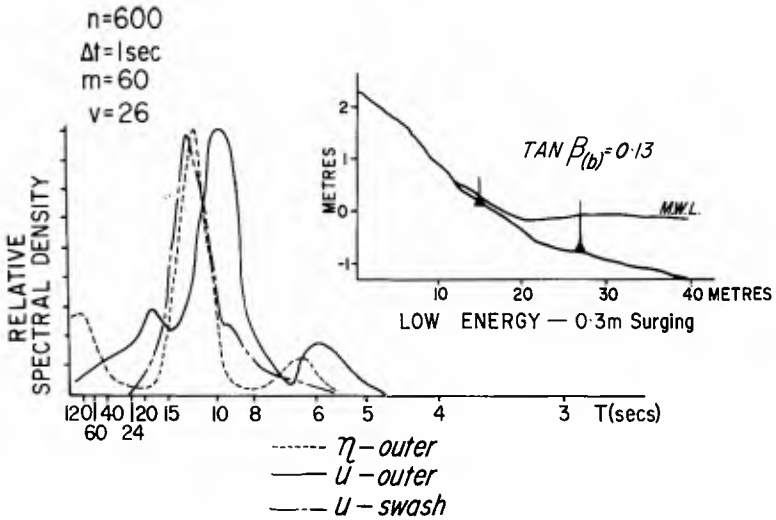


Figure 3: Typical run-up spectra from a low energy reflective beach.



Figure 4: Moderate energy reflective beach.

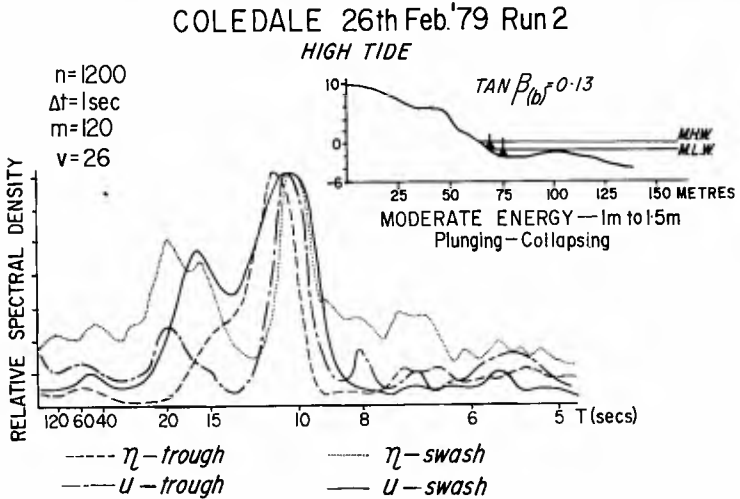


Figure 5: Typical run-up spectra from a moderate energy reflective beach.

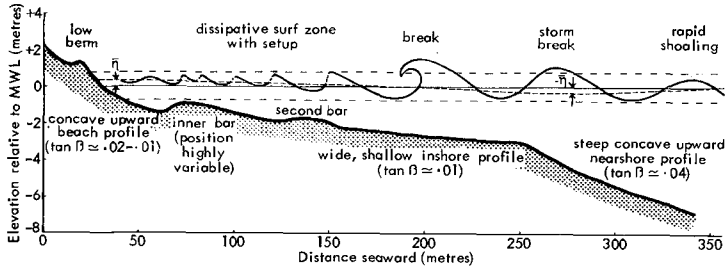


Figure 6: Typical cross section of a dissipative beach (after Wright et.al., 1979).

break point and about 5 metres seaward of the maximum run-up excursion. The figure reveals the following:

- (i) expected peaks for the outer instrument at both incident and infragravity (surf-beat) frequencies and for the inner instrument at infragravity frequency;
- (ii) a peak at half the incident wave frequency on both the inner and outer instrument, a phenomenon normally observed on steep beaches; and
- (iii) an unexpected peak at incident wave frequency at the inner instrument.

This last phenomenon can clearly be seen from visual observation of the surf zone and suggests that when low amplitude, long period swell acts on a flat profile, the beach does not eliminate high frequencies to the extent that was first described by Emery and Gale (1951) and later by Waddell (1973), Sonu et.al.(1974) and Huntley and Bowen (1975). The appearance of incident wave frequencies at the top of the beach face can be attributed to the low turbulence in the surf zone and also to the long period of the incoming swell which gives bores time to cross the entire surf zone before they are interfered with by those following.

Discovery of the nature and extent of subharmonics on flat, low energy beaches requires more experiment replication. During the particular experiment referred to in Figure 8, swash/backwash collisions resulting in short lived hydraulic jumps (or roll waves) were occurring regularly at the top of the swash zone, about 10 metres seaward of the inner instrument station. However, even after viewing time lapse film records it was not evident what effect the collision was having on the swash period landward of it.



Figure 7: Low energy dissipative beach.

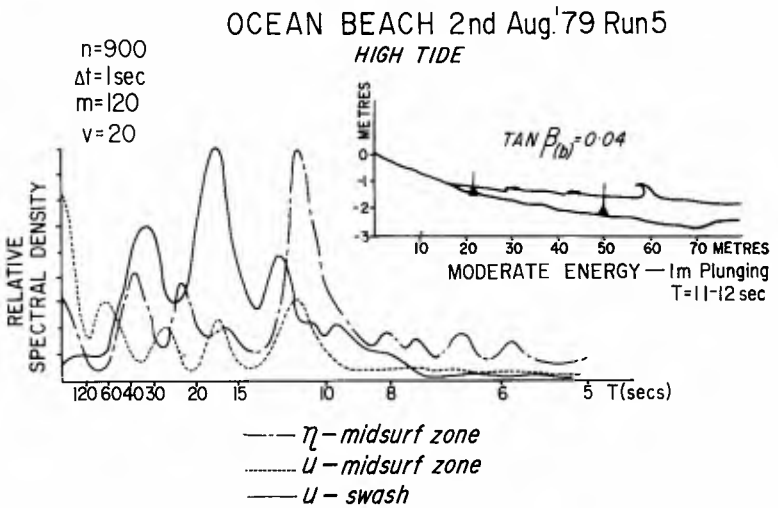


Figure 8: Typical run-up and surfzone spectra for a low energy reflective beach.



Figure 9: Moderate energy dissipative beach.

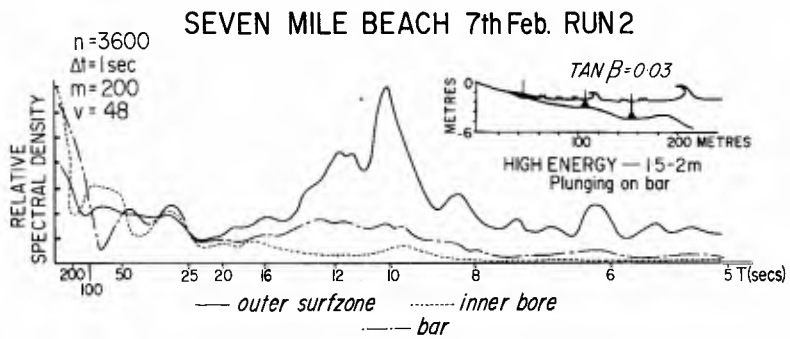


Figure 10: Typical run-up and surf zone spectra for a moderate energy reflective beach.

Figure 9 shows a dissipative profile in a much higher energy environment. Here a dual linear bar-trough system is present. Waves break on both bars and the resulting bores travel across a wide, highly turbulent surfzone. Larger bores often reform over the trough landward of the inner bar causing a secondary break higher up the beach.

The run-up spectrum for this moderate energy dissipative beach (Figure 10) shows a complete absence of energy at incident wave frequency and a dominance of energy in the low frequency infragravity domain. This is not only the case for shore normal currents at the top of the beach face but also for those over the inner bar. Compared to the low energy case these results correspond much more closely to those presented by workers such as Sonu et.al.(1974) and fit the classical view of the beach face as being an area dominated by low frequency oscillations.

Waddell (1973) presents evidence to show that the low frequencies on the beach face are not due to a simple low pass filtering effect but rather to a non-linear transfer of energy from high to low frequency, the result of collisions in the surf zone. Huntley and Bowen (1975) present similar results but suggest that the transfer is due to the interaction of many irregularly spaced breakers in the surf zone.

On the moderate energy dissipative beaches observed during the course of this study, it appeared that both mechanisms are important. It is certainly the case that there is a substantial modification of input frequencies as one moves across the lines of breakers and then into the turbulent bore zone. On moderate to high energy dissipative profiles the length of time that any one bore can travel shorewards without overrunning or being overrun by another bore is very short. However, backwashes with velocities greater than 1.5m/sec were recorded on many occasions and collision between these and shoreward moving bores resulted in roll waves lasting up to (and sometimes longer than) 10 seconds and with heights ranging to 0.5 metres. It is to be expected therefore that these are also considerably important in determining the range of frequencies operative on this type of beach.

3. Rhythmic Beaches

Many of the beaches on the Southeast Australian coast fall in between the two extremes discussed above and are characterised by complex rhythmic topography alongshore. Typically they consist of alternate anvil shaped shoals or transverse bars separated from each other and the beach face by well developed rips and feeder channels. Papers by Wright and Short (both in this volume) discuss the range of

complex morphologic types in greater detail; however an example from the New South Wales coast is shown in Figure 11.

Depending on the stage of the tide, run-up patterns on this type of beach will either be uniform in the longshore direction or will show marked variation as one moves alongshore. Wave height is also important in determining the form of the run-up along the entire beach.

At high tide, under both low and moderate energy, the shoals are usually sufficiently deep that no breaking occurs over them. Instead the waves surge or plunge on the steep beach face that lies landward of the shoals. Because the sections of beach in front of rip feeders present a reflective face to the incoming waves at all times, the overall picture at high tide is one of continuous reflectivity along the entire shore. An example of this condition was presented earlier in Figures 4 and 5.

At low tide shoals emerge and become active, leaving an inactive steep beach face behind them. The longshore pattern now changes to one of alternating zones of reflective and dissipative run-up. The beach face fronting rips and rip feeders continues to exhibit reflective characteristics while the shoal regions display the characteristics of a dissipative beach. Run-up spectra taken at intervals alongshore vary accordingly.



Figure 11: An example of well developed rhythmic topography.

CONCLUSIONS

A summary of the observations discussed in this paper is presented in Table 1. The following points arise:

(i) Sandy beaches can exhibit morphologic variability both between different beach systems and also within individual beach compartments. The data discussed and summarised in Table 1 show that run-up characteristics vary as a result of these spatial differences in beach face topography. This paper considers only the frequency of run-up to demonstrate the point but the same variability can be observed in all hydraulic and sedimentary processes operating on the beach face.

Given the wide variability of the processes under consideration, account should be taken of the morphology and wave conditions for the particular beach being investigated when analysing and presenting swash zone data. This is very important for purposes of meaningful data comparison.

(ii) Understanding of swash zone processes and the nature of their interrelationship with beach morphology will ultimately come only from studies conducted over a range of sandy beach environments. The question of the swash-backwash collision process and its effect on sediment entrainment and transport on different beach slopes is significant and may be a good starting point for more specific process investigations. Initial observations show that on a steep beach the collision at the bottom of the slope bears directly on short term changes in step morphology and also influences sediment transport higher up the slope through its controlling effect on run-up and backwash velocities. On flat beaches the area of interaction is less narrowly defined and the collision results in the temporary suspension of large volumes of sediment in the roll wave. Detailed studies in this area have yet to be carried out.

ACKNOWLEDGEMENTS

Data presented in this paper were collected as part of a program funded by the Australian Research Grants Committee and by the U.S. Office of Naval Research, Coastal Sciences Program, Task NR 388-157, Grant N-00014-80-G-0001. All members of the Coastal Studies Unit have participated at one time or another in the arduous task of collecting field data and I thank them for their assistance. Valuable help and discussion were also provided by I. Eliot, J. Lanyon and A. Learmonth. L.D. Wright reviewed the paper and J. Roberts and M. Rigney produced the diagrams.

Table 1: A summary of observed relationships between surf zone and swash zone morphology and characteristic run-up spectra.

MORPHOLOGIC TYPE		WAVE ENERGY		
		LOW (<0.5m)	MODERATE (0.5-2.0m)	HIGH (>2.0m)
STEEP (REFLECTIVE)		Incident dominant No subharmonic	Incident & subharmonic	
FLAT (DISSIPATIVE)		Incident, Subharmonic & infragravity (~40-60 sec)	Attenuation of incident subharmonic frequencies	Long period infragravity (>60sec) Rapid shoreward attenuation of incident frequencies
COMPLEX MORPHOLOGY (e.g. alternating transverse bars & troughs)	HIGH TIDE	Reflective run-up incident dominant	Reflective run-up incident & Subharmonic	As above
	LOW TIDE	Alternate zones of reflective & dissipative run-up	As for low energy	As above

REFERENCES

- Bendat, J.S. and Piersol, A.G., 1971, Random Data: Analysis and Measurement Procedures, New York: Wiley, 407 pp.
- Bradshaw, M.P., Chappell, J., Hales, R.S. and Wright, L.D., 1978, "Field monitoring and analysis of beach and inshore hydrodynamics", Proc. 4th Aust. Coastal and Ocean Engineering Conf., (Adelaide), pp.171-175.
- Chappell, J. and Eliot, I.G., 1979, "Surf-beach dynamics in time and space - an Australian case study, and elements of a predictive model", Marine Geology, 32: 231-250.
- Chappell, J. and Wright, L.D., 1979, "Surf zone resonance and coupled morphology", Proc. 16th Coastal Eng. Conf., pp.1359-1377.
- Emery, K.O. and Gale, J.F., 1951, "Swash and swash marks", Trans. Am. Geophys. Union, 32(1), 31-36.
- Huntley, D.A. and Bowen, A.J., 1975, "Comparison of the hydrodynamics of steep and shallow beaches", in J.R. Hails and A. Carr (Eds.), Nearshore Sediment Dynamics and Sedimentation, New York: Wiley, 316 pp.
- Meyer, R.E. and Taylor, A.D., 1972, "Run-up on beaches" in Meyer, R.E. (ed) Waves on beaches and Resulting Sediment Transport, (Academic Press, N.Y.)
- Sasaki, T., Horikawa, K. and Hoffa, S., 1977, "Nearshore current on a gently sloping beach", Proc. 15th Internat. Conf. Coastal Engineering, 624-644.
- Short, A.D., 1979, "Three-dimensional beach-stage model", J. of Geology, 87: 553-571.
- Short, A.D., 1980, "Beach response to variations in breaker height", Proc. 17th International Conf. Coastal Engineering, Sydney.
- Sonu, C.J., Pettigrew, N. and Fredericks, R.G., 1974, "Measurement of swash profile and orbital motion on the beach", in "Ocean Wave Measurement and Analysis", Am. Soc. Civ. Eng., 1: 621-638.
- Waddell, E., 1973, Dynamics of Swash and Implication to Beach Response, Coastal Studies Institute, Tech. Rept. 139, Louisiana State Univ., 49pp.
- Wright, L.D., Chappell, J., Thom, B.G., Bradshaw, M.P. and Cowell, P.J., 1979, "Morphodynamics of reflective and dissipative beach and inshore systems: Southeastern Australia", Mar. Geol., v.32., 105-140.

CHAPTER 68

BEACH PROFILES AND ON-OFFSHORE SEDIMENT TRANSPORT

by

Akira WATANABE, Yoshihiko RIHO and Kiyoshi HORIKAWA

Coastal Engineering Laboratory
Department of Civil Engineering
University of Tokyo
Bunkyo-ku, Tokyo
Japan

ABSTRACT

The on-offshore sediment transport due to waves on a sloping beach is studied by analyzing the laboratory test data on two-dimensional beach deformation. The net rates of sediment transport both inside and outside the breaker zone are evaluated from beach profile changes and are related to the nondimensional bottom shear stress or the Shields parameter. The importance of the critical shear stress and of asymmetrical to-and-fro water partical motion near the bottom is pointed out.

INTRODUCTION

Much effort has been devoted during the last few decades to elucidate sediment movement phenomenon in coastal zone, but it was not so long since intensive attempts were started to set up numerical models simulating beach processes. Prediction of beach transformation requires knowledge about the functional relationship of sediment transport rate to conditions of waves, currents, water depth, bottom configuration, sediment property and so on. There have been many, almost innumerable, studies on sediment transport rate, and considerable amount of knowledge on this problem has been accumulated so far. Yet it seems that we are still far from a reliable formula estimating the rate of sediment transport in particular perpendicular to coastline. This directional mode of sediment movements, or on-offshore sediment transport plays a vital role in the short-term beach deformation such as severe beach erosion due to storm surge. This may be also quite essential for more detailed understanding of longshore sediment transport, because the latter is expected to correlate with the former through the sediment sorting and entraining mechanics.

In the present study the on-offshore sediment transport was dealt with by analyzing the data obtained in laboratory experiments. In order to attain our purpose of getting the on-offshore transport rate formula of practical use in predicting beach deformation inside and outside the breaker zone, experiments were conducted under sloping beach condition. Two-dimensional beach deformations under various wave conditions were measured. Any equipment, such as a sand trap, to measure directly the sediment transport rate was not used in this test, because such apparatus would cause severe disturbance to the fluid motion and the sediment movement. Instead the net rates of sediment transport were estimated from the beach deformation data. Attempts to find the relationship between the net transport rates and wave conditions were then made.

EXPERIMENTAL PROCEDURES

Experiments were conducted in a two-dimensional wave flume, 25 m long, 1.5 m deep and 0.8 m wide. As mentioned above, the net rate of on-offshore sediment transport was evaluated from the beach profile changes. In order to make simple the experiments, data handling and interpretation of results, tests were limited to a uniform initial slope and to the wave action of one-hour for each wave condition, while wide range of wave conditions was adopted.

Table 1 is a list of experimental cases. Two kinds of quartz sand with mean diameters of 0.2 mm and 0.7 mm were used as bed materials, both being well sorted with the Trask sorting coefficient of 1.1. Combination of these two grain sizes, two initial slopes of 1/10 and 1/20, three wave periods of 1.0, 1.5 and 2.0 seconds, and four or five wave heights made fifty-eight experimental cases altogether.

In each experimental case, a beach with prescribed uniform slope, 1/10 or 1/20, was initially set up, and its deformed profile after one-hour wave action was measured. Measurement of beach profiles in this experiment was done by tracing them on transparent sheets attached on a side glass wall of the flume, although a bottom profiler of electrical-resistance type, by which continuous profile data can be recorded on a magnetic tape, has become available in the latest experiment. In the middle of wave action, wave profiles were measured by capacitance type wave gages at locations of 10 to 50 cm intervals above the beach as well as at the offshore end of the flume.

EXPERIMENTAL RESULTS

Beach Profile Change

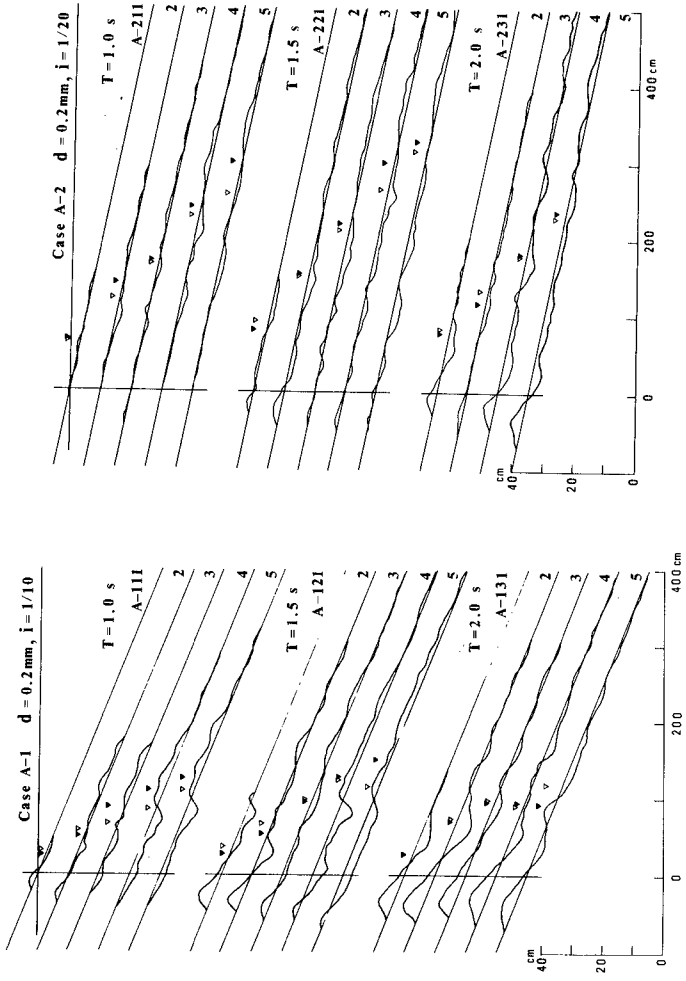
Figures 1 (a) to (d) show the beach profiles after one-hour wave action for all the cases listed in Table 1. It should be noted that profile changes in some cases with the initial slope of 1/20 and large wave heights stretch beyond the extent of these figures. The locations of breaking points are indicated by triangle symbols; open triangles for the initial stage and solid triangles for the final stage.

Table 1 Test cases and condition.

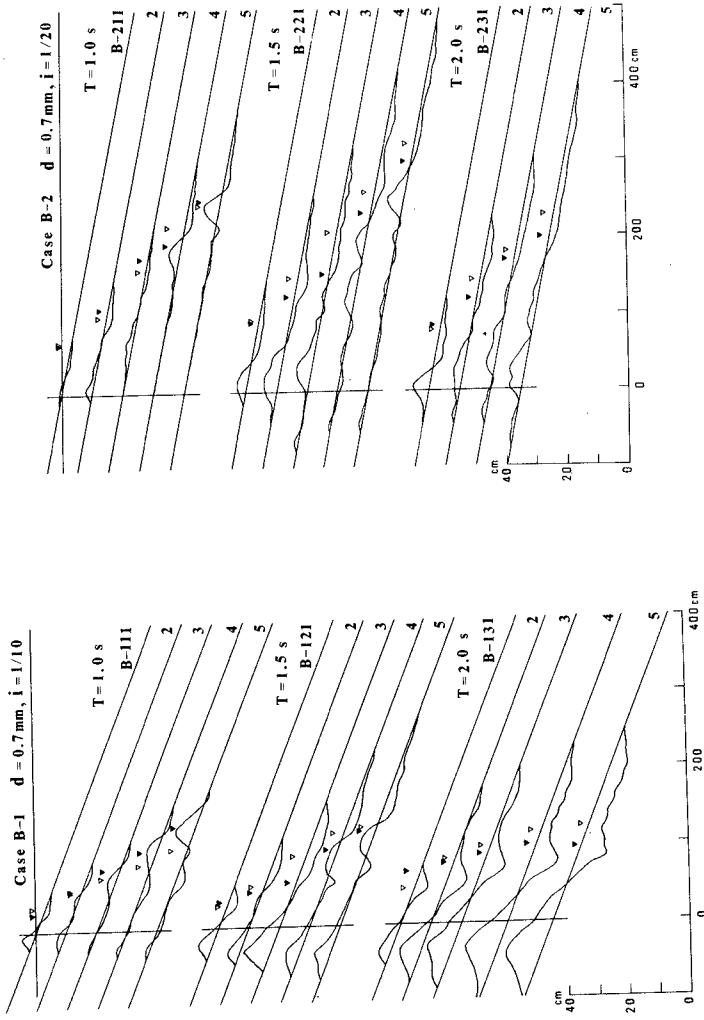
Case A-1 $\bar{d} = 0.2 \text{ mm}$ $i = 1/10$				Case B-1 $\bar{d} = 0.2 \text{ mm}$ $i = 1/10$			
Case No.	T (sec)	H_0 (cm)	H_0/L_0 ($\times 10^{-2}$)	Case No.	T (sec)	H_0 (cm)	H_0/L_0 ($\times 10^{-2}$)
A-111		2.6	1.7	B-111		2.6	1.7
2		5.1	3.3	2		5.0	3.2
3	1.0	6.9	4.4	3	1.0	6.4	4.1
4		8.9	5.7	4		8.5	5.4
5		10.5	6.7	5		10.0	6.4
A-121		3.2	0.9	B-121		3.0	0.8
2		5.8	1.7	2		5.3	1.5
3	1.5	8.3	2.4	3	1.5	7.7	2.2
4		10.5	3.0	4		10.5	3.0
5		12.1	3.5	5		11.3	3.2
A-131		3.1	0.5	B-131		3.5	0.6
2		5.4	0.9	2		5.3	0.9
3	2.0	6.1	1.0	3	2.0	6.7	1.1
4		7.5	1.2	4		8.2	1.3
5		9.2	1.5	5		9.6	1.5

Case A-2 $\bar{d} = 0.2 \text{ mm}$ $i = 1/20$				Case B-2 $\bar{d} = 0.2 \text{ mm}$ $i = 1/20$			
Case No.	T (sec)	H_0 (cm)	H_0/L_0 ($\times 10^{-2}$)	Case No.	T (sec)	H_0 (cm)	H_0/L_0 ($\times 10^{-2}$)
A-211		2.9	1.9	B-211		2.9	1.9
2		5.2	3.4	2		5.1	3.3
3	1.0	7.3	4.7	3	1.0	7.0	4.5
4		9.6	6.2	4		8.9	5.7
5		11.5	7.3	5		10.6	6.8
A-221		3.1	0.9	B-221		3.2	0.9
2		5.7	1.6	2		5.4	1.5
3	1.5	7.9	2.3	3	1.5	7.7	2.2
4		10.2	2.9	4		9.7	2.8
5		11.7	3.3	5		12.1	3.5
A-231		2.7	0.4	B-231		2.7	0.4
2		4.0	0.6	2		4.3	0.7
3	2.0	6.2	1.0	3	2.0	6.1	1.0
4		8.2	1.3	4		7.8	1.3

\bar{d} : grain diameter, i : initial beach slope, T : wave period
 H_0 : deep water wave height, H_0/L_0 : deep water wave steepness



(a) (b)
 Fig. 1 Beach profiles after one-hour wave action.



(d)

(c)

Fig. 1 Beach profiles after one-hour wave action (continued).

It is recognized by referring to Table 1 that the bar-type profiles are formed for relatively large wave steepness conditions, showing systematic increase in bar size with the increase of wave steepness. Under the condition of smaller wave steepness, a wide berm becomes noticeable in particular for the cases with initial slope of 1/10, implying the shoreward transport of nearshore bed material. It was observed during the experiment that the shoreward limits of significant beach change in most cases were determined by the locations of maximum runup. However no remarkable nearshore beach change took place for the cases with initial slope of 1/20 and wave period of 1.0 sec, where flow intensity of uprush was quite weak.

In case of 0.2 mm-sand, sand ripples always appeared outside the breaker zone and the sediment transport seemed predominantly in the form of suspension. When the initial slope was 1/20, sand ripples were observed in the surf zone as well, but vortex formation around those ripples were not so remarkable as it was in the offshore region.

By contrast, in case of 0.7 mm-sand, sand ripples were scarcely observed under those experimental conditions. Only in a few cases such as B-133 to 135, sand ripples appeared and vortex formation was recognized, but amount of suspended sands was pretty small. Predominant mode of sediment transport of 0.7 mm-sand was in general in the form of bed load.

Evaluation of Net Sediment Transport Rate

The net rate of on-offshore sediment transport is evaluated from two-dimensional beach deformation data as follows. Suppose a beach profile change as given in Fig. 2. In virtue of the conservation of the bed material amount, the local net transport rate $q(x, t)$ per unit width is related to the bed elevation $z(x, t)$ measured from a certain datum as:

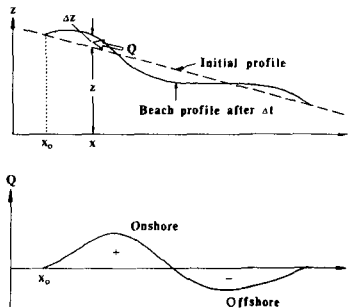


Fig. 2 Evaluation of net sediment transport rate.

$$\frac{\partial z}{\partial t} = \frac{1}{1-\epsilon} \frac{\partial q}{\partial x} \quad (1)$$

where ϵ is the sediment porosity. Therefore the effective net transport rate $Q(x)$ averaged over a time duration Δt of wave action is evaluated from the bed elevation change $\Delta z(x)$ during the same period by:

$$Q = \frac{\bar{q}}{1-\epsilon} = \int_{x_0}^x \frac{\Delta z}{\Delta t} dx \quad (2)$$

in which x is positively seaward and x_0 means the shoreward limit of beach deformation. After such calculation, we shall obtain the spatial distribution of transport rate $Q(x)$ as shown in the bottom of the same figure.

Figures 3 (a) to (d) show spatial distributions of the effective net transport rate $Q(x)$ averaged over one-hour of wave action thus evaluated from beach profiles given in Fig. 1. Positive values of Q indicates the net transport towards the onshore direction, while negative Q means the offshore transport. The abscissa x is the horizontal distance from the initial shoreline. The locations of breaking point are again indicated by triangle symbols.

It is seen from Figs. 3 (a) and (b) that in case of 0.2 mm-sand, sediment transport towards the offshore direction is predominant in particular outside the surf zone. In few cases such as A-131 to 135 with the initial slope of 1/10 and relatively small wave steepness, the onshore net transport dominates. It is interesting to note that this onshore transport was mostly replaced by the seaward transport for the initial slope of 1/20 even under the similar deep water wave conditions. (Compare Cases A-133 and 134 with A-233 and 234, respectively.)

Figures 3 (c) and (d) for 0.7 mm-sand indicate that, in contrast to the former cases of 0.2 mm-sand, the net transport is mostly shoreward, with the exception of some cases such as B-115 where the wave steepness as well as beach slope are large. Predominant shoreward transport might be simply explained by the asymmetric to-and-fro water particle motion under large amplitude waves, since the coarse sands are transported essentially as bed load.

DISCUSSIONS

Beach Profile Changes

Two-dimensional beach transformation has been intensively studied by numerous investigators. There are many attempts to determine parameters classifying beach profiles, such as by Johnson (1949), Iwagaki and Noda (1962), Nayak (1970), Sunamura and Horikawa (1974), and Hattori and Kawamata (1980).

Sunamura and Horikawa (1974) have proposed a beach profile classification based on the displacement of topography from the initial beach slope: Type I = a shoreline retrogresses and sand accumulates in offshore

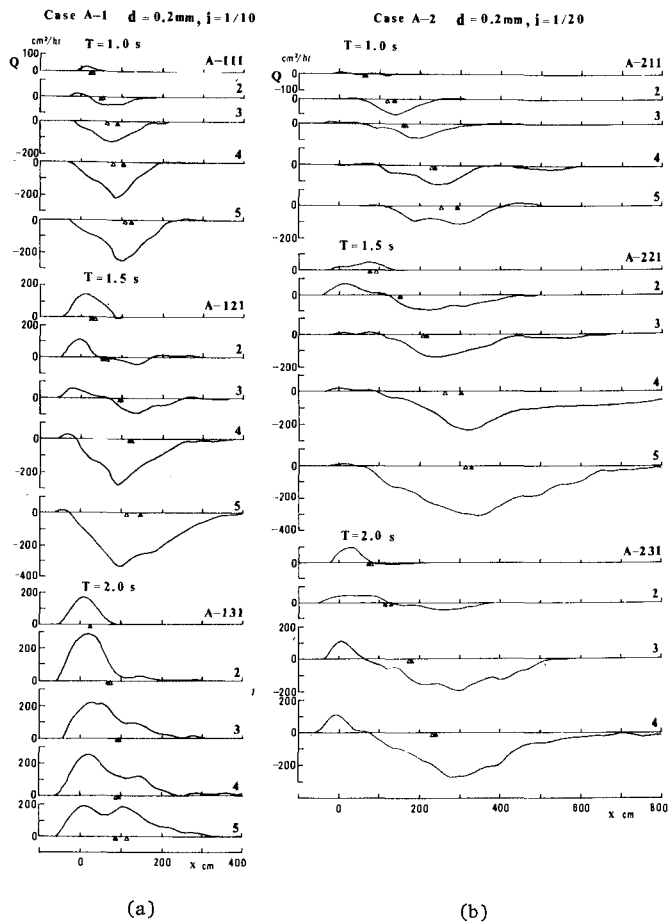


Fig. 3 Distributions of effective net transport rates.

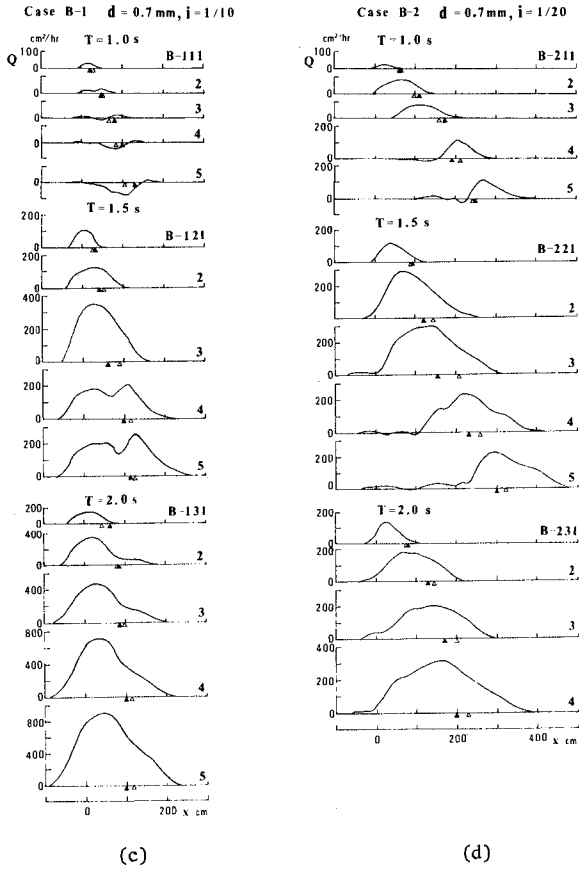


Fig. 3 Distributions of effective net transport rates (continued).

zone, Type II = a shoreline advances and sand piles up offshore, and Type III = a shoreline progresses and no sand deposition takes place offshore. According to them, these three types are distinguished by a nondimensional parameter,

$$C = (H_o/L_o) (\tan \beta)^{0.27} (d/L_o)^{-0.67} \tag{3}$$

as:

$$\text{Type I: } 8 < C, \quad \text{Type II: } 4 < C < 8, \quad \text{Type III: } C < 4 \tag{4}$$

where H_o and L_o : deep water wave height and length, $i = \tan \beta$: initial beach slope, d : grain diameter. Critical values of C have been determined based on the experimental results on the equilibrium beach profiles after more than 160-hour wave action.

Application of this classification to the present data given in Fig. 1 yields the result shown in Fig. 4. In spite of that the present data are for quite short wave duration, they are distinguishable by the proposed values of the parameter C .

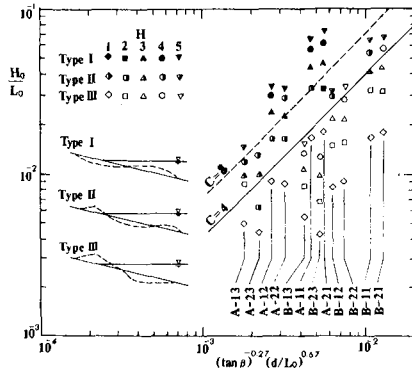


Fig. 4 Classification of beach profile changes.

Net Transport Direction of Suspended Sediment

As mentioned above, the predominant direction of net bed load transport is onshore, but that of the net transport of suspended load depends on conditions. For example, the predominant onshore transport in Cases A-133 and 134 are replaced by seaward transport in Cases A-233 and 234. One interpretation of the predominant directions of net suspended load in the present experiments will be given by Fig. 5.

Since the significant height of sediment suspension would be subject to the pitch of sand ripples, the abscissa $\lambda/w_o T$ was adopted as a param-

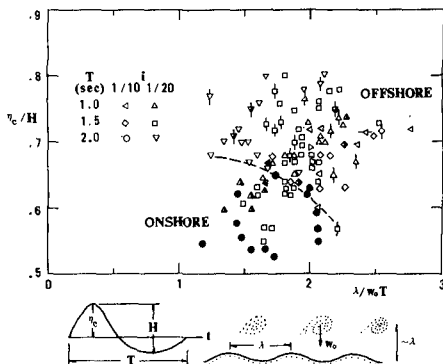


Fig. 5 Net transport direction of suspended sediment.

eter representing the excursion length of suspended sands, where λ is the ripple pitch, w_o the settling velocity of sands, and T the wave period. The ratio of the wave crest height η_c above the mean water level to local wave height H was chosen as another parameter in order to account for the effect of asymmetry of the to-and-fro water particle motion. Solid symbols mean the onshore transport, while open symbols the offshore transport. Figure 2 indicates that these two parameters are not always effective in classifying the sediment transport direction.

Inman and Tunstall (1972) have pointed out that the asymmetry of the sand ripple forms is important in determining the direction of the net sand transport. Although the present authors agree to their view, it should be mentioned that the asymmetry of ripple forms was not significant in the present experiment. The direction of sediment transport is indeed a very crucial problem and further intensive study on this point is definitely required.

Net Sediment Transport Rate and the Shields Parameter

Madsen and Grant (1976) have found that the so-called Shields parameter is effective in quantifying the fluid-sediment interaction in oscillatory flow as well as steady flow. They have proposed an empirical relationship of the sediment transport rate as:

$$\Phi' = 12.5 \Psi^3 \tag{5}$$

where $\Phi' = \bar{q}'/w_o d$: dimensionless transport rate, \bar{q}' : transport rate averaged over half a period of oscillatory flow, w_o : the settling velocity, d : the grain diameter, $\Psi = \tau_{om}/(\rho - \rho_s)gd$: the Shields parameter, ρ and ρ_s : the densities of fluid and sediment, respectively, and τ_{om} is the bottom shear stress amplitude defined by $\tau_{om} = f \rho u_{om}^2 / 2$ in which u_{om} is the maximum velocity at the bed and f the wave friction factor given by Jonsson

(1966). This formula is found to agree well with the experimental data for the bed load rates obtained by oscillating a plate containing sediment in still water. It should be mentioned that the quantity Φ' corresponds to the transport rate averaged over half a period, and that the net transport rate, which is directly related to beach deformation, must be evaluated as the difference between transport rates of onshore and offshore directions.

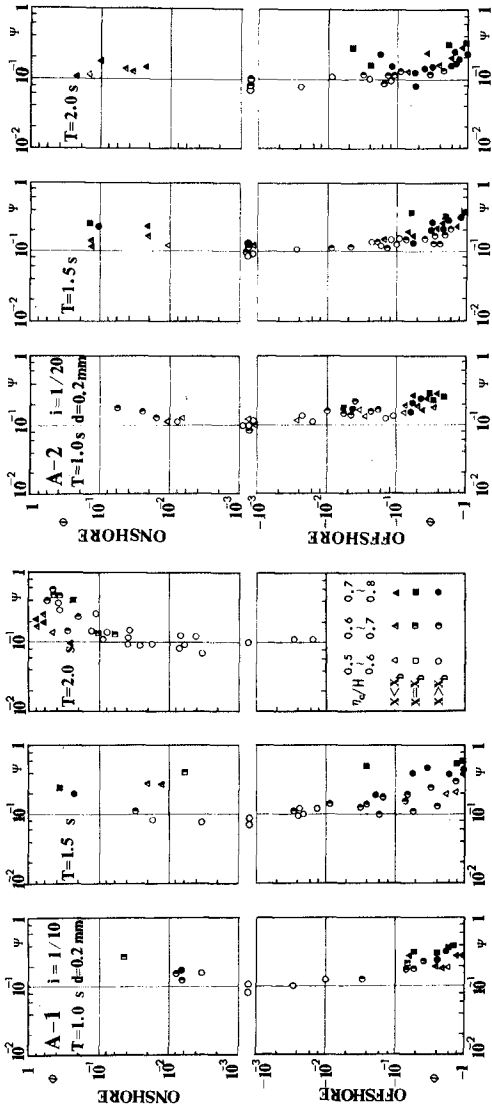
The dimensionless net transport rates $\Phi = \bar{q}/w_{\infty}d$ averaged over one-hour wave action were calculated from the present experimental data. The relations between Φ and Ψ are shown in Figs. 6 (a) to (d), where symbols are distinguished depending on the location; triangles are data obtained inside the surf zone, squares are at breaking point and circles are outside the breaker zone. Clear correlations between two parameters are recognized, though the overall scatter is not small enough.

It is interesting in particular that the relations of Φ and Ψ outside the breaker zone are almost identical, independently of bed slope, wave period and even of the transport direction. The values of Φ for a certain Ψ value inside the surf zone are mostly larger than outside; this should be investigated further by improving the estimation of bottom shear stress in the surf zone.

Now we shall consider only the data obtained outside the breaker zone. All of them are plotted together in Fig. 7 for 0.2 mm-sand and 0.7 mm-sand, respectively, distinguished by different symbols dependent on the transport direction and wave period. It is seen that the magnitude of Φ is somewhat larger for the offshore transport than for the onshore transport. Besides the larger wave period gives larger transport rate Φ .

The Madsen-Grant formula (Eq. 5) mentioned before is indicated by a broken straight line in each figure, and it seems by no means to fit well the experimental data. Since Eq. (5) corresponds to the transport rate averaged over half a period, it ought to overestimate the net rate which must be essentially the difference of the onshore and offshore transport rates. The tendency appearing in Fig. 7 is contrary to this expectation except for small Ψ values.

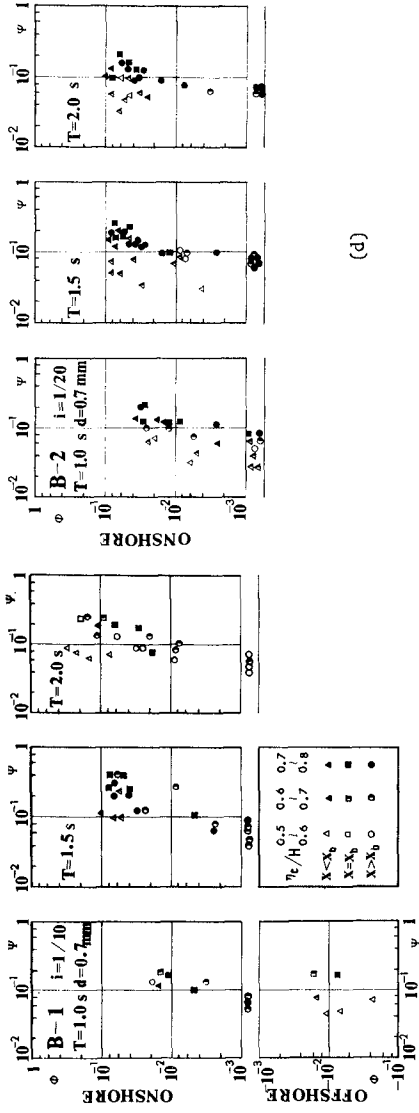
Experimental data shows the tendency that the Φ value increases rapidly with the Ψ value while the latter is small, but its increase rate gradually diminishes as Ψ increases; namely, the relation of Φ and Ψ is convexly nonlinear in logarithmic scales. This trend implies the importance of critical shear stress for the onset of sediment movement. According to the study of Madsen and Grant (1976), the critical value of nondimensional shear stress or the Shields parameter Ψ_{cr} is about 0.07 for fine sands and 0.05 for coarse material. Those values are found to fit well with the critical conditions of the so-called initial movement reported by Horikawa and Watanabe (1967). We shall find from the result of Horikawa and Watanabe (1967) that the critical Shields parameter for the onset of the general movement is to be around 0.11 for fine sands and 0.08 for coarse sands. (The terms, *coarse* and *fine*, are in fact not so appropriate because of their vague meaning. The terminology,



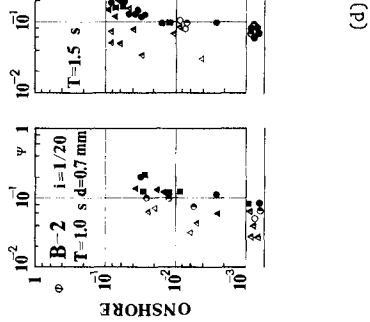
(a)

(b)

Fig. 6 Relationship between net transport rate and Shields parameter.



(c)



(d)

Fig. 6 Relationship between net transport rate and Shields parameter (continued).

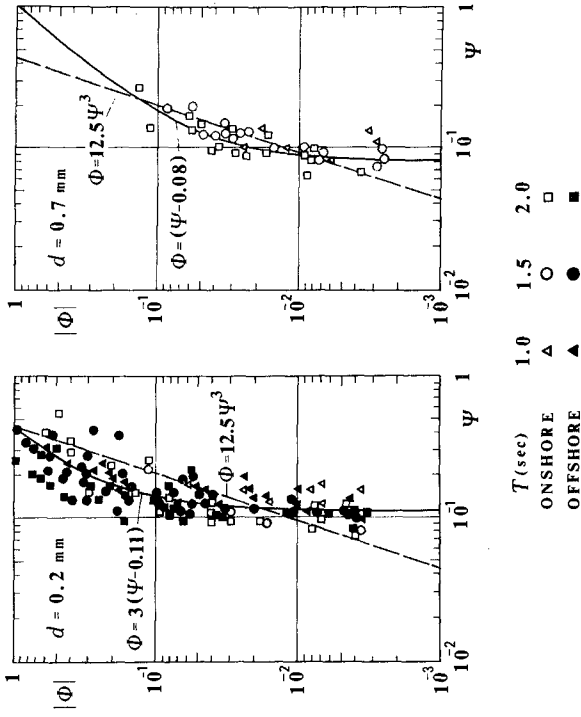


Fig. 7 Summarized relationship between net transport rate and Shields parameter.

hydrodynamically *smooth* and *rough*, will be better. See Horikawa and Watanabe (1967).)

We shall assume the net transport rate is proportional to the excess of Ψ value over its critical value for the general movement just mentioned as:

$$\Phi = A (\Psi - \Psi_{cr}) \quad (6)$$

The values of proportionality constants A to give good fit with the present data are 3.0 and 1.0, respectively, as shown in Fig. 7. It should be mentioned that Eq. (6) is just an empirical relation and is not physically well-founded yet. Probably we should not expect so simple relations between Φ and Ψ , because the net transport rate must be subject not only to the shear stress amplitude rather simply evaluated but also to the local bed slope, asymmetry of near-bed velocity, mass transport velocity, ripple form, and so on. Thorough investigation of the data and more physical consideration will be needed.

CONCLUDING REMARKS

Some interesting, though unsatisfactory yet, results on the on-off-shore sediment transport on a sloping beach have been gained by analyzing the experimental data of two-dimensional beach deformation. The authors are proceeding the study on wave deformation and near-bottom velocity field on a sloping beach in parallel with the laboratory tests similar to experimentation herein reported. Such investigation will be quite useful to improve the interpretation of experimental data.

REFERENCES

- Hattori, M. and R. Kawamata (1980): Onshore-offshore transport and beach profile change. Summaries of 17th Conf. Coastal Eng., pp. 254-255.
- Horikawa, K. and A. Watanabe (1967): A study on sand movement due to wave action. Coastal Eng. in Japan, Vol. 10, pp. 39-57.
- Inman, D. L. and E. B. Tunstall (1972): Phase dependent roughness control of sand movement. Proc. 13th Conf. Coastal Eng., pp. 1155-1171.
- Iwagaki, Y. and H. Noda (1962): Laboratory study of scale effects in two-dimensional beach processes. Proc. 12th Conf. Coastal Eng., pp. 194-210.
- Johnson, J. W. (1949): Scale effect in hydraulic model involving wave motion. Trans. A. G. U., Vol. 30, pp. 517-525.
- Jonsson, I. G. (1966): Wave boundary layers and friction factors. Proc. 10th Conf. Coastal Eng., Vol. 1, pp. 127-148.
- Madsen, O. S. and W. D. Grant (1976): Qualitative description of sediment transport by waves. Proc. 15th Conf. Coastal Eng., pp. 1093-1112.
- Nayak, I. V. (1970): Equilibrium profiles of model beaches. Proc. 12th Conf. Coastal Eng., pp. 1321-1340.
- Sunamura, T. and K. Horikawa (1974): Two-dimensional beach transformation due to waves. Proc. 14th Conf. Coastal Eng., pp. 920-938.

SECONDARY SAND TRANSPORT MECHANISMSBy A.W. Smith¹ and A.D. Gordon²

INTRODUCTION

The basic concept of coastal littoral drift consisting of a "river" of sand driven by the direct alongshore component of oblique waves has long been considered as a basis for littoral transport equations. This concept however is highly simplified since the actual littoral drift on real beaches represents only the final result of the inter-action of dozens or perhaps hundreds of secondary hydraulic processes which continuously occur in Nature. On many Coasts littoral transport is taken to represent the primary mechanism of beach recession or build-up but many of the secondary mechanisms themselves are only partially understood and their individual contributions to the primary process largely unexplored. This paper therefore discusses some of these secondary processes and since off-shore-onshore sediment transport is probably the most important of these a mechanism for this transport mode is suggested based upon the interaction between wave energy and a work capacity parameter for the beach sediments.

GEOGRAPHICAL FACTORS

In considering a coast in plan view many factors that might loosely be described as geographical are readily observed. Headlands and groynes generate complex hydraulic phenomena. Such "hard" surfaces not only generate re-alignments of the sea-bed sediment but they also discharge rip currents and shed vortices which may carry large volumes of sediment to distances exceeding a kilometer out to sea.

Creeks and river discharges may also behave as groynes with the tidal discharges into and out of the river acting as a hydraulic barrier "jet-stream". The barrier effect of tidal jets can be such that Nature must form extremely large delta deposits at the tidal outfall zone offshore of the beach before littoral transport can function within an effective combination of attenuated jet velocity, water depth and wave breaking energy.

1. Civil Engineer, Gold Coast, Queensland, Australia
2. Engineer, Coastal Branch, Dept. of Public Works, N.S.W. Aust.

A further obvious plan-form phenomenon of beaches, particularly within the unstable responsive state between fine weather small wave steep profile and high storm energy flat profile beaches is the development of cusped beach shapes at the water-aerial beach interface i.e. stages 2 to 5 of the Short Model (Ref 1). The hydraulic processes which generate these beach forms must be highly complex but they clearly must exert a profound effect on long shore littoral transport. Much evidence is beginning to emerge that suggests that sand transport occurs in slugs or pulses and cusped shapes have long been observed to migrate in the direction of the littoral drift as of the time.

Under long-shore transport conditions rip-currents become dominant hydraulic features of a beach during its cusped shape development and such currents have a dominant effect on beach cell water re-circulation and offshore sediment transport. In addition the inception of cusped topography leads to highly variable angles of incidence by the breaking wave even to the stage that any average or dominant angle of wave attack becomes meaningless under these circumstances. Nevertheless net littoral sand transport from cusped beach cells has been detected by tracer experiments and the driving force must consist of only the total hydraulic leakage from the cell. Clearly much study remains to be carried out on littoral transport on cusped beaches.

BEACH NORMAL PROCESSES

The most significant variability in beach response to energy input is clearly demonstrated by the hour to hour and day to day fluctuations in cross-sectional profile. The onshore-offshore movements of beach sediments call into motion much greater volumes of material in the short term, by a factor of many magnitudes, than those that can be measured as alongshore transport. If, as it seems likely, the actual littoral transport represents only the longshore component of onshore-offshore sediment movement under oblique wave energy input then it would seem essential to study the onshore-offshore processes in their own right before even addressing the ultimate problem of calculating littoral transport. It is for this reason that beach normal or onshore-offshore processes are considered as secondary mechanisms in this discussion.

SEDIMENT WAVE INTERACTION

There must certainly exist a profound but predictable interaction relationship between wave energy input and the behaviour of beach sediments. Waves change the beach shape and sediment distribution across the beach but the converse must also hold true, the behaviour of the beach sediment changes the form, shape and breaking behaviour of the waves. Beaches change slope according to wave height, offshore bars develop that induce multiple wave breaks and wave reformations with increasing size of deep water wave but why do these processes occur? Why do small swell waves generate a steep beach whilst great storm waves generate wide flat slopes? Why indeed do beach sediments exist at all? If waves destroyed energy entirely by hydraulic mechanisms the world's coast would surely all be rocky shelves. Beach sediments demonstrate a highly developed mobility in response to incident wave height, and to a lesser degree tidal variation, and it has long been taken as a basic tenet that the larger the beach particles the steeper the beach for the same wave input.

Clearly the properties of the beach particles themselves must exert a highly significant effect on the behaviour of any beach which cannot be explained by considering the properties of the waves in isolation, both form part of a highly sophisticated mechanism designed by Nature to ensure the most efficient dissipation of energy with a maximum conservation of natural resources. Many detailed descriptions exist of beach profile and wave responses with the work of Short (Ref 1) and Wright (Ref 2) probably representing the most definitive (and fascinating) statement of what might well be called an "Atlas" of beach and wave geography. It is tendered however that until the interaction between sediment properties and wave mechanics are included such work will remain largely descriptive.

SEDIMENT POPULATIONS

Beach and river sediments apparently exist in almost an infinite variety, to the extent that Nature seems to use whatsoever natural detritus that is available as of the place and the time and adjust the local geography to suit the energy demand of the ambient hydraulic process. Natural sediments do not consist of what might be described as "blocks" of particles all with the same properties but they occur in curious blends of all different sizes of particles from comparatively fine to comparatively coarse, all existing together within a finite volume.

Based on sediment grading curves as described in the literature, every natural beach sediment population contains a significant percentage of large particles and perhaps much more importantly an even more significant number of very fine particles. In normal grading analyses the "fine" contents in the "pan" are merely recorded for weight and thrown away but the fact remains that even on the most active beach exposed to the highest waves the largest particles found within the wave zone always contain a significant content of a matrix of fine particles dispersed within them.

It seems that Nature will never winnow out a sediment "blend" of particles to produce a neat-sized or gap-graded "mix", but always produces a full population encompassing the combination of a large number of particles over quite a wide range. Beach sediments thus exist and behave as integrated populations and not as groups of individual clusters of neat sized particles. It is perhaps for this reason that it is so difficult to calibrate model work carried out with sieved particles or beads almost all of the same size.

Because beach sediment populations are so wide a major difficulty is usually found in assigning some parameter that will describe the population, or its properties, in some meaningful way and if possible provide some average index of the parameter that also has some competent descriptive power. Tradition has been to adopt a "size" parameter to describe particles using either a sieve train or a settling tube to arrive at a nominal "diameter" size parameter. Whilst settling tubes should be well superior to sieving tests in that at least the settling tube tests particles within an hydraulic environment nevertheless both tests have a low standard of accuracy and reproducibility and in fact should only be reliable when they test one particle at a time.

The two major sampling and testing variables are:-

(a) Both devices are extremely sensitive to feed rate, that is the number of particles being tested together at one time. In the mineral industry sieves can be made to selectively either pass or concentrate particular particle densities, shapes or sizes by merely varying the feed rate and the analogous problems with settling tubes have been well reported e.g. McNown and Pin-Nam Lin see (Ref 3).

(b) Secondly both devices "pass" or "settle" high aspect ratio particles in a highly preferential manner, in sieves these particles pass through the mesh end-on with their greatest dimension normal to the mesh whilst the same particles settle in water with their greatest dimension horizontal and usually demonstrating some flutter or oscillation as well.

Finally in a settling tube the particles must settle under Laminar flow and surf zone dynamics must always be turbulent. It would not be surprising therefore if sediment transport equations based on some nominal size derived from either of these two tests display such wide scatter and poor correlation. The problem must result from the shape factors of the particles together with a significant contribution from their surface texture. By analogy to basic aerodynamics it might be expected that particle shape and aspect ratio might represent almost the dominant transport and drag mode and a preliminary appreciation appears to confirm this proposition for water as well. The most simple parameter available that quantifies any particles shape factor and weight is its specific surface - that is its total surface area divided by its weight. In mineral technology the term used is F and for normal beach particles the unit of mm^2/gram appears the most convenient.

Experiments carried out on a hydraulic spiral mineral separator under completely random turbulent input demonstrated that the migration of particles into high, medium and low energy zones across the spiral cross section was very strongly related to the particles specific surface and barely correlated at all with either sieve or settling tube diameters. It seemed therefore that the parameter of specific surface held much promise of providing a particle's energy response or work capacity indicator.

A most fortuitous discovery that when natural beach sediments are classified by particle specific surface is that the population is almost exactly Log-normal (See Fig 1) a property of sediments that has long been postulated but seldom detected by normal sizing methods. Intuitively the selection of specific surface to classify a particle seems reasonable also in that at least it provides a systematic integration and description of a particles properties of shape, texture, aspect ratio, specific gravity and thus weight and perhaps a good starting point for considering its overall hydraulic properties. In particular with a log-normal population distribution the ease with which borrow and native

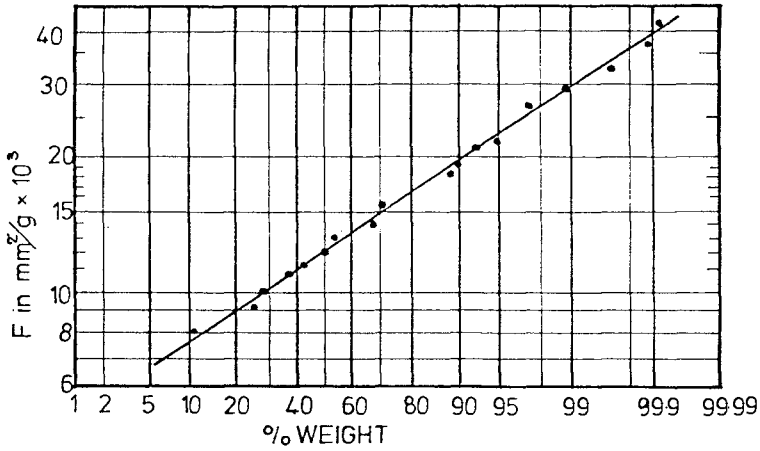


FIG.1 - SPECIFIC SURFACE : LOG PROBABILITY DIAGRAM FOR ONE SAND SAMPLE

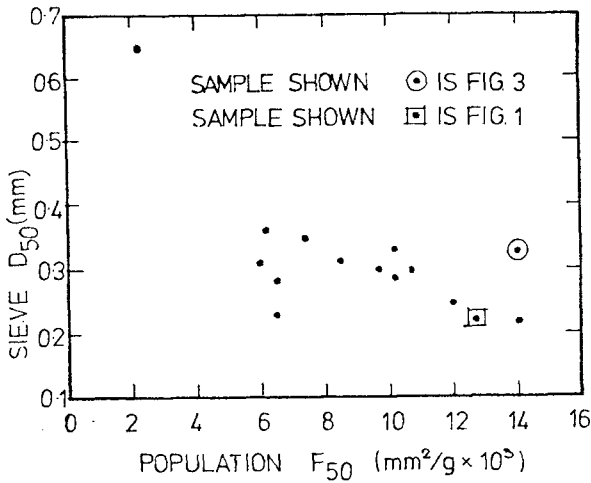


FIG.2 - COMPARISON OF D₅₀ ~ F₅₀

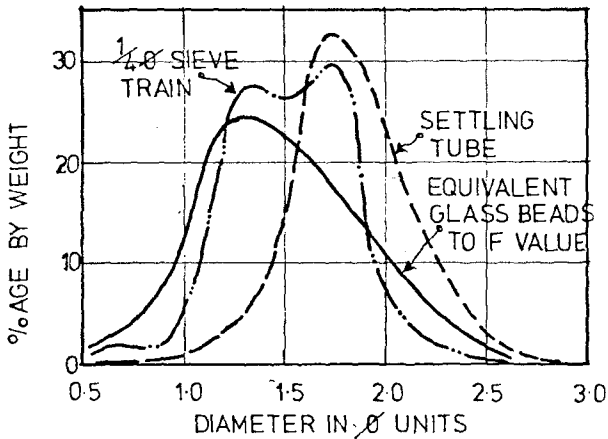


FIG. 3 — COMPARISON OF DIFFERENT PARAMETERS USED TO DESCRIBE SAME SAND SAMPLE

beach sands may be compared without recourse to deviation, skewness and kurtosis measures for example is also attractive.

As an indication of the absence of correlation between specific surface and sieve or settling tube diameter Fig 2 shows a plot of F50 against D50 for fifteen natural sediments taken up to 800 km apart on the Australian seaboard and Fig 3 shows a comparison of population diagrams as displayed by $\frac{1}{4} \phi$ sieving, settling tube and specific surface for the same sediment. Because specific surface cannot be plotted on the same graph as d or ϕ units the specific surface population has been shown as the size distribution for the actual sediment's F value converted to percentages of various sized purely spherical glass beads. The curve centroid offsets must be highly significant, and the bi-modal sieve population is typical of the local coast.

WORK CAPACITY

Because the parameter of specific surface does provide a log-normal distribution for natural beach sediments and thus probably close to representing a basic or perhaps the basic description of the particles it seems worth while to test this property with other basic parameters involved in fluvial mechanics. Unfortunately this is not entirely possible because most workers in the field have not recorded much in the way of shape factors for natural sediments and much work has been carried out with gap-graded or artificial particles, neither of which are found as populations in Nature.

However several workers have analysed parameters with large amounts of data generally using natural sediments and the larger the data-base the more reliable should be the average properties. For considering transport of sediment on beaches perhaps the two most significant parameters to consider might be the critical scour velocity and the critical tractive force. For the first case taking the boundary graph between erosion and transportation from the Hjulstrom diagram (Fig 4a) and making some reasonable appreciation of a shape factor the famous hooked curve can be re-plotted as Fig 5a as \bar{u} against F. If it is accepted that particles below approximately 0.1 mm dia as measured by sieves are in the silt range and entering the realm where water attraction and perhaps Van de Wals forces cause many particles to flocculate and behave as agglomerates the new graph, now straight lines, generates two branches when this zone of particle size is reached. Of more interest perhaps the relationship between critical scour velocity and specific surface appears to be quite close to:-

$$\bar{u}_{crit.} = \frac{k_1}{\sqrt{F}} \quad \dots (6.1)$$

In a similar fashion if the vast data array presented by Lane (1953) is similarly re-plotted to substitute F instead of D (see Figs 5a and 5b) there again seems a reasonable approach to:-

$$\tau_{o\,crit.} = \frac{k_2}{F} \quad \dots (6.2)$$

If the relationship of equation 6.2 can be substantiated within a reasonable envelope then the criteria of the threshold of a critical tractive force might be considered

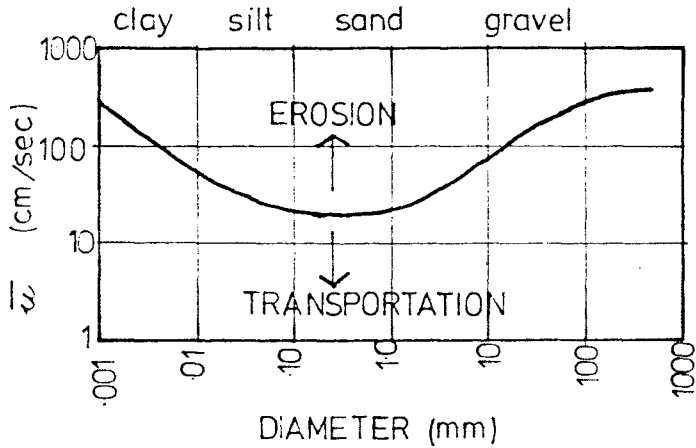


FIG 4_A - HJULSTROM DIAGRAM (1935)

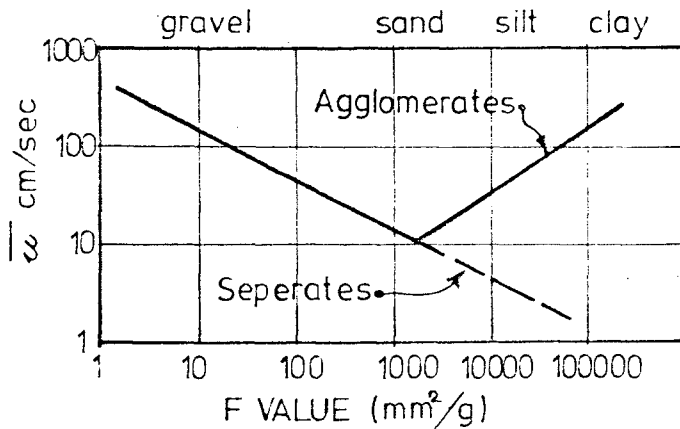


FIG.4_B - EQUIVALENT 'F' DIAGRAM

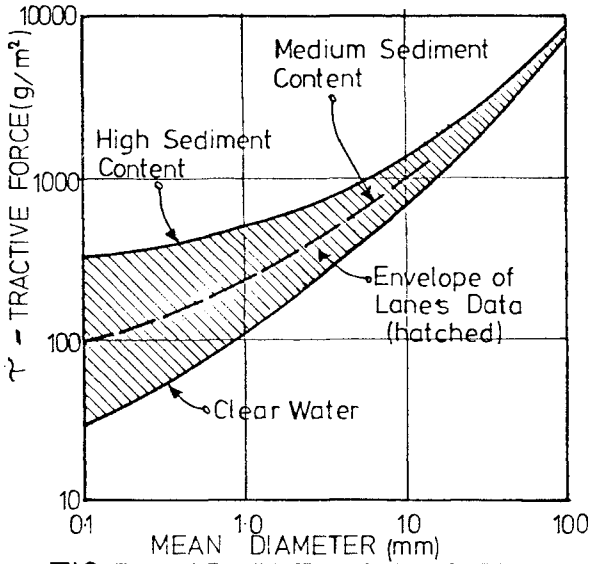


FIG 5A - ADAPTED LANE DIAGRAM (1953)

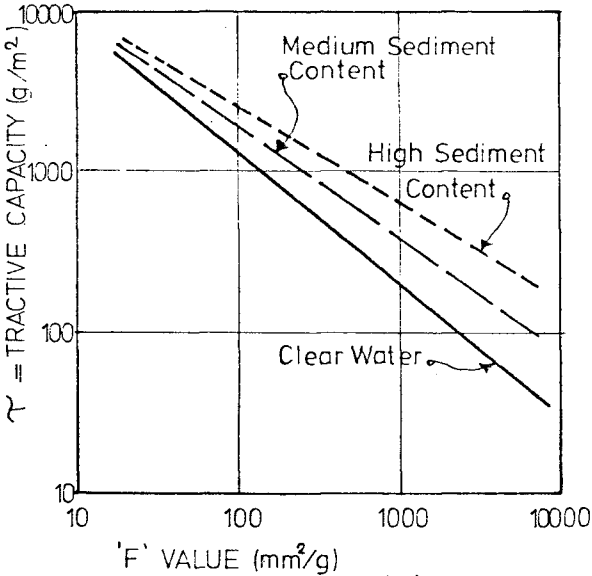


FIG 5B - EQUIVALENT 'F' DIAGRAM

as a measure of a particle populations ability to withstand hydraulic work input up to the stage where the particles are displaced and put entirely into suspension. If this concept is viable then τ_0 will represent the maximum work capacity of the sediment provided conditions are turbulent.

In Nature wave energy dissipation is a most complex phenomenon but suppose that the extreme case is considered, this being when the total average wave energy for one wave is completely absorbed by the active sediment volume of the beach. Further if it is assumed that a particular active volume of beach sediment multiplied by its average critical tractive force is required to absorb the total energy of the wave without washing away then:-

$$\text{Sediment Volume} \times \tau_{Av.} = \frac{\rho g H^2}{8} \quad \dots (6.3)$$

which reduces to:-

$$\text{Vol} = K_3 FH^2 \quad \dots (6.4)$$

this being for one wave. However in Nature some wave energy is dissipated by the breaking mechanism, some wave energy is reflected, some is deflected by currents, wind, hydraulic interference and suspended sand loadings so perhaps the best that might be expected under real conditions is:-

$$\text{Sediment Volume} \propto FH^2 \quad \dots (6.5)$$

. These approximate equations can only be considered for a simple case, in particular a wave break perfectly parallel to the beach and no rip currents or littoral drift but they may well allow for a crude first step model of onshore-offshore beach behaviour.

It would follow however that the higher the work capacity of the beach sediments the smaller the volume of sediment that would be required to absorb the same wave energy, therefore the lower the F value of the particles the steeper the beach for a constant wave climate, all very much as is always observed.

THE WORK PRISM

A question apparently seldom addressed is "how" do beach sediments in fact absorb wave energy? It can certainly be seen that they do - but how? It is straight forward to deduce that if all sediment transport and volumetric re-adjustment is caused purely by sea-bed current tractive

forces raising sand into suspension or as semi-suspended bed load then the thickness of the mobile bed must be extremely thin, often quoted as only a few grains in thickness. However recent work on beach tracers e.g. Chapman (Ref 4) and the consideration of the swept prism e.g. Chapman & Smith (Ref 5) has clearly demonstrated that on real beaches a vast volume of upper beach sediment extending to depths of at least 3 metres during storms turns over and/or intermixes continually representing a remarkably large active volume. Even under quite mild conditions with waves not exceeding 2m. high tracer grains have been recovered from depths exceeding 1m. below the beach surface on both Sydney and Gold Coast Beaches.

On the one hand it would seem absurd that a layer of sediment only a few grains thick on a beach could absorb any wave energy at all, yet how can the extremely large three dimensional movements and re-mixing of real beach sediments be explained. Beaches are traversed by waves and waves result in a variable hydraulic head pressure being exerted on the sea-bed. These fluctuations of hydraulic head will be followed by a variable hydraulic pore pressure within the sediment that composes the sea-bed. In its simplest case as a wave approaches a given sea-bed zone the inter-particle pore pressure will increase and once the wave has passed the pore pressure will reduce. This reduction in pore pressure will introduce an upwards vector of pore

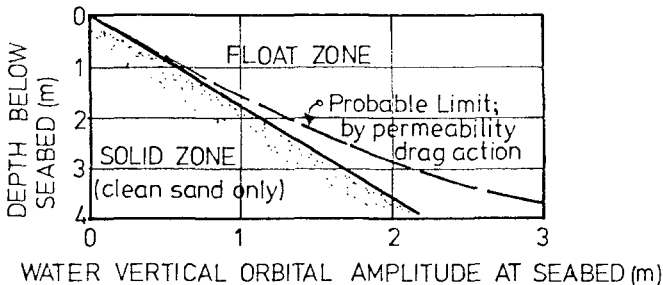


FIG.6- PORE PRESSURE INDUCED FLOAT ZONE

pressure and for the sea-bed sediments to remain at rest the shear strength of the sediments must exceed the pore pressure released stress. The most elementary equation for the development of "quick" conditions in purely frictional sediments is:-

$$\text{Pore pressure } \mu > \text{ soil shear strength } \tau \quad \dots(7.1)$$

and for critical stability:-

$$\mu = \tau = (\rho_s - \rho) h \tan \phi \quad \dots(7.2)$$

It is straight forward hence to construct a graph of pore pressure release against submerged sediment shear strength and a typical example is given as Fig 6. In the context of the graph the amplitude of pore pressure release may be taken as the wave height close to the breaking zone or the vertical amplitude of the orbital water movement for deep water conditions. Clearly the drag on hydraulic pressure transfer due to the permeability of the sediment population will decrease the depth of what is shown as the pure "float zone" and modified by the nominal only dashed line. The depth of sediment that is called the float zone need not of course go completely "quick" in the soil mechanics sense but even the vertical movement of only a few grain diameters of the total dead load of the float zone would absorb a great deal of dynamic energy in lifting it. Moreover a vertical movement of the sea-bed beneath a wave of the small amplitude postulated and within the short time scale involved would barely be noticed by an observer provided of course that he could hold his feet whilst the wave passed over him.

It might well be reasonable therefore to suggest a first approximating crude model of the energy absorbing mechanism of a sediment beach. If the sediment population has a finite and maximum capacity to absorb energy before it is washed away, if the cross sectional volume of the sediment population can be equated against wave energy input and the depth below the beach surface or seabed within which the sediment absorbing capacity may be called into action then it is possible to estimate what might be called the work prism of a beach that might be stable under any given wave energy input. What is here described as the work prism applies to each wave individually but the envelope of all work prisms on a beach may be represented by the swept prism concept described in Ref 5.

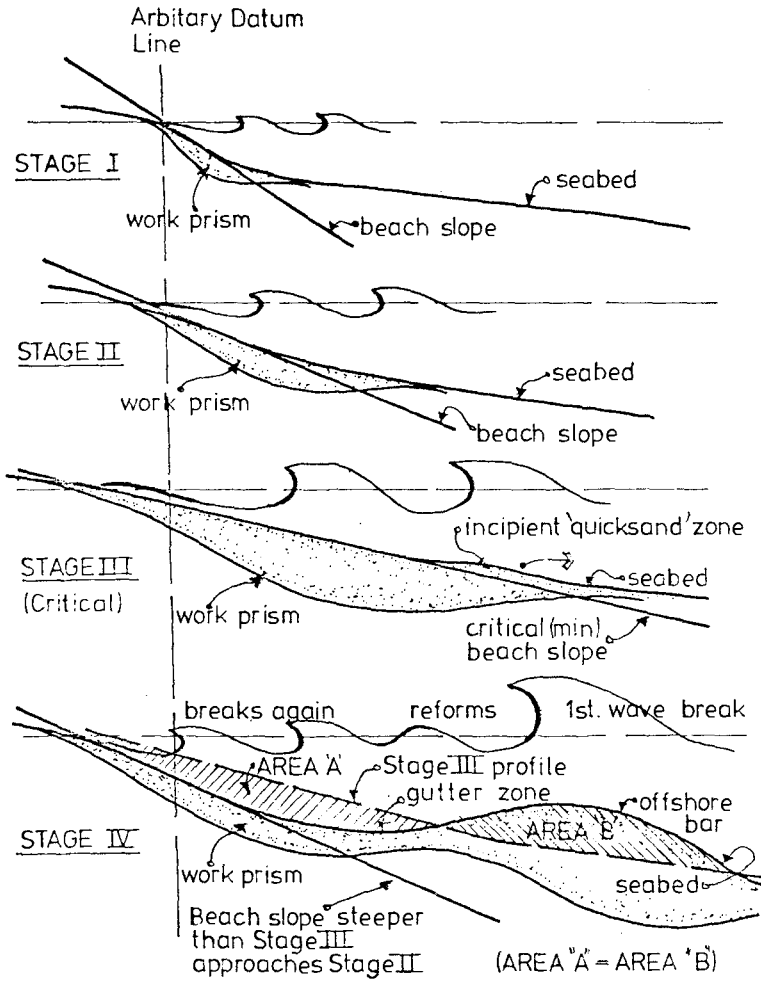
On real beaches some sediment is put into suspension and transported as such by even modest waves in the breaking zone but the rate of transport and the transport distances are often remarkably small and the phenomenon may even represent the inception of a beach slope adjustment. In great storms however vast volumes of sediment are placed in suspension but because of the great complexity of the hydraulic processes involved this factor has not been included in the simple model under consideration. The basic model is thus postulated largely for long term non-storm average conditions.

BEACH PROFILES

If a beach sediment has a maximum and limiting work absorbing capacity then an increasing wave energy input will demand a larger volume of the same sediment for equal wave dissipation. Since the thickness of the sediment work prism is not markedly sensitive to wave height and permeability must have a limiting effect on the thickness then the only way that more sediment may be called into play is to extend the prism in width across the beach and in Nature this can only be done by flattening the beach slope. The similarity to the concept of KD values for non-interlocking armour units might be noted.

As a first approximation therefore the hypothesis is that beach slope and width will be proportional to incoming wave energy. There must however be a critical slope beyond which the toe of the work prism is unstable and at this stage since most of the sediment in the prism will have reached its maximum work capacity already then all, or most, of the prism will liquify and flow offshore until it reaches a water depth where the energy input is again less than its maximum work capacity. This provides an explanation for the formation of offshore bars and demonstrates another of Nature's methods of conservation of resources because the development of an offshore bar causes the bigger incoming waves to break further offshore and the inner beach merely re-adjusts with a profile compatible with the reduced energy of the re-formed wave and on the beach the cycle may now be repeated. The generalised descriptive model of the proposed mechanism is shown in Fig 7.

This mechanism may also explain why the inner beach accretes during fine weather small swell conditions. In a simplified form, if say during a mildly variable wave energy input:-



NB.-All stages reversible at any time

FIG.7--RESPONSE OF BEACH PROFILE TO WAVE HEIGHT INPUT FOR CONSTANT BEACH SAND

- (a) The beach slope left by the previous wave is flatter than critical any sediment mobilised by the next wave will push up the beach to steepen it
- (b) If the beach slope is existing at critical slope there will be no change
- (c) If the beach slope left by the previous wave is steeper than the critical slope for the next wave then the slope will flatten and sediment will migrate offshore.

This simple model applies strictly on an individual wave basis, so that spectral and statistical measures would need to be applied to the wave climate before it might be possible to assess whether the model is reasonably valid in practice.

BEACH SORTING

A further process of considerable significance concerns the natural phenomenon of sorting on real beaches. Concentration areas of various apparent size fractions can readily be observed on beaches and there is much evidence to suggest that high energy particles tend to concentrate in high wave energy zones and vice versa. It would be only reasonable to expect Nature to apply resource conservation in this manner and optimise the total work capacity of the work prism by selective sorting and a similar mechanism might be expected for zeta bays where wave energy varies along the plan profile of the beach.

However within the concept of a total cross sectional work prism this sorting might well be considered as a micro-process existing as a dynamic internal fluctuation within the prism as depicted in Fig 8. The general discussion here considers average wave energy equated to the average work capacity of the prism and internal sorting within the prism might well then be represented by an extra efficiency factor that is greater than unity. It may even be that this internal sorting together with the localised humps and hollows that thus form within the beach profile, particularly on models, merely represent local variable fluctuations within an overall average beach slope and accordingly might be simply regarded as local "noise" impressed upon a general trend.

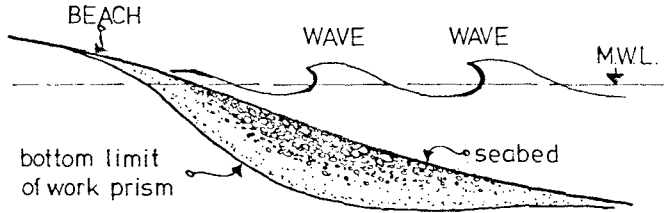


FIG. 8—DIAGRAM OF MICRO-SORTING OF SAND
WITHIN WORK PRISM
(LOWER 'F' VALUE DEPICTED BY LARGER PARTICLE)

If all the mobile sediment remains within the outer limits of the maximum work prism for the worst ambient wave energy then there has been no beach erosion, merely a cross sectional re-adjustment and as observed by Chapman (Ref 4) the appearance of the visible beach tells nothing about the work capacity of the total system, the real action always happens beneath the sea surface. The consideration of nett losses from the work prism into dunes, into offshore sinks and as littoral transport is of course another consideration to those discussed above.

CONCLUSION

(1) Secondary beach processes of remarkable complexity operate on natural beaches in both the micro and macro scale generally simultaneously such that it is extremely difficult to isolate the overall effects of each or assign their individual contributions to either beach stability or littoral transport.

(2) Many of these secondary processes are briefly discussed and for onshore-offshore transport in particular preliminary suggestions are made for modelling beach profiles not from wave data alone but from the interaction between beach sediments and wave energy following the application of a work capacity parameter to the sediments themselves.

APPENDIX - REFERENCES

1. Short, A.D. "Beach Response to Variations in Breaker Height" 17th International Conference on Coastal Engineering 1980.
2. Wright, L.D. "Modes of Beach Cut in Relation to Surf Zone Morphodynamics" 17th International Conference on Coastal Engineering 1980.
3. McNowen, J.S. and Pin-Nam Lin. "Sediment Concentration and Fall Velocity". 2nd Midwestern Conference on Fluid Mechanics, Ohio State University 1952.
4. Chapman, D.M. "Management of Sand Budget, Kirra Beach, Gold Coast" 4th Australian Conference on Coastal & Ocean Engineering. I.E.Aust. Publication No. 78/11, 1978.
5. Chapman, D.M. & Smith, A.W. "The Dynamic Swept Prism" 17th International Conference on Coastal Engineering, 1980.

CHAPTER 70

SAND TRANSPORT BY WAVES

By Jan van de Graaff* and
Wiel M.K. Tilmans**

1. Introduction

In coastal engineering practice frequently a distinction is made between two different modes of sand transport:

- longshore transport
- onshore-offshore transport

From a theoretical point of view the longshore transport phenomenon is not as complicated as the onshore-offshore phenomenon. In the longshore mode of transport, the variations in time (wave period scale) are less important since the current velocity component in the longshore direction is nearly constant in time. In the onshore-offshore direction both the time-variations of (orbital) velocities and sediment concentrations have to be considered in order to be able to compute the resulting net sediment transport. Since our quantitative knowledge of the time variations of the concentration is extremely poor at this moment, realistic calculations of the onshore-offshore transport, based on the actual physics involved, cannot be made. In many practical coastal engineering applications the onshore-offshore transports play an important role, however, and therefore a reliable description is urgently needed. Swart (1974;1976) presented an experimentally based computing method. The Coastal Engineering Group of the Delft University of Technology has been studying the onshore-offshore transport phenomenon since 1968. Since the beginning of the investigation a rather experimental research method has been used also since the measuring devices lacked to measure real concentrations. The outcome of the present investigation, however, is rather surprising in some aspects. Bijker, Van Hijum and Vellinga (1976) reported on some preliminary results. Later series of tests resulted in a change of the

* Senior Scientific Officer, Delft University of Technology;
Civil Engineering Department; Coastal Engineering Group
** Teaching Assistant Coastal Engineering Group
At present Project Engineer, Delft Hydraulics Laboratory;
De Voorst Laboratory.

preliminary ideas.

During the present investigation the (net) sediment transport due to waves over a horizontal sand bottom has been studied. Various grain sizes have been used for bottom material.

This paper describes some newer insights. The results at present can hardly be used for direct practical use. However, for a better understanding of the complex character of the onshore-offshore sediment transport, the test results are undoubtedly of interest.

This paper is a summary and uses the test results of the graduation theses of Vellinga (1975), Schepers (1978) and Tilmans (1979).

2. Small-scale tests

During the present experimental study, a wave-flume has been used in which regular waves can be generated (see Fig. 1). Over approximately 9 m the horizontal bed consists of well-sorted sand (see Fig. 2). At the "landward"-side of the flume a wave-absorbing slope has been constructed. The 1:10 slope is rather steep, resulting in some wave reflection.

In TABLE I a summary of the boundary conditions has been given. (In the present paper only tests with $T = 1.7$ s have been considered).

D_{50} (μm)	h (m)	H/h (-)	source
87 185	.20; .25; .30	.20; .25 .30; .35	Tilmans (1979)
125 465	.30	.30	Schepers (1978)
250	.20; .25; .30	.20; .30 .40	Vellinga (1975)

All tests $T = 1.7$ s.

TABLE I Boundary conditions

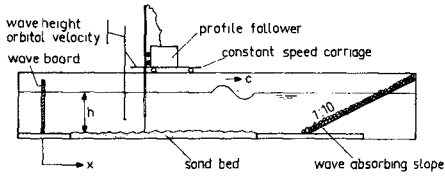


Fig. 1 Sketch of wave flume.

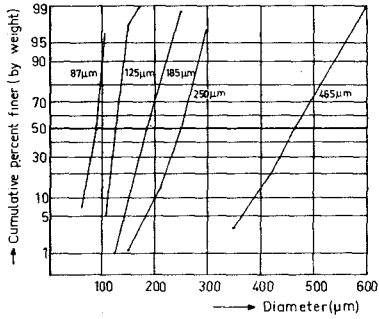


Fig. 2 Grain size distribution.

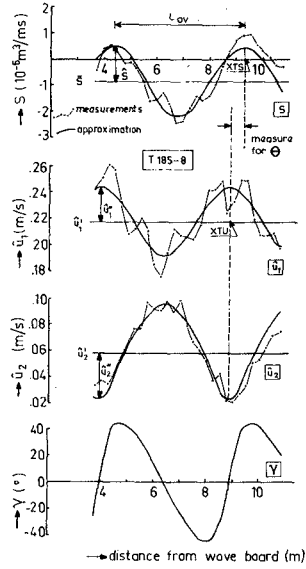


Fig. 3 Measurements; approximations.

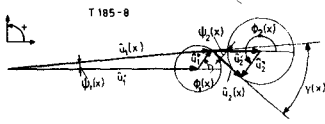


Fig. 4 Vector summation first and second harmonics.

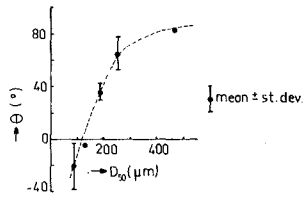


Fig 5 Effect of D_{50} on θ

Sediment transport

Before and after a test the bottom profile was measured with an electronic "bottom profile follower". The profile follower was attached to a constant speed carriage. It could be arranged by some electronics that the total volume of sand within 0.25 m sections was measured. By integrating the total volume of sand from the sand-less part of the bottom in front of the wave-generator to the sand-less part in front of the wave-absorbing slope and subtracting these values after and before a test, the net sediment transport at 0.25 m intervals could be computed (Fig. 3 gives an example). The bed profile was measured in three lines along the length of the flume; the mean value has been taken into account. Sometimes a slight adjustment was necessary to correct the differences in amount of material before and after a test. Normally the tests had a duration of 30 minutes.

Wave-heights

The form of the surface-elevation has been measured at cross-sections at 0.25 m intervals. A resistance type wave gauge was used for this purpose.

Water-motion

At 1/3 of the water depth (h) above the bottom the horizontal component of the orbital velocity was measured at the cross-sections at 0.25 m intervals with a micro-propeller. The propeller signal was sampled with a constant time-step. About 8 samples were obtained within a wave period.

The several harmonic components were determined afterwards with a harmonic analysis computer program:

$$u(t) = u_0 + \hat{u}_1 \cos \omega t + \hat{u}_2 \cos(2\omega t + \gamma) + \dots \quad (1)$$

where: $u(t)$: the momentary horizontal component of the orbital velocity; u_0 : mean resulting velocity; \hat{u}_1 , \hat{u}_2 : first and second harmonic components; ω : wave frequency; t : time and γ : phase

angle between the first and second harmonic component.

As can be seen from Fig. 3 the magnitude of the components \hat{u}_1 and \hat{u}_2 of Eq. 1 varies along the axis of the flume. That indicates the occurrence of secondary waves. Hulsbergen (1974) and Buhr Hansen and Svendsen (1974) described some aspects of the secondary wave phenomenon. The selected boundary conditions for the present study (especially the h/λ -values) are as such, that secondary waves do occur.

3. Test results

3.1. Theoretical considerations

Wave types

Due to the selected boundary conditions (see TABLE I) and the manner of wave generation (wave-paddle sinusoidally moving) various "waves" and hence orbital velocity components can be distinguished in the flume, viz.:

- main wave (third order Stokes wave)
- secondary wave (Fontanet wave)
- interaction waves

[See Kravtchenko and Santon (1957); Fontanet (1961); Hulsbergen (1974)]

The horizontal component of the orbital velocity under a third order Stokes wave can be described as:

$$u(t) = \hat{u}'_1 \cos \omega t + \hat{u}'_2 \cos 2\omega t + \hat{u}'_3 \cos 3\omega t \quad (2)$$

where: \hat{u}'_1 ; \hat{u}'_2 and \hat{u}'_3 : the Stokes components.

Due to the disagreements in velocity profile of a gravity wave and the translating wave board a "free" secondary wave (Fontanet wave) is generated. This wave with a frequency 2ω moves, contrary to the second order Stokes component with the same frequency, "free" with its own wave propagation speed through the wave flume. The corresponding maximum horizontal orbital velocity component is indicated by \hat{u}_2^* .

Due to non-linear interaction of the Stokes and the Fontanet waves, so-called interaction waves are generated. For the present analysis the interaction waves with the frequencies ω and 3ω are important. Both interaction waves have propagation speeds which are different from the "normal" celerities with respect to the frequencies. The orbital components are indicated by \hat{u}_1^* and \hat{u}_3^* .

As a result of the foregoing consideration each of the three basic Stokes components has thus a counterpart with the same frequency but with a different celerity. The various components are summarized in TABLE II.

Frequency	Stokes components		Interaction/Fontanet components	
	orbital velocity	celerity	orbital velocity	celerity
ω	\hat{u}_1'	c_1	\hat{u}_1^*	c_*
2ω	\hat{u}_2'	c_1	\hat{u}_2^*	c_2
3ω	\hat{u}_3'	c_1	\hat{u}_3^*	c_*

TABLE II Wave components

When two waves are present in a wave flume with the same frequency but with a different celerity, the phase difference ϕ between such two waves at a certain position x can be found again at the position $x + L_{ov}$ in which L_{ov} is the so-called overtake length defined as:

$$L_{ov} = \frac{\text{wave length slow wave}}{\text{celerity difference}} \cdot \text{celerity fast wave}$$

Thus for the second harmonic components results:

$$L_{ov2} = \frac{\lambda_2}{c_1 - c_2} \cdot c_1 \quad (3)$$

With $c_1 = \lambda_1/T$ and $c_2 = 2\lambda_2/T$, Eq. (3) yields:

$$L_{ov2} = \frac{\lambda_1 \lambda_2}{\lambda_1 - 2\lambda_2} \quad (4)$$

It can be proven that, with the theoretical values of c_x^* and c_x' (see TABLE II) for both L_{ov1} and L_{ov3} the same length as L_{ov2} results ($= L_{ov}$).

At the position x where $\phi_i = 0^\circ$ both components yield a resulting \hat{u}_i component with magnitude:

$$\hat{u}_i = \hat{u}_i' + \hat{u}_i^* \quad (5)$$

($i = 1, 2, 3$).

Where $\phi_i = 180^\circ$, results:

$$\hat{u}_i = \hat{u}_i' - \hat{u}_i^* \quad (6)$$

From the measurements of Fig. 3 it can be seen that for the first and the second harmonic component seemingly the same L_{ov} is found.

Furthermore, it can be detected that where $\phi_1 = 0^\circ$, $\phi_2 = 180^\circ$ results and vice versa. Fontanet (1961) did prove this theoretically.

In Fig. 4 the resulting vector summation of the first and the second harmonic component is given. From that figure the expression for $\hat{u}_i(x)$ ($i = 1, 2$) becomes:

$$\hat{u}_i(x) = \sqrt{(\hat{u}_i')^2 + (\hat{u}_i^*)^2 + 2\hat{u}_i' \hat{u}_i^* \cos \phi_i(x)} \quad (7)$$

$$\text{where: } \phi_1(x) = \frac{x-x_{1top}}{L_{ov}} * 360^\circ \quad (8)$$

$$\phi_2(x) = \frac{x-x_{1top}}{L_{ov}} * 360^\circ + 180^\circ \quad (9)$$

x_{1top} = x-ordinate where top in \hat{u}_1 -curve occurs.

Since the u_o^- , \hat{u}_3^- and further components in Eq. (1) turned out to be insignificantly small, they will be ignored in further analyses; thus only the first and the second harmonic components remain.

Sediment transports

Till now no sound physical description of the sediment transport as a

function of the water motion is known. It can be seen from Fig. 3 that the net sediment transports as a function of x do vary apparently with the same overtake length, L_{ov} , as the orbital components vary.

3.2. Results

As can be seen from Fig. 3 the actual test results show the general trends as discussed in section 3.1 quite well. Some fluctuations do occur however. For instance fluctuations due to measuring errors or wave reflection. In the further analyses it is useful to use mathematical descriptions for the water motion- (\hat{u}_1, \hat{u}_2) and transport- (S) parameters as a function of x . The basic measurements of the various tests (compare the measuring points of Fig. 3) have been approximated by three different curves with a least squares fitting-method. For the \hat{u}_1 - and \hat{u}_2 -curves an equation according to Eq. (7) was used. For the overtake length the theoretical values which can be computed with the help of the third order wave theory of Skjelbreia (1958), have been taken into account. In Eq. (7) three parameters, \hat{u}_1^1 , \hat{u}_1^* and the position of x_{1top} are to be approximated. TABLE III gives the results of the various tests. In Fig. 3 the ultimate approximation-curves have been given also. From TABLE III it can be seen that the maximum of the \hat{u}_1 -curve and the minimum of the \hat{u}_2 -curve (= max \hat{u}_2 -curve $\pm \frac{1}{2} L_{ov}$) are indeed nearly on the same x -position. In the further analyses the mean of the x_{1top} and $x_{2trough}$ position is taken into account (XTU in TABLE III).

The sediment transport curve, $S(x)$, has been approximated by a simple cosine-function with the overtake length L_{ov} as basis:

$$S(x) = \bar{S} + \hat{S} \cos \left(\frac{x-x_{1top}}{L_{ov}} * 360^\circ - \theta \right) \quad (10)$$

where: \bar{S} : mean sediment transport; \hat{S} : amplitude of the transport variation and θ : phase shift of the $S(x)$ -curve top with respect to the position of x_{1top} . Positive transport is in wave propagation direction.

For the time being the cosine-function has been adopted for simplicity reasons; no physical argument is known as yet. The \bar{S} -, \hat{S} - and θ -values

Test	\hat{u}_1	\hat{u}_1^*	\hat{u}_2	\hat{u}_2^*	\bar{s}	\hat{s}	x_{1tp}	x_{2tr}	XTU	XTS	L_{ov}	θ
	(m/s)				$(10^{-6} \text{ m}^3/\text{ms})$		(m)				$(^\circ)$	
T 87-1	.135	.011	.029	.015	-.18	.23	5.53	5.35	5.44	4.71	5.98	-44
T 87-2	.147	.006	.026	.013	-.10	.32	4.84	4.49	4.67	3.98	5.27	-47
T 87-3	.138	.002	.018	.011	-.03	.08	8.99	8.98	8.99	8.42	4.67	-44
T 87-4	.182	.026	.058	.031	-.80	1.87	4.80	4.55	4.68	4.47	5.68	-13
T 87-5	.185	.014	.040	.025	-.21	1.44	9.47	9.36	9.42	9.03	5.08	-28
T 87-6	.183	.012	.031	.022	.26	1.25	8.42	8.35	8.39	8.28	4.54	-9
T 87-7	.194	.037	.070	.036	-.87	3.39	10.17	10.06	10.12	9.86	5.43	-17
T 87-8	.191	.025	.046	.036	.09	3.17	9.02	9.07	9.05	8.97	4.88	-6
T 87-9	.227	.024	.041	.034	.30	2.61	7.57	7.42	7.50	7.38	4.41	-10
T 87-10	-	-	-	-	-	-	-	-	-	-	-	-
T 87-11	.233	.034	.059	.045	.92	6.31	8.91	8.80	8.86	8.82	4.69	-3
T 87-12	.238	.029	.048	.039	1.25	5.37	8.14	8.11	8.13	8.08	4.27	-4
T125-1	.193	.028	.030	.028	-.37	1.13	8.42	8.53	8.47	8.42	4.41	-4
T185-1	.149	.010	.039	.016	.01	.17	5.31	5.34	5.33	5.82	5.98	30
T185-2	.157	.007	.032	.016	-.10	.10	4.67	4.46	4.56	5.24	5.27	46
T185-3	.146	.004	.022	.015	.01	.06	9.01	9.06	9.04	9.46	4.67	32
T185-4	.186	.028	.055	.019	-.74	.75	4.59	4.80	4.70	5.50	5.68	51
T185-5	.193	.016	.049	.026	-.66	.65	9.26	9.31	9.29	9.77	5.08	34
T185-6	.194	.010	.033	.025	-.31	.50	8.48	8.54	8.51	8.98	4.54	37
T185-7	-	-	-	-	-	-	-	-	-	-	-	-
T185-8	.217	.026	.058	.037	-.84	1.37	8.80	8.88	8.84	9.30	4.88	34
T185-9	.208	.016	.041	.028	-.29	.71	8.39	8.42	8.41	8.78	4.41	30
T185-10	-	-	-	-	-	-	-	-	-	-	-	-
T185-11	.235	.040	.071	.049	-1.77	2.55	8.80	8.84	8.82	9.25	4.69	33
T185-12	.242	.027	.050	.041	-1.05	2.01	8.28	8.39	8.34	8.71	4.27	31
T250-10	.111	.006	.035	.011	.00	.00	5.53	6.00	5.77	-	5.98	-
T250-11	.163	.018	.060	.025	-.08	.39	5.63	5.64	5.64	6.41	5.43	51
T250-12	.190	.023	.073	.031	-.62	1.60	5.58	5.79	5.69	6.38	4.93	50
T250-13	.137	.006	.037	.012	-.03	.15	4.74	5.36	5.05	6.42	5.27	94
T250-14	.185	.009	.051	.019	-.50	.53	5.07	5.26	5.17	5.94	4.88	57
T250-15	.232	.014	.071	.018	-.55	1.90	4.60	5.17	4.89	5.77	4.52	70
T250-16	.155	.005	.035	.008	-.16	.17	4.27	4.43	4.35	5.09	4.67	57
T250-17	.203	.014	.052	.012	-.18	.62	4.16	4.23	4.20	4.98	4.41	64
T250-18	.250	.018	.064	.022	-.80	1.62	4.49	4.51	4.50	5.29	4.14	69
T250-19	.190	.021	.026	.026	.01	.36	8.60	8.67	8.64	9.49	4.41	69
T465-26	.202	.025	.034	.023	.02	.59	8.80	8.95	8.87	9.89	4.41	83

TABLE III Summary of harmonic components of orbital velocity and transport components.

- transverse oscillations

$$x_{1tp} = x_{1top}$$

$$x_{2tr} = x_{2trough}$$

T87-1: Test 1 with $D_{50} = 87\mu\text{m}$

for the various tests have been included in TABLE III.

A visual inspection of figures like Fig. 3 learned that indeed the sediment transport in the flume can be described according to Eq. (10). In particular the \bar{S} -components did not show a trend as to be a function of the x-ordinate.

4. Mutual relationships

The objective of this study is to find relationships between the sediment transport and the water motion. In the further analyses the following hypotheses have been adopted:

- A direct relationship does exist between the sediment transport at a certain position x and the horizontal orbital velocities at the same x-ordinate.

E.g. the gradients in both S- and \hat{u} -curves do not play a significant role.

- The water motion can be described sufficiently with only the first and second harmonic component.
- The velocities at 1/3 of the water depth above the bottom are considered to be crucial for the sediment transport.

In the next sections some examples of mutual relationships between sediment transport and water motion have been given.

4.1. Effect of D_{50} on θ

From TABLE III it can be seen that the phase shift θ of the top of the S-curve with respect to the top of the \hat{u}_1 -curve, varies apparently with the D_{50} -value. The θ -value is defined as:

$$\theta = \frac{X_{TS} - X_{TU}}{L_{ov}} * 360^\circ \quad (11)$$

Although the variation in θ -values for a specific bed material is rather large, a clear tendency can be observed. An increase in θ -value corresponds with an increasing bed material diameter. In TABLE IV the mean θ -values and the standard deviations have been summarized for the various D_{50} 's tested.

Fig. 5 gives a graph of that relationship.

D_{50} (μm)	θ (mean) ($^{\circ}$)	standard deviation ($^{\circ}$)
87	-20	17
125	- 4	-
185	36	7
250	65	13
465	83	-

TABLE IV Effect of D_{50} on θ .

It is felt to be very unlikely that a real constant θ -value exists for a specific bottom material. Thus, for instance to be irrespective of the actual order of magnitude of the water motion. During the preparation of this paper various attempts have been made to find a sounder physical basis for the observed differences; all attempts have been in vain however.

Nielsen (1979) proposes a computing method for this type of tests. In his Ch. 7 he compares his computing method with one of the Vellinga (1975) tests. (Not given in this paper since here only tests with $T = 1.7$ s have been summarized; that particular test had a wave period of $T = 1.5$ s). The Nielsen comparison is not that bad at a first glance (Fig. 7.6 of Nielsen's thesis). However Nielsen made a factor-5 mistake in plotting Vellinga's results. Although Nielsen's method is not entirely reliable, a comparable tendency can be distracted from his method with respect to the effect of D_{50} on θ . The authors did not work this out quantitatively for the present tests.

4.2. Transport as function of \hat{u}_1 , \hat{u}_2 and γ

In a specific test the two transport parameters, \bar{S} and \hat{S} , and the four velocity parameters, \hat{u}'_1 ; \hat{u}^*_1 ; \hat{u}'_2 and \hat{u}^*_2 , can be observed. To find relationships between these is the aim of this section.

It seems attractive to start with the assumption that the mean sediment transport \bar{S} is directly related to the constant part of the water motion; e.g. the combination of both Stokes components \hat{u}_1' and \hat{u}_2' . As an extension of this assumption the varying part of the transport, \hat{S} , could depend (among others) on the \hat{u}_1^* - and \hat{u}_2^* -components. For the $D_{50} = 250\mu\text{m}$ bottom material, Bijker, Van Hijum and Vellinga (1976) worked out these assumptions. They found rather simple linear relationships. The results of the tests with other D_{50} 's (see TABLE I), however, did not yield satisfying results. Also the approach of Bijker et al, to introduce the acceleration and deceleration of the water motion as important parameters to quantify the magnitude of \hat{S} , did not hold for the other D_{50} 's.

Therefore the foregoing approach has been abandoned in the further analyses. The four wave velocity parameters have been combined to calculate the actual velocities as a function of x . Three parameters viz.: \hat{u}_1 , \hat{u}_2 and γ result in that case. In Fig. 3 the resulting function $\gamma(x)$ belonging to the approximated \hat{u}_1 - and \hat{u}_2 -curves has been given also. At any position x , one sediment parameter S and three velocity parameters have to be taken into account now. An idea of the influence of the various velocity parameters can be obtained by taking one constant and the other two varying. Let us assume for instance $\gamma = 0^0$; thus at the x -positions where \hat{u}_1 (max) = $(\hat{u}_1' + \hat{u}_1^*)$ and \hat{u}_1 (min) = $(\hat{u}_1' - \hat{u}_1^*)$ do occur. The corresponding \hat{u}_2 -values are $(\hat{u}_2' - \hat{u}_2^*)$ and $(\hat{u}_2' + \hat{u}_2^*)$ respectively.

Every test then "contributes" two points to a $\hat{u}_1 - \hat{u}_2$ versus S graph. Fig. 6 shows the result for the various bottom materials for the choice of $\gamma = 0^0$.

In particular for the $D_{50} = 87\mu\text{m}$ -plot of Fig. 6, a positive and a negative transport part of the $\hat{u}_1 - \hat{u}_2$ -plane can be noted and further it can be detected that some tendencies in the sediment transport do occur in the $\hat{u}_1 - \hat{u}_2$ -plane. Furthermore, it can be seen from Fig. 6 that the boundary between positive and negative transports shifts to higher \hat{u}_1 -values as the bottom material diameter increases. This makes it attractive to see what happens when the \hat{u}_1 - and \hat{u}_2 -values are made

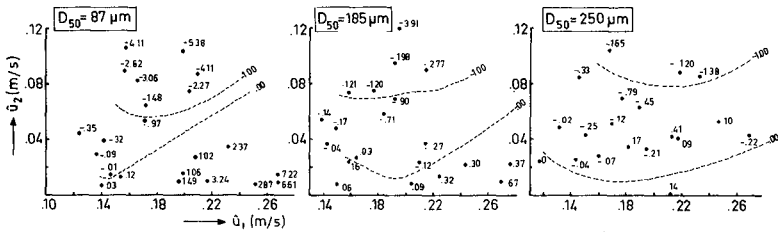


Fig. 6 Sediment transport as a function of \bar{u}_1 and \bar{u}_2 ($\gamma=0^\circ$). S in $10^{-6} \text{ m}^3/\text{ms}$

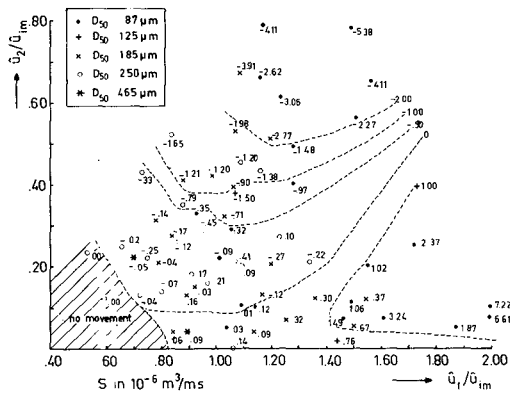


Fig. 7 Sediment transport ($\gamma=0^\circ$).

dimensionless and the various bottom materials are combined. Fig. 7 shows the result. The \hat{u}_1 - and \hat{u}_2 -values were divided by the critical orbital velocities for the various materials: \hat{u}_{im} . The initiation of motion values for a flat horizontal bed were computed according to Swart's (1977) formula:

$$\hat{u}_{im} = 4.58 D_{50}^{0.38} T^{0.043} \quad (12)$$

where: \hat{u}_{im} : initiation of movement-orbital velocity near the bed
and T: wave period.

Although in Fig. 7 some measuring points fall outside the general trends and although in some parts of the $\hat{u}_1/\hat{u}_{im} - \hat{u}_2/\hat{u}_{im}$ -plane the measuring points are rather scarce, it seems permitted to draw "iso-transport-lines".

The complex character of the net sediment transport due to waves can be seen clearly from vertical cross-sections in figures like Fig. 7. A vertical cross-section means a constant \hat{u}_1 -value and a varying \hat{u}_2 value. Let us take for example such a cross-section at 1.50 at the \hat{u}_1/\hat{u}_{im} -ordinate. Starting at $\hat{u}_2/\hat{u}_{im} = 0$ (a pure sine-wave!) a sediment transport of $S = 0$ can be expected. A slight increase of the \hat{u}_2/\hat{u}_{im} -value yields positive transports and a further increase of the \hat{u}_2/\hat{u}_{im} -value results, after first reaching $S = 0$ again, in negative transports. By taking a vertical cross-section at $\hat{u}_1/\hat{u}_{im} = 1.1$ in Fig. 7 for instance, an other picture results. In Fig. 8 the outcome is given for vertical cross-sections for measuring points in the ranges $1.04 \leq \hat{u}_1/\hat{u}_{im} \leq 1.16$ and $1.44 \leq \hat{u}_1/\hat{u}_{im} \leq 1.56$. For small \hat{u}_2/\hat{u}_{im} -ratios the differences are significant; for larger values of \hat{u}_2/\hat{u}_{im} it is remarkable that the differences in net transport are rather small, not withstanding the great differences in \hat{u}_1 -values.

The foregoing results hold for $\gamma = 0^\circ$. Similar results can be found for other γ -values. In Fig. 9 a review is given of vertical cross-sections in plots like Fig. 7 for points in the range $1.04 \leq \hat{u}_1/\hat{u}_{im} \leq 1.16$ for different values of γ . In some cases the measuring points

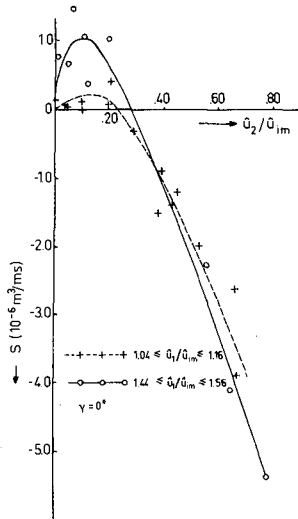


Fig.8 Effect of \hat{u}_2/\hat{u}_{im}

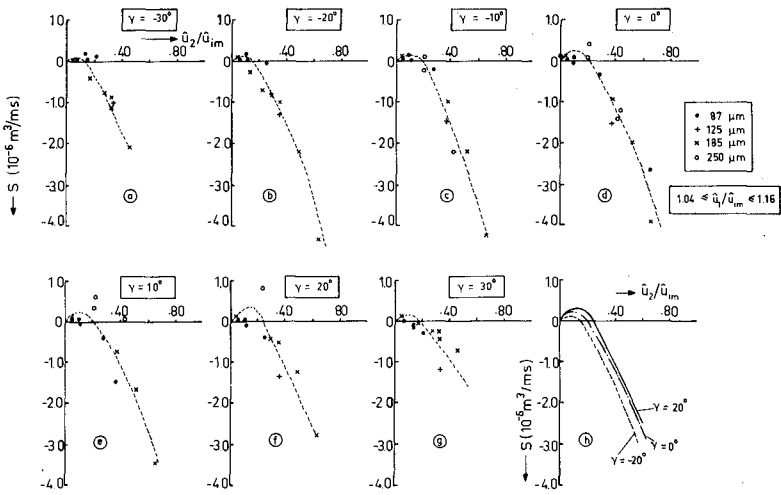


Fig.9 Effect of γ

of the tests with different D_{50} 's coincide fairly well. Sometimes however, a systematic difference between the various D_{50} 's seems to appear. The variation of the phase shift θ as a function of D_{50} (see section 4.1) can be the reason for these discrepancies. This means in fact, that it is not allowed to consider the various D_{50} 's together as is proposed in this section by dividing the orbital velocity components by the critical orbital velocity. As a preliminary analysing method, however, the results are not that bad. The curves in Fig. 9 are roughly sketched curves. In Fig. 9h an idea of the effect of the γ -value can be observed. The effect seems to be rather small. The unsolved dependence of the sediment transport as functions of the parameters \hat{u}_1 , \hat{u}_2 and γ (see Figs. 8 and 9) makes it unrealistic to believe in the reliability of the simple cosine function as an approximation of the sediment transport as a function of x (Eq. 10). An iterative method can be used to arrive at a more reliable and a more complicated transport function. Due to insufficient data this has not been carried out in the present paper.

5. Discussion

The outcome of the series of small-scale tests with different D_{50} 's has brought some surprising facts. As could be seen in section 4 the preliminary analyses did not solve the problems. Some results have been "seen" without, till now, understanding "why". This is rather disappointing since in the tests, in fact a very simple mode of onshore-offshore sediment transport (regular waves; horizontal bed) was considered. Even these simple tests yielded rather complicated results with clear tendencies as indicated for instance by the Figs. 5, 7 and 9. The authors tried to explain some tendencies qualitatively by taking into account the description of the actual transport by vortex formation and vortex ejection etc. as presented by Bijker et al (1976) and Nielsen (1979). They did not succeed. To find some more data just by carrying out more test with other velocity combinations is rather simple. Extended, and probably more reliable, graphs will result. However for direct practical use those graphs are useless. The velocity ranges as well as the set-up of these tests, e.g. a horizontal bed,

are quite different in prototype conditions. For a further increase in insight in the onshore-offshore transport mode a quantitative idea of concentration and velocity field as a function of time will be necessary. At the Delft University we intend to go that long road.

6. Summary and conclusions

- Small-scale tests with progressive waves over a horizontal bed in a flume with different D_{50} 's as bottom material show a net sediment transport which depends apparently on the water motion.
- The water motion, approximated by the first and the second harmonic component of the horizontal orbital velocity component, and the phase angle between both components, has been related to the sediment transport. Rather complex, till now not comprehended, predictive curves can be distracted from the measurements.
- These predictive curves show clear tendencies. The predictive curves, however, can hardly be used for practical purposes.
- The bed material diameter is an important parameter in the sediment transport process. A remarkable shift occurs in the position of the top of the S-curve with respect to the top of the orbital component curves when different D_{50} 's are used.
- To some degree the effect of the diameter of the bottom material can be taken into account by dividing the orbital velocity components by the critical orbital velocity (= maximum orbital velocity at the bed at initiation of movement).

References

- Bijker, E.W.; Hijum, E. van; Vellinga, P. (1976)
 Sand transport by waves
 Proc. 15th Coastal Eng. Conf., Honolulu
 Vol II, Chap. 68
- Buhr Hansen, J. and Svendsen, I.A. (1974)
 Laboratory generation of waves of constant form
 Proc. 14th Coastal Eng. Conf., Copenhagen
 Vol I, Chap. 17
- Fontanet, P. (1961)
 Théorie de la génération de la houle cylindrique par un
 batteur plan
 La Houille Blanche, nr 1 et 2.
- Hulsbergen, C.H. (1974)
 Origin, effect and suppression of secondary waves
 Proc. 14th Coastal Eng. Conf., Copenhagen
 Vol I, Chap. 22
- Kravtchenko, J.; Santon, L. (1957)
 Nouvelles recherches sur la houle de laboratoire
 7th General Meeting, I.A.H.R. Vol. II
- Nielsen, P. (1979)
 Some basic concepts of wave sediment transport
 Thesis, Institute of Hydrodynamics and Hydraulic Engineering
 Technical University of Denmark, Lyngby
- Schepers, J.D. (1978)
 Zandtransport onder invloed van golven en een eenparige stroom
 bij variërende korreldiameter
 Craduation thesis, Delft Univ. of Tech. (in dutch)
- Skjelbreia, L. (1958)
 Gravity waves; Stokes third order approximation, tables of
 functions
 Berkeley, Calif.: The Engineering Foundation Council on
 Wave Research
- Swart, D.H. (1974)
 Offshore sediment transport and equilibrium beach profiles
 Delft Hydraulics Laboratory, Publ. No 131, Delft
- Swart, D.H. (1976)
 Predictive equations regarding coastal transports
 Proc. 15th Coastal Eng. Conf., Honolulu
 Vol II, Chap. 66
- Swart, D.H. (1977)
 Weighted value of depth of initiation of movement
 Stellenbosch, Aug.
- Tilmans, W.M.K. (1979)
 Zandtransport in de golfrichting in relatief ondiep water
 Craduation thesis, Delft Univ. of Tech. (in dutch)
- Vellinga, P. (1975)
 Zandtransport door golven en de invloed van stoorgolven
 Craduation thesis, Delft Univ. of Tech. (in dutch)

CHAPTER 71

NEARSHORE SUSPENDED SEDIMENT LOAD DURING STORM AND POST-STORM CONDITIONS

Timothy W. Kana and Larry G. Ward¹

ABSTRACT

As part of the DUCK-X experiment at the CERC field research facility at Duck, North Carolina in September, 1978, suspended sediment measurements were made along the CERC pier. *In situ* bulk water samples were collected during a moderate northeast storm and two days later during post-storm wave conditions. Concentrations varied from approximately 0.01 g/l to over 10.0 g/l. Vertical arrays of suspended sediment samples indicated that concentration decreases rapidly up to two meters above the bed, then remains relatively constant, reflecting the nature of the suspension; intermittent suspension of sand near the bed, and continuous washload higher in the water column. Concentrations were at a maximum during storm conditions when measured values were 3 to 5 times higher than during non-storm conditions. The total load of sediment in a pier cross section during sampling periods in storm and post-storm conditions was calculated from arrays of 49 samples each. With $H_{1/3}$ exceeding 2.3 m and the surf zone width over 300 m during the storm, the total load of sediment in suspension was approximately 10 times higher than during post-storm conditions ($H_{1/3} = 1.2$ m and surf zone width approximately 100 m). Estimates of the longshore flux of suspended sediment indicate that as much as 60 times more sediment was transported during storm than during post-storm conditions. Longshore transport of sediment measured from 5 cm above the bed to the surface reached the equivalent of 22,330 m³/day. This value corresponds very closely to longshore transport predicted from wave energy flux. During post-storm conditions, on the other hand, transport of suspended sediment accounts for less than one-third of the transport predicted from wave energy flux.

INTRODUCTION

This report presents results of a field study of nearshore suspended sediment at Duck, North Carolina completed during the August-September 1978 DUCK-X experiment, sponsored by the Coastal Engineering Research Center. The goal of the DUCK-X experiment was to test the capabilities of the SEASAT-A satellite launched in June, 1978. Therefore, several experiments were conducted simultaneously at the CERC Field Research Facility at Duck to obtain ground truth data on waves, currents, suspended sediment and sand transport.

¹Research Scientists, Coastal Research Division,
Department of Geology, University of South Carolina,
Columbia, S. C. 29208

Numerous agencies were involved in the month-long experiment, including CERC, NASA, CRREL, NOAA, U.S. Navy and university groups from Johns Hopkins (Applied Physics Laboratory) and University of South Carolina (Department of Geology). Field support included the 600 m long CERC research pier and facilities at Duck, two LARC amphibious craft from Ft. Story, Virginia, the CRAB from Wilmington District, Corps of Engineers, and various aircraft for aerial surveys. Instrumentation included pier based and airborne radar, seven pier-mounted Baylor wave gauges, two wave rider buoys, several current meters, and tide gauges and various recording meteorological instruments.

The primary goals of the suspended sediment study, conducted 10-17 September 1978, included:

1. Measurement of the vertical and horizontal distribution of suspended solids from the surf zone to the end of the CERC research pier.
2. Measurement of the weight percent of organic and inorganic solids in suspension.
3. Estimation of the suspended sediment flux transport rate.
4. Correlation of suspended sediment flux transport rates with the longshore component of wave energy flux.

STUDY AREA

The CERC Field Research Facility is located on Currituck Bank approximately 2 km north of Duck and 20 km north of Kitty Hawk, North Carolina (Fig. 1). The facility included an approximately 600 m long concrete pier (Fig. 2) with piles spaced 12 m, extending to the 8 m MLW contour. Height of the pier deck is approximately 6 m above MSL.



Figure 1. Study area two kilometers north of Duck, North Carolina, U.S.A.



Figure 2. Oblique aerial photo of the CERC research pier on September 16, 1978. View looking south.

Beach Profiles

The typical beach and nearshore profile during the study period along the pier included a steep foredune ridge approximately 5-7 m high and a narrow berm with relatively steep beachface slope ($m = 0.10$). At the toe of the beachface was a 30 to 50 cm step dropping abruptly into a runnel 1 to 1.5 m below MSL. Seaward of the runnel was a ridge which sloped gently seaward. Along the beach at Duck, the innermost ridge was broken by numerous rip channels which directed the return flow of water from the runnel. Seaward of the inner ridge, mean nearshore slope was gentler ($m = 0.015$) with local variations due to the presence of low amplitude outer ridges.

Sediments

Beach sediments at Duck consist of a range of sizes. Coarse sand with a mean diameter of 0.75 mm and fine sand with a mean diameter of 0.17 mm predominates. A third mode of coarser sediments, including pea-gravel (grain size up to 15 mm diameter), is found as isolated lenses generally along the lower beachface or step. The exact proportion of sediment grain sizes was not determined. In general, the berm is a mixture of the two dominant grain size modes: the step is coarsest, the runnel ranges from pea-gravel to fine sand, and the ridge is well-sorted, fine sand.

Winds

Winds during the study are summarized in Figure 3 and the wind rose of Figure 4. The dominant wind was from the NNE occurring 13-14 September during the storm. A secondary component during pre- and post-storm periods occurred with winds from the SE. Maximum sustained wind velocity was 12.7 m/s (25 knots) occurring 13 September.

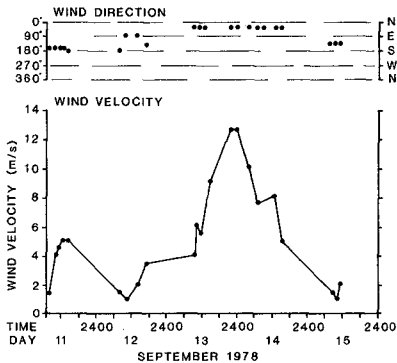


Figure 3. Average wind velocity and direction at the CERC Research Pier, Sept. 11-15, 1978.

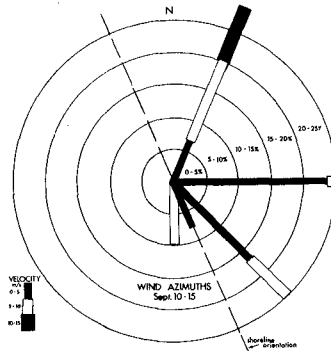


Figure 4. Wind rose for 10-15 September 1978 at the CERC Research Pier.

Wave Height

The beach at Duck is characterized by moderately high wave energy. During the present study, significant wave heights ranged from 1.0 to 3.5 m, as measured by pier-mounted wave gauges. This range is higher than the yearly average due to the presence of a moderate northeast storm occurring 13 September. Maximum recorded wave height during the study was 6.2 m at the seawardmost Baylor gauge, approximately 400 m offshore (D. Lichy, pers. comm.). Before and after the storm, waves were generally longcrested and smooth in form, characteristic of a swell wave environment. This is reflected in the range of recorded wave periods with shortest periods (6-8 seconds) occurring during the storm and long periods (greater than 10 seconds) during swell conditions. Figure 5 summarizes wave height and wave period as recorded by the innermost Baylor gauge located approximately 100 meters offshore (CERC station 6+20 on pier).

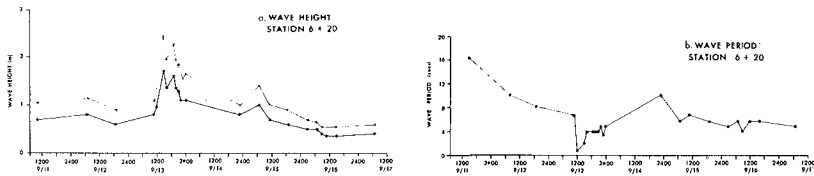


Figure 5. Distribution of wave height (a) and significant wave period (b) for 11-17 September 1978, measured by a pier-mounted Baylor gauge at station 6+20, approximately 100 m from the beach. Bold line in (a) is root mean square wave height; upper line is $H_{1/3}$.

Wave Direction

The distribution of wind velocities and directions caused two sediment transport reversals during the study. From September 10 through 13, waves arrived from the SE, causing sediment transport to the north. During the storm, 13-14 September, waves approaching from the northeast caused a transport reversal to the south. Following the storm, SE swell resumed, and transport was again to the north. Wave direction data was obtained from radar imagery and LEO observations.

PREVIOUS WORK

Several techniques have been used to measure suspended sediment concentrations in the surf zone. There are three basic methods: 1) pump systems for obtaining a time-integrated sample of water and sediment (Watts, 1953; Fairchild, 1972, 1977; and Coakley et al., 1978); 2) *in situ* collecting traps for obtaining relatively instantaneous bulk water samples (Kana, 1976; Inman, 1977); and 3) indirect measures which relate turbidity to light attenuation, back scatter of light or gamma absorption (Homma et al., 1965; Hattori, 1969; Kennedy and Locher, 1972; and Brenninkmeyer, 1976). There are certain disadvantages to any of these techniques, most important of which is the influence of the sampling apparatus on the flow field, a universal problem in studies

of suspended sediment.

Of the pump samplers, the most detailed results are reported in Fairchild (1977) in an updated version of an earlier paper (Fairchild, 1972). Working from ocean piers at Ventnor, New Jersey and Nags Head, North Carolina (approximately 35 km south of Duck), he collected over 700 time-averaged water samples seaward and landward of the breaker zone, using a tractor-mounted pump sampler. Sampling in waves from 40 to 120 cm high, Fairchild obtained concentration values ranging over 3 orders of magnitude to a maximum of 4.0 parts per thousand (\approx g/l). The sampler intake varied between 8 and 75 cm above the bed. Despite a great amount of scatter in the data, Fairchild isolated several trends, including: 1) Suspended sediment increases slightly with breaker height; 2) Concentration decreases away from the breakpoint in both the seaward and landward direction; and 3) Concentration decreases with elevation above the bed.

Leonard and Brenninkmeyer (1978), using the almometer developed by Brenninkmeyer (1973), indirectly monitored sediment suspensions during storm conditions at Nauset Beach, Massachusetts, documenting: 1) An increase in the number of suspension bursts from the bed during storms, and 2) A decrease in frequency of sediment movement with elevation and distance seaward from the shoreline. They also observed concentration inversions, which occur due to the shearing of tabular clouds of sediment moving in the upper layers. This produces a reverse gradient of higher concentration overlying a zone of lower concentration.

Utilizing a portable bulk water sampler (Figure 6), Kana collected over 900 suspended sediment samples primarily in the breaker or outer surf zone along South Carolina beaches. His data for waves up to 1.5 m high (Kana, 1977, 1979) indicate that suspended sediment at a point in the surf zone depends primarily on breaker type, distance from the breakpoint and beach slope. Wave height, wave period, and longshore current velocity during moderate swell conditions, have relatively little influence on mean concentration. A portion of Kana's data (summarized in Figure 7) indicates that plunging waves entrain almost an order of magnitude more sediment than spilling breakers. Typical concentration values range over 3 orders of magnitude with maximum values reaching 10.0 g/l at 10 cm above the bed in plunging waves on fine-grained beaches.

METHODOLOGY

Suspended Sediment Sampling

Of the previously-mentioned studies, the most comparable to the present experiment is Fairchild's since measurements were made from a pier. However, for the DUCK-X study, Kana's (1976) bulk water sampler was modified for use from the pier. Differences between the sampling techniques include:

- 1) The bulk water sampler obtains multiple instantaneous in situ samples in a vertical array compared to single time-averaged pump samples in Fairchild's apparatus.

2) The volume of water collected by the in situ sampler is 2 liters per sample compared to 152 liters per sample from the pump sampler.

3) The entire water sample collected with the in situ water bottles was retained to allow analysis of the organic- and fine-grained fractions. With the tractor-mounted sampler, only the sand fraction was retained.

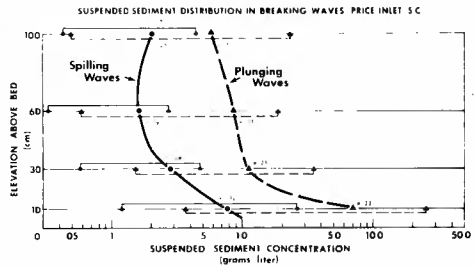


Figure 7. Mean concentration by elevation above bed for approx. 450 suspended sediment samples obtained using the in situ bulk water sampler in Fig. 6 (Kana, 1977).

Figure 6. Portable bulkwater sampler used to collect serial arrays of suspended sediment samples in the surf zone (from Kana, 1976).

The bulk water sampler used in the present experiment is designed to collect several closely-spaced simultaneous samples in a vertical array above the bed. It consists of a 2 meter long mounting pole, support brackets, and several 2 liter cast acrylic bottles closed off by hinged doors (Figure 6). A spring loaded trigger similar to that of a Van Dorn type water sampler, which holds each bottle door open, is mounted to the support pole. At the base of the trigger is a footpad which can be pushed up to open the trigger and simultaneously release all bottle doors.

The device has a relatively fast response time of less than one-half second, remaining off the bed until the sampling instant. Tests have shown that the collecting bottles are drawn shut before sediment thrown up by the apparatus reaches each sampling position. The lowermost bottle centered at 10 cm above the bed obtains sediment suspended between 4 and 16 cm off the bottom. The rigid mounting pole allows constant sample positioning with respect to the bed, making it possible to achieve consistency in results.

Minor modifications were made to the bulk water sampler for use from the CERC pier. The apparatus was rigged with rope and counterweights and a trip line for sampling remotely from the deck of the pier. (Note: The sampler is designed to trip as it is lowered onto the sea floor, unlike the standard technique of using a messenger released down a hydrographic wire for a Niskin or Van Dorn sampler).

Sampling Procedure from the Pier

A total of 13 pier stations were selected for obtaining vertical arrays of suspended sediment at approximately 1 m intervals above the bed. Each station was located midway between sets of pilings and away from any instrumentation already in place. In the present study, it was not feasible to boom the sampler over the updrift side of the pier, so all sampling had to be done through the center grates located along the pier deck. Approximate distance from sampler to closest piling was 7 m.

The typical array of samples collected were centered 10 cm, 90 cm, 170 cm, 300 cm, 400 cm, 500 cm, and so on above the bed. After each sample array was brought on deck, water volumes were measured and samples transferred into 2 liter Nalgene holding jars for processing in the lab. Thirteen vertical profiles were completed on 13 and 15 September, resulting in 98 usable samples.

Filtering and Combustion

Suspended sediment samples were filtered through Millepore filters (0.45 μ pore diameter) using standard vacuum apparatus and filtering flasks. All samples were rinsed with deionized water to eliminate dissolved salts, then dried for weighing. Suspended sediment concentration was determined as a weight of solids per unit volume of water (g/l) for comparison with other samples.

Approximately 40 samples out of 98 collected were combusted after determination of total concentration in order to calculate the percent organic fraction (assumed to be similar to the percent combustible). The combustion technique involved burning the filter and suspended sediment for 30 minutes at 500°C, then weighing the residual fraction to determine the proportion of noncombustibles and combustibles.

Data Contouring and Sediment Load Calculations

Suspended sediment concentrations were plotted for each sample run on a scaled cross-section of the nearshore zone along the pier. Based on previous results, which indicate an exponential decrease in concentration above the bed, a variable contour interval was used to depict the horizontal and vertical distribution of suspended sediment. The contour interval increases with concentration.

Total sediment load under a unit width pier cross-section was calculated by integrating areas between contours and applying a mean concentration to each portion of the cross-section. Contour diagrams were also prepared for the distribution of combustibles.

Estimation of Sand Fraction

In order to calculate the proportion of fine-grained material in each sample, the mean concentration of samples devoid of sand-sized particles was determined and assumed to be representative of the weight of sediment continuously in suspension. Particles larger than sand size (0.062 mm) were considered to represent intermittent suspensions origi-

nating from the bed under breaking waves. This procedure was necessary to estimate the effective suspended sediment flux transport rate of coarse bed material.

RESULTS

Distribution of Suspended Sediment

Suspended sediment sampling points and corresponding concentration values for 13 September during the northeast storm are plotted on Figure 8. Values ranged over $3\frac{1}{2}$ orders of magnitude from approximately 0.05 g/l to over 10.0 g/l with highest concentrations in the inner surf zone and near the bed. On 15 September, during post-storm moderate swell conditions, suspended sediment concentrations covered a lower range from 0.01 to over 4.0 g/l. Forty-nine samples were plotted for each date using virtually the same pier stations and sampling position.

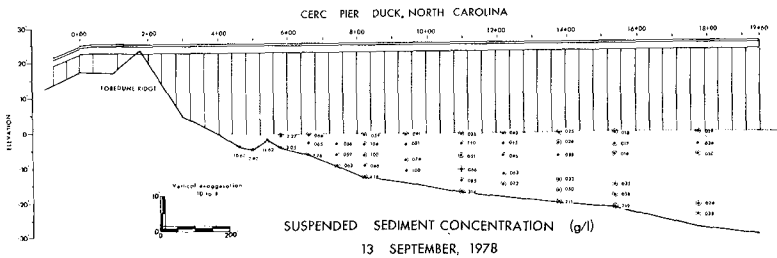


Figure 8. Suspended sediment sample positions and concentration values for 13 September 1979 during storm conditions.

To show the difference in suspended sediment between storm and post-storm surf conditions, mean concentration by elevation above the bed for each sample run is given in Figure 9. Note that, during the storm, suspended sediment concentrations, at a given elevation, were approximately 3 to 5 times higher than during post-storm conditions. As shown in Figure 9, there is an exponential decrease in concentration up to 170 cm above the bed, then concentration remains relatively constant to the surface. This distribution reflects an intermittent type of suspension: Coarse sediment originating from the bed in the lower elevations; and a continuous suspension: Washload of fine-grained sediments in the upper layers. The washload concentration on 13 September was approximately 2 times higher than the washload during post-storm conditions.

The horizontal and vertical distributions of suspended sediment for 13 and 15 September are given in the contoured pier cross-sections of Figure 10. Highest concentrations are found on the inner ridge and wash zone (lower beachface) and near the bed. On both sampling days, concentration decreased seaward from the inner ridge and with elevation above the bed.

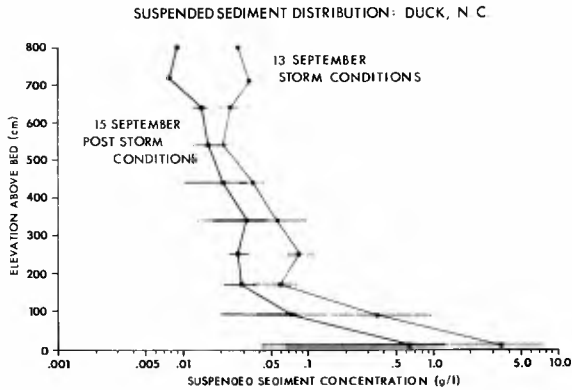


Figure 9. Mean suspended concentration vs. elevation above the bed for storm vs. calm conditions, 13 and 15 Sept., 1978, respectively. Note concentrations were three to five times higher, on average, during the storm.

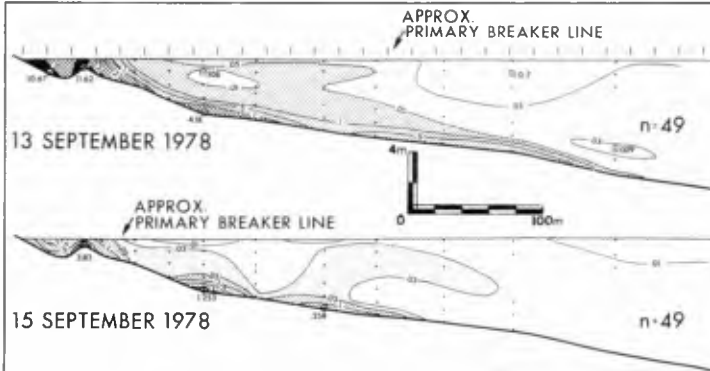


Figure 10. Suspended sediment contour diagrams along the CERC pier on 13 Sept. (upper) and 15 Sept. (lower) 1978. Total load of sediment in suspension was approximately ten times higher during storm conditions on 13 Sept. than during non-storm conditions on 15 Sept.

The primary difference between sample runs was, of course, the height of the waves and width of the surf zone. Figures 11 and 12 offer a comparison of wave conditions on the 13th and 15th. Significant wave heights during each sample run calculated from H_{rms} measured by the inshore Baylor gauge were 3.5 m on 13 September and 1.2 m on 15 September. As indicated on Figure 10, the seawardmost primary breakers were approximately 3 times farther offshore during the storm. Width of the surf zone was over 300 m on the 13th compared to less than 100 m on the 15th.



Figure 11. Wave conditions at approximately 1600, 13 Sept., 1978 at the CERC pier, Duck, N. C. View looking east. $H_{1/3}$ was approximately 3.5 m at the seaward end of the pier and 1.8 m in the inner surf zone.



Figure 12. Wave conditions at approximately 1430, 15 Sept., 1978. View looking north from the CERC research pier.

Percent Combustibles

The weight percent of combustibles in each sample was plotted on a pier cross-section and contoured as shown in Figure 13. In general, the proportion of combustibles was very low (less than 5%) with a slight increase in the seaward direction and vertically in the water column. This correlates well with the concentration data indicating the expected trend of increasing percentage of combustibles with decreasing total suspended solids. As indicated on the contour diagrams, the overall combustible fraction was slightly higher on the 15th during post-storm conditions. The percent combustibles ranged from less than 1% in the inner surf zone to a high of 15% at a seaward mid-depth station.

Suspended Load per Unit Width Cross-Section

Using the pier cross-section for reference frame, the total load of suspended solids per unit width (S) was calculated for each sample run by:

$$S = \rho \sum_{j=1}^m \int_{i=1}^n a_{ij} C_{ij} \quad (1)$$

where ρ = sediment density
 m = number of subsections normal to beach
 l = representative distance normal to beach
 n = numbers of samples over the depth
 a = the portion of the depth over which C was made
 C = concentration in subsection ij.

The total suspended load per meter width was 657.4 kg on 13 September and 118.5 kg on 15 September. Of these totals, an estimated 84.1 kg and 67.0 kg was washload (fine-grained sediment in continuous suspension) on the 13th and 15th, respectively (based on reference washload concentration of 0.03 and 0.022 g/l). Thus, the effective load of coarse-grained suspended sediment (Se) was 573.3 kg during the storm and 51.5 kg two days later, an order of magnitude difference.

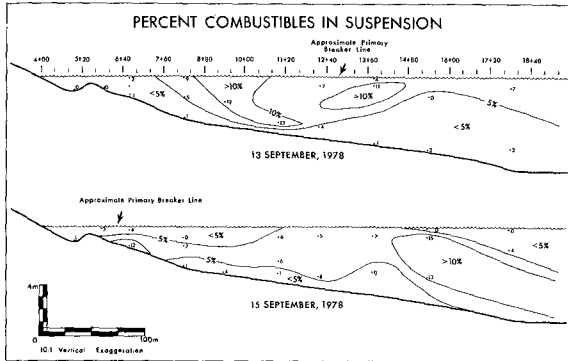


Figure 13. Distribution of combustible fraction in suspended sediment samples. In general, percent combustibles increases with distance from shore and elevation above the bed in contrast to a corresponding decrease in concentration.

ESTIMATION OF TRANSPORT RATES

Any estimation of suspended sediment transport rates in the longshore direction during the DUCK-X experiment must be an approximation, since the velocity field under the pier was not measured. However, to better appreciate the relative magnitude of storm vs. post-storm transport, two methods for estimating transport were performed. One was based on the suspended sediment load and an empirically determined longshore current velocity; the other on wave energy flux.

Suspended Sediment Flux Transport Rates

The total effective longshore transport rate (Q_s) of suspended sediment moving under the CERC pier during each sample run was estimated according to:

$$Q_s = 8.64 \times 10^4 Se \cdot V \quad (2)$$

where Se is the total effective sediment load, V is mean longshore current velocity, and the coefficient is a factor to convert an instantaneous transport rate to a daily rate giving Q_s in m^3/day .

Longshore current velocity, V , was calculated using the modified Longuet-Higgins (1970) equation as given by C.E.R.C. (1973, p. 4-48):

$$V = 20.7 m (gH_b)^{1/2} \sin 2\alpha_b \quad (3)$$

where m is slope, H_b is breaker height, α_b is the angle between breaker crest and shoreline, g is acceleration of gravity, and the coefficient is empirically determined using english units for all variables. The predicted longshore current speed in ft/s was then converted to m/s. Variables H_b and α_b were determined from the innermost Baylor gauge and pier-mounted radar imagery, respectively. The root mean square wave heights given by the gauges were converted to significant wave height ($H_{1/3}$) for use in the equation by:

$$H_{1/3} = 1.416 H_{rms} \quad (4)$$

which is based on the Rayleigh distribution function (see CERC, 1973, p. 3-5 to 3-10).

Based on the results summarized in Table 1, average velocities of 0.74 m/s and 0.15 m/s were used in equation (3) for 13 September and 15 September, respectively. Then solving equation (2), the effective transport rate, Q_s , was calculated to be approximately 22,300 m^3/day on the 13th and 383 m^3/day on the 15th. Thus, the effective transport rate of sand through the pier cross-section was as much as 60 times greater during the storm than on September 15.

Table 1. Calculation of Mean Longshore Current Velocity (V) given in Equation (3).

Date	Time	$H_{1/3}$ (ft)	α_b	$V(ft/s)$	$V(m/s)$
13 Sept	1200	4.5	2	0.26	0.08
	1400	8.1	20	3.21	0.98
	1600	6.5	28	3.71	1.13
	1900	7.5	21	3.21	0.98
	2000	6.5	14	2.10	0.64
	2200	6.0	14	2.02	0.62
15 Sept	1300	3.1	5	0.54	0.16
	1700	2.7	5	0.50	0.15

Note: $m = 0.015$; $g = 32.2 \text{ ft/s}^2$

Wave Energy Flux Transport Rates

It can be shown that daily longshore transport rate (Q) is related to the longshore component of wave energy flux by (metric equivalent of C.E.R.C., 1973, equation 4-40):

$$Q = 3.51 \times 10^{-7} P_{1s}, \quad (5)$$

where P_{1s} is an empirically determined factor of the longshore component of wave energy flux in ergs/m.s. Q is given in m^3/day . P_{1s} is given by the metric equivalent of CERC (1973) equation 4-35:

$$P_{1s} = 2.84 \times 10^{10} H_b^{5/2} \sin 2\alpha_b \quad (6)$$

where H_b is in meters.

Using recorded wave measurements for H_b and determining α_b graphically from radar imagery, values P_{1s} during each suspended sediment sampling period were calculated. On 13 September, P_{1s} averaged 6.89×10^{10} ergs/m.s; whereas, on 15 September P_{1s} was an order of magnitude less, averaging 3.54×10^9 ergs/m.s. The corresponding longshore transport rates, based on equation (5), were 23,400 m^3/day and 1,250 m^3/day , respectively. The transport rate during the storm is in surprisingly close agreement with Q_s calculated from suspended sediment flux (Table 2).

Table 2. Longshore Transport Rates from Suspended Sediment and Wave Energy Flux.

Date	$H_{1/3}$ (avg.) (m)	P_{1s} (ergs/m.s)	Q (from P_{1s}) (m^3/day)	Q_s (fm. sus. sed) (m^3/day)	Dir.
13 Sept.	1.99	6.89×10^{10}	23,400	22,300	S
15 Sept.	.88	3.54×10^9	1,250	385	N

DISCUSSION

Perhaps the most interesting aspect of the suspended sediment data is the comparison of suspended load during two greatly different surf conditions. In this case, scheduling of the sample runs was fortuitous. This may have been the first direct documentation of nearshore suspended sediment concentration during storm conditions.¹ Therefore, it is worthwhile to examine possible sources of error in these data.

Sources of Error

As with any sampling device used in the surf zone, there is always some effect of the apparatus on the flow field. This is undoubtedly true of the apparatus used in the present study. More recently, Inman and Hanes (1980) have used a portable bulk water sampler which "cores" the water column and may have less effect on the flow field than devices with hinged doors. Whatever effect the apparatus used in the present experiment has on the surf zone flow field is probably less important than the consistency of sampling technique. Departures of the apparatus from the vertical plane during sampling may possibly pro-

¹Leonard and Brenninkmeyer (1978) used the alcometer to obtain indirect measurements of suspended sediment in the surf zone at Nauset Beach, Massachusetts during a storm. Kana (1977) obtained single vertical arrays of direct samples during minor storm conditions ($H_{1/3} = 1.5$ m) on South Carolina beaches.

duce more anomalous values than any resulting from triggering and closure of the device. Given the wide range of concentrations occurring under breaking waves, it is extremely difficult to evaluate the performance of any sampler under prototype conditions. The extensive use of the present apparatus on South Carolina beaches (Kana, 1977, 1979) indicates that the sampler produces relatively consistent results and responds immediately upon contact with the bed minimizing the influence of sampler-induced suspensions. Furthermore, the concentration values obtained during the DUCK-X experiment are not abnormally high, suggesting the sampler did not bias the data on the high side. The range of concentration values obtained during storm conditions on the 13th are the same order as Fairchild's (1977) and those obtained on 15 September in the present study. The unusually high suspended sediment load on the 13th is due to the higher concentrations occurring throughout the water column and further offshore.

Another probable source of error is the scouring effect of the pier pilings. There is evidence that scour pits developed between pilings during the storm, and wakes of high concentrations were observed trailing from pilings in the inner surf zone on both sampling days. Some of the "plumes" at the foot of the inshore pilings sampled on 15 September were found to have concentrations approximately 50% higher than at a position 7 m from the pilings. Due to more intense wave action at the pilings on 13 September, no samples could be obtained for comparison.

With regard to the estimation of longshore transport from wave energy flux, there are three primary sources of error: 1) the longshore current velocity distribution was not directly measured and could only be estimated using presently existing theoretical models; 2) wave measurements were made under the pier possibly resulting in slight attenuation of the actual wave profile; and 3) wave approach directions, whether from radar or LEO observations, are imprecise at best.

Storm vs. Post-Storm Sediment Transport

Despite the possible sources of error listed above, the present data offer unique evidence that there is a great increase in suspended sediment transport during storm conditions. Measured point source concentrations ranging up to just 5 times higher during the storm, but extending significantly seaward and higher in the water column, produced an effective sediment load over 10 times higher. Estimated longshore current velocities 5 times higher during the storm resulted in a predicted transport rate over 60 times higher on the 13th than on the 15th. The close agreement on 13 September between suspended sediment transport and transport predicted from P_{1S} is probably fortuitous, but it is not unreasonable to believe these rates are of the right order.

The Importance of Suspended Sediment on Total Transport

An interesting result of these data is that during the storm, transport predicted from wave energy flux is totally accounted for by sediment 5 cm or higher in the water column. During post-storm swell conditions, however, suspended sediment flux only accounted for 30% of the transport predicted from P_{1S} . This may indicate that transport by sediment suspension is more important during storms, but may be secondary to bedload transport during post-storm swell conditions.

The data contained herein by no means resolve the controversy over the relative importance of suspended vs. bedload transport on beaches (Komar, 1978). However, they add an interesting twist. These results indicate that suspensions extend higher in the water column and farther offshore during storms. And, as Leonard and Brenninkmeyer (1978) reported, the frequency of suspensions may also be higher.

On the other hand, surf zone suspensions of sand during post-storm swell conditions appear to be lower in concentration, of lesser extent through the water column, and, perhaps, of lower frequency. This is analogous to the case for plunging vs. spilling waves reported by Kana (1979), where plunging waves suspend much greater quantities of sand. The present data, therefore, suggest that the suspension mode of transport is much more important during storms than during post-storm average conditions.

CONCLUSIONS

The present study at Duck, North Carolina provides some unique information on the relative quantities of sediment in suspension during storm and post-storm conditions. The following conclusions are offered:

1. Suspended sediment load in the surf zone is significantly higher during storms than post-storm swell conditions due to greater vertical and horizontal extent of the suspensions.
2. Sediment suspensions are relatively more important during storms in terms of their role in sediment transport.
3. Intermittent suspensions of sand from the bed are a less important component of longshore transport during post-storm recovery periods dominated by a swell wave environment.

ACKNOWLEDGMENTS

Support for the present study was provided by the U.S. Army under CERC Contract No. DACW72-78-M-0865. The authors wish to thank the staff from CERC who provided support, including David Lichy (DUCK-X coordinator), Curt Mason (Chief, Coastal Processes Branch), Phil Vitale (CERC technical monitor) and Charley Judge (CERC FRF manager). Data from radar and wave gauges were reduced by CERC before transmitting to University of South Carolina. Field assistance was provided by members of the Coastal Research Division at the University of South Carolina, including Aileen Duc, Kenneth Finkelstein, John Hodge, Tom Moslow, Pete Reinhart and Craig Shipp. Special thanks to Dag Nummedal and Shea Penland, Department of Geology, Louisiana State University who provided much technical assistance during the field work. The bulk of the data reduction was completed by Helen Johnson at the University of South Carolina. The manuscript and graphics were ably prepared by Pris Ridgell, Tom Vose, and Burk Scheper.

REFERENCES CITED

- Brenninkmeyer, B.M., 1973, Synoptic surf zone sedimentation patterns: Ph.D. Dissertation, Univ. of Southern California, 274p.
- Brenninkmeyer, B.M., 1976, In situ measurements of rapidly fluctuating high sediment concentrations: Marine Geology, Vol. 20, p. 117-128.
- Coakley, J.P., Savile, H.A., Pedrosa, M., and Larocque, M., 1978, Sled system for profiling suspended littoral drifts: Proc., 16th Conference on Coastal Engineering, ASCE, p. 1764-1775.
- Coastal Engineering Research Center, 1973, Shore Protection Manual: 3 Vols: U.S. Government Printing Office, Washington, D. C.
- Fairchild, J.C., 1972, Longshore transport of suspended sediment: Proc. 13th Conference on Coastal Engineering, ASCE, p. 1062-1088.
- Fairchild, J.C., 1977, Suspended sediment in the littoral zone at Ventnor, New Jersey and Nags Head, North Carolina: TO-77-5, Coastal Engineering Research Center, U.S. Army, Corps of Engineers, 97p.
- Hattori, M., 1969, The mechanics of suspended sediment due to standing waves, Coastal Engineering in Japan, Vol. 12, p. 69-81.
- Hom-ma, M., Horikawa, K., and Kajima, R., 1965, A study on suspended sediment due to wave action: Coastal Engineering in Japan, Vol. 8, p. 85-103.
- Inman, D. L., 1977, Status of surf zone sediment transport relations: Proc. Workshop on Coastal Sediment Transport with Emphasis on the National Sediment Transport Study, manuscript.
- Inman, D. L. and Hanes, D. M., 1980, Field measurements of bed and suspended load motion in the surf zone: Proc. 17th Conference on Coastal Engineering, Sydney, Australia, March 24-28, 1980.
- Kana, T. W., 1976, A new apparatus for collecting simultaneous water samples in the surf zone: Jour. of Sedimentary Petrology, Vol. 46, No. 4, p. 1031-1034.
- Kana, T. W., 1977, Suspended sediment transport at Price Inlet, S. C.: Proc. of Coastal Sediments '77, ASCE, p. 366-382.
- Kana, T.W., 1979, Suspended sediment in breaking waves: Tech. Rept. No. 18-CRD, Dept. of Geology, Univ. of South Carolina, 153p.
- Kennedy, J.F. and Locher, F. A., 1972, Sediment suspension of water waves: in Meyer, R. E. (ed.), Waves on Beaches and Resulting Sediment Transport, Academic Press, New York, p. 249-295.

- Komar, P.D., 1978, Relative quantities of suspension versus bed-load transport on beaches: Jour. of Sedimentary Petrology, Vol. 48, No. 3, p. 921-932.
- Leonard, J.E. and Brenninkmeyer, B.M., 1978, Periodicity of suspended sand movement during a storm: Proc. 16th Conference on Coastal Engineering, ASCE, p. 1744-1763.
- Longuet-Higgins, M.S., 1970, Longshore currents generated by obliquely incident sea waves, 1 and 2, Jour. of Geophysical Research, Vol. 75, No. 33, p. 6788-6801.
- Watts, G.M., 1953, Development and field tests of a sampler for suspended sediment in wave action: TM-34, Beach Erosion Board, U.S. Army, Corps of Engineers, Washington, D. C., 4lp.

CHAPTER 72

ONSHORE-OFFSHORE TRANSPORT AND BEACH PROFILE CHANGE

by

MASATARO HATTORI

Professor of Coastal Engineering, Chuo University, Tokyo, Japan

and

RYOICHI KAWAMATA

Research Assistant, Environmental Research Center,
University of Tsukuba, Ibaragi Prefecture, Japan

ABSTRACT

In this paper a model is presented to describe onshore-offshore sand transport in the surf zone. The model is based on the physical consideration that when the net transport attains a state of equilibrium, the power expended through gravitational force in suspending sand grains is balanced by that due to the uplifting force arising from the turbulence generated by breaking waves.

Two important parameters controlling sand transport are the dimensionless fall-time parameter and bottom slope. Using these parameters, the direction of onshore-offshore transport and the beach profile in the surf zone are expressed as

$$\begin{array}{l} (H_0/L_0) \tan \beta / \frac{w}{gT} < \quad \text{(onshore transport; accretive profile)} \\ \phantom{(H_0/L_0) \tan \beta / \frac{w}{gT}} = 0.5 \quad \text{(neutral; equilibrium profile)} \\ \phantom{(H_0/L_0) \tan \beta / \frac{w}{gT}} > \quad \text{(offshore transport; erosive profile)} \end{array}$$

INTRODUCTION

The aim of this study is obtain a better understandings of the mechanism governing onshore-offshore sediment transport and the transformation of beach profiles resulting from sediment transport across the surf zone. In treating coastal processes, sediment transport is usually divided into longshore and onshore-offshore components. It is generally believed that the longshore component controls relatively long-term systematic profile changes, whereas the onshore-offshore component has a marked connection with short-term profile changes, observed during either storm or post-storm wave climates.

The onshore-offshore shift of sand in the surf zone plays a very important role in shoreline migration as well as in the transformation of beach profiles. In other words, the beach profile has great bearing on coastal phenomena related to littoral sediment transport.

Since 1949, after Johnson proposed a criteria for beach profile classification in terms of the wave steepness in deep water, much effort has been devoted to clarify the mechanism of the profile change for two-dimensional beaches. Rector(1954), Iwagaki and Noda(1962), Nayak(1971), Watts(1954), Dean(1973); and Sunamura and Horikawa(1974) proposed certain parameters related to beach transformation and the direction of net sediment transport. The authors(1979) also obtained criteria for classifying the beach profile in terms of the "delay distance" (Kemp, 1960) and "surf similarity parameter" (Battjes, 1974). However, onshore-offshore processes, especially in the surf zone, have not yet been fully understood even under constant wave conditions.

Since the mechanics of sediment transport in the surf zone is more complex than in the offshore zone, all the relevant parameters can not be taken into account in a model description. In this paper, a model is developed on the basis of the concept of the balance of power expended on sand grains suspended by breaking waves.

DESCRIPTION OF MODEL

The turbulence generated by breaking waves acts as a stirring agent for suspending sediment particles. Using available field data of kinematic energy and momentum fluxes in the surf zone, Thornton(1978) presented a relationship between the ratio of the turbulent velocity intensity to the wave-induced velocity intensity and a parameter corresponding to the wave steepness.

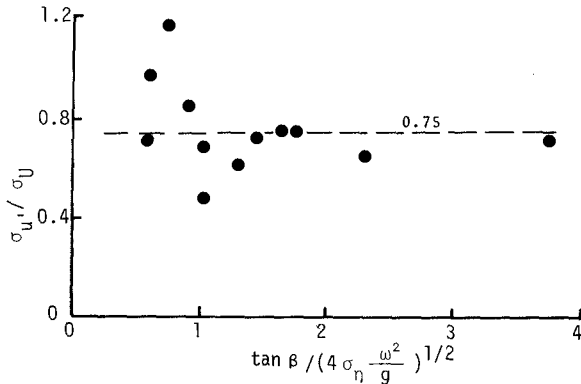


Fig. 1 Ratio of turbulent to wave-induced velocity intensity (Thornton, 1978)

ponding to the offshore parameter $\xi_0 = \tan\beta/\sqrt{H_0/L_0}$ (Battjes, 1974). His result is given in Fig. 1, in which σ_u and $\sigma_{\hat{u}}$ are the standard deviations of the turbulent and wave-induced velocities, σ_{η} is the standard deviation of the free surface calculated from the spectrum of the waves, ω is the angular frequency, and $\tan\beta$ is the bottom slope. Figure 1 indicates that the velocity ratio is almost constant regardless of the breaking type, which is represented by the value of the abscissa (Galvin, 1972).

Based on Thornton's result, the stirring power, P_s , for suspending sand grains due to turbulence as the stirring agent is written as Eq.(1),

$$P_s = a'W \hat{u} \tan\beta, \tag{1}$$

in which W is the submerged weight of sand grains, \hat{u} is the maximum wave-induced velocity, $\tan\beta (= h_b/X_b)$ is the bottom slope in the surf zone, h_b is the water depth at the breaking position, X_b is the width of the surf zone, and a' is a constant. Notations used are shown in Fig. 2.

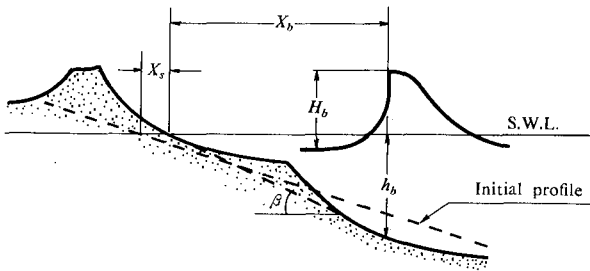


Fig. 2 Definition sketch.

Using the linear long wave theory, we have Eq.(2) as an expression for the maximum wave-induced velocity,

$$\hat{u} = 2\pi (H_b/L_b) gT, \tag{2}$$

where H_b and L_b are the wave height and length at the breaking position, T is the wave period, and g is the gravitational acceleration. Substituting Eq.(2) into Eq.(1), we have Eq.(3) for the expression of P_s ,

$$P_s = a'' W (H_b/L_b) g T \tan\beta, \tag{3}$$

where a'' is a constant.

Since it is considered that the resisting power against lifting sand grains from the bottom is due to the gravitational force, the resistive power expended on sand grains is written as Eq.(4),

$$P_r = a'' w_s(d), \quad (4)$$

in which $w_s(d)$ is the fall velocity of a sand grain of diameter d , and a'' is a constant.

If the stirring power, P_s , is greater than the resisting power, P_r , sand grains tend to keep in suspension due to breaking waves. Then, suspended sand grains would be transported seaward in the form of a sand cloud by wave-induced currents (Sunamura, 1980). If, on the other hand, the resisting power is greater than the stirring one, sand grains tend to roll and jump on the bottom surface. Then, sand grains are shifted shoreward as bed load.

It is, therefore concluded that the predominant or net direction of onshore-offshore sand transport, which has a close connection with beach profile change, can be described with the ratio of the above two powers, P_s and P_r . Combining Eqs.(3) and (4), the ratio P_s/P_r is written as

$$\begin{aligned} \frac{(H_b/L_b) \tan\beta}{w_s(d)/(gT)} &< && \text{(onshore transport)} \\ &= && C' \quad \text{(neutral)} \\ &> && \text{(offshore transport)} \end{aligned}, \quad (5)$$

in which C' is a constant.

As is well known, there are many difficulties in measuring wave and sediment processes within the surf zone, both in the laboratory and in the field. Most of the available data are usually represented by the wave characteristics in deep water and the median diameter of the sediment particles.

Wave steepness at the breaking position depends on the beach slope and incident wave steepness in deep water may be calculated within the limits of linear wave theory. Accordingly the wave steepness in Eq.(5) can be replaced with that in deep water. In addition, we write $w_s(d_{50})$ in place of $w_s(d)$ in Eq.(5), where $w_s(d_{50})$ is the fall velocity of sand grains determined from the median diameter of the sediment particles. Then Eq.(5) is rewritten as follows,

$$\begin{aligned} \frac{(H_0/L_0) \tan\beta}{w_s(d_{50})/(gT)} &< && \text{(onshore transport)} \\ &= && C \quad \text{(neutral)} \\ &> && \text{(offshore transport)} \end{aligned}, \quad (6)$$

in which C is a constant to be determined from laboratory and field data. It is noticed that Eq.(6), the final expression of the present model, is quite similar to the criterion proposed by Dean(1973), in which the effect of beach slope was not included.

By using the relation $L_0 = (g/2\pi)T^2$, Eq.(6) can be written as

$$\frac{H_0}{w_s (d_{50}) T} \tan\beta \begin{matrix} < \\ > \end{matrix} \frac{1}{2\pi} C. \quad (7)$$

Equation (7) indicates that two important parameters control onshore-offshore sand transport in the surf zone; the dimensionless fall-time parameter, $H_0/w_s T$, (SPM, 1977), and the relative width of the surf zone, $\tan\beta$. Dean (1973) also pointed out the importance of the quantity $H_0/(w_s T)$ for the prediction of accreted or eroded profiles.

COMPATIBILITY OF THE PRESENT MODEL

The present model emphasizes the importance of the beach slope for onshore-offshore sediment transport. Before discussing the validity of the model, it must be shown to be compatible with general observation both in laboratory experiments and in nature.

The beach slope in the surf zone may depend on the size of the beach material, the energy level of waves incident on the beach, the steepness of incident waves, the rate of percolation and the degree of sediment sorting of the beach, and the change in water level (Komar, 1976). Among these factors, the dependence of grain size on the beach slope has been investigated by geologists (Bascom, 1951; King, 1972; SPM, 1977).

The following has been deduced from previous studies:

(1) The beach slope of the foreshore depends mainly on grain size, and tends to increase with the median grain diameter. In addition, laboratory experiments with movable beds reveal that the specific gravity of beach material is an important parameter controlling the beach slope (Nayak, 1970). These facts imply that beach slope depends predominantly on the fall velocity, which is a function of the size, shape and specific gravity of the sediment particles.

$$(\tan\beta \sim w_s (d))$$

(2) For a given grain size, low-energy beaches have larger slopes than high-energy beaches.

(3) The effect of wave period (or, in effect, wave length) on the beach slope has been examined with both laboratory experiments and field investigations. The results indicate that the beach slope tends to increase with decreasing wave period.

$$(\tan\beta \sim 1/T \text{ or } \tan\beta \sim 1/L)$$

(4) The relationship between beach slope and steepness of incident waves is that the beach slope becomes flatter with increasing wave steepness (Rector, 1954; King, 1972).

$$(\tan\beta \sim 1/(H/L))$$

Combining the above results, we obtain the following relationship for the beach slope,

$$\tan\beta \sim \frac{w_s(d)/T}{(H/L)}, \quad (8)$$

which is essentially equivalent to Eq.(6).

TEST EQUIPMENT

In order to verify the present model and to determine the constant appearing in Eq.(6), laboratory experiments were performed in a two-dimensional wave tank, 0.4 m wide, 0.7 m deep, and 16 m long, with a glass wall on one side of the entire length. Figure 3 shows the general arrangement of the test equipment.

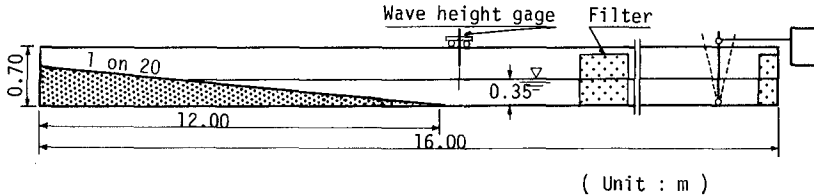


Fig. 3 General arrangement of test equipment.

The experiments were performed using monochromatic waves generated by a flap-type wave maker installed at one end of the tank. The incident wave height was measured by a capacitance type wave gage placed just offshore from the toe of the model beach. The breaker height was measured with a small capacitance type wave gage mounted on a carriage capable of moving with constant speed along the centerline of the tank. The horizontal distance from a base line on the model beach to the breaking position was measured with a ruler.

Beaches for the experiments were molded to an initial slope of 1 on 20 by using natural sand or Amberlite, a kind of plastic grain. The fall velocity of the bed materials was measured by means of a settling tube. Physical properties of the bed materials are given in Table 1.

Table 1 Physical properties of bed materials.

Bed Material	Amberlite	Natural Sand
Median Diameter (mm)	0.55	0.22
Specific gravity in Air	1.33	2.70
Fall Velocity (cm/sec)	3.20	2.60

Each experiment was performed in a series of runs. Beach profiles were surveyed along the centerline of the tank after each run using a specially designed bottom-touch type (Hattori and Kawamata, 1979). Immediately after starting a run, measurements of the incident wave height, and breaking characteristics were taken. Wave characteristics in the uniform depth of 0.35 m were determined from the threshold condition of sediment movement proposed by Horikawa and Watanabe (1967).

EXPERIMENTAL RESULTS AND DISCUSSIONS

As Sunamura and Horikawa (1974) have pointed out, from previous results obtained both in the laboratory and in the field, there exists some difficulty in grouping beach profiles into bar and step types according to the conventional criteria, because of the complexity of the beach configuration and of the tendency for shoreline migration. Figures 4 and 5, examples of the experimental results, show time changes of beach profiles of the accretive type. Arrows pointing toward the still water level represent the breaking position. As seen in Fig. 4, a break-point bar (King, 1972) moved shoreward gradually. It was noticed from the experiments that the breaking position also moved with the bar. When the migrating bar reached the beach face, the shoreline advanced considerably and the beach profile transformed to a step or reflective type profile (Hattori and Kawamata, 1979). On the other hand, sand outside the surf zone was shifted offshore. Due to this sand transport, the water depth around the breaking position deepened progressively, and the beach slope in the surf zone became steeper.

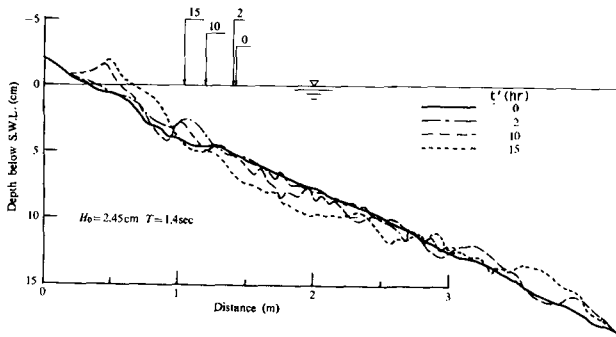


Fig. 4 Profile changes of accretive beach (Amberlite).

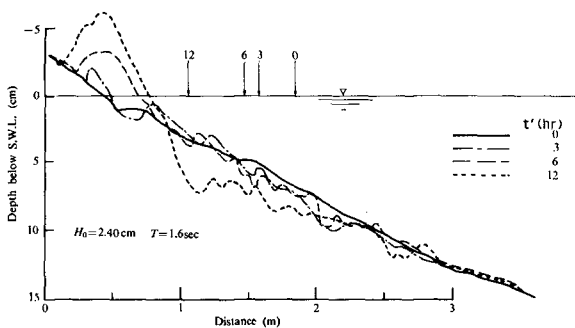


Fig. 5 Profile changes of accretive beach (sand).

Figures 6 and 7 illustrate profile changes of receding beaches. As the coastal berm eroded, sand shifted from the beach face was transported seaward and deposited in the offshore zone. Although an offshore bar sometimes formed at the breaking position, this bar tended to migrate offshore. With retreat of the shoreline, the beach slope within the nearshore zone became flatter and the width of the surf zone broadened in the course of time. It was also observed in the experiments that the breaker wave type changed from plunging to spilling.

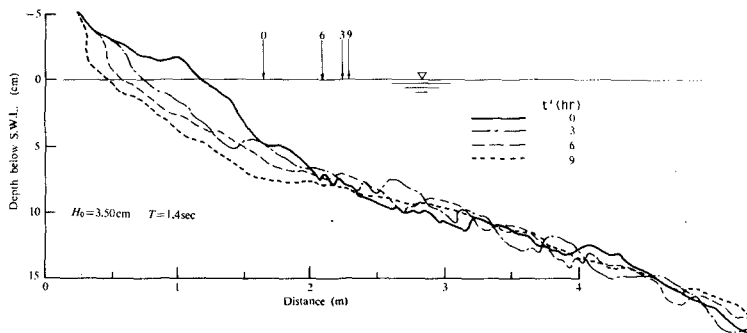


Fig. 6 Profile changes of erosive beach (Amberlite).

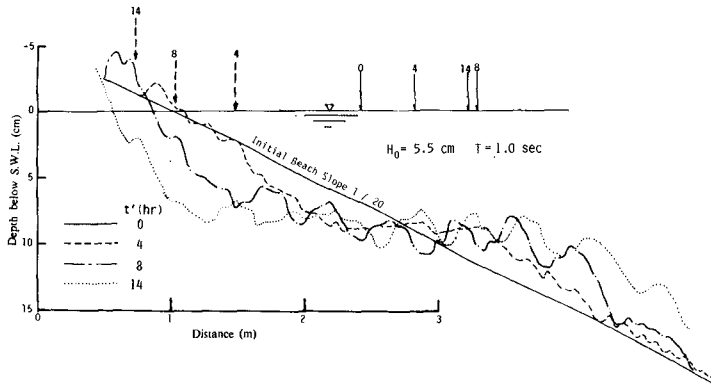


Fig. 7 Profile changes of erosive beach (sand).

When the cumulative time, t' , was greater than four hours, waves broke twice: by first spilling and then by plunging at the toe of the foreshore. Under these circumstances, as seen in Fig. 7, a step was formed at the foreshore face and the shoreline migrated seaward. In this figure, broken arrows pointing toward the still water level indicate the breaking position of reformed waves.

CLASSIFICATION OF BEACH PROFILE

On the basis of the experimental results, the authors classified beach profiles into the following three groups as determined by the direction of net sand transport inside and outside the surf zone as shown in Fig. 8.

TYPE I is the accretive beach profile with a step on the foreshore. For this profile a landward sand shift is dominant in the surf zone, and the shoreline advances.

TYPE III is the erosive or storm beach profile without bars. Intense offshore sand transport occurs in the nearshore zone.

On a beach of TYPE II, a bar is formed at the breaking position. This bar sometimes migrates either landward or seaward. Under certain conditions, which depend mainly on the wave characteristics in the nearshore zone, the TYPE II profile transforms to the TYPE I or to the TYPE III profile.

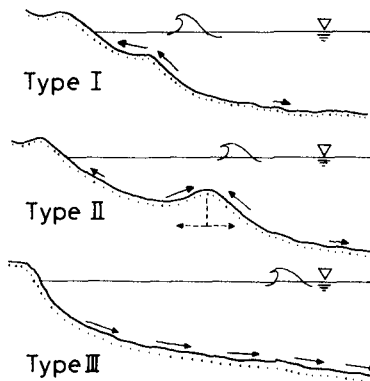


Fig. 8 Classification of beach profiles (Arrows denote the direction of net sand transport).

Figure 9 illustrates the method for determining the direction of net sediment transport adopted in the classification of beach profiles. The bottom figure shows two beach profiles surveyed at a time interval of three hours. From the difference between these two profiles, the rate of sediment transport in the onshore-offshore direction can be computed with the aid of the conservation equation of bottom sediment, given by Eq. (9),

$$\frac{\partial h}{\partial t} = \frac{1}{(1 - \lambda)} \frac{\partial q_s}{\partial x}, \quad (9)$$

in which h is the water depth, q_s is the sediment transport rate in the on-offshore or x direction, λ is the porosity of the bottom sediment, and t is the time. The distribution of the transport rate computed is given by the top figure. The dominant tendency of sediment transport inside and outside the surf zone in Fig. 8 was determined in connection with the beach profiles by calculation with Eq.(9).

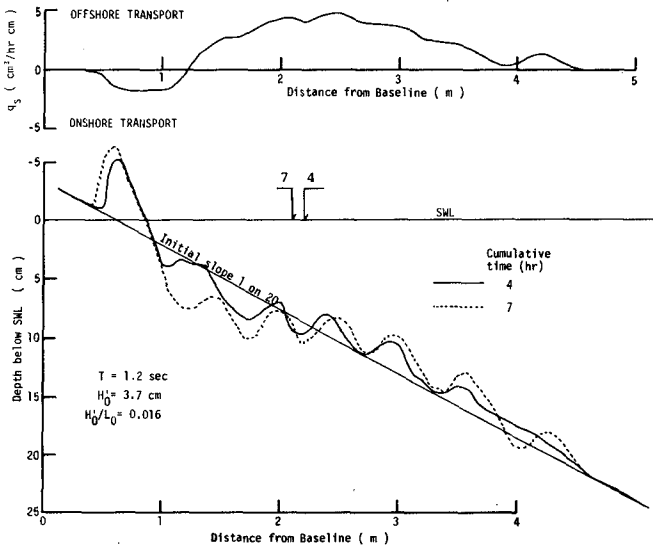


Fig. 9 Method for determining transport rate.

EVALUATION OF THE PRESENT MODEL

The evaluation of the present model is made on the basis of shoreline migration from the initial position of each test run, because the shoreline of the TYPE II profile exhibits considerable migratory tendencies. When the shoreline advances, a beach is termed as an accretive profile, whereas when the shoreline recedes, it is termed an erosive profile (Sunamura and Horikawa, 1974).

The criterion for the type of beach profile, erosive or accretive, based on this study is shown in Fig. 10 in terms of $(H_0/L_0) \tan \beta$ and $w_s (d_{50})/gT$. In this figure, the results of many other laboratory experiments are included to cover a wide range of characteristics of waves and bed materials. Open and solid symbols represent the accretive and erosive profiles, respectively.

It is noticed from Fig. 10 that regions of occurrence of the two beach profiles are distinctly separated by the line of $C = 0.5$, although there exists a mixed region bounded by $0.3 < C < 0.7$. The existence of this mixed region seems to have a close connection with the migration tendency of break-point bars.

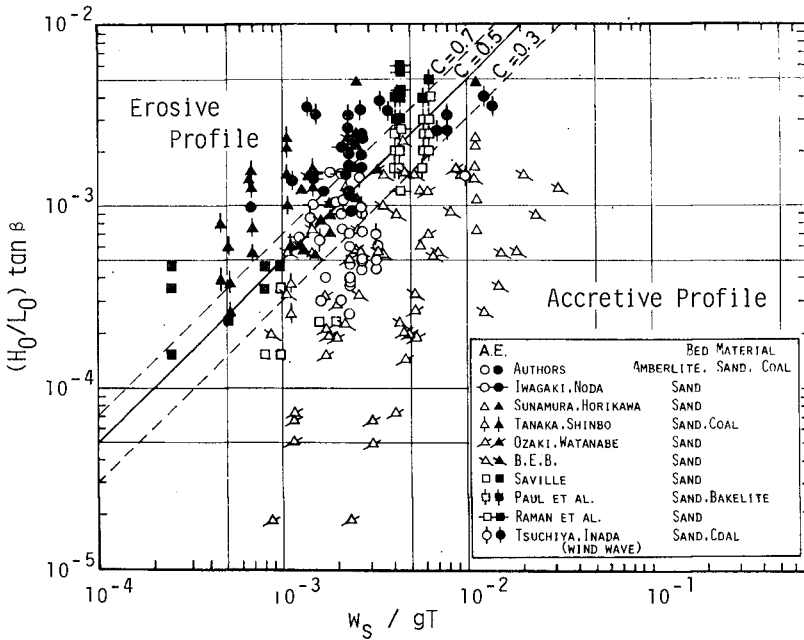


Fig. 10 Classification of erosive and accretive beach profile (Laboratory data).

Various kinds of light-weight bed materials have been widely used for movable bed experiments. Light-weight bed materials behave in very different ways under wave action from natural sand as a bed material (Nayak, 1970). Figure 10, however, indicates that the beach profile in the surf zone can be classified by the present model without respect to the specific gravity of bed materials. This implies that the fall velocity is a very important parameter controlling the beach transformation and sediment transport (Dean, 1973).

In applying results of model experiments to the prototype, we have to consider various factors resulting from the lack of dynamic similitude between the model and the prototype. Among these factors, the scale effect of model experiments and the effect of irregularity of wave characteristics on the onshore-offshore sand transport are examined in this study. Many previous studies have pointed out the importance of scale effects on the formation of beach profiles (Collins and Chesnutt, 1975; Noda, 1972). In the evaluation of the present model, experimental data obtained in a prototype wave tank by Saville (1957) are plotted on Fig 10 in order to obtain knowledge about the applicability of the present model to the prototype.

Tsuchiya et al. (1974) conducted a series of movable bed experiments in a wave tank installed in a wind tunnel. Their data, circles with a vertical bar, are plotted on Fig. 10 to examine the effect of irregularity of incident wave characteristics on beach profiles. In examining the irregularity effect of incident waves, the wave height in deep water in Eq. (6) is replaced with the mean wave height calculated from the significant wave height, which is calculated on the assumption that the wave height frequency distribution in the wave tank is expressible by the Rayleigh distribution function. It is noticed that the transformation of beach profiles under the action of irregular waves also is inferable fairly well from the criterion determined by the experimental results employing monochromatic waves.

The tendency for beach transformation due to changes in incident wave characteristics can be discussed with temporal variations of the C value of Eq. (6) and the shoreline position. The bottom figure of Fig. 11 shows the changes of C value with respect to the dimensionless cumulative time, t/T . The top figure is the time change in the relative displacement of the shoreline, X/L_0 (Fig. 2). The following statements are supported by the experiments: For cases of accretive beaches, $C_0 < 0.5$, the C -value tends to move progressively from the initial value to the value of 0.5. C_0 is the value at an initial stage of each test. For erosive beaches, $C_0 > 0.5$, the C -value also shifts toward the value of 0.5. It is therefore concluded that the line of $C = 0.5$ in Fig. 10 represents not only the criteria for the occurrence of beach profile type, but also the equilibrium condition of beach transformation in the surf zone.

When characteristics of both the incident waves and bottom sediment are prescribed, processes in beach transformations are represented by the vertical shift of data points on Fig. 10. It is apparent from Fig. 10 that the slope of an accretive beach becomes steeper due to the onshore sand transport in the surf zone in approaching an equilibrium beach profile, while the slope on the erosive beach becomes flatter due to the intensive offshore transport.

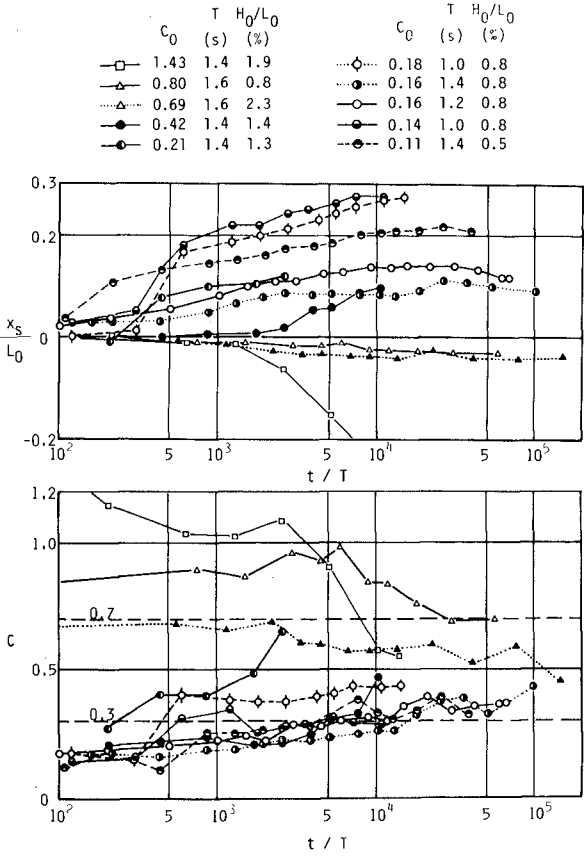


Fig. 11 Time changes of C-value and shoreline position.

BEHAVIOR OF BREAK-POINT BARS

In the classification of beach profiles, it was pointed out that the TYPE II profile occasionally exhibits unusual behavior, which may depend on the migratory tendency of a break-point bar. The occurrence and migratory tendency of break-point bars can be also discussed with the aid of the two parameters of this study. As seen in Fig. 12, a break-point bar is found both on the erosive and accretive profiles.

Most bars on the accretive profile migrate shoreward across the surf zone. Under constant wave conditions, this process is indicated by vertically upward shifts of data points in the accretive profile region of Fig. 12. In contrast, downward shifts of data points in the erosive region indicate the seaward migration of bars due to the intense sand transport beyond the breaking position. It is noticed from Figs. 10 and 12 that the mixed region, $0.3 < C < 0.7$, has a close connection with the growth and reduction of break-point bars, which depends on the direction of bar migration.

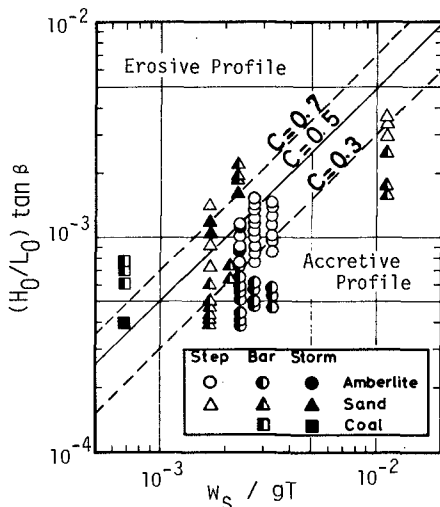


Fig. 12 Occurrence of break-point bars.

APPLICABILITY OF THE PRESENT MODEL TO THE PROTOTYPE

Figure 13 indicates the applicability of the present model to onshore-offshore sand transport in the prototype as well as to beach transformation. Analysis of previous field data, plotted in Fig. 13, is made on the assumption that two-dimensionality holds in shore processes. The examination of beach profiles, erosive or accretive, is decided by the shoreline displacement from its position at the beginning of each investigation term.

In examining the applicability of the model, the wave steepness in Eq.(6) is calculated by a method similar to that used in the examination of the effect of irregularities of wave characteristics as in Fig. 10. Some of the field data did not contain information on the characteristics of the breaking waves. In using such data, the breaking depth is calculated by using the breaker indices proposed by Goda(1970), and the surf zone width is estimated with the aid of a bathymetric chart. When the fall velocity was not prescribed in the data, it was calculated using the diagram for the fall velocity of quartz spheres (Sedimentation Engineering, 1975).

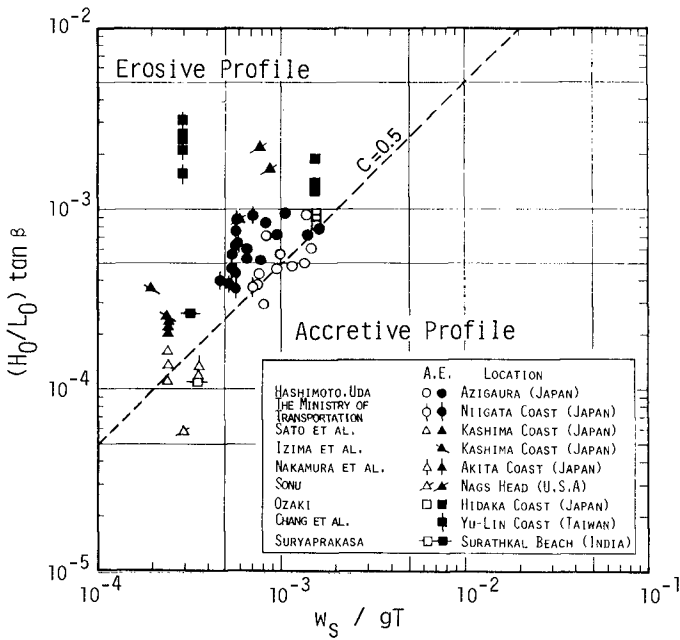


Fig. 13 Applicability of the model to the prototype.

In the analysis of the field data, the effect of time scale on the beach profile change was also included. Field data plotted on Fig. 12, except those of Hashimoto and Uda(1979), were obtained by investigations at intervals of three months or more. Hashimoto and Uda made weekly field surveys of the shoreline configuration and daily observations of the wave climate in the nearshore zone on Ajigaura beach facing the Pacific Ocean.

The long-term profile change appears to have good correlation with the wave height and period averaged over the field investigation. This implies that the beach profile change over the long-term depends on the mean energy level of the incident waves. On the other hand, the profile change over a short-term relates to the high-energy level wave climate during that term. It should be emphasized that the beach profile change in response to the wave field was found inferable from the same relation as that determined from the laboratory data.

CONCLUSIONS

In this study, a model describing onshore-offshore sand transport in the surf zone is developed on the basis of the concept of the balance of power expended on sand gains suspended by breaking waves. The derived relationship, Eq.(6), indicates that both the dimensionless fall-time parameter and the bottom slope in the surf zone, or the surf zone width, are very important parameters controlling on-shore-offshore sand transport.

To evaluate the present model, the authors classify beach profiles into accretive and erosive ones, which are determined by the shoreline migration from its initial position. According to experiments, the regions of occurrence of these two beach profiles are distinctly separated by the line of $C = 0.5$ (Fig. 10). This C -value also represents the equilibrium condition of profile change of two-dimensional beaches (Fig. 11).

The criterion obtained is as follows:

<	(onshore transport; accretive profile)
$C = 0.5$	(neutral; equilibrium profile)
>	(offshore transport; erosive profile)

From comparison with field data (Fig. 13), it is emphasized that this criterion is applicable to the prediction of the beach profile change in the prototype. The importance of the time scale involved in beach profile changes is revealed in the evaluation of the model.

ACKNOWLEDGEMENTS

The authors wish to express their gratitude to Dr. T. Sunamura, Associate Professor of the University of Tsukuba, for valuable discussions. A part of this study was supported by Scientific Research Fund from the Ministry of Education.

REFERENCES

- Bascom, W.H. (1951): The relationship between sand size and beach face slope, *Trans. AGU*, Vol. 32, 866-874.
- Battjes, J.A. (1974): Surf similarity, *Proc. of 14th ICCE*, 466-480.
- Chang, K.S.T. and F.L.W. Chang (1970): Studies on the shore process and wave features of the western coast of Taiwan, *Proc. of 12th ICCE*, 729-738.
- Collins, J.I. and C.B. Chesnutt (1975): Tests on the equilibrium profiles of model beaches and the effects of grain shape and size distribution, *Proc. of the Symposium on Model Technique, ASCE*, 907-926.
- Dean, R.G. (1973): Heuristic model of sand transport in the surf zone, *Proc. of Conf. on Engineering Dynamics in the Surf Zone, Sydney*, 208-214.
- Eagleson, P.S., B. Glenne, and J.A. Dracup (1961): Equilibrium characteristics of sand beaches in the offshore zone, *B.E.B. Tech. Memo.*, No. 126.
- Galvin, C.J. Jr. (1972): Wave breaking in shallow water, *Waves on Beach*, Ed. R.E. Meyer, Academic Press, New York, 413-456.
- Goda, Y. (1970): A synthesis of breaker indices, *Trans. of JSCE*, No. 180, 39-49.
- Hashimoto, H. and T. Uda (1979): Analysis of beach profile changes at Ajigaura by empirical eigenfunction, *Coastal Eng. in Japan, JSCE*, Vol. 22, 47-58.
- Hattori, M. and R. Kawamata (1979): Restoration of sandy beaches fronting seawalls, *Proc. of the Speciality Conf. on Coastal Structures '79, ASCE*, 388-404.
- Horikawa, K. and A. Watanabe (1967): A study on sand movement due to wave action, *Coastal Eng. in Japan, JSCE*, Vol. 10, 39-57.
- Ijima, T., S. Sato, and N. Tanaka (1964): Field study on littoral drift on Kashima Coast, *Proc. of 11th Coastal Eng. Conf. in Japan, JSCE*, 175-180. (in Japanese)
- Iwagaki, Y. and H. Noda (1962): Laboratory study of scale effect in two-dimensional beach processes, *Proc. of 8th ICCE*, 194-210.
- Johnson, J.W. (1949): Scale effects in hydraulic model involving wave action, *Trans. AGU*, Vol. 30, 517-525.
- Kemp, P.H. (1960): The relation between wave action and beach profile characteristics, *Proc. of 7th ICCE*, 262-276.

- King, C.A.M.(1972): Beaches and Coasts, 2nd ed., St. Martin's Press, New York, 314-334.
- Komar, P.D.(1976): Beach Processes and Sedimentation, Prentice-Hall, Englewood Cliffs, 303-321.
- Nayak, I.V.(1970): Equilibrium profiles of model beaches, Tech. Rept. HEL-2-25, Univ. of California, Berkeley.
- Noda, E.K.(1972): Equilibrium beach profile scale-model relationship, Proc. of ASCE, Vol. 98, WW 6, 511-527.
- Ozaki, A.(1964): On the effect of an offshore breakwater on the maintenance of a harbor constructed on sandy beach, Proc. of 9th ICCE, 323-345.
- Paul, M.J., J.W. Kamphuis, and A. Brebner(1972): Similarity of equilibrium beach profiles, Proc. of 13th ICCE, 1217-1234.
- Raman, H. and J.J. Earattupuzha(1972): Equilibrium conditions in beach wave interaction, Proc. of 13th ICCE, 1237-1256.
- Rector, R.L.(1954): Laboratory study of the equilibrium profiles of beaches, B.E.B. Tech. Memo., No. 41.
- Sato, S., N. Tanaka, and K. Sasaki(1974): The case history on variation of sea bottom topography caused by the construction works of Kashima Harbour, Rept. of the Port and Harbour Res. Inst., Vol. 13, No. 4(2). (in Japanese)
- Saville, T., Jr.(1957): Scale effects in two dimensional beach studies, Proc. of 7th General Meeting of IAHR, A.3-8.
- Sedimentation Engineering(1975): Manuals and Reports on Engineering Practice, No. 54, Ed. V.A. Vanoni, ASCE, 25.
- Shore Protection Manual(1977): U.S. Army Coastal Engineering Research Center, Vol. 1, 4-75-88.
- Sonu, C.J.(1968): Collective movement of sediment in littoral environment, Proc. of 11th ICCE, 373-400.
- Sunamura, T.(1980): Laboratory offshore sediment transport and a model for eroding beaches, Abstract-In-Depth, 17th ICCE, Sydney, 440-441.
- Sunamura, T. and K. Horikawa(1974): Two-dimensional beach transformation due to waves, Proc. of 14th ICCE, 920-938.
- Suryaprakasa Rao, P. and P. Kassim(1970): Field study of Surathkal Beach, Proc. of 12th ICCE, 1365-1381.
- Tanaka, N. and O. Shinbo(1973): The properties of coal grains as bed material in the model experiment on littoral drift, Rept. of the Port and Harbour Res. Inst., Vol. 12, No. 1, 3-45. (in Japanese)

Thornton, E.B.(1978): Review of status of energetics and momentum fluxes in the surf zone: Field data, Proc. of a Workshop on Coastal Sediment Transport, DEL-SG-15-78, Univ. of Delaware, 63-77.

Tsuchiya, Y. and K. Inada(1978): Experiments on the beach profile transformation due to wind waves - Criterion for occurrence of longshore bars - , Proc. of 21st Coastal Eng. Conf. in Japan, JSCE, 219-224. (in Japanese)

Watts, G.M.(1954): Laboratory study of effect of varying wave periods on beach profiles, B.E.B. Tech. Memo., No. 53.

APPENDIX
ON THE BEACH SLOPE IN THE SURF ZONE

The Shore Protection Manual(1977) provides a criteria for predicting the bar-berm profile in terms of the dimensionless fall time parameter, $F_0 = H_0/w T$. In this reference, the dimensionless fall time parameter is plotted against both wave steepness in deep water and wave height to grain size ratio (Figs. 4-29 and 4-30).

According to the results in SPM, the separation between bar-berm profiles, or erosive and accretive profiles, is given by a value of $F_0 = 1 \sim 2$, and the criteria in terms of F_0 is expressible as

$$\begin{array}{l}
 < & \text{(deposition onshore, accretive profile)} \\
 F_0 = 1 \sim 2 & \\
 > & \text{(deposition offshore, erosive profile)}
 \end{array}
 \tag{A.1}$$

On the other hand, the criteria obtained in the present study can be rewritten with respect to the dimensionless fall time parameter by using Eq.(7) and putting $C = 0.5$ as follows:

$$\begin{array}{l}
 < \\
 F_0 = \frac{0.08}{\tan\beta} \\
 >
 \end{array}
 \tag{A.2}$$

The effect of beach slope on the profile change can be evaluated by combining Eqs.(A.1) and (A.2). For the critical value of the beach profile classification, the beach slope in the surf zone becomes

$$\tan\beta = 1/12.5 \sim 1/25$$

The estimated beach slope is considered to be very reasonable in comparison with previous results obtained in laboratory experiments and in the field (SPM).

ON-OFFSHORE SEDIMENT TRANSPORT RATE
IN THE SURF ZONE

Toru Sawaragi

Professor of Civil Engineering
Osaka University, Osaka, Japan

and

Ichiro Deguchi

Research Associate of Civil Engineering
Osaka University, Osaka, Japan

ABSTRACT

In this paper, models of the distribution of net on-offshore sediment transport based on two-dimensional equilibrium beach profiles and an equation of continuity of sediment transport are proposed. Various parameters of net on-offshore sediment transport in those models are discussed. Further, the relative importance of bed load and suspended load in the two-dimensional beach deformation are examined by measuring both of them on model beach experiments.

1. Introduction

A problem of fundamental importance to the mechanics of sediment transport on beaches under wave and wave-induced current system is the relative magnitude of the littoral sand drift and on-offshore sediment transport. In the previous report (Sawaragi et al., 1978), the authors have formulated the littoral sediment transport rate considering long-shore current as a sediment transporting flow. However, as to on-offshore sediment transport rate, the authors could not evaluate quantitatively because of the complexity of mechanics of sediment transport.

The purpose of this study is to examine the relation between on-offshore sediment transport and the deformation process of two-dimensional beach profile. The first half of this paper will be constructed around a model of the distribution of net on-offshore sediment transport rate based on experimental results about two-dimensional beach deformation which were conducted by many investigators. The final part of this paper will examine a relative importance of suspended and bed load in the two-dimensional beach deformation by measuring directly suspended and bed loads in two-dimensional model beach experiments.

2. Model of the distribution of net on-offshore sediment transport rate along a beach profile

As suggested by Tanaka et al. (1973) and Horikawa et al. (1974), beach profiles which seem to reach a quasi-equilibrium condition can be classified into three types as shown in Fig. 1. The distribution of net

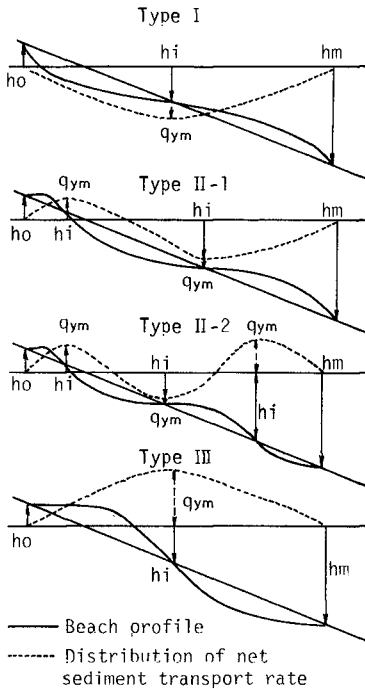


Fig.1 Model of the distribution of net on-offshore sediment transport rate

profiles, and calculated q_{ym} from the using the equation of continuity of sediment transport. In the following sections, these four characteristic quantities are analyzed by taking account of previous results obtained from the two-dimensional model beach experiments.

3. Analysis of h_0, h_m, h_i and q_{ym} which determine the distribution of net on-offshore sediment transport rate.

The four characteristic quantities will be expressed by the fluid density ρ , fluid kinematic viscosity ν , density of sediment ρ_s , median grain size d_{50} , wave height H , wave period T , beach slope i , gravity acceleration g , friction velocity u_* , wave running time t_s , and so on. Some important parameters such as the Shield's parameter

on-offshore sediment transport, which would have taken place in the processes of those beach deformation, can be modelled as dotted lines in Fig.1 from the equation of continuity of sediment transport. In Type I (erosion type), the direction of net on-offshore sediment transport is always toward offshore. In Type III (accretion type), onshore net sediment transport takes place in the entire range of beach profile. In Types II-1 and II-2, both onshore and offshore net sediment transport spring up.

The distribution of net on-offshore sediment transport rate can roughly determined by h_0, h_m, h_i and q_{ym} shown in Fig.1 where, h_0 and h_m : the critical height and depth of beach deformation, respectively, h_i : the depth of the point of intersection of two beach profiles measured in succession, i.e., the depth where the maximum net on-offshore sediment transport takes place, q_{ym} : the maximum net on-offshore sediment transport rate, and h_0 is taken upward, while h_m and h_i are taken downward from the still water level.

The authors rearranged about 80 experimental results on the two-dimensional beach deformation conducted by many investigators and evaluated h_0, h_m, h_i from the beach change of beach configurations by

$u_*^2/(\rho_s/\rho-1)gd_{50}$ and the surf similarity parameter $\xi=i/\sqrt{H_0/L_0}$ are already derived by combining above-cited variables to explain various phenomena in the surf zone. So far, however, there is no objective way to judge whether the beach profile reaches equilibrium or not. The authors, first, examine the time variations of h_o, h_m, h_i and q_{ym} to determine the wave running time for quasi-equilibrium beach profile.

3-1 Time-variations of the characteristic variables

Time-variations of h_o, h_m, h_i and q_{ym} of typical 2 cases in Type I and Type III are shown in Figs.2 and 3, respectively. In the figures, q_{ym} are calculated from differences of the water depth Δh , measured in succession with time interval Δt , by using the equation of continuity of the sediment transport. Therefore, they are given as average values taken over the time interval Δt . From Figs.2 and 3, the following results can be pointed out.

- 1) Net offshore sediment transport does not readily decrease even after a fairly long running time as seen in Fig.2. While, onshore net sediment transport decays soon, as seen in Fig.3.
- 2) In accordance with 1), h_o and h_m in Type I and h_m in Type II-1 increase after a large number of waves propagated. On the other hand, h_o and h_m

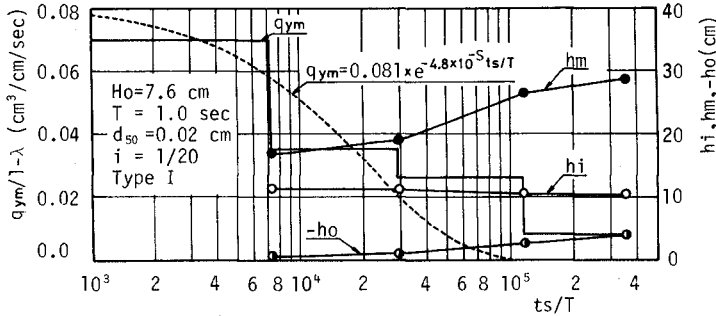


Fig.2 Time-variations of characteristic quantities of Type I

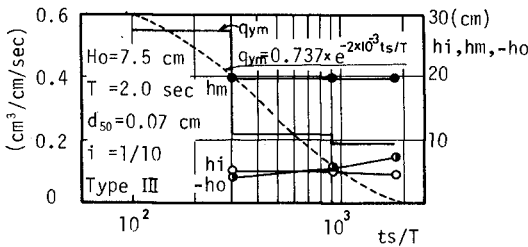


Fig.3 Time-variations of characteristic quantities of Type III

in Type III and Type II-2 almost remain constant or increase a little with increasing the running time.

3) h_i does not indicate significant changes with time.

Taking these results into account, beach profiles after 7.2×10^4 waves propagated were picked up to analyze h_o , h_m and h_i . In the case where the beach profile at this running time was not measured, we estimated those quantities by interpolating from the time-variations of them. The data, whose running time were less than $7.2 \times 10^4 T$, were omitted. However, experimental results of Saville (1957) who employed waves almost corresponding the full scale waves and Rector (1954) which have been quoted by many investigators were analyzed for reference, although they did not satisfy this limitation of running time.

On the other hand, we can assume the time-variations of q_{ym} expressed as Eq. (1) to clearly grasp the rate of decay of q_{ym} with running time.

$$q_{ym} = q_{ym0} \exp(-At_s/T) \quad (1)$$

where q_{ym0} is the initial value of q_{ym} and A is a constant. Here, q_{ym0} and A are calculated by the following procedure:

- 1) Select the data whose running times are more than $7.2 \times 10^4 T$ in which beach profiles were measured at least 3 times.
- 2) Let $t_s = 0, t_{s1}, t_{s2}, \dots$ be the times when the beach profile was measured and q_{ym1}, q_{ym2}, \dots be the maximum on-offshore sediment transport rate in the time interval $\Delta t_1 = t_{s1}, \Delta t_2 = t_{s2} - t_{s1}, \dots$
- 3) Calculate q_{ym0} and A by substituting $q_{ym} = q_{ym1}$ at $t_s = t_{s1}/2$ and $q_{ym} = q_{ym2}$ at $t_s = (t_{s1} + t_{s2})/2$.

In Figs. 2 and 3, Eq. (1) determined by the above-mentioned procedure are also shown by dotted curves. As can be seen from these figures, it is found that the time-variation of q_{ym} can be expressed fairly well by Eq. (1) and at $t_s/T = 7.2 \times 10^4$, the maximum onshore net sediment transport rate q_{ym} in Types III and II-2 almost diminish and the maximum offshore net sediment transport rate of Types I and II-1 become less than 25% of their initial value q_{ym0} .

3-2 Analysis of h_o

h_o will be determined by factors which control a wave run-up height and a change of shore line. The wave run-up height is said to be closely related to the surf similarity parameter ξ (Battjes, 1974). While, the change of shore line should be considered as one part of the whole beach deformation rather than related to local parameters near the shore line. Hence, the authors use the non-dimensional force, $N_s = H_o/T \sqrt{(\rho_s/\rho - 1)gd_{s0}}$ as the parameter to indicate the magnitude of the ability of the beach to deform. The derivation of N_s will be mentioned latter. Fig. 4 shows the relation between h_i/H_o and ξ with N_s as a parameter. From this figure, it is found that h_i/H_o increases with increasing ξ and that for the same value of ξ , h_i/H_o also increases with increasing N_s .

3-3 Analysis of h_m

In the initial stage of the beach deformation, h_m can not be deeper than the critical depth for an initial sediment movement. Generally,

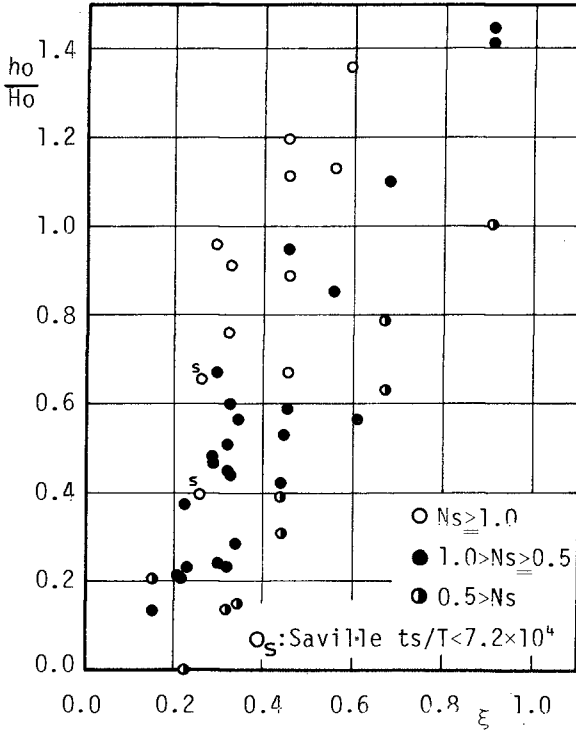


Fig.4 Relation between h_o/H_o and ξ

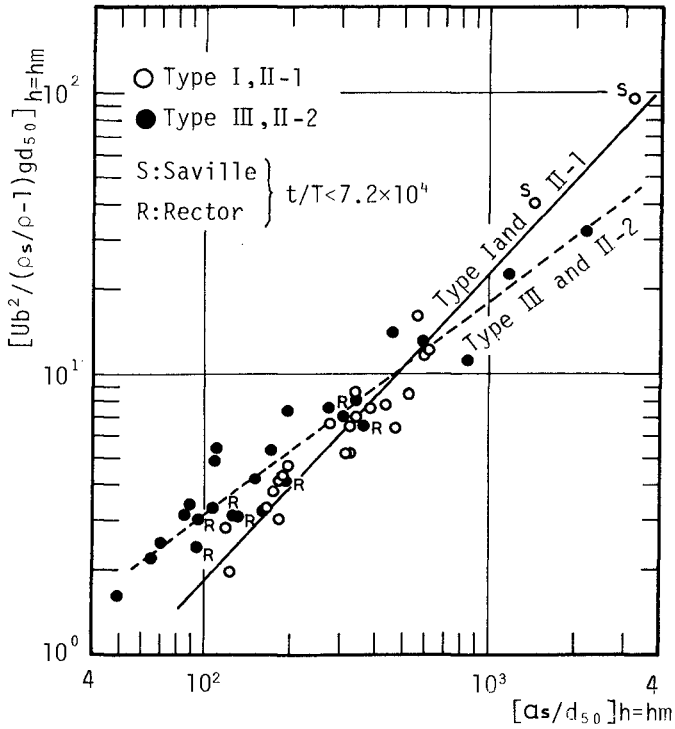


Fig.5 Relation between $U_b^2 / (\rho_s / \rho - 1) g d_{50}$ and a_s / d_{50} at $h=hm$

the critical depth for the sediment movement is determined from the balance between the forces acting on a grain and the resistance force of the grain which can be given as follow:

$$(\pi/6)gd_{50}(\rho_s-\rho)\tan\phi = K(\pi/4)d_{50}^2\rho f u_b^2 \quad (2)$$

where $\tan\phi$ is the friction angle of the sediment, f the friction factor, u_b the maximum water particle velocity at the bottom, and K the coefficient. f is usually expressed by $u_b\delta/\nu$ or $u_b^2 T/\nu$ in a laminar region and a_s/Z_o in a turbulent region where $\delta=(\nu T/2\pi)^{1/2}$, $a_s=Tu_b/\pi$ and Z_o the equivalent roughness height. However, the effect of Reynold's number on the initial movement of sediment seems to be small compared with a_s/Z_o (Dingler,1975). Hence, Eq.(2) can be given as follow:

$$u_b^2/(\rho_s/\rho-1)gd_{50}\approx 1/f\approx F(a_s/Z_o) \quad (3)$$

Assuming that the same relation as Eq.(3) holds with h_m , the authors calculated $u_b^2/(\rho_s/\rho-1)gd_{50}$ and a_s/Z_o at $h=h_m$ by using the linear wave theory. The results are shown in Fig.5. In this calculation, Z_o is taken equal to d_{50} in order to take account of only the skin friction regardless of the bottom configuration according to Madsen(1976). As seen from Fig.5, the relation between $u_b^2/(\rho_s/\rho-1)gd_{50}$ and a_s/d_{50} at $h=h_m$ can be approximated fairly well by the following equations:

$$u_b^2/(\rho_s/\rho-1)gd_{50} = B(a_s/d_{50})^n \quad (4)$$

in which,

$$\begin{array}{ll} B = 0.18 & n = 1.1 \quad \text{for Type I and Type II-1} \\ B = 0.10 & n = 0.75 \quad \text{for Type III and Type II-2} \end{array} \quad (5)$$

By using the linear wave theory and $N_s = H_o/T/\sqrt{(\rho_s/\rho-1)gd_{50}}$, Eq.(4) can be modified as Eqs.(6) and (7).

$$\{(H/H_o)(1/\sinh kh_m)\}^{-1} = CN_s(d_{50}/L_o)^m \quad (6)$$

$$\begin{array}{ll} C = 400 & m = 0.6 \quad \text{for Type I and Type II-1} \\ C = 20 & m = 0.3 \quad \text{for Type III and Type II-2} \end{array} \quad (7)$$

The left hand side of Eq.(6) is the function of h_m/L_o only. And if N_s and d_{50}/L_o are given, h_m/L_o can be calculated from Eqs.(6) and (7). Fig.6 shows the comparison of h_m calculated from Eq.(6) with h_m measured from the beach profile. From this figure, it is found that Eq.(6) together with Eq.(7) give a sufficiently accurate estimate of h_m .

3-4 Analysis of h_i

h_i is defined as the depth where the maximum on-offshore sediment transport takes place. The limit depth of "D-profile" proposed by Swart(1970), "cut-depth" defined by Hallermeier(1977) seem to correspond to h_i of Types I and II-1. "Stable point" proposed by Raman et al. (1972) may also equivalent to h_i . Although the concept of "D-profile" or "cut-depth" can be applied only to the beach of Types I and II-1, h_i as defined above, can be applied extensively to all types of beach profiles.

In the consideration of h_i , it is necessary to take into account the difference of the mode of sediment transport between Type I and Type III. The causes of net on-offshore sediment transport have been studied for long time and may be summarized as follows:

- 1) stational flow such as mass transport current due to waves.
- 2) asymmetry of water surface profile, ie, asymmetry of the time-vari-

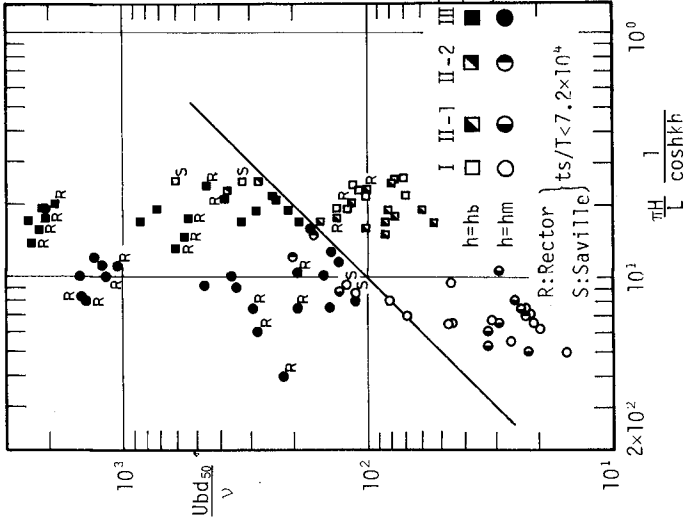


Fig. 7 Relation between Ubd_{50}/ν and $(\pi H/L)(1/\cosh kh)$ at $h=hb$ and $h=hm$

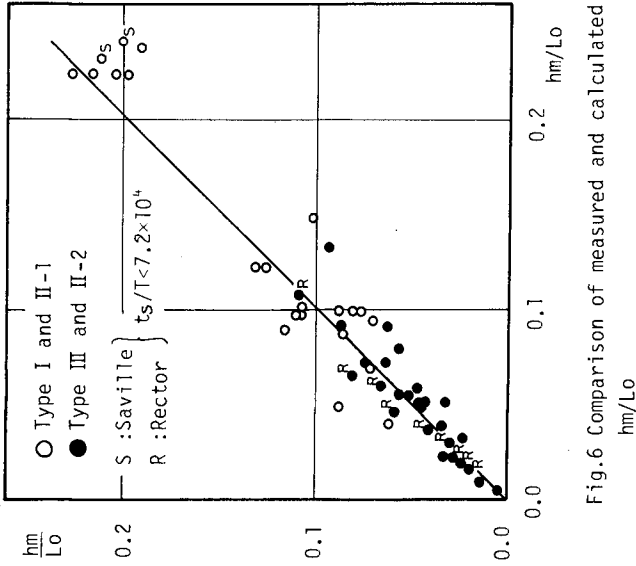


Fig. 6 Comparison of measured and calculated hm/Lo

ation of water-particle velocity.

3) effect of gravity, i.e., the existence of beach slope.

4) distorted profile of time-variation of the concentration of suspended sediment due to asymmetrical sand ripple or breaking waves.

Referring from theoretical and experimental results by Sato et al. (1962), Inman et al. (1963), Horikawa et al. (1974) and Bowen (1979), the necessary condition for the occurrence of net offshore sediment transport seems to be the existence of sufficient amount of suspended sediment, and net onshore sediment transport is mainly caused by bed load.

However, in the surf zone, although the asymmetrical property of time-variations of water-particle velocity increases, ripples usually disappear and the existence of the steady flow becomes dubious because of large turbulence brought by breaking waves. Hence, so far, the authors can not explain the reason why net onshore sediment transport can take place in the entire beach profile of Type III and net offshore sediment transport happens in the whole beach of Type I. Then, to begin with, the authors examine the direction of net on-offshore sediment transport in the offshore regions of three types of beach profiles by using two parameters proposed by Sato et al. (1962). They give the criteria for the occurrence of net on-offshore sediment transport on a horizontal bed by a function of sediment Reynold's number $u_b d_{50} / \nu$ and the amplitude of non-dimensional pressure gradient at the bottom by waves $(-1/\rho g)(\partial p/\partial x) = (H/L)(\pi/\cosh kh)$. They also found that asymmetrical ripples caused net offshore sediment transport by using radio active tracers. Although $u_b d_{50} / \nu$ is a non-dimensional parameter, it expresses a magnitude of drag force acting on a grain in a fluid and $(-1/\rho g)(\partial p/\partial x)$ indicates the relative magnitude of the acceleration of water-particle to that of the gravity. Fig. 7 shows the relation between $u_b d_{50} / \nu$ and $(H/L)(\pi/\cosh kh)$ at $h=h_b$, calculated from the new-breaker-index presented by Goda (1970), and $h=h_m$. Again, u_b and L were calculated by the small amplitude theory. Taking into account the direction of net on-offshore sediment transport of Type I and Type III, the direction of net on-offshore sediment transport can be distinguished by Eq. (8)

$$u_b d_{50} / \nu \begin{cases} < (H/L)(\pi/\cosh kh) \times 10^3 & \dots \text{ offshore} \\ > & \dots \text{ onshore} \end{cases} \quad (8)$$

Taking the ratio of $u_b d_{50} / \nu$ to $(H/L)(\pi/\cosh kh)$ and let the ratio be N_{sr} , the criteria of Eq. (8) can be written in a simple form,

$$N_{sr} = (u_b d_{50} / \nu) / \{(H/L)(\pi/\cosh kh)\} = g T d_{50} / 2 \pi \nu$$

$$N_{sr} \begin{cases} < 10^3 & \dots \text{ offshore} \\ > & \dots \text{ onshore} \end{cases} \quad (9)$$

However, as can be seen from Fig. 7, two data of Saville (1957) can not be classified by Eq. (8). He employed large waves as in the field and H_o/L_o of his experiments were larger than other cases. Therefore, to apply Eq. (8) or Eq. (9) to the large scale model beach as the field, some modifications including the effect of wave height itself or H_o/L_o explicitly seems to be required.

The direction of net sediment transport in Types II-1 and II-2 are also shown in Fig. 7, and they are classified by Eq. (9). This means that the change of the direction of net on-offshore sediment transport in

in these two types will occur in the surf zone.

As discussed above, the direction of net sediment transport in the offshore region can be determined by N_{sr} . On the other hand, h_i seems to be closely related to wave breaking as the first order action of fluid motion. So, the authors examine the relative depth of h_i to h_b , h_i/h_b of three types of beach profiles. Fig.8 shows the relation between h_i/h_b and N_{sr} . It can be seen from this figure that for the offshore net sediment transport of Types I and II-1, h_i/h_b ranges between $1.0 < h_i/h_b < 1.5$, for the onshore net sediment transport of Type III, $0.3 < h_i/h_b < 0.9$ and for the onshore net sediment transport of Type II-1, $-0.4 < h_i/h_b < 0.0$. This indicates that a longshore bar in a storm beach (Type I or Type II-1) has to be generated in the offshore region. For the beach of Type II-2, no significant tendency can be found out for the deficiency of the data.

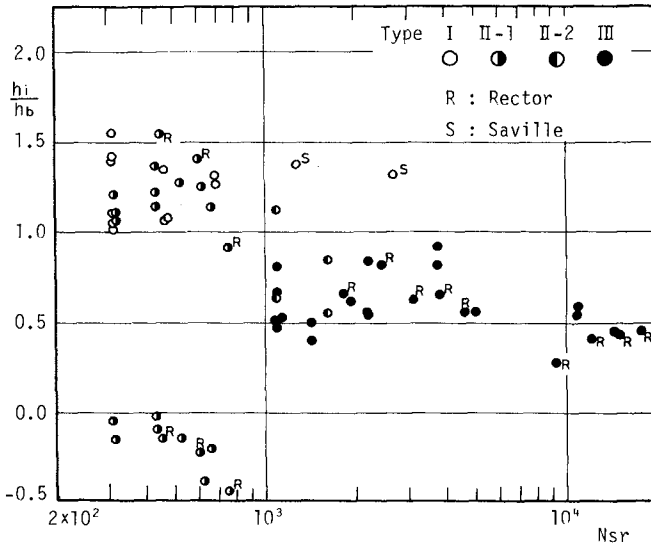


Fig.8 Relation between h_i/h_b and N_{sr}

Because h_i of Types I and II-1 appears outside the surf zone, the procedure proposed by Hallermeier(1977) seems to be effective. Hence, the authors compared h_s calculated according to Hallermeier with h_i measured from the beach profile of Types I and II-1. As a result, the correlation between h_i and h_s is relatively high for small scale experiments, however, h_s seems to give smaller values of h_i for large-scale experiments. On the other hand, within the breaker zone, wave characteristics and wave-induced flow pattern are controlled by H_0/L_0 and \bar{i}

(Nakamura et al., 1966). Hence, h_i for onshore net sediment transport of Type III may also be controlled by H_o/L_o and i . The authors also discussed the relation between h_i of Type III and those two parameters. It is found that h_i/h_b have a tendency to decrease with decreasing H_o/L_o , however, i seems to have little influence on h_i/h_b .

3-5 Analysis of q_{ym}

Referring Madsen's presentation (1976), the time averaged rate of on-offshore sediment transport by bed load \bar{q}_y , i.e., the amount of sediment which have a capacity to be transported as net on-offshore sediment transport, can be expressed as follow:

$$\bar{q}_y / W_o d_{s0} = D (u_*^2 / (\rho_s / \rho - 1) g d_{s0})^n \quad (10)$$

where D is a coefficient, W_o the settling velocity of sediment and $n=3$. Assuming that the same kind of relation as Eq. (10) can be applied to suspended load and that the direction and the rate of net sediment movement can be expressed by N_{sr} , H_o/L_o and i , net on-offshore sediment transport rate q_y will be given as a first order approximation by

$$q_y / W_o d_{s0} \approx q F_1 (N_{sr}, H_o/L_o, i) \cdot F_2 (t_s/T) \\ = D (u_*^2 / (\rho_s / \rho - 1) g d_{s0})^n \cdot F_1 (N_{sr}, H_o/L_o, i) \cdot F_2 (t_s/T) \quad (11)$$

Further, it seems reasonable to assume the turbulent flow condition near $h=h_i$ and consequently a constant friction factor. Then, for Types I and II-1, u_* at $h=h_i$ ($> h_b$) can be replaced by $(H_o/T)(H/H_o \sinh kh)_{h=h_i} = (H_o/T)F_3(h_i/L_o)$, and h_i/L_o is also expressed by H_o/L_o according to Hallermeier (1977). Hence, the maximum net sediment transport q becomes

$$q_{ym} / W_o d_{s0} = q_{ym0} \exp(-At_s/T) \\ = E (H_o/T / \sqrt{(\rho_s / \rho - 1) g d_{s0}})^{2n} F (N_{sr}, H_o/L_o, i) \exp(-At_s/T) \quad (12)$$

where $N_s = H_o/T / \sqrt{(\rho_s / \rho - 1) g d_{s0}}$ and E is the coefficient of proportionality. N_s was already used to analyze h_o and h_m . The authors further consider that Eq. (12) can be applied to Types III and II-2.

Fig. 9 shows the relation between A in Eq. (12) and N_s . It can be seen that A is closely related to N_s and the direction of net on-offshore sediment transport. Namely, the larger, the N_s , the faster net sediment transport decays. And onshore net sediment transport decreases faster than offshore sediment transport.

Finally, Fig. 10 shows the relation between non-dimensional net on-offshore sediment transport rate q_{ym0}^* and N_s . Here, q_{ym0}^* is derived by taking four parameters in Eq. (12) into account as follow:

$$q_{ym0}^* = (q_{ym0} / W_o d_{s0})^{2n} (1/\lambda) (1/N_{sr}) (H_o/L_o) \quad (13)$$

where λ is the porosity of sand. From Fig. 10, it is concluded that q_{ym0}^* is proportional to N_{sr} regardless of the direction of net on-offshore sediment transport. And the exponent n in Eq. (10) is 3. The result corresponds to that obtained by Madsen et al. (1976).

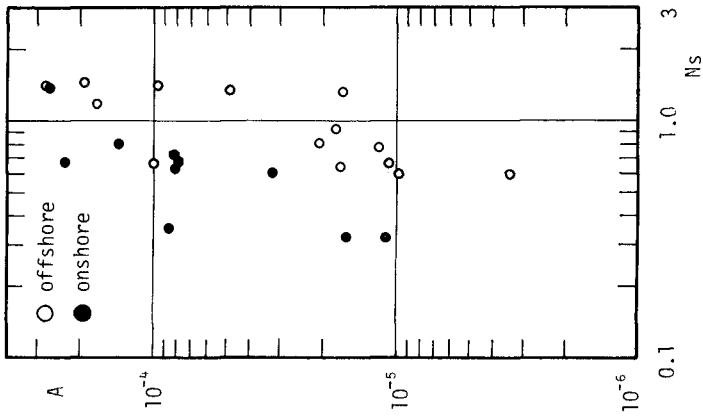


Fig.9 Relation between A and Ns

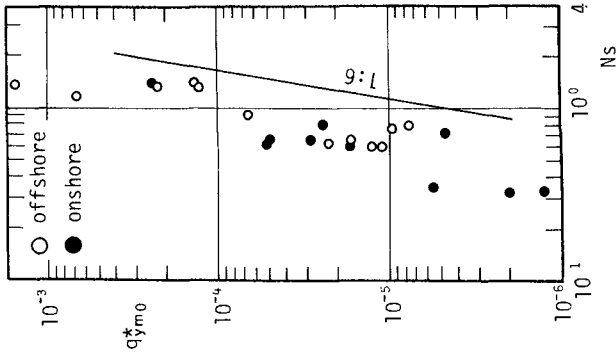


Fig.10 Relation between q_{yrmo}^* and Ns

4. Experiments to measure on-offshore sediment transport rate in the two-dimensional model beach

Since net on-offshore sediment transport discussed above includes both bed and suspended loads, the relative magnitude of bed load and suspended load can not be examined. In this section, based on the experimental results, relative importance of bed load and suspended load in the deformation of two-dimensional model beach is discussed.

4-1 Equation of continuity of the sediment transport including suspended sediment

Consider the co-ordinate system taken X-axis horizontal to the shore line, positive y-axis shoreward, positive Z-axis vertically upward from the stillwater level. The diffusion equation for any arbitrary volume is

$$\partial C / \partial t = -\nabla \cdot (\vec{C} \vec{V}_s) \quad (14)$$

where C is the sediment concentration, \vec{V}_s the sediment-particle velocity vector. After taking time average and integrating Eq.(14) from $z=-h$ (bottom) to $Z=\eta$ (free surface), the equation of continuity can be obtained as follow:

$$\frac{\partial}{\partial t} \left(\int_{-h}^{\eta} C \, dz + (1-\lambda)h \right) + \frac{\partial}{\partial x} \int_{-h}^{\eta} q_x \, dz + \frac{\partial}{\partial y} \int_{-h}^{\eta} q_y \, dz = 0, \quad (15)$$

where $(q_x, q_y) = (u_s C, v_s C)$, $\vec{V}_s = (u_s, v_s, w_s)$, $(1-\lambda)\partial h / \partial t = [w_s C]_{z=-h}$

In the previous section, the authors consider Eq.(11) as a first order approximation of $q_y = v_s C$. In Eq.(15), $z=-h$ corresponds to bed load and $z>-h$ to suspended load, respectively.

Based on these consideration, the authors examine the relative importance of bed load and suspended load by measuring directly bed load and suspended load in model beach experiments.

4-2 Experimental procedure

Two wave tanks of different dimension were used. One is 26m long, 1.5m wide and 1.8m high, and other one is 51m long, 0.64m wide and 0.97m high. Two kinds of beach materials, i.e. $d_{50} = 0.54\text{mm}$, $\rho_s = 2.65\text{gr/cm}^3$ and $d_{50} = 0.34\text{mm}$, $\rho_s = 2.68\text{gr/cm}^3$ were used to form a model beach of 1/20 initial beach slope. The bed load was measured by a sand trap composed of an outer casing and inner box made of a tin plate. The inner box has two compartments to separately measure the amount of onshore and offshore sediment transport rate. The dimension of this inner box is 10cm in width, 10cm in length and 5cm in depth. While the beach profile was developed, the inner box was not installed and the outer casing was buried into the bottom sand bed. Just before the measurement was conducted, the outer casing was pulled up to the bottom surface and sands in it were taken out to replace them with the inner box. Bed load was measured at 10 different locations covering from swash zone to the offshore zone, and the measured time was from 2 to 6min. The average sediment transport rate Q_{bt} and net sediment transport rate Q_{bnet} were calculated from the sum and the difference of the amounts of sediment trapped in both shoreward and seaward compartments respectively in the unit of (dry weight/cm/sec). The suspended load was measured by collecting the water samples through siphons with intake nozzles as shown in Fig.11. the reasons why such a

primitive apparatus was used are as follows:

- 1) by the optical method, the direction of suspended load can not be distinguished,
- 2) small babbles brought into water by breaking waves decrease the accuracy of the measurement by optical method,
- 3) direct measurement of the amounts of sediments is possible by collecting the sediment laden water samples by siphons.

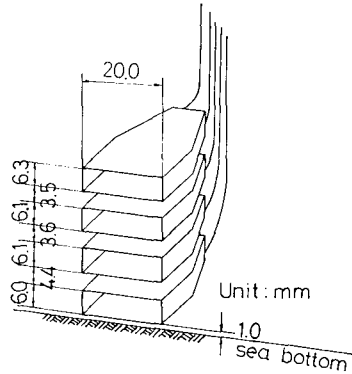


Fig.11 Sketch of the intake nozzles of siphon

The measurements of suspended sediment were done orienting the intake nozzle both toward onshore and offshore directions at each measuring point setting the lower part of the nozzle above 1mm from the bottom. Samples of 4 points distributed vertically at each measuring point were collected. Sampling time was from 40 to 80sec., and 200-400 CC was gathered. The concentration of suspended sediment \bar{C} and net on-offshore sediment transport rate q_{snet} are calculated from the following procedure. Let S_{ion} and S_{ioff} be weights of samples and dry net weights of sediments included in S_{ion} which was collected by orienting the intake nozzle offshore at $Z=Z_i$; height of the i th intake nozzle and S_{ioff} and S_{ion} be the amounts of those collected by orienting the intake nozzle onshore. The authors calculated \bar{C} at $Z=Z_i$ from

$$C(Z_i) = (S_{ion} + S_{ioff}) / (S_{ion} + S_{ioff}) \quad (\text{dry weight/weight}).$$

While net on-offshore sediment transport by suspension, q_{snet} was calculated from

$$q_{snet} = (1/T_s) [((S_{1on} - S_{1off}) / a_1) ((Z_2 + Z_1) / 2) + ((S_{2on} - S_{2off}) / a_2) ((Z_3 - Z_1) / 2) + ((S_{3on} - S_{3off}) / a_3) ((Z_4 - Z_2) / 2) + ((S_{4on} - S_{4off}) / a_4) (h - (Z_4 + Z_3) / 2)] \quad (\text{dry weight/cm/sec})$$

in which T_s is the sampling time and a_i is the area of i th intake nozzle. These method to separately measure the amount of onshore and offshore sediment transport by suspension is fundamentally based on the time-

variation of the velocity of fluid sucked through the intake nozzle which is calculated from the generalized Bernoulli's theorem; pressure equation. A head difference between the intake nozzle and the outlet was adjusted to coincide the intake velocity with the maximum water-particle velocity in both direction of offshore and onshore. However, when the orientation of intake nozzles directed onshore or offshore, a few sediments which were moving in the direction of offshore or onshore, seemed to be sucked. Consequently, the measured concentration might be little larger than the true concentration. Besides, due to an accuracy of weighing dry sands in the sample, the accuracy of concentration measured by this method decreases when C is less than 10^4 ppm.

The authors confirmed the reliability of the siphon by comparing the concentrations measured by the siphon with those of ductivity meter using an optical method.

Table-1 Experimental conditions

4-3 Experimental results

6 experiments were conducted. Their detailed conditions are shown in Table-1. In three cases of $N_{sr}=636$, suspended load will be expected to dominate and in the other three cases of $N_{sr}>1200$, bed load will be predominate.

H cm	T sec	d_{50} mm	ρ_s/ρ	N_{sr}
17.8	1.2	0.34	2.68	636
7.3	1.2	0.34	2.68	636
3.8	1.2	0.34	2.68	636
33.1	1.7	0.54	2.65	1431
12.4	1.7	0.54	2.65	1431
5.4	1.5	0.54	2.65	1263

i) Time-averaged on-offshore sediment transport by bed load Q_{bt} and suspended load Q_{st}

First, let's investigate the difference of the relative magnitude of Q_{bt} and Q_{st} between two beaches of different N_{sr} . Fig.12(a) and (b) show two examples of the distributions of Q_{bt} and Q_{st} . When $N_{sr}=636$, as shown in Fig.12(a), time-averaged suspended load Q_{st} clearly surpasses bed load Q_{bt} in amount. The ratio of the maximum time-averaged sediment transport rate Q_{st}/Q_{bt} is about 2.0. While in the case of $N_{sr}=1263$, as shown in Fig.12(b), suspended load is less than bed load and the ratio of the maximum transport rate Q_{st}/Q_{bt} is 0.5.

The authors also measured a bottom shear stress on a fixed flat bed by a shear meter. Details of the shear meter are described in the previous paper (Sawaragi et al., 1978). From Fig.12 and the results of the measured shear stress, it was found that Q_{st} was larger than Q_{bt} in the region of $U_* / W_0 > 0.8$, and Q_{bt} became larger than Q_{st} when $U_* / W_0 < 0.8$. However, U_* measured on a fixed bed, does not include the effect of the bottom roughness. So, in order to determine the strict criterion for the initiation of sediment suspension, it is necessary to clarify the sediment movements on the bottom which are closely related to the water-particle motion near the bottom.

ii) Relative importance of suspended load versus bed load to the beach deformation

Finally, the authors examine the relative importance of suspended load versus bed load to the beach deformation by investigating the relations among net sediment transport rate Q_{net} calculated from the time-variations of beach profiles, measured net on-offshore sediment transport rate by suspension Q_{snet} and bed load Q_{bnet} .

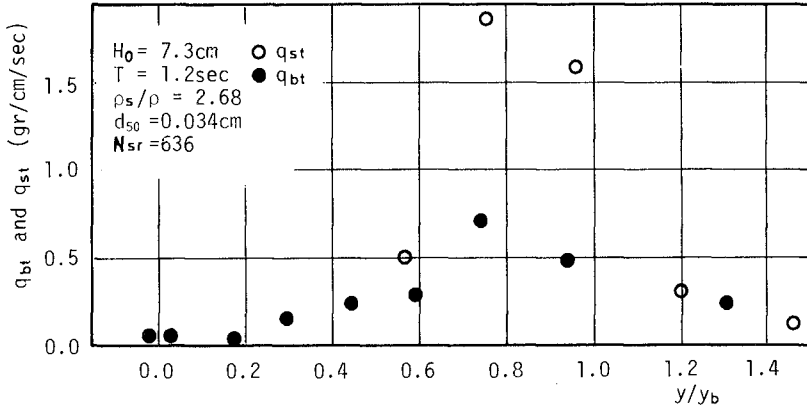


Fig.12(a) Distributions of q_{st} and q_{bt}
($N_{sr} = 636$)

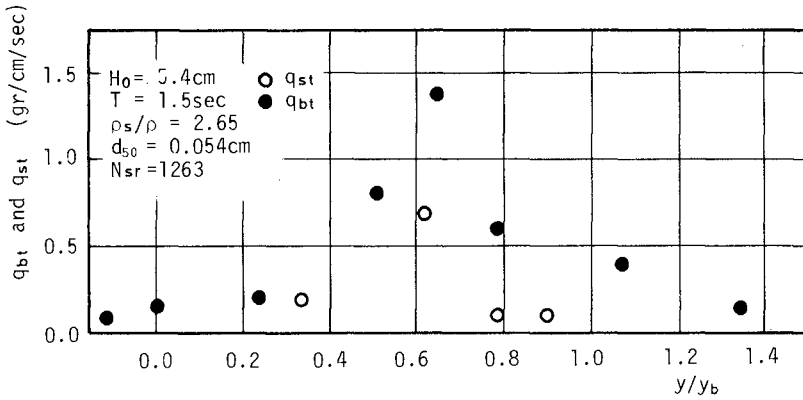


Fig.12(b) Distributions of q_{st} and q_{bt}
($N_{sr} = 1263$)

Fig.13 shows one example of the distribution of q_{ynet} , q_{bnet} and q_{snet} together with the beach profile of $N_{sr}=636$. q_{bnet} and q_{snet} were measured in a relatively short time compared with running time $t_s/T=1.5 \times 10^3$, in which the beach profile in Fig.13 was developed. So, they might change with running time. q_{ynet} is given as an average over $t_s/T=0 \sim 1.5 \times 10^3$. In Fig.13, the distribution of q_{bnet} is similar to that of q_{ynet} , and q_{snet} has a sharp peak at $y/y_b=0.75$ which corresponds to the location of the bar. To examine the relative importance of q_{bnet} and q_{snet} in the beach deformation, the authors calculated the change of water depth caused by q_{bnet} and q_{snet} by using the equation of continuity of sediment transport without considering the effect of time-change of concentration of suspended sediment indicated by the first term in Eq.(15). The result is shown in Fig.14. In this figure, Δh shown by solid line is calculated from the difference of beach profiles between $t_s/T=0$ and $t_s/T=1.5 \times 10^3$, Δh_b , shown by heavy line, is calculated from q_{bnet} and represents the changes of mean water depth between two neighboring measuring points and Δh_s , shown by broken line is calculated from q_{snet} as well as Δh_b . As can be seen from this figure, the bar near $y/y_b=0.75$, the typical beach profile of this case, seems to be created not only by bed load but also by suspended load. However, Δh_s gives fairly large beach deformation compared with Δh in this region. According to Eq.(15), this difference between measured and calculated water depths have to be compensated by the increase of concentration of suspended sediment. On the other hand, the measured concentration increased about 6ppt at $y/y_b=0.75$ during $t_s/T=1.5 \times 10^3$. This increment of concentration only accounts for few millimeter of erosion near $y/y_b=0.75$. This indicates that, even in the case where suspended load dominates bed load, the first term of Eq.(15) becomes less than 1/10 of other terms.

Fig.15 shows the relation between q_{ynet} , q_{bnet} and q_{snet} in the case of $N_{sr}=1263$. In this case, q_{bnet} is in the direction of onshore through the entire range of the beach profile and the distribution of q_{bnet} almost coincides with q_{ynet} . While the direction of q_{snet} is mainly offshore and its magnitude is less than 1/2 of q_{bnet} . Fig.16 shows the relation between Δh , Δh_b and Δh_s . Same notations and symbols as in Fig.14 are used. From this figure, it can be found that the fundamental mode of the beach deformation of Type III with deposition in the shallower region and erosion in the deeper region as shown in Fig.1 is mainly created by q_{bnet} . However, q_{snet} also seems to contribute to the beach deformation of secondary mode in addition to the fundamental mode.

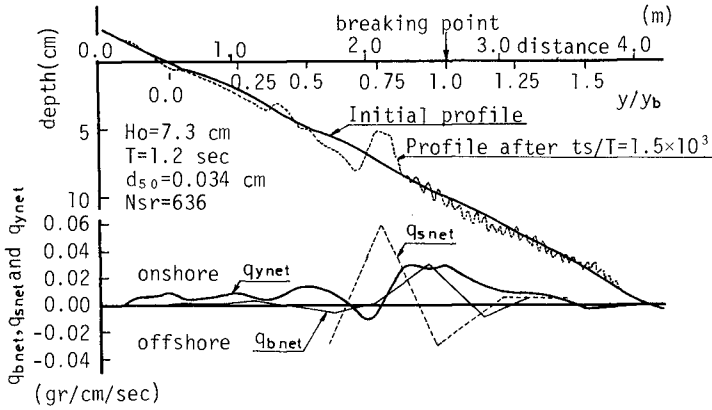


Fig.13 Beach profile and distributions of calculated and measured net on-offshore sediment transport rates ($Nsr=636$)

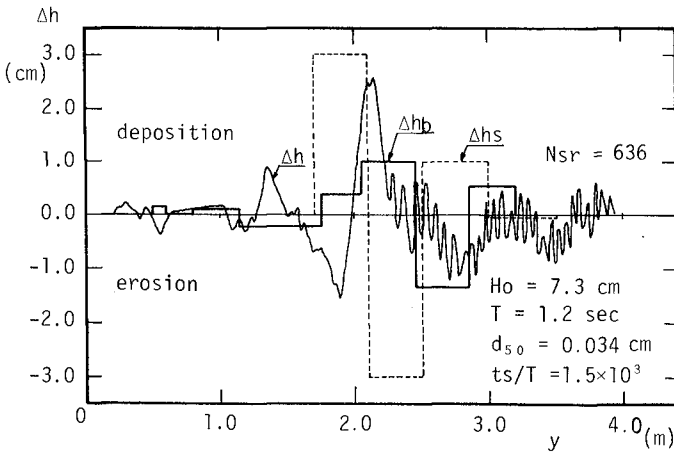


Fig.14 Comparison among Δh , Δhb and Δhi ($Nsr=636$)

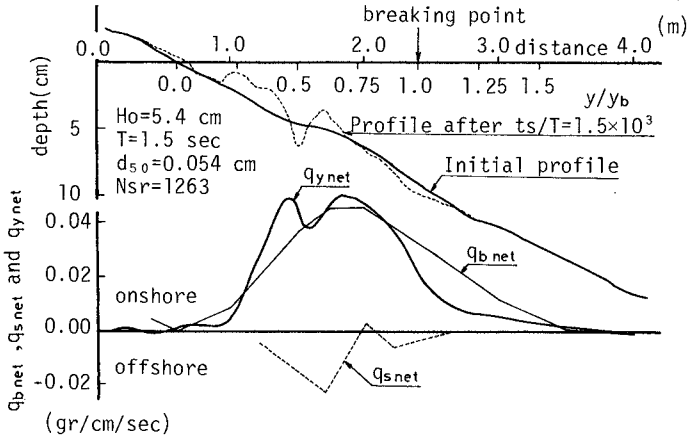


Fig.15 Beach profile and distributions of calculated and measured net on-offshore sediment transport rates ($N_{sr}=1263$)

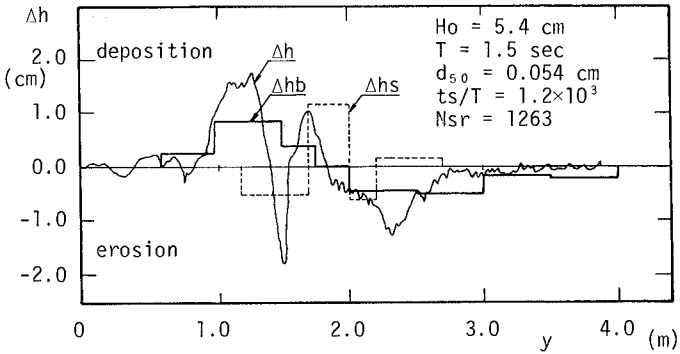


Fig.16 Comparison among Δh , Δh_b and Δh_i ($N_{sr}=1263$)

5. Conclusions

The authors analyzed experimental results about the two-dimensional beach deformation conducted by many investigators to propose the models of net on-offshore sediment transport rate and carried out two-dimensional model beach experiments to examine the relative importance of bed load and suspended load in the beach deformation. Following results are obtained.

- 1) When $N_{sr} = gT d_{50} / 2\pi v > 10^3$, the direction of net sediment transport is onshore (Type III) and when $N_{sr} < 10^3$, net offshore sediment transport is apt to take place (Type I). However, even when $N_{sr} < 10^3$, net onshore sediment transport may spring up near the shore line.
- 2) Net onshore sediment transport decays faster than that of offshore sediment transport. And when $N_s = H_o / T / \sqrt{(\rho_s / \rho - 1)} g d_{50}$ becomes large, net on-offshore sediment transport decays fast regardless of their direction.
- 3) The non-dimensional height of upper limit of beach deformation h_o / H_o increases with increasing $\xi = i / \sqrt{H_o / L_o}$ and N_s . And the non-dimensional depth of lower limit of beach deformation h_m / L_o can be expressed by Eq.(6).
- 4) The maximum net offshore sediment transport takes place in the offshore region and the maximum onshore sediment transport takes place in the surf and swash zones. Time-variation of the maximum sediment transport rate can be approximated by Eq.(1). And its maximum can be expressed by Eqs.(12) and (13).
- 5) When $N_{sr} > 1200$, time-averaged bed load surpasses time-averaged suspended load, and main beach deformation seems to be created by bed load.
- 6) When $N_{sr} < 640$, time-averaged suspended load surpasses time-averaged bed load, and beach deformation seems to be caused by both bed load and suspended load.
- 7) Suspended load becomes equivalent in amount to bed load when $u_* / W_o = 0.8$.

Acknowledgements

The authors gratefully acknowledge Dr. P.Eagleson, the former Associate Professor of Massachusetts Institute of Technology, Dr.B.Glenne the former Instructor of University of Colorado and Dr.J.Dracup, the former Assistant Professor of Oregon State College; Drs.M.Kurihara and K.Shinohara, the former Professors of Kyushu University, Dr.T.Tsubaki, the former Associate Professor of Yamaguchi University and Dr.M.Yoshidaka, the former Associate Professor of Miyazaki University; Dr.K.Hori-kawa, Professor of Tokyo University and Dr.T.Sunamura, the former Research Associate of Tokyo University; Dr.T.Izima and Mr.H.Aono, formerly Port and Harbour Technical Research Institute, Ministry of Transportation, Japan; Drs.R.Rector, T.Saville and G.Watts, formerly U.S.Army Beach Erosion Board; and Mrs.N.Tanaka and O.Shinbo, Port and Harbour Technical Research Institute, Ministry of Transportation, Japan for providing beach profiles for this report.

References

- Battjes, J.A., Surf Similarity, Proc. 14th International Conf. Coastal Engg. pp 466-480, 1974.
- Bowen, A.J., Simple Models of Near Shore Sedimentation ; Beach Profiles and Longshore Bars, Proc. Coastaline of Canada Conf., in press, 1979.
- Dingler, J.R., Wave-formed Ripples in Near Shore Sands, Ph.d. Dissertation, Dept. of Oceanography, University of Carifornia, San Diego, 1975.
- Goda, Y., A Synthesis of Breaker Indices, Proc. of JSCE, No.180, pp 339-350, 1970. (in Japanese)
- Hallermeier, R.J., Calculating a Yearly Limit Depth to the Active Beach Profiles, CERC Ft. Belvoir, Va., Tech. Paper 77-9, 1977.
- Horikawa, K., T. Sunamura and H. Kondo, A Study of Beach Deformation by Wave Action, Proc. 21st Japanese Conf. Coastal Engg. pp 193-199, 1974. (in Japanese)
- Inman, D.L. and A.J. Bowen, Flume Experiment on Sand Transport by Waves and Currents, Proc. 8th International Conf. Coastal Engg. pp 137-150, 1963.
- Madsen, O.S. and W.D. Grant, Quantitative Description of Sand Transport by Waves, Proc. 15th International Conf. Coastal Engg. pp 1093-1112, 1976.
- Nakamura, M., H. Shiraishi and Y. Sakai, Wave Decaying due to Breaking, Proc. 10th International Conf. Coastal Engg. pp 234-253, 1966.
- Rector, R.L., Laboratory Study of Equilibrium Beach Profiles, BEB Washington D.C., TM-41, Aug. 1954.
- Sato, S. and N. Tanaka, Sand Movement due to Wave Action on a Horizontal bed, Proc. 9th Japanese Conf. Coastal Engg. pp 95-100, 1962. (in Japanese)
- Saville, T., Scale Effects in Two Dimensional Beach Study, Proc. 7th IAHR, pp A3-1 - A3-10, 1957.
- Sawaragi, T. and I. Deguchi, Distribution of Sand Transport rate Across a Surf Zone, Proc. 16th International Conf. Coastal Engg. pp 1596-1613, 1978.
- Swart, D.H., A Schematic of On-offshore Transport, Proc. 14th International Conf. Coastal Engg. pp 884-900, 1974.
- Tanaka, N. and O. Shinbo, The Properties of Coal Grains as Bed Material in the Model Beach Experiment on Littoral Drift, Report of the Port and Harbour Research Institute, Ministry of Transport, Vol.12, No.1, pp 3-58, March, 1973. (in Japanese)

FIELD MEASUREMENTS OF SAND MOTION
IN THE SURF ZONE

by

Douglas L. Inman; James A. Zampol; Thomas E. White
Daniel M. Hanes; B. Walton Waldorf; and Kim A. Kastens

Shore Processes Laboratory A-009
Scripps Institution of Oceanography
La Jolla, California 92093

ABSTRACT

Forcing functions and sediment response were measured during two comprehensive surf zone experiments. The experiments included simultaneous measurements of waves and currents, and the movement of sediment as bed and suspended load. The longshore transport of suspended load was found to be about 10 to 20% of the tracer-measured load. Results from tracer measurements of the longshore transport of bed load indicate that previous measurements may have misestimated the effective "tracer layer thickness," and a more rigorous method is proposed.

1. INTRODUCTION

There is extensive competition for the use of nearshore areas for harbors, recreational beaches and swimming, as recipients of thermal and waste discharges, and for coastal construction. Therefore, understanding of sediment transport processes has become essential to coastal technology.

As a consequence, the Nearshore Sediment Transport Study sponsored by the U.S. Office of Sea Grant, NOAA, and funded in part by the Office of Naval Research, has been engaged in extensive field experiments since 1977. The overall objective of the study is the development of improved engineering prediction techniques for sediment transport by waves and currents in the nearshore region. The studies have been conducted jointly by research teams from five universities. The first field experiments were carried out at Torrey Pines Beach near San Diego, California, in March 1977 and November-December 1978 (Gable (ed), 1979; Seymour and Gable, 1980). Additional experiments have recently been conducted near Santa Barbara, California, in February 1980.

The purpose of this paper is to present the results from the two most comprehensive, high energy experiments conducted on 11 March 1977 and 6 December 1978. These experiments included simultaneous measurement of forcing functions (i.e., waves, winds and currents) from sensor arrays in and outside the surf zone, as well as sediment response in terms of bed and suspended load movement.

2. TORREY PINES BEACH SITE

A portion of Torrey Pines Beach in San Diego County, California, was selected as a site for this study. The site is located 5.5 km north of Point La Jolla, and 4 km north of the ocean pier of the Scripps Institution of Oceanography. A 3.0 km segment of this beach that has gently sloping offshore bathymetry and is terminated shoreward by 100 meter high sea cliffs was used for the beach and nearshore measurements (Figure 2-1). This beach satisfied the basic requirements for a straight beach with uncomplicated offshore bathymetry that is exposed to waves from all offshore quadrants. Chamberlain (1960) and State of California (1969) have estimated the net littoral transport in the vicinity of Torrey Pines Beach at about 200,000 m³ per year, to the south.

The study beach undergoes typical seasonal changes in configuration due to changes in wave climate. During summer wave conditions, the beach has a 30 to 60 meter wide backshore, a relatively steep upper foreshore, and a pronounced berm. Winter storm waves overtop the summer berm and erode the backshore, thus reducing the width of the exposed beach. Winter beach profile configuration is typified by a gently sloping beach foreshore that in places extends shoreward to the toe of the sea cliff. The beach profiles for the two experiments are shown in Figure 2-2. Generally the beach face slopes about 1:25, the surf zone 1:75, the section seaward to the 3 meter depth contour 1:35, while that portion from 3 to 10 meters depth slopes 1:50.

The sediments on the beach and shelf are predominantly fine quartz sand with minor amounts of feldspars and heavy minerals. Light minerals, that is those with a specific gravity of less than about 2.85, usually comprise 90% of the sample, while heavy minerals total about 10%. Of the light minerals approximately 88% is quartz, 10% feldspars and 2% shell fragments and miscellaneous material. Of the total heavy minerals hornblende is most plentiful, comprising about 60% (Inman, 1953). The size distributions for typical sediments obtained by grab samplers in the surf zone are listed in Table 2-1.

Table 2-1 Size distribution measures for sieved surf zone samples. Measures are from Inman (1952).

Date	11 March 1977			6 December 1978			
	Measure	Md microns	σ_ϕ	α_ϕ	Md microns	σ_ϕ	α_ϕ
Inner		184	.37	0	152	.43	-.26
Middle		200	.39	+.18	157	.51	-.14
Outer		215	.47	+.17	152	.63	-.23

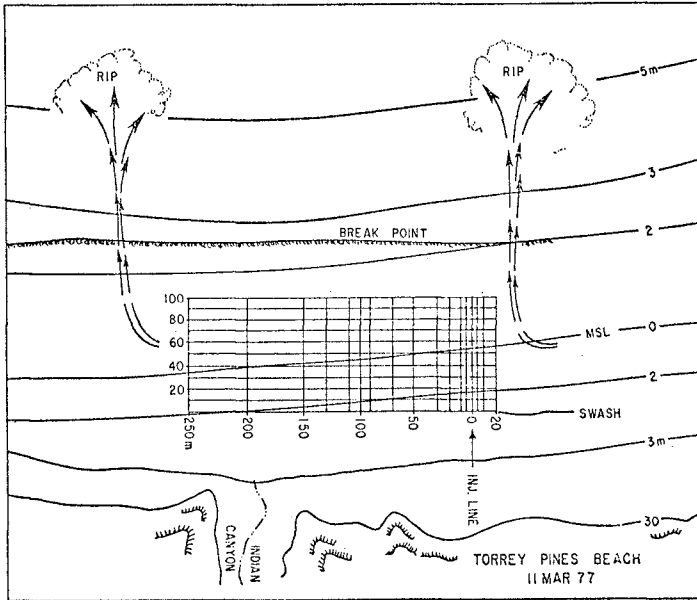


Fig. 2-1 Site and sampling grid for 11 March 1977.

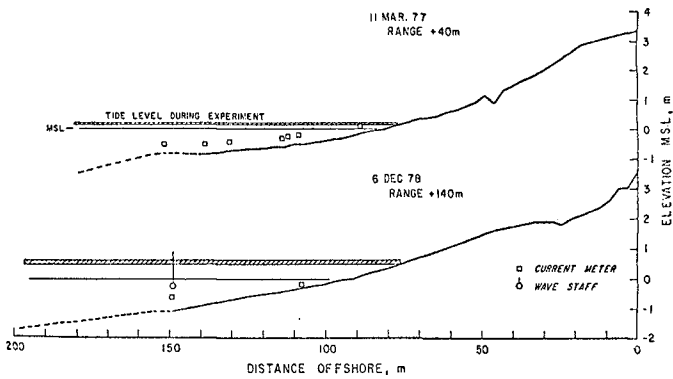


Fig. 2-2 Beach profiles and instrument locations for 11 March 1977 and 6 December 1978.

3. EXPERIMENT CONTROL

The dates and times of our tracer experiments were carefully selected to meet the following criteria: 1) fully operational status for the offshore wave array and other necessary sensors; 2) minimal change in tide elevation during a 3 hour period during daylight; 3) occurrence of dominant waves of sufficient height and breaker angle to generate a strong, unidirectional longshore current; and 4) absence of stationary rip currents across the sampling grid in the study area.

Figure 2-1 shows a stationary rip current pattern with separation between rip currents of 340 meters. In accordance with criterion 4, the injection line and sampling grid were placed within a 250 meter length of beach between rip currents. Reversal of longshore current during experiments resulted in the rejection of many of the experiments conducted on other days.

During the morning of the given day, Rhodamine-B dye was injected at several positions in the surf zone and observed from the cliff above the site. The dye dispersal patterns, such as that illustrated in Figure 4-4 indicated the approximate mean longshore current speed as well as the occurrence of complicating rip currents. If all conditions were satisfied, the injection location and sampling grid were determined appropriate to the current speed and direction, and flags marking the grid ranges were installed on the beach.

4. DRIVING FORCES

It is well known that the principal driving forces for longshore transport of sand in the nearshore waters are waves, currents, winds, and tides, in that order. Since strong winds did not occur during the two experiments described here, and because the experiments were scheduled to coincide with near still-stands in the tidal curve, neither wind nor tidal forces are considered to be important in these experiments. However, the stage of the tide may have some disequilibrium effect on the beach profile, as the water level during experiments was generally above mean sea level in order to cover the surf zone instruments. The tide in these waters is mixed, with a pronounced diurnal inequality. At the Scripps Institution of Oceanography pier the mean and spring tidal ranges are 3.6 and 5.2 feet (1.10 and 1.58 meters), and the mean tidal level is 2.7 feet (0.82 meters) above the datum of mean lower low water. During the experiments of 11 March 1977 and 6 December 1978 the water levels were about 20 cm and 60 cm respectively above mean tide level.

WAVES

The direction and flux of wave energy and momentum were measured from an array of wave pressure sensors placed parallel to shore in a water depth of 9.7 m below mean sea level, hereafter referred to as the 10 meter array. All data from it have been corrected to the actual depth of water at the times of the observations. Also, arrays of electromagnetic current meters, pressure sensors, and wave staffs were placed in and near the surf zone. Details of these near-surf arrays

are given in Guza and Thornton (1978, 1980) and Gable (ed 1979).

The spacings of the offshore line array were in a 1-2-4-5 and a 2-2-2-5 configuration with a unit lag of 33 meters and total array lengths of 396 and 363 meters respectively. The first was used on 11 March 1977 while the latter was used on 6 December 1978. The length of the array was designed for resolution of long period waves with directional peaks separated by 5° to 10° in ten meters of water. Data from the offshore array was telemetered back to the Shore Processes Laboratory of the Scripps Institution of Oceanography using the Shelf and Shore (SAS) system described by Lowe et al (1973).

The wave spectrum consists of the squares of the absolute values of the complex Fourier coefficients, which serve as estimates (having dimensions of length squared) of the energy density in each elemental frequency band. The sum of the energy densities under the spectral peak of the incident waves i.e., the variance, is the mean-square elevation $\langle \eta^2 \rangle$ of the water surface described by the time series. The mean wave energy per unit area of the water surface is given by the product of $\langle \eta^2 \rangle$ and the weight per unit volume ρg of the water,

$$E = \rho g \langle \eta^2 \rangle = \frac{1}{8} \rho g H_{\text{rms}}^2 \quad (4-1)$$

where H_{rms} is the root-mean-square wave height.

The energy spectrum was computed for time runs of about 17 minutes during which pressure was sampled two times per second ($\Delta t = 0.5$ sec), for a total number of data points $n = 2048$, which when transformed give 1024 elemental frequency bands. Energy and cross-spectra were computed from the summation of 8 ($q = 8$) elemental frequency bands, giving a total of 128 merged frequency bands and 16 degrees of freedom. The most important frequency bands were plotted, and examples are shown in Figures 4-1, 2.

Directional spectra were computed for every frequency band using the maximum likelihood estimator described by Capon (1969) and Davis and Regier (1977). Important frequency bands with high energy peaks were graphed, and examples are shown in the lower part of Figures 4-1, 2.

There is in general a flux of energy in the direction of wave propagation, which in the absence of refraction and dissipation is a constant per unit width of wave crest

$$ECn = \left[ECn \right]_{\infty} = \text{const} \quad (4-2)$$

where E is defined in relation (4-1), C is the wave phase velocity, and Cn is the wave group velocity.

Waves also transport momentum which is a tensor quantity consisting

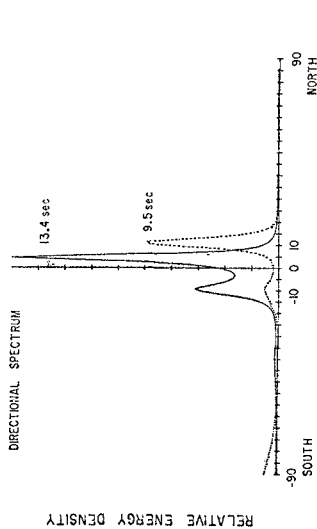
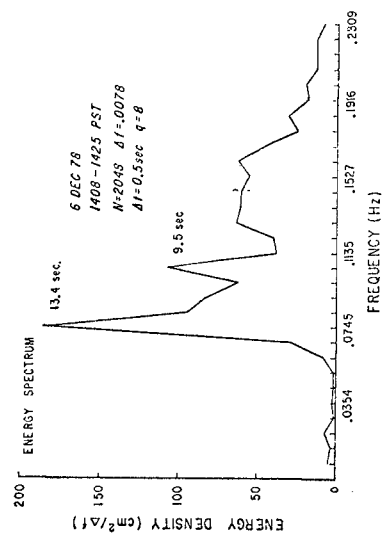


Fig. 4-2 Examples of wave energy and directional spectra for 6 December 1978.

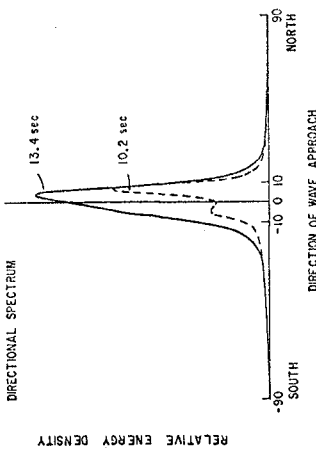
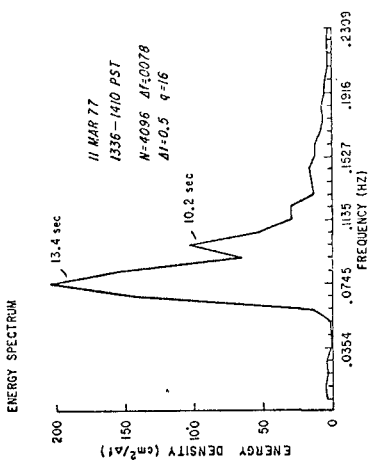


Fig. 4-1 Examples of wave energy and directional spectra for 11 March 1977.

of four components. The onshore flux of y -directed momentum S_{yx} has been shown to drive the longshore currents inside the surf zone (Bowen, 1969; Longuet-Higgins, 1972). Outside the surf zone S_{yx} is conserved, and is given by the relation

$$S_{yx} = En \cos \alpha \sin \alpha = (En \cos \alpha \sin \alpha)_0 = \text{const} \quad (4-3)$$

S_{yx} is obtained by integrating the energy, E , in the directional spectra with respect to $\cos \alpha \sin \alpha$ to obtain relation (4-3) for each 17-minute run.

The wave energy at the breakpoint was obtained by refracting each frequency band to an estimated breaker depth using Snell's law and relation (4-2). The actual breaker depth was then computed by combining equation (4-1) relating energy and wave height with the criterion for a breaking solitary wave, $\gamma_b = (H/h)_b = 0.78$ (Munk, 1949), and then recomputing the energy at the breakpoint, where h is the depth of water.

Wave heights at the breakpoint depth were then computed using equation (4-1); the radiation stress, S_{yx} , from equation (4-3). The phase velocities at the breaker depth were computed from the Boussinesq dispersion relation (Whitham, 1974, p. 462):

$$c_b^2 = \frac{9h_b}{1 + \frac{1}{3}(kh)_b^2} \quad (4-4)$$

It was then possible to estimate the power expended by the waves, $(CS_{yx})_b$, which has been related to the sand transport rate (Figure 6-1). Measured and computed wave parameters are summarized in Table 4-1.

Table 4-1. Forcing Functions

h (m)	11 March 77		6 December 78	
	Array 9.3 m	Breakpoint $h_b = 1.43\text{m}$	Array 6.0 m	Breakpoint $h_b = 1.65\text{m}$
α	Range	2.9-4.1	3.5-8.0	2.0-5.8
(degrees)	Mean	3.4	5.4	3.4
C	9.1-9.3	3.7-4.6	7.40-7.54	3.2-4.0
(m/sec)	9.2	3.9	7.5	3.6
C_n	8.5-8.7	3.7-4.6	6.90-7.03	3.2-4.0
(m/sec)	8.6	3.9	7.0	3.6
H (m)	0.67-0.83	0.99-1.19	0.91-0.97	1.26-2.70
	0.78	1.12	0.94	1.29
E	555-853	1198-1725	1008-1186	2089-2768
($\frac{\text{joules}}{\text{m}^2}$)	742	1529	1090	2483
S_{yx}	67.0-95.4	78.7-119.3	81.9-129.6	90.7-159.0
($\frac{\text{joules}}{\text{m}^2}$)	72.1	90.5	95.3	147.0
CS_{yx}	624-868	291-537	617-976	290-636
($\frac{\text{watts}}{\text{m}}$)	663	353	715	529

CURRENTS

The general circulation of water in the surf zone, although complex, appears to follow patterns shown schematically in Figure 4-3. Early measurements showed that outside the surf zone, and between rip currents, water tended to move onshore from surface to bottom (Shepard and Inman, 1950). However, inside the surf zone, surface, mid-depth, and bottom waters have different net directions: the surface water moves onshore and longshore and has the greatest speed; the mid-depth water moves on-offshore with a net longshore motion; while the bottom water has a very slow net offshore motion, even though the highest velocities during the passage of a bore are decidedly onshore. There is also an upward circulation associated with the passage of the breaking wave and its bore (Inman and Quinn, 1952; Inman and Nasu, 1956; Inman et al, 1971).

Surf zone currents in these studies were measured by three separate methods: 1) dye injection into the water; 2) weighted drift bottles; and, 3) electromagnetic current meters mounted at mid-depths in the surf zone. The first method gives a pattern of water motion and was particularly effective in locating rip currents (Figures 4-4). Drift bottles give Lagrangian trajectories which can be plotted as current velocities representative of the upper layers of the surf zone. The current meters give continuous measures of values of x-y current components, and are most representative of the mid-depth motion of the surf zone (Figures 4-5, 6). They are more fully described by Guza and Thornton (1978).

5. SEDIMENT RESPONSE

The sediment response to the action of waves and currents is complex and not understood. For our purposes we will group these complex motions into bed and suspended load components. Bed load is arbitrarily defined as sand transported on and within 10 cm of the bed; while

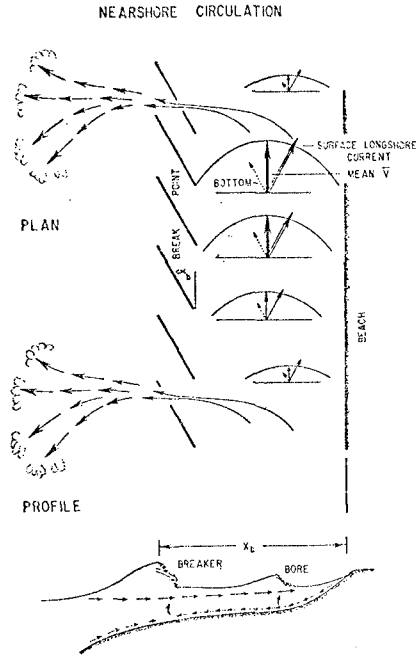


Fig. 4-3 Schematic of surf zone circulation.

DYE DISPERSION IN THE SURF ZONE
6 DEC 78

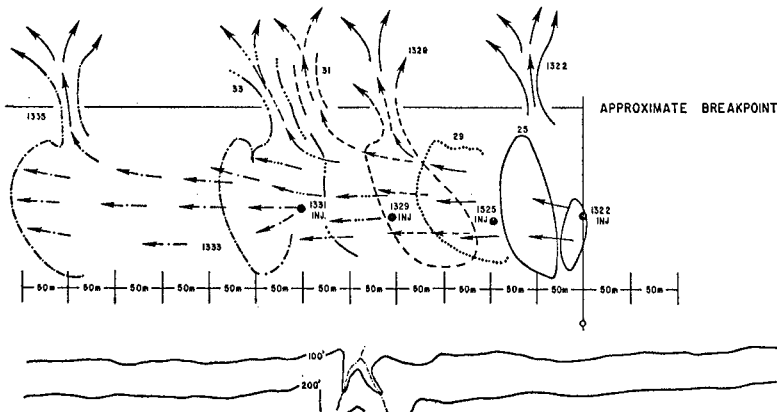


Fig. 4-4 Dye pattern from 13:22 injection.

suspended load is that transported in the water column from 10 cm to the water surface. This definition is used because our present suspended load samplers do not function properly when operated closer to the bed than 10 cm.

TRACER TECHNIQUE FOR BED LOAD

The only known means of estimating the "instantaneous" bed load transport in the field is by tagging the sand in some detectable manner and injecting the tracer into the surf zone (e.g., Inman and Chamberlain, 1959). More recently, fluorescent dyed sand grains have been used as tracers by several investigators (Aibulatov, 1961; Ingle, 1966; Komar and Inman, 1970) to study the motion of sand in the nearshore environment. The longshore transport of sand has been estimated by multiplying the rate of advection of sand tracer by the depth in the bed to which the sand tracer mixes (Inman, et al, 1968; Komar and Inman, 1970).

If sand motion consisted of uniform advection, then a line source of tracer sand placed across the surf zone would move at a velocity calculatable directly by sampling the bed at the proper time and distance following injection. However, granular diffusion in the bedload transport, turbulent diffusion in suspended load transport, and non-uniform advection tend to disperse as well as advect the original distribution of tracer. In view of these processes, a concentration-weighted mean velocity must be calculated in order to estimate the true advection rate of tracer and its admixed sand aggregate.

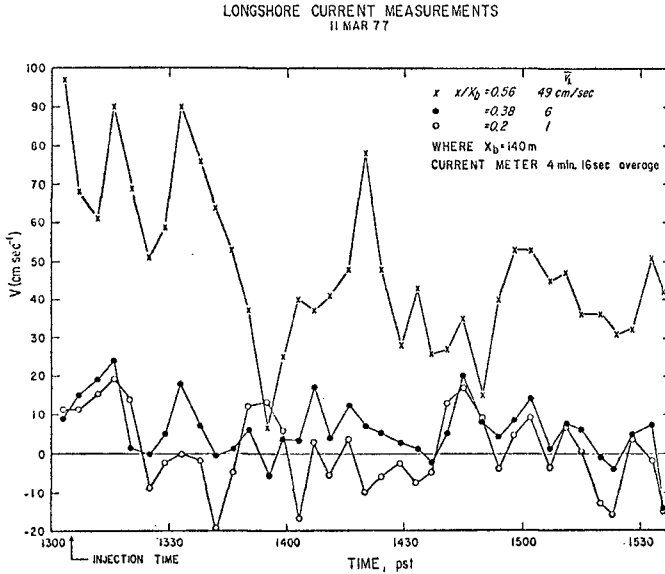


Fig. 4-5 Longshore currents from current meter array for 11 March 1977.

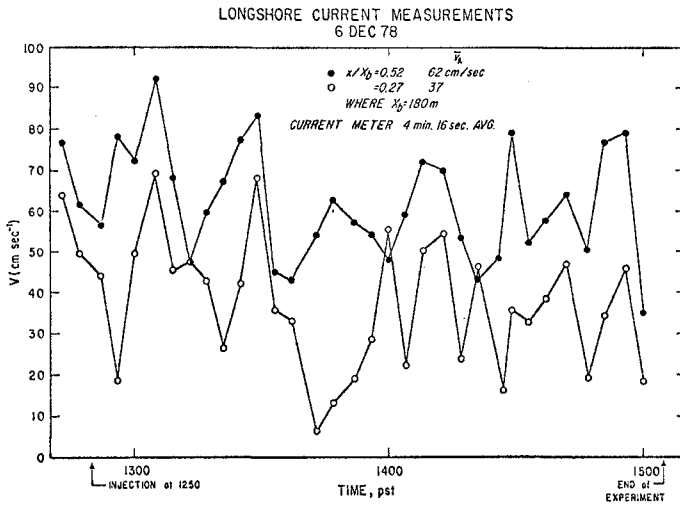


Fig. 4-6 Longshore currents from current meter array for 6 December 1978.

The tracer grain distribution was sampled following injection by two independent methods. The first method uses traditional "grab samplers" designed to sample the upper 2 cm of the sand bed, with the objective of surveying downcurrent as rapidly as possible to give a synoptic areal view of the tracer distribution at a given time. This method is referred to as "spacial sampling." The second method uses specially designed coring devices to repeatedly core the bottom along a fixed on-offshore range, downstream from the injection line and at constant intervals of time, and is analogous to sampling a dye plume in a river as it flows under a bridge. This method is called "temporal sampling." Each sample provides an estimate of the rate of advection. If a sample i is taken y_i meters from the injection line at an elapsed time t_i seconds after injection, then the sand velocity is given by $V_i = y_i/t_i$. If N_i is the tracer concentration of the sample, then a concentration weighted mean advection rate for sand in the longshore direction is given by

$$\bar{V}_L = \frac{\sum_{i=1}^n \left[N \frac{y}{t} \right]_i}{\sum_{i=1}^n N_i} \quad (5-1)$$

where n is the total number of samples. This definition of the advection rate V is also time weighted, thus freeing the transport calculation from bias introduced because all of the spacial samples cannot be taken at the same time. Spacial and temporal sampling concepts are shown schematically in Figure 5-1.

Tracer Layer Thickness

The vertical distribution of tracer in the cores was examined to determine the "tracer layer thickness," one of the most uncertain parameters in previous studies (Komar and Inman, 1970). Ideally the measured thickness is one which predicts the actual transport rate when multiplied by the advection rate and surf width. However, the determination of the tracer layer thickness from the core data has been highly subjective. In an effort to remove some of the subjectivity, we have chosen a concentration weighted depth to represent the "tracer layer thickness" Z_0 , defined as

$$Z_0 = 2 \frac{\int_{z=0}^{\lambda} N(z) z dz}{\int_{z=0}^{\lambda} N(z) dz} \quad (5-2)$$

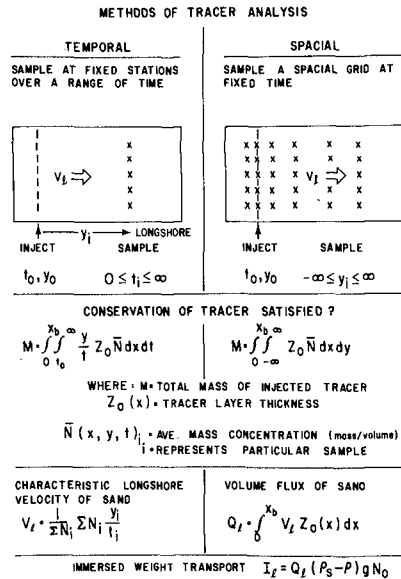


Fig. 5-1

where z is the depth in the bed, $N(z)$ is the tracer concentration at depth z , and λ is a depth in the bed greater than any tracer penetrates. It has been assumed here that the surface of the bed ($z = 0$) is fixed, with no erosion or accretion occurring. We realize that this definition is itself highly subjective, but it is an effort towards standardizing the determination of the tracer layer thickness. It is to be noted that the actual value of Z_0 can be greater than the measured value, and the velocity V_0 must grade from a maximum at the surface to zero at the bottom of the layer.

The longshore series of cores taken with the center grab sample on 11 March 1977 were analyzed for tracer layer thickness Z_0 using several systems including relation (5-2), and the results are plotted in Figure 5-2. The upper curve showing maximum thickness of tracer penetration more closely approximates the thickness used in previous studies (Komar and Inman, 1970); while the lower curve represents a more conservative cut-off thickness where the tracer concentration is 1 grain/gm or less.

BED LOAD TRANSPORT

The product of the tracer layer thickness Z_0 , the advection rate of sand and tracer V_0 , and the surf zone width X_b , results in an estimate of the longshore bed load sediment transport rate. This procedure is schematically depicted in Figure 5-1.

Tracer injections and bed load sampling

Tracer injections and bed load sampling were made on 11 March 1977 and 6 December 1978. On 11 March 1977, since only spacial sampling was attempted, a grid of $10 \times 18 = 180$ grab samples were recovered and 21 core samples. The grid is shown in Figure 2-1 and the contours of tracer concentration in Figure 5-3. On December 1978 two spacial and a temporal sampling were made, and the results are shown in Figure 5-4, 5. This procedure permits three independent estimates of transport, but with the same number of personnel, necessarily results in fewer samples per run.

The tracer layer thickness Z_0 as a function of surf zone width for both days is plotted in Figure 5-6. It is apparent that Z_0 is greatest in the swash zone and least in the central portion of the surf zone, and again increases towards the breakpoint. Separate investigation, not reported here, confirms this bimodal distribution of Z_0 , i.e., minimum values in the center of the surf zone. This bimodality was used to estimate transport rates near the breakpoint on these high energy days where breakpoint samples were not obtained.

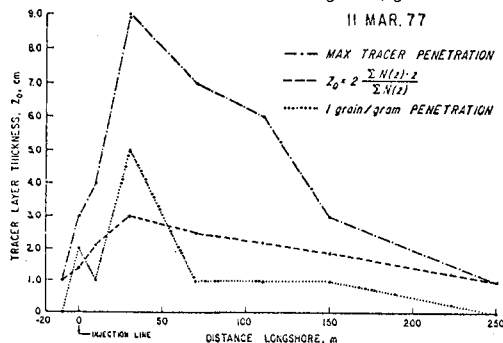


Fig. 5-2 Longshore variation of Z_0

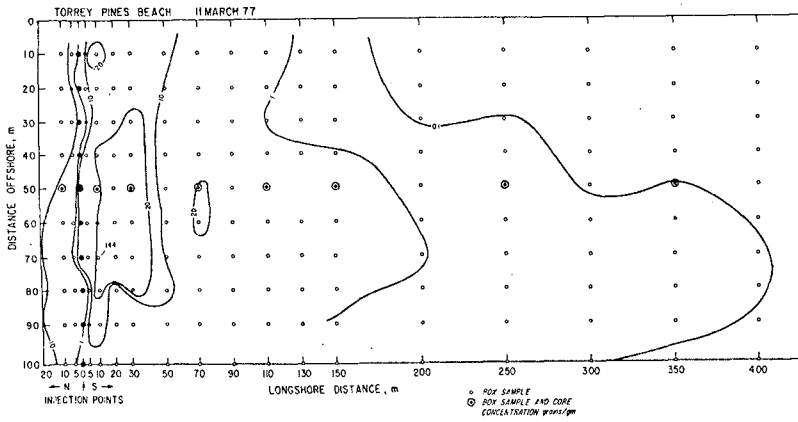


Fig. 5-3 Distribution of grab sample tracer concentrations on 11 March 77.

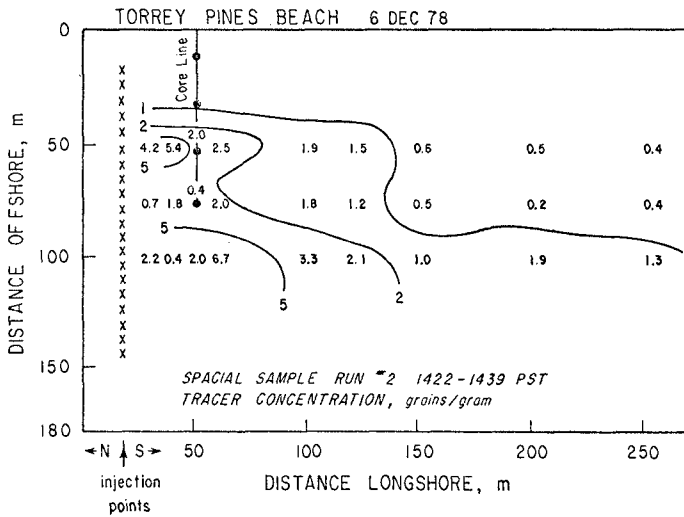


Fig. 5-4 Distribution of grab sample tracer concentrations on 6 December 78.

Three types of estimates for the transport rate were made in order to demonstrate the effect of the conceptual models in the interpretation of field data. The first estimate used the tracer layer thickness, Z_0 , as defined in eq. 5-2 and assigned the mid-surf value of Z_0 to the unsampled outer portion of the surf zone. The second estimate extrapolated the tracer layer thickness to the unsampled portion of the surf-zone using a bimodal distribution as described above. The final estimate equated Z_0 to the maximum thickness of tracer penetration and applied a bimodal distribution for the tracer layer thickness.

The percent recovery of tracer was calculated for both spacial and temporal methods. For the spacial method, each sample yields an estimate for the total amount of tracer in the region from which it was taken. These estimates can be summed over the experimental grid and compared with the known quantity of tracer injected over the same area. For the temporal method, the amount of tracer which advected across the sampling line is estimated, and compared to the amount of tracer injected in that portion of the surf zone covered by the temporal sampling line.

Table 5-1. Sediment Response

	11 March 77	6 December 78		
		Spacial		Temporal
		Run #1	Run #2	
Sampling Start (min. after inj.)	85	41	92	15
Sampling End (min. after inj.)	170	71	109	135
Tracer Recovery (%)	65	39	77	48
Immersed Wt. Longshore Transport Rate, I_b (nt/sec)				
1) Initial Estimate & Eq. 5-2	92	142	167	285
2) Bimodal Z_0 & Eq. 5-2	150	179	211	359
3) Max. Tracer Penetration & Bimodal Distribution	474	240	283	481
Suspended Load (nt/sec)				
Under Crest	34		60	
Average	23		33	
Tracer Amount Injected (kg)	113		90.7	
Surf Zone Width (m)				
Range	125-150		150-200	
Significant X_b	140		180	

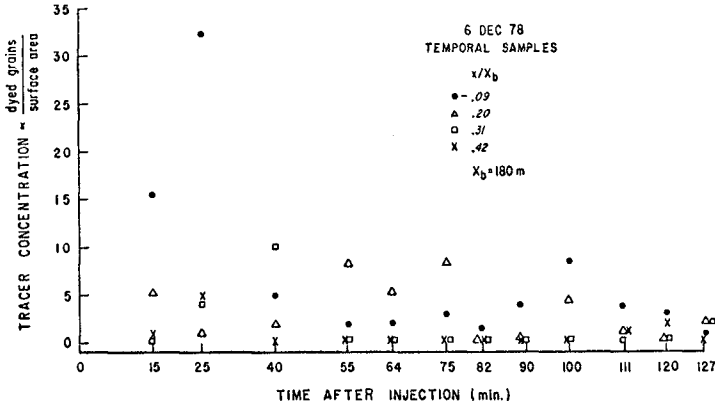


Fig. 5-5 Variation of core line tracer concentration with time after injection.

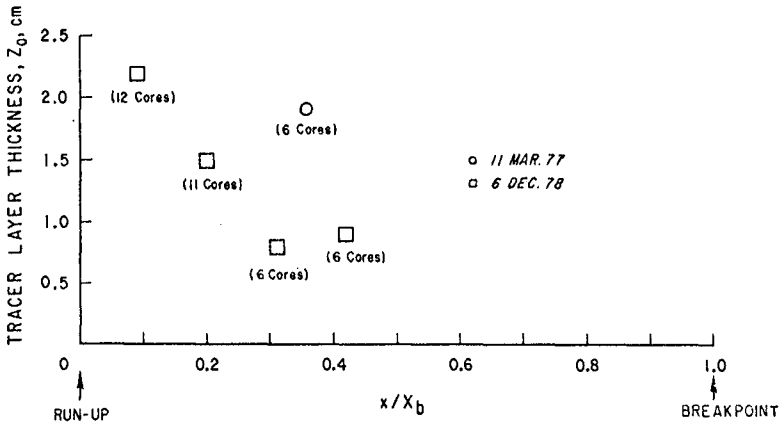


Fig. 5-6 On-offshore variation of tracer layer thickness (Z_0).

SUSPENDED LOAD

Suspended sediment samples were collected on 11 March 1977 and 6 December 1978 during the period between tracer sand injection and the start of grab sampling. The 11 March 1977 samples were collected at the offshore positions shown in Figure 5-7. Six sample series were collected below the crest of the bore, five series between bores, and five just before passage of the bore. On 11 March 1977 samples were taken where bore heights ranged from 30 cm to 102 cm. The breaker type on 11 March 1977 ranged from spilling to plunging, with some strongly plunging.

During the 6 December 1978 experiment suspended sediments were collected at four stations from under the passing crest of the bore. Because of high plunging breakers, these samples did not extend beyond the inner surf zone (Figure 5-8). Samples were collected under bores ranging in height from 49 to 72 cm on that day, with a total range of heights during the November-December 1978 experiments of 15 to 131 cm.

The suspended load was integrated over depth to give the suspended load in grams over a square meter of bed. The product of this load and the average longshore current was then assumed to give an estimate of the suspended load transport rate for that portion of the surf zone. These estimates, when integrated across the surf zone, give the estimates of total suspended load transport rate. The 11 March 1977 experiment provides data on the variation of suspension over a wave cycle. On this day the average suspended load over a wave was used to estimate the total suspended load transport rate. The 6 December 1978 rates were corrected using information from the 11 March 1977 experiment. The total suspended load transport rates are listed in Table 5-1.

FIELD AND LABORATORY PROCEDURES

The tracer experiment used natural Torrey Pines Beach sand dyed with either Florescein (green) or Rhodamine (red) dye. Plastic bags of wetted tracer sand were placed on the sand bed along the injection range to approximate a line source of tracer across the surf zone; then each bag was emptied simultaneously at the time of injection.

The grab samples were collected using a hand-held, scissors type, box grab sampler with the sample volume of 7.5 x 12.5 and 2.1 cm deep. The samples were transferred to plastic bags and labeled with date and grid location. Grab and core samplers were designed for both simplicity of operation in the surf zone and for recovery of sediment cores with undisturbed vertical structure, described in Waldorf and Zampol (in prep).

In the period between injection of tracer and grab sampling, the suspended load was sampled at a number of points across the surf zone. At each sample location a vertical series of 3 or 4 suspended load samples were taken using a "water-coring device" (Waldorf and Zampol, in prep). The swash was sampled with a mechanically closed "plastic bag" sampler.

After fresh water rinsing and drying, 10 gram sub-samples from each grab sample were spread to a single grain layer thickness on a counting grid. The fluorescent tracer grains in the sample were counted using a long-wave ultraviolet light in a completely darkened room. Using these techniques, tracer concentrations as low as 100 grains/kg are measured.

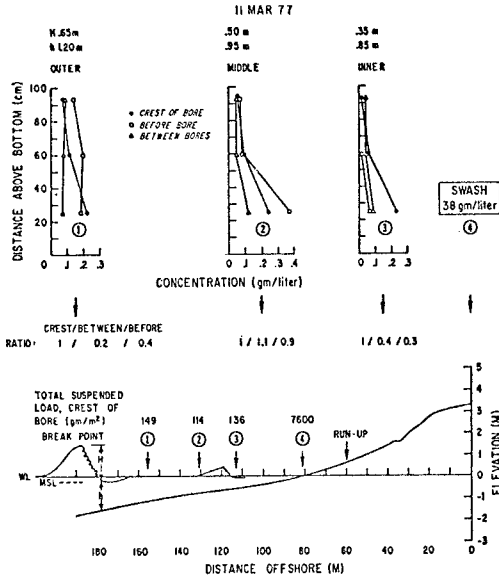


Fig. 5-7 Representative suspended load, profiles, and sampling locations for 11 March 77.

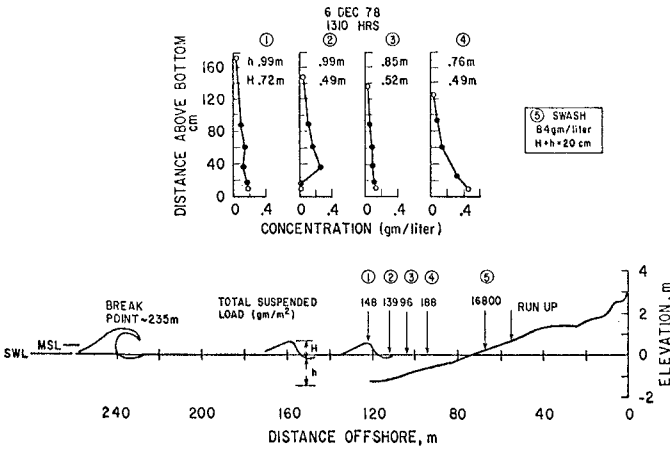


Fig. 5-8 Representative suspended load, profiles, and sampling locations for 6 December 78.

6. DISCUSSION

The bed and suspended load measurements presented here were made under the most intensely monitored forcing conditions yet reported for moderately high energy, dissipative beaches (gentle slope, wide surf zone). As a consequence more surf zone variables and their ranges are known than for previous field investigations. The measurements also showed some trends suggesting that previous simplistic models and methods of calculation should be revised.

FORCING FUNCTIONS

The surf zone width X_b varies with breaker height and type, and a rigorous definition is not generally possible. However, the old concept of a "significant surf zone width" determined by the average of the one-third highest breakers seems appropriate from the standpoint of energy and momentum fluxes.

The complex nature of the longshore and the on-offshore currents was clearly demonstrated by the three methods of current measurement employed, and portrayed schematically in Figure 4-3. The strongest currents were always near the midpoint of the surf zone, and no dyed water passed seaward of the breakpoint except in rip currents. Rip currents may be stationary (Figure 2-1), or may progress down current through the experiment area as in Figure 4-5. The effect of rip currents on the overall transport is not known, but must be considered as an important mechanism in the overall transport processes.

SEDIMENT RESPONSE

The on-offshore bimodality of the tracer layer thickness Z_0 was an unexpected finding, and clearly emphasizes the shortcoming of basing transport estimates on limited core information. The concepts of "tracer layer thickness" are of sufficient importance to merit much of the discussion in Section 5, and resulted in the definition given in relation (5-2). The differences between this definition and others is shown graphically by Figure 5-2. The upper curve of maximum tracer penetration more closely approximates the value of tracer layer thickness used previously by Inman et al (1968) and Komar and Inman (1970). Since the interpretation of sand tracer data depends upon the conceptual models of the processes involved, we have interpreted the data in accordance with several models in order to demonstrate the ranges in sand transport rates to be expected. For purposes of comparison, transport estimates are plotted together with the previous data of Komar and Inman (1970) in Figure 6-1.

The difference in transport rates between the spacial and temporal sampling on 6 December 1978 is not clear. However, the persistence of rip currents moving through the sampling grid (Figure 4-5) suggest tracer was lost offshore. This effect would be more pronounced in the spacial sampling which is sensitive to the entire grid length, than to the temporal sampling which was relatively close to the injection point (Figure 5-4). If this is the cause for the different transport rates, then the temporal sampling is the more accurate value.

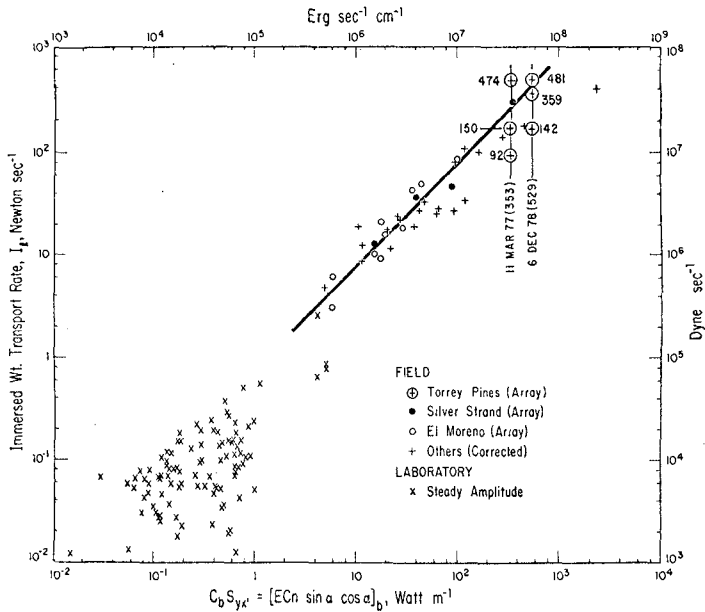


Fig. 6-1 Wave power vs. sediment transport rate (after Komar and Inman, 1970). Ranges of values for 11 March 77 and 6 December 78 are indicated.

Suspended load measurements emphasized the complex nature of suspension processes and demonstrate the need for continuous monitoring sensors vs. the discrete type samplers employed here. Even so, these data show the importance of the changes in concentration as a function of the phase of the bore. Other data taken during the 1977-78 period by this laboratory indicate the importance of the type of breaking wave. Plunging waves suspend much more sediment than spilling waves, especially near the breakpoint. There also appears to be a bimodal distribution of suspension, with maxima in the swash zone and near the breakpoint. The ratio of suspended transport rate to tracer-determined transport rate is 10 to 20% on 11 March 1977 and 6 December 1978. Thus, a comprehensive model of longshore transport as well as on-offshore transport will need to incorporate suspended load as a fundamental component of the total load.

REFERENCES

- Aibulatov, N.A., 1961, "Quelques données sur le transfert des sédiments sableux le long d'un littoral, obtenues à l'aide de luminophores," *Cahiers Oceanog.*, 13:292-300.
- Bowen, A.J., 1969, "The generation of longshore currents on a plane beach," *Jour. of Marine Research*, 27, 2:125-206.

- Capon, J., 1969, "High resolution frequency-wavenumber spectrum analysis," Proc. IEEE, 57:1408-1418.
- Chamberlain, T.K., 1960, "Mechanics of mass sediment transport in Scripps Submarine Canyon," Ph.D. thesis, Univ. of Calif., San Diego, 200 pp.
- Oavis, R.E. and L.A. Regier, 1977, "Methods for estimating wave spectra," Jour. of Marine Research, 35, 3:454-477.
- Gable, C.G., 1979, "Report on data from the Nearshore Sediment Transport Study experiment at Torrey Pines Beach, Calif., November-December 1978," Institute of Marine Resources, IMR Reference No. 79-8.
- Guza, R.T. and E.B. Thornton, 1978, "Variability of longshore currents," Proc. 16th Coastal Eng. Conf., Amer. Soc. Civil Eng., 756-775.
- _____, 1980, "Local and shoaled comparisons of sea surface elevations, pressures and velocities," Jour. Geophys. Res., 85, C3:1524-30.
- Ingle, J.C., Jr., 1966, "The movement of beach sand," Developments in Sedimentology, 5, Elsevier Publ. Co., New York, 221 pp.
- Inman, O.L., 1952, "Measures for describing the size distribution of sediments," Jour. Sed. Pet., 22:125-145.
- _____, and T.K. Chamberlain, 1959, "Tracing beach sand movement with irradiated quartz," Jour. Geophys. Res., 64, 41-47.
- _____, P.O. Komar and A.J. Bowen, 1968, "Longshore transport of sand," Proc. 11th Coastal Eng. Conf., Amer. Soc. of Civil Eng., 1:298-306.
- _____, and N. Nasu, 1956, "Orbital velocity associated with wave action near the breaker zone," Beach Erosion Board, Tech Memo 79,72 pp.
- _____, and W.H. Quinn, 1952, "Currents in the surf zone," Proc. 2nd Coastal Eng. Conf., Council on Wave Research, Univ. of Cal., 24-36.
- _____, R.J. Tait and C.E. Nordstrom, 1971, "Mixing in the surf zone," Jour. Geophys. Res., 76, 15:3493-3514.
- Komar, P.D. and D.L. Inman, 1970, "Longshore sand transport on beaches," Jour. Geophys. Res., 75, 30:5914-27.
- Longuet-Higgins, M.S., 1972, "Recent progress in the study of longshore currents," Waves on Beaches and Resulting Sediment Transport, Academic Press, New York and London, 203-248.
- Lowe, R.L., O.L. Inman and B.M. Brush, 1973, "Simultaneous data system for instrumenting the shelf," Proc. 13th Coastal Eng. Conf., Amer. Soc. of Civil Eng., 95-112.
- Munk, W.H., 1949, "The solitary wave theory and its application to surf problems," Ann. N.Y. Acad. Sci., 51:376-424.
- Seymour, R.J. and C.G. Gable, 1980, "Nearshore Sediment Transport Study Experiments," Proc. 17th Coastal Eng. Conf., Amer. Soc. of Civil Engrs., in press.
- Shepard, F.P. and O.L. Inman, "Nearshore water circulation related to bottom topography and wave refraction," Trans., Amer. Geophys. Union, 31, 2:196-212.
- State of Calif., 1969, "Interim Report on Study of Beach Nourishment Along the Southern Calif. Coastline," Dept. of Water Resources, Southern District, Sacramento, Calif.
- Whitham, G.B., 1974, Linear and Nonlinear Waves, John Wiley and Sons, New York, 636 pp.

AN APPROACH TO UNDERSTANDING COASTAL PROCESSES

A.D. Gordon, B.E., M. Eng. Sc., Engineer Coastal Process Investigation Section, N.S.W. Department of Public Works, Coastal Engineering Branch, Sydney, Australia.

D.B. Lord, B.E., Engineer Coastal Process Investigation Section, N.S.W. Department of Public Works, Coastal Engineering Branch, Sydney, Australia.

ABSTRACT

The approach adopted in N.S.W. for investigating coastal processes leading to development of a numero-descriptive model for management purposes is outlined. The technique involves the formation of a regional coastal model and its adaptation to site specific cases. This site specific conceptual model is then tested and modified on the basis of theoretical calculation and field data collection. Two specific case histories are outlined.

1. INTRODUCTION

With increasing pressure for development of the coastal zone, a growing community awareness of the nearshore environment, and the harsh economic realities of man's attempts to do battle with the sea, there has been a rapidly growing need for greater understanding of coastal process systems. Both planning and environmental impact requirements have necessitated the development of regional coastal process models to facilitate the assessment of factors which pattern the coastline.

It is desirable that such models be based on rigorous analytical solutions of mathematically described mechanisms. However, both the complex nature of coastal processes, and the recency of scientific endeavour in this field, have resulted in simplifying assumptions and empirically derived relationships being substituted for the more rigorous approach so that pressing problems may be attacked within an acceptable time frame.

In developing coastal models which can describe the historical coastal formation, determine present beach response and predict future trends, an accounting type philosophy has been adopted. "Sediment Budgeting", an expression of the conservation of mass principle, provides a useful framework within which a variety of techniques may be used to determine the coastal processes of a particular region. One further advantage offered by the flexibility of this budget philosophy is that the degree of sophistication to which mechanisms are described and calculations executed, can be tailored to the requirements of a particular study.

2. COASTAL PROCESS ANALYSIS

Two types of coastal process models have been developed for the New South Wales coastline; the criteria for categorisation being that of time scales.

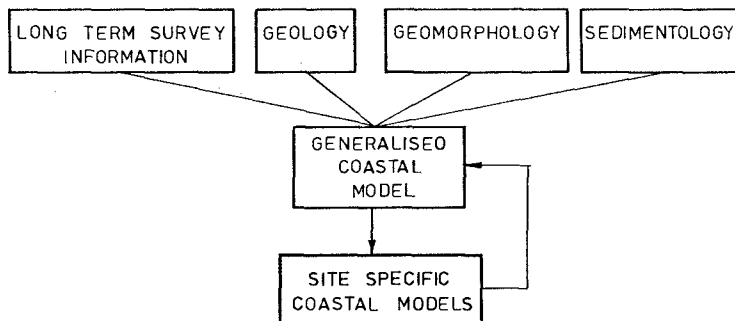
- (i) Engineering/planning time scale (1-100 years)
- (ii) Geological time scale (100 + years).

While it is recognised that far shorter time scales must be employed when considering specific mechanisms of the coastal processes within the sediment budget, it is argued that for the purpose of engineering/planning and environmental impact analyses, the time scales nominated above are most appropriate for model development.

Both the engineering time scale model (site specific), and the geological time scale model (generalised coastal), are developmental; each supplementing and complementing the other.

The remainder of this paper will be devoted to:

- . Outlining the generalised N.S.W. coastal model and demonstrating its relevance.
- . A documentation of the methodology used in developing site specific models and illustration of the strengths and shortcomings of the approaches and techniques employed.



GENERALISED COASTAL MODEL

FIG. 1.

3. GENERALISED COASTAL MODEL

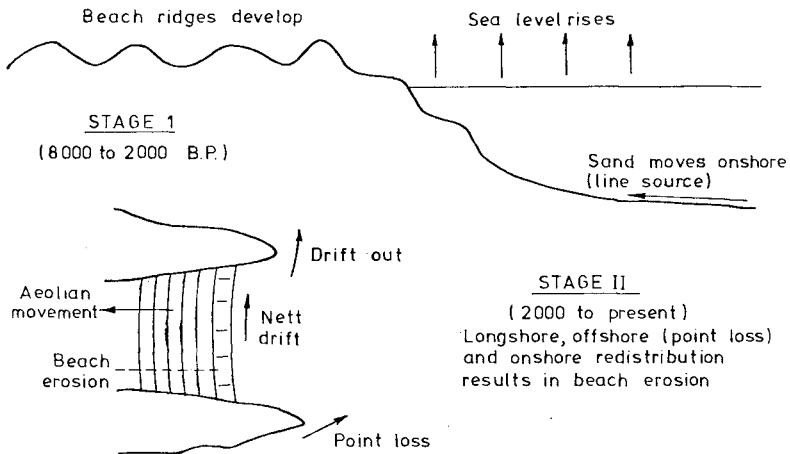
This is an overall coastal model which explains the historic development of the observed present day coastal features and is invaluable basic information for any site specific engineering study.

The methodology adopted in formulating the generalised coastal model is shown in Figure 1. In simplistic terms the resulting model for the New South Wales coastline can be presented as follows:

Three major natural factors have contributed to the present day coastal morphology.

- (i) Bedrock outcrops and sediment deposits which pre-date the Holocene sea level rise.
- (ii) The onshore movement of sand which accompanied the Holocene sea level rise.
- (iii) The alongshore and onshore/offshore re-working of coastal deposits by wind wave and current action.

While the contribution of the first factor may be obvious, the subtle inter-relationship of the other two is not so obvious. It is however essential that an understanding of this inter-relationship be developed in order that an apparent existing anomaly may be explained.



GENERALISED COASTAL DEVELOPMENT MODEL

FIG. 2.

Thom et. al. (1978) have shown at many locations along the N.S.W. coastline, that the development of beach ridges and barrier deposits followed the Holocene sea level rise and still stand (ref. Figure 2).

These accretionary features have resulted from the onshore movement of sand in response to the "new" sea level condition. Radio carbon dating carried out by Thom on N.S.W. beach ridge plains indicates that they were formed during the period approximately 8,000-2,000 years B.P. A decreasing rate of ridge formation is evident with time. Little evidence exists past 2,000-1,500 years B.P. of any general coastal accretion and in fact the reverse, a state of beach recession is now apparent on a majority of N.S.W. beaches. Hence an anomaly exists - coastal accretion having occurred approximately 8,000-2,000 years B.P., coastal erosion 2,000 years B.P. to the present.

Competing theories have been advanced to explain this apparent reversal in shoreline behaviour. The first is that there has been a major shift in weather patterns. The second theory which is favoured by the authors is that while longshore and aeolian redistribution mechanisms have operated throughout the 6,000 year still stand, during the period up until 2,000 years B.P., the onshore movement of sand dominated coastal development. The diminishing quantities of onshore moving sediment in the period 6,000-2,000 years B.P. reflected the decreasing availability of sand in the offshore region. By approximately 2,000 years B.P. the offshore source had been depleted to such an extent that longshore redistribution due to wave obliquity and onshore movement of sediments under aeolian processes dominated. In coastal compartments where longshore redistribution is possible, and the sediment losses to the compartment due to this redistribution exceed the onshore supply, a state of beach erosion exists.

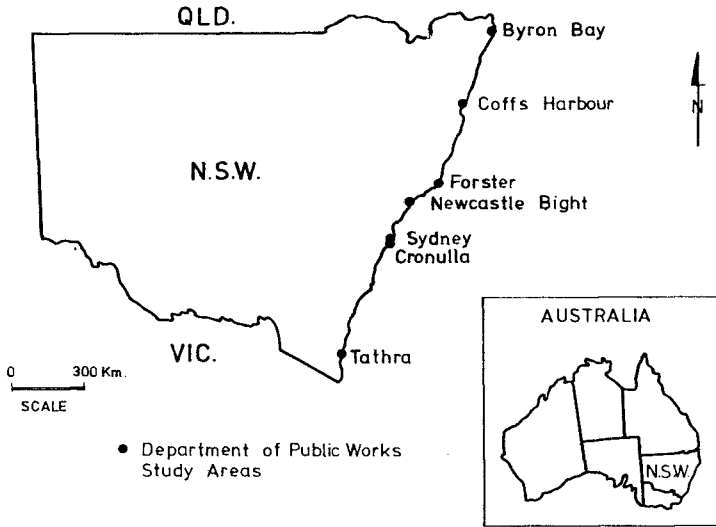
Thus the generalised coastal model predicts that at the present time, where there is no new source of suitable sediments, the beaches will be:

- (i) In a state of dynamic equilibrium where no longshore or aeolian losses occur.
- (ii) Undergoing long term erosion where either aeolian and/or longshore losses occur.

4. SITE SPECIFIC MODELS

Site specific models have been developed at a number of locations on the New South Wales coast (ref. Figure 3). While the aims of individual investigations may vary, the underlying philosophy of analysis adopted in each case is the sediment budget approach. Further, the application of this approach has taken a particular form:

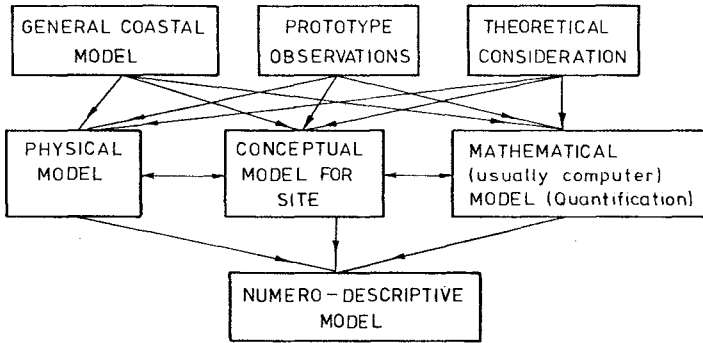
- . Development of a conceptual model.
- . Quantification of that model.
- . Formulation of a numero-descriptive (predictive) model.



LOCATION OF STUDY SITES

FIG. 3

An outline of this methodology is shown in Figure 4.



SITE SPECIFIC MODEL

FIG. 4

Boundary determination precedes model development. The onshore boundaries are usually obtained from morphological considerations while longshore boundaries are based on geomorphological criteria. Offshore boundary delineation is more complex as it is necessary to take into account sedimentological and/or bathymetric discontinuities as well as the hydrodynamic factors.

The final form of a site specific conceptual model is only obtained following a period of rigorous testing and modification. To facilitate this process of model development an extensive prototype data programme is required.

Data collection programmes have included:

- . Sea and swell data - height, period from Datawell Waverider Buoys, and directions from ship and shore observations supplemented by hindcast analysis.
- . Wind records - speed, duration and direction using Lambrecht anemometers at fixed locations and Ventimeters - hand held anemometers - for mobile stations.
- . Currents - Lagrangian patterns obtained by drogus tracking and Eulerian information using ONO directional and, more recently, Marsh McBirney X-Y electro-magnetic current meters. Rip currents - metered, surveyed and aerially photographed.
- . Bathymetry - 5.5 metre long twin hull boats powered by two 115 h.p. outboard engines give surf zone capability. These have been equipped with Raytheon type DE914 Fathometers and Motorola Miniranger Mk III position fixing equipment to enable accurate bathymetric data collection. This data is then reduced by a reduction/plot programme presently based on a VARIAN V75 computer.
- . Erosion history - including differential longshore, onshore and offshore movements. Standard terrestrial survey techniques are used onshore, and the technique outlined above is used offshore. Historical survey data collection from existing plans and photogrammetric analysis using stereo restitution instruments on present and historical photography. The latter is usually restricted to vertical aerial photography with a 60% overlap and scales typically in the range 1:4,000 to 1:50,000.
- . Sediment distribution patterns - spatial distribution of onshore and offshore sediment types, grain size parameters and lithology. This data is obtained from - dredge samples (a 75 mm x 300 mm steel tube with towing yoke at one end and sealed at the other is lowered to the sea floor and dragged a short distance by the survey boat); core samples up to 2 metre length obtained by divers using both suction coring equipment and hammer corers, diving is usually carried out from the survey boat; side scan sonographs produced using a Klein model 400 side scan unit operated from 15-25 metre trawlers. All position fixing is based on the

Motorola Miniranger system. Sand samples are examined under binocular microscopes to determine the composition and texture, and grain size characteristics are determined by both sieving and settling tube analysis. Further research is under way as to methods of classifying sediments under turbulent conditions (Smith and Gordon, 1980).

Geological and geomorphological history - analysis and age structure of sediment and bedrock: Sparker, boomer and magnetometer surveys to develop seismic profiles of both bedrock and the various sediment interfaces. The equipment is operated from the trawlers used for side scan operations with the same position fixing procedure. Auger boreholes are used to obtain material for dating from the back beach barrier ridge systems and to provide a check on seismic interpretation.

Bedforms - spatial and temporal distribution of ripples and dunes, their height, wave length, composition and direction of orientation. Data is collected by diver operations and from interpretation of side scan sonographs.

The quantification of the conceptual model requires an analysis of the various sources and sinks coupled with a mathematical description of the sediment movement between them. The techniques employed to quantify these sources and sinks will be illustrated in part in the following sections which deal with two site specific studies.

It is the quantification of sediment movements within the model boundaries which, of the coastal sciences, suffers most from the lack of adequate theoretical development. Hybrid modelling techniques have been employed in an attempt to offset these theoretical limitations.

Refraction and diffraction of waves provide particular problems. The accuracy of calculated longshore transport rates reflect to a considerable degree the ability to determine correctly the coastwise inshore wave energy distributions. Physical models, computer based mathematical models and prototype observations have been combined to synthesise inshore wave energy conditions. Because of inaccuracies in the available recorded wave data, particularly with respect to direction spectrum, the reliability of calculated values has been appraised by undertaking sensitivity analyses on the refraction and transport studies. Geomorphological and sedimentological indicators are also employed as independent references.

Sediment transport equations; the relationships between the driving forces and the sediment reaction to those forces, are in their infancy from the viewpoint of theoretical understanding.

The Bijker (1967) approach of increased bed shear under waves, represents a significant contribution to attaining a more scientific description of coastal sediment transport. However its inherent simplifications when applied to a beach system of complex morphology; rip cells and multiple offshore bars, has resulted in the continued

use of the more simplistic empirical approach outlined in the Shore Protection Manual (CERC, 1977); better known as the C.E.R.C. equation. More recent work by Longuett Higgins (1970, 1972) has lent some degree of theoretical credence to this relationship between wave thrust and longshore sand transport.

A mathematical model, at present based on a modified C.E.R.C. philosophy, has been adapted to local conditions and placed on a P.D.P. II computer for ease of calculation, alteration and testing against prototype data.

To illustrate the methodology employed in site specific model generation, and to highlight the shortcomings and strengths of both this approach and the theoretical considerations upon which it is based, two typical studies will be discussed. Both studies are from regions of the New South Wales coast which are believed to be undergoing long term recession.

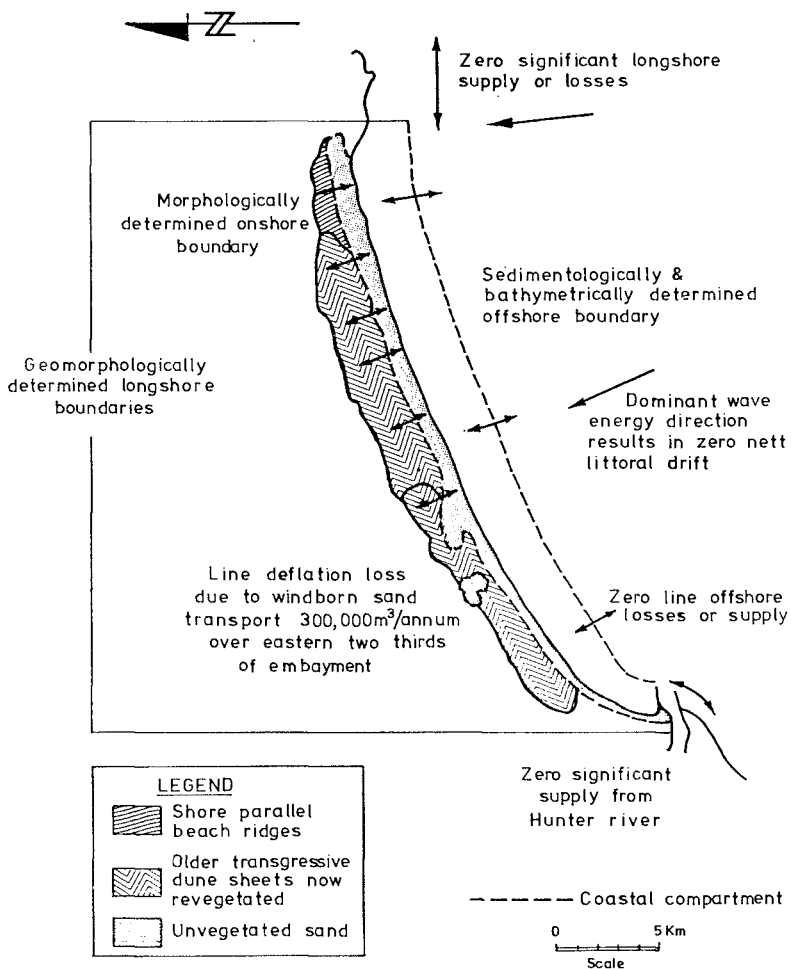
- . Newcastle Bight (Figure 3), a 30 kilometre long embayment located 120 kilometres north of Sydney. This is an example of a shoreline which is eroding due to aeolian losses.
- . Byron Bay - Hastings Point (Figure 3), a 30 kilometre long stretch of coastline located 750 kilometres north of Sydney. This is an area which is eroding due to an imbalance between overall coastal alignment and dominant wave energy approach direction. An interesting offshore loss mechanism intensifies the erosion problem.

4.1 Newcastle Bight

Newcastle Bight has a long history of beach erosion. It is backed by a massive transgressive dune sheet which is moving inland over forest and farming areas. Interest in the area followed a proposal to excavate a large new harbour in the transgressive dunes and to construct a breakwater protected entrance through the beach and surf zone.

The numero-descriptive model for Newcastle Bight has been summarised in Figure 5. It is not intended to discuss the study (Gordon and Roy 1977, D.P.W. 1977) in detail, but rather a number of interesting points have been singled out for presentation:

- . A major N.S.W. river discharges into the southern end of the coastal compartment. Calculations based on Colby's work (Colby 1964) showed that during major flood events the river had the capability to transport sand to the coast. Sand of suitable size was known to be present in the upper reaches of the river. Compositional and textural sedimentological studies showed no significant contribution of these terrestrial sands to the coastal sediment system. Further analysis of the flood data indicated that these events were infrequent, and that dry weather flows were incapable of transporting the material. The river was thus eliminated as a present day source of significant quantities of coastal sediments.



NUMERO-DESCRIPTIVE MODEL
NEWCASTLE BIGHT

FIG. 5

Initial calculations using hindcast wave statistics, the wave refraction programmes and sediment transport calculations gave a nett northerly drift of 200,000 cubic metres per year. Analysis of wave rider data showed that the hindcast statistics overestimated the frequency of waves of heights above 2-3 metres whilst underestimating the frequency of smaller waves. Using the waverider statistics, the calculated nett littoral drift was 135,000 cubic metres per year to the south (Table 1). Following doubts as to the accuracy of the recorded wave direction data, and particularly with respect to the assignment errors between True and Magnetic North (12 degrees), a sensitivity analysis was carried out on the effects of wave direction on transport volumes. It was found that a 7.5 degree shift in the nett energy flux pattern applied to the refraction programme resulted in a zero nett littoral drift condition for the embayment. Sedimentological evidence supported this latter finding (Gordon and Roy, 1977). As it was felt that at best, the wave directional data which was recorded to sixteen compass points was only accurate to ± 11.25 degrees, a model which predicted a zero nett littoral drift condition was adopted. The model was calibrated accordingly and the gross littoral drift quantities were adjusted.

TABLE 1

Deepwater Wave Approach Direction	Average Annual Sand Transport (m^3/yr) and Direction of Transport	
	From Wave Statistics based on True North	From Statistics based on Magnetic North (12° shift)
E	224,000 South	242,000 South
ESE	345,000 South	262,000 South
SE	235,000 South	86,000 South
SSE	212,000 North	304,000 North
S	457,000 North	396,000 North
Gross Drift	1,473,000	1,290,000
Nett Drift	135,000 South	110,000 North

The numero-descriptive model confirmed that the measured 1 to 2 metre per year (long term average) shoreline recession could be accounted for by the deflation losses associated with the landward moving transgressive dunes. The initial numerical analysis did not, however, produce this result. Aeolian transport was assessed by the Bagnold approach (Kadib, 1964) using long term wind data from anemometers located at both the southern end and the centre of the embayment. This formula was applied in the form:

$$Q = 1.8 \times t \times 3.6 \times 10^3 \sqrt{d/D \cdot \gamma/g \cdot U_*^3}$$

and

Q = total transportation in kg/year/metre

t = wind duration in hours/year

d = d_{50} diameter of sand in millimetres

D = 0.25 mm Bagnold standard sand particle size

γ = Specific weight of air kg/m³

g = gravitational acceleration m/sec²

U_* = shear velocity in m/sec

These calculations showed that some 20 cubic metres/year/metre of beach (long term average) was moving in an offshore direction. This resultant was 120 degrees opposed to the known landward transport obtained by direct measurements and aerial photographic interpretation which gave a landward encroachment of the transgressive dune sheet of from 5 to 10 metres per annum, landward transport of some 25 to 50 cubic metres/metre of beach. Examination of this anomaly showed that as the onshore movement was into a well vegetated region, the trapping effect of the trees, and their local modification of the wind field resulted in their acting as a 'sand diode'; selectively modifying the aeolian mechanism. Thus it was concluded that the nett movement was chiefly dependent on the onshore component of wind energy, and hence the aeolian transport calculations were modified accordingly.

Monthly surveys (D.P.W. 1977) and sand samples taken in the offshore zone produced evidence of a break in sediment characteristics and movement at depths of 12 to 14 metres throughout the Bight; shallower at the southern end in the hook of the zeta curve. This break was interpreted as being the base of the highly active inner nearshore zone and as such was useful in the further development of the "generalised model" and provided information relevant to the development of sediment transport models.

The quantity of material involved in the onshore-offshore movement during storm events was estimated from the profiling data. In March 1973 a 3 day storm occurred. The peak significant wave height from wave rider records was 6.2 metres while the maximum wave height was 9.9 metres. The recurrence interval of this storm

was estimated as 1 in 1 year. The storm produced an average 35 metre recession of the mean water mark and between 100 and 150 cubic metres/m of beach were removed from the sub aerial beach and placed on the offshore bar. Experience at other locations on exposed ocean beaches in N.S.W. indicate that for a more intense storm with wave heights of 10 to 12 metres this storm demand may be of the order of 200 to 400 cubic metres/metre of beach.

The accuracy of the final numero-descriptive model (Figure 5) constructed for Newcastle Bight was enhanced by the adoption of the approach outlined in Section 3 - the quantification of a conceptual model with emphasis on testing against prototype information and observations.

4.2 Byron Bay - Hastings Point

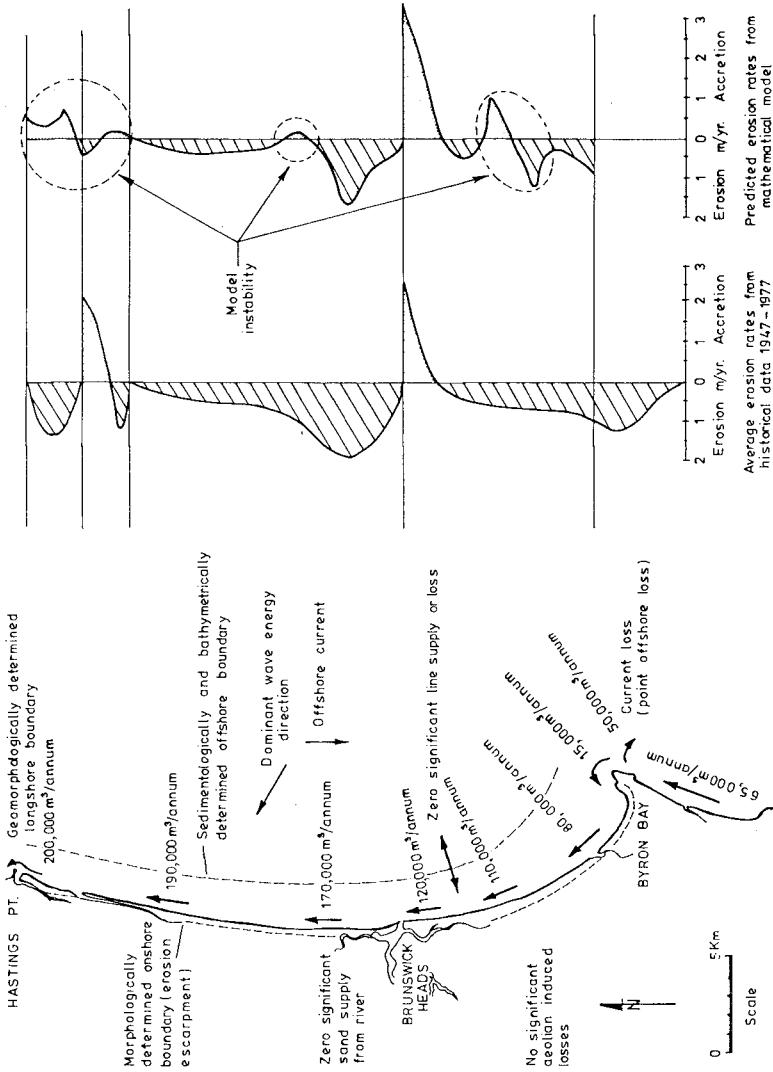
Shoreline recession in the Byron Bay - Hastings Point region was drawn to public attention dramatically with the loss of houses during the late 1960's and the severe damage to a small village located mid way along this stretch of coast. In 1972, after further severe cyclone activity, this village of 17 houses had to be totally abandoned. To provide a basis for future management and planning of the area, a site specific coastal study was undertaken (Gordon, Lord and Nolan, 1978).

This study showed that a time averaged nett longshore drift occurs from south to north throughout the Byron Bay - Hastings Point embayment, which is an open ended compartment. Throughout the embayment an unfavourable coastal alignment promotes a differential littoral drift situation which results in a greater quantity of sand leaving the compartment to the north than is entering it at the southern end.

The existing coastal sediments have responded to this increasing sediment demand, resulting in recession of the shoreline. This recession can be viewed as a "line source" of littoral drift material.

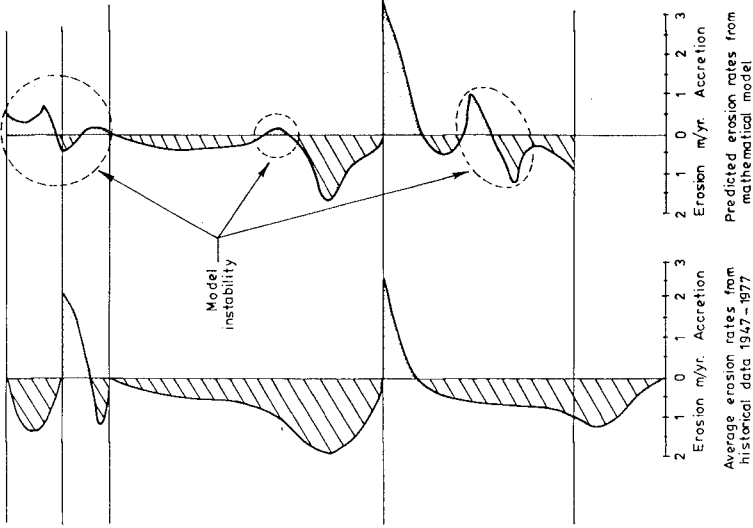
The numero-descriptive model which resulted from the study has been summarised as Figure 6. This study provided interesting insights into offshore loss mechanisms, and methods by which longshore transport formulae can be calibrated and used to reproduce time histories of differential shoreline recession.

Although it was recognised that littoral drift imbalance within the compartment was a major contributing factor to shoreline recession, it became apparent during the investigation that a significant offshore loss mechanism was active off the southern headland. Current studies, sedimentological evidence, and unusual bathymetric features (ref. Figure 7) off Cape Byron were examined to facilitate description and then quantification of this loss.

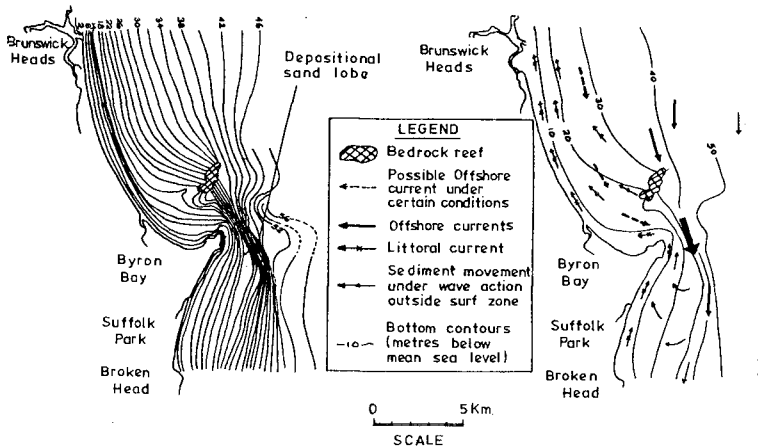


NUMERO-DESCRIPTIVE MODEL
BYRON BAY - HASTINGS POINT

FIG. 6



Intermittent excursions of the East Australia Coast Current onto the continental shelf in this region at certain times produce south bound currents in excess of 0.5 m/s close to the Cape where wave reflection from the near vertical cliffs ensure that sediment suspension occurs even under low wave conditions. Thus northerly drifting sand in the littoral stream which would normally bypass Cape Byron may, under certain conditions, be intercepted and transported offshore and to the south where it forms a prominent bathymetric feature; a sink for littoral material in some 30 to 50 metres water depth (ref. Figure 8). Using sedimentological



OFFSHORE BATHYMETRY
BYRON BAY

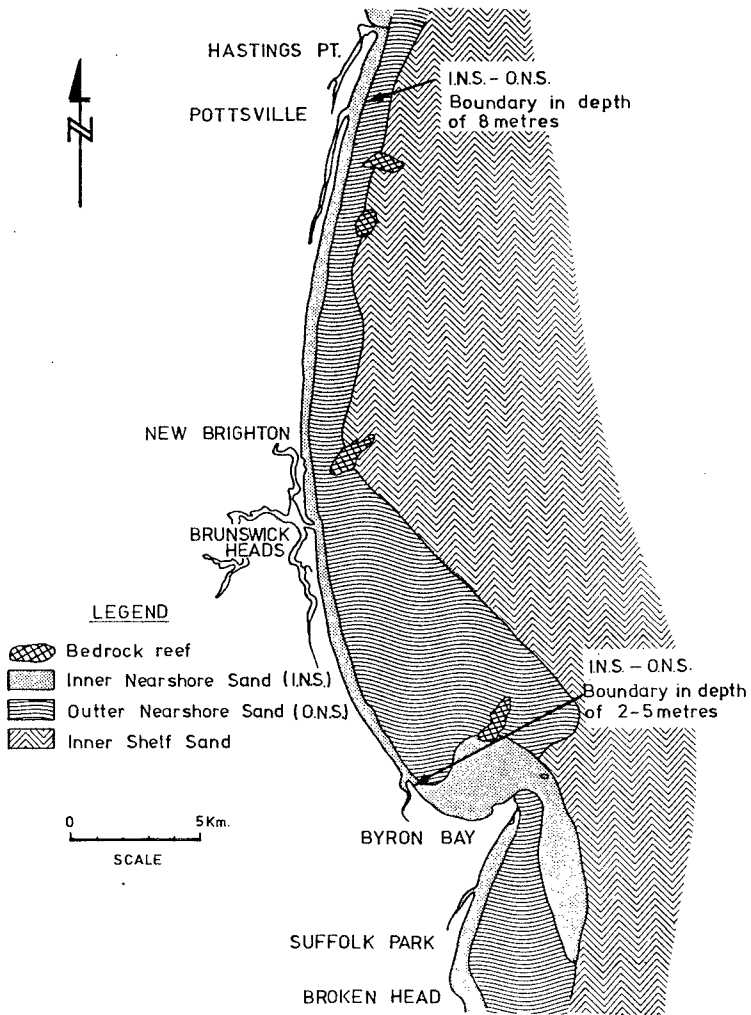
FIG. 7

OFFSHORE CURRENTS
AROUND CAPE BYRON

FIG. 8

analyses to define the extent of this feature, and bathymetric evidence to calculate the quantities of sediment lost to the sink, it was estimated that 50,000 cubic metres per annum of sand had been removed on average from the littoral drift system over the last 6,000 years. The assumption that this loss has occurred at a steady rate over 6,000 years is tentative. Further work is required to examine the validity and implications of this assumption.

To examine and predict the pattern of shoreline recession, a computer based transport model was adapted and extensively modified to this location. The model divided the coastal compartment into a number of shore normal elements (Figure 9). The wave refraction programme, sediment transport formula and local wave data were combined to calculate the longshore transport rate into and out of each element for discrete time steps. At each time step the "budget" of the individual elements



OFFSHORE SEDIMENT TYPES
BROKEN HEAD TO HASTING POINT

FIG. 9.

was assessed and sediment deficits or excesses were distributed to the adjacent elements. The onshore element boundary was flexible and reflected overall sediment gains or losses as beach erosion or accretion (Gordon, Lord and Nolan, 1978).

Instabilities occurred in the model at discontinuities such as breakwaters and in regions where refraction/diffraction patterns were complex or interacted (Figure 6). These instabilities were mainly associated with inappropriate selection of element size and the techniques employed to assign refraction, diffraction and bypass coefficients.

Model calibration was carried out by comparing the resulting shoreline recession patterns with those obtained historically from survey and photogrammetric analyses. The structure of this model, enabling it to be run both backward and forward from any point in time, allowed verification of the model against prototype data prior to its usage as a predictive tool for shoreline recession.

The model employed the C.E.R.C. formula in the form:

$$Q = K.C_g \frac{\rho g H^2}{8} \cdot \sin \alpha \cdot \cos \alpha$$

where

Q = longshore transport rate

K = an empirical coefficient which involves a number of parameters

C_g = wave group velocity

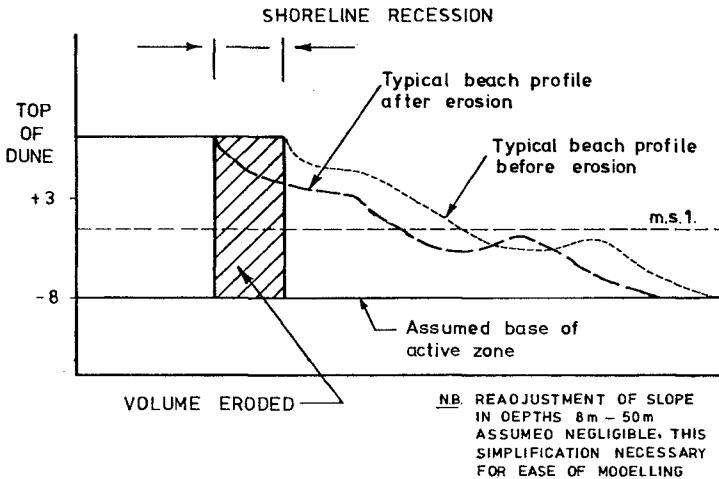
$\frac{\rho g H^2}{8} \cdot \sin \alpha \cdot \cos \alpha$ = wave thrust

Initial results using a K value obtained from the Shore Protection Manual (C.E.R.C., 1977) produced erosion and transport rates approximately three times those measured in the prototype. The K value was adjusted accordingly and the model was then used to predict future trends.

As with the Newcastle Bight study, offshore sediment patterns provided data on offshore boundary considerations. A marked change in sand type was noted at a depth of 8 metres in the exposed regions of the embayment, shallowing to 2-5 metres in the sheltered hook of Byron Bay.

The offshore boundary for the model elements was taken as the break in sediment patterns referred to above. The inner boundary was the back of the beach at the base of the erosion escarpment; typically +3 metres to +4 metres above I.S.L.W. In a fully

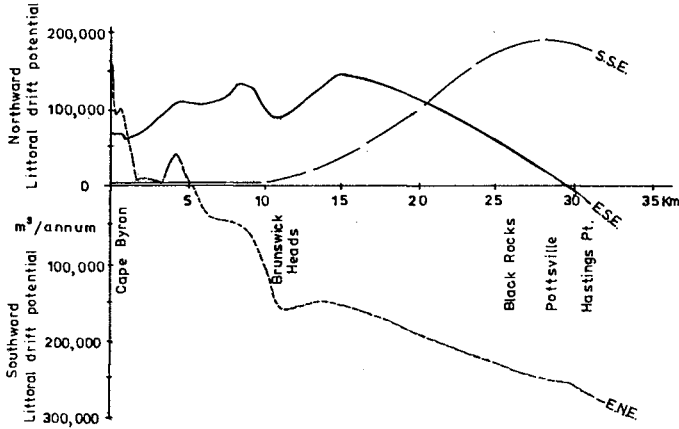
3-dimensional model, profile changes due to varying input data should be modelled as well as plan form changes in shoreline. It is argued that in a long term erosion situation, it is reasonable to assume that whilst dramatic day to day changes in profile shape may occur, the nett result is a mean profile which migrates landward as erosion progresses. Obviously, this is a gross simplification for the convenience of model operation. However it is believed that profile changes between depths of between 50 metres and 10 to 8 metres are subtle on an engineering time scale. It is further believed that no significant modification to the profile solely due to wave induced effects occurs at depths greater than 50 metres, although wave penetration to the bed may exceed this figure on certain occasions. Thus, the eroded volume per unit time, per unit length was obtained as illustrated in Figure 10.



ACTIVE ZONE ZONE

FIG 10

Sensitivity of the model to directional wave data was investigated by generating 100% occurrence nett transport rates along the embayment for three major offshore directions (Figure 11). It was then a simple process to test the effects of various directional distributions on the longshore transport rates and, hence, the erosion patterns.



100% OCCURENCE NETT TRANSPORT RATES
CAPE BYRON TO HASTINGS POINT

FIG 11

TABLE 2 - Sediment Budget

SOURCE	VALUE (m ³ /year)	SINK	VALUE (m ³ /year)
Q ⁺ ₁ (offshore point supply)	0	Q ⁻ ₁ (offshore current loss)	50,000
Q ⁺ ₂ (rivers and creeks)	0	Q ⁻ ₂ (inlet loss)	0
Q ⁺ ₃ (beach nourishment)	0	Q ⁻ ₃ (sand extraction)	0
Q ⁺ ₄ (longshore transport in)	65,000	Q ⁻ ₄ (longshore transport out)	200,000
q ⁺ ₁ x (offshore line supply)	0	q ⁻ ₁ x (offshore line loss)	0
q ⁺ ₂ x (dune and terrace erosion)	180,000	q ⁻ ₂ x (overwash and wind loss)	0
q ⁺ ₃ x (beach erosion and shell production)	0	q ⁻ ₃ x (beach storage and shell loss)	0
TOTAL of Sources	245,000	TOTAL of Sinks	250,000

The quantified conceptual model is presented in traditional sediment budget terms as Table 2. Emphasis has been placed on the use of point sources/sinks (Q) and line sources/sinks (q) because of their significance in this particular study. The total sediment budget therefore took the form:

$$\sum_{i=1}^4 Q_i + \sum_{i=1}^3 \left(\sum_o q_i x_i \right) = \sum_{i=1}^4 Q_i - \sum_{i=1}^3 \left(\sum_o q_i x_i \right)$$

In the Byron Bay - Hastings Point study, the adaptation of the methodology outlined in Section 3, enabled a model to be constructed which showed not only the total sediment budget of the coastal compartment, but also enabled predictions to be made concerning future differential shoreline movement throughout the compartment.

5. CONCLUSIONS

By invoking a conceptual model/numerical model approach the concept of sediment budgeting has been expanded to provide an insight into processes operating within the coastal compartment under study. The use of geomorphological and sedimentological indicators has assisted in quantifying and testing the models. The development of a general coastal model has provided an invaluable frame of reference and starting point for any site specific studies.

The modelling process is an ongoing development. Recognition that generalisation is dependent on mechanism understanding has resulted in increasing emphasis being placed on the methods used to calculate actual sediment movement paths.

Accuracy and confidence in results have been increased by the carrying out of sensitivity analyses and a process of constantly reviewing proposed mechanisms and transport paths against prototype observations and data.

Notwithstanding the above, it is plainly apparent that there exists a compelling need for greater understanding of sediment transport mechanisms, and hence the development of more appropriate formulae for both the aeolian and littoral regions of the coastal zone. In concert with this, far more sophisticated data collection is required, particularly with respect to inshore wave directional spectra, current information, and sediment characteristics.

The results of any computation are only as good as the input data and the validity of the assumptions used.

REFERENCES

- . BIJKER, E.W. (1967) "The Increase of Bed Shear in a Current Due to Wave Motion" - Delft Hydraulics Laboratory Publication No. 46, February 1967.
- . COASTAL ENGINEERING RESEARCH CENTER (C.E.R.C.) U.S. ARMY CORPS OF ENGINEERS (1977). "Shore Protection Manual" - Vol. I, II, III, Department of the Army Corps of Engineers.
- . COLBY, B.R. (1964). "Discharge of Sands and Mean Velocity Relationships in Sand Bed Streams." U.S. Geological Survey. Prof.Paper 462-A.
- . DEPARTMENT OF PUBLIC WORKS, N.S.W. (1977) "Sediment Movement in Newcastle Bight" Department of Public Works, N.S.W., Manly Hydraulics Laboratory Report No. 206, December 1977.
- . GORDON, A.D., LORD, D.B., NOLAN, M.W. (1978) "Byron Bay - Hastings Point Erosion Study". Department of Public Works, N.S.W., Coastal Engineering Branch Report No. PWD 78026, November 1978. ISBN 7240-2691-6.
- . GORDON, A.D. and ROY, P.S. (1977). "Sand Movements in Newcastle Bight". Third Australian Conference on Coastal and Ocean Engineering, Melbourne Victoria, Australian Institution of Engineers, April 1977.
- . KADIB, ABDUL-LATIF (1964). "Calculation Procedure for Sand Transport by Wind on Natural Beaches". U.S. Army Coastal Engineering Research Centre, Miscellaneous Paper No. 2-64, April 1964.
- . LONGUETT-HIGGINS, M.S. (1970). "Longshore Currents Generated by Obliquely Incident Sea Waves" - Journal of Geophysical Research, Vol. 75, No. 33, November 20, 1970. pp. 6778 to 6801.
- . LONGUETT-HIGGINS, M.S. (1972). "Recent Progress in the Study of Longshore Currents" - published in "Waves on Beaches and Resulting Sediment Transport". R.E. Meyer ed. 1972, Academic Press Inc. pp. 203-248.
- . SMITH, A.W., GORDON, A.D. (1980). "Secondary Sand Transport Mechanisms". Proceedings of the 17th International Conference on Coastal Engineering, Sydney. Published by American Society of Civil Engineers.
- . THOM, B.G., POLACH, H.A. and BROWN, G.M. (1978). "Holocene Age Structure of Coastal Sand Barriers in N.S.W., Australia" - Faculty of Military Studies Department of Geography, University of N.S.W., 1978.

Relationship Between Alongshore Wave Energy and Littoral Drift
in the Mid-West Coast at Taiwan

HO-SHONG HOU, ph.D., M., ASCE*

CHUNG-PAN LEE**

LUNG-HUI LIN**

ABSTRACT

Based on the wave pattern, the geographical location and the disposition of rivers, the littoral drift moves predominantly from NE to SW direction in section II as shown in Fig. 1. Seven rivers of rapid stream bring tremendous amount of sediments from the high mountain to the nearshore of this section in typhoon season (i.e. from June to September). But for the winter monsoon season, i.e. from October to the next April, the waves induced by NE monsoons migrate littoral drift from North toward South.

Applying the energy approach for unidirectional steady flow derived by Bagnold(1963), the theoretical relationship between the littoral immersed weight transport rate and the alongshore breaking wave energy is found out. It reveals that the relationship is not strictly linear, i.e. the larger part of the alongshore breaking wave energy is supplied for transporting the sediment as the former increases. But for a coast having a steady oceanographical condition, the relationship could be considered as linear relation since the alongshore breaking wave energy is not varying very much.

In this paper, the study of littoral drift vs wave energy at the Taichung Coast from the Ta-Chia River to the Ta-Tu River will be carried out. Using the wave records gained by the ultrasonic wave gauge at 19m depth and the littoral drift quantity obtained from long-term observation, the relationship between alongshore breaking wave energy and littoral immersed weight transport rate is found out.

First, the waves which have the same direction are summed up. Then from "THE WAVE CHARACTER COMPUTING PROGRAM", the incident directions of these wave groups at 19m depth are determined. Then the alongshore breaking wave energy per unit time per unit length of beach could be calculated by the same PROGRAM. Finally the relationship between alongshore breaking wave energy and littoral immersed weight transport rate of this coastal condition is obtained as $I_i = 0.55 (P_i)_b$

* Director and Prof., Graduate Institute of Harbor & Oceanic Eng., National Taiwan College of Marine Science & Technology, Keelung, Taiwan

**M.S., Graduate Institute of Harbor & Oceanic Eng., National College of Marine Science & Technology, Keelung, Taiwan

1. Introduction

The littoral transport rate is defined as the transport rate passing through a cross section which is perpendicular to the shoreline or contour line and the range of movement is considered between the threshold depth of sediment and the height of wave run-up.

To evaluate the littoral transport rate are classified into four different methods as follows:

(1). Using the littoral transport rate of neighbor coast, and considering the local conditions such as the shoreline configuration, the grain size and the source of sand, then modifying the neighbor littoral transport rate as the interest littoral transport rate.

(2). Using the nearshore bathymetry to evaluate the volume change of the total sediment along the shore, and estimate the littoral transport rate by groin or spit activity.

(3). Using the long-shore current to estimate the littoral transport rate.

(4). Using the along-shore breaking wave energy to compute the littoral transport rate.

Galvin(1972) derived the formula $Q_s = 2H^3$, where Q_s in unit 10^5 yd³/year and H (ft) is the mean breaking wave height of one year. But the formula is good only for suspended load due to its hypothesis. In fact, the quantity of the bed load is much larger than that of the suspended load.

Method (1) is more practical than the others, but the data of littoral transport rate are so few, therefore, the other methods are need to try. If the study area has not groin, break-water or spit to block completely the littoral transport, then the littoral transport rate is not easily to

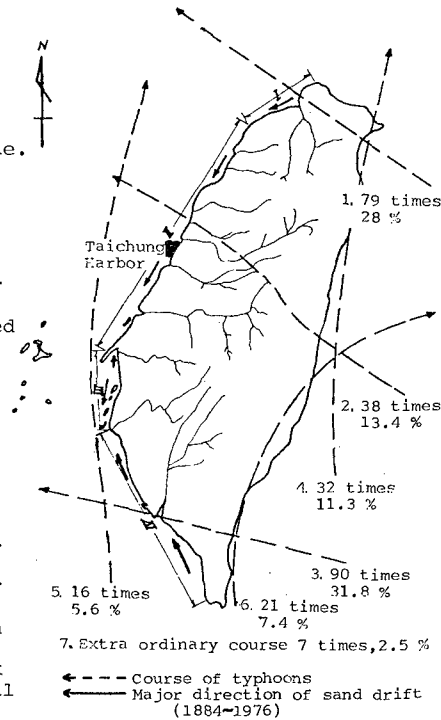


Figure 1. The sketch of the prevailing direction of littoral drift at Taiwan sandy coast.

estimate. The alongshore current is changing from place to place, from time to time, it is very difficult to find out a dominate value of alongshore current. Therefore, it is more often to use the alongshore breaking wave energy to estimate the littoral transport rate. If there is no wave records then the wave characters could be predicted from wind records.

Bagnold (1963) use the littoral immersed weight transport rate I_i to represent the littoral transport rate, where I_i has the same unit with the alongshore breaking wave energy $(P_i)_b$.

2. The theoretical consideration

2.1. The relationship between the bed load and the available power of fluid under wave action

Under wave action, the forces acting on the sand element (i.e. the free body m_b of containing sufficient sand particles) include the total driving force of fluid T_F , the tangential reactive force T_t due to collisions, the normal reactive force P_n due to collisions and its own gravity. T_F includes drag force, lift force and the pressure gradient stress. T_t and P_n is defined as shown in Fig. 2, where $\tan \phi' = T_t/P_n$ is the friction coefficient of solid phase. ϕ' is almost equal to the repose angle of sand, ϕ . Then

$$T_t = P_n \tan \phi \dots \dots \dots (1)$$

As shown in Fig. 3

$$T_t = \left[\left(\frac{\rho_s - \rho}{\rho_s} \right) g m_b \cos \alpha_B - T_{FV} \sin \beta \right] \tan \phi$$

where β is the angle between T_F and the bed. Since the sand moves up and down. From Newton's second law, i.e.

$$\left[\frac{(\rho_s - \rho) + \rho C_M}{\rho_s} \right] m_b \frac{du_{bb}}{dt} = T_{FV} \cos \beta - \left(\frac{\rho_s - \rho}{\rho_s} \right) g m_b \sin \alpha_B - \left[\left(\frac{\rho_s - \rho}{\rho_s} \right) g m_b \cos \alpha_B - T_{FV} \sin \beta \right] \tan \phi$$

and

$$T_{FV} = \left(\frac{\rho_s - \rho}{\rho_s} \right) g m_b \left\{ \frac{1}{\cos \beta + \sin \beta \tan \phi} \left[\frac{1}{g} \left(1 + C_M \frac{\rho}{\rho_s - \rho} \right) \frac{du_{bb}}{dt} + \sin \alpha_B + \cos \alpha_B \tan \phi \right] \right\} \dots \dots \dots (2)$$

Similarly

$$T_{FD} = \left(\frac{\rho_s - \rho}{\rho_s} \right) g m_b \left\{ \frac{1}{\cos \beta + \sin \beta \tan \phi} \left[\frac{1}{g} \left(1 + C_M \frac{\rho}{\rho_s - \rho} \right) \frac{du_{bb}}{dt} - \sin \alpha_B + \cos \alpha_B \tan \phi \right] \right\} \dots \dots \dots (3)$$

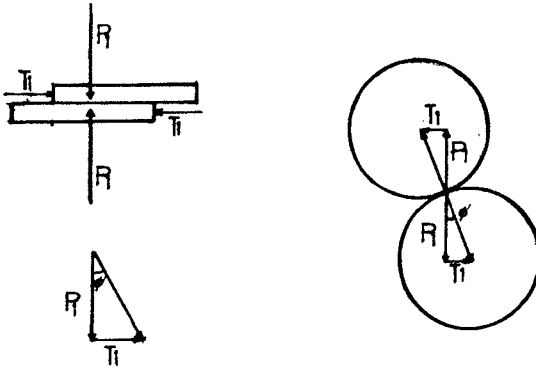


Figure 2. The diagram of definition of frictional coefficient in solid phase.

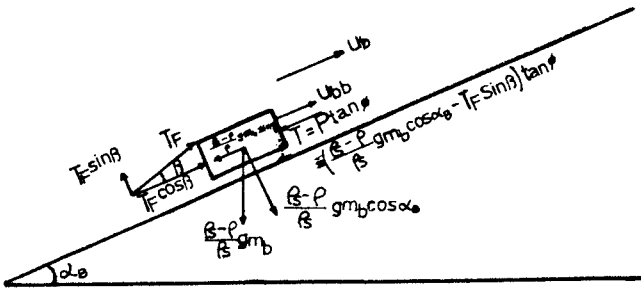


Figure 3. The force system acting on the bed load.

where T_{FV} is the upward driving force, T_{FD} is the downward driving force, u_{bb} is the velocity of sand and C_M is the virtual mass coefficient, while the volume concentration of sand is C_v .

$$C_M = \frac{1}{2} (1 + 1.59 \frac{C_v}{\pi}) \dots\dots\dots(4)$$

Then, as the sand element move up and down, the work done by fluid is

$$\begin{aligned} & |T_{FV} \cos \beta| |(u_{bb})_u| + |T_{FD} \cos \beta| |(u_{bb})_d| \\ &= \frac{\rho_s - \rho}{\rho_s} g m_b u_{bb} \left\{ \frac{2 \cos \beta}{\cos \beta + \sin \beta \tan \phi} \left[\frac{1}{g} (1 + C_M \frac{\rho}{\rho_s - \rho}) \right. \right. \\ & \quad \left. \left. \frac{du_{bb}}{dt} + \cos \alpha_B \tan \phi \right] \right\} \dots\dots\dots(5) \end{aligned}$$

where $(u_{bb})_u$, $(u_{bb})_d$ represent the upward and downward velocity of sand element respectively. Part of the force in Eq.(5) brings the sand away from the original place, i.e. to cause the net sediment transport, which is

$$\begin{aligned} & (\frac{\rho_s - \rho}{\rho_s}) g m_b \bar{u}_{bb} \left\{ \frac{\cos \beta}{\cos \beta + \sin \beta \tan \phi} \left[\frac{1}{g} (1 + C_M \frac{\rho}{\rho_s - \rho}) \right. \right. \\ & \quad \left. \left. \frac{dU_{bb}}{dt} + \sin \alpha_B + \cos \alpha_B \tan \phi \right] \right\} \dots\dots\dots(6) \end{aligned}$$

\bar{u}_{bb} is the net velocity of bed load. Set

$$i_b = (\frac{\rho_s - \rho}{\rho_s}) g \cdot m_b \cdot \bar{u}_{bb} \dots\dots\dots(7)$$

where i_b is the immersed weight transport rate. If ω is the available power of fluid, ϵ_b is the effective coefficient which is used to cause bed load. Then from eq.(6) and eq.(7), the relationship between the immersed weight transport rate of the bed load and the available power of fluid is as

$$\begin{aligned} & i_b \left\{ \frac{\cos \beta}{\cos \beta + \sin \beta \tan \phi} \left[\frac{1}{g} (1 + C_M \frac{\rho}{\rho_s - \rho}) \frac{du_{bb}}{dt} + \sin \alpha_B \right. \right. \\ & \quad \left. \left. + \cos \alpha_B \tan \phi \right] \right\} = \epsilon_b \omega \dots\dots\dots(8) \end{aligned}$$

Assume the sediment transport has completely developed, and the resultant force acts normal to the bed is in equilibrium, i.e. $P_t = 0$. Then

$$T_F \sin \beta = (\frac{\rho_s - \rho}{\rho_s}) g m_b \cos \alpha_B$$

$$T_F = \frac{1}{\sin \beta} (\frac{\rho_s - \rho}{\rho_s}) g m_b \cos \alpha_B \dots\dots\dots(9)$$

The work done by fluid to take sand element move up and down is

$$2 T_F \cos \beta u_{bb} = 2 \frac{\cos \alpha_B}{\tan \beta} \left(\frac{\rho_s - \rho}{\rho_s} \right) g m_b u_{bb} \dots \dots \dots (10)$$

But cause the net sediment transport is only equal to

$$T_F \cos \beta \bar{u}_{bb} = \frac{\cos \alpha_B}{\tan \beta} \left(\frac{\rho_s - \rho}{\rho_s} \right) g m_b \bar{u}_{bb} = \epsilon_b \omega$$

or

$$i_b \frac{\cos \alpha_B}{\tan \beta} = \epsilon_b \omega \dots \dots \dots (11)$$

It simply represents the relationship between the immersed weight transport rate of bed load and the available power of the fluid. Since T_F might change periodically, the equilibrium state of the assumption is existing temporarily and the sediment move up and down occasionally. But when the sediment transport has completely developed, the particles move up and down is considered as the same rate. Therefore, eq.(11) is quite reasonable.

2.2. The relationship between the suspended load and the available wave power

Since the suspended load is away from bed, its wall effect is less than that of bed load. The transport of suspended load is mainly caused by the mass transport due to nonlinear waves and the alongshore current. The motion of suspended load is considered as the resultant of the horizontal velocity u_s and the settling velocity w . The collision effect between suspended particles is ignored since the concentration of suspended load is low. The only external force on the suspended load is the driving force of fluid including the drag force, the lift force and the pressure gradient stress. It is shown in Fig.4. and yields

$$T'_F \cos \beta' = \left(\frac{\rho_s - \rho}{\rho_s} + C_M \right) m_s \frac{du_s}{dt} \dots \dots \dots (12)$$

where m_s indicates suspended load while u_s is its horizontal velocity, T'_F is the driving force of the fluid, β' is the angle of T'_F from horizontal direction. Fluid transports the suspended load by doing two actions. One is to make m_s move in the horizontal direction, the other is to keep m_s from falling with settling velo-

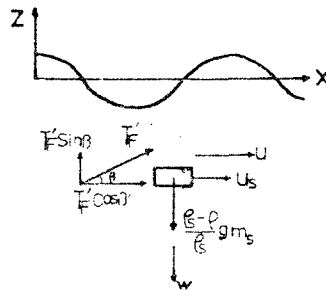


Fig.4 The force system on suspended load.

city w . Therefore, the power worked by fluid to transport the suspended load with net transport velocity \bar{u}_s is

$$[T'_F \cos \beta'] \bar{u}_s + [T'_F \sin \beta'] w = \epsilon_s (1 - \epsilon_b) \omega \dots (13)$$

If the sediment transport is fully developed, the suspended load may be considered statistically as move in the horizontal direction. Then

$$T'_F \sin \beta' = \left(\frac{\rho_s - \rho}{\rho_s} \right) g m_s \dots \dots \dots (14)$$

and

$$T'_F \cos \beta' = \left(\frac{\rho_s - \rho}{\rho_s} \right) g m_s \frac{1}{\tan \beta'} \dots \dots \dots (15)$$

From eq.(13), (14) and (15), then

$$\left(\frac{\rho_s - \rho}{\rho_s} \right) g m_s \bar{u}_s \left[\frac{1}{\tan \beta'} + \frac{w}{\bar{u}_s} \right] = \epsilon_s (1 - \epsilon_b) \omega \dots \dots (16)$$

is obtained, where i_s is the suspension efficiency, and next by

$$i_s = \left(\frac{\rho_s - \rho}{\rho_s} \right) g m_s \bar{u}_s \dots \dots \dots (17)$$

as the immersed weight transport rate of suspended load. Therefore,

$$i_s \left[\frac{1}{\tan \beta'} + \frac{w}{\bar{u}_s} \right] = \epsilon_s (1 - \epsilon_b) \omega \dots \dots \dots (18)$$

is the relationship between the suspended load and the available power of the fluid as the sediment transport is fully developed.

The total transport rate i is expressed as

$$i = i_b + i_s \dots \dots \dots (19)$$

$$i = \left[\frac{\epsilon_b}{\cos \alpha_s / \tan \beta} + \frac{\epsilon_s (1 - \epsilon_b)}{1 / \tan \beta' + w / \bar{u}_s} \right] \omega \dots \dots \dots (20)$$

Eq.(20) is derived from eq.(11) and (18). Let K be as follows.

$$K = \frac{\epsilon_b}{\cos \alpha_s / \tan \beta} + \frac{\epsilon_s (1 - \epsilon_b)}{1 / \tan \beta' + w / \bar{u}_s} \dots \dots \dots (21)$$

Eq.(20) represents the relationship between the immersed weight transport rate and the available power of the fluid. Because the action between sand bed and water mass is different as breaking wave type is changed, ϵ_b and ϵ_s will be affected by the breaking wave parameters. It is believed that the plunging wave causes seriously erosion than that of the other type of breaking wave. The settling velocity increases as grain size increases, therefore K will decrease as sand grain size increases. It is shown in eq.(21). Besides that, K becomes large as the net transport rate of suspended load increases.

Therefore, the littoral transport will be strengthened in the direction of alongshore current if there is a permanent or semi-permanent alongshore current. The parameter β (or β') reveals the magnitude of fluid acting on moving sediment, it grows up as the vertical fluctuation increases. Therefore, it will be larger in the shallower water or under the action of the bigger waves. And the K value will be larger in the shallower water and for the higher wave energy. The above reasons show that the K value is not always a constant. But, for the long-term climate, if the weather is steady at the same coast, the K value could be considered as a constant.

2.3. The definition of the available wave power

By Using the Airy wave theory, the energy density of a wave with wave height H is E

$$E = 1/8 \rho g H^2 \dots\dots\dots(22)$$

The power P transmitted between wave rays with distance Δb is

$$P = E \cdot C_g \cdot \Delta b \dots\dots\dots(23)$$

where C_g is group velocity, as shown in Fig.5, the angle between contour line and wave crest line is α and the power transmitted in the longshore direction is

$$P \sin \alpha = E \cdot C_g \cdot \Delta b \sin \alpha$$

where Δb is in term of the coast length Δl as

$$\Delta b = \Delta l \cdot \cos \alpha$$

Then, the alongshore wave energy per unit length of the coast is

$$P_l = E \cdot C_g \cdot \sin \alpha \cos \alpha = \frac{1}{8} \rho g H^2 \cdot C_g \cdot \sin \alpha \cdot \cos \alpha \dots\dots(24)$$

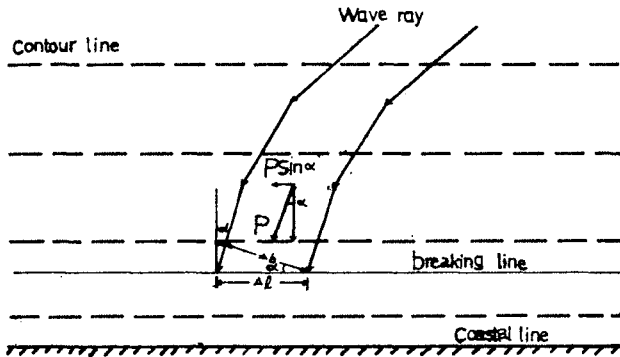


Fig.5. The diagram of the alongshore wave energy.

Eq.(24) is called the available alongshore wave power for transporting the coast sediment.

3.The experimental investigation

3.1.The estimate of littoral transport

At a straight sandy coast of infinite length, if characteristics of waves and characteristics of shore are kept the same along the straight sandy coast, then there is neither erosion nor accumulation. Because the movement of sediment transport is continuous. To estimate the littoral transport rate from the nearshore bathymetry, the groin or breakwater or spit is necessary installed to block the littoral transport. Therefore, the accumulation in the upstream area is the total littoral transport of this sandy coast.

The littoral transport rate of the Taichung coast is illustrated as follows.

There are the Ta-An and the Ta-Cha rivers in the north side of Taichung Harbor, while the Ta-Tu river is in the south side. In the typhoon season (From May to Oct.), Ta-Cha river bring about $1.13 \times 10^6 \text{ m}^3$ per year and Ta-Tu river bring about $1.20 \times 10^6 \text{ m}^3/\text{yr}$ into the coast. The orientation of the coastline from the Ta-Tu river to the Ta-Cha river is N 21.5 E and that of the Ta-Cha river to the Ta-An river is in the direction of N 42.5 E. This means that the neighborhood of the mouth of Ta-Cha river act as a spit which block a part of the littoral transport.

The bottom slope of depth contour from -0 m to -20 m is 1/75 in the neighborhood of the mouth of the Ta-Cha river and the slope of the Ta-Tu estuary is 1/100; the bottom slope from -20 m to -50 m is 1/80 in the mouth of the Ta-Cha river and it is 1/20 in the mouth of the Ta-Tu river. The width of the inter-tidal zone becomes wider from the Ta-Cha river to the Ta-Tu river. It reveals that the injecting flow of Ta-Tu river blocks the littoral transport and carries sediments toward offshore.

From the wind records, during winter season, wind blows from N to NE direction which is the predominant wind and occurs 80 % per year, and the speed is often beyond 10 m/sec. The induced wind wave is mainly $H=1 \sim 2 \text{ m}$, $T=6 \sim 6.4 \text{ sec}$. In summer, wind which blow in S to WSW direction occur 13 % Per year, and its speed is always below 5 m/sec unless in typhoon. The induced wind wave is always less than 0.7 m. Therefore, the littoral drift will migrate from north to south. The plot of the mean grain size distribution of the sediment confirms the result, as shown in Fig.6.

From the continuous bathymetry, using the mesh method, the volume change of the total sediment in the study area is found out as

$$\Delta V = \frac{A}{4} \left[\sum h_1 + 2 \sum h_2 + 3 \sum h_3 + 4 \sum h_4 \right] \dots \dots \dots (25)$$

where A is the grid area and h_j is the fluctuation of water depth at the point co-related to the i number of grids, as shown in Fig.7.

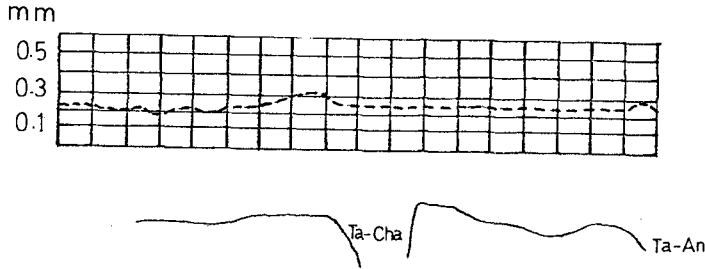


Fig.6. The distribution of the mean grain size.

After 1975, the north breakwater of Taichung Harbor has extended to the water depth of -5m, which is usually deeper than that of wave breaking, the north breakwater is completed at the October of 1976, the head of the north breakwater reached to the depth of -20m, as shown in the Table.

From Fig.8, it is found out that sea bottom fluctuated seriously before the head of the north breakwater reached -20m. This means that the littoral drift still passes through the north breakwater and moves southward before the time of July 1976. After the length of the north breakwater is prolonged, the area effected by the moving sediment to the place about 6Km south from south breakwater, which is always the change of erosion and accumulation, the littoral transport rate of the study area is equal to the accumulation between the Ta-Chia river and the place which is 6Km south from the south breakwater before July, 1976. The littoral transport rate is equal to the accumulated sand volume of the north side of the north breakwater after July, 1976.

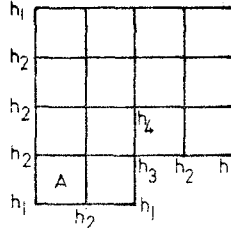


Fig. 7. The plot of the meth method.

Date		4, 1974	10, 1974	10, 1975	10, 1976	10, 1977
north breakwater	progress	+ 0 m	+ 142 m	+ 479 m	+ 462 m	+ 310 m
	the head's depth	± 0 m	- 3 m	- 5 m	- 10 m	- 20 m
north groin	progress	+ 0 m	+ 319 m	+ 6 m	+ 287 m	+ 200 m
	the head's depth	± 0.4 m	- 0.8 m	- 2 m	- 4 m	- 6 m

For computing the sand volume change rate by the mesh method, the yearly littoral drift of this area is shown as follows.

1971, 6 - 1972, 7	:	1,340,000 m/yr	
1972, 7 - 1973, 7	:	1,636,000 "	
1973, 7 - 1974, 7	:	1,458,000 "	
1974, 7 - 1975, 7	:	1,406,000 "	(26)
1975, 7 - 1976, 7	:	1,386,000 "	
1976, 7 - 1977, 8	:	2,028,000 "	
1977, 8 - 1978, 8	:	1,313,000 "	
1978, 8 - 1979, 8	:	1,307,000 "	

By representing the above results as the immersed weight of littoral transport rate, and using the formula

$$I_1 = (\rho_s - \rho) g a' Q \dots \dots \dots (27)$$

then the quantity of I_1 is, ($a' = 0.6$)

1971, 6 - 1972, 7	:	1.277 x 10	Kg m /sec/m-yr
1972, 7 - 1973, 7	:	1.588 x 10	"
1973, 7 - 1974, 7	:	1.389 x 10	"
1974, 7 - 1975, 7	:	1.339 x 10	"
1975, 7 - 1976, 7	:	1.320 x 10	"
1976, 7 - 1977, 8	:	1.929 x 10	"
1977, 8 - 1978, 8	:	1.251 x 10	"
1978, 8 - 1979, 8	:	1.245 x 10	"

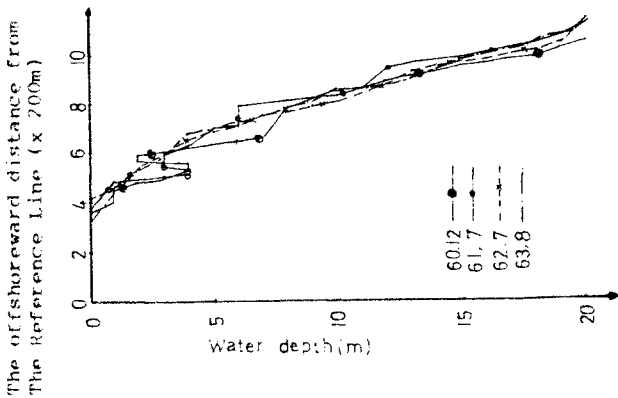


Figure 8.1. The change of the bottom slope at the north side of the north breakwater.

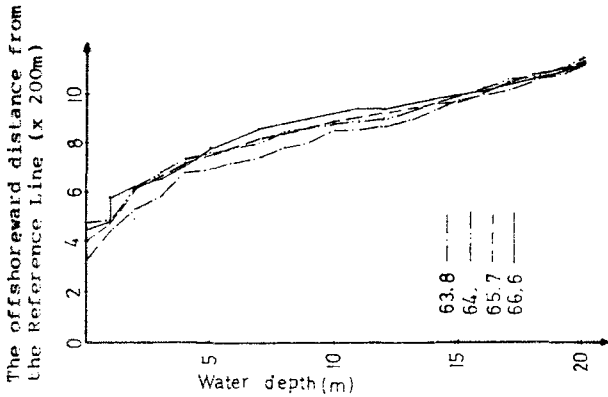


Figure 8.2. The change of the bottom slope at the north side of the north breakwater.

3.2 The calculation of the alongshore breaking wave energy :

The wave data are recorded by the ultrasonic wave gauge at the depth -19m per 2 hours from July 1972 to June 1976.

The wave is affected by the effects of shoaling, refraction, bottom friction and percolation. By neglecting the effects of bottom friction and percolation as wave is propagating toward the surf zone, there the breaking wave height is equal to

$$H = H_0 K_r K_s$$

where K_r and K_s are refraction coefficient and shoaling coefficient respectively. The mathematical representation is as follows

$$k_r = (B_0 / B)^{1/2}$$

$$k_s = (C_{g0} / C_g)^{1/2}$$

where B is the separation of the wave rays and prefix "0" represents the characters of deep water. As the bottom slope is smaller than 1/10, then K_r and K_s could be calculated from the four equations derived by Chao, Y.Y. (1970) as follows

$$C^2 = \left(\frac{g}{k}\right) \tanh kh$$

$$\frac{d\theta}{ds} = \frac{1}{c} \left(\sin \theta \frac{\partial c}{\partial x} - \cos \theta \frac{\partial c}{\partial y} \right) = -\frac{1}{c} \frac{dc}{dB}$$

$$H_0 (C_g)_0 B_0 = H^2 \cdot C_g \cdot B = \text{constant}$$

$$\frac{d^2 B}{ds^2} - P^{(1)} \frac{dB}{ds} + P^{(2)} B = 0$$

$$P^{(1)} = \frac{1}{c} \left(\cos \theta \frac{\partial c}{\partial x} + \sin \theta \frac{\partial c}{\partial y} \right)$$

$$P^{(2)} = \frac{1}{c} \left(\sin^2 \theta \frac{\partial^2 c}{\partial x^2} - 2 \sin \theta \cos \theta \frac{\partial^2 c}{\partial x \partial y} + \cos^2 \theta \frac{\partial^2 c}{\partial y^2} \right)$$

Where D is water depth, θ is the angle between X axis and wave direction, S is the distance along wave ray and C is the phase velocity. Use numerical method to get

$$D_{n+1} = D_n + \left(\frac{\partial D}{\partial x} \right)_n dx + \left(\frac{\partial D}{\partial y} \right)_n dy + \frac{1}{2} \left(\frac{\partial^2 D}{\partial x \partial y} \right)_n dx dy + \left(\frac{\partial^2 D}{\partial x^2} \right)_n dx^2 + \frac{1}{2} \left(\frac{\partial^2 D}{\partial y^2} \right)_n dy^2$$

$$P_{n+1} = \left[(4 - 2P_n^{(2)} \Delta s^2) / (2 - P_n^{(1)} \Delta s) \right] B_n - \left[(2 + P_n^{(1)} \Delta s) / (2 - P_n^{(1)} \Delta s) \right] B_{n-1}$$

The subscript "n" represents the value of the nth calculation, as shown in Fig.9, where X axis is taken parallel to the shoreline. Developing these numerical calculations to get "THE WAVE CHARACTER COMPUTING PROGRAM", the wave characters such as K_r , K_s , H , C_g and θ could be found out at any water depth $h=D$. Since $\theta = \frac{\pi}{2} - \alpha$ as shown in Fig.9, then

$(P_1)_b = \frac{1}{8} \rho g H_b^2 (C_g)_b \cos \theta_b \sin \theta_b$
is the alongshore breaking wave energy.

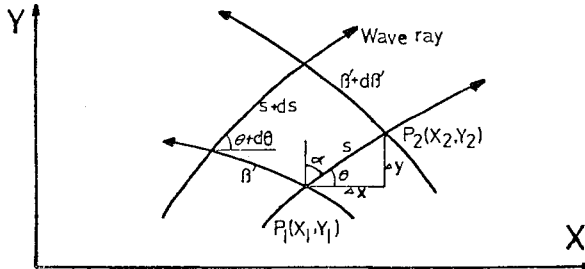


Figure 9.1. The diagram of the wave refraction.

Since there is no records of wave direction at -19m depth, the incident wave direction is found out by the above program using the deep water incident wave direction which is the wind direction as the wave gauge serves.

Consider only the waves which are moving onshore could cause littoral transporting. The waves which is the same incident direction is summed up. The root mean square value of their heights and the mean value of their periods are found out. Therefore, the total onshore acting waves are compiled to 8 equivalent waves which have the "rms" wave height H_{rms} , mean wave period \bar{T} . This is because

$$(P_i)_b \propto H^2 \cos \theta \sin \theta \propto H^2 \sin 2 \theta$$

$$\sum_{i=1}^M (P_i)_b \propto \left(\sum_{i=1}^M H_i^2 \right) \sin 2 \theta = M H_{rms}^2 \sin 2 \theta$$

Where M_j is the number of the waves which have the same wave direction θ_j , and H_{rms} is represented as

$$H_{rms}^2 = \frac{1}{M} \sum_{i=1}^M H_i^2$$

To compute the alongshore breaking wave energy, the input data including the water depths of the grid points, the water depths and the coordinates of the incident points, the H_{rms} values and the \bar{T} values of the equivalent waves with the incident wave direction θ at the depth -19m, are all considered.

The output results are $(SUM)_j$ which is the summation of the alongshore breaking wave energy of MN wave rays. Then the total alongshore breaking wave energy per unit beach length of one year is expressed as

$$(P_i)_b = \frac{7200}{MN} \sum_{j=1}^8 [M_j (SUM)_j]$$

where 7200 sec is the 2 hr wave acting duration.

The result of each year from July 1972 to June 1976 is shown as the Table 2,3,4 and 5.

3.3 The relationship between I_i and $(P_i)_b$

Equation (21) shown that the relationship between I_i and $(P_i)_b$ is not exact linearly proportional to each other, this is proved by Fig.10. which is originally prepared by Komar and Inman (1970) there is a upper limit $K=0.77$. Adding the data of equation(28) and Table 2 - 5 into Fig. 10, re-analyze the total data by the least square method to get a regression line which is expressed as $I_i = 0.154 (P_i)_b^{1.0695}$

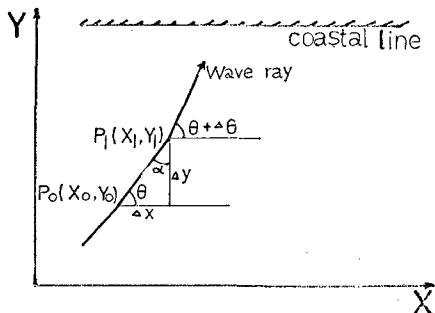


Figure 9.2. The diagram of the wave refraction.

Table 2. The resulting wave data and the alongshore breaking wave energy during July 1, 1972 to June 30, 1973.

MN=19	NNE	N	NNW	NW	WNW	W	WSW	SW
M_j	1802	657	248	120	76	86	123	502
H_{rms}	1.62	1.23	0.80	0.74	0.79	0.57	0.62	0.74
\bar{T}	5.6	5.4	5.2	5.0	5.0	5.1	4.8	5.1
θ_j at - 19.m	14.5°	35.6°	57.5°	80°	102.5°	125°	147.5°	170°
$(SUM)_j \times 10^4$	4.67	2.26	0.74	0.05	-1.06	-1.08	-0.77	-0.82
$(P_i)_b$	$3.59 \times 10^{10} \text{ kg m}^2 / \text{sec}^2 / \text{m-yr}$							

Table 3. The resulting wave data and the alongshore breaking wave energy during July 1, 1973 to June 30, 1974.

MN= 11	NNE	N	NNW	NW	WNW	W	WSW	SW
M_j	1830	682	226	159	153	126	194	234
H_{rms}	1.45	1.22	0.93	0.90	0.85	0.82	0.8	0.75
\bar{T}	6.3	5.7	5.5	5.2	5.2	4.5	4.6	4.8
θ_j at - 19.m	16°	35.6°	57.5°	80°	102.5°	125°	147.5°	170°
$(SUM)_j \times 10^4$	1.64	1.12	0.47	0.08	-0.91	-0.59	-0.91	-0.35
$(P_i)_b$	$2.24 \times 10^{10} \text{ kg m}^2 / \text{sec}^2 / \text{m-yr}$							

Table 4. The resulting wave data and the alongshore breaking wave energy during July 1, 1974 to June 30, 1975.

MN=11.	NNE	N	NNW	NW	WNW	W	WSW	SW
M_j	1021	617	105	61	57	71	79	127
$H_{r.m.}$	1.77	1.6	0.8	0.68	0.54	0.4	0.52	0.53
\bar{T}	6.1	5.9	5.0	5.6	5.3	4.0	4.2	4.4
θ_j at - 19.m	16°	35.6°	57.5°	80°	102.5°	125°	147.5°	170°
$(SUM)_j \times 10^4$	2.79	1.74	0.56	-0.03	-0.08	-0.17	-0.24	-0.21
$(P_i)_b$	$2.56 \times 10^{10} \text{ Kg m}^2 / \text{sec}^2 / \text{m-yr.}$							

Table 5. The resulting wave data and the alongshore breaking wave energy during July 1, 1975 to June 30, 1976.

MN=11	NNE	N	NNW	NW	WNW	W	WSW	SW
M_j	1375	455	120	97	83	76	106	196
$H_{r.m.}$	1.52	1.33	0.95	0.71	0.4	0.38	0.48	0.56
\bar{T}	5.8	5.5	5.5	5.2	5.3	5.2	5.3	5.4
θ_j at -19. m	14.5°	35.6°	57.5°	80°	102.5°	125°	147.5°	170°
$(SUM)_j \times 10^4$	1.67	1.82	0.89	0.6	-0.07	-0.12	-0.24	-0.17
$(P_i)_b$	$2.11 \times 10^{10} \text{ Kg m}^2 / \text{sec}^2 / \text{m-yr}$							

where I_i and $(P_i)_b$ are in units of cgs system.

But for the Taichung coast where the climate is so steady that the alongshore breaking wave energy fluctuate slightly, the relationship between I_i and $(P_i)_b$ could be expressed as

$$I_i = K(P_i)_b$$

where K is constant and is equal to 0.55. The equation is suitable for any unit system.

4. Conclusion and Discussion

Applying the energy approach for unidirectional steady flow (Bagnold, 1963), derive out the relationship between the alongshore breaking wave energy and the littoral immersed weight transport rate as $I_i = K(P_i)_b$. K is function of wave height, bottom slope, the grain size and the sediment transport pattern. It increases as the grain size decreases or it does either there exists an ocean current in the predominant littoral transport direction or under the action of the bigger waves. This reveals that the larger part of wave energy is supplied to transport sediment as the wave energy becomes larger. This is shown by the empirical relationship $I_i = 0.154 (P_i)_b^{1.0000}$. But for a coast, such as the Taichung coast, where the oceanographic condition is so steady that the alongshore breaking wave energy fluctuates slightly, the relationship between I_i and $(P_i)_b$ could be written as $I_i = K(P_i)_b$, where K is constant. Then the Taichung coast has the relation of $I_i = 0.55 (P_i)_b$. This equation could be applied for the coast of similar oceanographic conditions and beach characteristics to estimate the littoral transport rate. Such that the harbor planning and the shore protection could be based on.

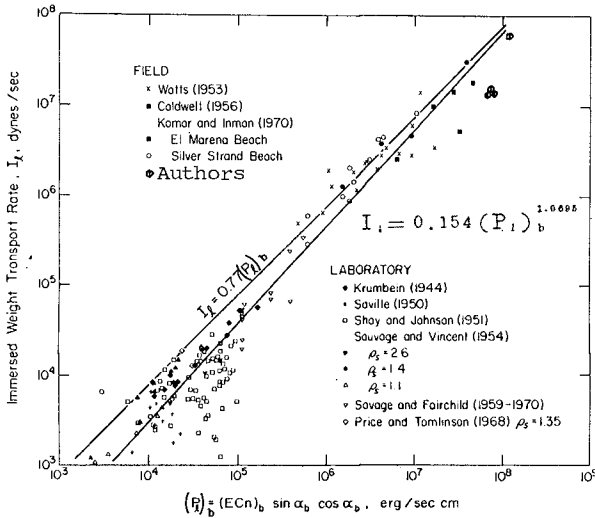


Figure 10. The relationship of the alongshore breaking wave energy and the immersed weight transport rate.

5. Acknowledge

The authors are grateful to the Taichung Harbor Bureau, Taiwan, R.O.C. for the observational wave records. Also the appreciation is given to Mr. Sen-Ho Chen, M.S., Harbor and Oceanic Engineering Institute, National Taiwan College of Marine Science and Technology, for his assistance to the computer program, and working personnel of The Computer Center at N.T.C.M.S.T.

6. Reference

- Babnold, R.A. (1963) "Mechanics of Marine Sedimentation" THE SEA, Interscience Publishers, New York, 3:507-528.
- Bruun, Per (1966) Tidal Inlets and Littoral Drift, University of Florida.
- Galvin, C.J., Jr. (1972) "Wave Breaking in Shallow Water", Waves on Beaches and Resulting Sediment Transport, edited by Meyer, R.E., 1972, Academic Press.
- "A Gross Longshore Transport Rate Formula", Proc. of the 13th Coast. Eng. Conf., Vancouver, B.C. Canada.
- Graf, W.H. (1971) Hydraulics of Sediment Transport, McGraw-Hill

Book Company, New York.

Komar, P.D. and D.L. Inman (1970) "Longshore Sand Transport on Beaches", J. of Geophysical Research, Vol.76, No.30.

Komar, P.D. (1971) "The Mechanics of Sand Transport on Beaches", J. of Geophysical Research, Vol.76, No.3.

Komar, P.D. and M.C. Miller (1973) "The Threshold of Sediment Under Oscillation Water Waves", J. of Sedimentary Petrology, Vol.43, No.4, pp.1101-1110.

_____ (1975) "Sediment Threshold Under Oscillatory Waves", Proc. 14th Conf. on Coast. Eng., PP.756-775.

Komar, P.D. (1976) "Longshore Transport of Sediments on Beaches", Chap.8, Beach Processes and Sedimentation.

Lee, Chung-Pan (1980) "The relation between the littoral transport and the surface wave", Theme of M.S., Institute of Harbor and Oceanic Eng., National Taiwan College of Marine Science and Technology, Keelung, Taiwan, R.O.C.

LeMeharte, B. (1976) An Introduction to Hydrodynamics and Water Waves.

Newman, J.N. (1977) Marine Hydrodynamics, Halliday Lithograph Corp., USA.

Raudkivi, A.J. (1976) "Movement of Sediment by Waves", Loose Boundary Hydraulics, 2nd ed., Robert Maxwell, m.c.

Shore Protection Manual, 1977, Department of The Army Corps of Engineering.

Tainan Hydraulics Laboratory (1970) "The Computation of Littoral Drift". Report on The Model Study and Sand Drift Investigation for Ta-Wu Harbor, Bulletin No. 12. The Tainan Hydraulic Laboratory, Tainan, Taiwan, R.O.C.

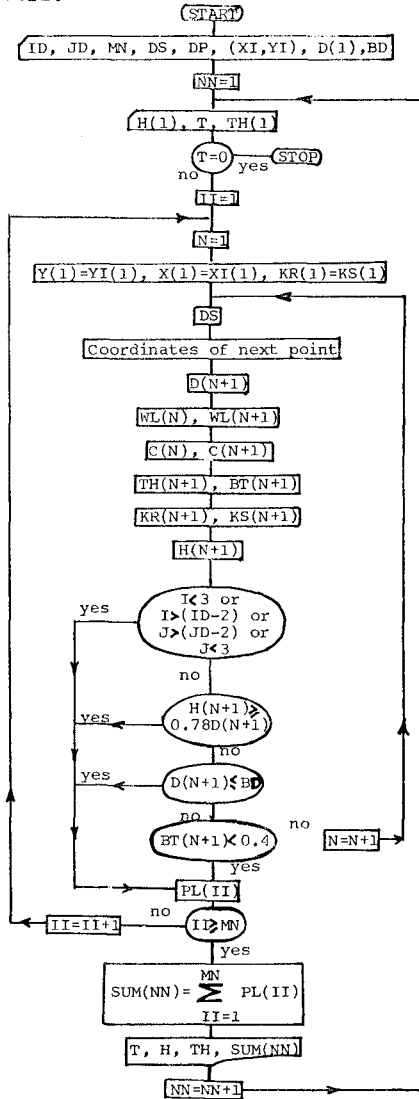
Tainan Hydraulics Laboratory (1972) "The Calculation of Refraction Coefficient". Report on The Model Test for Pa-Tou Fishery Harbor, Bulletin No.16. The Tainan Hydraulic Laboratory, Tainan, Taiwan, R.O.C.

Thornton, E.B. (1972) "Distribution of Sediment Transport Cross the Surf Zone", Proc. of the 13th Conf. on Coast. Eng., pp.1049-1068.

Walton, T.L., Jr. (1973) "Littoral Drift Computations Along The Coast of Florida By Means of Ship Wave Observations", Technical Report No.15, Univ. of Florida.

Yalin, M.S. (1972) Mechanics of Sediment Transport, Pergamon Press Ltd., Headington Hill Hall, Oxford.

Appendix: Flow Chart of THE PROGRAM OF COMPUTING WAVE CHARACTORS.



List of Notations

ID,JD: number of the grids for x-axis, y-axis, respectively
MN : number of the incident wave rays
DP : water depth of the grid point
XI,YI: the initial coordinates of x and y axis respectively
X,Y : the coordinates of the position for calculating wave character
D : water depth
BD : water depth to output
BT : the separation of wave direction ray
NN : the index of waves
H : wave height
T : wave period
WL : wave length
C : celerity
CG : wave group velocity
PL : wave energy of each incident wave ray
SUM : the total wave energy of all beach for each wave
TH : the angle between x axis and the wave direction
II : the order of incident wave rays
N : the index of calculating step
KR,KS: the refraction coefficient and shoaling coefficient respectively

CHAPTER 77

LONGSHORE WATER AND SEDIMENT MOVEMENT

by

D.H. Swart* and C.A. Fleming**

ABSTRACT

The mean sediment transport rate obtained by using six known longshore transport formulae, for which the input variables are determined consistently, is used as best estimate of the transport. A good comparison is obtained when this package deal approach is compared with a prototype situation where the transport rates are inferred from quarterly bathymetric surveys over two years. The accuracy of the input variables is reviewed theoretically and the results are used to perform a sensitivity analysis.

1. INTRODUCTION

The Inman/Bagnold/Komar formula (referred to below as the SPM formula) for the prediction of total longshore transport rates is suggested in the Shore Protection Manual (SPM, 1973) for use in the coastal environment. In the design of large coastal structures, such as the breakwaters for a harbour which can accommodate oil tankers and ore carriers, the length of the breakwaters is determined largely by navigational requirements and the longshore transport is important only for the determination of the method of sediment by-passing, if that should be required. In such instances the output as given by the SPM formula, that is, a total annual transport rate without any indication about the area within which this transport takes place, is mostly sufficient. However, the present-day trend is for more and more smaller coastal structures to be built, such as small fishing harbours or small-craft harbours. Navigational requirements only demand a water depth of, say, 7 m at the entrance to such harbours. This depth could quite easily fall within the active coastal transport zone, which implies that the sediment transport determines the entrance depth to the harbour. Therefore it is important to have both the longshore transport rate, as predicted by the SPM formula, and the distribution normal to shore of this transport. For this reason it is imperative that the longshore transport distribution normal to shore is predicted in terms of the local hydraulic parameters. Such formulae, which were called detail predictors by Swart (1976a), use the wave characteristics, hydraulic bed roughness and local longshore current velocity to predict instantaneous longshore transport rates. The accuracy of predicted sediment transport rates for given hydraulic input parameters is, even under steady-flow conditions, strongly dependent on the accuracy of the input variables. Even a small inaccuracy in the input velocity can, for example, cause substantial errors in the predicted transport rates. The input variables used for the prediction of longshore transport rates are usually also predicted, either because of difficulties in measuring the required parameters in the coastal environment, or because of the impracticability of measuring over a long period of time, say one year, to deduce seasonal trends from the input data. If the techniques used to predict the input variables, which are in

* Coastal Engineering and Hydraulics Division, National Research Institute for Oceanology, Stellenbosch, South Africa.

** Sir William Halcrow and Partners, Consulting Engineers, Swindon, U.K.

turn to be used to predict sediment transport rates, are not quite accurate, the computed longshore transport rates could be in error by an appreciable margin. For this reason it seems a sound practice to use as many reliable predictors for the longshore transport rate as are available, and to infer the best estimate of the longshore transport rate from the results of all these formulae. In addition, it is imperative to always use the same method of predicting the input variables, to eliminate the possibility of differences in predicted transport rates because of the use of different techniques to predict the input variables. This paper describes the elements of such a 'package deal' approach. The following *input variables* are required to allow the application of the package deal approach.

(1) *Wave data* are needed in either intermediate or deep water over the period for which transport rates are required (mostly one year to allow an evaluation of seasonal effects), that is,

- significant wave height $(H_s)_I$
- peak energy wave period T_p
- angle of incidence θ_I
- fraction of the time that every wave condition occurs f

Subscript I signifies 'input'.

(2) The following details of the *bed topography* are required:

- the topography of the whole area to allow the construction of wave refraction diagrams;
- beach profiles at the locations where transport computations are to be performed, to decide on the depths d_i in which transport rates are needed and to find the representative widths of the transport zones thus defined;
- the mean bed slope in the breaker zone at the locations where longshore current velocities are to be calculated.

(3) The *characteristics of the sediment* (bed material) influence the longshore sediment transport rates, namely,

- the relative apparent density $\Delta_s = (\rho_s - \rho_w)/\rho_w$ where ρ = mass density, subscript s refers to 'sediment' and subscript w to 'water';
- the distribution of grain sizes; $D_{10}, D_{16}, D_{35}, D_{50}, D_{65}, D_{90}$.

With the aid of the above input variables a comprehensive set of output variables is produced.

(1) The standard output of a *refraction study* is obtained, namely,

- significant wave height H_s
- wave length λ
- angle of incidence θ

in all water depths d_i , as chosen above in the area between the water line and a depth equal to four times the maximum depth in which wave breaking can occur. This area is referred to below as the 'test area'.

(2) A wide range of *wave characteristics* is calculated for water depths d_i in the test area. Included are, for example, the horizontal orbital velocity at the bed u_{bc} and the orbital amplitude a_0 at the bed. All computations regarding wave characteristics are at present performed with linear wave theory.

(3) *Bed-form characteristics* are computed at depths d_i in the test area by using the technique outlined by Swart (1976a) and are then used to compute the following:

- the hydraulic bed roughness $r = 25\Delta_r^2/\lambda_r$, see Swart (1976a) where Δ_r and λ_r are the bed-form height and length respectively;
- the wave friction factor f_w , found empirically by Swart and Loubser (1980) from 640 data sets for turbulent flow in the boundary layer, namely,

$$\text{For } a_o/r < 7 \quad f_w = \frac{0.30}{1+0.28\left(\frac{a_o}{r}\right)^{1.1}}$$

$$\text{For } 7 \leq a_o/r \leq 160 \quad f_w = 0.0066 + 0.483\left(\frac{a_o}{r}\right)^{-0.91}$$

$$\text{For } 160 < a_o/r \quad f_w = 0.0146\left(\frac{a_o}{r}\right)^{-0.157} + 0.483\left(\frac{a_o}{r}\right)^{-0.91} \quad \dots (1.1)$$

- the chezy roughness coefficient C_h , and
- the friction factor C_{LH} as used by Longuet-Higgins (1970) in his theory for the prediction of longshore current velocity.

(4) *Wave-induced properties* which are also functions of the bed roughness r are computed at depths d_i in the test area, namely,

- bed shear stresses, and
- wave power.

(5) *Longshore current velocities* v_i are computed for depths d_i in the test area, with the technique outlined in Section 2.

(6) At the same depths *longshore transport rates* are computed for five different detail longshore transport formulae, namely, the formulae of

- B yker (1971)
- Fleming (1976, 1977)
- adapted Engelund-Hansen (Swart, 1976b)
- Nielsen (1978, 1979)
- adapted Ackers-White (Swart and Lenhoff, to be published in 1980).

In addition the total longshore transport, as predicted by the SPM formula, is also obtained.

(7) *Statistical properties* of the computed transport rates are calculated, namely,

- the mean total transport μ obtained from the six formulae listed under (6), as well as the standard deviation σ around the mean,
- the mean transport/unit width normal to shore obtained from the five detail predictors listed under (6), as well as the standard deviation around the mean.

Similar means and standard deviations are also calculated for the gross transport and the total upcoast and downcoast transport.

The individual items of the package deal approach outlined above have mostly been reported on by various researchers in literature and are therefore not repeated in detail in this paper. The only exceptions are

the prediction of longshore current and the adaptation of the Ackers-White formula for the prediction of sediment transport under steady-state flow conditions. These two aspects are therefore discussed in more detail in Sections 2 and 3 below before the package deal approach is applied to a prototype example.

2. LONGSHORE CURRENT VELOCITY

The momentum balance in the longshore direction determines the strength and distribution of the longshore current, that is

$$\frac{\partial R_{yx}}{\partial y} - (B_x + \frac{\partial D}{\partial y}) = 0 \quad \dots (2.1)$$

where the x- and y-axes are assumed to be parallel and normal to the (straight) coastline, R_{yx} is the flux of longshore momentum across a line parallel to the shoreline, B_x is the bed shear in the direction of the longshore current and $(\partial D/\partial y)$ is the exchange of momentum due to horizontal turbulent eddies. The radiation stress term represents the driving force whereas the bed shear and the lateral mixing are the dissipative forces.

Longuet-Higgins (1970) formulated equation (2.1) and found a solution to this equation for regular waves breaking as spilling breakers on a gently sloping beach. The lateral mixing, which is the key factor in the determination of the shape of the velocity profile, that is, in the distribution of velocity across the breaker zone and beyond the breaker line, is difficult to determine quantitatively. Longuet-Higgins assumed the lateral mixing to increase with the distance offshore to the power 1.5, even outside the breaker zone. The lateral mixing depends to some degree on the rate of change of wave energy dissipation as the wave approaches the shore, that is, on the type of breaker that occurs, or stated differently, on the shape of the velocity profile itself. The area within which the wave energy is dissipated is greater in the case of irregular waves with a spectrum of wave heights (extends further offshore) than is the case for regular waves and in addition the local rate of energy dissipation is also lower for irregular waves than for regular waves. It therefore seems probable that the effect of lateral mixing on the velocity profile will be less in the case of irregular waves. Furthermore it is truer to nature since, although the assumption of spilling breakers will still be required, a spectrum of wave heights is assumed. With this in mind Swart (CSIR, 1978) developed an explicit formula for the prediction of longshore current which is valid for long-crested irregular waves. The main points of this derivation are outlined below.

The following *assumptions* are made:

- (1) Linear wave theory is used for all wave properties.
- (2) Random long-crested waves with a Rayleigh distribution of wave heights are assumed.
- (3) All waves in the spectrum break as spilling breakers with a constant breaker index $\gamma =$ ratio of wave height at breaking to mean water depth.
- (4) Each wave is assumed to retain a height equal to γ times the local water depth as it approaches the shoreline, that is, its wave height decreases at the same rate as the water depth in the breaker zone. In this manner a truncated wave height spectrum is formed, as assumed by Battjes (1974) in his treatment of random breaking waves.

- (5) Wave set-up is neglected.
- (6) The bed slope α in the breaker zone is assumed to be constant.
- (7) The friction coefficient is assumed constant over the breaker zone.
- (8) Lateral mixing is neglected.

Except for assumption (8), the other assumptions are the same as those made by Longuet-Higgins (1970). The resulting form of the three components in the momentum balance equation, based on these assumptions, is given below.

Radiation stress term ($\partial R_{yx} / \partial y$)

Longuet-Higgins (1971) showed that the radiation stress R_{yx} is given to the second order of approximation by

$$R_{yx} = En \sin \theta \cos \theta \quad \dots(2.2)$$

where E is the wave energy per unit surface area, n is the ratio group velocity to wave celerity and θ is the angle of wave incidence. Battjes (1974) showed that the wave energy in a breaking wave spectrum is reduced to a fraction q_b of the value it would have attained if shoaling and refraction had taken place uninterrupted, that is, if no breaking had taken place, when a fraction $(1-q_b)$ of the waves are breaking. It follows from the definition of the Rayleigh distribution that

$$q_b = 1 - \exp(-H_b^2 / H_{f,rms}^2) \quad \dots(2.3)$$

where H_b is the local breaker height ($= \gamma d$) and $H_{f,rms}$ is the root-mean-square wave height that would have been attained in the absence of wave breaking. Since the wave height cannot exceed a value (γd) this wave height is fictitious.

It therefore follows from equation (2.2) that the radiation stress R_{yx} is reduced to a fraction q_b of its fictitious value R_{yxf} in the absence of wave breaking, that is,

$$R_{yx} = q_b R_{yxf} \quad \dots(2.4)$$

where subscript f refers to 'fictitious'.

Since it is assumed that the fictitious waves do not break, R_{yxf} is independent of the distance offshore. Therefore

$$\frac{\partial R_{yx}}{\partial y} = R_{yxf} \frac{\partial q_b}{\partial y} \quad \dots(2.5)$$

With the aid of equations (2.2) to (2.5) it can be shown in an analogous manner to Longuet-Higgins' derivation for regular waves that

$$\frac{\partial R_{yx}}{\partial y} = \frac{5}{16} \rho \gamma^2 g d \exp\left(-\frac{\gamma^2 d^2}{H_{f,rms}^2}\right) \sin \theta \cos \theta \tan \alpha \quad \dots(2.6)$$

Bed shear term B_x

Longuet-Higgins (1970) showed that, provided that the longshore transport velocity v is much less than the maximum horizontal orbital velocity u_{bc} at the bed, the bed shear B_x can be approximated by

$$B_x = \frac{2}{\pi} C_{LH} \rho u_{bc} v \quad \dots(2.7)$$

For shallow-water waves the orbital velocity u_{bc} reduces to

$$u_{bc} = \frac{1}{2} \left(\frac{\bar{H}}{d} \right) (gd)^{\frac{1}{2}} \quad \dots(2.8)$$

$$\text{and therefore } B_x = \frac{1}{\pi} \rho C_{LH} \left(\frac{\bar{H}}{d} \right) (gd)^{\frac{1}{2}} v \quad \dots(2.9)$$

where \bar{H} is the mean wave height of the breaking wave spectrum in a water depth of d .

Solution

Since the lateral mixing is neglected, it follows from equations (2.1), (2.6) and (2.9) that the longshore current velocity v equals:

$$v = \frac{5\pi}{16} \frac{\gamma^2 (gd)^{\frac{1}{2}}}{C_{LH}} \left(\frac{\bar{H}}{d} \right)^{-1} \exp \left\{ \frac{-\gamma^2 d^2}{H_{rms}^2} \right\} \sin \theta \cos \theta \tan \alpha \quad \dots(2.10)$$

An example of the velocity profile as predicted by equation (2.10) is given in Figure 1. Both axes are non-dimensionalized, the vertical axis by dividing by a scaling velocity v_{OR} and the horizontal axis by dividing by the distance from the shoreline to the location in the profile where the significant wave height will start breaking, that is, where 13.5 per cent of the waves in the spectrum will have started to break. Also shown in this figure is the solution for regular waves of Longuet-Higgins, applied with a lateral mixing which can be shown to be the average of the possible mixings. The agreement between the two solutions is very good. This indicates that the assumption to neglect lateral mixing is justified for irregular waves and therefore equation (2.10) is used for the prediction of longshore current velocity in the package deal approach.

Longshore velocity friction factor C_{LH}

The magnitude of the friction factor C_{LH} must be known before equation (2.10) can be used to determine longshore current velocities. Galvin and Nelson (1967) compiled all available longshore current data. Each of these data sets can be used to determine a value for C_{LH} . Longuet-Higgins (1970) evaluated this information and concluded that C_{LH} is 'of order 0.01'. It is suggested in the Shore Protection Manual (SPM, 1973) that C_{LH} is actually less than 0.01. A value of $C_{LH} = 0.0071$ is suggested as the best estimate of C_{LH} . Using the same data, Komar and Inman (1970) found that

$$C_{LH} = 0.15 \tan \alpha \quad \dots(2.11)$$

Swart suggested that the friction factor should also be a function of the bed roughness r (CSIR, 1978). He showed theoretically that

$$C_{LH} = \Phi \left(\frac{f_{wb} g}{2C_{hb}^2} \right)^{\frac{1}{2}} \quad \dots(2.12)$$

where Φ is an unknown coefficient and subscript b refers to the significant breaker line.

Galvin and Nelson's data were then used to find a value for Φ , namely,

$$\Phi = 25 (\tan \alpha)^{0.85} \quad \dots(2.13)$$

that is,

$$C_{LH} = 25 \left(\frac{f_{wb} g}{2C_{hb}^2} \right)^{\frac{1}{2}} (\tan \alpha)^{0.85} \quad \dots(2.14)$$

Galvin and Nelson's data are plotted in Figure 2 for each of the above suggestions for the friction factor C_{LH} . From the four one-to-one plots of velocity listed in Galvin and Nelson's paper to predicted longshore current velocity it is quite apparent that the last alternative for C_{LH} , that is, equation (2.14), as given by Swart and Fleming (in CSIR, 1978) yields by far the best agreement between data and prediction, followed by Komar and Inman's equation (equation (2.11)). The value of C_{LH} as predicted from equation (2.14) is therefore used in the package deal approach.

3. PREDICTION OF LONGSHORE TRANSPORT RATES

As stated in Section 1, there are two types of formulae for the prediction of longshore transport rates, namely, overall predictors and detail predictors. Of the one overall predictor and five detail predictors listed in Section 1 only the adapted Ackers-White formula (Swart and Lenhoff, to be published in 1980) has not been reported on in the international literature. Therefore only a short summary is given of the first five transport equations, whereafter the adapted Ackers-White formula is discussed in more detail.

SPM formula (SPM, 1973; Swart, 1976a)

This formula is based on an empirical relationship between the longshore component of the energy flux due to wave action and the total longshore transport rate. No distribution is given of transport across the breaker zone. The formula for the total transport rate for each wave condition i is:

$$S_{SPM} = K(D) f_i T_p H_{OS}^2 K_{rb}^2 \sin 2 \Theta_b \quad \dots(3.1)$$

(in $m^3/year$)

where H_{OS} is the deep-water significant wave height, K_{rb} is the refraction coefficient at the significant breaker line and Θ_b is the angle of incidence at the significant breaker line. Swart (1976a) showed that the proportionality factor $K(D)$ is not a constant but is a function of the median grain size D_{50} of the bed material, namely,

$$K(D) = 91 \times 10^4 \log_{10} \left\{ \frac{0.00146}{D_{50}} \right\} \quad \dots(3.2)$$

Bijker formula (Bijker, 1971)

Bijker's formula, developed in 1967, was the first detail predictor and at the time constituted a major breakthrough in the prediction of longshore transport rates. It is built up of two components, namely, a bed load component and a suspended load component. The bed load formula was adapted from the Frýlink formula for sediment transport rates under riverine conditions by adapting the shear stress terms:

$$S_{bB} = 5 D_{50} \frac{v}{C_h} g^{\frac{1}{2}} \exp \left\{ \frac{-0.27 \Delta_s g D_{50}}{\mu(\tau_{wc}/\rho)} \right\} \quad \dots(3.3)$$

(in $m^3/m/s$)

where μ is a ripple factor defined by Bijker and the bed shear stress due to waves and current τ_{wc} is:

$$\tau_{wc} = \rho \frac{v^2 g}{C_h^2} \left(1 + \frac{1}{2} \left(\frac{\xi u_o}{v} \right)^2 \right) \quad \dots(3.4)$$

Swart (1976b) subsequently showed that $\xi = C_h (f_w / (2g))^{1/2}$. The suspended load was found from the Rouse-Einstein distribution of suspended material from bed to free surface and integrating the product instantaneous velocity times concentration of bed material with depth, resulting in:

$$S_{SB} = 1.83 S_{bB} \{ I_1 \ln \left(\frac{33d}{r} \right) + I_2 \} \quad \dots(3.5)$$

where I_1 and I_2 are elliptic integrals, for which Býker determined quantitative values by numerical integration. The total transport per metre in any given water depth d_i is then

$$S_B = S_{bB} + S_{SB} \quad \dots(3.6)$$

(in $m^3/m/s$)

Although the formula contains no incipient motion criterion, the transport rates predicted for velocities below the threshold velocity are very low.

Fleming formula (Fleming and Hunt, 1976; Fleming, 1977)

Fleming developed a transport formula by which the total load (bed plus suspended load) for wave action can be predicted. He defined a reference concentration C_e close to the bed (a small distance e above the bed). He used the force balance of bed particles to derive a theoretical expression for C_e , which contains an incipient motion criterion. Fleming assumed that the concentration at the bed cannot exceed 0.52 and that the eddy diffusivity is constant over the whole water mass above the elevation $z = e$. A simple one-seventh power rule was assumed for the variation with distance from the bed of the longshore current velocity. The following equations must be integrated numerically to find the total longshore transport at any water depth d_i :

For $0 \leq z \leq e$

$$C(z) = 0.52 \left(\frac{C_e}{0.52} \right)^{z/e} \quad \dots(3.7)$$

$$v(z) = \frac{8}{7} v \left(\frac{z}{d_i} \right)^{1/7} \quad \dots(3.8)$$

where z is the distance above the bed.

For $e < z \leq d_i$

$$C(z) = C_e \exp \{ J_m (1 - (z/e)^{0.75}) \} \quad \dots(3.9)$$

The velocity $v(z)$ is again determined from equation (3.8). Fleming presented equations for the finding of J_m and e . The resulting transport is given in $m^3/m/s$.

Adapted Engelund-Hansen formula (Swart, 1976b)

Swart adapted the original formula by Engelund and Hansen (1967) for the prediction of total sediment transport rates in any depth d_i under steady flow conditions in an analogous manner to the Býker formula. The resulting equation is:

$$S_{EH} = \frac{0.05 v C_h (\tau_{wc}/\rho)^2}{g^{5/2} \Delta_s^2 D_{50}} \quad \dots(3.10)$$

(in $m^3/m/s$)

Obviously, equation (3.10) contains no incipient motion criterion. For longshore current velocities below the threshold velocity the formula predicts longshore transport rates which are higher than those predicted by the Býker formula.

Nielsen formula (Nielsen et al., 1978)

Nielsen determined the distribution of suspended sediment with distance from the bed for breaking (spilling breakers) and non-breaking wave conditions in the laboratory. He used the data to determine empirically quantitative predictors for the eddy diffusivity ϵ , which he found is constant with distance from the bed for non-breaking waves and increases strongly with distance from the bed for breaking waves, and the concentration of suspended material at the top of the bed forms C_0 , which contains an incipient motion criterion. The effect of the spilling breakers was to increase the eddy diffusivity at the bed by two orders of magnitude. The variation of concentration of suspended material with distance from the bed for a nonuniform material is given by

$$C(z) = C_0 \left(\frac{1}{1+\sigma V} \right)^{1/V} \dots(3.11)$$

where $V = \text{var}(w)/w_{s0}^2$, with $w =$ fall velocity of bed material; and $\sigma =$ parameter including the eddy diffusivity. In the package deal approach the product of the concentration in equation (3.11) and the velocity in equation (3.8) is integrated numerically with respect to z to find the total load in any given depth d_i . The appropriate value of the eddy diffusivity (with or without wave breaking) is used inside and outside the breaker line.

Adapted Ackers-White formula (Swart and Lenhoff, to be published, 1980)

The original formula for the prediction of sediment transport rates under steady-state conditions was as follows (Ackers and White, 1971):

$$S = 1.45 v D_{35} C \underbrace{\left(\frac{P_{fg}/\rho}{v_* fg} \right)^n \left(\frac{P_{cg}/\rho}{v_* cg v_r} \right)^{1-n}}_{\text{efficiency term}} \left(\frac{F_{gr}}{A} - 1 \right)^m \dots(3.12)$$

where C , n , m and A are grain size dependent parameters, for which empirical relationships are given by Ackers and White; F_{gr} is the sediment mobility $= (v_{fg} v_{cg}^{1-n}) / (\Delta_s g D_{35})^2$; P is the stream power; v_r the resultant velocity $= v$ for steady state) and v_* is the shear velocity $= (\tau/\rho)^{1/2}$; subscripts 'fg' and 'cg' respectively denote the 'fine grain' and 'coarse grain' versions of the properties. The value for fine-grained sediment is obtained by using the actual bed roughness r , as described before, whereas the value for coarse-grained sediment is obtained by using the grain size D_{35} instead of r in the appropriate equations. For steady-state conditions the efficiency term reduces to $(v/v_* fg)^n$. At present there are four adapted versions of equation (3.12) which are used in coastal engineering application, each containing different assumptions.

(1) SWANBY-version (Swart, 1976b)

Only the fine grain component of the shear terms was adapted to include the effect of wave action, which has now been found to be incorrect. Both the fine grain and the coarse grain components should be adapted.

(2) Willis-version (Willis, 1978)

Willis concluded that the critical (incipient motion) value A of the mobility number is different for combined wave and current action from the value for current action alone. To compensate for this difference he

multiplied the wave-induced shear stresses by an empirical coefficient w_c^2 , where w_c^2 is a function of the grain size. Willis adapted both the fine grain and the coarse grain components of the shear stress to include the effect of wave action, but he used an erroneous equation for wave power $\{c_g \tau_{wc}$ (where c_g = group velocity of the waves) and the power was treated as a scalar instead of finding the mean value of the product (instantaneous resultant velocity at the bed times instantaneous bed shear stress)}, which yielded too high values for the power. The effect of this mistake on the predicted transport rates is masked because w_c^2 was computed by using the equation for longshore sediment transport rate with the erroneous expression for the wave power.

(3) V.d. Graaff and V. Overeem-version (V.d. Graaff and V. Overeem, 1979)

V.d. Graaff and V. Overeem added the effect of waves on the shear stresses to both the fine- and coarse-grain components, but used the same critical mobility number as for steady-state conditions and also used the steady-state version of the efficiency term instead of the actual wave power.

(4) Swart and Lenhoff-version (to be published, 1980)

All three versions discussed above are therefore erroneous in one way or another. Swart and Lenhoff therefore defined a fourth version, in which all previous shortcomings are eliminated. Three points are important.

a. The *instantaneous sediment mobility* $F_{gr}(t)$ for waves and currents is given by:

$$F_{gf}(t) = \frac{v_{*fg}(t)^n v_{*cg}(t)^{1-n}}{(\Delta_s g D_{35})^{1/2}} \quad \dots (3.13)$$

The 't' denotes time variation.

Instead of adapting the fine and coarse grain components of the shear stress individually by integrating each separately with respect to time, it is more logical to compute the average effect of the inclusion of waves on the mean mobility number by integrating the instantaneous mobility number with respect to time, that is

$$F_{wc} = \overline{F_{gr}(t)} = \frac{1}{T} \int_0^T F_{gr}(t) dt \quad \dots (3.14)$$

where F_{wc} is the mean sediment mobility for combined current and wave action.

b. Similarly, the *instantaneous value* $E_f(t)$ of the *efficiency term*, as given in equation (3.12), is averaged to obtain the mean value E_{fwc} of the efficiency term for combined current and wave action, namely,

$$E_{fwc} = \overline{E_f(t)} = \frac{1}{T} \int_0^T E_f(t) dt \quad \dots (3.15)$$

$$\text{where } E_f(t) = \left(\frac{P_{fg}(t)/\rho}{v_{*fg}(t)^3} \right)^n \left(\frac{P_{cg}(t)/\rho}{v_{*cg}(t)^2 v_r(t)} \right)^{1-n} \quad \dots (3.16)$$

$$P(t) = v_r(t) \tau(t) \quad \dots (3.17)$$

Values for the instantaneous resultant velocity at the bed $v_r(t)$ and the instantaneous shear stress at the bed $\tau(t)$ are found by vector addition of the contributions by the waves and the currents.

When applying the formula for sediment transport rates (equation (3.12)), values for F_{wc} and E_{fwc} are found by numerical integration.

c. A new empirical relationship for the *critical mobility number* A was determined from more than 800 data sets of four different types, namely:

- observed incipient motion data on a flat bed for waves only;
- observed incipient motion data on a rippled bed for waves only;
- observed incipient motion data on a flat bed for combined current and wave action;
- sediment load data over rippled beds for waves only as well as combined wave and current action.

In the case of the first three types the mobility number could be determined directly from the data. For the fourth type, however, all variables in equation (3.12) were known, except the critical mobility A , which could then be easily computed. The results are presented in Figure 3 in the form of a Reynolds number R_* ($= (\bar{\tau}_{cr}/\rho)^{1/2} D_{50}/v$, where $\bar{\tau}_{cr}$ is the mean shear stress at incipient motion and v is the kinematic viscosity) versus a dimensionless grain size D_* ($= (g\Delta_s/v^2)^{1/3} D_{50}$). This figure indicates that all four types of data follow the same relationship between R_* and D_* , namely,

$$\log_{10} (R_*) = 0.092 (\log_{10} D_*)^2 + 1.158 \log_{10} D_* - 0.367 \quad \dots(3.18)$$

The critical mobility is now simply

$$A = R_* D_*^{-1/2} \quad \dots(3.19)$$

This implies that equation (3.12) is in fact universally applicable to all types of flow, namely, to waves only, current only and combined waves and currents. Since the incipient motion data and sediment load data are completely independent and have been treated completely differently, it also implies that this fourth adapted version of the original Ackers-White formula is indeed correct. It is consequently also the only adapted version of Ackers-White which is included in the package deal approach.

4. PROTOTYPE APPLICATION

An example is now given to illustrate the results obtained with the package deal approach for a prototype application. The input variables are summarized in Figure 4. It can be seen that the location under consideration is situated on a high-energy coastline. Quarterly bathymetric surveys over a two-year period indicated that the beach under consideration was in overall equilibrium (see Figure 5) although a substantial seasonal variation took place in the total volume of sediment in the control area. Fleming (1976) showed that the offshore-directed transport through the seaward boundary of the control area was negligible and that the volumetric changes depicted in Figure 5 are associated with a distinct sloshing of the material in the bay. During the summer months with persistent southerly winds and wave conditions, accretion took place in the northern half of the control area and (less) erosion occurred in the southern half of the control area. The opposite process took place during the winter months when northerly winds and wave conditions are more predominant. The data therefore indicate a clear wave-driven sloshing in the bay, with a corresponding average transport residual per year maintained over two years of $1.45 \times 10^6 \text{ m}^3/\text{yr}$ (see Figure 5). The results obtained from the package deal approach are summarized in Figure 6. The data indicate that the

volume of material in the control area will increase during periods of northbound transport and will decrease during periods of southbound transport. This result agrees with the prototype data. The average value of the difference in transport capacity at the up- and down-coast boundaries of the control area is predicted to be $1.65 \times 10^6 \text{ m}^3/\text{yr}$ plus or minus about 20 per cent of this mean value, which agrees well with the observed value of $1.45 \times 10^6 \text{ m}^3/\text{yr}$. Furthermore, the theoretical results also indicate that the volume of material in the control area will return approximately to its initial value after each year ($+ 1.7 \times 10^6 - 1.6 \times 10^6$), which also agrees with the prototype data. Since the wave climate has a marked seasonal component, the package deal approach therefore indicates a wave-driven sloshing mode of the same magnitude as observed in prototype. Figure 7 indicates that the prediction of the distribution of longshore transport with distance offshore is very consistent for the five detail predictors. The 95 per cent confidence band of the mean predicted longshore transport rate is approximately twice the standard deviation, which means that it is possible to predict the mean annual transport rate from the six predictors with 95 per cent certainty to within plus or minus 40 per cent. *It can therefore be concluded that the six formulae used to predict annual longshore transport rates are consistent with the given input variables.*

5. POSSIBLE SOURCES OF INACCURACY IN THE INPUT VARIABLES

In order to investigate whether this consistent answer obtained by means of the package deal approach is necessarily the correct one, a few possible sources of inaccuracies in the input variables that have to be specified for the application of the package deal approach are discussed briefly below.

Wave characteristics

The wave height H , which is a very significant parameter in the determination of every wave-induced process, could have been obtained from measurements in either shallow or deep water. In both instances the obtained wave height could be inaccurate.

For waves *measured in shallow water* the method of analysis of the records determines the extent of the possible inaccuracies. The actual waves are non-linear, that is, they are not sinusoidal anymore. For that reason a random wave train in shallow water consists of a number of non-linear components. By assuming that all these non-linear components can be represented by Vocoidal waves (see Swart and Loubser, 1978) it can be shown that a normal Fourier analysis, that is, an analysis in the frequency domain, will underestimate both the significant wave height H_s and peak wave period T_p of wave records measured in shallow water (see Swart, 1980). This is the result of the decomposition into their higher-frequency components of the non-linear waves in the spectrum. An example of this behaviour is given in Figure 8a for a random shallow-water wave record, simulated by the random superposition of Vocoidal component waves. The input values for the example shown are the root-mean-square wave height $H_{rms} = 0.711 \text{ m}$ and the peak wave period $T_p = 14.621 \text{ s}$. The results of the normal Fourier analysis are denoted by a subscript '1' and are $H_{rms1} = 0.49 \text{ m}$ and $T_{p1} = 5.686 \text{ s}$. Also shown in this figure is the result of a higher-order analysis, developed by Swart (1980), in which the Vocoidal components (instead of the

sinusoidal components) are extracted from the original wave record. In the normal Fourier analysis the wave height can be underpredicted by up to 50 per cent, whereas the wave period can be underpredicted by up to 70 per cent. On the other hand, a Draper-analysis, in the time domain, of the same simulated record also underpredicts both height and period to the same extent as a normal Fourier analysis, in this instance as a result of the fact that the component waves are not symmetrical around the mean water level but do in fact have more pronounced crests. For the specific example shown in Figure 8a the Draper results are H_{SIGD} = 0.581 m and TZ (zero-crossing period) = 3.617 s.

Waves *measured in deep water* can be analysed properly, because all component waves are either sinusoidal or closely resemble sinusoidal waves. In this case it is the method of transfer (via shoaling/refraction) of the wave from deep to shallow water which determines the extent of the inaccuracies. Figure 8b shows the error, at the location where $H/d = 0.6$, in the wave height obtained from linear shoaling and refraction of a wave with a deep water angle of incidence of 20° , when compared to Vocoidal theory. This is a valid way of determining the errors, since Swart and Loubser (1979) have shown that Vocoidal theory shows both a good agreement with measured wave data and adheres closely to the theoretical boundary conditions. The wave height is consistently underpredicted by linear (Airy) wave theory. For the whole range of values of $T(g/d)^{1/2}$ given in Figure 8b the error in the angle of incidence at $H/d = 0.6$ is about -0.13 for the example under consideration, again as compared to Vocoidal theory. The corresponding errors in the radiation stress components R_{yx} (used in the determination of longshore current velocity) and R_{xx} (which determines the mean water level but is not as yet part of the package deal approach) are given in Figures 8d and 8c respectively. It is shown that linear theory consistently overpredicts the radiation stresses. The error in R_{yx} does not necessarily reflect the possible error in the longshore current velocity v , since the friction coefficient C_{LH} is determined empirically. Since it is, however, possible that the formula for longshore current is applied outside the area of empirical determination of the friction factor C_{LH} , the extent of errors in R_{yx} point to a very possible source of inaccuracy in the current velocity v .

Bed roughness

The bed roughness is determined by the geometry of the bed forms, which can consist of wave-induced ripples and completely three-dimensional dune and bar patterns. In the package deal approach only the wave-induced ripples are used for this purpose, because they are the only predictable bed forms. Although this approach has to date given quite satisfactory results, it is obvious that it is an obvious source of error in the determination of the roughness, which in turn affects the friction factors C_{LH} and f_w and therefore also the longshore current velocity and ultimately the predicted longshore transport rate.

Breaking waves

The package deal approach is applied throughout the whole sediment transport zone, that is, also in the breaker zone. This is for a few reasons not correct:

- (1) The wave characteristics inside the breaker zone, such as orbital velocities and wave profile, are definitely non-sinusoidal.

(2) The expressions for the determination of bed roughness and wave-induced bed forms, derived for non-breaking waves, are not necessarily valid inside the breaker zone.

(3) The amount of sediment in suspension is determined, not only by the bed-related turbulence structure, but also by the turbulence induced by wave breaking. Figure 8e contains an example of the sediment load in the breaker zone, as predicted by the technique of Nielsen et al. (1978) by alternatively assuming breaking and no breaking for the same wave conditions. Although for the example shown the case with breaking leads to a total load which is 173 per cent more than in the case without breaking, the average percentage underprediction due to the fact that the effect of breaking waves on the turbulence was not taken into account would have amounted to 33 per cent for the annual transport in the example in Section 4. This is significant, since the Nielsen formula is the only one of the five detail predictors which includes the effect of wave breaking in his formula.

(4) The longshore current profile across the breaker zone is determined to a large extent by the type of wave breaking which occurs. At present the computation performed in the package deal approach assumes, as is done by everybody else, that the waves break in the spilling mode.

Longshore current velocity

The effect of the bed roughness, friction factor C_{LH} and breaker type on the longshore current velocity have already been touched upon in the above discussion. The beach profile itself also affects the longshore current. At present a representative constant beach slope is assumed for the longshore current determination. In reality the beach profile is often of the bar-type, which contains a well-developed trough landwards of the breaker bar, in which the longshore current will tend to concentrate. Recent research by Dette (1980) is the first step towards understanding this phenomenon.

It is therefore apparent that all input variables could be subject to possible inaccuracies, which could affect all six longshore transport predictors used in the package deal approach.

6. SENSITIVITY ANALYSIS

For this reason a sensitivity analysis was carried out to establish the extent of the influence of inaccuracies in the prime input variables (that is, wave height H longshore current velocity v and bed roughness r) on the average annual longshore transport rate, as predicted for the situation outlined in Section 4 with the five detail predictors. These three input variables were allowed to vary in the following ranges, namely, $0.5 < r_r < 5.0$; $0.2 < r_v < 1.0$; and $0.5 < r_H < 2.0$. The definitions for r_r , r_v and r_H are given in Figure 9, which also contains the results of the sensitivity analysis. Two graphs are given in Figure 9 for each input variable (r , v , H). In each case the left-hand graph indicates the variation of S/S_{pm} with the ratio r_r (or r_v or r_H), where S is the mean computed transport for the five detail predictors and S_{pm} is the transport given by the SPM formula in the original package deal approach. The right-hand graph represents the

relative standard deviation σ/μ for the five detail predictors in terms of the ratio r_r (or r_v or r_H), where μ is the mean transport (equal to S in the left-hand graph) and σ is the standard deviation of the five elements of which μ is made up. Figure 9 indicates a few interesting things:

(1) The package deal approach, that is, $r_r = r_v = r_H = 1$, seems to yield the best correspondence with the SPM results of all ratios (of r_r , r_v and r_H) tested.

(2) The relative standard deviation σ/μ reaches a minimum value for $r_r = r_v = r_H = 1$, that is, for the package deal approach.

It can therefore be concluded that the package deal approach for the detail predictors yields the same annual transport rate as the SPM formula, which in a way contains empirically all the physical influences on the input parameters mentioned in Section 5, that is, the bed form and bed roughness, wave breaking and bar profiles. It is therefore reasonable to assume that the results obtained via the package deal approach at present represent the best estimate of annual longshore transport rates. Since both the overall and the detail predictors depend on the predicted wave characteristics, which have been shown to be possibly in error, the package deal results could be in error. The extent of the error will depend on the empirical relationships for the longshore friction factor C_{LH} and for the parameter $K(D)$ in the SPM formula, if both of these are determined from available data by using a good non-linear wave theory, for example, Vocoidal theory, for the prediction of shallow water wave characteristics instead of linear Airy wave theory.

7. CONCLUDING REMARKS

We have therefore at present got a *package deal* approach that yields consistent transport rates and distributions across the breaker zone, but we should do further research to improve our input variables, namely, (1) wave characteristics; (2) bed forms and bed roughness; (3) longshore current velocity and distribution across the breaker zone for bar-type beaches; (4) breaking wave phenomena in general; and (5) the effect on sediment suspension of increased turbulence due to breaking.

REFERENCES

- BATTJES, J.A. (1974). Computation of set-up, longshore currents, run-up and overtopping due to wind-generated waves. Ph.D. thesis, Technische Hogeschool, Delft.
- BIJKER, E.W. (1971). Longshore transport computations. Proc. ASCE, *Journal of the Waterways, Harbors and Coastal Engineering Division*, WW4.
- CSIR (1978). Koeberg Nuclear Power Station: Report No. 8: Sediment transport study: Current tests. CSIR Report, Stellenbosch, South Africa.
- DETTE, H.H. (1980). Migration of longshore bars. *Proceedings of 17th Coastal Engineering Conference*, Sydney.
- ENGELUND, F. and HANSEN, E. (1967). A monograph on sediment transport in alluvial streams. Teknisk Forlag, Copenhagen.
- FLEMING, C.A. (1977). The development and application of a mathematical sediment transport model. Ph.D. thesis, University of Reading, Reading.
- FLEMING, C.A. and HUNT, J.N. (1976). Application of a sediment transport model. *Proceedings of 15th Coastal Engineering Conference*, II, pp. 1184-1202.
- GALVIN, C.J. and NELSON, R.A. (1967). Compilation of longshore current data. Coastal Engineering Research Center, U.S. Army, Corps of Engineers, 19 pp.
- KOMAR, P.D. and INMAN, D.L. (1970). Longshore sand transport on beaches. *J. Geophys. Res.*, 75, pp. 5914-5927.
- LONGUET-HIGGINS, M.S. (1970). Longshore currents generated by obliquely incident sea waves, 1. *J. Geophys. Res.*, 75, pp. 6778-6789.
- NIELSEN, P. (1979). Some basic concepts of wave sediment transport. Institute of Hydrodynamics and Hydraulic Engineering, Technical University of Denmark, Series paper No. 20.
- NIELSEN, P. SVENDSEN, I.A. and STAUB, C. (1978). Onshore-offshore sediment movement on a beach. *Proceedings of 16th Coastal Engineering Conference*, II, pp. 1475-1492.
- SPM (1973). Shore Protection Manual. Coastal Engineering Research Centre, U.S. Army, Corps of Engineers.
- SWART, D.H. (1976a). Predictive equations regarding coastal transports. *Proceedings of 15th Coastal Engineering Conference*, II, pp. 1113-1132.
- SWART, D.H. (1976b). Computation of longshore transport. Delft Hydraulics Laboratory Report R968.
- SWART, D.H. (1980). The nature and analysis of random waves in shallow water. CSIR Research Report, to be published.

SWART, D.H. and LENHOFF, L. (1980). Wave-induced incipient motion of bed material. CSIR Research Report, to be published.

SWART, D.H. and LOUBSER, C.C. (1978). Vocoidal theory for all non-breaking waves. *Proceedings of 16th Coastal Engineering Conference*, I, pp. 467-486.

SWART, D.H. and LOUBSER, C.C. (1979). Vocoidal water wave theory, Volume 2: Verification. CSIR Research Report 360, Stellenbosch, South Africa.

SWART, D.H. and LOUBSER, C.C. (1980). Determination of friction factors and bed shear stresses under wave action: theory and experiment. CSIR Research Report, to be published.

VAN DE GRAAFF, J. and VAN OVEREEM, J. (1979). Evaluation of sediment transport formulae in coastal engineering practice. *Coastal Eng.*, 3(1), pp. 1-32.

WILLIS, D.H. (1978). Sediment load under waves and currents. *Proceedings of 16th Coastal Engineering Conference*, II, pp. 1626-1637.

The figures are given in the following sequence:

3; 9; 1; 2; 4; 5; 6; 7; 8.

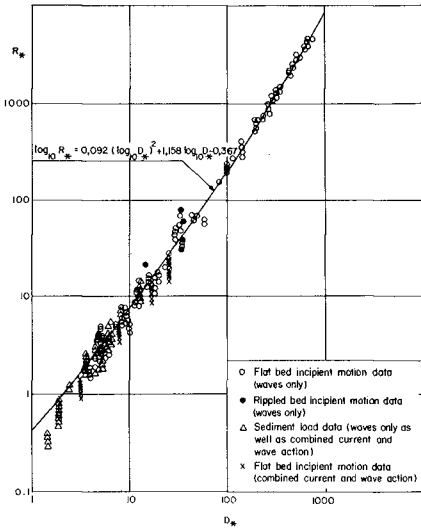


FIGURE 3
INCIDENT MOTION CRITERION FOR COMBINED CURRENT AND WAVE ACTION

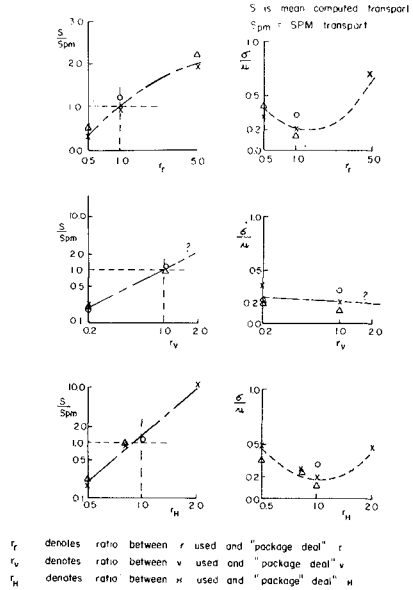


FIGURE 9 SENSITIVITY ANALYSIS ON ANNUAL LONGSHORE TRANSPORT RATE

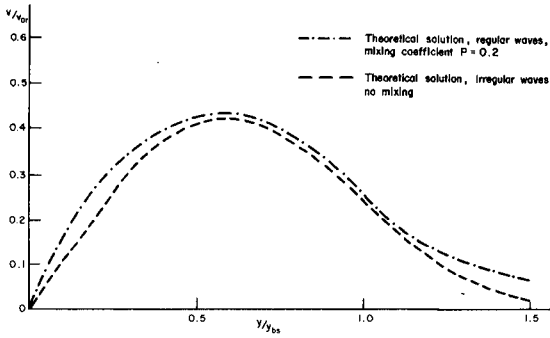


FIGURE 1
COMPARISON BETWEEN THEORETICAL SOLUTIONS FOR LONGSHORE CURRENTS
GENERATED BY REGULAR AND IRREGULAR WAVES

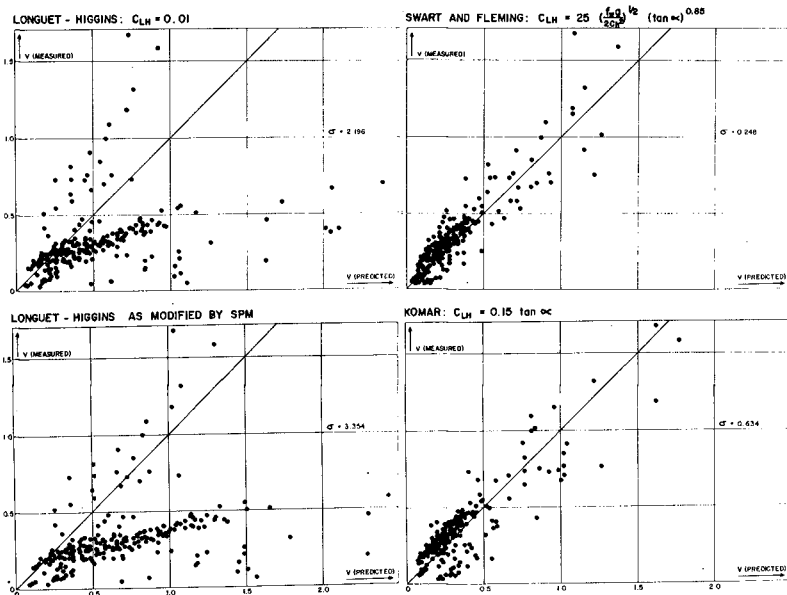


FIGURE 2
PREDICTED VERSUS MEASURED LONGSHORE CURRENT VELOCITIES BY FOUR DIFFERENT METHODS

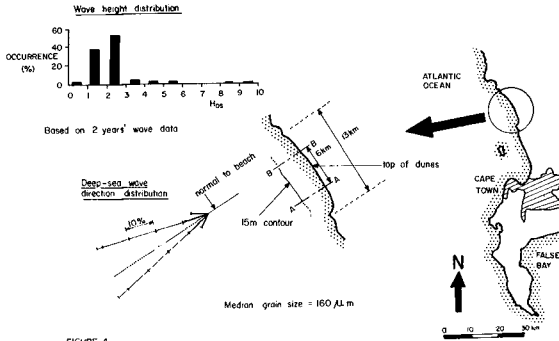


FIGURE 4
APPLICATION TO PROTOTYPE SITUATION

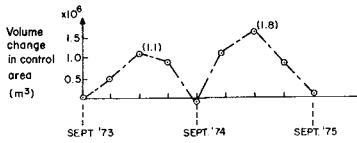


FIGURE 5
PROTOTYPE DATA OVER TWO YEAR PERIOD

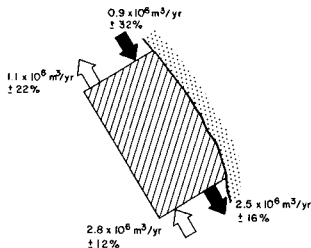


FIGURE 6
PACKAGE DEAL RESULTS FOR ONE YEAR

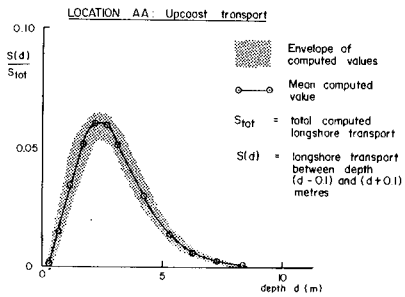


FIGURE 7
DISTRIBUTION NORMAL TO SHORE OF LONGSHORE
SEDIMENT TRANSPORT

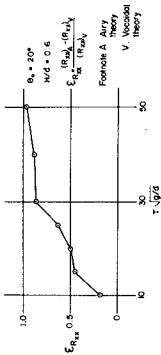


FIGURE 5
ERROR E_{R1} IN PRINCIPAL RADIATION STRESS R_{R1} AS OBTAINED AFTER REFRACTION WITH LINEAR (AIRY) WAVE THEORY

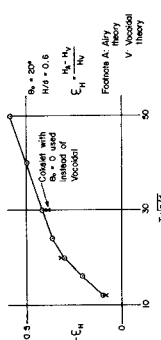


FIGURE 6
ERROR E_{C1} IN WAVE HEIGHT AS OBTAINED AFTER REFRACTION WITH LINEAR AIRY THEORY

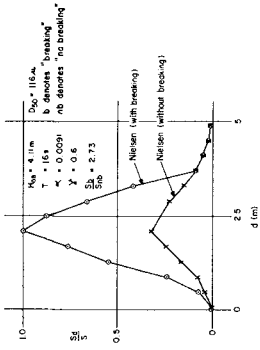


FIGURE 7
EFFECT OF INCREASED TURBULENCE DUE TO BREAKING ON LONGSHORE TRANSPORT

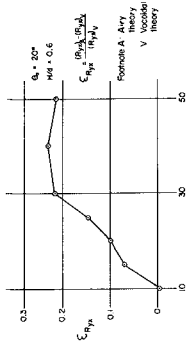


FIGURE 8
ERROR E_{R3} IN RADIATION STRESS R_{R3} AS OBTAINED AFTER REFRACTION WITH LINEAR (AIRY) WAVE THEORY

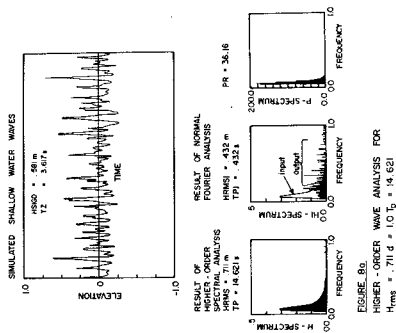


FIGURE 9
HIGHER-ORDER WAVE ANALYSIS FOR
 $H_{rms} = 7.11$ s $\cdot 1.0 T_p = 14.62$ s

CRITERION FOR STABILITY OF SHORELINE PLANFORM

JOHN D. WANG, Ph.D., Associate Professor
 BERNARD LE MEHAUTE, Ph.D., Professor and Chairman
 Ocean Engineering Division, Rosenstiel School of
 Marine and Atmospheric Science, University of Miami,
 4600 Rickenbacker Causeway, Virginia Key, Miami,
 Florida 33149, U.S.A.

INTRODUCTION

The problem of beach planform stability has been known for a long time: When does a small perturbation on a straight beach tend to grow with time and when does it tend to be flattened out? The interest in this problem arises from evidence of instabilities occurring in nature, but perhaps more importantly it is a problem that must be taken into account when formulating models for beach evolution and erosion. Existing mathematical models describing shoreline changes assume that the beach planform is stable and in equilibrium. It is therefore important to establish the range of wave conditions for which instabilities could occur, thereby invalidating such models. In the present case our interest is specifically directed towards determining conditions for which a model for shoreline evolution is intangible because of development of local instability.

Grijm (1960) gave an approximate mathematical analysis indicating that at the point where the longshore sediment transport Q as a function of wave angle is maximum the shoreline must either be straight or form a cusp. Under his assumption that Q is proportional to $\sin 2\alpha$ the maximum occurs for $\alpha = 45^\circ$. Le Mehaute and Soldate (1977) summarizes other studies that essentially arrive at the same results, viz. when the deep water wave angle is greater than 45° the shoreline is unstable. This result did not seem to be substantiated by field or laboratory observations.

In this study of shoreline planform we first derive a criterion for instability of straight beaches. Then assuming that longshore sediment transport is proportional to the alongshore wave energy flux component at the point of breaking we determine the range of deep water wave characteristics and beach slopes which would cause unstable situations to occur.

We consider only the longshore transport and exclude effects of on-offshore transport.

PLANFORM STABILITY CRITERION

Consider a straight beach along which an x-axis is defined, see Fig. 1. We shall take the usual definition of instability as a condition under which an initial infinitesimal disturbance grows in time. Accordingly, we introduce an infinitesimal protuberance on a straight shoreline, which is initially in equilibrium with

$\partial Q/\partial x = 0$. A mass balance on the control volume also shown in Fig. 1 is performed. The seaward boundary of the control volume is chosen at a depth large enough so that the longshore transport is zero there.

Two situations may arise:

- a) The longshore transport Q increases across the disturbance, i.e. $\partial Q/\partial x > 0$. To satisfy conservation of mass the increase in transport must come from erosion within the control volume and hence the protuberance is eroded until it disappears. The beach is stable for $\partial Q/\partial x > 0$.
- b) In the case of decreasing longshore transport, sediment accumulates in the control volume and the protuberance grows. The beach is unstable for $\partial Q/\partial x < 0$.

The above analysis applies to the case of a protuberance from the beach, the opposite conclusions would be derived for a recession. It is therefore useful to generalize the results by considering Q as a function of the breaking wave angle, i.e. $Q = Q(\alpha_b)$. According to our earlier assumption Q is also a function of deep water wave height, H_0 ; wave period, T ; and beach slope, S ; however these can be assumed unaffected by the small disturbance and independent of x .

We can then write

$$\frac{\partial Q}{\partial x} = \frac{\partial Q}{\partial \alpha_b} \frac{\partial \alpha_b}{\partial x}$$

and considering the sign for $\partial \alpha_b/\partial x$, which is positive for the protuberance and negative for the recession the criterion for stability becomes

$$\frac{\partial Q}{\partial \alpha_b} > 0 \quad \text{STABLE} \quad (1)$$

and similarly

$$\frac{\partial Q}{\partial \alpha_b} < 0 \quad \text{UNSTABLE} \quad (2)$$

Since α_b is a function of H_0 , T , S , and the deep water incident wave angle, α_0 , the condition $\partial Q/\partial \alpha_b = 0$ can also be given as a critical value of α_0 for given H_0 , T , and S . Expressing the stability criterion in terms of deep water wave characteristics makes it easier to determine whether given wave conditions would cause instability. In the following we use linear and nonlinear wave theories to determine those critical values of α_0 .

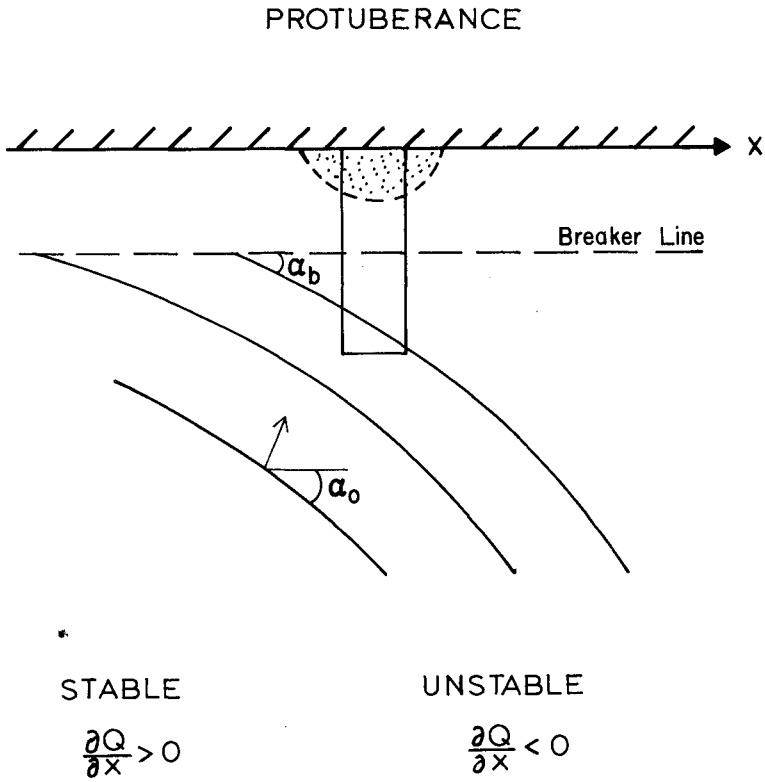


Figure 1. Local instability of a straight shoreline.

LINEAR THEORY

In the case of initially straight parallel contours, the deep water wave characteristics can easily be transformed into breaking wave characteristics by assuming conservation of energy flux between wave orthogonals.

If linear theory is used to express energy flux conservation, one obtains the following:

$$\frac{H_b}{H_o} = \sqrt{\frac{c_{go}}{c_{gb}}} \cdot \sqrt{\frac{\cos \alpha_o}{\cos \alpha_b}} \quad (3)$$

c_g = wave group velocity

Sub index o refers to deep water values and index b refers to breaking. By adding Snell's law; the dispersion relationship and the equation relating wave group velocity to wave phase velocity, c,

$$\frac{L_b}{L_o} = \frac{\sin \alpha_b}{\sin \alpha_o} \quad (4)$$

$$\frac{L_b}{L_o} = \tanh \frac{2\pi h_b}{L_b} \quad (5)$$

$$c_{gb} = \frac{1}{2} \frac{L_b}{T} \left(1 + \frac{\frac{4\pi h_b}{L_b}}{\sinh \frac{4\pi h_b}{L_b}} \right) \quad (6)$$

where h_b is the depth at breaking and L is the wave length, one has 4 equations to determine the 5 unknowns: H_b , h_b , L_b , c_{gb} and α_b . The fifth equation consists of a breaking criterion for which we use the empirical relation proposed by Le Mehaute and Koh (1967).

$$\frac{H_b}{H_o} = 0.76 \cdot S^{1/7} \left(\frac{H_o}{L_o} \right)^{-1/4} \quad (7)$$

Equation (7), which was derived for normal incident waves is modified to make it applicable to obliquely incident waves. The deep water wave height, H_o , is replaced by its unrefracted value

$$H_o \rightarrow H_o \frac{\cos \alpha_o}{\cos \alpha_b}$$

and the bottom slope is replaced by the slope

$$S \rightarrow S \cos \alpha_b$$

leading to the result

$$\frac{H_b}{H_o} = 0.76 \left(\frac{H_o}{L_o S^{4/7}} \right)^{-1/4} \cos^{3/8} \alpha_o \cos^{-13/56} \alpha_b \quad (8)$$

By straightforward manipulation of Eqs. (3) - (8), one obtains the following implicit equation for determining the breaking wave angle as a function of incident wave angle, α_o and the parameter $H_o/L_o S^{4/7}$

$$\begin{aligned} & 0.76 \left(\frac{H_o}{L_o S^{4/7}} \right)^{-1/4} \cos^{3/8} \alpha_o \cos^{-13/56} \alpha_b \\ &= \left(\frac{\sin \alpha_o}{\sin \alpha_b} \right)^{1/2} \left(\frac{\cos \alpha_o}{\cos \alpha_b} \right)^{1/2} \left\{ 1 + 2 \ln \left(\frac{\sin \alpha_o + \sin \alpha_b}{\sin \alpha_o - \sin \alpha_b} \right) \right. \\ & \left. \left[\frac{4 \sin^2 \alpha_o \sin^2 \alpha_b}{\sin^2 \alpha_o - \sin^2 \alpha_b} \right]^{-1} \right\}^{-1/2} \quad (9) \end{aligned}$$

The equation is solved numerically and the results are shown in Fig. 2.

LINEAR STABILITY CRITERION

The usual assumption is that longshore transport is proportional to the longshore component of wave energy flux at the point of breaking:

$$Q \propto H_b^2 c_{gb} \sin 2\alpha_b \quad (10)$$

We can normalize this expression with the constant $H_o^2 c_{go}$ to give the remarkably simple result

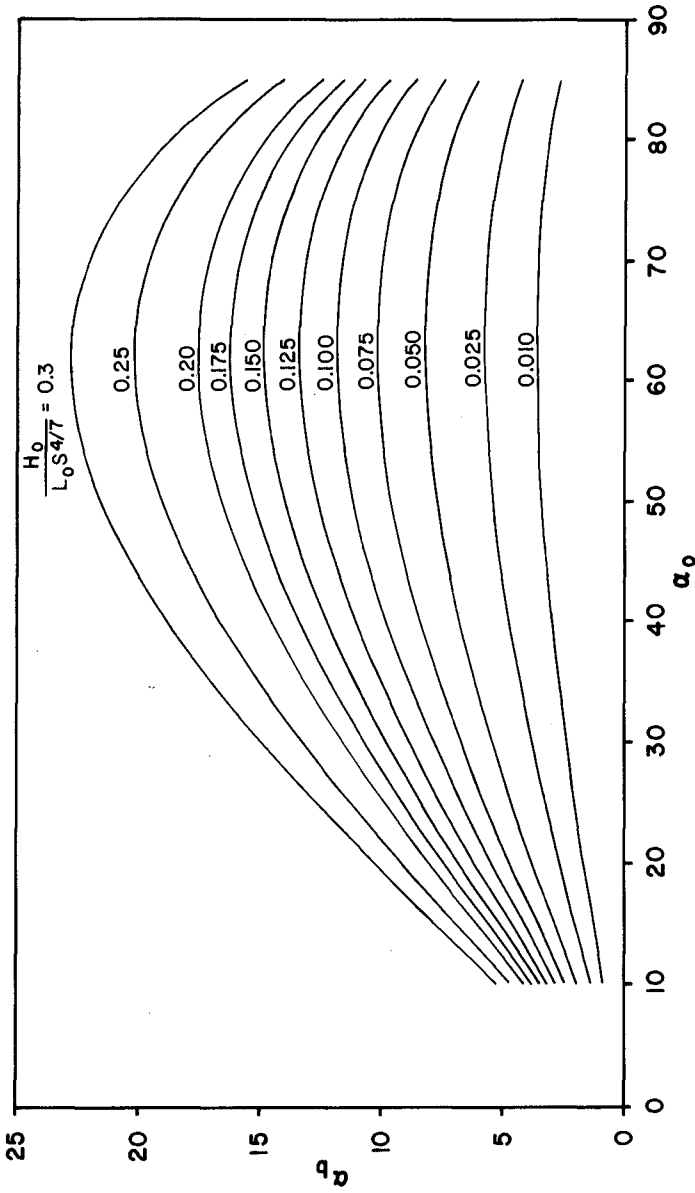


Figure 2. Breaking wave angle as a function of α_0 and $\frac{H_0}{L_0 S^{4/7}}$ linear theory.

$$\begin{aligned}
 Q &\propto \left(\frac{H_b}{H_o}\right)^2 \frac{c_{gb}}{c_{go}} \sin 2\alpha_b \\
 &= \frac{c_{go}}{c_{gb}} \frac{\cos \alpha_o}{\cos \alpha_b} \cdot \frac{c_{gb}}{c_{go}} 2 \sin \alpha_b \cos \alpha_b \\
 &= 2 \cos \alpha_o \sin \alpha_b
 \end{aligned} \tag{11}$$

Using Eq. (11) and (9) we can determine the critical value of α_o for which $\partial Q/\partial \alpha_b = 0$. This is again calculated numerically and the results are shown in Table 1. For each value of $H_o/L_o S^{4/7}$, two critical values of α_o are found. For incident wave angles between these two values the beach is unstable, otherwise it is stable.

The lower limit of the unstable region is almost invariant to the parameter $H_o/L_o S^{4/7}$ with a value of $\alpha_o = 42^\circ$ while the upper limit decreases with increasing $H_o/L_o^{4/7}$. The upper limit in terms of α_o varies between $59^\circ.8 \leq \alpha_o \leq 63^\circ.5$.

NON-LINEAR WAVE THEORY

It is well-known that linear wave theory underestimates the wave height near breaking. Since we are using an empirical breaking criterion derived from observations of real waves, we would expect that the predicted breaking depth is smaller than the real depth and thus the predicted limits for α_o and α_b are also smaller than the real waves. Wang and Le Mehaute (1980) have shown that better results can be obtained for large deep water wave steepness using a non-linear hybrid wave theory which uses cnoidal theory to predict wave height and linear theory for wave length. A detailed description of the rationale and verification of this model is given in that paper. Here, we use the hybrid theory with the breaking criterion (8) to determine critical values of α_o .

A problem arises because wave energy flux is not properly defined for the hybrid theory. We carried out the stability analysis using both the linear expression (11) and the normalized cnoidal energy flux given by

$$Q \propto \left(\frac{H_b}{H_o}\right)^2 \frac{L}{L_o} B \sin 2\alpha_b \tag{12}$$

B is a function of elliptic integrals:

$\frac{H_o}{L_o S^{4/7}}$	Lower Limit		Upper Limit	
	α_o	α_b	α_o	α_b
.005	41.9	2.18	63.5	2.57
.01	41.9	3.09	63.5	3.64
.05	41.9	7.00	63.4	8.26
.1	42.0	10.1	63.1	11.9
.2	42.0	15.0	62.5	17.6
.3	42.1	19.5	61.6	22.8
.4	42.3	24.8	59.8	28.7

TABLE 1

α_o limits for shoreline instability
linear theory.

S	H_o/L_o	I Lower Limit		I and II Upper Limit		II Lower Limit	
		α_o	α_b	α_o	α_b	α_o	α_b
.01	0.005	46.7	13.0	77.6	16.7	48.3	13.4
	0.01	46.7	16.4	79.5	21.4	48.3	16.8
	0.03	47.3	21.1	85.0	28.8	48.4	21.6
	0.03	47.7	25.4	>85.		49.2	26.1
.02	0.005	46.7	12.2	77.3	15.5	48.1	12.4
	0.01	46.7	15.1	78.5	19.4	48.2	12.4
	0.02	46.7	18.9	80.2	24.9	48.4	19.4
	0.03	46.9	21.8	83.2	29.4	48.5	22.4
	0.04	47.0	24.2	>85.		48.6	24.9
	0.05	47.1	26.6	>85.		49.0	27.6
0.03	0.005	46.4	11.7	77.7	14.9	48.2	12.0
	0.01	46.6	14.4	78.0	18.6	48.3	14.8
	0.03	46.7	20.5	80.0	27.1	48.4	21.1
	0.05	46.7	24.4	>85.		48.5	25.1
	0.07	46.4	27.5	>85.		49.2	29.0
0.05	0.005	46.5	11.1	77.3	14.2	48.1	11.4
	0.01	46.7	13.8	78.2	17.6	48.3	14.1
	0.03	46.4	19.2	79.2	25.2	48.3	19.8
	0.05	46.3	22.5	80.0	30.2	48.3	23.3
	0.07	46.0	25.0	>85.		48.5	26.1
	0.09	45.5	27.0	>85.		48.6	28.5
	0.11	45.0	28.7	>85.		49.0	31.0
0.1	0.005	46.2	10.4	77.2	13.3	48.2	10.8
	0.01	46.2	12.8	77.3	16.4	48.2	13.2
	0.03	46.3	17.9	77.9	23.2	48.2	18.5
	0.05	46.3	20.8	79.2	27.5	48.2	21.5
	0.07	45.6	22.8	80.2	30.8	48.2	23.8
	0.09	45.4	24.6	80.8	33.8	48.2	25.8
	0.11	45.3	26.0	82.5	36.6	48.2	27.4
	0.13	45.2	27.3	>85.		48.2	28.9
	0.15	44.8	28.4	>85.		48.3	30.0

Table 2

Lower and upper limits for unstable shoreline regimes. I is computed using linear wave energy transport Eq. 11. II is computed using cnoidal wave energy transport Eq. 12.

$$B = B(m) \equiv \frac{1}{m^2} \left[\frac{1}{3} (3m^2 - 5m + 2 + (4m - 2) \frac{E(m)}{K(m)} - (1 - m - \frac{E(m)}{K(m)})^2 \right] \quad (13)$$

$K(m)$ and $E(m)$ are complete elliptic integrals of the first and second kind respectively. The parameter m is given by, see e.g. Svendsen and Brink-Kjaer (1973):

$$m K^2(m) = \frac{3}{16} \frac{HL_c^2}{h^3} \quad (14)$$

where L_c is the cnoidal wave length parameter.

The critical values of α_0 and α_b corresponding to $\partial Q/\partial \alpha_b = 0$ are presented in Table 2. Again two values for α_0 are found indicating a bounded region of instability.

It is seen that as expected the critical values are somewhat greater than those computed using linear theory. The difference between using linear wave or cnoidal wave energy flux is small and only influences the lower limit. The upper limit is not affected by the choice of energy flux expression because it is determined practically by the maximum value of α_b for given S and H_0/L_0 .

Of greater importance is the fact that the non-linear theory predicts a larger zone of instability since the upper limit is significantly higher than predicted by linear theory. For large deep water wave steepness the upper limit for α_0 is greater than 85° , however, this may be due to the fact that we are outside of the region for which the breaking criterion and wave theory are verified. Another source of uncertainty derives from the empirical relationship between longshore transport and energy flux used in this study. When better parameterization of transport rates becomes available the same methodology can however be used to investigate for instabilities.

CONCLUSION

As part of our effort to develop useful models for the prediction of long term shoreline evolution we have investigated the practical limitations imposed on the models by the external conditions. The local instability phenomenon considered in this study is an example of such a limitation. Other areas that need further research involves the definition of an equivalent monochromatic wave from a multi-directional spectrum and the temporal discretization of an observed wave record.

ACKNOWLEDGEMENTS

This research was done under NSF sponsorship Contract No. ENG 79-11930.

REFERENCES

- Grijm, W. (1960). "Theoretical forms of Shoreline," Proc. 7th Coastal Engineering Conference.
- Le Mehaute, B., and Koh, R. C. (1967). "On the breaking of waves at an angle with the shoreline," J. of Hydraulic Research, Vol. 5, No. 1, pp. 67-88.
- Le Mehaute, B., and Soldate, M. (1978). "Mathematical modeling of shoreline evolution," XVIth International Conference on Coastal Engineering, Hamburg, Vol. II, Chapter 67, pp. 1163-1179.
- Wang, J. D., and Le Mehaute, B. (1980). "Breaking wave characteristics on a plane beach," submitted for publication.

ZETA BAYS, POCKET BEACHES AND HEADLAND CONTROL

by

R. Silvester,⁽¹⁾ Y. Tsuchiya⁽²⁾ and Y. Shibano⁽³⁾

ABSTRACT

The now familiar equilibrium shape of bay sculptured by waves between headlands can indicate to man the direction he could follow in stabilizing shorelines. The characteristics of these crenulate or zeta shapes are known and can be applied in design or defining limits of erosion. Some natural settings are discussed which introduce difficulties in identifying the correct bay shapes for applying these tools. The application of headland control to specific cases of instability is presented. The final requirement is emphasised of aiding Nature to protect the coastline by the formation of the offshore bar and its subsequent return to the beach without concurrent downcoast drift. The method currently receiving widespread support of placing offshore breakwaters in close proximity to each other is discounted as a viable protective alternative.

INTRODUCTION

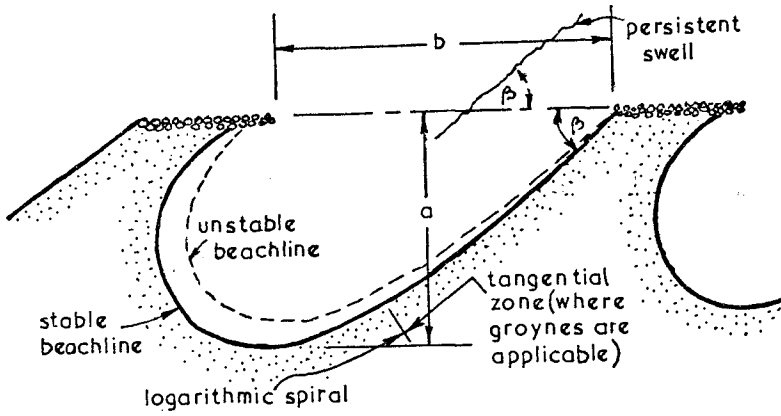
The occurrence of crenulate or zeta shaped bays between natural headlands when persistent swell approaches the coast obliquely is now observable and well known (1)(2)(3). These may be in dynamic equilibrium with the sediment supply and wave climate or in static equilibrium when no further littoral drift is taking place. (See Figure 1) In either condition the bay will have a curved section of logarithmic spiral form and some indentation dimension (a) that is some fraction of the space (b) between the headlands.

It is seen that the angle of wave crests to the line joining the headlands equals that between the tangential coast and this same alignment. Even when not in static equilibrium this beach extremity is very close to this final angle (β).

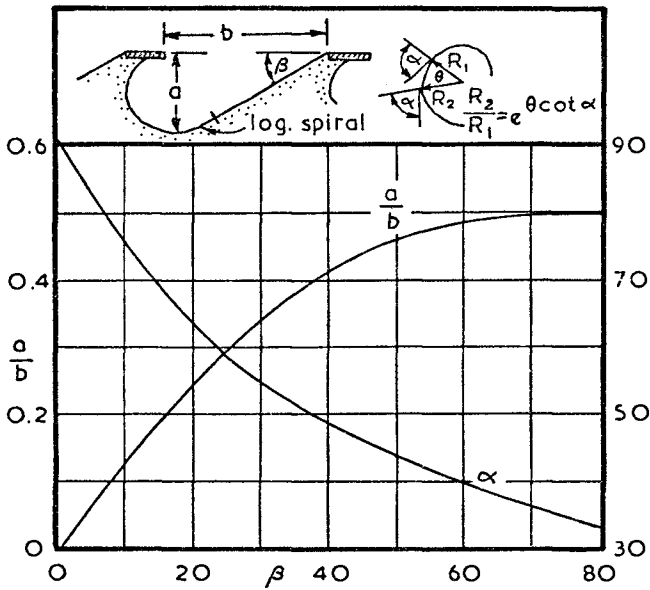
In the final stable form certain characteristics of the plan shapes are known from model tests and observations of prototype bays that are in this condition. (2)(4) As can be seen in Figure 2 the ratio of maximum indentation (a) to headland spacing (b) is fixed for a given obliquity of incident wave to headland alignments (β). In the same figure the relationship is shown between the constant (α) for the logarithmic spiral that the curved section of beach assumes.

With the above tools the stability of a bayed coast can be assessed, or the limit of erosion that can take place in the event of no further sediment being supplied, either from upcoast or from within the bay from

-
- (1) Assoc. Professor, Dept. Civil Engineering, University of Western Australia
 - (2) Professor, Disaster Prevention Res. Inst., Kyoto University, Japan
 - (3) Research Assistant, Disaster Prevention Res. Inst., Kyoto University



1. Definition sketch for crenulate shaped bay.



2. Parameters relating to bays in static equilibrium

a river. Such yard sticks can also be employed in designing headlands to stabilize an eroding bay or general coastline. In this final equilibrium condition persistent waves will be arriving normal to the complete periphery of the bay. At the tangential downcoast section waves will refract slightly but within the curved zone they suffer both diffraction and refraction before breaking parallel to the beach. Any wave thus breaks simultaneously around the complete bay shoreline.

POCKET BEACHES

There are situations where a deep indentation occurs and there is insufficient sand to saturate the bay and cause transport around the downcoast headland. These might be termed "pocket beaches", where it is more difficult to identify the control line from which the zeta bay can be tested for its stability. Extra variables entering the problem will be discussed to show how the true crenulate shape can be checked.

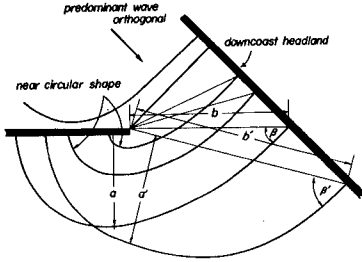
Protruding downcoast headland

Where the downcoast beachline does not reach the extremity of its headland (as pictured in Figure 3) due to lack of sediment, the control point should be the shoreline extremity. The figure shows the direction of the predominant or persistent waves, which determine the ultimate bay shape. The control line runs from the tip of the upcoast headland (on the left of the figure) to the intersection of the beach and the downcoast headland. This provides the measure of (β') from which (a'/b') and the logarithmic spiral constant (α') is determined from Figure 2. Since (b') is known the indentation (a') can be computed and the bay drawn.

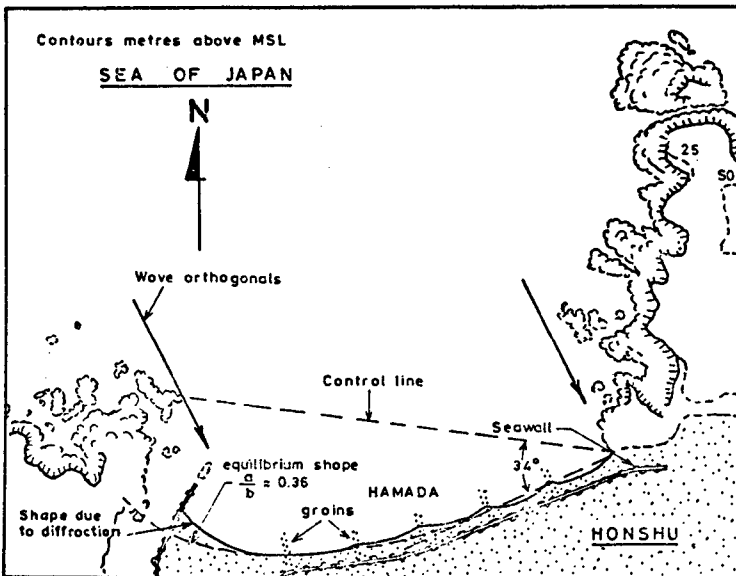
If renourishment by natural or man-made means were effected a new shape would emerge with a new contact point of the beach with the downcoast headland, as exhibited by angle (β) and indentation ratio (a/b) . A different value of (α) will also apply. Further addition of sediment will decrease the value of (β) which, as seen in Figure 2, will decrease (a/b) and make the curvature of the beach closer to that of a circular arc. After passing through the stage of a straight beach normal to the wave orthogonal, further accretion would result in a new bay shape which would be dictated by some headland or control point further upcoast.

The set-up as illustrated in Figure 3 would be ideal for further model verification of (a/b) and (α) , perhaps with a wave guide parallel to the downcoast headland to prevent reflection from this other headland.

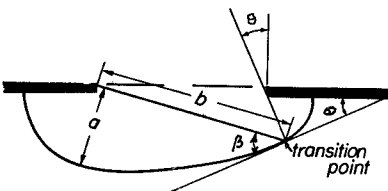
An example of this situation is contained in Figure 4, which is a bay of the Honshu coast facing the Sea of Japan. The wave orthogonals are normal to the tangential downcoast section of the bay. That on the left determines the control point of the upcoast headland whilst the control line intersects the meeting of the beach with the downcoast headland. The value of $\beta = 34^\circ$ gives $a/b = 0.36$ from which the equilibrium bay shape can be sketched, as shown dotted. It is seen that at the upcoast end extra accretion has occurred due to wave diffraction around the jetty constructed at a river outlet. Otherwise the existing coast is in static equilibrium or nearly so, which calls into question



3. Bays with no by-passing of downcoast headland.



4. Bay exhibiting downcoast control of beach with headland.



Bay with double curvature due to wave diffraction.

the need for the seawall and groynes constructed along the tangential section of beach. This is a case where sand renourishment might have solved the erosion problem.

Double curvature of bays

It has already been shown in Figure 4 that deviations from the logarithmic spiral curve can take place if a secondary headland, in this case a jetty causes local wave diffraction. Another example at the down-coast end of a bay is illustrated in Figure 5, where waves sculpture an almost circular beach which is asymptotic to the end of the log-spiral section. Any such change in curvature should indicate this extra control condition. As noted in the figure, the wave orthogonal must be normal to the tangent at the transition, from which β is obtained. The control line from which (b) is measured then provides the indentation (a) by which the static equilibrium shape can be assessed.

An example of this problem is given in Figure 6 which is a bay on the Shikoku coast of Japan facing the Pacific Ocean. The increased curvature at the western end of this pocket beach indicates diffraction by the protruding downcoast headland. The wave orthogonal must be normal to the transition tangent giving the control line shown. The resulting equilibrium bay can be drawn and compared to the existing shoreline for testing its stability. It is seen that the bay can be continued into the upcoast headland complex even though it cannot exist there.

Multiple upcoast headlands

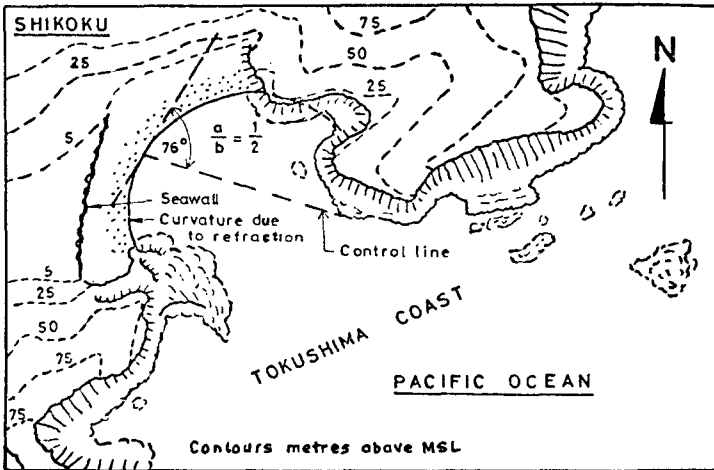
Figure 7 shows the complication of more than one headland in the upcoast region. It is necessary to determine which one controls the shape of the bay. The orthogonal of the persistent waves is normal to the tangential downcoast beach. This same orthogonal applies to the upcoast region as illustrated. In the absence of headland B point A becomes the control point and AC the control line by which β' is measured. This gives the indentation and curvature for the equilibrium beach from these controls. If this orthogonal intercepts the tip of headland B if it exists the new control line BC gives a new β value and completely different bay shape. It is obvious that the presence of headland C, even with A effecting control of the bay will cause greater curvature within its lee due to secondary diffraction.

In Figure 8 a bay on the Japanese coast is shown where the control point for the upcoast zone must be determined. It is another case of double curvature at the downcoast end so that a transition point must be determined to assess the line of the wave orthogonal. Once this is done the same alignment of wave approach indicates the protruding headland as the upcoast control point. The resulting equilibrium bay is much further inland than the existing coast indicating a great potentiality for erosion. This is displayed by the extensive seawalls shown, which have been provided to protect the road and rail links on the coast, a necessary feature around most of the Japanese coastline. A method of stabilizing this bay is indicated by headlands but will be discussed later.

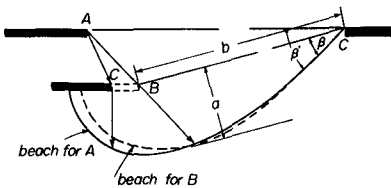
Orientation of headlands

It is convenient for considering bay characteristics to align headlands with the line joining the tips, about which waves diffract as in Figure 1. Natural conditions are never so easy and hence alignments as in Figure 9 must be accounted for. The original situation is presented by alignments A and E where the control line and spacing (b) fixes indentation (a) once (β) has been measured. If other headland orientations still have the same (b) the same plan form results. However, with alternatives B, C and D for the upcoast structure part of the bay will not exist. Even so the drawing of the remainder of the bay may help the determination of (a) within the hypothetical section in order that it, with portion of the logarithmic spiral, can be assessed.

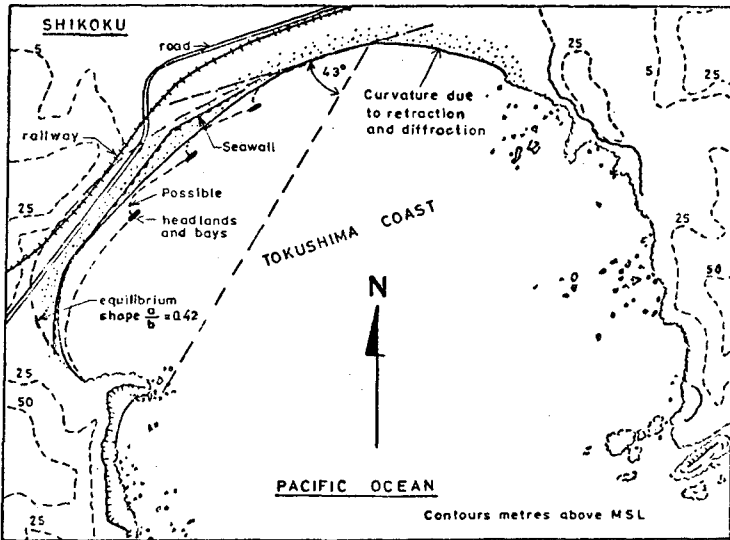
Similarly the orientation of the downcoast headland at G or F has no influence on the equilibrium bay formed by the control line as pertains to E. It is only when this structure protrudes into the bay, as with alternative H shown dotted in Figure 9, that a new control point is established. As seen a new (b') is operative as well as a different (β), from which a new (a) is derived and, of course, a changed log-spiral for the curved section of bay.



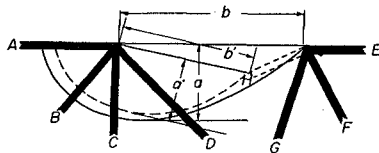
6. Example of bay with double curvature.



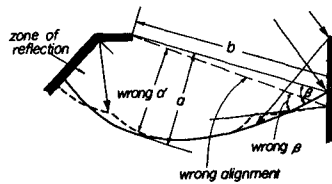
7. Bays formed by different upcoast headland control



8. Example of defining control by upcoast headland.



9. Effect of headland orientation on bay formation.



10. Influence of wave reflection on smooth beach line.

It is interesting to compare alternatives of breakwaters running parallel to the coast, as with A and E in Figure 9, to groynes running normal to it, as with C and between G and F. With the former a complete bay exists for a given spacing (b) between structures whereas only a fraction of it can result from the latter or groyne solution. Not only is a longer beachline possible with the breakwaters A and E, but material is prevented from being dispersed seawards during storm events. Any longshore drift during these sequences is forced into the deeply indented zone with perhaps deposition offshore. With the groyne alternative a rip current will form along the face of C in the figure and much material is thrown out to sea, possibly to return to the beach much further down-coast(5).

Influence of wave reflection

The crenulate shaped bays resulting from persistent waves from one direction will produce a uniformly curved beach of log-spiral form. Any deviation from this should indicate some secondary influence on the waves or the sediment motion. One of these could be a rocky shoal offshore which refracts the waves to produce a slight protuberance of the beach with possibly adjacent denudation. These aberrations should be smoothed out when determining indentation (a) or the log-spiral (α) value.

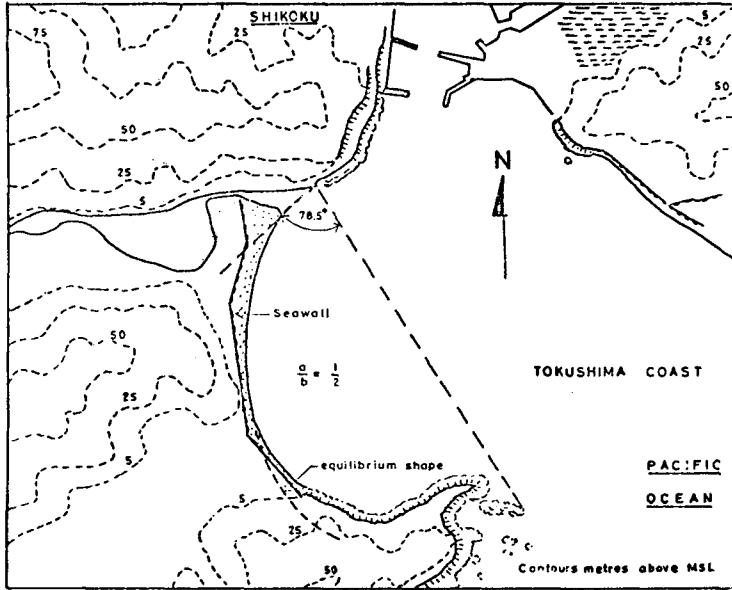
Another source of shoreline deviation would be reflection from headlands, two types of which are depicted in Figure 10. At the down-coast end orthogonals are drawn which show the extent of the reflected waves. The short-crested system so produced by these and incident waves is very conducive to sediment transport parallel to the wall, or headland in this case.(6)(7) Outside the bounding orthogonal of the reflected wave accretion will occur so that the shoreline shown dotted in the figure results. Using the intersection of this waterline with the headland as the control point is erroneous (as illustrated) as it should be derived from the smooth curve of this tangential or log-spiral curve.

The upcoast headland is also shaped to give the possibility of reflection. The incident orthogonals from the headland extremity will have varying angles of reflection but the bounding orthogonal is as shown. Here again material will be scoured and produce a shoreline as dotted in Figure 10. The deviation in the correct log-spiral curvature may cause a wrong assessment of indentation (a') instead of (a).

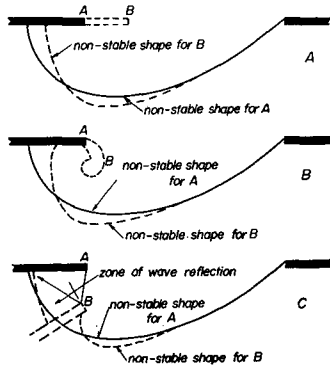
Figure 11 does not provide an example of reflected wave influence but it does indicate the need to extrapolate a bayed shoreline across a river mouth to the downcoast headland control point. It can be seen from the (β) measured and the (a/b) derived that the bay is in equilibrium except for a short length at the southern end where excess material is apparent. This is unlikely to be stable, as indicated by the presence of the seawall very close to this margin.

Changing control points

Figure 12 gives three examples of alterations in control points, those in A and C are man-induced whilst B could be a natural phenomenon.



11. Extrapolation of bay across river mouth to determine control line.



12. Examples of natural or man-made features that influence bay shape.

It is unfortunately a common practice to extend an upcoast headland in order to provide calmer water for the construction of a port in its lee. As seen in A of Figure 12, a control point is shifted from point A to point B, about which the persistent waves must now diffract. This results in accretion in the port location, probably before construction is commenced. In the case of the bay being close to equilibrium this siltation is at the expense of the adjacent beach.

The sand spit illustrated in B of Figure 12 will also produce a new control point B which will cause accretion in the lee of the breakwater, perhaps by denuding the adjoining beach by littoral drift being held within the spit.

In diagram C of the figure the reshaping of the coastline by the intrusion of a large structure, such as an airport runway, is illustrated. Between A and B reflection of waves can re-orient the beach as shown dotted. Downcoast of the new feature accretion will occur adjacent to it with concomitant erosion a little distance away, particularly if there is no sediment input into the bay.

HEADLAND CONTROL

Bays which are not in equilibrium can be stabilized by the installation of headlands within them. This results in smaller bays being sculptured by the persistent swell or predominant wave system. This is depicted in Figure 13 where the existing unstable shoreline is shown, together with the static equilibrium shape which would ensue in the event of all sediment supply being stopped (an eventuality quite possible in these days of dredging substantial channels to ports). To prevent the obvious loss of valuable land, which could be highly developed for commercial or recreational purposes, the suggested headlands could be located to give no net loss or complete gain of land area.

In determining (β) for each segment or bay it should be recognised that the persistent wave orthogonals at each headland location must be normal to the tangent at that section of the static equilibrium bay. The angle between the orthogonal and the normal to the control line joining adjacent breakwaters is (β) which gives indentation (a) from the value of (a/b) derived from Figure 2. Values are indicated in the figure. The bay can be sketched in by starting with the tangential section parallel to the static equilibrium section of coast and making the indentation line tangential to the curved section of the new bay. In the case of bay erosion the newly formed bays will be oriented in the same direction as the main bay, with the tangential sections to the right, for example, in Figure 13.

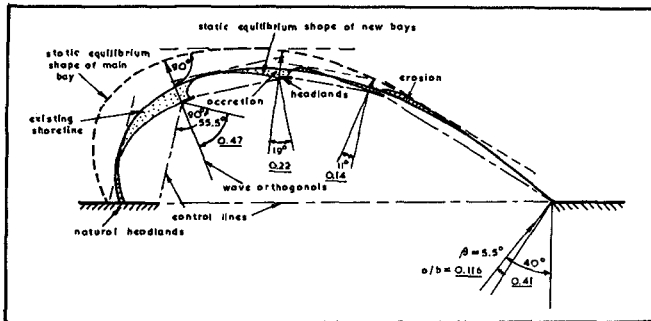
Another situation may arise where a bay is still building out to its static equilibrium limit. This possibility is displayed in Figure 14 where a deep indentation between two mountain structures has been virtually cut-off by a sand spit supplied from a source which is indicated is at the recognised downcoast zone of the bay being formed. The sediment still filling the bay will travel in the direction shown, towards the curved section of the coast. With the control points and (b) known, the angle (β) can define (a) and the log-spiral (α) so that the equilibrium bay can

be drawn. Whilst material is available for filling the coast will remain dynamically stable, with siltation continuing in the curved section of the bay. If however the supply is insufficient for the wave energy arriving, erosion will take place at the tangential downcoast end which is normally the most stable section.

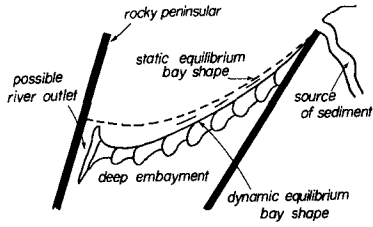
An example of this is given in Figure 15 which is a bay in Honshu facing the Sea of Japan. The Hino river in its natural state has over geologic time supplied an abundance of material to form the sandy spit reaching the Shimane Peninsular. However, the static equilibrium bay is far seaward of the existing shoreline, indicating the need for much more sediment before stability is reached. Since the river has been harnessed by dams upstream the discharge of sand has diminished substantially resulting in erosion near the Kaika coast.

A method of stabilizing this coast by headlands is suggested in Figure 14, in which the indentations of each bay is determined from the angle between the wave othogonals (normal to the static equilibrium line) and the normal to the control line of each bay (as detailed in Figure 13). It can be seen in this rather unique case that the stabilizing bays are oriented in the opposite direction to that of the major bay, due to this silting situation.

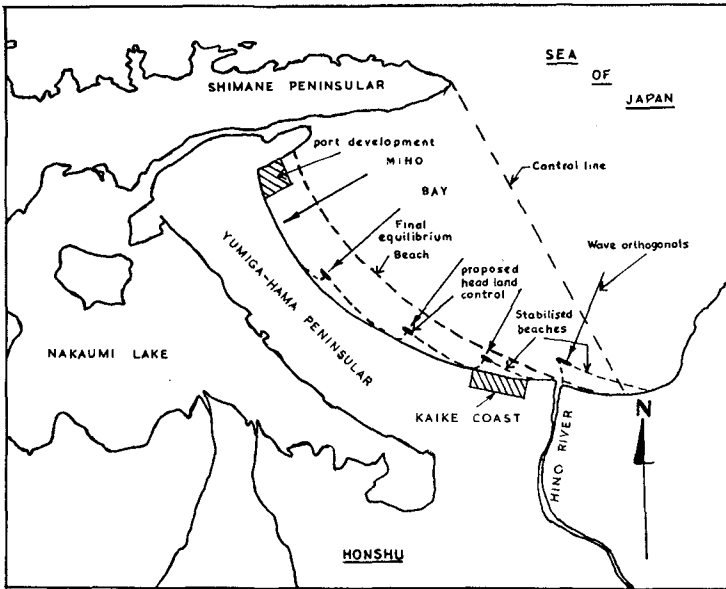
The solution proposed by Toyoshima (8), as in many other locations in Japan (9), is the installation of offshore breakwaters parallel to the coast but spaced very close together. The openings were, in fact, one quarter the length of the individual structures placed echelon fashion. This was after attempts at stabilisation by groynes and seawalls had failed. Figure 16 shows three of these breakwaters behind which tombolos have formed. However, also apparent are defensive blocks found necessary, in line with the openings between breakwaters. This indicates too close a spacing of the structures from the beachline desired. Although it was concluded that tombolo growth occurred during storm conditions, it would be during these events that a strong rip current would be generated through the openings as overtopping water and storm wave water entering the circular bays must return to the sea through these limited spaces. Toyoshima (9) suggests that counter-measures will always be necessary in this exposed zone.



13. Headland stabilization of an eroding bay.



14. Situation of a bay still filling to non-littoral drift state.



15. Example of bay accreting to equilibrium and method of stabilizing by headlands.

The sand finding its way behind the breakwaters will be that scoured by the reflected and incident waves seaward of these structures. The result of this can best be expressed in the conclusion of Toyoshima(8): "The most important problem is subsidence of the breakwaters".

The writer's concept of coast stabilization by headlands does not countenance offshore breakwaters placed so close together. It envisages a spacing in the order of ten times the length of each structure, in order that a zeta shape of coast can be sculptured. The alternative suggested by Toyoshima virtually constitutes a continuous wall being constructed offshore at great cost. The excessive reflection by oblique waves accelerates the transport of sediment that results in scouring of the bed and a resulting maintenance problem. The spacing of headlands from the existing shoreline can be such as to exchange some beach zone for accretion elsewhere or beach aggradation at all points. A renourishment scheme accompanied by headland installation will provide stable bays very quickly with no erosive effects downcoast of the system.

The suggested plan in Figure 8, to stabilize a highly developed coastal plain, contemplates (at first look) three headlands which would have cost much less than the seawalls finally constructed, even when nourishment of the bays is considered. It is worthy of note that such headlands only need to break the waves under the worst storm conditions. Even natural reefs have achieved the same results of maintaining sandy prominences leeward of such submerged features.

NATURE'S DEFENSE MECHANISM

The essence of the problem is to maintain a supply of sand for offshore bar construction by storm waves without the waterline continually receding. This implies that the bar material is brought back to the beach by subsequent swell exactly from whence it came. This is the case for bays in static equilibrium since persistence waves around their periphery arrive normally. Even with littoral drift occurring in a dynamic equilibrium situation, fluctuations in sediment supply will not be accompanied by such large beach recessions as for a long straight coast controlled by headlands at much greater spacing. The limiting indentation for no sand supply at all is predictable.

Man can do no better than observe natural processes and emulate them in his marine structures or operations, or by helping Nature to be more efficient. In this way he is copying natural scientists who try to enhance the productivity of Nature.

REFERENCES

- (1) Silvester R. "Stabilization of sedimentary coastlines" Nature (London) Vol. 188 (4749), 1960, 467-469.
- (2) Silvester R. "Development of crenulate shaped bays to equilibrium" Proc. ASCE J. Waterways and Harbors Divn. 96 (WW2), 1970, 275-287.

- (3) Silvester R. and S.K. Ho "Use of crenulate shaped bays to stabilize coasts". Proc. 13th Conf. Coastal Eng. 2, 1972, 1347-1365.
- (4) Silvester R. "Headland defense of coasts" Proc. 15th Conf. Coastal Eng. 2, 1976, 1394-1406.
- (5) Silvester R. "A new look at beach erosion control" Disaster Prevention Res. Inst., Kyoto Univ. Annual Rep. 22A, 1979, 19-31.
- (6) Silvester R. "Wave reflection at seawalls and breakwaters" Proc. Instn. Civil Engrs. 51, 1972, 123-131.
- (7) Silvester R. "Sediment transmission across entrances by natural means" Proc. 16th Congress IAHR, 1, 1975, 145-156.
- (8) Toyoshima O. "Changes of sea bed due to detached breakwaters" Proc. 15th Conf. Coastal Eng., 2, 1976, 1572-1589.
- (9) Toyoshima O. "Design of a detached breakwater system" Proc. 14th Conf. Coastal Eng. 2, 1974. 1419-1431.



16. Offshore breakwaters closely spaced at Kaika coast in Figure 15.

BEACHES: PROFILES, PROCESSES AND PERMEABILITY

Michael R. Gourlay

Department of Civil Engineering
University of Queensland, St Lucia, Australia.Abstract

Equilibrium beach profiles have been investigated in the laboratory for two beach materials, 0.22 mm marine sand and 1.55 mm crushed coal. Analysis of the results confirms that the dimensionless fall velocity H_0/Tw is an important parameter influencing both surf zone hydraulics and the form of the resulting equilibrium profile. Beach permeability also significantly influences the hydraulics within the beach face and it has been found that both H_0/Tw and the parameter w_f/w , the ratio of the fluidising velocity to the fall velocity, influence the form of the equilibrium profiles of permeable beaches.

1. INTRODUCTION

The problems involved in the interaction between waves and beaches are complex and while much research has been undertaken in this field, it is still not yet possible to predict on empirical grounds, let alone theoretical grounds, the shape of a beach after it has been subjected to given wave conditions. This situation applies both in the apparently simple two dimensional case where waves approach the beach with crests parallel to the shoreline and in the three dimensional case where matters may be further complicated by offshore wave refraction and geographical features such as headlands, rock bars, etc, as well as man made structures.

Investigation of this problem in the field involves an extremely complicated interacting system with many variables virtually none of which can be controlled. Moreover, the simultaneous measurement of all relevant variables over a sufficiently large area is in most cases completely impossible. On the other hand, investigation in the laboratory encounters problems concerning the reproduction of a sufficient number of the relevant variables in correct relationship to one another. Thus the laboratory investigator is confronted with the problems of

scale effects and of too simplistic a representation of the phenomena. Nevertheless, it is possible in the laboratory to investigate certain aspects of beach processes in a systematic manner so that the general behaviour may be established. For example, the work of Kemp and Plinston (1968) has shown the significance of the surf zone conditions, as expressed in terms of the ratio of uprush time to wave period, in determining the interaction between breaker type and beach profile. Again, the general influence of the height of a sand dune upon the amount of shoreline recession during a storm has been established by van der Meulen and Gourlay (1968), confirming what had been suspected but could not be proven from available field data.

While laboratory investigations provide a means for gaining further understanding of beach processes under controlled conditions, the solution of many practical coastal engineering problems cannot wait until complete understanding of these processes is obtained. Consequently a second very important purpose of laboratory beach profile investigations is to compare the behaviour of various model beach materials at laboratory scale with prototype conditions so that model scale relationships may be established for the design of movable bed coastal models used in the solution of real engineering problems involving coastal sediment transport. It has been a common procedure to use lightweight sediments in such movable bed models on the assumption that, because these materials are more easily moved by the flow or waves in the model, they will reduce the influence of scale effects. It has also been long recognised that such materials often give grossly distorted beach profile shapes particularly on the beach face and in the surf zone. The investigation described in this paper began as a study of the use of crushed coal as a model beach material to represent natural beaches of quartz sand but subsequently developed into a more general study of the processes which determine the shape of beach profiles formed in beach materials with different permeabilities.

2. FACTORS INFLUENCING BEACH PROFILE SHAPE

A large number of factors influence the shape of beach profiles in nature. These may be divided into active factors and passive factors. The former produce the actions which mould the latter into a given profile shape. At the same time changes in the profile shape modify the mechanisms by which the active forces mould the profile. The following are the more common factors involved:

Active factors

- waves, tides, winds, rainfall, temperature;
- duration of influence of active factors.

Passive factors

- beach material, initial profile shape;
- geology and/or other constraints.

In practice most model investigations neglect the effects of tides, winds and rainfall and reproduce only the action of waves upon various beach materials. The constraints of geology and/or artificial constructions are usually not included in tests but are replaced by the constraints imposed by the model test basin. The latter at one and the same time may both exclude prototype three dimensional effects produced by nearshore oscillations and circulation systems and introduce spurious three dimensional effects characteristic of the model basin. Moreover, wave generators producing regular waves in shallow water also generate parasitic secondary waves which can affect the form of the beach profile (Hulsbergen 1974).

Even with the very limited number of factors normally considered in model tests, still further simplifications are generally made. Most laboratory investigations of beach processes have been made with regular waves of constant height and period. Only a few investigations have involved irregular and/or wind generated waves (e.g. van der Meulen and Gourlay 1968, Kraai 1969, van de Graaff 1977 and Vellinga 1978). While numerous tests have been made with both quartz sand and various light-weight materials of different median sizes, systematic tests of the effects of variations in the grading and shape of beach sediments are very few (e.g. Collins and Chesnutt 1975). Opinion is divided as to whether the slope (and/or shape) of the initial profile affects the shape of the final equilibrium profile although it is recognised that it certainly affects the time taken to reach equilibrium. The fact that water temperature cannot be controlled in outdoor model basins and often has not been controlled in indoor ones means that many investigators have had difficulty in obtaining equilibrium profiles with fine sands whose motion relative to the fluid, as expressed by their fall velocity, is significantly affected by temperature (Chesnutt 1975).

3. BEACH PROCESSES AND SURF ZONE HYDRAULICS

3.1 The Equilibrium Beach Profile

The equilibrium beach profile is that profile shape which when subjected to a given wave condition dissipates and/or reflects all the wave energy reaching it in such a manner that no net transport of the beach/bottom sediment occurs anywhere along the profile. The sediment transport mechanisms involved in this process are complex and vary in nature along the profile. For instance offshore of the breakpoint sediment transport is initiated and maintained by the orbital motion of the waves which exerts a shear stress on the bottom material through the oscillatory boundary layer created by the waves. The process is complicated by the development of ripples on the bottom and the occurrence of complex interactions between the oscillatory flow and vortices formed in the lee of the ripples. At the breakpoint relatively large amounts of sediment may be thrown into suspension, particularly by plunging breakers, and the flow becomes highly aerated. High aeration and suspension of sediment particles may continue within the surf zone as the bore from the broken wave travels landward. At the shoreline

the uprush deposits its remaining sediment on the beach face as it percolates into the porous beach material before the backwash and/or outflow from the beach face mobilises the sediment again. The sediment transport processes acting to form the equilibrium beach profile are thus complex and cannot be related to a single simple model.

It has long been recognised that there are two basic forms of equilibrium beach profile (figure 1).

- (i) The step profile or swell profile formed when the waves are of low steepness (H_0/L_0 small) and/or the beach material is coarse.
- (ii) The bar profile or storm profile formed when the waves are of high steepness (H_0/L_0 large) and/or the beach material is fine.

The two profile types generally correspond with the concepts of reflecting and dissipative beaches as described by Short (1978). Transition profiles between these two limiting cases may exhibit rhythmic alongshore variations such as crescentic bars and beach cusps. In such situations the beach profile varies significantly in shape depending upon its location with respect to these rhythmic features.

Futhermore a bar profile may have one or more bars depending upon the wave steepness and/or the beach slope.

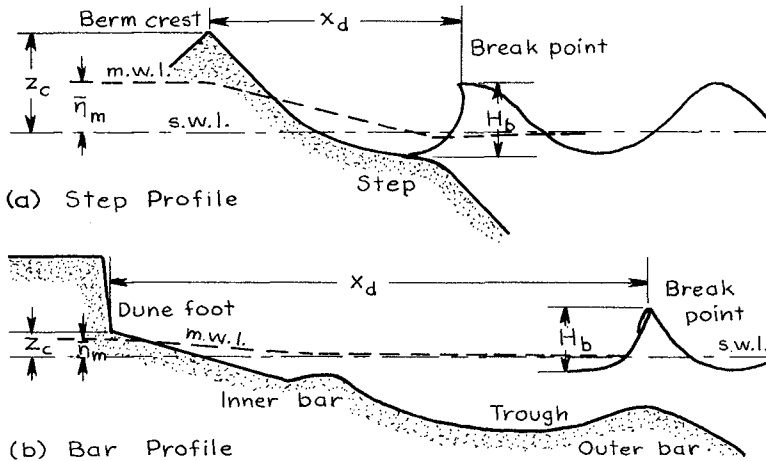


Figure 1

3.2 Dimensionless Fall Velocity H_0/Tw

In the search for model scale laws for beach process modelling, increasing attention is being paid to the use of the dimensionless fall velocity as a scaling parameter. For instance, Saville and Watts (1969) and Saville (1980) implicitly used this parameter in an investigation in which fine crushed coal was used to model larger scale beaches formed in fine to medium sand. Gourlay (1968) proposed the use of the parameter H_0/Tw for describing beach processes, pointing out that H_0/w represented "the time taken for a sand particle to fall a distance equal to the wave height. If this time is large compared with the wave period, any material stirred up by the breaking waves is likely to remain in suspension and to move as suspended load. If it is of the same order of magnitude or less than the wave period, bed load motion will predominate". Thus it was suggested that not only was the parameter H_0/Tw important in beach processes but that a value of the order of unity could be critical in determining the different sediment transport processes which lead to different profile forms.

Some time earlier Iwagaki and Noda (1962) had shown that the occurrence of the two main profile types, step profiles and bar profiles, depended upon the two parameters H_0/L_0 and H_0/d . Bar profiles occurred at relatively large values of both parameters and step profiles at small values. Subsequently Sitarz (1963) showed that the profile type depended upon the following parameter:

$$\frac{H}{T\sqrt{g(s-1)}d} < 0.6 \quad \text{step profile}$$

$$> 0.6 \quad \text{bar profile}$$

with bar profiles always occurring if $H_0/L_0 > 0.03$. This parameter is very similar to H/Tw since $w \propto \sqrt{g(s-1)d}/C_D$ where C_D , the drag coefficient of the sediment particles, is a function of the Reynolds number (wd/ν). Subsequently a number of researchers using data from various sources found that step and bar profiles could be separated on the basis of $H_0/Tw(d_{50})$.*

e.g. Dean (1973)	$H_0/Tw \lesssim 0.85$
C.E.R.C. (1973) based upon Kohler and Galvin	$\lesssim 0.6$ to 2.0 depending upon H_0/d
Gourlay (unpublished)	$\lesssim 1.55$ for fine sand (0.2 to 0.3 mm)
	$\lesssim 0.4$ for coarse sand/ fine gravel (2 mm)

In the last case the critical value of H_0/Tw decreased with increasing sediment size, indicative of the possible influence of beach permeability on profile shape.

* Unless otherwise specified the value of w used to calculate H_0/Tw is $w(d_{50})$, the fall velocity of the median sediment size.

More recently van Hijum (1974) found that for coarse material with $d_{90} \geq 6$ mm bar type profiles were formed when

$$\frac{H_o}{L_o} > 2.5 \frac{d_{90}}{H_o}$$

Assuming $C_D \approx 1.3$ for coarse natural sediments and $s = 2.65$ this reduces to

$$\frac{H_o}{T w(d_{90})} \lesssim 0.48$$

where $w(d_{90})$ is the fall velocity corresponding to the d_{90} size. In fact the beach material was very uniform and this relationship is probably equivalent to

$$\frac{H_o}{T w(d_{50})} \lesssim 0.54$$

which is the same order as that established for coarse material from the present author's earlier unpublished analysis.

A change in profile type also implies a change in beach slope. Kemp and Plinston (1968) found that the beach slope was a function of $H_b/Td^{3/2}$ which parameter is essentially the same as that used by Sitarz. Kemp and Plinston used the breaker height which is a more relevant wave height than H_o when the mechanics of the actual surf zone processes are being considered. For small values of $H_b/Td^{3/2}$ the beach slope decreased as $H_b/Td^{3/2}$ increased up to a critical value, above which the beach slope was constant. They also found that the critical value of $H_b/Td^{3/2}$ at which the beach slope changed significantly corresponded to the transition from surging/collapsing breakers to plunging breakers which occurred when the relative uprush time T_u/T , or "phase difference" of the uprush, was 0.7. Subsequently Nayak (1970) found that both the beach slope and the reflection coefficient decreased with increasing values of H_o/Tw . Moreover, reflection was smaller for coarser beach materials with the same value of H_o/Tw , apparently because of the increased permeability of the coarser materials. More recently Dalrymple and Thompson (1976) using data from a number of sources found that the beach slope at still water level decreased with H_o/Tw for step type beach profiles but tended to become constant for values of $H_o/Tw > 1$ when bar profiles were present.

Considering the problem of model scale relationships for dune erosion during a storm surge, van de Graaff (1977) and Vellinga (1978) have found that beach processes may be modelled using very fine sand, if H_o/Tw has the same value in both model and prototype. If this criterion cannot be met, then it is necessary to distort the model profile scales.

3.3 Initial Beach Slope

There has been some difference of opinion as to whether the initial slope of the beach profile affects the final equilibrium profile shape. For instance Dalrymple and Thompson (1976) found that initial slopes from 1:5 to 1:10 had no significant effect upon the equilibrium shape of beaches formed from 0.4 mm sand. Similarly van Hijum (1974) found the same result for the same initial slope range when the beach material was fine gravel. Earlier Nicholson (1968) claimed a similar result for 2 mm quartz sand with initial slopes from 1:5 to 1:20. On the other hand, Chesnutt (1975) found that equilibrium beach profiles formed in 0.2 mm sand may be affected by initial profile slopes when the latter was changed from 1:10 to 1:20. Sunamura and Horikawa (1974) found that initial profiles of 1:10, 1:20 and 1:30 influenced the final profile shape formed in 0.2 and 0.7 mm sands and proposed that profiles be classified on the basis of whether they resulted in erosion or accretion of the original beach face. Recently Hattori and Kawamata (1980) combined this concept of eroding and accreting profiles with a parameter which includes both the initial beach slope and the fall velocity, i.e.

$$\frac{(\frac{H_o}{L_o}) \tan \alpha}{w / g T} = 2\pi \frac{H_o}{T w} \tan \alpha$$

< - onshore transport
 = 0.5 - neutral (equilibrium)
 > - offshore transport

It is difficult to generalise on the effect of initial slope upon equilibrium profiles at the present time, but it seems possible that initial slope does not significantly affect the equilibrium profile when the initial profile is steep and no significant wave energy is dissipated offshore of the breakpoint. Under such conditions the breakers will normally be surging or plunging during the initial stages of profile development. On flat initial slopes where significant energy is dissipated offshore of the breakpoint and/or the breaking waves are spilling, it is possible that no equilibrium can be developed.

4. EXPERIMENTAL INVESTIGATION

The purpose of the present investigation was to compare the equilibrium beach profiles and associated processes produced by different kinds of breaking waves in two beach materials with very different permeabilities. The experimental work was divided into two parts:

- (i) the determination of all relevant properties of the beach materials;
- (ii) the formation of equilibrium beach profiles in a wave basin for each beach material for various wave heights at a constant wave period.

The two beach materials used in this investigation were:

- (i) a fine marine sand, $d_{50} = 0.22$ mm, typical of the beach sands on the exposed beaches of southern Queensland;
- (ii) a coarse crushed coal, $d_{50} = 1.55$ mm, with a similar relative particle size distribution to the sand.

The sediment properties determined were of two types:

- (i) those describing the sediment itself, e.g. specific gravity s , size distribution, porosity ϵ and angle of repose;
- (ii) those describing hydraulic characteristics associated with the sediment, e.g. fall velocity w , fluidising velocity w_f and permeability k .

The values of some of these properties are shown on figures 2 and 3 while the complete data is given in a separate report (Gourlay 1980).

The beach profile tests were made in a two dimensional wave basin 14.7 m long, 3.05 m wide, and 0.6 m deep equipped with a suspended paddle type wave generator. In each case the beach material was formed to an initial slope of 1 in 13. The water depth offshore of the beach h_i was 0.368 m. The wave period was 1.9 s for all tests and 8 or 10 tests were made for each material with deepwater wave heights varying from 23 to 183 mm.

Tests were run for sufficient time to reach equilibrium, the test durations varying from 4 to 30 hours. Equilibrium was taken as being reached when the wave uprush limit and breakpoint location did not alter position significantly with time. Once the profile had reached equilibrium the following quantities were measured:

- (i) incident wave heights and reflection coefficient along 10 equally spaced lines offshore of the beach;
- (ii) wave height transformation along centre profile, including crest and trough elevations, from offshore through the surf zone to the beach;
- (iii) location, height and type of breakers; location of plunge point, if any; location of uprush limit and time of travel of broken wave from breakpoint to uprush limit;
- (iv) wave set-down and set-up along centre profile from offshore to landward of uprush limit;

and after the wave generator was turned off:

- (v) beach profiles along 10 equally spaced lines over the full extent of the wave formed profile.

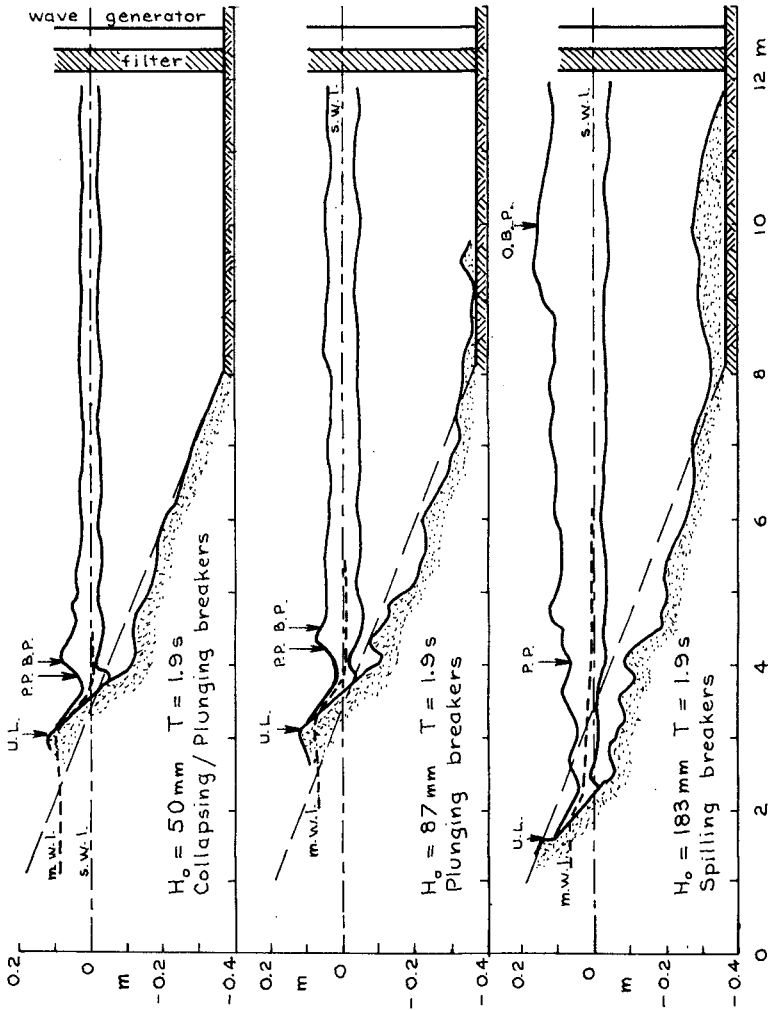
5. EXPERIMENTAL RESULTS

5.1 Beach Profiles and Mean Water Level

The experimental profiles measured along the centre of the wave basin together with wave heights and mean water levels are given for selected tests on figure 2 (sand) and figure 3 (coal). Steep reflective beaches with step type profiles were developed by low waves on both beach materials, while flat dissipative beaches with offshore bars were developed with the highest waves. In both cases the smallest waves produced erosion of the profile offshore of the breakpoint and accretion of the beach in the form of a large berm. Waves of intermediate height produced erosion of the offshore profile with accretion both on the beach and further offshore. Only the highest waves produced erosion of both the beach and inner surf zone and consequent deposition further offshore. The accreting, transition and eroding beaches generally corresponded with the occurrence of surging, plunging and spilling breakers respectively. For both beach materials the offshore profile seaward of the breakpoint was steepest just before the breakers changed from plunging to spilling.

Significant differences in detail were also evident between the profiles formed in the two different beach materials. All the beach profiles formed in sand had an almost constant beach face slope of 12° between the still water line and the berm crest (uprush limit). The sand beach behaved as an almost impermeable surface with both the uprush and the backwash flowing parallel to the beach face. Beach profiles in sand showed a breakpoint bar with plunging breakers. In contrast the beach profiles formed in the coal were much smoother in shape and a bar was not formed with plunging breakers. The most obvious feature of the coal beach profiles formed by low wave heights was the very steep berm which was built up at the uprush limit. With surging breakers this berm was very high and had a very steep face above the mean water level with a slope approaching 55° , the critical angle for stability of this beach material. On the other hand, the slope of the beach face at the still water line was very much less than this value, i.e. of the order of 4° for the higher waves. It is quite evident that the permeability of the coal beach was very important and the mechanism whereby this large berm was built up involved the uprush percolating into the steep berm face, draining vertically downwards through the deposited material, and then emerging as the backwash as the base of the beach below the mean water level.

Offshore of the breakpoint, the mean water level was almost horizontal with comparatively little wave set-down, particularly for the coal beach. Mean water level started to rise at the plunge point and the maximum elevation of mean water level (maximum wave set-up) occurred within the beach landward of the uprush limit. For the spilling breakers occurring with the largest waves, mean water level rose at a very flat slope between the outer and inner breakpoints. The mean water level gradient inshore of the inner breakpoint was significantly steeper than offshore but flatter than that for the lower wave heights.



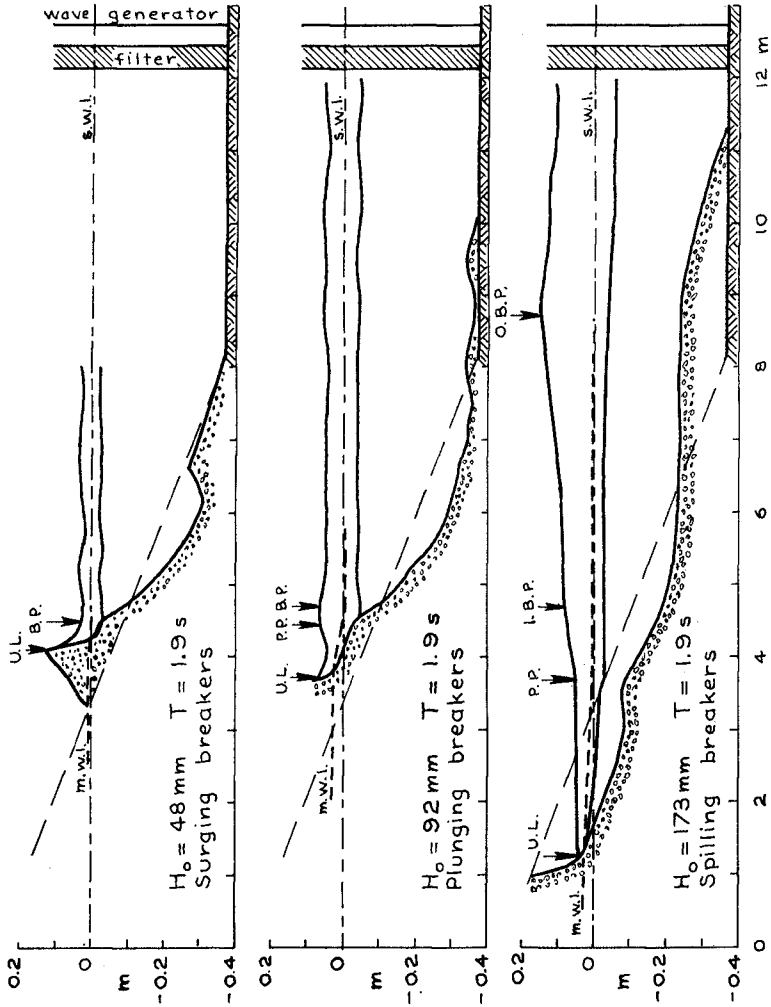
Marine sand

$d_{50} = 0.22 \text{ mm}$
 $e = 0.415$

$\sigma_g = 1.24$
 $w(d_{50}) = 27 \text{ mm/s}$

$s = 2.67$
 $w_f = 0.41 \text{ mm/s}$

Figure 2



$d_{50} \approx 1.55 \text{ mm}$
 $\epsilon \approx 0.51$

Crushed coal
 $\sigma_g \approx 1.27$
 $w(d_{50}) \approx 46 \text{ mm/s}$

$s \approx 1.34$
 $w_f \approx 2.7 \text{ mm/s}$

Figure 3

5.2 Beach and Surf Zone Parameters

The basic experimental data measured just before the end of each test and from the profiles surveyed just afterwards is presented elsewhere (Gourlay 1980). The parameters are breaking wave height H_b , wave reflection r , maximum wave set-up $\bar{\eta}_m$, berm crest/dune foot height z_c , surf zone width x_d , relative uprush time or "phase difference" T_u/T and beach slope at still water line $\tan \alpha_{swl}$. These parameters are plotted as functions of the basic independent variable, deepwater wave height H_0 on figure 4.

In virtually all cases the magnitudes of the various parameters are greater for the impermeable sand beach than for the very permeable coal beach. The quantity with the least difference is the breaker height but in most other cases the magnitudes of the coal beach parameters are about half those of the sand beach. In most cases the breaker type is seen to influence the form of the relationship. For instance the maximum berm height occurs when the surging breakers are just changing to collapsing breakers. Both plunging and spilling breakers dissipate more energy offshore of the beach with a consequent reduction in the wave uprush which determines the berm/dune foot height. The maximum wave set-up or wave induced groundwater level behind the beach also varies with breaker type but its maximum value appears to be associated with profile shape rather than breaker type. Both the surf zone width and maximum uprush time are different for each beach material with surging and plunging breakers but tend to similar values with spilling breakers.

As discussed earlier, the dimensionless fall velocity H_0/Tw is an important parameter influencing beach processes and beach profile shape. Its significance is shown on figure 5 where H_b/H_0 , $\bar{\eta}_m/H_0$, z_c/H_0 , x_d/L_0 and T_u/T are all plotted as functions of H_0/Tw or in actuality H_0/w since T is constant for these experiments. The following results are obtained:

- (i) The maximum wave set-up occurs at about $H_0/Tw = 1$ for both beach materials.
- (ii) $T_u/T = 0.5$ when $H_0/Tw = 1$ and profiles for $H_0/Tw < 1$ are definitely step type profiles. Bar type profiles are not formed until $H_0/Tw \approx 1.4$ to 1.5 .
- (iii) The relative berm height z_c/H_0 has a maximum value for the coal beach when $H_0/Tw < 0.6$.
- (iv) Both the relative surf zone width x_d/L_0 and the relative uprush time T_u/T are unique functions of H_0/L_0 for both materials except for the highest spilling breakers. The shapes of these functions indicate that x_d/L_0 is a function of T_u/T as shown by Sunamura and Horikawa (1974).

Since the wave period was not varied in these experiments, any parameter involving T or L_0 ($= gT^2/2\pi$) has not yet been justified. A detailed analysis of data from other sources has not yet been made, but

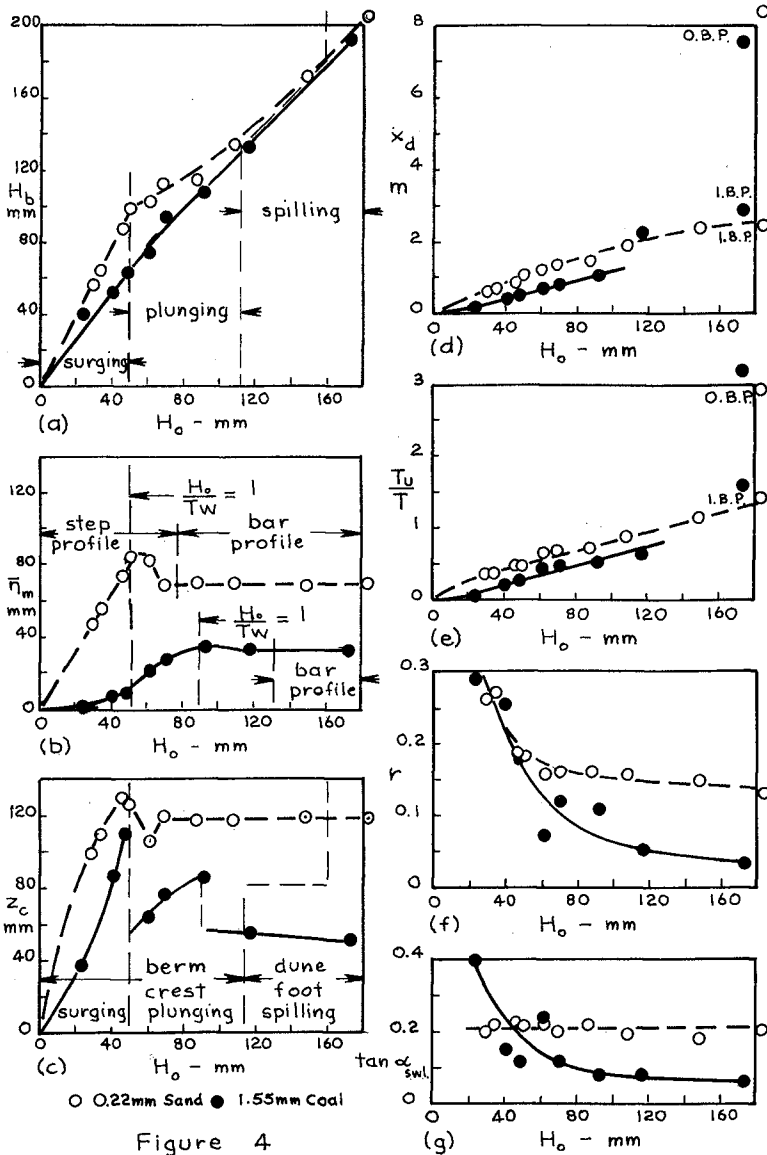


Figure 4

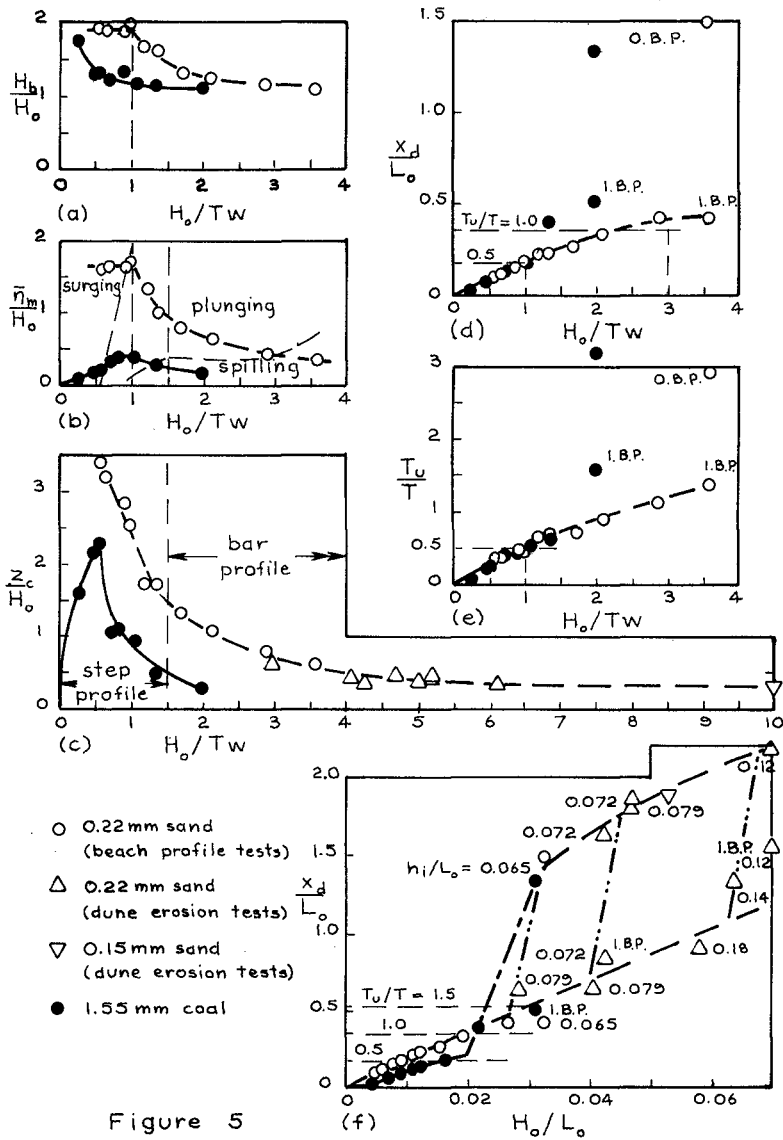


Figure 5

some data from earlier experiments on the erosion of sand dunes (Gourlay 1968, van der Meulen and Gourlay 1968) has been examined. This data is for 0.22 mm sand very similar to that used in the present tests, with one test with 0.15 mm sand. Wave periods varied between 1.04 and 1.63 s while wave heights were such that wave steepness H_0/L_0 was generally greater than the largest steepness used in the present tests. The only quantities conveniently available were dune foot height (uprush limit) z_c and surf zone width x_d . As indicated on figure 5c the relationship between z_c/H_0 for the dune erosion data and H_0/Tw is quite consistent with that for the present tests.

When x_d/L_0 for the dune erosion data was plotted as a function of H_0/Tw (not shown on figure 5d), no clear picture was presented since all the additional data was for $H_0/Tw \geq 3$ which was the region where this parameter tended to separate rather than unify the data from the present tests. On the other hand, it was found if x_d/L_0 were plotted against the deepwater wave steepness H_0/L_0 then a reasonably consistent pattern emerged (figure 5f). For $H_0/L_0 < 0.03$, x_d/L_0 is a simple function of H_0/Tw . For $H_0/L_0 > 0.03$ there are two possible surf zone widths. The narrower surf zone (small x_d/L_0) is an extension of the low wave steepness sand curve. It also includes surf zone widths inshore of the inner breakpoint on wide surf zones. Wide surf zones (large x_d/L_0) occur when significant deposition occurs on the level bottom of the wave basin seaward of the initial sand slope in the present tests or on a horizontal section of the offshore profile seaward of an approximately 1 in 10 slope in the dune erosion tests. Thus there appears to be an effect of initial profile shape present in the form of different values of h_i/L_0 where h_i is the depth offshore of the initial plane beach or the depth of the horizontal section of the initial profile in the dune erosion tests. As indicated on figure 5f the critical steepness of 0.03 for the initiation of a wide surf zone in these tests corresponds to $h_i/L_0 = 0.065$. About half the dune erosion tests have values of $h_i/L_0 = 0.072$ or 0.079 and those with $H_0/L_0 > 0.04$ have relatively wide surf zones. On the other hand, tests with $h_i/L_0 = 0.14$ and 0.18 lie on the narrow surf zone line with the former possibly on the point of transition to a wide surf zone at $H_0/L_0 \approx 0.06$. Certainly a test with $h_i/L_0 = 0.12$ and $H_0/L_0 > 0.06$ has a wide surf zone.

It appears from the preceding that the initial profile shape as typified by the ratio h_i/L_0 in these tests does affect the shape and particularly the surf zone width of the equilibrium profile when waves reach a certain critical steepness, the value of which increases with the magnitude of h_i/L_0 . This effect is possibly a consequence of significant energy dissipation occurring offshore of the original breakpoint during early stages of tests with relatively steep large waves. As suggested earlier, such an effect could be expected to occur on flat plane beaches, but not on steep ones. Hence the above results tend to confirm the idea that the initial profile shape affects the shape of the equilibrium profile when the former is flat but not when it is steep.

5.3 Beach Permeability

While it is evident that the parameter H_0/T_w is of considerable significance in representing the beach profile data particularly for x_d/L_0 and T_u/T when the latter parameter is less than 1.0, it is also evident from figure 5 that there are significant differences between the impermeable sand beach and the permeable coal beach with regard to other beach and surf zone parameters. These effects are almost certainly related to the differences in permeability of the two beach materials. In fact the magnitudes of these differences are in most cases directly related to the ratio between the fluidising velocity w_f and the fall velocity w as can be seen in figure 6 where w_f/w has been introduced as a multiplier to the various dependent variable parameters z_c/H_0 , \bar{r}_m/H_0 , etc. With the exception of figure 6a for H_b/H_0 , where the independent variable parameter H_0/T_w has been multiplied by w_f/w , all the other figures show that when the dependent variable is multiplied by w_f/w , the data points for both sand and coal beaches lie on the same curve when $H_0/T_w > 1$. Moreover there is a tendency for the modified parameters to become constant when $H_0/T_w > 3$.

The data plotted on figure 6 shows that there is no qualitative difference in behaviour between the two beach materials when $H_0/T_w > 1$, only a quantitative one. On the other hand, when $H_0/T_w < 1$ there are significant differences in the nature of the hydraulic processes within the surf zone, which is in fact confined to the uprush-backwash cycle, between the impermeable sand beach and the very permeable coal beach. The nature of these differences has been already indicated in the discussion on beach profiles. For the sand beach the hydraulic parameters involving H_b and \bar{r}_m are independent of H_0/T_w when the latter is less than 1.0 while the beach slope is essentially constant for all values of H_0/T_w . Both the modified wave reflection coefficient r_w/w_f and the modified surf zone similarity parameter $[(\tan \alpha_{sw})/\sqrt{H_0/L_0}]w_f/w$ appear to follow similar trends with H_0/T_w . Unfortunately the scatter of the data is too much to compare the relationship between these two parameters with that for a fixed plane beach.

The exact significance of the above results and particularly the ratio w_f/w has not yet been worked out in theoretical terms, but it seems quite certain that w_f is a very important sediment property which determines the shape of beach profiles formed in relatively large light weight sediments. w_f has been described as the fluidising velocity, that is it is the overall upward velocity of flow through a bed of sediment which just causes that sediment to be fluidised or to become unstable. It is related to the permeability k by the relationship

$$w_f = k i_c$$

where $i_c = (s-1)(1-\epsilon)$ is the critical hydraulic gradient at fluidization. On the other hand, w_f may be interpreted as the fall velocity of the sediment at maximum concentration of sediment particles. Under such conditions particle interference is a maximum and the fall velocity is very much less than that for widely separated particles in still water.

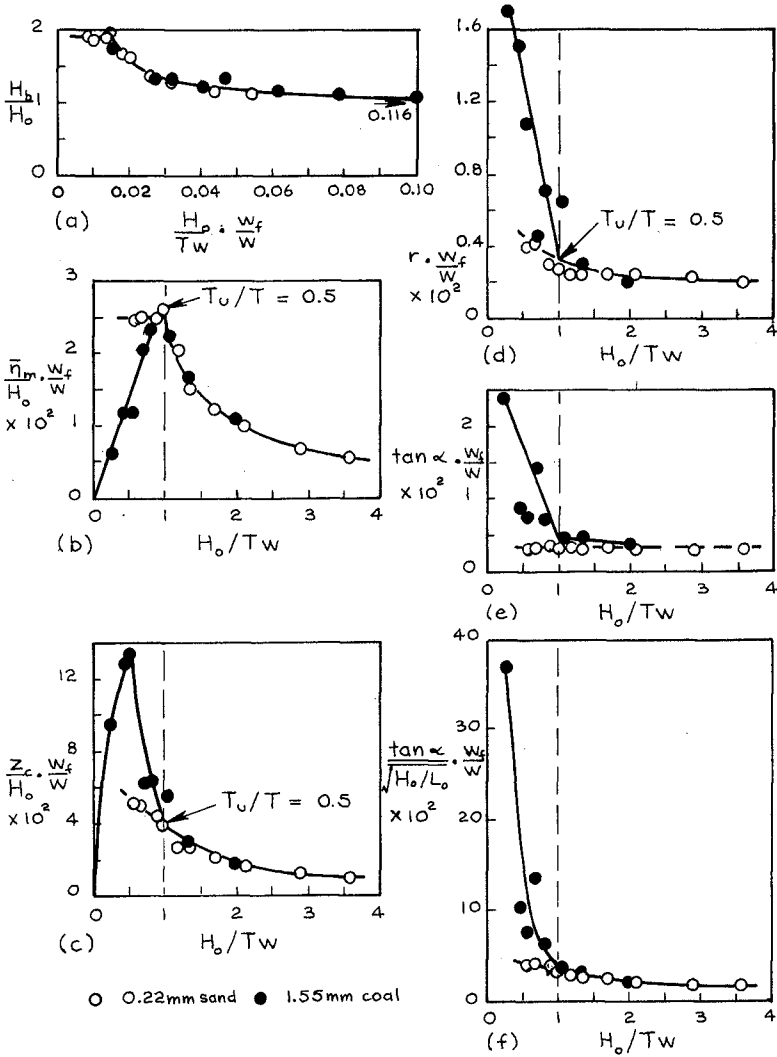


Figure 6

For spherical particles w_f/w is a constant for both very small and large particles, the magnitude of this ratio being a function of the dimensionless particle size $g^{1/3}(s-1)^{1/3}d/v^{2/3}$ and the porosity ϵ of the deposited sediment. This ratio w_f/w is smaller for small particles than large ones since the permeability and hence w_f of sediments decreases both as the porosity decreases and as the specific surface (surface exposed to fluid per unit volume of solid) increases.

6. SUMMARY AND CONCLUSIONS

(i) The dimensionless fall velocity H_0/Tw , which represents the behaviour of the sediment particles stirred up by the breaking waves in the surf zone, is an important parameter influencing surf zone hydraulics and the form of the equilibrium beach profile inshore of the breakpoint. In particular the wave set-up has a maximum value when $H_0/Tw = 1$ and both the relative surf zone width x_d/L_0 and relative uprush time T_u/T are unique functions of H_0/Tw when $T_u/T < 1$.

(ii) While H_0/Tw is a necessary and probably sufficient parameter for defining similarity conditions for model beaches formed in relatively impermeable sand, it is not sufficient for defining similarity conditions for model beaches formed in relatively permeable materials, particularly lightweight materials such as crushed coal. For permeable beaches the ratio w_f/w , which is the ratio of the maximum possible flow velocity within the deposited sediment to the maximum particle velocity in still water, is also important.

(iii) Similarity of the beach profile with respect to the beach face and its associated hydraulics is determined by both H_0/Tw and w_f/w as follows:

$H_0/Tw < 1$ - Hydraulic conditions within the beach face are significantly different for impermeable and permeable beach materials and no similarity is possible.

$1 < H_0/Tw < 3$ - Both H_0/Tw and w_f/w determine the similarity of the beach face.

$H_0/Tw > 3$ - Beach face parameters become independent of H_0/Tw and w_f/w is sufficient for similarity.

(iv) The shape of the initial profile does not appear to affect the shape of the equilibrium profile when the former is steep and offshore accretion is confined to the initial plane profile surface. If the initial slope is flat and/or offshore accretion occurs on the horizontal bottom of the wave basin or on an offshore horizontal section of the initial profile then either a wide or a narrow surf zone is possible. The occurrence of a wide surf zone depends upon the magnitude of both H_0/L_0 and h_1/L_0 .

(v) The results presented in this paper concerning the importance of w_f/w need to be extended with further experimental data for other beach materials including a permeable very coarse sand/fine gravel and a finer crushed coal. Further tests at various wave periods and initial profile slopes/shapes are also required to define the limits of the influence of H_0/T_w upon surf zone hydraulics and equilibrium beach profiles.

7. ACKNOWLEDGEMENTS

The author gratefully acknowledges the assistance of Jennifer Hacker, Peter Melloy, Warren Moreton and Shane Pearce in obtaining and analysing the experimental data for the beach profile tests.

The dune erosion test data was obtained by the author while working at the "de Voorst" laboratory of the Delft Hydraulics Laboratory, The Netherlands.

The beach profile tests were supported by a grant from the Australian Research Grants Committee.

REFERENCES

- C.E.R.C. (1973) Shore Protection Manual, 2nd edition, U.S. Army Coastal Engng Res. Center, Fort Belvoir, Virginia. Vol. 1, 1973.
- Chesnutt, C.B. (1975) Laboratory effects in coastal movable-bed models. A.S.C.E., Proc. Symp. on Modelling Techniques, San Francisco, 1975.
- Collins, I. and Chesnutt, C.B. (1975) Tests on the equilibrium profiles of model beaches and the effects of given shape and size distribution. A.S.C.E., Proc. Symp. on Modelling Techniques, San Francisco, 1975.
- Dalrymple, R.A. and Thompson, W.W. (1976) Study of equilibrium beach profiles. Proc. 15th Int. Conf. on Coastal Engng, Honolulu, 1976, Vol. 2, pp 1277-1296.
- Dean, R.C. (1973) Heuristic models of sand transport in the surf zone. Inst. Engrs Aust., Preprints 1st Australian Conf. on Coastal and Ocean Engng, Sydney, 1973, pp 208-214.
- Courlay, M.R. (1968) Beach and dune erosion tests. Delft Hydraulics Laboratory, Report No. M935/M936, May 1968.
- Gourlay, M.R. (1980) Beaches: Profiles, Processes and Permeability. Univ. Qld., Dept Civ. Engng. Res. Rep. CE14, June 1980.
- van de Craaff, J. (1977) Dune erosion during a storm surge. Coastal Engineering Vol. 1, 1977, pp 99-134.
- Hattori, M. and Kawamata, R. (1980) Onshore-offshore transport and beach profile change. Inst. Engrs Aust., Abstracts 17th Int. Conf. on Coastal Engng, Sydney, 1980, pp 254-255.

- van Hijum, E. (1974) Equilibrium profiles of coarse material under wave attack. Proc. 14th Int. Conf. on Coastal Engng, Copenhagen, 1974, Vol. 2, pp 939-957.
- Hulsbergen, C.H. (1974) Origin, effect and suppression of secondary waves. Proc. 14th Int. Conf. on Coastal Engng, Copenhagen, 1974, Vol. 1, pp 392-411.
- Iwagaki, Y and Noda, H. (1962) Laboratory study of scale effects in two dimensional beach processes. Proc. 8th Int. Conf. on Coastal Engng, Mexico City, 1962, pp 194-210.
- Kemp, P.H. and Plinston, D.T. (1968) Beaches produced by waves of low phase difference. Proc. Am. Soc. Civ. Engrs., Vol. 94, No. HY5, Sept. 1968, pp 1183-1195.
- Kraai, P.T. (1969) Comparison of wind wave and uniform wave effects on a beach. Shore and Beach. Vol. 37, No. 2, Oct. 1969.
- van der Meulen, T. and Courlay, M.R. (1968) Beach and dune erosion tests. Proc. 11th Int. Conf. on Coastal Engng, London, 1968, Vol. 1, pp 701-707.
- Nayak, I.V. (1970) Equilibrium profiles of model beaches. Univ. Calif., Berkeley, Hydr. Engng Lab. Tech. Rep. HEL-2-25, May 1970.
- Nicholson, J. (1968) A laboratory study of the relationship between waves and beach profiles. Inst. Engrs Aust., Conf. on Hydraulics and Fluid Mechanics, 1968.
- Saville, T. and Watts, G.M. (1969) Coastal regime - recent U.S. experience. P.I.A.N.C., Proc. 22nd Int. Nav. Congr, Paris, 1969, Sec. 11-4.
- Saville, T. (1980) Comparison of scaled beach deformation tests using sand and coal. Inst. Engrs Aust., Abstracts 17th Int. Conf. on Coastal Engng, Sydney, 1980, p 439.
- Short, A.D. (1978) Wave power and beach-stages: a global model. Proc. 16th Int. Conf. on Coastal Engng, Hamburg, 1978, Vol. , pp 1145-1162.
- Sitarz, J.A. (1963) Contribution a l'étude de l'évolution des plages a partir de la connaissance des profils d'équilibre. Travaux du Centre de Recherches et d'Études Océanographiques, Paris, Vol. V, Sept. 1963.
- Sunamura, T. and Horikawa, K. (1974) Two-dimensional beach transformation due to waves. Proc. 14th Int. Conf. on Coastal Engng, Copenhagen, Vol. 2, pp 920-938.
- Vellinga, P. (1978) Movable bed model tests on dune erosion. Proc. 16th Int. Conf. on Coastal Engng, Hamburg, 1978.

SAND BED-FORM LENGTHS UNDER OSCILLATORY MOTION

ARTHUR BREBNER*

ABSTRACT

Tests were carried out in the oscillating water tunnel to determine the bed-form lengths of sand ranging from 0.1 mm to 0.55 mm subjected to oscillatory motion of various orbital diameters ranging from 0.15 m to 1.5 m and of various periods ranging from 3 to 15 s. The relationship for the bed-form length is given in the accompanying graph in dimensionless form.

INTRODUCTION

Oscillatory motion over an initially flat bed can, under certain conditions, cause the formation of relatively stable bed-forms of trochoidal shape having a definite "wave-length" from crest to crest of Λ m and wave-height from crest to trough of Δ m. The purpose of the tests described herein is to provide more information on the bed-form lengths for fine sands of median diameter D of 0.1 and 0.2 mm and of density ρ_s (water density ρ) to compare these results with the results of previous tests. A test bed 15 m long and 0.15 m thick of sand was screeded off flat in the oscillating tunnel and the piston throw set to give a fixed value of orbital diameter Λ m. A starter from which the bed-forms would grow was created by heaping up a small quantity of the sand approx. 1 cm high across the tunnel normal to the oscillating motion.

This starter was not essential since the bed-forms would grow from any slight discontinuity, especially from the ends of the test section, but made the measurement of growth easier to record.

The oscillatory motion was then imposed on the bed with a very long period T s such that the maximum velocity just above the boundary

$$U_{\max} \left(= \frac{\pi \Lambda}{T} \right) \text{ m/s}$$

was incapable of creating motion. As the period was slowly decreased striations of negligible height and of about 5 cm wave length appeared, giving a mottled appearance to the bed. Bed-forms do not form until the mobility number

* Professor of Civil Engineering,
Coastal Engineering Laboratory,
Queen's University at Kingston, Canada.

$$\frac{U_{\max}^2}{g(\rho_s/\rho - 1)D}$$

(which is essentially the ratio of drag force to inertia force or Shields' parameter) is greater than 3. Under such conditions the bed-form will grow on either side of the starter, spreading to both ends of the test section, gradually growing in length and height until a stable form is attained. The number of oscillatory cycles, n , to achieve a sensibly constant length is a direct function of the value of the mobility number. The growth of the bed-form length with cycles is as shown on Fig. 1.

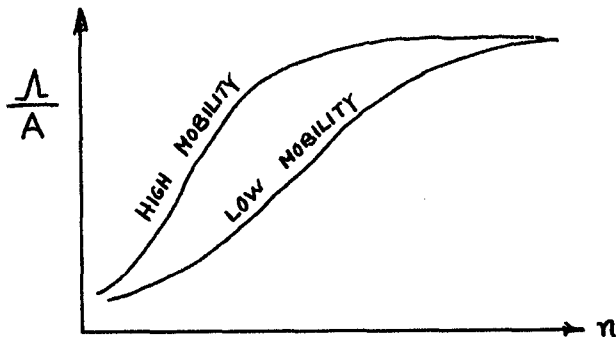


FIGURE 1

When a bed-form has been created and is sensibly stable if the period is reduced, so increasing the mobility number, the bed-form can be wiped out such is the amount of turbulence and material in suspension above the bed.

The author's results have been plotted on Fig. 2, as have the test results of Mogridge and Kamphuis (1) and Lofquist (2) for differing densities and sizes of bed material using the dimensionless group

$$\left(\frac{\gamma_s D^3}{\rho v} \right)^{1/2}$$

(proposed by Yalin and Russell (3)) to show why the bed-form length decreases with increasing mobility number for fine sands. Here γ_s is the submerged specific weight and v the kinematic viscosity of water. This group is essentially a fall velocity Reynolds Number.

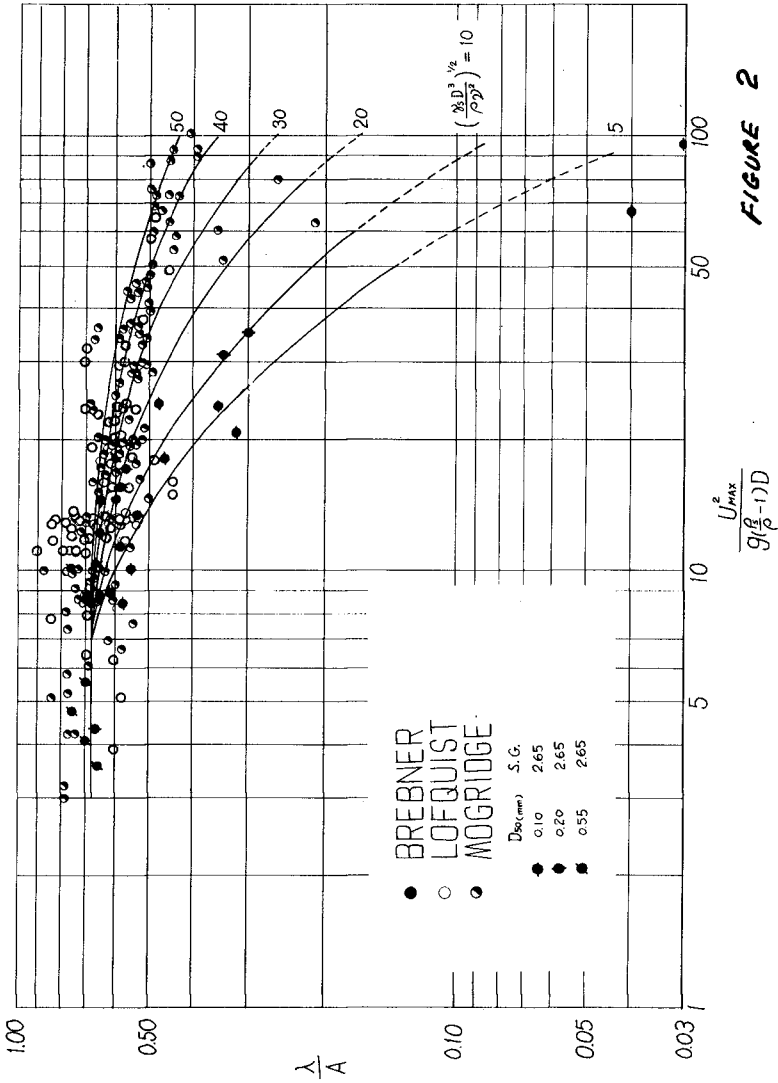


FIGURE 2

With regard to the ratio of bed-form "wave height" Δ to bed-form "wave-length" Λ , this ratio is given by $(\Delta/\Lambda)_{\max} = 0.14$ and the crest angle at this maximum steepness is 120° . These numbers are either remarkable or fortuitous — by water-wave theory for deep-water conditions the maximum water-wave steepness at breaking is 0.14 (i.e. $\pi - 3$) and Stokes' angle is 120° . Also, using typical soil mechanics figures for the natural angle of repose for loose sand, namely about 30° , this gives the internal angle of the crest as $(180^\circ - 2 \times 30^\circ) = 120^\circ$. The author leaves the explanation of this remarkable similarity of the two systems to erudite applied mathematicians such as Professor Longuet-Higgins.

In trying to relate this work to the extremely difficult task of modelling sea-bottom and beach processes one has firstly to keep in mind Fig. 1 where it is seen that the process is very time dependent. A 10 s prototype wave at a high mobility number will produce bed-forms in many less cycles than a 1 s model wave at perforce a smaller mobility number. Secondly, the model mobility number must be at least 3 to achieve any chance of bed-form formation — and hence material movement during the cycle. Lastly, for small sizes of sand (0.1 to 0.2 mm) which are very common on the world's best recreation beaches, a high prototype mobility number may result in no bed-form whatsoever and only massive amounts of sand in suspension above the bed which are easily moved by littoral or other currents. This may be impossible to reproduce in a model at lower mobility numbers unless one uses extremely lightweight material since the use of smaller model sizes of cohesionless material is not feasible. It is impossible for the same mobility number, by using say lightweight material in the model, to simultaneously have the same fall velocity Reynolds Number. Thus strict modelling of the motion of small size sand bed-forms under wave action is virtually impossible.

REFERENCES

- (1) Mogridge, G.R. and Kamphuis, J.W., "Experiments on Bed Forms Generated by Wave Action", Proc. 13th C.E. Conf., Vol. II, 1972.
- (2) Lofquist, K.E.B., "Sand Ripple Growth in an Oscillatory-Flow Water Tunnel", U.S. Corps of Engineers Tech. Paper 78-5, 1978.
- (3) Yalin, M.S. and Russell, R.C.H., "Similarity in Sediment Transport Due to Waves", Proc. 8th C.E. Conf., 1962.

CHAPTER 82

SEDIMENT TRANSPORT PROCESSES AND COASTAL VARIABILITY ON THE ALASKAN NORTH SLOPE

by

E. H. Owens

Woodward-Clyde Consultants, Victoria, B.C.

J. R. Harper

Woodward-Clyde Consultants, Victoria, B.C.

D. Nummedal

Ceology Department, Louisiana State University

ABSTRACT

Shoreline development and shore-zone sediment transport on the Alaskan North Slope are dependent upon levels of wave energy, sea ice conditions, and the ice-sediment characteristics of eroding tundra cliffs. Considerable variation exists between the coastal processes and the shore-zone morphology of the Chukchi and Beaufort Sea beaches, (respectively west and east of Point Barrow). The supply of coarse sediments (sands or gravels) and the volumes of material eroded from tundra cliffs are a function of the initial character of the cliff sediments and of the ice content of the exposed cliffs. As cliff heights decrease, the ice content of the cliff increases, erosion rates increase but the sediment supply rates decrease. Wave-energy levels are relatively high and maintain a constant level on the Chukchi coast. The transport system on this coast is continuous and is augmented by storm events. On the Beaufort coast, energy levels are much lower, transport processes discontinuous, and storm events are therefore more significant. Sediments supplied to the coastal zone on the Chukchi coast are derived largely from the erosion of tundra cliffs and the barriers are continuous, linear, and stable. Rivers are the primary source of coastal sediments on the Beaufort coast and the more variable energy levels produce unstable barriers that are subject to aperiodic transport processes.

INTRODUCTION

The shoreline processes and coastal form of the Alaskan North Slope between Cape Beaufort and Demarcation Point are characterized by considerable variability. These differences can be explained in terms of regional variations in geology, sediment supply, and sediment transport processes. This paper discusses the results and interpretations of work carried out since 1975 by the authors and by other workers in this area. The emphasis throughout is on the interaction between the sediments available for redistribution by shoreline processes and on the energy levels which control the redistribution of the littoral-zone sediments.

Although the same processes operate in the shore zone of the North Slope as in lower latitude regions, the role of ice is a key element in understanding the coastal geomorphology and the sediment dispersal patterns. The open-water season is less than 3 months each year and the shore zone is a low wave-energy environment due to the small fetch distances imposed by the perennial polar pack-ice. An additional role of ice is related to the ice content of the cliff sediments which is a critical factor in controlling the volume of sediments available to the shore zone for beach development. The ice content, which is a function of regional variations in cliff height, affects the rates of sediment supply and the construction of beach or barrier systems.

GEOLOGY

The geology of the Alaskan North Slope north of the Brooks Range is characterized by a series of thick (10-40 m) Quaternary sediments which form a low coastal plain. Outcrops of bedrock along the shoreline are limited to a few short sections of the Chukchi coast where Cretaceous sedimentary rocks outcrop at or near sea level. Apart from

these relatively few sections of bedrock, the remainder of the Alaskan North Slope coast is composed of unconsolidated materials. Relief is higher along the Chukchi coast than on the Beaufort Sea coast (Table 1). On the Chukchi shorelines 44.3% of the relief is greater than 5 m, whereas, on the Beaufort Sea coast only 11.3% of the relief is greater than 5 m (Hartwell, 1973). The primary effect of this regional variation in relief is that the drainage is predominantly towards the northeast. Although approximately 40% of the North Slope is adjacent to the Chukchi coast, about 80% of the drainage is into the Beaufort Sea (Walker, 1974). This drainage pattern, which results from the greater relief in the western coastal plain, is dominated by the Colville system which drains the majority of the hinterland area.

In terms of the surficial sediments it is possible to distinguish two major units that are found to the east and to the west of Oliktok Point. To the east there is a series of predominantly coalescing alluvial or glacial-outwash fans (sandy, gravel material), or outcrops of the Flaxman Formation (Hopkins and Hartz, 1978). The latter is a sandy, mud Pleistocene deposit which contains pebbles, cobbles and boulders. West of Oliktok Point, the Cubik formation, a Pleistocene marine deposit, is a pebbly sand which contains up to 65% of silt-clay in some sections; elsewhere the stoney muds of the Flaxman Formation outcrop. In all areas, these post-Pleistocene surficial sediments are mantled by a 2-3 m thick layer of thaw-lake sediments, which are predominantly peats and muds (Hopkins and Hartz, 1978).

In terms of broad characteristics, the Chukchi Sea has a coast of relatively high relief and straight shorelines with no large river systems or deltas. The more irregular coast of the Beaufort Sea is a

TABLE 1. Summary of Relief and Tundra Cliff Characteristics

	CHUKCHI COAST	BEAUFORT COAST
Bedrock	<ul style="list-style-type: none"> ● some coastal outcrops ● often near surface 	<ul style="list-style-type: none"> ● no coastal outcrops
Relief >5 m (%)	44.3	11.3
Cliff Heights		
mean	10 m	1 to 4 m
maximum	18 m	6 m
Average Retreat Rates (m/yr.)	0.3	1 to 3
Primary Cliff Sediments	clays gravels	silts
Estimated Overall Cliff Ice Content	≈25%	>90%

result of (i) shoreline erosion in this area of thaw lakes and low relief, and (ii) possible contemporary submergence (Hartwell, 1973). The Beaufort Sea coast has many sections of low cliffs, barrier islands, thaw lakes, and numerous large deltas.

The primary geological features of the North Slope that influence coastal zone processes and sediment transport systems are:

- (i) the near-surface bedrock on the Chukchi coast that affects relief, drainage and thaw subsidence,
- (ii) the variation in surficial sediments, with a higher fine fraction in the unconsolidated deposits on the Beaufort coast,
- (iii) the greater coastal relief on the Chukchi coast, and
- (iv) the greater number and size of the rivers that drain into the Beaufort Sea.

This geological background is essential to an understanding of the sediment sources and, therefore, of the sediment dispersal patterns on the North Slope.

The major sources of the sediments that accumulate in the beaches and in the lagoons of the North Slope are: (1) material eroded from tundra cliffs, and (2) sediments supplied to the littoral zone by rivers. Erosion of the barrier islands themselves may provide additional material to the nearshore system. The relative contributions from coastal and fluvial sources differ significantly between the Beaufort and Chukchi coasts. This difference can be attributed largely to: (a) the regional variation in tundra cliff characteristics and in the character of the unconsolidated deposits, and (b) the North Slope drainage pattern.

TUNDRA CLIFFS AND SEDIMENT SUPPLY

Tundra cliffs, comprised of unconsolidated Quaternary deposits and cemented by frozen interstitial pore water, are distributed widely along the Chukchi and Beaufort Sea coasts and are found on exposed outer shorelines as well as along lagoon shorelines. Estimates indicate that 50% to 75% of the coastline is backed by tundra cliffs.

Despite the geographical proximity of the two regions, fundamental differences in cliff morphology, stability and composition exist between the Chukchi and Beaufort Sea coasts. The major morphologic differences are caused by the regional variation in topography that has resulted from a stable to emergent coast with higher relief and near-surface bedrock, hence relatively high coastal cliffs, on the Chukchi Sea coast (Table 1) and from a submergent coast with widespread thaw

subsidence, hence relatively low coastal cliffs, along the Beaufort Sea coast (Table 1). This regional variation in relief between the two regions has important consequences to the coastal stability and littoral sediment supply.

Sediments become enriched with pore ice at the tundra surface as a result of normal periglacial processes. Ice contents are typically 75% ice-by-volume near the surface and decrease exponentially with depth to values of 40% at the six-meter depth (Sellman *et al.*, 1975). This means that near the tundra surface much of the bulk volume is actually comprised of ice, whereas, in sediments at lower depths only the normal void space is filled with ice. The important consequence of this phenomena is that the ice content of low cliffs is very high ("ice-rich") and of high cliffs is relatively low ("ice-poor"). Due to regional variations in topography (Table 1), the low, ice-rich cliffs are found primarily along the Beaufort coast and the high, ice-poor cliffs occur along the Chukchi coast.

The ice content of tundra cliffs is an important control on cliff stability, both in terms of rates of change and in terms of the mechanisms responsible for change. Surveys have shown that cliffs along the Chukchi coast are retreating at an average rate of 0.3 m/yr. (Harper, 1978), whereas along the Beaufort coast Lewellen's data (1977) indicate a mean cliff retreat rate of 2.7 m/yr. with local long-term retreat rates as high as 20 m/yr. Much of this order of magnitude difference in retreat rates can be attributed to the excess ice effect discussed above. In addition, large volumes of material may be eroded from low cliffs but these volumes would produce only small amounts of sediment for potential redistribution as these cliffs are largely comprised of

ice. The effect of excess ice is illustrated in Figure 1 which shows the relationship between cliff height, retreat rates and the volume of sediment produced by erosion. From this figure, a 2-m high "ice-poor" cliff retreating at 0.5 m/yr. would supply one cubic meter of sediment to the littoral zone. An "ice-rich" cliff of the same height would have to retreat at a rate of 0.9 m/yr. to produce the same volume of sediment. An important point illustrated in this figure is that the effect of ice content on sediment supply rates is most pronounced for

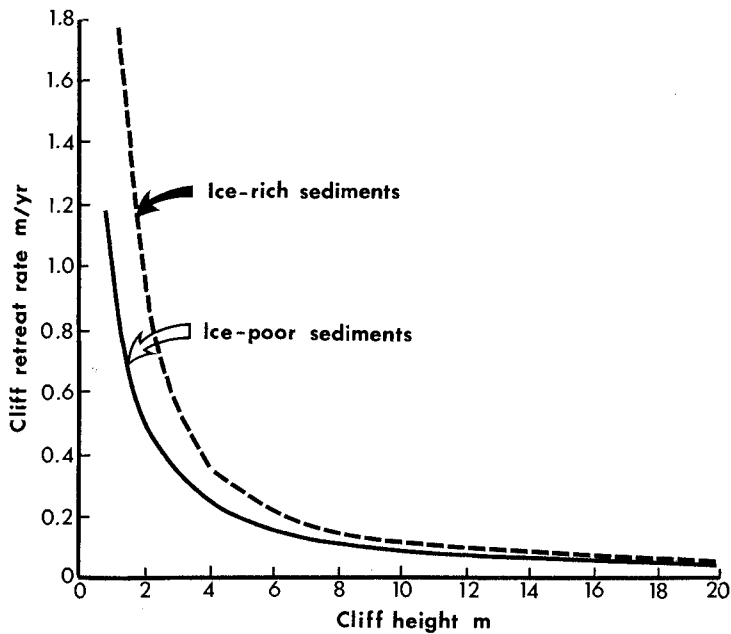


Figure 1. Cliff heights and cliff retreat rates required to produce $1 \text{ m}^3/\text{year}$ of eroded sediment from "ice-rich" cliffs (dashed line) and from "ice-poor" cliffs (solid line).

low cliffs (less than 3 m in height). The second important effect of the ice content in cliff sediments is a disproportionately high retreat rate for the low-relief, ice-rich cliffs.

An additional factor contributing to the large differences in retreat rate is lithology (Table 1). The Beaufort Sea cliffs are comprised primarily of silt; the sediment produced by erosion of these unconsolidated, fine-grained materials is rapidly transported offshore and lost from the littoral system. By contrast the gravel component of the Chukchi cliffs forms protective beaches at the cliff bases and can be reworked into constructional spits and bars.

As a result of the differences in cliff heights, ice-contents, and lithology between the two coasts, the rate of sediment supply from cliff erosion also differs significantly. Along the Beaufort Sea coast low, silty, ice-rich, rapidly retreating cliffs yield small amounts of sediment for reworking into constructional landforms, whereas on the Chukchi coast, high, gravelly, ice-poor, slowly retreating cliffs yield relatively large amounts of material which is available for redistribution into beaches, bars, spits and barriers.

The other major sediment source is from river input; this also differs significantly between the two coasts. Although the Beaufort Sea coast is 50% longer than the Chukchi Sea coast (Chukchi, 811 km; Beaufort, 1343 km; Hartwell, 1973) over 80% of the drainage of the North Slope is into the Beaufort Sea (Walker, 1974). The major river systems on the North Slope are the Colville, Sagavanirktok and the Canning, all of which drain into the Beaufort Sea. Preliminary estimates (Cannon, 1978) for the Beaufort Sea coast suggest that 82% of the material deposited in the lagoon system is derived from fluvial

input and that the remaining 18% is contributed from erosion of the tundra cliffs and of existing barrier islands. Sediment budget calculations for one section of the Chukchi coast indicate that less than 10% of the nearshore sediments are derived from fluvial input and that greater than 90% are contributed by erosion of the tundra cliffs (Harper, 1978).

Significant regional variations exist in terms of sediment sources. Material supplied from cliff erosion accounts for approximately 90% of the total sediment input to the Chukchi coast, whereas less than 20% of the sediment input on the Beaufort coast is from cliff erosion and over 80% is thought to be contributed by rivers. The effects of excess ice in the sediments and, to some extent, lithology are important in controlling these relative contributions.

No estimates are available on the absolute amounts of sediment input to the nearshore budget, however, knowledge of the relative contributions from cliff erosion versus fluvial input and observations of regional morphology suggest that total supply rates (in terms of reworkable material, i.e., sand or gravel) are much lower along the Beaufort than the Chukchi coasts. The net result is that: (1) erosion is exceeding supply along the Beaufort and the coastal system is experiencing a net sediment deficit, and (2) accretion is matching or exceeding erosion along the Chukchi and the coast is relatively stable. These regional variations in supply have important consequences to the stability and morphology of the constructional coastal landforms, particularly the barrier islands.

COASTAL PROCESSES

The single most important factor that controls shore-zone processes is the presence of sea ice on the adjacent coastal waters. The average open-water season on the North Slope decreases towards the northeast from Cape Beaufort to Point Barrow, from approximately 3 months to 1 month at Barrow, and increases to 2 months along the Beaufort Sea coast from Barrow towards Demarcation Point. In addition to open-water data, it is also important to consider the fetch distances and the presence of pack ice on the adjacent sea areas. Due to the location of the edge of the permanent polar pack the Chukchi Sea coast, which is exposed towards the west, has fetch distances in the order of 50-200 km during the open-water season. By contrast, fetch distances on the Beaufort Sea coast vary between 10 and a maximum of 200 km. Figure 2 presents the mean annual position of the 10% ice-cover line. The fetch areas adjacent to the coast are reduced from the southwest towards the northeast and into the Beaufort Sea area. In addition, pack ice assumes an increasingly important role in dampening existing waves. These factors combine to greatly reduce and limit the duration of the open-water period in the Beaufort Sea.

Although wave heights are low and wave periods are generally short throughout the entire area, there is a significant difference in shore-zone wave-energy levels between the Chukchi Sea and the Beaufort Sea due to the differences in potential wave generation. The coasts of the North Slope are low wave-energy environments and the role of storms is, therefore, significant as large pulses of energy are introduced to the shore zone in what would otherwise be relatively quiescent energy conditions. In particular, the southwest winds that affect the Chukchi

coast are characterized by frequent short periods of high wind velocities (Short, 1979). Onshore winds on the Chukchi coast occur between 30% and 40% of the open-water season. The relatively short duration of these onshore winds is offset by the higher velocities during storms that occur on this coast and by the longer fetch distances when compared to the Beaufort coast.

Wind data from Barter Island on the Beaufort Sea coast indicates that northeast winds occur between 60% and 70% of the duration of the open-water season. Although the frequency of onshore winds is greater than on the Chukchi coast, the velocities are lower and the fetch distances are smaller, so that overall wave-energy levels at the shoreline are considerably reduced. Although data are scarce for this region,

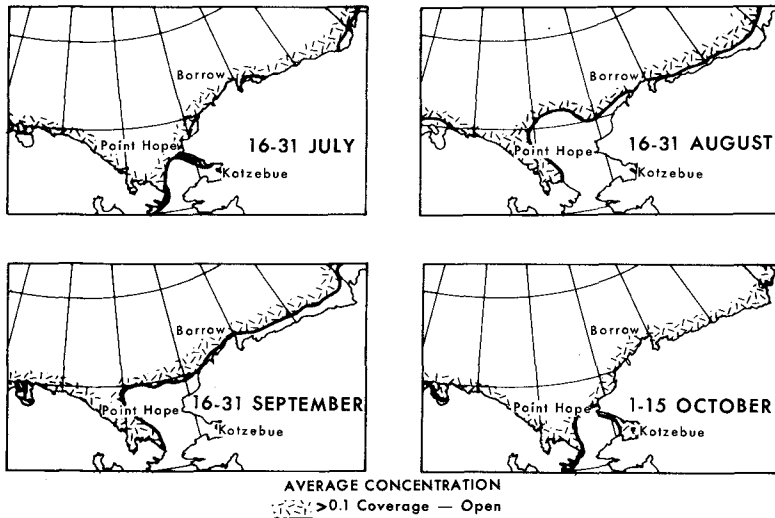


Figure 2. Mean position of the 0.1 (10%) ice-cover boundary for four different summer periods (from Selkregg, 1975).

wave heights greater than 1 m occur for approximately 10% of the open-water season on the Chukchi coast but for only 3% of the open-water season on the Beaufort coast. Brower *et al.* (1977) provide data on mean monthly wave heights for the Beaufort Sea which give values of 0.39 m for July, 0.48 m for August and 0.77 m for September. A secondary characteristic of the Beaufort Sea wave environment is that the angles of wave approach are generally high, due to the elongate nature of the wave generating zone. In addition to an increase in wave-energy levels from east to west along the Beaufort coast, which is a function of wind direction, the high-angle waves result in an east to west shore-zone sediment transport system.

Wave hindcasts for sites along the North Slope coast have been computed (Table 2) based on fetches derived from maps of the mean ice-margin position (Fig. 2). The wind speeds required to generate a fully arisen sea were determined for each of the fetch distances, based on Neumann (1953). The wave characteristics of the fully arisen sea were then related to wind velocities and the value \bar{H} is the mean wave height of the spectrum. The wave heights are therefore the theoretical maxima possible for each of the onshore directions. These data are summarized diagrammatically in Figure 3.

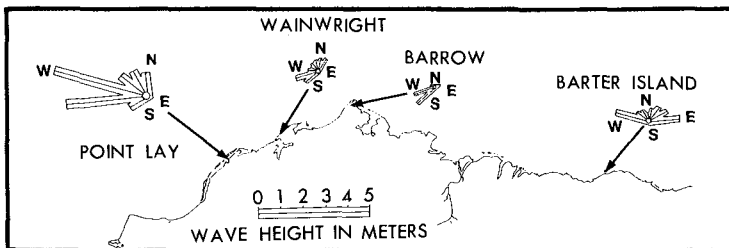


Figure 3. Hindcast maximum wave heights for September (data from Table 2).

TABLE 2. Measured fetch distances (F_m - in nautical miles) and mean wave heights (\bar{H} in meters) hindcast by the Pierson-Neumann-James method, for typical summer ice conditions on the Alaskan shore of the Chukchi and Beaufort Seas.

	<u>JULY</u>		<u>AUGUST</u>		<u>SEPTEMBER</u>		<u>OCTOBER</u>
	F_m	\bar{H}	F_m	\bar{H}	F_m	\bar{H}	
<u>Point Lay</u>							
SW	38	.85	38	.85	38	.85	N
WSW	30	.58	229	3.78	218	3.66	O
W	27	.49	290	4.57	272	4.36	
WNW	25	.43	245	3.96	76	1.58	N
NW	22	.37	60	1.34	60	1.34	E
NNW	30	.58	60	1.34	49	1.13	
<u>Wainwright</u>							
WSW	N		92	1.86	43	1.04	N
W			60	1.34	22	.37	
WNW	O		32	.61	16	.24	O
NW			32	.61	16	.24	
NNW	N		27	.49	20	.30	N
N			32	.61	19	.27	
NNE	E		38	.85	27	.49	E
<u>Point Barrow</u>							
SW	N		N		50	1.16	N
WSW	O		O		43	1.04	O
W	N		N		8	.15	N
	E		E				E
<u>Barter Island</u>							
WNW	N		21	.34	70	1.49	N
NW			11	< .15	32	.60	
NNW	O		10	< .15	27	.49	O
N			9	< .15	22	.37	
NNE	N		10	< .15	27	.49	N
NE			11	< .15	33	.67	
ENE	E		38	.85	28	.85	E
E			~100	1.98	60	1.34	

As these are low wave-energy environments storms assume an important role on both coasts in terms of shoreline wave-energy levels and of sediment transport. Storm-induced water level changes are greater than the astronomical tides. The tidal range is less than 50 cm on all coasts, whereas, storm-induced water level changes can reach 3 m (Reimnitz and Maurer, 1978). Under normal circumstances the tidal range is slightly greater on the Chukchi than on the Beaufort Sea coast, whereas, the storm surges are greater on the Beaufort Sea coast.

The computation of shore-zone energy levels provides an approximate guide to relative variations alongshore. Short (1979) indicates that approximately twice as much wave energy acts upon the Chukchi as upon the Beaufort Sea coast (Table 3). Of equal importance to the higher energy levels is the fact that wave processes are more continuous on the Chukchi Sea coast due to higher wind velocities (Owens, 1977). Energy levels on the Beaufort Sea coast are lower and the frequency and intensity of storm-generated waves are also lower. Therefore sediment transport in the shore zone is a relatively continuous process on the more exposed Chukchi Sea coast and transport is more intermittent and more variable on the Beaufort Sea coast. These differences in energy levels are reflected in the character of the beaches and the barriers. On the more exposed Chukchi coast the beaches are both straighter and higher, with better defined berm systems. On the Beaufort Sea coast, beach sediments are generally poorly sorted and often the berm is either low or not present. These basic differences in the profile characteristic of the beaches can be attributed directly to variations in both the frequency and the magnitude of peaks in the wave-energy spectrum.

TABLE 3. Summary of North Slope Process Characteristics

	CHUKCHI COAST	BEAUFORT COAST
Open-Water Season (months)	2 to 3	1.5 to 2
Average Open-Water Fetch (km)	50 to 200	10 to 100
Prevailing Winds	SW	NE
Frequency of Wave Heights >1 m (%)	10	3
Total Open-Water Wave Energy * (ergs x 10 ¹⁴)	6.5	3.0

(*Wiseman *et al.*, 1973)

SHORELINE DEVELOPMENT AND BEACH MORPHOLOGY

The regional variations in the geological and process parameters discussed above are clearly reflected in the character of the barrier beaches and in the sediment transport systems. Owens (1977) noted that the barriers of the Beaufort Sea coast have an irregular plan form, rarely have dunes, and are overwashed during storms. By contrast, the barriers between Point Hope and Barrow on the Chukchi coast are continuous, straight, and commonly have low dunes in the backshore. These differences are related directly to variations in both the frequency and magnitude of peaks in the wave-energy spectrum. Owens noted that longshore sediment transport processes on the more exposed Chukchi Sea coast are relatively continuous during the open-water season, whereas, energy levels on the Beaufort Sea coast are both lower and more variable.

The geometry of the barrier systems can be compared by referring to barrier height and barrier width values. Averages taken from survey profiles indicate that barrier heights on the Chukchi coast generally range between 1 and 3 m, whereas, barrier heights on the Beaufort coast greater than 1.5 m are rare. Similarly, barrier width values decrease from 150-350 m on the Chukchi coast to 100-200 m on the Beaufort coast. These morphological differences are a result of a combination of factors related to both wave-energy levels and sediment supply rates.

The paucity of sediments on the Beaufort Sea coast has given rise to a series of discontinuous and relatively unstable barriers which are generally crescentic in shape, are separated by wide tidal inlets, and are highly transgressive (Nummedal, 1979). Sediment transport on this coast takes place primarily as a series of storm-related pulses rather than as a continuous process. The Beaufort coast barriers are transgressive, with an average landward movement in the order of 3-5 m/yr. In response to the east-west sediment transport system (Short, 1979), many of the islands are also migrating towards the west at rates in the order of 20-30 m/yr. This overall sediment transport direction and migration pattern is not uniform, with frequent reversals related to storm winds. Due to the existence of wide inlets between many of the islands, many of the barrier islands are independent, self-contained systems rather than part of a longshore sediment transport continuum. This is in direct contrast to the long, continuous barrier systems of the Chukchi coast which form part of an integrated series of three large sediment transport cells.

The decrease in shoreline wave-energy levels towards the northeast and east along the coast of the North Slope results in an increasing

complexity of beach profile morphology and in an increasing variability of beach plan morphology. These trends are a simple reflection of the changes in wave-energy levels alongshore and in the change from a continuous to an aperiodic sediment transport system. Overall sediment transport rates range from 5,000 to 20,000 $\text{m}^3/\text{yr.}$ on the Chukchi Sea coast to 2,000 to 5,000 $\text{m}^3/\text{yr.}$ on the Beaufort Sea coast (Wiseman, *et al.*, 1973). Measured longshore sediment transport rates at Point Barrow (Nummedal, 1979) provide values in the order of 1,500 m^3 of sediment transport per day during a three-day storm in 1977 (Fig. 4). Thus this storm alone could have transported approximately 5,000 m^3 of sediment during that single event. Based on field observations and theoretical calculations, the entire annual sediment transport volume on the Beaufort Sea coast could be confined to one or several storm events.

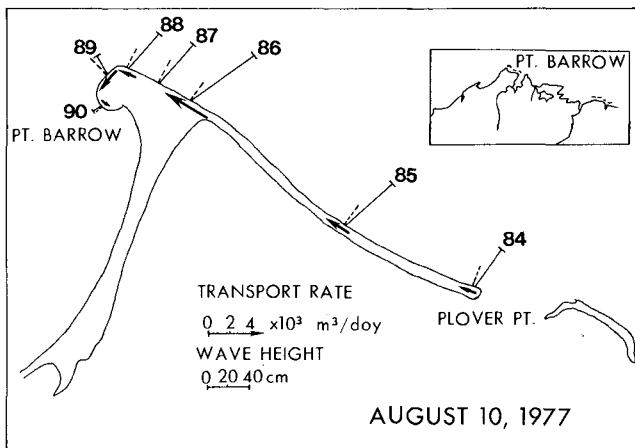


Figure 4. Sediment transport rates (arrows) based on measured longshore wave power and measured wave heights and wave orthogonal angles (bars) at Point Barrow. Numbers (84-90) refer to station codes (from Nummedal, 1979).

DISCUSSION

The assessment of the potential impacts of man's activities is important in engineering design studies. Sediment transport in the shore zone, cliff erosion rates, and the redistribution of beach materials are all critical and sensitive elements of the natural dynamics of the North Slope coasts. Many of the small, narrow, barrier islands of the Beaufort Sea coast are subject to major changes during large storms. The erosion and redistribution of sediments by overwash and by longshore transport can cause erosion and/or deposition on a large-scale during a period of only a few days. Site selection analyses for nearshore and onshore facilities must take into account the potential for such natural dynamic changes in morphology and in shoreline location on barrier islands as well as on the more obvious eroding tundra cliff coasts.

A knowledge and understanding of coastal processes can be used to advantage in the design process. For example, the orientation and shape of artificial islands placed in the nearshore zone can be varied to take into account local transport processes. Figure 5 provides a schematic example of this point. In this scenario an island oriented east-west would have a net shore-zone transport to the east, whereas, a 30° change in orientation to a northwest-southeast alignment would result in net transport towards the northwest. In both cases the calculated net transport rates are in the order of $10^5 \text{ m}^3/\text{yr}$. (Nummedal, 1979).

CONCLUSIONS

- (a) The supply of sand-sized sediments from cliff erosion for barrier development on the North Slope is controlled by wave-energy levels, cliff lithology, cliff height, and by the ice content of the exposed cliffs. Ice plays an important role in coastal process and in sediment supply variations.

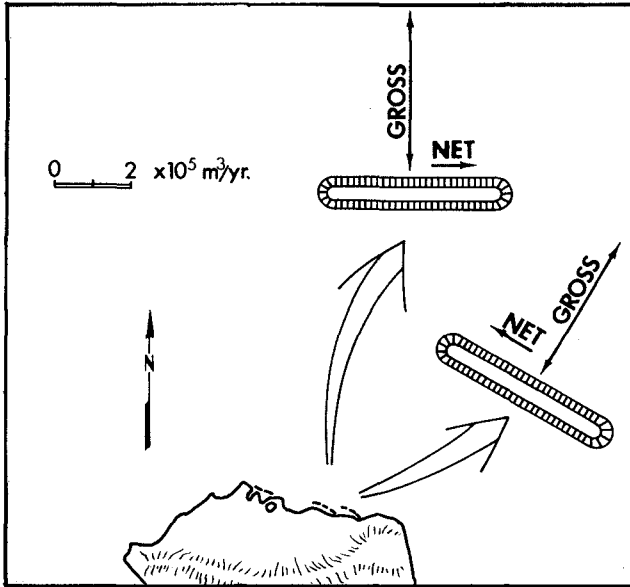


Figure 5. Sediment transport rates on hypothetical deep-water artificial islands.

- (b) Shore-zone wave-energy levels are controlled primarily by the distribution of sea ice which limits fetch distances. The ice content of exposed cliff sections is a function of cliff height due to periglacial processes that concentrate ice near the surface.
- (c) Variations in barrier and beach morphology between the Chukchi and Beaufort Sea coasts are dependent on the modifying effects of ice, both on the adjacent sea surface and, to some extent, within the cliff sediments.
- (d) The Chukchi coast has high tundra cliffs which supply comparatively greater volumes of sediment to the shore zone. Wave-energy levels are higher and barriers are straight, continuous, and stable.
- (e) Cliff heights, sediment supply rates and wave-energy levels are lower on the Beaufort coast. The barriers are more crescentic, complex, discontinuous, and transgressive.
- (f) Previous studies of arctic coasts have noted the important effects of ice in limiting shore-zone physical processes. On the Alaskan North Slope the effects of variations in ice content within the tundra cliffs also play a critical role in limiting sediment availability for barrier beach development.

ACKNOWLEDGEMENTS

The data discussed were derived primarily from research projects funded by the Geography Programs, Office of Naval Research, Arlington, Virginia, under a contract with the Coastal Studies Institute, Louisiana State University (Owens and Harper), and by the Outer Continental Shelf Environmental Assessment Program of NOAA (Nummedal).

REFERENCES

- Brower, W.A., Jr., H.W. Searby, J.L. Wise, H.F. Diaze, and A.S. Prechtel, 1977. Climatic atlas of the outer continental shelf waters and coastal regions of Alaska, Vol. III, Chukchi-Beaufort Sea; Arctic Environmental Information & Data Center, Anchorage, Alaska, 409 p.
- Cannon, J., 1978. Quoted in Coastal Geology and Geomorphology, Arctic Project Bulletin #20, OCSEAP, Fairbanks, Alaska, p. 2-3.
- Harper, J.R., 1978. The Physical Processes Affecting the Stability of Tundra Cliff Coasts; Ph.D. thesis, Dept. Marine Sci., L.S.U., 212 p.
- Hartwell, A.D., 1973. Classification and relief characteristics of northern Alaska's coastal zone; Arctic, 26(3), p. 244-252.
- Hopkins, D.M., and R.W. Hartz, 1978. Shoreline history of Chukchi and Beaufort Seas as an aid to predicting offshore permafrost conditions; OCSEAP, Annual Reports, 1978, Vol. XII, NOAA, p. 503-574.
- Lewellen, R., 1977. A study of Beaufort Sea coastal erosion, northern Alaska; OCSEAP, Annual Reports, Vol. XV(Transport), NOAA, p. 491-527.
- Neumann, G., 1953. On ocean wave spectra and a new method of forecasting wind-generated seas; U.S. Army, Corps of Engin., Beach Erosion Board, Tech. Memo No. 32, 42 p.
- Nummedal, D., 1979. Coarse-grained sediment dynamics - Beaufort Sea, Alaska; Proc. P.O.A.C. 1979, Trondheim, Norway, p. 845-858.
- Owens, E.H., 1977. Variations in coastal environments and beach morphology of northern Alaska; (abst.) AAPG Bull., 61(5), p. 818-819.
- Reimnitz, E., and D. Maurer, 1978. Storm surges in the Alaskan Beaufort Sea; U.S. Geol. Survey Open File Report 78-593, 26 p.
- Selkregg, L.L. (Coordinator), 1975. Alaska Regional Profiles - Arctic Region; Alaskan Environmental Data Center, Anchorage, Alaska.
- Sellman, P.V., J. Brown, R. Lewellen, H. McKim, and C. Merry, 1975. The classification and geomorphic implications of thaw lakes on the Arctic coastal plain, Alaska; CRREL, Hanover, N.H., Research Rept. 344, 21 p.
- Short, A.D., 1979. Barrier island development along the Alaskan-Yukon coastal plains; Geol. Soc. America Bull., Pt. II, v. 90, p. 77-103.
- Walker, H.J., 1974. The Colville River and the Beaufort Sea: Some Interactions; in The Coast and Shelf of the Beaufort Sea, (Reed, J.C. & Sater, J.E., eds.), Arctic Inst. of N.A., Arlington, Va., p. 513-540.
- Wiseman, W.J., Jr. et al., 1973. Alaskan arctic coastal processes and morphology; Coastal Studies Institute, L.S.U., Tech. Rept. 149, 171 p.

SEDIMENT DISPERSAL ON THE N.S.W. CONTINENTAL SHELF

Ron Boyd

Geology Department, University of Sydney,
N.S.W., 2006, Australia

ABSTRACT

This paper presents a semi-empirical model for describing sediment dispersal on the central New South Wales (N.S.W.) continental shelf. Results from a program of field experiments identify wind speed and direction, wave height and frequency distribution of near-bottom currents as being the dominant factors influencing near-bottom current asymmetry on this shelf. A combination of theoretical prediction and field experiment has been used to define the seaward limits for onshore/offshore sediment exchange and the modes of sediment transport operating within this active zone.

INTRODUCTION

A unified theoretical basis for continental shelf sediment dispersal is yet to be fully established. In such a situation, empirical models may provide useful tools in interpreting sediment dispersal patterns for specific shelf regions. This contribution presents such a model for the central N.S.W. shelf. Field data is used to identify the basic nature of the near-bottom flow field and resulting sediment transport on this shelf. The model also represents a framework from which future local investigations of sediment dispersal may be planned.

SIMPLIFICATIONS

A number of simplifying assumptions have been made which consist of eliminating those elements which account for only relatively minor contributions to the local sediment budget. These assumptions are:

- (i) Coastal streams do not supply significant quantities of sand-sized sediment to the shelf at the present time.
- (ii) Longshore transport is an ineffective dispersal mechanism along much of the compartmentised central N.S.W. coast.

- (iii) Coastal estuaries do not act as sinks for sediment derived from the adjacent shelf.
- (iv) The major contribution to the shelf sediment budget comes from onshore/offshore exchange.

FRAMEWORK OF THE MODEL

The model developed to document onshore/offshore exchange operates by rationalising the spectrum of atmosphere/ocean/substrate interactions into a finite number of categories. The resulting classification system is derived from four years of ocean observations in the Sydney region. These observations suggest a classification system based on parameters of average wave period (T_{av}), significant wave height (H_s), swell approach direction, wind speed and orientation to the coastline (Table 1). The wave period and height parameters define a number of alphanumeric

TABLE 1. SHELF WEATHER CLASSIFICATION

WAVE PARAMETERS	WIND PARAMETERS
<u>Average Wave Period (T_{av})</u>	<u>Wind speed</u>
A. $T_{av} \leq 7$ seconds	< 20 km/hr (av)
B. $7 \text{ seconds} < T_{av} \leq 10$ seconds	> 20 km/hr (av)
C. $T_{av} > 10$ seconds	
<u>Significant Wave Height (H_s)</u>	<u>Orientation of Wind to coastline</u>
1. $H_s \leq 1$ m	- Onshore (including S)
2. $1\text{m} \leq H_s < 3\text{m}$	- Offshore (including N)
3. $3\text{m} \leq H_s \leq 5\text{m}$	
4. $H_s > 5\text{m}$	
<u>Swell Direction</u>	<u>Key:</u>
- Arriving from the NE quadrant (including E)	< less than
- Arriving from the SE quadrant (including S)	> greater than
	\leq less than or equal to

divisions (A1-C4). Swell direction and wind parameters account for a further numeric subdivision (categories 1 to 49). The classification is informally referred to herein as the Inner Shelf Process-Response Model (I.S.P.R.M.)

EXPERIMENTAL PROGRAM

An experimental program was conducted at Palm Beach, some 30 km north of Sydney, to identify characteristic responses in the near-bottom current field and patterns of sediment transport for each category in the model. Data collection utilised a mechanical current meter based on a design by Summers *et al.* (1969).

NEAR BOTTOM CURRENT ASYMMETRY

Onshore/offshore sand transport depends on near-bottom current asymmetry. Initiation of sediment motion on wave-dominated coasts such as that of central N.S.W. depends on orbital velocities resulting from oscillatory wave currents. Rates and directions of sediment transport are determined by unidirectional currents superimposed on oscillatory wave motion (Bagnold, 1963). Unidirectional currents may be produced by the waves themselves (e.g. Longuet-Higgins, 1953) or they may result from other mechanisms such as wind stress (e.g. Murray, 1972), tidal motion (e.g. Huthnance, 1972), rip currents (e.g. Cook, 1970), or backwash (e.g. Kemp, 1975).

Under conditions such as those experienced during the Palm Beach field experiments, net water transport is expressed as inequality of onshore and offshore surges. For each cycle under shaling conditions, non-linear wave theories (e.g. Stokes theory) suggest onshore surges should become stronger while offshore surges should occupy a longer time interval. The field data from Palm Beach did not conform with these predictions. Current meter records exhibited current maxima in both the onshore and offshore directions. Similar variations occurred in the relative amount of time occupied by onshore and offshore flow. This data therefore indicates that other factors in addition to wave motion determine near-bottom currents at Palm Beach. To identify any other contributing factors, a statistical correlation analysis was performed on the data. In particular, investigations were made of the relationship between near-bottom currents and the parameters which define the I.S.P.R.M. such as wind velocity, wave height and wave period. Other parameters considered likely to influence near-bottom currents such as tidal motion or bedslope were also included for analysis.

Net bottom drift was the dependent variable chosen for correlation. This parameter is derived by summing individual current speed and direction values over an entire record. The resultant thus takes into account both current velocity and duration. Statistical tests for this analysis consisted of a diagonal correlation coefficient (D.C.C.) designed to identify relationships between directional parameters (such as net bottom drift and wave direction) and a rank correlation (R.C.) to identify relationships between parameters whose magnitude could be compared (such as wave height and net bottom drift).

The most significant correlations occurred between net bottom drift, wind and wave parameters. In particular, the direction of bottom drift correlated strongly with wind direction. Bottom drift magnitude correlated best with wave height and spectral distribution of near-bottom currents. Poor correlation resulted from the other parameters considered, including tidal motion and sea floor topography (Table 2).

1. Wind-Induced Effects

Wind direction and wind speed both showed good correlation with net bottom drift. A D.C.C. value of 0.77 (the highest value for all parameters investigated)

TABLE 2

PARAMETER	TEST	LEVEL OF SIGNIFICANCE	CORRELATION COEFFICIENT
Wind Direction	DCC	-	0.77
Wave Height	RC	>90%	0.56
Wind Velocity	RC	>90%	0.55
Spectral Distribution	DCC	-	0.50

Bed Slope	RC	<90%	0.30
Bed Roughness	RC	<90%	0.30
Depth	RC	<90%	0.30
Wave Period	RC	<90%	0.21
Tidal Direction	DCC	-	0.09
Wave Direction	DCC	-	0.02

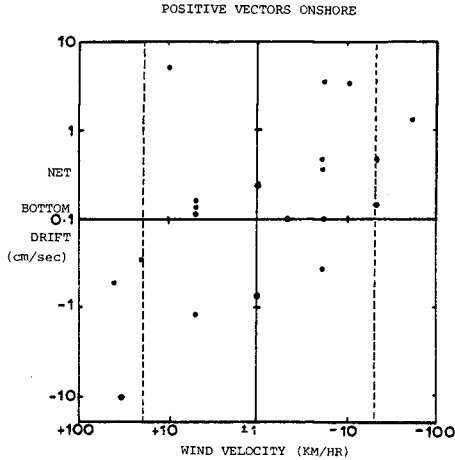


FIGURE 1
WIND VELOCITY VERSUS NET BOTTOM DRIFT

was found to exist for correlation between wind direction and the direction of net bottom drift. The R.C. test indicated a dependence existed between wind speed and net bottom drift magnitude at greater than the 90% level of significance. The correspondence between wind parameters and net bottom drift is graphically illustrated in Fig. 1. Data values tend to cluster in the upper right and lower left quadrants of the graph, with a further tendency to be along the diagonal between the two. This indicates onshore winds are associated with near-bottom currents directed offshore while offshore winds are associated with near-bottom currents directed onshore. Stronger winds tend to produce higher values of net bottom drift.

The above results are in agreement with comparable studies conducted by Cook and Gorsline (1972) and Murray (1972). A simple, steady-state model proposed by Jeffries (1923), adequately accounts for the observed generation of near-bottom currents by wind stress. On the N.S.W. coast, Jeffries' model predicts onshore-directed bottom currents to result from westerly winds and offshore-directed bottom currents from easterly winds on the inner shelf. Wind stress control over near-bottom currents may be generalised via the Jeffries model for inclusion in the I.S.P.R.M. classification. Strong offshore-directed current asymmetry, derived from wind stress effects, may

be found in Categories 5, 6, 11, 12, 17, 18, 23, 24, 29, 35, 36, 41, 42 and 49. Strong onshore-directed current asymmetry from the same source occurs in Categories 3, 4, 15, 16, 21, 22, 33, 34, 39, 40 and also 49.

2. Wave-Induced Effects

Wave height, wave period and water depth are the variables which occur in the expression for volume transport resulting from wave motion in both Stokesian and solitary waves (Inman in Shepard, 1963). Inspection of the Palm Beach data revealed wave height to be the most significant of these variables in determining net bottom drift. The magnitude of net bottom drift in the direction of wave advance increased exponentially with wave height (Fig. 2).

Values of net bottom drift also tended to increase with increasing wave period but here the relationship was less well established (Fig. 3). A similar result has been reported by Cook and Gorsline (1972). However, this result does not conform with theoretical predictions, such as the Longuet-Higgins mass transport concept (Longuet-Higgins, 1953), which suggest net bottom drift is inversely related to wave period. Several factors may help to interpret the Palm Beach results.

- a. Long average wave period is commonly associated with larger waves on the central N.S.W. coast. This was the case for all Palm Beach experiments. It was difficult (especially using in situ recording techniques) to monitor occasions where wave height remained constant over a range of wave periods.
- b. Conditions of low average wave period are commonly associated with a wide frequency distribution of wave energy rather than the monochromatic swell conditions for which theoretical relationships are derived. This is reflected in the high correlation found to exist between frequency distribution of near-bottom currents and direction of bottom drift. Narrow-band frequency distributions were associated with stronger onshore bottom drift. Wide-band frequency distributions often resulted in low and offshore-directed values of bottom drift. In addition, under field conditions, low average wave period is frequently the result of shorter-period wind waves generated by an onshore wind and superimposed on pre-existing swell.

3. Relationship of Current Asymmetry to the I.S.P.R.M.

Insufficient data has been collected during the present study to accurately determine the quantitative contribution of individual processes to current asymmetry. The value of the present work lies in identifying the parameters controlling current asymmetry and incorporating

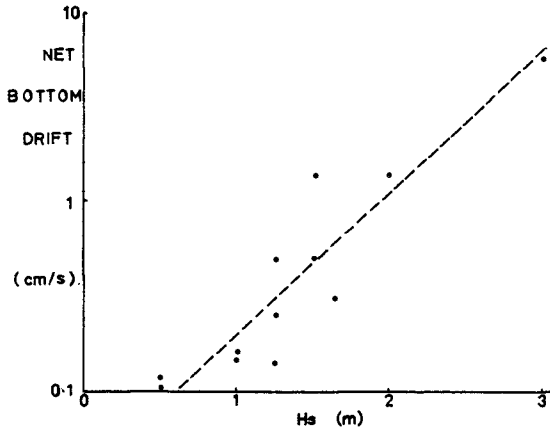


FIGURE 2
NET BOTTOM DRIFT VERSUS WAVE HEIGHT
(positive values only)

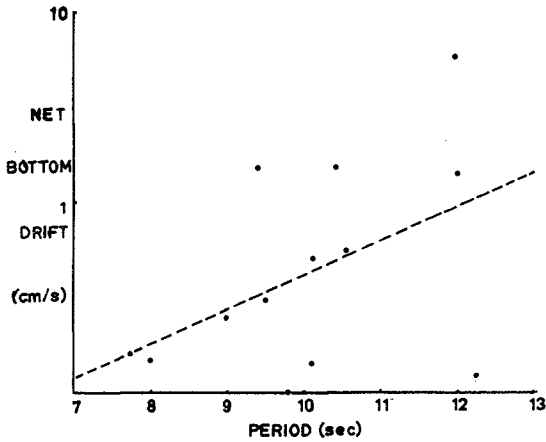


FIGURE 3
NET BOTTOM DRIFT VERSUS WAVE PERIOD
(positive values only)

these parameters into a qualitative model (the I.S.P.R.M.). The present form of the model is suitable for constructing a conceptual framework for shore-normal shelf dynamics which predicts the relative effectiveness of individual processes.

Wind stress provides the most effective control of current asymmetry. In the absence of a significant wind stress contribution, waves control the near-bottom current field. Wave control is most effective for conditions of larger waves which produce a concentration of near-bottom currents at low frequencies. Therefore, strong, onshore, near-bottom currents result from strong offshore winds, high energy swell conditions which produce oscillatory flows dominated by low-frequency components, and combinations of these two mechanisms. Such situations are present chiefly in I.S.P.R.M. Divisions C4, C3, C2 and B2, in Categories 49, 46, 44, 43, 40, 39, 38, 37, 34, 33 and to a lesser extent 20 and 19. Onshore flow extends to lower categories such as 22, 21, 16, 15, 4 and 3 under strong offshore wind conditions. Offshore near-bottom currents result from strong onshore winds and wide spectral distribution of oscillatory currents in Categories 5, 6, 11, 12, 17, 18, 23, 24, 29 and 30. Weak and variable near-bottom currents occur in the absence of higher energy swell or strong wind conditions such as in Categories 1, 2, 13 and 14, or when strong winds negate higher energy swell conditions. The above situations are summarised in Fig. 4.

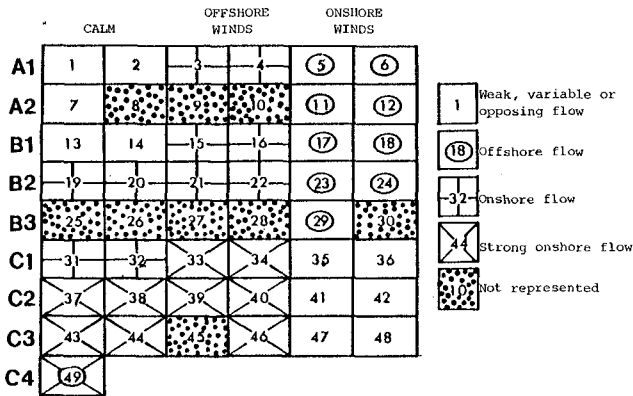


FIGURE 4
I.S.P.R.M. CLASSIFICATION OF NEAR-BOTTOM FLOW

SEDIMENT DYNAMICS

As a first step in determining sediment dynamics on the central N.S.W. shelf, the seaward limit to the zone of sediment activity resulting from wave processes was established for the range of shelf weather situations covered by the I.S.P.R.M. classification system. In addition, the modes of sediment transport operating within the active zone were observed and recorded during the field experiments at Palm Beach.

These field experiments conformed with a conceptual model of wave-generated sedimentary structures presented by Clifton (1976). Clifton recognised a typical shoaling sequence of structures resulting from wave-induced oscillatory flow. Beginning offshore and moving landward, these are (1) an inactive zone, (2) active symmetric ripples, (3) long-crested asymmetric ripples, (4) irregular asymmetric ripples, (5) asymmetric cross-ripples, (6) megaripples and (7) flat bed. This same sequence was commonly observed at Palm Beach.

Three important divisions exist within Clifton's model. These are:

- (1) A division between active and inactive zones. This division corresponds to the shelf location where initiation of sediment motion begins.
- (2) A division between symmetric and asymmetric bedforms. In the Palm Beach examples, this division also separated migratory and non-migratory bedforms. In the zone of symmetric bedforms, sediment was transported by grain translation close to the bed during each wave cycle and by intermittent suspension in ripple-lee vortices, formed as the oscillatory motion changed direction. In the zone of asymmetric bedforms, sediment transport was dominated by migration of individual bedforms and by the translation of a highly-concentrated, near-bed layer of suspended sediment.
- (3) A division between rippled beds and flat beds. This division corresponds to the appearance of a sheet flow mode of sediment transport.

It was decided to use the Clifton model as a basis for providing a conceptual documentation of sediment transport zones on the central N.S.W. continental shelf.

Sediment Transport Zones

For simplicity, Clifton's model was based on dimensional parameters derived from the work of Dingler (1974) and Komar and Miller (1973). It is generally accepted (see for example

discussion by Komar (1976)) that sediment transport criteria are best described by a shear stress concept, such as that proposed by Shields (1936). Therefore shear stress criteria have been used to construct continental shelf "fences" defining the initiation of sediment motion and the onset of sheet flow for each division of the I.S.P.R.M. Following the methods of Nielsen (1979), a non-dimensional shear stress

$$\theta' = \frac{\tau'_{\max}}{\rho(s-1)gd} \quad \text{eqn. 1}$$

has been used to calculate the sediment transport depth zonation. Here ρ is density of water, s is grain density, g the acceleration due to gravity and d is grain diameter. Nielsen found that the concentration of moving sediment is related more closely to the skin friction (τ') than to the total shear stress. τ'_{\max} may be calculated from the relationship;

$$\tau'_{\max} = \frac{1}{2} \rho f_w (a\omega)^2 \quad \text{eqn. 2}$$

where $\omega = \frac{2\pi}{T}$, a is water semi-excursion and f_w , a friction factor, is derived from Swart's (1976) formula

$$f_w = \exp [5.213 \left(\frac{k}{a}\right)^{1.94} - 5.977] \quad \text{eqn. 3}$$

Here k is the hydraulic roughness. Nielsen gives the critical θ' values for initiation of motion and onset of sheet flow as 0.045 and 1.0 respectively. An iterative solution was then developed (from eqn. 1) for critical water depths corresponding to θ' values of 0.045 and 1.0.

Bedform asymmetry is a function of near-bottom flow asymmetry. In Clifton's model, the transition between symmetric and asymmetric bedforms took place at velocity difference values between 1 and 5 cm/sec. Velocity difference is here defined as the sum of the maximum velocity under the wave crest in the direction of wave propagation (positive vector) plus the maximum velocity under the trough of the wave (a negative vector). In six of the seven examples of asymmetric bedforms observed at Palm Beach while simultaneously recording currents, the velocity difference lay between 1.1 and 9.5 cm/sec. It was thus concluded that the range of velocity difference between 1 and 5 cm/sec, proposed by Clifton, adequately defined the transition between symmetric and asymmetric bedforms. At present it is only possible to accurately predict the flow asymmetry derived from wave

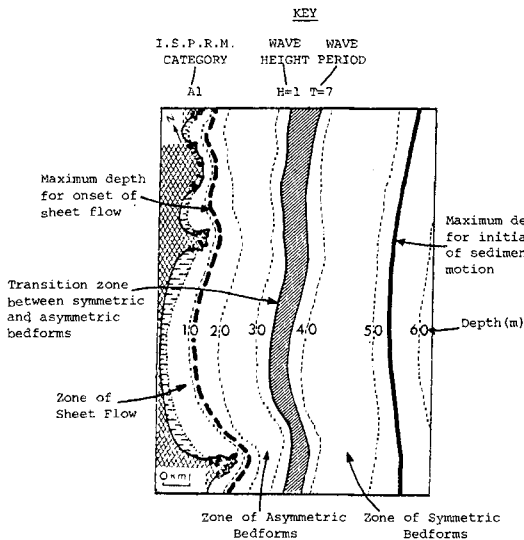
shoaling. In the following discussion other controlling influences of the near-bottom current field (such as wind stress) will not be considered. Velocity difference (V_d) values were quantitatively estimated from the Stokes second-order wave equations whereby

$$V_d = \frac{14.8H^2}{LT \sinh^4 kh} \quad \text{eqn. 4}$$

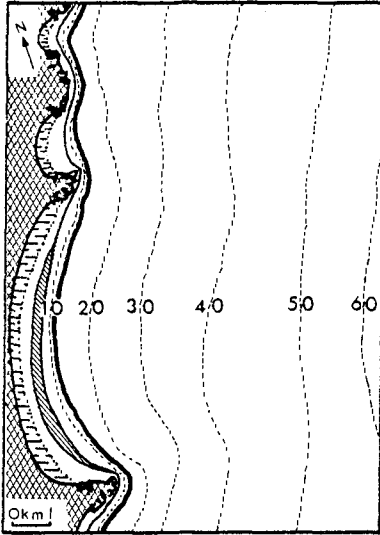
These values were used to construct a further continental shelf fence (for the development of asymmetric bedforms) in each I.S.P.R.M. division. The location of the three sediment transport zones defined by fences for the initiation of sediment motion, development of asymmetric bedforms and onset of sheet flow are shown for each I.S.P.R.M. division in Fig. 5.

A combination of low θ' values and a seaward increase in grainsize for sand on the inner shelf generally restricts

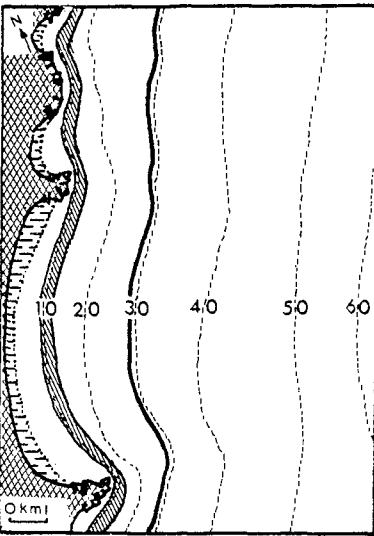
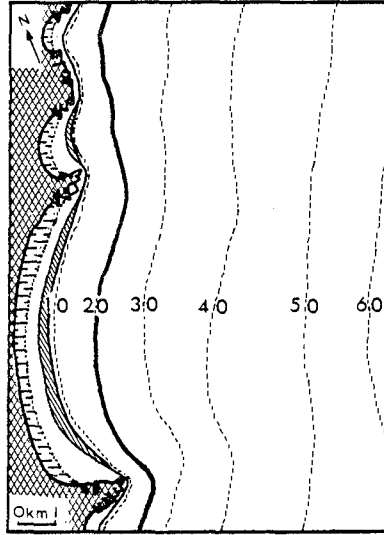
FIGURE 5
SHELF ZONATION FOR SEDIMENT DYNAMICS



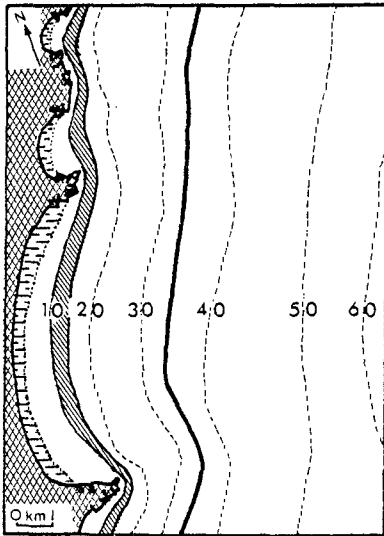
A1 H=0.5 T=7



A1 H=1 T=7

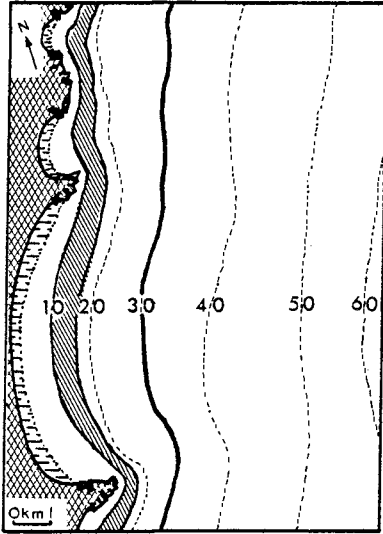


A2 H=2 T=7

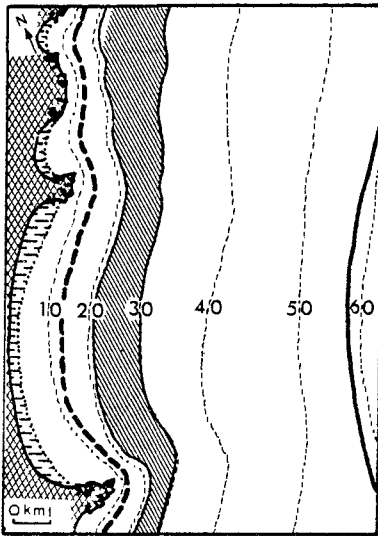
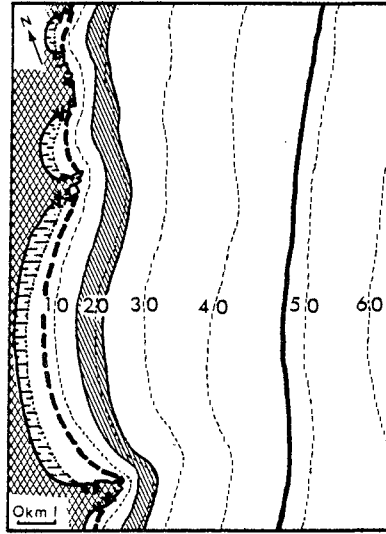


A2 H=3 T=7

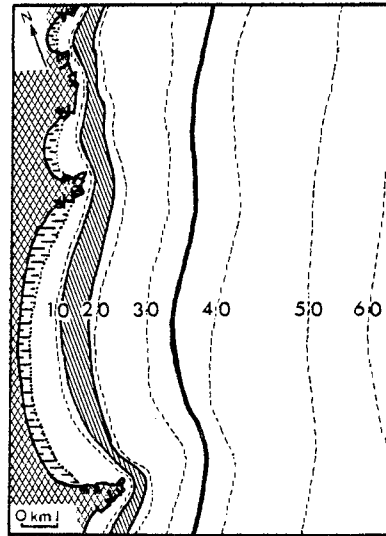
B1 H=1 T=10



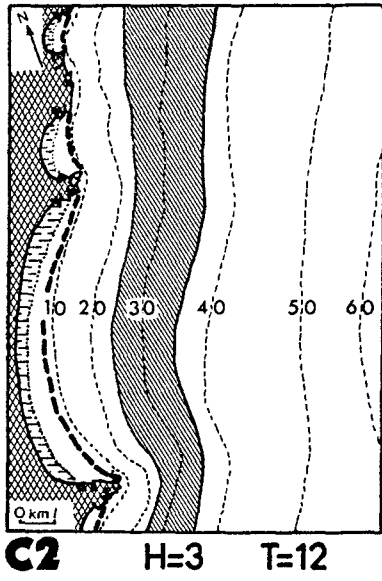
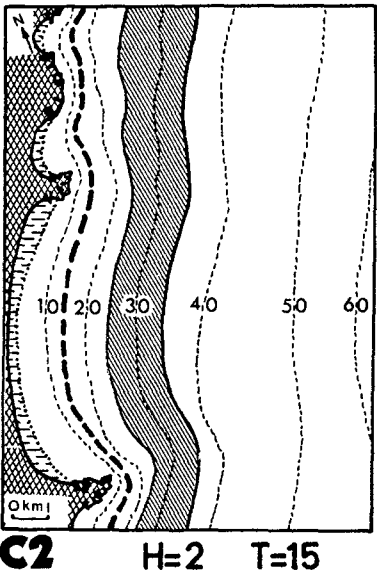
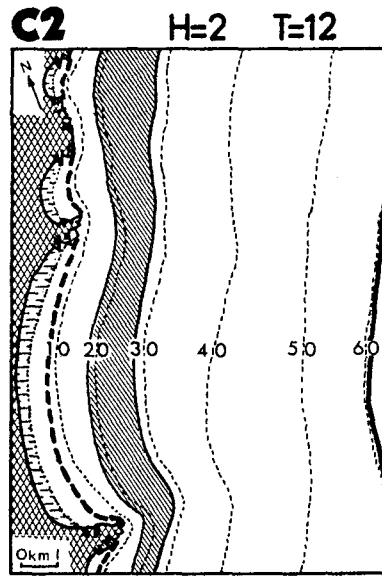
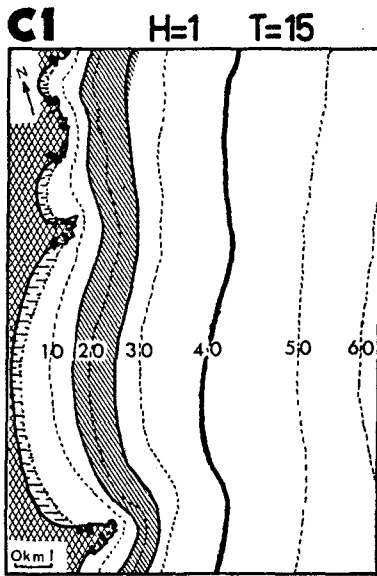
B2 H=2 T=10



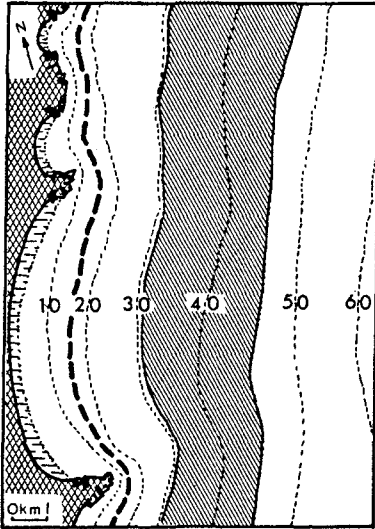
B2 H=3 T=10



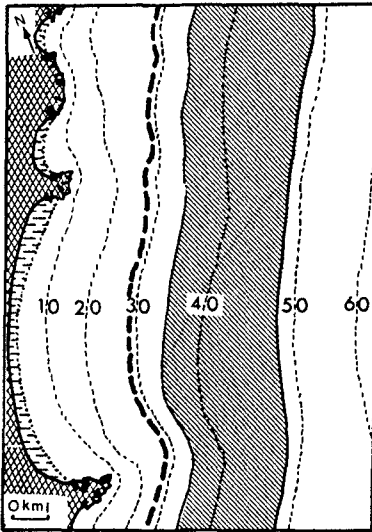
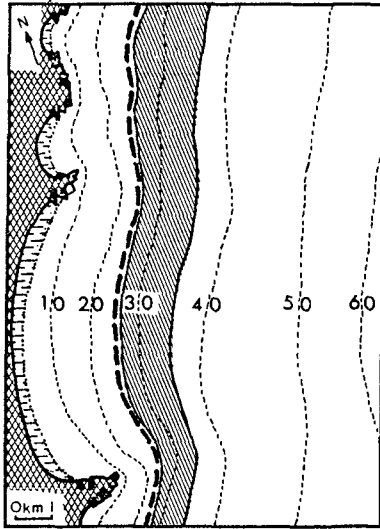
C1 H=1 T=12



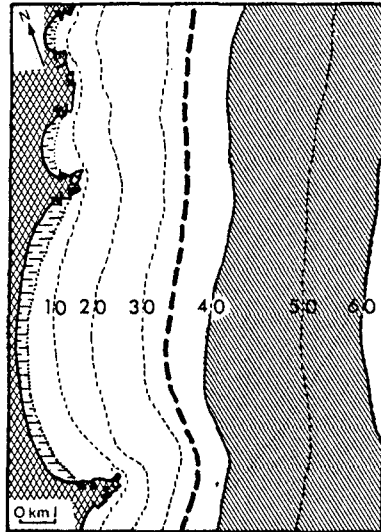
C2 H=3 T=15



B3 H=5 T=10



C3 H=5 T=12



C3 H=5 T=15

active bedform development to the shoreface, above the 30m isobath, for I.S.P.R.M. divisions A1, B1 and C1. Bedform activity in Divisions A2, B2 and C2 may extend onto the inner shelf while Divisions C3 and C4 create active sediment motion in all areas of the inner shelf and extend into the midshelf zone, below the 60m isobath. Fine sand modes (less than 0.5mm grainsize) in inner shelf sands are entrained at significantly deeper depths and under lower energy conditions than the coarser sand and gravel modes. Asymmetric bedforms are virtually restricted to the shoreface except for Divisions C2, C3 and C4. Sheet flow under flat bed conditions is entirely restricted to the shoreface except for extreme events in Division C4. In Divisions A1, B1 and C1 sheet flow is restricted to the vicinity of the surf zone.

DISCUSSION

The model which has been presented above contains several important implications for sediment dispersal on the central NSW continental shelf.

1. The dominant parameters identified as controlling near-bottom current asymmetry on this shelf are wind speed and direction, wave height and frequency distribution of near-bottom currents.
2. The active zone of sediment exchange, as defined in the fence diagrams, extends further offshore than is usually acknowledged on this coast. This is because the active zone limit has been previously correlated with a sharp sediment textural discontinuity at depths of 20-25m. Theoretical predictions for initiation of sediment motion, distribution of the asymmetric bedform zone (which contains migratory bedforms) together with corroborative data derived from bottom photographs and sediment volume measurements (Boyd, 1980) all indicate onshore/offshore sediment exchange may occur between the surf zone, the shoreface and the inner shelf on this coast.
3. The relative frequency of constructive versus destructive conditions (as defined in figure 4) is the primary determinant of both the short-term and long-term exchange budgets.

CONCLUSION

In its present form, the above model may be used to indicate direction and relative magnitude of near-bottom currents. For a wave-induced flow field, the model also indicates the modes of sediment transport and their areal distribution on the inner shelf. It thus represents a conceptual framework with which to interpret the general nature of sediment dispersal on the central NSW continental shelf.

ACKNOWLEDGEMENTS

This research was supported by the Warringah Shire Council. Critical discussion and data analysis was provided by members of the Coastal Studies Unit at Sydney University.

REFERENCES

- Bagnold, R.A. (1963). Mechanics of marine sedimentation. In Hill, M.N., ed., The sea, Vol. 3, New York, Wiley-Interscience, 507-528.
- Boyd, R. (1980). Sediment dispersal on the central N.S.W. continental shelf. Geology Department, University of Sydney, unpub. Ph.D. thesis, 319 pp.
- Clifton, H.E. (1976). Wave-formed sedimentary structures - a conceptual model: Beach and nearshore sedimentation. Soc. Econ. Paleontologists Mineralogists. Spec. Pub. 24, 126-148.
- Cook, D.O. (1970). Occurrence and geologic work of rip currents in Southern California. Mar. Geol., 9, 173-186.
- Cook, D.O. and Gorsline, D.S. (1972). Field observations of sand transport by shoaling waves. Mar. Geol., 13, 31-56.
- Dingler, J.R. (1974). Wave formed ripples in nearshore sands. Ph.D. dissertation, Univ. California, San Diego, unpub., 136 pp.
- Huthnance, J.M. (1972). Tidal current asymmetries over the Norfolk Sandbanks. Estuarine Coastal Mar. Sci., 1, 89-99.
- Jeffries, H. (1923). The effect of a steady wind on the sea level near a straight shore. Phil. Mag., 46, 114-125.
- Kemp, P.H. (1975). Wave asymmetry in the nearshore zone and breaker area. In Halls, J. and Carr, A., Nearshore sediment dynamics and sedimentation, an interdisciplinary review, London, Wiley-Interscience, 316 pp.
- Komar, P.D. (1976). In Stanley, D.J. and Swift, D.J.P. eds. Marine sediment transport and environmental management. New York, Wiley, 602 pp.

- Komar, P.D. and Miller, M.C. (1973). The threshold of sediment movement under oscillatory water waves. Journ. Sed. Petrol., 43, 1101-1110.
- Longuet-Higgins, M.S. (1953). Mass transport in water waves. Phil. Trans. Roy. Soc. London (A), 245, 535-581.
- Murray, S.P. (1972). Observations on wind, tidal and density-driven currents in the vicinity of the Mississippi River Delta. In Swift, D.J.P., Duane, D.B. and Pilkey, D.H. eds. Shelf sediment transport. Pennsylvania, Dowden, Hutchinson and Ross, 127-142.
- Nielsen, P. (1979). Some basic concepts of wave sediment transport. Institute of Hydrodynamics and Hydraulic Engineering, Technical University of Denmark, Series Paper 20.
- Shepard, F.P. (1963). Submarine Geology, 2nd Edition. New York, Harper and Row, 517 pp.
- Shields, A. (1936). Anwendung der Ähnlichkeitsmechanik und Turbulenz-forschung auf die Geschiebebewegung. Mitteil. Preuss. Versuchsamt; Wasser, Erd, Schiffsbau. Berlin, 26.
- Summers, H.J., Palmer, H.D. and Cook, D.O. (1971). Some simple devices for the study of wave induced surges. J. Sediment. Petrol., 41, 861-866.
- Swart, D.H. (1976). Predictive equations regarding coastal transports. 15th Int. Conf. on Coastal Engineering, Hawaii, 1113-1132.

FLUID MUD DYNAMICS AND SHORELINE STABILIZATION:

LOUISIANA CHENIER PLAIN

John T. Wells and Harry H. Roberts

Coastal Studies Institute, Louisiana State University

Baton Rouge, Louisiana 70803, U.S.A.

Abstract

The coast of western Louisiana is presently receiving a new influx of fine-grained sediment from the Atchafalaya River to the east, the first such sediment pulse in recorded history. The major effect of this sediment, which accumulates as fluid mud in the nearshore and at the shoreline, is to attenuate incoming wave energy, thus providing conditions favorable for further sedimentation. Examination of color infrared photography and comparison of observations from aerial overflights and information from ground reconnaissance undertaken periodically since 1969 indicate that mudflat sedimentation is increasing and appears to be moving to the west. When muds move ashore and begin to dewater after becoming "shore attached," they gain strength rapidly and can resist subsequent fair-weather wave scour if their bulk density exceeds $1.20-1.25 \text{ g/cm}^3$. An understanding of why and how these fluid muds accumulate and move subaqueously may provide us with the ability to predict areas of future erosion and accretion along the western Louisiana shoreline.

Introduction

The shoreline of Louisiana is extremely dynamic, and its history is complex. In contrast to the sandy beaches of the east and west coasts of the United States, shoreline sediments in coastal Louisiana are composed mainly of silts and clays that have entered the Gulf of Mexico via the Mississippi River. The predominance of fine-grained coastal sediments, particularly the soft gel-like "fluid muds," play a major role in many of the geologic and oceanographic processes on the inner continental shelf and at the shoreline, such as rate of wave attenuation and rate of shoreline erosion and accretion. This paper examines the source, transportation, and site of accumulation of fluid muds in western Louisiana and their importance to shoreline stabilization.

Traditionally, the coast of Louisiana has been eroding faster than that of any other state (USACOE, 1971), primarily because of the natural processes of wave and current scour, subsidence and consolidation of sediments, and sea level rise. Average annual rates of shoreline change for the period 1812-1954 were determined by Morgan and Larimore (1957) from 1:20,000 aerial photography and are given in Figure 1 for the western half of the state. Only three areas of accretion were reported by Morgan and Larimore, and two of these were the result of sediment entrapment by jetties east of both Calcasieu and Sabine ship channels (Fig. 1). In a third area, west of Marsh Island in the vicinity of Chenier au Tigre, coastal accretion had occurred naturally; much of this accretion resulted from new mudflat development initiated by an influx of muds during the 20-30 years prior to 1954.

Evidence provided in a detailed account of sedimentation on the western Louisiana coast (Morgan et al., 1953), along with results of the present study, indicates that the erosional trend is reversing and that the western half of the state is receiving a new pulse of sediment. This reversal in trend (stabilization and even progradation) is attributed to an influx of fine-grained sediment from the Atchafalaya River, a distributary of the Mississippi River which now carries 30 percent of total flow from the Mississippi. As will be discussed in the following paragraphs, an understanding of the dynamics of this new "fluid mud" in the nearshore and on the inner continental shelf may provide us with the ability to predict areas of future erosion and accretion at the shoreline.

Background and Study Area

The western half of the Louisiana coast, referred to as the chenier plain, has been dominated periodically by pulses of fine-grained sediment from the Mississippi River during the past 5,000 years (Howe et al., 1935; Russell and Howe, 1935). Development of the chenier plain and adjacent shelf was traced stratigraphically from cores using radiocarbon dating techniques (Gould and McFarlan, 1959) and is summarized below. As sea level rose from -5 m to its present level, a transgressive sequence of marine sediments was deposited over the dissected Pleistocene Prairie formation, first filling estuaries, then later spreading across shallow-bay and marsh environments (Fig. 2). High-resolution seismic profiles, such as that reproduced in Figure 2, provide thickness and location of Holocene sediments, older underlying channel fill deposits, silt horizons, and

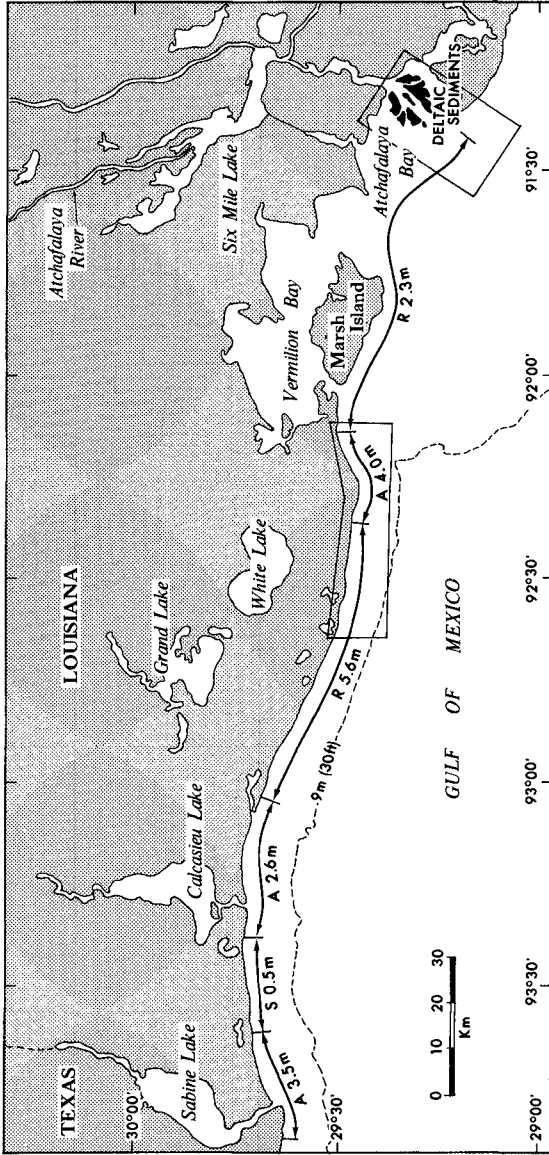


Figure 1. Coast of central and western Louisiana showing average annual rates of shoreline change from 1812 to 1954 (from Morgan and Larimore, 1957). A = accretion, S = stable, R = retreat. Enclosed areas of shoreline are major study sites.

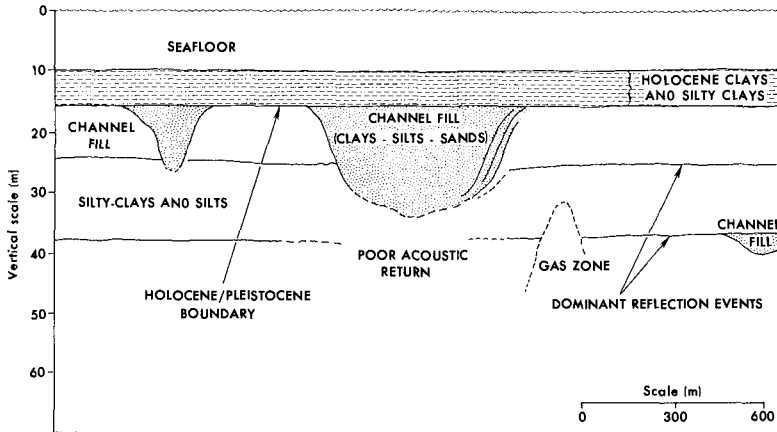


Figure 2. High-resolution seismic profile (E. G. and G. BOOM operated at 300 joules) across the western Louisiana shelf, approximately 10 km seaward of the shoreline south of White Lake. Note that Holocene clays and silty clays are approximately 6 m thick in this area. (Profile courtesy of Jim Hauser, Odom Offshore).

shell lenses.

During the final stage of post-glacial rise in sea level some 3,000 years ago, the chenier plain began to prograde rapidly, and eventually a wedge of recent sediments 6-8 m thick (Fig. 2) was deposited to a distance of 24 km offshore, thus placing the shoreline roughly where we see it today. Pulsations of sediment from the Mississippi River, transported by coast-parallel currents, were responsible for the progradational stage of development. At times when the Mississippi River introduced sediment in the vicinity of the present chenier plain, the shoreline shifted seaward; during periods when its course took the discharge farther east, sediment influx to the chenier plain was low and wave attack was able to slow or halt the advance (Could and McFarlan, 1959). Cheniers formed during these latter periods and now stand as "islands" in the marsh.

A new pulse of sediment, the first in some 1,000 years, began adding soft muds to the shoreline near Chenier au Tigre in the late 1940s, coincident with the subaqueous development of a new delta in Atchafalaya Bay (Morgan et al., 1953). Although the delivery of sediments from the Mississippi River down the Atchafalaya River had been in progress since the mid-1500s (Fisk, 1952), it was not until the mid-1900s that sedimentation in the bay and areas offshore became noticeable. This large-scale introduction of silts and clays to the coast occurred when the Atchafalaya basin to the north became essentially sediment filled and sediment began bypassing these basin-lakes for areas to the south. In the early 1950s Morgan et al. (1953) documented the occurrence of mud deposition along approxi-

mately 50 km of coast from Marsh Island to Rollover Bayou which, in places, formed broad mudflats up to 2 m thick. Today, the chenier plain is backed by extensive brackish and saline marsh and is fronted by ephemeral mudflats along the eastern one-third of its length (Fig. 3). Whereas the coastline and inner continental shelf may appear monotonous to a casual observer, they are in fact, on a small scale, extremely active morphologically.

Present Studies

Shoreline variations and areas of mudflat accumulation were determined from color infrared photographs taken in October 1974 and October 1978 (NASA Missions 74-293 and 78-148, respectively), from 1974 orthophotoquads, and from aerial and ground reconnaissance in 1974 and 1979. Color infrared photography is particularly useful for delineating vegetation/mudflat/open water boundaries since color enhances the vegetation, which during times of low primary productivity is difficult to distinguish from exposed mudflats or turbid water.

Results of these photo and ground comparisons, together with data given in Adams et al. (1978) for the period 1954-1969, are shown in Figure 4. Over the 10-year period from 1969 to 1979 the following patterns have been recognized: 1) simultaneous erosion and accretion at the shoreline,



Figure 3. Mudflat exposed at low tide, Louisiana chenier plain east of Rollover Bayou.

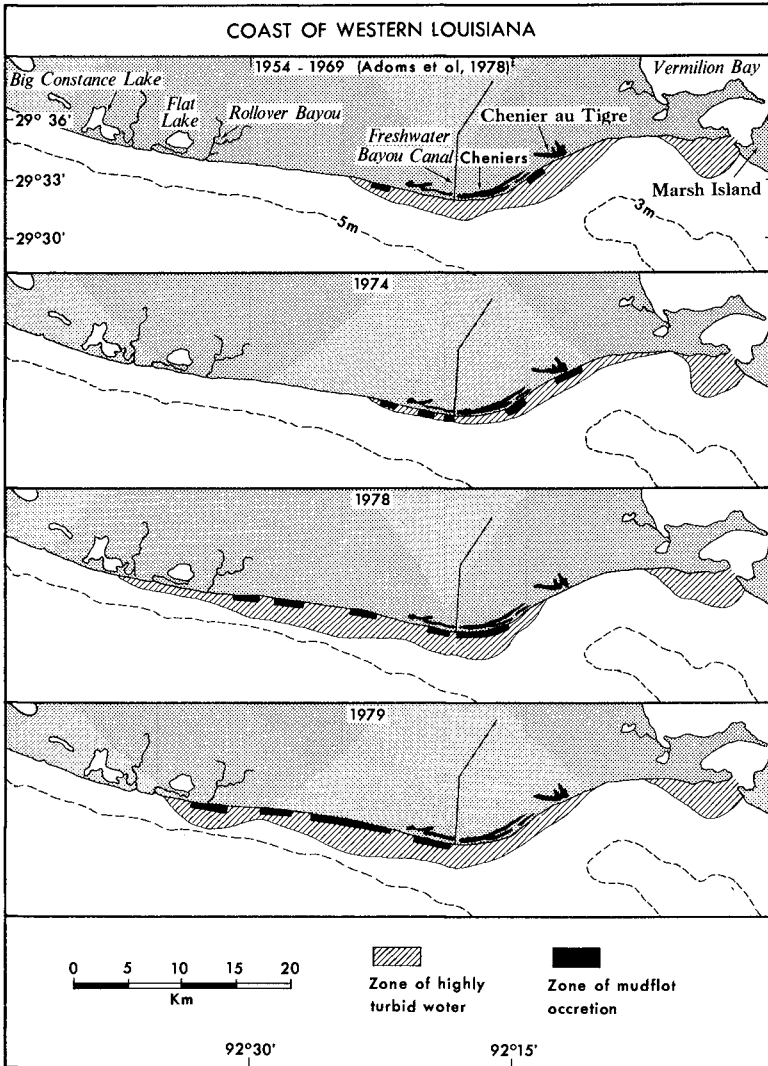


Figure 4. Areas of mudflat accretion from 1969 to 1979, Louisiana chenier plain. Segments of coast between mudflats are generally eroding. Note shift in sedimentation to the west.

2) increasing length of shoreline fronted by mudflats, and 3) shift in the locus of sedimentation to the west. No attempt has been made to plot previous shorelines, and our contention is simply that the presence of mudflats indicates a prograding shoreline. The basic question from an engineering standpoint, given the fact that simultaneous erosion and accretion do occur and that the system of mudflats is enlarging and spreading to the west, is, "How can future sites of erosion and accretion be predicted?" To begin answering that question requires field data from the sediment source, the pathway along which the sediment is carried, and the segments of coast that receive the sediment. To date we consider our findings in these areas to be of a reconnaissance nature.

Sediment source: Atchafalaya River. Field research in Atchafalaya Bay has been in progress for several years (Roberts et al., 1980), with emphasis presently on circulation and sediment transport. Earlier reports by Thompson (1955), Cratsley (1975), Shlemon (1975), and Rouse et al. (1978) have provided additional information on processes and rates of sedimentation, environments of deposition, and the initial phase of subaqueous delta growth. Information used in this and subsequent sections was gathered from many sources, including publications and files of the U.S. Army Corps of Engineers (USACOE), suspended-sediment analysis, current meter moorings, and aerial and ground surveys.

The volume of water delivered to the continental shelf from Atchafalaya River and the concentration of sediment in that water are factors presumed to be important to the growth of mudflats on the chenier plain. At present, nearly all of the sediment supplied to the chenier plain appears to be derived from the Atchafalaya River. Figure 5 shows the volume of sediment-laden water carried down the Atchafalaya River from 1956 to 1975. Mean monthly discharge averaged 5,126 cms from 1938 to 1972 (USACOE, 1974) and average annual peak flow, as shown by the dashed line (Fig. 5) is approximately 12,000cms.

Abnormally high waters were characteristic of the years 1973-1975. Average discharge was 8,864 cms with peak flows of approximately 20,000 cms in April 1973 and 18,000 cms in April 1975 (USACOE, 1975). During this period of high discharge, the Atchafalaya Delta emerged subaerially and evolved rapidly (Fig. 6).

Sediments that enter Atchafalaya Bay consist of fine sand, silt, and clay. Suspended-sediment concentrations at five stations within the bay (Fig. 6) taken during high-water discharge in 1980 show typical values of 200-300 mg/l, with highest concentrations occurring in bottom water (Table 1). Size analysis from USACOE data (Roberts et al., 1980) shows that 75-78 percent of suspended sediment in the river near its diversion point from the Mississippi River is silt and clay, whereas 63 percent of the sediment that eventually enters the bay is silt and clay sized.

Over the past 20 years sediments entering the bay have changed from a dominance of silt and clay to silt and fine sand. It is important to note, however, that, despite the increase in coarse sediment (sand) entering the bay, the volume of fine sediment (clay) also increased, but at a slower rate. The annual load of silt and clay to the bay is 61×10^6 metric tons,

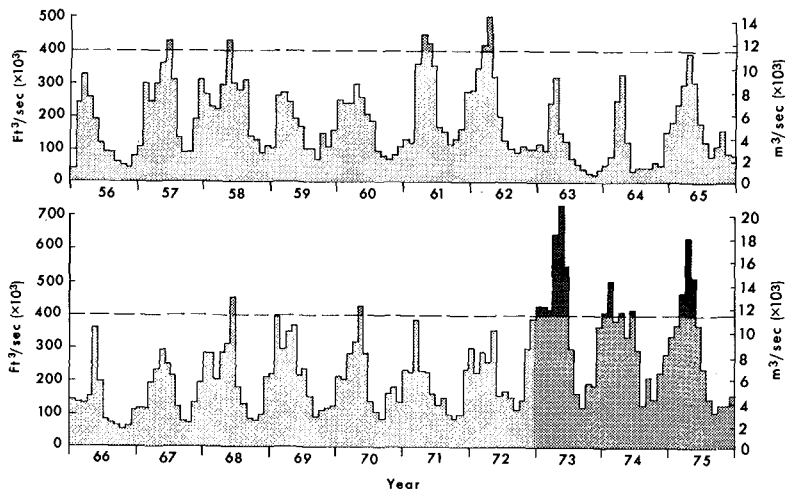


Figure 5. Mean monthly discharge from Atchafalaya River at Simmesport, Louisiana. Dashed line is average annual peak discharge.

or $146 \times 10^6 \text{ m}^3/\text{yr}$, using a mass to volume conversion of 425 kg/m^3 . Volumetrically, if one assumes that 80 percent of silt and clay leaves the bay for the inner shelf, then the shelf waters receive $117 \times 10^6 \text{ m}^3$ of fine-grained sediment each year.

The 3 years of abnormally high discharge (1973-1975) were also years of extreme sediment flux into and through the Atchafalaya system (Fig. 7). On average, annual suspended sediment (including sand) into the bay during

TABLE 1.--SUSPENDED-SEDIMENT CONCENTRATIONS IN ATCHAFALAYA BAY, FEBRUARY-JUNE 1980

Station	Depth	Concentration (mg/l)	
		Minimum	Maximum
1	Surface	95	207
	Bottom	115	587
2	Surface	102	416
	Bottom	137	179
3	Surface	230	603
	Bottom	68	238
4	Surface	116	328
	Bottom	89	372
5	Surface		



Figure 6. Photomosaic of Atchafalaya River delta 3 years after it first emerged subaerially. Stations 1-5 are locations of water samples used in suspended-sediment analysis.

these 3 years was 11.1×10^6 metric tons ($261 \times 10^6 \text{ m}^3$), nearly double that during the period 1965-1971. These flood events may be important in the subsequent development of mudflats on the chenier plain in that they provide perturbations to the already enormous sediment supply.

Sediment transport: coastal mud stream. Evidence that sediments which enter the Gulf of Mexico from Atchafalaya Bay are transported to the

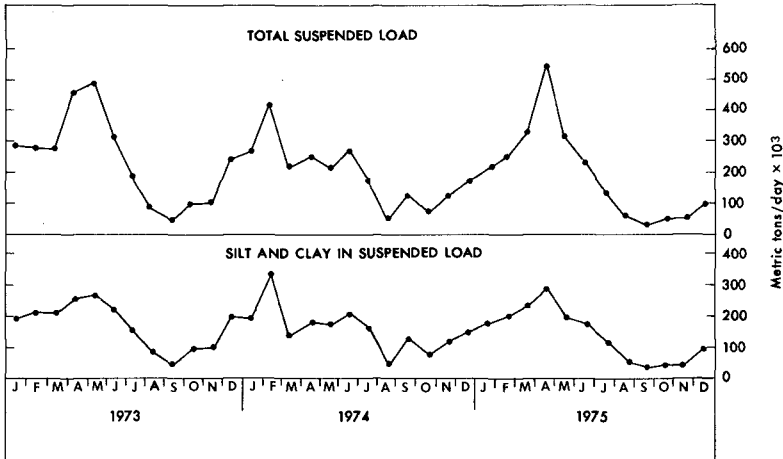


Figure 7. Total suspended load and silt and clay in suspended load during high discharge years 1973-1975.

west is provided by satellite imagery and current meter moorings. Figure 8 shows an ERTS Band 5 image that extends from Atchafalaya Bay to the eastern margin of the chenier plain. A turbid plume of water, shown as white, extends out from Atchafalaya Bay to a water depth of 5-10 m, then moves as a band along the south shore of Marsh Island and the western Louisiana coast. Similar bands of muddy water that originate from large rivers with high discharge of fine-grained sediments, such as those from the Mississippi, Amazon, and Po Rivers, have been referred to as mud streams (McCave, 1972) and we have applied this terminology to the Atchafalaya waters.

Current meter data taken at two stations seaward of Atchafalaya Bay in the spring of 1980 show residual currents to the southwest (parallel to the navigation channel) near the Point au Fer shell reefs and to the northwest farther out on the shelf (Fig. 9). Data at both stations are from mid-depth current meter moorings and were taken with Endeco 174 ducted-impeller, magnetic-recording current meters. Thirty-five days of data were obtained at station 1 and five days at station 2. Current speeds at station 1 are typically 10-30 cm/sec; direction of flow, although setting to the northwest, is influenced strongly by the passage of cold fronts every 5-7 days, which produce winds first from the southwest, then from the northwest. Current speeds at station 2 are 10-50 cm/sec and occur as well-defined pulses related to stage of the tide. Direction, however, does not reverse from tidal effects, but reflects a general flow to the south from Atchafalaya Bay with a strong westerly drift component from coastal waters.

Volume flux of silt- and clay-sized sediment into Atchafalaya Bay and onto the inner shelf is shown in Figure 10. To obtain an order-of-magnitude estimate of sediment transported northwest to the chenier plain, mass transport was calculated as

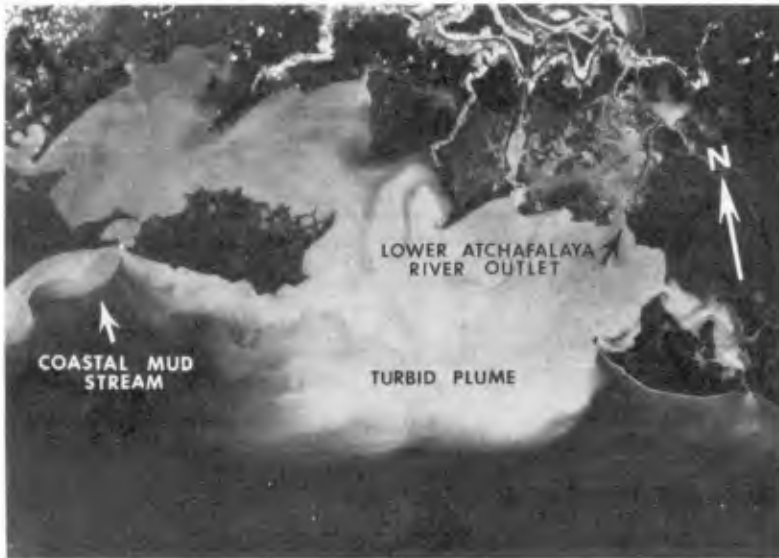


Figure 8. ERTS image (Band 5) of Atchafalaya Bay and central Louisiana coast taken in 1977.

$$T_M = \bar{c} \cdot \bar{v} \cdot A \quad (1)$$

where \bar{c} = average concentration of suspended sediment, \bar{v} = average velocity of residual current, and A = cross sectional area of the mud stream. Taking reasonable estimates of concentration (0.2 kg/m^3) and velocity (0.1 m/sec) through a 16-km-wide cross section normal to the coast resulted in a mass flux parallel to the coast of 640 kg/sec . To obtain an estimate of volume transport from mass transport,

$$T_v = T_m / \rho_c \quad (2)$$

was calculated, where ρ_c is sediment concentration of fluid muds in the nearshore and exposed as tidal flats (375 kg/m^3). When converted to transport per year, the volume of sediment moving in the Atchafalaya mud stream is $53 \times 10^6 \text{ m}^3$. This represents nearly one-half of the total sediment that leaves Atchafalaya Bay and is nearly an order of magnitude larger than longshore volume transport rates on high-energy sandy beaches.

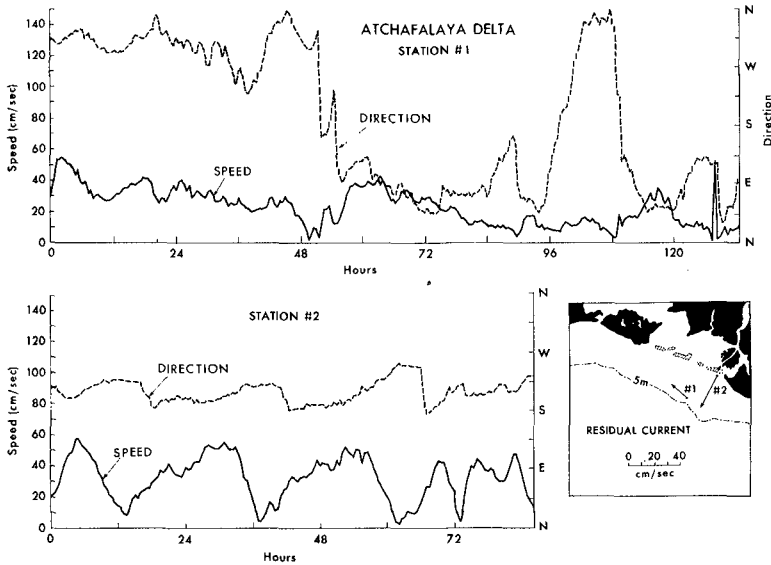


Figure 9. Examples of current speed and direction taken seaward of Atchafalaya Bay (see Fig. 10) in spring 1980. Residual currents are shown on the inset.

Sediment accumulation: chenier plain. Upon reaching the chenier plain, sediments accumulate as mudflats and subaqueous pools of fluid mud in the nearshore region. The initial accumulation of muds in the 1940s was attributed by Morgan et al. (1953) to a decrease in current strength in the vicinity of Chenier au Tigre as a result of the NE-SW shoreline configuration (see Fig. 4). Whereas the early mudflats were concentrated near Chenier au Tigre, they did extend as far west as Rollover Bayou. However, during the following 15 years (1954-1969) the intensity of mudflat progradation appeared to decrease, and, according to Adams et al. (1978), only two small segments of coast showed progradation in this time period (Fig. 4). The rapid mudflat progradation began again between 1969 and 1974.

The time correlation between years of abnormally high river discharge (1973-1975) and renewed mudflat development suggests that accretion, at least at the shoreline, follows sediment pulses from Atchafalaya River flood waters. During the time period between major flood events, sediment reaching the chenier plain may be deposited more gradually on the inner shelf as a blanket of silts and clays. If one computes the volume of a typical mudflat as $1-2 \times 10^6 \text{ m}^3$, then 25-50 such mudflats could form each year from the $50 \times 10^6 \text{ m}^3/\text{yr}$ of sediment derived from the Atchafalaya mud stream. Since new mudflats do not form at this rate, much of the sediment from the Atchafalaya River may be deposited as a uniform thin veneer over a

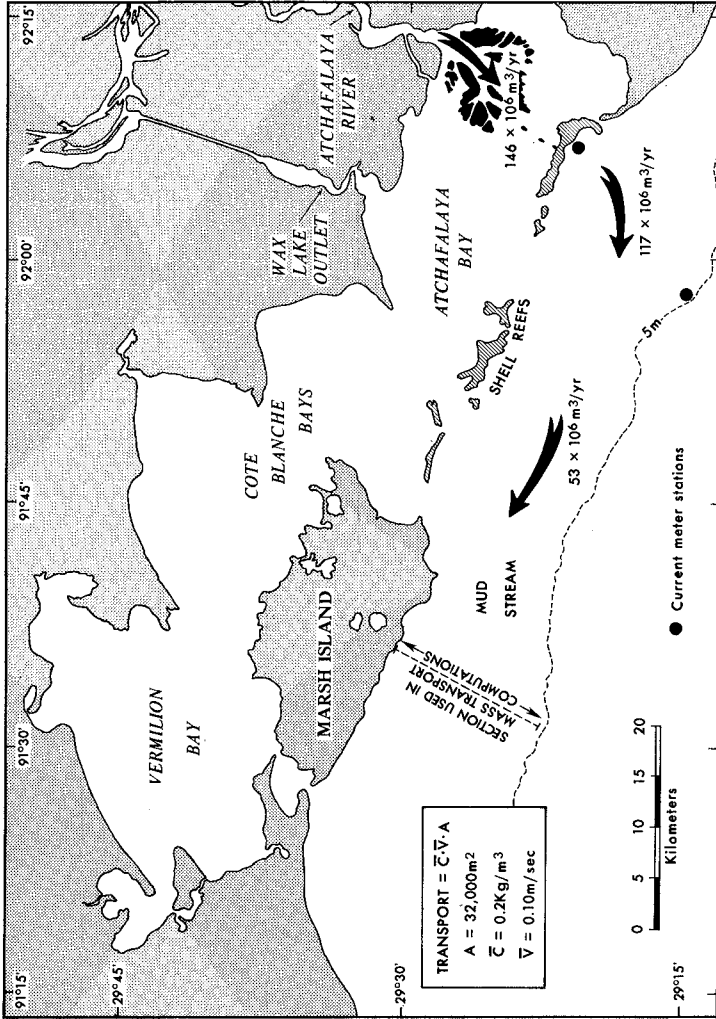


Figure 10. Central Louisiana coast showing computed values of volume flux of sediment into and through the Atchafalaya system. The coastal mud stream carries approximately 50×10^6 m³/yr of silt and clay to the chenier plain.

longshore distance of perhaps 100 km or more.

Longshore currents are responsible for transporting the muds to the west, as shown in Figure 4. These currents are driven by waves arriving at the shoreline from an angle. The most frequently occurring waves on the Louisiana shelf are from the southeast: 42 percent of all waves are 1-1.5 m high and arrive from the southeast with periods of 4.5-6.0 sec (Becker, 1972). Longshore transport of sediment to the west is consistent with currents induced by waves that arrive from the southeast quadrant. Generally, the wave climate is one of low wave energy at the shoreline (Fig. 11).

The clouds of turbid water that can be seen in color infrared photography, ERTS imagery, and aerial overflights are the result of soft, fluid mud which remains partly in a suspended state, even under low wave activity. Because of their low bulk density and high water content (Table 2), new muds are easily eroded and are often ephemeral features. Samples taken in May 1980 show that suspended-sediment concentrations between Freshwater and Rollover Bayous range from 25 to 200 mg/l in surface waters. The input of suspended sediment from local sources on the eastern chenier plain is low, and the sediments in suspension, in addition to being caused by wave scour, reflect the high turbidity of the Atchafalaya mud stream. Field reconnaissance and sampling have revealed areas of dense suspension near bottom and, on occasion, a poorly defined water-sediment interface.

Predicting Future Trends

The basic hypothesis proposed in this study is that, if the dynamics of fluid muds in the inner-shelf environment can be understood, particu-

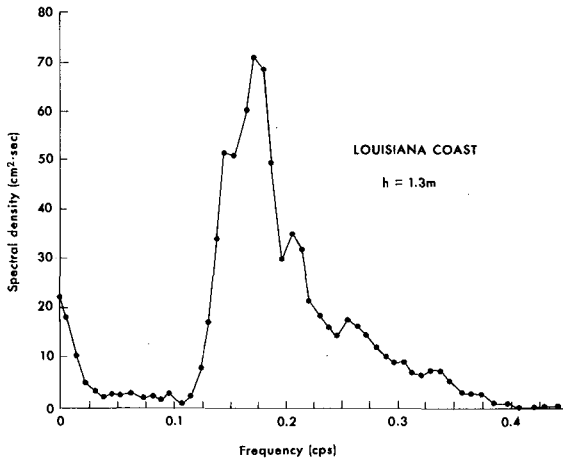


Figure 11. Spectrum of 6-sec waves from the southeast off Freshwater Bayou.

TABLE 2.--PROPERTIES OF COASTAL MUDS, LOUISIANA CHENIER PLAIN

Median diameter	1-5 microns
Bulk density	1.10-1.35 g/cm ³
Organic content	1-5%
Water content	61-89%
Viscosity	0.02-250 poises
Mineralogy	Montmorillonite:illite:kaolinite (3:1:1)

larly the question of where they accumulate and why they move, then areas of future erosion and accretion can be predicted. This hypothesis is based on the following rationale. First, wave energy is strongly attenuated when waves propagate over fluid muds; therefore, accumulation of muds on the inner shelf, such as at the "mud hole" (Morgan et al., 1953), will result in less wave attack at the shoreline itself (Fig. 12). Thus, segments of coast landward of fluid-mud accumulations should be areas of accretion as a result of the more favorable environment for fine-grained sedimentation. Second, fluid muds in the nearshore may periodically move onshore to become "shore-attached," thus causing the shoreline to prograde.

The rate of loss of wave energy on the inner shelf has been quantified from a similar environment in northeastern South America, where fluid muds blanket the bottom in layers 0.1-1.0 m thick (Wells, 1977). Figure 13 shows wave spectra constructed from simultaneous wave records taken at 22, 11, and 4 km offshore. By the time waves reach the station 4 km from shore in a water depth of 1.6 m, 94 percent of their energy has been lost. The shelf gradient in northeast South America is 0.0008, very close to the 0.001 gradient on the western Louisiana shelf. Often, waves never reach the shoreline, but are simply attenuated to nonexistence, without breaking (Wells, 1977; Wells et al., 1979). This sediment-water interaction is a true process-response relationship; muds attenuate waves,



Figure 12. Small waves propagating over a mudflat west of Freshwater Bayou.

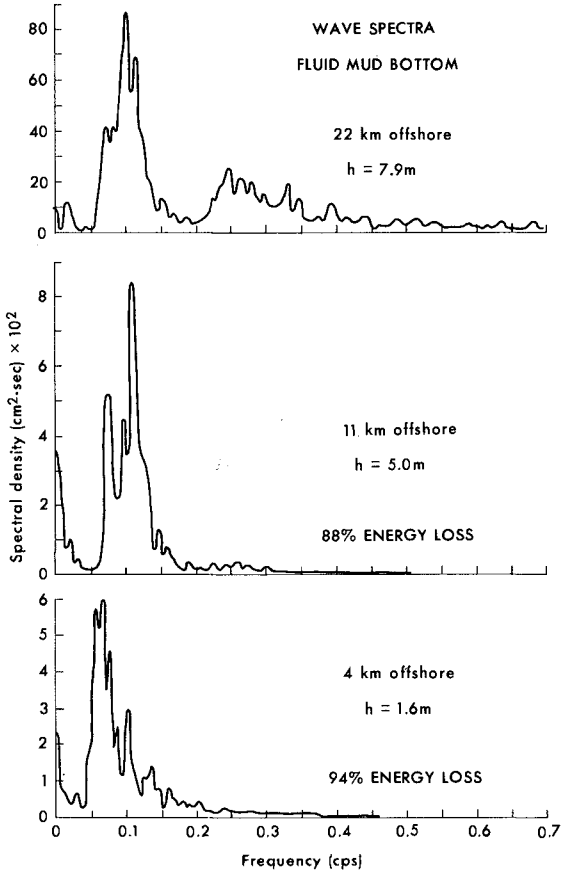


Figure 13. Wave spectra from simultaneous wave records taken off the coast of Surinam, South America. Bottom was blanketed by fluid muds similar to those in Louisiana.

which, because of their energy loss, allow even further sedimentation.

The mechanics of the process whereby muds move ashore are unknown, but have been suggested from results of research in other similar environments. Wells et al. (1979) have proposed that nonlinearity of shallow-water waves over soft muddy bottoms may produce a net drift in the direction of wave travel, thereby moving mud toward shore. The angle of wave

approach controls the magnitude of the longshore component, hence the ability to translate muds alongshore, even if waves do not break as spilling or plunging breakers. Others have suggested that inner-shelf circulation may carry highly turbid bottom water shoreward and less turbid surface water seaward, thus "trapping" muds in the nearshore (Cibbs, 1976), and still other researchers have explained mud accumulation on tidal flats as a result of settling lag (Postma, 1954) and scour lag (Van Straaten and Kuenen, 1957).

Once muds are exposed subaerially and begin to dewater, they gain strength rapidly. Figure 14 shows a plot of bulk density versus apparent viscosity for fluid muds in northeastern South America. A small linear increase in density as a result of dewatering and consolidation can lead to a large (exponential) increase in viscosity, which is related to sediment strength (Krone, 1963; Owen, 1970). If muds are exposed to conditions of drying and continue to dewater until density reaches 1.20-1.25 g/cm³, then shear strength may be sufficient to withstand normal wave attack. Coincident with this early stage of consolidation, vegetation becomes established. Barring catastrophic storm events, vegetation will flourish, and within a year the new mudflat will become permanently attached to form a wedge of Holocene sediments.

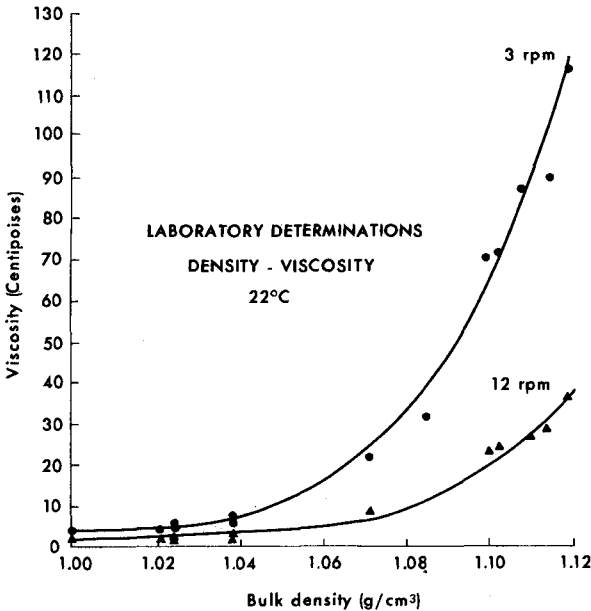


Figure 14. Plot of bulk density versus apparent viscosity in fluid muds from northeastern South America.

The process of mudflat sedimentation described above is altered significantly during major storms and the passage of hurricanes. For example, storm waves associated with Hurricane Audrey in 1957 caused higher than normal retreat rates on the western chenier plain, yet produced in only a few days' time near Freshwater Bayou two mud arcs 300 m wide, 2 m thick, and a total of 7200 m long (Morgan et al., 1958). At present we are unable to predict the effects of storms and hurricanes on coastlines fronted by fine-grained sediments.

Segments of coast between mudflats are typically eroding (Fig. 15), and the processes of erosion and accretion are cyclical in both time and space. Because of this cyclical nature of mudflat development, areas of future erosion and accretion have been predicted with moderate success in northeastern South America (Delft Hydraulics Laboratory, 1962; NEDECO, 1968) by studying locations of fluid mud accumulations. As in coastal Louisiana, conditions that favor fine-grained sedimentation in northeastern South America are 1) large supply of fine-grained sediments, 2) prominent westward drift, 3) strong wave attenuation, 4) shoreward movement of fluid muds, and 5) consolidation and increase in shear strength. Using this knowledge, studies are presently underway in Louisiana to locate and track fluid muds in the nearshore, and it is anticipated that future research into details of how fluid muds move will refine our predictive capabilities.

Acknowledgments

This research was supported by the Louisiana Sea Grant University Program, a part of the National Sea Grant University Program maintained by the National Oceanic and Atmospheric Administration of U.S. Department of Commerce. Additional support was provided by Coastal Sciences Program,



Figure 15. Eroding marsh near Rollover Bayou.

Office of Naval Research, Arlington, Virginia 22217. Illustrations were prepared by Mrs. Gerry Dunn.

References

- Adams, R. D., Banas, P. J., Baumann, R. H., Blackmon, J. H., and McIntire, W. G., "Shoreline Erosion in Coastal Louisiana: Inventory and Assessment," Final Report to Louisiana Department of Transportation and Development, 1978, 139 pp.
- Becker, R. E., "Wave Energy Studies along the Louisiana Coast," Report No. 12, Coastal Resources Unit, Center for Wetland Resources, Louisiana State University, Baton Rouge, 1972, 22 pp.,
- Cratsley, D. W., Recent Deltaic Sedimentation, Atchafalaya Bay, Louisiana, M.S. Thesis, Louisiana State University, Baton Rouge, 1975, 142 pp.
- Delft Hydraulics Laboratory, Demerara Coastal Investigation, Delft, The Netherlands, 1962, 240 pp.
- Fisk, H. N., 1952, "Geological Investigations of the Atchafalaya Basin and the Problem of Mississippi River Diversion," U.S. Army, Corps of Engineers, Mississippi River Commission, Vicksburg, Vol. 1, 1952, 145 pp.
- Gibbs, R. J., "Amazon River Transport in the Atlantic Ocean," Geology, Vol. 4, 1976, pp. 45-48.
- Gould, H. R., and McFarlan, E., Jr., "Geologic History of the Chenier Plain, Southwestern Louisiana," Transactions, Gulf Coast Association of Geological Societies, Vol. IX, 1959, pp. 1-10.
- Howe, H. V., Russell, R. J., McGuirt, J. H., Craft, B. C., and Stevenson, M. B., "Reports on the Geology of Cameron and Vermilion Parishes," Bulletin 6, Louisiana Geological Survey, 1935, 242 pp.
- Krone, R. B., "A Study of Rheologic Properties of Estuarial Sediments," Technical Bulletin No. 7, Commission on Tidal Hydraulics, U.S. Army Corps of Engineers, 1963.
- McCave, I. N., "Transport and Escape of Fine-grained Sediment from Shelf Areas," Shelf Sediment Transport: Process and Pattern, D. J. P. Swift, D. B. Duane, and O. K. Pilkey, eds, Dowden, Hutchinson, and Ross, Stroudsburg, Pennsylvania, 1972, pp. 225-248.
- Morgan, J. P., and Larimore, P. B., "Changes in the Louisiana shoreline," Transactions, Gulf Coast Association of Geological Societies, Vol. VII, 1957, pp. 303-310.
- Morgan, J. P., Nichols, L. G., and Wright, M., "Morphological Effects of Hurricane Audrey," Technical Report No. 10, Coastal Studies Institute, Louisiana State University, Baton Rouge, 1958, 53 pp.
- Morgan, J. P., Van Lopik, J. R., and Nichols, L. G., "Occurrence and Development of Mudflats along the Western Louisiana Coast," Tech-

- nical Report No. 2, Coastal Studies Institute, Louisiana State University, Baton Rouge, 1953, 34 pp.
- NEDECO, Surinam Transportation Study, Netherlands Engineering Consultants, The Hague, 1968, 293 pp.
- Owen, M. W., "Properties of a Consolidating Mud," Report No. INT 78, Hydraulics Research Station, Wallingford, England, 1970, 40 pp.
- Postma, H., Hydrography of the Dutch Wadden Sea, Thesis, Croningen. Arch. Neerland. Zoologie, X, 4e Livraison, 1954, 106 pp.
- Roberts, H. H., Adams, R. D., and Cunningham, R. H. W., "Evolution of Sand-Dominant Subaerial Phase, Atchafalaya Delta, Louisiana," Bulletin American Association of Petroleum Geologists, Vol. 64, 1980, pp. 264-279.
- Rouse, L. J., Roberts, H. H., and Cunningham, R. H. W., "Satellite Observation of the Subaerial Growth of the Atchafalaya Delta, Louisiana," Geology, Vol. 6., 1978, pp. 405-408.
- Russell, R. J., and Howe, H. V., "Cheniers of Southwestern Louisiana," Geographical Review, Vol. 25, 1935, pp. 449-461.
- Shlomon, R. J., "Subaqueous Delta Formation--Atchafalaya Bay, Louisiana," Deltas, M. L. Broussard, ed., Houston Geological Society, 1975, pp. 209-221.
- Stratten, L. M. J. U. van, and Kuenen, Ph. H., "Accumulation of Fine-Crained Sediments in the Dutch Wadden Sea," Ceologie en Mijnbouw, Vol. 19, 1957, pp. 329-354.
- Thompson, W. C., "Sandless Coastal Terrain of the Atchafalaya Bay Area, Louisiana," Finding Ancient Shorelines, J. L. Hough and H. W. Menard, eds., Special Publication No. 3, Society of Economic Paleontologists and Mineralogists, Tulsa, Oklahoma, 1955, pp. 52-76.
- U. S. Army Corps of Engineers, National Shoreline Study: Inventory Report--Lower Mississippi Region, New Orleans District Report, 1971, 57 pp.
- U.S. Army Corps of Engineers, Preliminary Draft Environmental Impact Statement, Atchafalaya Basin Floodway, New Orleans, 1974.
- U.S. Army Corps of Engineers, "Stages and Discharges of the Mississippi River and Tributaries in the New Orleans District," Annual Volumes 1973-1975, New Orleans, 1975.
- Wells, J. T., Shallow-water Waves and Fluid-Mud Dynamics, Coast of Surinam, South America, Ph.D. dissertation, Louisiana State University, Baton Rouge, 1977, 99 pp.
- Wells, J. T., Coleman, J. M., and Wiseman, Wm. J., Jr., "Suspension and Transportation of Fluid Mud by Solitary-like Waves," Proceedings, 16th Conference on Coastal Engineering, Hamburg, Germany, 1979, pp. 1932-1952.

NEARSHORE SEDIMENT TRANSPORT STUDY EXPERIMENTS
R. J. Seymour* and C. G. Gable**

INTRODUCTION

The Nearshore Sediment Transport Study (NSTS) is a multi-institutional research program with the objective of developing improved engineering predictive models for transport of sediment, both longshore and cross shore, by waves and currents. The program is sponsored by the Office of Sea Grant (OSG), an agency of the National Oceanic and Atmospheric Administration (NOAA). A general introduction to the objectives, schedule and organization of the NSTS program was presented at the 16th ICCE by Seymour and Duane (1979). Shortly after the Hamburg Conference, the first major field experiment was conducted at Torrey Pines Beach, California, in November, 1978. The second major experiment was conducted 14 months later in February, 1980 at Leadbetter Beach, in Santa Barbara, California. Each of these experiments involved levels of measurement intensity that appear to exceed by a large factor those of any similar work. Because of the large data sets obtained and the importance of these data to other investigators in coastal processes, the NSTS project is making them available promptly. In the following sections, a general description will be given for each of these experiments and information supplied on how the data may be obtained.

TORREY PINES BEACH EXPERIMENT, NOVEMBER, 1978

Torrey Pines Beach, north of the Scripps Institution of Oceanography (SIO) in La Jolla, CA, is a straight and regular beach, as shown in Figure 1. This regularity was considered a significant advantage for the initial experimental site, as was its proximity to SIO. The wave climate and beach response characteristics had been well studied and it was possible to select a month for the experiment when there would be a high probability of large waves, but prior to the extreme winter storms.

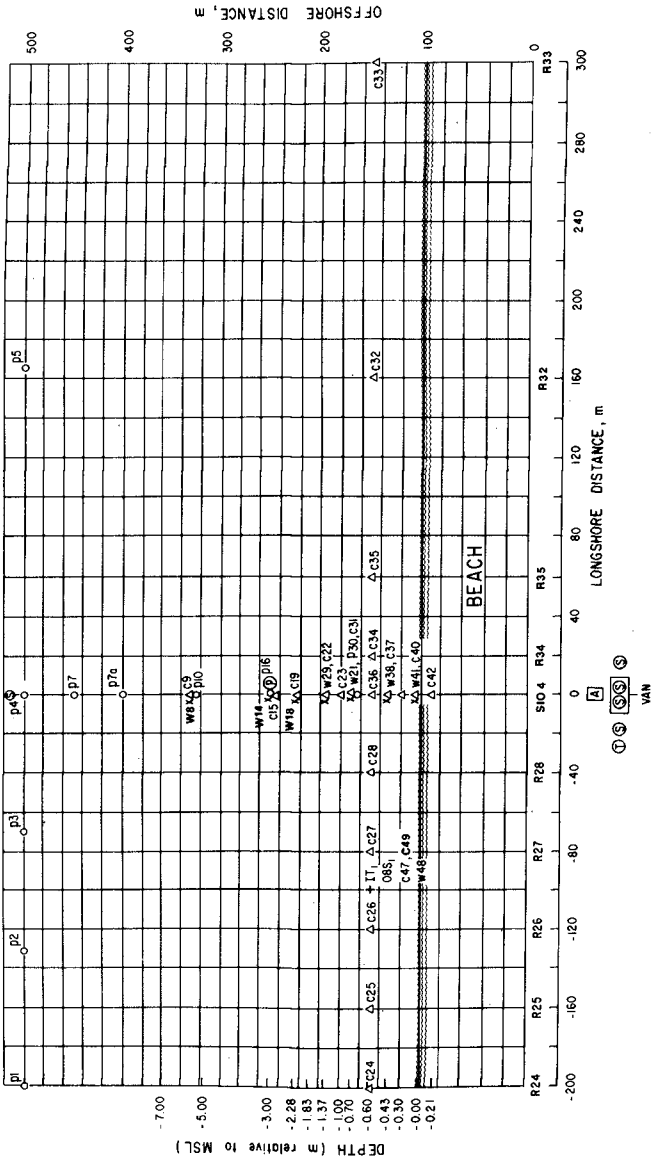
An instrumentation plan was developed by E. B. Thornton of the Naval Postgraduate School, R. T. Guza and S. S. Pawka of SIO to define the dynamics of the shoaling waves and of the surf zone. The arrangement adopted for Torrey Pines is shown in Figure 2. In this figure, the mean sea level intersection with the beach is at approximately 90 meters offshore of the arbitrary origin, and the typical breaker line is at about 180 meters during high tide. Therefore, it can be seen that the instrumentation extended several surf zone widths seaward, but with the highest density of instruments in the breaking zone and shoreward.

*Oceanographer, Ca. Dept. of Boating & Waterways & SIO
**Assoc. Dev. Engr., Scripps Institution of Oceanography



AERIAL VIEW OF TORREY PINES BEACH,
CA., SITE OF NSTS EXPERIMENT IN
NOVEMBER, 1978. SCRIPPS INSTITUTION
OF OCEANOGRAPHY PIER IN THE BACKGROUND.

FIGURE 1



INSTRUMENT PLACEMENT PLAN,
NSTS EXPERIMENT, TORREY PINES
BEACH, CA., NOVEMBER 1978.

FIGURE 2

The incident wave climate was measured with a 5 element linear array of pressure sensors at a depth of about 10 m. The array spacing was 2-2-2-5 with a 33 m. unit spacing. The linear array allowed the calculation of a directional spectrum so that the wave field could be refracted shoreward to any desired location. A main shore normal instrument line was established that is labelled SID4 in Figure 2. A shore normal array of pressure sensors, wave staffs and two-axis electromagnetic current meters was installed which extended shoreward to include a resistance type runup meter in the swash zone. A second, shore parallel, array of current meters was installed at a depth of approximately 0.6 m below MSL. A total of 22 current meters was employed, 20 of them in fixed locations within the instrument grid. Two current meters were arranged in portable frames which could be installed in locations suitable for obtaining measurements of rip currents. These measurements were made by R. A. Dalrymple of the University of Delaware. Ten pressure sensors and seven wave staffs were deployed, as well as an anemometer mounted on a tower on the beach. These instruments, as well as the 20 fixed current meters and the runup meter, were installed and operated by Thornton, Guza and Pawka.

During the experiment, R. W. Sternberg of the University of Washington deployed two prototype instruments for measuring suspended sediment. One operated on the principle of changing the natural frequency of a vibrating element with changing sediment concentrations. The second unit measured concentrations by determining the number of sediment grain impacts with a small sensing whisker. A third experimental suspended sediment meter was evaluated by D. L. Inman and R. E. Flick of SIO. This instrument measured backscatter from a polarized laser.

The data gathering and recording system used at Torrey Pines was developed by the Shore Processes Laboratory (SPL) at SIO. Signals from the deep water instruments were telemetered directly to SPL using a battery powered shelf and shore station at the linear array. Other instruments were cabled to the beach and then telemetered to SIO. Data were sampled at 64 hz from all instruments and were PCM encoded. The PCM data were transmitted by telemetry link and recorded on a 7 track tape recorder at SIO. Data runs were approximately four hours in duration on each of the 20 experiment days. When the data were converted to computer compatible tapes at a later time, the sampling rate was reduced to 8 hz by block averaging 8 adjacent data values. This resulted in a data output of nearly one-half billion words.

The principal emphasis of the Torrey Pines experiment, in contrast to later field work, was on characterizing the surf zone dynamics. However, a number of sediment

transport observations were made as well. D.L. Inman of SIO conducted three longshore transport experiments using dyed sand tracers which were timed to coincide with data runs. These experiments covered a variety of wave conditions. Suspended sediment measurements were made using a water column coring device. The amount of tracer in the bed, and its depth of burial, was determined from analysis of sediment cores taken using various spatial and temporal sampling schemes. Some results of this work are contained in Inman et al. (1980). Both the water column and the bed coring devices were developed by SPL.

Beach morphology changes were measured by R.J. Seymour of SIO. The ten ranges shown on Figure 2 were surveyed to wading depth every second day. The main range (SIO4) was surveyed daily. In addition, these ranges were extended to a depth of 10 m twice during the experiment using a boat mounted fathometer with electronic navigation. All of the beach profile and bathymetric data were digitized and recorded on magnetic tape. The beach changes included a number of erosional and accretional events associated with variations in the incident wave climate. These provide a data set on cross shore transport which can be correlated with the forcing functions obtained from the surf zone dynamics measurements.

Drift kelp was a major problem in this experiment. Particularly after an event of large waves, the mats of kelp could exceed 100 kg in weight and were capable of damaging or destroying any of the surf zone instrumentation. Guza and Thornton developed a breakaway mount for the current meters which allowed them to survive the kelp onslaughts and also devised a scheme for rapidly reinstalling and realigning the meters after the kelp was removed. Precise alignment of the two axis meters was critical in shallow water since wave approach angles are quite small, approaching the directional resolution of the meter. A storm midway through the experiment carried away all of the wave staffs and they were not replaced. However, all of the current meters were returned to service.

THE TORREY PINES DATA

One of the guiding policies of the NSTS program is that the experimental data be made available to the public promptly. The investigators are allowed 18 months after the completion of an experiment to analyze their data and to publish their findings. A large fraction of this time is spent in sorting out the records and editing the raw data. In July, 1979, NSTS sponsored a workshop at La Jolla in which the preliminary results of the Torrey Pines experiment were presented. In December, 1979, a comprehensive experiment report was published (Gable

[1979]). This report contained complete descriptions of the experiment site, the environmental conditions, the instrument locations, types and calibrations, and sufficient information to allow other investigators to extract meaningful data from the data tapes. In March, 1980, an announcement was made at the 17th ICCE that the data tapes were available to the general public. This was accomplished on schedule, 18 months after the experiment. The data require eight 2400 foot 9-track magnetic tapes. They include the profile data and the suspended sediment data from Sternberg's instruments as well as all of the surf zone dynamics measurements. The data from Inman's tracer studies, which could not be readily presented on tape, are included as an appendix to the experiment report.

Investigators wishing to acquire the Gable report or copies of the tapes should contact

National Oceanographic Data Center
Code D781
2001 Wisconsin Avenue, N.W.
Washington, D. C. 20235

THE SANTA BARBARA EXPERIMENT

A site selection study, conducted by R.G. Dean of the University of Delaware, recommended that the second NSTS experiment be conducted at Leadbetter Beach in Santa Barbara, CA. The second experiment was to place heavier emphasis on the measurement of sediment transport than the first, and Santa Barbara was selected principally because of the very satisfactory sediment trap provided by the harbor. As shown in Figure 3, Leadbetter Beach is a feeder beach for the sandspit formed in the shadow of the breakwater. The accumulation of sediment within the harbor is bypassed by intermittent dredging. The Santa Barbara experiment began in September, 1979 with the initiation of a year long trap study. The intensive experiment period, comparable to the Torrey Pines experiment, was conducted during the month of February, 1980. The experiment was directed by R.G. Dean for the sediment transport measurements and by R.J. Seymour for the wave climate measurements. The accumulation of sediment was measured at approximately six week intervals with profiles extending from the dry beach to a depth of approximately 10 m. These profiles were run at 50 m spacing along the feeder beach, the breakwater and the sandspit, as shown in Figure 4. Wading surveys were made on the shallow end of the profiles with the deep water portion conducted by fathometer surveys using an electronic location system on the boat. The incident wave climate was measured at least every six hours for the one year period of the experiment. Two slope arrays of the type described in Seymour et al. (1980) were



AERIAL VIEW OF SANTA BARBARA,
CA., LEADBETTER BEACH, SITE OF
NSTS EXPERIMENT IN FEBRUARY 1980
AS SHOWN ABOVE THE HARBOR.

FIGURE 3

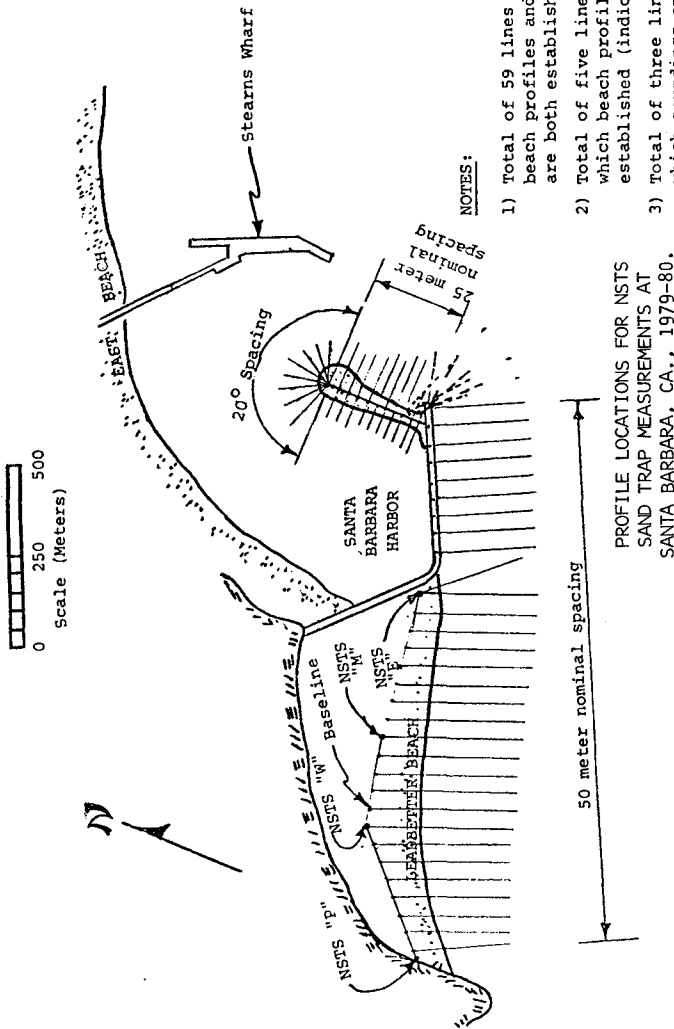


FIGURE 4

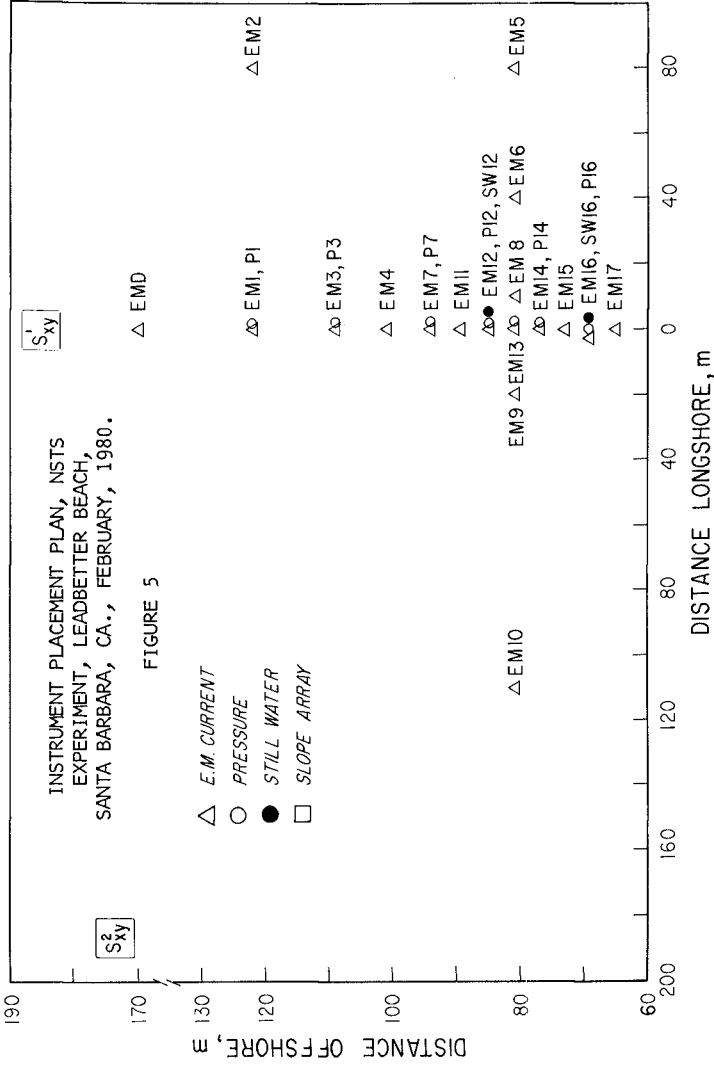
installed. These directional arrays provide a moderately well defined directional spectrum and well defined estimates of the longshore radiation stress. The wave data is collected automatically over telephone lines using the system described in Seymour and Sessions (1976) and is recorded at La Jolla.

During the February intensive experiment the instrument location plan followed the Torrey Pines scheme as shown in Figure 5. R. T. Guza and E. B. Thornton were again responsible for the surf zone dynamics measurements with R. A. Dalrymple making the rip current measurements. Twelve current meters were installed in the main cross shore range line and five meters were used in the longshore line. One other current meter was permanently installed, two were moveable for rip current measurements, and three were used for swash zone measurements. In addition to the eight pressure sensors in the slope arrays shown in Figure 5, there were seven additional pressure sensors in the cross shore main range line. Two still water level reference gauges were also installed in this line to measure setup.

In the Santa Barbara experiment, particular emphasis was placed on measurements in the inner third of the surf zone. Special portable space frames were developed to support instruments in very shallow water. These frames are shown in Figure 6. Typically, one frame would mount a two-axis current meter, a resistance type wave height probe, and two types of sediment concentration meters developed by R. W. Sternberg. The first of these was a refinement of the impact whisker type deployed at Torrey Pines. The second was a new miniaturized optical backscatter instrument with five sensors mounted at various heights off the bottom.

Measurements of integrated longshore current were obtained by R. E. Flick using a conventional metallic conductor GEK system and also a prototype seawater conductor unit. D. L. Inman and R. L. Lowe of Scripps Institution of Oceanography deployed a prototype bedload sensor employing three downward looking sonars. One sonar senses the bed thickness by discriminating the horizons at the sand surface and at the bottom of the moving bed. The other two, which look at the bottom at an angle, detect bedload speed components by Doppler shift. In addition to the swash zone instruments described earlier, R. W. Sternberg deployed two stacked 5 element suspended sediment meters of the backscatter type in deeper water.

Beach profile changes were measured by R. J. Seymour and by D. G. Aubrey of Woods Hole Oceanographic Institution. Five ranges were surveyed at least daily using wading survey techniques. In addition, an automatic profiling tractor was deployed to obtain continuous surveys to depths of 6 m. This vehicle is described in Seymour, et al. (1979).





The first two weeks of the month long experiment were characterized by moderate to low waves with high angles of incidence so that the longshore currents tended to be strong at all times. Midway in the experiment a storm of very unusual intensity attacked the site for about one week, resulting in severe erosion to the beach as shown by the profiles in Figure 7. During the high wave episode, which was also marked by exceptionally strong longshore currents, drift kelp necessitated the removal of all but the deepest instruments. The wave measurement system continued to function throughout the experiment.

D.L. Inman and R.E. Flick conducted seven tracer studies during this experiment. Four were before the storm and three were in the week following the storm when the beach had been flattened and narrowed considerably. These studies followed the methodology utilized at Torrey Pines.

At Santa Barbara, the data were all cabled directly to the recording system which was housed in a trailer adjacent to the beach. Because of increase in the number of channels of instrumentation and because of longer data runs, almost a billion words of data were recorded -- roughly twice that at Torrey Pines.

SANTA BARBARA DATA

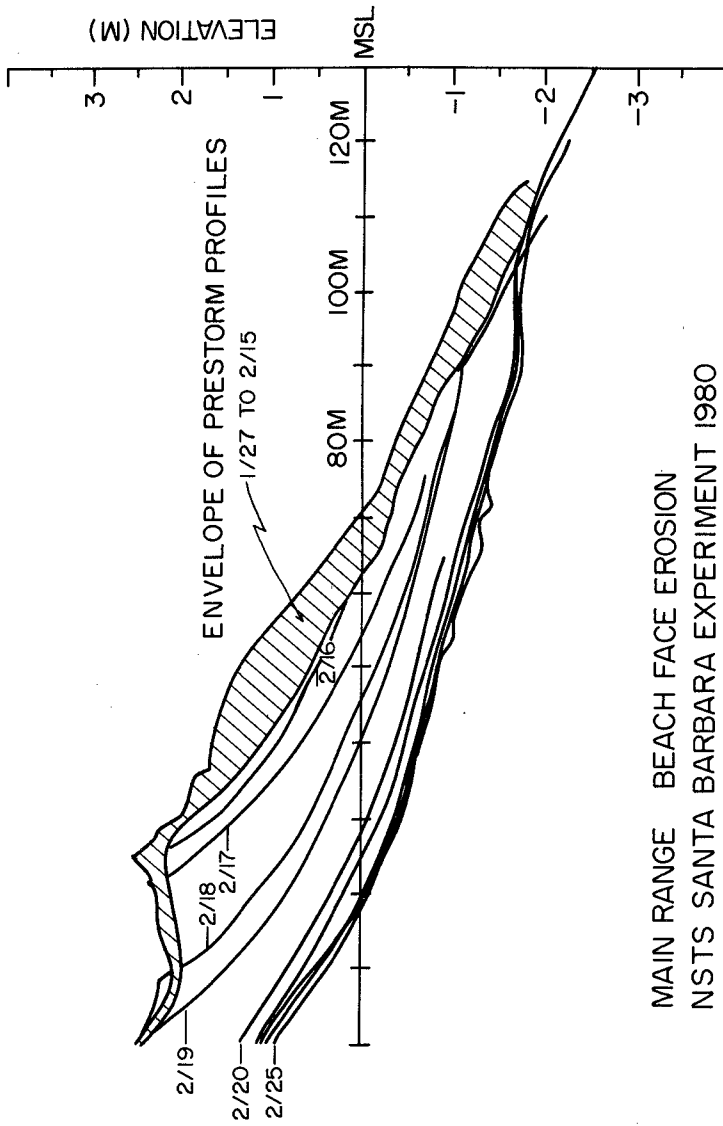
An experiment report and copies of the raw data tapes are expected to be available through the National Oceanographic Data Center in August 1981 for this experiment.

FUTURE EXPERIMENTS

The NSTS program plans one more major field experiment, patterned on the one at Santa Barbara, but on the eastern coast of the United States. The intensive portion of this experiment is tentatively scheduled for the fall of 1981. This third major experiment is expected to add a valuable data set on a barred coastline with steeper waves.

ACKNOWLEDGMENTS

The Nearshore Sediment Transport Study is supported by grants to the participating Sea Grant institutions from the Office of Sea Grant, National Oceanic and Atmospheric Administration.



MAIN RANGE BEACH FACE EROSION
NSTS SANTA BARBARA EXPERIMENT 1980

FIGURE 7

REFERENCES

- Gable, C.G., Ed.: 1979. "Report on Data from the Nearshore Sediment Transport Study Experiment at Torrey Pines Beach, California, November-December, 1978." University of California, San Diego, Institute of Marine Resources, IMR Ref. No. 79-8.
- Inman, D.L., J.A. Zampol, T.E. White, D.M. Hanes and K.A. Kastens: 1980. "Field Measurements of Sand Motion in the Surf Zone." 17th International Conference on Coastal Engineering, Sydney, Australia, 23-29 March 1980 (in press).
- Seymour, R.J. and D.B. Duane: 1979. "The Nearshore Sediment Transport Study." Proc., 16th Coastal Engineering Conference, Aug. 27-Sept. 3, 1978, Hamburg, Germany, Vol. II, pp. 1555-1562.
- Seymour, R.J., A.L. Higgins, and D.P. Bothman: 1979. "Tracked Vehicle for Continuous Nearshore Profiles." Proc., 16th Coastal Engineering Conference, Aug. 27-Sept. 3, 1978, Hamburg, Germany, Vol. II, pp. 1542-1554.
- Seymour, R.J. and M.H. Sessions: 1976. "Regional Network for Coastal Engineering Data." Proc., 15th Coastal Engineering Conference, July 11-17, 1976, Honolulu, HI., Vol. 1, pp. 60-71.

A SEDIMENT TRAPPING EXPERIMENT AT SANTA CRUZ, CA.

R. J. Seymour*
G. W. Domurat**
D. M. Pirie***

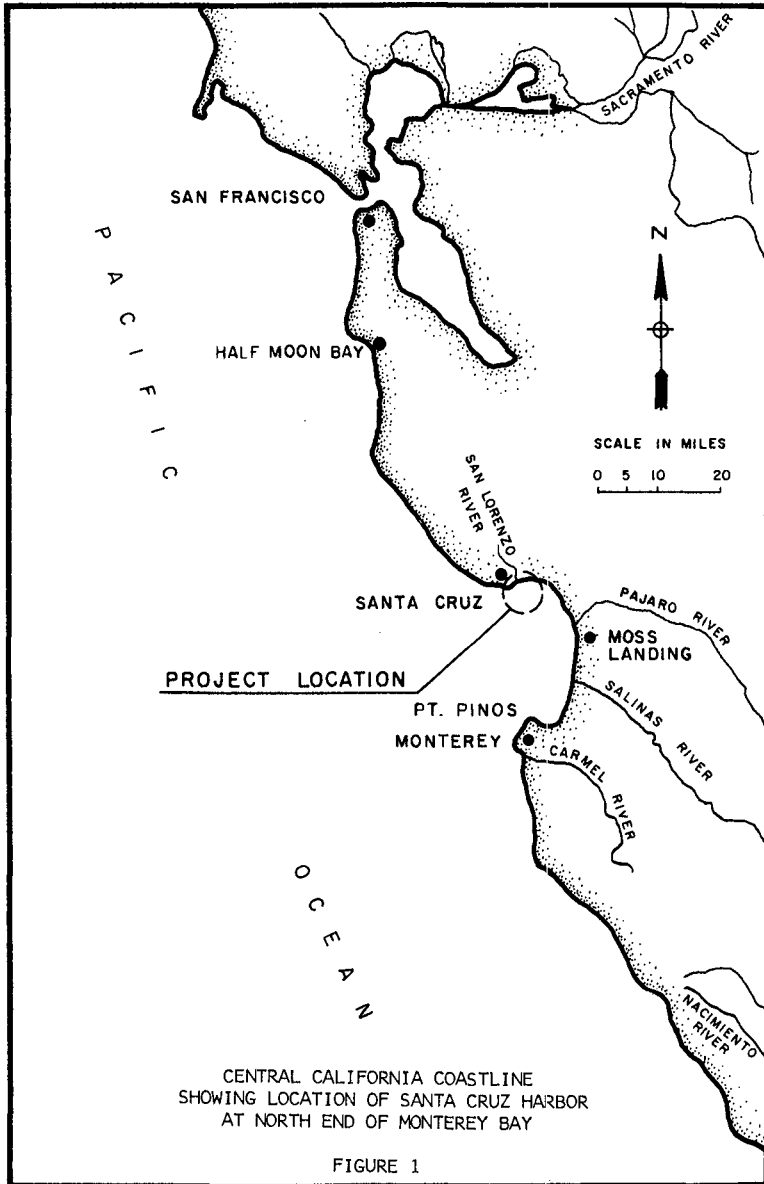
INTRODUCTION

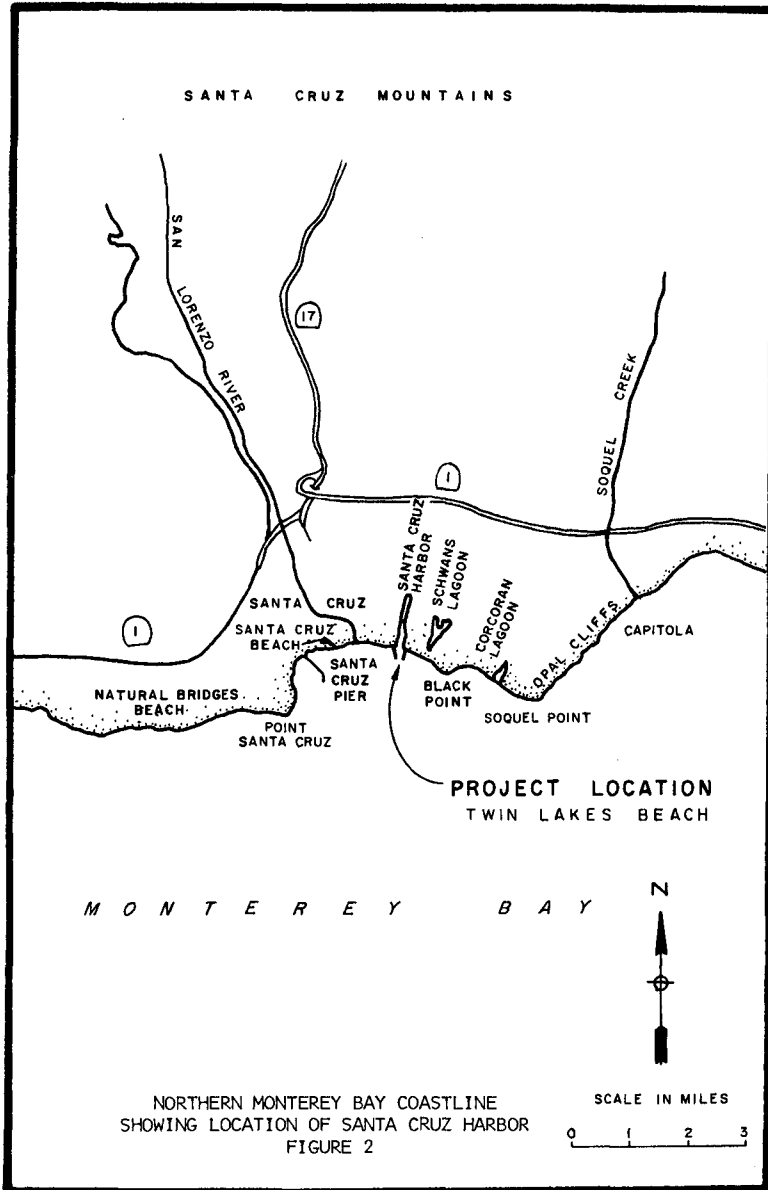
Santa Cruz Harbor is located on the northern coast of Monterey Bay, California, approximately 104 kilometers south of San Francisco and 22 kilometers north of Moss Landing, as shown in Figures 1 and 2.

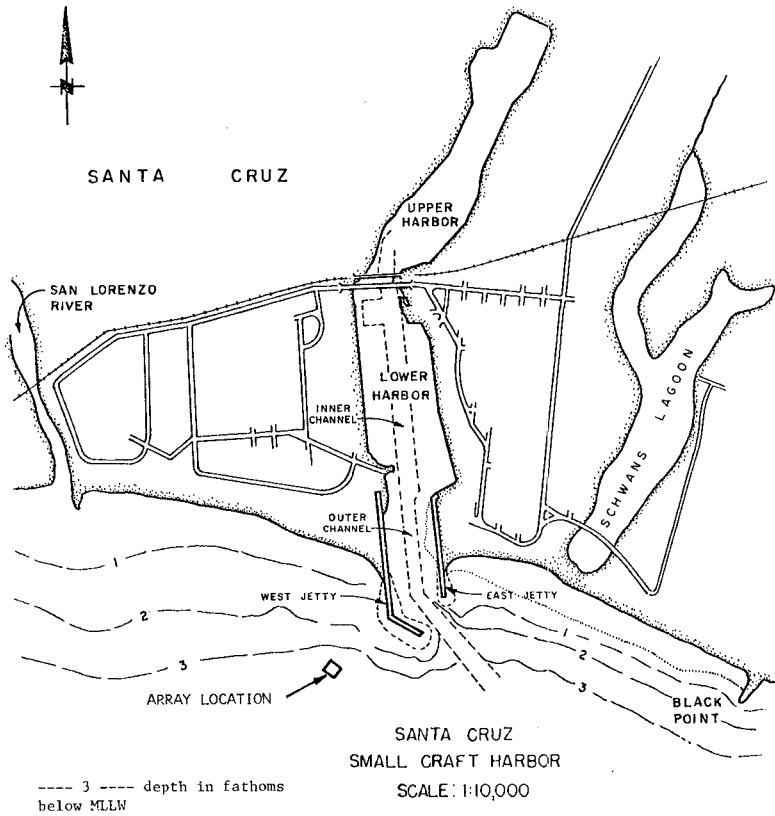
Harbor construction was authorized by Congress under the Rivers and Harbors Act of 1958, which provided for a harbor to accommodate light-draft vessels in Woods Lagoon at the eastern boundary of Santa Cruz. The authorized improvements included two rubblemound jetties 360 meters long and 243 meters long, on the west and east sides of an entrance channel, respectively -- an entrance channel approximately 270 meters long, 30 meters wide and 6 meters deep, reducing to 45 meters in depth at the same width for an additional 111 meters -- an inner channel, 240 meters long, 45 meters wide, 45 meters deep, reducing to 3 meters in depth at the same width for an additional 100 meters -- a turning basin approximately 90 meters long, 75 meters wide, and 3 meters deep, and a sand-bypassing plant. Figure 3 shows the project features. The armor units of the seaward side of the west jetty are 28-ton quadripods. The west jetty also has a concrete cap extending to elevation +4.8 meters MLLW.

Construction of the harbor was initiated in February of 1962 with the dredging of Woods Lagoon and the start of work on the west jetty. The west jetty was completed in February 1963. Then work began on the east jetty, and it was completed in April 1963. The entrance channel was dredged to the project dimensions in the summer of 1963. Construction of Santa Cruz Harbor was completed in November 1963, with the exception of the sand-bypassing plant. Construction of the sand-bypassing plant was deferred until the littoral drift rate could be more accurately determined.

*Staff Oceanographer, Ca. Dept. of Boating & Waterways
and Research Associate, Scripps Inst. of Oceanography, UCSD
**Oceanographer, U.S. ARMY Corps of Engrs., San Fran. Dist.
***Coastal Engr., U.S. ARMY Corps of Engrs., San Fran. Dist







PLAN OF SANTA CRUZ HARBOR
SHOWING WAVE GAGE ARRAY LOCATION

FIGURE 3

During and subsequent to construction of Santa Cruz Harbor jetties, the beach west of the jetties experienced rapid accretion, building out from the 1962 pre-project shoreline about 75 meters by 1965 and about 150 meters by 1977. The growth of the beaches has protected the bluffs along East Cliff Drive from rapid erosion by wave action. Soon afterward, substantial littoral transport during winter months would shoal the entrance to the harbor closing it to all vessel traffic.

In 1977, the U.S. Corps of Engineers undertook a study of the shoaling problem with the purpose to develop and evaluate alternative methods of mitigating the shoaling effects. The study defined the coastal processes and the resultant shoaling mechanism at the harbor entrance. The littoral processes study led to the conclusion that the net littoral transport rate was 230,000 cubic meters to 382,000 cubic meters per year from west to east. Shoaling of the channel has required annual maintenance dredging reported to be on the order of 76,400 cubic meters per year since 1965.

Estimated littoral transport rates used by Walker, et al. (1978) indicated that a potential for reversals in transport exists but that shoreline east of the harbor was so oriented that these reversals during the winter months were not likely to cause significant shoaling in the channel.

DEEPWATER WAVE CLIMATE

The waves arriving at Santa Cruz can be divided into three categories according to origin:

Northern Hemisphere swell, Southern Hemisphere swell, and seas generated by local winds.

The geometry and bathymetry off Santa Cruz allow swell to approach from the south clockwise through west-northwest, whereas locally generated seas can approach from the east clockwise through west-northwest. The following description of the wave climate is taken from Marine Advisors (1961).

Northern Hemisphere Swell. Most of the wave energy reaching Santa Cruz is from Northern Hemisphere swell generated primarily by extra-tropical cyclones in the northern Pacific. These cyclones, also referred to as Japanese-Aleutian storms, typically originate in the vicinity of Japan and move eastward across the higher latitudes to the Gulf of Alaska. These storms are most prevalent and intense during the winter and spring seasons. Infrequently, storms originating in the vicinity of the Hawaiian Islands move eastward across the mid-latitudes and

produce swell that reaches Santa Cruz. However, this southwesterly swell is rarely as large as that produced by the Japanese-Aleutian storms. Tropical storms and hurricanes, called chubascos, which develop off the coast of Mexico, during the months of July through October, rarely move as far north as Southern California, although they do generate moderate swell that reaches most of the California coast.

Southern Hemisphere Swell. During the austral winter, storms of great intensity and size occur in the high and mid-latitudes of the southern Pacific. The storms are comparable with the extra-tropical storms of the Northern Hemisphere but are often more severe. Swell generated by these storms occur from May through October, but are most common during August and September. Because of the great decay distances, these waves have low heights and long periods when they reach Santa Cruz. Typical southern hemisphere swell has heights between 0.3 and 0.9 meters and periods ranging from 13 to 21 seconds. These waves approaching Santa Cruz are from the south through southwest.

Data collected by the wave gage array for 1978 is summarized in Figure 4. This figure presents the measured height and period distribution functions.

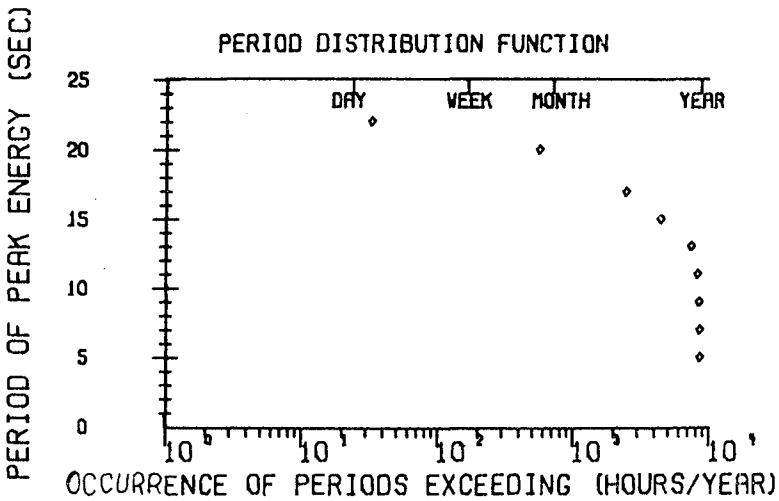
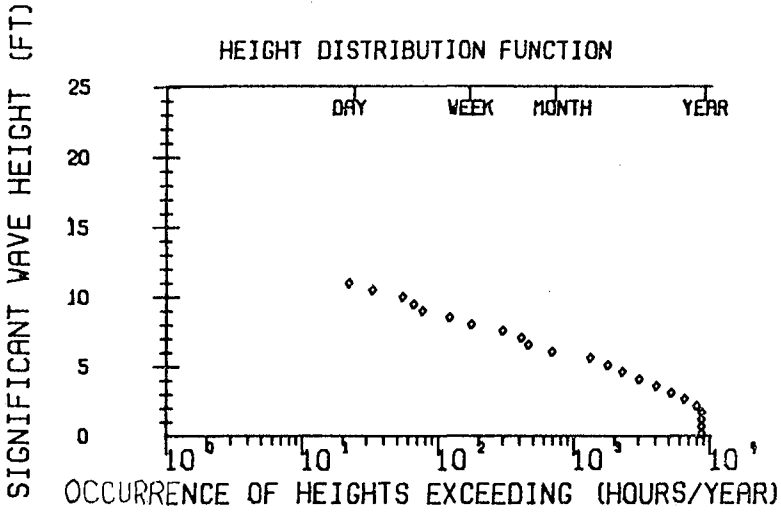
POTENTIAL SEDIMENT SOURCES

The shoreline region lying northwest of Santa Cruz, extending from Half Moon Bay to Point Santa Cruz, comprises sea cliffs and small pocket beaches which occur mostly at the mouths of small creeks. Wave-induced erosion of the sea cliffs is a possible source of littoral material at Santa Cruz. Sea cliffs comprise shale and cretaceous sediments in most of the southern two-thirds of this reach. However, these sediments may not be the significant contributors of beach material at Santa Cruz. Marine terrace deposits overlay the sea cliffs along the southern two-thirds of the region and may be the primary contributors of beach material.

Drainage in the region is typified by short, steep-gradient streams originating in the Santa Cruz mountain range. Near the ocean, the rivers have the character of drowned river valleys. The streams have small drainage areas, and flows are characterized by flash floods. No deltas are found offshore because the wave climate rapidly removes sediment and distributes them along the beach and offshore.

The reach of shoreline between Point Santa Cruz and Soquel Point includes Santa Cruz Beach, the San Lorenzo River, and stretches of sea cliffs. The San Lorenzo River, 0.8

SANTA CRUZ HARBOR JAN-DEC 1978



kilometers west of Santa Cruz Harbor, has a drainage basin of 355 square kilometers and an annual runoff of 0.1541 cubic kilometers. The heaviest runoff occurs during the winter months, October through April. Estimates made by the Corps of Engineers (1974) indicate that the annual sediment discharge of the San Lorenzo is between 67,232 and 101,612 cubic meters. Of this total, 20 percent, or 13,725 to 20,628 cubic meters was assumed to be of sand sizes found on beaches in the study area.

Offshore of the project site is a narrow continental shelf which drops off into the Monterey Canyon located in the middle of Monterey Bay. Figure 5 shows the general bathymetric features of the Santa Cruz embayment. The beach slopes steeply to the 6 meter depth contour, then slopes very gently to the south. The bottom comprises hard rock outcroppings which are partially overlain with unconsolidated sediment.

WAVE MEASUREMENT SYSTEM

In February, 1978 a directional wave measurement array was installed near the harbor entrance to assess the forcing function for longshore transport. Scripps Institution of Oceanography (SIO), under contract to the San Francisco District, U.S. Army Engineers, added this installation to the network of wave measurement stations as described in Seymour and Sessions (1976). The point of measurement is at a depth of 7 meters approximately 100 meters west, or updrift, of the jetties.

The wave measurement system consists of a directional array, a shore terminal containing suitable electronics to allow for remote automatic data logging and analysis, and the necessary interconnecting cable. The array is a square steel space frame, 6 meters on a side, with short vertical risers at the corners. At the top of each riser is a cylindrical container capable of storing approximately 15 meters of three conductor waterproof cable. Attached to these cables are pressure sensor instruments in waterproof housings. External pressure is transmitted to the instrument by means of an oil filled diaphragm. The use of the long cable allows divers to bring the pressure sensors to the surface, remove them for service or replacement, and reconnect the new instrument using reliable connectors that cannot be reconnected under water. The diaphragms are protected from marine growth by a pad of copper gauze coated with antifouling paint and contained in a perforated cap. The frame, which is made of steel pipe, serves as conduits for all branch cabling so that no cables are exposed after the system is installed. The main power and signal cable is polyurethane jacketed with internal steel armor and is strain relieved at the frame. The density of the cable is sufficient to insure rapid self burial under

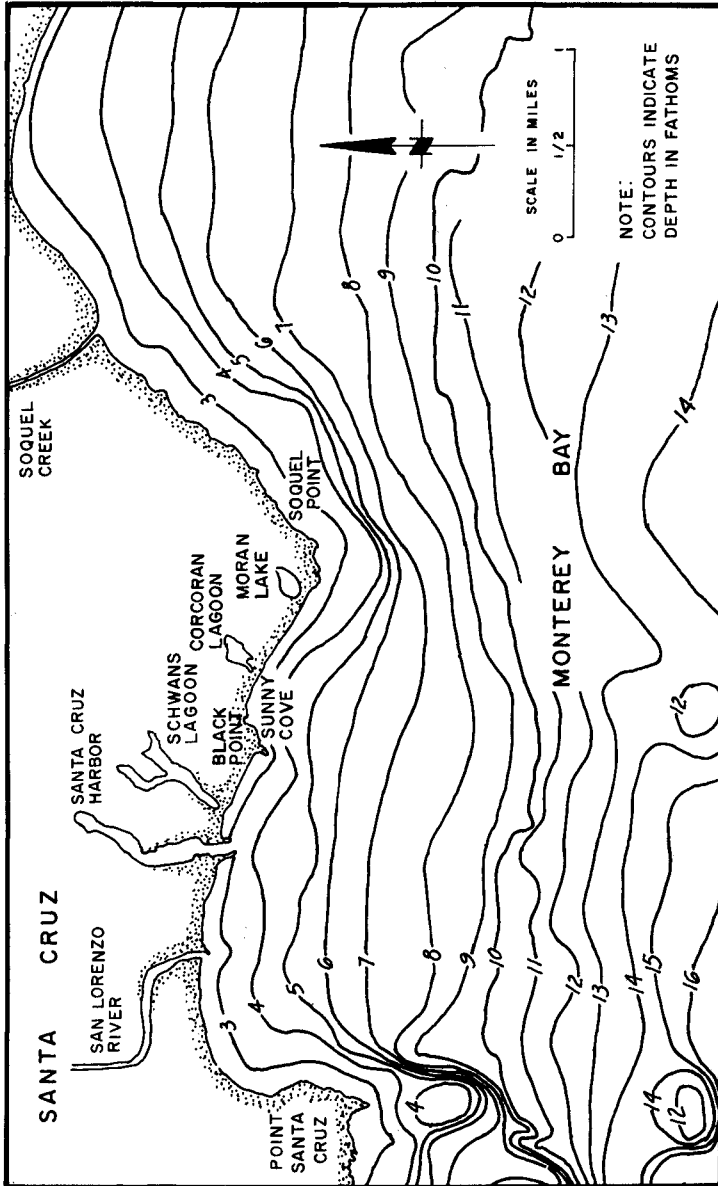


FIGURE 5 BATHYMETRIC FEATURES IN SANTA CRUZ REGION

even moderate wave conditions. Experience during several severe winter storms has shown that the cable will remain buried even during periods of gross beach erosion. The cable is trenched into the sand with a backhoe above the high water line. Figure 6 shows an array frame on the stern of a LARC amphibious truck prior to being towed to its installation site.

The shore terminal is a weatherproof enclosure, approximately one meter square containing the interface electronics. The analog output of each pressure sensor is converted to a frequency modulated signal within the sensor housing so that there are no line losses or distortion to contend with in the cable. This FM signal is then converted to a digital output sampled at 1 hz within the shore terminal for each sensor output. All sensors are sampled simultaneously so that phase relationships are accurately preserved for directional analysis. The digitized pressure values are stored in solid state memory using a pushdown scheme that retains the most recent 1024 values. This allows for storing slightly more than 17 minutes of data for each sensor.

The shore terminal is connected to an ordinary telephone line with a data coupler. When the assigned telephone number is dialed, the control circuitry locks the data in the memories, and transmits an identifying code followed by the data stream. The entire contents of the four memories are transmitted in less than one minute. Data are received by a dedicated computer at SIO and, after transmission quality checks, are written to magnetic tape. If the computer detects unusable data it will recall the station. If telephone company circuit overloads prevent a completed call after three attempts, the system will move that station to the end of the calling queue for a later attempt.

Wave data were collected at ten hour intervals during 1978 and part of 1979. During the fall of 1979, the interval between data runs was reduced to 6 hours.

DATA ANALYSIS METHODS

Longuet-Higgins, et al. (1963) shows that an estimate of the longshore component of the radiation stress, S_{xy} , can be obtained from knowledge of the surface elevation and the components of sea surface slope at a point. This methodology was developed for use with a pitch and roll measuring buoy in deep water but is equally applicable to shallow water if a method exists for measuring the slope components. In the present scheme, the components of sea surface slope are obtained from the differences between pairs of sensors. The components are rotated to a



DIRECTIONAL WAVE ARRAY FRAME
MOUNTED ON LARC VEHICLE PRIOR TO
BEING TOWED INTO POSITION. OIL
DRUMS ARE TEMPORARY FLOTATION.

FIGURE 6

coordinate system based upon the local onshore and longshore directions as determined by smoothing the bathymetry in the vicinity of the array. Since the estimate of S_{xy} is formed by cross-spectral analysis, the difference fourier coefficients can be corrected from pressure differences to surface elevation differences by linear wave theory, as described in Seymour and Higgins (1978).

Each data run obtained from the slope array is analyzed using the computer at La Jolla. The analysis products include:

- Significant wave height
- Period of peak energy
- Distribution of energy by frequency (energy spectrum)
- Distribution of S_{xy} by frequency

These statistics are published monthly and are made available to any investigators concerned with the study area. Figures 7 and 8 show typical examples of the analysis summaries for wave energy and S_{xy} .

The most commonly used estimator for longshore transport is the Bagnold-Inman-Komar model which is reported with the most recent values of the empirical coefficient in the CERC Shore Protection Manual. Seymour and Higgins (1978) shows that this formulation can be readily transformed so that transport is proportional to S_{xy} and to the square root of the significant wave height, resulting in an equation of the form:

$$Q = k S_{xy} (H_s)^{1/2} \quad (1)$$

where Q is the longshore mass transport,
 k is the proportionality coefficient,
and H_s is the significant wave height.

The assumptions embodied in Eq. (1) include:

1. The bathymetry between the measurement point and the breaker line is regular. Since the measurement point is in relatively shallow water, this is a reasonable approximation on almost all beaches. This assumption allows for conservation of S_{xy} .
2. S_{xy} is conserved to the break point.
3. The depth at breaking can be estimated from the significant wave height at the measurement point.

The advantage of the slope array for applications where sediment transport estimates are required is immediately

SANTA CRUZ HARBOR APR 1980				PERCENT ENERGY IN BAND (TOTAL ENERGY INCLUDES RANGE 2048-4 SECS) BAND PERIOD LIMITS (SECS)									
LOCAL DAY/TIME	SIG. (CM.)	HT (CM.)	TOT. EN (CM. SQ)	22+	22-18	18-16	16-14	14-12	12-10	10-8	8-6	6-4	
1	0405	67.0	280.4	9.4	9.2	3.3	4.2	32.7	19.4	7.2	8.2	6.8	
1	1007	63.3	250.7	7.1	7.1	6.5	6.3	22.2	18.6	7.2	9.6	15.9	
1	1610	66.7	278.1	3.3	6.8	16.8	3.3	21.5	18.3	12.6	8.0	9.9	
1	2205	66.6	277.2	8.6	11.9	15.2	10.5	14.5	12.2	11.7	8.6	7.3	
2	0405	71.0	314.6	5.2	5.0	24.4	12.4	15.5	10.6	10.3	8.7	8.4	
2	1005	82.1	421.0	4.6	5.4	19.6	21.9	13.2	12.1	6.2	8.5	8.9	
2	1607	65.8	270.8	2.8	6.6	14.1	15.9	27.6	8.9	7.0	10.2	7.3	
2	2205	70.2	307.9	5.0	8.1	9.8	39.0	20.6	4.3	2.5	4.7	6.4	
3	0405	66.8	278.5	5.5	9.3	18.5	26.5	19.2	6.9	2.6	4.9	7.0	
3	1005	56.7	201.2	4.3	1.9	10.2	24.7	28.4	9.0	5.1	7.4	9.4	
3	1610	74.5	346.5	3.4	2.7	18.3	41.1	13.4	8.2	1.9	5.6	5.8	
3	2205	66.2	273.8	4.0	1.9	9.3	54.0	14.7	6.2	2.0	3.5	4.9	
4	0405	71.2	316.5	5.4	1.8	14.4	26.0	34.5	8.5	1.6	4.0	4.2	
4	1005	68.8	295.8	3.7	0.9	11.8	29.7	33.6	5.8	1.7	4.0	9.3	
4	1605	79.2	391.8	2.9	0.9	8.1	8.8	18.7	10.8	7.3	4.4	38.6	
4	2205	118.6	879.5	1.3	0.6	2.5	4.6	7.6	4.9	1.8	28.2	49.0	
5	0405	131.8	1085.7	1.5	0.4	2.2	8.2	9.9	4.0	1.3	27.5	45.5	
5	1005	99.6	619.8	2.2	0.5	6.3	7.3	24.6	11.7	5.5	19.6	22.6	
5	1605	98.6	608.0	2.4	0.8	3.2	7.0	23.2	16.2	9.2	20.0	18.6	
5	2205	106.4	707.9	3.7	1.2	3.9	19.0	23.5	11.3	10.9	14.2	12.6	
6	0405	124.0	960.5	5.8	2.1	7.5	16.3	23.6	18.1	8.1	10.5	8.5	
6	1007	159.1	1581.9	6.2	1.7	18.1	22.9	17.3	8.6	7.3	11.3	7.1	
6	1011	159.1	1582.7	6.2	1.7	18.1	22.8	17.3	8.7	7.3	11.3	7.1	
6	1606	143.7	1290.8	6.6	1.1	5.4	36.0	24.7	5.6	4.2	11.5	5.4	
6	2205	122.6	939.5	7.4	1.5	3.7	25.7	34.9	6.5	5.3	10.3	5.1	
7	0405	128.1	1025.5	9.2	1.1	2.8	40.2	17.3	11.5	5.8	8.5	4.1	
7	1005	114.9	825.7	7.1	1.1	2.7	18.2	30.5	20.7	6.9	7.3	6.1	
7	1605	124.0	961.1	5.2	0.7	4.4	31.6	36.0	6.4	4.8	8.2	3.2	
7	2205	107.2	717.8	7.4	1.6	4.2	29.2	30.5	10.8	5.0	7.4	4.4	
8	0405	100.6	632.0	5.6	0.9	7.2	51.1	11.1	10.3	3.5	5.8	5.1	
8	1030	102.9	662.3	3.3	0.6	7.1	15.0	46.8	12.9	3.5	6.3	4.9	
8	1605	95.4	569.4	4.8	0.5	11.3	43.1	18.7	5.2	4.4	8.3	4.1	
8	2205	81.0	410.0	4.1	0.9	5.1	43.8	16.8	9.6	8.0	7.6	4.6	
9	0405	77.1	372.0	4.8	1.6	5.1	28.6	37.6	7.4	3.9	6.7	4.8	

TYPICAL DATA ON WAVE ENERGY AT
SANTA CRUZ HARBOR. FROM APRIL 1980
MONTHLY REPORT OF CALIFORNIA
COASTAL DATA COLLECTION PROGRAM

FIGURE 7

SANTA CRUZ HARBOR ARRAY
APR 1980

			ANGULAR DISTRIBUTION IN PERIOO BANOS (ANGLES IN DEGREES)								
LOCAL DAY/TIME	SIG. ANG (DEG)	TOT. SKY (CM. SQ)	BANO PERIOO LIMITS (SECS)								
			22+	22-18	18-16	16-14	14-12	12-10	10-8	8-6	6-4
1	0405	24.8	-1.8	18.4	14.2	16.6	19.7	31.5	26.6	30.9	33.4
1	1007	29.9	14.7	28.4	15.5	16.0	34.7	25.0	31.0	35.5	36.2
1	1610	24.0	-5.4	13.9	18.9	29.2	20.3	24.4	23.5	30.6	33.7
1	2205	26.0	2.5	14.1	17.2	21.7	36.4	25.1	24.4	26.7	35.3
2	0405	27.4	10.2	27.8	22.0	32.1	25.9	31.5	28.7	27.3	32.2
2	1005	26.6	8.9	21.3	20.1	23.2	37.3	29.0	27.8	27.5	29.7
2	1607	23.9	-4.7	29.2	14.7	22.0	29.2	25.3	18.0	24.9	28.9
2	2205	24.5	-2.3	16.9	16.0	20.0	35.3	30.4	30.1	28.0	21.7
3	0405	21.0	-15.5	18.5	18.2	17.5	21.0	32.8	30.1	24.8	23.8
3	1005	21.2	-12.4	11.0	18.6	17.5	19.6	26.9	19.3	24.6	33.1
3	1610	20.4	-24.8	8.8	14.6	19.8	26.0	21.5	33.5	19.5	23.3
3	2205	23.0	-8.2	7.3	22.7	22.1	24.6	25.3	25.6	25.5	24.8
4	0405	22.4	-13.1	21.4	12.3	20.1	26.7	26.2	18.0	24.0	27.9
4	1005	22.3	-12.8	11.6	17.8	17.5	24.8	34.9	17.6	26.7	27.1
4	1605	23.6	-6.7	12.2	17.8	18.2	27.1	26.0	32.2	32.8	21.3
4	2205	19.4	-60.6	-64.8	20.1	18.9	32.5	23.6	21.0	22.0	15.3
5	0405	13.2	-162.4	5.6	18.1	20.1	27.0	27.2	17.4	13.3	6.7
5	1005	22.5	-23.7	52.1	13.8	18.3	22.8	26.5	22.4	25.9	20.5
5	1605	25.1	3.8	20.5	21.0	19.8	33.8	23.3	27.5	23.4	19.9
5	2205	28.4	36.4	22.8	31.9	19.7	35.3	28.6	27.3	30.6	26.2
6	0405	27.1	30.7	14.4	21.9	23.8	34.1	25.4	26.1	25.7	24.6
6	1011	28.6	85.1	26.7	22.5	31.1	30.7	27.3	31.5	28.8	29.5
6	1606	28.3	63.8	34.4	21.7	23.4	36.9	31.1	33.2	27.5	25.4
6	2205	31.0	84.7	20.4	25.8	25.7	37.0	30.8	30.2	28.7	30.4
7	0405	28.6	54.8	5.0	24.5	27.8	28.6	31.6	30.1	28.1	29.5
7	1005	26.3	13.9	23.5	17.7	23.9	24.9	27.8	31.7	27.3	31.1
7	1605	29.1	62.2	30.7	22.5	27.5	32.7	24.5	28.3	27.0	33.0
7	2205	28.4	35.6	20.0	21.2	25.4	32.3	28.4	27.1	29.0	31.6
8	0405	25.4	1.6	8.1	22.8	21.0	37.7	28.9	26.5	32.1	34.0
8	1030	23.8	-14.7	24.2	5.1	22.4	24.0	28.6	31.2	26.3	30.6
8	1605	23.1	-18.3	45.7	21.7	21.7	22.8	29.2	24.9	24.5	33.5
8	2205	25.2	0.6	17.6	1.3	22.0	37.4	25.7	26.9	25.7	28.1
9	0405	27.7	14.4	8.2	18.8	25.6	28.2	28.1	36.8	34.5	31.7

TYPICAL DATA ON WAVE DIRECTIONAL
CHARACTERISTICS AT SANTA CRUZ
HARBOR. FROM APRIL 1980 MONTHLY
REPORT OF CALIFORNIA COASTAL
DATA COLLECTION PROGRAM.

FIGURE 8

apparent. This system produces an unbiased estimate of S_{xy} which can be readily converted to estimates of longshore transport by eq. (1). In theory, S_{xy} can be calculated from a knowledge of the directional spectrum. However, as shown in Higgins, Seymour and Pawka (1980), linear arrays designed to give good definition of directional spectra yield biased estimates of S_{xy} . Since linear arrays are characteristically much larger than the slope array and cannot be prealigned on the shore, they tend to be much more expensive to install. The slope array system offers, therefore, an inexpensive alternative which sacrifices some definition of the full directional spectrum to achieve the best definition of S_{xy} .

MODEL FOR SEDIMENT IMPOUNDMENT

Since the harbor is dredged to contract limits approximately at yearly intervals, at the end of the winter maintenance dredging season, the total amount of dredged material removed is a reasonable estimate of the annual amount of material impounded by the jetties. It has been assumed by many, including the authors, that a significant amount of the longshore transport is bypassed during the intervals when the harbor entrance is severely shoaled. Walker, et al. (1978), in a study of the dredging problem at Santa Cruz Harbor, suggest that the amount of material bypassing the entrance is much larger than the amount impounded. Nevertheless, in the present work, it was hypothesized that there was a correlation between the apparent longshore transport, as estimated by eq. (1), and the observed impoundment, derived from the dredging workload.

The period chosen for testing this hypothesis lays between two occasions when the dredging had been completed to design depth in the harbor entrance. The baseline was after the dredging completion in mid-March, 1978. This was assumed to be a zero level of accretion. The study extended to the next such event which occurred 15 months later at the end of May, 1979.

In the period including these events, from February 1978 to June, 1979, the slope array was sampled approximately 2500 times, or over 700 hours of actual wave data were collected. Each data run was analyzed to produce values of S_{xy} and H_s . These were then employed in Eq. (1) to provide a time history of estimated longshore transport. This series can be summed in a variety of ways to provide estimates of net or gross transport. In Figure 9, the transport estimates have been summed for complete months. It can be seen that the drift towards the east is dominant, but that intervals of small westward transport are predicted during the summer months.

ESTIMATION OF LONGSHORE TRANSPORT AT SANTA CRUZ HARBOR, CA.

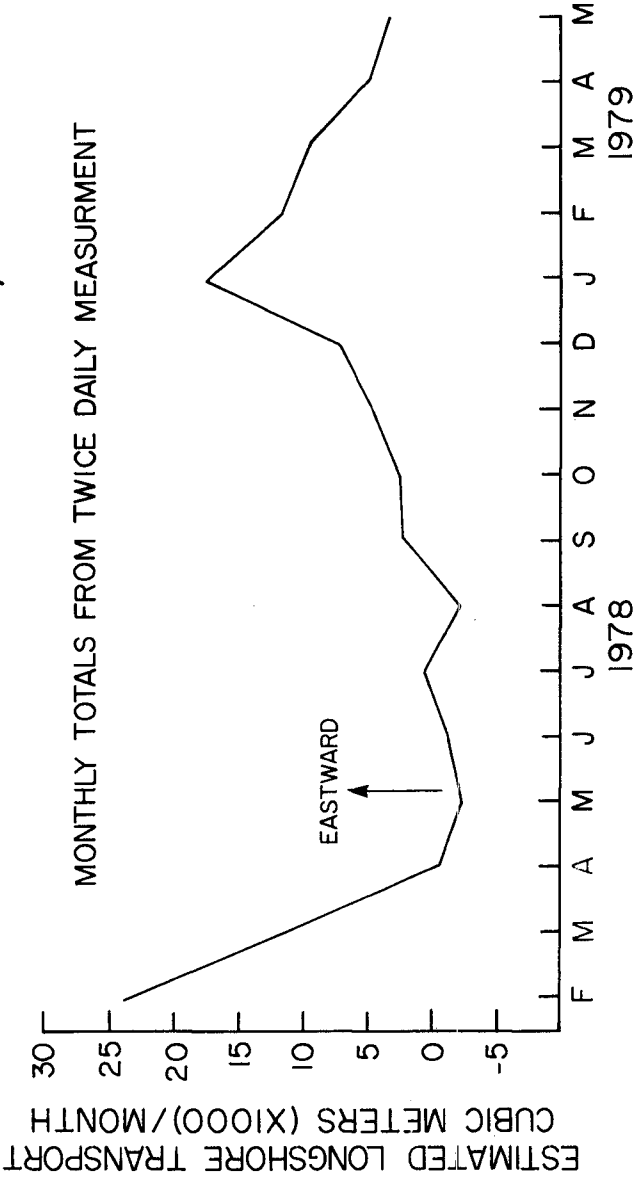


FIGURE 9

The authors then postulated a simple model for sediment impoundment in the harbor. Since the feeder beach to the west was characteristically full, it was assumed that all eastward transport would be trapped between the jetties. Conversely, since the eastern beach was usually stepped well shoreward of the jetty, it was assumed that the small amounts of westward transport would be stored in the eastern feeder beach and would not be carried around the jetty. The impoundment load in this model was then, simply, all of the eastward transport and none of the westward transport.

The impounded sediment volume, as a function of time, was then calculated by this scheme for the period between the two baseline dredging events. During this interval, there were two other dredgings. These were not made to the contract limits, but by subtracting their output volumes at the appropriate times, the accumulation time history could be made more realistic. The final accumulation volume was then reduced by the amount of the last baseline dredging episode. The residue or deficit volume would then represent the difference between the estimate of the impounded sediment and the actual value, since a perfect estimate of the accumulation would be exactly balanced by the dredging removals and the final volume would be zero.

Figure 10 shows the result of this estimation of the impounded volume. The estimate provided a residue of approximately 3000 cubic meters, which is about 5 percent of the total dredging load for the period. Therefore, the simple model for impoundment, and the closely spaced intervals of directional wave observation, provided a gratifyingly close estimate of the actual accumulation in the harbor entrance.

These same data can be employed to construct an annual net transport rate. The longshore transport estimate for the period from February, 1978 through January, 1979 is 62,000 cubic yards. It is interesting to compare this with an estimate made in Walker, et al. (1978). In this report, longshore transport was estimated by using deepwater wave statistics inferred from ships' observations and hindcasts from meteorological records. The deepwater waves were then refracted into shore and the same basic transport equation used to estimate a net longshore drift of 373,000 cubic meters. Since the transport relationships utilized were the same, this indicates that the hindcast thrust of the waves was six times that actually measured by the slope array.

OBSERVATIONS AND CONCLUSIONS

The slope array provides a convenient method for estimating the gross and net longshore transport of sediment in the

PREDICTION OF HARBOR SHOALING
AT SANTA CRUZ, CA.

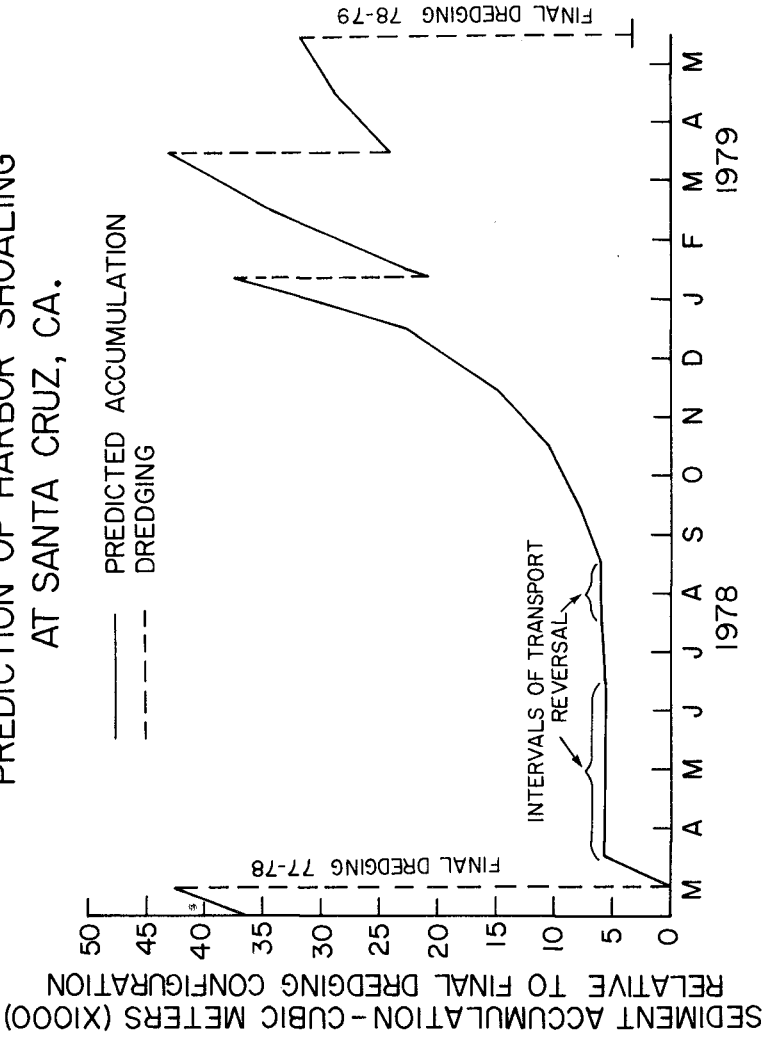


FIGURE 10

vicinity of the measuring point. For a particular 15 month period at Santa Cruz Harbor, CA, the net transport in the eastward, or dominant, direction provided a very efficient estimator of the sediment volume impounded in the harbor entrance.

There appeared to be little, or no bypassing of sand around the harbor entrance. During this particular winter storm period, staged dredging kept the harbor mouth from closing completely. This was not true during other winters, when there may have been substantial bypassing.

The longshore transport appears to be substantially less during the winter of 1978-79 than is predicted by using average deepwater wave climates refracted into this location.

The results suggest that a nearly complete trap of longshore transport was provided by Santa Cruz Harbor during the winter of 1978-79. It is believed that this is the first trap experiment of this duration in which accurate, continuous measurements of wave direction and energy were obtained. It provides another valuable data point confirming the efficiency of the presently accepted formulation for longshore transport.

ACKNOWLEDGMENTS

This research was conducted with funding from the San Francisco District, U.S. Army Engineers and the California Department of Boating and Waterways and this support is gratefully acknowledged.

REFERENCES

- Gable, C. G., Ed.: 1979. "Report on Data from the Nearshore Sediment Transport Study Experiment at Torrey Pines Beach, California, November-December, 1978." University of California, San Diego, Institute of Marine Resources, IMR Ref. No. 79-B.
- Inman, D. L., J. A. Zampol, T. E. White, D. M. Hanes and K. A. Kastens: 1980. "Field Measurements of Sand Motion in the Surf Zone." 17th International Conference on Coastal Engineering, Sydney, Australia, 23-29 March 1980 (in press).
- Seymour, R. J. and D. B. Duane: 1979. "The Nearshore Sediment Transport Study." Proc., 16th Coastal Engineering Conference, Aug. 27-Sept. 3, 1978, Hamburg, Germany, Vol. 11, pp. 1555-1562.
- Seymour, R. J., G. W. Domurat and D. M. Pirie: 1980. "A Sediment Trapping Experiment at Santa Cruz, Ca." Proc., 17th International Coastal Engineering Conference, March 23-29, 1980, Sydney, Australia.
- Seymour, R. J., A. L. Higgins, and D. P. Bothman: 1979. "Tracked Vehicle for Continuous Nearshore Profiles." Proc., 16th Coastal Engineering Conference, Aug. 27-Sept. 3, 1978, Hamburg, Germany, Vol. II, pp. 1542-1554.
- Seymour, R. J. and M. H. Sessions: 1976. "Regional Network for Coastal Engineering Data." Proc., 15th Coastal Engineering Conference, July 11-17, 1976, Honolulu, HI., Vol. I, pp. 60-71.

WAVE FORCING OF BEACH GROUNDWATER

Evans Waddell
Science Applications, Inc.
Raleigh, NC

ABSTRACT

A field project was conducted to measure swash and surf characteristics and related processes on a beach with a high tide range and very low slope. Variables measured were beach waterlevels in the surf and swash zones, beach groundwater levels, and on-offshore and alongshore currents. A variety of deployment patterns and instrument combinations were used. Results show a nonlinear transfer of wave energy from high to low frequencies. This appears to have occurred because finite amplitude waves and bores caused an onshore mass flux which produced an increased local waterlevel. Periodically, this impounded water was released. Groundwater records indicate that low frequency waterlevel oscillations on the beach face were the dominant forcing function for oscillations of the beach watertable. A model is generated which adequately predicts some of the response characteristics of the groundwater table.

INTRODUCTION

As one of a series of studies conducted to examine in detail the physical mechanisms which are active in a dynamic beach system, the field project discussed in this paper was designed to examine the relationship between waves, swash, and groundwater on a very low sloping beach. The specific process to be examined in this paper is the response of the beach groundwater and water table to forcing mechanisms occurring at frequencies ranging from input wave frequencies to several minutes. It is apparent from these results that on such a low sloping beach the understanding of the groundwater flow exceeds the understanding of the complexly coupled forcing mechanisms.

METHODOLOGY

This experiment was conducted on Little Talbot Island, Florida in May 1973. Little Talbot Island is a barrier island in the St. Johns River estuary. A typical cross beach profile at the experimental site is given in Figure 1. The slope is very shallow with an average of approximately 1:70. This site was chosen because of its low slope, high tide range, and medium sand-sized sediment.

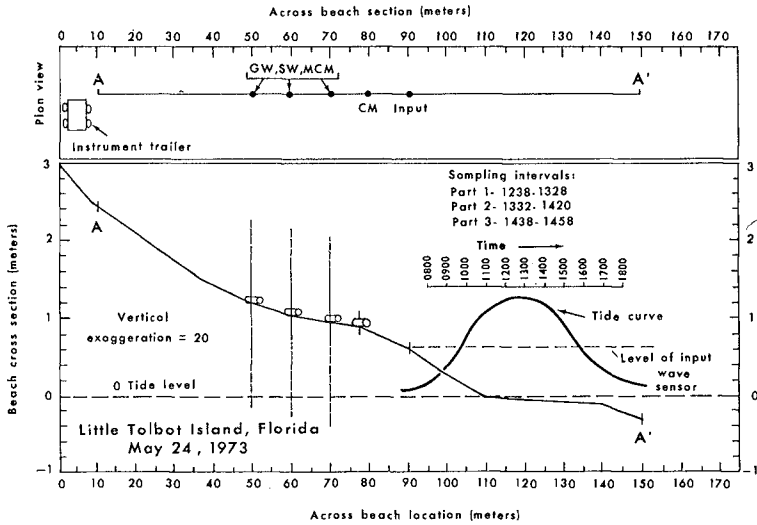


Figure 1. Beach profile, typical instrument deployment pattern, and representative tide curve. The plan view shows the cross beach locations of instruments where GW = groundwater well, SW = swash or beach waterlevel depth, input = input wave sensor. MCM and CM refer to current meters which are not discussed in this paper.

At the study site, the dominant semidiurnal tide was slightly tropic with a range of approximately 1.3 meters. This amplitude and period produced a beach face which rapidly migrated 120-150 meters during half a tidal period. For this discussion, beach is any region which is affected by swash at some time during a tidal cycle. During high tide, most of the beach was inundated and waves shoaled from the seaward or outer limit of the beach at approximately $x = 150$ meters. Waves and bores moved directly onshore, i.e., wave orthogonals were perpendicular to the shoreline and no complex refraction patterns occurred.

The beach cross section shown in Figure 1 remained rather static and exhibited no fundamental changes during the several day experiment. Small scale sedimentary features such as ripples and low amplitude sand waves would appear and disappear during a tidal cycle.

The general cross beach profile was composed of five zones distinguished on the basis of local slope. These zones correspond closely to processes active on the beach during particular portions of a tidal cycle. Zone 1, which extends seaward of $x = 140$ is the nearshore, which is continually inundated during all tidal phases except under exceptional conditions. Zone 2 ($110 < x < 140$) is a low tide terrace which is occasionally exposed or has only very shallow water during low tide. Zone 3 ($75 < x < 110$) is the low tide swash slope and a region over which swash migrates rapidly during rising or falling tide. Zone 4 ($50 < x < 75$) is a high tide terrace. This is a region of very shallow water during high tide. It is in this zone that most instruments were deployed. Zone 5 ($20 < x < 50$) is the high tide swash slope. The exact location of Zone 5 varies with a result of diurnal and fortnightly variability of high tide level.

Measurements were made between $x = 40$ and $x = 70$ m with most water-level measurements being made between $x = 50$ meters and $x = 70$ meters. In this region the beach slope was approximately 1:70. Measurements of input parameters were made between 80 m and 90 m, usually at approximately 90 m. Thus, input statistics reflect wave phenomena just prior to their transiting the very shallow Zone 4. It is in this region, Zone 3, in which waves make a transition to solitary waves and bores. Just seaward of the input wave sensor, water depth decreases from over a meter to less than .3 m.

Instrumentation and Data Runs

Three types of instruments were deployed on the beach face. Due to limitations in the number of analog recorders, all instruments were not used during all data runs. The three instruments were: (1) capacitance type waterlevel sensors which were used to measure waterlevel on the beach and in groundwater wells; (2) bidirectional, ducted impellor, current meters; and (3) a pressure transducer used to measure input surf conditions. These instruments are described and discussed by Sonu and Pittigrew (1974).

Instruments were deployed in different locations and combinations during various data runs. An example of the instruments and their deployments are given in Figure 1. Included on this figure is a representative vertically exaggerated cross beach profile and a tide level record plotted

relative to the profile datum. With this presentation water depths at any time and location can be readily determined.

Most data acquisition occurred during or near high tide. Conducting experiments during this period tended to minimize variations in local conditions that could cause a lack of stationarity in the processes active on the beach face.

Data was taken on several different days. For this discussion, primary instruments were swash probes and groundwater probes. Generally, a single instrument array was used each day. During a day, different data runs were conducted and these are referred to as Part 1, 2, or 3. A given data set is indexed by day and part. Thus "24-3" is part 3 on May 24th.

Analysis

Results of the measurement program were synchronous time series which represented variations in magnitude of the various phenomena measured. These records which have durations ranging from 10 minutes to over an hour were analyzed to give a frequency decomposition of the variance of each signal. In addition, physically related phenomena were analyzed for a frequency decomposition of the covariance of these processes. This technique permits isolation of major periodicities and associations which characterize the random processes being analyzed.

A standard method of spectral density analysis was used. In addition to spectral densities of individual time series, cross spectral densities were computed and the second order characteristics of coherence, transfer functions, and phase angle calculated. All data were demeaned and detrended during analysis to leave only periodic components of variability. Caution must be exercised when interpreting results of higher order spectral analysis. Many physical processes were related nonlinearly which can cause parameters such as coherence to be misleading.

RESULTS

Waterlevels

Design of this experiment required measurement of waterlevels in the region of the swash and surf zone. However, because of: (1) the desire to measure waterlevels during or immediately following high tide, (2) the diurnal variation in the elevation of high tide, (3) the necessity of putting instruments in place well in advance of high tide, and (4) the very low beach slope and hence very wide beach, it was not possible to have instruments in the same relative position during each data run. Therefore, during all data gathering periods, a given instrument or location does not measure or represent the same general environment. In fact, due to a lack of stationarity of still waterlevel, a given instrument may be sampling distinctly different environments in successive data runs; e.g., surf measurements in one run and swash measurements in the subsequent data run. As a

result, specific values of variance density can not be examined; however, patterns can be examined and these should reflect the processes occurring on the beach.

In almost all data runs, a critical, although at times minor, spectral peak occurred between .0667 Hz and .0769 Hz. This peak was observed at all across beach stations and was the lowest frequency peak which was uniform and consistently observed at each measurement station. The frequency of this spectral peak separates what will be referred to as high frequencies from low frequencies.

In these waterlevel spectra, Figure 2, two major features occurred: (1) higher frequency peaks apparently associated with input waves and bores, and (2) one or more low frequency peaks which are believed to have been locally generated by complex interaction of waves and topography. By local generation, it is meant that the process which produced this peak was not input to the beach system but rather was the result of local processes.

If time series of waterlevel at one location are considered as input and time series from a station further upslope are considered as output, then the relationship of the associated spectra can indicate whether spatial processes can be represented by a linear function in the frequency domain. If the spatial process is linear, then at any given frequency, the output is a linear multiple of the input; i.e.,

$$X_{out}(x_{out}, f) = |H(f)|^2_{x_1, x_2} X_{input}(x_{in}, f) \quad (1)$$

where $X(f, x)$ is the magnitude of the variance density at $x = X_{out}$ or x_{in} at frequency f , x = location on the beach relative to the arbitrary baseline in Figure 1 and $H(f)$ = frequency response function.

If the spatial processes are linear, then variance can not be redistributed in the frequency domain as the waves move from x_{in} to x_{out} . In the present beach system, it is anticipated that the linear multiple should be less than or equal to unity since energy is being dissipated as waves move upslope.

These data, Figure 2, suggest that the systems function for the entire spatial shoaling process is nonlinear. This must be concluded because of the apparent local generation and behavior of the low frequency spectral peak. The upslope increase in low frequency peaks and simultaneous upslope decrease in high frequency peaks, strongly suggests that some nonlinear process is causing variance to be redistributed in the frequency domain (Waddell, 1976).

If high and low frequency variance are viewed independently, then high frequency processes appear to be well behaved and quasi linear since there is a gradual upslope variance attenuation. This is what might occur if there was no spatial gradient in mass flux and there was simple upslope energy dissipation resulting in a continual decrease of wave or bore height. Such a situation may occur if Airy waves are gradually dissipated.

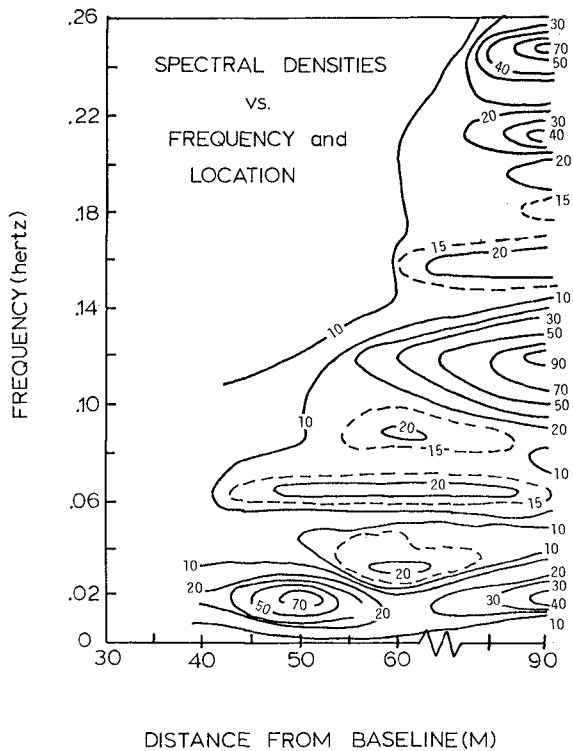


Figure 2. Contour plot of spectral density of beach waterlevels at each across beach location. The actual spectra at any location can be determined holding "distance from baseline" constant and examining changes in magnitude with frequency.

However, in the present situation, waves have definite nonlinear shape and there is most probably a spatial gradient in horizontal mass flux.

As indicated previously, for the environment being examined, local bore height depends on: (1) location, (2) initial wave energy, i.e., height, (3) rate of energy concentration, and (4) rate of energy dissipation. Therefore, it is expected that at some point on the beach face, total variance associated with the input bore spectral peaks will begin to decrease and will continue to decrease until completely attenuated. This complete attenuation may occur at the maximum limit of uprush or it may occur seaward of that point such that no wave induced uprush results (Le Mehaute, 1968).

An explanation of the cause and behavior of low frequency variance is much less straightforward. Possible sources for this variance are: (1) orderly variations in bore height causing variance at subharmonics of the input wave frequency; (2) a combined influence of radiation stress induced set-up in conjunction with arrival of wave groups, and (3) periodic impoundment and release of water moved onshore by shoaling waves and bores. One or more of these could occur simultaneously; however, in the present situation the last possibility seems the most probable.

If these low frequency peaks were the result of some orderly variation of the height of incident waves, then the low frequency peaks should occur at subharmonics of the dominant input periods. Additionally, since the dominant input spectral peak had a rather narrow bandwidth, such subharmonics should also be rather well defined. In the present data, there were no consistent patterns of low frequency variance at subharmonics of the input wave periods.

If orderly height variations caused the low frequency variance, then the magnitude of the low frequency peaks should be relatively small unless there were large differences between successive bore heights. If such were the case, there should be spatial changes in the period between successive bores because of the dependence of celerity on bore height, i.e.,

$$C = (g(h_0 + H_B))^{1/2} \quad (2)$$

where C = rate of change of location of bore front relative to the local water velocity, h_0 = initial water depth and H_B = change in water level across the bore front. If there were large sequential variations in bore height in water where H_B was the same order of magnitude as h ; i.e.,

$$O(H_B) \geq O(h) \quad (3)$$

then the band width of the input wave spectral peak should increase up-slope. No such pattern can be seen, in fact, the opposite generally occurs. As a result, it must be assumed that successive input waves did not display large sequential and orderly variations in height.

In these data some low frequency spectral peaks occurred at sub-harmonics of input wave spectral peaks, however, there was no consistent pattern and the magnitude of these spectral peaks was generally small.

It is expected that due to energy dissipation, a subharmonic peak should decrease in magnitude upslope unless secondary bores consistently rejuvenated primary bores. Even if this occurred, it is unlikely that such rejuvenation could account for low frequency spectral peaks having the magnitude of those observed.

If low frequency variance is associated with periodic set-up due to the arrival of wave groups, then the amplitude of the low frequency oscillation can be rather large. Examination of the original time series did not reveal clearly defined and repetitive wave groups, although there was some indication that small periodic variations of wave height might have been present at times. If such wave groups were the result of superposition of two deep water wave trains moving into shallow water, then it should be possible to identify the component waves in the input spectra and from these predict the approximate frequency of the low frequency oscillation. If there are two wave trains having similar amplitudes and angular frequencies ω_1 and ω_2 , then amplitude of the carrier wave will vary at a frequency of $\frac{(\omega_1 - \omega_2)}{2}$ and the variation in wave set-up will occur at $\omega_2 - \omega_1$.

All possible pairs of high frequency spectral peaks were evaluated for the frequency of the envelope wave which would be produced if they were superimposed. In all these data runs only a few high frequency peaks could be combined to produce the observed low frequency peaks. There is serious doubt as to whether this association was any more than random chance. This doubt arises because the peaks were not consistently observed across the beach face.

By elimination, impoundment and release of water from the beach appears to be the most likely explanation for the low frequency waterlevel oscillations. Since the component highly nonlinear waves caused a shoreward mass flux, a mechanism for onshore flux is readily available; however, an adequate explanation for the periodicity of impoundment and release is difficult to provide. It is possible that due to the low beach slope, wide beach zone and existence of multiple random waves in the shallow portion of the surf zone, some natural periodicity is established.

Groundwater

Spectra of groundwater indicate that low frequency oscillations of waterlevel on the beach dominated the forced groundwater oscillations (Figure 3). This is to be expected and has been documented previously (Waddell, 1973). These low frequency oscillations dominate for two major reasons: (1) the beach matrix and well point are low pass filters, and (2) groundwater was usually measured on the shoreward side of the experimental site where lower frequencies generally dominated the waterlevel spectra.

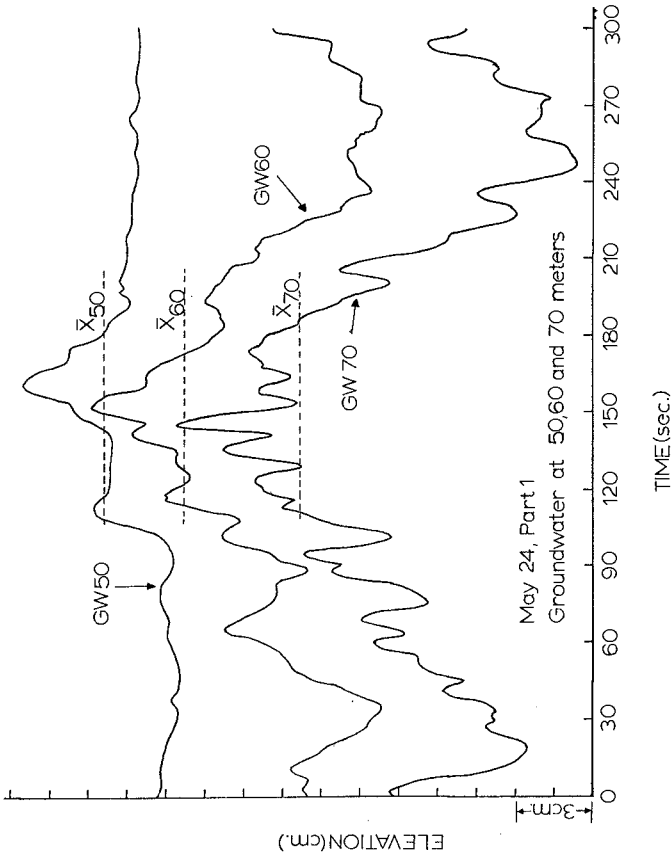


Figure 3. Groundwater oscillations at three beach stations 10 meters apart ($x = 50, 60,$ and 70 meters from baseline). The zero level or origin is shifted for each trace. Note the sequential upslope dominance of low frequency fluctuations. Also note the very slow fluctuation with a period of approximately 200 seconds.

As seen in Figure 4, examination of time-synchronized traces of beach waterlevel and well waterlevel shows that they correspond quite closely. This similarity suggests that possibly the local pressure gradient across the well wall may be the forcing function for the well waterlevel oscillations. Since velocities within the well are very small, especially at lower frequencies, pressure should be approximately hydrostatic. Also, pressure within a solitary wave is very close to hydrostatic (Ippen, 1962). Consequently, the time dependent hydrostatic spatial pressure gradient is probably the responsible forcing mechanism

A simplified model can be generated to explain the response of the beach waterlevel-well waterlevel system (Figure 5). Mass continuity dictates that flow through the well point is equal to the time rate of change of water within the well. Thus,

$$\rho Au = \frac{dQ}{dt} \quad (4)$$

where A = area of openings in the well point, u = spatial mean velocity of flow across the well point, ρ = density of water, Q = storage of water within the well. Storage within the well is given by

$$Q = \rho \pi r^2 h_w \quad (5)$$

where h_w = height of the waterlevel in the well and r = radius of the well and constant. Therefore,

$$Au = \pi r^2 \frac{dh_w}{dt} = \pi r^2 \frac{dh_1}{dt} \quad (6)$$

where h_1 is waterlevel relative to an arbitrary datum since only the time rate of change is being considered and this is independent of datum level. Let

$$u \propto (h_0 - h_1) \quad (7)$$

where h_0 = beach waterlevel and h_1 = well waterlevel, both being measured relative to the same arbitrary datum. Assuming a constant of proportionality K, then Eq. 7 is

$$u = K(h_0 - h_1) \quad (8)$$

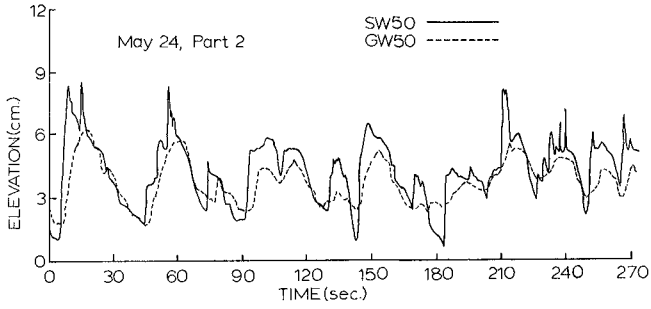


Figure 4. Synchronized beach waterlevel and ground waterlevel traces. The well waterlevels are attenuated relative to the swash fluctuations.

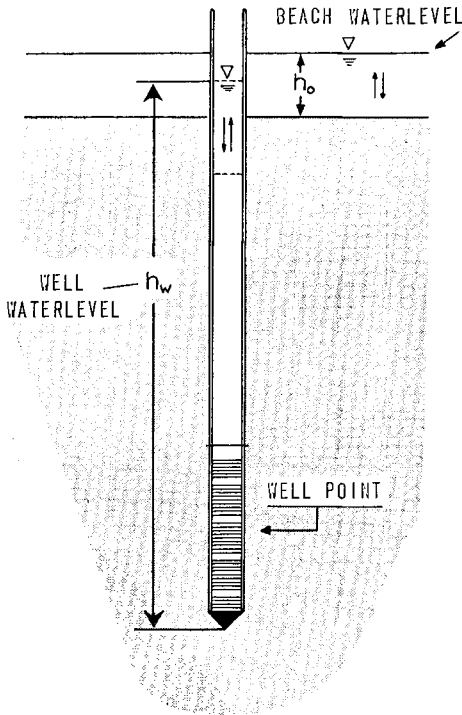


Figure 5. Schematic of groundwater well configuration and associated waterlevels.

Physically, $(h_0 - h_1)$ is the forcing function for the system and is a measure of the hydrostatic pressure gradient across the well point and can be expressed as

$$AK(h_0 - h_1) = \pi r^2 \frac{dh_1}{dt} \quad (9)$$

Let $F = AK$, $D = r$, and let $h_0 = H_b \cos(\omega t)$ where $\omega =$ angular frequency of beach waterlevel changes. Assigning values to h_0 establishes a datum level for h_1 and h_0 . Eq. 9 can be rewritten as

$$\frac{dh_1}{dt} - \frac{F}{D} h_1 = \frac{F}{D} H_b \cos(\omega t) \quad (10)$$

The solution to this equation is

$$h_1(t) = h_1(0) \exp\left(-\frac{F}{D}t\right) + \frac{F^2 H_b}{D^2 \omega^2 + F^2} \cos(\omega t) + \frac{F D \omega H_b}{D^2 \omega^2 + F^2} \sin(\omega t) \quad (11)$$

where $h_1(0) =$ waterlevel in the well at $t = 0$. The first term on the right side of the above equation represents the initial response to excitation of the beach-well system. To examine a well waterlevel response relatively unaffected by the initial well waterlevel, assume $t = t_1$ where t_1 is large so that $h_1(0) \exp\left(-\frac{F}{D} t_1\right) \rightarrow 0$. In the time domain where $t \geq t_1$, Eq. 11 reduces to

$$h_1(t) \doteq \frac{F^2 H_b}{D^2 \omega^2 + F^2} \cos(\omega t) + \frac{F D \omega H_b}{D^2 \omega^2 + F^2} \sin(\omega t) \quad (12)$$

The time derivative of Eq. 12 is evaluated for the first maxima, of $h_1(t)$, following a maximum in $h_0(t)$. This occurs at

$$t = \frac{1}{\omega} \tan^{-1} \left(\frac{D\omega}{F} \right) \quad (13)$$

where $t = \tau =$ lag of the well waterlevel maximum relative to the beach waterlevel maximum.

Given environmental parameters D and F , τ is frequency dependent. In this experiment $D = 45.6$. It remains to determine K , which can be viewed as incorporating a variety of effects generally associated with flow attenuation. For illustration it is assumed that K is a linear function of A , the surface area of the openings in the well point. Obviously, such a relationship would be dependent upon the geometry of the openings, but generally, given a geometry, as surface area increases for a given pressure gradient, the mean velocity would increase. This would be true for small openings where retarding forces due to boundaries of the openings and due to grain boundaries are significant.

$$\begin{array}{ll} \text{If} & K = mA \\ \text{then} & F = mA^2 \end{array} \quad (14)$$

For the present example we assume $F = 4$. Then,

$$\tau = \text{lag} = \frac{1}{w} \tan^{-1} (11.4w) \quad (15)$$

This argument can be reversed to use measured values of τ to calculate an estimate of K which relates velocity to the pressure differential.

Since the driving force for changes in these two waterlevels appears to be a hydrostatic pressure gradient which is a linear operator, it is expected that the systems function (filter function relating these two) will be linear. This means there should be a high coherence between the two signals. This was generally observed, e.g. Figure 6.

Phase lags of surf depth and well waterlevel are anticipated (Figure 4). As seen above, these occur as a direct result of the frequency response function $H(f)$, associated with the porous media and the well point, where

$$H(f) = |H(f)| e^{j\theta(f)} \quad (16)$$

and $\theta(f)$ is the frequency response phase angle and is numerically identical to the cross spectral phase angle, $\alpha(f)$. Thus, for a linear system, τ is a direct result of the amplitude attenuation of the signal by the system.

Figure 7 contains a plot of " τf " as determined from Eq. 15. Additionally, on Figure 7 are plotted some observed values of $\tau(f)$, suggesting that for sinusoidal input signal, Eq. 15 provides a rather accurate prediction of well waterlevel oscillations. Considering: (1) that the observed values of $\alpha(f)$ represent cumulative influence of all input signals at a given frequency and (2) that the input signal in Eq. 10 was strictly sinusoidal, the agreement in Figure 7 is very good.

In some data runs the lack of close agreement between predicted and observed values at higher frequencies may in part result because the

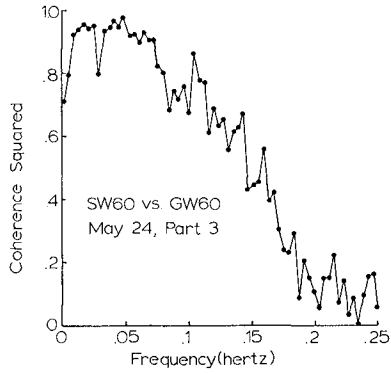


Figure 6. Coherence between waterlevels on the beach surface and in the groundwater wells. Note the coherence remains high at low frequencies ($f < .07$ hz) and decreases at higher frequencies.

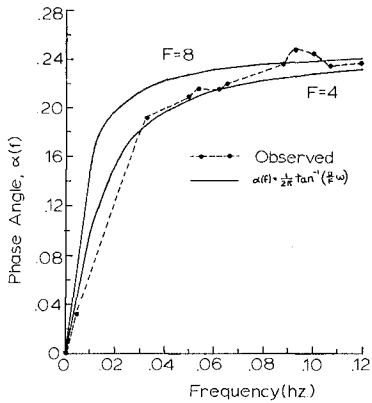


Figure 7. Phase angle or phase lag between the input signal (beach waterlevel) and the output signal (well waterlevel). Plotted are observed values and two examples of predicted phase lags from Eq. 15.

higher frequency signals were not sinusoidal but were more asymmetrical with a steep faced front and a more gradually sloping seaward side.

Specific frequency response functions between beach waterlevel and well waterlevel are, in part, dependent upon the depth of the well point below the beach surface. As suggested by the low pass characteristics of these functions, for a given beach, the deeper the well point, the lower the cut-off frequency of the filter function. Thus, in these experiments, if the well point had been closer to the surface, then the observed well waterlevels would have responded more vigorously to the input waves (i.e., 0.1 hertz).

Figures 8 and 9 are examples of the predicted response of well waterlevel to forcing functions of constant amplitude but having different frequencies. However, two identical wells placed in different locations can have different response characteristics as a result of differences in local sedimentary characteristics. Thus, to be useful in a predictive sense, each well must be "calibrated"; i.e., determine F in Eq. 13. If such a calibration is completed, nearshore wells could be used to identify slopes of oscillating nearshore waterlevels.

Since the flow parameter K is in reality dependent on the character and quantity of sediment above the well point, local changes in nearshore morphology can alter the frequency response function relating input and output signals.

High and low frequency pumping action may have very significant effects on local sediments. The pumping induced by the pressure gradient associated with the migrating bore front could cause dilation of surficial sediments. The depth of this layer would be limited by the frequency dependent amplitude attenuation which results from viscous flow through a porous media. However, low frequency pressure differentials could be transmitted to a much greater depth in the sediment deposit, thus causing flow and possible grain dilation to a much greater depth.

If spatial pressure gradients occur at high and low frequencies, it is possible that a rather thick sedimentary deposit could become fluidized. If this occurred, then such things as local shear strength of sediments could exhibit strong periodic components.

CONCLUSIONS

Waterlevel fluctuations on this low sloping, high tidal range beach exhibited a nonlinear transfer of energy from high to low frequencies. This spatial process appears to have resulted from the impoundment of water which was transferred onshore by bores and finite amplitude waves. Periodically this impounded water mass was released, resulting in low frequency waterlevel oscillations. These low frequency oscillations became increasingly dominant at the more shoreward stations. In some data runs near the mean shoreline these low frequency oscillations completely dominate almost to the exclusion of high frequency fluctuations. Thus, on the

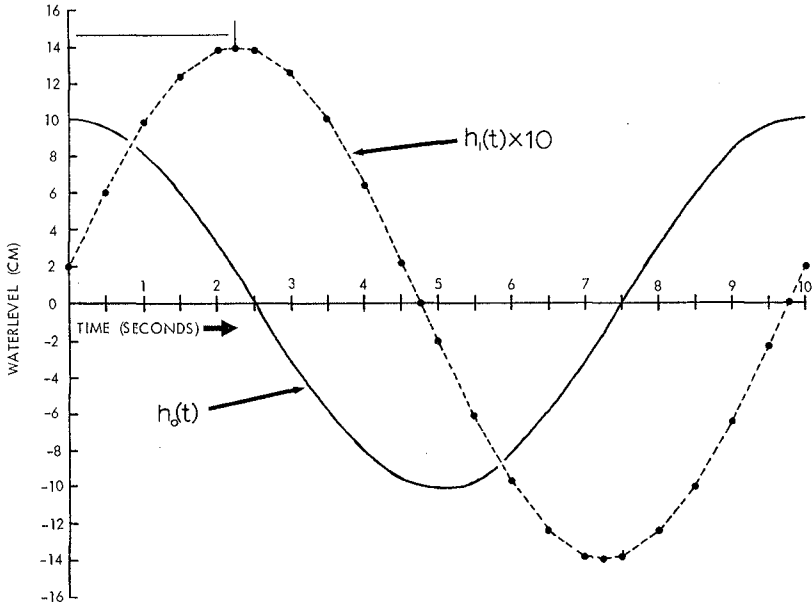


Figure 8. Input and output signals for high frequency ($f=.1$ hz) forcing. Note the low amplitude response to a 10 cm input amplitude.

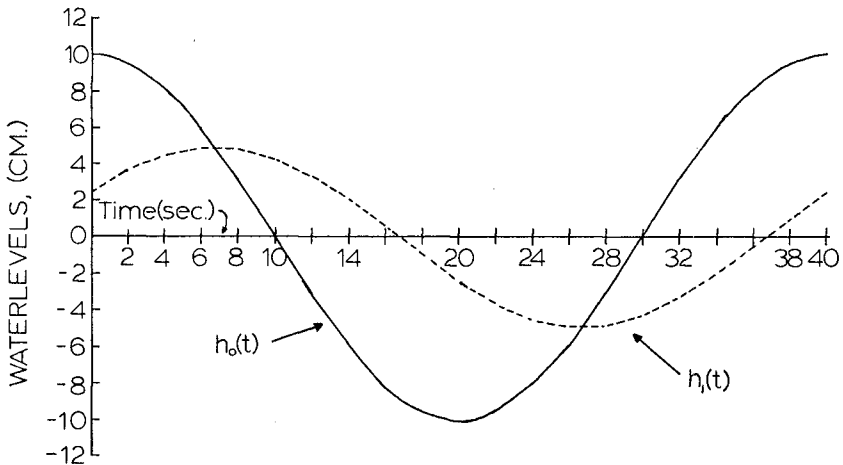


Figure 9. Low frequency response. Compare to Figure 8. Input signal has 10 cm amplitude but response is attenuated much less.

swash slope run-up due to individual bores may not even occur and periodic uprush and backwash may be associated with the low frequency waterlevel oscillations.

Watertable variance was dominated by lower frequency oscillations. This resulted because the beach acted as a low pass filter and the configuration of wells was such that high frequency fluctuations were almost completely attenuated at the depth of the well point. By assuming a form for the groundwater forcing function, it was possible to predict the lag of the groundwater maximum behind the beach waterlevel maximum. The influence of well placement and local sediment permeability and porosity are incorporated in parameters, F, D, which must be empirically determined.

ACKNOWLEDGMENTS

Field data used in this report was taken by personnel from the Coastal Studies Institute of Louisiana State University under the direction of Dr. C. J. Sonu, who is presently with Tekmarine, Inc. Use of these data are gratefully acknowledged as is the financial support of Science Applications, Inc.

REFERENCES

- Ippen, A.T., 1966, Estuary and Coastline Hydrodynamics, McGraw-Hill, New York, 744 p.
- Le Mehaute, B., 1963, On nonsaturated breakers and the wave run-up, Proceedings, VIII Coastal Engineering Conf., pp. 77.
- Waddell, E., 1973, The dynamics of swash and its implication to beach response, Coastal Studies Institute Tech. Rpt. No. 139, 49 p.
- Waddell, E., 1976, Swash-groundwater-beach profile interactions, SEPM Special Publication #24, pp. 115.

CHAPTER 88

LONGSHORE TRANSPORT EVALUATIONS AT A DETACHED BREAKWATER

by

R. O. Bruno¹, R. G. Dean², and C. G. Gable³

ABSTRACT

A field experiment was conducted by the Coastal Engineering Research Center (CERC) to develop correlations between wave characteristics and longshore sediment transport. The waves were measured by two near-bottom mounted pressure transducers and the average longshore sediment transport rates were determined from sequential volumetric surveys behind an offshore breakwater which was regarded as a total trap. The data analyzed herein encompass a period of nine months during which a total accumulation of 675,000 m³ occurred as documented by eight surveys. Spectral analyses of the wave data were conducted and yielded one direction per frequency. The correlations include immersed weight sediment transport rate, I , versus (1) longshore component of wave energy flux at breaking, $P_{\ell S}$, and (2) the onshore flux of the longshore component of wave-induced momentum, S_{xy} . The most widely used correlation constant, K , in the relationship $I = KP_{\ell S}$ is 0.77. The best-fit values found from the data were $K = 0.65$ and 0.92 for linear and log best-fits, respectively, as based on the $P_{\ell S}$ values directed toward the trap. The corresponding values of K_* (dimensional) relating I and S_{xy} are 4.98 m/s and 6.37 m/s, respectively. One feature of this type of trap is the potential for overtrapping if the waves are directed nearly normal to shore.

INTRODUCTION

The need for a quantitative relationship for longshore sediment transport is common to practically all coastal engineering projects. Examples include: channel deepening, design of coastal structures and beach nourishment programs. The most widely used predictor relates longshore sediment transport rate to longshore energy flux at breaking or to some measure of wave-induced momentum flux; these relationships require calibration with field and/or laboratory data. A survey of the available field data demonstrates that of the approximately 56 data points, none are based on both measured wave direction and volumetric accumulations in a total trap. Some are based on visually observed wave directions at a location quite distant from the measured wave heights. In addition, much of the sediment data is based on tracer studies with the attendant uncertainties in estimating depth of effective motion.

¹Chief, Chesapeake Bay Model Branch, Waterways Experiment Station, Stevensville, MD 21666; Formerly at Coastal Engineering Research Center, Fort Belvoir, VA 22060.

²Professor, Department of Civil Engineering and College of Marine Studies, University of Delaware, Newark, DE 19711.

³Associate Development Engineer, Scripps Institution of Oceanography, La Jolla, CA 92093; Formerly at Coastal Engineering Research Center, Fort Belvoir, VA 22060.

The present paper describes the analysis of a subset of the measurements carried out at Channel Islands Harbor by the Coastal Engineering Research Center (CERC) during the period 1974 to 1977. The data analyzed herein include wave height and direction measurements as determined from a pair of near-bottom mounted pressure gages located in a water depth of approximately 6 meters. The sediment "trap" is an off-shore breakwater in approximately 9 meters of water and the west jetty to the entrance to Channel Islands Harbor, see Figure 1. This "trap" is believed to be nearly complete. The volumetric accumulations over a period of nine months are documented by eight surveys, during which a total sediment volume deposition of 675,000 m³ occurred. Correlations are presented of longshore sediment transport as inferred from accumulation in the trap with $P_{\ell S}$, the longshore component of energy flux at breaking and S_{xy} , the flux in the onshore direction of the longshore component of momentum.

BACKGROUND

The relationship between immersed weight transport rate of sediment, I , and longshore energy flux at breaking, $P_{\ell S}$, is generally presented in terms of a non-dimensional constant, K

$$I = KP_{\ell S} \quad (1)$$

where for a single wave train of breaking height, H_b , and breaking direction, θ_b , relative to a normal to the beach, $P_{\ell S}$ can be expressed as

$$P_{\ell S} = \frac{\gamma H_b^2}{8} C_{G_b} \sin \theta_b \cos \theta_b \quad (2)$$

in which γ = specific weight of water and C_{G_b} is the wave group speed at breaking. A more useful form of Eq. (1) is obtained by noting that the immersed weight transport rate, I , and bulk longshore sediment transport, Q_s , are related by

$$Q_s = \frac{I}{\rho \left(\frac{\rho_s}{\rho} - 1 \right) g (1 - p)} \quad (3)$$

in which ρ and ρ_s are the mass densities of water and sediment respectively, g is the gravitational constant and p is the in-place porosity of the sediment. Combining Eqs. (1) and (3)

$$Q_s = \frac{K}{\rho \left(\frac{\rho_s}{\rho} - 1 \right) g (1 - p)} P_{\ell S} \quad (4)$$

It is noted that the above equations for longshore sediment transport do not account for sediment size, beach slope, porosity, etc. and thus it is very unlikely that "K" is a true constant; however, the tests conducted to date have not provided the ranges of independent

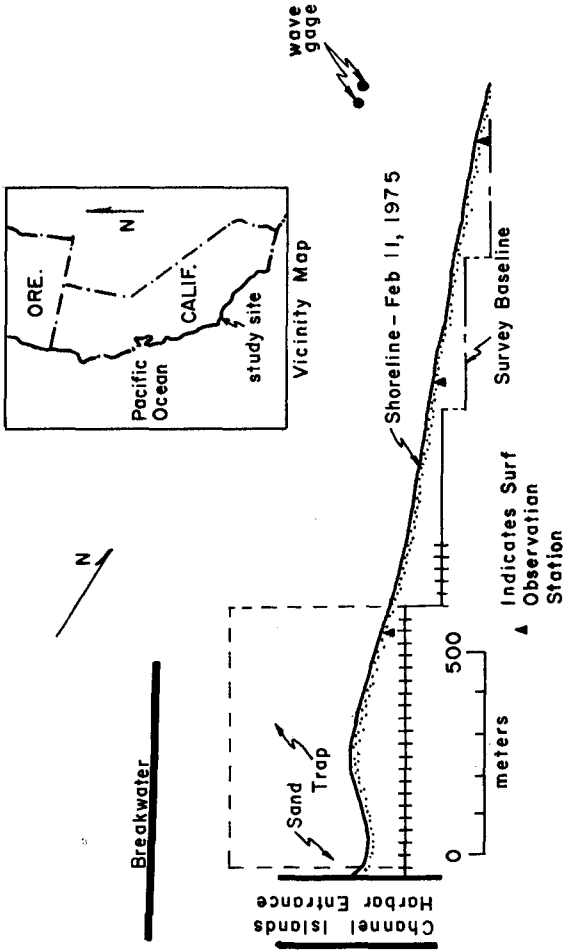


Figure 1. Location Map and Orientation of Field Area.

variables (e.g. sediment size) or accuracy necessary to distinguish the effects of these variables.

A brief review of previous field data is helpful in assessing the currently used relationship. In this review, the laboratory data will be omitted as they do not represent a properly scaled version of the prototype since the scaled sediment size is significantly larger than is usually present with sand-sized particles. The following review is presented in chronological order of the various investigations which have yielded the data. Other reviews have been presented by Das (1971, 1972) and Greer and Madsen (1978).

South Lake Worth Inlet, FL (Watts, 1953)

Longshore transport rates were based on quantities of sand transferred by a permanent sand bypassing plant on the north jetty of South Lake Worth Inlet. The pressure drop of the bypassing pump was correlated with sand discharge by a series of pumping events into a diked disposal area on the downdrift (south) side of the inlet and subsequent surveys of the associated volumes. Thereafter transport rates were inferred from the (calibrated) pressure drop of the pump. The wave characteristics were based on: (a) wave height measurements from a staff gage mounted on the South Lake Worth pier some 16 km north of the inlet, and (b) visual observations of wave direction at the surf line as obtained from a vantage point approximately 6 km north of the inlet. This study yielded four data points with a sediment diameter of approximately 0.4 mm. The average K value is 0.90 with a standard deviation of 0.11.

Anaheim Bay, CA (Caldwell, 1956)

Dredge material from the entrance to Anaheim Bay was placed on the downdrift (southeast) shore and repeated surveys of this area were conducted as the material was transported in a southerly direction. The changes in volume were interpreted as longshore transport rates and the estimates of longshore component of wave energy flux were based on (a) wave staff measurements from the Huntington Beach Pier, some 9 km to the south, and (b) wave directions based on hindcasts and recognition of the sheltering by the offshore islands for waves originating from certain directions. This study provided a total of five data points with a sediment diameter of approximately 0.40 mm. The average K value is 0.76 and the standard deviation is 0.38.

Cape Thompson, AK (Moore and Cole, 1960)

The growth of a spit and the associated waves were observed over a three-hour period. The spit volumes were measured by plane table survey and wave characteristics were based on visual estimates. Only one data point was obtained with a K value of 0.25 for a sediment size of 1.00 mm.

Santa Barbara, CA (Johnson, 1952 and Galvin, 1969)

These data are based on two separate sources. The volumetric data were developed by Johnson (1952) from spit accumulations in the shelter

of the terminus of the Santa Barbara breakwater. The longshore energy values were developed by Galvin (1969) and represent a combination of hindcast wave heights and wave directions selected to result in the maximum longshore energy flux and still be realistic. This data set includes a total of five points with average and standard deviation values for K of 1.60 and 0.70. The sediment size was approximately 0.20 mm.

Silver Strand, CA and El Moreno, Baja California (Komar and Inman, 1970)

These data represent transport over fairly short time intervals as determined from sand tracer measurements and wave energy fluxes derived from an array of wave sensors. Sand transport volumes were usually determined over a fraction of a tidal cycle as the product of the width of the surf zone, the longshore displacement of the center of gravity of the tracer and the thickness of tracer movement. The latter quantity was based on observations of the depth to which a cylindrical "plug" of tracer had been eroded over the observational period and depth of tracer in cores. Values of this depth ranged between 2 and 10.5 cm. These measurements yielded a total of 14 data points and the average and standard deviation values of K for Silver Strand (four data points) where the average sediment size was 0.18 mm are 0.77 and 0.18, respectively. These quantities for El Moreno (10 data points) where the average sediment size was 0.60 mm are 0.82 and 0.27, respectively.

Fernandina Beach, FL (Thornton, 1969)

Mechanical sand traps were placed at discrete locations across the surf zone and used to trap the lower 20 cm of the water column down to and including material in transit on the sand bed. The traps, which were operated from a pier, could be closed and the trapped material pumped up to the pier for measurement. Wave data (height and direction) were based on two wave gages located at the end of the pier. These studies yielded a total of 14 data points with average and standard deviation values for K of 0.048 and 0.027, respectively. The sediment diameter was approximately 0.20 mm.

Channel Islands Harbor, CA (Bruno and Gable, 1976)

These data were based on the same general field program that is the subject of the present paper. The sediment transport rates were inferred from volumetric accumulations behind the Channel Islands Harbor offshore breakwater and the longshore energy flux values were based on Littoral Environmental Observations (LEO). A total of 13 data points resulted with average and standard deviation K values of 1.61 and 1.19, respectively. The sediment size at this site is approximately 0.2 mm.

Discussion

The results presented above comprise a total of 56 data points which are summarized in Table I and presented in Figure 2. It is noted that the Thornton data are significantly lower than the rest and presumably the traps were not effective in collecting the entire sediment transport. Figure 3 represents an attempt to discern any effect of sediment size, D , on the quantity K . If the Thornton data are not con-

TABLE I
SUMMARY OF FIELD DATA AVAILABLE FOR LONGSHORE TRANSPORT CORRELATION AND CHARACTERISTICS OF RESULTING "K" FACTOR

Investigator	Location	Sediment Diameter (mm)	No. of Points	Methods			Characteristics of K			
				Transport	Waves		\bar{K}	σ_K	$\frac{\sigma_K}{\bar{K}} \times 100\%$	
					Height	Direction				
Watts (1953)	South Lake Worth Inlet, FL	0.40	4	Calibrated Bypassing Pump	M	0	0.90	0.11	19%	
Caldwell (1956)	Anaheim, CA	0.40	5	Surveys	M & H	H	0.76	0.38	50%	
Moore & Cole (1960)	Cape Thompson, AK	1.00	1	Measured Spit Growth	0	0	0.25	--	-	
Johnson (1952) & Galvin (1969)	Santa Barbara, CA	0.20	5	Surveys	H	Max.	1.61	0.70	44%	
Komar & Inman (1969)	Silver Strand, CA	0.18	4	Tracers	M	M	0.77	0.1B	23%	
Komar & Inman (1969)	El Morano Baja California	0.60	10	Tracers	M	M	0.82	0.27	33%	
Thornton (1969)	Fernandina Beach, FL	0.20	14	Bed Load Traps	M	M	0.048	0.027	56%	
Bruno & Gable (1966)	Channel Islands Harbor, CA	0.20	13	Offshore Breakwater Trap	0	0	1.61	1.19	74%	

KEY

1. M = Measured, O = Observed, H = Hindcast, Max. = Direction Selected to be Realistic and Yield Maximum Possible Transport.
2. I = K_{I_5} , I = Immersed Weight Transport Rate, I_{I_5} = Longshore Energy Flux of Waves.

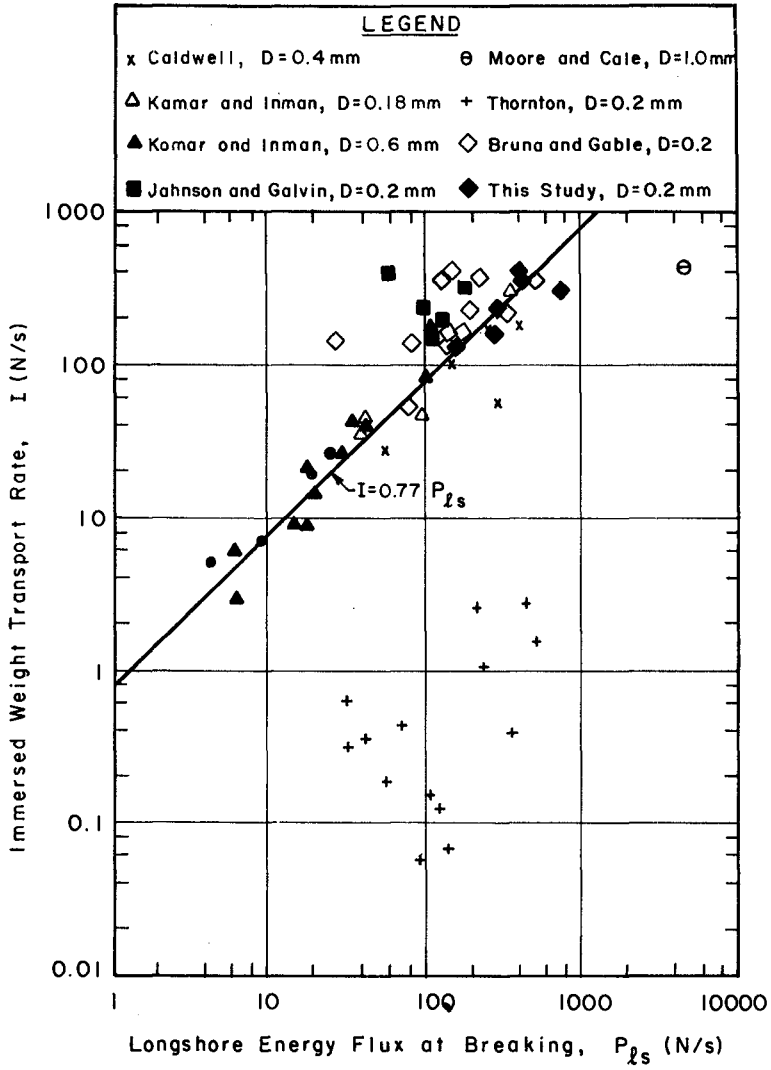


Figure 2, Summary of Field Data I vs. P_{ls} , Including Results of This Study.

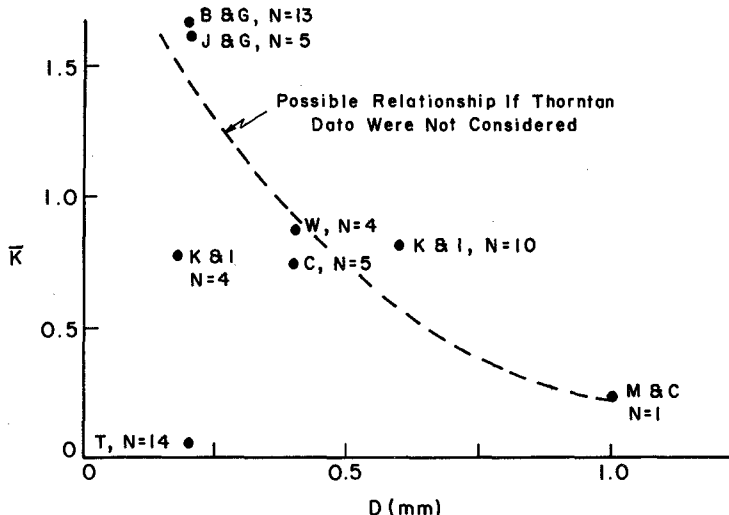


Figure 3. Plot of \bar{K} Versus Diameter, D . Initials and Numbers, N , Refer to Investigators and Number of Data Points Comprising K .

sidered, there is a fairly reasonable relationship of increasing K with decreasing sediment size, although there is only one data point for a sediment size exceeding 0.6 mm.

None of the studies of longshore sediment transport have attempted to present an error analysis of the results. Based on the normalized standard deviations (Table I), the results appear reasonably consistent within each data set, yet there is an enormous difference between the average K values of the various data sets, ranging from 0.05 for the Thornton data to 1.61 for the Bruno and Gable data. This would appear to be indicative of large biases in some of the measurements.

In general, it appears that none of the data sets were developed such that high confidence should be associated with both the wave and sediment volume data. In those studies for which the volumetric data were well-established, the wave data usually included one or more visually estimated wave parameters (height and/or direction). In the reported tracer studies, it is believed that the inferred sediment transport rates represent an overestimate of the actual transport. This expected bias is due to the estimate of the shore-parallel displacement of the center of gravity of tracer displacement being obtained from the upper 5 cm of the sediment column since a shear transport must exist within the sand bed with the upper layers moving most rapidly. Additionally, the use of a single value of thickness of transport based on the depth of erosion of a tracer plug should lead to an upward bias as the maximum erosion depth is expected to increase with time. Finally,

the longshore sediment transport in the surf zone is expected to be both spatially and temporally variable although these scales are presently unknown. Since the tracer studies represent longshore sediment transport over only a portion of a tidal cycle, it is surprising that they do not exhibit greater scatter, i.e. percentage standard deviations of 23% and 33% for the Silver Strand and El Moreno K values respectively. One of the advantages of a relatively long-term, complete sediment trap is that it integrates the temporal and spatial variability, thereby providing a good basis for investigating the mean structure of the transport phenomenon before attempting to measure and understand the fine structure.

The complexity of longshore sediment transport, the uncertainties and differences exhibited in the available data and the economic and functional impact of a valid quantitative predictor of transport certainly justify substantial future field and laboratory investigations.

SITE CHARACTERISTICS

Channel Islands Harbor (CIH) is located some 80 km northwest of Los Angeles, CA. The sediment trap is formed by an offshore breakwater parallel to the shoreline and the western jetty of the entrance to Channel Islands Harbor, see Figure 1. The offshore breakwater is some 700 m in length, is approximately 400 m offshore and is in a water depth of 9 m. The entrance to CIH was dredged in 1960-1961 and since that time the material impounded in the sediment trap has averaged approximately 1,000,000 m³/year. The capacity of the trap is approximately 2,000,000 m³ and usually the material is pumped (on a biennial basis) a distance of some two kilometers to the downdrift side of the entrance to Port Hueneme, CA, although material is occasionally placed in the "pocket beach" formed by the eastern jetty to CIH and the western jetty to the Port Hueneme entrance approximately 1.6 km to the east. An excellent description of the general characteristics of the site is presented by Herron and Harris (1966).

Although the net sediment transport is from northwest to southeast, periods of reversal do occur. The average sediment size at the site is approximately 0.20 mm; the textural characteristics of the material deposited in the trap have been reported by Bruno, Watts and Gable (1977).

One feature of an offshore breakwater is that it will tend to cause an "overtrapping" of material especially during times when the waves approach in a direction nearly perpendicular to the shoreline. This effect can be demonstrated by noting that even for waves propagating directly toward shore, the effects of diffraction will cause deposition in the form of a salient or tombolo behind the breakwater. If this deposited material is removed such that it no longer represents an equilibrium topography, more material will be transported behind the breakwater, etc. Unfortunately, the degree of overtrapping for different wave characteristics is, at present, unknown. A related question arises whether the impounded volumes should be correlated with the net or downdrift component of longshore energy flux. This will be discussed further in the "Analysis" section.

MEASUREMENT PROGRAM

The entire measurement program extended from April 17, 1974 to August 30, 1977. The portion of this program which will be presented in this paper corresponds to the period when two submerged pressure gages were operational and spans the period July 30, 1974 to May 6, 1975.

Wave Measurements

Two total pressure sensors were located near the bottom in a water depth of approximately 6 m. The gages were separated by approximately 23 meters; the geometric characteristics of the gage installations are presented in Figure 4. Pressure records were recorded in digital form approximately every two hours. The records contained 4096 data points at 0.25 sec. each resulting in a record length of 17.07 minutes. The procedure utilized in analyzing the wave records will be presented in a later section.

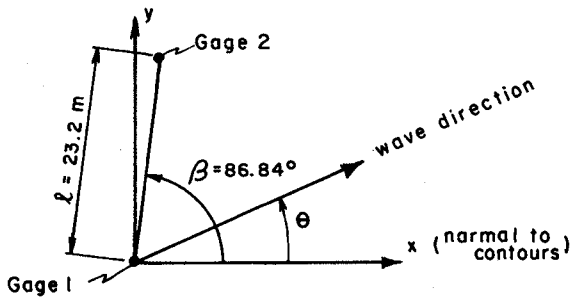


Figure 4. Characteristics of Two-Gage Array at Channel Islands Harbor, CA.

Sediment Volumes

A total of eight surveys were carried out during the period encompassed in this paper. Precision range-range equipment provided horizontal positioning and a standard fathometer was used to establish depths greater than could be obtained by shore-based leveling. The surveys were carried out using a LARC amphibious vehicle, thereby allowing a continuous profile to be obtained from the seaward limit of interest up onto the dry beach. When in water too shallow for the fathometer, a standard surveying rod was held over the side of the LARC and sighted on by a level from shore. This procedure ensured continuity over the entire profile.

The trap extended from the west jetty of the entrance to Channel Islands Harbor to a location 90 meters updrift of the western tip of the

offshore breakwater. In a shore perpendicular direction, the trap extended from the baseline landward of any wave activity, offshore to a distance of 425 meters. Within the trap area, the spacing of survey lines was 30.5 m and further updrift than 250 m from the updrift end of the offshore breakwater, the spacing was increased to 122 m.

ANALYSIS

As noted previously, the wave data consisted of simultaneous records of digitized pressure data from the two sensors located in approximately 6 m of water. In order to calculate $P_{\ell S}$ and S_{xy} at breaking, the following steps were carried out: (1) Calculation of the frequency-by-frequency wave direction and energy at the location of the wave gages; (2) Transformation of the wave spectrum to the breaker line, including shoaling and refraction effects, and (3) Computation of $P_{\ell S}$ and S_{xy} at the surf line. Each of these is described below.

Calculation of Wave Characteristics at Wave Gages

Each of the pressure records consisted of 4096 data points with a time increment of 0.25 sec. The time series were analyzed using a standard Fast Fourier Transform (FFT) program to determine the coefficients. For example, for the pressure time series from Gage 1

$$p_1(t_j) = \sum_{n=0}^{N-1} [a_1(n) - ib_1(n)] e^{-\frac{i2\pi nj}{N}} \quad (5)$$

in which $i = \sqrt{-1}$, and N is the total number of data points (= 4096) for each gage.

The FFT coefficients are defined in terms of the pressure time series as

$$a_1(n) - ib_1(n) = \frac{1}{N} \sum_{j=1}^N p_1(t_j) e^{-\frac{i2\pi nj}{N}} \quad (6)$$

and the $a_1(0)$ term represents the mean of the record. In calculating the FFT coefficients, there is a large number of "windows" or "tapers" that may be employed in an attempt to reduce the adverse effects of spectral leakage which arises due to representing an aperiodic time series by a periodic series (Harris, 1976). These tapers all have the form

$$p'(t_j) = w(j)p(t_j) \quad (7)$$

in which $p(t_j)$ is the measured pressure and $w(j)$ is a weighting factor. A characteristic of these tapers is that they are unity at the midpoint of the time series and decrease to a lesser value near the two ends. In the present analysis, through a number of test calculations, it was determined that although the effect of tapering at an individual frequency could be substantial, the overall effect on $P_{\ell S}$ and S_{xy} was quite small, generally less than 4%. Thus in the present analysis, no taper was employed.

The depth of water, Δh , overlying the pressure sensors is obtained from $a_1(0)$ and $a_2(0)$ as

$$\Delta h = \frac{0.5}{\gamma} [a_1(0) + a_2(0)] \quad (8)$$

in which γ is the specific weight of seawater. The total water depth, h , is the sum of Δh and the distance, S_G , of the pressure sensors above the bottom (0.3 m).

Each FFT pressure coefficient is transformed to a water surface displacement coefficient by the following linear wave theory relationship

$$\{a_n(n), b_n(n)\} = \frac{1}{\gamma K_p(n)} \{a_p(n), b_p(n)\} \quad (9)$$

in which $K_p(n)$ is

$$K_p(n) = \frac{\cosh k_n(S_G)}{\cosh k_n h} \quad (10)$$

In Eq. (10) k_n is the wave number associated with the angular frequency, σ_n as obtained from the linear wave theory dispersion relationship

$$\sigma_n^2 = gk_n \tanh k_n h \quad (11)$$

One of the disadvantages of measuring waves with near-bottom pressure sensors is evident by examining Eqs. (9) and (10). For the higher frequencies (shorter wave periods) K_p is very small resulting in very small pressure fluctuations near the seafloor for the higher frequency waves. Thus, to avoid contaminating the calculated water surface displacement, η , it is usually necessary to apply a high frequency cutoff, above which the pressure contributions are discarded. The proper selection of this high frequency cutoff depends on the signal to noise characteristics of the pressure sensor and signal conditioning system. For purposes of the present analysis, the high frequency cutoff was established at a wave period of 3.1 seconds. For a nominal water depth of 6 meters, and a height of the pressure sensor above the bottom of 0.3 m, the pressure signal is attenuated to approximately 16% of its surface value. In the area of interest, where reasonably long Pacific swell occur, it is probably justified to neglect wave energy for periods shorter than approximately 3 seconds.

Denoting hereafter the FFT coefficients for the water surface displacement as $a(n)$ and $b(n)$, it is noted that the coefficients have the following properties

$$\overline{\eta^2} = \sum_{n=1}^{N-1} [a^2(n) + b^2(n)] \quad (12)$$

$$\left. \begin{aligned} \frac{a_N}{2} + k &= \frac{a_N}{2} - k \\ \frac{b_N}{2} + k &= -\frac{b_N}{2} - k \end{aligned} \right\} \quad (13)$$

and thus

$$\overline{\eta^2} = 2 \sum_{n=1}^{N/2} [a^2(n) + b^2(n)] \quad (14)$$

Thus the total (kinetic plus potential) energy, $E(n)$, associated with a particular frequency component, n , is

$$E(n) = 2\gamma[a^2(n) + b^2(n)] \quad (15)$$

Wave Direction - Consider the definition sketch in Figure 5 and the following representation for $\eta(x,y,t_j)$

$$\begin{aligned} \eta(x,y,t_j) &= \sum_{n=1}^N d(n) e^{\frac{i2\pi nj}{N}} e^{-i(k_x(n) \cos \theta(n) + k_y(n) \sin \theta(n) - \epsilon(n))} \\ &= \sum_{n=1}^N [a(n) - ib(n)] e^{\frac{i2\pi nj}{N}} \end{aligned} \quad (16)$$

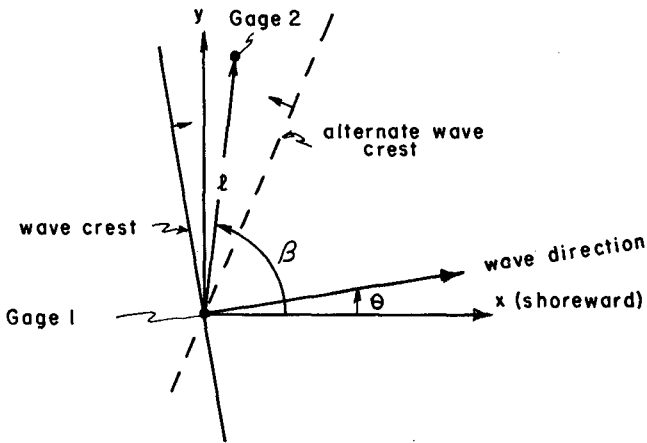


Figure 5. Showing Two-Gage Array Notation and Directional Ambiguity.

Denoting the water surface displacements at the two gage locations as $\eta(x_1, y_1, t)$ and $\eta(x_2, y_2, t)$ and calculating the cross-spectrum, $S_{12}(n)$,

$$S_{12}(n) = \overline{[a_1(n) - ib_1(n)]} [a_2(n) - ib_2(n)] \quad (17)$$

where the overbar denotes the complex conjugate,

$$\begin{aligned} S_{12}(n) &= [a_1(n)a_2(n) + b_1(n)b_2(n)] - i[a_2(n)b_1(n) - a_1(n)b_2(n)] \\ &= c_{12}(n) - iq_{12}(n) \end{aligned} \quad (18)$$

and $c_{12}(n)$ and $q_{12}(n)$ are the "co-spectrum" and "quad-spectrum", respectively of η_1 and η_2 . $S_{12}(n)$ can also be expressed as

$$S_{12}(n) = d^2(n) e^{-i[k(x_2 - x_1)\cos\theta(n) + k(y_2 - y_1)\sin\theta(n)]} \quad (19)$$

and noting from Figure 5 that the separation distance and orientation of a line joining the two gages are denoted by ℓ and β , respectively, $S_{12}(n)$ can be written as

$$\begin{aligned} S_{12}(n) &= d^2(n) e^{-ik_n \ell \cos(\theta(n) - \beta)} \\ &= d^2(n) \cos[k_n \ell \cos(\theta(n) - \beta)] - id^2(n) \sin[k_n \ell \cos(\theta(n) - \beta)] \end{aligned} \quad (20)$$

Comparing Eqs. (18) and (20), it is apparent that the wave direction, $\theta(n)$, relative to the x-axis can be expressed as

$$\theta(n) = \beta \pm \cos^{-1} \left\{ \frac{1}{k_n \ell} \tan^{-1} \left[\frac{q_{12}(n)}{c_{12}(n)} \right] \right\} \quad (21)$$

where the \pm is the result of a directional ambiguity associated with a two-gage array (Figure 5) and is avoided by choosing the minus sign which selects the wave arriving from the seaward half-plane adjacent to a line joining the two gages.

There are two conditions for which it was not possible to calculate the wave directions $\theta(n)$. These include poorly conditioned wave data, presumably due to spectral leakage, and spatial aliasing due to the fairly large separation distance (≈ 23 m) between the two gages. If the data are poorly conditioned for determining wave direction, the absolute value of the quantity within the brackets $\{ \}$ in Eq. (21) may exceed unity, clearly a physically impossible condition since the extreme values of the cosine function are ± 1 . This tended to occur for very long waves for which the energy was small and the value of k_n was also small. The percentage of energy within an individual record for which this condition occurred was relatively small, averaging 2% to 3% with a maximum of approximately 10%. The second condition is related to spatial aliasing

and requires that the wavelength be equal to or greater than twice the projection of the wave gage separation distance in the direction of wave propagation. Referring to Figure 5

$$L > 2\lambda [\cos(\theta - \beta)]_{\max} \quad (22)$$

which indicates that for the least adverse effects of spatial aliasing, the gages should be on an alignment parallel to the dominant orientation of the wave crests. In our case $\beta = 86.8^\circ$ and in general, the waves approach within approximately 40° of the shoreline. For purposes here, a variable aliasing frequency limit was developed for each record depending on the wave directions for the lower frequencies. Three frequency limits were considered, corresponding to $|\theta - \beta|$ values of 45° , 60° and 75° , with the 75° value associated with the highest frequency limit. Selection of the frequency limit required that 90% of the wave energy in a frequency range $\sigma_A/2$ to σ_A lie within the associated wave direction range, where σ_A is the frequency corresponding to the particular aliasing wave direction (Eq. (22)). For the water depth at the site, the three directional limits of 45° , 60° and 75° are associated with approximate wave periods of 5.3, 4.2 and 3.1 seconds, respectively. The percentage of energy associated with periods shorter than 5.3 s. was substantial in our data, amounting to 25-30%. In later calculations of P_{ℓ_S} and S_{xy} , an attempt was made to account for the energy above the aliasing frequency by augmenting the calculated values, illustrated for P_{ℓ_S} as follows, by

$$\left\{ P_{\ell_S} \right\}_{cm} = \left\{ P_{\ell_S} \right\}_c \frac{E_{TOT}}{E} \quad (23)$$

in which the subscripts "c" and "cm" indicate calculated and calculated modified respectively. E_{TOT} and E represent the total wave energy values and the energy below the spatial aliasing frequency. In a sense, this modification is equivalent to associating the effective direction as determined from the frequencies not affected by the aliasing consideration or poorly conditioned data to all the wave energy.

Transformation of Wave Spectrum to Breaker Line

Determination of Breaking Depth - At this stage, the wave energy and wave direction in the vicinity of the gages are determined. These values are then transformed to the breaker line accounting for shoaling and refraction.

To determine a breaking depth, a method suggested by T. L. Walton was employed in which the total onshore flux of wave energy was equated at the gages and at the breaker line with the requirement that the root-mean-square breaking wave height H_{rms} be related to the water depth by

$$\left(H_{rms} \right)_b = \kappa h_b \quad (24)$$

in which κ was taken as the usual spilling breaker value of 0.78. The total onshore energy flux, F_R , at the reference (gage) location is

$$F_R = 2\gamma \sum_{n=1}^{N/2} [a^2(n) + b^2(n)] C_{G_n} \cos \theta_n \quad (25)$$

in which the subscript "R" denotes the reference location. Considering shallow water conditions for breaking $C_{G_n} = C_G = \sqrt{gh_b}$ and $\cos \theta_b \approx 1.0$, the onshore energy flux at breaking is

$$F_b = \frac{\gamma H_b^2}{8} \sqrt{gh_b} = \frac{\gamma \kappa^2}{8} \sqrt{g} h_b^{2.5} \quad (26)$$

Equating F_R and F_b

$$h_b = \left[\frac{16 \sum_{n=1}^{N/2} [a^2(n) + b^2(n)] C_{G_n} \cos \theta_n}{\kappa^2 \sqrt{g}} \right]^{0.4} \quad (27)$$

It is worthwhile to note that neglecting wave refraction in the breaking depth determination does not result in very large errors. For example for a wave direction at the gages of 30° , the error in breaking depth would be less than 6%. For a more realistic overall wave direction of 20° , the associated error in breaking depth is less than 3%.

Transformation of Wave Components to Shore - With the breaking depth known, each wave component is transformed to shore accounting for both wave refraction and shoaling based on linear wave theory.

Wave refraction was computed in accordance with Snell's Law and the assumption that straight and parallel contours existed between the gage and breaking locations,

$$\theta_b(n) = \sin^{-1} \left[\frac{C_b(n)}{C_R(n)} \sin \theta_R(n) \right] \quad (28)$$

Shoaling was based on linear theory, resulting in the value of the sums of the squared FFT coefficients at the breaker line of

$$[a^2(n) + b^2(n)]_b = \frac{\cos \theta_R(n)}{\cos \theta_b(n)} \frac{(C_G(n))_R}{(C_G(n))_b} [a^2(n) + b^2(n)]_R \quad (29)$$

in which the first and second ratios on the right-hand side of the equation represent the effects of refraction and shoaling, respectively.

Computation of $P_{\ell S}$ and S_{xy} at the Surf Line

With the wave energy and direction known at the breaker line, the values of longshore component of wave energy flux, $P_{\ell S}$, and flux in the onshore direction of the longshore component of momentum, S_{xy} , are readily determined.

$$P_{\ell S} = G \left\{ 2\gamma \sum_{n=1}^{N/2} [a^2(n) + b^2(n)]_b \left(\frac{C_G(n)}{C(n)} \right)_b (\cos \theta(n) \sin \theta(n))_b \right\} \quad (30)$$

$$S_{XY} = G \left\{ 2\gamma \sum_{n=1}^{N/2} [a^2(n) + b^2(n)]_b \left(\frac{C_G(n)}{C(n)} \right)_b (\cos \theta(n) \sin \theta(n))_b \right\} \quad (31)$$

where the factor G is given by the ratio

$$G = \frac{E_{TOT}}{E} \quad (32)$$

as defined in and discussed in relation to Eq. (23).

It is worthwhile to comment on possible errors due to determination of the breaking depth, h_b . Under the condition of straight and parallel bottom contours as considered here, the value of S_{XY} at the gage and breaker line locations are identical. Since S_{XY} is independent of depth there is no associated error in this estimate and comparison of Eqs. (30) and (31) shows that $P_{\ell S}$ and S_{XY} differ only by the celerity, C_b , at the breaking depth. It follows that if breaking occurs under shallow water conditions (generally a good assumption), the associated error in $P_{\ell S}$ is proportional to the square root of the ratio of the respective water depths. For example, if the breaking water depth is overestimated by 20%, then the associated $P_{\ell S}$ value would be too large by 9.5%.

Determination of Gage and Shoreline Orientations

In the calculation of directional wave properties relative to the shoreline, it is extremely important to establish the orientation of the wave gage array and a representative shoreline orientation.

Orientation of Wave Gages - During the original study, the locations of the wave gages had been established by measuring angles with transits from two known shore stations on the project baseline. These angles were then translated into gage locations through standard geometric procedures. Two sets of such measurements had been carried out on June 24 and 26, 1974. The resulting gage characteristics are presented in Table II.

Although the gage separation distances as obtained from the two surveys differ somewhat more than desired, it is the gage orientations differing by 3.6° that is of particular concern. Thus on June 7, 1980, these variables were reestablished using range-range microwave equipment. Measurements were obtained from three combinations of shore-based locations, thus allowing a much better determination of gage orientation. These results are also presented in Table II and the averages of all values were adopted for purposes of this study.

TABLE II
GEOMETRIC CHARACTERISTICS OF TWO-GAGE ARRAY

Date	Gage Separation Distance	Gage Orientation With Respect to Baseline
June 24, 1974	23.55 m	10.81°
June 26, 1974	22.71 m	14.44°
June 7, 1980		
Trial 1	23.8 m	15.81°
Trial 2	23.2 m	12.74°
Trial 3	22.6 m	12.36°
Values Adopted For This Study	23.2 m	13.23°

Effective Shoreline Orientation - The determination of effective shoreline orientation proved to be a somewhat more difficult problem at this site than originally anticipated. One difficulty is that dredging and subsequent filling by longshore sediment transport in the impoundment area caused local anomalies in the bottom contours such that they were not quite straight and parallel. In particular, following a dredging event, the nearshore contours move landward more than the seaward contours. It is believed that this is an expression of the concentration of the longshore sediment transport in the nearshore zone.

The shoreline orientation was established by plotting and overlaying profiles located in the vicinity of the wave gages. The relative landward-seaward locations of the profiles were adjusted in the overlays to obtain best agreement by eye and the associated orientation determined. A range of orientations was obtained by matching the nearshore and offshore portions of the profiles. These ranges were qualitatively consistent with those determined from aerial photography, with the larger angles associated with the more seaward portions of the profiles.

TABLE III
SHORELINE ORIENTATION AS DETERMINED FROM BEACH AND OFFSHORE PROFILES

Date of Survey	Range of Effective Shoreline Orientation Relative to Baseline
May 8, 1974	9.95° to 11.33°
June 18, 1974	8.83° to 10.78°
Value Adopted In This Study	10.07°

Correlation of I with $P_{\ell S}$ and S_{xy}

In the correlation of $P_{\ell S}$ and S_{xy} with I, only the values directed toward the trap were used. The rationale is that during all periods when waves were directed toward the trap, there was sediment available for transport and therefore this variable provides the best basis for correlation.

The volumetric accumulations were interpreted as I values by Eq. (3) using $p = 0.35$ and by dividing by the time (in seconds) between surveys. The wave data were available nominally every two hours. The value of $P_{\ell S}$ (and S_{xy}) for a survey period was obtained by summing all $P_{\ell S}$ values directed toward the trap and dividing by the total number of wave recordings.

RESULTS

Table IV presents a summary of the analyzed data. A number of correlations were carried out to determine best fits of the transport data, I, with $P_{\ell S}$ and S_{xy} . These results are summarized in Table V.

TABLE IV
SUMMARY OF ANALYZED DATA

Survey Period	I (N/s)	$P_{\ell S_-}$ (N/s)	$P_{\ell S_+}$ (N/s)	S_{xy_-} (N/m)	S_{xy_+} (N/m)
July 30, 1974 to Aug. 20, 1974	182.1	120.3	49.9	22.3	10.3
Aug. 20, 1974 to Sept. 24, 1974	144.6	153.5	46.2	26.4	8.6
Sept. 24, 1974 to Nov. 6, 1974	171.2	295.8	158.2	39.2	25.6
Nov. 6, 1974 to Jan. 7, 1975	439.3	426.8	80.9	57.7	10.7
Jan. 7, 1975 to Feb. 11, 1975	401.4	446.6	0.0	57.0	0.2
Feb. 11, 1975 to March 4, 1975	245.8	330.9	144.5	45.7	17.5
March 4, 1975 to April 14, 1975	326.2	783.8	30.0	100.0	6.9

Note: $P_{\ell S_-}$ and S_{xy_-} represent fluxes toward the trap and

$P_{\ell S_+}$ and S_{xy_+} represent fluxes away from the trap.

TABLE V
 SUMMARY OF CORRELATIONS OF I WITH $P_{\ell S}$ AND S_{xy}
 ($P_{\ell S}$ and S_{xy} Are Values Directed Toward Trap)

Basis for Correlation	Coefficient	Percentage Standard Deviation in K or K_*
Least Squares Fit, Arithmetic Basis, $I = KP_{\ell S}$	$K = 0.65$	
Least Squares Fit, Logarithmic Basis, $I = KP_{\ell S}$	$K = 0.92$	
Individual Points $I = KP_{\ell S}$	$\bar{K} = 0.87$	39.6%
Least Squares Fit, Arithmetic Basis, $I = K_* S_{xy}$	$K_* = 4.98 \text{ (m/s)}$	
Least Squares Fit, Logarithmic Basis, $I = K_* S_{xy}$	$K_* = 6.37 \text{ (m/s)}$	
Individual Points $I = K_* S_{xy}$	$\bar{K}_* = 5.90 \text{ (m/s)}$	33.3%

Figure 6 presents a plot of the seven data points in the form of I vs. $P_{\ell S}$ where the energy flux value is directed toward the trap. In addition, a sensitivity analysis has been performed in which the horizontal bars represent the variation in $P_{\ell S}$ due to a $\pm 0.5^\circ$ variation in orientation of the offshore pressure gages. The vertical bars represent the variation in I due to a uniform variation in sand elevation of ± 5 cm over the area surveyed. The different bar lengths occur in $P_{\ell S}$ due to various effective wave approach angles and in I due to various volumes accumulated between surveys. It appears from Figure 6 that there is a low energy flux upward bias due to the tendency of the trap to collect material even for waves propagating directly toward shore.

SUMMARY AND CONCLUSIONS

Measurements of immersed sediment transport rate, I, as inferred from sediment accumulation in a near-total trap were correlated with longshore energy flux at breaking, $P_{\ell S}$, and the onshore flux of the longshore component of momentum, S_{xy} , as calculated from two pressure sensors mounted near the bottom.

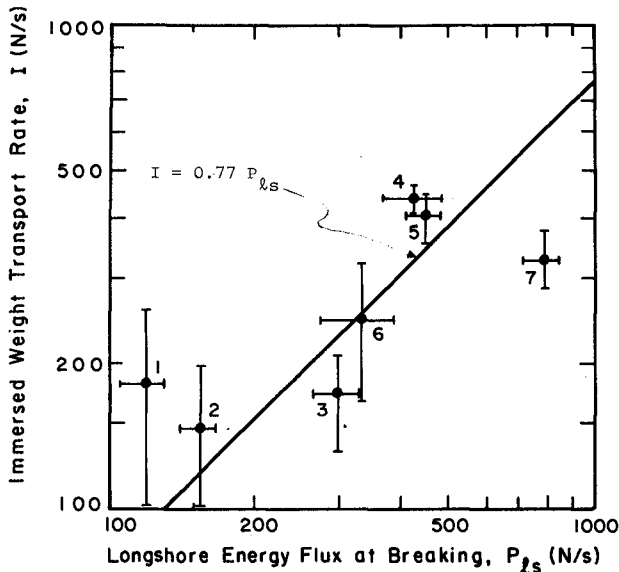


Figure 6. Plot of I vs. P_{ℓ_S} Results From Present Study. Horizontal Bars Represent $\pm 0.5^\circ$ in Offshore Gage Orientation. Vertical Bars Represent ± 5 cm Uniform Thickness of Sand. The Numbers Denote the Sequence of Intersurvey Periods.

Based on the analysis of seven volumetric accumulation periods, it is concluded that:

- (1) On an overall basis, the results agree reasonably well with some of the previous studies. Depending on the method of analysis, the best fit dimensionless constant K in the relationship $I = KP_{\ell_S}$ ranges from 0.65 to 0.92,
- (2) For the same seven intersurvey periods, the K values obtained here are substantially lower than those obtained by Bruno and Gable (1976) as based on visual wave estimates. Their average K value is 1.40 as compared to 0.87 obtained here.
- (3) A pair of wave gages appears to perform reasonably well to determine overall directional characteristics such as P_{ℓ_S} ; however, the quality of the detailed directional results could be improved substantially by a greater number of gages.
- (4) In calculating wave direction from an array of gages, it is extremely important to determine accurately the relative locations of the gages and the shoreline orientation. For

the present data, an angular misalignment of $\pm 0.5^\circ$ can cause an associated change in P_{gS} ranging from 8% to 18%. This effect is accentuated for small obliquity of the incident waves.

- (5) An offshore breakwater, if dredged below the equilibrium topography is expected to cause an upward bias in the volumes trapped. This effect appears present in the data; the points associated with small longshore energy flux values lie above the usual relationship. Moreover, there is a tendency for the individual K values to decrease as the trap fills (Figure 6). Unfortunately, at present, the magnitude of the bias exerted by an offshore breakwater on trapped quantities and the variation of this bias following a dredging event is unquantified. The best approach in the present case may be through the use of a detailed numerical model. It is expected that the K results developed in the present study contain an upward bias.
- (6) There are variations in the K values that cannot be explained through appeal to any evident mechanisms or processes. For example, the K value associated with the last (seventh) intersurvey period is approximately one-half the average of the values for the fourth and fifth intersurvey periods.
- (7) The environmental and economic significance of an improved quantitative predictor for longshore sediment transport justifies substantial future field programs to discern the effects of individual variables (e.g. grain size, beach slope, etc.) and in general, to develop a more accurate predictor.

ACKNOWLEDGEMENTS

The approval of the Coastal Engineering Research Center (CERC) to utilize the data forming the basis for this paper is appreciated. Dr. T. L. Walton of CERC offered helpful discussions and encouragement throughout the study. The Computing Center of the University of Delaware provided support for the required computer time.

REFERENCES

Bruno, R. O. and C. G. Gable, "Longshore Transport at a Total Littoral Barrier," Proceedings, Fifteenth International Conference on Coastal Engineering, Chapter 71, p. 1203-1222, 1976.

Bruno, R. O., Watts, G. M. and C. G. Gable, "Sediments Impounded by an Offshore Breakwater," Proceedings, ASCE Specialty Conference, Coastal Sediments '77, Charleston, SC, p. 1006-1025, 1977.

Caldwell, J. W., "Wave Action and Sand Movement Near Anaheim Bay, California," U. S. Army Beach Erosion Board Technical Memorandum No. 68, 1956.

- Das, M. M., "Longshore Sediment Transport Rates: A Compilation of Data," U. S. Army Coastal Engineering Research Center Miscellaneous Paper No. 1-71, September, 1971.
- Das, M. M., "Suspended Sediment and Longshore Sediment Transport Review," Chapter 54, Proceedings, Thirteenth Conference on Coastal Engineering, p. 1027-1048, 1972.
- Galvin, C. J., "Comparison of Johnson's Littoral Drift Data for Santa Barbara with the Empirical Relation of CERC TR 4," Memorandum for Record, Coastal Engineering Research Center, February 1969.
- Greer, M. N. and O. S. Madsen, "Longshore Sediment Transport Data: A Review," Chapter 93, Proceedings, Sixteenth Conference on Coastal Engineering, p. 1563-1576, 1978.
- Harris, F. J., "Windows, Harmonic Analysis, and the Discrete Fourier Transform," Report NUC TP 532, Naval Undersea Center, San Diego, CA, September 1976.
- Herron, W. J. and R. L. Harris, "Littoral Bypassing and Beach Restoration in the Vicinity of Port Hueneme, California," Proceedings, Tenth Conference on Coastal Engineering, ASCE, Chapter 38, pp. 651-675, 1966.
- Inman, D. L. and R. A. Bagnold, "Littoral Processes," in The Sea, Edited by M. N. Hill, Volume 3, Interscience, p. 529-533, 1963.
- Johnson, J. W., "Sand Transport by Littoral Currents," Institute of Engineering Research, Wave Research Laboratory, University of California at Berkeley, Technical Report Series 3, Issue 338, 1952.
- Komar, P. D. and D. L. Inman, "Longshore Sand Transport on Beaches," J. Geophys. Res., Volume 75, No. 30, p. 5914-5927, October 20, 1970.
- Komar, P. D., "The Mechanics of Sand Transport on Beaches," J. of Geophys. Res., Volume 76, No. 3, p. 713-721, January 20, 1971.
- Moore, G. W. and J. Y. Cole, "Coastal Processes in the Vicinity of Cape Thompson, Alaska; Geologic Investigations in Support of Project Chariot in the Vicinity of Cape Thompson, Northwestern Alaska - Preliminary Report," U. S. Geological Survey Trace Elements Investigations Report 753, 1960.
- Thornton, E. B., "Longshore Currents and Sediment Transport," Department of Coastal and Oceanographic Engineering, University of Florida, Technical Report No. 5, 1969.
- U. S. Army Corps of Engineers, Coastal Engineering Research Center, "Shore Protection, Planning and Design, Technical Report No. 4," 1966.
- U. S. Army Corps of Engineers, Coastal Engineering Research Center, "Volume I, Shore Protection Manual," U. S. Government Printing Office, 1973.
- Watts, G. M., "A Study of Sand Movement at South Lake Worth Inlet, Florida," U. S. Army Beach Erosion Board Technical Memorandum No. 42; 1953.

MIGRATION OF LONGSHORE BARS

by

Hans H. DETTE

1)

ABSTRACT

It is known that nearshore areas occupied by longshore bars constitute a zone of active migration of bottom deposit due to agitation by breaking waves and wave-induced on-/offshore currents and longshore currents. So far there is still a lack of actual data from the field itself concerning the magnitude and variability of single parameters involved in the stability and migration of longshore bar features.

This paper summarizes data collected from a comprehensive field study in the years from 1976 to 1979 when grain size distributions were obtained from a narrow grid of core samples and repeated soundings and continuous measurements of waves and wave-induced currents were carried out. With regard to the characteristics of different longshore bar feature relationships e. g. in between bottom gradients and mean grain sizes are analyzed. Furthermore distinct types of topographic response within the submarine belt occupied by longshore bars depending upon the variable intensity and position of breaking waves and the resulting magnitude and variability of wave-induced currents are pointed out and presented for discussion as a contribution towards a general understanding of longshore bar characteristics and changes.

1. Introduction

Sand bars extending mostly parallel to the shoreline are generally known as longshore bars. They are characteristic features of sandy beaches all over the world. Although varying considerably in size and form longshore bars belong to one of two general types; one type is predominant on non-tidal beaches and the other on beaches with a considerable tidal range.

1) Dr.-Ing. Div. of Hydrodyn. and Coastal Eng., Technical Univ. of Braunschweig, Germany

Longshore bars common to tidal seas are mostly fully developed and mainly located several hundred meters distant from the shoreline at the breaking position of large plunging breakers (see e. g. DETTE, 1980). Earlier it was proposed by KING and WILLIAMS, 1949) that this type of longshore bar might be referred to as "ridge and runnel" beach in order to distinguish this feature from that type of longshore bars predominant in non-tidal seas which should be referred to as "barred beaches".

Longshore bars in non-tidal seas occupy a definite belt on the submarine slope which KING and WILLIAMS (1949) defined as the nearshore area lying in between the waterline and the two-fathom line (approx. MSL - 3.5 m). Beach gradient figures since then mostly refer to that zone.

The belt covered by longshore bars usually extends over a third to a half of the total width of the submarine slope. ZENKOVICH (1967) concluded from extensive field observations in the Anapa region of the Black Sea that the lateral movement of material is fairly intensive in the bar zone. In regions in which longshore bars are well developed there may be up to four, five, or even six of them. Most frequently, however, there will be two, or even only one, which will be fairly close to the shore in relation to the total width of the nearshore area.

So far very few quantitative data are available on the relationships between wave action and topographic response of longshore bars. This study carried out in the non-tidal western part of the Baltic Sea (Kiel Bight) is an analysis of:

1. Grain size distribution obtained from core samples taken in a narrow grid within the area of investigation (12 kilometers in length and more than 1 kilometer distant from the shoreline)
2. Repeated soundings and beach levellings in the area of investigation
3. Longterm measurements of waves and wave-induced on-offshore and longshore currents at different points

within a selected submarine profile which is considered to be characteristic for the area of investigation

The data revealed two distinct types of topographic response within the belt occupied by longshore bars.

1. Changes that involve only shifting of the bed material in on-/offshore direction because, due to normal water levels, the breaker position of the highest breakers is located at the seaward slope of the outer bar. Only small waves ($H < 1.0$ m) pass over the bars and cause only weak longshore currents which in relation to the present grain size are not able to displace considerable amounts of material alongshore.
2. Changes that involve besides on-/offshore shifting major alongshore displacement of material. This process is connected with storm surge conditions occurring with a return period of approx. 5 years. During such events due to wind set-up, the still water level is increased by more than 1.5 m. Lasting sometimes for more than 100 hours the breaking position of the large breakers is shifted landward into the longshore bar belt. According to the water level increase higher waves pass over the bars and bring higher wave energy loads to corresponding points in the submarine profile compared to wave energy loads occurring with normal water levels. Due to the higher "breaking loose forces" (BRUUN, 1966) the longshore currents in response are increased considerably above the boundary values known for the initiation of sediment motion alongshore.

2. Presentation of data

2.1 About the study site

The field studies concerning the wave energy dissipation and magnitude of wave-induced currents as the impact forces and the topographical con-

figuration of the submarine slope as the response factor were carried out in the Kiel Bight (Fig. 1) located in the western part of the Baltic Sea which can be regarded as an enclosed sea in which waves are generated locally and have only little space in which to disperse before reaching a shoreline. The result of intermittent storm wave action typical for enclosed seas is a more or less distinct system of longshore bars because swell does not occur in order to sweep the bars back to shore. The longshore transport is almost completely confined to the surf zone which necessarily is wider than the surf zone on an oceanographic coast averaged throughout the year (SILVESTER, 1974).

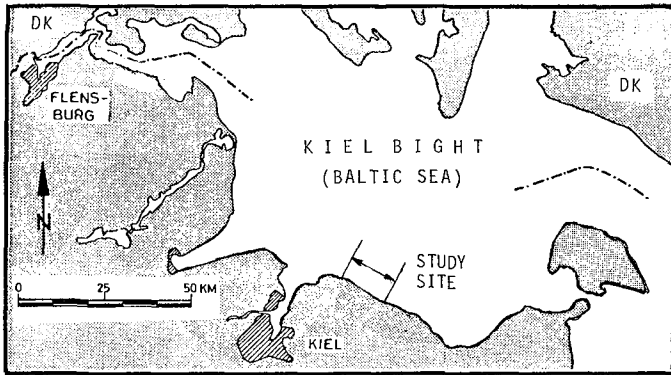


Figure 1: Location of the study site

Like in other enclosed seas, storm waves within the Baltic Sea are occurring mostly from a fairly narrow sector (DETTE and STEPHAN, 1979) so that a resultant vector applicable to any point on the coast can be derived and a predominant uni-directional alongshore transport can be assumed.

Figure 2 shows in more details the area of investigation which can be regarded as a physiographic unit consisting of an eroding feeder cliff which lies approx. 5 kilometers south-east of point 11 marked on the shoreline and an area of accretion located south-west of point 3. The zone between point 11 and point 3 can be considered as the transition area concerning alongshore transport.

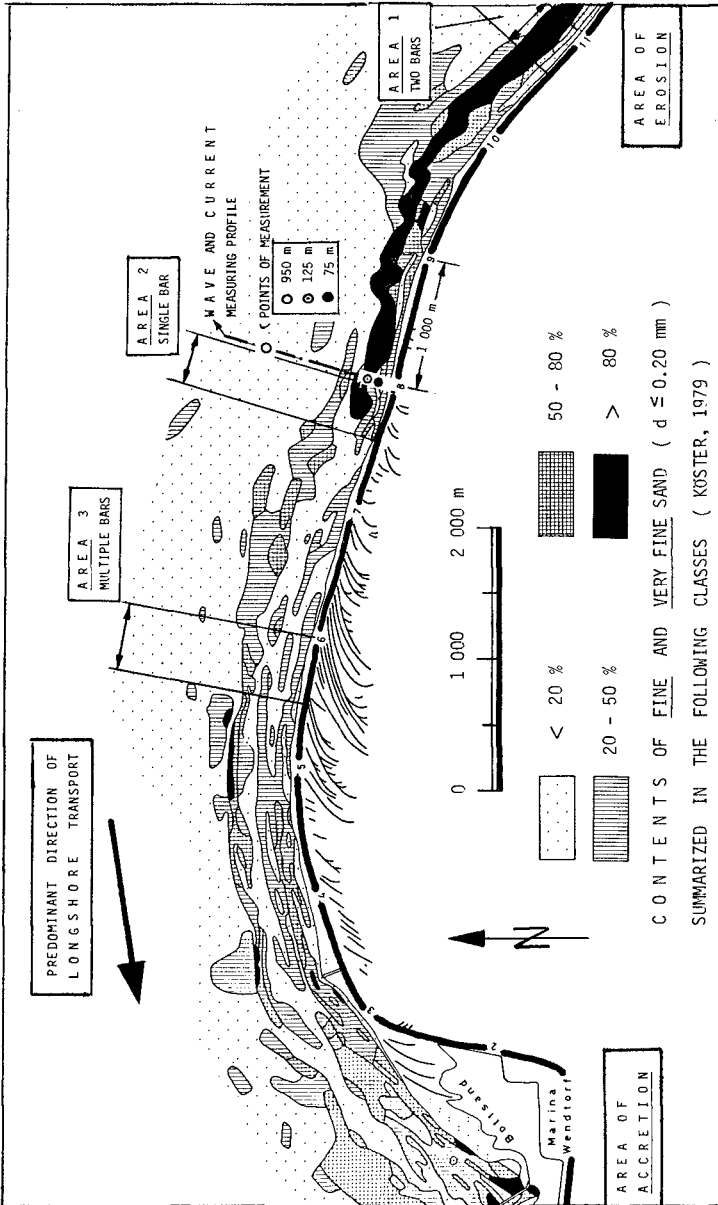


Figure 2: Plan view of the study site with indication of selected study sections (Area 1 to 3) and points of wave and current measurements in the nearshore zone (Position 75 m, 125 m, and 950 m)

In the study area storm waves approach from the sector North-East causing a predominant longshore transport in Western direction.

2.2 Characteristics of longshore bar features in relation to the grain size distribution

Within the study site, which can be considered as a physiographical unit of beach section, a system of different longshore bar features exists, lying generally upon silty clay and sometimes above troughs filled up in recent times. The bars consist of ridges with heights up to more than 1.0 m, widths of several meters and in length they sometimes extend over miles.

The topography of the submarine zone within the study site can be described by mean profiles which are found in Area 1, 2, and 3 (Fig. 2) and correlated with grain size distributions which have been analyzed by KÜSTER, 1979. In Figure 3 three different longshore bar features typical for this area are shown.

Within the eastern part of the study site represented by the mean profiles found in Area 1 and Area 2 (Fig. 2) where the sand transported alongshore is originating from a nearby cliff, mainly one or two bars can be detected. They are located fairly close to the shore in relation to the total width of the nearshore zone.

The inner bar here predominately consists of sand with maximum grain sizes between 0.18 mm to 0.25 mm (fine sand). The outer bar in this area, however, has maximum grain sizes below 0.18 mm (very fine to fine sand). In the troughs, however, coarser sediments are found.

In Area 2 (Fig. 2) a 'geological boundary' is obvious. This was detected by KÜSTER (1979) after plotting the band of sediment distribution containing more than 80 percent of grain sizes between 0.06 mm and 0.20 mm (Fig. 2). This band is connected with that part of the study site where one or two bars have been found to be the typical features.

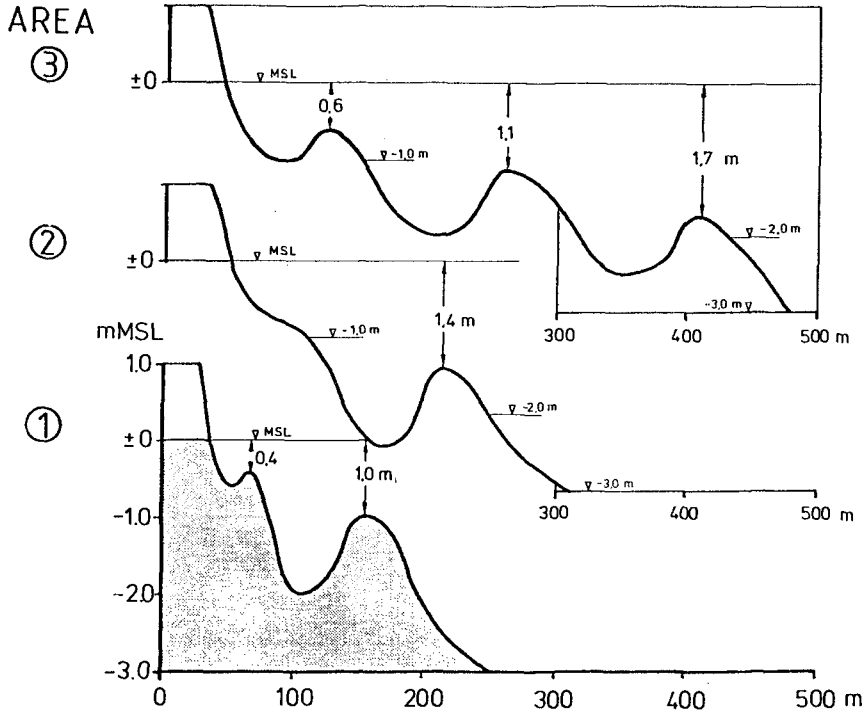


Figure 3: Mean longshore bar configurations within the study site
(Area 1, 2, 3 - see Fig. 2)

Towards the west from this boundary, that is in the direction of predominant longshore transport, a splitting-up of the longshore bar system into a multiple bar system takes place as is shown by the representative mean submarine profile for Area 3 (Fig. 2) in Fig. 3.

The bar pattern in the total study site furthermore can be evaluated from Fig. 2 by considering the areas representing contents of fine sand (0.06 mm to 0.20 mm) between 20 to 50 percent.

A typical phenomenon of the western study site is a considerable increase of the longshore bar belt in width compared with that in the Eastern part. This feature is directly related to an increase in grain size within the longshore bar belt up to a maximum between 0.25 mm and 0.35 mm which means medium sand without fine particles whereas grain sizes below 0.18 mm can be considered to be representative for the bar belt in the Eastern site.

Additionally to the investigations of fine and very fine contents of sand ($d \leq 0.20$ mm), KÜSTER (1979) analyzed the distribution of mean grain sizes (d_{50}) in different classes between $d < 0.18$ mm und $d > 0.5$ mm. Fig. 4 shows part of the results for the areas 2 and 3 which are representative of the two different longshore bar features; the crest positions of the single bars in Area 2 and 3 are marked for the purpose of orientation.

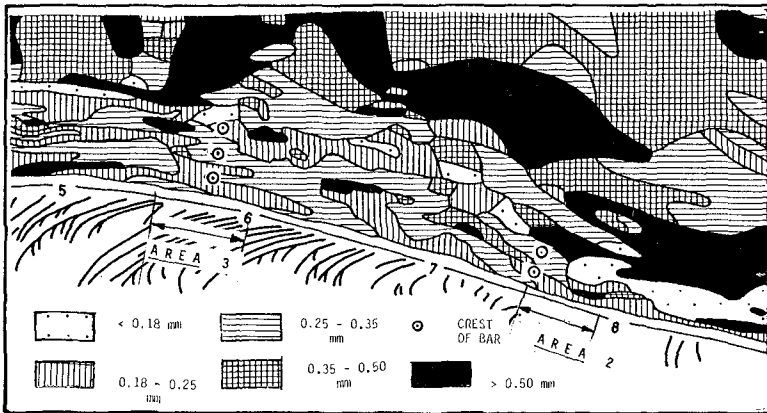


Figure 4: Distribution of mean grain sizes (d_{50}) summarized in five classes by KÜSTER (1979)

With regard to relations between longshore bar characteristics and grain size distributions within the study, the most important parameters are compiled in Table 1. From the results it can be concluded that a longshore bar system is characterized by a narrow range of materials and bottom gradients.

Table 1: Compilation of longshore bar characteristics and grain size distribution within the study site

		Area (see Fig. 2 and 3)		
		1	2	3
Bottom	A **)	1 : 75	1 : 90	1 : 150
Gradient	B ***)	1 : 110	1 : 125	1 : 220
Distance of outer bar from MSL		110 m	220 m	370 m
Crest height of outer below MSL		- 1.0 m	- 1.4 m	- 1.7 m
Mean grain size at outer bar		< 0.18 mm	< 0.18 mm	0.25 - 0.35 mm

**) Bottom gradient between MSL and MSL - 3 m

***) Bottom gradient between MSL and crest of the outer bar

The bottom gradients can be expected in the range between 1 to 50 and 1 to 200 (between MSL and the seaward boundary of the nearshore belt). When the gradient is slight, the number of bars increases. The bottom gradients are in turn connected with the nature of material. Longshore bars rarely will be found in areas where the mean size of the sand particles is greater than $d_{50} = 0.5$ mm and hardly ever found when particle sizes are smaller than $d_{50} = 0.1$ mm.

These findings are in good agreement with the investigations carried out in the Black Sea (ZENKOVICH, 1967).

2.3 Incoming waves and wave-induced currents in the nearshore zone

For the western part of the Baltic Sea within the Kiel Bight (Fig. 1) two typical storm conditions occurring intermittently were found out during the longterm field measurements:

1. Storm winds without causing considerable wind set-up (below + 1.0 m MSL)
 - Wind speeds: 20 to 30 knots
 - Wind direction: E to NE
 - Wind duration: Hours up to several days
 - Wave heights: $H_{\max} < 3.0$ m
 - Wave periods: $T_m = 3.0$ to 5.0 secs
 - Return period: 5 to 10 times per year

2. Storm winds causing storm surge conditions with considerable wind set-up (above + 1.5 m MSL)
 - Wind speeds: 30 to 50 knots
 - Wind direction: E to NE
 - Wind duration: Up to several days
 - Wave heights: $H_{\max} = 3.0$ m to 4.0 m
 - Wave periods: $T_m = 4.0$ to 5.5 secs
 - Return period: Once in 5 to 10 years

The time history of a storm surge event which lasted for more than 100 hours from December 28th, 1978 up to January 1st, 1979 is plotted as an example (Fig. 5). Measurements of wind and wave conditions were carried out during that event at intervals of 2 hours.

Storm events lasting for more than 100 hours but blowing with minor wind speeds and thus causing only negligible wave set-up also occurred during the period of measurements and were recorded.

For the two distinct events mentioned above, two representative records of wave heights and wave-induced on-/offshore currents and longshore currents measured at two locations within the surf zone are presented.

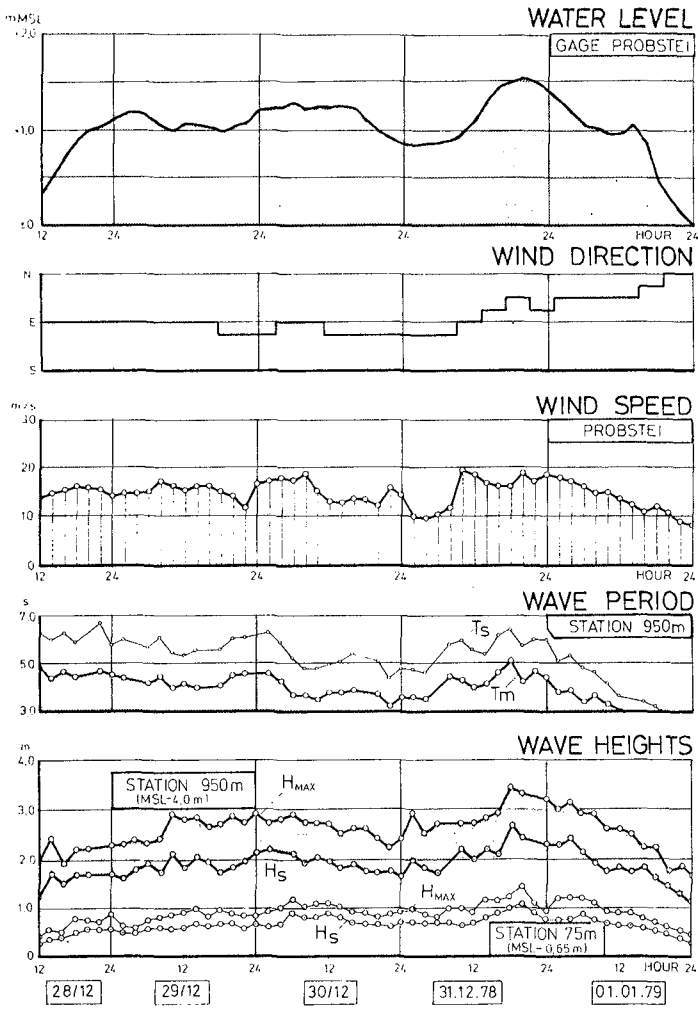


Figure 5: Time history of a storm surge event with wave set-up to +1.5 m MSL with regard to water level, wind, and wave conditions

Figure 6 is an example of storm winds causing negligible wave set-up and Figure 7 is an example of a storm surge event with wave set-up of 1.5 m above MSL.

By comparing Fig. 6 and 7, the location and width of the surf during both events appear to be more or less identical. The incoming waves break at identical locations of the submarine profile, but, are very much different because the water level increases up to 1.5 m above MSL and approx. 1.0 m higher breakers occur during storm surge conditions in comparison to the normal storm conditions.

The consequences of the large breakers and set-up are demonstrated by the rapid increase in the mean longshore velocities as well as the peak velocity components during a 10 minute record. During normal conditions (Fig. 6), the mean longshore current velocities are below $\bar{V}_L = 0.3$ m/sec which can be considered as the boundary value for the initiation alongshore transport of sediments found within the study site. Due to the higher breakers during storm surge conditions (Fig. 7) the mean longshore current velocities are increased considerably and reach mean velocities up to $\bar{V}_L = 0.8$ m/sec; accordingly a large alongshore flux of sediments can be assumed.

The changing and shifting of the longshore bar characteristics during periods without wave set-up (= normal conditions) and after a storm surge event with a return period of 5 to 10 years is demonstrated by comparing echo-sounded submarine profiles at distances of 100 m within Area 3 (Fig. 2). The erosions and accretions are plotted in Figure 8 (left side for a period without wave set-up and right side for a period with wave set-up over + 1.0 m MSL at a total of more than 100 hours).

3. Discussion

It is obvious that there exists a close relationship between the special longshore features, which may consist of one bar or multiple bars, and the grain size distribution.

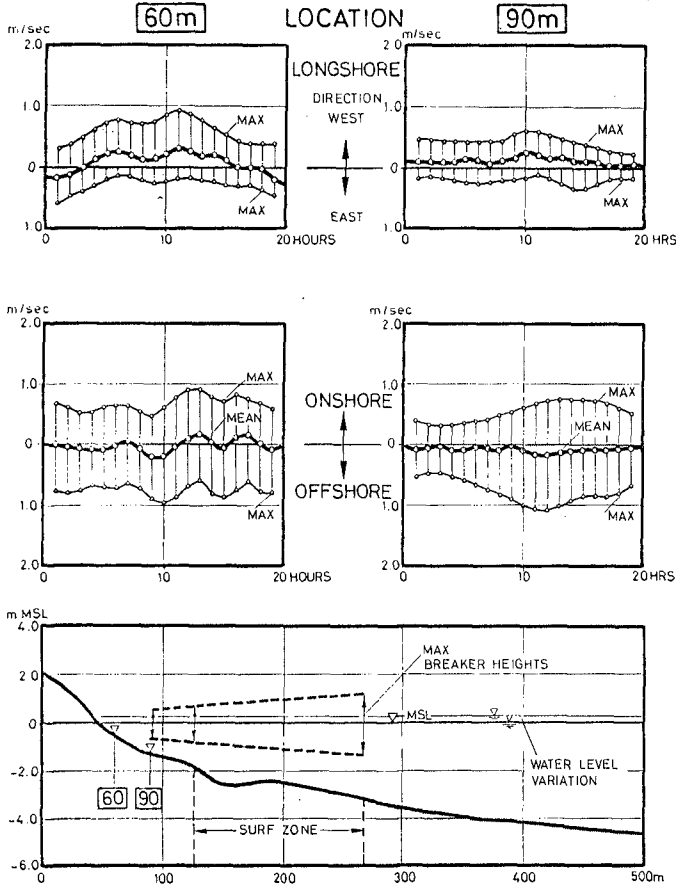


Figure 6: Location of the surf zone, envelope of max. breaker heights and wave-induced currents during normal storm winds causing negligible wave set-up

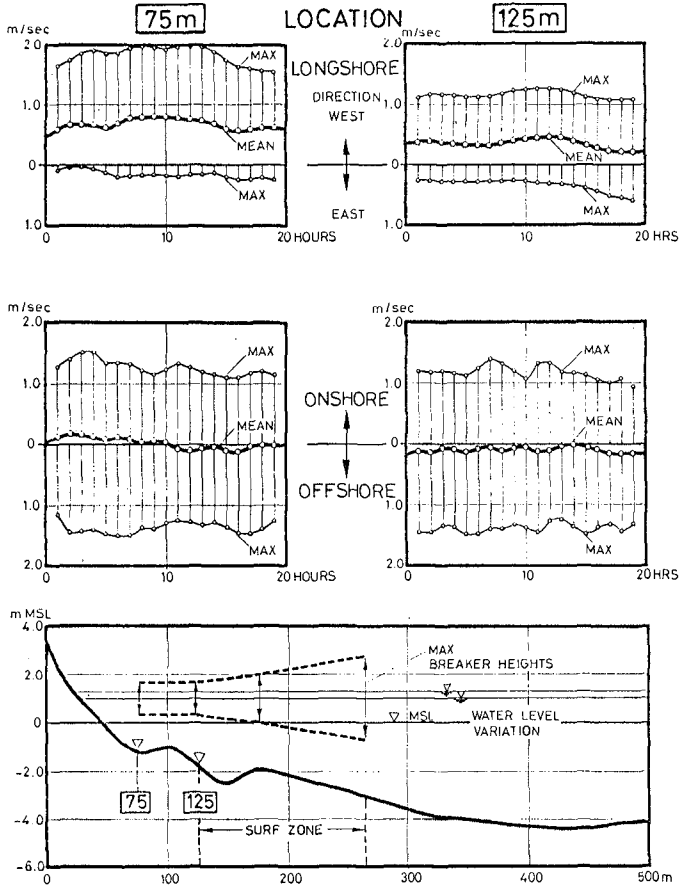


Figure 7: Location of the surf zone, envelope of max. breaker heights and wave-induced currents during storm surge conditions with a wave set-up of 1.5 m above MSL (see Fig. 5, measurements starting at 08.00 HOURS DEC. 29, 1978)

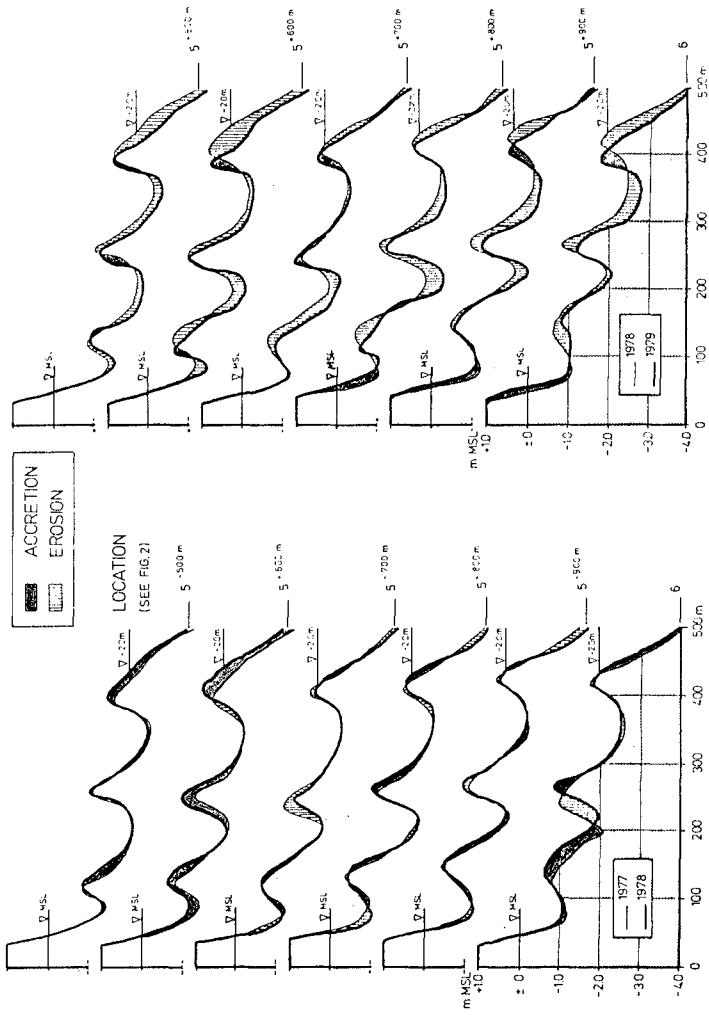


Figure 8: Changes and shiftings of the longshore bar characteristics after periods with normal storm conditions only (left side) and with storm surge conditions (right side)

With regard to the interactions of breaking waves and wave-induced currents, it can be concluded from the field study that the primary, or initial, effect on longshore bar formation and deformation is the breaking wave energy which causes the more intense on-/offshore oscillatory currents and greater magnitude and variability of longshore currents. Further investigations are necessary in order to study in more detail for example the different wave-induced currents in the vicinity of a bar trough or the bar crest. The present paper is thought as a contribution towards the collection of reliable data from the field itself as input data for further theoretical treatment of the problems.

4. Acknowledgements

The author wishes to express his thanks to the "AMT FÜR LANO- UND WASSERWIRTSCHAFT KIEL" which enabled the comprehensive field investigation programme and to Professor Köster from Kiel University who kindly placed at disposal his investigations concerning the sediment distribution within the study site.

5. References

- | | | |
|---------------------------------|------|---|
| BRUUN, P. | 1966 | Longshore currents in one and multi-bar profiles relation to littoral drift
Proceedings 10th Conference on Coastal Eng.,
Chapter 15, Tokyo, Japan, 1966 |
| OETTE, H. H. | 1980 | Migration of Longshore bars
Abstracts, 17th Intern. Conference on Coastal Engl,
Sydney, Australia, 1980 |
| DETTE, H. H.
STEPHAN, H.-J. | 1979 | Über den Seegang und Seegangswirkungen im Küstenvorfeld der Ostsee
Mitt. des Leichtweiss-Inst. der Techn. Univ. Braunschweig, Heft 65, 1979 |
| KING, C.A.M.
WILLIAMS, W. W. | 1949 | The formation and movement of sand bars by wave action
Geographical Journal, CXII, 1949 |

- KÖSTER, R. 1979 Die Sedimente im Küstengebiet der Probstei
- Ein Beitrag zu Sedimenthaushalt und Dynamik von
Strand, Sandriffen und Abrasionsfläche
Mitt. des Leichtweiss-Inst. der Techn. Univ. Braun-
schweig, Heft 65, 1979
- SILVESTER, R. 1974 Coastal Engineering
Vol. I and II, Elsevier Scientific Publishing
Company, Amsterdam, London, New York, 1974
- ZENKOVICH, V.P. 1967 Processes of Coastal Development
Oliver and Boyd, Edinburgh and London, 1967

CHAPTER 90

A PHASED-DREDGING PROGRAM FOR SANTA CRUZ HARBOR

By James R. Walker¹ and Peter J. Williams²

SUMMARY

This project was undertaken to define the littoral processes and resultant shoaling mechanisms at the Santa Cruz Harbor California, entrance channel and to develop and evaluate alternative methods of mitigating the shoaling effects. Since November 1963, when the construction of the entrance channel was finished, the channel has shoaled such that it was almost completely closed during the winter months. The study involved analysis of shoaling mechanisms and contour changes and review of past dredging procedures. Sixteen structural and non-structural alternatives for mitigation of shoaling were analyzed. A phased-dredging procedure was developed and tested over 3 winter seasons. The concept was to dredge the channel periodically each winter while shoaling occurs, thereby keeping the Harbor open to navigation most of the time. The experience gained at this site may be of benefit to others in solving a shoaling problem or in designing a new small-craft harbor.

INTRODUCTION

History

Santa Cruz Harbor, shown in figures 1 and 2, is located on the northern coast of Monterey Bay, about 65 miles south of San Francisco and 14 miles north of Moss Landing. Construction of the Harbor was authorized in 1958³. The authorized improvements included two rubble mound jetties, an entrance (outer) channel, an inner channel, a turning basin, and a sand-bypassing plant. The Harbor, figure 3, was created by dredging a 20-foot-deep channel, connecting a lagoon to the Ocean. The channel and Harbor are protected by two jetties that extend about 900 feet seaward of the beach that existed prior to the project. The jetties are 400 feet apart and the updrift (west) jetty is doglegged. The Harbor provides berthing facilities for 1,000 boats. Construction of the Harbor was initiated in February 1962 and the project was completed in November 1963, with the exception of the sand-bypassing plant which was deferred until the littoral-transport rate could be more accurately determined.

¹Senior Coastal Engineer, Ph.D., PE., M.ASCE, Moffatt & Nichol, Engineers, Long Beach, California

²Coastal Engineer, M.S., A.M. ASCE, P.R.C. Harris, Inc., Lake Success, New York.

³The River and Harbor Act of 1958, House Document No. 357, 85th Congress, 2nd Session.

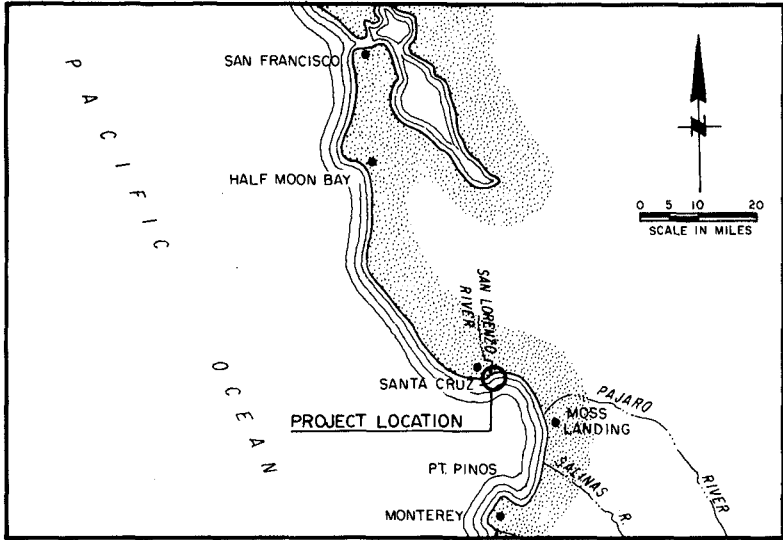


FIGURE 1: LOCATION MAP

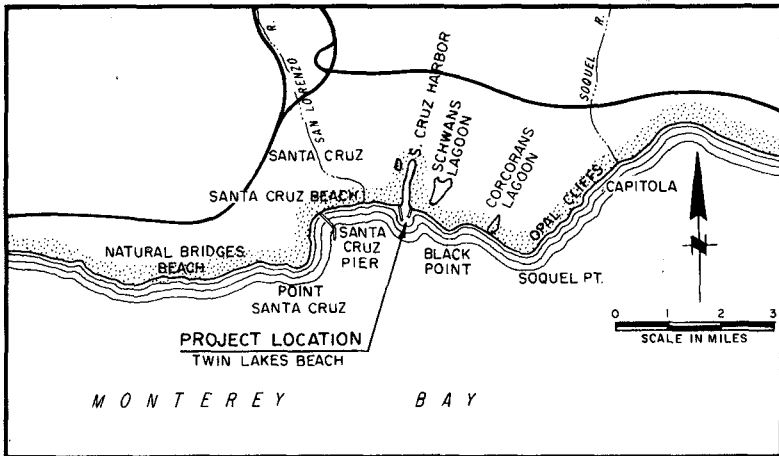


FIGURE 2: VICINITY MAP

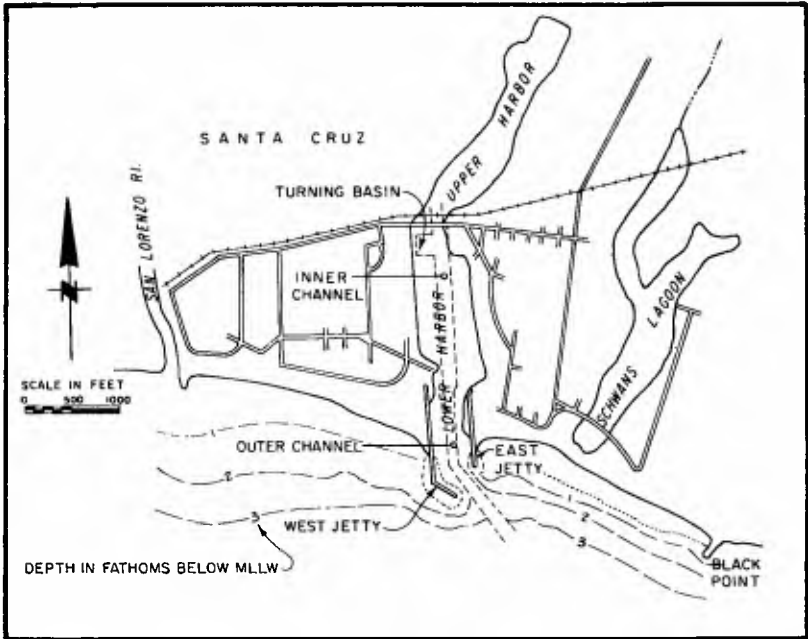


FIGURE 3: PROJECT FEATURES



PHOTO 1: SANTA CRUZ HARBOR IN SHOALED CONDITION

The entrance channel began to shoal in 1965 and navigation was severely impaired by a dangerous shoal, shown in photograph 1, for 4 months during each winter. Annual maintenance dredging on the order of 100,000 cubic yards per year had been required in the spring of each year from 1965 until 1977, when a multiyear, dredging program was implemented to maintain the channel during the winter season. In addition to the maintenance dredging, an experimental jet-pump bypassing system was installed in 1976 by the Waterways Experiment Station (WES) to field-test this new equipment. This eductor field test was terminated in March 1978.

Purpose and Scope

This study was conducted in 1977 to develop both short-term and long-term solutions to the shoaling problem with the short-term solution to suffice for the next few years. The objective was to define the littoral transport and shoaling mechanisms, with the view of developing a reliable engineering solution from existing data. This approach differs considerably from that of Seymour, et al. (1980), who were concerned with correlating potential littoral transport rates (predicted by analysis of results of a wave-gage array) with quantities of material dredged.

Physiography

The shoreline region lying northwest of Santa Cruz comprises sea cliffs and small pocket beaches, which occur mostly at the mouths of small creeks. Wave-induced erosion of the sea cliffs is a possible source of littoral drift at Santa Cruz. Near the Ocean, the steep-gradient streams originating in the Santa Cruz Mountain Range have small drainage areas and their flows are characterized by flash floods. The San Lorenzo River, 0.5 miles west of Santa Cruz Harbor, has a relatively small drainage basin of 137 square miles and an annual runoff of 125,000 acre-feet. The heaviest runoff occurs during the winter months, October through April. Estimates U.S. Army Corps of Engineers (1974) indicate that the annual sediment discharge of the San Lorenzo River is between 88,000 and 133,000 cubic yards. Of this total, 20 percent, or 18,000 to 27,000 cubic yards had sand sizes similar to those found on beaches in the study area. Yancey (1968) also determined, by studying minerals of the River basin and beaches, that the San Lorenzo River is not a primary contributor of beach sand.

Grain-size distributions for beach sediments indicate a medium-to-fine sand with sediments shoaled in the navigation channel being slightly finer than the sand found in the splash zone. The beach slope is 1 on 15 flattening to 1 on 20 toward the 20-foot depth contour, where it flattens to a very gentle slope. Most beach erosion and accretion has occurred shoreward of the 20-foot contour.

LITTORAL-TRANSPORT ANALYSIS

Wave-energy-flux calculations were made to estimate the potential for wave-induced littoral transport. Data from the wave gages described by Seymour (1980) were not available. Furthermore, a longer period of record was required to estimate long-term averages. Therefore, several sources of wave hindcasting and observation data were analyzed to compose a composite description of the wave climate.

The waves arriving at Santa Cruz can be divided into three categories according to origin: Northern Hemisphere swell, Southern Hemisphere swell, and seas generated by local winds. The landmass geometry of Monterey Bay and the bathymetry off Santa Cruz allow swell to approach from the east clockwise through west-northwest.

Most of the wave energy reaching Santa Cruz is from Northern Hemisphere swell generated primarily by extratropical cyclones in the Northern Pacific. These cyclones are most prevalent and intense during the winter and spring seasons, generating waves from the northwest that refract around Point Santa Cruz and have heights of up to 20 feet and periods ranging from 8 to 16 seconds. The National Marine Consultants (1960) 3 year hindcasts, modified by refraction and shoaling, were used for description of Northern Hemisphere swell.

Swells generated by storms in the Southern Hemisphere occurs from May through October, but are most common during August and September. Typical Southern Hemisphere swell has wave heights between 1 and 3 feet and wave periods ranging from 13 to 21 seconds. These waves approach Santa Cruz from the south through southwest. The Marine Advisors (1960) description of the Southern Hemisphere swell was used.

Locally generated seas at Santa Cruz are most severe from December through February. Predominant winds are from the northwest and north. Locally generated seas were described using the National Marine Consultants (1960) data set for waves from the south-southeast to west and were hindcast using the Summary of Synoptic Meteorological Observations (1976) (SSMO) wind rose for fetches exposed to the east and southeast.

Monthly variations of the longshore energy flux plotted in figure 4 were calculated for shoreline of various alignments by transforming the waves to their breaking position. The local seas and the Northern Hemisphere swell are the dominant factors during the winter between December and May. February has the most active contribution of wave-energy flux and the greatest longshore component of energy flux.

The longshore littoral-transport rate was estimated by applying an empirical factor to the longshore component of energy flux (P_{1s}):

$$Q = 7.5 \times 10^3 P_{1s}$$

where Q is the longshore transport rate in cubic yards per year and P_{1s} is the longshore component of energy flux in foot-pounds per second per foot.

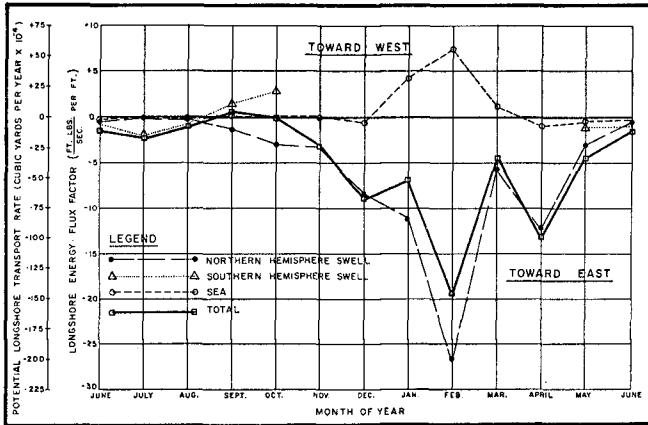


FIGURE 4: DISTRIBUTION OF MONTHLY POTENTIAL ENERGY-FLUX FACTOR

The variation of the potential longshore transport rate by month is also presented in figure 4. The potential net littoral-transport rate was estimated to be 488,000 cubic yards per year to the east. Approximately 80 percent of this transport occurs during the winter, between December and April. The Northern Hemisphere swell causes primarily an unidirectional eastward transport. During January, February, and March the local seas tend to cause a mild westward transport an order of magnitude less than the eastward transport.

CHANNEL SHOALING

The shoaling patterns of the entrance channel have been documented by monthly hydrographic surveys. Figure 5 shows a typical monthly progression of the 10-foot depth contour into the navigation channel during the winter season. Figure 6 shows a section of the channel between the heads of the two jetties. The patterns developed in similar fashion each year, with a tip shoal developing and then extending from the head of the west jetty across the channel toward the head of the east jetty. By January, the 10-foot depth contour had closed across the channel and the beach on the east side had receded. The influx of material into the channel during the winter appears to result primarily from sand bypassing the head of the sand-saturated west jetty. This is discussed in the following paragraph.

A fillet accreted west of the west jetty after the jetty was constructed in 1962. Figure 7, shows the advance of the shoreline at two range lines west of the west jetty. By 1965, the west jetty had trapped a fillet which extended the shoreline to 400 feet seaward of the preproject beach. The jetty was not long enough to trap additional material; therefore, in 1965, significant quantities of material bypassed the west jetty.

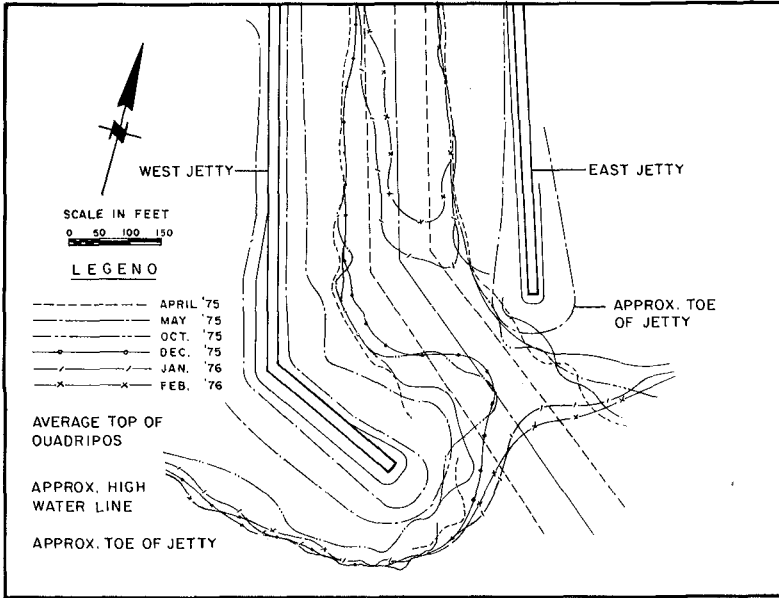


FIGURE 5: EVOLUTION OF CHANNEL SHOALING, 10 FT. CONTOUR

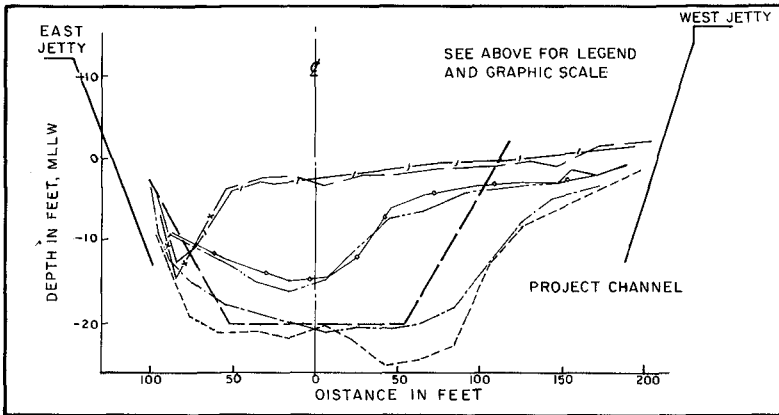


FIGURE 6: CROSS-SECTION BETWEEN HEADS OF JETTIES SHOWING SHOALING

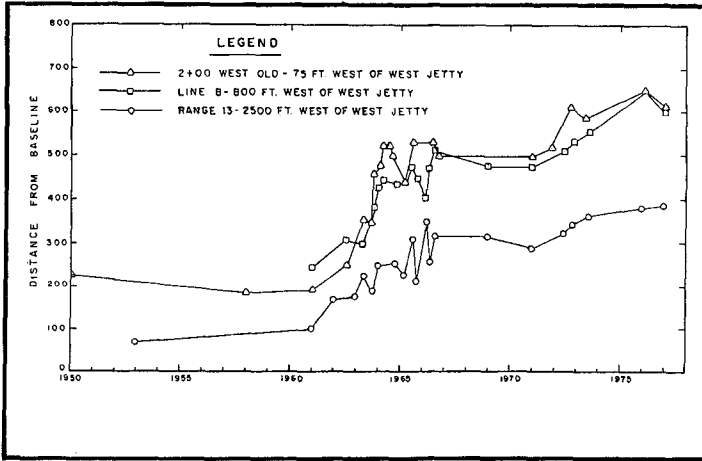


FIGURE 7: WEST BEACH SHORELINE CHANGES

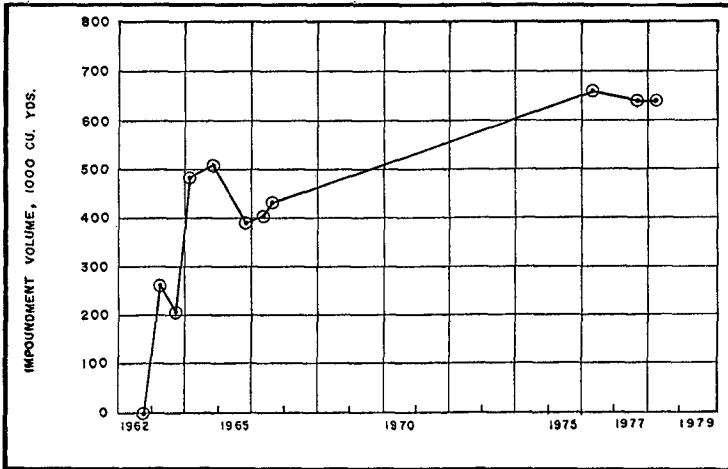


FIGURE 8: IMPOUNDMENT WEST OF WEST JETTY

Primary criteria for evaluation of the alternatives were cost effectiveness, engineering-feasibility, and minimization of adverse environmental effects. Bypassing was considered a satisfactory solution; however, material would still shoal the Harbor during storms unless the west beach were cut back to pre-1965 conditions. Citizens and homeowners who have become accustomed to a wide beach would object. Furthermore, some material would enter the Harbor by wind transport, leakage through the voids in jetty arm or units, and by reversals in littoral transport. A dredge would have to be mobilized for maintenance of the 20-foot project depth. Structural solutions would require considerable first costs; further, they would require bypassing of the net littoral transport into the area. Sealing the west jetty with a diaphragm would eliminate one of the shoaling mechanisms and reduce shoaling by about 10 percent of the total. The material would then bypass the head of the jetty, after which some material would bypass the channel and some would enter the channel. This is not considered a primary solution but could be implemented at a later date in conjunction with another system, such as an offshore breakwater. Maintenance dredging is the most direct method, wherein existing equipment and technology could be used. Therefore, a maintenance-dredging program was determined to be the most cost-effective, feasible, and reliable solution.

Figure 8 plots sand volumes impounded in the fillet west of the west jetty. Within the first 2 years of the project, 500,000 cubic yards were impounded; less than 200,000 more were impounded over the next 14 years. During this period of initial fillet-formation, the downdrift beaches experienced erosion, (Griggs 1975). The initial high rate of fillet impoundment may be partially be attributed to a relatively severe flood in 1963, which caused the San Lorenzo River to have a peak discharge rate of 13,400 cubic feet per second as compared to the long-term average of the annual maximum discharge rates of 7,961 cubic feet per second.

The shoreline east of the east jetty to Black Point had a more complex and variable evolution than that of the west beach. The jetties apparently shadow the predominantly westerly waves in the winter and cause a crescent-shaped beach to form near the east jetty. Comparison of the summer and winter shoreline configurations shows that the summer shoreline tends to rotate about 6 degrees clockwise relative to the winter shoreline.

MAINTENANCE-DREDGING RECORDS

The quantity of littoral drift that has shoaled in the entrance channel was determined through analyses of hydrographic surveys and maintenance-dredging records. Figure 9 shows the volume of littoral drift that accumulated between June 1972 and April 1978 within the control area shown in figure 10. The accumulation of material in the control area increased during each winter and was dredged in the late winter or in the spring. This dredging program was modified in 1977, when a series of multiyear, phased-dredging programs were implemented.

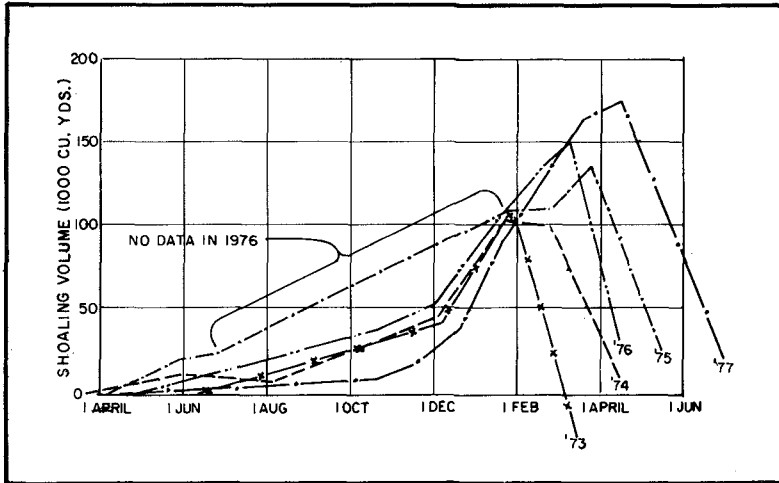


FIGURE 9: COMPARISON OF ACCRETION AND DREDGING QUANTITIES BY MONTH (1972-1977)

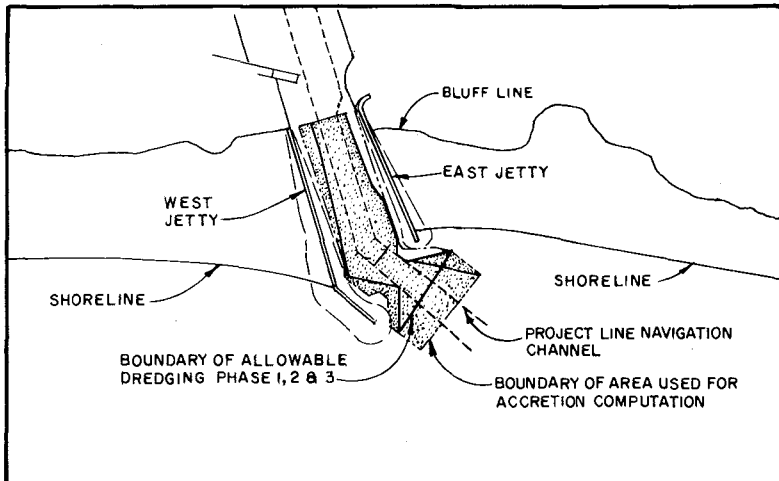


FIGURE 10: SHOALING BOUNDARIES

Maintenance-dredging records are plotted in figure 11. "Pay yardage" represents the quantity of material for which the Government agreed to pay the contractor. Pay yardage is not necessarily equal to the quantity of material actually removed. The dredgerman estimated that they actually removed as much as twice the pay yardage prior to 1977, when pay quantities were determined by comparing pre-dredging and postdredging surveys. This gave erroneous results when the dredging occurred simultaneously during the late winter and in the spring when shoaling also occurred.

The Waterways Experiment Station (WES) experimental jet-pump sand-bypassing system started operating on 26 June 1976. The bypassing system comprised three movable jet pumps operating in the channel off the west jetty, a movable jet pump at the head of the west jetty, and a stationary jet pump on the west side of the west jetty. The system was capable of bypassing about 100 cubic yards of sand per hour. The discharge area was 1,000 feet downdrift of the channel entrance, on the east beach. During the period July 1977 to June 1978, the WES plant dredged an additional 57,000 cubic yards.

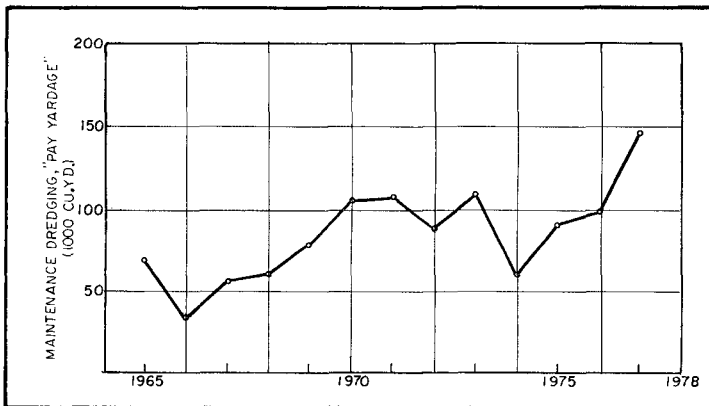


FIGURE 11: ANNUAL MAINTENANCE DREDGING HISTORY

SHOALING PROCESSES

Shoaling of the Santa Cruz Harbor entrance channel can be attributed to a number of disparate littoral processes, including: bypassing a saturated jetty (acting as a groin), leakage through voids in armor units on the jetties, wind transport, onshore transport, tidal-current transport, and updrift movement. This section describes each process and analyzes the history of shoaling to estimate the relative importance of each process. The nature of the available data and the state-of-the-art of defining littoral processes render it difficult to assign a definitive percentage of quantity of littoral transport to each process. However, for design purposes, it is often necessary to make certain assumptions in areas where precise quantification is not possible. Therefore, in order to prepare a plan to mitigate shoaling, estimates of the quantity of littoral transport attributable to each of the processes were made for design purposes.

Bypassing Saturated Jetty

Sand bypassing the head of the west jetty is the primary source of channel shoaling. Within 3 years after construction of the jetties, the west fillet had grown such that it reached the angle-point of the doglegged west jetty. As the west beach moved seaward during this period, maintenance-dredging pay yardage increased to quantities of more than 100,000 cubic yards per year.

Leakage Through Voids In Jetties

The west jetty is a rubble mound, armored with quarystone and quadripods. The seaward portion of the west jetty has a concrete cap, but the jetty is not impermeable and sand can be pumped through the voids in the large armor and underlayer stones of the structure. An estimated 20,000 cubic yards of sand leaks through the voids of the west jetty into the channel annually. The east jetty has a better seal and is exposed to less wave energy. The transport into the Harbor through the east jetty is estimated to be less than 1,000 cubic yards per year.

Wind Transport

The fine sand on the beaches is susceptible to windblown transport. An estimated 5,000 cubic yards are transported eastward over the west jetty annually while 2,000 cubic yards are transported westward over the east jetty.

Onshore Transport

Onshore transport of sediments near the Harbor entrance can be a source of shoaling; however, it is difficult to estimate the quantity involved. Long-term and seasonal bathymetric measurements of the offshore area indicate very little change in the bottom at depths of greater than 20 to 25 feet. This is consistent with a limit depth calculated by methods described by Hallermecier (1978). The contribution of offshore sources is therefore estimated to be relatively minor compared with that of longshore transport because the jetty 20 feet of water.

Tidal-Current Transport

The maximum tidal currents in the navigation channel are estimated to be less than 0.15 feet per second; therefore, the contribution of tidal-current transport to shoaling is minimal. The tidal prism of the Harbor is 9.8×10^6 cubic feet or 42 acres of water-surface area with a 5.3-foot mean tidal range. The cross-sectional area of the channel maintained a 400 square foot area as predicted from the O'Brien (1968) equation.

Updrift Movement

The total potential westward component of the littoral-transport rate is about 40 percent of the eastward component; however, conditions are appropriate for westward transport primarily during times of short-duration, local storm winds, at which time the east beach is well shoreward from the head of the east jetty. Thus, the actual updrift contribution to channel shoaling is smaller than the potential updrift contribution and is estimated to be 20,000 cubic yards per year.

Natural Bypassing

Some of the littoral drift that reaches the Harbor area is believed to bypass the Harbor entrance by natural processes. The sediment budget indicates that approximately 50,000 cubic yards of littoral drift shoals in the entrance each year. Some fraction of this is accumulating on the sides of the channel. Nearly twice as much drift as that which shoals in the channel may naturally bypass the Harbor via the bar that forms across the entrance during the winter. Removal of the bar during the winter by maintenance dredging would tend to increase the amount of material trapped in the Harbor and decrease natural bypassing. The long-term solution had to be designed with this large potential bypass taken into account.

ALTERNATIVE SOLUTIONS

The 16 preliminary alternative solutions for mitigating the shoaling of Santa Cruz Harbor were developed and evaluated. Alternatives were classified in three categories: maintenance, bypassing, and structural (table 1). Maintenance pertains to the removal of material from the project channel and disposal of the material on the downdrift beach. Bypassing is a preventive procedure wherein sand is trapped or intercepted outside of the project channel and transported to the downdrift beach. A structural alternative either provides protection for a dredge or prevents material from entering the Harbor. Structural solutions must be supplemented by some form of maintenance or bypassing. In all cases, sand was to be deposited on the downdrift beach.

TABLE 1 - ALTERNATIVE SOLUTIONS

- Maintenance
1. Annual Dredging - Floating Plant
 2. Phased Dredging - Floating Plant (selected plan)
 3. Hopper Dredge - "Currituck"
 4. Mechanical Dredging Systems
 5. Fixed Hydraulic System - Eductor
 6. Fixed Hydraulic System - Zipper
- Bypassing
7. Fixed Hydraulic System - Eductor
 8. Mobile Hydraulic System - Eductor
 9. Fixed Hydraulic System - Zipper
 10. San Lorenzo River Sediment Trap
- Structural
11. Long Offshore Breakwater - Annual Dredging
 12. Short Offshore Breakwater - Continuous Bypassing
 13. Extend West Jetty - Jetty
 14. Modify Both Jetties or Construct a New Entrance
 15. Weir Jetty or Groin - Continuous Bypassing
 16. Enhance Ebb Currents - Dredge basins

PHASED-DREDGING PROGRAM

Description

The philosophy of phased dredging is to maintain the entrance channel for a greater length of time each year by periodically in phases removing the shoaled material during the year rather than once annually. A phased-dredging contract would be awarded late in the calendar year to mobilize a dredge onto the site by November 15. The dredge would be activated several times between November 15 and April at times when the channel has shoaled to a minimum depth of 10 feet. A final dredging episode in April would bring the channel to over-depth and over-width project dimensions in order to create as large a storage capacity as feasible with the present entrance configuration and thus to maintain a navigable entrance channel until the following winter season.

A review of the dredging and accretion histories of Santa Cruz Harbor for the period between 1972-1977 indicates that the shoaling rate decreases between April and November and that dredging of the navigation entrance to the full project width and depth in April results in a navigable channel through the busy summer boating season. Periodic maintenance dredging would be required between November and April to keep the channel open to navigation. A total sand bypassing program with the existing Harbor entrance configuration would not be feasible because there is neither adequate protection to keep a dredge operating during storms nor sufficient storage capacity to create an effective sediment trap.

Two conflicting problems evolve. The channel should be wide and deep enough for safe navigation, yet narrow and shallow enough to maximize the natural bypassing of littoral drift during the winter. A compromise between these conflicting problems would be to reduce the project depth, at least during the winter. For example, if the navigation

channel could be maintained at a depth varying between 10 and 15 feet MLLW over a width of 100 feet, it should be reasonably safe for navigation (except during storm wave episodes) and yet not completely interfere with the movement of littoral drift that naturally bypasses the Harbor entrance seaward of the 10-foot depth contour.

Figure 12 shows the shoaling quantities and figure 13 shows the idealized phased-dredging program. Figure 13 also shows variation in shoaling quantities that have occurred and how the variation affects the program. Note a final dredge episode at the end of the winter season to clear the channel to project depth.

Results of Phased-Dredging Program

The phased-dredging program was initiated in the winter of 1977. The first contract was awarded for 2 years to Shellmaker, Inc. and the second 2 year contract was awarded to Watson, Inc. The purpose of a multiyear contract was to spread the cost of mobilization and demobilization of the dredge over more than 1 year. A longer contract period was considered; however, the experience gained during the first 2 years would benefit both contractors and the Government.

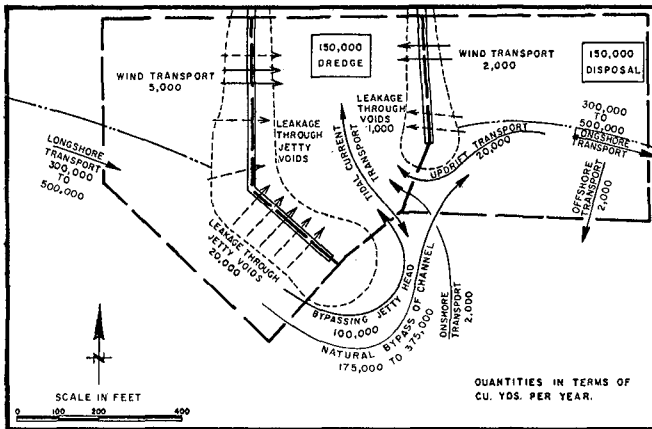


FIGURE 12: SEDIMENT BUDGET

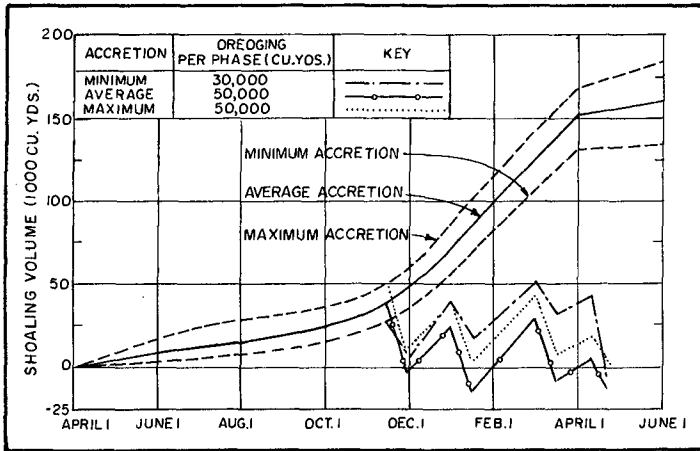


FIGURE 13: CUMULATIVE RATES OF ACCRETION AS MODIFIED BY PROPOSED DREDGE PROGRAM

TABLE 2-RESULTS OF PHASED-DREDGING PROGRAM			
PHASE	CONTRACTOR ESTIMATE CUBIC YARDS	PAY YARDAGE CUBIC YARDS	CONTRACT COST*
WINTER 1977-1978			
1	28,000	28,000	
2	42,000	36,000	
SPECIAL	34,000	24,000	
3	18,000	18,000	
FINAL	75,000	56,000	
WES Eductor Experiment	57,000	57,000	
Total	254,000	219,000	\$451,000
WINTER 1978-1979			
1	0	0	
2	35,000	22,000	
3	32,000	25,000	
FINAL	42,000	38,000	
TOTAL	109,000	85,000	
WINTER 1979-1980			
1	53,000	53,000	
2	75,000	43,000	
3	35,000	30,000	
FINAL (estimated)	50,000	40,000	
TOTAL	213,000	166,000	

*Includes mobilization and demobilization

Contractual and permit problems have delayed implementation of the project. The basic concept was to mobilize the dredge by 15 November each year; however, starting dates have been 19 December 1977, 19 January 1979, and 12 December 1979. The first and last delays were for legal reasons and resulted in several months of a partially closed harbor. The 1978 to 1979 winter was very mild and dredging was not required until mid-January.

The results of the first 3 years of the program are summarized in table 2. Two estimates of the quantities of material reportedly dredged during each episode and the total cost, including mobilization and demobilization for each dredging season are included. The Government pay yardage was estimated by taking leadline soundings from the back of the dredge as it operates and comparing them with predredging soundings. This method minimized the amount of material that can shoal during the dredging operation as was the case in measuring procedures prior to 1977; however, comparison of the contractor estimate compared with the government estimate reveals some large inconsistencies. In the cases revealing large inconsistencies, such as for phase 2 of the 1979-1980 winter, the contractor claimed that he dredged nearly twice the amount of material for which he was paid. The differential in estimates represents the amount of material that shoals from the time of predredge survey are taken until the time soundings were made. The dredging episodes typically last for 2 weeks. The average shoaling rate during a 2-week period is about 10,000 cubic yards. A severe storm over a 2-3-day period can deposit three times that amount. The dredgerman estimated a 26 percent greater total quantity than the Government allowed. The improved method of estimating dredged quantities has improved the differential between the amount the Government pays for and the amount the contractor claims he removes.

CONCLUSIONS

The phased-dredging program solved the shoaling problem at Santa Cruz during the first 3 years to the satisfaction of Harbor users. A large part of the success of the program is attributable to having an experienced and reliable dredgerman in charge of the operations. The system requires no initial capital expenditure for permanent structures and can be modified or adjusted to account for differences in littoral transport regimes seasonally. If at some future date, an efficient eductor system is developed and proven reliable, it can be installed at such a time.

The phased-dredging program has doubled the quantity of pay yardage compared with the previous system of dredging once in the spring. This is attributed to three factors:

1. unusually severe winters;
2. improved method of calculating pay yardage by taking soundings from the dredge; and
3. interruption of natural bypassing that occurs, when a shoal exists in the entrance channel.

RECOMMENDATIONS

1. The phased-dredging program should be considered as a viable nonstructural alternative to harbors with shoaling problems similar to those of Santa Cruz Harbor.
2. If in the future a structural solution is sought for Santa Cruz, careful consideration should be given to designing the capacity of the equipment to trap or handle an even greater quantity of material than the phased-dredging program has had to handle. For example, if a fixed eductor system is to be installed to maintain the channel to project depth, it should be prepared to remove at least 400,000 cubic yards per year.

ACKNOWLEDGEMENTS

The authors wish to thank Mr. Doug Pirie for his assistance on this project and to thank Col. J. Adsit, District Engineer, San Francisco District, Corps of Engineers, for permission to publish this summary. Mr. William Herron and Mr. Ogden Beeman participated in developing the phased-dredging procedure and Mr. James Dunham provided valuable comments.

REFERENCES

1. Criggs, C.B., and R.E. Johnson, "Effects of the Santa Cruz Harbor on Coastal Processes of Northern Monterey Bay, California," Environmental Geology, Volume 1, 31 October 1975.
2. Hallermeier, R.J., "Uses for a Calculated Limit Depth to Beach Erosion," Proceedings of the 16th Conference on Coastal Engineering, Hamburg, Germany, 1978.
3. Magoon, O.T., "Maintenance of Santa Cruz Harbor, California, USA," Proceedings of the 16th International Conference on Coastal Engineering, Hamburg, Germany, 1978.
4. Marine Advisors, "A Statistical Survey of Ocean Wave Characteristics in Southern California Waters," prepared for Los Angeles District, Corps of Engineers, 1961.
5. National Marine Consultants, "Wave Statistics for Seven Deepwater Stations along the California Coast," prepared for Los Angeles and San Francisco Districts, Corps of Engineers, 1960.
6. O'Brien, M.P., "Equilibrium Flow Areas of Inlets on Sandy Coasts" Journal of Waterways and Harbors Division, Proc. ASCE, Feb. 1969.
7. Seymour, R.J., C.W. Domurat, and D. Pirie, "Correlations Between Longshore Sediment Transport and Sediment Deposition at Santa Cruz Harbor, California." Proc. 17th Conf. on Coastal Engineering, Sydney, Australia, 1980.
8. "Summary of Synoptic Meteorological Observations - Pacific Coasts," SSMO - U.S. Naval Weather Service Command, Vol. 5, Area 35, May 1976.
9. Walker, J.R., P.J. William, and J.W. Dunham, "Santa Cruz Harbor Shoaling Study."
10. U.S. Army Corps of Engineers, "Beach Erosion Control Report on Cooperative Study of Santa Cruz Area, Pacific Coastline of California," San Francisco District, 1956.

11. U.S. Army Corps of Engineers "Environmental Statement-Maintenance Dredging (FY-1974), Santa Cruz Harbor, Santa Cruz, California," San Francisco District, 1974.
12. Yancey, T.E. "Recent Sediments of Monterey Bay, California", University of California, Hydraulic Engineering Laboratory, Tech. Rep. HEL-2-18, 1968.

CHAPTER 91

DESIGN OF ENCLOSED HARBORS TO REDUCE SEDIMENTATION

Craig H. Everts, M, ASCE¹

ABSTRACT

Sedimentation may be an important problem when quantities of suspended material are carried into an enclosed harbor on a flooding tide. In order to forecast future maintenance costs, two methods for predicting the sedimentation rate prior to harbor construction are proposed: 1) a sedimentation tank to be placed at the proposed harbor site, and 2) a mathematical model which uses sediment and hydraulic data collected at the harbor site.

Certain considerations in the design phase of a project may effect a reduction in harbor sedimentation. If feasible, the harbor may be sited in a region where suspended sediment concentrations are low and sediment sizes (settling velocities) are small. Proximity to river sediment sources may be a factor. Conversely, a harbor site in a clear-water river adjacent to a sediment-laden estuary may be desirable if bedload transport during freshets would not be a problem. Settlement of suspended material may occur in the channel which connects an enclosed harbor basin with navigable waters. This material may subsequently be resuspended and carried into the basin thereby increasing the sedimentation rate. To reduce that rate the channel should be designed as short as possible. A sill in the channel may also be used to reduce initial excavation costs and the sedimentation rate. Flotation for vessels in the basin will be provided at all times, but movement into and out of the harbor will be reduced to times of higher water. In high latitude areas where harbor use is limited to periods when ice cover is absent, the sedimentation rate may be reduced using a channel closure structure during non-use periods. Winter sedimentation rates can be predicted using the mathematical model for summer conditions, and when ice thickness is known.

INTRODUCTION

Special attention to sedimentation problems is warranted in the design of an enclosed harbor sited in a high tidal range, sediment-laden coastal area. Large quantities of suspended material will likely be carried into the harbor each floodtide. Because of the relatively quiescent conditions in the harbor when compared to outside waters, a part of the suspended sediment will probably settle out of suspension before being carried out on the ebb tide. Two important considerations are to predict the sedimentation rate prior to harbor construction in order to forecast future maintenance costs, and to site and design the harbor

¹Chief, Engineering Geology Branch, Coastal Engineering Research Center, Kingman Building, Fort Belvoir, VA 22060

to minimize sedimentation. These considerations are the subject of this summary paper. Deposition from suspension is assumed to be the only mechanism by which sediment infilling occurs. The only design criterion considered is that of minimizing the sedimentation rate.

In 1970, the Coastal Engineering Research Center (CERC) began a study for the U.S. Army Engineer District, Alaska, to address the problem of sedimentation in Alaskan small-craft harbors. Because of extremely high sedimentation rates and the attendant high dredging costs involved, the Alaska District requested that a means be developed to predict those costs before construction. It was noted that the feasibility of new harbor projects would, in some cases, hinge on maintenance dredging costs. The CERC study continued for 9 years. In that period, summer and winter monitoring of a prototype harbor at Dillingham, (Everts, 1976a) and measurements in Cook Inlet, Kenai River, and especially Knik Arm, Alaska, were made to identify and quantify the sediment and hydraulic mechanisms responsible for the harbor shoaling problem. A mathematical model (Everts, 1980) and a field measuring device (Everts, 1975) were developed to predict the sedimentation rate. Through the conduct of the study it also became apparent that certain considerations in the design of an enclosed harbor could effect a reduction in the sedimentation rate.

HARBOR CHARACTERISTICS AND SEDIMENTATION PROCESSES

For application of the results described in this paper, harbor conditions should conform to those described in this section. An enclosed harbor connected to coastal waters by a navigation channel is considered (Fig. 1). Because of high-velocity, tide-driven currents, and severe ice conditions, the protection offered by enclosed harbors is a special requirement in some of coastal Alaska. A sill in the navigation channel is a possible added design feature. It may be at any elevation. A sill, usually sited at the basin opening (Fig. 1), is used in high tidal range areas to reduce basin excavation costs. While providing flotation for vessels at low tidal stages, a sill restricts navigation in and out of the basin to times of higher tidal elevations. Harbors in Alaska with such sills are called "half-tide" harbors.

The harbor basin and channel may be of any size and shape as long as the rise and fall of the water surface inside the basin is nearly in phase with and of the same amplitude at that outside the basin (Everts, 1980). This means the volume of water that enters the basin as the water surface rises is equal to the volume of the basin above the sill. Basin and channel sidewalls may be sloping or vertical. If a sill is present, the basin is assumed stagnant below sill elevation. Therefore, when a suspended-sediment particle settles below that elevation it is considered deposited, even though it has not yet reached the bottom. Horizontal circulation within the basin is of such magnitude that sediment, once deposited or once it has settled below the sill elevation, it is not re-suspended.

Sedimentation results when suspended material settles from suspension. Bedload transport into the basin is assumed to be negligible. Sedimentation rates are assumed to be nearly equal throughout the basin; i.e., back eddies or other preferred depositional areas do not exist.

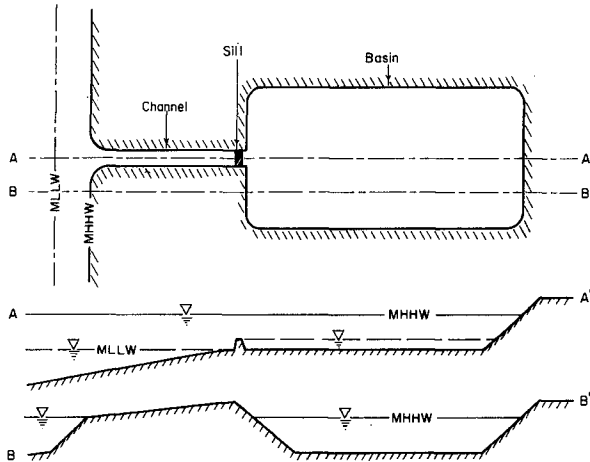


Figure 1. Definition sketch of an enclosed "half-tide" harbor illustrating major components: navigation channel, sill, and basin.

PREDICTION OF SEDIMENTATION RATE

To plan maintenance expenses before harbor construction in areas where sediment is carried in suspension, it is necessary to forecast future sedimentation rates. Two means for doing this were developed in the study: (1) a sedimentation tank, and (2) a mathematical model.

Prototype Harbor.

Dillingham Harbor, Alaska, was selected as the prototype on which to scale the tank and to test the model. Dillingham is located 500 km southwest of Anchorage, in the upper reaches of Nushagak Bay (Fig. 2). The local tidal range is 6 m and suspended-sediment concentrations vary from 50 to 1,500 mg/l of fine-grained material (1 to 100 micrometers). Local and transient fishing boats and commercial barges to 15-m long use the harbor. The harbor basin area is 21,500 m² at a project elevation of +0.6 m mean lower low water (MLLW). The sill elevation is +1.8 m MLLW and basin sidewall slopes are 1:5. Moorage is provided for 140 boats. Sedimentation has averaged almost 2 m/yr since the harbor was constructed in 1961. This requires nearly continuous dredging during the ice-free season.

June through September mean shoaling rates (5,400 m³/mo) are almost twice the mean October through May rate of 3,100 m³/mo (Fig. 3). Sediment infilling is nearly uniform throughout the basin when the basin bottom is below the elevation of the sill. An exception is a small

region near the sill that is scoured during the lower stages of a flood-tide. The channel has been stable in plan view and cross section since slightly after construction.

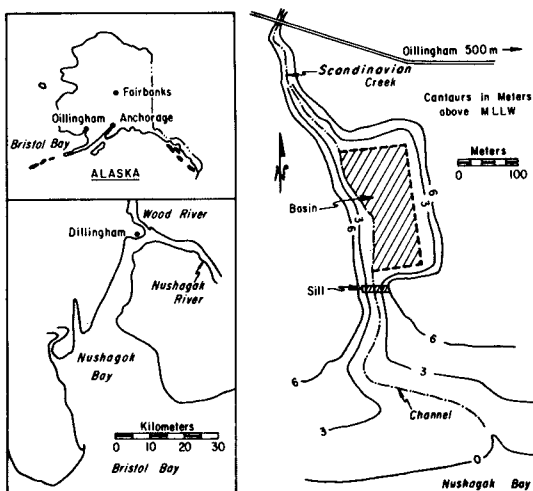


Figure 2. Location map of Dillingham Harbor, Alaska (Everts, 1976a). Discharge from Scandinavian Creek is negligible.

All sediment is transported into the harbor in suspension. At the sill, suspended concentrations are greatest as the rising tide initially passes over the sill (Fig. 4). More than 50 percent of the suspended material brought into Dillingham Harbor enters during the first hour of the 3-hour-long flood-tide cycle in the basin. The concentration at any given time is nearly uniform from the sill to the water surface. At any specific time the concentration is also nearly uniform throughout the basin at the water surface (samples within the water column in the basin were not taken). The bulk density of deposited material in the basin is about 1.5 gm/cm^3 .

Water velocities over the sill in the basin at any specific time are generally uniform from the water surface to the elevation of the sill. In the basin, the region below sill elevation appears to be near stagnant and a particle which settles below that elevation is not removed on an ebb-tide. Velocities above sill elevation are low enough in most of the basin that resuspension after deposition on the sidewalls does not occur. The basin appears to be turbulence-free and movements of fluid into and out of it are directed in line with the navigation channel.

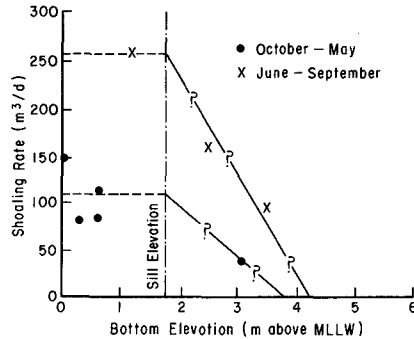


Figure 3. Shoaling rate in Dillingham Harbor, Alaska, as a function of bottom elevation in the basin (Everts, 1976a). Note the decrease in the shoaling rate as the bottom shoals above the sill elevation. This occurs because as the bottom elevation rises, less water and suspended sediment are carried into the harbor basin each floodtide, and consequently less sediment is deposited.

Sedimentation Tank.

A sedimentation tank was developed as an in situ instrument to obtain the shoaling rate as would be expected in an enclosed harbor (Everts, 1975). It was a hollow, upright cylinder fabricated of 5-mm steel, 9.1 m high and 3.7 m in diameter (Fig. 5). A narrow, vertical slot, 3 cm wide, 1.2 m long and of height sufficient to extend from the sediment-water interface to above the mean higher high water (MHHW) surface, was used to simulate the entrance channel. The tank was set in an excavated hole near the site of a proposed harbor in a tidal flat bordering Knik Arm, near Anchorage. The shoaling rate was obtained by monitoring the buildup of sediment within the tank during summer months of 1971 and 1972 (Fig. 6).

An important aspect of the study was to evaluate the tank. In most respects, depositional conditions within the tank were found to be similar to those at Dillingham Harbor. The study indicated the design could be modified to reduce fabrication, placement, and removal costs. The tank can not be scaled in its vertical dimension. However, it can be any plan shape or size, and a smaller plan area would serve the design purpose. Below the entrance slot the tank depth must be great enough to accommodate sedimentation expected during each field test. A critical aspect of the design is to provide an entrance which permits free exchange of water to or from the tank when the water surface rises or falls, but which inhibits in-tank circulation. The slot design (Fig. 5) worked well where waves were <0.6 m. In areas of higher waves the slot might be oriented away from the prevailing wave direction. The orientation, however, should be normal to the direction of the tidal current to inhibit

direct current access. The slot simulated a harbor entrance channel, but did not account for channel deposition and resuspension that could affect the amount of material that would be expected to enter a half-tide harbor. The result could be an underprediction of the actual shoaling rate if the proposed harbor is to have a navigation channel.

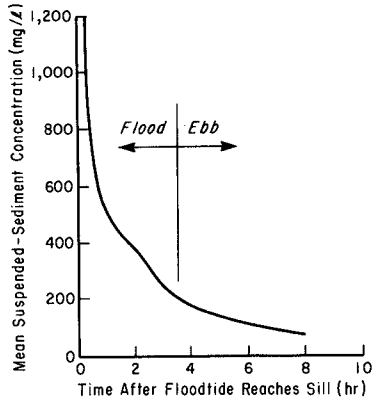


Figure 4. Suspended-sediment concentrations at the Dillingham Harbor, Alaska, sill over a harbor basin tidal cycle (Everts, 1976a). Concentrations are averaged through the water column and are based on sampling at the sill over five tidal cycles. Note the rapid decrease in concentration from the time the water level reached the sill until the time of high water.

Sedimentation Model.

Everts (1980) developed a model, posed in the Lagrangian representation, to simulate sediment shoaling. A mass of suspended particles is followed from the time and elevation at which it enters the basin in suspension until it is deposited or possibly removed from the basin during the outflow phase. The one-dimensional formulation has the essentials of the problem because the depositional process is assumed to be nearly uniform throughout the basin. The dependent variable is the mass of deposited sediment. Independent variables are the elevation and time - dependent mass of sediment discharged to the basin, the settling velocity distribution of that mass, and the harbor geometry. Data from the sedimentation tank and Dillingham Harbor were used to evaluate the model. In both cases the model results were between 10 and 12 percent less than the measured shoaling rate. Because of field sampling difficulties it is difficult to determine whether the errors are a result of an inadequacy in the model or are caused by sampling errors or omissions.

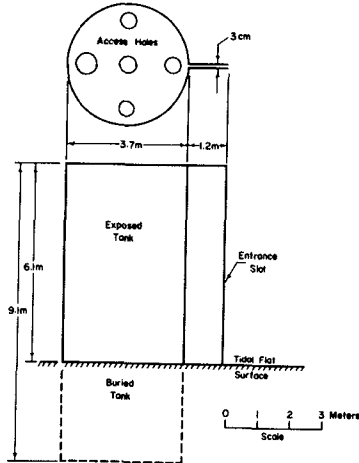


Figure 5. Side and plan view of sedimentation tank which was placed at half-tide elevation in a 500-m-wide tidal flat adjacent to Knik Arm near Anchorage, Alaska (from Everts, 1975). The median tidal range is 8.7 m. The entrance slot was oriented away from shore and normal to floodtide and ebb-tide currents.

The shoaling rate may be obtained in three steps: (1) Predict the total mass of sediment that will enter the harbor, (2) predict the part of that mass that will be deposited, and (3) predict the shoaling rate (bottom elevation increase).

(a) Step 1. During a rising tide the mass of sediment carried into a harbor is a function of the time-dependent concentration of entering suspended sediment, $c(t)$ time rate of water surface elevation, $\frac{dh}{dt}$ and the elevation-dependent plan area of the harbor basin at the water surface which is a function of time in the tidal cycle, $A(t)$. The total sediment mass which enters a harbor during a rising cycle, M_e , is

$$M_e = \int_{t_s}^{t_m} c A \frac{dh}{dt} dt \quad (1)$$

in which t_s = time floodtide reaches elevation of sill, and t_m = time floodtide reaches maximum elevation.

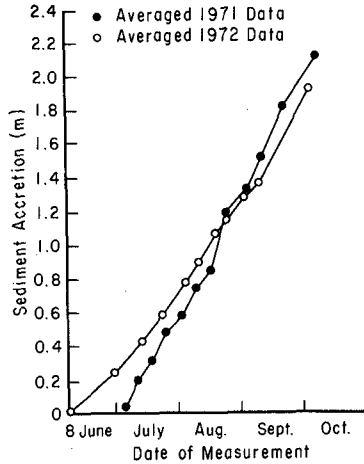


Figure 6. Sediment accretion in sedimentation tank in 1971 and 1972. Values are averages based on six measurement locations in tank. Note near-constant accretion throughout the summer and the 20 percent larger accretion rate in 1971.

(b) Step 2. That part of M_e deposited in the harbor is primarily dependent upon the settling characteristics of the sediment, the distance the sediment has to settle to be deposited, the time during which the suspended material settles, and the sill elevation. Figure 7 shows the part of the suspended material, P , that will be deposited as a function of tidal range and particle size. For diurnal and semidiurnal tides, the settling characteristics of disaggregated material less than 1 micrometer in diameter are such that little will be deposited in the harbor. Most particles larger than 32 micrometers will be deposited. Figure 7 is based on the mathematical model discussed by Everts (1980). Because all natural systems contain a range of sediment sizes, it is necessary to obtain M_e and P for each size grouping, then sum the individual masses to obtain the total deposited mass, M . In integral form this is

$$M = \int_{d_s=0}^{d_s=\infty} M_e P \, dd_s \quad (2)$$

in which d_s = suspended-sediment particle size. Figure 8, obtained using the model, shows the mass of sediment deposited per tidal cycle when sill

elevation, tidal amplitude, and particle size (fall velocity) are varied at the Anchorage sedimentation tank site.

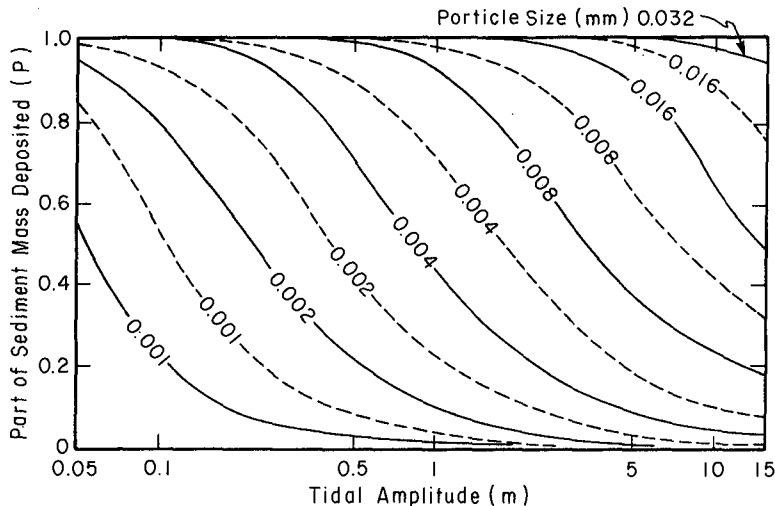


Figure 7. Part of sediment mass entering harbor basin which is deposited as a function of sediment particle size (based on sphere fall velocity in freshwater at 20°C) and tidal amplitude (from Everts, 1980). Solid lines are for a 12.4-hr. tidal period; dash lines are for a 24.8-hr. tidal period. Sill elevation is zero.

Sill elevation is not considered in Figure 7. At most, the increase in P will be 10 percent when the sill is at an elevation $A_0/2$ (half-tide elevation) and $P = 0.7$, where A_0 = tidal amplitude. When sill elevation = $A_0/4$ and $P = 0.7$ the increase is only 5 percent. In using Figure 7, the concentration of suspended sediment entering the harbor is not assumed to vary with time. If concentrations are highest early in the tide cycle, P will be larger than shown in Fig. 7. Suspended-sediment fall characteristics are assumed to be constant through time.

Particle aggregation may be an important factor in increasing the settling velocity of suspended material, especially in a saline estuary environment. In south-central Alaska, clay minerals constitute less than 2 percent of the total suspended-sediment load. Even there, however aggregation plays an important role which must be considered in harbor sedimentation (Fig. 9). Unless the settling velocities are obtained in the fluid in which they are collected (versus distilled

water used in some laboratory analyses) large errors in predicted sedimentation rates may result.

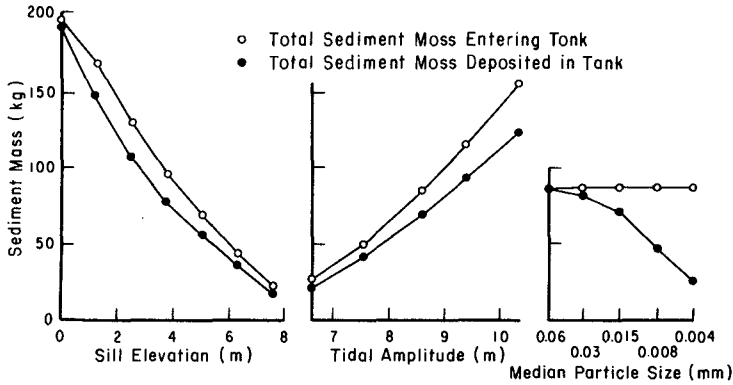


Figure 8. Sensitivity analysis of equations (1) and (2) using a mathematical model to predict sedimentation in a half-tide harbor (Everts, 1980). The model test basin was the sedimentation tank located in Knik Arm, Alaska. Predicted sediment mass entering and deposited in the tank is based on actual average values of all parameters except that shown.

The part of the sediment which enters the harbor and is subsequently deposited will probably be near constant from one tidal cycle to another, even though the total quantity which enters may vary widely (Everts and Moore, 1976; Everts, 1976a). Everts (1976a), for example, reported that the quantity carried into the basin at Dillingham Harbor varied by a factor of three between tidal cycles, but that the part deposited was near constant at 81 percent (range: 76 to 84.2 percent for five tidal cycles). Thus, to accurately predict M_e , a number of tidal cycles must be sampled to obtain representative concentration values.

(c) Step 3. If it is desirable to predict the rate of bottom elevation rise caused by sediment deposition, sediment mass deposited must be converted to sediment volume deposited. The part of a unit volume of deposited material with a density, ρ_d , which is composed of sediment of density, ρ_s , is V_s , given as

$$V_s = \frac{\rho_d - \rho_f}{\rho_s - \rho_f} \quad (3)$$

in which $0 \leq V_s \leq 1.0$, ρ_f = water density. Then the mass of sediment per unit volume of deposited material, m_v , is

$$m_v = \rho_s V_s \quad (4)$$

and the shoaling rate (per tidal cycle), S_r , in the basin is

$$S_r = \frac{M}{F m_v} \quad (5)$$

in which f = plan view area of the basin bottom.

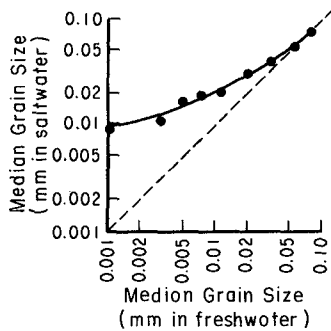


Figure 9. Comparison of median grain size, based on fall velocity, for duplicate samples of glacier-source sediment from Knik Arm using the hydrometer method with distilled water and with Knik Arm water (from Everts, 1976b). Sediment with a median grain size less than 0.075 mm settled at a faster rate in saltwater even though the clay mineral percentage was less than 2 percent.

HARBOR DESIGN TO REDUCE SEDIMENTATION

In the course of the study, a number of possible means to reduce the shoaling rate became apparent. These are summarized in the following sections.

Harbor Siting.

If a number of harbor sites are considered, the site where sediment concentrations are lowest and sediment sizes are smallest, all other conditions being equal, will experience the lowest sedimentation rate (see eq. 1 and Fig. 7). The size and concentration of sediments suspended in the water column may vary throughout an estuary and this may be a consideration in where a harbor is sited. Temporal variations in size and concentration may also be a factor. For example, a decision to close a harbor during certain nonuse times of the year may hinge on the predicted sedimentation rate during the closure period versus that of the remainder of the year.

In estuaries such as Knik Arm, most of the suspended sediment is contributed by glacier-fed rivers. High concentrations in the estuary are clearly related to the summer influx of river-borne sediments, although a phase lag appears in the estuary where autumn concentrations remain high (Fig. 10). Everts (1976b) found suspended-sediment concentration to be related to water discharge for the two largest contributors (Knik and Matanuska Rivers), but size was a function of water discharge only in the Knik River. A single year's water and sediment discharge record is not enough to predict average yearly suspended-sediment concentrations in a river-dominated estuary because yearly variations of 50 percent about the yearly mean may be expected. In addition, sediment discharge cannot be extrapolated from one river basin to another in glacial areas, even where the basins are adjacent. In south-central Alaska, river sampling during the 3 summer months (June, July, and August) is sufficient to determine the total yearly sediment load within 10 to 15 percent.

Floods may move a significant quantity of suspended material. In off-river harbors and harbors located near river mouths, the impact of flood discharge must be considered. A 2- to 5- day flood may discharge more than 50 percent of the yearly sediment contributed by a river. Sediment sizes carried by floodflows are considerably larger than the size carried during normal flow times.

Off-River Harbor Sites.

Siting a harbor beside or adjacent to a clearwater river may substantially reduce the sedimentation problem caused by fine-grained material. The reduction results because sediment-laden, landward-moving estuary waters are diluted by seaward-flowing, clear river waters. The decrease in suspended-sediment concentration, and in the predicted shoaling rate (eq. 5) can be obtained using data from a sediment sampling program during the time of floottide incursion near the proposed enclosed harbor site. Temporal variations in river-borne sediment concentration and size must be considered.

Potential problems exist in using an off-river harbor. Caution is advised to ensure that deposition of river-carried bedload sediments, and the river sediment load during flood times, will not mitigate the savings.

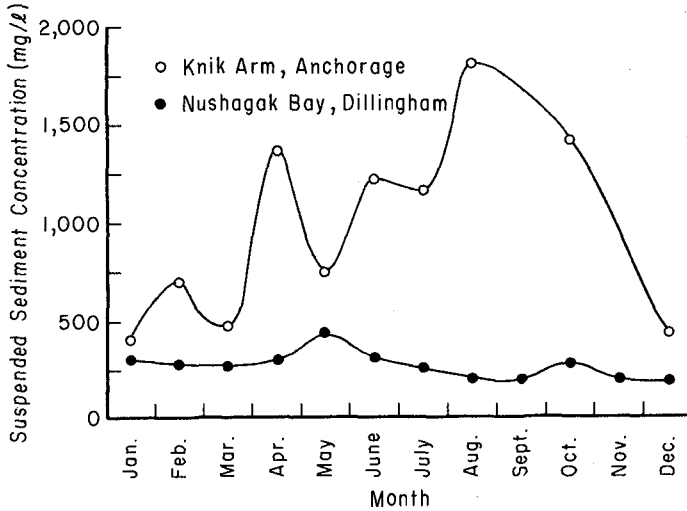


Figure 10. Average suspended-sediment concentrations in Knik Arm, an estuary in which much of the suspended material enters directly from glacier-fed rivers; and Nushagak Bay, an estuary where the material is continuously resuspended from the estuary bottom.

Channel Length.

Suspended sediment enters an enclosed harbor from two sources. The primary source is the adjacent estuary. An important secondary source may be the navigation channel between the harbor basin and estuary. At Dillingham Harbor, for example, current velocities in the channel are low when the tidal elevation is below the sill; consequently, suspended material settles in the channel during these times. As the next flood-tide rises over the sill, channel currents increase rapidly to accommodate the increased water discharge required to fill the basin. At that time, when the submerged channel cross-sectional area is smallest, the velocities are greatest and material previously deposited in the channel is resuspended. The amount of sediment entering Dillingham Harbor from the channel source is 40 percent of the total amount brought in.

Economies can be achieved when an entrance channel is designed to reduce the accumulation of channel sediment. Usually, this will require that the channel length be designed as short as possible.

Sill Design.

Sedimentation within a harbor may be reduced if the mass of sediment carried in each floodtide is reduced. One way to effect this is by placing a permanent sill in the entrance channel at an elevation above the harbor basin bottom and MLLW (Fig. 8). This reduces the tidal prism.

The design consideration, therefore, becomes one in which initial harbor cost plus future maintenance expense is balanced against the percent of time navigation is restricted into and out of the basin.

The period of restricted navigation can be easily calculated using the tidal hydrograph and sill elevation based on a consistent datum, and the draft and clearance required of the vessels using the basin. The mass of sediment carried into the harbor versus sill elevation can then be established (eq. 1).

Changes in suspended-sediment concentration with time differ greatly from one location to another. Everts and Moore (1976) measured an increasing concentration toward high water at the sedimentation tank site in Knik Arm, while Everts (1976a) found the concentration to decrease through the tide cycle in the estuary at Dillingham Harbor. Concentrations in Knik Arm seemed to be related to current speed and direction; the highest concentrations were measured on an ebbtide, i.e., sediment was moving away from a major riverine source. At Dillingham the concentration is greatest near midtide in Nushagak Bay where the fine-grained sediment source is the bay bottom and tidal flats. The channel resuspension mechanism greatly increases the early high concentrations.

Basin Closure.

When harbor use is seasonal, a channel closure structure may be warranted during nonuse periods. The cost-effectiveness of the structure and its emplacement and removal is determined by calculating the sediment volume that would be deposited during the nonuse period and the attendant maintenance cost for its removal.

Ice and winter conditions restrict the use of many harbors in Alaska to 6 months or less. Summer sedimentation rates do not prevail during ice-cover conditions. The submerged ice volume reduces the discharge volume of water and suspended sediment to the basin. That reduction can be estimated. A reduction in the amount of water and suspended sediment in an ice-covered channel will reduce the sediment mass inflow from that source. The mass of sediment which enters a harbor may also vary seasonally, especially where river discharge is an important source, as it is in Knik Arm. Wide seasonal variations, however, are not always the case. In Nushagak Bay the average monthly concentration of suspended sediment is near constant year round (Fig. 10). Sediment in Nushagak Bay comes from the suspension and resuspension of bottom sediment, not river discharge.

Because sediment size, water viscosity, and particle aggregation affect the settling velocity of suspended material in the basin, these factors must be considered on at least a seasonal basis. At Dillingham, median particle size varied from 0.014 mm in the summer to 0.005 mm in winter. Temperature affects water viscosity, and hence the fall velocity of the sediment particles. For example, at 0°C winter water temperature, the fall velocity of a particle 0.008 mm in diameter is about 70 percent the velocity it would be at 10°C. This must be considered. The effect of salt on the settling rate of clay minerals becomes distinguishable at seawater concentrations of about 1 to 2 parts per thousand (ppt).

Aggregation and hence the settling rate of the aggregated mass increase to seawater concentrations of 10 to 15 ppt. Suspended sediment in water samples with salt content of 0.5 ppt at Dillingham during the summer did not appear to aggregate. However, when the winter salinities reached 3 ppt, aggregation might have occurred.

At Dillingham, the winter shoaling rate (about 50 percent of the summer rate) was correctly estimated using these considerations. The major effects were decreased water and sediment discharge to the harbor because of the ice volume within the basin, and the reduction in sediment resuspended in the channel for which the ice cover was also responsible.

SUMMARY

This paper results from a 9-year study of enclosed harbors in Alaska. Two methods to predict harbor sedimentation rates prior to construction are presented and a number of design considerations to reduce sedimentation are suggested.

ACKNOWLEDGEMENTS

The analysis and results presented in this paper were based on research conducted at the Coastal Engineering Research Center under the Coastal Engineering Research Program of the U.S. Army Corps of Engineers. Much of the field work was done by the U.S. Army Engineer District, Alaska. Permission to publish this information is appreciated.

NOTATION

- P = deposited part of total suspended mass carried into harbor basin on floodtide
- c = suspended-sediment concentration
- h = water surface elevation
- A = plan area of harbor basin at water surface
- M_e = total sediment mass carried into harbor basin on floodtide
- t_s = time after low water that floodtide reaches sill elevation
- t_m = time after low water that floodtide reaches maximum elevation
- d_s = suspended-sediment particle size
- M = total mass deposited in harbor
- A_0 = tidal amplitude
- V_s = sediment part of unit volume of deposited material
- ρ_d = density of deposited material

ρ_s = sediment particle density

ρ_f = water density

m_v = mass of sediment per unit volume of deposited material

S_r = harbor shoaling rate per tidal cycle

F = plan area of harbor at basin bottom elevation

REFERENCES

- Everts, Craig H., "Shoaling Rate Prediction Using a Sedimentation Tank," ASCE, Proceedings of the Speciality Conference on Civil Engineering in the Oceans III, Newark, DE, 1975, pp. 294-312.
- Everts, Craig H., "Sedimentation in a 'Half-Tide' Harbor," in Assessment of the Artic Marine Environment: Selected Topics, Institute of Marine Science, University of Alaska, Fairbanks, 1976a, pp. 131-160.
- Everts, Craig H., "Sediment Discharge by Glacier-Fed Rivers in Alaska," ASCE, Proceedings of the Symposium on Inland Waterways for Navigation, Flood Control and Water Diversions, Fort Collins, CO, 1976b, pp. 907-923.
- Everts, Craig H., "Shoaling Rate Prediction for Enclosed Harbors," unpublished report, U.S. Army, Corps of Engineers, Coastal Engineering Research Center, Fort Belvoir, Va., 1980, 35 p.
- Everts, Craig H., and Moore, Harlan E., "Shoaling Rates and Related Data from Knik Arm Near Anchorage, Alaska," TP 76-1, U.S. Army, Corps of Engineers, Coastal Engineering Research Center, Fort Belvoir, Va; Mar. 1976, 84 p.

CHAPTER 92

OPENING AND MAINTAINING TIDAL LAGOONS & ESTUARIES

by

Scott A. Jenkins; Douglas L. Inman
Shore Processes Laboratory A-009
Scripps Institution of Oceanography
La Jolla, California 92093

and

James A. Bailard
Civil Engineering Laboratory
Port Hueneme, California

1. INTRODUCTION

Sedimentation in tidal lagoons and estuaries has become an acute problem, particularly where there has been over-dredging to accommodate today's deep draft vessels, 0(15m). The rise in mean sea level, which created natural estuaries, has not kept pace with the demand for greater draft ships. The limited number of navigable lagoons confronting a growing demand for more inland waterways has encouraged reconstruction dredging of some closed or partially filled lagoons.

Man's efforts to deepen existing or relict estuarine systems have disturbed the steady state equilibrium of the systems. Sedimentation acts continuously to restore this equilibrium by either of two processes. One is flocculation of fine-grained fluvial born sediments, a process accelerated when an estuary is deepened thereby allowing greater salt wedge intrusion. The other is the interception of the longshore transport of coarse grained beach sediments by the lagoon inlet. The larger tidal prism of an enlarged lagoon draws a greater percentage of the longshore transport into the lagoon from the adjacent surf zone. In the absence of wave suspension within the lagoon, very little of this sediment is carried back out of the lagoon on ebbing tides.

These sedimentation processes confront the coastal engineer with several distinct problems. A particular set of counter-measures are needed against accumulations of cohesive fines from the rivers, another set against accretion of cohesionless coarse grained sediments from the beaches. Still other methods are needed to reopen a closed lagoon.

Dredging has been the most widely practiced solution to all of these problems for the past 150 years. It is a solution we may not be able to afford indefinitely. In addition to intrinsic high rates of energy consumption and equipment breakdown, there are ever-growing costs associated with dredge spoils disposal. Ninety percent of the material annually dredged is contaminated by heavy metals, concentrated in the flocs from either natural erosion of country rock or industrial sources (Malloy, 1980). Further contamination results from chemical

and oil spills, sand blasting, paint removers and other shipyard and harbor activities. Sand is rarely contaminated because it is chemically inert. The contaminated sediments pollute the disposal sights, imposing additional costs to measure the pollution and minimize its effect. Recent climatic cycles and real estate developments have accelerated erosion and sediment runoff, ultimately bringing many spoils ponds to full capacity before their expected lifetime (N.E.S.O., 1976). Ocean dumping of poisoned spoils is environmentally unsound and strictly limited by environmental protection laws. Alternative spoils ponds are generally available only at great distance from the lagoon, requiring expensive booster stations and additional pumping capacity to transport the dredge spoils (Little, 1975).

This paper reports on five separate prototype scale field experiments that test alternative measures to dredging. Two of these experiments evaluate techniques of resuspension and exclusion for reducing fine sediment accumulations in quiet water, cul-de-sac berths, where the observed shoaling rates are greatest and dredging most difficult. These berths are essentially sediment settling basins where currents are insufficient to resuspend new deposits. The fine sediment control studies were performed in and around berths at Mare Island Naval Shipyard. Another two experiments involved by-passing sand around the inlet of Agua Hedionda Lagoon, California using fluidized trenches funnelling into a crater sink. The final experiment used open trench fluidization to reopen Penasquitos Lagoon, California.

2. SEASONAL AND EPISODIC MUD ACCUMULATION IN BERTHS

There is abundant data showing that the deposition rates of settled flocs in berthing areas and around structures within a tidal estuary exceed those in unobstructed navigation channels (NESO, 1978; Van Dorn, Inman, McElmury, 1977; 1978). This was dramatically shown in Mare Island Straits, California, during the record flood winter and spring of 1978 that brought an end to the California drought that began in 1945. Figure 1 compares the average bottom shoaling rates along a line extending across the navigation channel with the shoaling rates at two stations within the finger pier complex at Mare Island Naval Shipyard, pictured in Figure 2. Mare Island Straits are over-dredged to 13 m and situated at the confluence of the Napa and Sacramento Rivers on the eastern side of San Pablo Bay in the San Francisco Estuary. The shoaling at both stations within the finger pier berths at Mare Island were found to be three times the mean sedimentation rates across the navigation channel. Mud was found to accumulate at nearly uniform rates in both the channel and berthing areas through the wettest months of February and March, when the combined fresh water discharge of the Napa and Sacramento Rivers ran as high as $2.12 \times 10^3 \text{ m}^3/\text{sec}$, about 1/2 the tidal flux in Mare Island Strait. When the river discharge dropped to $1.13 \times 10^3 \text{ m}^3/\text{sec}$ by the end of April with subsidence of Pacific storms, the sedimentation rate in the finger pier berths abruptly increased. By this time 2 meters of new deposition occurred, 4 times the shoaling during the previous drought year of 1977 (Van Dorn, Inman, and McElmury, 1978).

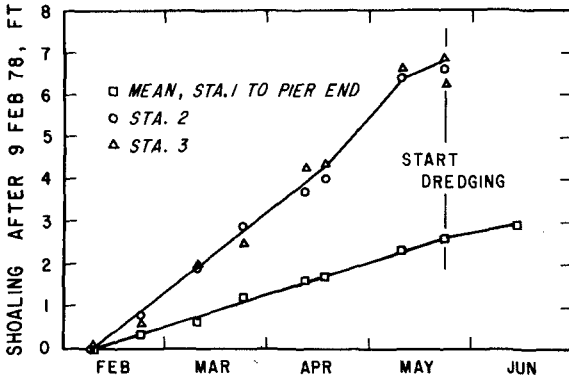


Figure 1 Shoaling history within a berth and across a navigation channel.

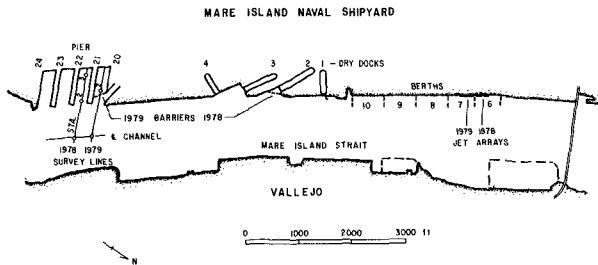


Figure 2 Mare Island Strait, ebb current and river flow to the left.

Initially new deposits of mud are fairly mobile, fluid mud, with a low threshold of motion of typically 15 cm/sec depending upon the time of immobility of the mud (Le Mer, 1962, and Van Dorn et al, 1977). In the navigation channels these threshold stress levels, $\approx (1 \text{ dyne/cm}^2)$ are exceeded more frequently, particularly if not over-dredged. Some fraction of the newly deposited fluid mud is resuspended and flushed out by tidal circulation. The remaining fraction of resuspended floc settles again next slack water, eventually reaching quiet water. The quiet water of the berthing areas allow for much less resuspension of fluid mud and greatly restrict circulation that might remove the resuspended material. Low density fluid mud (10-15 gm/l) which is not resuspended within 24-72 hours begins to compact under gravity, driving out interstitial water. After a week it becomes a high density (1.22 gm/cm³) anoxic mud, (Krone 1962) which can only then be moved by mechanical means. Eddies from pier piles, ship hulls and other vertical structures in and around the berth increase particle collisions and mix the higher salinity bottom water into the remainder of the water column,

further promoting flocculation. These factors all play a role in contributing to the higher siltation rates of berthing areas, although the relative importance of each may vary from place to place.

The seasonal variations of runoff in turn cause seasonal variation in sediment abundance and water properties. Figure 3 shows the vertical distributions of suspended sediment concentration, C, salinity, S, and temperature, T, from mid winter through summer 1978 at Station 3 inside the berth at Pier 23. Salinity and temperature are scaled on the horizontal axis in ‰ and °C along with concentration in gm/l. These data were collected during spring tides at four phases of tidal elevation labeled H, L, F and E for high, low, flood and ebb respectively. The salinity profiles show that the river discharge during the maximal rainfall months, from February until mid April, produced a thick lens of fresh water on the surface and rather low bottom salinities of 1-7 ‰. The salinity was uniform over depth at low tide indicating total retreat of the salt wedge from the berths by the end of ebbing tide. By mid June most of the Sierra snow pack had melted and the discharge of the Sacramento and Napa had fallen to $1.7 \times 10^4 \text{ m}^3/\text{sec}$. The fresh water surface lens then grew thinner into summer until finally an isohaline vertical distribution of 20 ‰ results from the tidal flux. The temperature distribution remains isothermal since thermal diffusivities $\approx (10^{-3} \text{ cm}^2/\text{sec})$ are large compared with diffusivities of salts, $\approx (10^{-5} \text{ cm}^2/\text{sec})$.

With the declining river discharge in late March, the salt wedge intrudes more freely into the berthing areas and bottom salinities reach the flocculation threshold of 7-10 ‰ (see Krone 1962). From this time on through summer, suspended sediment profiles show a high concentration toe, $\approx (100 \text{ mg/l})$ in the lower meter of the water column. The toe is due to the settling of flocs toward the bottom boundary and the re-suspension of those flocs by the tidal and eddy motion over pier piles, dredge banks and other bottom obstructions. However during periods of subthreshold salinities, e.g., following a train of local storms, 9 March 1978, the sediment remains uniformly distributed through the water column in spite of high sediment abundance.

The bi-weekly profiles of discrete properties in Figure 3 give a good resolution of the seasonal trends but may be somewhat aliased by weekly or daily variations. These short term fluctuations are most prevalent during the wet months as river discharge fluctuates daily in response to local storms passing over the water shed. As a result of these fluctuations, fine sediment deposition will exhibit episodes of extremely rapid build up, or "mud storms" when bottom salinities are near the flocculation threshold (7-10 ‰) while rivers remain laden with charged clay particles from recent runoff. Under these conditions four such mud storms, each depositing 0.6 m or more of new fluid mud at a time, were observed in the entrance to Pier 21 N at Mare Island during a near record flood winter in 1980 (see Figure 4). This echogram was taken using a 40 kHz echo transceiver. Each dated horizon is a veneer of loose floc trapped between thick layers of denser more consolidated fluid or anaerobic mud. The trapping of these floc layers implies that the subsequent build-up of mud occurred so rapidly that insufficient

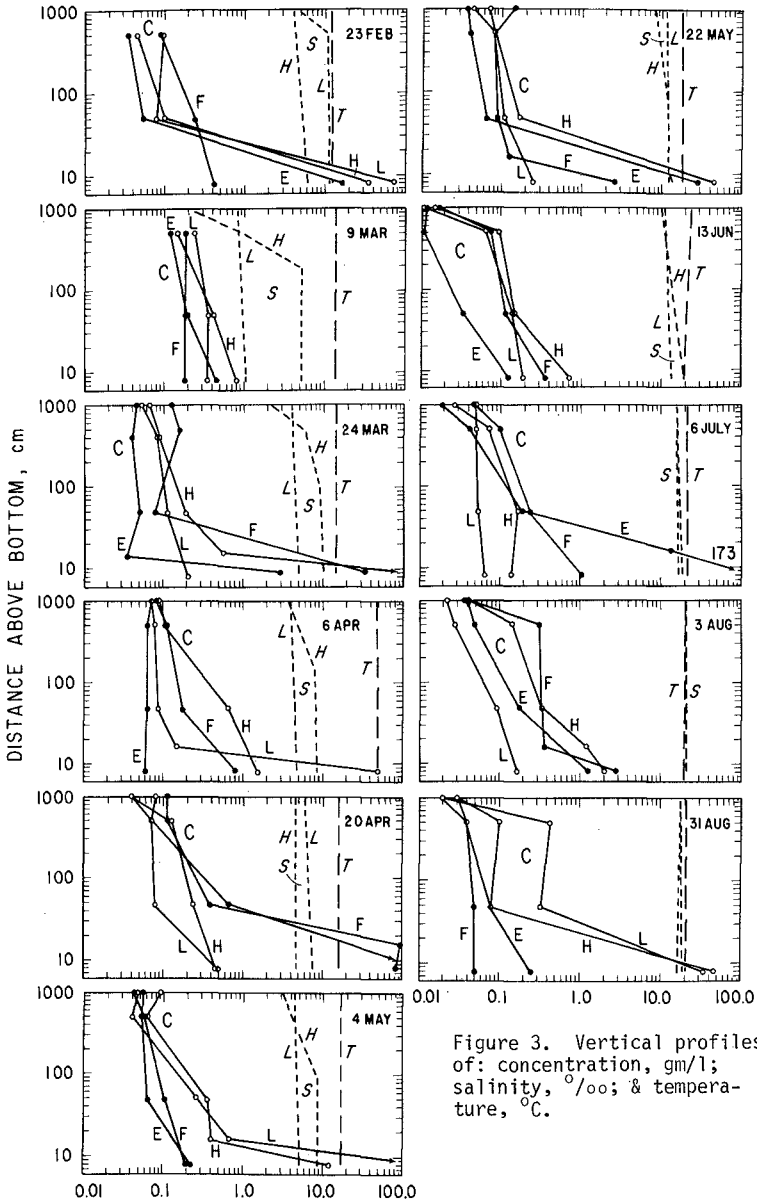


Figure 3. Vertical profiles of: concentration, gm/l; salinity, ‰; & temperature, °C.

time had lapsed for the water content of the floc layer to diminish. The accumulations of these mud storms are found between the dates of the horizons following the initial pulse of runoff from series of Pacific storms. The rise in bottom salinity in between these pulses triggers flocculation and a subsequent abrupt build-up in fluid mud. The flocs themselves appear as a speckled pattern in the water column between the surface reflection and the first bottom horizon on the echogram.

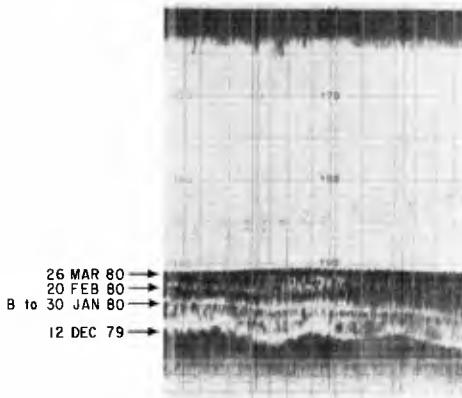


Figure 4

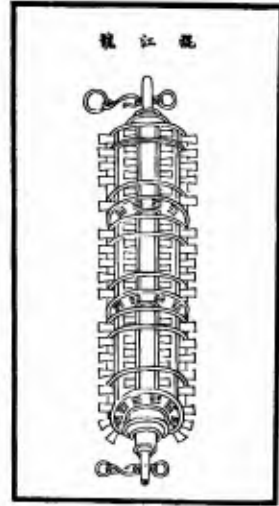


Figure 5

To a lesser degree the river discharge fluctuates during drier summer months, principally in response to manipulation of containment reservoirs and dam diversions. These fluctuations do not produce the episodes of rapid sediment accumulation found during the wet winter months. Shoaling in the summer months is characterized by a nearly steady state build up of about 0.25 cm/day. Whereas the controlling variable for shoaling in the winter is a bottom salinity of sufficient magnitude to induce flocculation in the presence of high sediment abundance, the summer shoaling rate in the presence of higher salinities appears strictly limited by the small amounts of suspended sediment brought in by the rivers. Krone (1959, 1960) has shown by tracer studies that suspended loads in the lower 80% of the water during the summer are in fact resuspended by wind waves over permanent shoals elsewhere in the estuary and carried subsequently into berthing areas by the density-stratified tidal flows.

Although these seasonal and episodic variations of water properties and fine sedimentation were observed at a single place, the mechanisms

of flocculation and resuspension are at work in most every tidal lagoon and estuary. The fact that these observations were made during an extreme in the weather cycle and covered maximum ranges of temperature, salinity, suspended sediment, and shoaling rate, should make them a useful design guide for sediment control measures anywhere.

3. CONTROL OF MUD ACCUMULATION BY RESUSPENSION

The first attempt to control mud accumulation by resuspending newly deposited layers of fluid mud date back to the Chinese in the 5th century A.D. Figure 5 shows a rolling suspensifier, the hun Chiang lung, first illustrated in the Ho Kung Chhi Chii Thu Shuo and reproduced here from Needham, 1974. This device was drawn along the bottom by a vessel or team of horses proceeding upstream. The teeth on the roller raised clouds of silt which were carried away on the ebbing tide.

The modern equivalent of the Chinese suspensifier is the tide actuated water jet array shown in Figures 6 and 7 tested on the water front of Mare Island at Berth 7 shown in Figure 1. The fundamental environmental constraint in the successful application of any such resuspending device is the presence of unidirectional currents for a sufficient period to advect away the material which has been resuspended. Berth 7 at Mare Island is ideal in this respect. This berth rests along the streamlined western shore of Mare Island Strait where 1200 m of unobstructed concrete quaywall stabilizes the bank against over-dredging to a depth of 10 m. Here bottom ebb current commences about 2.5 hours before high tide and persists for about 5 hours giving a rather long window to transport resuspended material. The weakest ebb current amplitudes at low river discharge, $10^2 \text{ m}^3/\text{sec}$, still produce near threshold stresses for newly deposited fluid mud, rising from 20 cm/sec at 0.5 meters above the bottom to 80 cm/sec on the surface. The tide actuated switching circuit entered in Figure 7 was synchronized for a 4 hour duty cycle through the period of maximum ebbing bottom currents.

The water jet array itself, Figure 6, was designed to operate from a fixed mounting on the quay wall where vulnerability to damage from dragging anchors and channel dredging activities is minimized. The most protruding components, the jet nozzles themselves, are secured to the discharge manifold by a quick-release Camlock clamp for easy diver replacement in the event of damage or malfunction. Ten equally spaced 7.3 cm diameter jet nozzles comprise the linear array 63 meters in length at a depth of 8.2 meters below MLL sea level. The jet array was driven by a 1910 gpm water pump at 92 psi powered by a 140 hp, 220 v electric motor. The automatic switching circuit, Figure 7, sequences the entire pump discharge through each individual nozzle one at a time beginning from the upstream side of the array. This was accomplished through an arrangement of pneumatically operated pinch valves operating on an inlet pressure of 67 psi. In this way each jet is able to produce a discharge velocity of 760 cm/sec, or nearly 1.65×10^7 dynes of static thrust. Wall jet experiments by Poreh, et al (1967) and Sforza and Herbst (1969) indicate that the bottom stress on an immobile boundary will decay with distance, r , from the jet as $r^{-2.3}$. These data suggest, that each jet will exert a super-critical bottom stress of 4.6 dynes/cm^2

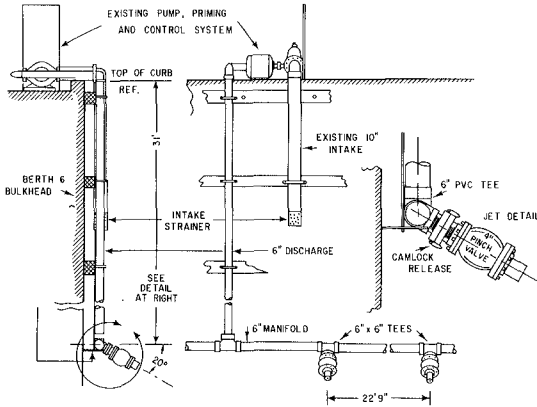


Figure 6: Quay wall Installation of Water Jet Array

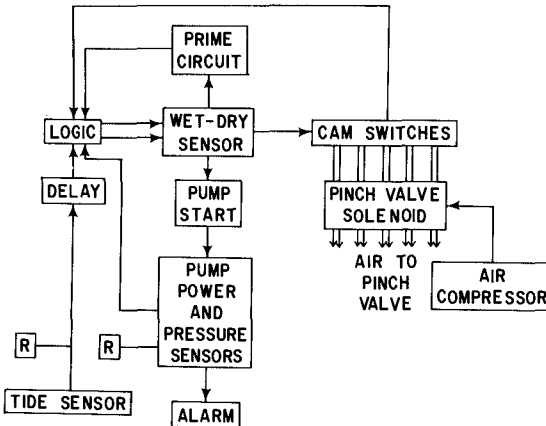


Figure 7 Tide Actuated Duty Cycle Control System for Jet Array

out to the design scour radius of 15.24 m, while not decaying to the threshold stress of fluid mud, 1 dyne/cm², until 30 m out from the quaywall. These ranges of coverages are sufficient to protect draft to beam ratios of most modern vessels.

The jet nozzles were inclined downward to allow the jet flow to be directed around the bottom of the hull of a moored ship, given the constraint of mounting the array above the over-dredged depth. A number of deflection angles were tested ranging from 20° to 45° of downward inclination. Figure 8 shows three time staggered bottom profiles along

three separate range lines measured out from the concrete quaywall. Those for the control were taken downstream in Berth 8 (see Figure 1). Another control area was monitored on the upstream side of the area in Berth 6. Curves for Jet 3 and Jet 8 compare the effects of different degrees of downward deflection. Jet 3 used 29° of downward deflection while Jet 8 was inclined 35° downward from horizontal. Bottom profiles labeled 30 March were taken just after the completion of dredging in Berth 7. Curves labeled 17 May show the build up of mud over 1 1/2 months while the jet remained inoperative pending Coastal Commission permits. The jet array became operational on 30 May. Therefore the curves labeled 9 August indicate the scour and protection provided by the array over a 2 1/3 month period. The most nearly optimum coverage

SURVEY ON TEN ELEMENT SWEEPING JET ARRAY

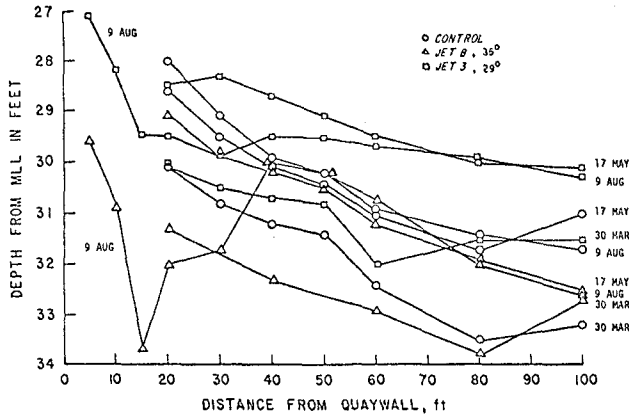


Figure 8

MUD ACCUMULATION NEAR QUAYWALL

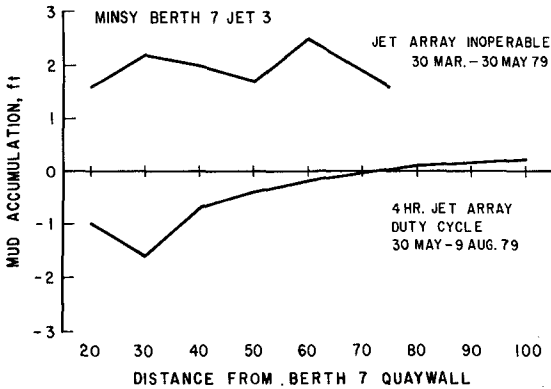


Figure 9

appears to have resulted from the 29° downward deflection provided by Jet 3. The larger downward deflection of Jet 8 is shown in Fig 8 to have excavated a 1.2 m deep impact crater extending from 3.05 to 12.19 m out from the quaywall, but depositing a mound beyond 12.19 out to 21.33 m. The lower curve of Fig 9 plots the net change due to Jet 3, showing scour out to 21.33 m and little new accumulation out to 30 m during the 2 month operational period. Integrating over all survey contours for the entire array, and comparing with the accumulations at the upstream control in Berth 6, it was determined that the jet array prevented or scoured 1200 cubic m of deposition in Berth 7 from 30 May to 9 August.

There was also an additional downstream influence from the jet array that can be found in the control contours from Berth B in Fig 8. Here only about 15 cm of new deposition was observed over the 2 1/3 month operational period as compared to an average of 45 cm during the same period at the upstream control in Berth 6. Factors which may have contributed to this apparent downstream influence were the presence of a 13 m diameter submarine and a highly stratified and stable water column with a Richardson's number, $R_i = g(d\rho/dz)/(du/dz)^2 \approx 10^5$ through May and June. Both these factors inhibit vertical mixing and keep the turbulent jet effluent confined near the bottom where it resuspends sediment while being advected downstream with the ebb flow.

The jet array resuspension technique is an attractive alternative to bucket and scow dredging presently used near structures. The jet array was also found to effectively prevent the new accumulations of mud along channel-side quaywalls during hopper dredging of the navigation channel.

4. CONTROL OF MUD ACCUMULATION BY EXCLUSION

Finding that the preponderance of suspended sediment is in the lower portions of the water column (Figure 3) led to the hypothesis that a flexible barrier, or curtain, could block these sediments from continuously circulating and settling into a berth by either tidal density-stratified currents or eddy motions. The finger pier complex notched out of the banks of Mare Island Strait (Figure 2) is well suited for this application. The entrance to the berth in between Pier 20 and



Figure 10

21 was partitioned off from the main channel by a 82.9 m long Hypalon curtain that extended from the bottom up to MLL sea level (see Figure 10). The lateral seal on the berth was provided by an undredged mud bank extending up to MLL water under Pier 21, and by a concrete quay-wall on the Pier 20 side. The 1.2-2.1 m gap over the curtain and mud bank between MLL and MHH water allows Berth 20-21 to equilibrate any sea surface inequality with the channel or neighboring berths during a tidal cycle. The lens of water overtopping the curtain and mud bank would be expected to transport a negligible amount of suspended sediment, even for the nearly isotropic conditions of peak rainfall periods, as during the 9 March extreme shown in Figure 3.

The curtain was constructed in 13 sections, each 6.4 m in length. The Hypalon curtain material on each section was anchored to the bottom by an 18 inch storm drain conduit filled with concrete aggregate weighing 8000 lbs. The 9.14 m high curtain sections were supported vertically in the water by curtain buoys constructed from 18 inch storm drain conduit filled with poly-urethane foam. A pair of air filled 10 inch diameter PVC pipes were retrofitted to the curtain buoys, seen in Figure 11, to trim the buoyancy against additional water absorption by the foam and concrete aggregate.



Figure 11 Rigging a curtain section for proper buoyancy

To raise the curtain as shown schematically in Figure 12, a second set of buoys at the surface are connected by a length of chain sufficient to extend down to the submerged buoy floats at a higher high water during spring tides. At the low tide preceding curtain opening, the surface floats and buoy floats are at nearly the same level, and the slack chain is drawn up and secured by a stopper arrangement. With the ensuing flooding tide, the additional buoyancy of the 24 inch diameter foam filled surface buoys are sufficient to gradually overcome the bearing stress of the fluid mud, about 20 dyne/cm², seen in progress in Figure 13. At high tide the curtain floats free of the bottom illustrated in Figure 11, whence it can be swung open into the berth by towing behind a small tug boat as shown in Figure 14. The end about which the curtain pivots was anchored to Pier 21 by cutting a notch in the slope of the mud bank and allowing the first curtain sections to become buried. The curtain rotates

about tongue and pin joints between the second and third sections. Consequently it was not necessary to raise the first two sections allowing surface floats adjacent to Pier 21 to be removed. This gave access to the berth by shallow draft barges while the curtain still remains closed and anchored (Figure 15).

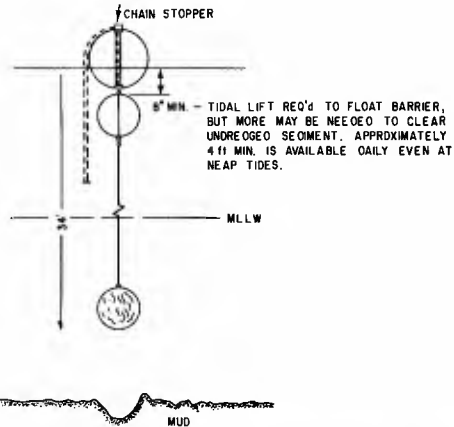


Figure 12 Curtain cross section in raised configuration



Figure 13 Surface buoys while raising anchored sections from the mud during a rising tide



Figure 14 The curtain being opened by the Sea Mule yard tug



Figure 15 The curtain in the closed and anchored configuration as seen looking into the Pier 20-21 berth

The shoaling with time averaged across the Pier 20-21 berth appears in Figure 16, comparing mean shoaling on two survey ranges inside the curtain with another two outside. The range lines were taken across the berth perpendicular to Pier 21 at positions measured from the shoreward end of the 228.6 m length Pier. The shoaling along these range lines is shown in Figure 17 to have been fairly uniform. Four months of

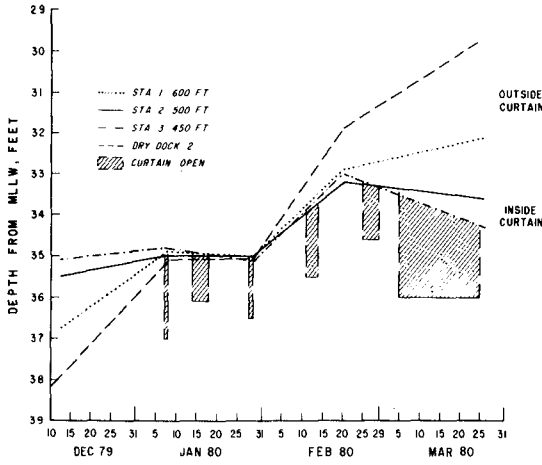


Figure 16 Shoaling history averaged across the berth

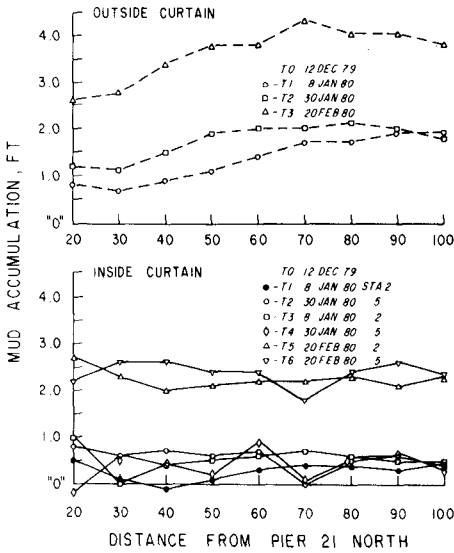


Figure 17 Mud accumulation across the berth beginning from 12 December 79

operational testing with six curtain opening cycles showed that only 0.46-0.76 m of new deposition occurred inside the curtain while 1.52-2.59 m accumulated in the unprotected waters outside the curtain. This represents a 70% effectiveness during high depositional conditions with several protracted periods in the open configuration necessitated by ship movements. An apparent dredging savings of between 18,000 to 30,000 cubic meters was achieved. This 4 month savings payed for the material costs of the curtain considering dredging costs at the present local value of \$2.50/yds³. Comparing the dates in Figures 16 and 17 with the mud storm events in Figure 4 it is concluded that most of the deposition behind the curtain occurred during February when the curtain was open for only one 3 day period. Only about 6" of deposition inside the curtain occurred in the months of December, January and March when there were 5 opening cycles adding up to 36 open days. Therefore the timing between mud storm events and curtain opening seems critical in achieving maximum protection of a berth by exclusion techniques. It was fortunate in this experiment that the curtain happened to be closed during the mud storms in December and early March when the large mud accumulations are shown in Figure 16 to have occurred outside the curtain.

5. CONTROL OF SAND ACCUMULATION BY CRATER-SINK/FLUIDIZATION

The crater-sink sand by-passing concept, which uses a crater shaped depression in the channel bed to capture sand, was first proposed by Inman and Harris (1970). Several systems based on this concept have been tested in both the laboratory and the field (Harris et al, 1976; McNair, 1976), and full scale systems are currently operating at Mexico Beach, Florida (Pekor, 1977), and at Rudee Inlet, Virginia.

One of the limitations of the crater-sink concept has been the relatively small trapping radius as compared with depositional patterns. Harris et al (1976) found that the trapping radius of a crater could be enlarged by feeding the crater with a fluidized trench cut across the depositional area. These trenches are themselves sinks to the sediment flux. The trench is both cut and maintained by a fluidizer pipe having a line of downward axially slanted water jets along its length. The jets fluidize the neighboring sand and impart momentum to the resulting slurry in the direction of the jet effluent. A momentum survey of the process in closed duct configurations is discussed in Bailard and Inman (1975).

The Agua Hedionda Lagoon selected for these experiments is located 30 miles north of San Diego, California. The lagoon consists of an outer, middle and inner section with a total area of $1.04 \times 10^6 \text{ m}^2$. The tidal prism is approximately $1.68 \times 10^9 \text{ m}^3$, passing through a stabilized inlet channel with a cross sectional area of 33.4 m^2 . One third of the tidal prism is removed from the lagoon each tide cycle and diverted through the cooling condensers of a power plant and discharged into the sea. The corresponding reduction in ebbing currents through the inlet which intercepts the longshore transport of sand results in an average influx of beach sands of about $11,000 \text{ m}^3/\text{month}$. This influx is deposited entirely in the outer lagoon where the utility company operates a

suction dredge on a yearly or bi-yearly basis.

A crater-sink/fluidization sand by-passing system was designed to intercept the inflow of sand and return it to the downdrift (south) beach face (Figure 18). The system was sited at two different locations between

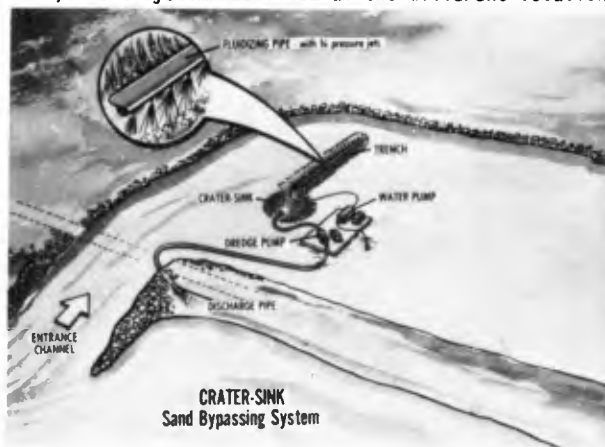
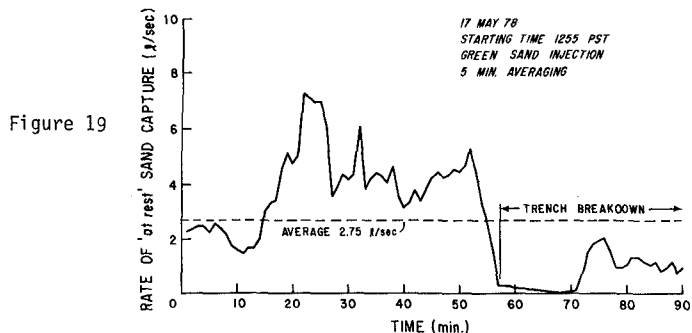


Figure 18

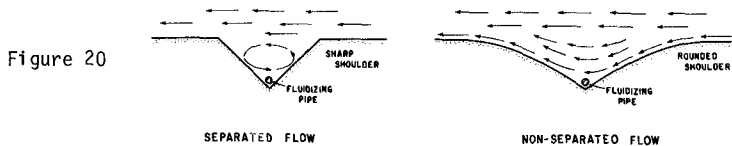
1978 and 1979 near the outer bank of the curved inlet where the centrifugal accelerations on a flooding tide direct the influx, depositing a sand bar. The latest of several system designs for Agua Hedionda Lagoon consisted of a 1-4 m deep crater excavated by a 6"x6", 150 hp centrifugal dredge pump connected to a 270 m long, 6 inch diameter discharge pipeline. A 50 m long fluidizer trench cut across the primary depositional bar powered by a 6 inch 100 hp water pump discharging into the crater on the interior downslope side of the bar. The fluidizer pipe was 4 inches in diameter with 0.282 cm diameter jets drilled at 45° angles and spaced 6.25 cm apart. The flow rate from the fluidizer drive water pump was 784 gpm at 100 ft total head pressure. One third of this discharge was diverted to a 2 inch diameter liquifier jet in the bottom of the crater, dropping the pressure to the fluidizer pipe down to 22 psi. The liquifier jet fluidized the sand at the crater suction inlet to minimize suction losses on the dredge pump. The flow rate through the dredge pump and sand discharge pipeline varied between 890 and 1000 gpm at 180 ft of total head, depending upon the amount of vertical lift required to remove the sand. To minimize the required suction lift, which varied between 2-6 m depending upon crater depth, tidal phase, and sand bar level, the pumping systems were operated from a moored barge.

To evaluate the ability of the system to capture and by-pass sand, the flow rate and sand concentration in the discharge line was monitored through the period of maximum flooding tide. Figure 19 shows the by-passing history during the 1978 experiment using a 60 cm deep fluidizing trench. The mean capture rate of 2.75 l/sec accounts for about 1/2 of the average sand influx rate, 4-6 l/sec. Flood currents during

this period peaked at 130 cm/sec on the surface above the fluidizer trench. If the sediment transport rate is taken to vary as the cube of



the velocity according to Bagnold (1966) then 1/2 the sand influx would be suspended load at these current speeds. Hence the capture efficiency of the system is in proportion to the bed load. Suspended load is transported over a shallow fluidizer trench. Furthermore underwater observations discovered that the initially sharp lip of the trench became rounded (Figure 20) after about 55 minutes of operation under currents in excess of 1 m/sec. With this round-off the flow no longer separated at the top of the trench, allowing the flood current to sweep into the



trench and carry away sand, as indicated in Figure 19 by the decline in sand capture with the onset of trench breakdown.

To avoid trench breakdown the 1979 experiment was moved further into the lagoon where flooding current amplitudes and suspended load were less. The fluidizer trench was deepened to 3 m to create a flow divergence over the trench that would drop the suspended load. Figure 21 shows by-passing time histories in which the average total sand influx (5-6 1/sec) was exceeded for extended durations without trench breakdown at current speeds as high as 110 cm/sec. However, these experiments were plagued by extra-normal amounts of kelp and bottom debris broken loose offshore by unseasonably high waves and subsequently swept into the lagoon on flooding tide. When captured by the system and mixed into the fluidized sand, the kelp would conglomerate in masses as large as 10 m in diameter which the system had insufficient power to move. A porous screen lid over the trench and crater successfully shielded the system for a two week period but required frequent diver maintenance. Another approach tested was to simply allow a kelp fouled system to become buried. Under the added pressure of the sand overburden kelp decays anerobically to a

SAND BY-PASS RATES FROM AQUA HEDIONDA LAGOON

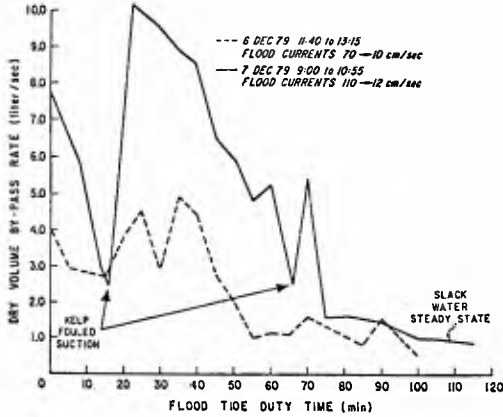


Figure 21

less fibrous black mulch which the system can move again in several days to a week. With a single fluidizer trench this procedure restricts the number of by-passing cycles. To circumvent that in future by-passing schemes, multiple fluidizing trenches extending out from a single crater in a fan arrangement could be alternately cycled and allowed to bury once fouled.

6. OPENING A TIDAL INLET BY OPEN TRENCH FLUIDIZATION

Pepasquitos Lagoon is a relatively small lagoon encompassing about $1.29 \times 10^6 m^2$ and is located approximately 10 miles north of San Diego. Past studies have shown that the normally closed lagoon inlet channel is periodically opened during times of high precipitation in which the lagoon

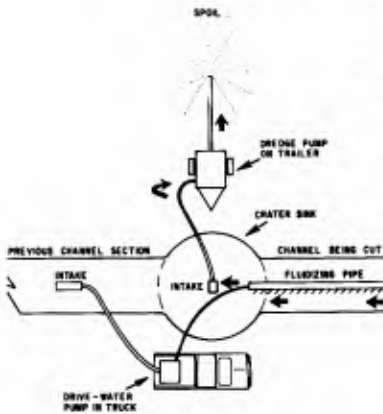


Figure 22



Figure 23

is filled to overflowing. The lagoon then remains open until it is closed by the longshore transport of sand. Closure is enhanced when high waves coincide with neap tides. This condition results in a large influx of sand into the lagoon and causes a sand plug to form in the seaward end of the inlet channel. An overwash fan then forms behind the sand plug, filling the channel with sand.

A crater-sink/fluidization system was designed to cut a new channel across the sand plug. The system consisted of a 6 inch, 100 hp dredge pump connected to a short discharge pipeline, and a 43 m long spiral wound fiberglass fluidizer pipe powered by a 4 inch, 30 hp water pump (Figure 22). The design of the pipe was based on a modified form of the analytic model developed by Bailard and Inman, (1975). The fluidizer pipe was 4 inches in diameter with 0.145 cm diameter jets angled at 45° and spaced 6.3 cm apart. The water flow rate to the pipe was 520 gpm at a pressure of 3.85×10^6 dynes/cm², (55 psi).

The procedure for cutting the channel consisted of starting at the lagoon and "leap-frogging" the system across the overwash fan. The system successfully cut a 210 m long channel in 5 steps (Figure 23) removing 600 m³ of sand. In fine sand the fluidizer moves sand at a rate of 100 m³ per hour; however due to the presence of extensive cobble beds, the maximum cutting rate of the system was 30 cubic meters per hour, cutting a 1.5 m deep, 3.7 m wide, 43 m long channel segment in approximately 3.5 hours.

7. REFERENCES

- Bagnold, R. A., 1966, "An approach to the sediment transport problem from general physics," U. S. Geological Survey, Report No. 422-J, 37 pp.
- Bailard, J. A. and D. L. Inman, 1975, "Analytic model of duct-flow fluidization," Proc. Sym. on Modeling Techniques, ASCE, San
- Harris, R., D. L. Inman, J. A. Bailard, and R. Oda, 1976, "Study and evaluation of remedial sand bypassing procedures," Rpt. no. H-76-1, WES, Vicksburg.
- Inman, D. L., and R. Harris, 1970, "Crater-sink sand transfer system," Proc. 12th Conf. Coastal Eng., ASCE, New York, vol. 2, p. 919-933.
- Krone, R. B., 1959, 1960, "Annual progress report on silt transport studies using radioisotopes," Hyd. Eng. Lab, Univ. of Calif., Berkeley.
- Krone, R. B., 1972, "A field study of flocculation as a factor in estuarial shoaling processes," Tech. Bul. No. 19, Com. Tidal Hydraulics, COE.
- La Mer, V. K. and R. H. Smellie, 1962, "Theory of flocculation, subsidence and refiltration rates of colloidal dispersions flocculated by polyelectrolytes," Proc. 9th conf. Clays & Clay Min., vol. 9, p. 295-314.

- Little, A. O., Inc., 1975, "Candidate environmental impact statement, Norfolk Naval Base Complex long range maintenance dredging program."
- Malloy, R. J., 1980, "U. S. Navy harbor maintenance dredging atlas," Proc. Dredge Sed. & Marine Organism Control, NAVFAC Washington, Apr. 23-24.
- McNair, E. C. Jr., 1976, "Sand by-passing system using a jet pump," Proc. 15th Conf. Coastal Eng., ASCE, Honolulu, HI, vol. 2, p. 1342-1360.
- Needham, J., 1974, Civilization and Technology of China, Oxford Univ. Press.
- N.E.S.O., 1976, "Composite baseline dredging report," Navy Environmental Support Office, Rpt. no. 11-008.
- Pekor, G. B., 1977, "Sand bypassing at Mexico Beach Florida," Shore and Beach Protection, Jan., p. 29-30.
- Poreh, N. Y., G. Tsuei and J. E. Cermak, 1967, "Investigation of a turbulent radial wall jet," Jour. Appl. Mech., 34, p. 457-463.
- Sforza, P. M. and G. Herbst, 1970, "A study of three-dimensional, incompressible, turbulent wall jets," AIAA Jour., Vol. 8.
- Van Dorn, W. G., O. L. Inman and S. McElmury, 1975, 1977, 1978, "Evaluation of sediment management procedures," Phase I, II and III Final Report, 1974-75, 1975-76, and 1976-77, SIO Ref. 75-32, 77-10, 78-18.

8. ACKNOWLEDGEMENTS

The Fine Sediment deposition control studies in this paper were funded by the Naval Facilities Engineering Command through the Geography branch of the Office of Naval Research, Contract No. N00014-76-C-0631. The 1977-78 Agua Hedionda and Penosquitos Lagoon experiments were sponsored by NOAA, Office of Sea Grant, U. S. Department of Commerce under grant number UCSD-R/CZ-33D.

The authors are grateful for the efforts of Dr. William Van Oorn, who was our colleague in the fine sediment studies prior to his retirement in August 1979. We have appreciated assistance and logistical support from Mr. James Oillard, technical assistant to the public works officer at Mare Island Naval Shipyard. We are further indebted to Marion Horna, plant manager, San Diego Gas and Electric Co. for the support of cable, barges, and electric power in the Agua Hedionda by-passing experiments.

RESEARCH IN SOUTHERN QUEENSLAND INTO
THE MANAGEMENT OF COASTAL SAND DUNES

James B. McKenzie¹ and David A. Barr²

1. INTRODUCTION

Queensland's Beach Protection Act (1968-1974) resulted, inter alia in the formation of the Beach Protection Authority, which is responsible for investigating coastal erosion, planning remedial works, recording and evaluating results of investigations, and various other functions.

Control of windblown sand and retention of vegetated and naturally stable coastal sand dunes are valuable means of decreasing coastal erosion and because of this the Authority implements a broad research program into the management of coastal dunes in Queensland. Field trials are carried out at the Authority's Dune Management Research Station on South Stradbroke Island to determine methods of repairing, stabilizing and managing coastal dunes.

The research program conducted so far consists of fifteen separate field trials within four general areas of investigation:-

(a) Dune Forming Fences

Two trials were installed in blown-out sections of the frontal dune to compare different types of semi-permeable fences (eg. wooden slats) and brush matting (a surface mulch of tree branches) on the basis of their ability to accumulate windblown sand and initiate dune formation.

(b) Dune Stabilization Techniques

Three trials were installed on bare dunal areas to evaluate methods of temporary sand surface stabilization (organic mulches and spray-on materials) as an aid in establishing dune vegetation.

(c) Dune Vegetation

Two trials were conducted to produce and compile information on the performance of important or potentially useful dune plants.

(d) Plant Nutrition

Eight trials using different combinations and rates of fertilizer were used to study methods of improvement of establishment and early growth of dune stabilizing plants, particularly sand spinifex grass (*Spinifex hirsutus*). Good establishment and rapid early growth is required in order to accelerate, improve, and decrease the costs of, the stabilization process.

-
1. Agronomist, Department of Harbours and Marine, Queensland, Australia.
 2. Principal Dune Conservationist, Department of Harbours and Marine, Queensland, Australia.

The trials carried out in each area of investigation are described below.

2. DUNE FORMING FENCES

Where there is a significant width of sand of suitable median grain size between high water mark and the seaward toe of the dune strong on-shore winds will transport large quantities of sand landwards.

In the absence of dune vegetation which traps and holds windblown sand, semi-permeable dune forming fences can be used for the same purpose. The fences function by lowering wind velocities adjacent to the fence below the critical threshold velocity required to keep sand moving. This results in sand accumulating on both sides of the fence, eventually burying it, and an artificial sand dune is formed.

Semi-permeable dune forming fences can be used to repair dune "blow-outs" or to initiate rebuilding of a new dune line. The most satisfactory types of dune forming fence in use are those constructed of spaced timber slats, brush material and moulded plastic or nylon materials.

(a) Trial 1

In 1971, a trial was installed in blown-out sections of frontal dune to measure and compare the rate of accumulation of windblown sand against three types of semi-permeable material attached to wooden post and wire fences. The semi-permeable materials used were spaced hardwood timber slats, 'Trical' (moulded polyethylene mesh) and 'Raschel' (woven polyethylene netting). Each fence material had a solid to space ratio of about 1:1. The fences were erected across each of three dune "blow-outs" and placed above, and parallel to high water mark. The fence treatments were replicated to enable statistical analysis.

Cross sections at each fence were surveyed to calculate volumes of accumulated sand. The cross section lines extended 6 m on both the seaward and landward side of the fence. Each fence was about 1 m high.

The volume of sand accumulated by each type of fence treatment, and the results of statistical analysis are presented in Table 1.

The slat fence initially accumulated windblown sand at a faster rate than the 'Trical' or 'Raschel' fence. During the 6 week period following installation the sand surface beneath the 'Raschel' fence suffered wind erosion (indicated by the negative value in Table 1). However, after 23 weeks the 'Raschel' fence was effectively trapping windblown sand. At 66 weeks after trial installation all fence treatments had completely filled with windblown sand.

(b) Trial 2

Another trial was installed in 1972 across a large blown-out section of frontal dune to compare the sand trapping ability of 6 types of semi-permeable material when attached to two parallel fences 6 m apart. The treatments used were: brush fence (pieces of brush attached to the fence wires), brush matting (successive layers of brush placed on the sand

TABLE 1: VOLUME OF SAND ACCUMULATED BY FENCE TREATMENTS

6 weeks after installation	Tr. C.V Sig.	Slats 1 089	Trical 146	Raschel -1 077
		L.S.D. = 1271 (P = 0.95)		
23 weeks after installation	Tr. C.V Sig.	Slats 2 423	Trical 1 357	Raschel 193
		L.S.D. = 1067 (P = 0.95)		
38 weeks after installation	Tr. C.V Sig.	Slats 6 059	Trical 4 511	Raschel 3 765
		L.S.D. = 756 (P = 0.95)		
66 weeks after installation	Tr. C.V Sig.	Trical 12 179	Raschel 12 009	Slats 11 839
		L.S.D. = 5676 (P = 0.95)		

Notes: Tr. = fence treatment

C.V = cumulative volume of sand ($\text{m}^3 \text{ km}^{-1}$)

Sig. = lines join treatment means not significantly different

L.S.D. = least difference necessary for significance.

surface), wooden slats, 'Trical', 'Easy Fencing' (plastic impregnated netting) and 'Sarlon' (loose woven polypropylene ribbon fabric). The parallel fences were placed above and parallel to high water mark. The experimental design used was that for a Randomised Complete Block:- 6 fence treatments randomly allocated within each of 3 replicates.

Cross sections at each fence treatment were surveyed to calculate volumes of accumulated sand, and the results are presented in Table 2.

Initial rates of sand accumulation were similar in all treatments but later in the trial brush matting showed a superior ability to accumulate windblown sand. The brush fence and wooden slats were similar in terms of rate and volume of sand accumulation and superior to the plastic materials ('Trical', 'Sarlon', 'Easy Fencing') which were the less effective sand accumulators. All fence treatments had completely filled with windblown sand after 128 days. The parallel fences in this trial accumulated sand more rapidly than the single fences in the first trial.

A wider dune having a more uniform profile of accumulated sand can be formed using two fences parallel to each other. Provided there is a sufficient quantity of sand blown landward from the beach both fences will fill quite rapidly with the seaward fence filling first.

To provide more permanently stability to the re-formed dune it is advisable to apply brush matting to prevent wind erosion and to plant the dune with suitable dune colonising vegetation.

TABLE 2: VOLUME OF SAND ACCUMULATED BY FENCE TREATMENTS

22 days after installation	Tr.	B.F	S	E.F	T	B.M	SA
	C.V	1 534	1 395	1 287	1 154	1 070	5 885
	Sig.	L.S.D. = 646 (P = 0.95)					
52 days after installation	Tr.	B.M	E.F	S	B.F	SA	T
	C.V	4 393	3 961	3 952	3 553	3 210	2 976
	Sig.	L.S.D. = 837 (P = 0.95)					
91 days after installation	Tr.	B.M	B.F	S	E.F	SA	T
	C.V	8 336	7 236	6 612	5 136	4 629	4 466
	Sig.	L.S.D. = 1653 (P = 0.95)					
128 days after installation	Tr.	B.M	B.F	S	E.F	SA	T
	C.V	16 843	11 467	8 470	7 733	6 608	5 885
	Sig.	L.S.D. = 3538 (P = 0.95)					

Notes: Tr. = fence treatment

viz. B.F = brush fence; B.M = brush matting; E.F = 'Easy Fencing';

S = timber slats; SA = 'Sarlon'; T = 'Trical'

C.V, Sig., L.S.D. = see notes for Table 1.

3. DUNE STABILIZATION TECHNIQUES

Initial sand surface stabilization using organic mulches and spray-on materials and rapid establishment of vegetation are integral parts of any program designed to stabilize exposed wind eroded coastal dunes. Surface stabilizing agents prevent wind erosion for a sufficient period of time to allow establishment of dune colonising vegetation which stabilizes the sand surface more permanently.

(a) Field Stabilization Trial

In 1971 a bare unstable dune area (4.6 ha) was selected to test the normally recommended method of frontal dune stabilization. Stabilization was to be a step-wise procedure utilizing the growing seasons and growth habits of annual and perennial plant species. The area was planted with sand spinifex grass (*Spinifex hirsutus*), marram grass (*Ammophila arenaria*) and cover crops consisting of cereal rye (*Secale cereale*), sand plain lupin (*Lupinus cosentii*), Zulu sorghum (*Sorghum vulgare*), Tamworth pearl millet (*Pennisetum typhoideum*) and Rhodes grass (*Chloris gayana*). Fertilizer containing nitrogen, phosphorus and potassium was applied at planting and throughout the trial period. The planted area was brush matted (about 10 tonne brush material per hectare) to prevent wind erosion. Tree seedlings of horsetail she-oak (*Casuarina equisetifolia* var. *incana*) and coastal wattle (*Acacia sophorae*) were also planted.

Ground cover estimates were used to assess development of a stabilizing vegetative cover. Brush matting provided initial sand surface stabilization, prevented wind erosion and allowed establishment of vegetation. Ground cover of vegetation averaged 60-65% within 30 months from planting and the trial area was completely stabilized by sand spinifex grass, Rhodes grass and the tree species. The annual plant species (cereal rye, sorghum) were dominant ground cover components early in the trial and were gradually replaced by the perennial species (sand spinifex grass, Rhodes grass) which stabilized the sand surface more permanently. The application of fertilizer (over 1 tonne ha⁻¹) throughout the trial period assisted establishment and growth of vegetation.

(b) Mulch Trial 1

In the winter of 1971 a plot trial was installed on a bare area of wind eroded dune to compare the effectiveness of various surface stabilizing agents in initially stabilizing sand and allowing establishment of vegetation. The trial area (0.4 ha) was planted with sand spinifex grass (28 kg ha⁻¹), marram grass (4 kg ha⁻¹), cereal rye (44 kg ha⁻¹), Zulu sorghum (11 kg ha⁻¹), Rhodes grass (11 kg ha⁻¹) and sand plain lupin (11 kg ha⁻¹). A mixed (N,P,K) fertilizer was applied at planting and the following treatments were applied to plots (9 m x 4.5 m) randomly allocated within each of four replicates: brush matting (2.5 kg brush m⁻²), straw mulch (0.62 kg straw m⁻²), 'Terolas' (bitumen emulsion mixed with 5 volumes of water and sprayed at 0.28 l emulsion m⁻²), 'Curasol' (poly vinyl acetate emulsion mixed with 30 volumes of water and sprayed at 0.05 l emulsion m⁻²), straw plus 'Terolas' and straw plus 'Curasol'. Fertilizer to promote plant growth was broadcast over the treatment plots during the 90 week trial period.

Measurements of plant establishment, ground cover and resistance to wind erosion were used to assess treatment effect. Each treatment gave sufficient surface protection to allow vegetation to establish and stabilize the sand. The brush matting treatment provided better conditions for plant establishment and growth than did most of the other treatments. In all treatments annual plants (particularly cereal rye) were dominant early in the trial but after 7 months the perennial plants, Rhodes grass and sand spinifex grass, were dominant. Ground cover in all treatments improved generally over the term of the trial (Fig. 1). Early ground cover was provided mainly by cereal rye and was slightly better in the treatment plots where this species established best i.e. in the treatments where straw was used. At the end of the trial (after 90 weeks) ground cover on the brush matting treatment was not significantly different from that on those treatments containing straw but it was significantly greater ($P = 0.95$) than ground cover on the 'Terolas' and 'Curasol' treatments. Rhodes grass was the dominant ground cover component in the brush matting treatment at the end of the trial. Visual ratings showed that brush matting had the greatest resistance to wind erosion. The surface seal provided by straw mulch was the first to deteriorate. The 'Terolas' and straw plus 'Terolas' treatments lasted slightly longer than the 'Curasol' and straw plus 'Curasol' treatments. The 'Curasol' and 'Terolas' treatments showed signs of deterioration at 10 months after application.

(c) Mulch Trial 2

A similar trial to the one above was installed in the summer of 1974. The trial area (1.2 ha) was sown (broadcast) with spikelets of sand spinifex grass at the rate of 67 kg ha⁻¹ and seed of Tamworth pearl millet at the rate of 11 kg ha⁻¹. A mixed (N, P, K) fertilizer was applied at planting and harrowed in with the seed.

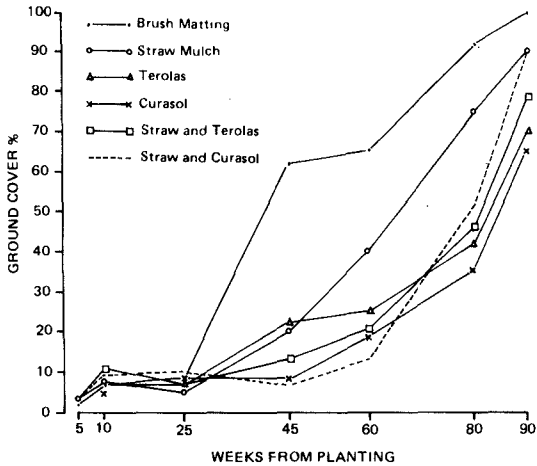


Figure 1. Ground cover on surface stabilization treatments.

Nine treatments were randomly allocated to plots (10 m x 5 m) within each of 4 replicates at 2 sites (each site 0.6 ha). The treatments applied were:-

Brush matting: 2.5 kg brush m⁻².

Straw mulch: 0.45 kg straw m⁻².

'Terolas': bitumen emulsion mixed with 4 volumes of water and sprayed at 0.36 l emulsion m⁻².

'Curasol': poly vinyl acetate emulsion mixed with 18 volumes of water and sprayed at 0.1 l emulsion m⁻².

'Unisol': synthetic latex and mineral oil emulsion mixed with 15 volumes of water and sprayed at 0.1 l emulsion m⁻².

Straw plus 'Terolas'.

Straw plus 'Curasol'.

Straw plus 'Unisol'.

Nil: bare sand without surface treatment.

The buffer strips between plots and all bare surrounding areas were brush matted to prevent wind erosion and sand encroachment onto treatment plots. Additional fertilizer was applied as required during the trial. Measurements of plant establishment, ground cover and resistance to wind erosion (longevity of surface seal) were used to assess treatment effect.

The nil treatment was completely ineffective and was brush matted to prevent sand blowing onto adjacent plots. All other treatments were initially effective in stabilizing bare wind-blown sand. Brush matting was again the most effective stabilizing agent and favoured establishment and growth of sand spinifex grass and Tamworth pearl millet. These plants also grew well in those treatments containing straw but establishment and growth were very poor in the 'Unisol' and 'Terolas' treatments.

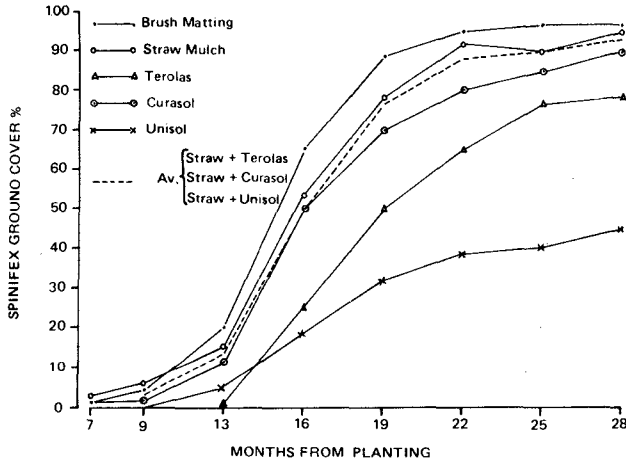


Figure 2. Spinifex ground cover on surface stabilization treatments.

The millet cover crop was the main ground cover component early in the trial and provided protection for establishing sand spinifex grass which was then the dominant ground cover for most of the trial. Development of spinifex ground cover during the trial period is shown in Fig. 2 and indicates that spinifex ground cover developed best in the brush matting treatment. Spinifex growth was also favoured by the 'Curasol' treatment and those treatments containing straw. There was poor development of spinifex ground cover in the 'Unisol' and 'Terolas' treatments.

All mulch treatments (except nil) initially stabilized the sand surface but as the trial progressed the surface seal provided by the treatments either rapidly or gradually deteriorated. Visual observations of the treatments indicated that the surface seals deteriorated in the following order:

nil (after 2 weeks); 'Unisol' (after 3 months); straw plus 'Unisol', straw, 'Curasol', straw plus 'Curasol' (after 7 months); straw plus 'Terolas', 'Terolas' and brush matting (seal still effective at trial completion).

4. DUNE VEGETATION

As coastal sand dune stabilization is usually based on the use of vegetation, it is necessary to make the best use of available species if the stabilization program is to be most effective.

(a) Spinifex Growth Pattern Trial

Sand spinifex grass is the most widespread and important primary coloniser of coastal dunes in southern Queensland and in the winter of 1971 a trial was installed on a bare section of frontal dune primarily to obtain information on the growth pattern of this perennial species.

The grass was planted in plots (about 14 m x 5 m) either by seed or by stolon tip cuttings, with nil, medium (500 kg ha⁻¹), or high (1000 kg ha⁻¹) rates of a mixed (N,P) fertilizer. The trial design was that of a 3 x 2 factorial in a randomised tri-replicated complete block. After planting brush matting was spread over the plots and surrounds to prevent wind erosion. When the grass had established, at about 6 months after planting, regular ground cover measurements were used to assess treatment effect. Observations were also made on the requirements for good seed set of spinifex plants grown from seed and stolon tip cuttings. Additional fertilizer applications were made as required to maintain growth during the trial.

Good establishment occurred both from seed and stolon tip cuttings. Vegetatively established plants grew faster than the seedlings. However the two methods of plant establishment produced similar ground covers. The higher plant numbers produced in plots established from seed compensated for the slower seedling growth. The development of spinifex ground cover over a 3 year period is shown in Fig. 3. Growth was best during the summer months with gradual die-back in winter. Ground cover was similar on plots receiving medium and high rates of fertilizer and ground cover on the fertilized plots was much higher than on unfertilized plots. The fall-off in ground cover after June 1973 was caused by the plots being inundated with windblown sand which occurred during a storm in July 1973. While fertilizer increases growth, climatic factors largely govern the plants growth pattern. The dramatic increase in ground cover after October 1972 is associated with increasing temperature and also the fact that 460 mm of rainfall occurred in late October 1972. Maximum ground cover was initially achieved in the fertilized and unfertilized plots at about 20 months after planting. The results indicate that where rapid stabilization is required fertilizer should be added. Plants raised from stolon tip cuttings produced more inflorescences than plants raised from seed in the first few years after planting. The addition of fertilizer markedly increased seed yield from both types of plant. To obtain maximum seed yield in the shortest possible time stolon tip cuttings should be planted and heavily fertilized.

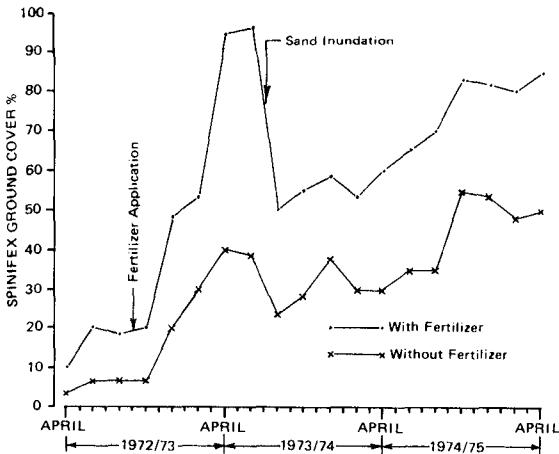


Figure 3. Development of spinifex ground cover over a 3 year period.

(b) Species Evaluation Trial

In 1974 a trial was installed to produce and compile information on the performance of important or potentially useful dune plants. Selected native and exotic species planted at 3 dunal sites of varying exposure are compared with sand spinifex grass (control species). Selected species are planted in duplicate 6 m long single rows at each site, either as seed or seedlings. Mixed (N, P, K) fertilizer is applied at 3 monthly intervals to all species except legumes (or other N-fixing species) which receive (P, K) fertilizer at 3 monthly intervals. Ground cover and vigour and persistence ratings appear to be the most useful measurements for comparing different plants.

The plants being studied include sea oats (*Uniola paniculata*), shoredune panicum (*Panicum amarulum*), beach grass (*Thuarea involuta*), green panic (*Panicum maximum* var. *trichoglume*), beach bean (*Canavalia maritima*), vigna (*Vigna marina*), vitex (*Vitex ovata*) and marram grass (*Ammophila arenaria*).

Ground cover, vigour and persistence of sand spinifex grass are generally superior to that recorded for all plants studied at each site. However sea oats, green panic, beach grass, vitex and beach bean may be suitable species for planting with sand spinifex grass on exposed frontal dunes. Sea oats, shoredune panicum, beach grass, green panic, vigna, vitex and marram grass have shown good growth at the less exposed sites but their vigour and persistence depends on season.

5. PLANT NUTRITION

Good establishment and rapid early growth of vegetation is required in order to improve the effectiveness of dune stabilization and to decrease costs by minimising the need for brush matting and repair work. Different combinations and rates of fertilizer were used in trials to improve establishment and early growth of dune stabilizing plants.

(a) Spinifex/Lupin/Nitrogenous Fertilizer Trial

In 1972 a trial was installed on the exposed seaward slope of the frontal dune to determine the effect of nitrogenous fertilizer on the growth of sand spinifex grass and sand plain lupin. Five rates of ammonium nitrate (34% N) fertilizer were applied to plots (9 m x 5 m) sown with spinifex and lupin seed. The rates used were 11.7, 23.4, 46.7, 93.4 and 186.8 kg N ha⁻¹ applied at planting and then at intervals of 3 months for 2 years. All plots received a basal dressing of all other essential plant nutrients at planting and the plots and surrounds were brush matted to prevent wind erosion. Treatments were randomly allocated within each of four replicates. Ground cover and dry matter yield were used to assess treatment effect.

The development of spinifex ground cover at 3 rates of nitrogen application is shown in Fig. 4. Accelerated growth and ground cover of sand spinifex grass occurred at 5 months after planting continuing until maximum ground cover was achieved at 15 months after planting. Increased spinifex growth was obtained by increasing the rate of application of nitrogenous fertilizer up to 934 kg N ha⁻¹ in 5 equal split applications over 15 months. Differences in spinifex ground cover in fertilizer treatments at 18 months after planting are shown in Table 3.

TABLE 3: SPINIFEX GROUND COVER IN TREATMENTS AT 18 MONTHS

Treatment ($\text{kg N ha}^{-1} \text{ 3 months}^{-1}$)	186.8	93.4	46.7	11.7	23.4
Ground Cover (%)	74.1	65.8	61.9	48.6	44.3

Note: 1. Values underlined are not significantly different ($P = 0.95$).

The application of increasing amounts of nitrogenous fertilizer increased dry matter yield of spinifex from about 1000 kg ha^{-1} to over 4300 kg ha^{-1} after 15 months. More frequent applications of nitrogenous fertilizer during the growing season are likely to improve growth, ground cover and yield of this grass. Heavy and frequent applications of nitrogenous fertilizer may be detrimental to lupin growth. No short term beneficial effect of using lupin as a nitrogen source for sand spinifex grass could be detected in this trial.

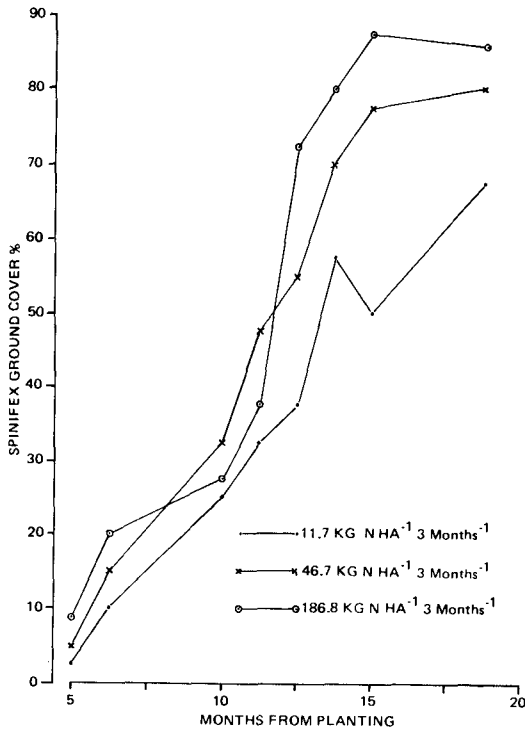


Figure 4. Effect of rate of application of nitrogenous fertilizer on spinifex ground cover.

(b) Spinifex/Superphosphate Trial

A trial was installed in 1972 on a bare section of frontal dune to determine the effect of superphosphate (9.2%P) on the growth of sand spinifex grass. Plots (9 m x 5 m) were sown with seed of sand spinifex grass at the rate of 112 kg ha⁻¹ and the plots and surrounds were brush matted to prevent wind erosion. Superphosphate was applied at the following rates: 126, 251, 502, 1004 and 2009 kg ha⁻¹. Each treatment was replicated 4 times in a randomised complete block design. Each plot was split and at planting each half of each plot received the appropriate fertilizer rate. Repeated applications of superphosphate were made at 6 monthly intervals for 2 years to the same half of each plot. All plots received adequate nitrogenous fertilizer during the trial. Dry matter yield was the main measurement used to assess treatment effect and the grass was harvested at 9 and 15 months after planting. The results obtained for each harvest are shown in Fig. 5. Establishment and growth of sand spinifex grass seedlings was unaffected by applications of superphosphate ranging from 126 to 2009 kg ha⁻¹ but the highest rate depressed early seedling growth. A yield increase at the 15 month harvest resulted from the application of superphosphate at moderate rates (502 kg ha⁻¹) when compared with the lowest rate (126 kg ha⁻¹). At each harvest date repeated applications of super produced marginally higher yields than the single application. An apparent yield suppression at the highest rate could not be confirmed statistically.

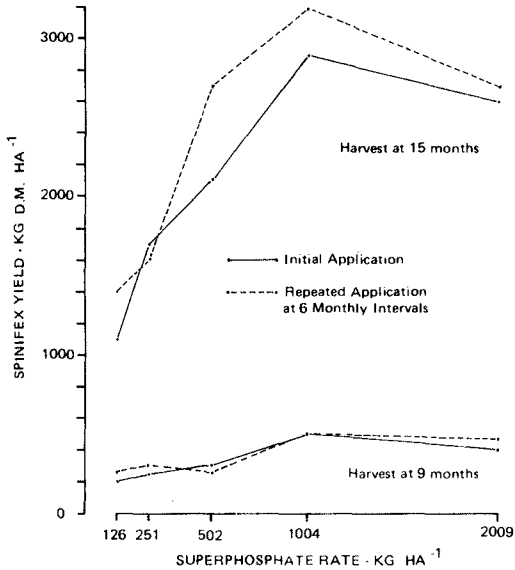


Figure 5. Effect of rate and timing of applications of superphosphate on spinifex dry matter yield.

(c) Millet Cover Crop/Fertilizer Trial

In 1973 a trial was installed in a semi-exposed bare area on the main dune to investigate the growth response of a cover crop of Tamworth pearl millet to different levels and combinations of potassium, sulphur and calcium fertilizers. Treatment plots (7 m x 7 m) were sown (broadcast) with millet seed at a rate of about 11 kg ha⁻¹. All plots received a basal dressing of nitrogen (40 kg ha⁻¹), phosphorus (30 kg P ha⁻¹), copper (10 kg ha⁻¹ of copper sulphate) and zinc (10 kg ha⁻¹ of zinc sulphate). The following rates (or levels) of nutrient elements were applied in factorial combinations: 0 and 26 kg K ha⁻¹; 4, 16, and 56 kg S ha⁻¹; 0 and 28 kg Ca ha⁻¹. Twelve nutrient element combinations were randomly allocated within each of 3 replicates. Statistical analysis of millet establishment counts indicated that there were significant differences between treatments in terms of plant establishment. The treatment plots were harvested 10 weeks after planting and dry matter yield was used to assess treatment effect. The effect of levels of K, S and Ca on millet dry matter yield is shown in Fig. 6. The application of potassium at 26 kg ha⁻¹ together with basal nitrogen and phosphorus increased dry matter production of Tamworth pearl millet. The application of calcium or sulphur had no significant effect on dry matter yield and there were no significant yield interactions between any of the levels of the 3 nutrient elements applied.

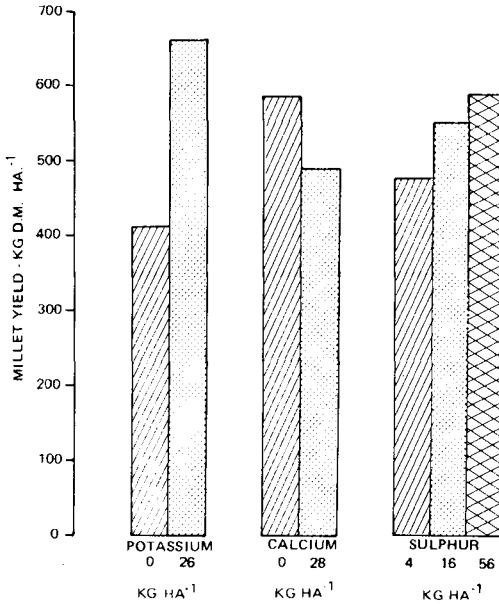


Figure 6. Effect of potassium, calcium and sulphur on millet dry matter yield.

(d) She-oak Nutrient Requirement Trial

In February 1975 a trial was installed at 2 sites on the main dune to investigate the nutrient requirements of horsetail she-oak seedlings. One site was exposed and the other was protected from onshore winds. The trial was an "omission" type with a randomised complete block design. Each site consisted of 24 plots (7 m x 7 m) in 3 replications of 8 plots. The plots and surrounds were brush matted to prevent wind erosion and planted with she-oak seedlings (about 20 cm high) on 1 m centres. The following fertilizer treatments were randomly allocated within each replicate at both sites: nil; complete (containing N, P, K, Ca, Mg, S and trace elements); complete minus N; complete minus P; complete minus K; complete minus Ca and Mg; complete minus S; and complete minus trace elements (Cu, Zn, Mo, B, Fe, Mn). The nutrients N, P and S were applied as split applications every 6 months and the remaining nutrients were applied annually. Tree height and basal diameter were the most useful measurements for assessing treatment effect. At the exposed site 15 months after planting there was no significant difference in height of trees in the following treatments: complete, -P, -K, -Ca/Mg, -S and -T.E (trace elements).

Trees in the nil and -N plots were significantly smaller in height than trees in other treatment plots. This marked difference in height was evident throughout the trial and is shown in Fig. 7. The -K, -Ca/Mg, -S and -T.E treatments are not shown as they are not significantly different from the complete and -P treatments.

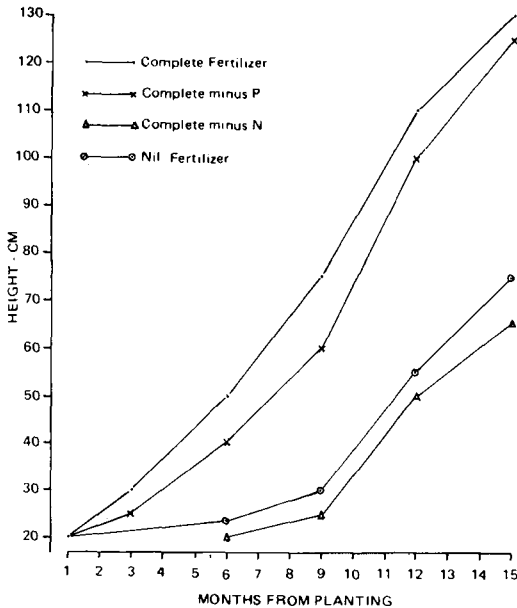


Figure 7. Effect of fertilizer treatments on the height of horsetail she-oak tree seedlings.

Similar trends for tree height within treatment plots were evident at the protected site. Results for basal diameter of trees within treatment plots at both sites showed similar trends to those for tree height. The trial has shown that nitrogen was the most important plant nutrient required for establishment and rapid early growth of horsetail she-oak seedlings.

(e) She-oak/Nitrogenous Fertilizer Trial

The she-oak nutrient requirement trial showed that nitrogen was the most important nutrient for growth of horsetail she-oak seedlings. Because of this a trial was installed in August 1975 on an exposed section of frontal dune to investigate the effect of different forms and rates of nitrogenous fertilizer on establishment and growth of she-oak seedlings. A randomised complete block design (with split plots) was used and consisted of 15 plots (18 m x 6 m) in 3 replicates of 5 plots. The plots and surrounds were brush matted to prevent wind erosion and planted with she-oak seedlings (about 20 cm high) on 1 m centres. The following fertilizer treatments were randomly allocated within each replicate: urea (46%N) plus basal P, K and T.E; blood and bone (4%N) plus basal K; di-ammonium phosphate (19%N) plus basal K and T.E; urea formaldehyde (38%N) plus basal P, K and T.E; and sulphur coated urea (36%N) plus basal P, K and T.E. Each nitrogenous fertilizer treatment was applied to split plots at rates equivalent to 100, 200 and 400 kg N ha⁻¹ yr⁻¹ in split applications every 6 months.

Tree height and basal diameter were used to assess treatment effect. Average height per tree in three fertilizer treatment over a period of 15 months from planting is shown in Fig. 8. At 15 months from planting the height of she-oak seedlings in the sulphur coated urea treat-

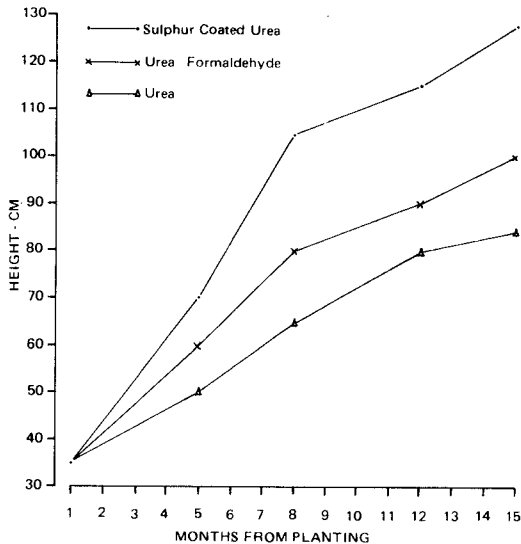


Figure 8. Effect of different forms of nitrogenous fertilizer on the height of horsetail she-oak tree seedlings.

ment was significantly greater than the height of seedlings in all other treatments. There was no significant difference in height of trees growing in the urea formaldehyde, blood and bone, di-ammonium phosphate and urea treatments. Increasing the rate of application of di-ammonium phosphate, urea or blood and bone did not result in any significant increase in tree height. However, sulphur coated urea and urea formaldehyde applied at the rate of $400 \text{ kg N ha}^{-1} \text{ yr}^{-1}$ produced trees that were significantly taller than those resulting when each fertilizer was applied at the rate of $100 \text{ kg N ha}^{-1} \text{ yr}^{-1}$.

The trends in basal diameter of she-oak trees are similar to those described for height. The application of sulphur coated urea or urea formaldehyde in split applications every 6 months at rates from 100 to $400 \text{ kg ha}^{-1} \text{ yr}^{-1}$ significantly increased growth of established she-oak seedlings. Both these fertilizers appear to be more beneficial to the nutrition of she-oak than the other forms of nitrogenous fertilizer. This is probably because forms of available nitrogen (eg. nitrate) are released from these fertilizers at a slower rate than they are from other fertilizers, and the nitrogen, which is easily leached from the root zone, is available to the trees over a longer period of time.

(f) Spinifex/Mycorrhiza Trial

In 1977 a small pilot trial was installed at a protected site on the main dune to investigate the effects that indigenous soil micro-organisms (mycorrhizas) may have on the phosphorus uptake and growth of sand spinifex grass. Data was collected but the results obtained were inconclusive.

(g) Spinifex/Superphosphate/Urea Trial

A trial to investigate the effect of various combinations and rates of superphosphate (9.2%P) and urea (46%N) on the growth of sand spinifex grass was installed on a bare section of the main dune in December 1977. The treatments consisted of 4 rates of superphosphate (0, 125.4, 250.8, and $501.7 \text{ kg ha}^{-1} \text{ yr}^{-1}$) applied in two ways, viz. "all-on" at planting and every 6 months, combined with 2 rates of urea (0 and $250.8 \text{ kg ha}^{-1} \text{ yr}^{-1}$) split into quarterly applications.

Ground cover of sand spinifex grass is being measured at intervals of 3 months. Early results clearly indicate the beneficial effect of quarterly applications of the nitrogenous fertilizer urea on growth and ground cover of sand spinifex grass. However the application of superphosphate did not seem to improve spinifex growth or ground cover.

(h) Spinifex/She-oak/Fertilizer Trial

In 1978 a trial was installed on a bare section of the main dune to determine optimum rates and timing for the application of nitrogenous and phosphatic fertilizers to horsetail she-oak tree seedlings planted into an established stand of sand spinifex grass. The trial will also determine the effect of competition between the trees and the grass on their respective growth rates. Data collection is still in progress.

6. INFORMATION GAINED FROM THE RESEARCH PROGRAM

The research program has produced quantitative and specific information on:

- (a) The rate of dune formation that can be expected using semi-permeable fences or brush matting.
- (b) The effectiveness of the recommended procedure for dune stabilization in immediately stabilizing base mobile coastal dunes and allowing rapid establishment of vegetation.
- (c) The relative effectiveness of organic mulches (eg. brush matting) and spray-on materials (eg. bitumen emulsion) in temporarily stabilizing bare coastal dunes and allowing establishment and growth of vegetation.
- (d) The likely value of a number of introduced and native sand colonising plants tested under field conditions for possible inclusion in dune management programs.
- (e) The growth patterns and nutrient requirements of sand spinifex grass and horsetail she-oak tree seedlings which are the two main species used in planting programs for dune stabilization in southern Queensland.

7. USING RESEARCH INFORMATION

Information gained from the research program is used to improve management of coastal dunes in Queensland as one means of decreasing rates of coastal recession. The information is used in the following ways:

- (a) It is progressively incorporated into a series of advisory leaflets on the vegetation and management of coastal dunes.
- (b) It is used by the Beach Protection Authority to provide free advice to coastal Local Authorities on establishment and management of dune vegetation.
- (c) It is tested and demonstrated in Field Trial Areas implemented on frontal dunes in co-operation with coastal Local Authorities.

Current and future trials in the research program will be aimed at improving all important aspects of coastal dune management in Queensland, and refining where necessary the information gained to date and presented in this paper.

8. ACKNOWLEDGEMENTS

Acknowledgement is made to the Queensland Department of Harbours and Marine and the Beach Protection Authority for supporting the research program and for giving permission to publish the results. Thanks is extended to Mr T.J. McDonald and the Queensland Department of Primary Industries for co-operation in the trial to investigate the growth pattern of sand spinifex grass, and to Dr I. Bevege and the Queensland Forestry Department for advice, assistance and co-operation in the horsetail she-oak trials. Sincere thanks is also given to Ms. E. Goward, Senior Biometrician, in the Queensland Department of Primary Industries for advice on trial design and subsequent analysis of results.

9. REFERENCES

Barr, D.A. & McKenzie, J.B. (1975), The establishment of vegetation on coastal sand dunes using mulches, *Proc. of 2nd Aust. Conf. on Coastal and Ocean Eng.*, pp. 75-84.

(1976), Dune stabilization in Queensland, Australia, using vegetation and mulches, *Int. J. Biometeor.*, 20, (1), 1-8.

(1977), Progress in coastal and sand dune stabilization and management experiments on South Stradbroke Island, Queensland, *Proc. of 3rd Aust. Conf. on Coastal and Ocean Eng.*, pp. 207-213.

Beach Protection Act 1968-1974, Queensland Government Printer, Brisbane, Australia.

Beach Protection Authority, *Dune Stabilization and Management Research Program* (report nos. D 01.1, D 01.2, D 01.3, D 01.4, D 02.1, D 02.2, D 02.3, D 02.4, D 02.5, D 02.6), Internal Report, Beach Protection Authority, Queensland, Australia (1979).

McDonald, T.J. (1979), Studies on Spinifex hirsutus with special reference to its use in the rehabilitation of coastal sand dunes, M.Sc. thesis, University of Queensland, Australia.

WIND AND SEDIMENT MOVEMENT IN COASTAL DUNE AREAS

JOHN R. HAILS

Director, Centre for Environmental Studies,
University of Adelaide, Adelaide, South
Australia

and

JOHN BENNETT

Flinders Institute of Atmospheric and Marine
Sciences, The Flinders University of South
Australia, Bedford Park, South Australia.

INTRODUCTION:

Little is known about how air-sediment interaction processes control the differential rates and direction of dune migration along the coast of South Australia. Information is needed on sand transport and dune formation in order to establish better guidelines for conservation and agricultural management programmes in areas that are undergoing erosion.

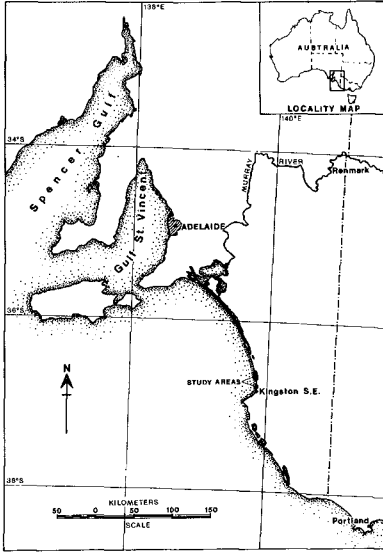
The writers, with financial support from the Coast Protection Board, Department for the Environment, South Australia, have commenced a pilot research project to examine dunes in the lower Coorong and adjacent areas in the southeast of the State (Figure 1). The aims of the project are -

To determine:

- (a) instantaneous surface stress values on the windward slopes of active transgressive dunes;
- (b) sand movement over the crestline as a function of surface stress on the windward slope in order to establish the life expectancy of stability of individual dunes;
- (c) the extent to which the local topography affects the wind regime in the dunal areas.

To obtain:

- (a) air trajectories over and around transgressive dunes;
- (b) information on dune geometry (slope inclinations, crest heights, base lengths, etc.).

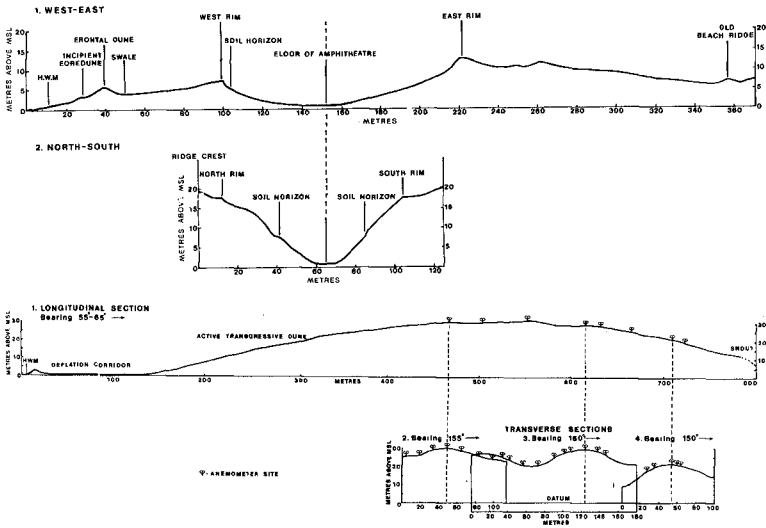


To measure thermal energy budgets so that time histories of the change in surface cohesion can be found - cohesion depending to a degree on moisture content, evaporation rate and surface temperature.

Monitoring stations have been established within an amphitheatre and along the crest of an active transgressive dune complex at the southern end of the Coorong in order to make a comparative study of the wind flow within, over and around different morphological features in dune fields (Figures 2 and 3) So far, field work has been conducted in the summer months with visits to the experimental areas in December and February.

← FIG. 1: Locality map to show study area.

↓ FIG. 2: Surveyed transects across the amphitheatre (top) and active transgressive dune complex (bottom).



Φ ANEMOMETER SITE



FIG. 3: Seaward and landward margins of active transgressive dune complex

FIELD TECHNIQUES:

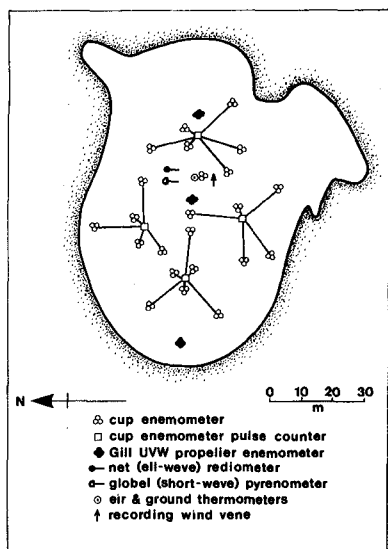
Miniature cup and Gill UVW propellor anemometers are used to determine the surface shear stress from profile measurements and eddy correlation techniques respectively. It is intended to relate the shear stress to the initiation, rate, and direction of sand transport at the monitoring stations. The complexity of the flow at sites where air is accelerated or decelerated by the topography makes the interpretation of data from shear stress measurements difficult. Results will be reported when further work has been completed.

The meteorological factors that control the cohesion of surface sand grains through the thermal energy and water budgets of the sand surface require the measurement of net radiant energy to it, the sensible (convective) and latent heat (water vapour) losses from it, and the conducted heat into the sand. The radiant energy is measured with a net all-wavelength pyranometer and the sensible heat flux is found from observation of the vertical profiles of air temperature and windspeed above the surface. Heat conducted into the dunes is estimated from records of temperature at two depths (2.5 and 13 cm) in the sand. The latent heat flux is to be determined from eddy correlation techniques combined with measurements of the sand moisture content.

The variations in wind speed through the active dune fields are measured with arrays of cup anemometers. In the amphitheatre, a total of twenty-four instruments were placed at regular intervals over the floor and sloping sides (Figures 4 and 5), while at the active transgressive dune, they were placed along and across the crest at three places (Figure 2, bottom). Because of the size of the dune, it was difficult to arrange

the anemometers so that a detailed wind pattern could be observed at one time. Since the direction and speed of the wind on the approach slopes were practically constant over several hours, more detail was obtained by moving part of the array to new sites on different occasions.

The cup anemometers are mounted 60-70 cm above and perpendicular to the sand surface, in order to measure the component of the wind parallel to the ground. The anemometers, manufactured after the design by Bradley (1969), have starting speeds of around 20 cm s^{-1} , and produce electrical pulses that are counted some distance away from the sensors.



← FIG. 4: Schematic diagram to show instrument layout within amphitheatre, February 13, 1980.



FIG. 5: Floor and west rim of amphitheatre

The mean wind speed is calculated from the counter readings by using the individual calibrations of the anemometers. For all the anemometers, the counting period began at almost the same time and had the same duration, so the mean speeds apply to effectively the same instant for one set of observations.

The wind direction is monitored with a portable, damped wind vane and magnetic compass.

The steadiness of the wind direction at both sites during the observation periods (generally to better than $\pm 10^\circ$) means that wind vectors, showing the speed and direction of airflow, can be constructed for each anemometer site. In addition, it is possible to construct isotach maps (showing lines of constant speed over an area) from the twenty-four average windspeeds centred at a particular time and measured at points across each site. This is done here from linear interpolations of the speed between adjacent anemometer stations.

Sand movement is measured with the aid of a 6-bin horizontal sand trap, with an effective downwind length of 1.5 metres. The mass of sand per unit time and per unit across-wind distance, in saltation and as surface creep, is calculated from the amount caught in the trap.

The textural (size distribution, shape, etc.) properties of the sand are determined by sieving and other standard sedimentological techniques.

RESULTS:

(a) Amphitheatre

The "surface" wind maps, showing the mean isotachs and wind vectors generally indicate that the velocities are higher near the floor of the amphitheatre and they progressively decrease towards the rim. The wind direction inside the depression depends strongly upon the direction of the undisturbed flow some distance from it. Two examples are illustrated in Figure 6.

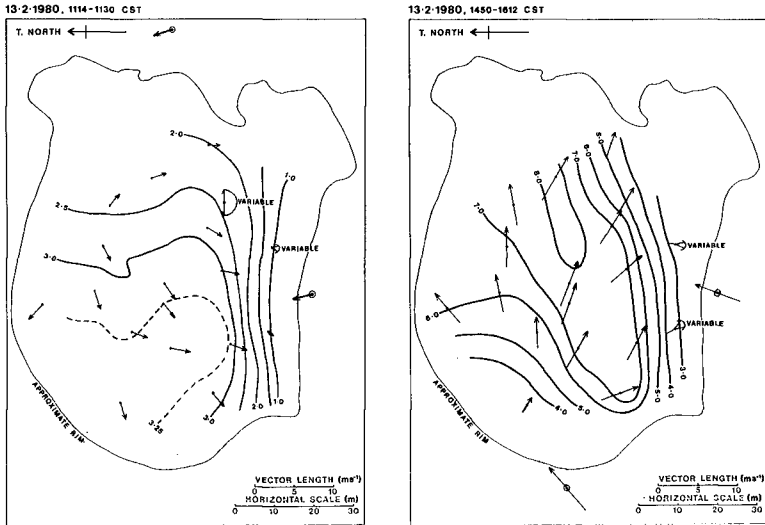


FIG. 6: Mean isotachs (ms^{-1}) and wind vectors in amphitheatre, 1114 to 1130 (left) and 1450 to 1612 (right), February 13, 1980.

The one on the left shows the isotachs for mid-morning, February 13, 1980, when the wind direction measured at the eastern rim was about 150° . At the time, the wind strength was insufficient to transport dry sand within the amphitheatre. On the same day, the wind veered to the southwest and freshened partly because of a change in the synoptic situation which reinforced a local sea-breeze. The one on the right applies to the later afternoon, by which time the wind speed was high enough to move sand on the north and south walls of

the amphitheatre. The isotachs show that the maximum speed was still confined to the floor, which was damp because of a shallow water table. No sand was moved from this relatively cohesive area.

Operation of a Gill UVW anemometer set erected on the east rim, when a strong and steady wind was blowing from the west in the amphitheatre, showed that the flow there was also quite steady. In addition, there was practically no evidence for any updraught from the amphitheatre.

It was observed that unobstructed airflow off the sea, as measured on the beach, had a more southerly component than at the western rim of the amphitheatre. Flow inside the depression had a decidedly westerly component, but the speeds on the beach and at the west rim were nearly identical.

The sand in the amphitheatre is predominantly medium to fine-grained, with mean values within the range 1.75ϕ to 2.10ϕ ($\phi = -\log_2$ diameter in mm). Standard deviation (sorting) values, in the range 0.35ϕ to 0.55ϕ , show that the sand is well to moderately-well sorted. The values for skewness, or the third moment measure, vary from $-.32$ to $+.52$. Coarser sand grains occur at the western (seaward) and eastern flanks of the amphitheatre, while poorer sorting has been identified along its west-east axis. The sign of skewness varies from site to site, and there is no clearly-defined trend with height above the floor of the depression. The skewness vs sorting is shown in Figure 7.

(b) Active Transgressive Dune

So far, observations indicate that the wind flow over one of a number of parallel, elongated active transgressive dunes and originating in an extensive deflation hollow, appears to be quite smooth and regular. Both the wind direction and strength were almost constant over an averaging period, although there was a freshening in the afternoons from the same cause as reported for the amphitheatre. When wind directions were around 190° (off the sea and at roughly 50° to the dune ridge) the isotachs were parallel and uniformly spaced down the windward and leeward sides of the ridge. The pattern was slightly displaced to windward of the crest. The highest speeds occurred along the crest rather than on the exposed upwind slopes with their long fetch across the relatively flat deflation hollow. The wind always slackened towards the snout of the dune while on the lee side, the lowest speeds occurred on the floor of the valley between neighbouring dunes. The speed there was 42-47% below the value on the crest.

The wind direction veered slightly from the windward side to the crest and backed a similar amount to the lee. An example of the wind distribution is given in Figure 8.

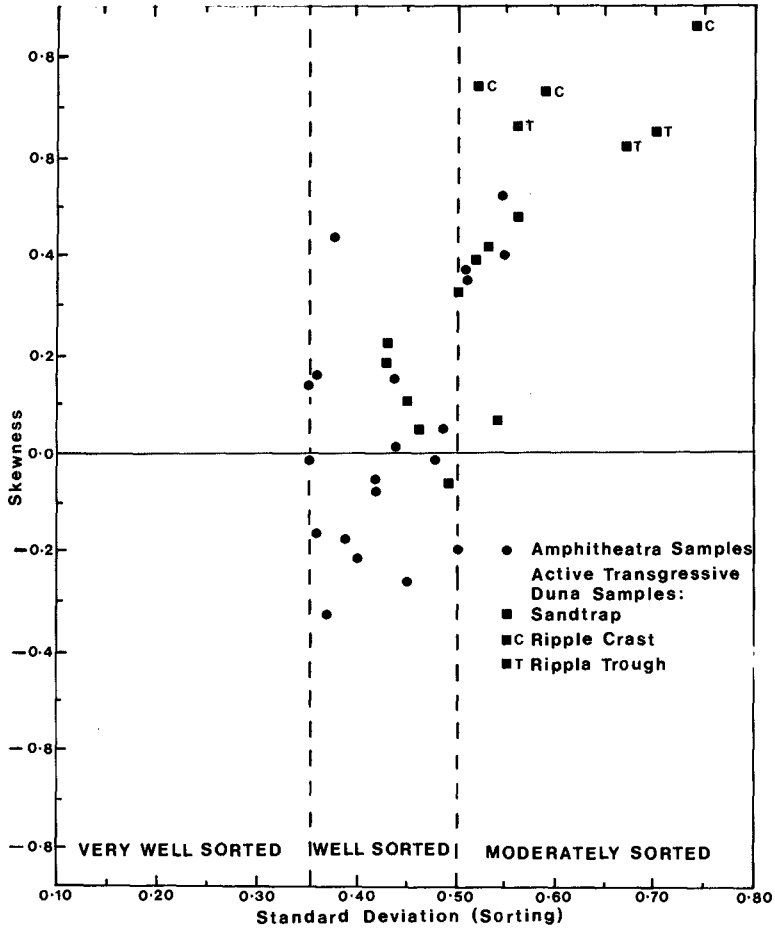


FIG. 7: Plot of the skewness versus standard deviation (sorting) for sand samples collected from the amphitheatre and active transgressive dune complex.

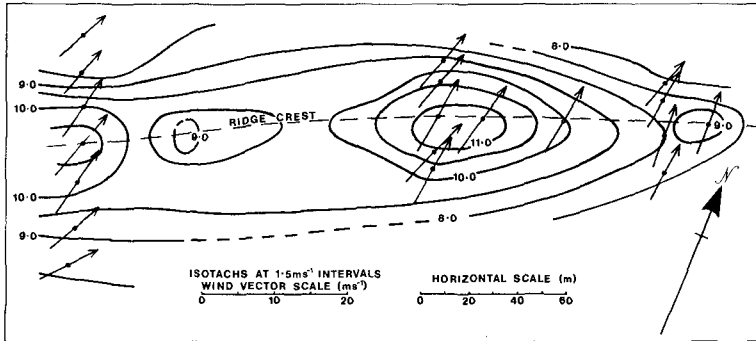


FIG. 8: *Isotachs and wind vectors for active transgressive dune, February 15, 1980,*

The windspeeds were sufficiently high to move a considerable volume of dry sand across the crest of the dune, and to carry fine dust high into the air. The amount of dry sand removed from some areas was sufficiently large to expose a moist, stable surface.

Analysis of the active transgressive dune sand shows that it is mainly medium-grained, with mean values between 1.65ϕ and 2.27ϕ . Overall, the dune sands are not so well sorted as those in the amphitheatre, with values in the range 0.43ϕ to 0.74ϕ . Except for one sample, the skewness values are positive and fall within the range $+0.05$ to $+0.86$ (see Figure 7). Such positive values are indicative of sands deposited under uni-directional flow conditions.

DISCUSSION:

The wind maps for each site show that, for the particular wind conditions recorded, the flow within the amphitheatre is much more complex than across the active transgressive dune. The wind vectors are the more informative parameters. At the amphitheatre, Figure 6 (left) shows that when the wind blows from 150° (as indicated by the two vectors at the eastern and southern sides outside the rim) there is pronounced reversal in the flow direction across the entire floor of the depression. This strongly suggests that a rotor forms in the lee of the southern rim for that particular wind direction. The nature of the circulation in both horizontal and vertical sections as deduced from Figure 6 (left) is sketched in Figure 9.

When the wind veered 50° from a direction along the crest of the main dune within which is the amphitheatre, the dominant contrary flow contracted to a small region high up on the southern wall, and was

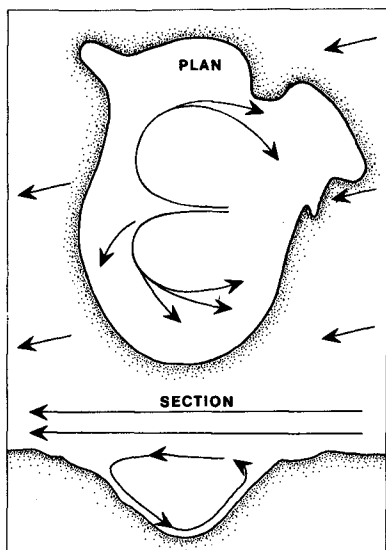


FIG. 9: Schematic diagram of wind circulation in amphitheatre (inferred from Figure 6, left)

replaced by a strongly-channelled flow through the amphitheatre from the west (Figure 6, right). The diminution in reversed flow is partly explained by the relatively low entrance to the amphitheatre from the west compared with the south (see sections in Figure 2, top). However, the main flow direction still differs appreciably from that of the unobstructed wind off the sea. Hence it is apparent that the foredune and main dune steer the flow to some degree, with the break in the main dune formed by the west rim, acting as a point of convergence for that flow. At the east rim, the flow was still from the west rather than the south-southwest, so the horizontal scale of any modification to the wind was of the same order as the length of the amphitheatre at least.

The wind observations in the amphitheatre suggest that the history of sand movement might be quite complicated in depressions. The sand could be moved from an area that is apparently sheltered from the unobstructed wind (but is

actually exposed to a reversed flow) to a new location that becomes exposed subsequently to winds from other directions. The observations also suggest that sand should be preferentially removed from the bottom and transported outside, or deposited on the walls of the depression. Here, however, because the floor was continually damp, even during the height of a hot and dry summer, it is unlikely that significant amounts will be transported from this part of the amphitheatre. The observations to date suggest that the driest sand on the walls moves first. There is active deposition on the east and south walls, while some sand moves through a small col on the northeast rim to add to a small dune behind it. The source of the mobile sand appears to be within the amphitheatre itself because a fresh supply of beach sand must cross a barrier of about 50 metres of thick vegetation before it reaches the depression. Old soil horizons are exposed on those parts of the north and west walls which are depleted of sand.

The distribution of windspeed across the amphitheatre might be expected to produce a corresponding variation in such statistical parameters as the first moment (mean), standard deviation (sorting), the third moment (skewness) and the fourth moment (kurtosis). Although the samples collected at different sites within the amphitheatre are generally well sorted, there is no marked trend in the degree of sorting from site to site, apart from poorer grain sorting along the west-east axis of the depression.

Figure 7 shows that 50% of the sand samples from the amphitheatre are negatively skewed, thus indicating a coarse-grained tail in the distribution. It is possible that the skewness values partly reflect the history of the sands, as well as the subtleties of air-sediment interaction, if the material in the amphitheatre has been reworked repeatedly over geologic time and can be described as both *polygenetic* and *polyeyelic*. However, higher moments are extremely sensitive to small changes and/or inaccuracies in the grain size distribution data, and therefore the values of these moments must be treated with caution (Hails, 1972). Obviously more analyses are needed to see if a relationship exists between environment-sensitive parameters and airflow within the amphitheatre.

Surprisingly, the airflow over the transgressive dune was comparatively simple. There was no reversal and only very slight steering of the wind by the dune itself. The absence of any lee eddy when the wind was blowing diagonally across the crest is presumably related to the smooth profile presented by that dune. The approximately 45% decrease in speed from the crest to the valley floor between adjacent dunes means that sand in transport on the crest would be dumped in the lee if the critical velocity for sand transport was higher than the actual velocity there. This feature would cause the dune crest to move downwind over an extended period of time, rather like a barchan dune.

In contrast to the amphitheatre sands, those comprising the active transgressive dune complex are positively skewed, except for one sample. This trend is characteristic of both modern and fossil dune sands and, in this instance, reflects the relatively simple uni-directional airflow over the dune system.

Figure 7 shows that, overall, the dune sands are less well sorted than those in the amphitheatre. The elongated shell fragments and sand comprising ripple crests are coarser than those in the troughs.

REFERENCES

- | | | |
|-------------|------|---|
| Bradley, | 1969 | A small sensitive anemometer system for agricultural meteorology.
<i>Agr. Met.</i> 6: 185-193. |
| Hails, J.R. | 1972 | The significance and limitations of statistical parameters for recognising sedimentary environments.
<i>Soc. Analyt. Chem. Proc.</i> 9: 115-118. |

SAND TRANSPORT UNDER THE ACTION OF WIND

by

Ulrich ZANKE¹⁾

1) Dr.-Ing., Head of a research group on Sediment-transport at SFB 79, Universität of Hannover, West-Germany

ABSTRACT

Field investigations on sand-transport by wind were carried out at German North-Sea coast. A special trap was constructed, which allows to measure bed load and suspended load seperated. In addition wind speed was measured up to 10 m over the bottom. The results of the field investigations were used to calibrate a transport-equation for sand-transport by wind.

1. INTRODUCTION

In coastal areas much sand is transported by the flow of wind. Hence wind generated sand movement on coasts can be a major factor in some areas, but very little is known about the basic meachnisms of the transport by wind yet. With growing use of artificial placement of sand for restoration and protection of beaches, wind generated sand movement shoreward of the waterline has become more and more a matter of interest.

In 1978 (4) the author presented a new transport equation which is valid for the calculation of bed load as well as suspended load in water flow, as it was demonstrated by many examples. Based on some results on the quantity of wind-generated sand transport given by KADIB (1964), O'BRIEN (1936) and EXNER (1928), the author demonstrated that the above mentioned equation is, in principle, also valid for wind generated sand transport. Either most of the earlier experimental results on wind transport were taken from tests in small wind tunnels and were carried out with sand-traps that did not separate the bed load and the suspended load, or the particular results for the two types of transport have not been published.

Hence, field measurements on sand transport under the action of wind were carried out at the German North Sea coast (Island of Spiekerog). Based on the results of these measurements, the transport equation was calibrated for the sediment transport by wind.

2. THEORY

The transport equation given by the author (4) is

$$q_b = a_1 \left(\frac{v_1^2 - v_{C1}^2}{w^2} \right)^2 D^{*4} v \frac{1}{p} \text{ for bed load} \quad (1a)$$

$$q_s = a_2 f(h) \frac{(v_1 - v_{C1}^2) (v_1^2 - v_{\ell 1}^2)}{w^4} D^{*4} v \frac{1}{p} f(\text{visc}) \quad (1b)$$

for suspended load.

Herein is

- q = transported volume per unit width and unit time
 v_1 = actual bottom velocity in the reference level
 $y_1 = 1$ cm over the bottom
 v_{C1} = critical velocity for start of bed load movement
(in $y_1 = 1$ cm)
 $v_{\ell 1}$ = critical velocity for start of suspension
 w = terminal settling velocity
 D^* = $(\rho'g/v^2)l/3d$
 d = grain-size
 g = coefficient of acceleration
 h = flow depth
 ρ' = $(\rho_s - \rho_f)/\rho_f$
 ρ_s = density of sediment
 ρ_f = density of fluid
 ν = kinematic viscosity
 p = 0,7; factor regarding the degree of compaction
of natural sands
 $f(h)$ = $\begin{cases} (h/h_1 \text{ with } h_1 = \text{reference level } y_1 = 1 \text{ cm,} \\ \text{for water flow;} \\ 1 \text{ for flow} \end{cases}$
 $f(\text{visc}) = \begin{cases} (\nu/\nu_0 - \nu)^{1/4} \text{ for water flow } (\nu_0 = \nu \text{ at } 0^\circ\text{C}) \\ 1 \text{ for air flow} \end{cases}$

The values of a_1 and a_2 are also different in the case of water or air flow probably because the turbulence structure, which is not directly included in Equ. (1), is different in both cases. (For water flow $a_1 = 10^{-7}$ and $a_2 = 10^{-8}$ (for air flow see 4. RESULTS)).

The critical velocity v_{C1} in Equ. (1) is

$$v_{C1} = A + B - \sqrt{AB} \quad (2)$$

$$A = C_1 \cdot 2,4 \cdot (\rho_s' g d)^{1/2} \quad (2a)$$

$$B = C_1 \cdot 7,78 \cdot (\rho_s' g \nu)^{1/3} \quad (2b)$$

$$C_1 = 1 \text{ for water flow} \quad / \quad 0.5 \text{ for air flow}$$

$$\rho_s^i = \rho' + \rho_a / \rho_F \quad (3)$$

where ρ_a is an "additional weight" effected by adhesion forces

$$\rho_a = \begin{cases} 9 \cdot 10^{-5} \text{ (cm}^2\text{)}/d^2 \text{ for natural sand in water;} \\ \text{function of moisture content for sand in air} \\ \text{(see 4. RESULTS)} \end{cases}$$

The critical velocity $v_{\ell 1}$ in Equ. (1b) is given by the author (4)

$$v_{\ell 1} = C_1 \cdot 3,14 w \quad (4)$$

where

$$w = \frac{11v}{d} (\sqrt{1 + 0,01 D^{*3}} - 1) \quad (5)$$

3. EXPERIMENTAL TECHNICS

For the calibration and test of the equation for wind flow, field measurements were carried out at the German North Sea coast over a duration of altogether 15 weeks in 1978 and 1979. During this time, wind-velocity profiles were measured up to 10 m over the bottom and sand-transport was measured seperately as bed-load and suspended load in two large traps. The inlets of the traps moved automatically into the direction of wind. The results were registrated continuously. In addition, air humidity, air temperature, air pressure and moisture content of the sand in the traps were measured. The following figures give an overview of the sand traps used during the field measurements. (The pictures were taken after heavy rainfall. Therefore the sand is wet).

Figure 1 is an overview of the test field: On a mast 5 wind-velocity-meters (variable hight) were installed. The apparatus in front of the mast is the suspended-load-trap.

Figure 2 is a view to the front inlet of the trap. Sand and air enter the trap and are seperated inside the trap. The wind-outlet is on the upper backside. The velocity-profile is not disturbed in front of the inlet. The sand is sampled inside the trap. The weight of the sampled sand is measured automatically and is plotted continuously.

Next, Figure 3, shows the entry of the bed-load trap. The sand moving near the bottom falls into an underground-trap. The axis of the inlet for the bed-load-material is always directed to the wind by the suspended-load-trap. Thus the area of the inlet is well defined every time. The weight of sand sampled in the bed-load-trap is also plotted continuously.



Fig. 1



Fig. 2



Fig. 3

4. RESULTS

Based on the measurements the following results were obtained:

1. ρ_a in Equation (3) can be approximated by

$$\rho_a = \frac{0,116 \ln (W^{1/2} + 1)}{d^2} \frac{(\text{cm}^2)}{(\text{cm}^2)} \text{ for } W > 0,0025 \quad (5a)$$

or

$$\rho_a = \frac{2,28 \ln (W + 1)}{d^2} \frac{(\text{cm}^2)}{(\text{cm}^2)} \text{ for } W < 0,0025 \quad (5b)$$

or

$$\rho_a = \frac{8 \cdot 10^{-3} \ln (H + 1)}{d^2} \frac{(\text{cm}^2)}{(\text{cm}^2)} \quad (5c)$$

where $W = \frac{\text{weight of wet sample} - \text{weight of dry sample}}{\text{weight of dry sample}}$
 $H = \text{relative humidity of air}$

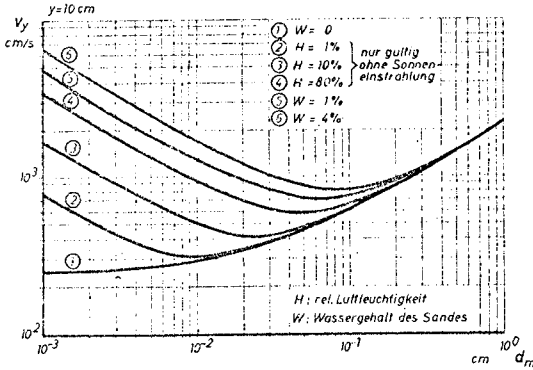


Fig. 4
Threshold velocities under wind action

Fig. 4 illustrated the dependence of threshold velocity on moisture content. Equations (5a) and (5b) are only valid for a short time after a rainfall. Then the sand is dried by the flow of wind and the critical velocity decreases. Nevertheless it is still impossible to set up a formula to calculate this decrease for each practical case, because in the nature sunshine, rainfall and wind speed can change rapidly. Moreover, some time after a rainfall, a layer of comparatively dry sand moves over a layer of more wet sand.

Equation (5c) is only valid, if there is no sunshine and if the moisture content is only effected by air humidity.

As a result of the measurements, calculations for practical use should at present therefore be carried out taking

$$\rho_a \approx 0 \text{ to } 5 \cdot 10^{-4} / d^2 \text{ for comparatively dry sand}$$

$$\rho_a \approx 2 \cdot 10^{-3} \text{ to } 4 \cdot 10^{-3} / d^2 \text{ for moved wet sand}$$

(din cm)

2. The values of a_1 and a_2 in Equations (1a, 1b) could be determined to be $a_1 \approx a_2 \approx 1.5 \cdot 10^{-6}$ in the case of sand-transport by wind.
3. For calculations of the quantity of wind generated sand transport in the nature the wind speed is, in general, only given for one level. Thus, to set the actual velocity in this given level in relation to the reference level of $y_1 = 1$ cm in Equs. (1), (2), (4), the velocity profile must be known. The investigations on the velocity profile gave the result that the velocity profile in the nature can be calculated by the Prandtl - Equation for rough boundary conditions with good agreement.

$$\frac{v_{y1}}{v_{y2}} = \frac{\ln \frac{30 \cdot y_1}{d}}{\ln \frac{30 \cdot y_2}{d}} \quad (6)$$

Equation (6) could be shown to be valid up to 10 m over the bottom for a velocity range between threshold and 20 ms^{-1} although the sand in the test field was comparatively fine ($d = 0.24 \text{ mm}$) (see Fig. 5). Effected by the irregularities of a natural sand bed in opposite to laboratory tests, a velocity distribution according to smooth conditions was never registered.

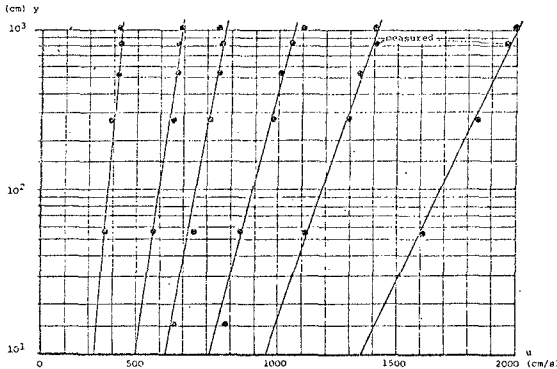


Fig. 5
Some examples of observed velocity profiles

5. SUMMARY AND CONCLUSIONS

A method for the calculation of the rate of wind generated sand-transport was developed in a half-empirical way. It could be demonstrated, that the critical velocity, v_C , increases rapidly if the sand becomes wet. Subsequently, depending on the duration and strength of wind, air humidity and rate of sunshine the layer of sand becomes drier and v_C decreases. On the functional coherences of these effects further research is needed.

For practical purpose an approximation for the calculation of v_C is given in this paper based on a great number of field investigations.

6. ACKNOWLEDGEMENTS

The investigations this paper is based on were financially supported by the SFB 79 (governmental found) and the Fran-

zius-Institut of the University of Hannover. Field investigations were carried out by friendly permission of the Bauamt für Küstenschutz, Norden, the Bezirksregierung Weser-Ems, Oldenburg, and the Gemeinde Spiekeroog. The author expresses his thanks to the Hermann-Lietz-Schule, Spiekeroog, for kindly supporting the field investigations.

7. REFERENCES

1. O'BRIEN, M.P. The Transportation of sand by wind.
RINDLAUB, B.D.: Civil Engineering, May 1936
2. EXNER, F.M.: Dünenstudien auf der Kurischen Nehrung,
Wien 1928
3. KADIB, A.L.: Sand Movement by Wind.
Techn. Memorandum No. 1, U.S. Army
Corps of Engineers, Addendum II. 1964
4. ZANKE, U.: Zusammenhänge zwischen Strömung und
Sedimenttransport, Teil 1.
Mitteilungen des Franzius-Instituts der
Universität Hannover, Heft 47. 1978

A NUMERICAL MODEL FOR DUNE DYNAMICS

by J. Sündermann, Prof. Dr. rer. nat., Institut für Meereskunde,
Universität Hamburg

H.-J. Vollmers, Prof. Dr.-Ing., Lehrstuhl für konstruktiven Wasser-
bau, Hochschule der Bundeswehr München

W. Puls, Dipl.-Phys., Sonderforschungsbereich 79, Technische Uni-
versität Hannover

Summary

A numerical sediment transport model is formulated that serves especially for the simulation of bedform mechanics. The model is based on the idea that sediment transport is determined by the erosion rate and the path length of bed material. Formulas for the erosion rate and the path length are derived from physical considerations and from measurements; they depend mainly on the local values of the shear velocity and the mean flow velocity near the bed. The behaviour of detached sediment is simulated by a Monte Carlo procedure, which is based on the mean flow velocities and the eddy viscosity. All flow properties that are needed for the sediment transport model are computed by a numerical flow model that includes two turbulence equations. Results of the flow model and the sediment transport model are compared with measured data.

NOTATION

A	eddy viscosity	$[\text{cm}^2 \text{s}^{-1}]$
D	mean grain diameter	$[\text{cm}]$
g	acceleration of gravity	$[\text{cm s}^{-2}]$
h	bed height	$[\text{cm}]$
H	mean water depth	$[\text{cm}]$
k	$= 0,5 (u'^2 + v'^2 + w'^2)$, turbulent kinetic energy (per unit mass)	$[\text{cm}^2 \text{s}^{-2}]$
p	pressure	$[\text{g cm}^{-1} \text{s}^{-2}]$
q_s	sediment transport rate	$[\text{cm}^3 \text{cm}^{-1} \text{s}^{-1}]$
u, w	local mean flow velocities in x- and z-direction	$[\text{cm s}^{-1}]$
u', v', w'	turbulent flow fluctuations in x-, y- and z-direction	$[\text{cm s}^{-1}]$
$u_{\text{bed}}, w_{\text{bed}}$	mean flow velocities 1 cm above the bed	$[\text{cm s}^{-1}]$
u_m	mean (depth integrated) flow velocity	$[\text{cm s}^{-1}]$
$-\overline{u' w'}$	Reynolds shear stress	$[\text{cm}^2 \text{s}^{-2}]$
$v_{cr,e}$	critical shear velocity for the end of grain movement	$[\text{cm s}^{-1}]$

v_*	effective shear velocity	[cm s ⁻¹]
v_*^k	shear velocity calculated from k	[cm s ⁻¹]
v_*^{cr}	critical shear velocity for material entrainment	[cm s ⁻¹]
x	horizontal coordinate in flow direction	[cm]
y	lateral horizontal coordinate	[cm]
z	vertical coordinate	[cm]
η	erosion rate of sediment	[cm ³ cm ⁻² s ⁻¹]
σ	path length of moving grains	[cm]

1 INTRODUCTION

Ripples and dunes develop in the lower regime of alluvial flows. Dunes are large-scaled bed structures which can have a height of about 0.25 of the water depth and which influence appreciably the transport of bed material.

Experimental research about bedforms has achieved a good deal of progress; most efforts were directed to laboratory experiments. On the other hand, theoretical knowledge about bedforms is meager. One reason for the lack of knowledge on this field is the complexity of the interdependencies between flow, sediment transport and bed deformation. An important point among this set of problems is the impact of turbulent flow fluctuations on the bed material.

2 FLOW COMPUTATION

We only consider two-dimensional (horizontal (x) - vertical (z)) flows. The flow model uses the Reynolds equations and the continuity equation in order to compute the pressure p and the mean flow velocities u and w (see Sündermann and Puls /1/), and it uses the equations derived by Launder and Spalding /2/ to compute the turbulent kinetic energy k and its dissipation rate ϵ . From k and ϵ we obtain the eddy viscosity A .

The flow equations are solved by a finite difference procedure. We only compute stationary flows. The flow model is the basis for the calculation of sediment transport. Therefore we must take care that especially the near bed flow is simulated as well as possible. Fig. 1 gives an idea of the grid being used both for the computation of the flow and the sediment transport.

Fig. 4 shows a comparison of measured and calculated flow quantities. It must be emphasized that discrepancies are not only caused by the shortcomings of the flow model, but also by shortcomings of the measurements (which is especially valid for turbulence measurements). But we don't want to find excuses if the measured and the computed data do not coincide: in some respects the model is really imperfect. This is especially valid for the simulation of large-scale turbulence structures. In addition, problems arise due to the numerical solution procedure: the transformation of differential terms of the flow equations into finite difference terms always causes a loss of physical information.

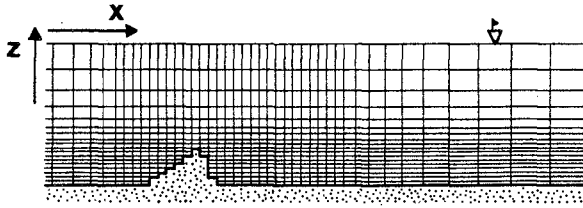


Fig. 1 : Computational Grid

The comparison of measured and computed data is performed by means of two flow examples: a flow above a negative step (Fig. 2) and a flow above a schematized dune (or to be more precise, a range of dunes, Fig. 3).

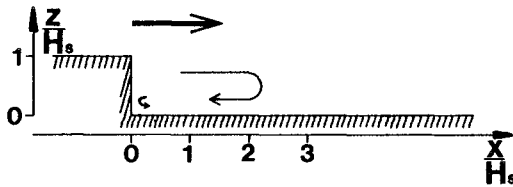


Fig. 2 : Negative Step Geometry

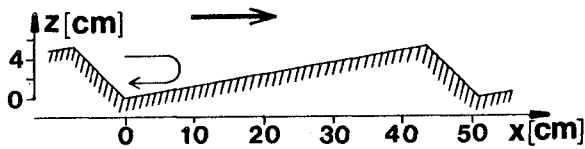


Fig. 3 : Dune Geometry

The experiment with the negative step was performed in a wind tunnel by Moss et al. /3/. The height of the wind tunnel is 84 cm, the step height H_s is 7.6 cm, the mean air velocity is about $u_m = 1000 \text{ cm s}^{-1}$, the kinematic viscosity is $15 \text{ cm}^2 \text{ s}^{-1}$. Fig. 4 shows vertical profiles

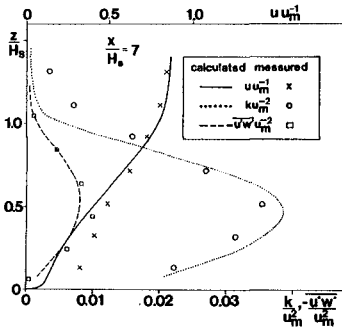
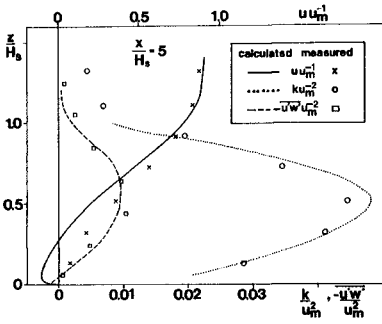
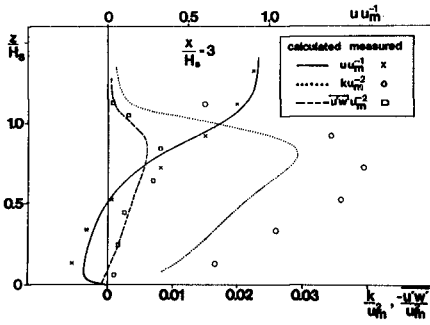


Fig. 4 : Vertical profiles of u , k and $-u'w'$; flow above a negative step, data from Moss et al. /3/

of measured and calculated values of the mean horizontal velocity u , the shear stress $-\overline{u'w'}$ (which is expressed in the model by $A \frac{\partial u}{\partial z}$) and the turbulent kinetic energy at the positions $x H_s^{-1} = 3, 5$ and 7 (compare Fig. 2). The length of the separation zone in the lee of the step is calculated to be $5.7 H_s$, while the measured value is $5 H_s$. This can be seen in Fig. 4 by the disagreement of measured and calculated u at $x H_s^{-1} = 5$ and 7 . Fig. 5 shows a comparison of the measured and the computed bottom pressure.

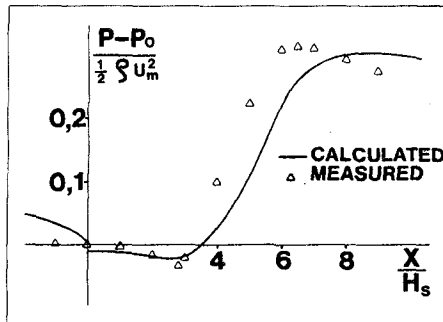


Fig. 5 : Bottom pressure; flow above a negative step, data from Moss et al. /3/

Rifai and Smith /4/ measured the water flow above dune-shaped bedforms in a flume. The water depth at $x = 0$ (see Fig. 3) is $H_0 = 30.5$ cm, the mean flow velocity at $x = 0$ is 57.65 cm s^{-1} . The measured quantities are $\overline{u'^2}$ and u . For the comparison of k and $\overline{u'^2}$, we assume $\overline{v'^2} + \overline{w'^2} = \overline{u'^2}$. Fig. 6 shows the comparison of measured and calculated vertical profiles of u and k . As well as in the case of the negative step, the agreement is satisfactory. The greatest differences appear at $x = 7.6$ cm (see Fig. 3), where at $z H_0^{-1} \approx 0.15$, the measured k is much larger than the calculated k . The reattachment point was measured at $x = 15$ cm; the same result is given by the model.

In addition to the two bed examples shown above, the model was also applied to other bed configurations.

On the whole, the flow model of course would need some corrections. However, being compared with the flow conceptions that are used till today for tackling sediment transport, our flow model is a real improvement, both concerning the structure of the mean flow and the turbulence.

3 SEDIMENT TRANSPORT MODEL

3.1 Formulation of the model

The sediment transport model serves for the small-scale simulation of sediment transport. The computation is based on a division of the bed into horizontal intervals. For any of these intervals, the flow model

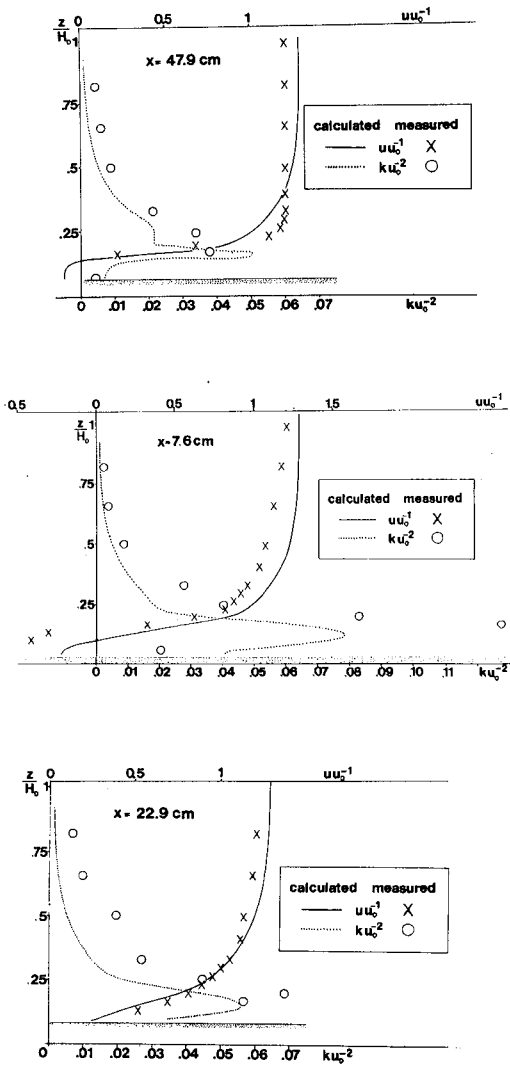


Fig. 6 : Vertical profiles of u and k ; flow above dunes, data from Rifai and Smith /4/

yields the near bed values for u , w , k and A .

One of the main faults of earlier works on bedform mechanics is the direct relation between the flow forces (usually in the form of the shear velocity v_*) inducing the sediment transport and the rate of sediment transport q_s . That this is wrong is easily shown by a simple example. Imagine a plane bed with a flow running above it; v_* is constant all over the bed. The upstream part of the bed is rigid, the downstream part is movable. Of course, q_s is zero on the rigid bed and develops from zero to an asymptotic value on the movable bed. Thus q_s varies over the movable bed though v_* is constant. A similar situation is found on bedforms downflow of the reattachment point. Therefore, in order to investigate bedform mechanics, the assumption of a direct relationship between v_* and q_s must be dropped.

Our device for the calculation of sediment transport is expressed by

$$(1) \quad \frac{\partial |q_s| (x)}{\partial x} + \frac{|q_s| (x)}{\sigma(x)} = \eta(x)$$

with σ being the path length a grain travels under homogeneous conditions from entrainment to deposition; η is the rate of material (measured by the total volume of bed material) being entrained from the bed per square unit and unit time. Equation (1) is valid for the absolute values of q_s only, because σ is positive definite. The sign of q_s is determined from the direction of the local mean flow near the bed. If η and σ are constant with respect to x , the differential term in (1) can be omitted, yielding

$$q_s = \eta \cdot \sigma$$

The next task is to get information about η and σ . There exist only a few experiments that have been concerned with direct measurements of η or σ . The erosion rate of non-consolidated mud was measured at HRS /5/. Takahashi, whose data is given by Nakagawa and Tsujimoto /6/, measured the probability of grains to be entrained on a flat bed. The information of both works can be expressed by ($v_* > v_*^{cr}$):

$$(2) \quad \eta = \text{const}_\eta \cdot D \cdot \frac{v_*^2 - (v_*^{cr})^2}{(v_*^{cr})^2}$$

with $\text{const}_\eta = 0.018 \text{ s}^{-1}$ from Takahashi's data and $\text{const}_\eta \approx 0.05 \text{ s}^{-1}$ from the HRS-data.

The path length σ was measured by Wulzinger and Liebig /7/ and by Nakagawa and Tsujimoto /6/. The quintessence of these measurements is a formula for the grain path length of bed load (for $v_* > v_*^{cr,e}$)

$$(3) \quad \sigma_{\text{bed}} = 820 \frac{\rho}{(\rho_s - \rho)_g} |u_{\text{bed}}| (v_* - v_*^{cr,e})$$

The values for $v_*^{cr,e}$ are taken from the Hjulstroem diagram (in Graf /8/).

The path length of suspended load cannot be deduced from direct measurements. The behaviour of suspended material is controlled by the settling velocity w_s and the eddy viscosity A . Our formula reads (for a derivation see Puls /9/)

$$\sigma_{\text{sus}} = \sigma_{\text{bed}} \left(1 + c_s \frac{A^S v_*^A}{w_s^3} \right)$$

A^S is an eddy viscosity being representative for the near bed zone, v_*^A is a shear velocity that is determined from A^S . c_s is a constant with the value $c_s = 30 \text{ s}^{-1}$.

The path length σ of total load (= suspended load + bed load) is determined by

$$\frac{1}{\sigma} = \frac{R_{\text{sb}}}{1 + R_{\text{sb}}} \frac{1}{\sigma_{\text{sus}}} + \frac{1}{1 + R_{\text{sb}}} \frac{1}{\sigma_{\text{bed}}}$$

with R_{sb} being the ratio of suspended load and bed load. Using the data of Guy et al. /10/, a rough formula for R_{sb} is

$$R_{\text{sb}} = 5 \frac{e^{-w_s z_s} (A^S)^{-1}}{1 - e^{-w_s z_s} (A^S)^{-1}}$$

with $z_s = 0.5 \text{ cm}$.

3.2 CALCULATION OF THE SHEAR VELOCITY

An essential point for calculating q_s is the choice of the shear velocity v_* . Because turbulence is the predominant factor for the capability of the flow to erode a grain and to prevent its deposition, v_* should be derived from the intensity of turbulence at the bed.

Using k_{bed} as the turbulent kinetic energy at the bed level, we obtain a shear velocity v_* from the equation

$$v_*^k = 0.51 (k_{\text{bed}})^{0.5}$$

Using v_*^k instead of v_* in (2) and (3), however, there is usually too much erosion in the reattaching zone of bedforms. Better results are achieved with

$$(4) \quad v_* = 0.7 v_*^k + 0.3 \cdot 0.07 (u_{\text{bed}}^2 + w_{\text{bed}}^2)^{0.5}$$

which uses the near bed mean flow velocities 1 cm above the bed. The weights 0.7 and 0.3 are found empirically in order to achieve acceptable agreement of the bed profile and the curve of q_s in Fig. 10.

3.3 BEHAVIOUR OF DETACHED SEDIMENT

The transport equation (1) is based on the assumption that σ is evaluated from v_* and u_{bed} being specific for the near bed region. This assumption is not fulfilled for particles being transported over a bedform's crest and which get caught in the separation zone in the lee of the bedform. In this case the particles are exposed to the local flow conditions which have nothing in common with the near bed values for the same x-coordinate. This is generally true if flow detachment occurs.

In such a case the transport of sediment is not calculated by (1) but by a Monte Carlo procedure (e.g. Maier - Reimer /11/). During this procedure, single (fictitious) particles are exposed to the direct influence of the local mean velocities and the local turbulence. The particles describe random walks like that plotted in Fig. 7.

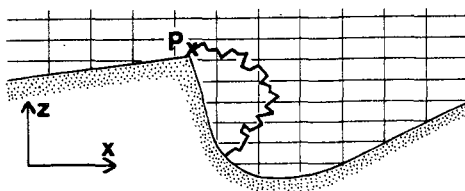


Fig. 7 : Random walk of a particle

The Monte Carlo procedure is tested by comparing its results with measurements of Allen /12/. Allen's experimental setup is shown in Fig. 8, simulating the lee slope of a bedform. Above the upper end of the slope,

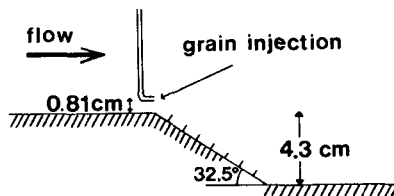


Fig. 8 : Experimental setup

sand grains are injected into the flow having a velocity u_g that equals that of the surrounding fluid. Touching the lee slope, the grains are arrested by a coat of glue. Measured and computed distributions of grains having settled down on the lee slope are shown in Fig. 9. On the

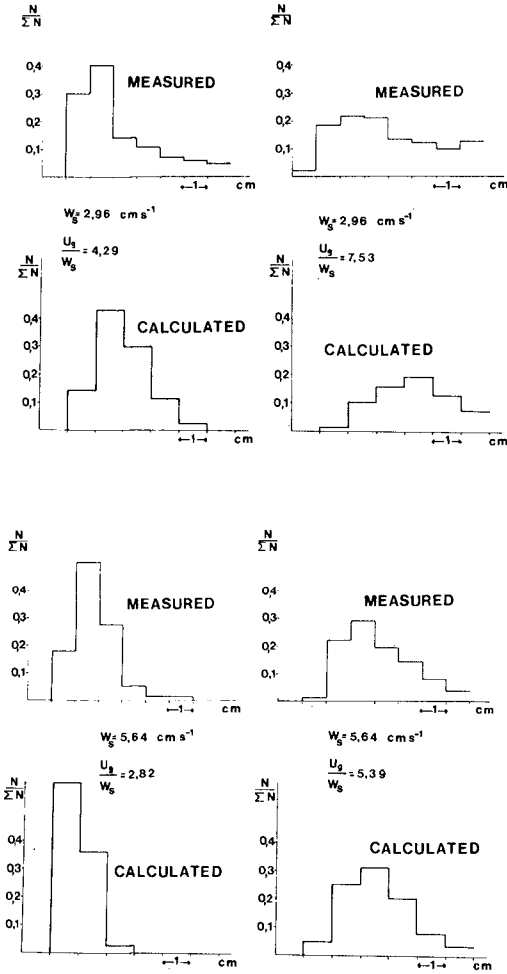


Fig. 9 : Distribution of settled particles

whole, the agreement is satisfactory; the centres of mass as well as the width of the distributions are reproduced quite well by the model.

4 SEDIMENT TRANSPORT OVER BEDFORMS

The transport model outlined above is applied to bedforms in unidirectional flow. For a bedform migrating with the velocity U_w without bed deformation, the relation

$$(5) \quad \frac{\partial q_s}{\partial x} = U_w \frac{\partial h}{\partial x}$$

is valid. The integration of (5) yields qualitatively

$$(6) \quad q_s(x) - q_{s,\min} \sim h(x) - h_{\min}$$

with $q_{s,\min}$ and h_{\min} being the minimum values of q_s and h respectively. The relation (6) fulfills the condition $q_s = q_{s,\min}$ at $h = h_{\min}$. For our comparison we consider three widely different bedforms: a laboratory ripple, a laboratory dune and a dune in the Elbe river. The Figures 10, 11 and 12 show the comparison of the measured bed profiles

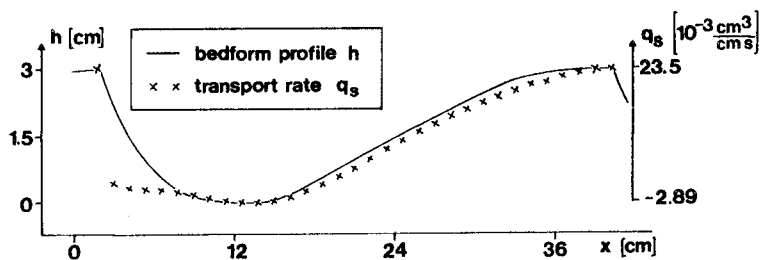


Fig. 10 : Comparison of h and q_s ; ripple profile taken from /13/,
 $u_m = 30 \text{ cm s}^{-1}$, $H = 13 \text{ cm}$, $D = 0,042 \text{ cm}$

$h(x)$ and the transport rates $q_s(x)$ that are calculated by the transport model. The values of h_{\min} and of $q_{s,\min}$ are placed on the same level. Further, the scale of q_s is chosen in order to obtain identical maxima for h and q_s . Thus if the relation (6) is really fulfilled, the curves of h and q_s must coincide irrespective whether U_w is simulated by the model or not. As we see from Figures 10, 11 and 12, the curves of q_s and h agree quite well. Of course, we must not forget that the model was drafted just in order to achieve the agreement of h and q_s . But nevertheless, we obtain the confirmation that our conception of sediment transport, i.e. the calculation of q_s with the help of η and σ , is able to yield good results.

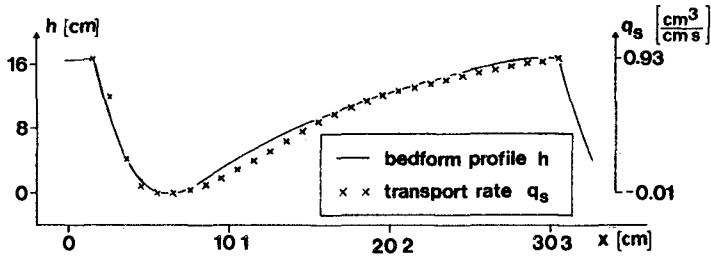


Fig. 11 : Comparison of h and q_s ; dune profile taken from /14/,
 $u_m = 62 \text{ cm s}^{-1}$, $H = 73 \text{ cm}$, $D = 0.026 \text{ cm}$

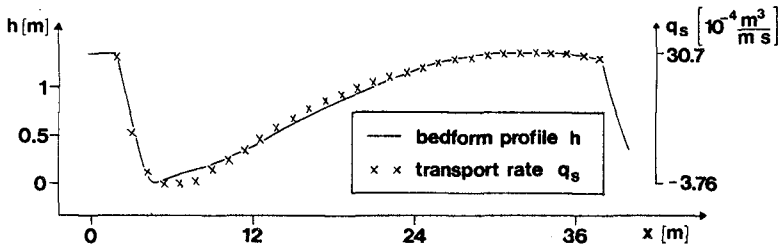


Fig. 12 : Comparison of h and q_s ; dune profile taken from /15/,
 $u_m = 120 \text{ cm s}^{-1}$, $H = 700 \text{ cm}$, $D = 0.04 \text{ cm}$

As stated above, the agreement of h and q_s is qualitative only. An additional quantitative comparison means to compare the absolute values of measured and calculated q_s .

No data is available for the dune in the Elbe river.

The transport rate over the ripple was measured to be $q_s = 6 \cdot 10^{-4} \text{ cm}^2 \text{ s}^{-1}$ whereas the calculated value is $q_s = 8 \cdot 10^{-3} \text{ cm}^2 \text{ s}^{-1}$ (using $\text{const. } \eta = 0.036 \text{ s}^{-1}$). The discrepancy could be caused by a "firmness" of the skin of the laboratory sand ripple (see also Guy et al. /10/): because of the low transport rate, a moving grain has a good chance to find a refuge in the bed, where it can easily resist to further flow attacks. Such a bed firmness decreases the erosion rate η appreciably.

For the laboratory dune, the qualitative comparison yields a better result: the measured migration velocity of the dune is $U_w = 0.049 \text{ cm s}^{-1}$,

while the calculated value is $U_w = 0.045 \text{ cm s}^{-1}$ (with $\text{const}_\eta = 0.036 \text{ s}^{-1}$).

The computed values of v_*^k , v_* , u_{bed} and σ over the three bedforms are shown in Figures 13, 14 and 15. The curves of v_*^k always have their

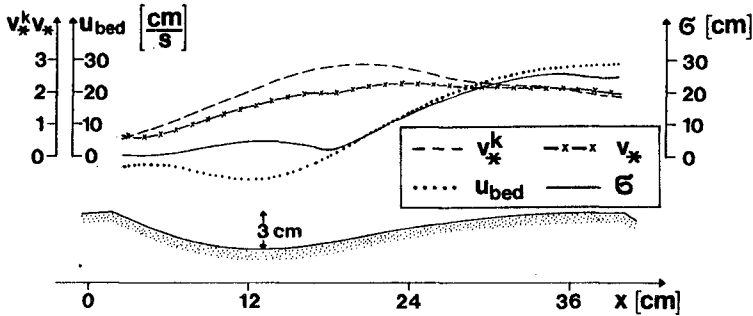


Fig. 13 : Computed values of v_*^k , v_* , u_{bed} and σ over the ripple taken from /13/

maximum in the reattaching zone. According to the influence of u_{bed} (see equation (4)), the curve of the effective shear velocity v_* is more smooth than that of v_*^k . The values of u_{bed} are negative in the recirculation zones. The most important point in Figures 13, 14 and 15 is the fact that σ is always in the order of the bedform length.

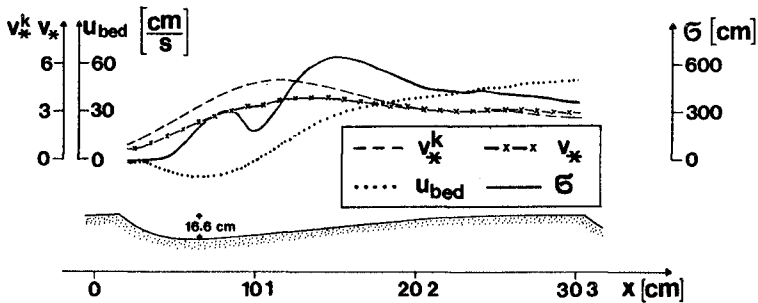


Fig. 14 : Computed values of v_*^k , v_* , u_{bed} and σ over the dune taken from /14/

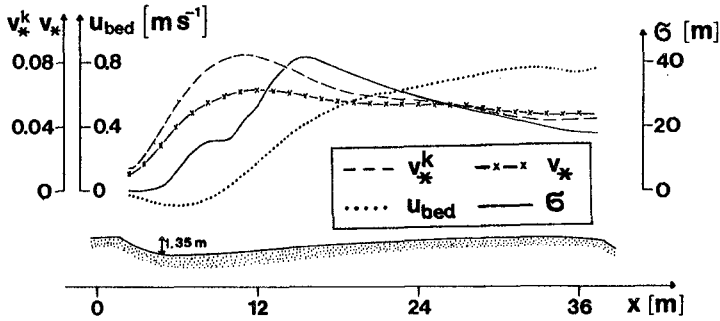


Fig. 15 : Computed values of v_*^k , v_* , u_{bed} and σ over the dune taken from /15/

CONCLUSION

Up to now, theoretical attempts to simulate in detail the sediment transport over bedforms and to explain the characteristics of bedforms have suffered from the following shortcomings:

- the flow was simulated in a simplified way only (e.g by using potential flow theory)
- turbulence was not included in the considerations
- a direct relationship between the flow parameters and the transport rate was assumed

The numerical model outlined in this paper avoids these shortcomings and is thus able to simulate in a physically adequate way the sediment transport over bedforms.

ACKNOWLEDGEMENT

The work reported in this paper was performed within the investigation program of the Sonderforschungsbereich 79, Hannover.

REFERENCES

- /1/ SÜNDERMANN, J. and PULS, W. (1980) Numerical modelling of sediment transport in coastal waters, in: Mathematical modelling of estuarine physics, Lecture notes on coastal and estuarine studies, editors: J. Sündermann and K.-P. Holz, Springer
- /2/ LAUNDER, B.E. and SPALDING, D.B. (1972) Mathematical models of turbulence, Academic Press, London.
- /3/ MOSS, W.D., BAKER, S. and BRADBURY, L.J.S. (1977) Measurements of mean velocity and Reynolds stress in some regions of recirculating flow, Symposium on turbulent shear flows, University Park, Pennsylvania, Vol. 1, 13 A

- /4/ RIFAI, M.F and SMITH, K.H.V. (1971) Flow over triangular elements simulating dunes, J. of the Hydr. Division, Proceedings of the ASCE, HY 7
- /5/ HRS (1977) Properties of Grangemouth mud, Report No. EX 781
- /6/ NAKAGAWA, H. and TSUJIMOTO, T. (1977) On probabilistic characteristics of motion of individual sediment particles on stream beds, in: Hydraulic problems solved by stochastic methods, editors: P. Hjorth, L. Joensson, P. Larsen, Proceeding, IAHR
- /7/ WULZINGER, W. and LIEBIG, W. (1979) Private communication
- /8/ GRAF, H.W. (1971) Hydraulics of sediment transport, McGraw-Hill Book Company
- /9/ PULS, W. (1980) Numerical simulation of bedform mechanics, Thesis (Ph. D.), University of Hamburg, to appear
- /10/ GUY, H.P., SIMONS, D.B. and RICHARDSON, E. V. (1966). Summary of alluvial channel data from flume experiments, Geologic Survey Professional Paper 462 - I
- /11/ MAIER - REIMER, E. (1980) On the formation of salt wedges in estuaries, Mathematical modelling of estuarine physics, edited by J. Sündermann and K.-P. Holz, Springer
- /12/ ALLEN, J.R.L. (1968) Current Ripples, North Holland Publishing Company, Amsterdam
- /13/ RAUDKIVI, A.J. (1963) Study of sediment ripple formation, J. of the Hydr. Division, Proceedings of the ASCE, HY 6
- /14/ BODE, E. and ZANKE, U. (1977) Private communication
- /15/ STEHR, E. (1975) Grenzschicht - theoretische Studie über die Gesetze der Strombank- und Riffelbildung, Hamburger Küstenforschung, Heft 34

ESTUARINE RESPONSE TO DREDGING
IN THE TWEED RIVER, AUSTRALIA

Bruce M. Druery
Supervising Engineer, Estuary Process Investigations
Department Public Works, State Office Block,
Phillip Street, Sydney. AUSTRALIA.. 2000.

ABSTRACT

Between mid 1974 and mid 1975, 760,000 m³ of sand was dredged from the bed of the Tweed River for the purpose of nourishing cyclone damaged beaches of the Gold Coast (Queensland). A comprehensive field data programme was established in 1976 to record the changes in the hydraulic processes of the Tweed River brought about by the dredging. The field measurements demonstrated that the dredged area was being infilled with sediments of both marine and estuarine origin. The dredging increased tidal ranges throughout the lower estuary, the effect being more pronounced at low water.

Sediment bedload rates were estimated from detailed measurements of bedforms and used to calibrate a sediment transport formula. The formula was used in conjunction with a 1 Dim. numerical model of tidal hydraulics to simulate estuarine shoal dynamics by means of a simple sediment routing technique. The results showed that the dredging had altered the tidal hydrodynamics so as to enhance the ebb transport of sediment towards the dredged hole. In the long term it was found that the sediment transport switched to a weak net upstream movement of sediment. The detailed hydraulic mechanisms involved are discussed. The study demonstrates that the impact of dredging can be minimised by location upstream of the entrance plug of marine sand.

1. INTRODUCTION

The coastal margins of a large number of estuaries in New South Wales (N.S.W.) have developed near regime channels in marine sands which were pushed against the coastline during the sea level transgressions of the late Pleistocene and Holocene epochs (Thom 1978). Typically the beds of these estuaries are composed of moderate to well sorted sands (D50 approx. 0.3 mm) and small scale sand extraction has been common place.

Areas of large scale sand extraction are associated generally with the building industry and are located well upstream of the estuary mouths. These upriver operations tend to have very little effect on the tidal hydrodynamics (N.B. fluvial hydrodynamics can be certainly affected though). Past dredging activities in the entrance reaches have been generally small scale, involving maintenance of navigation channels only.

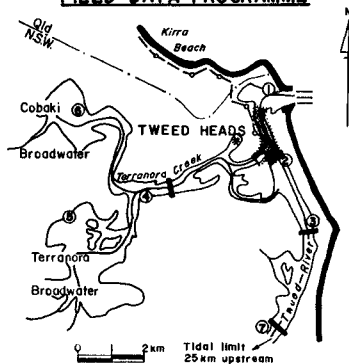
There is strong evidence to indicate that substantial portions of the N.S.W. coastline are receding (Gordon et al 1978, Roy 1980). Increased public acceptance of the realities of a receding coastline

LOCALITY MAP



creates more demand for coastal management techniques, such as beach nourishment, by which the amenity of the coast can be maintained. The lower reaches of estuaries are convenient sources of sand for beach nourishment but the quantities of sand required are no longer small and significant alteration of tidal hydrodynamics is possible. Consequently large scale sand extraction in estuaries should be examined closely so that all the environmental contraindications are identified.

FIELD DATA PROGRAMME



- DREDGE AREA (760,000m³) AND SURVEY CONTROL AREA
- Cross-sections at 30 metre intervals
- AUTOMATIC STAGE RECORDERS
- 1 Entrance
- 2 Letitia 1
- 3 Letitia 2
- 4 Dry Dock
- 5 Terranora
- 6 Cobaki
- 7 Barney's Pt.
- GAUGING LOCATIONS
- Velocity, Salinity and Temperature
- Sediment sampling undertaken throughout the whole area.
- SAND DELIVERY LINE
- THALWEG SOUNDINGS
- BAR SURVEYS
- * BOYD'S BAY DOCK HARBOUR

Figures 1 and 2

2. SAND EXTRACTION FROM THE TWEED RIVER

The Tweed River is the most northern river of N.S.W., located in part along the boundary between N.S.W. and Queensland - see fig. 1. Mean Spring Range at the estuary mouth is 1.3 m and is associated with a peak tidal discharge of 600 cumecs. The river catchment is relatively short and steep producing floods which are characteristically fast flowing but short lived. Fluvial flow is flashy with floods punctuating lengthy periods of low freshwater runoff.

Early in 1974 cyclones caused extensive damage to the Queensland resort of Kirra Beach - see fig. 2. The beach was restored by nourishment with 760,000 cubic metres of sand extracted from the Tweed River and pumped overland between July 1974 and October 1975. Once the dredging had been completed, however, there were reports of a number of marked changes in tidal levels, flows and phasing within the estuary, for instance:

Navigational difficulties were encountered by some of the larger craft operating from Boyd's Bay fishing harbour as a result of a reduction in low water levels.

Oyster farmers in Terranora Broadwater reported an increase in the range of the tide about their oyster racks.

Oyster farmers also reported a significant reduction in the tidal lag between Terranora Broadwater and the river entrance.

Whilst these reports would have involved some element of exaggeration and most of the reported consequences were of minor concern only, there was an overall concern that the effects could be "the tip of the iceberg" if further sand removal was carried out before the estuary had fully recovered. This concern was underlined by the Queensland authorities' desire to dredge similar quantities of sand from the river in the future.

3. FIELD MONITORING PROGRAMME

A comprehensive field monitoring programme was set up progressively from the end of 1976 - see fig. 2. The objective of the programme was to record the gradual recovery of the estuary and in so doing identify and quantify the real effects of the dredging. It incorporated the following:

- * A network of 7 automatic recorders.
- * Repetitive hydrosurveys of dredging area (in detail) and upper reaches (broad control).
- * Stream gauging of tides and floods.
- * Underwater photography of bedforms.
- * Measurement of bedform movement.
- * Sidescan and conventional sonar profiles.

3.1 Hydrographic Surveys

Seven hydrographic surveys were completed between December 1976 and March 1979, providing coverage of the dredged area at 30 metre intervals. Contour plans of each survey and isopach plots between successive surveys were prepared to illustrate the mode of shoaling. The surveys showed that the dredged area was undergoing both marine and estuarine infilling. The overall trend is summarised in fig. 3 which shows the total erosion and accretion over the period of the surveys (i.e. 2 1/4 years). Marine sand appears as a broad continuous shoal up to 3 m thick extending from the entrance. The estuarine sand appears as a 2-5 metre thick localised accumulation on the upstream edges of the dredged area. In the vicinity of chainage 1895 the two sands mix.

Fig 4. demonstrates the bathymetric impact of the April 1978 flood which had a probability of occurrence of 20%. The flood scoured the bed of the main arm upstream of the dredged area and the sharp reduction in sediment transport capacity, as the flood flow entered the deeper dredged area, caused deposition up to 1.5 metres in the confluence area. Deposition up to 2.5 metres occurred at the entrance to Terranora Inlet probably due to redistribution of flood deposits from the main arm. The entrance shoal of marine sand had restricted flood flow and considerable scouring of the surface had taken place.

The results of volumetric analyses of survey cross sections are presented in Table 1. Generally the estuarine infilling has been 10-20% of the total. The increasing trend of the estuarine infilling rate is probably indicative of the effect of mixing at the leading edge of the marine sand.

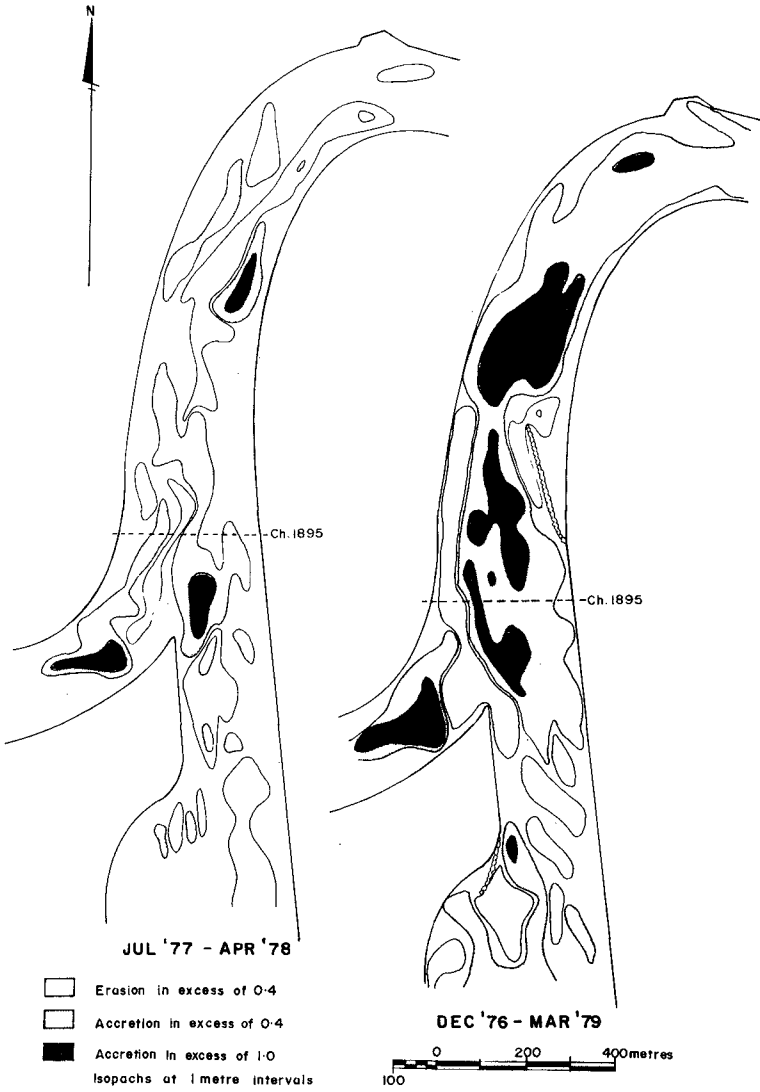


Figure 4
Hydrographic Surveys - Isopach Plots

Figure 3

TABLE 1 SEDIMENT INFILL RATES OF DREDGED AREA

SURVEY PERIOD DATES / DURATION (months)	TOTAL INFILL (m ³)	MARINE INFILL (m ³)	ESTUARINE INFILL (m ³)	MARINE INFILLING RATE (m ³ /yr)	ESTUARINE INFILLING RATE (m ³ /yr)
DEC '76 - JUL '77 (8.0)	68,300	62,200	6,100	93,300	9,100
JUL '77 - APR '78 (8.6)	28,000	66,900*	6,500*	93,300*	9,100*
APR '78 - OCT '78 (6.3)	48,700	38,000	10,700	72,300	20,400
OCT '78 - MAR '79 (5.4)	44,500	37,100	7,500	82,400	16,600

* Estimated from Dec. '76 - Jul. '77 survey period implying a flood scour of 45,400m³.

3.2 Tidal Gradients

Fig. 5 demonstrates the modification of the tidal wave which can take place due to shallow water effects.

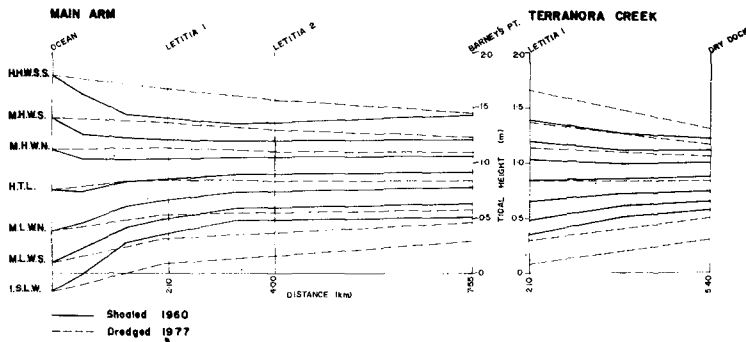


Figure 5 Comparison of Tidal Reference Planes

In 1977 the lower estuary was free of shoals because of the nourishment dredging and this contrasted with the heavily shoaled conditions of 1960. The constricted tidal ranges and the raising of half tide level are characteristics of the 1960 gradients (fig. 5) which signify the presence of pronounced shoaling. Considerable damping of the tidal wave, leading to high head losses, occurred within the first one to two kilometers from the entrance.

The determination of the tidal planes was based on the Range Ratio Method as developed by the Royal Navy Hydrographer (1969), using observations of high and low water over a period of one month in 1960 and 4 months in 1977. Druery and Curedale (1979) examined the inherent variability of local half tide levels and tidal amplitudes and concluded that for these short period observations the values of M.H.W.S. and M.L.W.S. could only be defined to ± 0.059 m and ± 0.032 m respectively

at Letitia 1 (95% Confidence Interval). Whilst this means that considerable caution must be exercised when making quantitative comparisons between different sets of tidal gradients, nonetheless, the behavioural trends described previously are well in excess of these confidence limits.

3.3 Bedform Dynamics

Suspended sediment sampling and underwater observation, during peak flows, indicated that away from the immediate entrance area the movement of the bed sediment ($D_{50} = 0.3$ to 0.35 mm) was restricted primarily to bedload. Individual sand grains either scudded across the surface or moved in discrete jumps which rarely extended more than 150 mm into the water column. During peak velocities (viz: 0.64 m/sec, 0.4 m above the bed) the majority of the dune surface was moving as either sheet flow, a few grains thick, or as short crested ripples of height 1-2 cm. Occasional boils of sediment occurred when one of the ripples disintegrated but the momentarily suspended sediment rapidly settled back to the bed and the ripple reformed a short distance downstream.

Detailed measurements of dune profiles were carried out at Letitia 1 (see fig. 2 for location) using an underwater frame to provide a fixed reference - see fig. 6. Bedform profiles were measured at slack water for a range of Spring and Neap conditions. Vertical and horizontal accuracy was $\pm 1-2$ cm.

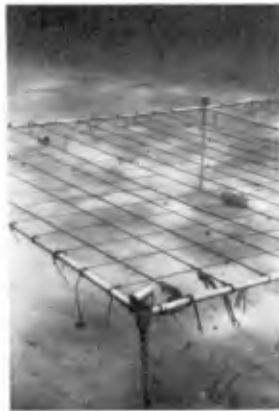


Figure 6 Underwater Bedframe

Typical profiles taken during Spring tide conditions are shown in fig. 7. Gross transport took place in the form of migrating dunes of typical amplitude 30-40 cm and 6 m wavelength in water depths varying from 2 m to 5 m across the estuary. During ebb tide the surface ripples migrated along the flat slope of the much larger dunes, passed over the crest and sand was deposited on the steep forward advancing face of the dune. In this manner the overall dune progressed downstream.

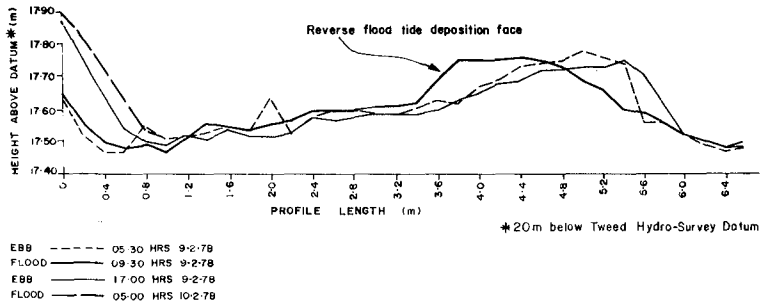


Figure 7 Dune Profiles at Letitia 1, Spring Tides

During the succeeding flood tide the ripples reversed and erosion of the downstream face of the dune occurred. The eroded sediment then proceeded to move upstream on the back face of the dune as a much smaller depositional face - see fig. 7. The dunes always preserved their downstream orientation due to the dominance of the ebb tide at Letitia 1 but the small reverse flood tide dune face was always eliminated by the following ebb tide. Nasner (1976) observed similar behaviour with large ebb oriented dunes on the bed of the Weser River, Germany, (D50 0.3 to 0.7 mm). He attributed a decrease in dune height during flood tide to a flattening of the steep lee slope and deposition of the eroded material on the luff slope. Allen (1974) also refers to a re-activation face during tidal flows counter to the orientation of the bedforms.

3.4 Determination of Estuarine Sediment Transport Rates

The gross sediment bedload per ebb or flood half tide was calculated as the volume of accretion or erosion, respectively, which occurred on the front face of the dune between successive slackwater profiles. This transport rate represents the gross bedload flux across the dune crest, expressed in m^3/m crest width.

Initially the gross bedload (Q_s) was calculated from profile measurements of a single dune using the bed frame (viz. 1.5 m x 6 m with 200 mm grid) and the results are shown in fig. 8A. However it was found that the bed frame could be replaced with a single line profile without significant loss of accuracy. The single line profile enabled accurate bed measurements over 20 m of river bed thereby allowing 3-4 consecutive dune profiles to be obtained. The gross bedload averaged over the multiple number of dunes is shown in fig. 8B. In addition the profiling was carried out simultaneously at three locations across the river width (viz. A, B. & C in fig. 8B).

The tendency for lower values of Q_s in fig. 8A stems from the single dune measurement. It was recognised on each occasion that the dune was not the largest in the dune field and hence the calculated transport rates were less than the later and more representative rates of fig. 9B. It was concluded that fig. 8B was a more realistic measure of the bedload rate, however the general trends of fig. 8A would still be applicable.

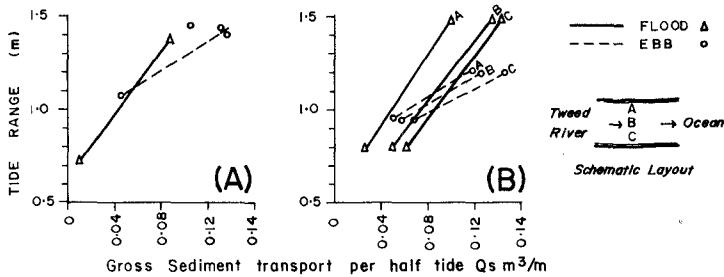


Figure 6 Results of Bedform Measurements at Letitia 1

4. DISCUSSION OF MEASURED BEDLOAD RATES

The peak gross bedload during Spring tides was measured to be 0.15 cubic metres/m/half tide which was approximately five times that for Neaps. Peak net transport was measured at approx. 0.1 cubic metres/m/day at Letitia 1 which is comparable to the bedload estimates obtained by Heathershaw and Carr (1974) from sand tracer studies in Swansea Bay, U.K., where sand transport took place primarily in response to strong tidal streams. Their studies indicated transport rates of 0.11 and 0.21 cubic metres/m/day in the deep and shallow areas of the bay respectively involving fine sands ($D_{50} = 0.21$ mm).

During Spring tides the difference between ebb and flood sediment transport was at its greatest leading to dune migration of up to 0.4 m per tide cycle. However during Neaps, conditions were near threshold and there was no substantial net transport of sediment and negligible dune migration.

Allen and Friend (1976) carried out continuous monitoring of dunes at Lifeboat Station Bank, Norfolk, U.K., over two consecutive Spring/Neap cycles and concluded that the largest "mature" dunes in a tidal dune field are tuned to the peak flow conditions at higher Spring Tides. Lesser tides had insufficient energy to significantly alter the dimensions of the mature dunes. If it is assumed that a fully developed tidal dune is functionally related to peak Spring Tide flow conditions, the work of Fredsoe (1979) can be applied. Fredsoe (1979) relates the ratio of dune height to wave length in alluvial conditions by the following expression:

$$h/L = 0.12 (1 - 0.06/\theta - 0.4\theta)^2$$

where θ is Shields shear stress parameter viz:

$$\theta = \tau_b / ((\gamma_s - \gamma) d) = RSf / (S-1) d$$

where R is the hydraulic radius, Sf is the friction slope, s is the relative density of sediment and d is the mean grain diameter.

Using typical Spring values at Letitia 1 of $R = 2.0$ m at the dune crest during ebb flow, $S_f = 38 \times 10^{-6}$, $S = 1.65$; $d = 0.0003$ m implies:

$$\theta = 0.21 \text{ and } h/L = 0.048$$

The actual values of h/L for all dunes ranged from 0.037 to 0.05 with an average of 0.044. Furthermore it can be shown from Fredsoe's transport formula viz:

$$q = [(S-1)g d^3]^{0.5} \left\{ 1 + \left(\frac{0.267}{\theta - 0.05} \right)^4 \right\}^{0.25} (0.5 - 0.7\theta^{0.5})$$

that the theoretical unit transport rate of a dune with $\theta = .21$ is 0.19 cubic metres/m/hour i.e. approx. 0.38 cubic metres/m/half tide which compares with the peak values, inferred from field measurements, of 0.2 - 0.25. It appears that the work of Fredsoe shows promise for possible quantified interpretation of tidal bedforms.

5. MODELLING OF TIDAL HYDRAULICS

5.1 Model Development

Tidal stage and discharge were modelled using a one-dimensional numerical model based on the specified time version of the method of characteristics as developed by Fischer (1970). The model was calibrated using stage and discharge data from a full Spring tide cycle and verified against two sets of neap data. Even though the estuary possessed some complex branching it was found that the one-dimensional schematisation adequately represented the bulk flow characteristics. The Spring tide calibration and a neap tide verification are shown in fig. 9.

5.2 Impact of Dredging on Tidal Hydraulics

The calibrated model was used to hindcast the changes in tidal levels caused by the sand extraction. The propagation of a Summer Solstice Tide using 1977 bed geometry is shown in fig. 10. The propagation of the same tide based on the bed geometry of the most recent comprehensive survey prior to the dredging (i.e. 1971) is also shown.

Fig. 11 portrays the same behavioural trends as fig. 5 however it is valid to draw quantitative conclusions from fig. 10. The numerical hindcasting demonstrated that the dredging produced a pronounced increase in the tidal range throughout the lower estuary, the effect being more pronounced at low water. The increase in range of 7 cm on Terranora Broadwater and the lowering of low water by 25 cm inside Terranora Inlet are substantial changes and are consistent with the observations reported in Section 2. Harten (1980) describes similar effects arising from channel deepening associated with port development in a number of German estuaries. The dredging produced an increase in tidal range roughly apportioned as one third due to an increase in high water and two thirds due to lowering of low water.

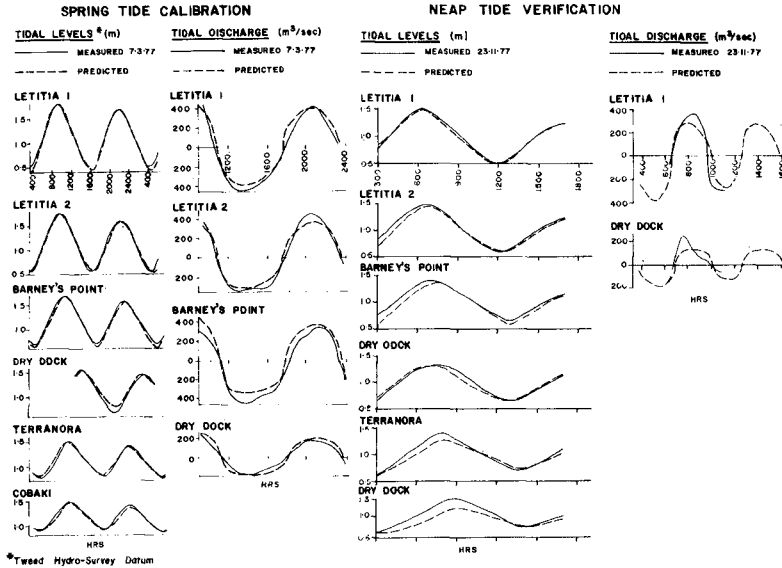


Figure 9 Numerical Model Calibration and Verification

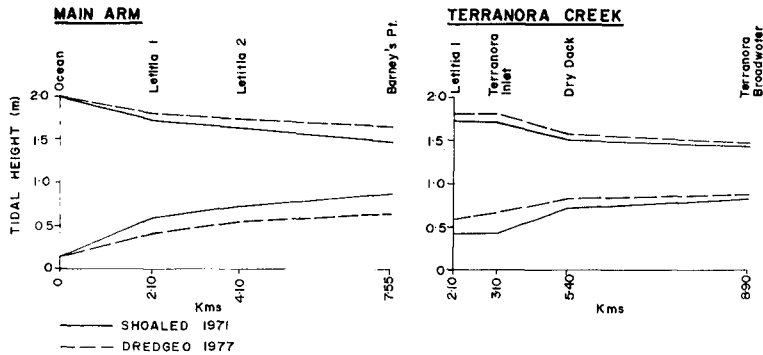


Figure 10 Predicted Tidal Propagation

6. MODELLING OF ESTUARINE SEDIMENT TRANSPORT

The foregoing numerical model of tidal hydraulics was incapable of assessing the recovery rates of the estuarine shoals or the long term impact of dredging on the estuarine sediment regime. Hence a sediment routing procedure was developed.

6.1 Selection of Transport Formula

Yalin (1976) undertook a fundamental examination of the transport of coarse bed material under conditions of oscillatory tidal flow and indicated that ebb and flood sediment transports can be viewed as separate unidirectional events. The result is a pattern of alternating, but intermittent, sediment motion. It was proposed that unidirectional theories could apply except near slack water where inertial effects become significant. Hence conventional formulae may be applicable during the bulk of the tidal cycle.

Based on a review of eight major transport equations by White, Milli and Crabbe (1975) the method of Ackers and White (1973) was adopted.

6.2 Sediment Transport Parameters

Friction Gradient (Sf)

The Ackers and White formula was developed from laboratory and field data under steady, uniform flow conditions in which the surface slope (Sw) and the friction slope (Sf) were identical. In order to facilitate the general application of the formula to tidal flows it was desirable to adopt Sw as the friction slope. Mehta et. al. (1976) concluded inertial effects were negligible except at slack water on the basis of field studies carried out on two tidal inlets of Florida. It was therefore considered that Sw was a reliable estimate of Sf for the majority of the tide during which sediment transport took place. When calculating the instantaneous sediment transport rate at any particular cross section the convention adopted was to set Sw equal to the water surface slope of the model element immediately upflow of the cross section.

Section Averaged Velocity

Initial predictions of sediment transport using the predicted cross section average velocity indicated no transport during low flow conditions such as Neaps. Even though net sediment transport approached zero during a full Neap tidal cycle, significant gross sediment transport occurred during each ebb and flood half tide - see fig. 8. This discrepancy occurred because the cross section average velocity in a 1 Dim. model will always be substantially less than the depth averaged velocity at any particular point. Hence an empirical correlation was established between the field values of depth averaged velocities and the predicted cross section average velocity. It was found that a single linear regression was sufficient to satisfy both Spring and Neap flow conditions at each gauging station.

6.3 Calibration of Gross Sediment Transport Rates

The individual bedload measurements at each Station A, B and C (see fig. 8B) were integrated across the river width and divided by the total cross section width to yield an average section transport rate per unit width. The result is shown in fig. 11. The general trend of fig. 8A was used to extrapolate fig. 11 at the higher tide ranges.

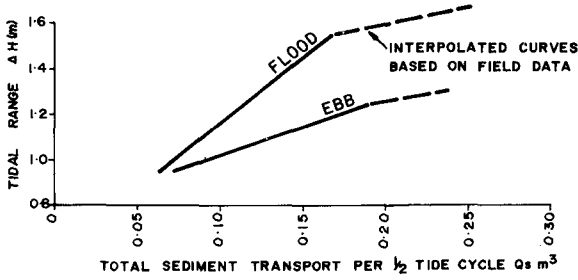


Figure 11 Integrated Bedload Transport Rates (Letitia 1)

A variety of tides of varying range were run through the numerical model to predict values of water surface slope and scaled velocities (at Letitia 1) at twenty minute intervals during each tide. Instantaneous sediment transport rates were calculated and a sediment flux curve was produced which was integrated with respect to time to determine the theoretical gross sediment transport for each half tide.

The theoretical gross transport rate per half tide was compared to the rate interpolated from the curves of field results for the same tidal range (i.e. fig. 11) - see fig. 12. It was found that the Ackers and White formula, using S_w and scaled velocities, gave reasonable results (\pm factor of 50%) for Spring conditions. However the greatest deviation occurred as the threshold condition was approached and hence sediment transport was still significantly underestimated under conditions of marginal velocity or gradient.

The general trend of fig. 12 was used to adjust the procedure for calculating sediment transport rates viz.:

- (a) If $.011 \leq p^1 \leq .15$
- $$P = 0.36 p^1 + 0.096$$
- (b) If $p^1 > 0.15$ then
- $$P = p^1$$

where:

p^1 = initial prediction of gross transport rate using Ackers and White with scaled model velocity, average depth and water surface gradient: cubic metres/m/half tide

P = Corrected prediction of gross transport rate: cubic metres/m/half tide

For values of $p^1 < .011$ a simple correlation with the peak velocity was developed. This corrected procedure for the calculation of sediment transport was used for all locations throughout the estuary.

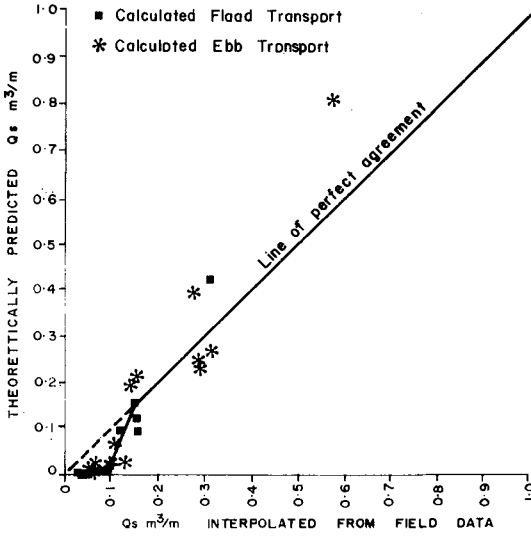


Figure 12 Comparison of Calculated and Measured Transport

6.4 Verification of Calibrated Transport Formula

Infilling of the dredged area during 1977, by the downstream transport of sediment, was predicted by the following procedure:

- (i) The Spring-Neap cycle at the River mouth was divided into six representative, symmetrical tide cycles of varying tidal ranges R_i - see fig. 13.

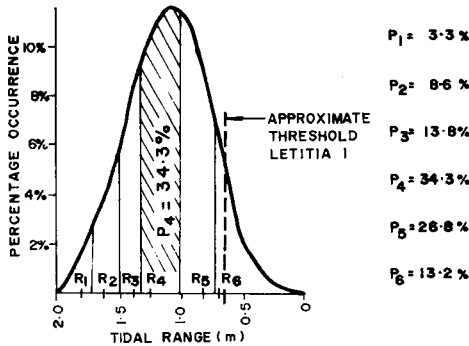


Figure 13 Annual Occurrence of Tides at Tweed Entrance

- (ii) The net sediment transport of each tide, q_i , was calculated at a number of locations throughout the estuary.
- (iii) Each representative tide cycle was assigned a size band within the 1977 tidal frequency curve. The relative percentage occurrence of each band, P_i , was determined as the proportional area under the curve.
- (iv) The annual transport of sediment at each particular location was calculated as:

$$700 \sum_{i=1}^{i=6} q_i P_i$$

where 700 is the number of tide cycles in one year.

The predicted total estuarine transport of sediment moving downstream in the Tweed main arm and Terranora Creek was $8,300 \text{ m}^3$ which is in reasonable agreement with the quantities of estuarine infill determined from hydrographic surveys (see Section 3.1). In addition the directions of net transport throughout the estuary agreed with all direct and indirect lines of evidence. This will be discussed further in the next section.

7. PREDICTED ESTUARINE SHOALING RATES

The impact of the nourishment dredging on the broad pattern of shoaling in the estuary by tides alone (i.e. ignoring the short term effects of floods and cyclones) was investigated with a sediment routing technique. The sediment routing incorporated interaction of bed levels with flow.

Except at the estuary mouth the predicted annual sediment transport values were increased by a factor of five to produce a coarse five year routing step. Because of the complexity of wave and current interaction at the entrance and the presence of strong secondary currents on the entrance bend, the predicted peak velocity and gradient were used to calculate an index of net sediment transport potential at the estuary mouth. When applying the first sediment routing step this index was assumed to represent the measured entrance sediment infeed rate of $93,000 \text{ m}^3 \text{ p.a.}$ (see Table 1). The entrance sediment infeed for all subsequent routing steps was reduced proportionately according to the predicted reduction in this index.

At the end of each five year routing step the channel geometry was reschematised according to the volumes of net accretion or erosion in each sediment routing compartment. Throughout the sediment routing it was necessary to assume that the empirical velocity scaling factors did not vary in time. The results are shown in fig. 14. While the results are not good for strict accuracy they do provide insight into the broad behavioural patterns of sediment movement and shoaling under pure tidal influence.

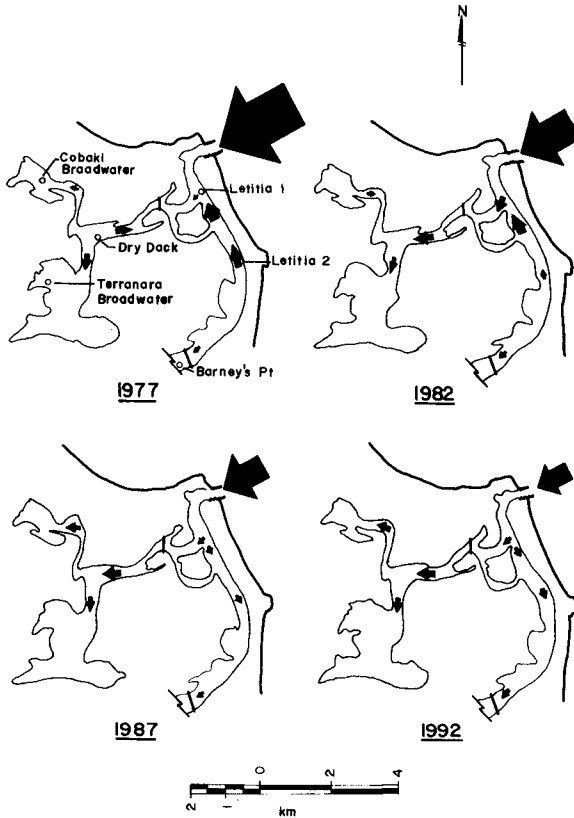


Figure 14 Results of Sediment Routing

7.1 Discussion of Predictions

Immediately after dredging (1977) there is a strong infeed of sand through the entrance. Immediately upstream of the dredged area the net sediment transport is downstream in both arms of the River.

By 1982 the dredged area is approx. 60% infilled and the impact on estuary flows is substantially reduced. Sediment reversal in Terranora Creek has occurred because the dredged area no longer has a significant influence on tidal flow patterns. Similarly in the main arm, at Letitia 2, the effect of the dredging on the sediment transport has diminished.

By 1987 the dredged area is completely restored and complete sediment transport reversal has taken place in the main area.

By 1992 the estuary is very shoaled due to continued sand feed (at a greatly reduced rate) from the entrance. The shoaling is causing considerable head losses in the lower estuary leading to a damping of velocities and gradients in the upper estuary where the net sediment transport is weakly directed upstream. The presence of the broadwaters in Terranora Creek helps to maintain relatively steeper gradients and higher sediment transport rates.

An interesting feature of these behavioural predictions is that the dredging produced a temporary reversal in the direction of net sediment transport immediately upstream of the dredged area. In the main arm this effect was predicted to extend upstream to some region between Letitia 2 and Barneys Point. Although no bedform survey was carried out prior to the dredging, partial verification of the predicted reversal point is shown in fig. 15. Further verification came from a careful study of all available aerial photography by Druery and Curedale (1979) which demonstrated that shoaling in Terranora Creek, near the Boyd's Bay fishing harbour, was due to the downstream movement of a shoal which had been stable for twenty years prior to any dredging of the lower estuary.

8. ESTUARINE SHOALING MECHANISMS

A detailed breakdown of the quantitative results of the numerical simulation of estuarine sediment dynamics is given in fig. 16 for a Summer Solstice tide. These will be discussed in order to obtain a better understanding of the hydraulic mechanisms involved.

8.1 Detailed Discussion Letitia 2

In Section 5.2 it was demonstrated that the immediate impact of the dredging was manifest as a drop in low water level and an increase in high water, the effect being more pronounced at low water. So, as the dredged area infills with time a progressive decrease in high water and a progressive increase in the level low water would take place. This is indicated by the decrease in the depth at peak flood tide velocity and the increase in depth at peak ebb tide velocity.

In terms of peak velocity at Letitia 2 there would be a tendency for the peak ebb velocity to decrease due to the increased depths and the opposite for the flood tide where velocities would tend to increase because of the decreasing depth. However there must also be an overall trend for reduction in velocities due to the decreasing peak discharge. Hence the depth effect results in the flood velocity decreasing to a much lesser extent than the ebb velocities.

Peak surface gradients show a decline with shoaling due to damping of the tidal wave but the peak flood gradient always remains higher than the peak ebb gradient.

The gross sediment transport per half tide is greatest on the ebb, initially, due to the depth effect providing greater enhancement of the ebb velocities. Hence there is net ebb oriented sediment transport. As the dredge area shoals, ebb velocities decrease due to the depth effect, both gradients diminish and the flood tide transport begins to dominate. So as shoaling takes place the net sediment movement reverts to the long term trend which is a weak net upstream movement of sediment.

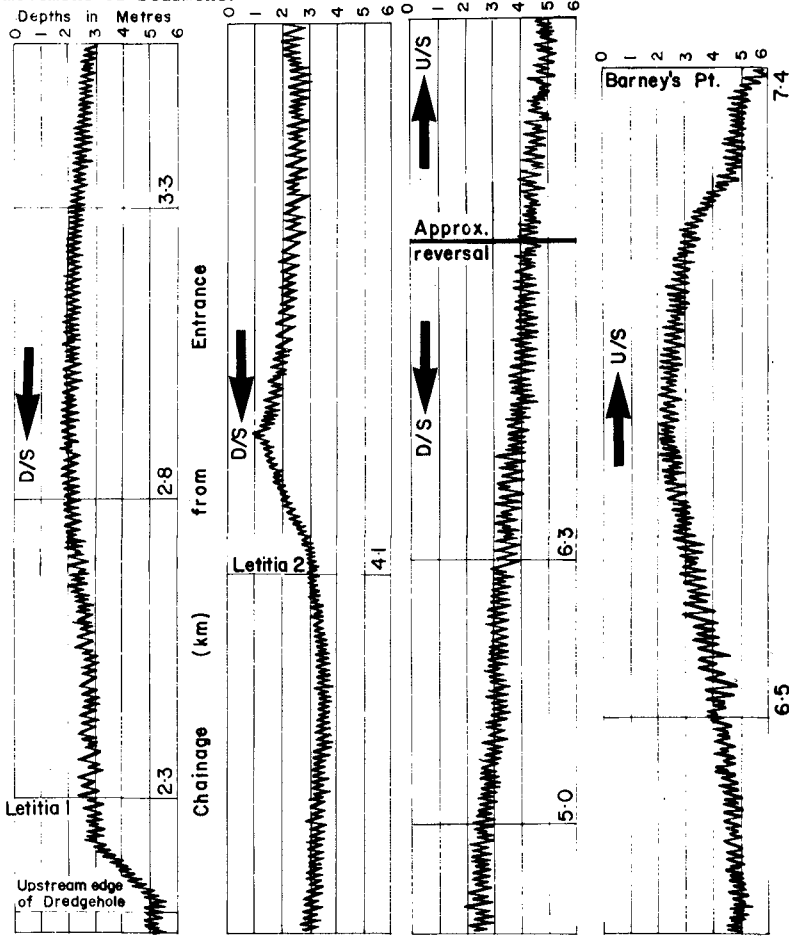


Figure 15 Longitudinal Echosounding Plot of Main Arm Showing orientation of bedforms. Note reversal between Letitia 2 and Barney's Point.

8.2 Terranora Broadwater

Looking quickly at Terranora Creek it is apparent that the presence of the broadwater suppresses any potential change in water levels and hence there is no significant depth effect. Velocities diminish at an equal rate in proportion to the decreasing discharge. The flood velocities and gradients are always greater than the ebb due to the different shapes of the discharge curves. Hence the overall trend is a net transport into the broadwaters.

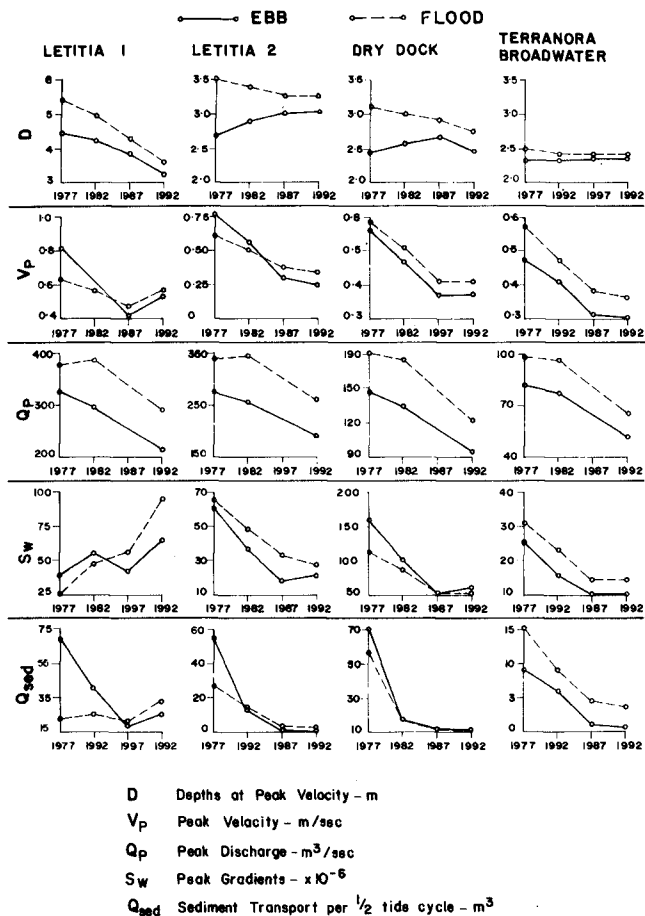


Figure 16 Variation of Hydraulic Parameters Due to Shoaling

8.3 Letitia 1

The picture is more complex at Letitia 1 because it is situated in the area of shoaling and this is reflected in the decreasing depths at both peak flows. Nonetheless a subtle enhancement of the peak flood velocities is discernable. Peak gradients increase due to the increasing head losses in the lower estuary, the flood gradient more so than the ebb. Ultimately the net transport reverts to the long term trend i.e. weak upstream movement of sediment.

9. CONCLUSIONS

- (1) Tidal propagation in a shallow estuary is very sensitive to the ruling channel depth within the initial 2-3 kilometres of the estuary. The extraction of 760,000 m³ of sand from the initial 2 km of the Tweed River had a significant effect on tidal levels and sediment dynamics throughout the estuary.
- (2) The dredging affected sediment movement for a distance of 3 km upstream in the main arm and 6 kms upstream in Terranora Creek.
- (3) Infilling of the dredged area initially took place at 100,000 m³ p.a. of which 85% was marine sand brought in through the entrance and 15% was derived from reworking of upstream estuarine sands.
- (4) In the long term the sediment transport throughout the estuary should trend towards a weak upstream movement of sediment.
- (5) The detailed monitoring of large scale bedforms can provide practical values of gross sediment transport rates provided the bed material is sandy and the transport mode is entirely bedload.
- (6) Sediment transport rates under Spring tides were five times that of Neap tide.
- (7) Points of reversal of net sediment transport were predicted and observed in the Tweed River. These are considered to be indicative of non regime conditions.
- (8) The hydraulic and environmental impact of large scale dredging in estuaries can be significantly reduced by location well upstream of the entrance.
- (9) Further field studies are needed to verify the broad behavioural trends predicted in this study and to evaluate the effect of floods and cyclones on estuary shoal regime.

10. ACKNOWLEDGEMENTS

The author acknowledges the tremendous effort and dedication of the late John Curedale to all phases of the investigation, particularly the preparation of the primary study report.

The author is grateful to Jan Iwaszkiewicz for his untiring assistance and initiatives in the field and Alan Dyson for his assistance and discussion in the computing side of the work.

11. REFERENCES

- Ackers & White (1973) - Sediment Transport : New Approach and Analysis. Jrnl. Hyd. Div., A.S.C.E., HY II, Nov. 1973.
- Allen & Friend (1976) - Changes in intertidal dunes during two spring-neap cycles, Lifeboat Station Bank, Sedimentology (1976) 23.
- Allen (1974) - Reaction, relaxation and lag in natural sedimentary systems. Earth Sci. Rev. 10, 263-342.
- Druery, B.M. & Curedale, J.W. (1979) - Tweed River Dynamics Study. Department of Public Works, N.S.W., Report No. 78009, Jan. 1979.
- Fredsoe, J. (1979) - Unsteady flow in straight alluvial streams : modification of individual dunes, J. Fluid Mech., Vol. 91, Part 3.
- Fischer, H.B. (1970) - A Method for Predicting Pollutant Transport in Tidal Waters, Uni. California, W.R.C., Berkeley.
- Gordon, A.D., Lord, D.B., Nolan, M.W. (1978) - Byron Bay - Hastings Point Erosion Study, Department of Public Works, N.S.W., Report No. 78026, Nov. 1978, ISBN 7240-2691-6.
- Harten, H. (1980) - Sea Ports, Studies to Hydraulic and Morphological Problems. Proc. 17th Int. Conf. Coast, Eng., Sydney Aust., 1980.
- Heathershaw, A.D. & Carr, A.P. (1977) - Measurements of Sediment Transport Rates Using Radioactive Tracers, Coast. Seds. 1977, 5th Symp. Wtway, Port, Coast and Ocean Division, A.S.C.E.
- Mehta, A.S., Byrne, R.J., De Alteris, J. (1976) - Measurements of Bed Friction in Tidal Inlets, 15th Int. Conf. Coast. Eng., Hawaii.
- Nasner, H. (1976) - Transport Mechanism in Tidal Dunes, Proc. 15th Int. Conf. Coast. Eng., Hawaii, 1976.
- Roy, P.S. (1980) - Responses of Sediment and Morphology to Nearshore Processes in Southeastern Australia. 17th Int. Conf. Coast. Eng.
- Royal Navy Hydrographer (1976) - Admiralty Manual Hydrographic Surveying.
- Thom, B. et al (1978) - Holocene Age Structure of Coastal Sand Barriers in N.S.W. Aust., Uni. N.S.W., Fac. Milt. Studs, Dept. Geog.
- White, Milli & Crabbe (1975) - Sediment Transport Theories : A Review. Proc. Inst. Civ. Engs. Part 2, 1975.
- Yalin, M.S. (1976) - Origin of Submarine Dunes. Proc. 15th Int. Conf. Coast. Eng., Hawaii, 1976.

NOOSA BEACH RESTORATION SCHEME

**R.J. Lloyd, B.E. (Civil), Executive Engineer, Beach Protection Branch,
Department of Harbours and Marine, Queensland, Australia.**

1. SUMMARY

A significant beach restoration scheme has been implemented at the coastal resort of Noosa in South-East Queensland. The scheme which cost \$1,400,000 involved sand nourishment, dune stabilisation works and the relocation of the entrance to the Noosa River using sand pumping techniques.

The effect of the scheme has been to greatly improve the quality of the main surfing beach at Noosa as a recreational facility and to provide much needed protection to a canal estate development which had been constructed within the Noosa River estuary close to the river entrance.

The successful implementation of this scheme also demonstrates that practical solutions to beach erosion problems are available and that sand pumping techniques may be used to economic advantage where relocation or closure of a river entrance is required and where local conditions and analysis indicate that such techniques can be applied.

Photograph 1 shows the completed restoration scheme.

2. SITE DESCRIPTION

Noosa Beach is located immediately south of the entrance to the Noosa River and seaward of the barrier dunes which separate the Noosa River estuary from the Pacific Ocean. The beach extends south east to the rocky headlands of Noosa Heads and is well known for producing excellent, safe surfing conditions.

The main commercial centre of Noosa is located precariously on the barrier dune landward of the surfing beach. Further landward is the Noosa River estuary and Hays Island - an area which was recently developed as a canal estate. Figure 1 shows the site of the restoration scheme.

The catchment area of the Noosa River comprises an area of approximately 87,000 ha. Most of this area is low lying with only two percent above 150 m above Mean Sea Level. The area is drained by a complex series of lakes and streams which finally join together to form the Noosa River which in turn meets with the ocean in the form of a wide unstable tidal estuary. Lake Cootharaba (3750 ha) and Lake Weyba (990 ha) are the major lakes of the drainage system and both are only slightly tidal with tidal ranges being less than 5 percent of the corresponding ocean tide ranges. Figure 2 shows the catchment area.

3. GEOLOGICAL DESCRIPTION

In terms of geological units the Noosa River estuary is defined as a Holocene Tidal Delta - an area of developed intertidal banks which represent successively abandoned channels.



PHOTOGRAPH 1 - The completed scheme (August 1979)



FIGURE 1 - Noosa River estuary showing the scheme of works

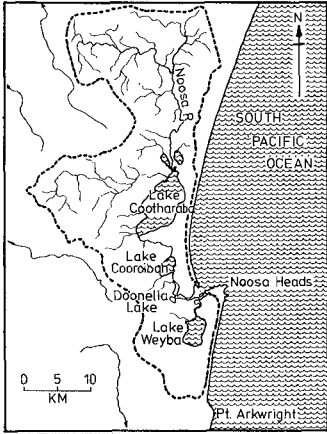


FIGURE 2 - Noosa River catchment area

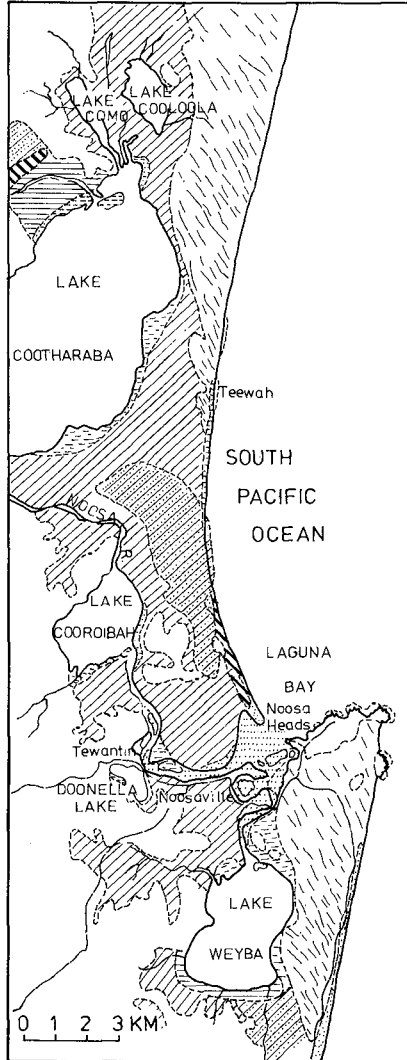
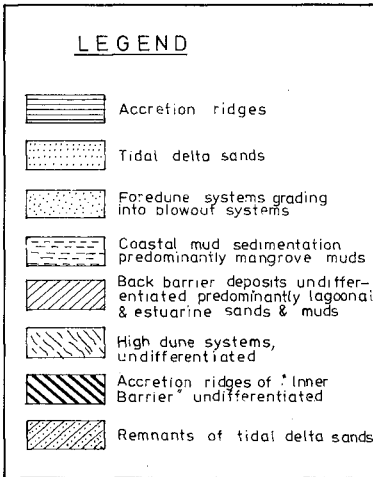


FIGURE 3 - Noosa area, geological units

The sand forming the delta has been shown to have been trapped from the beach system and to have its origins in the coastal rivers of Northern New South Wales to the south. The trapping mechanism could have been favoured by early increases in sea level.

The barrier dune which separates the estuary from the ocean is also of the Holocene epoch (probably formed in the past 10,000 years) and comprises well sorted quartz sands with minor heavy mineral deposits. Soil development on the fore dunes is minimal.

Reference 1 draws attention to alternating trends in dunal growth at Noosa and also to short term accretion trends within the estuary. Figure 3 shows the Noosa area subdivided into geological units.

4. EROSION PROBLEMS AT NOOSA

The main surfing beach at Noosa had suffered severely from erosion prior to implementation of the restoration scheme and following severe cyclonic storms in 1968 it had been necessary to construct a boulder wall full length along the beach to provide adequate protection to the development located on the barrier dune. The boulder wall was located in the swash zone and by partially dissipating wave energy in the form of turbulence and partially reflecting the waves established a process which further lowered the beach immediately seaward of the wall.

The canal estate developed on Hays Island within the Noosa River estuary had also been threatened as unforeseen movements of the main channel of the Noosa River had given rise to high velocity currents adjacent to the development. These had caused undercutting and partial collapse of some of the revetments to the development. Effectively the old channel on the northern side of the estuary which for many years had carried the main body of flow of the Noosa River was progressively abandoned in favour of a newer developing southern channel which in turn was in conflict with the canal estate development. Photographic records of the estuary indicate that the process of abandoning the older northern channel was quite natural and that the new southern channel adjacent to Hays Island was well established before any construction work at Hays Island commenced. Figure 4 shows the progressive changes which recently occurred in the estuary.

With the development of the new southern channel it was possible for waves entering the estuary through the river entrance to impinge on the works at Hays Island and the revetments had not been designed for such a contingency.

The development of the southern channel also had a direct impact on Noosa Beach. Coupled with the strengthening flow in the southern channel the river entrance moved south cutting into a camping reserve at Noosa Woods at the northern extremity of the commercial centre and at the same time reducing the length of the main surfing beach.

The overall effect was that by the time a decision was made to proceed with restoration works in 1977 Noosa Beach was virtually nonexistent.

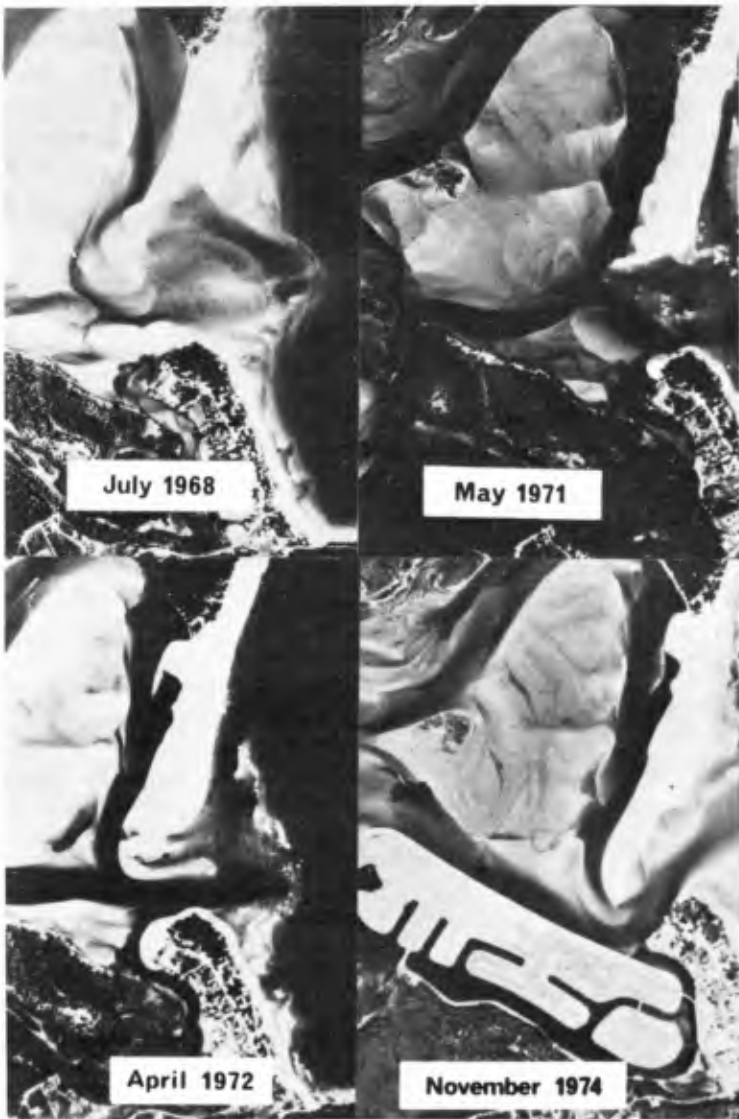


FIGURE 4 - Photographs showing progressive changes to the main channel within the Noosa River estuary

5. THE RESTORATION SCHEME

In seeking solutions to the erosion problems at Noosa model studies at the University of Queensland were initiated and several investigations commissioned (References 2 and 3). The findings of these investigations indicated that the Noosa River would have to be diverted away from Hays Island if the threat to the canal estate was to be removed.

The final scheme which was prepared in September 1977 after consideration of various alternatives was designed to provide a complete solution to all the problems previously outlined. It included the following works:-

- (a) Redevelopment of flow in the old northern channel of the river by opening a new entrance approximately 500 metres north of the existing river entrance.
- (b) The blocking of flow in the southern channel by means of sand pumping to form a closure bund across the original river entrance.
- (c) Development of a new beach system including a large dunal area north of the Noosa Woods camping area thereby reinforcing the closure of the southern channel and protecting the development at Hays Island from wave attack.
- (d) Sand nourishment of the original beach at Noosa at the rate of 250 cubic metres of sand per metre length of beach which would permit the establishment of a beach seaward of the existing rock wall.
- (e) The construction of a rock groyne and revetment on the southern side of the new river entrance to retain sand on the newly developed beach and also to prevent further southward migration of the new entrance.
- (f) The stabilisation and vegetation of all newly formed dunal areas (approximately 20 ha) to prevent damage by wind erosion.
- (g) The implementation of an effective monitoring program to record changes to Noosa Beach and within the Noosa River system.

Sand required for implementation of the works would be taken from borrow areas within the estuary. Figure 1 shows the location of the works including the designated borrow areas.

6. LIMITATIONS OF THE RESTORATION SCHEME

At the time the scheme was prepared its limitations were recognised. The more important of these were as follows:-

- (a) Undercutting of the rock groyne and revetment on the southern side of entrance might occur and maintenance could be required.
- (b) Erosion of freehold properties to the north of the new entrance could occur as northward movement or development of the new entrance would not be constrained by the scheme.

- (c) The new beach alignment would depend on the natural action of the sea and the supply of sand to the newly formed and restored beach.
- (d) A continuing maintenance commitment would be required to retain the newly vegetated dunal areas in satisfactory condition.
- (e) Maintenance of the beach in the form of additional sand nourishment following periods of severe storm wave attack might be required.
- (f) The scheme was not designed to control the behaviour and movements of channels within the Noosa River estuary.

7. CRITICAL PHASE OF THE SCHEME

The most critical phase of the restoration scheme was the closure of the original entrance to the Noosa River. While initially it had been expected that earthmoving plant might be required to effect final closure detailed examination showed that closure could be effected by sand pumping alone. Furthermore alternative techniques involving the use of earthmoving plant were found to be more costly.

Design calculations indicated the following:-

- * A continuous sand pumping rate of approximately 500 cubic metres per hour was required to construct a sand bund across the southern channel following the opening of a new entrance to the old northern channel.
- * The nett loss of sand from the works area during the closure operation would be minimal even though sand transport in the region of the closure bund would be high.

On this basis it was decided to adopt the sand pumping technique for the closure operation and the more costly techniques involving earthmoving plant were discarded.

In preparation of contract documents for implementation of the restoration scheme a sand pumping rate of 800 cubic metres per hour was specified for the entrance closure operation. This rate which was 300 cubic metres per hour in excess of the theoretically required sand pumping rate was considered necessary because of possible dredging plant failure.

8. CONSTRUCTION

Implementation of the restoration scheme comprised two distinct phases - the civil engineering works involving sand pumping and groyne construction and the dune stabilisation works.

Tenders for the civil engineering works were invited and five tenders ranging from \$1,263,435 to \$2,299,702 were received. The lowest tender was accepted and sand pumping works commenced on site on June 12, 1978 under the supervision of Departmental engineers. The specified sand pumping capacity was provided by these dredgers fitted with 250 mm diameter suction and delivery lines connected to pumps powered by diesel engines of 200 Kw rating.

Dredging commenced at the site of the new entrance with spoil being directed to the closure bund which was being developed from the northern side of the existing entrance. By June 20 the new entrance to the northern channel had been opened and by June 27 closure of the original entrance had been effected.

During the closure operation sand was pumped to the head of the closure bund to discharge points located well above water level. This resulted in much of the sand being deposited on the head of the closure bund above water level and rapid forward progress of the toe of the bund was made when slumping of this deposited material occurred.

While no technical problems were encountered with the entrance closure operation, the decision to specify a sand pumping rate of 800 cubic metres per hour was justified as actual records of dredging plant indicate that the average pumping rate achieved during the period June 12 to June 27 was only of the order of 600 cubic metres per hour because of dredging plant failures and the need to shift and maintain the associated equipment and dredge lines.

Following completion of the entrance closure operation, vehicular access to the site of the rock groyne became available and groyne construction was able to proceed. At the same time the final phases of sand pumping works were able to commence and all such works including the development of the beach and dunal areas north of the Noosa Woods camping area as well as sand nourishment of the original beach were completed by September 13, 1978.

During the progress of the works sand pumping rates being achieved by individual dredgers were measured. The rates varied between 280 and 370 cubic metres of sand per hour with only one test showing a result of less than 300 cubic metres per hour. Based on these measurements it is estimated that in excess of 1,000,000 cubic metres of sand were incorporated in the works. Of this approximately 150,000 cubic metres of sand were required for the entrance closure operation.

Progress of the civil engineering works is shown on Figure 5, a sequence of aerial photographs of the works.

After the completion of sand pumping works dune stabilisation works were able to proceed. These works proceeded on a day labour basis under the control and supervision of Departmental staff well experienced in dune stabilisation techniques.

Approximately 20 ha of the newly created dunal areas were initially stabilised against wind erosion by the establishment of a vegetative cover of grass. The speed with which this operation was carried out was greatly assisted by the balanced application of fertilizer.

In addition to establishing grasses, in excess of 20,000 creepers, shrubs and tree seedlings were planted and are now well established. Fencing and access paths were also constructed to control both vehicle and pedestrian movements in the stabilised areas.



FIGURE 5 - Photographs showing progress of the works

9. MONITORING

The restoration scheme included an extensive monitoring program as an integral part of the scheme. The major activities included in the program were as follows:-

- . Water level monitoring at four locations - three stations upstream of the development site on the Noosa River and a single station at Boreen Point on Lake Cootharaba.
- . Aerial photography at regular intervals.
- . Regular measurements of the tidal compartment.
- . Sand sampling.
- . Daily recording of wave and beach conditions at Noosa by a trained volunteer observer.

This monitoring program many aspects of which have remained in operation is providing valuable information on erosion and accretion trends of the restored beach and also on behavioural patterns of water level movements within the Noosa River and Lake Cootharaba.

10. BEHAVIOUR OF NOOSA BEACH SINCE IMPLEMENTATION OF THE RESTORATION SCHEME

The nett longshore transport at Noosa Beach is to the north. This conclusion is based on longshore transport calculations using observed and derived wave climates for Noosa Beach. It is also supported by the fact that available photographs of an old groyne which was constructed on Noosa Beach show sand build up on the southern side only. The nett longshore transport rates which have been derived are of the order of 140,000 cubic metres of sand per year to the north.

Since implementation of the restoration scheme the southern portion of Noosa Beach has receded visibly and successive surveys carried out along fixed lines spaced at 80 m intervals along the beach indicate that in excess of 100,000 cubic metres of sand has been lost in the 12 month period following implementation of the scheme. The bulk of these losses have been concentrated in the area above the -5 metre contour (relative to Mean Sea Level) and there has been no observable loss to offshore areas. The beach lines extend several kilometres offshore. The likely explanation of this behaviour is that the supply of sand to the southern portion of Noosa Beach has not been sufficient to make good sand losses from the area due to longshore transport to the north.

In the mid region of Noosa Beach adjacent to and to the immediate north of the Noosa Woods camping area surveys indicate that there has been little or no change in the quantity of sand on the beach in the 12 month period following implementation of the restoration scheme. While there have been some beach profile changes above the -7 metre contour (relative to Mean Sea Level) seaward of this contour the shape of the seabed profile appears to have remained relatively constant and any variations in level between surveys are considered to be caused primarily by the accuracy limitations of the survey techniques adopted. Based on the above it is considered that in the mid region of Noosa Beach there has been a balance between supply and loss of sand.

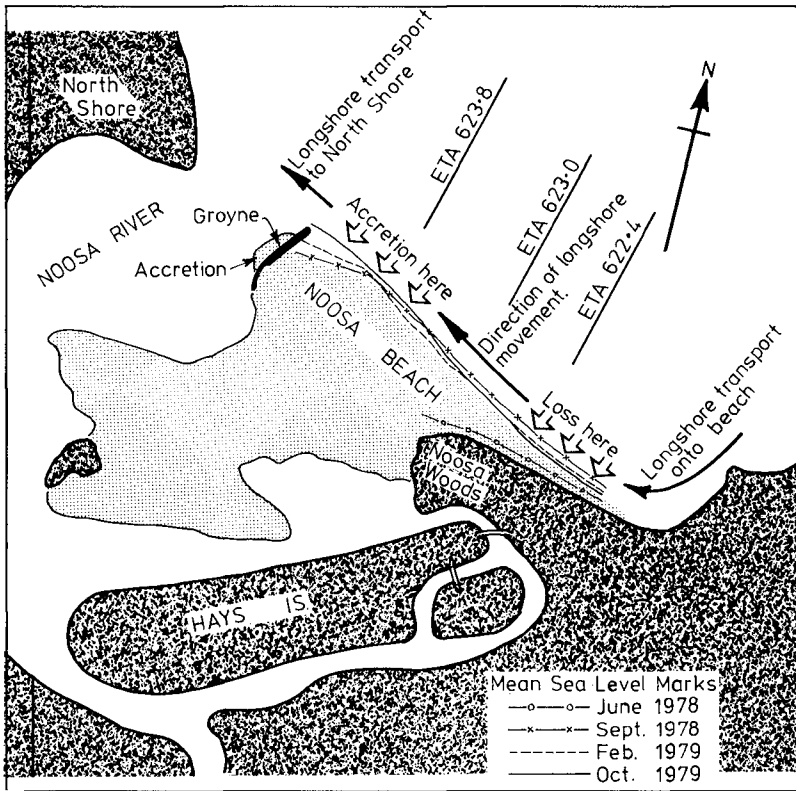


FIGURE 6 - Movements of the 0.0 contour (Mean Sea Level) as determined by beach surveys at Noosa

In the northern portion of the beach in the region of the rock groyne in the same period there has been obvious visible accretion and a substantial beach berm has developed. Beach surveys confirm this accretion and indicate that there has been accretion of sand of the same order of magnitude as the sand losses which occurred in the southern region of the beach. Virtually all profile changes were limited to the area landward of the -7 metre contour (relative to Mean Sea Level).

The nett result has been an overall change in beach alignment. Figure 6 gives an indication of this change in alignment and shows the 0.0 metre contours as determined from successive surveys carried out in June and September of 1978 and also in February and October 1979. The June 1978 survey was carried out prior to implementation of the restoration scheme. Figure 7 shows typical beach profiles obtained by survey.

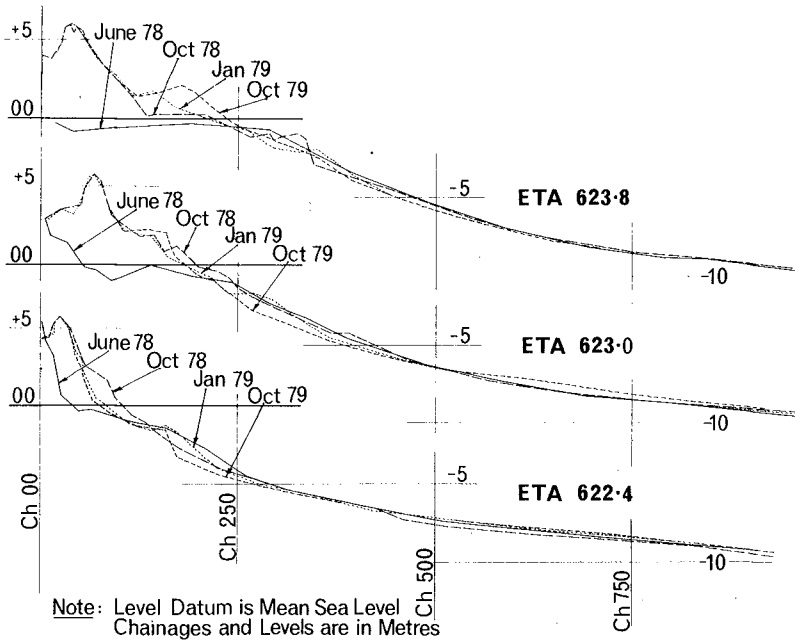


FIGURE 7 - Typical beach profiles at Noosa as determined by beach surveys. Location of beach lines is shown on Figure 6.

The accretion of sand in the northern region of Noosa Beach is attributed mainly to groyne action. However, sand bypassing has not been prevented by groyne construction as a large sandy spit has developed on the northern side of the groyne as a result of sand bypassing and the new entrance to the Noosa River has been displaced to the north.

The grain size of sand obtained from the estuary for beach nourishment purposes was generally coarser than the native beach material and it is not considered that sand losses at the southern extremity of the beach have been significantly increased by the loss of fine material. Figure 8 shows the results of sand sampling within the estuary and also on Noosa Beach.

It is postulated that the beach recession which has occurred along the southern portion of Noosa Beach has been caused by an intermittent sand supply from around Noosa Headlands. This argument is supported by photographic evidence which shows that the condition of Noosa Beach and the small pocket beaches between the headlands fluctuates with time. It is considered that the fluctuating condition exhibited by these beaches is the result of a fluctuating sand supply to these beaches and that the condition of the southern portion of Noosa Beach where restoration work has been carried out will continue to fluctuate under the influence of natural processes. The small pocket beaches between the headlands have not been in good condition since the restoration scheme was implemented. Thus it could be expected that the southern portion of Noosa Beach would currently be experiencing a period of recession.



FIGURE 8 - Photographs showing the fluctuating condition of beaches around Noosa Heads. Immediately south of Noosa Beach. The January 1978 photograph is typical of the condition which has existed since implementation of the restoration scheme.

11. BEHAVIOUR OF WATER LEVELS WITHIN THE NOOSA RIVER AND LAKE COOTHARABA

Monitoring of water levels within the Noosa River and further upstream in Lake Cootharaba has not shown that current water level behaviour differs greatly from that which was previously recorded prior to the restoration scheme being implemented.

Spring tide ranges at Munna Point (refer Figure 1) are as follows:-

- * Prior to Restoration Scheme being implemented -
 - 1974 - 0.77 m
 - 1975 - 0.70 m
 - May 1968 - 0.48 m
- * Following implementation of restoration scheme -
 - November 1978 - 0.73 m
 - July 1979 - 0.62 m
 - December 1979 - 0.62 m.

The above figures indicate that fluctuating spring tide ranges were a feature of water level behaviour within the Noosa River prior to the restoration scheme being implemented. Spring tide ranges based on data recorded since implementation of the scheme lie within the limits of previously recorded ranges.

12. MONITORING OF THE ENTRANCE CLOSURE OPERATION

During the entrance closure operation a sand bund with a crest level of approximately RL +4 metres (relative to Mean Sea Level) and a base width of approximately 150 metres at RL -2 metres was constructed across the entrance to the southern channel over a period of approximately 16 days. During this period regular surveys of the closure gap were carried out. The results of selected surveys are shown on Figure 10. Each of the surveys shows the presence of a deep channel located hard against the head of the closure bund. This channel was effectively pushed ahead of the closure bund as the closure operation proceeded.

The cross-sectional area of natural material eroded from the entrance is represented by the difference in cross-sectional area between the original channel profile and a line traced by the lower limit of the previously described channel as it was pushed ahead of the closure bund. This area which has been estimated to be 330 square metres is shown on Figure 9 as a cross-hachured area marked below the plot of the first survey of the entrance which was carried out on June 16, 1968.

Based on this survey information and aerial photography it was estimated that of the order of 30,000 cubic metres of sand was eroded from the natural bed of the entrance channel during the closure operation.

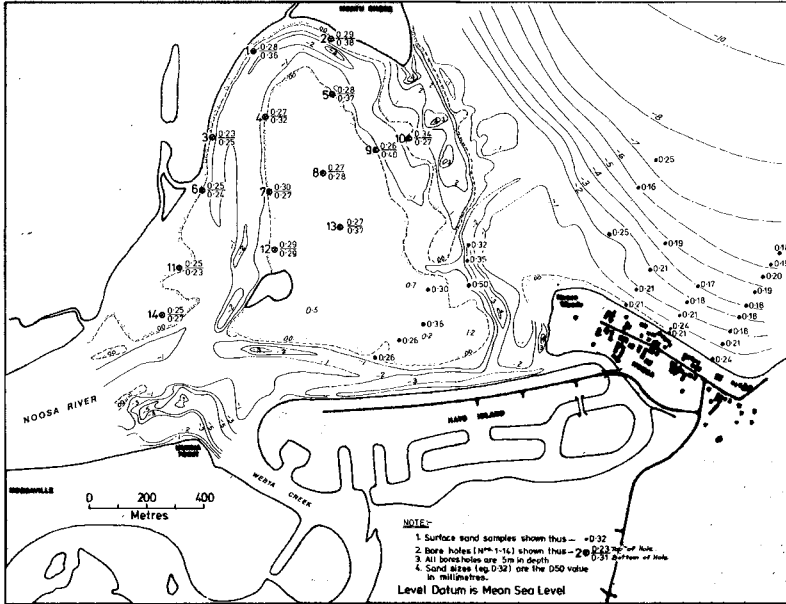


FIGURE 9 - Sand sampling results

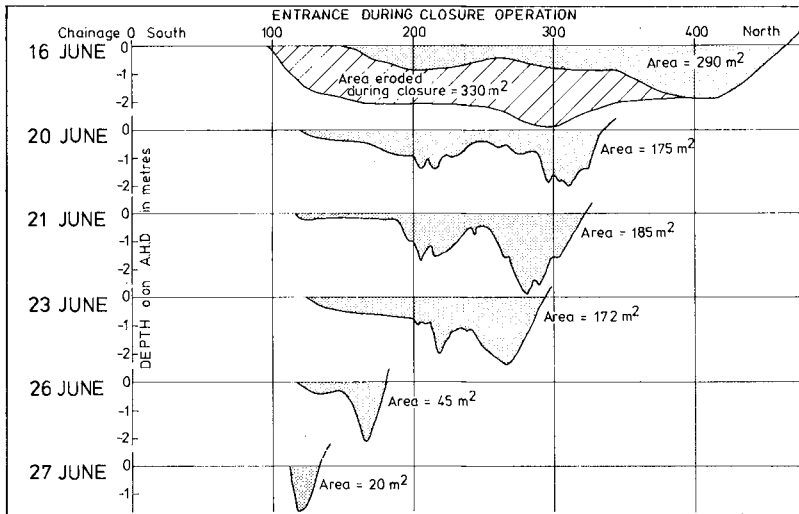


FIGURE 10 - Surveys of Noosa River entrance during closure operation

13. BEHAVIOUR OF NEW ENTRANCE

In the 18 month period following opening of the new entrance to the old northern channel of the Noosa River estuary on June 20, 1978 the entrance has continued to develop with the pattern of flow changing continuously. A new bar across the entrance has formed and surveys carried out in February 1980 show that this is continuing to extend seaward.

The cross-sectional area of the new entrance measured below Mean Sea Level as determined by survey in October 1979 was approximately 300 square metres. This is similar to the area which existed in 1896 when the entrance was first surveyed. It is also similar to that which existed when the restoration scheme was first investigated in September 1977.

As the cross-sectional area of an untrained entrance may be related to the tidal prism (Reference 4), the behaviour of the entrance would indicate that implementation of the restoration scheme has not had a significant impact on the tidal compartment of the Noosa River.

14. CONCLUSIONS

From a beach protection viewpoint the Noosa restoration scheme has been successful. The aerial photograph of the restoration scheme site which was taken after the artificially formed beach profiles had time to adjust to prevailing wave and current conditions shows that large areas of new beach are now available for a wide variety of recreational purposes whereas previously no such beach areas existed. Although there have been several periods of rough seas and high tides there is no evidence of a significant nett loss of sand from the beach system. In addition the new beach north of the Noosa Woods camping area has successfully withstood the attack of two cyclones without any damage to the artificially created frontal dune.

From the viewpoint of the development within the Noosa River estuary the threat of damage to revetments and property through undercutting and wave action has been removed.

From a technical viewpoint the success of the entrance relocation operation using sand pumping techniques has demonstrated for the first time in Queensland that both suitable plant and the necessary expertise are available locally to enable full use of this specialised low cost technique of entrance closure.

In view of the above, it is considered that the scheme has provided an effective solution to the erosion problems at Noosa and demonstrates clearly the benefits which can be derived from a well conceived beach restoration scheme.

REFERENCES

- (1) QUATERNARY GEOLOGY OF THE SUNSHINE COAST,
SOUTH EAST QUEENSLAND
Department of Mines, Record 1976/77, April 1976.
- (2) THE NOOSA RIVER AND ESTUARY, 1975
University of Queensland, Department of Civil Engineering, Report CH20.
- (3) SCHEME FOR PROTECTION OF HAYS ISLAND AND RESTORATION OF NOOSA
BEACH - Beach Protection Authority of Queensland, September 1977.
- (4) STABILITY OF COASTAL INLETS
P. Bruun and F. Gerritsen.

BEACH NOURISHMENT AS A MANAGEMENT TECHNIQUE

David M. Chapman,
Coastal Studies Unit,
University of Sydney, Australia

1) INTRODUCTION

Beach nourishment is considered an environmentally safe management technique, since an unsuccessful nourishment project would simply result in the redistribution of borrow material by wave action into environments more in keeping with a state of equilibrium. No permanent modifications of the beach and nearshore environment need result, and since no permanent structures are required for beach nourishment, the management commitment allows rapid project abortion if necessary. Beach nourishment monitoring has usually been concerned with evaluating changes in the extent of subaerial beach and/or retention of fill volume. These parameters are important, but it is also necessary to consider the way in which nourishment sand is taken up by the beach system since relationships between volume change, change in extent of subaerial beach, and changes in beach morphology are complex. This paper is concerned with evaluating beach nourishment on the Gold Coast (Figure 1), Australia's major resort, where 2.4 million cubic metres of fill were applied in the largest beach nourishment project attempted in this country at the time of writing.

Methodology, reported in Chapman & Smith (1977) and Chapman (1978a) included repetitive profile survey from backshore to point of zero change in inshore zone (over 400 profiles) using highly accurate techniques, and use of 38 tonnes of tracer, which was injected into the dredge line at a controlled rate.

2) BEACH BEHAVIOUR

2.1 Width/Volume Relationships

Analysis of Gold Coast survey data showed that subaerial (or "dry") beach width, taken alone, is a poor indicator of the volume of sand present in the active zone, or swept prism (Chapman & Smith, 1980), and is therefore not a reliable index of resistance to erosion. Correlation of subaerial beach width, per se, and sand prism volume is poor, and comparisons only become meaningful if beach morphologic states are taken into consideration.

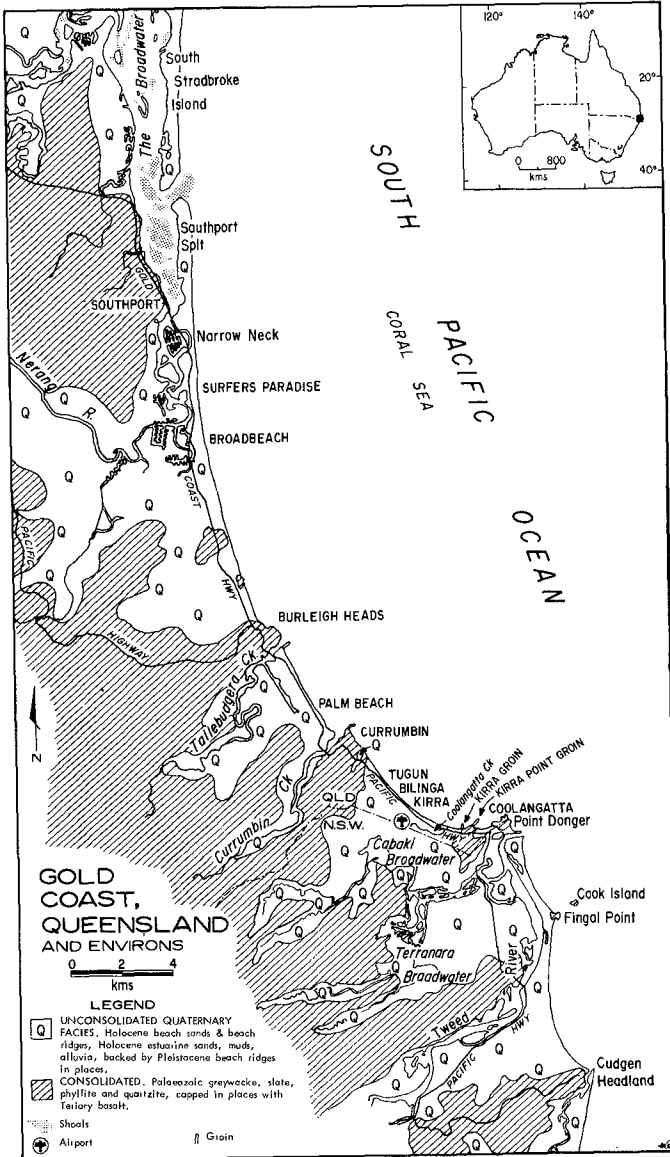


FIGURE 1

Net change in volume of the Lower Gold Coast beaches following nourishment is shown in Figure 2, with change in width of the sub-aerial beach shown in Figure 3. Datum in both cases is the beach state at commencement of survey. Although a net gain of volume occurred, Fig. 2 demonstrates that distribution of change at end of survey was very uneven, with the bulk of the fill remaining close to the delivery point in the form of two large "slugs", or parcels of sand. Comparison of Figures 2 and 3 also shows the importance of the subaqueous profile (or in-shore zone). Shoreline changes do not reflect the true state of erosion or accretion following beach nourishment. The total sand volume contained in the nourished area is critically dependent on the subaqueous profile. Shoreline recessions may be accompanied by accretion of the subaqueous profile. The lack of correlation between Figs. 2 & 3 is significant, showing as it does that width of subaerial beach is not a good indication of sand storage in the total beach system.

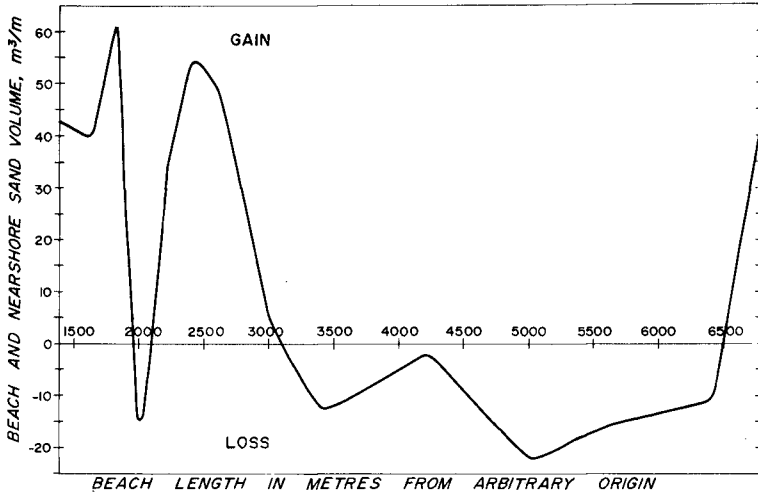
The large slug of sand centred on 2500 metres is almost wholly contained in the subaqueous part of the profile, being poorly reflected in added beach width, whilst small gains in beach width at 2000 metres and 3,500 metres do not reflect added volume in the beach prism at these points, but rather the reverse is true.

Most of the active zone of the beach is subaqueous (Chapman & Smith, 1980); a wide subaerial beach may give a deceptive appearance of security to resource managers, since the widest subaerial beach for a given fixed volume of sediment in the active zone, is associated with fully accreted, highly reflective beach states (cf. Short, 1978; Wright, *et al.*, 1979). Beaches in this condition are very sensitive to sudden increase in wave power, which causes rapid transfer of sediment to the subaqueous beach, and corresponding loss of subaerial beach width.

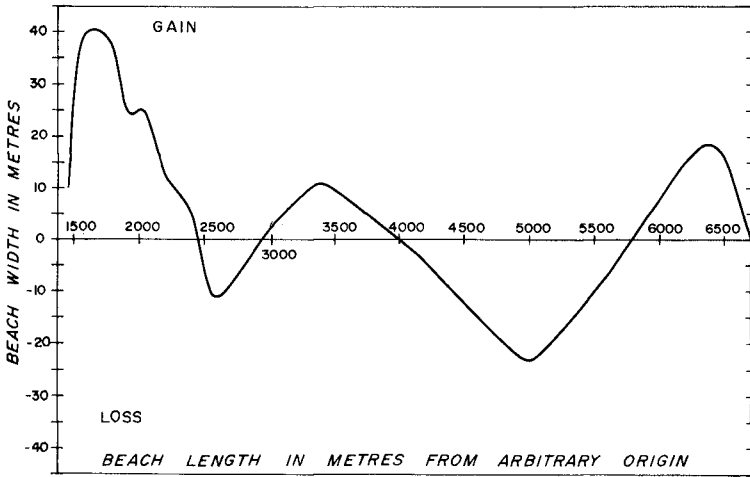
Re-distribution of beach sand by high energy waves was observed on the Lower Gold Coast seven months after project completion, when tropical cyclone "David" crossed the shoreline at about Lat 24°S. A reduction in dry beach width of over 20m occurred over the study area, with overall gradient being reduced from approx. 1:40 to approx. 1:80. The volume of the swept prism (Chapman & Smith, 1980) remained unchanged.

2.2 Manner of Sand Movement

It was found that the phenomenon of slugs of sand discussed above was not restricted to the nourishment project. Slugs of sand have been observed at three scales: (a) small-scale irregularities in beach volume revealed by survey as in Fig. 2; (b) medium-scale parcels of several hundred thousand cubic metres, usually associated with the flushing of flood-tidal deltas from estuarine inlets, and their subsequent accession to adjacent beaches; and (c) large-scale slugs of a million cubic metres or more, which appear as somewhat



CHANGE IN BEACH AND NEARSHORE SAND VOLUME
 FIGURE 2



CHANGE IN BEACH WIDTHS, KIRRA - CURRUMBIN
 FIGURE 3

subtle, low amplitude variations in subaerial and subaqueous sand storage over beach lengths of several kilometres.

Longshore transport, both in the short term of the nourishment monitoring study, and the longer term of some years, was effected by the alongshore migration of these slugs rather than as a continuous longshore flow of sand. Small and medium scale slugs tended to retain their identity whilst moving alongshore (drift direction is south-to-north, or left to right in Figs. 2 & 3) for distances of one or two kilometres, but then to diminish in amplitude and to coalesce into large-scale slugs.

Observations of large-scale slug movement, made over a period of 10 years, have revealed the slow longshore progression of forms illustrated schematically in Figure 4. Drift direction is from left to right; longshore movement of identifiable forms is indicated by the oblique arrows. The alongshore movement of the slugs of fill material from Kirra ($1.0 \times 10^6 \text{ m}^3$) and Surfers' Paradise ($1.4 \times 10^6 \text{ m}^3$) was particularly evident, since, although diffused with native sand, the fill slugs still exhibited a slightly different hue compared with the native sand in 1980. Calculations of volumes present in the slugs and rates of movement of their centroids indicated that longshore transport volume effected thereby was of the order of $2.0 - 2.5 \times 10^7 \text{ m}^3 \text{ yr}^{-1}$, a result remarkably similar to the figures of 2.84 and $2.52 \times 10^7 \text{ m}^3 \text{ yr}^{-1}$ derived for the Lower Gold Coast by intensive volumetric survey and tracer analysis (Chapman, 1978b).

The phenomenon of shore-parallel sediment movement in the form of discrete slugs has also been reported from the New Jersey coast of the U.S., where slugs of wavelength 4000-5000m were observed by Everts (pers. comm.)

2.3 Nourishment and Beach Topography

Fill application to the Lower Gold Coast resulted in a beach and inshore morphologic response similar to that observed on the beach sections adjacent to estuarine inlets following flushing by floods of flood-tidal deltas of marine sand contained in them, viz., amorphous inshore shoals, expansion of surf zone width, highly dissipative (as defined by Wright, *et al.*, 1979) conditions, and considerable wave setup.

As the slugs of fill moved alongshore, intensified and persistent rips developed ahead of them, leading to loss of beach width and volume as revealed in Figures 2 & 3. It is thought that a longshore gradient of radiation stress associated with wave setup over the fill slugs may have contributed to scour at the downdrift toe. The intensified rip at 3600 metres from the origin locally modified wave behaviour in the course of a short and relatively minor storm such that wave attack caused sea-wall collapse and property erosion behind the cell.

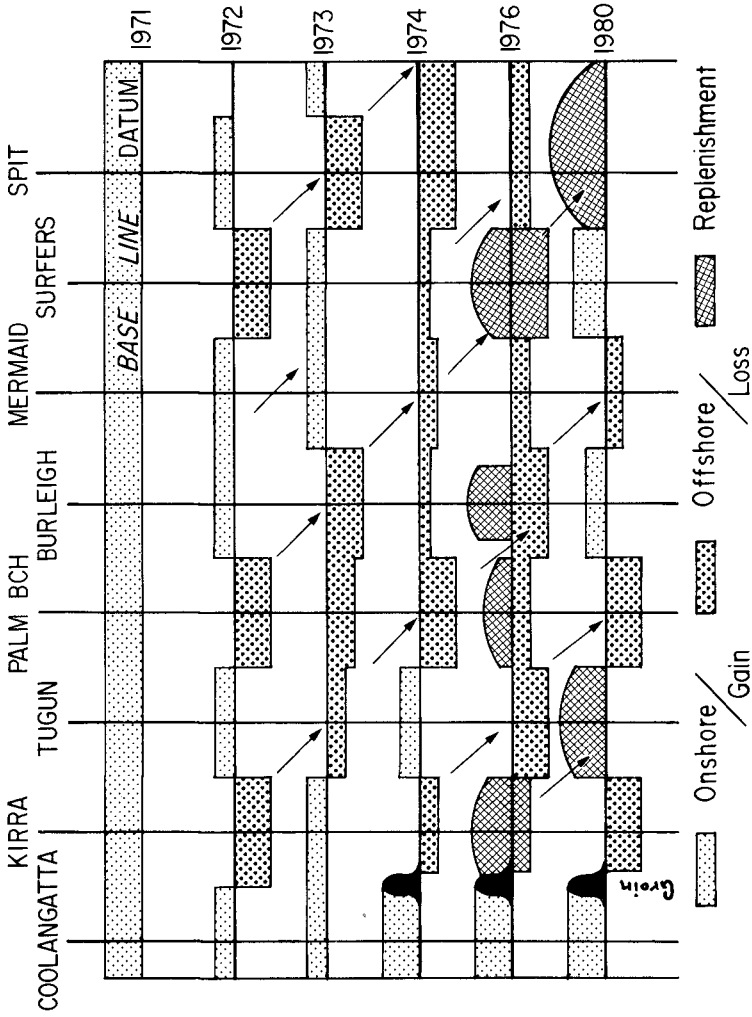


FIGURE 4

The phenomenon of scour at the downdrift end of fill on the Lower Gold Coast did not occur at the site of the contemporaneous nourishment project at nearby Surfer's Paradise. At Surfer's Paradise, it was more convenient for the contractor to place the fill by extending the delivery pipe incrementally in the opposite direction to the longshore transport system. No perturbations at the downdrift end of the nourished beach were observed.

3) FILL SELECTION & PLACEMENT

3.1 Fill Evaluation Criteria

A priori, one might expect that nourishment sand should be texturally matched to native sand if the "artificial" beach is to be successful. It may be anticipated that erosive forces would be less competent to remove sand of a coarser texture, hence use of nourishment sand substantially coarser than native might be expected to produce a more durable beach. Newman (1976) for example, considered that nourishment sand should have a median diameter $1\frac{1}{2}$ - 2 times that of native sand, and the well-known critical ratio concept has been developed around the foregoing assumption (Krumbein and James, 1965) to define the ratio of volume of nourishment sand required to be placed to the volume retained on the beach in equilibrium with shore processes. In most cases critical ratios considerably exceed unity, predicting that the proposed borrow material is less than ideal and that winnowing will selectively remove unsuitable fractions of the fill until it becomes compatible with the existing beach regime.

An alternative approach to evaluating the modification of nourishment sand by beach processes was proposed by James (1975), in the form of the re-nourishment factor which attempts to predict frequency of re-nourishment and to evaluate the long-term performance of proposed fill materials with regard to suitability, maintenance, and expense. The active beach system is considered a compartment which gains sediment through longshore transport and from gradual erosion of the store of sediments forming the backshore, and loses sediment by longshore and offshore transport beyond its boundaries. Fill is viewed as an increase to the backshore store. Sediment particle residence time in the compartment is longer for coarse grained material than for fine; thus a comparison between composite size distributions of native and borrow sediments is used to predict the "lifetime" of fill. A renourishment factor of $\frac{1}{2}$ means that borrow material would be expected to erode at half the rate of native material; renourishment with such borrow material should be required half as often as renourishment with sediment of identical composition to native material. Conversely a renourishment factor of 2 indicates that renourishment would be required twice as often as would be the case if native type sediment were used. The renourishment factor increases with an increasing difference between native and borrow means; the finer the borrow material compared with native, the higher the predicted retreat rate. Poorly sorted borrow material results lower predicted retreat rate since it contains a larger fraction of coarser material which is considered to provide a stable armour.

As the textural correspondence between native and borrow materials used in the Lower Gold Coast project was almost perfect, both the critical ratio and renourishment factor formulae gave values close to unity. However, using data derived from sediments actually present within the dynamic swept prism (Chapman & Smith, 1980) of the Lower Gold Coast, sensitivity analyses made on the formulae cast doubt on their validity. Aggregated samples varied between the limits (mean = 2.0ϕ , $s=0.4\phi$) and (mean = 2.5ϕ , $s=0.5\phi$), a remarkably homogeneous sand body; nevertheless both the critical ratio and renourishment formulae predicted that one or the other of these materials would generate quite marked changes in beach behaviour* in an environment where both were demonstrably in equilibrium.

Losses of beach nourishment material have often been ascribed to supposed winnowing of the finer fraction of such material, with the assumption that the fine sediment is lost to the system. Such is not necessarily the case, for, if a beach is moved into a different state by fill application, and redistribution of material to the inshore and inner nearshore takes place as a result, introduced material is not lost, but merely distributed in a different way to native material. In many cases the "lost" material will still be found within the dynamic swept prism (Chapman & Smith, 1980); absolute loss presupposes the existence of a sink. Accession of fill to the subaqueous part of the swept prism may produce a beach of lower overall gradient, with but slight increase in width, but one in which the swept prism has the capacity to absorb a great deal of wave energy without substantial withdrawal of sand from the subaerial part of the prism.

Introduction of finer-than-native material may well shift the beach regime into a more dissipative regime (cf. Wright, et al., 1979) with wider inshore zone, which could, by causing greater frictional dissipation of wave energy at greater distance from the backshore than in the pre-fill state, enhance erosion resistance. The fine sand, highly dissipative beach also requires more wave energy, compared to other beach states, to produce substantial erosion (Wright, 1980).

Use of coarser-than-native material, on the other hand, could conceivably cause a shift to a more reflective beach regime associated with a narrower inshore zone; this beach state is the one most delicately poised and subject to rapid collapse and removal of sand from the subaerial beach with input of increased wave energy (Wright, et al., 1979).

However, Gold Coast experience indicates that diffusion of fill into native sand may be rapid enough to warrant consideration of a new sand population formed as a mixture of fill and native materials. For the first two months after commencement of fill delivery, advection of added volume occurred principally over the first 1.5 km downdrift of the input point (Fig. 2) but diffusion of nourishment sand was very rapid, and revealed a high degree of over-turning within the sand prism.

* e.g. the renourishment factor varied between 0.41 and 1.92 in tests cited

Coring of the prism and analyses of tracer concentration (Chapman & Smith 1977) that the ratio of nourishment to native sand could be described by $r = e^{-(y/0.1)}$ where y is distance alongshore in kilometres.

Fill evaluation formulae as discussed above also presuppose the loss of the finest sand from the beach system. However, many microscopic examinations of beach sediments from a wide range of energy environments in eastern Australia have invariably revealed a significant tail of very fine sand, even in the extreme case where ϕ mean approached zero. Since Hobson & James (1978) have shown that elutriation of fines not in equilibrium with the beach environment can be very rapid, the persistent presence of very fine tails in beach sands suggests that these form part of the normal populations of the beaches concerned. Work in progress also suggests that behaviour of the sediments may be related to the frequency distribution of specific surface, as distinct from mean diameter (Smith & Gordon, 1980), in which case the fine tail achieves greater prominence.

The critical ratio and renourishment factor concepts appear to have evolved from the perception of a wide subaerial beach as the most desirable state, and assume uniform profile retreat under erosion. Rather than searching for field data for verification of the concepts, as has been suggested (e.g. Dean, 1976) it may be that criteria are required for the evaluation of fill suitability in terms of its effect on beach morphology within a given energy environment.

3.2 Fill Placement

Fill placement has usually been thought of in terms of a design profile of beach nourishment distribution (Delft, 1970; Silvester, 1974; Vallianos, 1975). Silvester suggested the calculation of an "equilibrium" profile form, whilst Vallianos used the concept of a design profile, complete with shaped dune form. Experience from the Gold Coast suggests that, whilst the design profile concept may be useful for calculation of fill quantities, it is of little value as a practical working criterion for the reconstruction of beaches by means of nourishment, since the procedure assumes both fill retention and morphology are predictable.

The concept of an artificially shaped profile, complete with formed dune, was an essential element in the scheme for the Gold Coast (B.P.A., 1973). The sand supplied to the beach was to be distributed above high water level by bulldozer and vegetation was to be established upon an artificially formed dune. The design concept envisaged that the fill would be placed as high on the beach as possible, covering any boulder walls present, and allowing the surplus only to escape to the swash zone.

However, execution of the concept proved impractical. Emplacement of fill sand in the design profile meant that the unnaturally high "berm" was scarpred at high tide. This not only gave the public the impression that fill was being lost by erosion, but made beach access

difficult for swimmers which resulted in public relations problems for the Local Authority.

The artificially formed "dune" concept also proved impractical. Immediately upon drying out, sand began to drift onto the backshore and encroach upon parking areas and esplanades. Moreover, attempts at establishment of the sand-binding grass, Spinifex hirsutus, in the pumped sand proved abortive. The tight packing characteristics and fines content of pumped sand were dissimilar to the lightly packed, free moving sand of the normal accreting foredune. It appears that the dissimilarity was great enough to inhibit Spinifex development.*

Much of the literature on beach management is imbued with static notions of beach equilibrium. The beach must be recognised as a dynamic system, and managed within its dynamic range, for management to be effective. The concept of the equilibrium inshore profile was shown by Chapman (1978b) to be a chimera. Use of an appropriate three-dimensional model allows a number of more-or-less discrete beach stages (or equilibria) to be recognized, as described by (e.g.) Short (1978) or Wright, et al., (1979). Viewed in this context, management of a beach by means of nourishment involves more than merely the addition to the active zone of sand having a suitable 'critical ratio' or 'renourishment factor'. Manipulation of the beach system could involve consideration of the characteristic morphologic states of the beach in question with their probabilities of occurrence spatially and temporally and in relation to most probable energy inputs. Given a variety of possible sediment sources it may be possible to induce beach behaviour of more dissipative or more reflective modes if these were considered desirable. Timing of application of nourishment with respect to existing or probable morphologic states and energy inputs, both from sea and wind, in order to maximise fill utility and encourage formation of backshore dunes, also may be seen as a management variable.

4) CONCLUSION

To the lay beach user, or even to the resource manager unfamiliar with inshore morphodynamics, a wide subaerial beach is interpreted as a sign of the presence of a large sediment volume. Results reported above show this perception may be quite erroneous.

A commonly applied guideline of one square foot of beach area gained per cubic yard of fill, may be seen in its general form as an attempt to relate subaerial beach area to volume of the sand prism; however it was shown above that width (or area) of subaerial beach is

* S.hirsutus is propagated by seed. Vegetative propagation is possible but not practical. The popular Ammophila spp. used in many cool temperate areas, A. Arenaria and A. breviligulata, were unsuitable for the Gold Coast as the sub-tropical location is beyond the environmental tolerance of the latter species.

poorly correlated with volume in the sand prism. Width will depend, inter alia, on beach state and on texture of added sediment.

Commonly-used renourishment factor or critical ratio concepts are unsoundly based; since both use simplistic data as basic input they can at best provide over-simplified approximations of the complex and dynamic beach regime, and no process terms are included in either. Basic to both concepts is the assumption that a coarser-than-native sediment is desirable for fill purposes, and is likely to prove more stable under the wave climate of the problem area. Whilst coarser non-cohesive sediment is less likely to be moved by any given wave than is fine sediment, it does not necessarily follow that coarser sediment will ultimately produce a more stable beach or more desirable beach state than native material.

A beach will be built, by waves, of whatever suitable material is available; high energy wave climates are not necessarily always associated with beaches of coarse sediment, or vice versa.

Sediment size is but one of a matrix of factors responsible for beach behaviour at a site under any given wave climate; varying sand grainsize may simply cause a shift into a different stage in the morphodynamic continuum rather than producing a beach of different erosion resistance.

The design profile concept is useful for computing required fill amounts by comparison with existing beach profiles; however, it assumes that both fill retention and morphology are predictable and that the design profile can be constructed. In practice, in a moderate-to-high energy environment, the concept may be operationally impractical, and establishment of vegetation by seed in pumped-sand "dunes" proved difficult. Fill redistribution by natural marine and aeolian processes proved more effective and economic than attempts to create an idealised profile. Apparent "losses" from the dry beach were accounted for by redistribution in the inshore zone.

Perturbations of the inshore system caused by fill application may affect local erosion patterns and longshore transport in ways which would be unexpected from observation of the beach in its normal state. Radiation stress gradients developed as a result of topography associated with nourishment may lead to intensified erosion adjacent to the filled beach.

If fill redistribution within the dynamic swept prism is seen as normal, and the movement of sediment to the subaqueous part of the prism as morphodynamic change rather than loss of material, it may be possible to consider a wide variety of potential nourishment sources to increase the erosion resistance of a given beach, and even to think of "tuning" to achieve desirable morphologic states.

5) REFERENCES

- B.P.A. (1973) Scheme Prepared by the Beach Protection Authority pursuant to the Beach Protection Act 1968-1970 for the Protection of all Beaches Situated at the Gold Coast. Brisbane, The Authority, 8pp. + maps.
- CHAPMAN, D.M. (1978a) Management of Sand Budget, Kirra Beach, Gold Coast. 4th Aust. Conf. Coastal & Ocean Eng., pp.19-24. The Institution of Engineers, Australia.
- CHAPMAN, D.M. (1978b) Management of Sediment Budget, Lower Gold Coast, Queensland. Ph.D. Thesis, University of Sydney, 279pp.
- CHAPMAN, D.M., SMITH, A.W. (1977) Methodology of a large scale tracer experiment. 3rd Aust. Conf. Coastal & Ocean Eng., pp. 185-189. The institution of Engineers, Australia.
- CHAPMAN, D.M., SMITH, A.W. (1980) The dynamic swept prism. Proc. 17th Coastal Eng. Conf., ASCE.
- DEAN, R.G. (1976) Beach erosion - causes, processes, and remedial measures. CRC Crit. Reviews in Envir. Control, 6 (3) 259-296.
- DELFT HYDRAULICS LABORATORY (1970) Gold Coast, Queensland, Australia-Coastal Erosion and Related Problems; Report 257 in 2 vols, Delft, The Laboratory.
- HOBSON, R.D. JAMES, W.R. (1978) Importance of handling losses to beach fill design. Proc. 16th. Coastal Eng Conf., ASCE, pp. 1873-1887.
- JAMES, W.R. (1975) Techniques in evaluating suitability of borrow material for beach nourishment. TM60, U.S. Army Coastal Engineering Research Center, Fort Belvoir, VA.
- KRUMBEIN, W.C. JAMES, W.R. (1965) A lognormal size distribution model for estimating stability of beach fill material. TM 16, U.S. Army Coastal Engineering Research Center, Washington, DC.
- NEWMAN, D.E. (1976) Beach replenishment - sea defences and a review of the role of artificial beach replenishment. Proc. Inst.,n Civ. Engrs., 60: 445-460.
- SHORT, A.D. (1978) Wave power and beach stages - a global model. Proc. 16th. Coastal Eng. Conf., ASCE, pp.1145-1162
- SILVESTER, R. (1974) Coastal Engineering. 2 vols., Amsterdam, Elsevier
- SMITH, A.W., GORDON, A.D. (1980) Secondary Sand Transport Mechanisms Proc. 17th Coastal Eng. Conf., ASCE

VALLIANOS, L. (1975) Beach-fill planning, Brunswick County, North Carolina. pp 93-114 in Hayden, B.P. (ed) The Present and Future of Coasts. Proc. 1st. Ann. Conf. Coastal Soc., Bethesda, M.D., The Society.

WRIGHT, L.D. (1980) Modes of beach cut in relation to surf-zone morphodynamics. Proc. 17th Coastal Eng. Conf. ASCE

WRIGHT, L.D., CHAPPELL, J., THOM, B.G., BRADSHAW, M., COWELL, P. (1979) Morphodynamics of reflective and dissipative beach and inshore systems, southeastern Australia. Mar. Geol. 32:105-140.

CAPRICORN COAST BEACHES

D.C. Patterson and L.R. Ford
 Engineers, Beach Protection Branch, Department of Harbours & Marine,
 Queensland, Australia

1.0 INTRODUCTION

The Beach Protection Authority of Queensland published in December 1979 a report outlining the results of its investigation into all the factors which determine the coastal behaviour of the 90 km strip of Central Queensland's coastline known as the Capricorn Coast (Fig. 1). The purpose of the investigation was to provide a detailed explanation of beach behaviour in this area including all the data necessary for the preparation of a comprehensive program of works and management strategies for improving beach conditions and minimising present and future erosion problems. This paper represents a brief summary of the contents of the published report.

2.0 OBJECTIVES

No previous studies have been made into the nature and behaviour of the Capricorn Coast beaches. It was clear from the location and wave exposure of this stretch of Queensland's coast that the behaviour of the beaches is unique and not easily related to other previously studied areas. Hence it was necessary to initiate a full scale investigation into all aspects affecting the beaches of this coastal region. The investigation into coastal behaviour along the Capricorn Coast was commenced in 1975 and carried out in compliance with the Beach Protection Authority's stated functions which include:-

- (a) The carrying out of investigations with respect to erosion or encroachment by the sea of or upon lands of the coast;
- (b) The investigation and planning of preventative and remedial measures in respect of erosion or encroachment by the sea of or upon lands of the coast;
- (c) The recording and evaluating of the results of such investigations and plans.

The primary objective of the study was to provide a firm basis for the preparation of an overall scheme of works and management for the beaches and dunes. The Beach Protection Authority's approach involves determining the extent of foreshore which is likely to be vulnerable to erosion in the future and attempting to restore or carefully manage this land so that it remains available as a buffer zone between the ocean and nearby development. The extent of buffer zone depends on -

- The rate of long term coastal erosion (R metres per year)
- The extent of the design cyclone erosion (C metres)

$BUFFER\ ZONE\ WIDTH = [(N \times R) + C] + F$ (metres)

where N = Planning period (years)

F = Factor of safety (metres).

Hence the investigation was directed toward quantifying the values R and C for each beach in the study area. The Beach Protection Authority has adopted a planning period of 50 years and a factor of safety of 40 metres for the Capricorn Coast area.

2.1 Data Collection

Data collection was carried out over the three years 1975 to 1977 inclusive. During that time repetitive surveys, wave recording, dune vegetation studies, geological investigations and current measurements were carried out.

This program of data collection provided data on -

1. the geological history of the region;
2. beach sediment properties;
3. beach profile forms and measured modifications under varying wave attack;
4. meteorological conditions;
5. incident wave conditions;
6. dune vegetation;
7. nearshore currents;
8. sea level fluctuations resulting from tides and storm surges;
9. beach and dune conditions;
10. the nature of the coast and the erosion problems.

2.2 Data Assessment

The task of assessing all of the available data was carried out by engineers and scientists of the Beach Protection Branch of the Department of Harbours and Marine. Assistance was also provided in respect of -

- (a) the geology of the area by geologists from the Geological Survey of Queensland and
- (b) dune vegetation by botanists from the Department of Primary Industries.

The principle aim of this data assessment was to provide an understanding of the active beach processes in the Capricorn Coast area with particular regard to -

- . sediment supply and distribution along the coast
- . erosion/accretion behaviour of the beaches in both the short and long term
- . the role of dune vegetation in beach and dune stability
- . buffer zone widths within which future dune erosion is likely to occur.

3.0 LOCATION AND TOPOGRAPHY

The Capricorn Coast is uniquely placed along Queensland's coastline (Fig. 1). Its location in relation to the Great Barrier Reef, the continental shelf and the shape of the adjacent coastline exposes it to wave, current and tidal forces different from those experienced elsewhere on our coast.

The physical appearance of this 90 kilometre stretch of coast is one of great contrasts. Prominent rocky headlands separate numerous sandy pocket beaches in the central sections while to the north and south long stretches of uninterrupted beach have developed (photo 1). The beaches of the Capricorn Coast are gently sloping, consisting of relatively fine sand containing a significant proportion of muds. The 4 metre ocean tidy typically rises and falls across a beach width exceeding 150 to 200 metres.

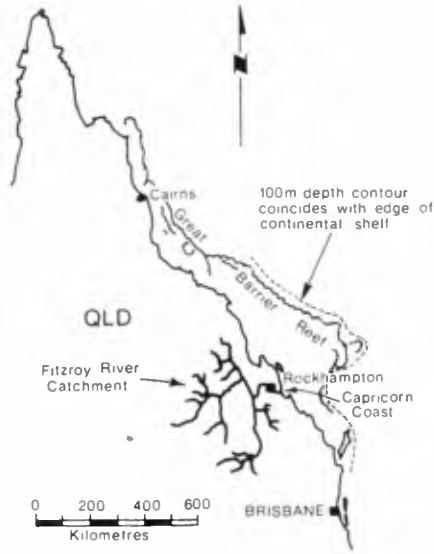


Fig. 1a Locality Plan

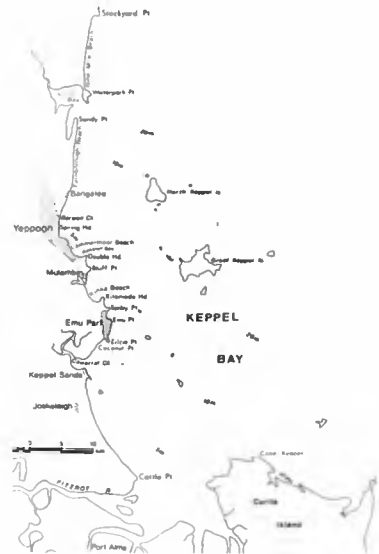


Fig. 1b The Study Area



Photo 1. The Yeppoon region of the study area.

The most common coastal landform along the beaches of the area is extensive sand dune development in various forms including recent foredunes, older parallel beach ridges, and both mobile and stabilised transgressive dune formations.

The Fitzroy River is by far the largest of the streams in this coastal region. This river has a comparatively large catchment area of about 14 million hectares. However the major part of the Fitzroy's catchment receives only 600-700 mm of rainfall per year on average, and significant fresh water flows in the river are typically associated only with cyclonic activity in the region.

4.0 GEOLOGICAL HISTORY

The present day topography of the Capricorn Coast and the beach processes taking place there are more readily understood when the past behaviour of the region is known. The beaches and dunes as we see them today have formed during the last 6000 years. The reason for this relates to the rise in sea level which ended at that time. Fluctuations of the sea level reaching about one metre above and below the present level have occurred since then. During the sea level rise, the position of the coastline moved landward from its former alignment resulting in large scale submergence of the former coastal plain to form the present day Keppel Bay. In the process many former mainland hills became headlands of the present shoreline or islands such as Great Keppel Island. The present day seabed topography of Keppel Bay is shown on Figure 2a. The present coastline has developed in response to the last 6000 years of wave and current influence and the input and output of sediment from offshore, alongshore and river sources.

4.1 Fitzroy River Sediments

The Fitzroy River carries with it vast quantities of sand and silt which are discharged to the sea and settle to the bed of Keppel Bay. These sediments have been eroded from the upstream catchment areas and exhibit characteristics which identify them as less mature than the pre-existing coastal sands of Keppel Bay. For example, the Fitzroy River sediments are finer grained and contain a significant proportion of muds. They also contain relatively large amounts of certain minerals such as feldspar which can be visually identified under microscopic examination and which break down in the coastal environment with time so that they are not present in mature sands. As well, sediment deposited from the river during floods has not been sorted (a winnowing process) by wave and current action and can be differentiated from the better sorted mature sands by grain size distribution analysis.

During the investigation nearly 700 samples of sand were collected from the seabed of Keppel Bay and from the beaches and dunes for analysis to identify these characteristics. This enabled the zone of deposition and transport of sediments supplied from the Fitzroy River during the last 6000 years to be delineated. This zone is shown on Figure 2 and is unusual in that it forms a well defined nearshore belt along the entire Capricorn Coast rather than extending directly seaward from the river mouth. Seismic profiling provided information on the total depth of the nearshore sands and the thickness of the Fitzroy River derived sediments. Using this information together with data on flow in the Fitzroy River during floods, it was estimated that an average quantity of 350,000 cubic metres of sand is supplied by the river each year.

The beaches and seabed in the vicinity of the Fitzroy River exhibit a very strong trend of accretion which diminishes with distance away from the river. This indicates that the rate of distribution of the input sediment is not as great as the rate at which the river supplies it. This has resulted in the flat shallow offshore profiles which characterise the southern Keppel Bay regions and which contrast with the steeper profiles further north.

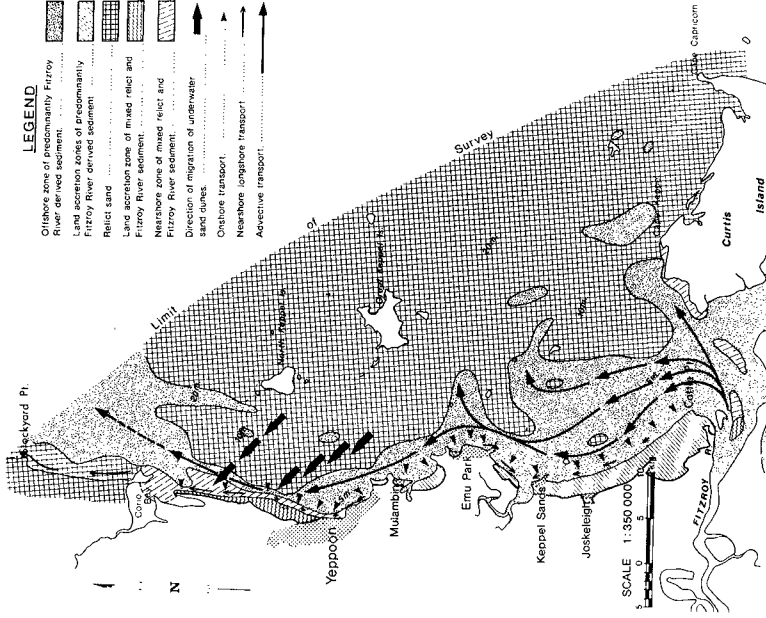


Fig. 2b Sediment Movements in Keppel Bay

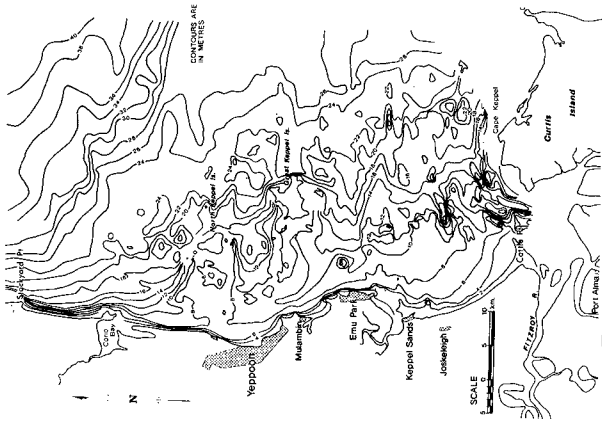


Fig. 2a Keppel Bay Contours

4.2 Offshore Sediment Distribution

The seabed sediments of Keppel Bay are being gradually distributed northwards away from the Fitzroy River (Fig. 2b). The sediment in motion includes both the relatively new Fitzroy River derived muddy sands and the older mature relict sands drowned by the sea transgression prior to 6000 years B.P. The mechanisms involved in this movement of sediment are not clearly understood but are thought to result from the combined action of waves and a northerly current induced by the predominant south easterly winds producing advective transport.

There are no established techniques readily available for calculating these advective transport rates using the available wave and current data. However an estimate has been made from the quantities of Fitzroy River derived sand which has been transported northwards past various locations over the last 6000 years (Table 1).

TABLE 1
NET NORTHWARD ADVECTIVE TRANSPORT IN KEPPEL BAY

Location	Total Holocene Sedimentation North of Location (cubic metres)	Net Northward Advective Transport (m^3/yr)
Cattle Point	2160×10^6	360,000
Keppel Sands	1146×10^6	191,000
Tanby Point	990×10^6	165,000
Double Head	900×10^6	150,000
Farnborough	726×10^6	121,000
Water Park Point	588×10^6	98,000

These rates of transport are large compared with the nearshore longshore transport rates particularly in the southern and central regions. Clearly advective transport represents the primary mechanism for the northward supply of sediment along the coast from the Fitzroy River.

4.3 Holocene Coastal Accretion

At the Capricorn Coast extensive accretion has occurred during the last 6000 years as a result of a persistent onshore movement of sand from the nearshore area of Keppel Bay. Most of this sand has come from the zone of Fitzroy River sediment delineated on Figure 2, and average rates of up to 2000 cubic metres per kilometre of beach per year have been assessed.

The land developed by this Holocene accretion (the "outer barrier") often has the form of a series of dune ridges and swales that correspond to erosion/accretion cycles probably associated with major cyclone events and are clearly evident from the air (Fig. 3 and photo 2). This dune ridge system is superimposed on a broader sequence of accretion features associated with six significant fluctuations in sea level which have occurred during the last 6000 years. During phases of high sea level the accretion sequence is truncated by sustained periods of erosion. Despite this however, the general landward movement of sediment from nearshore continues so that phases of falling sea level are accompanied by accelerated accretion.

As Fig. 2b shows, the beach areas strongly exhibiting this trend of long term accretion are -

- (a) the southern region between the Fitzroy River and Emu Park, including Keppel Sands (photo 2).
- (b) the deeply embayed shoreline of Mulambin and Kinka Beach.
- (c) the Farnborough area north of Yeppoon. In this area an additional input of the older mature sand from both nearshore and alongshore can be identified in the accreted dune sands.

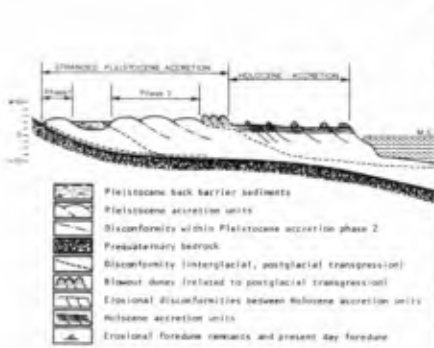


Fig. 3 Section of Holocene Accretion



Photo 2. Holocene accretion
Cattle Point to Keppel Sands

4.4 Persistently Eroding Beaches

In contrast to the strong accretion discussed above, those beaches where nearshore profiles are steep or where the onshore sand supply is moved away along the coast show little accretion and in some locations, general erosion.

Nine Mile Beach and the northern section of Farnborough Beach near Corio Bay show evidence of persistent erosion. This part of the Capricorn Coast is more exposed to the ocean wave conditions than the southern beaches which lie in the lee of the nearshore islands. Erosion by the rising sea level, longshore movement of sand and cyclones has led to persistently unstable foredunes and wind erosion on a large scale. Dune blows and extensive transgressive dune formations are thus the main landforms there (photo 3) and have allowed considerable vertical growth of the dunes reaching to over 150 metres above mean sea level inland of Nine Mile Beach.

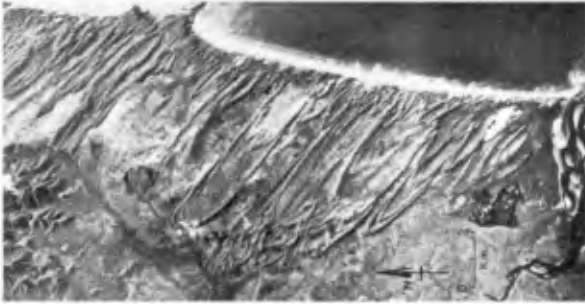


Photo 3. Transgressive dunes - Nine Mile Beach

5.0 NATURAL FACTORS INFLUENCING BEACH PROCESSES

5.1 The present day behaviour of the beaches varies from year to year, seasonally and from day to day depending on the occurrence of cyclones, climatic changes throughout the year and daily weather variations. Longshore transport and onshore/offshore transfer of sand were assessed on the basis of surveyed beach properties and measured forces such as the wind, waves and currents. The growth of dune vegetation which controls the stability of the dunes against wind erosion is determined largely by the climate and the nature of the dune soils.

Some of the natural factors influencing beach processes are outlined briefly below.

5.2 Meteorological Influences

Wind strengths at the coast are consistently moderate to fresh with velocities exceeding 20 km/hr about 50% of the time and essentially no calm days. Strong winds in excess of 50 km/hr occur less than 2% of the time. South east winds predominate and persist longer than all other winds.

There is considerable variation in annual rainfall along the Capricorn Coast with a predominant trend for average rainfall to increase from south to north (Table 2). This trend coincides with a general increase in relief in the coastal topography from south to north with minimum rainfall occurring in the low coastal plains at Cattle Point and maximum rainfall occurring in the coastal ranges inland from Stockyard Point.

TABLE 2
MONTHLY & ANNUAL RAINFALL DATA YEPPOON & EMU PARK

Recording Station	Recording Period	Average Rainfall (mm)												Year
		Jan	Feb	Mar	Apr	May	Jun	Jul	Aug	Sep	Oct	Nov	Dec	
Yeppoon	1891-1975	259	240	183	104	77	77	47	30	36	66	76	149	1344
Emu Park	1886-1976	203	201	145	78	59	60	43	24	30	46	71	123	1083

The incidence of tropical cyclones is a significant feature of the study area's climatology. On the average, the Capricorn Coast suffers the effects of tropical cyclones once every two years, although the occurrence of widespread cyclonic destruction in the study area is a much rarer occurrence.

TABLE 3
CYCLONE CENTRAL PRESSURE VS
PROBABILITY OF OCCURRENCE

Pressure Range	Representative Pressure	Probability
> 985	990	0.5
975-985	980	0.1
968-975	970	0.08
963-967	965	0.01
958-962	960	0.005
953-958	955	0.003
948-952	950	0.001
943-947	945	0.001
935-942	940	0.0002
< 935	920	0.00002

5.3 Dune Vegetation

Coastal processes would not approach or attain the dynamic equilibrium status common along many coasts without plants that tolerate salt spray, resist strong winds, trap and hold windblown sand and add organic soil components. The establishment, maintenance, and protection of vegetation within those zones affected by coastal processes, are important aspects of coastal management.

The type and distribution of coastal dune vegetation along the Capricorn Coast is highly variable and is determined by geology, landform/topography, climate and land use.

A field survey of vegetation in the Capricorn Coast study area was undertaken as a joint project by the Authority's Dune Conservation Section and the Botany Branch, Queensland Department of Primary Industries.

The survey was carried out to produce a vegetation map and report on the existing vegetation communities of the study area with special reference to beach and dunal areas.

The aggregation of plants in a coastal beach/dune system form, in general, three types of vegetative cover:-

1. a pioneer type composed mostly of herbaceous plants;
2. a heath/scrub type of woody shrubs, vines and small trees with a few associated herbs;
3. a woodland or forest type dominated by trees.

Nearly all the plants of the first two types are tolerant to salt spray, strong onshore winds and various degrees of soil salinity. The pioneer herbaceous vegetation occurs on foredunes nearest the beach. The scrub vegetation is found on the partly to fully stabilised older foredunes landward of the pioneer zone. The forest vegetation usually occurs towards the interior on the oldest and most stable dune/beach ridge systems.

Pioneer vegetation is the chief dune-forming agent. These herbaceous plants grow in a manner that enables them to help develop dunes in conjunction with wind action. Plants growing on the upper part of the beach trap windblown sand and initiate formation of a low frontal dune. Most of the pioneer plants occur on the seaward slope, crest and landward slope of the frontal dune.

Pioneer plants are the initial vegetation of the coastal succession or sequence of vegetation that finally develops into a climax community be it grassland, shrubland, heath, scrub, woodland, forest, or wetland. They increase the rate and height of dune formation and determine the pattern of vegetation development of the coastal dune system. They prepare the soil and other habitat conditions for the development of other vegetation communities (e.g. scrub) in the normal course of coastal succession.

Beach spinifex grass (Fig. 4a) is the most important pioneer sand stabilising plant occurring naturally on the frontal dune and foredunes and is usually the dominant species colonising the seaward slope of the frontal dune in exposed situations. It is tolerant to air borne salts, strong onshore winds, and has the ability to grow through accumulations of windblown sand.

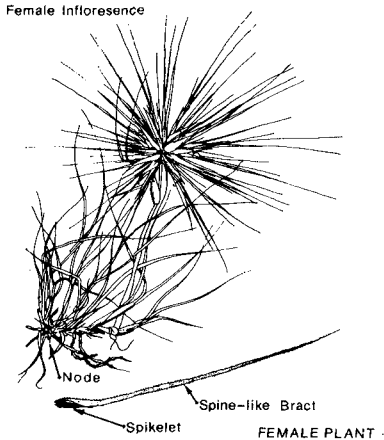


Fig. 4a Beach Spinifex Grass

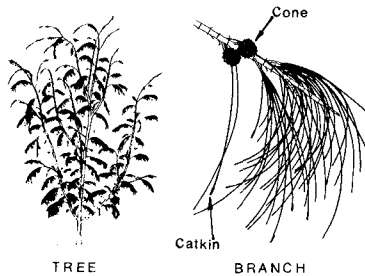


Fig. 4b Coastal She-Oak

Coastal she-oak (Fig. 4b) belongs to the genus: *Casuarina* which is the only non-legume genus native to Australia that can "fix" atmospheric nitrogen. Micro-organisms in the root nodules convert nitrogen from the air into a form which is more readily used by the plant. This process improves the nitrogen content of the sand/soil enable more nutrient demanding plants to establish.



Symbol	Plant	Map Unit	Commoner Designation	Vegetation Zone
	Mangroves	1	Mangroves, mudflats	Disturbed
	Mudflats	2		Littoral
	Spinifex	3	Spinifex - (former) Mt Bluff	Sand
	Scaevola	4	<i>Heterostichus scoparius</i> has been noted	
	Casuarina	5	At Mt Bluff, <i>casuarina</i> is noted	
	Casuarina	6	At Mt Bluff, <i>casuarina</i> is noted	
	Heath	7	Fringing dune heath scrub and open heath scrub	Fringing
	Scrub	8	Fringing dune scrub and open scrub	Beach Ridge
	Lantana	16	Lantana is present on the island and open scrub	
	Sodas	18	Shrubby mixed grassland	Wooded
	Mudflats	23	Rocky shore, low dune heath and open scrub	Rocky Shore
	Mudflats	24	Mudflats, low dune heath and open scrub	
	Heath	28	Coastal open heath and dune heath	Pebbly Dune
	Scrub	29	Coastal open heath and dune heath	

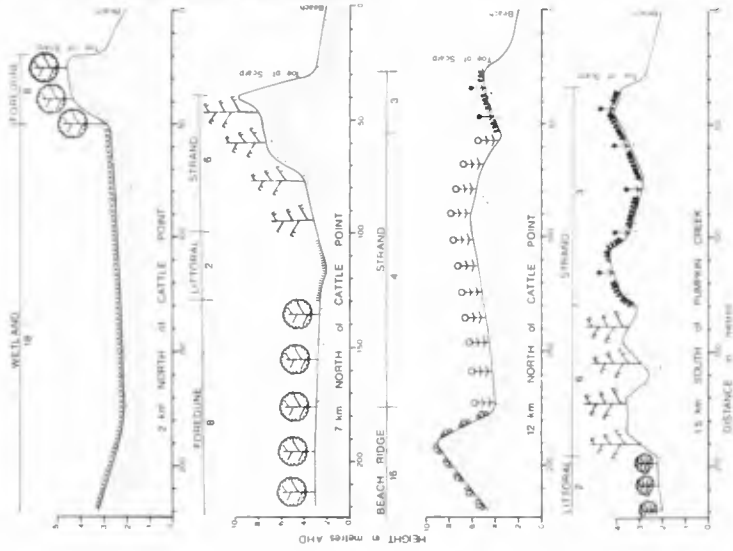


Fig. 5 Typical Vegetation on Dune Profiles

5.4 Sea Level Variations

Variations in sea level substantially influence beach behaviour through their effect on various wave phenomena such as refraction, shoaling and breaking, and the level at which the waves attack the beach. A significant change in sea level will upset a pre-existing equilibrium and result in changes to the original shoreline profile or plan form. Major sea level variations in the geological time scale are important in understanding contemporary coastal behaviour especially in relation to sediment distribution. During the Holocene period (last 10,000 years), the sea level has risen 20 metres. This rise occurred prior to 6,000 years ago and since then fluctuations in sea level of magnitude about ± 1 metre and period of almost 1,000 years have occurred.

Adopted values for the various tidal planes at the Capricorn Coast are as follows -

TABLE 4
TIDAL PLANES CAPRICORN COAST

Tidal Plane	Low Water Datum	Australian Height Datum
Mean High Water Springs:	4.0m	1.7m
Mean High Water Neaps:	3.1m	0.8m
Mean Low Water Neaps:	1.5m	-0.8m
Mean Low Water Springs:	0.6m	-1.7m

Three separate studies concerning storm surge statistics along the Capricorn Coast have been prepared over recent years. The most recent of these was carried out by the James Cook University, Townsville, for the Beach Protection Authority. It involved the numerical simulation of various cyclones in the Capricorn Coast region in terms of the cyclone intensity and direction of approach. Results from that study are outlined in Table 5.

TABLE 5
MAXIMUM SURGE AT VARIOUS LOCATIONS AS PREDICTED BY NUMERICAL MODEL

LOCATION	CYCLONE RETURN PERIOD		
	1 in 50yrs	1 in 100yrs	1 in 500yrs
Stockyard pt.	1.52	1.66	2.00
Water Park Pt.	1.67	1.83	2.19
Yeppoon	2.03	2.21	2.62
Emu Park	2.54	2.75	3.22
Fitzroy River	2.12	2.29	2.66
Cape Capricorn	1.11	1.21	1.41

5.5 Wave Climate

Waves affecting the Capricorn Coast may be generated locally within 100-500 kilometres of the study area or may arrive as decaying swell generated outside the vicinity of the region. The possible directions from which waves can arrive are confined to the seaward sector between north (0°) and south (180°), being the general alignment of the coast. Swell waves are further restricted by the shape of the coast and offshore reefs to directions between 60° and 120° , being intercepted by the Great Barrier Reef to the north-east and Fraser Island to the south-east. Recording of waves using the Dutch Waverider wave recording system was carried out at one location over the period November 1974 to April 1978. The recorder location was 33 km east of Yeppoon in 28 metres of water, being seaward of North and Great Keppel Islands and away from the sheltering effects of Cape Capricorn.

WAVEHEIGHT EXCEEDANCE

$$\text{AVE NO HOURS PER YEAR} = \frac{(pe)}{100} \times 8760$$

$$\text{AVE NO EVENTS PER YEAR} = \frac{(pe)}{Pm} \times 87.6$$

For a particular persistence _____

$$\text{AVE NO EVENTS PER YEAR} = \frac{(pe)}{Pm} \times 87.6 \times \frac{(pn)}{100}$$

$$\text{AVE RECURRENCE INTERVAL} = \frac{Pm}{0.876 (pe \cdot pn)}$$

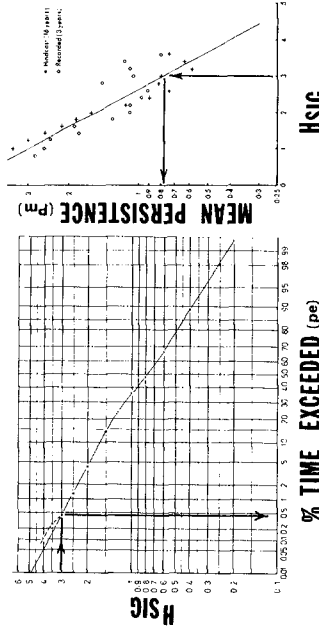
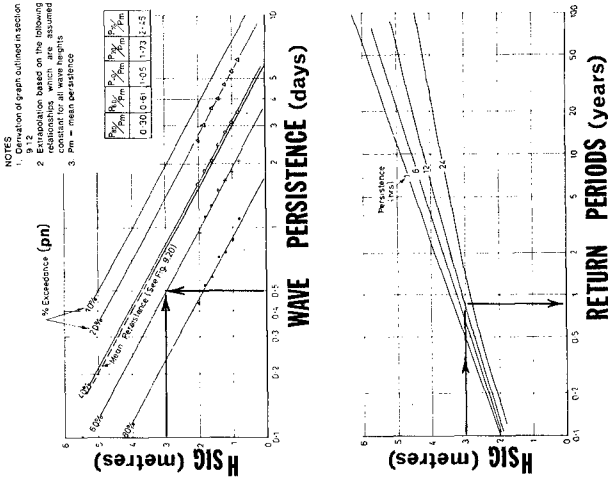


Fig. 6 Wave Climate - Capricorn Coast

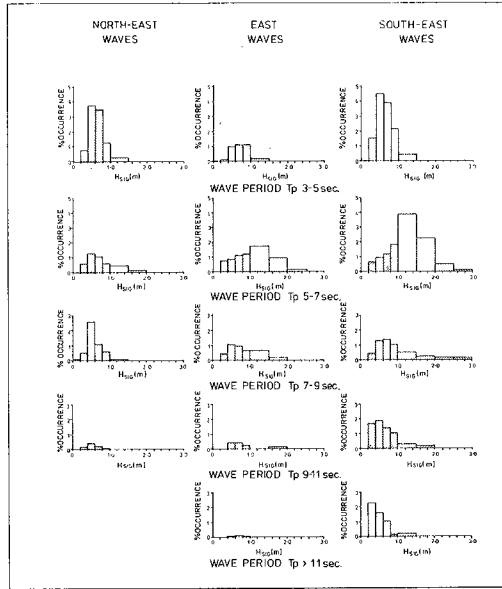


Fig. 7 Wave Height/Period/Direction Occurrence

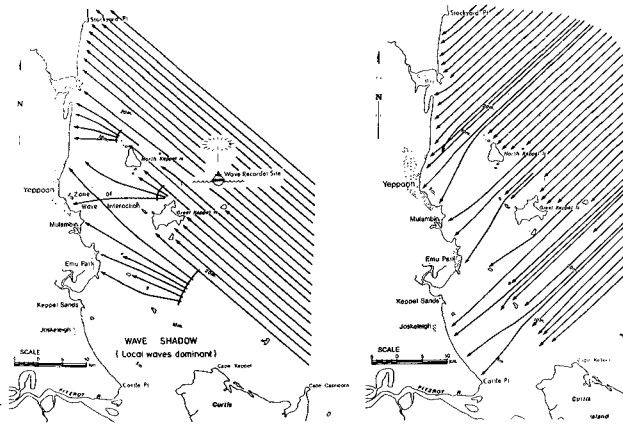


Fig. 8 Typical Wave Refraction

A wide range of basic wave parameters were analysed for each 20 minute wave record. However, the parameters considered most useful for determining beach processes were the significant wave height (H_{sig}) and the period corresponding to the peak of the energy spectrum (T_p). Hindcasting was also performed using twice daily wind data recorded at Cape Capricorn Lighthouse over a 17 year period. This involved the use of the revised S.M.B. empirical relationship for the non-deep water situation.

The reasons for hindcasting wave height data were -

- (a) to compare the results with recorded data to confirm a wave hindcasting/forecasting procedure for use in estimating wave heights during particular storm events either in the future or for past cyclones for which wind data is available.
- (b) to extend the time base of available wave data from the 3 years of recording to the period of available wind data namely 16 years in this region. This provides a better basis for statistical analysis of the less frequent high wave occurrences.

The calibrated hindcasting model provided wave height data showing good agreement with the recorded data over the three year period of recordings. Wave directions were assessed on a daily basis from synoptic charts and from wind data used in the hindcasting procedure.

Representative wave data for the Capricorn Coast determined from the wave study are outlined in Figures 6 and 7. The largest significant wave height recorded during the investigation was 4.26 metres associated with cyclone "David" in January, 1976.

Wave refraction procedures based on first order wave theory using peak energy wave periods were used to transfer the offshore wave data to the various locations along the coast (Fig. 8).

5.6 Nearshore Currents

Current measurements were undertaken both within the surf zone and nearshore outside the surf zone. Four types of currents were considered -

- Ocean Currents
- Nearshore Tidal Currents
- Nearshore Wind Drift Currents
- Wave Induced Currents

Measurement techniques involved the use of current meters outside the surf zone to provide the vertical velocity and direction profiles and float and dye tracking within the surf zone. It was found that both the wind and the tide contributed significantly with wave induced forces to the generation of longshore currents.

The data obtained was used to confirm or determine analytical expressions from the longshore current necessary as input to the calculation of the longshore transport of sand.

6.0 CYCLONE EROSION

Erosion of the beaches and dunes often accompanies the occurrence of major storms and cyclones in the region. Abnormally big waves attack the dunes during the high tides and accompanying storm surges and move sand in the offshore direction.

6.1 Measured Cyclone Erosion

The extent of erosion caused by Cyclone "David" in 1976 was monitored by surveys in terms of the quantity of sand eroded and the typical horizontal recession of the toe of the frontal dune. This is shown in Table 6 (terms defined on Fig. 9).

TABLE 6
EROSION DURING CYCLONE DAVID

Location	Quantity Eroded (m ³ /m)	Horizontal Recession (m)	Transition Level (m) (related to M.S.L.)	Offshore Limit of Deposition (m)	
				Related to M.S.L.	Below peak storm tide
Cattle Pt. to Keppel Sands	35	15	+1.0	-1.0	4.2
Keppel Sands	15	4	+1.5	0.0	3.2
Emu Park	30	13	+0.8	-3.0	6.2
Emu Pt. to Ritamada Headland	30	15	+1.0	-2.0	5.2
Kinka Beach	25	10	+1.5	0.0	3.2
Mulambin	10	5	+2.0	+0.5	2.7
Kemp Beach	20	7	+1.0	-1.5	4.7
Lammermoor	45	12	+1.0	-2.3	5.5
Yeppoon	30	N/A	+0.5	-3.0	6.2
Yeppoon to Bangalee	70	15	+0.5	-4.5	7.7
Nine Mile Beach	65	9	-1.0	-4.5	7.7

6.2 Erosion by the "Design" Cyclone

The method of Edelman for estimation of dune erosion during storms is based on the principle that a characteristic beach profile is developed by the cyclonic waves with sand eroded from the dune (Fig. 9).

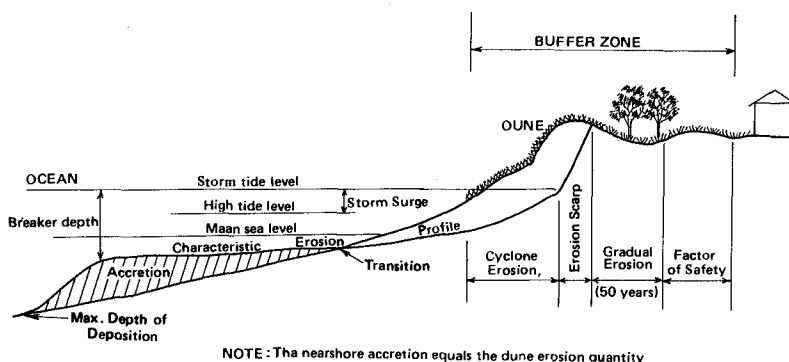


Fig. 9 Dune Erosion - Buffer Zone

Beach surveys immediately after cyclone David indicated that the Edelman profile closely approximated this characteristic profile for the Capricorn Coast beaches and could reasonably be used in the absence of more reliable information. Clearly sand grain size strongly influences the shape of this profile. For the estimation of erosion resulting from the adopted "design" cyclone conditions, the profiles actually developed during cyclone David were used for each individual beach along the study area.

The extent of cyclonic dune erosion depends also on the storm tide level and the wave height. Design wave heights were based on the recorded data as outlined in Section 5 with appropriate modification to allow for refraction. Design storm tide and wave heights for various beaches along the coast are shown in Table 7 along with the assessed dune erosion results.

TABLE 7
"DESIGN" CYCLONE DUNE EROSION

Location	Design Wave Height (m)	Design Storm Tide Level (m)	Erosion Quantity (cu m/m)	Erosion Distance (m)
Nine Mile Beach				
- High Fore-dune	5.9	3.40	50	20
- Low Fore-dune	5.9	3.50	140	35
Farnborough	5.3	3.60	175	35
Bangalee	3.0	3.75	75	25
Yeppoon	3.5	3.90	80*	40*
Lammermoor	3.5	3.90	130	50
Kemp Beach	3.5	4.00	50	35
Mulambin	3.8	4.00	115	50
Kinka Beach	3.8	4.20	65	50
Tanby/Ritamada	4.0	4.20	100	60
Emu Park/Zilzie	4.5	4.45	80	50
Keppel Sands	2.7	4.20	60*	20*
Cattle Point	2.2	4.00	50	50-150 ⁺

*Sections of beach protected by seawalls

⁺Large horizontal erosion where overtopping of fore-dune occurs.

7.0 LONGSHORE TRANSPORT

At the Capricorn Coast where the offshore profiles are relatively flat and wind and tide induced currents are frequently large compared with wave induced currents, the transition from the offshore advective transport to the nearshore longshore transport is not a clear one.

Several methods were used to estimate the gross and net longshore transport rates for the various beaches (refer Fig. 1b). These were -

- the "CERC Method which is based on the assumption that all transport is caused by wave forces alone
- the Bijker method which allows the input of the appropriate longshore current velocity together with wave, sediment and profile parameters
- a method developed by the Authority for estimating longshore transport using observed daily wave and longshore current information from the COPE stations.

The results are summarised in Tables 8 and 9. Greater reliability is expected of the COPE data results as they incorporate longshore current directions and velocities obtained by direct measurement and include the influence of the tide and wind.

8.0 GRADUAL EROSION

Persistent gradual erosion may result from a differential in the longshore transport along a beach, the effects of a rising sea level or wind erosion. Historical information given by the geological study and successive surveys or aerial photography is available, together with the assessed longshore transport data, to quantify the gradual erosion for each beach. Rates in the range 0-4 metres per year have been obtained.

TABLE 8
SEDIMENT TRANSPORT CALCULATED FROM WAVE DATA

Site	SEDIMENT TRANSPORT						
	Refracted Offshore Waves		Wave Generated Within Keppel Bay		Total Sediment Transport		
	Upcoast	Downcoast	Upcoast	Downcoast	Upcoast	Downcoast	
Net							
Nine Mile Beach	368,000	64,000			368,000	64,000	+ 304,000
Sandy Spit	138,000	86,000	43,000		181,000	86,000	+ 95,000
Farnborough		86,000	43,000		43,000	86,000	- 43,000
Barwell Ck.	29,000	60,000			29,000	60,000	- 31,000
Yeppoon	55,000	63,000			55,000	63,000	- 8,000
Lammermoor	69,000	50,000			69,000	50,000	+ 19,000
Mulambin	83,000	80,000			83,000	80,000	+ 3,000
Ritamada	67,000	57,000			67,000	57,000	+ 10,000
Emu Park	34,000	38,000			34,000	38,000	+ 4,000
Keppel Sands	11,000		7,000	2,000	18,000	2,000	+ 16,000
Cattle Point - Keppel Sands			46,000	2,000	46,000	2,000	+ 44,000

* Keppel Sands Transport rates apply only at the beach, above the tidal flats.

NOTE: (+) Upcoast
(-) Downcoast

TABLE 9
LONGSHORE SEDIMENT TRANSPORT CALCULATED FROM COPE DATA
MONTHLY AND ANNUAL NET RATES

	SITE		
	Barwell Creek	Yeppoon (Main Beach)	Lammermoor
January	1,700	-10,000	0
February	800	- 2,700	7,000
March	500	- 4,000	4,400
April	+ 700	- 3,300	6,300
May	1,300	- 1,200	4,200
June	700	- 600	2,300
July	600	0	4,800
August	0	0	1,200
September	0	0	600
October	-1,000	- 3,000	300
November	-2,800	- 1,500	-2,700
December	-6,000	- 1,500	3,800
Net Annual Transport	- 4,500	-27,800	32,200

9.0 BUFFER ZONES AND BEACH PROTECTION SCHEMES

Using the assessed rates of gradual erosion over the adopted 50 year planning period and the extent of the design cyclone erosion for each beach, the buffer zones have been calculated as outlined in Section 2.0. Typical results are outlined in Table 10.

Existing and potential erosion problems have been identified and recommendations for protection (including restoration where necessary) of the beaches are outlined in the published Beach Protection Authority report. While several beaches require works such as beach nourishment, groynes or seawalls, most of the beaches can be protected by careful dune management and control over adjacent residential development.



Photo 4. Natural Dune Vegetation



Photo 5.
The residences and access road at Keppel Sands is perilously close to the eroding beach.

Fig. 10 Recommended Beach Restoration at Yeppoon

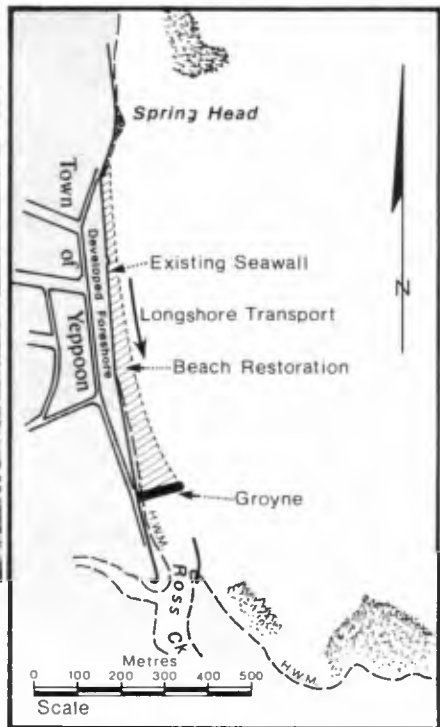


TABLE 10
BUFFER ZONE WIDTHS

Location	Gradual Erosion (m)	Cyclone Erosion (m)	Dune Scarp Component (m)	Factor of Safety (m)	Buffer Zone Width (m)
Nine Mile Beach					
High Fore-dune	50	20	30	40	140
Low Fore-dune	50	35	10	40	135
Farnborough	40	35	10	40	125
Bangalee	25	25	10	40	100
Yeppoon	0*	40	10	40	90
Lammermoor	15	50	10	40	115
Kemp Beach	10	35	10	40	95
Mulambin	10	50	10	40	110
Kinka Beach	0-75	50	10	40	100-175
Tanby/Ritamada	10	60	10	40	120
Emu Park/Zilzie	10	50	10	40	110
Keppel Sands	50	20	10	40	120
Cattle Point to Keppel Sands	0-200	50	10	40	100-300

*Protected by seawall.

10.0 CONCLUSION

The provision of adequate buffer zones between development and the sea and the protection of the dunes contained within them by careful dune management is clearly the best way of protecting both the beaches and the nearby development. Every effort should be made in future town planning schemes to make such provisions. However some beaches are already experiencing erosion problems where development has been permitted too close to the sea in the past and has come under threat of erosion by cyclonic wave action. Determination of the most appropriate remedial action is not simple and depends on the individual beach behaviour. The consequences of incorrect decisions in beach protection matters can be financially severe and physically disastrous for the beach itself. To date the financial resources available for beach protection measures has been limited. It is important that available funds are directed towards the most appropriate solutions which do not create other problems. It is therefore necessary for beach protection proposals to be based on a thorough knowledge of local behaviour.

The Capricorn Coast Beaches investigation has provided an explanation of beach behaviour in that area in quantitative terms based on actual field data with the additional testing and use of empirical and theoretical predictions.

The Beach Protection Authority is convinced that such detailed investigations are necessary to determine the optimal use of the limited money resources available for the improvement of existing beach conditions and the minimising of future erosion problems.

ACKNOWLEDGEMENT

The permission of the Chairman of the Beach Protection Authority of Queensland and Director of the Department of Harbours and Marine, Mr. J. Leech to publish this paper is gratefully acknowledged.

CHAPTER 101

THE BEACH IMPROVEMENT PROGRAMME : NEW SOUTH WALES

Neale A. Philip and Philip H. Whaite¹.

1. INTRODUCTION

The Coastal Engineering Branch of the Public Works Department N.S.W administers the Beach Improvement Programme, a programme of works with an average annual expenditure of one million dollars, for the improvement of the State's public recreational beach amenities.

Priority is given to beaches with highest usage, resulting in the first two years' funds being allocated to the densely populated coastal strip between Newcastle and Wollongong.

Priority is also assigned to various types of works:-

1. Preservation, conservation or restoration of the beach itself by sand nourishment, dune stabilisation, seawall demolition;
2. Erosion control where appropriate, by seawall and revetment construction and land acquisition;
3. Provision of facilities such as car parks, access roads, dressing sheds and toilet blocks;
4. Beautification such as grassing and tree planting.

The near city beaches in Sydney, Newcastle and Wollongong have mostly been fully developed with seawalls and promenades behind the beach berm, while in outer Metropolitan areas, the beaches have been left in a more natural state, with some development such as car parks and dressing pavillions on or behind the sand dunes.

2. BACKGROUND

The New South Wales coastline experiences the highest recreational pressures on it of all Australian States. With the shortest coastline length and the highest population this pressure is overwhelming by Australian standards.

1. The Authors are Engineers in the Coastal Engineering Branch of the Public Works Department, New South Wales.

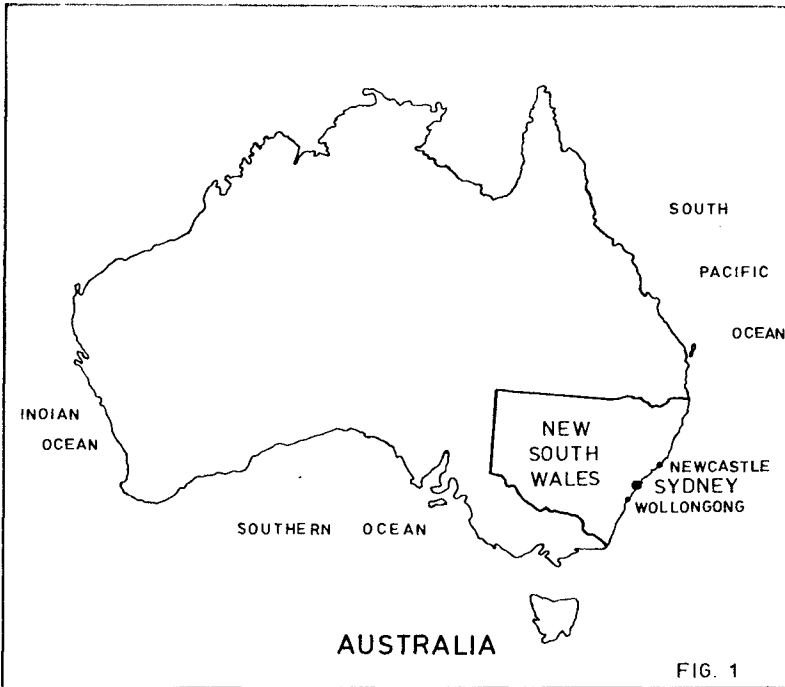


FIG. 1

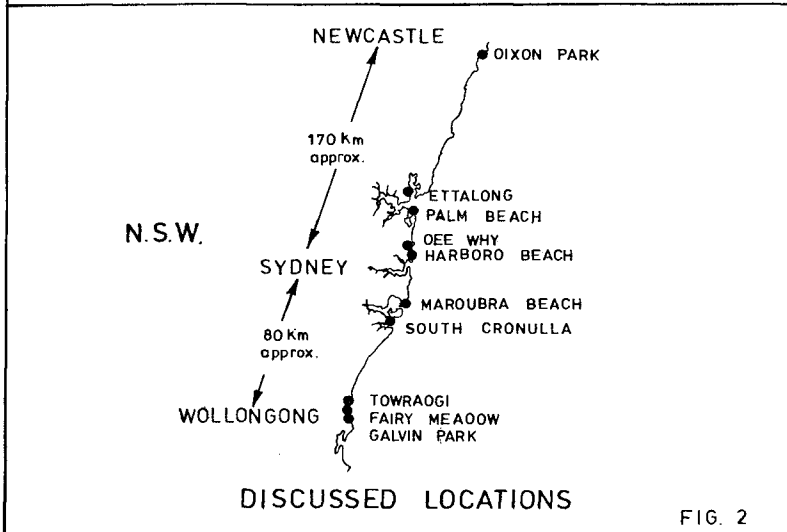


FIG. 2

Given this high potential demand on the recreational resources of the New South Wales coast and the later documented evidence confirming the suspicion that the New South Wales coastline is receding, the State Government, four years ago, introduced the Beach Improvement Programme.

3. BEACH USAGE

Although it is obvious that the population density along the New South Wales coast is low when compared to the European or U.S. situation, usage of beaches for recreation is encouraged by the climate, the availability of the free beach resource and the high mobility of the community.

A study of the accessibility of beaches to the population of the Sydney region (approximately 2.8 million in 1976) (Whaite, 1979) provides a measure of the potential customers for beach usage in that region. This study utilised travel times from the Sydney Area Transportation Study (1974) and Australian Bureau of Statistics population data (1977).

Table 1 indicates how close the regions population is to an ocean beach.

TABLE 1 : MINIMUM TRAVEL TIMES TO A SYDNEY BEACH
FOR PERCENTAGE OF REGIONS POPULATION

Travel times (mins.)	30	60	120
Percentage of population taking less than travel time	21	59	97

A more detailed study at a relatively inaccessible beach in the region (Palm Beach) reveals that 72% of all users at this beach come from local government areas which are not coastal and that only 13% of users are local residents. It is also interesting to note that 5% of users travel for more than two hours. This fact is related to the particularly scenic location of this beach.

This example illustrates how local government Councils have beaches accessible to large populations from outside their areas of responsibility. Local government is responsible for the upkeep of the beaches. The need for some State involvement in improvement work at beaches with high usage is apparent. Thus the Beach Improvement Programme, by offering grants to local government for beach works, has helped to distribute the burden of upkeep of this valued recreational resource.

4. PROGRAMME MANAGEMENT

Expert technical input to investigation and/or design of projects can come from the Department, the State Soil Conservation Service or consultants. The Department provides coastal engineering and/or landscape architectural expertise, the Soil Conservation Service provides dune stabilisation expertise, and the consultants, where used, provide coastal and structural design or architectural expertise.

Local councils initiate proposals and carry out the works. In an advisory capacity at the proposal stage, the Department has conducted a number of beach management studies in which a beach system has been examined, overall beach management strategies have been formulated and improvement works recommended.

5. MANAGEMENT STUDIES

5.1 Dee Why Study

In 1977 the Department carried out a proto-type Coastal Management Study at Dee Why, a beach situated in Sydney's northern beach region. The Dee Why area was an obvious choice for a proto-type study as a large amount of research into the local coastal system was available from studies undertaken by various government authorities and the three Universities in Sydney.

The area is interesting for study purposes as it consists of a lagoon/beach system which is relatively common along the New South Wales coast. Further, the area is surrounded by urban development and the resulting pressures of human activity highlight the need to develop appropriate management strategies.

The management study proposed a number of alternative strategies, namely:

1. 'No Nothing' Strategy
2. Minimum Management Strategy
3. Desirable Management Strategy
4. Back to Nature Strategy

The Beach Improvement Programme has funded works which are contained in the Desirable Management Strategy. The works include dune stabilisation and reno-mattress training works at the lagoon entrance designed to stabilise the lagoon breakout zone.

This is an example of how the Beach Improvement Programme by providing financial incentives, has encouraged local councils to consider various management options available for coastal areas and make decisions that will improve an area's capacity to withstand future usage and natural forces.

5.2 Maroubra Beach Management Study

The Maroubra Beach Management Study (D.P.W., 1978) employed the combined expertise of coastal engineers and landscape architects from the Department, and consultant architects.

During the study, interviews were held with all authorities having an involvement with the beach and with members of the public who use the beach. These interviews, subsequently interpreted by the varied expertise possessed by the study personnel, and combined with the latter's observations, identified a number of problems existing at the beach and works solutions were recommended where appropriate.

The major recommendations were :-

- revised landscaped parking scheme and new landscaped area linking the major beach buildings
- the reconstruction of the existing pavilion to house a kiosk; new change rooms and beach inspectors room and paved terrace areas
- stabilisation of dune system with a programme of fenced plantings and access ways over an area measuring 50 metres wide by 400 metres long.

Many aspects were examined to reach appropriate conclusions regarding management of the beach and recommendations on improvement works. Aspects studied included beach behaviour, beach management, visual character, parking and general access, vegetation and services proved to the public.

The dune stabilisation recommendation has been implemented and landscaping work will commence shortly.

6. PROJECTS

6.1 Dixon Park Project

Dixon Park Beach (D.P.W., 1978) is part of a small embayment approximately 1 kilometre long, bounded by a minor headland to the north and a headland to the south.

The objectives of the project were as follows:-

- (i) Restoration of the beach amenity in the form of a large beach area.
- (ii) Erosion control in the form of revetment construction.
- (iii) Improved access by way of steps, paths and boat ramp.
- (iv) Provision of amenities such as picnic area.
- (v) Beautification such as grassing, shrubbery and aesthetic restoration.

The design of the revetment used the basic Hudson's formula approach but the usual secondary under layer of rock was not used as the slag fill behind contained material of this size. This also reduced the number of steps required in the construction procedure. The armour stone was keyed into firm material at the toe.

6.2 Beach Nourishment Projects

The programme has been and is currently involved in a number of beach nourishment projects.

Nourishment of South Cronulla Beach, the most southerly major beach in the Sydney region (Foster, Gordon, 1978) involved the placing of some 130,000 cubic metres of sand onto the beach berm in two stages commencing in July 1977 over 3 months and again in May 1978 over a further 3 months period. The local Council undertook the work which involved trucking from the sand source, a major transgressive dune system some three kilometres north of the beach.

Another beach nourishment project currently in progress is at Ettalong Beach an estuarine beach north of Sydney. Delay of commencement to that project was necessary to avoid interference with summer holiday recreational activities. This project is a consequence of a Departmental Report (Ray, Hoffman, 1978) which proposed so called 'soft' management techniques to restore 'natural' sand circulation in the estuary. The borrow area is a shoal within the estuary and a dredge is being utilised to move some 60,000 cubic metres of sand to nourish the beach and nearshore channel.

In both the above projects monitoring programmes are being undertaken to gauge the success of the works and provide information for any future works of this nature in both ocean and estuarine environments in general and of the needs for periodic nourishment in the actual works location.

6.3 Wollongong Region Projects

A beach system where a number of works have been constructed is situated near Wollongong.

Terminal revetments have been constructed at Towradgi and Galvin Park to protect recreational amenities at each end of the embayment, and in between dune stabilisation is under construction from Fairymeadow to Towradgi.

The terminal revetment at Towradgi and Galvin Park are of Reno mattress construction, and as such are world leaders in the application of this structure in a wave climate as severe as is experienced on this section of the Australian coast.

Mattresses were selected both for economic reasons, and as a trial structure to assess their effectiveness. Aesthetic treatment of the revetment has been provided by sand cover planted with marram grass. Board and chain walkways provide access over the structure onto the beach.

Along the shoreline between these two structures, is several kilometres of dune stabilisation work. Where necessary, sand in the hind dune area has been excavated and placed in the frontal dune area to rebuild a continuous and effective frontal dune system.

To reduce costs, marram grass has been planted by mechanised methods, and the entire frontal dune area has been fenced, with access ways at appropriate locations.

6.4 Eastern Suburbs Beaches

Beaches in Sydney's eastern suburbs (the coastline from Sydney Harbour to Botany Bay), surrounded by urban developments, attract high user concentrations. The beach accessibility study (Whaite 1979), showed that these beaches are the most accessible to the greater proportion of Sydney's population.

The involvement of the Beach Improvement Programme in this region to date has been in the form of landscaping and beautification such as the financing of retaining walls, turfing, shrub plantings and irrigation systems. Landscape architecture input has been used to guarantee high aesthetic standards and to ensure selection of plant species tolerant to the harsh foreshore climate.

6.5 Harbord Project

Harbord Beach on Sydney's northern beach region provides an example of how the Beach Improvement Programme has funded a variety of works at one site. The original proposal from the local council formed the basis for discussions between council staff, the State soil conservationists and Public Works' coastal engineers and landscape architects. The resulting final design represents a major change in the previously degraded character of the beach and surrounding area.

The works have rebuilt sand dunes, re-organised parking by providing limited asphalt spaces with grassed overflow areas and have diverted drainage lines.

Although this beach was not subject to a formal Beach Management Study, the multi-disciplinary approach produced the integrated nature of the components which constituted the final design. Major schemes of this nature, or works forming part of a major scheme are proving to be the most successful projects in improving the beach amenity.

6.6 Cost of Works

Table 2 summarises the costs of a number of works discussed. A cost of works per metre of coast is included to enable some comparison between the different types of works.

TABLE 2 : BEACH IMPROVEMENT WORKS : COST COMPARISONS

Project Location	Type of Work	Total Cost A\$(x 1000)	Cost per Metre (A\$/m)
Dixon Park	Rubble revetment	275	1100
South Cronulla	Sand nourishment	250	600
Towradgi and Galvin Park	Reno-mattress revetment	350	800
Fairymeadow/ Towradgi	Dune reshaping and stabilisation	100	75
Maroubra	Dune stabilisation	60	100
Harbord	Dune re-building and stabilisation	60	200

7. CONCLUSIONS

In the four years since the commencement of the Beach Improvement Programme works at over thirty sites have been undertaken. A trend has developed towards a total scheme concept where beach preservation/restoration works, such as dune stabilisation or beach nourishment, are complemented by provision of back beach amenities, such as landscaped and car parks areas. The use of management studies to define management options, utilising knowledge of the local coastal system, has proved of great benefit by providing a basis for discussion concerning an area's possible development which ultimately results in preparation of beach improvement proposals suiting their environment and acceptable to the public.

8. REFERENCES

1. WHAITE P.H.
ACCESSIBILITY OF BEACHES IN SYDNEY -
Survey of beach users
Part of requirements for M. Eng. Sc.
degree from University of N.S.W. 1979
2. Coastal Engineering Branch - Department
of Public Works, N.S.W.
DEE WHY LAGOON - MANAGEMENT STUDY
November 1977
3. Department of Public Works, N.S.W.
MAROUBRA BEACH MANAGEMENT STUDY
Report No. 78030, September 1978.
4. Department of Public Works - Newcastle
District Office
DIXON PARK - CONSTRUCTION REPORT
September 1978

REFERENCES Cont.

5. FOSTER D.N. and A.D. GORDON
BEACH PROTECTION, CRONULLA
Fourth Australian Conference on Coastal
and Ocean Engineering, November 1978.
6. RAY, N.S.W. and J.G. HOFFMAN
ETTALONG BEACH EROSION STUDY AND
MANAGEMENT PROGRAMME
Fourth Australian Conference on Coastal
and Ocean Engineering, November 1978.

EDDY CURRENTS AND SEDIMENT TRANSPORT OFF THE DAMIETTA NILE

S. P. Murray, J. M. Coleman, H. H. Roberts, and M. Salama*

Coastal Studies Institute, Louisiana State University

Baton Rouge, Louisiana 70803, U.S.A.

Abstract

Current meter observations indicate that a trapped eddy with a high-speed outer limb is formed downcurrent of the Damietta Nile promontory. This eddy is instrumental in the formation of the highly mobile sand body that extends seaward from the Damietta mouth, out onto the shelf, and curves back toward the coast just east of the Suez Canal entrance. Orientation of sand waves along the sand belt mirrors the direction of current flow within the eddy and indicates that the zone of reattachment of the separation streamline is located to the east of the Suez Canal. Dissipation of this sand belt will likely result in increased coastal erosion locally.

*Coastal Protection Branch, Institute of Oceanography and Fisheries, Academy of Scientific Research and Technology, Alexandria, Egypt

Introduction

Between September 1964 and October 1966 the monthly discharge from the Nile River decreased by an order of magnitude, from $1.9 \times 10^{10} \text{ m}^3/\text{month}$ to $4 \times 10^9 \text{ m}^3/\text{month}$, as a result of the closure of the High Dam at Aswan. The corresponding decrease in sediment brought to the coast resulted in the marked acceleration of an already serious coastal erosion problem and the transition of the inner shelf from one dominated by riverine processes to one dominated by marine processes, i.e., waves and currents. The resulting erosion problems along the entire coast fronting the Nile Delta have been the subject of exhaustive studies originally sponsored by the United Nations and continued under the auspices of the Academy of Scientific Research and Technology (ASRT), Cairo. For extensive summaries see UNDP (1976, 1977). These studies emphasized changes in beach morphology as an indication of coastal retreat and relied heavily on large-scale oceanographic cruises (e.g., Summerhayes and Marks, 1976) and reinterpretation of earlier shelf sediment surveys (Misdorp and Sestini, 1976) for knowledge of sedimentation on the adjacent shelf.

Because of wartime conditions, access to the shelf by the U.N. project was greatly restricted, and, according to Nielsen (1977), essentially prohibited east of the Damietta promontory. Accordingly, the start of a joint United States-Egyptian bathymetric resurvey in 1978 of the continental shelf from Damietta eastward past Port Said, at the Suez Canal entrance (Fig. 1), presented an excellent opportunity to further our understanding of the physical processes and sediment transport active in this area. A combined team from the Coastal Studies Institute and the Institute of Oceanography and Fisheries, ASRT, Cairo, was provided space and logistical support on the survey ship U.S.N.S. Harkness to carry out scientific studies of the currents and bottom sediment behavior. The most conspicuous geomorphic features along the coast of the delta are the large promontories or cusped capes at the mouths of both the Rosetta and the Damietta branches. As earlier work (e.g., Murray and Wiseman, 1976) had documented the intermittent presence of a large eddy downstream (west) of the Mississippi delta promontory, it was suspected that the Nile capes might also exert a significant influence on the local current field. A similar suspicion was voiced by Misdorp (1977) to explain the sand distribution east of the Damietta promontory. Thus current observations were concentrated immediately downcurrent or eastward of the Damietta promontory.

In this report we shall emphasize the results of the current studies and the interaction of currents with the bottom. A brief review of physical processes in the local area will be followed by a discussion of the current velocities, temperatures, and salinities obtained during our measurement program. The current velocity field will be shown to have a highly coherent spatial structure intimately related to the geometry of the Damietta promontory. A composite model of the current field constructed from theoretical, experimental, and numerical studies will then be compared to both the observed current field and the observed patterns of sediment movement. The presence of a mesoscale eddy trapped in the lee of the Damietta promontory and its strong control on bottom sediment transport is established, and its implications on the future of the coast between Damietta and Port Said are discussed.

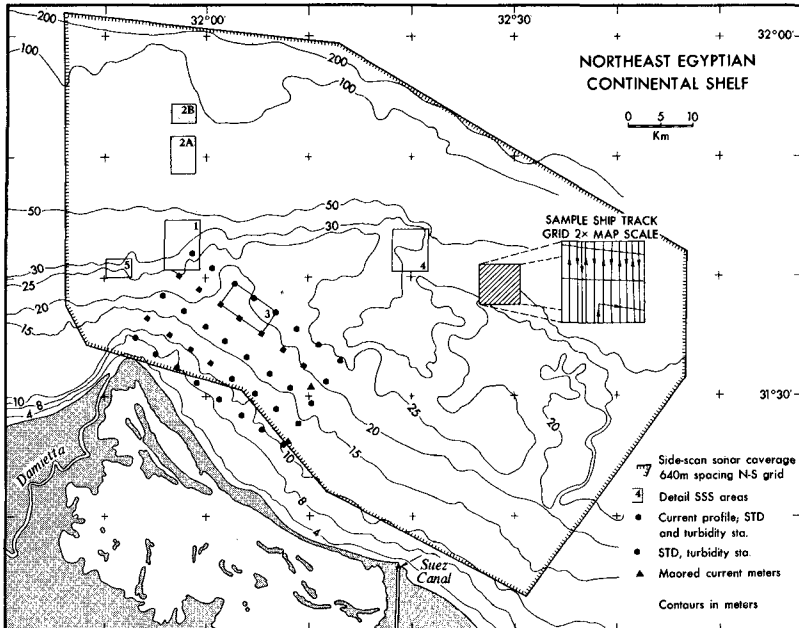


Figure 1. Location map of study area off the Damietta branch of the Nile River. The inset shows a survey grid typical of those carried out over the entire area.

Background Processes

The average properties of winds and currents are obtained from the data archived at the U.S. National Oceanographic Data Center (Fig. 2). A good correlation is clearly seen between the wind direction and the current direction. The modal wind direction is clearly to the southeast from May through October. A strong secondary peak of winds blowing toward the northeast is present from December through March. Both of these winds, with east-going components, can be seen to produce east-flowing currents in the Damietta-Port Said area. Other peaks of wind direction, to the southwest in April-May and October-November, are seen to reverse the dominant current drift to the east and drive the surface currents westerly. Representative background current speeds from this data set are seen to be 15-20 cm/sec.

Direct observations of currents along the Nile Delta coast are discussed in Manohar (1976); Manohar et al. (1977); and Tebelius (1977). Unfortunately, again for security reasons, these measurements were

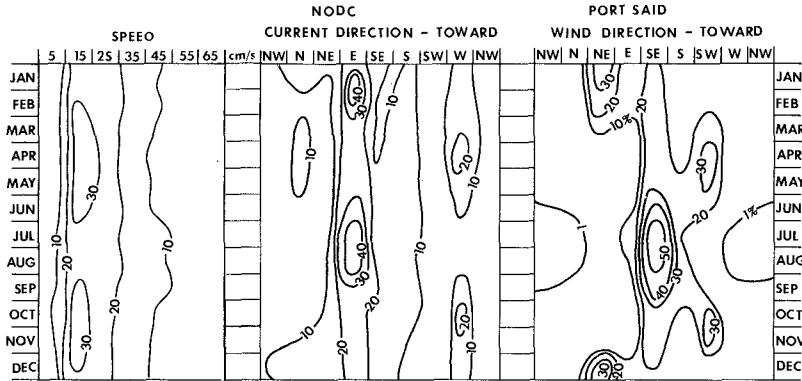


Figure 2. Percentage distribution of current speed and current direction throughout the year for the Port Said 1°-square from NODC data. Percentage distribution of wind direction throughout the year at Port Said from the Sailing Directions.

restricted largely to the surf zone. Manohar (1976) did show current speeds up to 600 m from shoreline in water depths of 2-4 m to reach 30-40 cm/sec, but he noted that these data were as yet unanalyzed. Tebelius (1977) presents a discussion of a current measurement program in Abu Quir Bay, near the mouth of the Rosetta Nile, but, as with Manohar's data, these results do not apply to the inner shelf (10-30 km offshore), which is the focus of this paper.

Perhaps the best source of modern data on the background drift current along the Egyptian Mediterranean coast is Gerges (1978). Analysis of the return data from Woodhead surface drifters released monthly for 18 months in 1976 and 1977 (total of 2,664 drifters) indicated a general easterly drift of 10-15 cm/sec. The May 1977 drifter returns clearly showed the intermittent westerly setting current reversal suggested in Figure 2.

Physical Oceanographic Measurements

Data were collected through the 40-station grid along lines normal to the coast (034° M), moving west to east (Fig. 1). Current meter profiles requiring an anchor station were restricted to the outer, middle, and inner stations on each line; all stations also included a vertical profile of salinity, temperature, and turbidity. Thirty-eight of the forty stations were occupied in the 6-day interval 29 April - 4 May 1978, during which period winds always had onshore components blowing from NNW to NE at 5-10 m/sec.

The current meter profiles at the anchor stations which are of principal interest here were taken from a 12-m-long LCVP, which, while open and rough-riding, proved to be an excellent vehicle for the current studies. Even in light winds the boat swing at anchor was minimal, and good current

data were the rule. The current meter used was a Marine Advisors Q-15 ducted impeller meter with a bidirectional sensing capability designed to mechanically and electronically filter out "noisy" wave motion. A Plessey STD Model 9060 gave in situ measurements of salinity and temperature with a 20-40 ppt salinity range. Wind velocities were measured on the Harkness and LCVF, but the most reliable data were obtained from the Suez Canal Research Center at Port Said.

In addition to the spatial coverage of the current field provided by the anchor stations, two current meter moorings equipped with acoustic releases were installed at the eastern end of the grid, as shown in Figure 1. Each mooring had two Marine Advisors Q series meters in line which had the same response characteristics as the Q-15 profiling meter described above.

Station data. The complete data set on the current field obtained from the anchor stations is presented in Figure 3. Stations on the western most line (1-5) reflect the expected background easterly drift current, but note the unexpectedly strong (~30 cm/sec) surface layer currents at the outer two stations (1 and 3). Also note the sharp deceleration in current speed from station 5 to station 6, which were taken within 1 hour of each other at a time of steady northerly winds. On the following day (30 April) stations 10 and 11, only 4 km apart and taken within 90 minutes of each other, show extreme horizontal current shear. Station 11 is particularly remarkable; speeds of 40 cm/sec throughout the water column from the surface to the bottom were directed seaward essentially against a weak north-northeasterly wind of 2-3 m/sec on that day. It appears likely from the stations that this seaward-directed high-speed zone is only 1-2 grid units (4-8 km) across.

Four stations on the middle and inner lines (13, 15, 16, 18) were next occupied, on 1 May. All four showed a westerly directed current of 10-15 cm/sec against the regional drift, which cannot be accounted for by the weak winds of that day. Clearly a convergence or zone of stagnation exists in the area between stations 6-8 and 13-15. On 2 May the apparently narrow jet of seaward-directed high speeds was again penetrated by stations 21 and 23. It was extraordinary to note the entire water column moving seaward at speeds in excess of 50 cm/sec. The great difference in speed and direction between stations 20 and 21 and between 23 and 25, each taken within 90 minutes of the other, strongly indicate a relatively narrow, highly coherent local circulation system. It appears that the high-speed zone had migrated from the vicinity of station 11 on 30 April, easterly to the vicinity of station 21, 2 days later, on 2 May.

The remaining stations, all located outside the zone of strong seaward flow, must be examined carefully for wind-driven effects in the surface and mid-depth layers. For example, at the shallow nearshore stations (e.g., stations 26, 35) and at deeper stations outside the high-velocity jet, where the speeds are generally lower (e.g., stations 30, 31), the onshore surface layer currents clearly result from local wind driving. In contrast, the remarkably strong seaward motion near the bottom, directed toward the high-speed zone at stations 28 and 33 and again at 26 and 35, indicates that the forces driving the circulation pattern are barotropic, i.e., they extend throughout the water column down to the bottom, where

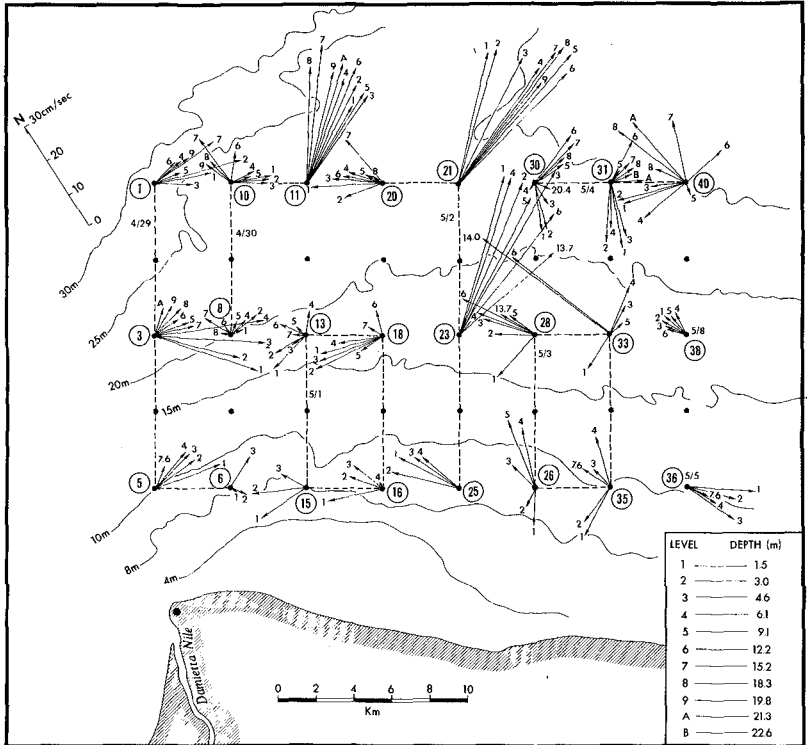


Figure 3. Vertical profiles of current velocity at each grid anchor station. Depth of observation is coded by a level number or letter except where actual depth is stated in metres. Stations occupied on same day are connected by a dashed line.

they overpower the frictional forces associated with wind driving.

Salinity, temperature, and velocity cross sections. Considerable insight into the spatial pattern of the flow field is also obtained by inspecting hydrographic sections. Two offshore lines that were completely covered in 1 day are shown in Figures 4 and 5, the westernmost section off the Damietta promontory and the central section through the core of the offshore jet, respectively. In the Damietta section (Fig. 4A) the along-shore speed component (parallel to the grid) shows a distinct offshore jet with a surface maximum of 25-30 cm/sec located 15 km offshore. Alongshore speeds decrease monotonically with depth. The cross-shore speed component is directed onshore (negative values) only in a shallow near-surface prism in the center of the section. The bulk of the section has offshore components reflecting the shunting of the background flow seaward by the curvature of the Damietta promontory. The salinity values of about 38 ppt are typical of the eastern Mediterranean but are interesting in that they still reflect coastal drainage by slight increases of a few tenths parts

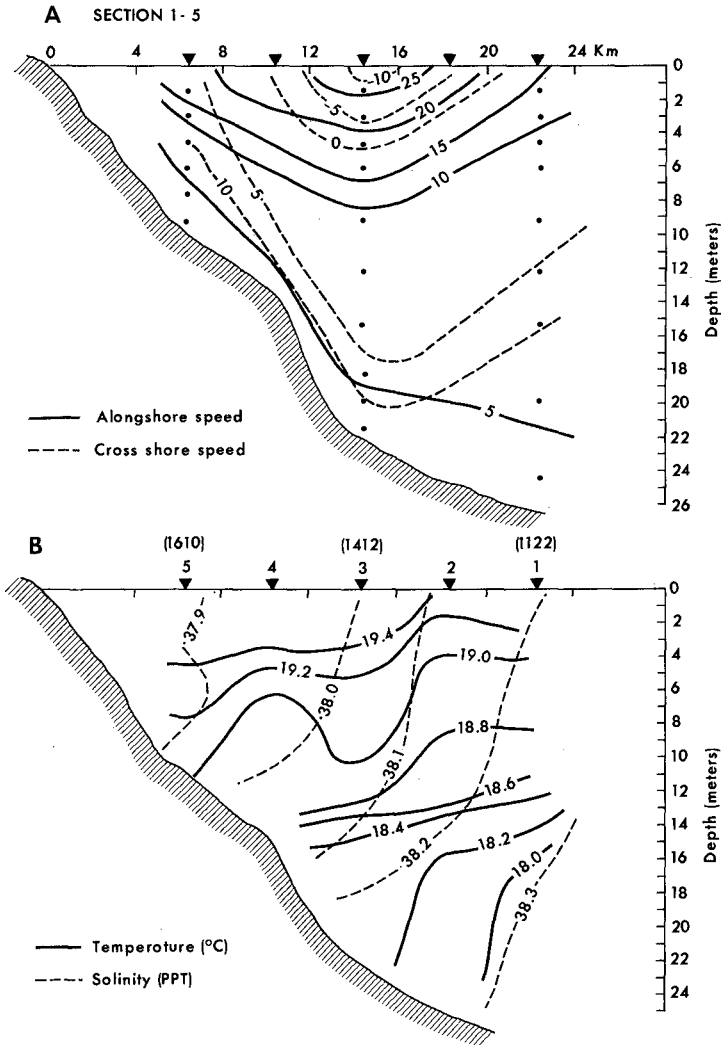


Figure 4. A, alongshore and cross-shore current speed components and, B, salinity and temperature distribution along the cross-shore line through stations 1-5 on 29 April 1978. Cross-shore speeds are positive offshore; alongshore speeds are positive downdrift or to the southeast. Time station was occupied is given above station number.

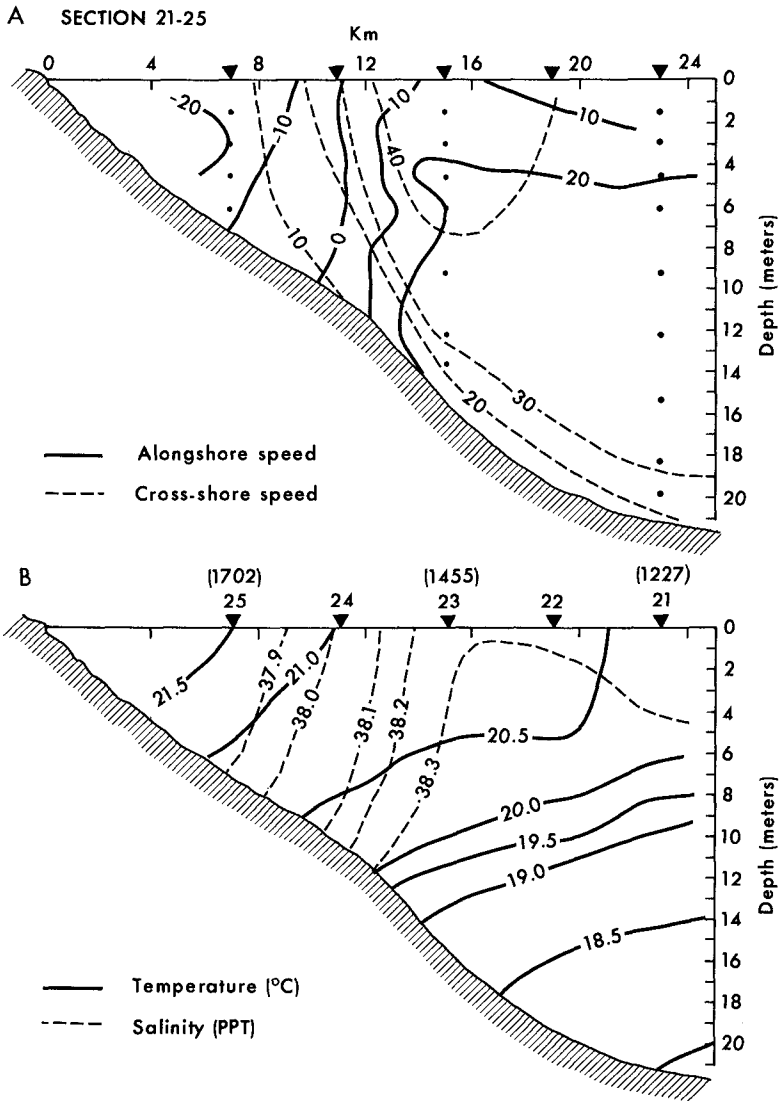


Figure 5. Same as Figure 4 except stations 21-25 on 2 May 1978.

per thousand both with depth and in the offshore direction. The temperature distribution in Figure 4B shows a thermocline at the 12-14-m depth.

Only 3 days later the section through stations 21-25 (Fig. 5), taken 16 km downcurrent (southeast), is in marked contrast to the picture along the Damietta line (Fig. 4). Here the cross-shore speed is the dominant component, showing offshore (positive) values across the entire section, with a maximum of over 40 cm/sec located 16 km offshore. Continuity, of course, demands an inflow somewhere to supply the volume transported offshore in this jet. Equally instructive is the alongshore speed component. Seaward of station 24 (11 km offshore) the flow is entirely downcurrent or southeasterly, while shoreward of this mark the flow is entirely upcurrent or northwesterly. Here, then, is the inshore return flow to resupply the jet. The water temperatures here (Fig. 5B) are consistently higher, by as much as 1-2°C, than in the Damietta section, nicely reflecting the inshore origin of the jet water. The salinities, however, remain a puzzle, requiring further analysis to understand why high salinities (38.2-38.3) characterize the warm offshore jet.

Combining knowledge of the background drift current from the literature with our own current observations (Figs. 3, 4, 5), we can infer a streamline pattern for the flow field around the Damietta promontory, excluding wind effects on the surface layer, as shown in Figure 6. The easterly background longshore flow of 15-20 cm/sec is shunted seaward by

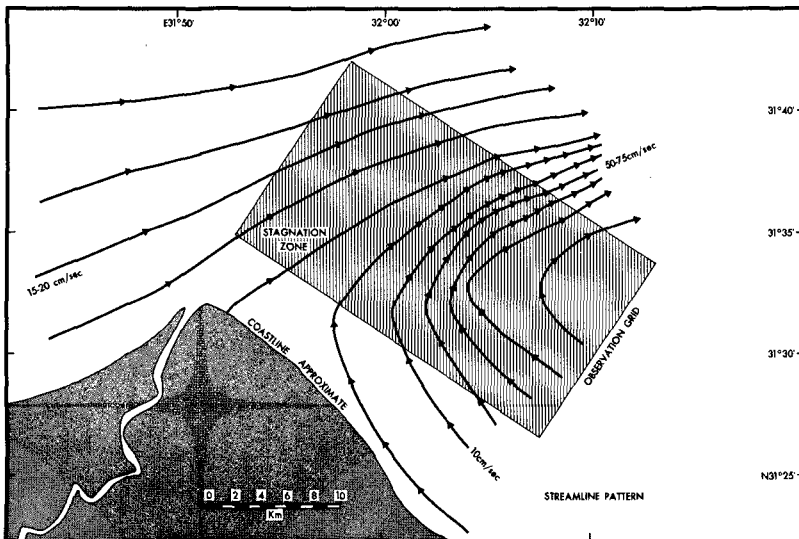


Figure 6. Streamline pattern interpreted from interior layer currents shown on Figure 3. Note narrow zone of high speed exiting seaward edge of grid.

the curvature of the Damietta promontory. Flow separation takes place several kilometres downstream (eastward) of the river mouth and induces a seaward-flowing high-speed jet as the northern limb of a topographically trapped eddy. A broad, slow northwesterly return flow forms as the southern limb of the eddy. The separation streamline must, of course, return to the coast somewhere downstream and form another stagnation zone of divergent currents flowing westward to feed the eddy and eastward to reestablish the background drift current.

A laboratory visualization (Prandtl and Tietjens, 1957) of the type of eddy we believe forms in the lee of the Damietta promontory is shown in Figure 7. The upward (seaward) shunting of the background flow, the high-speed jet, and the inshore return flow are all present, but of course we expect the natural scale eddy to be more elongate alongshore and diffuse due to the gentler angles involved.

Moored current meters. Figure 8 is an example of the current meter data obtained from the outer mooring (Fig. 1). The temporal behavior of the current velocities at these two levels are consistent with the interpretation of the current structure based on the station data. Note that between 27 April and 1 May the upper level currents are generally weaker than the deep currents, except for two short-lived events apparently asso-



Figure 7. Eddy trapped behind tapered edge. (Reproduced from Prandtl and Tietjens, 1957, with permission of Dover Publications.)

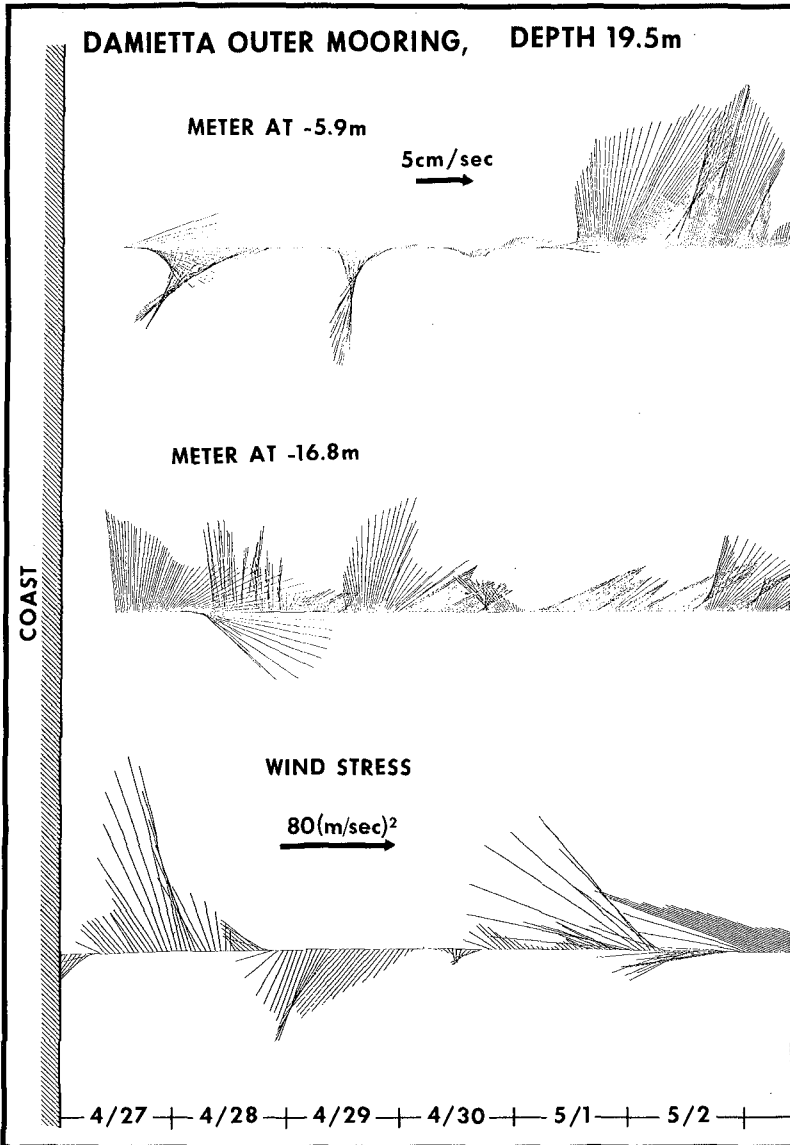


Figure 8. A stick diagram of current vectors at the outer mooring compared to the wind at Port Said (Suez Canal entrance on Fig. 1). The horizontal time lines lie on azimuths to the coast of 215° .

ciated with wind decelerations at 0400 on 28 April and a wind acceleration at 0600 on 29 April. The deeper currents are persistently more energetic, generally showing an upcurrent or north to northwesterly motion toward the narrow zone of strong seaward flow, thus again indicating the influence of the circulation of the trapped eddy on the currents below the wind-driven surface layer. It is probable that the sudden episode of strong, persistent currents at the upper level on 1 and 2 May reflect the increased influence of the eddy as it migrated southeasterly toward the mooring on 1 and 2 May, as suggested by the station data of Figure 3.

The data from the inner current meter mooring is heavily influenced by accelerations and shifts in the wind. Further analysis will be necessary to establish any relationship between these meters and the eddy circulation system. As anticipated, the current meter records show the tidal current to be on the order of only 5-8 cm/sec, and thus the lack of synopticity of the station data does not seriously disturb the inferred flow field of Figure 6.

Bottom Morphology--Side-Scan Sonar

While performing its primary mission of a detailed bathymetric survey, the Harkness towed side-scan sonar (SSS) over the 4,450 sq km of the Egyptian shelf outlined in Figure 1. The survey grid consisted of north-south track lines spaced at 650 m with a side-scan scale of 400 m (total swath width was 800 m), giving a 150-m overlap on each adjacent line. While these SSS data were taken to assist the bathymetric survey, experienced users can interpret morphologic features, sediment type, and sediment mobility from the same data. Our results from such an interpretation are shown in Figure 9.

After mapping of bottom morphology from the SSS data taken by the Harkness was completed, several areas of special interest in differing types of shelf morphology were chosen for a more closely spaced survey grid with a higher resolution range on the side scan (detail areas 1-5, Fig. 1). In these regions the line spacing was 150 m, with a swath width of 200 m set on the side scan, giving a 50-m overlap on each line. In addition, bottom samples were collected within each area to assess the sediment type composing each morphologic unit. Thus this survey allowed coverage of a large shelf area in greater detail than any other previous survey of the eastern Nile shelf.

Perhaps the most exciting discovery from these data was the presence of a broad sand belt extending from off the mouth of the Damietta eastward and finally curving landward along the eastern boundary of the survey region in the vicinity of the Suez Canal (Fig. 9). This sand belt lies in water depths of 25 to 60 m, and the belt ranges in width from 5 to 20 km. This belt consists typically of large sand ribbons which display small migratory sand waves and fields of large-scale migratory bedforms or sand waves. These features are similar to the sand ribbons described by Kenyon (1970) in European tidal seas, Kenyon and Belderson (1973) in the Mediterranean, and Swift and Ludwick (1976) on the east coast of the U.S. While the major morphologic features forming on the sand belt are the sand ribbons, there are areas where large patches of sand waves are present. Figure 10 shows the detailed mapping of area 1 (see Fig. 1 for location)

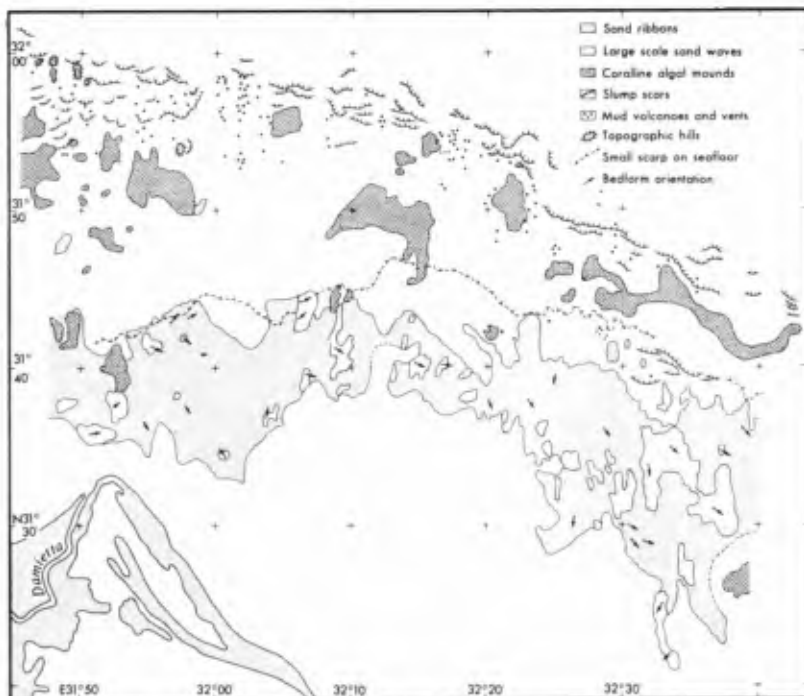


Figure 9. Bottom morphology of the Nile shelf as mapped from side-scan sonar data. Small arrows give direction of movement as determined from bedform orientation.

within the sand belt. Notice that the sand ribbons vary in size considerably, ranging from 150 m wide and 1 km long to much larger, 1-2.5 km wide and 10-18 km long. The sand ribbons display heights above the general sandy silt sea bottom that range from less than 2 m to 10 m. Small-scale sand waves are often found on the ribbons, especially on the larger features, where the ribbons obtain some elevation above the bottom. The sand waves normally display crest lines that are generally perpendicular to the long axis of the ribbons.

Figure 11 is an enlargement of actual side-scan data taken from a sand wave field on one of these ribbons. The sand waves are seen to be about 50 m long and 3-5 m high. Clearly, strong, persistent currents are necessary to mold the bottom to this condition. Utilizing the side-scan sonar data, the orientation of the various bedforms could be mapped, and these are shown on Figure 9. Near the Damietta distributary the bedforms show a general NNW orientation and near the seaward edge swing toward the

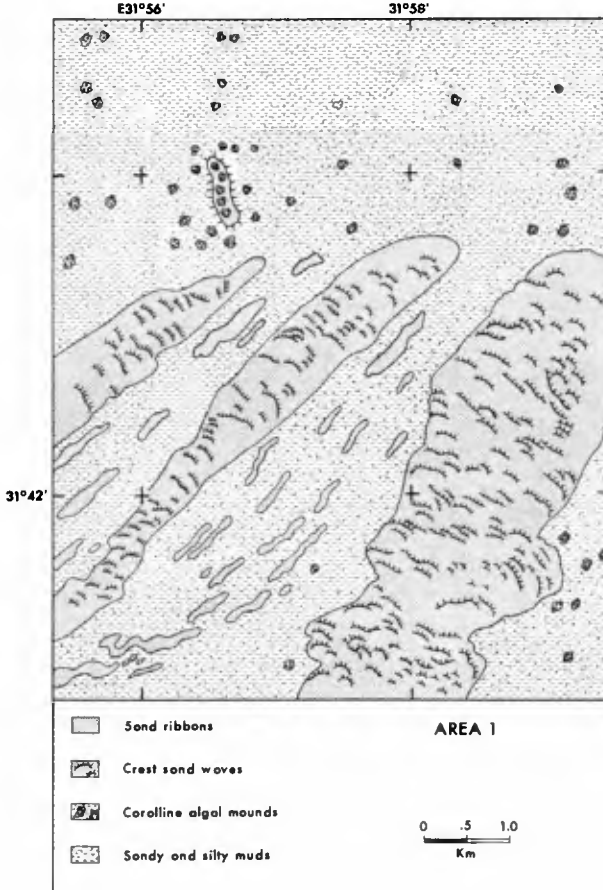


Figure 10. Detailed morphology of sand ribbons and sand waves moving over a mud bottom in area 1 (see location on Fig. 1).

east and ESE. In the central part of the sand belt the bedforms show a general east and southeast direction of sediment migration. Along the easternmost edge of the study region the bedforms display a general southern or toward-shore migration pattern. Note also in this area that there is a large accumulation of sand, and the contour map (Fig. 1) shows the presence of a large shoal just east of the Suez Canal. It is highly probable that this sand migration pattern has been responsible for the sediment accumulation in the Suez Canal region. The pattern of sand wave

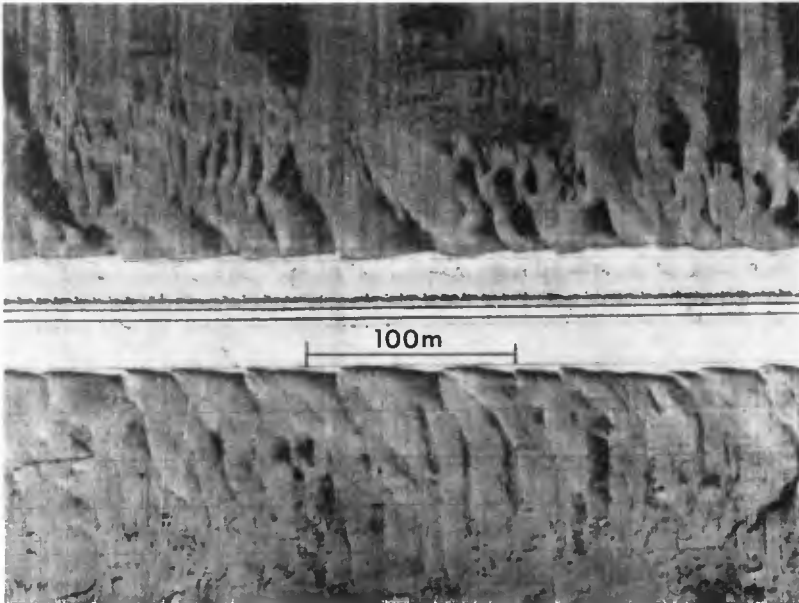


Figure 11. Side-scan sonar image illustrating bedforms on the crest of a sand ribbon. Ship track run parallel to the long axis of the sand ribbon. Lateral scale is in increments of 15 m. Sand waves are 3-5 m high.

movement certainly appears to be with the eddy current structure inferred from Figure 3. This will now be examined in more detail.

Model of Eddy Circulation East of Damietta

Fluid flow around obstacles is a frequent topic for laboratory experimentation in hydro- and aero-dynamics. The experimental results from flow around flat plates and blunt obstacles such as seen in Figure 7 have been used successfully in formulating models of flow separation, cavity (trapped eddy) formation, and return flow for design of nuclear reactor shells (Halitsky, 1968). Only recently have analytical and numerical techniques been successful in describing the air flow over hills. Jackson and Hunt (1975) presented an analytical treatment of the velocity field over gently sloping hills, while Mason and Sykes (1979) recently described a numerical model which treated hills steep enough to produce flow separation.

The essential results of these three approaches, experimental, analytical, and numerical models, have been synthesized in Figure 12 and applied to the Damietta promontory, considered as an obstacle to flow. According to Jackson and Hunt (1975), the background flow U_0 approaching

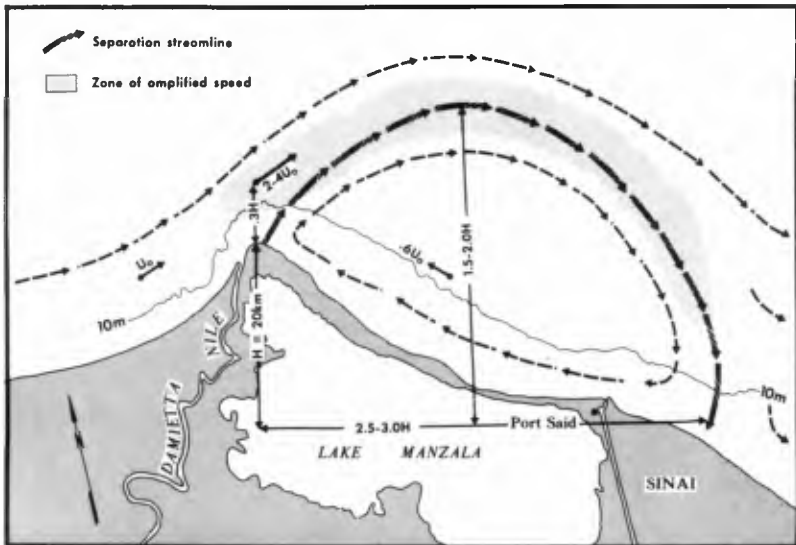


Figure 12. Composite model of flow field around an obstruction, synthesized from experimental, analytical, and numerical studies.

the promontory is amplified into a free jet with a magnitude 2 to 4 times U_0 , located at a position above the obstacle equal to three-tenths of its height (H). Experimental work indicates that the cavity or trapped eddy will resemble an ellipsoid of revolution with a downstream dimension of at least $2.5-3H$ and a cross-stream dimension of $1.5-2.0H$. In the center of the eddy there will be a return flow of $0.6U_0$. The zone of high speed will follow the separation streamline deflected cross-stream by the obstacle. The essential features of these models were reproduced in the elegant numerical solutions of flow over steep topography by Mason and Sykes (1979).

In Figure 13 the basic geometry of the trapped eddy is compared to the current velocity observations and the sand body mapped by side-scan sonar. The zone of high-speed currents first identified in the station data is clearly the right magnitude and location to be on the seaward limb of the trapped eddy. The return flow along the coast at the inner line of stations also fits the model rather well. There can be little question that the high-speed outer limb of the eddy is interacting strongly with the bottom as the curvature of the inner shelf sand body follows the predicted axis of the eddy quite closely except at its eastern end. Far more striking is the agreement among the direction of movement of sand waves shown on the figure, the observed current velocities, and the current speeds and directions expected from the flow separation-trapped eddy model.

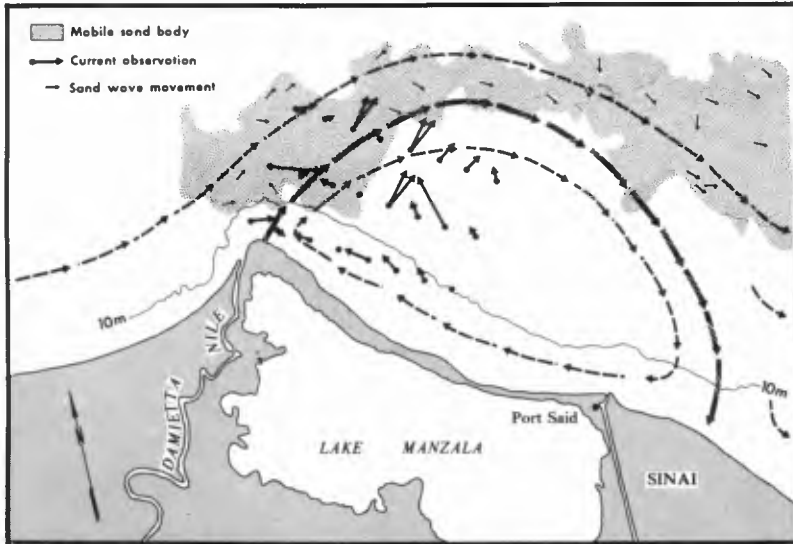


Figure 13. Observations of currents and sand wave movements compared to the composite model of a trapped eddy shown in Figure 12.

Implication to future coastal erosion. The coastline between the Damietta promontory and the Suez Canal is already undergoing severe erosion (Nielsen, 1977). As closure of the Aswan High Dam has cut off the input source of sand for the sediment transport system driven by the Damietta eddy, we expect the arcuate sand ribbon belt to gradually consume itself. The tail or western boundary of the sand belt will migrate easterly due to lack of replenishment, and the height of individual sand ribbons will gradually lessen as the arcuate sand belt dissipates, allowing increasingly higher levels of wave energy to impact the coast, accelerating the erosion rate.

Summary and Conclusions

The closure of the High Dam at Aswan on the Nile River markedly accelerated an already severe erosion problem along the Mediterranean coast of Egypt. In 1978 the U.S.N.S. Harkness, while performing a bathymetric resurvey of the shelf between Damietta and a line eastward of the Suez Canal entrance, obtained side-scan sonar coverage of the entire survey area. On the basis of these data a combined program of physical oceanographic and marine geologic measurements was made at a much finer resolution in an area immediately east of the Damietta Nile promontory and leads us to the following conclusions.

1. A seaward-directed jet of high-speed current 4-8 km across forms

off the Damietta promontory and shoots out northeasterly against the prevailing wind. Flow separation occurs a few kilometres east of the vertex of the promontory.

2. A broad, slow return flow to the northwest forms in the shallower waters along the coast. This return flow is highly influenced by the local wind.

3. These two zones are elements of a mesoscale (~50 km) eddy trapped in the lee of the promontory.

4. The spatial and velocity characteristics of the eddy are consistent with a composite model of eddies induced by flow separation based on analytical, numerical, and experimental studies. Further observations of the temporal and spatial behavior of such an important feature are clearly warranted.

5. Detailed side-scan sonar surveys of bottom morphology indicate that the eddy is underlain by a highly coherent, mobile sand belt that extends about 50 km downcurrent (east). Orientation of sand waves reflects the measured currents in the eddy and indicates that reattachment of the separation streamline occurs about 10 km to the east of the Suez Canal entrance.

6. As a principal source or input of sediment to the eddy driven sand belt was shut off by the closure of the Aswan High Dam, we expect the relief on the sand belt (up to 10 m) to diminish gradually, allowing greater wave energy to impact the coast, thus aggravating the local erosion problem.

Acknowledgments

We gratefully acknowledge the highly capable assistance of the officers and men of the U.S.N.S. Harkness during the work at sea. Captain J. R. McDonell, Dr. William E. Hart, and Mr. Dodd Ouellette of the U.S. Naval Oceanographic Office, Commander William Friskin of the Royal Navy, and Dr. James Bailey of the U.S. Office of Naval Research provided essential assistance in our utilization of the Harkness. Drs. A. R. Bayoumi and A. A. Khafagi, of the Academy of Scientific Research and Development, Cairo, arranged cooperative efforts with the Egyptian scientific community. The Port Said wind data were supplied by Dr. M. El Ghamry of the Suez Canal Research Center. This work was carried out under a contract between the Coastal Sciences Program, Office of Naval Research, Arlington, Virginia 22217, and Coastal Studies Institute, Louisiana State University.

References

- Coleman, J. M., Roberts, H. H., and Murray, S. P., "Morphology and Dynamic Sedimentology of the Eastern Nile Delta," Proceedings of SANDS Symposium, 7-17 July 1980, Paris, France, 26th International Geological Conference, in press.
- Gerges, M., "Trajectories and Speeds of Surface Currents near the Egyptian Mediterranean Coast as Deduced from the Movement of Surface Drifters," IV Journées Etud. Pollutions, Antalya, C.I.E.S.M., 1978, pp. 573-587.
- Halitsky, J., "Gas Diffusion near Buildings," Meteorology and Atomic Energy, U.S. Atomic Energy Commission, Oak Ridge, Tenn., 1968, pp. 221-252.
- Jackson, P. S., and Hunt, J. C. R., "Turbulent Wind Flow over a Low Hill," Quarterly Journal Royal Meteorology Society, Vol. 101, 1975, pp. 926-956.
- Kenyon, N. H., "Sand Ribbons of European Tidal Seas," Marine Geology, Vol. 9, 1970, pp. 25-39.
- Kenyon, N. H., and Belderson, R. H., "Bedforms of the Mediterranean Undercurrent Observed with Side-scan Sonar," Sedimentary Geology, Vol. 9, 1973, pp. 77-99.
- Manohar, M., "Dynamic Factors Affecting the Nile Delta Coast," Proceedings of Seminar on Nile Delta Sedimentology, Academy of Scientific Research and Technology, 1976, pp. 104-129.
- Manohar, M., Nafaa, M., and Sharaky, N., "Longshore Currents along the Nile Delta Coast," Proceedings of Seminar on Nile Delta Coastal Processes with Special Emphasis on Hydrodynamical Aspects, Academy of Scientific Research and Technology, Cairo, 1977, pp. 255-273.
- Mason, P. J., and Sykes, R. I., "Separation Effects in Ekman Layer Flow over Ridges," Quarterly Journal Royal Meteorology Society, Vol. 105, 1979, pp. 129-146.
- Misdorp, R., "The Nile Promontories and the Nile Continental Shelf," Proceedings of Seminar on Nile Delta Coastal Processes with Special Emphasis on Hydrodynamical Aspects, Alexandria, 2-9 October 1976, Academy of Scientific Research and Technology, 1977, pp. 456-551.
- Misdorp, R., and Sestini, G., "Notes on a Sediment Map of the Nile Delta Continental Shelf, Based on the Endeavour Survey of 1919-1922," Proceedings of Seminar on Nile Delta Sedimentology, Alexandria, pp. 191-205, 1976.
- Murray, S. P., and Wiseman, Wm. J., Jr., "Current Dynamics and Sediment Distribution in the West Mississippi Delta Area," Proceedings, First Interdisciplinary Conference on Marine and Freshwater Research in Southern Africa, Port Elizabeth, 1976.

- Nielsen, Ev, "Coastal Protection and Improvements," Proceedings of Seminar on Nile Delta Coastal Processes with Special Emphasis on Hydrodynamical Aspects, Academy of Scientific Research and Technology, Cairo, pp. 612-624, 1977.
- Prandtl, L., and Tietjens, O. G., Applied Hydro and Aerodynamics, Dover, New York, 1957, 311 pp.
- Summerhayes, C., and Marks, N., "Nile Delta: Nature, Evolution and Collapse of Continental Shelf Sediment System," Proceedings of Seminar on Nile Delta Sedimentology, Alexandria, 1976, pp. 162-191.
- Swift, D. J. P., and Ludwick, J. B., "Substrate Response to Hydraulic Process: Grain-size Frequency Distributions and Bedforms," Marine Sediment Transport and Environmental Management, D. J. Stanley and D. J. P. Swift, ed., John Wiley and Sons, New York, pp. 159-196, 1976.
- Tebelius, U., "Bottom Currents in Abuquir Bay," Proceedings of Seminar on Nile Delta Coastal Processes with Special Emphasis on Hydrodynamical Aspects, Academy of Scientific Research and Technology, Cairo, 1977, pp. 255-273.
- UNDP, Proceedings of Seminar on Nile Delta Sedimentology, Academy of Scientific Research and Technology, Cairo, 1976, 257 pp.
- UNDP, Proceedings of Seminar on Nile Delta Coastal Processes with Special Emphasis on Hydrodynamical Aspects, Academy of Scientific Research and Technology, Cairo, 1977, 624 pp.

A Comparison between Dredge Induced Sediment Resuspension and that
Produced by Natural Storm Events

W. Frank Bohlen
Marine Sciences Institute
and
Marine Sciences Department
University of Connecticut
Avery Point
Groton, Connecticut
U.S.A.

Abstract

Field observations indicate that the effect of dredge-induced resuspension on sediment transport within small estuaries is generally negligible in comparison to the transport induced by natural storm events. Data obtained in the Thames River, near New London, Connecticut show dredge-induced resuspension to be essentially a near field phenomenon. The resultant plume of material increases total suspended load in the river by approximately 25% but extends over less than 2.5% of the total estuarine area. In contrast storms are observed to increase total suspended load by a factor of three, influencing concentration levels throughout the estuary. These factors, in combination with the lower frequency of dredging vis-a-vis significant storm events, appear to effectively limit the influence of dredge-induced resuspension.

Introduction

During the past ten years dredging operations intended to maintain the viability of navigable waterways within the northeastern United States have often been surrounded by intense environmental debate. These coastal areas typically contain sediments contaminated by a variety of organic and inorganic pollutants and concerns have centered on both the short and long-term biological impacts associated with dredge-induced resuspension and disposal related dispersion of these materials. In many cases these concerns have served to slow project completion, forcing rescheduling and, on occasion, have provided a basis for legal injunctions, completely blocking further dredging.

Unfortunately, many of the above activities have proceeded despite the absence of hard data. This has been particularly true for the case of dredge-induced resuspension where, until recently, essentially no information has been available detailing the characteristics of the downstream plume of materials or the significance of this source of suspended sediments vis-a-vis naturally occurring storm events. Within the past three years this situation has improved to some extent and several investigations have been conducted providing insights into the factors governing the distribution of dredge resuspended sediments and the spatial extent of the resultant plume (Bohlen, 1978; Bohlen, et al., 1979). In addition, the increasing amounts of field data have also served to provide a basis for the development of predictive modeling schemes applicable to both clam-shell (Cundy and Bohlen, 1979) and hydraulic (Wilson, 1979) dredging operations.

The detail provided by the above investigations is sufficient also to permit an initial evaluation of the magnitude of dredge-induced resuspension relative to that produced by natural storm events. This paper presents the results of such an evaluation.

Study Area

Since 1974 the Thames River estuary (Fig. 1) located in southeastern Connecticut, approximately 120 km east of New York City, has been the site of several major dredging projects. This stream represents a typical small New England estuary. Annual streamflow varies between 70 and 76 m³/sec while the mean tidal range equals 0.78 m at New London. The combination serves to distribute sediments supplied from both upstream terrestrial and downstream marine source areas. Typically, these materials consist of fine sands and silts with minor fractions of clay. The effect of winds on these distributions in the estuary appears to be negligible.

Sediment deposition and the resultant shoaling requires periodic dredging to maintain the assigned depth of the navigational channel. Operations usually employ floating cranes equipped with large volume (10 m³) clam-shell buckets. Spoils are placed in hopper barges for transport to an offshore disposal site. The frequency of those operations over the past six years has provided ample opportunity to study the characteristics of dredge-induced resuspension.

Survey Methods and Procedures

The characteristics of the suspended material field within the Thames River have been the subject of intensive study since 1974. During 1974-76 surveys of a network of 12 stations (selected numbers shown in Fig. 1) were conducted monthly to determine ambient concentrations and the degree of spatial and temporal variability. At each station water samples were obtained at the surface, mid-depth and near bottom, using a 5 l Van Dorn bottle. Samples were placed in pre-washed and rinsed glass bottles and returned to the laboratory. By weight concentrations of total suspended solids were determined for each sample by vacuum filtration, using dried and preweighed Nuclepore filters (0.40 μ pore size, 47 mm dia.) mounted in a standard Millipore filtration apparatus. After careful washing to remove salts each filter was dried and reweighed. Surveys were, in general, confined to the ebb tidal cycle.

In 1977-78 primary emphasis was placed on determinations of the characteristics of the dredge-induced plume of sediments. Several surveys were conducted while the dredge operated near the northern limit of the study area (Fig. 1). The methods used in the surveys have been described in detail in an earlier paper (Bohlen, et al., 1979). Very briefly, optical techniques were used to define the limits of the plume and to establish a network of stations along the defined centerline. Sampling techniques employed at each station and the procedures used to determine the suspended material concentration in each sample were the same as those used for the large scale surveys described above. Here again surveys were conducted only during the ebb phase of the tidal cycle.

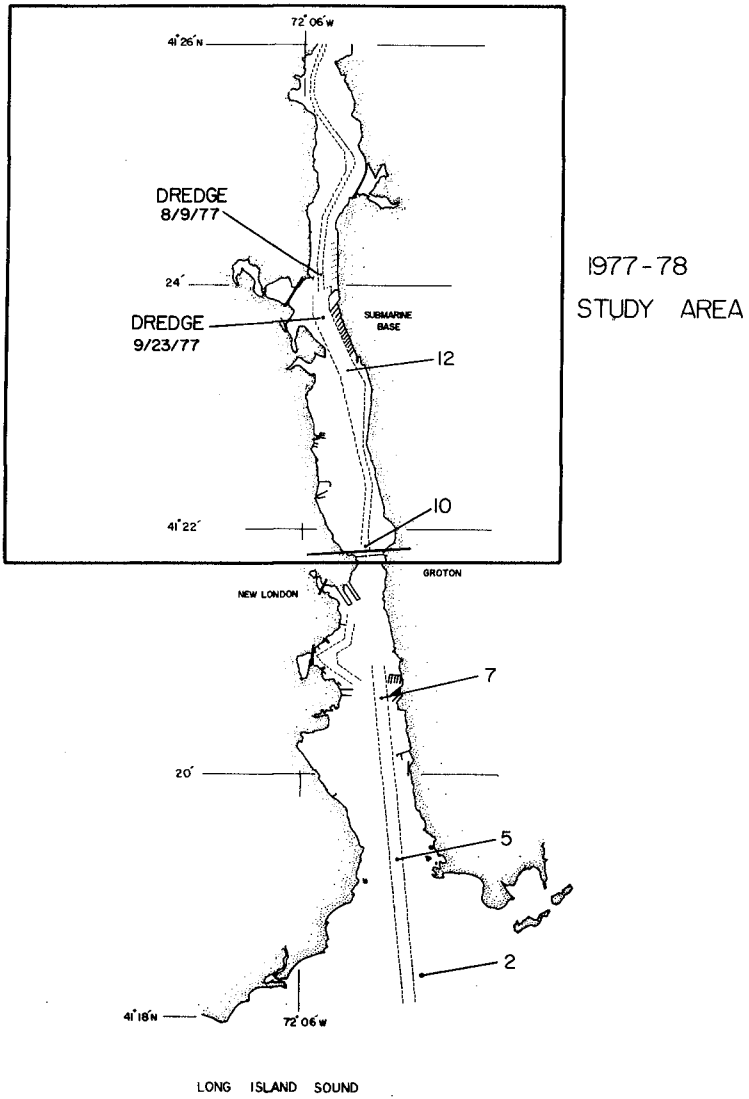


Fig. 1. Lower Thames River Estuary

Results and Conclusions

a. Storm induced resuspension: The suspended material field within the Thames River displays no well-defined seasonal variability (Fig. 2). At each of the main channel stations concentrations averaged between 4.0 and 5.0 mg/l during the major portion of the survey period and displayed only minor variations over the vertical.

The first major concentration anomaly, contrasting sharply with the otherwise persistent homogeneity, occurred on February 1, 1976 coincident with a major storm event. This storm, characterized by long periods (i.e., >24 hrs) of high wind stress and relatively minor precipitation, served to increase material concentrations within the lower river by a factor of four. Proceeding upstream, the magnitude of the increase becomes progressively less with concentrations simply doubling by Station 12. This trend implies that the observed increase is produced by an upstream transport of sediments resuspended by the storm within adjacent Long Island Sound rather than either local resuspension within the estuary or streamflow driven downstream transport. These latter factors would favor distributions differing sharply from that observed. Significant local resuspension tending to produce perturbations of similar magnitude at each station while streamflow dominated transport would favor upstream rather than the observed downstream maxima. This dominance of the offshore source area appears representative of the majority of coastal embayments in southern New England.

A second storm event occurred during March 1977. However, the resultant increase, despite similar storm intensity and duration, was substantially less than that observed during the February event and was largely confined to near bottom waters. Again concentrations decreased progressively with distance upstream further supporting the dominance of the offshore source area.

The response of the suspended material field in the Thames River to the events of February and March, 1976 indicates that storms have the potential to significantly increase the mass of sediments in suspension throughout much of the estuary. At concentrations of 5 mg/l, a reasonable background value (see Fig. 2), approximately 25×10^7 gr of sediment would be suspended in the estuary. The storm event of February 1, 1976 increased this load by approximately a factor of three to 75×10^7 gr. This was an estuary-wide increase and persisted for nearly two days, the duration of the storm. It is against this response that the effects of dredge-induced resuspension should be evaluated.

b. Dredge-induced resuspension: In contrast to the large scale effects of storms, dredge-induced resuspension appears to be essentially a near field phenomenon. Although the field surveys (Figs. 3 and 4) show that concentrations in the area immediately adjacent to the dredge exceed background by more than a factor of 40, values tend to decrease rapidly with distance downstream. Surface concentrations decay most rapidly and appear to reach background within 200 m downstream of the dredge. Mid-depth and near-bottom values are persistently higher than surface values and approach background within approximately 700 m downstream of the dredge. Under those conditions the surface area impacted by the dredge resuspended plume equals less than 2.5% of the total area of the estuary.

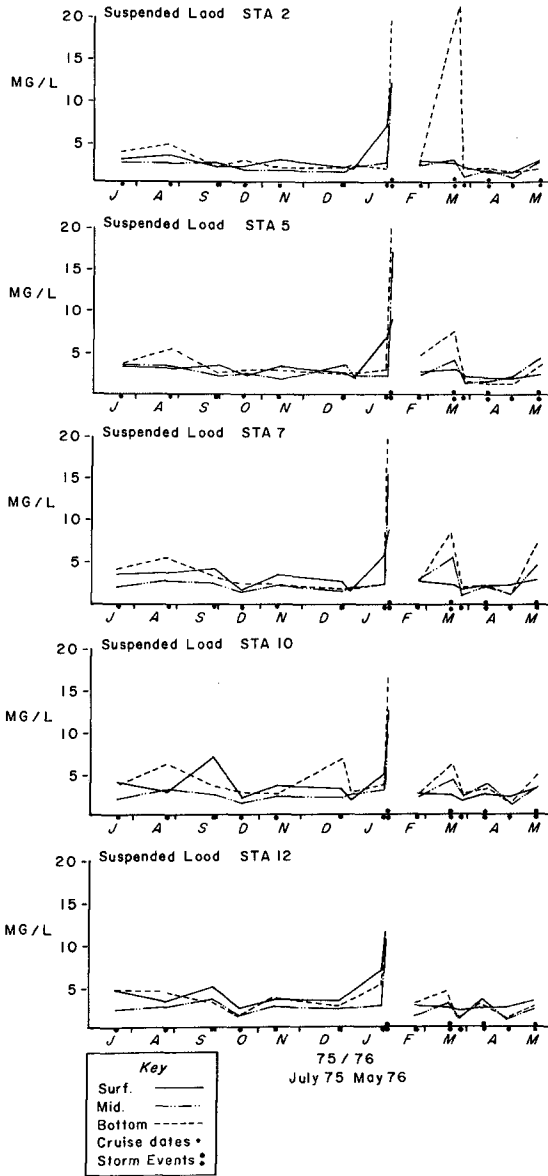


Fig. 2. Suspended Material Concentrations Thames River 1975-1976

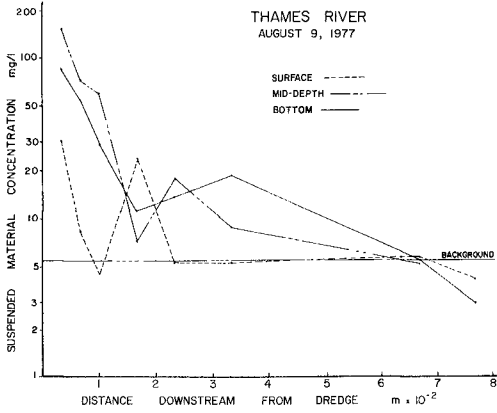


Fig. 3. Suspended material concentrations along the centerline of the plume downstream of the operating dredge, August 9, 1977. (from Bohlen, et al., 1979).

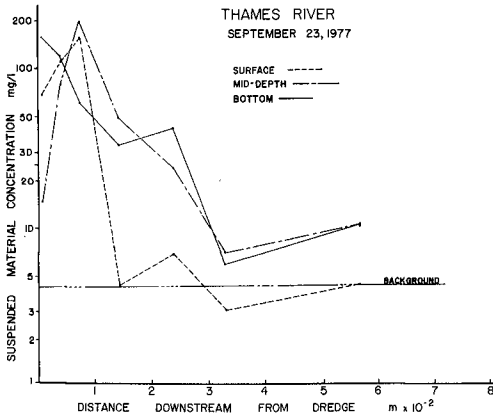


Fig. 4. Suspended material concentrations along the centerline of the plume downstream of the operating dredge, September 23, 1977. (from Bohlen et. al., 1979).

Estimates of the mass of sediment contained in the dredge-induced plume cannot be simply realized since the field measurements were confined to the longstream axis and provide no indication of the cross-stream distributions and concentration levels. Using the optical data to define the plume width, a "worst-case" estimate can be developed assuming that the suspended material concentrations are constant across each lateral section. Using the observed centerline values to define the concentrations at each section, this approach indicates that the plume contains approximately 6×10^7 gr of sediment. Comparison of this value with the above estimate of total suspended load indicates that the dredge has the potential to increase the mass of sediment suspended in the estuary by approximately 25%. In terms of transport, however, these re-suspended sediments must be considered to be of negligible import since they settle rapidly affecting an extremely small area.

Discussion - Dredge vs. Storm Induced Resuspension

The above observations suggest that the effect of dredging on the suspended material field within the Thames River is generally negligible relative to that produced by naturally occurring storm events. The mass of sediment introduced by the storm exceeds that suspended by the dredge by nearly an order of magnitude. In addition the storm affects an estuary-wide increase whereas the dredge impacts an area representing less than 2.5% of the total river. Dredge effects appear to be further reduced by the characteristic frequency of occurrence of storms as compared to dredging. Reviews of the local meteorological data indicate that storms having an intensity similar to that of the February and March 1976 events can be expected to occur 1 to 3 times each year. Dredging, on the other hand, typically recurs at a rate of once every ten years or so. This combination of light sediment load, small spatial extent and low frequency of occurrence effectively limits the impact of the dredge resuspended plume on the local sediment system.

These conclusions, however, cannot be presented without some qualification. In particular, it's important to remember that this analysis concerns only the suspended sediment transport system and the relative effects of dredging and storms on that system. Although this system will also affect the local biological community and the variety of geochemical cycles, conclusions regarding its response to storms and/or dredging should not be applied haphazardly to these latter systems. The processes governing the interactions between sediment resuspension and the local biological community and geochemistry are clearly complex and require additional work. The above comparison is only intended to provide some initial physical insights to complement this work.

Acknowledgements

This research has been supported by the U.S. Navy through Contract N00140-77-C-6536.

References

- Bohlen, W.F., 1978. Factors governing the distribution of dredge-resuspended sediments. Proc. 16th Coastal Eng. Conf., Amer. Soc. of Civ. Eng., Hamburg, Germany, 1978, 2001-2019.
- Bohlen, W.F., D.F. Cundy and J.M. Tramontano, 1979. Suspended material distributions in the wake of estuarine channel dredging operations. Estuarine and Coastal Marine Science, 9:699-711.
- Cundy, D.F. and W.F. Bohlen, 1979. A numerical simulation of the dispersion of sediments suspended by estuarine dredging operations. In: Estuarine and Wetland Processes: with Emphasis on Modeling. Plenum Press (in press).
- Wilson, R.E., 1979. A model for the estimation of the concentrations and spatial extent of suspended sediment plumes. Estuarine and Coastal Marine Science, 9:65-78.

SEDIMENTATION IN CHANNELS AND TRENCHES

E.W. Bijker*

1. Introduction

In this paper the siltation in approach channels and trenches due to cross currents and waves is discussed. It is in this respect not necessary that the current crosses the channel at a right angle. When the current crosses the channel obliquely simply a greater distance over which the water flows over the greater depth is introduced. Deviations in the flow pattern - see figure 1 - due to the channel are neglected. When the flow pattern is known, either from measurements in nature or in model this effect can easily be introduced. The influence of the waves is introduced through the introduction of an increased bed shear and subsequently higher diffusion coefficient (see Bijker, 1971, [3]).

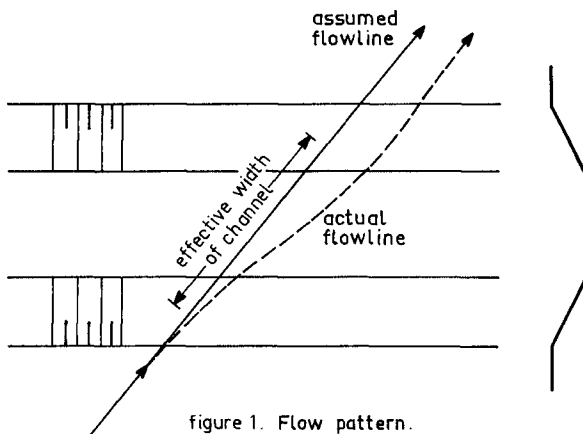


figure 1. Flow pattern.

Although computer programs are available to compute the siltation under the above described circumstances, an attempt will be made to come to a relatively simple method which enables a quick estimate of the siltation to be expected without the requirement of a big computer. This method could be especially usefull for the engineer in the field who has to make the first appraisal for the various solutions.

* Professor of Coastal Engineering, Delft University of Technology

2. Basic equations

For the water motion a logarithmic velocity profile and a first order linear wave theory are applied. The vertical distribution of the suspended sediment is described by:

$$w c + \epsilon dz/dz = 0, \quad (1)$$

with w = fall velocity of the sediment in still water, c = concentration at height z above the bed and ϵ = diffusion coefficient for the suspended material at height z . For ϵ the same value as for the diffusion coefficient for the momentum is used, which is acceptable for relative fine material ($D \leq 300 \mu\text{m}$). Applying the logarithmic velocity distribution and the linear shear stress distribution the following expression of ϵ is obtained.

$$\epsilon = \kappa v_* z(1-z/h), \quad (2)$$

in which v_* = the bed shear velocity, κ = the constant of Von Karman and h = the total water depth.

This expression of the diffusion coefficient gives the well known concentration gradient which is after Einstein also used by Bijker (1971, [3]). However, experiments by Coleman (1970, [4]) indicate that with reasonable accuracy a constant diffusion coefficient for the whole depth can be applied. Kerssens and Van Rijn (1979, [7]) use a constant value for the upper half of the depth and a logarithmic distribution for the lower half. Although this represents the available data certainly better, in this case nevertheless one constant value is assumed in order to keep the procedure as simple as possible. This gradient of ϵ determines the vertical sediment concentration. Since in this case the decrease of this vertical sediment concentration with the distance over the channel is, rather than the actual form, the main item, this inaccuracy is accepted. For the constant value of ϵ is assumed:

$$\epsilon = \kappa v_* h/2,5 = 0,16 v_* h = 0,16 \bar{v} h \sqrt{g/C}, \quad (3)$$

in which \bar{v} = the mean value of the uniform flow, g = acceleration of the earth gravity and C = the resistance coefficient after Chezy and equal to $18 \log(12h/r)$ with r as apparent bed roughness. With this value of ϵ the following expression for the vertical sediment concentration is obtained:

$$c = c_b \exp(-w z/\epsilon), \quad (4)$$

with c_b = concentration at the bed.
The average silt concentration is

$$\bar{c} = (c_b \epsilon/w h) [1 - \exp(-w h/\epsilon)] \quad (5)$$

With this it is implicitly assumed that the total suspended load is $S_s = \bar{c} h$. This assumption is checked against the strict computation $S_s = \int_0^h v c dz$. Although for current alone the errors are less

then 10%, it can be expected that for conditions with waves and currents the errors could be more. In that case the form of the decrease of the sediment load and therefore the mechanism of the siltation will, nevertheless, be the same. The actual values of the transport can be calculated then with the more strict formula, while for the decrease the method described in this paper is used. This will be demonstrated in the example with waves and currents. When the suspended load is related to the bed load, the concentration c_b at the bed is calculated from this bed load. Bijker (1971, [3]) found for this relation via the velocity distribution close to the bed:

$$c_b = S_b / 6,34 r \sqrt{\tau_c / \rho} = S_b C / 6,34 \bar{v} r \sqrt{g} \quad (6)$$

in which S_b = bed load, τ_c = bed shear and ρ = density of the water. As well the bed load as the concentration are expressed in volumes of deposited material with the normal porosity coefficient. The wave influence is taken into account through an increased bed shear as derived by Bijker originally in 1966 and 1967 ([1] and [2]). According to this derivation

$$v_{*cw} = v_{*c} \left[1 + \frac{1}{2} (\xi u / \bar{v})^2 \right] \quad (7)$$

in which v_{*cw} and v_{*c} are the bed shear velocities due to waves and current and current alone, \hat{u} = amplitude of the horizontal orbital velocity at the bed and

$$\xi = C \sqrt{f_w / 2g}, \quad (8)$$

with f_w = friction coefficient as derived by Jonsson (1966, [6]). (See Swart, 1974, [8], and Van de Graaff and Van Overeem, 1979 [5]). This friction factor can be written as:

$$f_w = \exp \left[-5,977 + 5,213 (a_o / r)^{-0,194} \right] \quad (9)$$

in which a_o = amplitude of horizontal orbital motion at the bed. This adjusted value of u_{*} is introduced in the formula for ϵ .

Since, as has been demonstrated by Van de Graaff and Van Overeem (1979, [5]), the transport formula as given by Bijker in 1971 [3] gives for the combination of waves and current better results than the adapted Ackers and White and Engelund and Hansen formulae, this formula is also used here. The bed load is then written according to the adjusted Kalinske-Frijlink formula as:

$$S_b = (B D \bar{v} \sqrt{g} / C) \exp \left[-0,27 \Delta D C^2 / \mu \bar{v}^2 \left(1 + \frac{1}{2} (\xi \hat{u}_o / \bar{v})^2 \right) \right] \quad (10)$$

in which B = coefficient ≈ 5 , D is the grainsize of the bed material, Δ = relative density of the bed material and μ = a ripple coefficient = $(C_{D90} / C)^{3/2}$, with C_{D90} = bed resistance coefficient for a flat bed consisting of grains with a diameter of D_{90} ; that is that grainsize which is exceeded by only 10% of the bed material.

3. Sedimentation

The sedimentation in the channel is determined by an equation of the type of eq. (1).

So the first thing to do is to study the behaviour of ε and dc/dz above the channel. Since c is a property of the water, the value of c will remain constant in the first instance. The vertical gradient of the sediment concentration will, however, immediately decrease by a factor h_1/h_2 , h_1 and h_2 being the depth upstream and in the channel. (See figures 2 and 3).

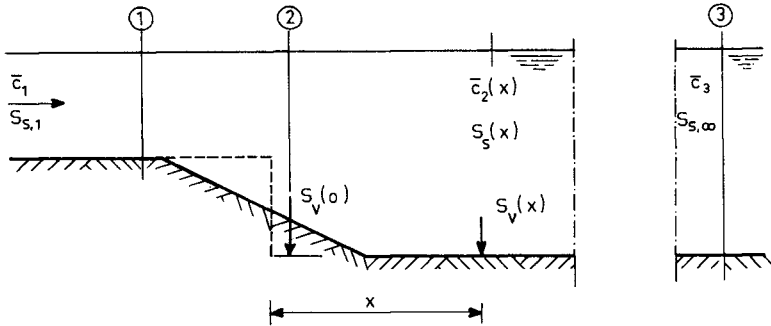


figure 2. Mechanisme of sedimentation.

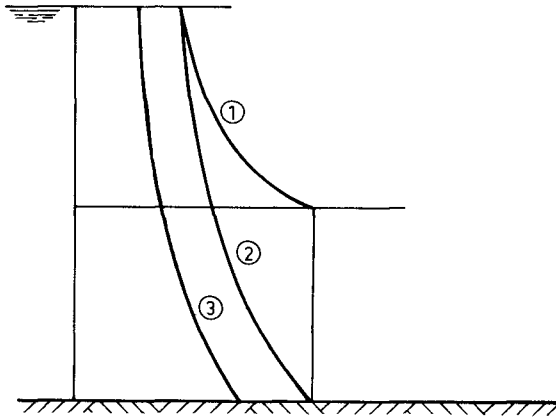


figure 3 Concentration verticals.

Since the actual sedimentation, or vertical transport is determined by the condition just above the bed this vertical transport reads then

$$S_v = w c_{b2} + \epsilon (dc/dz)_b, \quad (1)$$

in which the subscript b indicates the situation at the bed and ϵ is not yet determined. Due to the greater depth ϵ will eventually decrease. It is not known with certainty how fast this will happen. Since it is assumed that with normally occurring slopes of the channel banks the current will follow the bed, it is assumed that also ϵ will adapt immediately to the new situation. The value to be used above the channel will be then

$$\epsilon_2 = 0,16 v_{*2} h_2 = 0,16 \bar{v}_2 h_2 \sqrt{g/C_2} = 0,16 q \sqrt{g/C_2} \quad (11)$$

The vertical sediment concentration distribution at the most upstream side of the channel, before any sedimentation has taken place, is:

$$c = c_b \exp(-w h_1 z / \epsilon_1 h_2). \quad (12)$$

The vertical gradient is in this case:

$$(dc/dz) = -(h_1 w / h_2 \epsilon_1) c_b \exp(-w h_1 z / \epsilon_1 h_2). \quad (13)$$

The average sediment concentration is at that moment:

$$c_2 = (\epsilon_1 / w h_1) c_{b,1} \left[1 - \exp(-w h_1 / \epsilon_1) \right] \quad (5)$$

which is - as it should be - equal to the average sediment concentration just upstream of the channel. Since it is assumed that the value of the diffusion coefficient would adjust itself rather soon to that for the situation above the channel, the sedimentation - or vertical transport - at the most upstream side of the channel is:

$$\begin{aligned} S_v &= w c_{b,2} + \epsilon_2 (dc/dz)_b = \\ &= w c_{b,2} - w \frac{h_1 \epsilon_2}{h_2 \epsilon_1} c_{b,2} \exp(-w h_1 z (=0) / \epsilon_1 h_2) = \\ &= w c_{b,2} \left(1 - \frac{h_1 \epsilon_2}{h_2 \epsilon_1} \right) \end{aligned} \quad (14)$$

With $w h / \epsilon = h_{*}$, this equation reads

$$S_v = w c_{b,2} (1 - h_{*,1} / h_{*,2}) \quad (14)$$

The vertical transport S_v is expressed in m^2/s per unit of bed surface. The suspended load of the stream will decrease as result of the sedimentation until a new equilibrium is obtained.

This equilibrium is determined again by equation (1) which reads

$$w c_3 + \varepsilon_2 (dc/dz)_3 = 0 \quad (15)$$

with subsequently:

$$c_3 = c_{b,3} \exp(-w z/\varepsilon_2). \quad (16)$$

$$\bar{c}_3 = (c_{b,3} \varepsilon_2/w h_2) \left[1 - \exp(-w h_2/\varepsilon_2) \right] = (c_{b,3}/h_{x,2}) \left[1 - \exp(-h_{x,2}) \right] \quad (17)$$

$$(dc/dz)_{b,3} = -(w/\varepsilon_2) c_{b,3} \quad (18)$$

The vertical transport at that moment is

$$S_{v,3} = w c_{b,3} - \varepsilon_2 (w/\varepsilon_2) c_{b,3} = 0 \quad (19)$$

A positive value for S_v indicates a downward transport, that means sedimentation. The value of $c_{b,3}$ is for the moment unknown, but it is assumed that in the equilibrium situation it is again determined by the relationship of equation (6), and it will be written as

$$c_{b,3} = \alpha c_{b,2} = \alpha c_{b,1} \quad (20)$$

The equation of motion for the suspended load is

$$dS_s(x)/dx + S_v(x) = 0 \quad (21)$$

in which x = distance along the flow line from the upstream side of the channel.

For the solution of the continuity equation (21) two possibilities exist.

a). Assume that $S_s(x)$ decreases exponentially with x , so

$$S_s(x) = f (\exp(-\beta x)) \quad (22)$$

With the boundary conditions:

$$S_s(0) = S_{s,1} \quad (23)$$

$$S_s(\infty) = S_{s,3} \quad (24)$$

equation (22) can be written as

$$S_s(x) = (S_{s,1} - S_{s,3}) (\exp(-\beta x) - 1) + S_{s,1} \quad (25)$$

When this is substituted in the continuity equation (21) the following expression for β in S_s and S_v is obtained:

$$-\beta (S_{s,1} - S_{s,3}) \exp(-\beta x) + S_v(x) = 0 \quad (26)$$

$$-\beta (S_s(x) - S_{s,3}) + S_v(x) = 0 \quad (27)$$

$$\begin{aligned} \text{For } x = 0 & \quad S_v = S_v(0) \\ \text{For } x = \alpha & \quad S_v = 0 \end{aligned}$$

This results in the following expression for β .

$$\beta = S_v(0)/(S_{s,1} - S_{s,3}) \quad (28)$$

- b). Assume that the sedimentation, that is the vertical transport S_v , is linearly proportional to the ratio between the differences between the actual and equilibrium concentration and the original and equilibrium concentration.

Then the following equation will hold:

$$S_v(x) = S_v(0) \left[\frac{(\bar{c}(x) - \bar{c}_3)}{(\bar{c}_1 - \bar{c}_3)} \right] \quad (29)$$

And with $S_s = \bar{c} q$ this equation can be written as

$$S_v(x) = S_v(0) \left[\frac{(S_s(x) - S_{s,3})}{(S_{s,1} - S_{s,3})} \right] \quad (30)$$

Equation (30) is also obtained after substituting eq (28) in eq (27), so both approaches give the same result.

When $S_v(0)$, $c(x)$, \bar{c}_1 and \bar{c}_3 are expressed in the bed concentration the following expressions are obtained.

$$\begin{aligned} S_{v,0} &= w c_{b,1} (1 - h_{*,1}/h_{*,2}) \\ \bar{c}(x) &= (c_b(x)/h_{*,2}) \left[1 - \exp(-h_{*,2}) \right] \\ \bar{c}_1 &= (c_{b,1}/h_{*,1}) \left[1 - \exp(-h_{*,1}) \right] \\ \bar{c}_3 &= (c_{b,3}/h_{*,2}) \left[1 - \exp(-h_{*,2}) \right] \\ c_{b,3} &= \alpha c_{b,1} \end{aligned}$$

$$\begin{aligned} S_v(x) &= w c_{b,1} (1 - h_{*,1}/h_{*,2}) \frac{\bar{c}(x) - \bar{c}_3}{(c_{b,1}/h_{*,1})(1 - \exp(-h_{*,1})) - (\alpha c_{b,1}/h_{*,2})(1 - \exp(-h_{*,2}))} = \\ &= w (\bar{c}(x) - \bar{c}_3) \frac{h_{*,1}(h_{*,2} - h_{*,1})}{h_{*,2}(1 - \exp(-h_{*,1})) - \alpha h_{*,1}(1 - \exp(-h_{*,2}))} = E w (\bar{c}(x) - \bar{c}_3) \end{aligned} \quad (31)$$

Equation (27) can be also written as follows:

$$S_v(x) = \beta q (\bar{c}(x) - \bar{c}_3)$$

from which follows that $\beta = E w/q$, (32)
and the equation (25) for $S_3(x)$ reads than

$$(S_{s,1} - S_s(x))/(S_{s,1} - S_{s,3}) = 1 - \exp(-E w x/q) \quad (33)$$

Or also

$$(S_s(x) - S_{s,3})/(S_{s,1} - S_{s,3}) = \exp(-E w x/q) \quad (34)$$

These equations make it possible to compute in a quick and simple manner the sedimentation above the channel or trench.

4. Results

In this chapter two cases will be computed and the results will be compared by those computed with the program "Susleuf" of the Delft Hydraulics Laboratory, which is described by Kerssens, Prins and van Rijn [7].

For only current the following situation has been computed:

$$\begin{aligned} D_{50} &= 0.2 \cdot 10^{-3} \text{ m} & r &= 0.1 \text{ m} & w &= 2.5 \cdot 10^{-2} \text{ m/s} & D_{90} &= 0.3 \cdot 10^{-3} \text{ m} \\ h_1 &= 5 \text{ m} & \bar{u}_1 &= 1 \text{ m/s} & q &= 5 \text{ m}^2/\text{s} & h &= 10 \text{ m} & \bar{v}_2 &= 0.5 \text{ m/s} \\ C_1 &= 50 \text{ m}^{1/2}/\text{s} & C_{D90} &= 95 \text{ m}^{1/2}/\text{s} & \mu &= 0.38 \\ v_{*1} &= 6.3 \cdot 10^{-2} \text{ m/s} & \epsilon_1 &= 0.16 v_{*1} & h_1 &= 5 \cdot 10^{-2} \text{ m}^2/\text{s} & h_{*1} &= w h/\epsilon_1 = 2.5 \\ C_2 &= 55 \text{ m}^{1/2}/\text{s} & C_{D90} &= 101 \text{ m}^{1/2}/\text{s} & \mu &= 0.40 \\ v_{*2} &= 28 \cdot 10^{-2} \text{ m/s} & \epsilon_2 &= 0.16 v_{*2} & h_2 &= 4.5 \cdot 10^{-2} \text{ m}^2/\text{s} & h_{*2} &= 5.56 \end{aligned}$$

With $B = 5$;

$$\begin{aligned} S_{b,1} &= 3.486 \cdot 10^{-5} \text{ m}^2/\text{s} & \text{and } c_{b1} &= 0.88 \cdot 10^{-3} \\ S_{b,3} &= 0.192 \cdot 10^{-5} \text{ m}^2/\text{s} & \text{and } c_{b3} &= 0.106 \cdot 10^{-3} \\ \alpha &= 0.12 & E &= 1.59 \end{aligned}$$

For the Susleuf program the following distribution of the diffusion coefficient has been applied.

$$\begin{aligned} z/h < \frac{1}{2} & \epsilon_1 = v_*^4 z(1-z/h) \left[0.13 + 0.20(w/v_*)^{2.12} \right] \\ z/h \geq \frac{1}{2} & \epsilon_2 = v_*^4 h \left[0.13 + 0.20(w/v_*)^{2.12} \right] \end{aligned}$$

Although this expression for ϵ gives an illogical trend for ϵ from upstream of the channel to above the channel, the most important value of ϵ , namely ϵ_2 is in reasonable agreement with the ϵ applied in the method of this paper.

In the following tabel the values of $(S_{s,1} - S_s(x))/(S_{s,1} - S_{s,3})$ as follow from the Susleuf computation and this method are given.

Deposit of suspended material as fraction maximum possible deposit as function of distance from upstream edge of channel.

x (m)	Susleuf program	This method
25	.22	0.18
50	.37	.33
75	.47	.45
100	.55	.55
125	.62	.63
150	.67	.70
175	.71	.75

The correspondence is reasonable.

For the combination of waves and current the following conditions are applied.

$$D_{50} = 0.2 \cdot 10^{-3} \text{ m} \quad r = 0.05 \text{ m} \quad w = 2.5 \cdot 10^{-2} \text{ m/s} \quad D_{90} = 0.27 \cdot 10^{-3} \text{ m}$$

$$h_1 = 5 \text{ m} \quad \bar{v}_1 = 1 \text{ m/s} \quad q = 5 \text{ m}^2/\text{s} \quad h_2 = 10 \text{ m} \quad \bar{v}_2 = 0.5 \text{ m/s}$$

$$C_1 = 55.4 \text{ m}^{1/2}/\text{s} \quad C_{D90_1} = 96.2 \text{ m}^{1/2}/\text{s} \quad \mu = 0.44$$

$$C_2 = 60.8 \text{ m}^{1/2}/\text{s} \quad C_{D90_2} = 101 \text{ m}^{1/2}/\text{s} \quad \mu = 0.46$$

$$H = 1 \text{ m} \quad T = 6 \text{ s}$$

For the Susleuf program the following distribution for ϵ has been applied this time

$$z < h/2 \quad \epsilon = \kappa \bar{v}_* z(1-z/h)$$

$$z \geq h/2 \quad \epsilon = 0.25 \kappa \bar{v}_* h$$

This results in $\bar{\epsilon} = 0.0883 \bar{v}_* h$ which is about half the value which is suggested by the author. In order to be able to compare the results of this method with that of Susleuf here also this lower value of $\bar{\epsilon}$ will be applied. The various values are given upstream and above the channel.

upstream of the channel
depth 5 m

$$u_o = 0.568 \text{ m/s}$$

$$a_o = 0.542 \text{ m}$$

$$v_{*cw} = 0.093 \text{ m/s}$$

$$C_1 = 55.4 \text{ m}^{1/2}/\text{s}$$

$$C_{D90_1} = 96.2 \text{ m}^{1/2}/\text{s}$$

$$\mu_1 = 0.44$$

$$\bar{\epsilon}_1 = 0.0388 \text{ m}^2/\text{s}$$

above the channel
depth 10 m

$$u_o = 0.309 \text{ m/s}$$

$$a_o = 0.295 \text{ m}$$

$$v_{*cw} = 0.0557 \text{ m/s}$$

$$C_2 = 60.8 \text{ m}^{1/2}/\text{s}$$

$$C_{D90_2} = 101.1 \text{ m}^{1/2}/\text{s}$$

$$\mu_2 = 0.46$$

$$\bar{\epsilon}_2 = 0.0464 \text{ m}^2/\text{s}$$

$$\begin{aligned}
 h_{*1} &= 3.22 & h_{*2} &= 5.39 \\
 S_{b1} &= 4.49 \cdot 10^{-5} \text{ m}^2/\text{s} & S_{b2} &= 1.4 \cdot 10^{-5} \text{ m}^2/\text{s} \\
 c_{b1} &= 2.51 \cdot 10^{-3} & c_{b2} &= 1.71 \cdot 10^{-3} \\
 \alpha &= 0.78 \\
 E &= 2.33
 \end{aligned}$$

The suspended load is computed with the original procedure as suggested by Bijker in 1971 [3] and described also by Van de Graaff and Van Overeem [5].

The following values are then obtained

$$\begin{aligned}
 w/\kappa v_{*wc1} &= 6.72 \cdot 10^{-1} & w/\kappa v_{*wc2} &= 1.12 \\
 S/S_b &= 19 & S/S_b &= 7 \\
 S_{s,1} &= 8.53 \cdot 10^{-4} \text{ m}^2/\text{s} & S_{s,3} &= 0.98 \cdot 10^{-4} \text{ m}^2/\text{s} \\
 S_{s,1} - S_{s,3} &= 7.55 \cdot 10^{-4} \text{ m}^2/\text{s} \\
 S_{\text{tot}}(x) &= S_s(x) + S_{b,2}
 \end{aligned}$$

In order to calculate the transport in ton/ms, a porosity of 0.4 and a density of the dry material of 2.65 is assumed.

Deposit of material as fraction of maximum possible deposit as function of distance from upstream edge of channel.

This method			Susleuf		
$S_{\text{tot}}(x)$	$\frac{S_{\text{tot}}(x)}{S_{\text{tot},1}}$	Fraction of deposit	$S_{\text{tot}}(x)$	$\frac{S_{\text{tot}}(x)}{S_{\text{tot},1}}$	Fraction of deposit
in ton/m's					
$1.43 \cdot 10^{-3}$	1.00		$1.5 \cdot 10^{-3}$	1.00	
$1.13 \cdot 10^{-3}$.79	.21	$1.20 \cdot 10^{-3}$.75	.25
$0.93 \cdot 10^{-3}$.65	.35	$0.92 \cdot 10^{-3}$.58	.42
$.78 \cdot 10^{-3}$.55	.45	$0.72 \cdot 10^{-3}$.45	.55
$.65 \cdot 10^{-3}$.45	.55	$0.61 \cdot 10^{-3}$.38	.62
$.55 \cdot 10^{-3}$.38	.62	$0.53 \cdot 10^{-3}$.33	.67
$.48 \cdot 10^{-3}$.34	.66	$0.46 \cdot 10^{-3}$.29	.71
$.42 \cdot 10^{-3}$.29	.71	$0.41 \cdot 10^{-3}$.26	.74
$.36 \cdot 10^{-3}$.25	.75	$0.36 \cdot 10^{-3}$.23	.77

The agreement is again reasonable.

In the case the transport is calculated via $S = q \bar{c}$ higher values for the actual transport are obtained. This last approximation is apparently - as was expected - acceptable for the computation of the rate of sedimentation, but not for the actual transports.

Acknowledgement:

I like to thank the Delft Hydraulics Laboratory for the runs of the Susleuf program they made available for comparison with this method and Mr. J. van Overeem for the discussions on this subject.

- [1] Bijker, E.W., The increase of bed shear in a current due to wave motion. Proc. 10th C.E. Conf., Tokyo 1966, pp 746-765.
- [2] Bijker, E.W., Some considerations about scales for coastal models with movable bed. DHL publ. No 50.
- [3] Bijker, E.W., Longshore transport computations. Proc. A.S.C.E., Journal of Waterways, Harbours and Coastal Engineering Division WW4, Nov. 1971.
- [4] Coleman, N.L., Flume studies of the sediment transfer coefficient. Water Resources Research, vol. 6, nr. 3, June 1970.
- [5] Van de Graaff, J. and van Overeem, J., Evaluation of sediment transport formulae in coastal engineering practice. Coastal Engineering vol. 2, no 3, pp 1-32.
- [6] Jonsson, I.G., Wave boundary layers and friction factors. Proc. 10th C.E. Conf., Tokyo 1966, vol. 1, Ch. 10.
- [7] Kerssens, P.J.M. and van Rijn, L.V., Model for non-steady suspended sediment transport. 17th I.A.H.R. Congr., Baden-Baden 1977, also DHL publ. no. 191.
- [8] Swart, H.D., Offshore sediment transport and equilibrium beach profiles. DHL publ. no. 131, 1974.

CHAPTER 105

SEDIMENTATION IN DREDGED NAVIGATION CHANNELS

BY

Lars Mikkelsen *

Preben Mortensen *

Torben Sorensen **

1. INTRODUCTION

The feasibility of a harbour project, which involves dredging of an access channel, may to a large extent depend on the future maintenance dredging in the channel. It is therefore important to be able to calculate sedimentation in dredged channels with sufficient accuracy.

In 1974 and 1975 the Danish Hydraulic Institute (DHI) carried out a study of the most feasible access channel to Warri Port situated in the Western Niger Delta, Nigeria. Two alternative entrances were studied and in conclusion it was recommended to improve the existing access channel through Escravos Entrance

* Senior Hydraulic Engineer, M.Sc., Danish Hydraulic Institute, Copenhagen, Denmark.

** Director, Danish Hydraulic Institute, Copenhagen, Denmark.



Fig. 1 Location Map

as this solution would yield much smaller maintenance dredging quantities as compared to an access channel through Forcados Entrance, see Ref. /1/

In 1978 it was decided to improve the accuracy of the sedimentation estimates for a dredged channel through Forcados Entrance and therefore it was recommended by DHI to dredge test pits in the alignment of the channel and to carry out a pertinent monitoring programme.

The paper presents

- The test pit monitoring programme and results including a discussion of measurement techniques.
- calculation of sediment transport in combined currents and waves and comparison with the monitoring results.

- discussion of some important sedimentological aspects.

2. SUMMARY AND CONCLUSIONS

On the basis of the test pit monitoring and the measured current and wave parameters it has been possible to calibrate the sediment transport rates in combined waves and currents. The test pit results has been used to obtain a satisfactory expression for the sediment diffusion coefficient ϵ_s and hence the concentration profile.

Using the calibrated transport rates, the theoretical sedimentation model and the wave and current statistics it has been possible to calculate the expected annual sedimentation in the dredged channel. Further, it has been possible to predict the consequences of changes in the depth ratio D_1/D_2 and in the channel width and hence to produce an optimal design of the channel.

In conclusion the sedimentation model has proved itself to be a very useful tool for studies of expected sedimentation quantities, particularly if the transport rates can be calibrated through pertinent field studies.

3. TEST PIT LOCATION AND PLANNING OF MONITORING

A test pit was dredged outside Forcados Bar at an undisturbed depth of app. 7 m MSLW (Mean Spring Low Water), see location map. The aim of the test pit investigation was not to provide a direct estimate of the future annual maintenance dredging quantities. This would be unrealistic due to the following reasons:

- 1) The test pit experiment took place during a limited part of the year only.
- 2) The depth in the test pit was decreasing contrary to the maintained depth of the access channel.
- 3) Suspended sediments would settle from the test pit ends contrary to the settling in a continuous access channel.
- 4) A continuous channel could tend to "attract" the current in the alignment of the channel.

The aim of the test pit investigation was therefore to calibrate a sedimentation model and thereby be able to understand and control the effects mentioned under 1 through 3.

Based on experiences from channels under similar conditions it was estimated that the effect mentioned under 4 was of minor importance.

In conclusion it was decided to dredge a rectangular test pit with bottom width 200 m equivalent to the future access channel width and bottom length 400 m in order to eliminate the major part of the "artificial" infill from the ends of the pit (effect 3). The test pit volume was about 350.000 m^3

4. FIELD MEASUREMENTS

The test pit was dredged in April 1979 and a monitoring programme was carried out from May to September 1979. Below is briefly outlined the most important hydrographic parameters and the methods of test pit monitoring.

Hydrographic Parameters

Currents

Recording current meters and float trackings revealed current velocities of 10-30 cm/sec without any dominating direction at the location of the pit. Some deviation between the surface and bottom current directions could be observed.

Waves

The wave trains consisted of swell waves approaching from W-SW with typical periods between 10 sec. and 18 sec. superimposed by local wind waves with periods between 3 sec. and 8 sec.

The wave heights (spectrum derived significant wave height H_{mo}^{mo}) varied between 0.7 m and 2.2 m. About 70% of the time H_{mo} was between 0.8 m and 1.4 m.

Bottom Material

At the location of the test pit the seabed consisted of coarse silt with fine sand and minor portions of finer sediments could be found. A median grain size of 0.05 mm was characteristic.

Suspended Sediment Sampling

The suspended sediment sampling was carried out by using a tripod frame, see fig. 2.

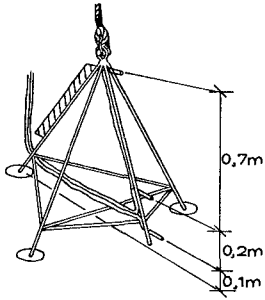


Fig. 2 Tripod Frame

The tripod was lowered to the undisturbed seabed and samples were sucked from fixed levels above the bottom layer, the lowest level being 0.1 m above bed. Results are presented in section 5.

MONITORING OF SEDIMENTATION

Methods

Preliminary calculations had revealed severe potential sedimentation, but even with high sedimentation rates it was foreseen to be difficult to detect the sedimentations with sufficient accuracy due to the swell waves. It was decided to measure the sedimentation by using two different methods:

- 1) Echo-sounding in lines crossing the test pit. The wave disturbance of the echo-sounding was eliminated by repeating the lines a sufficient number of times, see data processing below.
- 2) A pressure cell mounted on a sledge was pulled across the pit at the bottom. By averaging over a sufficient period of time the waves were eliminated. The position of the sledge was determined by underwater positioning equipment, see fig. 3.

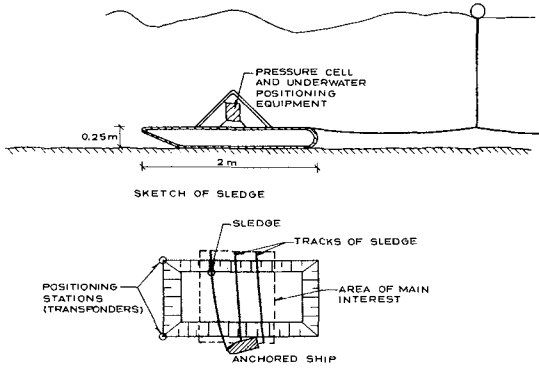


Fig. 3 Pressure Cell Method

DATA PROCESSINGEcho-soundings

The wave disturbed depth soundings of the echosounders (200 khz and 30 khz) were smoothened out for the individual sounding lines, see fig. 4. The repetitions of the same line were plotted to the same scale and an average of the cross section was elaborated, see fig. 5.

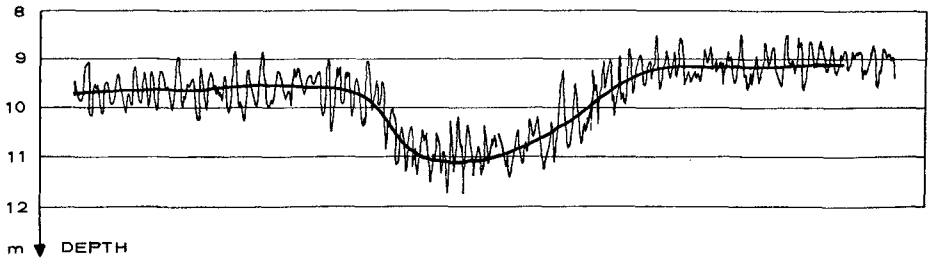


Fig. 4 Echogramme

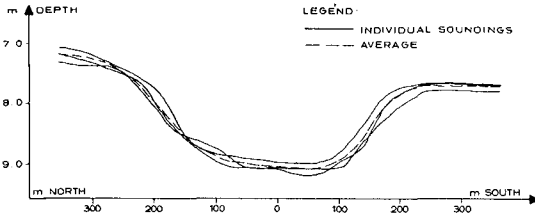


Fig. 5 Characteristic Profiles.

It is seen in fig. 5 that the deviations of the individual soundings from the average is in the order of 10 cm. The pitch and roll of the ship had some effects at the slope of the pit. However, performing echosounding during relatively calm periods it was concluded that repetition of each sounding line three times yielded satisfactory results.

Since the middle of the pit was flat and the velocity of the waves large compared to the speed of the survey vessel, this method was in principle the same as the averaging of the pressure cell at a specific position, see below.

Pressure_Cell_Method

In fig. 6 the cross section obtained from the average of the three cross sections shown in fig. 5 is compared to the results of pressure cell soundings in a number of check-points.

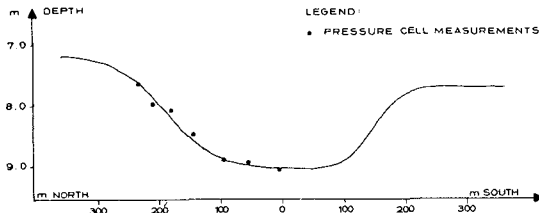


Fig. 6 Comparison of Sounding Methods

It is seen that the differences are small, averagely in the order of 5 cm.

The points were obtained by averaging over 30 seconds which was an adequate timelength, but the method as such turned out to be fairly complicated and time consuming.

Sedimentation_Rates

The soundings of the pit took place with app. 3 weeks interval. The cross section of the middle of the pit is presented

in fig. 7.

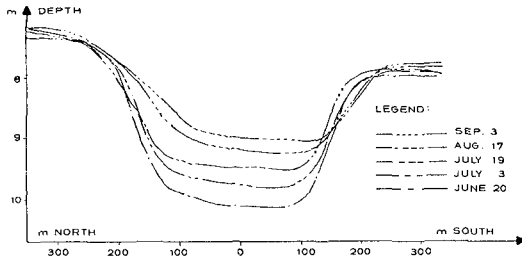


Fig. 7 Sedimentation in the middle cross-section of test pit.

The sedimentation was fairly evenly distributed over the width of the pit indicating slow settling of fine suspended sediments.

During the first period a sedimentation rate of app. 1.7 cm/day was observed, while later on a rate of 1.2 cm/day appeared. Using the sedimentation model this decrease was explained by the depth reduction in the pit.

Also longitudinal profiles of the pit showed that the sedimentation was fairly evenly distributed, see Fig. 8

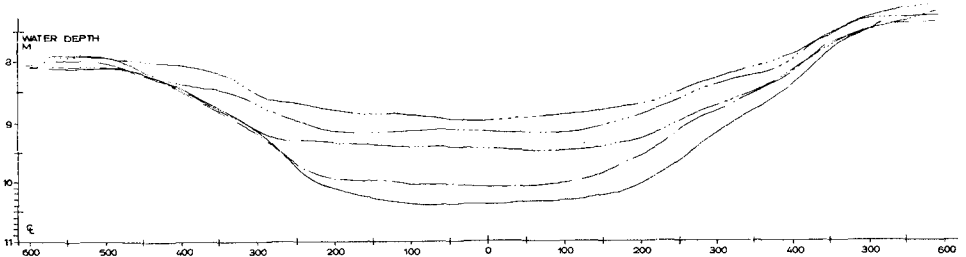


Fig. 8 Longitudinal test pit profile.

Fig. 9 shows the sedimentation rate between two soundings. The rates are seen to be strightly higher along sides of the pit than in the centerline of the pit.

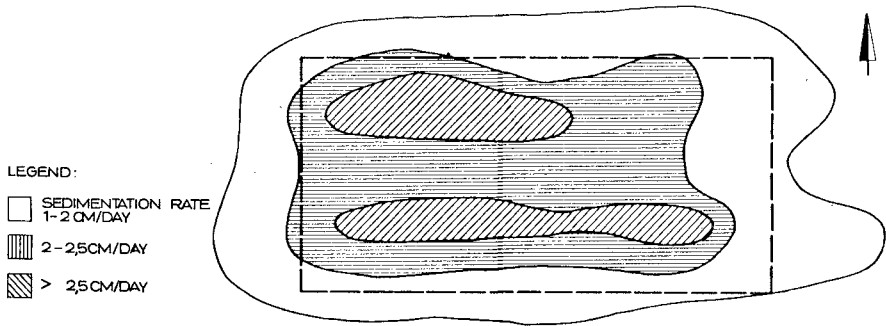


Fig. 9 Sedimentation between two soundings

5. SEDIMENTATION MODEL

In Ref /1/ it was shown that the sedimentation in a dredged channel, q_r , originating from settling of suspended sediments could be calculated as follows

$$q_r = \left\{ q_{10} \left(1 - e^{-\frac{w}{\epsilon} \frac{w}{v} \frac{D_1}{D_2} \frac{B}{\cos \alpha}} \right) - q_{20} \left(1 - e^{-\frac{w}{\epsilon} \frac{w}{v} \frac{B}{\cos \alpha}} \right) \right\} \cos \alpha$$

- where:
- q_{10} = transport of suspended sediments, equilibrium conditions at depth D_1
 - q_{20} = transport of suspended sediments, equilibrium conditions at depth D_2
 - w = settling velocity of suspended material
 - ϵ = eddy viscosity
 - v = current velocity
 - B = channel (test pit) width at the middle of the slope
 - α = angle between the direction of the current and normal to the test pit alignment
 - D_1 = undisturbed depth
 - D_2 = channel (test pit) depth

The calculation of the equilibrium transports q_{10} and q_{20} of suspended sediments in combined currents and waves has mainly been based on parameters calculated from field data. Further, the measured sedimentation in the test pit has offered a possibility to determine the unknown sediment diffusion coefficient ϵ_s near the bottom. In the following some of the basic parameters are discussed.

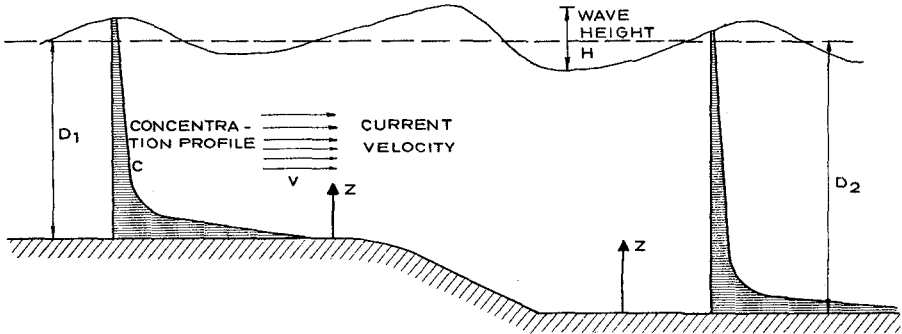


Fig. 10 Parameters

Wave Parameters

The thickness δ of the wave boundary layer was calculated by formulae given in /2/. In the calculation it was assumed that the wave amplitude a and the horizontal particle velocity U_w could be determined by sinusoidal wave theory.

Current Velocity Profile

The description of the current velocity profile at the bed is essential as the concentration of suspended sediment near the bed increases enormously.

The friction velocity $U_f = \sqrt{\frac{\tau}{\rho}}$ (where τ is the shear stress and ρ the density of water) in combined currents and waves can be determined by iteration in the following way:

1. The instantaneous particle velocity U_0 just above the wave boundary layer is determined by adding the current velocity U_c and the wave particle velocity U_w vectorially
2. The instantaneous shear stress is found by using U_0 and Johnsons wave friction factor f (/2/) calculated from:

$$\frac{1}{4\sqrt{f}} + \log \frac{1}{4\sqrt{f}} = -0.08 + \log \frac{A}{k}$$

where k is the bed roughness. The amplitude A may be taken as one half of the maximum excursion of a particle in the combined currents and waves.

3. The instantaneous shear stress projected in the current direction is integrated over a wave period yielding an expression for U_f .
4. The current velocity profile $U = U(z)$ near the bottom is then determined by

$$U_f^2 = \epsilon \frac{\partial U}{\partial z}$$

where ϵ is the total turbulent eddy viscosity in the current direction and z the distance above the bottom. The eddy viscosity for waves has been determined from /3/.

5. Finally current velocity U_0 just above the wave boundary layer is used in 1. for the determination of U_f and the "circle" is closed.

Above the wave boundary layer the current velocity profile has been assumed to be logarithmic.

Suspended Sediment Concentration Profile

Bottom Concentration

The bottom concentration has been assumed to be a function of the dimensionless shear stress (Shield's Parameter):

$$\theta = \frac{1}{2} f \frac{U_0^2}{(S-1)gd}$$

where U_0 is the instantaneous particle velocity just above the wave boundary layer, f the friction factor, S the relative density, g acceleration of gravity and d the grain diameter. By using formulae in /4/ and integrating over a wave period the average bottom concentration were obtained.

Concentration at the bed (wave boundary layer)

The time-averaged concentration C of suspended sediment a distance z above the bed was determined by

$$\epsilon_s \frac{\partial C}{\partial z} + WC = 0$$

W being the settling velocity of the grains and ϵ_s the sediment diffusion coefficient.

Laboratory experiments have indicated that for specific conditions ϵ_s is constant near the bed. However for the present study conditions none of the experiments were pertinent and instead another approach was needed.

Since no ripples were present it was natural to assume that ϵ_s at the bed basically could be expressed as a product of a characteristic length, a, characteristic velocity, U_f , i.e.:

$$\epsilon_s = n_1 (aU_f)^{n_2}$$

n_1 and n_2 being constants, n_1 nondimensionless.

n_1 and n_2 were then determined from the results of the test pit monitoring as they should satisfy the following conditions:

1. Integration of the sedimentation with current and wave statistics should yield measured sedimentation.
2. The calculated sediment concentration profiles should correspond with the measured profiles.

n_1 has been calculated to be $2.4 \times 10^{-4} \text{ (m}^2/\text{s)}^{0.45}$, n_2 to be 0.55

Concentration above the wave boundary layer

Above the wave boundary layer the sediment diffusion coefficient has been assumed to be equivalent to the momentum exchange coefficient

$$\epsilon_s = 0.4 U_{fcw} z \left(1 - \frac{z}{D}\right)$$

U_{fcw} being the time-integrated "friction velocity" without projection in the current direction.

6. DISCUSSION

Suspended Sediment

Fig.11 shows the suspended sediment concentration as function of wave height and current velocity as well as the theoretical concentration lines. A large scatter is observed but it can be concluded that

- The current has no significant effect on the amount of sediment in suspension.

The amount of sediment in suspension increases with increasing wave height (determining n_2 , discussed above).

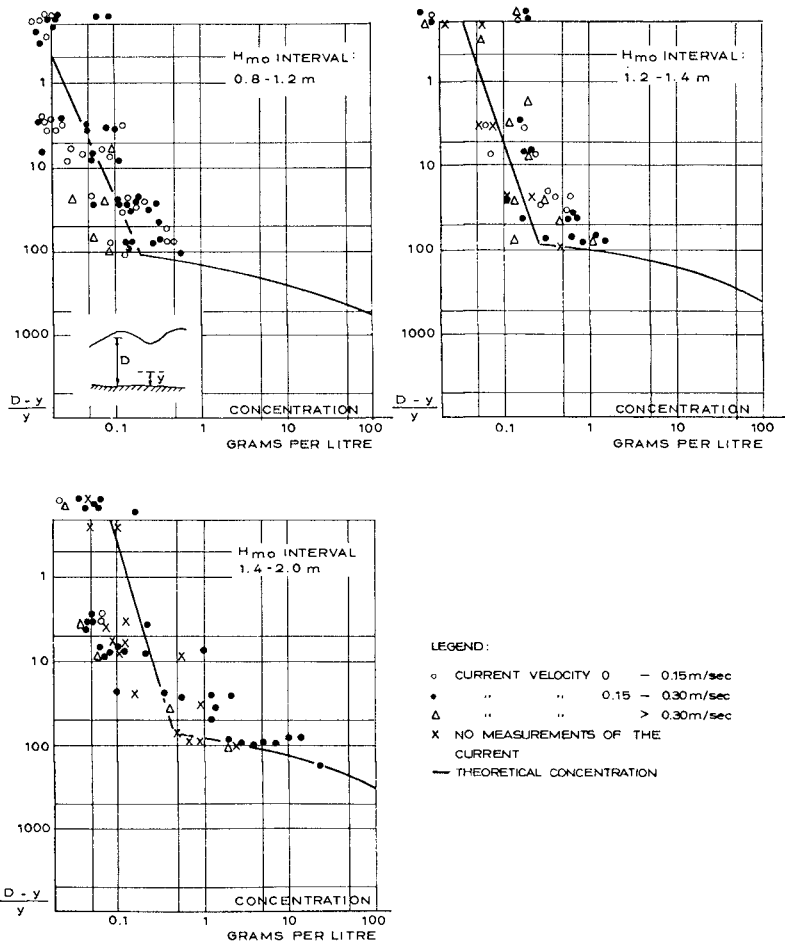


Fig. 11 Suspended Sediment

On the basis of the information that

the field measurements revealed that fairly large quantities of sand was settling in the pit and practically no sand in suspension was found above level 0.1 m above the bed and the concentrations of suspended sediment above this level were too small to explain the sedimentation -

it was concluded that very large concentration gradients exist at the bed in the wave boundary layer (5-10 cm thickness) and that it is essential to have a description of the suspension within and above the boundary layer.

Fig. 12 shows theoretical concentration profiles. The extreme concentration gradient at the boundary layer clearly proves the importance of the waves as the determining parameter.

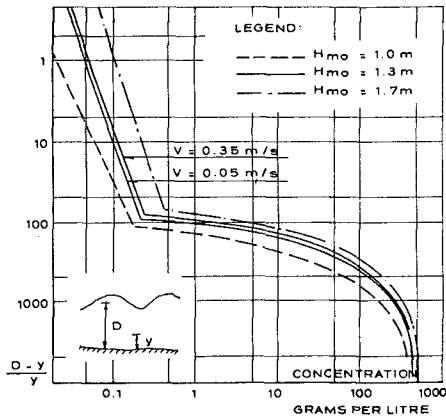


Fig. 12 Theoretical concentration lines

Sedimentation in the Test Pit

The rates of sedimentation as function of wave and current parameters calculated from the sedimentation model is shown in Fig. 13 (only one current direction shown).

The sedimentation model yielded that the current was hampered by the waves at the bed mostly when current and wave particle motion was parallel. Hence the sedimentation in the pit was

significantly largest when the current was perpendicular to the alignment of the pit and the wave direction parallel to it.

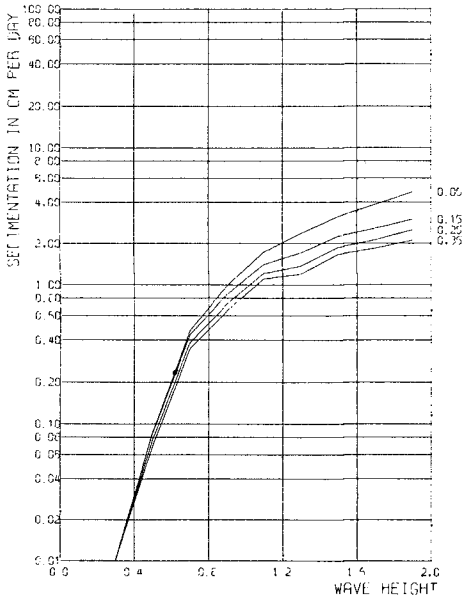


Fig. 13 Sedimentation Rates

Using the sedimentation model the decrease of the sedimentation rate in the pit in the monitoring period was very satisfactorily explained as caused mainly by the depth reduction of the pit and not because of changes of wave and current climate.

7. ACKNOWLEDGEMENT

The test pit investigations has been carried out on the demand of the Nigerian Ports Authority, whom we thank for the opportunity of working with a very interesting programme.

8. REFERENCES

- /1/ Mayor-Mora, Mortensen and Fredsøe, CEC 15, Hawaii, 1976
- /2/ J.G.Johnson and H.A.Carlsen. Experimental and Theoretical Investigation in an Oscillatory (Rough) Turbulent Boundary Layer. J. Hydr. Res, Vol 14, No. 1, 1976
- /3/ H. Lundgren. Turbulent Currents in the Presence of Waves, CEC, Chapter 33, 1972.
- /4/ F. Engelund and J. Fredsoe. A Sediment Transport Model for Straight Alluvial Channels. Nordic Hydrology 7, 1976.

CHAPTER 106

SOME ASPECTS OF COASTAL ENGINEERING RESEARCH WORKS IN CHINA

by

Professor Yen Kai

China has a long coastline. Only for the continental part of China, the length of coastline amounts to 18,000 km and, when including the coastline of more than 6,400 islands, an overall length of more than 32,000 km may be counted. As far as the geographical features are concerned, China is characterized by the prevalence of plateaux in the west, such as plateaux of Tibet and Sinkiang regions and plateaux of Yunnan and Kweichow provinces. There are nearly a hundred rivers, the most prominent of which are: the Yangtze River, the Yellow River, the Pearl River etc., flowing from west to east into the Pacific, and carrying about 2,000 million tons of sediment each year to the sea. As a result, silty coasts prevail in the vicinity of estuaries while sandy coasts emerge from a distance away. Generally speaking, the depth of coastal waters is comparatively small, especially along the silty coasts, where the beach profile presents a very gentle slope, varying from 1/50 to 1/500, and in some extreme cases even to 1/2000. Hence the maintenance of water depth in coastal harbours and estuaries has become one of salient problems of coastal engineering in our country. A brief description of our research on the sedimentation of harbours along silty and sandy coasts as well as rivermouth regulation, wave protection etc. is given as follows:

President, Chinese Society of Ocean Engineering, Nanking, China
President, East China College of Hydraulic Engineering, Nanking, China
Director, Nanking Hydraulic Research Institute, Nanking, China

(A) Research on siltation of harbours on silty coasts

To this the New Port of Tianjing may be taken as a typical example. This harbour was constructed on a mud flat, the material composing the beach is very fine, with mean particle diameter of 0.005 mm, and the beach slope is only 1/1000 to 1/2000. Heavy siltation took place in the water area of the harbour due to the combined action of waves, tidal currents and river discharge. Therefore, the study of reduction of harbour siltation becomes an urgent task. The key to solving such a problem lies in gaining a clear idea of the cause and process of siltation. For this reason we must get an insight into the physico-chemical properties of the sediment deposited in the harbour, have a thorough understanding of the behavior of sediment movement under the action of waves and currents, and investigate the inflow process of the sediment and estimate its rate of transport on the basis of the analysis of field measurements so as to devise the siltation reduction schemes. According to the requirements mentioned above systematic experimental studies of the sediment deposits in the port were performed and then siltation reduction schemes developed on the basis of the comprehensive analysis of field observation data and scale model studies as well. These projects have been carried out in succession over the past decade. At present the water depth in the navigation channel has been increased to 9.0 m below mean L.W., and is safe for vessels of 15,000 tons to enter the port at any time, while general cargo carriers of 40,000 tons can enter at high water.

(B) Research on siltation of harbours on sandy coasts

Along sandy coasts runnels are generally formed on the beaches due to the breaking of waves, and littoral transport of sediment comes into being. Natural coasts are in a state of relative equilibrium when a material balance is reached after a long-term interaction between the dynamic forces of the sea and the coasts. The construction of port results in disturbing the original state of equilibrium and, consequently siltation takes place. Experiments with scale models were conducted with several

sandy coast harbours, indicating that the locations and shapes of runnels were basically similar to those in nature. Despite difference in harbour layouts, such as the use of detached breakwaters, jetties, or even open-type structures, the littoral drifts were more or less intercepted and deposition on the updrift side would occur. The sediment accumulation gradually extends seawards, leading to the formation of a new coastline. It is the depositional behavior of the sediments and the rate of siltation as well as the measures to reduce siltation that are stressed in our present studies.

(C) Research on estuary regulation

Along the Chinese coast about 100 rivers empty into the sea. All the chief rivers, such as the Yangtze River, the Pearl River, the Chientang River, the Liao River etc., are navigable and highly important to the development of our national economy and the realization of four modernizations. A brief description of the regulation of some main estuaries is given as follows:

(1) Yangtze River Mouth

The Yangtze, more than 6,300 km long, is the first largest river in China. The Yangtze River Mouth, serving as a vital passage for the foreign trade of six provinces and the gateway to the biggest port of China, the Shanghai port, is of great concern to the development of our national economy. The Estuary is bifurcated into the North Branch and the South Branch. The South Branch is again bifurcated into the North Pass and the South Pass, and the latter in turn is divided into the North Channel and the South Channel. At present the South Channel is the main entrance channel. Because of the high river discharges and strong tidal currents, drastic channel changes take place, which has become a hindrance to navigation. For the purpose of improvement, large quantities of field observation data have been collected since 1958. Based on the analysis of the data, a relatively comprehensive knowledge of the characteristics of the channel process has been gained.

Diversified as the phenomena are, they can be classified as two problems. One is the susceptibility of the channels of the south branch to changes, and the other is the difficulties of maintaining adequate depths at the entrances of the navigation channels due to severe siltation. Now a tidal model with a horizontal scale of 1:1600 is available, its overall length is some 140 m and the maximum width is 34 m. A comprehensive experimental study is being performed for the planning of regulation works. The regulation works will be carried out in stages in combination with farmland reclamation.

(2) Chientang River Mouth

The Chientang River Mouth is famous for its strong tide. Low river discharge, strong tidal current and high sediment transport from the sea are the contributing factors in the formation of a huge sandbank inside the entrance. Owing to the fact that the river there is very wide and shallow, along with strong tidal currents and roaring bores, the main channel swings frequently between the two banks, and severe scour takes place once a new channel is formed. In conformity with these natural features our principle of regulation is such that at first we confine the tidal flow by reclaiming the foreshore of the river mouth, so as to reduce the inflow of water and sediment during the flood tide. It is hoped that by so doing the main channel will be stabilized and sandbank lowered. The final program consists of building tidal gates at the mouth of the river (in the vicinity of Jianshanhuang) to control the river discharge and tidal flow. A series of theoretical analysis and model studies have been performed for the above-mentioned programs. In the meantime, reclamation of the foreshores has been carried out in stages. Up to now 50,000 hectares of land has been reclaimed, and the river mouth has got its course initially stabilized.

(D) Research on wave protection works

Along the Chinese coast water depths and wave heights are comparatively small and most of the breakwaters are of rubble-mound type. Apart from model tests of rubble type breakwaters,

large numbers of experiments have been conducted to investigate the stability of artificial armor units such as tetrapod blocks, Akmon blocks, tetrapod hollow blocks, I-blocks, wing blocks, frog blocks etc., as well as breakwaters armoured with the artificial units mentioned above. Some of the above types have already been adopted in engineering practice. In addition, wall type breakwaters of caisson and concrete block construction are also in use at many harbours. Recently not a few experimental studies have been performed with a view to further improving the stability of the breakwater, reducing its cross section and saving its engineering costs. For instance, owing to the adoption of a sloping breast wall, we got chamfered upright breakwater which, as compared with the conventional wall type breakwater, bears a low horizontal wave pressure at high water and, what is more, the vertical wave pressure is increased, thus resulting in much improvement in the stability of the breakwater. This kind of breakwater is already in use in Tsingtao, Proving successful in withstanding the attack of severe waves. Recently the construction of deep water harbours has given a stimulus to the study of floating breakwaters.

The problem of the effect of typhoon waves on breakwaters and the damage resulting therefrom has aroused broad interest of all the coastal engineering circles both at home and abroad since the attack of Typhoon No.3 on the Gulf of Pohai with associated heavy damage in 1972. Special technical discussions were held and, later, special studies made on the selection of the frequency of occurrence of design waves. Now a method, which conforms to the particulars of China, has been developed of selecting wave height and wave period corresponding to a certain frequency.

In the field of theoretical investigation on waves, methods which conform to China's particulars, are developed for sea wave prediction, calculation of wind wave elements and so on. Our research work also includes some basic problems such as loss of wave energy due to turbulence and the like.

Furthermore, in the aspect of coast protection and seawalls, systematic studies of the height of wave run-up on sloping,

embankments have been conducted by laboratory tests along with analysis of field data. The results of investigation are already used in the design of seawalls.

Above is only a brief account of our research works on coastal engineering. As China has a long coastline, many problems remain to be solved. Despite all the above efforts we still lag behind what the development of our national economy demands of us. Now, it is for the first time that we, the Chinese delegation, take part in the activities of the International Conference on Coastal Engineering. We come here chiefly for the purpose of learning the advanced experiences from our friends, as well as carrying on academic exchanges, which, we think, would further promote the friendship and mutual understanding among us.



Offshore loading facilities at Hay Point, Queensland

PART III

COASTAL STRUCTURES AND RELATED PROBLEMS

Green Island on the Great Barrier Reef



SIMULTANEOUS WAVE AND CURRENT FORCES ON A PIPELINE

David A. Knoll, M.S., M.A.S.C.E.
Shell Oil Company
New Orleans, LA 70160

and

John B. Herbich, Ph.D., P.E., M.A.S.C.E.
Professor and Head, Ocean Engineering Program
Texas A&M University
College Station, TX 77843

INTRODUCTION

The hydrodynamic loads on an offshore pipeline resting on the ocean bottom are a function of parameters associated with waves and currents acting near the pipeline. There have been many studies conducted to develop the criteria needed to estimate the hydrodynamic loads imposed by waves and currents. Many of these studies have investigated the effect of these phenomena individually, but to date only limited research has been directed towards evaluating the combined effect. In general, the investigations of the interaction of waves and currents and their effect on the fluid force have been directed toward vertical piles^{1,2,3,4,5} and structures in a random wave field with a current present;^{6,7,8,9} however, the fluid force of waves in the presence of currents on pipelines has not been directly addressed.

The purpose of this research was to investigate the interaction of waves and currents and its relationship to the forces on submerged pipelines. A model pipeline in a wave-flume was used to obtain experimental values which were compared to values predicted by the Morison equation in conjunction with the superposition of the waves and a current.

The Morison equation¹⁰ was used to evaluate the forces on a horizontal cylinder resting on the bottom. The two major input parameters required by this equation are (1) the water particle kinematics of velocity and acceleration; and (2) the coefficients of drag and inertia. The testing program investigated the drag forces developed by the combined waves and a current. The inertia forces were assumed small when compared to the drag forces since a relatively small diameter cylinder was used in the experiments, thus the accelerations were small.

The coefficient of drag was obtained directly by simultaneous measurements of the water particle kinematics and the fluid force on the cylinder. The horizontal velocity, predicted by Airy and Stokes third order wave theories in still water, was combined with a current by the algebraic addition of their respective horizontal velocity fields at a specific elevation. These velocities were compared directly to experimentally-determined values. Measured forces were then compared

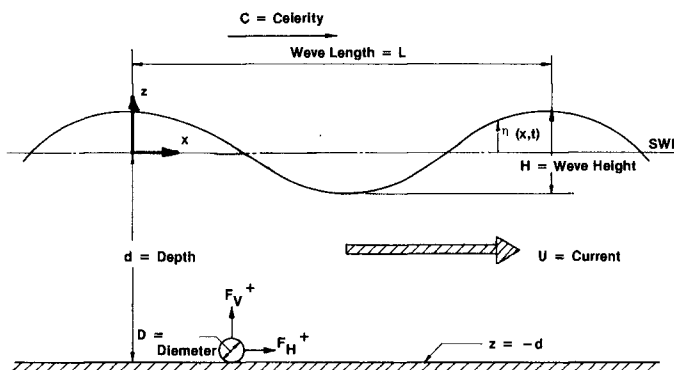
to the forces obtained by the Morison equation, using the coefficients determined in this research and the kinematics of the modified Airy and Stokes third-order wave theories. The error associated with the algebraic addition assumption was investigated.

Many wave and current orientations are possible in the field, but only the case of a wave propagating in the direction of the current was investigated. It is felt that this orientation represents the most severe conditions that will be experienced in the field. Further investigations will be needed to verify this assumption. In order to develop the basic knowledge needed to understand the error associated with the superposition-principle assumption, the fundamental problem of mono-chromatic waves and currents must be evaluated before other effects such as random waves can be attempted.

The primary purpose of this research was not to develop explicit prototype design criteria, but to provide the design engineer with an insight into the parameters governing fluid force in combined wave and current conditions. The parameters for fluid force are affected by the interaction of waves and currents and the variation of these parameters are presented.

DATA ANALYSIS

The definition sketch of the idealized two-dimensional wave-current problem for offshore pipelines is given in Fig. 1. This



DEFINITION SKETCH OF THE PIPELINE PROBLEM

FIGURE 1

configuration may represent a pipeline resting on the ocean bottom. The cylinder has both horizontal and vertical forces acting on it due to the passing wave and current. Only the horizontal drag force is investigated in this research.

The Morison equation considers the total horizontal force (f_H) as the sum of the horizontal drag force (f_D) and the horizontal inertial force (f_I)(all forces expressed per unit length of cylinder):

$$f_H = f_D + f_I \dots \dots \dots (1)$$

The drag force is a function of both a drag coefficient (C_D) and the horizontal component of the water particle velocity if the structure were absent (u), or:

$$f_D = \frac{C_D}{2} \rho D u |u| \dots \dots \dots (2)$$

where D = diameter of cylinder
 ρ = mass density of the fluid

The inertia force is a function of the inertial coefficient (C_I) and the horizontal particle acceleration (\dot{u}), or:

$$f_I = C_I \frac{\rho \pi D^2}{4} \dot{u} \dots \dots \dots (3)$$

Two of the major input parameters required by the Morison equation are the coefficients of drag and inertia. These coefficients must be determined experimentally. This is accomplished by measurements or theoretical predictions of the horizontal water particle kinematics in conjunction with fluid-force measurements. The coefficient of drag can be determined when the horizontal acceleration equals zero by the following equation:

$$C_D = \frac{2f_D}{\rho D u |u|} \dots \dots \dots (4)$$

when $f_I = 0$.

The coefficient of drag is generally presented as functions of two dimensionless parameters. The first parameter is the Reynolds number (N_{RE}). The Reynolds number indicates the dimensionless ratio of the inertial forces to the viscous forces in fluid motion, or:

$$N_{RE} = \frac{Du}{\nu} \dots \dots \dots (5)$$

where D = characteristic length (diameter)
 u = horizontal component of the particle velocity if the structure were absent at the time of interest
 ν = kinematic viscosity

The second parameter, developed by Keulegan and Carpenter, is related to the coefficients of drag and inertia. This dimensionless parameter is also known as the "period parameter" and it relates the maximum amplitude of the oscillating particle velocity, including both wave and current (u_{max}), the period of the oscillatory motion (T) to the diameter of the cylinder (D):

$$N_{KC} = \frac{u_{max}T}{D} \dots \dots \dots (6)$$

This parameter has been found to be related to the coefficients of drag and inertia for a very wide range of data.

The coefficient of drag determined experimentally in this research is presented as functions of these parameters.

Two other major input parameters required by the Morison equation are the particle kinematics of velocity and acceleration.

For a pipeline located near the ocean bottom, the water particle orbits are flattened (parallel to the bottom) for waves where the wave lengths are large compared to the water depth. The orbital motion changes to a horizontally oscillating flow when the water depth is small compared to the wave length; therefore, in this condition the variation of velocity over the height of the pipe is insignificant. This fact allows the velocity at the mid-point of the cylinder to represent the velocity used in the calculation of the fluid force by the Morison equation.

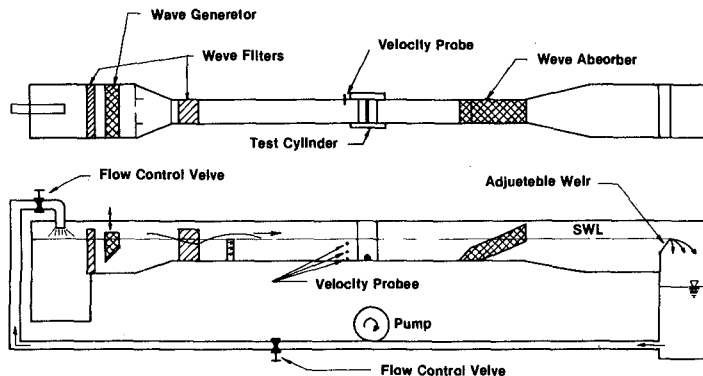
Airy and Stokes third-order wave theories are used in conjunction with the current to predict the combined flow field. In this case the parameters of wave height (H) and period (T) are considered to be the properties of a wave progressing in still water. These parameters are used with the water depth (d) to predict the velocities under a wave if no current were present. These resulting wave velocities are combined algebraically with the current velocity profile to predict the combined velocity profile. The equations and methods to determine the horizontal wave particle velocities predicted by Stokes third-order wave theory were those presented by Skjelbreaia¹¹.

The effect of the viscous boundary layer of the wave was neglected in the calculation of the horizontal velocity near the bottom. Since the actual current velocity profile was used for superposition, the boundary layer due to the current was taken into account. Therefore, any error in the boundary layer was due to neglecting the boundary layer in velocity prediction of the wave theories.

The forces on submerged pipelines are related directly to the velocity field near the structure. Accurate prediction of the horizontal velocity fields is essential for the proper prediction of the forces on submerged pipelines. The error associated with the prediction of the combined horizontal velocity field is directly related to the error in the calculation of the horizontal force of a submerged pipeline.

EXPERIMENTAL METHODS AND EQUIPMENT

The experimental study was conducted in a two-dimensional wave-flume facility of the Ocean Engineering Program at Texas A&M University. The dimensions of the wave flume are 45.72 m (150 ft) in length, 0.46 m (1.5 ft) in width, and 1.22 m (4.0 ft) in depth. The test section was located approximately 18.29 m (60 ft) from the wave generator. Fig. 2 shows the general layout of the test facilities.



WAVE-CURRENT TEST FACILITY

FIGURE 2

The wave flume is constructed of a metal and wood frame, with one wall consisting of plywood and the other of plexiglass. Currents are produced by a pumping system capable of developing currents of 1.22 m/sec (4.0 ft/sec). The water depth for any specific flow rate was controlled by an adjustable weir located at the end of the tank.

A wave absorber was specially constructed for this investigation to reduce the reflection of the waves as shown in Fig. 3. The design permitted large volumes of water to be transmitted through the absorber so that significant currents could be produced.

The facilities included two measurement stations. Station one was for the measurement of surface parameters and water particle kinematics and station two was for fluid-force determination. Station one was used to gather the information for comparing the predicted water particle to the theoretical values. Station two was used to determine the fluid force on the test structure. Since the distance between the two stations is 1.26 m (4.13 ft), it is assumed that the wave characteristics do not change between the stations. Therefore, the results obtained at station one can be used at station two.

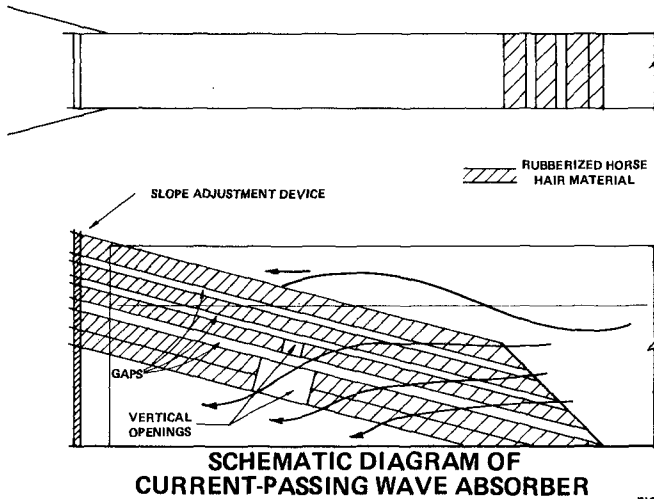
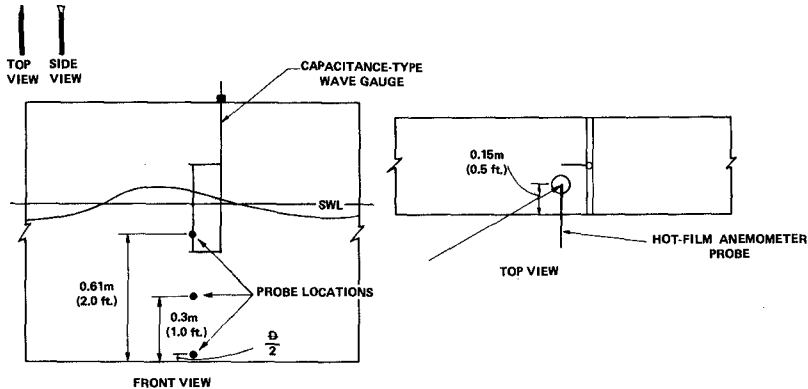


FIGURE 3

The test cylinder was constructed of polyvinyl chloride (PVC) pipe. Its outside diameter was 44.5 mm (1.75 in). The pipe was located 1.58 mm (.0625 in) above the bottom of the tank. This small gap provided for the free movement of the cylinder so that the unrestricted movement was transmitted to the load cell which converted this movement to an applied force. Since only horizontal components of force were being measured the effect of the gap was minimized. The test cylinder extended through the walls of the test tank. This extension helped to reduce end effects, which supported the two-dimensional assumption.

Measuring devices at station one consisted of a capacitance-type wave gauge and a hot-film anemometer probe as shown in Fig. 4. The capacitance-type wave gauge was used for surface profile measurements of wave height and period because of its availability and linearity. The results were recorded on a Hewlett Packard Model 74024 oscillographic strip recorder. This recorder was capable of providing a time reference on the recorded data. The period of the wave was determined by measuring the time between two successive wave crests. The capacitance-type wave gauge was used with a Hewlett Packard Model 17403A Carrier preamplifier. This preamplifier contained the full-bridge network required by the capacitance-type wave gauge. The output of the hot-film anemometer was amplified by a Hewlett Packard Model 17402A Low-Gain preamplifier before the output was recorded on the strip recorder.

A Thermo-Systems Model Series 1050 hot-film anemometer was used for the particle velocity measurements. This series consisted of a Model 1050A constant-temperature anemometer, a Model 1051 monitor and power supply, a Model 1055 linearizer, and a Model 1057 signal conditioner.



STATION ONE, SURFACE PROFILE AND VELOCITY MEASUREMENTS

FIGURE 4

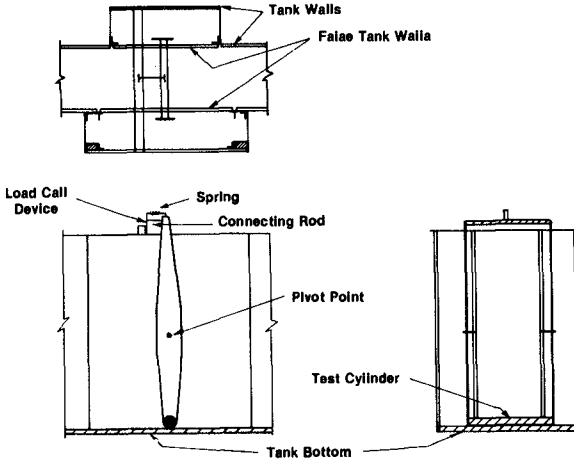
The transducer used with the anemometer is a small resistance element which is heated and controlled at an elevated temperature. A Model 1210-20 hot-film transducer (probe) was used in this research. The amount of electrical energy dissipated in the sensor is a measure of the cooling effect of the fluid flowing past the heated sensor. The cooling effect of the fluid passing over the sensor depends on both the mass flow and temperature difference between the sensor and the fluid.

In operation, a current flows through the bridge. The amplifier senses any off balance, and feeds back more or less current until the bridge comes into balance. This additional electrical energy is outputted as a bridge voltage which is amplified and recorded on the oscillographic strip recorder.

It can be seen from Fig. 4 that three locations were used for water particle measurements. They were at 0.61 m (2.0 ft), 0.31 m (1.0 ft) and at the mid height of the cylinder at the bottom of the tank. The particle kinematics were compared at these elevations. The particle velocity at the mid height of the cylinder was used with the measured fluid force to determine the coefficient of drag. The probe was extended into one side of the tank a distance of 0.15 m (0.5 ft). This distance was selected so that the measured particle velocity would be out of the boundary layer, but the distance was short enough to reduce the effect of probe vibrations due to vortex shedding. The orientation of the probe in the fluid flow is important, because by aligning the probe perpendicular to the flow, only the horizontal component of the velocity is measured. The velocity parallel to the probe is not significant and can be assumed to be zero. With the orientation shown in

Fig. 4, only the horizontal velocity component was recorded. Only horizontal velocities and forces were investigated in this research.

Measurements at the second station consisted of a capacitance-type wave gauge and a mechanism to transmit the horizontal forces on a horizontal circular cylinder resting near the bottom to a load-cell device. A sketch of station two is shown in Fig. 5. The cylinder was connected



**SCHEMATIC DIAGRAM OF STATION TWO,
MODEL LOAD TEST STATION**

FIGURE 5

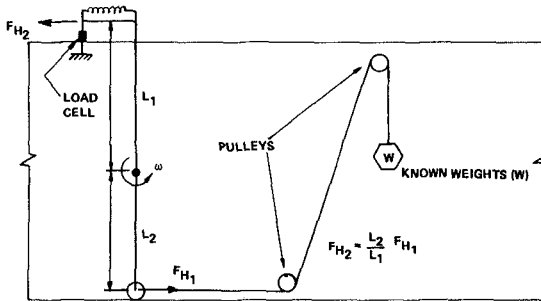
by two arms which rotated about a pivot point. This rotation transmitted the horizontal fluid force on the cylinder to a load cell located on the top of the tank. The load cell had a capacity of 1500 grams (≈ 3.0 lbs). The load cell was connected to the rotating mechanism by a rod which was pointed on both ends and which was held in place by a stiff spring. These pin-point connections were used to reduce friction. This total mechanism was capable of transmitting the positive or negative fluid force to the load cell without disrupting the fluid flow near the model. This device was found to be very effective in measuring the fluid force on the horizontal cylinder.

CALIBRATION AND PROCEDURE

All the equipment used in this investigation was calibrated using known values which were related to the output on the oscillograph recorder. All equipment was re-calibrated at each major test except for the hot-film anemometer which had to be calibrated periodically during the testing due to drift of the output.

The load cell was calibrated and balanced in a manner recommended by Hewlett-Packard. A known load was applied to the test cylinder, and

the output of the bridge network was recorded on the oscillograph recorder display. The applied load was transferred through a system of pulleys and weights described by the schematic diagram shown in Fig. 6.



SCHEMATIC DIAGRAM OF LOAD-CELL CALIBRATION APPARATUS

FIGURE 6

The total force applied to the cylinder was equal to the suspended weight multiplied by the length ratio of the arms around the pivot point. Any losses due to friction were neglected. The known load was related to the output voltage recorded on the oscillography display by a linear ratio.

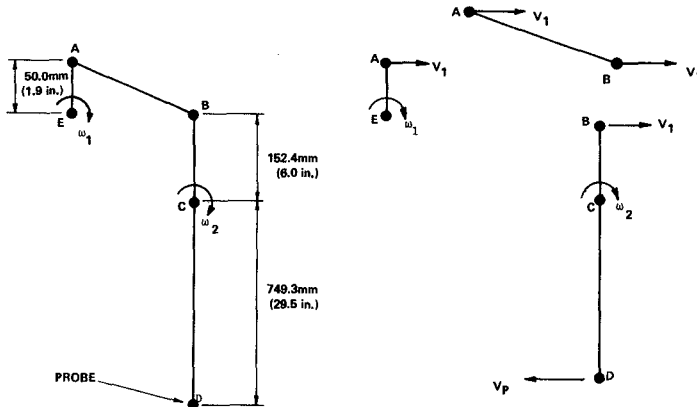
Calibration of the hot-film anemometer proved to be difficult, due to its non-linear output and the constant drift of the output voltage. The hot-film anemometer was calibrated by means of known velocities created by a forced pendulum. A schematic of the forced pendulum is shown in Fig. 7. The angular velocity (ω_1) of the driving mechanism is related to the velocity of the probe by the following equation:

$$V_p = \text{velocity of probe (ft/sec)} = 0.7857 (\omega_1) \dots \dots \dots (7A)$$

$$V_p = \text{velocity of probe (m/sec)} = 0.2395 (\omega_1) \dots \dots \dots (7B)$$

Four known velocities were used as calibration points for the hot-film anemometer. These velocities were measured using the same apparatus as the wave particle kinematics. The number of divisions for each calibration point was related to the velocity by fitting the data to a power curve.

An inherent problem of the hot-film anemometer is that the calibration will drift in a relatively short period of time. It was determined that significant drift occurred in a period of several hours. To



SCHEMATIC DIAGRAM OF THE FORCED PENDULUM FOR VELOCITY CALIBRATION

FIGURE 7

overcome this problem, the drift as a function of time was investigated. The drift was determined by running successive calibration tests during a period of one hour. The drift during the hour period was reasonably linear. Calibration tests were run periodically during the test periods. This procedure proved successful for calibrating the hot-film anemometer.

The testing program was divided into two major stages. One stage was the determination of the water particle kinematics at three elevations with the wave surface parameters; the other was the measurement of the simultaneous fluid-force measurements and particle kinematics measurements required to determine the coefficient of drag.

All data were recorded on the oscillograph recorder and digitized and then used as input for a computer program which fitted the velocity data to a power curve. This program then wrote the calibrated data and other parameters of the particular test to a computer data file, where it was stored for computer analysis.

DATA ANALYSIS AND RESULTS

The results obtained from the testing program were based on several assumptions. First, the wave reflections from the sides and end of the wave tank were considered to have very little effect on the measurements. Secondly, the flow was assumed to be essentially two-dimensional. This was supported by the fact that the aspect ratio of the model was 10.274. Thirdly, the flow was considered irrotational, and the fluid was

inviscid. This assumption, which is vital for the validity of the superposition principle, has been found to be incorrect for currents with a varying velocity profile. The quantification of the error associated with this assumption was the basic goal of the research.

The thrust of the data analysis was two-fold. One task was to determine the error associated with the superposition of the current velocity field and the velocity field generated by a wave propagating in still water. This was accomplished by directly measuring the error over a specific range of waves and currents. The velocity field of the waves was predicted by both Airy and Stokes third-order wave theories.

The other task was a comparison of the measured forces on the pipeline model with the forces predicted by this superposition principle. The experimental drag coefficients were determined by simultaneous measurements of horizontal fluid velocity and fluid force. Comparisons were then made to the coefficients determined from the superposition principle using Airy or Stokes third-order wave theories.

For the first task, kinematic measurements were taken at three elevations as discussed previously. The second task employed a fourth test to measure forces on the model pipeline. The range of wave parameters and currents tested are presented non-dimensionally in Table 1. Since tests Nos. 3 and 4 were conducted simultaneously, the range of values for both tests were identical.

TABLE 1
RANGES OF WAVE AND CURRENT
PARAMETERS FOR TESTING PROGRAM

TEST	$\frac{H}{d}$	$\frac{H}{gT^2}$	$\frac{d}{gT^2}$	$\frac{U}{u}$	$\frac{H}{L}$
1. HORIZONTAL PARTICLE VELOCITY MEASUREMENT ELEVATION = 0.61 M (2.0 FT.)	0.1358-0.291803	0.0415-0.0230	0.0639-0.1102	0.1439-1.0179	.09896-.09186
2. HORIZONTAL PARTICLE VELOCITY MEASUREMENT ELEVATION = 0.30 M (1.0 FT.)	0.1715-0.2912	0.0107-0.0238	0.0561-0.1253	0.0000-5.3316	.07265-.12429
3. HORIZONTAL PARTICLE VELOCITY MEASUREMENT ELEVATION = 0.02 M (0.145 FT.)	0.1155-0.2407	0.0128-0.0197	0.0563-0.1155	0.0000-4.9602	.06899-.12508
4. HORIZONTAL FORCE MEASUREMENT	0.1155-0.2407	0.0128-0.0197	0.0563-0.1155	0.0000-4.9602	.06899-.12508

The raw data for tests Nos. 1-3 consisted of wave heights, wave periods, and a continuous measurement of horizontal fluid velocity over the wave period. The raw data for test No. 4 included a continuous record of horizontal fluid force over the period. The estimated error associated with each of these input variables is presented in Table 2.

TABLE 2
ESTIMATED ACCURACY OF
EXPERIMENTAL MEASUREMENTS

VARIABLE	MAXIMUM ERROR	MAJOR SOURCE OF ERROR
WAVE HEIGHT	2 TO 5 PERCENT	STABILITY AND LINEARITY OF BRIDGE NETWORK AND RECORDING DEVICE; WAVE REFLECTION
WAVE PERIOD	± .05 SECONDS	DETERMINATION OF WAVE CREST FROM RECORDING DEVICE
WATER DEPTH	6 MM (.25 IN.)	VARYING WATER DEPTH DUE TO CURRENT
FLUID FORCE	2 TO 3 PERCENT	DETERMINATION FROM RECORDING OUTPUT; STABILITY AND LINEARITY OF BRIDGE NETWORK
FLUID VELOCITY	1 TO 8 PERCENT	CALIBRATION AND DRIFT OF HOT-FILM ANEMOMETER (THIS ERROR IS GREATEST AT LOW VELOCITY DUE TO CURVE FIT PROCESS OF OUTPUT VOLTAGE TO VELOCITY)

The largest error was associated with the fluid velocity measurements of the hot-film anemometer. The error reached its maximum at the lower velocities, which were not within the range of the calibration curves.

The relative error of the superposition principle of the horizontal velocities can be expressed as a dimensionless difference (E):

$$E = \frac{u_{mea} - u_{tot}}{\frac{\pi H}{T}} \dots \dots \dots (8)$$

- where u_{mea} = the measured horizontal velocity at elevation (z),
- u_{tot} = the algebraic sum of the horizontal particle velocity at elevation (z) predicted by either Airy or Stokes third order wave theory and the current velocity,
- H = wave height, and
- T = wave period.

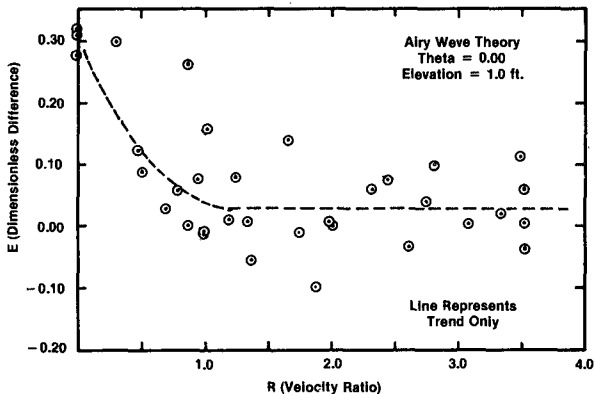
Dividing by the Airy deepwater horizontal velocity at the still water elevation the difference was non-dimensionalized.

The dimensionless difference (E) was found to be a function of a dimensionless parameter (R) relating the magnitude of current to the horizontal particle velocity of the wave in still water:

$$R = \frac{U}{u_{calc}} \dots \dots \dots (9)$$

where U = current velocity at elevation (z),
 u_{calc} = horizontal particle velocity predicted by either Airy or Stokes third order wave theories in the absence of a current at elevation (z).

The relationship between the dimensionless difference (E) and the velocity ratio (R) for an elevation of 1.0 ft above the bottom under the wave crest is shown in Fig. 8 for Airy wave theory and Fig. 9 for Stokes third-order wave theory.



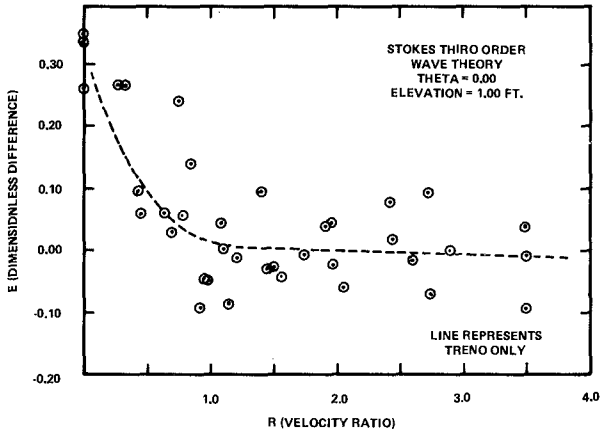
DIMENSIONLESS DIFFERENCE VERSUS THE VELOCITY RATIO FOR AIRY WAVE THEORY AT ELEVATION 1.00 FT (THETA = 0.00)

FIGURE 8

Several interesting results can be noted from these figures. The wave theories tend to under-predict (positive dimensionless difference) the horizontal velocity at elevation (z) when no current is present ($R = 0.0$). As the current velocity increased relative to the wave particle velocity, the error decreased to approximately zero for values of $R > 1.0$. This trend is represented by the dotted lines on each of the figures. This trend seems to indicate that the superposition of the velocity fields approaches reasonable agreement with the measured values for $R > 1.0$.

A slight tendency exists for Stokes third-order wave theory to predict the superimposed velocity superior to that of Airy prediction. This can be seen by the mean error which is closer to the zero error line.

The fluid force data were analyzed at the crest to determine the drag coefficient. At this point the acceleration is equal to zero and



**DIMENSIONLESS DIFFERENCE VERSUS VELOCITY
RATIO FOR STOKES THIRD ORDER WAVE THEORY
AT ELEVATION 1.00 FT. (THETA = 0.00)**

FIGURE 9

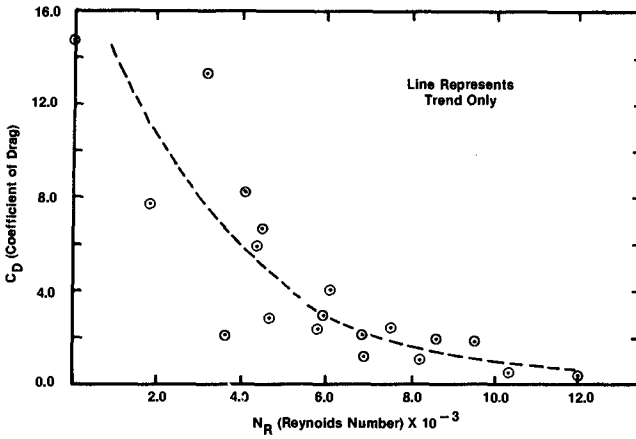
only the drag force is present. The coefficients of drag were determined by three methods. The first method used simultaneous measurements of the horizontal fluid force and velocity.

The second and third methods were based on the predicted velocities of the superposition principle using Airy and Stokes third-order wave theories to calculate the coefficient of drag. A comparison of the three methods was made to demonstrate the differences in the coefficient of drag.

The coefficient of drag is related to the Reynolds Number (N_R). The coefficient of drag was plotted as a function of the Reynolds number in Fig. 10 as computed by the simultaneous measurements of fluid force and fluid velocity; Fig. 11 as computed using the superposition principle with Airy wave theory; and Fig. 12 as computed using Stokes third-order wave theory.

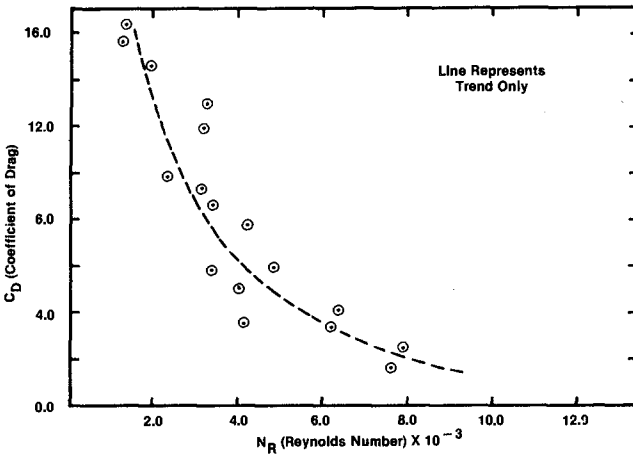
These figures all show the same general trend of reduction in the coefficient of drag with increasing Reynolds numbers.

Figures 10 and 11 show that the coefficient of drag was less when computed from the measured velocity as opposed to the Airy or Stokes III velocities for the range of Reynolds numbers shown. This is related to the fact that the wave theories used in conjunction with the superposition principle have a tendency to under-predict the horizontal velocity near the bottom boundary.



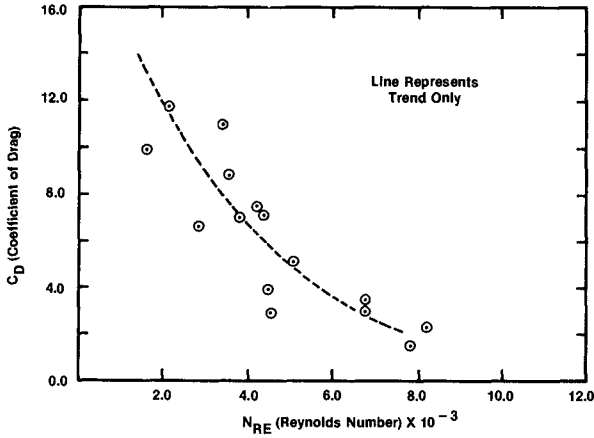
COEFFICIENT OF DRAG VERSUS REYNOLDS NUMBER FROM SIMULTANEOUS FORCE AND VELOCITY MEASUREMENTS

FIGURE 10



COEFFICIENT OF DRAG VERSUS REYNOLDS NUMBER FROM COMPUTATIONS USING AIRY WAVE THEORY

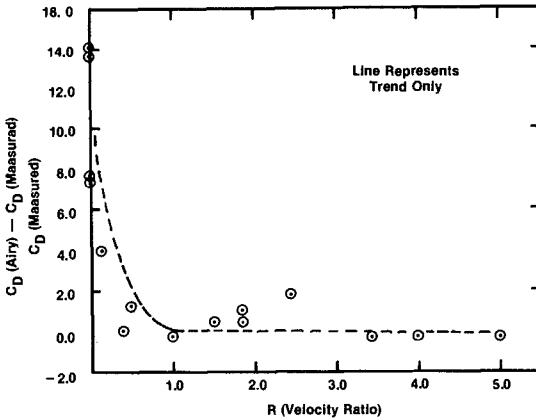
FIGURE 11



COEFFICIENT OF DRAG VERSUS REYNOLDS NUMBER FROM COMPUTATIONS USING STOKES THIRD ORDER WAVE THEORY

FIGURE 12

The relative difference between the coefficients of drag computed by Airy wave theory and those computed from measured values are shown in Fig. 13. This figure demonstrates at low velocity ratios (R) the coefficients computed using Airy wave theory are greater than the actual values, but this difference decreases with increasing currents.

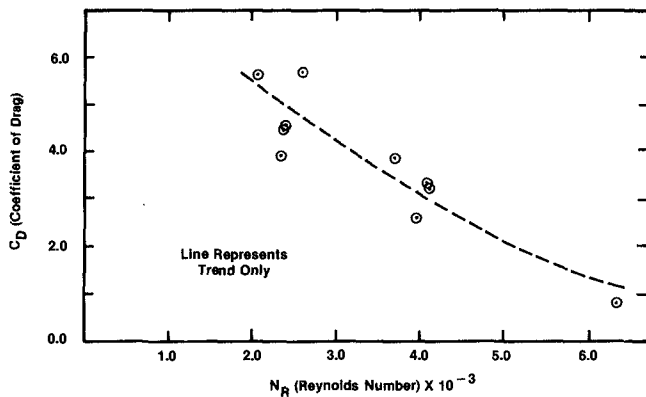


RELATIVE DIFFERENCE OF C_D FOR AIRY WAVE THEORY AND MEASURED VALUES VERSUS THE VELOCITY RATIO

FIGURE 13

The coefficients of drag computed by the simultaneous measurements of the horizontal fluid force and velocity are, by definition, the actual values. These coefficients can only be used if the actual horizontal velocity can be predicted. This supports the fact that the coefficients of drag are dependent on the method used to determine the horizontal velocity. Therefore, the prediction of forces on a cylinder should be consistent with the method which was used to determine the coefficients.

For the steady-state current condition, Fig. 14 shows the actual coefficient of drag for the horizontal cylinder.



COEFFICIENT OF DRAG VERSUS REYNOLDS NUMBER (STEADY-STATE CURRENT CONDITION)

FIGURE 14

The primary purpose of this research was to determine the drag forces associated with the horizontal velocity. The drag forces were determined when the velocity was maximum and the acceleration was zero. Therefore, no inertial effects were present and the coefficient of drag was unaltered by this effect.

CONCLUSIONS AND RECOMMENDATIONS

The following conclusions were evident from the testing program for the range of values tested.

1. Airy and Stokes third-order wave theories in conjunction with the superposition principle predict the horizontal velocity reasonably well for velocity ratios ($R = \frac{U}{u}$) greater than one. The velocities are under-predicted for u values of R less than one.

2. The coefficients of drag computed from Airy and Stokes third order wave theories in conjunction with the superposition principle are greater in magnitude than the values determined by the simultaneous force and velocity measurement. This difference decreases with increasing velocity ratios.

The conclusions were based on a limited testing program. These results can be extended over a greater range of waves and currents by further tests. These additional tests will indicate whether any scale effects are important.

Other conditions related to the pipeline problem, such as the distance of the cylinder from the boundary, the transverse (lift) force, relative roughness and orientation angles, should be investigated for the combined wave-current condition.

Other theories developed for the interaction of waves and currents should be tested experimentally to determine their accuracy for the prediction of fluid force and particle kinematics.

REFERENCES

1. Dalrymple, Robert A., "Models for Nonlinear Water Waves on Shear Currents," Offshore Technology Conference, 1974, Paper No. 2114.
2. Dalrymple, Robert A., "Waves and Wave Forces in the Presence of Currents," Civil Engineering in the Oceans, Vol. 2, pp. 999-1018.
3. Davis, D. A. and Ciani, J. B., "Wave Forces on Submerged Pipelines - A Review with Design Aids," Naval Facilities Engineering Command, Technical Report No. R844, July 1976, 55 pages.
4. Dean, R. G., "Stream Function Representation of Nonlinear Ocean Waves," Journal of Geophysical Research, Vol. 70, No. 18, September 15, 1965.
5. Garrison, C. J. and Rao, U. S., "Interaction of Waves With Submerged Objects," Journal of the Waterways, Harbors and Coastal Engineering Division, American Society of Civil Engineers, Vol. 97, No. WW2, May 1971, pp. 259-277.
6. Tung, Chi Chao and Huang, Norden E., "Combined Effects of Currents and Waves on Fluid Force," Ocean Engineering, Vol. 2, No. 4, 1973, pp 183-193.
7. Tung, Chi Chao and Huang, Norden E., "Influence of Wave-Current Interactions on Fluid Force," Ocean Engineering, Vol. 2, No. 5, 1973, pp 207-218.
8. Tung, Chi Chao and Huang, Norden E., "Influence of Current on Statistical Properties of Waves," Journal of the Waterways, Harbors and Coastal Engineering Division, Vol. 100, 1974, pp. 267-278.
9. Wu, Song C. and Tung, Chi Chao, "Structural Response to Wave and Current Forces," Civil Engineering in the Oceans, Vol. 2, 1975, pp. 849-864.
10. Morison, J. R., O'Brien, M. P., Johnson, J. W. and Schaaf, S. A., "The Force Exerted by Surface Waves on Piles," Petroleum Transactions, American Institute of Mining, Metallurgical, and Petroleum Engineering, Vol. 189, 1950, pp. 149-154.

11. Skjelbreia, Lars, "Gravity Waves: Stokes Third Order Approximation, Tables of Functions," Council on Wave Research, The Engineering Foundation, 1959, p. 336.

WAVE FORCES ON AN INCLINED CIRCULAR CYLINDRICAL PILE

by

Toshiyuki Shigemura
Associate Professor of Ocean Engineering
National Defense Academy, Yokosuka, Kanagawa, Japan

ABSTRACT

This paper describes experimental results on the in-line and lift forces acting on inclined circular piles which are placed in two different planes: (1) a vertical plane parallel to the direction of wave propagation; and (2) a vertical plane parallel to the wave crest.

The in-line and lift force formulas for an inclined pile are formulated by referring to the conventional Morison and lift force formulas, respectively. Stokes third order wave theory is used for the estimation of flow kinematics induced around a pile. Based on these formulas, the time-independent and time-dependent values of the drag, mass and lift coefficients are determined by using several methods. Further, the time-dependent coefficients are expanded into Fourier series which consist of several significant components.

Reliability of these coefficient values are studied by examining the relative deviation of the predicted wave forces based on these coefficient values from the measured ones. The analysis finds that relative deviations of the in-line and lift forces exceed in many cases 15% and 100%, respectively, when the time-independent coefficients are used for the prediction of wave forces, but that they are reduced to 5% and 15%, respectively, when the time-dependent coefficients are used for it.

INTRODUCTION

It is commonly recognized that two types of wave forces are induced on a slender cylindrical pile subject to the motion of unbroken waves. One is called in-line force which acts on the pile to the direction of wave propagation and the other is called lift force which acts on the pile transversely to the direction of wave propagation. For the present, the in-line force is calculated by the Morison formula which evaluates the in-line force as a linear sum of the drag force and the inertia force. The lift force is calculated by the lift force formula which is same as that in a steady flow. However, when one attempts to predict these wave forces by the above formulas, one has to get reliable information on: (1) the flow kinematics induced around an inclined pile; and (2) the values

of the hydrodynamic coefficients $[C_D]$ and $[C_M]$ included in the Morison formula and of the lift coefficient $[C_L]$ included in the lift force formula. It is currently common practice to estimate the flow kinematics by using appropriate wave theories. Airy's wave theory has been widely used because of its simplicity although Stokes wave theory of higher order and Dean's stream function theory have also been used recently for the estimation of the flow kinematics. Hence, determination of C_D , C_M and C_L values experimentally has become one of the major themes in the present research of the wave forces.

Since Morison(1950) developed his unique method of determining C_D and C_M values experimentally, many distinguished works have been conducted on wave forces and coefficient values have been determined by several methods. Table 1 summarizes some of the representative works in which unique methods have been either developed or used to determine the coefficient values. Through a brief review of these previous works, the following facts can be noted:

1. Coefficient values for either vertical or horizontal piles have been determined mainly by the methods shown in Table 1.
2. There has not been sufficient study conducted to determine which method will provide the most reliable coefficient values for the prediction of wave forces.
3. Inasmuch as only a few works have been done on the wave forces acting on inclined piles, there is a limited amount of information available on the coefficient values for inclined piles.

It should be noted, however, that jacket-type offshore structures generally consist of many steel piles which are inclined in various planes at different angles. Thus, it is quite doubtful whether the coefficient values determined for either vertical or horizontal piles can be used directly for the evaluation of wave forces exerted on inclined piles.

Based on this, a basic experiment is performed in this study to investigate the characteristics of in-line and lift forces which act on inclined piles placed in two different planes: (1) a vertical plane parallel to the direction of wave propagation; and (2) a vertical plane parallel to the wave crest. The conventional Morison and lift force formulas are modified, respectively, to predict the in-line and lift forces acting on the inclined piles which are placed in each of both vertical planes. Further, Stokes third order wave theory is used to estimate the flow kinematics induced around the inclined piles. Based on these formulas, the time-independent and time-dependent values of C_D , C_M and C_L are determined by using either the methods shown in Table 1 or the methods which are derived by modifying the previous ones.

The analysis is focussed to determine: (1) whether the inclinations of piles affect the coefficient values; (2) which method will provide the most reliable coefficient values for the prediction of respective wave forces; and (3) how the inclinations of piles affect the ratio of the maximum lift force to the maximum in-line force exerted of an inclined pile over a wave cycle.

Table 1. Representative works on the wave forces acting on the piles.

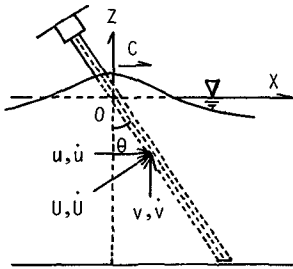
Authors	Contents of investigations	Methods used for determining coefficient values
Morison (1950)	Circular and H-shaped piles and flat plates were placed vertically in progressive waves, and total in-line forces on them were measured.	C_D and C_M values were determined at two specific phases within a wave cycle where either the drag or inertia term became zero, respectively. This method determines time-independent values of each coefficient, and is called hereafter the "two-point method".
Keulegan and Carpenter (1958)	Circular piles and flat plates were placed horizontally at the nodal points of standing waves, and total in-line force on them were measured. Flow patterns were also observed photographically.	C_D and C_M values were determined by Fourier analysis: (1) by the primary coefficient of Fourier series; and (2) by the Fourier series of fully expanded. The former method determines time-independent values, and does the latter time-dependent values of each coefficient. The former method is called hereafter the "Fourier-averaged method".
Al-Kazily (1972)	Circular piles were placed horizontally in progressive waves, and total in-line, transverse and uplift forces on them were measured. Some experiments were also made on wave forces exerted on inclined piles.	C_D and C_M values were determined by the two-point method. These values were also determined by solving Morison formulas provided at successive phases, t and $(t+\Delta t)$ simultaneously where Δt is an incremental phase. This method determines the time-dependent values of each coefficient, and is called hereafter the "Al-Kazily's method".
Sarpkaya (1975)	Circular piles and spheres were placed horizontally in oscillatory flows generated in the U-shaped tunnel, and total in-line and lift forces on them were measured.	C_D and C_M values were determined by the Fourier-averaged method and C_L values were determined at a specific phase where the lift force became maximum. This method also determines time-independent values of C_L , and is called hereafter the "one-point method".
Chakrabarti et al (1976)	Circular piles were placed vertically in progressive waves, and total and sectional in-line and lift forces on them were measured.	C_D and C_M values were determined by the least square method, which also determines time-independent values of them. This method is called hereafter "the least square method". C_L values were determined by the Fourier analysis.

THEORETICAL CONSIDERATION

This study employs an essential assumption that the in-line and lift forces exerted on any inclined piles can be evaluated by the conventional Morison and lift force formulas if certain modifications are made on them. This assumption is the basis of this research.

Wave Force Formulas for an Inclined Pile

Figure 1 shows a sketch of a circular pile with an outer diameter, D , placed in a vertical plane parallel to the direction of wave propagation at an inclining angle, θ , and the coordinate system used for the analysis. For the convenience of later discussion, this vertical plane will be called hereafter the "Plane A".



In this figure, u and v represent the horizontal and vertical velocity components of an induced flow at an arbitrary position, (x, z) on the circular pile, at an arbitrary phase, t . Similarly, \dot{u} and \dot{v} represent the acceleration components of u and v , respectively. Here assume that the velocity component normal to the pile axis, U and its acceleration, \dot{U} can be composed into the following equations:

Figure 1. Schematic drawing of an inclined pile placed in the Plane A.

$$U = u \cos\theta + v \sin\theta \dots\dots\dots(1)$$

$$\dot{U} = \dot{u} \cos\theta + \dot{v} \sin\theta \dots\dots\dots(2)$$

Then, the total in-line force, $F_{txA}(t)$ which acts on the inclined pile at an arbitrary phase, t , will be evaluated by the following equation:

$$F_{txA}(t) = \int_{-h}^{\eta} C_{DU} \frac{1}{2} \rho D U |U| \sec\theta dz + \int_{-h}^{\eta} C_{MU} \frac{1}{4} \rho \pi D^2 \dot{U} \sec\theta dz + \frac{1}{4} \rho g \pi D^2 \eta \tan\theta \dots\dots\dots(3)$$

where C_{DU} and C_{MU} represent the drag and mass coefficients of the inclined pile, and the last term represents the buoyancy caused by the fluctuation of the surface elevation, η .

Similarly, the total lift force, $F_{tLA}(t)$ which acts on the inclined pile at the same phase, t will be evaluated by the following equation:

$$F_{tLA}(t) = \int_{-h}^{\eta} C_{LU} \frac{1}{2} \rho D U^2 \sec\theta \dots\dots\dots (4)$$

where C_{LU} is the lift coefficient of the inclined pile.

Figure 2 shows a sketch of a circular pile with an outer diameter, D , placed in a vertical plane parallel to the wave crest at an arbitrary inclining angle, θ , and the coordinate system used for the analysis. For the convenience of later discussion, this vertical plane will be called hereafter the "Plane B".

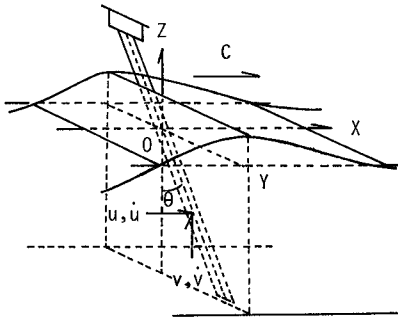


Figure 2. Schematic drawing of an inclined pile placed in Plane B.

In this figure, u and v represent the horizontal and vertical velocity components of an induced flow at an arbitrary position, (y,z) on the pile at an arbitrary phase, t . Similarly, \dot{u} and \dot{v} represent the acceleration components of u and v , respectively.

Here assume that the in-line force which acts on the inclined pile consists of the in-line force caused by u and \dot{u} , and the lift force caused by v . Similarly, assume that the lift force which acts on the inclined pile consists of the in-line force caused by v and \dot{v} , and the lift force caused by u .

Then, the total in-line force, $F_{txB}(t)$ which acts on the inclined pile at an arbitrary phase, t , will be evaluated by the following equation:

$$F_{txB}(t) = \int_{-h}^{\eta} C_{Du} \frac{1}{2} \rho D u |u| \sec\theta dz + \int_{-h}^{\eta} C_{Mu} \frac{1}{4} \rho \pi D^2 \dot{u} \sec\theta dz + \int_{-h}^{\eta} C_{Lv} \frac{1}{2} \rho (v \sin\theta)^2 \sec\theta dz \dots\dots\dots (5)$$

where the first two terms in the right-hand side of Eq.(5) represent the in-line force caused by u and \dot{u} , and the last term represents the lift force caused by v .

Similarly, the total lift force, $F_{tLB}(t)$ which acts on the inclined pile at an arbitrary phase, t , will be evaluated by the following equation:

$$F_{tLB}(t) = \int_{-h}^{\eta} C_{Lu} \frac{1}{2} \rho D u^2 \sec\theta \, dz + \int_{-h}^{\eta} C_{Dv} \frac{1}{2} \rho D v |v| \sin\theta \tan\theta \, dz + \int_{-h}^{\eta} C_{M\dot{v}} \frac{1}{4} \rho D^2 \dot{v} \tan\theta \, dz + \frac{1}{4} \rho g D^2 \eta \tan\theta \dots\dots\dots(6)$$

where the first term in the right-hand side of Eq.(6) represents the lift force caused by u and the second and third terms represent the in-line force caused by v and \dot{v} . Eqs. (3), (4), (5) and (6) were all derived by referring to the Morison and lift force formulas.

Determination of Coefficient Values

It is known that the coefficients in each of the above equations are functions of certain variables associated with the characteristics of the flow kinematics induced around a pile and of the pile itself. Thus, these coefficients may have different values from one point to another over the submerged portion of the pile.

In this study, however, the representative values of each coefficient over the submerged portion will be determined. Thus, the coefficients in each integral term of Eqs.(3), (4), (5) and (6) can be taken out of each integral sign. Consequently, Eqs.(3) and (4) can be rewritten as follows:

$$F_{txA}(t) = C_{Du} F_{Du}(t) + C_{M\dot{u}} F_{I\dot{u}} + F_B(t) \dots\dots\dots(7)$$

$$F_{tLA}(t) = C_{Lu} F_{Lu}(t) \dots\dots\dots(8)$$

where $F_{Du}(t)$ and $F_{I\dot{u}}(t)$ in Eq.(7) represent the corresponding integral terms in Eq.(3), and $F_B(t)$ represents the buoyancy term in Eq.(3).

Similarly, Eqs.(5) and (6) can be rewritten as follows:

$$F_{txB}(t) = C_{Du} F_{Du}(t) + C_{M\dot{u}} F_{I\dot{u}} + C_{Lv} F_{Lv}(t) \dots\dots\dots(9)$$

$$F_{tLB}(t) = C_{Lu} F_{Lu}(t) + C_{Dv} F_{Dv}(t) + C_{M\dot{v}} F_{I\dot{v}}(t) + F_B(t) \dots\dots(10)$$

where $F_{Du}(t)$, $F_{I\dot{u}}(t)$ and $F_{Lv}(t)$ in Eq.(9) represent the corresponding integral terms in Eq.(5), and $F_{Lu}(t)$, $F_{Dv}(t)$ and $F_{I\dot{v}}(t)$ in Eq.(10) represent the corresponding integral terms in Eq.(6).

As it can be noted from these equations, both time-independent and time-dependent values of each coefficient can be determined once the flow kinematics around an inclined pile and measured values of the wave forces are known. In advance of determining these coefficient values, all integral terms in Eqs.(7), (8), (9) and (10) are calculated at every incremental phase of 0.01 second over a wave cycle, based on the information of flow kinematics estimated by the Stokes third order wave theory.

Further, recorded data of incident waves and wave forces are quantized at the corresponding phases and punched on input cards automatically by a special A-D converter.

1. Coefficient Values for Inclined Piles Placed in Plane A

Based on the data provided previously, the time-independent values of C_{DU} and C_{MU} in Eq.(7) are determined in this study by the two-point method and by the least square method which are shown in Table 1. Similarly, the time-independent values of C_{LU} in Eq.(8) are determined by the one-point method and by the least square method.

The time-dependent values of C_{DU} and C_{MU} at every incremental phase are also determined in this study by Al-Kazily's method which is shown in Table 1. Similarly, the time-dependent values of C_{LU} are determined by solving Eq.(8) directly at the same incremental phases. The time-dependent coefficients are all expanded into Fourier series in which several significant components are involved. The details of this method has been shown in Shigemura and Nishimura's paper(1979).

2. Coefficient Values for Inclined Piles Placed in Plane B

Eqs.(9) and (10) include three unknown coefficients in themselves. Thus, data should be provided at least at three successive phase for each equation to determine these coefficient values.

The time-independent values of these coefficients are determined by the following procedures:

1. Divide a wave cycle into four equal divisions. Further, determine three phases in each division by dividing it into four equal subdivisions.
2. At each division, establish three equations for both of Eqs.(9) and (10), based on the data provided at the three phases mentioned above.
3. Solve each pair of three equations simultaneously to determine the respective coefficient values in each division.
4. Calculate the arithmetic means of the respective coefficient values obtained in the four divisions.

This method will be called hereafter the "three-point method". The least square method is also used to determine the time-independent values of these coefficients.

The time-dependent values of each coefficient in Eqs.(9) and (10) are also determined by a method similar to the Al-Kazily's method. Namely, three equations are provided first for each of Eqs.(9) and (10), based on the data provided at three successive phases, $(t-\Delta t)$, t , and $(t+\Delta t)$ where Δt is an incremental phase. Two pairs of these three equations are then solved simultaneously under the assumption that each coefficient

keeps constant value at the three successive phases. The coefficient values determined by this method are also expanded into Fourier series which consist of several significant components.

Reliability of Coefficient Values

Based on the coefficient values determined, theoretical values of each wave force are calculated at every incremental phase of 0.01 second over a wave cycle by Eqs.(7), (8), (9) and (10), respectively. To determine the reliability of each coefficient value quantitatively, relative deviations of theoretical wave forces from the measured ones are calculated by the following equation:

$$\delta F(\%) = \frac{\sqrt{\sum_{t=1}^N [F_m(t) - F_t(t)]^2 / N}}{[F_t]_{\max} - [F_t]_{\min}} \times 100 \quad \dots\dots\dots(11)$$

In this equation, $F_m(t)$ and $F_t(t)$ represent the measured and theoretical values, respectively, of a wave force at an arbitrary phase, t . Further, $[F_t]_{\max}$ and $[F_t]_{\min}$ represent the maximum and minimum values, respectively of the theoretical wave force over a wave cycle, and N is sample number used for the calculation of δF . Note that δF also measures the propriety of formulation of each wave force formula.

EXPERIMENTAL SETUP AND PRECEDURES

A 4.5 meters wide, 1.2 meters deep and 12.0 meters long wave channel was used for this experimental study. This wave channel has a flap-type wave generator at the back of the channel. A self-driven truck sits astride the channel so that it can run from the wave generating paddle to the wave absorber installed at the front end of the channel. This truck was locked at a position of 6 meters from the wave generating paddle.

At a point below the main beam of this truck, a chuck was fixed in such a way that it could rotate around an axis parallel to the direction of wave propagation and around an axis parallel to the wave crest. This chuck allows placing a force meter on the beam. A commercialized force meter, or a three-component loadcell was clamped firmly by this chuck. This loadcell is designed to detect the electrical signals produced by two components of forces, F_x and F_y which are perpendicular to each other, and by a component of the bending moment caused by either F_x or F_y , simultaneously. This force meter was connected to an oscillograph through proper amplifiers.

A total of twelve model piles used in this experiment were made of aluminum and acrylic acid resin tubes having circular cross sections. The upper portion of each pile was fabricated so that it could be connected to the force meter, and its lower portion was cut off so that the cut face

would be parallel to the bottom of the channel when the pile was connected to the force meter. The cut face of each pile was also shielded by vinyl sheet to avoid edge effects.

It was decided to give seven different angles of 0° , $+10^\circ$, $+20^\circ$ and $+30^\circ$ to each model pile placed in an allotted plane. These angles are those measured against an axis normal to the still water surface. Here, the plus sign in front of each angle indicates that a pile is inclined away from the direction of wave propagation and the minus sign means that a model pile is inclined towards the direction of wave propagation. This is the case when a model pile is placed in Plane A. In the case of model pile placed in Plane B, the plus sign indicates that a model pile is inclined towards the left side of the wave channel when one views the channel from the side of wave absorber, and the minus sign means that the pile is inclined towards the right side of wave channel. It was also decided to perform all tests at a constant water depth of 0.8 meters and seven waves were chosen as the experimental waves. Table 2 summarizes experimental conditions used in this study.

Table 2. Experimental conditions used in this study.

Characteristics of Model Piles				
Materials of Model Pile		Aluminum Tube	Acrylic Resin Tubes	
Outer Dia. of Model Pile(cm)		2.2	3.0	4.0
Inner Dia. of Model Pile(cm)		1.9	2.2	3.2
Placement of Model Piles				
Planes for Placing Model Pile		Plane A and Plane B		
Inclining Angles of Model Pile		0° , $\pm 10^\circ$, $\pm 20^\circ$ and $\pm 30^\circ$		
Characteristics of Experimental Waves				
Wave No.	Wave Period T(sec)	Wave Height H(cm)	H/L	h/L
1	0.86	2.8	0.024	0.693
2	0.94	4.4	0.032	0.576
3	1.02	5.9	0.036	0.489
4	1.14	6.7	0.033	0.395
5	1.27	8.3	0.034	0.325
6	1.46	8.3	0.027	0.257
7	1.69	9.2	0.024	0.208

A total of 273 tests were conducted. In each test, both in-line and lift forces exerted on the model pile were recorded on the oscillograph. Characteristics of the incident waves were also measured simultaneously by a capacitance-type wave gage which was placed at a position 15 cm from the right side of the model pile by aligning the gage front carefully with the intersection of model pile and still water surface, and were recorded on the same oscillograph.

RESULTS AND DISCUSSIONS

Values of Drag, Mass and Lift Coefficients for Inclined Piles

Time-independent and time-dependent values of drag, mass and lift coefficients were determined for inclined piles placed in both Plane A and Plane B, by using the methods described in the previous Chapter, and characteristics of these coefficient values were studied.

1. Time-Independent Values of Drag, Mass and Lift Coefficients for Inclined Piles Placed in Plane A

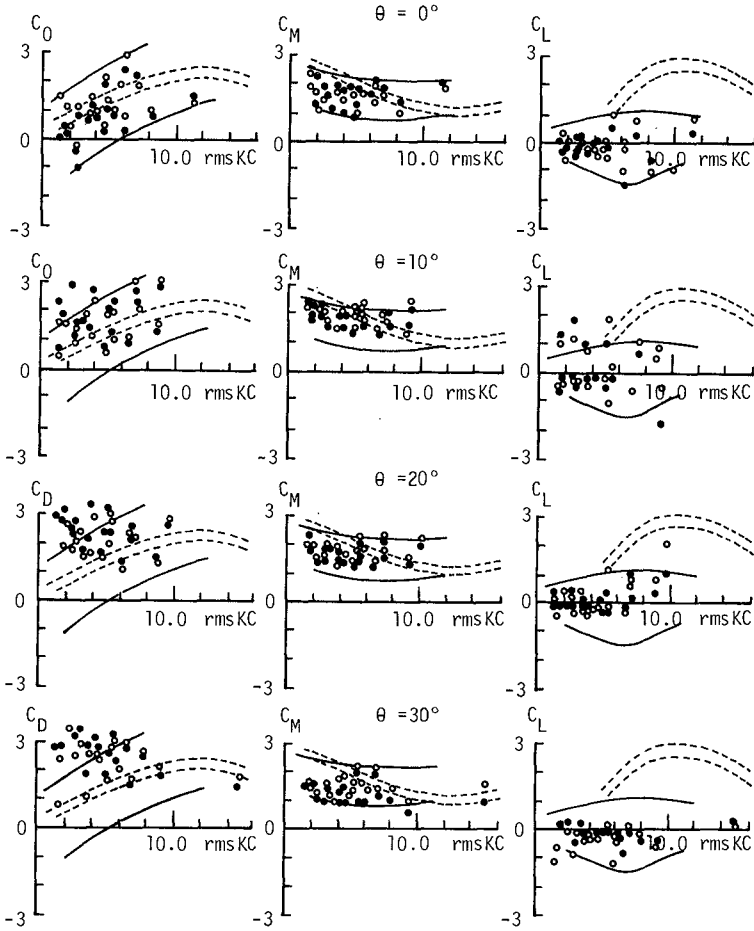
Time-independent values of the drag and mass coefficients in Eq.(7) were determined by the two-point method and by the least square method, respectively. Similarly, those of the lift coefficient in Eq.(8) were determined by the one-point method and by the least square method, respectively. For the convenience of later discussion, the following notations were given to the values of these coefficients:

- C_{DU2} : value of the drag coefficient determined by the two-point method.
- C_{DUL} : value of the drag coefficient determined by the least square method.
- C_{MU2} : value of the mass coefficient determined by the two-point method.
- C_{MUL} : value of the mass coefficient determined by the least square method.
- C_{LU1} : value of the lift coefficient determined by the one-point method.
- C_{LUL} : value of the lift coefficient determined by the least square method.

As mentioned previously, it has been pointed out by many researchers that the time-independent values of drag, mass and lift coefficients for either vertical or horizontal piles have some functional relationships with the period parameter or the Keulegan-Carpenter number. To determine whether this is true in the case of the coefficient values for inclined piles, coefficient values determined were plotted against the value of the rmsKC number, at every inclination of the pile. Here, the rmsKC number is the Keulegan-Carpenter number evaluated by $\sqrt{U^2} T/D$ where $\sqrt{U^2}$ is the root mean square of the velocity component, U, T is a wave period and D is a pile diameter.

Figure 3 shows the plots of the coefficient values determined for the piles inclined away from the direction of wave propagation. In this figure, the dotted lines show the Sarpkaya's results(1975) which were obtained for the piles placed horizontally in oscillatory flows, and the solid lines represent the variation ranges of each coefficient obtained in this study for the vertical piles. From this figure, the following facts were noted:

- (1). Both C_{DU2} and C_{DUL} increase their values first as the rmsKC number



- :variation curves of each coefficient determined by either the one-point or the two-point method.
- :variation curve of each coefficient determined by the least square method.
- :variation curves found by Sarpkaya for horizontal piles.
- :variation curves found by the writer for vertical piles($\theta=0^\circ$).

Figure 3. Variations of the coefficient values versus rmsKC number for circular piles placed in Plane A at plus inclination.

increases its value up to approximately 10.0, then start decreasing their values as the rmsKC number increases its value farther, although values of both coefficients scatter considerably.

- (2). Variations of C_{DU2} and C_{DU1} values versus rmsKC number agree considerably well to that found by Sarpkaya except for some data obtained for the piles inclined at 20° and 30°. It should be noted that these coefficients tend to decrease their values as the rmsKC number increases its value up to approximately 6.0.
- (3). Both C_{MU2} and C_{MU1} decrease their values first as the rmsKC number increases its value up to approximately 10.0, then start increasing their values as the rmsKC number increases its value farther. In this case, both coefficient values do not scatter as greatly as the values of drag coefficient.
- (4). Variations of C_{MU2} and C_{MU1} values versus rmsKC number agree considerably well to that found by Sarpkaya although inflection points of each variation curve appear at smaller value of the rmsKC number than the value of the KC number at which inflection point appears in the variation curve found by Sarpkaya. Further, distinct effect of pile inclination is not found on the variations of these coefficient values versus rmsKC number.
- (5). Many of C_{LU1} and C_{LU2} take minus values over the whole range of the rmsKC number. Further, the values of both coefficients scatter considerably over the whole range of the rmsKC number.
- (6). Variations of C_{LU1} and C_{LU2} values versus rmsKC number do not show any agreement with the variation curve found by Sarpkaya, although distinct effect of the pile inclination is not found on the variations of these coefficient values versus rmsKC number.

Similar plots were also made for the coefficient values of the piles inclined towards the direction of wave propagation. These plots found that variations of each coefficient value versus rmsKC number were quite similar to those found for the coefficient values of the piles inclined away from the direction of wave propagation except for the fact that many of the drag coefficient took minus values in the range where the value of the rmsKC number was smaller than approximately 6.0.

These facts found above may be caused partially by the following reasons:

- (1). Coefficient values determined here are a sort of representative values averaged over the submerged portions of inclined piles. Thus, effects of the water depth for these coefficient values are not evaluated properly.
- (2). The rmsKC number is used for the analysis of these coefficient values instead of the conventional period parameter.
- (3). Experiments have been conducted in the range of relatively small values of rmsKC number where the inertia force is predominant in comparison to the drag force.

2. Time-Independent Values of Drag, Mass and Lift Coefficients for Inclined Piles placed in Plane B

Time-independent values of drag, mass and lift coefficients in Eqs.(9) and (10) were determined by the three-point method and by the least square method, respectively. Many of these coefficients, however, took incredibly large values. This might be caused by the defect of the determination methods which require each force term in Eqs.(9) and (10) to share equal weight for the determination of each coefficient value regardless to its magnitude. Then, the following ratios were calculated to find some information which help minimize this defect:

$$RX1(t) = F_{Du}(t)/F_{mxB}(t) \times 100(\%)$$

$$RX2(t) = F_{I\dot{u}}(t)/F_{mxB}(t) \times 100(\%)$$

$$RX3(t) = F_{Lv}(t)/F_{mxB}(t) \times 100(\%)$$

$$RL1(t) = F_{Lu}(t)/F_{mLB}(t) \times 100(\%)$$

$$RL2(t) = F_{Ov}(t)/F_{mLB}(t) \times 100(\%)$$

$$RL3(t) = F_{I\dot{v}}(t)/F_{mLB}(t) \times 100(\%)$$

In the above equations, $F_{mxB}(t)$ represents measured value of the in-line force exerted on a pile placed in Plane B at an arbitrary phase, t , and $F_{mLB}(t)$ represents measured value of the lift force on the same pile at the same phase. Hence, these six ratios measure the relative magnitude or the contribution rate of each force term in Eqs.(9) and (10) to the corresponding wave forces. These calculations found that values of $RX3(t)$ were always quite small comparing to the values of the other ratios. Namely, the maximum values of $RX3(t)$ within a wave cycle were always smaller than 5% when piles were inclined at an inclination less than or equal to 20°. Further, some of $RX3(t)$ surely exceeded 5% when piles were inclined at 30°, but they did not exceed 10% in these cases.

Based on this finding, it was assumed that contribution rate of $F_{Lv}(t)$ in eq.(9) to its total in-line force, $F_{tXB}(t)$ is negligibly small in the cases of runs where the maximum value of $RX3(t)$ is less than 5%, and the values of only C_{Du} and $C_{M\dot{u}}$ in Eq.(9) were determined in these cases again by the two-point method and by the least square method, respectively. For determining the coefficient values in Eq.(10), it was further assumed that the values of $C_{M\dot{v}}$ in Eq.(10) are approximately equal to the values of $C_{M\dot{u}}$ determined previously since values of $C_{M\dot{u}}$ were almost constant over the range of rmsKC number experienced in this study. Based on this assumption, values of only C_{Lu} and C_{Dv} in Eq.(10) were determined again by the two-point method and by the least square method, respectively.

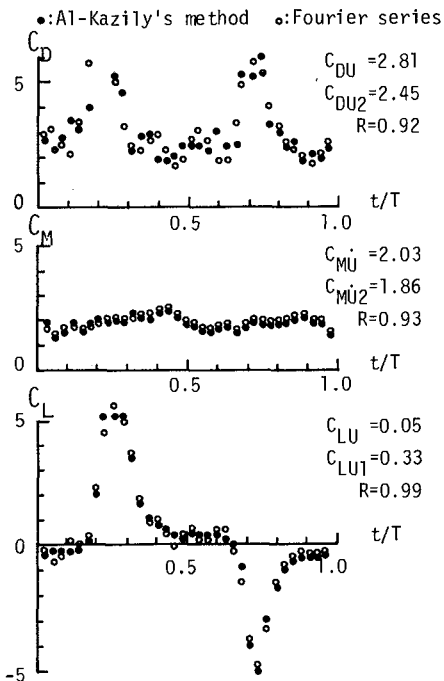
Coefficient values determined by these procedures were also plotted similarly against the values of the rmsKC number. As a result, it was found that the values of these coefficients also showed quite similar variations to those of the corresponding values of the coefficients found for the inclined piles placed in Plane A.

3. Time-Dependent Values of Drag, Mass and Lift Coefficients for Inclined Piles

Time-dependent values of drag, mass and lift coefficients for inclined piles placed in Plane A were determined by the same methods as described in the previous Chapter. Namely, time-dependent values of drag and mass coefficients in Eq.(9) were determined by the Al-Kazily's method, and those of the lift coefficient in Eq.(8) were determined by solving Eq.(8) at every incremental phase of 0.01 second over a wave cycle.

In the determination of time-dependent values of each coefficient for the piles placed in Plane B, however, coefficient values were determined by using the same procedures as developed previously for the determination of their time-independent values. Namely, the time-dependent values of each coefficient in Eqs.(9) and (10) were determined by the Al-Kazily's method when the contribution rate of each force term was less than 5%, although coefficient values were determined by the three-point

method described in the previous Chapter when the contribution rates of all force terms were greater than 5%.



Coefficient values determined by these methods were expanded into Fourier series which consist of six significant components whose frequencies are the multiples of the frequency of incident wave. As a result, it was found that correlation coefficients between determined values of each coefficient and the values of the corresponding coefficient estimated by the Fourier series reached approximately 0.8 in average.

Figure 4 shows some comparisons of the time-dependent values of each coefficient determined by the Al-Kazily's method, with those estimated by the Fourier series mentioned above. It can be noted clearly from this figure that coefficient values are not constant but vary considerably within a wave cycle, and that Fourier series of significant components can trace determined values of each coefficient quite satisfactorily.

Figure 4. Variation of the time-dependent coefficients ($\theta = +20^\circ$, $D = 4.0\text{cm}$, rmsKC No. = 2.80)

Reliability of the Coefficient Values

To check the reliability of the time-independent and time-dependent values of each coefficient determined above, quantitatively, relative deviations of the calculated wave forces from the measured ones were computed by Eq.(11) which was shown previously. This computation was made for both in-line and lift forces exerted on all piles placed in Plane A and Plane B. To distinguish these relative deviations, two suffixes were further added to the notations indicating the relative deviations of the in-line force, δF_x and that of the lift force, δF_L , respectively. Namely, the first suffix of the two indicates the plane where piles were placed: suffix [A] represents Plane A; and suffix [B] represents Plane B. On the other hand, the second suffix indicates the coefficients used for the calculation of wave force: suffix [1] represents the coefficient determined by the one-point method; suffix [2] represents the coefficients determined by the two-point method; suffix [L] represents the coefficients determined by the least square method; and suffix [F] represents the coefficients determined by the Fourier series of six significant components. These values were plotted against the rmsKC number at every inclination of a pile.

Figure 5 shows the relative deviations of the in-line force exerted on the piles placed in Plane A and Plane B at plus inclinations, respectively. Namely, the left half of this figure shows the variations of relative deviations versus rmsKC number in the cases when the time-independent coefficients were used for the calculation of in-line force, and the right half of it shows the variations of the relative deviations versus rmsKC number in the cases when the time-dependent coefficients determined by the Fourier series were used for the calculation of in-line force. From this figure, the following facts were noted:

- (1). Relative deviations calculated basing on the time-independent coefficients are less than 10% mostly, regardless of the placing plane or the inclination of the piles, although some of them exceed 10% in the case of vertical pile ($\theta = 0^\circ$). It is further noted that these relative deviations tend to increase slightly as the rmsKC number increases although some scatters are found among them in the range of the rmsKC number smaller than approximately 4.0.
- (2). Relative deviations calculated basing on the coefficients determined by the least square method are always few percents smaller than those calculated basing on the coefficients determined by the two-point method, regardless of the placing plane or the inclination of the piles.
- (3). Relative deviations calculated basing on the time-dependent coefficients determined by the Fourier series are less than 5% mostly over the whole range of the rmsKC number, regardless of the placing plane or the inclination of the piles.

Similar facts were also found in the cases when piles were placed at minus inclinations. These facts found above may indicate that the time-independent coefficients can be used for the prediction of the in-line force exerted on the inclined piles although usage of the time-dependent coefficients is more desirable for that purpose. These facts may also

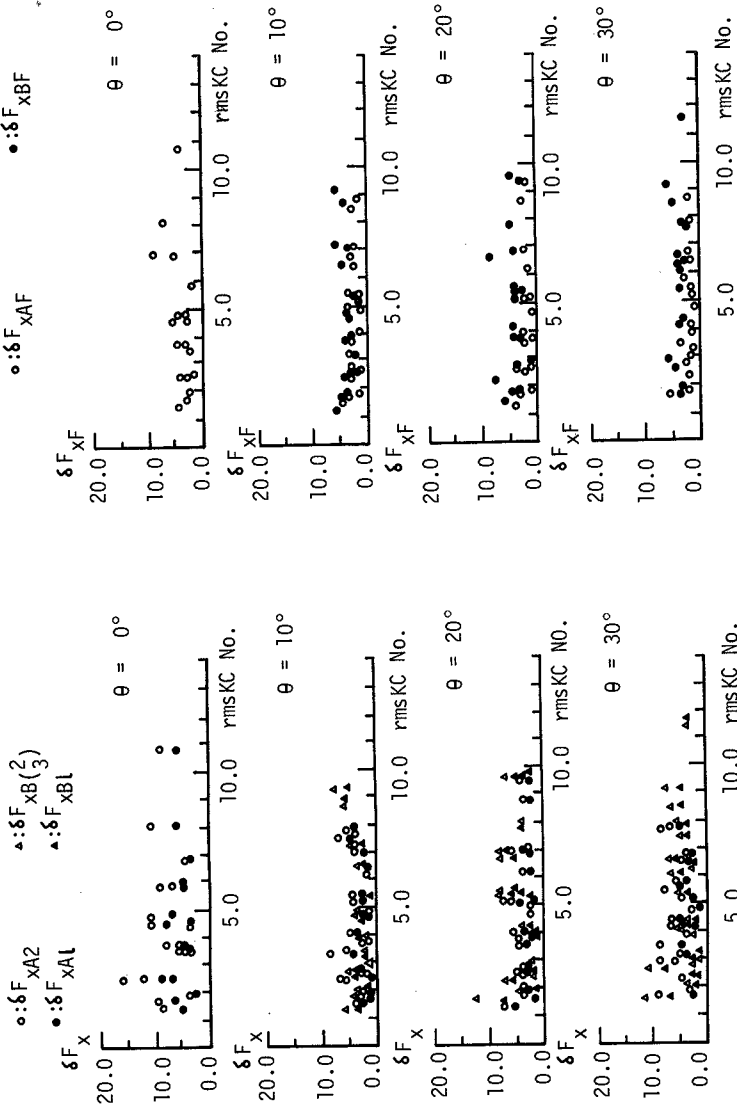


Figure 5. Relative deviation of in-line force plotted against rmsKC number.

endorse the propriety of wave force formulas formulated in this study for the inclined piles.

Figure 6 shows the relative deviations of the lift force exerted on the piles placed in Plane A and Plane B at plus inclinations, respectively. Namely, the left half of this figure summarizes variations of the relative deviations versus rmsKC number in the cases when the time-independent coefficients were used for the calculation of the lift force, and the right half of it summarizes those in the cases when the time-dependent coefficients determined by the Fourier series were used. From this figure, the following facts were noted:

- (1). Relative deviations calculated basing on the time-independent coefficients scatter considerably over the whole range of the rmsKC number, regardless of the placing plane or the inclination of the piles, and some of them exceed 200%.
- (2). Relative deviations calculated basing on the time-dependent coefficients are decreased significantly, irrespective of the placing plane or the inclination of the piles. Further, they tend to decrease as the rmsKC number increases, and most of them become approximately 10% when the rmsKC number reach 10.0.

Similar facts were also found in the cases when piles were placed at minus inclinations. The above facts may indicate that considerable amount of error would be induced if the time-independent coefficients are used for the prediction of lift force acting on the inclined piles, and that it is desirable to use some sorts of time-dependent coefficients such as the ones determined by the Fourier series for the prediction of lift force acting on the inclined piles.

Ratio of the Maximum Lift Force to the Maximum In-Line Force

Bidde(1971) conducted laboratory tests on the lift force acting on vertical circular piles and found that ratio of the lift force to the in-line force increased steadily as KC number increased, and that the ratio reached about 0.6 at the KC number of approximately 15 although it stopped increasing at the range of KC number greater than 15.

Sarpkaya(1975) also measured the lift force acting on horizontal circular piles and found that the ratio of the maximum lift force to the maximum in-line force varied with two humps while KC number increased up to about 30 although it kept almost constant value of about 0.8 at the range of KC number greater than 30. Further, he found that the ratio reached the maximum value of about 1.3 at one of the humps which appeared at the KC number of about 18.

In this study, ratio of the maximum lift force to the maximum in-line force recorded within a wave cycle were checked for all test cases and plotted at every inclination against the rmsKC number. Figure 7 shows these ratios found in the cases of the tests where piles were placed at plus inclination. In this figure, solid lines show the variation range of the ratio found by Bidde(1971). From this figure, the following facts were noted:

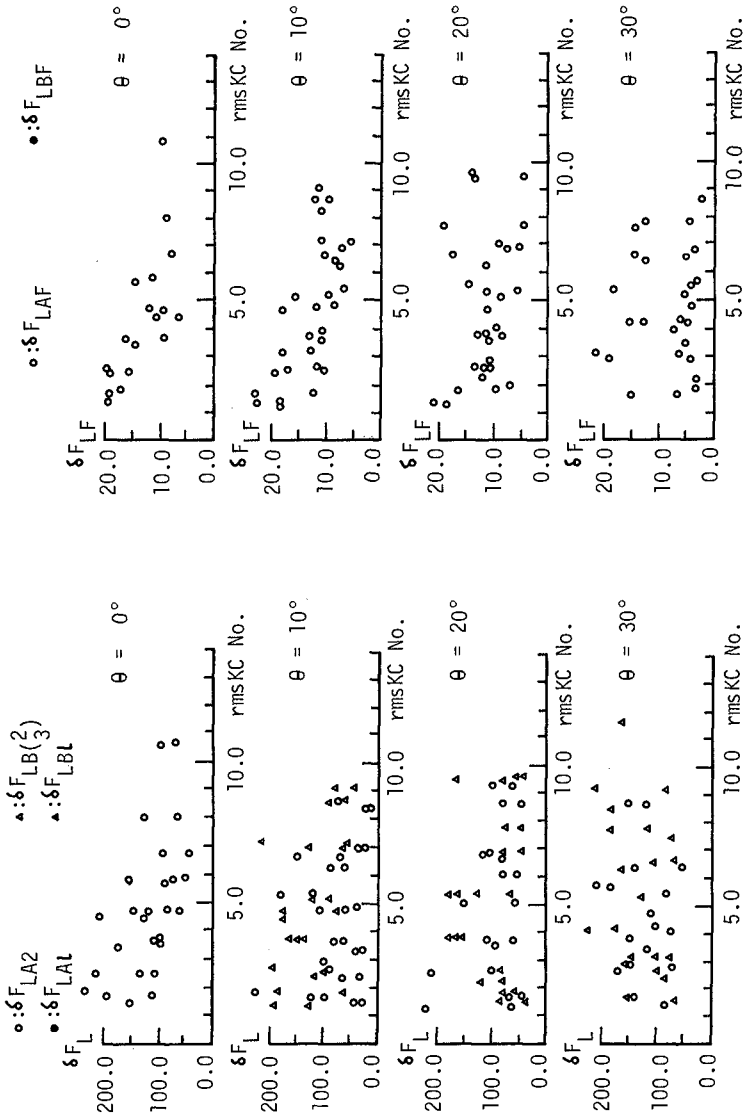


Figure 6. Relative deviation of lift force plotted against rmsKC number.

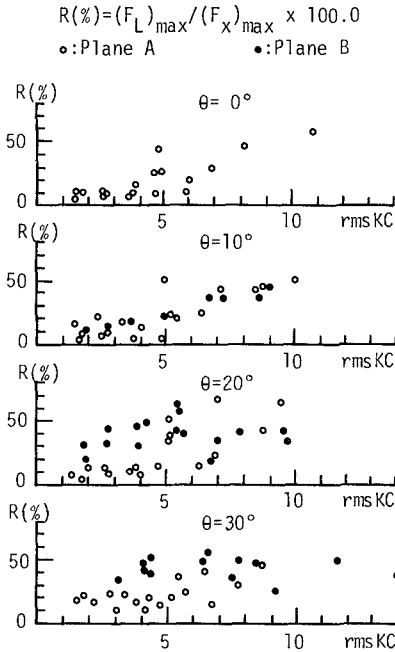


Figure 7. Ratio of the maximum lift force to the maximum in-line force versus rmsKC number (in cases of plus inclinations).

recognize the fact that considerably large lift force may possibly appear even at the small value of rmsKC number when piles are inclined more than 20°.

CONCLUSIONS

Both time-independent and time-dependent values of drag, mass and lift coefficients for inclined piles were determined by several methods, based on the respective wave force formulas which were derived by referring to the conventional Morison and lift force formulas. Reliability of these coefficient values were examined by checking the relative deviations of the calculated wave forces from the measured ones. Further, ratio of the maximum lift force to the maximum in-line force was also studied. As a result, the following conclusions were drawn:

- (1). Time-independent values of drag and mass coefficients can be used for the prediction of in-line force acting on the inclined

- (1). Ratio of the maximum lift force to the maximum in-line force tend to increase generally as the rmsKC number increases. Further, variations of the ratios versus rmsKC number agree quite well to the upper envelope of the variations found by Bidde, when piles are inclined at the inclination equal to or less than 10°.
- (2). When piles are inclined at the inclination equal to or greater than 20°, some scatters appear among the values of the ratios for the piles placed in Plane B. Namely, in this case, the ratios become almost constant ranging from approximately 0.3 to 0.6.

Similar facts were also found in the cases where piles were inclined at minus inclination.

The fact described in (2) may be caused partially by the effect of vertical velocity component of the induced flow. In any rate, readers should

- piles. Relative deviation calculated basing on these coefficients increases as the rmsKC number increases, but it will be 10% at most if the rmsKC number is smaller than about 12.0.
- (2). Time-independent values of lift coefficient can not be used for the prediction of lift force acting on the inclined piles. If they are used for prediction, relative deviation is about 100% in average over the whole range of rmsKC number. Lift coefficient determined by the Fourier series of six significant components will be a good one to be used for the prediction of lift force. If this coefficient is used for prediction, relative deviation is 20% at most. Further, it will decrease as the rmsKC number increases.
 - (3). Ratio of the maximum lift force to the maximum in-line force increases slightly as the rmsKC number increases, and variation of the ratio versus rmsKC number agrees quite well to the upper envelope of the variation of the ratio versus KC number found by Bidde, as long as the pile inclination is equal to or less than 10°. However, considerably large value of the ratio is found at the small value of rmsKC number if the piles are inclined more than 20°.

REFERENCES

1. Al-Kazily, M. F., "Forces on Submerged Pipelines Induced by Water Waves," University of California, Berkeley, Technical Report, HEL 9-21, October 1972, p.197.
2. Bidde, D. D., "Laboratory Study of Lift Forces on Circular Piles," Journal of the Waterways, Harbors and Coastal Engineering Division, Proceeding of ASCE, November 1971, pp.595-614.
3. Chakrabarti et al., "Wave Forces on Vertical Circular Cylinder," Journal of the Waterways, Harbors and Coastal Engineering Division, Proceeding of ASCE, WW2, May 1976, pp.203-220.
4. Keulegan, H. G. and L. H. Carpenter, "Forces on Cylinders and Plates in an Oscillatory Fluid," Journal of Research of the National Bureau of Standards, Vol. 60, No. 5, May 1958, pp.423-440.
5. Morison, J. R. et al., "The Force Exerted by Surface Waves on Piles," Petroleum Transactions, AIME, Vol. 189, 1950, pp.149-154.
6. Sarpkaya, T., "Forces on Cylinders and Spheres in a Sinusoidal Oscillating Fluid," Journal of Applied Mechanics, Transaction of ASME, March 1975, pp.32-37.
7. Shigemura, T. and K. Nishimura, "Simulation of Wave Forces on Inclined Cylindrical Piles," Proceedings of the Speciality Conference on COASTAL STRUCTURE 79, ASCE, March 1979, pp.134-153.

CHAPTER 109

WAVE-INDUCED SEEPAGE EFFECTS ON A VERTICAL CYLINDER

by

Thomas J.P. Durand¹ and Peter L. Monkmeyster², M. ASCE

ABSTRACT

This study deals with the seepage effects experienced by a large, vertical, circular cylinder resting on a submerged bed of sand when planar water waves interact with it. Potential theory is used to describe the seepage flow field. The sea bottom pressure condition is determined from the water field velocity potential derived by MacCamy and Fuchs (1954) in the case of planar waves diffracted by a large impervious cylinder. Consideration is also given to cylinders with a thin circular base whose diameter exceeds that of the cylinder itself.

The problem formulation as well as the initiation of the analysis apply to the general case of a bed of sand with finite depth.

For the case of infinite depth of the porous medium, theoretical solutions for the seepage pressure are obtained in the form of infinite integrals. Theoretical solutions for the pressure along the cylinder circular base are then derived, leading by integration to closed form expressions for the wave-induced seepage uplift force and overturning moment exerted on the cylinder. These expressions for the force and moment, which are presented in non-dimensional form are shown to be universal functions of a unique variable. Graphs are provided so that very few computations are required to determine the uplift force and overturning moment exerted on a cylinder. A comparison with various approximate theories reveals the present theory to be the only one which gives reliable results in general.

The amplitude and phase angle of the oscillating wave-induced pressure along the cylinder base are determined numerically. Results for the pressure amplitude are presented as non-dimensional ratios to the amplitude of the pressure that would prevail if no cylinder were disturbing the wave field.

Expressions for the exit gradient around the cylinder base are also determined. Contours of the ratio of the exit gradient to the one that would prevail in the absence of a cylinder are presented.

Laboratory measurements of uplift pressure amplitudes on a circular cylinder show good agreement with theoretical calculations.

INTRODUCTION

The rapid development of offshore construction in recent years has led to some complex technological problems, not the least of which are those concerned with the foundation and the possibility of foundation

-
- 1 Research Assistant, Department of Civil and Environmental Engineering, University of Wisconsin, Madison, Wisconsin 53706
 - 2 Professor of Civil and Environmental Engineering, University of Wisconsin, Madison, Wisconsin 53706

failure. There is some indication that such failure may be due to wave-induced seepage in the porous sea bed. Dynamic seepage pressures are believed to induce erosion phenomenon around the foundation of some structures as well as the cyclic uplift forces which act on the underside of a structure resting on the sea bottom. As a result, research dealing with the dynamics of wave-induced seepage in sea beds has been conducted by a number of investigators.

Most of the past research on the subject has focused upon the mathematical formulation required to obtain a realistic model of the physical phenomenon involved. Although work on this matter is still in progress, it may be useful to summarize the assumptions and governing equations used by some of the contributors. Sleath (1970) performed experiments which strongly support Putnam's (1949) use of potential theory, thereby suggesting that elastic effects can be neglected. Later, however, Moshagen and Tørum (1975), by including a water compressibility term in the continuity equation, derived a "heat conduction type" equation for the pressure. In the case of coarse sand, solutions to their equation approach those of Putnam, using potential theory, asymptotically. The results deviate only slightly for fine sands and are quite different for silts and silty clays. Yamamoto (1977), using the consolidation theory of Biot (1941), derived and solved a system of partial differential equations taking into account the compressibility of the water and the skeleton. Interestingly enough his solutions are very similar to those obtained from potential theory in the case of coarse sands and slightly different in the case of fine sands. Madsen (1978) also considered compressibility of water and skeleton as well as other soil properties. He concluded that for fine sands, as well as coarse sands which are isotropic, the effect of compressibility of fluid and skeleton is negligible.

It should be emphasized that all the previously mentioned studies apply only to planar waves unaffected by any structure. No consideration was given to the presence of a structure until Moshagen and Monkmeyer (1979) completed an investigation in which an embedded vertical cylinder was subjected to horizontal, wave-induced seepage forces. For a more detailed literature review the reader is referred to their paper.

The objective of this study is to analyze the dynamic seepage pressures and forces exerted on the base of a single, vertical, circular cylinder resting on a bed of sand when linear progressive waves interact with it. The cylinder does not penetrate the sea bed but its base can have a larger radius than the cylinder body itself. This extended circular base, when it is considered, is assumed to be infinitely thin. (See Fig. 1.)

The good agreement among the solutions of the various theories mentioned previously, when applied to sands (especially coarse sands), together with the great simplification it provides, makes potential theory the logical choice for the present study, especially in view of Sleath's experimental confirmation. The coupling condition between the sea water field and the pore water seepage field is obtained by means of a pressure matching procedure along the sea bottom. To accomplish

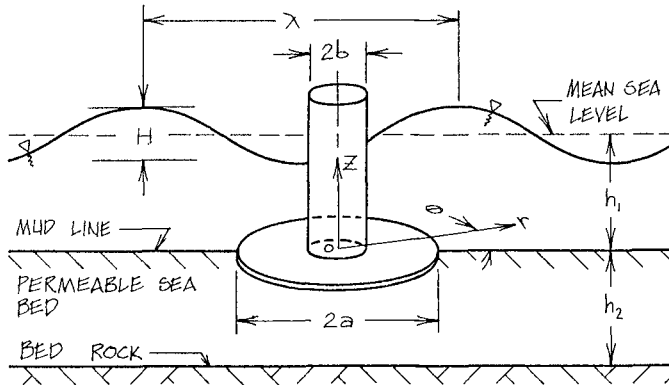


Fig. 1. Definition Sketch

this, MacCamy and Fuchs' (1954) potential function, describing both the incident and diffracted waves of the sea water flow field, is used to derive an analytic expression for the sea water pressure on the sea bottom. This pressure distribution provides a coupling boundary condition for the dynamic seepage field. The various additional boundary conditions are also stated for the seepage potential function. Although the analysis is initiated for the general case of a porous medium of finite thickness, theoretical solutions for the seepage pressures in the sea bed are only presented for the case of a porous medium of infinite thickness. Indeed, only in that case do the solutions lead to relatively simple expressions for the pressure distribution along the underside of the cylinder base. The uplift force and overturning moment exerted on the cylinder base by the dynamic seepage can then be obtained by integration.

THEORETICAL ANALYSIS

Governing Equation

The seepage flow field in the porous medium is assumed to follow Darcy's law,

$$\vec{q} = \nabla \phi_2 \quad (1)$$

$$\text{with} \quad \phi_2 = -K[p_2/\gamma + z] \quad (2)$$

where ϕ_2 = velocity potential [L^2/T]

γ = specific weight of water [M/L^2T^2]

p_2 = pressure [M/LT^2]

\vec{q} = specific discharge [L/T]

K = hydraulic conductivity [L/T]

z = vertical coordinate [L]

Assuming a completely saturated soil and neglecting the various effects due to the compressibilities of the water, porous skeleton and sand grains themselves, the continuity equation takes the form:

$$\nabla \cdot \vec{q} = 0 \quad (3)$$

By substitution of Eq. 1 into Eq. 3, the governing equations for seepage then lead to Laplace's Equation,

$$\nabla^2 \phi_2 = 0 \quad (4)$$

so that under the assumption of essentially incompressible water flowing through a saturated, rigid, isotropic porous medium, potential theory may be used to describe the seepage flow field, as noted before.

Boundary Conditions

In order to couple the sea water field to the seepage flow field, the pore water pressure distribution along the mud line is matched to the corresponding sea water pressure distribution. To this end, use is made of the well-known MacCamy and Fuchs (1954) velocity potential for small amplitude water waves diffracted by a vertical circular cylinder of radius b .

$$\phi_1(r, \theta, z, t) = \frac{gH}{2\omega} e^{-i\omega t} \frac{\cosh(kz)}{\cosh(kh_1)} \sum_{m=0}^{\infty} \frac{\epsilon_m i^m C_m(kr)}{H_m^{(1)'}(kb)} \cos(m\theta) \quad (5)$$

where $C_m(kr) = J_m'(kb) H_m^{(1)}(kr) - H_m^{(1)'}(kb) J_m(kr)$

$$\epsilon_m = \begin{cases} 1 & \text{if } m = 0 \\ 2 & \text{if } m \geq 1 \end{cases}$$

and where g = acceleration due to gravity [L/T^2]
 H = wave height [L]
 ω = $2\pi/T$ = wave frequency = [$gk \tanh(kh_1)$] $[T^{-1}]$
 k = wave number [L^{-1}]
 h_1 = elevation of mean sea level above sea bottom [L]
 b = cylinder radius [L]
 $J_m(\)$ = Bessel function of the first kind of order m
 $H_m^{(1)}(\)$ = Hankel function of the first kind of order m

where the primes indicate differentiation with respect to the argument. It should be emphasized at this point that MacCamy and Fuchs' velocity potential is valid for cylinders large with respect to the wave dimensions. More specifically, since the MacCamy and Fuchs theory neglects drag but considers inertial effects it is only valid when drag effects are minimal. As Dean and Harleman (1966) point out, this is the case when H/b is small and kh_1 is large.

By substituting Eq. 5 into the linearized dynamic pressure equation,

$$\frac{\partial \phi_1}{\partial t} + \frac{p_1}{\rho} = 0 \quad (6)$$

where ρ = mass density $[M/L^3]$,

one can derive an expression for the dynamic pressure at the bottom of the sea. The next step is to equate the pore water pressure immediately below the mud line to the corresponding sea water pressure immediately above.

$$p_1 = p_2 \quad \text{at } z = 0 \quad \text{for } r \geq a \quad (7)$$

where a = radius of the cylinder circular base $[L]$.

Making use of Eq. 2 one finally obtains the following condition for ϕ_2 along the mud line

$$\phi_2 = \frac{K}{g} \frac{\partial \phi_1}{\partial t} = -\frac{iK}{g} \omega \phi_1 \quad \text{at } z = 0 \quad r \geq a$$

or, henceforth dropping the subscript 2,

$$\phi(r \geq a, \theta, z=0, t) = -i \frac{KH e^{-i\omega t}}{2 \cosh(kh_1)} \sum_{m=0}^{\infty} \frac{\epsilon_m i^m C_m(kr)}{H_m^{(1)}(kb)} \cos(m\theta) \quad (8)$$

The impervious condition at bed rock is

$$\frac{\partial \phi}{\partial z} = 0 \quad \text{at } z = -h_2 \quad (9)$$

while the impervious condition along the circular disc of radius a on the underside of the base of the structure is

$$\frac{\partial \phi}{\partial z} = 0 \quad \text{at } z = 0 \quad r \leq a \quad (10)$$

It should be noted that the radiation condition associated with the present potential problem - such a condition is needed to insure the uniqueness of the solution - turns out to be implicitly integrated in the pressure matching condition along the mud line so that no additional requirement need be prescribed.

The governing Laplace equation, Eq. 4, is therefore constrained by its boundary conditions, Eqs. 8, 9 and 10. It clearly appears that a Neumann type condition and a Dirichlet type condition are prescribed on different parts of the same boundary, namely the upper plane $z = 0$, so that the potential problem to be solved is of the mixed boundary value type.

Solution

Due to the non-axisymmetric diffracted wave pattern, the analysis is initiated in three dimensions using a non-dimensional coordinate system

$$r^* = r/a \quad z^* = z/a \quad h_2^* = h_2/a \quad (11)$$

The stars are dropped for simplicity of the notation.

The particular form of the pressure matching condition, Eq. 8, suggests that the unknown potential function be expressed in a Fourier expansion of the polar angle,

$$\phi(r, \theta, z, t) = -i \frac{KH e^{-i\omega t}}{2 \cosh(kh_1)} \sum_{m=0}^{\infty} \frac{\epsilon_m i^m \phi_m(r, z)}{H_m^{(1)}(kb)} \cos(m\theta) \quad (12)$$

where the functions $\phi_m(r, z)$ are the new problem unknowns satisfying the reduced partial differential equation

$$\frac{\partial^2 \phi_m}{\partial r^2} + \frac{1}{r} \frac{\partial \phi_m}{\partial r} - \frac{m^2}{r^2} \phi_m + \frac{\partial^2 \phi_m}{\partial z^2} = 0 \quad (13)$$

A solution of Eq. 13, satisfying the bed rock condition, Eq. 9, can be obtained through a Hankel integral transform and is given by

$$\phi_m(r, z) = \int_0^{\infty} p A_m(p) [e^{pz} + e^{-p(z+2h_2)}] J_m(pr) dp \quad (14)$$

where $A_m(\)$ is a new unknown function which can be determined by making use of the remaining boundary conditions, Eqs. 8 and 10,

$$\int_0^{\infty} p \tanh(ph_2) F_m(p) J_m(pr) dp = 0 \quad 0 \leq r < 1 \quad (15)$$

$$\int_0^{\infty} F_m(p) J_m(pr) dp = C_m(kar) \quad 1 \leq r$$

where

$$F_m(p) = p A_m(p) [1 + e^{-2ph_2}] \quad (16)$$

Eqs. 15 are known as Dual Integral Equations. They obviously result from the mixed nature of the boundary value problem. Sneddon (1966) presents a thorough treatment of these equations. Closed form solutions of Dual Integral Equations have been obtained in the case of $h_2 \rightarrow \infty$, which corresponds to the physical case of infinite depth of the porous medium, and therefore this analysis will be restricted to the infinite depth case only.

For $h_2 \rightarrow \infty$, Sneddon reports Titchmarsh's solution as

$$p A_m(p) = -\sqrt{\frac{2p}{\pi}} \int_1^{\infty} t^{m+1/2} J_{m+1/2}(pt) dt \frac{d}{dt} \int_t^{\infty} \frac{C_m(kau) du}{u^{m-1} \sqrt{u^2 - t^2}} \quad (17)$$

which, after some rearrangement and then substitution into Eq. 14, leads to

$$\phi_m(r, z) = \int_0^{\infty} \sqrt{kap} e^{pz} J_m(pr) dp \int_1^{\infty} t J_{m+1/2}(pt) C_{m+1/2}^*(kat) dt \quad (18)$$

where

$$C_{m+1/2}^*(kat) = J_m'(kb) H_{m+1/2}^{(1)}(kat) - H_m^{(1)'}(kb) J_{m+1/2}(kat) \quad (19)$$

It should be pointed out that Eq. 18 together with Eq. 12 provide an exact expression for the wave-induced potential distribution throughout the entire seepage field when a cylinder is resting on a bed of sand of infinite thickness.

Although some simplifications of Eq. 18 can be performed by making use of the Hankel inversion formula and of a known indefinite integral for the inner integral, this would only apply for the Bessel function of first kind, $J_m(\cdot)$, but not for $H_m^{(1)}(\cdot)$ so that no equation for ϕ_m , more suited to computational purposes, could be derived.

RESULTS OF THE THEORETICAL ANALYSIS

Pressure Distribution along the Cylinder Base

Substituting $z = 0$ in Eq. 18, inverting the order of integration, and performing the inner integration leads to

$$\phi_m(r \leq 1, 0) = \sqrt{\frac{2ka}{\pi}} r^m \int_1^\infty \frac{C_{m+1/2}^*(kat) dt}{t^{m-1/2} \sqrt{t^2 - r^2}} \quad (20)$$

which can in turn be transformed into

$$\phi_m(r \leq 1, 0) = C_m(kar) - \sqrt{\frac{2ka}{\pi}} r^m \int_r^1 \frac{C_{m+1/2}^*(kat) dt}{t^{m-1/2} \sqrt{t^2 - r^2}} \quad (21)$$

Hence the exact solution for the wave-induced pressure distribution along the circular base of the cylinder is, dropping the hydrostatic term,

$$p(r \leq 1, \theta, 0, t) = \frac{\gamma_H e^{-i\omega t}}{2 \cosh(kh_1)} \sum_{m=0}^{\infty} \frac{\epsilon_m i^{m+1} \phi_m(r, 0)}{H_m^{(1)'}(kb)} \cos(m\theta) \quad (22)$$

where, for computational purposes, Eq. 21 is transformed into

$$\phi_m(r \leq 1, 0) = C_m(kar) - \sqrt{\frac{2kar}{\pi}} \int_0^{\cosh^{-1}(\frac{1}{r})} \frac{C_{m+1/2}^*(kar \cosh u)}{(\cosh u)^{m-1/2}} du \quad (23)$$

Tabulated numerical results for the wave-induced dynamic pressure amplitude along the cylinder base are presented as non-dimensional ratios to the amplitude of the pressure that would prevail if no cylinder were disturbing the wave field, namely

$$P_{LT} = \frac{\gamma H}{2 \cosh(kh_1)} \quad (24)$$

Hence only the infinite sum in Eq. 22 is tabulated. Table I shows the values of these pressure ratios for $ka = kb = 0.2, 1.0$ and $ka = 2kb = 2.0$.

Table I

DIMENSIONLESS PRESSURE AMPLITUDE ON THE CYLINDER BASE

$ka = kb = 0.2$	$r/a = 0.2$	$r/a = 0.4$	$r/a = 0.6$	$r/a = 0.8$	$r/a = 1.0$
$\theta = 0^\circ$.85260	.85978	.87580	.90536	.99894
$\theta = 30^\circ$.85285	.85979	.87500	.90288	.99067
$\theta = 60^\circ$.85369	.86052	.87450	.89949	.97643
$\theta = 90^\circ$.85525	.86321	.87782	.90283	.97724
$\theta = 120^\circ$.85728	.86779	.88568	.91518	1.00101
$\theta = 150^\circ$.85905	.87233	.89420	.92962	1.03179
$\theta = 180^\circ$.85976	.87423	.89789	.93599	1.04562

$ka = kb = 1.0$	$r/a = 0.2$	$r/a = 0.4$	$r/a = 0.6$	$r/a = 0.8$	$r/a = 1.0$
$\theta = 0^\circ$.33957	.25847	.26442	.40492	.88819
$\theta = 30^\circ$.35685	.28891	.27930	.36903	.74425
$\theta = 60^\circ$.40360	.38152	.39463	.46184	.73888
$\theta = 90^\circ$.46534	.50802	.58878	.73176	1.17128
$\theta = 120^\circ$.52368	.62174	.75669	.95830	1.52487
$\theta = 150^\circ$.56391	.69448	.85453	1.07523	1.67346
$\theta = 180^\circ$.57809	.71879	.88496	1.10795	1.70708

$ka = 2kb = 2.0$	$r/a = 0.2$	$r/a = 0.4$	$r/a = 0.6$	$r/a = 0.8$	$r/a = 1.0$
$\theta = 0^\circ$.05838	.10355	.22347	.40757	.92881
$\theta = 30^\circ$.06704	.09116	.18303	.33408	.78076
$\theta = 60^\circ$.09431	.11759	.19394	.34493	.83519
$\theta = 90^\circ$.13022	.18857	.30615	.52746	1.27124
$\theta = 120^\circ$.16014	.23754	.36243	.58202	1.38303
$\theta = 150^\circ$.17771	.25566	.35972	.52815	1.21639
$\theta = 180^\circ$.18326	.25908	.35205	.49587	1.11703

Uplift Force and Overturning Moment on the Structure

In addition to providing a simplifying transformation, the Fourier expansion, as performed at the beginning of the analysis, also has the well-known advantage of extracting from the pressure the very terms required for calculating the uplift force and overturning moment exerted on the cylinder base. More specifically, when performing the integration of the pressure, only the zero or first order terms of the Fourier infinite series make a non-zero contribution to the force or moment respectively. Furthermore, in both cases, the corresponding integration of Eq. 21 involves two integrations which can be inverted and performed analytically. Various straightforward algebraic manipulations - for the detailed derivation see Durand (1978) - finally yield closed form expressions for the wave-induced seepage uplift force and overturning moment exerted on the cylinder base as follows:

$$F = \frac{\gamma H}{\cosh(kh_1)} \frac{\pi a^2}{ka} A_0(kb) \cos(\omega t + \alpha_0(kb))$$

$$\{J_1(kb) [Y_1(ka) + \frac{2}{\pi} \frac{\cos ka}{ka} + \frac{2}{\pi} \sin ka]$$

$$- Y_1(kb) [J_1(ka) - \frac{2}{\pi} \frac{\sin ka}{ka} + \frac{2}{\pi} \cos ka]\}$$
 (25)

$$M_o = - \frac{\gamma H}{\cosh(kh_1)} \frac{\pi a^3}{ka} A_1(kb) \sin(\omega t + \alpha_1(kb))$$

$$\{J_1'(kb) [Y_2(ka) - \frac{4}{3\pi} (\cos ka (1 - \frac{3}{(ka)^2}) - \frac{3 \sin ka}{ka})]$$

$$- Y_1'(kb) [J_2(ka) + \frac{4}{3\pi} (\sin ka (1 - \frac{3}{(ka)^2}) + \frac{3 \cos ka}{ka})]\}$$
 (26)

where

$$\tan[\alpha_i(kb)] = \frac{Y_i'(kb)}{J_i'(kb)} \quad i = 0, 1$$
 (27)

$$A_i(kb) = [J_i'(kb)^2 + Y_i'(kb)^2]^{-1/2} \quad i = 0, 1$$
 (28)

It should be noted that Eq. 26 can be simplified when $kb = ka$ by making use of the identity,

$$J_1'(ka) Y_2(ka) - Y_1'(ka) J_2(ka) = - \frac{2}{\pi (ka)^2}$$
 (29)

Eq. 25 may be normalized with expressions for the amplitude of the force based on two approximate theories. First, assuming that the oscillating pressure has the same amplitude and phase across the cylinder base, one obtains (see curve A in Fig. 2)

$$F_{LT_1} = \frac{\gamma H}{2 \cosh(kh_1)} \pi a^2$$
 (30)

The second approximate force is derived by taking into account the spatial variation of the pressure that would prevail across the cylinder base if no cylinder were present, (see curve B in Fig. 2)

$$F_{LT_2} = \frac{\gamma H}{\cosh(kh_1)} \pi a^2 \frac{J_1(ka)}{ka}$$
 (31)

Eq. 26 may also be normalized with an approximate expression for the amplitude of the moment derived for conditions similar to those of Eq. 31. (The moment vanishes for the conditions of Eq. 30.)

$$M_{o_{LT}} = \frac{\gamma H}{\cosh(kh_1)} \pi a^3 \frac{J_2(ka)}{ka}$$
 (32)

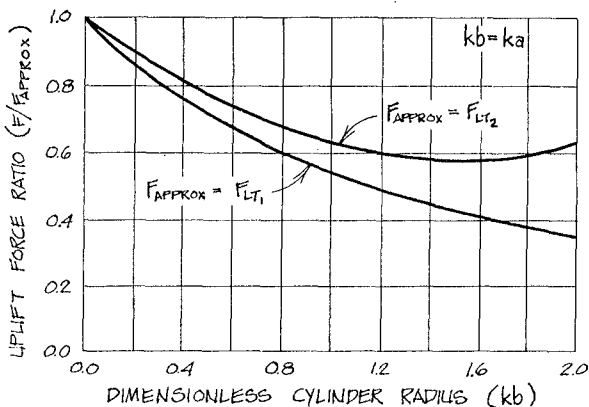


Fig. 2. Uplift Force Ratios

The ratios of the amplitude of the uplift force and overturning moment to the above normalizing quantities are plotted in Figs. 3 and 4 with ka as the variable and kb as parameter. For the most common case of $a = b$, each result is restricted to a universal graph because the above ratios are universal functions of a unique variable, ka .

Vertical Velocity Distribution along the Mud Line

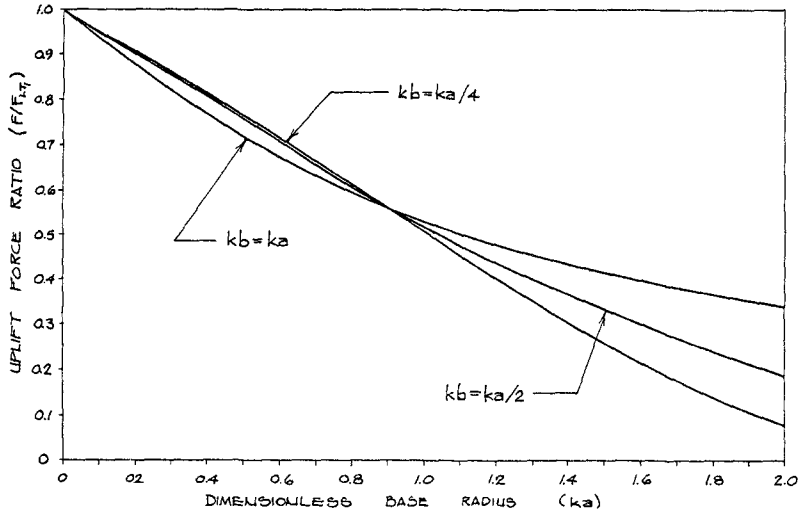
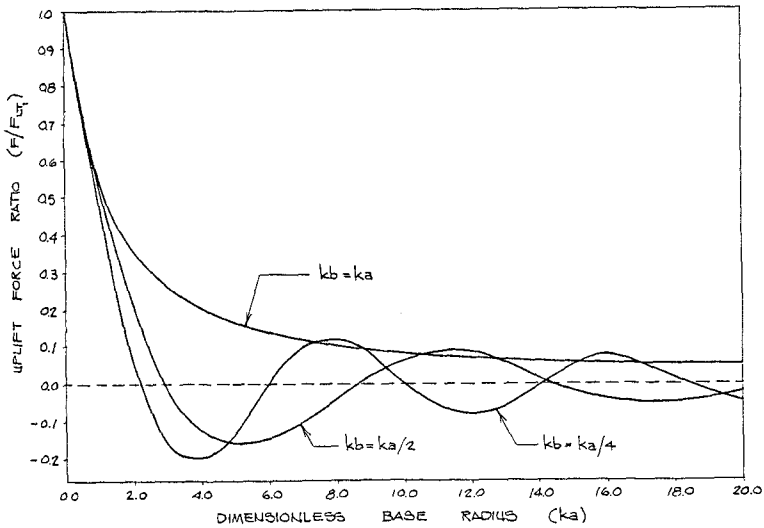
It is important to note that Sneddon (1966) provides an alternate method to derive Eq. 20 directly from the Dual Integral Equations themselves. Interestingly enough he also provides a direct solution for the vertical velocity $\frac{\partial \phi}{\partial z}$ at the mud line through an expression for $\frac{\partial \phi}{\partial z}^m (r > 1, z = 0)$ which can take the form

$$\frac{\partial \phi}{\partial z}^m (r > 1, z = 0) = ka C_m^*(ka r) + \sqrt{\frac{2ka}{\pi}} r^{-m} \int_0^1 \frac{u^{m+3/2} C_{m+1/2}^*(kau)}{(r^2 - u^2)^{3/2}} du \quad (33)$$

Hence Eqs. 12 and 33 enable one to determine the vertical component of the specific discharge along the mud line and therefore the exit gradient. This quantity obviously appears to become infinite at the end of the cylinder base, $r = a$, but one may extract the singularity from Eq. 33 as

$$\sqrt{\frac{2ka}{\pi}} \frac{C_{m+1/2}^*(ka) r^{-m-1}}{\sqrt{r^2 - 1}} \quad (34)$$

so that the singularity of the seepage velocity field is clearly of the same weak nature as the well-known seepage velocity singularity occurring at the toe of an impervious dam resting on the top of a porous medium.

Fig. 3.a. Uplift Force Ratio: $ka \leq 2.0$ Fig. 3.b. Uplift Force Ratio: $ka \leq 20.0$

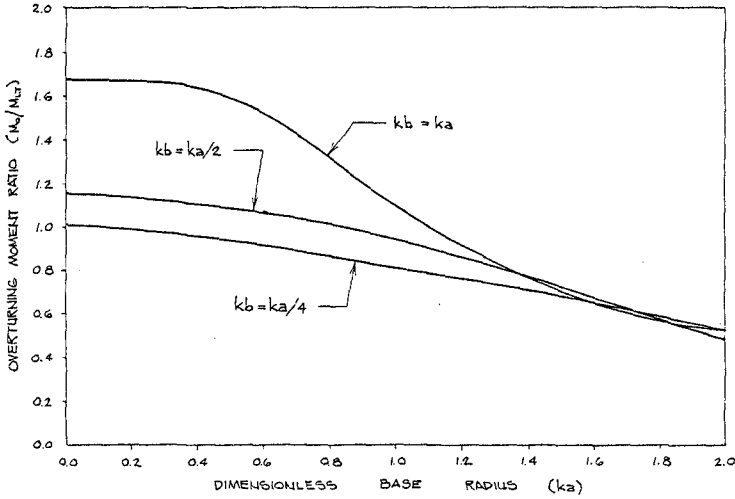


Fig. 4. Overturning Moment Ratio

The vertical component of the specific discharge can then be obtained from Eq. 12 so that the exit gradient

$$I_e = \frac{1}{K} \frac{\partial \phi}{\partial z} (r > 1, 0, 0, t) \tag{35}$$

is

$$I_e = - \frac{kH e^{-i\omega t}}{2 \cosh(kh_1)} \sum_{m=0}^{\infty} \frac{\epsilon_m i^{m+1}}{ka H_m(1)'(kb)} \frac{\partial \phi_m}{\partial z} (r > 1, 0) \cos(m\theta) \tag{36}$$

One may use the notion of critical gradient by comparing the amplitude of the oscillating exit gradient as given by Eq. 36 to the well-known expression

$$I_{cr} = \frac{Y'}{Y_w} = \frac{S_s - 1}{1 + e} \tag{37}$$

which for sands is approximately equal to 1.

If no cylinder were disturbing the wave field, the amplitude of the exit gradient to be used in place of Eq. 36 would simply be

$$I_e = \frac{kH}{2 \cosh(kh_1)}$$

so that it appears to be useful to simply compute the quantity

$$S(r, \theta) = \left| \sum_{m=0}^{\infty} \frac{\epsilon_m i^{m+1}}{H_m(1)'(kb)} \frac{1}{ka} \frac{\partial \phi_m}{\partial z} (r > 1, 0) \cos(m\theta) \right|$$

after substituting from Eq. 33.

A stability condition is then given by

$$\frac{kH}{2 \cosh(kh_1)} S(r, \theta) \leq I_{cr} = \frac{S_s - 1}{1 + e} \approx 1$$

in which the cylinder effect has been concentrated in a single coefficient, $S(r, \theta)$.

EXPERIMENTAL STUDY

In order to check the validity of the above theory, actual uplift pressure amplitudes along the base of a rigidly fixed, vertical, circular cylinder resting on a bed of sand were measured in the wave tank of the Hydraulics Laboratory of the University of Wisconsin-Madison. The sand used in the experiments was a fairly uniform coarse sand (about 1 mm in diameter). Although the depth of the porous medium had to be finite, it was kept large enough with respect to the wave length to permit the use of infinite-depth theory. More specifically the quantity kh_2 was equal to 2.1 so that $\tanh(kh_2)$ was close to 1, or more precisely 0.97. The tank used was 26 ft (7.92 m) long, 4 ft (1.22 m) wide and 2 ft (61 cm) deep but the inclusion of a bed of sand reduced the depth to 1 ft (30.5 cm). The sinusoidal progressive waves generated were in the following approximate ranges

$$.7 \text{ s} \leq T \leq .9 \text{ s} \quad 2.4' \leq L \leq 3.5' \quad 2.2'' \leq H \leq 2.85''$$

$$(73.2 \text{ cm}) \quad (106.7 \text{ cm}) \quad (5.59 \text{ cm}) \quad (7.24 \text{ cm})$$

Pressure measurements were made on the underside of the base of a vertical, circular cylinder mounted in the tank on top of the sand bed. Only one cylinder having a diameter of 5.72 in (14.5 cm) was tested with a sea water depth of 8 in (20.3 cm). A Pace transducer was used to measure pressures along the underside of the cylinder base at $r_1 = .991$ in (2.52 cm) and $r_2 = 1.963$ in (4.99 cm) while variation of the polar angle θ was obtained by rotation of the cylinder. The cylinder base had the same radius as the cylinder itself: $b = a$. See Fig. 5.

The measured pressures were normalized with respect to the pressure that would have prevailed if no cylinder had been disturbing the incoming waves. To this end, the normalizing quantities were determined by substituting the physical values into Eq. 24.

Spring and Monkmeyer (1975) studied the effect of wall confinement on pressure measurements along a cylinder placed in a tank of finite width. Correction coefficients resulting from their theoretical analysis of confinement were also used. In all cases, however, this coefficient turned out to be very close to 1 because their results and recommendations had made it possible to avoid those very parameter values based on wave length, tank width, cylinder radius for which confinement effects are important.

In Table II typical laboratory results are compared with the theory. The non-dimensional theoretical results were computed from

DIRECTION OF WAVE ADVANCE
→

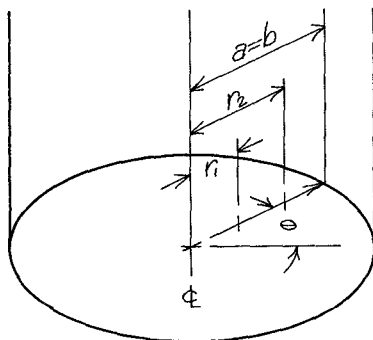


Fig. 5. Position of the Pressure Taps

Eqs. 22, 23 and 24. In combination with two values for r , r_1 and r_2 , five values for the polar angle θ were used.

DISCUSSION

Table I clearly shows that the maximum pressure amplitude generally occurs at $r = a$, $\theta = 180^\circ$ while the minimum is generally found at $\theta = 0^\circ$, between $r = 0.0$ and $r = 0.4a$. For small values of $ka = kb$ (cylinder radius small with respect to the wave length) the maximum pressure amplitude is only 1.2 times the minimum so that the pressure amplitude variation across the cylinder base is not very significant in this case. For larger values of ka , e.g. $ka = kb = 1.0$, however, the maximum amplitude may be as much as 7 times larger than the minimum and 1.7 times larger than the value expected if no cylinder were disturbing the incoming wave field. A strong damping effect is also demonstrated by the small value of the amplitude of the oscillating pressure at the point of minimum pressure amplitude (about 25% of the expected value at that point if no cylinder were there). For the same cylinder, $kb = 1.0$, with an extended base, $ka = 2.0$, the pressure amplitudes around the edge of the base are not as affected by the diffracted waves as they are in the immediate vicinity of the cylinder wall, e.g. when $ka = kb$. However the damping effect taking place across the extended base is more striking.

Typically the value of the parameter ka for conditions corresponding to large oil tanks in the North Sea ($2a = 100$ m) with the century wave ($L = 320$ m) is about 1.0. Interestingly it was found that for values of ka of order 1, the pressure amplitude variation across the cylinder base is quite significant.

The graphs presented on Figs. 3 and 4 show how the pressure variation across the cylinder base affects the uplift force and overturning

TABLE II

COMPARISON OF SELECTED EXPERIMENTAL PRESSURE RATIOS
WITH PRESSURE RATIOS PREDICTED BY THEORY

kb (=ka)	Experimental Data		Theory	
	r/a	θ	R_{exp}	R_{th}
0.6133	0.3465	180	0.719	0.75602
		135	0.657	0.71614
		90	0.549	0.62555
		45	0.547	0.55224
		0	0.548	0.53048
	0.686	180	0.970	0.99319
		135	0.813	0.90817
		90	0.707	0.71096
		45	0.581	0.58945
		0	0.558	0.58829
0.4235	0.3465	180	0.777	0.78260
		135	0.744	0.76181
		90	0.718	0.71926
		45	0.705	0.69016
		0	0.729	0.68278
	0.686	180	0.903	0.92851
		135	0.804	0.87648
		90	0.750	0.77613
		45	0.728	0.73250
		0	0.741	0.73619

Note: Waves approach from $\theta = 180^\circ$

moment. The pressure damping in the sea bed as ka increases, clearly has the effect of decreasing the force and moment with respect to what approximate theories would predict. This is consistent with what intuitive consideration would suggest but a quantitative rather than qualitative statement about the uplift force and overturning moment is quite important for design purposes. As an example for $ka = 1$, the force is about 50% smaller than that which simple approximate theories would predict.

Although not presented here in detail, additional studies led to the following conclusion: From the standpoint of minimizing the net uplift force and net overturning moment exerted on a cylinder of given radius b , also taking into account the effect of the pressure distribution along the upperside of the extended base, it appears that a cylinder without an extended base ($a = b$) rather than one with an extended base ($a > b$) is preferable. In the latter case one might have expected the dynamic pressure exerted along the upperside of the extended base to somehow compensate for the increase in the underside contribution from the dynamic seepage. But this was not the case. In other words, to minimize the force and moment, other considerations aside, an extended base should be avoided.

Insofar as an extended base does not remove the seepage velocity singularity occurring around the edge of the cylinder base such a base has little or no value in preventing erosion. Rather the technique of laying a rock filter around the cylinder base would seem more appropriate because it stabilizes the sand, while not increasing the net uplift force and overturning moment on the structure itself. The specific area to be protected around the cylinder base should be determined by calculating the exit gradient. As an example of what Eqs. 12 and 33 can provide, a contour of value 2.0 for the ratio of the hydraulic gradient amplitude to its value if no cylinder were there, namely of the coefficient $S(r,\theta)$, is shown on Fig. 6. Obviously for practical purposes, the critical exit gradient corresponding to the conditions of a specific problem should be determined and thus a critical contour around the cylinder base could be drawn, delimiting the area to be protected. As usual a safety factor should be introduced.

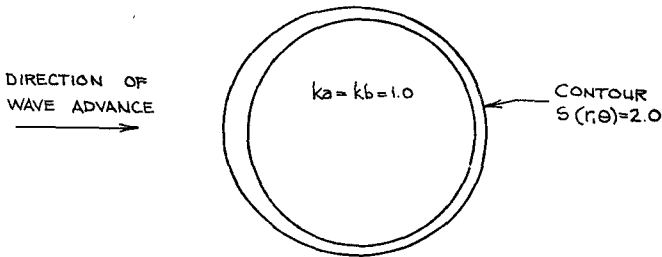


Fig. 6. Hydraulic Gradient Ratio

Table II shows that good agreement was found between experimental and theoretical results. Possible reasons for the small but persistent discrepancies include experimental error, difficulty in achieving a truly isotropic and homogeneous sand bed, and compressibility effects in the porous medium. In general these effects were not very significant.

CONCLUSIONS

1. The theory presented allows calculation of seepage pressure, uplift force and overturning moment values for a single vertical circular cylinder resting on a bed of sand of infinite depth. Evaluation of the exit gradient around the cylinder base is also possible. The nature of the seepage velocity singularity is shown to be similar to the singularity encountered at the toe of an impervious dam.

2. Normalized forms of the force and moment appear to be universal functions of two non-dimensional parameters ka and kb (k is the wave number, b the cylinder radius, and a the radius of the cylinder base), reducing to one when $a = b$. Graphs for these functions are provided so that once the physical characteristics of the problem are known, little additional computation is required.

3. A cylinder base extending beyond the cylinder radius does not remove the exit gradient singularity at the edge of the base. Furthermore, for a given cylinder radius, the effect of an extended base is to increase the maximum value of the net uplift force and overturning moment exerted on the cylinder. As a preferred protection against possible piping below and around the structure foundation, the use of a rock filter is recommended.

4. The theoretical results for the pressure appear to be in good agreement with data from a limited experimental program in a wave tank at the Hydraulics Laboratory of the University of Wisconsin-Madison.

5. The graphs presented in Fig. 2 show that approximate theories generally can not predict the wave-induced seepage effects on the cylinder.

ACKNOWLEDGMENTS

This material is based upon work supported by the National Science Foundation under Grant #ENC77-20030. Support was also provided by the Graduate School of the University of Wisconsin.

The writers are grateful to Professor Ben. Noble for his advice on dual integral equations, to Mr. R. Hughes for his technical assistance and to Mrs. R. Wyss for assistance in preparing the manuscript.

REFERENCES

1. Biot, M. A. (1941), "General Theory of Three Dimensional Consolidation", Journal of Applied Physics, Vol. 12, pp 155-164.
2. Dean, R. G. and D. R. F. Harleman (1966), "Interaction of Structures and Waves", chapter 8 of Estuary and Coastlines Hydrodynamics, Ippen (Editor), McGraw Hill Book Co., New York, N.Y.
3. Durand, T. J. P. (1978), Wave-Induced Seepage Effects on a Single Vertical Circular Cylinder Resting on a Bed of Sand, unpublished Independent Study Report, Department of Civil and Environmental Engineering, University of Wisconsin-Madison.
4. MacCamy, R. C. and R. A. Fuchs (1954), "Wave Forces on Piles: A Diffraction Theory", Technical Memorandum No. 69, U.S. Army Coastal Engineering Research Center (formerly Beach Erosion Board).
5. Madsen, O. S. (1978), "Wave-Induced Pore Pressures and Effective Stresses in a Porous Bed", Ceotechnique, Vol. 28, No. 4, pp 373-393.
6. Moshagen, J. and P. L. Monkmeyer (1979), "Wave-Induced Seepage Forces on Embedded Offshore Structures", Proc. Civil Eng. in the Oceans/IV Conf., San Francisco, Cal.
7. Moshagen, J. and A. Tórum (1975), "Wave-Induced Pressures in Permeable Sea Beds", Journal of the Waterways, Harbors and Coastal Engineering Division, Proc. ASCE, Vol. 101, No. WW1, Feb. 1975.

8. Putnam, J. A. (1949), "Loss of Wave Energy due to Percolation in a Permeable Sea Bottom", Trans. A.C.U., Vol. 30, No. 3, June 1949.
9. Sleath, J. F. A. (1970), "Wave-Induced Pressures in Beds of Sand", Journal of the Hydraulics Division, Proc. ASCE, Vol. 96, No. HY2, Feb. 1970.
10. Sneddon, I. N. (1966), Mixed Boundary Value Problems in Potential Theory, North Holland Publishing Company.
11. Spring, B. H. and P. L. Monkmeier (1975), "Interaction of Plane Waves with a Row of Cylinders", Proc. Civil Engineering in the Oceans/III Conf., Newark, Delaware.
12. Watson, G. N. (1966), A Treatise on the Theory of Bessel Functions, Cambridge University Press.
13. Yamamoto, T. (1977), "Wave-Induced Instability in Seabeds", Coastal Sediments '77, ASCE, Charleston, South Carolina, Nov. 1977.

STABILITY ANALYSIS OF SEAFLOOR FOUNDATIONS

TOKUO YAMAMOTO, Ph.D., Associate Professor
 Ocean Engineering Division, Rosenstiel School of
 Marine and Atmospheric Science, University of Miami,
 4600 Rickenbacker Causeway, Virginia Key, Miami,
 Florida 33149, U.S.A.

and

YASUMASA SUZUKI, Research Engineer
 Port and Harbour Research Institute
 Ministry of Transport
 Yokosuka, Japan

ABSTRACT

Stability analysis of homogeneous and inhomogeneous seabed foundations under attack by storm waves are made by calculating the wave induced effective stresses. Wave induced effective stress analysis of homogeneous seabed is made using the theory previously developed by the senior author which is based on the poro-elastic theory by Biot. Effective stresses in inhomogeneous seabeds induced by waves are calculated by approximating an inhomogeneous bed by many layers of homogeneous soils each of which has different geotechnical properties of soils. A good agreement is obtained between the theory and the pore pressure data in situ field measurements. For a given wave length, it is found that there exists a most unstable thickness of homogeneous seabed when the seabed thickness is one-fifth of the wave length. As a realistic example of an inhomogeneous bed, the effective stresses in a typical seabed formation at the Mississippi Delta area of the Gulf of Mexico under the attack of design storm waves are calculated. The numerical results indicate that the storm waves induce a continuous submarine landslide which extends as deep as 9 m from the mud line. Numerical calculations also indicate that such landslides and liquefaction of seabeds can be prevented by placing a layer of concrete blocks or rubbles on the top of the seabeds.

INTRODUCTION

As ocean waves propagate over the continental shelf, turbulent boundary layers developed on the mud line and submarine sediment deposits experience wave-induced pore pressure and effective stresses. Consequently the wave energy is dissipated by the turbulence in the boundary layers, percolations and soil internal frictions in the seabed and the seabed is disturbed by the wave induced effective stresses. Because overall wave-seabed interaction is rather complicated, only the wave induced effective stresses and pore pressures are considered in this paper. The

problem of the wave damping due to the turbulent boundary layers, percolations and internal friction of seabed soils is out of the scope of this paper.

If the wave induced effective stress state in the submarine soils exceed the limit equilibrium, the seabeds will fail and may result in the liquefaction and submarine landslides. Such wave induced liquefaction and slide of seafloor foundations are evidenced as the flotation of buried pipelines at Australia coasts, the uneven settlements of gravity-type oil drilling rigs at North Sea and toppling of several jacket-type oil drilling rigs and numerous pipeline failures at the Mississippi Delta area.

The senior author has solved the effective stress state in homogeneous and isotropic seabeds induced by ocean waves based on the Biot's (1941) three-dimensional consolidation theory (Yamamoto, 1977). An almost identical theory was later published by Madsen (1978) except he assumed unisotropic soil permeabilities while assuming an isotropical elasticity of the soil. However, as pointed out by Biot (1955) such assumption is physically inconsistent. Mei and Foda (1980) developed the so-called boundary layer method approximating Yamamoto's (1977) exact solution which considerably simplify the numerical calculations. The theory by Yamamoto (1977) has been substantiated by a laboratory experimentation (Yamamoto, et al., 1978). Further verification of the theory is made in this paper by comparing the theory with the pore pressure data from *in situ* measurements in fine-grained sediment bed at the Mississippi Delta area by Bennett and Faris (1979).

The real seabeds on the continental shelves are usually not homogeneous but the geotechnical properties of soils vary with the distance from the sea-seabed interface or the mud line. The purpose of this paper is to extend the existing theory by the author for the homogeneous seabeds to more realistic inhomogeneous seabeds. An inhomogeneous seabed is approximated by many layers of homogeneous soils each of which has different values of geotechnical properties and the thickness of the sublayers. Seed and Rahman (1978) computed the wave induced pore pressures in a multi-layered seabed assuming that soils are rigid and pore water is incompressible. However such solution is only applicable to very permeable seabeds as pointed out by Yamamoto (1978). Furthermore, their theory provides no information on wave induced effective stresses in seabed which are provided by the present theory.

As illustrative examples, the typical seabed formations at the North Sea and the Mississippi Delta area under attack of design storm waves are analyzed. The results indicate high potential of massive landslide and liquefaction of submarine

seabed foundation. The numerical calculations suggest that such liquefactions and landslides of seabed can be prevented by placing a layer of concrete blocks or rubbles on the top of the seabeds.

PORO-ELASTIC THEORY FOR MULTI-LAYERED SEABEDS RESPONSE TO WATER WAVES

An inhomogeneous seabed is approximated by many layers of homogeneous soils each of which has different values of geotechnical properties and thicknesses. Figure 1 shows a definition sketch of a two-dimensional water wave propagating over a multi-layered seabed. The wave propagates from right to left. The x-axis is taken on the mud line and the positive z-axis is taken downward from the mud line. Soils in each sublayer of seabed are assumed to respond linearly to waves. Assuming that displacements of soils and pore water are relatively small, the inertia of soils and pore water are neglected. For soft clays, the inertia terms may not be negligibly small as indicated by Dawson (1978). Nonetheless, the error due to neglect of the inertia terms is considered to be small compared to the errors due to the uncertainty of geotechnical properties of submarine soils. The results including the inertia terms will be published in a future paper.

The continuity equation is given as,

$$\frac{k_j}{\gamma_j} \nabla^2 p_j = \frac{n_j}{K'_j} \frac{\partial p_j}{\partial t} + \frac{\partial \epsilon_j}{\partial t} \quad (j = 1, 2, \dots, N) \quad (1)$$

where p_j is the excess pore-water pressure, ϵ_j is the volume strain of the porous medium, t is the time, k_j is the coefficient of permeability of the soil, γ_j is the unit weight of the pore-water, n_j is the porosity, and K'_j is the apparent bulk modulus of pore-water. The subscript j indicates the j -th layer and N is the total number of layers. The volume strain of the soil matrix for the two-dimensional problem is

$$\epsilon_j = \frac{\partial u_j}{\partial x} + \frac{\partial w_j}{\partial z} \quad (2)$$

where u_j is the horizontal component of soil displacement and w_j is the vertical component of soil displacement.

From the effective stress concept and Hooke's law, the equation of equilibrium is

$$G_j \nabla^2 u_j + \frac{G_j}{1-2\nu_j} \frac{\partial \epsilon_j}{\partial x} = \frac{\partial p_j}{\partial x} \quad (3)$$

$$G_j \nabla^2 w_j + \frac{G_j}{1-2\nu_j} \frac{\partial \epsilon_j}{\partial z} = \frac{\partial p_j}{\partial z} \quad (4)$$

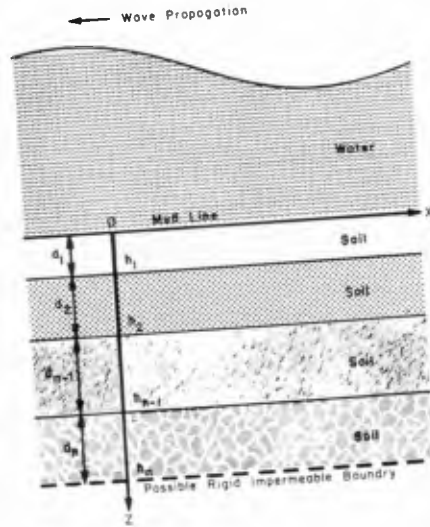


Figure 1. The definition sketch of a multi-layered seabed.

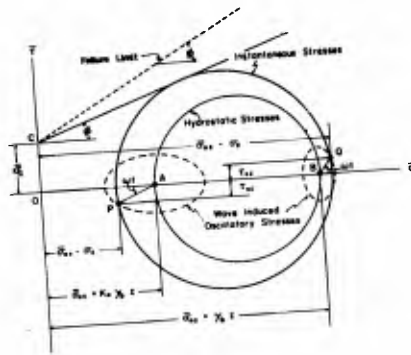


Figure 2. The Mohr's circle diagram of wave induced effective stresses.

where G_j is the shear modulus of the soil, and ν_j is Poisson's ratio for the soil.

Equations (1), (3) and (4) from the governing equations of the pore-water and the soils to be solved for p_j , u_j and w_j .

The effective stresses are related to the strains by Hooke's law as

$$\left(\sigma'_x\right)_j = 2G_j \left[\frac{\partial u_j}{\partial x} + \frac{\nu_j}{1-2\nu_j} \epsilon_j \right] \quad (5)$$

$$\left(\sigma'_z\right)_j = 2G_j \left[\frac{\partial w_j}{\partial z} + \frac{\nu_j}{1-2\nu_j} \epsilon_j \right] \quad (6)$$

$$\left(\tau'_{xz}\right)_j = G_j \left[\frac{\partial u_j}{\partial z} + \frac{\partial w_j}{\partial x} \right] \quad (7)$$

wherein $(\sigma'_x)_j$ is the effective normal stress in the x-direction, $(\sigma'_z)_j$ is the effective normal stress in the z-direction, and $(\tau'_{xz})_j$ is the shear stress in the z-direction on the plane perpendicular to the x-axis.

In the case of a sinusoidal wave propagating over the seabed, the response of the seabed to the wave is considered to be periodic in both time and space. Then, it is reasonable to assume that p_j , u_j and w_j are also periodic in time and space, or

$$p_j = p_j(z) \exp(i\theta) \quad (8)$$

$$u_j = U(z) \exp(i\theta) \quad (9)$$

$$w_j = W(z) \exp(i\theta) \quad (10)$$

where,

$$\theta = \lambda x + \omega t \quad (11)$$

λ is the wave number, ω is the angular wave frequency, and i is the imaginary unit ($i^2 = -1$). The right hand sides of Eqs. (8), (9) and (10) are complex. U_j , W_j and P_j are the function of z only.

Substituting Eqs. (9), (10) and (11) into the governing Eqs. (1), (3) and (4), the three simultaneous ordinary differential equations of second order can be obtained. The differential equations are linear and homogeneous and the characteristic equation is given as:

$$(D^2 - \lambda^2)^2 (D^2 - \lambda_j^2) = 0 \quad (12)$$

where D is the operator, d/dz , and λ_j is given as

$$\lambda_j^2 = \lambda^2 + i \frac{Y_j}{K_j} \omega \left[\frac{n_j}{K_j} + \frac{(1-2\nu_j)}{2(1-\nu_j)G_j} \right] \quad (13)$$

From Eq. (12) the general solutions of U_j , W_j and P_j are:

$$U_j = a_{1j} \exp[\lambda z] + a_{2j} \exp[-\lambda z] + a_{3j} \frac{z}{h_j} \exp[\lambda z] \\ + a_{4j} \frac{z}{h_j} \exp[-\lambda z] + a_{5j} \exp[\lambda_j' z] + a_{6j} \exp[-\lambda_j' z] \quad (14)$$

$$W_j = b_{1j} \exp[\lambda z] + b_{2j} \exp[-\lambda z] + b_{3j} \frac{z}{h_j} \exp[\lambda z] \\ + b_{4j} \frac{z}{h_j} \exp[-\lambda z] + b_{5j} \exp[\lambda_j' z] + b_{6j} \exp[-\lambda_j' z] \quad (15)$$

$$P_j = c_{1j} \exp[\lambda z] + c_{2j} \exp[-\lambda z] + c_{3j} \frac{z}{h_j} \exp[\lambda z] \\ + c_{4j} \frac{z}{h_j} \exp[-\lambda z] + c_{5j} \exp[\lambda_j' z] + c_{6j} \exp[-\lambda_j' z] \quad (16)$$

in which h_j is the depth of the lower boundary of the j -th layer, and a_{mj} , b_{mj} and c_{mj} ($m=1, \dots, 6$; $j=1, \dots, N$) are arbitrary constants. However, the coefficients a_{mj} , b_{mj} and c_{mj} are not independent on each other, and the relationship can be obtained from Eqs. (1), (3) and (4) as:

$$\left. \begin{aligned} b_{1j} &= -ia_{1j} + i(A_{1j}/h_j)a_{3j} \\ b_{2j} &= ia_{2j} + i(A_{1j}/h_j)a_{4j} \\ b_{3j} &= -ia_{3j} \\ b_{4j} &= ia_{4j} \\ b_{5j} &= -i(\lambda_j'/\lambda)a_{5j} \\ b_{6j} &= i(\lambda_j'/\lambda)a_{6j} \end{aligned} \right\} \quad (17)$$

$$\left. \begin{aligned}
 c_{1j} &= -i(A_{2j}/h_j)a_{3j} \\
 c_{2j} &= i(A_{2j}/h_j)a_{4j} \\
 c_{3j} &= c_{4j} = 0 \\
 c_{5j} &= A_{3j} a_{5j} \\
 c_{6j} &= A_{3j} a_{6j}
 \end{aligned} \right\} \quad (18)$$

where

$$\begin{aligned}
 A_{1j} &= \frac{1}{\lambda} \left[1 + \frac{n_j G_j}{K'} \frac{3 - 4\nu_j}{1 - 2\nu_j} \right] / \left[1 + \frac{n_j G_j}{K'} \frac{1}{1 - 2\nu_j} \right] \\
 A_{2j} &= 2G_j / \left[1 + \frac{n_j G_j}{K'} \frac{1}{1 - 2\nu_j} \right] \\
 A_{3j} &= 2\gamma\omega G_j (1 + \nu_j) \left[\frac{n_j}{K'} + \frac{1 - 2\nu_j}{2(1 - \nu_j)G_j} \right] / \left[\lambda k_j (1 - 2\nu_j) \right]
 \end{aligned} \quad (19)$$

Thus, in order to calculate U_j , W_j and P_j , unknown constants a_{1j} , a_{2j} , ..., a_{6j} ($j = 1, 2, \dots, 6$) should be determined in each layer. These $6 \times N$ constants can be determined from boundary conditions at the bed surface, at the interfaces between the sublayers, and at the bottom bed rock boundary.

In general, because of the interaction between the water waves and the seabeds, the properties of the waves will be changed under the influence from the seabeds. In this paper, we assume that the changes of wave properties are negligible, or the relative acceleration between water particles and soils are very small. Therefore, the boundary conditions at the bed surface are that the vertical effective stress is zero, that the shear stress is negligibly small, and that the sinusoidal pressure fluctuation exists, or at $z = 0$.

$$(\sigma'_z)_1 = 2G_1 \left[\frac{\partial \omega_1}{\partial z} + \frac{\nu_1}{1 - 2\nu_1} \left(\frac{\partial u_1}{\partial x} + \frac{\partial \omega_1}{\partial z} \right) \right] = 0 \quad (20)$$

$$(\tau'_{xz})_1 = G_1 \left(\frac{\partial u_1}{\partial z} + \frac{\partial w_1}{\partial x} \right) = 0 \quad (21)$$

$$p_1 = p_0 \exp(i\theta) \quad (22)$$

where $(\sigma'_z)_1$ is the effective normal stress in the z direction in the first layer, $(\tau'_{xz})_1$ is the shear stress in the z direction on the plane perpendicular to the x axis in the first layer, p_1 is the pore-water pressure in the first layer, and p_0 is the amplitude of pressure fluctuation at the bed surface.

The boundary conditions at the interfaces between the sublayers are that of the soil stresses, the pore-water pressures, the pore-water flow, and the soil displacement are continuous, of at $z = h_j$:

$$\left. \begin{aligned} (\sigma'_z)_j &= (\sigma'_z)_{j+1} & , & & (\tau'_{xz})_j &= (\tau'_{xz})_{j+1} \\ p_j &= p_{j+1} & , & & k_j (\partial p_j / \partial z) &= k_{j+1} (\partial p_{j+1} / \partial z) \\ u_j &= u_{j+1} & , & & w_j &= w_{j+1} \end{aligned} \right\} \quad (23)$$

If the lowest layer (N - th layer) is on an impermeable and rigid bed, the boundary conditions are that no soil displacements at the boundary and no flow across the boundary are allowed, or at $z = h_n$:

$$u_N = 0, w_N = 0, \partial p_N / \partial z = 0 \quad (24)$$

For a semi-infinite half-plane, the boundary conditions may be given as:

$$u_N, w_N, p_N \rightarrow 0 \text{ as } z \rightarrow \infty \quad (25)$$

From Eqs. (14), (15), (16), (17) and (18), this means that:

$$a_{1N} = 0, a_{3N} = 0, a_{5N} = 0 \quad (26)$$

FAILURE ANALYSIS

So far, only the wave induced incremental changes in stresses and pressures in soils from the initial equilibrium state have been considered. In this section the failure mechanisms of soils induced by waves are considered. From this point on, the traditional sign convention for stresses in the soil mechanics will be used, i.e., a stress is positive when it acts as a compression. The subscript j

for the effective stresses are omitted for simplicity in the following development.

The total effective stress, $\bar{\sigma}_z$, in the z-direction is given as

$$\bar{\sigma}_z = \bar{\sigma}_{oz} - \sigma'_z \quad (27)$$

where $\bar{\sigma}_{oz}$ = effective normal stress in the z-direction at initial equilibrium and given as:

$$\bar{\sigma}_{oz} = \gamma_b z = \gamma(G_s - 1)z \quad (28)$$

where γ_b = buoyant unit weight of the soil, γ = unit weight of water (9800 N/m³), and G_s = specific gravity of soil grains σ'_z in Eq. (28) is the incremental effective stress given by Eq. (6). The total effective normal stress, $\bar{\sigma}_x$, in x-direction is given by:

$$\bar{\sigma}_x = \bar{\sigma}_{ox} - \sigma'_x \quad (29)$$

where $\bar{\sigma}_{ox}$ is the effective stress at the initial hydrostatic equilibrium and may be given as:

$$\bar{\sigma}_{ox} = K_o \bar{\sigma}_{oz} = K_o \gamma_b z$$

where K_o is the coefficient of earth pressure at rest and is related to the Poisson ratio, ν , as:

$$K_o = \frac{\nu}{1-\nu} \quad (31)$$

σ'_x in Eq. (29) is given by Eq. (5). The values of K_o for soils range from 0.4 to 1.0 (Scott, 1963).

Since the shear stresses on horizontal and vertical planes are zero at the initial equilibrium, the total shear stress, $\bar{\tau}_{xz}$, is related to the incremental shear stress, τ'_{xz} , of Eq. (17) as

$$\bar{\tau}_{xz} = -\tau'_{xz} \quad (32)$$

Equations (27), (29) and (32) may be represented by the Mohr's circles as shown in Fig. 2. The Mohr's circle at a given instance is illustrated by a heavy solid circle passing through points P and Q. The point P and Q rotates on the shear ellipses shown by dashed lines at wave angular frequency, ω , as the waves progress over the seabed.

The failure condition for a given soil may be given as

$$\bar{\tau}_f \geq \bar{\sigma}_f \tan \phi_f + c \quad (33)$$

where ϕ_f = angle of internal friction of the soil, c = cohesion of the soil, τ_f = shear stress on the failure plane, and $\bar{\sigma}_f$ = effective normal stress on the failure plane. The limiting failure condition given by Eq. (33) is shown by the dashed straight line in Fig. 2.

Let the angle, ϕ , between the tangent to the instantaneous Mohr circle from point C (0,c) and the horizontal in Fig. 2 be defined as the "stress angle." Then the failure criteria of the soil element at a given point at a given instance may be defined as

$$\phi(x,z,t) \geq \phi_f \quad (34)$$

The stress angle, ϕ , is related to the stresses on the vertical and horizontal planes as

$$\frac{\bar{\sigma}_z + \bar{\sigma}_x}{2} \sin \phi + c \cos \phi = \left[\frac{\bar{\sigma}_z - \bar{\sigma}_x}{2}^2 + \bar{\tau}_{xz}^2 \right]^{1/2} \quad (35)$$

COMPARISON BETWEEN THEORY AND FIELD DATA

The pore-elastic theory presented in this paper has been substantiated by laboratory experiments of a coarse sand bed and fine sand bed (Yamamoto, et al., 1978). In order to further verify the theory, the theory is compared with the wave induced pore-pressure data from in situ measurements in the field available in the literature. Bennett and Faris (1979) measured the wave induced pore-pressure in fine-grained submarine sediments at the East Bay area of the Mississippi Delta in 12.5 m of water. They measured the 30 min. time history record of the pore-pressures at 6.3 m and 15.3 m below mud line as well as the bottom pressure. The 30 min long records are divided into three and the average values of the peak to peak pressures are calculated. The significant wave length is 52 m from the linear theory. The geotechnical properties of the sediments are estimated as the shear modulus, $G = 1.0 \times 10^6$ N/m², the Poisson ratio, $\nu = 0.333$, the porosity, $n = 0.5$, and the permeability, $k = 1.0 \times 10^{-6}$ m/s. Infinite thickness of a homogeneous isotropic seabed is assumed in the theoretical calculations. Since up to 10% by volume of undissolved gas in the sediments are reported, both saturated case as well as the case of 90% saturation are computed in the numerical calculations. The comparisons between the theory and the field measurements for the ratio, p/p_0 , of the amplitude of pore pressure and the amplitude of bottom pressure vs. the depth d are shown in Fig. 3. The field data fall in between the theoretical curves of 90% saturation and 100% saturation. Considering the limited information about the geotechnical properties of these sediments, Fig. 3 shows an excellent agreement between the theory and the field measurements. This agreement supports the credibility of the present theory in some degree.

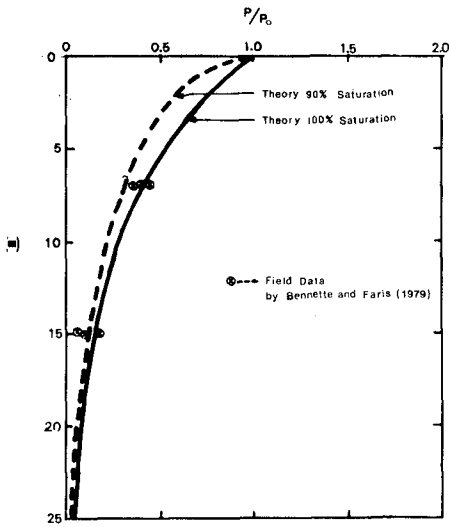


Figure 3. Comparisons between theory and field data of wave induced pore pressures. Data from Bennett and Faris (1979).

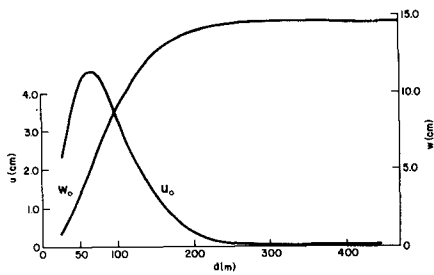


Figure 4. The horizontal displacement, u_0 , and the vertical displacement, w_0 , of the soil at the mud line vs. the bed thickness, d .

EFFECTS OF THE BED THICKNESS ON THE BED RESPONSE

In order to investigate the effects of the bed thickness on the bed response to waves, a single homogeneous soil bed with varying bed thickness, d , on an impermeable rigid bedrock is first considered. The North Sea design condition of wave characteristics and the geophysical properties of soil is used in calculations; wave period $T = 15$ s, wave length $L = 324$ m, wave height $H = 24$ m, water depth $h = 70$ m, shear modulus $G = 1.0 \times 10^7$ N/m², permeability $k = 1.0 \times 10^{-4}$ m/s, porosity $n = 0.3$, Poisson ratio $\nu = 0.333$, cohesive strength $c = 0$ bulk modulus of pore water $K' = 2.3 \times 10^9$ N/m³. The amplitude of bottom pressure calculated from the linear wave theory is $p_0 = 5.60 \times 10^4$ N/m².

The plots of the horizontal displacements, u_0 , and the vertical displacement, w_0 , of the soil at the mud line vs. the bed thickness, d , are shown in Fig. 4. The horizontal displacement u_0 first increases as the bed thickness d increases, reaches the maximum value of 4.6 cm at $d = 61.8$ m, then decreases thereafter and vanishes as d tends to infinity. The vertical displacement w_0 monotonously increases with d and reaches a constant value of 14.5 cm as d tends to infinity. This suggests that there exists the most unstable bed thickness when $d = 0.20 L$. Figure 5 shows the distribution of stress angle ϕ in the seabed of infinite thickness which is evaluated from Eq. (35) which represents Mohr's effective stress diagram illustrated in Fig. 2. $x = 0$ represents the location of wave crest and $x = 162$ m represents the location of wave trough. Although the distribution of ϕ in the bed is not exactly symmetrical with respect to $x = 0$, it is nearly symmetrical and only the region of a half wavelength is shown in Fig. 5. The wave induced effective stresses are small for this case and the maximum value of $\phi = 27.2^\circ$ occurs 1.5 m below the mud line under the wave crest. If the failure limit ϕ_f of the soil is 30° , the bed withstands the wave loading and therefore the bed is stable. Figure 6 shows the distribution of ϕ in the bed if bed thickness $d = 61.8$ m. For this case, the stress state becomes most unstable. Under the wave crest, the stress angle ϕ becomes very large near the mud line. If the failure limits, ϕ_f , of the soil is 30° , the top portion of the bed as deep as 15 m fails by wave loading. Since the entire bed continuously fails as the wave progresses, the top portion of bed up to 7 m may be liquefied and result in a continuous landslide if the bed surface has even a slight angle to the horizontal. Therefore, if the footing of an offshore structure is less than 15 m, the structure suffers from an uneven settlement. Pipelines buried shallower than 15 m may float. Since the bed thickness at the North Sea varies from 15 to 80 m, it may be said that the submarine seabed foundation at the North Sea is usually unstable against large storm waves. Some protection work may be needed.

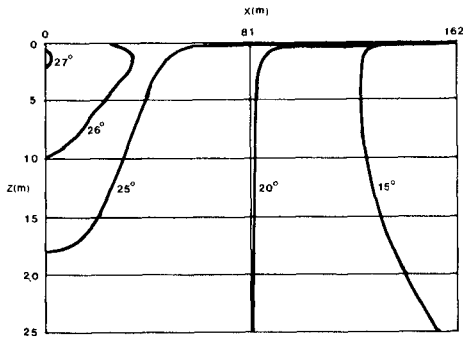


Figure 5. The distribution of the effective stresses in the seabed in terms of stress angle ϕ in degrees for an infinitely thick bed $d = \infty$.

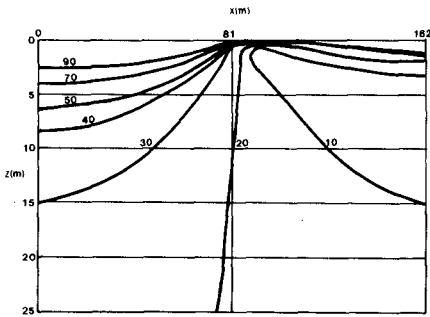


Figure 6. The distribution of the effective stresses in the seabed in terms of stress angle ϕ in degrees for a fine bed thickness $d = 61.8$ m.

RESPONSE OF INHOMOGENEOUS BEDS TO WAVES-STABILITY ANALYSIS
OF MISSISSIPPI DELTA CLAY BED WITH "CRUST PROFILE"

As a practical example of inhomogeneous seabeds, the behavior of the seabed at the offshore area surrounding the Mississippi River Delta under attack of a design storm wave is analyzed. A bottom supported platform and numerous buried pipelines were destroyed by massive submarine landslides in this area induced by the storm waves during hurricane "Camille" in 1969 (Bea and Arnold, 1973). The seabed soil formation is characterized by the so-called "crust profile" where a relatively stiff top soil layer and a very weak sublayer exists above a normally consolidated deeper layer. Some of the geotechnical properties of the soils at the area are given in Bea and Arnold (1973). For the numerical calculations, the seabed is subdivided into five layers with different soil properties and thicknesses which approximates the *in situ* data by Bea and Arnold (1973) and are tabulated in Table 1. For this case the total bed thickness is infinite. The design storm wave condition is; $T = 14$ s, $L = 152.4$ m, $H = 4.52$ m, and $h = 13.5$ m. The bottom pressure amplitude calculated from the linear wave theory is $p_0 = 1.91 \times 10^4$ N/m².

The vertical distributions of the horizontal displacement, the vertical displacement of the soil and the wave induced pore pressure are shown in Fig. 7. Although the total bed thickness is infinite, a large horizontal displacement of 2.2 m exists at the mud line contrary to the case of homogeneous infinite bed. The pore pressure is maximum and equal to 1.7 KN/m² at $z = 20$ m. Therefore, the weak sublayer experiences large horizontal displacements and large pressure fluctuations. The stress distribution is shown in Fig. 8. As can be seen, large stresses penetrate deep in the seabed under the wave crest. Assuming the failure limit of the soils $\phi_f = 25^\circ$, the top portion of the bed up to 12 m below the mud line fails from the wave loading. Since the mud line is sloped in this area, the wave induced stress instability is predicted to induce a massive continuous landslide which causes toppling of bottom based platforms and pipeline failures as has happened during hurricane "Camille" in 1969.

PROTECTION OF SEABEDS BY CONCRETE BLOCKS AND RUBBLES

Stabilizing effects of concrete blocks and natural rubbles on the seabed response to waves are considered in this section. The present theory is applied to the problem of concrete blocks or rubbles placed on the seabeds to protect them from wave actions. The geotechnical properties of the sand used in the calculation are: $k = 10^{-4}$ m/s, $G = 10^7$ n/m², $\nu = 0.3$, $n = 0.3$, $d = 30$ m and $G_s = 2.7$. The seabed is on an impermeable and rigid bed, and the water depth is 10 m. The soil responses to the wave of $T = 8$ s,

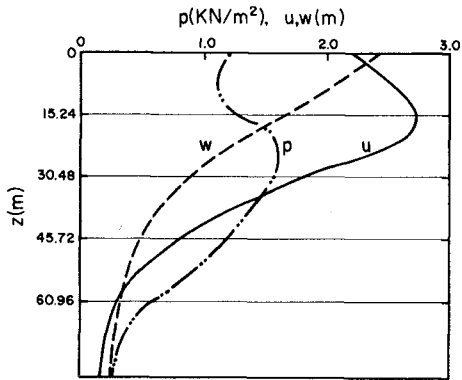


Figure 7. The vertical distributions of the horizontal displacement, u , the vertical displacement, w , of the soil and the wave induced pore pressure, p , in the Mississippi Delta clay seabed.

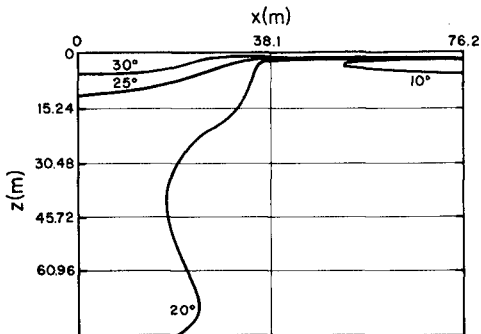


Figure 8. The distribution of the effective stresses in terms of stress angle ϕ in the Mississippi Delta clay seabed.

$H = 4$ m and $L = 71$ m are shown in Figs. 9 and 10. Figure 10 shows the distribution of the stress angle between the wave crest and the wave trough. (The crest exists at $x = 0$ and the wave propagates to the left). The distribution of the stress angle for $x < 0$ is again almost the same as this. Figure 10 shows that if the internal friction of the sand is 40° , the penetration depth of failure zone is maximum at a wave crest and about 1.5 m. Therefore, the seabed will fail in the failure zone and may cause liquefaction and sliding of the bed.

In order to protect the seabed from wave action, concrete blocks may be placed on it. The amplitudes of the soil displacements and pore-water pressure, and the distributions of the stress angle for the seabed covered by blocks of 3.0 m in thickness are shown in Figs. 11 and 12. The physical properties are: $G = 10^8$ N/m², $k = 1.0$ m/s, $\nu = 0.4$, $n_s = 0.4$, $G_s = 2.2$. It can be seen from Fig. 9 and Fig. 11 that the amplitudes of soil displacements and pore-water pressure are hardly influenced by the blocks placed on the seabed. However, the distributions of the stresses shown in Fig. 12 become much smaller than those in Fig. 10. This is due to an increase in vertical and horizontal effective stresses by the weight of concrete blocks.

As discussed above, it has been verified theoretically that covering over seabeds by blocks is effective to protect them from waves. The optimal properties of the blocks can also be determined by using the theory.

We have also analyzed the effectiveness of the asphalt mats laid under the blocks. However, the results for such seabeds are similar to those shown in Figs. 11 and 12, and no additional effectiveness is noticed from the numerical results. It is predicted from the numerical results that the seabeds will fail from the storm waves and continuous landslides may result in the top portion of the bed 12 m from the mud line without a concrete block layer.

The numerical calculations suggest that such liquefaction and sliding of the seabed from waves can be prevented by placing a layer of concrete blocks or rubbles.

SUMMARY AND CONCLUSIONS

The response of multi-layered poro-elastic beds to water waves has been treated analytically in this paper. The number of layers, the thicknesses of the layers and geotechnical properties of the soil in each layer can all be arbitrary. The theory has been verified by the data of wave induced pore pressures from in situ measurements at the offshore area of the Mississippi River Delta by Bennett and Faris (1979).

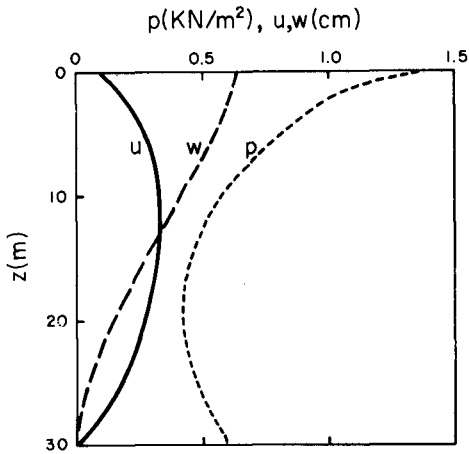


Figure 9. The vertical distribution of the horizontal displacement, u , the vertical distribution, w , and the wave induced pore pressure, p , in the seabed without a concrete block layer.

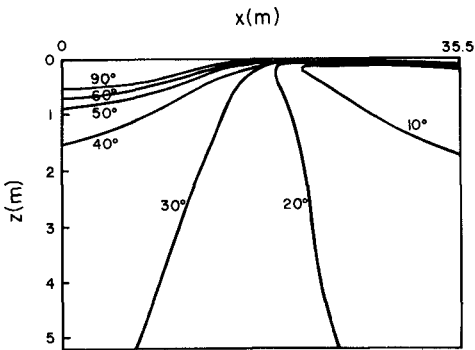


Figure 10. The distribution of the effective stresses in terms of the stress angle ϕ in degrees in the seabed without a concrete block layer.

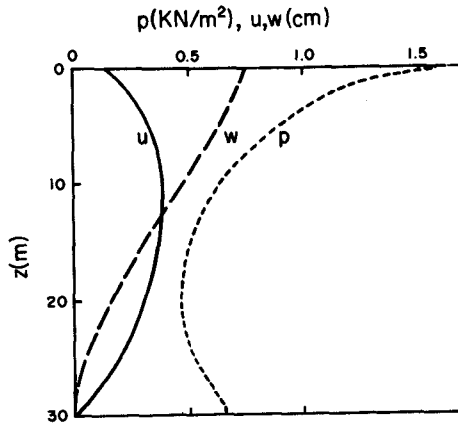


Figure 11. The vertical distribution of the horizontal displacement, u , the vertical distribution, w , and the wave induced pore pressure, p , in the seabed with a concrete block layer.

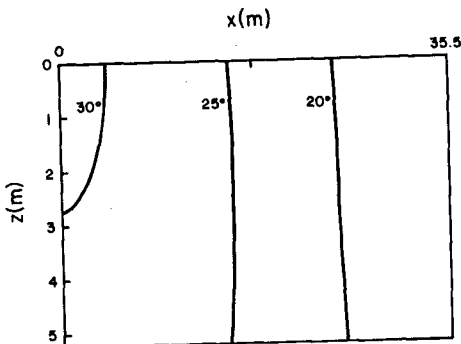


Figure 12. The distribution of the effective stresses in terms of the stress angle, ϕ , in the seabed with a concrete block layer.

The theory has been applied to the problem of the seabed response to the design waves at the North Sea. The theoretical results indicate that, for a given wave condition, there exists a critical bed thickness, $d_c = 0.20 L$, which creates the most unstable stress state in a homogeneous seabed. It has been indicated that generally the seabeds at the North Sea become unstable from large storm waves due to the relatively thin thickness of the seabeds.

As an example of inhomogeneous seabeds, the response of the soft clay beds with "crust profile" in offshore area of the Mississippi River Delta has been analyzed under attack of design storm wave. The numerical results indicate that large soil displacements, pore pressure fluctuations and stresses are induced by waves in the crust layer and the weakly consolidated sublayer below the crust.

The numerical results indicate that such wave induced stress instabilities can be prevented by covering the bed by a layer of concrete blocks and rubbles.

ACKNOWLEDGEMENTS

This work was entirely supported by the National Science Foundation, Grant No. CME 8009528. The authors are grateful for the support. The authors also wish to thank Dr. Richard Bennett for providing the pore pressure data and consultation on the structure of the submarine sediment.

REFERENCES

1. Bea, R. G. and Arnols, P., 1973. "Movements and forces developed by wave-induced slides in soft clays," Preprints of Offshore Technology Conference, OTC1899, Houston, Texas, May.
2. Bennett, R. and Faris, J., 1979. "Ambient and dynamic pore pressures in fine-grained submarine sediments in Mississippi Delta," Applied Ocean Research, Vol. 1, No. 3, pp. 115-123.
3. Biot, M. A., 1941. "General theory of three-dimensional consolidation," Journal of Applied Physics, Vol. 12, pp. 155-164.
4. Biot, M. A., 1955. "Theory of elastically and consolidation for a porous anisotropic solid," Journal of Applied Physics, Vol. 26, No. 2, pp. 182-185.
5. Dawson, T. H., 1978. "Wave propagation over a deformable sea floor," Ocean Engineering, Vol. 5, pp. 227-234.

6. Madsen, O. S., 1978. "Wave-induced pore pressures and effective stresses in a porous bed," *Geotechnique* 28, No. 4, pp. 377-393.
7. Mei, C. C., and Foda, M. A., 1980. "Wave-induced responses in a fluid-filled poro-elastic soil with a free surface-A boundary layer theory," to be published.
8. Scott, R. F., 1963. "principles of soil mechanics," Addison-Wesley Publishing Company, Massachusetts.
9. Seed, H. B., and Rahman, M. S., 1978. "Wave-induced pore pressure in relation to ocean floor stability of cohesionless soils," *Marine Geotechnology*, Vol. 3, No. 2, pp. 123-149.
10. Yamamoto, T., 1977. "Wave-induced instability in seabed," *Proc. of ASCE Spec. Conf., Coastal Sediments '77*, pp. 898-913.
11. Yamamoto, et al., 1978. "On the response of the poro-elastic bed to water wave," *Journal of Fluid Mechanics*, Vol. 87, Part 1, pp. 193-206.

TABLE 1. The values of geotechnical properties of soils at the Mississippi Delta are used in numerical calculations.

Layer	1	2	3	4	5
d (m)	15.24	15.24	15.24	15.24	∞
k (m/s)	1×10^{-6}	1×10^{-6}	1×10^{-6}	1×10^{-6}	1×10^{-6}
G (N/m ²)	8×10^4	3×10^4	8×10^4	2×10^5	1×10^6
v	0.45	0.45	0.45	0.45	0.45
n	0.3	0.3	0.3	0.3	0.3
γ_s	2.7	2.7	2.7	2.7	2.7
c (N/m ²)	8×10^3	3×10^3	8×10^3	2×10^4	1×10^5

WAVES FORCES ON OFFSHORE PIPELINES

by

N. Jothishankar* and V. Sundar**

INTRODUCTION

Transportation of offshore oil and gas is mostly carried out by means of offshore pipelines. Depending on the ocean environment these pipelines are either buried or made to rest on the ocean bed or placed on excavated trenches. In cases where the sea bed is mostly of rock, pipelines can be laid on the bed and anchored to the ocean floor by suitable supports. In certain instances pipelines are also placed on saddles leaving a clearance between pipe and the sea floor. The design of these pipelines requires an accurate assessment of wave induced loads acting on them.

The objective of this paper is to present the experimental results of wave forces exerted on a model pipeline, of diameter 5 cms at different clearances from the bed of the flume. Hydrodynamic coefficients namely Drag and Inertia are computed from the measured forces and their correlation with the non-dimensional parameters, Reynold's Number, Keulegan-Carpenter Number and relative clearance from the bed are presented.

LITERATURE REVIEW

The relationship between the hydrodynamic coefficients C_D , C_M , C_L and the environmental forces which can be represented in terms of non-dimensional flow parameters is essential for the prediction of wave forces acting on pipelines. Several investigations (Brater, E.F., and Wallace, R. (1972), Johansson, B. (1968), Keulegan, G.H., and Carpenter, L.H. (1958), Sarapkaya, T. (1976), Nath, J.H. and Yamamoto, T. (1974), Grace, R.A. and Nicinski, S.A. (1976), Wright, J.C., and Yamamoto, T. (1979), have been carried out regarding this aspect and there is a

* Senior Lecturer, University of Singapore, Department of Civil Engineering, Singapore 0511.

** Research Scholar Hydraulic Engineering Laboratory, Indian Institute of Technology, Madras, India.

considerable variation in their results in respect of the coefficients.

Beckmann, H. and Thibodeaux, M.H. (1962) recommended values of $C_D = 0.5$, $C_L = 0.5$ for the case of rough pipes resting on the bed and $C_D = 0.5$ and $C_L = 0$ for a freely suspended pipe. Johansson, B. (1968) performed experiments with 3 inches (7.5 cms) diameter pipeline with Reynold's Number varying from 3×10^3 to 2×10^4 and observed that for a constant clearance varying 0 to 1.0 D. C_M varied from 4.0 to 2.8 and C_L from 6.0 to 1.8. As the clearance increased it was found that values of C_D , C_M and C_L decreased. Grace, R.A. (1971) reanalysed Wallingford wave force data (1961) on a 1-1/2 inches model pipeline just clear of the bed and concluded that C_D roughly decreases with increase in the Reynold's Number from about 3.8 at $Re = 9 \times 10^3$ to 1.8×10^4 . The value of C_L was found to decrease with increase in Reynold's Number from 3.1 at $Re = 7 \times 10^3$ to 0.8 for $Re = 1.8 \times 10^4$. The inertia coefficient varied from 2.4 to 8.5 with an average value of 4.7.

Grace, R.A. (1971) conducted experiments on a 3 inch dia aluminium pipe and obtained the horizontal force coefficients for $Re = 2.5 \times 10^4$ as given in table 1.

Table 1 : Horizontal Force Coefficients
Grace R.A. (1971)

e/D	C_M	C_D
0.042	3.50	2.53
0.083	3.54	2.73
0.167	1.81	3.61
0.292	1.17	3.17

The values of the coefficients were obtained using the data of peak horizontal force and the phase of the peak force.

Several studies on submarine pipelines are reported in literature wherein the viscous effects are negligible and the forces are predominantly inertial (Ref: Nath, J.H. and Yamamoto, T., (1974)). Recently Wright, J.C. and Yamamoto, T. (1979) have reported the results of their study on wave forces on a horizontal cylinder 12 inches dia subjected to regular waves. The variation of force coefficients of inertia, drag and lift with respect to relative clearance (e/D) have been presented.

EXPERIMENTAL SET UP - PRESENT STUDY

Experiments were conducted in a 29 m long x 0.9 m deep x 0.9 m wide wave flume to determine the wave forces acting on a 5 cm dia plexiglass pipe positioned at different clearances from the simulated ocean floor. The pipe was subjected to regular waves produced by a plunger type wave generator with a parabolic section. The wave period ranged from 1.0 to 2.0 secs and the wave height from 5.0 cms to 16.0 cm in a water depth of 40 cm. Force transducers working on strain gauge principle were encased in the model pipeline on cantilever beams which were supported at the sides of the flume on roller bearings. Proper

care was taken to water proof the ends of the pipe. The cantilever beam and the associated strain gauge bridge was used to measure the horizontal and vertical forces. The test module used is similar to the one used by Garrison et al (1975). Suitable arrangements were made for positioning the pipeline at different clearances from the bed of the flume.

The outputs from the two force transducers are fed into a 3 channel carrier frequency amplifier the outputs of which are fed to two channels of Kempf and Remmers three-channel strip chart recorder. A resistance type wave probe is mounted in alignment with the central line of the model to record the time histories of the water surface elevation. The leads from the wave probe are connected to a wheatstone bridge the output of which is fed into the third channel of the recorder.

The model pipeline was kept at spacings of 3 cms, 5 cms and 7.5 cms from the bed of the flume and subjected to the action of regular waves. Fig. 1 shows the definition sketch of the model pipeline subjected to regular waves. The pipeline was immersed atleast five cylinder diameters below the free surface to avoid any free surface effect on the measured forces.

ANALYSIS

Consider a horizontal pipeline of diameter D at a spacing of e from the sea floor subjected to the action of a regular progressive wave train of wave height H in water of depth d as shown in Fig. 1. The

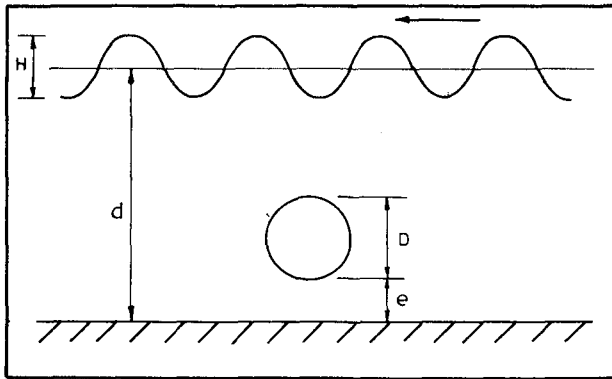


FIG. 1 DEFINITION SKETCH

maximum horizontal or vertical component of force per unit length acting on the pipeline can be expressed as a function of the following physical parameters.

$$\frac{F_x(\max)}{\ell} \text{ or } \frac{F_y(\max)}{\ell} = f(v, g, D, u_{\max}, e, b, T \text{ or } L) \quad (1)$$

in which F_{\max} = maximum force, ℓ = length of cylinder, D = cylinder diameter, g = acceleration due to gravity, T = wave period, L = wave length, e = clearance of bottom of pipe from sea floor, b = depth of submergence of the pipe centre line below the still water level, and ν = fluid viscosity.

Expressing Eq. (1) in non-dimensional form one gets, in the horizontal direction

$$\frac{F_x(\max)}{\frac{\rho}{2} D \ell u_{\max}^2} = f(e/D, D/L, u_{\max} T/D, u_{\max} D/\nu, \frac{u_{\max}}{\sqrt{g(d-b)}}) \quad (2)$$

as drag form or

$$\frac{F_x(\max)}{\rho \left(\frac{\pi D^2 \ell}{4} \right) 2\pi \frac{u_{\max}}{T}} = f(e/D, D/L, u_{\max} T/D, u_{\max} D/\nu, \frac{u_{\max}}{\sqrt{g(d-b)}}) \quad (3)$$

as an inertia form.

For a cylinder far away from the free surface as is the case studied here, the effect of free surface can be neglected, in which case the Froude Number $u_{\max} \sqrt{g(d-b)}$ can be ignored in the equations (2) and (3). For $D/L > 0.2$ the diffraction effects become dominant (Ref: Hogben et al (1977) and for $D/L < 0.2$ Morison Equation is applicable. In the case considered here D/L is less than 0.2 and the influence of D/L in this range may be neglected. With these reasonings equation 2 and 3 can simply be written as

$$\frac{F_x(\max)}{\frac{\rho}{2} u_{\max}^2 (D\ell)} \text{ or } \frac{F_x(\max)}{\rho \left(\frac{\pi D^2 \ell}{4} \right) 2\pi \frac{u_{\max}}{T}} = f(e/D, u_{\max} T/D, u_{\max} D/\nu) \quad (4)$$

DETERMINATION OF HYDRODYNAMIC COEFFICIENTS C_D and C_M

The analysis of the experimental data is based on the wave force trace and wave profile trace obtained at the central line of the pipe for different clearances of the pipeline from the simulated sea floor. The drag and the horizontal inertia coefficient are obtained from the horizontal force trace while the lift and vertical inertia coefficients are computed using the vertical force profile. The coefficients are assumed to be constant over a wave period. The coefficients C_D and C_M

are obtained based on the peak force and the phase at which the peak force occurs. If F_T is the total force per unit length of the pipeline, then using Morison's formula

$$F_T = F_D + F_I$$

in which

$$F_D = \frac{1}{2} C_D \rho D u |u| \quad (5)$$

and

$$F_I = C_M \frac{\pi}{4} D^2 \dot{u} \quad (6)$$

in which D = pipe diameter, ρ = mass density of water; u = horizontal particle velocity at the central line of the pipe; and \dot{u} = corresponding horizontal water particle acceleration. Using Airy's theory it can be shown that the maximum total force on the pipe is

$$\frac{F_{\max}}{\frac{\rho}{2} u_{\max}^2 (D\kappa)} = C_D \left(1 + \frac{C_M}{C_D} \frac{\pi^2}{2} \frac{1}{K^2} \right) \quad (7)$$

where K = Keulegan-Carpenter number = $u_{\max} T/D$. The phase at which the maximum force occurs is given by

$$\sin \theta = \frac{C_M}{C_D} \frac{\pi^2}{2} \frac{1}{K} \quad (8)$$

Using measured values of F_{\max} and θ from the force trace, C_D and C_M can be computed using Equations 7 and 8.

RESULTS

Experimental runs yielded Reynolds Number in the range 5×10^3 to 1.7×10^4 and Keulegan-Carpenter number in the range 1 to 9.

Typical plots showing the variation of C_D and C_M with the wave Reynolds Number $u_{\max} D/\nu$ are shown in Figs. 2 and 3, for a relative clearance of $e/D = 1.0$. The least square fit of the data is also shown in the figures. Similar plots were obtained for relative clearances 0.60 and 1.50. The lines of least square fit for the three clearances tested are shown in Figs. 4 and 5, for C_D and C_M respectively. The results indicate that within the Reynolds number range of data, C_D tends to decrease with increasing Reynolds number. Similar results were obtained by Brater et al (1972) and Grace, R.A. (1971) on analysing Wallingford's (1962) data. It is also seen that for a given Reynolds number the value of C_D decreases with increasing clearance. C_D varies from 4.3 to 0.8 for e/D varying from 0.6 to 1.5.

The variation of C_D with Keulegan-Carpenter Number is shown in Fig. 6 for the e/D ratios tested. Only the lines of the best fit are shown in this figure to simplify the presentation of the data. Within the range of Keulegan-Carpenter Numbers tested (2 to 9) it is observed that C_D decreases with increase in Keulegan-Carpenter Number. Similar results were reported by Grace and Nicinski (1976), who plotted the

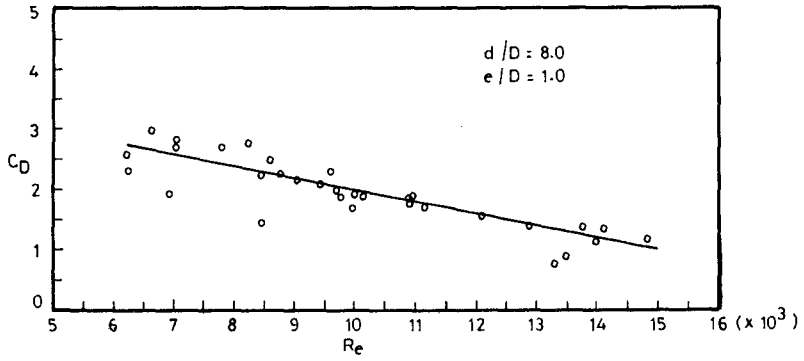


FIG. 2 VARIATION OF C_D WITH REYNOLD'S NUMBER

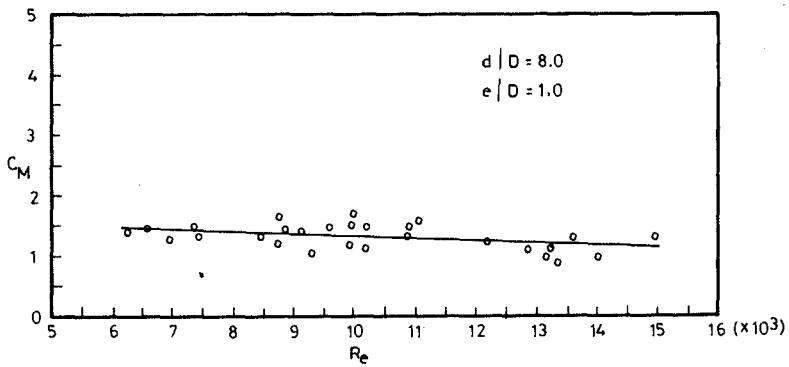


FIG. 3 VARIATION OF C_M WITH REYNOLD'S NUMBER

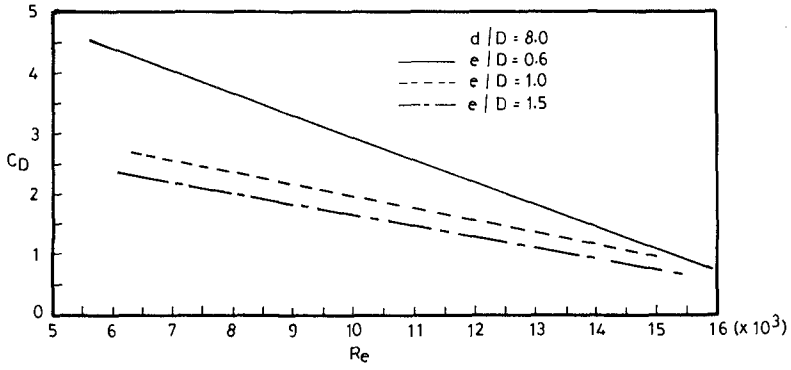


FIG. 4 DRAG COEFFICIENT Vs REYNOLD'S NUMBER FOR VARIOUS CLEARANCES

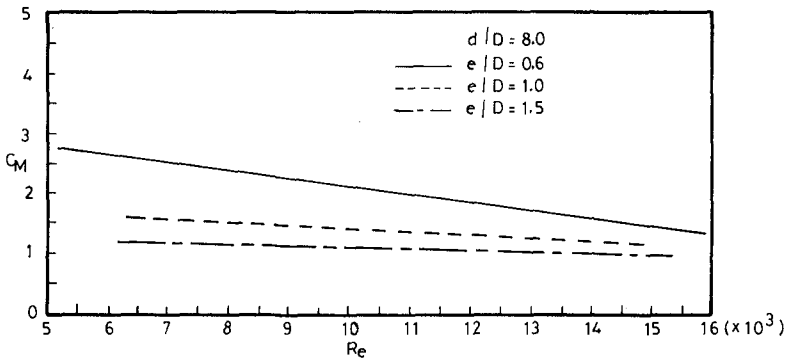


FIG. 5 INERTIA COEFFICIENT Vs REYNOLD'S NUMBER FOR VARIOUS CLEARANCES

values of C_D against relative distance of water particle travel. This trend may be due to the interaction between two boundaries (plane bottom boundary and cylinder itself) and the generation and behaviour of eddies. High Drag Coefficients of the order of 3.75 are obtained at Keulegan-Carpenter Number around 3.0 for $e/D = 0.6$. For $e/D > 1.0$ the variation in the value of C_D with e/D tends to become small. This is to be expected since far away from the boundary the effect of boundary will diminish and the C_D values would approach those found for $e/D = \infty$ as pointed out by Sarapkaya, T. (1976).

For a relative clearance of $e/D = 0.6$, C_M is found to decrease from 2.7 at $Re = 5 \times 10^3$ to 1.5 at $Re = 1.6 \times 10^4$. For the other two increasing clearances C_M values are not very sensitive to variation in Reynold's number. It is also inferred that C_M decreases with increase in clearance for the range of Reynold's number tested.

The variation of Inertia Coefficient with Keulegan-Carpenter number is shown in Fig. 7 for the three clearances. It is clearly seen from these plots that the inertia coefficient decreases with increase in the clearance. Within the Keulegan-Carpenter number range of 2 to 9 the variation of C_M is insignificant. For $e/D > 1.0$ the variation of C_M with e/D becomes small. It is also inferred that C_M is dominant at smaller Keulegan-Carpenter number values when the relative clearance is less.

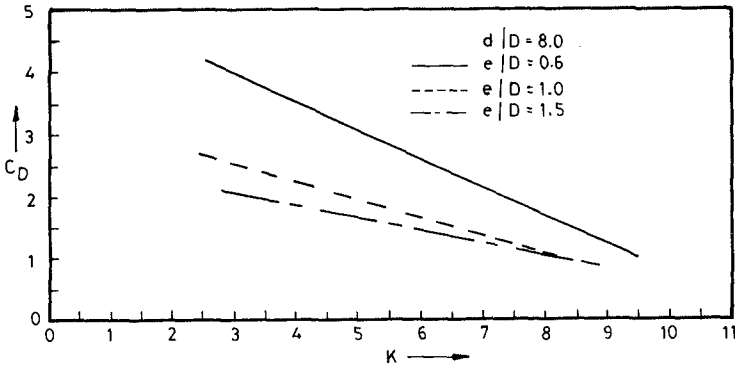


FIG. 6 DRAG COEFFICIENT Vs KEULEGAN-CARPENTER NUMBER FOR VARIOUS CLEARANCES

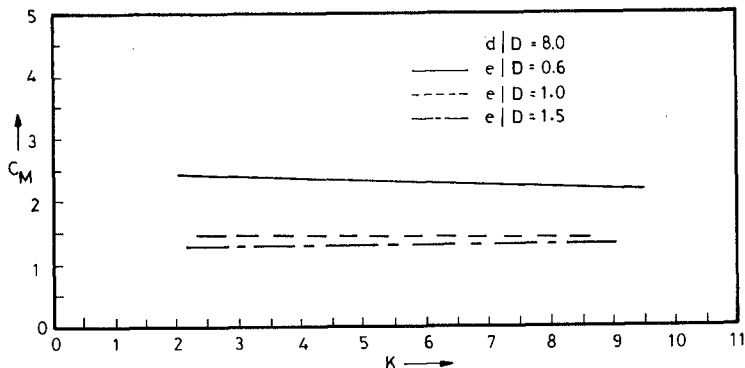


FIG. 7 INERTIA COEFFICIENT Vs KEULEGAN-CARPENTER NUMBER FOR VARIOUS CLEARANCES

CONCLUSIONS

The analysis of wave forces on pipelines at different clearances from the simulated ocean floor has shown that the hydrodynamic coefficients C_D and C_M computed from measurement of horizontal force are functions of relative clearance, Reynold's number and Keulegan-Carpenter number. The drag coefficient is found to decrease with the Reynold's number while the inertia coefficient is fairly constant over the Reynold's Number range (5×10^3 to 1.7×10^4).

As the Keulegan-Carpenter number increases it is found that the C_D value decreases. However, the variation of C_M with the Keulegan-Carpenter number is insignificant in the range tested. The values of both C_D and C_M are found to decrease with increase in clearance. The analysis of vertical force coefficients namely C_{MV} and C_L will be reported in a future paper.

ACKNOWLEDGEMENT

The laboratory investigation on which this paper is based was done in the Hydraulic Engineering Laboratory, Civil Engineering Department, Indian Institute of Technology, Madras, India. The authors wish to thank the authorities for the encouragement given to publish this paper.

The authors wish to thank Subbiah, K., Research Scholar,

Hydraulic Engineering Laboratory, Indian Institute of Technology, Madras, for his help in carrying out the experiments.

REFERENCES

1. Anonymous (1961), "Model Investigation of the Wave Forces on Submarine Pipelines", Hydraulic Research Station, Wallingford, England, Report Ex 158, July.
2. Beckmann, H. and M.H. Thibodeaux (1962), "Wave Force Coefficients for Offshore Pipelines", Journal of Waterways, Harbours and Coastal Division, ASCE, Vol. 88, No. WW2, Part 1, May.
3. Brater, E.F. and R. Wallace (1972), "Wave Forces on Submerged Pipelines", Thirteenth Coastal Engg. Conf., Vancouver, B.C., Canada, July 10-14, Vol. III, pp 1703-1721.
4. Garrison, C.J., M. ASCE, F.H. Gehram and B.T. Perkinson (1975), "Wave Forces on Bottom Mounted Large Diameter Cylinder", Journal of Waterways, Harbours and Coastal Engg. Div., ASCE, Vol. 101, No. WW4, Nov. pp 343-356.
5. Grace, R.A., (1971), "The Effects of Clearance and Orientation on Wave Induced Forces on Pipelines: Results of Lab Experiments", Univ. of Hawaii, Look Lab of Oceanographic Engineering, Technical Report No. 15, April.
6. Grace, R.A. and S.A. Nicinski (1976), "Wave Force Coefficients from Pipelines Research in the Ocean", Offshore Technology Conf., Vol. III, May 3-6, Houston, Texas, paper No. OTC 2676.
7. Hogben, N., B.L. Miller, J.W. Searle and J. Ward (1977), "Estimation of Fluid Loading on Offshore Structures", Proc. Inst. Civ. Engrs., Part 2, 63 Sept., 515-562.
8. Johansson, B., (1968), "Wave Forces on a Pipe at the Bottom of the Sea", Royal Institute of Tech., Stockholm, Sweden, Division of Hydraulics, Bulletin, No. 71.
9. Keulegan, G.H. and L.H. Carpenter (1958), "Forces on Cylinders and Plates in an oscillating Fluid", Journal of Research of the National Bureau of Standards, Vol. 69, No. 5, May, pp 423-40.
10. Nath, J.H. and T. Yamamoto (1974), "Forces from Fluid Flow Around Objects", Proc. Fourteenth ASCE Conf. on Coastal Engg., Copenhagen, Denmark, pp 1808-27.
11. Sarapkaya, T. (1976), "Forces on Cylinders near a Plane Boundary in a Sinusoidally oscillating Fluid", Journal of Fluid Engg., Trans. ASME, Vol. 98, No. 3, pp. 499-505.
12. Wright, J.C., A.M. ASCE and T. Yamamoto (1979), "Wave Forces on Cylinders near Plane Boundary", Journal of the Waterway, Port, Coastal and Ocean Division, ASCE, Vol. 101, No. WW1, Feb., pp 1-13.

WAVE IMPACT PRESSURES ON COMPOSITE BREAKWATERS

by

G.R. Mogridge and W.W. Jamieson*

ABSTRACT

Wave impact pressures and forces on composite breakwaters have been measured in the laboratory. A solid wall breakwater and a perforated breakwater were instrumented with small pressure transducers in a study designed to estimate the relative effectiveness of perforated breakwaters in reducing impact loads caused by breaking waves.

Experimental results of maximum pressures and forces measured on the breakwater walls are presented as cumulative probability distributions. It is concluded that the perforated breakwater experiences significantly lower breaking wave loads although local impact pressures may be as high as those measured on the solid wall breakwater. Further studies are required on the perforated breakwater and alternative designs to determine the most suitable caisson type for the reduction of wave impact forces.

INTRODUCTION

With the trend in recent years to deep water harbours exposed to unfavourable wave climates, rubble mound breakwaters have become increasingly more expensive relative to composite breakwaters. The massive quantities of rock required for mounds with the gentle slopes necessary for stability, the limited strength of concrete armour units, and the effect of wave groups on armour unit stability, pose problems in the design of rubble mound breakwaters which are not easily solvable. The composite breakwater, consisting of concrete caissons founded on a rubble mound, does not require large quantities of quarry stone and in addition has a considerable advantage at some locations where the wave climate allows only a short construction time, because the caissons are constructed in dry dock and then towed to the site. However, there are also problems in designing composite breakwaters. In the past, composite breakwaters in deep water have been designed assuming total reflection of the waves, but it is now generally recognized that wave breaking can occur even on a composite breakwater with a low rubble mound in deep water. The resulting impact pressures, although occurring infrequently, for an extremely short

* Associate Research Officers, Hydraulics Laboratory,
National Research Council of Canada, Ottawa, Canada,
K1A 0R6.

duration and over a very localized area, are enormous. Such pressures can cause severe local damage to the structure, and in the case of lower less localized pressures can cause sliding failure of the breakwater. It is apparent that composite breakwaters should be designed to avoid the possibility of severe impact pressures occurring. Thus, Lundgren and Graveson (3), have proposed breakwaters constructed using vertical cylindrical caissons and also caissons with the upper surfaces sloping away from the wave attack. Measurements of impact pressures on cylindrical caissons are described by Graveson et al. (1). Richert (9) has also shown the effectiveness of a sloping wall in reducing impact pressures. Onishi and Nagai (7) and Nagai and Kakuno (6) have conducted studies in which impact pressures were measured on slit-type breakwaters.

In the laboratory study described in this paper, wave impact pressures were measured on a composite breakwater with plane vertical solid walls. Tests were also conducted on a perforated Jarlan-type breakwater with plane vertical walls in order to determine whether impact pressures are reduced on such a breakwater. Although similar comparative tests have not been carried out previously, many others have measured impact pressures on plane solid walls and Nagai and Kakuno (6) have measured impact pressures on walls with perforations consisting of vertical slits. However, there are many inconsistencies in the experimental data produced from previous studies, mainly because of wide differences in the quality of the experimental equipment used.

EXPERIMENTAL EQUIPMENT

It has been found that the same incident waves breaking on a composite breakwater can produce widely varying magnitudes of impact pressure because of slight differences in timing and position of the breaking wave. This phenomenon has been observed by numerous other researchers such as Mitsuyasu (4) and Moutzouris (5). Therefore, it was essential in order to obtain a valid comparison of caisson designs, to run many tests and plot the results as cumulative probability distributions. The height and period of the regular incident waves were chosen such that every wave in the wave train broke on the vertical walls of the breakwaters. Irregular waves were not used in these tests, nor was any effort made to produce different types of breakers. Thus, the possibility should not be overlooked that the results of this study may not be applicable to situations with breaker types other than the plunging breakers produced in the present experiments.

It is well known that the impact pressures measured on composite breakwaters depend on many design variables such as slope and height of the berm, top width of the berm and water depth above the berm. In addition there are the variables describing the incident waves and the caisson design.

In this study, the berm dimensions were chosen to produce severe wave impact conditions to facilitate the comparison of caisson types.

A sketch of the model breakwater is shown in Fig. 1. The water depth in the wave flume was 75.6 cm and the depth above the berm was 29.2 cm. The berm had a slope of 1:3 and was constructed of stone fill with a cement outer layer approximately 4 cm thick. The model breakwaters were 1.22 m wide and were tested in a wave flume 64 m long and the same width as the breakwaters. The caissons were constructed high enough that no overtopping occurred and were held rigidly in position by a massive concrete and steel structure at the rear of the breakwaters. A solid wall caisson was constructed of wood with walls 3.8 cm thick and internal chambers such that after testing as a solid wall caisson, holes were drilled in the front wall so converting it into a perforated wall caisson. The chamber width from front to rear walls was 30.5 cm, giving a ratio of chamber width to incident wave length of 0.06. This is considerably smaller than the ratio of approximately 0.2 usually recommended to minimize wave reflection; however, it is approximately the ratio suggested by Nagai and Kakuno (6) to reduce impact pressures on slit-type breakwaters. Transverse walls with low porosity were included at 23 cm centres for structural rigidity. One of these walls may be seen through a transparent end wall in the photographs in Fig. 5. The perforations on the front wall of the caisson were circular holes 3.8 cm in diameter spaced at 5.7 cm centres giving a relatively high porosity of 34.9%. Pressure transducers mounted on a thick brass plate were located in the centre of the caisson at elevations as shown in Fig. 2. The locations were the same on the front wall for both the solid and perforated breakwaters, being midway between the rows of holes in the perforated wall. A maximum of seven transducers could be used at any one time, so pressure distributions on the front and rear walls of the perforated breakwaters were measured in consecutive test series.

The pressure transducers were 7.6 mm in diameter with semi-conductor strain gauges mounted on a thin metal diaphragm. Temperature compensation was provided but was not entirely satisfactory. The linear range of the transducers was 0-25 psi or 0-172 kPa (kN/m^2) with a combined non-linearity and hysteresis of $\pm 0.25\%$. The transducer calibrations supplied by the manufacturer were confirmed by static pressure tests. The resonant frequency in air was 20 000 Hz and in water approximately 12 000 Hz.

Outputs from the pressure transducers were amplified one hundred times by amplifiers with a frequency response of 15 000 Hz, before going to two transient recorders. Basically, these recorders are high speed analog to digital converters which have a resolution of 10 bits or 1 in 1000. Each transient recorder has four data channels each capable of storing in memory 1024 data words. The sampling rate can

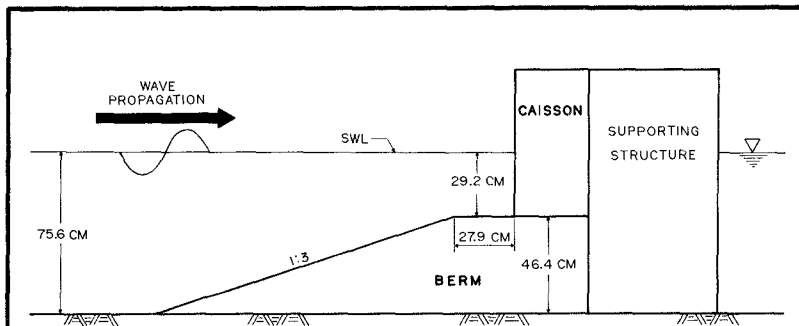
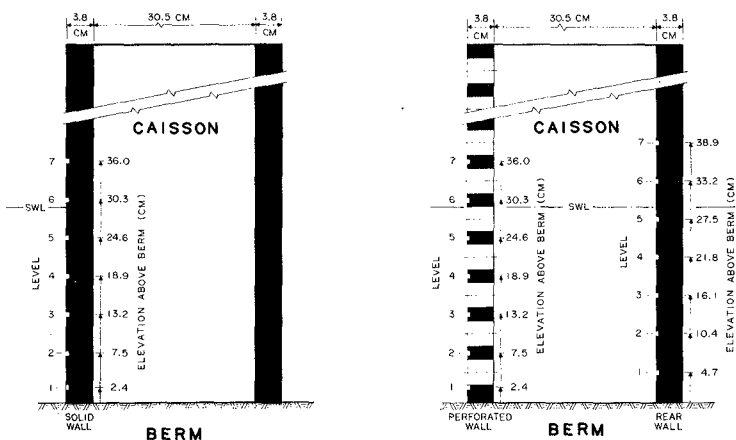


FIG. 1 SKETCH OF MODEL COMPOSITE BREAKWATER



(A) SOLID WALL CAISSON

(B) PERFORATED CAISSON

FIG. 2 LOCATIONS OF PRESSURE TRANSDUCERS

be chosen as high as 100 000 samples per second, which corresponds to a sample interval of 0.01 ms. At this sample interval the total record length is 0.01 s.

Because fast sampling rates are necessary for accurate measurement of sharp pressure peaks, total record lengths are short. Thus, it is important to commence sampling immediately before a pressure peak occurs, to ensure its inclusion in the record. This is possible using the pre-trigger function of the transient recorders. In this mode of operation the recorders sample the pressure transducer outputs continuously and the data simply overflows from the memory. When a rise in pressure exceeding a certain pre-set level is sensed at any input channel, the recorders interrupt sampling after continuing to sample for a pre-set length of time referred to as the pre-trigger delay. For example, in the present experiments with the pre-trigger delay set at 0.90, the recorders continue to sample and store 0.9 times 1024 data words after the pressure rise is sensed. Then on completion, the channel memory contains 0.1 times 1024 data words recorded previous to and 0.9 times 1024 data words recorded following the increase in pressure. The two transient recorders are interconnected so that the time base is identical for all channels and a pressure rise on any one channel will trigger both recorders simultaneously. After the data from one wave is stored in the memories of the two recorders, it is transmitted to the disk of a digital computer for storage. The transfer of 7168 data words is accomplished fast enough that the system is ready for sampling the pressures caused by the next wave impact.

The rate of sampling by the transient recorders must obviously be chosen sufficiently fast that the peak pressures measured are not attenuated. However, because the memory of each data channel is limited to 1024 words, fast sampling rates result in short records. If the record length is too brief, then pressure rises at locations distant from the point of initial contact of the wave will not be recorded. This in turn means that when the pressures are integrated over the breakwater, the resulting force record may not contain the maximum force on the breakwater. Thus, the choice of sample rate is quite important.

Pressure records measured at different sample rates are shown in Fig. 3. The well-known form of the records of wave impact pressure can be seen when the rate of sampling is slow. A rate of 1000 samples per second conveniently includes the complete pressure record for this wave period of 2.1 seconds; however, this speed is not sufficient to accurately define pressure peaks. For the present experiments, a rate of 20 000 samples per second was chosen, that is, a sample interval of 0.05 ms. The total record length is therefore approximately 0.05 s and this length is illustrated on all the pressure records in Fig. 3 to show the relatively small part of the total record being sampled.

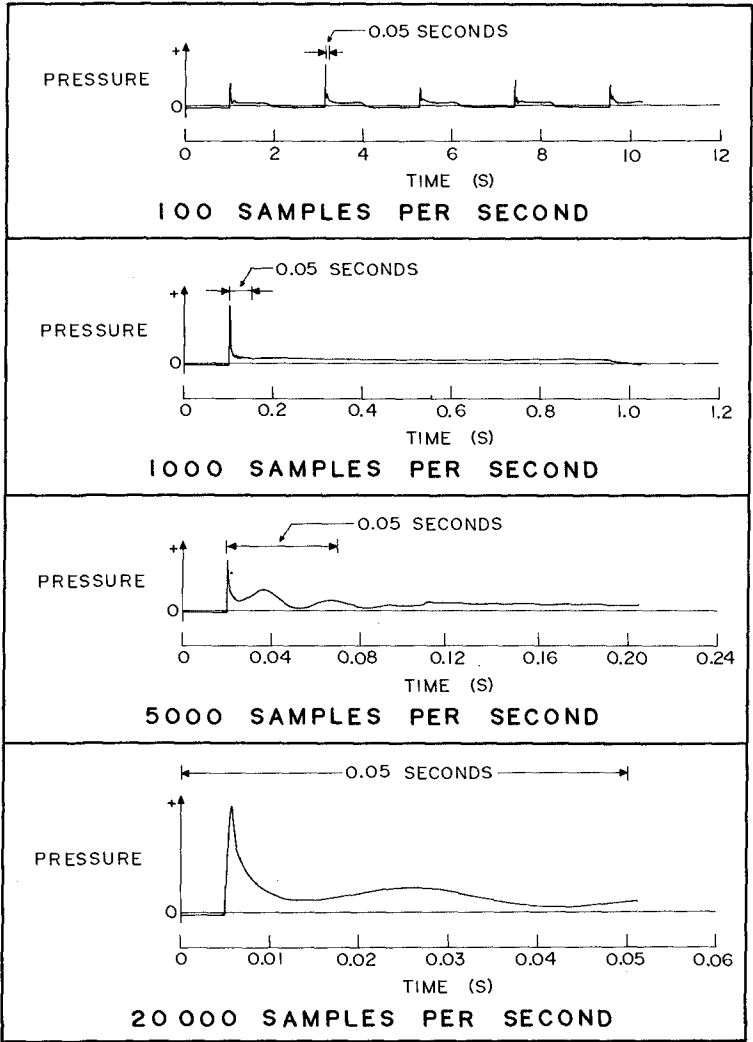


FIG. 3 PRESSURES AT DIFFERENT SAMPLE RATES

TEST PROCEDURE

Scale factors and bias values for the transient recorders were determined at the start of each day. Trigger levels of the recorders were set at approximately 3.5 kPa so that each breaking wave would trigger data collection. Zero readings for the pressure transducers were taken when the water in the wave flume was calm at the beginning of each test series. Thus, zeros were taken with hydrostatic pressure on the transducers so the pressure records produced were the dynamic pressures of the wave impacts.

A train of regular waves was generated using voltage signals produced by a digital computer as input to the wave machine, to ensure repeatable sequences of waves from start-up to finish. A short series of waves was produced so that there would be no disturbance caused by secondary reflections returning from the wave generator board. The height of the incident waves was 37 cm and the wave period was 2.1 s. Wave reflection from the solid wall breakwater was approximately 60% and from the perforated breakwater was 30%.

Ten wave impacts were measured in each wave train, after which it was necessary to allow the agitation in the wave flume to settle before running more tests. The data from sixty wave impacts or 430 000 words were stored on disk before it was necessary to transfer the data to magnetic tape. Because of the wide variation in wave impact pressures even when incident waves varied in height by only $\pm 4\%$, approximately 300 tests were run with pressure transducers on each breakwater wall so that the results could be treated statistically. To estimate the total force on a perforated breakwater, it is necessary to know the pressures on the interior walls of the chamber. Thus, pressures were also measured on the rear wall of the chamber, although it was assumed that pressures on the interior side of the perforated wall were negligible. In all, approximately 900 tests were run to obtain pressure distributions on the solid wall breakwater and the front and rear walls of the perforated breakwater.

The series of photographs in Fig. 4 show how the incident waves broke against the solid wall breakwater. The numerals on the right hand side of each photograph show the locations of the pressure transducers on the brass plate which is just visible in the centre of the breakwater. The first two photographs show the approach of a wave crest to the caisson wall and the instant before impact. An air pocket is just beginning to form and it appears that the maximum pressure in this case will occur where the crest first hits the wall at level 4. Immediately after the wave impact the water surface begins to rise and large pockets of air can be seen plastered against the caisson wall. The remaining photograph shows the wave run-up and the high density of air bubbles in the water caused by the wave breaking.

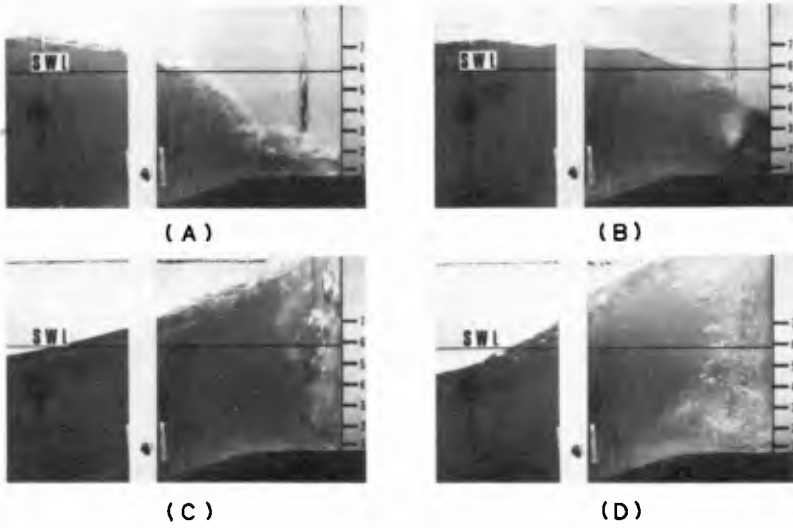


FIG. 4 WAVE BREAKING ON SOLID WALL BREAKWATE

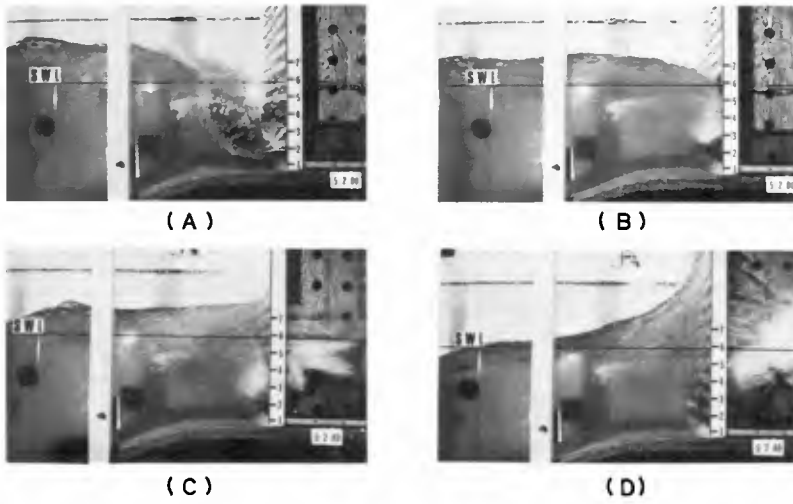


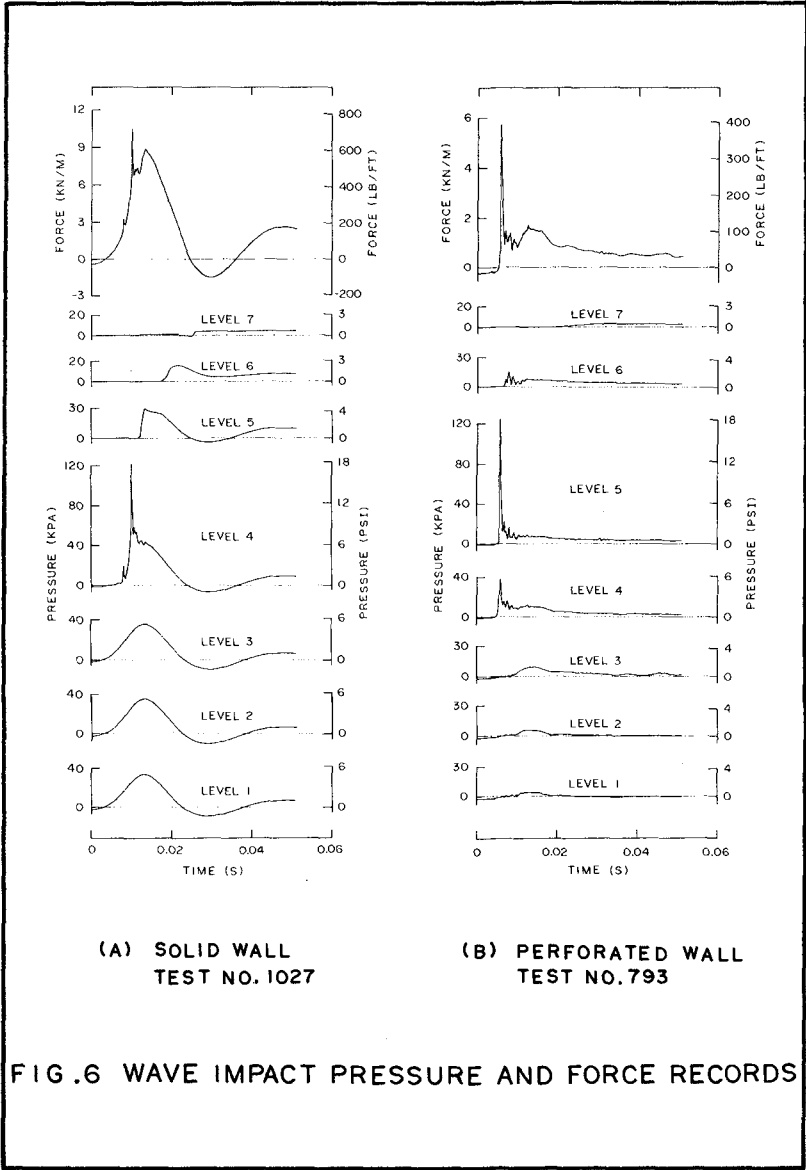
FIG. 5 WAVE BREAKING ON PERFORATED BREAKWATER

A wave breaking against the perforated breakwater is shown in Fig. 5. The first photograph shows the wave crest approaching the caisson and the water still draining from the caisson chamber. The water level inside the chamber does not reach level 3 before the crest hits the wall as seen in the second photograph. A small air pocket is formed between levels 1 and 3. The third photograph shows an instant after the initial impact of the wave crest. Water jets have not yet contacted the rear wall and the water surface inside the chamber has been deformed by jets entering between levels 1, 2 and 3. The remaining photograph shows the continued run-up against the front wall of the caisson with water jets entering at higher levels and the extreme turbulence and high air entrainment of the flow against the rear wall.

EXPERIMENTAL RESULTS

Wave impact pressure records are shown in Fig. 6(a) for tests on the solid wall breakwater and the perforated breakwater. The pressure on the solid wall in this particular test reached a maximum of 122 kPa (17.6 psi) at level 4. The pressure records at levels 1, 2 and 3 show the characteristics of compression shocks caused by the presence of an air pocket, that is, a slow rise and fall of pressure. The record at level 4 is somewhat unusual because it apparently is a combination of a sharp pressure increase caused by a hammer shock and the smoother curve of a compression shock. The similarities in the lower four pressure records indicate that in this case the spacing of the transducers was sufficiently close for a relatively accurate determination of the total force on the wall. The pressure records from levels 4 to 7, in which the pressure increase occurs at progressively later times, show the effect of the run-up of the wave crest on the caisson wall.

Pressures recorded in a test on the front wall of the perforated breakwater are shown in Fig. 6(b). The most obvious difference to the previous records is that compression shocks are absent because of the rapid dissipation of air pockets through the perforations in the wall. However, there is a very large hammer shock present at level 5 with a magnitude of 125 kPa (18.1 psi) and a rise time of 0.25 ms indicating that the perforated wall does not completely eliminate the occurrence of high impact pressures. In fact the highest impact pressure recorded in all tests was 142 kPa (20.6 psi) and occurred on the front wall of the perforated breakwater. Fortunately, such high pressures do not occur over a wide area. In Fig. 6(b) the peak pressure is recorded at level 5, but at level 4 this peak has already dropped to one third and at level 6 it is even less. The high frequency oscillations in these records are due to structural vibration of the breakwater. They are not the compression oscillations measured by many investigators



(A) SOLID WALL
TEST NO. 1027

(B) PERFORATED WALL
TEST NO. 793

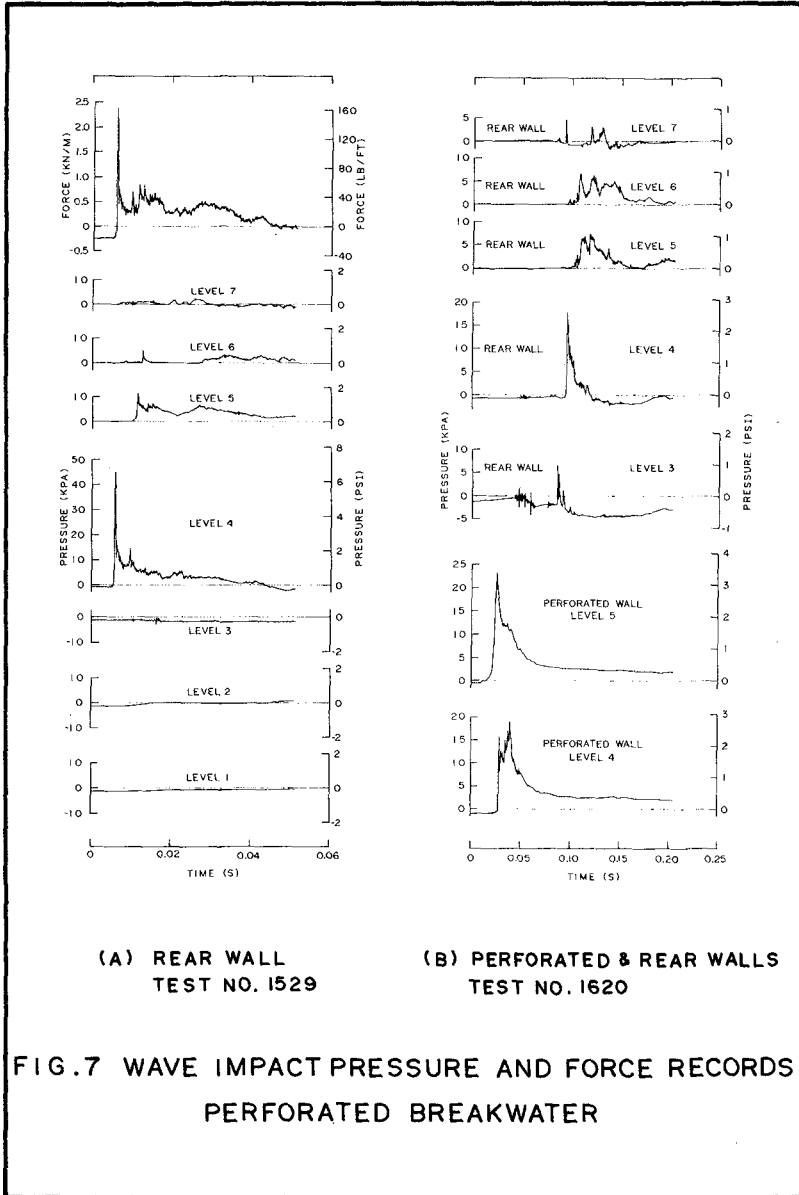
FIG. 6 WAVE IMPACT PRESSURE AND FORCE RECORDS

(Mitsuyasu (4) and Rankema (8)) because such oscillations are generally at frequencies less than 500 Hz, although in the present tests similar low frequency oscillations were occasionally observed.

By integrating the pressure over the vertical height of the caisson, the total horizontal force on the wall is obtained in units of kN per metre width of caisson. Thus, the force records for the solid and perforated walls are also shown in Fig. 6. The effect of the compression shock pressures on the solid wall is to produce a force record with a relatively slow rise time. The maximum force is obviously caused by the hammer shock recorded at level 4, but it is important to note that the peak of the force caused by the compression shock is almost 90% of the maximum force. The total force on the model breakwater which is 1.22 m wide is 12.76 kN (2870 lbs) which emphasizes the importance of the massive supporting structure. The maximum force measured in all tests on the solid wall breakwater was 14.78 kN/m or a total force for the width of the model of 18.03 kN (4050 lbs).

The force record in Fig. 6(b) for the perforated wall test has a peak force due to the hammer shock pressure at level 5 which occurs for a short duration of approximately 1 ms. It should be noted in this case that a correction has been made for the porosity of the wall. Thus, the pressure has been integrated only over the solid area of the wall and the resulting force is therefore only 65% of the force that would have been obtained if the wall contained no perforations.

To determine the total force on the perforated breakwater, it is necessary to take into account the additional pressures on the internal walls of the chamber. However, pressures on the interior side of the perforated wall were not measured, as it is thought that these pressures would be small. In any event, it is conservative to omit these pressures as they act in the opposite sense to those on the other surfaces. Approximately 300 tests were conducted with seven pressure transducers located on the rear wall of the perforated breakwater as shown in Fig. 2(b). An example of the type of pressure records measured is in Fig. 7(a). The initial impact of the water jets produced by the perforated wall is sensed at level 4 on the rear wall. The pressure peaks at levels 5 and 6 are displaced in time slightly and are much smaller in magnitude. In a number of the pressure records measured on the rear wall, the rise times were very fast indeed. In fact several were measured with a rise time approaching that of the sample interval. This obviously means that the sampling rate was not nearly fast enough to measure such pressure peaks accurately. In addition, when the pressure rose so rapidly, the transducer diaphragm vibrated giving an oscillation on the pressure record that was unmistakably due to the excitation of the resonant frequency of the transducer.



The pressure records measured on the rear wall of the perforated breakwater were not always as clean as shown in Fig. 7(a). The turbulent fluid motions occurring on the rear wall after the initial wave impact, caused irregular pressure records such as shown in Fig. 7(b). This figure illustrates the time difference between pressure peaks occurring on the two walls of the perforated breakwater. Because pressures could not be measured simultaneously at 14 locations on the perforated and rear walls, an accurate estimate of the total force on the perforated breakwater could not be obtained. However, to help understand how the total force is produced, two pressure transducers were placed at levels 4 and 5 on the perforated wall, and the remaining five at levels 3 to 7 on the rear wall. Triggering of the transient recorders was initiated by either of the two transducers on the perforated wall, and tests were conducted to determine the most suitable sampling rate. The sample interval of 0.05 ms used for the earlier tests was too fast in this case because the water jets did not reach the rear wall within the 0.05 s record length. A sample interval of 0.20 ms was chosen and approximately 60 tests were conducted with the pressure transducers located as described above. A typical set of pressure records is in Fig. 7(b). There is a pronounced time difference between the occurrence of peak pressure on the perforated wall and that on the rear wall. This time difference varies between different records, but it can be estimated as approximately 0.075 s and is the time taken for the jets of water formed by the perforated wall to reach the rear wall. The resulting displacement of pressure records appears to be large enough that as a result of integrating pressure over the two walls, the peak total force on the breakwater would not be significantly greater than the maxima recorded separately on either the front or rear walls. However, further investigations are necessary to obtain accurate estimates of total force on the perforated breakwater. It is important to note that the maximum force on the breakwater will depend on the chamber width, not only because of the effect of wave reflection but because if the rear wall is too close to the perforated wall, peak pressures will occur at approximately the same time.

For comparison of breakwater types, approximately 300 tests were conducted on each of three walls, that is, the solid wall breakwater, and the front and rear walls of the perforated breakwater. For each test the maximum pressure at each transducer was extracted along with the maximum force from the force record. Using these figures, cumulative probability distributions were plotted for the maximum pressures occurring at each level on the walls and also for the maximum forces. Since the transducer elevations for the solid and perforated walls are identical and in order to provide a direct comparison, probability distributions for these two walls are plotted together in Fig. 8. As an exam-

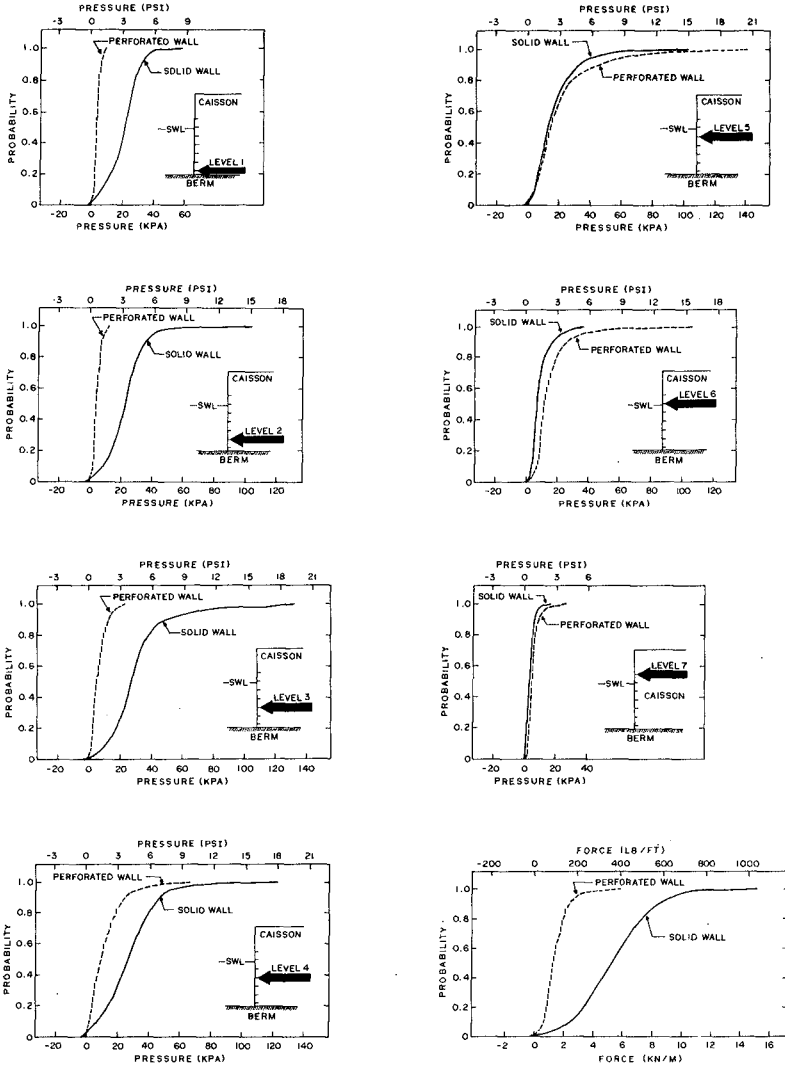


FIG.8 CUMULATIVE PROBABILITY DISTRIBUTIONS
SOLID AND PERFORATED WALLS

ple of how these figures may be read, taking a probability of 0.9 at level 1 on the solid wall shows that 90% of the maximum pressures measured at this location were less than approximately 31 kPa (4.6 psi).

From levels 1 to 4 in Fig. 8, the pressures on the solid wall are considerably larger than those measured on the perforated wall, but from levels 5 to 7 the pressures are larger on the perforated wall. The maximum pressure occurs at level 5 on the perforated wall and is 142 kPa (20.6 psi). However, because the pressures are more localized, the cumulative probability distribution curves show that the force on the perforated wall is very much less than that on the solid wall. At probabilities of 0.5 and 0.9 the maximum force on the perforated wall is consecutively 25% and 29% of that on the solid wall.

Fig. 9 shows the cumulative probability distributions for the maximum pressures measured on the rear wall of the perforated breakwater. These pressures are generally much smaller than those occurring on the front wall; however, peak pressures of up to 100 kPa (14.5 psi) were measured. The probability distribution for force also shows that the force on the rear wall is less than that on the perforated wall. At a probability of 0.9, the maximum force on the rear wall is 58% of that on the perforated wall, and 17% of the force on the solid wall breakwater.

The distributions of maximum pressure in Fig. 10 have been plotted by taking the maximum pressures at probabilities of 0.5, 0.9 and 1.0 for each transducer location from the cumulative probability distributions. The pressure distributions for the three walls are superimposed. The curves for probabilities of 0.5 and 0.9 show that the pressure on the solid wall is usually a maximum at level 3, while that on the perforated wall is usually a maximum at level 5. This is a result of the different characteristics of the breakers striking the two walls. Although the incident wave is the same in both cases, the reflection from the perforated breakwater is about half that from the solid breakwater, causing the wave to trip slightly closer to the perforated wall. The pressure distributions at a probability of 0.9 show pressure peaks similar in magnitude for both the perforated and solid walls, but the solid wall has a higher pressure over a greater area of wall. Pressures are lower at the base of the perforated wall because of the absence of compression shocks. The plot for a probability of 1.0 shows the maximum pressures measured at the pressure transducer locations and so the curves are not as smooth as the previous plots. Also, Fig. 10(d) shows examples of instantaneous pressure distributions. The pressures plotted are from tests 1027, 793 and 1529 for which the pressure records are in Figs. 6 and 7, and are the pressures occurring at the same time as the maximum pressure on the wall which also corresponds to the pressures at the time of maximum force. However, it should be pointed out that in some tests the

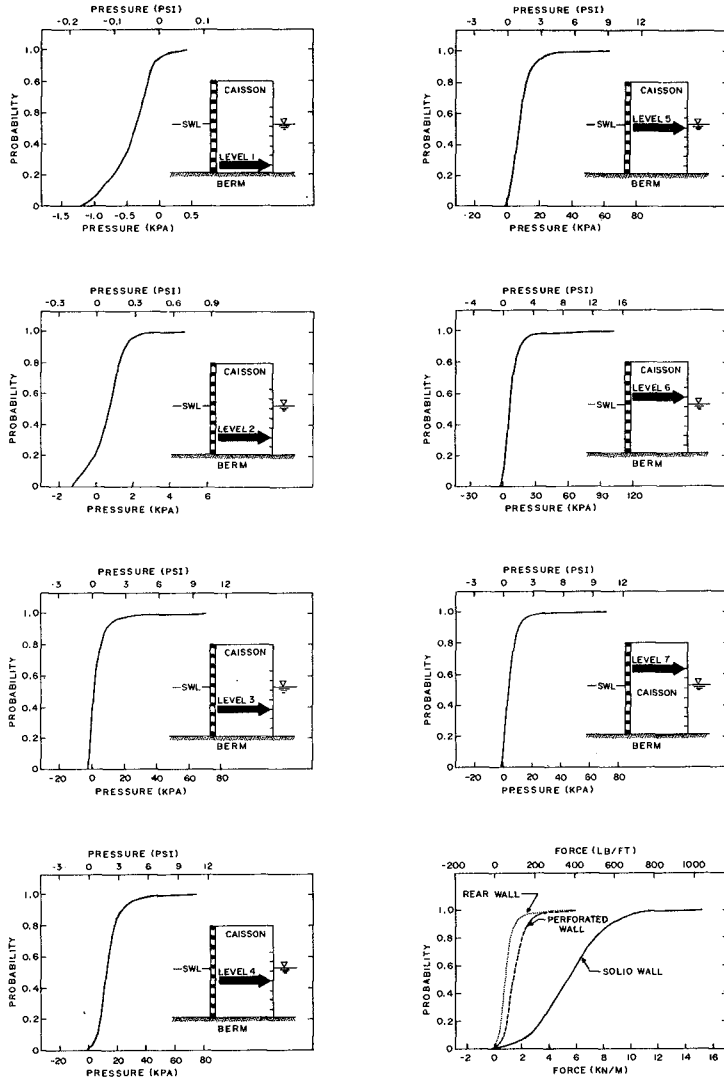
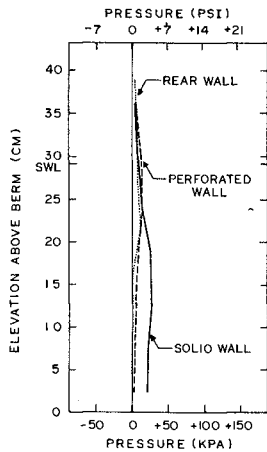
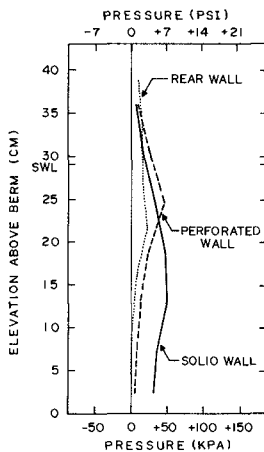


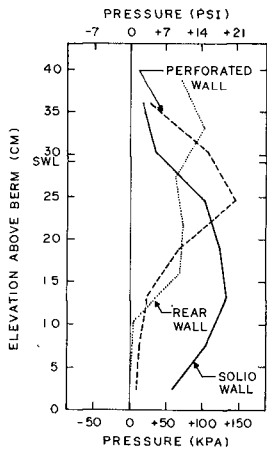
FIG.9 CUMULATIVE PROBABILITY DISTRIBUTIONS
REAR WALL OF PERFORATED BREAKWATER



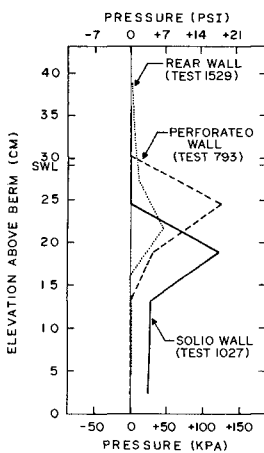
(A) PROBABILITY = 0.5



(B) PROBABILITY = 0.9



(C) PROBABILITY = 1.0



(D) INSTANTANEOUS PRESSURE DISTRIBUTIONS

FIG.10 PRESSURE DISTRIBUTIONS

maximum force occurs at a different time to the maximum pressure and therefore would not result in the same pressure distributions.

RESEARCH PROBLEMS

The experimental results clearly show the importance of good instrumentation, since the peak pressures measured are much higher than in many previous studies in which inferior instrumentation was used. The frequency response of all components must be fast enough that resonance problems are eliminated and pressure peaks are not significantly attenuated. Even with the present equipment, these difficulties were obviously present in a number of tests, particularly on the rear wall of the perforated breakwater. However, it is essential to make a decision as to how fast peak pressures need to be measured in view of the probability that breakwaters are not adversely affected by high pressures if the duration of pressure is extremely brief. Evaluation of the relative importance of high frequency pressures and forces is necessary, but unfortunately the response of breakwaters to wave impact loads has received little attention in the literature. However, breakwater response must be considered using the latest wave impact pressure data before more highly sophisticated instrumentation is deemed necessary.

The estimation of total force on breakwaters as complex as the perforated breakwater, requires numerous pressure transducers to give reasonable accuracy. This could be an unnecessarily expensive proposition when it may be possible to design force dynamometers which are sufficiently stiff for high frequency response. Also an alternative to the use of pressure transducers is the possibility of strain-gauging the structure itself, as described by Graveson et al. (1).

There is still no generally accepted method of scaling impact pressures from model to prototype conditions. The compression laws of Lundgren (2), Mitsuyasu (4) and Rankema (8) may improve predictions but still rely on measurements in models which are not dynamically similar to the prototype. Consideration should be given to very large model tests and the measurement of impact pressures on existing full-size breakwaters.

The data presented in this paper demonstrates the extreme variability of impact pressures and forces under controlled conditions, when attempting to reproduce exactly the same incident waves. Natural sea states are so much more complex that the frequency of occurrence of high impact pressures in real seas is still largely a matter of speculation.

CONCLUSIONS

1. A large variation was observed in the impact pressures caused by incident waves with a variation in height of only $\pm 4\%$ at the most. For example, extremes of maximum pressure occurring at a single location on a breakwater were as much as ten times the average peak pressure. Means and standard deviations (S.D.) of maximum pressures and forces are as set out in Table I.

TABLE I
MEANS AND STANDARD DEVIATIONS
OF MAXIMUM PRESSURES AND FORCES

Pressure (kPa) at Level	Solid Wall		Perforated Wall		Rear Wall	
	Mean	S.D.	Mean	S.D.	Mean	S.D.
1	21.2	9.6	3.4	2.0	-0.4	0.3
2	23.9	11.6	4.5	2.5	0.7	0.8
3	32.6	20.6	7.1	4.8	3.6	6.2
4	29.8	17.2	12.5	10.7	14.7	8.2
5	17.8	13.0	22.2	19.9	9.2	6.9
6	9.2	5.9	16.4	11.7	9.5	9.6
7	3.9	2.4	6.0	3.3	5.7	6.0
Force (kN/m)	5.5	2.4	1.6	0.8	0.9	0.6

2. The perforated wall virtually eliminated compression shocks caused by the entrapment of air pockets.
3. Although impact pressures were generally lower on the perforated wall than on the solid wall caisson, there were locations where the pressures recorded were higher than on the solid wall. In fact, the highest pressure recorded in all tests, that is 142 kPa (20.6 psi), was measured on the perforated wall. However, the frequency of occurrence of high pressures on the perforated wall was lower than that on the solid wall.
4. Peak pressures measured on the rear wall of the perforated breakwater were significantly less than those occurring on the front wall and occurred at a time displaced from the peaks on the front wall dependent on the chamber width.
5. The mean force measured on the perforated wall was only 28% of that on the solid wall caisson. The total force on the perforated breakwater was not measured but is estimated to be considerably less than the force on the solid breakwater.

- 6.⁶ This experimental study has enabled an evaluation of the advantages of the perforated breakwater over the solid wall breakwater, but further investigations are necessary before it can be concluded that the structurally complex perforated caisson would be preferable to other alternative caisson designs.

ACKNOWLEDGEMENTS

Although the task of high speed transmission of data from two transient recorders a distance of 120 m to a digital computer, may not seem difficult, it caused much grief particularly for Arnold Wiegert and Tony Edwards. The authors appreciate their perseverance in developing a data acquisition system which made possible the rapid processing of vast quantities of experimental data.

REFERENCES

1. Graveson, H., Brodersen, F.P., Larsen, J.S. and Lundgren, H., "Cylindrical Caisson Breakwater: Strain Model Tests", Proc. Fifteenth Coastal Engineering Conf., Honolulu, July 1976, pp. 2357-2370.
2. Lundgren, H., "Wave Shock Forces: An Analysis of Deformations and Forces in the Wave and in the Foundation", Proc. Research on Wave Action, Delft, July 1969, pp. 1-20.
3. Lundgren, H. and Graveson, H., "Vertical Face Breakwaters", Sixth International Harbour Congress, Antwerp, May 1974, pp. 2.11/1-2.11/11.
4. Mitsuyasu, H., "Shock Pressures of Breaking Wave", Proc. Tenth Coastal Engineering Conf., Tokyo, September 1966, pp. 268-283.
5. Moutzouris, C., "Probabilistic Analysis of the Peak Pressures Due to Wave Breaking on a Coastal Structure", Atti del XVI Convegno di Idraulica e Costruzioni Idrauliche, Torino, September 1978, pp. B21.1-B21.12.
6. Nagai, S. and Kakuno, S., "Wave Pressures on Slit-Type Breakwaters", Proc. Sixteenth Coastal Engineering Conf., Hamburg, August 1978, pp. 2360-2377.
7. Onishi, H. and Nagai, S., "Breakwaters and Sea-Walls with a Slitted Box-Type Wave Absorber", Coastal Structures 79, Alexandria, March 1979, pp. 9-28.
8. Ramkema, C., "A Model Law for Wave Impacts on Coastal Structures", Proc. Sixteenth Coastal Engineering Conf., Hamburg, August 1978, pp. 2308-2327.
9. Richert, G., "Shock Pressures of Breaking Waves", Royal Institute of Technology, Stockholm, Bulletin No. 84, 1974, 139 pp.

CONSTRUCTION AND MODEL INVESTIGATION
OF STORMWATER OUTFALL

by
K A Heathcate¹ and G W Brittan²

1. INTRODUCTION

Posford Povry Sinclair and Knight were commissioned in 1976 to design a new stormwater outfall off one of Sydney's surfing beaches. The location of the outfall was dictated by a previous outfall which had been built in the dry when the beach line was much further seaward but which had been destroyed by wave action when the beach line retreated to the 1976 position (a distance of approximately 50 metres (Figure 1)).

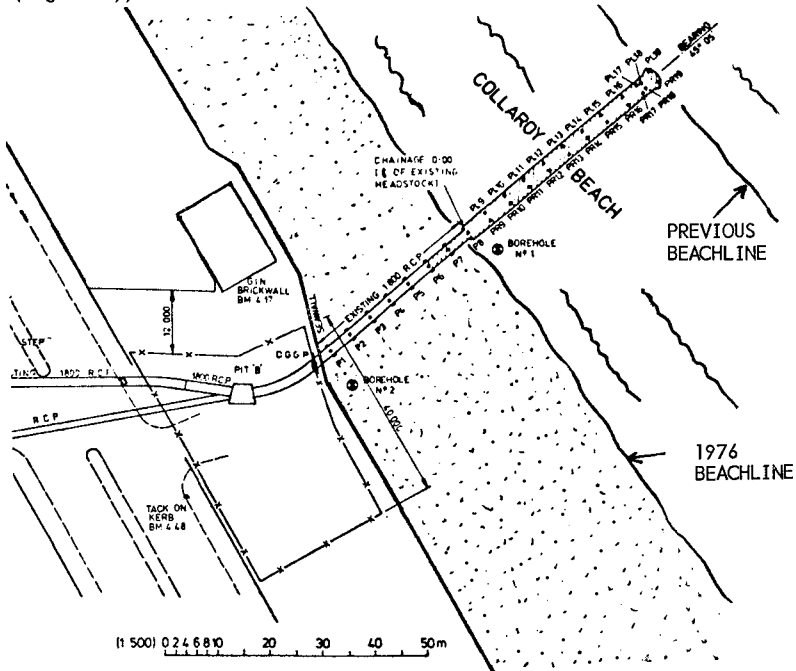


FIGURE 1 LOCATION PLAN OF OUTFALL

1. B.E., M.ENG.SC., M.COM., Engineer, Posford Pavry Sinclair & Knight, Sydney, Australia
2. B.E.(Civil), Engineer, Department of Public Works, NSW, Australia

2. CONSTRUCTION

Because of difficulties in locating plant in the surf zone, it was decided to construct the outfall out of precast reinforced concrete box sections (Figure 2) using a "leopfrogging" method of construction whereby all construction operations were carried out by a crane/pile driver located on top of previously placed units.

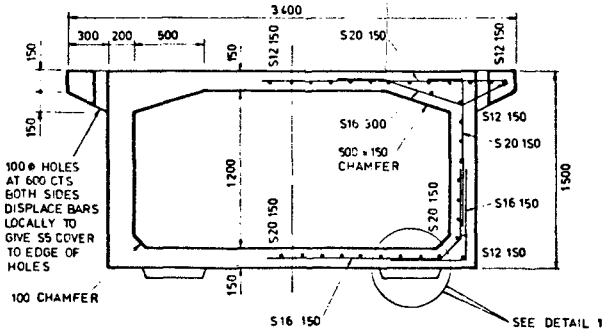


FIGURE 2 CROSS-SECTION OF BOX UNIT

The first stage of construction involved building a temporary support platform to enable a crane to get from the corpark to the waterline. This ramp was built level with the top of the concrete box units. A crane travelled down this ramp and proceeded to drive the two pile bents (Figures 3 and 4). Each pile bent consisted of two steel H piles of 1 metre centres. Precast unreinforced concrete protective jackets were then jettied around the H piles to provide scour protection (Figure 5).

The second stage involved placing precast reinforced concrete headstocks (Figures 6 and 7) on top of the pile bents, levelling them off by means of a special level adjustment device, locking them into place to prevent their displacement by waves, and then grouting them up to form a fixed connection with no pile steel exposed (Figure 7).

The third stage in the construction process necessitated the crane lifting up a box unit which had been wheeled down from the costing yard to a position behind the crane, swinging it around and placing it on the headstocks (Figure 9). The stainless steel bolts in the headstocks were fed through slatted holes in the base of the box units and stainless steel pods clamped the box units to the headstocks once in place (Figure 8). The slotted holes accounted for any longitudinal misalignment of the piles.

STAGE 1—DRIVE PILES FROM PREVIOUSLY
ERECTED BOX UNIT AFTER SETTING TO
REQUIRED LEVEL. DROP SHORBRACE UNIT
INTO HOLES IN STIFFENERS AND FIT
RETAINING NUTS (SEE CONNECTION
DETAILS ON DWG. N° 1956/104.)

SUGGESTED CRANE
UNIT TO BE A
N C K 60S WITH
91S WIDE TRACKS

PILING GUIDE
CONSTRUCTED
TO SUIT.

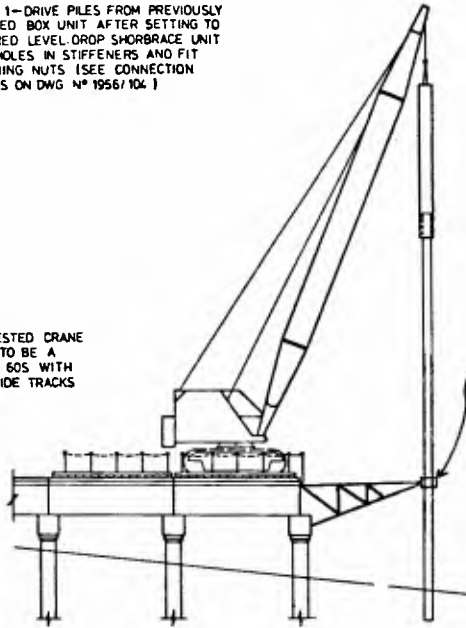


FIGURE 3 STAGE 1 CONSTRUCTION PROCEDURE



FIGURE 4 PILE DRIVER BEING LIFTED INTO POSITION



FIGURE 5 JACKETS BEING JETTED IN AROUND PILES

STAGE 2—DROP CONCRETE PIPE OVER PILE AND
JET TO REQUIRED LEVEL. DROP R C CAGE
DOWN PIPE. LIFT PRECAST HEADSTOCK
UNIT INTO PLACE AND FIX DOWN WITH
CLEAT SEAL BETWEEN HEADSTOCK AND
CONCRETE PIPE AND PLACE GROUT UP TO
TOP OF HEADSTOCK.

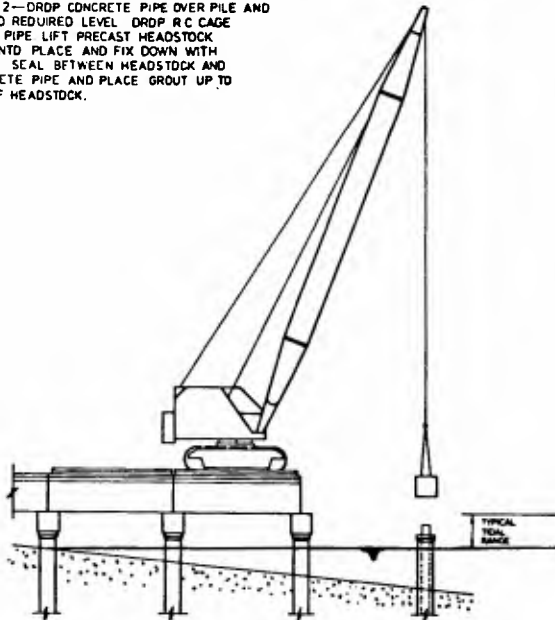


FIGURE 6 STAGE 2 CONSTRUCTION PROCEDURE



FIGURE 7 PRECAST REINFORCED CONCRETE HEADSTOCKS

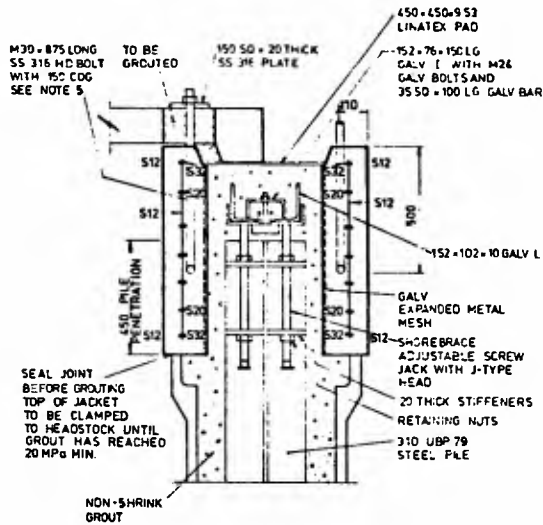


FIGURE 8 SECTION THROUGH HEADSTOCK IN PLACE

This procedure was repeated for a total of nine box units (each approximately 4.9 metres long) and a special precast outlet unit was then placed on four piles at the seaward end (Figure 10). This outlet unit was designed to prevent blockage of the outlet should the shoreline extend out to its previous level. At the shoreward end, a transition piece connected the box units to the existing circular 1.83 metre diameter reinforced concrete stormwater pipes.

STAGE 3--WHEN IN-SITU CONCRETE IN HEADSTOCK HAS ATTAINED A STRENGTH OF AT LEAST 30 MPa, LIFT PRECAST BOX UNIT INTO PLACE AND BOLT DOWN. ADVANCE CRANE AND REPEAT PROCESS.

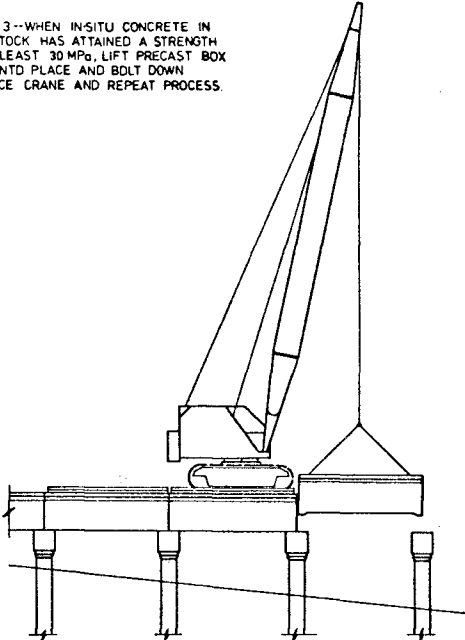


FIGURE 9 STAGE 3 CONSTRUCTION PROCEDURE

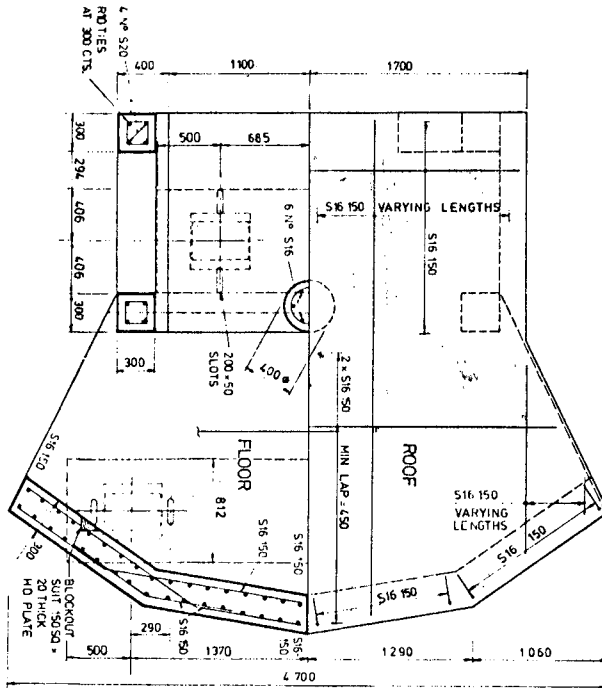


FIGURE 10 SPLIT PLAN OF OUTLET UNIT

In retrospect, the construction procedure worked very well. However a short time after the sixth box unit had been placed, reasonably heavy seeps were experienced. This particular unit broke up in the region of the holding down bolts. Evidence of site stiff present at the time indicated that the nuts of the holding down bolts had worked loose and the unit had been pounding up and down under the action of the waves. It was at this stage that the possibility of high shock pressures on the slab immediately adjacent to the headstocks occurred to us, and a rough model test was carried out to indicate the magnitude of this effect. The tests indicated that the wave pressures on the underside of the slab were sufficiently high (of the order of 60 KPa prototype) to warrant a full scale model investigation. Details of this investigation are presented in Section 3.

At the same time as the work was being carried out to determine what wave loading to use in checking the box units, further investigation and analysis was carried out to determine the inherent strength of the box units. It had been assumed in the design stage that the

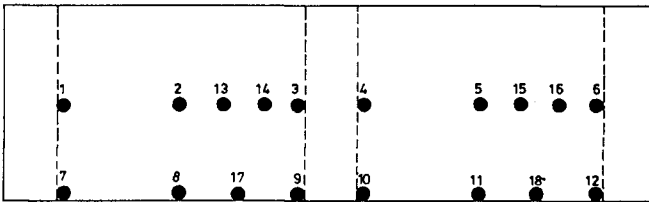
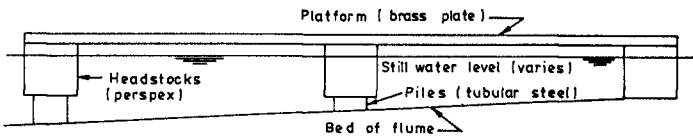
outlet unit would shield the box units from direct wave attack and no allowance had been made for any vertical wave loading. The box units had been designed for a static water pressure of 12 kPa and were only nominally reinforced in the base slab. A finite element analysis was carried out for a wave loading of around 360 kPa (based on an increase in wave energy as water depth increased) and for the crane loading during construction. The analysis revealed a shear weakness in the construction case and indicated that for the assumed wave loading, the box unit would stay intact but with severe cracking occurring. Both these problems were exacerbated by the Contractor's omission of reinforcement in critical areas. The problem of the shear weakness during construction was easily remedied by the insertion of packing plates and further holding down bolts were put in to enable the bottom of the box units to act more as a two way slab and thus have greater flexural strength under wave attack.

The outfall was completed on this basis and it was decided to re-evaluate the question of further strengthening when the detailed model tests were completed.

3. HYDRAULIC MODEL INVESTIGATION

3.1 Model and Instrumentation

The nature of the breaking wave uplift pressures on the underside, or soffit, of the stormwater outfall was investigated in a laboratory wave flume 0.9 m wide using a model of two bays of the stormwater outfall constructed at a scale of approximately 1 in 12 (Figure 11).



NOTE


1. Location for transducer and number shown thus 

FIGURE 11 MODEL OF OUTFALL

To enable measurement of the uplift pressure a total of 18 holes were drilled through the horizontal platform of the model, comprising 9 through the centre-line and 9 along the edge, in which could be positioned a pressure transducer flush with the platform soffit. Only one single pressure transducer was used throughout the investigation and therefore simultaneous measurement of uplift pressures over the platform could not be achieved.

The pressure transducer was a Stothom differential pressure transducer Model PM1311C. This transducer is a flush diaphragm construction with a working range of ± 175 cm H₂O and natural frequency 3,500 hertz. The response of the transducer to wave pressures was amplified and displayed on a Tectronix 912 storage cathode oscilloscope via a low pass filter. The low pass filter attenuated the effects of component frequencies above 1,000 hertz which it was thought could excite vibration of the transducer at its natural frequency.

3.2 Experimental Conditions and Procedure

The model was placed centrally in the wave flume on a beach slope of 1 in 20, approximately 17.5 m from a periodic progressive wave generator. Throughout the testing the model wave period was maintained constant at 2.3 seconds (8 seconds prototype). Incident waves were always made to break seaward of the model by variation of the stroke of the wave paddle. The wave motion impinging on the model was therefore the surge formed after breaking.

The work of previous researchers had shown that wave pressures exerted on horizontal platforms (and vertical walls) were characterised by an initial impact pressure of high magnitude and short duration followed by a pressure of longer duration and lesser magnitude. The nature of the initial short duration impact pressure was the prime concern of this investigation and was studied in two stages. The first stage was aimed at establishing temporal characteristics of the impact pressure and involved simultaneous measurement of both impact pressure rise time and magnitude. Readings were taken for only the centre-line transducer locations and for still water levels 10 mm and 20 mm below the soffit of the platform. The elevation of the soffit above the bed of the flume was such that the most seaward headstock rested on the bed (Figure 1).

The second stage of testing was concerned with determining the distribution of the magnitude of the impact pressure over the platform as well as a study of the slowly varying pressure. In this case readings were taken at each of the 18 locations for the transducer. The difference between the soffit and still water level was varied, in steps of 10 mm, between a lower water level value at which no contact occurred between the incident wave and the soffit and an upper water level value at which impact pressures ceased to occur (see Section 1.3.4). In addition, two elevations of the

platform soffit above the bed of the flume were considered. Initially the elevation of the soffit was set as described for the first stage of testing. A second series of tests was then undertaken with the soffit raised 25 mm by insertion of spacers into the support piles.

Both the magnitude and rise time of the initial impact pressure were subject to considerable variation from impact to impact for a given test condition. In order that meaningful average values were obtained 20 readings of impact pressure magnitude and rise time were taken for each combination of transducer location, difference between soffit and still water level and soffit elevation above the bed. The magnitude of the slowly varying pressure was much more regular and a representative value was taken from the display of 3 to 4 waveforms only.

Over the range of conditions studied in the model investigation the variation in the breaking wave height in the model was from 7 cm to 19 cm (0.85 m to 2.3 m prototype) and in the water depth along the structure was from 2 cm to 15 cm (0.25 m to 1.8 m prototype).

3.3 Results and Discussion

3.3.1 General

Although the experimental equipment comprised essentially only a single pressure transducer and storage cathode ray oscilloscope, several informative and interesting conclusions could be drawn from the hydraulic model investigation.

As expected, when impact occurred, and irrespective of the location of the transducer on the platform, the recorded pressure in general comprised an initial impact pressure of potentially high magnitude and short duration (of the order of milliseconds) followed by a slowly varying pressure of longer duration, which was typically first positive then negative.

The nature of the slowly varying pressure is fairly well understood and can be related to the hydrostatic effects with due allowance made for the influence of vertical fluid acceleration. It is therefore proposed only to discuss here some of the important aspects of the impact pressure. Accurate measurement of the impact pressure is difficult because of its extremely short rise time and the finite size of the pressure transducer's sensitive diaphragm. Together these factors may lead to a so called "transducer area defect", related to the transducer's spatial resolution (French, 1969).

French proposed that a transducer would not accurately record a pressure distribution unless the characteristic half-length of the pressure pulse (the product of the rise time and wave celerity) was greater than about three times the radius of the pressure transducer's sensitive diaphragm. If this was not the case a record of

time-dependent pressure would be produced in which the recorded pulse was of longer duration and of lesser amplitude than a record produced by a transducer of vanishingly small area or simply of somewhat smaller area. A correction procedure developed by French increased the recorded impact pressures in his study by a few percent to as much as 50% although it is stated that the procedure cannot be applied with certainty.

The Statham PM131TC transducer used in this investigation did not satisfy the above criterion for "accurate measurement" proposed by French. As the purpose of the investigation was to establish the nature of the breaking wave impact pressures no attempt has been made to correct the results for the above factors. It is therefore likely that the results presented in the following sections may tend to underestimate the magnitude of the impact pressure and overestimate its rise time. Use of the low pass filter could be expected to contribute to this tendency.

3.3.2 Rise Time of Impact Pressure

The rise time of the impact pressure was defined as the duration of time between the initial sharp rise of the pressure above static level and the peak of the pressure response.

For the centre-line gauges and the two water levels tested the average rise time of the impact pressure varied between 1.8 milliseconds and 8.5 milliseconds. Although subject to considerable variation from impact to impact there did appear to be a relation between the rise time and magnitude of the impact pressure, such that the shorter the rise time the higher was the magnitude of the impact pressure. This relationship has in fact been reported by previous researchers, notably Bagnald (1939) and Rass (1954), who found that the area enclosed by the pressure-time curves tended to approach, but never exceed, a definite value. This area of the pressure-time curves up to the peak of the impact pressure was found to be a fraction of the wave momentum and is thought to be related to the destruction of the original momentum of the kinetic mass involved in the impact.

3.3.3 Longitudinal Variation of Impact Pressure Head

Figure 12 shows the variation in magnitude of the impact pressure head along the centre-line of the structure for the two elevations of the soffit relative to the bed of the flume. Impact pressure head is measured in centimetres of water and each plotted point represents the average of twenty readings of the impact pressure for a given difference between the soffit and still water level.

It should be noted that the plotted points do not represent a simultaneous envelope of impact pressure on the structure. The impact pressure is in fact considered to be a phenomenon travelling with the line of initial contact between the wave and the soffit and at any one time to be confined to this immediate vicinity. (This was

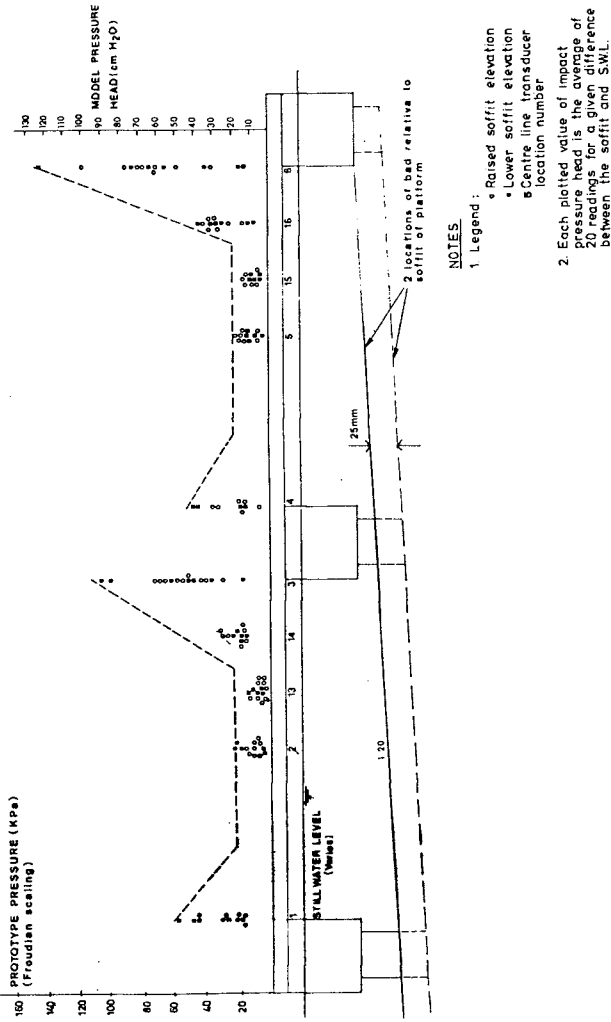


FIGURE 12 LONGITUDINAL VARIATION OF IMPACT PRESSURE HEAD

first proposed by French and confirmed by observation during this investigation.) An estimate of the spatial extent over which the impact pressure acts can be obtained from the product of the wave celerity and the rise time. From the results of this investigation the extent is of the order of only millimetres (model). This means that only very localised regions of the structure, each of wave length order, are subject to the impact pressure at any one instant. Quite a considerable length, however, could be subject to the slowly varying pressure at any one time.

The effect of the headstocks on the magnitude of the impact pressure head is immediately evident. Impact pressures are higher in the regions immediately seaward and shoreward of the headstocks with the effects most pronounced immediately seaward of the headstocks. (Note that the plotted points represent pressures caused by incoming waves and not backwash. The effect of backwash for the conditions tested was found to be negligible.) The influence of the headstocks appears to extend over a region either side of the headstock, equal to about the projection of the headstock below the soffit.

The highest average magnitude of the impact pressure head recorded in the model was 123 cm H₂O (or about 12 kPa) at transducer location 6 immediately seaward of the most shoreward headstock (Figure 12). If scaled according to Froude's Law, which is generally considered to overestimate pressures of this type (Richert, 1974), a prototype pressure of 150 kPa would be predicted. These pressures are clearly extremely high in comparison to normal design loads and their magnitude alone suggests that they would be of concern in the design of prototype structures. Before their effect on a structure could be evaluated, however, the structure's response to the spatial and temporal characteristics of the pressures would need to be established.

In regions of the platform remote from the effect of headstocks the magnitude of the impact pressures are much lower. The results of this investigation are in agreement with the work of previous researchers who studied impact pressures on horizontal platforms (without vertical obstructions) and found that the magnitude of the impact pressure head rarely exceeded 5 times the height of the incident wave above still water level (French, 1969; Wong, 1970; Massel et al, 1978).

3.3.4 Variation of Impact Pressure Head with Difference Between Soffit and Still Water Level

Figure 13 shows the manner of the variation of average impact pressure head with difference between the soffit and still water level for transducer locations 6 and 3. The manner of the variation is typical for each of the transducer locations but is best illustrated by the results of locations 6 and 3 due to the wide range in the magnitude of the impact pressure head recorded at these locations.

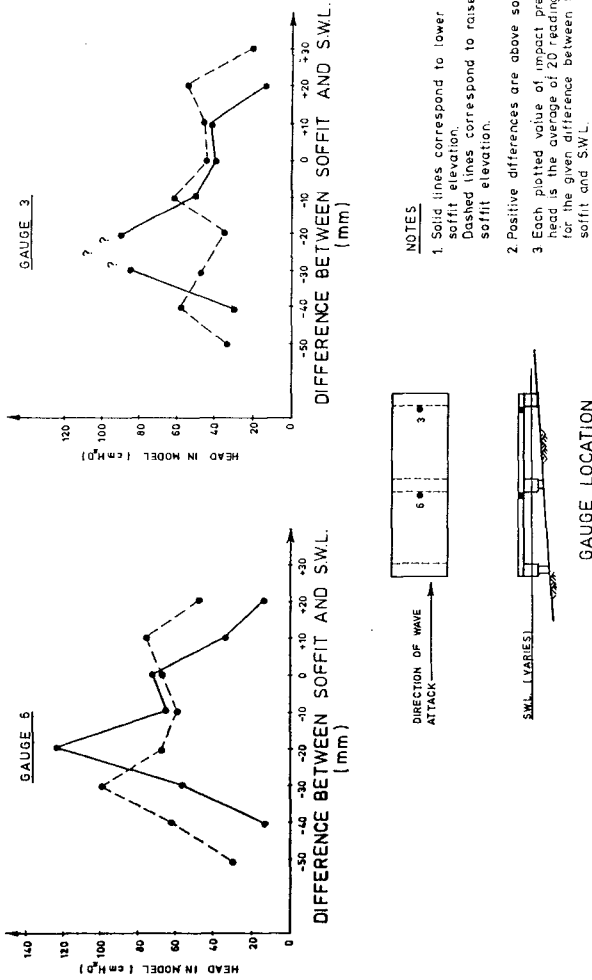


FIGURE 13 VARIATION OF IMPACT PRESSURE HEAD WITH DIFFERENCE BETWEEN SOFFIT AND S.W.L.

The highest single impact pressure recorded in the model was 300 cm H_2O , also at transducer location 6, and if scaled in the same way corresponds to about 360 kPa in the prototype.

Most evident from Figure 13 is that impact pressures at a location on the platform occur only over a certain range of differences between soffit and still water level (or alternatively, for a certain range of water depths). The lower limit of the range is the trivial case of when the water level is so low that no contact is made between the incident wave crest and soffit of the platform. The upper limit of the range appears to be for the case of when there is no air gap between the body of water in front of the incident wave and the soffit of the platform. In this case the impact pressure appears to be "drowned" and the record of wave pressure comprises the slowly varying pressure only. This observation lends support to French's conclusions that impact pressures on a horizontal platform are associated with a wave propagating into an empty air filled space (French, 1969).

An important inference from the above results is that providing wave activity is present and the water level is within the "critical range" wave impact pressures will always occur and furthermore will continue to occur, at the wave frequency, until the water level varies outside the limits of the "critical range" or the waves themselves cease to propagate. This is in direct contrast to breaking wave impact pressures on vertical obstructions which are extremely sensitive to the form of the breaking wave at the point of contact with the obstruction and are therefore by nature infrequent.

4. CONCLUSIONS

The main conclusions of the hydraulic model investigation are:

- (1) Short duration impact pressures occurring on the soffit of the precast units vary in magnitude along the unit. Prototype pressures predicted by Froude's law are of the order (maximum) of 150 kPa seaward of headstocks, 60 kPa shoreward of headstocks and 20 kPa in the central region between headstocks. (It should be remembered that the equivalent prototype height of incident breaking waves was of the order of only 1 to 2 metres.) The region of influence of the headstocks appears to extend from the face of the headstock for a distance about equal to the projection of the headstock below the soffit of the units.
- (2) The rise time of the impact pressure is extremely short, of the order of milliseconds and observation during testing confirmed that the impact pressure is a phenomenon confined to the immediate vicinity of the wave front and travelling with the wave velocity. These two aspects imply that only a narrow lateral strip of the box units is subject to wave impact loading at any one instant.

- (3) Impact pressures on the soffit at the precast box units occur for only a certain range of water levels and can be related to the difference in elevation between the soffit of the box units and the still water level. Within the range of water levels there is a "critical" water level for which maximum impact pressure occurs. Far lower or higher water levels the impact pressure is reduced even though for the case of the higher water level the breaking wave height is increased. For the particular conditions studied in this investigation the water levels within which impact pressures occurred extended over a vertical range of about 65 mm in the model, corresponding to approximately 0.75 m in the prototype.

The above conclusions have the following implications with respect to the prototype:

1. The wave loading predicted by the model tests is much higher than that assumed in design. The finite element analysis showed that the structure can safely withstand an overall pressure of around 10 kPa on the underside of the units combined with an impact pressure peaking from 10 kPa at a distance equivalent to the headstack depth away from the headstack to a maximum of around 60 kPa in the region of the headstack. This is significantly less than the maximum pressure envelope predicted by the model tests.



FIGURE 14 WAVE IMPACTING ON OUTLET UNIT

2. Because of the location of the soffit of the units at mean sea level combined with a tidal range of 1.33 metres it is extremely likely that the units have in the two years since completion been frequently subjected to wave forms which the model tests indicate produce high impact loading (Figure 14). For example 8 second waves over a tidal period of 6 hours represent 2700 waves and a significant proportion of these would strike the headstock when the water level was at or around the critical level.

Despite the above the structure has remained intact and a recent inspection revealed no obvious signs of distress. One can only assume from this fact that:

- (i) Non-idealised conditions in the prototype and/or the use of Froude's law result in the model tests overestimating actual prototype wave impact pressures.
- (ii) The response of the structure to the temporal and spatial disruption of actual wave pressures is such that significant redistribution and damping of internal stresses result.

It is likely that in practice a combination of the above factors probably occurs. The relative importance of these two factors is expected to become clearer when a prototype wave pressure study of the outfall (planned to be undertaken shortly by the Department of Public Works, NSW) is completed.

The aim of the paper has been to highlight the manner in which site-specific conditions govern design and construction in the surf zone, and in particular the need for wave loading to be fully evaluated in addition to normal functional loads. The results of the model tests have given the authors a valuable insight into the nature of wave loading on horizontal platforms in the surf zone and, whilst several questions still remain unanswered, it is hoped that the paper will be of assistance to designers and provide the basis for a better understanding of the performance of structures located in the surf zone.

5. REFERENCES

1. ALLGOOD, J.R. & SWIHART, G.R. (1970). Design of Flexural Members for Static and Blast Loading. ACI Monograph No 5.
2. ACKERMANN, N.L. & PING-HO CHEN (1974). Impact Pressures Produced by Breaking Waves. Proceedings, Fourteenth Conference on Coastal Engineering.
3. BAGNOLD, R.A. (1939). Interim Report on Wave Pressure Research. Journal of Institution of Civil Engineers, Vol. 12.

4. CHUANG, S.O. (1970). Investigation of Impact of Rigid and Elastic Bodies with Water. Novel Ship Research and Development Center, Report 3248.
5. CHUANG, S.L. (1970). Slamming Tests of Three-Dimensional Models in Calm Water and Waves. Novel Ship Research and Development Center, Report 4095.
6. DALTON, C. & NASH, J.M. (1976). Wave Slam on Horizontal Members of an Offshore Platform. Offshore Technology Conference, Paper No. 2500.
7. DENNY, D.F. (1951). Further Experiments on Wave Pressures. Journal of Institution of Civil Engineers, Vol. 35.
8. DENSON, K.H. (1972). Wave Forces on a Platform with a Ribbed Bottom. Proceedings, Thirteenth Conference on Coastal Engineering.
9. FRENCH, J.A. (1969). Wave Uplift Pressures on Horizontal Platforms. W.M. Keck Laboratory of Hydraulics and Water Resources, California Institute of Technology, Report No. KH-R-19.
10. FRENCH, J.A. (1971). Discussion of Water Wave Pressure on Horizontal Plate. Proceedings, A.S.C.E., Journal of the Hydraulics Division, Vol. 87, No. HY4.
11. FURUDOI, T. & MURATA, A. (1966). Wave-Induced Uplift Forces Acting on Quay-Aprons, Reprinted from Technology Reports of the Osaka University, Vol. 16, No. 734.
12. GARCIA, W.J. (1968). An Experimental Study of Breaking Wave Pressures. U.S. Army Engineer Waterways Experiment Station, Research Report H-68-1.
13. HAYASHI, T. & HATTORI, M. (1958). Pressure of the Breaker Against a Vertical Wall. Coastal Engineering in Japan, Vol. 1.
14. KAMEL, A.M. (1970). Shock Pressure on Coastal Structures. A.S.C.E., Journal of the Waterways, Harbour and Coastal Engineering Divisions, Vol 96, No WW3.
15. KAMEL, A.M. (1968). Shock Pressures Caused by Waves Breaking Against Coastal Structures. U.S. Army Engineer Waterways Experiment Station, Research Report H-68-2.
16. KAPLAN, P. & SILBERT, M.N. (1976). Impact Forces on Platform Horizontal Members in the Splash Zone. Offshore Technology Conference, Paper No. 2498.

17. MASSEL, S.R., OLESZKIEWICZ, M. & TRAPP, W. (1978). Impact Wave Forces on Vertical and Horizontal Plates. Proceedings, Sixteenth Conference on Coastal Engineering.
18. MINIKIN, R.R. (1950). Wind, Waves and Maritime Structures, London.
19. MITSUYASU, H. (1966). Shack Pressure of Breaking Waves (I). Coastal Engineering in Japan, Vol. 9.
20. MITSUYASU, H. (1966). Shack Pressure of Breaking Waves. Proceedings, Tenth Conference on Coastal Engineering.
21. NAGAI, S. (1960). Shack Pressures Exerted by Breaking Waves on Breakwaters. A.S.C.E., Journal of the Waterways and Harbours Division, Vol. 86, WW2.
22. NAGAI, S. (1958). Researches of the Shack Pressures of Breaking Waves on Breakwaters. Proceedings Fifth Conference on Coastal Engineering, Interim Report (in Japanese).
23. OCHI, M.D. & BONILLA-NORAT, J. (1970). Pressure-Velocity Relationship in Impact of a Ship Model Drapped onto the Water Surface and in Slamming in Waves. Naval Ship Research and Development Center, Report 3153.
24. RAMKEMA, C. (1978). A Model Law for Wave Impacts on Coastal Structures. Proceedings, Sixteenth Conference on Coastal Engineering.
25. RICHERT, G. (1974). Shack Pressures of Breaking Waves. Hydraulics Laboratory, Royal Institute of Technology, Stockholm, Bulletin No. 84.
26. ROSS, C.W. (1954). Shack Pressure of Breaking Waves. Proceedings, Fourth Conference on Coastal Engineering.
27. RUNDGREN, L. (1958). Water Wave Forces. Institution of Hydraulics, Institute of Technology, Stockholm, Bulletin No. 54.

28. SILVESTER, R. (1974). Coastal Engineering. Elsevier Scientific Publishing Company.
29. VENNARD, J.K. (1961). Elementary Fluid Mechanics, 4th Edition, Tokyo.
30. WANG, H. (1970). Water Wave Pressure on Horizontal Plate. Proceedings, A.S.C.E., Journal of the Hydraulics Division, Val. 96, No. HY 10.
31. WANG, H. (1971). Closure of 'Water Pressure on Horizontal Plate'. Proceedings, A.S.C.E., Journal of the Hydraulics Division, Val. 97, No. HY 4.

FULL SCALE NEAR SURFACE WATER PARTICLE VELOCITIES AND
PRESSURES ACTING ON AN INCLINED TUBULAR MEMBER

by

Fritz Büsching ¹⁾ and Eckehard Martini ²⁾

ABSTRACT

A field investigation programme on simultaneous wave force and water particle velocity measurements is described with reference to an inclined tubular member subjected to offshore wave kinematics. First measurements at supercritical Reynolds numbers indicate strong irregularities in successively taken pressure distributions on the circumference of the test section as well as in the velocity vectors.

The influence of superimposed tidal currents is obvious.

1. INTRODUCTION

For want of anything better, MORISON's equation is still used for the calculation of wave forces on circular cylindrical structural members. Most experiments are based on it both in the laboratory and in the field. However, usually only water level deflexions and wave forces on a test section are measured, and the velocities and accelerations as input to MORISON's equation are determined using some suitable wave theory. As is well known, this procedure turns out to be one of the reasons for the wide range of scatter in the reported force coefficients.

Contrary to the respective investigation technique, DEAN (1976) pointed out the necessity of also measuring undisturbed flow characteristics down in the fluid. KIM and HIBBARD (1975) measured the local water particle velocities in a full scale experiment and similar measurements are being carried out at present in the Christchurch Bay Tower experiment, see for instance PEARCY and BISHOP (1979) and HOLMES and TICKELL (1979).

High enough REYNOLDS's numbers in the laboratory experiments to be applicable to prototype were only obtained by applying special model techniques for instance SARPKEYA (1976), HOGBEN (1976), YAMAMOTO and NATH (1976).

It remains, however, still a question as to how well the laboratory results apply to real wave motion, and especially to irregular waves with varying directions of propagation.

¹⁾ Chief-Engineer, Dr.-Ing. ; ²⁾ Dipl.-Ing.

Div. of Hydrodyn. and Coastal Eng. Techn.Univ.Braunschweig, F.R.G.

Being also aware of additional uncertainties arising from

- a) different roughness characteristics due to marine fouling,
- b) the coincident presence of waves and (tidal and wind induced) currents,
- c) different shapes of test sections (vertical or inclined),
- d) different wave kinematics (deep versus shallow water) etc.

the authors initiated a field wave force investigation programme which is sponsored by the GERMAN MINISTRY OF RESEARCH AND TECHNOLOGY (project number MTK 0053).

The experiments are performed on the GERMAN RESEARCH PLATFORM "Nordsee" about 100 km offshore in a water depth of approx. 30 m. There is also another measuring programme under way on the island of NORDERNEY (German North Sea Coast) involving substantially differing kinematics of shallow waves.

Both investigation programmes are at first restricted to the measurement of near surface wave forces (derived from the measured pressure distribution on the circumference of tubular members), water level deflexions (waves) and to the measurement and analysis of the ambient flow characteristics including tidal, wind and wave induced currents.

In the future the research programmes will be extended by the measurement of directional spectra (from an array of 3 sonar devices) in the offshore programme and the near shore measuring configuration shall be combined with measurements of additional forces exerted by wave spray loadings, see FÜHRBÖTER (1977).

At present the MTK-project deals with the wave loadings exerted on an inclined member of a platform leg, and the near shore measuring configuration consists of a vertical pile structure for the force measurement with a satellite measuring station for the measurement of water level deflexions and particle velocities.

Because of the lack of space, only the offshore measuring configuration is described in the following including the test structure, the measuring devices, some data processing routines and preliminary evaluations are outlined. Additional remarks on the near shore measuring configuration are contained in BÜSCHING, MARTINI and SPARBOOM (1979).

2. MEASURING CONFIGURATION

The measuring devices of the test section (Fig. 1) consist of a packing ring clamped on a member of a platform leg which is inclined 30.225° with reference to the vertical axis. This tubular structure (5 m long, 1.92 m diameter) contains 24 KISTLER-pressure transducers on its circumference centered about 5 m below mean low water spring (MLWS).



Fig. 2 : Test section clamped on an inclined member of the platform substructure to be seen on extremely low tide water level at storm conditions. Baylor wave staff on the left hand side.

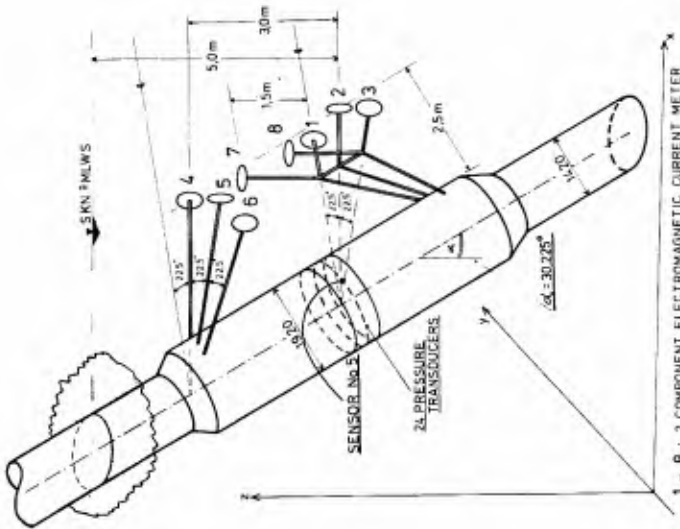


Fig. 1 : Sketch of the measuring configuration

At the same elevation are located 3 two-component electromagnetic COLNBROOK-current meters (No. 1 - 3) oriented in such a way (angular spaced 22.5° and 2.5 m distant from the test section) that the particle velocities in certain vertical planes containing the respective main wave propagation direction can be determined from the measurements to a high degree of reliability. For the direct measurement of the wave propagation direction and the phase velocities, the current meters No. 7 and 8 are used, each measuring two velocity components in a horizontal plane 3.5 m below MLWS.

Additionally only 2 m below MLWS, there is a third horizontal measuring plane again containing 3 current meters (No. 4, 5 and 6) for another measurement of the water particle kinematics in vertical planes with reference to the above mentioned current meter positions No. 1, 2 and 3.

The corresponding water level deflexions are measured at a certain distance from the test section by a BAYLOR wave staff, see Fig. 2. Additional wave data can also be received from a set of 3 sonar devices fixed to different members of the platform structure, see LONGREE (1976).

3. MEASUREMENTS

Because of the many interpretation difficulties arising due to the inclination of the tubular member, superimposed currents and reflexion effects (resulting from the neighbouring platform substructure elements) etc. the authors found it to be reasonable as an initial attempt at data interpretation to consider the simplest loading case in which the main wave propagation direction is in the vertical plane of the inclined member.

As can be seen from Fig. 3, such a configuration occurs when wind and waves come from south westerly directions which unfortunately are not in correspondence with the direction of maximum reliability of current meters 1 - 6 measuring rotating orbital vectors in vertical planes. Hence, the description of actual force creating wave kinematics can only be based on the measurement of

- the water level deflexions,
- the pressure distribution on the circumference and
- the horizontal velocity components (of current meters No. 7 and 8),
which are most reliable for maximum values only.

As an example, such an irregular wave trace measured by the BAYLOR wave staff on November 15th, 1978, 10.11 p.m. at a distance of about 2 m from the test section is shown in the upper part of Fig. 4, and the total set of synchronously taken pressure traces from the circumference of the test section is shown below. Additionally Fig. 5 and 6 contain the corresponding velocity traces of current meters No. 7 and 8 respectively each split into magnitude and direction. All of these traces cover a measuring period of 12.8 sec which are sampled at intervals of 0.2 sec giving 64 phase points also indicated in the graphs.

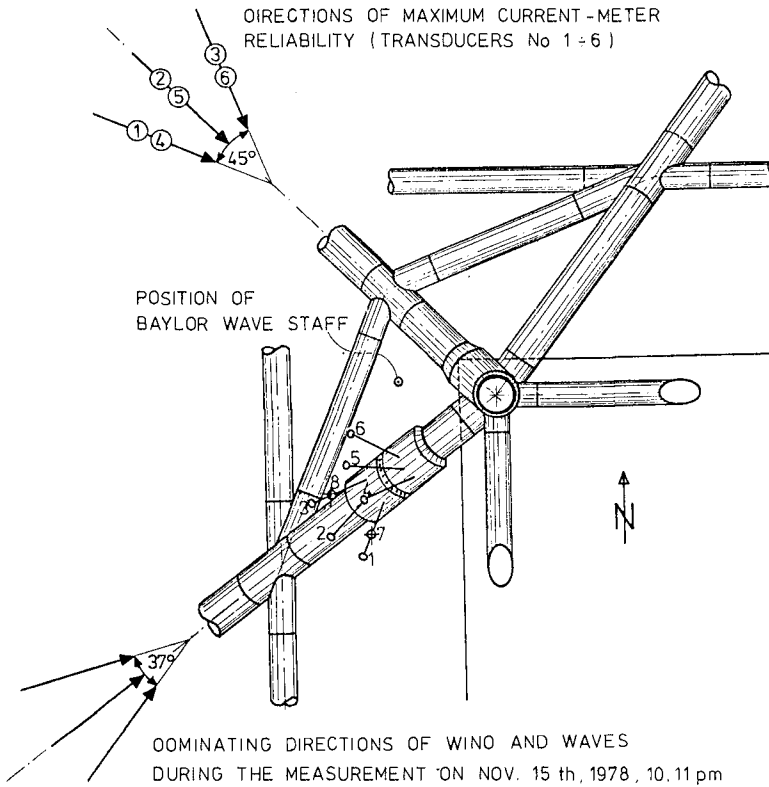


Fig. 3: Orientation of the test section with reference to different directions of wave propagation

The pressure measurements shown in Fig. 4 do not contain any different hydrostatic components corresponding to their respective location below the water level. Hence, the zero mark shown is arbitrary only. The different behaviour of the curves is due to the processes taking place in the boundary layer at specific transducer locations on the circumference and depends on the actual wave propagation direction. This is examined in detail in Fig. 7 showing the pressure distributions (on the circumference of the test section) corresponding

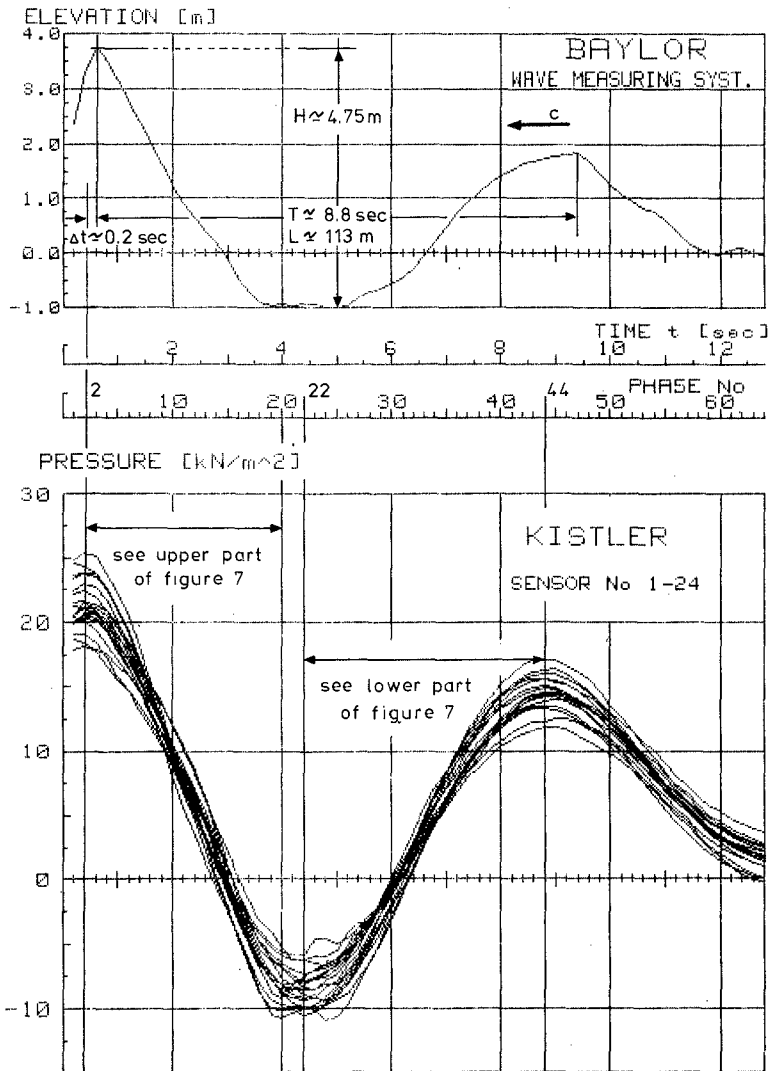


Fig. 4 : Synchronously measured wave trace and pressure traces on the test section circumference on November 15th, 1978, 10.11 pm

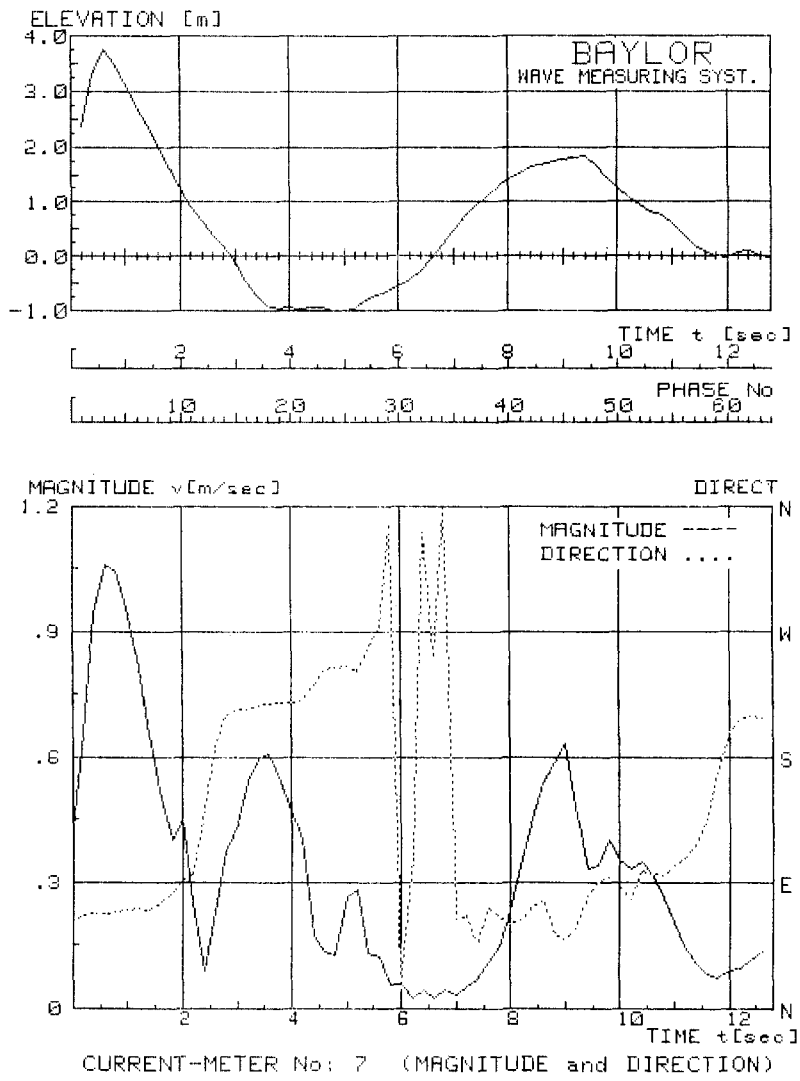


Fig. 5 : Synchronously measured wave and velocity traces on November 15th, 1978, 10.11 pm

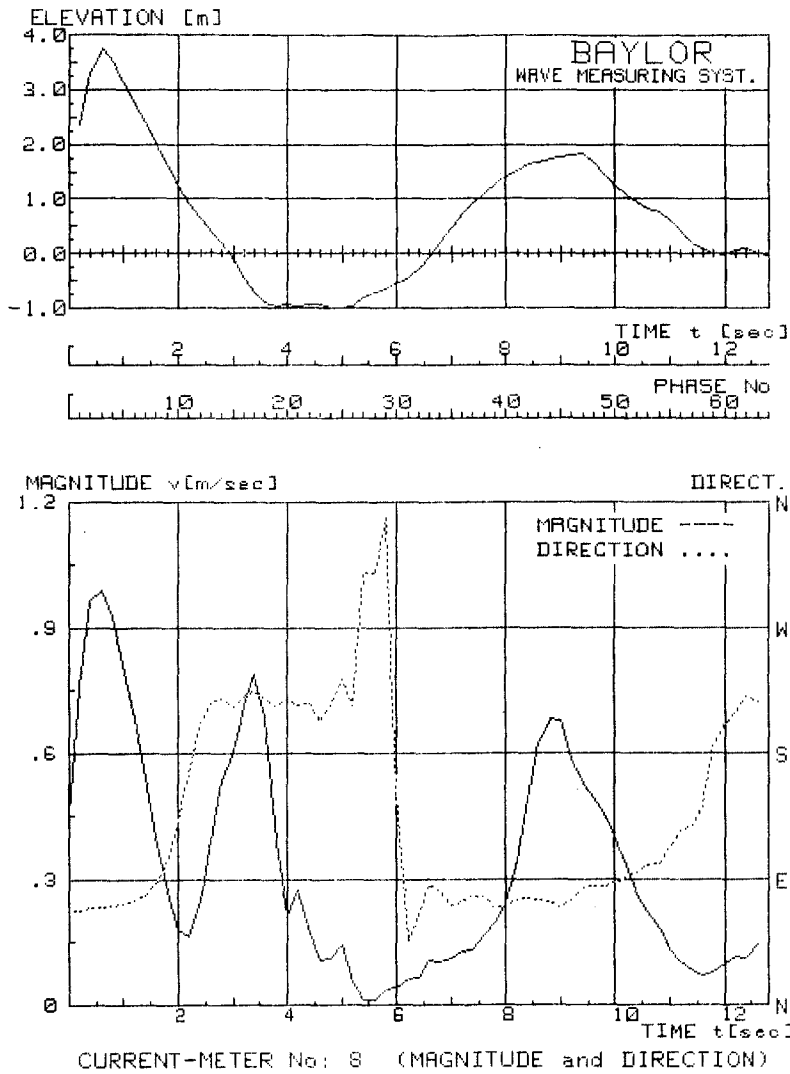


Fig. 6 : Synchronously measured wave and velocity traces on November 15th, 1978, 10.11 pm

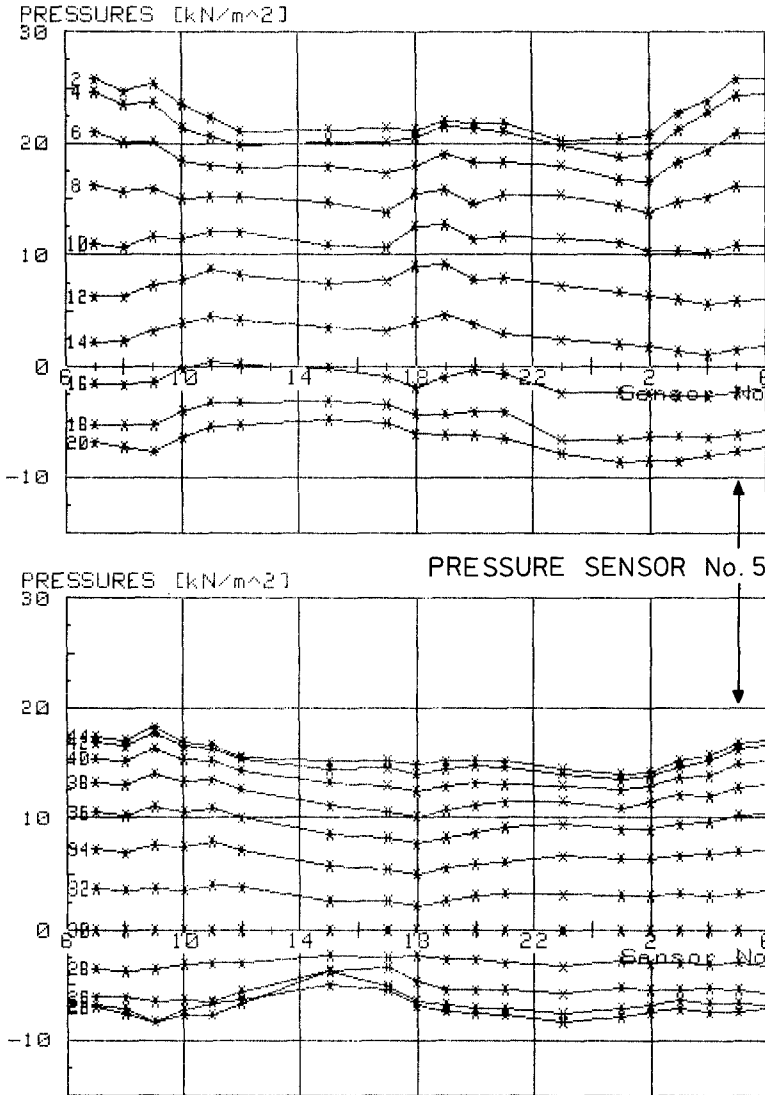


Fig. 7 : Variation of pressure distributions on the circumference of the test section with wave phase

to phase intervals of 0.4 sec. The respective development from phase Na. 2 to No. 20 (marked by numbers on the left hand side), is shown in the upper part of this Fig. and the measurements corresponding to phase numbers 22 to 44 are shown below.

For example, pressure sensor Na. 5 (indicated by arrows) located at the highest point on the circumference (see also Fig. 1) shows the absolute maximum pressure value near the first wave crest position (phase No. 2), intermediate values (with respect to other transducers) corresponding to trough phase numbers 18 to 26 and comes back to a relatively high value at the next crest position (phase No. 44).

Because of erroneous offsets in some of the transducer signals in this case all the distributions refer to that of phase no. 30 whose raw data showed minimum deviations from zero. As a consequence in this kind of presentation its pressure values are zero everywhere, cf. lower part of Fig. 7.

4. CONCLUSIONS

With the vertical distance between the first wave crest and the following trough

$$H \approx 4.75 \text{ m}$$

and the time between the two crests

$$\begin{aligned} T &\approx 8.8 \text{ sec} && \text{corresponding to a wave length} \\ L &\approx 113 \text{ m} && \text{(at a water depth of about 30 m)} \end{aligned}$$

both taken from Fig. 4 and

$$\max. u_c \approx 1 \text{ m/sec}$$

from Fig. 5, the data may be characterized roughly by calculating the following quantities :

REYNOLDS's number

$$R_n = \frac{\max u_c \cdot D}{\nu} \approx \frac{1 \cdot 1.92}{10^{-6}} = 1.92 \cdot 10^6$$

KEULEGAN-CARPENTER number

$$N_{KC} = \frac{\max u_c \cdot T}{D} \approx \frac{1 \cdot 8.8}{1.92} = 4.58 \text{ and}$$

DEANS's reliability ratio (cf. DEAN (1976) Fig. 5)

$$R_D = \frac{F_{D \max}}{F_J \max} \approx 0.4$$

Hence, at least at the wave crest position the conditions are well within the rough turbulent flow regime and the data turn out to be more appropriate for extracting C_M rather than C_D . Because of the insufficient velocity measurement, however, at the present stage the authors do not find it reasonable to apply routines for extracting any force coefficients until the actual flow pattern around the inclined member can be described in general and particularly with reference to varying directions of wave propagation. The following remarks contribute to that aim.

Although there are strange irregularities to be seen from the pressure distributions in Fig. 7, a certain similarity to the well known supercritical stationary flow case is obvious. This is most distinct at the wave crest position (phase no 2) with maximum pressures at the front face and a secondary pressure maximum on the opposite side of the test section circumference. With the flow direction changing the secondary pressure maximum becomes the absolute maximum (near sensor numbers 15 and 17 at phase numbers 22 and 24 respectively) and vice versa, however with its exact location changing from wave to wave. After integrating the pressure distributions (at phase intervals of 0.2 sec), the irregular behaviour can also be observed in the resultant force vectors which are plotted with the wave phase in the two alternative presentations of Fig. 8.

The trace of successive force vectors is shown in the upper part and the same data are given below with reference to 0. Both traces are numbered consecutively.

Up to phase number 8 the forces are directed easterly and have south-westerly components at phases 9 to 30.

Maximum forward and backward force vectors differ by angles of $\alpha = 69^\circ$ and $\beta = 91^\circ$ respectively (see lower part of Fig. 8). A similar change can be seen from the following wave cycle. An inspection of the velocity data is helpful in order to check out how much these changing force directions are influenced by the inclination of the tubular member.

The respective presentations - similar to that of the resultant forces - are shown in Fig. 9 and 10 respectively. It is apparent from these graphs that there also exist differences in the forward and backward directed flow, but the difference angles between maximum velocities (most reliably measured) are in the range of 13° to 30° only (see upper part of Fig. 9).

A speculation that the deviations are due to superimposed currents can be true, if tidal velocities are considered:

As an example Fig. 11 shows the behaviour of the tidal currents at the same location as during the measuring period from February 15th to 20th, 1977. In particular it can be seen from this graph that maximum tidal velocities (1 hour average values) occur with magnitudes of about $V_T \approx 0.3$ m/sec setting easterly at increasing water levels and north-westerly with the water level decreasing. By inserting the vectors U_{CR} and U_{TR} from Fig. 9 into Fig. 11 at a tide phase similar to that of the measurements on November 15th, 1978, the asymmetry between U_{TR} and U_{CR} can be explained by a superimposed tidal current of $V_T \approx 0.3$ m/sec. The even stronger asymmetry in the force vectors of Fig. 8 than in the velocity vectors (of Fig. 9 and 10) is because an inclined member

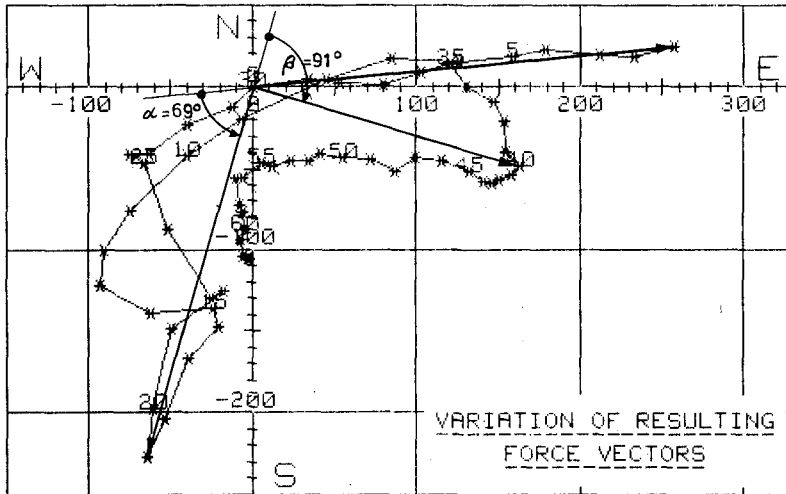
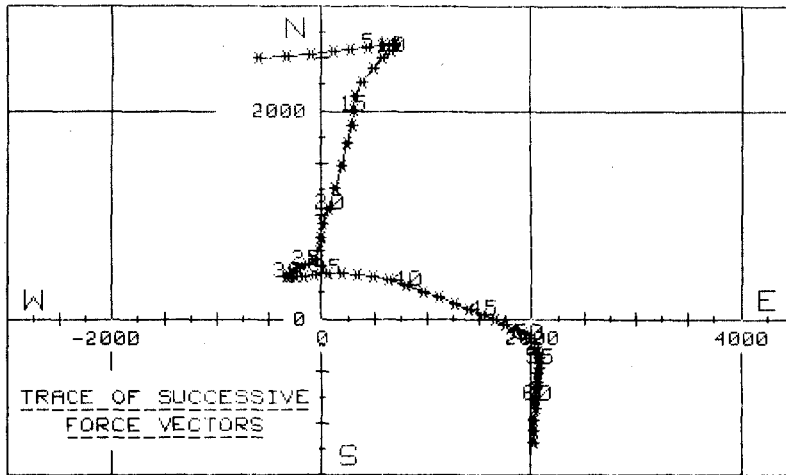
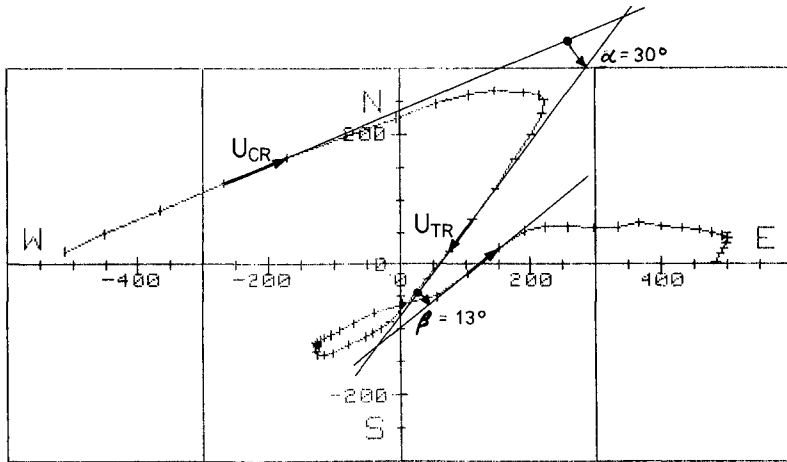
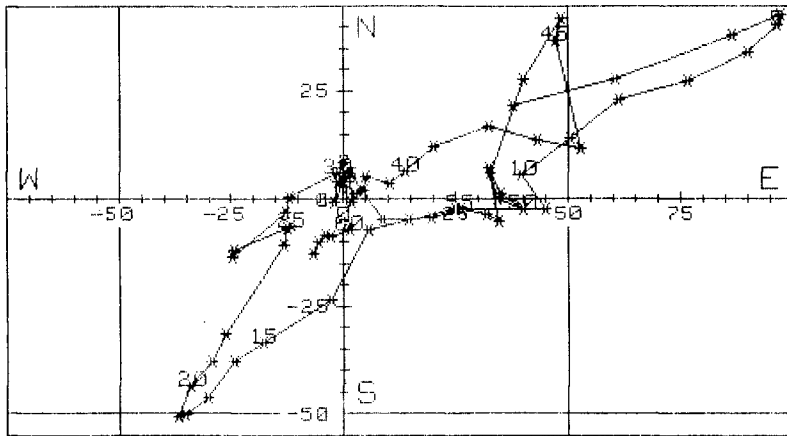


Fig. 8 : Variation of resultant force vectors with wave phase



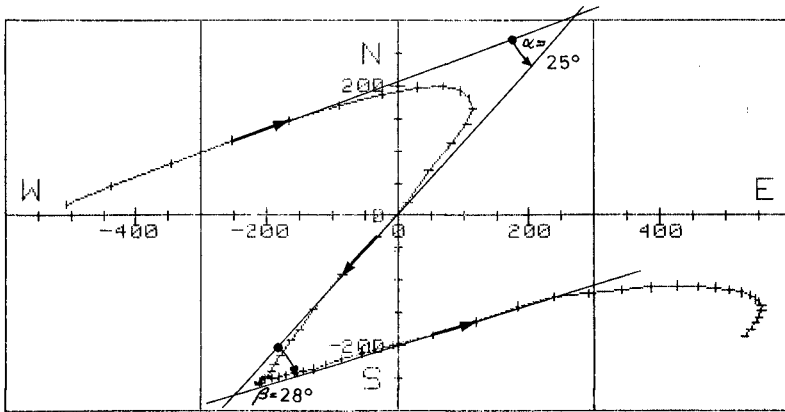
TRACE OF SUCCESSIVE VELOCITY VECTORS



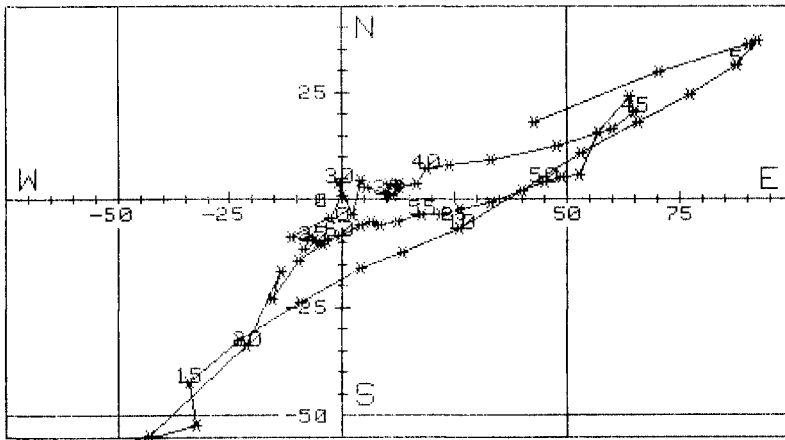
VARIATION OF VELOCITY VECTORS

CURRENT-METER No : 7

Fig. 9 : Variation of velocity vectors with wave phase



TRACE OF SUCCESSIVE VELOCITY VECTORS



VARIATION OF VELOCITY VECTORS

CURRENT-METER No: 8

Fig. 10 : Variation of velocity vectors with wave phase

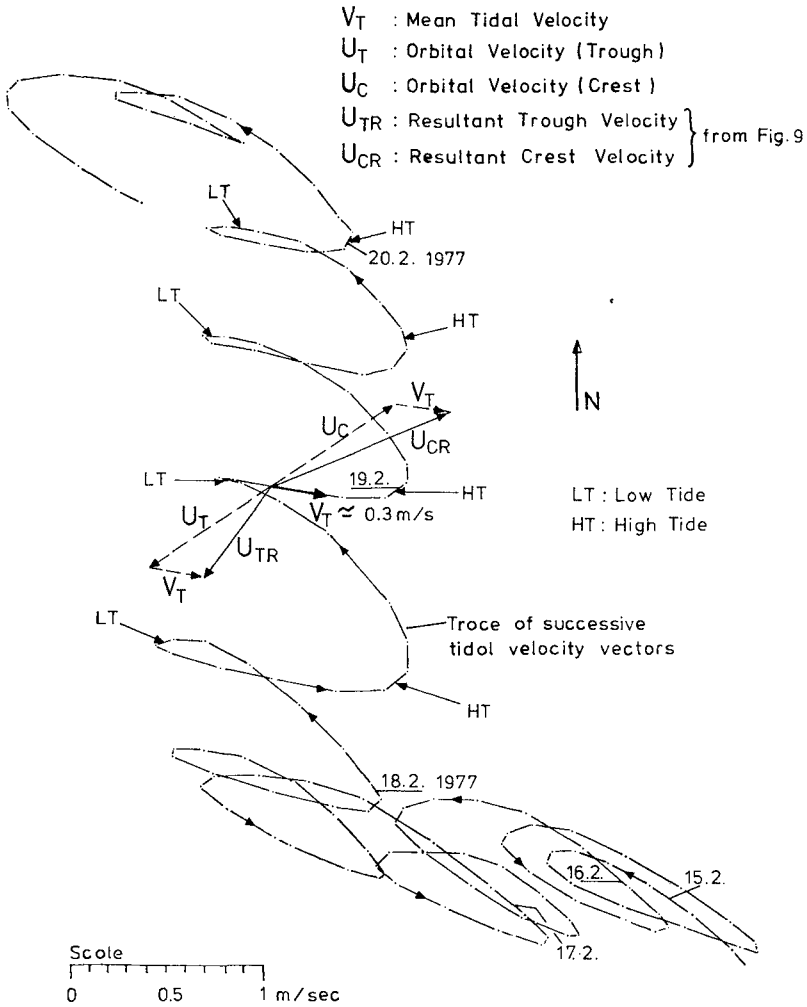


Fig. 11 : Variation of tidal stream vectors from February 15th to 20th, 1977

is (more) sensitive to an asymmetric flow condition resulting in an amplification of the force creating processes.

The evaluations shall be continued in the future. In particular, the synchronous measurements, reported here, shall be compared to the actual tidal velocity as calculated from the long term velocity measurements.

5. REFERENCES

- BÜSCHING, F., MARTINI, E., SPARBOOM, U. (1979) Measuring Equipment for Field Investigations on Near Surface Wave Forces Proc. BOSS'79, Imperial College, London England
- DEAN, R. G. (1976) Methodology for Evaluating Suitability of Wave and Wave Force Data for Determining Drag and Inertia Coefficients. Proceedings of BOSS'76. Norwegian Institute of Technology, Trondheim.
- FÜHRBÖTER, A. (1977) Remark on the influence of Wave Spray on Wind Load, Safety of Structures under Dynamic Loading, Vol. 2, Topir; Norwegian Inst. of Technology, Trondheim.
- HOGBEN, N. (1976) The Wavedozer: A Travelling Beam Wave-maker, Proc. 11th ONR Symposium on Naval Hydrodynamics, London.
- HOLMES, P., TICKELL, R. G. (1979) Full Scale Wave Loading on Cylinders. Proc. BOSS'79, Imperial College, London, England.
- KIM, Y. Y., HIBBARD, H. C. (1976) Analysis of Simultaneous Wave Force and Water Particle Velocity Measurement, Paper 2192, OTC.
- LONGREE, W.-D. (1976) Aspects of the Instrumentation and Measurement Performances of the Research Platform NORDSEE, Proc. BOSS'76, Norwegian Inst. of Technology, Trondheim.
- PEARCEY, H. H., BISHOP, J. R. (1979) Wave Loading in the Drag and Drag Inertia Regimes; Routes to Design Data, Proc. BOSS'79, Imperial College, London, England.
- SARPKAYA, T. (1976) Vortex Shedding and Resistance in Harmonic Flow about Smooth and Rough Circular Cylinders. Proceeding of BOSS'76, Norwegian Institute of Technology, Trondheim.
- YAMAMOTO, T., NATH, J. H. (1976) Hydrodynamic Forces on Groups of Cylinders, OTC 2499.

ENERGY TRANSMISSION OVER BREAK WATER
- A DESIGN CRITERION ? -

- P. BADE, Research Assistant, Technical University of Berlin, Federal Republic of Germany
- H. KALDENHOFF, Professor of Hydraulic Engineering, Technical University of Berlin, Federal Republic of Germany

1. INTRODUCTION

The wave transmission from seaside to lee of break waters depends on structural parameters as well as on the initial wave climate. Transmission coefficients for special boundary conditions are known, but information about wave parameters are often not available or they cover often only special cases. Again a case study, undertaken for the break water at the proposed deep water harbour at Scharhoern/Neuwerk, Germany, documented this lack. The results of the case study using conservative wave parameters did not answer the important questions of energy transmission sufficiently, thus we investigated the characteristics of the initial and transmitted wave spectra. A special case was treated initially and subsequently more general situations were examined. These tests were carried out using a physical model of a length scale of 1:10 under conditions described by Froude's law.

2. MODEL TESTS

The cross section of the proposed break water is seen in Figure 1. It consists of several layers with a cover layer of concrete cubes. The break water was built into the wave channel under simulated prototype conditions, i.e. under water and having waves in the flume. This was done to simulate also the settling of the structure.

The wave flume itself is about 90 m long, 4 m wide and has a water depth of 1.6 m. The model was located about 60 m away from the wave generator. A dividing wall was set up so that the width of the structure was only 2 m. Thus it was possible to measure the wave heights in front and

beside the break water as well as behind in order to get information about the energy transmission and reflection.

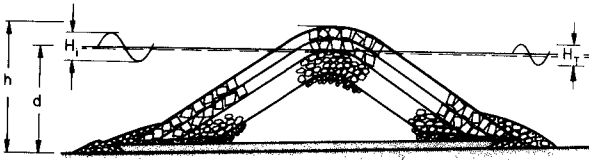


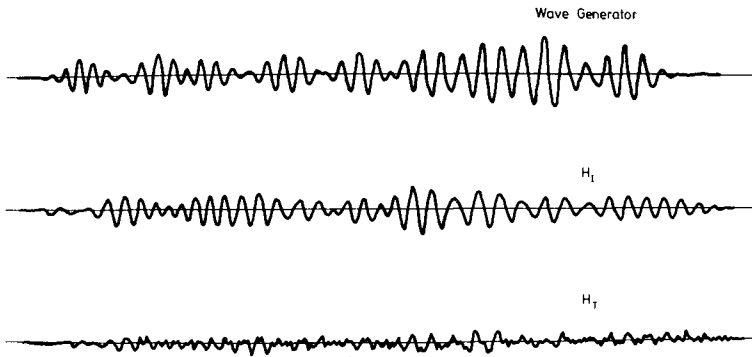
Figure 1: Cross section of the break water
Scharhoern/Neuwerk

In order to avoid misleading test results, wave groups which were reproducible but limited in time length were used. The main reason for using this kind of model waves is to compensate the effects of energy reflection. Figures 2 to 5 show four different wave trains with the time-amplitude relation of the wave board, initial wave and transmitted wave.

The wave train is generated by the superposition of different wave packets, which gives two advantages:

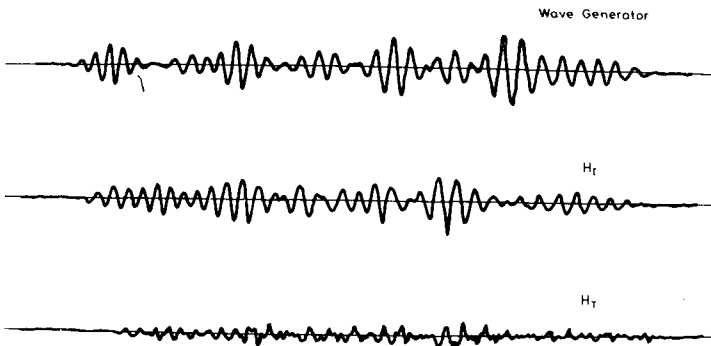
1. The wave train can be limited in time to avoid the influence of reflection at the wave board, but all wave components are simulated.
2. The oscillation of the water surface at any point of the channel can be predetermined in period and amplitude.

Assumption of this method is that the wave packet is describable by an analytical function. It was proved and



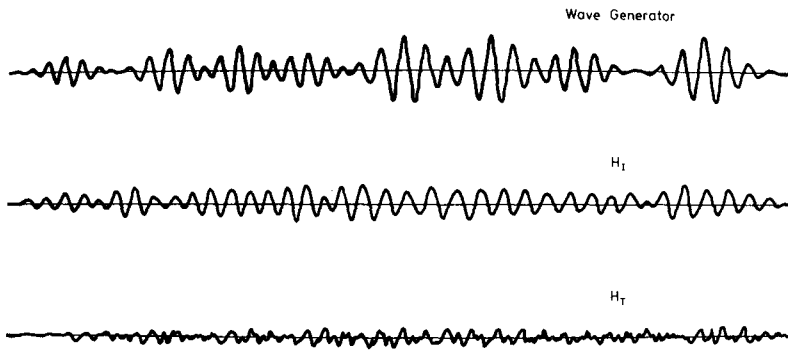
WG 903 C

Figure 2: Wave group 903 C



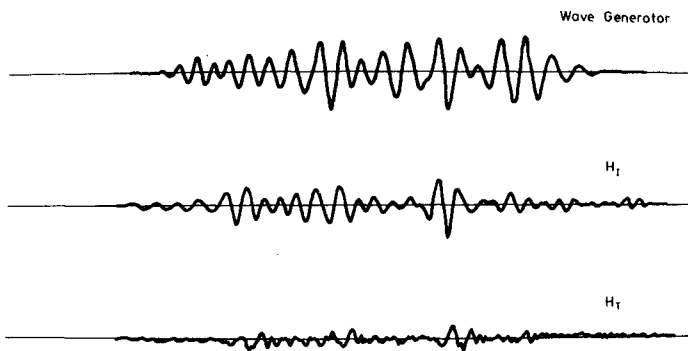
WG 903 D

Figure 3: Wave group 903 D



WG 912 A

Figure 4: Wave group 912 A



WG 915 A

Figure 5: Wave group 915 A

analyzed by Coulson 1949 that the Gaussian wave packet does fulfill this assumption. Additionally it has the following characteristics:

- The energy peak is well marked and travels with the group velocity adequate to the wave length of the energy peak.
- The amplitudes in front of and behind the energy peak decay exponential. The wave length in front of the energy peak increases, and behind it the wave length decreases.
- This kind of Gaussian wave packet describes the surface motion of the sea in shallow waters pretty well, specially a wave train with a well marked energy peak. The energy spectra covers a wide frequency band and the amplitude distribution does follow the Rayleigh distribution.

The superposition of several of these wave packets results in the wave train which statistical and group properties can be varied in a wide range. But this variation is not random but predetermined.

The water depth was varied from $h/d = 0.9$ to $h/d = 1.0$ and $h/d = 1.1$ that is 10 % below break water crest even and 10 % over. Each test series consisted of 16 different wave trains (those four already shown but each of it with four different frequencies). The runs were controlled by an 'on line' computer. The data were collected and stored by magnetic tape for later analysis.

3. EVALUATION OF MODEL TESTS

The conventional evaluation of the damping efficiency of break waters relates the transmitted wave height to the initial wave height. But this method gives no information about possible relationships of wave period and steepness in the luv and lee of the structure. Thus, a frequency analysis was included in the programme for the data analysis. The spectral distribution of the wave energy gives some information about the transmission which is indeed dependent on the wave frequency. The transmission coefficient is defined as $K_t = H_t/H_1$. Using its regular waves the coefficient was calculated by comparing the mean values of waves, i.e.:

$\bar{K}_t = \bar{H}_t / \bar{H}$ and in an analog manner, the transmission coefficient for 33 % and 10 % highest waves. The wave generation system enabled us to shift the energy maximum to different frequencies and to test the influence of wave grouping.

4. RESULT OF MODEL TESTS

The transmission coefficients evaluated for different water depth and wave heights as a function of the normalized run-up $\Delta h = 1 - h-d/H_{1/3}(n)$ is given in Figure 6.

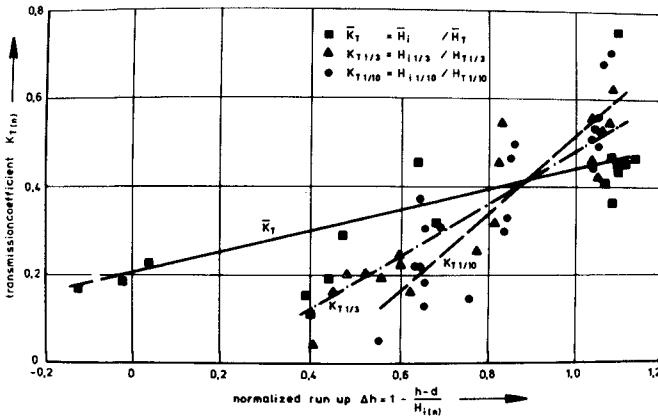


Figure 6: The results and regression of the transmission coefficient $K_T(n)$ for the normalized run-up

This graph includes the linear regression, which has an interesting behaviour, particularly at $\Delta h = 0.88$. At values of $\Delta h < 0.88$, the transmission coefficient drops for extreme values of $H_{1/3} = H_{1/10}$ faster than for $H_{1/3} = H_{1/3}$. At higher values of Δh the depending is vice versa.

That means, that if $h-d = 12\%$ of H_i (which is $H_i^{1/3}$, $H_i^{1/10}$ or \bar{H}) the transmission coefficient has the same value of about 0.4 no matter of the kind of significant wave we were looking at. In front of this point, the K_T values are smaller for higher significant waves when the difference ($h-d$) is about 60% of H_i . This is a quite amazing result, but it may be explained by the energy dissipation of the breaking waves which are of course the higher ones. If $(1 - h-d/H)$ raises, that is if the break water crest is not significantly above the still water level, the assumed result can be found: the higher the waves, the higher the K_T -values.

The scatter of K_T -values is considerable and does not allow an exact calculation of the influence of wave grouping, but the trend is obvious, i.e. wave trains of significant grouping characteristic create higher K_T -values. Because the wave train portions of different frequency and different energy percentage do not provide useful results by means of an extreme value analysis, a spectral analysis became necessary. The test results showed a strong amplitude and energy damping near the energy maximum of the initial wave train but the damping rate depends on the mean frequency of the wave train. An example is given in Figure 7, $h/d = 1.0$

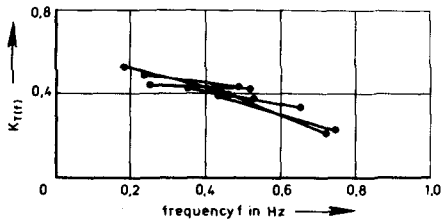


Figure 7: Transmission function $K_T(f)$ of one wave train generated by four different frequencies, $h/d = 1.0$

All tested wave trains had almost an equal character of the $C_{1/3}$ -quotient $H_{1/3}/\bar{H} = 1.5$, but the frequency of the maximum energy was different. The transmission function $K_T(f)$, assumed to be linear in the range of the energy peak, increases with decreasing frequency.

Taking a brief look to the spectra analysis we will see on Figure 8 to 11 the energy spectra of the initial and the transmitted waves and the transmission function.

The higher curve in the first graph is the auto spectrum which is the magnitude squared of the linear: spectrum which is the Fourier transform of the signal $x(t)$, thus $S_x(f) = F(x(t))$, that is

$$G_{xx}(f) = S_x(f) \cdot S_x(f)^* \quad * = \text{conjugate of function}$$

The second curve in the first graph and the second graph shows the cross power spectrum which is a measure of the mutual power between two signals at each frequency and it is defined as:

$$G_{yx}(f) = S_y(f) \cdot S_x(f)^*$$

The transfer function in the third graph is the mathematical description of the input - output relationship of a system. For single inputs and outputs it is defined to:

$$H(f) = \frac{G_{yx}(f)}{G_{xx}(f)}$$

The frequency range, which includes about 95 % of the wave energy is marked. Each wave train gives a different transfer function. They are taken together to show the frequency behaviour of the transmission function and are plotted in Figure 12 to 15.

There seems to be a general tendency. In case of relative low water ($h/\bar{d} = 1.1$) the group characteristic dominates the wave transmission in such a way, that wave trains of strong grouping create higher $K_T(f)$ values, and there is also the frequency related tendency for the transmission

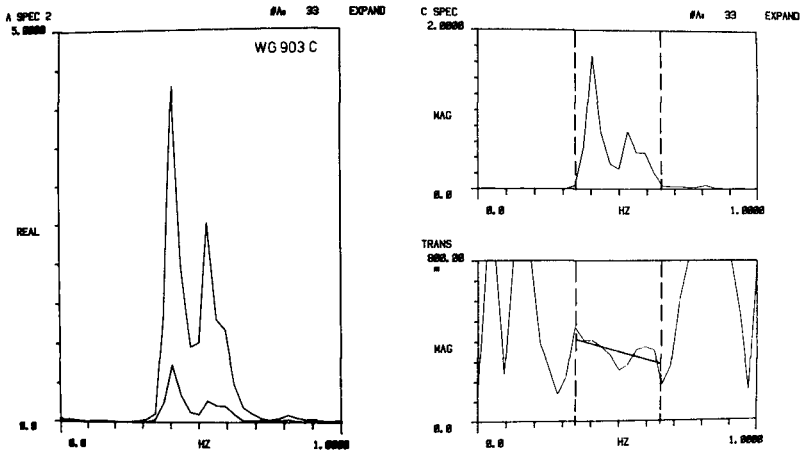


Figure 8: Energy spectra of the initial and transmitted waves and the transmission function, wave group 903 C

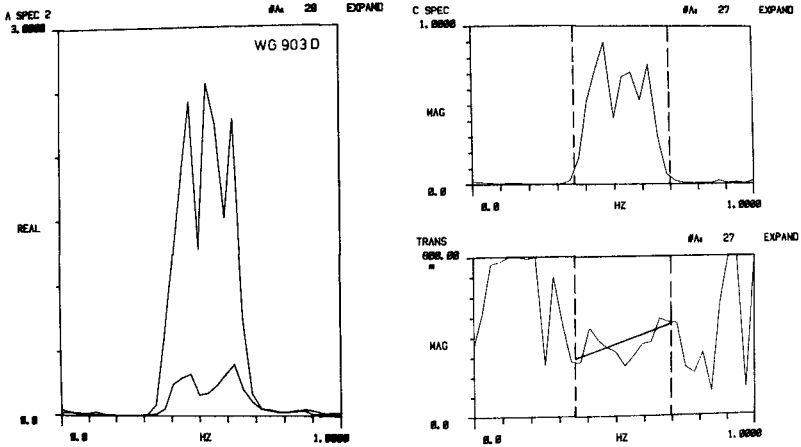


Figure 9: Energy spectra of the initial and transmitted waves and the transmission function, wave group 903 D

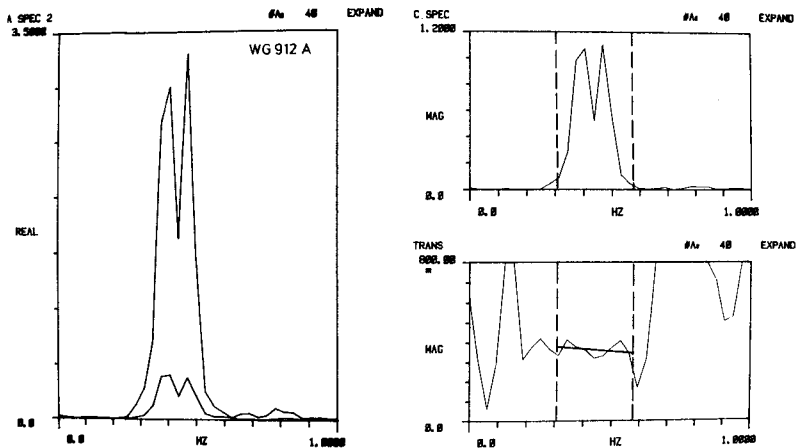


Figure 10: Energy spectra of the initial and transmitted waves and the transmission function, wave group 912 A

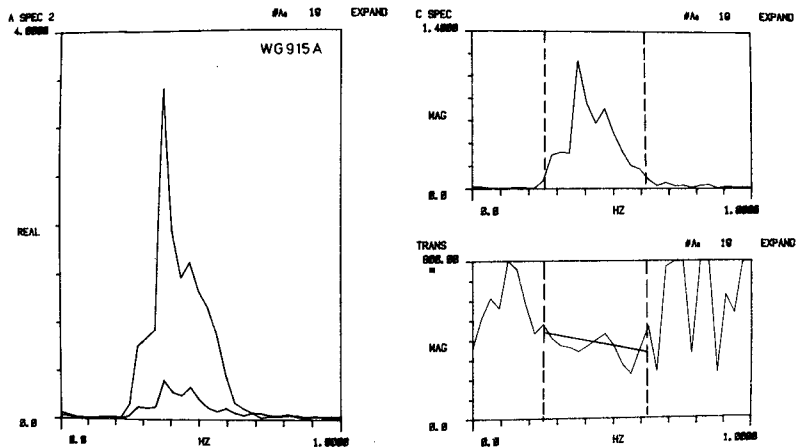


Figure 11: Energy spectra of the initial and transmitted waves and the transmission function, wave group 915 A

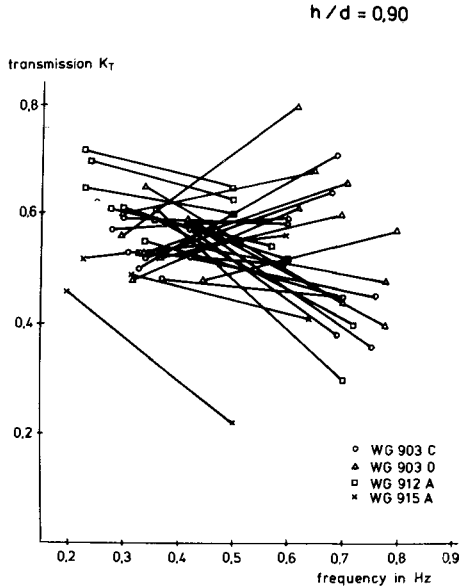


Figure 12: Transmission function of different wave trains, $h/d = 0.9$

coefficient. In case of high water ($h/d = 0.9$) the frequency relation is not obvious. This may be explained by energy fronts, which are more marked in wave trains of high waves and strong grouping. These energy groups transmit a large amount of wave energy during a small time range. Additionally, the peak of energy density function is shifted to higher frequencies.

As H/gT^2 , the so called normalized wave period, is an indicator of frequency dependence, the test results were evaluated to prove a frequency relationship.

$h/d = 1.10$

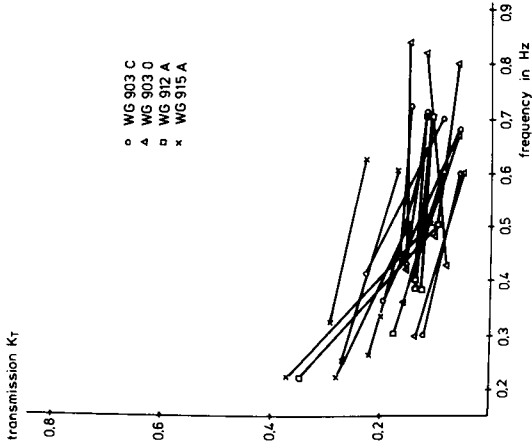


Figure 14: Transmission function of different wave trains, $h/d = 1.1$

$h/d = 1.00$

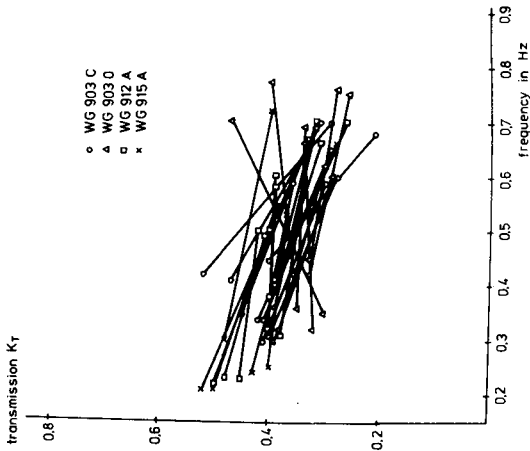


Figure 13: Transmission function of different wave trains, $h/d = 1.0$

It could be shown that the normalized wave period H/gT^2 of the significant wave height $H_{1/3}$ is not a sufficient parameter to indicate the frequency behaviour, see Figure 15.

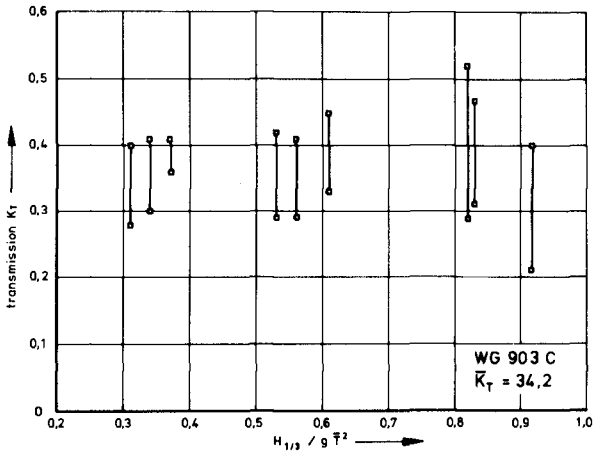


Figure 15: Wave transmission depending on normalized wave period, wave group 903 C

The results for the other wave groups look more or less the same.

Summarizing, it may be stated that the damping efficiency of overtopped break waters is related to the wave height and its distribution as well as the frequency of the energy maximum. Moreover, a grouping characteristic of the initial wave train is of influence. More research on this phenomenon is of high interest.

The Design Concept of Dual Breakwaters
and its Application to Townsville, Australia.

W. Bremner⁽¹⁾, D.N. Foster⁽²⁾, C.A. Miller⁽³⁾ and
 B.C. Wallace⁽⁴⁾.

1. Introduction

In Central and North Queensland the coastline is protected by the Great Barrier Reef over a length of some 1900km from Gladstone in the south to the tip of Cape York (Fig. 1).

The fetch distance from the reef to the coastline is very variable from about 15km to 140km. Hence the coastal areas north of Gladstone have moderate to low wave climates except during abnormal weather events such as cyclones or long time interval bands of strong winds. In these events larger storm waves of significant wave heights of 10m may be superimposed, in the case of cyclones, on storm surges several metres in height.

The design of breakwaters and shoreline structures for protection against all except cyclonic and strong wind band effects requires, in the main, readily available sizes of armour rock and relatively low crest elevations.

To offer similar protection against cyclonic weather events often requires the use of artificial armour units of concrete and a substantial increase in crest heights. The resulting increase in costs makes many of the small projects uneconomic.

In this paper the concept of using an offshore breakwater which is designed to fail under extreme wave conditions to protect an inner breakwater or revetment is examined and the results applied to Townsville Harbour where cost savings of the order of 40 percent were achieved over a conventional design.

2. Rossllyn Bay Breakwater

The design concept arose from studies and observations of the damage to the Rossllyn Bay breakwater during cyclone David (see Fig. 2) and the subsequent protection provided by the breakwater following damage (Foster, Bremner and McGrath, 1978). Features of this damage were:-

- (1) Principal, Blain Bremner & Williams, Consulting Engineers
- (2) Associate Professor, Water Research Laboratory, University N.S.W.
- (3) Principal, C.A. Miller & Associates, Associate Consultant to WRL
- (4) Principal, B.C. Wallace & Associates, Associate Consultant to WRL

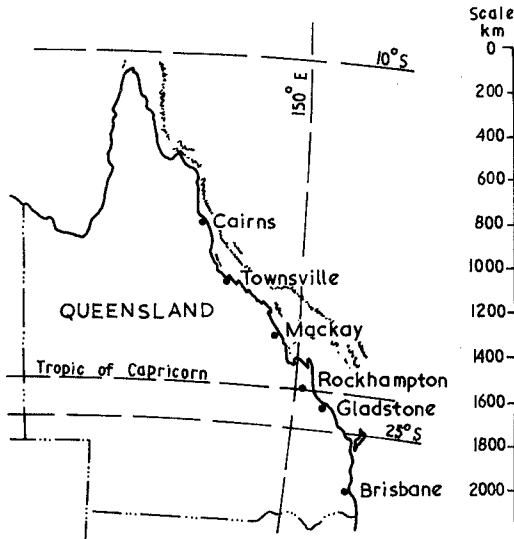
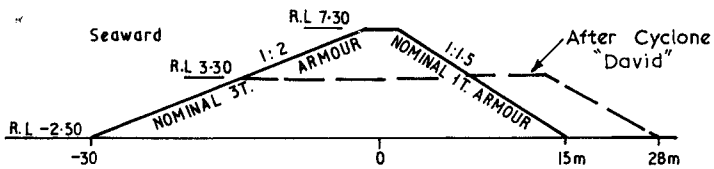
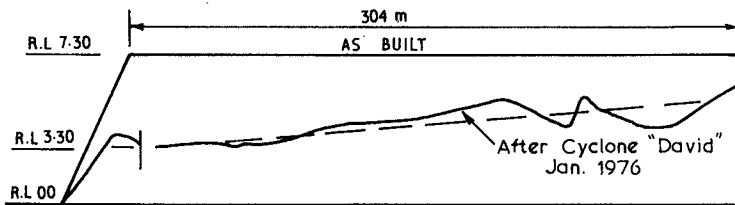


FIGURE 1: LOCALITY SKETCH



TYPICAL CROSS SECTION

FIGURE 2: DAMAGE TO ROSSLYN BAY BREAKWATER BY CYCLONE DAVID

- (i) Failure occurred in a controlled manner with material being displaced from the crest and deposited on the leeward slope, forming a widened and lowered profile. The breakwater was composed of 3t nominal armour rock on the seaward face, $\frac{1}{2}$ to 1 tonne filter rock and less than 150mm core material.
- (ii) Failure to the breakwater was closely simulated by model studies.
- (iii) Reconstruction of the breakwater was not commenced until 2½ years after failure. During this period the breakwater acted as a submerged breakwater and continued to provide substantial wave protection within the harbour. Over this period waves of up to 1.8m height were experienced. All small boats continued to stay on their piled and bottom moorings and there was no damage to boats, moorings or shoreline revetments.

These observations triggered the idea that if a controlled submerged breakwater could successfully be built then a significant reduction in costs may well be possible. The interesting design problem was then posed of building a breakwater of sufficient initial stability to allow safe construction but when subjected to the designed forces, due to carefully chosen extreme and fairly rare weather events that result from cyclones, it would be reshaped in a controlled and predictable manner to become a stable and partially submerged structure and retain its wave attenuation ability.

(It should be noted that in Australia large floating plant is not available for breakwater construction and all breakwaters are constructed in the dry. This precludes the construction of an initially stable offshore submerged breakwater).

It is of interest to note that the repair to the Rosslyn Bay breakwater as reported by Bremner, McGrath and Foster (1978), which used a combination of rock and modified cubes, has been completed and in 1980 was subjected to waves of 3.2m in height during cyclone Simon. There was no damage to the breakwater.

3. Townsville Harbour

3.1 General

To provide additional port facilities it is proposed to reclaim a significant area on the eastern side of the harbour as shown in Figure 3. Wave protection to this reclamation was to be provided by an offshore breakwater or by conventional armouring of the seaward face of the revetment. Initial design and economic assessment showed that the second proposal was approximately 60 percent more expensive and detailed designs were not undertaken. This cost saving resulted from:-

- (i) use of locally available low cost rock in the offshore breakwater which was designed to "fail" under extreme wave and storm surge conditions and provide a partially submerged offshore breakwater;

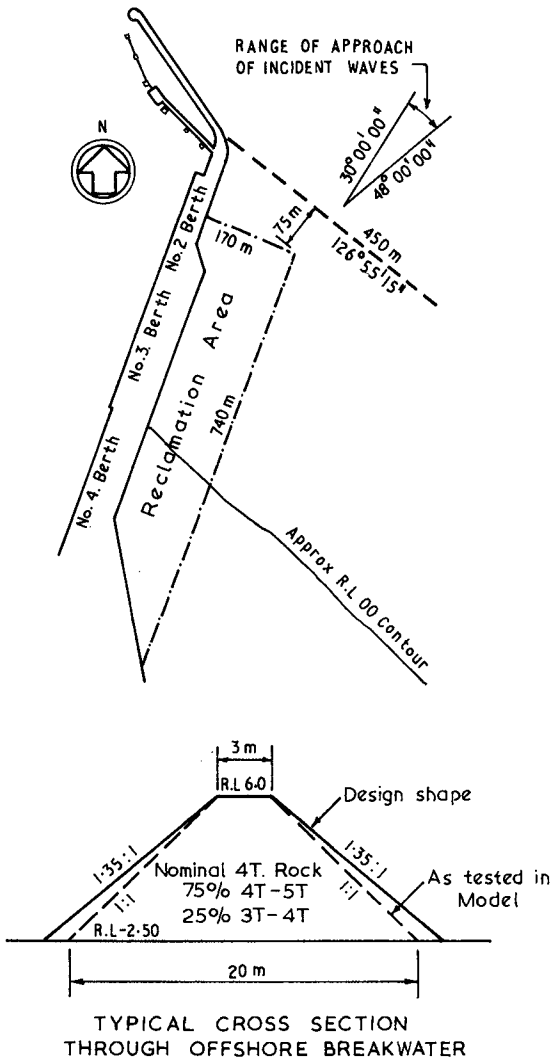


FIGURE 3: TOWNSVILLE HARBOUR

- (ii) reduction in wave height at the revetment thereby reducing the height of reclamation required and the use of low cost readily available rock armour.

3.2 Design Conditions

Design wave and surge conditions have been extensively studied by Blain Bremner and Williams (1978), Harper and Stark (1977), Sobey, Rossow and McConagle (1978), and are summarised in Table 1 below:-

Table 1: Design Storm Conditions

Return Period (yrs)	Tide (MHW) (RLm)	Cyclonic Conditions			
		Storm Surge (m)	Design SWL (RLm)	H _s (m)	T _s (sec)
50	2.45	1.68	4.13	3.76	6.0
100	2.45	2.00	4.45	4.15	6.3
500	2.45	2.76	5.21	5.26	7.2

Tidal data based on Townsville Harbour Board datum of RL0.0 are as follows - HAT 3.6m, MHWS 2.9m, MHW 2.0m, MSL 1.6m, MLWN 1.2m, MLWS 0.4m, LAT -0.2m.

3.3 Offshore Breakwater

A typical section through the proposed offshore breakwater is shown in Figure 3. It basically is composed of nominal 4t rock placed at its natural angle of repose with a range of rock sizes between 3 and 5t. Crest level at completion of construction is at RL 6.0 which will be overtopped only under extreme wave and surge conditions.

3.4 Model Tests

Extensive model tests of the scheme were undertaken by the Water Research Laboratory of the University of N.S.W. (Foster, Miller and Wallace 1980). A summary is given in this paper and the reader is referred to the above reference for more complete details.

Preliminary stability tests were run at constant water levels for the design peak water levels and wave heights shown in Table 1. The tests were run for two nominal rock sizes (M) of 2t and 4t, having approximate gradings of 75% between M and 1.25 M and 25% between 0.5M and M. Test duration was 7 hours. (Prototype).

Collapse of the breakwater was ordered with some stone being displaced seaward, flattening the seaward slope and the remainder being displaced landwards resulting in a broadening and reduction in elevation of the crest which is similar to that observed during the failure of the Rosslyn Bay breakwater (Foster, Bremner and McGrath 1978). The majority of damage occurred in the first two hours and basically stopped when a water cushion formed over the crest. Because of the higher water levels damage was less for the less frequent events, the highest damage being associated with the 1 in 50 year event. All further tests

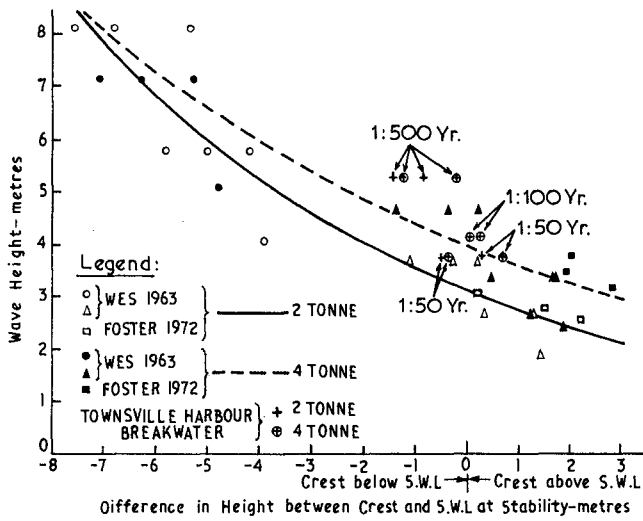


FIGURE 4: VARIATION OF CREST STABILITY WITH WAVE HEIGHT—CONSTANT WATER LEVEL

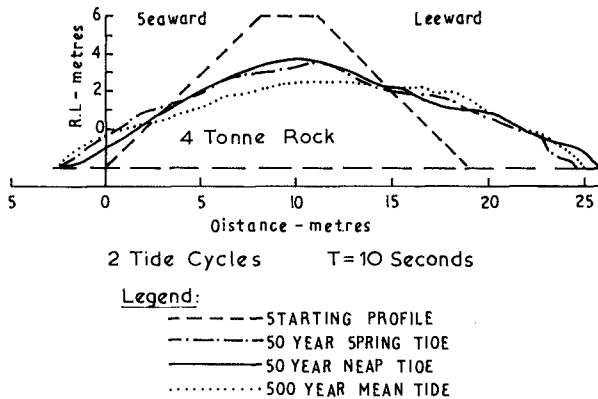


FIGURE 5: BREAKWATER DAMAGE

were undertaken with tide variation reproduced in the model so that the structure was subjected to the design wave under varying water levels.

The relation between crest level and S.W.L. at stability under constant water level is shown in Figure 4 together with results of similar studies undertaken by U.S. Army Corps of Engineers (1953) and Foster (1972) using Froudian scale factors to convert the results to equivalent 2 and 4t nominal rock. Figure 5 indicates that the results are within the range obtained in previous studies. However, the difference in damage for the 4t and 2t rock sizes is smaller than indicated by the lines of best fit (exponential). This may be due to the fact that the previous studies were carried out on conventional breakwaters having separate core, filter and primary armour layer.

In the second series of tests the breakwater was subjected to the design wave height and storm tide resulting from tide plus the design storm surge. Wave period was 10 seconds. Spring, neap and mean tidal cycles were tested. Typical results are shown in Figure 6. The mode of failure was similar to that for the constant water level tests but the degree of damage was substantially larger as the crest is exposed to higher wave forces as the tide changes. Damage was not strongly dependent upon the tidal cycle chosen.

During the tests maximum incident and transmitted waves were monitored and the results are shown in Figure 7. Wave breaking occurred over the crest and the transmitted wave was measured 65m landward of the structure after the wave had reformed.

Rather surprisingly these results indicate that the transmitted wave is not strongly dependent upon the amount of damage and implies a considerable degree of safety in the design. The reason for this appears to be, that the effect of increasing crest width as a result of failure tends to largely counterbalance the effect of increasing water depth relative to the crest. Similar results have been observed by Saville (1963) (see Appendix 1). The overtopping tests were undertaken in the laboratory's 1m wide monochromatic wave flume. The model scale was 1 to 27.4.

The three dimensional model tests to study the effects of diffraction around the head of the breakwater and wave heights along the revetment were undertaken at a scale of 1 to 57. In these tests the transmitted waves past the breakwater agreed closely with the larger scale tests which indicates that scale effects are small and that the major component of the transmitted wave results from wave overtopping.

The three dimensional tests undertaken to study diffraction indicated that during overtopping wave heights were not substantially increased in the lee of the breakwater as a result of diffraction which enabled the initial design length of the breakwater to be substantially reduced in the final design.

4. Conclusion

Model tests have shown that the concept of constructing a break-

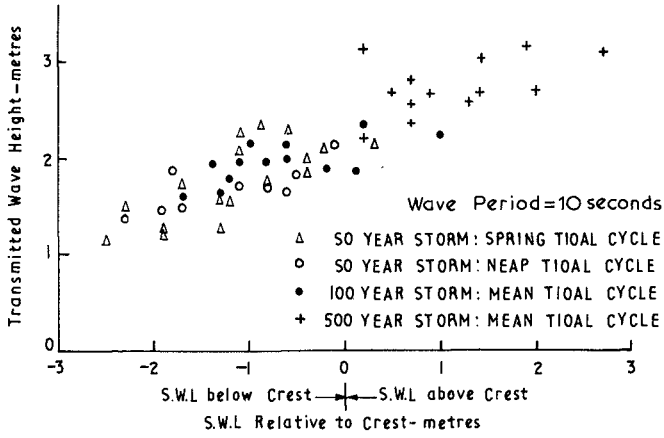


FIGURE 6: VARIATION OF TRANSMITTED WAVE HEIGHT WITH S.W.L. RELATIVE TO CREST

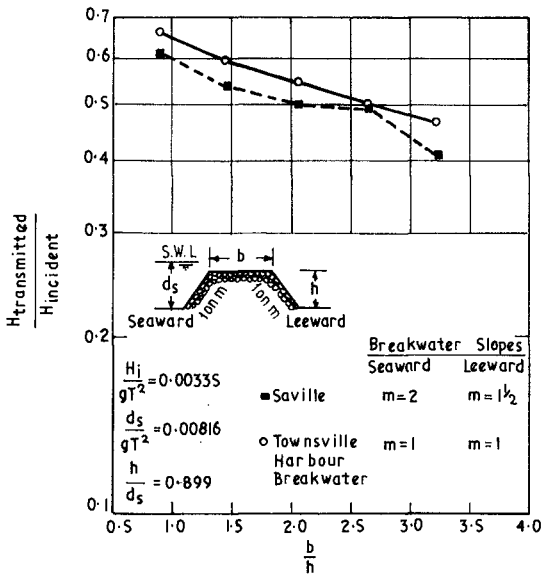


FIGURE 7: WAVE TRANSMISSION FOR VARYING CREST WIDTH

water to form a submerged structure after failure is an effective method of reducing wave heights at inshore structures. Tests indicate that the transmitted wave past the breakwater is relatively independent of incident wave conditions, rock size and depth over the crest. Although more damage occurs for the longer return period events and the smaller rock sizes the correspondingly wider crest tends to counterbalance the increased depth over the crest resulting in relatively small increases in the transmitted wave. Hence a considerable degree of safety is provided against the design conditions being exceeded.

In the view of the authors the important features of the design concept are:-

- (i) The high degree of tolerance inherent in the design against the design conditions being exceeded.
- (ii) The relative ease of construction which does not require large radius heavy cranes and leads to rapid construction and substantial cost benefits.
- (iii) The size of rock is contained to economic winnable and handable natural rock sizes.
- (iv) Wave run-up on the inshore structure is reduced, enabling lower crest levels to be adopted.

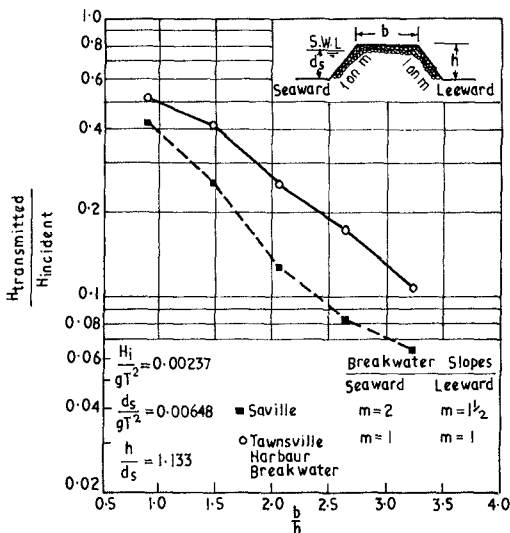


FIGURE 8: WAVE TRANSMISSION FOR VARYING CREST WIDTH

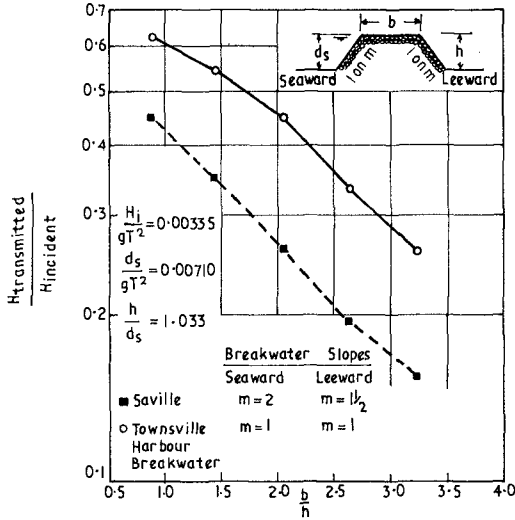


FIGURE 9: WAVE TRANSMISSION FOR VARYING CREST WIDTH

Appendix 1.

There are little data on wave transmission coefficients over permeable breakwaters of relatively narrow crest widths. Model tests for substantially broader crest widths are described by Saville (1973). These show that the transmitted wave is reduced with increasing width of crest. This fact has been used to explain why the present results indicate only a slow change in the transmission coefficient even though the breakwater crest is substantially lowered during failure.

In order to quantify the comparison with Saville's results supplementing tests were undertaken on the rock used in the model studies for the same dimensionless geometric and wave parameters. Results are shown in Figures 6 - 8. All tests follow similar trends to that observed by Saville. However, for S.W.L. below the crest transmission coefficients were found to be 20 to 40 percent higher. For S.W.L. above the crest the results agree closely. The differences are believed to result from the different rock sizes used in the tests. The results for SWLs below the crest tend to indicate that permeability and therefore wave energy transmission through the structure are higher for the submerged breakwater in the present studies. For SWLs above the crest, difference in permeability has only a marginal effect on transmitted wave since the majority of energy is transmitted by overtopping.

References

Blain, Bremner and Williams, 1978, "Eastern breakwater extension: Design report for hydraulic model analysis" Internal report Nov. 1978.

Foster, D.N. 1972, "Breakwater stability Kirra Beach": The Univ. of N.S.W. Water Research Lab. Tech.Report 72/13, Aug. 1972.

Foster, D.N., McGrath, B.L. and Bremner, W. 1978: "Rosslyn Bay breakwater, Queensland, Australia". Proc. 16th International Conf. on Coastal Engineering, Hamburg, Aug. 1978.

Foster, D.N., Miller, C.A. and Wallace, B.C. 1980. "Townsville Harbour eastern breakwater extension, hydraulic model studies". The Univ. of N.S.W., Water Research Lab.Tech.Report 80/1, Jan. 1980.

Harper, B.A. and Stark, K.P. : "Probabilities of water levels at Townsville resulting from the combined effects of cyclonic storm surge, tides and waves". Report, James Cook Univ. December 1977.

Saville, T. Jr. (1963), "Hydraulic model study of transmission of wave energy by low-crested breakwaters" : Reproduced in U.S. Army Corps of Engineers, Coastal Eng. Research Centre, Shore Protection Planning and Design 1973 pp7-56 to 7-60.

Sobey, R.J., Rossow, D.J. and McConagle, C.T. , "Long term wind wave frequencies at Cleveland Bay and Rosslyn Bay": Report, James Cook Univ., July 1978.

W.E.S. 1953, "Stability of rubble-mound breakwaters - hydraulic model investigation": U.S. Army Corps of Engrs., Waterway Expt. Station, Vicksburg Tech.Memo 2-365, June 1953.

DESIGN OF AN OVERTOPPING BREAKWATER

- P.D. TRELOAR, Consulting Engineer, Lawson and Treloar Pty. Ltd., N.S.W. Australia.
- B. NAGLE, Design Engineer, The Maritime Services Board of N.S.W., Australia.

1. INTRODUCTION

The Maritime Services Board of New South Wales, Australia, is constructing a major new port facility on the northern foreshores of Botany Bay. A principal part of this project has been the construction of a large armoured revetment from the northern shores.

The entrance to Botany Bay faces south-east and it is from this direction that a large proportion of offshore wave energy arrives. Some of the wave energy which is directed onto the Bumborah Point revetment is reflected towards Yarra Bay on the northern shores of Botany Bay. Yarra Bay is largely undeveloped, but a sailing club has stood for many years on the beach at the southern end. As a consequence of this reflected wave energy being directed towards Yarra Bay, its wave climate has been changed considerably so that during the storms of May-June, 1974, Foster (6), damage was suffered by the club-house. Additionally the more severe wave climate and consequent steeper beach have made it much more difficult to launch sailing boats. The Maritime Services Board is charged with the responsibility to carry out remedial works where damage is caused by the port development. Figure 1 shows the revetment and sailing club site.

To assist in coastal engineering design aspects of the port development, a large fixed bed wave model of Botany Bay has been built to an undistorted scale of 1:120. This model, some aspects of which have been described by Lawson (4), has pneumatic wave generators which enable offshore wave directions between east-north-east and south to be generated with prototype periods in the range of 5 to 16 seconds. A pneumatic tide generator enables a sinusoidal tide to be generated.

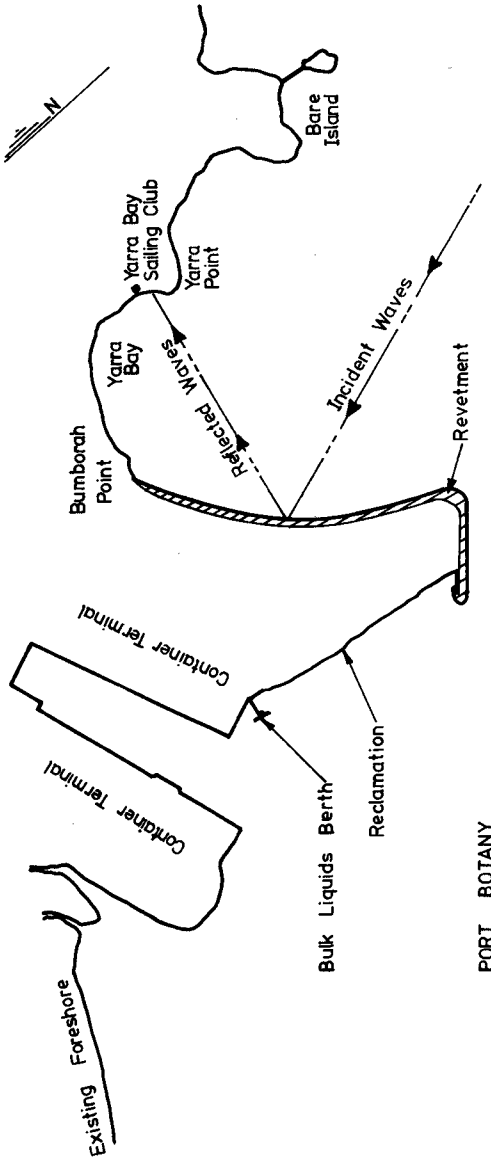


FIG. 1

PORT BOTANY

The effect of tide stage and velocity on wave propagation is important in Botany Bay because it is relatively shallow.

Wave-height exceedance statistics have been gathered for a number of years using Datawell Waverider Buoys. The installation has been maintained for more than 8 years about 2 kilometres offshore of the entrance to Botany Bay and programmed gathering of data 4 times a day for 20 minutes carried out. Another buoy was installed in Yarra Bay for about 2 years.

The breakwater had to fulfill the following requirements :-

- (a) Return wave climate and run-up in front of the club house to pre-port-works condition;
- (b) Offer adequate rigging area on the beach;
- (c) Provide an adequate gap between its outer end and the shoreline to provide a 10 boat-length space, based on a 5 metre boat length;
- (d) Be no more visually obtrusive than necessary.

This last requirement meant than an over-topping breakwater would be desirable.

2. HYDRAULIC STUDIES

The hydraulic studies required for successful design of a shore structure must investigate the following aspects :-

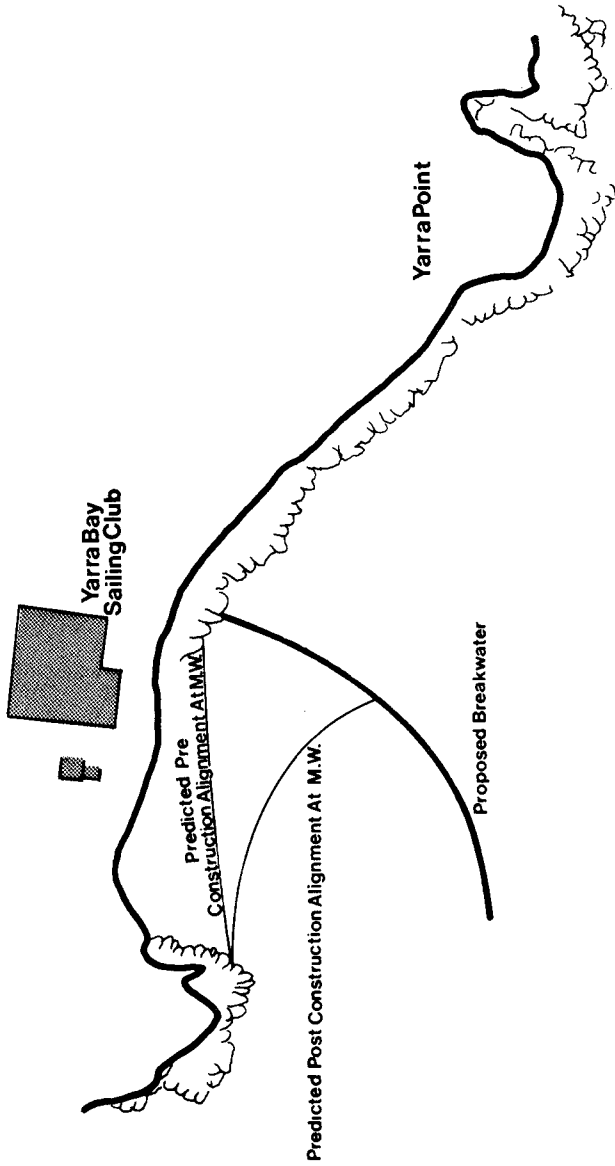
- (a) optimisation of the performance of the breakwater taking due consideration of benefit-cost relationships.
- (b) provide design wave-height data based on probability levels.
- (c) investigate the changes in beach alignment which construction of the breakwater will cause.

2.1 Breakwater.

In order to determine a suitable breakwater length and alignment, various breakwaters were constructed in the Botany Bay Hydraulic Model. These were built so that no overtopping occurred. It was decided to calculate this aspect separately; the scale of 1:120 being considered too small for adequate run-up and overtopping determinations. Figure 2 shows the final design alignment. Breakwater lengths of 10m greater and smaller length were also tested in the model. The alignment shown in Figure 2 is the centre-line and fulfils the 10 boat length requirement taking into consideration the physical size of the structure.

Previous testing in the Botany Bay Hydraulic Model enable wave-height coefficients to be determined for the offshore directions east-south-east, south-east and south-south-east, combined with periods of 8, 10, 12 and 14 seconds at position A shown in Figure 2. These conditions contribute the major proportions to the wave energy reaching Yarra Bay as the entrance to Botany Bay faces south-east. The direction of reflected waves arriving in Yarra Bay varies very little with offshore direction-period combination and there is very little incident wave energy. It was therefore decided not to carry out this full range of 12 tests for the breakwater, but instead examine results available for position A and then, on the basis of partial probabilities of wave-height exceedance, carry out tests for the 5 most important conditions.

Two positions on the lee side of the breakwater were chosen and wave-height coefficients measured relative to position A, Figure 2. The tests were conducted at tide levels of 0.2m, 0.9m (M.W.) and 1.5m, these levels allowing probabilities of occurrence to be apportioned as 0.25, 0.5 and 0.25 respectively for tide level intervals spanning these values. Highest Astronomical Tide is 1.9m and the datum is Indian Springs Low Water, 0.0m. Depth at the breakwater head was 3.1m at I.S.L.W. Coefficients for the untested wave conditions were estimated by extrapolation.



● A
FIG. 2

Overtopping coefficients, K_t , were determined following Cross and Sollitt (3). Their envelope equation is :-

$$K_t = 0.65 \left(1.1 - \frac{H_b}{R} \right) \quad (1)$$

where H_b is breakwater crest elevation above Still Water Level.

R is run-up.

Run-up was determined using data presented in the Shore Protection Manual (7) for run-up on permeable rubble slopes, a slope of 1:1.5 being used. K_t values were determined for a range of unrefracted deep water wave-heights at the same tide levels used in the model tests.

It was then assumed that wave coefficient in the lee of the breakwater, K , could be conservatively estimated by :-

$$K = K_A K_t + K_A K_{di} \quad (2)$$

where K_{di} was determined from model tests.

K_A is the wave coefficient at position A, seaward of the breakwater.

Adoption of this method is considered to be conservative. K was evaluated for the different tide levels and for different breakwater crest elevations, 2.0m and 3.0m above I.S.L.W. Equations like (2) were used to determine plots of lee-side wave-height versus offshore wave-height; this not being a linear relationship. Then, following Lawson, (4), and applying weights of 1, 2 and 1 to the low, mean and high water level tests, partial probabilities of wave-height exceedance for the two lee positions were obtained. Summation of all these partial probabilities produced wave-height climate data which could then be used to calculate expected wave run-up on a statistical basis. The breakwater length and crest height were chosen to provide acceptable wave run-up conditions to the clubhouse.

However, wave run-up (i.e. in the horizontal plane) depends upon beach alignment and it was necessary to determine the expected ultimate mean alignment to be able to finalize the design. Additionally, in the final design, tribar armour units were used at the outer end of the breakwater. Run-up on these units is approximately 20% greater, Foster (5), than on rubble mound structures and so this change had to be included in the final calculations.

2.2 Beach Alignment.

Following the beginning of construction of the Bumborah Point revetment and the consequent change in wave climate in Yarra Bay, the beach was forced to realign, Treloar (8). In general this produced a wider beach in front of the sailing club, but the much higher waves and steeper beach lead to run-up being increased and dangerous boat launching conditions. A beach survey programme was begun in 1971 with surveys being at 3 monthly intervals. These surveys recorded beach levels at 12 cross-sections along the beach and extended from the frontal dune to a depth of about 4m below I.S.L.W. At the northern end the frontal dune soon disappeared and storm waves began eroding the bund protecting an old rubbish tip. Curve fitting to the survey data and calculations based on data measured in the Botany Bay Hydraulic Model were carried out to determine the expected ultimate mean beach alignment, Treloar (8). Statistical analysis of the survey data enabled the 95% confidence limits, based on a postulated normal distribution of beach width, to be obtained. This figure is approximately + 10m and results from onshore-offshore movement of sand, slope changes, alignment fluctuations and survey error. It is believed that this is a good estimate of the width band within which a beach contour (at Mean Water) will lie in Yarra Bay.

In 1974 about 30,000 cubic metres of sand were placed on the beach in Yarra Bay to overcome the problems caused by re-alignment. Beach surveys were continued and inclusion of this sand quantity in the beach alignment calculations enabled a predicted pre-construction alignment to be determined.

The pattern of diffracted waves behind the breakwater was used to determine an estimate of ultimate beach alignment. Circular wave fronts were drawn, centred at the breakwater seaward end and tangential to the predicted ultimate mean beach at the limiting orthogonal. This procedure assumes that the sand volume which will move in behind the breakwater will be sufficiently small to produce minimal narrowing of the beach in the remainder of the bay. The process of sand moving in behind the breakwater commenced soon after construction began. However, the plan shape of this "fillet" developed beyond the calculated circular arc alignment, this development being caused by the radiation stress resulting from the lee-side wave-height gradient. Sand will be transported by the current caused by this radiation stress gradient until the lee beach develops sufficiently for the gradient to become zero and a condition of stability established. Based on the circular arc beach and wave data on the lee side, run-up to the clubhouse was established for the various test conditions.

On the exposed side a complicated wave pattern was to be expected. An interference zone, formed essentially from waves reflected from the Bumborah Point revetment and waves reflecting again from the curved alignment of this breakwater, would cause further re-alignment of the small beach area between the breakwater and Yarra Point to the south. This re-alignment would take the form of a reduction in beach width near the breakwater. In order to avoid undermining of the breakwater toe 3,000 cubic metres of sand were placed on this beach area after construction was completed. It was considered that a larger quantity would not remain "entrapped" on the beach and might tend to move away around the rocky headland of Yarra Point.

2.2 Design Wave-Height.

The design wave-height information was obtained using wave-height coefficients at position A, Figure 2, and 5 years of Waverider buoy data obtained from the offshore deep water installation. This data has been collected with directional information and log-normal wave-height

exceedance distributions determined for direction - average zero crossing period combinations. The model mono-chromatic wave periods were related to the prototype zero crossing periods by considering proportions of energy in frequency bands spanning each monochromatic frequency in a Moskowitz spectrum defined for each zero crossing period. These data were used in the structural design of the breakwater. Table 1 shows wave-height exceedance data for significant wave-height as well as data obtained from 440 days of wave records measured by a Waverider buoy installation at position A. These latter data were not available at the design stage but confirm, with reasonable accuracy, the model results.

<u>Probability of Exceedance in Days/Year</u>	<u>Significant Wave-height (m)</u>	
	<u>Model</u>	<u>Prototype</u>
1	1.9	1.8
2	1.6	1.5
3	1.5	1.3

TABLE 1: Design and Measured Wave-Height Data

3. STRUCTURAL DESIGN

As indicated earlier the need to construct this breakwater became more urgent as the work on the major revetment in the port development progressed (Figure 1).

Increasing lengths of exposed core and completed armour at different construction stages of the revetment, and their various effects on reflection of waves to this site during the storms which occurred in the years 1974-75, produced damage to the club house resulting in the urgent need for ameliorative works to be undertaken.

In order that protection could be afforded prior to the principal storm period of May-June 1976 the design of the breakwater was completed without wave flume tests.

The structural design of the breakwater was thus based on a survey of information contained in the literature. Figure 3 indicates

site details for the final design.

3.1 Materials Available.

At the wave heights indicated, use of concrete armour tribars sized at 2½ tonnes and 6 tonnes was possible as a result of their use on the main revetment in the Port.

Rock armour sizes of 1 and 2 tonnes were similarly being used in that project. This material was being won from a quarry on the south coast of N.S.W., a road haul of approximately 120km.

Suitable core material was available up to 2 tonnes R.O.Q. within 60km from the site. Sizing of this material was 65% finer than 1 tonne.

The urgency of construction indicated the need for use of these available materials, if possible, in this breakwater.

3.2 Wave Height

In keeping with design wave heights for other port works, the significant wave height corresponding to a 0.01% probability of exceedance was considered appropriate for the structural design of the breakwater. At this probability, significant wave height is exceeded for a total of nine hours in 10 years.

As earlier indicated overtopping to some extent could be tolerated.

3.3 Crest Elevation.

A major requirement for this breakwater construction was to keep the crest elevation as low as possible. Additionally, so that the core material could be placed at normal stages of the tide, a crest elevation of approximately 3 metres above I.S.L.W. would achieve this aim. The depth at the breakwater's head is approximately 3.1 metres below I.S.L.W.

3.4 Head.

As reflected in the Shore Protection Manual's recommendations, (7), a structure head

is more conservatively treated for armour design.

The most commonly used formula for estimating armour sizes for non-overtopped breakwaters subject to breaking and non-breaking waves is the Hudson formula. This formula is based on a no damage stability criterion, defining permissible damage as displacement of up to 5% of the armour cover layer.

The largest available rock armour size was 3 tonnes for placing in two layers, but at the design stage this size of rock was not stockpiled at any possible source. Data available indicated that the cost increased by 50% for 3 tonne rock above 1 to 2 tonne size.

For minor overtopping, the Shore Protection Manual (7), recommends a K_d of 2.9 on a slope of $1\frac{1}{2}$ to 1 with levels of damage from 0 to 5%.

Foster (5), indicated damage co-efficient K_d values of 4 and 8 for 3 tonnes rock at slopes of $1\frac{1}{2}$ to 1 and 2 to 1 would lead to damage levels of 10% and 5% respectively for no overtopping. The data compares favourably with the Shore Protection Manual recommendations.

A conclusion reached by Lording (2), indicated that damage of a rock armour breakwater head should be restricted to 3%. Even though the testing in that report was limited, it was concluded that the most critical design for the tested structure was for S.W.L. just below crest level. For all tide stages this condition applies at the site of this breakwater for the design crest level.

Thus on the above data it appeared that damage levels of 3% for 3 tonne rock might occur at the 0.01% probability wave height.

Investigation of a concrete armour alternative was then pursued as flatter slopes than 2 to 1, and larger rock size may not have ensured the desirable lower damage levels of 3% at the head. Additionally, rubble deposited in the lee of the breakwater head may need to be removed to ensure adequate navigation.

Construction of the major port works, having included the use of single layers of tribars of 2½ and 6 tonne, enabled easy availability of these armour unit forms. For the 0.01% exceedance wave height the co-efficient of damage for 2½ tonnes tribars is 6.9, just below recommendations in the Shore Protection Manual (7) for minor overtopping. It is noted that in these recommendations the margin of uniform tribars (1 layer) over random placed tribars (2 layers) on the structure trunk is not maintained for the structure head. This presumably results because uniform placing makes greater use of frictional resistance than does random placing and this gain becomes less significant when the breakwater face is convex and the lateral reactions between blocks are somewhat reduced. For overtopping the damage co-efficient of 6.9 is not conservative for a breakwater head when looking at the Shore Protection Manual recommendations, (7) if the tribars are placed in one layer. However, the construction cost saving in placing tribars in one layer is significant.

To increase the size of tribar units for which forms were readily available, namely 6 tonnes, meant that the elevation of the core material would be below M.H.W.M. as armour unit and underlayer size is increased and this would be an unsatisfactory working level for a contractor.

In tests by Jackson (1), random placing of tribars in two layers on a convex surface of 1½ to 1 slope indicated a crest level to block dimension (C/D) ratio of 0.5 and still water level radius to block dimension ratio of 5. In this design these ratios are 0.8 and 3.4 indicating a tighter proposed head geometry when compared to the tests. Jackson recommended a damage co-efficient of 6 based on the Shore Protection Manual density of placement for two layers of random placed tribars.

In other work in the port tribars have been pattern placed ensuring leg to leg contact between adjacent tribars. This technique achieves lower placing densities and higher stability than placing uniformly to the Shore Protection Manual recommendations (7), Foster (5). However, pattern placing is difficult below water and a pattern could not be achieved in construction on the convex face at the head.

Foster's data (5), indicates for single layer tribar tests a damage co-efficient, K_d of 7 for a damage percentage level of 2%. That level of model damage is viewed by the writers to indicate a virtually maintenance free structure.

While Lording's data (2) applied to a rubble mound structure it indicated that critical damage occurred more to the crest and lee side for water levels just below the crest. Movement of tribars would be restricted in these areas by ensuring that :-

- (a) they were anchored in a substantial toe, achieved during excavation for trimming of the core; and
- (b) at the intersection of the sloping face and the crest adjacent tribars would be placed under close supervision to ensure leg to leg contact.

It was concluded that, provided tribars were placed to achieve the density stated in the Shore Protection Manual, with tight packing on the head, armouring of the crest, seaward and lee slopes in 2½ tonnes tribars would give an economical maintenance free head. The design adopted at the head is indicated in Figure 4.

3.5 Trunk.

The head design adopted continued for approximately 44 metres along the centreline of the breakwater where the bed is reasonably level. From that point, chainage 100m, water depth decreases rapidly.

For the design of the trunk it was proposed to use an armour stone of similar size for both crest and side slopes due to the short length to be armoured. Lording (2), concluded that a limit of 6% displacement of rock armour would ensure structural integrity of the trunk. At the design stage the Maritime Services Board had a commitment for over supply of 1 tonne rock in other port works.

Lording (2) indicated that crest armour size necessary for stability with 6% displacement

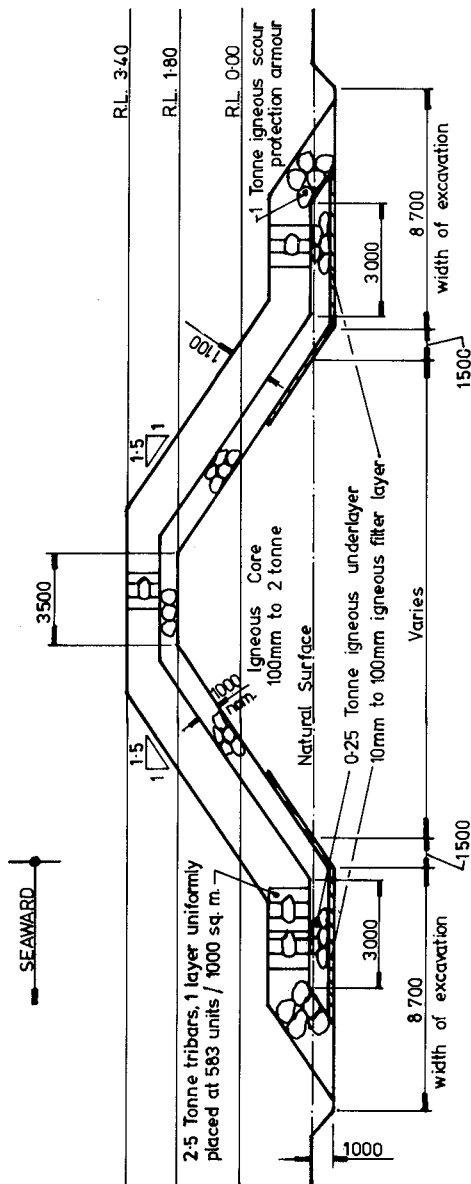


FIG. 4

appeared more critical at critical still water depths. Additionally identification of the critical still water depth for a given armour zone may permit estimation of armour sizes for that zone by an empirical formula (such as Hudson's) with a degree of accuracy not greatly inferior to that achieved for the non-overtopped criteria. For the $1\frac{1}{2}$ to 1 seaward and leeward slopes tested, a K_d of 7 corresponds to a satisfactory displacement of 6%. The maximum armour size was less than that required for non-overtopped breakwater.

The 1 tonne armour size, readily available, corresponded to a 6% damage level, at a wave height of 2.5 metres on a $1\frac{1}{2}$ to 1 slope, equivalent to a damage co-efficient, K_d of 7.

The structural integrity of the breakwater would not be lost at that damage level. In view of the low probability of higher wave heights mentioned herein, greater damage could be expected, but the structure would protect the club house to allow repair when necessary.

The trunk design adopted is shown in Figure 5.

3.6 Post Construction Performance.

Since completion of the breakwater, damage to the trunk section only has occurred following a storm of maximum significant wave height of 2.5 metres at position A (Figure 2). The principal reason for damage was undersize rock in this area. However, the breakwater was not breached and damage occurred to the seaward part of the crest and the seaward face between chainages 70 and 90 metres. At the area of damage, during construction, some slumping of the unprotected core occurred due to inferior quality of core rock. If all the unsatisfactory rock was not detected and replaced prior to armouring the breakwater, storm damage may have been triggered by local slumping of the core during the storm in question.

The quantity of rock placed to repair this section represented less than 3% of the total 1 tonne rock placed on the seaward and lee slopes and the crest of the trunk. The repair rock was sized 2 to 3 tonnes and the cross section (Figure

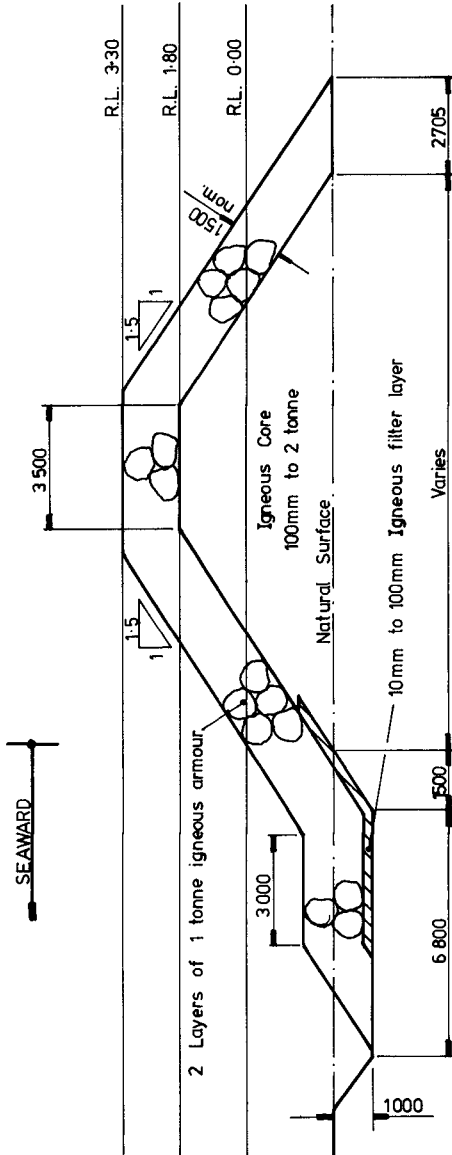


FIG. 5

5) was reinstated.

On the cost information available, the repair demonstrated the saving in construction cost if the trunk had been armoured in larger rock size, and/or by using a flatter slope. However this saving is demonstrated only for this short breakwater trunk.

For an overtopped breakwater it is not recommended that reduction of rock armour size below that for a non overtopped breakwater be adopted unless wave flume tests are undertaken. Additional protection would have certainly been given to this breakwater because of depth limitations at the site.

REFERENCES

1. Jackson R.A. - "Stability of Rubble Mound Breakwater, Nassau Harbour, Nassau, New Providence, Bahamas" - U.S. Army Engineers, Waterways Experiment Station, Technical Report No. 2-697, October 1965.
2. Lording, P.T. and Scott, J.R. - "Armour Stability of Overtopped Breakwater" - Journal of the Waterways, Harbors and Coastal Engineering Division, Proceedings of the American Society of Civil Engineers, pp. 341-354, WW2, May 1971.
3. Cross, R.H. and Sollitt, C.K. - "Wave Transmission by Overtopping" - Journal of the Waterways, Harbors and Coastal Engineering Division, Proceedings of the American Society of Civil Engineers, pp. 295-308, WW3, August 1972.
4. Lawson, N.V., Abernethy, C.L. and Treloar, P.D. - "The Probabilistic Interpretation of Wave Height Data from the Botany Bay Model" - First Australian Conference on Coastal Engineering, Sydney, Institution of Engineers, Australia, pp. 16-20, May 1973.

5. Foster, D.N. and Gordon, A.D. - "Stability of Armour Units Against Breaking Waves" - First Australian Conference on Coastal Engineering, Sydney, Institution of Engineers, Australia, pp. 98-107, May 1973.
6. Foster, D.N., Gordon, A.D. and Lawson, N.V. - "The Storms of May-June 1974, Sydney, N.S.W." - Second Australian Conference on Coastal and Ocean Engineering, Gold Coast, Queensland, Institution of Engineers, Australia, pp. 1-11, 1975.
7. U.S. Corps of Engineers - "Shore Protection Manual" - U.S. Army Engineering Research Centre, Department of the Army, 1975.
8. Treloar, P.D. - "Determination of the Ultimate Beach Alignment for a Small Bay Under Changed Wave Climate" - Third Australian Conference on Coastal and Ocean Engineering, Melbourne, Australia, Institution of Engineers, Australia, pp. 131-136, 1977.

FULL SCALE TRAILS OF DOLOSSE TO DESTRUCTION

by

Hans F. Burcharth*

ABSTRACT

It is well known that the relative dynamic strength of unreinforced slender concrete units decreases as the size increases. Big units can resist relatively smaller movements than small units. When model tests of cover layer stability are performed the determination of the damage criterion that should be adopted must therefore be based on knowledge of the dynamic strength of the corresponding prototype units.

With the purpose of establishing a relation between the size and the dynamic strength of unreinforced units some full scale tests to destruction of 1.5 and 5.4 t units were performed. The set up and the procedure of the tests which simulates the impact from rocking of the units and from concrete pieces that are thrown against the units are designed to make a comparison between the behaviour of units of different sizes possible. The test method is described and proposed as a standard method.

The theoretical expression for the dynamic strength is compared with the test results and it is shown that if the units are allowed to move there is an upper limit for the size of unreinforced units where a balance between the hydraulic stability of the cover layer and the strength of the units exists. Different ways of improving the strength of the units are discussed on the basis of the results from tests with different types of concrete.

The tests included an investigation of the influence of reinforcement, and of different types of concrete and surface cracks on the performance of the units.

* Prof. of Marine Civil Engineering, Aalborg University, Denmark

1. INTRODUCTION

It is well known that rubble mound breakwaters with armour layers of relatively small Dolos units - say up to 10 tons weight - have proved to be very successful structures, while there have been problems in a number of cases where very big Dolos units have been used.

There are probably many reasons to account for this. This paper deals with one of them, which could be expressed as the "lack of balance between the hydraulic stability of the units and their physical strength".

From hydraulic model tests it is known that the hydraulic stability of Dolos armour layers is extremely good if we allow the units to move, and usually a damage criterion is adopted where rocking of a number of units and displacement of a few units take place. The model units can be moved around during the tests without going into pieces, but in nature it is different as we know from experience that especially big slender units cannot resist much movement.

Unfortunately nobody has been able to make model block material with strength properties scaled correctly and it is doubtful whether it can be done at the moment at reasonable costs as for theoretical reasons both the compression and the tensile strength, the density and the dynamic Youngs modulus must be controlled in a certain combination.

In 1978 the Hydraulics Laboratory, Ottawa, Canada made a very good attempt to simulate the strength by inserting a thin slice of a weak material into the stem of the model units, but correct, quantitative data cannot be obtained from this type of model units.

There is, therefore, a missing link. This in fact makes it impossible to apply the model test results directly for the design of big, slender concrete units, and at the moment sufficient practical experience of the behaviour of these units does not exist.

On this background some full scale tests of the dynamic strength of 1.5 and 5.4 t Dolos units have been performed with the purpose of getting a better understanding of the behaviour of big units and thereby find ways for an improvement of the units.

2. TEST SET UP

Two different types of tests were used. A drop test, which simulates the wave introduced rocking of the units, and a pendulum test, which simulates the impact from pieces of broken units that are thrown around by the waves.

Figure 1 shows the drop test and Figure 2 the pendulum test.

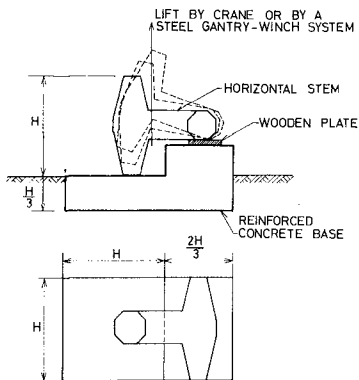


Figure 1 Drop test set up

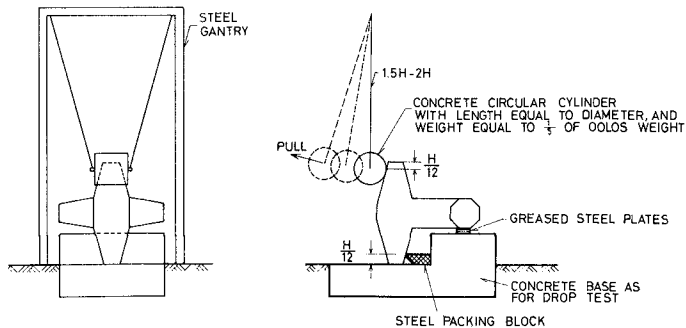


Figure 2 Pendulum test set up

In the drop test one end of the unit is lifted a predestinated height and then dropped by means of a quick release hook. In the pendulum test the weight is pulled back a certain distance and then released.

From practical experience it is known that in most cases when a Dolos is damaged it is fractured through the stem at a position close to the fluke. Therefore, the support of the unit and the direction and point of attack of the hitting force must be chosen in such a way as to ensure breakage in the stem. Besides this the support system should be well defined, thus allowing for the calculation of stresses in the unit. Figure 1 and Figure 2 show set up systems that make allowance for these points of view.

It is seen from the figures that all the dimensions of the test rig and the pendulum weight are related to the size of the Dolos unit. The idea is to introduce a standard method that makes it easier to compare the behaviour of units of different sizes, cf. the theory in chapter 5. This is a very important point since it is known that the strength of relatively small units is satisfactory, and by testing such small Dolosse and comparing the results with the results from tests of bigger Dolosse one can obtain information on the relations between the strength and the size and material of the units. Only if based on such information can a relation be established between the size of the units and the damage criterion which should be used in the hydraulic model tests.

The horizontally placed stem has the advantage that the height to which the unit can be lifted in the drop test without shifting the point (or line) of support is sufficient to ensure fracture. The unit will also hit the base with the full area of the fluke end and thus prevent that crushing in the contact zone takes place. The base should be made of good quality reinforced concrete to avoid cracking after a few drop tests.

Full scale drop tests of Dolos units have been performed by others before the tests described in this paper. But to the author's knowledge the test set up has been as shown in Figure 3. Here the unit is resting on the ground or on a relatively thin steel or concrete slab and one end of the unit is lifted and dropped.

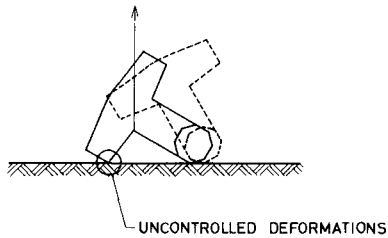


Figure 3 Inappropriate drop test set up

However this set up makes it impossible to compare different test results. This is mainly because the impact force will not be well defined, since the deformation from the crushing of the end of the Dolos leg and the deformation of the ground vary too much. Moreover, a test procedure where the threshold of the fall height is determined by increasing the fall height gradually cannot be used because of the uncontrolled crushing of the Dolos.

It may be argued that also the set up shown in Figure 1 implies uncontrolled impact forces caused by unknown variations in the soil characteristics at different sites. This is true, but for practical and economic reasons a much thicker concrete base, which is desirable, is not realistic. It is believed that the proposed relatively heavy and thick base will ensure applicable results as long as the base is founded on normal soils.

As the purpose of the pendulum test is to simulate the impact from a piece of a Dolos, e.g. a leg, thrown around by the waves a pendulum weight of $1/5$ of the Dolos weight is chosen. From an experimental point of view the same weight is adequate when combined with a pendulum length of 1.5 to 2 the Dolos height, since the draw back distance - or lifted height - of the pendulum required to destruct the unit will then be of a magnitude that can be measured accurately.

The pendulum should be made of the same type of concrete as used for the units and should be cast in a steel plate cylinder with wall

thickness of approximately 1/50 of the pendulum diameter. The steel cylinder serves as a mould and prevents damage of the surface from taking place during the tests.

A control of the impact energy from the pendulum is possible only if the movement of the pendulum when released is guided to ensure a central hit. The pendulum is therefore suspended in two non-parallel wires, the length of which should not be more than twice the Dolos height, see Figure 2. In this respect it is also important to use a good quality trigger mechanism (quick release hook) which does not cause undesirable movements of the pendulum when released. The mutual position of the Dolos and the pendulum should be so that the pendulum, when hanging at rest in vertical wires, should just touch the Dolos.

3. TEST PROCEDURE

Before the tests the surface of the units was carefully examined and photos were taken of possible surface cracks.

Since the influence of the load history on the dynamic strength was not known the load history was kept the same for each size of units. The history was chosen in such a way that failure occurred after approximately 6 to 8 impacts. In the drop tests the fall height, which was defined and measured as the vertical distance from the base to the centre of the fluke end, was gradually increased. For the 5.4 t units the initial drop was 100 mm, the second drop was 150 mm, and thereafter the increment was 20 mm. In the pendulum tests for the 5.4 t units the draw back distance, which was defined and measured as the shortest distance between the surface of the weight and the struck point on the Dolos unit, was gradually increased from 400 mm in the first strike to 450 mm in the second strike, and thereafter in increments of 20 mm.

Because of the rebound the unit was jerked back against the steel packing block after each pendulum blow.

The concrete surface was carefully examined after each stroke and in the case of reinforced units the width and the extent of the cracks were registered.

For the unreinforced units failure was taken as occurring at the first sign of fine cracks appearing in the unit. By soaking the unit with water these fine cracks could be seen as dry lines as the water was sucked by capillary action into the cracks.

For the reinforced units failure was taken as occurring when the crack width exceeded 0.1 mm. According to recent investigations of concrete structures in the North Sea this is a conservative value where no corrosion takes place.

With the purpose of examining the fracture the loading was continued until the unit broke into two pieces.

Where the fracture went through the surface cracks that existed before the test started the approximate extension of these cracks could be seen as wet areas.

For each unit the age and the specifications and density of the concrete mix were registered. The tensile strength was found indirectly from cylinder splitting tests and/or estimated from cylinder or cube compression strengths. The dynamic modulus of elasticity (the dynamic Youngs modulus) was found partly from the measurement of the velocity of ultrasonic pulses in the concrete and partly from static stress - strain graphs.

4. TEST PROGRAMME

Besides some pilot tests a total of 62 units were tested. Of these 27 were 1.5 t units and 35 were 5.4 t units. The tests were divided into

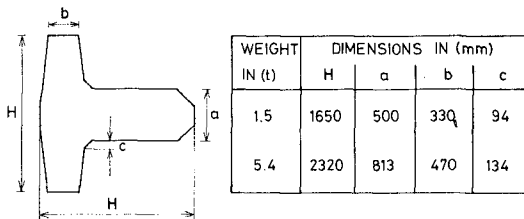


Figure 4 Geometry of Dolos units

6 series each containing approximately 10 units, of which one half was used for drop tests and the other half for pendulum tests. The geometry of the units is shown in Figure 4 and the specifications for the different series are given in Table 1.

Series No.	1	2	3	4	5	6
Weight of unit $M(\text{kg})$	1500	1500	1594	5400		
Density $\rho(\text{kg mm}^{-3})$	$2.33 \cdot 10^{-6}$	$2.33 \cdot 10^{-6}$	$2.47 \cdot 10^{-6}$	$2.4 \cdot 10^{-6}$		
Height of unit $H(\text{mm})$	1650			2320		
Waist ratio $\tau = a/H$	0.303			0.350		
Weight of pendulum $m(\text{kg})$	294			990		
Cement content (kg m^{-3})	291	291	392	385		
Water-cement ratio	0.50	0.55	0.24	0.46	0.46	0.44
Aggregate	Not crushed, max. 32 mm			Crushed basalt, max. 40 mm		
Additives	4-5% air	4-5% air	78 kg fine particles (mainly Silicadust) and 23 kg plastisizer per m^3	1% Plasto- crete OC	1% Plasto- crete OC	4-5% air and 1% Plasto- crete OC
Mean static compression strength; 100 x 200 mm cylinder. $\sigma_c(\text{Nmm}^{-2})$	28.9	26.6	88.4	45.5*)	45.5*)	39.2*)
Mean static tensile strength; cylinder splitting test. $\sigma_T(\text{Nmm}^{-2})$	2.95**)	2.79**)	5.74**)	4.38***)	3.56***)	4.18***)
Mean dynamic modulus of elasticity $E(\text{Nmm}^{-2})$	$3.6 \cdot 10^4$	$3.6 \cdot 10^4$	$7.0 \cdot 10^4$	$5.2 \cdot 10^4$	$4.96 \cdot 10^4$	$4.50 \cdot 10^4$
Particulars	Reinforcement of stem, see Figure 6			Cracks in stem-fluke corners, see Figure 5		

*) Calculated from 150 mm cube tests by multiplying the cube strength by 0.74.

***) Determined from cylinders cast during the production.

***) Determined from cores taken from the units.

Table 1 Specifications of the test series

As seen from Table 1 different concrete mixes with a considerable variation of the strength properties were used. Also a test series with units exhibiting serious surface cracks in the stem fluke corners was performed.

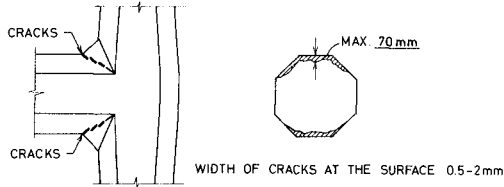


Figure 5 Typical extension of surface cracks in test series No. 5

Different degrees of reinforcement were used in some of the 1.5 t units with the purpose of investigating the relation between development and sizes of cracks and degree of reinforcement, see Figure 6. Because of limitations in the test program only the stem, being the weaker part of the unit, was reinforced. As a reinforced stem is much stronger than an unreinforced leg these tests could also give information about the dynamic strength of unreinforced legs. The concrete cover layer thickness was chosen to 70 mm in accordance with recommendations for concrete structures in the North Sea.

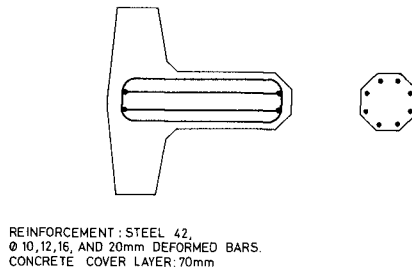


Figure 6 Reinforcement of 1.5 t Dolos units in test series No. 2

5. THEORETICAL BACKGROUND FOR ANALYSIS OF THE TESTS

5.1 Dimensional Analysis of Impact.

Consider a class of geometrically similar systems, in which the size of a structure and the size of an impinging body are both determined by a characteristic length and both made of the same material.

If the moving body strikes the structure the maximum stress σ at any point of the structure depends on the mass m and the velocity V of the incident body, the characteristic length L , the elastic modulus E , Poisson's ratio ν , and the mass density ρ . As an approximation E and ν are taken as constants that characterize the material, which means that the effects of rate of strain on stress are not taken into account.

By dimensional analysis we obtain,

$$\frac{\sigma}{mV^2L^{-3}} = f\left(\frac{EL^3}{mV^2}, \frac{m}{\rho L^3}, \nu\right) \quad (1)$$

As the proposed test system implies a constant ratio between the masses of the impinging body and the structure, and also because ν has a negligible influence on the phenomenon (we are dealing with concrete mixes with small variations in ν) equation (1) takes the simpler form,

$$\frac{\sigma}{mV^2L^{-3}} = f\left(\frac{E}{\rho V^2}\right) \quad (2)$$

This equation can be used to describe both the drop test and the pendulum test.

5.2 Drop Test Formular

In the case of the drop test the unit itself is the impinging body having a mass of M and a potential energy of Mgh , when the unit's centre of gravity is lifted vertically a distance h . As $V^2 = gh$ equation (2) yields,

$$\frac{\sigma}{MghH^{-3}} = f\left(\frac{E}{\rho gh}\right) \quad (3)$$

Until now only geometrically similar units have been considered. However, Dolos units are not always geometrically similar since the waist ratio $\kappa = a/H$ (see Figure 4) varies from 0.30 to 0.35 or more.

By calculating the unit's momentum as a function of M , H , κ and h and taking the duration of the impact as proportional to H/c , where $c = \sqrt{E/\rho}$ is the speed of a longitudinal wave in the concrete, an expression for the mean impact force can be established. From this the maximum stress in the stem cross section close to the fluke corner is found to,

$$\frac{\sigma}{MghH^{-3}} = C \frac{1+\kappa}{\kappa^2} \sqrt{\frac{E}{\rho gh}}, \quad 0.3 \leq \kappa \leq 0.4 \quad (4)$$

where C is a constant factor. Equation (4) does not include the negligible stresses caused by the weight of the unit.

5.3 Pendulum Test Formular

In this case the impinging body is a pendulum with a mass m equal to or approximately equal to 1/5 of the mass of the Dolos unit. The potential energy of the pendulum is mgh when pulled back to a position where the centre of gravity is lifted vertically a distance h . The maximum velocity of the pendulum is $V = (2gh)^{0.5}$. Equation (2) is valid only if the size of the pendulum and the Dolos are both determined by a characteristic length. Since Dolos units have varying waist ratios and also because the size and the weight of the pendulum for practical reasons are not always fixed parts of the size and the weight of the Dolos, equation (2) is not suitable for practical calculations. By using the same assumptions and calculation procedure as described for the drop test the following formula for the maximum stress in the stem cross section close to the fluke corner is obtained,

$$\frac{\sigma}{mghH^{-3}} = K \frac{1}{\kappa^3} \sqrt{\frac{E}{\rho gh}}, \quad (5)$$

where K is a constant factor. Equation (5) does not include the negligible stresses caused by the weight of the unit.

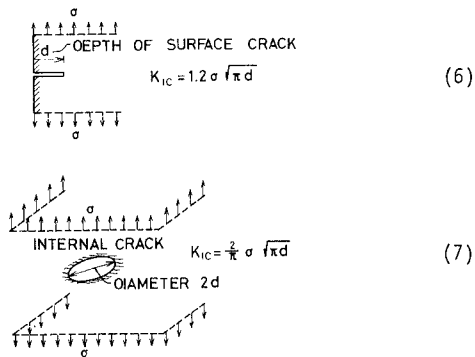
5.4 Analysis of the Influence from Cracks on the Dynamic Strength

The influence from cracks on the strength of the units can be looked into by means of fracture mechanics theory. An estimate on this influence can be made by using the fracture toughness parameter K_{IC} (critical stress intensity factor) for a static load situation on a linear elastic body of homogeneous and isotropic material. In K_{IC} the subscript I refers to the crack opening mode of crack propagation and the subscript C refers to the critical value of K_I , i.e. the onset of rapid fracture.

Although the assumptions related to K_{IC} are incorrect for concrete, many investigators have generally assumed that the approximations involved in the application of linear elastic fracture mechanics to concrete are reasonable.

For concrete K_{IC} values are found in the range from about 0.45 to 1.40 $\text{MN m}^{-3/2}$ for a static load situation. As an approximation the static load theory and the mentioned range of K_{IC} values are assumed valid for a dynamic load situation.

For plain strain conditions the critical sizes of surface cracks and internal cracks can be found from the equations (6) and (7), (see Figure 7), in which σ is the tensile stress at some distance from the crack.



(6) $K_{IC} = 1.2 \sigma \sqrt{\pi d}$

(7) $K_{IC} = \frac{2}{3} \sigma \sqrt{\pi d}$

Figure 7 Fracture toughness parameters

As the tensile stress σ generally varies between 2.5 and 5 Nmm^{-2} the range of the critical crack sizes will be as shown in the diagram, Figure 8.

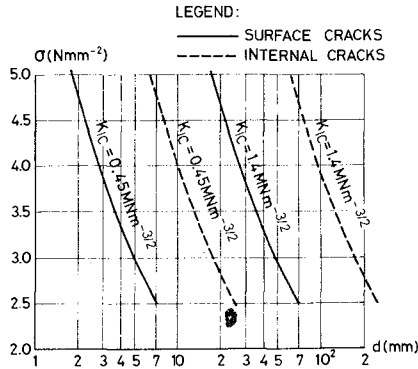


Figure 8 Critical sizes of surface cracks and internal cracks

It is seen from the graphs that if the tensile strength of the concrete is approximately 3 Nmm^{-2} and K_{IC} is in the range from 1 to 1.4 $\text{MNm}^{-3/2}$ then the surface cracks can have depths of up to 25-50 mm without altering the performance of the unit.

6. TEST RESULTS

6.1 Unreinforced Units

The test results are summarized in Table 2. C and K are found by replacing the tensile stress by the static tensile strength in eq. (4) and eq. (5). This is an approximation but since it is believed that the ratio between the static and the dynamic tensile strength is constant the approximation is acceptable.

The average and the standard deviation of C are 0.16 and 0.02 respectively, and the average and the standard deviation of K are 0.69 and 0.14 respectively.

Series No.	1	3	4	5	6
Drop height h for centre of gravity in drop tests. Average (mm)	153	171	117	115	138
Stand.dev. (mm)	14.5	5.0	9.4	20.9	22.5
Lifted height h of pendulum in pendulum tests. Average (mm)	46.5	45.8	40.5	39.9	39.9
Stand.dev (mm)	2.9	4.0	1.9	2.2	2.1
C, factor in eq. (4)	0.128	0.165	0.184	0.155	0.174
K, factor in eq. (5)	0.469	0.681	0.807	0.677	0.835
α , average of angle of rotation in drop tests	13 ⁰ 8	15 ⁰ 5	7 ⁰ 5	7 ⁰ 3	8 ⁰ 9

Table 2 Test results for unreinforced units

In the drop tests, the cracking started at the top of the stem and spread to the bottom of the stem leading to a fracture of the type shown in Figure 9. The start of the cracking at the top side instead of at the bottom side is due to the big horizontal momentum of the top leg caused by the pivoting of the unit. In a few of the drop tests (mainly in series No. 1) the fracture developed first through the middle part of the stem and not in the stem-fluke corner.

In the pendulum tests the cracking started at the bottom of the stem and spread to the top, leading to a fracture of the type shown in Figure 9.

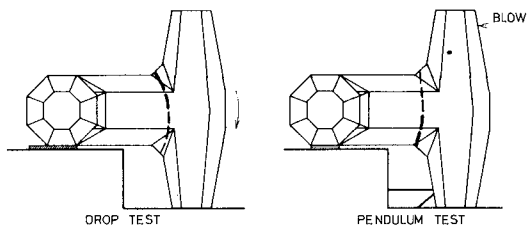


Figure 9 Typical fractures in unreinforced units

6.2 Reinforced Units

The results from test series 2 are summarized in Table 3 a and b.

Drop test No.	Reinforcement, deformed bars, steel 42		Drop height h for centre of gravity (mm)	Observations
	Size	%		
1	8 \emptyset 10 mm	0.29	160	fine crack in stem
	-	-	174	fine crack in top leg
	-	-	222	top leg fractured, crack width in stem ≤ 0.1 mm
2	8 \emptyset 12 mm	0.41	206	fine crack in stem
	-	-	238	crack in top leg
	-	-	268	top leg fractured, crack width in stem ≤ 0.07 mm
3	8 \emptyset 16 mm	0.73	181	fine crack in top leg
	-	-	210	fine crack in stem
	-	-	286	bottom leg crushed, crack width in stem ≤ 0.01 mm
4	8 \emptyset 20 mm	1.14	201	top leg fractured, no visible cracks in stem

Table 3 a Test results for reinforced units, Drop tests

Pendulum test No.	Reinforcement, deformed bars, steel 42		Lifted height h of pendulum (mm)	Observations
	Type	%		
1	8 \emptyset 10 mm	0.29	87	fine crack in stem top leg fractured, crack width in stem \leq 0.1 mm
	-	-	112	
2	8 \emptyset 12 mm	0.41	119	fine crack in stem top leg fractured, crack width in stem \leq 0.03 mm
	-	-	136	
3	8 \emptyset 16 mm	0.73	107	top leg fractured, no visible cracks in stem
4	8 \emptyset 20 mm	119	top leg fractured, no visible cracks in stem	

Table 3 b Test results for reinforced units, Pendulum tests

Figure 10 shows typical positions of cracks in the reinforced units.

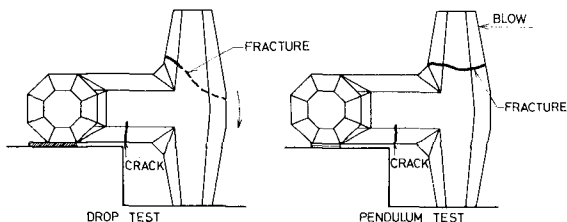


Figure 10 Typical cracks and fractures in reinforced units

7. CONCLUSIONS AND RECOMMENDATIONS

The presented theory for the dynamic loading of Dolos units should be regarded as a first approximation. In spite of this and in spite of the scatter in the values of C and K (Table 2), it is believed that the theory (eq. 4 and eq. 5) can be used to estimate the relative dynamic strength of units of different sizes, different waist ratios, and different concrete mixes. It should be noted that a considerable

scatter in the C and K values is expected because the determination of the tensile strength and of the dynamic modulus of elasticity is subject to big uncertainty. A careful determination of these two quantities is therefore an important part of the full scale tests.

Before a final conclusion about the presented theory can be made tests with big units (10-30 t) should be done and the influence of the load history should be investigated. This can be done by determination of the relation between the number of blows that will lead to fracture and different loads, e.g. 60%, 70%, 80% and 90% of the failure load that corresponds to the load history in the presented tests:

Both the test results and the theory show that the relative dynamic strength of unreinforced units decreases considerably with increasing size of the unit, other things being equal. Although the strength can be improved by increasing the waist ratio it is not always possible to compensate for the reduction of the strength. This can be explained by an example.

Let us assume that we know from experience that the dynamic strength of some 7.5 t Dolos units with a waist ratio of 0.3 is just sufficient to resist the rocking that takes place when the units are exposed to the design storm waves. Let us then assume that we perform some hydraulic model tests for a Dolos breakwater on a much more exposed place. In the model tests, units with a waist ratio of for example 0.34 is used, and from the tests it is concluded that the weight of the prototype units will be 26 t if the damage criterion that corresponds to the design wave situation for the 7.5 t units is used. For simplicity we will now assume that the same concrete mix is used for both sizes. From the drop test formula it is then found that the big Dolos unit must have a waist ratio of 0.39 to resist the same rocking - or angle of rotation - as the small units. From Figure 11 it is seen that by increasing the waist ratio that much, the shape of the unit is completely altered, and so is the hydraulic stability. Therefore, a new series of hydraulic model tests with more bulky Dolos units has to be done, but since such tests lead to a demand for even heavier units than the 26 t, a bigger waist ratio than 0.39 must be applied to obtain sufficient strength of the prototype units, etc.

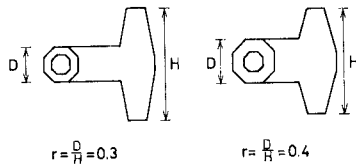


Figure 11 Influence of waist ratio on Dolosse of the same weight

From this it can be concluded that the design criterion which are adopted in hydraulic model tests must correspond to the dynamic strength of the prototype units.

Moreover it can be concluded that if a design criterion which implies movements of the units is adopted there will exist a maximum size of unreinforced units for which there is a balance between the hydraulic and the physical stability. Units heavier than this maximum size can, of course, be used if a non-rocking design criterion is adopted. However, this will lead to a demand for relatively heavier units.

From the test series No. 1 and No. 3 and from the theory it is seen that it is difficult to improve the dynamic strength by using a stronger concrete, even if a super-strong concrete, as the one in series No. 3, is used. This is so, because stronger concrete mixes are more brittle as they have relatively poorer tensile strength and relatively higher modulus of elasticity. It should be stressed that this conclusion must not lead to the use of weak concrete mixes, because the surface resistance and the long term durability of the units are very much dependent on the strength and the compactness of the concrete.

From a comparison of the test series No. 4 and No. 5 it can be concluded that an unreinforced unit can suffer from relatively deep surface cracks, even in the stem-fluke corners, without losing much of its dynamic strength. This matter, which can be explained by fracture mechanics theory, is caused by the low stress level and the relatively good fracture toughness of concrete. From the theory it can also be

concluded that even relatively big internal cracks have a negligible influence on the strength of the units. It should be noted that surface cracks should of course be avoided, since the freeze-thaw resistance and the long term durability of the units are affected by the cracks.

The age of the units, when tested, varied from 28 days to half a year. No correlation between age and dynamic strength was found.

On exposed locations, where very big armour units are needed, it is presumably advantageous to improve the dynamic strength by reinforcing the units. From test series No. 2 it can be concluded that, even with a small degree ($\leq 1\%$) of ordinary reinforcement, it seems possible to double the impact energy and still restrict the width of the cracks to sizes well below the critical size (0.1-0.3 mm), where corrosion of the bars takes place. This conclusion holds also for the more realistic situation where a unit, besides the dynamic loading, must carry a static load, e.g. from the weight of one or two other units. By comparing the test results from series No. 1 and No. 2 it is seen that the legs of a Dolos are considerably stronger than the stem. It is therefore a question whether it does pay to reinforce the legs (or some part of them) as it complicates the production of the units considerably. Very little is known about reinforced Dolosse, but in the few places where they have been used, e.g. in the Humboldt Jetties, investigations of the state including recording of the width of possible cracks should be performed.

Prestressed, posttensioned and fibre reinforced concrete are other possibilities, which should be looked at, but in this respect the importance of an easy production method should be stressed, since the production of ordinary Dolos units is difficult enough.

Although the described tests were performed with Dolos units the qualitative results and conclusions hold also for other types of slender concrete armour units.

8. ACKNOWLEDGEMENTS

The tests were performed in co-operation with mr. Hans Halskov (formerly student at Aalborg University Center), The Danish Governmental Coast Authority, Aalborg Portland Cement and Concrete Laboratory, Denmark, South of Scotland Electricity Board, James Williamson & Partners, Scotland and Sir Robert Mc Alpine and Sons, U.K.

9. REFERENCES

- Beeby, A.W., 1978. Concrete in the Oceans, Cracking and Corrosion, Technical Report No. 1. Cement and Concrete Association, Department of Energy, U.K.
- Magoon, O.T., Shimizu, N., 1971. Use of Dolos Armour Units in Rubble-Mound Structures e.g. for Conditions in the Arctic. Proc. POAC Conf., 1971, Vol II, pp. 1089-1108.
- Mansard, E.P.D., Ploeg, J., 1978. Model Tests of Sines Breakwater. LTR-HY-67. Hydraulics Laboratory, National Research Council of Canada, Ottawa, Ont. Canada.
- Minders, S., Lawrence, F.V., Kesler, C.E., 1977. The J-Integral as a Fracture Criterion for Fiber Reinforced Concrete. Cement and Concrete Research, Vol. 7, pp. 731-742.

DOLOSSE

PAST, PRESENT, FUTURE?

by

J.A. ZWAMBORN, D.E. BOSMAN AND J. MOES*

SUMMARY

Information is presented on 38 dolos projects in various parts of the world. Some of the data were collected by means of questionnaires and the remainder are based on publications, reports and personal visits. Information is given on design conditions, structure details, model tests and site experiences. *Past* dolos research is discussed briefly.

Present experience of damage to various dolos structures is described, particularly that to the 2 km long Sines main breakwater. The results are discussed of research initiated by differences in accepted design and model test conditions and the recent dolos failures. This research concerned dolos packing densities, dolos movements (damage criteria) and structural failure of armour units.

There is little doubt that dolosse will be used effectively and economically, in the *future* for many small and medium-sized coastal structures. However, special attention will have to be given to deep-water structures of any kind, with regard to representative design conditions, the effect of the larger waves in the spectrum and the possibility of structural failure of armour units. A few practical suggestions are made for the design of safer dolosse, in the interim, but it is recommended that a major effort be made to collect reliable data on existing structures as well as to develop representative and, preferably, standardized design and model test techniques.

1. INTRODUCTION

The dolos, invented by East London Harbour Engineer E.M. Merrifield, was used for the first time in 1964 when 18 t dolosse were placed on the East London breakwater to repair sections of the 37 t rectangular block armour which had sustained serious storm damage. After 15 years in service, this dolos protection is still in satisfactory condition while sections of the breakwater where there is no dolos protection have been damaged further.

This early success led to the mounting of a series of hydraulic model tests with dolosse at the CSIR laboratory in Pretoria in 1965; these tests showed that dolosse have very high stability factors of between about 20 and 40 for small percentages of damage. After the first publication on dolosse appeared in 1966 (Merrifield and Zwamborn) the results of the initial tests were substantially confirmed by other laboratories and, thereafter, dolosse have been used for coastal works in numerous parts of the world.

* Coastal Engineering and Hydraulics Division, National Research Institute for Oceanology, Stellenbosch, South Africa.

Because of the high stability of the dolosse found in the model tests these units have been used for ever-larger projects, in greater water depths and in more severe wave climates. The major dolos failure at Sines, Portugal, however, has thrown serious doubts, *firstly*, on the reliability of accepted model test techniques, *secondly*, on the adequacy of generally-accepted design criteria and, *thirdly*, on the suitability of concrete armour units, in general, and dolosse, in particular, under these severe conditions, especially with regard to their structural behaviour.

2. PAST EXPERIENCES

2.1. Dolos Structures

A survey has been made of existing dolos structures by means of a detailed questionnaire. Detailed information was received on 18 projects (Table I) of the 38 known to the authors.

TABLE I KNOWN DOLOS PROJECTS

DETAILED INFORMATION AVAILABLE, BASED MAINLY ON RETURNED QUESTIONNAIRES			INCOMPLETE INFORMATION AVAILABLE, ABSTRACTED FROM LITERATURE AND PERSONAL CORRESPONDENCE		
LOCATION	COUNTRY	YEAR	LOCATION	COUNTRY	YEAR
<i>East London</i>	<i>South Africa</i>	<i>1964</i>	Mossel Bay	South Africa	1967/69
<i>Port Elizabeth shore protection</i>	<i>South Africa</i>	<i>1966/68</i>	Cap aux Meules	Canada	1970
<i>St. Helena Bay</i>	<i>South Africa</i>	<i>1967/68</i>	Turton shore protection	South Africa	1973
<i>Gans Bay</i>	<i>South Africa</i>	<i>1968/70</i>	Reef runway for airport	Hawaii	1973
<i>Cape Town</i>	<i>South Africa</i>	<i>1968/72</i>	Crescent City	U.S.A.	1973
Humboldt	U.S.A.	1971/72	Kuwait	Kuwait	1974
<i>Hirtshals</i>	<i>Denmark</i>	<i>1971/73</i>	Jubail	Saudi Arabia	1976
<i>Richards Bay</i>	<i>South Africa</i>	<i>1973/76</i>	Azzawiya	Libya	1976/77
Sines	Portugal	1973/79	Maianae	Hawaii	1977
High Island water scheme	Hong Kong	1974/75	Gioia Tauro	Italy	1978
<i>Port Elizabeth</i>	<i>South Africa</i>	<i>1975/77</i>	Gans Bay new design	South Africa	1979
Kahului	Hawaii	1975/77	St Thomas runway	Virgin Islands	1979 (?)
Baie Comeau	Canada	1976	Botany Bay	Australia	
<i>Oranjemund</i>	<i>South-West Africa</i>	<i>1976/77</i>	Carboneras	Spain	
San Ciprian	Spain	1978/79	Gabarus	Canada	
<i>Koeberg Nucl. power station</i>	<i>South Africa</i>	<i>1978/80</i>	Llanddulas shore protection	North Wales U.K.	
<i>Hay Point</i>	<i>Australia</i>	<i>1978</i>	Mackay	Australia	
Beach Haven Atl. gen. station	U.S.A.	1980 (?)	Rivière aux Renard	Canada	
			Tristan da Cunha	South Atlantic	
			Saline di Montebello	Italy	

Note : The names of projects for which data were obtained solely from questionnaires, are typed in italics.

The questionnaire included questions on *design conditions, structure details*, including information on the *dolos armour*, and the *underlayer stone, hydraulic model tests, construction methods, in-service performance and costs*. A summary of the available detailed information is given in Table II (blank spaces indicate no information available while '-' was used in some returned questionnaires instead of 'no' or 'negligible'). Information gathered on the other 20 projects is summarized in Table III.

The following are extreme values of some of the main parameters:

- design-wave height (H_s or H_{mo}) 2 to 11 m
- dolos masses (W) 0,5 to 56 t
- water depths at the structures 0,8 to 52 m

Figure 1 shows a correlation between water depth and dolos mass. It will be seen that all the structures were built in relatively shallow water, except for the Sines breakwater.

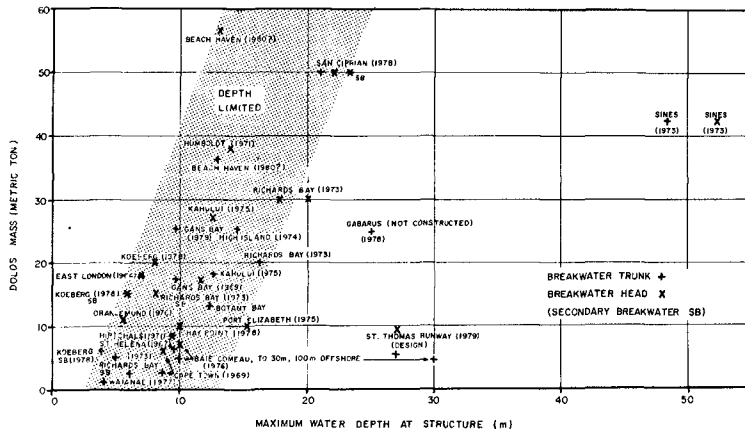


Fig. 1 Dolos mass versus water depth

The dolos protection designed for the St. Thomas Runway in the Virgin Islands runs into a water depth of 27 m and falls also outside the general trend shown in Figure 1. The actual water depth at the breakwater at Baie Comeau is 10 m but only 100 m away from the breakwater, the depth is about 30 m and this project could therefore be affected by deep-water conditions.

A correlation of dolos mass versus design wave height is shown in Figure 2. The figure again shows definite trends but the variation in dolos mass for a given design wave height is very large. It is interesting to note that Sines follows the general trend.

TABLE II. SUMMARY OF RELEVANT INFORMATION ON KONGS INDOUS PROJECTS

Project & details	Design conditions			Structure geometry			Dolos armouring particulars					
	Wave height H(m)	Wave period T(s)	Wave angle to structure (°)	Armour layer height (m)	Structure depth (m)	Structure width (m)	Block height (m)	Block width (m)	Block density (t/m ³)	Block spacing (m)	Block density (t/m ³)	Block spacing (m)
East London harbour	3.5	12.0		0.8	8.5	4.0	7.0	17.9	3.35	0.34	2.26	30.0
1964-1964	8.5	12.0	90	0.8	7.6	4.0	7.0	17.9	3.35	0.34	2.26	30.0
Port Elizabeth coast	2.0	8.0		0.67	4.1	1.1	1.1	2.6	2.05	0.30	2.39	31.0
1963-1972	2.5	12.0	90	0.67	4.1	1.1	1.1	2.6	2.05	0.30	2.39	31.0
St James Bay harbour	6.1			0.51	4.7	3.8	9.7	6.4	2.66	0.31	2.43	34.5
1962-1968												1.02, 0.63-4
Gans Bay harbour	6.0	12.0	30	2	0.67	5.3	7.3	9.7	17.1	3.66	0.30	2.4
1968-1970	6.0	12.0	30	2	0.67	5.3	7.3	11.7	17.1	3.66	0.30	2.4
METS				2	0.80	2.3	5.1	5.7	4.5	2.26	0.33	2.4
Cape Town harbour	2.0	12.0	90	0.67	5.0	4.5	6.0	3.0	1.92	0.31	2.4	30.0
1963-1972	2.5	12.0	90	0.67	3.7	6.8	0.8	3.0	1.92	0.31	2.4	30.0
1971-1972	12.2		90	0	0.25	6.9	14.0	12.9	30.0	4.50	0.33	2.6
Humboldt harbour	12.2		90	0	0.25	5.6	14.0	15.0	38.0	4.50	0.33	2.6
1971-1972												42.0
MIRZAPUR harbour	3.9	8.0	45	0.67	4.0	4.0	9.5	8.4	2.80	0.33	2.35	34.3
1971-1973	3.9	8.0	45	0.50	3.0	4.0	9.5	8.6	2.80	0.33	2.35	34.3
Richards Bay harbour	7.2	11.5	30	2	0.67	7.1	14.9	16.3	20.0	3.71	0.33	2.4
1973-1976	7.0	11.5	30	2	0.50	7.1	14.9	16.3	20.0	3.71	0.33	2.4
1973-1976	7.0	11.5	30	2	0.50	7.1	14.9	16.3	20.0	3.71	0.33	2.4
1973-1976	7.0	11.5	30	2	0.50	7.1	14.9	16.3	20.0	3.71	0.33	2.4
Slanes harbour	11.0	16.0	100	1	0.67	16.0	15.0	48.0	42.0	4.54	0.35	2.5
1973-1979	11.0	16.0	100	1	0.50	16.0	15.0	52.0	42.0	4.54	0.35	2.5
High Island water	10.7	15.0		2	0.5	14.8	14.6	14.6	23	3.86	0.35	
1973-1972 scheme												1.16, 6.1
Port Elizabeth bay	6.4	12.0	50	0.58	5.3	13.3	15.3	9.7	3.03	0.31	2.38	30.0
1975-1972												1.02, 0.5-2
Kaunui harbour	10.4	18.0	45	0.3	5.0	7.0	15.4	16.0			2.4	
1973-1977	10.4	18.0	45	0.3	5.0	7.0	15.4	16.0			2.4	
Male Comau St	10.0		30	0.59	5.3	8.0	10.0	4.5	2.29	0.30	2.4	
1976	10.0		30	0.5	5.3	8.0	10.0	4.5	2.29	0.30	2.4	
Orange Bay (Tinkale)	7.7	11.5	25	4.0	6.7	7.8	5.3	10.1	3.00	0.31	2.35	40.0
1976-1971												1.15, 1.5-2
San Clemente harbour	13.0	15.5	4	0.5/0.8	13.7	15.3	21	50.0	4.85	0.35	2.41	0.98 > 7
1978-1979	13.0	15.5	90	4	0.5	13.7	15.3	21	50.0	4.85	0.35	2.41
1978-1979	13.0	15.5	90	4	0.5/0.7	13.0	15.3	23	50.0	4.85	0.35	2.41
1978-1980	13.0	15.5	90	4	0.5/0.7	13.0	15.3	23	50.0	4.85	0.35	2.41
Kobe (Shel. Power)	5.0	16.0	45	2	0.67	7.3	9.0	6.0	15.0	3.33	0.34	2.4
1976-1980	5.0	16.0	45	2	0.67	7.3	9.0	6.0	15.0	3.33	0.34	2.4
1976-1980	5.0	16.0	45	2	0.67	7.3	9.0	6.0	15.0	3.33	0.34	2.4
1976-1980	5.0	16.0	45	2	0.67	7.3	9.0	6.0	15.0	3.33	0.34	2.4
Bay Point Harbour	6.1	10.0	45	0.59	10.4	7.1	10.1	10.0	3.01	0.32	2.35	35.0
1978												0.72
Beach Haven Gali.	12.0	13.5	100	2	0.2	18.7	13.0	14.0	36.4	4.22		
1980(1) Gen. St.	12.0	13.5	100	2	0.2	18.7	13.0	14.0	36.4	4.22		
1980(1) Gen. St.	12.0	13.5	100	2	0.2	18.7	13.0	14.0	36.4	4.22		

* NRT/MNR - Main Breakwater Trunk/Head; SRT/SBR - Secondary Breakwater Trunk/Head; SF - Shore Protection NRTIS - NRT inner Slope

** All depths are to mean sea level (MSL)

TABLE 11. (CONTINUED) 2. DETAILED INFORMATION ON KNOWN DOLDS PROJECTS

Project & details Name and period of construction	Hydraulic Model Tests		Site Experience								Storm wave height (m) H _{max}	Storm wave store (t) H _{max}	Number of dolds used	Unit cost (US\$)
	Part*	3D, Reg. scale No	2D, Irr. scale No	28 day com- pression (days)	28 day com- pression (days)	Breache of dolose (%) during storm	Initial factor	Final factor	Storm wave height (m) H _{max}					
East London harbour 1964-1964	MHT	No	No	1	3	28	0.15	0.5	0.25	-	-	2000	-	
Port Elizabeth coast 1965-1985	SPT	No	No	1.5	1.5	28	2.25	0.5	-	-	-	13343	22	
St. John's Bay, Nam. 1967-1968	MHT	No	No	1	7	28	41.5	0.5	0.2	0.3	-	11689	21	
Gana Bay harbour 1968-1970	MHT	30	80	7.3	2	28	31.7	-	-	-	6.1	12	1651	
MBH	No	80	7.3	2	7	28	31.7	-	-	-	6.1	16	1500	
MHTS	No	80	7.3	2	7	28	31.7	-	-	-	6.1	16	1000	
Cape Town harbour 1969-1972	MHT	No	No	1	6	28	0.8	0.1	0	-	-	9371	56	
MBH	No	No	No	1	6	28	0.8	0.1	0	-	-	9277	56	
SP	No	No	No	1	6	28	0.8	0.1	0	-	-	9366	40	
Humboldt harbour 1971-1973	MHT	No	50	14.2	1	14	28	34.3	0.4	0.4	0.4	0.4	2396	
MHT	No	50	14.2	1	14	28	34.3	0.4	0.4	0.4	0.4	2396		
MBH	No	50	14.2	1	14	28	34.3	0.4	0.4	0.4	0.4	2396		
Richards Bay harbour 1973-1976	MHT	50	100	10.6 (9.8)	0.5	6	28	38.0	0.38	0.36	0.01	-	13397	
MHT	50	100	10 (9.8)	0.5	6	28	38.0	0.14	0.3	0.01	-	2194		
MBH	50	100	10 (9.8)	0.5	6	28	38.0	0.14	0.67	0.01	-	8832		
SPT	50	100	10 (9.8)	0.5	6	28	38.0	0.14	0.67	0.01	-	8832		
SPT	50	100	10 (9.8)	0.5	6	28	38.0	0.14	0.67	0.01	-	8832		
St. John's Bay, Nam. 1973-1979	MHT	62	-	15	10.5	2.2	7	28	43.0	0.51	1.58	0.29	-	
MHT	62	-	15	10.5	2.2	7	28	43.0	0.51	1.58	0.29	-		
MBH	62	-	15	10.5	2.2	7	28	43.0	0.51	1.58	0.29	-		
High Island Water 1975-1975 scheme	MHT	50	No	-10	-10	2	7	28	49.0	0.5	1.5	<5	9.5	
MHT	50	No	-10	-10	2	7	28	49.0	0.5	1.5	<5	9.5		
MBH	50	No	-10	-10	2	7	28	49.0	0.5	1.5	<5	9.5		
Port Elizabeth har- bour 1975-1987	MHT	No	No	2	7	28	37.0	-	-	-	-	8500	201	
MHT	No	No	No	2	7	28	37.0	-	-	-	-	8500		
MBH	No	No	No	2	7	28	37.0	-	-	-	-	8500		
Bay's Causeway, St. John's, Nam. 1976	MHT	No	No	54.0	-	-	-	-	-	-	-	4.3	30	
MHT	No	No	No	54.0	-	-	-	-	-	-	-	4.3		
MBH	No	No	No	54.0	-	-	-	-	-	-	-	4.3		
Oranjevallei (Innate) 1976-1977	MHT	50	No	9	-	-	-	-	-	-	-	4.3	30	
MHT	50	No	9	-	-	-	-	-	-	-	-	4.3		
MBH	50	No	9	-	-	-	-	-	-	-	-	4.3		
San Ciprian harbour 1978-1979	MHT	Scale	Scale	16	0.2	0.3	28	34.0	0.7	1.0	<5	3.6	3-15	
MHT	Scale	Scale	Scale	16	0.2	0.3	28	34.0	0.7	1.0	<5	3.6		
MHT	Scale	Scale	Scale	16	0.2	0.3	28	34.0	0.7	1.0	<5	3.6		
MBH	Scale	Scale	Scale	16	0.2	0.3	28	34.0	0.7	1.0	<5	3.6		
Konberg (Nocl. Power 1978-1980 St.)	MHT	50	80	5.0	0.8	3	10	50.0	1.0	2.0	<5	7.0	-	
MHT	50	80	5.0	0.8	3	10	50.0	1.0	2.0	<5	7.0	-		
MBH	50	80	5.0	0.8	3	10	50.0	1.0	2.0	<5	7.0	-		
SPT	50	80	5.0	0.8	3	10	50.0	1.0	2.0	<5	7.0	-		
MHT	50	80	5.0	0.8	3	10	50.0	1.0	2.0	<5	7.0	-		
MBH	50	80	5.0	0.8	3	10	50.0	1.0	2.0	<5	7.0	-		
Bay West harbour 1978	MHT	-	-	-	-	-	-	-	-	-	-	-	-	
MHT	-	-	-	-	-	-	-	-	-	-	-	-	-	
MBH	-	-	-	-	-	-	-	-	-	-	-	-	-	
Beach Haven (A.C.L. 1980(?)) Gen. St.)	MHT	35	-	14.6	-	-	-	-	-	-	-	-	-	
MHT	35	-	14.6	-	-	-	-	-	-	-	-	-	-	
MBH	35	-	14.6	-	-	-	-	-	-	-	-	-	-	

*MHT/MBH - Main Washbasin Tank/Head; SPT/MBH - Secondary Breakwater Tank/Head; SP - Shore Protection; MBHIS - MBT Inner Slope
 †Period variation only. ()
 ‡Xero-type damage as indicated in the questionnaire, except for Sines, Kahluli, Bains Causeway and San Ciprian which were obtained from other sources
 ††All days after casting

TABLE 111: SUMMARY OF INCOMPLETE INFORMATION OBTAINED FROM LITERATURE AND PERSONAL CORRESPONDENCE

PROJECT & DETAILS		DESIGN CONDITIONS		STRUCTURE GEOMETRY		DOLOS ARMOURING			HYDRAULIC MODEL TESTS		NUMBER OF DOLOSSE	UNIT COST (U.S. \$)
NAME AND CONSTRUCTION PERIOD	PART *	H(m)	T(s)	Armour slope 1:2	Water depth (m)	Dolos 1:1 ratio	Dolos 1:1 ratio	Underlayer 1:1 ratio	2D scale	3D scale	Design dredge (m)	
Nossel Bay harbour 1967-1969	MBT	3,0		0,67		2,7	0,33	1,8				3 420
	MBH	3,0		0,67		5,4	0,33	2,7				2 630
Cap aux Heules 1970-1970	MBT			0,67	5,5	3,6						7 600
	MBH			0,67	6,1	5,5						4 600
Turton shore 1970 protec.	SP					3,0						
Reef Rumay 1973-1973	MBT			0,67	7,6	3,6	0,30					
	MBH			0,67	8,0	5,5	0,30					
Crescent City 1973	MBT					42,0						
Kuwait harbour 1974	MBT			0,67		1,4	0,36					
	MBH			0,67		0,5						
Jubail harbour 1976	MBH	5,0		0,50	9,0	5,0				28		
Azzawiya harbour 1976-1977	MBT	6,0		0,67	5,0	5,5			30	50		
	MBH	7,0		0,50	6,0	11,0			40	50		
Moanae harbour 1977	MBT			0,5	4,0	1,4				22		
Ghia Tauro harbour 1978	MBT	8,0	11,5	0,6	15,0	15,0	0,32	3,0		58		
	MBH	9,0	11,5	0,5	20,0	30,0		6,0		58		
	SBT	8,0	11,5	0,6	15,0	15,0	0,32	3,0		58		
	SBH	9,0	11,5	0,5	20,0	30,0		6,0		58		
Gms Bay (New design) 1979	MBT	8,5	12,0	0,67	9,7	25,0	0,35			80	1,0	
	MBH	8,5	12,0	0,67	11,7	25,0	0,35			80	1,0	
	MODCB			0,67	20,0	12,4	0,34			80	1,0	
	MBTIS			0,80	12,4	0,33				80	1,0	
St Thomas Rumay 1979(?)	MBT	7,0		0,67	27,0	5,5		2,0				2 400
	MBH	7,0		0,67	27,0	9,1		2,0				
Bonany Bay harbour	MBT	7,8			11,3	13,2	0,32		52		2,0	2 500
Carboneras harbour	MBT	7,0		0,75	16,5	10,0				42		
Gabarus (design) (?)	MBT			0,5	25,0	25,0				42		
Llanddulas shore protec.	SP1	6,0		0,5		4,3	0,32		40			
	SP2	6,0		0,5		1,0	0,32					
Hackay harbour	MB			0,67		8,0						
Rivière aux Renard	MB											
Tristan da Cunha	MBT					2,0						
Saline di Monte- bello	MBT			10,0	15,0	0,32						
	SBT			10,0	15,0	0,32						

* MBT/MBH - Main Breakwater Trunk/Head; SBT/SBH - Secondary Breakwater Trunk/Head; SP - Shore Protection;
MODCB - Modified Caisson Breakwater; MBTIS-MBT Inner Slope

** All depths are to mean sea-level (MSL)

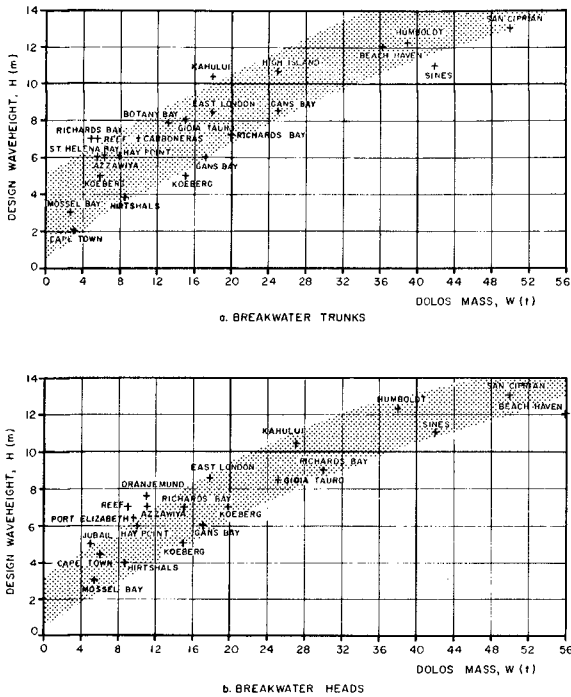


Fig. 2 Correlation of dolos mass with design-wave height

Table II shows that the relative packing densities, ϕ , are generally above $\phi = 1,0$ (ϕ is defined by $N = \phi V^{-2/3}$ where N is the number of dolosse per unit area and V is the dolos volume). They range from 0,73 for Hay Point harbour to 1,47 for Cape Town harbour; well outside the values $\phi = 0,83$ for *light*, 1,00 for *mean* and 1,15 for *dense* packing, as defined by Zwamborn (1978).

Table II also indicates that only two projects were tested using fully irregular waves while a large number of projects were not model-tested at all (only limited irregular-wave tests were done for Sines).

Total breakage of dolosse during manufacture and handling never exceeded 5 per cent and, on average, was between 1 and 2 per cent. Breakages during initial shake-down were also *estimated* to be below 5 per cent, with an average of 1 to 2 per cent.

Apart from at Sines, very *little general damage* has been reported on dolos structures (the Sines breakwater was built in very deep water, see Figure 1). Storm damage occurred at Baie Comeau where deep water is close to the breakwater, while the damage at Gans Bay was concentrated at the junction between the rubble mound and the vertical wall sections of the breakwater.

It may, therefore, be *concluded* that the approximately 173 000 dolosse of various sizes have generally performed satisfactorily in water depths of up to about 20 m.

A correlation of dolos mass versus the cost, in U.S. dollars, for one unit is shown in Figure 3.

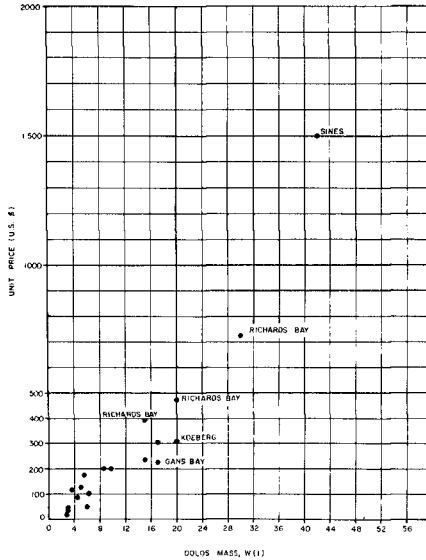


Fig. 3 Unit cost, in U.S. \$ versus dolos mass

2.2. Dolos Research

Most of the research carried out on dolosse was applied research, that is, specific projects were model tested for stability. Details of these model tests are given in Tables II and III.

Basic model test results on dolos stability have been reported by Merrifield and Zwamborn (1966), Ouellet (1972), Foster and Gordon (1973), Brorsen (1977), Carver and Davidson (1977 and 1978) and Zwamborn (1978).

The high stability factors found in the original tests (minimum $K_D \approx 25$ for 2 per cent damage) were confirmed by Ouellet ($K_D \approx 25$ both for regular and irregular waves), Carver and Davidson ($K_D \approx 31$ for non-breaking waves) and Zwamborn (average $K_D \approx 24$ based on 2 per cent displaced units). However, there are large variations in individual tests results ($15 < K_D < 40$ for 2 per cent displacement) and in test conditions as well as damage criteria, making direct comparisons between test results of different laboratories, at least, questionable. Inconsistency in dolos packing densities and corresponding layer thicknesses were also found to be responsible for large differences (Zwamborn, 1978).

Clear definitions for packing densities have therefore been proposed and *standardization* of this aspect to ensure compatibility of test results is being pursued (Zwamborn, 1978 and 1980).

In the original model tests, dolosse which were *seen* to be rocking, were also included in the total damage because it was considered that these units would probably break (Merrifield and Zwamborn, 1966). However, insufficient attention has been given to the structural strength of armour units, in general, and to that of dolosse, in particular, since that time (Magoon and Baird, 1977 and Brindley, 1977).

3. PRESENT SITUATION

3.1. Damage to Dolos Structures

Unfortunately, the amount of data on the performance of the various structures is extremely limited and damage figures are often only *estimates* (Table II).

It has been reported that there has been moderate damage to the 4,5 t and 7,3 t dolos armour of the Baie Comeau breakwater (Québec), and minor damage (10 per cent) to the 42 t Crescent City dolosse and to the 38/39 t Humboldt breakwater dolos armour (Edge and Magoon, 1979).

A detailed above- and underwater survey of the main *trunk* section of the Gans Bay breakwater provided *quantitative* data on the performance of the 17,1 t dolos (Bosman and Zoutendyk, 1979). The survey showed a total breakage of about 10 per cent but shank breakages amounted to only 0 to 2 per cent. This breakwater was built some nine years ago and wave heights of up to the local design wave height of 8,5 m have been recorded on various occasions during this period.

The partial failure of and major damage to the 42 t dolos armour of the Sines breakwater during a near-design storm in February, 1978, is by far, the most important (Figure 4). From a detailed analysis of the causes of the damage Zwamborn (1979) concluded that failure of the armour was caused mainly by:

- (i) *large and long waves* in the spectrum which, because of the great depth of water in front of the breakwater (Figure 1), were not reduced in height by breaking;
- (ii) wave concentration due to *refraction*;
- (iii) *breakage* of dolosse caused by excessive movement of the units during the storm.



Fig. 4 Peak storm waves, Berth No. 1, 26 February 1978

The damage to the Sines breakwater came as a shock because the design wave height ($H_s = 11$ m) was not exceeded during the storm while conventional model tests, including irregular wave tests, had indicated that the dolos armour would be stable under wave conditions up to the design wave height.

Surveys after the storm, however, showed that dolos armour had been removed completely over a distance of approximately 0,5 km of the 2 km long breakwater, resulting in the collapse in the superstructure of two sections, 150 and 300 m long, while a significant percentage of the dolosse in the non-failed areas had been broken and moved down the slope. Although the incident significant wave height during the storm did not exceed 10 m, waves of maximum height of up to about 17 m must have occurred, and these, due to refraction, may have increased in height to 20 m at certain points along the breakwater. Combined with peak energy periods of 18 to 20 s these large waves had lifted single or clusters of dolosse out of the slope and when these waves retracked, the dolosse had either rolled down the slope or had dropped back and probably broken on impact.

The Sines disaster highlighted again the importance of *reliable field data*. For most damaged dolos structures, available information is very incomplete, making it difficult to draw definite conclusions regarding the underlying causes. Much work was done *after* the Sines failure to establish the causes of the damage but uncertainties in the final conclusions will remain because of, *inter alia*, the lack of such basic data as 'as-built' surveys of the armour and wave records during the storm.

3.2. Recent Research

In the past, differences in dolos packing densities were largely responsible for differences in reported stability factors (K_D).

Carver and Davidson (1978), using data from different laboratories, suggested that the K_D value of dolosse increases with relative packing density, ϕ . They considered ϕ values from 0,6 to 1,0 with corresponding K_D values from 16 to 38 (Figure 5).

Zwamborn (1978) has suggested that there should be an *optimum* packing density for dolosse, namely, $\phi = 0,87 \approx 0,9$ when the layer thickness is equal to the dolos height, because such conditions would result in maximum interlocking.

A series of comparative model tests was therefore carried out in a 3 m wide regular-wave flume using relative packing densities $\phi = 0,65; 0,83; 0,87; 1,00; 1,15$ and 1,50. Results of the tests, Figure 5, show the mean K_D values, corresponding to different ϕ values for 2 per cent damage (displaced units).

The data reveal some interesting trends, namely,

- (i) an increase in stability from low ϕ values to $\phi = 0,87$, which corresponds to the optimum double-layer packing ($\phi \approx 0,9$);
- (ii) reduced stability for $\phi = 1,15$;
- (iii) increased stability for $\phi = 1,50$, which is close to that for a four-layer system ($\phi \approx 1,7$).

Figure 5 shows the results of the tests as well as the extreme values, from which it is clear that the results can, at the most, show only general trends. The tests were done under closely *controlled conditions*, but the variation in individual test results was nevertheless very large, which is worth noting. Notwithstanding these large variations the general trend is displayed, not only by the mean, but also by the extreme values.

In practical terms it means that one should aim at a packing density of $\phi = 0,9$ but, because it will be virtually impossible to achieve the ideal packing in the field, it would be better to use $\phi = 1,0$ as a minimum *average* relative packing density for the design. Even if $\phi = 0,9$ is used, it would be unwise to adopt a *mean* value of K_D greater than about 24 (Zwamborn, 1978) or a *minimum* K_D factor greater than about 16.

Differences in stability, particularly for the lower damage levels, are also caused by *differences in packing*. Because the stability of the dolos armour depends in part on the degree of interlocking of the units, randomly-placed units will, inherently, show considerable variations in the stability of the uppermost layer of dolosse. This was shown effectively in recent tests carried out by Price (1978) who measured the forces required to lift different blocks of various types off an armour slope. These tests also indicated an optimum slope for dolosse of between 1 in 1,5 and 1 in 2,5 for a static force normal to the armour slope which was applied in the tests.

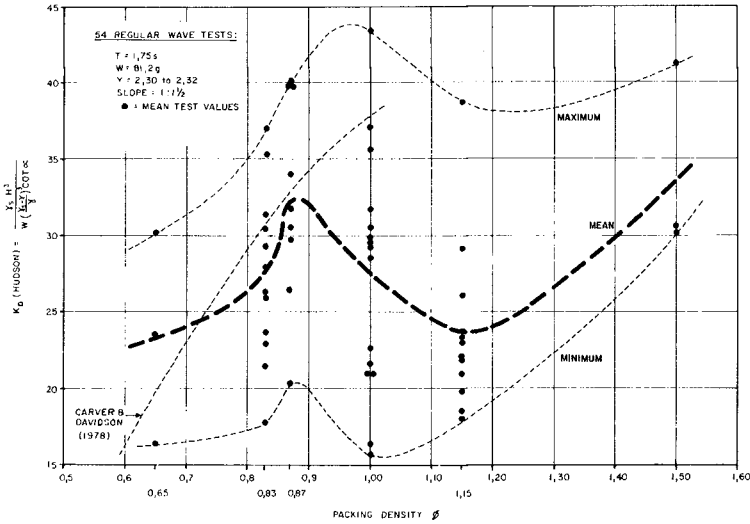


Fig. 5 Dolos stability versus packing density - test results for 2 per cent damage

Damage to armouring is related normally only to the percentage of displaced units, mainly because of the difficulty in measuring accurately the percentage of moving and rocking units. A time-lapse cine technique, however, makes it possible to get reliable data on *continuously* and *intermittently rocking* units. This provides a more accurate picture of the damage to the armouring. It was found, in regular-wave model tests, that the extent of damage based on the number of displaced and rocking dolosse was about *twice* that derived from only the number of displaced units (Zwamborn, 1978). This applies to the lower damage levels (2 per cent displacement); for the higher damage levels, the increase was much smaller.

If the design of a dolos structure is to be safe, knowledge of the percentage of rocking dolosse is essential; this knowledge is also an important factor in understanding the structural failure of dolosse.

An attempt was made by Mansard and Ploeg (1978), to reproduce dolos breakage by means of a model. A breaking plane was introduced in the shank of the model dolosse which had a linearly-scaled tensile strength, so that the units would break under wave action. The results showed clearly the effect on stability of dolos breakage, but this technique needs further development because a single breaking plane does not simulate accurately the *initiation of breakage*, which should form the basis of safe design.

Much of this work was initiated as the result of, or intensified after, the Sines disaster, which, together with the preceding (1976) damage to the Bilbao (35 m depth, 65 t cubes) breakwater in Spain (Tørum *et al.*, 1979) emphasized the lack of knowledge of representative *design-wave conditions* and the inadequacy of present *model-test techniques*.

Successful dolos-armoured structures were built in relatively shallow water which masked possible shortcomings in the designs. Since most stability factors (K_D) are based on tests done with relatively shallow conditions in which regular waves represent natural conditions reasonably well, they *cannot* be applied to structures built in deep water. Moreover, structural damage to artificial armour units, particularly those of the interlocking type such as the dolos, must be taken into account in the design stage.

4. FUTURE APPLICATIONS

4.1. Shallow- Versus Deep-Water Structures

There is little doubt that dolosse provide an effective and economic means for protecting many small and medium-size coastal structures, although more attention should, in future, be given to the effect of rocking motions of *all* artificial armour units, particularly when the design-wave height is not depth-limited. Rocking can be reduced by using *heavier units* which, in many instances, could still provide an optimum solution and, in some cases, may even be more economical.

For major structures in *deep* water realistic and representative *design-wave conditions* will have to be adopted. It must be realized that, if a Rayleigh wave-height distribution is assumed, 5 per cent of the waves will exceed $1,22 H_s$ and 1 per cent $1,52 H_s$ and, when there is no depth limitation, these waves will attack the breakwater armour.

Figure 6 shows curves for the reserve stability for non-breaking dolosse, based on regular wave tests at a slope of 1 in 1,5 (Zwamborn, 1978), and a Rayleigh wave-height distribution. This figure shows that a dolos armour designed on the basis of 2 per cent damage for a regular wave of height H_s , may fail when the wave height is barely 25 per cent higher than the design-wave height. In the case of breakable units, the reserve stability will be even less. As may be seen from other data plotted in Figure 6, which is also based on tests with regular waves but using a slightly steeper slope of 1 in 1,33 (Paape and Walter, 1962), this problem is not unique to dolosse.

The obvious answer is to *increase* the unit *mass*, for instance by basing the initial design on H_5 or even H_1 instead of H_s ($H_s = H_{1,3,5}$). The design must then be carefully model tested, using realistic waves (e.g. time series) up to and well in excess of the design wave condition. Both displaced and rocking units should be counted and, when deciding on an acceptable percentage damage, possible cumulative effects must also be taken into account.

When the mass of dolosse is increased, however, tensile stresses should increase linearly with the height of the dolos, if the basic shape remains the same (Figure 7). This applies to above-water conditions (free-fall). If the dolosse are under water, drag resistance will reduce impact forces and under-water stresses will therefore increase with a lower power of the dolos height, say, a power of 0,5 (Figure 7).

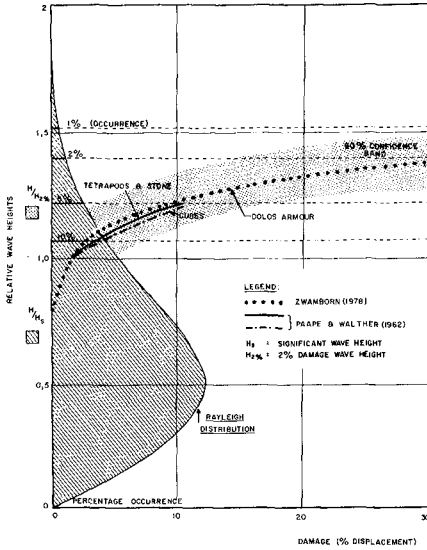


Fig. 6 Dolos reserve stability

To reduce the stresses in the larger dolosse, the dolos *waist thickness* could be *increased*, for instance, in accordance with the earlier suggested relationship $r = 0,34 \sqrt[6]{W/20}$, where r is the waist ratio and W the dolos mass (t) (Zwamborn and Beute, 1972). This formula is based on the assumption that a 20 t dolos with a waist ratio of 0,34 is sufficiently strong to avoid breakage during design load conditions, an assumption which is supported by considerable prototype evidence. Figure 7 shows the effect of the increased waist ratio. If these dolosse are under water, the stresses do not increase with dolos mass and if they are above water, the increase is drastically reduced. Waist ratios of up to about 0,4 do not materially affect the shape of the dolos (Figure 8) but their hydraulic efficiency may be reduced at the higher r values (model tests with dolosse of waist ratios from 0,27 to 0,35 showed no measurable difference in porosity, layer thickness and stability; Zwamborn and Beute, 1972 and Zwamborn, 1978).

Another method of increasing the strength of large dolosse is to *increase* their *tensile strength*, either by using better quality concrete, or by using, for example, steel fibres. Figure 7 shows that with an increase in tensile strength of 10 to 20 per cent, the dolos size could be increased safely by, at least, a factor of two. The original 20 t dolosse used at

East London had a rupture strength $< 3,5$ MPa. If these dolosse are accepted as being sufficiently strong, which they appear to be, 40 t dolosse with $r = 0,38$ would also be satisfactory, provided a minimum rupture strength of about 4 MPa could be achieved (Figure 7).

Conventional steel-reinforced dolosse were used at Humboldt Bay, Kahului (Hawaii) and for the provisional repair work at Sines. This type of reinforcing is, however, neither very effective (Figure 9), nor economical. For example, a 0,6 per cent reinforcing (by volume) used at Sines resulted in a 20 to 25 per cent increase in strength while the cost of a 42 t dolos increased by 50 per cent. There is also the problem of corrosion, and central reinforcing, using for instance, scrap rails may be more attractive (Standish-White and Zwamborn, 1978).

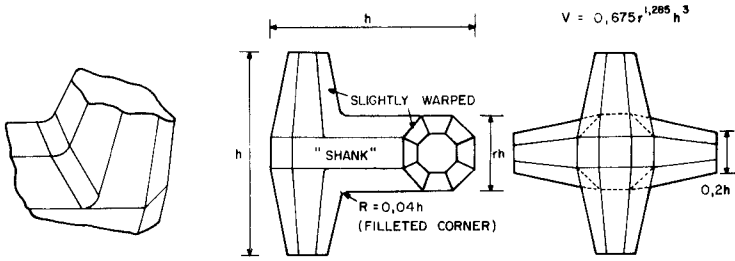
This paper deals with past, present and possible future use of dolosse. It goes without saying that particularly for deep-water conditions, *alternative structures* should also be considered. Moreover, because deep-water design conditions are, inherently, ill-defined the adopted structure should have considerable reserve stability, that is, complete failure should not occur with higher than design waves.

4.2. Research Needs

In the above, problems relating to deep-water breakwater structures have been discussed and some practical suggestions made to allow for the typical deep-water effects in the design of dolos structures.

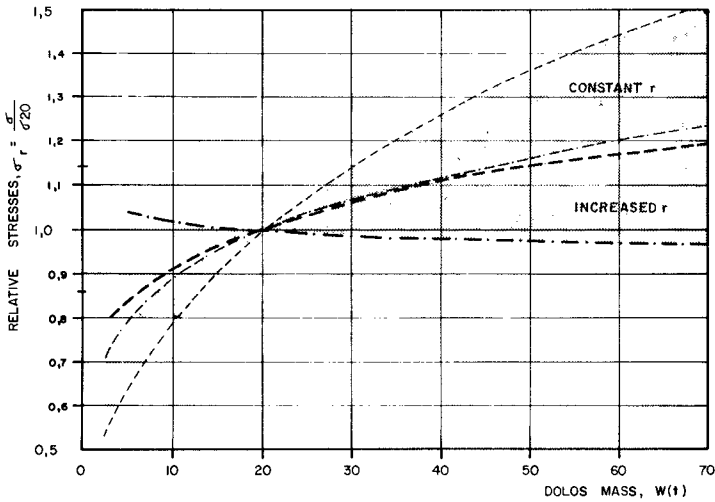
After the Sines disaster, designs will, however, tend to be conservative and there is thus an urgent need for more research to ensure *safe* and yet *economic designs*, namely:

- (i) more information is required on realistic design wave conditions and representative reproduction of these conditions in, preferably, three-dimensional models;
- (ii) research into the structural behaviour, under extreme load conditions, of artificial armour units, in general, and dolosse, in particular, is needed; such studies should include surveys of existing dolos structures (Bosman and Zoutendyk, 1979), hydraulic model tests to determine the loads on the units, stress analysis for these load conditions and structural tests (Tait and Mills, 1980) to determine acceptable degrees of movements;
- (iii) for deep-water conditions, structures with a high reserve stability should be developed;
- (iv) model test techniques should be investigated further and standardized as far as possible to ensure compatibility between test results of different laboratories (Zwamborn, 1980).



FILLETED CORNER DETAIL

a. BASIC DOLOS SHAPE



b. STRESS INCREASES WITH DOLOS MASS

LEGEND

- $r = \text{CONSTANT}$ (ABOVE WATER)
- $r = \text{CONSTANT}$ (BELOW WATER)
- INCREASED WAIST RATIO (ABOVE WATER)
- INCREASED WAIST RATIO (BELOW WATER)

INCREASED WAIST RATIO:
 $r = 0,34 \sqrt{\frac{W}{20}}$

Fig 7 Basic dolos shape and effect of increased waist ratio

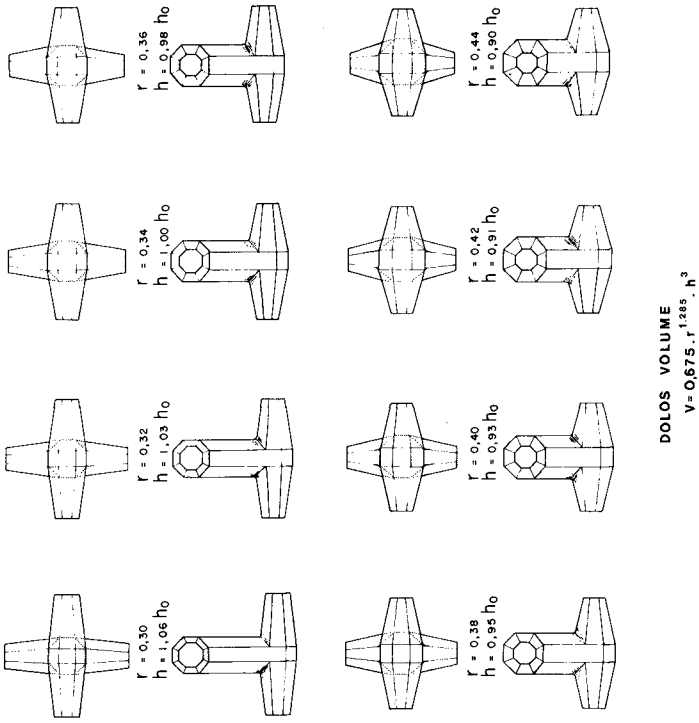


Fig. 8 Constant volume dolosse with various waist ratios



a. Typical fluke breakage



b. Broken reinforced dolos

Fig. 9 Sines breakwater, damage to unreinforced and reinforced 42 t dolosse

ACKNOWLEDGEMENTS

The assistance from various authorities and persons who completed the dolos questionnaire is hereby gratefully acknowledged. The photograph used for Figure 4 has been made available by Messrs. Condotte d'Acqua.

REFERENCES

- BOSMAN, D.E. and P.J. ZOUTENDYK (1979). Dolos survey - pilot study. CSIR Report, Sea 7918, Stellenbosch.
- BRINDLEY, J.S. (1977). Rubble mound breakwaters - state of the art. Dock and Harb. Auth., Vol. LVII, No. 678.
- BROSEN, *et al* (1974). Stability of dolos slopes. Bulletin No. 9, Aalborg Universitetscenter, Denmark.
- CARVER, R.D. and D.D. DAVIDSON (1977). Dolos armor units used on rubble-mound breakwater trunks subjected to non-breaking waves with no overtopping. Techn. Report H-77-19, WES, Vickburg.
- CARVER, R.D. and D.D. DAVIDSON (1978). Dolos-armoured breakwaters: special considerations. Proc. XVth Cost. Eng. Conf., Hamburg.
- EDGE, B.L. and O.T. MAGOON (1979). A review of recent damages to coastal structures. Proc. Coastal Structures 79, ASCE Speciality Conference, Alexandria, Virginia.
- FOSTER, D.N. and A.D. GORDON (1973). Stability of armour units against breaking waves. Proc. Inst Austr. Conf. Coast. Eng. Dyn. of Coast Zone, Inst. of Eng., Australia.
- MAGOON, O. and W.F. BAIRD (1977). Breakage of breakwater armour units. Proc. Symp. on Design of Rubble Mound Breakwaters, Isle of Wight.
- MANSARD, E.P.D. and J. PLOEG (1978). Model tests of Sines breakwater. Report LTR-HY-67, NRC, Ottawa.
- MERRIFIELD, E.M. and J.A. ZWAMBORN (1966). The economic value of a new breakwater armour unit 'dolos'. Proc. Xth Coast. Eng. Conf., Tokyo.
- OUELLET, Y. (1972). Effects of irregular wave trains on rubble-mound breakwaters. ASCE Journ., Waterways, Harbours and Coast. Eng. Div., Vol. 98, No. WW 1.
- PRICE, W.A. (1978). Static stability of rubble mound breakwaters. Report, HRU, Wallingford (not published).

STANDISH-WHITE, D.W. and J.A. ZWAMBORN (1978). Problems of design and construction of an offshore seawater intake. Proc. XVI Coast. Eng. Conf., Hamburg.

TAIT, R.B. and R.D.W.B. MILLS. An investigation into the material limitations of breakwater dolosse. SANECOR Newsletter, No. 11, Stellenbosch.

TØRUM, A. *et al* (1979). Reliability of breakwater model tests. Proc. Coastal Structures 79, ASCE Speciality Conference, Alexandria, Virginia.

VONK, A.P.M. (1976). Breakwater armour units - influence of packing density and porosity on stability. Proc. Marine/Fresh Water Conference, S 22, Port Elizabeth.

WHILLOCK, A.F. (1977). Stability of dolos blocks under oblique wave attack. Report No. IT 159, HRS, Wallingford.

ZWAMBORN, J.A. (1978). Dolos packing density and effect of relative block density. Proc. XVth Coast. Eng. Conf., Hamburg.

ZWAMBORN, J.A. (1979). Analysis of causes of damage to Sines breakwater. Proc. Coastal Structures 79, ASCE Speciality Conference, Alexandria, Virginia.

ZWAMBORN, J.A. (1980). Measuring techniques, dolos packing density and effect of relative block density. CSIR Research Report 378.

ZWAMBORN, J.A. and J. BEUTE (1972). Stability of dolos armour units. ECOR Symposium, S 71, Stellenbosch.

A DETACHED BREAKWATER SYSTEM FOR BEACH PROTECTION

by James R. Walker¹, Denton Clark², and Joan Pope³

SUMMARY

Three segmented, detached breakwaters were constructed in the fall of 1977 at Lakeview Park, Ohio, on Lake Erie, to protect a beachfill to be used for recreation and shore protection. This paper documents the design procedures which established the configuration of the breakwaters and the beachfill, and determined the need for a terminal groin. The beachfill has been monitored by aerial photography and bathymetric profiling. During the second year, a storm of near design intensity generated severe waves concurrently with high Lake levels and eroded the updrift beach; however, the initial beach configuration was partially restored by natural processes during the following summer season. The project has functioned well, with very little loss of sand from the system and without adverse impacts on the downdrift coast.

INTRODUCTION

Lakeview Park is a lakeside recreational area in Lorain, Ohio, on the southern shore of Lake Erie (figure 1). The Park provides 1,500 feet of beach serving the recreational needs of north central Ohio. Prior to implementation of this project, the beach had eroded due to high Lake levels and an inadequate supply of littoral drift.

Studies were conducted in 1974 to plan and design a beach-restoration project within the Park boundaries to satisfy the recreational needs of the tributary area. The study was undertaken at the request of the City of Lorain and was authorized by Congress. Alternative designs included groin fields and artificial headlands. An existing groin field at the project site had not worked well, although properly designed groins and heavy nourishment may have retained a beach. The potential for offshore loss of littoral drift with a groin field would result in innumerable greater annual costs for groin-field shore protection than for protection with offshore breakwaters. Artificial headlands (see Silvester, 1972) were a relatively new concept during the planning process. Although the headland plan would probably have functioned properly, it would have affected reaches of shoreline both up- and downdrift of the project. These up- and downdrift shorelines are privately owned. The Federal

-
1. Chief Coastal Engineer, Ph.D, P.E., M.ASCE, Moffatt & Nichol, Engineers, Long Beach, California
 2. Chief Coastal Engineering, Buffalo District, Corps of Engineers, Buffalo, New York
 3. Coastal Geologist, SEPM, M.A.A.A.S. Buffalo District, Corps of Engineers, Buffalo, New York

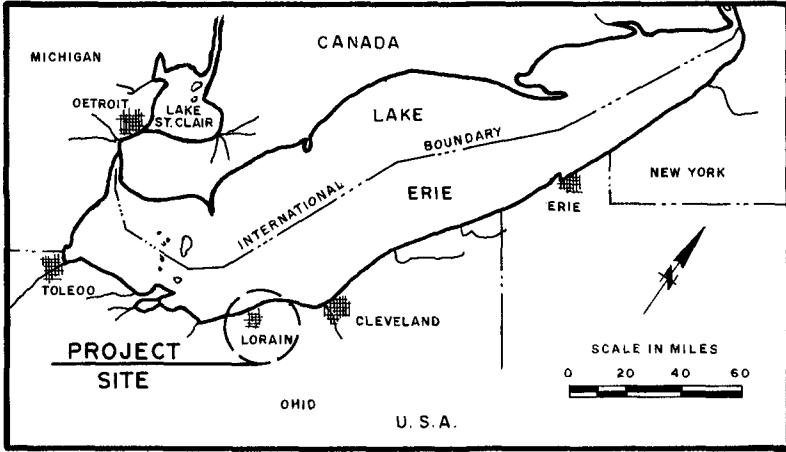


FIGURE 1: VICINITY MAP

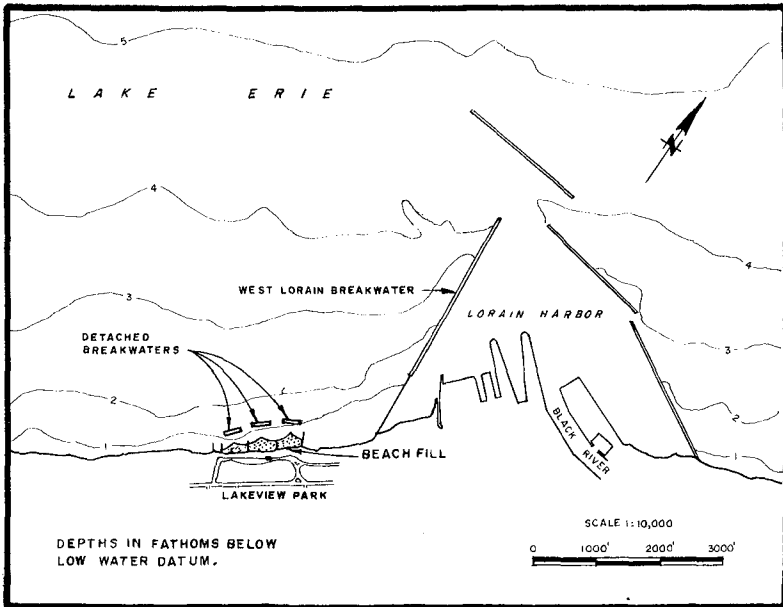


FIGURE 2: AREA MAP

Government does not cost-share in developing recreational beaches for protecting private property.

The design procedures presented herein are therefore state-of-the-art as of 1974 for construction of a small project. The design was done in less than a year without the use of mathematical or hydraulic models, which were not available during the design period. The project construction was completed in October 1977 and a post-construction monitoring program was initiated.

DESCRIPTION OF PROJECT SITE

Location

The project site is located in Lakeview Park in the city of Lorain, Ohio, which is 25 miles west of Cleveland. Lakeview Park is a lakeside recreational facility situated $\frac{1}{2}$ mile west of Lorain Harbor as shown in figure 2. Lorain Harbor has several breakwaters that extend 5000 feet lakeward from shore. The shoreline in the vicinity of the project site comprises both heavily protected and eroding glacial till and shale bluffs on reaches to the west. The preproject site had six existing groins of various construction, ranging in length from 70 feet to 150 feet. The groins which did not represent a consistent design, were not long enough to trap the meager littoral transport in sufficient quantity to provide an adequate recreational beach, nor were they high enough to prevent sand from moving over them during extremely high Lake levels.

Geology

Lake bottom surveys indicated the bottom 300 feet offshore is 8 feet below low water datum (LWD) and comprises a 12- to 18-inch stratum of medium to coarse sand with gravel and traces of laminae of silty clay. Underlying this stratum is 2 to 12 feet of stiff-to-hard, gray, silty clay. Shale bedrock underlies these strata.

Lake Levels

Water levels on Lake Erie vary from year to year and from month to month, and fluctuate on an hourly basis. The yearly variations are due to long-term climatic cycles. The seasonal variations consist of high levels in the spring and early summer and low levels in the winter. Short-term hourly fluctuations are caused by local meteorological disturbances. Astronomical tides are negligible. Low water datum, LWD=0, is 568.6 feet above the International Great Lakes Datum, 1955, (IGLD) based on mean water level at Fathers Point, Quebec. The highest recorded monthly mean Lake level was 573.5 feet and the lowest was 567.5 feet. The monthly mean was 570.4 feet from 1960 to 1970. The greatest annual fluctuation of monthly mean lake level was 2.75 feet. A 1.5-foot storm surge has a recurrence interval of 1 year.

The design water level with a statistical recurrence period of 20 years is 5.5 feet above LWD and comprises a 2.0-foot storm surge and 3.5-foot LWD monthly mean lake level.

Waves

The project site is directly exposed to fetches from the west clockwise through the north. The fetch length to the west is 36 miles and that to the north is 55 miles. The fetches in the Lake for directions east of north are 150 miles; however, the Lorain Harbor breakwaters shelter the project site from direct northeasterly wave attack. The wave climate used for the design of structural features was done by hindcasts that used a 24-year wind record taken at Cleveland. Calculation of littoral transport potential was derived from refraction, shoaling, and diffraction transformations of a 3-year hindcast of waves on Lake Erie by Saville (1953). The published data were for a station 28 miles east of Lorain; therefore, appropriate corrections were made to reflect the differences in fetches between the two sites. The hindcast data were corrected for effective fetches and a 44-foot Lake depth over the generating area. The wave heights approaching the project site range up to 8 feet annually, and periods range up to 7 seconds. The wave climate for littoral transport calculation assumed waves arrived at the shore only during the typical ice-free period from April through November. The 20-year recurrence design wave was from the northwest with a height of 10 feet and a period of 8 seconds.

Littoral Transport Analysis

Analysis of the potential for littoral transport is a key element in designing beach-stabilizing structures. The analysis was conducted by reviewing historical aerial photographs, site observations, and calculations of the potential littoral transport rate by wave-energy flux methods.

The existing preproject beach at Lakeview Park comprises a medium sand with traces of gravel, some of which is debris derived from remnants of decomposing updrift to the west shore-protection structures. The beach slope is 1 on 12 above water and 1 on 18 below water. Immediately west of the project site, the shoreline comprises eroding shale bluffs. Glacial till and decomposing bulkheads on the bluffs are a source of littoral drift. The west Lorain Harbor breakwater, 1,500 feet east of the project site, has been accumulating a fillet of sand on its west side at a rate of between 5,000 and 8,000 cubic yards per year. The existing groins in the project site had trapped some sediment out of the littoral system, but material apparently was bypassing them to deposit in the fillet at the west Lorain Harbor breakwater.

The general trend of the shoreline is an orientation of a 58-degree relative to north. The analysis of aerial photographs taken in 1948, 1956, 1968, and 1974 indicates that the preproject groin

field trapped fillets aligned on 50- to 55-degree azimuths. This indicates a west- to-east littoral transport.

The potential littoral transport rate was estimated by determining the longshore component of wave-energy flux. This was accomplished by transforming the incident waves to their breaking properties of height and direction of propagation. The energy flux is given by:

$$P = \frac{\rho g}{8} H_b^2 C \cos \alpha_b$$

where ρ is the density of water;

g is the acceleration due to gravity;

H_b is the breaking wave height;

α_b is the angle of the wave crest relative to depth contours at breaking; and

C is the wave celerity.

The incident deep water wave climate was transformed to the project site by diffraction about the Lorain Harbor breakwaters and by refraction and shoaling analyses. The sheltering effect of the Lorain Harbor breakwaters decreases with distance to the west. This is illustrated in figure 3, which plots the total and longshore components of energy flux as a function of distance from the west Lorain Harbor breakwater. The plot indicates a net eastward littoral transport at the project site; however, the net transport reverses to the west 1,500 feet west of the site. Furthermore, the total energy flux increases with an increase in distance from east to west. This clearly illustrates the influence of the Lorain Harbor breakwaters. The potential littoral transport rate is estimated by multiplying the longshore energy flux by an empirical coefficient described in the Shore Protection Manual (1974), where the potential longshore transport rate (Q_s) is

$$Q_s = 7.5 \times 10^3 P_{1s}$$

where Q_s is in cubic yards per year and

$$P_{1s} = P \sin \alpha_b \text{ (where } P_{1s} \text{ is the longshore component of energy flux in foot-pounds per second per foot of beach.)}$$

The potential longshore rate is 21,500 cubic yards per year to the east project site. This potential is not realized due to an inadequate supply of littoral drift. The 5,000 to 8,000 cubic yards per year that is accreting in the west Lorain Harbor-breakwater fillet is a more reliable indication of the actual transport rate. Figure 4 shows the distribution of total energy flux and the longshore component of energy flux at the project site. The distribution of wave-energy flux indicates a well-balanced potential for littoral

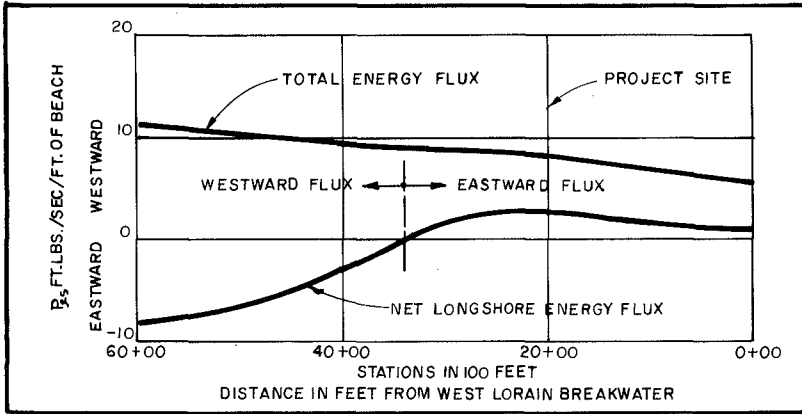


FIGURE 3: WAVE ENERGY FLUX ALONG COASTLINE

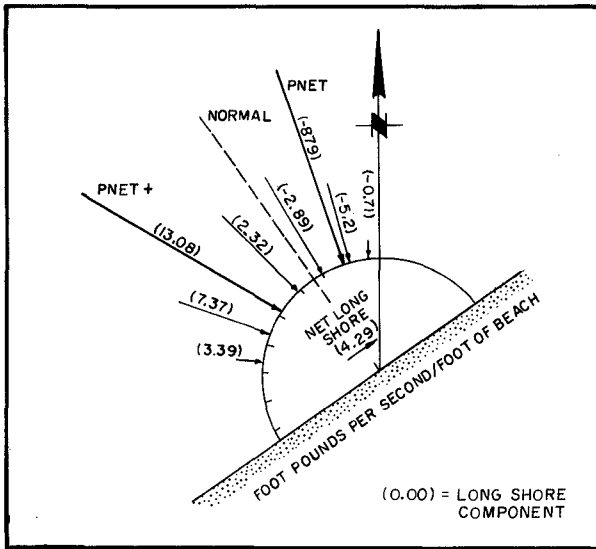


FIGURE 4: ENERGY-FLUX P_{25} AT THE PROJECT SITE

transport; i.e., the tendency for reversals in littoral transport due to waves from the east is nearly two-thirds of the potential transport for waves from the west. The sheltering effect of the Lorain breakwater therefore is partially offset by the greater fetches to the east.

PROJECT DESIGN

Alternative Studies

The primary purpose of the project is to provide a recreational beach and protect the Park from erosion. Beach-protection structures should not increase the erosion of up- and downdrift properties. This is a Federally sponsored project, which can protect only publicly owned lands. This ruled out the use of a massive beachfill or a large groin field extending to the Lorain breakwater. Artificial headlands would also affect a larger segment of shoreline than just the Park. Several groin fields of various lengths and spacing were considered; however, detached breakwaters were selected because they would decrease offshore sand movement. Each alternative considered would require imported sand to nourish and maintain the beach.

Plan Description

The detached-breakwater configuration is shown in figure 5. Three detached rubble-mound breakwaters, each 250 feet long, are arranged along a flat-arc alignment convex lakeward in water with a depth of -8 feet LWD. The breakwaters are spaced 160 feet apart. The west end of the west breakwater is 450 feet offshore and the east end of the east breakwater is 500 feet offshore. The breakwaters protect 1,500 feet of shoreline. An existing groin on the east side of the project site was increased in elevation and extended from 150 to 350 feet offshore. The crest of one of the groins on the west side of the park was also raised 2 feet to maintain the updrift beach profile during periods of high Lake levels. A medium-sand beachfill with an average of 200 feet, was placed behind the breakwaters. The initial beachfill of 110,000 cubic yards was placed on a 1 on 5 slope, with a berm elevation of +8 feet LWD. The project was completed in October 1977 at a cost of about \$1,700,000. The Federal Government paid for 70 percent of the construction costs and the local government paid for 30 percent. The planning document also allowed for periodic nourishment, at a rate of 5,000 cubic yards per year, to be placed on the beach as nourishment, or on the downdrift beach if the project induces downdrift erosion.

Design Analysis

Several configurations of detached breakwaters were investigated. The primary function of the breakwater is to regulate incident waves and to reduce offshore littoral transport. For initial design, the breakwaters were assumed to be situated in constant water depth, to be impermeable, and to not be overtopped. The shoreline was assumed

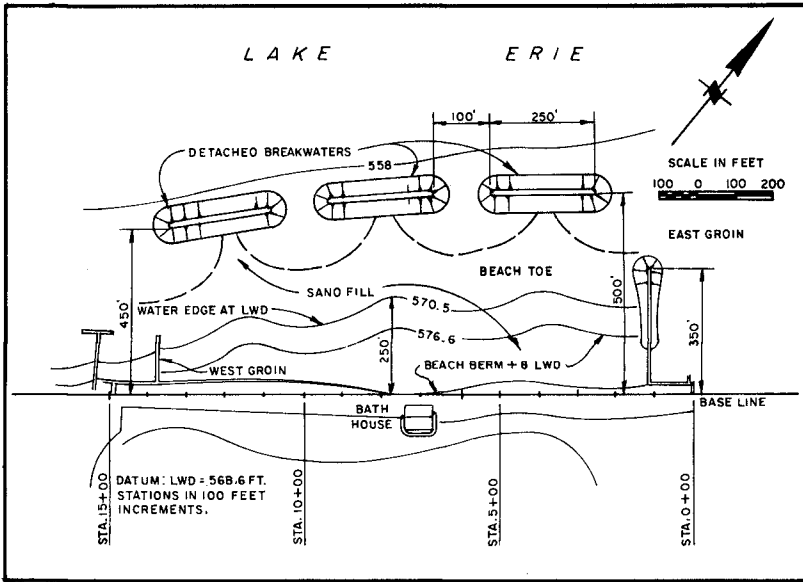


FIGURE 5: PLAN OF IMPROVEMENTS

to adjust to equilibrium in response to the predominant waves. The shoreline planform was assumed to be in equilibrium when the shoreline is coincident with the transformed wave crests; otherwise, waves arriving at an angle to the shore would induce longshore transport. The predominant wave was selected as being the wave from the direction associated with the net direction of energy flux. Figure 6 shows one of the simple diffraction analyses used in the design analysis. The heavy lines of variable thickness are wave crests that are weighted according to the diffraction coefficient. The resultant shoreline is shown to generally parallel the incident wave crests; however, the salients are more accentuated to account for refraction effects. A salient is located near the center of the geometric shadow of each breakwater. The apex of the salient shifts in response to incident waves. The updrift shoreline (to the west) must have continuity with the existing shoreline. The downdrift shoreline, similarly, must have continuity with the project shoreline. This was not feasible; therefore, the existing east groin was extended in length from 150 feet to 350 feet. The toe of the beach at the east groin had to intersect the existing Lake bottom at the groin head as shown in figure 7 to stabilize the project beach with a desired 200-foot width.

The salient in the geometric shadow of each breakwater is formed by littoral drift being transported into the sheltered region by diffracted wave crests. If the breakwaters are too close to shore, or are too long, the shadow region becomes too effective a barrier, and insufficient wave energy is left for littoral transport. The salient continues to grow and eventually becomes a tombolo. Once a tombolo is formed, natural nourishment of the downdrift beaches is denied, increasing the tendency of these beaches to erode. Because this is naturally an eroding reach of shoreline with a limited supply of littoral drift, a considerable period of downdrift starvation would be experienced before tombolo formation and before natural bypassing would continue. Therefore, formation of a tombolo was not considered desirable.

A tombolo can be prevented from forming by designing the breakwater lengths and distances offshore such that variation in directions of incident waves will allow sufficient energy to enter the shadow to transport littoral drift. The variations in wave attack were incorporated into the design by considering the net westerly and net easterly directions of energy flux, as shown in figure 4. The net easterly and westerly components each represent a weighted, long-term average potential to transport littoral drift. The predominant waves move sand toward the salients. If the variations in wave energy from various directions are adequate to move appreciable material past the salients, no tombolos should form.

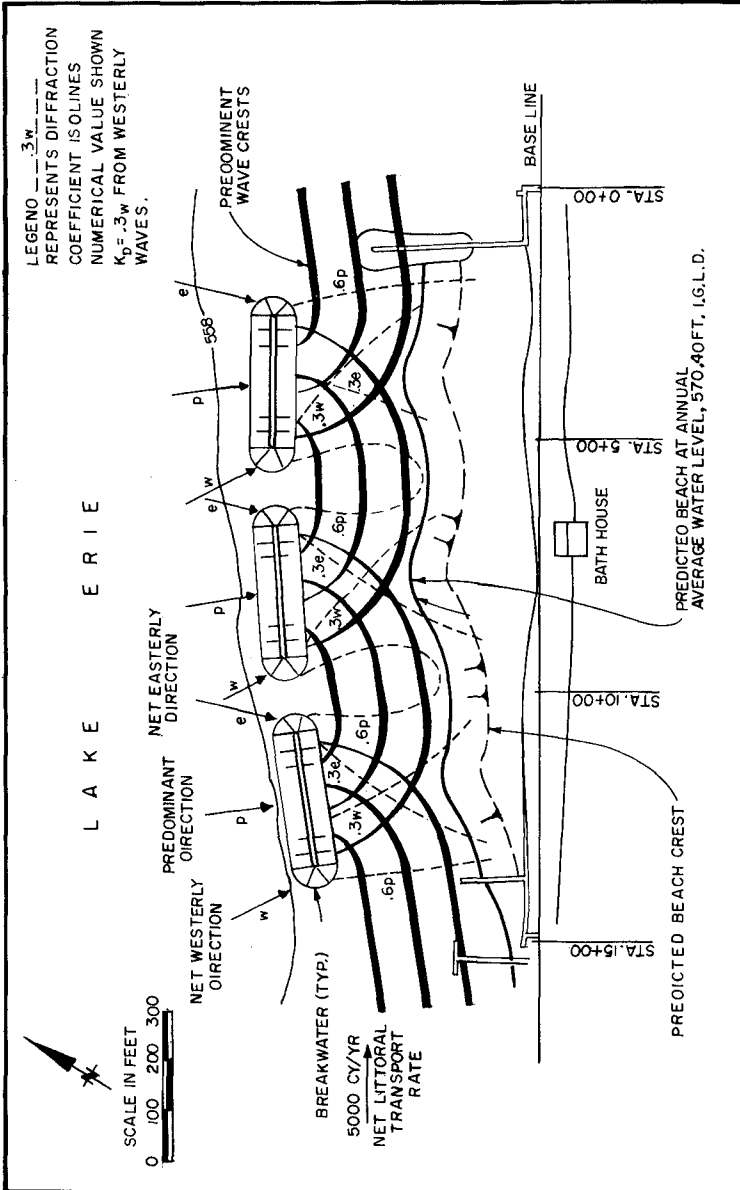


FIGURE 6: DIFFRACTION ANALYSIS

The amount of wave energy required to prevent tombolo formation is not accurately known; however, observations of several detached breakwaters in southern California by James Dunham^{1/}, led to the hypothesis that if the shoreline were landward of the intersection of the diffraction coefficient (K_D) isolines where $K_D = 0.3$ for the easterly and westerly wave components derived from the energy-flux analysis, a tombolo would not form. A case-in-point is the Venice, California, detached breakwater. This breakwater, built about 1902, is 600 feet long and was then 1,200 feet offshore. A small salient formed in the lee of the breakwater; however, the salient never advanced to more than 200 feet from the original shoreline. A 14 million-cubic yard sandfill, placed along 5 miles of the local beach in 1947 and 1948, advanced the shoreline about 500 feet, and a tombolo soon formed in the lee of the breakwater. Dunham discovered that the intersection of $K_D = 0.3$ isolines of waves diffracting about the heads of the breakwater was just shoreward of the advanced shoreline when the fill was first placed. This finding roughly checked with beach built-outs behind other breakwaters in southern California, and the principle was used successfully in siting two new breakwaters in the next few years so as to prevent unwanted tombolo formations. As a result of this experience, the same principle was adopted for design in Lake Erie. Apparently, the rule works because the wave energy is nearly an order of magnitude less than the incident wave energy where $K_D = 0.3$. Storm waves generally have an order of magnitude more energy than the daily predominant waves. Therefore, during storm conditions, there would be as much wave energy reaching the apex of the salient as the prevailing waves bring to unshielded segments of the beach. This energy is adequate to prevent tombolo formation.

The intersections of the $K_D = 0.3$ isolines for waves from directions representative of the net easterly and westerly component of the energy-flux waves vectors are shown in figure 6. The intersections are well offshore, thus ensuring that, even at low Lake levels, a tombolo should not form. The $K_D = 0.6$ isolines from the predominant wave direction are also shown for reference. The primary function of the breakwaters is to regulate the direction of wave approach. The lengths of the breakwaters, the distance offshore and the spacing between the breakwaters dictate the shape of the beach. The updrift and downdrift shorelines also control the lakeward extent of the shoreline behind the breakwaters.

The resultant beach was designed to be normal to the predominant wave approach. The flat-arc configuration of the breakwaters resulted from the design process of matching adjacent shoreline boundary conditions in the project area. In order to maintain natural transport to downdrift beaches, the net transport behind the breakwater had to

^{1/} Senior Coastal Engineer, Moffatt & Nichol, Engineers, Long Beach, California; formerly with the U.S. Army Corps of Engineers

be slowly eastward. With the east end of the project shoreline designed to be 300 feet lakeward of the natural shoreline, blending of adjacent shore segments as was done at the west end was not feasible, therefore, a terminal groin at the east end was designed to maintain the advanced position of the beach in that area. This groin was designed to be impermeable to sand, but short enough to allow the littoral drift that enters the system from the updrift shoreline to bypass around its head. This would prevent any acceleration of erosion of the downdrift beaches due to the project structures.

Figure 7 illustrates the design of the east groin. The pre-project concrete-sheet-pile groin was raised 2 feet to prevent sand from overtopping it during high Lake levels, and it was extended lakeward sufficiently to retain the new beach in its design configuration. An important feature of this groin is the impermeable diaphragm along its centerline. This membrane is of steel-sheet-pile construction; however, concrete poured in place between the voids in armor rock could also have been used.

The typical breakwater cross section is shown in figure 8. The crest elevation, at +8 feet LWD is designed to allow minor wave overtopping during storm conditions. A transmitted height of 1 foot was allowed. A lower crest elevation would have resulted in greater wave overtopping, which would induce a higher wave runup on the lee beach and generate a wave setup in the water. The setup would induce rip currents between the gaps and around the ends of the two outboard breakwaters, thereby increasing offshore loss of littoral drift. The rip-current scour might also undermine the breakwater ends. This actually occurred in model studies of an offshore breakwater system designed and tested by the Corps of Engineers in conjunction with erosion-prevention planning for Imperial Beach, California (U.S. Army Corps of Engineers, 1978).

MONITORING PROGRAM

Description of Program

The Corps of Engineers initiated a 5-year monitoring program immediately after construction to document littoral transport and the wave climate in the vicinity of the project site. The purpose of the monitoring program is to provide information on required operations and maintenance, such as beach-nourishment needs, to assist in developing design criteria for detached breakwater systems, and to provide data that will lead to a better understanding of nearshore processes in the Great Lakes.

The monitoring program comprises aerial photography, bathymetric and topographic surveys, sand samplings, Littoral Environment Observations (LEO), site inspections, and installation of a wave gage. Color aerial photographs are taken three times a year over a 6-mile reach of shore to document morphological changes. The photographs are at a scale of 1:4800 and have 60 percent overlap. Surveys are

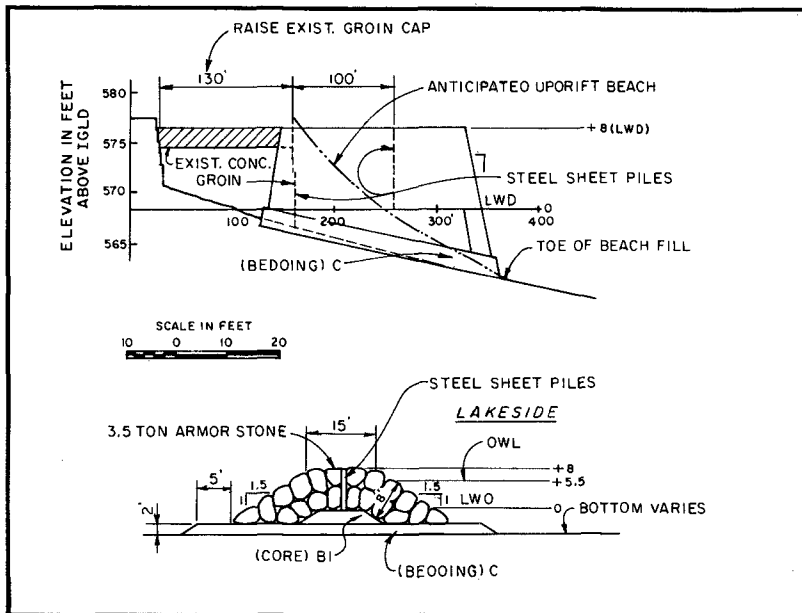


FIGURE 7: EAST GROIN PLAN

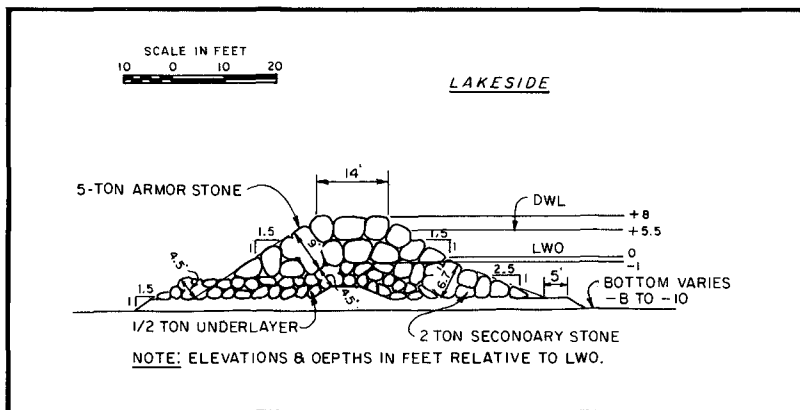


FIGURE 8: DETACHED BREAKWATER PLAN

taken twice a year, once in the spring and once in the fall. The survey area extends 2,000 feet east and 3,000 feet west of the project site, and range lines are at 100-foot intervals within the project site. Each line is surveyed from the backshore out to a depth of -20 feet LWD. Surface sediment grab samples are taken once a year, in the fall.

A local observer documents daily wave and beach conditions under the LEO program. The LEO data have not yet been reduced nor analyzed at the time of this writing. Site inspections are made three times a year to describe beach morphology and conditions. A wave gage will be installed in 1981 and records kept for a period of 1 year.

FINDINGS

The project construction was completed in October 1977. Photograph 1 shows that the planform quickly adjusted to the shape predicted by the design. Salients soon formed in the lee of each of each breakwater, and the beach slopes flattened. Photograph 2 shows the configuration of the beach in May 1980. Figures 9 and 10 show the morphology of two representative beach and offshore profiles. Figure 9 was a section taken in the gap between the east and central breakwater and figure 10 was a section taken behind the west breakwater. The profiles in these figures show that the offshore slope during the first 6 months adjusted to 1 on 20 behind the breakwaters (figure 10), and to 1 on 15 in the gaps (figure 9). The foreshore slopes in both cases are 1 on 12. These slopes remained essentially the same, although the most recent survey (in November 1979) showed that the west end of the beach had eroded to within 20 feet of a seawall on the east side of the west groin at station 13 + 75. (Stations are at 100-foot incremental distances west of the east end of the Park, as shown in figure 5).

The project was subjected to a storm from the west in May 1979. The storm generated waves of near design conditions at near record high Lake levels. The west end of the beach eroded severely; however, normal wave action restored much of the beach later in the year. Since that storm, other storm waves from the west have eroded the west end, but, again, the normal wave activity partially restored the lost sand.

A volumetric analysis was made to determine the changes in quantities of sand within the project boundaries. October 1977 was the base year. The initial beachfill comprised 110,000 cubic yards of medium sand. The volume of sand was measured by topographic and bathymetric surveys along the range lines shown in figure 5. Volumes were computed by the average-end-area method. The downdrift shoreline did not experience noticeable erosion. The total project area behind the breakwaters has accumulated sand. Figure 11 summarizes the volumetric changes behind each of the breakwaters as a function of time. The changes indicate that the project rapidly gained 4,000 to 6,000 cubic yards of sand, but that the volume of sand retained



PHOTO 1: IMMEDIATELY AFTER CONSTRUCTION, OCTOBER, 1977



PHOTO 2: TWO AND A HALF YEARS AFTER CONSTRUCTION, MAY 1980

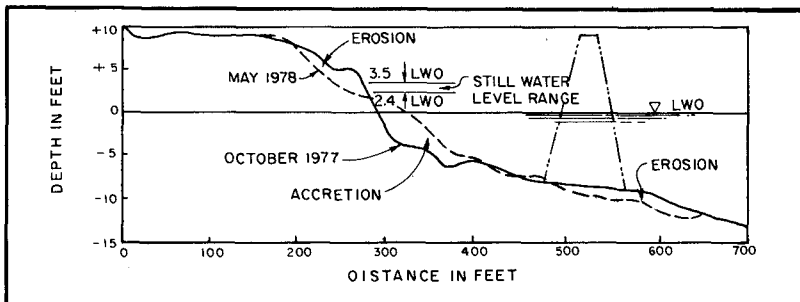


FIGURE 9: COMPARISON OF BEACH PROFILES
STATION 6+00W
(GAP BETWEEN EAST AND CENTRAL BREAKWATERS)

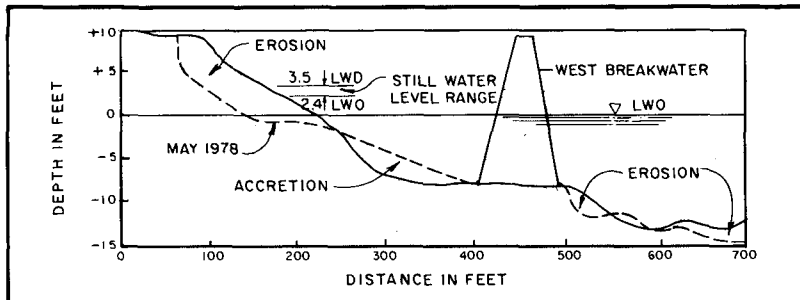


FIGURE 10: COMPARISON OF BEACH PROFILES
STATION 13+00W
(IN LEE OF WEST BREAKWATER)

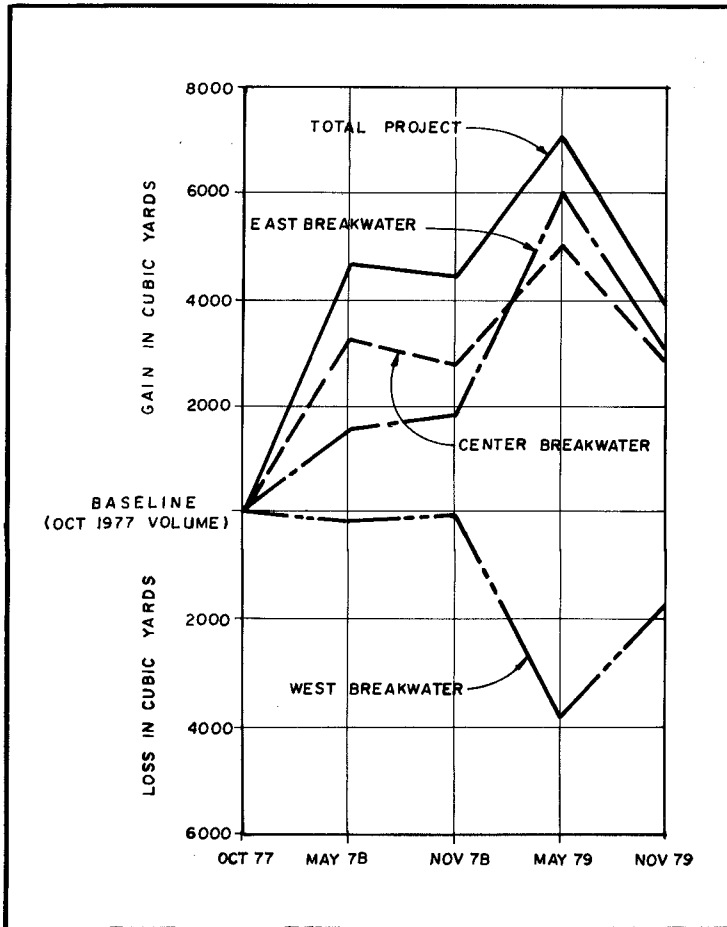


FIGURE 11: CHANGES IN LEE OF BREAKWATERS

behind the structures fluctuates. Both the central and eastern breakwaters now retain more material than was initially installed; however, the west breakwater has lost material. The areas of gain and loss can be seen in figure 12 as a function of survey period.

The overall project has gained about 5,000 cubic yards of material. The beach has become aligned in a slightly more westward-facing orientation than predicted. This is evident by erosion of the west end. Although the project has been in place for 2 ½ years, no maintenance has been performed. Nourishment is planned for 1980 to replenish the west end of the project with 6,000 cubic yards of sand.

The project has been exposed to several severe storms from the west during periods of high Lake levels, but no damage to the breakwaters or groins has resulted.

Proper analysis of the project will require several years, in order to include observations during periods of low Lake levels. The intensity and frequency of storms from the west during the early years of the project may not be representative of the relative frequency of long-term, typical wave conditions. Furthermore, the winter of 1979-1980 was very mild, and Lake ice which normally protects the shoreline from severe winter storms did not form. Therefore, the project was subjected to severe winter storm waves had not been taken into account in the design analysis.

CONCLUSIONS

The beach-restoration project performed well despite being subjected to atypical severe westerly storms, high Lake levels, and a winter with no ice. The beach is the focal point of a popular recreational facility. The project has required little maintenance and has not induced erosion of the downdrift shoreline.

The simplified diffraction analysis using the predominant wave direction from the littoral transport analysis for prediction of beach planform appears to have worked reasonably well. Designing the beach landward of the $K_D = 0.3$ isoline intersections of diffraction diagrams drawn for the easterly and westerly resultants of wave-energy flux has precluded formation of a tombolo. The effects of wave attack due to severe individual storms may have a significant impact on localized areas such as the west end of the beach. Perhaps a greater safety margin should have been provided by making the initial beach wider or by extending the breakwater system farther westward.

Significant erosion has not been induced on the Lake bottom between the breakwater gaps. The height of the breakwater was sufficient to preclude wave overtopping from inducing a strong rip current that would scour the Lake bottom.

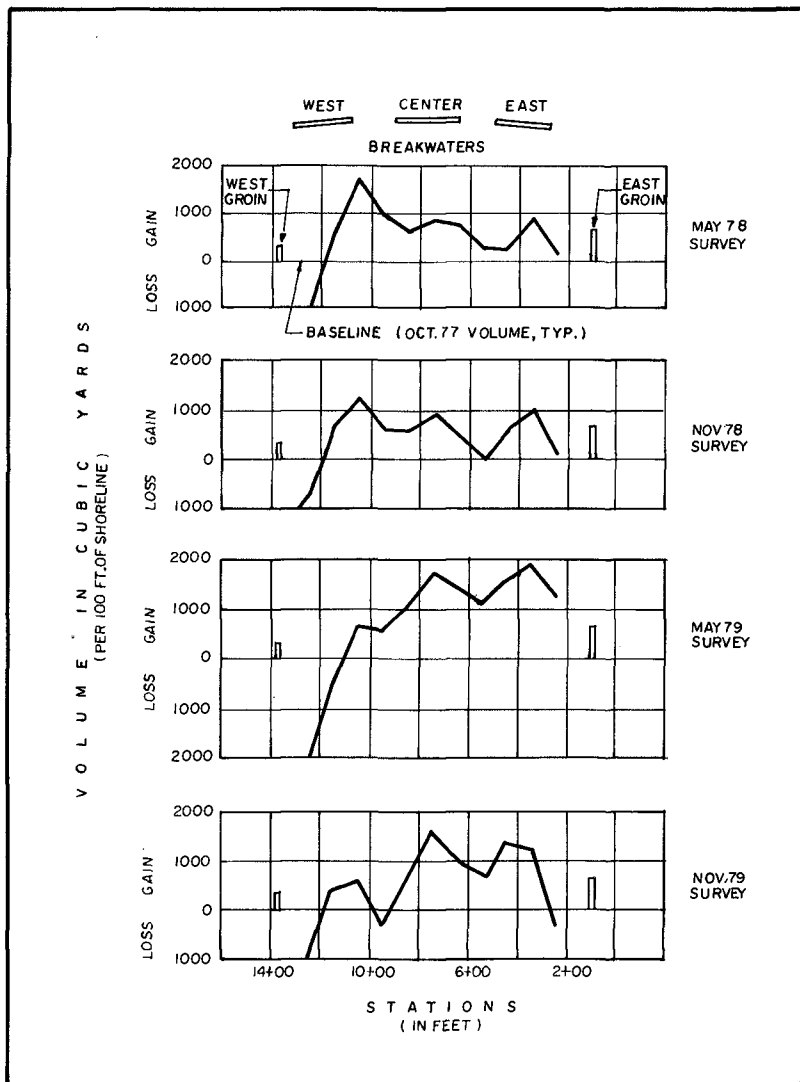


FIGURE 12: SAND VOLUME CHANGES RELATIVE TO OCTOBER 1977

RECOMMENDATIONS

The beach project at Lakeview provides a case history of a beach protection design using detached breakwaters. Insufficient funding was available to conduct a hydraulic model study or to develop a rigorous mathematical model prior to project implementation. Since the Lakeview design, Dean (1978) and others have developed shoreline evolution mathematical models that more accurately incorporate the effects of wave diffraction through segmented breakwaters. It would be useful to use a case study such as the Lakeview Park project to calibrate movable- or semimovable-bed hydraulic models and mathematical models.

Detached breakwaters have been shown to be a feasible method of protecting a beach. They should be considered where strict regulation of the beach planform is required. The gap spacings, the length and distance offshore, and the crest height should be designed by use of a rational procedure, giving adequate attention to sediment supply, the potential for littoral transport, variations in wave direction, the potential effects of single storms, and the consequences of variation in planform resulting therefrom.

ACKNOWLEDGEMENTS

The authors wish to thank Col. G.P. Johnson, District Engineer, Buffalo District, Corps of Engineers, for permission to publish this paper, and to thank Mr. James Dunham for extending the benefits of his experience in the project design and the review of this paper.

REFERENCES

1. Dean, R.G., "Diffraction Calculation of Shoreline Planforms," Proceedings of the 16th International Conference on Coastal Engineering, ASCE, Hamburg, Germany, 1978.
2. Saville, T., "Wave and Lake Level Statistics for Lake Erie," U.S. Army Corps of Engineers, B.E.B. T.M. 37, 1953.
3. Silvester, R., and S. Ho, "Use of Crenulate Bays to Stabilize Coasts," Proceedings of the 13th International Conference on Coastal Engineering, ASCE, Vancouver, B.C. 1972.
4. Toyohira, O., "Design of a Detached Breakwater System," Proceedings of the 14th International Conference on Coastal Engineering, ASCE, Washington, DC 1974.
5. U.S. Army Corps of Engineers, "Cooperative Beach Erosion Control Project at Lakeview Park, Lorain, Ohio," General Design Memorandum, Phase II - Project Design, Buffalo District, Corps of Engineers, Buffalo, New York, June 1975.
6. U.S. Army Corps of Engineers, "Imperial Beach, Erosion Control Project, San Diego County, California." General Design Memorandum 4, Los Angeles District, Corps of Engineers, Los Angeles, California, April 1978.

STABILITY OF RUBBLE MOUND BREAKWATER

J. FEUILLET*

M. SABATON*

ABSTRACT

The stability of a rubble mound breakwater section, with 3 in 2 armour slope, was tested under random waves attack. Tests analysis shows that the equivalent wave height characterizing the spectrum to be used in a stability formula elaborated with regular waves (for instance the Hudson's formula) is the upper twentieth height of the distribution for a storm duration of 6 hours. An analytical expression of the damage evolution as function of time modulates this choice according to the storm duration. The same rubble mound breakwater was also tested under the action of regular breaking waves. The damage was expressed in terms of the four following parameters :

H_0 : wave height

T : wave period

D_p : water depth at the toe of the structure

D_b : breaker depth without the breakwater

For a given wave height, the most important damage occur when :

$$\frac{D_p}{D_b} = 1$$

In this case the design wave height must be increased by about 30 % when using a stability formula elaborated for non breaking waves.

1 - INTRODUCTION

The use of breakwater stability formula (e.g. Hudson's formula) [1] to determine the weight of armour units of rubble mound breakwater raises two questions :

What wave height do we have to choose to represent the action of a random sea and is this dependant upon the duration of the design storm ?

* Laboratoire National d'Hydraulique - E.D.F. CHATOU FRANCE.

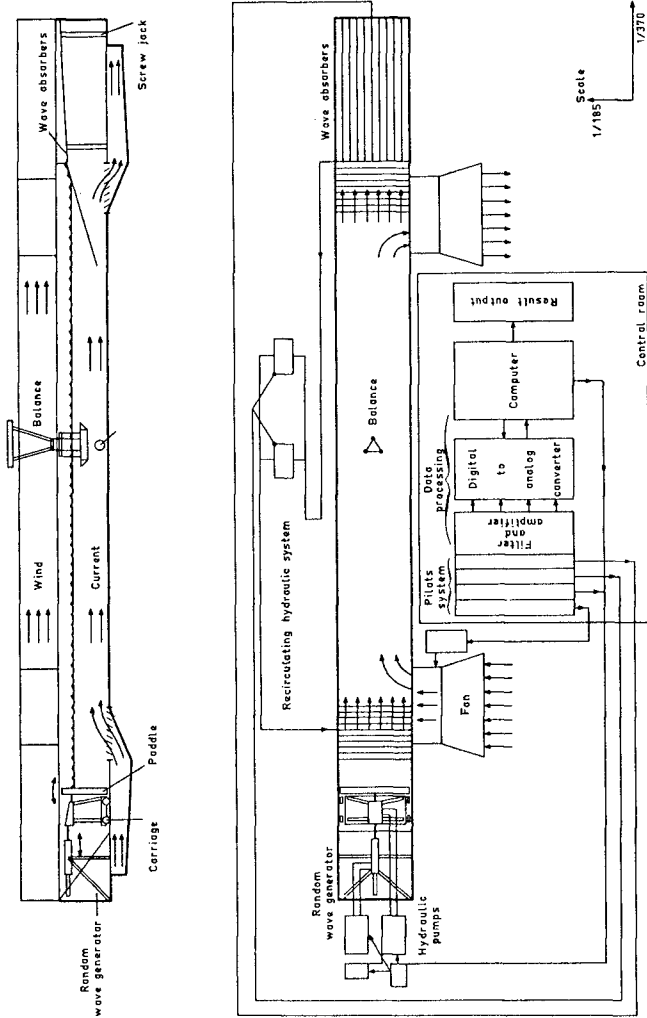


Figure 1

SCHEMATIC OF THE EXPERIMENTAL INSTALLATION

How can we take into account the effect of breaking waves ?

It has been generally accepted that the destructive effect of random waves is equivalent to that of regular waves having a height equal to the significant wave height characterizing the real sea state and the armour blocks weight is often calculated with this criterium. Is this approach correct ? The paper presents the results of three series of tests of breakwater stability on a reduced scale model with random non breaking waves, regular non breaking waves and regular breaking waves.

II - DAMAGE EVOLUTION IN RANDOM WAVES AS COMPARED WITH REGULAR WAVES

II.1 - Test procedure

. wave flume : A sketch of the wave tank layout is shown in figure 1. The flume is sixty meters (185 ft) long, five meters wide (15,4 ft) and 1,6 meters (4,9 ft) deep. The wave generator consists of a carriage rolling on rails laid on the flume bottom and of a plane paddle, hinged on this carriage, swinging around an axle located near the flume bottom. Carriage and paddle are operated by hydraulic pistons fed with two variable output pumps. The two movements, translation and rotation are independant. This wave generator is able to simulate random or monochromatic waves. In random waves the control signal is provided directly by a digital computer. Wave heights and periods were measured with resistance type wave gages. A fast measurement central unit ensures the analog switching and the analog digital conversion of wave data. These last one are analysed by the computer which gives harmonic, spectral, and statistical analysis of the data.

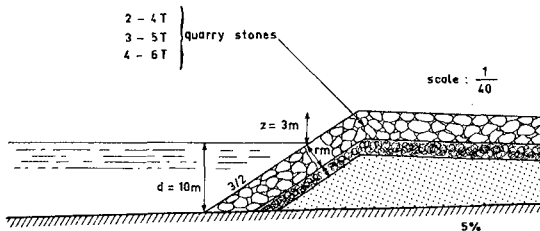


Figure 2

BREAKWATER MODEL FOR RANDOM WAVES

. Breakwater model : A simplified sketch of the cross section of the model studied is shown in figure 2. The scale was 1/40. The armour layer was composed of blocks with a weight in the range 2-4 T (mean 2.6 T) and a specific weight of 2.6 T/m³. Its slope was 3 in 2. The water depth at the toe of the breakwater was 10 m (30,8 ft). The bottom slope in front of the breakwater was 1 in 10.

. Test conditions : In order to make comparisons possible, the same model was submitted to the attack of regular waves and irregular waves. The storm duration was lower than 20 hours (30 mn at model scale).

The incident wave was measured using 3 wave gages, according to the method described by GODA [7].

II.2 Test results and analysis

II.2.1 - Results in regular waves

Figure 3 shows that the results obtained in regular waves compare well with Hudson's results. The stability number N_s is defined as :

$$N_s = \frac{H}{\left(\frac{w}{\gamma_r}\right)^{1/3} (S_r - 1)} \quad \text{with} \quad S_r = \frac{\gamma_r}{\gamma_w}$$

The damage D is defined as the ratio of the number of removed blocks to the total number of armour layer blocks.

II.2.2 - Results in irregular waves for a storm duration of 6 hours.

In order to define a design wave height in random waves for a storm duration of 6 hours, we have compared the values of N_s obtained by Hudson in regular waves to the values obtained in random waves for different typical wave heights :

$$\left(H_{Z, \frac{1}{3}}, H_{Z, \frac{1}{10}}, H_{Z, \frac{1}{20}}, H_{Z, \frac{1}{50}} \right)$$

The best agreement between N_s values calculated in regular waves and random waves is obtained for the wave height $H_{Z, 1/20}$ (figure 4), which characterizes the action of random waves for a storm duration of 6 hours. This wave height will be noted H_D . But this result has to be modulated because the storm duration has a great effect upon the rubble mound breakwater stability.

III.2.3 - Effect of the storm duration in random waves

The purpose of this study was to compare the damage evolution in regular and irregular waves, considering random waves as a succession of independant waves, and to obtain a literal formula expressing the damage evolution under random waves action as function of a characteristic height and of the storm duration. Two different methods have been explored. In the first one we determine in regular waves a law describing evolution as a function of the wave height and the time, and then deduced by integration a law in irregular waves.

This method leads to the following expression :

$$D = \frac{1}{T_{\text{moy}}} \int_0^t \int_0^{\infty} DPV \cdot p(h) \, dh \, d\tau. \quad (1)$$

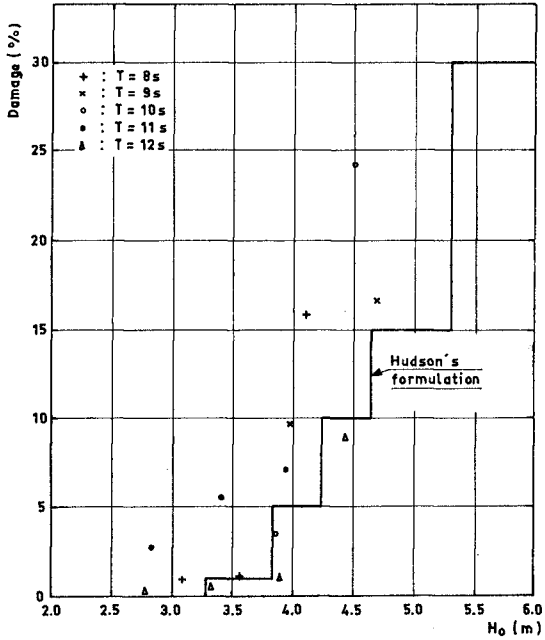


Figure 3

COMPARISON OF EXPERIMENTAL RESULTS WITH HUDSON'S
FORMULA IN REGULAR WAVES.

with $p(h)$: probability law of wave height ;

T_{moy} : mean period ;

D : damage ;

t : storm duration ;

DPV : function expressing damage provoked by one wave of height h attacking the breakwater at time τ .

The values given by this formula compare well with experimental results (figures 5 and 6).

In the second method we have obtained directly a literal formulation of damage evolution in random waves by a statistical adjustment of the experimental results with a least squares fitting through all the experimental points.

By this method we have obtained the following expression [5] :

$$D = \frac{2.78}{T_p} H_{Z, \frac{1}{10}}^{3.9} t^{0.37} \quad (2)$$

with D : damage expressed as number of removed blocks ;

t : storm duration in hours ;

T_p : peak period ;

$H_{Z, \frac{1}{10}}$: the upper tenth mean height of the distribution.

This statistical adjustment has been obtained with a good correlation coefficient ($\rho \approx 0,96$).

The results obtained by this method are represented in dashed lines on the figures 5 and 6.

II.2.4 - Application to the determination of the design wave height H_D

The results obtained in [4], and presented in II.2.2, lead for a storm duration of 6 hours to the relation :

$$H_D = H_{Z, \frac{1}{10}} \# 1.1 H_{Z, \frac{1}{10}} \quad (t=6) \quad (3)$$

expressing the equivalence (for the damage) between a regular wave of height H_D acting till the stabilization of the breakwater and a random wave of height $H_{Z, \frac{1}{20}}$ acting during 6 hours.

From equation (2) can be derived the relation :

$$H_{Z, \frac{1}{10}} = kt^{-0,095} \quad (4)$$

Which expresses that for given blocks and damage (e.g. $k = \text{constant}$)

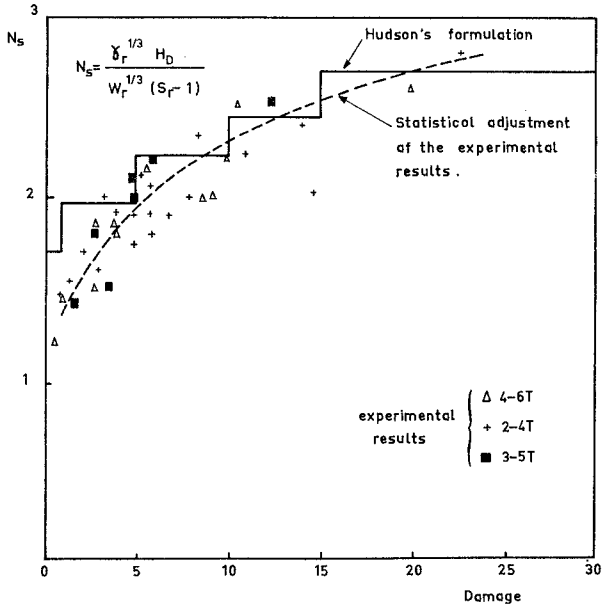
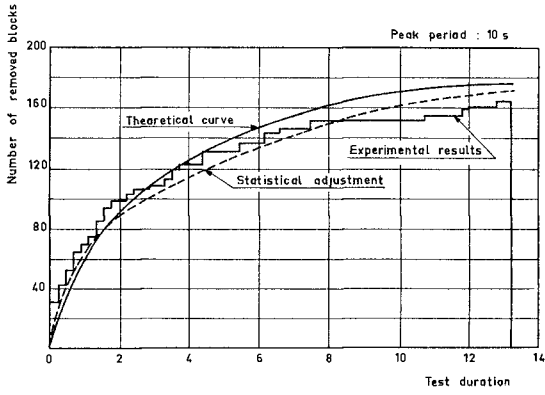


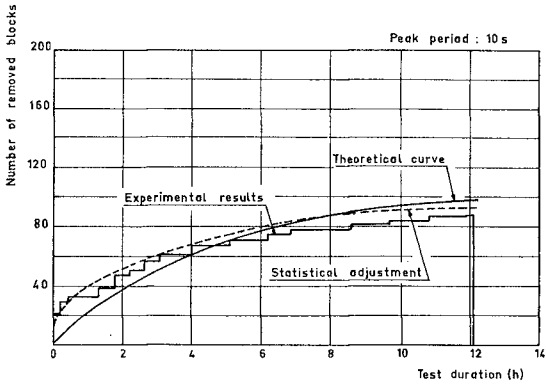
Figure 4

COMPARISON OF EXPERIMENTAL RESULTS
 WITH HUDSON'S FORMULA

N_s estimated with $H_z \cdot \frac{1}{20}$ for a storm
 duration of 6 hours



Quarry stones 2-4T
 $H_s = 2.70\text{m}$



Quarry stones : 2-4T
 $H_s = 2.27\text{m}$

Figure 5

DAMAGE EVOLUTION IN RANDOM WAVES

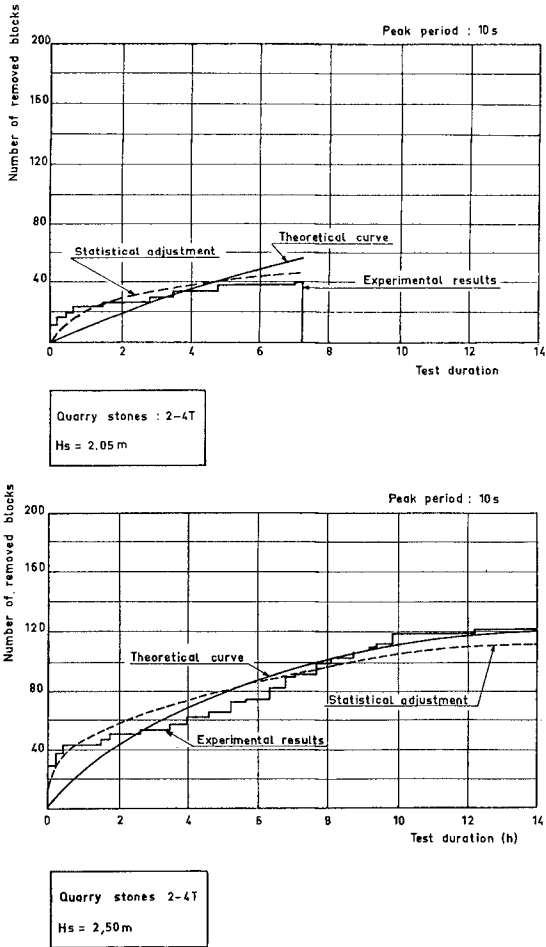


Figure 6

DAMAGE EVOLUTION IN RANDOM WAVES

the wave height $H_Z, \frac{1}{10}$ at which the rubble mound breakwater resists, decreases when the storm duration increases.

The relation (4) allows us to write (figure 7) :

$$H_Z, \frac{1}{10} (t=6) 6^{0,095} = H_Z, \frac{1}{10} (t) t^{0,095}$$

and, taking into account the relation (3) :

$$H_D = f(t) H_Z, \frac{1}{10} t^{0,095}$$

with $f(t) = 0,93 t$

This last formula expresses the design wave height H_D to be used in a stability formula established in regular waves as a function of storm duration and wave height $H_Z, \frac{1}{10}$ characterizing the random sea spectrum.

The variations of the design wave height with the storm duration (for a duration greater than 3 hours) are relatively small (figure 8).

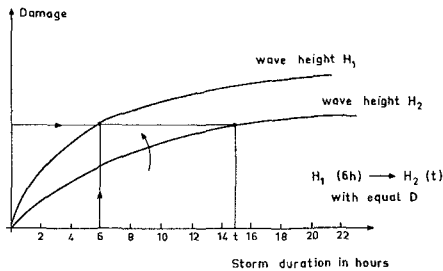


Figure 7 : Method used for the determination of H_d for a storm duration t .

But the choice of $H_Z, 1/3$ as design wave height usually adopted seems to underestimate the effect of random waves, whatever the storm duration may be. $H_Z, 1/20$ is approximately 40 % higher than the significant wave height and this leads to an important difference in armour units weight, this last one being generally proportionnal to the height to the cube (figure 8).

III - EFFECTS OF BREAKING WAVES

These tests were conducted only in regular waves, in a smaller flume which is 50 m long and 0,60 m wide. The rubble mound breakwater model was the same as the one describes above but the median armour stone weight was 5,37 T.

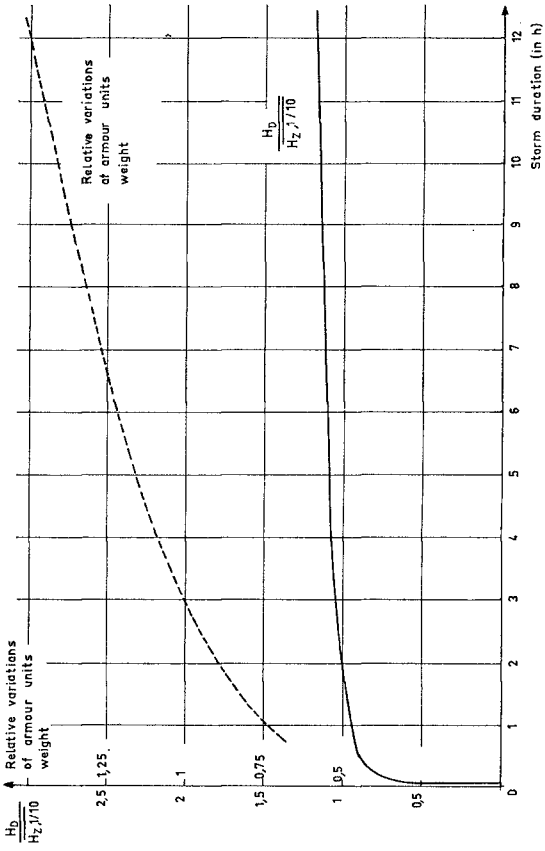


Figure 8

DETERMINATION OF THE DESIGN WAVE HEIGHT AS A
FUNCTION OF THE STORM DURATION

The water depth at the toe of the structure varied from 3 m to 10 m and the wave height from 3 m to 5 m. Three periods were tested : 8, 10, 12 s.

Damage was expressed in terms of the four following parameters :

- wave height H_0 ;
- wave period T ;
- water depth at the toe of the structure D_p ;
- breaker depth D_b without the rubble mound breakwater.

III.1 - Multicomponents analysis

The statistical study of all the results has pointed out that the stability is strongly influenced by two parameters : the height H_0 as usually expressed by the stability formula and the ratio D_p/D_b characterizing the position of the breakwater in the surf zone. This result is illustrated by the figure 10.

Interpretation of the figure 10 :

- the correlation coefficient between two variables may be characterized by the distance separating these variables ;
- each axis may be interpreted as a variable to be defined ;
- the correlation coefficient between an axis and a variable is given by the projection of the variable on the axis.

So the observation of the figure 10 allows to establish that :

- the damage D and the wave height H_D are strongly correlated ;
- Oy axis may be interpreted as the ratio $\frac{D_p}{D_b}$;
- the correlation coefficient between the damage D and the ratio D_p/D_b is important.

III.2 - Expression of the damage D as a function of $\frac{D_p}{D_b}$ an H_0

Although there is a great scatter of the tests results, a statistical adjustment has been made (figure 9). For a given wave height, the most important damage occurs when $\frac{D_p}{D_b} = 1$.

So a rubble mound breakwater is submitted to the worst attack of waves when it is located just in the breaker zone corresponding to design storm conditions.

When the ratio $\frac{D_p}{D_b}$ is great, that is when in non breaking conditions, the curves presented on the figure 9 are in good agreement with Hudson's results.

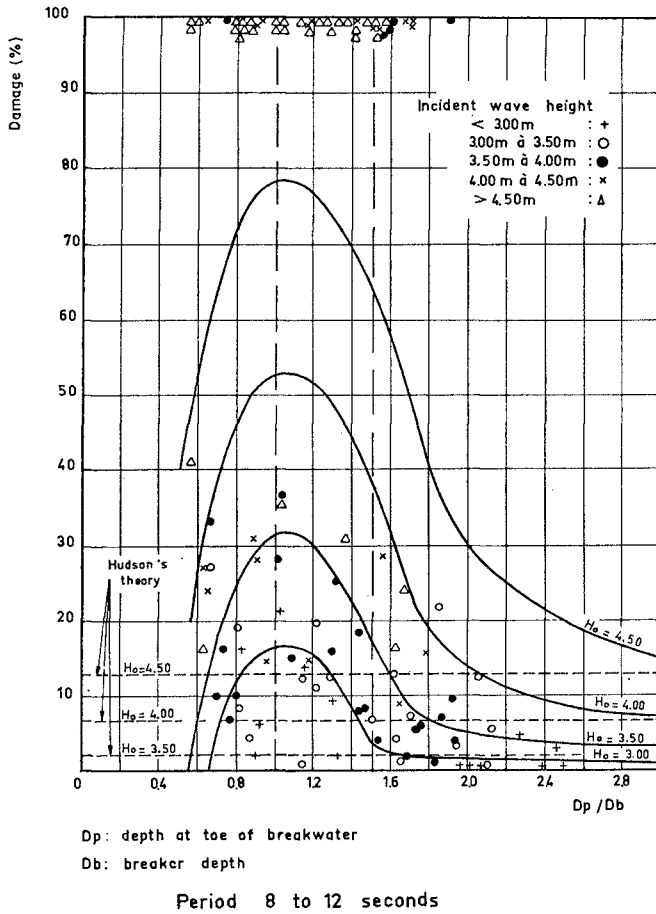


Figure 9

DAMAGE EVOLUTION WITH THE BREAKWATER
 POSITION AND THE WAVES HEIGHT

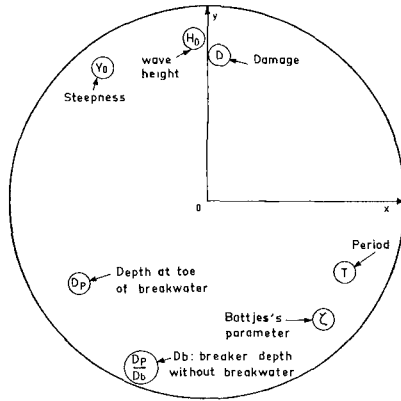


Figure 10 : Détermination of the most influencing parameters (multicomponents analysis)

III.3 - Application to the determination of the design wave height

This statistical adjustment has permitted to express the design wave height as a function of $\frac{D_p}{D_b}$ and H_0 . This function is represented graphically on the figure 11.

This figure shows that in the most unfavourable case ($\frac{D_p}{D_b} = 1$), the design wave height must be increased by about 15 to 40% when using a stability formula elaborated for non breaking waves. Again this leads to significantly increased armour units weights.

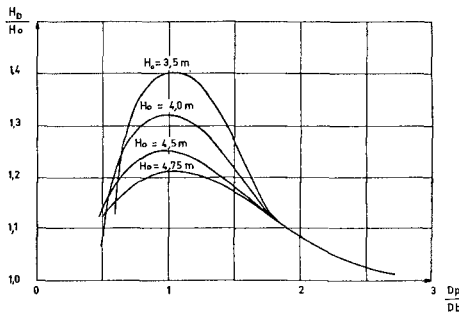


Figure 11

Variations of the ratio $\frac{H_d}{H_0}$ versus $\frac{D_p}{D_b}$ and H_0

IV - CONCLUSIONS

However these tests have been run for conditions which are limited in comparison with the range of conditions to be handled in practice, (e.g. artificial blocks eventually with interlocking effects), they have pointed out that the design wave height to use in a stability formula is higher than the significant wave height of the spectrum and depends of the storm duration.

For a storm duration of 6 hours the design wave height should be approximately $H_z \frac{1}{20}$.

Furthermore this choice must be modulated according to the location of the rubble mound breakwater in the breakwater zone of the most severe storms.

REFERENCES

- [1] HUDSON R.Y.
Laboratory investigation of rubble mound breakwater.
Journal of the waterways and Harbors division, September 1959.
- [2] AHRENS P.
The influence of breaker type on riprap stability.
Proceedings of twelfth conference on Coastal Engineering, 1970.
- [3] THORTON B, CALHOUN J.
Spectral resolution of breakwater reflected waves.
Journal of the waterways, Harbors and Coastal Engineering division
Proc. ASCE November 1972.
- [4] LEPETIT J.P., FEUILLET J.
Etude de la stabilité d'une digue en enrochement en houle aléatoire.
Comparaison avec la stabilité en houle régulière.
Rapport E.D.F. HE42/78.44.
- [5] LEPETIT J.P., FEUILLET J.
Etude de la stabilité d'une digue en enrochement en houle aléatoire.
Quantification de l'effet de la durée d'action.
Rapport E.D.F. HE42/79.15.
- [6] FEUILLET J.
Etude de la stabilité d'une digue en houle déferlante.
Rapport E.D.F. HE42/78.36.
- [7] CODA SUZUKI
Estimation of incident and reflected waves in random wave
experiments.
Conference Coastal Engineering, 1976.
- [8] CARTERS T., TORUM A., TRAUETTEBERG A.
The stability of rubble mound breakwater against irregular waves.
Conference Coastal Engineering, 1970.

ARTIFICIAL RESORT BEACH PROTECTED BY
OFFSHORE BREAKWATERS AND GROINS

by

Shoji SATO and Norio TANAKA
Port and Harbour Research Institute, Ministry of Transport
1-1, 3-chome, Yokosuka, JAPAN

INTRODUCTION

In Japan, area of natural beaches has decreased in the vicinity of cities, towns and villages, in consequence of constructing ports and harbours, reclaiming shore and beach, and building storm-surge prevention structures like sea dikes and sea walls. On the other hand, the demand of people for recreation area is increasing year by year with the improvement of living and economic conditions. Therefore, since several years ago, local governments have extensively been constructing artificial beaches and restoring eroded beaches on many places by the aid of the central government.

Such artificial beaches, however, need large amount of natural sand, in spite of the deterioration of sand supply and the soaring of sand price. Moreover, local governments are able to get subsidiary payments of the central government for the construction of artificial sand beach, but not for replenishing sand lost by wave action after the completion of the construction works. Therefore, most artificial beaches in Japan are usually protected by groins and offshore breakwaters in order to retain artificially filled sand. But in summer when sea is in calm condition, pollutant produced by sea-bathing people or discharged from the land is likely to stagnate in the vicinity of the shoreline on account of such structures.

From the above-mentioned, coastal engineering problems on construction and restoration of sand beach in Japan are:

- (1) suitable arrangement of offshore breakwaters and groins from standpoint of artificial beach protection
- (2) keeping the sea water of the beach clean
- (3) estimation of profile change of the artificial beach due to wave action after its construction.

This paper presents the results of investigations conducted with the aim of solving the above coastal engineering problems related to artificial beach constructions at Suma and Ito beaches. The investigations are mainly conducted using model experiment.

SUMA BEACH

Natural Condition of Suma Beach

Suma Beach is located in the western portion of Kobe City along Osaka Bay as shown in Fig. 1. Fig. 1 shows a bathymetric map of Suma Coast surveyed just before the start of the construction of the

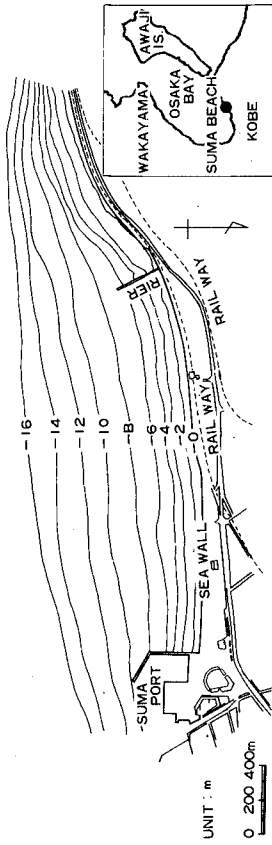


Fig. 1 Bathymetric map of Suma Coast

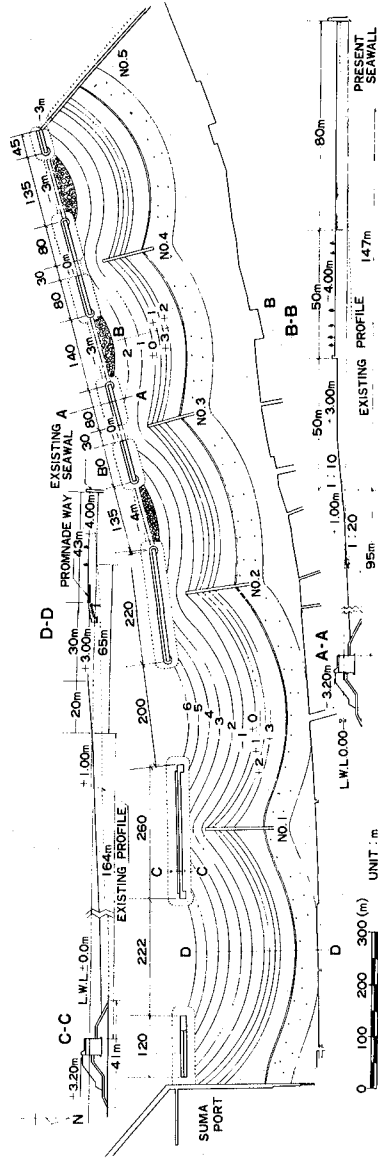


Fig. 2 The scheme of artificial beach at Suma of Kobe City

artificial beach, in 1973. The height of the backshore is 3 m above L.W.L., and the beach slope is nearly 1/10 on the foreshore and 1/20 - 1/30 between 1 and 6 m deep. The median diameter of the beach materials are several mm on the foreshore and 0.3 to 0.5 mm between 1 and 6 m deep. Usually waves are so small and significant wave heights are less than 0.5 m. Waves of more than 1.5 m in $H_{1/3}$ come only a few times a year. But, in very rare cases, the beach is attacked by severe waves due to typhoons. The estimated past maximum $H_{1/3}$ is 4.75 m. Tidal currents are going and returning in parallel with the shore, showing maximum velocity of about $50 \text{ cm}\cdot\text{s}^{-1}$ on the offshore of about 10 m deep at spring tide. The mean spring tidal range is 1.8 m.

Scheme of The Artificial Beach Construction

In 1973, Kobe municipal city has decided to construct the wide artificial beach on the stretch of about 2 km long between Suma Port, which is a leisure and fishery port, and the pier, which is a permeable type and is used to load materials for the reclamation of the area of Kobe Port. At that time, short groins of several ten meters long had existed on the whole stretch of the beach with space intervals of 100 m or so in order to prevent beach erosion, and behind the beach there was sea wall of 5 m high above L.W.L. in its crown height.

Fig. 2 shows the present scheme of the artificial beach designed on the basis of the model experiment which will be mentioned in the following paragraphs. The beach is divided into five parts by five long groins of No. 1 to 5, and there are six offshore breakwaters in order to protect the artificial beach from the wave action. The groins are of impermeable cellular type and the offshore breakwaters of composite type. The beach is filled with natural sand to form arch-shaped plane shape. The beach width, from the promnade way to the shoreline of mean water level, is about 50 m at the center of arch-shaped beach in the east portion. The green belt is behind the promnade way. In the west part of the stretch, the width of the coastal area is increased by the reclamation and the artificial beach is made in front of the reclaimed land, because houses densely exist just behind it. Therefore, the width of artificial beach become so narrow that submerged rubble mound is constructed between the offshore breakwaters so as to retain the seaward end of the beach slope. The construction of the artificial beach began in 1973 and the most of the east portion in the figure will be completed in 1980 fiscal year.

Model Test on Sea Water Exchange in The East Part of The Beach

Model tests on sea-water exchange between inshore and offshore have been conducted using a fixed bed model with the reduced scale of 1/100 in both vertical and horizontal. Fig. 3 shows a pattern of the currents measured in the model of the east part of Suma Beach without the artificial beach, which corresponds to the state of the maximum of current velocity in flood tide at the site. There is a circulation of currents at the lee of the breakwater of Suma Port while the tidal currents in the offshore zone flow in parallel with the shore line. Under the steady current with such flow pattern, the dispersion of fluorescent

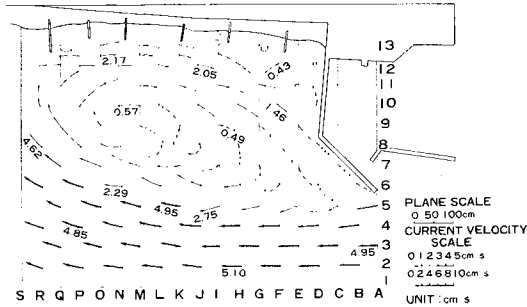


Fig. 3 Pattern of the fastest currents during flood tide at the east part of Suma Beach before the beach nourishment

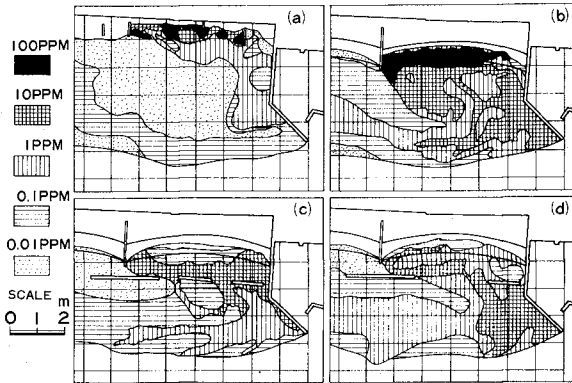


Fig. 4 Dispersion patterns of dye discharged on the shoreline in the east part of Suma Beach

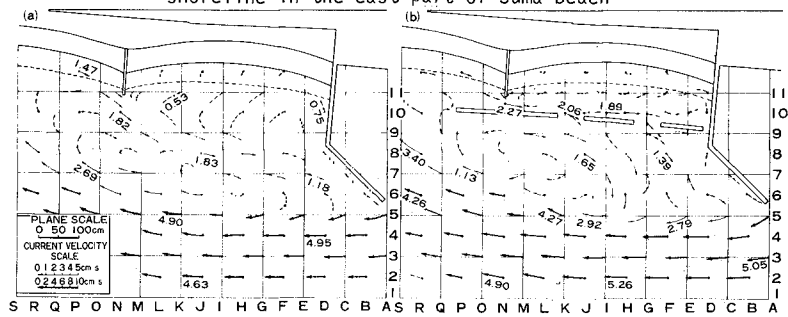


Fig. 5 Current patterns of the cases with and without offshore breakwaters

dye discharged on the shoreline has been investigated for cases with and without the artificial beach.

Fig. 4 shows the patterns of spreading dye at 60 minutes after the start of discharge of dye, though the dye of 500 ppm in density has been discharged only during the first 15 minutes at 8 points on the shoreline. The discharging rate is $0.222 \text{ cm}^3\text{s}^{-1}$ per point. These diagrams were drawn by eyes on the base of colored pictures taken from the ceiling together with dye samples of 0.1, 1, 10 and 100 ppm in density placed on the edge of the model. In the figure, Case (b) of artificial beach with only groins is worse in offshoreward dispersion of dye than Case (a) without artificial beach, but Cases (c) and (d) with offshore breakwaters in addition to groins are better in it than the Case (a). It is because there are fast currents along the landward side of offshore breakwaters as well as circulating currents between offshore breakwaters and the shoreline at Cases (c) and (d), as seen from the patterns of currents shown in Fig. 5. The figure shows the result of test conducted under the same hydraulic condition as the above-mentioned Fig. 3. In comparison of Cases (c) and (d) in Fig. 4, the latter is better than the former. In these cases, the offshore breakwater is apart from the tip of the groin because it had been verified in the preliminary test that attaching them makes the water exchange worse between inshore and offshore.

Model Test on Beach Evolution in The Eastern Part of The Beach

Model tests on the beach evolution have been conducted using a movable bed model of 1/60 in vertical and horizontal scales. Fine sand of 0.19 mm in median diameter was used as sediments. Fig. 6 shows the comparison of depth contour lines before and after 6 hours run of waves of 4 cm in height and 1.03 s in period, which correspond respectively to 2.4 m and 8 s in the prototype on the basis of Froude's law. The direction of wave is south, and the still water level is equal to M.W.L. which is 1 m above L.W.L. in prototype. In the figure, the part of 1 to 3 m deep in the vicinity of the beach center is eroded by the wave action. The counter measures to prevent such erosion were tested under the same wave condition.

Fig. 7 shows the changes of the levels of the bottom between before and after 6 hours run of the same wave as Fig. 6 for each counter measure. Case 1 in the figure has a submerged breakwater of 3 m deep in crown level between offshore breakwaters, Case 2 it of 2 m deep in crown level on 6.5 m deep contour line, and Case 3 it of 2 m deep in crown level on 4.5 m deep contour line. In these cases having a submerged breakwater, the foreshore in the center of the arched beach erodes, and its backshore and the foreshore of both ends of the beach accrete. Case 3, which has a submerged breakwater in the nearest place to the foreshore, is the most elosive at the foreshore in the center of the arched beach. The submerged breakwater seems to be difficult to prevent the recession of the center part of the shoreline. Therefore, a small breakwater of 2 m above L.W.L. in crown level was placed in front of the foreshore, that is, on the 2 m deep contour lines. Its result is shown at (d) of the figure, where there are seen no erosion on the foreshore

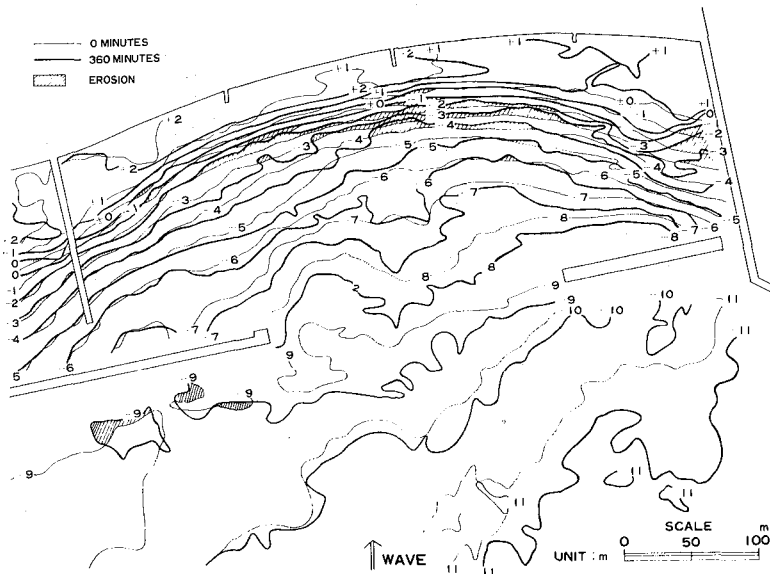


Fig. 6 Comparison of depth contour lines between before and after 6 hours wave action in the east part beach ($H = 2.4 \text{ m}$, $T = 8 \text{ sec}$)

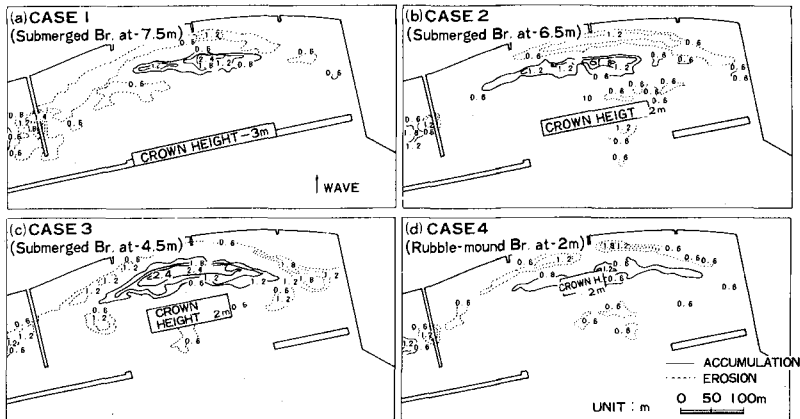


Fig. 7 Changes of the levels of bottom between before and after 6 hours wave action ($H = 2.4 \text{ m}$, $T = 8 \text{ sec}$)

just behind of the small breakwaters, though the areas around both tips of it are a little eroded.

Fig. 8 shows the change of bottom profile of the central part for each the above mentioned case. In every case except Case 4, the offshore side of shoreline is eroded by wave actions. This erosion is severer in the cases with a submerged breakwater than the case without any countermeasures. Therefore, Case 4 is recommended as the countermeasure against the recession of the center portion of the arched beach, but, at the site, the beach have been remained without any such a countermeasure at present. The reason is why such a structure is not welcomed from the view point of recreation and the model tests have a scale effect in their results. It will be again considered if such countermeasure is necessary or not after finishing scheduled beach filling.

The Change of Bottom Topography in The East Part of The Beach

In the site, the beach filling was conducted every autumn from 1973 to 1977 at the east end portion, the total volume of filled sand being 180,000 m³. Fig. 9 shows the changes of L.W.L. shoreline after the filling in September 1977, when 83,000 m³ of sand was supplied so as to shift the foreshore seawards. The supplied sand was 1.6 mm in median diameter and 2.6 in Task's sorting coefficient. The shoreline of L.W.L, which was of nearly straight line, has receded in center and advanced in the both ends with the time. But, the latest change from December 1973 to June 1979 is very small, especially in the center part. It means that the shape of the shoreline has reached the state of equilibrium in nearly one year. This equilibrated shoreline is nearly similar to that of the model test shown in Fig. 6.

Fig. 10 shows the changes of the beach profile at the center and the both sides of the beach. The profile of Section B at the center has changed mainly in the part above one meter deep, while these change appeared in the part above 3 m deep in the model test, as shown in the first section of Fig. 8. It seems to be because the most waves were less than 1.5 m in height at the site during the duration. The eroded sand in the center of the beach may have been transported along the foreshore to the both ends of the beach by the wave action. As the results, the foreshores of Section A and C have advanced and have become steeper than in the center portion. Despite such a bottom change, the total loss of filled material was only 2,500 m³ in volume the period from September 1977 to March 1979.

Model Test on The Beach Evolution in The West Part of The Beach

The west part is, as described above, planned to be made in front of the reclamation land. The typical plane shape of artificial beach, which have been tested using a movable model of 1/80 in horizontal and 1/50 in vertical scale, are shown in Fig. 11. The three beaches are perfectly separated each other in Case 1 and are connected through the tip of the groin each other in Case 2 and 3. For each case, the crest level of the offshore breakwaters and the submerged breakwaters are 3.2 m above and 3 m below L.W.L., respectively. Moreover, Case 3 has the

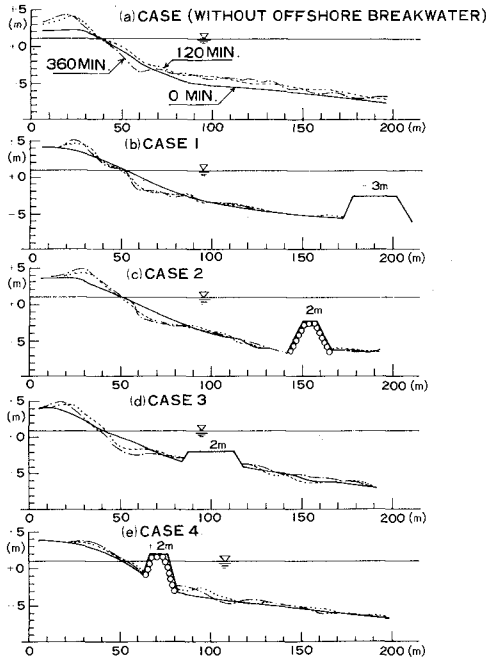


Fig. 8 Comparison of change of bottom profile along the central section

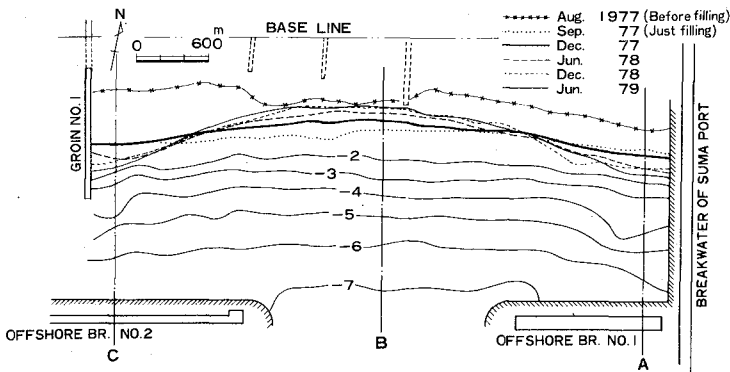


Fig. 9 Change of the shoreline of 10 m after the sand filling in Sep. 1977 at the site

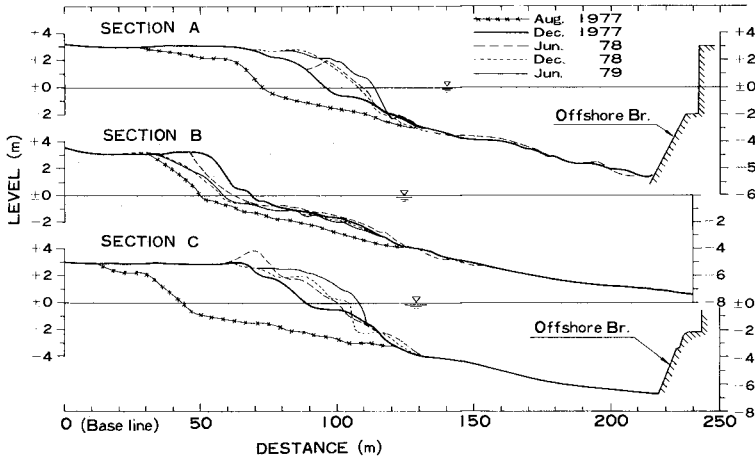


Fig. 10 Change of beach profile of the east part of the beach at the site

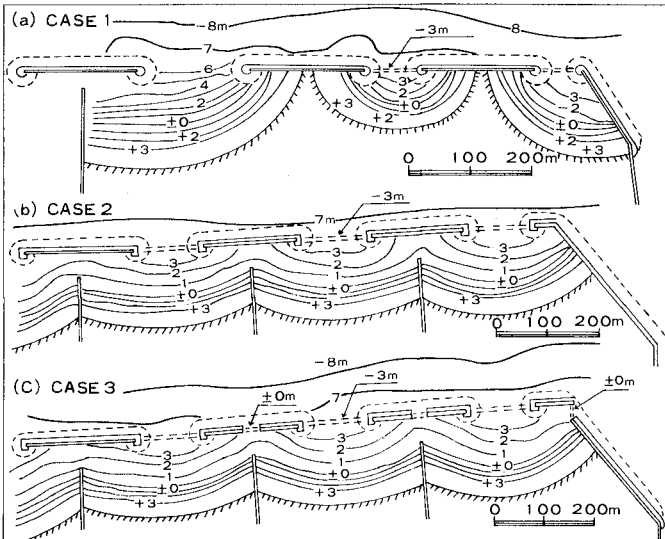


Fig. 11 Typical layouts of the artificial beach tested for the west portion

small open part of ± 0 m deep in the center of the offshore breakwater. Fine sand of 0.29 mm in median dia. was used as sediments.

(a) Comparison between Cases 1 and 2

Fig. 12 shows the change of the water depth between before and after 6 hours run of waves of 5 cm in height and 0.85 s in period. The model waves correspond to the prototype waves of 2.5 m height and 6 s in period on the basis of Floude's law. The waves come from SSW and the bottom topography before the run is the same as that in Fig. 11. For both cases, each beach is eroded in the part directly facing the incident waves and accreted in its either side sheltered by the offshore breakwaters. However, the quantity of water depth changes and the recession of shoreline at the center are severer in Case 1 than in Case 2 and more sand was lost seaward of the breakwater in the former case than in the latter case.

Fig. 13 shows the pattern of the currents caused by the waves for these two cases. The currents are measured by following by eyes the movement of a plastic ball of 0.7 cm in dia., the inside of which is filled with water so as for the ball to be a little heavier than the water. In Case 1, there are strong currents going outwards out of the open mouth of the western two beaches, but, in Case 2, there is not such current except weak currents in the central compartment. In Case 2, most currents approaching toward the offshore tip of either groin from the center of the beach flow towards the next compartment through the gap between the groin and the offshore breakwater. This difference of the current pattern is the cause that the sand loss in Case 1 is larger than that in Case 2. The seaward currents transport out the sands suspended on the beach by wave action.

(b) Comparison between Cases 2 and 3

Case 2 has rather large accumulation of sand in the vicinity of the tip of groin, as seen in Fig. 12. This accumulation is likely to grow up gradually and obstruct the current flowing toward the next compartment through the gap. Case 3 is a arrangement devised to prevent such obstruction, having the small open part of ± 0 m in its crown level in the center of the breakwater as mentioned previously. Fig. 14 shows the effect of the small open part, this is, the change of water depth between before and after 6 hours run of the same wave as (a) mentioned above but in SSE direction. In Case 3 with the small open parts, the vicinity of the tip of the groins is scoured and the recession of the shoreline at the center is smaller than in the Case 2.

The comparison of depth contour lines of the central compartment in these two cases is shown in Fig. 15 with the wave height ratio of Case 3 against Case 2. It is seen from the figure that the small open part makes wave height behind the offshore breakwater 3 - 1.5 times as large as the case without it, giving rise to currents running from it towards the base of the groin. As the results, the area around the tip of the groins is scoured and the accumulating area behind the offshore breakwater shifts toward the center of the compartment. Therefore, the sand transported along the shoreline from the central area of the compartment toward the both side decreases in volume, which prevent the recession of the shoreline at the center area of the compartment.

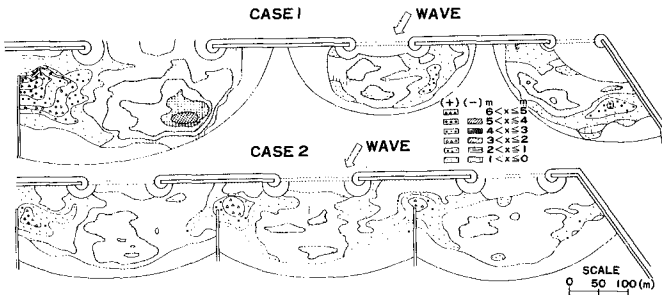


Fig. 12 Comparison of depth changes by wave action between Cases 1 and 2

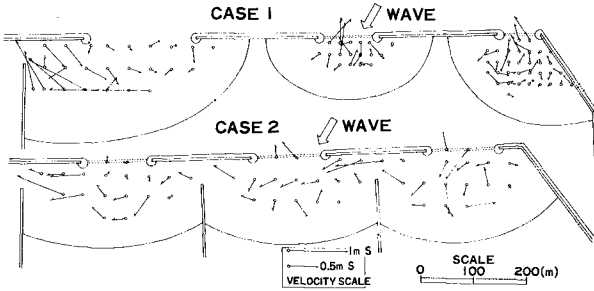


Fig. 13 Current patterns of Cases 1 and 2

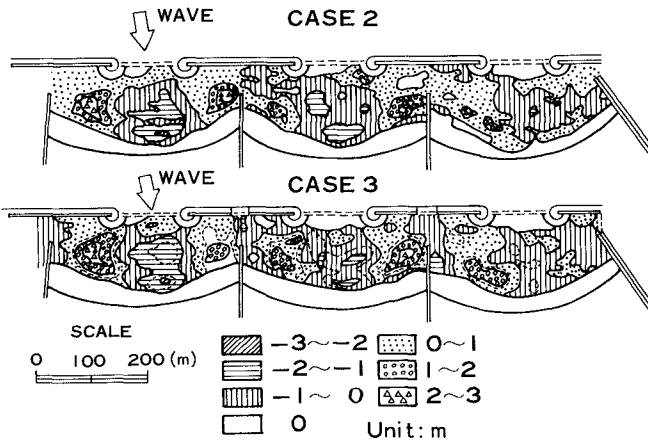


Fig. 14 Comparison of depth changes by wave action between Cases 2 and 3

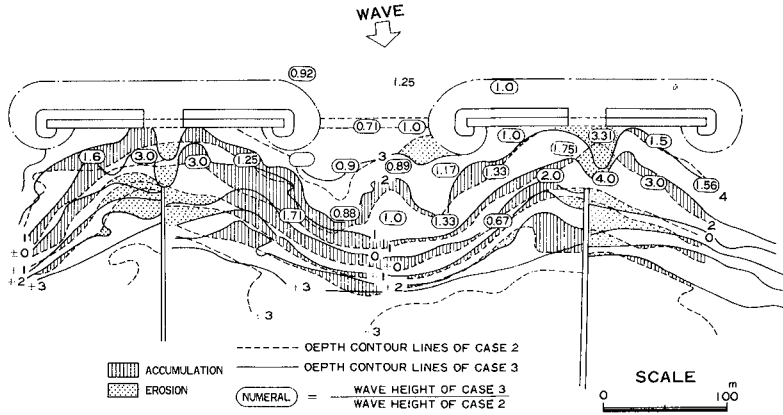


Fig. 15 Comparison of the depth contour lines between Cases 2 and 3

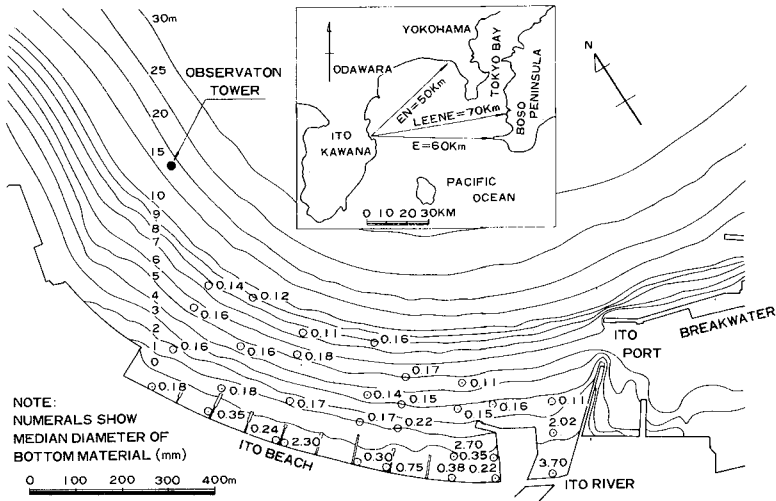


Fig. 16 Bathymetric map of Ito coast

ITO BEACH

Natural Condition of Ito Beach

Ito City is located at the east coast of Izu Peninsula which is about 100 km southwest from Tokyo as shown in Fig. 16. The figure shows bathymetric map of Ito Coast just before the beginning of the construction of the artificial beach, in 1973. The height of the backshore is 3 - 4 m above L.W.L. and the beach slope is nearly of 1/10 on the foreshore and 1/25 - 1/30 between 1 and 6 m. But the deeper part than 10 m deep has steeper slope of about 1/10. The median diameter of sea-bed material is 0.2 - 0.5 mm on the foreshore and 0.2 - 0.12 mm on the offshore until 6 m deep.

The beach is sheltered by the head land of Kawana against southerly waves, as estimated from Fig. 16. Therefore, northerly waves are predominant at the beach, but their height is almost 1.5 m in H1/3 except when typhoons pass near the beach in summer and autumn. Tidal current flowing in nearly parallel with the coast in the offshore forms reverse circulating currents in the nearshore the velocity of which is weak and the order of several $\text{cm}\cdot\text{s}^{-1}$. The mean range of spring tide is nearly 1.5 m.

Scheme of Artificial Beach Construction

The beach of nearly 900 m long, which is to the west of Ito port as shown in Fig. 16, is at present protected by 8 groins of 40 - 60 m long and has the sea wall of 4.8 m above L.W.L. in crest height. The road just behind the sea wall is very jammed by traffic in resort season. Ito City, which is a tourist resort with hot springs, has decided in 1973 with the aid of the central government to change the beach into a more beautiful and cleaner resort place after widening the road seaward by 7.5 m. Therefore, the authors have conducted the model experiment to make the plan of artificial beach.

Fig. 17 shows a plane view and a beach profile of the scheme of artificial beach which has been decided on the basis of the model experiment. A fishing basin of the east side and a slope way for fishery boats of the west side accommodate small fishery boats scattering on the beach at present. The present seawall is shifted seaward by 7.5 m as mentioned above, the green belt of 12.5 m wide is made, and artificial beach is arranged in front of the green belt. The beach is protected by three offshore breakwaters of 3.0 m above L.W.L. in crown height and three long groins, of which the two groins in the both side also work to protect the fishery boat area. The short wing parts parallel with the shore are attaching at the tip or its vicinity of each groin, which serves to stabilize sea-bed as shown later. The offshore breakwater are of rubble mound type covered with artificial brocks and the groin is of impermeable type of concrete blocks. Moreover, the tip part of each groin is protected with wave absorbers of artificial concrete blocks.

Model Test on Sea Water Exchange

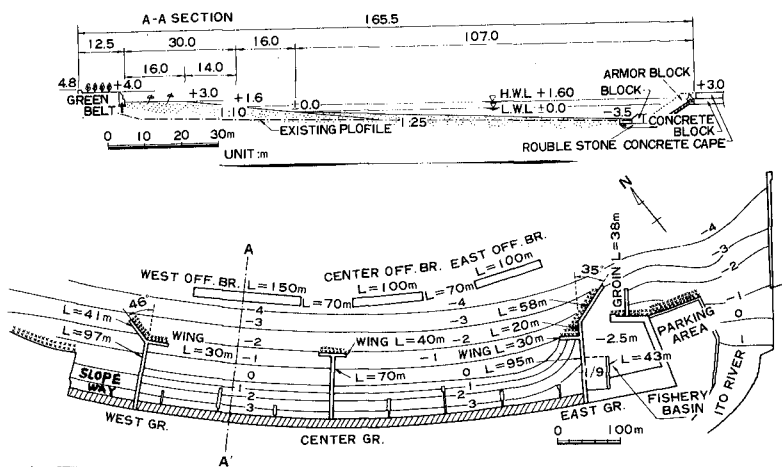


Fig. 17 Scheme of the artificial beach at Ito

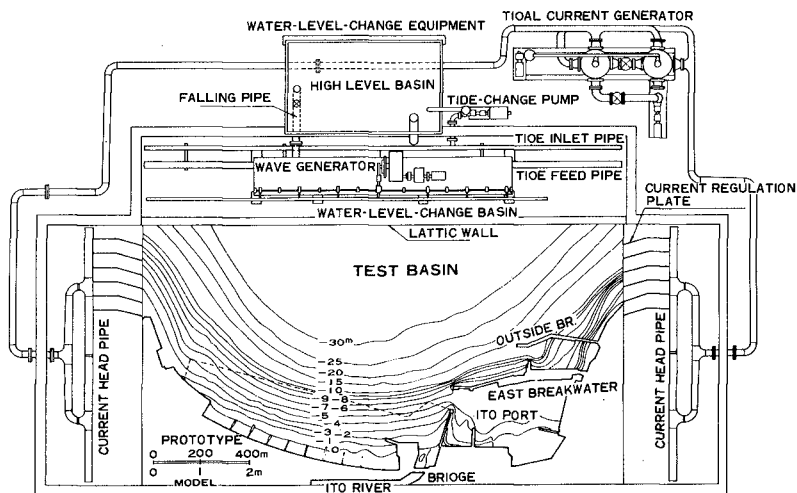


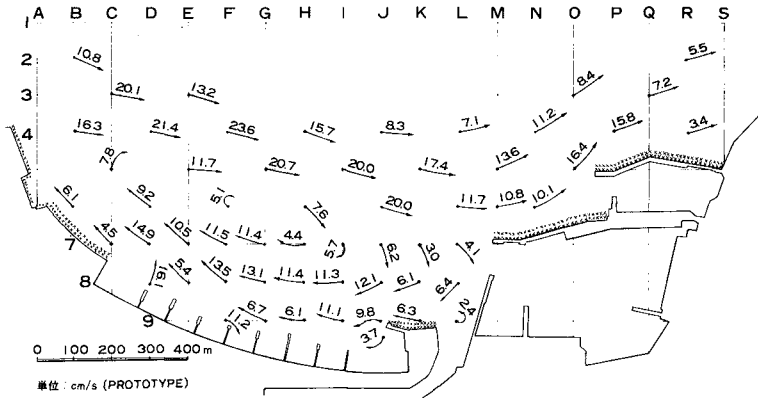
Fig. 18 A plane view of the model for sea-water exchange test

Fig. 18 shows a plane view of the model for the test on sea water exchange conducted in order to determine the above-mentioned scheme of Ito artificial beach. The model is of concrete mortar floor with the reduced scale of 1/200 in horizontal and 1/100 in vertical, in which the part deeper than 30 m deep below L.W.L. is made as the constant depth of 30 m deep. A tidal current generator, of which the main part is shown in the right upper part of the figure, produces cyclic currents flowing from right to left or from left to right in the test basin by means of a pump and rotating valves. The water level in the basin is periodically changed by a water-level-change equipment, which pumps up some suitable volume of water from the water-level-change basin to the high-level basin together with falling down some water by gravity from the latter basin into the former basin through a falling pipe. The water-level-change basin is separated by a lattice wall from the test basin so that the water is able to commute between these two basin freely. A wave generator is arranged in the water-level-change basin so as not to disturb currents in the test basin.

Fig. 19 shows the patterns of currents when both steady currents and waves are in force. The velocity of the steady currents corresponds to the maximum velocity of current at falling tide. The steady waves are 30 cm in height and 10 s in period which correspond to swells in summer. In the figure, numerals beside arrow marks of current direction show velocity in unit of $\text{cm}\cdot\text{s}^{-1}$. In (a) of the figure, there are reverse currents in the shallower area against the main currents flowing from left to right, and the currents of $10 \text{ cm}\cdot\text{s}^{-1}$ or so seen in the vicinity of the shoreline are caused by breaking waves. In (b) of the figure, there are comparatively strong currents flowing out from the open parts among offshore breakwaters and groins, though the current velocity inside the offshore breakwaters is nearly the same order as the existing state without offshore breakwaters and groins. The similar phenomenon appears also in the case of rising tide in which the main currents flow from right to left.

In order to check the influences of offshore breakwaters and groins on the sea water exchange between the onshore and offshore sides of these structures, fluorescent dye was discharged at 7 points on the M.W.L. shoreline only for 9 minutes at the time of the first H.W.L. and its dispersion was traced by taking the colour pictures from the ceiling under the condition that the sine curves of tide and current are generated to simulate the state of mean spring tide in addition to swells in summer. Discharged fluorescent dye is 700 cm^3 in volume and 500 ppm in density for each test. The current distribution at the M.W.L. of falling tide is the same as one shown in the above-mentioned Fig. 19. Fig. 21 shows the time changes of dye dispersion for the cases without and with the artificial beach, where each figure of 9 and 45 minutes corresponds to the first H.W.L. and the second H.W.L., respectively, as shown in Fig. 20. Currents flow from left to right in the offshore and from right to left in the nearshore during 9 minutes to 27 minutes. The dye discharged on the shore is transported offshoreward by current and diluted by mixing with the surrounding water. The case with the artificial beach is seen to be a little better than the case without it in offshoreward dispersion of fluorescent dye. It is because the offshore breakwaters serve as training walls against the

(a) Existing state



(b) State with the artificial beach

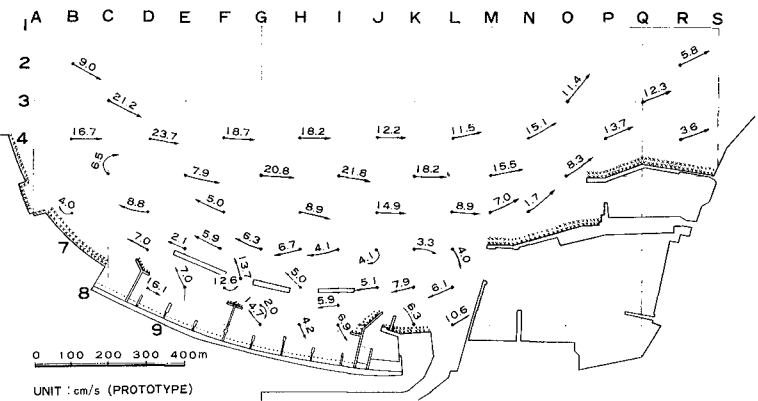


Fig. 19 Patterns of the fastest currents falling tide with summer swells

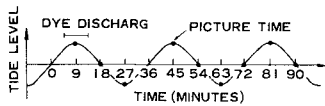


Fig. 20 Relation between tide and the time when dye-pictures were taken

current in their vicinity, as assumed from the current distribution in Fig. 19.

Model Test on Beach Evolution

For the model test on the evolution of artificial beach, in the model basin shown in Fig. 18, the area in the vicinity of the shore bounded with the dotted line was changed to the movable bed of fine sand of 0.17 mm in median diameter and the area deeper than 10 m deep was remolded to become constant depth of 10 m deep. Moreover, the wave generator was moved onto this part of constant depth and set to be parallel with the lattice wall. In this test, the water level was always M.W.L. and tidal currents was not generated.

Fig. 22 shows the changes of equi-depth lines due to wave action in the first proposed scheme. Model wave is 3 cm in height and 1 s in period which corresponds to the prototype wave of 3 m in height and 10 s in period by Floude's law. (a) and (b) in the figure corresponds respectively to before and after 3 hours of the run. As (b) is compared with (a), the foreshore near each groin of West and Center remarkably erodes and the area behind of each offshore breakwater remarkably accretes. Moreover, the mouth of the fishery basin in the eastside also shoals. As the countermeasures against such remarkable changes of the bottom topography, short wing breakwaters were attached at the tip or its vicinity of each groin and short jetty was added at the east side of the entrance of the fishery basin. Their effects are shown in Fig. 23, where the seawall is shifted seaward by 20 m in order to keep the space of the green belt and the widened road. Comparing this figure with Fig. 22, the changes of topography is much less remarkable. It means that the wing breakwater attached on the groin serves not only to prevent the erosion at the foot of the groin but also to restrain the accumulation behind the offshore-breakwater. The accumulation at the entrance of the fishery basin also has been moderated by the installation of the short jetty.

Change of Equi-Contour Lines at The Site

Construction of the West Offshore Breakwater has started in autumn of 1974, and its part of 120 m long has been completed until 1979. Fig. 24 shows the comparison of equi-contour lines between 1974 and 1979. Though the contour lines were in parallel with the shore-line in 1974, there are remarkable accumulation at the lee of the offshore breakwater in 1979. Especially the contour lines of ± 0 and 2 m deep advance toward the offshore breakwater and the slope between 2 and 4 m deep is steeper than 1974. These tendency of sea-bed change in the lee of the offshore breakwater can be observed in the model test shown in Fig. 22 and 23, though the value of contour lines which changed remarkably is a little different from the site. At the areas of the both side of the offshore breakwater, the area deeper than ± 0 m are scoured, especially the contour lines of 1 to 3 m deep receding landwards. But, the contour lines higher than ± 0 m deep do not recede on account of the existance of shore groins.

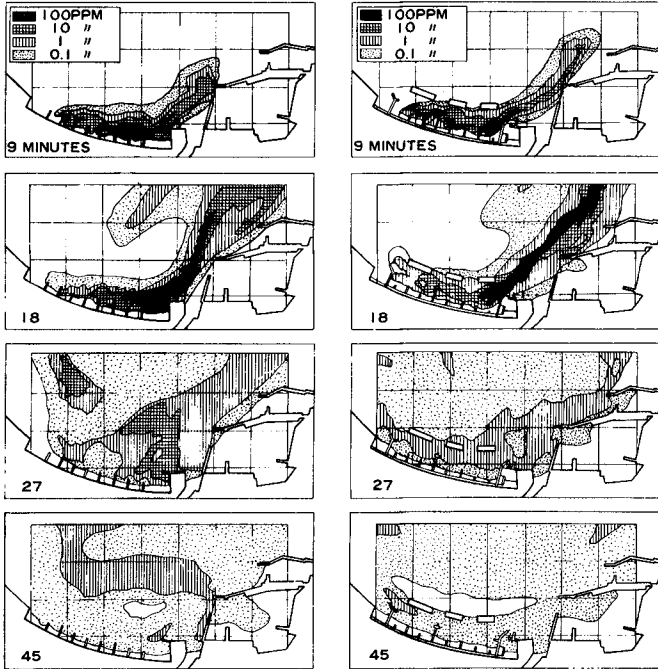


Fig. 21 Time change of dye dispersion

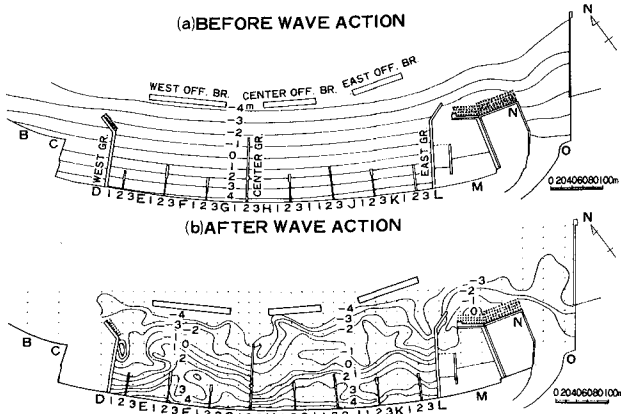


Fig. 22 Change of equi-depth line due to wave action for the first proposed scheme

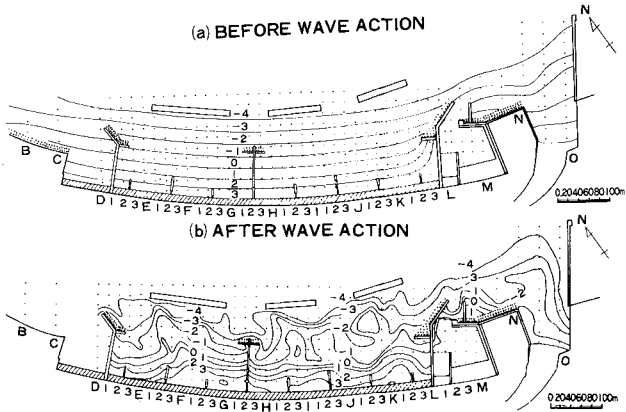


Fig. 23 Changes of equi-depth lines due to wave action for the artificial beach

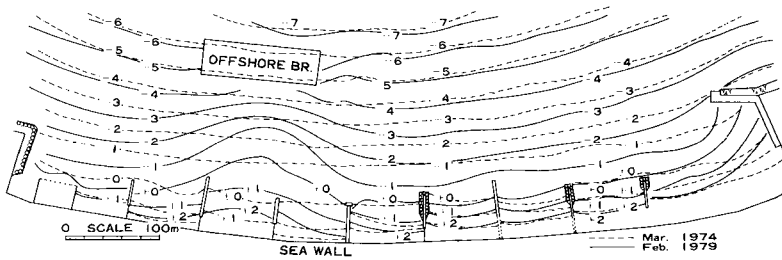


Fig. 24 Changes of equi-contour lines by the construction of west offshore breakwater at the site

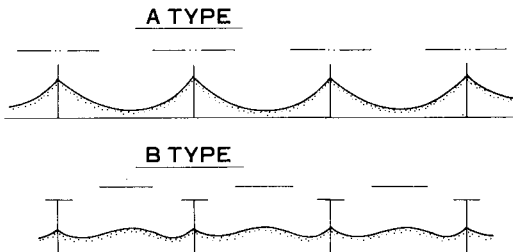


Fig. 25 Typical layouts of structures for the protection of an artificial beach

Conclusion

There are two types on the layout of the structures at artificial resort beach in Japan as shown in Fig. 25, one is the layout where a groin is installed behind an offshore breakwater as in Suma Beach and the other is the one where a groin is installed at the open part between offshore breakwaters as in Ito Beach. In the following description, the former layout is called A type and the latter one B type. The followings can be remarked from the above-mentioned tests:

- (1) In A type layout, the shoreline of each compartment between groins is likely to change to concave one with recession at its center and advancement at its either side. The bottom-slope just in front of the foreshore becomes flatter in the middle part and steeper in the either side part. In this case, placement of a submerged breakwater near the foreshore in the middle of the compartment is not effective to prevent the recession of the middle part.
- (2) In B type layout, the shoreline of each compartment tends to change to convex one with advancement at the center and recession at the either side. The bottom-slope of the middle part becomes steeper in the offshore far out of the foreshore though the part near the foreshore becomes flatter, and it of the either side becomes flatter in front of the foreshore.
- (3) In A type layout, the groin must not be connected with the offshore breakwater from the stand-point of the prevention against the loss of the beach sand outwards of the offshore breakwater and the stagnation of polluted water in the inside of the offshore breakwater. Moreover, lowering the crown level of a little part in the center of the offshore breakwater serves to moderate the erosion at the middle part of the beach as well as the accumulation at the either side part of it.
- (4) In B type layout, the groin should have a short wing breakwater at its tip. It serves to moderate the erosion near the groin as well as the accumulation behind the offshore breakwater.

ACKNOWLEDGEMENT

The authors express grateful thanks to the authorities of Kobe and Ito Cities for their presentation of many field data and to Messrs Hisao Kimura and Hideo Osanai in the same institute as the authors for their hearty cooperation in the model test.

CHAPTER 123

SEAWALLS IN DEEP SEAS

by

Shoshichiro Nagai¹, F. ASCE and Shohachi Kakuno²

ABSTRACT

Features in wave overtopping of two new types of seawalls designed to be built in considerably deep sea conditions are presented herein. One of those is the seawall of concrete caisson with a parapet wall and armor blocks on the top of the caisson, and another one is the seawall with a slitted box-type wave absorber.

The former type of seawall has successfully been constructed in the Japan Sea and the Seto Inland Sea and is also to be constructed at a site directly exposed to an open sea of the Pacific Ocean in 1980 and 1981. The latter type of seawall was proposed in 1977 after numerous experiments and has been under construction in the Port of Osaka since 1978.

The results of the experiments on the wave overtopping over the slit-type seawall were compared with the calculated results, obtained by an analysis in which the wave overtopping over a parapet wall was considered similar to the phenomenon of flow over sharp-edged weirs having time-dependent overflow-head. The calculated curves obtained are in good agreement with the experimental results.

The designs of these two types of seawall are also presented herein.

INTRODUCTION

In recent two decades in Japan, a special type of seawall, in front of which a 1 : 1.5 slope covered with concrete armor blocks is built, has been constructed to protect reclaimed lands and coastal areas from overtopping of waves during typhoons. The water depths at the sites have been several meters to about ten meters or a little more. The heights of the design waves were several meters and the

¹ Professor Emeritus, Director of Harbor and Coastal Engineering Laboratory, Osaka City University, Osaka, Japan

² Research Associate of Hydraulic Engineering, Faculty of Engineering, Osaka City University, Osaka, Japan

periods of them were 8 sec to 13 sec. Most of the seawalls, designed after experiments had been carried out at scales of 1/20 to 1/30, have been proved to be successful after attack of storm waves [1].

However, when the water depths where a seawall is built become so large as about 15 m to 25 m or more and the design waves are more than several meters in height and 13 sec to 15 sec in period, the section of the seawall mentioned above becomes very large; therefore its cost of construction becomes extremely high.

From such a reason, a new type of seawall was proposed in 1969 after numerous experiments had been carried out in the wave channel with a wind blower in our laboratory. This type of seawall is composed of a big concrete caisson with a parapet wall and concrete armors on the top. It has already been constructed at one place on the shore of the Japan Sea and one in the Seto Inland Sea, and has been under construction at a place on the shore of the Pacific Ocean since 1980.

In 1977 another type of seawall for deep seas was proposed. This type of seawall, called slit-type seawall, is composed of a concrete caisson and a slitted box-type wave absorber attached to it. It has been under construction in the Port of Osaka since 1978 [2].

CLASSIFICATION OF BEHAVIORS OF OVERTOPPING

As shown in Table 1, the behavior and quantity of overtopping waves over seawalls have been classified and judged in Japan the appropriateness of the seawalls by the relative overtopping quantity, q/q_0 , in which q denotes the quantity of overtopping over the unit length of a seawall for a wave period and q_0 is the volume of water transported shoreward over the unit length of the seawall by a shallow water wave for a wave period ($= HL/2\pi$, H : wave height, L : wave length) [1].

As known from Table 1, the limiting relative overtopping quantity for a seawall is $q/q_0 = 5 \times 10^{-3}$, that is, when $q/q_0 \leq 5 \times 10^{-3}$ the seawall can be effectively adoptable in the field.

TABLE 1.- Classification of Behaviors of Overtopping

Classification	Behavior of overtopping	q/q_0	Appropriateness
I	Only spray overtops (very well absorption of wave)	0 to 10^{-4}	Ade- quate for seawall
II	Lumps of water overtop (higher limit applicable to a seawall)	10^{-4} to 5×10^{-3}	
III	A substantial part of wave over- tops (imperfect absorption of wave)	5×10^{-3} to 10^{-2}	Inade- quate for seawall
IV	Large volume of wave overflows (poor absorption of wave)	10^{-2} to 10^{-1}	

SEAWALL OF CONCRETE CAISSON WITH A PARAPET WALL AND ARMOR BLOCKS ON THE TOP

The latest seawall of concrete caisson with a parapet wall and armor blocks on the top has been under construction since 1980 at a site, Gobo, directly exposed to an open sea of the Pacific Ocean, as shown in Fig. 1, to protect a reclaimed land of about 350,000 m² for a thermal power station from wave overtopping during typhoons. Fig. 2 shows the cross-section of the seawall. The water depth at the site is about 18 m below Datum Line (D.L.), and the design wave height and period are $H_{1/3} = 9$ m and $T_{1/3} = 13$ sec at the design sea level of 3.6 m above D.L.. The sea-bottom in front of the seawall has a slope of 1/100. N-shaped blocks are used as the concrete armors to be placed on the top of the caisson because they have much greater stability against wave attack than other specially-shaped concrete armors, in addition to their distinguished ability for absorbing wave energy [3].

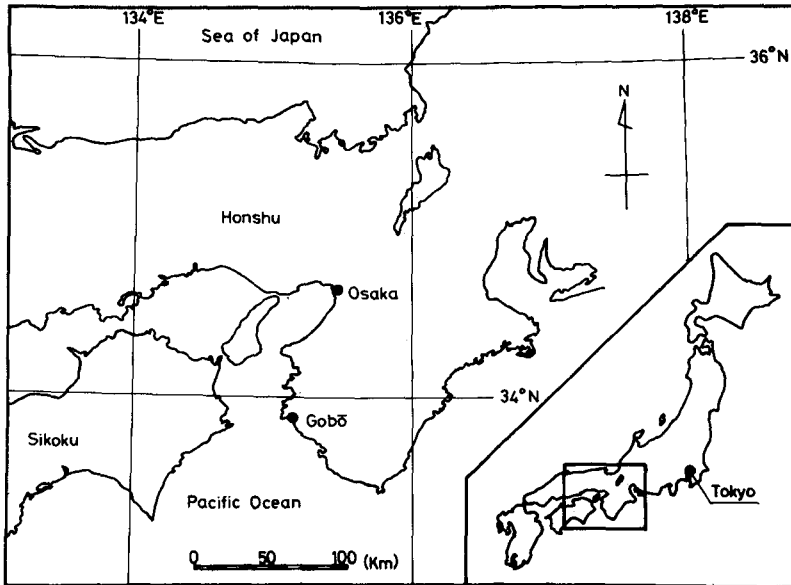


Fig. 1.- Location Map of Seawalls

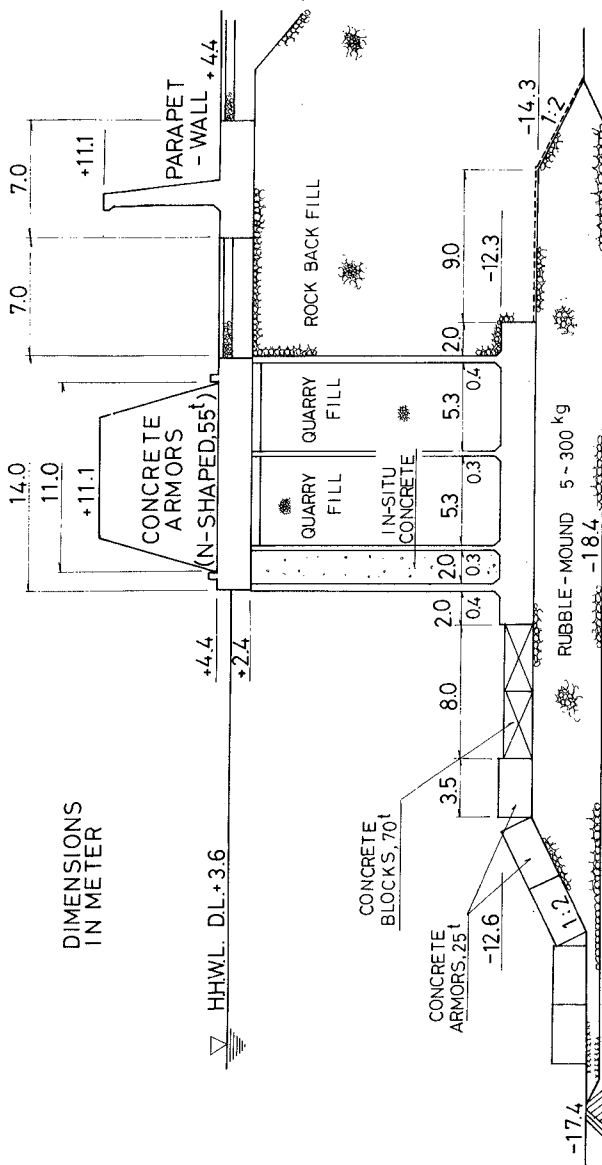


Fig. 2.- Seawall of Concrete Caisson with a Parapet Wall and Armor Blocks on the Top

Experimental Equipment and Procedures

In order to measure wave overtopping quantity over the seawall shown in Fig. 2 and to examine the stability of the concrete armors against wave attack, a great number of experiments were carried out at a scale of 1/35 using a wave channel with a wind blower, 100 m long, 1.2 m wide, and 2.0 m high, shown in Fig. 3.

The characteristics of the waves and winds used in the experiments are shown in Table 2.

Winds of velocities of 10 m/sec were blown in models over the waves in the wave channel to simulate the circumstances of the actual overtopping waves and sprays over the seawalls in the field.



Fig. 3.- Wave Channel (100 m long) with a Wind Blower

TABLE 2.- Characteristics of Waves and Winds in the Experiments

Wave characteristics (prototype)		Wind velocity (model)	Sea level (prototype)
Period T_p (sec)	Height H_p (m)	V_m (m/sec)	D.L. + (m)
13	8.7 to 12.4	10	3.6
10	8.5 to 12.6		
15	9.0 to 10.1		

As listed in Table 3, four conditions of the armor blocks were tested in the experiments. Fig. 4 shows the N-shaped block of 6 ton, and Fig. 5 shows the way of placing of the N-shaped blocks in two layers on the top of the caisson.

TABLE 3.- Conditions of the Armor Blocks
on the Top of the Caisson

Cross-section	Armor blocks	Weight (ton)	Placing	Width of placing (meter)	Top of armor blocks (meter)	Top of parapet wall (meter)
I	N-shaped	28	2 layers (5,4) rows	15.8	D.L. + 9.5	D.L. + 11.1
II		28	3 layers (5,4,3) rows	15.8	D.L. + 11.5	D.L. + 10.1
III		55	2 layers (3,2) rows	11.0	D.L. + 11.1	D.L. + 11.1
IV		55	2 layers (4,3) rows	14.8	D.L. + 11.1	D.L. + 10.1



Fig. 4.- N-Shaped Block



Fig. 5.- N-Shaped Blocks in Two Layers

Experimental Results

Stability of the armor blocks was firstly examined using the cross-sections-I and -II with 28-ton N-shaped blocks in two or three layers. The results of the experiments for the waves used in the experiments showed that the N-shaped blocks of 28 tons were stable and the relative wave overtopping quantity, q/q_0 , for both sections was about 1×10^{-3} , smaller than the limiting quantity of 5×10^{-3} , if they were placed on the top of the caisson in two or three layers.

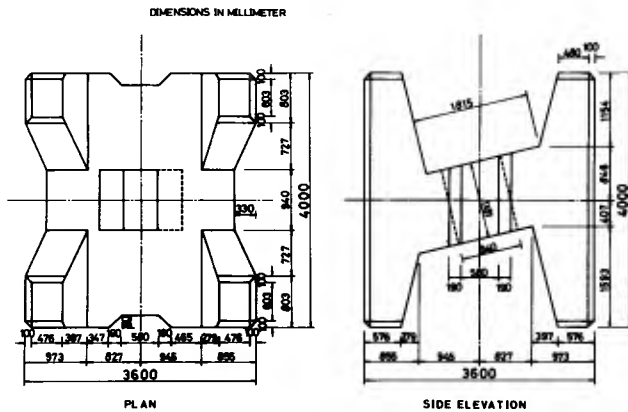


Fig. 6.- Detail of 55-Ton N-Shaped Block

Reinforced 55-ton N-shaped blocks, shown in Fig. 6, however, were decided to use in practice for more safety. Fig. 7 shows the results of q/q_0 as a function of wave height, H , for the seawalls with the 55-ton N-shaped blocks of the sections-III and -IV.

From Fig. 7 it may be stated that the overtopping quantities in the sections-III and -IV are almost same if the characteristics of the waves are same, and q/q_0 for the design wave of $T_{1/3} = 13$ sec and $H_{1/3} = 9$ m is about 1×10^{-3} in these two sections. Therefore, the seawalls with these sections are adoptable to the seas, as known from Table 1.

The section-III, shown in Fig. 2, was decided to adopt as the design section, because the width of placing of the armor blocks, 11.0 m, is smaller than the width of the caisson, 14.0 m.

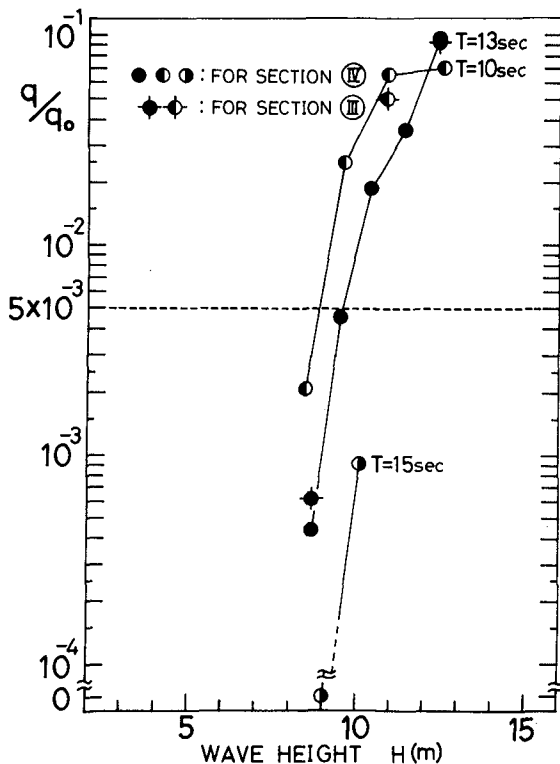


Fig. 7.- q/q_0 as a Function of Wave Height

SLIT-TYPE SEAWALL

The slit-type seawall, shown schematically in Fig. 8, is composed of a concrete caisson founded on a rubble mound and a box-type wave absorber, attached to the caisson, with a slitted vertical front-wall and a slitted horizontal bottom-wall. Experimental results have already proved that this type of structure has features of low reflection and distinguished reduction in wave pressures [4, 5], and also has an ability of reduction in wave overtopping to a considerable extent if it is used as a seawall.

Experimental Equipment and Procedures

The experiments were carried out at a scale of 1/25 by using a wave channel with a wind blower, 50 m long, 1.0 m wide, and 1.75 m high.

The heights and periods of the waves used in the experiments are $H = 2.0$ m to 6.0 m, and $T = 6.0$ sec to 12.0 sec. The velocity of wind used is constant $V = 23$ m/sec in prototype through the experiments. The widths of wave chambers of the slitted box-type wave absorbers are $l = 3.75$ m and $l = 2.50$ m in prototype. The void ratios of the vertical front-wall and horizontal bottom-wall are constant $\lambda = 0.24$ and $\lambda' = 0.14$, respectively, through the experiments. The depths of water where the seawalls locate are $h = 12.2$ m, 13.2 m, 14.2 m, and 15.3 m. The rubble mound on which the caisson is founded has a top width of $B = 10.5$ m in prototype and a sea-side slope of 1 : 2.

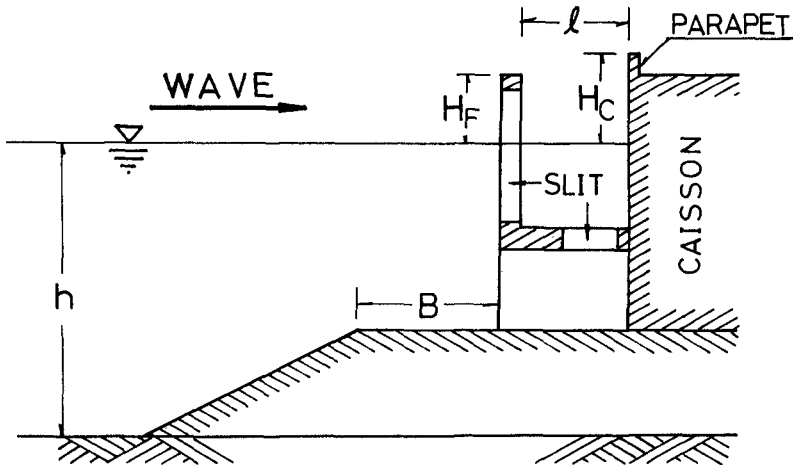


Fig. 8.- Schematic Cross-Section of the Slit-Type Seawall

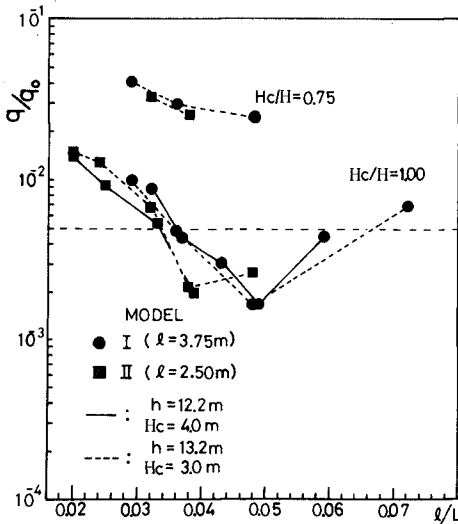


Fig. 9.- Relationship between q/q_0 and l/L .

0.05 of l/L for the minimum relative overtopping, $(q/q_0)_{\min}$, of the slit-type seawalls are less than half of 0.13 to 0.18 for the minimum reflection coefficient, $(K_R)_{\min}$, of the slit-type breakwater or quay-wall [4]. Because the horizontal velocities of the waves plunging into the wave chamber are attenuated by making the value of the relative chamber width to be 0.04 to 0.05.

The relations between q/q_0 and H_c/H in association with the characteristics of waves may be much of interest in the design of the seawalls. Figs. 10 through 13 show the relationships between q/q_0 and H_c/H when the values of l/L fall within the range of 0.04 to 0.05 for $(q/q_0)_{\min}$. From these figures it can be seen that the values of q/q_0 and H_c/H are in a certain relation regardless of the incident wave heights, and the values of q/q_0 become smaller than the limiting relative wave overtopping quantity of 5×10^{-3} , if H_c/H is taken to be larger than 1.0 and H_F/H , in which H_F denotes the height of the top of the vertical front-wall above the design sea level, is taken to be larger than or equal to 0.70.

Comparisons of wave overtopping quantities of the slit-type seawalls with those of other types showed that the slit-type seawalls give much smaller values of q/q_0 in most cases [2].

Experimental Results

The values of relative overtopping quantity, q/q_0 , for the slit-type seawall depend mainly upon the relative wave chamber width, l/L (wave chamber width/wave length). The minimum value of q/q_0 is obtained to be about 1×10^{-3} at the range of about 0.04 to 0.05 of l/L , if the relative parapet wall height $H_c/H = 1.0$, as shown in Fig. 9, in which H_c denotes the height of the top of the parapet wall above the design sea level. The range of about 0.04 to 0.05 of l/L where the minimum value of q/q_0 is obtained does not vary even though H_c/H becomes larger than 1.0. The values of 0.04 to

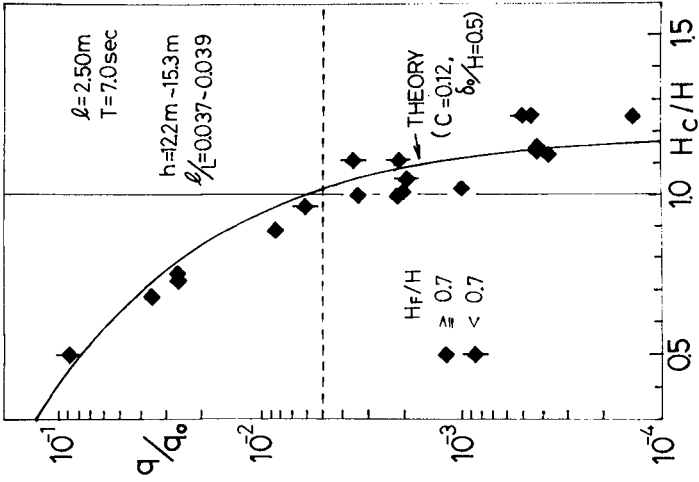


Fig. 11.- Relationship between q/q_0 and H_c/H

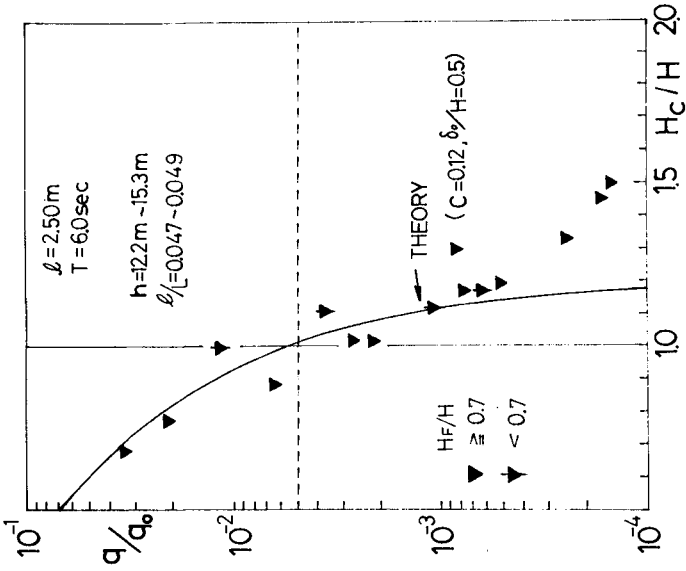


Fig. 10.- Relationship between q/q_0 and H_c/H

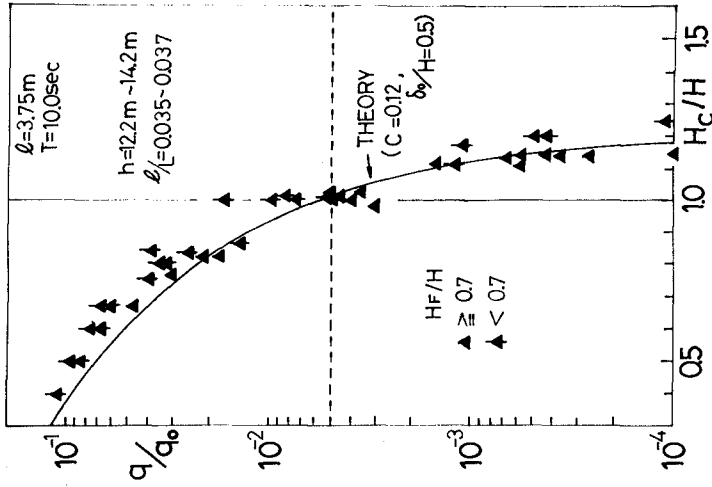


Fig. 13.- Relationship between q/q_0 and H_c/H

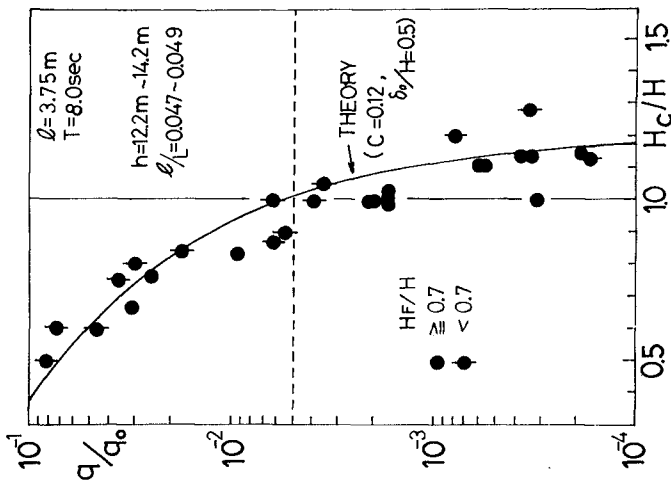


Fig. 12.- Relationship between q/q_0 and H_c/H

Calculations of Overtopping Quantities for the Slit-Type Seawall

When the water level inside the wave chamber of the slit-type seawall becomes higher than the top of the parapet wall, water flows over the parapet wall. The overflow was observed to occur calmly if $1/L$ was smaller than 0.06. This phenomenon implies that the analytical approach on wave overtopping over vertical seawalls [6] can also be useful for the analysis on the wave overtopping over the slit-type seawall with the values of 0.04 to 0.05 of $1/L$.

(1) Assumptions and analysis

The surface elevation inside the wave chamber is considered to be a perfect standing wave with the wave height of $2\gamma_T \cdot H$, in which γ_T is the transmission coefficient of the perforated (slitted) walls of the absorber and H denotes the incident wave height, because it is composed of the transmitted wave, η_T , through the perforated wall and the reflected wave, η_{TR} , from the solid back-wall, as previously described [4].

Therefore the time history of the surface elevation inside the wave chamber can be written

$$\eta(t) = \gamma_T \cdot H \cdot \sin(2\pi t/T) + \delta_0 \quad (1)$$

in which T is the period of the wave, $\eta(t)$, and is identical with that of incident waves, and δ_0 is the mean water surface elevation from the still water level at the solid-back wall, which can be observed in the experiments and could be subject to the characteristics of the incident waves, water depths, wave chamber widths, and the profiles of the rubble mounds.

Supposing that the parapet wall of the seawall is a sharp-edged weir, and that the overflow-head for it is $\eta(t) - H_C$, varying with time, one gets the overtopping quantity over the unit length of the seawall for a wave period as

$$q = 2 \int_{t_1}^{t_2} \frac{2}{3} \cdot C(t) \cdot \sqrt{2g} \{ \eta(t) - H_C \}^{3/2} dt \quad (2)$$

in which t_1 is the time when $\eta(t)$ equals H_C , t_2 is the time when $\eta(t) = \eta(t)_{\max} = \gamma_T \cdot H + \delta_0$, and $C(t)$, termed the coefficient of wave overtopping in this paper, is the coefficient corresponding to the discharge coefficient used in the expression for the discharge of the flow over weirs.

Supposing that the coefficient of overtopping is constant with time, i.e., $C(t) = C$, and substituting Eq.(1) into Eq.(2), one can get

$$q = \frac{4\sqrt{2}}{3} \cdot C \cdot (\gamma_T \cdot H)^{3/2} \int_{t_1}^{t_2} \left\{ \sin \frac{2\pi}{T} t - \frac{1}{\gamma_T} \left(\frac{H_C}{H} - \frac{\delta_0}{H} \right) \right\}^{3/2} dt \quad (3)$$

Dividing Eq.(3) by $q_0 = H \cdot L/2\pi$ to express Eq.(3) in the form of the relative overtopping quantity, and putting $t' = 2\pi t/T$ to express the integral term of Eq.(3) in non-dimensional form, one eventually obtains

$$q/q_0 = \frac{4\sqrt{2}}{3} \cdot C \cdot \gamma_T^{3/2} \cdot \frac{T\sqrt{gH}}{L} \int_{t_1'}^{t_2'} \left\{ \sin t' - \frac{1}{\gamma_T} \left(\frac{H_C}{H} - \frac{\delta_0}{H} \right) \right\}^{3/2} dt' \quad (4)$$

in which $t_1' = \arcsin \left(\frac{H_C}{H} - \frac{\delta_0}{H} \right) / \gamma_T$ and $t_2' = \pi/2$.

(2) Comparison with the experimental results

The full lines in Figs. 10 through 13 show the calculated results by Eq. (4). The value of $\gamma_T = 0.70$, which is the same value used in the calculations for the reflection coefficient of the box-type wave absorber [4], is used in the calculations. The values of C and δ_0/H in Eq. (4) are assumed to be $C = 0.12$ and $\delta_0/H = 0.50$ in order to fit the calculated results to the experimental results. The height of incident waves used in the calculations except the case of $T = 6.0$ sec is $H = 4.0$ m, which is the average value of the wave heights used in the experiments. For the case of $T = 6.0$ sec, $H = 3.0$ m is used to avoid the excessive wave steepness. The water depth used in the calculations is $h = 12.0$ m, which is about the same value as used in the experiments.

Figs. 10 through 13 show that the calculated curves obtained by the use of Eq. (4) with $C = 0.12$ and $\delta_0/H = 0.50$ are in good agreement with the experimental results. Most of the experimental results with the values of $H_F/H < 0.7$ in Figs. 10 through 13 are larger than the experimental results with the values of $H_F/H \geq 0.7$ and the calculated curves. The reason is that the upper portion of the wave crest just outside the front-wall plunges into the wave chamber over the top of the front-wall, and then it strongly hit the back-wall, to cause large sprays.

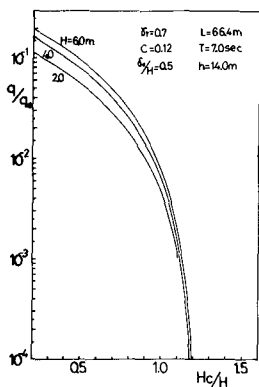


Fig. 14.- Effect of Wave Height

The calculated results also show that the effect of the incident wave heights on q/q_0 is not significant in the region of $H_C/H \geq 1.0$, as shown in Fig. 14.

Slit-Type Seawall in the Port of Osaka [2]

The slit-type seawall of 3,700 m length, the cross-section of which is shown in Fig. 15, has been under construction in the sea in the Port of Osaka, where the water depth is about 10 m to 12 m below the D.L., and the height and period of the design wave are $H_{1/3} = 3.3$ m and $T_{1/3} = 7.0$ sec.

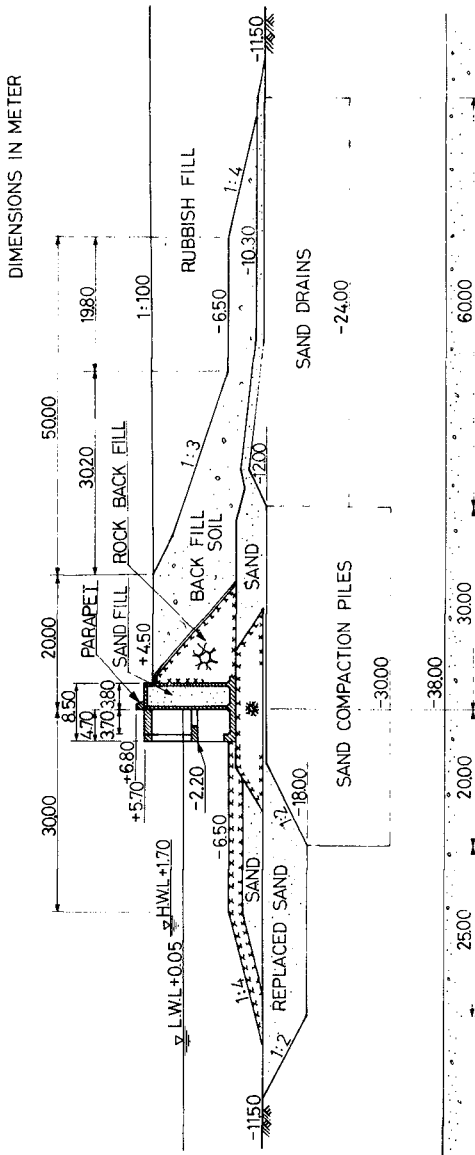


Fig. 15.- Cross-Section of Seawall in the Port of Osaka

The width of the wave chamber was taken $l = 3.7$ m to make the relative chamber width, l/L , equal to 0.15 for waves with a period of 4 sec, which occur most frequently when small fishing boats are in operation in the sea. Then the reflection coefficient takes the minimum values, $(K_R)_{\min} = 0.10$ to 0.20. The void ratios of the front-wall and bottom-wall were taken to be $\lambda = 0.22$ and $\lambda' = 0.14$, respectively. The height of the top of the parapet wall was taken D.L. + 6.8 m to make the relative wave overtopping quantity $q/q_0 \approx 1 \times 10^{-3}$ for the design sea level of D.L. + 3.5 m and the design wave, by taking $H_c/H = 1.0$ and $l/L \approx 0.05$, as shown in Fig. 9, for the wave period of $T = 7.0$ sec, which is the period of storm waves during typhoons.

Fig. 16 shows the completed caisson of the seawall, and Figs. 17 and 18 show the upper part and lower part of the seawall taken from the inside of the wave chamber.



Fig. 16.- Completed Caisson for Seawall



Fig. 17.- Upper Part of Wave Chamber of the Seawall



Fig. 18.- Lower Part of Wave Chamber of the Seawall

REFERENCES

- [1] Nagai, S., "Researches on Sea-Walls", Proc. of the 12th Coastal Engineering Conf., Washington, D.C., Sept., 1970, pp.1431 - 1450.
- [2] Onishi, H., and Nagai, S., "Breakwaters and Sea-Walls with a Slitted Box-Type Wave Absorber", Proc. of the Specialty Conf. on COASTAL STRUCTURES 79, Alexandria, March, 1979, pp. 2 - 28.
- [3] Nagai, S., "Stable Concrete Blocks on Rubble-Mound Breakwaters", J. of Waterways and Harbors Div., A.S.C.E., Vol. 88, No. WW3, Aug., 1962, pp. 85 - 115.
- [4] Nagai, S., and Kakuno, S., "Slit-Type Breakwater : Box-Type Wave Absorber", Proc. of the 15th Coastal Engineering Conf., Honolulu, July, 1976, pp. 2697 -2716.
- [5] Nagai, S., and Kakuno, S., "Wave Pressures on Slit-Type Breakwaters", Proc. of the 16th Coastal Engineering Conf., Hamburg, Aug., 1978, pp. 2360 - 2377.
- [6] Shi-igai, H., and Kono, T., "Analytical Approach on Wave Overtopping on Levees", Proc. of the 12th Coastal Engineering Conf., Washington, D.C., Sept., 1970, pp. 562 - 573.

PROBABILISTIC DESIGN OF SEA DEFENCES

by W.T. Bakker¹⁾ and J.K. Vrijling²⁾

0. ABSTRACT.

Designs of dikes and dunes according to current Dutch guidelines, based on a deterministic approach, are not consistent with probabilistic philosophy. This statement is amplified in the present paper as a pilot investigation; a rough outline for a probabilistic method of dune and dike computation is given. Numerical comparison of probabilistic and deterministic methods is hampered due to the fact that the results according to the deterministic approach depend on engineering instinct in the choice of boundary conditions and because the probabilistic approach is not as yet operational. Illustrative computations show differences of a factor 1000 in failure probability, starting from dimensioning according to the same standards, following deterministic guidelines.

1. INTRODUCTION.

Sea defences are constructed to safeguard the population against storm surges. The rich tradition in the field of dikes in Holland shows however, that complete safety is unattainable. Realizing this, a method to assess the probability of failure (or safety) of a system of sea defences has to be developed. All possible causes of failure have to be analysed and consequences determined. For this aim, the "fault tree" is a good tool (figure 1).

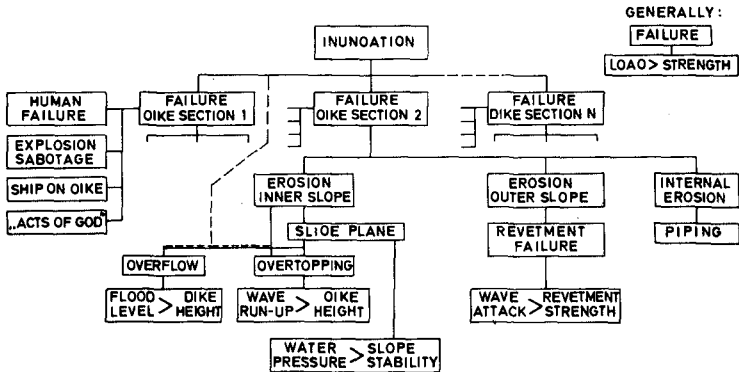


Fig. 1 Simplified fault tree for a dike circle, consisting of N sections.

1) Head of the Advisory Department Flushing, Rijkswaterstaat, Netherlands

2) Project Engineer, Delta Department, Rijkswaterstaat, Netherlands.

The fault tree combines four categories of events, that may cause the inundation of a polder:

- human failure; management faults;
- aggressive human action;
- "acts of God";
- technical failure of structural elements.

Although all four categories of events are equally important for the overall safety of the polder, the engineers responsibility is mainly limited to the technical and structural aspects. Therefore this paper deals only with technical failure of structural elements.

In the fault tree, all possible modes of failure of elements can eventually lead to the failure of a dike section and to inundation. This reflects good engineering practice, where attention should be given to all failure mechanisms of the construction under design. A common approach in the design of concrete or steel structures.

In dike and dune design, limit-state analysis is not yet established, although it has many useful features in clarifying technical problems as will be shown in this paper.

The ultimate limit-state (u.l.s.) of a failure mechanism describes the situation, wherein the acting loads are just balanced by the strength of the construction. The probability of occurrence of this u.l.s. for each technical failure mechanism can be found from a "convolution integral" (CIRIA, 1976).

Starting from a probability density function (p.d.f.) of the boundary condition one finds with a transferfunction the p.d.f. of the loads on the structural element, called $f_L(\lambda)$, being a function of the load λ . Combining the last-mentioned p.d.f. with the p.d.f. of the strength s of the structural section, called $f_S(s)$, gives the failure probability p_f of the element:

$$p_f = \int_0^{\infty} \int_0^{\lambda} f_S(s) ds f_L(\lambda) d\lambda \quad (1.1)$$

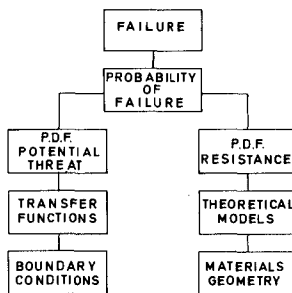


Fig. 2 The concept of the ultimate limit-state of a failure mechanism.

This concept is applicable in coastal engineering, when the narrow definitions of load and strength are widened to potential threat and resistance. The adapted concept of the ultimate limit-state of a failure mechanism is given in figure 2.

First, all basic variables that play a role in the theoretical relationships on which the design of a particular element is based, have to be specified. The main categories of basic variables are "resistance" and "potential threat". The category contains basic variables

that can be defined as threatening boundary conditions for the construction e.g. wind velocity extremes, water levels or a ship's mass.

The resistance of the construction is derived from the basic variables by means of theoretical models. The relations that are used to derive the potential threat from the boundary conditions are called transfer functions.

The safety margin between "potential threat" and "resistance" must guarantee a sufficiently low probability of failure.

Three different philosophies are currently available in construction practice:

1. deterministic philosophy;
2. quasi-probabilistic philosophy;
3. probabilistic philosophy.

The present dutch guidelines for dike and dune design follow a philosophy, that lies between the deterministic and the quasi-probabilistic approach. The ultimate potential threat is derived from extreme storm surge levels with a very low probability of exceedance (1% per century) and equated with the average resistance of the dike without any apparent safety margin. In this paper it will be shown that designs according these guidelines are not consistent with the probabilistic philosophy.

Beside the ultimate limit-state, there are situations, where the ever continuing presence of a load causes a deterioration of constructional resistance in time, without any imminent danger of failure (e.g. fatigue, creep).

However, this deterioration of constructional resistance can cause an unexpected failure in extreme conditions. The serviceability of the construction can also diminish without leading to collapse (e.g. settlements, deformation).

The serviceability limit-state is principally treated in the same way as the ultimate limit-state. However, attention is rather given to loading situations that occur very frequently during the lifetime of the construction than to extreme conditions.

A point of great practical importance is that a serviceability limit-state, i.e. a deterioration of constructional resistance in time, can be solved in two ways:

1. improving the resistance of the construction to guarantee sufficient strength during the service life;
2. the deterioration of constructional resistance can be controlled by inspection and maintenance procedures.

The second solution, however, introduces a certain non-technical risk, because constructional safety depends on the care of other people.

In some fields of dike and dune design the application of the limit-state conception as described above is cumbersome because a theoretical description is not available. This is especially true for erosion and scour problems, which govern the design of dunes and dikes. Neither transfer functions to transform waves and tide into forces on grains nor a theoretical model for the stability of grains are known.

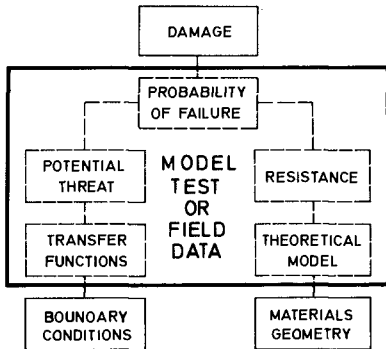


Fig. 3 The solution of a limit state by black box approach.

simplified dike designs according to the present dutch guidelines will be made. Afterwards the design will be checked with probabilistic methods.

As an example, two alternative designs situated in the mouth of the Eastern Scheldt, one facing Northwesterly storms and the other, a dike with a southeastern orientation (no wave attack), will be studied.

According to the guidelines (DELTA COMMITTEE, 1960) the starting point of the design of a dike that protects economically less important regions is a storm surge level with a frequency of exceedance of $2.5 \cdot 10^{-4}$ p.a. This storm surge level is determined by statistical extrapolation of empirical data at NAP +5.50 m. The design wave is also found by statistical extrapolation from wave data (vide cross in figure 6):

$$H_s = 5.00 \text{ m} \quad T_z = 7.7 \text{ sec.} \quad T_p = 12.0 \text{ sec.}$$

where:

H_s = significant wave height
 T_z^s = mean zero crossing period
 T_p = peak period of the wave spectrum

To calculate the wave run-up, a transfer function of the following form¹⁾ is applied (T.A.W., 1972):

1) In practical design calculations the wave run-up is evaluated with the formula $r_{2\%} = 8 H_s \tan \alpha$, which gives smaller values.- Theoretically, lastmentioned formula is only valid for a wave steepness $H/L \sim 0.05$. However, up'til now, this theoretical error has not caused serious problems due to run-up reducing phenomena.

To overcome this problem, a scheme to simulate all possible combinations of natural boundary conditions in a scale model of the construction and to correlate the damage done to the boundary conditions can be developed (figure 3). Of course, field data of boundary conditions, resistance parameters and damage are preferred as base for correlation, if they are available in sufficient amount.

2. CALCULATION OF DIKE HEIGHT ACCORDING TO THE PRESENT DUTCH GUIDE LINES.

As an illustration of the concepts developed in the foregoing paragraph three simplified dike designs according to the present dutch guidelines will be made. Afterwards the design will be checked with probabilistic methods.

simplified dike designs according to the present dutch guidelines will be made. Afterwards the design will be checked with probabilistic methods.

As an example, two alternative designs situated in the mouth of the Eastern Scheldt, one facing Northwesterly storms and the other, a dike with a southeastern orientation (no wave attack), will be studied.

According to the guidelines (DELTA COMMITTEE, 1960) the starting point of the design of a dike that protects economically less important regions is a storm surge level with a frequency of exceedance of $2.5 \cdot 10^{-4}$ p.a. This storm surge level is determined by statistical extrapolation of empirical data at NAP +5.50 m. The design wave is also found by statistical extrapolation from wave data (vide cross in figure 6):

$$H_s = 5.00 \text{ m} \quad T_z = 7.7 \text{ sec.} \quad T_p = 12.0 \text{ sec.}$$

where:

H_s = significant wave height
 T_z^s = mean zero crossing period
 T_p = peak period of the wave spectrum

To calculate the wave run-up, a transfer function of the following form¹⁾ is applied (T.A.W., 1972):

1) In practical design calculations the wave run-up is evaluated with the formula $r_{2\%} = 8 H_s \tan \alpha$, which gives smaller values.- Theoretically, lastmentioned formula is only valid for a wave steepness $H/L \sim 0.05$. However, up'til now, this theoretical error has not caused serious problems due to run-up reducing phenomena.

$$r_{2\%} = 0.7 T_p \sqrt{g H_s} \tan \alpha \quad (2.1)$$

where:

g = acceleration of gravity
 α = angle of the outer slope
 $r_{2\%}$ = wave run-up, that is exceeded
 by 2% of the waves

A minimum wave run-up of 0.50 m always has to be accounted for. Seiches and gust bump are estimated to have amplitudes of 0.24 and 0.25 m respectively. According to the guidelines, the amplitude of the gust bump B may be reduced if a combination with wave run-up occurs. The advised reduction R is:

$$R = \frac{B}{B + \xi \cdot r_{2\%}} \quad (2.2)$$

Now the minimum dike height can be calculated. However, three factors affect the height of the dike during its lifetime, i.e. secular change of the chartdatum (NAP), settlement of the dike and settlement of the deep soil. The first effect is estimated at 0.10 m per century (DELTA COMMITTEE, 1960). Soil-mechanical calculations have to provide an insight in the amount of settlement.

The dike height is now determined by the addition of all phenomena (table 2.1).

Table 2.1	transfer function	NW slope 1 : 6	NW slope 1 : 8	SE slope 1 : ?
storm surge level (NAP)		+ 5.50 m	+ 5.50 m	+ 5.50 m
wave run-up	$r_{2\%} = 0.7 T_p \sqrt{g H_s} \tan \alpha$	9.90 m	7.42 m	0.50 m
seiches	S	0.24 m	0.24 m	0.24 m
gust bump	$\frac{B}{B + \xi r_{2\%}} \cdot B$	0.03 m	0.04 m	0.18 m
design water level z (NAP)		+15.67 m	+13.20 m	+ 6.42 m
change of chart datum		0.15 m	0.15 m	0.15 m
settlement dike		0.10 m	0.10 m	0.10 m
settlement subsoil		0.50 m	0.50 m	0.50 m
dike height $\xi = \frac{1}{5}$ (NAP)		+16.42 m	+13.95 m	+ 7.17 m

2.1 Probabilistic calculation and evaluation of the dike height.

In the designs of the previous paragraph all parameters, except the storm surge level and the waves, have been thought of as specified constants. For an advanced analysis, all parameters should be specified as stochastic, which implies that their exact magnitude is not known with certainty.

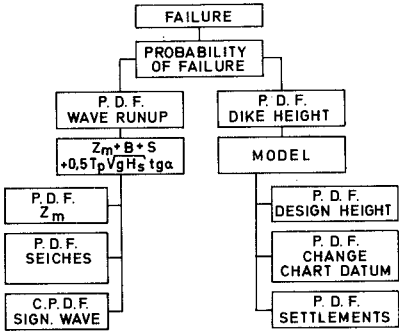


Fig. 4 Ultimate limit-state caused by wave run-up.

In figure 4 the ultimate limit-state caused by wave run-up is given in the schematical way developed in par. 1, whereby all relevant parameters are specified as probability density functions or distributions.

The distribution of the storm surge level z is based on the already mentioned set of empirical data. After a correction for the influence due to the Delta Works, the distribution has the form:

$$P_r (z > z) = \exp(-2.3 \frac{z-2.94}{0.696}) \quad (2.3)$$

$$z = [m]$$

Due to the extrapolation of the distribution to very low probabilities of exceedance, some uncertainty is introduced which is supposed to be normally distributed. The standard deviation is defined as a function of the storm surge level (DELTA COMMITTEE, 1960).

$$\sigma_z \geq 0.11 (z - 2.25) \quad \sigma_z = [m] \quad (2.4)$$

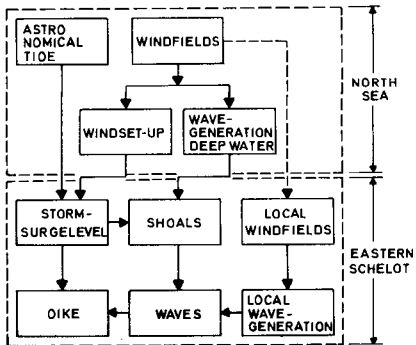


Fig. 5 Model to predict the sea state in the Eastern Scheldt.

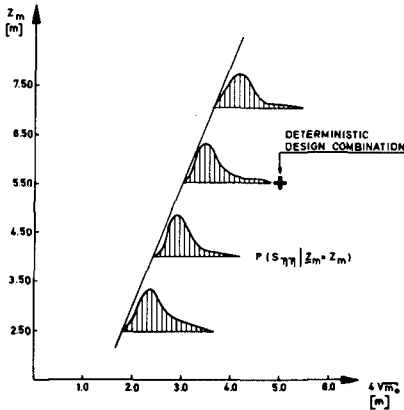
A study of the sea states in the Eastern Scheldt has shown that the wave energy comes from two sources (VRIJLING and BRUINSMA, 1980).

1. Wave energy penetrates from the North Sea. This energy is reduced as a function of the water level by breaking on the shoals in front of the coast.
2. Local windfields generate wave energy in the area between the shoals and the dike.

This system analysis enabled the determination of the probability density function of the wave spectrum $S_{\eta\eta}$ as a function of the storm surge level z_m . Figure 6 shows the conditional probability density function of wave energy and storm surge level.

Now the joint probability density function of wave spectra and storm surge levels can be determined:

$$p(S_{\eta\eta} \cdot z) = p(z) \cdot p(S_{\eta\eta} | z = z)$$



Seiches in dutch coastal waters are irregular waves with a period of 10 to 50 minutes, that show no correlation with the storm surge level.

Assuming a Rayleigh distribution for the relative maxima and estimating the number of maxima during a storm at N, the probability density function of the highest maximum is (BATTJES 1972):

Fig. 6 Conditional probability density function of wave energy and storm surge level.

$$p(S_{max}) = \frac{S}{m_{0S}} \cdot N \cdot \exp\left(-\frac{S^2}{2 m_{0S}}\right) \cdot \exp\left(-N \exp\left(-\frac{S^2}{2 m_{0S}}\right)\right) \quad (2.5)$$

where:

$$m_{0S} = 0.08 \text{ m}$$

$$N = 12$$

This function can be approximated by a Gaussian distribution with the parameters:

$$\mu_S = 0.18 \text{ m}$$

$$\sigma_S = 0.04 \text{ m}$$

Gust bumps are single pronounced elevations of sea level. Lacking statistical data, a Gaussian distribution is assumed with the parameters:

$$\mu_b = 0.15 \text{ m}$$

$$\sigma_b = 0.05 \text{ m}$$

Now the natural boundary conditions are reduced to three dimensions by combining the uncertainty of the exceedance curve of storm surge level, the seiche and the gust bump in one variable h. Assuming statistical independence the result is

$$\mu_h = \mu_S + \mu_b = 0.33 \text{ m} \quad \sigma_h = \sqrt{\sigma_Z^2 + \sigma_S^2 + \sigma_b^2} \quad (2.6)$$

In the case studied here the transfer functions are trivial, except for the transformation from waves into wave run-up. A relation similar to (2.1) is used, which contains more spectral information (T.A.W., 1972):

$$r_{sign} = \frac{\gamma}{1.40} T_p \sqrt{g H_{sign}} \tan \alpha \quad \text{in which } \gamma = 0.48 + 0.37 \epsilon \quad (2.7)$$

where

$$\varepsilon = \frac{m_0 m_4 - m_2^2}{m_0 m_4} \quad \text{spectral width}$$

$$m_n = n - \text{th spectral moment}$$

Further it is assumed that the wave run-up r is Rayleigh-distributed.

$$P_r(\underline{r} > r) = \exp\left(-2\left(\frac{r}{r_{\text{sign}}}\right)^2\right) \quad (2.8)$$

Damage will only be done if the wave run-up exceeds the dike height several times during a storm. Based on the binomial distribution one finds for the probability distribution of wave run-up, which exceeds a given level at least m times in a storm containing N waves:

$$P(r_m) = 1 - \sum_{k=0}^{m-1} \frac{N!}{k!(N-k)!} \cdot P_r(\underline{r} > r)^k \cdot \{1 - P_r(\underline{r} > r)\}^{N-k} \quad (2.9)$$

This distribution is conditional on the occurrence of the sea state $S_{\eta\eta}$.

For numerical reasons the three-dimensional space $z, S_{\eta\eta}, h$ of natural boundary conditions is divided in small elements with dimensions $\Delta z, \Delta S_{\eta\eta}$ and Δh . The probability of occurrence $P_r(z, S_{\eta\eta}, h)$ of a combination of boundary conditions falling within these elements is:

$$P_r(z, S_{\eta\eta}, h) = p_r(z) \cdot p_r(S_{\eta\eta}|z) \cdot p_r(h|z) \quad (2.10)$$

where $p_r(z)$, $p_r(S_{\eta\eta}|z)$ and $p_r(h|z)$ denote the respective (conditional) probability densities times Δz , $\Delta S_{\eta\eta}$ and Δh respectively.

The potential threat, representative for this element now can be found by adding the storm surge level z and the seiche-gust bump combination h -giving together the still-water level z_m - and adding the wave m run-up r over and above that:

$$\tau = z + h + r \quad (2.11)$$

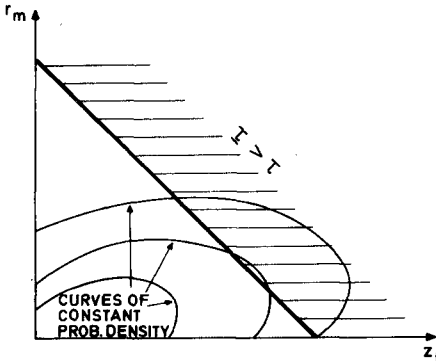
The probability of occurrence is evaluated as:

$$P_r(\tau) = P_r(z, S_{\eta\eta}, h) \cdot p(r_m | S_{\eta\eta}) \Delta z \quad (2.12)$$

Now the joint probability density function of still water levels and m -times exceeded wave run-up heights can be found by repeating the calculation for all possible combinations of boundary conditions.

The probability of exceedance of a specific potential threat can now be evaluated by integrating the two dimensional probability density function of still water levels and wave run-ups (figure 7).

$$P_r(\underline{r} > \tau) = \iint_{\underline{r} > \tau} p(z_m, r_m) dz_m dr_m \quad (2.13)$$



The probability of exceedance curve, which is numerically evaluated, appears to be of the form:

$$P_r(\tau > \tau) = \exp\{(8.36 - \tau) / 0.452\}$$

$$\tau = [m] \quad (2.14)$$

Having derived the probability of exceedance curve, it is interesting to compare the potential threat with a probability of exceedance of $2.5 \cdot 10^{-4}$ p.a. with the design level calculated according to the guidelines (table 2.2).

Fig. 7 Probability of wave run-up as part of the probability mountain.

	slope 1 : 6	slope 1 : 8	SE	
guidelines	NAP +15.67	NAP +13.20	NAP +6.42	heights in m
probabilistic	NAP +12.21	NAP +10.50	NAP +5.95	

An even more interesting experiment is to evaluate the probability of failure of the simplified dike designs of the preceding paragraph. Because the real failure mechanisms are not expressed in mathematical form, failure will be arbitrarily defined as the exceedance of the dike height by at least 12 wave run-ups during a storm.

On the side of the "resistance", the height of the dike also presents some uncertainty. When a storm occurs at some time in the future the effects, that are accounted for in the difference between the planned dike height and the design water level, are realized to some uncertain extent. In fact, the theory of the serviceability limit-state developed in ch. 1 applies.

heights in m levels: NAP	NW		SE	σ	cp table 2.1
	slope 1 : 6	slope 1 : 8	SE		
dike height	+16.42	+13.95	+ 7.17		
change of chartdatum	- 0.10	- 0.10	- 0.10	0.025	0.15
settlement dike	- 0.07	- 0.07	- 0.07	0.02	0.10
settlement subsoil	- 0.35	- 0.35	- 0.35	0.10	0.50
tolerance	-	-	-	0.10	-
	+15.90	+13.43	+ 6.65	0.14	0.75

This means, that the real dike height differs from the planned one unless a proper maintenance scheme is carried out. The real height can be approximated by normal distribution (table 2.3). Now the probability of failure caused by overtopping of the dike can be evaluated by integrating:

$$P_r(\text{failure}) = \int_0^{\infty} P_{\tau}(x) \cdot p_{\text{dike height}}(x) \cdot dx \quad (2.15)$$

$$= \int_0^{\infty} e^{-\frac{8.36-x}{0.452}} * \frac{1}{0.145\sqrt{2\pi}} e^{-\frac{1}{2}\left(\frac{15.92-x}{0.145}\right)^2} dx$$

The probability of failure is given in table 2.4.

Table 2.4

	NW		SE
	slope 1 : 6	slope 1 : 8	
$P_r(\text{failure})$	$5.8 * 10^{-8}$	$2.2 * 10^{-7}$	$4.1 * 10^{-5}$

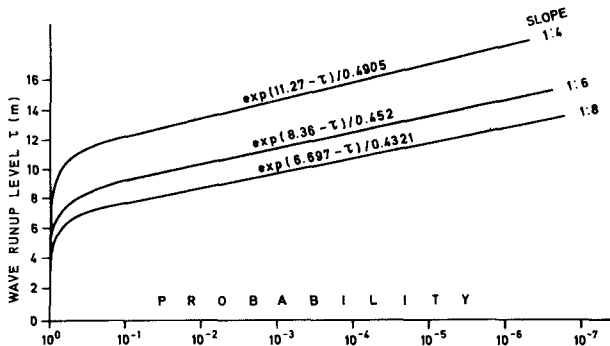


Fig. 8 Exceedance probability of wave run-up as function of revetment slope.

From the results (figure 8) it appears that the probability of overtopping of the dikes designed according the guidelines is not of the same order for various cases. Reducing the dike height by flattening the outer slope increased the chance of overtopping c.q. failure by a factor of nearly 4. The dike facing SE is even more unsafe. Here the potential threat, formed by the still water level without waves exceeding the dike height, will certainly cause inundation. So failure of this dike is at least 1000 times likelier than the dikes facing North West.

This illustrates that, under simplifying assumptions, designs according the present dutch guidelines are not able to be compared without further attention.

3. DUNE DESIGN.

At the same place, where in chapter 2 a dike has been designed, a dune will now be constructed.

3.1 Calculation of dune breadth according to the present Dutch Guideline.

The present Dutch "guideline for the Calculation of Dune Erosion during Storm Conditions" is based on the following assumptions (v.d. GRAAFF (1977) and VELLINGA (1978)):

1^o During a storm surge the coastal profile is reshaped, to a uniform profile, the "stormprofile", described by the formula:

$$y = 0.415 (\lambda x + 4.5)^{0.5} - 0.88 \quad (3.1)$$

in which:

y = depth in meters below the maximum surge level

x = distance in meters from the point of the profile lying at maximum surge level

λ = coefficient, lying between .8 and 1.25, dependent on the grain diameter; λ equals 1 when $D_m = 200\mu$

The profile is given in figure 11.

2^o The depth d_b to which the storm profile applies is equal to 1.28 times the height of the significant wave H_s at the breaking point. Thus defining the "width of spreading" B as the width of the stormprofile, over which the eroded sand from the dunes settles, one finds inversely from (3.1):

$$B = \frac{(2.41 d_b + 2.12)^2}{\lambda} - \frac{4.5}{\lambda} \quad (3.2)$$

3^o The inclination of the outer slope of the eroded dune is assumed to be 45°. The seaward side of the outer slope i.e. the "foot" of the dune-coincides with the origin of the x,y-coordinate system.

4^o During the storm surge, the coastal profile is reshaped, in such a way that the total area of the eroded sand equals the area of the settled sand.

5^o Losses of sand, either to the regions outside the breaker zone, or in landward direction or by a longshore gradient of the littoral drift are neglected.

With respect to necessary dune dimensions, one should take into account a very low beach level in the initial situation before the surge; after the surge a dune breadth of 10 m at surge level should remain.

Starting from the same data as in chapter 2.1, i.e. $H_s = 5.0$ m, a surge level of N.A.P. + 5.50 m and a beach level lying .30 m lower than the mean beach level, for a dune, which has to offer Delta protection during 10, 20 or 50 years respectively, one finds the dune dimensions given in table 3.1.

	MAINTENANCE PERIOD		
	10y	20y	50y
storm erosion	44.58	44.58	44.58
yearly erosion	3.75	7.50	18.75
minimum body	10.00	10.00	10.00
dune dimension	58.33	62.08	73.33

3.2 Probabilistic calculation and evaluation of the dune breadth.

3.2.1 General considerations.

The technical failure mechanisms, which can be distinguished for a dune, acting as sea defence, are principally the same as those for dikes: a. failure outer slope c. failure inner slope
b. submerging d. internal failure

With respect to d, internal failure, apart from failure by hydrologic overpressure, one should also take rabbit holes into consideration as these may occur in the most landward side the dunes.

In the following, the failure mechanism mentioned in b and c are combined by assuming that there will be inundation when the water level rises above a certain given level z_s . This water level will be lower than the dune height, because of wave set-up and wave run-up.

It will be assumed, that a certain "body" of dune should remain, of which the width is assumed to be known, in order to avoid internal failure (figure 9).

The most important failure mechanism for dunes is the "failure" of the outer slope. Therefore this mechanism will be considered in the first place.

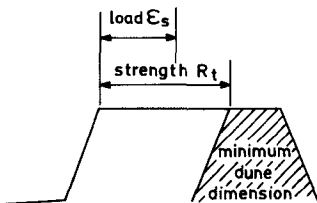


Fig. 9 Definitions of load and strength.

Generally, failure occurs when the load on a construction is larger than the strength. The simultaneous probability of this occurrence is found by convolution of the probability density functions of load and strength. The following definitions of load and strength will be used (see also figure 9):

- The load e_s is defined as the dune erosion, caused by surges combined with waves.
- The strength R_t at time t is defined as the dune breadth, above a certain minimum, necessary to avoid failure mechanisms other than erosion of the outer slope.

Consider first the strength R_t , composed of three components.

$$R_t = R_0 + \epsilon_t + \epsilon_b \quad (3.3)$$

It depends upon:

- a. the initial conditions R_0 ;
- b. the effect ϵ_t of gradual erosion¹⁾ and, in the event, periodical supply;
- c. the effect on the erosion ϵ_b of the beach level at the moment of the occurrence of a severe storm.

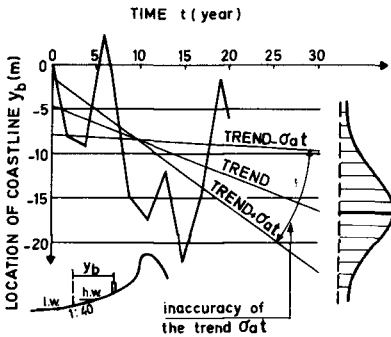


Fig. 10 Location of the coastline in the course at time.

With respect to gradual erosion, it is assumed that the future trend can be found in principle by linear extrapolation of the trend in the past:

$$\epsilon_t = \underline{a} t + \underline{b} \quad (3.4)$$

Figure 10 gives an example: it shows the location of the coastline in a certain range, perpendicular to the coast, with respect to a reference pole; the "coastline" is defined as the mean between the high- and low-water line.

However, given this registration, the trend cannot be properly determined, and a uncertainty remains.

Therefore \underline{a} and \underline{b} are coefficients with a stochastic character. $E(\underline{a})$, $\sigma(\underline{a})$ and $\sigma(\underline{b})$ are found by linear regression from the registration in the course of time, of the coastline; $E(\underline{b})$ is assumed zero and determines the reference, from which ϵ_t is taken.

The dune erosion ϵ_s during storm conditions depends upon the beach level ζ at the moment of the storm. In the mathematical model, this may be simulated by assigning to the strength R_t a normally distributed stochastic component ϵ_b with mean zero and standard deviation $\sigma(\epsilon_b)$, which is related to the standard deviation of the beach level $\sigma(\zeta)$ in the following way:

$$\sigma(\epsilon_b) = \frac{\partial \epsilon_s}{\partial \zeta} \cdot \sigma(\zeta) \quad (3.5)$$

The used data and transfer functions are mentioned in table 3.2.

1) In this paper the dimensioning of an eroding dune will be considered, as this case is more intricate than an accreting dune.

Table 3.2 Data and transfer functions used for finding $E(\underline{R}_t)$ and $\sigma(\underline{R}_t)$.

$E(\underline{a})$		-0.375	m/y	
$\sigma(\underline{a})$		0.326	m/y	$\sigma(\underline{\epsilon})$ 0.30 m
$E(\underline{b})$		0		$\frac{\partial \underline{\epsilon}_s}{\partial \tau}$ 11.79
$\sigma(\underline{b})$		7.21	m	
$E(\underline{\epsilon}_t)$	$E(\underline{a}) \cdot t + E(\underline{b})$	-0.375 t	m	$\sigma(\underline{\epsilon}_b)$ 3.54 m
$\sigma(\underline{\epsilon}_t)$	$\sqrt{\sigma^2(\underline{a}) \cdot t^2 + \sigma^2(\underline{b})}$	$\sqrt{0.326^2 t^2 + 7.21^2}$	m	

From (3.3) and (3.4) one finds, assuming $\underline{\epsilon}_t$ and $\underline{\epsilon}_b$ statistically independent:

$$E(\underline{R}_t) = R_0 + E(\underline{a}) \cdot t$$

$$\sigma^2(\underline{R}_t) = \sigma^2(\underline{a}) \cdot t^2 + \sigma^2(\underline{b}) + \sigma^2(\underline{\epsilon}_b) \tag{3.6}$$

Further considerations concerning the strength depend upon the applied strategy and are given in chapter 3.2.2 and 3.2.3. Consider next the load.

Replacing in figure 5 the dike by a dune and using the same schedule as explained in chapter 2.1 for all possible combinations of still water level z_m and wave heights H_s the dune erosion ϵ_s can be numerically calculated using the assumptions 1° to 5°, given in chapter 3.1.

Thus, one finds the probability distribution for the dune erosion by surge (cf (2.14)):

$$P_r = (\epsilon_s > \epsilon_s) = \int_{\epsilon_s} \int p(z_m, H_s) d z_m d H_s \tag{3.7}$$

Starting from the initial profile, given in figure 11, the distribution found is shown in figure 12.

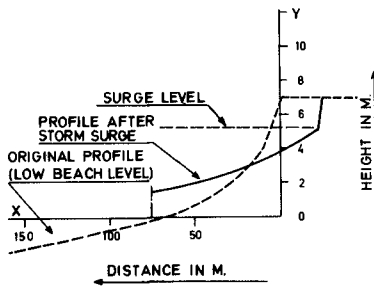


Fig. 11 Dune profile before and after storm surge.

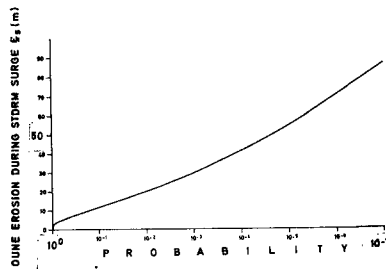


Fig. 12 Exceedance probability of dune erosion during storm surge.

Table 3.3
(values in m)

	MAINTENANCE PERIOD		
	10y	20y	50y
$E(\underline{R}_t)$	$R_0 - 3.75$	$R_0 - 7.50$	$R_0 - 18.75$
$\sigma(\underline{R}_t)$	8.67	10.35	18.17

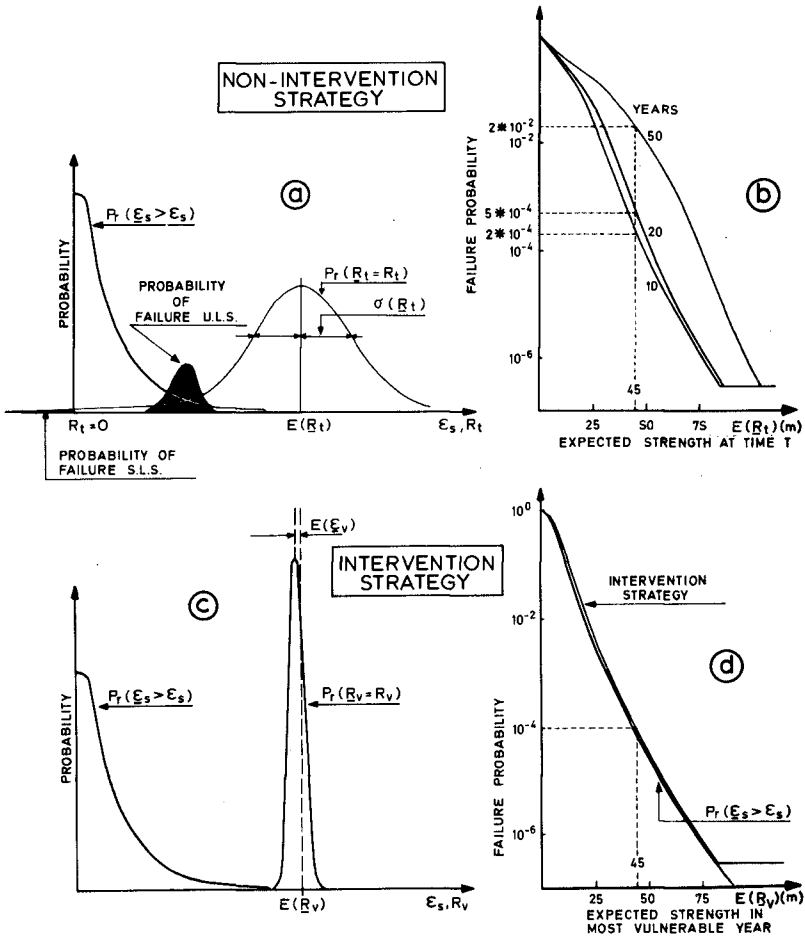


Fig. 13 Failure probability according to non-intervention and intervention theory.

3.2.2 Non-intervention strategy.

Now load and resistance will be combined.

In the numerical model, three examples have been elaborated starting from a period of non-intervention in the coastal processes of 10, 20 and 50 years respectively. Table 3.3 gives $E(R_t)$ and $\sigma(R_t)$ after these periods. Figure 13a shows an example of, on the one hand the probability density of the strength R_t , and, on the other hand the exceedance probability of the load ϵ_t . The figure shows two classes of failure: the ultimate limit-state, where the load surpasses the strength, and the serviceability limit-state, where the dune collapses, just because the gradual erosion is more than expected.

By convolution, one can calculate the total probability of failure as a function of the expected strength $E(R_t)$ at time t (figure 13b).

The upper part of the curves has a Gaussian character, determined mainly by the serviceability limit-state (gradual erosion more than expected). The middle part has a more or less negative-exponential character, determined by the ultimate limit-state. The lowest part, the horizontal line, is determined by the risk of submergence of the dunes.

The results are discussed in the evaluation.

3.2.3 Intervention strategy.

This strategy implies a sand supply to a seaward line 0 as soon as the dune foot surpasses a landward line L in landward direction (figure 14a,b). In the example treated, the line L has been chosen in such a way, that when the dune foot coincides with L, the strength necessary according to the deterministic approach was just available (i.e., that R_t equals 44.58 m, cf table 3.1). It has been assumed, that if in one year measures, that the eroding dune foot surpasses the limit L in landward direction, it takes another year for preparing and carrying out the dune replenishment. The distance OL depends upon the desired expectation of the return period of sand supply. Starting from the assumptions given in figure 14, one finds a probability density of the location of the dune foot in the course of many years as sketched in figure 14c, either by a numerical Monte Carlo simulation, or by analytical computations (BAKKER 1980). As it is the yearly probability of inundation that counts, the situation has to be considered in the year in which the dune is most vulnerable¹⁾. Figure 14c shows (interrupted line) the probability density of the location of the dune foot, under the condition, that it is measured in the year after the one, in which the landward surpassing of the line L was recorded and on the other hand before the supply to line 0 took place.

1) This means that in other years a "hidden safety" will be present. In this way, the average safety over, say 100 years of a dune will be higher than the one for a dike (with respect to this aspect).

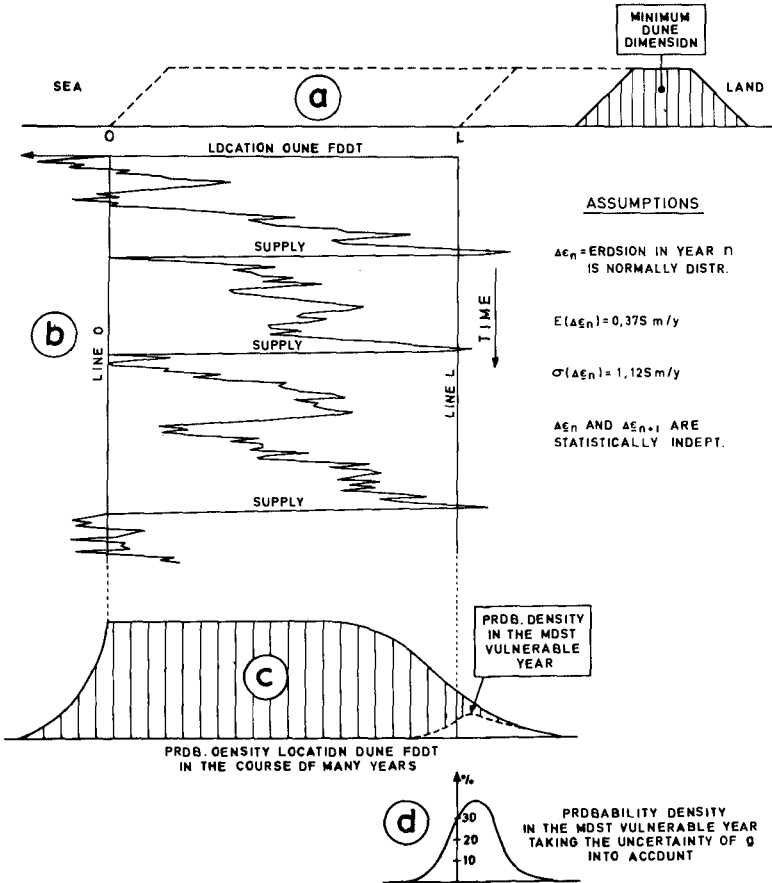


Fig. 14 Probability density of dune foot location in the year that the dune is most vulnerable.

Figure 14d gives the same probability density, but now taking into account, that the rate of erosion a cannot be properly determined from the measurements, as stated in chapter 3.2.1. To this end, the computation of the last-mentioned probability density has been repeated for various values of the yearly expected erosion, assuming fixed values for the yearly variation of the erosion $\sigma(\epsilon_n)$ and for OL . After this, these probability density distributions are combined again, by giving each a weight, proportional to the occurrence.

probability -found from $E(a)$ and $\sigma(a)$, table 3.2- and adding. The result found does not depend very much on OL, when the expected return period is not too small. Analogous to figure 13a and 13b, figures 13c and 13d are constructed, where R_v , the strength in the year the dune is the most vulnerable, replaces R_t from (3.3):

$$R_v = R_L + \epsilon_v + \epsilon_b \quad (3.8)$$

in which R_L denotes the strength when the dune foot coincides with the line L; ϵ_v (of which the probability density is shown in figure 14d, indicates the gradual erosion with respect to L in the most vulnerable year and ϵ_b has the same meaning as in (3.3). In the example, $E(\epsilon_v)$ and $\sigma(\epsilon_v)$ are found to be 1.05 m and 1.31 m respectively.

Evidently, the standard deviation of R_v in figure 13c is much less than that of R_t in figure 13a. Consequently, as figure 13d shows, the failure probability according to the intervention strategy is nearly determined by the probability of erosion, $P_r(\epsilon_v > \epsilon_s)$, during storm surge. It shows that for equal values of $E(R_t)$ and $E(R_v)$, the intervention strategy (with the given reaction time of 1 year) gives more safety than the non-intervention strategy.

3.3 Evaluation of deterministic and probabilistic approach of dune breadth computation.

In chapter 3.1, a value of 44.58 m for the dune erosion during "super surge" with exceedance probability $2.5 \cdot 10^{-4}$ was found. Following the non-intervention strategy this value should be compared with the expected necessary strength $E(R_t)$ at time t, given in figures 13a,b.

Then, for $t = 10, 20$ and 50 years, figure 13b gives probabilities of failure of $2 \cdot 10^{-4}$, $5 \cdot 10^{-4}$ and $2 \cdot 10^{-2}$ p.a. respectively, when $E(R_t)$ equals 44.58 m.

Following the intervention theory, the wanted expectation of the strength $E(R_v)$ determines the location of line L (cq. (3.8)). When $E(R_v)$ equals 44.58 m, figure 13d gives the probability of failure in the year the dune is the most vulnerable as $8 \cdot 10^{-5}$ p.a.

Table 3.4

	MAINTENANCE PERIOD			
	10y	20y	50y	
dune breadth in m acc. to guideline	58.33	62.08	73.33	exceedance prob. $2.5 \cdot 10^{-4}$
failure probability for above-ment. dune	$2 \cdot 10^{-4}$ $8 \cdot 10^{-5}$	$5 \cdot 10^{-4}$ $8 \cdot 10^{-5}$	$2 \cdot 10^{-2}$ $8 \cdot 10^{-5}$	non-intervention intervention
dune breadth in m acc. prob. theory	57.75	65.50	89.0	non-intervention
failure prob. $2.5 \cdot 10^{-4}$	50.25	54.00	65.25	intervention

1) positive in seaward direction.

In table 3.4 these values have been summarized. Furthermore this table gives the dune width following the guide line as given in table 3.1.

Another comparison can be made in a way similar to that in table 2.1, i.e. instead of fixing the strength $E(R_t)$ and finding the failure probability, one fixes the failure probability and finds the necessary strength $E(R_t)$. Choosing a probability of $2.5 \cdot 10^{-4}$, as has been done for a dike (table 2.2), the results are summarized in table 3.4.

The intervention strategy results in smaller dune breadth for achieving the same safety as in the deterministic approach, because of the rather extreme choice of the wave boundary condition ($H_S = 5$ m where $z = +5.50$ m NAP, cf figure 6)¹⁾. As figure 13d shows, during storm surge the erosion ϵ_S with exceedance probability $2.5 \cdot 10^{-4}$ equals 36.5 m instead of 44.58 m, as found from the deterministic approach (table 3.1); this illustrates the fact that the wave height $H_S = 5$ m is too high to be representative. Apart from this fact, it shows, that in the case non-intervention strategy is applied, the deterministic method gives values too low, especially for long return periods.

4. DISCUSSION.

The theory, developed in this paper is far from operational. Further developments are in preparation in working groups of the Dutch Technical Advisory Committee on Water Defences. Questions which remain to be solved are:

- a. The failure probability of a sea defence system, surrounding a protected area²⁾ should be less than the probability of a (super) surge, which the system in any case should be able to withstand³⁾. Standards will have to be made for the allowable risk to areas to be protected.
- b. In the paper, only the probability of failure of the sea defence system in one cross-section is considered. Considering n cross-sections in a sea defence circle, the risk will be multiplied by a factor n , unless failure of one section implies failure of another. The length of the circle will affect the dimensions.
- c. The assumption of failure of a dike by 12 wave run-ups is quite unsatisfactory: here soil mechanics and hydraulics (overflow discharge) will have to come into the picture.

1) It may be pointed out, that this wave height was originally a boundary condition for the storm surge barrier. Thus it is clear, that a "safe" value has been chosen. For dimensioning of dunes in the same region a less pessimistic estimate is usual. This illustrates that the accuracy and the result of a deterministic approach depends upon (subjective) "engineers instinct".

2) This will be called a "sea defence circle".

3) DELTACOMMITTEE (1960): to withstand: each surge 10^{-4} p.a.; failure probability: $8 \cdot 10^{-6}$ p.a.; storm surge barrier project group (1979): failure probability storm surge barrier 10^{-7} p.a.

- d. With respect to dunes, the expectation and the variation of the width of spreading B (chapter 3.1 and 2^o) should replace eq (3.3). The failure mechanisms b, c and d (chapter 3.2.1) should be considered in more detail.

Considering the method as a whole, it may be pointed out that inaccuracy or uncertainty is translated into extra dimensions of the sea defence system. This gives an operational tool for steering coastal research, as the benefit of this research can be rated and weighted against the costs.

5. CONCLUSIONS.

- a. The probabilistic method is more consistent than the deterministic method.
- . Failure probability may differ considerably for various constructions, when using the same deterministic standards.
- b. The probabilistic approach offers more opportunity for taking "hidden safeties" into account,
- . the uncertainty in structural strength, including the effect of various strategies of maintenance;
 - . a better comparison is found for the safety of dunes and dikes.
- c. The method gives a general approach to the goal pursued: safety for the hinterland.
- . it gives a better insight in the relationships between the various failure mechanisms and better evaluation of the failure mechanisms itself;
 - . one is obliged to trace non-technical failure mechanisms.
- d. The financial value of accuracy and maintenance can be determined. This gives a tool for steering coastal research.

6. ACKNOWLEDGEMENT.

This paper is based upon a report of a preliminary working group of the Dutch Technical Advisory Committee on Water Defences (1979). The authors wish to thank the other contributors of this working group. Also the effect of discussions in other groups is gratefully acknowledged.

REFERENCES.

- BAKKER, W.T. (1980) Prob. design of dunes, acting as sea defence. Rijkswaterstaat, Department Coast and Sea, Nota WWKZ-80.VO13.
- BATTJES, J.A. (1972) Stat. eig. stat. processen. Ingenieur 84, nr. 27.
- CIRIA (1976) Rationalisation safety factors struct. code. Rpt. 63.
- DELTACOMMITTEE (1960) Rept. Deltacommissie. Staatsdr. & Uitg. Bedr.
- GRAAFF, J.A. v.d. (1977) Dune erosion during storm surge. Coastal Engineering 1, nr. 2.
- T.A.W. (Technical Advisory Committee on Water Defences) (1972a) Wave run-up and wave overtopping.
- T.A.W. (1972b) Guidel. for Calc. of Dune Erosion during Storm cond.
- T.A.W. (1979) Report Prel. Group Probabilistic Method.
- VELLINCA, P. (1978) Model tests on dune erosion. Proc. 16th ICCE Ch. 132.
- VRIJLING J.K. and BRUINSMA J. (1980) Hydraulic Boundary Conditions Symposium Hydraulic Aspects of Coastal Structures.

THE EFFECTS OF CONSTRUCTION TECHNIQUES & BULK TERMINAL OPERATIONAL REQUIREMENTS ON THE DESIGN CRITERIA FOR ISLAND BREAKWATERS

A.G.F. EDDIE

Managing Partner, Connell Eddie & Associates, Melbourne, Australia.

J.O. LAWSON

Professor of Civil Engineering, University of Melbourne, Australia.

H.R. GRAZE

Senior Lecturer, Department of Civil Engineering, University of Melbourne, Australia.

B.K. DEAN

Senior Engineer, John Connell & Associates, Melbourne, Australia.

SYNOPSIS

The title of the paper contains two important key words - CONSTRUCTION and ISLAND. The techniques for safe and economical construction of an island breakwater located some distance from the shore in exposed waters are radically different from the techniques required for conventional breakwaters with one end attached to the land. The differences in construction technique are so profound as to change the preferred basic design selection from rubble mound to caissons.

The paper discusses:-

1. The circumstances in which island breakwaters will become increasingly necessary for unloading of bulk ships.
2. Reasons why prefabricated caisson breakwaters are preferable for construction in an offshore situation.
3. The economy to be gained by using the caissons as the structural support for ship unloading machinery.
4. A consequent necessity to develop a caisson breakwater configuration with adequate design criteria to ensure total safety of the equipment supported on it.
5. A research program aimed at deriving these criteria.

INTRODUCTION

The concepts discussed in this paper are based on the experience of Connell Eddie & Associates in the planning of two bulk unloading terminals, one in the Mediterranean and one in Western Australia. Both require deep water for large ships, and located 1500-2000 metres offshore outside existing sheltered ports.

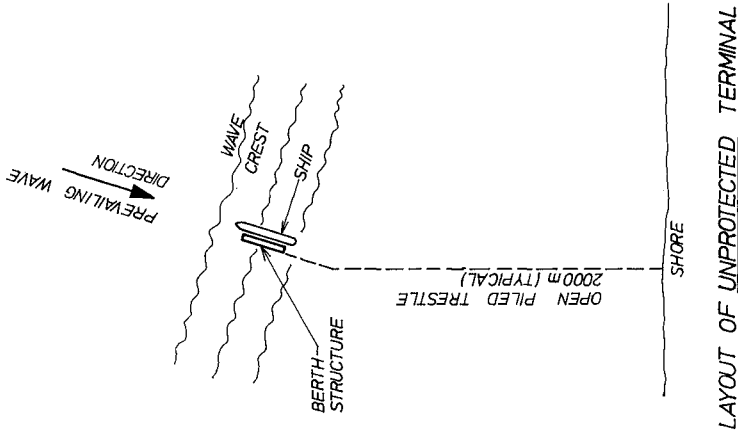


FIG. 1a

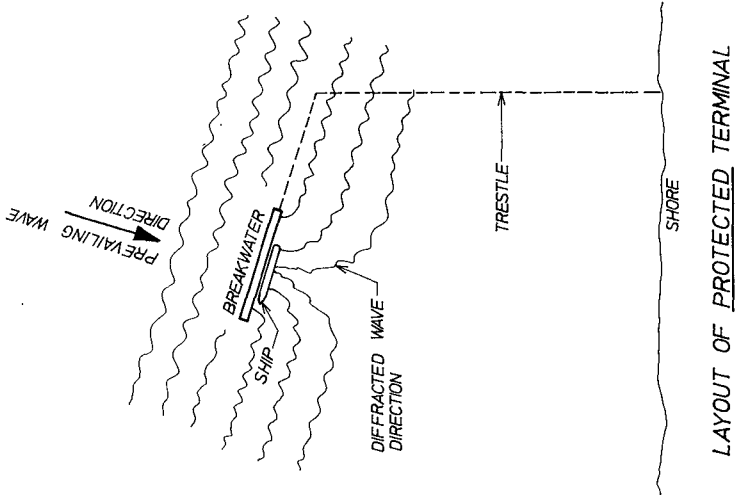


FIG. 1

There is adequate experience world wide, and particularly in Australia to confirm that large bulkships can be loaded at exposed offshore terminals without requiring the protection of a breakwater.

There is no experience of unloading large bulk carriers other than in sheltered harbours. However the consensus of opinion is that unloading operations at an unprotected offshore berth would be rendered impossible in sea conditions much less severe than those which cause the cessation of loading operations.

The differences arise because loading equipment need never be in contact with the ship or its cargo, the bulk material being loaded through a telescopic chute suspended above the ship's hold. Therefore pitching, rolling and heaving of the ship have negligible effect on the loading operation. However, unloading equipment (grabs, screws, bucket chains etc) are immersed in the bulk cargo and hence movement of the ship can endanger the unloading equipment.

In the current world energy crisis situation, a rapidly escalating world trade in bulk coal can be expected, using ever larger vessels. Unloading of these vessels at existing ports causes high capital dredging costs and environmental problems, such as urban aesthetics involving coal stockpiles and power stations.

LIMITING OPERATIONAL CONDITIONS FOR BULK TERMINALS

In planning an offshore bulk terminal (i.e. one which is not in a sheltered harbour), the most important issue is whether a breakwater is necessary.

FIGS 1 & 1a show typical arrangements of protected and unprotected terminals respectively. In typical circumstances, such terminals are about 2km offshore.

The protected terminal is at right angles to the dominant wave direction, whilst the unprotected terminal is oriented in the same direction as the dominant waves. In both cases the waves arriving at the ship are travelling in the direction of the longitudinal axis of the ship and hence cause minimum disturbance to the ship.

In the case of the unprotected terminal, waves varying from the dominant direction will cause significantly increased ship disturbance. In the breakwater case, a change in wave direction has little effect because, (subject to adequate breakwater length) the diffracted waves are still travelling parallel to the breakwater when they arrive at the ship position.

Thus a breakwater has two effects which reduce the disturbance of the ship

- . Attenuation of wave height;
- . Virtual elimination of increased ship disturbance due to variation in wave direction.

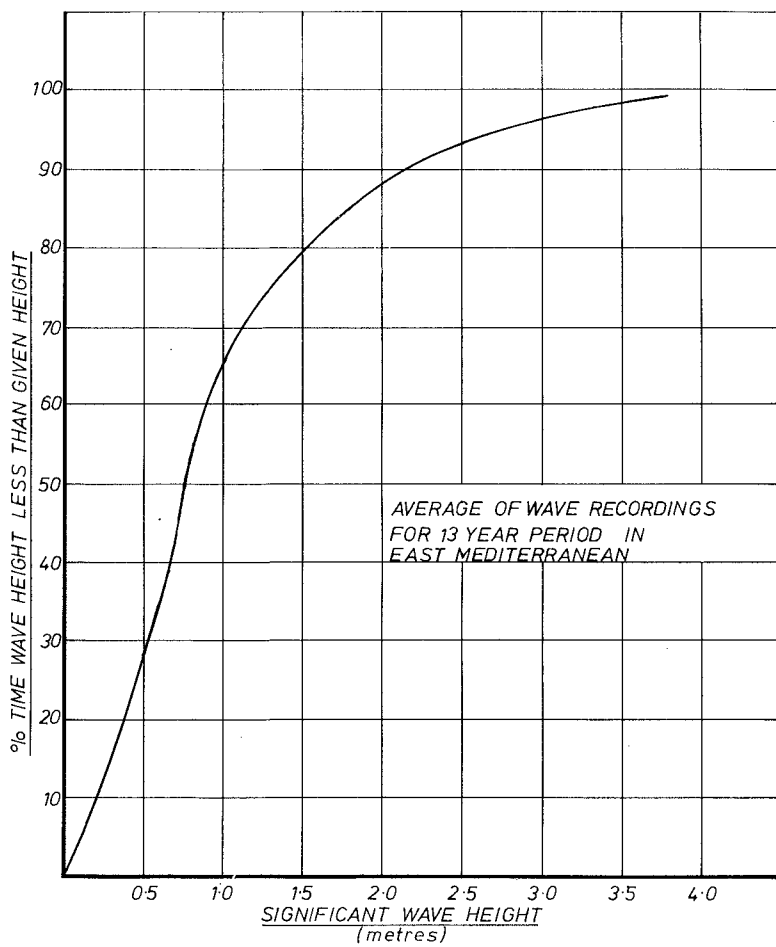


FIG. 2.

Experience at a number of Australian loading terminals has provided good information on the limiting wave conditions which cause loading operations to cease. For unloading terminals there is no information available world-wide, but enquiries made of a number of operators and equipment manufacturers suggest the figures in TABLE 1.

TABLE 1

Wave direction relative to ship heading	Limiting Wave Height (metres)	
	Loading	Unloading
0°	2.5	1
45°	1	0.5

There are of course many other factors affecting the limiting conditions for safe operation (e.g. wave period, wind, ship size and inertia characteristics).

A full analysis would include all these factors, but the authors believe that a good first approximation to the berth availability equates with the amount of time each year that the waves fall into the categories shown in TABLE 1.

At offshore loading terminals so far constructed in Australia (1980) sufficient berth availability has been obtained without using a breakwater. Availability is normally required in the range 90-95%, but in some circumstances (e.g. low annual throughput tonnage) much less may be quite satisfactory. In periods of unavailability, the berth is shut down and if there is a ship in port it is taken off and anchored in deep water awaiting favourable weather. This type of off-shore terminal operation differs from the usual concept of all-weather port operations and must be understood in the context of this paper.

The planner of an unloading terminal is much less likely to find adequate berth availability if the berth is unprotected by a breakwater. FIGS 2, 3 & 3a show a typical wave climate such as the authors found at a proposed terminal site in the Mediterranean. If no breakwater is provided, the availability of an unloading terminal would correspond to the wave conditions shown in the last column of TABLE 1. Thus FIG 2 suggests an availability of 65%. However, FIG 2 represents the average of 13 years wave recordings and the authors wish to draw attention to the dangers of basing terminal planning on average statistics.

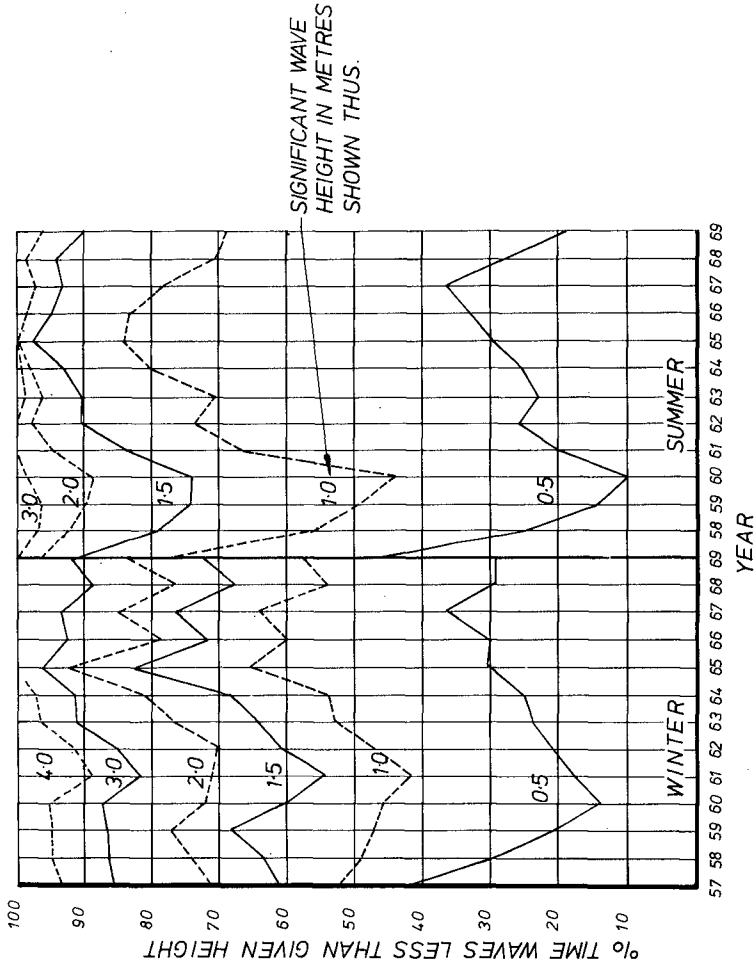


FIG. 3

FIG 3 shows the same figures broken down into winter and summer for each of the 13 years separately. This shows that in a bad winter (such as 1961) availability would be only 42%. FIG 3a shows the 1961 winter figures broken down into wave directions, and again using the criteria of TABLE 1, it can be seen that the availability is reduced to 30%.

In these circumstances, a high annual throughput installation would not be feasible with a single unprotected berth. Even a two-berth installation, whilst providing in theory sufficient unloading time, would be subject to long shut-down periods of both berths simultaneously. Accordingly, the authors believe that a single berth protected by a breakwater is the preferred solution.

The layout shown in FIG 1 is consequently the subject of this paper. It will be seen from FIG 3 that if the breakwater is capable of attenuating 4 metre incident waves to 1 metre at the berth, there will be 90% availability even in the worst recorded winter period. (As stated earlier, the variation of incident wave direction does not significantly affect a breakwater protected terminal).

Such an installation would be operated in the same way as the existing unprotected loading terminals in Australia - i.e. when the sea conditions prevent operations, a ship in berth would be taken off and anchored in deep water to await favourable weather.

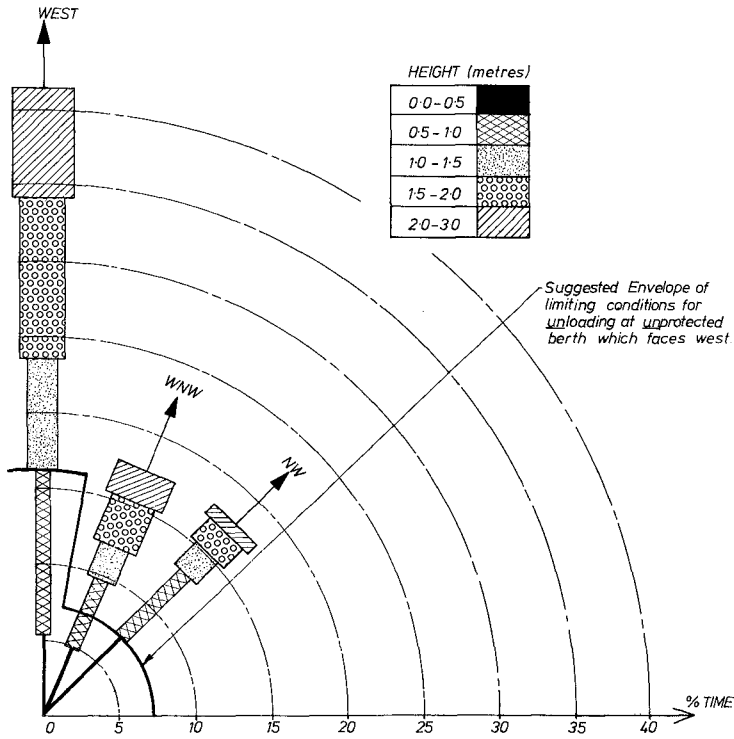
DESIGN & CONSTRUCTION CONSIDERATIONS

New style offshore terminals satisfying the aforementioned availability requirements give rise to design and construction problems which necessitate further research.

The proposed offshore terminal differs from traditional concepts in two important ways.

1. The breakwater is not required to provide a safe anchorage on its lee side for 100% of the time, but only when the incident waves are 4 metres high or less. Operation of the terminal is not required when waves greater than 4 metres are allowed to overtop. This concept is termed a "limited availability breakwater".
2. The breakwater is an island structure, and this raises construction problems which have a profound effect on the design concept.

The required island breakwater is in fact connected to the shore by a piled trestle. For operational purposes, this trestle carries one or more conveyor belts and a roadway. Thus it may be argued that this trestle can be built first and used for access by trucks to construct a conventional rubble mound breakwater by end-over-end tipping.



FIGURES SHOW PERCENTAGE OF TOTAL TIME WAVES ARE WITHIN STATED HEIGHT AND DIRECTION RANGE WORST RECORDED WINTER PERIOD.

FIG. 3a

However, in practice this is un-economic for two reasons. Firstly it requires an unacceptably long time to construct the trestle and breakwater sequentially. Secondly the roadway on the trestle would have to be strengthened significantly above the standard required for operation of the berth.

The fundamental economics of construction dictate that the break-water must be constructed as an offshore operation, without use of the trestle for construction access. An offshore operation is defined by the authors as an operation in exposed waters with no access during construction other than by boats or helicopters. This requires the use of floating construction equipment and daily use of barges, tugs and other vessels for the transfer of men and equipment. These activities cannot generally be carried out safely when the waves exceed about 1 metre. Thus it can be seen that in a typical situation such as shown in FIGS 2 and 3, there may be an average of 35% downtime, with a maximum of 58% in a bad winter and a minimum of 16% in a good summer. These figures are not untypical of previous experience in the construction of offshore loading terminals (Ref.1).

Weather down-time in an offshore operation is very costly because it shuts down the entire construction establishment, which after each shut-down requires some time to restart. Furthermore, the wide variability of shut-down time from 16% to 58% makes effective planning of the operation very difficult.

In offshore operations such as construction of the North Sea oil platforms, these problems are so obvious that there is no economic alternative to total onshore pre-fabrication of the structure followed by very rapid offshore installation. The whole purpose of this concept is to reduce the required offshore working time to a minimum by making maximum use of onshore pre-fabrication.

The type of offshore terminal shown in FIG 1 shares the same problems. Instead of being 100km or more from the shore like an oil platform, it is only 2km. Therefore whilst it becomes feasible to adopt "conventional" construction such as would be used for the same structure if it were in sheltered waters, the authors believe that maximum onshore pre-fabrication is economically essential. In the context of a break-water this means caissons. The "conventional" alternative of a rubble mound requires the piecemeal offshore construction of both the break-water and a complete separate berth structure.

A number of eminent authorities have pointed out the disadvantages of caisson breakwaters (Ref. 2). It is the primary purpose of this paper to draw attention to the construction advantages of pre-fabricated caissons for the particular case of a detached bulk unloading terminal, and the consequent necessity to develop design criteria which adequately overcome the various objections to caissons. In the authors' opinion, the disadvantages of caisson breakwaters apply almost entirely to vertical wall fully reflecting structures. Caissons do not need to be fully reflecting or to have vertical walls.

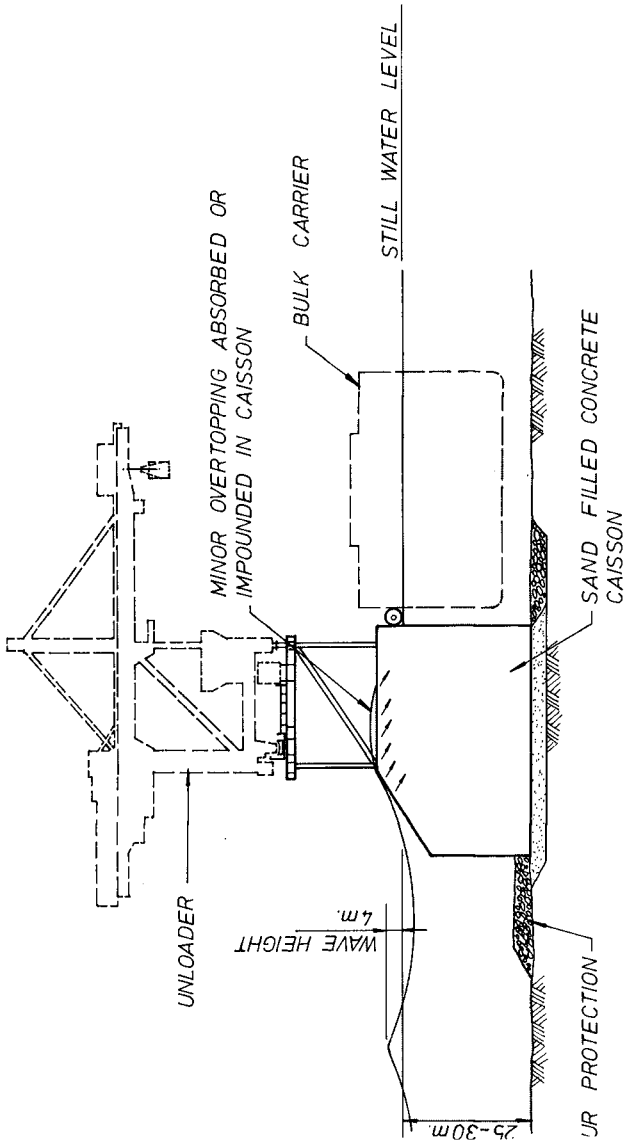


FIG 4 (a)

Previously published work has suggested the concept shown in FIG 5 for the type of terminal shown in FIG 1. The Danish Hydraulic Institute (Ref 5) have recognised the advantages of an overtopping breakwater but suggested that a high reflecting wall, as shown in FIG 5, is necessary in cases where equipment is mounted on the caisson.

However, the maximum design wave load on the caisson depicted in FIG 5 can be shown to be 2 or 3 times that on a sloping face overtopping caisson, and furthermore it suffers all the other disadvantages of vertical wall structures, such as scour at the base.

Accordingly, the authors have developed the concept shown in FIGS 4a & 4b. This meets all the operational availability requirements discussed earlier. Incident waves up to 4 metres high are diffracted round the ends but do not overtop, creating safe conditions for unloading. Waves higher than 4 metres pass over the caissons but under the elevated plant deck. Under these circumstances the berth is shut down and ships taken off to await favourable weather.

The concept is based on the type of breakwater developed by the Danish Hydraulic Institute (Ref 5) but goes a step further by mounting the berth structure on an elevated deck. This retains all the advantages of a sloping face overtopping caisson without endangering the equipment.

The Danish Hydraulic Institute's published work (Ref 5) also draws attention to the fact that much of the advantage of a sloping face breakwater is lost when the tide level falls below the bottom of the sloping section.

The authors consider that from the construction point of view it is not essential to extend the vertical wall up to still water level. Accordingly, it is proposed to include in the research program the concept shown in FIG 6, with the slope extended below low tide level. Such a caisson would require temporary buoyancy tanks to assist flotation and installation. Its potential advantages are further reduction of the maximum wave load on the caisson, and reduced scour.

The paper so far has discussed operational and constructional requirements and demonstrated that these factors combine to create a need for research to establish suitable design criteria for the concept shown in FIGS 4 & 6.

The next part of the paper discusses the requirements of the research program proposed by the authors.

PROPOSED RESEARCH AND DEVELOPMENT

The proposed island breakwater concept (see FIGS 4 & 6) has to meet three principal design criteria:

- (i) its geometry must ensure that the wave climate at the berth behind the breakwater provides the required percentage time availability for unloading, i.e. it must have the specified attenuation factor.

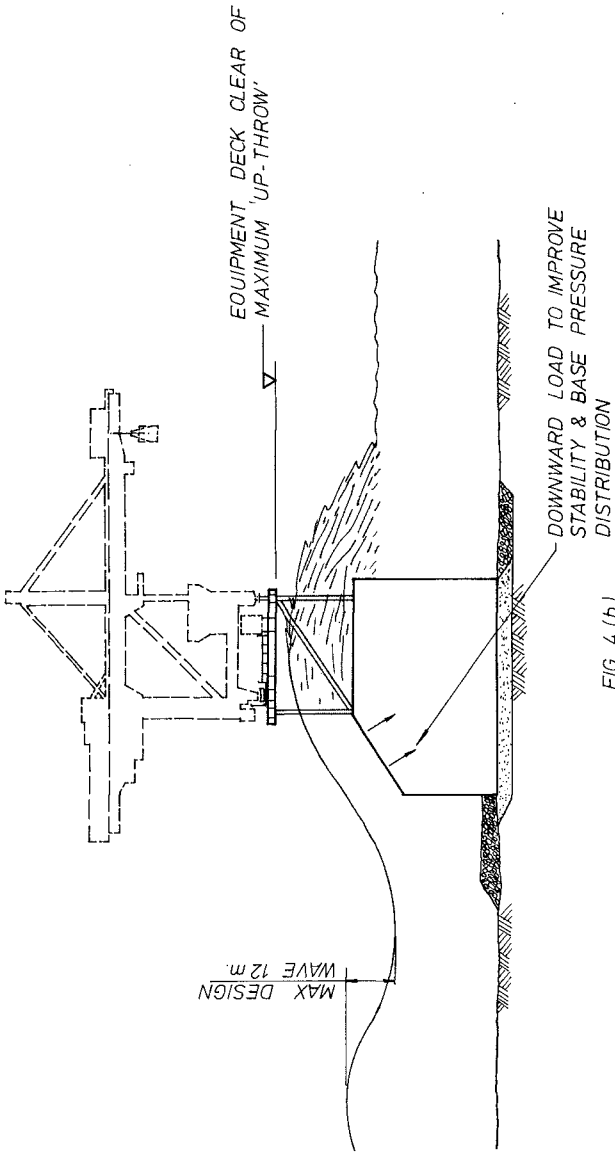


FIG 4 (b)

- (ii) the breakwater must have an adequate factor of safety against a stability failure commensurate with the risk to personnel and unloading equipment.
- (iii) the breakwater geometry should minimise the "up throw" of overtopping waves in order to limit the require deck elevation.

These three criteria require opposing solutions with respect to the breakwater's height and seaward wall geometry, and hence a compromise design must be selected. In general terms a profile which minimises the loads on the structure will also create more overtopping.

Breakwater Stability

The basic requirement of the breakwater stability design comprise:

- (a) provision of the required factors of safety against sliding and overturning of the breakwater when subjected to the maximum design wave.
- (b) prevention of scour at the base such that the foundations are not progressively undermined.

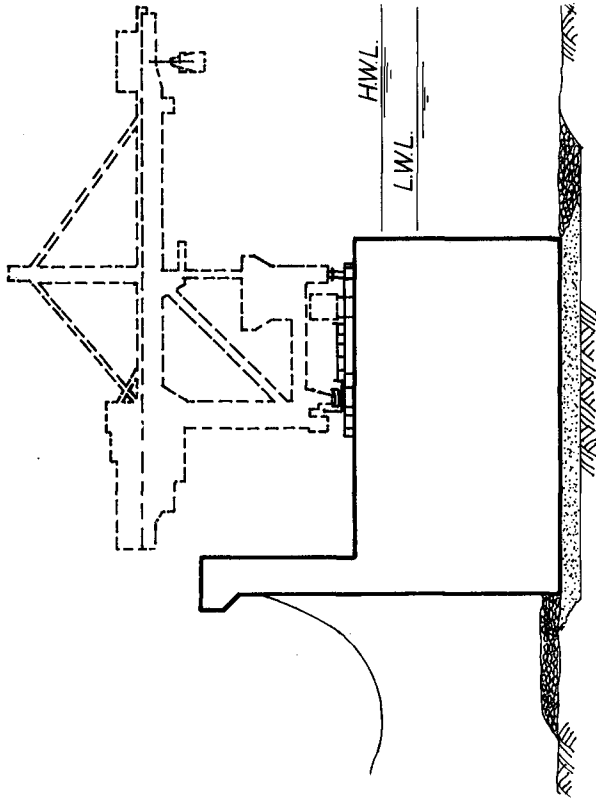
The authors consider that ideally the factor of safety against an overturning failure or base failure, which would have catastrophic consequences for the installation, should be significantly higher than that against sliding. A slide of a few centimetres need not be classed as irreparable damage as it can be rectified by adjustments to the rails carrying the ship unloading equipment. It is of interest to note that most of the documented caisson breakwater failures have in fact involved slides (Ref 3).

Effect of Breakwater Profile with Respect to Stability

If a vertical wall caisson is first considered the wave forces can, as expected, be significantly decreased by allowing the higher waves to overtop instead of totally reflecting them. The graphs in FIG 7 were derived using the MICHE-RUNDGREN theory with the approximations discussed in Refs. 3 & 4. Both the horizontal force and the overturning moment are lower for the overtopping structure. More importantly, the rate of increase of moment with respect to wave height, is significantly reduced. Hence, the overtopping breakwater is considerably less sensitive to an unforeseen increase in the design wave height.

These points are also demonstrated by previous model test results (Ref 5) particularly as the wave conditions approach breaking.

It is possible to further reduce the wave forces and scour erosion of the overtopping breakwater by providing an inclined face to the seaward wall.



FULLY REFLECTING VERTICAL WALL
BREAKWATER

FIG. 5

Model tests (Ref 6) show that the pressure distribution acting on an overtopping inclined face breakwater are of the form shown in FIG 8. This diagram demonstrates another advantage of allowing waves to overtop, namely the stabilising effect of the downward component of the water pressure acting on the inclined face. Besides increasing the friction resistance to sliding this downward component can also be used to counteract some of the overall overturning moment.

Furthermore, model tests have shown that the shock pressures as well as the overall horizontal wave force can be reduced by inclining the seaward wall (Ref 5).

The model test results in Ref 6 indicate that by inclining the front face, the uplift force is also reduced, with further stability benefit.

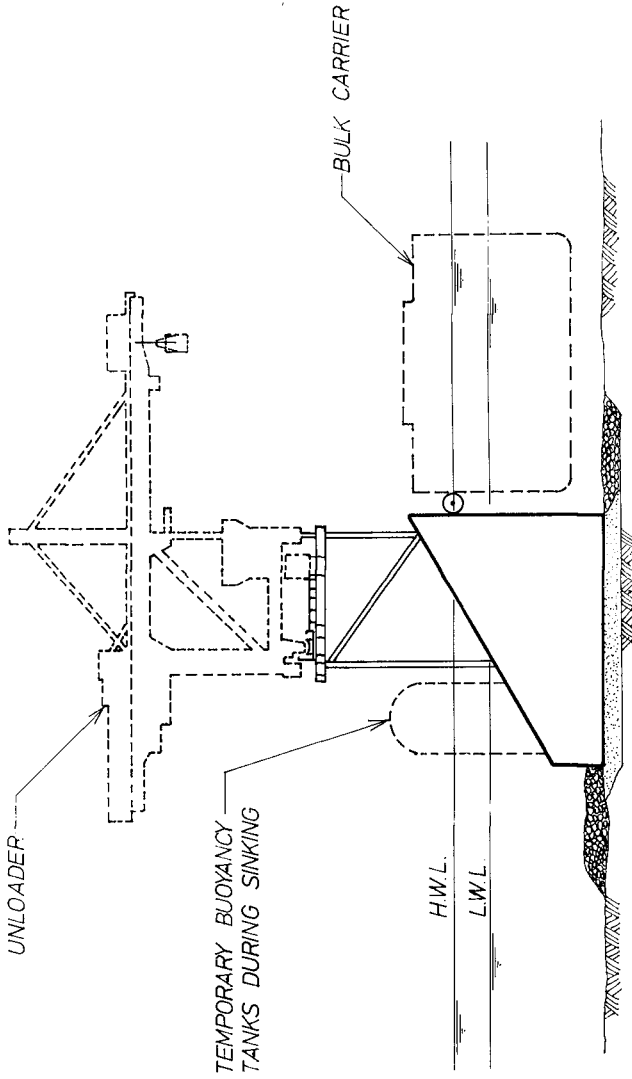
The inclined wall breakwater has a further advantage in relation to scour effects. Waves breaking against a vertical wall are deflected both upward and downward and the latter effect results in high water velocities at the seabed which can lead to foundation erosion (Ref 4). The downward effect is substantially reduced by an inclined seaward face.

PROPOSED MODEL TEST PROGRAM

It can be seen that the attenuation and stability criteria require opposing solutions with respect to the breakwater's profile. Hence a model test programme is proposed to investigate optimum profiles.

A summary of recent relevant literature (Ref 5) suggests the following criteria may be pertinent to the test program:

- (i) physical models are valuable in deriving design criteria for stability of structures and wave forces on structures.
- (ii) the design of a shock-sensitive structure requires that the inertia of the structure and the stiffness of the foundation be taken into consideration in a dynamic analysis. Further, it is common that the natural period of a caisson-type breakwater on its soil foundation is about an order of magnitude smaller than the mean wave period, thus suggesting that the characteristics of the individual wave are all-important.
- (iii) acceptable values of shock forces may be expected on physical models of caissons providing air entrainment is unimportant in both model and prototype. Further, the shock forces are sensitive phenomena such that a large scatter in results is likely unless repetitive tests are carried out - 1000 waves minimum and preferably 3000-5000 waves have been suggested. Even with a random or model-reproduced natural wave train generation, due care should be taken in accepting one single random field record due to the large scatter in force reproductibility.



PROPOSED ALTERNATIVE
BREAKWATER

FIG. 6

- (iv) the maximum force on a vertical-faced structure increases with wave height up to the stage where the wave breaks on the face and begins to overtop. For higher waves the maximum force remains approximately constant or reduces.
- (v) sloping face structures cause less reflection than vertical faces because of energy loss and likely overspill.
- (vi) there are problems with model tests of reflecting structures due to re-reflections within the wave tank.
- (vii) wave height and water level with respect to the structure are the most important independent variables for structural stability analysis.
- (viii) for the same wave height, the longer the period the larger is the force.
- (ix) it is commonly considered erroneous to design structures on the basis of tests with regular waves of design height.

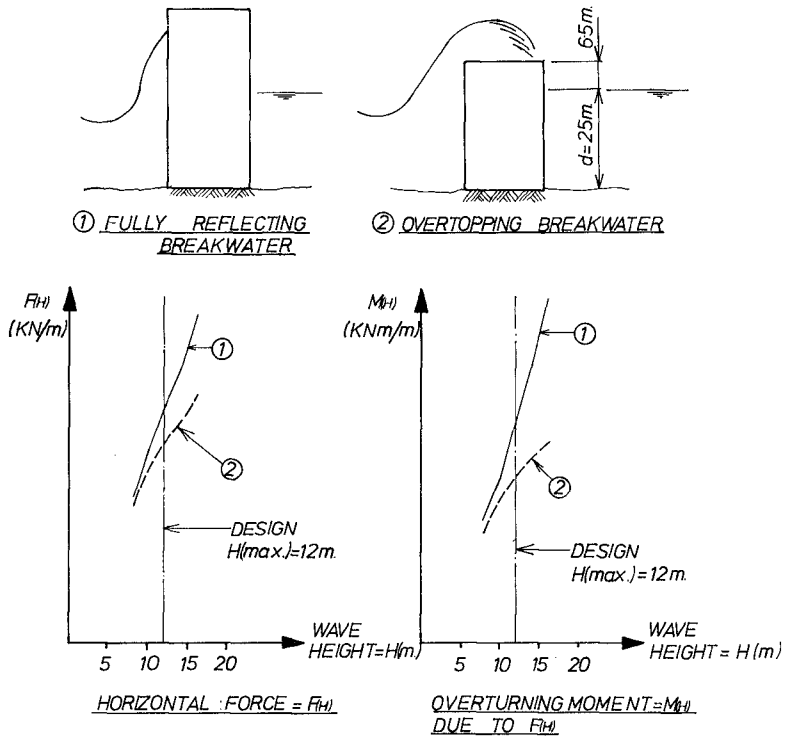
A wave tank 60 metres long and 1.83 m x 1.83 m in section will be used to contain physical models of scale 1:50 to study waves of height up to 5m and periods up to 30 sec. in water up to 50m deep. A larger model (scale 1:20) will be used for confirmatory pressure distribution studies, with waves up to 2m high. In view of the criterion (ii) above applying, and despite criterion (ix), regular waves are considered satisfactory for these tests, recognising re-reflections as a problem.

Additional to the physical tests, it is planned to examine the fully overtopping phenomenon by means of numerical techniques for wave force determination. This will provide valuable guidance as to the type of profile likely to produce the best results in the physical models.

The cross-section configuration of the caisson will likely be similar to that in FIGURES 4 & 6. However the length and angle of sloping front face, level and length of top face of caisson, freeboard height above caisson to plant deck are all variables to be examined. A free-draining wave-absorbing stilling basing set into the top face of the caisson may also be examined, as a possible way of lowering the caisson profile whilst still preventing overtopping.

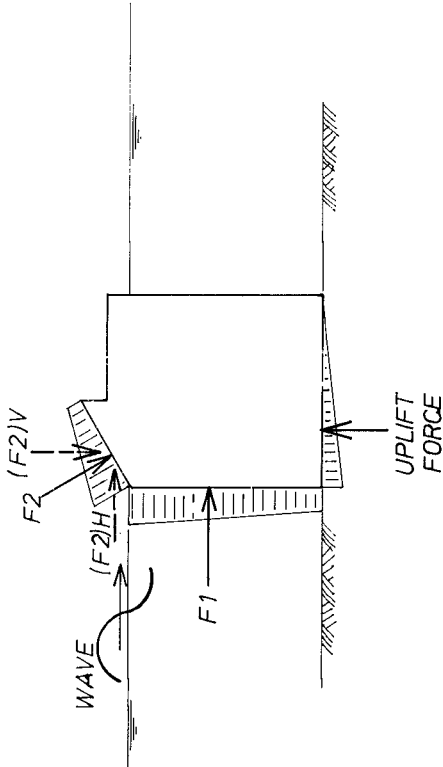
It is too early to report the findings of these various studies in this paper. Instead, comment is invited on, especially, the usefulness and pitfalls associated with the numerical modelling envisaged.

This paper does not consider the very important issue of foundation strength and stability. Apart from considerations of sliding, shearing, overturning, and uplift pressure distribution, the foundation will be subject to erosion forces, the severity of which will depend on wave climate, water depth, and foundation configuration and composition.



NON-BREAKING WAVE FORCES USING MICHE - RUNDGREN FORMULAE (12 SECOND PERIOD WAVE)

FIG. 7



TYPICAL WAVE PRESSURE
DISTRIBUTION FOR OVERTOPPING
BREAKWATER

NOTE:

The forces shown are those additional to the hydrostatic and gravity loads.

FIG. 8.

CONCLUSIONS

- . The construction of bulk unloading terminals in deep water will require the use of detached island breakwaters.
- . For construction reasons related to the delay risks when working in an offshore situation, pre-fabricated caisson breakwaters are preferable in this situation.
- . Significant cost savings can be achieved if the caissons forming the breakwater are also used as the structural support for the ship unloading equipment.
- . Significant further cost savings can be achieved if the highest 5% to 10% of waves are allowed to overtop the caisson.
- . Sloping face caissons supporting an elevated plant deck above the crest of the highest overtopping waves offer the most attractive solution.
- . Further research is required to define wave loads and other parameters with an adequate degree of assurance for safety of the equipment. The paper makes recommendations for the required research.

REFERENCES

1. EDDIE, A.G.F., GERWICK, Prof. Ben C., LEE, J.O.T. - 24th International Navigation Congress, Published by PIANC, Leningrad 1977. Design and Construction Aspects of Exposed Offshore Bulk Mineral Export Terminals in Australia.
2. PIANC - Final Report of the International Commission for the Study of Waves
3. GODA, Yoshimi - New Wave Pressure Formulae for Composite Breakwaters Proc 14th Coastal Engineering Conference, Copenhagen, 1974.
4. U.S. ARMY COASTAL ENGINEERING RESEARCH CENTRE - Shore Protection Manual, Volume II, 1975.
5. GRAVESEN, H. - Published by Danish Hydraulic Institute, January 1979, Design of Caisson Breakwaters
6. BRAGADIN, G.L. - Published by International Association for Hydraulic Research XVII Congress - Baden-Baden, 1977, Hydraulic Behaviour of Overflow Breakwaters.

THE DESIGN AND CONSTRUCTION OF THE NEW
OIL PORT IN DALIAN, C.P.R.

Xin, Zhu-zhuang,

Qiu, Da-hong, Li, Yu-cheng and others
(Dalian Institute of Technology)

Abstract

The construction of New Oil Port in Dalian, C.P.R., was started from the end 1974 and completed in autumn 1976. In this paper a summary of the essential considerations in design and construction of this oil port, such as the planning of the pier, the determination of exciting forces (namely wave forces, forces due to earthquake, mooring line forces and berthing forces due to the impact of tanker on the fenders) on structures, the design of the large cylindrical caisson with a diameter of 9m and a height up to 19.7m and the construction of connecting bridges by two types, is presented.

General description

The New oil port is situated in Dalian, Liao-Ning, People's Republic of China, it is a terminal of the Da-Ching Oil Field. The design capacity of the export of crude oil is 15,000,000 tons per year.

Fig(1) is the general plan of the New Oil Port. The jetty is of cylinder-pier type and is located about one kilometer from the shore line. The direction of the axis of the jetty runs $N150^{\circ}$, which gives an efficiency of 85-90% utilization of the berth every year. The depth of the water alongside the jetty is 17.85 meters at low water level, which is sufficient for the berthing of 100,000 tonnage oil tanker.

The jetty is 421.3 meters long, consisting of an operating platform, two berthing piers and six mooring piers, as shown in fig(5). Fig(2) is its general view.

There are four spans of steel pipeline bridge between the operating platform and the piers No.6,7,8,9 and four spans of steel foot bridge between the operating platform and the piers No.4,3,2,1. The span lengths of these bridges are 24.2 meters, 2-30.7 meters and 51.5 meters respectively. The distances between the piers are determined mainly according to the adequate angles of mooring lines and the requirement of the berthing of the tankers. In this design, the arrangement of the piers is fitting for the berthing of 30,000 tonnage up to 100,000 tonnage oil tankers.

The water depth alongside the jetty at low water level is determined mainly according to the following considerations: (1) the berthing tanker will not touch the sea bed under the wave action of the operating condition, (2) the increase of the draft of the tanker when it navigates out of the port, (3) the reserved depth for deposition and

other factors.

Under the wave action, the draft of the berthing tanker will be increased due to the heave, roll and pitch motion of it .

The results of the 1:60 scale model tests are shown in table (1) for the beam sea and in table(2) for the oblique sea with an angle of 30° between the wave direction and the longitudinal axis of the tanker.

From the results shown in tab.(1), the increase of the draft under the beam sea does not exceed 0.94m. in the general case, and in the case of long period swell with the wave height less than 1.0m., its extreme value does not exceed 2.58m.

Under the action of oblique sea, in the test the amplitude of the motion of heave and roll decreased rapidly, but a pitch motion was produced. Although the amplitude of the pitch motion was not very large, due to the fact that the length of the ship was much longer than its width, the small pitch motion still caused a significant increase in the draft of the tanker. From the results shown in tab.(2), the increase in draft , generally did not exceed 1.17m. at high water level (HWL) and 0.57m. at low water level (LWL), and in

the case of long period swell, its extreme value did not exceed 2.54m. at HWL and 1.09m. at LWL.

The elevations of all the pier tops are +10.0m, and those of the top deck and low deck of the operating platform are +12.0m and +10.0m. respectively. The determination of these elevations is mainly due to the following considerations: (1) no overtopping of waves will occur, (2) no strong wave action on the pipeline bridge will occur, (3) the inclination angles of the mooring lines are adequate, (4) the operating range of the oil loading arm is sufficient for

different tonnage berthing tankers.

The jetty is connected to the shore by a 111.75m.long mole consisted of rubble mounds and 9 spans of steel bridge. Each span of the bridge is 100 meters long. The bridges are supported on the cylinder piers, which are spaced 106m. apart center to center. The axis of the connecting bridge runs out in the east direction, and makes an angle of 120° with the axis of the jetty. Fig (3) is the general view of the connecting bridge.

The construction of the piers

The piers are all of gravity type using the reinforced concrete cylinder caissons as the underwater structure. The soft top layer of the sea bottom was dredged and stones weighing 15 to 100 kg. for rubble mounds were deposited in the dredged cavities up to the design level, then the cylinder caissons were rested upon these rubble mounds. The largest cylinder caissons used are 9.0m. in diameter and 19.7m. high, the bottom of the caissons is octagonal in shape. The thickness of the wall of the cylinder is 30cm. and that of the bottom is 100cm. The superstructures of the piers over the caissons were three layers of solid or hollow precast reinforced concrete blocks, which were interlocked with each other by filling concrete in the concrete in the connecting holes with reinforcement in it. As an example, the construction of the operating platform is shown in fig (4).

The forces acting on the piers

The forces acting on the piers consist of the following forces: (1) wave forces, (2) forces due to earthquake, (3) mooring line forces, and (4) berthing forces due to the impact of tanker on the fenders.

The wave force exerted on single pier is calculated by Morison equation. In order to estimate the influence of the

pier group, a 1:60 model test were made in the laboratory. According to the test results, a coefficient was used to modify the calculated result for single pier. For the operating platform this coefficient is 0.9-1.1, and for the berthing pier, 1.0-1.4.

The mooring line force of the berthing tanker is caused mainly by the wind, current and wave action on the tanker. For the offshore jetty, the dominant condition is the wave action. This action is very complex, because it not only depends on the scale and the direction of the wave, but also on the loading condition of the tanker, the characteristics of the mooring lines and fenders, and the arrangement of mooring lines when in berthing. Model tests of the 100,000 tonnage tanker with 1:60 scale were made for measuring mooring line forces and impact force and energy of the berthing tanker on the fenders. The mooring line arrangement in the test is shown in fig(5). The test data are tabulated in table(3).

From analysis of the test data, the following informations can be drawn:

(1) The maximum mooring forces are produced by the beam sea, if the wave direction is at an angle with the longitudinal axis of the tanker, the mooring forces will be reduced rapidly. The maximum mooring forces will occur at the ballast loading condition. For the beam sea from the outside of the berth, the mooring line forces of a tanker in full loading condition are increased as the wave height and wave period increase. As for the tanker in ballast loading condition, the mooring line forces will be maximum when the wave period coincides with the natural roll period of the tanker. For the oblique sea and head sea, the mooring line forces are also increased as the wave height and wave per-

iod increase. For the beam sea however, the mooring line forces inside of berth will be greater than that outside of the berth due to the tendency of pushing the tanker away from the berth.

(2) When nylon breast lines are used, the mooring lines work normally for all test conditions, only for long period beam sea when the wave height reach 1.4-1.6m., the mooring lines will be broken occasionally. When the steel breast lines are used, the mooring line will be broken in most cases during test, it can work in normal condition when wave height is less than 1.5m. and wave period less than 4 sec. for beam seas and wave height less than 2.4m. and wave period less than 5.3 sec. for oblique and head seas.

According to the test results, the mooring line breaking force is used as the control force of the mooring line in design. This is mainly dependent upon the arrangement and the size of the mooring line selected. In design for the 100,000 tonnage tanker the 10" nylon line was selected and the arrangement of the mooring line is shown in fig (5).

The impact force of the tankers on the berthing piers is mainly due to the following two causes: (1) the kinematic energy produced by the approaching velocity of the tanker during berthing, (2) the kinematic energy produced by the motion of the berthing tanker due to wind, current, especially the wave action. For offshore jetties in the open sea, the latter is the controlling case for determining the impact energy in design.

The model test results of the impact energy of 100,000 tonnage tanker due to wave action are shown in table 4. From these test data we can see that the wave condition has great influence on the impact energy of the tanker.

Therefore in the design we must first determine reasonably the wave condition for safe loading operation of the berth. This is a complex problem because it depends upon many factors such as the management of the loading operation of the berth, the design criterion of the jetty, the requirement of the loading capacity of the berth per year and others. In this design, the wave condition for safe loading operation is tabulated in table (5).

From the test results and the analysis of the moored ship, we can get a semi-empirical formula for calculating the impact energy of the tanker.

$$E/H^2 = \alpha_1 \alpha_2 \alpha_3 \alpha_4 (1.4-2.7 \frac{D}{B}) \frac{LoA}{260} T^{2.5} (t-m/m^2)$$

Where: H, T—wave height (m.) and wave period (sec.) :

D, B, LoA—draft, breadth and total length of the moored tanker;

α_1 —the coefficient due to eccentric impact of the tanker,

$\alpha_1 = \frac{1}{1 + (L/r)^2}$, L is the distance between the fender and the center of gravity of the tanker on the cross section, r is the radius of gyration of the cross section of the tanker;

α_2 — the coefficient due to the change of the water level, for the case of tidal range less than 4.0 m. and small reserved depth for safety for the berth, $\alpha_2 = 1.0$;

α_3 — the coefficient due to the loading condition of the tanker and the influence of the elasticity of the mooring line, for the case of full loading, $\alpha_3 \cong 1.0$, for the case of ballast loading : $\alpha_3 = 1.0$ for all nylon mooring lines, $\alpha_3 = 1.5$ for steel spring lines with nylon lines for others, and

$\alpha_3=2.2$ for steel breast lines with nylon lines for others;

α_4 — the coefficient due to different wave direction,
 $\alpha_4 = 0.05 + 0.95 \sin^4 \alpha$, α is the angle between the wave direction and the longitudinal axis of the tanker;
 for beam sea from inside of the berth, $\alpha_4 \leq 0.6$.

The formula is applicable for the condition of wave period equal to or less than 7sec..

It is necessary to determine the dynamic characteristic of the piers for calculating the earthquake reaction. For this purpose, the natural frequency and the damping ratio of the completed connecting bridge piers No.1,2,3 and the jetty pier No.8 under construction, shown in table 6, were measured in site. The coefficient of the rigidity of foundation K calculated from the measured data was used to design the dynamic model test of the completed jetty pier No.8. The test results of the first mode of vibration of the dynamic model test were very close to the calculated values, as shown in table (7). The sketch for calculation is shown in fig(6).

Using the dynamic characteristic of the pier obtained from the test, we can calculate the deformation process of the pier during berthing and the earthquake force and its distribution along the pier.

The design of the large cassion

The construction of the reinforced concrete cassion is shown in fig. (7). The wall of the cassion is a cylindrical shell which is rigidly connected on the base plate of the cassion. In design, the following items are considered: (1) the strength and the stability of the cylindrical wall against crack, under the action of the external and internal pressure, (2) the stability of the cylindrical shell under the combined action of axial force and be-

nding moment,(3) the local strength of the shell due to the impact of the construction ships.

The cassion was built in two stages. In the first stage, the cassion was built up to a height of 12m. on land, and then slipped into sea on the slipway. In the second stage, it was built up to the full height of 19.7m. along the wharf under floating condition. Because the draft of the cassion floating vertically in state is larger than the water depth of the navigation channel, the cassion was towed by the tug at inclined position. The process of sinking down the cassion during the rising of tide and the reaction acted on the edge of the base of the cassion during sinking were checked in a 1:30 scale model test. The test results agreed closely with the calculated values.

The construction of the bridges

The all-welded Vierendeel trusses in parabolic shape are used in the construction of the connecting bridge. This is because the main loads of the bridge are uniformly distributed dead loads which occupy almost 84% of the total loads, and the moving loads are also essentially uniformly distributed.

The all-welded steel plate-girders strengthened by struts are used in the construction of the pipeline bridge along the jetty, because the total height of the bridge is limited in a small range of 4 meters. The result of using this type of structure is satisfactory in economy and service.

The span of the vierendeel truss is 100 meters, which is divided into 12 panels. The ten intermediate panels are 9 meters in length each, and the two end panels are 5 meters in length each. The distance between the trusses is

7.6m. and the total width of the bridge is 12m. The height of truss at mid-span is 12.5m., which gives a rise-span ration of $1/8$. The joints of the truss are strengthened, and the wedge-shape plate girders with an integral box section are used to strengthen the end panels. The sketch of the connecting bridge is shown in fig.(8).

The height of the plate-girder of the pipeline bridge is 2.0 meters. There is an elbow at each end of the girder to support the strengthening strut. Vertical members are spaced at 6.4m. apart to connect the plate girder and the strut. The distance between main girders is 5 m. center to center, and the width of the bridge is 9.0m. at the lower deck for carrying pipes and 5.0m. at the top deck. The sketch of the pipeline bridge is shown in fig.(9).

For checking the reliability of the design, several tests were made during construction.

For the Vierendeel truss, a photo-elastic model test and a 1:3 structural model test for the joint have been carried out and an overload (total load 840 t.) test for the whole bridge and a test for the non-uniform settlement of the supports were made on the assembly ground on the shore. The dynamic characteristics of the Vierendeel truss under different loading condition have also been measured, the results are shown in table (8).

Photo-elastic model tests of 1:100 scale for the whole span of the pipeline and 1:20 scale for the elbow part of the girder were made during design. The deflections of the bridge in prototype under the service loading condition were measured, the value agreed closely with the theoretical value with a deviation of about 5%.

The members of the bridges were fabricated in workshops and then assembled into a complete unit on the assembly ground, which was specially constructed for the assembly work of the

bridges. After a whole span of the bridge has been assembled, the pipes, traffic deck, and all accessories were installed on it, and then it was pulled on the shipway to the end of a mole. The assembled span was hoisted on the floating crane which was navigated by towing tugs to the bridge site and the span was finally erected on the piers.

Tab.1

Wave height H(m)	Wave period T(s)	amp.of heavy(m)		heavy below W.L(m)		roll θ	
		mean	max.	mean	max.	mean	max.
1.5	≤ 8	< 0.3	< 0.6	< 0.22	< 0.42	$< 55'$	$< 1^{\circ}30'$
1.0	11	< 0.6	< 1.2	< 0.55	< 1.0	$< 3^{\circ}40'$	$< 4^{\circ}38'$

Tab.2

depth (m)	Wave height H(m)	wave period T(s)	amp.of heavy		pitch		ψ
			mean	max.	mean	max.	
H.W.L.	~ 1.5	5.0~8.0		0.28			23'
		9.3~11.0	0.39	0.7	25'	48'	
		5.0~8.0		0.24	27'	39'	
21.5 ^m	2.0~2.5	9.3~11.0	0.51	0.84	26'	45'	
		5.0~8.0		0.15		11'	
		9.3~11.0		0.2		19'	
L.W.L.	~ 1.5	5.0~8.0		0.25		14'	
		9.3~11.0		0.26	17'	22'	
		2.0~2.5					

Tab.3

Wave height H(m)	Wave period T(s)	Condition of Loading and Mooring	Outside beamsea		Inside beamsea		Oblique sea 300		stern sea	
			breast line(t)	spring line(t)	breast line(t)	spring line(t)	b.l. (t)	s.l. (t)	b.l. (t)	s.l. (t)
1.4	5.0	B.L. ny. b.l. st. b.l.	<55 broken	<25 <27	<45	<20 may be broken	<10 <8	<10 <8	<10 <8	<10 <8
~ 1.7	~ 8.0	F.L. ny. b.l. st. b.l.	<31 broken	<11 5	/	/	<5 6	<5 6	<5 6	<5 6
1.9	5.0	B.L. ny. b.l. st. b.l.	<67 broken	<27 35	<145	<75 broken	<25 10	<15 10	<15 10	<15 10
~ 2.5	~ 8.0	F.L. ny. b.l. st. b.l.	<59 broken	<20 20	/	/	<10 /	<14 /	<10 /	<13 /
1.1	9.3	B.L. ny. b.l. st. b.l.	<134 /	<69 /	<80	<75	/	/	/	/
~ 1.15	~ 11.0	F.L. ny. b.l. st. b.l.	<45 broken	<25 10	/	/	/	/	/	/
1.4	9.3	B.L. ny. b.l. st. b.l.	<92 broken	<92 49	<96	<123	<10 broken	<5 105	<7 105	<15 16
~ 1.6	~ 11.0	F.L. ny. b.l. st. b.l.	<88 broken	<20 15	/	/	<35 /	<10 /	<8 /	<22 /
1.9	9.3	B.L. ny. b.l. st. b.l.	/	/	/	/	<27 broken	<45 20	<20 broken	<20 15
~ 2.4	~ 11.0	F.L. ny. b.l. st. b.l.	/	/	/	/	<38 /	<18 /	<12 /	<20 /

B.L.:ballast loading
 F.L.: full loading
 ny. b.l.: nylon breast line
 st. b.l.:steel breast line

Tab. 4

Wave height H(m)	Wave period T(s)	Condition of loading and Mooring		Outside beamsea Emax (tm)	Inside beamsea Emax (tm)	Obliquesea Emax (tm)	Sternsea Emax (tm)
1.4 ~1.7	5.0 ~8.0	B.L.	ny. b.l.	< 420	< 260	< 40	< 16
			st. b.l.	< 660	—	< 55	< 13
1.9 ~2.5	5.0 ~8.0	F.L.	ny. b.l.	< 320	—	< 30	< 20
			st. b.l.	< 370	—	—	—
1.9 ~2.5	5.0 ~8.0	B.L.	ny. b.l.	< 680	< 143	< 75	< 16
			st. b.l.	< 1950*	—	< 80	< 22
1.1 ~1.15	9.3 ~11.0	F.L.	ny. b.l.	< 570	—	< 50	< 28
			st. b.l.	< 450	—	—	—
1.1 ~1.15	9.3 ~11.0	B.L.	ny. b.l.	< 830	< 330	—	—
			st. b.l.	—	—	—	—
1.1 ~1.15	9.3 ~11.0	F.L.	ny. b.l.	< 450	—	—	—
			st. b.l.	< 420	—	—	—

1.4 ~1.6	9.3 ~11.0	B.L.	ny. b.l.	$\leq 1520^*$	≤ 360	≤ 80	≤ 17
		F.L.	st. b.l.	$\leq 1930^*$	—	≤ 95	≤ 22
1.9 ~2.4	9.3 ~11.0	B.L.	ny. b.l.	$\leq 1370^*$	—	≤ 95	≤ 27
		F.L.	st. b.l.	$\leq 1010^*$	—	—	—
		B.L.	ny. b.l.	—	—	≤ 140	≤ 21
		F.L.	st. b.l.	—	—	≤ 320	≤ 37
		F.L.	ny. b.l.	—	—	≤ 180	≤ 29
			st. b.l.	—	—	—	—

*When $E_{max} > 1000$ t.m., the data is usually not true, because $E_{exp} > (E_{fen.})_{crit}$.

Tab.5

direction of waves	wave height H(m)	mean period T (s)
E, ENP, NE	≤ 1.0	< 6
other direction of waves	≤ 1.5	$< 7 \sim 8$

Tab.6

No of cylinder piers	direction of vibration	nat.freq, f	ratio of damping ζ
No 1 pier of connecting bridge	per. to axis	1.98	0.06
	par. to axis	2.16	
No 2 pier of connecting bridge	per. to axis	2.36	
	par. to axis	2.44	
No 3 pier of con.bri.	per. to axis	2.34	0.044
	par. to axis	2.49	
No 8 pier of jetty (before constructed)	per. to axis	2.06	0.060
	par. to axis		

per.: perpendicular

par.: parallel.

Tab.7

	η	1.208	1.0	0.8	0.6	0.4	0.2
first mode of vib.	Y (1) meas. by acc. meter type SHQ-8A	1	0.740	0.622	0.445	0.334	0.289
	Y (1) meas. by acc. meter type DS-1	1	0.600	0.609	0.376	0.184	/
	Y (1) (cal.)	1	0.813	0.626	0.446	0.279	0.125
Second mode of vib.	Y (2) (cal)	-1	0.281	1.500	2.130	1.980	1.140

Tab. 2

loading condition	mode of vib.	curve of vib. mode	nat. freq. f (s^{-1})	exp. ratio of damping δ	duration of damping(s)
whole bridge 316 t.	1 st mode	antisym.	1.58	0.122	11.9
	2 nd mode	sym.	2.33	0.134	7.7
whole bridge 388 t. (with 5 pipelines)	1 st mode	antisym.	1.48		
	2 nd mode	sym.	2.13		
whole bridge 460 t. (with 10 pipelines)	1 st mode	antisym.	2.14	0.205	5.4
	2 nd mode	sym.			

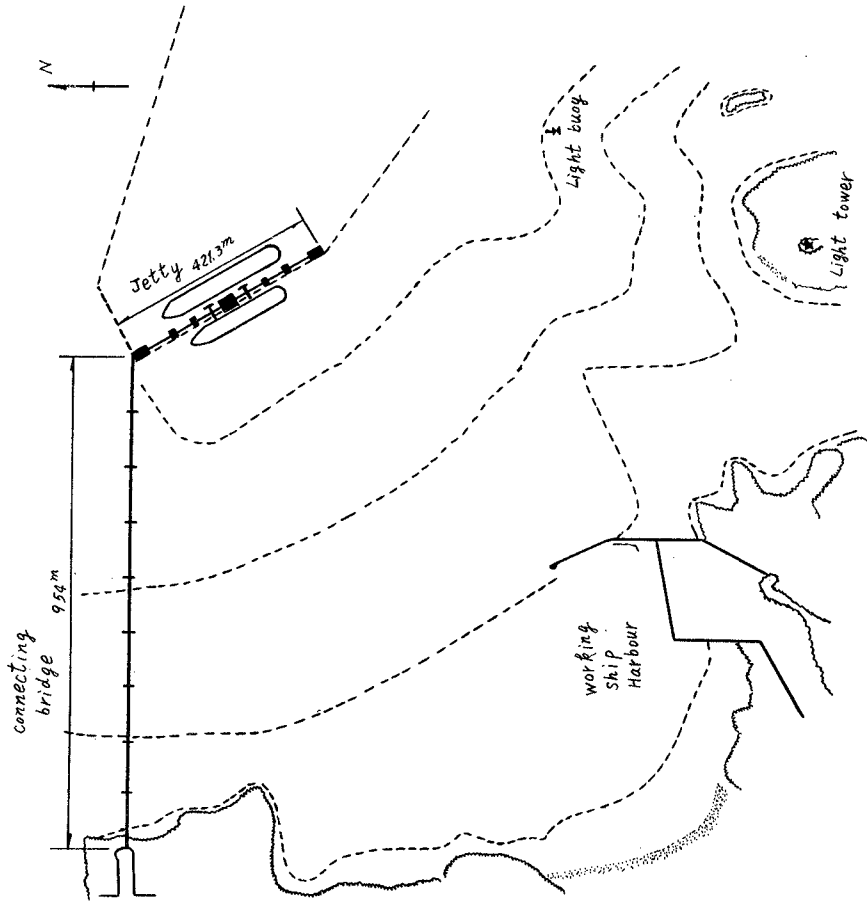


Fig 1



Fig 2



Fig 3

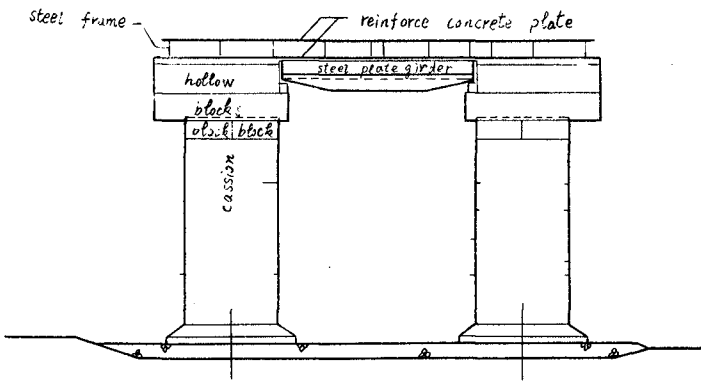
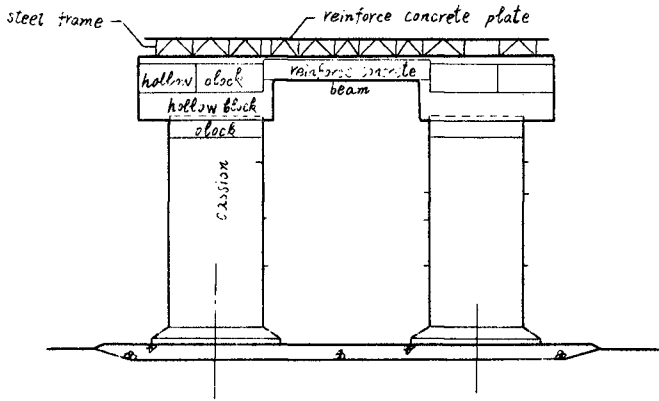


Fig 4

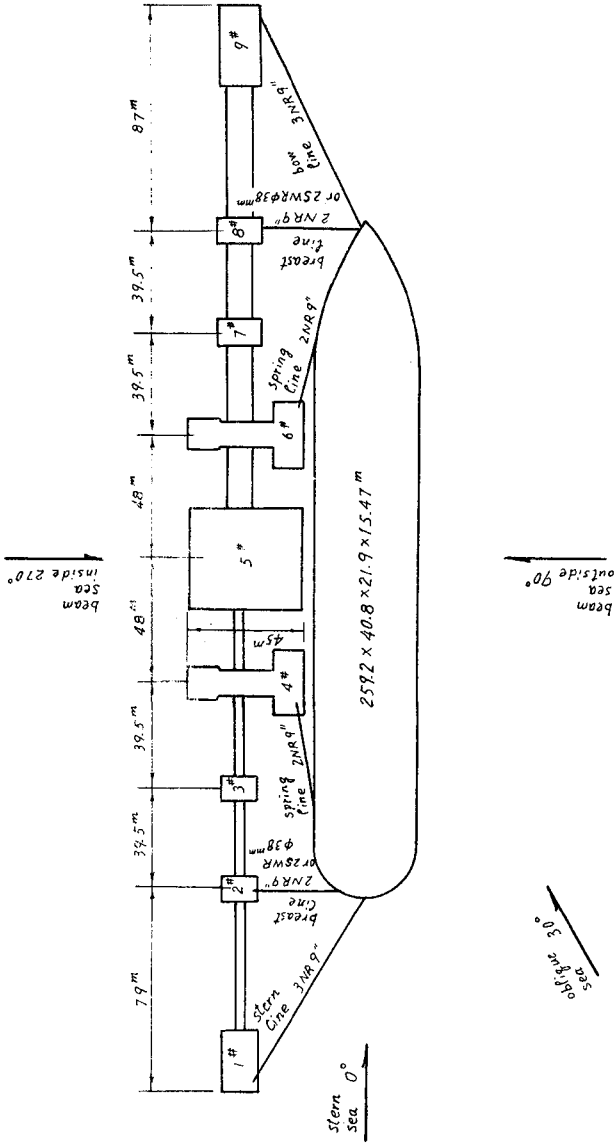


Fig 5

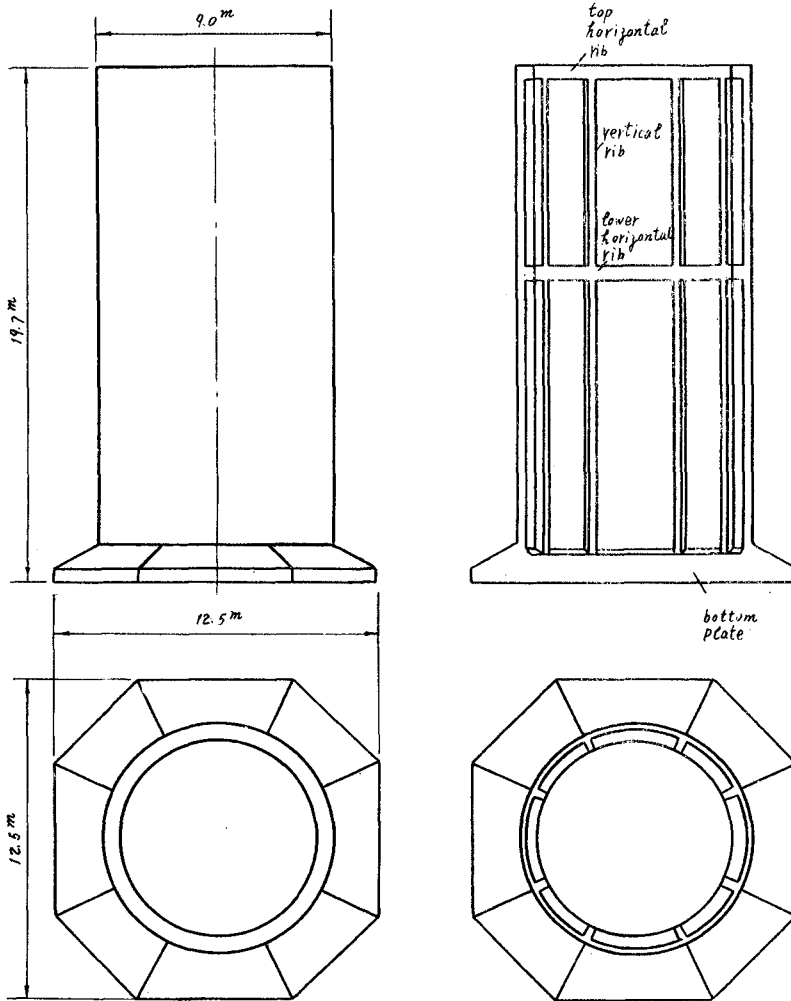


Fig 7

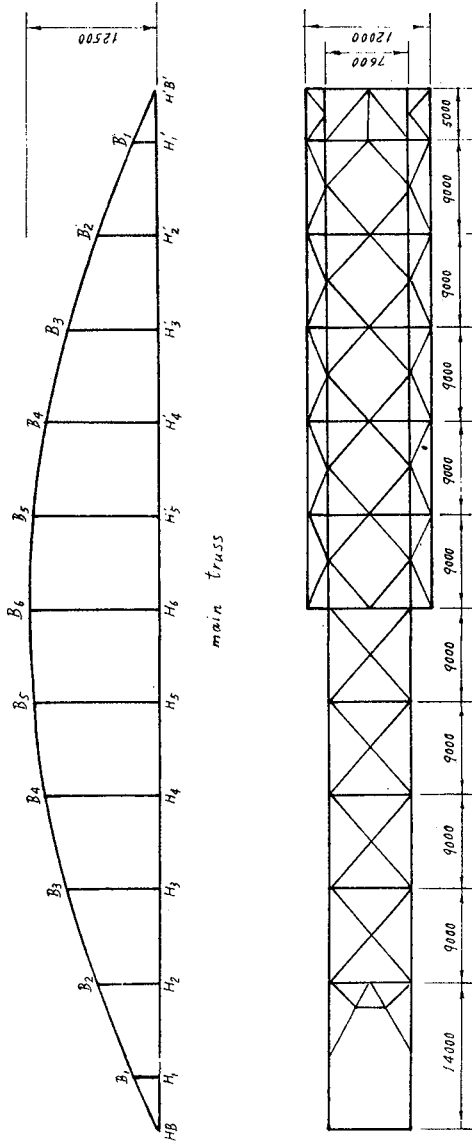


Fig 8

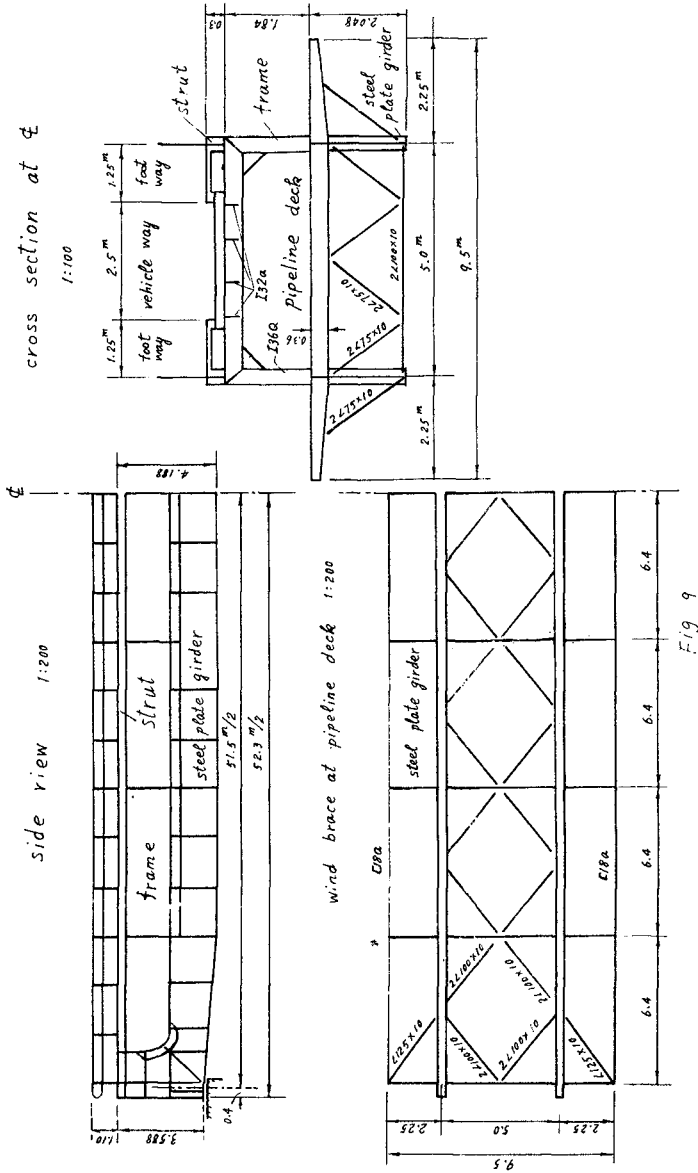


Fig 9

SITING AND DESIGN CRITERIA OF DOCK STRUCTURES IN THE
MARSHALL ISLANDS

by

R.M. Noble¹, K.C. Leslie² and D. O'Day³ABSTRACT

In the summer of 1978, a siting/design investigation for dock structures (Marshall Islands Dock Project) was conducted at 15 atolls within the Marshall Islands group (see Figure 1). The Marshall Islands are within the U.S. Trust Territory of the Pacific Islands (TTPI), located in the North Pacific. The Marshall Islands Dock Project is part of the Capital Improvements Program currently underway in the Marshalls. The program, aimed towards making the Marshall Islands more self-sufficient in preparation for their independence in 1981, includes the construction of low cost dock structures for use by the design vessels described in this paper to load/unload agricultural products, supplies, and passengers. This study did not include the feasibility of this approach versus other alternative loading/unloading approaches.

This investigation included site selection, development of design criteria, and the design and alignment schemes for 12 new dock structures. In addition, design criteria and plans were developed for the upgrading of three existing dock structures. The site selection was performed using a multi-disciplinary approach which considered environmental, sociological, and archaeological impacts, in addition to the usual technical site selection. This paper only discusses the technical considerations to site selection.

Overall responsibility for the project was assumed by the Pacific Ocean Division of the U.S. Army Corps of Engineers on behalf of the Government of the Trust Territory of the Pacific Islands. Our work was performed for Alfred A. Yee & Associates, Inc., the structural engineer and prime contractor for the project, and in collaboration with R. M. Towill Corporation.

¹ Associate, Dames & Moore, Los Angeles

² Staff Engineer, Dames & Moore, Los Angeles

³ Project Engineer, Dames & Moore, Honolulu

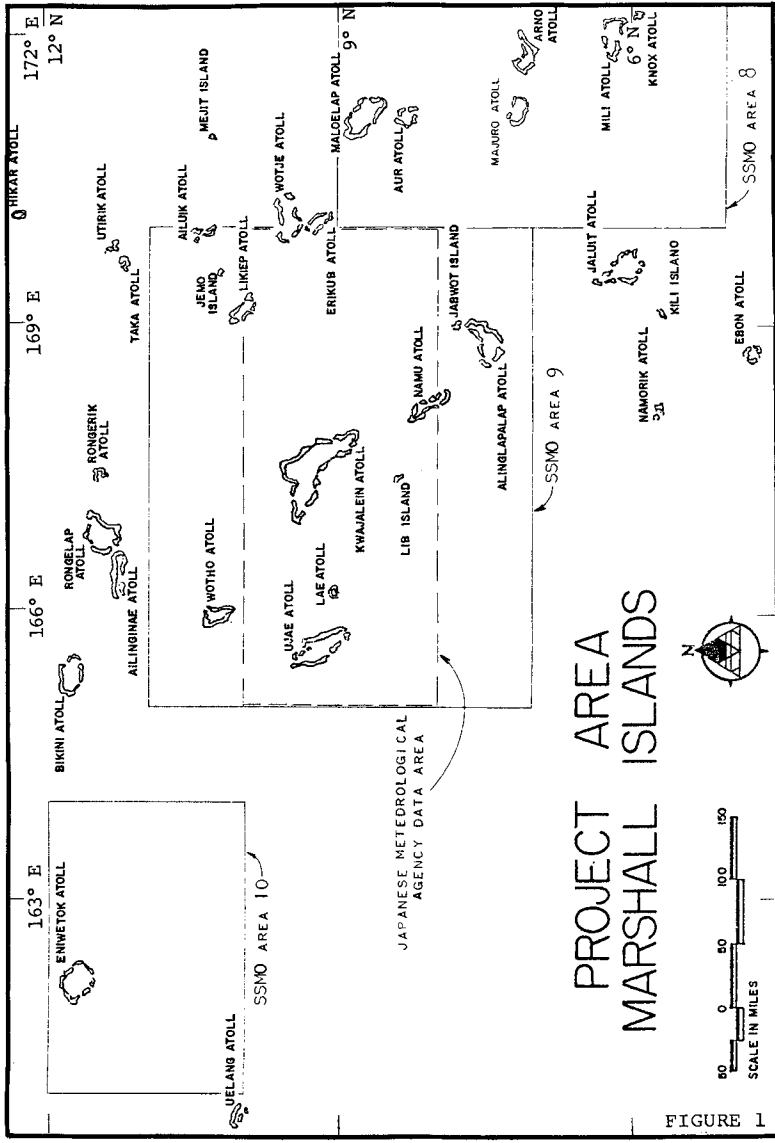


FIGURE 1

INTRODUCTION

The Marshall Islands group is composed of two roughly parallel, northwest-trending island chains approximately 500 miles long in the North Pacific. There are about 25 atolls and several islands in the Marshall Islands chain. The atolls are typically comprised of a number of elongated low lying islands and coral reef segments that enclose a lagoon.

This project involved the recommendation of sites and alignment schemes and development of design data for new docks in 12 island atolls, and recommended alignment schemes and developed design data for the upgrading of existing pier structures at three island atolls (Wotje, Jaluit and Ebeye). It is hoped that by providing centrally located dock facilities in the primary outer atolls, inter-atoll vessels could be put on a fixed schedule and copra production in the outer atolls could be increased. (Copra, the dried meat from coconuts, is a major, yet underdeveloped resource in the Marshall Islands.) In addition, one of the upgraded docks, Ebeye, was to serve for larger international vessels. The specifications of the design vessels (inter-island and international) are presented below.

	<u>M/V Eigamoiya</u> (Namu Pal Line, Melbourne, Australia)	<u>Micro Chief</u> (TTPI)
Length (feet)	368.5	185
Beam (feet)	55.0	25*
Draft (feet)	24.5	14.5
Displacement Dead Weight (tons)	5,700	800
Use	International containerized cargo	Inter-island cargo

* Estimated

The Marshall Islands Dock Project was different than most full scale siting/design investigations due to time and budget constraints and the remoteness of the Marshall Islands. A team of individuals were asked to perform a 3-day site investigation at each atoll to select sites, develop design criteria and determine dock alignment schemes. In U.S. coastal waters, a site selection and design investigation for a project such as this would involve a site-specific data gathering effort lasting many months.

OBJECTIVES

The following objectives were undertaken to complete the assigned task within the allotted time.

- Prefield program--Existing regional data including wind and wave information and atoll bathymetric charts and aerial photographs were reviewed and assessed in order to select candidate sites for each of the atolls. Design wind and waves for return periods up to 100 years were developed from the compiled regional wind and wave information.
- Field program--During the field program, which generally lasted 3 days per atoll, the following was performed:
 - Reconnaissance of candidate sites--Usually more than one site had been pre-selected for evaluation on each island. Each was briefly examined for its coastal characteristics;
 - Meetings with residents--Meetings were held with the local officials and the probable users of the facility;
 - Site selection--Based on previously-collected data, candidate site inspections, and local input, tentative site selections and alignment determinations were made considering all major factors;
 - Site investigations--Site-specific data were then gathered for use in the design phase. A recording current meter was deployed for approximately 2 days at each site, and general reconnaissance was undertaken onshore and offshore. Limited soil sampling and jet probing were performed using SCUBA diving equipment. Wind, wave, and tidal information was collected, and on- and offshore site processes, such as littoral transport and flooding potential, were evaluated.
 - Field report preparation--Preliminary reports including the data gathered in the field were prepared with tentative alignments and preliminary design recommendations.
- Formulation of recommendations--Upon returning from the Marshall Islands, field bathymetric/topographic data were reduced and maps drawn, current meter data records were interpreted, limited soils laboratory testing was completed on bottom samples, a number of

meetings between the project participants were held, final alignments were selected, and design recommendations were formulated.

- Report preparation--A final report documenting our efforts and including the results of the literature search, field and laboratory data, and discussions and recommendations was prepared for submittal.

BASELINE DATA

The Marshall Islands, lying approximately between 4 degrees and 12 degrees north, are within the northeasterly trade wind belt. The trade winds dominate the regional wind regime in the area. They blow strongest (average wind speed of 10 to 18 knots) and most steadily from December to March, but weaker (average wind speed of 5 to 10 knots) and less steady from July to November. Maximum trade wind speeds are in the 30 knot range. A representative wind rose for the Marshall Islands is presented on Figure 2. These data are based upon eight years of observational wind data contained in the Summary of Synoptic Meteorological Observations (SSMO, 1971).

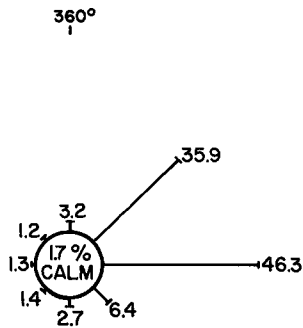
Typhoons are uncommon in the Marshall Islands, but do occur. The winds, sometimes in excess of 100 knots, and accompanying battering waves, can alter an atoll island so radically that it is not recognizable (National Ocean Survey, 1976). The typhoon season in the Marshall Islands usually extends from July to October, although typhoons have been reported throughout the year. Approach direction of the typhoons is generally east to southeast. Violent gales, sometimes severe enough to endanger shipping and cause widespread destruction on an island, occasionally occur from August through November (National Weather Records Center, 1943). The most frequent approach directions are southeast to southwest. Thunderstorms are fairly common, except during the winter months when they are relatively infrequent. Most of the thunderstorms come from the northeast, east or southwest, but a few originate in the north, south, or southwest.

Return period estimates of surface wind speeds based on observational wind data (SSMO, 1971) are presented on Figure 3. Extreme wind speeds associated with typhoons are apparently not represented in the data base. Consequently, the extreme winds for a 100 year return period (non-typhoon condition) are on the order of 40 knots and reflect primarily the trade wind condition.

WIND ROSE- MARSHALL ISLANDS

Percent Frequency by Direction (8 pt. Compass Direction)

SSMO AREA 9



NOTE: AREAL COVERAGE OF DATA
GIVEN ON FIGURE 1

180°

REFERENCE: SSMO, 1971.

FIGURE 2

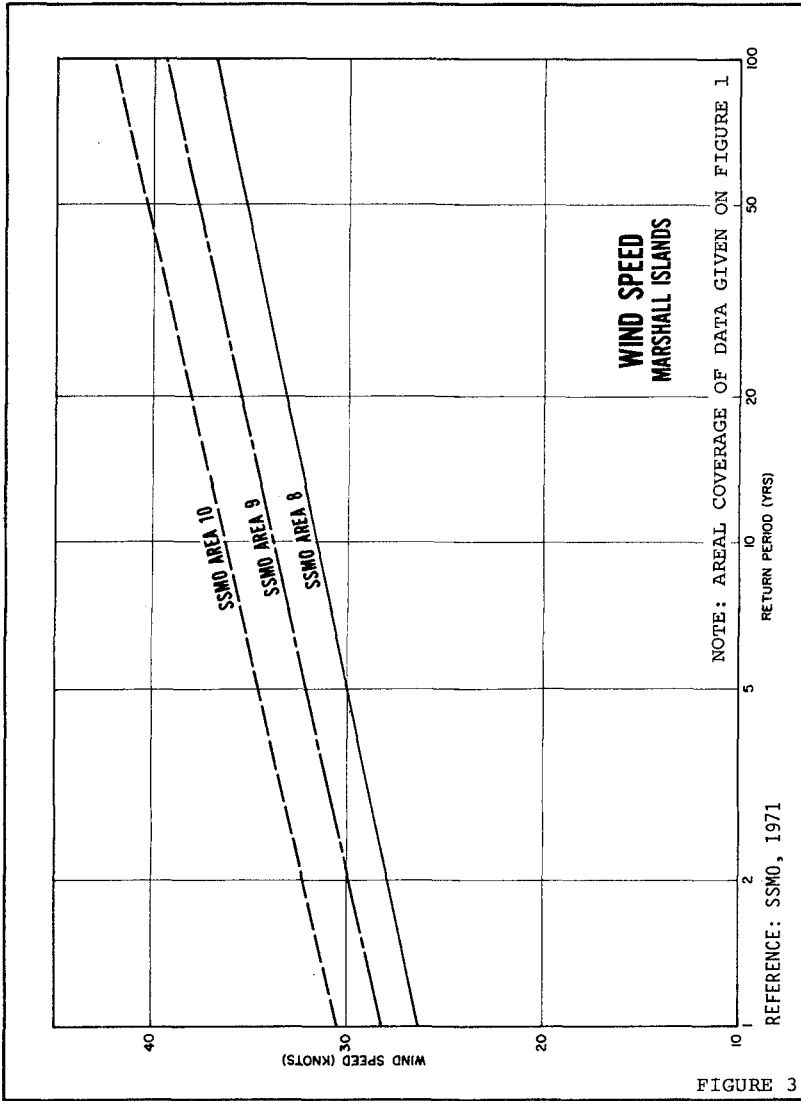


FIGURE 3

The predominant wave approach directions within the Marshall Islands area are northeast to east, which is a consequence of the persistent northeast trade winds. Wave data based upon wave observations made aboard ship over an eight- to ten-year period and compiled in SSMO (1971) and Japanese Meteorological Agency (1971-1978) are presented on Figure 4. These data indicated that less than two percent of the waves observed in the Marshall Islands area have heights exceeding 12 feet. The maximum wave height observed in either of the two data bases was a long period, 22-foot-high wave, directed from the northeast. Return period estimates of wave heights based on observational wave data (SSMO, 1971 and Japanese Meteorological Agency, 1971-78) are shown on Figure 5.

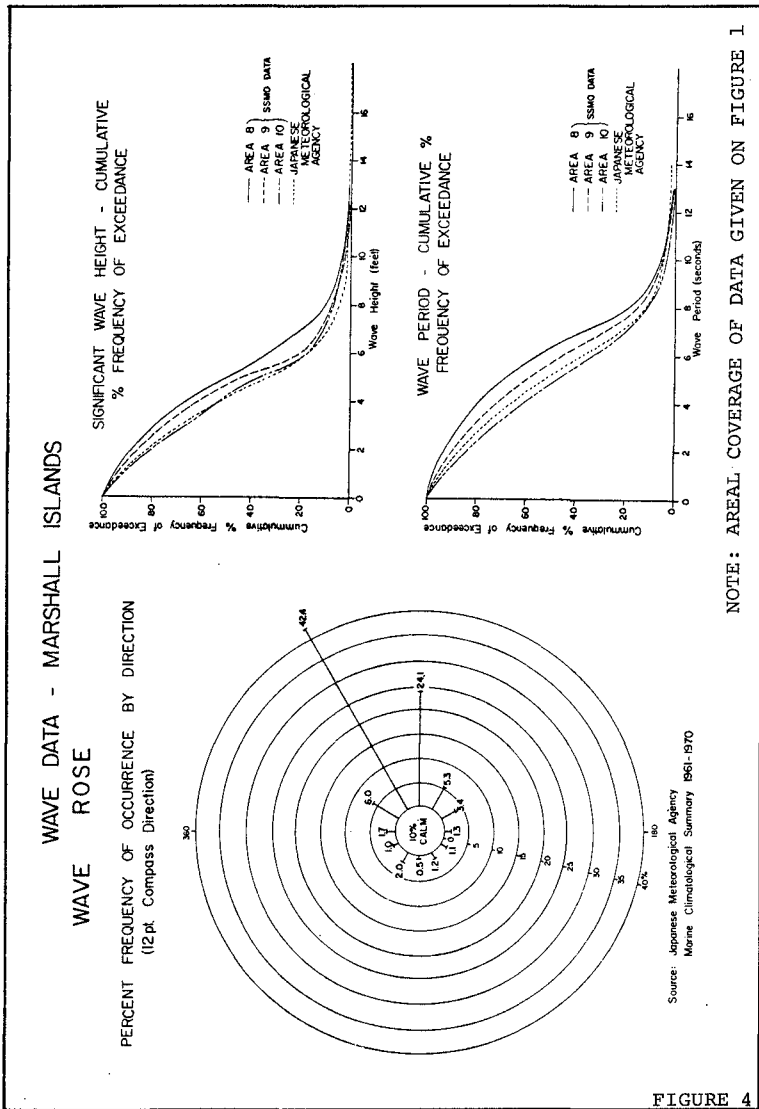
The protection afforded by the encircling islands and reef segments forming the atoll rim shelter the lagoon from incoming oceanic waves. Wave heights were calculated within the lagoons along critical approach directions using a 20-knot wind speed and the wind speed associated with a 50-year return period. The wave heights calculated using the 50-year return period wind speed ranged from 3.0 to 7.8 feet, depending primarily upon fetch length and degree of exposure, and were in close agreement with the maximum wave height observed by atoll residents.

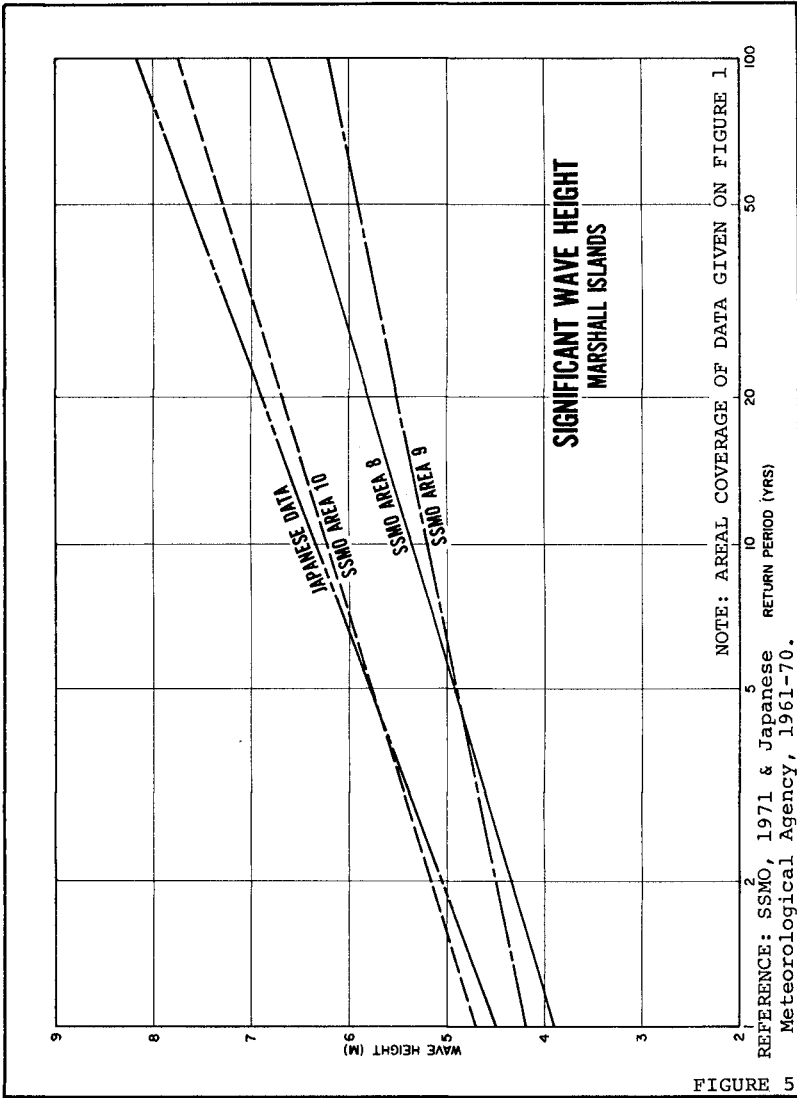
Currents within the lagoons of the Marshall Islands atolls are generally wind dominated. The wind generated currents have speeds generally less than 0.5 knots. Tidal current speeds as great as 5 to 10 knots have been reported in some of the passes of the atolls.

Seiching was observed in several of the lagoons where a reference, such as the face of an existing pier, was available. It is likely that the seiching occurs as a result of lagoon excitation produced by incoming wave trains passing through the channels and passes.

The Marshall Islands are, in essence, coral atolls. Fringing reefs, sometimes rising above sea level to form islands, encircle the atoll, creating a protected lagoon. Deep drilling studies indicate the coral atolls are underlain at depth by basaltic bedrock (Emery and others, 1954). It is generally accepted that the volcanic masses once reached a near- or above-sea level elevation, and that during subsidence, upward growth of the coral has kept pace with the subsidence, thus preserving the near-sea level feature.

The reefs forming the atoll rim have adjusted to the prevailing wind, wave and current forces. Emery and others (1954) investigated the marginal reefs of Bikini and nearby atolls, and were able to correlate reef type with prevailing





oceanographic conditions. In general, the windward reefs, the more vigorous of the reefs investigated, had characteristic well-developed algal growth (Lithothamnion ridge) that appeared to be a consequence of an adjustment to strong, steady surf. The leeward reefs generally lacked this prominent ridge, were slower growing, wide, and had steeper seaward slopes. The reefs on the southern shore are adapted to weak surf conditions, as this is the lee shore, but are subject to severe damage during periods of southern storms (Emery and others, 1954). Large blocks of coral torn from the reef edge during storms litter the reef flat.

Between the reef segments are passes or channels that link the lagoon to the open ocean. The passes are characteristically deeper, and have flatter sea floor bottoms than the channels. Tidal currents maintain these passageways.

Shallow lagoons lie within the encircling reefs. The maximum depth of the lagoons is generally less than 200 feet. Beach or near-beach deposits are often present around the outside margin of the lagoon. Coral knolls and pinnacles rising near- or above-sea level are common features within the lagoons.

SITE INVESTIGATION

The site investigation team consisted of six professionals from Dames & Moore, Alfred A. Yee & Associates, Inc. and R. M. Towill Corp. Represented were experts in coastal/ocean engineering, geotechnical engineering, environmental/oceanographical sciences, surveying and structural/construction engineering. Also traveling with this team were one or two representatives of the U.S. Army Corps of Engineers and one or two representatives of the TTPI.

Key siting criteria were established for use in both pre-site and final site selection. Due to the short duration (average of 3 days per atoll) site visits, it was extremely critical to rapidly perform final site selection at each atoll where a docking facility was to be established. Therefore, all pertinent data, including navigational charts and aerial photographs, were thoroughly reviewed in advance of the site investigations to pre-select the most desirable sites. Siting criteria considered were as follows:

- Exposure
- Navigation
- Water depths near shore
- Bottom conditions
- Location/access within atoll
- Available landside area
- Environmental considerations

Of prime consideration in pre-site selection were: site exposure to or protection from oceanographic/meteorological conditions such as waves, winds, surge, currents, sediment transport, etc.; navigational approach to the site, sufficient water depths along approach, potential navigational hazards, transit through inlet passes for lagoon sites, vessel exposure to currents, waves, winds, etc.; and, proximity of deep water nearshore for more economical dock facilities.

Whenever possible, lagoon sites were selected over open ocean sites due to their usual better protection from wave conditions which resulted in lower design conditions, safer navigational approach, and longer duration of operational time during the year.

Just prior to the site investigations, a quick reconnaissance was performed to assess pre-selected sites. In addition, meetings were held with the local Marshallese to confirm preferred site locations. Preliminary diving and land surveys were then performed to select a final site and a possible alternative. This involved consideration of such added factors as: offshore bottom conditions from design, construction and environmental viewpoints; available landside area for storage and dock facilities; and, the site location relative to the atoll's population, copra production, and roads.

The means for performing physical site investigations were kept as simple as possible due to time, budget, weight, and maintenance constraints. On several occasions, we were left on atolls where we were totally self-sufficient by transporting all living supplies and field equipment (approximately 3,000 pounds) across several hundred feet of coral reef to a camp location. Field equipment consisted of such items as SCUBA gear, tanks, compressor, boat, outboard engines, gasoline, survey instruments, current meters, jet probe and pump, fathometer, weights, floats, etc. Field equipment had to be dependable as we could only handle a limited number of spares and selected maintenance equipment.

Site surveys consisted of both onshore surveys and offshore diver reconnaissance surveys. Offshore surveys consisted of a bathymetric survey, installation of an in situ current meter, jet probing into bottom sediments along the proposed pier alignment, mapping of bottom conditions including extent of coral, mapping of existing structures, and an environmental inventory. Onshore surveys consisted of a topographic survey, shoreline conditions, site exposure, onshore geologic structure, available land area and access, socioeconomic considerations, availability of construction materials, etc.

RECOMMENDATIONS

Site field data were reduced and assessed along with the analysis of available historical data to develop appropriate design criteria for the design and construction of dock structures. Design criteria consisted of the following:

- Water levels--deck height
- Wave/wind conditions--pier alignment
- Wind/impact loads
- Wave uplift forces
- Setback
- Pier support

A pile-supported trestle/pier structure with mooring dolphins was recommended. Gravity structures, such as landfills or permanent cofferdams, were ruled out for economic and environmental reasons. The basic pier design adopted consists of a 16-foot-wide approach trestle terminating at a 24- by 80-foot loading/unloading platform at the pier head. A dolphin off each end of the pier head was recommended to provide proper mooring, while minimizing the length of the pier head required to handle cargo and passengers. Preliminary vertical pile loads were estimated at 20 tons per trestle pile and 40 tons per pier head pile. The approach trestle was recommended for extension landward of the intertidal zone beyond the upper limits of wave uprush. This was recommended to reduce environmental and construction concerns if a landfill causeway had crossed the beach area to connect with the trestle. A pier deck height of +10 to +12 feet (chart datum) was recommended to account for the effects of tide, storm surge, wave, and wave runoff.

The following recommendations were of major importance in the final design and construction of dock facilities:

- Minimize
 - Dock lengths
 - Dredging
 - Maintenance
- Standardize
 - Dock configurations
 - Construction materials
 - Construction techniques
- Maximize
 - Precast concrete

It is recommended that standardized concrete modular units be prefabricated elsewhere and then transported to the sites. By use of a construction barge with a crane and pile driver and use of standard construction techniques, docks

would be assembled on location with minimum on-site construction. The above are recommended due to the remoteness of the sites, the unavailability of supplies and laborers, and to keep construction costs to a minimum. Concrete is recommended from a corrosion maintenance standpoint.

Due to the high cost of mobilization to the sites, additional field work to gather supplementary data was not economically feasible. Therefore, it is expected that some changes to the designs may be required in the field.

BIBLIOGRAPHY

- Emery, K. O., and others, 1954. Geology of Bikini and Nearby Atolls, in Bikini and Nearby Atolls, Part 1, Geology, U.S. Geological Survey Prof. Paper 260-A.
- Japanese Meteorological Agency, 1971-1978. Marine Climatological Summary - Marshall Islands area, 8°-10° north latitude, 165°-170° east longitude. Covers period 1961-1970.
- National Ocean Survey, 1976. Sailing Directions for the Pacific Islands. Publ. 82, Vol I (revised from first edition, 1964), published by the Defense Mapping Agency, Hydrographic Center.
- National Weather Records Center, 1943. Meteorology of the Marshall Islands. Strategic Bulletins of Oceania, No. 2, compiled by the Cross-Cultural Survey, Institute of Human Relations, Yale University.
- U.S. Naval Weather Service Command, 1971. Summary of Synoptic Meteorological Observations, Vol. 3, Area 8 - Majuro, Area 9 - Kwajalein, Area 10 - Eniwetok.

Coast Protection Against
the Action of Waves and Currents

Leren P. Mikhailov Cand.Sc.(Eng.)
Director of Hydroproject Institute

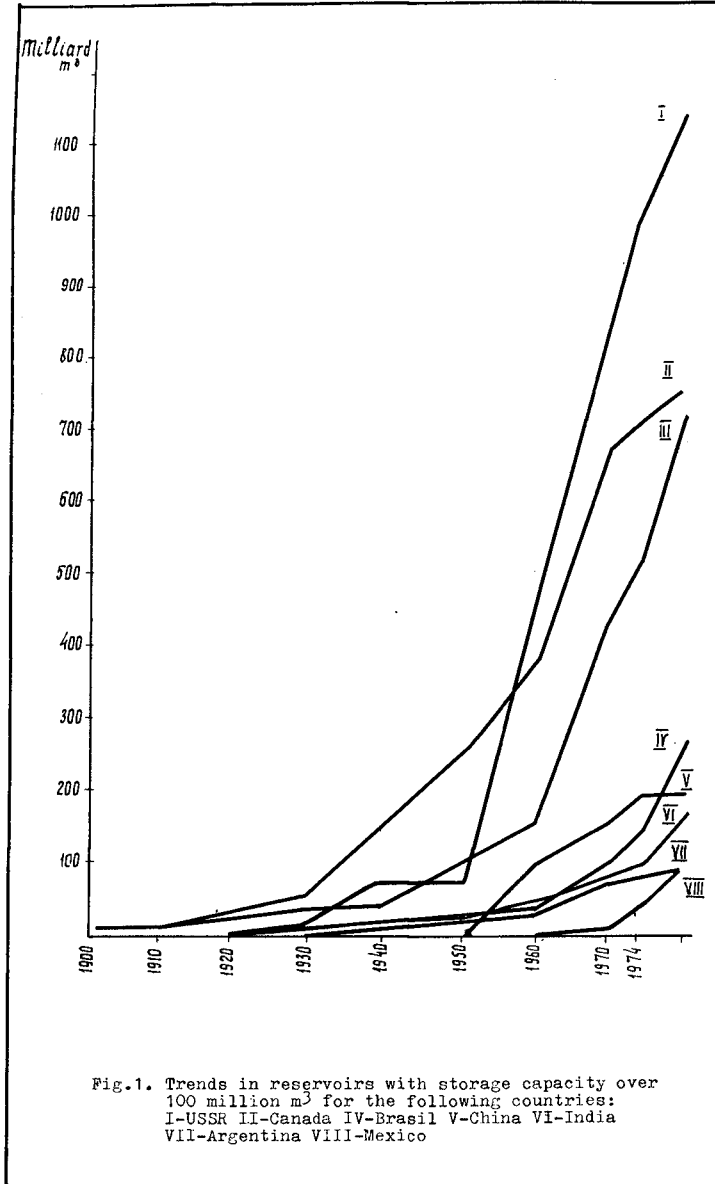
Sergei M.Uspenskii Eng., Chief of
Reservoir & Environmental Protection
Department Hydroproject Institute

According to the information available in the USSR, now in the world there are more than 13000 reservoirs with storage capacity over 1 million m³ in service and under construction. The largest ones are illustrated in Table 1. In some countries these storage reservoirs constitute rather a great per cent relative to all the reservoirs of the given country. (Table 2).

Lately, such reservoirs have substantially grown in number in many countries of the world, especially in the USSR and USA, what is seen from the chart (Fig.1).

In this connection, one can conclude on the great area of some reservoirs (reaching sometimes thousands of square kilometers), on their importance in the balance of the controlled runoff, making up in some countries over 95 per cent and on the intensive increase of their storage capacity beginning from the fifties of the present century. The above said is one of the reasons of greater interest in the action of waves and currents of the shore line showing up most intensively on the largest storage reservoirs.

The length of the shore line of the USSR reservoirs is over 40000 km. The length of the erosion shores of storage reservoirs at the hydroelectric projects on the Volga and Dnieper River make up more than 30 per cent of the total shoreline of these reservoirs, while that of the reservoirs on the Kama River - 35 per cent. Most intensively the erosion is going on in the first decades of the operation of the reservoirs. The action of waves on the shore results in formation of the underwater slope with a gradient at which the wave energy is dissipated on the shoal, and the shore erosion slows gradually down until it ceases completely. However, it is rather difficult now to determine the period of the shore formation attenuation process in view of the fact that the problem of distribution of wave energy between all the phenomena taking place here is not properly studied yet and it is not also clear what width and gradient of the shoal can fully baffle the wave energy and how much time it will take for such a shoal to get formed. The observation carried out on the natural water bodies well prove it. On the Seligher Lake (2) the shores of some large



Main data of the world largest storage reservoirs

Table 1

Storage reservoir	River, lake	Country	Back-water curve, m	Area, km ²	Reservoir volume	
					gross, km ³	live, km ³
1. Owen Falls	Victoria-Nile, Victoria Lake	Uganda Tanzania Kenya	22	76000	204.8	204.8
2. Bratsk	Angara	USSR	106	5470	169.3	48.2
3. Kariba	Zambezi	Zambia	100	4450	160.3	46.0
4. Nasser	Nile	ARE				
5. Volta	Volta	Sudan	95	5120	157.0	74.0
6. Daniel Johnson	Manicouagan	Chana	70	8480	148.0	90.0
7. Krasnoyarsk	Yenisei	Canada	154	1950	141.9	85.9
8. Gordon M. Shrum	Peace-River	USSR	100	2000	73.3	30.4
9. Zelsk	Zeya	Canada	105	1683	70.1	37.0
10. Ust-Ilim	Angara	USSR	90	2419	68.4	32.1
11. Kuibyshev	Angara	USSR	88	1870	59.4	2.8
12. Bukhtarma	Volga	USSR	25	6448	58	34.6
13. Irkutsk	Irtish and Lake Zaisan Angara and Lake Baikal	USSR	67	5490	49.6	30.8
		USSR	31	32966	48.5	46.0

Ratio of reservoirs with storage capacity 100 million m³ and over to the total number and gross volume of all reservoirs in the respective countries, %

Table 2

Country	In percent to the total number and gross volume of reservoirs	
	number	volume
USSR	16	99
Spain	16	86
India	14	93
Japan	2	47
China	28	96
The Union of South Africa	10	92
USA	17	84
Canada	26	98
Brasil	22	94
Average for the above countries	15	96

islands have retreated during the last thirty years by 50-80 m with the shoal width varying from 64 m to 210 m. The signs of recent erosion of the shores have been discovered on the Kish-Lake with the shoal width being 80 m. In view of the variability of wave regime and, especially, level fluctuation in the reservoirs, it is believed that the wave erosion of the shores can proceed for rather a long period of time.

In proper studies the action of waves and currents on the shoreline of the reservoirs is explained by the availability of a number of circumstances, complicating the studies, as compared to the sea and lake conditions. First of all, it is the geological and geomorphological factors and, especially, considerable water level fluctuations which influence the waves and currents formation. These factors are most effectual in the first decades of the reservoirs operation. In this period the length of the longshore currents owing to a sinuous shoreline is not great. As the shoreline simplification proceeds, the currents become stronger and lengthy. One of the causes of a more complex relation of the wave growth vs. the duration and fetch length is the size of water bodies and their volume, which are less as compared with the sea ones. The height of waves on the reservoirs is less than on the sea and is usually not more than 3m. As a rule the waves here steeper than on the sea. Owing to a less volume of water in the reservoir, the wind waves here attenuate very quickly, contrary to the sea condition, where the swell remains long. The water circulation in the zone of waves disruption is caused by the setup of the longshore currents and of compensating currents (countercurrents or rip currents, being a particular case of the first ones). All this governs the complexity and variability of the hydraulic regime of the littoral zone in which the protection works are located. When working the problem of building the protection works the economic analysis is usually made which includes the study and comparison of the following alternatives:

- absence of protection works, and as a consequence necessity arises to relocate or remove the national economy projects; there are land losses caused by shore transformation and flooding;
- provision of protection works after five-ten and even more years of the reservoirs operation. In view of the transformation and flooding of the shores during this period it becomes necessary to take into account the protection measures to be undertaken and the conditions of construction of the coast engineering works with account for the developed underwater and above-water shore slopes;
- construction of the protection works during the period of creating the reservoirs.

The above analysis makes it possible either to discard the protection works or choose the constructive solutions,

which from the viewpoint of their designation can be divided into two large categories:

- shore erosion protection works and
- shore flooding protection works

The first category of works include the shore protection walls made of stone, concrete, reinforced concrete; shore revetments made of rock, concrete, reinforced concrete, asphalt-concrete and cement-earth mixture; groins, breakwaters, sand inwash, planting and different combination of the above protection works. Depending upon the hydrogeological conditions and usage of the littoral area, the construction of drainage can be required. The length of the protected shoreline of the storage reservoirs at the hydro projects on the Dnieper River is over 400 km.

The second category of works include the works which protect the shores against erosion and flooding. very often it is a complex of protection works, including levees, pump stations and drainage arrangements. Such protection works can afford a considerable saving, especially, in case of protecting the towns against floods.

So, vast areas of valuable arable lands near many storage reservoirs in the USSR have been protected against flooding.

Only near the reservoirs on the Dnieper River over 200000 hectares of lands have been protected what gave a 30 per cent saving in land easement. On the Lower Kama and Cheboksary storage reservoirs which are being constructed now, the work is under way also to protect about 50000 hectares of lands. Rock and concrete are widely used in protection works.

If rock is available, it is possible to use riprap. Its advantage is easy and simple placement procedure and repair and suitability for all types of underlying soils. The job is easily mechanized and can be carried on at any time of the year.

The merits of the protection of continuous and cellular precast and cast-in-situ concrete slabs are the following; strength watertightness, possibility of wide mechanization (and for precast slabs-possibility of prefabrication) and carrying the job in winter.

Among the demerits are the necessity of importing such materials as cement, reinforcing steel and aggregates; rigidity and low roughness of structures and for precast slabs - thorough slope levelling; difficulties in concreting the joints and in repair. The analysis of malfunction of such types of protection has shown that the underestimation of one or another factor such as the upper limit of water level fluctuation, wave action, ground water seepage velocities and deformation properties of the underlying soil had a great effect.

The analysis of the state of the structures in service affords a valuable information that can be used in their designing.

The most interesting is the analysis of the behaviour of the works under the extreme conditions which allow for revealing the reliability and disadvantages of the construction.

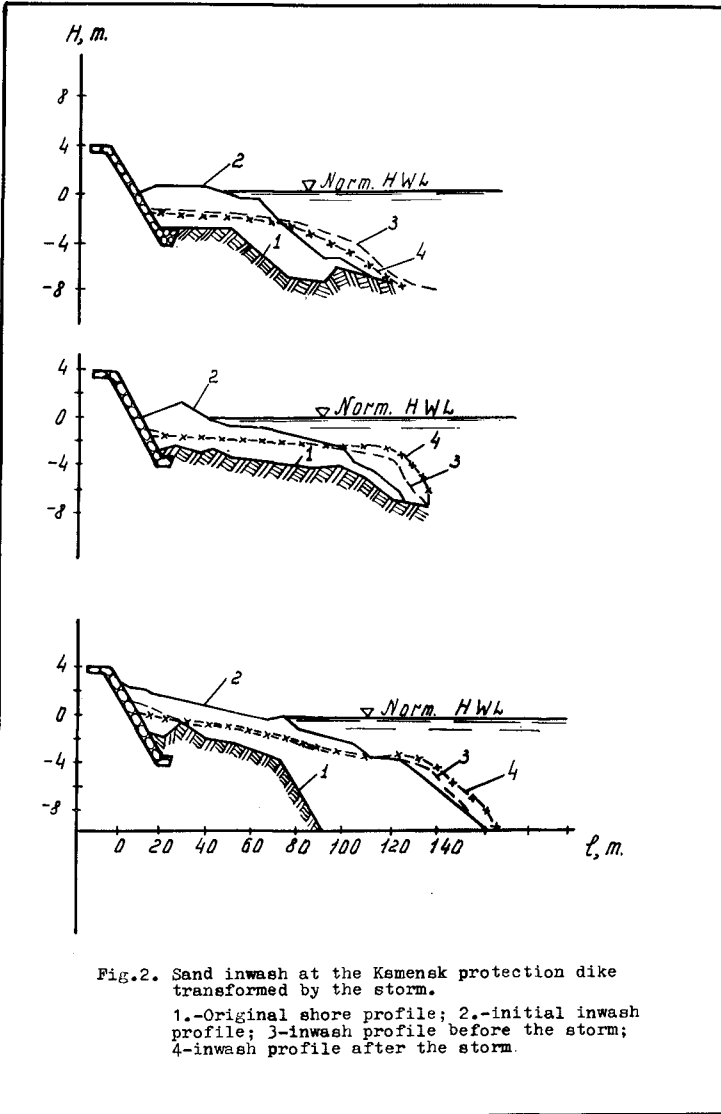




Fig.3a) Upstream slope of the Kamensk dike during the rock toe repair

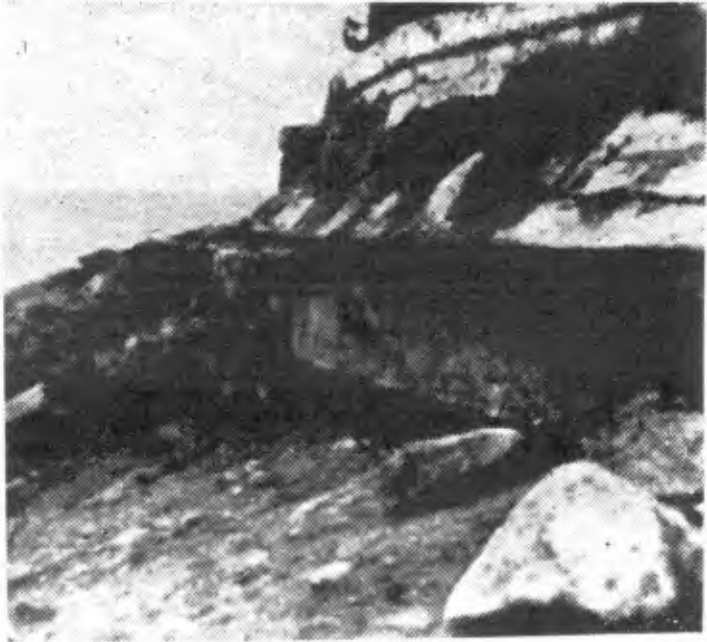


Fig.3b) Shore protection in the town of Kakhovka after the storm.

Such conditions appeared on a number of storage reservoirs on the Dnieper River where a storm of rare frequency was recorded in October, 1969. With the wind velocity of about 35-40 m/s in the area of the Kamensk dike on the Kakhovka reservoir the wave reached 2.5 m in height. The upstream slope of the dike is made $m=3$ and protected with a riprap layer 0.55-0.7 m thick, placed over an inverted filter 0.7 m thick.

To protect the downstream cut-off the sand inwash 0.5-2.0 m was provided, that appeared to be a very reliable means of protection. The transformation of the inwashed fill during the storm followed the pattern: erosion - in the water edge zone and soil accretion at the outer side of the inwashed fill (Fig.2). The visual observations proved that the disruption of high waves had taken place on the outer side of the inwash at a distance of 90-120 m from the water edge. No evidence of the dike slopes damage was traced. The inwashed fill had undergone inconsiderable transformation (Fig.2), while the Znamensk dike on the same reservoir had been damaged. The upstream dike slope is $m=3.0$, the downstream slope is $m=2.5$. The upstream slope is protected with stones weighing 40-180 kg and placed over a double-layer inverted filter 60 cm thick. To prevent the underwashing of the cut-off, silty sand was sluiced in one place, while the rock banquette was built in the other place. The crest of the sluiced sand fill was 3-3.5 m below the Norm. HWL, that is why its effect in the waves extinction was insignificant. The slope protection was damaged locally with scours which appeared two meters above and below the Norm. HWL and reached 84-480 m². Here, the filter material had been washed out and stone had subsided. So, about 864 m² of slope protection and 2400 m³ of rock banquette had been destroyed (Fig.3)a)b). In so far as the sluiced sand fill its lowered top elevation (3-3.5 m below Norm. HWL) did not promote the extinction of waves, the Znamensk dike slope protection was damaged. The comparison of behaviour of structural elements of practically the similar design illustrated how effective in wave energy dissipation the sluiced sand fill was. The cause of damage of the Znamensk dike slopes was the unjustified lowering of the sluiced fill crest by 3-3.5 m, below the Norm. HWL.

The cost analysis of the coastal engineering projects showed that the most expensive structures are the dike of economical section with concrete protected slopes; their cost makes up 70-80 per cent of the total cost of the coastal engineering, and the cost of slope protection is about 40 per cent of the dike construction cost (5). That is why, one of the most important trends in searching the rational design solutions is finding out of the ways to reduce the cost of the slope protection or to eliminate it. The latter, to some extent, be met by the dikes with gentle slopes.

On the reservoirs at the hydroprojects on the Dnieper River the length of such dikes is about 200 km; 120 km of the dikes are with a "beach" upstream slope (1:25-1:50) and downstream slope (1:4).

The dikes of this type have been built to protect the shallows and shores against the waves not more than 1.5 m in height. The height of dikes is 6-7 m and soil particles $d_{50} = 0.18-0.25$ mm (6).

When the dike is over 7-8 m in height and wave is over 1.5 m in height the smooth slopes are economically inefficient. Under such conditions the "beach" slopes are protected against the currents and waves with the help of rockfill groins and underwater intermittent breakwaters.

The advantages of the dikes with gentle slopes are the following:

- good stability of the dike body;
- elimination in many cases of drainages in the dike body and on the protected area;
- safety of the dikes founded on the easily compressible soils;
- elimination of imported materials (concrete and rock);

However, a demerit of the dikes in question is rather a great area they occupy.

The construction of the above dikes affords a saving of 8-10 per cent as compared with the other dike types; the running costs are only 10-15 per cent higher than these of the economical section dike and for some of them they are practically the same (6).

Quite promising are the shore protection works of economical design worked out by the Institute of Hydromechanics, AS Uk SSR, using the method of "natural analogues". The essence of the method consists in simulation of the natural process of transformation of the erosion shore into the stable accretion one under the dynamic action of waves and currents.

The designation of the protection structures using the principle of "natural analogues" is that they direct the energy of the wave flow to the transformation of unstable shore (intensively transformed by waves and alongshore currents) into the dynamically stable ones. Owing to this, on cessation of the unidirectional shore transformation, the protection works which had been used to control the wave energy, become its permanent elements and maintain the shore in the dynamically stable condition. Thus, the protected shore become a hydraulic structure functioning as an "artificial analogue" of the self-protection element of the shore that had transformed to the dynamically stable one.

The protection structures employed lately in coastal engineering are the intermittent protection of the shore and double-groins (tombolo).

The intermittent protection of the shore makes it possible to stop the development of the shore and transform it into the bay-shaped shore, dynamically stable at any wave (Fig. 4) and it can be used in the cases, when the

shore retreat deep into the territory is permissible. When it is not permissible (Fig.4, b), the double-groins shall be used.

The relationship between the size of protection and the dynamically stable shore shape depending on the zone of the alongshore drift (transit and sediment pick-up zones) is illustrated in Fig. 4, where T-the coefficient of the dynamically stable slope for the design waves and normal wave approach to the shore (7). Under the action of waves every adjacent couple of double-groins and the length of the protected shore enclosed between them from "bays". In time, the shore profile in plan changes in accordance with the shape of the waves getting into the water area and curved due to diffraction and refraction. So, the frontal approach of waves to the water wedge is provided lengthwise the whole perimeter of the bay irrespective of the direction of initial wave what ensures the development of the bay shape with dynamically stable surface of the underwater shore slope. Being completely transformed the bays take the form of semicircumferences, with the radius $L = \frac{1}{2}S + \frac{2}{3}S$ (Fig.4) (8). The construction of the above protection works makes it possible:

- to transform the eroding shore into the stable bay-shaped one by a directed harnessing of the energy of waves eroding it, thus eliminating the possibility of development of the unique alongshore wave flow, as one of the causes of the shore erosion;
- to cut down the requirements in building materials (concrete, rock) considering the intermittent protection, as compared with the conventional breakwaters;
- to facilitate the execution of work, since it can be done ashore and during the reservoir operation.

The economic analysis proves that the intermittent protection works in some cases are 1.5-3 times cheaper than the continuous riprap protection (3).

Provided the rock is available, the reservoir coasts are protected by riprap of graded and ungraded rock placed in two layers: the upper layer consists of large-size material, the lower layer-of rock with fraction size decreasing towards the protected surface. Based on the results of the study of the riprap behaviour and in order to facilitate the work execution the double-layer riprap protection has been substituted now by a single-layer riprap protection, i.e. by a mixture of all fractions which form two layers. However, it didn't eliminate the work on leveling the slope before placing the riprap to protect it and the construction of the rock toe (cut-off) at the base of the slope revetment. When the reservoir was filled, the work was much more complicated and the cost grew up.

Provision on a number of storage reservoirs of the transforming banquettes of rock muck designed on the principle of "natural analogues" allowed for eliminating the mentioned shortcomings of the employed revetments of rock muck.

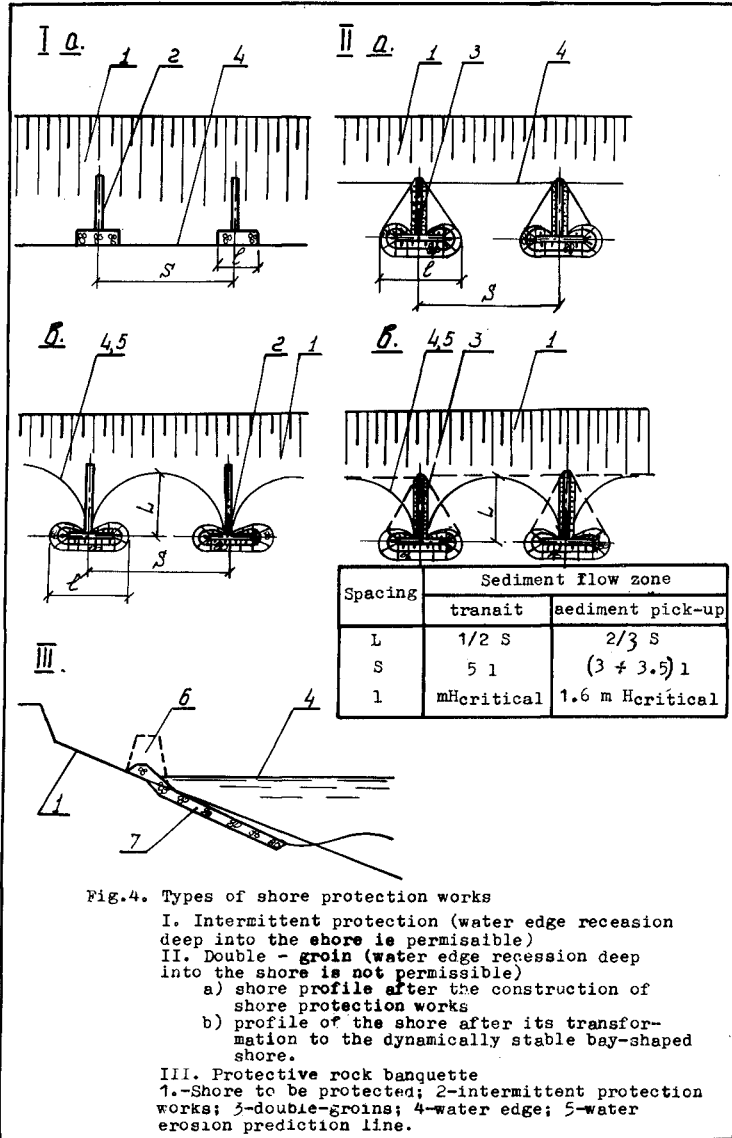


Fig.4. Types of shore protection works

I. Intermittent protection (water edge recession deep into the shore is permissible)

II. Double - groin (water edge recession deep into the shore is not permissible)

a) shore profile after the construction of shore protection works

b) profile of the shore after its transformation to the dynamically stable bay-shaped shore.

III. Protective rock banquettes

1.-Shore to be protected; 2-intermittent protection works; 3-double-groins; 4-water edge; 5-water erosion prediction line.

The natural analogue of the above construction was the shoals at the erosion shores with their body composed of highly desintegrated rocks.

Immediately after its completion, the banquette is a prism filled of rock muck lengthwise the shore to be protected at the level of water edge with natural (for this material) angles of repose for the upstream and downstream slopes (Fig.4).

Under the action of waves and alongshore currents a part of the shoal in front of the structures is washed out and the front end of the banquette gets deformed. The rock muck in this case rolls down onto the coast shoal at the banquette base and spreads to form a train of V-shaped cross section. At the same time the rock muck brought by waves to the train body is segregated as if in the inverted filter, thus making the protection stable to the wave hydrodynamic loads and preventing the beach shoal from being eroded.

The applied methods of calculations (8) enable one to choose the main dimensions and construction work quantities for the structures of different service life. Among the above tasks to be solved when designing the banquette are the substantiation of the design parameters of wind waves; calculation of movement of the load under the wave action within the length of the protection structure and on the adjacent shore sections; choosing of the grain size distribution of the rock muck to be used for the banquette according to the wave parameters and characteristics of soil composing the beach shoal.

This structure, depending upon its designation and proposed lifetime, can be considered as the temporary, permanent or, constructed in several stages.

The operation of the similar type structures on the Kakhovka reservoir and designing of the shore protection on the Volgograd reservoir attests that the use of a rock muck banquette to protect the shore against erosion is 18-38 per cent cheaper than the conventional type of protection - riprap protection; a combination of concrete re-vestment and riprap and others (9).

Besides, the design of the rock banquette makes it possible to mechanize practically all construction operations, to employ the unskilled labour and, what is most important, to carry all the work under conditions of the filled reservoir. The same advantages are characteristic of the structures isolating the shallows and simulating the natural accumulation forms, such as spurs, bay-bars and bars.

The approach to such structures differs from the traditional one, i.e. when the alignment of the structures is chosen on the principle of their longitudinal axis orientation along the most elevated points of the reservoir bed. However, this principle is unacceptable, if such

structures are considered as the artificial analogues of the natural accumulation form. In this case their shape in plan shall follow the natural accumulation forms stable to the action of waves and currents which could develop under the natural conditions with a required amount of sediment available and under the action of prevailing winds. Such works, creating the natural "analogues" (spurs, doublegroins, bars) by the directed utilization of the energy of waves and alongshore currents, provide the isolation of shallows and comparatively cheap protection of shores against erosion.

The coastal engineering works make possible at the same time, the rational development of the natural resources and are of importance for nature conservation, namely:

- protection of arable lands, mineral deposits, historical and architectural monumental against underflooding, flooding and banks collapse;
- improvement of sanitary and hygienic conditions of the water bodies by slowing down the intensity of water "bloom" and by reducing the shallow areas;
- selection of the hydroelectric project site and Norm. HWL that guarantees the most rational utilization of natural resources by all the users.

In the USSR the coastal engineering works protecting the shores and agricultural lands against flooding and erosion find expanding application. The protection works are being erected on the reservoirs under construction as well as on the existing reservoirs. Carrying out of these works in an even increasing scale is dictated by the considerations of nature conservation stated in the USSR Constitution and in other legislative documents.

Conclusions

1. Intensive increase of the number of large storage reservoirs, a considerable share in control of the total runoff, great length of erosion shores and complex action of waves and currents on the reservoir shores prove the urgency of the problem of elaborating the economical designs of the protection works;

2. The most expensive elements of protection works are revetments. One of the progressive trends in studies aimed at working out the structural solutions which enable one either to reduce the quantities of work involved or to eliminate the protection is the "method of natural analogues";

3. The protection works allow the rational utilization of natural resources and at the same time they conserve the nature, namely, they conserve the land resources, prevent the shore erosion, improve the sanitary and hygienic conditions in the reservoirs etc.

References

1. A.B.Avakyan, B.A.Sharapov and others. "World Storage Reservoirs", "Nauka" Publishers, 1979
2. E.F.Vasilieva "Erosion of Storage Reservoirs Shores and Its Forecast", Proceedings of the Central Institute of Forecasting", Issue 75, 1958.
3. B.A.Pyshkin "Dynamics of Storage Reservoirs Shores", "Naukova Dumka" Publishers, Kiev, 1973.
4. A.I.Tomiltseva "Action of Storm on the Protection Works on the Kakhovka Storage Reservoir", "Gidrotekhnicheskoye Stroitelstvo i Melioratsia, No 5, 1972.
5. S.M.Uspenskii "Reservoir Activities and Rational Utilization of Natural Resources", Gidrotekhnicheskoye Stroitelstvo, No 8, 1976.
6. T.P.Dotsenko, V.F.Kanarskii "Dams and Dikes with Gentle Slopes", "Energiya" Publishers, 1975.
7. Yu.N.Sokolnikov "About Applying Natural Analogues in Designing Shore Erosion Protection Works", Book "Dynamic of Waves and Circulation Flows", "Naukova Dumka" Publishers, Kiev, 1966.
8. Yu.N.Sokolnikov, E.S.Tsaits, V.V.Khomitskii "Protection of Storage Reservoirs Shores by Rock Muck, Banquettes", "Naukova Dumka", Kiev, 1974.
9. Yu.N.Sokolnikov, V.V.Khomitskii, E.S.Tsaits, S.M.Uspenskii "Construction of Bank Protection Banquettes of Rock Muck in Reservoir Areas of the Volga and Dnieper Cascades of Hydroelectric Power Plants", Vestnik A.S. Ukr. SSR 1975, No 9 (in Ukrainian).
10. Yu.N.Sokolnikov, A.L.Onufrienko "Problems of Isolation of Shallows in Large Storage Reservoirs", Proceedings of the IVth All-Union Hydrological Congress", Vo 1.5, 1975.

PROCEEDINGS
OF THE

Seventeenth Coastal Engineering Conference

March 23 to 28, 1980
Sydney, Australia

Volume III

Sponsored by
ASCE Coastal Engineering Research Council
ASCE Waterway, Port, Coastal and Ocean Division
and
The Institution of Engineers, Australia



Published by the American Society of Civil Engineers
345 East 47th Street, New York, N.Y. 10017

Copyright © 1981 by the American Society of Civil Engineers,
All Rights Reserved.
Library of Congress Catalog Card No. 80-69156
ISBN 0-87262-264-9
Manufactured in the United States of America.

FOREWORD

The Seventeenth International Conference on Coastal Engineering was extremely important in many ways to those who attended the conference and to those who will benefit from use of these *Proceedings*. The Seventeenth Conference marked the 30 year point in the history of the coastal engineering conference series and a change in leadership. Since the first conference was held in Long Beach, California in October 1950, Dean Morrrough P. O'Brien and Professor Joe W. Johnson have provided the continuity, direction, and motivation that have made the International Coastal Engineering Conferences so successful. For thirty years Dean O'Brien has served as Chairman and Professor Johnson as Secretary of first the Council on Wave Research and now the Coastal Engineering Research Council. Because of the importance of their contributions to the coastal engineering conferences the Council decided that these *Proceedings* will be dedicated to these two leaders. A summary of the accomplishments of each in coastal engineering is presented here.

MORROUGH P. O'BRIEN

His distinguished career in coastal engineering has been much too full to cover adequately in this space; only a sketch of his accomplishments are included here. M. P. O'Brien retired as Dean of the College of Engineering at the University of California, Berkeley, in 1959. His tenure at Berkeley included an impressive record of teaching, research and university administration. During this interval, through his students and research, he established the reputation of "The Father of Coastal Engineering." After leaving his post at Berkeley he has been very active in industrial and governmental research and development projects. At his present age, 78, Dean O'Brien is still an extremely active professional in coastal engineering.

Dean O'Brien graduated from Massachusetts Institute of Technology in 1925 and pursued graduate work at Purdue University. In 1927 he was awarded the ASCE John R. Freeman Scholarship which allowed him to attend the Technische Hochschule, Danzig, and the Royal College of Engineering, Stockholm, to study hydraulic structures and machinery. He has received honorary degrees from Northwestern University, D.Sc.; Purdue University, D.Eng.; and University of California, Berkeley, LL.D.

He joined the Mechanical Engineering Department at the University of California becoming Department Chairman in 1936 and Dean of the College in 1943. During his tenure as Dean he was instrumental in the development of graduate education and research and in the modernization of the undergraduate program.

In 1929, Dean O'Brien organized and initiated a program of research on shoreline processes and coastal engineering for a board appointed by the Chief of Engineers of the Army; subsequently, Congress established this work on a permanent basis under the U.S. Beach Erosion Board. Dean O'Brien has served as a member of this board and its successor, the Coastal Engineering Research Board from 1938 to 1980. He has maintained an active interest in ocean waves and shoreline phenomena. During the war years, this interest led to work on the design of landing craft, on forecasting surf conditions,

and on intelligence studies of landing beaches. Following the war he served as Chairman of the ad hoc committee on Amphibious Operations of the National Research Council which reviewed the plans for modernization of the Marine Corps. Consulting engagements in the field of coastal engineering included restoration of the beach at Santa Barbara, regulation of the estuary of the Columbia River, Dos Bocas Harbor in the Gulf of Campache and other similar coastal projects.

Dean O'Brien's research on hydraulic machinery led to many practical applications by industry. Most of the jet pumps sold in the United States follow the designs of O'Brien and Gosline. Application of the theory of airfoils to the design of propeller pumps and fans by O'Brien and Folsom provided the basis for extensive production of low-head, high-capacity pumps for irrigation and drainage. Consulting engagements on hydraulic machinery during this period included Byron Jackson, Food Machinery, Fairbanks-Morse, Becker Pump, Navy Department, Corps of Engineers, and many other governmental agencies. His experience with turbo-machinery led to his appointment in 1949 as a consulting engineer by the Aircraft Gas Turbine Division of the General Electric Company, an association which has continued to the present. He is now a consultant to the Technical Systems and Materials Sector of General Electric, dealing with both technical and management problems of jet engines, missiles and space vehicles, ordnance, and electronic systems.

During the war years, Dean O'Brien directed the University of California's program of engineers' science and management war training for technical and professional personnel in the aircraft and shipbuilding industries. During the four years of its existence, this program included 1800 instructors and 46,000 students. Concurrently, he served as dean of the college and as consultant in the research section of the Bureau of Ships on problems of submarine propeller noise, and on amphibious operations. In 1946, he participated in Operation Crossroads at Bikini as a consultant on the measurement of waves generated by the bomb tests; most of the photographs of the Baker tests, which appeared in the press, were taken by the tower and aerial cameras which Dean O'Brien and his associates operated for wave measurements.

Twice, he has taken full-time leave from academic duties to engage in engineering practice; once, 1947 to 1949, to serve as director of research and engineering with the Air Reduction Company and, again in 1953, to join General Electric Company's Aircraft Nuclear Propulsion Project. He has held membership on many influential boards and commissions, among them the Coastal Engineering Research Board, formerly the Beach Erosion Board; the National Science Foundation's panel of engineering consultants; the Army Scientific Advisory Panel; the Atomic Energy Commission's personnel security board; the Maritime Research Advisory Committee and the Advisory Board on Education of the National Academy of Sciences, National Research Council; and the board of directors, McGraw-Hill Publishing Company. In 1958 President Eisenhower appointed him a member of the Board of the National Science Foundation. During 1958-1959, he was a visiting institute professor at the Massachusetts Institute of Technology, and a visiting research fellow at Harvard University.

Among awards he has received are the Army-Navy Certificate of Appreciation; the Distinguished Civilian Award, Department of the Army (twice); and the Bliss Medal of the Society of American Military Engineers. In 1968 he received the ASEE's Lamme Award, and in 1969 a building at the University of California's Berkeley Campus was named after Dean O'Brien.

He has written more than 100 published articles on technical subjects and engineering education, and is co-author of "Applied Fluid Mechanics," published by McGraw-Hill in 1937. The bibliography is his own selection of the papers which he most enjoyed

writing. He is a registered professional engineer in the states of California and New York, and a chartered Mechanical Engineer in Great Britain. In 1969 he was elected to the National Academy of Engineering. He is an Honorary Member of both the ASCE and ASME.

Selected Bibliography

- Entrance Area Related to Tidal Prism, *Civil Engineering*, 1931.
- Checks on the Model Law for Hydraulic Structures, *Trans. Amer. Geo. Union*, 1932.
- Review of the Theory of Turbulent Flow and its Relation to Sediment Transportation, *Trans. Amer. Geo. Union*, 1933.
- Model Law for Motion of Salt Water through Fresh (with John Chuno), *ASCE Trans.*, vol. 99, 1934.
- The Transportation of Bcd-Load by Streams (with B. B. Rindlaub), *Trans. Amer. Geo. Union*, 1934.
- The Water Jet-Pump (with J. E. Gosline), *Univ. Calif. Publ. in Eng.*, vol. 3, no. 3, 1934.
- A Summary of the Theory of Oscillatory Waves, TR No. 2, Beach Erosion Board, 1941.
- The U.S. Tidal Model Laboratory, *Shore & Beach*, vol. 3, no. 2, 1935.
- Velocity of Large Bubbles in Vertical Tubes (with J. E. Gosline), *Indust. Eng. Chem.*, vol. 27, December 1935.
- Models of Estuaries, *Trans. Amer. Geo. Union*, 1935.
- The Transportation of Sound by Wind (with B. B. Rindlaub), *Trans. Amer. Geo. Union*, 1936.
- The Design of Propeller Pumps and Fans (with R. G. Folsom), *Univ. Calif. Publ. Eng.*, vol. 4, no. 1, 1939.
- Some Problems of Horizontal Steady Flow in Porous Media (with J. A. Putnam), *Am. Inst. Min. & Met. Eng.*, paper 1349, 1941.
- Model Experiments on Impulsive Waves in Shallow Water, *Trans. Amer. Geo. Union*, April 1947.
- Lag and Reduction of Range in Tide-gage Wells, Beach Erosion Board Bulletin, vol. 4, no. 3, 1950.
- The Nature of Engineering, *Jour. Eng. Educ.*, November 1950.
- The Force Exerted by Waves on Objects (with J. R. Morison), *Trans. Amer. Geo. Union*, February 1952.
- The Engineering of Large Systems, *The World of Engineering*, Chapter 9, McGraw-Hill, 1964.
- The Equilibrium Flow Areas of Tidal Inlets on Sandy Coasts, Tenth Int. Conf. on Coastal Eng., ASCE, 1966.
- Hydraulic Coefficients of Tidal Inlets (with R. Clark), Coastal & Oceanographic Engineering Laboratory, Univ. of Florida, 1974.
- Hydraulic and Sedimentary Stability of Tidal Inlets (with R. G. Dean), ASCE, Thirteenth Int. Conf. on Coastal Engineering, 1972.

JOE W. JOHNSON

Professor Johnson has had a long and very distinguished career in coastal engineering. His reputation extends around the world, reaching forth from his consulting, his research and especially his students. In 1975 he retired as Professor of Civil Engineering from the University of California, Berkeley. Professor Johnson is also well known for his excellent handling of the *Proceedings* of all sixteen prior coastal engineering conferences. Since his retirement from the University of California he has been extremely active in his consulting practice and professional duties.

Professor Johnson graduated from the University of California, Berkeley, in 1931 with a B.S. in Civil Engineering and in 1934 with an M.S. degree. Following a brief stay at the Waterways Experiment Station he devoted eight years to studying sediment transport with the Soil Conservation Service. He then returned to the University of California and enjoyed a very fruitful career of teaching, research and public service.

He has been consultant to many international projects involving shoreline development including: an ore port in Vitoria, Brazil; harbor development along the coast of Venezuela; port development in Northwest Australia; port development in Damietta, Egypt; sedimentation at Bahia Blanca, Argentina; Hay Point Coal Port, Australia; and wave action and sedimentation in Brazil. His associations with coastal engineering projects in the United States are equally extensive; a brief list follows of his involvement: Rio Grande Valley, wind tides in Lake Okeechobee, wave analysis of Marina del Rey, San Francisco Bay Area Rapid Transit, Turkey Point Power Plant in Florida and beach erosion at the Zion Atomic Power Plant.

In addition Professor Johnson has been a member, since 1974, of the Shoreline Erosion Advisory Panel created by the U.S. Congress. His expertise in coastal engineering has been quite instrumental in the success of this research and development program. He also has been selected as the chairman of the U.S. Delegation to the U.S.-Japan Cooperative Seminar on Coastal Engineering held in Japan. Professor Johnson has been appointed to numerous other boards and committees. He was the Secretary of the Council on Wave Research during its existence from 1950 to 1964, and then of the subsequent organization, The Coastal Engineering Research Council of the ASCE. He has been very active in the AGU holding key positions and has been a major driving force behind the American Shore and Beach Preservation Association as Vice President and Editor of *Shore and Beach*.

In 1976, Professor Johnson was elected to membership in the National Academy of Engineering and in 1979, he received the distinguished honor of Honorary Member of the ASCE. He is also the recipient of the Guggenheim Fellowship, The Outstanding Civilian Service Medal for his service in the field of coastal engineering and the Berkeley Citation. A selected listing of his over ninety publications are given below. Professor Johnson has been and still is a very active and important part of international coastal engineering.

Selected Bibliography

- The Transportation of Sediment by Streams: Bed Load, *Inter. Union Geod. and Geophys.*, 1939.
- Transportation of Sediment by Flowing Water, *Soil Conserv.*, vol. 6, 1941.

- A Distinction Between Bed Load and Suspended Load in Natural Streams (with Einstein and Anderson), *Trans. Amer. Geo. Union*, 1940.
- “War-time research on waves and surf.” *The Military Engineer*, June 1947.
- “Refraction of surface waves by currents.” *Trans. Amer. Geo. Union*, 1947.
- “The force exerted by surface waves on piles,” (with J. R. Morison, M. P. O’Brien, and S. A. Schaaf), vol. 189, 1950.
- “The Damping Action of Submerged Breakwaters,” (with R. A. Fuchs and J. R. Morison), *Trans. Amer. Geo. Union*, vol. 32, 1951.
- “The March 1962 Storm on the Atlantic Coast of the United States,” (with M. P. O’Brien), Proc. Eighth Conference on Coastal Engineering, 1963.
- “Ship Waves in Shoaling Water,” Proceedings Eleventh Conference on Coastal Engineering, 1968.
- “Lessons in Coastal Engineering,” Symposium on Coastal Engineering, Stellenbosch, South Africa, 1970.
- “Closure of Tidal Entrances,” Proc. Fourteenth Conference on Coastal Engineering, 1974.
- “Littoral Processes at Some California Shoreline Harbors,” *Shore and Beach*, vol. 43, no. 1, April 1975.

The omissions from the accomplishments of Dean O’Brien and Professor Johnson are solely the responsibility of the writer; however, the magnitude of their contributions to coastal engineering has forced the writer to condense their many activities. Indeed a detailed listing of their individual efforts would fill a volume.

While listening to the discussions of the mechanics of sand waves by Professor Arthur Brebner, Professor Longuet-Higgins was able to tie some of Brebner’s findings with the theoretical work he (Longuet-Higgins) had done on water waves of maximum steepness. Since Professor Longuet-Higgins’ Keynote address begins the *Proceedings*, it was felt proper to end them with a brief summary explaining the application of his limiting wave theory to sand bed-forms. His discussion can be found on page 3107.

Billy L. Edge, Secretary
 Coastal Engineering Research Council
 American Society of Civil Engineers

ACKNOWLEDGMENTS

ORGANIZING COMMITTEE

Mr. J. G. Betty, Chairman,
Macdonald Wagner & Priddle Pty. Ltd.
Mr. G. Evans,
Department of Public Works of N.S.W.
Professor D. N. Foster,
The University of New South Wales.
Mr. W. J. Kerle,
Department of Public Works of N.S.W.
Mr. N. Lawson,
Maritime Services Board of New South Wales.
Mr. W. M. Lewis,
Esso Australia Ltd.

LADIES COMMITTEE

Mrs. D. E. Betty,
Wahroonga, N.S.W.
Miss K. Winter,
Maritime Services Board of New South Wales.
Miss J. Shaw,
The University of New South Wales.

SUPPORT

The Institution of Engineers, Australia, in collaboration with the Coastal Engineering Research Council of the American Society of Civil Engineers, acknowledges the support and encouragement given by the following organizations:

Department of Public Works, N.S.W.
Esso Australia Ltd.
Macdonald, Wagner & Priddle Pty. Ltd.
Maritime Services Board of New South Wales
New South Wales State Government
The Sydney County Council
The Exhibiting Companies
The University of New South Wales.

INTERSTATE CORRESPONDING COMMITTEE MEMBERS

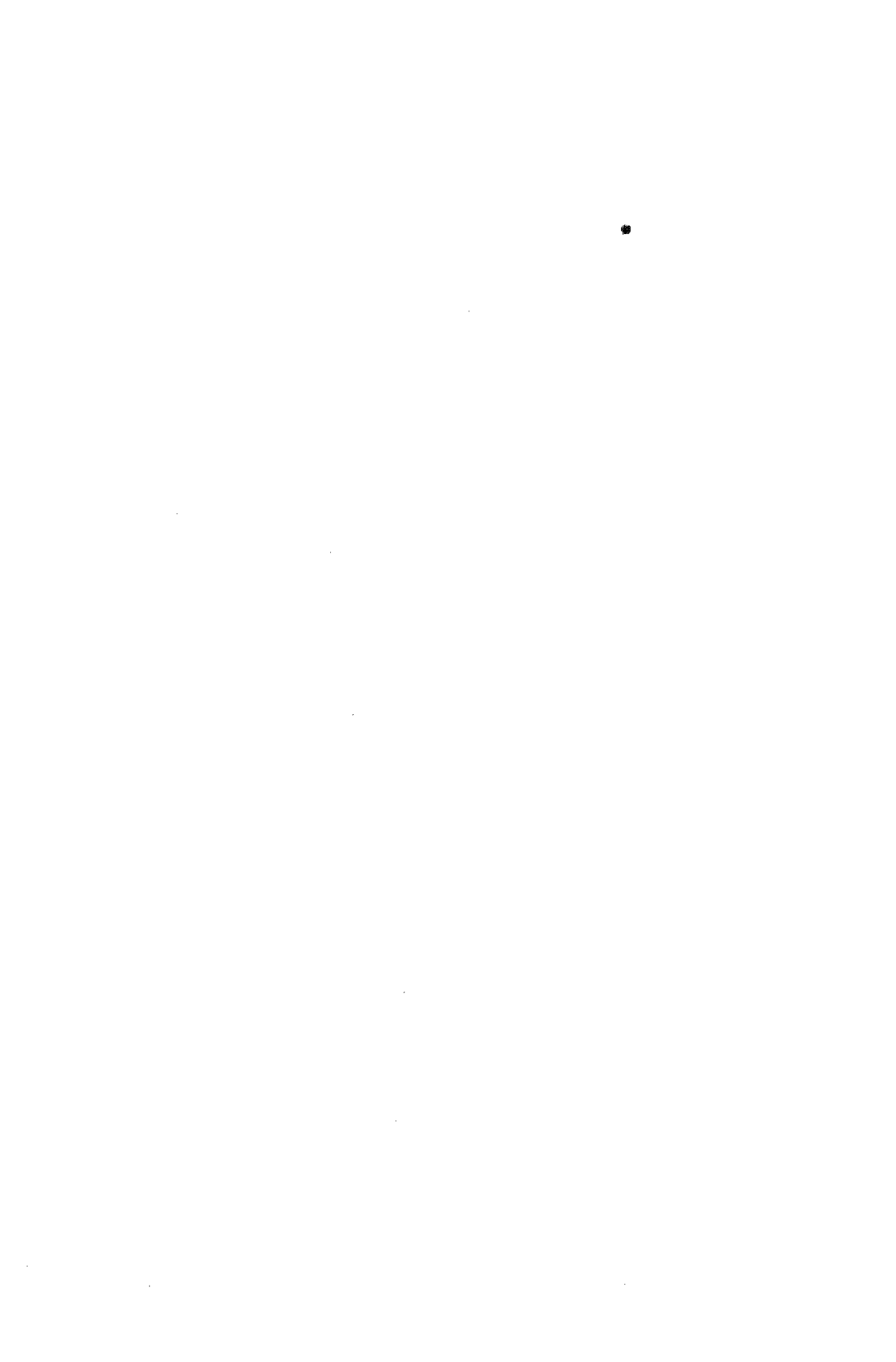
Mr. R. Culver, Dept. of Mechanical Engineering, The University of Adelaide,
South Australia 5000.
Dr. J. Hinwood, Dept. of Mechanical Engineering, Monash University, Clayton,
Melbourne, Victoria, 3168.
Mr. B. McGrath, Dept. of Harbours and Marine, G.P.O. Box 2195, Brisbane,
Queensland, 4001.
Professor R. Silvester, Dept. of Civil Engineering, University of Western Australia,
Perth, 6009.



Morrrough P. O'Brien



Joe W. Johnson



CONTENTS

FOREWORD	iii
ACKNOWLEDGEMENTS	ix

INVITED LECTURE

THE UNSOLVED PROBLEM OF BREAKING WAVES

by

M. S. Longuet-Higgins
Institute of Oceanographic Sciences
Wormley, Surrey, England

PART I

THEORETICAL AND OBSERVED WAVE CHARACTERISTICS

Chapter 1	
SOME IMPLICATIONS OF RECENT ADVANCES IN WAVE THEORIES	
J. R. Chaplin and K. Anastasiou	31
Chapter 2	
ACCURATE NUMERICAL SOLUTIONS FOR NONLINEAR WAVES	
J. D. Fenton and M. M. Rienecker	50
Chapter 3	
MASS TRANSPORT IN PROGRESSIVE WAVES OF PERMANENT TYPE	
Yoshito Tsuchiya, Takashi Yasuda and Takao Yamashita	70
Chapter 4	
RAY CURVATURE AND REFRACTION OF WAVE PACKETS	
J. Ernest Breeding, Jr.	82
Chapter 5	
VERIFICATION OF A WAVE REFRACTION MODEL	
G. Henderson and N. B. Weber	101
Chapter 6	
WAVE SHOALING CALCULATED FROM COKELET'S THEORY	
T. Sakai and J. A. Battjes	121
Chapter 7	
A SURVEY OF "RANDOM" WAVE GENERATION TECHNIQUES	
J. Ploeg and E. R. Funke	135
Chapter 8	
THE MEASUREMENT OF INCIDENT AND REFLECTED SPECTRA USING A LEAST SQUARES METHOD	
E. P. D. Mansard and E. R. Funke	154
Chapter 9	
ORBITAL VELOCITIES IN IRREGULAR WAVES	
F. C. Vis	173

Chapter 10	
INVESTIGATIONS ON IRREGULAR WAVES IN HYDRAULIC MODELS	
Karl-Friedrich Daemrich, Wolf-Dietrich Eggert and Soren Kohlhase	186
Chapter 11	
METHOD OF ANALYSIS OF RANDOM WAVE EXPERIMENTS WITH REFLECTING COASTAL STRUCTURES	
Pierre Gaillard, Michel Gauthier and Forrest Holly	204
Chapter 12	
WAVE HEIGHT DISTRIBUTION AROUND PERMEABLE BREAKWATERS	
Shintaro Hotta	221
Chapter 13	
NON-RESONANT WAVE AGITATION IN SMALL CRAFT HARBOURS	
J. W. Kamphuis and D. A. Y. Smith	241
Chapter 14	
EXPERIMENTAL INVESTIGATIONS OF PERIODIC WAVES NEAR BREAKING	
J. Buhr Hansen	260
Chapter 15	
AN HEURISTIC MODEL OF WAVE HEIGHT DISTRIBUTION IN SURF ZONE	
Masaru Mizuguchi	278
Chapter 16	
RESONANCES OF COASTAL WATERS BETWEEN PERTH AND GERALDTON (WESTERN AUSTRALIA)	
H. Allison, A. Grassia and R. Litchfield	290
Chapter 17	
A CLOSELY RESPONDING, VERSATILE WAVE TUNNEL	
C. H. Hulsbergen and J. J. Bosman	310
Chapter 18	
CONDITIONAL SIMULATIONS OF OCEAN WAVE PROPERTIES	
Leon E. Borgman	318
Chapter 19	
WIND WAVES TRANSMISSION THROUGH POROUS BREAKWATER	
Stanislaw R. Massel and Piotr Butowski	333
Chapter 20	
FIELD MEASUREMENTS OF WIND WAVE KINEMATICS	
J. A. Battjes and J. van Heteren	347
Chapter 21	
HF RADAR MAPPING OF EXTENSIVE OCEAN WINDFIELDS	
P. E. Dexter and R. C. Casey	363
Chapter 22	
SOURCES OF MEASURED WAVE DATA	
Laurence Draper	372
Chapter 23	
VISUALLY OBSERVED WAVE DATA AT PT. MUGU, CALIF.	
Christine Schneider and Richard Weggel	381
Chapter 24	
WAVE HINDCASTS AND MEASUREMENTS - BASS STRAIT	
M. N. Silbert, T. P. Barnett, D. J. H. Peters and R. C. Hamilton	395

Chapter 25		
REALTIME WAVE ANALYSIS, NEWCASTLE, AUSTRALIA		
N. V. Lawson and P. H. Oull	412
Chapter 26		
FLORIDA COASTAL DATA NETWORK		
Gary Howell	421
Chapter 27		
A MEASUREMENT OF SLOPE, CURVATURE, AND DIRECTIONAL SPECTRA OF WIND WAVES IN LAKE MICHIGAN		
Paul C. Liu	432
Chapter 28		
WAVE ATTENUATION AND WAVE SET-UP ON A COASTAL REEF		
Franciscus Gerritsen	444
Chapter 29		
LONGSHORE CURRENT FLOWS IN A WAVE BASIN		
P. J. Visser	462
Chapter 30		
DYNAMIC CHARACTERISTICS IN THE NEAR SHORE AREA		
Kiyoshi Horikawa and Masahiko Isobe	480
Chapter 31		
VELOCITY FIELD IN A STEADY BREAKER		
J. A. Battjes and T. Sakai	499
Chapter 32		
THE FLUID MECHANICS OF WAVES APPROACHING BREAKING		
D. H. Peregrine, E. D. Cokelet and P. Melver	512
Chapter 33		
A SIMILARITY MODEL IN THE SURF ZONE		
Hsiang Wang and Wei-Chong	529
Chapter 34		
VELOCITY AND PRESSURE FIELD IN SPILLING BREAKERS		
M. J. F. Stive	547
Chapter 35		
DIRECTIONAL WAVE SPECTRA AND WAVE KINEMATICS IN HURRICANES CARMEN AND ELOISE		
G. Z. Forristall, E. G. Ward and V. J. Cardone	567
Chapter 36		
PREDICTION OF THE SEVEREST SIGNIFICANT WAVE HEIGHT		
Michel K. Ochi and Joseph E. Whalen	587
Chapter 37		
PREDICTION OF DOMINANT WAVE PROPERTIES AHEAD OF HURRICANES		
Omar H. Shemdin	600
Chapter 38		
LONG PERIOD DISTURBANCES DUE TO WAVE GROUPS		
E. C. Bowers	610
Chapter 39		
TWO-DIMENSIONAL SURF BEAT		
Reinhard E. Flick, Douglas L. Inman and Robert T. Guza	624

Chapter 40		
LONG WAVES GENERATED BY COMPLEX BOTTOM MOTIONS		
J. L. Hammack and F. Raichlen		639
Chapter 41		
TSUNAMIS ALONG WEST COAST OF LUZON, PHILIPPINES		
R. L. Wiegel		652
Chapter 42		
TSUNAMI PRONE FRICTION FACTORS FROM WIND MEASUREMENTS		
Charles L. Bretschneider		672
Chapter 43		
RUN-UP OF TSUNAMIS BY LINEAR AND NONLINEAR THEORIES		
Chiaki Goto and Nobuo Shuto		695
Chapter 44		
ON THE CORRECTION OF LAND-BASED WIND MEASUREMENTS FOR OCEANOGRAPHIC APPLICATIONS		
S. A. Hsu		708
Chapter 45		
NUMERICAL MODELLING OF TROPICAL CYCLONE STORM SURGE		
Rodney J. Sobey, Bruce A. Harper, and George M. Mitchell		725
Chapter 46		
A NUMERICAL MODEL OF STORM WAVES IN SHALLOW WATER		
A. Hauguel		746
Chapter 47		
THE GENERATION OF LONG WAVES IN THE LABORATORY		
Derek Goring and Fredric Raichlen		763
Chapter 48		
CORRECT REPRODUCTION OF LONG GROUP INDUCED WAVES		
N. -E. O. Hansen, S. E. Sand, H. Lundgren, T. Sorensen and H. Gravesen		784
Chapter 49		
AN ELECTROMAGNETIC ANALOGY FOR LONG WATER WAVES		
G. W. Jackson and D. L. Wilkinson		801
Chapter 50		
INTERACTIONS OF WAVES WITH SUBMARINE TRENCHES		
Jiin J. Lee, Robert M. Ayer and Wen L. Chiang		812
Chapter 51		
TRANSIENT FINITE-DIFFERENCE TSUNAMI CALCULATIONS		
Ove Skovgaard and Ivar G. Jonsson		823
Chapter 52		
AN INVESTIGATION OF WAVE SHELTERING BY ISLANDS		
S. V. Hsiao, J. E. Vesecky and O. H. Shemdin		840
Chapter 53		
THE DISSIPATION OF WAVE ENERGY BY TURBULENCE		
Yu Kuang-ming		850

PART II
COASTAL SEDIMENT PROBLEMS

Chapter 54	
BEACH CUSPS AT POINT REYES AND DRAKES BAY BEACHES, CALIFORNIA	
Robert G. Dean and E. M. Maurmeyer	863
Chapter 55	
BARRON RIVER DELTA INVESTIGATION	
D. A. Robinson, D. J. Cook and J. G. Barff	885
Chapter 56	
SOFT DESIGNS FOR COASTAL PROTECTION AT SEABROOK ISLAND, S.C.	
Miles O. Hayes, Timothy W. Kana and John H. Barwis	897
Chapter 57	
GEOLOGICAL CONTROLS ON PROCESS-RESPONSE, S.E. AUSTRALIA	
P. S. Roy and A. W. Stephens	913
Chapter 58	
BEACH EROSION-ACCRETION AT TWO TIME SCALES	
B. G. Thom and G. M. Bowman	934
Chapter 59	
PHYSICAL PROCESSES AND SEDIMENT FLUX THROUGH REEF-LAGOON SYSTEMS	
Harry H. Roberts	946
Chapter 60	
INSHORE-NEARSHORE MORPHODYNAMICS-A PREDICTIVE MODEL	
John Chappell	963
Chapter 61	
BEACH CUT IN RELATION TO SURF ZONE MORPHODYNAMICS	
L. D. Wright	978
Chapter 62	
BREAKER TYPE AND PHASE SHIFTS ON NATURAL BEACHES	
Peter J. Cowell	997
Chapter 63	
BEACH RESPONSE TO VARIATIONS IN BREAKER HEIGHT	
A. D. Short	1016
Chapter 64	
THE DYNAMIC SWEEPED PRISM	
David M. Chapman	1036
Chapter 65	
A LABORATORY STUDY OF OFFSHORE TRANSPORT OF SEDIMENT AND A MODEL FOR ERODING BEACHES	
Tsuguo Sunamura	1051
Chapter 66	
NEARSHORE CURRENTS ON A PARTIALLY ROCKY SHORE	
T. O. Sasaki, H. Igarashi and S. Harikai	1071

Chapter 67	
TOPOGRAPHIC CONTROL OF RUN-UP VARIABILITY	
Mark P. Bradshaw	1091
Chapter 68	
BEACH PROFILES AND ON-OFFSHORE SEDIMENT TRANSPORT	
Akira Watanabe, Yoshihiko Riho and Kiyoshi Horikawa	1106
Chapter 69	
SECONDARY SAND TRANSPORT MECHANISMS	
A. W. Smith and A. D. Gordon	1122
Chapter 70	
SAND TRANSPORT BY WAVES	
Jan van de Graaff and Wiel M. K. Tilmans	1140
Chapter 71	
NEARSHORE SUSPENDED SEDIMENT LOAD DURING STORM AND POST-STORM CONDITIONS	
Timothy W. Kana and Larry G. Ward	1158
Chapter 72	
ONSHORE-OFFSHORE TRANSPORT AND BEACH PROFILE CHANGE	
Masataro Hattori and Ryoichi Kawamata	1175
Chapter 73	
ON-OFFSHORE SEDIMENT TRANSPORT RATE IN THE SURF ZONE	
Toru Sawaragi and Ichiro Deguchi	1195
Chapter 74	
FIELD MEASUREMENTS OF SAND MOTION IN THE SURF ZONE	
Douglas L. Inman, James A. Zampol, Thomas E. White, B. Walton Waldorf, Daniel M. Hanes and Kim A. Kastens	1215
Chapter 75	
AN APPROACH TO UNDERSTANDING COASTAL PROCESSES	
A. D. Gordon and D. B. Lord	1235
Chapter 76	
RELATIONSHIP BETWEEN ALONGSHORE WAVE ENERGY AND LITTORAL DRIFT IN THE MID-WEST COAST AT TAIWAN	
Ho-shong Hou, Chung-Pan Lee, and Lung-Hui Lin	1255
Chapter 77	
LONGSHORE WATER AND SEDIMENT MOVEMENT	
D. H. Swart and C. A. Fleming	1275
Chapter 78	
CRITERION FOR STABILITY OF SHORELINE PLANFORM	
John D. Wang and Bernard le Mehaute	1295
Chapter 79	
ZETA BAYS, POCKET BEACHES AND HEADLAND CONTROL	
R. Silvester, Y. Tsuchiya, and Y. Shibano	1306
Chapter 80	
BEACHES: PROFILES, PROCESSES AND PERMEABILITY	
Michael R. Gourlay	1320
Chapter 81	
SAND BED-FORM LENGTHS UNDER OSCILLATORY MOTION	
Arthur Brebner	1340

Chapter 82	
SEDIMENT TRANSPORT PROCESSES AND COASTAL VARIABILITY ON THE ALASKAN NORTH SLOPE	
E. H. Owens, J. R. Harper and D. Nummedal	1344
Chapter 83	
SEDIMENT DISPERSAL ON THE N. S. W. CONTINENTAL SHELF	
Ron Boyd	1364
Chapter 84	
FLUID MUD DYNAMICS AND SHORELINE STABILIZATION: LOUISIANA CHENIER PLAIN	
John T. Wells and Harry H. Roberts	1382
Chapter 85	
NEARSHORE SEDIMENT TRANSPORT STUDY EXPERIMENTS	
R. J. Seymour and C. G. Gable	1402
Chapter 86	
A SEDIMENT TRAPPING EXPERIMENT AT SANTA CRUZ, CA.	
R. J. Seymour, G. W. Domurat and D. M. Pirie	1416
Chapter 87	
WAVE FORCING OF BEACH GROUNDWATER	
Evans Waddell	1436
Chapter 88	
LONGSHORE TRANSPORT EVALUATIONS AT A DETACHED BREAKWATER	
R. O. Bruno, R. G. Dean, and C. G. Gable	1453
Chapter 89	
MIGRATION OF LONGSHORE BARS	
Hans H. Dette	1476
Chapter 90	
A PHASED-DREDGING PROGRAM FOR SANTA CRUZ HARBOR	
James R. Walker and Peter J. Williams	1493
Chapter 91	
DESIGN OF ENCLOSED HARBORS TO REDUCE SEDIMENTATION	
Craig H. Everts	1512
Chapter 92	
OPENING AND MAINTAINING TIDAL LAGOONS & ESTUARIES	
Scott A. Jenkins, Douglas L. Inman and James A. Bailard	1528
Chapter 93	
RESEARCH IN SOUTHERN QUEENSLAND INTO THE MANAGEMENT OF COASTAL SAND DUNES	
James B. McKenzie and David A. Barr	1548
Chapter 94	
WIND AND SEDIMENT MOVEMENT IN COASTAL DUNE AREAS	
John R. Hails and John Bennett	1565
Chapter 95	
SAND TRANSPORT UNDER THE ACTION OF WIND	
Ulrich Zanke	1576
Chapter 96	
A NUMERICAL MODEL FOR DUNE DYNAMICS	
J. Sundermann, H. -J. Vollmers and W. Puls	1584

Chapter 97	
ESTUARINE RESPONSE TO DREDGING IN THE TWEED RIVER, AUSTRALIA	
Bruce M. Druery	1599
Chapter 98	
NOOSA BEACH RESTORATION SCHEME	
R. J. Lloyd	1619
Chapter 99	
BEACH NOURISHMENT AS A MANAGEMENT TECHNIQUE	
David M. Chapman	1636
Chapter 100	
CAPRICORN COAST BEACHES	
D. C. Patterson and L. R. Ford	1649
Chapter 101	
THE BEACH IMPROVEMENT PROGRAMME: NEW SOUTH WALES	
Heale A. Philip and Phipp H. Waite	1669
Chapter 102	
EDDY CURRENTS AND SEDIMENT TRANSPORT OFF THE DAMIETTA NILE	
S. P. Murray, J. M. Coleman, H. H. Roberts and M. Salama	1680
Chapter 103	
A COMPARISON BETWEEN DREDGE INDUCED SEDIMENT RESUSPENSION AND THAT PRODUCED BY NATURAL STORM EVENTS	
W. Frank Bohlen and Marine Sciences Department., Univ. of Conn.	1700
Chapter 104	
SEDIMENTATION IN CHANNELS AND TRENCHES	
E. W. Bijker	1708
Chapter 105	
SEDIMENTATION IN DREDGED NAVIGATION CHANNELS	
Lars Mikkelsen, Preben Mortensen, and Torben Sorensen	1719
Chapter 106	
SOME ASPECTS OF COASTAL ENGINEERING RESEARCH WORKS IN CHINA	
Yen Kai	1735

PART III
COASTAL STRUCTURES AND RELATED PROBLEMS

Chapter 107	
SIMULTANEOUS WAVE AND CURRENT FORCES ON A PIPELINE	
David A. Knoll and John B. Herbich	1742
Chapter 108	
WAVE FORCES ON AN INCLINED CIRCULAR CYLINDRICAL PILE	
Toshiyuki Shigemura	1761
Chapter 109	
WAVE-INDUCED SEEPAGE EFFECTS ON A VERTICAL CYLINDER	
Thomas J. P. Durand and Peter L. Monkmeyer	1781

Chapter 110	
STABILITY ANALYSIS OF SEAFLOOR FOUNDATIONS	
Tokuo Yamamoto and Yasumasa Suzuki	1799
Chapter 111	
WAVE FORCES ON OFFSHORE PIPELINES	
N. Jothishankar and V. Sundar	1819
Chapter 112	
WAVE IMPACT PRESSURES ON COMPOSITE BREAKWATERS	
G. R. Mogridge and W. W. Jamieson	1829
Chapter 113	
CONSTRUCTION AND MODEL INVESTIGATION OF STORMWATER OUTFALL	
K. A. Heathcote and G. W. Britton	1849
Chapter 114	
FULL SCALE NEAR SURFACE WATER PARTICLE VELOCITIES AND PRESSURES ACTING ON AN INCLINED TUBULAR MEMBER	
Fritz Busching and Eckehard Martini	1869
Chapter 115	
ENERGY TRANSMISSION OVER BREAKWATER—A DESIGN CRITERION?	
P. Bade and H. Kaldenhoff	1885
Chapter 116	
THE DESIGN CONCEPT OF DUAL BREAKWATERS AND ITS APPLICATION TO TOWNSVILLE, AUSTRALIA	
W. Bremner, N. N. Foster, C. A. Miller and B. C. Wallace	1898
Chapter 117	
DESIGN OF AN OVERTOPPING BREAKWATER	
P. D. Treloar and B. Nagle	1909
Chapter 118	
FULL SCALE TRIALS OF DOLOSSE TO DESTRUCTION	
Hans F. Burcharth	1928
Chapter 119	
DOLOSSE: PAST, PRESENT, FUTURE?	
J. A. Zwamborn, D. E. Bosman and J. Moes	1948
Chapter 120	
A DETACHED BREAKWATER SYSTEM FOR BEACH PROTECTION	
James R. Walker, Denton Clark, and Joan Pope	1968
Chapter 121	
STABILITY OF RUBBLE MOUND BREAKWATER	
J. Feuillet and M. Sabaton	1988
Chapter 122	
ARTIFICIAL RESORT BEACH PROTECTED BY OFFSHORE BREAKWATERS AND GROINS	
Shoji Sato and Norio Tanaka	2003
Chapter 123	
SEAWALLS IN DEEP SEAS	
Shoshichiro Nagai and Shohachi Kakuno	2023
Chapter 124	
PROBABILISTIC DESIGN OF SEA DEFENCES	
W. T. Bakker and J. K. Vrijling	2040

Chapter 125	
DESIGN OF CAISSON BREAKWATERS	
A. G. F. Eddie, J. D. Lawson, H. R. Graze and B. K. Dean	2060
Chapter 126	
THE DESIGN AND CONSTRUCTION OF THE NEW OIL PORT IN DALIAN, C.P.R.	
Xin Zhu-Zhuang	2080
Chapter 127	
SITING AND DESIGN CRITERIA OF DOCK STRUCTURES IN THE MARSHALL ISLANDS	
R. M. Noble, K. C. Leslie and D. O'Day	2106
Chapter 128	
COASTAL PROTECTION AGAINST THE ACTION OF WAVES AND CURRENTS	
Leren P. Mikhailov and Sergei M. Uspenskii	2120
Chapter 129	
FLOATING BREAKWATER PERFORMANCE COMPARISON	
Volker W. Harms	2137
Chapter 130	
LITTORAL DRIFT OF SAND NEAR PORT OF OARAI	
Kazumasa Mizumura	2159
Chapter 131	
LONG-TERM EXPERIENCE WITH THE USE OF SYNTHETIC FILTER FABRICS IN COASTAL ENGINEERING	
Georg Heerten	2174
Chapter 132	
BREAKWATER WITH SAND BITUMEN CORE	
E. Loewy, K. G. Witthaus, R. J. Maddrell and J. P. Wood	2194
Chapter 133	
HARBOUR DESIGN INCLUDING SEDIMENTOLOGICAL PROBLEMS USING MAINLY NUMERICAL TECHNIQS	
B. Latteux	2213
Chapter 134	
NEW JETTIES FOR TUNG-KANG FISHING HARBOUR, TAIWAN	
Chi-Fu Su	2230
Chapter 135	
MAJOR RECLAMATION SCHEME FOR MARINA CITY, SINGAPORE	
S. Y. Chew and J. Wei	2245
Chapter 136	
SHIP-BRIDGE-PIER PROTECTIVE SYSTEMS	
Akira Iwai, Hitoshi Nagasawa, Kazuki Oda and Kuniaki Shoji	2261
Chapter 137	
WAVE-WAVE INTERACTIONS, CURRENT-WAVE INTERACTIONS AND RESULTING EXTREME WAVES AND BREAKING WAVES	
Soren Peter Kjeldsen and Dag Myrhaug	2277
Chapter 138	
CAN WE DEVELOP NEW BREAKWATER ARMOUR FORMULAE?	
John Dorrington Mettam	2304

PART IV
COASTAL, ESTUARINE, AND ENVIRONMENTAL PROBLEMS

Chapter 139	
SEPARATION OF CLIMATIC FLUCTUATIONS AND IMPACTS OF ENGINEERING ACTIVITIES IN ESTUARIES	
G. Krause	2325
Chapter 140	
WAVE ENERGY DISTRIBUTION IN AN ESTUARY	
Volker Barthel	2340
Chapter 141	
HYDRAULIC RESEARCH IN THE OOSTERSCHELDE ESTUARY	
Anton W. Walther	2360
Chapter 142	
PORT OF BRISBANE SILTATION STUDY	
N. V. M. Odd and T. Baxter	2377
Chapter 143	
A 3-D MODEL FOR PENOBSCOT BAY, MAINE	
Bryan R. Pearce, Bruce R. Fidler and Adrian C. Humphreys	2397
Chapter 144	
THE USE OF ARRAY PROCESSORS FOR NUMERICAL MODELLING OF TIDAL ESTUARY DYNAMICS	
D. Prandle, E. R. Funke, N. L. Crookshank and R. Renner	2413
Chapter 145	
PARAMETER IDENTIFICATION IN ESTUARINE MODELING	
Wen-Sen Chu and William -G. Yeh	2433
Chapter 146	
AUTOMATIC CALIBRATION OF NUMERICAL TIDAL MODELS	
K. -P. Holz and U. Januszewski	2450
Chapter 147	
TIDAL INLET BEHAVIORAL ANALYSIS	
A. F. Nielsen and A. D. Gordon	2461
Chapter 148	
SEDIMENTATION PROCESSES IN TIDAL CHANNELS AND TIDAL BASINS CAUSED BY ARTIFICIAL CONSTRUCTIONS	
E. Renger and H. W. Partensky	2481
Chapter 149	
ARTIFICIAL ROUGHNESS IN PHYSICAL MODELS OF ESTUARIES FOR STORM SURGE INVESTIGATIONS	
D. Berndt, E. Giese, H. Schwarze, and H. -J. Vollmers	2495
Chapter 150	
COMMENTS ON TIDAL ENTRANCES ON SANDY COASTS	
Morrough P. O'Brien	2504
Chapter 151	
TIDAL PRISM-INLET AREA RELATIONS FOR SMALL TIDAL INLETS	
R. J. Bryne, R. A. Gammisch and G. R. Thomas	2517
Chapter 152	
A COASTAL INLET WITH FIXED BED AND MOBILE SIDES	
R. C. Nelson and A. J. Keats	2534

Chapter 153	
INLETS/ESTUARIES DISCHARGING INTO SHELTERED WATERS	
H. P. Riedel and M. R. Gourlay	2550
Chapter 154	
THE CORPS OF ENGINEER'S GENERAL INVESTIGATION OF	
TIDAL INLETS	
Robert M. Sorensen	2565
Chapter 155	
SATELLITE APPLICATIONS ON A COASTAL INLET STABILITY	
STUDY	
Yu-Hwa Wang	2581
Chapter 156	
BOUNDARY CONDITIONS FOR ANALYSIS OF FLOW IN TIDAL	
INLETS	
T. C. Gopalakrishnan and J. L. Machemehl	2595
Chapter 157	
MECHANISMS OPERATING AT A JETTIED RIVER ENTRANCE	
Bruce M. Druery and Alexander F. Nielsen	2607
Chapter 158	
STABILITY OF ESTUARY MOUTHS IN THE RHINE-MEUSE DELTA	
J. van de Kreeke and J. Haring	2627
Chapter 159	
BARDEN INLET, N.C.: A CASE STUDY OF INLET MIGRATION	
Limberios Vallianos	2640
Chapter 160	
STUDY ON VORTEX CURRENT IN STRAIT WITH REMOTE-SENSING	
Sotoaki Onishi and Tsukasa Nishimura	2655
Chapter 161	
DYNAMIC SIMILARITY OF TRANSPORT PHENOMENA	
M. S. Yalin and F. Gerritsen	2671
Chapter 162	
MOORING FORCES INDUCED BY PASSING SHIPS—MEASUREMENTS	
IN PROTOTYPE	
K. Haffke	2691
Chapter 163	
NUMERICAL MODELLING OF NEARSHORE CIRCULATION	
Bruce A. Ebersole and Robert A. Dalrymple	2710
Chapter 164	
MODELLING OF PLANFORM INFLUENCE ON CIRCULATION IN	
HARBOURS	
Roger A. Falconer	2726
Chapter 165	
HYDRAULIC CIRCULATION PERFORMANCE OF A CURVILINEAR	
MARINA	
Jeffrey A. Layton	2745
Chapter 166	
THE EFFECT OF BREAKING WAVES ON THE MIXING OF LIQUID	
POLLUTANTS INTO THE SEA	
Arvid Naess	2760

Chapter 167	
ON A ROLE OF THE INTERFACIAL FROUDE NUMBER	
Masakazu Kashiwamura	2780
Chapter 168	
DISPERSION OF COOLING WATER FROM A COASTAL LNG PLANT	
P. Ackers, J. D. Pitt, G. Thompson and K. G. Rippin	2796
Chapter 169	
EXPERIMENTAL STUDY OF THE BUOYANT SURFACE JET WITH	
THE PRESENCE OF BOTTOM BOUNDARY AND CROSS CURRENT	
B. Safaie	2816
Chapter 170	
DESIGN OF AN INTERMITTENTLY OPERATED OUTFALL	
Roger W. Lindquist and George J. Murphy	2837
Chapter 171	
EXPERIMENTAL EVALUATION OF HEAT EXCHANGE BETWEEN	
WATER SURFACE AND ATMOSPHERE	
Gunther Barg, Horst Schwarze, and Gerhard Visscher	2851
Chapter 172	
DYNAMICS OF SILT IN ESTUARY, RESIDUAL CURRENT OR	
FLOCCULATION WHICH PREVAILS?	
J. P. Lepetit and M. Davesne	2861
Chapter 173	
FOR DISPOSAL: 10 m cu m OF CALCIUM CARBONATE SLURRY	
L. Summers and C. A. Fleming	2874
Chapter 174	
AN EXPERIMENT ON CLAY SUSPENSION UNDER WATER WAVES	
Prida Thimakorn	2894
Chapter 175	
CONSIDERATIONS IN THE DESIGN OF AN OFFSHORE DATA	
COLLECTION PROGRAM	
Cortis Cooper and German Febres	2907
Chapter 176	
THE GERMAN "MORAN" PROJECT	
Winfried Siefert and Volker Barthel	2927
Chapter 177	
ENVIRONMENTAL ASPECTS OF OIL AND GAS PIPELINE LANDFALLS	
IN NORTHEAST SCOTLAND	
William Ritchie	2938
Chapter 178	
STATISTICAL PROPERTIES OF RANDOM WAVE GROUPS	
Akira Kimura	2955
Chapter 179	
ON THE SYNTHESIS OF REALISTIC SEA STATES	
E. R. Funke and E. P. D. Mansard	2974
Chapter 180	
A COMPARISON OF NATURE WAVES AND MODEL WAVES WITH	
SPECIAL REFERENCE TO WAVE GROUPING	
Hans F. Burcharth	2992

Chapter 181	
WATER MOVEMENT STUDIES REQUIRED FOR PORT PLANNING	
Graeme C. Dandy, Desmond A. Mills and Jon B. Hinwood	3010
Chapter 182	
INTEGRATION AND COMPUTATION IN AN EXPERIMENTAL STUDY	
J. B. Hinwood, J. E. Watson and D. M. Burrage	3027
Chapter 183	
SOME RECENT RESULTS FOR WAVE INDUCED MOTIONS OF A SHIP IN SHALLOW WATER	
P. A. Madsen, I. A. Svendsen and C. Michaelsen	3043
Chapter 184	
REPORT ON THE DAMAGES TO THE SINES BREAKWATER, PORTUGAL	
William F. Baird, Joseph M. Caldwell, Billey L. Edge, Orville T. Magoon and Donald D. Treadwell	3063
Chapter 185	
DISCRETE-TIME MODELLING OF DISPERSION IN ESTUARIES	
T. Wood	3078
Chapter 186	
MEASUREMENTS OF OSCILLATORY DRAG ON SAND RIPPLES	
Karl E. B. Lofquist	3087
Contribution to the Discussion During Session C, Coastal Processes, Friday, March 28, 2:00 p.m., M. S. Longuet-Higgins, Institute of Oceanographic Sciences, Wormley, Surrey, England	
SUBJECT INDEX	3109
AUTHOR INDEX	3163

FLOATING BREAKWATER PERFORMANCE COMPARISON

Volker W. Harms

Lawrence Berkeley Laboratory
University of California
Berkeley, California 94720

ABSTRACT

Wave-transmission and mooring-force data of the Tethered-Float Breakwater and Pole-Tire Breakwater (PT-Breakwater) were compared, and the basic costs (without mooring system) of two equivalent breakwaters determined. It was found that, for short-fetch applications, the PT-Breakwater was an order of magnitude less costly than the Tethered-Float Breakwater. The PT-Breakwater is a more effective wave-energy filter than a Tethered-Float Breakwater of equal size. For open ocean conditions neither of these breakwaters has so far been proven to be economically feasible.

1. INTRODUCTION

An increasing demand for mooring space and the simultaneous depletion of suitable construction sites that are naturally sheltered from wave action creates a need for artificial low-cost protection of marinas and harbors [1]. Floating breakwaters are frequently chosen to provide this protection, particularly in locations where large water depths, poor foundation conditions or large seasonal water-level changes have to be considered [1]. Although the basic concept of using floating structures as wave-attenuation devices is certainly not new [4,11], the idea of utilizing automobile tires or tethered floats as major functional components is [16,12]. The Floating-Tire Breakwater and Tethered-Float Breakwater are two innovative breakwater concepts that have received considerable attention in recent years from researchers, users and the public press and, as a consequence, are increasingly considered in the solution of wave-protection problems. For short-fetch applications (fetch less than approximately 10 km), or semi-protected regions, both appear to be technically and economically feasible [3,6,9]. For large-fetch exposed locations this has not been demonstrated to date.

In the endeavor to meet a particular wave-protection problem with a functional cost-effective engineering design, the practicing engineer is generally faced with the important task of assessing the relative merits of several technically feasible solutions. Using the available data on

the tethered-float and floating-tire breakwaters, such an assessment is difficult to perform. It is our aim here to provide needed information on the relative cost, wave-attenuation performance and mooring forces associated with these structures. Additional factors such as breakwater size, useful life, aesthetics, maintenance and repair are certainly involved, but the two primary design factors to be considered here are the wave-attenuation performance and cost of the basic structure. For a specified degree of wave attenuation, the coastal engineer should be able to estimate and compare the cost of alternative structures able to provide this protection. Using presently available data, this cannot be done in the case of the tethered-float breakwater (TF-Breakwater) and floating tire breakwater.

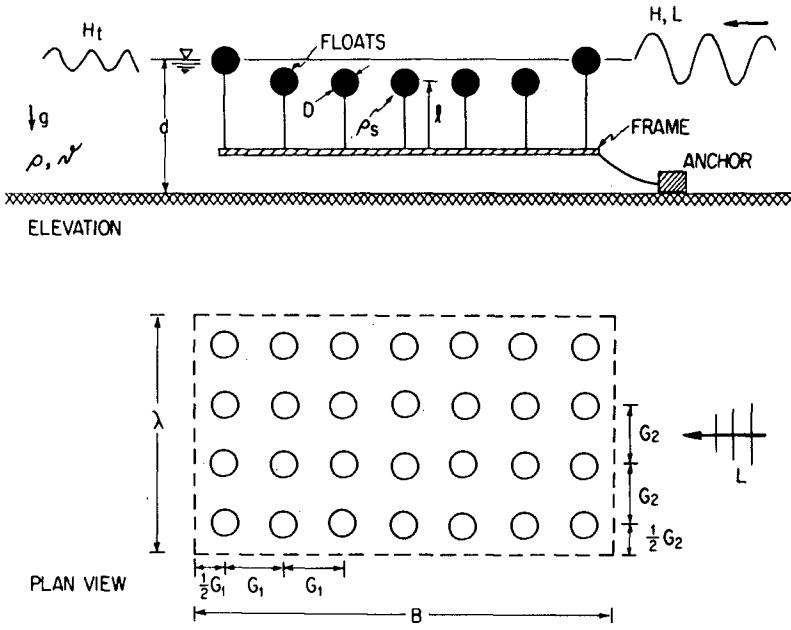
The generic name of floating-tire breakwater is generally applied to three types of floating structures using pneumatic tires as construction components: the Wave-Maze Breakwater [8,10,16], the Goodyear Breakwater [3,5,7], and the Pole-Tire Breakwater [5,6]. For purposes of this report, the most recent entry into the field, the Pole-Tire Breakwater (PT-Breakwater) was chosen as a basis of comparison for the Tethered-Float breakwater (TF-Breakwater). This is particularly appropriate since the PT breakwater has exhibited very promising survival capabilities and wave-damping characteristics in waves up to 2 m in height during recent tests (1979) at the U.S. Army Corps of Engineers Coastal Engineering Research Center.

2. BASIC DESIGN FEATURES

Most breakwaters function primarily as wave reflectors. Although some of the intercepted wave energy is indeed dissipated upon the structure, the larger portion is generally redirected seaward again. The converse is true for the breakwaters considered here: they are predominantly dissipators of wave energy. Most of the incident wave energy is transformed into turbulence within and around the many components of these structures, while only a small portion is reflected. For the PT-Breakwater, ten times as much energy is typically dissipated as is reflected [5].

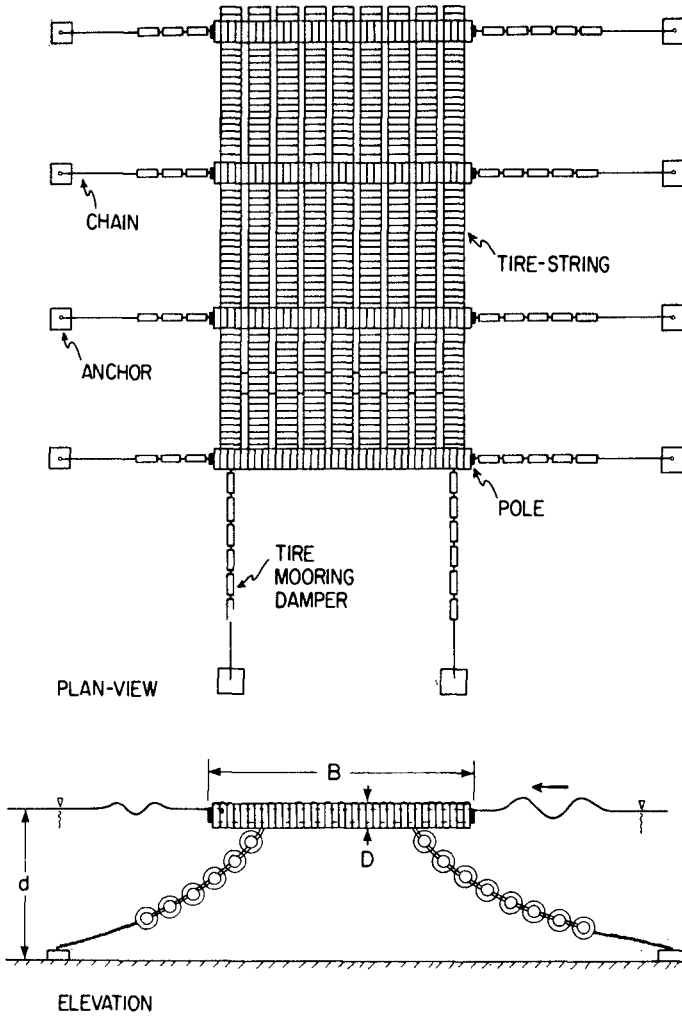
In the TF-Breakwater the basic energy dissipation units are oscillating spherical floats that are individually tethered to a rigid submerged frame. The frame, shown in Fig. 1, is ballasted to provide proper float submergence and transmits all wave-induced loads to the mooring system. A portion of the incident wave energy is converted into turbulence by the pendulum-like wave-induced oscillations of the tethered buoyant floats. The tethered float constitutes a tuned, selective wave-energy filter. Waves that are able to excite the float into high-amplitude oscillatory motions, out of phase with the wave water-particle motions, experience substantial levels of drag-related turbulent energy dissipation. Relatively long waves that cause the float to move in phase with the wave water-particle motions experience little decrease in energy, as do, on the other end of the spectrum, very short waves that are not able to set the float into motion at all. Some important design features of the TF-Breakwater are [14,15]:

- 1) Optimum tether length in deep water is approximately 10% of the peak energy wave length of the spectrum.



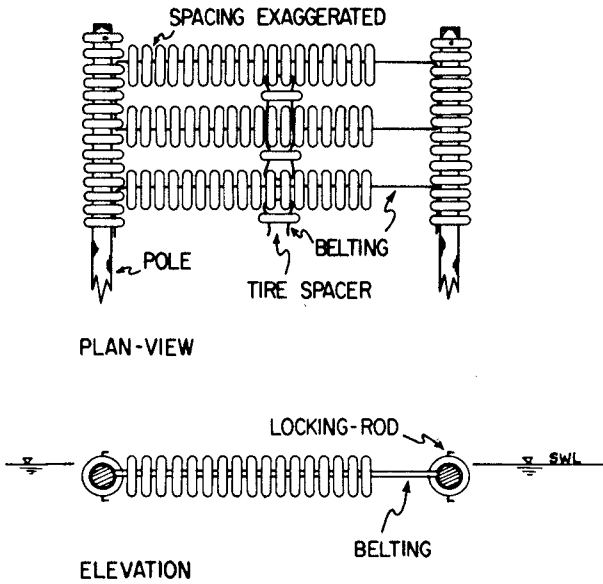
XBL 799-4200

Fig. 1. Definition sketch for Tethered Float Breakwater.



XBL 799-2997

Fig. 2. Schematic of Pole-Tire Breakwater.



XBL 799-4201

Fig. 3. Basic tire arrangement in Pole-Tire Breakwater.



Plate 1. PT-Breakwater before testing at Coastal Engineering Research Center, Ft. Belvoir, Virginia: truck tires/steel pipe on left and automobile tires/telephone pole on right.



Plate 2. Assembly of PT-Breakwater.

CBB790-14041

- 2) Best performance in deep water is attained with floats totally submerged approximately one-quarter diameter beneath the surface. Some floats must pierce the surface in order to provide reserve buoyancy.
- 3) Ballast frames must be flexibly interconnected and frames must be kept small with respect to the peak energy wavelength. This is necessary in order that both frame and floats follow the sea surface and thus prevent emergence of floats in the wave trough (avoiding associated shock loadings during resubmergence).
- 4) A flexible terminator or boot must be provided at the base of the tether in order to reduce bending stresses and ensure reasonable life expectancy of the tether assembly.
- 5) Reasonable diameters of the TF-Breakwater will be of the same order as the significant wave height.

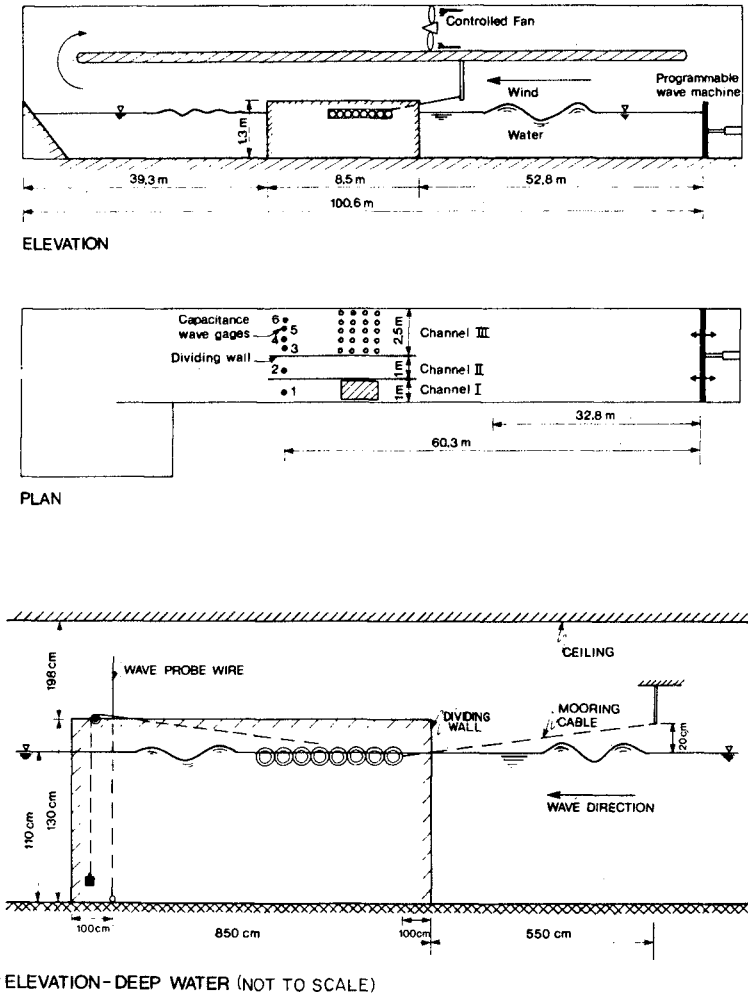
In the case of the PT-Breakwater the basic energy dissipation units and major structural components are discarded pneumatic tires (truck, automobile, earthmover, etc.). These are interconnected and, in conjunction with a rigid longitudinal member (telephone pole, steel or concrete pipe, etc.), form an integral part of the structure, as can be seen in Figs. 2 and 3 and Plates 1 and 2. The PT-Breakwater is essentially a dense mat composed of a large number of interconnected tires floating near the surface, with approximately 85% of the structure submerged. It functions predominantly as a wave-energy dissipator: most of the incident wave energy is transformed into turbulence in and around the many elements of the structure, with only a small portion being reflected. The breakwater is interconnected with conveyor belting [2], as shown schematically in Fig. 3.

3. LABORATORY DATA AND ANALYSIS

3.1 Experimental Conditions

Models of the TF and PT-Breakwaters were tested in the large wind wave tank (109 m × 4.5 m × 1.5 m) of the Hydraulic Laboratory at the Canada Centre for Inland Waters in Burlington, Ontario, shown in Fig. 4 and Plate 3. Additional full-scale tests of the PT Breakwaters were performed at the University of Delaware and the U.S. Army Coastal Engineering Center. Models of the TF Breakwater were constructed at two scales using 5 cm spherical styrofoam floats and 15 cm pressurized plastic balls. They were constructed according to guidelines given by Seymour [14,15]. Tires from a 1/8-scale model automobile were utilized in the construction of the PT-Breakwater models. Telephone poles were modeled from wooden hand-rail material.

In the test section shown in Fig. 4, the tank was subdivided into three channels (1 m, 1 m, and 2.5 m wide) so that two breakwaters as well as the undisturbed incident wave could be monitored simultaneously. For each breakwater the transmitted wave and mooring force on the seaward mooring line were recorded. Waves were generated with a programmable piston-type wave machine. Most experiments were performed with regular



XBL 799-2995

Fig. 4. Schematic diagram of wave tank at the Canada Centre for Inland Waters.



Plate 3. One-quarter scale model of TF-Breakwater in drained wave tank at Canada Centre for Inland Waters (model of Goodyear Breakwater in foreground).

waves, but machine-generated and wind-generated wave spectra were also investigated. In the case of irregular waves, the transmission coefficient $C_t = H_t/H$ and wave steepness H/L were evaluated using the peak-energy wave length and the average wave height as obtained from time-series analysis of the water surface elevation.

3.2 Dimensional Analysis

For the breakwater configuration shown in Fig. 1 we assume that the transmitted wave height H_t is an unknown function of the following variables:

$$H_t = f(H, L, d, \rho, \nu, g, D, \rho_s, \ell, B, \lambda, N) \quad (1)$$

Here H, H_t = incident and transmitted wave height; L = wave length; d = water depth; ρ = fluid density; ν = kinematic viscosity; g = gravitational acceleration; D = float diameter; ρ_s = float density; ℓ = tether length; B = beam dimension of breakwater; λ_s = length of breakwater; N = number of floats in breakwater. Note that the transmitted wave height H_t is assumed to depend only upon the total number of floats N , not their geometrical arrangement, as long as no interference between balls occurs. According to Buckingham's Pi Theorem, this is equivalent to the following non-dimensional relationship:

$$H_t/H = f[L/B, H/L, \ell/d, \ell/D, \rho_s/\rho, B/D, \lambda/D, \sqrt{B\lambda/ND^2}, D\sqrt{gH/\nu}] \quad (2)$$

Note that the last term is a Reynolds number and that the next to last term is simply a measure of the float spacing, e.g., with $G_1 = G_2$, $\frac{B}{\lambda} = nG_1$, $\lambda = mG_2$ in Fig. 1 and $N = nm$ = number of floats; it follows that $\sqrt{B\lambda/ND^2} = G_1/D$. We simplify this expression by:

- i) Keeping some terms the same in all models $\rho_s/\rho, \ell/D$;
- ii) Considering only quasi-two-dimensional tests,
i.e., no diffraction influences from ends λ/D ;
- iii) Assuming that some parameters are of second-order importance if they are sufficiently large ... $B/D, D\sqrt{gH/\nu}$

For such experiments:

$$C_t \approx f[L/B, H/L, \sqrt{B\lambda/ND^2}, \ell/d] \quad (3)$$

i.e., the transmission coefficient $C_t = H_t/H$ depends primarily upon the relative wave length L/B , the wave steepness H/L , the effective float spacing $\sqrt{B\lambda/ND^2}$ and the relative draft ℓ/d . For the mooring force we obtain, similarly:

$$F/\gamma B^2 = f[L/B, H/L, \sqrt{B\lambda/ND^2}, \ell/d] \quad (4)$$

For the PT-Breakwater, following procedures similar to those applied above, we may anticipate a relationship of the form

$$C_t = f[L/B, H/L, B/D, D/d] \quad (5)$$

$$F/\gamma B^2 = f[L/B, H/L, B/D, D/d] \quad (6)$$

where D now designates the tire diameter.

3.3 Wave-Attenuation Performance

In Fig. 5 the wave-height transmission ratio C_t has been plotted as a function of relative wave length L/B for three models of the TF-Breakwater. These models were constructed according to guidelines given by Seymour and are similar to structures tested in San Diego Bay, California [14,15]. An averaged wave-height transmission curve representing Seymour's predictive model [14] for several wave spectra with peak energies at $L/B = 0.6, 1.0$ and 1.7 has been included for comparison. Agreement in basic trends is evident, but measured C_t values are generally larger. Although Reynolds' numbers appear to be sufficiently high for proper modeling of float dynamics (and to maintain the turbulent character of the drag-related energy dissipation mechanism that governs at larger scales), it is possible that some Reynolds-number influences are being observed in the case of the small breakwaters. Seymour performed laboratory and field experiments on the TF-Breakwater and found his predictive model to be satisfactory [14]. For purposes of comparison it will be assumed that Seymour's predictive model describes the wave-transmission characteristics of the TF-Breakwater correctly.

In Fig. 6 the wave transmission curve for the PT-Breakwater is shown as a dashed line that increases monotonically as a function of L/B . This curve corresponds to $H/L = 0.04$ and is based upon extensive data, both model and full-scale. The data will not be included here because it is already well documented [5,6]. This performance curve was originally established using tires 8.4 cm in diameter, but has also been confirmed by full-scale experiments with truck and automobile tires 64 cm and 100 cm in diameter. A fundamental difference in the filtering characteristic of these structures is evident in Fig. 6: the TF-Breakwater is a tuned discrete filter that is most effective around $L/B = 0.7$, and becomes increasingly less effective at wave lengths other than this (either shorter or longer), whereas the PT-Breakwater is a monotonic filter that becomes increasingly more effective as the wave length decreases. It is apparent that the PT-Breakwater offers substantially more wave protection (lower C_t levels) than a TF-Breakwater of equal size.

3.4 Mooring Forces

The data presented here applies to a single-point mooring that provides an essentially horizontal restraining force on the seaward side of the breakwater, similar to the anchor line depicted in Fig. 1. Only the peak mooring force recorded during the experiment is reported (excluding wave-generator stop-start transients). Although accurate scaling of elastic properties and damping characteristics of the mooring system could not be assured, it was found that satisfactory agreement with full scale measurements existed for similar breakwaters tested in the past [5,6]. In tests with irregular waves the wave length corresponding to the spectrum energy peak is utilized in the wave length parameter L/B .

Mooring force data for the TF-Breakwater is plotted in Fig. 7 for large wave steepness ($H/L > 0.04$), and Fig. 8 for low wave steepness

($H/L < 0.04$). For comparison, the corresponding mooring force curve for the PT-Breakwater ($H/L = 0.06$, $D/d = 0.06$) has also been included in Fig. 7. It is evident that the peak mooring force for the PT-Breakwater is larger than that of a TF-Breakwater of equal size, but it should be recalled that such a PT-Breakwater is also more effective (Fig. 6). In previous studies [5] a useful empirical relationship for the peak mooring forces on a PT-Breakwater was determined to be

$$F/\gamma B^2 = 0.15(H/L)^2(L/B) \tanh(L/B) \quad (7)$$

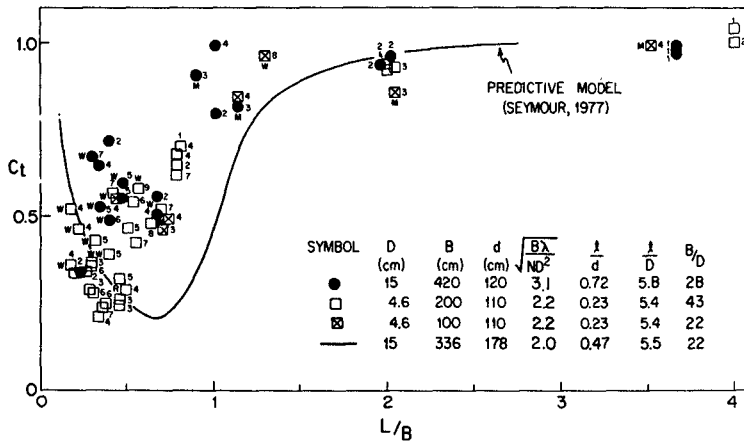
This indicates that for a given wave length and structure the peak mooring force grows rapidly as a function of wave height. Mooring force measurements performed by Seymour with waves of very low steepness are also included in Fig. 8. It is apparent that these forces are significantly higher than those from this investigation. The two force measurements at a low wave steepness of $H/L = 0.02$, for example, are as high as those for $H/L = 0.06$ in the present study.

4. COST COMPARISON

The following material is intended to be of assistance to the coastal engineer in a preliminary assessment of relative costs associated with the TF- and PT-Breakwaters. The principle of "equal wave protection" has been utilized here in order to arrive at meaningful, comparable cost figures for the different structures. This implies that the size of each structure was first fixed so as to provide equal levels of wave protection from the same incident wave. The associated breakwater costs were then determined using these dimensions. The resulting cost figures may therefore be meaningfully compared as costs associated with two equivalent solutions to a particular wave protection problem. Cost estimates are given for major cost-contributing components of the structure, the mooring system, has not been included.

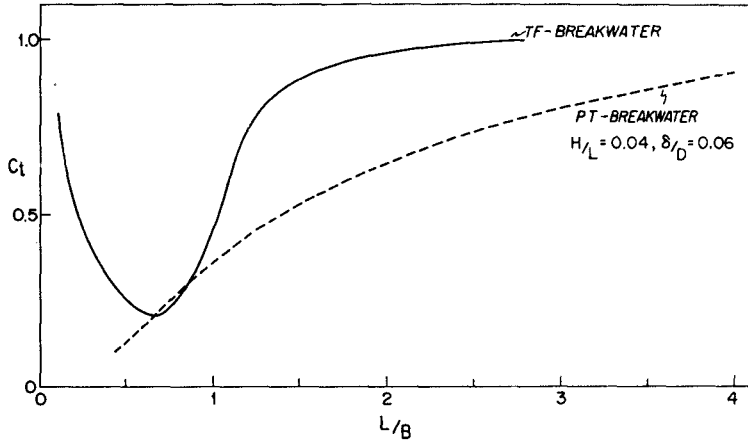
4.1. Equivalent Breakwaters

Figure 6 indicates that over practically the full spectrum of wave lengths L/B , the wave attenuation performance of the PT-Breakwater is superior to that of a TF-Breakwater of equal size. The only exception to this is a narrow band of essentially equal wave attenuation from $L/B = 0.65 - 0.85$. This narrow region would be of importance only in the case of monochromatic laboratory waves and not with regards to the broader wind-generated spectra encountered in actual design cases. In view of this disparity in wave attenuation performance, it is clear that one should not compare the cost of two breakwaters of equal size, for different "amounts of wave protection" would then be purchased with each structure. We therefore determine first how large a TF-Breakwater must be in order to provide approximately the same level of wave protection as a PT-Breakwater. In Fig. 9 a PT-Breakwater with beam B is compared to a TF-Breakwater with beam dimension $B_{TF} = 1.5B$, and from this conclude that approximate equivalence of wave protection has been attained. In the simple design procedure used here, the beam dimension of the TF-Breakwater is chosen so that the region of maximum effectiveness of the breakwater (the trough



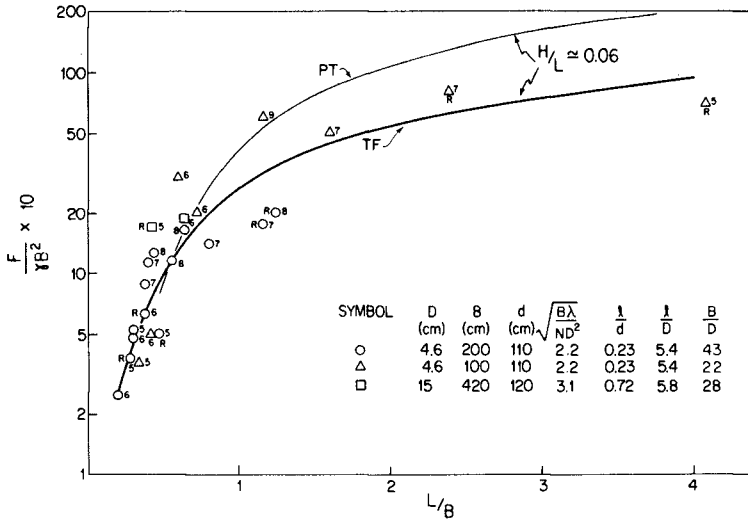
XBL 799-2993

Fig. 5. Wave-height transmission data for TF Breakwater.



XBL 799-2994

Fig. 6. Wave transmission curves for TF and PT Breakwaters of equal size.



XBL 799-2998

Fig. 7. Peak mooring force data for the TF Breakwater and $H/L > 0.04$ (curves for TF and PT Breakwaters, $H/L \approx 0.06$).

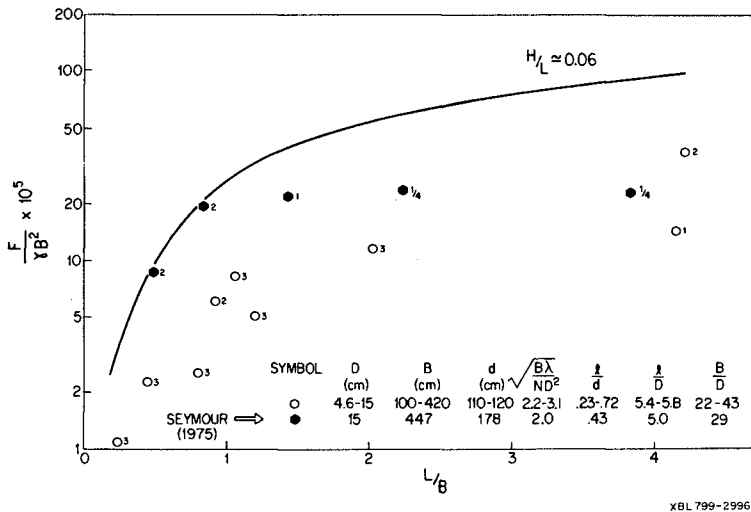
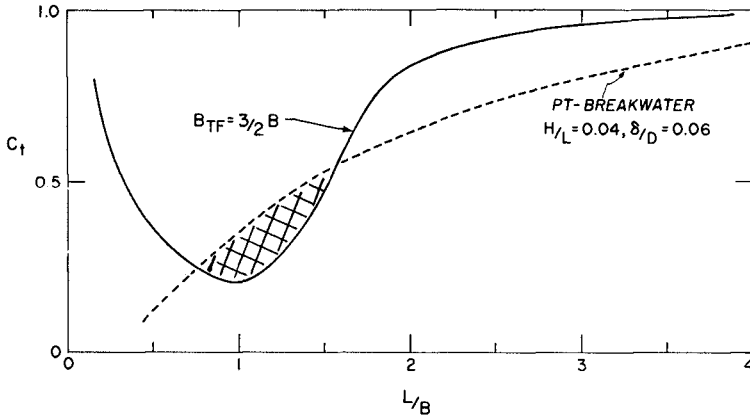


Fig. 8. Peak mooring force data for the TF Breakwater and $H/L < 0.04$ (curve for $H/L \approx 0.06$).



XBL799-2999

Fig. 9. Wave transmission curves for PT Breakwater and larger TF Breakwater ($B_{TF} = 3/2 B$).

region at $L/B = 1$) corresponds to the design wave length or, equivalently, the peak energy wave length of the incident spectra. With this in mind, and recognizing that most short-fetch wave spectra are much broader than the cross-hatched region around the incident wave-energy peak at $L/B = 1$, it is reasonable to conclude that the two breakwaters are, for most practical purposes, equal in wave attenuation performance. The beam-size relationship to be used in the cost comparison is consequently $B_{TF} = 1.5B$, i.e., the TF-Breakwater requires a 50% larger planform area.

Considering the case of a design-wave period (or peak energy period) of $T = 3.0$ sec and a wave height of $H = 1.0$ m, and assuming deep-water conditions, one finds that $L = 14.0$ m and $H/L = 0.07$. This wave length should correspond to $L/B = (3/2)L/B_{TF} = 1.0$ in Fig. 9 in order to maximize the effectiveness of the TF-Breakwater. The beam dimension necessary to achieve this is consequently $B_{TF} = 3/2 L = 21.0$ m. To attain comparable performance with the PT-Breakwater requires a beam dimension of $B = 1.0 L = 14.0$ m. The corresponding peak mooring forces can be determined from Fig. 7 using $H/L = 0.06$ as an approximation. For both the TF-Breakwater ($L/B = 2/3$) and the PT-Breakwater ($L/B = 1.0$), the peak mooring forces turn out to be very nearly equal, $F = 780 \text{ Nm}^{-1}$.

4.2 Cost Estimates

The following cost comparison is based predominantly upon the cost of major structural components required for assembly of the breakwater. Construction labor costs are also included, but mooring system costs and expenditures for construction equipment that may be utilized during assembly and launching are not. In the absence of site-specific data on mooring and launching costs, the total component cost figures given here become useful first approximations of the installed cost, particularly in the case of the TF-Breakwater for which the neglected cost items (mooring system and launching) are generally only a small fraction of the total.

Cost data for the TF-Breakwater were obtained from a 1977 "Feasibility Study to Evaluate the Commercial Market for a Tethered Float Breakwater System" [Maritime Administration, U.S. Department of Commerce]. Cost figures for the PT-Breakwater reflect recent construction experience (1979) with two breakwaters at the State University of New York in Buffalo: these utilized telephone poles and steel pipes 12 m in length in conjunction with automobile and truck tires, respectively. The utilization of automobile tires is financially attractive particularly because they can generally be obtained in large quantities at no cost. In the US the cost associated with the disposal of a truck tire is typically US \$1 (landfill sites generally charge user fees and, to improve compaction, also demand that tire casings be cut up prior to disposal). Trucking and tire-recapping firms are consequently willing to not only supply tires, but deliver them to the breakwater construction site as well: in most cases they still save money. All cost figures were adjusted to 1980 levels by assuming annual price increases of 10%.

COMPONENT COST ESTIMATES: TETHERED FLOAT (TF) BREAKWATER

Module Dimensions : B = 21.0 m, λ = 3.80 m

Materials : Spherical floats (D = 38 cm, γ = 0.04 gm cm⁻³),
 Tethers and flexible tether terminals,
 Steel ballast frames with flexible couplings
 (3 frames 7.00 m × 3.00 m per module),
 Concrete ballast.

<i>Item</i>	<i>Quantity</i>	<i>Unit Cost (US \$)</i>	<i>Total (US \$)</i>	<i>Cost per meter (US \$)</i>
Float unit (float, tether, flex. terminals)	135	24.30*	3279.30	863.00
Ballast frame (incl. flexible couplings)	3	465.90*	1397.60	367.80
Concrete ballast	4.2 m ³	113.10*	475.20	125.00
Assembly (labor only)	14 hrs	6.00	84.00	22.10

Cost per meter of breakwater = \$1377.90
 (excluding mooring system)

*Source: Ref. (9)

COMPONENT COST ESTIMATES: POLE-TIRE (PT) BREAKWATER

Module Dimensions : B = 14.0 m, λ = 4.00 m

Materials : Automobile tires (typically 0 = 64 cm),
 Telephone poles (4 m spacing),
 Conveyor belting (3-ply, 14 cm wide, 5000 N cm⁻¹
 breaking strength),
 Nylon bolts, nuts, washers (13 mm or equivalent).

<i>Item</i>	<i>Quantity</i>	<i>Unit cost (US \$)</i>	<i>Total (US \$)</i>	<i>Cost per meter (US \$)</i>
Tires	403	none	none	none
Tying material (conveyor belting)	180 m	0.90	162.40	40.60
Nylon bolts, nuts, washers	105	0.55	57.80	14.40
Telephone poles	1	50.00 (salvage @ 15% new)	50.00	12.50
Assembly (labor only)	18 hrs	6.00	108.00	27.00

Cost per meter of breakwater = \$94.50
 (excluding mooring system)

Note: The use of steel pipe (41 cm diam, 6 mm wall) and truck tires will increase the cost by approximately \$130 per meter.

5. CONCLUSIONS

- 1) The Tethered-Float and Pole-Tire Breakwaters are technically feasible solutions to wave protection problems in short-fetch (say, less than 10 km) or semi-protected locations.
- 2) The Pole-Tire Breakwater is a more effective wave-energy filter than a Tethered-Float Breakwater of equal size.
- 3) In a typical short-fetch design case, a Tethered-Float and Pole-Tire Breakwater were found to compare as follows (for equal levels of wave protection):
 - a. The Pole-Tire Breakwater costs less than one-tenth as much as the Tethered-Float Breakwater.
 - b. Peak mooring forces are approximately the same.
 - c. The Pole-Tire Breakwater requires less space.

6. ACKNOWLEDGMENTS

This research was sponsored in part by the New York Sea Grant Institute under a grant from the Office of Sea Grants, National Oceanic and Atmospheric Administration, and in part by the Energy Technology/Solar Division of the U.S. Department of Energy under Contract No. W-7405-ENG-48. The writer would like to express his appreciation to T. M. Dick of the Hydraulics Research Division of the Canada Centre for Inland Waters (CCIW) for making the laboratory tests at CCIW possible. The valued assistance of Tom Bender, graduate student at State University of New York at Buffalo, is gratefully acknowledged.

7. REFERENCES

- [1] Chen, K. and Wiegel, R., "Floating breakwater for reservoir marinas," Proceedings of Twelfth Conference on Coastal Engineering, ASCE, Vol. III, pp. 1647-1666 (1977).
- [2] Davis, A.P., Jr., "Evaluation of tying materials for floating tire breakwaters," Marine Technical Report No. 54, University of Rhode Island, Kingston, R.I. (April 1977).
- [3] Giles, M.L. and Sorenson, R.M., "Prototype scale mooring load and transmission tests for a floating tire breakwater," Technical Paper No. 78-3, U.S. Army Corps of Engineers, Coastal Engineering Research Center, Fort Belvoir, Virginia (April 1978).
- [4] Griffin, O.M., "Recent designs for transportable wave barriers and breakwaters," Marine Technology Society Journal Vol. 5, No. 2, pp. 7-16 (March/April 1972).
- [5] Harms, V.W., "Design criteria for floating tire breakwaters," Proceedings, ASCE Journal of the Waterway, Port, Coastal and Ocean Divisions, Vol. 105, No. WW2, pp. 149-170 (March 1979).

- [6] Harms, V.W., "Data and procedures for the design of floating tire breakwaters," Dept. of Civil Engineering, State University of New York, Buffalo, WREE Report No. 7901 (March 1979).
- [7] Harms, V.W. and Bender, T.J., "Preliminary report on the application of floating tire breakwater design data," Water Resources & Environmental Engineering Research Report No. 78-1, Dept. of Civil Engineering, State University of New York at Buffalo (April 1978).
- [8] Kame1, A.M. and Davidson, D.D., "Hydraulic characteristics of mobile breakwaters composed of tires or spheres," U.S. Army Engineer Waterways Experiment Station Technical Report No. H-68-2, Vicksburg, Mississippi (1968).
- [9] Moffatt & Nichol Engineers, "Feasibility study to evaluate the commercial market for a tethered float breakwater," Report No. MA-RD-970-77077, Maritime Administration, Washington, D.C., pp. 88-90 (March 1977).
- [10] Noble, H.M., "Use of wave-maze flexible floating breakwater to protect offshore structures and landings," Presented at the May 3-6, 1976, Eighth Annual Offshore Technology Conference, Houston, Texas.
- [11] Richey, E.P. and Nece, R.E., "Floating breakwaters - state of the art," Marine Technical Report Series No. 24, Floating Breakwater Conference Papers, University of Rhode Island, pp. 1-19 (1974).
- [12] Seymour, R.J. and Isaacs, J.D., "Tethered float breakwaters," Marine Technical Report Series No. 24, T. Kowalski, editor, Floating Breakwater Conference, University of Rhode Island, pp. 55-72 (1974).
- [13] Seymour, R.J., "Wave induced loads on multi-element structures," Proceedings of Symposium on Modeling Techniques for Waterways, Harbors and Coastal Engineering, San Francisco, California, pp. 1552-1567 (September 1975).
- [14] Seymour, R.J. and Hanes, D.M., "Performance analysis of a tethered float breakwater," California Dept. of Navigation & Ocean Development and Institute of Marine Resources, University of California, Sea Grant Publication No. 55 (January 1977).
- [15] Seymour, R.J., "Tethered float breakwater: a temporary wave protection system for open ocean construction," Paper No. OTC-2545, Eighth Annual Offshore Technology Conference, May 1976, Houston, Texas.
- [16] Stitt, R.L., "Wave-maze floating breakwater," Brochure, 10732 Freer St., Temple City, California (1963, revised 1977).

CHAPTER 130

LITTORAL DRIFT OF SAND NEAR PORT OF OARAI

by

Kazumasa Mizumura

ABSTRACT

To study the main direction of littoral drift of sand near the Port of Oarai, field observations were made. Through the analyses of the results the following facts were obtained.

- (1) The relative changes of foreshore gradients alongshore were correlated with the characteristics of beaches.
- (2) By investigating sand grain sizes on the coast the predominant direction of littoral drift of sand could be illustrated.
- (3) The direction of littoral drift of sand was almost coincident with the main nearshore currents.

INTRODUCTION

Problems on coastal changes are important and have attracted many engineers. The most reliable work for the shore protection before the construction of ports and harbors is considered to be field observations. Stillmore, the success of hydraulic model tests is also dependent on the data analysis of field observation. To investigate the plan of extension at the Port of Oarai in regard to coastal changes, field observations were done before the start of the plan. Herein, the characteristics of the coast near the Port of Oarai are studied using the results of field observations. Therefore, beach profiles, littoral materials and nearshore currents were measured in July of 1977.

Since the predominant direction of littoral drift of sand was determined, the groin of 400m in length had been constructed in September of 1977.

Associate Professor, Dept. of Civil Engineering, Kanazawa Institute of Technology, Kanazawa, Japan

GENERAL

The Port of Oarai is located north of Tokyo, Japan and faced to the Pacific Ocean as illustrated in Fig.1. In the south of the port there is a sandy Kashimanada Coast which has an arcuate form and almost 70 km in length. To the east of the port there exist Oarai Headland and Oarai Coast. Contours along the Kashimanada Coast and the Oarai Coast are almost linear and parallel to the shoreline except near Oarai Headland as shown in Fig.1. Because there exist marine ridges in the offshore of Oarai Headland. Therefore, the incident wave energy converges to the headland and shows the shoreline of erosion. In the west of the Port of Oarai some breakwaters remain as represented in Fig.1. This was the old Port of Isohama and tried to construct about 60 years ago. But this was stopped during the construction of breakwaters because of the deposition of much sand. At the present, the sandy beach forms a good bathing place in summer. The arm of the south breakwater is expanded to the south and it causes erosion problems along the segment of the opposite coast to the breakwater. It can be observed that the position of erosions moves down to the south as the south breakwater expands.

WIND AND WAVES

Wind directions and velocities were measured at the position which is located 4.5 km in SE direction of the Port 1973 to 1975. The wind directions from ENE to N are predominant and occupy almost 40 % of the total. Wave conditions offshore were measured at the south point of 9 km from the port. ENE direction is predominant and reaches more than 50 % of the total as shown in Fig.2. The percentage of the periods from 9.0 sec to 13.0 sec attains almost 58 % of all available data as illustrated in Fig.3. Especially, 11 sec and 12 sec are predominant and about 14 %. The percentage of wave height more than 3.0 m is almost 4 % and less than 1.5 m amounts to 75 % as given in Fig.4. It can be seen that the coming wave height is low and seasonal changes are not found.

FORESHORES AND BEACH PROFILES

To study the characteristics of beaches near the port, beach profiles, specially foreshores were surveyed at 8 points as numbered in

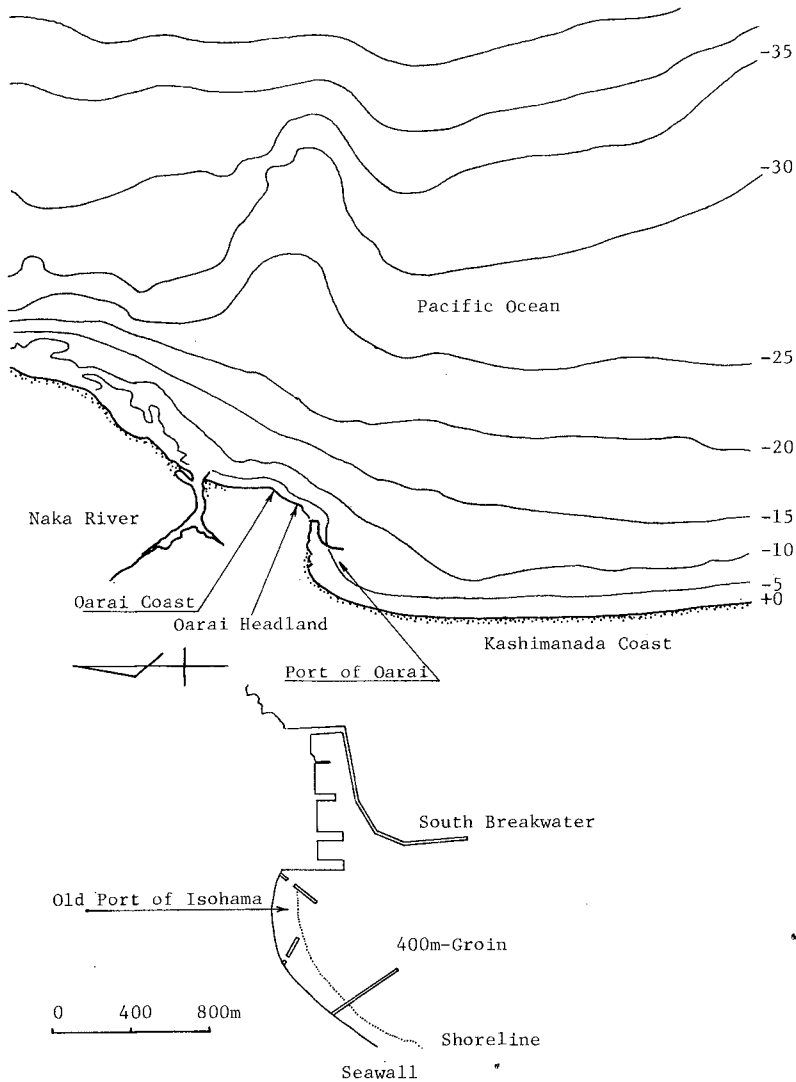


Fig. 1. - Study Area and Port of Oarai

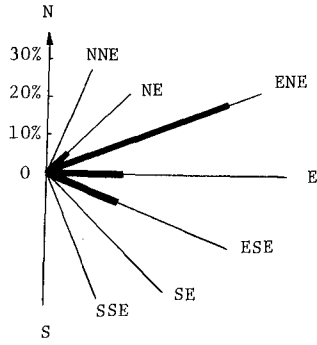


Fig. 2. - Distribution of Wave Directions

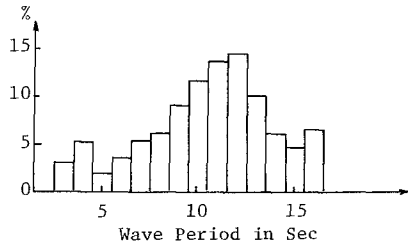


Fig. 3. - Distribution of Wave Periods

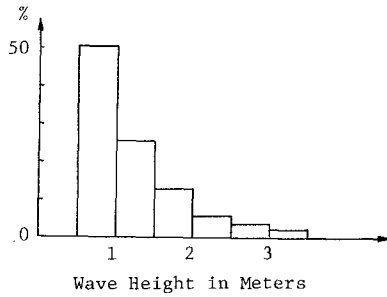


Fig. 4. - Distribution of Wave Heights

Fig.5. These points correspond to the sampling points of bed materials on the beaches. The beaches in the sheltered zone by the south breakwater are very wide and sand grains are fine there. The slopes are milder than $1/100$. The zone between the sheltered zone by the south breakwater and the zone which is not influenced by coastal structures is for simplicity defined as the intermediate zone in this study. The shore in the intermediate zone recedes to the seawall partly and shows the shore of erosion by the existence of the system of small offshore breakwaters and groins for shore protection. The slopes are steeper than $1/30$. The southward beaches which are far from the south breakwater have no influence from any coastal structures and are called open beaches. The slopes are about $1/60$. The shape of beach profiles on each point are represented in Fig.6.

LITTORAL MATERIALS

Sand was sampled by dredges at 48 points as illustrated in Fig.5 and its physical properties such as specific gravities and size distributions were investigated. The specific gravities are almost constant and equal to 2.65. Fig.7 represents the relationship between sea bottom slopes and mean diameters of sand grains. This means that very fine sand exists on sea bed with milder slope and vice-versa. The grain diameters in breaking zones are large due to the wave sorting effect. Moreover, Fig. 8 shows "curves of equi-mean diameter" based on the sampled data at 48 points. On the southward beach which does not have any influence from coastal structures, the curves are almost parallel to each other and the shoreline. In the intermediate zone the intervals of the curves become narrow and the curves approach to the shoreline. If imaginary curves were drawn from the south to the north until near the port in parallel condition to the shoreline, it can be understood that the curves in this zone shift more landwards than they are drawn in the south. This suggests that the shifting is caused by sand movement and the predominant direction of littoral drift of sand is landward. In the sheltered zone by the south breakwater the pattern of the curves changes. That is, the curves are not parallel to the shoreline, but almost perpendicular to that. By considering the imaginary curves of the equi-mean diameters previously discussed, the real

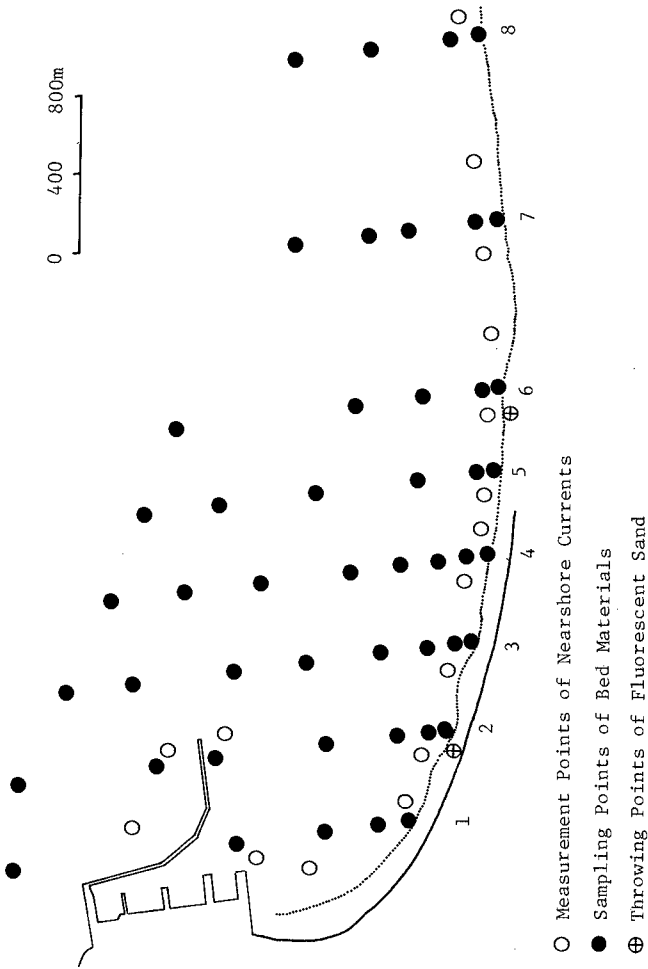


Fig. 5. - Map of Field Observations

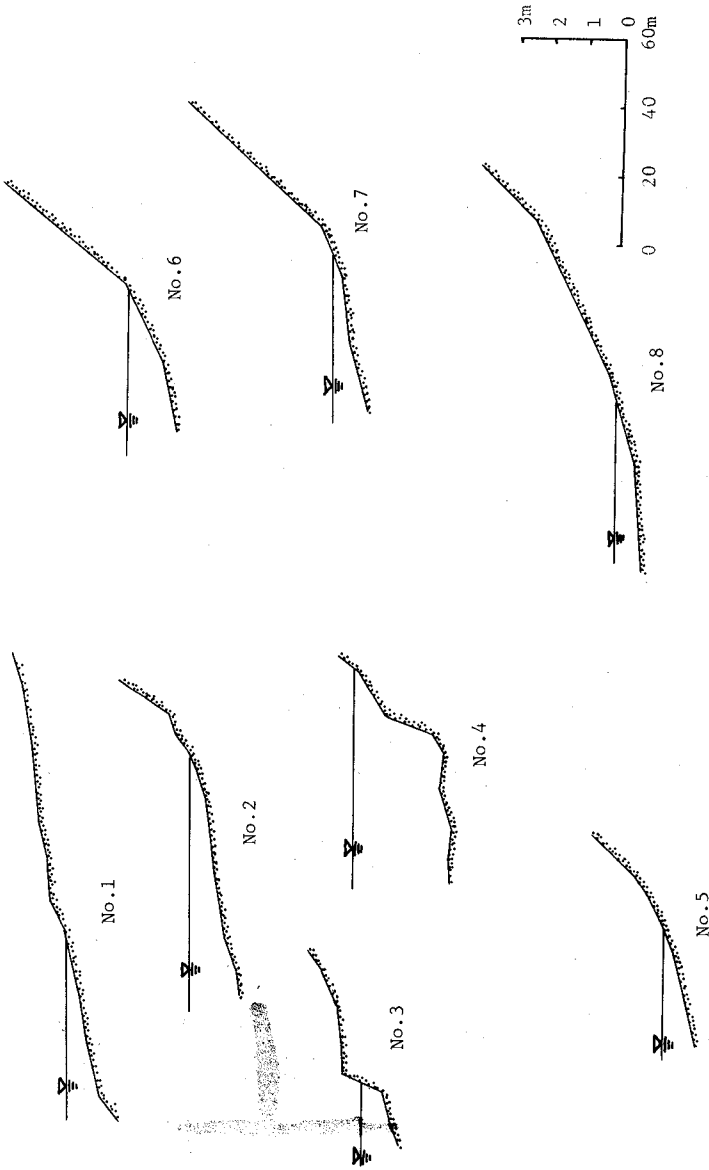


Fig. 6. - Beach Profiles

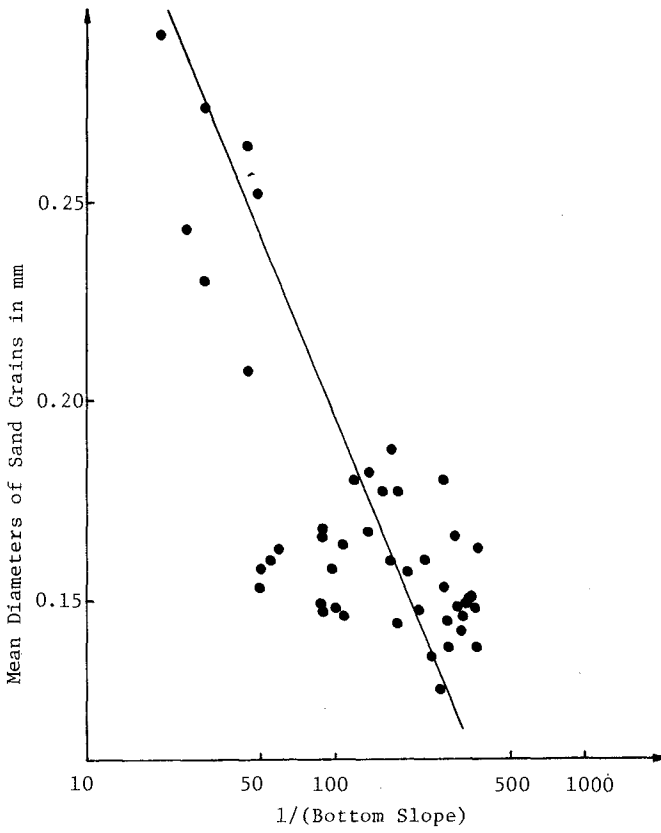


Fig. 7. - Relationship between Mean Diameters of Sand Grains and Bottom Slopes

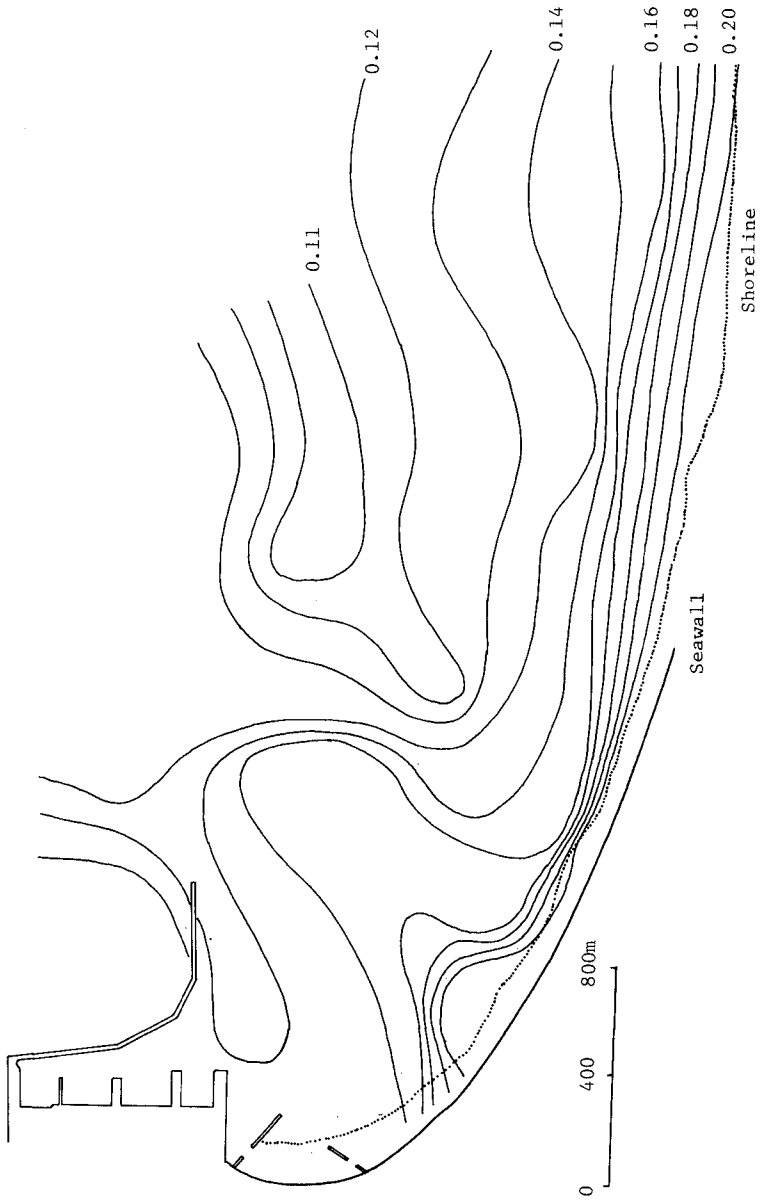


Fig. 8. - Curves of Equi-Mean Diameters

curves drawn in the figure can be recognized to shift seawards. This shows that the shifting is caused by sand movement and the predominant direction of littoral drift of sand is seaward in this zone. The combination of the above two directions of littoral drift of sand gives the direction of that between the two zones. Namely, the transported sand from the offshore in the intermediate zone moves alongshore and deposited in the sheltered zone. The one part of the transported sand moves seawards and deposits in the port. The other part moves alongshore, reaches near the old Port of Isohama and deposits there.

NEARSHORE CURRENTS

The nearshore currents in the breaking zones of 17 points as illustrated in Fig.5 were measured by floats when the wave direction and the wave height were E or ENE and 0.5 m to 0.8 m, respectively. The measured average velocities of nearshore currents are represented in Fig.9.

Simple modeling of the measured flow pattern shows the existence of a circulatory current in the lee of the south breakwater. The cause of the circulatory current is explained as follows. The incident waves from the predominant direction ENE are diffracted by the south breakwater and this produces the difference of breaking wave heights along the shore. Moreover, this generates the difference of the mean water level along the shore by the radiation stresses. Therefore, the regular and stationary circular current is induced alongshore from high to low water levels. In the intermediate zone the component of the circulatory current flows landwards and erodes the shore. In the sheltered zone, the component of the circulatory current forms the longshore current and it transports sand alongshore into the port. This fact is also proven by the movement of fluorescent sands as illustrated in Fig.10a and b. The throwing points of the fluorescent sands are located on the beach in the sheltered zone as shown in Fig.5. All sands move definitely alongshore to the port.

COMPARISONS OF PAST SURVEYS AND AERIAL PHOTOS

The comparisons of each contour between June of 1977 and December of 1973 are represented in Fig.11. Solid lines and dotted lines show the contours in June of 1977 and December of 1973, respectively.

Therefore, erosion area is illustrated by the zone of hatching and

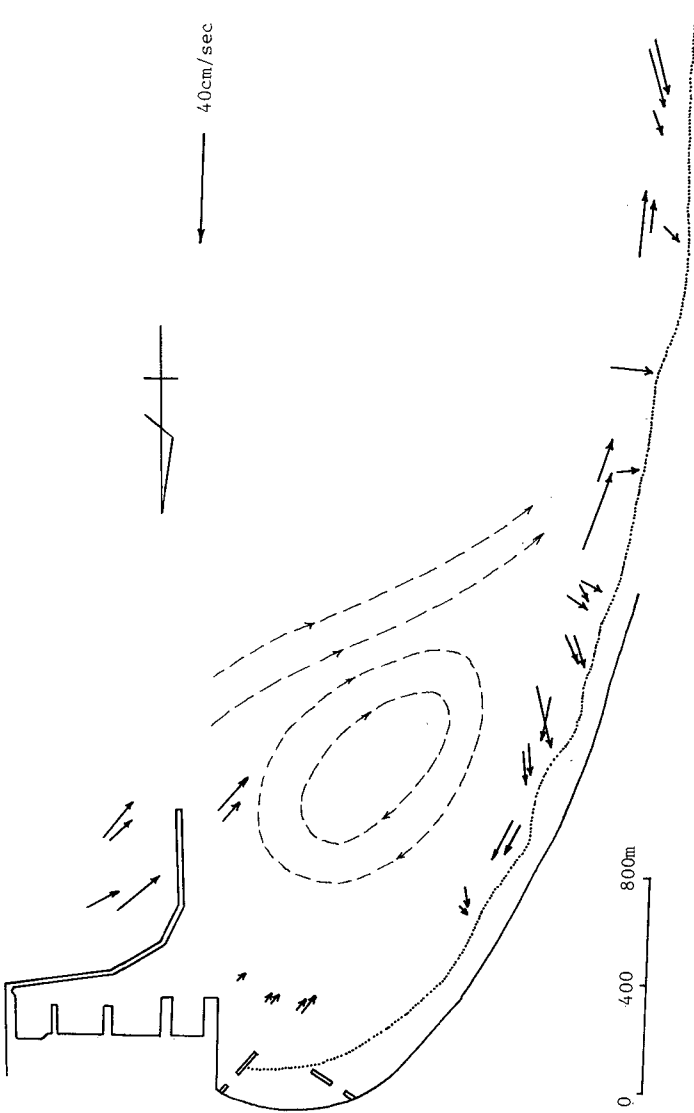


Fig. 9. - Measured Nearshore Currents

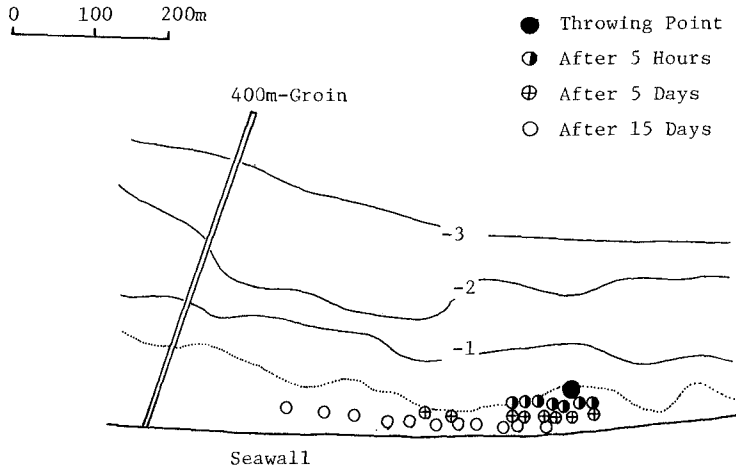


Fig.10a. - Movement of Tracers

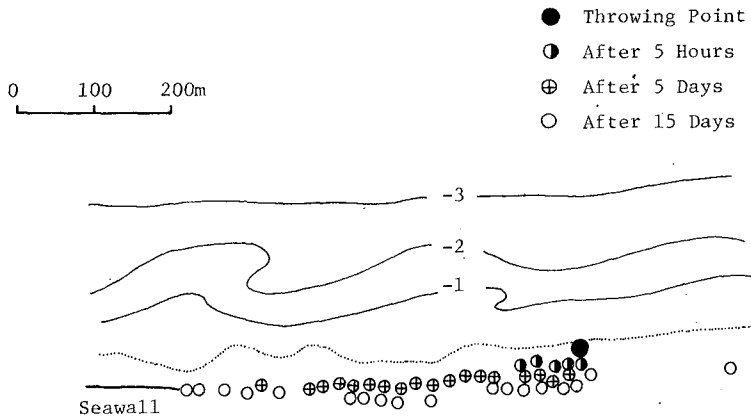


Fig.10b. - Movement of Tracers

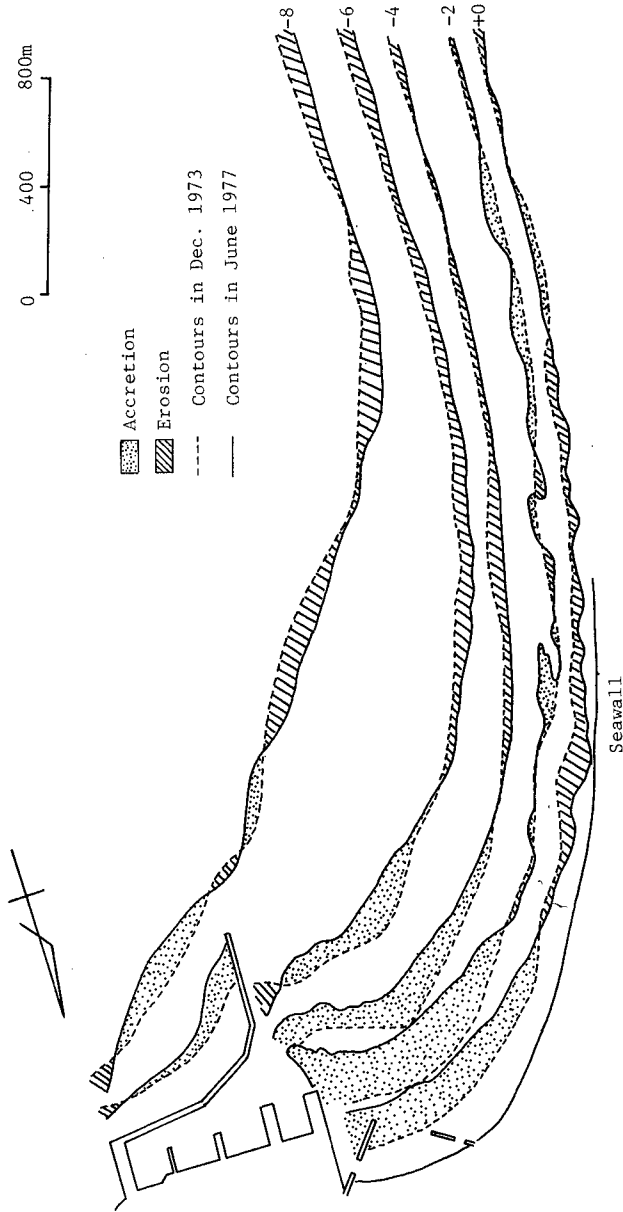


Fig.11. - Comparison of Past Surveys



Fig.12. - Aerial Photo in Dec. of 1969

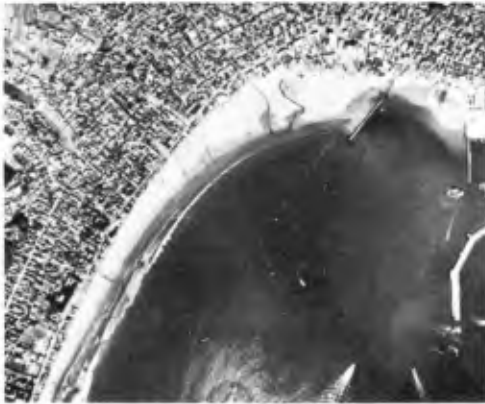


Fig.13. - Aerial Photo in Jan. of 1975

accretion area is shown dotted in the same figure. As previously discussed severe erosion occurs in the intermediate zone, the eroded sand is transported near the old Port of Isohama and forms accretion area.

The maximum advance of the shoreline in the accretion area is almost 120 m in 3.5 natural years. Moreover, aerial photos in December of 1969 and in January of 1975 are shown in Fig.12 and Fig.13, respectively. The comparison illustrates the remarkable accretion phenomena near the old Port of Isohama. Namely, in December of 1969 the shoreline had touched the old breakwaters, but in January of 1975 the shoreline moved more seawards and much sand accumulated around the old breakwaters.

SUMMARY AND CONCLUSIONS

The following conclusions are made for characteristics of the coast near the Port of Oarai under the field observations used in this study.

- (1) The foreshore gradient on the eroded beach is steep and that on the accreted beach is mild, relatively.
- (2) The sizes of sand grains are correlated with the sea bottom slopes.
- (3) The curves of equi-mean diameter obtained by size distributions of sand grains can indicate the predominant direction of littoral drift of sand.
- (4) There exists the circulatory current in the lee of the south breakwater and the direction of this current is coincident with that of littoral drift of sand.

LONG-TERM EXPERIENCE WITH THE USE OF SYNTHETIC
FILTER FABRICS IN COASTAL ENGINEERING

by

Georg HEERTEN ¹⁾

1)

Dr.-Ing., Scientific Assistant, Franzius-Institut of the
University of Hannover, Germany

ABSTRACT

Various types of synthetic filter fabrics are available for geotechnical applications. Especially in the field of coastal engineering a lot of experiences are generally known. Unfortunately technical recommendations and testing regulations for specific implementations of geotextiles are not generally available and some actual examples of damage of coastal structures urgently require investigations on long-term resistance. A research program oriented towards the development of guidelines for testing geotextiles, the development of filtration rules and the clarification of long-term resistance of fabrics was carried out. This paper deals with testing procedures associated with the estimation of the opening size and the permeability to water of fabrics. Results of investigations on long-term resistance are described and filtration rules for selecting a fabric according to the special requirements of the application are given.

INTRODUCTION

For more than 10 years the use of synthetic filter fabrics in various types is a standard in coastal engineering works at the North sea coast.

We can distinguish the following applications to filter fabrics:

- as a filter-layer in revetments of seadikes and shore lines

- as a filter- and separation-layer for the foundation of groins and breakwaters
- as a flexible filter-layer for the bottom protection against scouring for example at tidal- and stormsurge-barriers and when closing a dike
- as sand filled bags or tubes as construction elements of groins and embankments.

Designing coastal structures, a synthetic filter fabric almost is represented only by a "synthetic filter fabric" named line (Fig. 1). At first this designation seems to be

REVETMENT OF A SEADIKE WITHOUT FORELAND
(NORTHFRISIAN COAST)

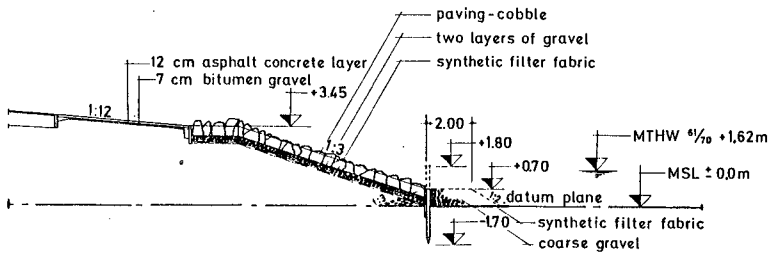
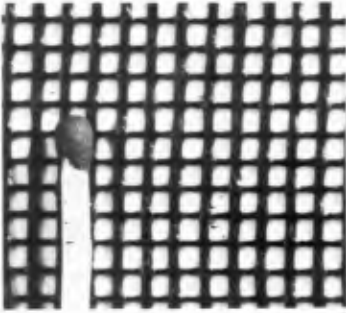


Fig. 1

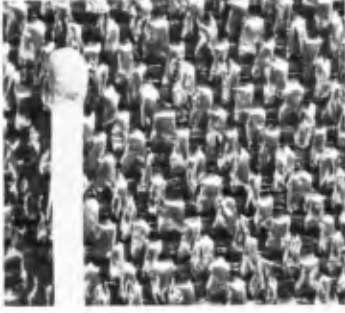
without problems but when selecting a suitable fabric for a special application the engineer has to recognize that there are a lot of conditions to be considered. He has to notice that various types of synthetic filter fabrics (woven, non-woven and combinations) are offered, produced of different polymers.

TYPES OF FABRICS

Of the variety of offered filter fabrics Fig. 2 only gives an impression by showing some of the most important kinds of woven and non-woven fabrics.



mesh netting



tape fabric

woven fabrics



fibre fabric



spun fabric

non-woven fabric

Fig. 2
Different kinds of geotextiles

The properties of fabrics are very different, influenced by the polymer properties and by the manufacturing process. For woven fabrics for example we have to distinguish the kinds of threads (multi-filament, mono-filament, tapethreads), the kind of weaving, the used polymer and the finish (e.g. PVC-coating). Non-woven fabrics also are produced by different polymers and we have to distinguish the method to obtain the cohesion of the fibres or filaments.

THE GIVEN SITUATION IN USING FILTER FABRICS

For dimensioning and selecting a fabric a comparison of product datas and the requirements of the buildings, given by dimensioning rules or other proved standard values, is necessary. If there are two or more fabrics performing the requirements - a comparability of the testing methods is provided - a selection can consider economical aspects.

Unfortunately there exists a lot of different testing methods used by the manufacturers to estimate the properties of the fabrics, so that the product datas of different fabrics are not comparable in many cases. Therefore an optimal selection of a fabric is very difficult and sometimes impossible.

It is an additional difficulty too, that there are no sufficient technical recommendations up to now to select a fabric according to the special requirements of the application. Therefore it doesn't wonder, that the present situation in the extensive use of woven and non-woven fabrics is characterized by a selection based on local experiences or on the costs per square meter.

Up to now there was no serious doubt about a sufficient long-term resistance of the synthetic fabrics covered by soil materials and protected against ultra-violet irradiation. But actual examples of damage of coastal structures urgently require investigations to estimate the long-term resistance of fabrics, especially in comparison to the time of use of the structures (30 to 50 years).

RESEARCH PROGRAM

The specified uncertainties in the use of synthetic filter fabrics lead to a special research program carried out at the FRANZIUS-INSTITUT FOR HYDRAULIC RESEARCH AND COASTAL ENGINEERING OF THE UNIVERSITY OF HANNOVER.

The investigation program consists of three parts:

1. extensive questionnaires were sent to the coastal engineering authorities to evaluate the experience in the use of the synthetic filter fabrics.

2. testing methods were development to estimate the filtration properties of fabrics.
3. various filter fabrics being in function for many years were diged out of coastal struktures.

From this investigations the following results can be presented:

TESTING METHODS

To estimate the filtration properties of fabrics the developed testing methods allowed the determination of the effective opening size and the permeability as a function of superimposed load. The testing methods can shortly be described as follows:

To estimate the effective opening size we used a wet sieving with a defined testing sand. In the test, the fabric has to operate as a sieve (Fig. 3). The complete testing equipment for the wet sieving shows Fig. 4.



Fig. 3

Placing of the fabric for sieving operation

A grain-size analysis of the retained and the passing material leads to the effective opening size as a essential filtration parameter by a fixed evaluation method (4).

For testing the permeability of the filter fabrics we used a permeability test with constant hydrostatic head, generated by two overflow reservoirs, as proposed by BOURDILLON (1).



Fig. 4
Testing equipment for the estimation
of the effective opening size of geotextiles

Fig. 5 shows the test lay out. In the permeability cell a sample of several layers of the fabric is placed and after measuring the flow, the difference in piezometric level, the water temperature and the settlement of the sample a DARCY-coefficient can be determined. Repeating this procedure for various superimposed loads the permeability as another essential filtration parameter can be given as a function of load conditions.

This two tests may be like a standard for testing the filtration properties of synthetic filter fabrics. Only in special cases or for testing woven fabrics an additional test can be carried out, testing the system of fabric and original soil material. In cases of testing non-woven fabrics in combination with soil material it has to be considered that the testing conditions in the laboratory are very different to natural conditions. This is a result of field investigations on coastal structures. It can be seen that in non-woven fabrics-diged out of coastal structures - the incorporation of soil material is a multiple in nature than in a comparatively short laboratory test.

FIELD INVESTIGATIONS

The field investigations on coastal structures mentioned before were the most important part of the research program.

EQUIPMENT FOR WATER PERMEABILITY TEST

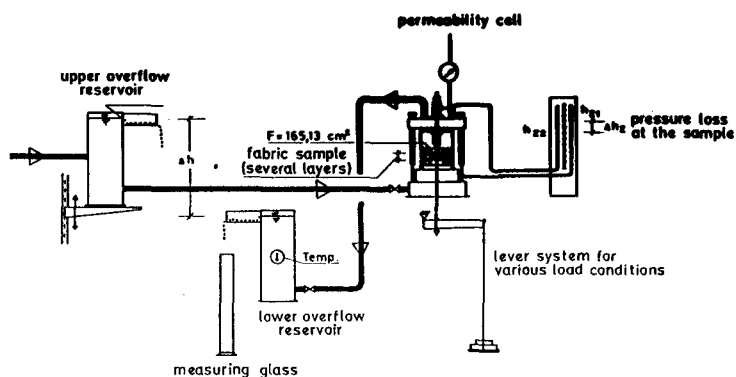


Fig. 5

At 13 locations at the Northsea coast of the German Bight sampling operations were carried out and samples of 39 fabrics were taken.

16 samples were diged out of revetments of seadikes and 23 samples of woven fabrics were taken from sandbags and sand filled tubes.

Fig. 6 shows the revetment of the seadike without foreland at the Dithmarscher Bight at the Northfrisian coast and Fig. 7 gives an impression of the sampling operation at this location and in Fig. 8 a non-woven fabric is shown after removing the cover layers of the revetment.

The photographs in Fig. 9 and Fig. 10 give an example of the application of sand filled tubes. First as small dams in land reclamation fields in the tidal flats in front of the seadikes (Fig. 9) and second as stabilizing elements in a beach feeding area (Fig. 10).

From the sandbags and sandfilled tubes two different samples were taken, one of the weathered upper side and one of the



Fig. 6

Seadike at the Dithmarscher Bight at the Northfrisian coast



Fig. 7

Digging out a fabric



Fig. 8
Non-woven fabric after removing the cover layers



Fig. 9
Sand filled tube in a land reclamation field



Fig. 10
Sand filled tube in a beach feeding area

protected bottom side. By this it is possible to calculate the influence of weathering on the long-term resistance of the fabrics.

For fabric samples diged out of revetments the following individual investigations were carried out:

1. Condition and changing of the profile of the revetment
2. Condition of the fabric
3. Testing the tensile strength
4. Testing the filtration properties
5. Testing the fabric weight and soil content
6. Grain-size analysis and permeability test of the subsoil

For fabric samples of sand bags and sand filled tubes the research program is reduced to the following individual investigations:

1. Condition of the fabric
2. Testing the tensile strength
3. Estimation of effective opening size
4. Grain-size analysis of packed soil.

Essential results of the investigations of the seadike revetment are the registered extensive filling of the coarse-layers with sand and mud particles and the considerable incorporation of soil in the non-woven fabrics. Caused by the filling of the coarse-layers with sand and mud, shown by Fig. 11, the boundary layer of fabric and subsoil was protected against dynamic wave attack.



Fig. 11

Coarse layers filled up with sand and mud particles

This situation also gave a stability in revetment sections with fabrics of too large opening size according to actual knowledge.

The extensive incorporation of soil in the non-woven fabrics lead to the assumption as mentioned before to doubt about the similarity to nature of laboratory test with non-woven fabrics and soil. Fig. 12 gives an example of an non-woven fabric with an incorporation rate of about 9000 grams per squaremeter by a fabric weight of about 1000 grams per squaremeter.

Additional investigations lead to the perception that the sand and mud particles in the coarse-layers mostly came from the seaside of the construction and not from the bottom side. Some significant profile changes with a flater slope of the revetment were perhaps caused by soil-liquefaction under wave impact but certainly not by a washout through the filter-fabrics.

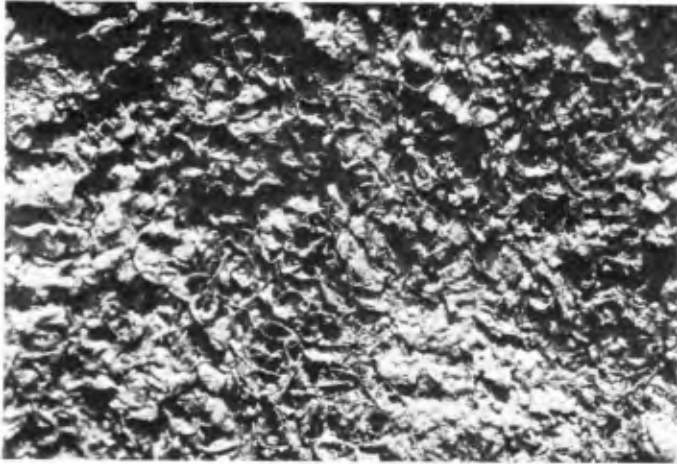


Fig. 12

Non-woven fabric filled up with sand and mud particles

RESULTS ON LONG-TERM RESISTANCE

A usual method to give some informations about the long-term resistance of synthetics is a comparison of tensile strength of the new and of the aged material. The strength testing procedure used corresponds to the conventional textile strip test like the German standard (DIN 53857).

In the following some examples of the results of the investigations about long-term resistance of the synthetic filter fabrics are presented.

In Fig. 13 the relative residual strength determined for different fabrics of nylon (PA 6.6) as a function of exposure time by unprotected weathering is shown. The minimum value of residual strength is about 20 percent after an exposure time of 20 years. By protection against ultra-violet irradiation, the residual strength decreased only to values of about 70 percent after an exposure time of 20 years (Fig. 14).

The next examples give an impression of the long-term resistance of all fabrics examined in the research program. For each of the basematerial of the fabrics average values of residual strength were determined.

Fig. 15 shows these average values for fabrics by unprotected weathering. It can be seen that the residual strength

TENSILE STRENGTH AS A FUNCTION OF EXPOSURE TIME
FOR MULTI-FILAMENT FABRICS OF POLYIMIDE 6.6
(unprotected weathering)

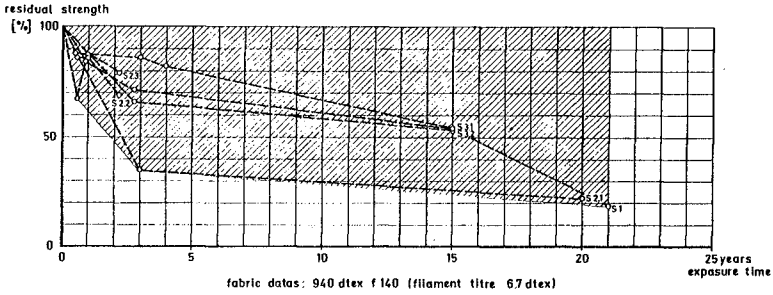


Fig. 13

TENSILE STRENGTH AS A FUNCTION OF EXPOSURE TIME
FOR MULTI-FILAMENT FABRICS OF POLYIMIDE 6.6
(protected against ultra-violet irradiation)

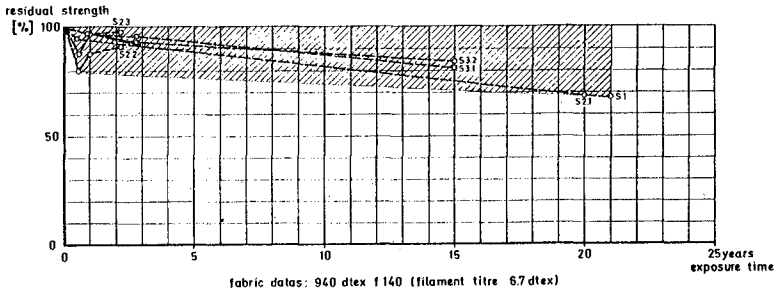


Fig. 14

TENSILE STRENGTH AS A FUNCTION OF EXPOSURE TIME
FOR FABRICS OF VARIOUS TYPES AND POLYMERS
(unprotected weathering)

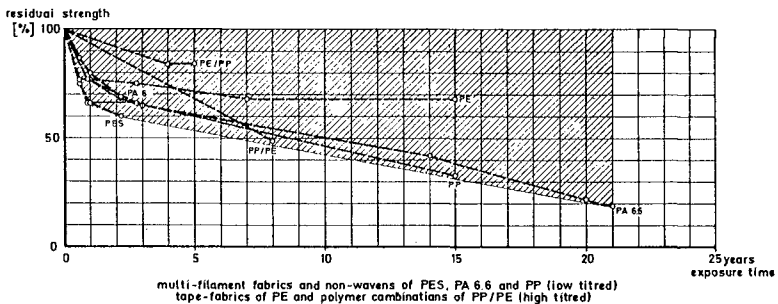


Fig. 15

TENSILE STRENGTH AS A FUNCTION OF EXPOSURE TIME
FOR FABRICS OF VARIOUS TYPES AND POLYMERS
(protected against ultra-violet irradiation)

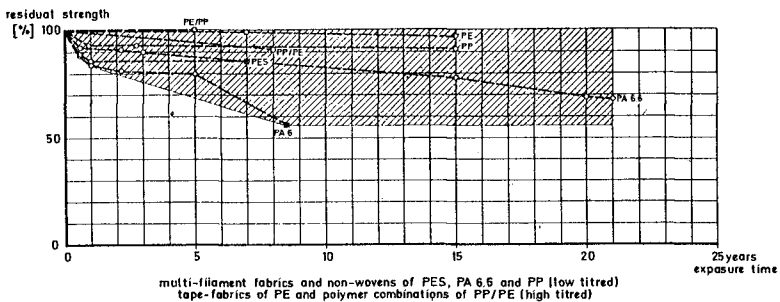


Fig. 16

of tape-fabrics with polyethylene or polypropylene as base material is higher than the residual strength of multi-filament fabrics of polyester, polyamide and polypropylene. Comparable results are given by protection against ultra-violet irradiation (Fig. 16), but nevertheless in general the decrease in residual strength is lower as seen in Fig. 15.

By the interpretation of these results we have to consider that the fibre fineness is of great influence in long-term resistance of fabrics. Therefore the good results of the tape-fabrics, produced of relative thick tape threads, doesn't surprise. - The fibre fineness of the tape-threads is about some hundred dtex whereas the fibre fineness of filaments is only 5 to 10 dtex.

In addition we have to consider that the results determined at samples of the salt-water region could be influenced by a lot of parameters like suspended load of the seawater, duration of tidal overflow, covering of the fabrics by mud, seaweed, mikro-organism or rubble and their temporary variation. The damage of fabrics could also be caused by wave-action, drifting-wood, ice, shipping or tourists. Most of the parameters only influenced the sections with unprotected weathering like the upper sides of the sandfilled tubes. Synthetic filter fabrics in revetments protected by several cover-layers are less endangered but there is to pay attention that there is no damage of the fabrics during construction time.

Finally we can say that the most important parameters influencing the long-term resistance of fabrics in the salt-water region of the northsea coast are the ultra-violet irradiation and the raw material and fibre fineness of the fabric. Ageing by biological and chemical damages is of lower importance. Attention has to be paid that there is no damage of fabrics during construction time.

This results show fair agreement with results of investigations carried out on the woven synthetic filter fabric being a construction element of protection against scouring at the Eider stromsurge barrier. The protection against scouring was damaged but the first supposition that the damage was caused by an insufficient long-term resistant of the woven fabric could not be confirmed.

In addition to the investigations on long-term resistance filtration rules have been development.

FILTRATION RULES

A new dimensioning method to select a fabric allows, to fulfil and calculate the requirements of sand-tightness as well as the requirements of the hydraulic permeability of

fabrics. Fig. 17 shows a flow diagram which explains the procedure to select a fabric according to the characteristics of the subsoil and the construction. In the first step we have to estimate the effective opening size D_w . D_w is given by filtration rules as a function of the particle distribution curve of the soil and the load conditions.

In the second step the hydraulic conditions have to be controlled. To prevent over-pressures in a revetment-construction the permeability of the filter fabric has to be higher than the permeability of the subsoil. Special investigations were carried out to consider the decrease of the permeability of woven fabrics by blocking and non-woven fabrics by clogging. Now, as a result of the investigations, it is possible to estimate a permeability-reduction factor as a function of fabric data and soil characteristic. Only for non-woven fabrics, when the effective opening size is small in relation to the diameter of soil particles, an additional restriction is given by $D_w < 0.5 \cdot d_{10}$ leading to a η_V value $\eta_V = 1.0$. The permeability of the fabric is sufficient when

$$\eta_V / G \cdot k_f \geq k.$$

The filtration rules to fulfil the sand-tightness are determined as follows:

Static load conditions and $u \geq 5$	$D_w < 10 \cdot d_{50}$ and $D_w \leq d_{90}$
Static load conditions and $u < 5$	$D < 2.5 \cdot d_{50}$ and $D_w \leq d_{90}$
Dynamic load conditions	$D_w < d_{50}$

Fig. 18 shows the diagram to estimate η_G . η_G is given as a function of the standard test permeability coefficient k_f and the soil parameter d_{10} .

η_V is given as a function of the fabric parameters k_f and P (Fig. 19). k_f is the standard test permeability coefficient and P is named porosity of the fabric. P is defined as a product of the

voids ratio n
fabric thickness d under a load of 2 kN/m^2
and effective opening size D_w .

At times the application of this diagram is limited by the particle distribution of the investigated soils at the sampling locations. The range of the particle distribution curves are shown in Fig. 20.

Further investigations will be carried out to complete the diagram with η_V as a function of the soil parameter d_{10} .

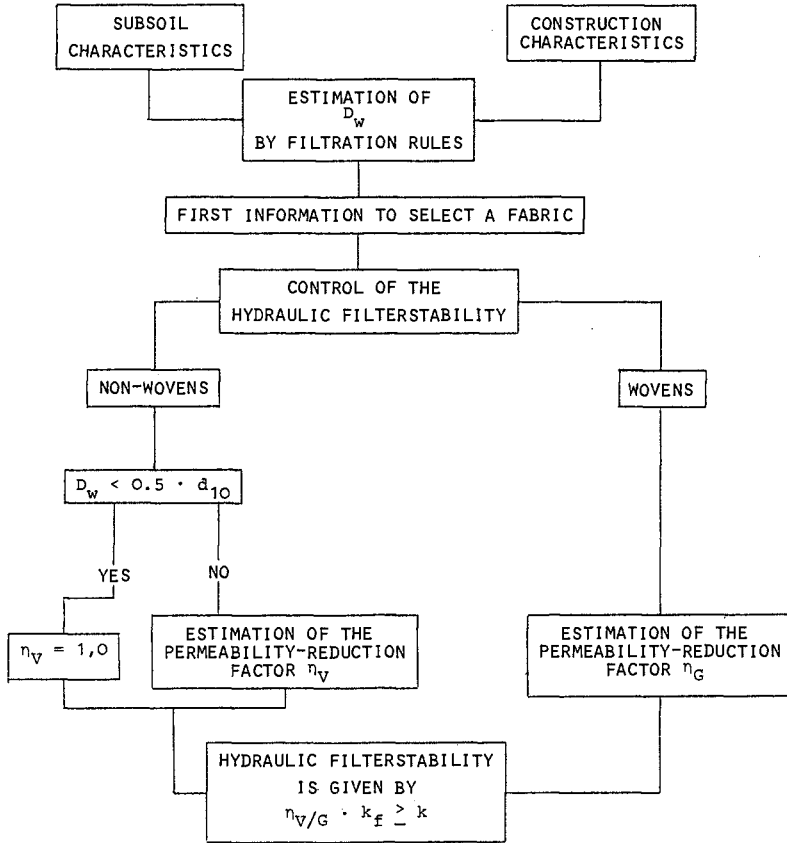


Fig. 17

Flow diagram to check the filtration properties of geotextiles

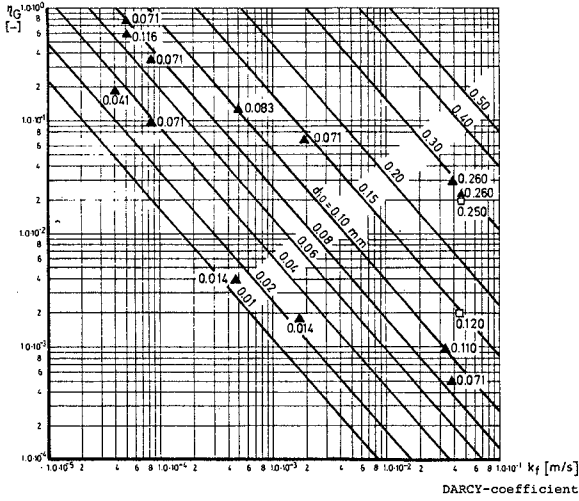


Fig. 18
Diagram to estimate the permeability-reduction factor η_G for woven fabrics

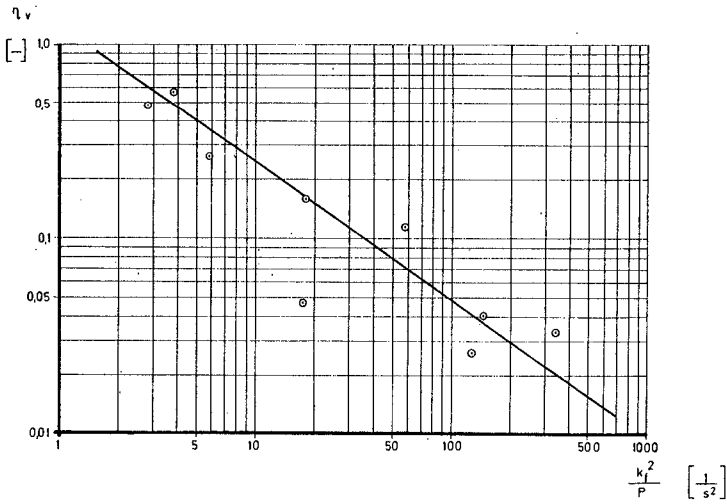


Fig. 19
Diagram to estimate the permeability-reduction factor η_V for non-woven fabrics

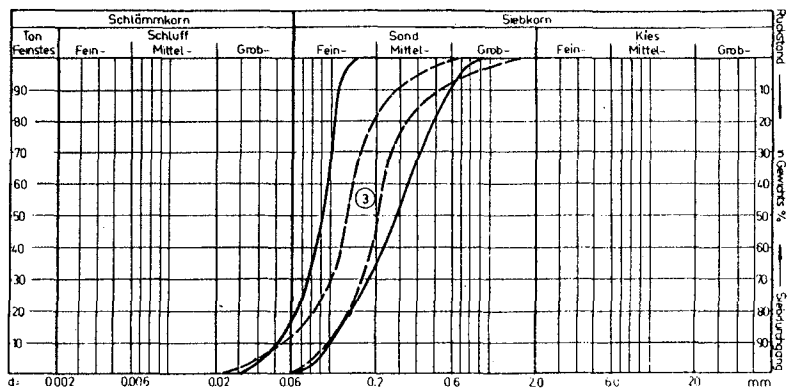


Fig. 20

Particle distribution curves at the sampling locations

CONCLUSION

For applications in coastal engineering in the salt-water region of the Northsea coast the investigations on long-term resistance of fabrics lead to first satisfying results. The given filtration rules make it possible to select a geotextile according to the special requirements of the application given by the particle distribution curve and the DARCY-coefficient of the soil. Some additional investigations will be carried out at the FRANZIUS-INSTITUT in the near future.

REFERENCES

1. BOURDILLO, M.: Utilisation des textiles non-tissés pour le drainage. Laboratoire central des Ponts et Chaussées, Lyon, 1976
2. ERCHINGER, H.F. u. SNUIS, G.: Kunststoffgewebeschläuche im Küstenwasserbau. Wasser und Boden, 24. Jahrg. (1972), Heft 1
3. GIROUD, J.-P. u. PERFETTI, J.: Classification des textiles et mesure de leurs propriétés en vue de leur utilisation en géotechnique. International Conference on the Use of Fabrics in Geotechnics, Paris, 1977, Vol. II

4. HEERTEN, G.: Geotextilien im Wasserbau - Prüfung, Anwendung, Bewährung. Mitteilungen des FRANZIUS-INSTITUTS für Wasserbau und Küsteningenieurwesen der Universität Hannover, Heft 51, 1980
5. ZITSCHER, F.F.: Kunststoffe für den Wasserbau. Bauingenieur-Praxis, Heft 125, Verlag W. Ernst & Sohn, Berlin 1971

BREAKWATER WITH A SAND BITUMEN CORE

E. Loewy	B.Sc., A.C.G.I., C. Eng., F.I.C.E., M.A.S.C.E. Partner, Watermeyer Halcrow and Partners.
K.G. Witthaus	B.Sc., Pr. Eng., F.I.C.E., Partner, Watermeyer, Halcrow and Partners.
R.J. Maddrell	B.Sc., Ph.D., M.I.C.E., Senior Engineer, Sir William Halcrow and Partners.
J.P. Wood	B.Sc., M.I.C.E., Resident Engineer, Marine Works, Koeberg Nuclear Power Station.

SUMMARY

Sand bitumen was used in the core of a rubble mound breakwater to form an impermeable barrier, essentially to inhibit the recirculation of warm water exhausted from a power station outlet back into the intake pumps. The core had a secondary advantage in permitting the placing of bitumen grouting to the rock on the lee face of the breakwater to stabilise it against wave overtopping.

The paper describes the reasons which led to the adoption of this unique method on a very exposed coastline. It also outlines some of the measured properties of the sand bitumen and the methods used and experience gained in its mixing and placing.

The sand bitumen, which has not to our knowledge been used for this purpose and as a core material previously, is proving to be successful.

1. INTRODUCTION

In 1967, the Electricity Supply Commission of South Africa (ESCOM) decided upon the location of Africa's first nuclear power station at a coastal site adjacent to the Atlantic Ocean, some 35 kilometres to the north of Cape Town. The first phase of development of this project is for the construction of two reactors, each of 920 MW, which should be commissioned by 1984. Further development has been allowed for in the future immediately to the north of the station which could eventually increase its capacity.

The site was selected, inter alia, because of its proximity to unlimited supplies of cooling water coming from the Antarctic in the cold Benguela current. However, this section of coastline is extremely exposed and devoid of any naturally deep and protected

area from which to draw the water. The wave climate is severe with the deep water significant wave height exceeding 2 metres for about 38% of the time and maximum wave heights of 11 metres have been recorded. It is axiomatic that power station cooling water should not contain heavy concentrations of sediment and, on this coast, with its severe wave climate and 1 in 60 to 1 in 100 bed slopes, one of the problems relating to the abstraction of cooling water is that considerable quantities of sand are suspended in a very wide surf zone. The firm of Watermeyer, Halcrow and Partners, which is a joint partnership between Watermeyer, Legge, Piesold and Uhlmann and Sir William Halcrow and Partners was retained by ESCOM to advise on the best means of obtaining cooling water and, later, to undertake the detailed engineering design and supervision of construction of the scheme that was finally adopted.

Feasibility studies on a number of possible schemes, which included tunnels with offshore intakes, concluded that the most suitable and economic solution would be to situate the pump houses within a dredged basin, protected by rubble mound breakwaters.

The configuration and detailed design of this basin had to satisfy the parameters of:-

- (a) stability of the breakwaters under wave action;
- (b) limiting wave penetration and wave heights at the intakes;
- (c) controlling sediment build-up around and, in particular, in the basin; and
- (d) restricting recirculation of warm exhaust water.

Detailed site measurements of the local marine environment (1), were combined with physical model studies of the breakwaters and a mathematical modelling of sediment build-up (2) to examine items (a) to (c) above. These considerations essentially determined the final configuration.

As illustrated in Figure 1, the pump intakes are located along the original shoreline and are protected by the main (south) breakwater which is 933 m long and the north breakwater which is 578 m long. The basin entrance is in about 8 metres of water at high water.

In this first phase of station development the pump intakes will draw in a total of about 80 cumecs of seawater at ambient temperatures ranging between 8 and 16° C. This water will be heated through a range of about 10° C in its passage through the turbine condensers and will be discharged through a shallow outfall channel into the surf zone just to the south of the main breakwater (see Fig. 1).

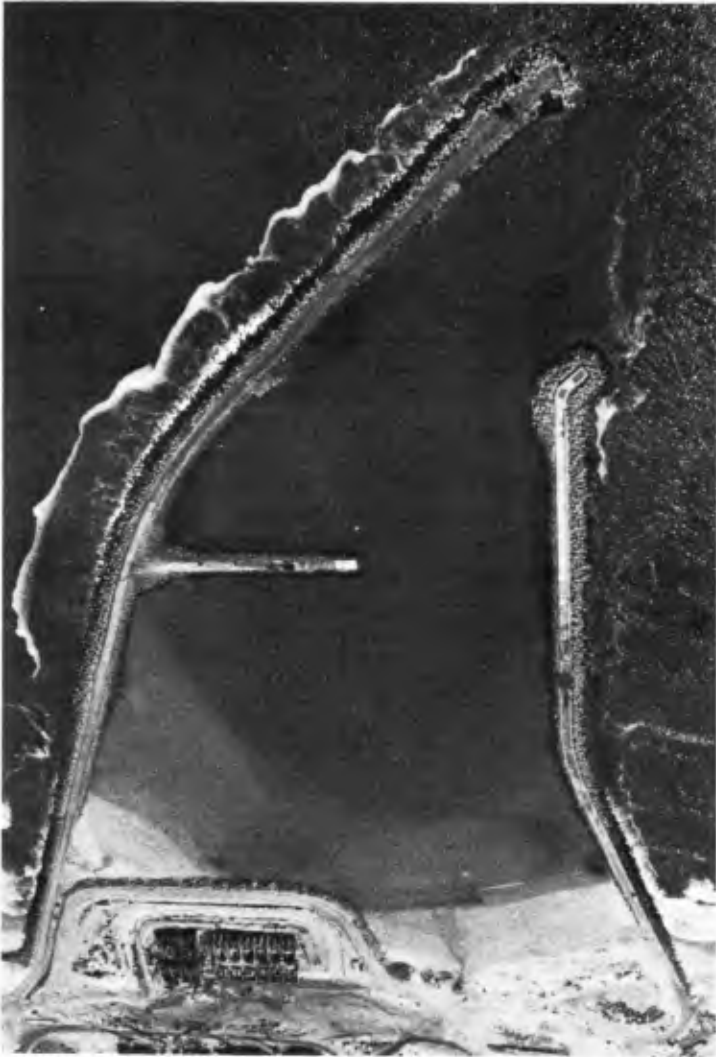


Figure 1. CONFIGURATION OF INTAKE BASIN

It was feared that, in connection with (d) above, the warm outlet water could pass through the rubble mound of the south breakwater in significant quantities and re-enter the pump intakes during certain times of the year. Field observations using dye were made of the transmission of water through the breakwaters at Richard's Bay which confirmed these fears.

The flow through a rubble mound breakwater without an impermeable core was also studied theoretically. Because of turbulence, Darcy's formula was inappropriate and Hazen's formula for permeability was adopted. For the purposes of this calculation, wave set-up outside the basin was assumed whilst the cooling water pumps were drawing sea water from within. This produced low flows in the order of about 3 cumecs over 300 m of breakwater length. However, when it was assumed that the breakwater contained a network of very twisted rough pipes, the flow became significant e.g. for 500 kg and 1 000 kg rock over a 300 m length of breakwater the calculated equivalent flows through the structure were 28 and 55 cumecs respectively.

Similar recirculation problems were solved, following construction, at Fukushima nuclear power station in Japan by driving steel sheet piles parallel with and close to the breakwater inside the basin. This arrangement was examined for Koeberg, as well as several other alternative solutions involving grouting, sand bitumen, slicework and blockwork. Eventually it was decided to construct an impermeable core to the breakwater with a mixture of sand and bitumen. This construction material had been used previously in the United States and, more notably, in the Netherlands but, as far as is known, never before in this manner as a breakwater core material.

The sand bitumen core offers a further benefit at the seaward, more exposed end of the south breakwater. Normally the crest of the structure in this area would have to be heightened and/or the lee face reinforced with additional and possibly heavier armour units as a safeguard against wave overtopping. Fortunately, however, the sand bitumen core acts as a barrier against the transmission of air/water pressure through the rubble mound, and permits the use of relatively light rock on the lee face, grouted to act as a spillway for overtopping waves. Without the impermeable sand bitumen core, air and water pressure within the rubble mound caused by wave attack on the seaward face would almost certainly dislodge the grouted rock on the leeward face. The rock grouting was also carried out with a sand bitumen grout, but since the characteristics required were different, the constituents and mixing proportions differed from the sand bitumen core.

Breakwater construction commenced in October, 1977, and placing of the rubble mound and sand bitumen was completed in December, 1979. The construction has proved successful and the resistance to erosion of the sand bitumen core when exposed to the force of the waves at the scar end during construction was found to be surprisingly good - better in fact than the filter layers of rock on either side of it.

2. DESIGN CONSIDERATIONS

Two possible methods of constructing a barrier within the heart of the south breakwater to impede the passage of water through the rubble were examined in detail, namely:

- (i) the installation of large precast hollow concrete rectangular boxes with compatible curved front and rear faces placed in contact with each other on a bed of prepared rubble (i.e. a type of slicework construction).
- (ii) a sand bitumen core.

Solution (i) would have provided a relatively impermeable boundary only between the levels of - 1.0 m and + 2.0 m G.M.S.L. However, the rock above it would have been grouted and it was considered that this form of construction would provide an adequate barrier to the passage of heated exhaust water because the heated water will largely be confined to the surface layer.

Solution (ii), because the column of sand bitumen would be continuous, provided an impermeable barrier throughout the depth of the breakwater. It did, however, require the provision of filter layers to protect the core during the life of the breakwater.

The feasibility of construction of the breakwater utilising the hollow concrete box solution was tested in a 3D model, as it was suspected that the boxes might be unstable during the construction stage. It was envisaged that the core area would be partly protected from wave action, along the most exposed length of breakwater, by rock mounds on either side. Although tests showed the boxes to be vulnerable during periods of severe wave action, it was concluded that construction was feasible.

The comparative study showed that the sand bitumen core was clearly the better of the two solutions. No special method of placing was required (i.e. it could be placed in a similar manner to the rock). Its use, unprotected in temporary works in Europe,

had shown it to be a reasonably tough, resilient, material. It would provide a complete barrier between sea bed level and the underside of the concrete cap. And it was significantly cheaper than the precast concrete alternative when all factors were taken into account.

It was envisaged that the sand bitumen would be placed, from trays, in the form of a Christmas tree, the Contractor using the same plant to transport both the sand bitumen and rock. However, only minimum thicknesses for the sand bitumen core and its adjacent filter layers were specified, giving the Contractor freedom to choose his own method of placing (Figure 3). In the event, the Contractor chose to adopt a Christmas tree similar to that originally envisaged (Figure 4).

It was appreciated that, during storms, some large rocks might be washed into the core area. This could pose long-term stability problems because, if the bitumen on placing were to span a large void, this could gradually "pipe" through the sand bitumen, its size only marginally decreasing. Consequently, it was thought that, if necessary, after storms a sand bitumen mix with a higher bitumen content could be placed, at higher temperature, in order to provide a material of higher plasticity and minimise the likelihood of large voids in the core area. In the event, however, no increase in bitumen content for this purpose was required.

The presence of an impermeable core offers the advantage of permitting the lee face of the breakwater to be grouted. However, it also means that the transient pressure which would normally be transmitted through a rubble structure must be contained or dissipated within the seaward half of the structure. As may be seen on Figure 3, blow holes some 6 m apart, were provided through the cap on the seaward side of the core to dissipate these pressures.

Consideration was also given to the effect that the impermeable core might have in decreasing the wave energy absorption capacity when compared with a normal rubble mound breakwater. This might result in a need for heavier dolosse armour units than would otherwise be the case. Consequently, the stability of the breakwater with the impermeable core was extensively model tested both in a flume and in a 1:80 scale 3D model.

In making these tests, it was realised that the 3D model would tend to give conservative answers (i.e. less energy would be destroyed in the model than in the prototype) because of Reynolds scale effects. Another conservative factor was that, for site safety reasons, extreme environmental conditions were considered

in the breakwater design. However, even when applying an estimated "one-in-a-million" storm condition (including surge plus wave set-up plus run-up) the design wave remains depth limited, and the stability of the outer armour units was found to be acceptable.

The sizes of the dolosse armour units adopted on the south breakwater were 6 t, 15 t and 20 t and, on the north breakwater, 6 t and 15 t. In fixing dolos sizes, consideration was also given to available crane capacities, overall cost, and the requirement that the need for future maintenance of the breakwater should be minimized.

3. SAND BITUMEN PROPERTIES

3.1 Contract Requirements and Trial Mixes

The Contract Specification required sand, won locally from sand dunes on the site, to be mixed with 80/100 pen. straight run bitumen. The bitumen content could be fixed, subject to trial mixes, at between 3 and 6 percent by weight. The grading limits were specified to lie anywhere between 2 mm and 0.063 mm sieve sizes.

At the commencement of the Contract suitable dunes were located. Table 1 below shows a typical grading curve which indicates that the sand was fine and essentially single-sized.

Sieve Sizes (mm)	Percentage Passing
1,18	100
0,600	99
0,300	92
0,150	6
0,075	0

TABLE 1. Typical Grading of Local Dune Sand

Before construction commenced, trial mixes were undertaken with bitumen contents ranging from 3 to 6% in half percent increments as specified in the Contract Document. In the

absence of documented methods of judging their suitability, each of the mixes was appraised by both the Engineer and the Contractor on a somewhat subjective basis. It was observed that the mixes containing 3 and $3\frac{1}{2}\%$ bitumen had little inherent strength or cohesion and looked unstable. The 4% mix showed a remarkable improvement whilst the $4\frac{1}{2}\%$ mix was marginally better still. Further increases in bitumen content did not appear to improve the properties of the mix. In view of likely batching inaccuracies (see ASTM D1663-74) of $\pm \frac{1}{2}\%$ the bitumen content was set at $4\frac{1}{2}\%$ in the knowledge that if it dropped to 4% the resulting mix would be acceptable.

In practice, it was found that the tolerances on the batches provided by the Contractor were very much better than $\pm \frac{1}{2}\%$ and in a sample of 119 bitumen content tests (of many more taken) the standard deviation on the bitumen content was 0.128%.

3.2 Laboratory Testing

With the exception of routine bitumen content and sand grading tests, no other laboratory testing was required under the Contract.

Apart from the data published by van Asbeck (4), Visser (5) and Kerkhoven (6), very little data could be traced on the behaviour and testing of sand bitumen. It seemed important to carry out some objective tests on this unique material in order that:

- a record could be made of the physical state of the material during construction for future reference should deterioration ever occur;
- to give an indication of the properties of the materials that are actually in place in the breakwaters;
- to provide at least some data for others in the future.

Therefore the ensuing tests were undertaken, although it should be noted that the results are not necessarily definitive. They should be interpreted with care, as the material actually used in the breakwater was placed under a wide variety of physical conditions and was not compacted. Its properties in-situ may therefore be variable and the laboratory test results may not be truly representative of the actual sand bitumen core.

Finally, it should be pointed out that the characteristics of any bituminous mix are dependent upon numerous variables such as sand grading, temperature, bitumen content, bitumen grade, etc., and that these results are therefore not necessarily universally applicable.

3.2.1 Marshall Testing

Two samples with 4 $\frac{1}{2}$ % bitumen were tested by the Standard Marshall Method (ASTM D1559).

The results are given below.

	Sample No.	
	1	2
Briquette compacted by	10 blows each side	5 blows each side
Density of Mix tonnes/m ³	1,8	1,8
S.G. of Sand	2,6	2,6
Voids in Mineral Aggregate %	30,8	30,8
Stability kN	0,61	0,24
Flow mm	0,46	9,0

TABLE 2.

MARSHALL DATA

3.2.2 Durability Testing

This test was made in an attempt to obtain some quantitative index of the durability of the sand bitumen in service in the breakwater. The mix contained 4 $\frac{1}{2}$ % bitumen and the test was the "Wet-Dry Durability Test" adapted for sand bitumen. The procedure for testing is given in the South African Standard Methods of Testing Materials Method A19 which is almost identical to ASTM D558.57 and D559-57. Samples, compacted in a standard fashion, were subjected to repeated cycles of brushing with a wire brush and the

loss of weight recorded. Tests were carried out for five cycles of brushing on four sets of four samples. Figure 2 summaries the results obtained.

3.2.3 Permeability Tests

Three specimens of the 4½% content mix were tested by filling a 76 mm dia. ring 18,75 mm thick with sand bitumen at 120° C and allowing it to cool. Standard falling head permeameter tests were performed with water at 12° C.

The results are given in Table 3 below.

Test No.	Dry Density (kg/m ³)	Coefficient of Permeability (m/s)
1	1685	3.7 x 10 ⁻⁵
2	1681	3.7 x 10 ⁻⁵
3	1751	2.3 x 10 ⁻⁵

TABLE 3. RESULTS OF PERMEABILITY TESTS

3.2.4 Shear Strength Tests

Three undrained, unconsolidated triaxial tests were carried out on the 4½% mix. Samples were prepared by filling a 75 mm dia. x 150 mm deep mould with sand bitumen heated to 120° C and allowing it to cool to testing temperature. Tests were conducted at temperatures considered representative of the sea adjacent to the breakwaters.

A shear box test was also carried out in an attempt to assess the strength of the cold joint between adjoining layers. Here the lower layer was permitted to cool before the overlying layer was added.

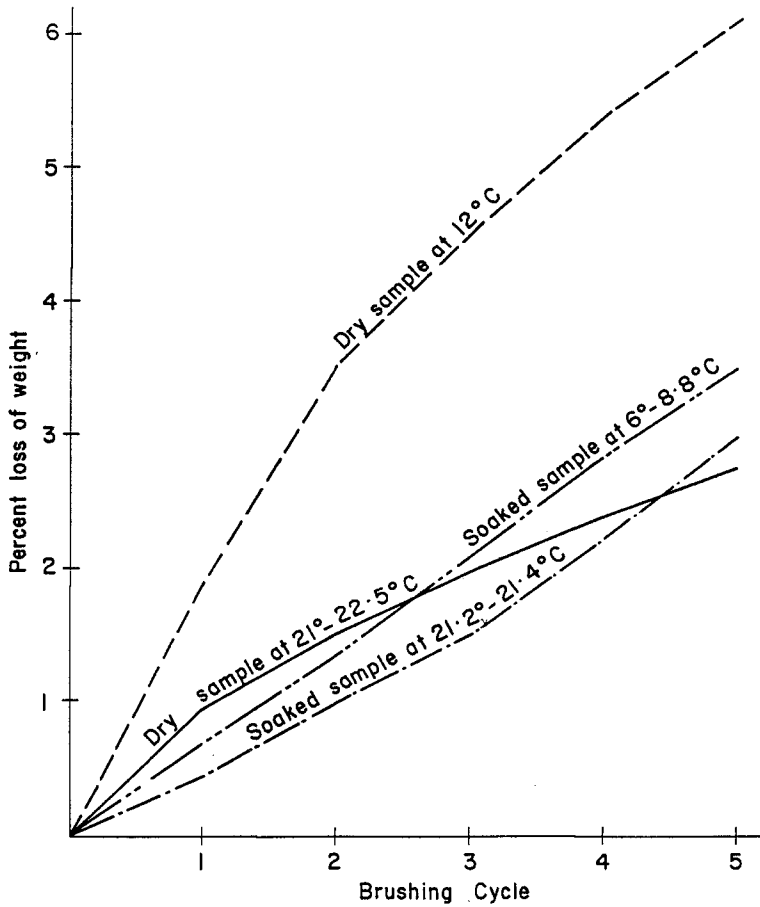


Figure 2. RESULTS OF BRUSHING TESTS

Test Type	Test Temp.	Apparent Cohesion	Friction Angle
	° C	KPa	°
Triaxial UU	8	175	53°
"	12	90	46°
"	16	60	45.5°
Shear box	12	74	45°

TABLE 4. RESULTS OF SHEAR STRENGTH TESTS

4. APPLICATION

The Main Contractor for the construction of the breakwaters sensibly employed a specialist asphaltting firm as sub-contractor to produce the sand bitumen and bitumen grout mixes. This sub-contractor established a continuous drum mixer on the site which could reach an output of about 40 tonnes of material per hour.

The bitumen was added by nozzle at the entrance to the drum and the flow rate was regulated by a load cell on the sand supply conveyor. This proved extremely satisfactory.

Batching proceeded on a daily basis and the materials were generally mixed at about 115° to 130° C. The material was placed in storage bins to cool down to placing temperatures that could range between 40° and 95° C. In practice, it was found that the optimum temperature for placing material in the sea was about 60° C. At higher temperatures the mix held together poorly and the washout losses were high whilst at lower temperatures the transport lorries had difficulty in getting the material to tip out. It should be noted that the material retains its temperature for many days thus it is both possible and reasonable to specify the placing temperature. In the height of summer, it still had ample heat to be used after a week. In winter it had to be used within 4 days. Heating elements were built into the bin walls and these were occasionally used to heat up mixes which had fallen below the minimum specified temperature. This procedure was sometimes supplemented by mixing cold and freshly mixed hot batches with a front-end loader.

Sand bitumen was loaded from the bins into tipper trucks and transported to the breakwater. There it was tipped into the rock tray of the breakwater crane which then positioned the load according to a predetermined pattern and tipped it into the sea. Some 37 000 cu. metres of sand bitumen were placed in this manner in individual loads of about 7 tonnes.

Figure 3 shows a typical idealised cross-section through the breakwater with its sand bitumen core. The core itself is protected on either side by graded rock filters with the seaward face armoured with dolosse units. In practice, the Contractor could not, of course, construct this idealised cross-section and dumped the rock and sand bitumen in a succession of layers, resulting in the "Christmas Tree" cross-section. This is shown on Figure 4.

Although the sand bitumen is protected by the rock filters in its permanent state in the breakwater, it was exposed to wave attack at the scar end during construction. Under these conditions it proved highly resistant to wave attack and this is well illustrated in Figure 5 which shows sand bitumen being placed at about water level. As can be seen, the mix stands up well to the erosive force of the waves. No doubt its long-term erosion resistance is poor and it requires the filter armouring but this property was extremely useful during the short construction phase.

Very soon after placing, the cold sea hardened the outer shell of the sand bitumen which must have greatly improved its early erosion resistance. Many instances of this property were observed during construction, where wave action removed the rock on either side of the sand bitumen, leaving the core standing proud.

Another helpful aspect of this material was found to be its ability to envelop discrete boulders. As previously mentioned, it was foreseen at the design stage that boulders could be washed by the sea or accidentally dropped by the Contractor into the core area. Observations during construction of the breakwater and core samples obtained by drilling indicated that such boulders become totally surrounded by sand bitumen thus preserving the integrity of the core. These boreholes also indicated that at lower sections, the core area sometimes tended to become filled with sand before the sand bitumen was placed on top. In one instance a pocket of sand over 1 metre thick was located in a borehole between the underside of the core and the top of the small rock foundation blanket.

Two sets of prototype tests, using dye placed on the south of the breakwater during strong south to south east winds have indicated that little or no transmission of water is taking place through the core.

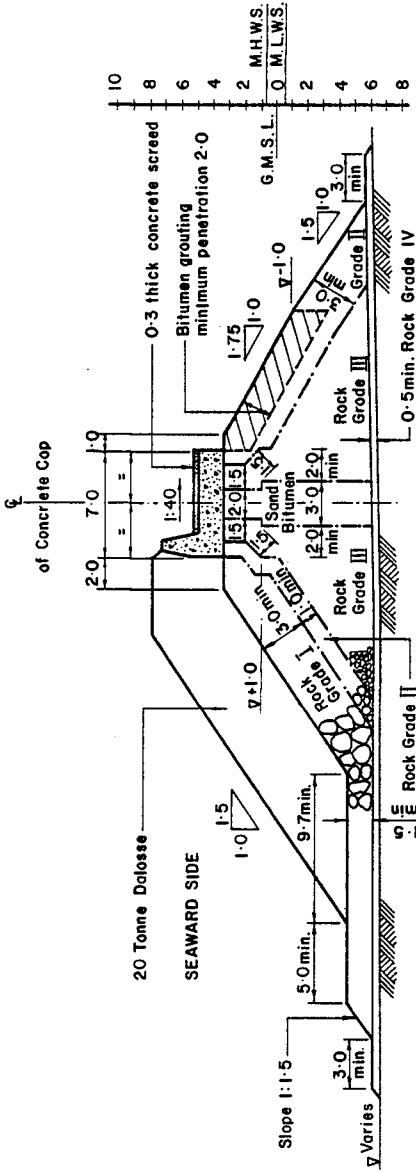


Figure 3. IDEALISED CROSS-SECTION THROUGH BREAKWATER

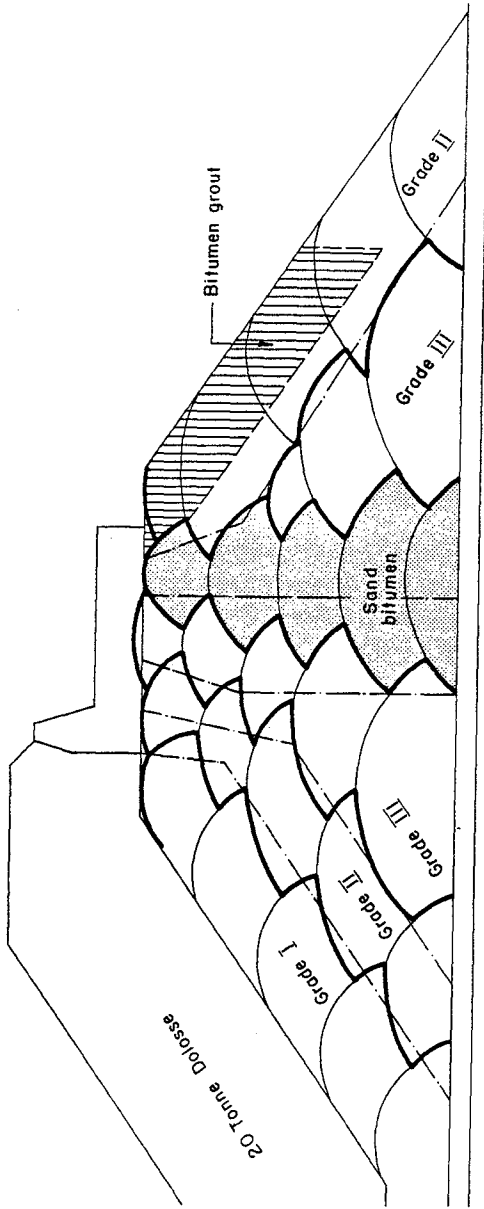


Figure 4. ACTUAL BREAKWATER BUILDING PROFILE



Figure 5. SAND BITUMEN BEING PLACED IN BREAKWATER



Figure 6. BOULDER SURROUNDED BY SAND BITUMEN

5. CONCLUSIONS

The use of sand bitumen in this instance as an acceptably impermeable core material has, so far, proved successful.

Its unit cost was higher on this occasion than the quarry run which would normally be used. However, it could find application as a general breakwater material in areas where rock is expensive. Because of high wave activity and sediment transport, the lower portion of the breakwater core became contaminated with sand before the bitumen could be placed.

On this project a net saving in the total cost of breakwater construction might be claimed as the presence of the sand bitumen core permitted grouting to the lee face, thus obviating the need for increasing its crest height and providing lee face armouring towards the seaward end. The extra cost of the sand bitumen and grout thus tends to be balanced by the savings in crest height armour units.

Care is necessary in the design of the armour layer as a breakwater with an impermeable core may not absorb as much wave energy as a conventional rubble mound and some of the wave energy within the breakwater may be reflected. The design should therefore be model tested.

6. ACKNOWLEDGEMENTS

The authors would like to thank ESCOM for their assistance in compiling this Paper and permission to publish it.

7. REFERENCES

1. LOEWY, E., WITTHAUS K.G., SUMMERS L., MADRELL R.J. (1976)
Data collection and analysis for coastal projects.
Coastal Engineering Conference Vol. 1, pp. 43 - 59.
2. FLEMING C.A., HUNT J.N. (1976)
Application of a Sediment Transport Model.
Coastal Engineering Conference Vol. 2, pp. 1184 - 1202.
3. HINO M., (1974)
Theory on Formation of Rip-Currents and Cuspidal Coast.
Coastal Engineering Conference Vol. 2 , pp. 901 - 919.
4. VAN ASBECK W.F. (1964)
Bitumen in Hydraulic Engineering Vol. 2, 1st Ed.
Holland, Elsevier.

5. VISSER W. (1968)
Coast Protection with Bitumen
Symposium on Hydraulic Uses of Bitumen, University of
Nottingham.

6. KERKHOVEN R.E. (1965)
Hydraulic Applications in the Netherlands
Shell International Petroleum Co. Ltd.
MOR110F

CHAPTER 133

HARBOUR DESIGN INCLUDING SEDIMENTOLOGICAL PROBLEMS USING MAINLY NUMERICAL TECHNIQS

by
B. LATTEUX⁺

ABSTRACT

For most of the needed studies for the design of Calais harbour enlargement works, the "Laboratoire National d'Hydraulique" chose to use numerical models. This approach includes the determination of currents around and inside the new outer-harbour, just as the evaluation of the project sedimentologic impact and of the long-term evolution of a bank named "le Riden de la Rade", edging the access channel.

Current studies were performed using four nested bidimensional computer models fitted on field data and supplying in each point the depth-averaged velocity and the total water height. These four models are based on an implicate finite difference fractionnal step method. Besides for the very near field model the method is especially elaborated to enable the detailed reproduction of eddies and flow separations.

The sedimentological numerical study is based upon current models results : the bed-load transport is computed from the depth-averaged velocity and the water height previously determined using an empirical formula, and the continuity equation applied to this load transport gives then the bed evolution. As soon as the ceptn variation is significant enough to react on the flow pattern, current fields are readjusted by a simple method based on flow continuity equation.

This numerical model, applied to the near field, has given an evaluation of the sedimentological impact of the harbour enlargement project :

- strong erosion in front of the new harbour due to current strengthening ;
- accretion on each side of this erosion area, especially in the channel ;
- bar formation at the harbour entrance.

1. INTRODUCTION

Due to the increase of the passengers traffic between Calais and the United Kingdom, Calais Harbour is going to be equiped with supplementary car-ferry berths ; this development required an enlargement of the outer-harbour which will enable in a second stage the harbour spreading towards East (fig. 1).

⁺ Division Hydraulique Maritime. Laboratoire National d'Hydraulique.
Electricité de France. Chatou. France.

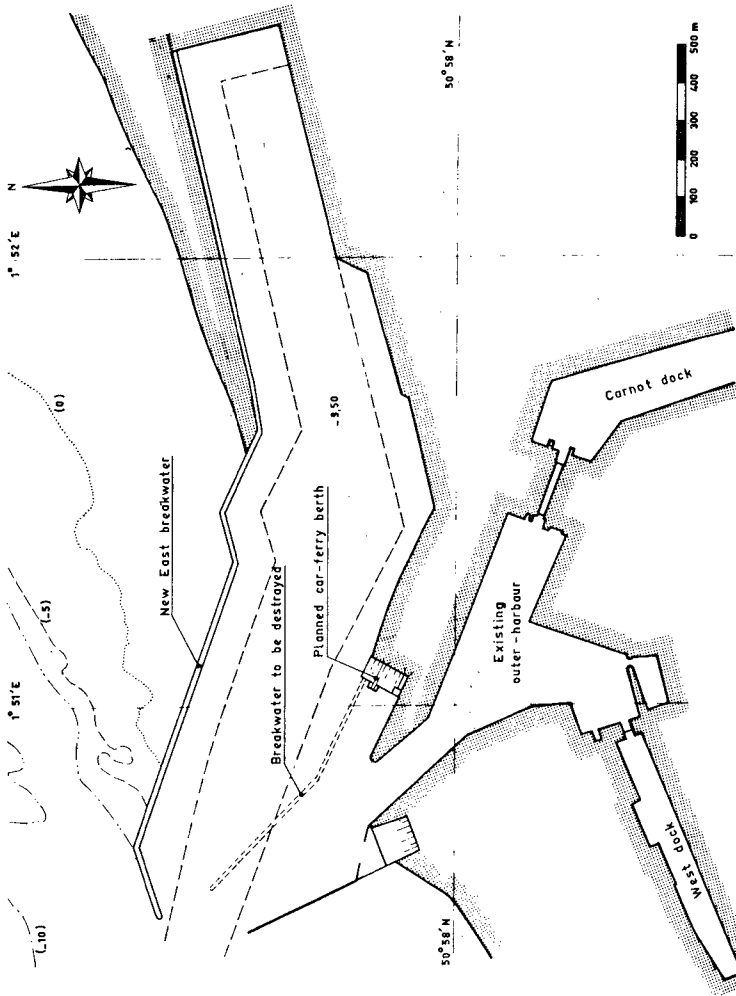


Fig.1 - CALAIS HARBOUR : NEW OUTER-HARBOUR LAYOUT

Hydraulic and sedimentological studies required by this development have been performed using mainly computer models : wave refraction off the harbour and diffraction inside were thus numerically studied by the "Service Central Technique des Ponts et Chaussées" ; the determination of tidal currents around and inside the new outer-harbour, just as the evaluation of the project sedimentological impact on bed-load transport, both presented here, were carried out in the same way by the "Laboratoire National d'Hydraulique". Only breakwater structure adjusting and final tests of wave agitation inside the harbour have required physical modelling.

2. NOTATION

C = Chezy's bottom friction factor ;
 C_S = Strickler's bottom friction factor ;
 d_m = mean particle diameter ;
 g = gravitational acceleration ;
 h = water height ;
 K = dispersion coefficient reckoning velocities vertical heterogeneity in ;
 K_S = porosity coefficient ;
 t = time variable ;
 T = bed-load transport rate ;
 U, V = components of flow discharge per unit width ;
 v = depth-averaged velocity ;
 x, y = space variables ;
 Z_0 = bottom elevation related to the horizontal reference level ;
 λ = mean latitude in the model's field ;
 ω = water specific weight ;
 ω_s = particle specific weight ;
 τ = bottom shear stress ;
 τ_c = critical bottom shear stress ;
 Ω = angular rotational velocity of the Earth.

3. STUDY OF THE CURRENTS

3.1. Presentation

Tidal stream and level distribution have been computed on mean spring tide conditions by means of four nested bidimensional numerical models (fig. 2 and 3) fitted on field data :

- a global model of the Southern part of the North Sea (5 kilometers mesh-grid) ;
- a regional model of the Dover Strait (one kilometer mesh-grid) ;
- a local model of Calais region (250 meters mesh-grid) ;
- a very near field model representing outer and inner parts of the harbour (variable mesh down to 30 m).

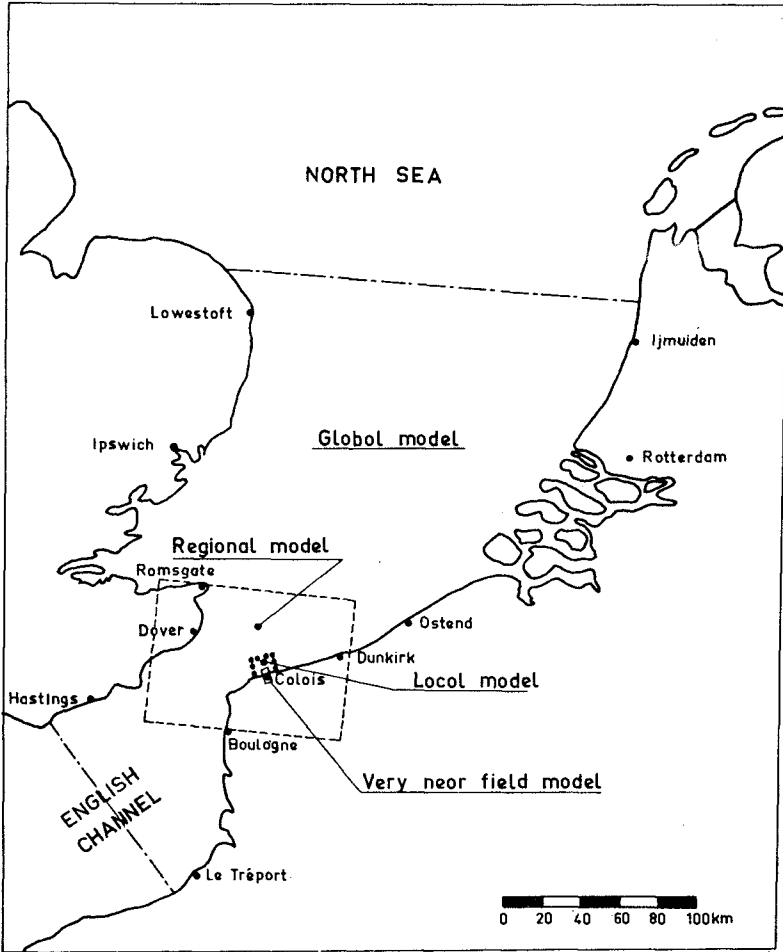


Fig.2 - AREA COVERED BY THE DIFFERENT NUMERICAL MODELS

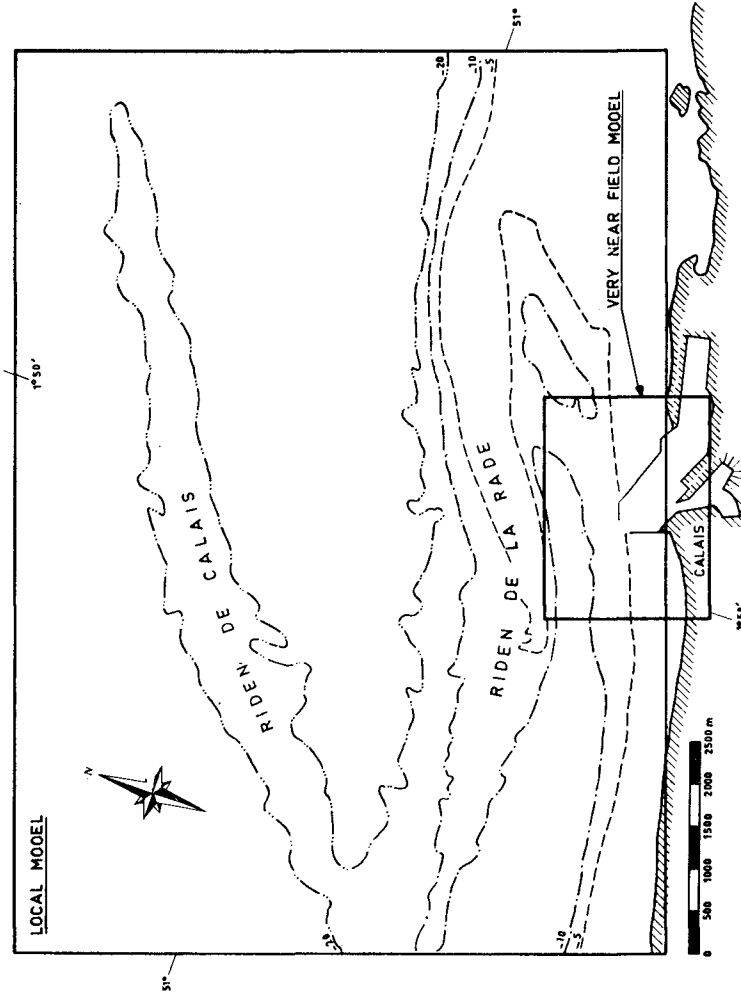


Fig.3. AREA COVERED BY THE LOCAL AND VERY NEAR FIELD MODELS

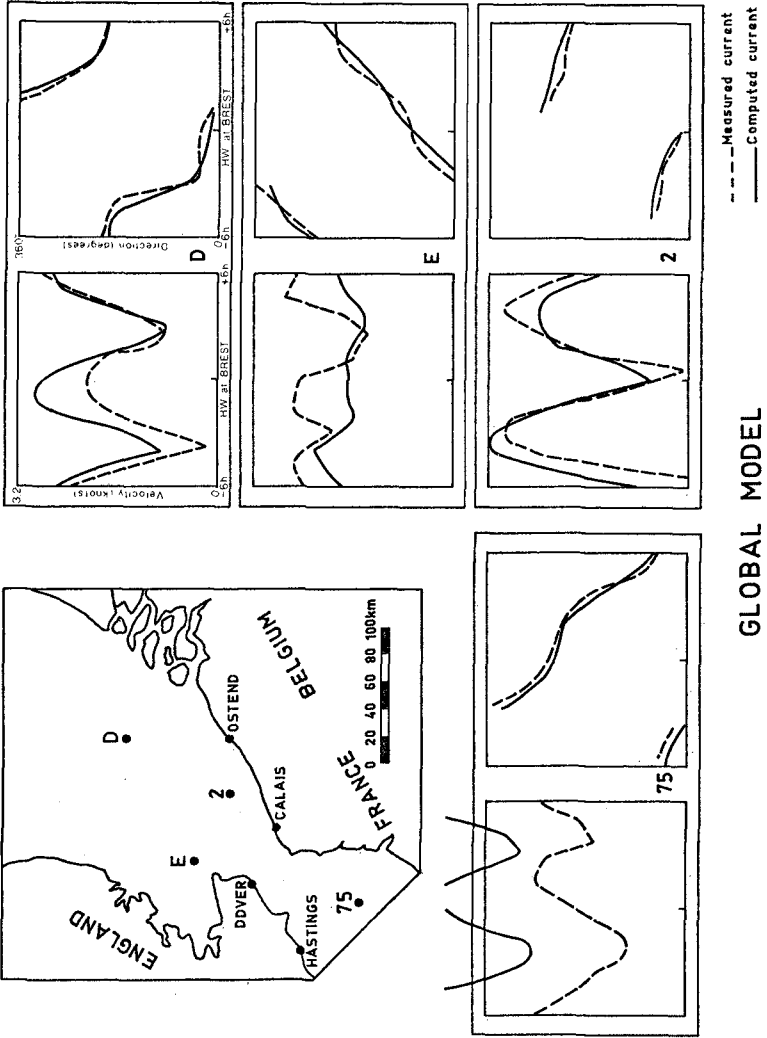


Fig. 4 - COMPARISON BETWEEN COMPUTED AND MEASURED CURRENTS

Only the last two models are directly within the goal of the study, allowing the evaluation of the project nautical conditions and serving as input to the sedimentological investigation ; the first two models, extending very far off the studied area, are only used to solve the problem of the boundary conditions : the few field measurements near Calais are not sufficient to give by interpolation adequate conditions ; limits must then be pushed away so far as computed current near the harbour depends on the well-known bed and coast topography and on the global boundary conditions rather than on the distribution of these conditions.

3.2. Model principle

The model is based upon the assumptions of an hydrostatic pressure, slight curvature of the bottom and the free surface and a vertical quasi-homogeneity of the current. Sun and moon attractive forces are neglected in the model's field (they are included only in the boundary conditions). The model computes then the depth-averaged velocity and the total water height using the classical Saint-Venant equations including bottom friction and Coriolis force :

$$\frac{\partial h}{\partial t} + \frac{\partial U}{\partial x} + \frac{\partial V}{\partial y} = 0 \quad (1)$$

$$\frac{\partial U}{\partial t} + \frac{\partial}{\partial x} (U^2/h) + \frac{\partial}{\partial y} (UV/h) + g h \frac{\partial h}{\partial x} = - g h \frac{\partial Z_b}{\partial x} - g \frac{U\sqrt{U^2 + V^2}}{C^2 h^2} + 2 \Omega V \sin \lambda + K \Delta U \quad (2)$$

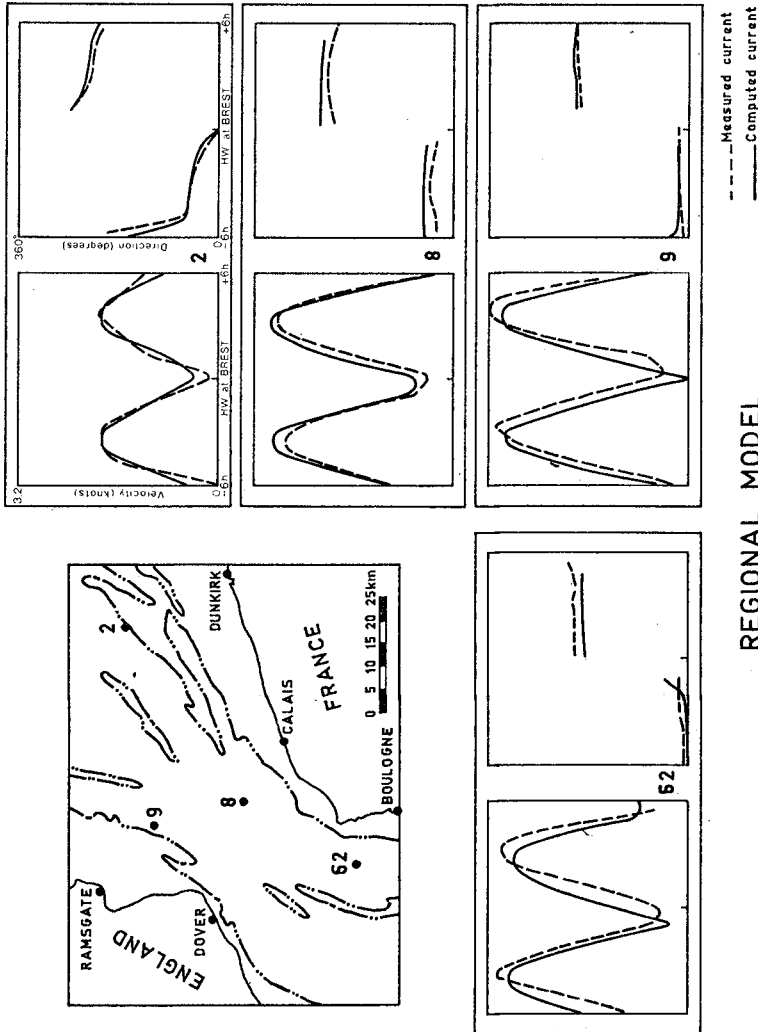
$$\frac{\partial V}{\partial t} + \frac{\partial}{\partial x} (UV/h) + \frac{\partial}{\partial y} (V^2/h) + g h \frac{\partial h}{\partial y} = - g h \frac{\partial Z_b}{\partial y} - g \frac{V\sqrt{U^2 + V^2}}{C^2 h^2} - 2 \Omega U \sin \lambda + K \Delta V \quad (3)$$

The solving method is an implicate finite difference fractional step scheme using an orthogonal grid. Boundary conditions (water height, flow discharge or tidal wave) are coming partly from field data, partly from the results of another global model in the case of the largest one. The finer models are successively feeded with boundary conditions interpolated from the results of the preceding one.

3.3. Results

3.3.1. Global model

This model includes the Southern part of the North Sea and the Eastern part of the English Channel from Great - Yarmouth - Ijmuiden to Hastings - Le Tréport with a 5 kilometers mesh. On



REGIONAL MODEL
Fig.5 -COMPARISON BETWEEN COMPUTED AND MEASURED CURRENTS

the northern boundary, crossing an amphidromic point, surface level and flow discharge were fixed basing on field data ; on the southern boundary were imposed both components of flow discharge, supplied by the results of another preexisting numerical model, covering the whole English Channel.

The complex tidal range distribution due to the superposition of two tidal waves, one coming from the English Channel, the other from the North Sea, is generally well reproduced except near the Dover Strait, too narrow compared with the mesh to be correctly described. Figure 4 shows the comparison between measured and computed current for some of the calibration points ; it reveals a rather good agreement concerning flow direction, even when his value is continually changing (points E and 75), and a less accurate simulation of the velocities.

3.3.2. Regional model

Dover Strait is considered in more details in the regional one kilometer mesh model. Boundary conditions, supplied by the global model, are the two components of flow discharge.

Tide law is rather improved ; as displayed on figure 5 for some calibration points, velocity, direction and phase of the tidal stream are accurately reproduced, except on narrow banks, badly described in the grid system, where velocities are often overrated.

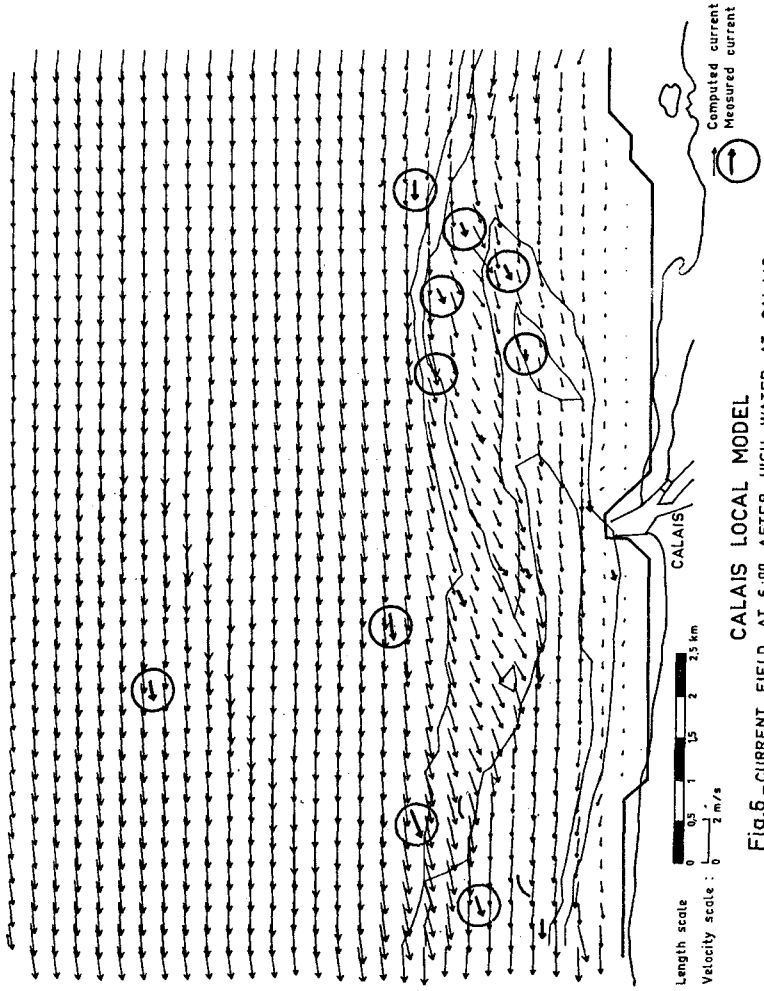
3.3.3. Local model

This 250 meters mesh model covers the whole "Riden de la Rade" (fig. 3), a sand bank edging the access channel to Calais Harbour, whose evolution has to be computed with and without the influence of the new outer-harbour.

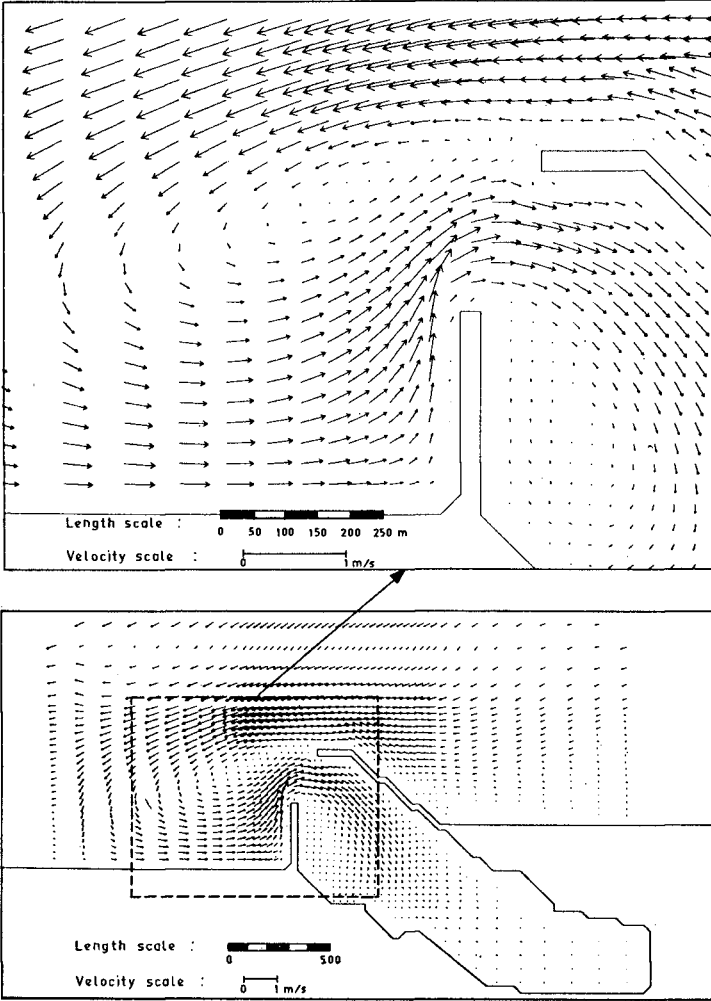
The flow pattern peculiarities involved by this bank are effectively achieved by the model in spite of the two-dimensional representation of the actually three-dimensional flow configuration. Figure 6 gives the computed stream distribution 6 hours after high water, compared with current measured in a few points : natural current deflection on the bank induced by the feeding of the southern channel, just as the ebb flow reducing in this channel are rather well reproduced.

3.3.4. Very near field model

The last model, representing the enlarged outer-harbour and its close vicinity, uses a variable mesh grid (down to 30 m), allowing an accurate representation of the harbour entrance and inner parts while having at the same time boundaries far enough to get there a flow pattern not disturbed by the harbour enlargement. The solving method is especially suited to enable the detailed reproduction of eddies and flow separations ; these flow configurations can be reproduced



CALAIS LOCAL MODEL
Fig.6 -CURRENT FIELD AT 6:00 AFTER HIGH WATER AT CALAIS



CALAIS HARBOUR VERY NEAR FIELD MODEL

Fig.7- CURRENT FIELD AT 3:00 BEFORE HIGH WATER

owing to the zero velocity assigned on solid boundaries, whose effect is carried inside the model field by the diffusion terms. Both components of flow discharge are imposed on eastern and western fluid boundaries ; on the northern one, rather near to the harbour, it has proved better to impose water level and tangential component of flow discharge, thus allowing contingent flow lines deflection by the new breakwater even on the boundary.

Flow pattern has been computed for two stages of the harbour development and for two different considerations of the west breakwater one being permeable. The model results show a significant flow strengthening and deflection northward of the harbour during flood, slighter during ebb, and the development of two eddies, the largest one occurring to the west of the harbour at the end of ebb (fig. 7). In the harbour entrance velocities do not exceed 30 cm/s ; inside, the flow is rather slow, slightly vortical at the end of filling.

These results yield an estimate of the nautical conditions, which seem rather better than the present ones, point out the most propitious time for the harbour access and give precious informations concerning the access handling.

4. SEDIMENTOLOGICAL STUDY

Current results are used to compute by means of a two-dimensional bed-load transport model the sedimentological effect of the harbour enlargement.

4.1. Model presentation

Besides assumptions considered for current determination, following ones are made :

- flow and bottom evolutions are slow ;
- bed-load transport has the same direction as the depth-averaged velocity.

Bed-load transport induced by tidal current is computed using Meyer-Peter's formula :

$$T = 8 K v \sqrt{\frac{g}{\bar{w}}} \frac{1}{\bar{w}_s - \bar{w}} (\tau - \tau_c)^{3/2} \quad \text{pour } \tau > \tau_c \quad (4)$$

$$T = 0 \quad \text{pour } \tau < \tau_c$$

Where τ is given by Strickler's law :

$$= \frac{\bar{w}}{C^2} \frac{v^2}{h^{1/3}} \quad (5)$$

and τ_c by Shield's law :

$$\tau_c = A (\omega_s - \bar{\omega}) d_m \quad (6)$$

where A is a coefficient between 0,02 and 0,06 (0,047 according to Meyer-Peter).

Continuity equation applied to the bed-load transport provides then the bed evolution :

$$\frac{\partial Z_b}{\partial t} + \text{div } \vec{T} = 0$$

Numerical solving is based upon an explicite finite difference method using an orthogonal grid. Boundary conditions have to be imposed only when flowing in ; sea bed is then kept fixed on the bound mesh.

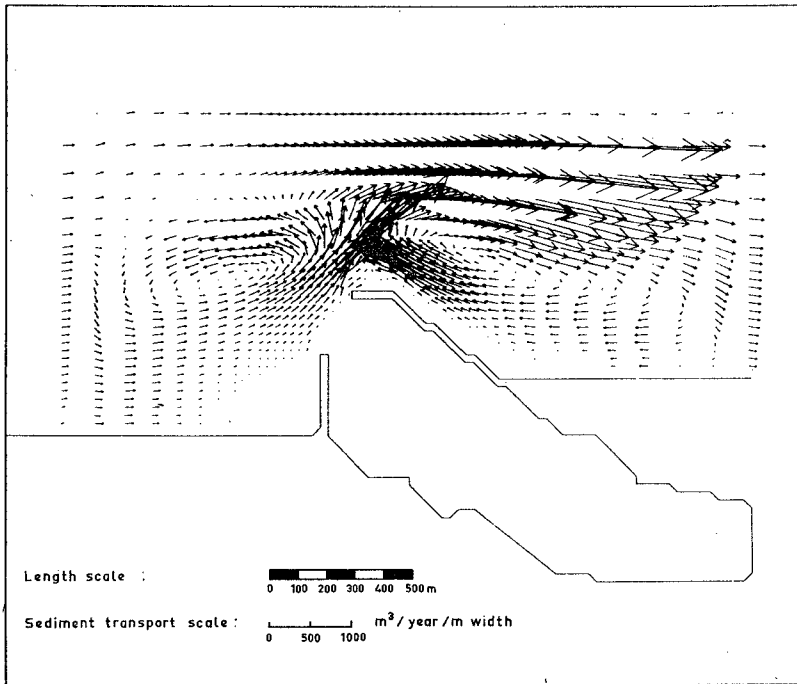
In order to avoid a prohibitive number of computation steps, tide is filtered by expanding sedimentological time step with respect to hydraulic one (so a lengthened tide represents several tides, in the same way as it is made on scale models). At every step velocity is readjusted according to the new water depth assuming that the initial flow discharge remains the same at the same time of the tide.

This model has already been applied in a similar case, related to the sea bed evolution induced in the building of the new outer-harbour of Dunkirk, about 40 kilometers away from Calais : mathematical model results turned out to be close to those achieved on the physical movable bed model operated for the study, themselves well corroborated afterwards by the natural bed evolution.

4.2. Results

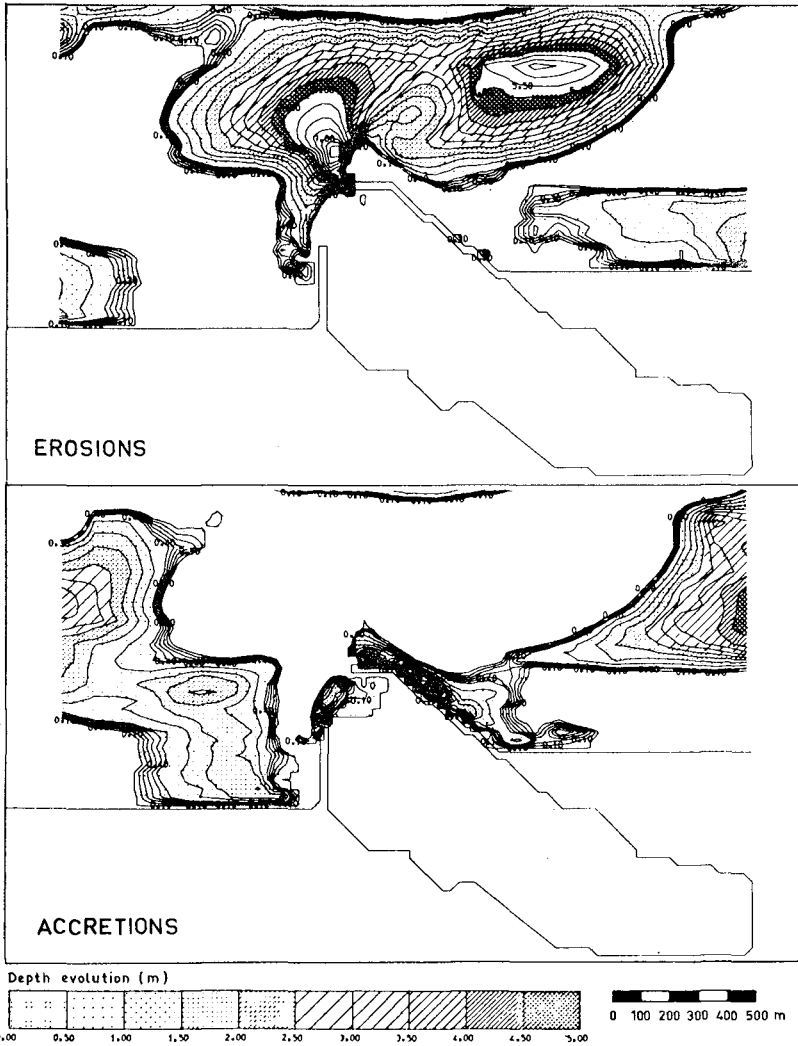
Based on the results of the very near field current model, the bed-load transport model, using the same grid as the current one, has supplied an evaluation of the sedimentological impact of the final enlargement project.

Figure 8 displays, in the initial state, the computed distribution of tidal-averaged sediment transport rate : it points out predominance of flood action, especially northward of the harbour where current strengthening inferred from the new breakwater building is then much more significant than during ebb ; in this area sediment transport rate reaches 1 500 m³/year/m width, i.e. ten times as much as on the eastern and western bounds. On each side of the harbour occurs a sediment transport "eddy" caused by unequal distribution of both ebb and flood current downstream the harbour, strengthened in the north and reduced in the south in the of the breakwaters. As time elapses maximum transport rates decrease gradually because of mutual adjustment of flow distribution and bottom topography.



CALAIS NEW OUTER-HARBOUR

Fig.8 - COMPUTED PATTERN OF NET SEDIMENT TRANSPORT
(INITIAL STATE)



CALAIS NEW OUTER-HARBOUR

Fig.9 - COMPUTED EVOLUTION AFTER 5456 TIDES (8 YEARS)

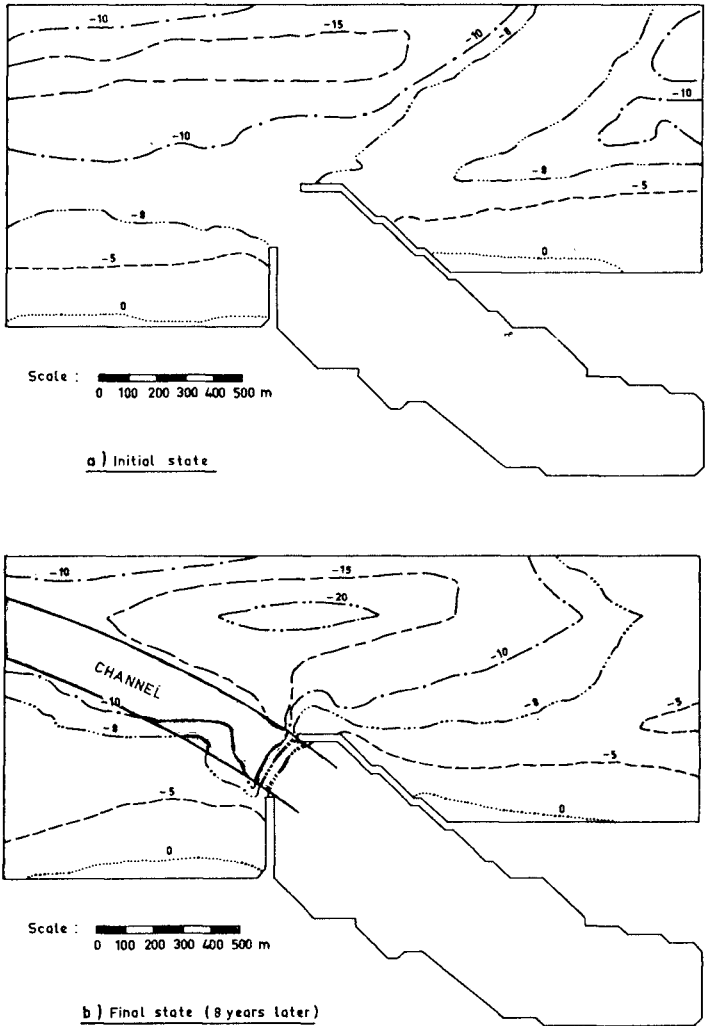


Fig.10- CALAIS - COMPUTED BED EVOLUTION NEAR THE NEW OUTER-HARBOUR

Figure 9 presents the bed evolution computed after 8 years of tidal current action ; it shows a large area of erosion from the north-west to the north-east of the harbour with deepening exceeding 8 m near to the new breakwater head ; slighter accretion occurs on each side, especially at the edge of the access channel ; in the harbour entrance the current velocity gradient brings out the development of a bar of rather limited size.

Figure 10 yields the comparison between present and final bottom topography, showing up the necessity of maintenance dredging in the harbour entrance and in the south of the outer channel.

The results of this bed-load transport study show that a bed protection has to be placed at the toe of the new breakwater ; they also give an estimate of the sand volume to be dredged to maintain the harbour access.

Bed evolution owing to suspended sediment, notably prevailing inside the harbour, will be separately examined using a method of balance calibrated from the present state data.

5. CONCLUSION

Among hydraulic studies needed by the enlargement of Calais Harbour, both stream distribution and sedimentological impact of the project have been dealt by means of numerical technics : current computer simulation, involving four bidimensional nested models, has enabled the detailed determination of nautical conditions in relation with the design of the new outer-harbour, pointing out the most propitious time for the harbour access and giving information for access handling ; current results have then been used to compute from a bidimensional bed-load transport model, validated on a similar study, the effect of the harbour extension on the bed evolution, yielding definitions of bed protection and forecast of channel dredging rates. This computer model will be used afterwards to study the evolution of a bank named "Riden de la Rade" (fig. 3) which could threaten in a very distant future the harbour access.

Physical modelling was required only for items needing little equipment and able to be quickly dealt with : final tests of wave agitation and breakwater structure adjusting.

This procedure of comprehensive numerical harbour design study is of moderate cost, of great flexibility and rather fast compared with scale modelling.

NEW JETTIES FOR TUNG-KANG FISHING HARBOR, TAIWAN

Chi-Fu Su
Manager
Engineering Department
Taiwan Fisheries Consultants, Inc.
Taipei, Taiwan

INTRODUCTION

Tung-Kang Fishing Harbor, which is about 16 km to the south of Kaohsiung Harbor, is a river harbor on the south-west coast of Taiwan. This harbor is located at the estuary of the Niu-Pu River, which meets the Tung-Kang River and the Kao-Ping River on the north side. (see Fig. 1) The original north and south jetties were constructed in 1959. Because the entrance is located at the meeting of the three rivers and the water depth at the entrance is shallower than that in the breaking zone, the entrance is easily choked with sand during the summer season when the south-west wind and waves are strong. Therefore, dredging is always necessary to maintain the required depth. On the other hand, because of the increasing number of fishing boats and deeper draft, the port cannot function effectively. Therefore, how to keep the required water depth at the entrance and to obtain a wider and stable water basin is an urgent problem with this harbor.

Based on the sounding of 1973, the littoral drift is mainly from the south. In the next year the construction of a 176 m long new south jetty was begun to protect the entrance and to facilitate the sedimentation study. In 1975, the Taiwan Fisheries Consultants was appointed to undertake the investigation and long-term planning work. This project includes littoral process study, planning, model test and design. Finally it is recommended that an adequate layout of south and north jetties can solve the problem of accretation of the harbor entrance.

The purpose of this paper is to describe some aspects with emphasis on how to prevent the shoaling of the entrance channel located at the meeting of the rivers.

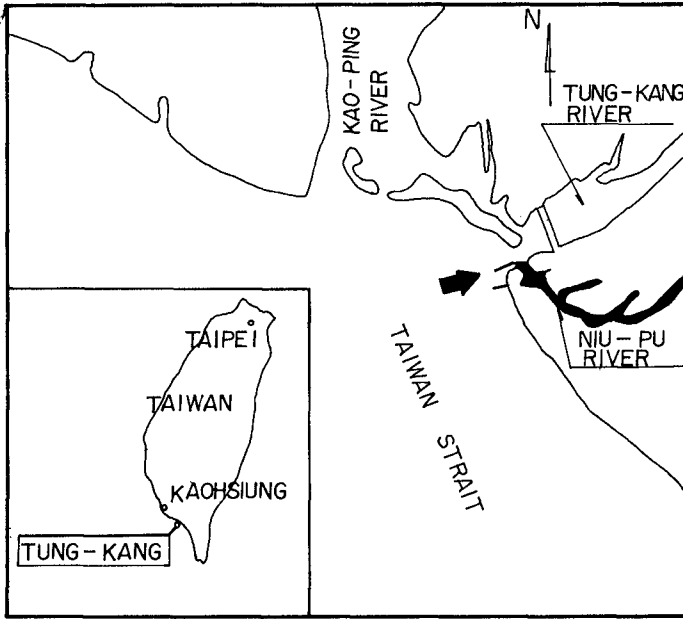


Fig-1 SITE LOCATION

LITTORAL ENVIRONMENTAL CONDITIONS

Wind

Because of the lack of site data, those observed at Kaohsiung are referable. The wind data from 1951 through 1970 were analyzed. (2) Winds from north-northwest occur in the greatest part of the time and prevail during the months of September through April. Higher velocities are associated with typhoon passing this area or tropical depression which occurs in the South China Sea mainly during June through September. The strongest longshore winds with speeds ranging from 5.4 to 13.8 m/sec occur during the summer season and predominantly from the southeast.

Waves

Based on the wave data measured in 12^m of water at Kaohsiung Harbor, the predominant wave height is 0.5-1.0^m, with wave period of 7-8^{sec} and from southwest. The higher waves occur during the summer season, especially in the typhoon period.

Tide

The spring tidal range is 1.3^m, the maximum water level was observed in 1969 at 2.7^m above low water level. This is due to the combination of spring tide and storm surge. The measured current speeds of both ebb and flood tide are below 0.5 m/sec.

Rivers

There are four rivers in the study area (see Fig. 1); except the three of them meeting at Tung-Kang Harbor, the Lin-Ben River is 10 km to the south of this harbor. The maximum measured discharge of the Kao-Ping River is 18,000^{cms}, 1,470 the Tung-Kang River and 2,950^{cms} the Lin-Ben River. The discharge in the Niu-Pu River is too small and negligible. The estimated annual sand volume transported by Kao-Ping River is 24 million cubic meters, 0.5 million cubic meters the Tung-Kang River and 1.5 million cubic meters the Lin-Ben River.

Topography off Tung-Kang Coast

Fig. 2 shows a deep marine canyon off this coast. Therefore most of the sediment discharged from rivers are trapped in it.

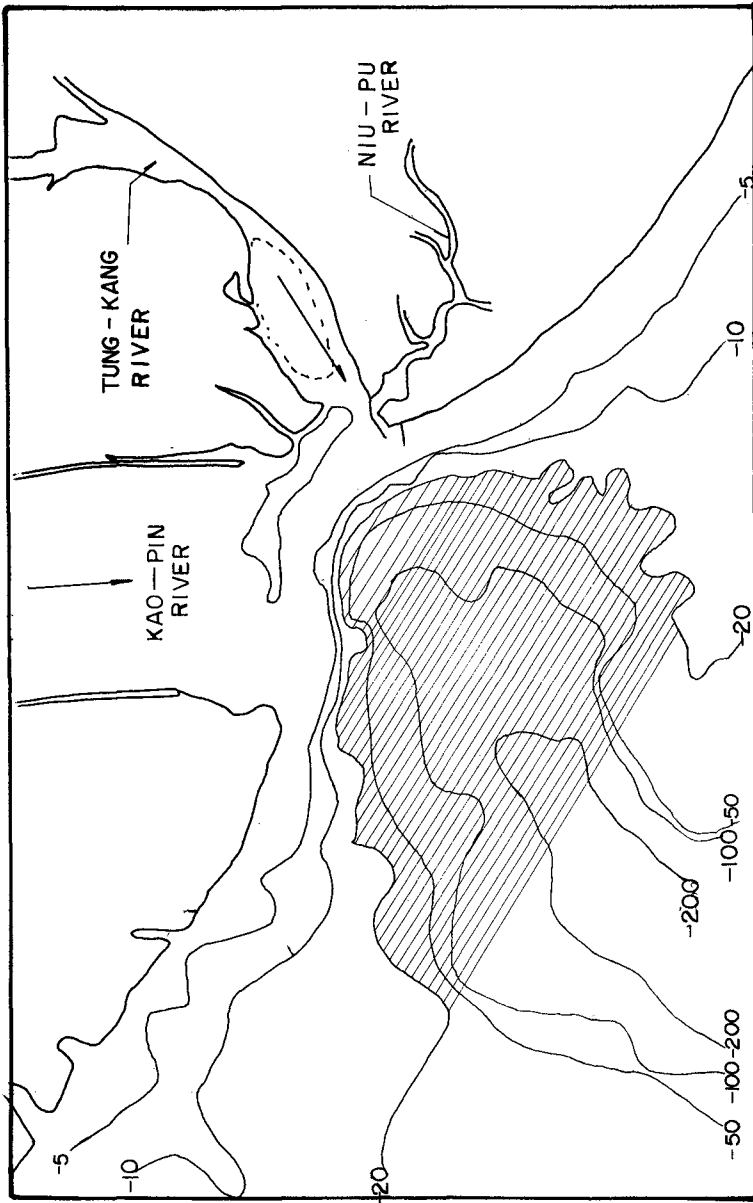


Fig-2 Marine , Canyon Of TUNG-KANG Coast

LITTORAL PROCESS

Bathymetry

From the bathymetric survey of September 1973, it was found that the littoral drift was mainly from the south. As shown in Fig. 3, the sand bars were formed at both heads of the original north and south jetties. In the next year the construction of a 176^m long new south jetty (see Fig. 7) was begun to protect the entrance and to facilitate the sedimentation study. For further study, three other soundings were conducted in May 1975, September 1975 and June 1976. The lengths of the newly constructed south jetty in these three soundings were 120^m, 176^m and 216^m, and the depths at the jetty head were 1.8^m (below low water level), 2^m and 4^m respectively. The results of the sounding were used for comparing changes of contour. So the sand sources and seasonal sea bottom change in the region between shoreline and some water depth contour could be interpreted. The influence of the newly constructed south jetty on the behavior of littoral drift was also evaluated.

Grain size Distribution

With the last two soundings littoral materials were also sampled for analyzing grain size and size distribution in the study area.

The median grain size was analyzed, from the size distribution overall the study area, the following results could be obtained. 1. The June 1976 data showed that the relatively coarse sands were distributed in the range from -2 to -3^m depths, while those of September 1975 were in -5 to -6^m depths. They were positioned in breaking zone, and during typhoon period the position moved seaward. 2. At the mouth of the Tung-Kang River, the median size D50 was up to 0.6^{mm} which was rather coarser than at the other place. From this we can know that they came from the Tung-Kang River or the Kao-Ping River. The finer sands were transported by wave current and the coarser ones remained behind. 3. At the entrance of the harbor, the sand was fine because of low wave energy there.

Dredging Record

To provide the required navigation channel, dredging work was conducted during the period from 1973 through 1975. The monthly dredging volume is listed in Table 1, which shows the annual volume to be around 100,000^{m³}.

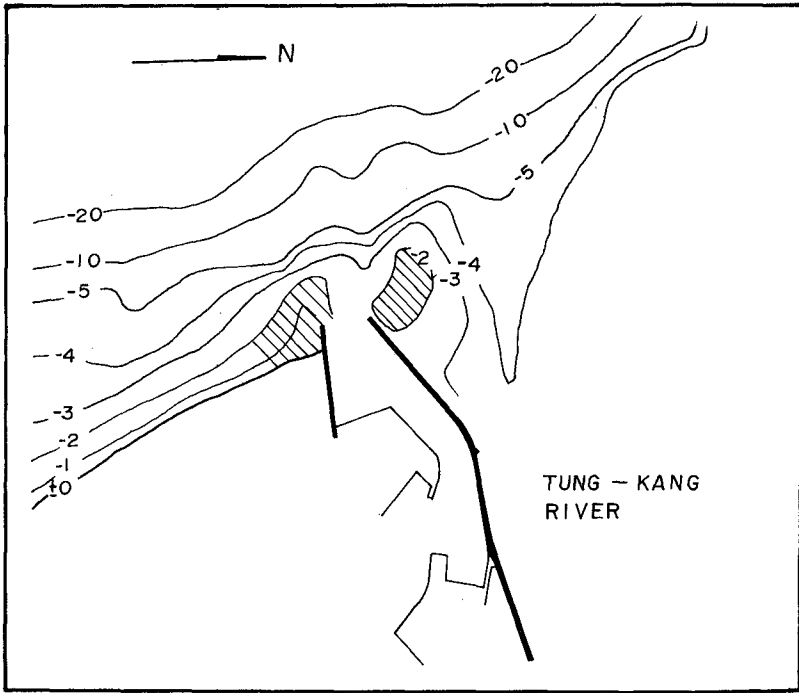


Fig-3 SOUNDING OF SEPTEMBER 1973

Table 1. Records of Dredging Volume

Month	Volume	Year			
		1973	1974	1975	1976
1		3,400	6,300	13,442	7,600
2		9,100	9,450	5,600	7,400
3		9,270	11,600	10,000	-
4		7,250	9,200	11,000	-
5		10,410	8,400	13,300	-
6		11,415	6,800	6,300	-
7		3,970	8,000	9,200	
8		5,970	4,900	1,200	
9		14,580	11,400	9,750	
10		7,160	9,600	5,560	
11		8,200	8,240	9,600	
12		6,480	9,270	9,200	
total		97,250	103,610	104,152	

Seasonal Changes of Shore

They were analyzed by comparing the survey of May 1975, September 1975 and June 1976.

Summer Season: In the area immediately south of the new south jetty, the rip current induces by the jetty was obvious and deeply affected the foreshore and inshore topography. Along the shoreline accretion and erosion occurred at different positions relative to the new south jetty. Due to the action of waves arriving from WSW to SSW, accretion occurred in the area from the south jetty to a line approximately 200^m south. From the 200^m line to the line of 600^m south, the concentrating rip current made this area eroded evidently. While southwards the rate of erosion decreased

and accumulation occurred by the supply of the southerly sand. Inspecting the onshore-offshore change, the influence of rip current was down to the depths between -4^m and -6^m . Deeper than this, there was accumulation because of slower current and abundant supply of material.

The area north of the new south jetty was mainly affected by the sand from the Tung-Kang River and the Kao-Ping River. Two impounding zones could be found in the lee of the south jetty and in the zone immediately north of the north jetty respectively. In the former case, littoral material moved along the outer face of the jetty and deposited in the relatively calm water in the lee of the structure. While in the latter case, sand transported by the rivers accumulated in the zone between the north jetty adjacent to the Tung-Kang River, due to slower water flow and wave current on the reverse at the river mouth. The accumulated sand may be transported by diffraction waves to deposit at the entrance. Fortunately, most of the sand there is moved by northward longshore current to the deep marine canyon off the mouth of the Kao-Ping River. This is why the small scale Tung-Kang Fishing Harbor could be maintained by dredging about $100,000^m^3$ of sand every year, as shown in Table 1.

Winter season: During the winter months, the approaching waves shift to the west direction and more perpendicular to the shoreline. So both the impounding capacity of the new south jetty and the southerly littoral drift are decreased. Although the rip current becomes slower, the shortage of sand supply made the erosion area moved northward. While to the south of the 600^m line, the volume accumulated still increased and also moved northward due to the continuous supply of sand. Rapid erosion in the area north of north jetty is due to the decrease of sand from rivers during the winter months. The bar formed during the summer season was moved northward or transported seaward to the deep marine canyon by waves.

From the above analysis, the deep marine canyon is an effective sink to trap the large volume of sand transported from the Kao-Ping River. The orientation of the coast makes the direction of advancing wave toward the shore stable, and create a coast-longshore current from south to north, these two local conditions are very important for solving the entrance stabilization problem.

HYDRAULIC MODEL TEST

To prevent the sand from entering the entrance, both the newly constructed south jetty and the north jetty should be adequately extended. This was studied by using hydraulic model test conducted in the laboratory of Chung Hsing University⁽⁴⁾.

The south jetty is mainly to stop the southern longshore drift and let it bypass the entrance. The extended north jetty is not only to provide a deeper entrance channel but also to reflect the waves to transport the sand at the head to the north. Besides, some short groins connected to the south bank of the Tung-Kang River can change the flow direction so as to discharge the sand away from the entrance. Based on these principles, the jetties were arranged and verified by model test.

A distorted scale (1:75 vertical and 1:150 horizontal) movable-bed model in which fly-ash with median diameter $D_{50}=0.08\text{mm}$ and specific gravity $S_m=2.02$ was used as bed load. The wave generator was only 9m long. In order to have a larger scale model, the model was divided into two parts. (see Fig. 4) Part A included the area from the entrance to a point 1000m from the south of the new south jetty. The test was principally on the southern longshore drift. Part B included the area between the lines 300m to the south and 1000m to the north of the entrance. This part covered the estuary of the Tung-Kang River. The test was mainly on the sand from the river. The test was carried out with a number of cases with different layout of jetties.

In part A, five cases and thirteen runs were carried out with various wave conditions and durations. The results suggested a layout in which the south jetty was 410m including the shore connected portion of 350m long, then turning to the north-west and widening the north jetty so as to have a longer head for reflection waves. (see Fig. 5) In this case, no obvious accretion took place in the entrance channel; accretion occurred around the north jetty where the counterlines moved seaward. The current induced by the new south jetty transported sand in the south-west direction. This corroborate the field investigation results.

In part B, five cases and seven runs were carried out. Besides various wave conditions and durations, the discharge and sand from the Tung-Kang River was also simulated. The results suggested a layout in which

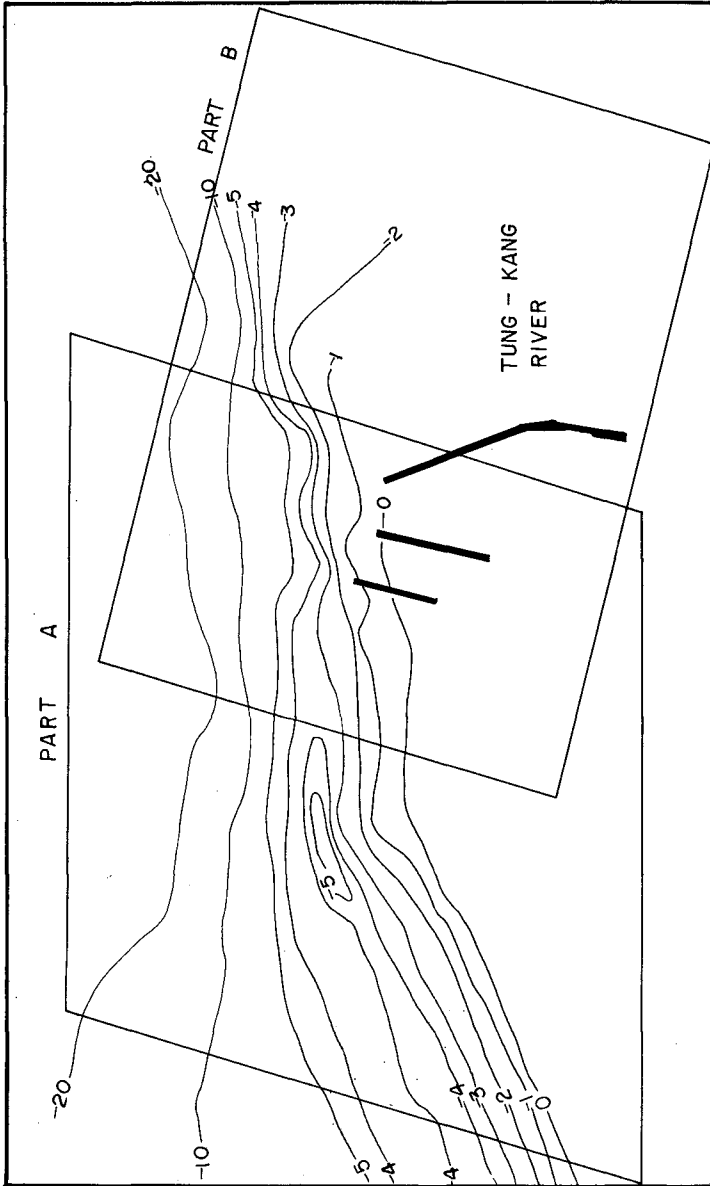


Fig-4 The Scope Of Part A & Part B Test

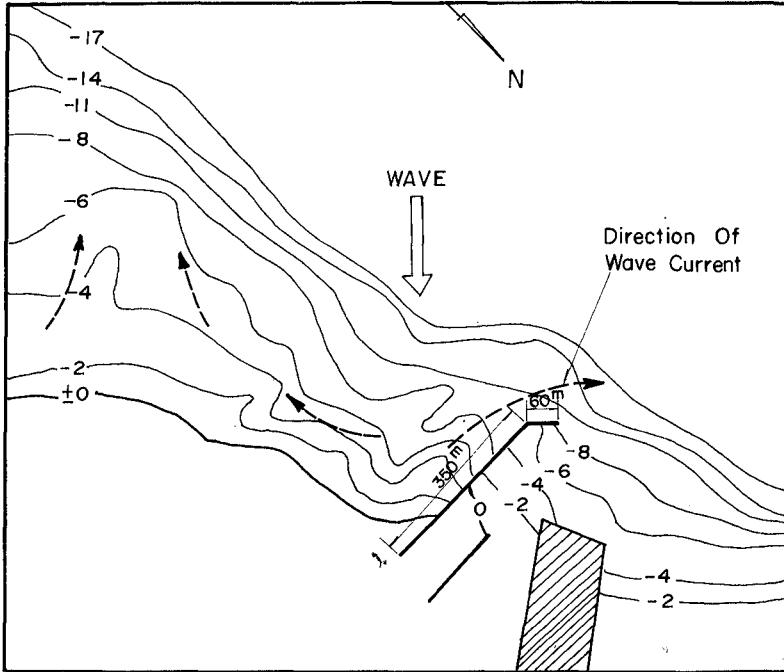


Fig-5 PART A TEST

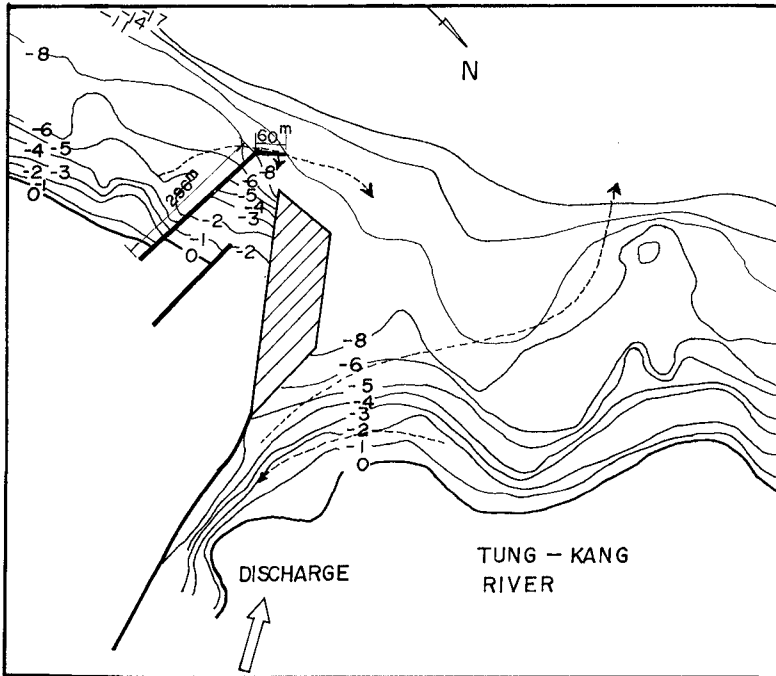


Fig-6 PART B TEST

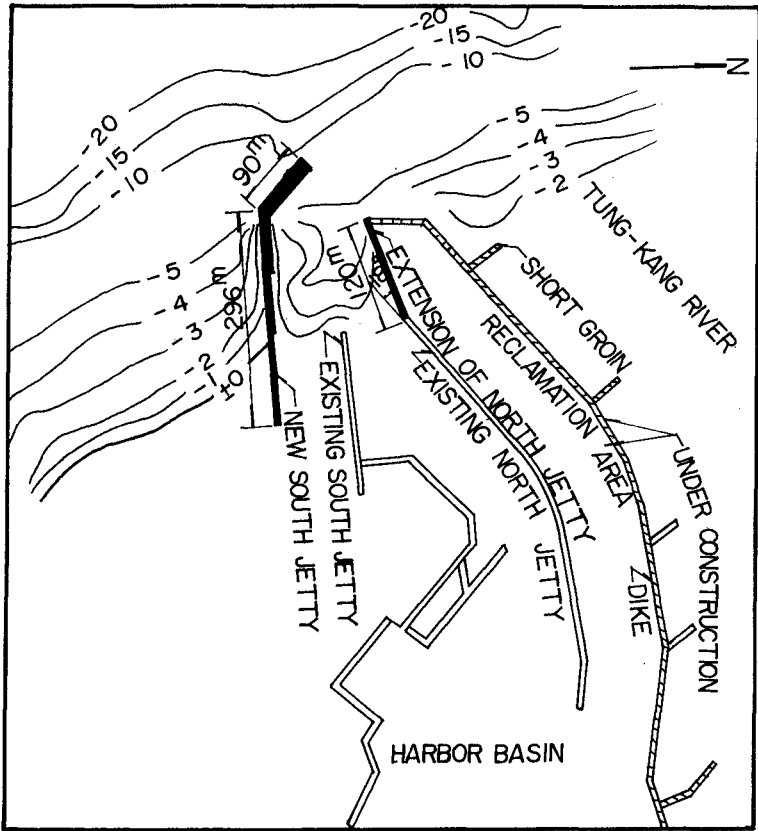


Fig-7 LAYOUT OF NEW JETTIES

the length of the new south jetty was 356m including the shore connected portion of 296m then turning to the north-west, and the north jetty was turned clockwise by 18° from the head of the existing north jetty and lengthened by 120m. (see Fig. 6) To reflect the waves at the head of north jetty so as to transport the sand apart, a reclamation area on the north side of the north jetty was suggested so as to have a wider head to reflect the incident waves. In this case, the southern longshore drift could by-pass the entrance without accretion because of the reflected waves from the north jetty head. The sand discharged from the Tung-Kang River was far away from the entrance due to the action of reflected waves and the effect of the reclamation area.

FINAL LAYOUT AND STRUCTURE TYPE

The final layout is as shown in Fig. 7. The new south jetty was lengthened by 30m so as to have a calmer basin. The first 176m section was rubble mound type armoured with holtripod. The other portion of 60m long was composite-caisson type. The width of caisson at head section is 15m, 8.5m high and 12m long. Composite-Caisson type was also adopted for north jetty. The construction work of the new south jetty and the extension of the north jetty was completed on 1979. The reclamation area, dike and short groins will be built in the following years.

CONCLUSIONS

- (1) A careful field investigation of littoral process is helpful to the study of a small scale harbor which is located at the meeting of rivers.
- (2) A prototype jetty (if possible) for aiding the study of longshore drift is very effective.
- (3) A physical hydraulic model is proved to be an important tool for the functional design of jetty system for entrance channel with complicated littoral drift phenomena.
- (4) An adequate arrangement of jetties can make the diffraction and reflection waves play important roles in the sand bypassing system.

REFERENCES

1. Taiwan Fisheries Consultants, Inc. (1977), Report on the Entrance Improvement and Long-Term Planning of Tung-Kang Fishing Harbor.
2. Central Weather Bureau (1974), Summary Report of Meteorological Data Taiwan, Vol. III. 1961-1970. pp. 466-471
3. Kaohsiung Harbor Bureau (1968), Report on the Planning of the Second Entrance of Kaohsiung Harbor, pp. 37-199.
4. Chung Hsing University and Taiwan Fisheries Consultants Hydraulic Laboratory (1977), Report on the model Studies of Tung-Kang Fishing Harbor, Rep. No. 5.

CHAPTER 135

MAJOR RECLAMATION SCHEME FOR MARINA CITY, SINGAPORE

S.Y. CHEW
Manager, Building and Development Division,
Housing and Development Board, Singapore

and

J. WEI
Principal Civil Engineer, Building and Development Division,
Housing and Development Board, Singapore.

SUMMARY

One of the most ambitious coastal reclamation projects in the Republic of Singapore to reclaim 360 hectares is now in progress and, when completed in 1985 at an estimated cost of S\$385 million, will provide a major portion of the lands required for the development of Singapore's new city centre to be known as Marina City. This paper describes the various activities involved in the planning, design and construction of the project.

INTRODUCTION

The island republic of Singapore with a very small land area of only slightly over 600 square kilometres saw rapid industrial and housing development in the early 1960's. This prompted the government to embark upon an intensive reclamation programme to provide new lands to meet the urgent needs.

Following a small pilot scheme reclamation in 1963 the East Coast Reclamation Scheme was launched and the following phases were executed (Figure 1):-

- (i) Phase I reclamation of 405 hectares commenced in April 1966 and was completed in April 1970 at a cost of S\$45 million. (Unit cost approximately S\$11 per sq metre)
- (ii) Phase II continued westwards from Phase I to reclaim 53 hectares. Work commenced in April 1970 and was completed in May 1971 at a cost of S\$10 million. (Unit cost approximately S\$19 per sq metre)
- (iii) Phase III to reclaim 67 hectares commenced in March 1971 and was completed in December 1975. The project cost was S\$23 million. (Unit cost approximately S\$34 per sq metre)
- (iv) Phase IV reclaimed 486 hectares from May 1971 to February 1976 at a total project cost of S\$44 million. (Unit cost approximately S\$9 per sq metre)

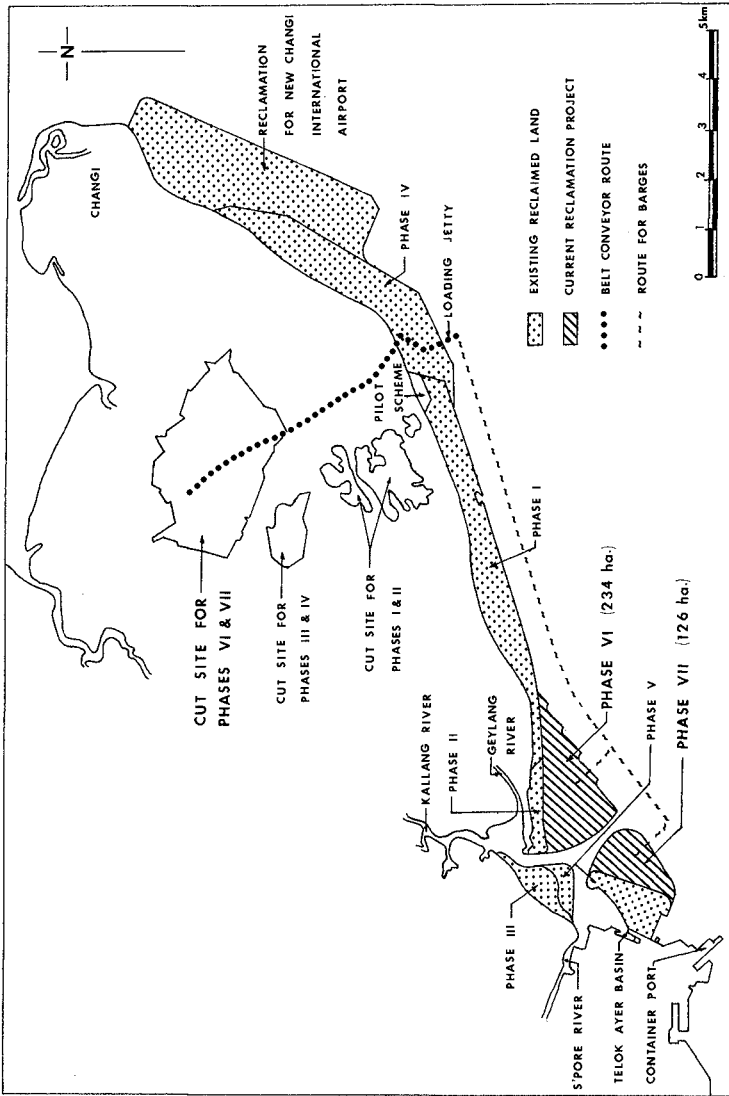


Figure 1 PLAN SHOWING THE LAYOUT OF VARIOUS PHASES OF EAST COAST RECLAMATION SCHEME, SINGAPORE.

(v) Phase V to reclaim 154 hectares commenced in April 1974 and was completed in December 1977 at a total project cost of S\$106 million. (Unit cost approximately S\$69 per sq metre)

Altogether, between 1966 and 1977 a total of 5 phases were completed, providing 1165 hectares of new land at a total cost of S\$228 million. The Housing and Development Board as agent for the Government carried out the planning, design and supervision of construction of these 5 phases of reclamation.

The proposed shifting of the international airport to Changi by 1982 has lifted planning constraints on areas adjacent to the existing city centre which are now under the flight path. Planners and architects were therefore able to plan a city of the future to meet the Republic's needs for the year 2000 and beyond. As a result, the concept of the Marina City was mooted and it became necessary to reclaim more land to meet the requirements of the proposed development. Thus Phases VI and VII of the East Coast Reclamation Scheme were initiated. When completed in 1985 these 2 phases together with some of the lands reclaimed under earlier phases will provide 660 hectares of new land for the Republic's city of the future.

Figures 1 & 2 show some of the main features of the project.

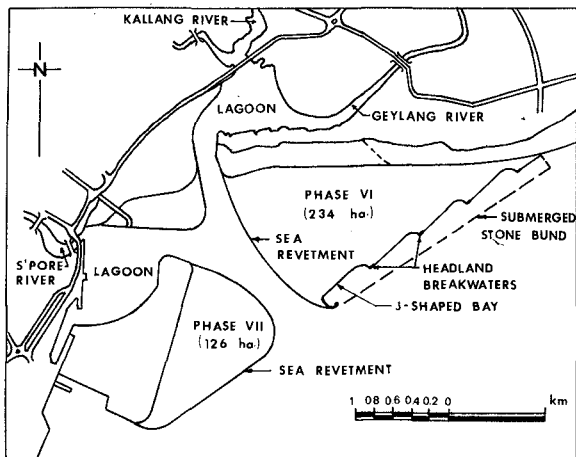


Figure 2 LAYOUT OF EAST COAST RECLAMATION SCHEME PHASES VI & VII

COASTAL PROCESS PARAMETERS

During the implementation of the earlier phases of the East Coast Reclamation Scheme various data such as waves, currents and tides were monitored (1) to enable studies to be carried out on the behaviour of the new coastline (2) as well as to provide information for the planning and design of the new reclamation projects.

From the field investigations it has been established that the southeast coast of Singapore is essentially a low energy coast throughout the year with waves coming from the southeast quadrant and a nett westward littoral drift is present. The area is considered as rather sheltered and winds from the north during the northeast monsoon (December to March) do not have a large influence except through refracted swell from the South China Sea. Higher waves are experienced during the northeast monsoon. Recordings showed a maximum wave height of 1.14 m with a zero-crossing period of 3 seconds and the highest probable maximum wave was 1.37 m.

It was found that the tides are essentially semi-diurnal of a mixed type and the current patterns appear to bear little relationship with the rise and fall of tide. Results of the field measurements also suggest that the tidal current is not a significant factor for distribution and transportation of bed material.

MODEL STUDIES

The data obtained from the investigations just mentioned as well as other data such as peak discharge values, distribution of direct run-off against time and water quality data of several rivers with outlets near the reclamation area were used in subsequent model studies to investigate the following:-

- (i) whether the proposed reclamation shapes or modifications thereof would limit the increase of water levels of the lagoons by no more than 5 cm above existing levels after reclamation (taking into account the coinciding of a 5-year flood with the high tide);
- (ii) whether adequate flushing of the lagoons would be possible;

(iii) the flow patterns resulting from the proposed reclamation on condition that this should not adversely affect the navigation of vessels leading to the Container Port, smaller craft to Telok Ayer Basin and Kallang Basin and movement of vessels in the general vicinity and

(iv) siltation aspects arising from the proposed shapes of reclamation.

The items (i) to (iv) above were carried out on the Singapore Tidal Model at Pōona (3). Horizontal and vertical scales of 1:700 and 1:120 respectively were used.

It was observed that of the different stages of flow viz. east-going ebb, east-going flood, west-going ebb and west-going flood, with and without freshet discharge, two flow conditions viz. east-going ebb and west-going ebb produced the bad flow conditions. Accordingly results of east-going ebb and west-going ebb when rivers carry their peak freshet discharge are considered.

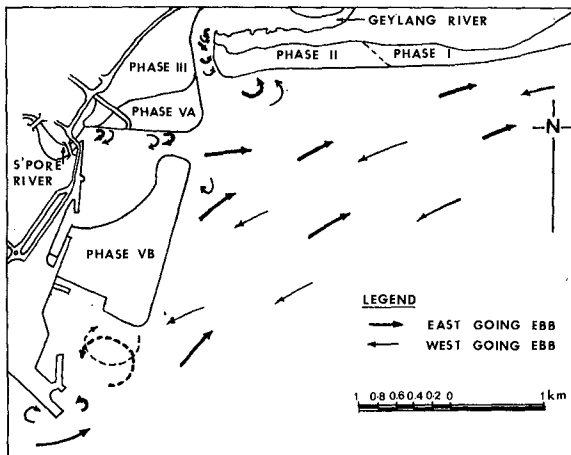


Figure 3 FLOW PATTERN FOR EXISTING CONDITION

Figure 3 shows the flow pattern for existing conditions, ie with the completed Phase V reclamation. Eddies were observed near the entrance to the new basin off the mouth of Singapore River and also near Kallang River mouth and south of Phase II. Eddies were also observed at the east and west of the Container Port for both east-going and west-going flows.

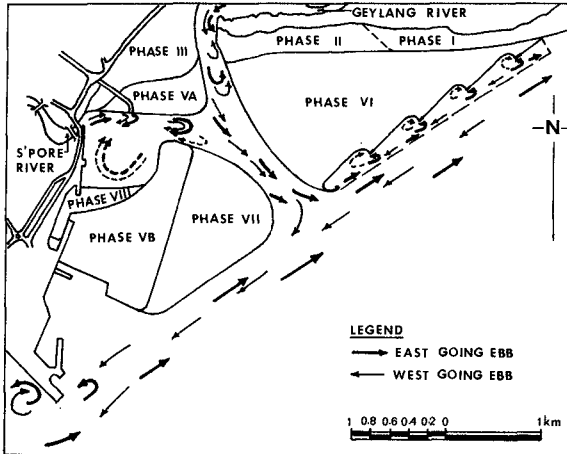


Figure 4 FLOW PATTERN WITH PHASES VI, VII & VIII

Figure 4 shows the flow pattern with Phases VI, VII & VIII. Phase VIII, incidently is not being implemented under the current project. It was observed that the flow pattern along the seaward faces of Phases VI and VII as well as in the channel between Phases VI and VII was good. However eddies were observed near the entrances to the new basin and Kallang Basin during the ebb phase of the tide. Eddies were also formed to the east and west of the Container Port during both east-going and west-going flows. The eddies in front of the Container Port which were observed for existing conditions (Figure 3) were not seen after simulating Phases VI, VII & VIII on the model.

With slight modifications introduced to the proposed reclamation profiles the flow pattern improved, as shown in Figure 5.

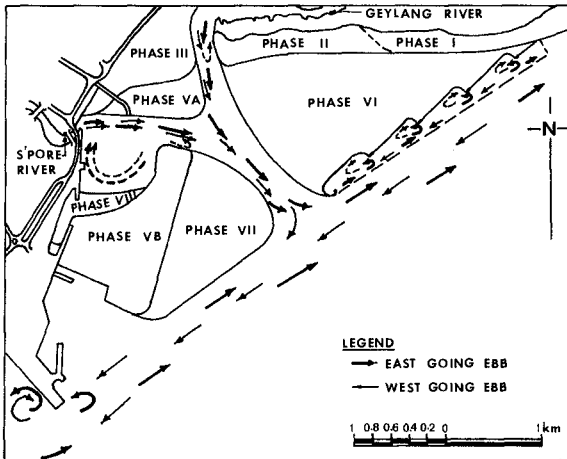


Figure 5 FLOW PATTERN WITH PHASES VI, VII & VIII
(with slight modifications)

From float track observation it was found that the average current velocity along the seaward face of Phase VII during east-going ebb was of the order of 0.36 to 0.38 m/sec. while that along the seaward face of Phase VI beyond the submerged stone bund was of the order of 0.42 to 0.47 m/sec. During west-going ebb the average current velocity along the seaward face of Phases VI & VII was of the order of 0.41 m/sec and that in the channel between Phases VI & VII was from 0.35 to 0.40 m/sec. The average current velocity between the submerged stone bund and the J-shaped bays of Phase VI varied from 0.17 to 0.23 m/sec.

It is however not practicable to modify the existing Phase V revetment because it had already been completed and the modification cost would be very high. In any case the flow pattern is no worse than that for the existing conditions, ie without Phases VI & VII.

To study the flushing characteristics of the lagoons, experiments were conducted on the tidal model by injecting fluorescent water soluble dye in the lagoons. A solution of fluorescent dye of known strength representing the pollutant was injected at a known uniform rate in the rivers and its dispersion under tidal activity with and without freshet discharge was studied over a period of 4 consecutive tides. It was observed that the strength of pollutant in the lagoons remained constant. Further experiments were conducted on the model by polluting only the lagoon water by fluorescent dye and its dispersion was studied with and without freshet discharge. It was observed that tidal activity equivalent to a 1-day duration for a tidal range of 3 m without freshet discharges from the rivers provided a dilution ratio of 5.5 in the new basin at Singapore River mouth and 23 in the Kallang Basin. With freshet discharge from rivers dilution ratios of 13.8 and 43.2 respectively were achieved at the end of a period equivalent to 1 day.

Results of the studies can be summarized as follows:-

- (i) Rise of water level in the lagoons caused by discharge (5-year flood) of various rivers coinciding with high tide would only be slightly over 3 cm. This was not measured on the tidal model because of the small vertical scale of the model. Instead the result was obtained by computation.
- (ii) Flushing characteristics of the lagoons would be satisfactory as indicated by no accumulation of pollutant in the model tests.
- (iii) Flow patterns would be satisfactory.
- (iv) Siltation characteristics would not change significantly with the construction of the proposed reclamation.

DESIGN OF SEABED STABILIZATION & REVETMENT

Because of the presence of thick soft marine clay strata at the reclamation site it is necessary to carry out seabed stabilization works in the form of dredged and sand filled trench, ie sand key.

Dimensions of sand key and ancillary components of stone bund and sea revetment were obtained by the method of slip circle analysis using the Bishop equation.

With known soil strength parameters obtained from offshore soil investigation and the trial dimensions for a given section as inputs for using a proprietary computer programme (Bishop method) numerous analyses were carried out to obtain a design with a minimum factor of safety of 1.30 against slip failure.

Final design sections adopted have factors of safety slightly over 1.30 and are founded on firm clay layer between upper and lower marine clay strata. An example of the results of one actual slip circle analysis is shown in Figure 6.

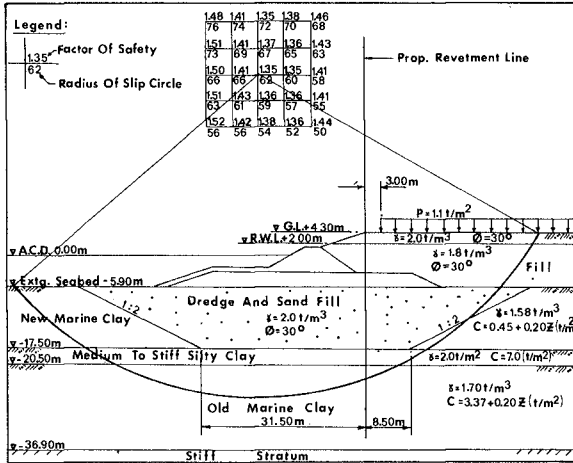


Figure 6 EXAMPLE OF SLIP CIRCLE ANALYSIS

Typical design sections for the stabilization works are shown in Figures 7 & 8.

Details of revetment are designed in accordance with the methods given in the Shore Protection Manual of the U.S. Army Corps of Engineers (4). The design wave height used is 1.7 m (25-year probable maximum height) (2) with a 5-second wave period.

Typical details of revetment are shown in Figure 9.

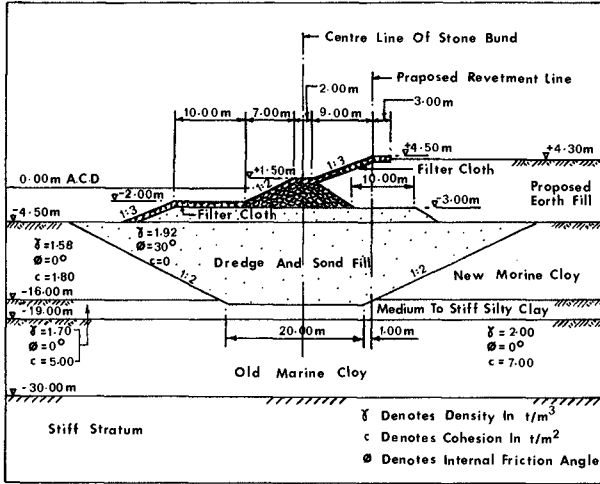


Figure 7 TYPICAL SECTION OF SEA REVETMENT

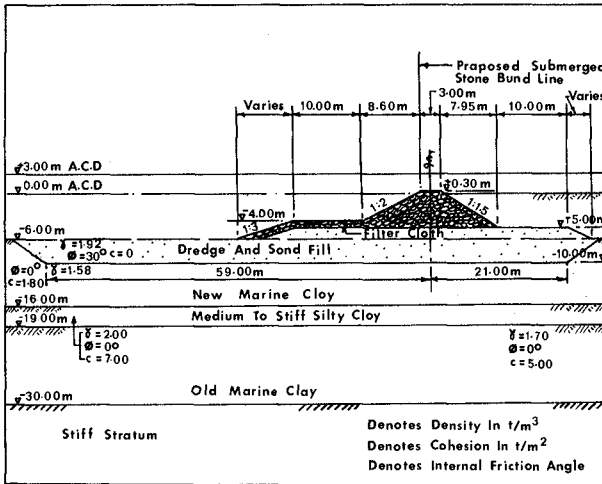


Figure 8 TYPICAL SECTION OF SUBMERGED STONE BUND

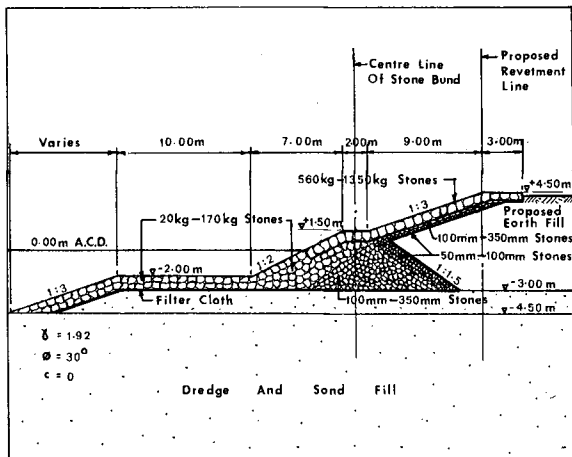


Figure 9 DETAILS OF STONE BUND AND REVETMENT

It can be seen that the sizes of the armouring units of granite blocks are generally somewhat bigger than those required by the design calculations. The reason for this is that the sizes adopted are those normally produced by local granite quarries and it would be uneconomical for contractors to break down the supplied sizes to the calculated sizes.

SHORE PROTECTION

For the whole of Phase VII and the western part of Phase VI shore protection in the form of sea revetment is adopted. However, in order to provide beaches for recreation, the southern edge of Phase VI is designed as an offshore platform with J-shaped bays between rip rap headland breakwaters. This method is based on a new concept (5) of protecting newly reclaimed shoreline by a series of shore-attached headland breakwaters (1), (2) and was first tried out successfully on earlier phases of the East Coast Reclamation further to the east (Plate 1).



Plate 1. Typical J-shaped bay between headland breakwaters
(Phase I reclamation).



Plate 2. Bucketwheel Excavator.

EXECUTION OF THE PROJECT

Execution of the current 2 phases of reclamation requires excavation of about 45 million cubic metres of earth from the Cut Site at Tampines (Figure 1). This excavation will pave the way for the development of Tampines New Town which will eventually house 225,000 people.

Excavation is being done by 2 large bucketwheel excavators (Plate 2) and the earth transported about 7 km by belt conveyors to a loading jetty (Plate 3) from which barges are loaded for transportation of the earth by sea over a distance of 12 km to the fill sites. The bucketwheel excavators and the entire conveyor system including the ship loader on the loading jetty are all electrically driven with a total power rating of about 10 MVA. Earthworks by this method has the advantage of very low noise and dust pollution as compared to the conventional method using traxcavators and tipper lorries.

Each bucketwheel excavator has a rated output of about 2,000 tonnes per hour while the conveyor system can handle up to about 5,000 tonnes per hour. Barges of various sizes ranging from 4,000 tonnes to 10,000 tonnes are used for the transporting operation.

The first stage of the construction involved dredging of the trench (Plate 4) for sand key to the design profiles followed by sand filling of the dredged trench. Depths of dredging are in the order of 16 m below A.C.D. (low low water level). A total of 4.5 million cu m and 5.5 million cu m of dredging and sand filling respectively are involved. At the same time the cut site and belt conveyor route preparations were carried out with construction of loading jetty, electrical system, overhead bridges and underpass across existing roads going on simultaneously.

Stone bund (Plate 5) was constructed over the sand filled trench to the design levels followed by temporary works of silt barricade. Two types of silt barricade, one using stone-filled gabions and the other using a floating screen are used to limit siltation in the adjacent port waters. Once a substantial portion of stone bund and silt barricade was completed the reclamation filling commenced, the timing being such that by then the cut site and conveyor system operations were ready.

Excavating, transporting and filling is now being carried out round-the-clock. At present about 60,000 tonnes per day are being executed. Initially direct dumping of fill material is possible until draught limitation necessitates unloading of the barges by reclaimer (Plate 6) and conveyor system on the newly reclaimed land.



Plate 3. Loading of fill material from the belt conveyor onto barges.



Plate 4. Dredging for sand key.



Plate 5. Stone bund at Phase VII reclamation site.



Plate 6. Reclaimer unloading fill material from barge into the sea to form reclaimed land.

The average median size of fill material from the cut site is 0.2 mm. After sorting by wave action it is expected that the average median size at mid-tide level will vary from 0.7 mm to 2 mm based on the results obtained in the earlier phases of reclamation(2).

Filling, grading and compaction to the final levels will be carried out by a combination of conveyor system and conventional equipment. The standard of compaction specified is a minimum dry density of 90% Modified AASHO Density at a level of 1 m below the finished level.

Other items of work such as construction of outlet drains, sea revetment, headlands and landscaping will form the last activities of the project.

CONCLUSION

The current Phases VI & VII of the East Coast Reclamation Scheme is one of the most prestigious and challenging projects ever carried out in Singapore.

Based on the current rate of progress it is anticipated that the Phase VII part of the reclamation will be completed by 1982 while the Phase VI part will be completed by 1984.

By early 1985 Singapore will have another 360 hectares of land on which will be built its city of the future.

REFERENCES

1. Chew, S.Y., Wong, P.P. & Chin, K.K. (1974) "Beach development between headland breakwaters", Proceedings of the 14th Coastal Engineering Conference, Copenhagen, Denmark, ASCE.
2. Chew, S.Y. (1976) "Processes and Beach Development between headland breakwaters, S.E. Coast of Singapore". Thesis for the Degree of Master of Engineering, University of Singapore (unpublished).
3. Central Water & Power Research Station Poona, India (1976) Note No. 24 Hydraulic Model Studies for proposed Reclamation Scheme Phases VI, VII & VIII (unpublished).
4. U.S. Army Corps of Engineers (1973) "Shore Protection Manual".
5. Silvester, R. (1960), "Stabilization of Sedimentary Coastlines" Nature Vol. 188, No. 4749.

SHIP-BRIDGE-PIER PROTECTIVE SYSTEMS

by

Akira Iwai¹, Hitoshi Nagasawa², Kazuki Oda³ and Kuniaki Shoji⁴

ABSTRACT

This paper describes the analytical and experimental studies on the behaviors of a ship subjected to a sheering flow induced around a rectangular solid-type marine structure, and also deals with ship-structure protective systems against ship impacts.

Large bridge piers, which are constructed in a narrow waterway with strong tidal currents, are treated herein as one of the typical solid-type marine structures.

INTRODUCTION

Owing to the recent increase of marine traffic and marine structures such as bridge piers in navigable waters, ship collision accidents with the structures have been increasing.

The collapse accidents of the Tasman Bridge of Australia in 1975, the Tjorn Bridge of Sweden in 1980 and the Sunshine-Skyway Bridge of America in 1980 were brought about by the very ship collision.

The national big projects for bridge construction aiming to link the Shikoku Island to the Main Land of Japan are put into practice at the present or under planning at different three routs by the Honshu-Shikoku Bridge Authority.

Most of their piers are being constructed or planning to be constructed in narrow straits with strong tidal currents where numerous marine accidents have occurred every year.

-
- 1 Professor of Navigation, Tokyo University of Mercantile Marine, Tokyo, Japan
 - 2 Director of Ship Structure Division, Ship Research Institute, Tokyo, Japan
 - 3 Associate Professor of Hydraulic Engineering, Osaka City University, Osaka, Japan
 - 4 Associate Professor of Marine Engineering, Tokyo University of Mercantile Marine, Tokyo, Japan

When a solid-type structure comparably large to a ship size is placed in strong tidal currents, sheering flows induced around the structures may cause serious navigational problems to the ships from the viewpoint of the safety maneuvering.

In this paper, bridge piers with a large rectangular cross section are treated as one of the marine structures, and the behaviors of ships navigating under the effects of sheering flows around the pier are predicted by means of an analytical method. And on the basis of the analytical results on the ship behaviors, the required minimum clearances between the ship courses and the pier to avoid collision accidents are proposed.

Moreover, the impact forces in the bow collision are estimated on the basis of the test results of the load-deformation characteristics of ship bows. And the load-penetration characteristics of proposed buffering devices are described.

SHIP BEHAVIORS NEAR THE PIER

Model experiments were carried out in a flow channel of Osaka City University, which is 35 m long, 4.0 m wide and 75 cm deep, to obtain the data of hydrodynamic exciting forces exerted on the ship due to sheering flows around the pier under conditions of reverse currents and zero ship speed.

One kind of ship model and three kinds of pier models were used. The length of the ship model was 100 cm. Though the length of the lateral side was maintained at 27 cm in all models, the length ratios of the longitudinal side to the lateral side, L_p/B_p , were varied 1.67, 2.00 and 2.33. The pier model of $L_p/B_p = 1.67$ was mainly used in the experiments. The length ratio of the lateral side of the pier model to the ship model, B_p/L_s , were varied 0.27 and 0.54.

The flow direction and the longitudinal axis of the ship model were kept normal to the lateral side of the pier model.

Hydrodynamic swaying forces and yawing moments on the ship model were measured by using dynamometers. And the hydrodynamic coefficients of swaying forces and yawing moments were obtained from Eqs. (1) and (2).

$$C_Y = Y_C / \frac{1}{2} \rho L_s d v^2 \quad (1)$$

$$C_N = N_C / \frac{1}{2} \rho L_s^2 d v^2 \quad (2)$$

where Y_C and N_C are respectively swaying forces and yawing moments, C_Y and C_N are coefficients of swaying forces and yawing moments; L_s and d are the length and the draft of the ship model; and v is the flow velocity; ρ is density of water.

Fig. 1 shows one example of the experimental results of the distribution of coefficients of swaying forces and yawing moments obtained from Eqs. (1) and (2) in case of $B_p/L_s = 0.27$ and $L_p/B_p = 1.67$. It may be said from Fig. 1 that both coefficients of swaying forces and yawing moments decrease exponentially with an increase of the dimensionless coordinates of the ship center x_0/B_p (or x_0/L_p) and y_0/B_p .

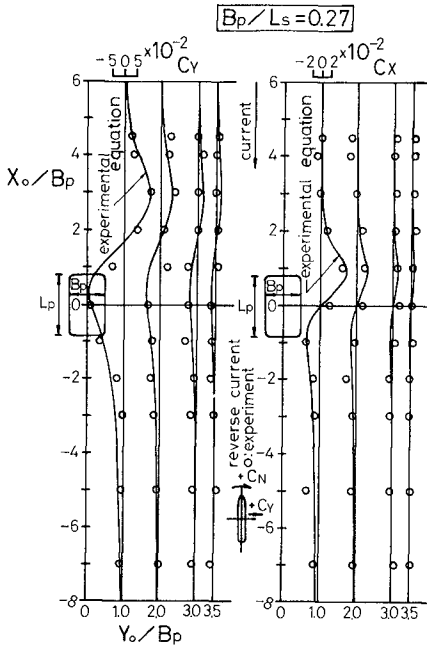


Fig. 1 Distribution of the hydrodynamic coefficients of swaying forces and yawing moments

For the purpose of the estimation of coefficients of swaying forces and yawing moments in numerical calculations of the ship motions, the following empirical equations were derived as functions of x_0/L_p and y_0/B_p on the basis of the whole experimental results.

$$C_Y = \begin{cases} \frac{0.266y_0/|y_0| (x_0/L_p - 1) \exp[-0.86(|y_0|/B_p - 1)]}{1 - (x_0/L_p - 1)^3} & ; x_0/L_p \leq 1.0, y_0/B_p \geq 0.5 \\ \frac{0.196y_0/|y_0| \cdot (x_0/L_p - 1) \exp[-0.86(|y_0|/B_p - 1)]}{1 + (x_0/L_p - 1)^4} & ; x_0/L_p > 1.0, y_0/B_p \geq 0.5 \end{cases} \quad (3)$$

$$C_N = \left\{ \begin{array}{l} \frac{0.110y_0/|y_0| \cdot (x_0/L_p - 1) \exp[-0.98(|y_0|/B_p - 1)]}{1 + 4(x_0/L_p)^2} ; x_0/L_p \leq 1.0, y_0/B_p \geq 0.5 \\ \frac{0.935y_0/|y_0| \cdot (4x_0/3a) \exp[-0.98(|y_0|/B_p - 1)]}{1 + (4x_0/3L_p)^5} ; x_0/L_p > 1.0, y_0/B_p \geq 0.5 \end{array} \right. \quad (4)$$

where x_0 and y_0 are the coordinates of the ship center in O-X₀Y₀ coordinate system shown in Fig. 1.

The solid lines in Fig. 1 denote the coefficients estimated from Eqs. (3) and (4).

Substituting these hydrodynamic forces and moments estimated from the empirical equations as nonlinear external disturbances into the equations of ship maneuvering motions expressed by simplified Eq. (5) and solving the equations of ship motions by numerical techniques, ship trajectories in the vicinity of the pier are obtained.

$$\left. \begin{array}{l} (m + m_x)\dot{u} = mvr \\ (m + m_y)\dot{v} = Y_{vV} + (-mu + Y_r)r + y\delta\dot{\delta} + Y_C \\ (I_{ZZ} + J_{ZZ})\dot{r} = N_{vV} + N_r r + N\delta\dot{\delta} + N_C \end{array} \right\} \quad (5)$$

where m = mass of the ship; m_x and m_y = respectively added masses in sway and yaw motion; I_{ZZ} and J_{ZZ} = moment of inertia and added moment of inertia of the ship about the vertical axis through the center of ship gravity; u , \dot{u} , v , \dot{v} = respectively components of the ship velocity and acceleration in X and Y axis direction (referred to Fig. 2); r and \dot{r} = angular velocity and acceleration about the vertical axis; Y_v , N_v , Y_r and N_r = hydrodynamic coefficients concerning damping forces and moments respectively; Y_δ and N_δ = hydrodynamic coefficients of swaying forces and yawing moments induced by steering; δ = rudder angle; Y_C and N_C = exciting swaying forces and yawing moments given by Eqs. (1) and (2).

It was assumed in the calculation that the ship comes up to the pier with an initial course parallel to the longitudinal side of the pier. Steering simulation was performed so as to give a rudder angle of 15 degrees to the occurrence of yaw angle deviation of 2 degrees from the initial straight course.

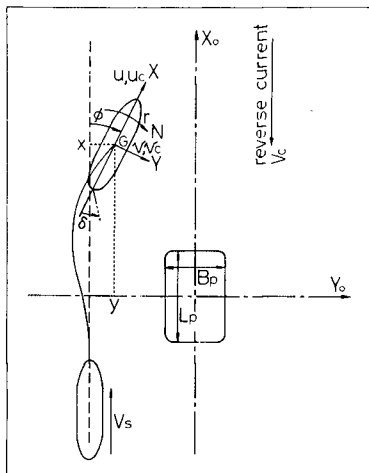


Fig. 2 Coordinate system

Values of added masses, added moment of inertias and other hydrodynamic coefficients concerning damping forces and moments used in the calculation are given in Table 1.

Table 1 Values of hydrodynamic coefficients used in the calculation of ship moments

Swaying motion		Yawing motion	
$\frac{m + m_x}{\frac{1}{2} \rho L_s^3}$	0.018	$\frac{I_{zz} + J_{zz}}{\frac{1}{2} \rho L_s^5}$	0.0015
$\frac{Y_v}{\frac{1}{2} \rho L_s^2 V}$	-0.01434	$\frac{N_v}{\frac{1}{2} \rho L_s^3 V}$	-0.00460
$\frac{Y_r - \mu u}{\frac{1}{2} \rho L_s^3 V}$	0.00456	$\frac{N_r}{\frac{1}{2} \rho L_s^4 V}$	-0.00296
$\frac{Y_\delta}{\frac{1}{2} \rho L_s^2 V^2}$	-0.00332	$\frac{N_\delta}{\frac{1}{2} \rho L_s^3 V^2}$	0.00165

where V is the ship velocity relative to currents.

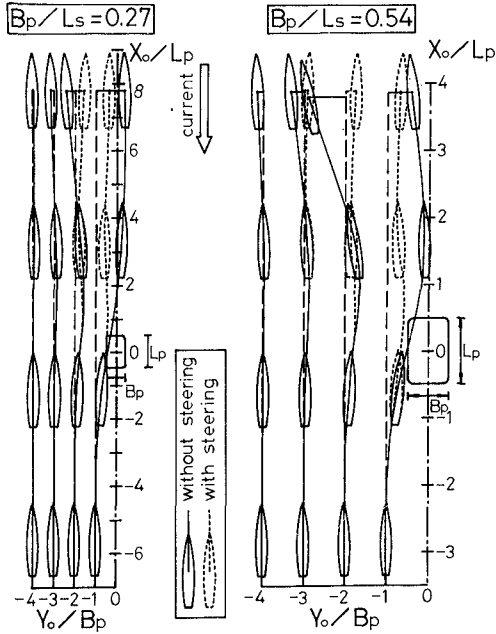


Fig. 3 Examples of the calculated ship trajectories ($v_c/v_s = 0.75$)

Fig. 3 shows two examples of the ship trajectories calculated under the condition of $v_c/v_s = 0.75$ in the cases of $B_p/L_s = 0.27$ and 0.54 respectively. Herein, v_c is the current velocity and v_s is the ship velocity.

It can be said from Fig. 3 that the effect of sheering flow around the pier on the ship course keeping becomes larger with an increase in the length ratio of the lateral side of the pier to the ship, B_p/L_s .

REQUIRED SHIP COURSE CLEARANCE TO THE PIER

The maximum normalized sway deviation $\Delta y_m/L_s$ and yaw deviation $\Delta\phi_m$ from the initial straight course are shown in Fig. 4 (a) and (b) respectively for the case of $B_p/L_s = 0.27$ and $B_p/L_s = 0.54$ with respect to the normalized coordinate of the initial ship course, y_0/B_p . Herein, Δy_m and $\Delta\phi_m$ are the maximum sway and yaw deviation caused within a distance of one ship length away from the upstream side of the pier.

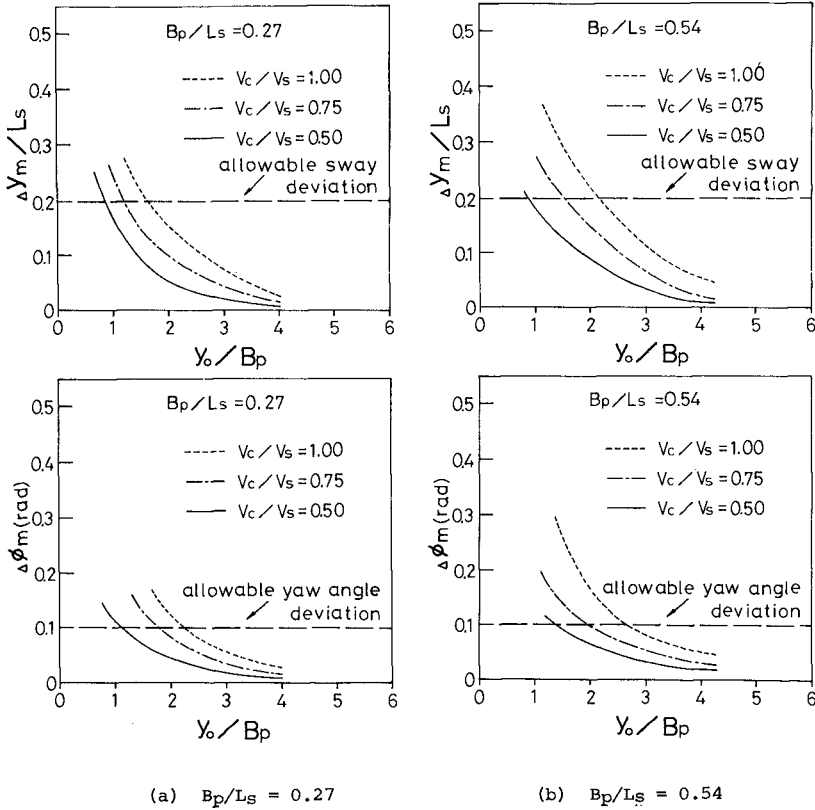


Fig. 4 Relationship between the maximum normalized sway deviation and the normalized coordinate of the initial ship course

If the allowable deviation of ship motions from the initial course are limited to 0.1 radian (about 5.7 degrees) in yaw angle and 0.2 time the ship length in sway displacement from the viewpoint of safety ship handling, the minimum required distance of the ship course from the pier center needed to avoid the collisions of the ship to ship as well as the ship to pier may be determined in the manner which is shown in Fig. 4 (a) and (b).

The minimum required distances from the pier center obtained in the manner mentioned above are shown in a solid line for the case of $B_p / L_s = 0.27$ and in a dotted line for the case of $B_p / L_s = 0.54$ in Fig. 5.

It may be said from Fig. 5 that the minimum required distance become larger with an increase in the velocity of tidal currents relative to the ship velocity.

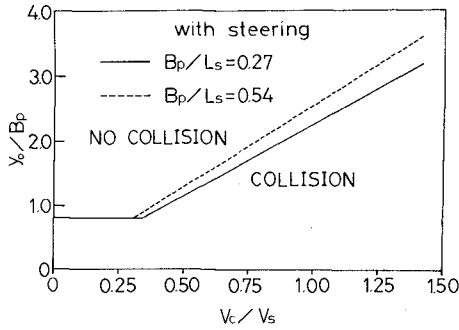


Fig. 5 The minimum required distance of the ship course from the pier center

Fig. 5 is interpreted that for instance, when $V_c/V_s = 1.0$ in the case of $B_p/L_s = 0.54$, ships are recommended to navigate more than 2.6 times the length of lateral side of the pier away from the pier center in the distance. In other words, ships should pass near the pier having a clearance more than about 2.1 times the length of the lateral side from the longitudinal side.

COLLIDING FORMS OF THE SHIP

The behaviors of a drifting ship due to currents were experimentally observed in the vicinity of the pier by means of taking sequent pictures using a auto-driven camera.

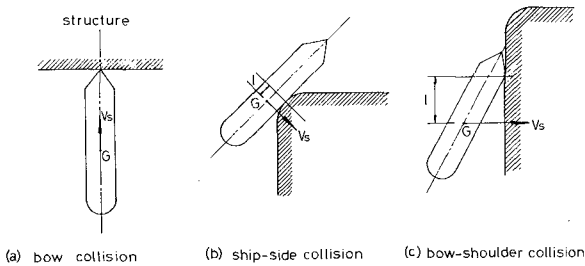


Fig. 6 Classification of the main colliding forms of the ship

Through the examinations of the ship behaviors in both navigating and drifting near the pier obtained by means of the previous description, colliding forms of the ship against the pier may be classified mainly into three cases as shown in Fig. 6.

It may be said from the viewpoint of designing protective systems that the most serious case is the bow collision among these colliding forms.

LOAD-DEFORMATION CHARACTERISTICS OF THE SHIP BOW

Static collapse tests were conducted to examine the load-deformation characteristics using steel bow models which simulate the transversely framed structure of cargo-type ships of 500 G.T. and 4,000 G.T.

The models are made in a scale of 1:4 for 500 G.T. ship and in a scale of 1:8 for 4,000 G.T. ship.

For 500 G.T. ship, two kinds of bow models with a raked stem and with a vertical stem while only one kind of model with the vertical stem was used for 4,000 G.T. ship. The models with the vertical stem were used for the simplification of the tests. Fig. 7 shows a diagram of the one-fourth scale bow model of 500 G.T. ship with the raked stem.

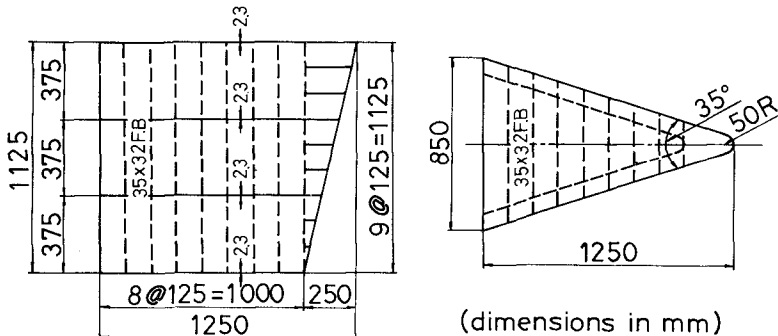


Fig. 7. One-fourth scale bow model of 500 G.T. ship

Fig. 8 shows the test results of the load-deformation characteristics of the 500 G.T. type bow model with the vertical stem in comparison with the test results for the bow model with the raked stem. In Fig. 8, a solid line denotes the test results for the case of the vertical stem, and a broken line for the case of the raked stem.

It can be seen in Fig. 8 that there is little difference between the load-deformation curves for the bow models with the raked stem and with the vertical stem in the range of the deformation larger than the

length of the raked stem while the collapse loads near zero deformation show the great differences between them.

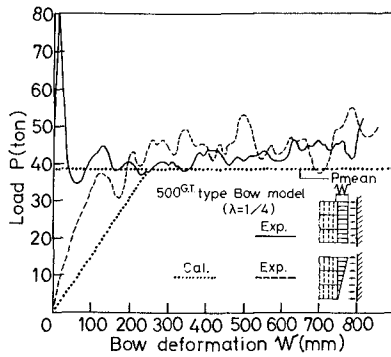


Fig. 8 Comparison between the load-deformation curves for two kinds of bow models of 500 G.T.

Fig. 9 also shows the characteristics of the load-deformation of one-eighth scale bow model of 4,000 G.T. with the vertical stem.

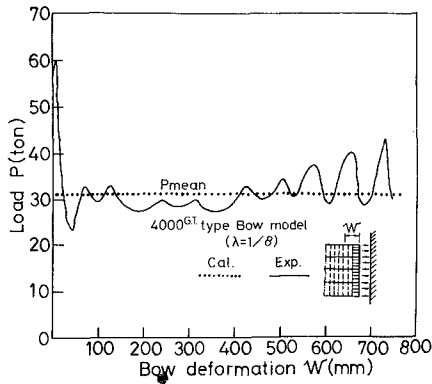


Fig. 9 Load-deformation curves of a one-eighth scale bow model of 4,000 G.T.

From these test results, it was found that the relationship between the load and the bow deformation is characterized by the buckling strength of a rectangular panel hull plate between the transverse frames (referred to Fig. 10) and the load-bow deformation curve can be simplified and represented as shown in Fig. 11.

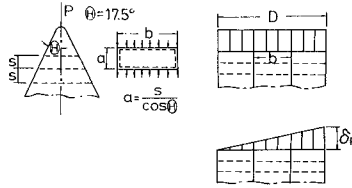


Fig. 10 Definition diagram of the rectangular panel hull plate

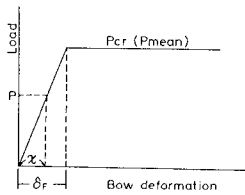


Fig. 11 Simplified load-bow deformation curve

In Fig. 11, δ_f is a raked stem length which is equal to about a quarter of the depth in usual ships and P_{CR} is the component of a buckling load of the rectangular panel hull plate of the bow in the direction of the longitudinal ship axis which is expressed by Eq. (6)

$$P_{CR} = 2Dt \cos\theta \times \sigma_{CR} \tag{6}$$

where D = the depth of the ship; t = the thickness of the hull plate; θ = the entrance angle of the bow; and σ_{CR} = the buckling stress of the rectangular panel plate expressed by Eq. (7).

$$\sigma_{CR} = \kappa \left\{ \frac{\pi^2 E}{12(1 - \nu^2)} \right\} (t/b)^2 \tag{7}$$

where κ = buckling coefficient; E = Young's modulus; ν = Poisson's ratio; and b = the depth of the panel.

The dotted lines in Figs. 8 and 9 represent the calculated results by Eqs. (6) and (7) in comparison with the experimental results. Generally, it can be stated that the agreement between the calculated and the experimental results is satisfactory.

ESTIMATIONS OF THE IMPACT FORCES

Using the simplified load-deformation curve of the bow hull, ship impact forces can be estimated at the bow collision with a right angle against a vertical flat plane of a rigid bridge pier. The estimated results herein are graphically shown for the ship collision ranging from 500 G.T. to 4,000 G.T. in Fig. 12.

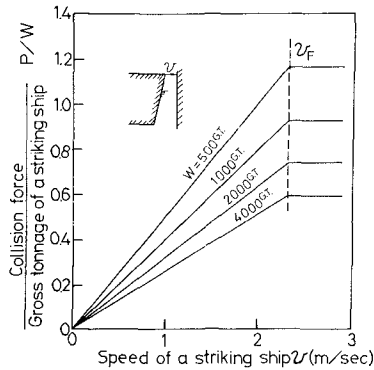


Fig. 12 Estimated impact forces at the bow collision

In Fig. 12, V_F is the speed of the striking ship resulting in the full collapse of the part of the raked stem. According to Fig. 12, V_F is equal to about 2.3 m/sec for every ship ranging from 500 G.T. to 4,000 G.T., and the maximum impact forces are estimated to be about 580 tons for the 500 G.T. ship and about 2,400 tons for the 4,000 G.T. ship.

Judging from the viewpoint of designing the ship-pier protection, it may be said that the striking ship speed should be less than the value of V_F using other detached-type fendering systems, or the impact forces should be reduced to the values less than the buckling loads of the bow hull plate by means of effective buffer devices installed on the pier. Herein, the ship-pier protective systems based on the latter idea were described.

PROPOSED BUFFER DEVICES AND THE FORCE-DEFORMATION CHARACTERISTICS

Four kinds of buffer devices were proposed which are coarse grid-type, dense grid-type, grid-composite-type filled up with hard polyurethane foam and composite-type filled up with hard polyurethane foam.

The schematic diagrams of the models of the proposed buffer devices are shown in Fig. 13 and the model dimensions of the coarse grid-type and the composite-type are shown in Fig. 14. The compressive strength of hard polyurethane foam used in the tests are 1.4 Kg/cm^2 .

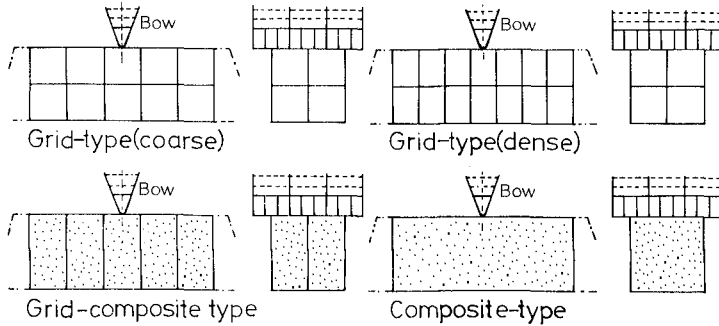


Fig. 13 Schematic diagram of the models of the proposed buffer devices

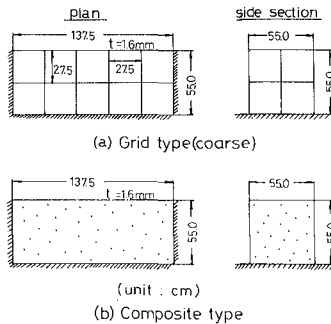


Fig. 14 Model dimensions of the coarse grid-type and the composite-type

The comparisons between the force-bow penetration curves for the preceding four kinds of buffer devices are shown in Fig. 15. They were obtained from the static fracture tests performed by the use of a one-eleventh scale rigid bow model of 4,000 G.T. ship.

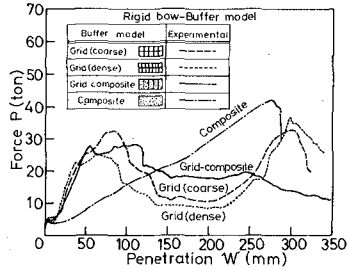


Fig. 15 Comparisons between the force-bow penetration curves for four kinds of buffer devices

It appears from Fig. 15 that the composite-type buffer device has almost linear characteristics in the relationship between the force and the ship penetration while other three kinds of buffer devices have somewhat complicate characteristics.

Every ship has a different bow collapse load because it depends on the size and the structure of the bow itself. The composite-type buffer device has the characteristic capable of absorbing the impact energies in relatively small reactive forces. Therefore, it can be stated from the viewpoint of practical designing that the composite-type is the most suitable buffer device among the proposed ones.

It was found from the further static fracture tests using a elastic bow model which simulates an actual bow that the linear superposition of the independent load-deformation characteristics of the bow itself and the buffer itself can be adapted for the estimation of the combined load-deformation characteristics in the ship-buffer collision.

The composed deformations of the bow and the respective buffer devices at the 4,000 G.T. ship collision were estimated in prototype values on the basis of the test results as shown in Fig. 16.

Fig. 16 shows that the composite-type has much larger deformation in comparison with the other three types. Fig. 17 shows the estimated results of the impact forces versus the penetration at the 4,000G.T. ship collision against the composite-type buffer device 4.0 m broad in which t and q represent the thickness of the steel plate of the

buffer and the compressive strength of hard polyurethan foam respectively.

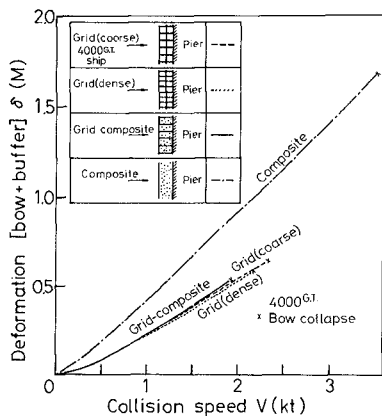


Fig. 16 Composed deformations of the bow and the respective buffer devices at the 4,000 G.T. ship collision

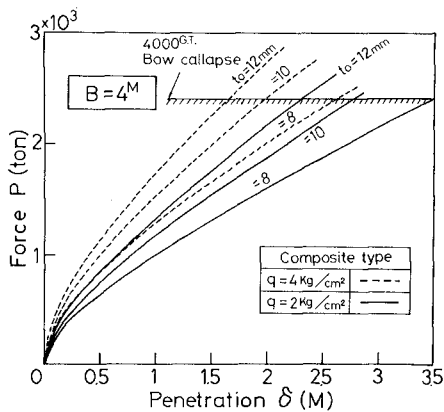


Fig. 17 Impact forces versus the penetration at the 4,000 G.T. ship collision against the composite-type buffer device

SUMMARY AND CONCLUSIONS

In this paper, the behaviors of ships navigating under the effects of sheering flow around the solid-type bridge pier were predicted by means of the numerical analyses and the experiments in the flow channel.

Based on the previous predicted results, the minimum clearances between the ship course and the longitudinal side of the pier, which are required to avoid the ship-pier collision, were proposed.

The load-bow deformation characteristics for the ships ranging from 500 G.T. to 4,000 G.T. were examined by the bow collapse tests and were represented by the simplified equation.

Using the simplified load-bow deformation curve, the impact forces were estimated at the bow collision with a right angle against the vertical flat plane of the rigid bridge pier without any buffer devices.

The composite-type buffer device filled up with hard polyurethane foam was selected as the most suitable one among the proposed four kinds of buffer devices. And the impact forces at the 4,000 G.T. ship collision against the composite-type buffer device were estimated.

ACKNOWLEDGEMENT

The authors are grateful to Dr. S. Nagai, Professor Emeritus of Osaka City University and Dr. H. Tani, Professor of Tokyo University of Mercantile Marine for their guidance and encouragement given during this study.

WAVE-WAVE INTERACTIONS, CURRENT-WAVE INTERACTIONS
AND RESULTING EXTREME WAVES AND BREAKING WAVES

by

SØREN PETER KJELDTSEN & DAG MYRHAUG
Senior Research Engineers

Norwegian Hydrodynamic Laboratories
Trondheim, Norway

ABSTRACT

The influence of an opposing current on highly non-linear transient breaking waves in deep water is described quantitatively from experiments. 3 new parameters that describe crest front steepness and wave asymmetry are introduced. Further, joint probability density distributions are obtained from an analysis of field data containing nearly 25000 storm waves. Thus, a tool is provided from which estimates for probabilities for occurrences of steep breaking waves in deep water, may be obtained.

1. INTRODUCTION

Detailed knowledge of the kinematics, dynamics and frequencies for occurrences of large breaking waves in deep water is important, and has many practical applications, due to the following reasons:

- 1) Experiments have now confirmed that transient, near breaking and breaking waves attain velocities up to 2.8 times the first order phase velocity. Local accelerations in the wave can attain values somewhat above 3 times the gravity acceleration (KJELDTSEN et al., 1980). Such results may be applied to evaluation of the operation and stability of ships under severe sea conditions. Further,

such results provide the basis for the estimation of wave drag and inertia forces from extreme breaking waves in deep water with many applications to the design and safety of offshore structures.

- 2) The large breaking waves give rise to the largest environmental pressures, both on fixed and floating structures, in the form of shock or impact impulses with a duration of some milliseconds.
- 3) The breaking waves give rise to the most effective mechanism for transfer of momentum from the wind to a mean surface current, (dominant compared with dissipation of non-breaking waves, LONGUET-HIGGINS, 1969). This implies that a detailed knowledge of ratios of breaking waves compared to the total number of waves has important practical applications for the evaluation of dispersion of pollution (e.g. hydrocarbons).

In order to evaluate safety at sea, a basic need is a prediction of the characteristics of extreme sea states. There is an extensive literature on the subject of the mysterious disappearances of ships, both large and small. A high percentage of these mysteries can be solved by even a cursory study of so-called 'freak waves' (a freak being 'capricious change'), which are more correctly termed extreme waves. In the following the term extreme waves will be used, since these are recurring events along the continental margins. Extreme waves occur in virtually all such areas during certain predictable times of the year, but the origin of these waves is not fully understood. It is believed that a shoaling mechanism, unique to a certain geographic location, as well as particular random phase relationship between waves, can account for the phenomenon. However, also an opposing shear current might change the wave conditions in an abrupt way, in particular in areas where the waves travel against a current gradient. Known areas of destructive waves are the Nova Scotia coast, the Bermuda rise, the water off Greenland, the coast of North West India, and the water off the South East African coasts, where the Agulhas current opposes the main dispersion direction of the waves. Also certain parts of the Norwegian Continental Shelf seem to contain areas where such extreme waves occur. In the

period 1970-1979, 26 Norwegian trawlers and freighters were lost due to capsizing in very rough seas. Reports from the Courts of Inquiry show that for 13 of these vessels surviving members of the crew confirmed a capsizing in extreme waves. In 13 other cases the vessels disappeared in very bad weather, the reasons being unknown, but capsizings in extreme waves were concluded to be the most probable. Altogether 72 lives were lost. (NEDRELID, 1978.)

In 1978 a new project, "SHIPS IN ROUGH SEAS", was initiated by a coordinating board with the Royal Norwegian Council for Scientific and Industrial Research, the Norwegian Fisheries Research Council and the Norwegian Maritime Directorate as sponsors. The aim is to use theoretical and experimental work and practical experience to improve the understanding of manoeuvring, rolling and capsizing, i.e. the response of ships to severe conditions in the form of extreme movements. Further, it is the aim of the project to try to establish new criteria for the stability of the vessels on the basis of knowledge of extreme environmental conditions and the motion properties of the vessel. This will be an improvement compared to the established stability criteria which consider movement of a ship in calm water or in regular waves. One of the main activities for this new project is:

To locate exposed areas in Norwegian waters where the probabilities for occurrences of extreme waves and breaking waves are most pronounced, and contribute to the development of forecast methods for such areas.

Results of a survey of areas on the Norwegian Continental Shelf with typical large scale refraction and current-wave interaction effects are shown in Fig. 1 (KJELDEN & MYRHAUG, 1978). Also, positions and estimated headings are shown for 24 of the lost vessels.

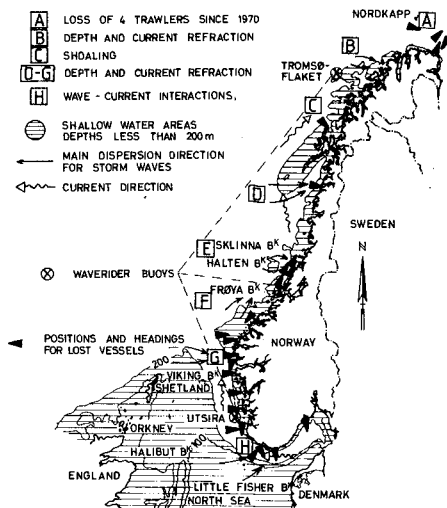


Fig. 1. Exposed areas on the Norwegian Continental Shelf, with positions and headings for lost Norwegian vessels. Foreign vessels lost in the same area are not shown.

An inquiry to all pilot offices in Norway has now indicated several local areas where probabilities for occurrences of extreme waves are believed to be higher than the average, under certain weather conditions. It is now remarkable that such 'Red Areas' agree very well with the mapping of earlier accidents, shown in Fig. 1. Altogether 19 local 'Red Areas' are now identified. (DAHLE, 1979.)

2. BASIC DEFINITIONS

A well defined quantitative description of transient highly asymmetric waves of finite amplitude approaching the point of breaking is needed. In general, finite amplitude storm waves at sea will not appear with a symmetric shape (as a high order Stokes wave), but will have a pronounced asymmetry, both with respect to a vertical and a horizontal axis. This is due to a sheltering effect, which gives rise

to pressure differentials over the upwind and leeward side of the crests. Further, the common wave steepness defined as $s = H/L$, where H is the total wave height and L is the wave length, does not represent a unique definition of steepness for extreme waves, as several asymmetric waves can exist with the same total steepness s , both with very different steepnesses of the wave crests.

The present study utilises the advantages that are contained in a zero-downcross analysis. This analysis uses the wave trough and the proceeding wave crest in the definition of a single wave, and defines the wave height as the difference between these water levels, Fig. 2. (The conventional zero-upcross analysis defines a single wave as a wave crest and the following wave trough, and *thus obtains a wave height behind and not ahead of a possible breaking wave.*) The zero-downcross analysis is therefore believed to be the only analysis which provides parameters that are a representation of the physical conditions with relevance to breaking waves, and thus, the only parameters which should be correlated with measurements of ship response or shock pressures.

Furthermore, careful observations show that the wave trough ahead of a breaking wave always appears with a certain and very characteristic shape, and finally the zero-downcross wave height is the only height corresponding to visual wave observations. It is thus only oceanographic wave data treated with the zero-downcross analysis that represents a reasonable basis for a comparison with the vast amount of existing wave observations, made from observers on ships and shore, collected and distributed by national meteorological institutions.

The present study provides a more accurate description of steepness and asymmetry in transient near breaking waves, when the three following parameters are introduced:

Crest front steepness:

$$\epsilon \equiv \frac{n'}{L'}$$

Vertical asymmetry factor:

$$\lambda \equiv \frac{L''}{L'}$$

Horizontal asymmetry factor:

$$\mu \equiv \frac{n''}{H} \quad (1)$$

The definitions are shown in Fig. 2. Here η' is the crest elevation measured from mean water level, while L' and L'' are horizontal distances defining the position of the wave crest relative to the zero-crossing points. It is generally accepted that use of the crest elevation for design applications provides a basic parameter more relevant to finite amplitude wave geometry than the wave height. Observations of breaking waves show that these waves can be characterized by a very steep crest front and high asymmetry factors. The ϵ -parameter is thus a mean front crest inclination.

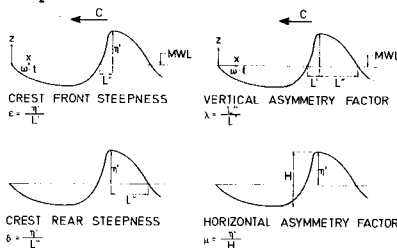


Fig. 2. Basic definitions for asymmetric waves of finite height. (KJELDSEN & MYRHAUG, 1978.)

In this study the mean water level, MWL is defined as the still water level in a wave flume before the start of an experiment. For field data the mean water level is defined as the arithmetic mean of a 20 minutes recording period of surface fluctuations.

Thus, in our definition λ describes asymmetry with respect to the vertical axis in the crest, while μ describes asymmetry with respect to a horizontal axis in the mean water level. It is now possible to obtain the crest rear steepness directly as: $\delta \equiv \epsilon/\lambda = \eta'/L''$.

In the following deterministic experiments in the laboratory with extreme deep water waves will be described in section 4. A range of variation and maximum values of the parameters ϵ , μ and λ will be given, both for the case with interacting deep water waves, and for the case with interacting waves superposed upon an opposing shear current.

Then, in section 5 results from a statistical analysis of 25000 storm waves from Norwegian waters are given. This

analysis provides joint probability density distributions that relate the ϵ -parameter to a particular sea state. Thus, a tool from which estimates for probabilities for occurrences of steep and breaking waves in deep water might be obtained.

3. EXPERIMENTAL ARRANGEMENT

A new transient test technique is developed for generation of extreme storm waves in deep water. The waves appear as plunging breakers, deep water bores and spilling breakers, together with very steep near breaking waves, and are created from wave-wave interactions of several individual single wave components.

In deterministic laboratory experiments extreme waves are obtained at a specified time and location. At the Norwegian Hydrodynamic Laboratories this new technique is now developed to a level where on-line testing of fixed and floating structures under extreme deterministic conditions is possible and already undertaken. However, in this study only test series with extreme waves freely dispersing without interaction with structures will be discussed. The test arrangement is shown in Fig. 3.

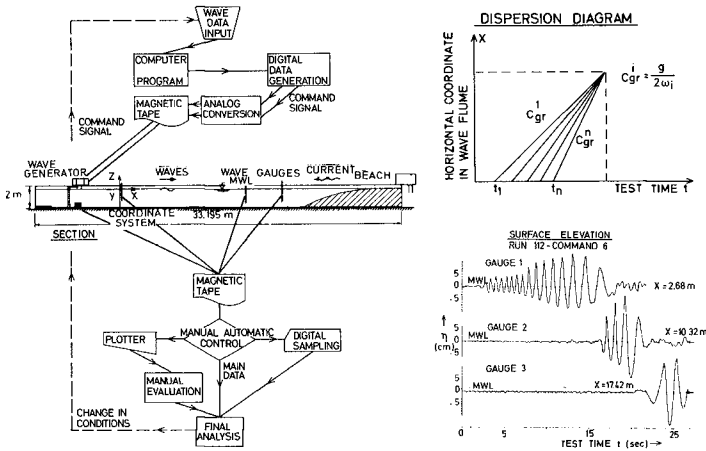


Fig. 3. Arrangement for wave-wave and current-wave interaction experiments.

Comprehensive series of experiments were performed in a 33 m long, 1 m wide and 1.60 m deep wave flume, equipped with a computer controlled hinged flap type wave generator at one end, and an energy absorbing parabolic beach at the other end. Further, it was possible to introduce a surface current at the beach with a discharge of $0.050 \text{ m}^3/\text{sec}$. The current opposes the dispersion direction of the waves and is extracted in front of the wave generator. The extreme breaking waves in deep water were obtained using several methods. One of them was to utilize the dispersion properties of gravity waves in a wave train. When the rate of change of the cyclic frequency for the wave train was kept constant, a transient event was obtained, where all available wave energy was concentrated at one nodal point in the flume, 12 m from the wave generator, Fig. 3. Surface elevations were measured with wave staffs, and fluctuating particle velocities with electromagnetic current meters.

Synoptic recordings of the surface form and breaker development were obtained with a high-speed movie camera operated with 300 frames/sec. synchronously with the wave staffs. The obtained synoptic wave profiles were then digitized with great accuracy in a motion analyzer.

In a model basin there are major difficulties in obtaining accurate measurements of breaking waves, or of the response of structures to breakers. One is that of generating highly non-linear finite amplitude water waves without scale effects in the flume (without correspondence to the ocean). Such sources of inaccuracy are:

- 1) Generation of higher harmonics which propagate with phase velocities other than the basic wave. Superposition of such harmonics on the basic wave gives rise to disturbances in the breaking process itself.
- 2) The wave-induced mass transport is not reproduced correctly in a wave flume. In the ocean, non-linear waves give rise to a drift velocity in the direction of propagation. In a wave flume this net drift is reflected by the beach and returns to the wave generator, and thus a circulation pattern is obtained, with the result that the kinematic profiles in the waves have no mean drift and therefore are not similar to the kinematic profiles in the ocean.

The new transient test technique avoids some of these difficulties, and takes advantage of the small time domain in which progressing waves occur with the correct drift velocity, before unwanted harmonic transients from the wave generator reach the section of observation.

4. EXPERIMENTAL RESULTS

A striking result of the experiments with breaking waves in deep water, is that the observed wave-wave interaction phenomena lead to the generation of breaking waves which can all be classified as (belonging to) three distinct types of wave forms, Fig. 4. It is obvious that many different forms of breaking waves can exist in deep water during advanced sea states. However, when only two-dimensional waves are considered, the number of wave forms decreases rapidly.

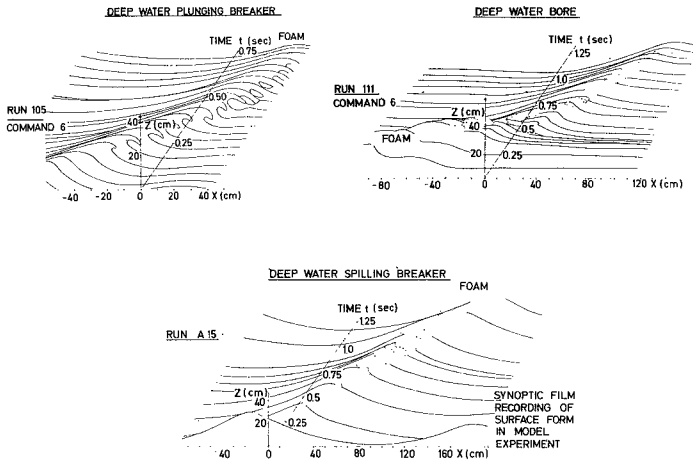


Fig. 4. Classification of breaking waves in deep water.

The first type is a deep water plunging breaker, which is a violently breaking wave, generated by interaction of several individual waves. The second type is a deep water bore. This breaker appears as a result of a highly non-linear wave-wave interaction phenomenon, in which one wave phase overtakes another. The overlying wave proceeds in a way which can be observed to be very similar to the travel of a tidal bore. The duration of the breaking is much longer than for a normal spilling breaker, and the asymmetry is very pronounced, with crest elevations which can approach 90% of the total wave heights. When the two wave phases finally meet, the whole front is nearly vertical and breaking.

The third breaker type, observed as results of wave-wave interaction experiments, is the spilling breaker, commonly known as "white capping". This breaker is a very symmetrical breaking wave. This study reports experimental evidence of all three. It is therefore a contribution to the classification of types of breaking waves in deep water, akin to the work by GALVIN (1968), in which breaking waves on beaches were classified.

Particular attention should be given to the results concerning the particle velocities in breaking waves. Fig. 5 gives a map of the horizontal velocity component at five levels for a situation with a plunging breaker, generated from a highly non-linear interaction of several waves in a wave train. In these experiments the rate of change of cyclic frequency was kept constant. The map is obtained as the mean of 26 plunging breakers, which all broke at the same nodal point under identical test conditions. Standard deviations for the measured surface elevations are plotted on the surface contour in order to demonstrate the accuracy of the experiments. The current meter was installed beneath the point where the wave profile became vertical, and the map gives the development in time of the particle velocity and the surface elevation at this position. The linear phase velocity c_{0B} corresponds to the measured wave period at the point of breaking. A considerable phase lag is found between the wave crest and the point where the maximum in the horizontal particle velocity appears. This effect is partly due to limitations in the dynamic response of the current meters. In deep water plunging breakers approximately one wave amplitude below mean water level, the measured particle velocities showed only minor deviations from linear theory.

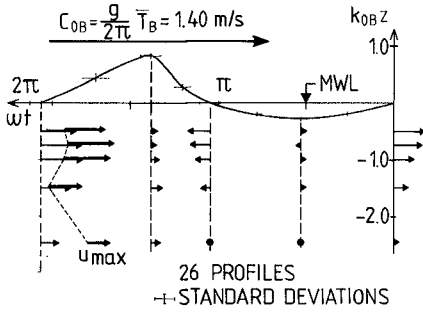


Fig. 5 Non-dimensional plot of surface elevation and horizontal particle velocities in plunging breakers as functions of time

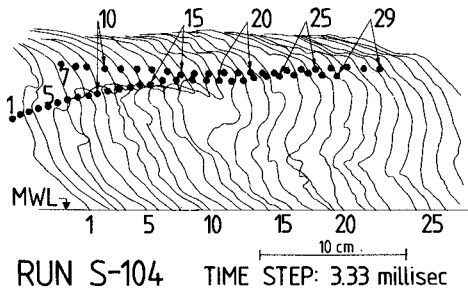


Fig. 6 Particle trajectories in the crest of a plunging breaker

Fig. 6 gives an example of the particle trajectories for a Stokes wave disturbed by a subharmonic with equal amplitude. Results are obtained from a high-speed film (300 frames/sec) with neutrally buoyant styropor particles as tracers. The map shows subsequent particle positions in the wave crest near the breaking zone. Particle velocities up to 3.76 m/sec, corresponding to 2.8 times phase velocity c_{OB} for a wave period $T_B = 0.85$ sec at the point of breaking, were recorded.

In a numerical model (VINJE & BREVIG, 1980), the development of the (breaking) wave profile, the particle velocities and the accelerations within the wave are simulated. The results are achieved up to the point where the overhanging crest hits the wave front. Comparison of the plunging breakers generated in the wave flume and calculated numerically, shows good agreement with respect to

the wave geometry. The measured and calculated velocities also agree well at depths larger than approximately one wave amplitude below the mean water level. In the wave crest near the plunging jet, the measured velocities are, however, 1.5 times as large as the calculated velocities. This may be due to the difference in the method of generating the plunging breakers in the two cases (KJELDSEN, VINJE, MYRHAUG, BREVIG, 1980).

It is a common observation at sea, that steep waves have a tendency to break, sometimes as plunging breakers when they disperse into an area with an opposing surface shear current with a vertical velocity gradient. However, experiments with this particular phenomenon have never been attempted. Therefore, in the following, particular attention will be given to two experiments; one is a case with wave-wave interactions which create a deep water plunging breaker in still water. The other experiment is performed with the same deterministic command signal to the wave generator, but now the wave-wave interaction takes place on a weak steady shear current, which opposes the dispersion direction of the waves. Fig. 7 shows the profile of the current as it was obtained from a film recording, using styropor particles as tracers.

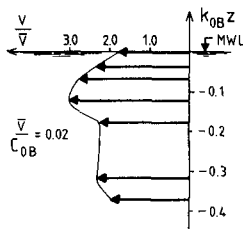


Fig. 7. Current profile before start of transient wave experiment. Total depth is $K_{OB}z = 7.02$. Mean current velocity is $\bar{v} = 0.03$ m/sec.

Fig. 8 shows the time developments of two deep water plunging breakers. T_B is the period of the breaking waves obtained from wave staffs at the position of breaking. Relative time $t/T_B = 0$ indicates the moment when the wave front becomes vertical. To the left is shown the development with no shear current present. A small jet develops and plunges down in the front of the wave at

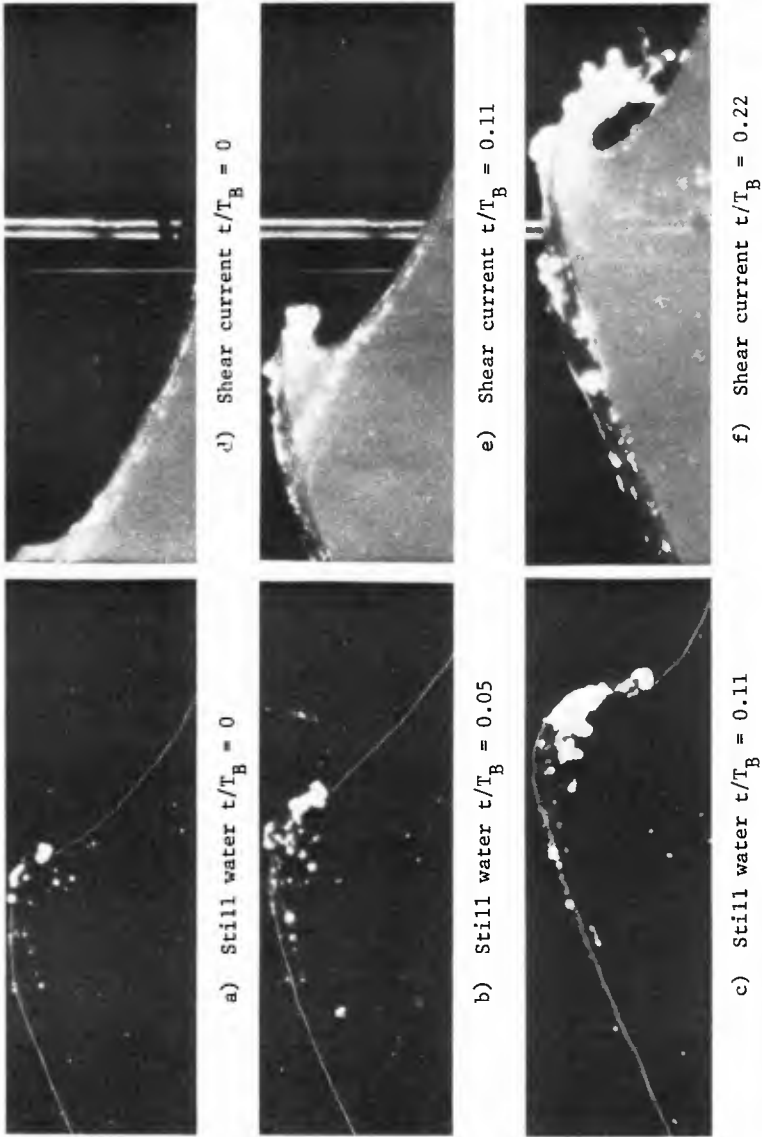


Fig. 8. Comparison of developments of deep water plunging breakers in still water and in water with an opposing shear current.

time 0.05. At time 0.11 air has been entrained and development of the breaking on the front increases. Here a large eddie that curls down on the front face of the wave appears, and more and more air is entrained.

To the right is shown the development when a steady shear current is present. The mean current velocity is only 2% of the linear phase velocity computed for the breaking wave. However, the result is remarkable. A much more violent plunging breaker with a very strong jet in the wave crest appears. It shoots forward with a very characteristic shape at time 0.11 and hits the front of the breaking wave at time 0.22. Thus, the duration of the breaking is much longer, and displays the breaking of a much more violent wave.

Fig. 9 shows the development of the two breakers displayed by the ϵ parameter. Data is obtained from a frame to frame analysis of the film with time steps 10 millisecond. At the time the wave fronts become vertical both breakers have ϵ values near 0.70. For the case with the shear current ϵ increases during the breaking to a value near 0.83, returning to values near 0.70. For the breaker development in still water, on the other hand, 0.73 is the maximum value, and ϵ then decreases when breaking takes place.

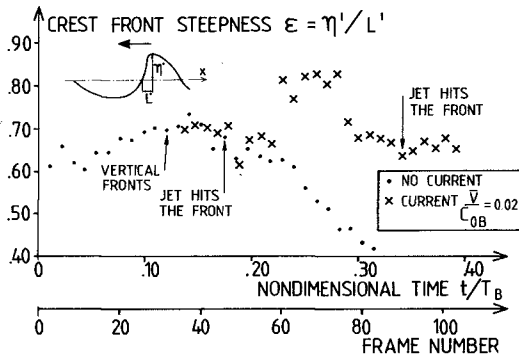


Fig. 9. Amplification of crest front steepness by a shear current.

Also the μ -parameter displays the development in a similar way, Fig. 10. When the wave fronts become vertical, both breakers show ratios of crest elevation to the wave heights as high as 0.75-0.80. For the case with a shear current the values of the μ -parameter then increases to nearly 0.90. For the case with no current, the μ -value slowly decreases when the breaker develops.

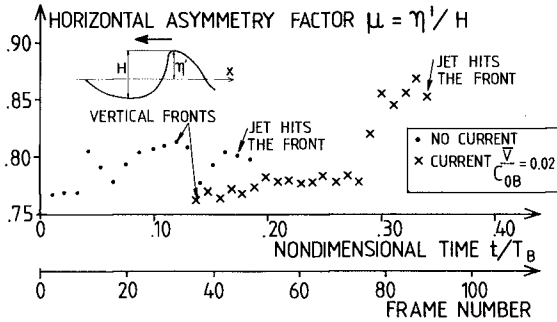


Fig. 10. Amplification of horizontal asymmetry factor by a shear current.

The amplification on the plunging breaker can be described as the relative increase in the ϵ and μ parameters:

$$\Delta\epsilon = \frac{\overset{\text{current}}{\epsilon_{\max}} - \epsilon_{\max}}{\epsilon_{\max}} = \underline{13\%} \quad \Delta\mu = \frac{\overset{\text{current}}{\mu_{\max}} - \mu_{\max}}{\mu_{\max}} = \underline{6\%} \quad (2)$$

Here ϵ_{\max} is the maximum value for a wave-wave interaction experiment, while $\overset{\text{current}}{\epsilon_{\max}}$ is the maximum value for a wave-wave interaction experiment with a shear current superimposed. Similar symbols are used for the μ -parameter. It is striking that a weak current (only 2% of the phase velocity) is able to create such drastic changes in the wave dynamics. The steepening of linear waves in the same shear current is very modest. This means that when a very asymmetric highly non-linear wave is triggered by even a weak energy flux, remarkable non-linear effects can be obtained.

Neither analytical nor numerical models are yet able to describe the phenomenon observed here. Such a high degree of amplification of breakers might lead to serious problems for mariners in smaller vessels in cases where high and steep waves approach even a weak current with a modest gradient. The phenomenon observed in deep water is a parallel to the well-known development of a plunging breaker on a beach, where return flow from the preceding wave can be observed to trigger the development of the following wave, in such a way that it might break as a plunging breaker. (KJELDSSEN & OLSEN, 1968.)

5. RESULTS FROM FIELD DATA

Storm Model

No single mathematical model for extreme wave statistics has gained universal acceptance. NOLTE (1973) used storm models which contained the most probable maximum wave height during a storm as a stochastic parameter. ARHAN et al. (1979) used a similar model based on significant wave height. MO, VIK & HOUMB (1978) used a model where consecutive values of $H_{1/3}$ exceed a threshold level, under the condition that also a higher level later is exceeded within a given time.

In the present study a storm model is given by the probability distribution:

$$S(H^*) = \sum_{i=1}^N \theta(H_{1/3}^i - H^*)/N \quad (3)$$

where the Heaviside unit function is defined by:

$$\theta(x-\xi) = \begin{cases} 1 & \text{for } x \geq \xi \\ 0 & \text{for } x < \xi \end{cases} \quad (4)$$

Here $H_{1/3}^i$ is the significant wave height for the i^{th} storm, N is the total number of storms and H^* is a wave height threshold level. This threshold level is taken as a definition of 'a gale' for the model. In this study only sea state 6, 7, 8 and 9 will be of importance, and a gale will therefore be defined as an event where the significant wave height exceeds 4 m.

With the assumption that storms are statistical independent events, no grouping correction is required. In this way the present model is superior to other methods. Only waves with zero-downcross wave heights exceeding 5 m were found to be significant for evaluation of stability and safety (from capsizing) for the vessels under consideration in the project "SHIPS IN ROUGH SEAS". From available field measurements on the Norwegian continental shelf, nearly 25000 single storm waves with heights exceeding 5 m were analyzed statistically. (KJELDSEN & MYRHAUG, 1978.) Approximately 8% of the most severe sea states in 26 gales were then selected for a closer study, and joint probability density distributions as well as marginal density distributions for relevant parameters were obtained. (KJELDSEN & MYRHAUG, 1979a.) The field data were sampled in the period 1974-78 with 3 wave rider buoys, located at Tromsøflaket, Halten and Utsira, Fig. 1. 20 minutes of recording was obtained every 3 hours, starting 20 minutes before 0 time GMT. The properties of the obtained probability density distributions show that data obtained from the 3 locations can be regarded as belonging to the same statistical population. This means that common statistical distributions can be obtained, which are representative for the wave dynamics in the whole area. (KJELDSEN & MYRHAUG, 1979b.) R.m.s.-values are used for normalisation, and dimensionless plots of probability density distributions are then obtained. The resulting data base provides a coupling to sea state, wind velocity and wave spectral parameters.

Probability density distributions of crest front steepness and asymmetry factors for waves with $H > 5$ m

Fig. 11 shows the probability density distributions of the crest front steepness ϵ , the vertical asymmetry factor λ , and the horizontal asymmetry factor μ , respectively, for 1754 storm waves with wave heights exceeding 5 m. For all distributions correlation coefficients are obtained using the Pearson χ^2 -test.

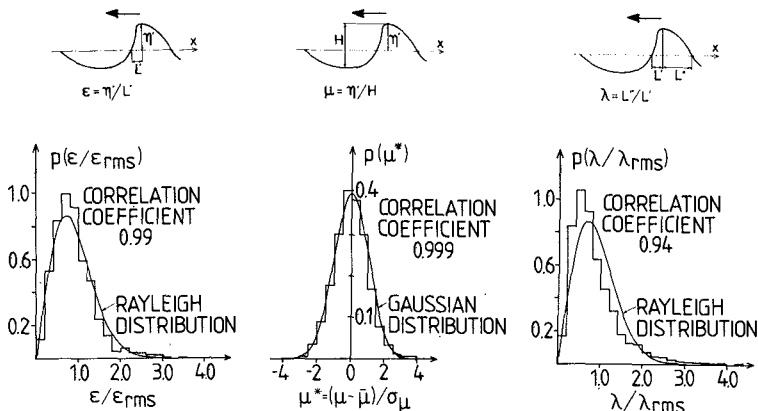


Fig. 11. Probability density distributions for ϵ , μ and λ .

The histogram of the crest front steepness ϵ is compared with the Rayleigh distribution:

$$p(x) = 2x \cdot \exp(-x^2) \tag{5}$$

where in this case $x = \epsilon/\epsilon_{rms}$ is the normalized crest front steepness. ϵ_{rms} is calculated for wave heights exceeding 5 m. A good correlation with a correlation coefficient of 0.99 is obtained. A two-parameter Weibull distribution is also fitted to the histogram of the crest front steepness. According to the two-parameter Weibull distribution, the cumulative probability is given by:

$$P(x \leq x_c) = 1 - \exp\left(-\left(\frac{x}{B}\right)^\gamma\right) \tag{6}$$

where x_c is a specific value. The result is given in Table 1. (The Rayleigh distribution corresponds to $\gamma = 2$ and $B = 1$.) The distribution of the vertical asymmetry factor λ also shows a good correlation with the Rayleigh distribution with a correlation coefficient of 0.94. The Weibull parameters are given in Table 1. The horizontal asymmetry factor shows a very good correlation with the Gaussian distribution given by

TABLE 1. WEIBULL PARAMETERS FOR MARGINAL DISTRIBUTIONS

	Normalized wave height h/ξ			Normalized crest front steepness ϵ/ϵ_{rms}			Normalized total wave steepness s/s_{rms}			Normalized wave period t/ξ			Normalized vert. asymmetry factor λ/λ_{rms}		
	Y	B	Corr. coef.	Y	B	Corr. coef.	Y	B	Corr. coef.	Y	B	Corr. coef.	Y	B	Corr. coef.
	H \geq 5 m				1.67	.91	.997								
All waves	2.02	.94	.998	1.45	.83	.998	1.85	1.00	.99	3.67	.93	.997	1.44	.86	.99

Two-parameter Weibull distribution $P(x \leq x_c) = 1 - \exp(-(\frac{x}{B})^\gamma)$

TABLE 2. WEIBULL PARAMETERS FOR CONDITIONAL DISTRIBUTIONS

Normalized wave height h/ξ	Normalized crest front steepness ϵ/ϵ_{rms}			Normalized total wave steepness s/s_{rms}			Normalized wave period t/ξ		
	Y	B	Correlation coefficient	Y	B	Correlation coefficient	Y	B	Correlation coefficient
	0-0.2	1.55	1.10	.98	2.96	1.52	.92	3.11	.51
0.2-0.4	1.70	1.08	.99	1.80	1.17	.996	3.61	.67	.96
0.4-0.6	1.39	.84	.997	1.77	.99	.99	3.81	.80	.99
0.6-0.8	1.33	.73	.995	1.66	.91	.98	4.43	.97	.97
0.8-1.0	1.43	.68	.99	1.87	.85	.99	5.12	1.10	.92
1.0-1.2	1.50	.76	.997	1.98	.92	.99	5.09	1.20	.93
1.2-1.4	1.71	.90	.99	3.25	1.22	.93	5.30	1.25	.90
1.4-1.6	1.89	.95	.996	2.37	1.09	.99	5.35	1.35	.87
1.6-1.8	2.22	1.24	.99	4.25	1.50	.94	5.41	1.22	.90
1.8-2.0	3.22	1.38	.95	3.61	1.44	.98	5.54	1.29	.87
2.0-2.2	3.24	1.37	.94	3.52	1.41	.97	5.55	1.39	.83
2.2-2.4	5.17	1.99	.91	4.80	1.78	.93	5.65	1.33	.83
2.4-2.6	5.32	1.70	.88	5.62	1.90	.87	5.51	1.63	.76

$$p(\mu^*) = \frac{1}{\sqrt{2\pi}} \cdot \exp(-\frac{1}{2} \mu^{*2}) \quad (7)$$

where $\mu^* = (\mu - \bar{\mu})/\sigma_{\mu}$. Here $\bar{\mu}$ is the mean value of μ and σ_{μ}^2 is the variance of μ in the respective registration period calculated for wave heights exceeding 5 m. A correlation coefficient of 0.999 was obtained.

Joint probability density distribution of crest front steepness and wave height

Fig. 12 shows the joint probability density distribution of crest front steepness and wave height combined for all three locations, representing 6353 storm waves.

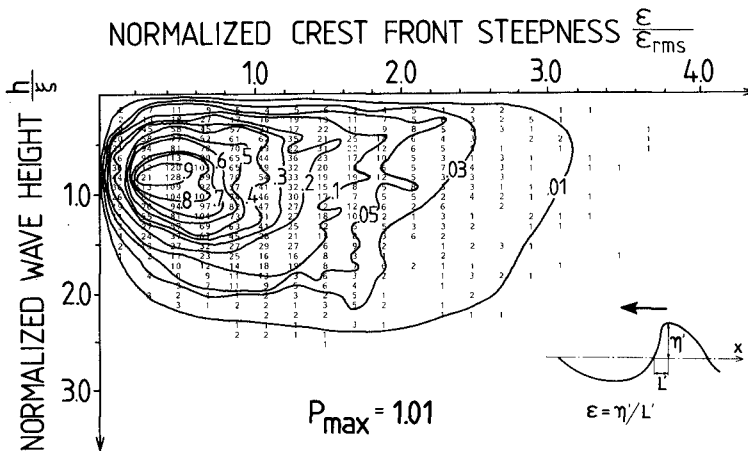


Fig. 12. Joint probability density distribution of ϵ and H .

The marginal distributions of the wave height and the crest front steepness are given in Fig. 15, showing good correlations to the Rayleigh distribution. Correlation coefficients of 0.98 were obtained for both distributions. Weibull parameters and correlation coefficients for the marginal distributions are included in Table 1. Further, the Weibull distribution given in (6), was fitted to the conditional distribution of the crest front steepness.

Weibull parameters and correlation coefficients corresponding to the best fit for each wave height interval are given in Table 2. If the crest front steepness and the wave height were uncorrelated, then the conditional distribution of the crest front steepness for given wave heights would be a Rayleigh distribution. However, the degree of correlation between ϵ and H is given in Table 2.

Joint probability density distribution of total wave steepness and wave height

Fig. 13 shows the joint probability density distribution of total wave steepness and wave height combined for all three locations. The marginal distribution of total wave steepness is given in Fig. 15, and corresponds well to the Rayleigh distribution with a correlation coefficient of 0.92. Weibull parameters are given in Table 1. The Weibull parameters for the conditional distribution of the total wave steepness for each wave height interval are given in Table 2. A marginal distribution of s that follows the Rayleigh distribution is in agreement with earlier results (BATTJES, 1976), but in our study use of the rms-value is recommended for normalisation. The s - H distribution shows a similar general shape as the ϵ - H distribution, and is included here in order to obtain a comparison of different types of steep waves.

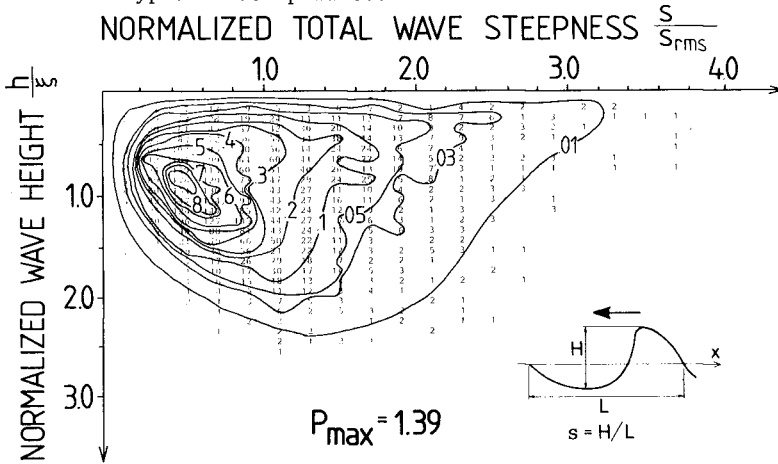


Fig. 13. Joint probability density distribution of s and H .

Joint probability density distribution of wave height and wave period

Fig. 14 shows the joint probability density distribution of wave height and wave period combined for all three locations. The wave period was normalized with the parameter $\zeta^2 = (\overline{T^4})^{1/2}$, related to the rms-value of the wave period squared. The marginal distribution of the wave period is given in Fig. 15. The histogram is compared with the Rayleigh distribution of the wave period squared, i.e.

$$p\left(\frac{t}{\zeta}\right) = 4\left(\frac{t}{\zeta}\right)^3 \cdot \exp\left(-\left(\frac{t}{\zeta}\right)^4\right) \tag{8}$$

and shows a good correlation with a correlation coefficient of 0.98. Weibull parameters are given in Table 1. (The distribution of the wave period in (8) corresponds to $\gamma = 4$ and $B = 1$. The Weibull distribution is also fitted to the conditional distribution of the wave period for each wave height interval, Table 2. The joint probability density distribution of wave height and wave period shows asymmetry with respect to wave periods for lower waves and symmetry for higher waves, having the same general behaviour as the joint distribution given by CAVANIE et al. (1976).

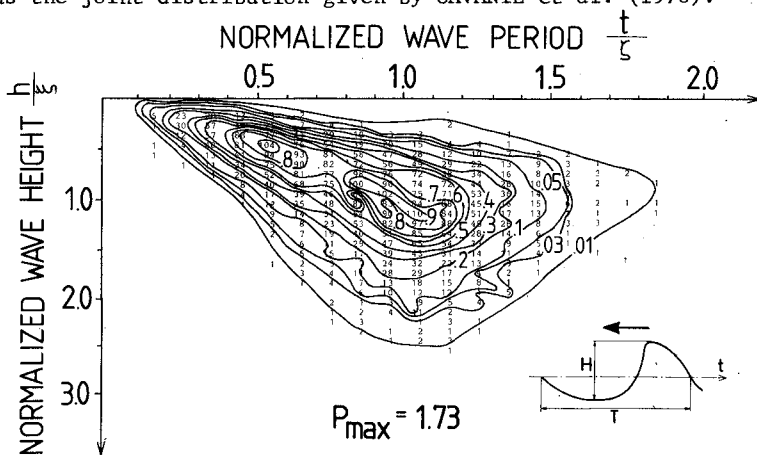


Fig. 14. Joint probability density distribution of H and T.

Assuming a narrow band spectrum, LONGUET-HIGGINS (1975) found a theoretical joint distribution of H and T with an axis of symmetry at the mean period of the spectrum. This describes the observed joint distribution for high waves. A detailed comparison of LONGUET-HIGGINS and CAVANIE et al.'s theory is given by GODA (1978).

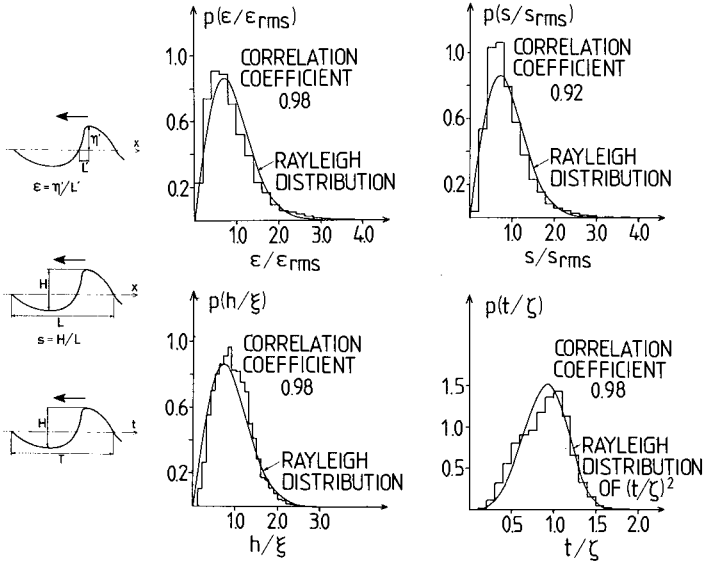


Fig. 15. Marginal distributions of ϵ , s , H and T .

6. DISCUSSION OF RESULTS

An analysis of 6353 storm waves showed that asymmetric waves with heights $H > 5$ m and vertical asymmetry factor $\lambda > 2$ appeared more frequently in wave groups than asymmetric waves with $H > 5$ m and horizontal asymmetry factor $\mu > 0.67$. (KJELDEN & MYRHAUG, 1979a.)

Fig. 11 shows that the horizontal asymmetry factor follows a Gaussian distribution for $H > 5$ m. An application of this result is that for waves with a given specific wave height (h), 16% of these waves will have crest heights that exceed:

$$\eta' = (\bar{\mu} + \sigma_{\mu})h \quad (9)$$

while 2.5% of the waves with the specific wave height, h , will have crest heights that exceed:

$$\eta' = (\bar{\mu} + 2\sigma_{\mu})h \quad (10)$$

This result has obvious important applications for the evaluation of both safety and design.

A very rough sea state can only be satisfactorily described as an event that contains both high values for the wave heights and high values for steepness and asymmetry parameters. High values of steepnesses combined with low values of wave heights describe a choppy sea, but this is not disastrous. Low values of steepnesses combined with high values of wave heights describe a heavy swell. *It is therefore the joint probability density distributions for high values of both steepnesses and wave heights that describe a very rough sea, and not the percentage of breaking waves itself.* Thus, the term *extreme waves* used earlier, describes a condition with high values of both wave height and crest front steepness.

When estimates of probabilities of occurrences of breaking waves are made, then the joint distribution of wave height and wave period is commonly used. A breaking criteria is then formulated in terms of the total wave steepness s . However, the parameter s does not define a steep asymmetric wave uniquely. Several asymmetric waves can exist, with the same total wave steepness s , but with very different crest front steepnesses, see Fig. 16.

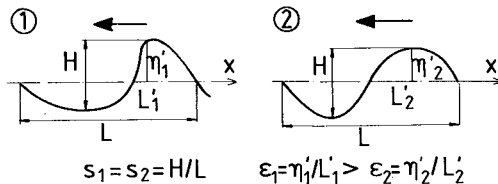


Fig. 16. *The total wave steepness s does not define an asymmetric wave uniquely.*

Thus, the joint probability density distributions of s and H or of H and T are not suited, when estimates for probabilities for occurrences of breaking waves are made.

This study has shown that the crest front steepness is the most relevant parameter describing the mean inclination of the wave profile ahead of the crest, while the zero-downcross wave height is obtained ahead of a breaking wave. Therefore, when estimating probabilities for occurrences of breaking waves, the use of the joint distribution of crest front steepness and zero-downcross wave height is recommended.

7. CONCLUSIONS

- 1) The experiments show that all two-dimensional breaking waves generated by wave-wave or current-wave interactions in deep water can be classified as belonging to one of three distinct types, namely deep water plunging breakers, deep water bores, and deep water spilling breakers.
- 2) The difference in phases between a basic wave and a disturbance is crucial for the creation of a deep water plunging breaker.
- 3) A weak opposing shear current with a mean velocity of only 2% of the linear phase velocity for the breaking wave, was able to amplify a deep water plunging breaker violently. Thus, the relative increase in the μ -parameter became 6%, while the relative increase in the ε -parameter became 13%.
- 4) Recommendations for analyzing of steep asymmetric waves are to use:
 - zero-downcross analysis defining the wave height as the height ahead of the wave crest, giving a parameter relevant for the description of the development of the breaking process, and for the response of ships and structures.
 - the crest front steepness ε , the vertical asymmetry factor λ and the horizontal asymmetry factor μ in order to describe the zero-downcross wave uniquely.

- 5) Field data from the Norwegian Sea shows that the probability density distributions of the crest front steepness ϵ , and the vertical asymmetry factor λ follows the Rayleigh distribution. The horizontal asymmetry factor μ follows the Gaussian distribution. It was found that for waves with wave heights beyond 5 m, a high vertical asymmetry factor λ was obtained more frequently than a high horizontal asymmetry factor μ . Maximum values obtained in the field data and the laboratory experiments were $\lambda = 7.7$, $\epsilon = 0.83$ and $\mu = 0.92$. A high μ -value indicates that the crest height is very near the total wave height. *In other words, the wave is nearly entirely above mean water level.* This latter result is obviously important both for evaluations of safety and design.
- 6) Joint probability density distributions of the following zero-downcross wave parameters are given:
- . *Crest front steepness and wave height*
 - . *Total wave steepness and wave height*
 - . *Wave height and wave period*

Conditional distributions for given wave heights are presented as two parameter Weibull distributions. The joint distribution of H and T shows asymmetry with respect to wave periods for lower waves, and symmetry for higher waves, in the same general pattern as the one given by CAVANIÉ et al. (1976). Since s does not define steep asymmetric waves uniquely, neither the joint distribution of s and H nor the joint distribution of H and T should be used to estimate probabilities of occurrences of breaking waves.

- 7) Severeness of a particular sea state, containing estimates for the probabilities of occurrences of breaking waves, should be evaluated from the given joint probability density distribution of crest front steepnesses and wave heights *for individual zero-downcross waves*. This method will be superior to a method using mean parameters such as a mean wave period and a significant wave height.

8. ACKNOWLEDGEMENTS

Experiments with current-wave interactions were performed as a part of the project "Shock Pressures from Breaking Waves" sponsored by the Royal Norwegian Council for Scientific and Industrial Research (NTNF).

Other experiments and analysis of field data were performed as a part of the project "Ships in Rough Seas" sponsored by the Royal Norwegian Council for Scientific and Industrial Research (NTNF), the Norwegian Maritime Directorate and the Norwegian Fisheries Research Council (NFFR).

9. REFERENCES

ARRAN, M.F., CAVANIE, A.G., EZRATY, R.S., 1979: "Determination of the Period Range associated to the Design Wave". Paper No. 3643. Proc. Offshore Technology Conf., Houston, Texas.

BATTJES, J.A., 1976: "Probabilistic Aspects of Ocean Waves". International Research Seminar on Safety of Structures under Dynamic Loading, Trondheim 1977, Vol. 1, pp. 387-439.

CAVANIE, A., ARRAN, M. & EZRATY, R., 1976: "A Statistical Relationship between Individual Heights and Periods of Storm Waves". Proceedings BOSS '76, Vol. II, pp. 354-360.

DAHLE, L.A., 1979: "Waves and Weather Conditions on the Norwegian Continental Shelf - Mapping of Dangerous Areas", Report, Ships in Rough Seas, Part 4, Norwegian Hydrodynamic Laboratories, Trondheim, Norway (in Norwegian).

GALVIN, C.J., 1968: "Breaker Type Classification on Three Laboratory Beaches". Journal of Geophysical Research, Vol. 73, No. 12, June.

GODA, Y., 1978: "The Observed Joint Distribution of Periods and Heights of Sea Waves". Proc. 16th Conference on Coastal Engineering, Hamburg, Vol. 1, pp. 227-246.

KJELDSEN, S.P., VINJE, T., MYRHAUG, D., BREVIC, P., 1980: "Kinematics of Deep Water Breaking Waves", Paper No. 3714, Proc. 12th Offshore Technology Conf., Houston, Texas.

KJELDSEN, S.P., MYRHAUG, D., 1979a: "Formation of Wave Groups and Distributions of Parameters for Wave Asymmetry", Report No. STF60 A79044. Ships in Rough Seas, Part 4. Norwegian Hydrodynamic Laboratories, Trondheim, Norway.

KJELDSEN, S.P., MYRHAUG, D., 1979b: "Wave-Wave and Wave-Current Interactions in Deep Water", Proc. 5th POAC Conference, Trondheim, Vol. III, pp. 179-200.

KJELDSEN, S.P., MYRHAUG, D., 1978: "Kinematics and Dynamics of Breaking Waves", Report No. STF60 A78100, Ships in Rough Seas, Part 4. Norwegian Hydrodynamic Laboratories, Trondheim, Norway.

KJELDSEN, S.P., OLSEN, G.B., 1968: "Breaking Waves" (16 mm film). Institute of Hydrodynamics and Hydraulic Engineering (ISVA), Technical University of Denmark, Copenhagen.

LONGUET-HIGGINS, M.S., 1975: "On the Joint Distribution of the Periods and Amplitudes of Sea Waves". Journal of Geophysical Research, Vol. 80, No. 18, pp. 2688-2694.

LONGUET-HIGGINS, M.S., 1969: "A Non-Linear Mechanism for the Generation of Sea Waves". Proc. Roy. Soc. A, 311: 371-389.

MO, K., VIK, I., HOUMB, O.G., 1978: "Wave Statistics at Station "M" with Special Reference to Duration and Frequency of Sea States". Division of Port & Ocean Engineering at The University of Trondheim, Norway.

NEDRELLID, T., 1978: "Analysis of Earlier Capsizing Accidents", Report, Ships in Rough Seas, Part 3, Norwegian Hydrodynamic Laboratories, Trondheim, Norway (in Norwegian).

NOLTE, K.G., 1973: "Statistical Methods for Determining Extreme Sea States". Proc. 2nd POAC Conf., Reykjavik, Iceland.

VINJE, T., BREVIC, P., 1980: "Numerical Simulation of Breaking Waves", 3rd Int. Conference on Finite Elements in Water Resources, Univ. of Mississippi, USA.

<p>10. NOMENCLATURE</p> <p>C_{OB} linear phase velocity at point of breaking ($\frac{g}{2\pi} T_B$)</p> <p>H zero-downcross wave height</p> <p>h specific zero-downcross wave height</p> <p>K_{OB} wave number at point of breaking ($\frac{2\pi}{gH}$)</p> <p>L zero-downcross wave length</p> <p>L' forward length from zero-upcross point to crest</p> <p>L'' backward length from crest to zero-downcross point</p> <p>S total zero-downcross wave steepness</p> <p>I zero-downcross wave period</p> <p>T_B zero-downcross wave period at point of breaking</p> <p>t time coordinate</p> <p>u specific zero-downcross wave period</p> <p>u horizontal particle velocity in breaking wave</p>	<p>$V(xk_{OB})$ current velocity at level $z'k_{OB}$</p> <p>\bar{V} mean current velocity</p> <p>x horizontal coordinate</p> <p>z vertical coordinate, origin at MSL</p> <p>δ crest rear steepness ($= \eta'/L'$)</p> <p>ϵ crest front steepness ($= \eta/L$)</p> <p>ζ parameter related to rms-value of squared wave period ($\zeta^2 = \frac{\sigma^2}{A^2}$)</p> <p>$\eta'$ crest elevation</p> <p>λ vertical asymmetry factor ($= L'/L$)</p> <p>μ horizontal asymmetry factor ($= \eta'/H$)</p> <p>μ^* ($= (\lambda-\mu)/\zeta$) normalisation of μ</p> <p>$\bar{\mu}$ mean value of μ</p> <p>$\bar{\mu}^2$ root-mean-square of the zero-downcross wave height</p> <p>ξ standard deviation of μ</p> <p>C_u</p>
---	---

CAN WE DEVELOP NEW BREAKWATERARMOUR FORMULAE ?

John Dorrington Mettam*

Introduction

The purpose of this paper is to draw attention to the limitations of present empirical methods for the design of rubble mound breakwaters, particularly those using concrete armour units. Although it is unlikely that analytical techniques could become an adequate substitute for model testing, they should contribute significantly to a major advance in our understanding of breakwater behaviour. This is now long overdue and the art of breakwater design should be capable of substantial development.

Hudson's Formula

$$W_r = \frac{\gamma_c \cdot H^3}{K_D \left(\frac{\gamma_c}{\gamma_w} - 1 \right)^3 \cot \alpha} \quad (1)$$

During the last quarter of a century, most engineers and research workers have used Hudson's formula (ref: 1) for comparing different types of breakwater armour and for other purposes such as the design of simple breakwaters and the interpretation and correction of hydraulic model tests. Other formulae, such as Iribarren's formula have also been used to a lesser extent.

As new types of armour unit have been developed, their effectiveness has generally been measured by quoting the value of K_D in Hudson's formula in relation to their behaviour in model tests. However, Hudson's formula was originally developed to represent the behaviour of natural rock-type materials which retain their stability under wave action principally by their own weight and without any significant interlock with adjacent units.

In representing the behaviour of armour units of this basic type, Hudson's formula has been a very convenient tool even though in a single formula it over simplifies a very complex situation.

* Partner in the firm of Bertlin and Partners, Consulting Engineers of Redhill, Surrey, U. K.

The development of new types of artificial armour units, which to varying degrees do not behave in the same way as rock, has highlighted the limitations of Hudson's formula. The best-known such unit is the dolos which relies principally upon its interlock with a number of surrounding and underlying units to prevent displacement. For this reason dolos units may be less than a third of the weight of the natural rocks required to resist similar conditions. The unsuitability of the Hudson formula for dolos units has long been apparent (refs: 2, 3 & 4) e. g. it is necessary to quote different K_D values according to slope for these units. This has made it very difficult to interpret the results of different model tests.

It is also important to consider whether there are any other factors influencing stability which were not found to be of significance when Hudson's formula was developed for gravity-type armouring and which become of increased importance with units in which interlock is a major or predominant feature. There are indications from recent model testing (ref: 5 & 6) that contact friction between armour units could be one such important factor and that wave steepness may well be another.

What is now becoming very clear is that breakwater designers must appreciate the circumstances under which Hudson's and Iribarren's formulae were developed and the conditions for which they were designed. To use these formulae out of their original context is likely to be misleading and even dangerous. The application of Hudson K_D values to dolos and other interlocking units is convenient in comparing their weight-for-weight effectiveness against more traditional forms of breakwater armour; however, we must not be deceived into thinking that Hudson's formula therefore represents their behaviour or that such comparisons are valid.

Although most engineers would only advocate use of Hudson's formula for direct design purposes in the simplest cases, and would prefer to rely upon specific model tests for any important breakwaters, they would nevertheless in most cases have recourse to Hudson's formula for correcting hydraulic model test results for errors in modelling such as in water and material densities.

However, the fact that certain variables such as contact friction (or natural angle of repose) are not included in the formula does not imply that they are necessarily insignificant nor that they may be ignored with impunity when constructing and operating hydraulic models.

Before considering what other phenomena may be important to breakwater stability and then suggesting how breakwater design techniques might be developed, it is worth studying in some detail the development and derivation of Iribarren's formula.

Development and Derivation of Iribarren's Formula

The formula was first published in 1938 (ref: 7) in the form:

$$P = \frac{N A^3 d}{(f \cos \alpha - \sin \alpha)^3 (d - 1)^3} \quad (2)$$

It followed an earlier formula by Castro in 1933 (ref: 9).

A number of modifications have been suggested to the original formula. Some of these are expressed below using symbols defined in the legend

$$W_r = \frac{K' \gamma_c \mu^3 H^3}{(\mu \cos \alpha - \sin \alpha)^3 (S_r - 1)^3} \quad (3)$$

after Hudson (ref: 1)

$$W_r = \frac{\gamma_c \mu^3 H^2 L_p}{K_o \left(\frac{\gamma_c}{\gamma_w} - 1 \right)^3 (\mu \cos \alpha - \sin \alpha)^3} \quad (4)$$

after Gravesen et al (ref: 6)

The derivation of the term $(\mu \cos \alpha - \sin \alpha)$ shown in figures 1 and 2, is very simple but is worth mentioning to clarify thinking.

This derivation represents the stability of an isolated block tending to slide down a slope (α) with a coefficient of friction between the slope and block of $\mu = \tan \phi$ where ϕ is the angle of repose. Compared with $\cot \alpha$ in Hudson's formula it has the merit that $(\mu \cos \alpha - \sin \alpha)$ tends to zero as α approaches the angle of repose ϕ ; the weight of armour required therefore tends to the infinite.

Let us now remind ourselves of the derivation of the other main components of Iribarren's formula.

Disturbing force

$$\text{Water velocity} \quad V \propto \sqrt{gH}$$

$$\text{Drag force} \quad \propto M.V.A_{\text{area}}$$

$$\text{or } \gamma_w V V \left(\frac{W}{\gamma_c} \right)^{2/3} \text{ or } \gamma_w g H \left(\frac{W}{\gamma_c} \right)^{2/3} \quad (5)$$

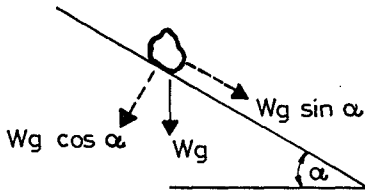
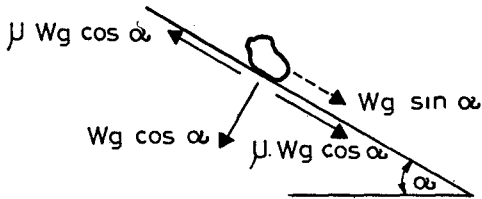


FIG. 1.



For simple shapes μ = coefficient of friction

FIG. 2.

Force required for movement

Sliding down - $W_g (\mu \cos \alpha - \sin \alpha)$

Sliding up - $W_g (\mu \cos \alpha + \sin \alpha)$

If submerged x $\frac{(\gamma_c - \gamma_w)}{\gamma_c}$

Stabilising force (resisting down-rush)

$$\frac{Wg}{\gamma_c} (\gamma_c - \gamma_w) (\mu \cos \alpha - \sin \alpha) \quad (6)$$

Equating these and re-arranging

$$\gamma_w g H \left(\frac{W}{\gamma_c} \right)^{2/3} \propto \frac{Wg}{\gamma_c} (\gamma_c - \gamma_w) (\mu \cos \alpha - \sin \alpha) \quad (7)$$

$$W^{1/3} \propto \frac{\gamma_w H \gamma_c^{1/3}}{(\gamma_c - \gamma_w) (\mu \cos \alpha - \sin \alpha)}$$

$$\text{or } W \propto \frac{\gamma_c H^3}{\left(\frac{\gamma_c}{\gamma_w} - 1 \right)^3 (\mu \cos \alpha - \sin \alpha)^3} \quad (8)$$

It will be seen that the derivation of the modified form of the formula clearly represents the stability of the slope in resisting drag forces caused by wave down-rush. The formula does not represent the effects of impact forces on the armour units, nor does it consider stability of units subject to uprush (Hedar drew attention to this in 1960).

Some further points may be worth mentioning.

It will be seen that the third power relationship between W and most of the other factors arises from the basic fact that the main stabilising forces must be proportional to the volume of the units whilst the main disturbing forces must be proportional to the exposed area.

If W were not proportional to H^3 it would not, of course, be possible to use hydraulic models for testing breakwaters. This involves an assumption that the pressures of water on the armour units are proportional to the height of approaching waves and that the velocity of water within the armour layer is proportional to \sqrt{H} . An examination of the limitations of this assumption would be a fruitful area for further research and with the great advances of recent years in mathematical analysis of waves, this may perhaps be an area for mathematical research.

In the case of wave uprush it should also be considered whether impact forces obey the same relationship and over what range of conditions.

If the function $\left(\frac{\gamma_c}{\gamma_w} - 1 \right)^3$ is now considered it will be seen that it comes partly from the disturbing force and partly from the stabilising. The function does, however, appear to be fundamentally appropriate to the third power as in the Hudson and Iribarren formulae.

In 1972 Zwamborn (ref: 2 and 3) advanced the view that some other power may be more correct in the case of dolosse. One might rather question whether dolosse used in tests with different specific gravities may also have had some other differences such as different co-efficients of friction as this could provide an explanation of the effects reported by Zwamborn.

Factors which might affect Slope Stability

In considering the possibility of improving on present techniques of designing rubble mound slopes and the need to develop new tools for new types of armour unit and new applications, we must take a fundamental look at breakwater behaviour. Although the stabilising and disturbing forces must be related to the factors included in Hudson's and Iribarren's formulae, we can identify a number of other phenomena which may be of differing relative importance for different types of armour and in different circumstances but which do not appear in these formulae. These would include:-

- (a) Wave uprush.
- (b) Effect of surface slope angle and porosity on the wave behaviour.
- (c) Effect of bed depth and slope on the wave behaviour.
- (d) Incident wave steepness.
- (e) Dynamic and static stresses in armour units.

Development of New Formulae

If one starts to break the problem into its constituent parts it soon becomes clear that the single K_D factor of Hudson or the comparable factor in any of the versions of Iribarren cannot be expected to behave as a constant even for a particular armour unit. If we separate K_D into a number of functions (not factors) related to each element of the problem, each of these functions is necessarily a complex combination of many different variables.

Figs: 3 and 4 illustrate the problem and indicate functions f_1, f_2, \dots, f_7 . The different elements which can be expected to enter into each function are tabulated in Tables 1 and 2.

In addition to functions f_1 to f_7 which relate to different aspects of stabilising and disturbing forces, one more function, f_8 has been added to represent the damage condition at which the formula is being applied.

STABILITY FUNCTIONS

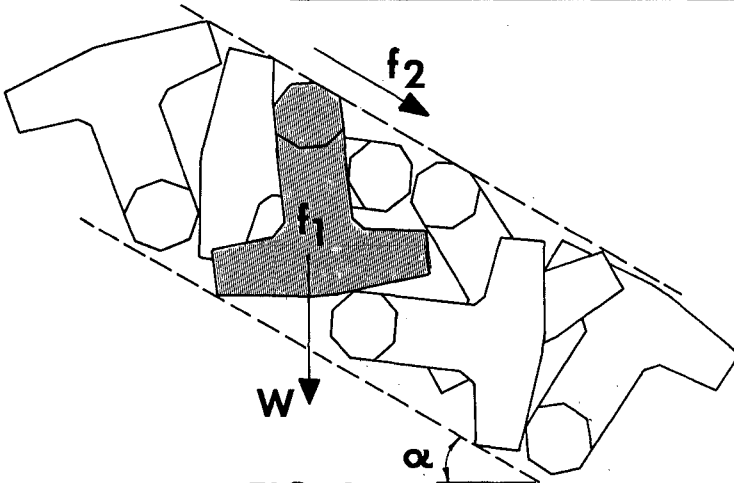


FIG. 3

DISTURBANCE FUNCTIONS

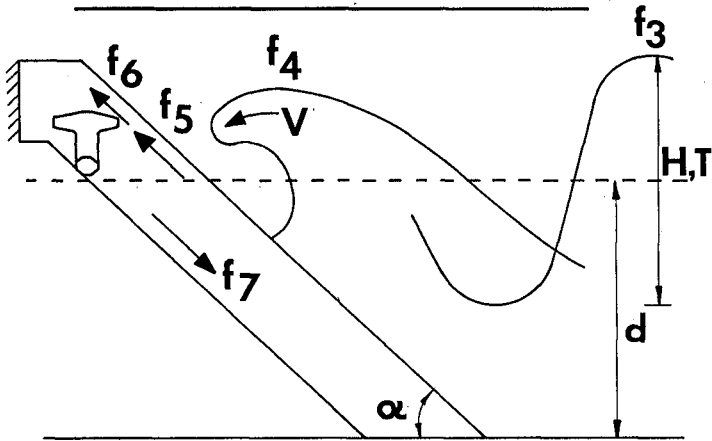


FIG. 4

TABLE 1 - Stability Functions

Function	Adjusting	Possible Factors
f_1	Effect of W as stabiliser (downrush)	1. Unit type 2. Interlock achieved 3. Surface friction
f'_1	Same as for uprush	Similar
f_2	Effect of interlock (downrush)	1. Unit type 2. Method of placing 3. Surface friction 4. Extent to which disturbing force acts on adjacent units
f'_2	Ditto (uprush)	Similar but 4 may be very different
S	Factor of safety	Possibly made up from S_1 . related to block type/size S_2 . related to quality of wave data

TABLE 2 - Disturbance Functions

Function	Adjusting	Possible Factors
f_3	H approaching	H/d Period T (or steepness) Bed slope Reflections, α
f_4	V Velocity at face of armour	Type of breakwater, bed slope, wave steepness, resonance effects, α , porosity, crest detail
f_5	Drag coefficient	Shape of arms of unit Shape of voids
f_6	Uprush velocity in armour	Slope type of unit, porosity, roughness, armour underlayers
f_7	Downrush velocity	As for f_6 , plus wave period or resonance effects crest detail
f_8	Degree of damage	Storm duration Wave spectrum Wave grouping

If we write the Iribarren formula in a form which keeps the stabilising and disturbing forces separate and insert the various functions $f_1 \dots \dots \dots f_8$ and a factor of safety S these become clearer.

$$\frac{Wg}{\gamma_c} (\gamma_c - \gamma_w) (\mu \cos \alpha - \sin \alpha) \propto \gamma_w g H \left(\frac{W}{\gamma_c}\right)^{2/3} \tag{7}$$

$$f_1 W (\gamma_c - \gamma_w) f_2 (\mu \cos \alpha - \sin \alpha) = S f_3 f_4 H f_5 f_6 f_7 f_8 \frac{W^{2/3}}{\gamma_c^{2/3}} \tag{9}$$

We may also consider the up-rush case as below:-

$$f'_1 W (\gamma_c - \gamma_w) f'_2 (\mu \cos \alpha + \sin \alpha) = S f_3 f_4 H f_5 f_6 f_8 \frac{W^{2/3}}{\gamma_c^{2/3}} \tag{10}$$

In equations 7, 9 and 10 the functions $(\mu \cos \alpha \pm \sin \alpha)$ are included to emphasise the point that up-rush and down-rush are different effects. It must, however, be admitted that these functions of μ and α may not be correct and that it may be better to consider f_2 and f'_2 separately.

Looking at equations 9 and 10 together with Tables 1 and 2, there will be many whose immediate reaction will be to despair of ever finding a solution. Indeed, in the sense of finding a single formula for all conditions, we may expect this to prove impossible.

In the same way that a structural engineer does not expect to use a single formula to analyse bending, shear, bond and torsion, we cannot expect to develop a single formula to represent all the phenomena involved in wave action on armoured slopes. We must therefore expect the development of a range of interrelated design formulae. In the meantime we must recognise the uses and the limitations of Hudson's and Iribarren's formulae.

Further Research

It is advocated that research into this subject should be carried out in a coordinated manner so that:-

- (i) The new formulae can be developed as rapidly as possible.
- (ii) Costs of the necessary model testing can be minimized and the greatest benefit obtained.
- (iii) Testing methods and procedures may be standardized.

In addition to development of the formulae, it will be necessary to carry out statistical studies. Even if we identify and correct the empirical coefficients for all the phenomena and influences which are identified, we shall not be able to correct for all the random elements involved. We may therefore expect a certain scatter in our test results and in the performance of prototypes. It will be necessary to have some sort of quantification of the risk element involved in using the formulae.

To commence development of new formulae it is advocated that research should be directed at determining the effect of each of the many parameters (such as slope, water depth and wave steepness) on the stability of the armour layer - not by just adding for each parameter one new function which attempts to represent all the effects of varying that parameter, but rather by considering separately the many different effects. As we use hydraulic models for design of breakwaters it is natural to use them to test the effect of varying the different factors which should be taken into account in any stability formula. This method has serious weaknesses, in particular:-

- (1) It can be extremely difficult to vary one factor while keeping all others constant.
- (2) The results of flume tests, in the form of numbers of units moving or displaced, necessarily show an enormous scatter. This must to a large extent be because of the human element involved in their measurement; the counting of units relies very largely on the judgement of those conducting the tests. The results are not as accurate as the numbers might imply.
- (3) The inherent soundness and stability of the model is likely to vary each time the model is rebuilt for new tests. Results are likely to vary randomly from test to test.

As indicated in Tables 1 and 2, changing one factor such as face slope can have a number of quite unrelated effects on different aspects of the disturbing and the stabilising forces.

This paper has indicated that the path ahead will not be easy but that it is important that we should at least attempt it. The means of progress will be an integrated programme of both theoretical research and model testing.

In planning such research it is suggested that effort should be directed chiefly to the problems of armouring rubble mound breakwaters in deep water. The work may well cast light also on the behaviour of breakwaters in the depths where breaking of waves limits the severity of wave attack but

this is an area where experience gives engineers a better basis for design (even though not as yet a rational analysis).

Having posed the general problem in broad terms, it may be helpful to discuss in more detail three aspects which have not always received sufficient attention. These are the importance of contact friction, the wave shape characteristics and structural strength.

Importance of Contact Friction

When natural rock armouring is represented in scale model testing, natural stone of suitable shape and size is used, preferably from the quarry from which the armour will be obtained. Its contact friction is similar in value to the rock it models. Similarly, early tests of concrete armour units were carried out using model units of cement mortar which again gave reasonable representation of contact friction. New techniques have recently been developed for moulding model armour units from other materials (ref: 10 and 11). These techniques are quicker and cheaper and are more reliable in terms of dimensional accuracy and specific gravity of the units. However, these model units often have very different contact friction values to the concrete armour which they represent and laboratory tests (ref: 5 and 6) show that this difference has a major influence on slope stability. This is hardly surprising as a change in contact friction alters the direction of the forces acting between units at the limiting condition when movement occurs; it must therefore alter the natural angle of repose of the units and this has been shown to be so. Methods to measure the natural angle of repose of an armour slope are described by Iribarren (ref: 8), Hedar (ref: 12) and Gravesen (ref: 6).

Fig. 5 shows the relationship between angle of repose and angle of contact friction for dolos units with extrapolation carried out for maximum and minimum repose angles. The curve is based on the values obtained for concrete mortar and DHP*plastic units (ref. 6). Tests on model dolosse from two other laboratories (Types A and B) have given lower values of contact friction although measurement of their natural angles of repose was not possible owing to the few samples available. (The values of contact friction were similar to those reported by Gravesen for porcelain and glazed porcelain). Angles of repose for types "A" and "B" have been estimated by reference to possible extrapolations of values on the curve of Fig. 5.

Taking Iribarren's Modified Formula (3) and rearranging it we get:-

$$\left(\frac{\mu \cos \alpha - \sin \alpha}{\mu} \right) = H^3 \frac{\sqrt{K' \gamma_c}}{\sqrt{W_r (S_r - 1)^3}} \quad (11)$$

* DHI Danish Hydraulic Institute

RELATIONSHIP BETWEEN ANGLE OF REPOSE AND ANGLE OF CONTACT FRICTION FOR DOLOS UNITS

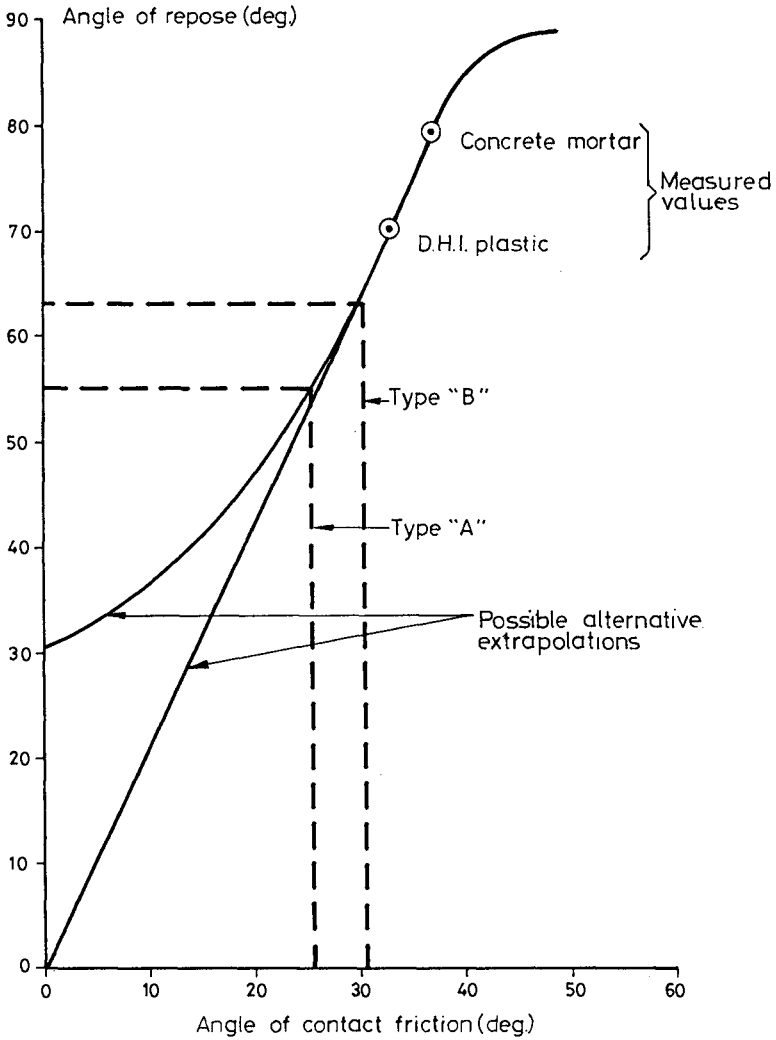


FIG. 5

If, for a given type and weight of armour, we consider the effect of contact friction and face slope angle we may consider C to be a constant where:-

$$C = \sqrt[3]{\frac{K' \gamma_c}{Wr}} \quad (12)$$

and plot curves of H, C against ϕ (where $\phi = \tan^{-1} \mu$) for different slope angles; this is done in Fig: 6. The angles of repose of the various types of dolos mentioned have been plotted onto Fig: 6 and it can be seen that the influence of the natural angle of repose of armour units on their stability under wave attack is significant. It is not claimed that the results shown are precise, further tests are required, but it is fair to conclude that this effect is too important to be ignored as it has been by the majority of laboratories until now.

In view of the wide variety of materials being used for model armour units for test purposes, it is essential that contact friction should be represented correctly at least until we know how to correct for errors in modelling contact friction. It seems unlikely that mathematical analysis will assist us in this and it will be necessary to devise modelling techniques which enable contact friction to be varied without varying any other factors, such as specific gravity or hydraulic drag forces.

Wave Characteristics

Applying a significant wave height parameter to the Hudson equation does not seem suitable to a structure which has to withstand a spectrum including some waves which are considerably greater than this height. Care in selection of wave height was suggested by Hudson (ref: 1) with limits $H_{\frac{1}{5}} < H < H_{\frac{1}{100}}$ recommended by Morais (ref: 13).

Wave steepness is an important factor in terms of the disturbing force acting on the armour units. The steeper waves plunge whereas the flatter ones surge onto the breakwater.

Losada et al (ref: 14) carrying out tests on height-period interactions defined joint values of (H min, T) and (H, T min) which caused initiation of damage on breakwaters. (H min, T) therefore gives an optimum value of T for initiation of damage pertinent to each set of breakwater characteristics and also an optimum value of T for any wave height greater than H min, which causes the greatest amount of damage for that particular wave height.

Brunn (ref: 15) explained these optimum values of T as the occurrence of resonance between the wave period and the down-rush period. Peak forces perpendicular to the slope are set up by the collapsing-plunging wave repeatedly breaking, with the previous wave down-rush being in the same low position.

RELATIONSHIP BETWEEN ANGLE OF REPOSE
AND SIGNIFICANT WAVE HEIGHT

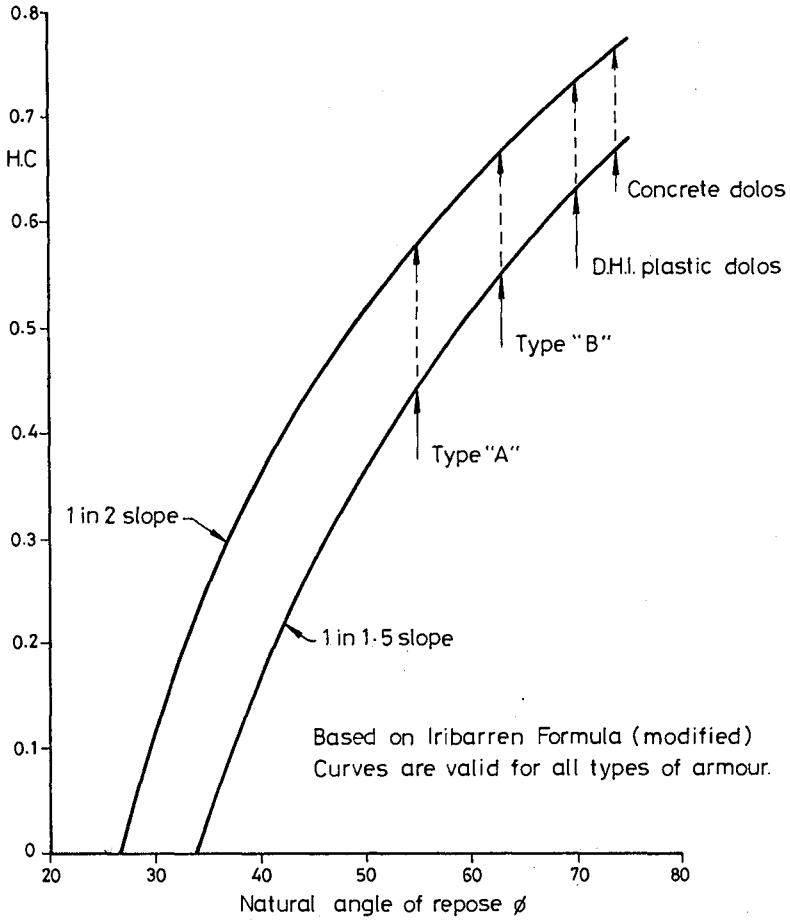


FIG. 6

Considering the rate at which energy is transmitted (wave power) towards a breakwater; it is directly proportional to wave period.

$$\text{Wave power} \quad P = \frac{g^2 H^2 T}{32\pi} \quad \text{/Sec.} \quad (13)$$

However, it has been found that as the wave period increases there is an increase in wave reflection (ref: 2) and a corresponding decrease in near surface orbital velocities. An optimum wave period for maximum damage is therefore anticipated.

The wave form itself is influenced by depth limiting factors such as refraction, shoaling, bed friction, bed permeability and wave breaking. On interception with the breakwater the wave characteristics are modified by both the armour slope and the porosity of the breakwater cover layers. Consideration of these influences is therefore necessary prior to determination of H in a stability equation and for determination of the wave field in model tests.

It is envisaged that mathematical analysis could now contribute significantly to our understanding of the nature of many of these effects.

Structural Strength

With the recently developed interlocking units, which rely on linkage with adjacent units rather than on their own weight, there are greater possibilities of movement and oscillation of units under wave action. These oscillations result in impacts, and it is necessary for the units to be sufficiently sturdy to resist these impacts. This has been recognized since the initial development of such units as has the possibility that structural strength problems might increase with size of unit (assuming a consequent increase in wave height). Considerably more full scale testing of armour units is required to increase our understanding of the strength of large concrete units. It is not possible yet to measure the amplitudes, velocities and acceleration of the oscillations of the armour units or to predict the amount of movement which will cause breakage. However, model tests using breakable armour units with inserts of material with reduced strength have been used in hydraulic flume tests (ref: 11). The results were interesting and indicate that this could prove to be a valuable method for determining the strength requirements of interlocking armour units. It will however be necessary to find a modelling material (not just an insert) with correct strength characteristics as well as correct specific gravity and surface friction.

Until such techniques have been developed it would be advisable to include in our formula a specific factor of safety against the conditions under which model testing shows the degree of movement likely to result in breakage.

Conclusions

We may conclude in summary that:-

- (i) Research into breakwater design and behaviour is now urgently needed to reduce reliance upon existing formulae which are no longer suitable for modern armour units.
- (ii) An integrated programme of theoretical analysis and model testing will be required.
- (iii) Future design methods will include more carefully controlled hydraulic model testing and the use of a range of new formulae.
- (iv) Until the new techniques have been developed, tested and proved, we must recognize the limitations of the present formulae and be very careful indeed not to use them out of their intended context.

REFERENCES

1. Hudson. R.Y., "Laboratory investigation of rubble-mound breakwaters." A.S.C.E. Waterways & Harbours Div. September 1959.
2. Zwamborn, J.A., and Beute "Stability of dolos armour units" ECOR Symposium, Stellenbosch, Nov. 1972
3. Zwamborn, J.A. Discussion. Conference on Coastal Engineering, Vancouver. 1972.
4. Zwamborn, J.A. "Dolos-packing density and effect of relative block density." Conference on Coastal Engineering. Hamburg 1978.
5. Brorsen, M., Burcharth, H.F., and Larsen, T., "Stability of dolos slopes." Conference on Coastal Engineering. Copenhagen. 1974.
6. Graveson, H., Jansen, O.J. and Sorensen, T. "Stability of rubble mound breakwaters." Conference on Coastal Engineering. Hamburg, 1978. Additional Paper.

7. Iribarren, R., "Una formula para el calculo de los diques de escollera." July, 1938. Translated Fluid Mechanics Laboratory, Univ. Calif., Berkeley, Tech. Rep. HE-116-295, 1948.
8. Iribarren, R., "Formula pour le calcul des diques en enrochements naturels ou elements artificiels." XXI Int. Navigation Congress. Stockholm. 1965 Sec. II Theme I.
9. Castro, E., "Diques de escollera" - Revista de Obras Publicas, Madrid, April 1933.
10. Funke, E.R., and Haines, S.A. "Production of model armour units for scale breakwaters" Hydraulics Laboratory, Division of Mechanical Engineering, Ottawa, Canada. Report LTR-HY-52, August 1976.
11. Mansard, E.P.D. and Ploeg, J. "Model tests of Sines Breakwater" Hydraulics Laboratory, Division of Mechanical Engineering, Ottawa, Canada. Report LTR-HY-67 Oct. 1978.
12. Hedar, P.A., "Stability of rock-fill breakwaters" London. Heinemann. 1960.
13. Morais, C.C. "Irregular wave attack on a dolos breakwater" Conference on Coastal Engineering. Copenhagen, 1974.
14. Losada, M.A. and Gimenez-Curto, L.A. "The joint effect of the wave height and period on the stability of rubble mound breakwaters using Iribarren's number" Coastal Eng., 6. 1979.
15. Bruun, P. and Johannesson, P. "Parameters affecting stability of rubble mounds" A.S.C.E. Waterways and Harbours Division. May 1976.
16. Mettam, J.D., "Larnaca : new port for Cyprus" The Dock & Harbour Authority. Vol. 1. No. 584 June 1969.

LEGEND

W_r	=	armour block weight
K_D	=	Hudson's dimensionless stability coefficient
γ_c	=	concrete density
γ_w	=	water density
α	=	inclination of armour face from horizontal
H	=	design wave height
N	=	Iribarren's stability coefficient
A	=	incident wave height
P	=	armour block weight
$\mu = f$	=	friction coefficient of the armour blocks $f = \tan \phi$
ϕ	=	natural angle of repose
$S_r = d$	=	relative density of armour block $= \frac{\gamma_c}{\gamma_w}$
K_o, K'	=	dimensionless stability coefficients
L_p	=	wave length
T	=	wave period



Port Botany, New South Wales

PART IV

COASTAL, ESTUARINE, AND ENVIRONMENTAL PROBLEMS

Tribar and DoLos revetment, Port Botany, New South Wales



Separation of climatic fluctuations and impacts of
engineering activities in estuaries

G. Krause

Institute of Marine Research
Bremerhaven, Federal Republic of Germany

Abstract

Using salinity as an example of dissolved substances in estuarine waters it is shown how the long term trend of concentrations can be split up into a man-made and a climatic contribution. The understanding of long term mixing processes and adequate sampling techniques are essential for this purpose. The physical state of the estuary can be described in terms of 3 basic variables, the river discharge, the filtered water level and the filtered salinity. The river discharge represents the climatic fluctuations in the catchment area, and the filtered water level is a record of the large scale weather pattern over the adjacent ocean basin. Salinity trends which cannot be attributed to these two variables must originate from man-made actions, such as dredging or other engineering activities which change the geometry of an estuary.

Two models are used for the trend analysis, the simplest possible mixing equation (which always holds for a sufficiently long time scale), and a salt flux consideration.

1. Introduction

In many cases environmental impacts of coastal engineering activities in estuaries are not easily assessed because it is necessary to separate the man-made changes from climatic fluctuations. Moreover, variables such as water level current velocity and salinity depend not only on tidal conditions and river discharge, but also on external forces like wind set-up, atmospheric pressure gradients, presence of shelf waves and changes of the large scale water circulation of the adjacent ocean basin.

Therefore, methods have to be developed that allow to eliminate all of these natural effects from measured data prior to any trend analysis which aims at assessing human impacts. For the variable salinity suitable methods will be described for a well-mixed estuary. They are derived from a case study using observations of a typical tidal estuary of the North Sea.

2. Area description and observations

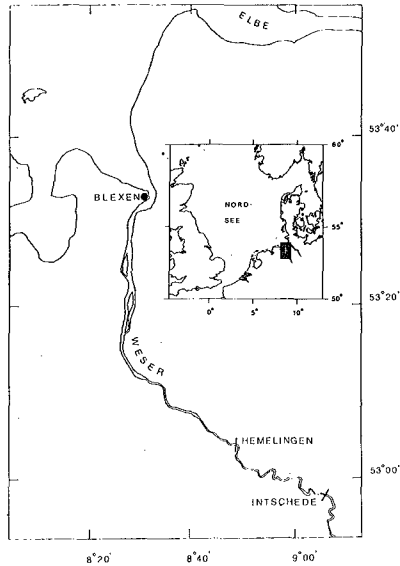


Fig. 1 The river Weser estuary. The tidal range extends up to Hemelingen. The river discharge is measured at Intschede, all other data were obtained from a jetty at Blexen

Fig. 1 shows a map of the river Weser estuary. The mean tidal elevation is 3.40 meters, there are strong tidal currents up to several knots, and a weak stratification of salinity occurs only for two or three hours around slack waters.

The Weser river is an important shipping channel which connects the old Hanse town Bremen with the North Sea. Dredging of the channel has been carried out ever since the introduction of effective techniques.

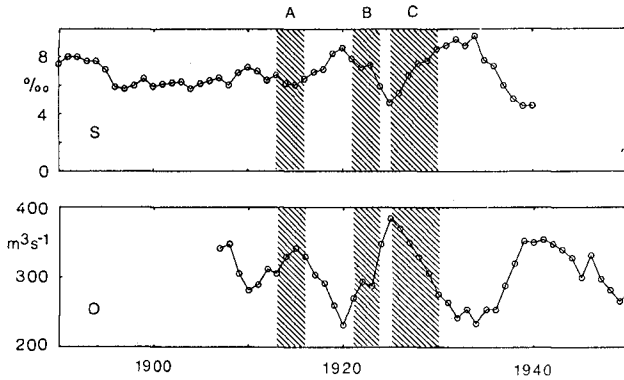


Fig. 2 5 year averaged salinity and river discharge together with major dredging operations A, B and C during which the river was deepened from 5 down to 7 meters

Fig. 2 displays the development of salinity near the mouth of the river (Blexen) together with the river discharge covering the period from 1887 to 1940.

People were alarmed by the increase of salinity which followed the first extensive period of dredging, but it is seen that salinity just reflects the influence of the variable river discharge whereas effects of dredging are not obvious from the data.

However, there is biological and other evidence that salinity must have changed especially after deepening the river further upstream. Obviously, the large fluctuations of the river discharge mask the effects of dredging. It could also be the case that salinity sampling was not adequately carried out with respect to the problems to be studied. The old data set of fig. 2 just served as an in-

roduction into the problem of a long term trend analysis. The intention of this paper is to outline a method how man-made changes and natural fluctuations of salinity can be separated.

For this purpose another data set will be used which is represented in fig. 3. It was measured at a rather high sampling rate ($\Delta t = 1$ hour), and it covers 368 days of salinity, water level and river discharge observations.

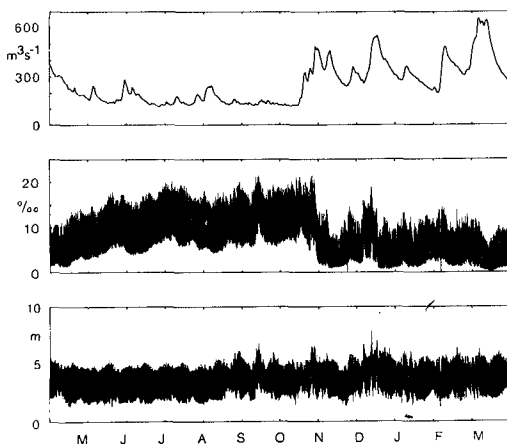


Fig. 3 The data set (river discharge, salinity, water level) used for this investigation. Time scale is one year, sampling interval is one hour

3. Fundamentals of trend analysis of salinity

3.1 Scale considerations

The duration of a tidal cycle can be considered as a basic estuarine time scale. Mixing of river and sea water appears as a very complicated process within this scale. It involves turbulence, density effects, bottom friction, river discharge and many others amongst which are the water depth and other geometrical properties of the channel.

In order to predict salinity changes as a result of dredging the complicated mixing process is usually modelled, and respective parameters are systematically changed.

This usual engineering approach will not be adopted here. Man-made changes to salinity distributions in estuaries occur not only by single operations but also by many minor actions in the course of years or decades, and on these very long time scales one cannot consider all the details of mixing which take place within a single tidal cycle.

If a long term observer looks upon salinity in an estuary, the time averaged salinity \bar{S} can only be a function of the averaged volume ratio of fresh water to sea water \bar{q} , and the salinity of the adjacent ocean water S_0 , i.e.

$$\bar{S} = S(S_0, \bar{q}) \quad (1)$$

The volume ratio \bar{q} depends on the position within the estuary, on the geometrical dimensions, and on the amount of fresh water which is given by

$$F = Q + (P - E) \quad (2)$$

where Q is the river discharge, P is precipitation and E stands for evaporation. Restricting the discussion to one fixed position, assuming a channel-like estuary, neglecting $(P-E)$ compared with Q , and assuming salinity of the ocean water to be constant, then eq. (1) reduces to

$$\bar{S} = f(Q, \bar{h}) \quad (3)$$

where \bar{h} is the mean water depth. Eq. (3) indicates that the averaged salinity is a function of climatic fluctuations in the catchment area, and that it is also dependent on all external processes that change the mean water level. Such processes can be wind set-up, seiching, presence of shelf waves or atmospheric pressure gradients. Eventually, the mean water depth depends on the dredging operations in the area.

No particular mixing process has been assumed. If data are sufficiently averaged it does not matter how river and sea water is mixed, whether this is due to tidal or other currents or whether there exists a stratification or not for some periods of time. The basic question is only over what period of time the averaging procedure has to be extended so that the above arguments will hold. This can only be answered with the aid of observations, and the data set of fig. 3 serves for this purpose.

3.2 Selecting the time scale

The result of the previous discussion can also be put this way: Whenever the mean water level changes sea water is moved into or out of the estuary in addition to the tides. Given enough time this additional water mass will be mixed completely with the estuarine water.

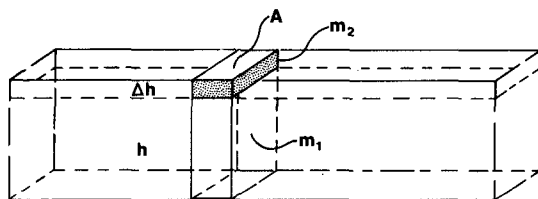


fig. 4

If m_1 denotes the mass of water in a control volume and m_2 an additional water mass, then the equation

$$m_1 S_1 + m_2 S_2 = (m_1 + m_2) S \quad (4)$$

must hold after complete mixing. S_1 , S_2 and S are the respective salinities. Relating the masses to respective water levels (fig. 4) yields for small changes

$$\Delta S = \frac{S_2}{h} \Delta h \quad (5)$$

Near the mouth of the river S_2 can be considered constant (ocean salinity), it varies very much less than the salinity in the estuary. Therefore, one should expect a linear relationship between mean salinity and mean water level fluctuations. This can serve as a criterion for finding the characteristic time after which complete mixing has taken place.

With the frequently sampled time series available, the most obvious averaging procedure is filtering by a low pass filter.

For the river Weser estuary it was found (KRAUSE 1979) that mean data of salinity and water level satisfy eq. (5) after being filtered with a pass band between 35 h and 3000 h. The filtered time series are shown in fig. 5.

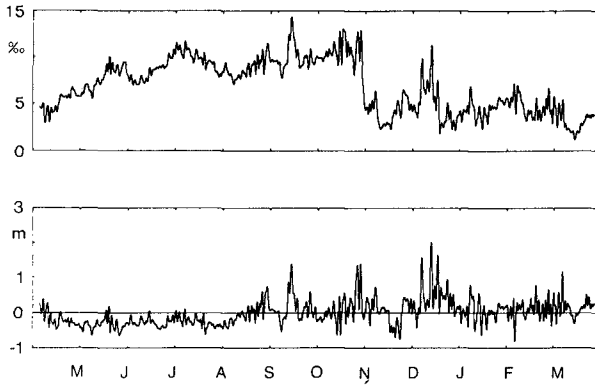


Fig. 5 Filtered salinity and water level

Fig. 6 shows an enlarged section of the filtered time series, and in fig. 7 the same data are plotted against each other.

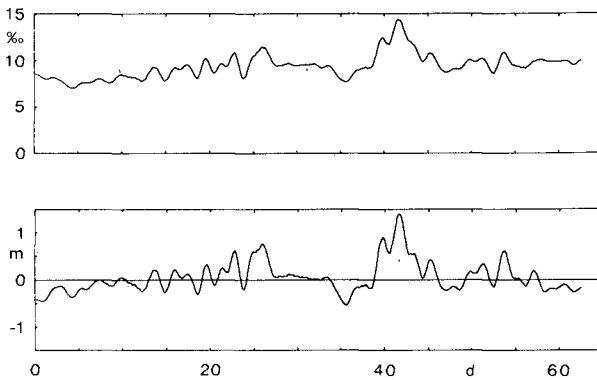


Fig. 6 Filtered salinity and water level during September/October

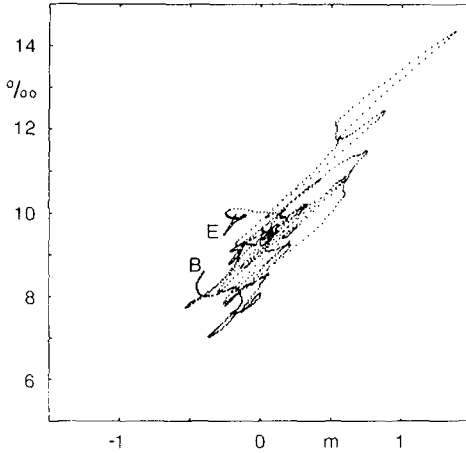
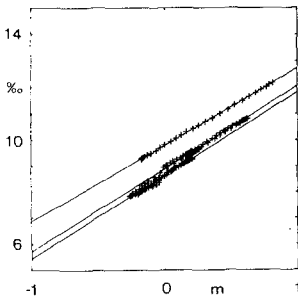


Fig. 7 The data fig. 6 plotted against each other. B: begin, E: end

This picture appears confusing at the first glance, but this results only from the variable river discharge. For short times of almost constant discharge there holds a linear relationship which cannot be better fulfilled as indicated by fig. 8.



$$S_F = AH_F + B$$

A	B	R	Q (m^3s^{-1})
3.16	8.89	1.00	157
3.18	8.36	0.99	146
2.92	9.74	1.00	130

$$\Delta S = 3.02 H_F$$

Fig. 8 Regression lines through successive data points of fig. 7 (3 examples). R is the correlation coefficient and the last column is the river discharge. S_F denotes filtered salinity, H_F filtered water level and $\Delta S = H \cdot H_F$

It was assumed that the empirical relationship in fig. 8 holds throughout the record.

The physical significance of this result is that in the Weser river a time of about 3 tidal cycles (35 h) is sufficient to mix an additional water mass, associated with a change of the mean sea level, completely with the water already present at the observation site.

3.3 Rejection of external forces

The filtered sea level fluctuations in fig. 5 are closely related to the large scale weather patterns over North Sea and North Atlantic Ocean. However, it is not necessary to elaborate on the mechanism of this response. Whenever the filtered water level changes, water is moved into or out of the estuary. The filtered water level is simply a record of external forces on the estuary. The associated salinity fluctuations can be computed using the empirical relationship given in fig. 8. The result is displayed in fig. 9, and it is seen that the fluctuations are of considerable magnitude.

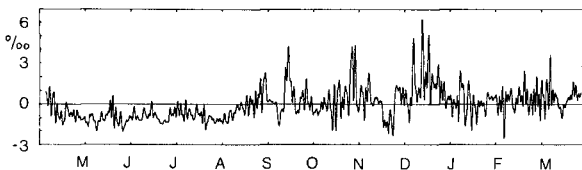


Fig. 9 Salinity fluctuations as a result of external forces on the estuary

They do not contribute to a man-made trend, they only contaminate the data. Therefore, they are subtracted from the filtered salinity time series of fig. 5. The result, presented in fig. 10 is a rather smooth curve which is almost the mirror image of the river discharge.

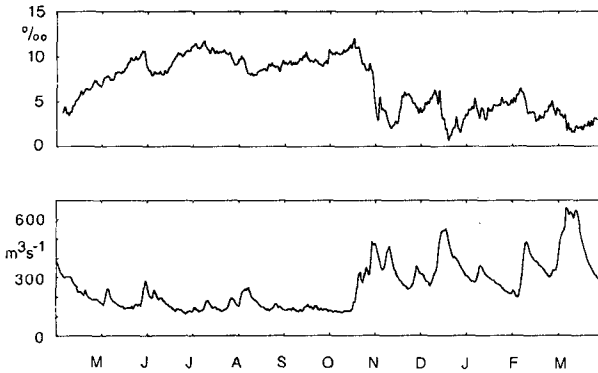


Fig. 10 Reduced salinity and river discharge

3.4 Rejection of climatic fluctuations in the catchment area

Under the assumptions of stationary conditions, constant bathymetry, constant salinity of the adjacent ocean basin and mixing processes being independent of the river discharge Q , the mean in- and outgoing salt fluxes through a cross section of the estuary would be in balance and be constant.

The outgoing salt flux is

$$f_{\text{out}} = \rho U_0 \bar{S} \quad (6)$$

where \bar{S} is salinity averaged over the cross section and over time, ρ denotes density and

$$U_0 = \frac{Q}{A} \quad (7)$$

is the outgoing velocity according to river discharge Q and cross sectional area A .

Under the above assumptions one has

$$f_{\text{out}} = - f_{\text{in}} \quad (8)$$

both being constant. Therefore, the total outgoing flux (mass per second) must also be constant, i. e.

$$\Sigma QS = \text{const} \quad (9)$$

and the ingoing flux needs not to be known. As indicated by eq. (7) a dredging operation which changes the cross sectional area A would change the constant in eq. (9).

To a first approximation eq. (9) can be used to eliminate the variable river discharge which expresses the climatic fluctuations in the catchment area of the river. The flux according to eq. (9) has been calculated, and the result is displayed in fig. 11. It is seen that most of the time the assumption of stationary conditions is violated. When a flood wave enters the estuary the flux increases, and salt is washed out of the estuary. Nevertheless, there are also times of almost constant discharge, which enables the observer to determine the constant in eq. (9). In the present case the constant is 1200 kg s^{-1} .

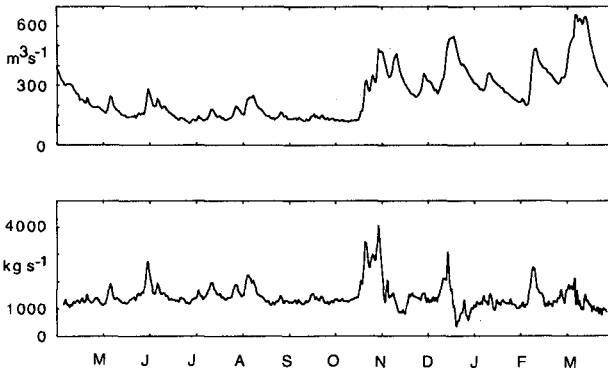


Fig. 11 River discharge and total outgoing salt flux

Observations taken at times of variable discharge cannot be used for the trend analysis under study. Fig. 12 gives some insight into the complicated response of salinity due to variable river discharge, and it supports the above argument.

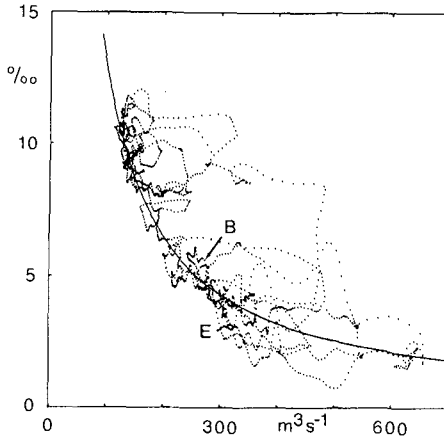


Fig. 12 River discharge - salinity diagram. The solid curve corresponds to a constant flux of 1200 kg s^{-1} which had been determined from fig. 11

3.5 Results

The decisive processes which govern the subtidal variability of salinity in an estuary originate from the adjacent ocean basin and from climatic fluctuations in the catchment area. Resulting fluctuations mask the man-made changes. However, it is possible to recover the very weak signal of human impacts by regarding the other fluctuations as "noise" which contaminates all data gathered.

The salinity fluctuations as a result of external forcing are very well understood. On time scales beyond 3 tidal cycles in case of the Weser, they are linearly related to the filtered (mean) sea level, and corresponding salinity fluctuations are easily removed from observed salinities.

The response of salinity to the variable river discharge involves the previous history of the salinity distribution and depends also on magnitude and time history of the discharge. Only salinity data gathered during periods of almost constant river discharge are reliable for assessing man-made trends.

It is obvious that results derived for salinity will also hold respectively for other dissolved substances, pollutants, turbidity, current velocity and for sediment transport processes. Attention to the difficulties in estimating mean flow conditions in estuaries has been pointed out by WEISBERG (1976).

4. Applications

4.1 Monitoring strategies

With respect to the long-term development of salinity or other variables it is important to realize that in spite of the predominance of tidal variability, a tidal estuary is a meteorologically governed area of the sea. This prescribes the sampling rate to be adopted by monitoring schemes.

In order to demonstrate this more clearly, the salinity data set of fig. 3 (again as an example) can be resampled according to various schemes.

If one assumes an observer who could take a sample at every high water the result would be the trace in fig. 13. In case of pollutants such frequent sampling is beyond any hope of achievement.

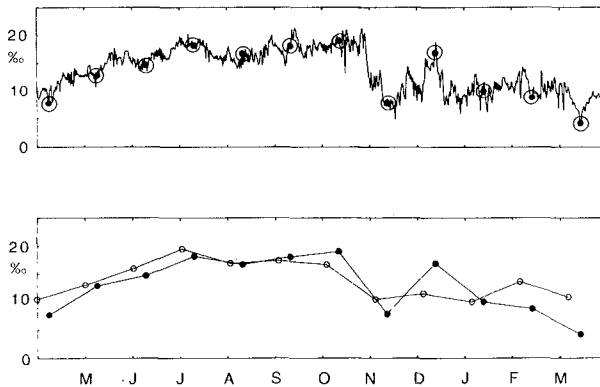


Fig. 13 Results of various monitoring schemes. Trace: Sampling at each high water, dots: sampling on monthly intervals.

Sampling on monthly cruises gives rise to serious errors in trend calculations as indicated in fig. 13. Data of such schemes e.g. depend on the starting time.

A suitable monitoring strategy can only be based on the 3 basic variables water level, salinity and river discharge. They are easy to measure continuously and they characterize the physical state of the estuary. One can apply the reduction procedures outlined before, and this can also be carried out on-line. Based on the results (i.e. stable or unstable conditions due to variable river discharge, mean sea level fluctuations etc.) other measurements can be assessed or perhaps be corrected. One can also adopt a flexible approach. A costly field investigation is only carried out when the conditions are right.

4.2 Assessment of available data sets

The results of chapter 3 enable the assessment of existing data of an estuarine environment also in cases where no salinity measurements have been carried out. It is necessary to know the time history of mean sea level and river discharge to have an indication of the usefulness of data with respect to trend analyses.

4.3 Calibration of mathematical models

Numerical models designed to predict salinities or other variables rely on a data set for calibration that only depends on processes which have been modelled. As has been demonstrated before, estuaries are seldom in a stationary state and field data depend on the previous history. Therefore, great care is necessary to measure a suitable data set that ensures the general validity of the model parameters.

5. Conclusions

- (i) The basic element for a long term trend analysis of estuarine variables is the fact that an estuary is a meteorologically governed area of the sea in spite of the predominance of tidal variability.
- (ii) The long term trend of the concentration of a conservatively dissolved substance depends only on the large scale weather patterns over the adjacent ocean and the catchment area of the river.

- (iii) Whereas other authors (e.g. ELLIOT and WANG, 1978; SMITH, 1978; WANG, 1979) have studied the influence of atmospheric forcing on estuaries in detail, this is not necessary for a long term trend analysis. The filtered (mean) sea level is the record of all external forcing mechanisms.
- (iv) In well-mixed estuaries only a few tidal cycles have to elapse until the simplest possible mixing equation describes adequately the response of salinity to external forces which change the filtered water level. Filtered water level fluctuations are natural "experiments" by which the time scale can be determined.
- (v) Filtered salinity, filtered water level and river discharge are the basic variables which describe the physical state of an estuary. They can be used to design monitoring schemes and to assess available data, mathematical tidal models and impacts of engineering activities on estuaries which are masked by large climatic fluctuations.

Literature

- Elliot, A.J. and D.P. Wang, 1978: The effect of meteorological forcing on the Chesapeake Bay: The coupling between an estuarine system and its adjacent coastal waters. In: J.C.J. Nihoul (ed.) Hydrodynamics of estuaries and fjords. (Elsevier Oceanogr. Ser. 23, 127-145).
- Krause, G., 1979: Grundlagen zur Trendermittlung des Salzgehalts in Tide-Ästuarien. Dt. Hydrogr. Z. 32, 233-247.
- Smith, N.P., 1978: Long-period, estuarine-shelf exchanges in response to meteorological forcing. In: J.C.J. Nihoul (ed.), Hydrodynamics of estuaries and fjords. (Elsevier Oceanogr. Ser. 23, 147-159).
- Wang, D.P., 1979: Subtidal sea level variations in the Chesapeake Bay in relations to atmospheric forcing. J. Phys. Oceanogr. 3, 413-421.
- Weisberg, R., 1976: A note on estuarine mean flow estimation. J. mar. Res. 34, 387-394.

Wave Energy Distribution in an Estuary

by
Volker Barthel *

Abstract

A field investigation program on waves in the Weser Estuary, German Bight of the North Sea, was started to learn about the complex wave climate in this region. The comparison of results in the various locations shows that most of the wave energy is transferred from deep water across the reef region to the wadden area. The comparison of spectra in the different sites and the parametrization of these multi-peak-spectra gives another feasibility to describe estuarine waves.

Introduction

Waves coming from deep water and entering an estuary generate a very complex wave climate. In addition to the influence of wind and shoaling water (refraction, diffraction etc.) nonlinear wave-to-wave-interactions occur. Therefore it is very difficult to find a reasonable prediction method as a basis for the design of all structures and for shipping purposes in the region in question. A field investigation which for economical reasons has to be restricted to a few locations in a strongly divided area of an estuary normally can only give a limited view. But with a sophisticated choice of the sites the comparison of the results can give valuable references of the behaviour of waves in this area.

In 1976 a field investigation program on waves was started in the Weser Estuary (German Bight of the North Sea) (Fig. 1).

* Dipl.-Ing., Federal Waterways Administration,
Wasser- und Schifffahrtsamt Bremerhaven, F.R.Germany

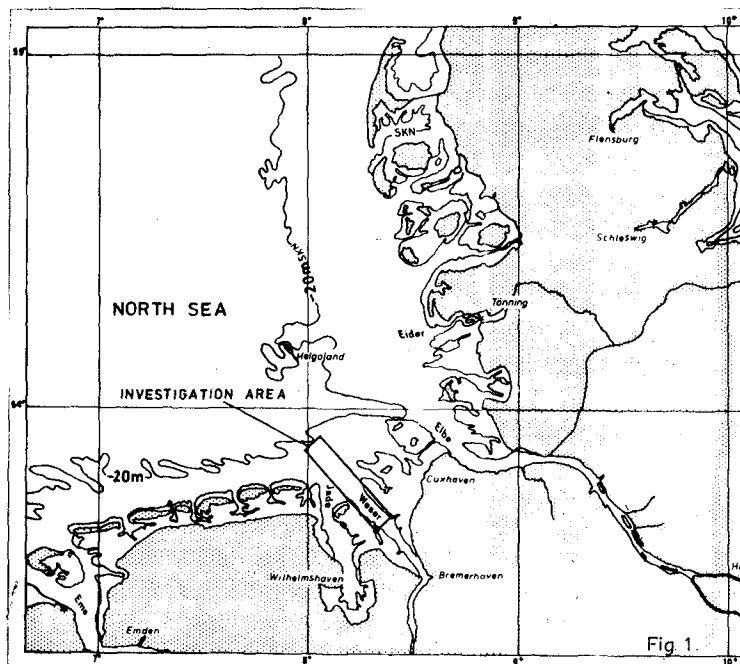
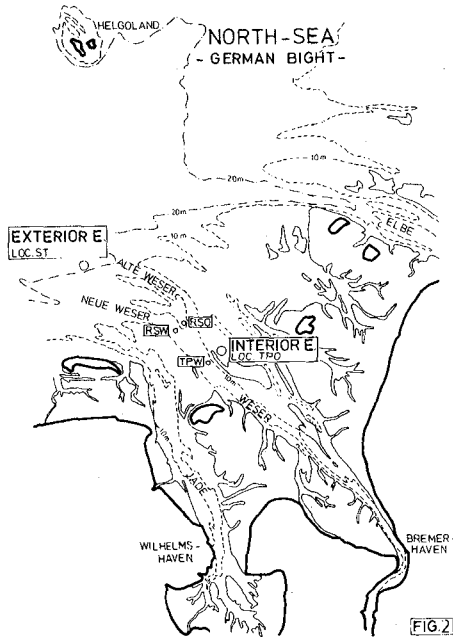


Fig 1

The measurements were carried out by the German Federal Waterways Administration which is part of the Federal Ministry of Transportation. They were supported by the German Coastal Engineering Board (KFKI).

Fig. 2 gives a better view of the investigation area with the single sites. The location ST lies at a water depth of about 20 m below MLW and is to registrate the waves coming from the open sea. RSW lies on the edge of the deep shipping channel "Neue Weser".



The water depth is 10 m below MLW. RSO lies behind the bar "Roter Grund", where the water depth is 7 - 8 m below MLW. Finally the location TPW on the edge of the shipping channel is to record the change in wave height and period in the interior estuary in front of the wadden area. On most of these locations waverider buoys were installed, the radio-signals of which were received and recorded on a light-house in the near-by wadden area.

Though a lot of records with nearly all wind directions and - velocities could be gathered the following analysis was only worked out for a series of records with strong winds from WNW during a minor storm surge. Previous measurements had shown that already slight changes in wind-direction in this area very promptly exercise an influence on wave parameters.

Three of the main ideas of this program were:

- a) to find a reasonable site for a permanent measuring station, which could lead to predictions for the whole estuary,

- b) to find out whether long waves could penetrate the estuary causing a possible danger for deep-drawing ships
- c) to express multi-peak-spectra by parameters, which can be correlated with different influence factors.

Loss of Wave Height or Energy on the Reef

Fig. 3 shows the significant wave height H_s ($H_{1/3}$) versus the wind-velocity as an example for the location RSW. The distinctions between ebb - or flood - currents were not regarded in this case. The results of a lot of measurements as far as this correlation is concerned made it possible to complete the plot of the variations of

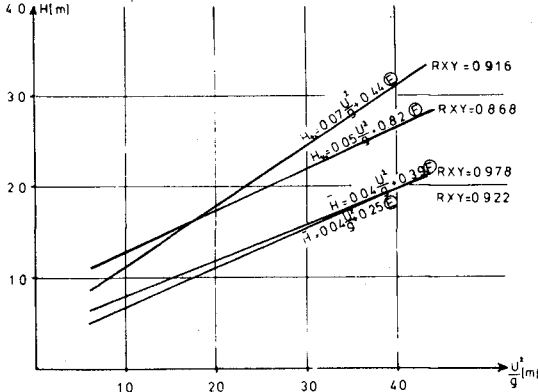
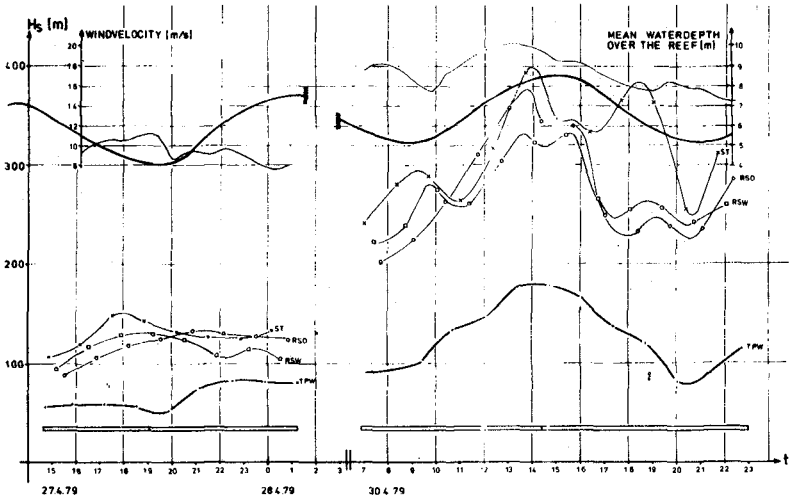


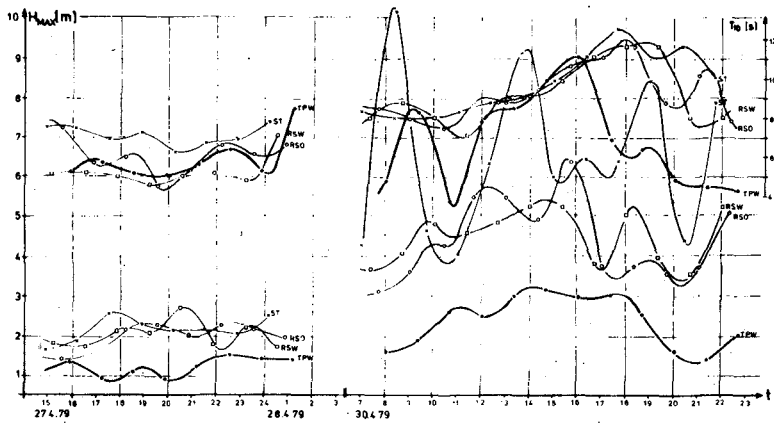
Fig. 3 H_s versus $\frac{u^2}{g}$ (m) - Loc. RSW; WIND SW - NNW

wave heights and periods on all locations though the technical equipment allowed a 20 - minutes - record every 80 minutes only. Fig. 4 shows the variations of wave parameters of 4 locations on April 27th and 30th, 1979. While in the left part only minor wind-velocities occur they rise up to 20 m/s on April 30th. In accordance with this and the mean waterdepth over the reef between RSO and ST the significant and maximum wave height H_s and H_{max} and the peak-period T_{f0} react. The first task was to find interdependencies between the wave parameters of the different regions of the estuary. In this study the significant wave height H_s was looked at in detail. The waves coming from the open sea and entering the estuary at location ST are hardly affected by the sea bottom if they aren't too high under severe storm conditions.



VARIATIONS OF WAVE HEIGHT H_s , WIND AND TIDE

FIG. 4



VARIATIONS OF WAVE HEIGHT H_{max} AND PEAK PERIOD FIG. 4

First influences are to be expected in the reef region and were to be recorded at the locations RSW and RSO. We expected to find a considerable loss of wave-energy and therefore wave - height in the reef region.

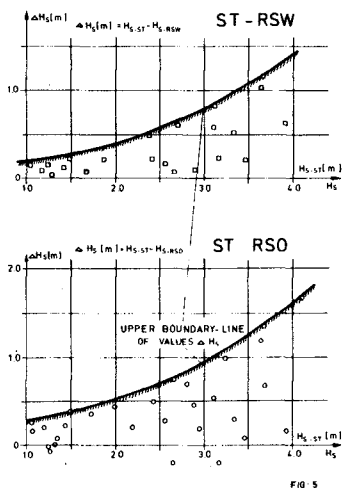


Fig. 5: ΔH_S versus H_S

Fig. 5 shows the difference of the significant wave height ΔH_S between ST and RSW respectively ST and RSO as a function of H_S at ST. With no reference to the water depth on the reef this is an accumulation of single points, which can be delimited by curves. These boundary lines weren't transgressed after the evaluation of a lot of additional records with the same wind-direction either. Though the slope of the curve ST - RSO is a little bit steeper the difference between RSW and RSO is smaller than expected.

Regarding the further course of waves into the inner estuary we found out a fairly good dependency between RSW resp. TPW.

Fig. 6 shows that the damping of wave height resp. the loss of wave energy between RSW and TPW decreases with increasing H_S at RSW.

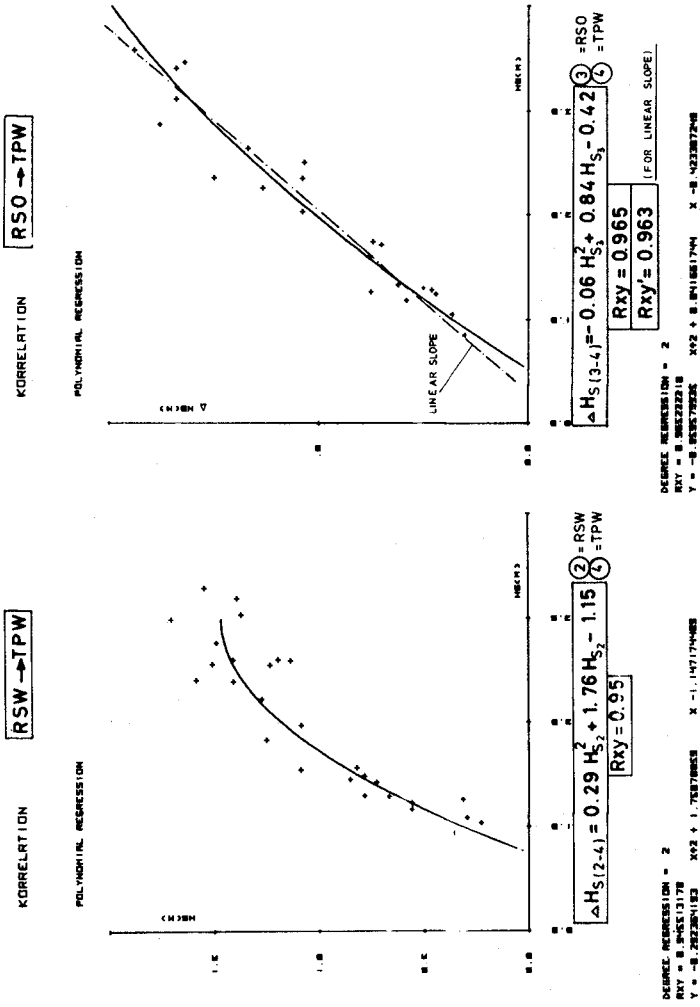
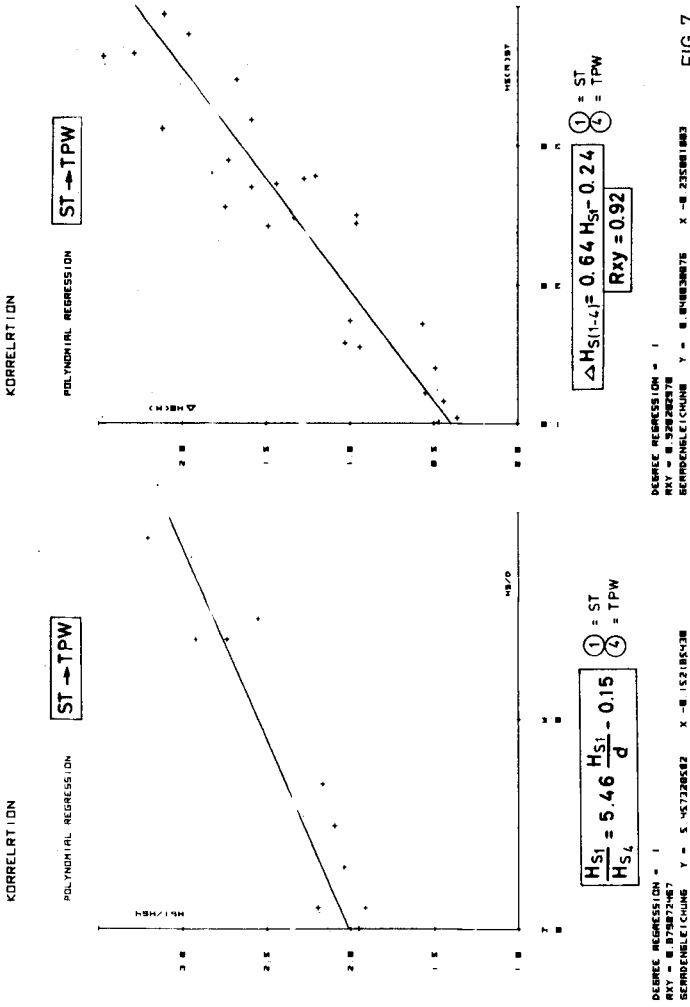


Fig. 6: Damping of wave height RSW - TPW and RSO - TPW



That seems to be an indication for the direct connection between both locations in the deep channel, which becomes better with increasing wave height. That is not so evident with RSO and TPW where the slope is nearly linear.

A certain correlation with the inclusion of the waterdepth over the reef resp. the water level in this area was only to be found between ST and TPW directly.* The scattering of values may be due to the oscillating tide currents, the influence of which is to be recognized at TPW predominantly. Tidal currents in this region can have a velocity up to 2.0 m/s. The following table gives a view of some of the results of the measurements:

Table of significant wave height H_s and water depth d over the reef

1 ST	2 RSW	3 RSO	4 TPW	Depth d
2.42	2.20	1.92	0.90	5.75
2.81	2.31	2.12	0.95	5.20
2.89	2.80	2.43	1.12	5.30
2.65	2.57	2.84	1.37	6.40
3.17	2.92	3.38	1.54	7.40
3.94	3.31	3.77	1.80	8.30
3.80	3.20	3.41	1.79	8.50
3.47	3.27	3.39	1.76	8.60
3.35	2.80	3.00	1.51	8.10
3.66	2.49	2.29	1.32	6.80
3.64	2.62	2.47	1.12	5.90
2.56	2.40	2.27	0.78	5.30
3.12	2.55	2.59	0.96	5.30

H_s and d in (m)

Results of the correlation:

$$\frac{H_{s1}}{H_{s2}} = 1.07 \frac{H_s}{d} + 0.66 \quad (R_{xy} = 0.59)$$

$$\frac{H_{s1}}{H_{s3}} = 2.17 \frac{H_s}{d} + 0.17 \quad (R_{xy} = 0.69)$$

$$\frac{H_{s1}}{H_{s4}} = 5.45 \frac{H_{s1}}{d} - 0.15 \quad (R_{xy} = 0.88)$$

*Fig. 7

The three equations at the bottom of the table show once more that there is a poor correlation between ST, RSW and RSO - in other words: water depth over the reef or the reef itself doesn't play an important part for the decrease of height or energy. To summarize the results of the investigations concerning loss of energy resp. damping of wave height Fig. 8 shows the mean proportional

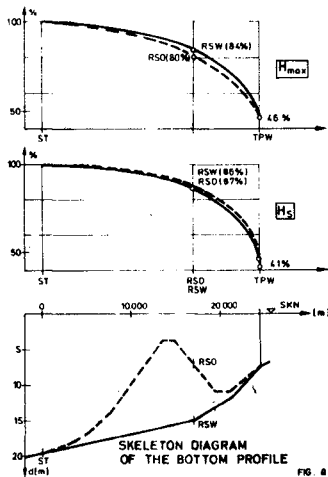


Fig. 8: Mean proportional decrease of wave height H_s and H_{max}

decrease of wave height H_s and H_{max} . It is shown that waves having travelled across the reef or via the deep channel still have 86 - 87% of the original height. Only when having arrived at TPW there was another decrease of 38 - 45 %. (The lower part of the graph shows a skeleton diagram of the bottom profiles in the different routes.) This means that the maximum part of wave energy isn't lost in the reef region, as one could have expected especially for higher waves. More than 40 % are lost on the way between the reef region and the wadden area. That is an important conclusion for planning and design of all structures.

Discussion of Spectra

Normally the records were evaluated statistically and with the Fast-Fourier-Transformation of COOLEY and TUKEY a power spectrum was calculated. The comparison of a series of plotted energy spectra in Fig. 9, 10 and 11 gives an indication of the alteration of waves more obviously:

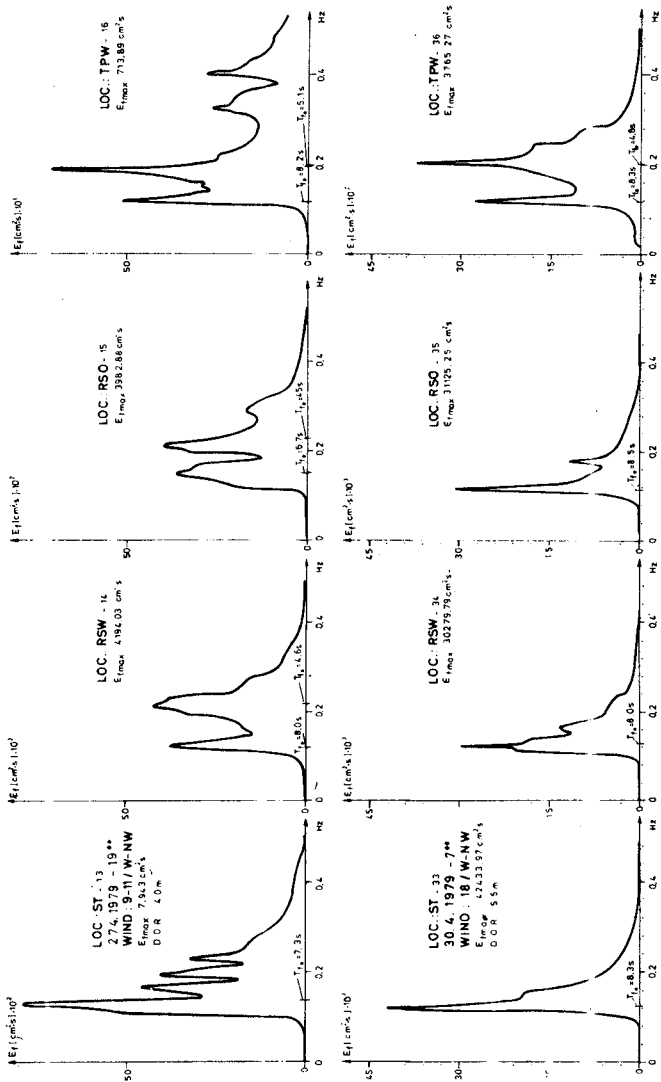


Fig. 9: Energy spectra in the Weser Estuary

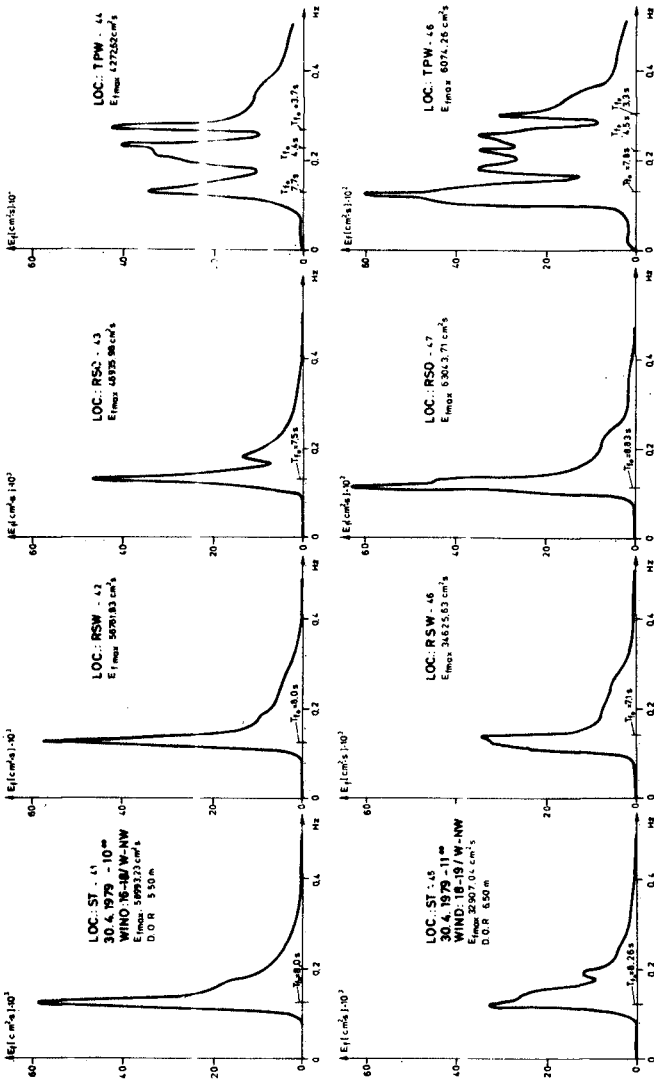


Fig. 10: Energy spectra in the Weser Estuary

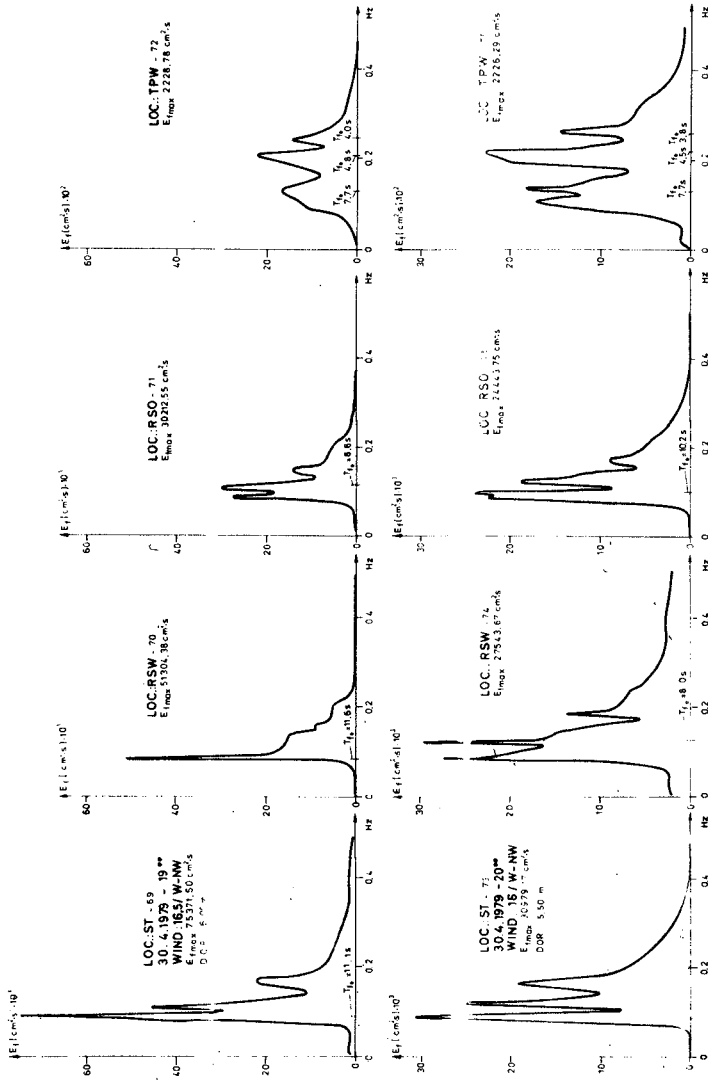


Fig. 11: Energy spectra in the Weser Estuary

Fig. 9: On loc. ST the spectrum shows energy shares of higher frequencies with a peak at 7.3 s. With low wind-velocities a max. height of 2.5 m arises. Waves with longer periods penetrate the estuary and are to be found with a small increase of the peak-period T_{fo} . The spectral shape varies strongly and shows the presence of more than one wave system. The spectra of April 30th, 7.00, show a normal shape at ST and energy shares of the locally arisen sea at RSW and RSO. At TPW the maximum of energy density lies in the region of higher frequencies, but the penetrating long-period-waves with $T_{fo} = 8.3$ s can be recognized clearly.

Fig. 10 shows two additional series of energy spectra with higher wind-velocities, still increasing. This time one can see a typical spectral shape at loc. TPW. This - as we called it - 3-peak-spectrum shows the complexity and variety of waves in an estuary. This shape could be detected again and again at this location. Among others it points out that waves with longer periods penetrate the estuary without remarkable alteration of period or length. This is important knowledge for ships with only a small underkeel-clearance, which enter the narrow channels of an estuary. The two additional systems at this location can be explained by locally arisen sea and reflexion or refraction.

Fig. 11 shows another two series of energy spectra with decreasing wind-velocity and the 3-peak-shape at loc. TPW again. There is a lot of additional information in this graph, which can be extracted either by further discussion or computer analysis. Though the frequencies of the long-period-waves don't change very much while penetrating the estuary the energy contents within certain frequency ranges can shift.

Fig. 12 shows the proportional shares of the spectral energy $m_o = \int E(f)df$ for three frequency ranges. The situation is presented for a) minor wind-velocity (increasing), b) high wind velocity (still increasing) and c) high wind-velocity (decreasing). It can be recognized that with minor wind velocities the spectral energy is concentrated within the frequencies 0,1 - 0,25 $1/s$ with a decreasing tendency into the inner estuary. Increasing wind-velocities generate longer waves with an increasing share into the inner estuary. With decreasing high wind-velocities this development has a downward movement with a high percentage of waves with periods 4 - 10 s in the interior estuary.

Parametrization of Spectra in Estuaries

The above mentioned analysis or discussion is very largescale as far as the evaluation of energy-shares and the description of spectral shape is concerned. But there is of course a possibility to have that done by a computer. To express the alteration of energy spectra or to describe them in a simple way we have the possibility of parametrization.

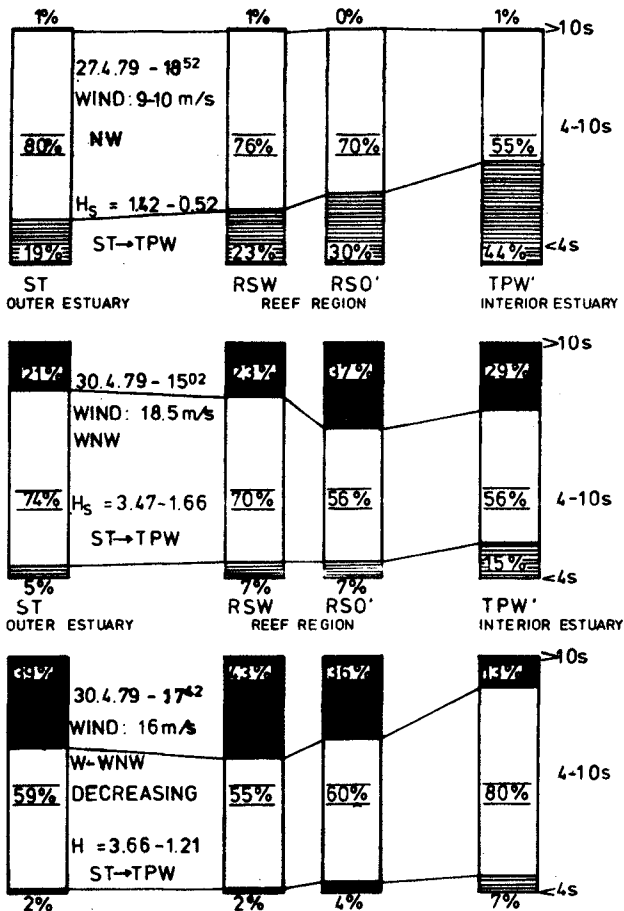


Fig. 12: Proportional energy shares for three frequency ranges.

Examples for that are given by the BRETSCHNEIDER-Spectrum, the PIERSON-MOSKOWITZ-Spectrum or the JONSWAP-Spectrum, which is expressed by the equation:

$$S(f) = \alpha g^2 (2\pi)^{-4} \cdot f^{-5} \cdot \exp\left(-\frac{5}{4}\left(\frac{f}{f_0}\right)^{-4}\right) \cdot \exp\left(-\frac{(f-f_0)^2}{2\delta^2 f_0^2}\right)$$

Several attempts to express an estuary-spectrum in the JONSWAP-form were very unsuccessful because there was no possibility to register more than one peak. So we tried to divide a two-peak-spectrum into two parts, to approximate the measured (Hamming-smoothed) partial spectra to the JONSWAP-form and to superpose them again. One gets a 10-parameter-spectrum then:

$$\begin{aligned}
 f_K(p) &= \text{SPECTRAL FUNKTION} \\
 S(f)_p &= \text{PARAMETRIZED SPECTRUM} \\
 S(f)_H &= \text{"HAMMING" - SMOOTHED SPECTRUM} \\
 f_K(p) &= S(f)_p - S(f)_H \rightarrow \text{CONSTRAINT MINIMUM SEARCH}
 \end{aligned}$$

$$\text{MIN. } \sum (f_K(p))^2$$



$$\text{MIN. } \sum f_K(p+\Delta p)$$

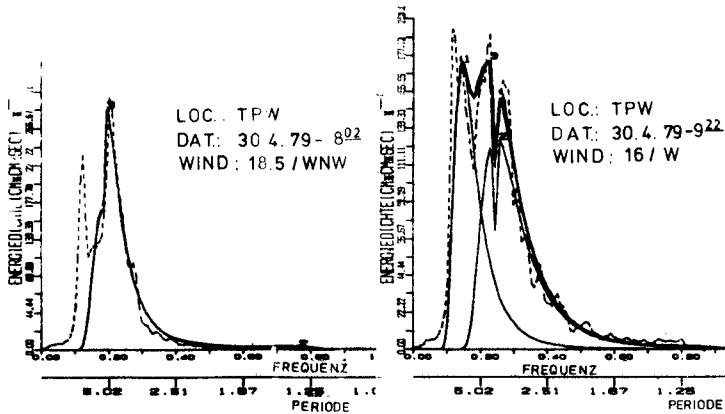


TWO - PEAK - SPECTRUM

$$S(f) = S_1(f_{01}; \alpha_1; \gamma_1; \xi_{ab1}) + S_2(f_{02}; \alpha_2; \gamma_2; \xi_{ab2})$$

Fig. 13 shows the results of a first attempt for three spectra.

1. APPROXIMATION - 10 PARAMETER-SPEKTRA



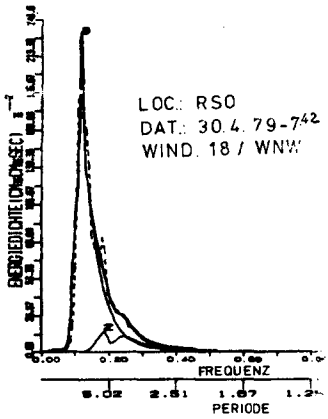
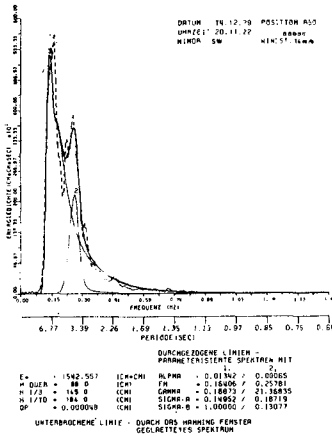
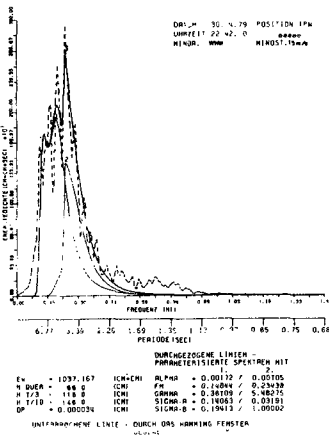


Fig. 13:
First Approximation-10-Parameter-
Spectra

But this solution wasn't sufficient yet because of the shifting of the peak-frequencies f_{01} and f_{02} during the calculation resp. the approximation process.

Because of the inadequacies we defined the peak frequencies and gave them a fixed value after looking at the Hamming-smoothed spectrum. So we got a spectrum with 8 parameters which can describe a two-peak-spectrum in a sufficient way.

Fig. 14 shows 3 examples with a fairly good correspondence between measured and calculated spectra.



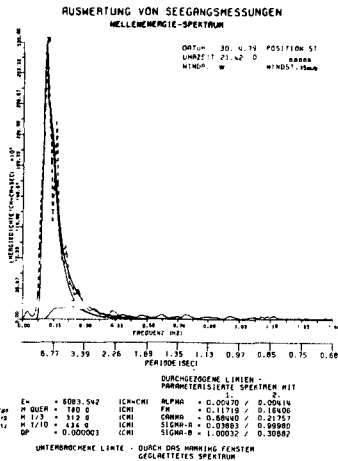


Fig. 14:
8-Parameter-Spectra in the
Weser-Estuary
(the continuous line shows the
superposed spectrum whereas
the dotted line gives the
measured (Hamming-smoothed)
spectrum)

It is possible either to combine JONSWAP- and PM-Spectra in case of the parameter $\chi < 1$ or to superpose more than two partial spectra if necessary.

Conclusions

The evaluation of a lot of wave records in the Weser Estuary gives a basis for a sufficient prediction system. With a permanent reference location it would be possible to predict wave heights and periods for the various regions of the estuary. The comparison of the height of waves in the exterior and interior estuary and the energy loss on the way prove that there is hardly any shelter by the submerged bars in the reef region so that the high waves can get to the wadden area. This fact has to be taken into account for nautical purposes too.

The wave-energy loss together with the tidal currents in this region cause a high amount of sand transport. Fig. 16 gives an idea of the morphological changes in the area of TPW and TPO. The erosion rate within one year per km² is 260.000 m³ resp. 120.000 m³ (Fig. 16).

The parametrization of estuary-wave-spectra has to be developed and tested for another series of more difficult cases. The description of a complicated multi-peak-spectrum by a couple of parameters and their correlation with the factors of influence is another step for the analysis of the complex wave climate in an estuary.

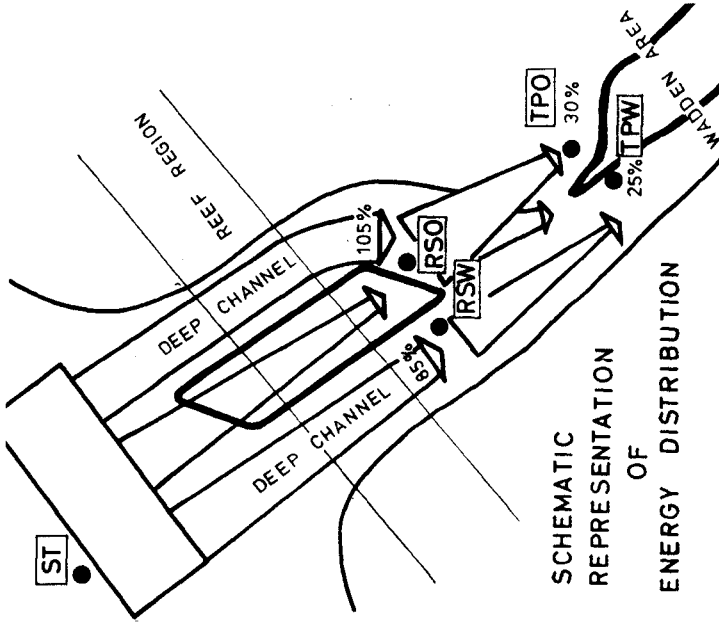


Fig. 15: Energy distribution in the Weser Estuary

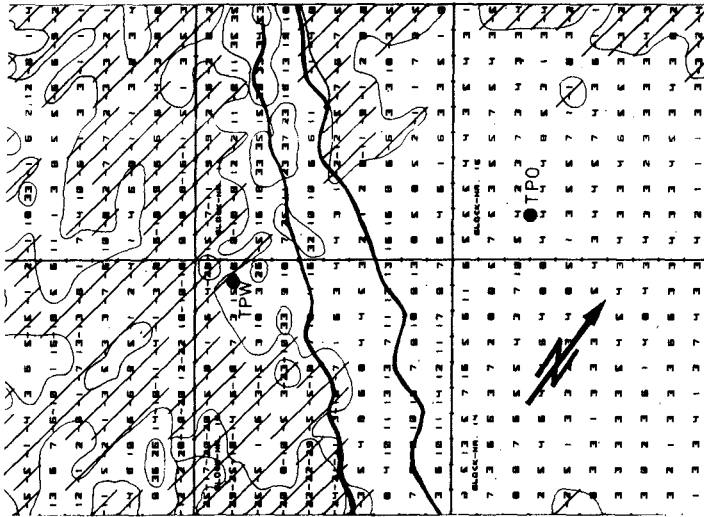


Fig. 16: Morphological changes in the Weser Estuary
+ = erosion, - = sedimentation

REFERENCES:

- Barthel, V.: Analysis of Storm Tide Waves, Proc. 16th Conf. on Coast.Eng.,Hamburg 1978
- Bretschneider, C.L.: Field Investigation of Energy Loss in Shallow Water Ocean Waves, B.E.B. Techn. Mem. No. 46, 1954
- Büsching, F.: Wave Deformation Due to Decreasing Water Depth, Mitt. Leichtweiß Inst. der TU Braunschweig, H. 63, 1978
- Cooley, J.W.,
Tukey, J.W.: An Algorithm for the Machine Calculation of Complex Fourier Series, Math. of Computation, Vol. 19, 1965
- Hasselmann et,al.: Measurements of Wind-Wave Growth and Swell Decay During the Joint North Sea Wave Project (JONSWAP), Deutsche Hydrograf. Zeitschrift, H.12, 1973
- IBM - Scientific Library, SL. Math., 1979
- Siefert, W.: Über den Seegang in Flachwassergebieten, Mitt. Leichtweiß Inst. der TU Braunschweig, H.40, 1973

CHAPTER 141

Hydraulic research in the Oosterschelde Estuary.

A.W. Walther

Head of Hydraulics Division, Delta Department of the
Ministry of Transport and Waterways, The Netherlands.

In 1974 a major policy change was made to the Delta plan (fig. 1) to close the Oosterschelde (East Scheldt). For ecological reasons it was decided to replace the originally planned barrier dam with a storm surge barrier. This could be opened to allow normal tidal movement or closed during storm surges.

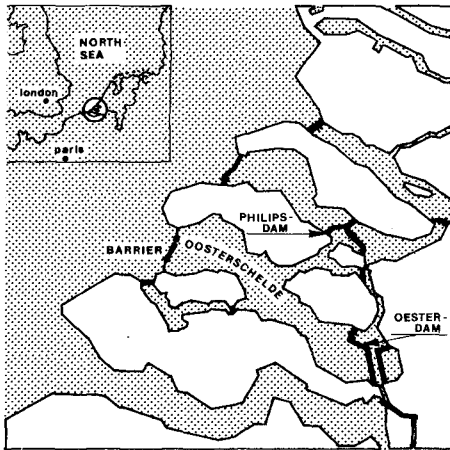


Figure 1: Delta Plan, Netherlands.

Instead of completing the dam in 1978, the new structure (fig. 2) would be finished in 1985. The vertical tidal movement in the estuary would be reduced to about 80 per cent of the original tidal range, while under storm surge conditions the storm surge barrier (with a cross-sectional area of about 15,000 sq.m.) could be closed, thus serving both ecology and safety at the same time. This new concept

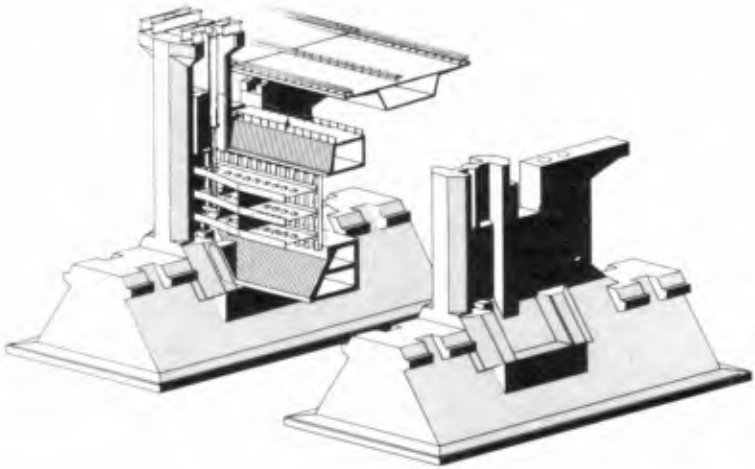


Figure 2: Storm Surge Barrier.

required a large number of new investigations in coastal engineering and soil mechanical fields.

In the "Driemaandelijks Bericht Deltawerken", an illustrated quarterly Dutch magazine with English abstracts (1), both the design of the barrier and the investigations are described.

The soil mechanical research was reported in the "International Symposium on Soil Mechanics Research and Foundation Design for the Oosterschelde Storm Surge Barrier" in 1978 (2).

The results of the hydraulic research will be presented during a symposium in August 1980 (3).

This paper gives a general description of some of the hydraulic investigations.

In the design stage of the storm surge barrier a probabilistic approach of the hydraulic loading conditions of the structure was made. The barrier must survive a force with a frequency of exceedance of 2.5×10^{-4} per annum. The starting point in the determination of this force is formed by the three-dimensional probability density function of storm surge levels, wave energy and basin levels. Basically there are two ways of extrapolating the measured data of these parameters and their correlation into regions of low probability of occurrence, where measured data are not available viz. statistical extrapolation or extrapolation by means of mathematical models based on physical laws and checked with measured data. A combination of these methods has been used in finding the probability density function of storm surge levels and the conditional probability density functions of wavespectra and basin levels, from which the three-dimensional probability function is derived.

The probability density function of the storm surge level is based on 40 years of historical data; extremes are predicted by statistical extrapolation. The knowledge of the physical laws governing this phenomenon has been used to see whether predicted extremes could be reached.

The conditional probability density function of basin levels depends at least partly on the closing strategy of the barrier during storm surges. A simple model was developed based on the fact that a storm is formed by a random combination of wind set up and astronomical tide. From this model the conditional probability density function of basin levels (conditional on storm surge level) could be derived for different closing strategies. The basin level was found to be virtually statistically independent of the wave energy.

Studies were made on local wave and wind conditions, and their relationship with conditions in the North Sea. It was found that not only the wind but also the water level, currents and swell entering from the sea exerted influence on the wave movement.

In addition, waves were greatly influenced by the shallows in this area. The wave spectra near the barrier show in general two peaks. It appeared from the data that a loose correlation exists between the storm surge level and the significant wave height. Lack of data prevented a reliable extrapolation of this two-dimensional probability function by purely statistical methods. Therefore a mathematical model has been developed. It is based on the hypothesis that the typical double peaked form of the wavespectrum is caused by the fact that the wave energy originates from two sources. Waves entering the estuary from deep water via the shoals near the mouth of the estuary are influenced by processes of breaking, bottom dissipation and refraction by depth and current. The wave energy reaching the barrier depends strongly on the storm surge level. In addition, waves generated by local windfields, show a loose relation to the general storm intensity. In fig. 3 the outline of the idea is given. A numerical model which incorporates all these effects is tested in a hindcast of several storms. For these storm conditions the model is in good agreement with the measurements (fig. 3).

The input for this mathematical model are the wave conditions on the border of the Oosterschelde, the storm surge level and the local wind-speed. It is clear that for extrapolation to extreme circumstances these quantities have to be known. As reliable statistics of the windfield are difficult to get, starting point is the probability of exceedance curve of the storm surge level. Using a model that relates the wind set up to the windspeed and the maximum storm surge level to the wind set up and the astronomical tide, the two-dimensional probability function of maximum storm surge level and windspeed is obtained. A theory of wavegrowth and wave propagation on water of limited depth gives, combined with the two-dimensional probability density function of windspeed and storm surge level, the two-dimensional probability function of maximum storm surge levels and significant wave heights on the border of the Oosterschelde.

The introduction of the breaker criterion for the shoals shows that nearly all wavefields generated on the North Sea during an extreme storm will break on the shoals. Therefore the wave height at sea will not influence the energy penetrating in the Oosterschelde. The maximum storm surge level is the only parameter that matters for the penetration.

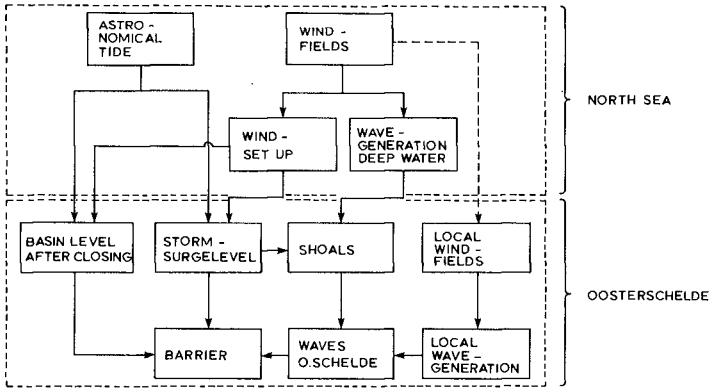
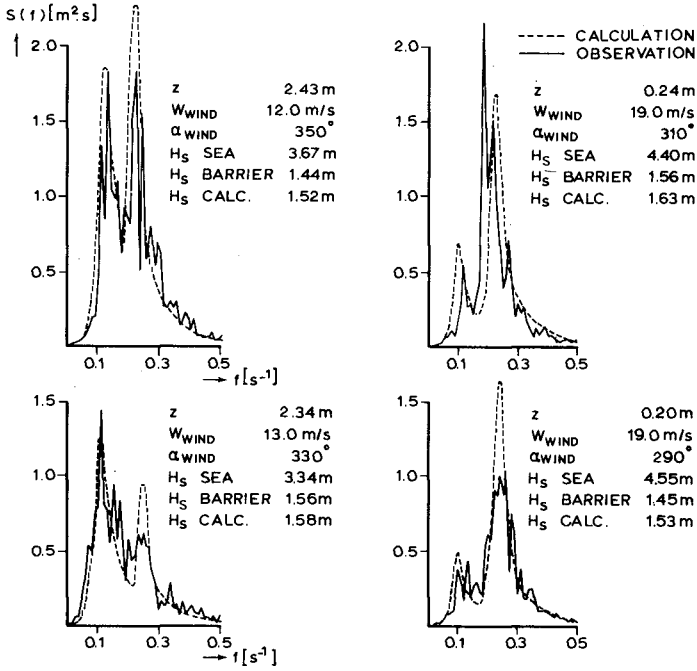


Figure 3: Wave model and results of hindcasts.

The second source of wave energy near the barrier is related to the local windspeed. A relation between local windspeed and the windfields at sea has been established.

The barrier will be maximally loaded during the maximum storm surge level, because the differences between sea level and basin level and the amount of low frequency wave energy penetrating from the North Sea are both maximal.

By joining together the above mentioned models the two-dimensional probability function of maximum storm surge levels and local windspeeds is obtained, where for every combination the wave spectrum near the barrier is known. By adding this to the conditional probability density function of basin levels, the three dimensional probability density function of maximum storm surge levels, wave energy and basin levels is derived. This function is used as input in the calculations of the probability distribution of the hydrodynamic load on the storm surge barrier.

The construction of the barrier across the Oosterschelde mouth will affect the tidal regime in the estuary. Reducing the present 80,000 sq.m. cross-sectional area across the mouth of the Oosterschelde to an effective aperture of 14,000 sq.m. will decrease the discharges through the aperture. As a consequence the tidal range in the basin will be reduced. The tidal regime will not only be affected by the construction of the barrier, however, but also by the construction of compartment dams. Two compartment dams, the Philipsdam and the Oesterdam, (fig. 1), will be incorporated to aid water management and to provide a tide-free shipping route between Antwerp and the Rhine passing through the rear of the Oosterschelde. Due to the compartment dams the storage area of the Oosterschelde basin will be reduced to about 80% of its original value. The tidal movement in the estuary was studied by means of field measurements, one- and two-dimensional mathematical models, a one-dimensional electric analogue model, stationary hydraulic models and a non-stationary overall hydraulic model (fig. 4).



Figure 4: Hydraulic model of the Oosterschelde

The boundary conditions of the models were obtained from extensive measurements in the prototype (fig. 5).



Figure 5: Flow measurements near the Philipsdam.

A comparison between the various types of models shows that each type has its specific advantages and specific drawbacks. Numerical one-dimensional network models can be applied when the estuary is mainly composed of gullies separated by shallow areas. Water levels and discharges are the relevant quantities. Two-dimensional numerical models (two-dimensional in a horizontal plane) are used in coastal areas and seas and in wide estuaries where the current direction is not related directly to the bottom geometry. Hydraulic models are applied for estuaries with complex bottom geometries where information about current velocity distributions is very important. It should be stated, however, that recent development in numerical solution techniques make it more and more advantageous to apply

numerical models instead of hydraulic models. However, there is one important exception: near sluices and closure gaps the flow pattern is so very complicated that only a three-dimensional description is adequate.

For the closure-operations of the Brouwershavense Gat (1971) three methods for predicting the velocities were used simultaneously. The concrete caissons could be sunk only during low water slack tide. With higher velocities the forces acting on the caissons would be too large for positioning. A combination of the predictions of the hydraulic model and the electric analogue model Deltar is given in fig. 6 (prediction Deltar).

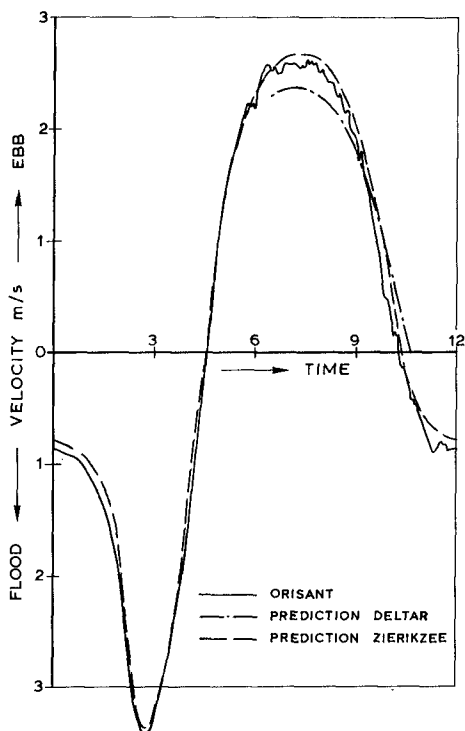


Figure 6: Predicted (see text) and observed (Orisant) velocities during Brouwershavense Gat closure 27 april 1971.

The observations of nature were used of about one tidal period preceding the closure operation. In the figure also a curve is given of a prediction based on the analysis of the measurements of a large number of tidal curves preceding the operation (prediction Zierikzee in fig. 6). This method in general proved to be somewhat more accurate. An example is shown in the figure. From this example the importance of field measurements can be derived.

Knowledge of tidal movements in an estuary is also important for the study of the salinity since the salinity distribution is mainly influenced by tidal motion and fresh water input. In the case of the Oosterschelde the main fresh water input is controlled by sluices and kept approximately constant. The discharge of the river Rhine into the North Sea may also influence the salinity in the Oosterschelde under certain circumstances. With northerly winds especially, the water from the Rhine forms a large proportion of the coastal water around the mouth of the Oosterschelde. The construction of the storm surge barrier is intended to maintain the ecological function of the Oosterschelde. An example is given in fig. 7, depicting the number of species living in the water as a function of the chlorinity.

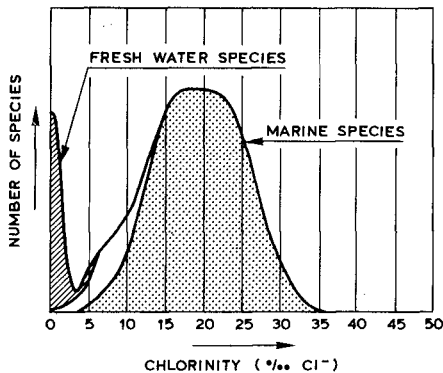


Figure 7: Remane-curve: number of species as a function of chlorinity.

This ecological function depends, amongst others, on the salinity which must be kept as high as possible. This suggests that the fresh water input has to be reduced in order to compensate the decrease of salinity intrusion due to the reduction of the tidal motion.

For the study of the influence of the tidal reduction on the salt intrusion several means have been used:

- the hydraulic model of the Oosterschelde with horizontal scale 1/400 and vertical scale 1/100 (fig. 4),
- the two-dimensional depth integrated mathematical model (4) and
- a one-dimensional tidal averaged mathematical model.

The hydraulic and two-dimensional mathematical model can only deal with vertical homogeneous conditions. In the main part of the Oosterschelde this condition is satisfactory. Because of the small fresh water input the longitudinal salinity gradient is too small to create important density currents and stratifications. This is also the case in the present situation with a much larger fresh water supply. The one-dimensional model may also be used for situations where moderate density currents are present, but it needs more information about the mixing processes than the two other models. This information is contained in the longitudinal dispersion coefficient D . It is not possible to obtain a general theoretical expression for the dispersion coefficient as a function of tidal parameters and characteristic geometrical and morphological quantities. For particular transport processes in simple geometrical configurations one may deduce from theory the dependance of D on tidal parameters, yielding $D = \gamma u_0^2 T$. Here u_0 is the amplitude of the tidal velocity and T the tidal period. The parameter γ may still depend on the tidal parameters in various ways according to the considered transport mechanism. Simulations of the present salinity distribution in the Oosterschelde with the hydraulic scale model by means of a permanent rhodamine injection showed that the tidal flushing was larger in the model than in nature, which might be related to the relative large depth of the model. The influence of the tidal reduction on the salinity distribution in the model was in agreement with $D = \gamma u_0^2 T$ with no significant dependance of γ on tidal parameters. Predictions for the salinity distribution were made with the one-dimensional model using a dispersion coefficient reduced proportional to u_0^2 with respect to its value in the present situation. The study of the salt intrusion in the Oosterschelde is focused on the following questions:

- Which constructions are necessary in order to regulate the salinity regime in the estuary?
- How must the locks and the storm surge barrier be operated in order to prevent low salinities?

Possible constructional devices are:

equipment in the locks to keep the salt and the fresh water separated as much as possible during the passage of ships, as will be discussed later on,

connections with other estuaries through which water can be flushed so that circulation in the connected estuaries is increased.

Finally one might consider the possibility of opening and closing certain gates in the storm surge barrier alternately during flood and ebb, stimulating circulatory currents between the different main channels in the estuary.

The use of such interventions depends on the occurrence of external conditions such as intense rainfall or large Rhine discharges in the coastal area. Therefore studies have been undertaken concerning the intensity and the frequency of these circumstances and their influence on the salinity distribution on the Oosterschelde.

In the Philipsdam and Oesterdam, which are to be built in the eastern part of the Oosterschelde, shipping locks will be constructed. These locks

form the connection between the fresh water lake called Zoommeer and the salt Oosterschelde.

The locks are to be equipped with systems to prevent, as much as possible, the intrusion of salt into the Zoommeer and fresh water into the Oosterschelde caused by passing ships. These systems are called fresh/salt-separation systems.

In the Philipsdam five locks will be built, three large locks, dimensions $24 \times 280 \text{ m}^2$, and two small locks, dimensions $9 \times 80 \text{ m}^2$. The fresh/salt-separation system is, like the lock in the Oesterdam, based on the difference in specific weight between fresh and salt water. During the exchanging of salt and fresh water, the interface between it moves vertically. A similar system has already been designed for a lock in the channel of Mardyck near Dunkirk in France and for the Kreekrak-lock in The Netherlands (5).

When designing the locks in the Philipsdam, it became clear that the quality of the fresh/salt-separation system depends strongly upon the stability of the interface layer between the fresh and salt water. This layer needs to be as thin as possible, as the stability diminished with the thickness of this layer.

In the framework of the study for the locks in the Philipsdam, with a hydraulic model, the factors which influence the mixing during the exchanging process have been investigated. The way fresh water flows into the lock chamber through openings in the wall turns out to be an important factor in the mixing process. As the Kreekraklocks have been designed with valves, that are halfway in the culverts through the walls, the locks in the Philipsdam will be equipped with valves that are on the lock chamber side of the wall.

Two-dimensional model studies show that the thinnest interface layers occur when the valves move in such a way during the beginning of the downward movement of the interface layer, when fresh water flows into the lock chamber, that at this moment a situation exists in which a practically resting salt tongue is above the valve, over which fresh water flows towards the middle of the lock chamber. Therefore the movement of the lock chamber depends in principle upon the drop of head of the fresh water through the culverts, and upon the difference in density across the locks.

Model studies (scale 1:20) show that with valves and culverts of the Kreekrak locks, interface layers of approx. 2 m thickness occur while under comparable circumstances with valves and culverts of the Philipsdam locks, this thickness is reduced to approx. 1 m. Compared with the Kreekrak locks an improvement of the quality of the fresh/salt-separation system is expected with the Philipsdam locks system, based on the possibilities of optimizing the movement of the wall culvert valves of the Philipsdam locks.

The lock that is to be built in the Oesterdam and equipped with a fresh/salt-separation system, has a lock chamber area of $10 \times 90 \text{ m}^2$, incidentally to be enlarged to $14 \times 100 \text{ m}^2$ later. This system differs from that of the locks in the Philipsdam, although this system also means that during the passage of ships the water in the lock chamber around the ships changes with closed gates from salt to fresh water or vice versa. The difference, however, is that this exchange in the Oesterdam lock takes place by moving a large basin, filled with salt water, in a vertical direction.

A ship, sailing from the Oosterschelde towards the Zoommeer, sails into this basin, which is surrounded by fresh water. The edges of the basin are about 10-20 cm above level of the fresh water. After entry the gate is closed and the basin moves downward underneath the ship, while fresh water flows around the basin towards the ship (fig. 8). A similar movement in the opposite direction is performed with a ship sailing towards the Oosterschelde. Such a system is called a submersible salt basin lock.

The submersible salt basin system was chosen for the Oesterdam, as the ecosystem of the Oosterschelde, nearest to the Oesterdam, is more sensitive to fresh water than the part of the Oosterschelde near the Philipsdam.

The sediment movement during and after construction of the barrier is important. The sediment consists mainly of fine sand, mean grain size approximately 0.2 mm. Part of the foundation-bed of the piers and part of the layers of the sill have to be constructed in trenches dredged across the riverbed in all gaps. Siltation in these trenches during the construction may lead to the formation of sandlayers, which may be washed out at extreme storm surge conditions due to the very high pressure gradients over the foundation, when the gates of the barrier are closed. If the sand is washed out unequal settlements may occur which will affect the stability of the barrier.

The degree of siltation per construction stage depends on the duration of the stage, on the supply of sediment, on the hydraulic conditions (wave action and flow) and on the shape of the trench. These factors vary along the alignment of the barrier. The amplitude of the tide is about 3 m, maximum velocities are about 1.5 m/sec.

In order to make a prognosis a calculation method should be available to determine the rate of siltations as function of the above mentioned parameters. A mathematical model¹⁾ to determine the siltation in trenches in tidal rivers with mainly suspended load was already available. Application of this two dimensional model is only useful for trenches with relatively gentle slopes of non cohesive bed material in quasi steady flow conditions.

As in the design relatively steep slopes were introduced for the trenches, the mathematical DHL-model had to be adjusted accordingly. An additional adjustment had to be made to assess the effects of the grainsize distribution of the sediment in suspension. Finally, the calculation method had to be adjusted to non-stationary situations in which the time lag of settling respective resuspension has to be taken into account. Oblique flow towards the trenches and currents in bends will cause secondary flows and inherent sediment transport in longitudinal direction.

It soon became clear, that it was impossible to develop a model that could well reproduce the three-dimensional hydraulic circumstances within the fixed period of time. Moreover, it is expected that three-dimensional effects will occur only locally in the immediate vicinity of the banks. It was therefore decided to develop two dimensional models (streamlines perpendicular on the axis of the trenches).

The DHL-model was extended and Svasek Engineering Consultants developed the SGB-model²⁾.

1) developed by the Delft Hydraulics Laboratory (DHL).

2) SGB stands for the initials of the members of the team which set up the model: J.N. Svasek, M.B. de Groot and A.J. Bliet.

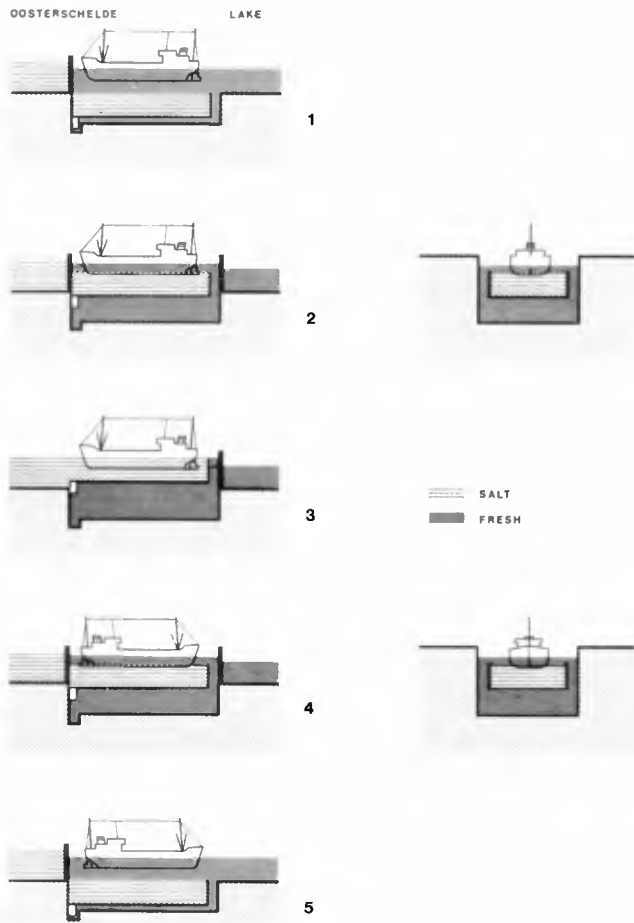


Figure 8: Oosterdam ship lock with vertical shiplift 1-3: Ship traveling from the fresh lake to the salt Oosterschelde, 4-5 ship traveling from Oosterschelde to the lake.

Field tests were made to determine the sediment transport across the alignment of the storm surge barrier and the sedimentation of sand during the construction phase. To establish the reliability of the models the results of the computations were tested against field measurements in trial trenches. Current velocities and sediment concentration were measured simultaneously. The grainsize distribution of the sediment thus collected was analyzed. At the same time the boundary conditions for the flow and the sediment transport could be derived from these field measurements. The storm surge barrier will be built in the three flow channels present in the mouth of the Oosterschelde (see figure 9).

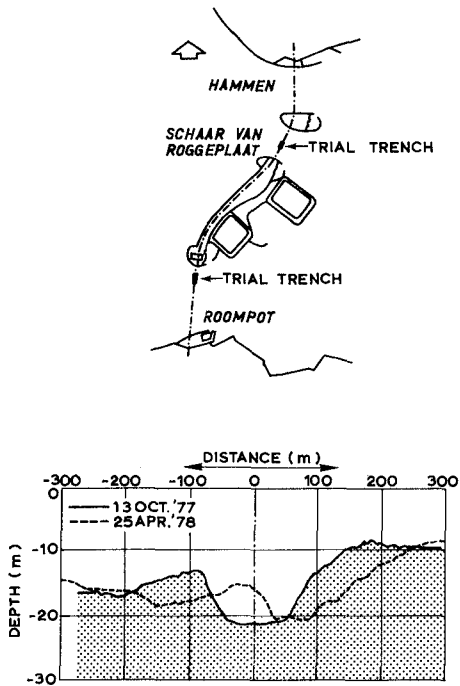


Figure 9: Situation of trial trenches in the mouth of the Oosterschelde. Cross section of trial trench Roompot.

The northern channels, the Hammen and especially the Schaar van Roggenplaat, present a reasonable two-dimensional flow field. The flow field in the Roompot presents a strong three-dimensional character. The two northern channels can be well compared as far as the sediment transport and the presence of a bed protection is concerned. Therefore the result of measurements taken in one of these channels holds also for the other. Measurements taken in a trial trench in one of these channels would be well suited to test the developed mathematical models.

A trial trench was dredged in the Schaar van Roggenplaat as conditions to take measurements there were generally more favourable than in the Hammen. To determine the influence of the three dimensional effects a trial trench was also dredged in the Roompot.

In the trial trench in the Roompot a significant rate of siltation was only found on the steep western slope (1:4); the siltation increased from south to north. Due to the difference in siltation the alignment of the slope rotated and shifted in eastern direction with an average of 0.02 m/day in the southern part and an average of 0.35 m/day in the northern part. As shown in figure 9 the eastern slope was eroded.

The figure shows that the eastern slopes are stable (irrespective of the shifting) and that the eastern slopes are fading away. At the same time on the eastern slope large sand waves have been formed.

Over the whole area of the trial trench in the Schaar van Roggenplaat continuous siltation took place. According to the sounding results a siltation of 0.01 m to 0.02 m/day takes place over the whole of the trial trench Schaar, whereas the area outside the trench remains stable. On the bottom of the trench, ripples were formed up to a height of 0.5 m. In general the slopes of the trenches decrease with time.

In order to gain more insight into the local variations of sediment-increase, divers placed nine measuring tubes in two sections, which protruded right after the installation 1 meter from the bottom.

Periodically the tubes were measured from top to the sand level. It appeared that local significant variations can occur, even more than 0.6 m in a three-day period. This variation is probably caused by migrating bed-ripples.

The rate of deformation of a sandy trench bed was investigated by means of echo soundings. Immediately after having dredged the trial trench in the Roomport, trying to keep the bottom as level as possible, the irregularities proved to be smaller than 20 cm in vertical direction. During the tidal period following the levelling of the trench, ripples were formed up to a height of approximately 1 meter. There was little or no difference between the characteristics of the ripples found one week after dredging the trenches and several months later. The ripples in and adjacent to the trial trench Roompot proved to be approximately twice as high and as long compared to those in the trial trench Schaar, whereas the slopes were more or less equal.

From the results of the field tests and the models, it was concluded that the siltation rate in the trenches will be very high even if short periods are considered. An adaptation of the construction schema was needed so that as many layers of the foundation-bed as possible are constructed in one run. The sandlayers sedimentated in the interval between two runs have to be removed. The period between the removal of the sediment and the next run must be kept very short, less than a few hours. To this end special equipment was developed.

Around 1985 when the Oosterschelde barrier will be completed, the hydrodynamic regime will change and as a result, the sedimentation and erosion pattern will change too.

Under the present conditions the bottom of the Oosterschelde consists mainly of sand. Only the border of the estuary is built up of silt and very fine sand. This area with tidal flats, outer-dike saltings and mudflats, is of very high ecological value. For this reason and because of the use of the shallow areas of the estuary for fishing, a change in silt and clay movement can have important consequences. Silt consists of organic and inorganic matter. Silt can be transported; it is affected by erosion and sedimentation; it can be consumed. The silt concentration is also influenced by mineralisation and primary production. It is obvious that a full understanding of this complex matter is extremely difficult especially with respect to the consequences for the fauna.

As a first approximation a simple erosion-sedimentation-model was used. This model will not supply a new concentration distribution but will merely indicate areas with possible future silt sedimentation. Erosion of a silt layer takes place when the velocity of the current causes a bottom shearstress (τ), larger than a critical value (τ_c). Expressed in terms of shear velocity (v_{*c}) the following relation between erosion and shear velocity is given by Partheniades (6):

$$\frac{dm}{dt} = M \left[\frac{v_*}{v_{*c}}^2 - 1 \right]$$

m is mass of eroded matter per unit area and
 M is constant.

Sedimentation of silt will occur when τ is smaller than the critical shear stress for sedimentation (τ_1).

As the value of τ_1 is smaller than τ_c , there can be a period during the tidal cycle in which sedimentation and erosion are in balance. Krone (7) gives the following relation, expressed in terms of shear velocity:

$$\frac{dm}{dt} = cw \left[1 - \frac{v_*}{v_{*1}} \right]$$

c is concentration of the suspension and
 w is fall velocity.

The constants in the relations are derived from literature and no comparison with field data is yet available. The following values for the constants were used:

$$v_{*c} = 0.03 \text{ m/sec}, v_{*1} = 0.009 \text{ m/sec}, w = 3 \cdot 10^{-4} \text{ m/sec and}$$

$$M = 0.210^{-3} \text{ kg/m}^2/\text{s}.$$

The values of v_* are derived from a one dimensional tidal model.

Figure 10 shows the schematisation of the one dimensional tidal model and the potential silt sedimentation under present conditions. It is remarkable that sedimentation appears only in branches which come to a dead end. This phenomenon corresponds with collected field data. This is also the case for the sedimentation in the channel which was closed in 1972 near the future storm surge barrier. Computations with this simple model show that after completion of the storm surge barrier and the secondary dams the areas with silt sedimentation will expand.

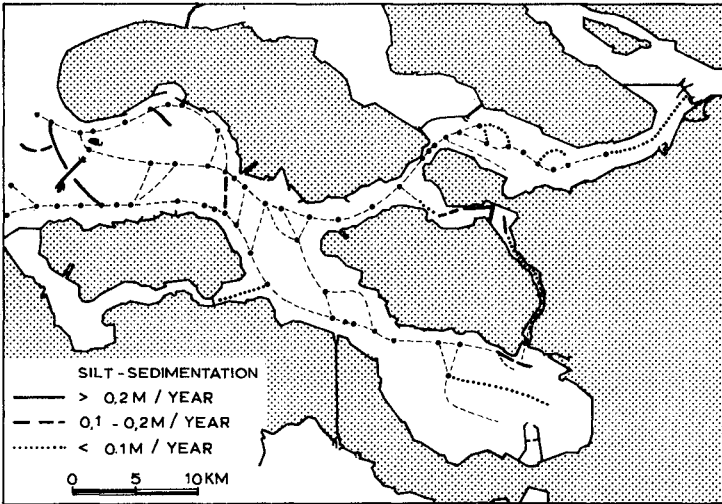


Figure 10: Results of simple siltation model (present situation).

Acknowledgement

The work reported in the paper was performed by the hydraulics division of the Delta Department in close cooperation with the Delft Hydraulics Laboratory .

The author expresses his gratitude to those who assisted him in preparing the paper and are listed below.

Dr. J. Bruinsma and H. Vrijling (waves and probabilistic design methods), J. Voogt and W.J. van de Ree (tides), dr. J. Dronkers (transport phenomena in estuaries), C.P. Ockhuysen (ship locks), H. Speekenbrink (sand transport) and R.H.W. van Vechgel (siltation models).
Mrs. J. den Elzen prepared the manuscript.

References

1. Driemaandelijks Bericht Deltawerken, Staatsuitgeverij Den Haag, The Netherlands (quarterly with English summaries).
2. International Symposium on Soil Mechanics Research and Foundation Design for the Oosterschelde Storm Surge Barrier. Delft, The Netherlands, October 9-12, 1978, Proceedings volume 1-3.
3. Symposium on hydraulic aspects of Coastal Structures, The Netherlands 1980.
4. Van de Ree, W.J. Voogt, J, and Leendertse, J.J. A tidal survey for a model of an offshore area. 16th International Conference on Coastal Engineering, Hamburg 1978.
5. Kolkman, P.A. and Slagter, J.C. The Kreekrak locks on the Scheldt-Rhine connection. Rijkswaterstaat Communication no. 24, 1976.
6. Partheniades, E, Thesis, 1962, University of California and Shen, H.W. (Ed.), River mechanics, Vol. II, Chapter 25, 1971 Fort Collins, Colorado.
7. Krone, R.B. Flame studies of the transport of sediment in estuarial shoaling processes, University of California, 1962.

CHAPTER 142

PORT OF BRISBANE SILTATION STUDY

N V M ODD

Hydraulics Research Station, Wallingford, UK

and

T BAXTER

Port of Brisbane Authority, Queensland, Australia

SUMMARY

The paper describes the constituent parts of a combined field and mathematical model investigation into the processes causing siltation in the Port of Brisbane. It describes the methods of collecting and using field data and laboratory results in conjunction with a variety of mathematical models which were employed to simulate and predict the interaction of tidal and fluvial flows, saline intrusion and sediment transport in the Brisbane tidal river. A newly developed X-Z-T model was used to simulate the unsteady patterns of mud transport and siltation resulting from the interaction of tidal flows with short flashy fluvial floods, which are the main cause of shoaling in the Port. The paper discusses the structuring of the investigation which involved a carefully phased schedule of desk, field, laboratory and mathematical model investigations with the aim of solving the problem with minimum effort and cost. The paper does not discuss predictions.

INTRODUCTION

The recently formed Port of Brisbane Authority (PBA) is developing new port facilities on Fisherman Islands near the mouth of the Brisbane tidal river. The proposed work in the estuary includes lengthening, deepening and widening the existing swing basin area, and deepening the approach channel. PBA also wish to cease or reduce maintenance dredging upstream in the existing port area some 19km from Moreton Bay, Fig 1. In January 1977, PBA commissioned the Hydraulics Research Station (HRS) at Wallingford in the UK to undertake a field and mathematical model study to determine the processes causing siltation in the Port and to predict the effects of the proposed engineering works on sediment transport and siltation in the tidal river. This paper only deals with the collection and use of the field data in developing a variety of mathematical models for simulating and quantifying the processes causing siltation in the Port. The paper describes the structuring of the investigation which involved a carefully phased schedule of desk, field, laboratory and mathematical model investigations with the aim of solving the problem with minimum effort and cost. It does not discuss predictions.

Mr Baxter is the Assistant General Manager for the Port Authority with responsibilities for planning and development of new port facilities. Mr Odd was responsible for the technical direction of the project at HRS, which had about twelve constituent parts involving fifteen different specialists at HRS. The project also involved a number of staff of the Port Authority who carried out a series of observational programmes in the period 1977/79.

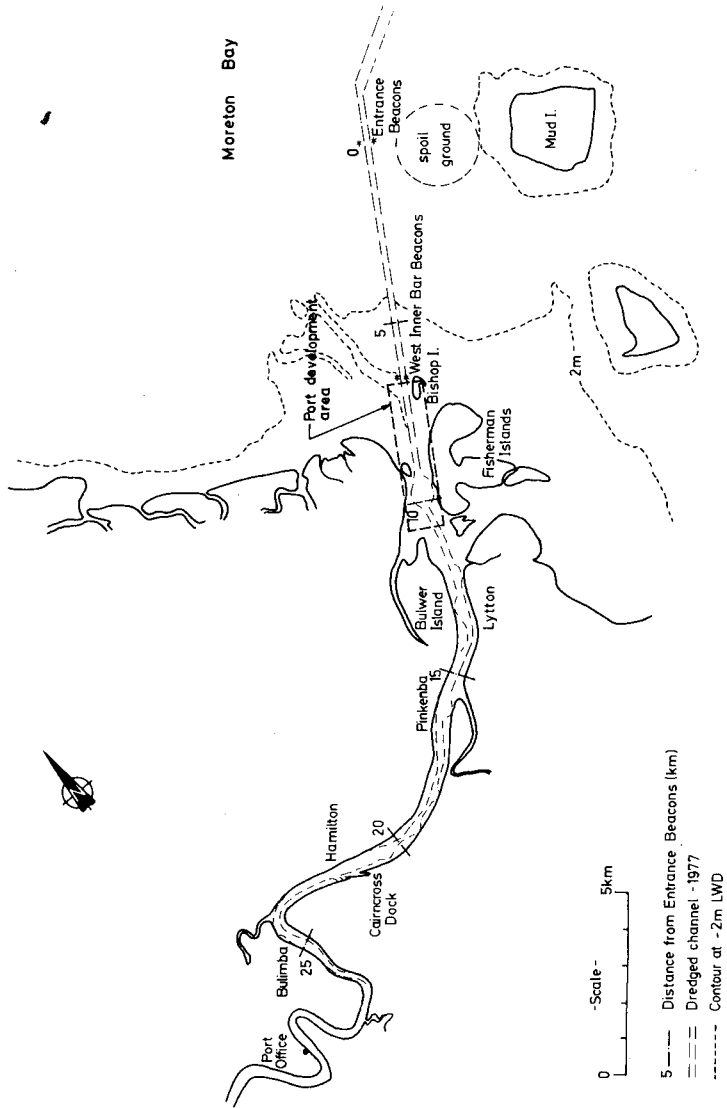


Fig.1 Brisbane River - Port area

Mathematical model techniques were chosen in preference to a physical model because the depositional and erosional properties of muddy sediments cannot be scaled correctly in physical models. The Brisbane study is the first case in which HRS has applied its latest multi-layer (X-Y-T) multi-process, tidal mathematical model, which was developed during the course of the study.

OBJECTIVES OF THE INVESTIGATION

The main objectives of the investigation were to identify, quantify and simulate the processes causing siltation in the navigation channels, swing basins and berths in the seaward reaches of the Brisbane river estuary. And secondly, to predict the effect of capital dredging works associated with port developments at Fisherman Islands and changes in the pattern of maintenance dredging in the existing port area, on siltation in the tidal river.

CONSTITUENT PARTS OF THE STUDY

The study could be considered to be divided into five constituent parts. The type of work and an approximate estimate of the relative effort put into each part of the study in terms of cost were as follows:

	RELATIVE EFFORT(%)	
	HRS	PBA
1. Collection of field data in the tidal river	25	80
2. Analysis of data	25	20
3. Laboratory experiments	5	-
4. Construction and validation of mathematical models	25	-
5. Use of models to predict the effect of engineering works	20	-
	<u>100</u>	<u>100</u>

The above table shows what a large proportion of the effort went into collecting and analysing field data and the relatively small amount of effort that went into the final use of the models to predict the effect of engineering works.

The field studies for the investigation were planned to provide data to determine and quantify processes of tidal propagation, saline intrusion and sediment transport in the estuary, and to validate three types of mathematical model.

HRS supplied the PBA Survey Team with a rapid-drop profiler which was mounted on a fast launch and used to monitor suspended solids and salinity profiles throughout the length of the estuary at regular intervals.

THE BRISBANE RIVER ESTUARY

The river has a typically flashy hydrograph with long periods of practically no flow interspersed with short flood events, which usually occur

in the months between December and April and last on average about twelve days. The tidal regime in Moreton Bay is a mixed one with significant diurnal and semi-diurnal constituents. The M_2 semi-diurnal tidal constituent is the largest one with an amplitude of 0.724 metres.

The tidal compartment of the Brisbane river is narrow compared to its length, which is about 100km from the entrance in Moreton Bay to Mount Crosby weir. The original port was about 30km upstream from Moreton Bay. In 1860, there was a shallow bar across the entrance to the river, and its lower reaches consisted of braided channels. During the past 100 years the channel in the lower estuary has been gradually trained and deepened to accommodate the increasing size of vessels using the Port. The deepest berths have moved progressively seaward during this period.

The dredged channel silts up with muddy sediments at the rate of about 1.5 million cubic metres per annum. The bulk of the siltation being located in the existing port area especially in Hamilton reach (Fig 1). There had been no previous investigation of the physical processes causing siltation in the Port.

INTERACTION OF TIDAL AND FLUVIAL FLOWS IN THE ESTUARY

There are two very well defined conditions that prevail in the estuary. Firstly, in the dry season there are negligible fluvial flows for several months and the limit of saline intrusion moves steadily inland. The estuary is in a vertically well-mixed condition but there are significant longitudinal density currents. In these conditions there are deep, sluggish periodic tidal flows in the port area with peak velocities in the order of 0.5 metre a second, superposed on a longitudinal gravitational circulation.

Secondly, there are short flashy fluvial floods, which last about twelve days with the peak discharge being reached on the second or third days. The peak velocity in the upper estuary may exceed three metres per second and most of the fresh water leaves the estuary via the surface layers flowing over a saline wedge, which forms in the port area. Conditions are very unsteady and strongly dependent on the magnitude and duration of the fluvial flows.

DISTRIBUTION OF BED SEDIMENTS

A study was made of the geology and recent sedimentology of the estuary with the aim of defining the distribution of river bed surface sediment types. A variety of historical data was examined including a mixture of seismic, drilling logs, grab sampling analyses and side scan sonar plots. This historical data was supplemented by a series of new field investigations undertaken by HRS and PBA in the top one or two metres of the river bed. This included collection of bed surface grab samples, vibratory core samples, and bulk density profiles using a radioactive transmission probe.

The main findings of this investigation were that the sediments below the dredged project depth were generally in-erodible rock, gravel or clay. The main silting material in the existing port area is a slightly sandy mud with the following average properties.

Total Bulk Density - 1.3 tonnes/m³
Total Dry Density - 0.5 tonnes/m³
Sand Fraction (60 - 150 microns) about 25% by weight
Bulk Density of Mud Matrix - 1.25 tonnes/m³
Dry Density of Mud - 0.4 tonnes/m³

SOURCES OF SEDIMENTS CAUSING SILTATION

A recurrent problem in all estuarine siltation investigations is the identification of the source of the sediments causing shoaling, namely whether they come from the river catchment or from the coastal region at the mouth of the estuary. This problem was investigated by analysing historical gauging records of discharge and suspended solids at Mount Crosby Weir at the head of the tidal compartment; undertaking velocity and suspended solids sampling in the entrance to the tidal river, and undertaking a radioactive tracer study of the movement of dumped spoil in Moreton Bay.

The main findings of these studies were that fluvial floods carry large mud loads which increase in proportion to the square of the peak discharge, and that the suspended sediment flux at the mouth of the estuary is usually in balance, except in the case of large fluvial floods which flush saline water and suspended sediments out of the estuary. Finally, dredged spoil dumped in Moreton Bay near the approaches to the port hardly moved after an initial period of spreading. However, as usual there was still some doubt about the role of local wave action stirring up mud on the bed of intertidal mud flats which surround the mouth of the estuary.

SUSPENDED MUD LOAD OF THE RIVER

HRS made an analysis of the discharge and suspended sediment records of the Brisbane and Bremer rivers with the aim of determining the frequency and distribution of fluvial flows and the quantities of suspended sediments brought into the estuary. The analysis showed that the river has a typically flashy hydrograph with long periods of practically no flow interspersed with short flood events, which usually occur in the months between December and April. An approximate correlation was established between the mean daily discharge and the suspended sediment load of the rivers. The recent history of the rate of influx of mud (clay particles) from the catchments into the tidal compartment was hindcast by application of the calibrated sediment rating equations to the Mount Crosby Weir flow records for the period January 1972 to August 1977. The analysis showed that the annual influx of mud into the head of the estuary varied from about 30 000 tonnes in 1975 to over 5 000 000 tonnes in 1974. It is estimated that on average about 600 000 tonnes of mud enters the estuary every year from the rivers, which is equivalent to about 1.4 million m³ of siltation. This rate of influx matches the reported long-term average rate of maintenance dredging in the port.

Extreme flood events such as occurred in 1974 tend to flush nearly all their load of suspended sediment into Moreton Bay. Medium floods are incapable of flushing the saline wedge from the estuary and hence a large proportion of the total suspended load, which may be as much as 300 000 tonnes in one flood, is trapped within the estuary by the longitudinal

gravitational circulation and is redistributed and deposited in the deep reaches where the bed stresses are low. The rate of maintenance dredging in the port can be fully accounted for by the influx of suspended fluvial sediments washed down annually by the Brisbane and Bremer rivers, excluding extreme floods such as the 1974 event.

An analysis of the port dredging records showed that in the years prior to the construction of the Fisherman Islands Swing Basin in 1965, over sixty percent of the siltation occurred in Hamilton Reach. There was relatively little maintenance dredging required in any of the reaches seaward of Hamilton Reach. After the construction of the Fisherman Islands Swing Basin there was evidence to suggest that the distribution of maintenance dredging altered so that on average about twenty percent of the siltation occurred in this new swing basin with proportionately less occurring in the Hamilton Reach. HRS are of the opinion that this redistribution can be explained in terms of the gravitational circulation in the port area and the trapping efficiency of the Fisherman Islands Swing Basin.

Although the rivers bring down considerable quantities of sand and gravel in the case of extreme floods, this sediment does not cause a significant shoaling problem in the port area. There is reason to believe that the trapping efficiency of the estuary in its present configuration is high except for extreme floods.

MUD PROPERTIES

A mineralogical analysis of mud from the bed of the tidal river showed that it had an appreciable proportion of montmorillonite, which has a high cation exchange capacity, indicating that it has probably been recently eroded from the land surface. Laboratory flume and viscometer tests were made at HRS to determine the critical stress for the initiation of erosion as a function of the density of the exposed mud layer and the rate of erosion as a function of excess shear stress for erosion varied between 0.1 and 3.0 N/m² for a range of surface densities varying between 0.1 and 0.4 T/m³. The tidal currents near the bed in the port area exert a peak shear stress on the bed of less than about 1 N/m², which is not sufficient to cause erosion of the main body of the mud bed.

Krone¹ has postulated that when flocculated marine muds settle to the bed they form into a series of very thin layers which have shear strengths in the same order as that required to erode it. A consideration of the over-burden pressure exerted by an increasing thickness of these fluffy surface deposits show that they can only be in the order of a few millimetres thick. As a result the only mud available for resuspension in the port are these thin "slack water deposits". During a phase of deposition as each slack water deposit is covered it is consolidated to form the main body of the bed.

An HRS Owen Tube was used to determine the in-situ settling velocity of mud flocks in the estuary as a function of the concentration of mud in suspension. This was found to be negligible in the fresh water region of the estuary and in the range 0.1 - 1.0 millimetres per second in the saline reaches.

SIMULTANEOUS OBSERVATIONS IN THE PORT AREA

HRS and PBA mounted two identical 2-day long intensive simultaneous observations at seven sections between km 4 and km 26 in the port area in the dry season in August 1977 and again during the passage of small fluvial flood in April 1978. An analysis of simultaneous observations of velocity, salinity and suspended solids throughout the depths at the seven sections during spring tides showed that in the absence of wave action very little mud entered the estuary from Moreton Bay. During low fluvial flows the estuary is only weakly stratified. However, the longitudinal density gradients generate small but significant gravitational flows in the landward direction near the bed in the port area. The gravitational circulation tends to hold suspended mud in the middle and upper reaches of the estuary during the dry season. The concentrations of mud in suspension during spring tides in the deep navigation channels were low in the dry season having a maximum value of about 200 ppm. A calculation of the flux of suspended mud passing each section during the flood and ebb phases of the tide at three levels showed that there was a tendency for a net upstream movement of suspended sediment near the bed and a seaward movement near the surface in the port area. However, the net rate of sediment transport was only about 100 tonnes per tide in the upstream direction.

A similar exercise was undertaken during the latter stages of a moderate fluvial flood in April 1978, which is estimated to have carried about 10 000 tonnes of suspended mud into the tidal compartment, increase suspended solids concentration about four-fold at the landward limit of saline intrusion, which was near km 40 and also in the lower layers of the flow in the port area, compared with the dry-season conditions. This exercise showed that very little of the suspended sediment brought down by the river left the estuary.

It appears that most of the fluvial flood water passes fairly rapidly out of the estuary via the surface layers without greatly affecting the longitudinal salinity distribution in the lower layers in the port area. However, there are considerably longer periods of slack-water in the saline wedge near the bed on the ebb tide in Fisherman Islands Swing Basin and in the Hamilton Reach compared to conditions in the dry-season.

Each fluvial flood carries an extra load of mud into the estuary and uniquely and temporarily alters the pattern of tidal propagation, saline intrusion and sediment transport for a period of several weeks. The suspended sediment moves progressively seaward in each tidal cycle until it becomes flocculated by the seawater, periodically eroded, transported and deposited by the tides, and translated by the gravitational circulation until it settles in the deep dredged reaches of the lower estuary where the currents are no longer strong enough to resuspend it.

The rate and pattern of siltation in any one wet season depends on the frequency, magnitude, duration and sediment load carried by each fluvial flood and the manner in which it interacts with the tidal flows. It seems very likely that the sediment brought into the estuary during fluvial floods is reworked and eventually deposited in the deep dredged areas several months after the flood event.

MATHEMATICAL MODELS

Three types of mathematical model were used in the investigation. Firstly, a one-dimensional bulk-flow model was used to quantify the general characteristics of tidal propagation in the estuary, the longitudinal distribution of roughness on the bed of the estuary, the relative flow carrying capacity of the old and new bar cuttings at the mouth of the estuary, peak fluvial flood levels in the estuary and discharge boundary conditions for the second model.

The second one was a steady-state, two-dimensional-in-plan, vertically averaged mathematical model used for the simulation and prediction of peak tidal currents, bed stress and mud deposition patterns in the wide swing basin area at Fisherman Islands between Km 7 and Km 11.

The third one was a two-dimensional-in-depth, laterally-averaged mathematical model of the whole tidal river, which was used to simulate the interaction of fluvial and tidal flows on the scour, transport and deposition of mud in the estuary during flash fluvial floods.

PBA supplied HRS with 1:2500 scale sounding charts of the estuary dating from the years 1974 and 1976. A total of 268 cross-sections were obtained from these charts to provide the basic data for defining the geometry of the estuary in all three models. For the purpose of the bulk flow and two-dimensional in depth model the estuary was divided into 101 storage elements whose length varied between about 500 and 2500 metres, overlapping a similar set of flow or conveyance elements. The results from the survey of sediments in the surface layers of the bed of the estuary were used to prescribe the weight of sand and mud in a series of horizons or layers in each model element.

A viable mathematical model requires sets of equations to describe the processes represented in the model which should be based on well grounded physical concepts and theory and experiments. Certain aspects of the processes of mixing, energy dissipation and sediment transport, as yet, can only be defined by semi-empirical relationships based on field observations and laboratory experiments. The physical equations and functional relationships determine the structure of the model but the results depend heavily on the values of the constants and engineering coefficients applied to a particular calculation. A viable model from the point of view of engineering applications requires an efficient and reliable and accurate method of solution of the equations, giving due regard to the quality of the data and the accuracy required from any predictive calculation. In the case of the Port of Brisbane investigation HRS employed implicit six point finite difference schemes with second order accuracy and a time-step varying between 5 and 10 minutes depending on the particular application of the model. Such a short time-step is required to define the rapidly varying flows and conditions for scour and deposition that occur at the bed of the estuary at certain stages of the tidal cycles.

A model of sediment transport in an estuary requires boundary conditions in terms of water levels and salinities and suspended solids on the incoming tide at the seaward boundary, and the fluvial discharge and suspended concentrations at the landward boundaries. The main problem

in the case of the Brisbane river was defining the salinity and suspended solids at the seaward boundary on the incoming tide during large fluvial floods. The models required a mass of bathymetric and sediment data to define the geometry and distribution and grading of sediments in and along the bed of the estuary. A second mass of field data in terms of water levels, velocity, salinities and suspended solids was required to prove and validate the model for a range of tidal and fluvial conditions.

THE ONE-DIMENSIONAL MODEL OF TIDAL FLOW IN THE ESTUARY

The bulk-flow, area-averaged model of tidal flow in the estuary extended from Km 0 at the Entrance Beacons to the head of the estuary representing both the Old Bar Cutting distributary at the mouth, and the Bremer river a tributary near the head of the tidal compartment. The longitudinal distribution of roughness was adjusted until the model simulated a repeating spring tidal cycle.

The model was then used to simulate a neap spring cycle of tides during the dry season. The results from the model with a smooth bed and with the optimum distribution of roughness were compared with month-long tidal level records made by the Department of Physics at the University of Queensland at nine stations along the estuary in 1974. Both the observations and the results from the model were subjected to a species analysis to define the phase and amplitude of the main constituents of the vertical tide as shown in Fig 2. The length of the tidal compartment is such that the semi-diurnal tide is close to the first resonant mode, with a tendency for the tidal amplitude to increase continuously in the landward direction, as occurred in the case with the smooth bed. However, the middle and upper reaches of the tidal river are hydraulically rough causing a high rate of energy dissipation which damps the resonating semi-diurnal tidal constituents. It should be noted that the muddy bed in the lower reaches of the estuary including the port area acts as an effectively smooth bed, which minimises the shear stress of the bed for a given tidal discharge. A species analysis of the model results showed that the tidal flow in the Brisbane river estuary is mainly semi-diurnal in character as regards the strength of the tidal velocities, which are the main agency for scouring and transporting sediment. The diurnal tidal velocities account for only about 15% of the peak velocities during spring tides. The effect of a high rate of energy dissipation in the middle and upper reaches of the estuary is to keep mud in suspension and to maintain a clear cross-section. The amplitude of the semi-diurnal tidal velocity averaged about 0.5 m/sec over the first 60 km length of the tidal river, except in the vicinity of the swing basins in the port area, where it was considerably lower.

The model showed that the Old Bar Cutting carries only about 10% of the tidal flows entering and leaving the estuary. The tidal discharge at the main run of the flood and ebb phases of a mean spring tide in the Fisherman Islands reach was about 2 600 cumecs. This was used as a boundary condition for the two-dimensional model.

It has been postulated that there is a unique relationship between the peak tidal discharge and local cross-sectional area of an estuary, which is in long-term equilibrium. That is to say that the cross-section is

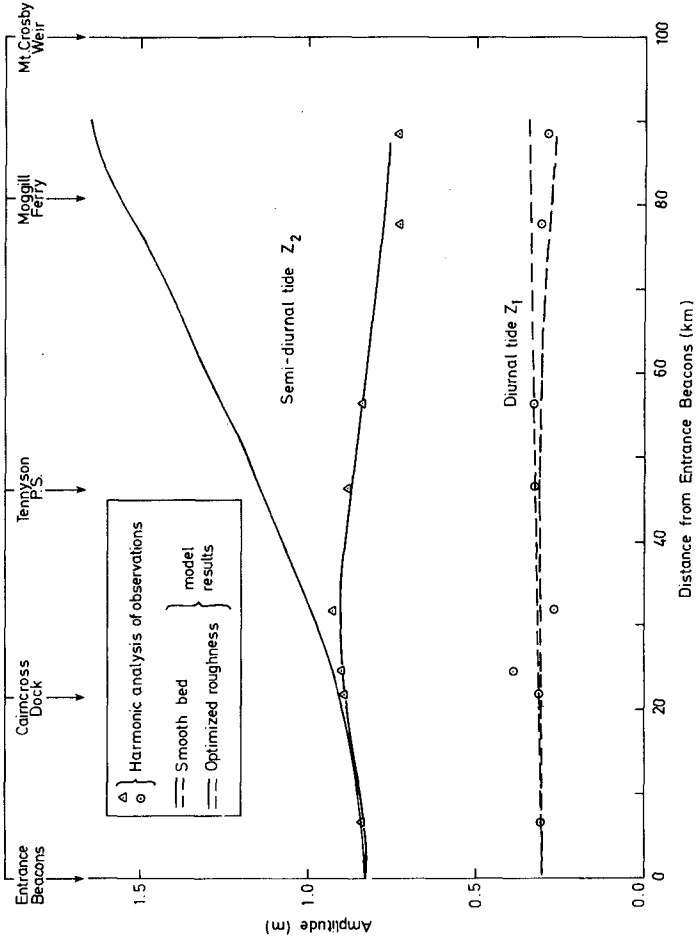


Fig. 2 Effect of bed roughness on tidal amplitudes

neither silting nor eroding over a period of many years. This condition probably applies to the middle reaches of the Brisbane tidal river. The results of the model did in fact show that there was an approximately linear correlation between peak tidal discharge on spring tide and the local cross-sectional area below mean tide level. The fluvial discharges from the infrequent floods appear to have little effect on maintaining the cross-sectional area below mean tide level. In fact during fluvial floods the water level is much higher. The linear correlation implies that a peak tidal velocity of about 0.5 m/sec averaged over the cross-section is sufficient to maintain equilibrium. The consideration of the actual cross-sectional area in the port area suggests that they greatly exceed the equilibrium area in reaches which contain swing basins.

The bulk-flow model was also used to simulate conditions during the peak of the 1974 fluvial flood event. At a peak discharge of 9,600 cumecs, the water level at the head of the estuary rose over 20m above mean sea level. To achieve a good comparison with observed water levels it was necessary to increase the friction factor of the channel by about 24% compared to the dry season proving tests to allow for the bend losses, which become significant with area-mean velocities exceeding 3.5 metres/second.

X-Y MODEL OF PEAK TIDAL FLOW AND MUD DEPOSITION PATTERNS IN SWING BASINS

A steady-state, two-dimensional-in-plan, vertically-averaged mathematical model was used for the simulation and prediction of peak tidal velocities and mud deposition patterns in the Fisherman Islands swing basin and the Inner Bar Cutting reach. The main purpose of this study was to quantify the velocity and bed shear stress distribution pattern in the turning basin and hence help define future patterns of siltation. The boundary conditions of the two-dimensional model were determined from the results of the aforementioned one-dimensional model of the whole estuary. The model was used to hindcast conditions at times of peak flood and ebb discharges during a spring tide, that is to say 2,600 cumecs. The bed of the estuary was assumed to be smooth and the coefficient of lateral exchange momentum was increased until there was a condition with no significant flow reversal in the re-entrance at either side of the swing basin, as shown by float tracks made in May 1977. The bed stress patterns were used to define areas which would be subject to mud deposition at the peak run of the tide and hence at all other stages of the neap/spring cycle (Fig 3). An analysis of the bed surface sediment types and information supplied by PBA based on experience of the dredge master confirmed that the general pattern of mud siltation simulated by the model for conditions in 1977 in the swing basin agreed with reality. The model was then used to predict conditions for different stages of development of Fisherman Islands Reach. Comparisons were made by comparing the results with the base condition in 1977.

X-Z-T MULTI-PROCESS MODEL OF THE WHOLE ESTUARY

The third mathematical model employed in the study was a two-dimensional-in-depth, laterally-averaged mathematical model of tidal propagation, saline intrusion and mud and sand transport in the whole of the tidal river upstream from the West Inner Bar Cutting Beacons. This is the first case in which HRS has used the model which was developed during

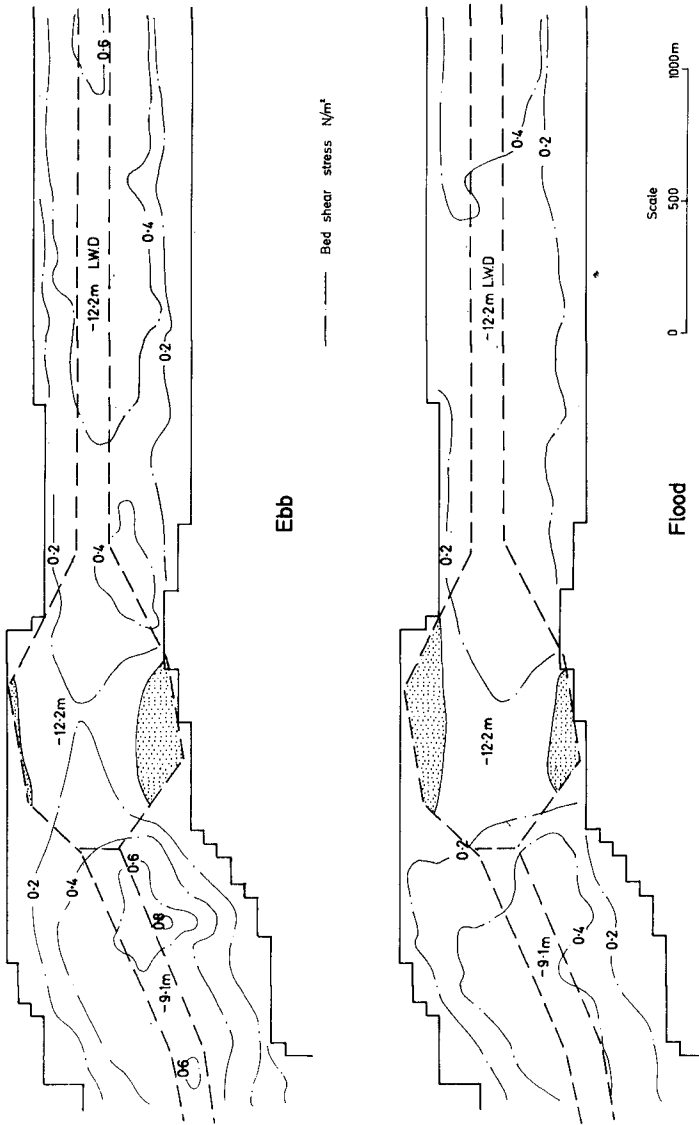


Fig.3 Simulated peak bed shear stress and siltation patterns - 1977

the course of the study as part of HRS's basic research programmes. The method was therefore untried and its application to the Brisbane Siltation Study rather a speculative venture. However, such techniques are the only method of simulating and predicting mud transport and siltation in deep, partially stratified estuaries such as the Brisbane tidal river.

The main purpose of the model was to simulate and predict the interaction of tidal and fluvial flood flows and the resulting pattern of mud transport and siltation for different depths of dredged channels in the port area.

The geometry of the estuary and its roughness were derived from the one-dimensional mathematical model studies, the longitudinal and vertical distribution of bed sediments were determined from an examination of the mixture of seismic, drilling logs, grab sample analyses, sidescan sonar plots, vibratory core samples and density profiles measured with a radioactive transmission probe. The settling properties of Brisbane mud were determined from measurements with an Owen tube in the estuary. The erosional properties of the mud were defined from flume and viscometer tests. The vertical mixing functions employed in the model which took into account the damping effects of saline stratification were based on recent research work² undertaken at HRS.

The tide curve at the seaward boundary was prescribed using harmonic constants determined from long-term records at the West Inner Bar Cutting Beacon. The fluvial discharges into the head of the estuary were based on observations made at the Mount Crosby Weir. The flux of suspended mud into the head of the estuary was based partly on observations and partly on a calibrated sediment load function for the river.

The model was as far as possible based on established laws of physics. However, certain aspects of mixing and sediment transport can only as yet be described by semi-empirical functions based on the analysis of field data. The aim was to prescribe the values of all the various coefficients before the model was used and thereby avoid the complications of a protracted proving process in which the coefficients are adjusted by a trial and error process as has been done in the past. The main unknown was the coefficient of longitudinal dispersion in each of the flow filaments caused by lateral variations in the estuary. However a common scaling factor for the whole estuary was adjusted until the simulated pattern of saline intrusion was in satisfactory agreement with observations.

SIMULATION OF CONDITIONS DURING THE DRY SEASON

Initially, the model was set-up to simulate a repeating 25 hour spring tidal cycle during the dry season. The results from the model were compared with observations made during the simultaneous exercise made in August 1977. This test showed that it satisfactorily simulated the pattern of tidal propagation but there was some difficulty in simulating the absolute values of the salinity in the port area. This was caused in part by the problem of defining the initial conditions from observations solely in the port area and which in the case of the dry season were suspect. However, the model simulated correctly the important features of the pattern of tidal currents in terms of their phase and amplitude throughout the depth (Fig 4). It should be noted that the results from

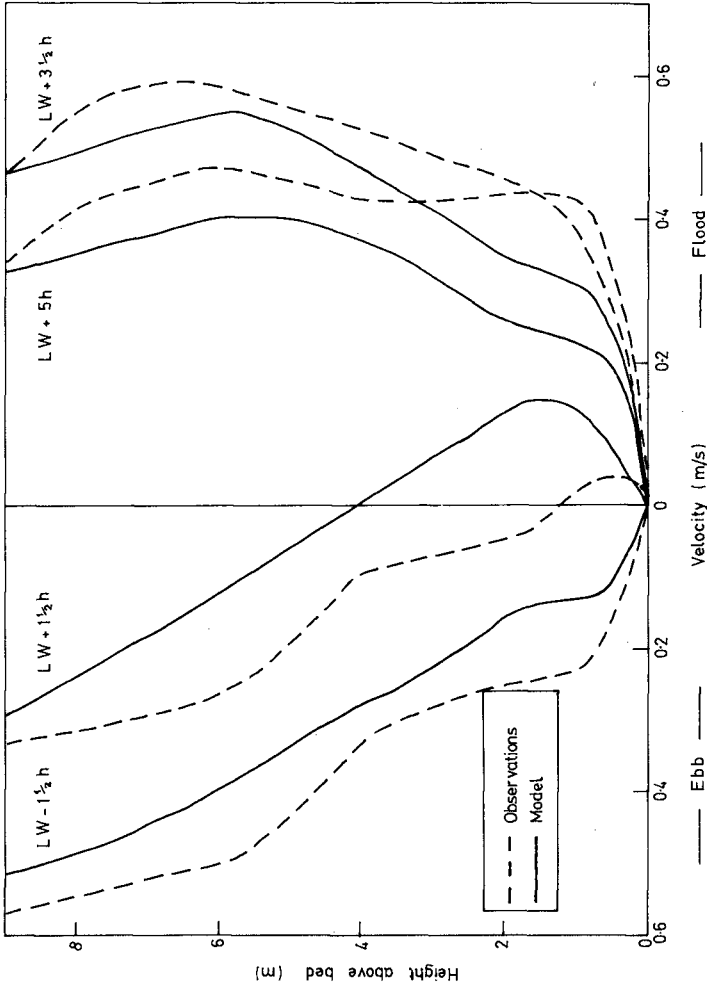


Fig 4 Tidal velocity profiles in the Port area — dry season

the model refer to laterally averaged values, whereas the observations were generally made at mid-stream in the deepest point of the section. As a result the observed velocities are generally higher than the computed laterally averaged velocities. The two-dimensional model studies demonstrated that there are large lateral variations in the velocity especially in the widened reaches of the estuary. The model simulated the important features of the pattern of suspended mud transport. The actual concentrations in suspension and rate of transport are relatively small and unimportant in terms of siltation in the port. The model simulated how muddy sediment is retained in the estuary by the gravitational circulation, and the longitudinal distribution of siltation in the dry season period. This pattern showed that there are two potential zones of siltation in the dry season, one near the toe of the saline wedge upstream of the port and the second one in the deep port area itself.

SIMULATION OF CONDITIONS DURING AND IMMEDIATELY AFTER A FLUVIAL FLOOD

The x-z-t model was then used to simulate the passage of a moderate fluvial flood that was observed in April 1978 after a long period of low fluvial flows. Such fluvial floods are considered to be the main cause of siltation in the port. The interaction of the tide and such flashy fluvial floods result in a very unsteady pattern of sediment transport which is unique to each flood event and which can be only simulated in an x-z-t type model. The results from the model showed that it simulated all the gross features of the unsteady pattern of tidal propagation, saline stratification and the processes of scour, transport and deposition of mud over a period of about two weeks (Figs 5, 6, 7). The results showed that a large proportion of the load of mud brought into the estuary by the fluvial flood would settle in the upper reaches of the dredged port area. It takes a considerably longer time for the mud to reach the lower estuary than for the fluvial water to be evacuated from the estuary. This occurs because a considerable fraction of the new sediment is periodically resuspended and carried up the estuary in the lower layers on the flood tide, whereas the fluvial water passes fairly rapidly out of the estuary via the surface layers without greatly affecting the longitudinal salinity distribution in the lower layers of the flow. The model showed that the mud trapping efficiency of the port area is enhanced during periods of fluvial floods because there are considerably longer periods of slack-water in the saline wedge near the bed on the ebb tide in the Fisherman Islands Swing Basin and in Hamilton Reach compared with conditions in the dry season.

TRAPPING EFFICIENCY OF THE ESTUARY

The investigation has shown that the trapping efficiency of the estuary and the location and longitudinal distribution of siltation is a function of the volume of each individual fluvial flood and the artificial geometry of the lower estuary imposed by capital and maintenance dredging works. For practical purposes one can assume that most floods in the Brisbane river have a duration of about twelve days and that the volume of flood water is approximately proportional to the peak discharge. The mud load of a flood on the other hand increases with approximately the square of the peak discharge. Observations and mathematical model calculations show that almost the entire sediment load of small and medium

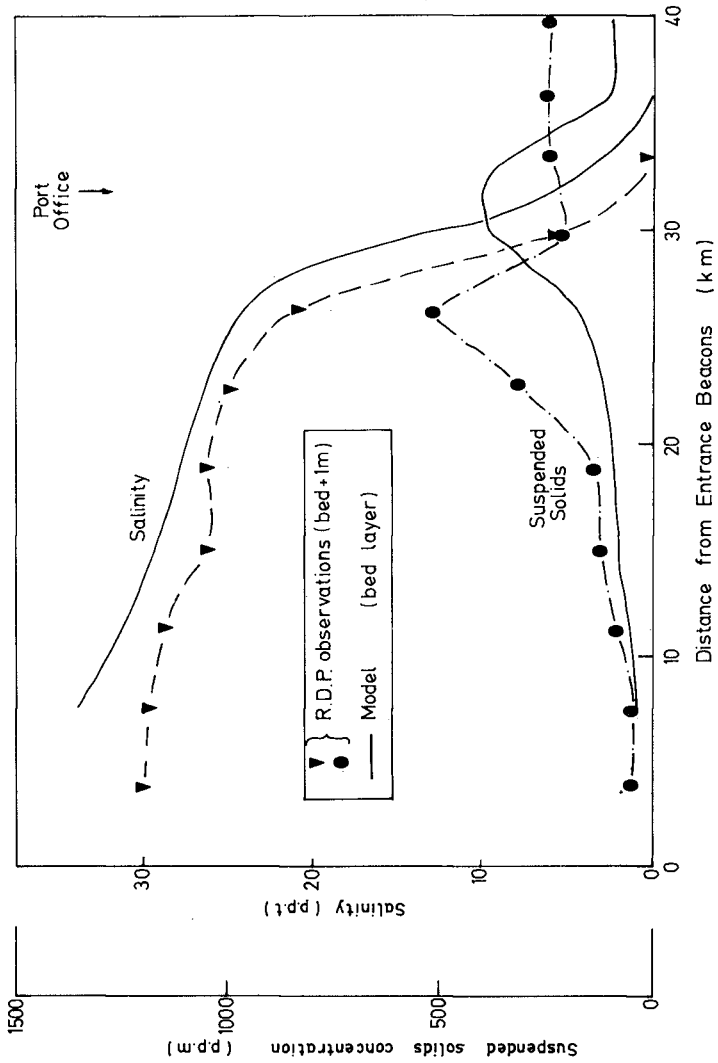


Fig. 5 Longitudinal profiles on flood tide
 - wet season, 4 April 1978

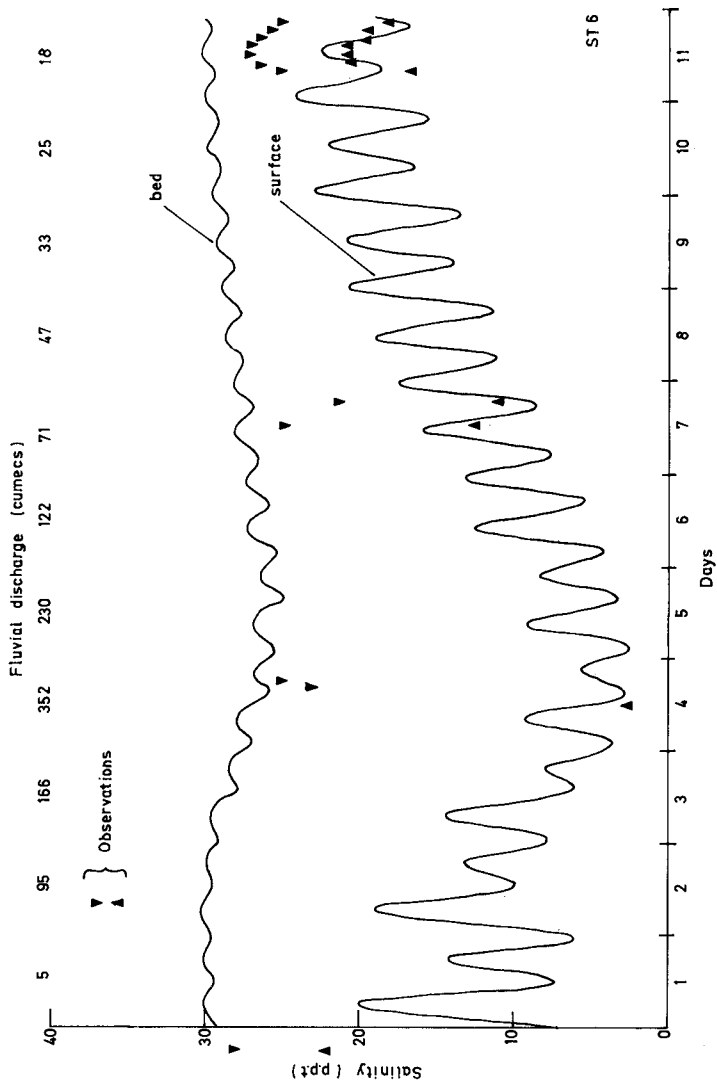


Fig. 6 Simulated salinities in Hamilton Reach during the passage of a small flood, 1-12 April 1978

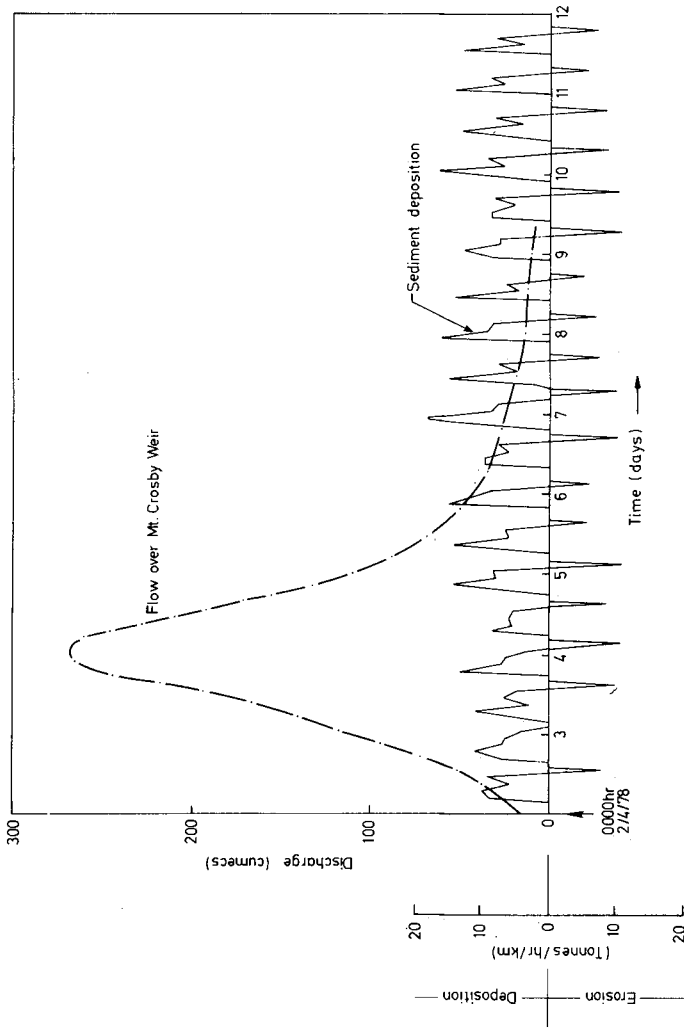


Fig. 7 Pattern of deposition and erosion in Hamilton Reach, 2-12 April 1978

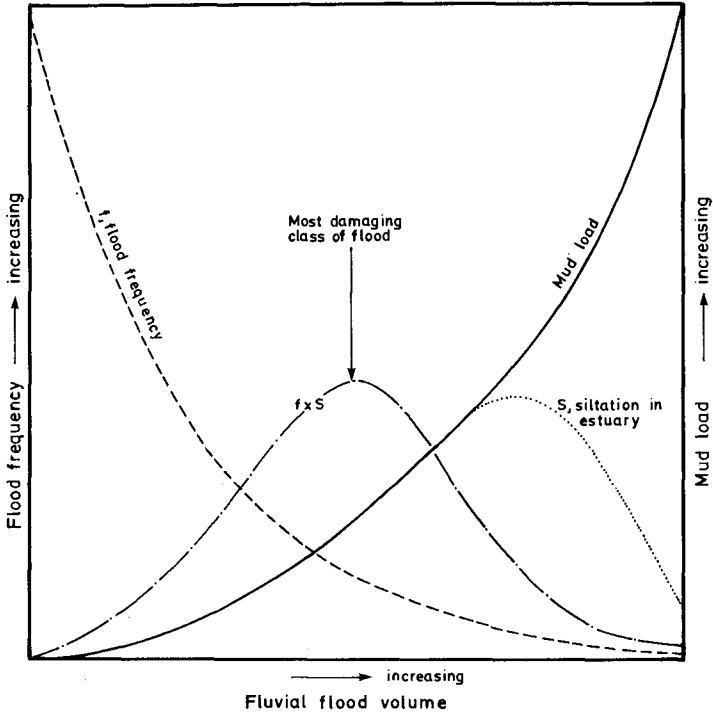


Fig.8 Trapping efficiency of the estuary

floods is trapped within the estuary with little loss to Moreton Bay. The effect of the larger floods is to push the centre of gravity of siltation further seaward and to spread the zone of siltation over a longer reach.

At some critical flood stage, depending on the depth of the estuary, the fluvial discharge is big enough to flush the saline wedge out of the estuary, which allows a large proportion of the mud load brought down by the flood to pass out of the estuary. The flood causing the worst amount of siltation is therefore not the largest one. For example the 1974 flood caused little damage to the port in terms of mud siltation. A consideration of the frequency of given flood events shows that there is some smaller flood which on average causes the most damage to the port. The relationship between the trapping efficiency of the estuary and the size of the fluvial flood is illustrated in Fig 8. The main purpose of the x-z-t multi-process model was to calculate the trapping efficiency of the estuary for a range of flood magnitudes and for several different dredged channel configurations in the lower estuary.

CONCLUSIONS

The paper showed how an analysis of historical data, a programme of intensive field observations using traditional and specialised techniques, laboratory experiments, and a combination of different mathematical model techniques can be used to identify, quantify and simulate the main processes causing siltation in an estuary and be used to predict the effect of engineering works on that pattern.

ACKNOWLEDGEMENTS

The investigation was commissioned by the Port of Brisbane Authority and carried out by the Hydraulics Research Station, Wallingford, UK. Mr N V M Odd was responsible for the technical direction of the project which involved staff from Mr M J Crickmore's Field Studies Section, Dr G V Miles' Coastal, Tidal Hydraulics Section, Mr M F C Thorn's Mud Properties Study Group, the staff of the Port of Brisbane Authority and Mr B M Druery on study leave at HRS from the Coastal Engineering Branch of the Department of Public Works, NSW. Dr J G Rodger was responsible for the development of the x-z-t model and Dr P Cole was responsible for the application of the x-y model. Mr K Mann was responsible for the analysis of the field observations, which were collected under the supervision of Mr C J Teal.

REFERENCES

1. R B Krone A Study of Rheologic Properties of Estuarine Sediments SERC Report No 63-8 University of California 1963.
2. N V M Odd and J G Rodger Vertical Mixing in Stratified Tidal Flows ASCE Paper 13599 J Hyd Div HY3 March 1978.

A 3-D MODEL FOR PENOBSCOT BAY, MAINE

by

Bryan R. Pearce¹, Bruce R. Fidler², Adrian C. Humphreys³Introduction

Penobscot Bay is a deep, geometrically complex, partially stratified estuary (Figures 1 & 2) lying on Maine's Atlantic Coast. Like other Maine estuaries, the Penobscot supports economically important fisheries and tourist industries, and is a significant transportation artery. It is frequently proposed as a region suitable for new industrial and port development. Once heavily polluted by upstream paper-mills, the estuary has today been substantially restored by enforcement of discharge regulations under the National Pollution Discharge Elimination System. The goal of this study was to improve our knowledge of

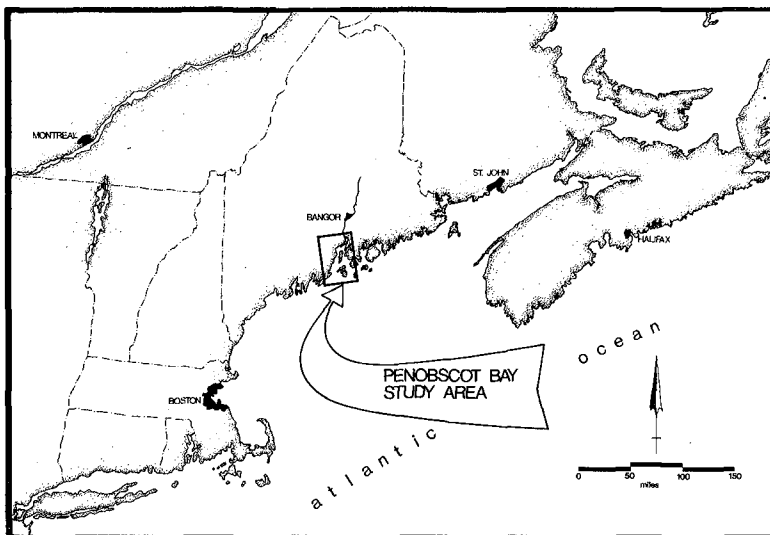


Figure 1: Study Area

¹Associate Professor, Civil Engineering, University of Maine at Orono.

²New England Coastal Engineers, Inc., Bangor, Maine.

³Research Assistant, University of Maine at Orono.

the Penobscot estuary's circulation patterns, as an important factor in maintaining the estuary's water quality and economic resource capacity. A previous effort to model Penobscot Bay (Fidler, 1978) laid the foundation for this study, but concentrated on instantaneous tidal velocities, and was hampered by a shortage of data suitable for model tuning and for comparison of modelled output. The present study concentrated on modelling residual currents, which are somewhat more interesting than instantaneous currents from the point of view of pollution control. In addition, an extensive data set, hitherto largely unanalyzed, became available for tuning and comparison.

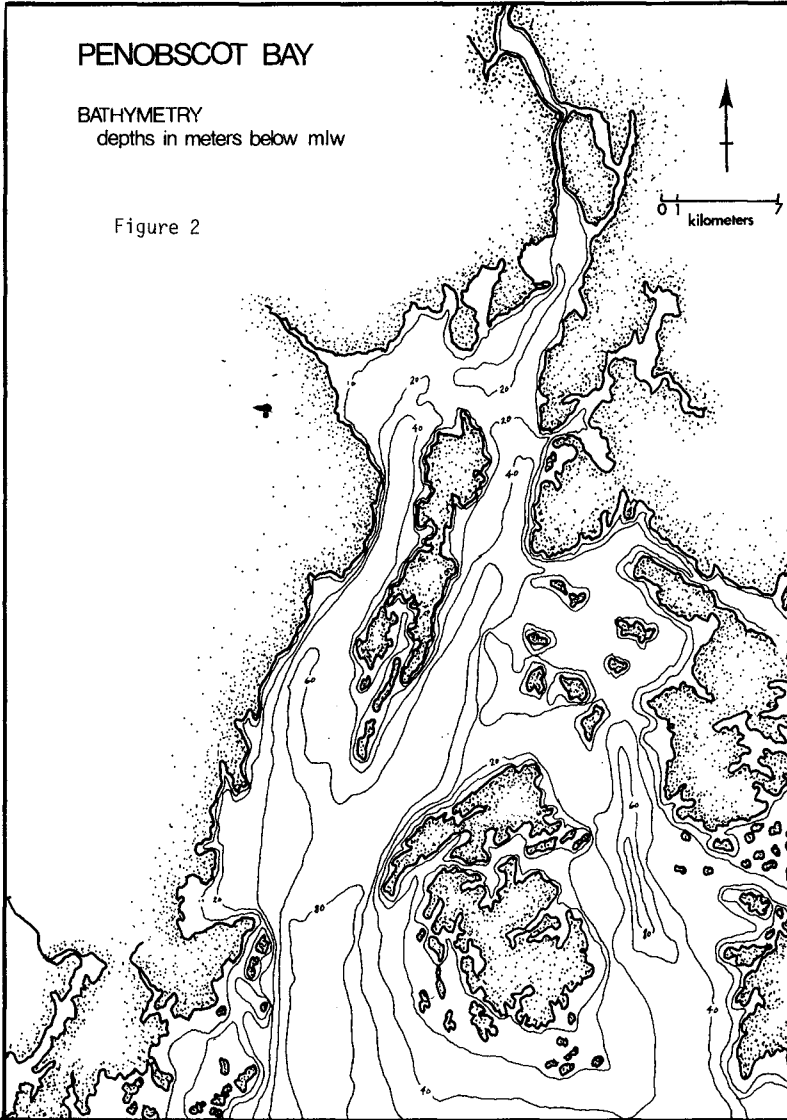
The numerical model "GAL" was applied to a 36 km by 51 km rectangular grid covering the entire lower estuary from Fort Point to the southern end of Vinalhaven Island (Figure 3). Developed by Pearce, et al (1978), it is a three dimensional model which has a finite difference formulation in the horizontal but is continuous in the vertical. Model inputs are bathymetry, vertical eddy viscosity, wind velocity, tidal excitation at the seaward boundary, and a river inflow. Model outputs are current velocities at each grid element for specified depths, velocity profiles and net drift information.

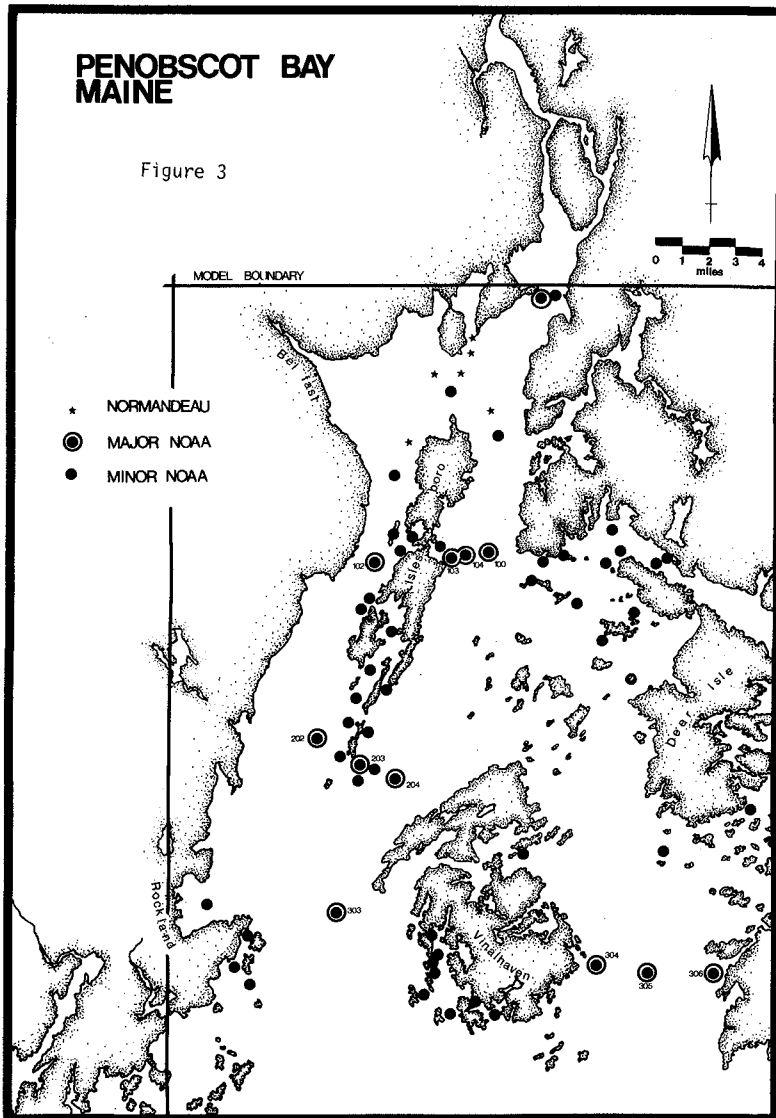
Data

The National Ocean Survey collected current data at 37 stations in Penobscot Bay during the spring and summer of 1969; at 103 stations in 1970. In addition, extensive salinity/temperature data was taken coincidentally with the 1970 current survey. Photo-Geodyne meters were used during the 1970 survey; several stations had up to five meters on a mooring. Monitoring periods ranged from a few days to three months. Because of the coincident density information and larger data set available, most of the data analysis was conducted on the 1970 data and particularly on those stations which had simultaneously collected data during the period 23 May to 6 June.

Maximum recorded velocities were 1.3 kts (0.67 m/s) at the near-surface meters at the mouth (southern end) of the bay, which if reduced by a factor of 0.25 to allow for wave rectification, means that actual maximums were on the order of 1 knot (0.5 m/s). In general, the current records were dominated by the semi-diurnal tide, although the near-surface records (meters positioned at 4.6 meter depth) were quite noisy, due to wave action on the surface buoy that was typical of the mooring installations.

In order to examine the residual current characteristics of the estuary, progressive vector plots were made of the data at those stations with the same record period (21 May to 8 June). A typical set of plots is shown as Figure 4. The resultant vector in each case (drawn from the origin to last point of record) represented the residual current with tidal components removed. The resultants are plotted in Figure 5 and indicate the general pattern of the residual circulation in the estuary. Bold arrows indicate data taken during the indicated time period; light arrows show data taken during non-coincident time periods, but also in





the spring. Residual speeds are on the order of 1 to 5 kms/day (1 to 6 cms/sec), and generally trend down estuary in the upper layers and up-estuary in the low layers, although station 201 presents an anomaly at several depths.

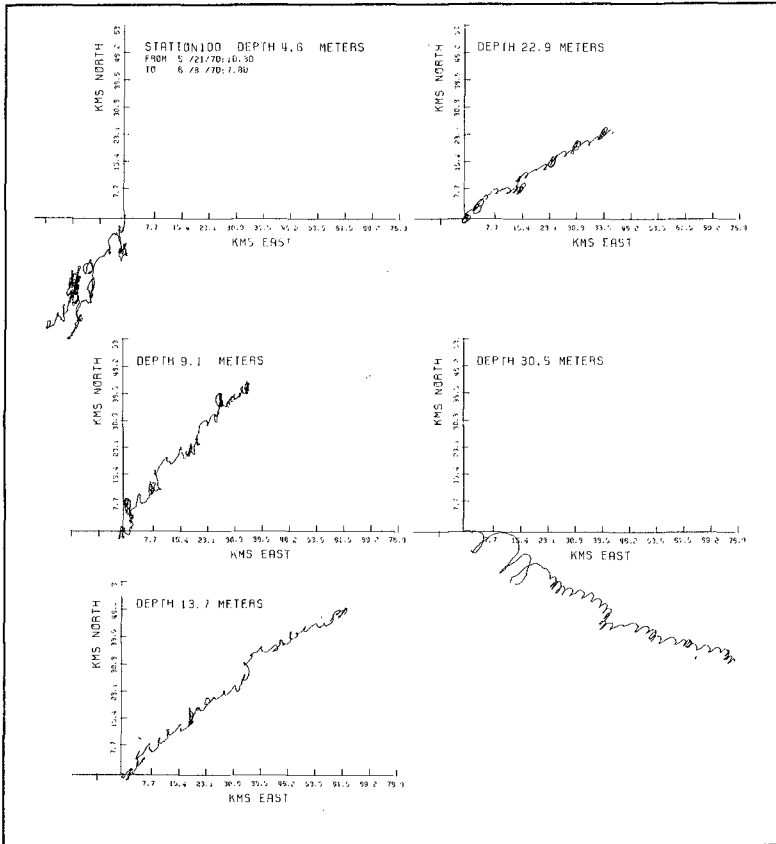


Figure 4: Progressive Vector Plots

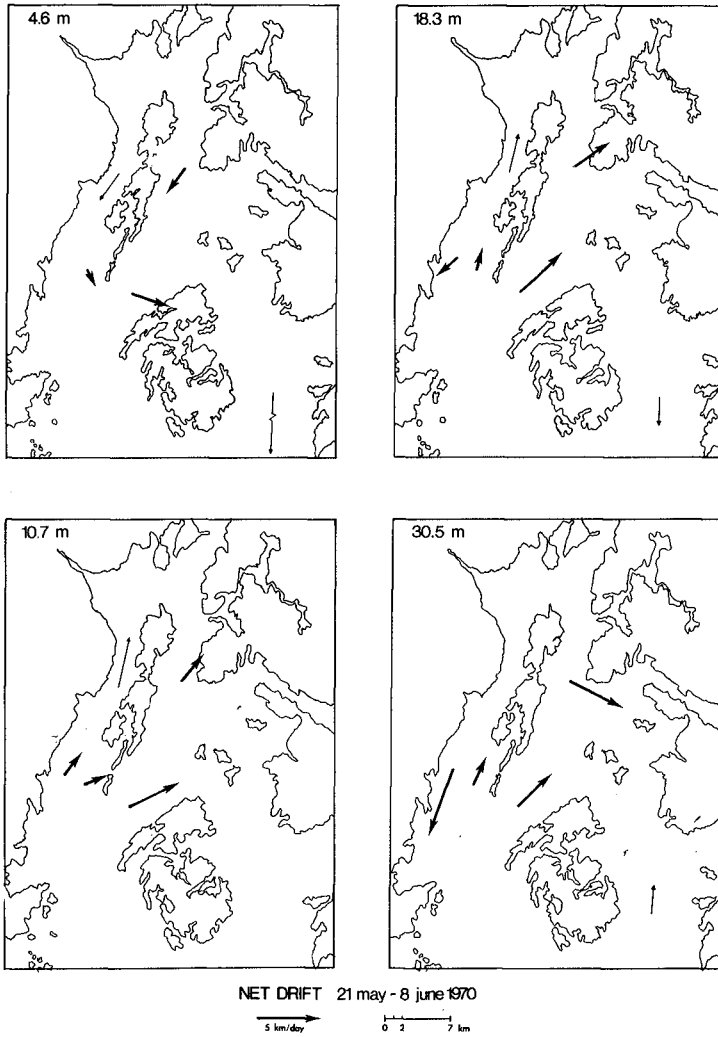


Figure 5

Salinity and temperature data provided some insights into the layered structure of the estuary. Figure 6 shows densities across the bay at several points on both sides of Islesboro Island, confirming earlier work by Haefner (1967) that a deeper fresh water layer lies on the west side of Islesboro. The order of magnitude of the observed data is predicted by application of the Margueles equation (Neumann and Pierson, 1966):

$$\tan \gamma = \frac{-f}{g} \left(\frac{\rho_2 v_2 - \rho_1 v_1}{\rho_2 - \rho_1} \right) \quad (1)$$

where: γ = transverse slope of the density interface
 f = coriolis parameter
 ρ_1, ρ_2 = densities of upper and lower layers
 v_1, v_2 = longitudinal current velocities

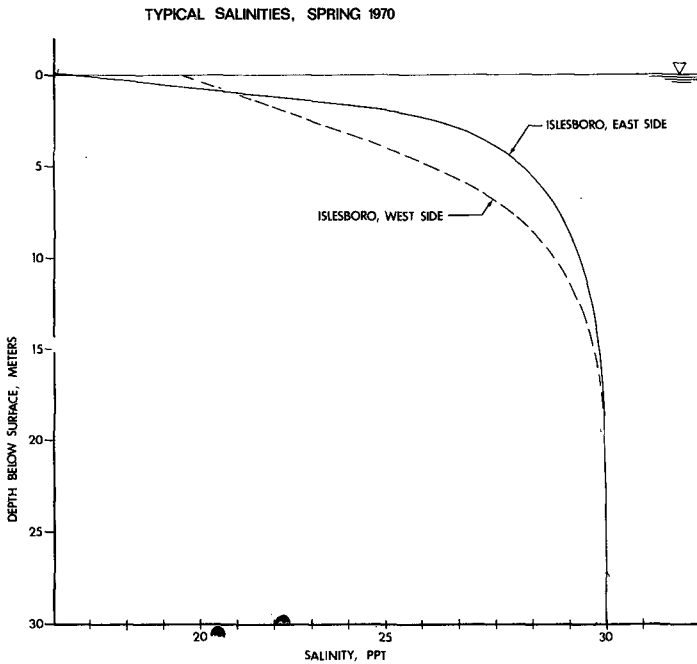


Figure 6

Within the range of observed transverse density gradients and with velocities of 5 cm/s upstream and downstream, equation (1) predicts that the pycnocline would be about 0.5 to 1.0 meter deeper on the western shore of the bay than on the eastern shore. Using the longitudinal density slope of the interface (from figure 7), it is possible to estimate the current velocities due to the density gradient alone (no wind) (after Defant, 1961):

$$i_2 = \frac{-2N_z \gamma}{g} \quad (2)$$

$$\gamma = \frac{-i_2 g}{2 N_z} \quad (3)$$

$$u_2 = A(z + h_1)(z + h_2) \quad \text{with } A = -4a\left(\frac{h_2}{h_1} - 1\right)^{-3} \quad (4)$$

$$\gamma = \frac{\rho_1}{\rho_2 - \rho_1} a \left[1 - \frac{\rho_2}{\rho_1} A \right] \quad (5)$$

where: i_2 = slope of the density interface (taken as 3×10^{-4} m/m)
 N_z = vertical eddy viscosity (taken as $0.01 \text{ m}^2/\text{s}$)
 h_2 = depth to bottom (taken as 25m.)
 h_1 = depth of surface layer (taken as 5 m.)
 ρ_1 = density of upper layer (1.025)
 ρ_2 = density of lower layer (1.012)

For small A, iterative solution of equations (2) through (5), suggests that density driven currents on the order of 2 km/day could exist in the Penobscot estuary. Although this is the same order of magnitude as the observed residual currents, this analysis is suggestive only, since the calculated velocity is critically dependent on the observed slope of the density interface. A further test was made of the importance of the density driven flow to the net circulation in the estuary, by applying the numerical model without including the density driven terms. Successful simulation of observed currents would indicate that the density terms could be safely ignored. Failure to achieve reasonable results would require that further modelling efforts be made with the computationally more complex (and expensive) version of the model incorporating the density terms.

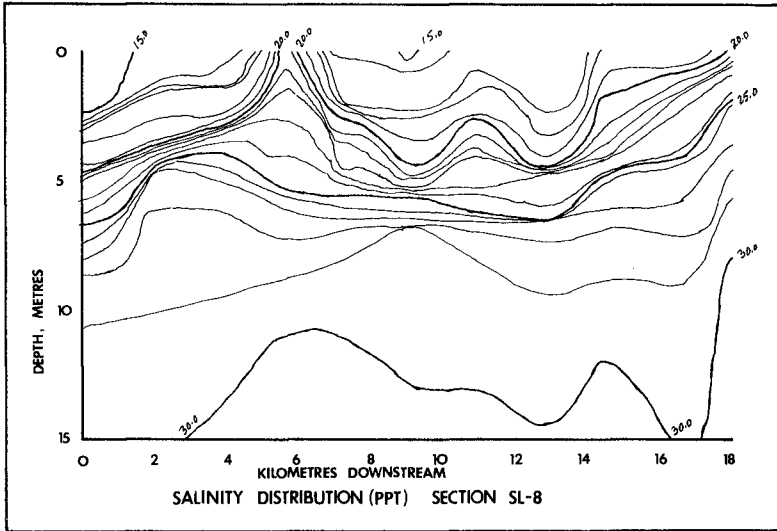


Figure 7

The Computer Model

The three-dimensional computer model "GAL" (Galerkin), described in detail in Pearce, et al. (1978), was used in this study to simulate currents in the Penobscot estuary. It uses the following expression of the Navier Stokes equation, neglecting vertical accelerations, density driven currents, and atmospheric pressure gradients:

$$\frac{\partial u}{\partial t} + u \frac{\partial u}{\partial x} + v \frac{\partial u}{\partial y} + w \frac{\partial u}{\partial z} = -g \frac{\rho_s}{\rho} \frac{\partial \eta}{\partial x} + fv + \frac{\partial}{\partial x} (N_H \frac{\partial u}{\partial x}) + \frac{\partial}{\partial y} (N_H \frac{\partial u}{\partial y}) + \frac{\partial}{\partial z} (N_V \frac{\partial u}{\partial z}) \tag{6a}$$

in the y direction,

$$\frac{\partial v}{\partial t} + u \frac{\partial v}{\partial x} + v \frac{\partial v}{\partial y} + w \frac{\partial v}{\partial z} = -g \frac{\rho_s}{\rho} \frac{\partial \eta}{\partial x} - fu + \frac{\partial}{\partial x} (N_H \frac{\partial v}{\partial x}) + \frac{\partial}{\partial y} (N_H \frac{\partial v}{\partial y}) + \frac{\partial}{\partial z} (N_V \frac{\partial v}{\partial z}) \tag{6b}$$

The surface boundary condition is specified as a set of horizontal shear stresses:

$$\tau_{sx} = -\rho_s N_V \frac{\partial u}{\partial z} ; \quad \tau_{sy} = -\rho_s N_V \frac{\partial v}{\partial z} \quad (7)$$

A linear slip coefficient defines the bottom boundary:

$$\frac{\partial u}{\partial z} = \frac{-C_b u_b}{N_b} ; \quad \frac{\partial v}{\partial z} = \frac{-C_b v_b}{N_b} \quad (8)$$

where: N_V = vertical component of the eddy viscosity

N_b = value of the vertical eddy viscosity at the bottom boundary

N_H = horizontal component of the eddy viscosity

C_b = bottom slip coefficient

u, v = x and y components of velocity

τ_{sx}, τ_{sy} = x and y components of wind shear stress at surface

u_b, v_b = velocities at the bottom boundary in the x and y directions

η = height of water surface above still water level

ρ_s = water density at surface

ρ = water density at any depth

g = acceleration of gravity

f = coriolis parameter

These equations are solved by assuming a trial solution which specifies the x and y components of velocity as a continuous function of depth, z. The functions used here are:

$$\hat{u} = \frac{\tau_{sx} z^2 (z-H)}{\rho_s H^2 N_b} + \frac{\tau_{sx}}{\rho_s \alpha} \ln \left(\frac{N_b}{N_V} \right) + \sum_{I=1}^{I'} c_I \cos \left(\frac{a_I z}{H} \right) \quad (9a)$$

$$\hat{v} = \frac{\tau_{sy} z^2 (z-H)}{\rho_s H^2 N_b} + \frac{\tau_{sy}}{\rho_s \alpha} \ln \left(\frac{N_b}{N_V} \right) + \sum_{I=1}^{I'} d_I \cos \left(\frac{a_I z}{H} \right) \quad (9b)$$

where the a_I 's are given by the solution to:

$$a_I \tan a_I = \frac{c_b H}{N_b}$$

and where:

$$\alpha = \frac{\partial N_V}{\partial z}$$

c_I, d_I = undetermined parameters whose values represent a solution at location x, y , and time t , and

H = still water depth

Equations (9a) and (9b) are substituted into the Navier-Stokes equation. Since the trial functions are not the exact solutions, there will be an error, or residual, R , associated with this substitution, where:

$$R = \frac{du}{dt} + \frac{\rho_s}{\rho} g \frac{\partial \eta}{\partial x} - \frac{\partial}{\partial x} (N_H \frac{\partial u}{\partial x}) - \frac{\partial}{\partial y} (N_H \frac{\partial u}{\partial y}) - \frac{\partial}{\partial y} (N_V \frac{\partial u}{\partial z}) - fv$$

$$+ \frac{1}{\rho} \frac{\partial P}{\partial x} \neq 0 \quad (10)$$

The Galerkin technique is used to minimize the error by specifying that the sum of the residuals, multiplied by an arbitrary weighting function, over the depth of the water column be zero:

$$\int_{-\eta}^H R \Omega_I dz = 0$$

The weighting function chosen here is:

$$\Omega_I = \cos \left(\frac{a_I z}{H} \right)$$

which takes advantage of the orthogonality of the cosine function to simplify the integrations in the resulting Galerkin statement:

$$\int_0^H R \Omega_I dz = \int_0^H \left\{ \frac{d\hat{u}}{dt} + g\rho_s \frac{\partial \eta}{\partial x} \frac{\Omega_I}{\rho} - \left[\frac{\partial}{\partial x} (N_H \frac{\partial \hat{u}}{\partial x}) + \frac{\partial}{\partial y} (N_H \frac{\partial \hat{u}}{\partial y}) \right] - \left(\frac{\partial N_V}{\partial z} \frac{\partial \hat{u}}{\partial z} \right) - N_V \frac{\partial^2 \hat{u}}{\partial z^2} - f\hat{v} + \frac{1}{\rho} \frac{\partial P_a}{\partial x} \right\} \Omega_I dz = 0 \quad (11)$$

Equations (11) are integrated under the following additional assumptions:

- (a) the convective terms are small and may be neglected
- (b) a linear approximation to the horizontal shear stress terms is appropriate
- (c) η is small with respect to H .

This results in the reduction of the original second order, non-linear momentum equations and the non-homogeneous vertical boundary conditions to a set of $2I'$ linear, first-order partial differential equations in $2I' + 1$ unknown parameters, c_I (x component), d_I (y component), and η . These are coupled to the continuity equation:

$$\frac{\partial u}{\partial x} + \frac{\partial v}{\partial y} = \frac{\partial \eta}{\partial t} \quad (12)$$

and the horizontal boundary conditions. These equations are discretized and solved explicitly for the coefficients by a "split-time" finite difference scheme. The coefficients are substituted into the Galerkin trial solutions (Equations (9)) to yield values for u and v at each grid element.

Model Applications: Inputs

1. Vertical eddy viscosity. GAL should prove useful in modelling stratified flow since the model uses a vertically varying vertical eddy viscosity, N_V . For this application, two different methods of specifying N_V were tried, figure 8. In both cases, the break-point in the piece-wise linear form occurred at the assumed density interface, 5 meters below the surface.
2. Wind. A southwest wind at 5 m/s was applied to the modelled estuary, ramped up from zero to maximum velocity in one tidal cycle. The appropriateness of this input was confirmed with lighthouse keepers' observations of wind at Matinicus Rock (26 kms. south of the study area's southern boundary). They had been taken at approximately 3 hour intervals and showed that southerly winds prevailed during the study period.

3. Other input parameters. River discharge was taken as $1300 \text{ m}^3/\text{s}$. This is near the maximum discharge for the Penobscot and is a representative flow for the study period.

The bottom slip coefficient was used as a tuning parameter and varied in magnitude from 0.01 to 0.001 m/s.

A rectangular grid spacing of 1016 meters was chosen as the maximum that could place at least three grid elements across the narrowest section of the bay. With less than three elements in the transverse direction, the no-flow horizontal boundary condition leads to spurious results at those points. The Courant condition, equation (13), governed model stability with the result that for the maximum depths of 130 meters encountered, a maximum time step of 20 seconds was used in the model runs.

$$\Delta t \leq (2gh_{\max})^{-1/2} \Delta L \quad (13)$$

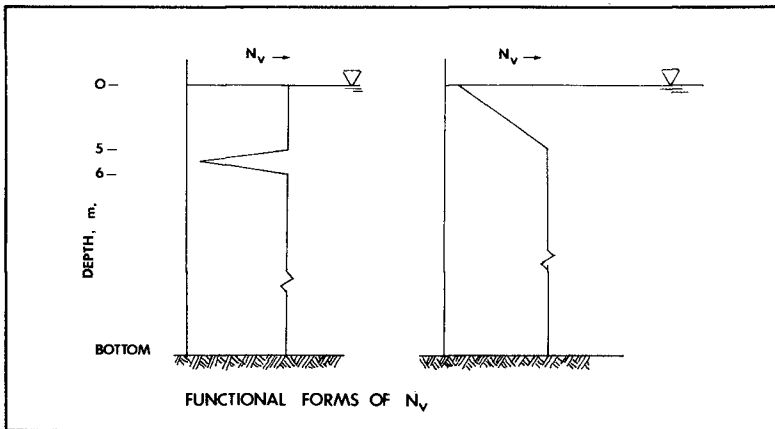


Figure 8

Model Application: Results

The model provides a reasonable representation of the instantaneous currents as shown by a typical velocity profile, Figure 9 (Figure 9 shows the modelled currents at maximum flood and five profiles of the measured data taken about the time of maximum flood). Residual currents were not well represented. Figure 10 shows a plot of the residual currents from one of the most encouraging runs to date. While the magnitudes compare favorably to data, directions are merely suggestive of those found in the data.

We conclude, based on these comparisons and on the evidence cited earlier, that during the time of spring runoff, the density driven residual currents are of the same order of magnitude as the residual currents from other causes. In order to properly consider density driven currents, the model GAL is now being appropriately modified.

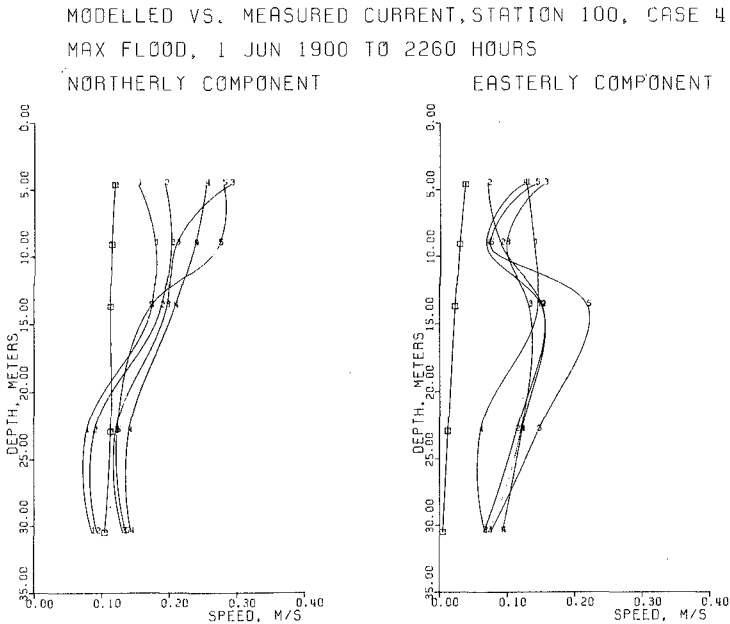


Figure 9

CASE 4, 2 EV'S, RIVERFLOW=45KCF5, 6 TIDAL CYCLES, WIND SW 5 M/S

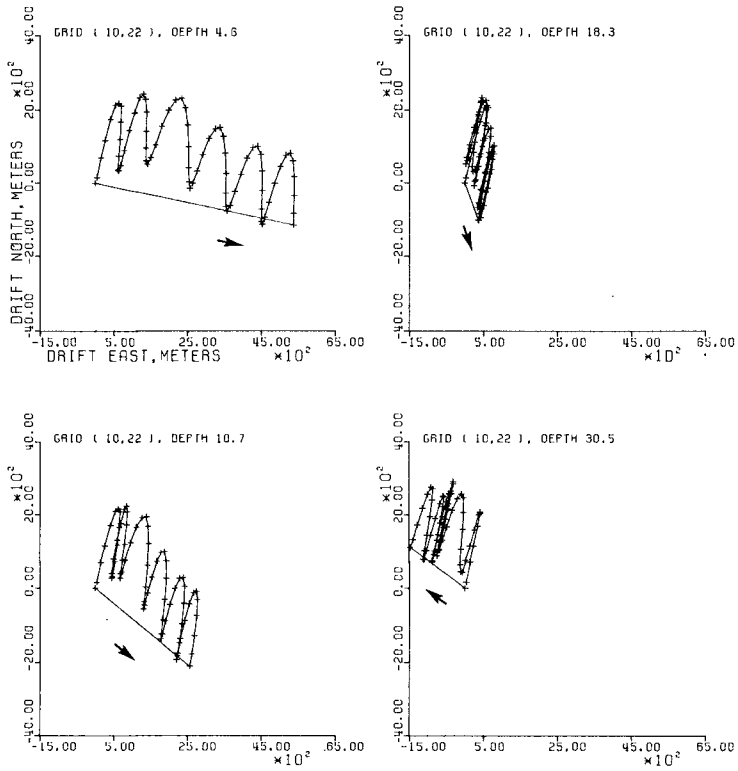


Figure 10: Residual Currents

REFERENCES

1. Defant, A., Physical Oceanography, Vol. I., MacMillan, New York, 1961.
2. Fidler, R.B., An Approach for Hydrodynamic Modeling of Maine's Estuaries. Master's Thesis, University of Maine, Orono, Maine.
3. Haefner, P.A., Jr., Hydrography of the Penobscot River Estuary, J. Fisheries Research Board of Canada, 24 (7), 1967.
4. Neuman, G., and W.J. Pierson, Jr., Principles of Physical Oceanography. Prentiss-Hall, Englewood Cliffs, N.J., 1966.
5. Pearce, B.R., C. Cooper, S. Nelson, GAL: A 3-Dimensional Numerical Model to Calculate Currents with a Depth Varying Vertical Eddy Viscosity. Technical Report, University of Maine, Orono, Maine.

The Use of Array Processors for Numerical Modelling
of Tidal Estuary Dynamics

by D. Prandle*, E.R. Funke**,
N.L. Crookshank*** and R. Renner****

1.0 INTRODUCTION

The use of array processors for the numerical modelling of estuarine systems is discussed here in the context of "hybrid modelling", however, it is shown that array processors may be used to advantage in independent numerical simulations. Hybrid modelling of tidal estuaries was first introduced by Holz (1977) and later by Funke and Crookshank (1978). In a hybrid model, tidal propagation in an estuary is simulated by dynamically linking an hydraulic (or physical) scale model of part of the estuary to a numerical model of the remaining part in a manner such that a free interchange of flow occurs at the interface(s). Typically, the elevation of the water surface at the boundary of the scale model is measured and transmitted to the numerical model. In return, the flow computed at the boundary of the numerical model is fed directly into the scale model.

This approach enables the extent of the scale model to be limited to the area of immediate interest (or to that area where flow conditions are such that they can be most accurately simulated by a scale model). In addition, since the region simulated by the numerical model can be extended almost indefinitely, the problems of spurious reflections from downstream boundaries can be eliminated.

In normal use, numerical models are evaluated on the basis of computing requirements, cost and accuracy. The computer time required to simulate one tide cycle is, in itself, seldom of interest except in so far as it affects the above criteria. However in hybrid modelling this parameter is often paramount since concurrent operation of the numerical and scale models requires that the former must keep pace with the latter.

The earlier hybrid model of the St. Lawrence (Funke and Crookshank, 1978) involved a one-dimensional numerical model of the upstream regions of the river. However, future applications are likely to involve extensive two-dimensional numerical simulation. Consequently the

* Visiting Scientist, **Senior Research Officer, ***Systems Manager, Hydraulics Laboratory, National Research Council of Canada, Ottawa, Canada.
**** Chief Scientist, Canadian Astronautics Ltd., Ottawa, Canada.

computational power required will be considerable and almost certainly in excess of the power of present-day mini-computers. The use of a substantial main frame machine is complicated by both the cost and the requirement for a high priority real time service. Thus the use of an array processor/mini-computer combination was examined to bridge this gap in computational power.

Section 2 describes a hybrid model of the Bay of Fundy with the details of the numerical scheme given in section 3. Sections 4, 5 and 6 describe, in some detail, various aspects relating to the usage of the array processor. Finally section 7 provides a comparison of the performance of the array processor against that of both a mini-computer and two main frame machines.

2.0 THE BAY OF FUNDY HYBRID MODEL

In order to subject the development project to the rigors of a practical application, a suitable estuary was selected. The Bay of Fundy offered several advantages. For one, there exists a proven explicit model (Greenberg, 1976) which covers both the Bay of Fundy and the Gulf of Maine, down to the Continental Shelf. Secondly, there is a considerable interest in the electric power potential of the Fundy tide and it was felt that the experience gained from the pilot model study may benefit future investigations whenever the Bay of Fundy tidal power development progresses to the engineering design stage. With these considerations in mind, the construction of a pilot hybrid model was initiated with Cumberland Basin and Shepody Bay forming the physical model and the remainder of the estuary down to the Continental Shelf forming the numerical model. Fig. 1 illustrates the general outline of this estuary, and includes the schematization employed for the finite difference scheme. The small "boxed-in" area in the upper right hand corner of the diagram is simulated by a physical model. Fig. 2 illustrates the outline of this scaled model and its relationship to the numerical model. The computer in this hybrid model serves the dual functions of being both host to the array processor and at the same time, being the data acquisition system and feedback controller for the discharge control pump (Funke, Crookshank and Wingham, 1980).

Fig. 3 gives the timing diagram of a typical hybrid model. It should be noted that the "hatched" pulses represent the regular clock pulses which, for the Bay of Fundy model, occur every 0.3 seconds. Shortly after each pulse, a data transfer takes place which transmits the last calculated discharge value Q_I from the array processor to the control computer. The data acquisition phase follows immediately, monitoring among other variables, the water elevation H_I which is then transmitted back to the array

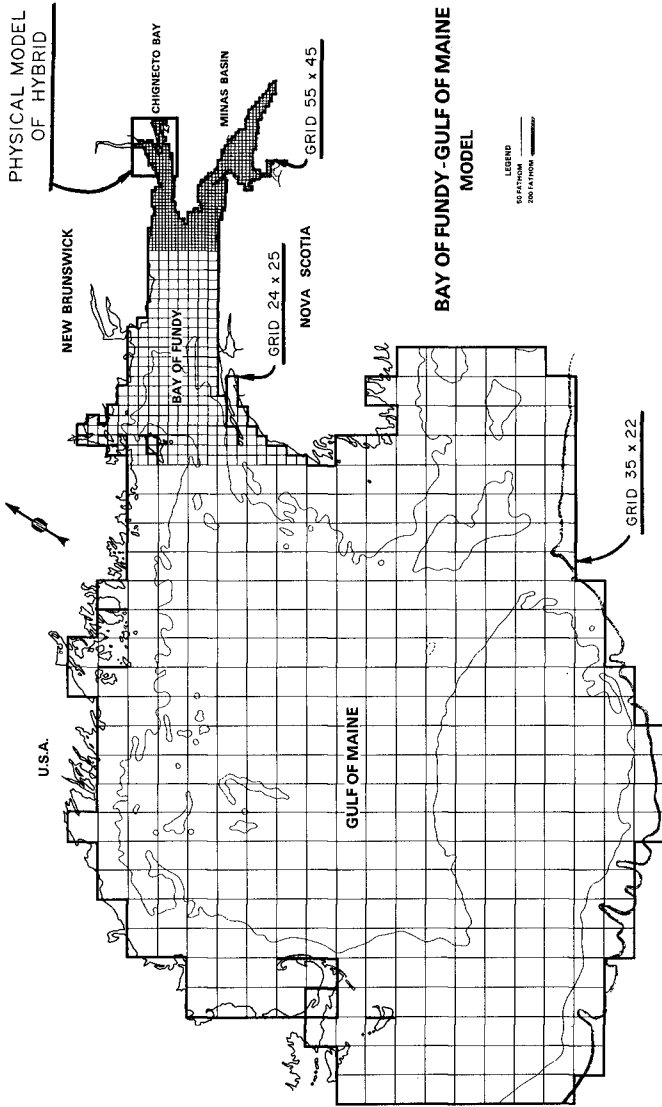


FIG. 1
SCHEMATIC REPRESENTATION OF BAY OF FUNDY

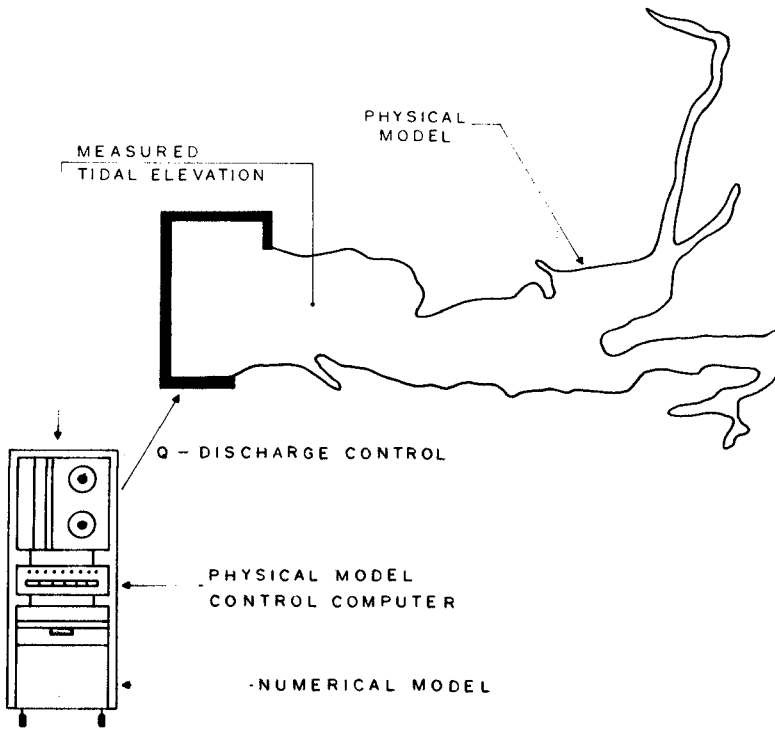
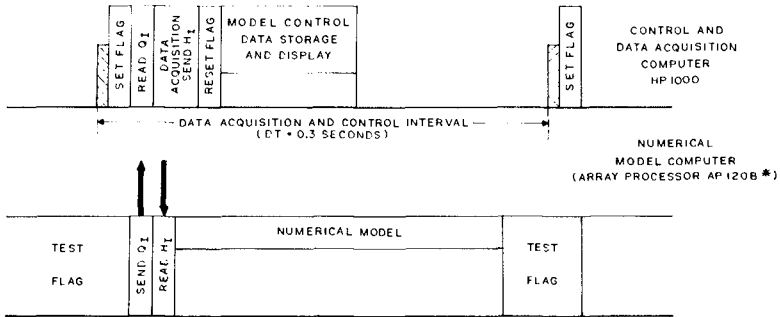


FIG. 2 HYBRID MODEL OF CUMBERLAND BASIN AND SHEPODY BAY

processor. Next comes the model control phase and while the control computer is engaged in achieving the required discharge, the array processor must solve one time step of the numerical model. Since clock pulses for the Bay of Fundy hybrid model occur every 300 milliseconds, the computational time available for one time step of the numerical model must be somewhat smaller. In fact, sufficient time must remain to complete all the data acquisition and the data transfer between the host computer and the array processor. In addition one wants to have some margin of safety so that the "ping-pong" interchange between the two machines can never get out of synchronism.



H₁ * PHYSICAL MODEL WATER ELEVATION AT THE INTERFACE BOUNDARY FOR THE INSTANCE 1

Q₁ * THE CALCULATED MODEL DISCHARGE AT THE INTERFACE FOR THE INSTANCE 1-Δt

* MANUFACTURED BY: FLOATING POINT SYSTEMS INC.

FIG. 3 TIMING DIAGRAM FOR HYBRID MODEL

3.0 THE EXTENT OF THE MATHEMATICAL MODEL

The estuary dynamics of the mathematical model for the present Bay of Fundy is based on the following equations:

$$\text{x-motion: } \frac{\partial U}{\partial t} + g \frac{\partial Z}{\partial x} + f \frac{U \cdot (U^2 + V^2)^{1/2}}{(D + Z)} - \Omega \cdot V = 0$$

$$\text{y-motion: } \frac{\partial V}{\partial t} + g \frac{\partial Z}{\partial y} + f \frac{V \cdot (U^2 + V^2)^{1/2}}{(D + Z)} + \Omega \cdot U = 0$$

$$\text{continuity: } \frac{\partial Z}{\partial t} + \frac{\partial}{\partial x} [U \cdot (D + Z)] + \frac{\partial}{\partial y} [V \cdot (D + Z)] = 0$$

where U and V are the velocities in the x and y direction,
 D is the depth below mean water,
 Z is the tidal elevation about the mean,
 f is the friction term, and
 Ω is the Coriolis parameter.

Fig. 4 shows the schematization using a finite difference, explicit method with a staggered mesh and forward difference

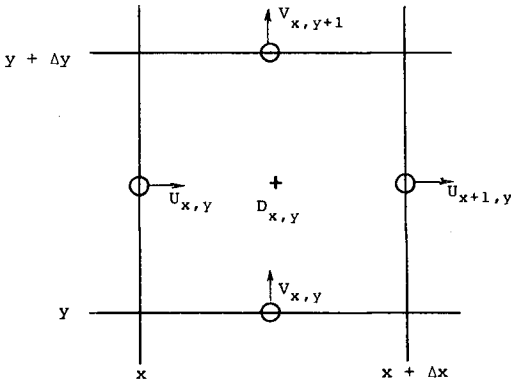


FIG. 4 DEFINITION OF FINITE GRID ELEMENT

in time. The differential equations are thus approximated by the following.

$$U'_{x,y} = (U_{x,y}/\Delta t + g(Z_{x,y} - Z_{x-1,y})/\Delta x - \Omega \cdot \bar{V}) / (1/\Delta t + F_x)$$

where:

$$\bar{V} = (V_{x,y} + V_{x-1,y} + V_{x,y+1} + V_{x-1,y+1})/4$$

and

$$F_x = f \cdot (U_{x,y}^2 + \bar{V}^2)^{1/2} / ((D_{x,y} + D_{x-1,y} + Z_{x-1,y})/2)$$

$$V'_{x,y} = (V_{x,y}/\Delta t + g(Z_{x,y} - Z_{x,y-1})/\Delta y + \Omega \cdot \bar{U}) / (1/\Delta t + F_y)$$

where:

$$\bar{U} = (U_{x,y} + U_{x+1,y} + U_{x,y-1} + U_{x+1,y-1})/4$$

and

$$F_y = f \cdot (\bar{U}^2 + V_{x,y}^2)^{1/2} / ((D_{x,y} + D_{x,y-1} + Z_{x,y} + Z_{x,y-1})/2)$$

and

$$Z'_{x,y} = \left(Z_{x,y}/\Delta t + [U_{x+1,y} \cdot (D_{x+1,y} + D_{x,y} + Z_{x,y} + Z_{x+1,y}) - U_{x,y} \cdot (D_{x,y} + D_{x-1,y} + Z_{x,y} + Z_{x-1,y})] / (2 \cdot \Delta x) + [V_{x,y+1} \cdot (D_{x,y+1} + D_{x,y} + Z_{x,y+1} + Z_{x,y}) - V_{x,y} \cdot (D_{x,y} + D_{x,y-1} + Z_{x,y})] / (2 \cdot \Delta y) \right)$$

Fig. 1 shows that the area to be modelled is subdivided into three zones. The Gulf of Maine is represented by a 35 x 22 grid. The Bay of Fundy area has three times the resolution with a 24 x 25 grid. Finally the upper reaches of the Bay have again three times the resolution with a 55 x 45 grid.

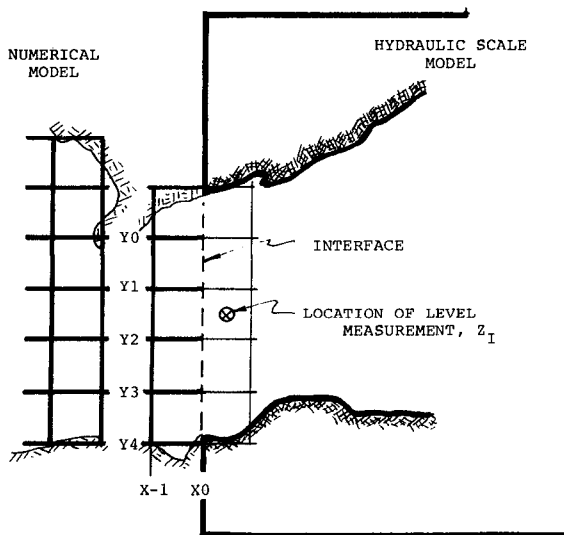
Fig. 5 shows that five finite grid elements form the boundary with the scaled model. It is anticipated that each of these five elements could control an appropriate interface pump. However, for the pilot model now under construction, only one elevation, Z_I , is measured and the numerical model supplies the average discharge through the boundary by means of the averaging formula given in Fig. 5.

4.0 A BRIEF DESCRIPTION OF ARRAY PROCESSOR HARDWARE

An array processor (AP) is a digital data processor which is specifically and optimally designed to process long data vectors. Typically, one can say that the longer the data vector or vectors, the more advantageous is the array processor as a "number cruncher".

Array processors are peripheral to so-called host computers. Their advantage must, of course, be measured relative to their host computer. For this reason, it is quite common now to find array processors interfaced to mini-computers rather than to larger main frame machines. The list of references suggests some papers which offer more technical information on various array processors.

Fig. 6 shows the major components of a typical array processor "Floating Point Systems Inc. AP120B", i.e. the machine used for this particular study. From this diagram several pertinent features can be recognized:



ASSUME: $Z_{X_0, Y_0} = Z_{X_0, Y_1} = Z_{X_0, Y_2} = Z_{X_0, Y_3} = Z_{X_0, Y_4} = Z_I$

$$Q_I = \sum_{i=Y_0}^{Y_4} \Delta y \cdot U_{x_0, i} \cdot (D_{x_0, i} + D_{x-1, i} + Z_{x_0, i} + Z_{x-1, i}) / 2$$

FIG. 5 INTERFACE DETAILS BETWEEN NUMERICAL AND SCALED MODEL

- (a) The AP has separate and independent memory components for data, program store and table constants. This permits not only some parallel processing but also an optimum choice of word length for instructions and data respectively. For example, the AP120B has a 64 bit instruction word which may control up to ten different operations more or less at the same time. On the other hand, the data word is 38 bits long with 28 bits used as mantissa and 10 bits as exponent. This is a worthwhile improvement over the usual 32 bit data formats especially for the type of problem described by this paper.
- (b) The AP has parallel arithmetic processors which may operate on data concurrently.
- (c) Data processing may take place in a "pipeline" fashion so that data words move progressively through successive stages. Each stage may require in the order of

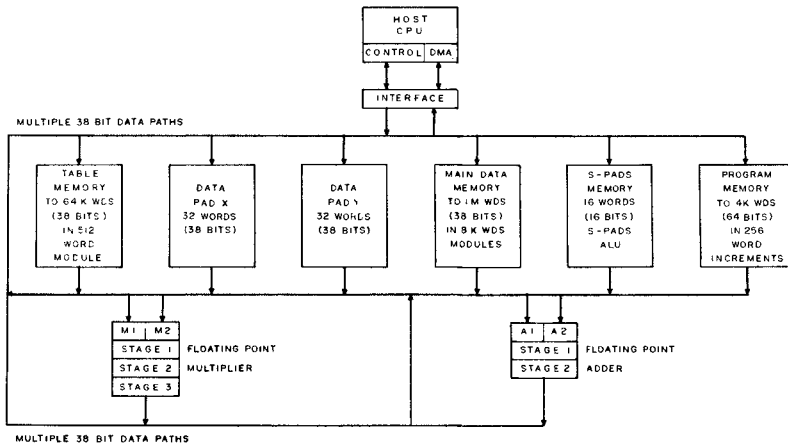


FIG. 6 GENERAL SYSTEM DIAGRAM FOR AP122B ARRAY PROCESSOR

167 nanoseconds. Once the "pipeline" is filled, solutions are returned back to the data memory at the same 167 nanosecond rate. It is both the parallel processing and the "pipelining" which gives these processors their phenomenal speed.

- (d) The interface between the host computer and the AP is of particular importance in appreciating the operation of the machine in relation to its host. In the usual configuration depicted by Fig. 6, all AP-programs and data come from the host and results are returned to the host. An executive program in the host keeps track of the programs which are required in the AP program store and if a particular program which is being called is not, at that time, resident in the AP, it must be transferred there into whatever free area is available. If the program store is filled to capacity, then the last program in will be the first program to be overlaid, and hence destroyed.

Data transfer to and from the AP is usually costly in time. Consequently an awareness of these operational and hardware features can affect the manner in which an AP program is written for best performance.

5.0 ARRAY PROCESSOR APPLICATION TO BAY OF FUNDY MODEL

Fig. 7 illustrates the particular computer and

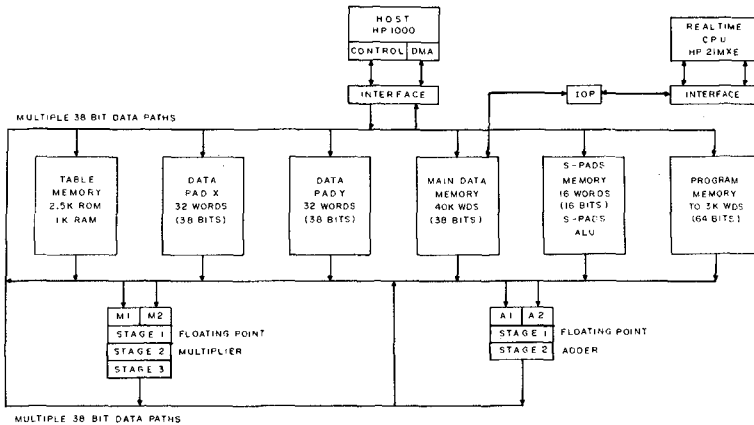


FIG. 7 THE ARRAY PROCESSOR CONFIGURATION AS FOR B OF F MODEL

array processor configuration which is being used for the Bay of Fundy pilot hybrid model. It may be noted that the host computer is a Hewlett-Packard HP-1000 model 45, while the data acquisition and on-line, digital control computer is the HP-21MXE computer. Although the configuration of Fig. 6 could have served the requirements of the hybrid model, the configuration of Fig. 7 was selected in order to get a better overall system utilization. This is of particular importance since the hybrid model is not the only real time activity which is being supported concurrently by this H.P. computer system (Funke, Crookshank and Wingham, 1980).

The DMA interface to the host computer in Fig. 7 is the usual channel for transmission of AP-programs and for initial model constants. The entire Bay of Fundy numerical model, as described in section 3.0, is down-loaded in this way prior to commencement of actual model operation. Once in operation, data related to the tidal elevation is transmitted from the data acquisition computer to the AP via the input/output processor box (IOP) and the resultant discharge data travels on the same channel in the opposite direction. In this manner, the array processor is an autonomous, dedicated numerical model, completely freeing the host computer for other activity.

A suitable "logical" switch was provided to run the numerical model of the Bay of Fundy either as a hybrid model or as a completely independent numerical model. In the former case a boundary exists at the entrance to the Cumberland and Shepody Basins and boundary information is transmitted via the IOP. In the latter case, this boundary does not exist as the two basins are included in the numerical model.

In order to monitor the progress of tidal propagation through the numerical model, the solutions for tidal elevation at each grid point are also transmitted to the data acquisition and control computer at each control step. In this manner one may treat the data in a similar fashion to other data which were acquired through instrumentation on the physical model.

6.0 PROGRAMMING ARRAY PROCESSORS

Whereas the array processors offer substantial improvements in processing speed, the effort required to exploit their power may still be substantial. For this reason it is a definite advantage to have the help of an expert consultant who can quickly solve the usual "teething" problems and who can pilot the project around the various pitfalls.* However, there is a significant and promising development in progress which may overcome many obstacles.

There are four different ways by which the Floating Point Systems Inc. AP120B may be programmed. Each of these offers certain advantages or disadvantages which must be traded off.

6.1 FORTRAN Calls to Existing Library Subprograms

Fig. 8 gives a typical example of a program task which requires various vector and matrix operations. The first portion in Fig. 8 describes this task as a conventional FORTRAN code. Following this, one may recognize calls to various subroutines which serve

- (a) to initialize the AP,
- (b) to transfer data from the host to the AP, and
- (c) to cause a wait until the transfer of data is complete.

It is worth noting that the data memory in the AP is addressed here in terms of absolute addresses and these must be generated before the data transfer calls can

* Canadian Astronautics Ltd.
1024 Morrison Dr., Ottawa, K2H 8K7 Canada.

```

C***** POTENTIAL CALCULATION *****
C
C=====
C   ORIGINAL FORTRAN
C
C   SUBROUTINE EX2
C   COMMON /B/PHIB(100,10),HB(100,10),PKB(100),DS12
C   DO 1 J=1,9
C   DO 1 I=1,100
C 1   PHIS(I,J+1)=PHIB(I,J)+DS12*PKB(I)*(HB(I,J+1)+HB(I,J))
C   RETURN
C   END
C=====
C
C   SUBROUTINE EX2
C   COMMON /B/PHIB(100,10),HB(100,10),PK(100),DS12
C-----AP MEMORY LAYOUT
C   IDS12=0
C   IPKB=1
C   IHB=IPKB+100
C   IPHIB=IHB+1000
C-----INITIALIZE THE AP
C   CALL APINIT (0,0,STATUS)
C   IF (STATUS.LT.0) CALL ERROR
C-----PUT OUT THE DATA TO AP
C   CALL APPUT (PHIB,IPHIB,1000,2)
C   CALL APPUT (HB,IHB,1000,2)
C   CALL APPUT (PKB,IPKB,100,2)
C   CALL APPUT (DS12,IDS12,1,2)
C   CALL APWD
C
C-----DO THE COMPUTATION
C
C   AP COMPUTATION TIME IS 2.3 MS FOR 167 NS MEMORY, 3.7 MS FOR
C   333NS MEMORY, EXCLUSIVE OF HOST SYSTEM OVERHEAD
C
C   CALL VSMUL(IPKB,1,IDS12,IPKB,1,100)
C   CALL VADD (IHB+100,1,IHB,1,IHB,1,900)
C   JHB=IHB
C   DO 1 J=1,9
C   CALL VMUL(IPKB,1,JHB,1,JHB,1,100)
C 1   JHB=JHB+100
C   CALL VADD (IPHIB,1,IHB,1,IPHIB+100,1,900)
C   CALL APWR
C-----GET THE RESULTS FROM AP
C   CALL APGET (PHIB(1,2),IPHIB+100,900,2)
C   CALL APWD
C   APRLSE
C   RETURN
C   END

```

FIG. 8 EXAMPLE AP PROGRAM FOR CALLS ON AP-MATHEMATICAL LIBRARY

be made. Other arguments specify typically how many elements are to be transferred and what format conversion is to take place.

The subsequent calls deal with the actual solution of the problem. One may recognize vector multiply and vector addition operation which make reference to the various arrays in terms of their addresses in AP memory. In order to make these routines as general as possible, they have been designed to permit operation either on consecutive elements (i.e. arguments No. 2, No. 4 and No. 6 are set to 1) or on alternate or arbitrarily spaced arguments. It is typical for the list of arguments to be organized as "SOURCE1", "SOURCE2" and "DESTINATION". For each of these the order is always "WHERE", "HOW MANY" and "NUMBER OF SKIPS - 1". Prior to the data transfer from AP to host a "WAIT FOR AP READY" must also be invoked.

It should be noted that the DO-loop and the calculation of the "JHB" parameter are executed in the host computer and for each pass through the DO-loop a transfer of subroutine arguments to the AP will be implemented. This is not the fastest way of running the solution but it does offer a relative simplicity in implementation.

The disadvantages of this approach are:

- (a) Programming is limited to existing algorithms in the various libraries supplied by the manufacturer,
- (b) Special requirements, such as conditional branches, require FORTRAN coding in the host computer with the consequent loss of speed due to repeated interchange of information between the host and the AP,
- (c) Addressing of variables and arrays in the AP must be implemented in terms of absolute addresses with a subsequent loss of the convenience and power of a mnemonic address structure which is inherent to FORTRAN and
- (d) Although each AP subprogram has been coded in an optimum fashion, any special requirements, which could benefit from some of the various hardware features of the AP, cannot be accommodated.

6.2 Programming with the Vector Function Chainer Language

The Vector Function Chainer is an AP programming language of a somewhat higher power than the simple calling of precoded library subprograms. This language allows not only the creation of new AP library subprograms, but it also permits some simple, FORTRAN-like statements for execution in the array processor rather than the host computer.

Fig. 9 gives an example of a subprogram for a

```

***** MVADD = MATRIX/VECTOR ADD *****
"
"   DEFINE MVADD(A,I,B,J,C,K,NRC,NCC)
"
"   ADD VECTOR B TO EVERY ROW OF MATRIX A, PUTTING THE RESULT IN C
"
"   A - ADDRESS OF MATRIX A
"   I - INCREMENT BETWEEN ELEMENTS OF A
"   B - ADDRESS OF VECTOR B
"   J - INCREMENT BETWEEN ELEMENTS OF B
"   C - ADDRESS OF DESTINATION MATRIX C
"   K - INCREMENT BETWEEN ELEMENTS OF C
"   NRC - NUMBER OF ROWS IN C (AND A)
"   NCC - NUMBER OF COLUMNS IN C (AND A)
"
"THE MATRICES ARE STORED IN COLUMN ORDER. THUS I AND K ARE INCREMENTS
"BEWEEN ELEMENTS IN A COLUMN. WE MUST COMPUTE THE INCREMENT BETWEEN
"ELEMENTS IN A ROW.
"
"   LOCAL AR,CR
"
"   AR = I * NRC           "COMPUTE 'A' ROW INCREMENT
"   CR = K * NRC           "COMPUTE 'C' ROW INCREMENT
"
LOOP: CALL VADD(A,AR,B,J,C,CR,NCC)      "ADD TO A ROW
      A = A + I                    "ADVANCE 'A' POINTER
      C = C + K                    "ADVANCE 'C' POINTER
      NRC = NRC - 1                "DECREMENT ROW COUNTER
      IF NRC < 0 GOTO LOOP          "GO BACK IF NOT DONE
      END
"
"

```

FIG. 9 EXAMPLE AP PROGRAM USING VECTOR FUNCTION CHAINER

matrix/vector addition which was created using the vector function chainer. This example illustrates some of the features of this language such as the calling of other existing subprograms, the creation of absolute addresses by arithmetic statements and the use of the logical IF-statement.

Fig. 10 shows the procedure by which a vector function chainer program is implemented. The source code of the program is first processed by the vector function chainer and the resultant output is a "second stage" source code in the AP assembler language. This assembler must also process the code which is then fed through the AP linking loader which serves to satisfy calls to the AP-library. The result of these operations leads to a third-stage source code which is in the host FORTRAN language. However, this code is quite unreadable as it consists of no more than a subroutine definition and termination statements and a long list of DATA statements with integer values. Each integer word is a quarter of a 64 bit instruction word which forms part of the desired AP program.

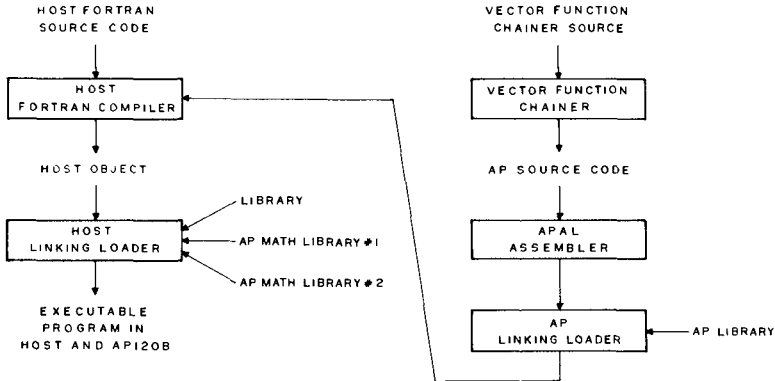


FIG. 10 USE OF VECTOR FUNCTION CHAINER

This third stage source program now represents the newly created member of an AP subprogram library. Before execution it must be compiled together with its calling FORTRAN program by the host FORTRAN compiler and then loaded in the usual fashion.

The vector function chainer offers greater programming power than the approach described under section 3.1. It is equally cumbersome in the management of absolute addresses but since addresses and additional branches defined by the vector function chainer language are computed within the AP, the repeated information transfer between the host computer and the AP is eliminated and a considerable speed-up of the solution times is achievable. The explicit model of the Bay of Fundy was coded in this manner.

6.3 Programming by Using the AP-FORTRAN Compiler

A more recent addition to the bag of tricks for programming is a FORTRAN compiler for the array processor. It offers potentially many significant advantages over any other approach and promises to make the array processor a truly general purpose computer which can bring low cost, high speed computation into the reach of anyone who has a need for it.

In order to code a task in AP FORTRAN, it is necessary to define that portion of a program which is to run on the array processor as distinct from the host computer. This portion must be coded as a standard FORTRAN subprogram. If all of the task is to run on the AP, it is still necessary to have a host program that simply states:

```

READ ARG1,ARG2
CALL NAME(ARG1,ARG2, ... ARGN)
WRITE ARGN
END

```

The subroutine NAME must be processed by the AP FORTRAN compiler which will take care of all data transfers to and from the AP and the associated wait-calls. It can handle any type of linear or non-linear functional relationships and any multi-dimensional array configuration. However, the usual data input/output function via the host computer's peripherals must be looked after by the host computer.

Fig. 11 shows the procedure for implementing an AP pro-

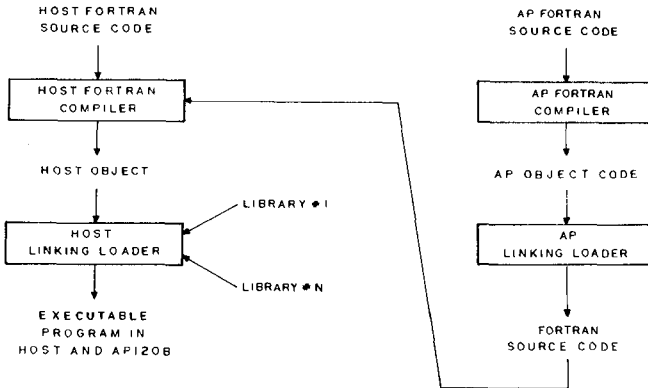


FIG. 11 USE OF AP FORTRAN COMPILER

gram by the AP FORTRAN compiler. The source code of the subroutine 'NAME' is first processed by the AP FORTRAN compiler. This must be done on a larger 32 bit computer as the compiler is not, at present, operational on 16 bit computers. However, its output may be run on 16 bit host computers which provide, after linking-loading, a secondary source code in host FORTRAN. As before, this source code consists substantially of DATA statements only and looks quite similar to the third stage source code produced by the vector function chainer described in section 6.3.

At this time, the community of users of an AP-FORTRAN compiler is still relatively small and general experience in its use must yet be established. However, for the purpose of the Bay of Fundy hybrid model study, an investigation was carried out for the purpose of:

- (a) establishing the suitability of either the explicit or the implicit method for numerical models with regard to array processor operations, and
- (b) establishing the effectiveness of the AP-FORTRAN compiler vis à vis the Vector Function Chainer as a means for implementing the implicit model on the AP.

Table 1
COMPARISON OF AP-FORTRAN WITH VECTOR FUNCTION CHAINER

	AP PROGRAM STORE WORD	PROCESSING SPEED PER TIME STEP**	NO. OF DAYS WORD TO IMPLEMENT PROGRAM*
VECTOR FUNCTION CHAINER	2700	1.5 s	7 days
AP-FORTRAN COMPILER	2200	1.5 s	1 day

* From an original statement of the model in terms of a correctly working program in host computer FORTRAN.

** 48 steps per tidal cycle

The comparison of Table 1 favours the AP-FORTRAN compiler. This came as a surprise because other users had indicated that both the required program store and the solution time would increase as a consequence of using the AP-FORTRAN compiler.* It may be possible that the nature of the particular program or the manner in which the program was coded using the vector function chainer could both affect the results. Nevertheless the authors' experience has been most encouraging even though there still are some minor errors in the AP-FORTRAN compiler.

6.4 Programming by Using the AP Assembler Language

In order to get the greatest processing speed with the least amount of required program store, it is necessary to use assembly language. This option was considered as a last resort for the Bay of Fundy hybrid model if other programming methods had not brought the solution speed within the real time constraints imposed by the physical model.

* Verbal communications

The assembly language permits direct control over all registers, data buses and arithmetic units. The price for this additional flexibility and power is the greater language complexity. As a result it is difficult and costly to learn the language and very time consuming to create an error-free program. Coding by the AP assembly language is considered practical only for those situations where the additional speed justifies the additional cost in program development effort.

7.0 COMPARISON OF AP PERFORMANCE TO OTHER COMPUTERS

Comparisons between computers are meaningful only in terms of specific benchmark programs which contain a specific mix of computational operations. For this reason it is necessary to point out that this comparison applies strictly to the solution of a system of finite difference equations describing estuary dynamics.

The original numerical model of the Bay of Fundy (Greenberg, 1976) uses an explicit method, a schematization similar to Fig. 1 and a time step of 30 seconds in prototype time. Because of the particular interests in the Minas Basin, that area was originally schematized with a finer grid than the one shown in Fig. 1. However, the hybrid model of the Cumberland and Shepody Basins does not require this detailed representation of the Minas Basin and therefore the schematization of Fig. 1 could be adopted. As a consequence, the time step could also be increased to 1 minute in prototype time. The execution times which are listed in Table 2 apply to one semi-diurnal cycle of a tide and, the execution times for the explicit model are based on a time step of 1 minute.

Since the original Greenberg model was not run under exactly these conditions, the time for the CDC CYBER 74 (equivalent to a CDC 6600) can only be estimated.

A finite difference implicit model of the Bay of Fundy was tested with 15 minute time step in prototype time. For the particular requirements of the hybrid model, this implicit method is not considered economically justified. At \$1.00 per word for AP data storage, this model is substantially more expensive to implement.

In assessing the results shown in Table 2, one additional factor is the usefulness of an in-house machine for other applications. In buying time on a main-frame machine, the cost involved includes a significant proportion relating to peripheral equipment which may not be required for present purposes. Thus while it is difficult to obtain accurate costs for main frame time, Table 3 shows that the complete array processor/mini-computer package costs less

than \$150 000 - a figure considerably less than the annual expenditure involved with many large model studies.

Table 2
Comparison of Execution Times for Fundy Models

	EXPLICIT MODEL 1 MINUTE TIME STEP 750 STEPS/CYCLE		IMPLICIT MODEL 15 MINUTE TIME STEP 48 STEPS/CYCLE	
	MINUTES	MEMORY	MINUTES	MEMORY
CDC CYBER 74	2 to 2.5			
IBM 3032	5			
HP1000, MOD. 45	75.	60K	128	145K WDS*
AP-120B	2.5	40K WDS**	1.2	40K WDS

* A modification to the algorithm reduced this to 75K WDS

**Considerable memory savings could be achieved with additional programming effort.

Table 3
CAPITAL COST FOR MINI-COMPUTER/AP SYSTEM

(January 1980)

1.	HP1000, MODEL 45 - 128 K WORDS MEMORY	
	- 20 MBYTE DISC,	
	- 2648 VIDEO GRAPHICS TERMINAL	\$45 000.
2.	AP-120B ARRAY PROCESSORS WITH	
	- 3K PROGRAM STORE, - 1K TABLE RAM,	
	- 40K DATA MEMORY (167 ns), - IOP	\$81 130.
	- EXTENDED SOFTWARE	\$ 8 475.
	- AP-FORTRAN COMPILER	\$ 8 500.
		<u>U.S. \$143 105.</u>

8.0 GENERAL REFERENCES

- Funke, E.R. and N.L. Crookshank (1978), "A Hybrid Model of the St. Lawrence River Estuary", Proc. 16th Coastal Engineering Conf., Hamburg.
- Funke, E.R., N.L. Crookshank and M. Wingham (1980), "An Introduction to GEDAP - An Integrated Software System for Experiment Control, Data Acquisition and Data Analysis", Hydraulics Laboratory Technical Report LTR-HY-75, NRC, Ottawa, Canada.
- Greenberg, D.A. (1976), "Mathematical Description of the Bay of Fundy-Gulf of Maine Numerical Model", Technical Note No. 16, Marine Environmental Data Service, Environment Canada, Ottawa.
- Holz, K.P. (1977), "Hybrid Models, A Study on Their Principle and Realization", Proc. 7th Conf. IAHR, Vol. 6, pp. 674-678.

9.0 ARRAY PROCESSOR REFERENCES

- Alexander, P. (1979), "Array Processors", Machine Design, pp. 87-92, August 23, 1979.
- Caspe, R.A. (1978), "Array Processors", Mini-Micro Systems, pp. 54-64 (Comparison of Processors).
- Hufnagel, S.P. (1979), "Comparison of Selected Array Processor Architectures", Computer Design, pp. 151-158, March.
- Strelchun, J. (1979), "Array Processor Responds in Real Time", Electronics, pp. 118-124, August 16, 1979.
- Wiley, P. (1979), "Interfacing Peripherals Directly to an Array Processor", Computer Design, pp. 158-164, August 1979.
- Wittmayer, W.R. (1978), "Array Processor Provides High Throughput Rates", Computer Design, pp. 93-100.

PARAMETER IDENTIFICATION IN ESTUARINE MODELING

Wen-Sen Chu¹ and William W-G. Yeh²

INTRODUCTION

Parameter Identification (PI) algorithm is an optimization procedure that systematically searches the parameters embedded in a mathematical model. These parameters are not measurable from a physical point of view. The optimization is based on the minimization of a selected norm of the differences between the solution of the mathematical model and scattered observations collected from the system.

Parameter identification (or inverse problem) has been studied in groundwater systems extensively for the past decade (15), and it has also drawn many researchers in the fields of open-channel flow and estuarine modeling since 1972 (1,2,9,17). All the past estuarine PI works in the literature are confined to the one-dimensional case, and hydrodynamics and transport equations are treated separately.

This study deals with PI in a two-dimensional vertically-averaged estuarine salinity model. The salinity transport equation is coupled with the hydrodynamics equations. The coupled relationship introduces extra density terms in the hydrodynamics equations, which must be solved simultaneously with the transport equation.

One of the most difficult problems in PI is the collection of needed observations from the system which is being modeled. With limited exception, the currently available data from the prototype estuaries are not adequate for the purposes of developing a PI algorithm. This is usually critical in quantity (the number of stations and/or the period of time) and in quality (noise of data). However, if an operational hydraulic model is available, the data could then be obtained economically and accurately under an ideally controlled environment. The large amount of data that can be collected from a hydraulic model of an estuary will provide a sufficient number of observations and the required initial and boundary conditions for the development of a PI algorithm. The use of the estuary hydraulic model could provide a better source of prototype data than would be available from the real estuary. It will be much easier to distinguish between the inadequacy of the mathematics and the inadequacy of our understanding of the prototype. Thus, it will give us an idea of how well we could expect to mathematically model the real estuary if we had an unlimited amount of prototype data. Additionally, when these types of data are used in PI, parameters can be optimally identified and the mathematical model can then be used conjunctively with the hydraulic model for prototype applications, provided that the mathematical model is consistently formulated. How well a hydraulic model simulates the prototype estuary is not considered in this study.

¹Assistant Professor, Department of Environmental Resources Engineering, Humboldt State University, Arcata, California 95521. (Formerly, Graduate Student, School of Engineering and Applied Science, University of California, Los Angeles, California 90024).

²Professor, School of Engineering and Applied Science, University of California, Los Angeles, California 90024.

A tidally averaged approach is adopted to furnish the mathematical model solutions for the purpose of PI. This particular approach solves the dynamic steady-state conditions of the variables as represented by their time-averaged values. The mathematical model of this type is a boundary-value problem, and it is solved by an implicit-explicit iterative scheme (3,4). The rationale of using a tidally averaged model in PI is based upon the assumption that the parameters to be identified are time-invariant, i.e., the parameters have the same values in the transient and dynamic steady-state conditions.

The Error Function Method (1,4) is used with minimax criterion in the optimization. Error function is linearized so that when it is used with the minimax criterion, the optimization problem can be transformed into a Linear Programming (LP) problem.

TIDALLY AVERAGED APPROACH

In order to formulate the two-dimensional vertically averaged mathematical model (See Figure 1) that approximates the prototype conditions as represented by the fixed-bed hydraulic model, the following transient equations are used (11,12):

$$\frac{\partial u}{\partial t} + u \frac{\partial u}{\partial x} + v \frac{\partial u}{\partial y} + g \frac{\partial \xi}{\partial x} + g \langle i \rangle_x + g \frac{u(u^2 + v^2)^{1/2}}{C^2 H} = 0 \quad (1)$$

$$\frac{\partial v}{\partial t} + u \frac{\partial v}{\partial x} + v \frac{\partial v}{\partial y} + g \frac{\partial \xi}{\partial y} + g \langle i \rangle_y + g \frac{v(u^2 + v^2)^{1/2}}{C^2 H} = 0 \quad (2)$$

$$\frac{\partial \xi}{\partial t} + \frac{\partial (Hu)}{\partial x} + \frac{\partial (Hv)}{\partial y} = 0 \quad (3)$$

$$\frac{\partial (Hs)}{\partial t} + \frac{\partial (Hus)}{\partial x} + \frac{\partial (Hvs)}{\partial y} - \frac{\partial}{\partial x} \left(HD_x \frac{\partial s}{\partial x} \right) - \frac{\partial}{\partial y} \left(HD_y \frac{\partial s}{\partial y} \right) = 0, \quad (4)$$

in which u , v are the velocities in x , y directions; ξ is a tidal elevation with respect to mean sea level h ; $H = \xi + h$; s is salinity; C is the Chezy's coefficient; D_x and D_y are the dispersion coefficients; g is gravitational acceleration; and $\langle i \rangle_x$ and $\langle i \rangle_y$ are the density slope terms induced by salinity. The density terms can be represented in English unit system by (12, 14):

$$\langle i \rangle_x = \frac{1.94 \times 10^{-3}}{1.94 + 1.94 \times 10^{-3} \sigma_t} \frac{\partial \sigma_t}{\partial x} \cdot \frac{H}{2} \quad (5)$$

$$\langle i \rangle_y = \frac{1.94 \times 10^{-3}}{1.94 + 1.94 \times 10^{-3} \sigma_t} \frac{\partial \sigma_t}{\partial y} \cdot \frac{H}{2} \quad (6)$$

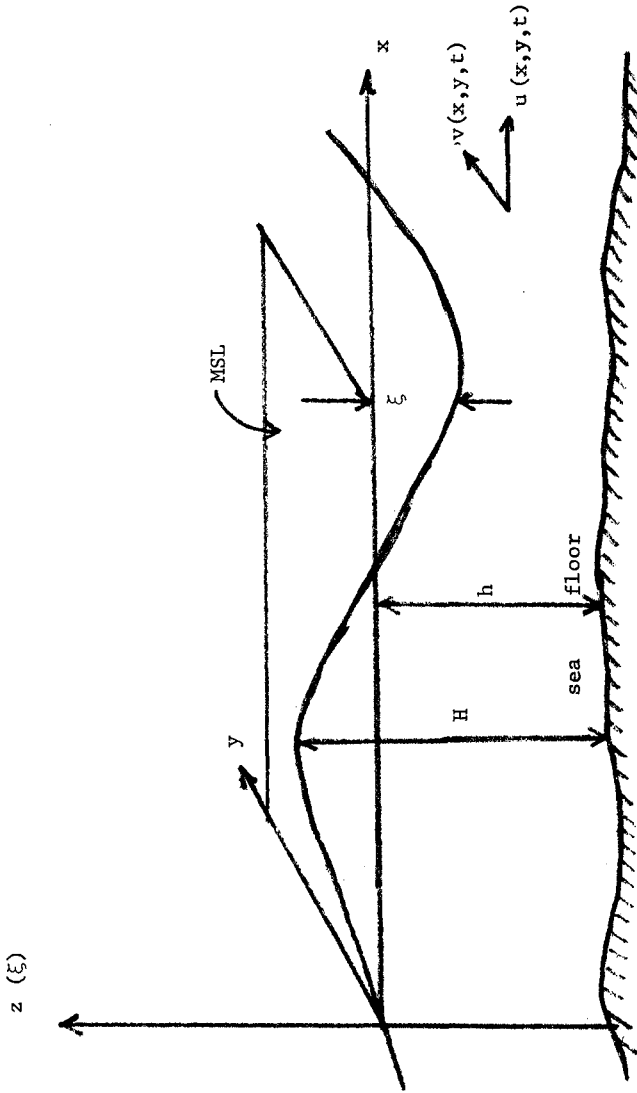


Fig. 1.- Two-Dimensional Estuarine Coordinate System

in which σ_t is the oceanographical sigma-tee function whose values depend upon salinity and temperature.

Coriolis force and wind stress are not included in Eqs. (1) and (2) to conform with the hydraulic model conditions.

For the purpose of this study, the following equation is used for Chezy's C:

$$C = \sqrt{2g/f} \quad , \quad (7)$$

in which f is the Darcy's roughness coefficient, which can be assumed to be time-invariant (5).

Using previous findings (8,10,11), the dispersion coefficients can be written as:

$$D_x = DCX \cdot H \cdot |u| \cdot g^{1/2} \cdot C^{-1} \quad (8)$$

$$D_y = DCY \cdot H \cdot |v| \cdot g^{1/2} \cdot C^{-1} \quad , \quad (9)$$

in which DCX and DCY are assumed to be constants representing the characteristics of the particular estuary; and $|u|$, $|v|$ are the velocities in x and y directions.

When the boundary conditions of the transient model can be assumed to be periodic, all transient variables will reach a dynamic steady-state after a long period of time. These dynamic steady-state variables are constant over time when they are averaged over the period. They are defined as tidally averaged variables when the period used is a tidal cycle.

When Eqs. (1) to (9) are tidally averaged, they can be written as (3,4):

$$U \frac{\partial U}{\partial x} + v \frac{\partial U}{\partial y} + g \frac{\partial \hat{\xi}}{\partial x} + g \langle \bar{i} \rangle_x + g \frac{U(U^2+V^2)^{1/2}}{C^2 H} = 0 \quad (10)$$

$$U \frac{\partial V}{\partial x} + v \frac{\partial V}{\partial y} + g \frac{\partial \hat{\xi}}{\partial y} + g \langle \bar{i} \rangle_y + g \frac{V(U^2+V^2)^{1/2}}{C^2 H} = 0 \quad (11)$$

$$\frac{\partial (\bar{H}U)}{\partial x} + \frac{\partial (\bar{H}V)}{\partial y} = 0 \quad (12)$$

$$\frac{\partial}{\partial x} (\bar{H}US) + \frac{\partial}{\partial y} (\bar{H}VS) - \frac{\partial}{\partial x} \left(\bar{H}D_x \frac{\partial S}{\partial x} \right) - \frac{\partial}{\partial y} \left(\bar{H}D_y \frac{\partial S}{\partial y} \right) = 0, \quad (13)$$

and,

$$\langle \bar{i} \rangle_x = \frac{1.94 \times 10^{-3}}{1.94 + 1.94 \times 10^{-3} \sigma_t} \frac{\partial}{\partial x} \sigma_t \cdot \bar{H} \quad (14)$$

$$\langle i \rangle_y = \frac{1.94 \times 10^{-3}}{1.94 + 1.94 \times 10^{-3} \bar{\sigma}_t} \frac{\partial \bar{\sigma}_t}{\partial y} \cdot \frac{\bar{H}}{2} \quad (15)$$

$$C = \sqrt{2g/f} \quad (16)$$

$$\bar{D}_x = DCX \cdot \bar{H} \cdot |U| \cdot g^{1/2} \cdot C^{-1} \quad (17)$$

$$\bar{D}_y = DCY \cdot \bar{H} \cdot |V| \cdot g^{1/2} \cdot C^{-1}, \quad (18)$$

in which U , V , $\hat{\xi}$, S , $\langle i \rangle$ are the tidally averaged values of u , v , ξ , s , $\langle i \rangle$; and \bar{H} is equal to $h + \hat{\xi}$. The detailed mathematics of this approach are given by Chu and Yeh (3) and Chu (4) which will not be included here. The key assumption for the averaging process is that all the transient variables have small amplitudes in time. The concept of the averaging process is similar to the one that was used in vertical averaging by Leendertse (11).

The parameters to be identified in the above tidally averaged model are the Darcy's roughness coefficient f , and the two dispersion constants DCX and DCY . The parameters, by the previous assumptions, will have the same values in both the transient and the tidally averaged models.

The distinct advantage of using the tidally averaged approach, despite the above-mentioned assumptions, is the saving of computing cost. If a transient model is used for PI, long term integration is likely to be required to generate solutions that are commensurate with observations. Since most of the identification schemes require an iterative search process, such long term integration can easily discourage the modelers' desire for PI, let alone their concerns over the accumulated errors generated by such extended runs.

Equations (10) through (18) are solved by an implicit-explicit, alternating direction, iterative finite difference scheme developed by Chu and Yeh (3). The method is conceptually similar to the multi-operational, implicit-explicit scheme by Leendertse for the transient problem (11). Instead of integrating in time, an acceleration parameter is used for each iteration. The convergence of the proposed scheme is fairly rapid for hydrodynamics and slow for salinity transport. Since its development, the algorithm has been numerically verified through a series of test problems (3,4). These test problems include various initial and boundary conditions. The results showed that the numerical model is applicable to any two-dimensional estuarine problem. Detailed computational aspects of the scheme are given in Chu and Yeh (3) and Chu (4) and they will not be covered here.

PARAMETER IDENTIFICATION ALGORITHM

The selected norm for this study is the minimax criterion, which minimizes the absolute value of the maximum error among all observation stations in the domain. Mathematically, it is to

$$\min_{\vec{D}} \max_{1 \leq i \leq M} \sum_{k=1}^L |w_{ik} \epsilon_{ik}|, \quad (19)$$

in which \vec{D} represents the parameter vector in the model; and ϵ_{ik} is the error at station i of the k th variable which is collected as observation. Equation (19) implies that all k variables are observed at the same stations, $i = 1, \dots, M$. w_{ik} in Equation (19) is a weighting factor. These weighting factors are necessary to reflect widely differing numerical values and units.

If tidal elevations and salinities are available at stations $i = 1, \dots, M$, we can rewrite Equation (19) as:

$$\min_{\vec{D}} \max_{1 \leq i \leq M} \left\{ |w_{i1} \epsilon_i| + |w_{i2} \eta_i| \right\} \quad (20)$$

$$\epsilon_i = \hat{\xi}_i - \xi_i^* \quad (21)$$

$$\eta_i = S_i - S_i^* \quad (22)$$

in which $\hat{\xi}^*$ and S^* are the observations.

In this study, ϵ_i and η_i are assumed to be functions of the parameters only; i.e., it is assumed that the differences between the model solutions and the observations are due to incorrect quantification of the model parameters. Given this assumption, error function can be written in vector notation as:

$$\vec{\epsilon}(\vec{D}) = (\epsilon_1(\vec{D}), \dots, \epsilon_M(\vec{D})). \quad (23)$$

$$\vec{\eta}(\vec{D}) = (\eta_1(\vec{D}), \dots, \eta_M(\vec{D})). \quad (24)$$

The parameter vector \vec{D} can be written as $\vec{D} = (\vec{F}, DCX, DCY)$, in which DCX and DCY are assumed to be pure constants.

By Taylor's theorem, Equations (23) and (24) can be expanded at some initially estimated parameters \vec{D}^0 as

$$\vec{\epsilon}^1(\vec{D}^1) = \vec{\epsilon}^0(\vec{D}^0) + J(\vec{\epsilon}^0, \vec{D}^0)(\vec{D}^1 - \vec{D}^0) + \text{H.O.T.}, \quad (25)$$

$$\vec{\eta}^1(\vec{D}^1) = \vec{\eta}^0(\vec{D}^0) + J(\vec{\eta}^0, \vec{D}^0)(\vec{D}^1 - \vec{D}^0) + \text{H.O.T.}, \quad (26)$$

in which the superscript 1 represents the new estimates; H.O.T. are the higher order terms; and $J(,)$ is the Jacobian matrix.

When H.O.T. are dropped, Equations (25) and (26) become linear with the Jacobian being approximated by finite difference. The finite difference version of the Jacobian is referred to by Becker and Yeh (1) as the Influence Coefficient Matrix.

After transforming Equation (20) to a linear objective function, the optimization problem becomes a linear programming problem. Physical constraints representing parameter lower and upper bounds can be imposed for optimization to ensure realistic solutions.

The solutions of the LP will provide the minimized error and a set of new parameters \hat{D}^1 . These new parameters then become the initial estimates for the next iteration. The algorithm continues until the convergence criteria are satisfied. Two types of convergence criteria are proposed in this method; they are 1) stop when $|J^K| < \delta_1$, and 2) stop when $|J^{K+1} - J^K| < \delta_2$, in which J^K is the objective value of the LP solution at the Kth iteration, and δ_1 and δ_2 are two arbitrarily selected small constants.

The most important merit of the proposed method is that it is independent of the mathematical model, and it can be implemented and solved efficiently in any modern computer facility where packaged routines are available for linear programming problems.

NUMERICAL EXAMPLE

Suisun Bay in California was selected for this study (see Figure 2). Tidal elevations and salinities were obtained in the Suisun Bay portion of the San Francisco Bay - Delta Hydraulic Model in Sausalito, California (13). The finite difference schematization of Suisun Bay is shown along with the installed observation stations in Figure 3. Bathymetric schematization was obtained according to the actual blueprints for the construction of the model (13).

The first PI attempt assumes that all the unknown parameters are constant valued in the domain. The physical bounds set for the parameters are: 1) $0.01 < f < 0.1$ (which corresponds to the Chezy's C values between 25 ft $^{1/2}$ /sec and 80 ft $^{1/2}$ /sec), 2) $1000 < DCX < 7000$, and 3) $1000 < DCY < 5000$. These physical bounds are determined not only by the physical laws but also by computational experience through sensitivity analyses of the parameter values. For example, through various test runs, it was determined that the dispersion constants DCX and DCY would have to be enlarged in order to "reflect" the boundary salinities toward the interior of the domain.

The PI algorithm started with a set of initial estimates of: 1) $f^0 = 0.05$, 2) $DCX^0 = 3500$, and 3) $DCY^0 = 3000$. The computed solutions using the estimated parameters are compared with the observations in Table 1. The convergence property of this run is shown in Table 2.

The second attempt of the PI is much more refined. The roughness coefficient is assumed to be spatially distributed in Suisun Bay. The dispersion constants remain constant valued because of their insensitivity in the model simulations.

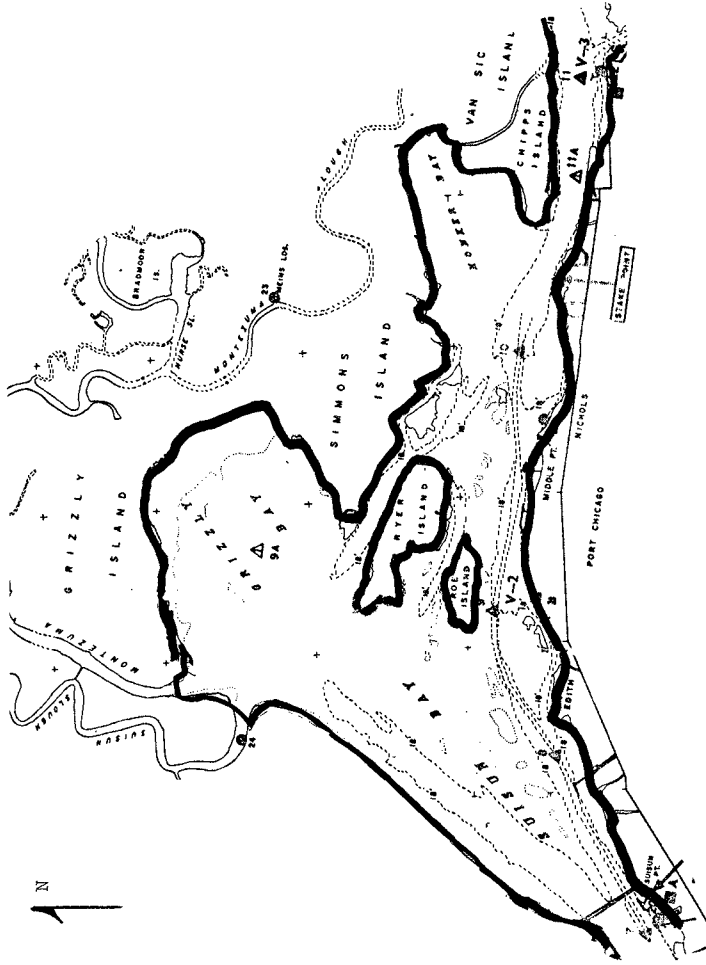


Fig 2. Map of Suisun Bay. (Courtesy of U.S. Army Corps of Engineers, San Francisco District.)

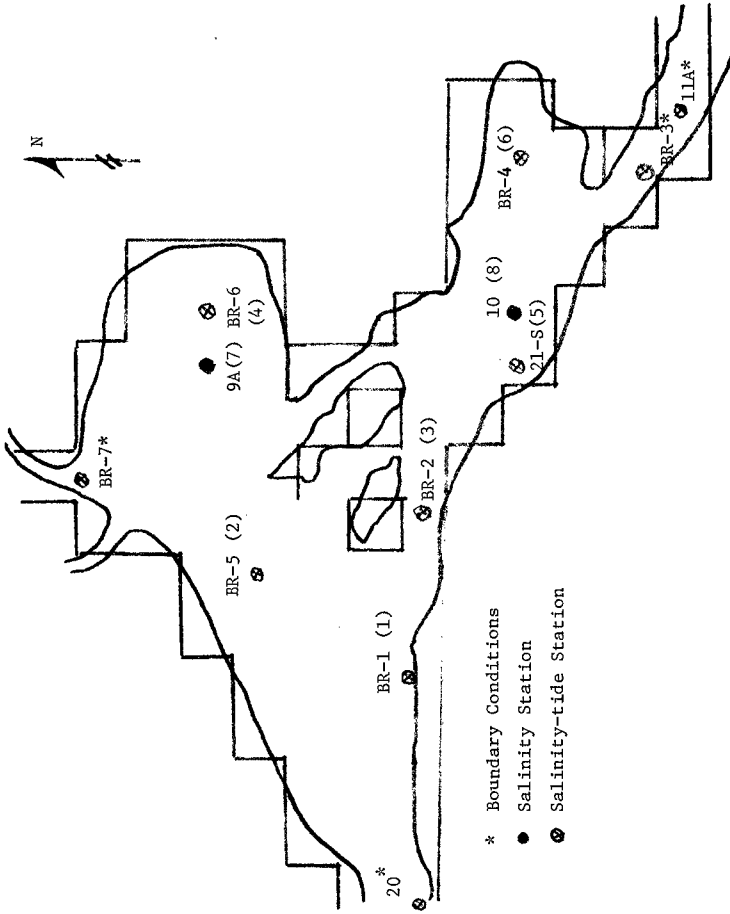


Fig. 3-Finite Difference Schematization and Observation Stations in Suisun Bay

TABLE I.- Summary of Computational Results
(Lumped Parameter Case⁴)

Station No.	Obs. $\frac{\Delta \xi}{\xi}$	Comp. $\frac{\Delta \xi}{\xi}$	Obs. S^3	Comp. S^3	ϵ^2	η^2
1	0.27	0.17	11.09	9.29		
2	0.32	0.19	7.99	6.92		
3	0.23	0.20	8.45	6.40		
4	0.41	0.21	5.40	7.05	0.19	1.74
5	0.29	0.25	5.0	3.56		
6	0.40	0.27	3.2	3.15		

- 1 $\frac{\Delta \xi}{\xi}$ is net tide in ft.
- 2 Minimized maximum errors
- 3 S is tidally averaged salinity in ppt
- 4 Optimal parameters: $f = 0.06$ ($C = 32 \text{ ft}^{1/2}/\text{sec}$)
 $DCX = 7000.$
 $DCY = 5000.$

Boundary conditions used for parameter identification (calibration):

Ocean boundary: $\frac{\Delta \xi}{\xi} = 0.12 \text{ ft}$
 $S = 13.71 \text{ ppt}$

Fresh Water Inflows: U (Sacramento River) = -0.34 ft/sec
 S (Sacramento River) = 2.5 ppt
 V (Montezuma Slough) = -0.1 ft/sec
 S (Montezuma Slough) = 5.68 ppt

TABLE 2. - Summary of Successive Approximations
(Lumped Parameter Case)

<u>Iteration</u>	<u>f</u>	<u>DCX</u> ($\times 10^{-3}$)	<u>DCY</u> ($\times 10^{-3}$)	<u>J</u>
0	0.05	3.5	3.0	4.85
1	0.07	7.0	4.5	2.00
2	0.10	5.3	5.0	1.95
3	0.06	7.0	5.0	1.94

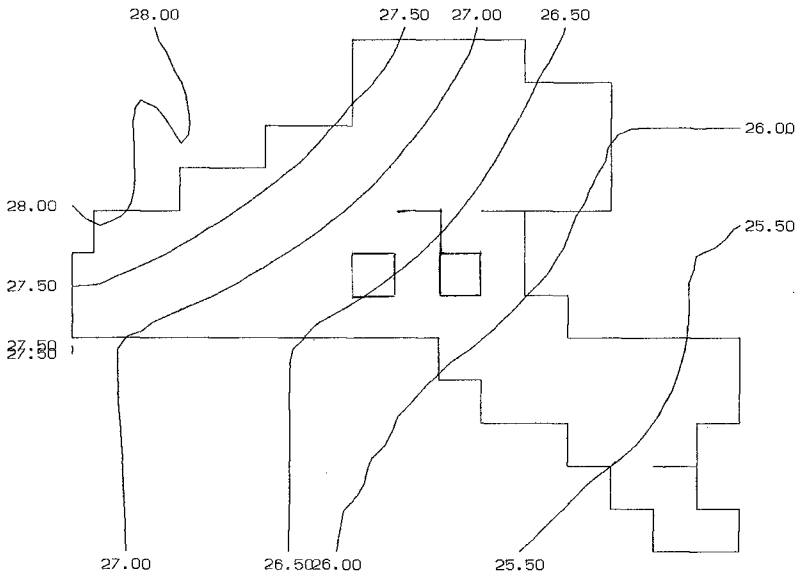


Figure 4. Spatial Distribution of Chezy's C.

Given the above proposed distributed parameter assumption, the PI algorithm would have to identify roughness coefficient at all nodal points. This is such a large task that it is almost impossible to accomplish with the fastest computer available. Furthermore, parameter values between the nodes show discontinuities which do not have any physical meaning. This difficulty has been resolved with the help of the finite element concept by Yeh and Yoon (16) and Yoon and Yeh (18) in PI problems of groundwater flow.

It appears that roughness parameter space in Suisun Bay can be adequately represented by the four corner nodes with bilinear basis functions (4,16). Mathematically, it is

$$f(x,y) = \sum_{i=1}^4 f_i \phi_i(x,y), \quad (27)$$

in which f_i 's are the corner nodal values; and ϕ_i 's are the bilinear basis functions. With Equation (27), the parameter values in any grid point of Suisun Bay could be calculated given nodal values of f_i 's. The algorithm is then to identify the four nodal values (f_i 's) instead of searching through all the grid points.

The physical bounds and the initial estimates for the parameters remained the same in this run. The algorithm converged in eight iterations. The optimally estimated roughness parameters vary from 0.07 to 0.1, which correspond to the Chezy's values of 25 ft ^{1/2}/sec to 30 ft ^{1/2}/sec. The distributed values as estimated by the PI algorithm are shown in Figure 4. The optimal dispersion constants converged to be at 7000 and 1000. The computed solutions using the optimal parameters are compared with the observations in Table 3. The convergence property of this run is shown in Table 4.

To validate the results of calibration, the optimized parameters were used as input data along with a different set of boundary conditions, which were consistent with the experimental set up, in the tidally averaged numerical model to produce solutions. These solutions were compared with the experimental data taken from the San Francisco Bay-Delta Hydraulic Model. The boundary conditions (fresh water inflow and tide) used in the verification and the corresponding experiment were different from the boundary conditions used in the calibration.

Since there is no significant difference in results between the lumped parameter and distributed parameter approach (see Tables 1 and 3), the lumped parameters were used for verification. The verification run started with a set of initial conditions (identical to the ones used in calibration), boundary conditions, and the optimized parameters which are: 1) $f = 0.06$, 2) $DCX = 7000$, and 3) $DCY = 5000$ (see Table 1). The verification results and the boundary conditions used are presented in Table 5.

DISCUSSION AND CONCLUSION

Although the tidally averaged numerical model can save a signifi-

Table 3. Summary of Computational Results
(Distributed Parameter Case⁴)

Station	Obs. $\hat{\xi}^1$	Comp. $\hat{\xi}^1$	Obs. S^3	Comp. S^3	ε^2	η^2
1	0.27	0.17	11.09	9.71		
2	0.32	0.19	7.99	7.37		
3	0.23	0.20	8.45	6.95		
4	0.41	0.23	5.40	7.35	0.18	1.45
5	0.29	0.27	5.00	3.86		
6	0.40	0.30	3.20	3.33		
7	-	-	5.49	6.33		
8	-	-	4.39	3.66		

1 $\hat{\xi}$ is net tide in ft.

2 Minimized maximum errors

3 S is tidally averaged salinity in ppt.

4 Optimum parameters:

$$f \text{ in nodal values } \left\{ \begin{array}{ll} f_1 = 0.07 & C_1 = 30 \text{ ft }^{1/2}/\text{sec} \\ f_2 = 0.10 & C_2 = 25 \text{ ft }^{1/2}/\text{sec} \\ f_3 = 0.10 & C_3 = 25 \text{ ft }^{1/2}/\text{sec} \\ f_4 = 0.10 & C_4 = 25 \text{ ft }^{1/2}/\text{sec} \end{array} \right.$$

DCX = 7000.

DCY = 1000.

TABLE 4. - Summary of Successive Approximation
(Distributed Parameter Case)

Iteration	f_1	f_2	f_3	f_4	DCX ($\times 10^{-3}$)	DCY ($\times 10^{-3}$)	J
0	0.05	0.05	0.05	0.05	3.5	3.0	4.85
1	0.05	0.01	0.10	0.08	7.0	5.0	2.02
2	0.06	0.10	0.10	0.10	7.0	5.0	1.73
3	0.07	0.01	0.10	0.01	7.0	5.0	1.90
4	0.07	0.10	0.10	0.10	7.0	1.0	1.52

Table 5. Results of Steady-State Model Verification

Station No.	Obs. ξ^1	Comp. ξ^1	Obs. S^2	Comp. S^2
1	0.09	0.04	16.89	14.81
2	0.06	0.04	13.95	12.41
3	0.10	0.06	14.81	11.86
4	0.26	0.08	11.77	10.62
5	0.15	0.11	11.60	9.28
6	0.28	0.13	9.39	8.99

Boundary conditions used for verification:

Ocean boundary: $\xi = -0.01$ ft

$S = 19.31$ ppt

Fresh water inflows: U (Sacramento River) = -0.33 ft/sec

S (Sacramento River) = 8.34 ppt

V (Montezuma Slough) = -0.01 ft/sec

S (Montezuma Slough) = 12.19 ppt

1 net tide in feet

2 tidally average salinity in ppt.

cant amount of computing time in PI, the convergence of the solution scheme is still slow; especially when the transport equation is coupled with the hydrodynamics. The solutions of hydrodynamics alone will usually converge within 200 iterations with variable acceleration parameters (3,4). Nevertheless, when salinity transport equation is calculated with hydrodynamics, the algorithm will typically require 400 iterations to converge. The convergence of salinity values depends on the corresponding hydrodynamics. When the magnitudes of hydrodynamics (velocities and tides) are small, the convergence property of salinities is also influenced by the initial conditions of salinity (3,4). This particular computational problem is solved by a series of semi-heuristic rules that are determined from the computational experience (4).

When the transient numerical model is simulated, the outputs of the model are generally insensitive to different values of dispersion constants (DCX, DCY). In one particular simulation for example, two sets of dispersion constants which differed in value as great as 100 times produced only 1 to 5% changes in salinities in ten tidal cycles. Nevertheless, when tidally averaged numerical model is simulated with the true boundary values collected from the hydraulic model, it was found that the dispersion constants would have to be enlarged in order to "reflect" the ocean boundary salinities toward the interior of the domain. One of the conceivable reasons for this phenomenon is the strong net outflow from the delta to the ocean. This limited increase of the internal salinity values in the domain in tidally averaged numerical model is due to the inherent nature of the boundary value problems (Eqs. 10 to 14). Other factors that may cause the inflation of the dispersion constants include: the finite difference schematization, the vertical averaging, the tidal averaging, and the various model approximations.

The proposed PI algorithm is independent of the numerical model by virtue of the error function approach. By the definition of error function and the problem formulations, the identification algorithm can be programmed separately from the numerical model. In other words, the method can be easily implemented with any numerical model for PI purposes, provided that enough data are available.

The calibration and verification of the tidally averaged numerical model have been successfully performed. In both attempts, the maximum deviations between the model results and field observations came from the particular station in Grizzly Bay. In the schematization of the entire study area, the inflow from Suisun Slough which is next to Montezuma Slough was ignored. The performance of the mathematical model depends not only on its parameter values, but also on the schematizations. Other important factors that could contribute the discrepancies include noises in observations and errors in data processing of boundary conditions and observations (4).

In each iteration of PI, the numerical model has to be solved once for each parameter in order to generate the influence coefficient matrix. In the lumped parameter approach, (three constant parameters for the entire domain), it took three iterations for the PI scheme to converge. (The numerical models had been solved by $3 \times 3 + 3 = 12$ times.) This lumped parameter PI case used 20 minutes of IBM 360/91 computing time at a cost of \$150 dollars.

ACKNOWLEDGMENTS

The research leading to this report was supported by the OFFICE OF WATER RESEARCH AND TECHNOLOGY, USDI, under the Matching Grant program of Public Law 88-379, as amended, and by the University of California Water Resources Center, as part of Office of Water Research and Technology Project No. B-191-CAL and Water Resources Center Project UCAL-WRC-W-530. The writers wish to thank Shiao-Kung Liu, Leonard Becker, Young S. Yoon for their helpful suggestions and discussions. The continued support and encouragement of Donald Herbert and Richard Kristof is gratefully acknowledged.

REFERENCES

1. Becker, L. and Yeh, W. W-G., "Identification of Parameters in Unsteady Open-Channel Flows," Water Resources Research, Vol. 8, No. 4, August 1972, pp.956-965.
2. Bennett, J. P., "Calibration of Branched Estuary Models," Proceedings of the Fifteenth International Conference on Coastal Engineering, American Society of Civil Engineers, Vol. 3, 1976, pp.3416-3434.
3. Chu, W-S. and Yeh, W. W-G., "Two Dimensional Tidally Averaged Estuarine Model," Journal of the Hydraulics Division, ASCE, Vol. 106, No. HY4, April, 1980, pp 501-518.
4. Chu, W-S., "Parameter Identification of Two-Dimensional Estuarine Model," dissertation presented to the University of California at Los Angeles, California in 1979, in partial fulfillment of the requirements for the degree of Doctor of Philosophy.
5. Daily, J. W. and Harleman, D. R. F., Fluid Dynamics, Addison-Wesley Inc., Reading, Mass., 1966, pp.297-298.
6. Davidson, B., Vichnevetsky, R., and Wang, H. T., "Numerical Techniques for Estimating Best-Distributed Manning's Roughness Coefficients for Open Estuarial Systems," Water Resources Research, Vol. 14, No. 5, October 1978, pp 777-789.
7. Dronkers, J. J., "Tidal Theory and Computations," Advances in Hydroscience, V. T. Chow, Ed., Vol. 10, Academic Press, Inc., New York, N. Y., 1975.
8. Fischer, H. B., "Analytical and Numerical Methods for Predicting Dispersion Coefficients in Natural Stream," Professional Paper 582-A, United States Geological Survey, Washington, D.C., 1968.

9. Fread, D. L. and Smith, G. F., "Calibration Technique for 1-D Unsteady Flow Models," Journal of the Hydraulic Division, ASCE, Vol. 104, No. HY7, Proc. Paper 13892, July 1978, pp.1027-1044.
10. Holley, E., "Unified View of Diffusion and Dispersion," Journal of the Hydraulics Division, ASCE, Vol. 95, No. HY2, Proc. Paper 6462, March 1969, pp.621-631.
11. Leendertse, J. J., "Water Quality Model for Well-Mixed Estuaries and Coastal Seas, Vol. I, Principles of Computation," RM-6230-RC, Rand Corporation, Santa Monica, California, 1970.
12. Pritchard, D. W., "Two-Dimensional Model," Chapter II of Estuarine Modeling: An Assessment, Ward, G. H. and Espey, W. H., Ed., TRACOR, Inc., Austin, Texas, February 1971, pp.22-33.
13. U. S. Army Corps of Engineers, "San Francisco Bay - Delta Model, Technical Memo No. 1," San Francisco District, San Francisco, California, June 1976.
14. U. S. Naval Oceanographic Office, Handbook of Oceanographic Office, Bialek, E. I. Compiled, Special Publication No. SP-68, Washington, D. C., 1966.
15. Yeh, W. W-G., "Aquifer Parameter Identification," Journal of the Hydraulics Division, ASCE, Vol. 101, No. HY9, Proc. Paper 11582, September 1975, pp.1197-1209.
16. Yeh, W. W-C. and Yoon, Y. S., "A Systematic Optimization Procedure for the Identification of Inhomogeneous Aquifer Parameters," Proceedings of the Symposium on Advances in Groundwater Hydrology, American Water Resources Association, September 1976, pp.72-82.
17. Yih, S-M, and Davidson, B., "Identification in Nonlinear, Distributed Parameter Water Quality Models," Water Resources Research, Vol. 11, No. 5, October 1975, pp.693-704.
18. Yoon, Y. S. and Yeh, W. W-C., "Parameter Identification in an Inhomogeneous Medium with Finite Element Method," Society of Petroleum Engineering Journal, AIME, August 1976, pp. 217-226.

AUTOMATIC CALIBRATION OF NUMERICAL TIDAL MODELS

K.-P. Holz

Professor, Chair of Fluid Mechanics,
Hannover University,
Federal Republic of Germany

and

U. Januszewski

Dr.-Ing., Gew. Brigitta Elwerath, Hannover,
Federal Republic of Germany

1. Introduction

Numerical models for the simulation of tidal waves in estuaries have become a standard tool of coastal engineers. Before they can be applied to practical problems, they have to be calibrated against nature. The basis for calibration is normally a representative set of tidal curves (natural field data), which has to be reproduced by the numerical model. Generally, the calibration is performed by empirically tuning certain parameters, until a fairly good agreement between measured and calculated quantities is obtained. In most cases, this is a "trial-and-error" process which may become very time-consuming, and which strongly depends on the intuition and experience of the user.

In order to make the process of calibration more effective, and to ensure that the best possible agreement between nature and numerical model is achieved, a calibration method has been developed to determine the parameters of the numerical model automatically by means of a mathematical method of optimization. The method is applied to a one-dimensional numerical model of the Elbe River.

2. Numerical Model

For the numerical river model, the common assumptions of vertically and horizontally averaged velocities, and of hydrostatic pressure distribution are made. The basic equations are derived from the conservative principles for momentum

$$\int \left(\frac{1}{gA} \frac{\partial Q}{\partial t} + \frac{1}{g} \frac{Q}{A^2} \left(\alpha + \frac{b_s}{b} \right) + \left(1 - \frac{\alpha}{g} \frac{Q^2}{A^3} b_s \right) \frac{\partial h}{\partial s} - I_s + I_v \right) ds = 0 \quad (1)$$

and for mass

$$\int \left(b \frac{\partial h}{\partial t} + \frac{\partial Q}{\partial s} \right) ds = 0 \quad (2)$$

where A stands for the stream area, b_s for the stream width, and b for the top width. s is the space coordinate along the river axis, Q the flux in this direction, and h gives the variation of the free surface.

The quantity I_s stands for the bottom slope, I_v for the friction losses, and α is a velocity coefficient.

These integral formulations are integrated directly. Adopting a finite element concept, and using linear trial functions in space and time for the description of the water level h and the flux Q , an implicit formulation of second order accuracy is obtained. The scheme is identical with that proposed by Preissmann (1960), and can alternatively be derived from a finite difference formulation for a finite control scheme. An analysis of the numerical properties of this scheme was presented by Evans (1977).

The numerical model was applied to the Elbe river, covering its tide-influenced length of 139.1 km from the North Sea (Cuxhaven) to Hamburg (St. Pauli) and further upstream to Geesthacht (Fig. 1). The model had to take into account islands and banks. For the discretization an average element length of about 1 km was chosen. A rather high resolution of the topography was thus obtained.

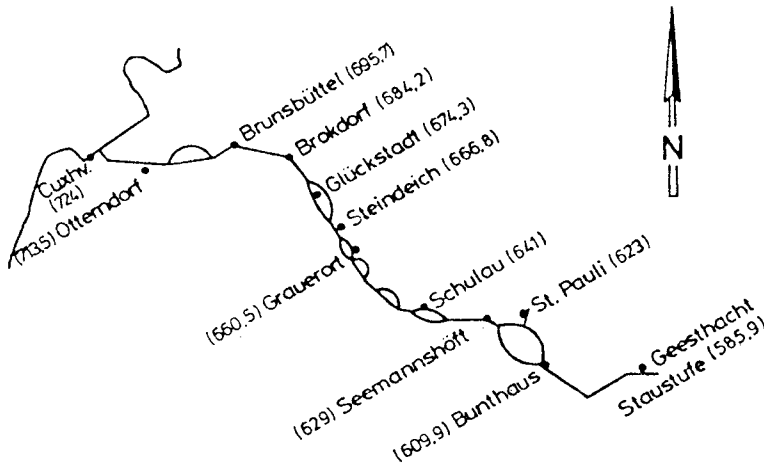


Fig. 1: One-dimensional Elbe model

For the description of bottom friction, the Taylor formulation

$$I_v = \frac{r|v|v}{g h} \quad (3)$$

was used, r is the friction parameter.

3. "Trial-and-Error" Calibration

The numerical model calculates the time-dependent variation of the free surface, and the water flux along the river. The calculated values depend

on a chosen set of friction parameters. They have to be determined from a calibration of the model, which aims at hindcasting some typical measured states in nature. Normally the calibration is performed with respect to a set of tidal curves only, since data on velocities are more difficult to get. During the process of calibration, the friction parameters are varied empirically until a fairly good agreement between calculated and measured data is obtained. So the calibration is actually performed in a "trial-and-error" manner. In each iterative step, the "degree of agreement" between computed and measured data should be determined according to some analytic criteria. This can be done efficiently on the computer only, unless the criteria for the calibration are strongly simplified.

The really crucial point of any "trial-and-error" calibration, however, is the estimate of a new parameter set for the next iteration step. It is difficult to make a good guess, due to the non-linearity of the numerical model. The model user needs a good deal of experience and intuition. In order to overcome this drawback, an automatic calibration method (Januszewski, 1980) was developed, based on the theory of mathematical optimization. This method is independent of any user's "feeling" and determines an optimal parameter set in accordance with any user-defined criteria and error bounds.

4. Optimized Calibration

The strategy for an automatic and optimal determination of friction parameters leads to a closed optimization system which is shown in Fig. 2. The numerical model is the basic element of this system. In the later application on the Elbe river, a numerical model will be used, for which the initial and boundary conditions z_o and z_R must be prescribed.

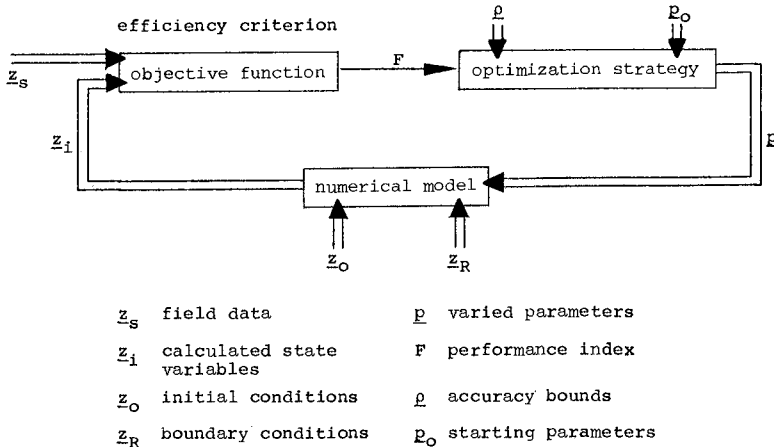


Fig. 2: Strategy for Optimized Calibration

\underline{z} is the vector of state variables which are the free surface and the fluxes or velocities at any cross-section. These quantities are either computed by the numerical model, giving the vector \underline{z}_1 , or measured in the field, and then giving the vector \underline{z}_2 . The computed vector \underline{z}_1 depends on the parameter vector \underline{p} which contains the friction parameters.

In the closed calibration loop an initial parameter set \underline{p}_0 has to be chosen as input for the numerical model, which calculates the vector \underline{z}_1 . This vector has to be compared with the corresponding field data set in \underline{z}_2 . For the Elbe model, this comparison was made for the water levels, as they were the only available field data. The analytic criterion, in accordance to which the comparison is being made, and the definition of which is open to the model user, is called the objective function. The comparison between calculated and measured state variables results in a scalar quantity, the performance index F . This is a measure for the agreement achieved between measured and calculated values.

The performance index is now the input for the optimization strategy, which generates a new set of parameters. This new parameter vector \underline{p} is the output of the optimization strategy and in turn the input for a second cycle of the closed optimization system.

The iteration stops following a convergence test which is made during each cycle just before a new parameter set is calculated. For this test, the model user has to define the wanted accuracy bound ρ , according to which three tests are made:

a comparison of the actual values and those of the preceding iteration step, for all elements of the parameter vector \underline{p}

$$p_v - p_{v-1} \leq \epsilon \quad (4)$$

a test on the achieved improvement of the performance index F

$$|F_v - F_{v-1}| \leq \eta_1 \quad (5)$$

and a test on the performance index itself

$$F \leq \eta_2 \quad (6)$$

Calibration is completely automatized in the outlined closed loop. The model user influences the calibration run only by specifying the error bounds, and by defining the objective function. So he is still controlling the physics of the calibration, but has got rid of a lot of manual work.

4.1 Objective Function

The objective function describes the error between calculated and measured data. It should define a scalar non-negative quantity, the performance index F , which depends on the parameter set \underline{p} . The optimal parameter set \underline{p} is obtained when the error between computed and measured data is minimized. The obtained minimum should be a global one.

For the application to the Elbe model, the objective function was defined as the sum of the squares of the differences between measured and calculated state values taken at all time steps for the tidal period and at

all locations for which field data were given.

$$F(\underline{p}) = \int_{t_0}^{t_1} (\underline{z}_s(t) - \underline{z}_i(t, \underline{p}))^T (\underline{z}_s(t) - \underline{z}_i(t, \underline{p})) dt \quad (7)$$

The advantage of this formulation lies in the fact that the differences over the total time of the tidal period are equally weighted, i.e. the differences are minimized with respect to phase and amplitude.

In order to find the optimal parameter vector \underline{p} , the objective function has to be differentiated with respect to all components of the vector \underline{p} .

$$\left. \frac{\partial F(\underline{p})}{\partial p_j} \right|_{\underline{p}=\underline{p}^*} = 2 \int_{t_0}^{t_1} (\underline{z}_s - \underline{z}_i)^T \left. \frac{\partial \underline{z}_i}{\partial p_j} \right|_{\underline{p}=\underline{p}^*} dt = 0, \quad 1 \leq j \leq n \quad (8)$$

A minimum for $F(\underline{p})$, at least in a local sense is obtained, when the derivative is equal to zero. The parameter vector \underline{p}^* corresponds to $\min F(\underline{p})$. This condition is fulfilled in three cases.

- 1) The derivative of computed state values

$$\frac{\partial \underline{z}_i}{\partial p_j}$$

is independent of the friction parameters, which means that the problem is not correctly posed.

- 2) The product

$$(\underline{z}_s - \underline{z}_i)^T \frac{\partial \underline{z}_i}{\partial p_j}$$

is equal to zero, which means that both functions $(\underline{z}_s - \underline{z}_i)$ and $\frac{\partial \underline{z}_i}{\partial p_j}$ are orthogonal, and thus independent of each other.

This result is meaningless.

- 3) The deviation $(\underline{z}_s - \underline{z}_i)$ is equal to zero. This is exactly the desired result for a perfect calibration.

The first derivative, however, does only give a necessary condition for a local minimum. A global minimum is obtained, if the second derivative is positive - semi-definite. This can be shown for each iteration step, as long as the objective function is based on an error-squared formulation.

The numerical model is integrated for discrete steps in the time domain, and thus the objective function too has to be formulated in a discrete manner.

$$F(\underline{p}) = \sum_{k=1}^{T_{\max}} (\underline{z}_s - \underline{z}_{i,k}(\underline{p}))^T \underline{A} (\underline{z}_s - \underline{z}_{i,k}(\underline{p})) \quad (9)$$

To this formulation, a symmetric matrix \underline{A} is added, which allows for an arbitrary weighting of different elements of the error vector $(\underline{z}_s - \underline{z}_i)$.

Depending on the model user's experience and on the application he has in mind, it is also possible to use other objective functions. For the Elbe model

computations, the correlation coefficient $r_{j,si}$ was alternatively introduced:

$$F(\underline{p}) = \sum_{j=1}^N (1 - r_{j,si}) \quad (10)$$

which is based on an error-squared formulation, too. Other statistical measures can also be used.

The error computation must refer to all the tidal curves, as in the case of the Elbe model. It can be extended to include the velocities, too, or it can be restricted to tidal high and low water alone. The choice of the objective function is open to the user, and this means that automatic calibration does not become a black-box system.

4.2 Optimization Strategy

Optimization strategy is a mathematical procedure for finding the minimum value of the performance index. Due to the non-linearity of the St. Venant equations (1,2), it is impossible to find the minimum \underline{p}^* of the objective function, i.e. $\underline{p}^* = \min F(\underline{p})$, in an explicit way. So the second method of Powell (1964), which is a method taken from the scope of non-linear programming, is applied for finding the minimum by a sequential search strategy. It is based on a direct searching technique which avoids the computation of derivatives for the objective function $F(\underline{p})$, which in turn depends on the non-linear St. Venant equations, and is rather complicated.

The principle of the searching strategy is explained by figure 3.

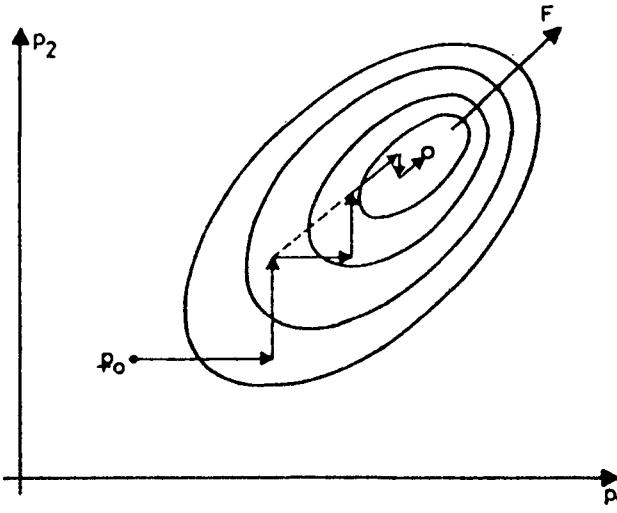


Fig. 3: Second Method of Powell

It is assumed that the objective function $F(\underline{p})$ is a convex function. In a three-dimensional representation which is chosen for reasons of simplicity of the graphical sketch, the objective function $F(\underline{p}) = \text{const.}$ defines isolines in the $p_1 - p_2$ domain. Starting from an initial estimate \underline{p}_0 , two linear independent searching directions are defined. The minimum of $F(\underline{p})$ is determined subsequently and independently in each direction. This leads to a new parameter vector \underline{p}_1 . This procedure is repeated iteratively. To make the searching process efficient, a test is performed after each iteration step to find out whether the search directions should be the same for the next step, or whether they should be varied. A criterion on this is given by the determinant of the search directions. It will attain its maximum for orthogonal, and thus linear independent searching directions. So for each iteration step a new direction, which is defined from the starting value $F(\underline{p})$ to the computed value $F(\underline{p})$ at the end of the step, is introduced and tested. If the direction determinant, computed by omitting the first search direction and including the new one, is bigger than it was in the step before, the new direction is accepted. The search for the minimum for $F(\underline{p})$ in each independent direction is effected by means of the method of quadratic interpolation, which avoids the computation of derivatives. An example for this strategy is given by figure 4.

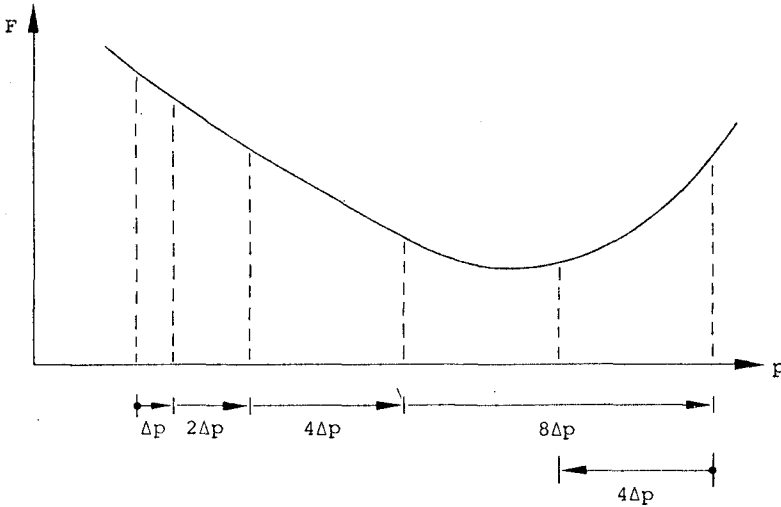


Fig. 4: Quadratic Interpolation

Starting with a value $F(\underline{p})$, neighbouring values

$$F(\underline{p} + \Delta \underline{p}), F(\underline{p} + 3\Delta \underline{p}), F(\underline{p} + 7\Delta \underline{p}), F(\underline{p} + \dots)$$

are computed, until the last value is bigger than the preceding one. An

additional value is computed in the center of the last interval, and then the minimum is determined by quadratic interpolation. This procedure is rather efficient, as it basically corresponds to a binary searching strategy.

5. Results

The suggested method for optimized automatic calibration was applied to the section from Grauerort Geesthacht of the described Elbe river model (Fig. 1). This section, which is also given in figure 6, has a length of 74.6 km. The one-dimensional model for this part of the river was divided into 17 branches to include the islands and the highly branched Hamburg harbour (St. Pauli). Measured data were available at 5 locations along the river, which are marked by dots in figures 1 and 6. The model was run with constant inflow prescribed at Geesthacht, and a tidal curve given at Grauerort.

It was assumed that for this river section the friction parameters may be independently varied within 4 areas as shown in figure 6. At least one measured data set has to be available within each area, as otherwise no performance index can be determined for this area, and consequently the problem would not have a unique solution.

Figure 5 shows a comparison between "trial-and-error", or manual, and the optimized automatic calibration for the location Seemannshöft.

The calibration was performed for the first 12.5 hours of the tidal curves shown in figure 5, which correspond to the first tide on August 22, 1975.

The objective function for the manual calibration was the difference between measured and calculated values at tidal high and low water only. In the manually-performed calibration, friction parameters which depend on the flow direction were used. The obtained calibration is nearly perfect at high and low water, but not so good for the gradient at falling water.

For the automatic calibration, the friction parameters were assumed to be constant over the tidal period. Moreover, as a time-step of 10 minutes was used in the numerical model, the error was also minimized at about 75 points per tidal period, and per location, for which measured data were given. So amplitude and phase error equally weighted and in more detail were taken into account by this strategy. The phase error reduction leads to a much better agreement of the tidal curves. This will probably result in a much better representation of the velocities, the wave height, however, is too small.

The automatic calibration was performed to an accuracy of less than 0.005 m per location and time-step. The obtained friction parameters are given in the table of figure 6.

The variation of the parameters is explained from the typical cross section shapes of the river, which are approximately trapezoidal in area I, and much more complicated in areas III and IV. Moreover, the system is highly branched in the areas II to IV, and especially in the harbour area II simplifications with respect to the discretization have been made.

The given results were obtained by using the sum of the squares of the differences between measured and computed values as objective function.

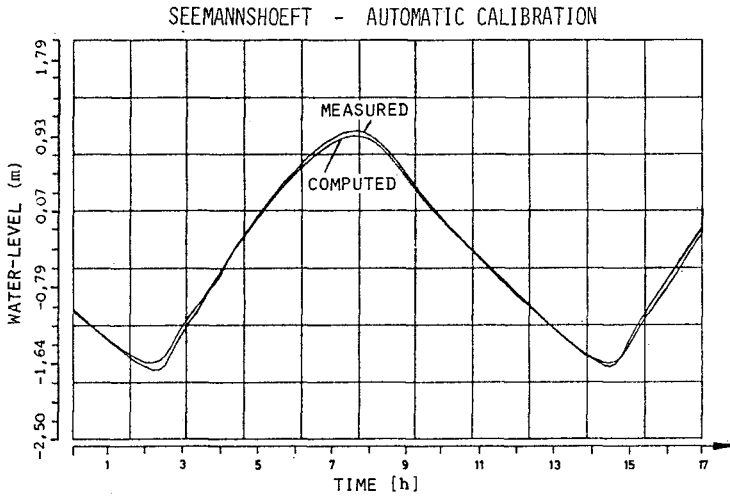
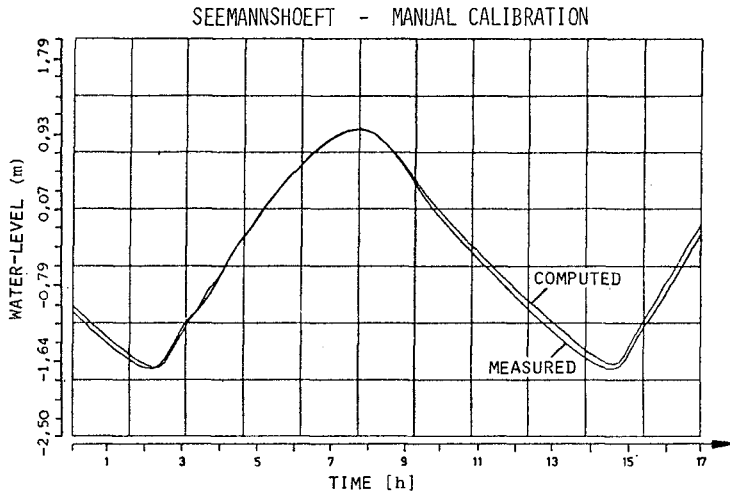


Fig. 5: Comparison Manual to Automatic Calibration

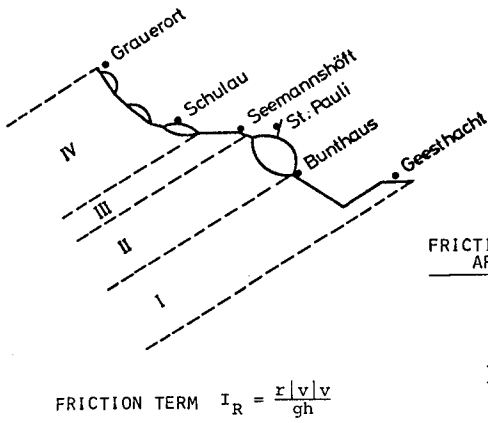


Fig. 6: Friction Parameters after Calibration

Alternatively, a calibration was performed, using the correlation coefficient (ρ) as objective function. For the same error bounds, a correlation coefficient of 0.99965 was obtained. The correlation as well as the relation of computed versus measured data is given in figure 7. The computation time for the calibration was reduced by about 20 % in comparison with the error-squared function.

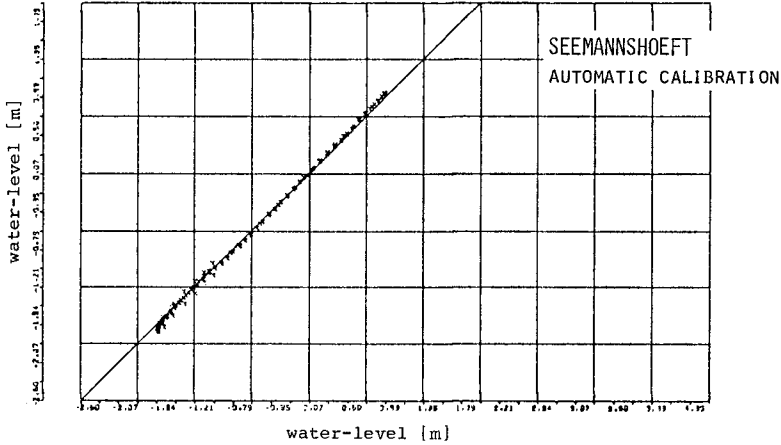


Fig. 7: Calibration using Correlation Coefficient

During calibration it was found that the numerical model was very sensitive to all parameter changes. Small increments on the optimal parameter set increased the value of the objective function considerably. This might easily lead to many poor estimates on new parameter sets in the "trial-and-error" calibration. It is confirmed by a comparison of the internal statistics, which was made over the number of computer runs for manual and automatic calibration. The optimization strategy required 33 runs for the given bounds, whereas about 60 variations of the parameter were necessary for the manual calibration. The manual calibration demanded for a careful and time-consuming data analysis, and repeated plotting. A trained engineer was kept busy by this job for weeks. The automatic calibration was performed within one computer run in one night. The obtained results cannot be improved, unless the error bounds are reduced. Moreover, the actual bound up to which the calibration was performed, is a useful information for the model user 's prognostic applications of the model.

6. Conclusion

A method from the field of mathematical optimization was applied for the calibration of a one-dimensional river model. The model starts from the St. Venant equations which are solved numerically. The optimization leads to a closed system, so that the calibration can be performed automatically within one computer run. This leads to considerable savings in manpower and computer time. The physical transparency for the hydraulic engineer is maintained. The engineer still defines the criteria according to which the calibration is performed. The parameter set finally obtained is the best and only combination of parameters which is obtainable within a given error bound.

References:

- PREISSMANN, A., "Propagation des intumescences dans les canaux et les rivières", 1er Congrès de l'Association Française de Calcul, Grenoble (1960)
- EVANS, E.P., "The Behaviour of a Mathematical Model of Open Channel Flow", Proc. 17th IAHR-Congress, Vol. 2, pp 173 - 180, (1977)
- JANUSZEWSKI, U., "Automatische Eichung für ein- und zweidimensionale hydrodynamisch-numerische Flachwassermodelle", Dissertation, University Hannover, (1980)
- POWELL, M.J.D., "An Efficient Method for Finding the Minimum of a Function of Several Variables without Calculating Derivatives", The Computer Journal, Vol. 7, (1964)

TIDAL INLET BEHAVIOURAL ANALYSIS

A.F. Nielsen, B.E. Engineer, Coastal Process Investigation Section,
Coastal Engineering Branch, N.S.W. Department of Public Works,
Sydney, Australia.

A.D. Gordon, B.E., M. Eng. Sc. Engineer, Coastal Process Investigation
Section, Coastal Engineering Branch, N.S.W. Department of Public
Works, Sydney, Australia.

ABSTRACT

For many years stability theories have been used both to design inlets and to appraise the performance of them. There are a variety of approaches to the formulation of stability criteria ranging from the purely empirical (Stevenson, 1884 - cited by Bruun & Gerritsen, 1958; O'Brien, 1931; Bruun, 1977) to the generalised analytical (Escoffier, 1940; Bruun & Gerritsen, 1958; Keulegan, 1967; O'Brien and Dean, 1972).

In 1966 a seemingly small perturbation made to the inlet of Wallis Lake resulted in significant changes to the estuary. The direct application of existing stability theories was of marginal value in explaining these changes and predicting the stable regime that the estuary may ultimately reach. This paper highlights some of the limitations of existing stability theories, presents a new method of



Plate 1 Wallis Lake inlet in 1952 and 1974
(northern breakwater constructed in 1966).

dynamic behavioural analysis, outlines the case study of an estuary to which existing stability theories could not be effectively applied but to which the behavioural analysis produced interesting results, and recommends the direction in which further research could yield beneficial results.

1. INTRODUCTION

The twin towns of Forster and Tuncurry are sited on the banks of the entrance channel to Wallis Lake (Figure 1); an estuary located 220 km north of Sydney on the New South Wales coastline. The economic viability of the towns is based on the fishing, oyster and tourist

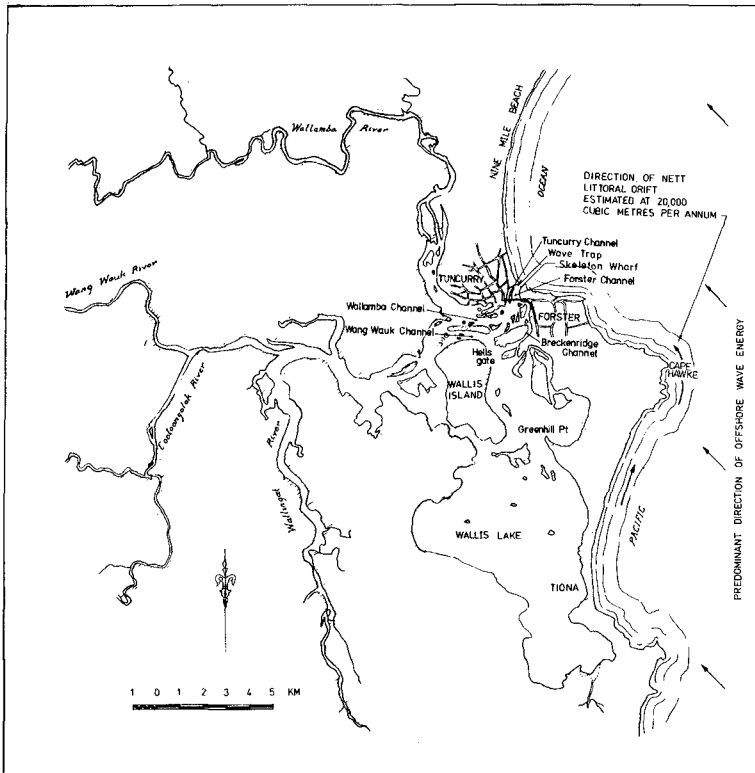


Figure 1 Locality Sketch

industries which focus on the amenity of the estuary and nearby coastal waters. Hence, the entrance conditions and hydraulic characteristics of the estuary are vital factors regarding the existence and development of the region.

Wallis Lake has a plan area of 100 square kilometres and an average depth of 3 m. Three rivers - the Coolongolok, the Wang Wauk and the Wallingat - enter the north-western sector of the estuary. The Wallamba River enters the northern part of the estuary amongst a confusion of small islands and channels. Whilst the four rivers and the lake all share the same ocean entrance, three major and several minor channels connect the river/lake system to the coast. In the vicinity of the ocean inlet the channel system simplifies to the Tuncurry (northern) and Forster (southern) channels.

The average daily fresh water flow in these rivers is small compared with the tidal flows and only extreme flood events have any influence on the estuarine channels. The tidal prism at the higher spring tides is some 18×10^6 cubic metres (ocean tidal range 1.93 m). The average annual flood has a total discharge of about 30×10^6 cubic metres, but the stilling basin effect of the lake greatly damps the potential of floods to scour the entrance channels. This century there has only been one very large flood through the system. This flood occurred in 1929 and had an estimated total discharge of 250×10^6 cubic metres. It caused considerable scouring of the entrance channels.

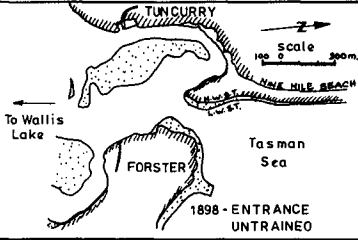
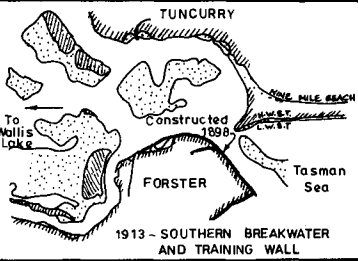
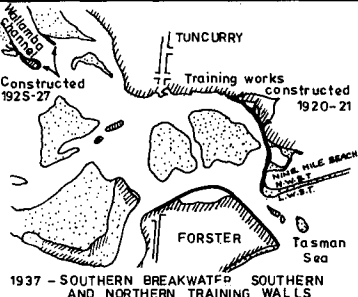
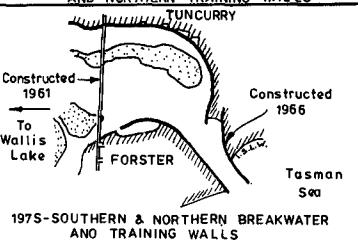
The inlet is located on a moderate to high energy coastline. However, the entrance is somewhat protected from the predominant southeasterly swells by Cape Hawke (Figure 1). The nett littoral drift is northerly and is estimated to be in the order of 20,000 cubic metres per annum. Studies are presently underway to further assess this littoral drift estimate and to develop a more detailed description of the coastal processes in this region.

2. HISTORICAL DEVELOPMENT AND EFFECTS OF ENTRANCE WORKS

In its natural state prior to the construction of any training works the inlet comprised a series of sandy, shoal filled channels that meandered across a wide, beach ridge plain. Both the location and cross-section of the ocean entrance varied with time. Over the past 82 years various entrance training works have been constructed to improve the navigability of both the entrance and estuarine channels and to cater for the historical trend towards larger ocean going trawlers. These works are summarised in Table 1.

It was not possible to fully assess the impact of works carried out before 1966 on the estuary/inlet system due to the paucity of data. However, indications are that from 1898 to 1966 the estuary mouth exhibited many of the typical features of single breakwater inlets. These features include an asymmetrical entrance bar with a channel that meandered across it, large shifting swash shoals, a marginal flood tide channel on the unprotected (northern) side and shifting shoals in the lower entrance channel region. Immediately inside the inlet a twin flood/ebb channel system had developed.

Table 1 History of Entrance Works taken from Hydrographic Plans

YEAR OF SURVEY	DESCRIPTION	
1898	Untrained entrance	
1913	<p>Southern breakwater and training wall</p> <p>In 1898 a contract was let for the construction of a breakwater (500m) and training wall (560m) along the southern (Forster) embankment</p>	
1937	<p>Northern training works and bay shoal stabilisation attempt.</p> <p>In 1919 further works at the entrance were carried out by constructing a 380m long training wall on the northern (Tuncurry) side of the inlet.</p> <p>The work was completed in 1922 and was followed in 1925 and 1928 by the construction of training walls within the estuary in an attempt to stabilise the internal sand bars.</p>	
1975	<p>Northern breakwater and extension of southern breakwater.</p> <p>By 1966 a 460m long breakwater had been constructed on the Tuncurry side of the inlet and the Forster breakwater had been extended by 90m.</p> <p>The width between the breakwaters is 120m.</p>	

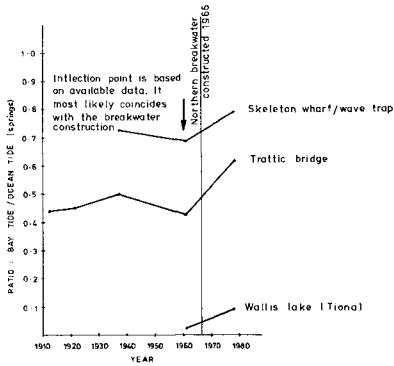


Figure 2 History of Estuary Tidal Ranges

The Forster (southern) channel predominantly conveyed the flood tide whereas the Tuncurry (northern) channel predominantly conveyed the ebb. Tidal gradients presented on hydrographic charts indicate that prior to 1966, entrance works had no significant impact on tidal ranges or phasings throughout the estuary.

Following the construction of the northern breakwater in 1966 there was a dramatic increase in tidal ranges throughout the estuary (Figure 2). Associated with this change was an accentuation of the distortion between flood and ebb tidal hydrographs, a marked change in the predominance of tidal channels and the scouring of the entire 3 km estuary channel system; a scouring mode which is showing no sign of reversal to the present day.

3. STABILITY THEORIES

Approaches to the formulation of the most commonly used stability criteria fall into two basic categories:

- (i) The empirical approach - the identification of parameters relating cause and effect followed by the development of simple relationships between these parameters using coefficients which have been derived from many field observations.
- (ii) The generalised analytical approach - the development of generalised formulae from mechanism understanding and description.

3.1 Empirical Approach

Bruun and Gerritsen (1958) outlined the history of stability theories from Stevenson (1884) through the work of O'Brien (1931) up to that proposed by Bruun and Gerritsen in their 1958 paper.

One of the most popular empirical approaches is based on the work of O'Brien (1931). O'Brien proposed that the stable inlet cross-sectional area could be determined from the tidal prism using the relationship:

$$A = 1000 \left(\frac{\Omega}{640} \right)^{0.85} \quad (1)$$

where

A = inlet cross-sectional area
 Ω = tidal prism

Considerable embellishment of this model has been carried out by O'Brien (1969) and others, the most notable being Jarret (1976) who has presented prism/area relationships for estuaries with various inlet configurations and tidal conditions.

These predictive prism/area relationships are of marginal value to analytical work. The reasons for this are that firstly, the scatter of field data points around the predictive curve implies that the relationship is at best approximate and secondly, for estuaries with long and complex entrance channels connecting the water body to the ocean it is virtually impossible to relate an equivalent theoretically determined stable channel cross-sectional area to channels in the field.

Bruun (1977, 1978) has advanced the empirical approach by proposing a method which considers the relationship between littoral drift and the tidal prism of the estuary. This approach represents a shift in emphasis of pertinent parameters from the morphological (cross-sectional area) to those describing forces (sediment transport). In essence, this approach is concerned with entrance bar conditions. Bruun contends that the stability of an inlet must be analysed in terms of the ability of the tidal flow to flush out the sediments that are carried by wave and current action to the inlet gorge. On this basis he proposes that inlets be classified in terms of Ω/M ratios, where

Ω = tidal prism
M = sediment feed to the gorge

Low ratios (less than 50) are indicative of poor entrance conditions whereas high ratios (greater than 150) are indicative of good entrance conditions. This approach is simply one of classification by parameter ratios and has severe limitations if it is to be used as a predictive tool.

However, it is important to be aware of the development, limitations and strengths of the empirical approaches as they represent significant steps down the path of understanding inlet dynamics.

3.2 Analytical Approach

Of the generalised analytical approaches, that presented by O'Brien and Dean (1972) is a significant contribution to inlet mechanism understanding. It is based on the earlier well documented work of Escoffier (1940) and Keulegan (1967). This method relates the bay tide phasing and amplitude to that of the ocean tide through the hydraulic characteristics of the entrance channel. The approach is applicable to small inlets and large tidal estuaries on shorelines where littoral drift is small. It favours estuaries with relatively short and regular entrance channels connecting the water body to the ocean. With this method of analysis, through the construction of an Escoffier diagram,

the status of an inlet at any point in time can be examined and the ultimate stable cross-sectional area of the entrance channel can be predicted. The O'Brien and Dean method is outlined below as it forms a basis from which the analytical approach adopted for the Forster/Tuncurry study was developed.

Keulegan developed the relationships between the repletion coefficient K and the tidal phase lag, and the ratio of the bay-to-ocean tidal amplitudes, a_b/a_o . These relationships are shown in Figure 3. The repletion coefficient may also be expressed as a function of the hydraulic and geometric properties of the estuary in the following way:

$$K = \frac{T}{2\pi a_o} \cdot \frac{Ac}{Ab} \cdot \sqrt{\frac{2gR}{Ken + Kex + \frac{fl}{4R}}} \quad (2)$$

where

- T = tidal period
- a_o = amplitude of the ocean tide
- Ac = inlet cross-sectional flow area
- Ab = surface area of the basin
- g = gravitational constant
- Ken, Kex = entrance and exit head losses of the entrance channel
- f = friction factor
- l = friction length
- R = hydraulic radius of entrance channel

Keulegan also presented the relationship between the repletion coefficient and the dimensionless maximum velocity in the inlet $V'max$, as shown in Figure 4. The maximum velocity through a specific inlet is given by equation (3):

$$Vmax = V'max \cdot \frac{2\pi}{T} \cdot a_o \cdot \frac{Ab}{Ac} \quad (3)$$

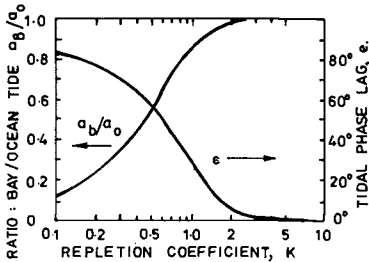


Figure 3

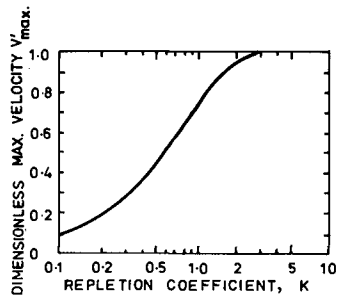


Figure 4

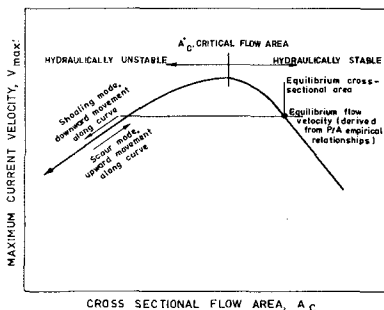


Figure 5 Generalised inlet hydraulic stability curve, or "Escoffier Diagram".

Where equations (2) and (3) and Figure 4 are used together a range of inlet hydraulic conditions can be calculated in terms of the maximum velocity versus cross-sectional flow area. The inlet mechanics are portrayed by the inlet stability curve (Escoffier diagram - Figure 5).

It can be seen from this diagram that an induced change in the cross-sectional flow area of an hitherto hydraulically stable inlet will result in either a change in inlet current velocity which will work to return the inlet towards its equilibrium size by appropriate deposition or scour, or, if the induced area change is so large as to reduce the cross-sectional area below the critical flow area, making the inlet

hydraulically unstable. An hydraulically unstable inlet is characterised by increasing friction with decreasing cross-sectional area. The result is that if any natural or man-induced change in flow area occurs this is accompanied by a change in the flow velocity which will, by inducing scour or deposition, perpetuate the induced area change. Since area changes are perpetuated, an hydraulically unstable inlet will either continuously scour until a stable flow area is achieved (unstable scour mode) or its will continuously shoal until inlet closure (unstable shoaling mode).

Many limitations of this model have been documented by Bruun (1977, 1978). In particular, major difficulties are encountered in determining the equivalent length and cross-sectional area of a long and complex entrance channel system. However, the major failing of the model is that it can not be used as a predictive tool in situations where significant perturbations such as those associated with the construction of breakwaters are or will be made to the entrance bar of the inlet. Moreover, if it is desired to predict the effect of such perturbations the O'Brien and Dean model cannot be used for the reason that an Escoffier diagram representing the range of future likely hydraulic characteristics cannot be constructed if more than one parameter (A_c and consequently R) is varied.

Following on from the O'Brien and Dean approach, Bruun (1978) shifted the emphasis to sediment transport considerations on the basis that stability must reflect the ability of sediment to move through the inlet in such a way that nett deposition does not occur. Bruun suggests that inlet analysis be undertaken by calculating sediment transport:

- (i) in the gorge (entrance channel),

- (ii) in the region between the inlet and the ocean bar,
- (iii) in the ocean channel including its passage over the bar, and
- (iv) in the bay channels.

It is then possible to construct a quantitative sediment budget from which erosion and depositional areas may be identified, hence a model of estuary/inlet behaviour can be constructed.

The limitations of the Bruun approach are less obvious than those of O'Brien and Dean. There are difficulties in accurately carrying out many of the required calculations. The sediment budget determination may in many cases be very sensitive to these inaccuracies. Further, there is no well documented method to determine sediment transport in the region of the ocean bars for differing inlet configurations. Finally the method is not readily adapted to situations where relatively long channels connect the bay to the ocean.

4. INLET BEHAVIOURAL APPROACH

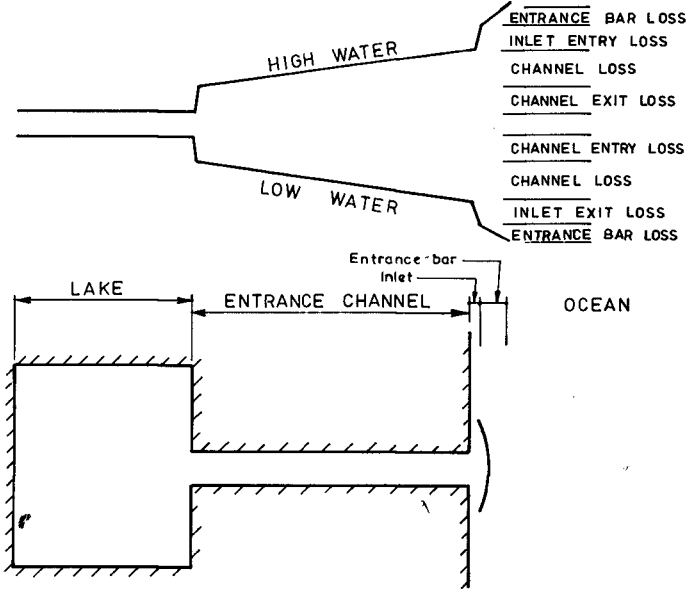
The concepts of O'Brien and Dean and Bruun may be modified and used in a complimentary manner when studying the changes induced by major inlet forcing works such as breakwater construction. Extension of these approaches has led to the development of an inlet behavioural approach which allowed studies to be undertaken on typical New South Wales inlets. This behavioural approach included the recognition and inclusion of the following:

There are two major sources of head loss between the forcing function (ocean tide) and the bay response. These are the head loss over the entrance bar and the losses associated with the hydraulic characteristics of the inlet and entrance channel (Figure 6). When constructing the Escoffier diagram for a particular estuary the following approach is used (Czerniak, 1977 - see Section 3.2):

- (i) A_b/a_o is calculated from existing data and K is determined from Figure 3.
- (ii) Equation (2) is solved for l using K and known values of R, Ac, T, a_o , Ab, f, Ken and Kex. The latter six parameters are assumed not to vary.
- (iii) The hydraulic stability curve is computed using equations (2) and (3) and Figure 4 with only Ac (and consequently R) varying over the entire range.

In equation (2), four head loss parameters (Ken, Kex, f, l) are used to describe the total impedance of the tidal inlet and entrance channels to the flow. This implies that the forcing function a_o (the amplitude of the ocean tide) is applied immediately outside the inlet. Hence, a_o is not a true ocean tidal amplitude unless entrance bar losses are negligible.

SCHEMATISED ESTUARINE HYDRAULIC LOSSES



SCHEMATISED PLAN OF ESTUARY

Figure 6 Generalised head loss diagram for inlet/estuary system

Accordingly, a_0 should be defined as the amplitude of the tide immediately outside the inlet. This is not in accord with Bruun's recommendation that a_0 be determined from outer coast ranges.

Sediment budgeting as proposed by Bruun can be modified by the application of regime theory to the inlet hydraulics both

before and after the perturbation to provide a predictive numerical-descriptive model.

5. APPLICATION OF BEHAVIOURAL ANALYSIS

It has been identified that changes to head loss over the ocean bar are important when considering the impact of inlet modification on estuary behaviour because such modifications can significantly affect the forcing function of the system. Moreover, changes to tractive stresses and the regions over which they act can be expected to radically alter sediment transport paths and the quantities of sediment involved in the budget.

An essential part of inlet behavioural analysis includes an examination of changes to the hydraulic and sediment transporting characteristics of the ocean bar following inlet modification works. The changes to the hydraulic characteristics can be analysed in terms of alterations to the head loss over the bar and in the inlet due to modifications to the inlet cross-sectional shape, velocities and frictional properties. The modification of sediment supply to the inlet gorge must include examination of:

- (i) Changes to tractive stress patterns resulting from modifications to tidal flow patterns across the bar.
- (ii) Changes to velocity profiles resulting from increased/decreased inlet efficiency.
- (iii) Changes to the sediment entrainment and depositional rates resulting from morphological modifications to the ocean bar and hence areas over which increased bed shear due to wave effects occur.
- (iv) Changes to wave setup effects, hence their relationship to flood/ebb hydraulic gradients.

Having determined the changes in head loss characteristics, the regime equations of Engelund and Hansen (1967 - cited by Bruun, 1978) can be considered with the Manning formula to predict changes to the friction slope in the estuary channels. The Engelund-Hansen equations can be expressed in the following way:

$$B \propto Q^{0.525} \quad (4)$$

$$D \propto Q^{0.317} \quad (5)$$

$$A \propto Q^{0.842} \quad (6)$$

$$V \propto Q^{0.158} \quad (7)$$

Using equations (5) and (7) with Manning's formula in the form:

$$S = \left(\frac{v_m n}{R^{2/3}} \right)^2 \quad (8)$$

and with D approximating R for wide shallow channels, the behavioural change slope ratio is:

$$\frac{S_{ultimate}}{S_{prior}} = \left(\frac{Q_{ultimate}}{Q_{prior}} \right)^{-0.107} \quad (9)$$

Finally, with the above information and certain assumptions the response rate of the estuary from the pre-perturbated condition to the "ultimate" condition can be mapped. From this history, using an appropriate sediment transport formula, it is possible to predict sediment movements and future scour/depositional patterns.

The analysis of the Wallis Lake estuary will be used to illustrate the method.

6. APPLICATION OF INLET BEHAVIOURAL ANALYSIS TO WALLIS LAKE ESTUARY

The construction of the northern breakwater at Forster/Tuncurry in 1966 resulted in profound changes to the Wallis Lake estuary. The inlet behavioural analysis was used to predict the ultimate configuration and size of the inlet channels, to predict the response time of the estuary to the perturbation and to assess the impact of proposed further perturbations in the lower estuary regions.

6.1 Ocean Bar/Inlet Morphology and Flow Patterns (also see Druery and Nielsen, 1980)

Figure 7 shows typical current flow paths, velocity distributions and sediment transport paths pertaining to the inlet before the northern breakwater was constructed. During ebb flow sediments were entrained on the channel shoals and carried to sea through the inlet. As the ebb jet expanded the flow velocity reduced. The asymmetrical nature of the jet expansion resulted in a skewed velocity distribution and sediments were deposited in the low energy region along the edge of the swash shoals. A large separation eddy developed on the northern side of the jet resulting in an inlet directed current through the northern marginal flood tide channel (see Figure 7). This feature resulted in the formation of an opposing current on the northern side of the entrance and produced a head loss to the ebb tide flow. Wave action from the predominant southeasterly swells carried sediment northward along the swash bars. During flood tide sediments were entrained on the swash bars and carried into the inlet.

The construction of the northern breakwater in 1966 resulted in significant alterations to the bar morphology, tidal flow paths and sediment movement patterns (Figure 8). On ebb tide the jet expansion became more symmetrical. The interception of the marginal flood tide channel and large swash shoals by the breakwater resulted in the elimination of the large flow separation eddy and the inlet directed

current during ebb flow. The breakwater has also caused a redirection of the flood tide flow which became orientated along the centreline of the breakwaters. Figure 9 summarises the pertinent changes caused by the northern breakwater construction, the salient points being the reduction to the sediment entrainment area of tidal currents over the entrance bar during flood tide, the reduction in area on the bar affected by increased bed shear due to wave effects and the increase in ruling depths on the bar.

6.2 Head Loss at the Entrance

A significant reduction in the total head loss over the entrance bar has occurred. An estimate of this reduction was obtained by comparing the tidal envelopes measured before (1961) and after (1978) the breakwater construction (Figure 10). On the assumption that the tidal envelope in the region of the bar approximates the peak instantaneous head loss over the bar, the head losses for the higher spring tide ranges have been reduced from 0.19 m to 0.11 m (0.08 m reduction) for high waters and from 0.24 m to 0.18 m (0.06 m reduction) for low waters.

It is estimated that the inlet losses have reduced from about 0.1 m to about 0.05 m which is a measure of the increased hydraulic

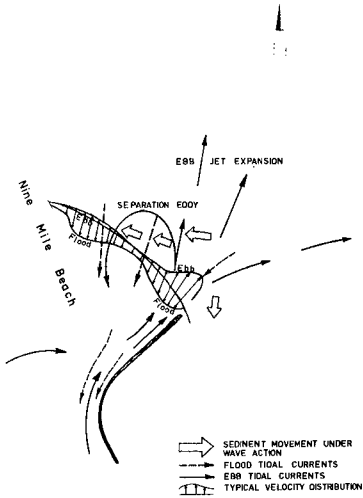


Figure 7 Littoral processes at a single breakwater entrance

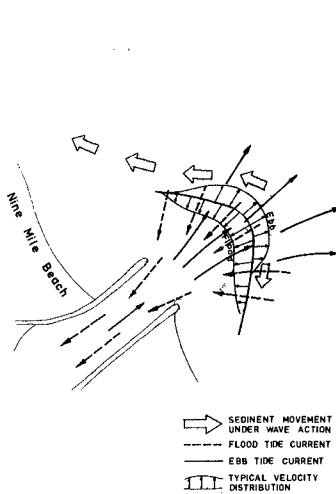


Figure 8 Littoral processes at a double breakwater entrance

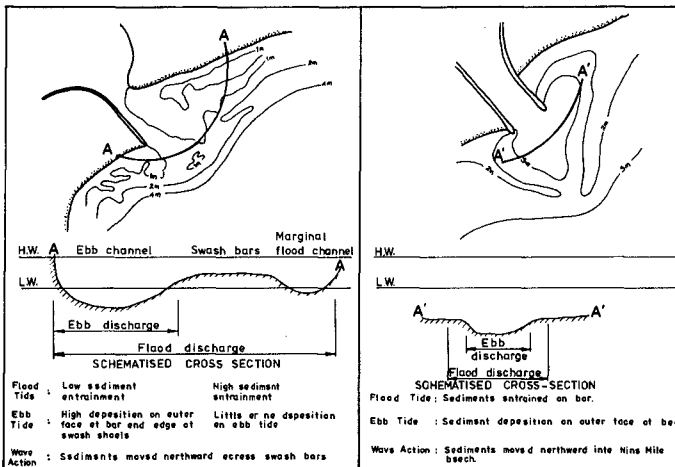


Figure 9 Differences between single and double breakwater entrances

efficiency of the new trapezoidal section between the breakwaters, as outlined by Bruun (1978).

In the O'Brien and Dean approach the inlet entry losses are accounted for by Ken, the entry head loss coefficient. The entry head loss is:

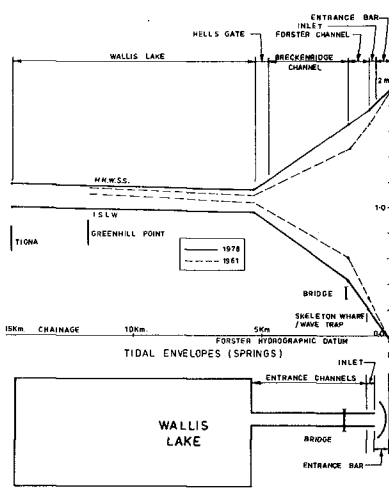
$$\text{Ken} \cdot \frac{u^2}{2g}$$

Dean (1971, cited by Bruun, 1978) recommends a value of Ken = 0.25 for inlets with exposed breakwaters. O'Brien and Dean (1972) recommend a value of Ken + Kex = 1.3. As a value of Kex = 1 is usually adopted (Bruun, 1978) then this sets Ken = 0.3. These values were also adopted by Czerniak (1977).

In this application, given peak velocities of about 2 m/s during the highest spring tides and for a measured inlet head loss of about 0.05m, a value of Ken = 0.25 was calculated. This value is in accordance with the recommended values cited above. It is clear that the generalised analytical model of O'Brien and Dean does not take into account head losses that occur over the ocean bar.

6.3 Regime/Gradient Analysis

An estimate of the ultimate stable channel regime and the total response time of the estuary was made by a generalised analytical appraisal of the channel hydraulics. The assumptions made include:



SCHEMATISED PLAN OF ESTUARY

Figure 10 1961 and 1978 tidal envelopes for Wallis Lake inlet/estuary system

- (i) The ultimate head loss values between the traffic bridge and the ocean were reached within a short period of time after the northern breakwater was constructed.
- (ii) The channels are erodable between the traffic bridge and the lake, hence regime equation apply.
- (iii) The hydraulic gradients at peak flows are proportional to the gradients of the tidal envelope at spring tides.
- (iv) The tidal range in the lake is proportional to the tidal prism and discharge.
- (v) Manning's "n" in the various channels remains constant throughout the response period, that is, there will be no significant change in the composition of the sediments or in bed forms in the channels.
- (vi) The tidal prism in 1966 is equal to the tidal prism in 1961 - necessary because of lack of data.

Based on assumptions (i), (iv) and (v) a relationship between discharges and hydraulic gradients was developed:

$$\frac{Q_{1966}}{Q_{1966}} = \frac{(1.65 - 0.37 \frac{S_{ult}}{S_{1966}})_{HHWSS} - (0.43 + 0.43 \frac{S_{ult}}{S_{1966}})_{ISLW}}{0.06 \text{ (lake tidal range, 1966)}} \quad (10)$$

Equations (9) - Section 5 - and (10) were solved graphically (Figure 11) resulting in the following regime parameters:

- (i) Tidal prism (HHWSS) = 67,000 cubic metres, a tenfold increase.
- (ii) Lake range = 0.60 m (increase from 0.06 m).
- (iii) Channel velocities increase by 44%.
- (iv) Channel depths double.
- (v) Channel widths treble.

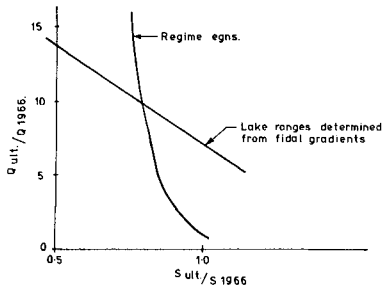


Figure 11 Solution of regime/gradient equations

Given that there was a threefold increase in tidal prism between 1967 and 1978 (see Figure 10), and assuming that the rate of increase was and will remain constant, it will take 50 years from 1967 for the estuary to fully respond to the northern breakwater construction.

The assumptions and the basis for these predictions are at this point of time felt to be suboptimal. However, the methodology employed is considered to be reasonable. In the case of Forster/Tuncurry a number of factors will further influence the ultimate result:

- The presence of indurated sands at some locations in the estuary will act to control and modify channel erosion patterns, hence the predicted tidal range in the lake may never be realised.
- The extent of the oyster leases throughout the estuary will have an effect on erosion patterns and may invalidate the Mannings "n" assumption.

6.4 Sediment Budget Analysis

The increase in the efficiency of the inlet has resulted in an increase in bar depths with a resulting reduction in wave setup effects. There has also been a reduction to the area on the entrance bar over which threshold shear stresses are exceeded during flood tide. The nett result of these effects has been to enhance the ebb tide sand transporting capabilities and to reduce the sediment feed to the inlet during flood tides.

Sediment transport rates under tidal current action were calculated at various locations in the lower entrance region using the Ackers and White (1973) approach. This approach was used for reasons of convenience as the computational steps have been automated on our office computers. The results at each gauging station were plotted in terms of transport rate vs velocity and a curve in the form:

$$Q = kv^n \quad (11)$$

where

- Q = sediment transport rate
- k = constant
- v = average channel velocity

was fitted to each set of results. It was found that n varied from about 4 to about 6 over the monitoring stations. The mean grain size of the sand is about 0.3 mm and depths of flow were in the order of a few metres. This result is therefore in close agreement with the A.S.C.E. recommendation which sets $n = 5$, and it is also in accord with the analysis carried out by Costa and Isaacs (1977).

For each tidal gauging sediment transport rates were calculated at hourly and, in some instances, half hourly intervals. The transport rate/time curve was integrated to give the sediment load for the tidal gauging. Annual sediment transport rates were calculated based on statistics of annual tidal ranges and derived relationships between tidal ranges and tidal discharges.

To check the validity of this approach it was assumed that the sediment transport rates remained constant over the period since the northern breakwater was constructed and the sediment budget was calculated (Figure 12) and compared with that obtained from the analysis of hydrographic surveys. The analysis was carried out for two sections of the estuary (see Figure 12). Limitation to the extent of the hydrographic surveys dictated that different time periods for the two sections were analysed. However, it was felt that this in itself provided further proof of consistency of the results.

The values are given in Table 2 from which it can be seen that a remarkably good agreement was obtained.

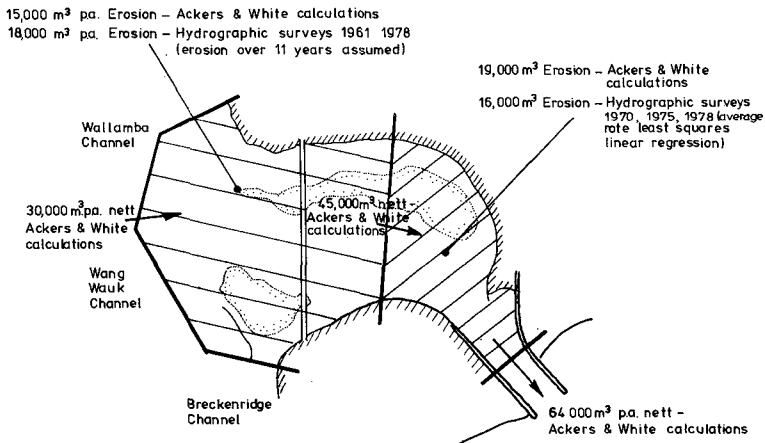


Figure 12 Sediment budget for lower entrance channel region at Forster/Tuncurry

TABLE 2

Comparison of Theoretically Determined and Measured Erosion Rates

Section (See Figure 12)	Period of Analysis	Erosion of entrance shoals (cubic metres per annum)	
		As predicted by Transport Calcs.	As given by Hydro-survey
From breakwater to section D/S of bridge	1970 - 1978	19,000	16,000
From section D/S of bridge to section U/S of bridge	1967 - 1978	15,000	18,000

The calculated sediment budget for the estuary was therefore adopted. From this it can be seen that the nett sediment movement has been directed out of the estuary, considerable scour has occurred in the lower entrance channel region and, as sediments are not carried into the entrance channels from the lake during ebb tide, the upper region of the entrance channel system is scouring. These effects have been dramatically borne out in the field where scouring has resulted in severe subsidence of the traffic bridge with piers settling 400 mm, erosion of the untrained channel banks throughout the estuary with some channels doubling in waterway cross-sectional area, increased upstream penetration of marine sand flood tide deltas. Further; a significant accretion on nine mile beach has occurred since 1966 as a result of the sediment being supplied to the coastal littoral system from the "point source" generated within the estuary by the breakwater construction.

7. CONCLUSIONS

The construction of a northern breakwater at Forster/Tuncurry converted the previous single breakwater entrance into a double breakwater entrance. This perturbation, unlike the previous one occasioned by the construction of the first breakwater, caused significant changes to the tidal prism, the inlet entry and exit head loss characteristics and the entrance bar morphology. Existing stability theories were unable to describe the changes or predict the future consequences of the perturbation. The long and complex estuary channel system connecting the ocean inlet to the "bay" region, Wallis Lake, provided additional complications.

It was necessary to adopt a new approach of "Inlet Behavioural Analysis" which was based on a combination and extension of past methods.

The major features of this approach included:

Examination and description of changes to ocean bar morphology, current patterns and entrainment condition in order to identify

the relevant parameters and their importance with respect to the changes.

- . Determination of the impact of the perturbation on ocean bar/inlet efficiency. That is, determination of head loss variation caused by changes to bar morphology, flood/ebb current patterns and cross-sectional optimality at the entrance - particularly between the breakwaters.
- . Use of a regime type approach to predict the propagation and distribution of the changed hydraulic conditions at the entrance throughout the inlet-estuary system.
- . The development of a predictive sediment budget model based on sediment transport formula and the calculated hydraulic conditions from the regime analysis.
- . The use of this sediment budget model and conceptual hydraulic model to chart the future of the estuary and determine the time span over which impacts from the perturbation will occur.

Application of this approach to Forster/Tuncurry produced interesting results which at this point of time - 14 years after the perturbation - are in good agreement with field observations.

The magnitude of the "ultimate" changes, that is, a tenfold increase in tidal prism (a threefold change has already occurred), a doubling of channel depths, a trebling of channel widths and a 50 year adjustment period is difficult to contemplate. This end result may however never be realised due to the simplistic assumptions which were made in the analysis and the development of controls such as the exposure of indurated sand rock bars, which were not considered in the study.

The increasing need to be able to adequately predict long term impacts of entrance training works has shifted the emphasis away from the static "stability analysis" approach towards the more dynamic one of "behavioural analysis". The methodology outlined in this paper is seen as an attempt by the authors to respond to this need.

The authors keenly look forward to discussion and guidance on this matter. An exciting field of future research must be undertaken to overcome many of the crude assumptions and simplifications which have been made to date.

8. REFERENCES

1. Ackers, P. and White, W.R. (1973). "Sediment Transport : New Approach and Analysis". A.S.C.E. Journal of the Hydraulics Division, Vol. 99, No. HY11, November, 1973.
2. Bruun, P.M. and Gerritsen, F. (1958). "Stability of Coastal Inlets". A.S.C.E., Journal of the Waterways, Harbours and Coastal Engineering Division, Vol. 84, No. WW 3.

3. Bruun, P.M. (1977). "Design of Tidal Inlets on Littoral Drift Shores". Coastal Sediments '77. Proc. Fifth Symposium of the Waterway Port, Coastal and Ocean Division of A.S.C.E. Charleston, pp 754-773.
4. Bruun, P.M. (1978). "Stability of Tidal Inlets." Elsevier Scientific Publishing Company. Amsterdam.
5. Costa, S.L. and Isaacs, J.D. (1977). "The Modification of Sand Transport in Tidal Inlets." Coastal Sediments '77. Proc. Fifth Symposium of the Waterway Port, Coastal and Ocean Division of A.S.C.E. Charleston, pp 946-965.
6. Czerniak, M.T. (1977). "Inlet Interaction and Stability Theory Verification". Coastal Sediments '77. Proc. fifth Symposium of the Waterway Port, Coastal and Ocean Division of A.S.C.E. Charleston, pp 754-773.
7. Druery, B.M. and Nielsen, A.F. (1980). "Mechanisms Operating at a Jettied River Entrance". Proc. 17th International Conference on Coastal Engineering. Sydney.
8. Escoffier, F.F. (1940). "The Stability of Tidal Inlets." Shore and Beach, Vol. 8, No.4, pp 114-115.
9. Jarret, J.T. (1976). "Tidal Prism - In let Area Relationships", GITI Report 3, U.S. Army, Corps of Engineers, Coastal Engineering Research Centre, Fort Belvoir, Va., and U.S. Army Engineer Waterways Experiment Station, Vicksburg, Miss., Feb. 1976.
10. Keulegan, G.H. (1967). "Tidal Flow in Entrances Water Level Fluctuations of Basins in Communication with Seas". Committee on Tidal Hydraulics U.S. Army, Corps. of Engineers. Tech. Bulletin No. 14.
11. O'Brien, M.P. (1931). "Estuary Tidal Prism Related to Entrance Areas." Civil Engr., Vol. 1, No. 8.
12. O'Brien, M.P. (1969). "Equilibrium Flow Areas of Inlets on Sandy Coasts". A.S.C.E., Journal of the Waterways and Harbours Division, Vol. 95, No. WW1.
13. O'Brien, M.P., and Dean, R.G. (1972). "Hydraulics and Sedimentary Stability of Coastal Inlets." Proc. 13th Coastal Engineering conference. Vancouver, pp 761-780.

SEDIMENTATION PROCESSES IN TIDAL CHANNELS AND TIDAL
BASINS CAUSED BY ARTIFICIAL CONSTRUCTIONS

by

E. RENGER

Senior Research Engineer, Landesamt für Wasserhaushalt
und Küsten, Kiel, Federal Republic of Germany

and

H.W. PARTENSCKY

Professor and Director, Franzius-Institut für Hydraulic
and Coastal Engineering, University of Hannover
Federal Republic of Germany

1. INTRODUCTION

Tidal basins and tidal rivers especially in areas of agricultural and industrial interest are more and more regulated and improved for different reasons such as draining, disposal of waste water, shipping and storm flood protection. This is - up to now - mainly done by dams, dikes, training walls, channel dredging, storm surge control barriers, etc..

In general, the tidal motion (tidal range and tidal velocities) in the whole system is affected by these man-made changes in the cross-sectional area of the tidal river. The hydrographical effects caused by such artificial constructions in tidal rivers have been outlined in the papers of H.G. WITTMER and al.(12). However, the morphological consequences of such measures are largely unknown.

The analysis of a real system, such as the EIDER-Estuary at the German Bay, which was affected by both a reduction in its tidal prism by the construction of a tidal dam in 1936, and by a reduction of its cross-sectional area by a storm surge control barrier in 1972, must therefore be highly appreciated.

In general, the most important changes of a tidal regime are caused by two different types of artificial influences:

- horizontal reductions of the tidal volume (for instance by damming-off a tidal river)
- vertical reductions of the cross-section(s) at any particular part of the tidal regime (for instance by storm surge control barriers or training walls)

In both cases the existing equilibrium conditions are disturbed and the relationships between the horizontal and vertical components of the tidal motion are distorted more or less according to the distance from the structure. As a con-

sequence, the resulting pattern of flow and sediment transport is changed into a net flood-oriented flow. This leads to a very heavy siltation in the tidal system and consequently to a shrinking of the cross-sections.

An exact prediction of the sedimentation rates to be expected in tidal basins as a consequence of artificial constructions is not possible so far. However, the application of some simple equilibrium conditions, as have been used for the hindcasting of the sedimentation rates in the Eider-Estuary, seems to prove that an approximate evaluation of the morphological changes in a tidal system is nevertheless possible.

2. EQUILIBRIUM CRITERIA

Stability investigations of tidal basin inlets show the most important relationship between the cross-sectional area (F) and the associated mean tidal prism (V). Estuaries and tidal rivers follow - within certain boundary conditions - nearly the same relationship.

All the existing equilibrium criteria are based on the fundamental concept of correlating characteristical horizontal and vertical parameters of the system. In the following, two discharge oriented approaches shall be discussed in this paper.

W. HENSEN (2) defined a stability parameter (c_f) as an average flood current velocity under natural flow conditions as follows:

$$c_f = \frac{V}{D_f \cdot F_{fm}} \quad (1)$$

with: V = mean tidal prism
 D_f = duration of flood
 F_{fm} = mean cross-sectional area (about half-tide)
 c_f = average flood current velocity

Due to HENSEN, the equilibrium condition of a tidal system is given if the calculated c_f -value remains a constant, i.e.

$$c_f = c_{eq} = \text{const.} \quad (2)$$

Although no fundamental research about this regime constant has been carried out, the average flood and ebb current velocities in tidal basins and tidal rivers with fine sand and silt seem to be of the order of $c_f \sim 0,67 \text{ m/s}$ (2).

A more detailed and especially vertically differentiated relationship was elaborated by E. RENGGER (10).

When the continuity equation for non-steady flow is applied

to any cross-section (s_i, z_i) of a tidal basin within the mean tidal range (ζ) the mean current velocity (\bar{u}) can be derived with a good accuracy as follows:

$$\bar{u} = \frac{A}{F} \cdot \bar{v} \quad \text{or} \quad \frac{u}{v} = \frac{A}{F} = \varphi(\zeta) \quad (3)$$

with: A = horizontal cross-section within the
 F = vertical cross-section mean tidal
 \bar{v} = mean velocity of tidal range $\zeta = z'/H$
 rise and fall

The equilibrium conditions of a tidal system were found to depend on a certain general vertical distribution $\varphi^m(\zeta)$ and on a reference value $\varphi_R(H)$.

The morphological characteristic $\varphi^m(\zeta^m)$ is significant for the type of the tidal regime, whereas the reference value ($\varphi_R(H)$) obviously seems to depend on the mean tidal range (H).

3. GENERAL REMARKS ON THE REGIME CHANGING CONCEPT

As has been pointed out before, the two most important effects on a tidal regime are changes in the horizontal and vertical cross-sections. In both cases the existing hydrodynamical equilibrium is disturbed by the artificial constructions. The morphological reactions of the system (in most cases heavy sedimentation) show at first an increasing tendency but tend to reach a new state of equilibrium with time.

The mean flow characteristics of the system $u(z')$ and c_f are directly related to the morphological changes of the tidal basin. This can be shown by the two formulas mentioned before:

$$\text{from (1)} \quad c_f \sim \left[\frac{V}{F_{fm}} \right] = \left[\frac{\int_0^H A dz'}{F_{fm}} \right] \quad (4)$$

$$\text{from (2)} \quad u(z') \sim \left[\frac{A(z')}{F(z')} \right] \quad (5)$$

where F_{fm} and $F(z')$ are the terms in which morphological changes are represented.

As a first step and for a rather good estimate of the expected changing of the regime, only the morphological terms of both formulas need to be analyzed. The most important assumption for this analysis is, however, that the equilibrium criterias mentioned before can be applied furthermore to the remaining tidal influenced part of the system. In other words, the hydrodynamical components of the equilibrium approaches ($c_f = c_{eq}$, D_f , $u(z')$ and $v(z')$) are of an universal importance and remain of the same numerical order as given in the former state.

4. STAGES OF MORPHOLOGICAL REACTIONS

With respect to the general remarks on the regime changing concept of tidal basins due to artificial constructions four typical stages of morphological reactions can be distinguished (Table 1):

Stage of time	Criteria		Stability
I. $t_1 = t_{eq}$ (exist) existing condition	$C_{f1}/C_{eq} \approx 1$	$u_1/u_{eq} \approx 1$	stable (assumed)
II. t_2 , just influenced by artificial construction	$C_{f2}/C_{eq} \gtrless 1$	$u_2/u_{eq} \lesseqgtr 1$	non stable
III. t_3 period of change	$C_f(t)/C_{eq} \rightarrow 1$	$u(t)/u_{eq} \rightarrow 1$	different degrees of instability towards stability
IV. $t_3 = t_{eq}$ (exp.) expected new equilibrium	$C_f/C_{eq} = 1$	$u/u_{eq} = 1$	stability

TABLE 1: Stages of morphological reactions

In stage II the two alternative signs indicate either reduction (symbol <) or enlargement (symbol >) of the tidal system.

The different morphological time stages for a schematic reduction of a tidal basin - for instance by the construction of a tidal dam - are shown for the two equilibrium approaches of HENSEN and RENGGER (in figure 1 and 2, respectively). The figures show a schematical tidal basin and the parameters of state used in the approaches. The morphological changes to be expected are indicated for the different stages. The equations for the calculation of the corresponding cross-sections F are listed in Table 2 for the two different approaches.

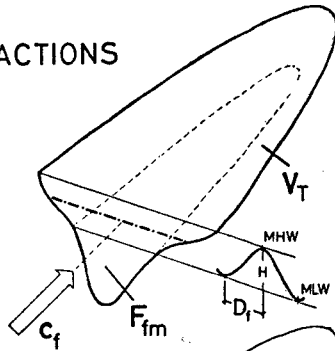
Stage I: Existing condition

The existing condition is assumed to be in a dynamical equilibrium, i.e. no net sediment transport between ebb and flood current exists. The equilibrium state is represented by the c_f - and u - values, which vary within the mean tidal range ($0 \leq z' \leq H$). The equilibrium condition is shown

STAGES OF MORPHOLOGICAL REACTIONS OF TIDAL BASINS

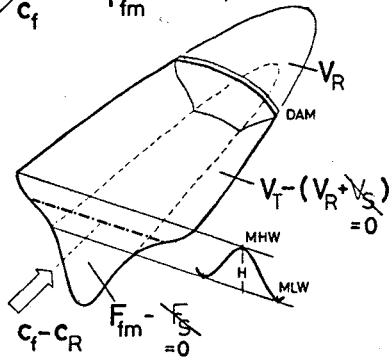
I. EXISTING CONDITION:

$$c_f = \frac{V_T}{D_f \cdot F_{fm}} \quad (\text{Hensen})$$



II. REDUCTION OF VOLUME V_T :

$$c_f - c_R = \frac{1}{D_f} \cdot \left[\frac{V_T - V_R}{F_{fm}} \right]$$



III. PERIOD OF CHANGE:

$$D_f = \text{CONST.}$$

$$c_R \rightarrow 0$$

$V_S F_S$ INCREASING BY SEDIMENTATION

IV. EXPECTED EQUILIBRIUM:

$$c_f = \frac{1}{D_f} \cdot \left[\frac{V_T - (V_R + V_S)}{(F_{fm} - F_S)} \right]$$

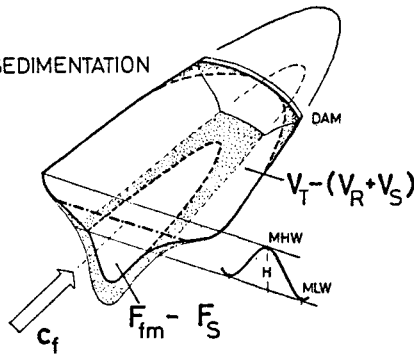
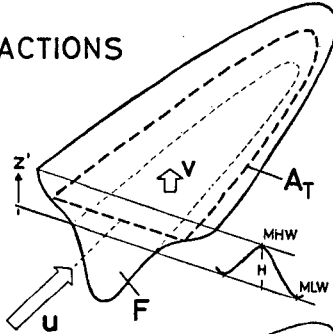


Figure 1

STAGES OF MORPHOLOGICAL REACTIONS OF TIDAL BASINS

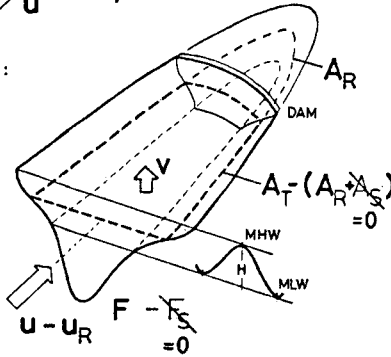
I. EXISTING CONDITION

$$u \cong v \cdot \left[\frac{A}{F} \right] \text{ (Renger)}$$



II. REDUCTION OF VOLUME A(z):

$$u - u_R \cong v \cdot \left[\frac{A_T - A_R}{F} \right]$$



III. PERIOD OF CHANGE:

u_R DECREASING
 A_S, F_S INCREASING BY SEDIMENTATION
 $v = \text{CONST.}$

IV. EXPECTED EQUILIBRIUM:

$$u \cong v \cdot \left[\frac{A_T - (A_R + A_S)}{(F - F_S)} \right]$$

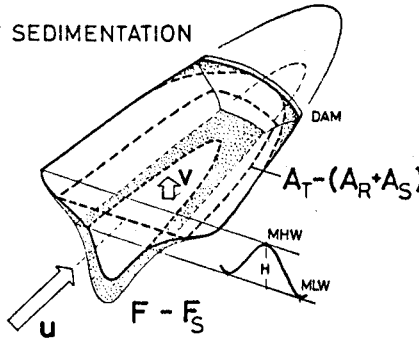


Figure 2

in figure 1 and 2 for the two approaches.

Stage II: Directly after reduction of the tidal volume

The initial change of the significant parameter is caused by the man-made construction (tidal dam, see figure 1). Due to the location of the dam and the corresponding reduction of the tidal volume (V_R and $A_R(z')$, fig. 1 and 2), the velocity-pattern within the remaining part of the tidal basin will also change ($c_f - c_R$, $u - u_R$) as a natural hydrodynamical reaction.

Stage III: Period of time dependent morphological changes

As a consequence of the reduction in tidal volume, the existing sediment transport is changed into a resulting flood-oriented sediment transport. The latter will cause a continuous reduction in the cross-sections (F) of the remaining part of the tidal basin. The shrinking of the tidal basin will in turn affect the tidal motion in it (see fig. 1 and 2 - stage III). This process of morphological and hydrological changes will continue until a new state of equilibrium is reached.

Stage IV: Expected new equilibrium

The expected new state of equilibrium at the end of the time dependent morphological and hydrological changes in the tidal basin can only be predicted by means of a rough approximation. This is due to the fact that in both methods only the vertical and horizontal morphological parameters are considered to be variable, whereas all other variables are kept constant. The calculated cross-sections (F_{calc}) must therefore be considered as an upper limit of the expected ones, i.e. (see figure 1, stage IV and table 2):

$$F_{exp} < F_{calc} = F_{fm} - F_S \quad (6)$$

In the following, the approximated forecasting equations are applied to the case of the Eider-River at the German Bight where a considerable part of the tidal volume was dammed-off by the construction of a tidal dam in 1936 and a storm-surge barrier was built at its ocean entrance in 1972.

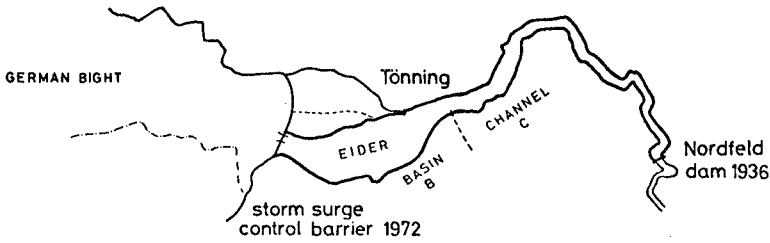
5. APPLICATION OF THE FORECASTING METHODS TO THE EIDER RIVER

General remarks: The tidal river of the Eider which flows into the inner German Bay had been dammed-off by a tidal dam at Nordfeld in 1936 (see figure 3).

Due to the construction of the dam, the initial tidal volume of the estuary was reduced by approximately 12 Mio m^3 . As a result of this reduction in tidal volume, a heavy accumulation of silt and sediment was observed downstream of the tidal dam in the following 30 years. By means of

Stage of Reactions	Approaches for the calculation of the cross-sections (F)	Method of E. RENGER (1978)
I. Existing equilibrium condition	Method of W. HENSEN (1937) $F_{f_m} \sim \frac{V_T}{C_f}$	Method of E. RENGER (1978) $F \sim \frac{A_T}{u}$ (all variables vary with (z') within the mean tidal range)
II. Stage directly after the reduction of the tidal volume	$F_{f_m} \sim \frac{ V_T - V_R }{ C_f - C_R } = \frac{\text{calc. } V}{(C_f - C_R)}$	$F \sim \frac{ A_T - A_R }{ u - u_R } = \frac{\text{calc. } A}{(u - u_R)}$
III. Period of time dependent morphological changes	$F_{f_m}(t) = F_{f_m}(I) - F_S(t)$ $F_{f_m}(t) \sim \frac{ V_T - V_R - V_S}{(C_f - C_R)} = \frac{\text{calc. } V - V_S}{(C_f - C_R)}$ with: $Df(t) \approx \text{const.}$ $C_R \rightarrow 0$ $V_S \sim \text{increasing from zero}$ $F_S \sim \text{increasing from zero}$	$F(t) = F(I) - F_S(t)$ $F(t) \sim \frac{(A_T - A_R) - A_S}{(u - u_R)} = \frac{\text{calc. } A - A_S}{(u - u_R)}$ with: $v(t) \approx \text{const.}$ $u_R \sim 0$ $A_S \sim \text{increasing from zero}$ $F_S \sim \text{increasing from zero}$
IV. Expected new equilibrium	$\exp F_{f_m} < \text{calc. } F_{f_m} \sim \frac{\text{calc. } V - V_S}{C_f(\text{eq})} < \frac{\text{calc. } V}{C_f(\text{eq})}$	$\exp F \cdot F < \text{calc. } F \sim \frac{\text{calc. } A - A_S}{u(\text{eq})} < \frac{\text{calc. } A}{u(\text{eq})}$

Table 2 :



Volume below... mNN	MEASURED IN 1936	1967	HINDCASTING OF THE influence of 1936	FORECASTING OF THE influence of 1972
... MHW +1.64	100.56	49.65	52 ... 43 (-12)	30 ... 18 (-12)
MTR 3.28m	54.82	35.67	40 ... 36 (-11)	27 ... 16 (-11)
... MLW -1.64	45.74	13.98	7 ... 9 (-1)	3 ... 2 (-1)
			E(B•C) E(B)+C	(C)

Figure 3

soundings carried out at certain intervals, a total sedimentation of about 50 Mio m³ has been determined downstream of the dam covering an area of about 25 km² over a length of 30 km. A detailed description of the time-dependent morphological changes in the Eider basin can be found in reference (4) .

In the following, an attempt is made to hindcast the observed morphological changes in the Eider river by means of the two methods discussed before. In particular, the shrinking of the tidal volume below MHW and MLW is investigated and compared with the prototype measurements (7,8,9).

Hindcasting of the cross-sections: As has been outlined before, the new cross-sections to be expected after the construction of the tidal dam and the restoration of a new morpho-dynamical equilibrium (see figure 1, stage IV) can be determined by means of the following equation:

$$\text{calc } F_{fm} = \frac{\text{calc. } V}{D_f \cdot c_f(\text{eq})} = \frac{V_t - V_R}{D_f \cdot c_f(\text{eq})} \quad (7)$$

For reasons already discussed before, the calculated F_{fm} -values according to equation (7) are somewhat higher than the actual values (exp F_{fm}) to be expected for each cross-

section, i.e. calc. $F_{fm} > exp.F_{fm}$. The former can therefore be considered as an upper limit of the expected new cross-sections.

In Table 3, the results of the calculations for two different cross-sections of the Eider-River (profiles 78 and 115, see figure 3) are presented for four different years. The first calculation was carried out for year 1935, when the tidal dam was not yet built (Figure 1, stage I). The second calculation (1936) corresponds to stage II (fig.1), i.e. summarises the situation after the construction of the dam, whereas the calculations for the years 1967 and 1976 show the situation in the Eider river during the morphological changes (stage III and IV, respectively).

All parameters used for calculating the new cross-sections F_{fm} had to be taken from the tidal system at stages I (existing condition) and II (situation directly after the completion of the tidal dam). These values are printed in bold in Table 3.

CALCULATION OF THE EXPECTED CROSS - SECTIONS
OF THE EIDER

year	Vol (10 ⁶ m ³)		D _l (min)		F _{fm} (m ²)		c _t (m/s)		
	PROFILE 78	115	78	115	78	115	78	115	
1935	17.9	26.2	352	362	1600	1790	0.52	0.67	
1936	5.9	14.2	310	320	1600	1790	0.20	0.41	
1967	5.3	12.8	315	320	500	820	0.53	0.81	
1976	5.1	12.3	320	322	324	640	0.82	0.98	
CALCULATED:					530	970	m ²		

Table 3

As can be seen from the figures in Table 3, there is a reduction of 12 Mio m³ in tidal volume due to the construction of the tidal dam. The remaining tidal volumes of 14,2 Mio m³ (profile 115) and 5,9 Mio m³ (profile 78) decrease, however, with time due to the heavy accumulation of silt and sand in the upper part of the estuary.

An even more pronounced effect could be observed for both profiles in the decrease in cross-sectional area (Table 3). The measurements obtained for 1976 might already be slightly affected by the influence of the new tidal control barrier which was built in 1972 at the ocean entrance of the Eider river. The values obtained for 1967 show, however, a fairly good agreement with the calculated F_{fm} -values according to equation (7).

Hindcasting of tidal volumes: During the last 6 years, systematic evaluations of about 25 existing tidal basins of the inner German Bay, were carried out by the Franzius-Institute, University of Hannover/Germany, which led to some general stability criteria for these tidal basins with a mean tidal range of about 3,0 m. It could be shown that the tidal volume V of a basin depends clearly on its drainage area E . The empirically determined relationship for the volumetric capacity of the tidal basin at MLW as well as for the mean tidal volume V_{Tm} are as follows (8,10):

$$\text{Mean tidal volume: } V_{Tm} = 1,65 \cdot E^{1,036} \quad (8)$$

$$\text{Capacity at MLW : } V_{MLW} = 4,39 \cdot E^{1,643} \quad (9)$$

where volumes V are in $(10^6 \cdot m^3)$ and drainage areas E in (km^2) .

The two equations were applied to the Eider basin between the dam at Nordfeld (built in 1936) and the storm surge barrier (built in 1972) at its ocean entrance (see figure 3).

Because of the complex form of the Eider basin, two different approaches were used in the attempt to hindcast the observed sedimentation rates. For this, the Eider basin was subdivided into a basin (B) and a channel part (C), as shown in figure 3.

In the first approach, the sum of the areas B and C was used as significant drainage area, i.e. $E = B + C$, whereas in the second approach only the drainage area of the basin part (B) was used as variable and the remaining volume of the channel part (C) of about 12 Mio m^3 was added to the tidal volumes calculated by means of equations (8) and (9).

The results are shown in the table of figure 3. The calculations were carried out for 2 different tidal levels (MHW and MLW) and for the mean tidal range (MTR). As can be seen from the results, the hindcasted volumes (in Mio m^3) are in a rather good agreement with the values obtained by systematic soundings in 1967 (see table in figure 3).

6. FORECASTING OF THE INFLUENCE OF THE STORM SURGE CONTROL BARRIER, BUILT IN 1972

As has been pointed out in the introductory remarks, a change in the morphology of a tidal basin can also be caused by a local narrowing down of the existing cross-section of the basin, as for example by a storm surge control barrier. An artificial construction of this kind acts like a singular discontinuity within the horizontal distribution of the cross-sections along the river axis.

The effect of such discontinuities on the morphological reaction of a tidal system has been recently investigated by

several authors (6,8,11). In general, an abrupt narrowing down of an existing cross-section of a tidal basin by means of an artificial construction leads to a distortion of the tidal wave with a partial reflection of the latter. The horizontal and vertical velocity components $u(t)$ and $v(t)$ of the tidal motion are changed which results in a distorted flow pattern on both sides of the construction. As a result, the transport capacity of the tidal flow is changed with a higher concentration of silt and sediment in the upper layers. This leads to an increase in the transport range of the sediments, especially under flood conditions.

The net effect of the narrowing down of the cross-section will be an accumulation of sediment and silt on both sides of the construction, the amount of which depending upon the degree of contraction.

At the new storm surge control barrier at the mouth of the Eider river (figure 3), heavy sedimentation was observed upstream and seaward of the construction since its completion in 1972.

By applying the tidal basin concept to the Eider basin restricted by the control barrier, an attempt can be made to forecast the sedimentation rates to be expected within the remaining basin. Using the two different approaches as mentioned before, an upper and lower limit for the reduced tidal volume to be expected could be determined. The results are shown in the table of figure 3. As can be seen from the calculated values, some additional 22 to 25 Mio m^3 of silt and sedimentation must be expected under MHW within the Eider basin (compared with 1967) until a new state of morphological equilibrium is reached (7). The evaluated soundings along the Eider river since 1972 seem to support this prediction (see figure 4).

7. CONCLUSIONS

The knowledge of morphological changes to be expected in tidal rivers and basins as a result of man-made constructions such as dykes, dams and tidal control barriers is of high interest for future decisions in tidal regions of agricultural and economical value. It was the aim of this paper to present two empirical approaches by means of which a prediction of the morphological reaction of a tidal system and an estimate of expected sedimentation rates is possible.

By using prototype measurements from the Eider River, it could be shown that the observed sedimentation rates were in fairly good agreement with obtained theoretical values from the two empirical approaches. Although further systematic research is needed in this respect, it seems that the two methods discussed in this paper promise to be a

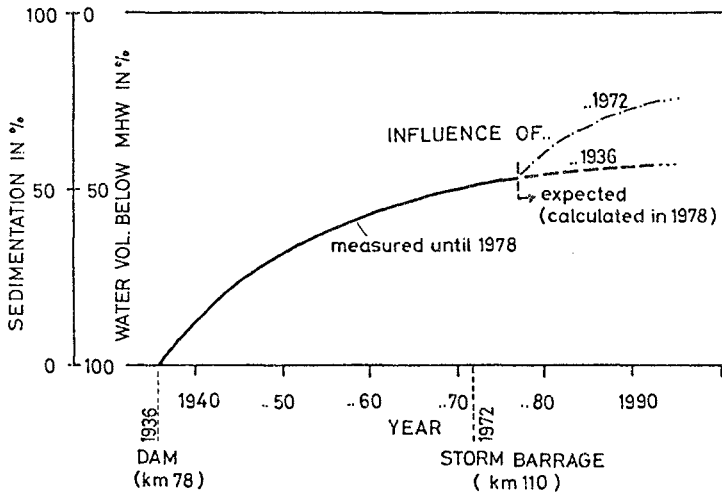


FIGURE 4

good tool in the prediction of sedimentation rates to be expected in tidal basins and tidal rivers due to artificial constructions in the tidal regime.

8. REFERENCES

- (1) BRUUN, P.G. and GERRITSEN, M.: "Stability of Coastal Inlets", Journal of the Waterw.a.Harb.Div., Proc.of the ASCE, WW3, May 1958.
- (2) HENSEN, W.: "Umrechnung von Strömungsgeschwindigkeiten in Tideflüssen auf Mittelwerte", Bautechnik, vol.8,1937
- (3) HENSEN, W.: "Ausbau der seewärtigen Zufahrten zu den deutschen Nordseehäfen". Hansa, No.15, 1971
- (4) KÜSTENAUSSCHUSS NORD- UND OSTSEE, GUTACHTERGRUPPE EIDER: "Gutachten über die Vorschläge zur Behebung der Schwierigkeiten in der Eider", Die Küste, Jg. 12, 1964

- (5) O'BRIEN, M.P.: "Equilibrium Flow Areas of Inlets on Sandy Coasts", Journ.of Waterw. and Harbors Div., Proc.of the ASCE.vol.15, No WWI, Feb.1969
- (6) PARTENSKY, H.W.: "Neue Erkenntnisse über das Stabilitätsverhalten und den Sedimenttransport in Watt-Prielsystemen", Mitt.Franzius-Inst., Univ.Hannover, vol.50,1980
- (7) PARTENSKY, H.W.
and
RENGER, E.: "Gutachtliche Stellungnahme zu den Regimeveränderungen in der Eider durch den Betrieb des Sturmflutsperrwerkes". (unpublished report, 1978).
- (8) RENGER, E.: "Quantitative Analyse der Morphologie von Watteinzugsgebieten und Tidebecken",Mitt.Franzius-Inst.,Univ.Hannover, vol.43,1976
- (9) RENGER, E.: "Grundzüge der Analyse und Berechnung der Morphologie von Watteinzugsgebieten und Tidebecken", Mitt.Franzius-Inst., Univ. Hannover, vol.46, 1976
- (10) RENGER, E.: "Two-dimensional Stability Analysis of Tidal Basins and Tidal Flats of Larger Extent", Proc. 16th Int.Conf.on Coastal Engin. Vol. II, 1978
- (11) RODLOFF, W.: "Über Wattwasserläufe" Mitt.Franzius-Inst. Univ. Hannover, vol. 34, 1970
- (12) WITTMER, H.: "Tideänderungen durch Einbauten in Tideflüssen", Mitt. Franzius-Inst., Universität Hannover, vol. 13, 1958

ARTIFICIAL ROUGHNESS IN PHYSICAL MODELS OF ESTUARIES FOR STORM SURGE INVESTIGATIONS

BY

D. BERNDT,¹⁾ E. GIESE,²⁾ H. SCHWARZE,³⁾ H.-J. VOLLMERS⁴⁾

- 1) Dipl.-Ing., Bundesanstalt für Wasserbau (Hydraulics Laboratory of the Federal Government), Hamburg
- 2) Ing.grad., Bundesanstalt für Wasserbau (Hydraulics Laboratory of the Federal Government), Hamburg
- 3) Dr.-Ing., Chief Engineer, Franzius-Institut, University Hannover
- 4) Professor, Hochschule der Bundeswehr (University of the Armed Forces) in München

1. INTRODUCTION

One of the characteristics of the North Sea between the British Isles, the Netherlands, Germany and Denmark is the occurrence of heavy storm surges especially in autumn and winter with heights of about 4 m above spring highwater. Coastal areas and especially the estuaries of the tidal rivers are hit by these storm surge events. The mean tidal range at the German coast comes to about 3 m with relatively low daily and semimonthly inequalities of less than 0.5m.

Within the framework of long-term developments of the navigation channels of the estuaries as well as of the storm surge protection works, physical model tests had to be carried out in order to predict the influences of such measures on the storm surge heights to be expected.

2. GENERAL REMARKS ON THE SIMULATION OF TIDES IN PHYSICAL MODELS

In connection with these model tests the question as to the artificial roughness pattern in distorted tide models necessary for simulating different types of storm surges had to be investigated. The simulation of unsteady alternating currents and water level elevations of a mean tide in a physical model of an estuary can be attained by a roughness pattern of artificial elements fixed over the total tidal cycle. For mean tides, determined as the mean of a long-term sequence of tides in an estuary which is morphologically in a state of equilibrium (morphology of the model), a roughness pattern denoted as "similar to prototype" can be defined. In principle, a roughness pattern different from the "similar to prototype" roughness should be neces-

sary for the simulation of other tides in this particular morphological state of the model.

It must certainly be taken into account that the "similar to prototype" roughness will be more and more restricted to the calibration tide and to the corresponding morphological situation with increasing distortion of the model.

Storm tides can only be reproduced incompletely in long models of estuaries when conventional methods are used, i.e. appropriate tide generation without reproducing wind effects and fixing the roughness pattern in the model. Specific current distributions basically different from current distributions of mean tides must be considered.

3. INVESTIGATIONS ON THE INFLUENCE OF TIDAL FLAT ROUGHNESS

The results of several tests within the framework of basic investigations at the University of Hannover as well as in the Laboratories of the Federal Government in Hamburg will show the influence of the roughness pattern in a model and especially its importance on the success of each investigation.

The subject of the investigations were storm surges in the Elbe Estuary in Germany. The Outer Elbe is characterised by wide tidal flats on both sides of the navigation channel. Upstream of the real coastline the dominant portion of the cross section of the Elbe River is the navigation channel accompanied by more or less wide smaller flats partly higher than mean highwater. For this case a physical tidal model with a distortion of 5, that means 1:500 for the lengths and 1:100 for the depths, of the Elbe Estuary was constructed (Fig. 1). The overall length of the part of the Elbe reproduced in the model is about 170 km from the seaward boundary up to the tidal boundary fixed by a weir.

Figure 2 shows schematically a longitudinal section of high-water elevations of a special type of storm surge in the Elbe Estuary.

The black line shows the storm surge highwaters actually measured along the estuary.

The dashed line represents the highwaters found in the model which had been equipped with conventional roughness elements such as barbed wire or small concrete blocks. In this model it was not possible to achieve a course of storm surges really similar to prototype. In the downstream area of the estuary with wide tidal flats the water level elevations do not follow the real highwater line well-known from the event in the nature. Only in that region where the cross sections of the estuary are reduced, are the model line and the nature line at least parallel to each other.

In order to raise the model highwaters up to the natural highwaters the storm surge curve of the control station was

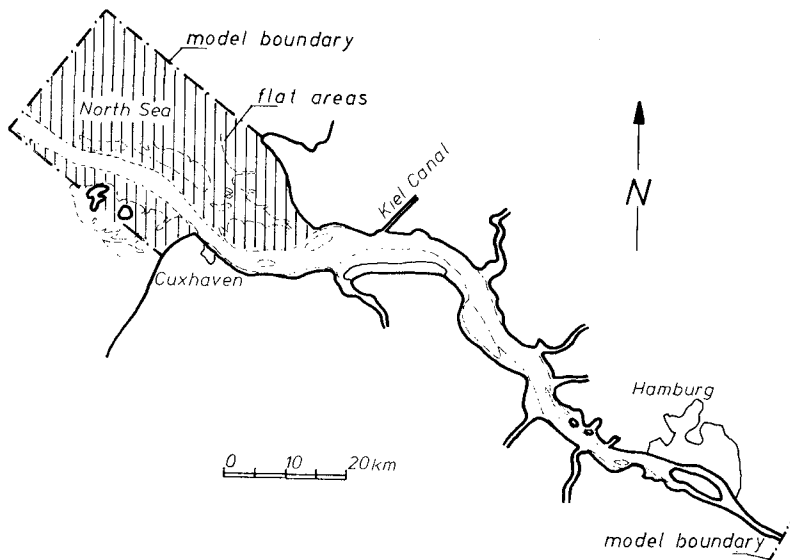


Fig. 1

General map of the Elbe Estuary and model boundaries

raised to a certain height above the real height. The result is demonstrated with the dotted line. It is obvious that the highwater line in the model was only raised nearly parallel to the dashed highwater line. So this measure was not successful in obtaining a highwater line similar to prototype.

On the other hand, similar problems did not arise in reproducing storm surges in another physical tide model of the Elbe Estuary with the same scales but with a seaward boundary upstream of the flat areas.

4. IMPORTANCE OF REAL SIMULATION OF TIDAL FLAT ROUGHNESS

The outstanding result of the tests described above was the realization of the importance of the flat areas in the downstream areas of the model. The flat areas, even in a model with a distortion of 5, seem to be hydraulically too rough, and this is caused by the shallow water depths and a model bottom surface with a relative roughness which is too great. The influence of roughness in the flat areas must not be neglected. It is a serious mistake to accept a storm tide in a model under the assumption that the model tide which occurs accidentally is only one of a great number of different possible storm surge tides. In order to show the

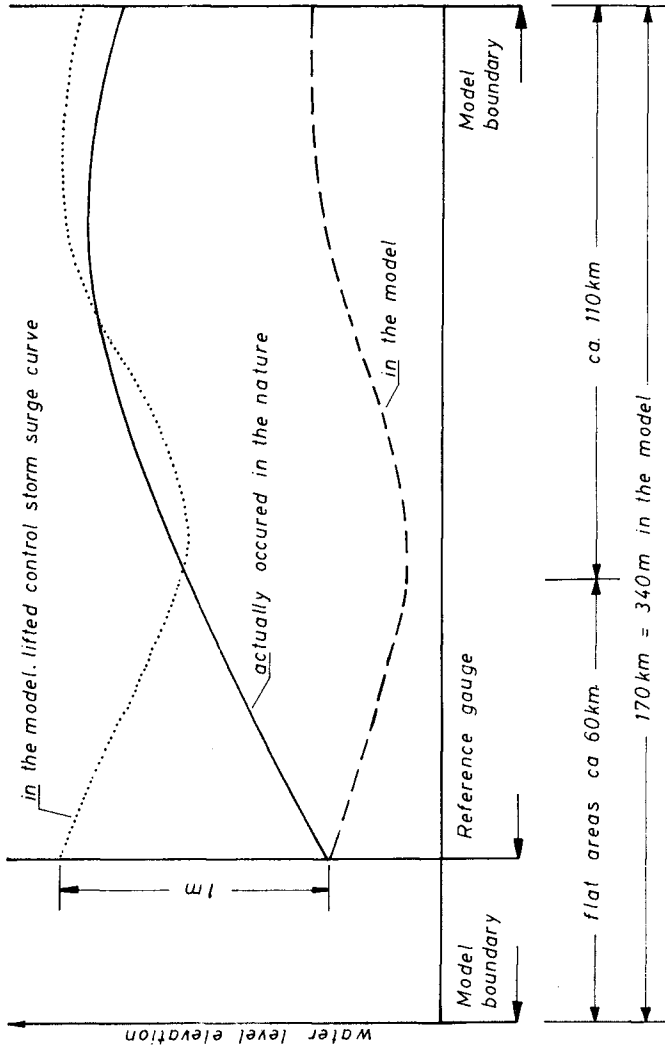


Fig. 2
Storm surge highwaters in the prototype and in the model
(schematically)

importance of the demand for the real simulation of the roughness pattern on the flats, that means a smoothing of the relative roughness, some tasks of storm surge investigations are to be briefly mentioned.

Model investigations of storm surges in general refer to the prediction of storm surge heights to be expected after more or less serious artificial changes of the morphological situation of an estuary (Fig. 3). Basically two types of changes can be imagined.

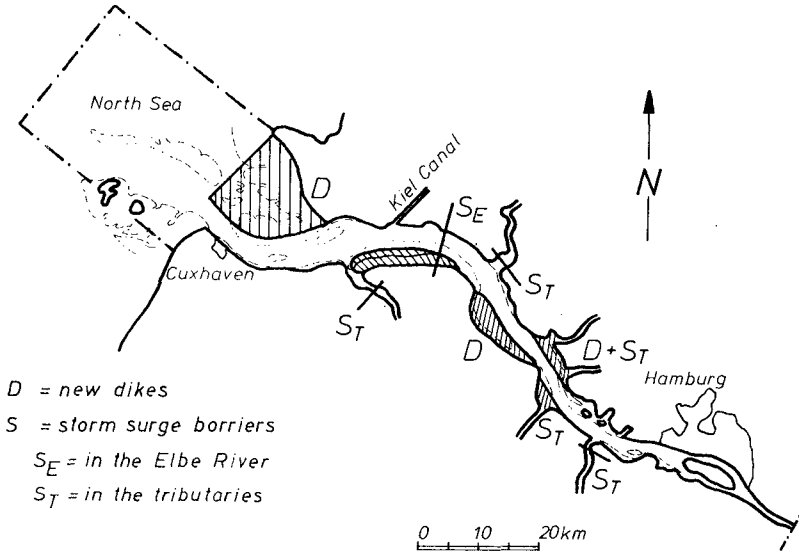


Fig. 3

Storm surge protection works in the Elbe Estuary

1. Because of the development of a harbour in the upper region of an estuary, such as Hamburg on the Elbe River about 100 km upstream of the point where the Elbe flows into the North Sea, deepenings of about 4 m as well as enlargements of the width of the navigation channel in several steps over a couple of decades became necessary.

In this case the deepening will result in an increase of the amplitude of a storm surge wave, which results in higher highwaters.

In addition, basic considerations confirmed by SIEFERT (1) led to the conclusion that with the increasing depths of the navigation channel the efficiency of the discharge in the deepened portion of the estuary increases. From

the MANNING-STRICKLER formula it can be derived that, assuming certain simplifications, the efficiency is increased by nearly the square of the additional water depth. When the main channel of the estuary is deepened the remaining efficiency of the flat areas becomes less and less important for the course of the storm surge.

2. In order to minimize the risk of flooding in lower regions on both sides of the estuary, existing storm surge protection facilities have to be reinforced or new structures such as dikes in front of newly reclaimed areas for human and industrial settlements have to be planned. This means that certain portions of the cross sections, in general with low efficiency of the discharge, will not yet be available for the filling and emptying of the upper estuary. The effect on the storm surge heights is dependent on the importance of these portions of the cross sections for the discharge. The resulting effect on the storm surge in an estuary caused by reducing the cross section by means of dikes is, in any case, an increase of roughness, which leads to higher partial reflections of the tidal wave downstream of the construction measure and to corresponding reductions of the amplitude of the tidal wave upstream.

5. DEVELOPMENT OF EFFECTIVE ROUGHNESS ELEMENTS

5.1 GENERAL REMARKS

A method therefore had to be found for overcoming the roughness effect of the tidal flat areas including the effect of winds blowing in the direction of the floodstream which cannot be reproduced directly in a physical model. The rise of storm surges had to be accelerated in order to obtain higher peak water elevations in the lower region of the estuary. On the other hand, the fall of the storm surges in the lower regions had to be decelerated in order to postpone the turn of the flood currents in the upper region of the estuary.

5.2 MOMENTUM JETS

On the basis of an idea being developed in the Hydraulics Laboratories of the Federal Government in Hamburg, momentum jets were used to achieve the required effect.

This new method was proved in pretests in a plume with a width of 1 m. 8 jets of about 4 up to 8 cm³/s each were pressed out of nozzles with diameters of 3 mm, located in horizontal tubes arranged at a distance of about 2 m across the plume (Fig. 4). Jets were injected in the direction of the plume flow as well as against the plume flow. The discharge of the plume came to about 16 l/s with a water depth of about 20 cm.

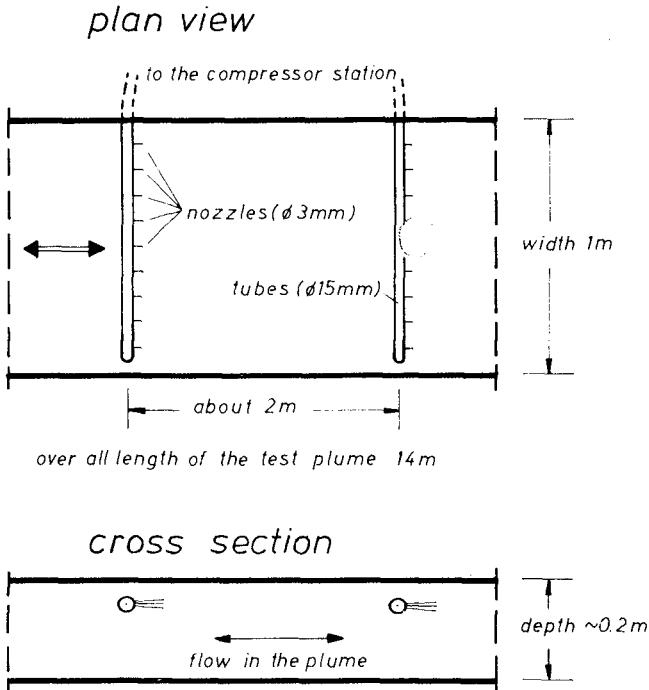


Fig. 4
Test facilities for momentum jets

The results of the pretests showed a remarkable decrease of the longitudinal gradient of water level elevations, which means an increase of the roughness coefficient of MANNING-STRICKLER. In this case increasing the roughness coefficient means increasing smoothness.

The momentum jets were found to be even still more effective when directed against the flow. It was possible to achieve remarkable roughness effect which led to an increase of the gradient, for instance, from 1 ‰ to 6 ‰ .

Dependent on the distribution of momentum jets in the model as well as on the control of the jet intensity, the desired gradients of the flow can be achieved in a limited range.

The use of the jets in the flat areas of the downstream region of the estuary (Fig. 5) was as successful as expected.

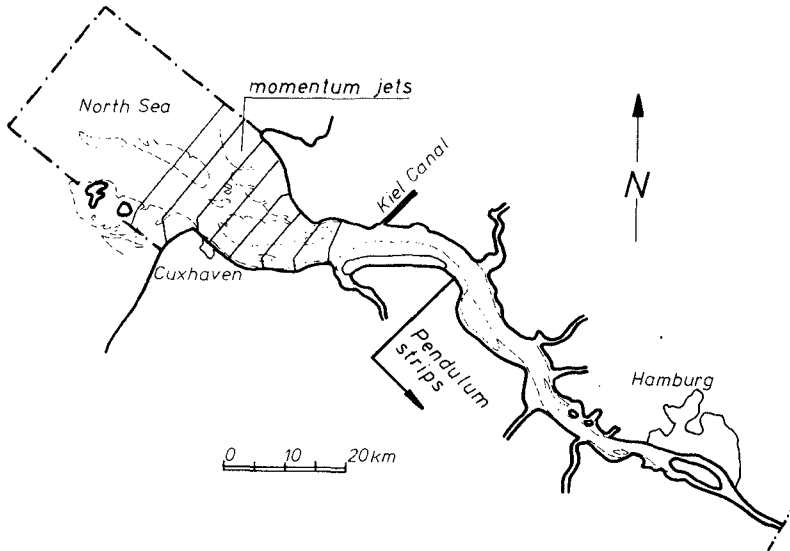


Fig. 5
Location of momentum jets in the model

The course of the storm surge over the whole estuary was in almost good agreement with the natural course.

5.3 PENDULUM STRIPS

However, the fall of the storm tide after highest highwater had to be corrected by additional roughness elements effective only in the ebbstream phase. Fixed roughness elements for the simulation of mean tides are thus modified by flexible roughness elements in the form of pendulum strips (Fig. 6). These strips are raised by flood currents and placed in a vertical position by ebb currents, which causes increased friction in the flow direction, while the flood currents are not influenced by this kind of roughness element. The use of flexible roughness elements yielded a still better agreement between model and prototype storm surges.

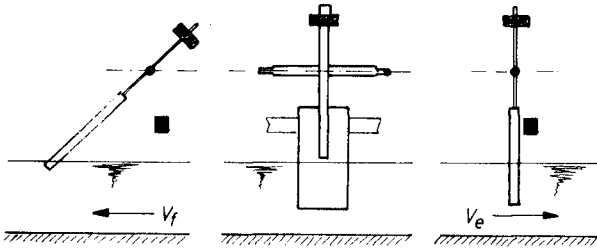


Fig. 6
Pendulum strips

6. CONCLUSION

It was possible to find out the reason for the difficulties in reproducing storm surge events in physical models of estuaries with wide flat areas. The importance of the necessity of not underestimating the influence of flat areas on the simulation of storm tides was pointed out.

On this basis a new method for such investigations including the consideration of the influence of local winds was developed and successfully applied. By means of momentum jets and pendulum strips it was possible to achieve a good agreement with natural courses of storm surges.

Finally it should be pointed out that up to now the idea for this new method and its application exists for one physical tide model after some basic tests in a plume. However, further research is needed, in particular to modify the facilities of this new development.

7. REFERENCE

- (1) SIEFERT, W.: Über das Sturmflutgeschehen in Tideflüssen (On storm tides in rivers) Mitteilungen des Leichtweiß-Instituts für Wasserbau der Technischen Universität Braunschweig, Heft 63 (1978)

CHAPTER 150

COMMENTS ON TIDAL ENTRANCES ON SANDY COASTS

by

Morrrough P. O'Brien, * Hon.M. ASCE

FLOW AREA-TIDAL PRISM

The information necessary for computation of the tidal prism is available in charts and tide tables for many inlet-bay systems. Empirical correlations have been developed by Le Conte in 1905, O'Brien in 1931 and 1969, and others, which showed the flow area to be a unique function of the tidal prism for the sets of data studied. However, the data underlying these correlations were derived from inlets with semi-diurnal tides, typical of the Atlantic and Pacific Coasts of the United States. Jarrett in 1976 showed that such correlations are not valid for diurnal and mixed tides, such as occur along the Gulf Coast.

Stevenson in 1874 pointed out that the scouring capacity of the tide must include the number of tidal cycles per year. Since the number of tidal cycles in any period of time is inversely proportional to their duration, the integrated scouring capacity of the tidal flow through an inlet channel should be independent of the duration of the tidal cycle and should depend primarily on the tidal discharge. If the maximum rate of tidal discharge (Q_{\max}) and the variation of discharge throughout the tidal cycle are identical for two inlets subjected to tidal cycles of different duration, the scouring capacity of the two inlets would be the same over equal periods of time. The conclusion is that Q_{\max} should provide a more generally valid basis for correlation with the flow area than does the tidal prism alone and one which may be valid at hydraulic model scale and for inlets maintained by the seiching of nontidal lakes, as at Duluth. Bruum (1978) used the correlation of the flow area with Q_{\max} in his studies.

Keulegan's (1951) analysis of inlet flow yielded the relationship

$$Q_{\max} = \pi CP/T \quad (1)$$

Here, C is a coefficient which ranges from 0.81 to 1.0, with 0.86 as a generally applicable value. The minimum flow area A_C should be correlated with either Q_{\max} or (P/T) to be applicable to diurnal, semi-diurnal, and mixed tides and to periodic flows in general.

If the maximum rate of discharge to be correlated with the flow area has been measured directly, rather than derived from the tidal prism through Eq. 1, this value must be corrected to that which would occur on a standard range of tide. This correction will require, in

* Dean Emeritus and Professor Emeritus, College of Engineering, University of California, Berkeley.

effect, the establishment of a rating curve, or discharge coefficient for the inlet. Furthermore, the corrected maximum rates of discharge on flood and ebb are seldom equal and a choice must be made as to which phase is generally more effective in maintaining the flow area. The first correlations were based on Pacific Coast data where the tide shows a diurnal inequality, with the "long-runout" following higher high water and the diurnal range, and the related strong ebb current was selected for the correlation. This characteristic is not found in Atlantic and Gulf coast tides and, for these inlets, the spring range has usually replaced the diurnal range. Although the ratio of the spring range to the mean range is numerically about equal to that of the diurnal range, the hydraulic effects may be very different, since ebb may not be dominant over flood at the time of the spring range. In future studies of the correlation between tidal discharge and flow area, use of the mean tidal range would probably be more significant. The generalized correlation between tidal flow and flow area might be

$$A_c = f(Q_{\max}) \text{ or } f\left(\frac{\pi CP}{T}\right) \quad (2)$$

depending upon whether the measured flow or the or the tidal prism, from charts and tide gages, is the source of data.

HYDRAULIC CHARACTERISTICS

Brown-Keulegan Analysis - Brown (1928) analyzed the flow through a tidal inlet on the basis of the following simplifying assumptions:

- The tidal variations in both ocean and bay are sinusoidal.
- The flow area of the inlet channel (below MSL) is constant (prismatic) from ocean to bay.
- The surface area of the bay does not vary with the tide stage in the bay.
- The surface of the bay remains horizontal throughout the tidal cycle.
- The depth of the inlet channel is large as compared with the range of tide.
- The difference in head necessary to accelerate the mass of water in the inlet channel is neglected.
- There is no surface runoff into the bay.

These assumptions are repeated here to emphasize the degree to which Brown's inlet-bay system was idealized; the configurations of almost all real inlets differ markedly from these assumptions.

Keulegan (1951) recognized that a sinusoidal tide in the ocean would not produce a sinusoidal tide in the bay because the flow through the inlet channel is proportional to the square root of the difference in head; otherwise, he made the same assumptions as Brown. He found

that the ratio of the tide in the bay to that in the ocean, the lag of slack water in the inlet channel after HW or LW in the ocean, and the maximum velocity in the inlet channel could be represented as functions of a dimensionless quantity which he designated as the repletion coefficient,

$$K = \frac{T}{2\pi a_0} \frac{A_C}{A_B} \sqrt{\frac{2ga_0}{F}} \quad (3)$$

The quantities in Eq. 3 are the major variables affecting inlet flow. This coefficient provides a useful means of ordering and analyzing inlet flow data, even though it is based on highly idealized assumptions. Keulegan compared his results with those of Brown in the high range of K-values, where the difference should be greatest, and found that Brown's method yielded values of maximum velocity between 10 and 15 percent greater than did his method. Probable errors in the data usually available are of the same magnitude as the difference between the relationships developed by Brown and Keulegan and Brown's method is much simpler in application. Following Brown, assume that the tidal fluctuations in the bay are sinusoidal. High water in the bay occurs at slack water in the inlet channel; the amplitude of the bay oscillation (a_b) is related to the ocean amplitude (a_0) and the lag of slack water after HW or LW in the ocean (ϵ , deg) as

$$a_b = a_0 \cos \epsilon \quad (4)$$

If the flow conditions in the inlet are as assumed, the difference, Δ , defined as

$$\Delta = \frac{a_b}{a_0} - \cos \epsilon \quad (5)$$

should be zero. When Δ is plotted as a function of inlet size, small inlets show a random scatter about the zero line but, with increasing size of inlet, the values of Δ become increasingly positive. Refinement of the value of Δ by using the more precise method of Keulegan plus corrections for the effects of variations in the flow area and the bay area with tide stand and of the inertia of the mass of water in the inlet channel would probably reduce the scatter of points somewhat but would not explain the systematic increase of Δ for large entrances. The entrances included in this study show fairly good agreement with the flow area-tidal prism correlation.

The explanation of the increasing value of Δ with size of inlet is believed to be that the flow through the inlet channel is not wholly of the "hydraulic" type assumed but is, in some degree, that of a long wave. A good illustration of this difference is the flow at the mouth of the St. Johns River (Florida) where the value of Δ is approximately 0.95; the strength of flood very nearly coincides with HW and the strength of ebb with LW; the lag of slack water is 92° and the ratio of the ranges, a_b/a_0 is 0.90. This entrance leads into a river channel leaving substantially constant average depth and width; the characteristics of the flow are those of a long wave in shallow water.

Considering tidal entrances of increasing width, the depth does, in general, not increase in proportion to the width, and it seems reasonable that the tide should enter large entrances primarily as a wave. If this is the case, the average velocity in the channel should follow approximately the equation

$$u = a_0 \left(\frac{g}{h} \right)^{1/2} \quad (6)$$

Comparing Eq. 6 with the average of flood and ebb currents reported in the Current Tables for a few representative entrances:

	Mean Ocean Range (ft)	Mean Inlet Range (ft)	Lag Slack Water (deg)	Average Depth (ft)	u_w (ft/sec)	From Tables
Narrows	4.5	4.5	64	61	3.3	3.1
Delaware	4.4	4.1	44	38	2.0	3.1
Chesapeake	3.5	2.9	116	25	2.0	2.1
Port Royal	6.4	6.4	51	40	2.9	3.0
St. Johns R.	5.4	4.9	92	31	2.7	3.5
San Francisco	4.2	4.0	56	176	0.9	5.3

The ocean range shown in this table is the range on the outer coast remote from the entrance; the range at "inlet" is that at the station at or inside the throat. At San Francisco, the throat section (Golden Gate) is bounded by rock and the width there is small in proportion to the depth.

If the calculation of the lag angle and of the ratio of ranges is refined by considering the effects of inertia, flow area, bay surface area and surface runoff, the positive value of Δ may be an indicator of the extent to which the flow through the inlet channel is "hydraulic," as assumed by Brown and Keulegan, or "long wave."

Corrections for the effects of deviations from the simplifying assumptions of Brown and Keulegan have been studied by Oliveira (1970), King and Shemdin (1974), Seelig and Sorensen (1978), Mehta and Ozsoy (1978), Escoffier and Walton (1979), and others.

Other useful approximate relationships, derived on the assumption that the tide in the bay is sinusoidal, are that the maximum head difference between ocean and bay and the maximum channel velocity

$$h_{\max} = 2a_0 \sin \epsilon \quad (7)$$

$$V_{\max} = \left(\frac{2ga_0 \sin \epsilon}{F} \right)^{1/2} \quad (8)$$

Equation 8 is a convenient means of determining the impedance of an entrance because a_0 , ϵ , and V_{\max} can be obtained for many entrances

from the tide and current tables. If ϵ and V_{\max} are not available, they may be measured at the throat section with little difficulty.

O'Brien and Clark (1973) used Eq. 8 to compute the value of the impedance (F) for a number of inlet channels having simple geometry and to determine the value of the friction coefficient (f) and the Manning roughness coefficient (n) from

$$F = 1 + \frac{fLc}{4Rc} \quad (9)$$

$$n = 1.48 Rc^{1/6} \left(\frac{f}{8g} \right)^{1/2} \quad (10)$$

Entrances	Lc(H)	Rc(H)	F	f	n
Fire Island	33,100	13.8	16	0.025	0.022
E. Rockaway	11,100	13.7	10.5	0.047	0.022
Indian River	4,200	10.6	15.3	0.143	0.051
St. Marys	15,200	32.8	7.6	0.057	0.039
Lake Worth	1,900	20.9	5.9	0.220	0.071
Humboldt B.	2,690	17.9	5.1	0.110	0.049
San Diego	18,860	40.9	6.7	0.049	0.038

Keulegan measured the friction loss in the relatively uniform inlet channel at Indian River between the ocean and the seaward side of the bridge; his value of n was 0.046. The value in the table included the head loss through the bridge piers. No direct measurements were available for comparison with the other figures in the table, but the close agreement for Indian River lends credence to the other values.

STABILITY OF INLETS

Escoffier (1940) treated the stability of an inlet from the purely hydraulic standpoint by assuming progressive changes in the flow area and hydraulic radius and computing the corresponding maximum tidal velocity during a tidal cycle. He showed that there is a critical flow area at which the maximum tidal velocity is greatest and concluded that, at larger areas, the inlet will be stable because a decrease in area will cause increases in the maximum velocity and in the scouring capacity. Conversely, at areas less than the critical area, an inlet will be unstable because a decrease in area will cause a decrease in velocity. O'Brien and Dean (1972) modified this approach by making assumptions regarding the manner in which sediment encroachment would change the effective length as well as the flow area and hydraulic radius. Their results also showed a critical flow area and maximum tidal velocity with implications regarding stability similar to those of Escoffier.

Bruun (1978) treats inlet stability in terms of the balance between the scouring capacity of the tidal flow, represented by

Q_{\max} , and the magnitude of the littoral transport. This approach, which is believed to be basically sound, considers the two major factors affecting inlet stability, but its quantitative application is limited by the uncertainty over the magnitude of the littoral transport at many inlets, especially regarding the local sand movement under storm wave intensity. Oliveira (1970) broadened the Brown-Keulegan analysis of inlet flow by including the effects of varying both flow area and lagoon surface area during the tidal cycle and computed the scouring capacity of the tidal currents; he showed that the bed load capacity reached a maximum value when the Keulegan coefficient of repletion was within the range $0.6 < K < 0.8$. His other results of significance were that the duration of the ebb phase exceed the flood and that the mean level in the bay was above that in the ocean.

Consider first an inlet-bay system which fulfills the Brown-Keulegan assumptions. The maximum hydraulic power available for scouring the channel occurs when the head and the related rate of discharge are at their maximum values; the maximum head available is a function of the phase difference between the ocean and bay tides.

$$\begin{aligned}
 P_{\max} &= w Q_{\max} h_{\max} \text{ (Max. Power)} \\
 Q_{\max} &= \frac{\pi C P}{T}; \quad P = 2 a_b A_B \\
 a_b &= a_o \sin \epsilon; \quad h_{\max} = 2 a_o \cos \epsilon \\
 P_{\max} &= \frac{4w\pi C}{T} A_B a_o^2 \sin \epsilon \cos \epsilon \quad (11)
 \end{aligned}$$

Consequently, the maximum hydraulic power would be available in the inlet channel under the idealized conditions assumed if the lag angle ϵ is 45° , corresponding to $K \cong 0.63$. The total energy available on either the flood or ebb phases would be

$$E = \frac{8}{\pi} \cdot A_B a_o^2 \cos \epsilon \sin \epsilon \quad (12)$$

Again, the maximum value corresponds to $\epsilon = 45^\circ$ and $K \cong 0.63$.

These relationships are pertinent to the analysis of the stability of an inlet because the energy available will increase or decrease as changes in the geometry or the hydraulic characteristics change the value of K . If $K > 0.64$, a decrease in K would cause an increase in the energy available for scouring the channel; such a decrease might be caused by a choking down of A_b , or an increase in F , or both. Conversely, if $K < 0.64$, a decrease in K will bring a decrease in the energy available, which may then lead to a further decrease in the value of K .

The obvious disparity between the simplifying assumptions made by Brown and Keulegan and the configuration of real inlet-bay systems and between their theoretical results and field measurements has led to studies of the effects of deviations from the assumed conditions, as

mentioned earlier, and it is now possible to correct, at least approximately, for such effects as are caused by variations in the surface area of the bay, the inertia of the mass of water in the inlet channel and so forth. The coefficient of repletion

$$K = \frac{T}{2\pi a_0} \frac{A_C}{A_B} \sqrt{\frac{2ga_0}{F}} \quad (13)$$

includes the major variables affecting the hydraulics of an inlet-bay system, and it appears to be the most illuminating single descriptor of such systems. Of the variables entering K , the impedance, F , is usually that one most in question; its value may be determined, at least approximately, by methods described earlier.

The coefficient of repletion should be regarded as one of a number of dimensionless parameters which may be used to describe quantitatively real inlet-bay systems. Used in this sense, the quantitative relationships between K and the magnitude and occurrence of maximum energy and other variables will probably be altered to some degree by the interaction with the other parameters. As mentioned earlier, Oliveira (1970) employed a numerical model to determine the effect of systematic variations of the flow area and the surface area on the scouring capacity at the throat and found that this capacity had a maximum value in the range $0.6 < K < 0.8$ for the conditions he considered, indicating that the maximum for real inlets may not lie far from that of the idealized models of Brown and Kuelegan.

It should be emphasized that this discussion has dealt only with the energy available for maintaining an inlet channel. The effectiveness of this energy in doing so will depend upon the initial configuration and hydraulic conditions and on the character of the changes which occur subsequently. A large value of the coefficient of repletion should signify a strong capability for maintaining a stable channel and a low value, the reverse; corrections for the effect of variations in flow area, inertia and other effects will improve the accuracy in predicting the actual value of K at which the energy would be a maximum. Such calculations require, however, assumptions regarding changes in the configuration or the hydraulic conditions which would induce a change in K ; the uncertainty here is of the same nature as that involved in the other approaches to stability, previously discussed.

The energy considerations discussed here may shed some light on the method of formation of barrier islands and inlets. If an embayment is gradually enclosed by the growth of a sand spit, the value of the repletion coefficient would be very large initially but would decrease as the spit continued to grow and to reduce the flow area; this process would increase the energy available for scouring the opening and presumably this process would continue until the tidal discharge becomes capable of sweeping away the littoral transport and establishing an equilibrium condition. However, the maximum energy potentially available for maintaining an inlet might not be sufficient to balance the littoral transport, in which case the spit would continue to grow and gradually close

the opening, passing through a condition of marked instability before closure. On the other hand, if the barrier has been developed as a continuous ridge, such inlets as are formed in it might have any initial coefficients of repletion.

INLET CLOSURE

The final closure of natural inlets occurs primarily under storm conditions. It is also true that waves and surge from extreme storm conditions occasionally enlarge or open inlets. These notes deal with the closure of inlets by wave conditions which are abnormal relative to the local wave climate but which are not so extreme as to overwash or break through the adjacent sand spits. There are examples of inlets which have been closed under non-storm conditions by a persistent or excessive littoral transport, but these inlets were, for the most part, small artificial cuts; under such conditions of excessive transport, natural inlets are usually found to be long-since closed, leaving a fresh-water lagoon as the evidence that an inlet once existed.

An important factor in the conditions which determine whether or not an inlet will be closed is the configuration of the shore and bottom seaward of the throat; the volume of sand in offshore shoals, jetties, overlapping or offset spits, rocky headlands and other natural or artificial features in the vicinity of the channel may affect both the volume of sand movement required for closure and the rate of deposition. The variety of such conditions is almost unlimited; data on the conditions which have caused closure should be categorized under inlet configurations. These notes consider a simple inlet channel without jetties through a straight, sandy shoreline with ebb-tide outer bar and zero offset. On a segment of coast exposed to essentially the same wave climate under normal weather conditions, storms may produce substantial differences in winds, wave characteristics and surge within relatively short distances and over short time intervals. Observations on the conditions which actually caused closure are subject to considerable uncertainty and much scatter of the data is to be expected. The duration of storms is at most a few days and is the same for small and large inlets on the same segment of coast. Closure of an inlet requires time for the movement of material and the closure of a large inlet should require either a longer duration or a greater intensity of wave-induced sand movement than for the closure of a small one.

There have been a number of studies of the conditions under which inlets close. Johnson (1974), Sedwick (1975) and Mehta and Hou (1974) have proposed criteria which differ in detail but which, in essence, compare the sand-transporting capacity of the wave climate with the potential scouring capacity of the tide and have located a boundary zone between closed and open inlets by examples from the Pacific Coast, Florida and Long Island. Data on this phenomenon are not plentiful and almost none pertain to the actual conditions at the time of closure. If an inlet has been closed for some time, the data regarding tidal prism and scouring capacity consist of the surface area of the lagoon and the tide range and duration in the ocean; hydraulic analysis of the flow

conditions would be questionable, and the potential tidal prism has been used. On the other side of this boundary are the small inlets which are still open; the specific wave intensities to which they have been subjected is usually uncertain, and a representative figure has been derived from the wave climate. Apparently, there is only one example of the measurement of waves and tides during closure of a natural inlet, and that a very small one (Mehta and Hou, 1974); there is one set of laboratory tests on closure (Saville and Simmons, 1957). However, despite these limitations these studies have served to define approximately criteria which separate closed and open inlets and which clearly show an upward trend in the required wave intensity with increasing tidal prism.

The studies of closure just mentioned yielded criteria which were based upon average or representative conditions, such as the tidal prism on a mean range of tide or the annual or seasonal average wave intensity; they are not representative of the actual conditions existing at the time of closure and, consequently, they should be regarded as an indication of the vulnerability of an inlet to closure; over an extended period of time, an inlet with a value of the criterion in the "closed" region will probably close sometime, but it may not do so. The equilibrium condition of an inlet is really the statistical average of conditions which change somewhat with every change in incident waves and tide range; perhaps what is visualized as the equilibrium conditions is the bathymetry "frozen" in a survey. If the concept of equilibrium as the balance between wave-induced sand movement and tidal scour is correct, even the most stable inlets must experience continuous changes under the influence of the sequence of tidal ranges and the variations in normal wave conditions. Littoral transport along the adjacent shore moves sand toward or away from the vicinity of the inlet; waves plus flood and ebb currents bypass sand across the inlet, store it in ebb or flood shoals, or carry it to deep water. What is the nature of the changes in this regimen caused by an abrupt transition to storm conditions? The littoral transport is a function of the alongshore component of wave power per unit length of shore. The tidal currents may be altered slightly by the storm surge and consequent super elevation of the bay. The volume of sand movement onshore or offshore from the ebb shoal and bottom is probably some function of the tidal currents plus the component of wave power perpendicular to the shore, multiplied by the width of the inlet opening. Under the normal range of wave and tide conditions, sand movements balance and change is minimal but a drastic increase in wave power probably results in a strong shoreward sand movement, which is large as compared with the concurrent littoral drift. Considering the conditions existing at the time of closure, a criterion suggested is

$$M = \frac{W \cdot I_p \cdot T_F}{P_E a_b} \quad (14)$$

where:

- W = width of throat
- I_p = component of wave power perpendicular to shore per unit length
- T_F = duration of flood

a_b = range of tide in bay
 P_E = volume of the ebb tide.

This criterion is the ratio of the energy delivered by wave action during the flood phase of the tidal cycle studied to the energy available in the ebb flow of the same tidal cycle. Since the tide range and the wave intensity will vary during a storm, this criterion should be computed, if possible, for each cycle during a storm. Other quantities might be substituted, if more convenient. The concept represented is that the wave energy delivered over the width of an inlet will dominate the sand movement during a storm and will be the principal agent of closure.

Data necessary for developing a quantitative criterion of closure will be extremely difficult to obtain in nature. Hydraulic models may offer a means of establishing, at least qualitatively, the relative importance of the variables, such as the onshore component of wave power. Although surface wave models may not be distorted and this requirement leads to large models, a compensating factor is that the turbulence of breaking waves seems to permit smaller models for similarity. The experiments of Mayor-Mora (1973) and the CERC-WES program (Saville and Simmons, 1957) seems to show that movable-bed wave models of reasonable size responded to waves and currents in a manner similar, in flow characteristics, to the behavior of natural inlets.

REFERENCES

- Brown, E. I., "Inlets on Sandy Coasts," *Proc. Amer. Soc. of Civil Engrs.*, Vol. 54, Part 1, Feb., 1928, pp. 505-523.
- Bruun P., *Stability of Tidal Inlets: Theory and Engineering*, Elsevier Scientific Pub. Co., 1978, 510 pp.
- Escoffier, E. E., "The Stability of Tidal Inlets," *Shore and Beach*, Vol. 8, No. 4, Oct., 1940, pp. 114-115.
- Escoffier, E. F., and Walton, T. L., "Inlet Stability Solutions for Tributary Inflow," *Jour. Waterways, Port, Coastal and Ocean Div.*, ASCE, Vol. 105, No. 4, Nov. 1979, pp. 341-355.
- Jarrett, J. T., "Tidal Prism-Inlet Area Relationships." *GITI Report No. 3*, Coastal Engineering Research Center, Corps of Engineers, 1976.
- Johnson, J. W., "Characteristics and Behavior of Pacific Coast Tidal Inlets," *Jour. Waterways, Harbors and Coastal Engrg. Div.*, ASCE, Vol. 99, No. WW3, Aug. 1974, pp. 325-339.
- Keulegan, G. H., "Water Level Fluctuations of Basins in Communications with Seas," *Third Progress Report on Tidal Flow in Entrances*, U. S. Beach Erosion Board, 1951.

- Keulegan, G. H., "Tidal Flow in Entrances. Water-Level Fluctuations of Basins in Communication with the Sea," *Tech. Bulletin No. 14*, Committee on Tidal Hydraulics, Corps of Engineers, 1967.
- Keulegan, G. H., and Hall, J. V., "A Formula for the Calculation of the Tidal Discharge Through an Inlet," *U. S. Beach Erosion Board Bulletin*, Vol. 4, No. 1, 1950, pp. 15-29.
- King, D. B., and Shemdin, O. H., "Dynamics of Inlets and Bays," *Tech. Report No. 22*, Coastal and Oceanographic Engrg. Lab., Univ. of Florida, Gainesville, 1974.
- Kondo, Hideo, "Design Procedure of Artificial Channels for Tidal Entrances," *Coastal Engineering in Japan*, Vol. 21, 1978, pp. 191-199.
- LeConte, L. J., Discussion of "Notes on the Improvement of River and Harbor Outlets in the United States" by D. A. Watt, *Trans. Amer. Soc. Civil Engrs.*, Vol. LV, Dec. 1905, pp. 306-308.
- Mayor-Mora, R. E., "Hydraulics of Tidal Inlets on Sandy Coasts," *Hyd. Engrg. Lab. Tech. Report HEL 24-16*, Univ. of California, Berkeley, Aug. 1973, 241 pp.
- Mehta, A. J., and Hou, H. S., "Hydraulic Constants of Tidal Entrances II: Stability of Long Island Inlets," *Tech. Report No. 23*, Coastal and Oceanographic Engrg. Lab., Univ. of Florida, Gainesville, 1974.
- Mehta, A. J., and Ozsoy, E., Chapter 3, "Inlet Hydraulics," in *Stability of Tidal Inlets: Theory and Engineering* by P. Bruun, Elsevier Scientific Pub. Co., 1978, 510 pp.
- O'Brien, M. P., "Estuary Tidal Prism Related to Entrance Areas," *Civil Engineering*, Vol. 1, No. 8, 1931, pp. 738-739.
- O'Brien, M. P., "Equilibrium Flow Areas of Inlets on Sandy Coasts," *Jour. Waterways and Harbors Div.*, ASCE, Vol. 95, No. WW1, 1969, pp. 43-52.
- O'Brien, M. P., and Clark, R. R., "Hydraulic Constants of Tidal Entrances I: Data from NOS Tide Tables, Current Tables, and Navigation Charts," *Tech. Report No. 21*, Coastal and Oceanographic Engrg. Lab., Univ. of Florida, Gainesville, 1973.
- O'Brien, M. P., and Dean, R. G., "Hydraulics and Sedimentary Stability of Coastal Inlets," *Proc. 13th Conference on Coastal Engrg.*, ASCE, Vol. II, Chap. 41, 1972, pp. 761-780.
- Oliveira, I. B. Mota, "Natural Flushing Ability of Tidal Inlets," *Proc. 12th Conference on Coastal Engrg.*, ASCE, Vol. III, 1970, pp. 1827-1845.
- Saville, T., Jr., and Simmons, H. B., "Preliminary Report: Laboratory Study of the Effect of an Uncontrolled Inlet on Adjacent Beaches," *Tech. Memo 94*, Beach Erosion Board, 1957.

Sedwick, E. A. "Hydraulic Constants and Stability Criterion for MOB Inlet," M.S. thesis, Coastal and Oceanographic Engrg. Lab., Univ. of Florida, Gainesville, 1975.

Seelig, W. N., and Sorensen, Robert M., "Numerical Model Investigation of Selected Tidal Inlet-Bay Characteristics," *Proc. 16th Conference on Coastal Engrg.*, ASCE, 1978, p. 1302.

Stevenson, Thomas, *Design and Construction of Harbors: A Treatise on Maritime Engineering*, 2nd edition, Edinburgh, 1874.

SYMBOLS

a_b	range of tide in bay
a_o	amplitude of the ocean tide (range = $2a_o$)
a_B	amplitude of tide in the bay
A_B	surface area of the bay
A_C	flow area at the throat below MSL
b	surface width of inlet throat at MSL
c	Keulegan coefficient to correct the tidal prism for nonsinusoidal tide in bay
E	potential tidal energy available for scouring the channel on either phase of the tide
F	impedance of the inlet channel ($= \Sigma k + f L_c / 4 R_c$)
f	friction coefficient
g	gravitational force per unit mass
h	difference between surface elevations of ocean and bay
I_p	component of wave power shore normal per unit length of shore
k	coefficient of velocity head loss
K	coefficient of repletion
L_c	length of hypothetical channel of area A_C having same friction loss as real channel
M	criterion of closure
n	roughness coefficient in Manning's equation
P_{max}	maximum tidal power
P	volume of the tidal prism
P_E	volume of a particular ebb tide

Q_{\max}	the maximum rate of discharge during either phase of the tidal cycle
R_c	hydraulic radius of A_c
T	duration of the tidal cycle
T_F	duration of flood
W	width of throat
ϵ	lag of slack water after HW or LW

CHAPTER 151

TIDAL PRISM-INLET AREA RELATIONS FOR SMALL TIDAL INLETS

R.J. BYRNE, R.A. GAMMISCH and G.R. THOMAS

Virginia Institute of Marine Science
College of William and Mary
Gloucester Point, Virginia, 23062, U.S.A.

ABSTRACT

Fourteen tidal inlets within the lower Chesapeake Bay were studied to examine whether significant differences existed in their hydraulic behavior relative to the larger oceanic inlets hitherto studied. Measurements included simultaneous external and internal tides, gaging of discharge through a tidal cycle, measurements of inlet geometry, and basin area. The results indicate that: a.) smaller inlets ($A_c < 100 \text{ m}^2$) depart from the relationship between inlet throat area and tidal prism developed for oceanic inlets; b.) examination of inlet width versus depth indicates the departure from ocean inlet geometry occurs at A_c values between 100 and 500 m^2 ; c.) the maximum velocity in smaller inlets is significantly less than oceanic inlets (~ 0.35 vs 1.0 m/s); d.) tidal phase lags and tidal range ratio were generally equal. However, for conditions of significant tide range reduction, the low water phase lags more closely approximated the tide range ratio.

INTRODUCTION

It is generally recognized that inlets possessing a stable entrance cross-section reflect a dynamic balance between wave driven sand transport processes tending to close the entrance and the tidal flows tending to maintain the channel. A relationship between the tidal prism and the inlet throat cross-sectional area was presented by O'Brien (1969, and earlier); for inlets without jetties

$$A_c = 2.0 \times 10^{-5} \Omega, \text{ (FT)} \quad (1)$$

Jarrett (1976), analyzing a larger data set of inlets on the U.S. coasts, found differences between the Atlantic, Pacific and Gulf Coasts which he attributed to wave climate and tidal characteristics.

Rather than base the correlation upon the integral of the discharge, Bruun (1978, and earlier work) has related the throat area with maximum discharge as it, or the maximum velocity, more clearly designates the relevant bottom shear stress. For inlets of large depth relative to the tide range, Keulegan's analysis (1967) indicates the maximum discharge is proportional to the discharge. Thus, under simplified conditions, the two approaches are closely related. In both cases, the correlation between minimum flow area and the hydraulic parameter are taken to represent the condition of sedimentary equilibrium.

Departures from "equilibrium" conditions have also been considered by Escoffier (1940, 1977) and O'Brien and Dean (1972), who utilized the

analysis of Keulegan (1967). Basically, the approach gives an estimation of the resulting maximum velocity due to a change in the inlet area which is then compared with the velocity associated with the corresponding "equilibrium" area as derived, under simplifying assumptions, from Equation 1 or similar plots. The procedure provides a basis for prediction as to whether the inlet area will tend to return to "equilibrium" or toward closure. It is important to note that the method depends upon the empirically derived relationship between flow area and hydraulic parameters.

PURPOSE OF THE STUDY

Most previous studies have focused on oceanic inlets with relatively large entrances (throat areas $> 10^2 \text{m}^2$) or in small models (throat areas $< 10^{-1} \text{m}^2$). This study focuses on natural tidal inlets, the dimensions of which fall between oceanic inlets and the model scale. Interest in this mid-range exists because of increasing demand to improve navigability into such inlet-basin systems fringing the Chesapeake Bay. Moreover, the model results of Mayor-Mora (1977) suggested that very small systems may depart from the relationships developed for oceanic inlets. Those results showed that for a given tidal prism, the inlet area was an order of magnitude higher than that predicted by extrapolation of the oceanic inlet data.

Fourteen tidal inlets without jetties, Figure 1, in the lower Chesapeake Bay were studied in 1978 and 1979. The cross-sectional area of the channel throats varied between 25m^2 and 0.5m^2 so the data set extends the observed range of natural inlets by two orders of magnitude. The data set for each inlet includes basin and "ocean" tides, discharge gaged through a full tide cycle, the geometrical characteristics of the inlet channel, and the planform characteristics of the basin. The exposure to wave action varied widely with the fetch ranging between fractions of a kilometer to tens of kilometers. To insure that true inlet systems were considered, only those entrances connecting to basins with a tide range reduction or inlets whose histories otherwise demonstrated a dynamic balance between littoral drift and tidal scour were selected. A complete description of the inlet-basin systems, including available aerial photography, is given in Byrne, *et al.* (1980).

This paper reports on: a.) the observed inlet area-tidal prism relationship; b.) the geometry of the inlet throat; c.) the observed maximum channel velocity; d.) the observed phase lags between ocean and basin tides.

METHODS

Tides. The external and basin tidal fluctuations were measured either with Fisher-Porter recording gages, recording bubbler gages, or graduated plastic tubes with a small orifice to filter out wind wave action. In most cases, the external and internal tide measuring devices were leveled to a common datum.

Discharge. Instantaneous tidal discharge was obtained as the sum of area weighted velocity readings from an array of current meter across the channel. The vertical position of the small ducted impellor meters (Byrne and Boon, 1973) was maintained at 0.6 the water depth and values determined were accepted as local vertically averaged mean velocity.

Throat geometry. Channel cross-section profiles were obtained with level and rod reference to the tide recorders.

Basin area. Basin area was determined from aerial photography or plane table mapping with separate consideration given to total basin area and the fraction filled by marsh. The area-height relationship of the basins is currently under study (see also Boon and Byrne, 1981).

DISCUSSION OF RESULTS

Tidal prism-inlet area relationship

The relationship between tidal prism and inlet area, for semi-diurnal tidal conditions, is shown in Figure 2 for 15 Chesapeake Bay inlets, the model results of Mayor-Mora (1977) with tide and waves, and 34 Atlantic coast inlets (without jetties) presented by Jarrett (1976). The least square fit for these data sets are, in metric units:

$$\begin{array}{l} \text{Jarrett data:} \\ m = 34 \end{array} \quad \begin{array}{l} A_C = 6.954 \times 10^{-6} \Omega^{1.14} \\ \text{corr. coeff. } (r) = 0.97 \end{array} \quad (2)$$

$$\begin{array}{l} \text{Chesapeake Bay:} \\ m = 15 \end{array} \quad \begin{array}{l} A_C = 9.902 \times 10^{-3} \Omega^{0.61} \\ r = 0.87 \end{array} \quad (3)$$

$$\begin{array}{l} \text{Mayor-Mora:} \\ m = 17 \end{array} \quad \begin{array}{l} A_C = 7.61 \times 10^{-3} \Omega^{0.68} \\ r = 0.95 \end{array} \quad (4)$$

$$\begin{array}{l} \text{Chesapeake Bay plus Mayor-Mora:} \\ m = 32 \end{array} \quad \begin{array}{l} A_C = 8.079 \times 10^{-3} \Omega^{0.64} \\ r = 0.98 \end{array} \quad (5)$$

For the Chesapeake Bay data set (Tables 1 and 2), the tidal prism could be calculated either from the product of the open basin area and the spring tide range or from the integrated discharge curves which were then linearly scaled to spring tide range.

The ratio of the two prism values was found to vary directly with the open water fraction of the total basin area. This result may be expected since the calculation of prism as the product of tide range and open water basin area neglects the actual basin area-height conditions of the system. The values plotted in Figure 2 are the tidal prisms calculated from the discharge.

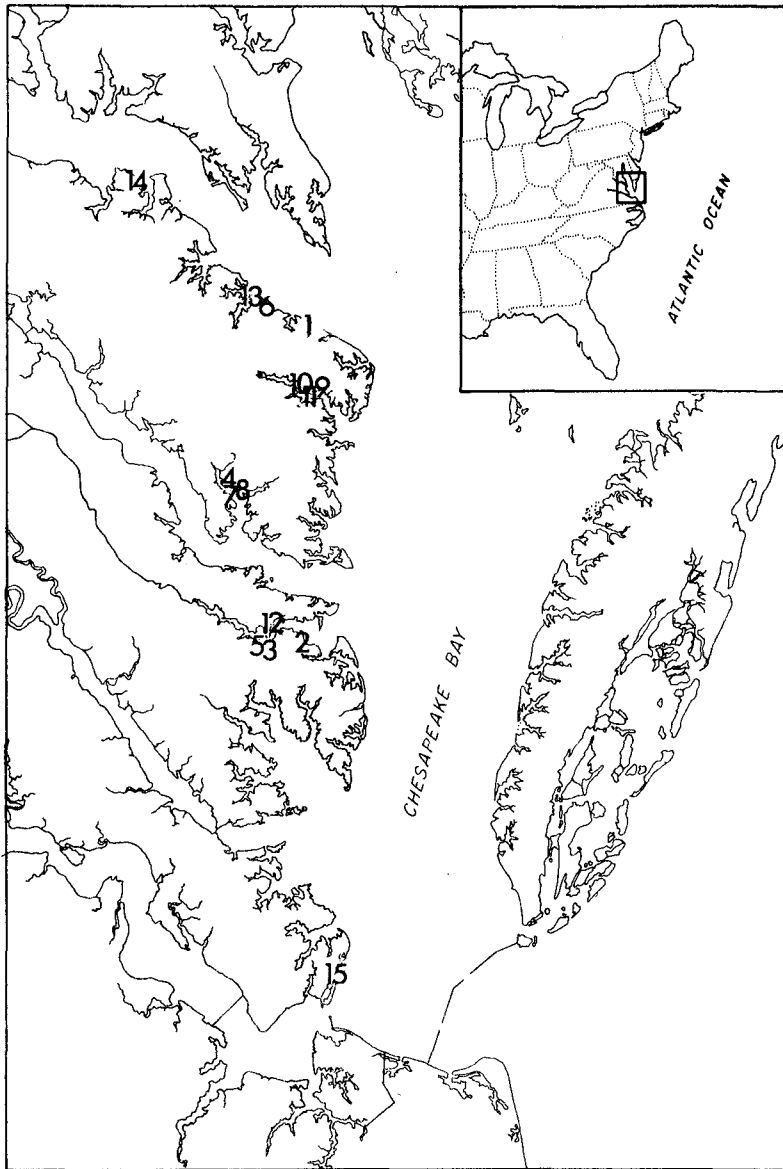


Figure 1. Location map; numbers identify inlets in Table 1.

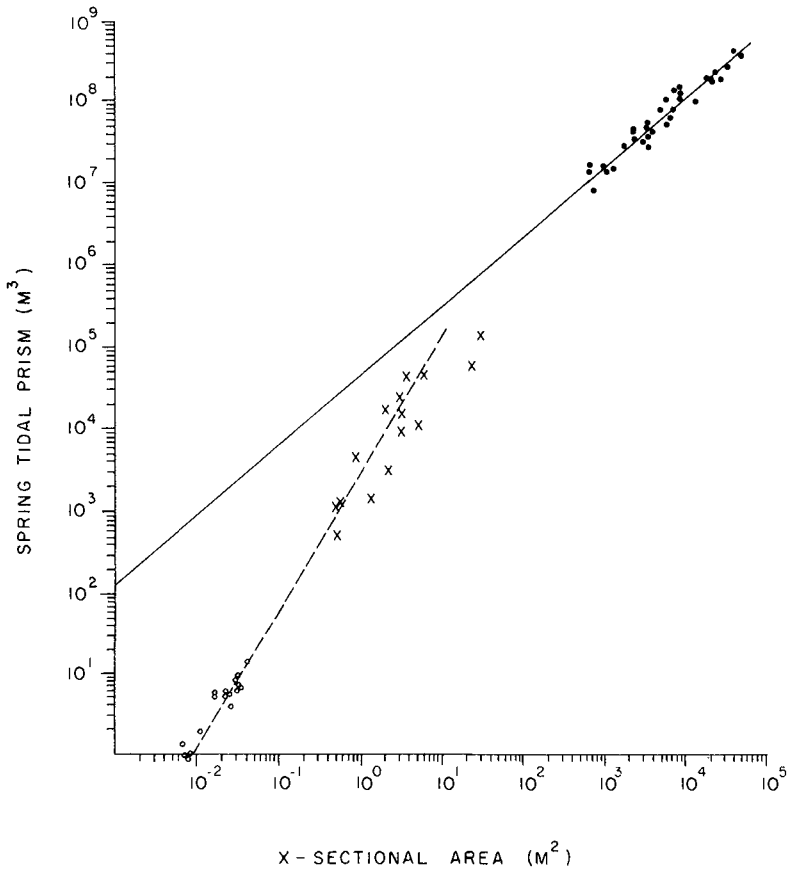


Figure 2. Tidal prism versus inlet throat cross-sectional area. Open circles are from Mayor-Mora (1977); closed circles are from Jarrett (1976); crosses represent Chesapeake Bay Inlets. All cases are inlets without jetties.

Table 1. Geometrical Characteristics of Inlet Systems.

NO.	INLET NAME	BASIN AREA PARAMETERS				CHANNEL PARAMETERS				
		TOTAL* (km ²)	PLUS WATER (m ²)	OPEN WATER (m ²)	% OPEN	Ac (MTL) m ²	AH AL	W (MTL) m	W/D	
1	CUBITT	9.11	874,900	709,000	81	3.90	2.2	15.2	58	
2	CHAPEL	2.89	166,700	118,700	71	3.20	2.6	6.6	14	
3	WADINGER	2.71	48,690	25,693	53	3.46	5.2	11.3	36	
4	JOHN	2.15	113,300	88,200	78	25.27	1.6	27.4	30	
5	BOUNDARY	0.65	12,733	6,638	52	0.91	3.6	3.4	13	
6	COD	0.34	62,100	62,100	100	2.13	3.2	4.2	8	
7	PALMER	0.33	27,700	26,700	96	5.67	2.4	11.3	22	
8	SCHOONMAKER	0.23	18,500	17,500	95	3.30	2.9	7.3	16	
9	MARINA	0.23	8,253	7,319	87	2.32	4.3	8.2	29	
10	HEADLEY	0.07	2,438	2,159	88	1.41	6.6	5.8	24	
11	KILDUFF	0.06	2,966	1,419	48	0.50	9.5	2.7	15	
12	LITTLE WILLIS	0.03	1,467	1,356	92	0.58	5.5	2.2	8	
13	LITTLE COD	0.04	3,894	3,203	82	(0.56)+	-	(1.5)	4	
14**	CABIN POINT	2.97	450,000	120,000	27	(6.4)	-	(16.7)	44	
15	SALT PONDS	4.04	530,000	200,000	38	(31.0)	-	-	-	

*Area of total drainage system, upland plus tidal basin.

**From Seelig, W.H., 1976.

+(), estimates.

Table 2. Hydraulic Characteristics of the Inlet Systems.

INLET NO.	TIDAL PRISM (SPRING) m^3	OCEAN SPRINC TIDE RANGE m	AVE. SPRING TIDE V_{max} m/s	DIMENSIONLESS DURATION OF TIDE		TIDE RANCE RATIO R_b/R_o	PHASE LAC $\cos \epsilon$	
				ebb	flood		ebb	flood
1	4.25×10^4	0.43	0.19	0.70	0.30	0.16	-	-
2	2.40×10^4	0.43	0.46	0.66	0.34	0.34	0.34	0.39
3	1.57×10^4	0.49	0.36	0.66	0.34	0.83	0.88	0.80
4	6.03×10^4	0.49	0.16	0.50	0.50	1.04	0.99	1.00
5	4.46×10^3	0.49	0.36	0.57	0.43	0.84	0.89	0.99
6	1.71×10^4	0.43	0.56	0.66	0.34	0.68	0.69	0.95
7	1.08×10^4	0.49	0.30	0.54	0.46	1.04	1.00	1.00
8	9.09×10^3	0.49	0.31	0.48	0.52	1.06	1.00	1.00
9	3.05×10^3	0.43	0.40	0.68	0.32	0.61	0.75	1.00
10	1.40×10^3	0.43	0.12	0.55	0.45	0.97	1.00	1.00
11	1.12×10^3	0.43	0.28	0.68	0.32	0.86	0.85	1.00
12	1.22×10^3	0.49	0.35	0.52	0.48	1.00	1.00	1.00
13	5.23×10^2	0.43	-	0.67	0.33	0.38	0.98	0.82
14	4.60×10^4	0.61	-	-	-	-	-	-
15	1.37×10^5	0.85	-	-	-	-	-	-

Mayor-Mora's experiments were conducted with combined scaled tidal action and waves. Tidal prism was calculated as the product of basin area and tide range. Since a natural quartz sand distribution $d_{50} = 0.34$ mm) was used, scale effects may be important.

Review of extant aerial photography indicates that the Chesapeake Bay inlets included in this study have existed for at least a decade which suggests they are not ephemeral. When only a single survey is performed on an inlet, the observed correspondence between inlet channel area and hydraulic parameters (prism, discharge, etc.) is assumed to approximate the condition of sedimentary equilibrium. Modulations around an average equilibrium flow area occur with changes in wave conditions and tidal height variations but recovery from extreme events may take only days (Byrne, et al., 1974). The inlet sites herein presented are exposed to relatively weak littoral drift so disturbances from "equilibrium" may require longer recovery times. Moreover, those systems with relatively large upland drainage basins (i.e. No. 1, Cubitt Creek) may have periodically large freshwater outflow which temporarily enlarge the channel throat area.

Given the assumption that the inlets studied do approximate conditions of sedimentary equilibrium, the results displayed in Figure 2 indicate the inlet area-tidal prism relationship deduced for oceanic inlets does not apply to smaller natural inlets. Inspection of the plotted points and the least squares analyses suggests that the transition zone between the oceanic and smaller inlets occurs near $A_c \approx 100 \text{ m}^2$ to 500 m^2 .

Geometry of the inlet throat

Oceanic inlets are generally considered to be hydraulically wide (hydraulic radius \approx mean depth). However, for smaller channels to remain stable, the cross-section must become more efficient. For example, for the oceanic inlets plotted in Figure 2 (Jarrett, 1976), the average value of $W/R \approx 337$ whereas the average value of $W/D = 23$ for the smaller Chesapeake Bay inlets herein reported. A dimensionless downstream view of channel geometry, scaled to a reference semi-circular cross-section, is shown in Figure 3. For comparison, a channel cross-section from Mayor-Mora's model results are included.

The departure of the width-depth characteristics of mid-range and model inlets from the ocean inlets is shown in Figure 4 (Mehta, 1976; Winton, 1979). While there is appreciable scatter in the data, the departure zone between the trend of the larger oceanic inlets alone and that of a smooth curve through all of the data appears to lie at an inlet area of about 100 to 500 m^2 , the same zone observed in the inlet area-tidal prism plot (Fig. 2).

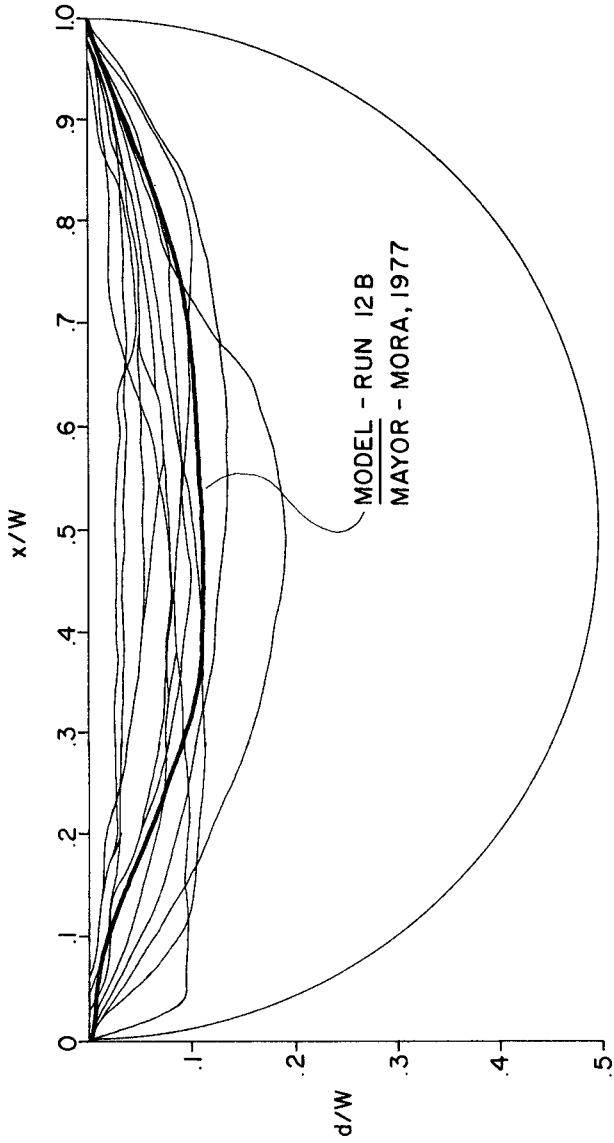


Figure 3. Dimensionless inlet throat geometry.

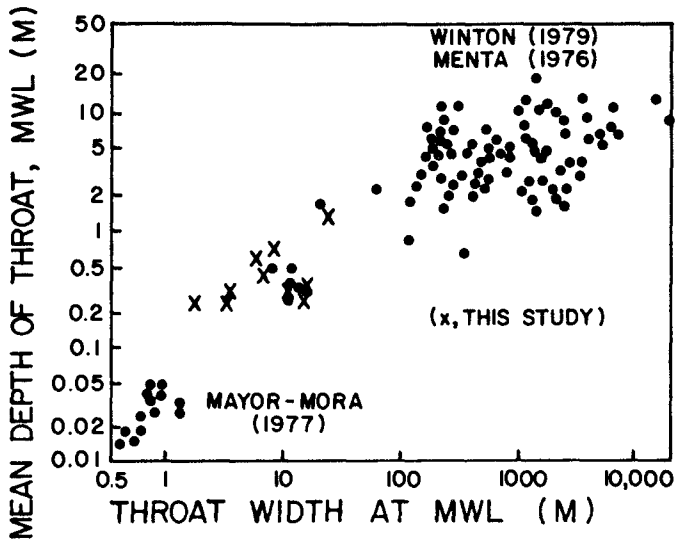


Figure 4. Width-depth relationship for inlets without jetties. After Winton, 1979.

Maximum velocity versus inlet area

As previously mentioned, the scouring capacity of the tidal current to maintain the inlet entrance may be represented by the maximum discharge ($Q_{\max} = A_c V_{\max}$). If the constraints leading to a sinusoidal time variation in discharge are accepted, the "equilibrium" relationship between channel area and tidal prism may be used to calculate the corresponding Q_{\max} or V_{\max} (Keulegan and Hall, 1950; O'Brien, 1969; Bruun, 1974). Following O'Brien:

$$\Omega = \int_0^{T/2} a v dt ,$$

and if $v = V_{\max} \sin \frac{2\pi t}{T} ,$

then $\Omega = \frac{A_c V_{\max} T}{\pi}$ or $Q_{\max} = \frac{\pi \Omega}{T} .$ (6)

Equation 6 may be expected to hold when $A_c \approx$ constant, and by definition, the duration of the ebb and flood currents are equal.

Combining Equations 1 and 6 and with $T = 12.4$ hours, O'Brien found $V_{\max} = 1.06$ m/s (3.5 fps). This value corresponds rather closely with values of $V_{\max} = 1.0 \pm 15\%$ m/sec reported by Bruun (1967) and Jarrett (1976) for a number of oceanic inlets.

Keulegan and Hall (1950) tested Equation 6 against gaged discharge at four oceanic inlets and concluded that a coefficient was required to account for deviations from a sinusoidal discharge ($Q_{\max} = C(\pi\Omega/T)$, $C = 0.86$). In his later theoretical development of inlet hydraulics for conditions of constant basin and channel areas, Keulegan (1967) found that the coefficient, C , may vary between 0.8 and 1.0.

The purpose of this section is to examine the relationship between V_{\max} and A_c for the smaller tidal inlets studied. As shown in Table 1, the channel cross-sectional area changes appreciably during the tidal cycles giving rise to distortions in the velocity time history. For comparative purposes, Figure 5 presents the measured values of V_{\max} with those calculated from Equation 6 for a smooth curve drawn through the combined data in Figure 1. That segment of the V_{\max} versus A_c curve derived from the Jarrett (1976) data ($A_c > 10^2$ m) indicate a decrease in V_{\max} as A_c increases. This result would arise as well from the application of Equation 6 to Equation 2 since the exponent in Equation 2 is greater than 1. This is likely to be an anomaly arising from a limited data set.

Three data sets are presented in Figure 5. Data associated with channel areas less than 10^{-1} m² are V_{\max} values averaged for flood and ebb from the model results from Mayor-Mora. The mid-range inlets of

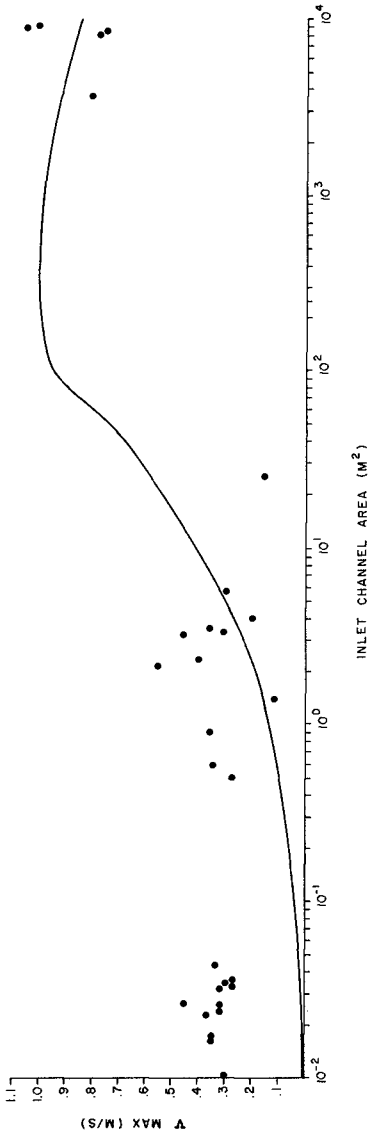


Figure 5. Observed maximum velocity versus throat cross-sectional area, A_c . Solid line is derived from smooth curve through points in Figure 2 and application of Equation 6. Data points for $A_c > 10^2 \text{m}^2$ from Jarrett (1976), points for $A_c < 10^2 \text{m}^2$ from Mayor-Mora (1977).

Chesapeake Bay ($10^{-1}\text{m}^2 < A_c < 10^2\text{m}^2$) represent the ebb and flood averaged values of V_{\max} after adjusting to spring tide conditions with $V_{\max}/\sqrt{ga_0}$ as the scaling parameter (Table 2). The unadjusted V_{\max} values were taken from curves of $\bar{v}(t) = q(t)/a_c(t)$ for each inlet. The data for $A_c > 10^3\text{m}^2$ are taken from Jarrett (1976) for inlets on the Atlantic U.S. Coast.

Inspection of Figure 5 indicates that V_{\max} for the model and mid-range (Chesapeake Bay) inlets cluster around the value of $V_{\max} \approx 0.35$ m/s. This may represent a limiting condition for the active transport of medium to fine sand sized sediments in the entrances and thus act as the limiting V_{\max} for stable inlets.

Phase lags and durations of flow

The analysis of Keulegan (1967) indicates that for a sinusoidal "ocean" tide and a horizontal water surface response in the basin (basin small relative to tide wave length), the tide range ratio (R_o/R_b) should equal the cosine of the phase lag between the times of high (low) water in the "ocean" and those of the lagoon. Keulegan's analysis was based, as well, on the assumption that the inlet depth was large relative to the tide, and that the inlet hydraulics were controlled by local head differences rather than a progressive wave through the entrance. O'Brien and Clark (1973) attempted to test the theoretical expectation for U.S. inlets using available current and tide data. Recognizing the appreciable scatter in the data, they concluded that for smaller entrances ($A_c/(\frac{1}{3}R_o)^2 < 10^4$) the theoretical expectation was reasonably approximated.

For small tidal inlets, the channel cross-sectional area may vary significantly during the tidal excursion which results in a distortion of the velocity time history such that a longer ebb flow duration over a reduced flow area is required to balance an equivalent tidal prism. Such were the conditions considered by Mayor-Mora in model experiments. He found the ebb flow durations to be greater than the flood durations and, correspondingly, that the phase lags between high waters were shorter than predicted in the Keulegan analysis while the low water lags were longer.

The mid-range inlets herein reported have significant variation in entrance channel area during the tidal excursion (high water area to low water area ranging between 1.6 to 9.5, Table 1). Accordingly, the observed distortions in the ebb and flood flow durations may be expected (Table 2). However, variations in the basin area with tidal stage induce an opposing effect leading to longer flood durations (Mota-Oliveira, 1970; Boon and Byrne, 1981).

Given the distorted durations of flow, Seabergh (1979) indicates that the phase lags may be weighted by the duration of ebb and flood flow:

$$\epsilon = \frac{\Delta t \text{ between basin and ocean high (low) tide}}{\text{duration of flood (ebb) flow}} \times 180^\circ$$

Inspection of Table 2 indicates there is generally good agreement between the tide range ratio, R_b/R_o , and $\cos \epsilon$. In those cases where there is substantial reduction of the basin tide range (inlets 2, 3, 5, 6, 9, 11), the ebb phase lag more closely corresponds to the resultant tide range ratio. Inlet 13 is an anomalous case arising from the fact that this entrance, crossing the foreshore of a beach, becomes perched at low tide which controls the basin tide range.

CONCLUSIONS

- 1.) The data on smaller tidal inlets indicate significant departures from the oceanic inlets in the relationship between throat cross-sectional area and tidal prism. For the cases studied, namely inlets on the Atlantic United States coast subject to semi-diurnal tides, the departures appear to exist for inlet areas less than 500 m^2 .
- 2.) Examination of the relationship between inlet width and depth also suggests a departure between the oceanic inlets and the smaller natural and model inlets at throat area values between $100\text{-}500 \text{ m}^2$.
- 3.) Within smaller tidal inlets characterized by large flow area variations with tidal stage, the maximum velocity is significantly lower than that observed in the larger inlets (0.35 m/s vs 1 m/s). It is suggested that these low maximum velocities may represent the limiting condition of inlet stability.
- 4.) The idealized relationship (Keulegan, 1967) between the tide range ratio and tidal phase lag,

$$R_b/R_o = \cos \epsilon$$

was found generally to hold when the time lag between "ocean" and basin tides were scaled by the duration of ebb or flood flow. When there was substantial reduction in the basin tides, the low tide phase lags more correctly predict the tide range ratio. This is probably due to the higher inlet impedance at low tide.

ACKNOWLEDGEMENTS

This work is a result of research sponsored in part by the Virginia Institute of Marine Science, College of William and Mary, Sea Grant Program, supported by the Office of Sea Grant, NOAA under grant number NA-79-AA-D-00055. The U.S. Government is authorized to produce and distribute reprints for governmental purposes notwithstanding any copyright notation that may appear hereon.

SYMBOLS

A_c	Inlet throat cross-sectional area at mean tide level (MTL)	m
$A_H(L)$	Inlet throat cross-sectional area at high (low) water	m
a	Instantaneous channel area	m
a_o	Amplitude of "ocean" tide	m
D	Inlet throat mean depth at MTL	m
d	Local channel depth, as $f(x)$	m
Q_{max}	Maximum of discharge	m^3/s
R	Hydraulic radius at MTL	
$R_o(b)$	Tide range in ocean (basin)	m
T	Period of tide	hrs
V_{max}	Maximum velocity averaged over flow area	m/s
v	Instantaneous velocity averaged over flow area	m/s
W	Inlet throat width at MTL	m
x	Local distance across channel	m
ϵ	Phase lag between external and internal high (low) tides	hrs
Ω	Spring tidal prism	m^3

REFERENCES

- Boon, J.D., III and R.J. Byrne (1981), "On Basin Hypsometry and the Morphodynamic Response of Coastal Inlet Systems", accepted for publication in Marine Geology.
- Bruun, P. (1967), "Tidal Inlets and Littoral Drift; Stability of Tidal Inlets", Vol. 2, 193 p.
- Bruun, P. (1978), "Stability of Tidal Inlets", Elsevier Scientific Publishing Co., Amsterdam, 506 p.

- Byrne, R.J. and J.D. Boon, III (1973), "An Inexpensive, Fast Response, Current Speed Indicator", Chesapeake Science, Short Papers and Notes, Vol. 14, No. 3, p. 217.
- Byrne, R.J., J.T. DeAlteris, and P.A. Bullock (1974), "Channel Stability in Tidal Inlets: A Case Study", Proceedings, 14th Coastal Engineering Conference, American Society of Civil Engineers, New York, p. 1585-1604.
- Byrne, R.J., G.R. Thomas, and R.A. Gammisch (1980), "Chesapeake Bay Inlets", Special Report in Applied Marine Science and Ocean Engineering, No. 238, Cloucester Point, Va.
- Esoffier, F.F. (1940), "The Stability of Tidal Inlets", Shore and Beach, Vol. 8, No. 4, p. 114-115.
- Esoffier, F.F. (1977), "Hydraulics and Stability of Tidal Inlets", CITI Report 13, U.S. Army, Corps of Engineers, Coastal Engineering Research Center, Fort Belvoir, Va., and the U.S. Army Engineer Waterways Experiment Station, Vicksburg, Miss.
- Jarrett, J.T. (1976), "Tidal Prism-Inlet Area Relationships", CITI Report 3, U.S. Army, Corps of Engineers, Coastal Engineering Research Center, Fort Belvoir, Va., and the U.S. Army Engineer Waterways Experiment Station, Vicksburg, Miss.
- Keulegan, C.H. (1967), "Tidal Flow in Entrances Water-Level Fluctuations of Basins in Communications with Seas", Technical Bulletin No. 14, Committee on Tidal Hydraulics, U.S. Army Engineer Waterways Experiment Station, Vicksburg, Miss.
- Keulegan, C.H. and J.V. Hall (1950), "A Formula for the Calculation of Tidal Discharge Through an Inlet", U.S. Beach Erosion Board Bulletin, Vol. 4, No. 1, p. 15-29.
- Mayor-Mora, R.E. (1977), "Laboratory Investigation of Tidal Inlets on Sandy Coasts", CITI Report 11, U.S. Army, Corps of Engineers, Coastal Engineering Research Center, Fort Belvoir, Va., and the U.S. Army Engineer Waterways Experiment Station, Vicksburg, Miss.
- Mehta, A.J. (1976), "Stability of Some New Zealand Coastal Inlets", New Zealand Journal of Marine and Freshwater Research, Wellington, New Zealand, letter to the Editor, Vol. 10, No. 4, p. 437-742.
- Mota-Oliveira, I.B. (1970), "Natural Flushing Ability of Tidal Inlets", Proceedings, 12th Coastal Engineering Conference, American Society of Civil Engineers, New York, p. 1827-1845.
- O'Brien, M.P. (1969), "Equilibrium Flow Areas of Tidal Inlets on Sandy Coasts", Journal of the Waterways and Harbors Division, ASCE, Vol. 95, No. WW1, Proc. Paper 6405, p. 43-52.

- O'Brien, M.P. and R.R. Clark (1973), "Hydraulic Constants of Tidal Entrances 1: Data From NOS Tide Tables, Current Tables and Navigation Charts", Coastal and Oceanographic Engineering Laboratory, Technical Report No. 21, University of Florida, Gainesville, 49 p.
- O'Brien, M.P. and R.G. Dean (1972), "Hydraulics and Sedimentary Stability of Coastal Inlets", Proceedings, 13th Coastal Engineering Conference, American Society of Civil Engineers, New York, p. 761-780.
- Seabergh, W.C. (1979), "Model Testing of Structures at a Tidal Inlet", Coastal Structures, 79, American Society of Civil Engineers, New York, p. 690-709.
- Seelig, W.H. (1976), "Environmental Effects of Inlet Improvement at Cabin Point, Virginia", U.S. Army, Corps of Engineers, Coastal Engineering Research Center, Fort Belvoir, Va., unpublished.
- Winton, T.C. (1979), "Long and Short Term Stability of Small Tidal Inlets", Coastal and Oceanographic Engineering Laboratory, Report 79/004, University of Florida, Gainesville, 135 p.

A COASTAL INLET WITH FIXED BED
AND MOBILE SIDES

R.C. Nelson

Senior Lecturer, Civil Engineering Division,
Deakin University, Australia.

and

A.J. Keats

Engineer, Geelong Waterworks
and Sewerage Trust, Australia.

1. INTROOUCTION:

The coastal inlet dealt with in this paper has a fixed bed of exposed rock and mobile side boundaries of sand that overlies the bed rock platform.

The work was undertaken to investigate the response of the throat section to natural hydraulic and meteorological events and to observe the nature and rate of recovery of the inlet after the more extreme events. These events included sea and swell states, wind, freshwater flood flows and short term changes in mean sea level (storm surges or meteorological tides). The three year study involved the inlet at the mouth of the Barwon River, Victoria, Australia (see Figure 1). The work forms part of a continuing study to assess the impact of engineering works on the stability of the estuary and inlet, and was required to assist in delineating the natural inlet variability from that due to engineering works. The study described here looked specifically at the inlet throat section which refers to the short narrow waterway connecting the estuary with the sea. The inlet throat section at Barwon Heads is well defined and is shown in Figure 1.

The inlet itself is free of training walls and is normally flanked by sandy beaches. However, the depth of the inlet is limited by a bed of rock (see Figure 2), there being, in effect, unlimited mobility on a side boundary only. The study therefore included

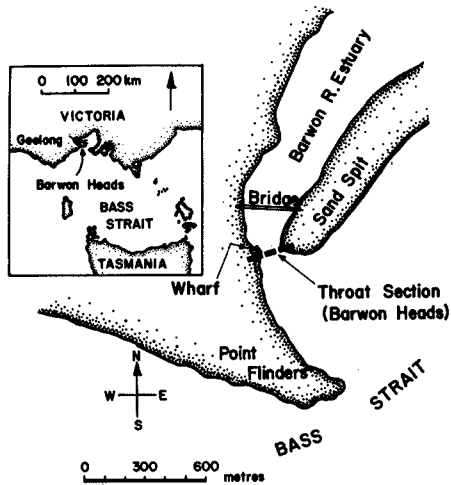


FIGURE 1: LOCALITY SKETCH

an investigation to see if such an inlet conformed to equilibrium criteria developed from inlets with unrestricted bed mobility.

Some results of previous investigations on the estuary and inlet were reported by Nelson (1977).

2. DESCRIPTION OF INLET:

The Barwon Heads inlet is located west of Port Phillip Heads and is backed by an estuary 9 km long, joining Lake Connearre with the sea. The lake is 9 km² in area. The tidal limit lies on the river 1.5 km upstream of the lake. The tide at the inlet is semidiurnal with significant diurnal inequality. The mean spring tide range at the inlet (astronomical tide) is 1.56 m and in the lake is 0.15 m. Superimposed on this astronomical tide is a significant meteorological tide range observed to be at least 0.8 m. An investigation of the meteorological tide has been reported elsewhere (Keats, 1979). During the three year study the maximum and minimum still water levels observed on the gauge at the inlet were 2.48 m and 0.02 m respectively. The mean sea level for the three year period of study was 1.03 m on the gauge.

The total catchment area above the inlet is 4400 square kilometres with an average annual catchment rainfall of about 660 mm, of which only 80 mm per year, on average, passes the catchment outlet as runoff. Higher runoff proportions occur during heavy storm or prolonged wet periods. Most flood flows occur as a result of heavy winter and early spring rainfalls.

For at least 80 per cent of the time the inlet experiences insignificant freshwater inflows. The peak tidal discharges at the inlet during these dry periods range from 230 m³/s (measured) on a mean spring tide range to 80 m³/s (measured) on a neap tide.

The tidal prism of the inlet, as determined by continuous monitoring of discharge over a tide cycle, is 2.3 million cubic metres for a mean spring tide range.

Winds in Bass Strait have a predominant westerly component and therefore, sea states from the south west predominate in the region of Barwon Heads. Swell from the south west is also dominant and originates in the Southern Ocean. The result is a net littoral transport along the coast from west to east in the region of Barwon Heads.

Sand samples taken from the inlet from time to time indicate a median diameter of 0.20 mm to 0.25 mm.

3. DATA COLLECTION:

3.1 Tidal Discharges and Tidal Prism:

The tidal prism of the inlet was obtained by tidal gauging where continuous observation of velocities was made during a tide cycle at a cross section several hundred metres upstream of the throat section. Area velocity methods were used to convert this data to a relationship of discharge versus time, from which the tidal prism was readily obtainable. The measurements were made from a boat using a fan type current meter. Velocity measurement traverses were made over both width and depth and the process continually repeated. The exercise was done for several different tide ranges ensuring the availability of reliable data on tidal discharges and prism.

3.2 Inlet Throat Survey Data:

The variation with time of the area below mean sea level (Figure 4) was generated from regular surveys of the inlet throat section, supplemented by visual assessments made during intermediate inspections. The latter were generally made following extreme events or during weekly maintenance visits to the tide recorder located at the cross section. All surveys were made at the same cross section located as shown in figure 1. The cross section was retrievable from fixed markers and was always at the point of minimum width no matter what the overall geo-

metric characteristics of the inlet were at any point in time. The survey of other cross sections from time to time confirmed that this point of narrowest width was in fact the point of minimum cross section area. An echo sounder was used to obtain bed levels in submerged regions and normal level survey methods used for above water regions. Surveys were undertaken, where possible, at or near low tide when sea and swell penetration were minimum. The mean sea level used was the average for the 3 years of the study, namely 1.03 metres on the Barwon Heads tide gauge.

3.3 Bed Rock Levels:

Bed rock levels are shown in figure 2. Where natural surface was above low tide level, rock levels were obtained using a mobile drilling rig. Rock levels in the channel were obtained using steel rod probing techniques immediately after floods when most of the underwater rock was cleared of sand and exposed by the flood.

3.4 Barwon River Freshwater Flows:

River flow (figure 4) was monitored using a rated river flow station at Geelong. River levels were obtained using a staff gauge, read at least once daily, and more frequently, as required during floods. River levels were converted to river discharges using a rating curve generated from a total of 40 river discharge gaugings, covering the whole range from near zero flow up to a maximum measured discharge of 735 cubic metres per second. The highest estimated discharge at Geelong during the three year investigation was 580 cubic metres per second (figure 4) and therefore no extrapolation of the rating curve was required.

3.5 Surface Winds and Sea State:

Regional surface wind velocities and direction (figure 4) were estimated indirectly from isobaric pressure gradients. The data was extracted from Australian Region, Sea Level Synoptic Charts at six hourly intervals for the duration of the study. The charts used were those corresponding to 0000, 0600, 1200 and 1800 hours G.M.T. Average offshore regional winds were thought to have more meaning in this study as sea state activity can be inferred from it. No recorded offshore wave data was available and since wave action and associated littoral drift has an important influence on inlet geometry, it was necessary to identify severe sea state occurrences and its general direction. These can be identified from the graph showing average daily wind vectors. Prevailing sea state conditions and direction over longer periods can be inferred from the graph showing average monthly wind vectors.

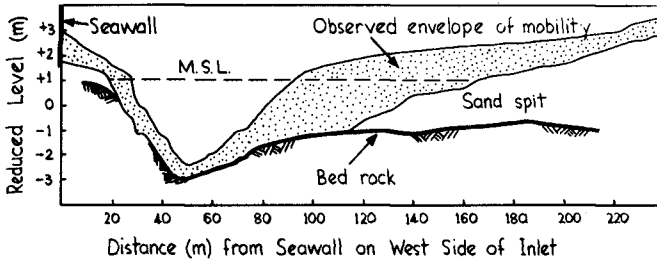


FIGURE 2: INLET THROAT CROSS SECTION

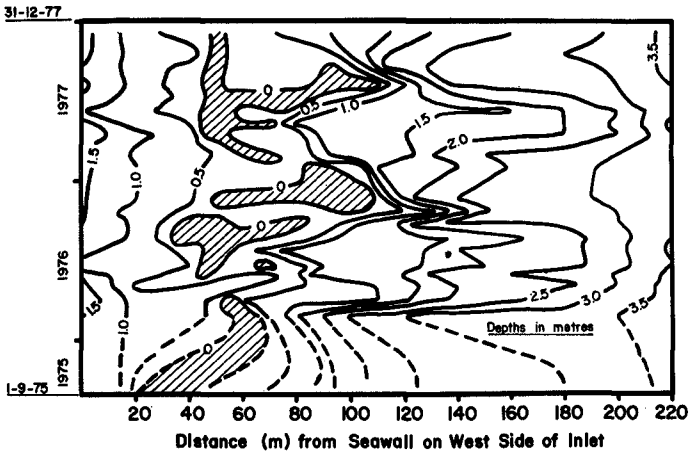


FIGURE 3: DEPTH OF SAND OVER BED ROCK

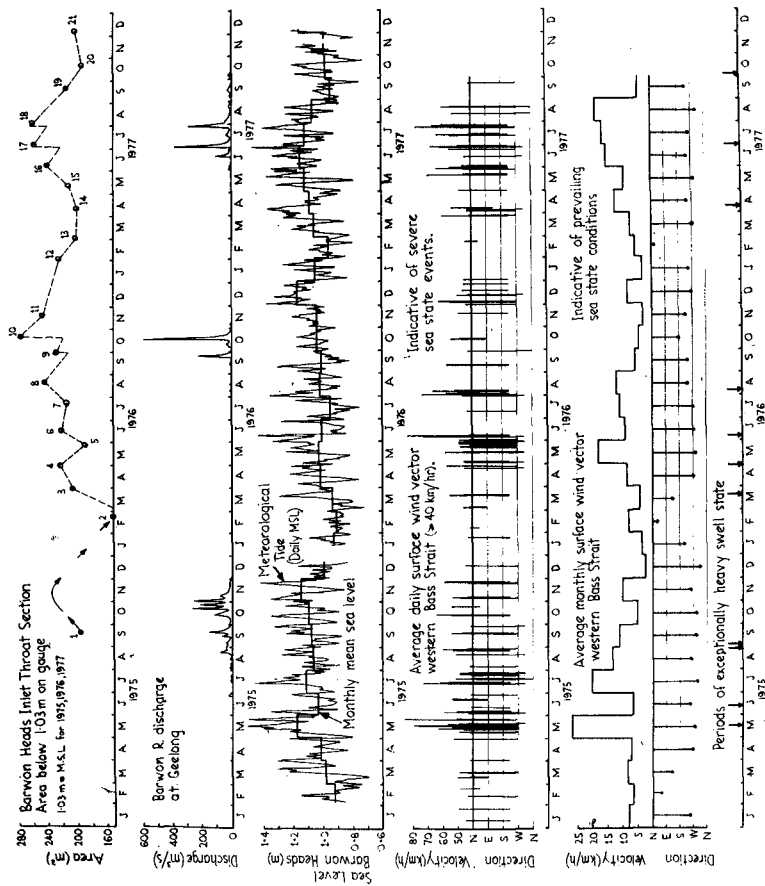


FIGURE 4: CHRONOLOGICAL SUMMARY OF DATA RECORD

TABLE 1

SUMMARY OF INLET DATA

Cross Section No.	Date of Survey	Area (A) Below MSL (m ²)	Width (w) at MSL (m)	Hydraulic Radius (R) at MSL (m)	W/R at MSL
1	19. 9.75	195	91	2.0	45
2	22. 2.76	149	71	2.1	34
3	30. 3.76	205	128	1.8	72
4	30. 4.76	222	128	1.7	76
5	28. 5.76	188	108	1.7	64
6	16. 6.76	220	124	1.7	74
7	23. 7.76	213	118	1.7	69
8	19. 8.76	243	133	1.8	74
9	1. 10.76	227	99	2.2	45
10	22.10.76	276	126	2.1	59
11	19.11.76	246	101	2.2	45
12	2. 2.77	223	115	2.0	57
13	2. 3.77	200	116	2.0	59
14	13. 4.77	200	131	1.6	84
15	11. 5.77	210	140	1.4	97
16	8. 6.77	240	144	1.6	90
17	7. 7.77	258	131	1.9	69
18	5. 8.77	260	110	2.3	48
19	21. 9.77	214	88	2.4	37
20	19.10.77	192	88	2.1	41
21	6.12.77	202	114	1.7	66

Two wind recording stations do exist within a 16 km radius of Barwon Heads, one on the coast and one inland, but these are influenced by diurnal and topographic effects and would not be indicative of the offshore regional influences responsible for sea state conditions.

The data in figure 4 demonstrates the predominance of westerly winds. The only months during the study where an easterly component predominated over a westerly component were February and March.

3.6 Swell State:

The data in figure 4 were obtained from visual estimates made by the lighthouse keeper at Point Lonsdale, 10 km to the east of Barwon Heads. The estimates were for swell conditions and not sea conditions, a distinction which was made by the observer. The reliability of the data was dependent on the experience of the observer.

3.7 Sea Levels:

These were obtained from a tide recorder located at the throat inlet section for the duration of the three year study. The data was recorded in analogue chart form and digitised manually at one hourly intervals for computer analysis. The daily mean sea levels (meteorological tide) shown in figure 4 demonstrate that high levels (storm surges) were associated with strong and sustained westerly winds and unusually low levels were associated with easterly gales. A study of weather and associated sea levels at Barwon Heads has been reported elsewhere (Keats, 1979). Generally speaking the average monthly mean sea levels were lowest in February.

4. INLET BEHAVIOUR:

4.1 General Variability:

The cross section area below mean sea level varied from a minimum of 149 m^2 to a maximum of 276 m^2 . The envelope of sand surface elevation over the study period (figure 2) represents the prism of sand worked over during that period. The prism of sand below mean sea level was 171 m^3 per metre length of inlet and 331 m^3 per metre length of inlet for the whole cross section. The gross volume changes (absolute sum of the changes between each survey) were 501 m^3 per metre length of inlet below mean sea level and 912 m^3 per metre length of inlet for the whole cross section. Nevertheless, net changes within the cross section between the first and last survey were only small being $+7 \text{ m}^3$ per metre length of inlet below mean sea level and $+30 \text{ m}^3$ per metre length of inlet for the whole cross section.

The maximum depth of sand movement within the total cross section was 2.9 m. Bed rock was always exposed in the bottom of the

inlet restricting the water depth that could be attained (figure 3). The maximum depth of the inlet, therefore, varied little. Major adjustments in cross section area were achieved by movement of the inlet's eastern boundary as the sand spit extremity forming that boundary, retreated or advanced over the bed rock.

The inlet itself remained fixed in general location, this being attributable in no small way to the influence of Point Flinders.

4.2 Inlet Area Enlargement:

Flood flows, even if relatively small, had a significant influence on the area below mean sea level. The two flood flows of 1976, which occurred within a four week period, increased the cross section considerably, mainly by removing sand from above the base rock on the east side of the inlet. At Geelong, the larger of these two floods had a return period of ten years and the smaller a return period of three. Enlargement was again detected during the two floods of 1977 which also occurred within a four week period. The enlargement was again effected by the removal of sand from above the base rock on the east side of the section. The larger of these two floods had a return period at Geelong of five years and the smaller flood a return period of four years. The results are not inconsistent with a relationship where the inlet throat area after a flood is highly dependent on the magnitude of the flood peak such that the larger the flood peak the larger the resulting cross section area.

It should be understood that the peak flood discharge through the inlet occurs four to five days after the storm which produced it. Therefore it need not be coincident with extremes of other parameters such as gale force winds, high seas and high daily mean sea levels, which may have accompanied the storm responsible for the flood flows. The flood peaks shown for Geelong in figure 4 would have occurred two to three days after heavy rainfall on the upper catchment. The peak flows through the inlet at Barwon Heads would have occurred about 36 hours later again and would have been attenuated considerably below the peak at Geelong. Investigations undertaken so far, indicate that major flood peaks at Barwon Heads are at least 20 to 30 percent less than those observed at Geelong.

Other inlet enlargements did occur during periods well isolated from flood events, when river flows approached cease to flow conditions. Typically, these were periods which experienced -

- a. High daily mean sea level events (storm surges).
- b. Prolonged west to south west wind events where the average daily surface wind speed in Bass Strait exceeded 40 km per hour for 5 or more consecutive days. This also implies prolonged periods of high sea state from the south west.
- c. Exceptionally heavy swell events from the south fo west quarter.

Those periods immediately preceding cross sections 6, 8 and 16 fall into this category.

Enlargement during severe storm periods is contrary to expected behaviour. Most investigators report inlet channel reduction during such periods because of increased littoral drift rates. One possible explanation is that during exceptionally high tides, significant amounts of sea and swell do penetrate to the throat region and impinge on the sea wall on the Barwon Heads side of the inlet. This is particularly so during south westerly gales when high tide still water levels of 2.4 m are not uncommon and this is often sufficient to submerge the base of the sea wall on the west side of the inlet. The waves are reflected from the wall obliquely across the inlet, interacting with the incident waves, creating severe turbulence in the shallower edge regions on both sides of the estuary. The turbulence would tend to keep sand in suspension, it then being moved out of the region by prevailing tidal currents.

One enlargement that does not fit the patterns previously described is that resulting in cross section 3. The river was near cease to flow condition and strong winds from the south west exceeded average daily values of 40 km/hr in only one storm that lasted for only two consecutive days. There was, however, an earlier easterly gale when average daily surface winds exceeded 40 km/hr for two consecutive days. Despite the fact that this was only a two day event, and that daily mean sea levels were unusually low, the inlet's greater exposure to the easterly direction, combined with the later south westerly storm, must have enabled enough wave energy to reach the inlet to create sufficient turbulence to remove sand from the region.

4.3 Inlet Area Reduction:

The data record shows that periods of reducing cross section area are typically those which -

- a. Follow the winter and spring flood periods.
- b. Have falling or more moderate monthly mean sea levels.
- c. Are free of prolonged, extreme wind events when the daily average surface wind speed in Bass Strait exceeds 40 km/hr for three or more consecutive days. That is when more moderate sea states prevailed.
- d. Are generally free of exceptionally heavy swell events.

These characteristics are evidenced in all three years of the data record following winter and spring floods. The fact that these four characteristics are linked together is not surprising because they are not mutually independent. Low river flows, less extreme mean sea levels and less severe sea and swell states are associated with more moderate wind and weather conditions (Nelson and Keats 1978).

The rate of area reduction can be both rapid and sustained following a flood period. After the floods of September and October 1976, the cross section reduced at a peak rate of 30 square metres per month for a 28 day period immediately following the flood and sustained an average reduction rate of 16 square metres per month for a 131 day period, to produce a total reduction of 76 square metres. Following the floods of July and August 1977 the cross section reduced at a peak rate of 28 square metres per month over a 47 day period immediately following the flood and sustained an average reduction rate of 26 square metres per month over a 74 day period to produce a total reduction of 68 square metres.

The bulk of the material responsible for the area reduction was, in both instances, deposited on top of the base rock on the east side of the cross section so that the east side boundary gradually encroached toward the centre of the section. This is contrary to the general west to east movement of littoral drift prevailing along the coast. Sand tracer experiments have not been made to determine the precise cause of this local behaviour but wave pattern observations suggest the following explanation. The predominant south westerly waves refract and diffract around Point Flinders resulting in a wave direction near the end of the sand spit favourable to the movement of material back into the inlet from the east side. This material would be that washed out by flood flows together with some which appears to be deposited on a shallow bank on the east side of the inlet after bypassing the inlet from west to east.

The inflow of material from the east side and its deposition in the throat section only occurs during milder wave conditions. Severe and prolonged south west gales and their associated abnormally high sea levels cause the opposite effect as described in section 4.2.

4.4 Overall Influence of Floods:

Figure 5 is a plot of inlet throat area below mean sea level against peak river discharge at Geelong immediately preceding the inlet survey. Included is one survey taken after the flood of November 1978 which was the largest flood since 1952. While this is well isolated from the continuity of the main study period it is very valuable in assessing the inlet's response to flood flows. The area range shown on the zero discharge line, represents inlet surveys well isolated from flood events. It indicates the range of cross section area that can occur under the influence of varying wind, wave and meteorological tide conditions. Those points shown coupled with significant river discharges, demonstrate that the range of cross section area possible during flood flows is reduced, being minimised when the peak flood flows at Geelong are about 250 m³/s to 300 m³/s. For higher flows at Geelong the cross section area at the inlet is a function of the freshwater discharge only and independent of prevailing wind, wave and sea level conditions.

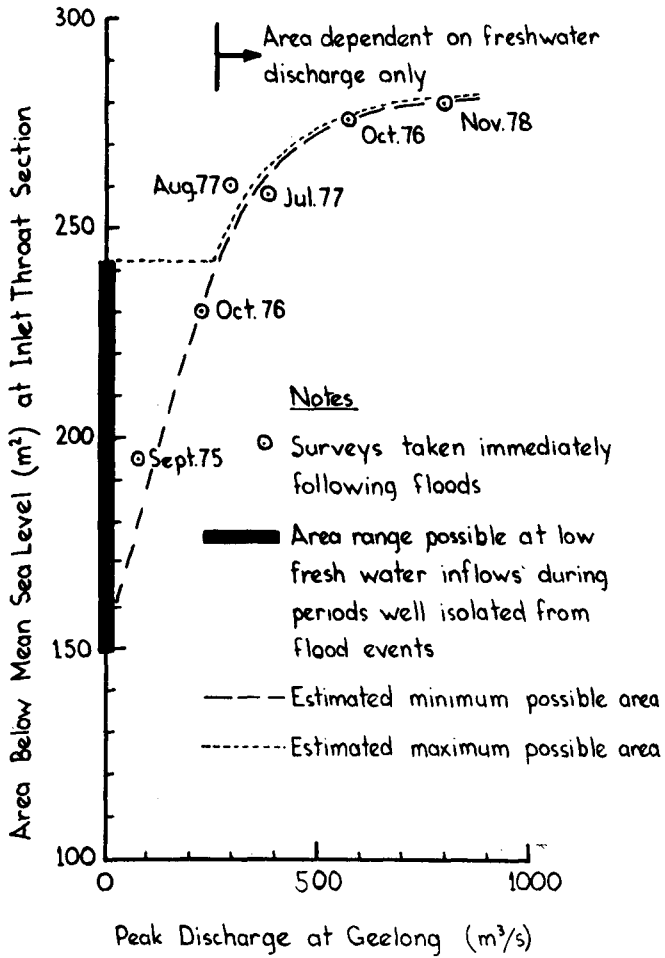


FIGURE 5: FLOOD FLOW INFLUENCE

5. EQUILIBRIUM CRITERIA CONSIDERATIONS:

Table 1 and figures 2, 3 and 4 demonstrate the geometric variability of the Barwon Heads inlet over the period of investigation. Of particular interest was the variability of the cross section area below mean sea level (1.03 m).

The mean area was 218 square metres with a standard deviation of 28 square metres representing 13 percent of the mean. The minimum observed area was 149 square metres and the maximum 276 square metres representing a range of from minus 32 percent to plus 27 percent of the mean. For comparative purposes discussed below, the standard deviation in log A was required and was determined to be 0.058. Investigators have found that the area below mean sea level depends primarily on the tidal prism of the upstream water body. Linear regression analysis on the logarithms of these two parameters yield equations of the form

$$A = bP^c$$

where A is the cross section area below mean sea level, P is the tidal prism and 'b' and 'c' are constants. Figure 6 shows a plot of data for eight North American inlets without training walls, published by O'Brien (1969). The cross section area at each inlet was generally estimated from one set of survey data. Data for the Barwon Heads inlet is also shown, based on the mean of twenty-one surveys. Linear regression analysis on the nine points yields equation (1).

$$A = 1.08 \times 10^{-4} p^{0.97} \quad (1)$$

where A is in square metres and P is in cubic metres. A measure of the data scatter and the degree of uncertainty involved in using this equation is given by the standard error in log A which was 0.066. The standard error in log A must be used since the linear regression analysis was done on the logarithms of A and P. However, an indication of the physical significance is obtained by realising that a standard error of 0.066 in log A represents a range of from minus 14 percent to plus 16 percent about the most likely value of A.

The standard error associated with log A in equation (1) approximates the standard deviation associated with the 21 observed values of log A at Barwon Heads. It seems the entire uncertainty associated with equation (1) could be explained by the natural variability associated with each inlet. Therefore, attempts to reduce the uncertainty associated with equation (1) by investigating the influence of other parameters, such as grain size or by improving the accuracy, resolution and compatibility of the various data used to estimate areas and prisms at each inlet will, on their own, produce minimal rewards. They must be coupled with observations of the variability induced at individual inlets by varying hydraulic and meteorological conditions.

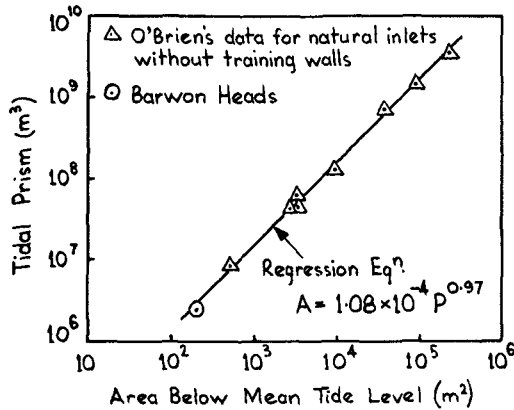


FIGURE 6: INLET AREA VERSUS TIDAL PRISM

The Barwon Heads data demonstrates that inlet area based on one survey (or even two or three surveys) can give quite misleading information as to the prevailing or average geometric characteristics. When a group of such data is assembled from different inlets (eg. O'Brien's data of figure 6), the degree by which the observed area varies from the mean will differ from inlet to inlet depending on the antecedent conditions experienced at each inlet prior to it being surveyed.

Of further interest in this study was whether an inlet like Barwon Heads conformed to equilibrium criteria developed from inlets with unrestricted bed mobility. Two empirical criteria are considered here. The first concerns the relationship between an inlet's cross section area and its tidal prism. The data plot of figure 6, together with the regression analysis indicate that the Barwon Heads data fall well within the expected range as determined from inlets with unlimited bed mobility. The second criterion refers to the inlet's mean maximum tidal velocity for a mean spring tide. Bruun and Gerritsen (1960) demonstrated that

$$Q_{\max} \dot{=} A \quad (2)$$

This implies that the maximum tidal velocity for a stable inlet is approximately 1.0 m/s. At Barwon Heads the ratio of the maximum

discharge (mean spring tide) to the mean cross section area below mean sea level is 1.06 m/s. However, if the phasing between the discharge and water level variations with time are taken into account the actual maximum velocity is nearer 0.9 m/s. The data again agree closely with those determined from inlets with unlimited bed mobility.

6. SUMMARY AND CONCLUSIONS:

- a. While the depth of the inlet remained fixed by the bed rock, the variation in cross section area and width were such that their maximum observed values were approximately double their minimum values. Major adjustments in cross section area were achieved by the retreat or advance of the inlet's sandy eastern boundary across the underlying rock platform.
- b. Freshwater flood flows had by far the most significant influence on inlet area change (enlargement) but recovery was both rapid and sustained. High meteorological tides combined with severe and prolonged south westerly sea and swell states also created area enlargements, contrary to expected behaviour. Area reduction always occurred following floods and during periods when more moderate seas and swell prevailed together with more moderate mean sea levels.
- c. Bed rock was always exposed in the bottom of the inlet restricting the depth that could be attained. Despite this, the inlet's tidal prism and average cross section area below mean sea level, conformed closely to equilibrium criteria developed from inlets with unlimited bed mobility. The same finding applied to the inlet's mean maximum tidal velocity.
- d. The statistical uncertainties associated with predicting an inlet's equilibrium cross section area from existing equilibrium equations, are approximately the same as those associated with the natural variability of any one inlet, if the Barwon Heads observations are typical. Therefore, attempts to refine equilibrium equations will not be profitable unless coupled with studies, over a period of time, of the response of individual inlets to varying hydraulic and meteorological conditions.

7. REFERENCES:

- Bruun, P. and Gerritsen, F. (1960), "Stability of Coastal Inlets", North Holland Publishing Co.
- Keats, A.J. (1979), "Meteorological Influences on Coastal Sea Levels West of Port Phillip and their Engineering Significance". Deakin University, Victoria, Australia, Master of Science Thesis.

- Nelson, R.C. (1977), "The Relative Sensitivity of Estuaries and Coastal Inlets to Engineering Works", Third Australian Conference on Coastal and Ocean Engineering, Melbourne, 1977. Institution of Engineers, Australia, Publication No. 77/2
- Nelson, R.C. and Keats, A.J. (1978), "Abnormal Sea Levels on the Otway Coast - Their Nature, Cause and Effects", Deakin University, Civil Engineering Division Research Report No. CE1/78, 1978.
- O'Brien, M.P. (1969), "Equilibrium Flow Areas of Inlets on Sandy Coasts". Journal of the Waterways and Harbours Division A.S.C.E., Vol.95, No.WW1.

INLETS/ESTUARIES DISCHARGING INTO SHELTERED WATERS

H.P. Riedel¹M.R. Gourlay²SUMMARY

Tidal prism - cross sectional area relationships and tidal velocities have been measured for inlet entrances and along the length of the estuary for four creeks entering the sheltered waters on the South East Queensland coast, Australia. It has been found that the inlet entrance tidal prism - cross-sectional area relationship is controlled by the magnitude of littoral drift. The tidal prism - cross-sectional area relationship along the estuary is believed to be common to all tidal estuaries landward of the region where littoral drift has an influence.

For tidal inlets on sheltered coasts with tidal prisms of the order of 10^6 m^3 , the mean maximum velocity during spring tides at the inlet entrance is about 0.3 to 0.4 m/s.

1. INTRODUCTION

For the design of a new international airport at Brisbane, it was necessary to reclaim an existing stable creek and to divert floodwaters to an artificial inlet. In order to design an artificial inlet which would be stable, or at least have predictable characteristics, a study was undertaken by and for the design authority, the Australian Government Department of Housing and Construction, to investigate the characteristics of inlets and estuaries discharging into sheltered waters.

The site for the airport is shown in Figure 1 where Serpentine Creek will be reclaimed and an artificial inlet excavated about two kilometres to the north. Both Serpentine Creek and the artificial inlet discharge into Moreton Bay which is approximately 30 km wide by 50 km long. It follows that the wave climate at the inlet entrance will be mild with wave periods and heights rarely exceeding 5 seconds and 1.5 metres respectively. Littoral drift rates are consequently low, probably less than $10,000 \text{ m}^3$ per annum. With these considerations, it was thought that the economic design of an artificial inlet should not be based on relationships derived for tidal inlets on open coasts; e.g. O'Brien (1969), Bruun (1978), Jarrett (1976).

In order to obtain relationships upon which the design of a predictable inlet and estuary may be based, field studies were undertaken to measure the characteristics of inlets in protected waters.

1. H.P. Riedel, Director, Riedel & Byrne Consulting Engineers Pty. Ltd., Australia
2. M.R. Gourlay, Senior Lecturer, University of Queensland, Aust.

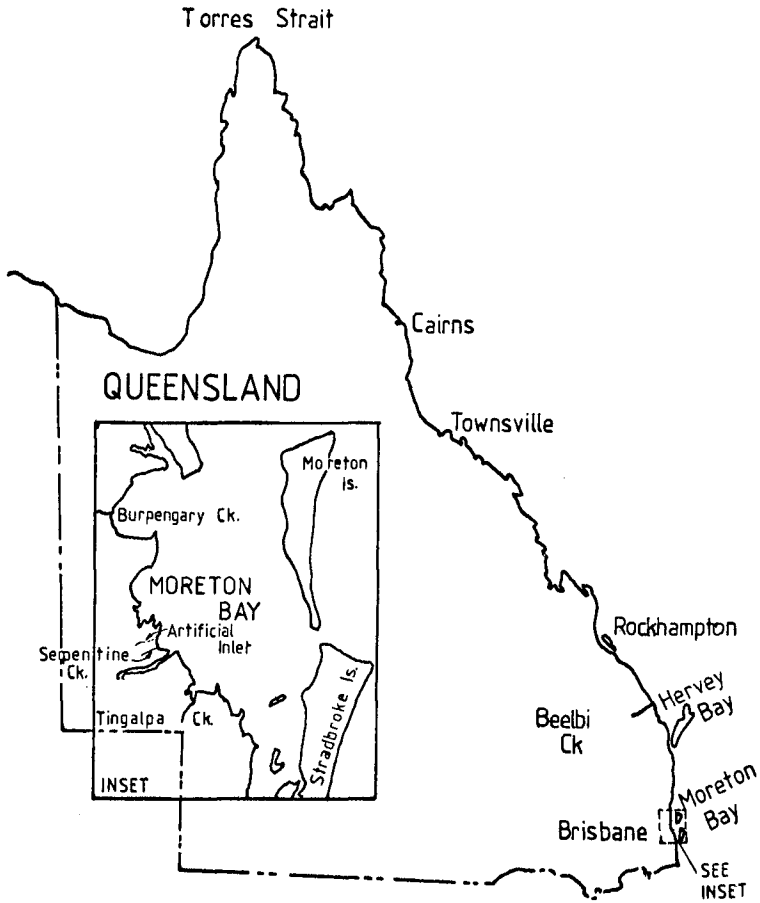


FIGURE 1 Locality Plan

Comparisons were also made with data obtained by others. Geomorphological and sedimentological studies of Serpentine Creek and adjoining areas were also undertaken to obtain an understanding of the recent (Holocene) geological history and sedimentation processes; Gourlay (1979).

2. PREVIOUS STUDIES

An understanding of the stability of inlets/estuaries must be based on a sound understanding of the tidal hydraulics, flood flows, wave mechanisms and sedimentary aspects. However, the degree of importance of each of these influences depends to some extent on the exposure of the inlet to the open ocean.

There have been numerous studies of tidal inlets on exposed coasts. Summaries of these studies and the factors controlling these inlets have had wide publication, in particular those of O'Brien (1969) and Bruum (1978). These studies relate mainly to inlets between the ocean and bays, rather than inlets and an associated tidal estuary. Information on tidal inlets and estuaries discharging into bays or a sheltered section of the ocean is fairly scarce, and there is little published data. Very recently, Byrne et al (1980) have obtained a comprehensive set of data for inlets in Chesapeake Bay. Also, because of the variability possible in bay shape and bathymetry, the generalisations possible for the open coast may not be possible for sheltered inlets.

For Australian inlets/estuaries discharging into relatively sheltered waters very few publications have been found which are quite relevant to this study. Many of these publications are internal to their relevant organisations, which indicates that there may be other data obtained by others which has not been reported in an accessible form. It is possible that a similar situation exists in other countries where, because the studies for small inlets tend to be small scale, the results are not readily accessible. Consequently, a literature search of data obtained outside Australia has not been attempted for sheltered inlets.

Perhaps the most relevant study to this investigation is that published by Apelt (1977) which investigates the existing Serpentine Creek. Figure 2 shows a plot of tidal prism vs cross-sectional area along the Serpentine estuary. It also includes the data from other relatively sheltered estuaries for which information was available, namely Georges River, N.S.W. (Munro et al 1967), Mooloolah River, Qld. (Nittim 1974) and Pine River, Qld. (Cameron McNamara 1978). The Mooloolah River in South East Queensland discharges into the ocean at a rather sheltered location on an exposed coastline about 150 km north of Brisbane where the littoral drift is relatively small. The Georges River, N.S.W., discharges into Botany Bay south of Sydney. The Pine River discharges into Moreton Bay, but is a much larger estuary than the other estuaries in Moreton Bay considered in this paper.

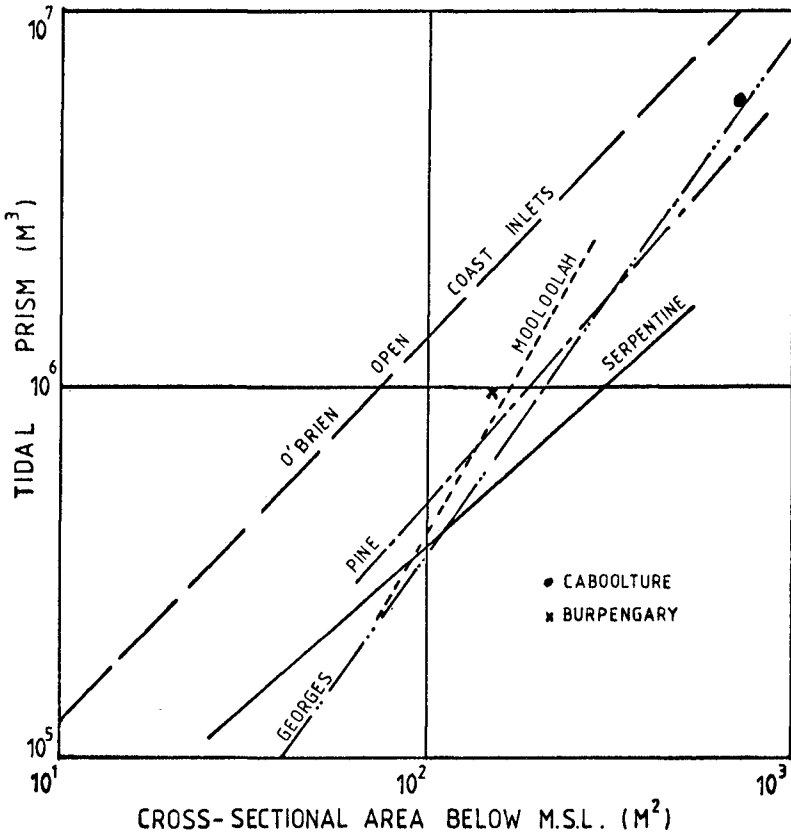


FIGURE 2 AUSTRALIAN INLET-ESTUARY DATA
SHELTERED LOCATIONS

For reference, O'Brien's line for exposed inlet entrances has been included. Figure 2 shows that for each of these Australian inlets the tidal prism characteristics at the entrance and along the estuary fall well below the open coast inlet line.

Figure 2 also shows tidal prisms for the entrance to Burpengary Creek and the Caboolture River in Moreton Bay which also fall well below the open coast line. These sets of data do show quite a wide scatter and were considered inadequate for the purposes of designing an artificial inlet and estuary. Much of the scatter may be attributed to a large variation in scale of the estuaries, and to river flows that may dominate tidal flows. For the system under study, it was expected that tidal characteristics would control the long term shape of the inlet and estuary.

3. FIELD MEASUREMENTS

Tide, current and limited hydrographic data were obtained for four inlets and associated estuaries in South East Queensland. Chosen were:

Beelbi Creek in Hervey Bay, and
Tingalpa, Serpentine and Burpengary Creeks in Moreton Bay.

Each inlet was selected because its scale, tidal range and exposure were similar to that of the proposed artificial inlet. For each creek the spring tidal range is about 2 metres outside the entrance, and the tidal prisms ranged from $0.8 \times 10^6 \text{ m}^3$ for Burpengary Creek to $1.4 \times 10^6 \text{ m}^3$ for Beelbi Creek.

The prevailing wind system for this section of coast is south easterly, as typified by the wind rose for Cape Moreton in Figure 3. The wind rose for Cape Moreton may give an exaggerated impression of the dominance of the south east wind, because the recording station has direct exposure to this wind direction. Winds within Moreton Bay and Hervey Bay would be slightly modified by the adjacent land masses.

From Figures 1 and 3 it is apparent that each of these creek entrances is well protected from swell waves, as well as receiving a large degree of protection from short period waves generated from the dominant south east wind direction.

Perhaps the most variable factor between the selected creeks was the nature of the sediments. All the creeks entering Moreton Bay have similar sediments, with silts and clays on the banks and fine sand on the creek bed. In the downstream areas the depth of these fine materials is generally in excess of 1.5m. The upstream reaches show more variability, with Tingalpa Creek crossing several rock bars within the region of tidal influence.

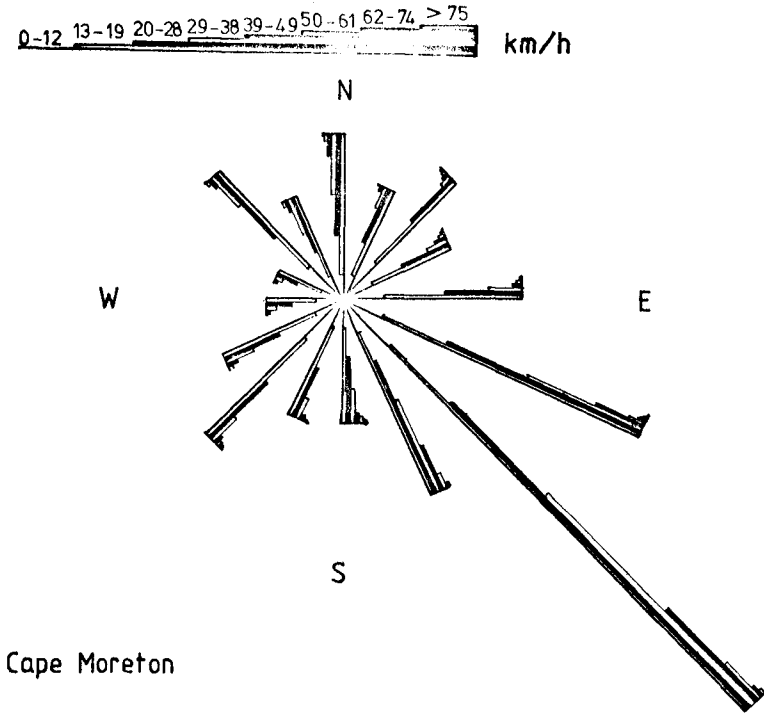


FIGURE 3 WIND ROSE

Beelbi Creek has much coarser sediments throughout its length. Areas showing fine sand or silt on the bed are only superficial deposits and much of the creek bed is underlain with gravel. Silt or fine sand thickness rarely exceeds 0.5m within the creek bed. There are quite coarse sediments at the downstream end of Beelbi Creek, particularly in the flood channel. A detailed sedimentological study of these creeks was beyond the scope of this paper, although this type of study has been completed for the Serpentine Creek (Gourlay 1979).

4. DATA

The data obtained consisted of:

- (a) Tide records at three or four stations along each creek during at least one spring tide.
- (b) Tidal velocities at up to four sections along each creek during the period for which tidal records were made.
- (c) Hydrographic survey of each creek sufficient to define cross-sectional areas and tidal prisms along the length of the estuary.

The data was reduced to give mean maximum velocity across each section monitored over a mean spring tidal range (V mean max.), and the cross-sectional area (A) and tidal prism (P) at sections every 0.5 to 1 kilometre along the estuary. Figure 4 shows the V mean max. for both flood (F) and ebb (E) tides for each creek as a function of distance upstream from the creek mouth. With the exception of the flood data point at the 5 km mark of Beelbi Creek, the data points show a consistent picture, with velocities at the creek entrance of about 0.3 to 0.4 m/s dropping to 0.2 to 0.3 m/s at the upstream limit of tidal influence. There was negligible rainfall (river flow) before or during all the measurement periods.

Figure 5 shows the data for tidal prism vs cross-sectional area for the length of the estuaries to the limit of the tidal influence. The data for Serpentine Creek has been modified from that shown in Figure 2. A correction has been made by deducting the tidal prism of Schultz canal - an excavated channel at the upstream end of Serpentine Creek. This correction has been justified on the basis that the lower reaches of the Serpentine have not had time to readjust to the extra tidal prism introduced by the Schultz channel. This correction results in a better agreement between the four sets of data.

5. DISCUSSION

It is quite clear from the data presented that the stability characteristics of small inlets discharging into sheltered waters are quite different from those for large systems connected through an exposed shoreline.

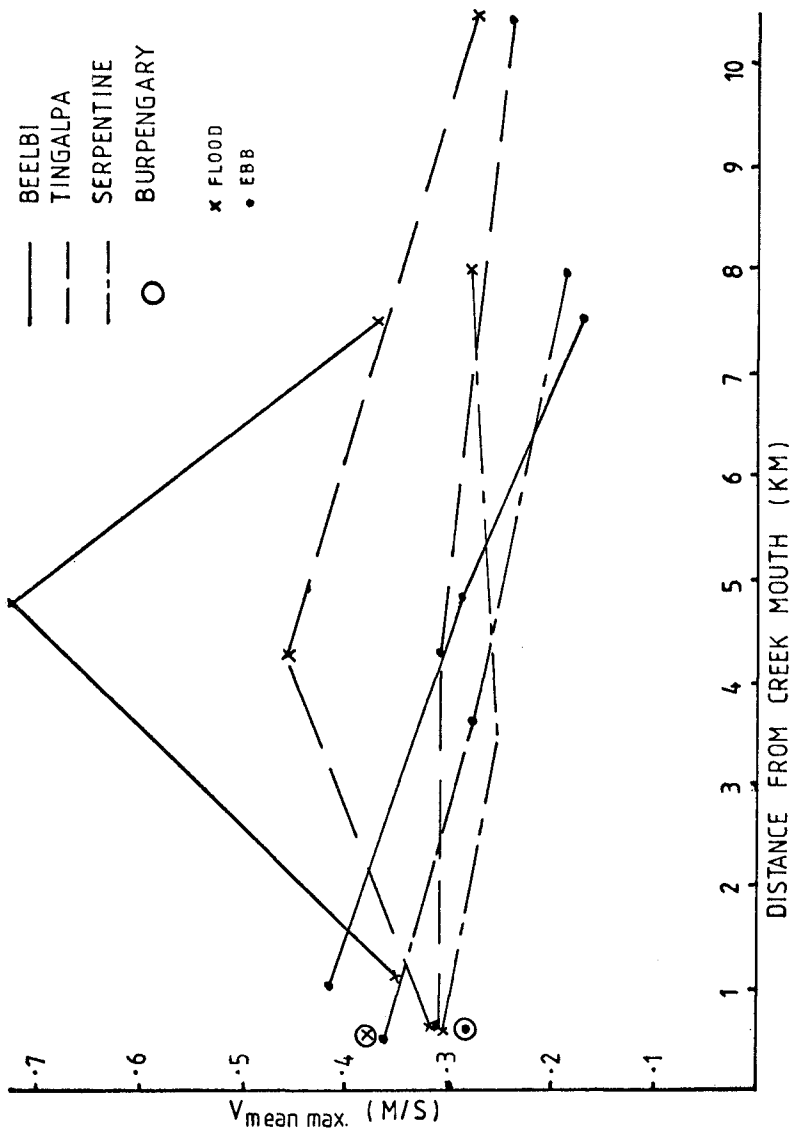


FIGURE 4 INLET/ESTUARY TIDAL VELOCITIES

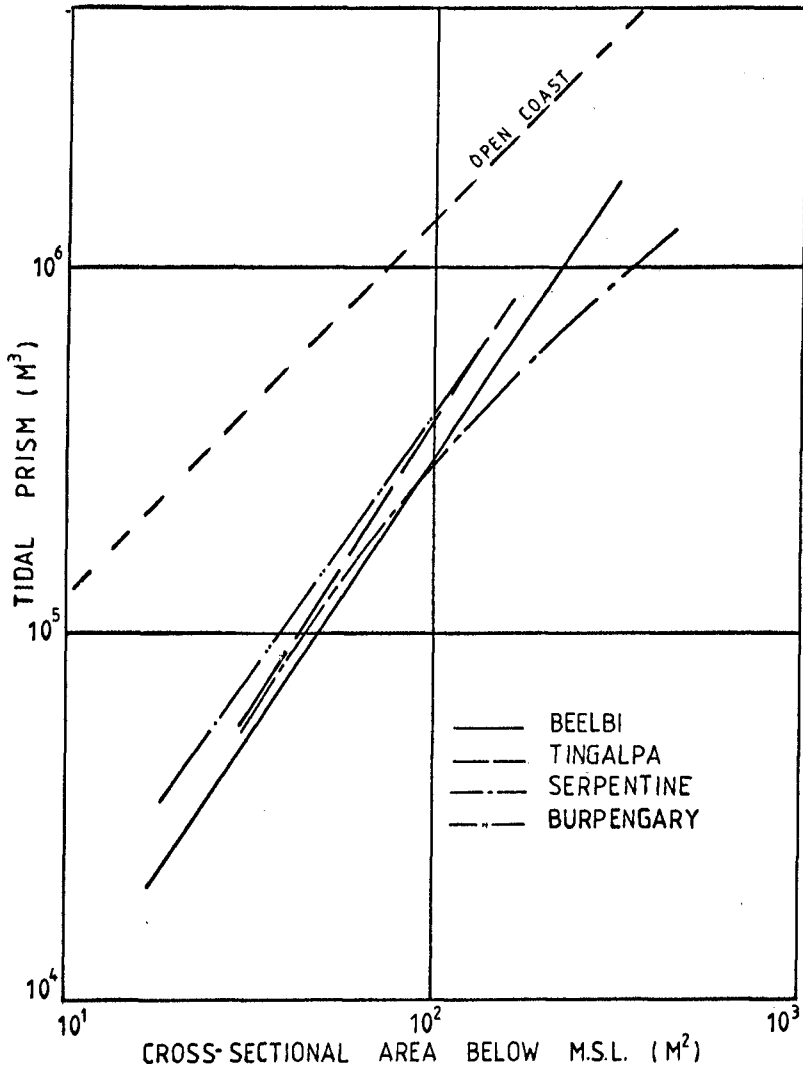


FIGURE 5 S.E. QUEENSLAND INLET/ESTUARY DATA
SHELTERED LOCATIONS

However, it is suggested that the difference is purely in terms of scale. The mechanisms are the same in both instances.

5.1 Inlet Only

Table 1 summarises the velocity at the inlet entrance for each of the four creeks considered.

TABLE 1

V mean max. : FOR CREEKS ENTERING SHELTERED WATERS ON THE SOUTH EAST QUEENSLAND COAST

Creek	V mean max. (m/s)	
	Flood Tide	Ebb Tide
Serpentine	0.30	0.31
Tingalpa	0.31	0.32
Burpengary	0.37	0.29
Beelbi	0.35	0.42

By comparison, for about 50 inlets on exposed coasts on the U.S.A. and in Europe, Bruun (1978) reports that in almost all cases $0.8 < V \text{ mean max.} < 1.2 \text{ m/s}$. In a similar manner, Figure 5 shows that for a given cross-sectional area of the inlet entrance, the tidal prism for exposed coast inlets is roughly 2 to 3 times those of the sheltered inlets reported herein.

An explanation for the marked difference between the four creeks and those reported for open coasts is that the littoral drift is on order of magnitude lower for the shorelines across which the South East Queensland creeks discharge.

The effect of the littoral drift is to try to infill the entrance of the inlet, whereas the tidal flow through the inlet entrance combats this by moving at a velocity fast enough to scour any material deposited in the entrance. If the tidal velocity is not large enough, the entrance will reduce in size until either the velocity increases to a sufficiently high scouring velocity, or the entrance is closed. With the large littoral drift on exposed shorelines, it follows that a large quantity of sediment must be moved by tidal velocities each tidal cycle, and this velocity for a stable inlet is of order of 1 m/s.

In contrast, for sheltered inlets the littoral drift rate is small and, consequently, a much smaller volume of material needs to be moved out of the entrance each tidal cycle. Figure 5 shows that the tidal cross-sectional area of the entrance to sheltered tidal inlets is much larger than for exposed inlets for a given tidal prism, and, it follows that velocities will be much lower. The measured velocities of 0.3 to 0.4 m/s are sufficient to initiate sediment motion for the sediments encountered, and, although

the velocities are low, they are sufficient to counteract the low littoral drift rates.

Confirmation of the consistency of the P - A relationships of the inlets reported here, and those of others, is strengthened by the results reported by Byrne et al (1980). Figure 6 shows the inlet P - A relationships for exposed coasts, sheltered coasts, very small natural inlets and model scale inlets.

5.2 Estuary

Confirmation of the influence of littoral drift upon inlet tidal prism - cross-sectional area relationships is found when the relationship between P and A along the estuaries is considered. Figure 7 combines data from Figures 2 and 5 and includes the Yaquina River in Oregon, U.S.A., which discharges into the ocean on an exposed coast. Goodwin et al (1970).

For all these estuaries the P - A relationship is approximately the same as the P - A relationship for the entrances of the four small estuaries studied here, and this relationship is very different from that for inlet channels on exposed coastlines. The entrance channel data of Byrne et al (1980) for inlet entrances are an order of magnitude smaller than these South East Queensland entrances, and are consistent, as can be seen on Figure 6. All the estuaries have entrance cross-sections with greater areas than indicated by the open coast line, except the Yaquina River whose cross-section falls on the O'Brien line. This is consistent with its exposed location. The inference is that for estuaries where tidal flow, rather than flood discharge, determine the form, a stable P - A relationship may be predicted, provided the littoral drift rate is known. The littoral drift rate effectively controls the entrance cross-sectional characteristics, but upstream from the limit of influence of littoral drift all the estuaries investigated have a similar P - A relationship.

As previously proposed by Nelson (1977) this inference can be taken one step further by postulating on Figure 6 a generalised estuary (tidal) P - A line for the estuary outside the region of littoral drift influence. See Figure 8. The underlying assumption, which is validated by the data examined for inlet estuary systems, is that any littoral drift tends to choke the entrance area. Field data for a range of tidal estuaries would be required to completely test this hypothesis.

6. CONCLUSIONS

- (A) Tidal prism - cross-sectional area (P - A) relationships may be used for describing tidal inlets, provided a distinction is drawn between the entrance and locations along the length of the estuary.

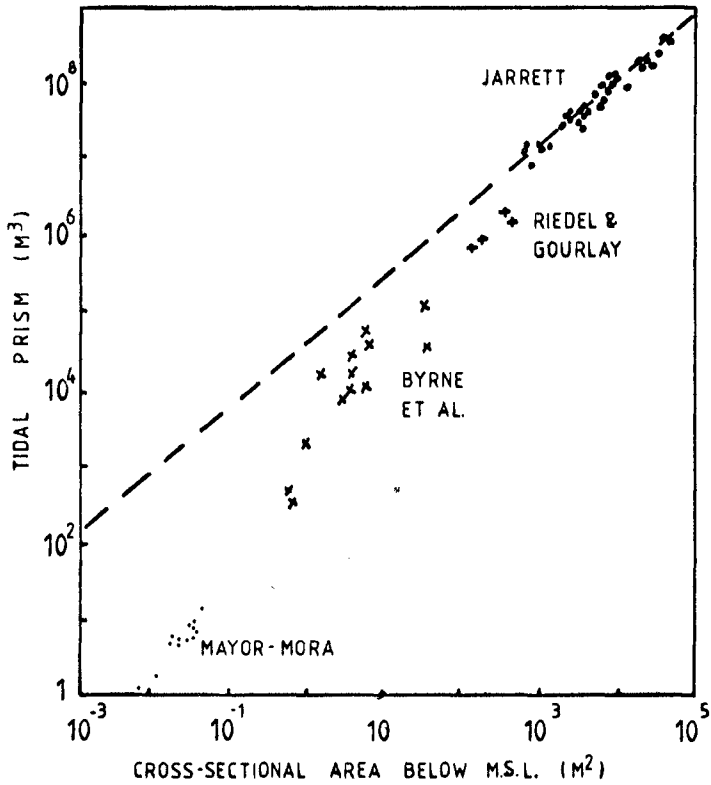


FIGURE 6 INLET ENTRANCES
ALL SCALES

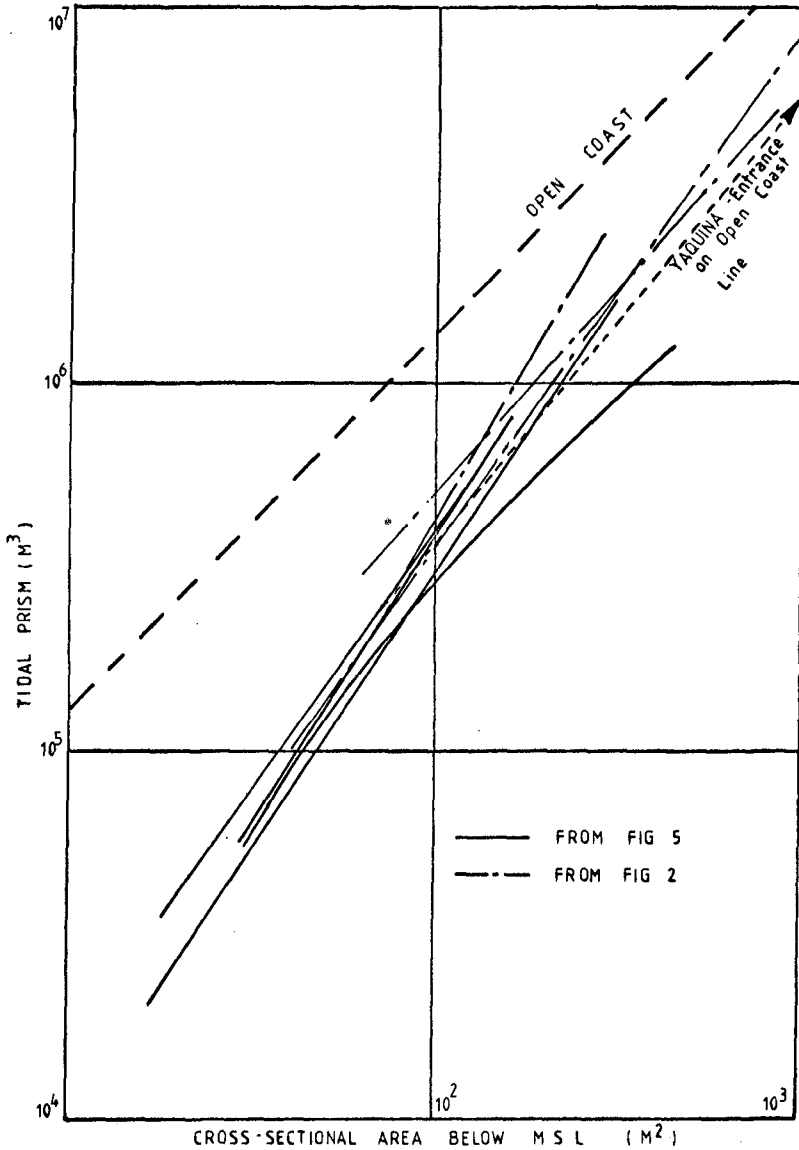


FIGURE 7 INLET - ESTUARY COMPARISON

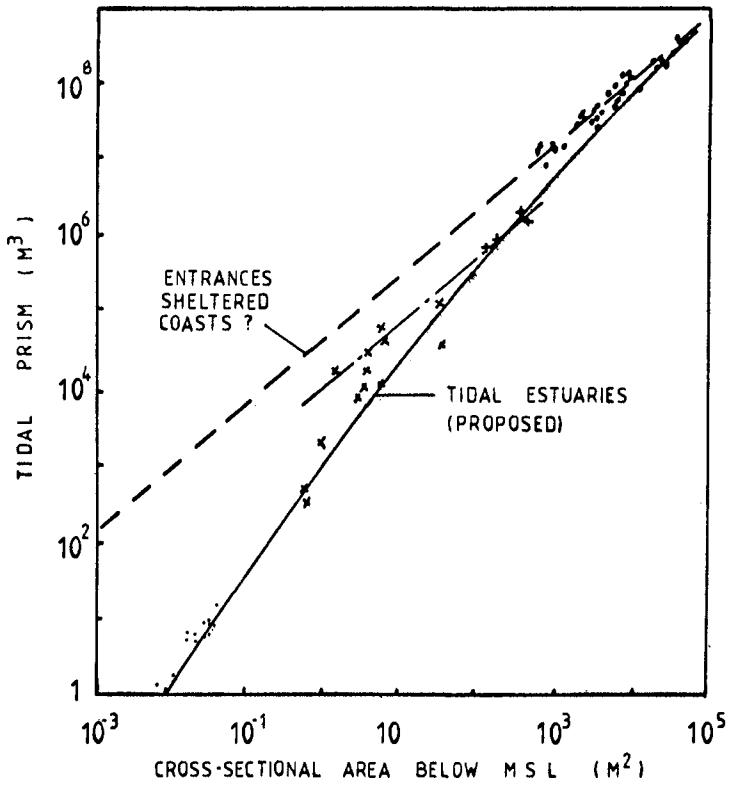


FIGURE 8 PROPOSED TIDAL ESTUARY LINE

- (B) The O'Brien P - A representation holds for exposed coasts where there is a large littoral drift. At the other end of the scale are inlets with small littoral drift which fall on a P - A line well below the exposed coast line.
- (C) The P - A line for inlet entrances lies above the P - A line for the length of the estuary. As littoral drift reduces for smaller inlets which are permanently open, the estuary line approaches the inlet more closely.

7. ACKNOWLEDGEMENTS

The authors wish to thank the Secretary of the Department of Housing and Construction for permission to publish this paper, and gratefully acknowledge discussions with colleagues in the Maritime Works Branch. The work was undertaken while Dr. Riedel was employed by this Department. Nevertheless, the opinions expressed herein are those of the authors.

8. REFERENCES

- APELT, C.J. "Brisbane Airport Development Floodway Studies". Univ. of Qld, Dept. Civ. Engng., Bull. No. 19, 1977.
- BRUUN, P. "Stability of Tidal Inlets". Elsevier Publications, 1978.
- BYRNE, R.J., GAMMISCH, R.A., THOMAS, G.R. "Tidal Prism - Inlet Area Relations for Small Tidal Inlets". 17th Int. Conf. on Coastal Engng. I.E. Aust. Abstracts in Depth Conf. Publ. 80/1 pp 244-245. 1980.
- CAMERON, McNAMARA & PARTNERS. Report to Co-ordinators General Dept. Qld. "Pine River Sand and Gravel Extraction Study". Jan. 1978.
- GOODWIN, C.R., EMMETT, E.W. and GLENNE, B. "Tidal Study of Three Oregon Estuaries". Bull. No. 45, Civil Engng. Dept., Engng. Experiment Station, Oregon State Univ, May 1970.
- GOURLAY, M.R. "Redevelopment of Brisbane International Airport Sedimentation Investigations". Univ of Qld, Dept. Civ. Engng. Report CI 24 - 79, Aug. 1979.
- JARRETT, J.J. "Tidal Prism - Inlet Area Relationships". GITI Report 3, U.S. Army Corps of Engineers CERC, Fort Belvoir, Va., and U.S. Army Engineer Waterways Experiment Station, Vicksburg, Miss. 1976.
- MUNRO, C.H., FOSTER, D.N., NELSON, R.C. and BELL. "The Georges River Hydraulic, Hydrologic and Reclamation Studies". Water Research Lab. Rep No. 101, Univ of N.S.W., Dec. 1967.
- NELSON, R.C. "The Relative Sensitivity of Estuaries and Coastal Inlets to Engineering Works". I.E. Aust. Papers, 3rd Aust. Conf. on Coastal and Ocean Engng. Melb. 1977. pp137-142.
- NITTIM, R. "Mooloolah River Tidal Investigations". Univ of N.S.W., Water Research Lab. Tech. Rep No. 74/13, 1974.
- O'BRIEN, M.P. "Equilibrium Flow Areas of Inlets on Sandy Coasts". Proc. ASCE, J. Waterways and Harbours Div. Vol 95, WN 1 Feb. 1969, pp43-52.

CHAPTER 154

THE CORPS OF ENGINEER'S GENERAL INVESTIGATION OF TIDAL INLETS

Robert M. Sorensen*

Introduction

During the past decade the U.S. Army Corps of Engineers has been conducting a General Investigation of Tidal Inlets (GITI). The GITI was an applied research program through which a wide range of inlet phenomena relating to Corps responsibilities for coastal navigation and recreation, prevention of beach erosion, and control of coastal flooding were investigated. The program was managed by the U.S. Army Coastal Engineering Research Center (CERC); specific research projects were conducted by CERC, the U.S. Army Waterways Experiment Station (WES), private consultants, and universities.

The various GITI research efforts can be divided into five categories: 1) field studies of the hydraulics and sedimentary dynamics of selected inlets, 2) analysis of historic field data, 3) numerical models of inlet hydraulics, 4) movable and fixed-bed physical inlet models, and 5) other miscellaneous inlet studies. Research results are being published in a special report series. The number, title, author and date of each report are listed in the Appendix - GITI Reports.

The intent of this paper is to summarize GITI research efforts and, based on key results of this research as well as recent Corps field experience, to recommend new areas for research.

Field Studies of Tidal Inlets

Corpus Christi Water Exchange Pass in Texas is a two mile long prismatic channel (8 ft by 120 ft) with short entrance jetties that was dredged across the barrier island to connect Corpus Christi Bay and the Gulf of Mexico. Field studies of the pass and adjacent beaches were conducted from the time of channel construction in 1972 to 1975 (GITI 8, 9).

Water levels were continuously measured at each end of the channel and twenty tidal-cycle discharge surveys were conducted over the three-year study period to document tidal cycle, lunar, seasonal and longterm changes in channel hydraulics. During the first year of pass operation, average channel frictional resistance increased by approximately 50 percent and even greater resistance variability was observed during individual tidal cycles. This is demonstrated by typical plots of Manning's n and water level differential versus time (Figure 1). At times there was a strong progressive increase in resistance as flood or ebb flow

* Chief, Coastal Processes and Structures Branch, U. S. Army Coastal Engineering Research Center, Ft. Belvoir, Virginia 22060

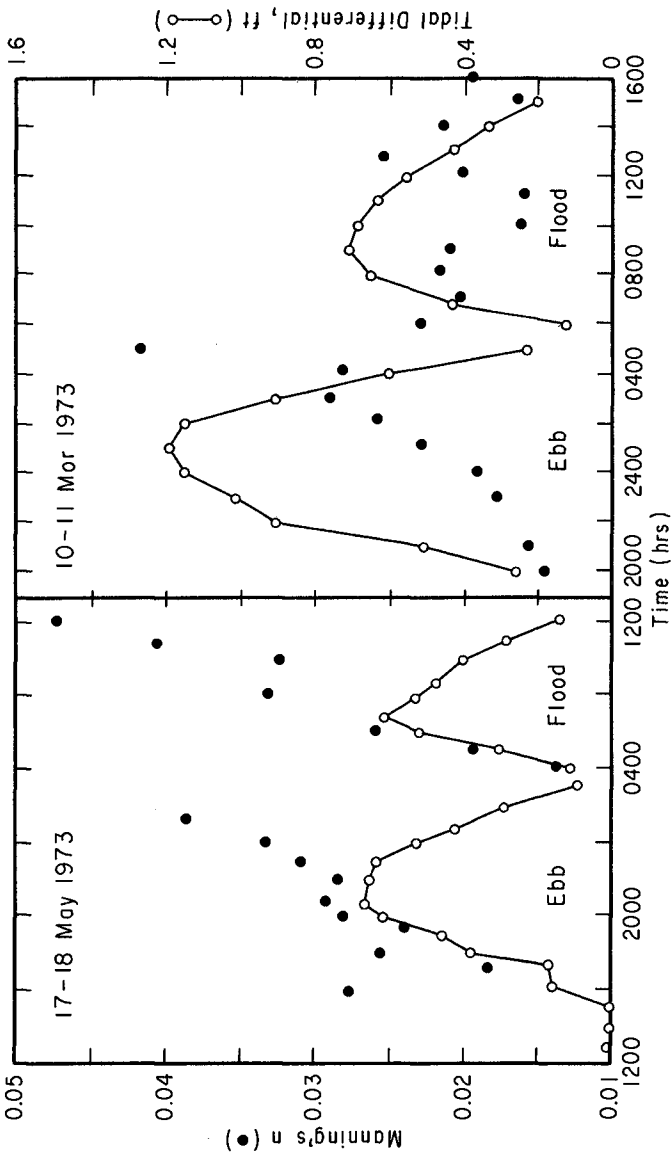


Figure 1 Temporal variation of Manning's n and tidal differential, CCWEP, Texas (GITI 10)

developed followed by a rapid drop as flow reversed; at other times no trend in channel resistance was observed.

Temporal flow resistance variations of the magnitude demonstrated in Figure 1 will have a significant impact on inlet flow regimes as well as on our ability to accurately predict inlet hydraulic response by applying physical and numerical models. There is a strong need for additional field and possibly laboratory investigations to define the causes for this resistance variation and the field conditions under which it can occur.

Periodic bathymetric surveys of the bay and gulf entrances, the pass, and adjacent beaches were also made and results related to wave climate (visual observations), gulf tide levels, local winds, channel discharge, and estimated longshore transport rates. Inlet stability analyses proposed by O'Brien (1931, 1969), Escoffier (1940), and Bruun and Gerritsen (1960) concur with the continuing channel shoaling observed during the field study period.

The other GITI field study involved a two-year program of data collection at North Inlet, a natural tidal inlet in South Carolina (GITI 10, 16). Water level differentials and inlet discharge were measured, visual wave observations were made to determine longshore energy flux and sediment transport, beach profiles and inlet hydrography were periodically measured and compared to historic hydrographic charts, and sediment samples were collected and analyzed.

Calculated values of Manning's n show a similar range of values as those found at the Corpus Christi Water Exchange Pass. Also, occasional less well defined progressive increases in Manning's n were observed during the flood and ebb phases of the tidal cycle. The average peak ebb/flood velocity ratio in the inlet gorge was 1.22, the ebb dominance being attributed to the greater efficiency of water exchange at high tide because of a significantly larger bay surface area.

This and other field studies of tidal inlets have investigated sediment transport modes and patterns, and resulting erosion and deposition environments in the inlet and vicinity. Additional field work is needed to thoroughly define natural inlet sediment bypassing mechanisms as a function of inlet geometry, tidal range, and incident wave climate. The results must then be used to develop artificial inlet bypassing schemes that will maintain a navigable channel with a minimum of dredging and construction of permanent structures. Most typical bypassing schemes consist of fixed structures that establish a sediment trap and control the navigation channels. Such schemes are too costly to construct at many inlets. The ideal bypassing system would employ a dredging program that is flexible and reacts to the natural channel and sediment bypassing conditions.

Inlet channels stabilized by jetties may maintain an adequate

channel between the jetties but it is usually necessary to conduct maintenance dredging across the outer bar (seaward of the jetties). Additional field and possibly laboratory and analytical studies are needed to define the rates and patterns of shoaling to be expected in this portion of the channel. Better understanding of the shoaling patterns will allow a more effective program of overdredging in anticipation of the subsequent shoaling that will occur.

Analysis of Historic Field Data

Using data primarily for the Pacific coast inlets, O'Brien (1931, 1969) established a power function relationship between the mean cross-section area of the inlet throat and the diurnal or spring range tidal prism. Combining O'Brien's data, data from a few other sources (92 data points total) and an analysis of additional Atlantic and Gulf coast inlets (70 data points), Jarrett (GITI 3) developed tidal prism-inlet area relationships for a total of 108 inlets (162 data points). His tidal prism data development used both the "cubature method" which employs measured tide ranges throughout the bay at the instant when slack water occurs at the inlet, and the "NOS current data method" based on current measurements at the inlet throat.

The prism-area data were presented for combinations of three physical categories (all inlets, unjettied and single jetty inlets, and dual jetty inlets) and four geographical categories (inlets on all coasts, Atlantic inlets, Pacific inlets, Gulf inlets). Power function regression curves were fit and 95% confidence limits were established. Figure 2 is a typical result. The prism-area relationships for unjettied and single jetty inlets did vary somewhat for the three coasts, probably because of the differences in tidal and wave characteristics. In no cases was there significant variation from the original O'Brien relationship.

It is reasonable to expect that other relationships besides that relating tidal prism and inlet throat area could be formed between pairs of inlet geometric parameters. An investigation of hydrographic charts and air photographs for 67 natural inlets in the U.S. was conducted: "to isolate a set of parameters than can be used to quantify inlet geometry, to analyze relationships between the basic parameters selected, and to analyze the relationships between inlets based upon the parameters selected" (GITI 20). Over 50 parameters were evaluated and 13 were selected for detailed investigation. They are the inlet channel length and minimum width; the average and maximum depth of the inlet channel at the minimum width; the depth at the crest of the outer bar; the area of the ebb tidal delta; and eigenvectors of the minimum width channel cross section (three), the channel thalweg profile (two), and the ebb tidal delta shape (two).

Linear regression and R^2 analyses of all combinations of pairs of the 13 parameters were performed. Several strong relationships were found. For example $AED = 3.92 \times 10^{-7} L^{1.71}$ ($R^2 = 83.4$ percent) where AED is the area of the ebb tidal delta (square miles) and L is length of the channel from the point of minimum channel width to the

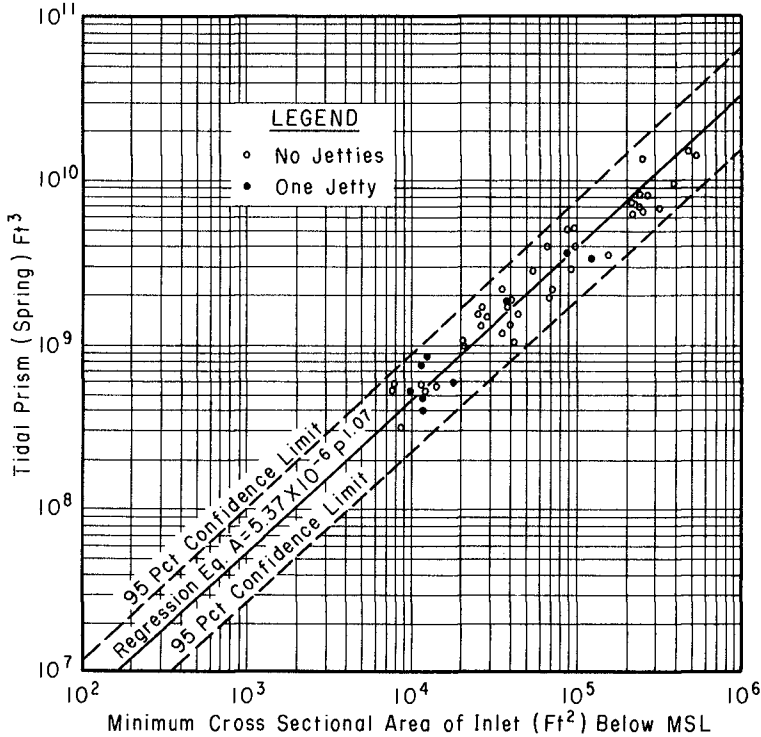


Figure 2 Prism vs area for Atlantic coast inlets with one or no jetties. (GITI 3)

crest of the outer bar (feet).

The parameters defining the gross scale dimensions and shape of the ebb tidal delta and the channel showed a strong relationship to the minimum width channel cross-sectional area (represented by the product of the average depth and width). However, there was no strong correlation with either the channel width or average depth separately. Apparently, the channel width and depth at the minimum width are free to adjust to the wave climate while the cross sectional area is controlled by the tide (tidal prism).

The multivariate statistical method of cluster analysis was used to evaluate tendencies for the various geometric parameters to define groups or clusters of inlets. Then, discriminant analysis was used to

test the strength of these clusters

The 67 inlets can be grouped into six well defined clusters plus five inlets that do not form a cluster or fit into any of the basic six clusters. The various clusters do exhibit some stratification based on size and some based on geographic location but these factors are not strong enough to solely explain the resultant clustering. As an example, Figure 3, shows the channel width and length groupings for the six clusters.

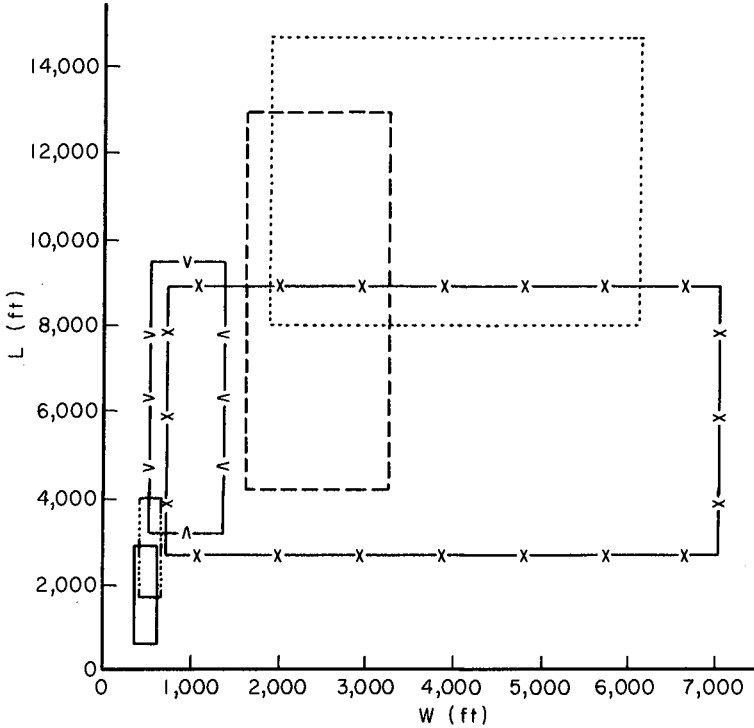


Figure 3 Channel width-length relationships for six inlet clusters. (GITI 20)

An analysis of the dynamic nature of inlet geometry was conducted by determining the temporal variation of selected inlet geometric parameters (GITI 21). This effort employed from four to twenty-one air photographs at each of 51 inlets. Geometric parameters used included the minimum entrance width, the channel length, and the thalweg position and orientation. These parameters were quantified from the air photographs and non-dimensionalized to remove size effects; then the temporal rates of change of the dimensional and non-dimensional parameters were evaluated. Somewhat arbitrary limits were set on each parameter to delineate stable and unstable inlets and to allow grouping or classification based on this delineation.

Both the geometric pattern and stability analyses provide much insight into the geometric characteristics of natural inlets but the information has not been related to causative factors e.g. wave climate, tide characteristics, net and gross longshore sediment transport. The important next step will be to conduct these analyses. Another, potentially fruitful area of research will be to evaluate the specific changes in the various geometric parameters as inlet structures are constructed (realizing that some of the parameters would be strongly controlled by structures such as dual jetties).

In 1957 an eight-mile channel was dredged across Padre Island and Laguna Madre to the Intracoastal Waterway at Port Mansfield, Texas. Gulf and laguna tide elevations, channel current velocities, and channel hydrographic data were collected periodically from 1957 to 1975. Longshore transport rates were estimated from wave hindcast data for the Gulf.

These data were analyzed to evaluate the channel's hydraulic response, shoaling patterns, and resulting stability (GITI 12). Strong channel instability, indicated by channel shoaling patterns and a required dredging rate of 350,000 cubic yards/year is in agreement with the stability criteria proposed by O'Brien (1931), Escoffier (1940), and Bruun and Gerritsen (1960). The length of the channel across the barrier island (3 miles) and the small Gulf tidal range are such that no channel crosssectional area would develop sufficient scouring velocities to eliminate the need for maintenance dredging.

Another effort was a study of thirteen tidal inlets each having a single updrift or downdrift jetty in order to evaluate the response of the entrance channel to jetty construction (GITI 19). This effort used information from periodic hydrographic charts, some of which date back to the 1890's.

In all cases, the channel thalweg was driven toward the jetty by wave action and the resulting longshore sediment transport, regardless of the inlet-bay orientation and resulting tidal flow patterns, the direction of net longshore sediment transport, or the orientation of the jetty. Channel cross section areas decreased up to 40 percent with the construction of a single jetty. In some cases the tendency of a channel

to migrate toward a jetty was so strong that undermining of the jetty occurred. In cases where two jetties were eventually constructed and one had deteriorated so sand could move over or through the jetty, channel movement toward the underiorated jetty was observed.

Numerical Models of Inlet Hydraulics

Available mathematical models for inlet hydraulic calculations vary greatly in complexity and commensurate cost (time, money, expertise) of application. They range from the simple one-dimensional model (e.g. Keulegan, 1967; King, 1974) which makes very restrictive assumptions about channel and bay geometry, sea water level time-histories, bay surface level variations, etc. to the complex two-dimensional finite difference numerical models that compare with physical hydraulic models in capability. The former are useful for simple quick preliminary calculations while the latter, operated by specialists, will provide the detailed flow pattern and water level information necessary for final design of major inlet developements. There was a need for an intermediate level model that would yield information on the velocity pattern at an inlet for relatively complex inlet-bay hydrography and nonsinusoidal sea water levels but that could be operated by Corps field offices without the need for special expertise and substantial investment of time and money. To satisfy this need a spatially integrated quasi two-dimensional numerical model was developed (GITI 14).

To apply the model, a somewhat subjective net of subchannels and cross sections is drawn at the inlet (see Figure 4). GITI 14 provides guidance for drawing the net. The one-dimensional equation of motion, with the friction term at each time step being evaluated by spatially integrating over the net, is solved simultaneously with the continuity equation for the inlet-bay in a time-marching fashion. This yields the inlet discharge and bay water level at each time step. Given the instantaneous inlet discharge, the velocity at each grid section can be calculated. Important capabilities of the model include: any sea level variation as a function of time (tsunami, storm surge, complex tide) may be specified; more than one inlet can connect the sea and bay; river inflow and surface runoff can be considered; and the bay surface area can vary with the surface elevation. Limitations include: wind stress and Coriolis effects are neglected, and the bay water surface is assumed to remain horizontal.

As part of an effort to evaluate the effectiveness of mathematical and physial models of tidal inlet hydraulics, an RFP was issued and studies were funded to calibrate and apply three mathematical models for predicting water-surface time histories and current velocities at Masonboro Inlet, N.C. (GITI 6, Appendices 2, 3 and 4).

One was a simple lumped parameter model that extended the method developed by Keulegan (1967) by allowing for variable bay surface area, a nonprismatic inlet channel, a nonsinusoidal ocean tide, inclusion of inertial effects, and surface inflow to the bay. The other two were two-dimensional (vertically integrated) finite difference model using explicit solution schemes and having their genesis in the hurricane

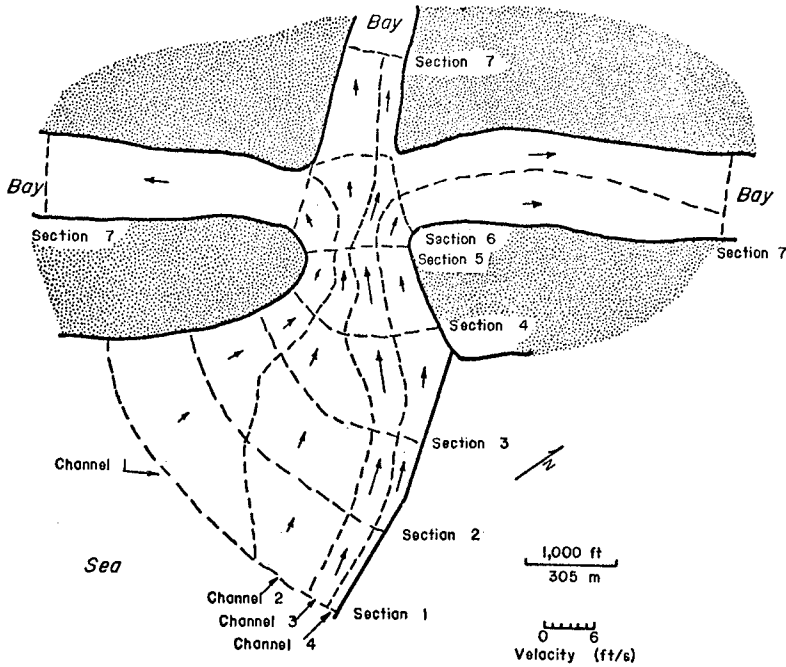


Figure 4 - Net and flood flow velocity distribution, Masonboro Inlet, N.C. (GITI 14)

surge model of Reid and Bodine (1968). GITI 6 is a summary discussion of inlet hydraulic models and a comparison of the effectiveness of the three mathematical models applied to Masonboro Inlet. Figure 5 shows a typical calculated flood flow pattern at the entrance to Masonboro Inlet using one of the two-dimensional models.

Implicit and explicit finite difference models of inlet hydraulics have been steadily improved since the applications discussed above were completed in the early 1970's. They now provide an extremely effective tool for detailed inlet investigations. The next development should be to include sediment transport in inlet numerical models. Perhaps this should be done in two steps. The first step would be to develop a model in which regions of erosion and deposition are determined without quantifying transport rates and the resulting changes in hydrography. The second step would be to develop a complete interactive hydraulic/sediment transport model that quantifies sediment transport rates, resulting bed elevation changes, and resulting tidal flow modifications.

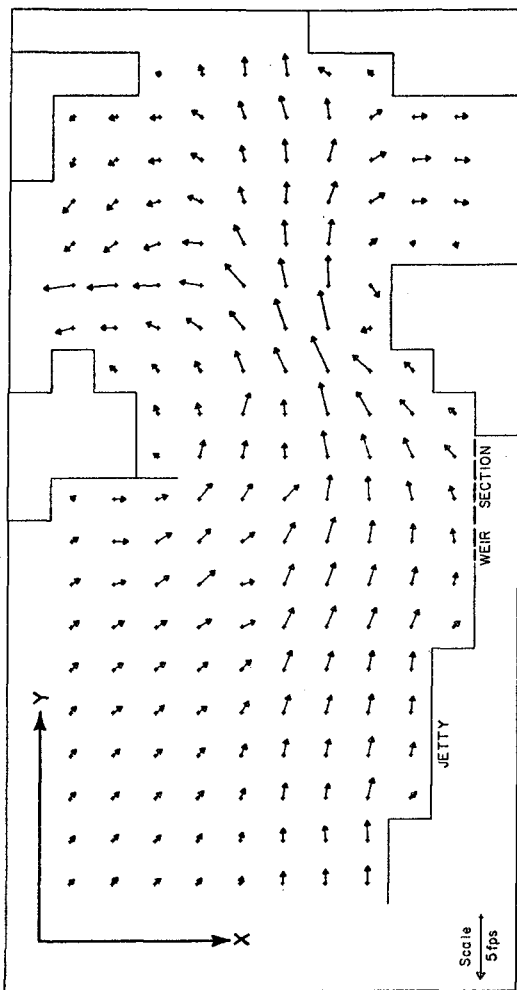


Figure 5 - Flood flow pattern at Masonboro Inlet entrance calculated using two-dimensional finite difference model (GITI 6 App. 2).

Movable and Fixed Bed Physical Models

A concrete distorted scale hydraulic model of Masonboro Inlet was included in the evaluation of the effectiveness of mathematical and physical tidal inlet hydraulic models (GITI 6, Appendix 1; GITI 15). The model, constructed (at WES) to a 1:60 vertical scale and 1:300 horizontal scale, was run with and without waves to evaluate the effect of waves on tidal flow patterns. The general result of the comparison (GITI 6) is that the physical model and the two-dimensional finite difference numerical models are about equally effective in predicting resulting flow velocities and water level time-histories in the inlet and bay. The physical model can include the effects of waves which can improve simulation of flow patterns on the ocean bar and inlet throat as well as resulting bay water levels. It also simulates finer scale turbulence. Numerical models, which are less expensive to operate and easier to store for future use, can simulate wind stress, Coriolis acceleration, and atmospheric pressure gradients.

To further evaluate numerical and physical inlet hydraulic models, additional tide, current, wave and hydrographic data were collected at Masonboro Inlet at a later date (July 1974). The models were operated for the new ocean tide and inlet channel hydrographic conditions to predict channel velocities and bay levels for comparison with measured data. For details of the comparison see GITI 22. Generally, the conclusions of GITI 6 were confirmed.

Before the Masonboro Inlet physical model was destroyed a variety of supplementary tests was conducted (GITI 18). These included an evaluation of: 1) the effects of various level weirs in a proposed south jetty as well as in the existing north jetty (see Figure 4), 2) the effects on inlet flow patterns of closure of any of the three interior channels (see Figure 4), and 3) the efficacy of various sediment tracer materials (sand, expanded shale, ground pumice and plastic) in qualitatively predicting observed shoal and scour trends.

A movable bed (0.34 mm sand) model investigation of basic tidal inlet behavior was conducted at the University of California Hydraulic Engineering Laboratory (GITI 11). Jettied and unjettied prismatic channels of various cross sectional areas were cut across a barrier island to connect an ocean and bay. Experiments were run with a sinusoidal ocean tide and, in some runs, ocean waves or steady bay inflow. Data collection included bay and ocean tide levels, wave characteristics, channel velocities, channel cross sections and centerline profiles, and overhead photographs to define bed forms.

Calculations using simple mathematical models (Keulegan 1967; GITI 6, Appendix 4) satisfactorily predicted the maximum channel velocity and the bay tide range, high and low water time lag, and superelevation.

Comparison with tidal prism versus channel area relationships for prototype inlets (GITI 3) showed that for a given tidal prism the area was an order of magnitude larger than the area predicted by an extrapolation of the prototype curve. Wave action reduced these areas up to 40 percent.

One tool for evaluating the effects of proposed structures and other modifications on tidal inlets is the movable bed hydraulic model. They are the most difficult of all movable bed models because the entrance to a tidal inlet is a region of strong current and wave effects combined. The only known U.S. movable bed tidal inlet models were the seven conducted by WES from 1939 to 1969. GITI 17 presents an evaluation of the effectiveness of six of these models as well as a review of the state-of-the-art of movable bed model similitude requirements and suggested similitude conditions that should be observed in future movable bed inlet model studies.

Movable bed model calibration is achieved by operating the model to produce changes observed in the field between successive hydrographic surveys. If additional field surveys are available the model is operated to verify that it predicts these changes. Five of the WES models were evaluated by quantitatively investigating the accuracy of calibration as no field data were available for subsequent model verification. A sixth model (Galveston Harbor Entrance) had post channel modification data available for evaluation of model verification.

In general, the report concludes that calibration of the five models was unsatisfactory in terms of their reproduction of prototype hydrographic changes between field surveys. Entrance channel shoaling rates and patterns predicted by the Galveston model were not in agreement with subsequent prototype observations.

Deficiencies observed are believed to be caused by: scale and lab effects caused by nonsimilarity between model and prototype processes and conditions; insufficient historical and contemporary data to allow adequate model calibration and operation; and oversimplification of prototype conditions in the model.

In an appendix to the report WES provides background information on the purposes for conducting the model studies, practical limitations encountered, and results of positive practical value achieved by the model studies.

Miscellaneous

Information compiled on over 6000 inlet photographs during the search for imagery for the inlet geometry and stability classification studies is listed in GITI 2. Included are: inlet name and geographic coordinates, photograph date and scale, georef grid square, agency holding photograph, and NOS chart covering the inlet.

An indepth annotated bibliography of over 1000 books, journal

papers, and published and unpublished reports on the geologic, hydraulic and engineering aspects of tidal inlets has been compiled in GITI 4. It covers material dated up to 1973.

GITI 5 is a collection of memoranda by M.P. O'Brien giving miscellaneous thoughts on the hydraulic behavior and stability of tidal inlets. It also recommends a series of field and laboratory studies.

In GITI 13 Escoffier reviews most of the important basic developments concerning analysis of the hydraulics and stability of tidal inlets. He also summarizes functional design requirements for the development of inlets and briefly presents four case studies. The most valuable contribution of this report is the extension of his original inlet stability concept (Escoffier 1940).

In 1940 Escoffier presented a diagram in which the mean channel velocity (ordinate) was plotted against the channel cross-sectional area (abscissa) for a range of areas starting from zero. He assumed that a constant channel velocity (horizontal line) defines equilibrium conditions for the inlet, and its intersection point with the first curve defines the stable inlet area. In GITI 13 Escoffier uses O'Brien's prism-area relationship to show that the equilibrium velocity is not constant but increases with channel area. He presents the new version of his diagram (Figure 6) as a plot of dimensionless mean velocity, v , versus Keulegan's repletion coefficient, K to yield the inlet stability point B.

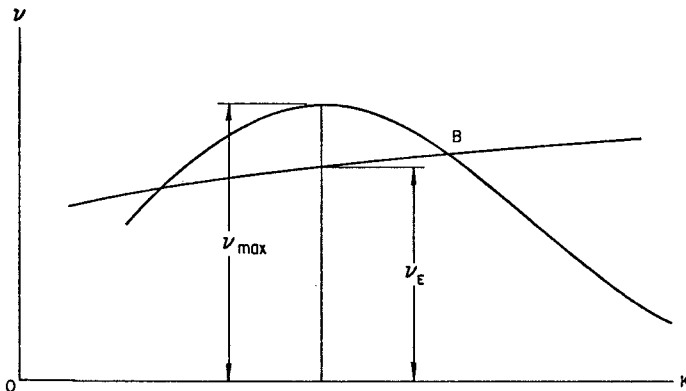


Figure 6 - Escoffier inlet stability diagram (GITI 13).

He further reasons that an indication of the stability of an inlet is given by $\lambda = \frac{v_{max}}{vE}$. When $\lambda < 1$ no channel area could be stable for the given channel length, bay area and ocean tide. When $\lambda > 1$ a stable channel is possible, the degree of stability being indicated by the magnitude of λ . An evaluation of this concept using data for a series of inlets of known historic stability is needed.

Summary

The General Investigation of Tidal Inlets was a varied and effective program of inlet studies that has made significant contributions to supporting the Corps' Civil Works effort. However, continued inlet research is needed and should receive high priority as part of the Corps' coastal engineering research program.

Acknowledgement

The analyses and results presented in this paper, unless otherwise noted, were based on research conducted under the Coastal Engineering Research Program of the U.S. Army Corps of Engineers. The findings of this paper are not to be construed as official Department of the Army position unless so designated by other authorized documents. Permission to publish this information is appreciated.

Appendix - GITI Reports

1. "Reanalysis of BEB TM 94" E.C. McNair (in press).
2. "Catalog of Tidal Inlet Aerial Photography" J.H. Barwis, June 1975.
3. "Tidal Prism-Inlet Area Relationships" J.T. Jarret, February 1976.
4. "Annotated Bibliography on the Geologic, Hydraulic and Engineering Aspects of Tidal Inlets" J.H. Barwis, January 1976.
5. "Notes on Tidal Inlets on Sandy Shores" M.P. O'Brien, February 1976.
6. "Comparison of Numerical and Physical Hydraulic Models, Masonboro Inlet, North Carolina" D.L. Harris and E.R. Bodine, June 1977 (plus four separate appendices on individual models by various authors).
7. "Model Materials Evaluation" E.C. McNair, June 1976.
8. "Hydraulics and Dynamics of New Corpus Christi Pass, Texas: A Case History, 1972-73" E.W. Behrens, R.L. Watson, and C. Mason, January 1977.

9. "Hydraulics and Dynamics of New Corpus Christi Pass, Texas: A Case History, 1973-75" R.L. Watson and E.W. Behrens, September 1976.
10. "Hydraulics and Dynamics of North Inlet, South Carolina, 1974-75" R.J. Finley, September 1976.
11. "Laboratory Investigation of Tidal Inlets on Sandy Coasts" R.E. Mayor-Mora, April 1977.
12. "A Case History of Port Mansfield Channel, Texas" J.M. Kieslich, May 1977.
13. "Hydraulics and Stability of Tidal Inlets" F.F. Escoffier, August 1977.
14. "A Spatially Integrated Numerical Model of Inlet Hydraulics" W.N. Seelig, D.L. Harris and E.E. Herchenroder, November 1977.
15. "Physical Model Simulation of the Hydraulics of Masonboro Inlet, North Carolina" R.A. Sager and W.C. Seabergh, November 1977.
16. "Hydraulics and Dynamics of North Inlet, South Carolina, 1975-76" D. Nummedal and S.M. Humphries, September 1978.
17. "Evaluation of Movable Bed Tidal Inlet Models" S. Jain and J.F. Kennedy, February 1979.
18. "Physical Model Simulation of the Hydraulics of Masonboro Inlet, North Carolina - Supplementary Tests" W.C. Seabergh and R. Sager, June 1980.
19. "Tidal Inlet Response to Jetty Construction" J.M. Kieslich (in press).
20. "Ceometry of Selected Tidal Inlets" C.L. Vincent and W.D. Corson, May 1980.
21. "Stability of Selected Tidal Inlets" C.L. Vincent and W.D. Corson, (in press).
22. "Evaluation of Physical and Numerical Models - Masonboro Inlet, North Carolina" J. McTamany (in press).
23. "General Investigation of Tidal Inlets - A Summary" R.M. Sorensen (in preparation).

References

Bruun, P. and F. Cerritsen (1960), Stability of Coastal Inlets North Holland Publishing Co., Amsterdam.

- Escoffier, F.F. (1940), "The Stability of Tidal Inlets" Shore and Beach Magazine, Vol. 8, No. 4, pp. 114-115.
- Keulegan, G.H. (1967), "Tidal Flow in Entrances, Water-Level Fluctuations of Basins in Communication with Seas" Tech. Bull. 14, comm. on Tidal Hydraulics, Army Corps of Engineers, 100p.
- King, D.B. (1974), "The Dynamics of Inlets and Bays" Tech. Rept. 22, Coastal and Ocean Engineering, University of Florida, Gainesville.
- O'Brien, M.P. (1931), "Estuary Tidal Prisms Related to Entrance Areas" Civil Engineering Magazine, Vol. 1, pp. 738-739.
- O'Brien, M.P. (1969), "Equilibrium Flow Areas of Inlets on Sandy Coasts" ASCE Waterways and Harbors Division, February, pp. 43-52.
- Reid, R.O. and B.R. Bodine (1968), "Numerical Model for Storm Surges in Galveston Bay" ASCE Waterways and Harbors Division, February, pp. 33-57.

SATELLITE APPLICATIONS ON A
COASTAL INLET STABILITY STUDY

Yu-Hwa Wang
Maritime Systems Engineering Department
Texas A&M University at Galveston

INTRODUCTION

It is known that longshore drift of alluvial material occurs along sandy barrier islands. Inlets between these barrier islands intercept the normal littoral drift, resulting in a net loss of sand from the beaches. During a flood tide, sand is brought into the inlet and part of it is retained to form the inner bar; during ebb cycle, part of the sand is jettied out into the ocean to form an outer bar. The reversing flows of flood and ebb cycles may also cause deposition or scouring on the bottom of inlet channels.

There are two sets of parameters pertinent to the behavior of inlets. The first set deals with the changes in the dynamic bottom configuration (i.e. the movement of inner and outer bars, the choking or scouring of the inlet channel). The second set of parameters regards the driving forces of the coastal system (i.e. wave climate, tide, wind and currents). Understanding the interrelationship of these two sets of parameters lead to the solution of stabilizing the inlet. The time sequential dynamic interrelationships and natural tendencies of inlets are well-portrayed on available Landsat imageries.

The techniques of mapping the sand bars and their movements are traditionally done by a sounding boat and survey team. The derived point and line information are then used to produce the contour map of the bottom. Extensive interpolations are needed because many details between the points and lines are missing. The operation is expensive and the procedures are time consuming. Techniques using remote sensing can be used to monitor the changes that take place, reducing costs and increasing efficiency.

Eventhough standard procedures have not yet been established, the satellite sensing of bottom features has progressed considerably in recent years. Sherman (1975), Middleton and Barber (1976), Hubbard (1977), and Lyzenga and Thomson (1978) all demonstrated that it is possible to correlate the radiance values of multi-spectral images, such as Landsat imagery, with the depth related information in shallow water. The present study is one more example of such an effort.

IMAGE ANALYSIS AND INTERPRETATION

Two Landsat magnetic tapes (1974 and 1976) covering Pinellas County shoreline was obtained and displayed on the screen of an IMAGE 100 computer. Spectral radiance values were derived from the magnetic tape for various key locations in the Clearwater Beach area as it is shown by the dark squares in Figure 1. These radiance values were later used to compare with ground truth observation and measurement. Typical scene of the image manipulations are given in Figures 2 through 7. Figure 2 shows a cluster rendition of the study area in general. The land water boundary is nicely shown in Figure 7. These two figures are used as reference figures for the comparison with the specific signatures, their extent and location in Figures 3, 4, 5 and 6. In Figure 3, the large shaded dark area in the left one third (approximately) of the picture represented the area of water depth greater than 10 feet. The dark shaded area in Figure 4 was identified as the grass bed. Figure 5 showing the intermediate water depth region of 4 to 10 feet was found to surround the barrier island chain. The extremely shallow water areas were found in Figure 6.

The natural navigation channel at Clearwater Pass can be clearly observed in the enlargement picture on the north-east corner of Figures 8 and 9. Figure 9 is a binary computer printout showing the results of Golay Cluster techniques. The enlargement picture in Figure 10 (also a binary printout) gave the location of shoals.

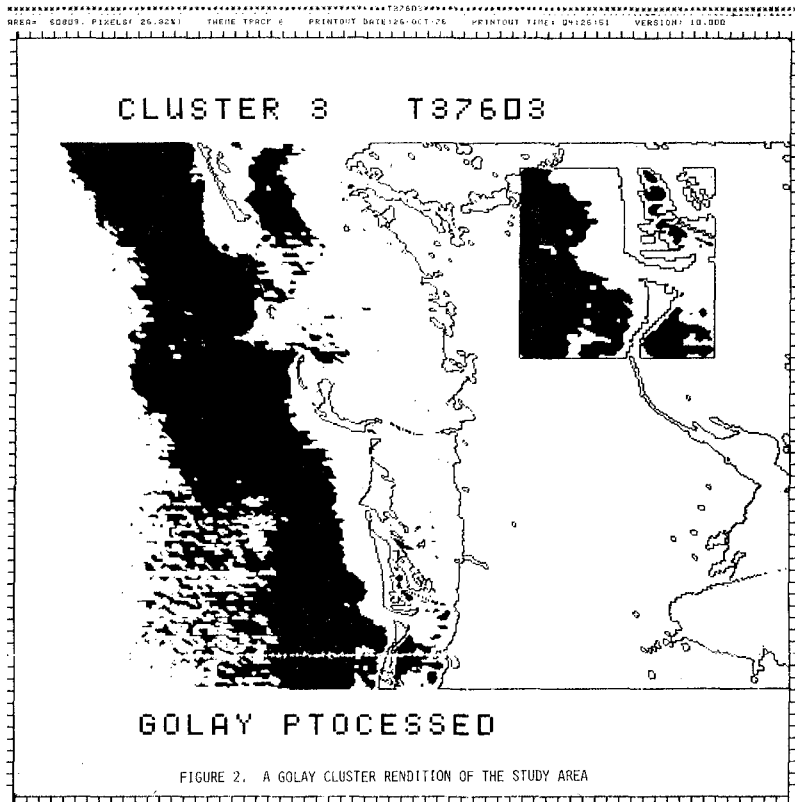
GROUND TRUTH

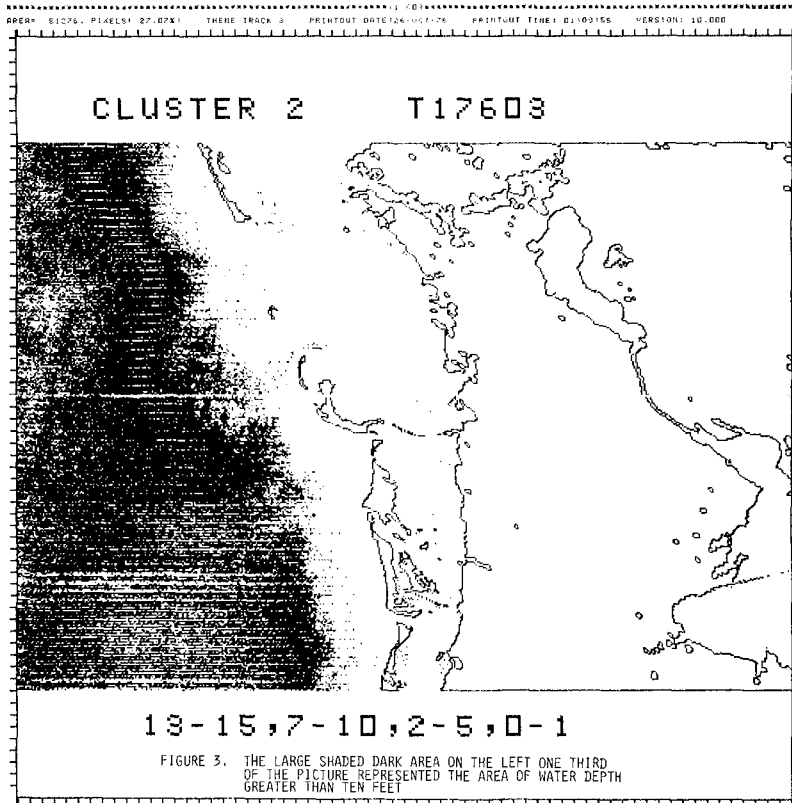
A team equipped with survey instruments and sounding gear were sent to determine shallow water bottom conditions. The inlets cross sectional area and the shoaling region were measured by sounding and survey. These ground truth observations were used for the comparison with radiance values of the Landsat imagery.

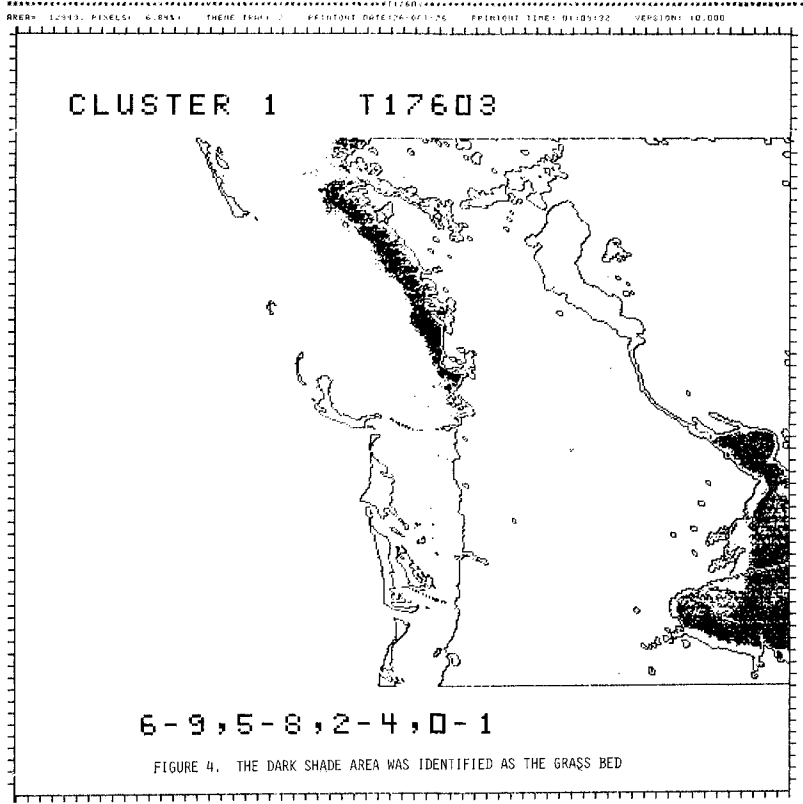
The difficulty encountered during ground truth operations was the identification of the bottom condition by boat. An analogy to this would be best described by an old saying: "When you are in the forest, you don't see the trees." To improve the situation, two flights were flown to collect low altitude photographs. The first set of photos covered a shoreline of approximately ten miles in length, and the flight line was along the beach. The second flight emphasized on the Clearwater Pass and on the bay area.

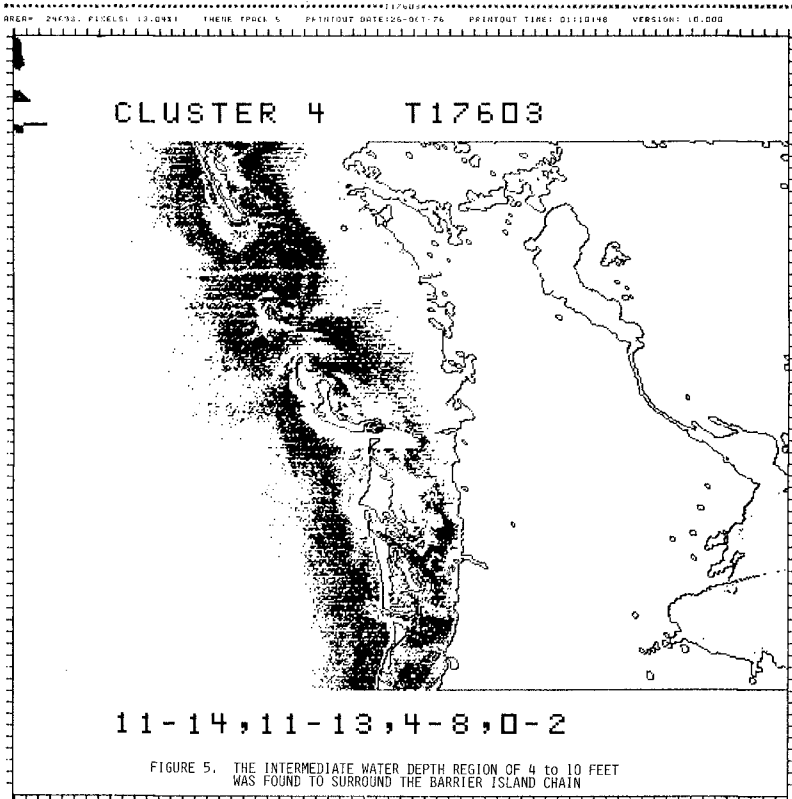
The hydrographic measurements together with the aerial photos constitute the basis of ground truth for interpretation and calibration of the Landsat imageries. The reader is directed to the two reports by Wang, et al (1977) for ground truth details.

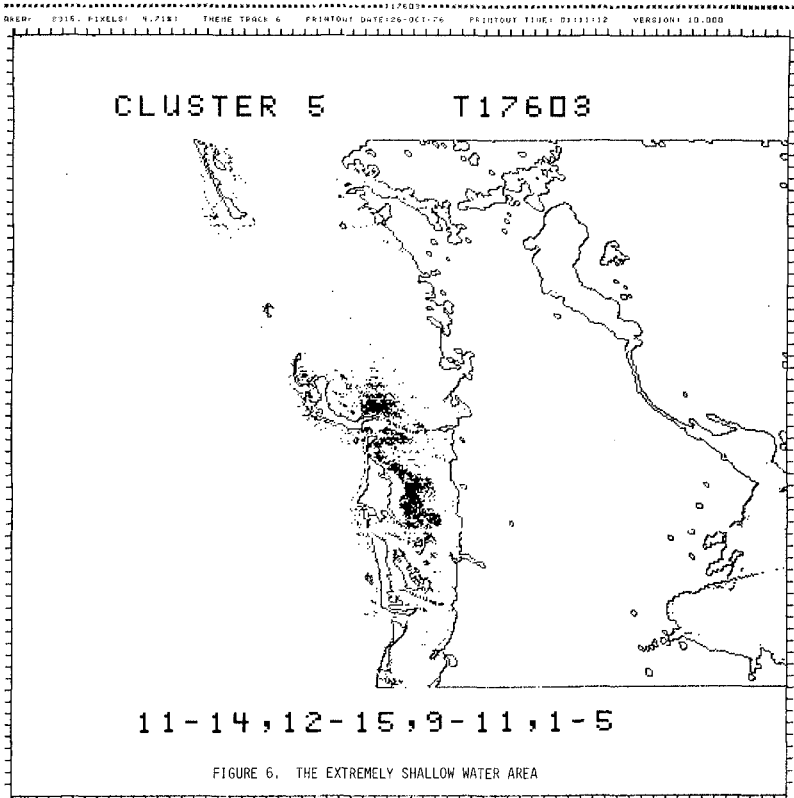


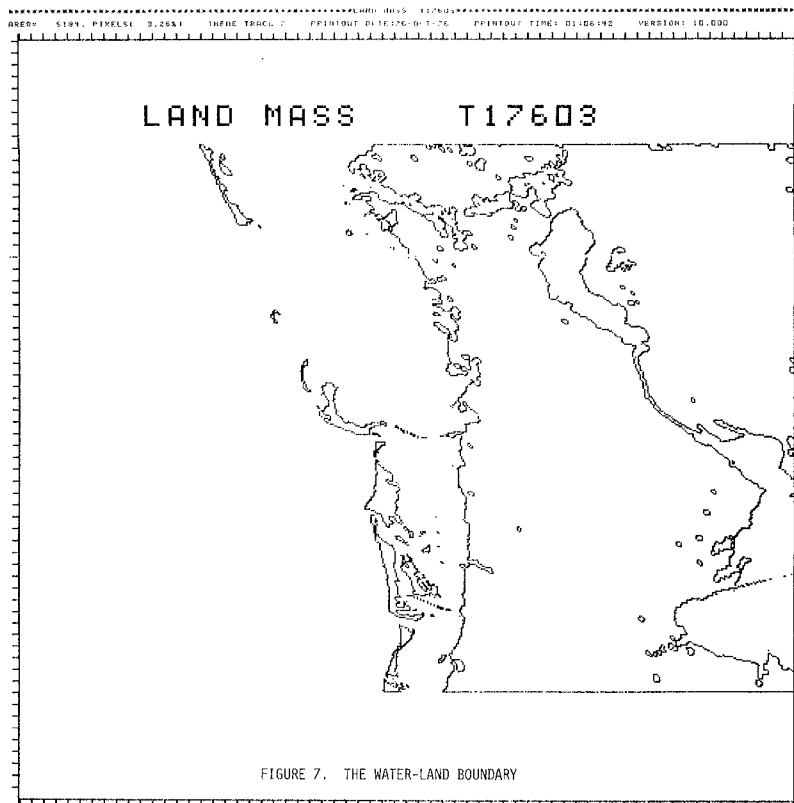


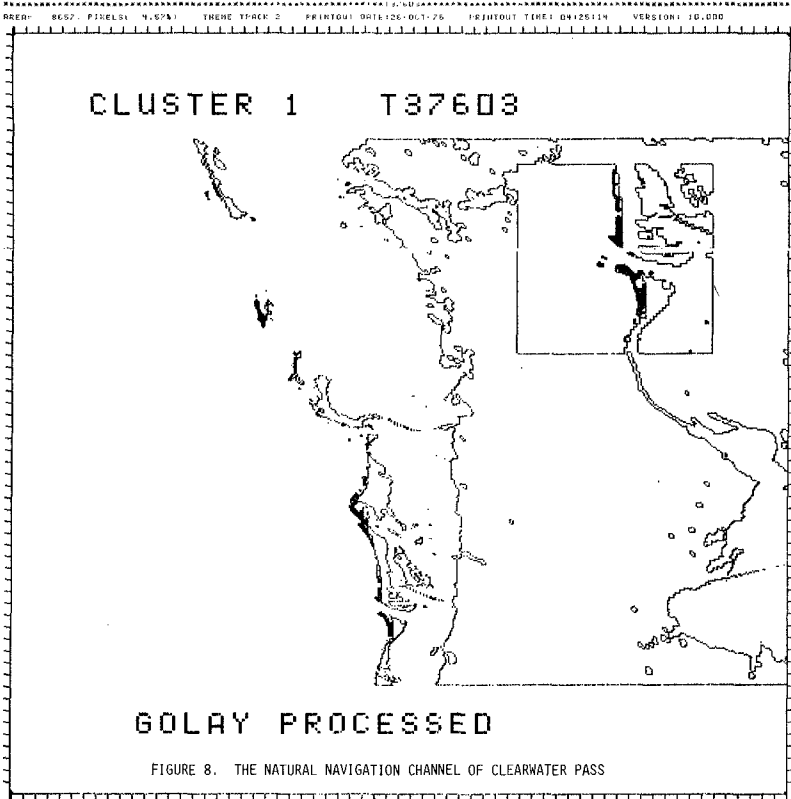


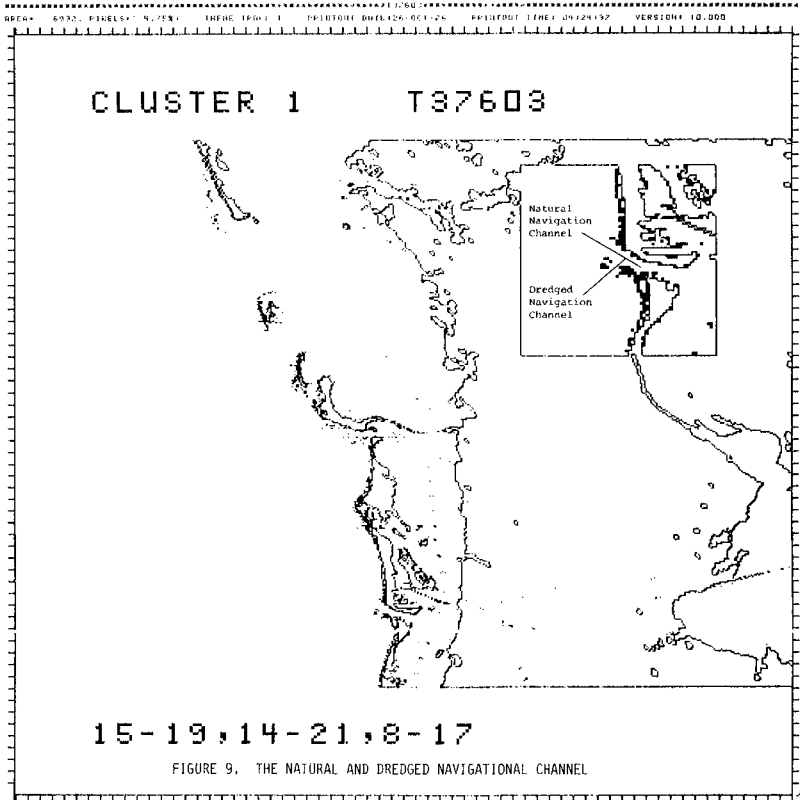


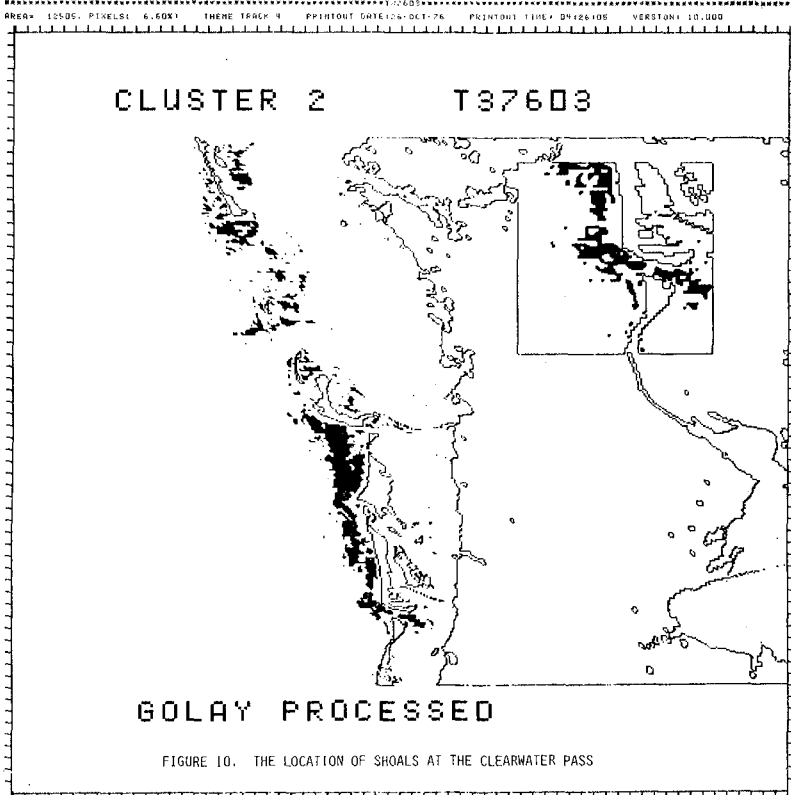












ENGINEERING ASSESSMENT FROM LANDSAT DATA

1. Identification of the pass's natural channel: Spectral analysis of the Landsat imagery (see Figures 8 and 9) has revealed the direction of the natural course of the inlet channel. The main stream (deep part) along the inlet has been eccentric and parallel to the north bank of the inlet. As a result, the beach erosion is likely to occur at south end of the Clearwater beach. It is also clear that the dredged navigation channel at the inlet mouth deviates from the inlet's natural channel course (see Figure 9).

2. Location of shoals:

A. Outer bars: The extremely shallow region and outer bars, such as the bathing zone and the second bar parallel to shoreline, are identifiable by the shaded regions in Figure 6. These regions correspond well with the area identified on the aerial photos. The identification of the bar location at the inlet mouth (Figure 9) has helped to reveal the need for realignment of the navigational channel for the following reasons: (i) the existing dredged navigation channel turned towards the outer bar and cut through the middle of the outer bar; this means the dredged channel may be filled with sand more rapidly and therefore will require more frequent dredging; (ii) the 35° turn that the channel made at the inlet mouth would create navigational hazards, since the current at the inlet mouth is strong and the wave field is variable there, particularly in bad weather; (iii) since the bar location is known the realignment of the navigational channel should be chosen in such a way that a straighter course cutting through the trough between two shoaling areas is possible.

B. Inner bars: The identification of the inner bar location in the bay area (see Figure 10) is important with regard to the future dredging practice in connection with the inlet stability problem. The inner bars slowed down the flow by increased bottom friction. As a result, the bay flow pattern was concentrated in two streams at the inlet throat. One was along the east bayshore where the navigation channel is maintained, the other was parallel to the west bayshore between the bridge and the toll booth. This flow concentration pattern focused its momentum on one part and was weakened in other regions of the inlet channel. Therefore, it was responsible for the scouring at the bridge pier and silting along the south jetty.

CONCLUDING REMARKS

This study has demonstrated the following:

1. The multi-spectral imagery, such as the Landsat imagery, can

be used to study many coastal phenomena and monitoring changes that take place. Navigation channel alignment, shoal locations and water depths are among the good examples.

2. Remote sensing by satellite should and can reduce cost and increase efficiency. It only needs a few training sites and ground truth measurements.

3. Formulation of engineering judgement and opinion from Landsat data are illustrated.

REFERENCES:

1. Hubbard, C. (1977), "Offshore Hydrographic Survey Utilizing Multi-Spectra Sensor Data," Conference on Satellite Applications to Marine Operation, New Orleans, Louisiana
2. Lyzenga, D. and F. Thomson (1978), "Basic Remote Sensing Investigation for Beach Reconnaissance," Final Technique Report No. 108900-11-F, ERIM
3. Middleton, E. M. and J. L. Barber (1976), "Hydrographic Charting From Landsat Satellite: A Comparison with Aircraft Imagery," Ocean '76
4. Sherman, J. W. III (1975), "Working Paper on a Possible Change In The Landsat-C Green Band for Improved Bathymetry Application," National Environmental Satellite Service, NOAA, Washington, D.C.
5. Wang, Y. H., M. Smutz, B. E. Ruth and H. K. Brooks (1977), "Satellite Applications To A Coastal Inlet Study, Clearwater Beach, Florida," Technique Report UFL/COEL-77/025, Coastal and Oceanographic Engineering Laboratory, University of Florida
6. Wang, Y. H., S. Hughes, and M. Smutz (1977), "Monitoring Study of Clearwater Pass, Clearwater Beach, Florida," Technical Report UFL/COEL-77/008, Coastal and Oceanographic Engineering Laboratory, University of Florida

BOUNDARY CONDITIONS FOR ANALYSIS
OF FLOW IN TIDAL INLETST. C. Copalakrishnan¹ and J. L. Machemehl²

INTRODUCTION

One-dimensional gradually varied flow analysis of flood routing and inlet flows (Mahmood and Yevjevich, 1975; Amein, 1975 and Hinwood and Wallis, 1975) has been a subject of study in the last few decades and many mathematical models have been developed based on those studies. A common feature in all these models is that the boundary conditions at the ends of the channel reaches are supplied from measured values of stage, discharge or velocity. These boundary conditions form an integral part of the mathematical models. In the case of implicit schemes, without the supply of these boundary conditions there will be more unknowns than equations. Even though in the explicit schemes they are not required in order to supply sufficient equations, it is obvious that the flow will not be properly simulated without imposing proper end conditions of flow.

Normally two end conditions will be required, the upstream and downstream conditions, even though in a network of channels there will be more than two end conditions. Of these two the upstream condition is usually the forcing function and the downstream one is the result of the flow due to the forcing function. The downstream condition depends on what happens to the flow outside the system. In other words, it depends on the shallow water wave reflections from the continuation of the channel beyond the downstream end of the system considered. These reflections are characterized by the expansion or contraction of the channel, the rate of change of the side slopes and other channel characteristics. As mentioned earlier, the downstream end condition is supplied from measured values of flow parameters so that the channel features (outside the system) mentioned above are automatically simulated. However, if it is required to know the response for any given forcing function, the corresponding measured downstream values may not be available. This means that the downstream boundary condition cannot be imposed in the usual way. This paper describes a method by which the downstream boundary condition can be imposed in the absence of measured downstream response to a given forcing function. However, the method presupposes

¹Assistant Professor, Ocean Engineering Centre, Indian Institute of Technology, Madras, India 600 036.

²Associate Professor, Department of Marine Science and Engineering, North Carolina State University, Raleigh, N. C. 27650.

that measured values for at least one forcing function are known as part of the features of the channel or channel system.

FLOW PARAMETERS

The rate of change of velocity or stage at a point is a function of geometric and dynamic parameters. The geometric parameters include the shape of the channel cross section and the rate of change of that section beyond the point under consideration. The stage and velocity themselves at the point form the dynamic parameters, in addition, of course, to the acceleration due to gravity. However, when looking for the rate of change of velocity or stage at an end section, it should be recognized that such rates can be different for the same stage and velocity depending on whether the flow is accelerating or decelerating and whether the flow is inward or outward of the inlet. Thus, the following four situations are:

- 1) Flood tide - accelerating flow
- 2) Flood tide - decelerating flow
- 3) Ebb tide - accelerating flow
- 4) Ebb tide - decelerating flow

By grouping the geometric and dynamic parameters to form appropriate non-dimensional numbers that govern the flow, it is possible to predict with a degree of accuracy the time rate of change of velocity or stage at the end sections of a channel system. In the present study, the rate of change of velocity, $\partial U/\partial t$, has been used as the downstream boundary condition.

Application of the Π - Theorem

A functional relationship of the dynamic parameters involved can be written as follows, remembering that we are looking for, $\partial U/\partial t$:

$$F(\dot{U}, U, g, \eta) = 0$$

where, U , is the velocity, \dot{U} , is time-derivative, g , the acceleration due to the gravity and, η , the water level.

Using, η , and, g , as the repeating variables, the non-dimensional numbers, Π_1 , and, Π_2 , are:

$$\Pi_1 = \eta^a g^b \dot{U}$$

$$\Pi_2 = \eta^{a_1} g^{b_1} U$$

On applying the dimensional equations, it is found that $a = 0$, $b = -1$, $a_1 = -\frac{1}{2}$ and $b_1 = -\frac{1}{2}$. Therefore:

$$\Pi_1 = \dot{U}/g$$

$$\Pi_2 = U/\sqrt{gn}$$

As expected, the Froude number of flow is a governing factor.

Steps to Arrive at $\partial U/\partial t$

From a given set of velocity-stage relationship at a given end of a channel system a relationship between the two non-dimensional numbers, Π_1 , and, Π_2 , is obtained using a least squares fit of a fourth order polynomial. From this relationship one can compute, $\partial U/\partial t$, once the velocity and stage at the point for a given time is known. The, $\partial U/\partial t$, is then imposed as the downstream boundary condition. The steps involved in the procedure are shown in Figures 1 and 2.

APPLICATION TO THE CAROLINA BEACH INLET

The procedure mentioned was tested with the field data obtained for Carolina Beach Inlet, North Carolina, USA. The inlet (Fig. 3) has a small inlet-channel connecting the ocean to the Atlantic Intracoastal Waterway. That part of the channel system studied is shown in Fig. 3. The Galerkin finite element approach coupled with a Hermitian Cubic shape function (Zienkiewicz, 1971) was used to analyze the inlet. Details of this method have been reported independently. (However, the type of the numerical analysis is irrelevant at this point). The channel system requires the rate of change of velocity, i.e. $\partial U/\partial t$, at the two points Range 1 and Range 2. Independent relationships between Π_1 and Π_2 were obtained for these two points in order to impose the two downstream boundary conditions. The upstream boundary condition was the forcing function which is the tidal fluctuation at the mouth of the inlet.

The relationship between Π_1 , and Π_2 for flood tide at Range 2 and ebb tide at Range 1 for both accelerating and decelerating trends are shown in Figs. 4 and 5. The figures shown indicate a fairly smooth relationship in all cases. The inlet was analyzed using these relations for a complete tidal cycle. The best way to test the method would be to use two sets of tidal data, one to construct the relationship between Π_1 , and, Π_2 , and other to compare measured computed values. As two sets of data were not available for the inlet, a hypothetical tidal input was used as a second forcing function, the first one being from the records. Figs. 6 and 7 show the measured and computed tidal fluctuations at Ranges 1 and 2. The hypothetical forcing function was taken as 0.8 times the tide used for the first set of computations.

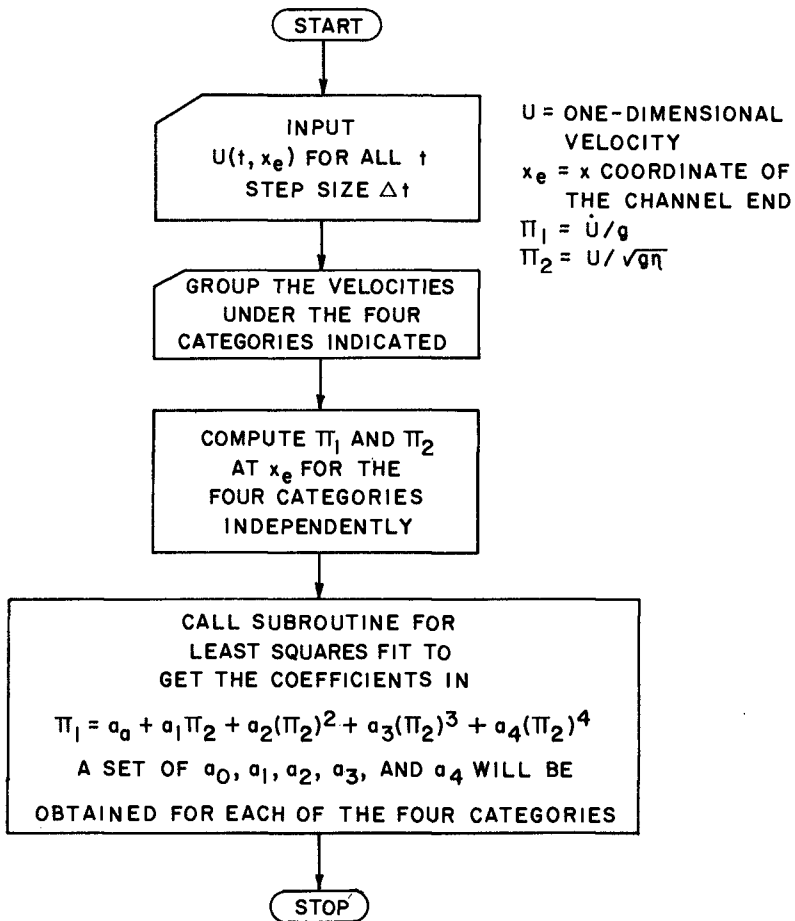


FIGURE 1. FLOW CHART NUMBER ONE.

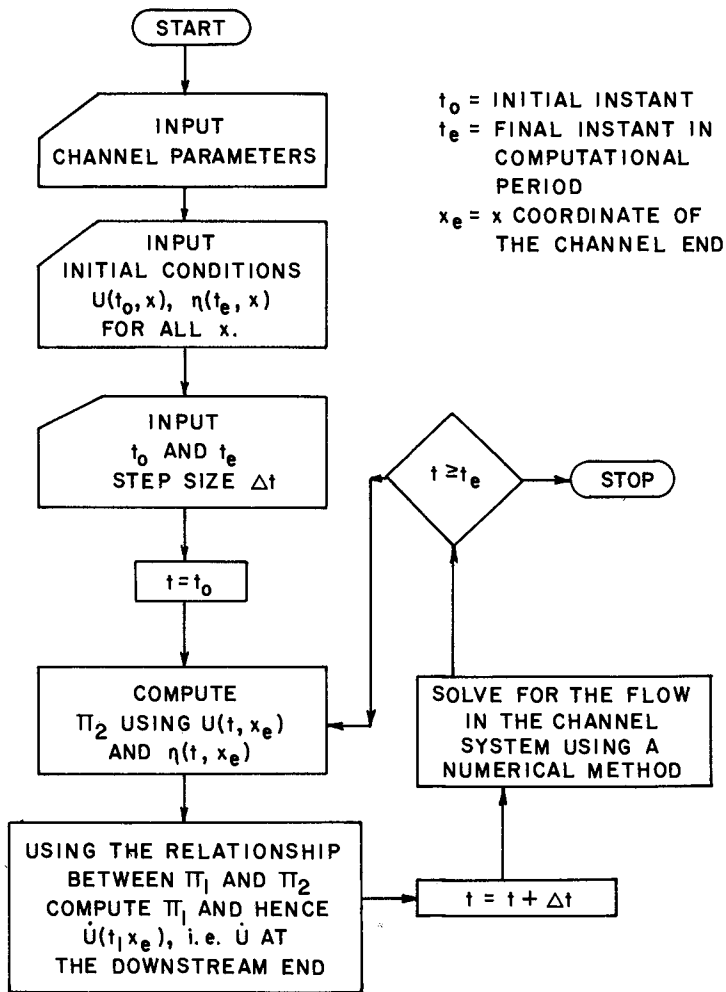


FIGURE 2. FLOW CHART NUMBER TWO.

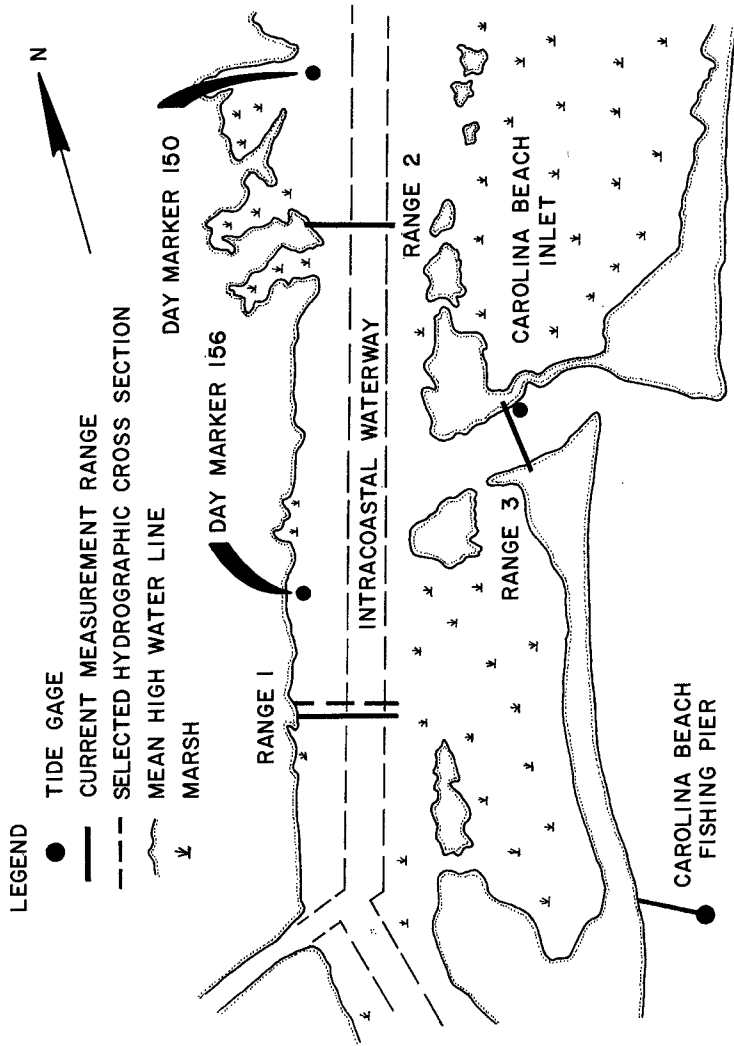


FIGURE 3. CAROLINA BEACH INLET

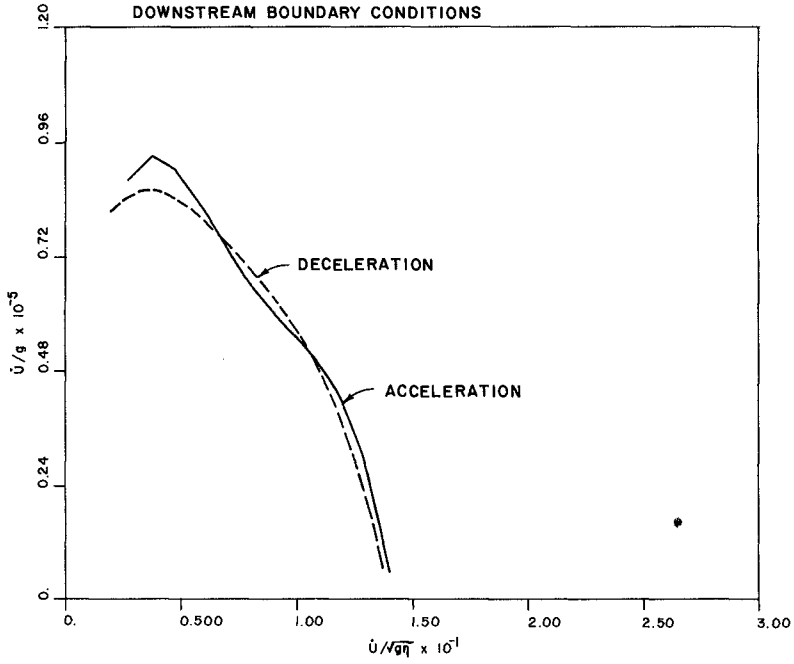


FIGURE 4. FLOOD TIDE AT RANGE NUMBER 2

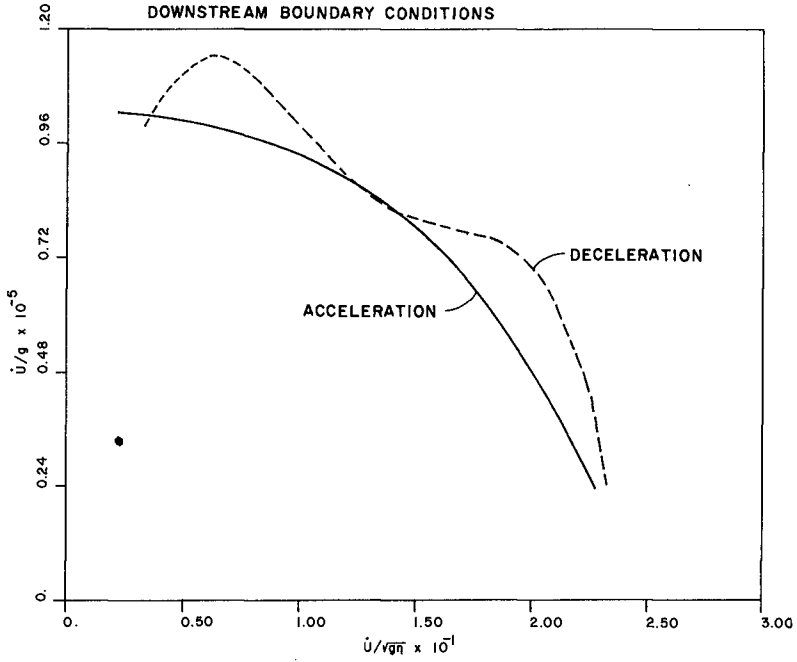


FIGURE 5. EBB TIDE AT RANGE NUMBER 1

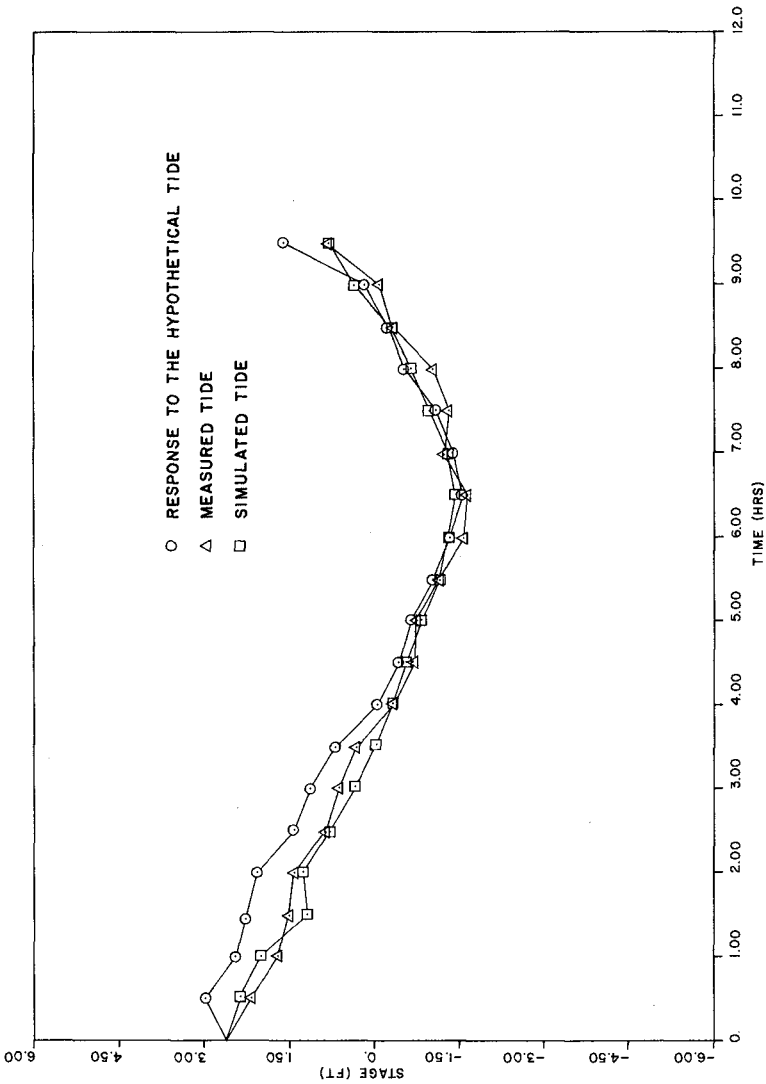


FIGURE 6. TIDAL FLUCTUATIONS AT RANGE NUMBER 1

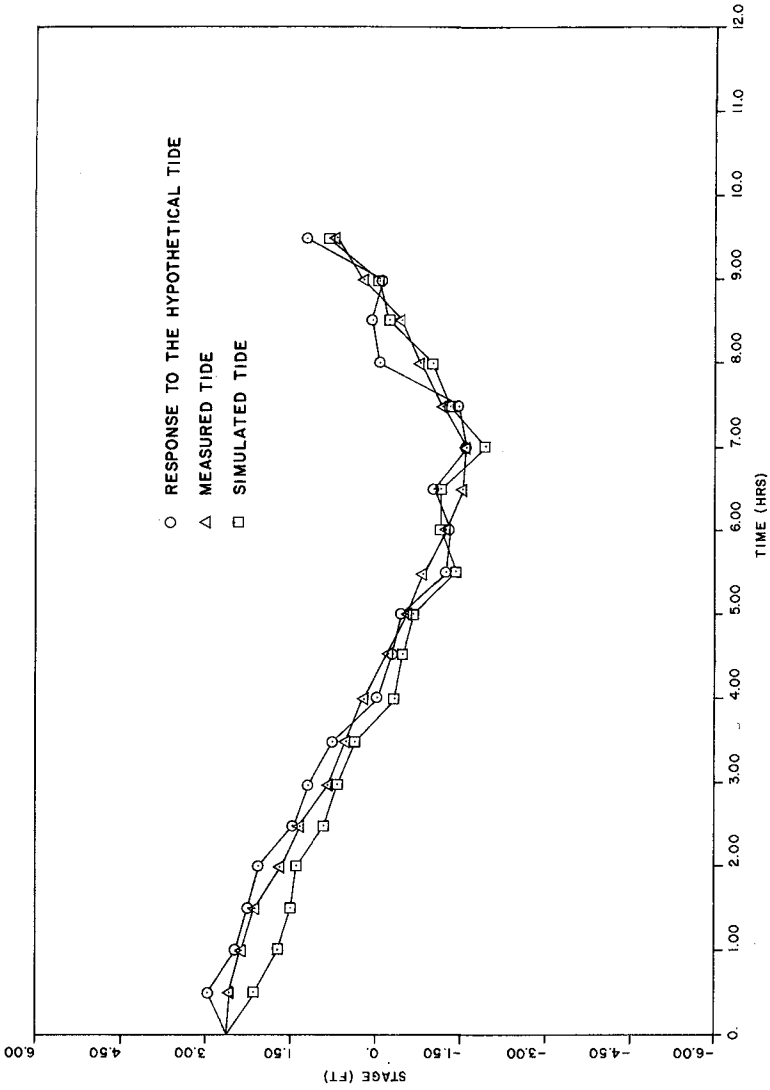


FIGURE 7. TIDAL FLUCTUATIONS AT RANGE NUMBER 2

CONCLUSIONS

A method for supplying downstream boundary condition in the absence of measured data for any given forcing function has been developed. This method is based on non-dimensional numbers which govern the dynamics of flow. These numbers were determined by a simple application of the Π - Theorem to the dynamic parameters of flow.

The above method was applied to the Carolina Beach Inlet, N. C. analysis. As shown by Figs. 6 and 7 the method yield values which are in good agreement to the measured tide at the two points considered. This, no doubt, depends on the numerical method of analysis also. The non-dimensional numbers can be used to yield the downstream boundary conditions for any numerical method chosen to analyze the flow provided. $\partial U/\partial t$, is the downstream condition needed for all time. If it is, $\partial \eta/\partial t$, then a different set of non-dimensional numbers are required.

The advantage of the method developed here is that one can know the response of a channel system to a hypothetical but possible forcing function for which measured downstream values are not available. This situation is especially relevant to power canals and inlet channels where the flow is affected by man-made alterations in river discharge or construction, etc.

ACKNOWLEDCEMENT

This study was partly supported by the Center for Marine and Coastal Studies, North Carolina State University. The data for the analysis were obtained from the reports of the Army Corps of Engineers, Wilmington, North Carolina, USA.

APPENDIX I - References

- Amein, M., 1975, "Computations of Flow Through Masonboro Inlet, N. C.", Journal of the Waterways, Harbours and Coastal Engineering Division, ASCE, Vol. 101, No. WWI, Proc. Paper 11124, Feb., pp. 93-108.
- Hinwood, J. B., and Wallis, I. C., 1975, "Review of Models of Tidal Waters", Journal of the Hydraulics Division, ASCE, Vol. 111, No. HY11, Proc. Paper 11693, November, pp. 1405-1421.
- Mahmood, K., and Yevjevich, V., 1975, Unsteady Flow in Open Channels, Vol. 1, Water Resources Publications, Fort Collins, Colorado.
- Zienkiwicz, O. C., 1971, The Finite Element Method in Engineering Science, McCraw Hill Book Co., New York, N. Y.

APPENDIX II - Notation

The following symbols are used in this paper:

a, b, a_1, b_1 = powers of variables while applying the Π -Theorem

g = acceleration due to gravity

x = independent variable, space

t = independent variable, time

U = the one dimensional velocity in the x direction

$\dot{U} = \partial U / \partial t$

η = water level with regard to a horizontal datum

Π_1, Π_2 = the non-dimensional numbers \dot{U}/g and $U/\sqrt{g\eta}$ respectively.

MECHANISMS OPERATING AT A JETTIED RIVER ENTRANCE

Bruce M. Druery
Supervising Engineer,
Estuary Process Investigations

Alexander F. Nielsen
Engineer
Coastal Process Investigations

Department of Public Works, State Office Block,
Phillip Street, Sydney, AUSTRALIA. 2000

ABSTRACT

Between October 1976 and July 1977 a northern rubble mound jetty was constructed at the mouth of the Hastings River, transforming the entrance from a single to a double jettied system. Prior to the jetty construction the entrance was characterised by the presence of a substantial swash bar (alternatively called an ebb delta marginal shoal) which was a continuous feature over 100 years of hydrographic survey records. However, construction of the northern jetty triggered an unprecedented onshore movement of the swash bar. This movement was well documented by a field monitoring programme incorporating hydro-surveys, aerial photographs, tidal gaugings, sediment sampling, float tracking and nearby wave rider buoy information.

A semi-quantitative model was developed to aid understanding and quantification of the macro sedimentary processes associated with this phenomenon. The model demonstrated that the sudden reduction of the swash bar was due to the disruption of a circulation of sand which had previously aided the dynamic stability of the bar. The quantitative predictions of the model agreed well with subsequent entrance behaviour. The philosophical development of the model and its findings are discussed in detail.

In the literature there is a general lack of attempts to quantify the sediment transport relationships between the gross morphologic features of tidal entrances. This paper presents a methodology for assessing the sedimentary process at tidal entrances.

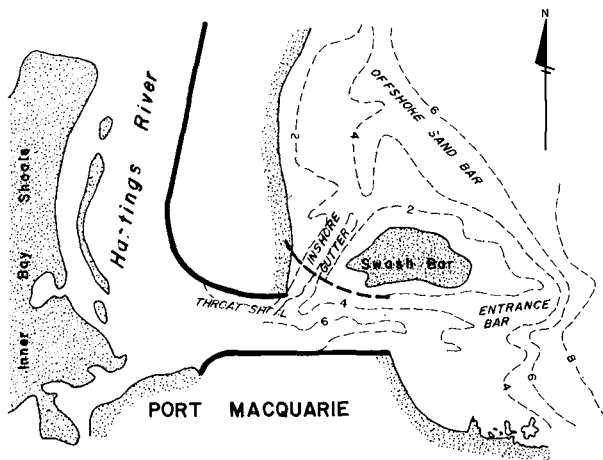
1. INTRODUCTION

The coastline of New South Wales has over thirty jettied river entrances. Their physical setting varies from the sandy (albeit eroding) coastline of the north, characterised by relatively high littoral drift rates, to the southern coastline where pocket beaches and prominent rocky headlands extending into deep water testify to an impoverished littoral drift. Virtually all these entrances have river mouth bars and entrance jetties have been constructed to satisfy, to varying degrees, the navigational requirements of increased depth, safer navigation and/or stability of inlet location. This paper is a critical review of the response of the Hastings River, Port Macquarie, to recent entrance jetty construction.

Port Macquarie is located at the mouth of the Hastings River, in the mid-north coast of N.S.W. - See fig. 1. Tides are semi-diurnal



PORT MACQUARIE DEFINITION SKETCH



- KEY**
- Low water (L.W.O.S.T.)
 - Early training works - Southern 1897
- Northern 1940
 - New entrance jetty 1977/78
 - - - Contours - metres, 1966 survey
- metres 0 200 400

Figures 1 and 2

with a Mean Spring Tide range, at the entrance, of 1.26 m associated with a peak tidal discharge of 1600 cumecs. Fluvial flows are flashy but significant. The peak fluvial discharge is 7100 cumecs, estimated from height records spanning the last 50 years. The wave climate is moderate to high with offshore significant wave heights of 1.5 m being exceeded 50% of the time (Lawson and Abernathy 1975).

Since its discovery in 1819 by Captain John Oxley the Hastings River entrance has been hazardous

to navigate. Records are replete with accounts of vessels running aground on the bar or being swamped and even wrecked. Navigation of any entrance bar is never easy and the Hastings River bar can be treacherous because it is unusually wide, has a steep seaward face and a shifting channel.

2. HISTORY OF ENTRANCE WORKS AT PORT MACQUARIE

The first attempts to stabilise the entrance were made in 1897 when construction was started on the southern training wall and jetty - see fig. 2. These works proved to be largely ineffectual with the entrance varying in position over a distance of 1 km along the northern beach. The pattern was for floods to cut through the northern sandspit and the new entrance to migrate slowly southwards.

A northern training wall and jetty were completed in 1940 but the works were gradually out flanked by the prograding profiles of the adjacent beaches.

During the last decade the entrance has been host to a broad expanse of shoals through which the channel has shifted seasonally according to the prevailing wave pattern. The deterioration of the bar has had a deleterious effect on the local fishing and commercial fishing industries and prevented Port Macquarie from realising its full tourist and pleasure craft potential (Posford, et al 1974). Hence in October 1976 construction of a new northern jetty commenced with the objective of creating a more stable, safer bar for navigation.

Since the commencement of construction a field monitoring programme has been in operation and considerable data relating to the morphologic changes in the entrance area has been obtained.

3. SEDIMENTARY PROCESSES

To facilitate discussion of sedimentary processes the study area has been subdivided into a number of coastal cells - see fig. 3. The cells have been chosen because they comprise a number of discrete hydraulic processes and it is useful to discuss the interactions of these processes within relatively self-contained cells. Interactions between cells link them together as a complete dynamic system. The detailed discussion of data and the quantification of the processes is given by Druery and Nielsen (1979) and only the key findings will be discussed below.

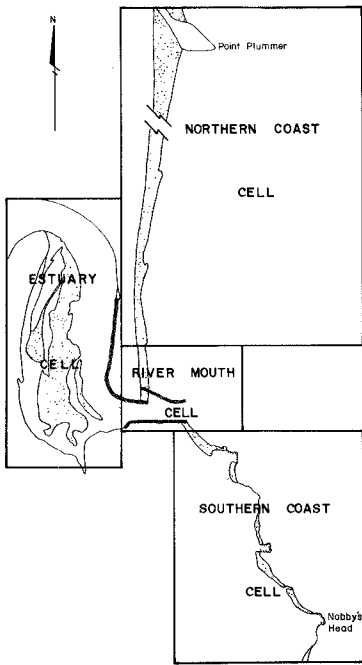


Figure 3 Coastal Cells

3.1 Estuary Cell

This cell is defined as that part of the river upstream of the entrance throat and includes the inner bay shoals. An analysis of 14 hydrographic surveys, from 1881 to 1972, demonstrated that the inner shoals showed an early tendency towards accretion due to the high sand infill rates prior to the construction of the northern training wall in 1940. Since that time the inner shoals have tended to stabilise

and the contemporary growth rate was estimated at $50,000 \text{ m}^3$ per year.

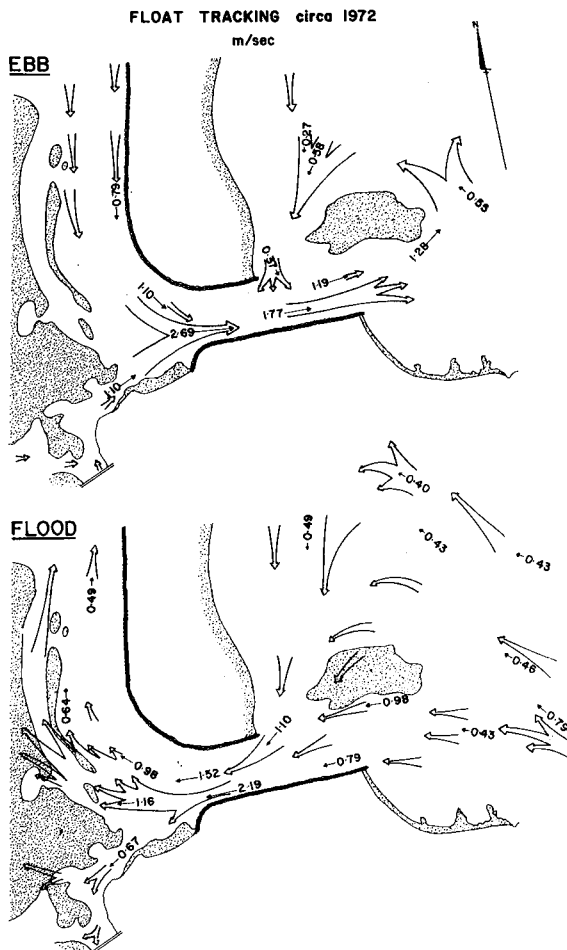


Figure 4 shows the results of float tracking carried out in 1972. The flood tides promote accretion of the inner bay shoals due to the direct impingement of the flood tide velocities. The ebb velocities are basically parallel to the training wall and hence tend to interact little with the bulk of the inner shoals. This tendency for net flood tide accretion manifests itself as a growth of parallel, crescentic shaped shoals on the eastern edge of the inner shoals - see fig. 5. There appears to be a functional relationship between accretion and the throat shoal as seen by the close association of the more recent

Figure 4 Float Tracking Results

crescent (fig. 5) with sand coming from the throat shoal.

Tidal velocities and surface gradients, over a full ebb and flood tide cycle, were measured approx. 1 km upstream from the seaward tip of the southern jetty under conditions of Spring, Neap and intermediate tides. Using these measurements in the sediment transport formula of Ackers and White (1973), the annual transport of sediment by tidal action was estimated to be approximately 200,000 m³ p.a. for the flood tide and 150,000 m³ p.a. for the ebb. Similar sediment transport calculations in the entrance throat indicated a maximum tidal transport capacity of 500,000 m³ p.a. However analysis of bed sediments indicated that the sediments in the entrance throat were coarse and probably predisposed towards armouring. It was considered that because of the high likelihood of channel armouring, the annual transport in the throat would not differ greatly from that estimated for the upstream location. (i.e. there would be 100% throughput of sediment supplied to the throat).

Apart from the tidally active eastern edge of the inner shoals, the bulk of the shoals are relatively stable. Further inland on the shoals diver observations revealed active bioturbation and a surface growth of algae both of which are indicative of immobile sediments. The only note of instability associated with the inner shoals is scouring by floods which tend to remove portions of the crescentic shoals on the eastern margin.

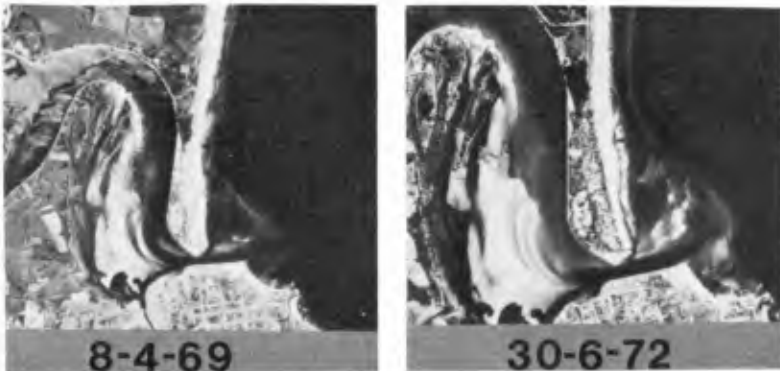


Figure 5 Aerial Photographs showing growth of Inner Shoals.

3.2 River Mouth Cell

The dominant morphologic features of this cell (re: fig. 2) are the entrance bar, the offshore bar, the swash bar, the inshore gutter which separates the swash bar from the beach and the jettied entrance channel and throat shoal.

Current trackings carried out in 1972 (see fig. 4) are typical of the general current patterns which existed prior to the northern jetty construction. While the current trends would depend largely on the conditions pertaining to the particular day of measurement, discussion with the local navigation authority confirmed that fig. 4 is a fair representation of the persistent current features.

A significant feature of the ebb current pattern is the development of a large eddy centred about the swash bar. This is a common feature of tidal inlets, particularly when there is only one entrance jetty (Komar and Terich 1976, FitzGerald et al 1976, Dean and Walton 1975). At Port Macquarie it is considered that the eddy was produced by a combination of factors viz:

1. Viscous drag between the ebb tide jet stream and adjacent water (Dean and Walton 1975).
2. A strong current driving mechanism in the inshore gutter would have been created by the coupling of set down against the northern wall, due to superlevation of the main ebb flow as it was forced around the severe approach bend, and set up due to breaking waves on the swash bar.
3. Refraction of the dominant southeast waves around the swash bar would tend to produce an inlet directed longshore current (Hubbard 1976, Dean and Walton 1975).

During the flood tide the currents seawards of the entrance were generally 50% less.

Irrespective of the state of the tide the currents in the inshore gutter were inlet directed and showed a tendency to increase when the main entrance flow was ebbing. The commitment of the inshore gutter to flood tide currents produced a strong bias in favour of flood tide velocities and sediment transport against the northern training wall.

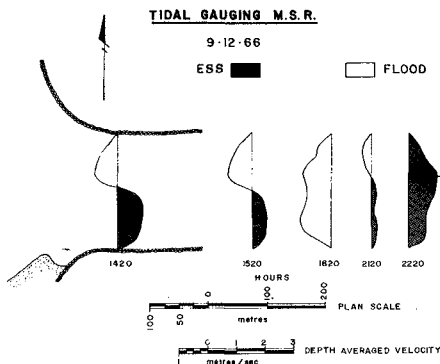
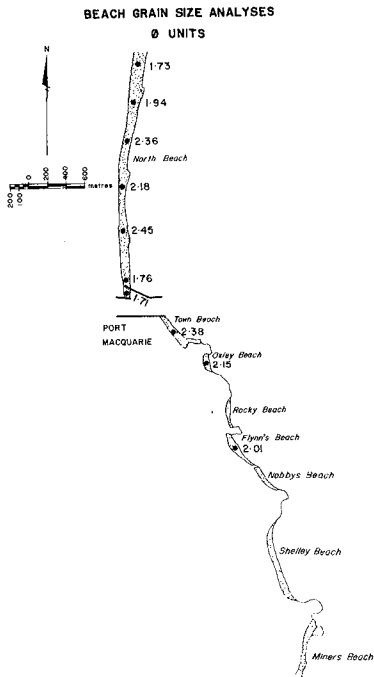


Figure 6 Horizontal Velocity Distribution at Entrance.

Fig. 6 shows portion of comprehensive tidal gaugings carried out in December 1966. Towards the end of the ebb tide the flood tide commenced two hours early against the northern training wall. During the commencement of the ebb tide it persisted for approx. one hour. Hence against the northern wall the flood flow had a duration of 8 hours thus indicating a strong potential for flood tide transport against the northern wall.

Sediment sampling and diver observation, during jetty construction, showed that the landward face of the bar was gravelly comprising well rounded and highly polished shell fragments and lithic pebbles. The surface was formed into symmetrical long crested ripples 7-10 cm in height and 0.3 - 0.6 m wavelength. There was no observed movement of the gravel during conditions of small swell. The seaward face of the bar, however, was composed of shell free quartzose sand and substantial movement of the sand took place (as sheet flow) in response to the orbital velocities of small swell.



The intrinsic difference between the surficial sediments of the inner and outer faces of the bar is intriguing. It is considered that it reflects possible differences in the ebb and flood sediment paths. The ebb tide would tend to jet most of its sediment onto the seaward face of the entrance bar, developing an armouring of the bed of the main channel in the process. During flood tides, the return of that sediment would take place by combined wave and current action on the swash bar and inshore gutter.

On a day to day basis the entrance bar and swash bar constitute a balance between the seaward movement of sediment by the ebb tide and landward transport by waves and the flood tide. The ebb tide would deposit sand on both the entrance bar and the swash bar. Shoaling of waves would induce sediment movement across the surface of the swash bar either onto North Beach or directly onshore and into the inshore gutter.

Figure 7

The inshore gutter would then feed sediment directly into the estuary at all states of the tide and during each ebb tide a significant portion of the inshore gutter sand feed would be carried back onto the swash bar and recycled.

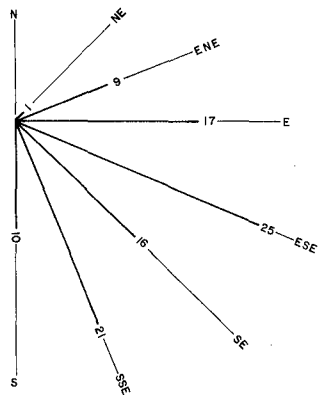
3.3 Southern Coast Cell

This cell comprises small beaches which contain limited sand and are well pocketed between rocky cliffs - see fig. 7. Sedimentological studies identified a distinct northward fining of the beach sands and an absence of lithic minerals, setting them apart from the beach sands of the northern coast cell. All indications pointed to the existence of a weak, intermittent littoral transport which is probably associated with temporary development of offshore bars during major storms and is considered to be of the order of $20,000 \text{ m}^3 \text{ p.a.}$

3.4 Northern Coast Cell

North Beach is zeta shaped with a well developed offshore bar. Historical hydrosurveys revealed episodes of successive onshore and offshore movement of sediments. The offshore sediment movement, resulting from storm events, was of the order of $100-200 \text{ m}^3/\text{m}$ storm whereas onshore movement rates, during calmer periods, were much less and of the order of $30 \text{ m}^3/\text{m/year.}$

PERCENTAGE OCCURRENCE OF WAVE DIRECTION



DATA SOURCE: Wave Rider Buoy;
Coffs Harbour Jun.'75-Nov.'79

Wave refraction analyses were carried out with the aim of assessing longshore sediment transport rates at a number of locations on the beach. The direction of wave approach was divided into two directions; north easterly and south easterly. The percentage occurrence of waves from each direction was set at 19% and 81% respectively, based on four years of wave rider buoy data at Coffs Harbour - see fig. 8. For each direction, four classes of wave height were considered and a representative significant wave height was assigned to each class. From relationships of significant wave height and period derived from the wave rider buoy data a significant wave period was assigned to each representative significant wave height. These parameters are set out in Table 1.

Figure 8

TABLE 1. Representative Wave Statistics used in Refraction Analysis

Significant Wave Height Class	Hs (m)	Representative Wave Height Hs (m)	Wave Period Ts (s)
0 - 1		0.5	6.4
1 - 2		1.5	7.7
2 - 5		3.5	8.9
> 5		7.5	10.2

The occurrence of each representative wave height was determined from wave height exceedence curves presented by Lawson and Abernathy (1975).

The inshore wave breaking height obtained from the wave refraction analyses, the angle of shore break from aerial photographs and the values of % exceedance were used to estimate the littoral sediment transport. The CERC formula exhibited extreme sensitivity to the wave direction data but the overall result was one of zero net longshore drift on North Beach. However, historical aerial photographs showed that an occasional offshore bar forms around the northern headland of the beach (Point Plummer). This suggests that there is an intermittent northward leakage of sand from the compartment which is consistent with the zeta shape of the beach and the existence of rudimentary transgressive dunes in the far north of the beach. Hence it is considered that there is a weak net northerly longshore drift along North Beach.

Gross sediment transport rates calculated at a point on the northeastern edge of the swash bar indicated a strong net onshore transport, the amount of movement being on order of magnitude higher than that estimated for North Beach.

The gross sediment transport rates calculated using the CERC formula were unrealistically high. Gordon et al (1978) also found this to be the case in studies of other beaches along the New South Wales coastline. Hence, it was not considered valid to directly apply the CERC formula which has been empirically developed from measurements on USA beaches. Nevertheless, it was considered that the CERC formula would provide a reasonable indication of the relative magnitude of transport rates calculated at various locations within a littoral system. Hence the net sediment transport rates along North Beach and the northeastern edge of the swash bar were assigned values of "x" and "10x" respectively. The absolute values of the rates were then determined implicitly using the interaction equations of the sediment budget model (Section 7).

4. LONG TERM SEDIMENT DYNAMICS

On a day to day basis the entrance bar/swash bar appears to constitute a relatively stable dynamic system. However long term

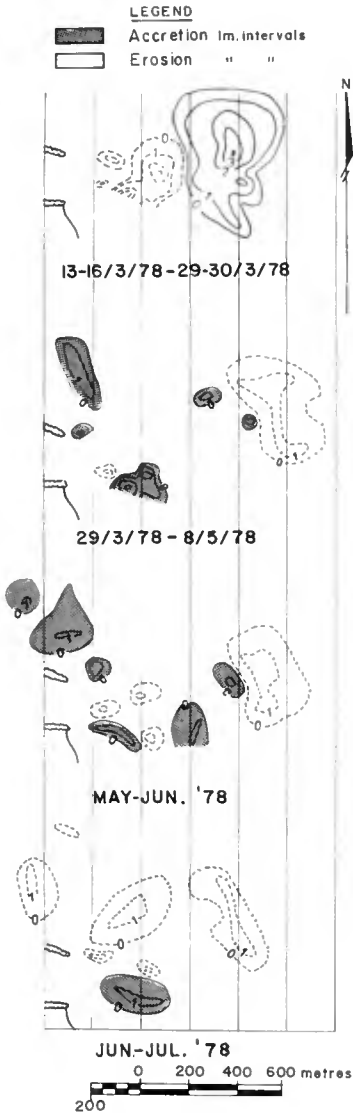


Figure 9 Offshore Isopachs

data (hydrographic surveys and aerial photographs) indicated a cyclicality which can be attributed to the interplay of floods and waves.

Floyd and Druery (1976) found that the seaward face of an entrance bar undergoes movement largely as a result of deposition by floods. Floods deposit sediment on the seaward face in depths of 10 m and less. Hydrographic surveys of the Hastings River bar indicate that the volumes of deposition range from 400,000 m³ to 200,000 m³ for major and moderate floods respectively. Deposition by floods is sudden (i.e. 2 to 3 days). Initially the conditions for navigation on the bar would be good because major floods tend to gouge a gutter through the crest of the bar. This reduces the effective width of the bar and increases the ruling depth, making navigation less hazardous. However Floyd and Druery (1976) showed that any flood deposit, on the seaward face of the bar, would undergo reworking by waves and the pre-flood location of the seaward bar face would tend to be re-established. The onshore movement would be slow and therefore the improved bar conditions would persist for a time varying from six months to two years depending upon the magnitude of the flood. As the relatively slow onshore movement began to have effect, the bar channel would become infilled and conditions on the bar would noticeably deteriorate. The onshore movement would continue until the swash bar invaded the entrance channel. A new flood would restart the cycle.

On 20-23 March 1978 a flood occurred on the Hastings River. Figure 9 shows isopachs of hydrosurveys carried out before and after the flood. It can be seen that the flood deposited sediment on the seaward face of the bar (in depths less than 10 m). The total

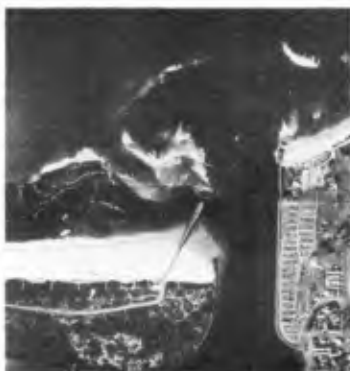


Figure 10 16th June '77

Figure 11 15th July '7



Figure 12 26th August '77



Figure 13. 19th December '77

17th July '78
Considerable shore movement
still occurring



21st February '80
Notice shoal area immediately
offshore North Beach

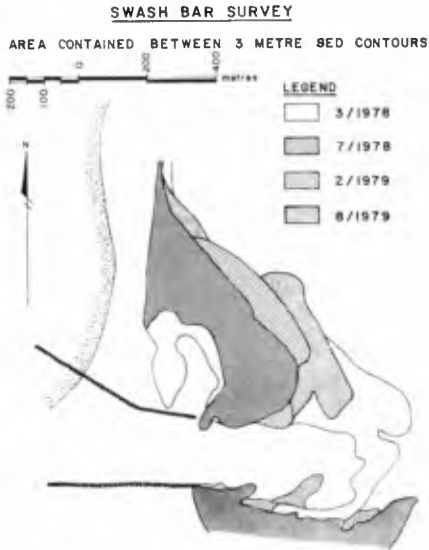


Figure 14

of the sand moving onshore from the swash bar had become attached to the jetty and North Beach as a fillet and the inshore gutter was becoming severely pinched between the tip of the jetty and the advancing slug of sand. The advancing slug of sand had shoaled and its surface was exposed at low water. By August (fig. 12) the slug of sand had completely inundated the inshore gutter and attached itself to North Beach. A portion had been intercepted by the end of the jetty causing the wave trap to be overwhelmed with sand. Spillage of sand from the wave trap had given birth to a fledgling throat shoal. By December (figure 13) the fillet of sand against the base of the jetty had been redistributed along North Beach in the form of a series of wave berms.

The onshore movement of sediment continued well after the completion of construction (viz. July 78) as shown by offshore surveys in figure 14. Between March 78 and August 79 the swash bar progressively reduced in size as a result of this onshore movement.

6. CONCEPTUAL MODEL OF SEDIMENTARY PROCESSES

The investigation of coastal processes in each cell led to the formulation of a conceptual model of the sedimentary processes of the

volume deposited was 280,000 m³ of which 60,000 m³ was derived from scouring of the inner face of the bar. The sequence of post flood surveys shows the seaward face of the bar undergoing reworking and moving slowly onshore as a series of sand slugs.

5. EFFECT OF NORTHERN JETTY

The construction of the northern jetty triggered rapid changes in the estuary mouth morphology - see Figures 10 - 13.

The jetty began to intrude into the surf zone in May 1977 at which time the swash bar occupied a substantial area and the throat shoal had been removed by a small fresh in early May. A month later further extension of the jetty had taken place and a portion of the swash bar had begun to move onshore. See fig. 10. During July (figure 11) some

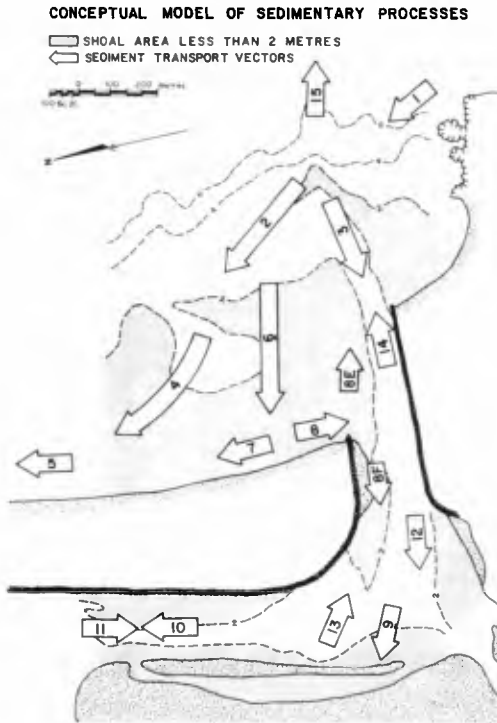
entrance bar and its environs - see Figure 15. In order to test the coherence of the conceptualisation an attempt was made to quantify the various model elements.

6.1 Interaction Equations

Consideration of local sediment budget led to the following interaction equations:

- (1) Sediment moving onshore across the swash bar, Q(2), can either head towards the inshore gutter, Q(6), or travel along the offshore bar (i.e. the outer edge of the swash bar) to North Beach, Q(4).

Hence: $Q(2) = Q(4) + Q(6)$



- (2) Sediment is carried into the estuary, Q(12), by flood currents moving across the entrance bar, Q(3), and via the swash bar/inshore gutter complex, Q(8F).

Hence: $Q(8F) + Q(3) = Q(12)$

- (3) The quantity of sediment dumped on the entrance bar and swash bar each ebb tide, Q(14), is derived from the estuary, Q(11), and the recycled component of the inshore gutter sand feed, Q(8E).

Hence: $Q(14) = Q(8E) + Q(11)$

- (4) Within the estuary the flood tide, Q(12), produces some accretion of the eastern edge of the inner shoals, Q(9), and the rest remains in the active tidal sediment flux, Q(10).

Hence: $Q(12) = Q(9) + Q(10)$

Figure 15 Conceptual Model

- (5) The sediment moving directly onshore from the Swash Bar, Q(6) can split into longshore components Q(7) or Q(8) and Q(8) can be broken down into its ebb and flood constituents.

$$\text{Hence : } Q(6) = Q(7) + Q(8); Q(8) = Q(8E) + Q(8F)$$

- (6) Prior to jetty construction North Beach was relatively stable i.e. $Q(5) = Q(4) + Q(7)$.

6.2 Functional Relationships

- (1) It was assumed that 90% of the flood tide sediment transport took place via the swash bar and inshore gutter i.e. $Q(3) = 0.1 Q(8F)$.

- (2) The ebb and flood sediment transport potential against the inside of the northern training wall was calculated from tidal current measurements assuming transport potential was proportional to the cube of the velocity (Maddock 1969). This indicated that the recycled ebb tide constituent of the inshore gutter sand feed was approximately half the flood tide constituent, therefore

$$Q(8E) = 0.3 Q(8)$$

- (3) The application of the CERC formula to determine the net littoral transport along North Beach, Q(5), and the onshore transport on the Swash Bar, Q(2), was discussed in Section 3.4 where it was argued:

$$Q(2) = 10 Q(5)$$

6.3 Calculated Values

A number of the model elements were known or estimated viz:

- (1) $Q(1) = 20,000 \text{ m}^3 \text{ p.a.}$ (See section 3.3)
- (2) Because currents in the inshore gutter were always inlet directed (Section 3.2) it was assumed that all sand feed would be inlet directed i.e. $Q(7) = 0$
- (3) $Q(9) = 50,000 \text{ m}^3 \text{ p.a.}$ (Section 3.1)
- (4) $Q(12) = 200,000 \text{ m}^3 \text{ p.a.}$ (Section 3.1)
- (5) $Q(11) = 150,000 \text{ m}^3 \text{ p.a.}$ (Section 3.1)
- (6) $Q(13) = \text{Erosion during flood event only}$ (Section 3.1)
- (7) $Q(15) = \text{Deposition during flood events}$ (Section 4)

6.4 Effect of Northern Jetty Construction

The foregoing equations and relationships were adjusted so as to

represent the hydraulic impact of the northern jetty. The impact was divided into the "short term" (i.e. within the first 2-5 years say) and the "long term" (i.e. 10 years or more).

Short Term :

- (1) Because of the elimination of the inshore gutter the majority of sediment moving directly onshore from the swash bar, Q(6), would not find its way into the estuary.

$$\text{i.e. } Q(8) = Q(8F) = Q(8E) = 0$$

- (2) The jetty construction would greatly increase the flood tide velocities across the entrance bar and the tip of the northern jetty and hence the sediment transport capacity of Q(3) would greatly increase. It was considered that the net result would be a reduction in the infeed of sediment into the estuary and hence Q(12) was reduced from its pre-jetty value of 200,000 m³ p.a. to 150,000 m³ p.a.

$$\text{i.e. } Q(12) = 150,000 \text{ m}^3 \text{ p.a.}$$

- (3) It was assumed that initially accretion of the inner shoals would not change i.e. Q(9) = 50,000 m³ p.a.

Long Term :

- (1) After a long period of onshore movement the swash bar would tend to disappear and only an ebb delta bar would remain, similar in shape to other entrances in N.S.W. (Floyd 1968). The only throughput of sediment would be that necessary to bypass the net southerly drift.

$$\text{i.e. } Q(2) = Q(1) = 20,000 \text{ m}^3 \text{ p.a.}$$

- (2) Based on experience of the effects of entrance works at the mouths of other similar estuaries in N.S.W., it was considered that tidal propagation in the estuary would not change significantly and therefore the unusual estuary instability associated with entrance jetty construction at Forster (Gordon and Neilsen, 1980) would not occur.

It was considered that within the estuary a balance would be established but the general level of sediment movement would be less i.e.:

$$Q(10) = Q(11) = 100,000 \text{ m}^3 \text{ p.a.}$$

$$Q(9) = 0$$

Effects of Floods:

It needs to be stressed that the "long term" was considered within the context of no flooding. Floods will tend to place new deposits on the entrance bar (Section 4) which would have the effect of reversing the situation towards the immediate post construction condition.

7. RESULT OF CONCEPTUAL MODEL

All the various functional relationships and known values were applied to the interaction equations for each of the three cases i.e.

- (1) prior to construction
- (2) after construction in the short term
- (3) after construction in the long term

The results are shown in Table 2.

TABLE 2 - Quantification of Conceptual Model

Model Element	Prior to Jetty Const.	After Jetty Short Term	After Jetty Long Term
Q(1)	20,000	20,000	20,000
Q(2)	290,000	290,000	20,000
Q(3)	18,000	150,000	100,000
Q(4)	29,000	29,000	20,000
Q(5)	29,000	29,000	29,000
Q(6)	260,000	260,000	N.A.
Q(7)	0	260,000	N.A.
Q(8)	260,000	0	N.A.
Q(8E)	78,000	0	N.A.
Q(8F)	182,000	0	N.A.
Q(9)	50,000	50,000	0
Q(10)	150,000	150,000	100,000
Q(11)	150,000	100,000	100,000
Q(12)	200,000	150,000	100,000
Q(13)		EXTREME EVENT	
Q(14)	228,000	150,000	100,000
Q(15)		EXTREME EVENT	
Swash Bar Removal Rate i.e. $Q(2) + Q(3) - Q(14) - Q(1)$	60,000	270,000	N.A.
Sediment Feed to North Beach $Q(4) + Q(7)$	29,000	289,000	20,000

The main effect of the jetty construction was the elimination of the inshore gutter which used to drive a circulation of sand and therefore tended to perpetuate the swash bar. The recycled component of the inshore gutter sediment feed (i.e. Q(8E)) was of the order of 100,000 m³ p.a.

After jetty construction the swash bar removal rate increased dramatically. This would explain the unprecedented onshore movements observed during the jetty construction (Section 5).

The elimination of the inshore gutter greatly increased the quantities of sediment reaching North Beach and North Beach would therefore be expected to accrete markedly.

The model predicted long term erosion of North Beach viz.:

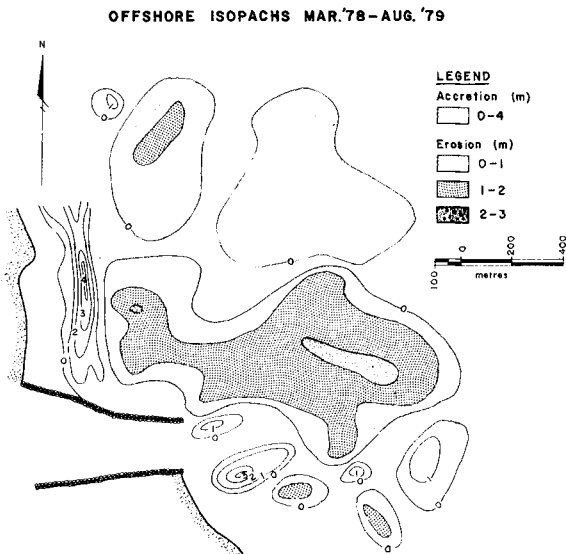
$$Q(5) - Q(4) = 9,000 \text{ m}^3 \text{ p.a.}$$

However, this would tend to be offset (to an unknown extent) by sediment injected into the system by fluvial floods i.e. $Q(15)$.

8. MODEL VERIFICATION

The conceptual model and its predictions were completed by the end of the jetty construction in July 1978. Hence the predictions of the model can be tested against the results of subsequent entrance monitoring.

The progressive decrease in areal extent of the swash bar has already been demonstrated in Figure 14. An Isopach plot between the March and August surveys is shown in figure 16. The broad area of erosion from the swash bar is directly related to pronounced accretionary structures on North Beach (viz. recent beach ridges). Volume calculations indicate a net erosion from the swash bar at a rate of $280,000 \text{ m}^3 \text{ p.a.}$ which compares remarkably well with the estimate of $270,000 \text{ m}^3 \text{ p.a.}$ obtained from the conceptual model.



The pronounced build up of North Beach is compatible with the predicted increase in the sediment supply to North Beach. Estimates of beach accretion were not possible because sediment was dispersed northwards beyond the control area of the beach surveys.

Recent monitoring of the entrance has indicated that the entrance bar has reduced in width and there has been an improvement in bar depth.

Figure 16 Swash Bar and Beach Isopachs

9. CONCLUSIONS

1. For over 40 years the entrance to the Hastings River was host to a large swash bar the presence of which created hazardous navigation conditions. The recent construction of a northern entrance jetty in, 1977-78, triggered an unprecedented onshore movement of the swash bar. The cause can be related to the elimination of a daily circulation of sand which had previously aided the dynamic stability of the swash bar.
2. Monitoring of post-construction changes has indicated that the swash bar will not return to its former size and there has been a substantial reduction in the width of the bar.
3. The long term configuration of the entrance bar and swash bar is linked to the occurrence of major floods. It was possible to discern past cycles of deposition by floods and subsequent slow onshore movement of the flood deposits.
4. It was possible to construct a conceptual model of entrance sedimentary processes which was suitable for predictions of morphological response. Although the model was based on elementary considerations of sediment budget, it was a highly effective tool for elucidating the subtleties of sediment transport relationships between the gross morphologic features of a tidal entrance.

Considerable fundamental research is necessary before full process understanding of tidal entrances will be achieved. Conceptual models as put forward in this paper are a useful interim step which combine the art and the science of coastal engineering and offer a means for assessing the impact of coastal works on macro coastal processes.

10. ACKNOWLEDGEMENTS

The authors acknowledge the assistance of Graeme Levien and Stuart Green in the computation and collation of field data.

11. REFERENCES

- Ackers & White (1973) - Sediment Transport : New Approach and Analysis. Jnl Hyd. Div. ASCE HY11.
- Dean and Walton (1975) - Sediment Transport Processes in the Vicinity of Inlets with Special Reference to Sand Trapping. Est. Res. Vol. 11, Acad. Press.
- Druery & Nielsen (1978) - Port Macquarie Entrance Study. Department of Public Works, N.S.W., Report PWD 78005.

11. REFERENCES (Cont'd).

- Fitzgerald, Nummedal & Kana (1976) - Sand Circulation Pattern at Price Inlet, South Carolina. Proc 15th Int. Conf. Coast. Eng., Hawaii 1976.
- Floyd & Druery (1976) - The Results of River Mouth Training on the Clarence River Bar, N.S.W. Aust., Proc. 15th Int. Conf. Coast. Eng., Hawaii.
- Floyd (1968) - River Mouth Training in New South Wales Proc. Int. Cont. Coast. Eng., 1968.
- Gordon, Lord, Nolan (1978) - Byron Bay - Hastings Point Erosion Study, Department of Public Works, N.S.W., Report No. 78026.
- Komar & Terich (1976) - Changes due to Jetties at Tillamook Bay, Oregon. Proc. 15th Int. Conf. Coast. Eng., Hawaii.
- Lawson & Abernathy (1975) - Long Term Wave Statistics of Botany Bay. 2nd Aust. Conf. Coast & Ocn. Eng., Gold Coast, Queensland.
- Maddock (1969) - The Behaviour of Straight Open Channels with Moveable Beds U.S. Geol. Survey, Prof. Paper 622-A, 70P.
- Nielsen & Gordon (1980) - Tidal Inlet Behavioural Analysis. Proc. 17th Int. Conf. Coast. Eng., Sydney, 1980.
- Posford, Pavry, Sinclair & Knight (1974) - Port Macquarie Economic Study. Report for Department of Public Works.

STABILITY OF ESTUARY MOUTHS IN THE RHINE-MEUSE DELTA

J. VAN DE KREEKE, Professor of Ocean Engineering, Rosenstiel School of Marine and Atmospheric Science, University of Miami, Miami, U.S.A.

JAC HARING, Research Engineer, Deltadienst, Rykswaterstaat, The Hague, Holland

1 GENERAL CHARACTERISTICS OF THE RHINE-MEUSE DELTA

The Rhine-Meuse Delta in the southwestern part of the Netherlands covers an area of approximately 60 x 60 km; see Fig. 1. The Delta consists of sediment deposits of the Rhine and the Meuse in which tides and river flow have scoured an intricate system of channels. The four major estuaries are from south to north Eastern Scheldt, Brouwershavense Gat, Haringvliet and Rotterdam Waterway. The connection between estuaries and rivers is formed by a system of branching channels, referred to as tidal rivers. The flow in the tidal rivers is constrained by dikes, revetments and groynes. It is in this region where most of the sand fraction of the sediments carried by the rivers Rhine and Meuse is deposited. Extensive maintenance dredging is required to maintain a sufficiently large cross-section for navigation. The mud fraction (all sediments with grain size $< 62 \mu$) of the river sediments is carried further seaward and is partly deposited in the estuaries and partly in the offshore underwater delta.

Average tidal ranges at the seaward boundary of the Delta decrease going from south to north and vary between 3.78 m at Flushing to 1.58 m at Hook of Holland. The ratio average tidal range to average spring tidal range is approximately 0.86. Tides are predominantly semi-diurnal. The average annual discharges of the Rhine and Meuse are respectively 2200 m³/sec and 250 m³/sec. Discharges of both rivers show seasonal fluctuations with a maximum in the winter and a minimum at the end of the summer. The river water is distributed over the estuaries in varying proportions. E.g. in 1959 the ratios of the average river volume to the average flood volume for the estuaries Eastern Scheldt, Brouwershavense Gat, Haringvliet and Rotterdam Waterway were respectively 0, 0, 0.25 and 0.53.

In the offshore region there exists a longshore sand motion to the north with a transport rate on the order of 50,000 m³/year. Associated with the longshore motion is a fining of the bottom sand when going from south to north. Typical values for the mean grain diameter of the sand are 200 μ for the mouth of the Eastern Scheldt and 150 μ for the mouth of the Haringvliet. Terwindt (1973).

The present shape of the Delta is to a large extent the result of man's interference with the natural sedimentation processes, the expansion of the port of Rotterdam, maintenance dredging and in particular the Delta project. The Delta project envisions the closure

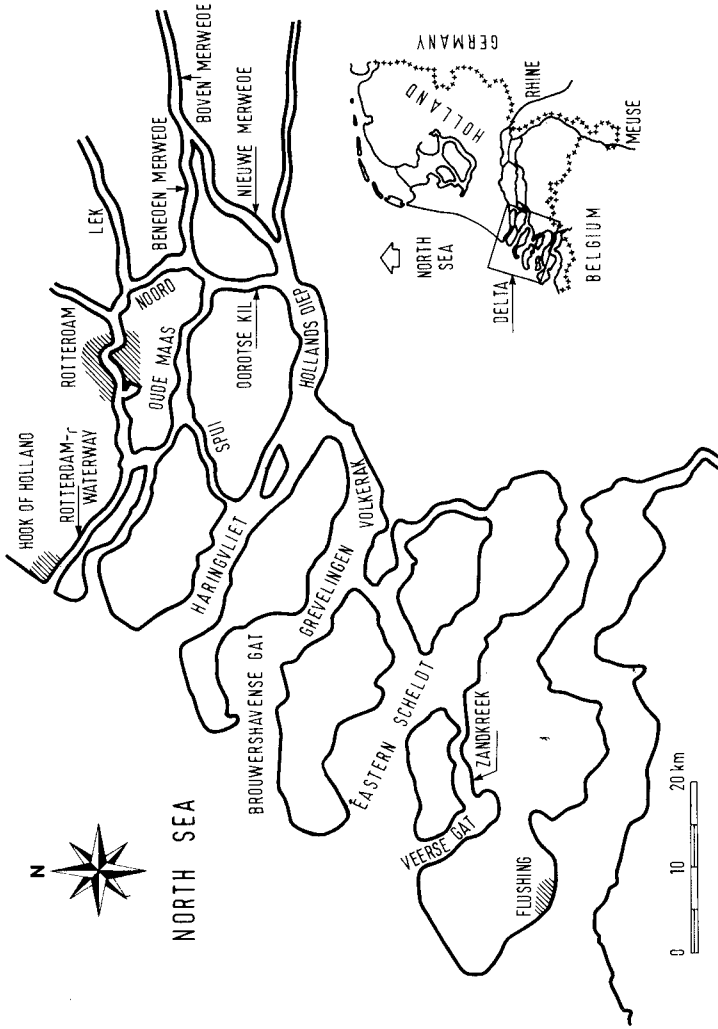


Figure 1. Rhine-Meuse Delta prior to 1953.

of the Eastern Scheldt, Brouwershavense Gat and Haringvliet. To properly manage the Delta and in particular to minimize maintenance dredging and to prevent dike calamities it is important to be able to predict scour and shoaling associated with the various man-made modifications. For this purpose, empirical relations between characteristics of cross-section and flow are derived using observations in the Rhine-Meuse Delta, prior to the Delta project.

2 EQUILIBRIUM FLOW AREAS

The important parameters governing the cross-sectional area at the mouth of the estuaries are the sediment transport capacity of the tidal currents, Q_{tc} , and the littoral drift, Q_l . Assuming that during the major part of the tidal cycle the bottom shear stress is considerably larger than the critical shear stress for sediment motion, the sediment transport capacity of the tidal currents can be expressed as, Leliavsky (1966).

$$Q_{tc} = f(b, F, \rho_s, \rho_w, g, d) \left(\frac{Q}{A}\right)^n \quad (1)$$

in which

Q_{tc}	= sediment transport (m^3/sec)
b	= inlet width
F	= bottom friction
ρ_s	= density of sediment
ρ_w	= density of water
g	= gravity acceleration
d	= grain diameter
Q	= discharge
A	= cross-sectional area

Depending on the investigator, n varies between 3 and 5.

It is postulated that for long term equilibrium conditions

$$\overline{Q}_{tc} :: \overline{Q}_l \quad (2)$$

where the overbar denotes a long term (yearly) average, and thus,

$$\overline{\left(\frac{Q}{A}\right)^n} :: \frac{\overline{Q}_l}{f} \quad (3)$$

For tidal inlets with zero fresh water inflow $\overline{Q} = \text{const.}$
 \hat{Q} where \hat{Q} is the maximum discharge during the tidal cycle.
 Assuming a constant area $A = A_c$, Eq. (3) can be written as

$$\overline{\left(\frac{\hat{Q}}{A}\right)^n} :: \frac{\overline{Q}_l}{f} \quad (4)$$

From observations and restricting attention to inlets in the same geographical area, it follows $\hat{Q}/A_c \approx \text{constant}$, Jarrett (1976), Byrne et al. (1980). Thus, with regard to the long term equilibrium, the magnitude of the littoral drift and the sediment characteristics appear to be of secondary importance. Note that for $n = 3$ the left-hand side of Eq. (4) can be interpreted as the work done by the tidal currents on the inlet bottom per sec.

Similarly to the inlets an attempt is made to correlate the cross-sectional area at the mouth of the estuaries in the Rhine-Meuse Delta with the maximum tidal discharge \hat{Q} . Because in general estuaries have fresh water inflow, the tidal discharge follows from

$$Q(t) = Q_r + \hat{Q} \sin \omega t \quad (5)$$

$Q(t)$ = instantaneous discharge

Q_r = river discharge

$\omega = 2\pi/T$ = angular frequency of the tide

T = tidal period

In this study, the maximum tidal discharge, \hat{Q} , is computed from the measured value of the tidal volume (tidal volume is sum of flood volume and ebb volume) using the equation.

$$TV = \hat{Q} T \left[\frac{Q_r}{\hat{Q}} + \frac{2}{\pi} \sqrt{1 - \left(\frac{Q_r}{\hat{Q}}\right)^2} \right] \quad (6)$$

This equation assumes $Q_r < \hat{Q}$.

For the purpose of this discussion, the cross-section characterizing the estuary mouth is taken at the location where there exists a pronounced change in the rate of change of the cross-sectional area; see Fig. 2. It appears that at this location the characteristic velocity, \bar{v} , defined as the tidal volume divided by the tidal period is a maximum.

For the mouths of the estuaries values of cross-sectional area and maximum tidal discharge are plotted in Fig. 3. To a very good approximation

$$A_c = 1.17 \hat{Q} \quad (7)$$

Here the maximum discharge, \hat{Q} , in Eq. (7) refers to average tide conditions. The corresponding maximum tidal velocity for the estuary mouths is:

$$\hat{u} = 0.85 \text{ m/sec} \quad (8)$$

This value varies slightly for the different estuaries and ranges between 0.82 m/sec and 0.86 m/sec; see van de Kreeke and Haring (1979). For spring tide conditions, the corresponding maximum tidal

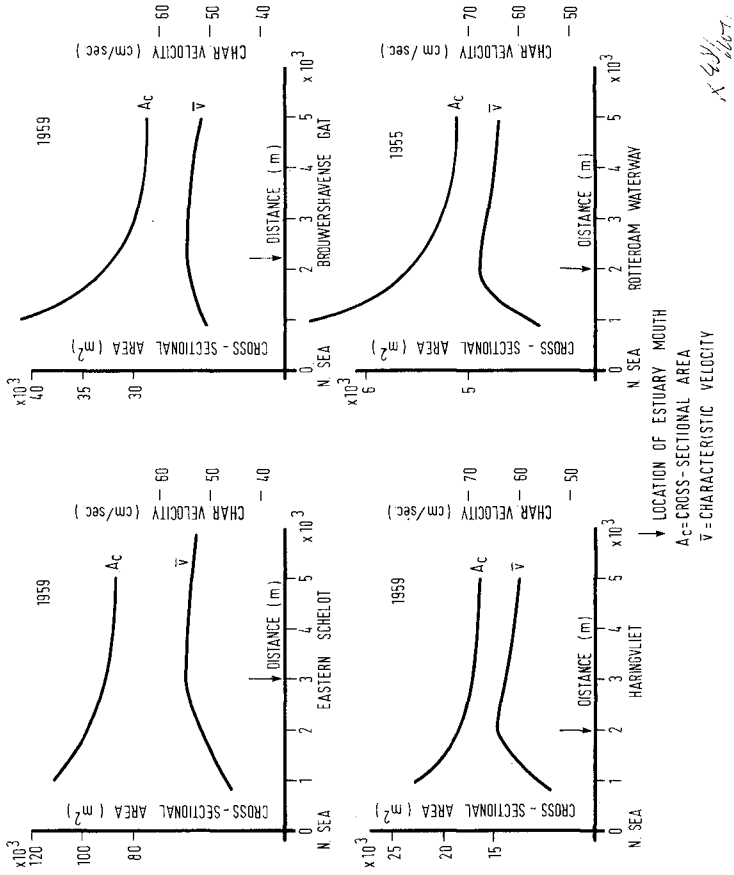


Figure 2. Variation in cross-sectional area and tidal velocity, \bar{v} , along longitudinal axis of estuaries.

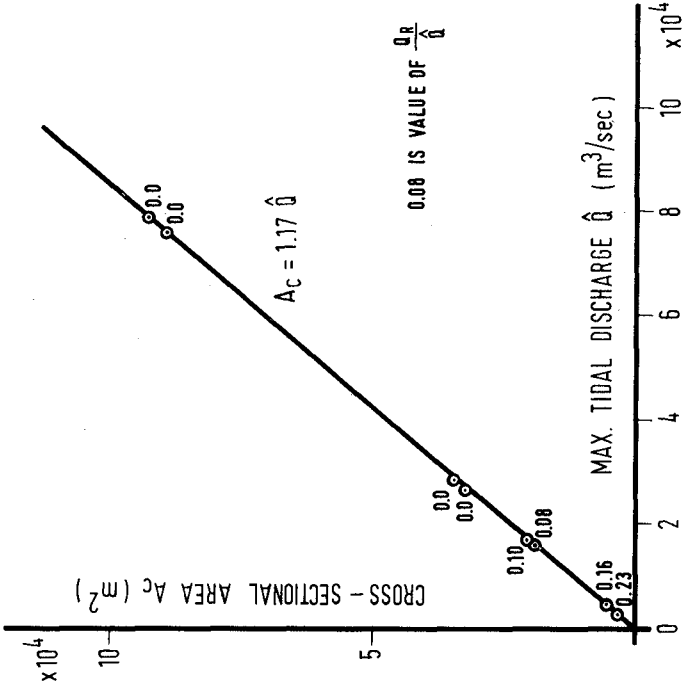


Figure 3. Relation between equilibrium flow area and maximum tidal discharge for estuary mouths.

velocity in the estuary mouths is:

$$\hat{u} = 1 \text{ m/sec} \quad (9)$$

For the values encountered in the Rhine-Meuse Delta, $Q_r/\hat{Q} < 0.25$, the effect of the ratio Q_r/\hat{Q} on the equilibrium flow area appears to be negligible. This is somewhat unexpected as it is generally believed that for constant values of the maximum tidal discharge \hat{Q} , the equilibrium flow area increases with increasing values of the river discharge Q_r . A possible explanation is that the increased cleansing effect resulting from the increased ebb velocities is offset by the inward-directed density currents along the bottom.

It is shown in van de Kreeke and Haring (1979) that Eq. (7) implies that for the Rhine-Meuse Delta the cross-sectional areas at the mouths of the estuaries is proportional to the flood volume rather than the tidal volume.

3 STABILITY CONSIDERATIONS

Because of the time varying nature of the sediment transport capacity of the tidal currents, Q_{TC} , and the littoral drift, Q_d , it is to be expected that cross-sectional areas show variations in time about the long term equilibrium profile. As an example the observed variations in the cross-sectional area of Wachapreague Inlet, Virginia are presented in Fig. 4. The record clearly shows a yearly cycle. Variations are on the order of 10% of the yearly mean value of the cross-sectional area.

If as a result of the short term fluctuations, the cross-sectional area decreases below a certain value, the estuary mouth could conceivably close. This will be explained using Fig. 5 which is taken from Escoffier (1940).

In Fig. 5 the solid curve, further referred to as closure curve is analogous to the well-known relation between inlet velocity and cross-sectional area for bay-inlet systems. In principle, for estuary mouths the closure curve can be obtained by computing the tidal velocity for various values of the cross-sectional area at the mouth. E.g., see Dronkers (1964), chapter XII. The exact shape of the curve depends among other things on how the cross-sectional area is varied i.e., by a change in width or a change in depth. Here it will be assumed that the cross-sectional area, A_c , is gradually decreased by decreasing the water depth. In that case for larger values of A_c , a decrease in cross-sectional area leads to an increase in tidal velocity, \hat{u} . For smaller values of A_c frictional effects become increasingly important and a decrease in cross-sectional area will lead to a decrease in tidal velocity. The horizontal line in Fig. 5 represents Eq. (8), and will be further referred to as the sediment curve.

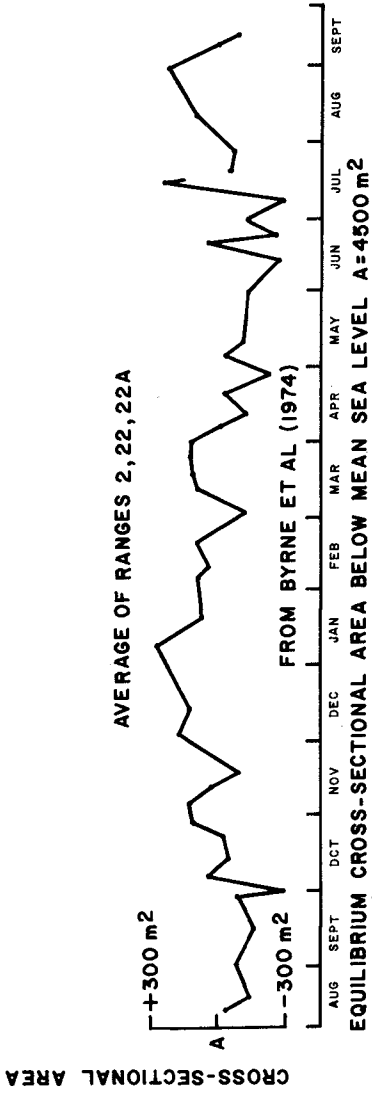


Figure 4. Variations in cross-sectional area for Wachapreague Inlet.

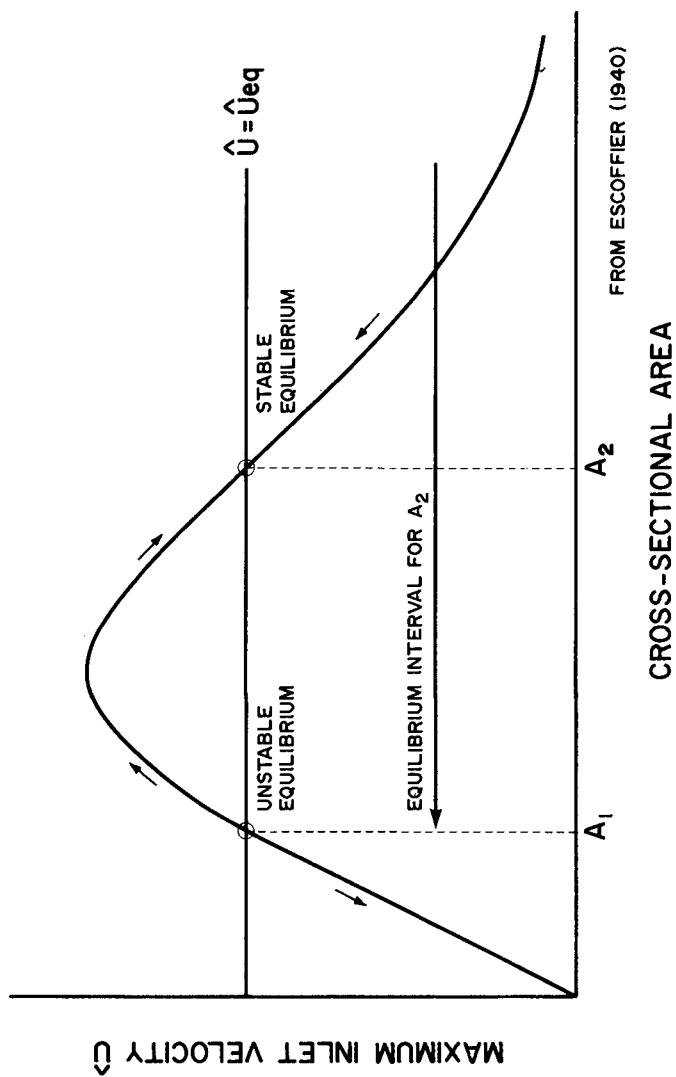


Figure 5. Escoffier diagram.

It follows from Fig. 5 that for values of the cross-sectional area are smaller than A_1 , tidal velocities are too small to maintain the cross-sectional area; the estuary mouth will shoal. For values larger than A_1 the tidal velocity is larger than the velocity required to maintain the cross-sectional area; the estuary mouth will enlarge until the cross-sectional area reaches the value A_2 . Estuary mouths with cross-sections larger than A_2 will shoal until the cross-section reaches the value A_2 . Thus the long-term equilibrium condition for an estuary mouth is represented by the second intersection of the closure and sediment curve.

The foregoing implies that a condition for an estuary mouth to remain open is that the closure curve and sediment curve intersect. As a measure of the degree of stability the ratio $(A_2 - A_1) / A_2$ is introduced. Multiplying by hundred this ratio yields the percentage by which the equilibrium flow area can be reduced before the estuary closes.

As an application of the concepts presented in the previous section variations in the cross-section of the mouth of the Rotterdam Waterway covering the period 1885-1958 are explained. Dredging activities and construction of new harbors during the period 1885-1958, have resulted in a considerable increase of the cross-section at the mouth of the Rotterdam Waterway. A time history of the cross-sectional area and the tidal velocity, u , at the mouth of the estuary, the tidal range at Rotterdam and the various construction activities is presented in Fig. 6. Two equilibrium periods can be identified. The first period between 1897 and 1909 shows a cross-sectional area of 3720 m². During the second period 1944-1958, the equilibrium flow area equals 5600 m².

Closure curves pertaining to the year 1885 and the previously mentioned equilibrium periods together with the sediment curve are indicated in Fig. 7. It is emphasized that the closure curves are not exact but rather show qualitatively the trend of the maximum tidal velocity when changing the cross-sectional area. In 1885 the cross-sectional area of 3000 m², in Fig. 7, was larger than the equilibrium cross-sectional area, a in Fig. 7. During the succeeding period the cross-section would have returned to the equilibrium value were it not for dredging upstream of the mouth. Dredging led to a change in closure curve and caused the cross-sectional area to increase until it reached an equilibrium value of 3720 m² in 1897, in Fig. 7. The cross-sectional area then remained constant until about 1909, when port expansion led to an increase in storage and a change in closure curve. The value of the tidal velocity became larger than the equilibrium value of 0.85 m/sec which led to scour at the mouth of the estuary. However, the process of natural adjustment could not keep pace with the increased storage associated with the construction of harbor basins. Only after 1923 when the pace of harbor construction and dredging reduced did the value of the tidal velocity decrease, in Fig. 7. With the additional help of dredging in the mouth, the cross-sectional area reached a new equilibrium value of 5600 m² in 1944, in Fig. 7. Because relatively little

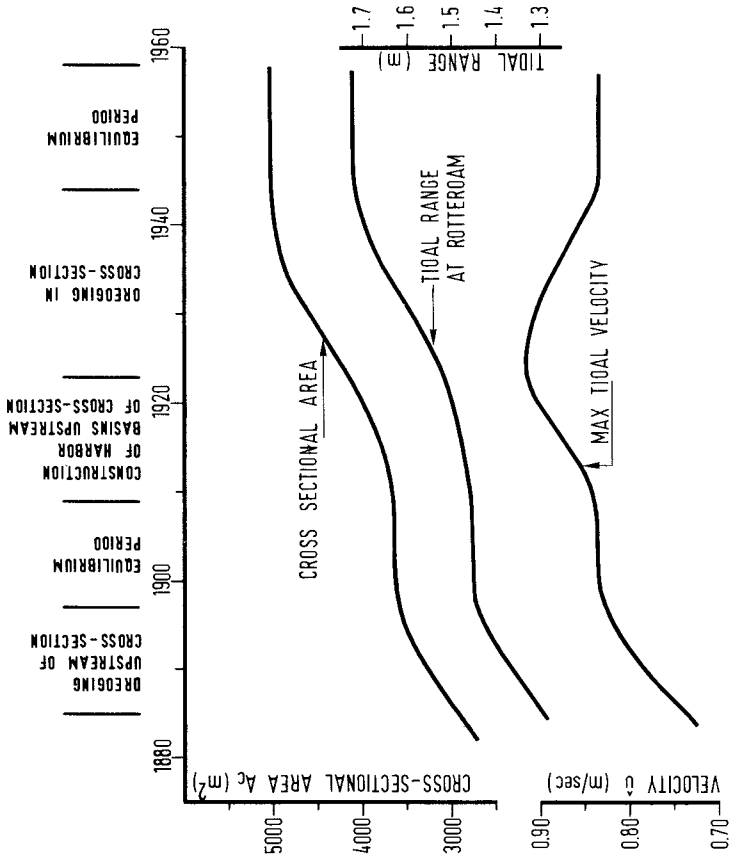


Figure 6. Mouth of Rotterdam Waterway; variations in cross-sectional area, tidal range and maximum tidal velocity during the period 1885-1958.

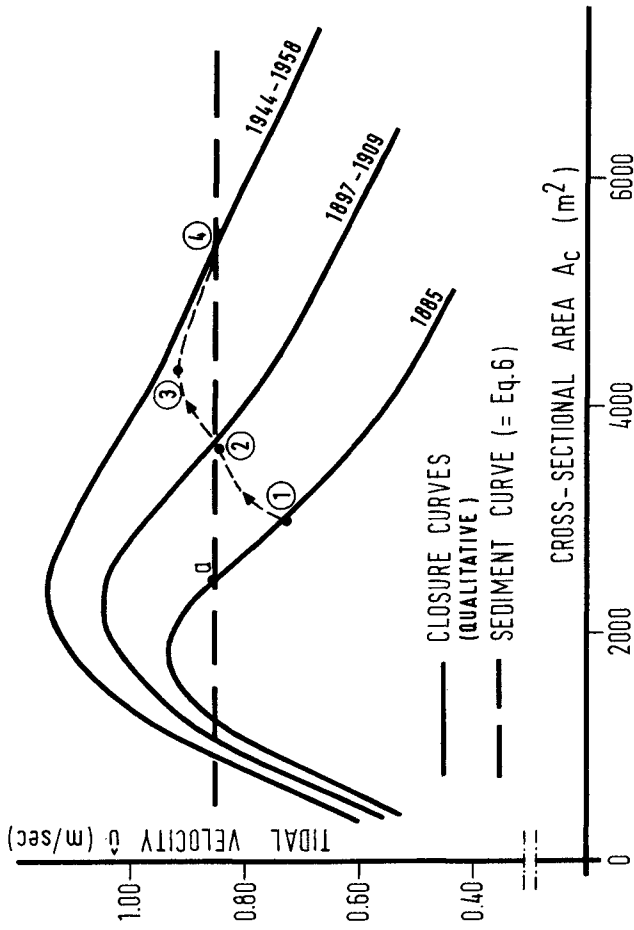


Figure 7. Mouth of Rotterdam Waterway; closure curves and sediment curve.

construction and dredging was carried out during the following period, stable conditions prevailed until 1958. Note that during the period 1885-1958 the stability index for the mouth had considerable increased.

5 CONCLUSIONS

For equilibrium conditions the maximum tidal velocity in the estuary mouths is constant and for average tide conditions equals 0.85 m/sec. For the estuaries with freshwater inflow this implies an approximately constant ratio between flood volume and cross-sectional area. For the estuaries with zero freshwater inflow the implication is a constant ratio between tidal prism and cross-sectional area.

Variations in the cross-sectional area at the mouth of the Rotterdam Waterway during the period 1885-1958 are explained using closure curves and a sediment curve (Escoffier diagram).

REFERENCES

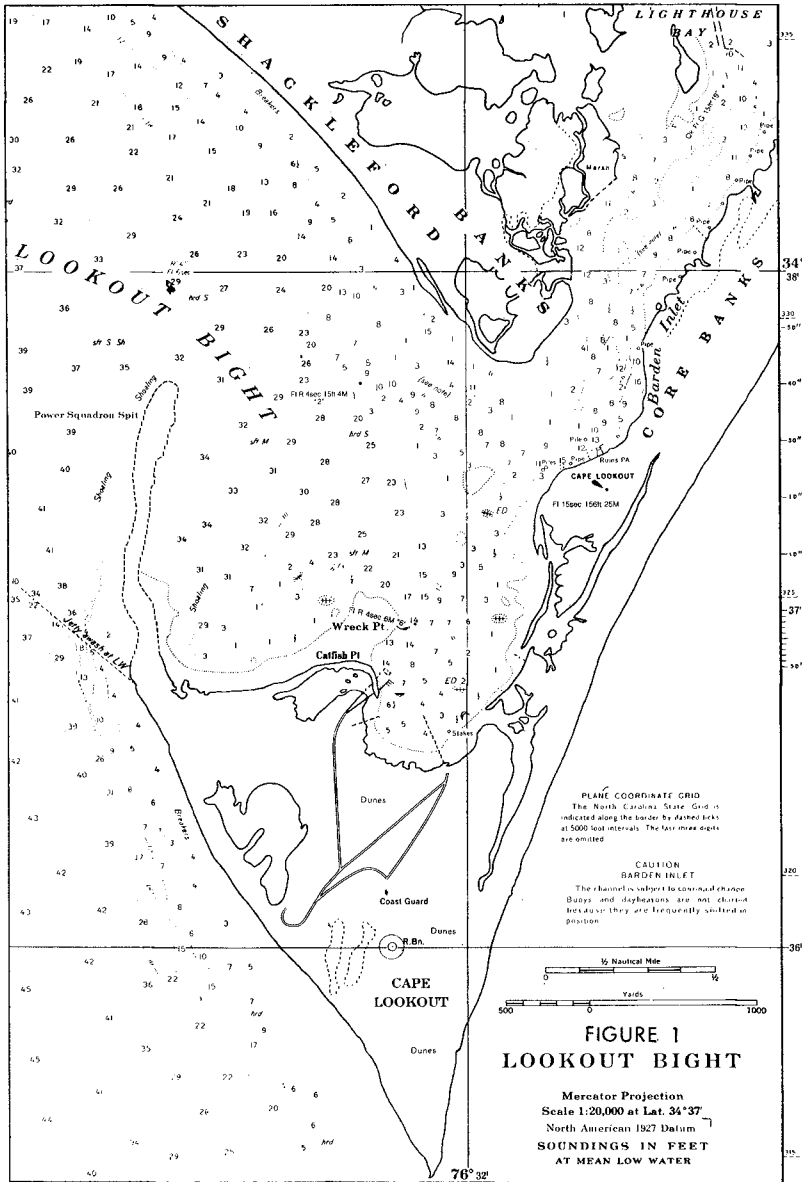
- BYRNE, R.J., J.T. DeALTERIS and P.A. BULLOCK, (1974). "Channel Stability in Tidal Inlets: A Case Study," Proceedings 14th Coastal Engineering Conference, Copenhagen, Vol. II.
- BYRNE, R.J., R.A. GAMMISCH and G.R. THOMAS, (1980). "Tidal Prism-Inlet Area Relations for Small Tidal Inlets," Proceedings 17th Coastal Engineering Conference, Sydney.
- DRONKERS, J.J., (1964). "Tidal Computations in Rivers and Coastal Waters," North Holland Publishing Co., Amsterdam.
- ESCOFFIER, F.F., (1940). "The Stability of Tidal Inlets," Shore and Beach, Vol. 8. No. 4.
- JARRETT, J.T., (1976). "Tidal Prism-Inlet Area Relationships," Department of the Army, Corps of Engineers, U.S. Army Coastal Engineering Research Center and U.S. Army Engineers Waterways Experiment Station, CITI Report No. 3.
- LELIAVSKY, S.L., (1966). "An Introduction to Fluvial Hydraulics," Dover Publications, Inc., New York.
- TERWINDT, J.H.J., (1973). "Sand Movement in the In - and Offshore Tidal Area of the S.W. Part of the Netherlands," Geol. Mynbouw, 52(2): 69-77.
- VAN DE KREEKE, J. and J. HARING, (1979). "Equilibrium Flow Areas in the Rhine-Meuse Delta," Coastal Engineering, 3, 97-111.

BARDEN INLET, N.C.
A CASE STUDY OF INLET MIGRATIONLimberios Vallianos, Chief, Coastal Engineering Studies Section
U. S. Army Engineer District Wilmington, Wilmington, N.C.ABSTRACT

The migratory pattern of a small coastal inlet was examined in terms of the factors generally acknowledged to control inlet behavior. That is, the tidal discharge which acts to flush the inlet and, on the other hand, the intrusive littoral materials depositing in the inlet environment. Specifically, a "flow conveyance index" was computed and compared to shoreline movements. The "flow conveyance index" was defined as the ratio of the mean distribution of the overall planform area of the throat of the inlet to the mean distribution of the planform areas of shoals within the throat of the inlet. High and low "flow conveyance index" values would correspond, respectively, to periods of relatively high and low inlet flushing conditions. A consistent pattern obtained from this analysis, wherein high and low index values corresponded with high and low shoreline movements. Additionally, the plot of rates of shore movements against rates of change of "flow conveyance index" was fitted with a simple linear regression line having a positive correlation coefficient of 0.85. Further analyses of the mean distribution of the shoals within the throat of the inlet demonstrated the cause of time-varying rates of movement of points along the spiriferous east shoreline of the inlet. Shoreline movement rates were plotted on a time-space plane and isolines of shore movement rates contoured. The result was a three-dimensional image of shore movement rates over time and distance. The position of the centroid of the inlet shoal distribution at different times was superimposed upon the three-dimensional image. This revealed that variations of shoreline movement rates along the shore at any point in time are dependent on the mean position of the inlet shoal distribution. Also, the direction of movement of the mean position of the inlet shoal distribution appeared to indicate the predominant direction of flushing action, that is, flood or ebb tides.

1 INTRODUCTION

Barden Inlet is located along the central portion of the North Carolina coastline and constitutes the physiographic juncture of Shackleford Banks and the south end of Core Banks, see figure 1. This inlet is characterized by an expansive shoal protruding into the inlet's throat from Shackleford Banks, and a resulting curvilinear main flow-conveyance channel juxtaposed with the east or Core Banks shore of the inlet. The effect of flow concentration on the east bank of the inlet has been to mold that shore into a spiraliform indenture. The continuous migration of the primary inlet channel (natural gorge) and concomitant erosion of the Core Banks shore is now threatening eventual damage and possible destruction of the historic Cape Lookout Lighthouse and related peripheral structures located near the inlet. On recognizing the hazard posed by the easterly migration of Barden Inlet, a study was undertaken



by the U.S. Army Corps of Engineers to determine the causative factors contributing to the problem and to develop appropriate corrective measures. This paper focuses on the evaluation of cause and effect relationships of the problem. It is remarked that prior to initiation of the study reported here, it was suggested by some parties having interest in the problem that the primary cause was the effects of dredging operations conducted in the maintenance of navigation channels approaching the throat of the inlet through its ebb and flood-tide deltas. Accordingly, the first steps in the problem evaluation involved a comparison of the pattern of movements of the shorelines adjacent to the inlet with the record of maintenance dredging in the channels approaching the inlet from its seaward and bay sides. This comparative analysis failed to demonstrate any relationship between dredging and shore movements or inlet migration. Therefore, the next phase of the evaluation examined those factors generally acknowledged to control inlet behavior on sandy shores, viz, sediment influx and tidal discharge. In this case, a very good correlation developed between the intensity and direction of shoreline movements, and an index value representing the relative magnitudes of sediment influx and tidal discharge. Further analyses of the distribution of shoal accumulations within the throat of the inlet demonstrated the cause of time-varying rates of movement of points along the eroding shore on the east side of the inlet.

2 EFFECTS - SHORELINE MOVEMENT HISTORY

The pattern of shoreline movements over time was established through the use of aerial photographs of the study area. The available record consisted of 21 photographic coverages during a 37.5-year period extending from October 1940 to April 1978, thus allowing for the evaluation of 20 discrete time spans. Standard methods of evaluating the shoreline movements were employed, that is, a measurement baseline or reference was selected and superimposed on each of the aerial photographs. The baseline was divided into stations at which measurements to the shorelines were made on the respective photographs and compared to determine shoreline movements and rates of movements during the time periods between successive photographs. The baseline passed through the center of the base of the Cape Lookout Lighthouse on a bearing of N 31° E which approximates the orientation of the longitudinal axis of the throat of Barden Inlet. A total of 35 baseline stations, numbered consecutively 1 through 35, were established at a spacing of 30.5 meters (100 feet), with station number 6 being located at the lighthouse. Distances to the shoreline(s) were measured at these stations along transects perpendicular to the baseline and extending toward the inlet. In the evaluation, stations 1 through 35 were utilized to obtain shoreline movement measurements pertaining to the overall Core Banks shoreline of the inlet, and measurements made at stations 4 through 8 were selected to represent conditions of the shoreline in the immediate vicinity of the Cape Lookout Lighthouse building complex, and the transects and related measurements at stations 20 through 27 were extended across the inlet to develop the general pattern of shoreline movement along the inlet's Shackelford Banks shoreline.

In terms of the single longest time span, that is October 1940-April 1978, the results of the photographic analysis were that: (a) the average movement of the entire east shore or Core Banks side of Barden Inlet had been eastward for a distance of 361 meters, giving an average rate of movement of 9.6 m/yr or 0.8 m/mo; (b) the segment of the inlet's east shore in the immediate vicinity of the Cape Lookout Lighthouse had moved easterly for a distance of 388 meters, resulting in an average movement rate of 10.3 m/yr or 0.9 m/mo and by April 1978, this segment of shoreline was within 49 meters of the lighthouse keeper's dwelling and 105 meters from the base of the lighthouse; and (c) the inlet's west shore or Shackleford Banks side had moved westward over a distance of 38 meters, giving an average rate of movement of 1 m/yr or approximately 0.1 m/mo. In regard to short time spans, the rates of shoreline movement deviated substantially from the long-term averages enumerated above. For example, the average movement rate of the east shore varied from as high as 4.4 m/mo in an easterly direction, to as much as 2.8 m/mo in a westerly direction. Additionally, in any given time span, there was great variability in the rates of shoreline movement experienced along the various station transects used in the analysis. In this connection, graphs of the cumulative movements of transect stations were plotted and superimposed, see figure 2. This superposition demonstrated that variations in shore movement rates, transect to transect, were generally occurring in the form of a gradual transition. This occurred because of the remarkably smooth planform curvature of the indentured east bank of Barden Inlet. Indeed, the major portion of this eroding shoreline at the various times that it was photographed could be precisely duplicated by the equation of a logarithmic or equiangular spiral, as illustrated by figure 3.

3 CAUSAL FACTORS

In search of a rational causal factor(s) resulting in the inlet channel migration and attendant erosion of the inlet's east bank, the first consideration was given to dredging activities associated with maintaining the seaward and bayward channels approaching the inlet gap. It is remarked that the primary inlet channel (gorge) flowing against the eroding east bank is naturally wide and deep and does not require dredging. With respect to dredging related to the inlet's approach channels through the ebb and flood-tide deltas, the existence, or lack thereof, of two primary trends was sought in terms of the comparison of dredging quantities and shoreline movements, namely: (a) high or low shoreline movement rates corresponding directly with high or low dredging quantities; and (b) high or low shoreline movement rates immediately following high or low dredging quantities. The first comparison to be made was the superposition of histograms of the shoreline movement rates and dredging quantities over time. This comparison failed to indicate any relationship between shoreline behavior and dredging. This was followed with simple linear regression analyses of shoreline movement rates and dredging quantities, considering both the overall indentured east bank of the inlet having a length of 1,036 meters, and a segment of that same shore having a length of 150 meters situated in the immediate vicinity of the Cape Lookout Lighthouse. With shoreline movement rates

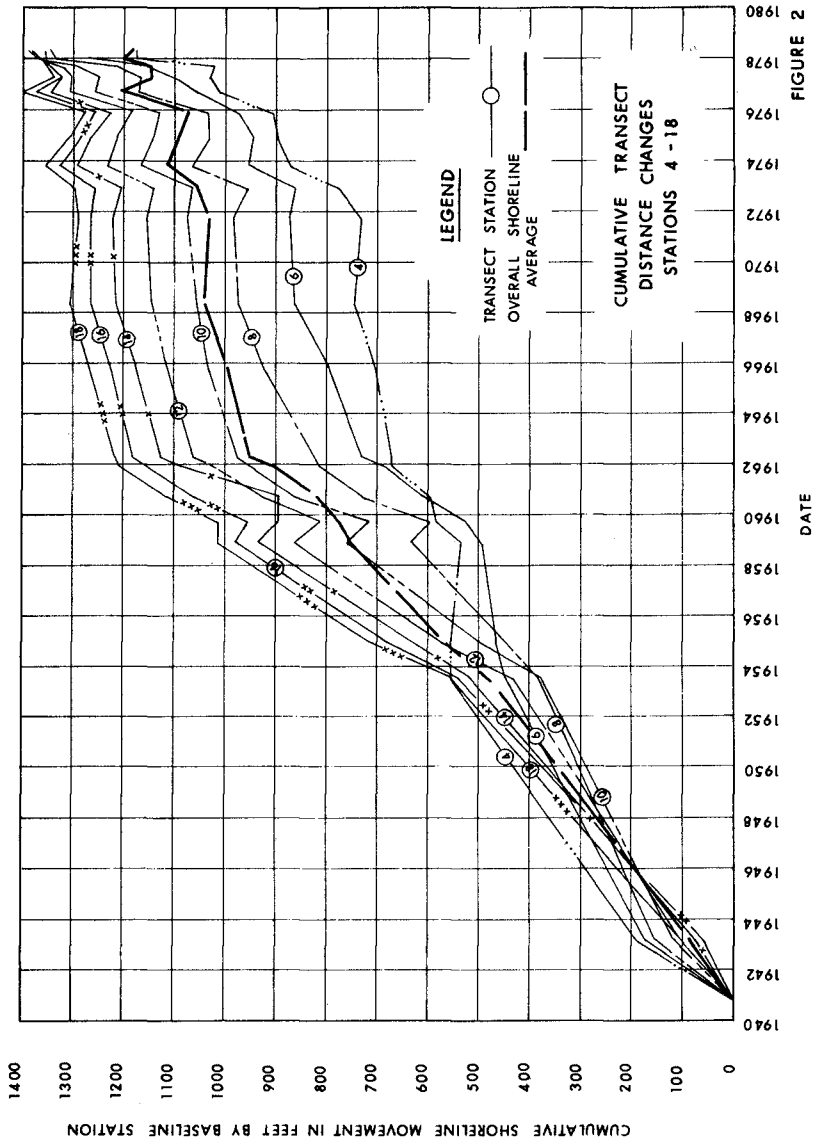


FIGURE 2

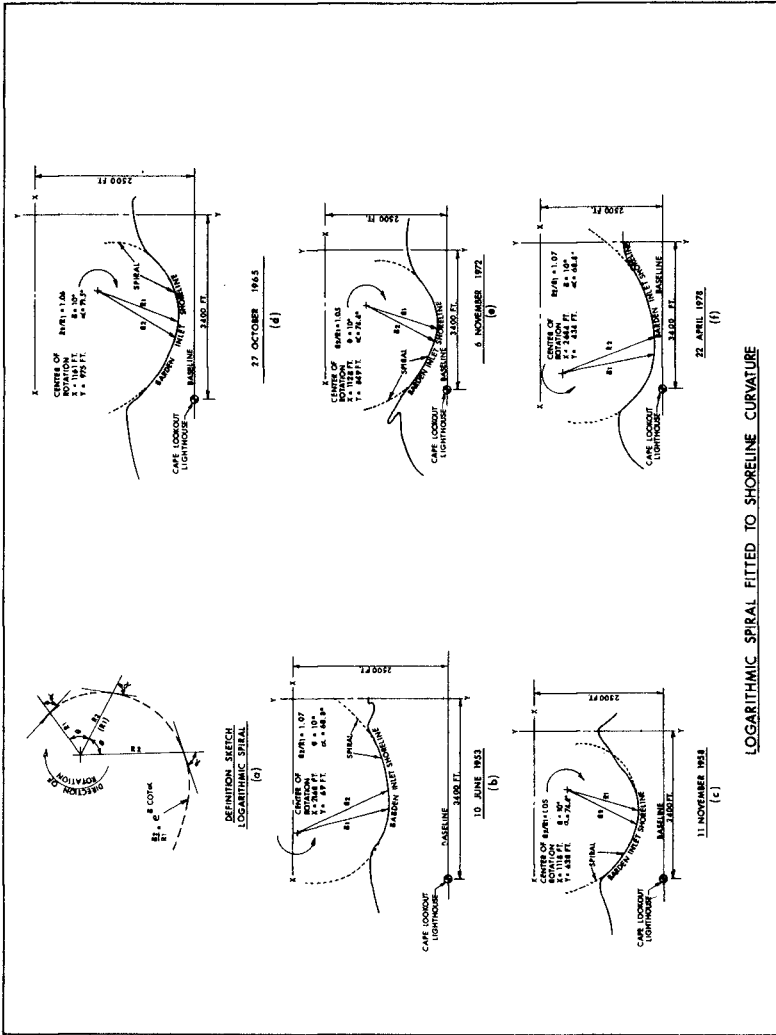


FIGURE 3

and dredging quantities as the dependent and independent variables, respectively, the lines of regression fitted through the data points had correlation co-efficients of -0.03 for the overall east bank of the inlet and -0.24 for the small segment of east shore near the lighthouse, see figure 4. This demonstrated numerically that which was evident on inspection of the scatter diagrams, to wit, there was no apparent association between dredging operations in the approach channels and movement of the east bank of the inlet. This was not a particularly startling revelation inasmuch as many inlets on the coast of North Carolina at which there are no navigation channels through the ebb and flood deltas have experienced higher rates of primary inlet channel migration and attendant erosion of the downcoast inlet shoulders than has been experienced at Barden Inlet.

The next step in the evaluation was to examine the available data in terms of the factors generally acknowledged to control inlet behavior on sandy shores. That is, the tidal discharge which acts to flush the inlet and, on the other hand, the intrusive littoral materials depositing in the inlet environment. In the case of Barden Inlet, there was not sufficient data for a quantification of the relative magnitudes of the two opposing factors over the various time periods in which shoreline movements were determined. Accordingly, an implicit approach was taken in analyzing the relative magnitudes of the flushing and siltation factors as reflected in the shoaled and deeper water portions of the throat of Barden Inlet depicted by the available aerial photography. The aerial photographs selected for analysis were those dated 15 July 1960, 3 May 1962, 27 October 1965, 12 April 1968, 15 August 1971, 6 November 1972, 5 October 1973, 15 November 1974, 15 August 1976, 10 August 1977, and 22 April 1978. These particular photographs were selected due to their generally high resolution of submerged features. Moreover, the time spans between photographs were approximately in the range of 1 to 3 years, which should be sufficient time for the inlet to adjust to changed conditions but not so long as to miss important changes.

The analysis of inlet characteristics depicted on the selected photographs was performed on the basis of the geometric framework defined on figure 5, where the X-X and Y-Y axes are identical to those previously described. The longitudinal extent of the inlet was defined as the water area confined between the Y-Y axis and a line extending from and perpendicular to the X-X axis to the Core Banks shoreline through the point of maximum seaward protrusion of the platform shoal which projects into the throat of Barden Inlet from the Shackleford Banks side. The size and distribution of the overall inlet on a given photograph within this framework was characterized by its areal size, the X and Y distances to its centroid, and the first moments of the area taken about the X-X and Y-Y axes. Similarly, the size and distribution of the shoal areas within the inlet framework were defined by their combined areal size, centroidal distances, and first moments about the X-X and Y-Y axes. A measure of the flow conveyance of the inlet was established as the ratio of the first moment of the overall inlet area about the X-X axis to the first moment of the shoal areas about the X-X axis (M_{X-X} (inlet) / M_{X-X} (shoal)). This ratio is referred to here as the "flow

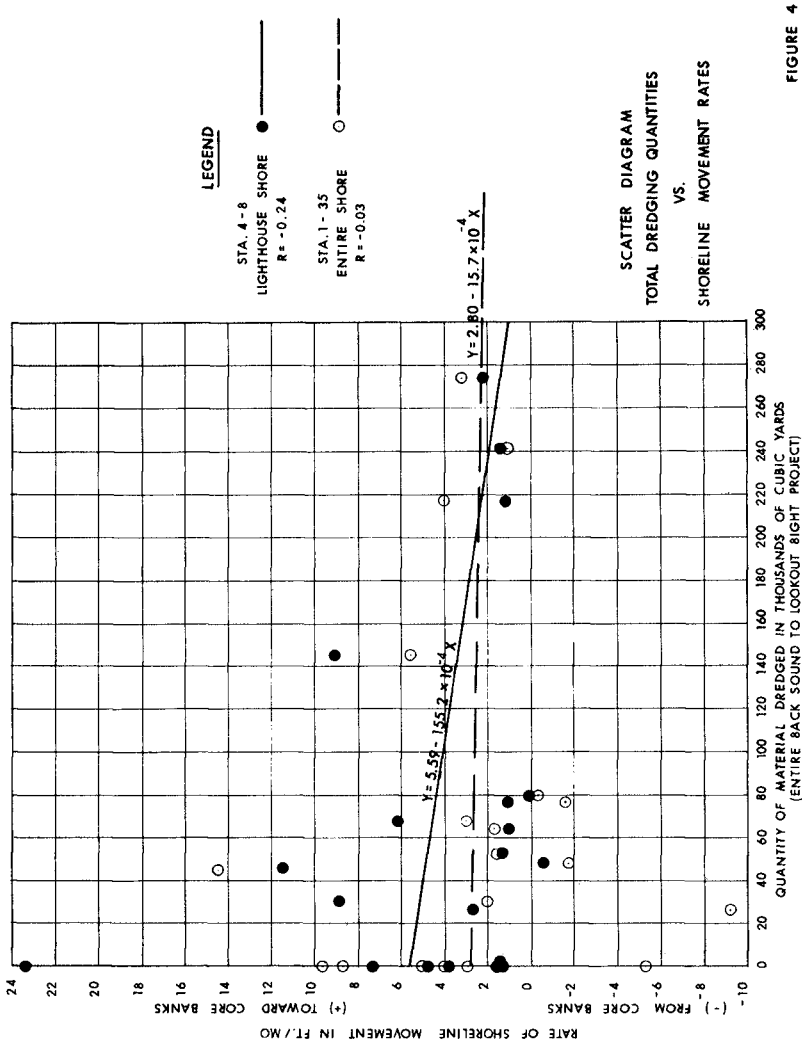


FIGURE 4

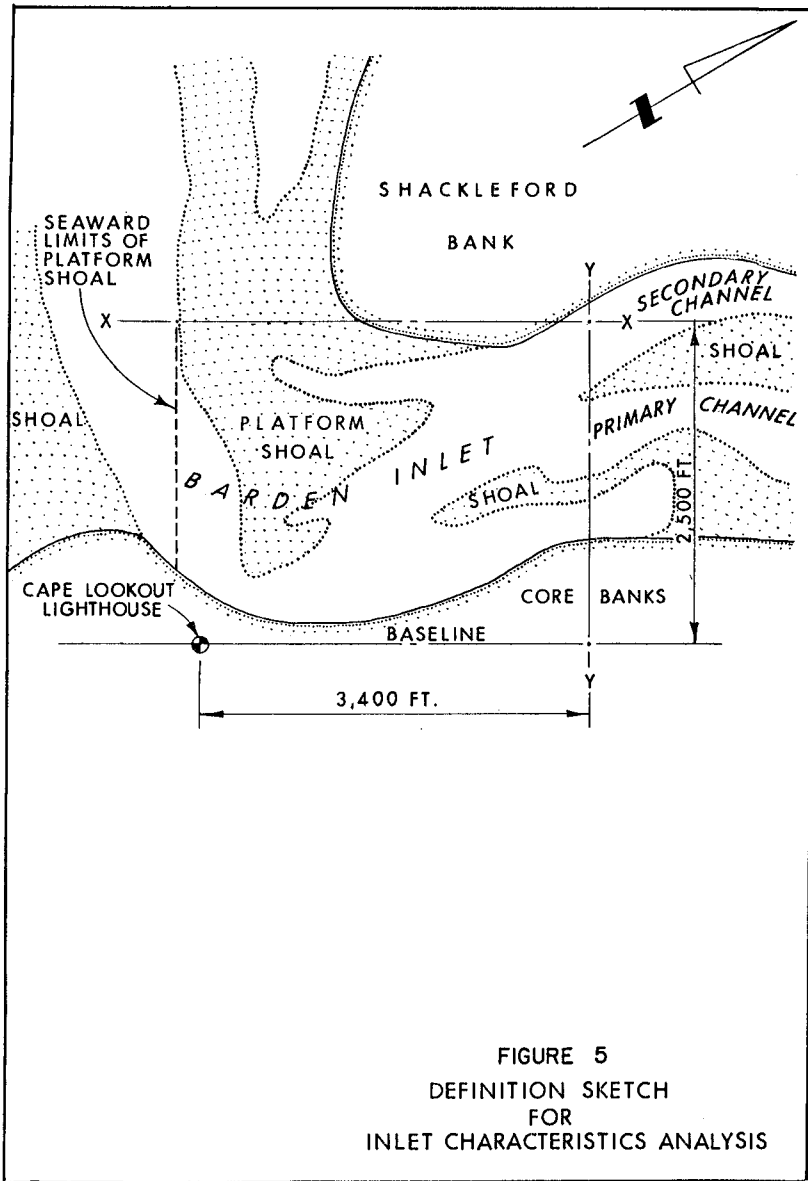


FIGURE 5
 DEFINITION SKETCH
 FOR
 INLET CHARACTERISTICS ANALYSIS

conveyance index." In other words, if the mean distribution of the overall inlet is large by comparison to the mean distribution of the shoal areas therein, it can be expected that the inlet's flow conveyance and flushing capability is high compared to a case where the flow conveyance index is relatively low. The values of inlet and shoal areas, centroidal coordinate distances, first moments about the X-X and Y-Y axes, flow conveyance indices, rates of change of flow conveyance indices, and the weighted average rates of shoreline movements between sequential photographs are listed in table 1. The reader will note the distinctly consistent pattern in which the rates of shoreline movement increase and decrease in accordance with increasing or decreasing flow conveyance indices. This trend is graphically displayed on figure 6 which is a scatter diagram and associated simple linear regression line for shoreline movement rates plotted against the rates of change of the conveyance indices. The linear correlation coefficient (R) has a value of 0.85. In view of the trends described above, it is concluded that the general shoreline behavior on the Core Banks side of Barden Inlet is basically dictated by changes in the tidal flow exchange through the inlet as controlled by increasing and decreasing littoral influx associated with changes in wave energy reaching Shackelford Banks, and increasing and decreasing flushing action which is primarily controlled by wind energy and attendant wind tides and wind drift (movement of water due to wind stress) over the estuarial waters comprised of Pamlico-Core Sounds and Bogue-Back Sounds.

Another important output of the inlet characteristics analysis was the evaluation of the changes in rates of movement of the spiriferous shoreline indenture on the Core Banks side of Barden Inlet generally confined between transect stations 4 and 32. Data plotted on figure 7 graphically display the influence of the longitudinal position of the inlet shoal distribution on the magnitudes of shoreline movement rates at specific points along the indentured shoreline. It will be noted that figure 7 provides a three-dimensional image consisting of a time-space plane on which isolines of shoreline movement rates are plotted. The isolines were contoured from shoreline movement rates of alternate transect station values plotted at the midpoints of the time periods for which the values were computed. Superimposed on the three-dimensional image are the positions (dots) of the centroids of the inlet shoal distributions with respect to the Y-Y axis as referenced to the transect station numbers. The influence of the longitudinal positions of the shoal distribution centroid on the magnitude of shoreline movement rates along the spiriferous shore indenture is clearly evident. During the 1960-1962 period, the shoal centroid position moved bayward with high shore movements being concentrated on the bayward end of the shore (transect stations 22 through 32). This was followed by a gradual seaward movement of the shoal distribution centroid over the period 1962-1972 during which the Core Banks shore retreated at a moderate rate, was stable, or in a state of accretion. This, in turn, was followed by a rapid seaward movement of the centroid in the 1972-1973 period, with concomitant high shore retreat rates concentrated along the seaward end of the shore near the lighthouse. Then, the centroid moved bayward with an accompanying stable or accreting state of the shoreline over the

TABLE 1
 Geometric Properties of Inlet Platform Features
 Flow Conveyance Indices and Shore Movement Rates

Date	Area			Centroidal Coordinates				1st Area-Moment				Flow Conveyance Index M_{x-x} Inlet M_{x-x} Shoals M_{x-x} Shores	Rate of Change of Flow Conveyance Index $(10^{-2} \text{ mo}^{-1})$	Weighted ^{2/} Average Rate of Shoreline Movement (ft/mo)
	Overall		Inlet Shoals	\bar{X}	\bar{Y}	M_{x-x}		M_{y-y}		Overall \bar{Y} Area				
	(10^6 ft^2)	(10^6 ft^2)	(ft)	(ft)	Inlet Shoals (10^8 ft^3)	Inlet Shoals (10^8 ft^3)	Inlet Shoals (10^8 ft^3)	Inlet Shoals (10^8 ft^3)						
15 Jul 60	4.47	2.38	1,300	1,384	939	655	58.13	32.92	41.99	15.58	2.70	+4.82	5.9	
3 May 62	4.82	2.07	1,260	1,230	999	634	60.78	25.49	48.19	13.14	3.76	-2.39	1.1	
27 Oct 65	5.70	2.72	1,463	1,446	995	754	83.24	39.39	56.61	20.54	2.76	-0.30	1.6	
12 Apr 68	6.12	3.03	1,551	1,574	1,030	777	94.92	47.77	63.04	23.58	2.67	-0.67	-0.3	
15 Aug 71	6.09	3.36	1,530	1,679	1,021	771	93.14	56.40	62.15	25.90	2.40	+1.08	1.7	
6 Nov 72	6.07	3.06	1,491	1,641	1,035	802	90.54	50.15	62.85	24.51	2.56	+9.07	5.6	
5 Oct 73	6.36	2.78	1,545	1,745	1,049	677	98.3	48.52	66.76	18.82	3.55	-5.78	1.8	
15 Nov 74	6.08	3.15	1,489	1,572	1,042	723	90.56	49.48	63.37	22.76	2.78	+9.33	5.3	
15 Aug 76	6.75	2.68	1,612	1,991	1,098	584	108.75	53.35	74.07	15.64	4.74	-8.42	-4.7	
10 Aug 77	6.70	2.76	1,630	1,835	1,085	707	111.91	50.67	73.0	19.52	3.73	+1.07	4.5	
22 Apr 78	6.89	2.64	1,653	1,866	1,084	724	113.92	52.01	74.71	19.58	3.82			

^{1/} Positive and negative rates refer to increasing and decreasing rates of change, respectively.
^{2/} Rates of movement for entire Core Banks shoreline averaged over transect station 1 thru 35.

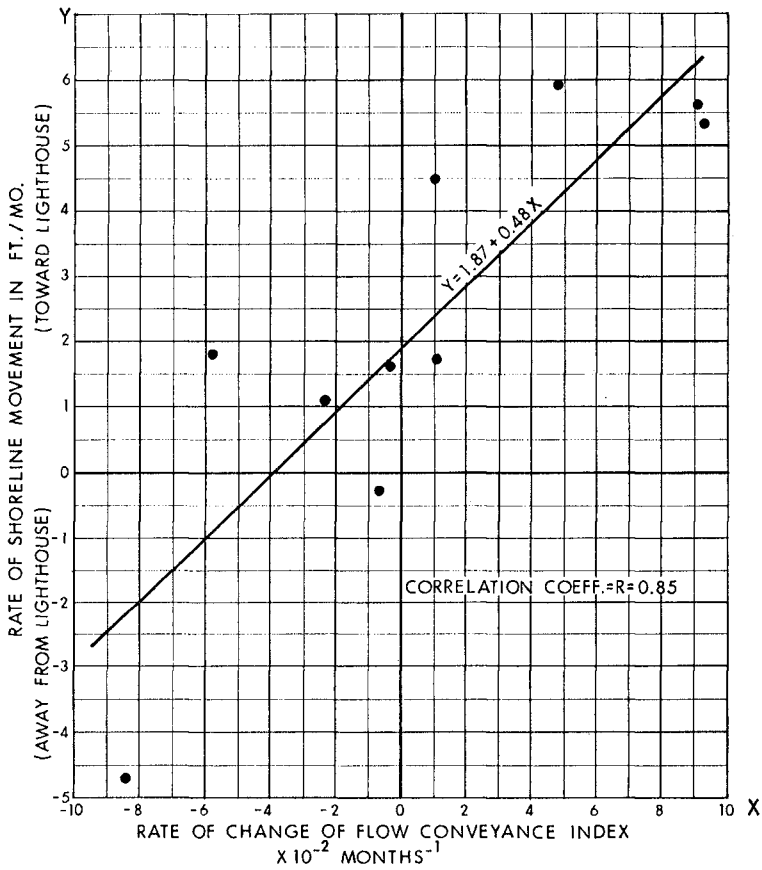


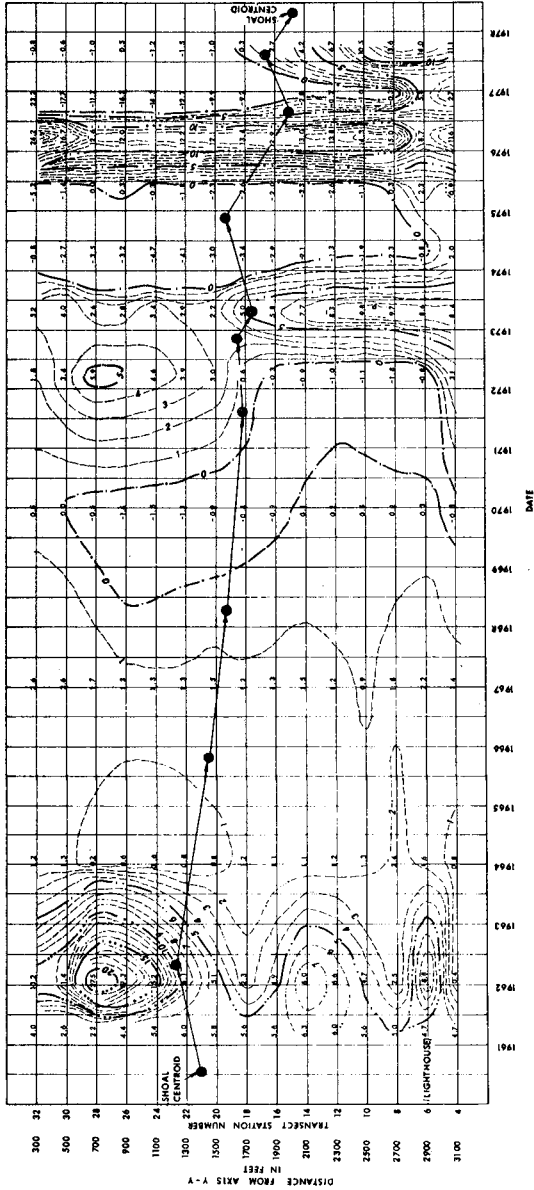
FIGURE 6
SCATTER DIAGRAM
 SHORELINE MOVEMENT RATE
 -vs-
 RATE OF CHANGE
 OF
 FLOW CONVEYANCE INDEX

1973-1974 time period. Again, in the period 1974-1976, the centroid moved seaward at a rapid rate with generally high erosion rates along the entire shoreline, followed by a bayward centroid movement in the 1976-1977 period with shore accretion developing. From 1977 to 1978, the centroid moved seaward with high rates of movement occurring along the lighthouse area at the seaward end of the shoreline. Thus, we see that the rates of shoreline movement along different points of the Core Banks side of the inlet are basically controlled by the position of the shoal distribution relative to the shoreline. This, of course, comes from the fact that the shoal distribution also relates to the major channel positions and orientations and, therefore, the points at which flows are concentrated.

The fundamental cause of the movement of the inlet shoal distribution can be attributed to the direction of the primary inlet flushing action. Major flushing occurs when strong perennial winds from the general northeasterly direction act over the expansive, shallow waters of Pamlico-Core Sounds. This wind action superelevates and forces water movement toward and through Barden Inlet, while concurrently suppressing onshore wave action and littoral materials transport along Shackleford Banks. Thus, the tidal ebb flows are highly efficient in flushing Barden Inlet when winds come from a general northeasterly direction. The results of this phenomenon are reflected in the general trend of seaward movement of the shoal-distribution centroid over the period 1962 to the present; see figure 7. The bayward movement of the shoal-distribution centroid from July 1960 to May 1962 as shown in figure 7 was, in all probability, caused by the high bayward flushing action generated by Hurricane Donna. This storm passed over the inlet on 12 September 1960 and was the last hurricane, to date, causing a significant ocean storm tide along the Shackleford Banks coastal zone. Indeed, it was not only the last significant ocean surge event, but was also the highest storm surge of record for that area. The Donna ocean storm tide reached an elevation of 3.3 meters above mean sea level. At the time of the recorded peak ocean tide, the bay water level was measured at 1.4 meters above mean sea level. Thus, a maximum water level differential of 1.9 meters existed between ocean and bay waters. The flood current velocity through Barden Inlet, as generated by this condition, was computed at 2.4 meters per second. Such a high flow would unquestionably flush the inlet shoal accumulations in a bayward direction. Moreover, as Hurricane Donna moved northward, its radius of maximum winds traversed a line coincident with the long axis of Pamlico Sound, thus tilting the water up at the north end of Pamlico Sound and depressing the water levels in Core Sound and the south end of Pamlico Sound. This resulted in an unusually long period of bayward flushing at Barden Inlet.

4 CONCLUSIONS

The investigation of Barden Inlet in reference to migration of the primary inlet channel (gorge) and the attendant erosion of the east bank demonstrates that one cannot, a priori, relate dredging operations through the ebb and flood-tide deltas of small coastal inlets with inlet migration in general nor with the rates of migration. The availability



ISOLINES OF RATE OF SHORELINE MOVEMENT IN FEET PER MONTH WITH RESPECT TO TIME AND SHORELINE STATIONING

FIGURE 7

of aerial photographs of Barden Inlet allowed for an implicit analysis of the causal factors associated with inlet processes at that site, resulting in findings consonant with the accepted concepts of factors influencing inlet behavior, namely, tidal discharge and the influx of littoral material.

STUDY ON VORTEX CURRENT IN STRAIT
WITH REMOTE-SENSING

by

Sotoaki Onishi
Professor of Civil Engineering Department,
Science University of Tokyo, Noda-Chiba, Japan

Tsukasa Nishimura
Researcher of Civil Engineering Department,
Science University of Tokyo, Noda-Chiba, Japan

INTRODUCTION

With rapid increases of industrial activity in present time, water pollution in the coastal environment has become an urgent problem to cope with. This problem is especially serious in enclosed bays or inland seas. Hydrodynamic character of the strait connecting the inland sea to the open ocean must be understood well in order to analyse the diffusion of pollutants in the inland sea, because its character determine boundary conditions in the mathematical models of the water pollution problem. So far however, it is seemed that the main efforts exerted by coastal engineers have concentrated mainly on the development of mathematical models, lacking satisfactory knowledge of the boundary conditions through field measurements. One reason of this state is resulted from the fact that the relating phenomena in the field are of too large scale, in general, to perform the field measurements.

Connecting with this point, the authors present in this paper, that remote-sensing technology is very useful to get information of the hydrodynamical phenomena occurring in the water body around the strait. To show the above, the authors selected as an object of the study, Naruto Strait in the Seto Inland Sea, which is world famous for the existence of rapid tidal currents and dynamic vortices. Remote-sensing data both from the airplanes and from a space satellite Landsat are analysed with the aid of theoretical considerations and hydraulic model tests to disclose the behavior of the vortices of various scales and the roles of them in the sea water mixing phenomena at the strait.

1. VORTEX DISTRIBUTION IN NARUTO STRAIT

Naruto Strait, being well known with the existence of dynamic vortices, is located between Shikoku and Awaji Island in Japan (Fig-1). Fig-2 is an aerophoto of the Naruto Strait. The left side on the figure is Harima Sea forming a part of the Seto Inland Sea and the right side is Kii Channel leading to the Pacific Ocean. The width of the Naruto Strait is, as shown in Fig-3 (a), contracted by shoals stretching out from both Oge Island in Shikoku and Tozaki Headland in Awaji Island. The most contracted section in the strait has V-shaped configuration as indicated in Fig-3 (b), in which the water surface is of 1,100m width, and the maximum depth is more than 80m. Each of the tidal levels in the Harima Sea and the Kii Cannel turns reversly with the period of 12hours,

Fig-1 Location of the Naruto Strait

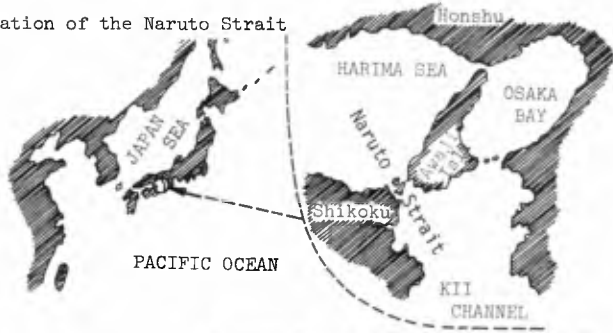


Fig-2 Aerophoto of the Naruto Strait

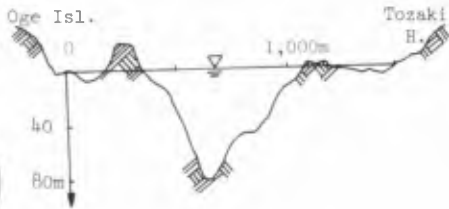
0 500m



Fig-3 Topography of the Naruto Strait

(a) plan view

(b) section view of the Naruto Strait



producing rapid tidal currents, the maximum velocity of which is about 10 knot, the dynamic vortices that are asserted roughly into coherent vortices along the free boundary layers leaving from both of the headlands, and vortex-pairs of large scale as schematically indicated in Fig-4. On the Fig-2, one can see the dynamic coherent vortices behind the headlands. Fig-5 shows the closer view of the coherent vortices. On the figure, one can see some aspects of the process through which rather smaller vortices amalgamate into the coherent vortices of larger size.

The authors investigated hydraulic character of these vortices through two different ways of field survey. The first of those is the remote-sensing with aero-photography, main purpose of which is to study the hydraulic character of the coherent vortices along the free boundary layer. The second way of the survey is the remote-sensing by Landsat, the purpose of which is to disclose the distribution of the larger scale vortex-pairs appearing as a result of amalgamation of the small scale coherent vortices.

Fig-4. Vortices associated with tidal current at Naruto Strait

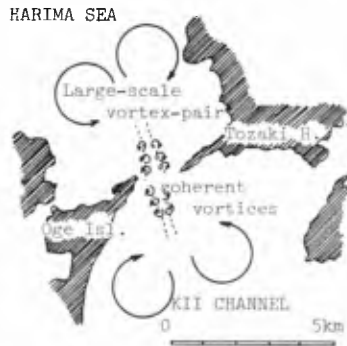


Fig-5 Amalgamation process of small scale vortices to larger scale ones

(aerophoto from 300m altitude)



2. INVESTIGATION OF COHERENT VORTICES THROUGH SOLID AERO-PHOTOGRAPHY

2-1 Field observation

The aero-photographic surveys at Naruto Strait were done using a pair of airplanes at the altitude of 800m under the flood tide conditions of spring and autumn in 1978. Several series of aerophotos of the strait were synchronously obtained by the pair of airplanes at 3 sec time intervals and analysed through a stereoscope to map the hydraulic character of the strait such as unevenness of the water surface, direction of the tidal current, distribution of the vortices along the free boundary layers, upwelling currents and so on. Fig-6 is an example of the map gained. One of the interesting aspect is the existence of upwelling region, indicated by dotted line on the figure, on the water surface in the region opposite to the tidal current. Relations between the vortices and the upwelling current will be discussed in the paragraph 2-4 later.

Another example of the results obtained through the field survey is Fig-7 which represents the unevenness of the water surface. This figure was yielded through the solid aerophoto and will be used in the estimation of the vortex strength as described below.

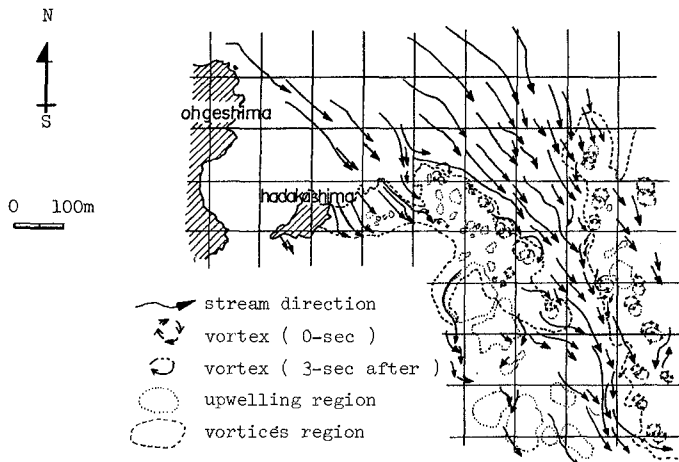


Fig-6 Distribution of tidal currents, coherent vortices and upwelling regions

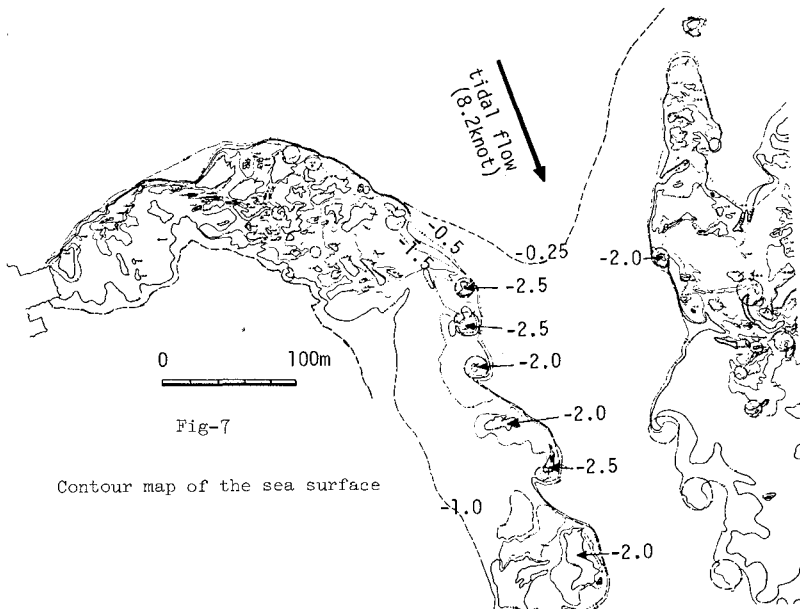


Fig-7

Contour map of the sea surface

2-2 Strength of the Coherent Vortices

From hydrodynamical view point, the vortex strength Γ in the practical sea water region with large scale such as the strait is quite an interesting subject to study. But, because of the unsteadiness as well as huge scale of the related hydraulic phenomena, the field measurement of the vortex strength by means of conventional instruments shall be considerably difficult. In this respect, the remote-sensing technology by the airplane and/or the satellite Landsat is quite useful. Here, authors present several ways to estimate the vortex strength with the data obtained through the remote-sensing.

(1) Estimation on the basis of " Rankine-Vortex " model

By applying the Rankine-vortex model to the individual vortex on the Fig-7, the vortex strength Γ_1 can be estimated by

$$\Gamma_1 = 2\pi R \sqrt{g \Delta h} \tag{1}$$

where R : vortex radius, g : acceleration of the gravity
 Δh : concavity of the water surface on the vortex axis

On the Fig-7, we can obtain Δh directly and R by the fact that the vortex radius is equal to the radius of the contourline of the concavity of $\Delta h/2$.

(2) Estimation on the basis of "Concept of vorticity flux conservation"

Referring to Fig-8 and assuming that the strength of vorticity generated at the point P will be preserved during transport to the downstream direction along the free boundary layer, the vorticity flux passing through the control section I in a unit time can be estimated as follows.

Volume flux of the fluid passing through an element of thickness dy in the unit time is $u dy$, where u is the velocity in the direction normal to the y -axis. The vorticity ω in the fluid of unit volume is

$$\omega = du / dy$$

therefore, the vorticity flux ω_{flux} passing through the control section I becomes

$$\omega_{flux} = \int_{-\infty}^{\infty} u \, dy = \int_{-\infty}^{\infty} \frac{du}{dy} u \, dy = \frac{1}{2} (U_1^2 - U_2^2) \quad (2)$$

where, U_1 and U_2 are the velocities above and below the boundary layer as shown in Fig-8 (a) respectively. With assumption that the free boundary layer consists of the group of coherent vortices, each of which is distributed in a constant space interval of b and possesses a shifting velocity of C as shown in Fig-8(b), the strength of each coherent vortex Γ_2 becomes

$$\Gamma_2 = \omega_{flux} \cdot \tau = \frac{1}{2} (U_1^2 - U_2^2) \frac{b}{C} \quad (3)$$

where, $\tau = b/C$ is the average shedding period of the vortices.

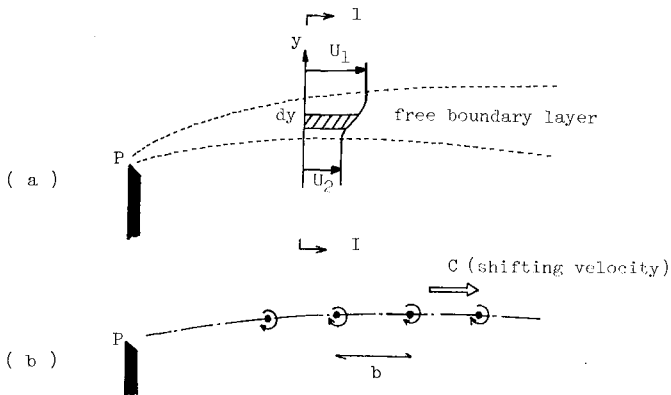


Fig-8 Concept of vorticity flux conservation

- (5) The sediment moving directly onshore from the Swash Bar, $Q(6)$ can split into longshore components $Q(7)$ or $Q(8)$ and $Q(8)$ can be broken down into its ebb and flood constituents.

$$\text{Hence : } Q(6) = Q(7) + Q(8); Q(8) = Q(8E) + Q(8F)$$

- (6) Prior to jetty construction North Beach was relatively stable i.e. $Q(5) = Q(4) + Q(7)$.

6.2 Functional Relationships

- (1) It was assumed that 90% of the flood tide sediment transport took place via the swash bar and inshore gutter i.e. $Q(3) = 0.1 Q(8F)$.

- (2) The ebb and flood sediment transport potential against the inside of the northern training wall was calculated from tidal current measurements assuming transport potential was proportional to the cube of the velocity (Maddock 1969). This indicated that the recycled ebb tide constituent of the inshore gutter sand feed was approximately half the flood tide constituent, therefore

$$Q(8E) = 0.3 Q(8)$$

- (3) The application of the CERC formula to determine the net littoral transport along North Beach, $Q(5)$, and the onshore transport on the Swash Bar, $Q(2)$, was discussed in Section 3.4 where it was argued:

$$Q(2) = 10 Q(5)$$

6.3 Calculated Values

A number of the model elements were known or estimated viz:

- (1) $Q(1) = 20,000 \text{ m}^3 \text{ p.a.}$ (See section 3.3)
- (2) Because currents in the inshore gutter were always inlet directed (Section 3.2) it was assumed that all sand feed would be inlet directed i.e. $Q(7) = 0$
- (3) $Q(9) = 50,000 \text{ m}^3 \text{ p.a.}$ (Section 3.1)
- (4) $Q(12) = 200,000 \text{ m}^3 \text{ p.a.}$ (Section 3.1)
- (5) $Q(11) = 150,000 \text{ m}^3 \text{ p.a.}$ (Section 3.1)
- (6) $Q(13) = \text{Erosion during flood event only}$ (Section 3.1)
- (7) $Q(15) = \text{Deposition during flood events}$ (Section 4)

6.4 Effect of Northern Jetty Construction

The foregoing equations and relationships were adjusted so as to

Fig-10 Karman vortex street formed by cloud behind Cheju Island

(from Tsuchiya¹⁾)

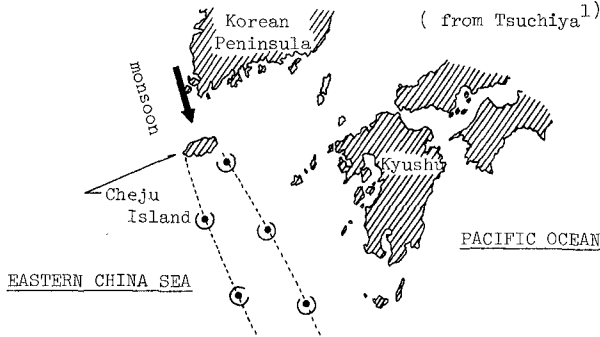


Table-1 Strength of vortices behind Cheju Island

Date	1969 Mar.05	1969 Mar.17	1969 Mar.22	1971 Jan.14	1971 Mar.13	
a km	36.8	44.0	61.3	48.8	35.4	
b km	110.8	71.0	86.1	121.8	76.2	
C m/sec	7.0	6.5	7.2	6.0	6.9	
U m/sec	9.2	10.5	12.0	8.3	10.5	
Γ_4 $10^9 \text{m}^2/\text{sec}$	6.3	5.9	8.4	6.6	6.1	←(eq. 5)
Γ_2 $10^9 \text{m}^2/\text{sec}$	6.7	6.0	8.6	7.0	6.1	←(eq. 3)
Γ_3 $10^9 \text{m}^2/\text{sec}$	10.2	7.5	10.3	10.1	8.0	←(eq. 4)

2-3 Strength of the Coherent Vortices in Naruto Strait

In order to estimate the strength of the coherent vortices in Naruto Strait, remote-sensing data from the airplanes were hydrodynamically interpreted using the above equations. On the Fig-7, one can estimate the surface concavity on the vortex axis to be $\Delta h = 1.0\text{m}$, the radius of the contourline of the concavity $\Delta h/2$ to be $R = 8\text{m}$. Putting these data into eq.(1), it is shown that the vortex strength amounts to about $160 \text{m}^2/\text{sec}$, when the velocity of the tidal current is 8.2 knot. The space interval of the vortices b , and the shifting velocity C were measured on the aerophotos to get the results presented in Table-2, where the velocity of the tidal current U was gained from the onsite data, and the velocity in the dead water region was considered to be negligible. The strength of the vortices on the basis of eq.(3) is estimated to be $50 \sim 100 \text{m}^2/\text{sec}$ in the case of the tidal flow velocity of 6.6 knots and $130 \sim 200 \text{m}^2/\text{sec}$ in the case of 10 knots, respectively. The vortex strength gained by eq.(1), (3) and (4) is considered to agree well each other.

Table-2 Strength of the coherent vortices in Naruto Strait

(Vortex No. 1, 2, (1', 2',) means a vortex positioned in the right(left) hand free boundary layer ; X means distance between the numbered vortex and its generated point)

Date	Vortex No.	U m/sec	X m	b m	C m/sec	τ sec	$\sqrt{2}$ m ² /sec	$\sqrt{3}$ m ² /sec	
1977 Apr. 1st	1	3.7	100	17	2.1	8	60	60	
	2	-	120	28	3.1	9	60	100	
	3	-	160	63	4.2	15	100	230	
	4	-	240	90	3.8	24	160	330	
	5	-	340	96	4.6	36	240	360	
	6	-	440	163	4.0	41	280	600	
	1'	-	170	73	3.5	21	140	270	
	2'	-	240	74	2.9	25	270	170	
	3'	-	320	66	2.1	32	220	250	
	4'	-	380	86	3.3	26	180	320	
	5'	-	490	129	4.6	28	190	480	
	6'	-	630	143	4.2	34	230	530	
	1977 Jul. 2nd	1	4.1	150	80	3.9	21	170	330
		2	-	230	74	4.0	19	160	300
3		-	300	66	3.5	19	160	270	
4		-	360	80	3.3	24	200	330	
5		-	460	96	4.5	21	180	390	
1977 Mar. 8th	1	4.4	100	58	2.5	23	220	250	
	2	-	160	59	3.4	17	170	260	
	3	-	220	64	2.8	23	220	280	
	4	-	290	73	2.5	29	280	320	
	5	-	360	114	4.1	28	270	500	
	1'	-	160	58	2.9	20	190	250	
	2'	-	220	76	2.8	27	260	340	
	3'	-	310	70	3.0	23	230	310	
	4'	-	360	84	2.7	31	300	370	
	5'	-	480	123	3.0	41	390	540	
1978 Feb. 24th	1	4.55	120	44	2.8	16	160	200	
	2	-	160	52	4.2	12	130	240	
	3	-	220	86	4.7	18	190	390	
	4	-	340	82	3.3	25	260	370	
	5	-	390	66	3.5	19	190	300	
	6	-	470	100	4.0	25	260	460	
	1'	-	280	56	4.0	14	140	250	
	2'	-	340	50	3.2	16	160	230	
	3'	-	380	48	2.8	17	180	220	
	4'	-	430	76	3.4	23	230	350	
	5'	-	530	100	5.3	19	200	450	

2-4 Consideration of the Upwelling Current
Associated with the Coherent Vortices

Onsite field observations and analysis of the solid aerophotos disclosed the existence of strong upwelling regions adjacent to the coherent vortices as shown in Fig-6. Theoretical considerations²⁾ using tornado-model show that a single line vortex around a vertical axis terminating at the sea surface and at the sea bottom, induces strong upward flow from the bottom due to the friction along the bed surface. Deducing from these results of a single line vortex, the observed upwelling phenomena at the strait are considered to be strictly related to the coherent vortices along the free boundary layer.

In order to estimate the upward volume flux in Naruto Strait, hydraulic model tests were carried. In a test basin of 0.6m-width and 25m-length, a single line vortex was generated by putting suddenly a plate of 0.3m-width into the uniform flow with the velocity of 7.0cm/sec, keeping it standing still in a moment, and finally drawing out abruptly. Both of the strength and diameter of the vortex could be changed by controlling the degree of the small shifting motion of the plate toward the upstream. The vertical profiles of the water surface of the vortex were measured by a wave gauge set in the course of the vortex path. The vortex motion and the induced upwelling motion were coloured with respective different dyes and their side views as well as their plan views were photographed every one second. Experiments were carried under the two different conditions of bottom surface, that is, smooth surface and rough one with pasted sand of 1.7mm ~ 2.2mm diameter. The wave gauge was set at 0.5m downstream from the vortex generating point. Experimental conditions are presented in Table-3, in which H is water depth, C is shifting velocity of the vortex and Γ is the vortex strength estimated by eq.(1) with the surface concavity gained by the wave gauge.

Case No.	1	2	3	4	5	6	7	8	9	10	11	12	13	14	15	16	17	18	19	20	21	22
Vortex velocity C (cm/sec)	7.7	8.0	7.2	7.5	5.5	8.3	8.0	8.3	7.0	5.6	7.7	7.0	8.2	7.2	7.8	7.5	7.8	8.0	8.2	8.0	7.9	6.8
Vortex radius a (cm)	2.08	3.60	3.02	3.82	3.96	1.62	2.28	2.74	3.36	3.19	3.28	2.31	2.58	3.67	4.21	1.91	3.28	3.36	4.18	3.12	2.61	3.57
Vortex concavity Δh (cm)	0.63	0.35	1.18	0.88	1.88	0.42	0.70	0.86	1.16	1.93	0.25	0.93	2.46	1.25	1.03	0.82	0.31	0.31	0.39	1.18	2.30	2.38
Vortex strength Γ (cm ² /sec)	325	419	645	705	1068	207	375	498	712	871	319	438	796	807	840	340	359	368	513	667	778	1038
Water depth H (cm)	20					20					30					30						
Bottom roughness	smooth					rough					smooth					rough						

Table-3 Experimental conditions

Fig-11
Upwelling due to
a line vortex
(Case 1)

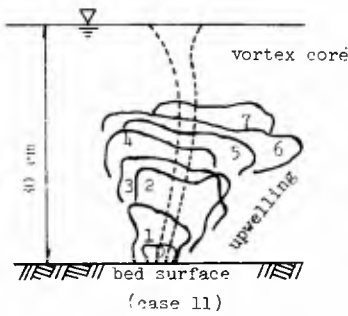
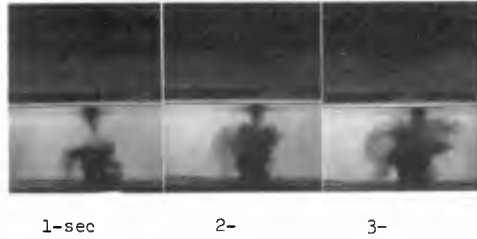


Fig-12

Successive picture of
upwelling flow

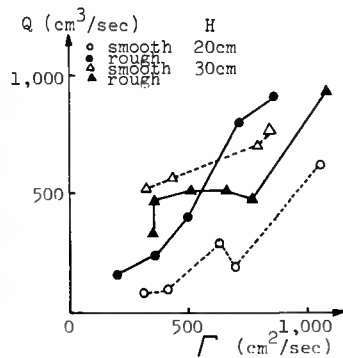


Fig-13

Upwelling flux as a function
of vortex strength

When the vortex comes into the observation section, red colored dye set on the bottom surface moves along the bottom surface and turns its direction upward. In case of the vortices of weak strength, the upwelling flow concentrates near the vortex axis and breaks itself down before arriving at the water surface (Fig-11). According as the vortex strength increases, the downward flow along the vortex axis appears and increases its diameter, and the upwelling flow takes the shape of a ring. In the case of the rough bottom surface, the diameter of the upwelling flow becomes larger, and breaks down more easily because of the rotating energy consumption by the friction due to the bottom roughness.

Fig-12 shows the successive pictures of the upwelling flow mapped from a series of photos with the time interval of 1 sec. The upward volume flux associated with the upwelling motion was estimated from such figures gained respectively in each case of the experiments of Run 1~22 of Table-3. Fig-13 shows the relation of the upward volume flux to the vortex strength.

The upward volume flux at Naruto Strait was estimated by using these experimental data on the basis of the Froude similitude. In the experiments, the upward volume flux of $500\text{cm}^3/\text{sec}$ was observed to be induced by the vortex of 3cm-diameter, water surface concavity of 0.8cm and vortex strength of $500\text{cm}^2/\text{sec}$ in the case of water depth of 20cm. Basing on the Froude similitude, the upward volume flux of $280\text{m}^3/\text{sec}$ is expected to be induced by a vortex of 6m-diameter, 1.6m-concavity and $150\text{m}^2/\text{sec}$ strength in the case of water depth of 40m, which is of approximately equal scale to the coherent vortices in the free boundary layer generated at Naruto Strait in the flood tide condition. At Naruto, about a dozen of vortices are existing as shown in Fig-2, and then the total volume of upward flux is roughly estimated to be $3,000\text{m}^3/\text{sec}$. The total volume flux of the tidal current under the flood tide condition is about $100,000\text{m}^3/\text{sec}$. Therefore, at Naruto, the vertical sea water mixing caused by the upwelling motion induced by the coherent vortices is estimated to be a few percents of the total volume flux of the tidal current passing the strait.

3. LARGE SCALE VORTEX-PAIR OBSERVED BY LANDSAT

3-1 Remote-sensing by Landsat

As shown in Fig-4, the coherent vortices along the free boundary layers amalgamate into a pair of vortices of larger scale. This amalgamation phenomena have too large scale to observe from the airplane, but the satellite Landsat may present us these clearly. For example, Fig-14 shows a result of the analysis of the Landsat data obtained on August 1st, 1976. On this figure, one can see the vortex-pair of larger scale under the northward tidal current of the maximum velocity of 7.6 knot. Fig-15 is another example and shows the flow pattern on October 24th, 1972. In this case, the northward tidal flow maximum velocity of which is 10.2knot have just finished and the current is under the slack condition. The fully grown vortex-pair of large scale can be observed on this figure. Finally, Fig-16 obtained from the Landsat data on December 30th, 1975 shows the situation that the tidal current is flowing in the southward direction with about maximum velocity of 7.6knot while the vortex-pair left behind in the Harima Sea is still leaving away the strait with its self-induced velocity U_v , which is theoretically described by

$$U_v = \frac{\Gamma}{2\pi\ell} \quad (6)$$

where

$$\Gamma : \text{strength of each vortex} = \alpha \int_0^{6\text{hour}} \frac{1}{2} u^2(t) dt$$

ℓ : distance between each vortex

α : amalgamation efficiency factor

$u(t)$: velocity of the tidal current

Fig-14

Midst of the formation process
at the maximum northward flow
condition



Fig-15

Final stage of the formation
process at the slack



Fig-16

Vortex-pair progressing into the
Harima Sea against surrounding
sea water at the maximum
southward flow condition



The above three different phases of large scale vortex-pair are summarized in the Fig-17. These Landsat data present clearly the various patterns of the vortex-pair formed by northward flow under each characteristic stage of the tidal cycle. On the other hand, patterns of vortex-pair formed by northward flow are not presented so clearly, although the vortex-pair can be vaguely recognized in Kii Channel in the case of Fig-16.

With the expectation to obtain more clear feature of the vortex-pair, the authors did measurements of thermal image of the flow from the air-plane at the altitude of 4,000m. Fig-18 shows the thermal image gained at 11:00 A.M. Aug. 23rd 1979, being 2 hours after the southward flow began. Again the existence of the vortex-pair in the Harima Sea can be definitely recognized. Fig-19 shows the situation at 12:00 A.M. on the same date. The tidal condition at this moment is southward maximum flow. On this figure, one can see the vortex-pair in Kii Channel as expected and strong water mixing proceeding at the strait.

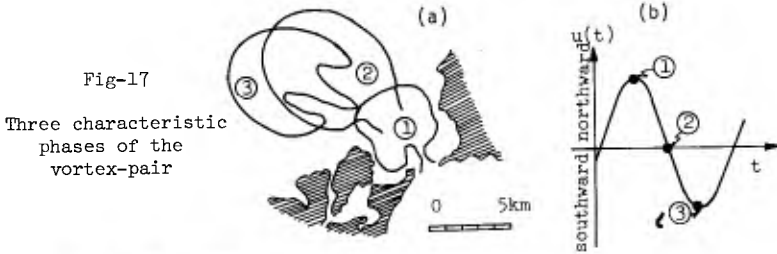


Fig-18 Thermal image at 11:00



Fig-19 Thermal image at 12:00

3-2 Consideration of Tidal-Exchange by Vortex-Pair

The mechanism of the tidal-exchange through the narrow strait such as Naruto Strait is explained using vortex-pair model as shown in Fig-20, in which A-①~③ represent the growing process of the vortex-pair, each of which corresponds to the typical phase of the cyclic tidal current at the strait as shown as B-①~③.

- ① Tidal current is flowing with the maximum speed at the strait. The vortex-pair is being generated by the amalgamation process of the coherent vortices along the free boundary layer. At the same time, the vortex-pair advances forward with the self-induced propulsive force, pushing aside the surrounding water body.
- ② The first half of the tidal-cycle as well as the growing process of the vortex-pair are over.
- ③ Tidal current is running with the maximum speed in the reversal direction. Vortex-pair left behind is still leaving away the strait, with its self-induced velocity U_v defined by eq.(6). Under this situation, the water mass passing the strait, which has been pushed aside by the vortex-pair in the former processes, generates another vortex-pair in the opposite side of the strait.

Thus tidal-exchange is inspired by the self-propelling motion of the vortex-pair.

The water mass forming the vortex pair corresponds to the magnitude of the tidal-exchange during one tidal cycle, which is estimated to be 10^9 m^3 in Naruto Strait as the result of the analysis of the remote-sensing data and onsite data as well. The self-propelling motion, which plays an important role in the tidal-exchange process through the strait, is also expected to contribute to the mixing process in the open sea neighboring the strait. Analyses of the remote-sensing data from Landsat show that the self-induced velocity of the vortex-pair at Naruto-Strait is about 0.8 knot, from which the strength of the vortex is estimated to be $10^4 \text{ m}^2/\text{sec}$. Thus, about 10% of the vorticity generated at the strait is expected to amalgamate to the large scale vortex-pair via the form of the coherent vortices along the free boundary layer.

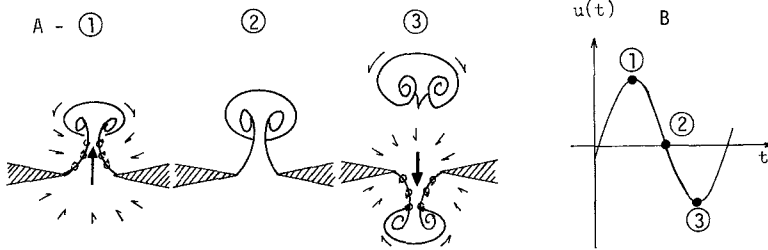


Fig-20 Schema of tidal-exchange mechanism

CONCLUSION

Usefulness of the remote-sensing from airplanes and Landsat in the study of tidal current in straits was discussed, choosing Naruto Strait as the object of the onsite study. Solid aerophoto provides various information of small scale hydrodynamical character of the tidal current including the distribution of the coherent vortices in the free boundary layer, surface concavity at the vortex axis and radius of the vortices, through which the strength of each coherent vortex can be estimated. Regarding the estimation of the vortex strength, the authors presented four formulas of eq.(1), (3), (4) and (5), of which fitness was studied by means of aerophotos. Among these, eq.(3) is considered to be most convenient in the case when we apply aerophotos in the study, because all variables in the equation can be obtained directly on the aerophotos.

The small scale coherent vortices amalgamate during a half of the tidal cycle, 6 hours, finally into a large scale vortex-pair, the self-propelling motion of which takes an important role in the tidal-exchange through the strait. The scale of the vortex-pair is generally too large to observe on the aerophotos. In that case, Landsat is quite useful as shown in Fig-14. The self-propelling motion of the vortex-pair is also considered to promote the mixing of the water from the inland sea with the water in the open sea. In the case of Naruto Strait, about 10% of the vorticity generated at the strait is expected to amalgamate in the vortex-pair via the form of small scale coherent vortices, and a few percents of total volume flux of the tidal current passing the strait is estimated to mix with the surrounding water body due to the upwelling current induced by the coherent vortices.

REFERENCES

- 1) Kiyoshi Tsuchiya (1974) : " Cloud Features Associated with Mesoscale Phenomena during Cold Season as Revealed by Meteorological Satellite Pictures", The Geographical Magazine, vol-37, No.1, pp49-94
- 2) Sotoaki Onishi and Tsukasa Nishimura (1979) : " Field Observations of Upwelling Associated with Vortex and Considerations of Generating Mechanism of These Phenomena", Coastal Engineering in Japan, vol-22 pp123-138

CHAPTER 161

DYNAMIC SIMILARITY OF TRANSPORT PHENOMENA

by

M.S. Yalin,
Professor, Dept. of Civil Engineering,
Queen's University, Kingston, Canada
(Consultant, Dept. of Ocean Engineering, University of Hawaii)

and

F. Gerritsen
Professor of Ocean Engineering
University of Hawaii

ABSTRACT

The discharges issued by OTEC plants, thermal power plants and other engineering devices, give rise to the transport of "foreign" properties and substances into the natural ocean environment. In order to predict the functioning of such structures and assess their environmental impact, physical modelling has already been utilized. Since the simultaneous fulfillment of both Reynolds and Froude criteria is impossible (in a conventional small scale model operating with the prototype fluid) in the models mentioned the transport phenomenon was reproduced on the basis of the densimetric Froude number (Fr) only, the influence of the Reynolds number (Re) being neglected. On the other hand, the identification of the scale of Fr (viz λ_{Fr}) with unity can lead to substantial differences between the model and prototype values of Re . (Because $\lambda_{Fr} = 1$ yields $\lambda_{Re} = \lambda_\ell^{3/2}$ where λ_ℓ is the linear model scale.) Yet many of the pertinent aspects of a turbulent diffusion (energy dissipation, thickness of mixing zones, separation processes, etc.) are strongly dependent on Re , and therefore an appreciable distortion of Re ($\lambda_\ell^{3/2} \ll 1$) can lead to some substantial errors with regard to the similarity of these aspects.

The central theme of the approach presented in this paper can be outlined as follows: Why should any of λ_{Fr} or λ_{Re} necessarily be identified with unity? If Π_A is the dimensionless version of a quantitative property A of the transport phenomenon, then $\Pi_A = \Phi_A(Re, Fr, \dots)$. The modelling of A means the approach of λ_{Π_A} to unity as close as possible. But, if so, then there should exist such (optimal) scales $\lambda_{Fr} = \alpha$ and $\lambda_{Re} = \beta$ (both $\neq 1$) which would yield

$$|\lambda_{\Pi_A} - 1| \rightarrow \text{minimum}$$

The proposed determination of α and β rests on experimental basis; it rests on the calibration of the model by adjusting the model velocity v so that the last equation becomes valid.

Since $\frac{\partial A}{\partial Re}$ cannot be expected to be the same for all the properties of the transport phenomenon each A will in general require "its own" scales α and β .

1. INTRODUCTION

Transport phenomena form a large class of problems whereby discharges from a source induce certain changes in the natural environment. The transported element may be matter (salinity) or temperature but may also refer to fluid properties such as momentum. The overall objective of this paper is to describe a method by which transport phenomena can be tested in a hydraulic model. In such phenomena both Froude number and Reynolds number play a role in their model simulation.

The method developed in this paper may also be useful in other hydraulic phenomena, in which both the Reynolds number and the Froude number play a role.

The reason to undertake this study was the present development of O.T.E.C. plants in the Hawaiian environment. In addition to the vast number of technological problems that have to be solved before O.T.E.C. plants can be operable and can deliver power to the network, the induced circulation and the effect of OTEC plants on the ocean environment have to be evaluated quantitatively. This is particularly important if one visualizes a large number of OTEC plants operating in the tropical oceans.

To the authors' opinion the environmental impact aspects of OTEC power plants have not been given adequate consideration in the research planning by the DOE and other agencies involved in OTEC developments.

Studies on environmental impact of these plants can be accomplished in three different ways:

- . by field studies on pilot plants
- . by laboratory investigations with hydraulic models
- . by mathematical modelling.

The question is often raised which of those methods would be preferable. In the authors' opinion all three are necessary in order to arrive at satisfactory and reliable answers.

Of these three methods a mathematical model is the most versatile tool. After the formulation of the model has been worked out and the algorithm has been developed, a large number of varying conditions can be investigated at a relatively low cost. There is no doubt that the mathematical model will be the ultimate method of analysis for the future. However such model utilizes physical concepts, parameters and constants, the values of which are only known for a limited degree of accuracy for a given situation. Of interest is the numerical model developed by Yamashita (Yamashita, 1979). This model has been developed for a shore-based OTEC plant at Keahole Point on the island of Hawaii, but can easily be extended into an offshore floating OTEC plant.

The answers that the mathematical model provides depend heavily on the numerical values of essential parameters and therefore verification is required. There is no doubt that the best way to verify the value

of physical constants is from the prototype. However, such verification requires a large number of points for the measurement of velocities, temperatures and salinities, both in the near field and in the far field.

Such program will be extremely costly, if at all feasible.

The scope of the field experiment can be strongly reduced if a combination of laboratory and field studies is employed to verify the physical constants. In the field, measurements can then be limited to observations in a number of strategically located points. The laboratory studies will provide the opportunity for taking a great number of detailed measurements in a controlled environment, whereby verification with the field conditions is possible from data obtained in corresponding points of prototype and model.

Having stated that hydraulic model experiments are an indispensable tool in the study of OTEC-related phenomena we will have to determine which scale relationships to apply to convert model data to prototype conditions. Before we discuss this matter in detail we will give a short description of the OTEC concept.

2. DESCRIPTION OF OTEC CONCEPT

Ocean Thermal Energy Conversion (OTEC) is presently one of the major development thrusts for energy extraction from the ocean. Other areas in which efforts may become fruitful are tides, currents, waves and salinity gradients.

In the OTEC concept the temperature difference between the warm surface water and the cold bottom water is utilized as a source of power generation.

The vast expanse of the oceans covers nearly three-quarters of the earth's surface and stores sufficient energy to fulfill the needs of everyone for many years to come (Richards and Vadus, 1980).

The study of OTEC-related problems in Hawaii has come to the forefront because Hawaii has been chosen for three major R&O OTEC research projects: the Mini-OTEC (50 kWe), OTEC-1 (1 MWe) and OTEC 10/40 MWe pilot plants.

Of these pilot projects the Mini-OTEC pilot project was in operation in Hawaiian waters during the summer and fall of 1979. It proved that the OTEC concept is workable.

Temperature, density and salinity profiles for offshore Hawaiian waters are summarized in Table 1. See also Bathen (1975).

Mini-OTEC was the world's first at-sea OTEC plant to produce net power.

Table 1. Density Profile (Offshore Hawaiian Waters)

Depth	Field Data		Computation with Constant Salinity (35‰)
	Temperature	Density	
0m	24.30°C	1.0236 (gm/liter)	1.0237
200	17.40	1.0254	1.0254
400	8.40	1.0267	1.0271
600	6.35	1.0270	1.0274

The system was developed by a private consortium of organizations including the University of Hawaii, Lockheed Missiles and Space Co., Oillingham Construction & Dredging Co., and Alfa-Laval.

An interesting feature of Mini-OTEC was that the cold water pipe (length 630m, diameter .6m and built of polyethelene), through which cold water is pumped from the deep to the plant, also serves as a part of a single mooring system.

As another step in the development, OTEC-1, a converted government-owned T-2 tanker, the Chepachet, will arrive at its test site off Keahole Point, westside of the island of Hawaii, in the summer of 1980.

The schematics of an OTEC seawater system is shown in Figure 1.

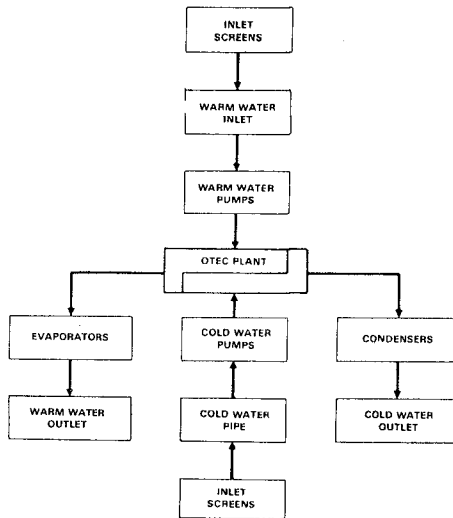


Figure 1. Schematics of OTEC Seawater System
(from Richards and Vadus, 1980)

Warm water of the surface layers of the ocean is used to evaporate a working fluid (ammonia) in an evaporator.

The vapor drives a turbogenerator, after which it passes through a condenser and a pressurizer. The condenser is cooled with the cold water pumped from the deep ocean layers.

The above-described system is the so-called closed cycle, which has been emphasized in ongoing research. Other cycles such as the open cycle, the hybrid cycle and the lift cycle offer other possibilities (Richards and Vadus, 1980).

When passing through the installation the warm water loses some of its heat, whereas the cold water gets warmer. Both are being discharged into the ambient ocean, either separately in two outlets or mixed in one discharge opening.

The location (depth) of the discharge jets is to be chosen in such a manner that no shortcuts in the circulation will develop; such short-cuts will necessarily lead to a reduction in the available potential.

The efficiency of an OTEC system is primarily determined by the difference in temperature between the warm and cold water. In Hawaiian waters this difference is about 20°C. The second law of thermodynamics specifies that the best efficiency of an OTEC system is of the order of 6%. If energy losses are taken into account (for pumping and other system components) the expected energy producing efficiency is 2-3%.

Despite the low efficiency the system may still be economically feasible, since no fuel is required for its operation.

Present research on OTEC systems is concentrated on the technological aspects of system components. Major problem areas are the bio-fouling of heat exchangers, and the design of the cold water pipe, and of the mooring system.

So far only little attention has been given to the aspects of induced ocean circulation and environmental impact, particularly if more than one plant will be built in a specified area. This area of study needs more attention in the near future. Laboratory studies can assist in providing the required information.

3. PHYSICAL MODELLING OF OTEC PLANTS

3.1. Objectives of Study

In the study of the functioning of OTEC plants by means of laboratory investigations (hydraulic models) two types of problems are particularly relevant:

problems concerned with the circulation near the plant (near-field) with the objective of determining the required distance between intake and discharge opening in order to avoid short

circuiting, having adverse effects on the available temperature potential.

problems of the flow field away from the plant (far-field) with the principal objective to determine the ocean area affected, and the required distance between plants if several plants are to be built in the same region.

Changes induced by the plants in the far field furthermore will be indicative of the effects, if any, on climatological conditions.

In order to achieve a reliable prediction from mathematical models it has been noted that the quantitative formulation of the phenomenon must be known. In the case of OTEC plants, it is the discharge flow, which manifests itself in the form of a turbulent jet, that is the main source of the flow phenomenon and its consequences.

At present the turbulent flow in general and the "free turbulence" (to which the jet flows belong) in particular have not yet been understood completely.

Consequently the mathematical formulation of the free turbulence is also far from being complete and thus reliable. This is especially so for the conditions presented by OTEC plants, where the fluid which constitutes the discharge flow has different temperature (and thus density and viscosity) in comparison to the ambient fluid and where the ambient fluid is not homogeneous (temperature decreases with the depth) and very often not even static (ocean currents). Considering this it will not be difficult to realize that mathematical modelling whose output accuracy is completely dependent on the knowledge and thus accuracy of the mathematical formulations forming the impact, cannot be regarded as more reliable than physical modelling which does not depend on the mathematical formulations, i.e. on the knowledge of the quantitative relations among the parameters involved but which is dependent only on the knowledge of the parameters themselves. Admittedly very often the knowledge of the parameters and thus of the criteria of similarity does also not mean that a reliable physical model can be immediately designed. Indeed, some criteria of similarity may turn out to be conflicting (and in the case of OTEC plants where both the densimetric Froude number (Fr) and the Reynolds number (Re) are involved this is just so), nonetheless to find a "way out" in such cases by means of a special research is considerably more feasible than the formulation of the free turbulence and its consequences for heterogeneous fluids; it should be sufficient to recall that the research on turbulence is being carried out since the beginning of the century and yet, with the exception of some very simple cases (parallel flows, rectilinear flow boundaries, homogeneous fluids, etc.), no generally accepted formulation of this elusive phenomenon has been found so far.

In view of the above it is not surprising that efforts dealing with the physical modelling of OTEC plants have been limited.

To the authors' opinion the work done by Jirka et al. (1977) has

been the only work of this kind, and in their view the approach used in their study is very innovative.

These authors have used an inverted model approach. The study was conducted at a scale 1:200, in which only the body of water above the thermocline was considered, giving the physical model a very shallow depth.

Results of their experiments agreed with those of a mathematical model. Because of the concerns expressed above there is no guarantee that the results also represent prototype conditions without further verification.

In the study by Jirka et al. (1977) the time averaged fields of temperature and velocities were measured and some pertinent aspects of these fields were determined.

In order to study the quantitative aspects of the phenomena in a physical model the authors believe that additional measurements are necessary.

It is recommended that the results of a small scale model (e.g. 1:50) be compared with the results of another, several times larger physical model (e.g. 1:10) and subsequently with the full scale (prototype).

The prototype in question could be the Mini-OTEC plant, when it will be back in operation for prototype testing, such as planned.

It is furthermore suggested to measure in the model the fields of some fluctuating properties of turbulence (viz of the root mean square values of the fluctuating velocities u' , v' and w' and also the Reynolds stresses $-\rho \overline{u'v'}$).

The overall picture of the phenomenon is characterized by its time average properties and therefore it is only reasonable to start the investigation of similarity by using the time average properties. It is perfectly possible that the rejection of the Reynolds criterion may not affect noticeably the similarity of the time average velocity fields in model and prototype but it may affect the similarity of the fluctuating velocities and thus the similarity of the internal structure of turbulence and its consequences (such as energy dissipation, diffusion, etc.).

3.2. Facilities For Proposed Research

Because of the large water depth involved model facilities need to be of large size in order to allow testing the phenomenon at a desirable scale.

Such facilities are limited on a worldwide basis. The new ocean tank of the Norwegian Hydrodynamic Laboratories in Trondheim, Norway (size 50 x 50 x 10m³) would be an excellent facility for such testing.

At the University of Hawaii's JKK Look Laboratory, the large steel circular model tank would be a suitable facility. The tank has an opening at the top and on the side.

The tank is 9.14m in diameter and 12.34m high. (See Figure 2.)

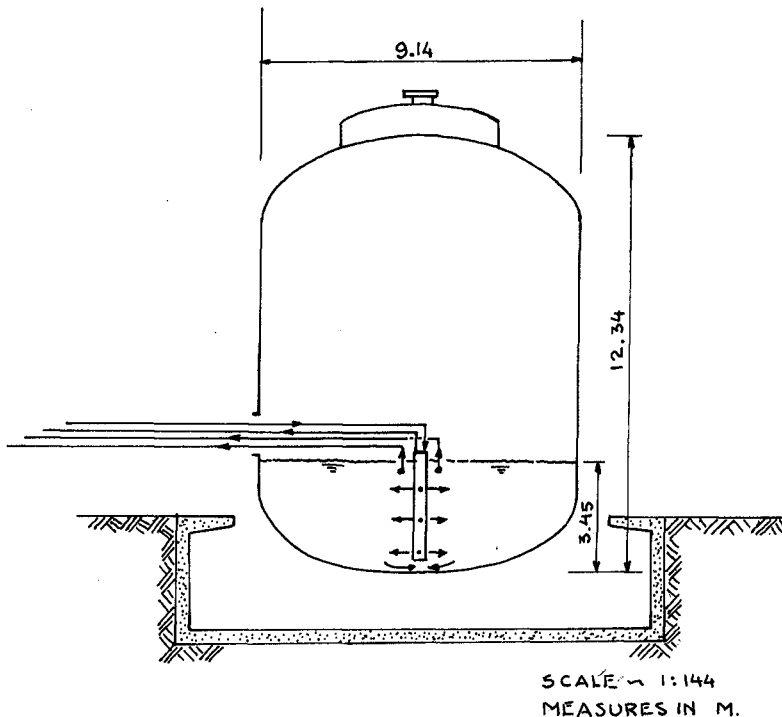


Figure 2. University of Hawaii's Large Circular Testing Tank

An analysis was made to determine if this tank could be made suitable for the testing of OTEC plants. The results were promising (Lee, 1978). Experiments can be carried out by using either the lower portion of the tank or by utilizing its full water depth.

The facility is considered suitable because it allows the simulation of ocean depths at a reasonable scale.

Heaters and coolers will have to be added for the establishment of a vertical temperature gradient in the tank and for the heating and cooling of the circulating fluid.

The circuits that provide the water circulation will be able to simulate the following conditions:

1. Skimming of "hot" water from the upper layers.
2. Discharging warm water at varying levels.
3. Pumping cold water from the deep portion of the tank.
4. Discharging cool water at varying levels.
5. Combining the warm water and cool water effluent into a single discharge arrangement at various levels. (Mini-OTEC arrangement)

4. THEORETICAL BASIS FOR MODEL SCALE DETERMINATION

From the pioneer work of Jirka et al., carried out in MIT in 1977, it is clear that the most relevant dimensionless variables determining the flow phenomenon around an OTEC plant are the densimetric Froude number Fr and the Reynolds number Re . If the geometry of the OTEC plant is specified then the velocity U which appears in both of these numbers can be any "typical velocity" of the system. If the undistorted model operates with the prototype fluid, that is with water having the same temperature, then, as is well known, a simultaneous fulfillment of both Froude and Reynolds criteria is impossible. Thus Jirka et al. made an attempt to achieve the dynamic similarity by identifying the model and prototype values of the Froude number only ($Fr'' = Fr'$), i.e. by identifying the scale of the Froude number with unity ($\lambda_{Fr} = 1$) and disregarding the Reynolds number completely (Re). This method of modelling is yet another example of the contemporary modelling convention, where a dimensionless variable, such as the Reynolds number, is rejected on the ground that its "influence on the phenomenon is negligible". This statement often is more a convenient justification of our conventional modelling methods than a reflection of truth. Indeed a physical phenomenon has an unlimited number of various properties which are different functions of the dimensionless variables defining that phenomenon. But if so then the influence of a certain variable, such as the Reynolds number, may indeed be irrelevant with regard to one set of the properties and yet it may turn out to be quite relevant with regard to another.

Notations.

For the analysis the following notations are utilized.

1. Model values are specified by ("), prototype values by (').
For example if α is a quantity to be studied then

α'' is the model value of α
 α' is the prototype value of α

and $\frac{\alpha''}{\alpha'} = \lambda_{\alpha}$ is the scale of α . (Yalin, 1971).

2. The ambient values (i.e. the values undisturbed by the OTEC plant) of any value of α is denoted by $\bar{\alpha}$. (See Figure 3.)

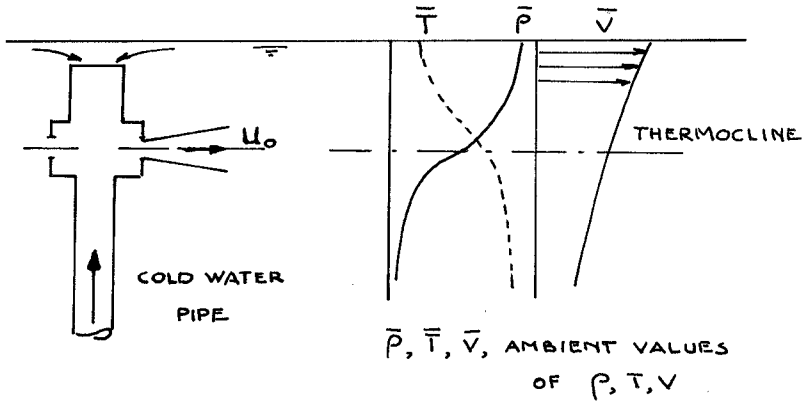


Figure 3. Schematics of OTEC Circulation and Ambient Ocean Conditions

Characteristic Parameters.

It is assumed that the model is undistorted and that it operates with the prototype fluid.

Since

$$\rho = f_1(T, S) \quad \text{and} \quad \mu = f_2(T, S) \quad (1)$$

the geometrically similar distribution of the ambient temperature and salinity in the model will yield the geometrically similar distributions of $\bar{\rho}''$ ($= \bar{\rho}'$) and $\bar{\mu}''$ ($= \bar{\mu}'$) [the same applies for ρ_0 and μ_0]. Accordingly, it is assumed, that the necessary distribution of the ambient temperature and thus of $\bar{\rho}''$ and $\bar{\mu}''$ is provided. Similarly, we assume that the model has the geometrically similar distribution of \bar{V}' (even if the scale λ_V' will be revealed later on).

If the ambient conditions are specified then the flow phenomenon in the region under investigation will be dependent only on the geometry of the plant and on the nature of its functioning, i.e. it will be dependent

- a) on the geometric parameters (lengths and angles) L_1, L_2, L_3, \dots
 $\theta_1, \theta_2, \dots$

- b) on the kinematic parameters (which in the steady state case under consideration are velocities only)
 $U_1, U_2, U_3, U_4, \dots$
- c) on the physical properties (ρ, μ) of "in" and "out" flows*
 $(\rho_1, \mu_1), (\rho_2, \mu_2), (\rho_3, \mu_3), \dots$

and

- d) on the acceleration due to gravity g .

Hence any quantitative property A of the present phenomenon must be expected to vary as a certain function of the position in space (x, y, z) and of the parameters above:

$$A = f_A(x, y, z, L_i, \theta_j, U_k, \rho_l, \mu_m)** \tag{2}$$

The subscript A in f_A indicates that the form of the function (2) depends on the quantity A under consideration: different properties A of a phenomenon are different functions of the same parameters (describing that phenomenon).

Let L, U, ρ, μ be some (single) parameters selected from the groups L_i, U_k, ρ_l, μ_m (as their "representatives"), e.g. one can identify L, U, ρ, μ with L_4, U_3, ρ_3, μ_3 respectively. In this case the (dimensional) relation (2) can be brought into the dimensionless form

$$\Pi_A = \phi_A \left[\frac{x}{L}, \frac{y}{L}, \frac{z}{L}, \frac{L_i}{L}, \frac{U_k}{U}, \frac{\rho_l}{\rho}, \frac{\mu_m}{\mu}, \frac{UL\rho}{\mu}, \frac{U}{\sqrt{gL}}, \theta_j \right] \tag{3}$$

Here Π_A is the "dimensionless version" of the property A under investigation

$$\Pi_A = \rho^\alpha L^\beta U^\gamma A \tag{4}$$

where depending on the dimension of A the exponents α, β, γ must be determined so that the power product (4) becomes dimensionless.

Dynamic Similarity, Model Scales

If all Π_A are identical in model and prototype, i.e. if

$$\Pi_A' = \Pi_A'' \quad \text{or} \quad \lambda_{\Pi_A} \equiv 1 \quad (\text{for any } A) \tag{5}$$

is valid then model and prototype are dynamically similar (and the predictions obtained from the model are reliable).

Since Π_A is given by the dimensionless variables shown in (3) the model and prototype identity of all Π_A [as implied by (5)] can certainly be achieved if the identify of all variables [on the right of (3)] is provided.

* T&S need not be included

** $i=1,2,\dots, N_L, j=1,2,\dots, N_\theta, \dots$ etc. where N_L, N_θ, \dots are the numbers of all the pertinent lengths, angles, ...etc.

Now, the identities

$$\left(\frac{L_i}{L}\right)' \equiv \left(\frac{L_i}{L}\right)'' \quad \text{and} \quad \theta_j' \equiv \theta_j'' \quad (6)$$

are provided: because model is geometrically similar.

The identities

$$\left(\frac{\rho_1}{\rho}\right)' \equiv \left(\frac{\rho_1}{\rho}\right)'' \quad \text{and} \quad \left(\frac{\mu_m}{\mu}\right)' \equiv \left(\frac{\mu_m}{\mu}\right)'' \quad (7)$$

are also provided, because model is supposed to operate with the prototype fluid and the similarity in the distribution of the ambient temperature and salinity is provided.

The identities

$$\left(\frac{x}{L}\right)' = \left(\frac{x}{L}\right)'', \quad \left(\frac{y}{L}\right)' = \left(\frac{y}{L}\right)'', \quad \left(\frac{z}{L}\right)' = \left(\frac{z}{L}\right)'' \quad (8)$$

are also valid, since the measurements and predictions will be carried out for corresponding points (of the space occupied by flow).

Since all velocities will be scaled down in the same proportion λ_U (whatever its value may be!) the identity

$$\left(\frac{U_k}{U}\right)' = \left(\frac{U_k}{U}\right)'' \quad (9)$$

is also satisfied. Thus the identity of all Π_A , i.e. the dynamic similarity depends entirely on the model and prototype identity of the Reynolds and Froude numbers

$$X = \frac{UL\rho}{\mu} \quad \text{and} \quad Y = \frac{U}{\sqrt{gL}} \quad (10)$$

At this state it should be mentioned that in the present phenomenon the free surface is not disturbed significantly and therefore the main role of the acceleration due to gravity g is not so much to reflect the influence of the free surface, but to reflect the influence of the gravity difference of the fluid layers having different densities. In other words the role of g consists of acting on various ρ_ℓ and generate various specific weights $g\rho_\ell$ and their differences such as

$$g\rho - g\rho_\ell = g(\rho - \rho_\ell) \quad (11)$$

Since g will thus appear in the expression of any Π_A in the form (11), one could consider the form (11) in the first place, i.e. one could take, say, $g(\rho - \rho_\ell)$, rather than simply g , (when writing d). In this physically more meaningful (and yet mathematically equivalent) approach we would have

$$Y_* = \frac{U}{\sqrt{gWL}} \quad (*) \quad (\text{with } W = 1 - \frac{\rho_1}{\rho}) \quad (12)$$

[rather than $Y = U/\sqrt{gL}$ in Eqs. (3) and (10)].

The mathematical equivalence with regard to model tests follows from the fact that

$$Y_* = Y \cdot (1 - \frac{\rho_1}{\rho})^{-\frac{1}{2}} \quad (13)$$

since in the present case the model and prototype values of ρ_1/ρ are identical. The model and prototype identity of Y -numbers implies automatically the model and prototype identity of Y_* -numbers and vice versa.

Hence in accordance with convention established in the field we replace consideration of (10) with that of

$$X = \frac{UL}{\nu} \quad Y_* = \frac{U}{\sqrt{gWL}} \quad (14)$$

As is well known the simultaneous identity of model and prototype values of X and Y_* (i.e. $\lambda_X = 1$ and $\lambda_{Y_*} = 1$) cannot be achieved (if the small scale model operates with the prototype fluid). Indeed

$$\lambda_X = 1 \quad \text{yields} \quad \lambda_U = \frac{1}{\lambda_L} \quad (15)$$

whereas

$$\lambda_{Y_*} = 1 \quad (\text{or } \lambda_Y = 1) \quad \text{gives} \quad \lambda_U = \sqrt{\lambda_L} \quad (16)$$

(e.g. if $\lambda_L = 1/16$ then Reynolds criterion requires $\lambda_U = 16$ whereas Froudian criterion demands $\lambda_U = 1/4$).

In the situations such as above the conventional approach is to ignore one of the criteria. Accordingly in the present field, one usually finds some justifications and states that "the influence of the Reynolds number X is negligible with regard to the present phenomenon and thus that it can be ignored". Accordingly, the condition $\lambda_X = 1$ and thus $\lambda_U = 1/\lambda_L$ are excluded and the flow velocities are scaled down according to $\lambda_Y = \lambda_{Y_*} = 1$, i.e. as $\lambda_U = \sqrt{\lambda_L}$. The weakness of this seemingly reasonable statement lies in the word "phenomenon", which is used as if it were a single entity. In fact, however, the term "phenomenon" stands for a multitude of the quantitative properties A

$$A_1, A_2, A_3, \dots, A_k, \dots \quad (17)$$

Indeed it is the sum total of these unlimited number of properties that constitute a physical phenomenon, e.g. A_1 may be the temperature at the space point m_1 , A_2 the temperature of a point m_2 , A_3 - root mean square value of the vertical component of the fluctuating velocity of turbulence at a point m_3 , A_4 the rate of energy dissipation at yet another location...etc. So, when saying that " X is unimportant"...which

* Referred to as "densimetric Froude Number"

property do we have in mind? A_1 or A_3 ...or which one?... Each of these properties A_n are different functions ϕ_{A_n} (of the same variables) and therefore some of them may vary indeed with X only in a feeble manner, but some others may vary with X strongly... It follows that the statement "X is unimportant" is rather sweeping and shallow. Being a different function of X , Y_* ,...etc. every property A has "its own degree of importance" with regard to the variables X , Y_* ...etc., the "measure" of the degree of importance of X , say, on any A_k can be reflected by the partial derivative of A_k with respect to X viz by

$$\frac{\partial A_k}{\partial X} \quad (18)$$

If $\frac{\partial A_k}{\partial X} \rightarrow 0$ then X can be neglected with respect to that A_k . If however $|\frac{\partial A_k}{\partial X}| \gg 0$ then the influence of X cannot be neglected (for that A_k).

Alternative Approach to Dynamic Similarity*

In the modelling of the present phenomenon all dimensionless variables, other than X and Y_* are identical in model and prototype. Thus any A_k can be regarded as a function of X and Y_* only:

$$\Pi_{A_k} = \phi_{A_k}(X, Y_*) \quad (19)$$

Consider the total differential $\delta \Pi_{A_k}$ implying the difference between the model and prototype values of Π_{A_k} :

$$\delta \Pi_{A_k} = \Pi_{A_k}'' - \Pi_{A_k}' = \Pi_{A_k}' (\lambda_{\Pi_{A_k}} - 1) \quad (20)$$

On the other hand

$$\delta \Pi_{A_k} = \frac{\partial \Pi_{A_k}}{\partial X} \cdot \delta X + \frac{\partial \Pi_{A_k}}{\partial Y_*} \cdot \delta Y_* \quad (21)$$

where

$$\begin{aligned} \delta X &= X'' - X' = X' (\lambda_X - 1) \\ \text{and} \quad \delta Y_* &= Y_*'' - Y_*' = Y_*' (\lambda_{Y_*} - 1) \end{aligned} \quad (22)$$

Hence

$$\Pi_{A_k}'' - \Pi_{A_k}' = \frac{\partial \Pi_{A_k}}{\partial X} X' (\lambda_X - 1) + \frac{\partial \Pi_{A_k}}{\partial Y_*} Y_*' (\lambda_{Y_*} - 1) \quad (23)$$

What is actually required is the identity of the model and prototype values of Π_{A_k} ; i.e. that $\Pi_{A_k}' \equiv \Pi_{A_k}''$ or that

* Outlined in the "invited opening lecture" by M.S. Yalin in the 15th International Congress of the IAHR-BadenBaden, Germany W., Aug. 1977

$$\Pi_{A_k}'' - \Pi_{A_k}' \equiv 0 \tag{24}$$

As seen from (23), the requirement (24) can be achieved if

$$\frac{\partial \Pi_{A_k}}{\partial X} \cdot X' (\lambda_X - 1) + \frac{\partial \Pi_{A_k}}{\partial Y_*} \cdot Y_*' (\lambda_{Y_*} - 1) = 0 \tag{25}$$

is provided.

Clearly if $\lambda_X = 1$ and $\lambda_{Y_*} = 1$ (i.e. if the model and prototype values of X and Y_* were identical) then (25) and thus (24) are satisfied and the dynamic similarity is achieved for any A_k . If, however, accordance with the usual practice $Y_*' = Y_*''$, i.e. $\lambda_{Y_*} = 1$ is provided but the equality of X numbers is ignored (i.e. if $X' \neq X''$ and $\lambda_X \neq 1$) then

$$\delta \Pi_{A_k} = \Pi_{A_k}'' - \Pi_{A_k}' = \frac{\partial \Pi_{A_k}}{\partial X} \cdot X' (\lambda_X - 1) \neq 0 \tag{26}$$

and

$$\Pi_{A_k}'' \neq \Pi_{A_k}' \tag{27}$$

In this case the dynamic similarity is violated, for the model and prototype values of Π_{A_k} are not identical and as seen from (26) the difference between Π_{A_k}'' and Π_{A_k}' (i.e. the error) increases in proportion to

$$\frac{\partial \Pi_{A_k}}{\partial X} \cdot X' \text{ and the deviation of } \lambda_X \text{ from unity.}$$

But why the requirement (24), reflecting the dynamic similarity of the property A_k , should necessarily be achieved by identifying one of the scales of the dimensionless variables (in our case λ_{Y_*}) with unity? If the purpose of the exercise is to fulfill the requirement (24) then this can be achieved by any pair $\lambda_{Y_*} = \alpha$ and $\lambda_X = \beta$ which constitute the solution of the equation (25):

$$\frac{\partial \Pi_{A_k}}{\partial X} X' (\beta - 1) + \frac{\partial \Pi_{A_k}}{\partial Y_*} Y_*' (\alpha - 1) = 0 \tag{28}$$

Clearly, in this case neither α nor β may be equal to unity ($\alpha \neq 1, \beta \neq 1$).

Denoting for brevity

$$\frac{\partial \Pi_{A_k}}{\partial X} = \Pi_X \text{ and } \frac{\partial \Pi_{A_k}}{\partial Y_*} = \Pi_Y \tag{29}$$

we determine from (28)

$$\frac{\beta - 1}{\alpha - 1} = \frac{\pi_y \cdot Y'}{\pi_x \cdot X'} \quad (30)$$

where X' and Y' are always positive ($X' > 0$, $Y' > 0$). It follows then

- (i) if π_y and π_x have different signs (i.e. if π_{A_k} is an increasing function of Y_x but is a decreasing function of X or vice versa) then $(\beta-1)$ and $(\alpha-1)$ have also different signs: i.e. one among α and β is larger than unity whereas another is smaller than unity, i.e.

$$\text{if } \pi_y = -\pi_x \text{ then } \left. \begin{array}{l} \text{either } \alpha > 1 \text{ while } \beta < 1 \\ \text{or } \alpha < 1 \text{ while } \beta > 1 \end{array} \right\} \quad (31)$$

- (ii) The Eq. (30) (which is in fact (28) and which thus implies (24) reflecting the similarity of the property A_k) does not have a unique solution. Indeed for the given values of π_x , π_y , X' and Y' and thus for the given value (C , say) of its right hand side, the Eq. (30) can be satisfied for an infinite number of pairs α and β :

$$\frac{\beta - 1}{\alpha - 1} = C \quad (32)$$

(as it is one equation for two unknowns). e.g. if $C = -2$ and thus (32) is

$$\frac{\beta - 1}{\alpha - 1} = -2$$

then any of the pairs:

$$\left. \begin{array}{l} \alpha_1 = 1/2, \beta_1 = 2 \\ \alpha_2 = 1/4, \beta_2 = 2.5 \\ \alpha_3 = 0.7, \beta_3 = 1.6 \\ \alpha_4 = 1.2, \beta_4 = 0.6 \dots \text{etc.} \end{array} \right\} \quad (33)$$

are the solutions [note, that since $C < 0$ (which means that $\pi_y = -\pi_x$), then when one of the scales (α & β) is larger than unity the other is smaller than unity, as predicted by (31)].

- (iii) Clearly the solution of (32) would be most elegant if α and β would deviate from unity as little as possible. This can be achieved with the aid of the straight-line diagram of α_j versus β_j e.g. the values (33), which correspond to $C = -2$, are forming the straight line shown in Figure 4. From this diagram it is clear that the solutions α_3 , β_3 and α_4 , β_4 should be regarded as more preferable than α_1 , β_1 and α_2 , β_2 .

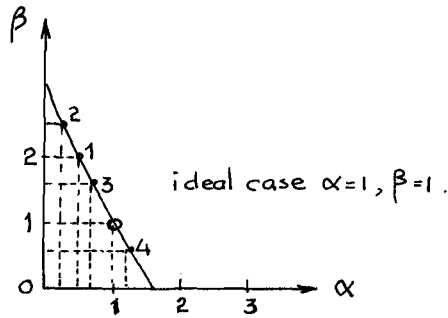


Figure 4. Combinations of Model Scales

- (iv) The selection of scales can be based on the simultaneous consideration of several properties A_1, A_2, \dots, A_N . Consider e.g. only two A_1 and A_2 :

$$\frac{(\Pi_y)_1(Y')_1}{(\Pi_x)_1(X')_1} = C_1 \quad \text{and} \quad \frac{(\Pi_y)_2(Y')_2}{(\Pi_x)_2(X')_2} = C_2 \quad (34)$$

in this case

$$\frac{\beta - 1}{\alpha - 1} = C_1 \quad \frac{\beta - 1}{\alpha - 1} = C_2 \quad (35)$$

and we have two lines (intersecting at $\alpha=1; \beta=1$) which can be shown e.g. as in Figure 5

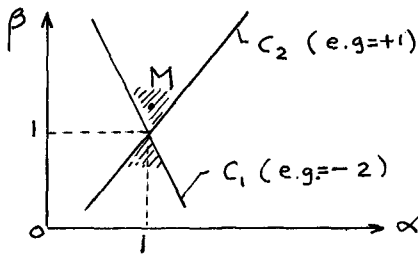


Figure 5. Intersecting Model Scales

As has been mentioned earlier each A_j requires "its own" scales α and β for its dynamically similar modelling. Hence A_1 and A_2 will require some pairs of α and β lying on their respective straight lines (C_1 and C_2 in the figure above). On the other hand if the

lines do not diverge from each other substantially and if the scales are selected in the neighborhood of the point $\alpha=1, \beta=1$ (shaded regions in figure above) then one can consider the α and β values of a point such as M somewhere in between. Admittedly, in this case neither A_1 nor A_2 will be rigorously reproduced. On the other hand the deviation from the rigor may be insignificant while the sacrifice of the rigor may be regarded as compensated by the advantage of studying both properties (A_1 & A_2) in the same model [or with regard to OTEC models "by the advantage of studying both A_1 and A_2 for the same model velocity u " (i.e. during the same run)"]

Clearly the idea above can be generalized to overall properties provided that their respective straight lines (e.g. C_1, C_2, C_3, C_4) do not diverge much from each other and/or the point M corresponding to common solution is reasonably close to the point $\alpha=1; \beta=1$

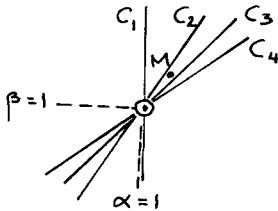


Figure 6. Intersecting Model Scales for Several Properties

- (v) All the considerations above rest on the assumption that the values of

$$X', Y', \frac{\partial \pi_{A_k}}{\partial X}, \frac{\partial \pi_{A_k}}{\partial Y}$$

corresponding to the property A_k are known (or estimated from some preliminary experiments) in the region X', Y' under investigation. If however this is not so then an "experimental model" should be adopted which is outlined in Figure 7.

1. Take prototype values X' and Y_{*}' and find the point M' (on the X, Y_{*} plane)
2. Let λ be the model scale. It is assumed that model is undistorted and that $\lambda_{\rho} = \lambda_{\mu} = 1$.
 - (i) if the model were Froudian: $\lambda_{Y_{*}} = 1 \rightarrow Y_{*}'' = Y_{*}'$ and $X'' \ll X'$ (point $M_{Y_{*}}$)
 - (ii) if it were a Reynolds model $\lambda_X = 1 \rightarrow X'' = X'$ and $Y_{*}'' \gg Y_{*}'$ (point M_X)

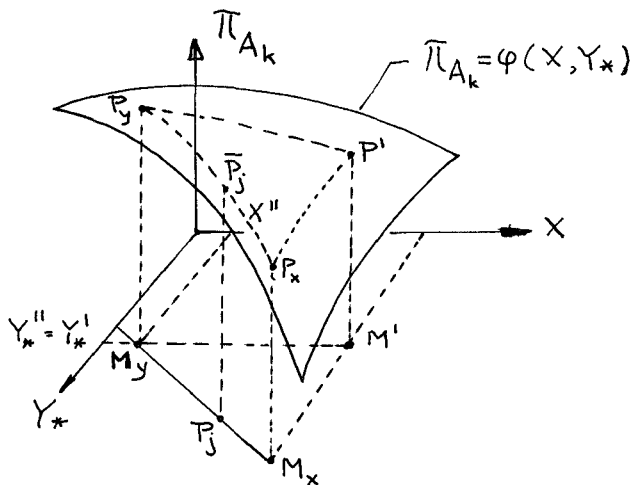


Figure 7. Graphical Presentation of Π_{A_k} as Function of X and Y_*

3. For a Froudian model $\lambda_u = \sqrt{\lambda}$ and thus $u'' = u'(\lambda)^{1/2}$
 For a Reynolds model $\lambda_u = \lambda^{-1}$ and thus $u'' = u'(\lambda)^{-1}$

i.e. the exponent ω of λ is distributed along the straight line interval $M_x M_y$ as in Figure 8

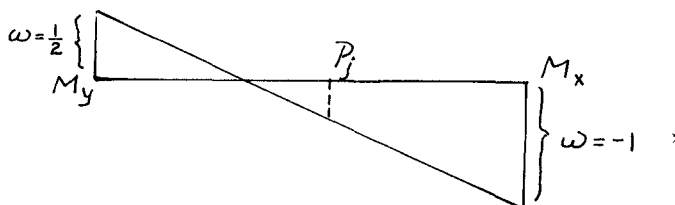


Figure 8. Variation of Exponent ω of λ

4. Now if $\frac{\partial \Pi_{A_k}}{\partial X}$ and $\frac{\partial \Pi_{A_k}}{\partial Y}$ have different signs, e.g. if Π_{A_k} increases with Y_* but decreases with X (which is likely to be the case) then

$$\overline{P_y M_y} > \overline{P' M'} \quad \text{while} \quad \overline{P_x M_x} < \overline{P' M'}$$

where $\overline{P' M'}$ signifies the prototype value $\Pi_{A'}$.

5. Now alter the model velocity u'' in the interval

$$(u' \lambda^{1/2}) < u'' < (u' \lambda^{-1}) \tag{36}$$

(and thus move along the straight line $\overline{M_x M_y}$) until such a point P_j is found where the ordinate $P_j P_j$, implying Π_A'' , becomes approximately equal to $P' M'$ implying (beforehand measured) prototype value Π_A' . Knowing thus "the solution point P_j " determine the corresponding exponent ω from Figure 8. The coordinates of P_j are model values X_j'' and Y_{*j}'' . Form the ratios X_j''/X' and Y_{*j}''/Y' ; these ratios are the scales β and α sought:

$$\alpha = \frac{Y_{*j}''}{Y'} \quad ; \quad \beta = \frac{X_j''}{X'} \quad (37)$$

5. CONCLUSIONS AND RECOMMENDATIONS

- 1) The potential effect of one or more large OTEC plants on the ocean environment requires further investigations.
- 2) In these investigations, field studies, laboratory investigations (physical modelling) and mathematical (numerical) modelling support each other and are all required to provide satisfactory answers.
- 3) In the physical modelling of OTEC plants special consideration has to be given to the similarity criteria to be used to convert model data to prototype values.
- 4) In the past the similarity criteria utilized can hardly be regarded as satisfactory. Since the simultaneous fulfillment of both Reynolds and Froude criteria is impossible (if the model is operated with prototype fluid), contemporary practice often uses one of these criteria as dominant, the other criterion being ignored. This practice may lead to erroneous results in model interpretation.
- 5) The present paper is intended as a step in improving the modelling technique. Rather than supposing that one of the parameters (e.g. the Reynolds number) is irrelevant and that similarity is based on the other parameter (the Froude number) a method is proposed in which the influence of both numbers is compromised.

6. REFERENCES

- 1) Bathen, K.H. (1975). "An evaluation of oceanographic and socio-economic aspects of nearshore ocean thermal energy conversion pilot plant in subtropical Hawaiian waters". Final report for NSF/RANN, ERDA, April 1975.
- 2) Jirka, G.H., Johnson, R.P., Fry, D.J. and Harleman, D.R.F. (1977). "Ocean Thermal Energy Conversion Plants" experimental and analytical study of mixing and recirculation". Ralph M. Parsons Laboratory to Water Resources & Hydrodynamics, Dept. of Civil Engineering, M.I.T., Report No. 231.
- 3) Lee, T.T. (1978). "Assessment of the impact of OTEC power plant on the near-field environment". Proposal to University of Hawaii Sea Grant College, 1978.
- 4) Richards, William E. and Vadus, Joseph R. (1980). "Ocean Thermal Energy Conversion: Technology Development". Journal M.T.S. Feb.-Mar. 1980. Vol. 14-No. 1, pp. 3-14.
- 5) Yalin, M.S. (1971). "Theory of Hydraulic Models". London MacMillan.
- 6) Yamashita, Yoshihiko (1979). "Three-dimensional mathematical model for Ocean Thermal Energy Conversion system operations". PhD dissertation, Univ. of Hawaii, Dept. of Ocean Engineering.

MOORING FORCES INDUCED BY PASSING SHIPS

- MEASUREMENTS IN PROTOTYPE -

by

K. HAFFKE¹⁾

ABSTRACT

In the present study the mooring systems of four bulk carriers which were moored at a jetty located parallel to a navigable water were investigated with special regard to forces due to passing ships. The objective of this study was to verify in praxi the present knowledge of moored vessels berthed at more protected sites and to prove proposed models of forcing functions by passing ships as well as numerical models for the computation of ship mooring systems. For that purpose the mooring forces and also those data which characterized the properties of the mooring systems were recorded. On the basis of the also recorded wind and current data and the data of the passing ships with which the external forces could be estimated the mooring forces were computed. These computed forces are compared with the measured mooring forces.

1. INTRODUCTION

In recent years ship mooring problems arose at existing or projected berths located not only in exposed areas but also at comparatively protected sites. Among the more protected facilities also jetties rank which are located in close proximity and parallel to much frequented navigable waters (Laucht, 1976). For ships moored at these jetties in general not only forces due to wind and current and possibly due to waves have to be taken into account but also forces which are induced by passing ships. These forces can be of considerable significance when the passing distances of the ships are small or the velocities which are generally limited to a certain minimum to ensure sufficient manoeuvrability increase largely.

¹⁾ Research Assistant, Technische Universität Braunschweig, Federal Republic of Germany

The forces on moored ships due to wind and current can be estimated with sufficient accuracy, for instance with the data given by the Oil Companies International Marine Forum (1977) or by Remery and van Oortmerssen (1975), just as the behavior of moored ships in regular and irregular seas as well as in long waves (van Oortmerssen, 1976). Compared with this, the knowledge about those forces which are induced by passing ships is incomplete till now. One of the few theoretical works to this subject which provides more extensive results is that of Wang (1975), who replaces both vessels by idealised bodies with semicircular cross sections and a parabolic sectional-area distribution. Results of model investigations as well as of theoretical work are given by Remery (1974) and Muga and Fang (1975). Field investigations to this complex however are rare up to now. In 1972 measurements were carried out in Rotterdam at the Kalandkanal Quay by the Gemeendewerken Rotterdam and in 1976 the author performed measurements at the Kiel Canal (Haffke, 1976).

The behavior of moored ships can be described in general by a set of six simultaneous second order differential equations

$$\{M\} \{x\} + \{F_h\} + \{F_b\} + \{F_l\} + \{F_f\} + \{F_r\} = \{F_w\} + \{F_a\} + \{F_c\} + \{F_p\} \dots (1)$$

in which the mass forces $\{F_m\} = \{M\}\{x\}$, the hydrodynamic forces $\{F_h\}$, the hydrostatic forces $\{F_b\}$, the restoring forces due to the mooring and the fender system $\{F_l\}$ and $\{F_f\}$ and the fender friction forces $\{F_r\}$ face the external forces due to waves, wind, current and passing ships $\{F_w\}$, $\{F_a\}$, $\{F_c\}$ and $\{F_p\}$.

A comprehensive mathematical model of the non-linear oscillating system in which the hydrodynamic forces are frequency dependent functions of the accelerations and velocities in the six modes of motion was given by van Oortmerssen (1976) who investigated a moored ship in a quay-side position for various quai-distances and underkeel clearances due to wave excitation. In a similar manner Cuthbert and Seidl (1976) analysed the design layout of an offshore terminal mooring system. The time domain solution they used was, for the study of ship motions, originally formulated by Cummins (1962) and is based on the well known impulse response function technique.

Although a derivation of this technique is beyond the scope of this paper, some of the expressions may be given. Here for example the hydrodynamic force $F_{h,kj}$, the force in the k -th mode due to motion in the j -th mode

$$F_{h,kj} = m_{kj} \ddot{x}_j + \int_{-\infty}^t K_{kj} (t - \tau) \dot{x}_j(\tau) d\tau \quad \dots \dots \dots (2)$$

where: $K_{kj}(t) = \frac{2}{\pi} \int_0^{\infty} b_{kj}(\omega) \cos \omega t d\omega \quad \dots \dots \dots (3)$

with m_{kj} = a high frequency asymptotic value of the added mass

and b_{kj} = the frequency dependent damping coefficient

Substituting the hydrostatic forces as linear forces, equation (1) can be written

$$\sum_{j=1}^6 (M_{kj} + m_{kj}) \ddot{x}_j + c_{kj} \dot{x}_j + \int_{-\infty}^t K_{kj} (t - \tau) \dot{x}_j(\tau) d\tau + F_{1,k} + F_{f,k} + F_{r,k} = F_{w,k} + F_{a,k} + F_{c,k} + F_{p,k} \quad \dots \dots \dots (4)$$

$$k = 1, 2, \dots, 6$$

where the wave forces may also include drift forces. These equations can then be solved by a time stepping procedure. In those cases where the forces due to wind and current, which in a practical engineering approach can be considered as quasi-static forces, dominate or at locations where ship oscillations are not allowed a pure static analysis of the problem is sufficient.

The forces due to a passing ship are in general functions of the geometric properties of both ships and the waterway, the velocity and the distance of the passing ship and the properties of the fluid and may be

described as follows

$$\frac{1}{\rho (v - u)^2} \left\{ \frac{F_{p,1}}{B_1 T_1}, \frac{F_{p,2}}{L_1 T_1}, \frac{F_{p,3}}{L_1 B_1}, \frac{F_{p,4}}{L_1 T_1^2}, \frac{F_{p,5}}{L_1^2 B_1}, \frac{F_{p,6}}{L_1^2 T_1} \right\}$$

$$= \phi \left[\frac{B_1 T_1}{L_1^2}, \frac{B_1}{L_1}, r_1, \frac{L_2}{L_1}, \frac{B_2 T_2}{L_2^2}, \frac{B_2}{L_2}, r_2, \right.$$

$$\left. \frac{v}{v - u}, Fn, Rn, \frac{a}{B_1}, \frac{b}{L_1}, \frac{d}{L_1}, \frac{2c}{L_1 + L_2} \right] \dots \dots \dots (5)$$

where $F_{p,1}, F_{p,2} \dots F_{p,6}$ denote the forces and moments in the six modes of motion: surge, sway, heave, roll, pitch, yaw and L_1, B_1, T_1 and L_2, B_2, T_2 denote the length, the beam and the draught of the moored and the passing ship respectively. Further in this simplifying scheme the form parameter of both hulls are summarized by r_1 and r_2 , v denotes the velocity of the passing ship, u a characteristic current velocity in the navigable water, b the passing distance, c the distance of the transverse centerlines, a the distance from a vertical quay and d the water depth.

In nearly all practical cases the Froude numbers based on length of the passing ship are so small that the effect of the Kelvin-type wave pattern can be neglected and hence the influence of the Froude number too. A larger influence however is due to viscous effects especially cross-flow separation forces. Nevertheless approaches based on potential theory give good results when the geometric properties can be well approximated. Forces and moments i. e. their Euler numbers are therefore essentially functions of the geometric boundary conditions given by the ships and the navigable water. For engineering purposes simpler geometric models are possible.

For practical approaches the forces in surge, sway and yaw are the important ones. Due to the mostly large hydrostatic restoring forces and the small restoring forces of the mooring and the fender system in heave, roll and pitch the forces in these modes which are in a similar manner nearly even or odd functions of the normalized distance of the transverse centerlines of the ships can usually be ignored.

In the present study the mooring systems of four ships were investigated with special regard to forces induced by passing ships. The objective of this study was to verify and complete in praxi the present knowledge of moored vessels berthed at more protected sites and their mooring systems and to prove models of forcing functions by passing ships as well as numerical models for the computation of ship mooring systems.

2. FIELD INVESTIGATIONS

The investigations were performed at the "Asbestos Anleger" Nordenham, a jetty located in close proximity and parallel to the navigable water of the Weser near Bremerhaven (Figure 1). The structure has vertical quay walls and is equipped with mooring dolphins on both sides; the depth of the navigable water is SKN - 9,50 m. At this location forces due to passing ships, wind forces and distinct current forces have to be considered; due to the comparatively protected site wave forces have no influence.

Subject of the investigations were the mooring systems of four bulk carriers of conventional form and design which needed at this berth on an average six days to discharge their cargo (asbestos). The three ships of the first, the third and the fourth measuring period, the "Ouivendrecht", the "Deltadrecht" and the "Oordrecht" are sister ships with a loading capacity of 42 550 tdw (L = 187,00 m, B = 29,00 m, T = 11,90 m) the ship of the second measuring period, the "Scherpendrecht", has a loading capacity of 65 350 tdw (L = 224,00 m, B = 32,30 m, T = 13,60 m).

The ships were moored in the usual way with up to twenty mooring lines wire ropes with polyamid tails as well as fibre ropes, and in some cases the tension winch equipment was used. Figure 2 shows the bow mooring of the "Oordrecht" and Figure 3 the mooring at the stern.

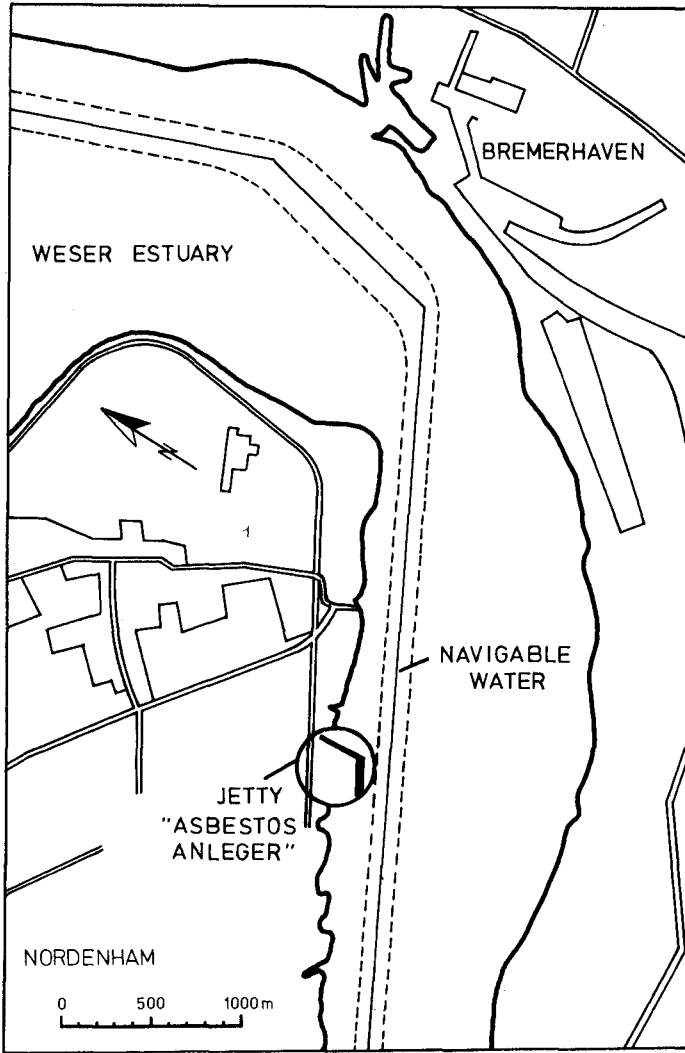


Fig. 1: Location of the "Asbestos Anleger"



Fig. 2: Bow mooring of the "Dordrecht" .



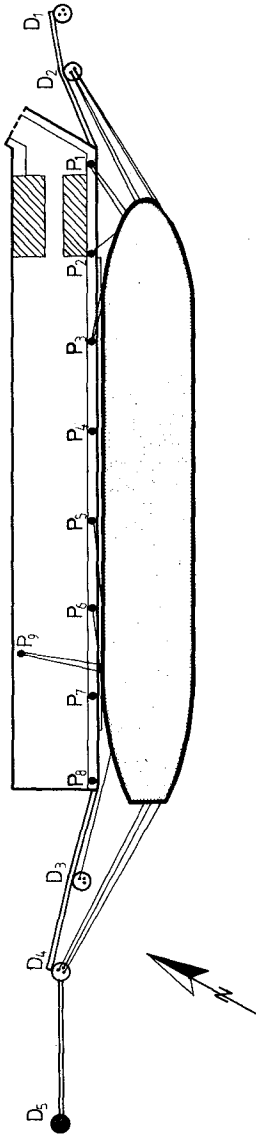
Fig. 3: "Dordrecht"-mooring at the stern

The mooring forces were measured by means of a special measuring equipment, strain gauge force transducers with a capacity of 750 kN which were connected to the mooring lines during the whole berthing time of each ship. In cases in which the number of mooring lines exceeded the number of transducers being available those lines were not connected which ran over mooring winches or which as reserve lines remained without effect. Consequently also in these cases, apart from some failures, the complete response of the mooring systems could be recorded since the forces adjusted at the tension winches were known. An example of a mooring line layout is given with Figure 4 with again the "Dordrecht". The mooring forces were recorded during the passage of ships just as in fixed intervals without a passing ship; in addition permanent measurements were performed in the first and in the second measuring period. For measurements only those passing ships were chosen by which larger forces could be expected. Velocity and distance of these ships whose main dimensions were known were recorded separately. Furthermore the geometric properties of the mooring systems, the draught of the moored ships and the waterlevel fluctuations were recorded as well as wind and current velocities at selected points. An example of a mooring force record is given in Figures 5 and 6.

In the first and second measuring period 56 passing ships were recorded, the number of ships recorded in the third and fourth measuring period was 51. The permanent measurements had a total length of 60 hours.

3. COMPUTATIONS

In the first stage of the study the described dynamic model was assigned for the computation of the mooring systems. In view of the relatively inaccurate hydrodynamic data being available for both ships however this model wasn't used since in all cases the oscillations of the ships and with that the mass and damping forces were negligible. Hence a static model was applied which includes also the reaction of tension winches, hydrostatic forces and fender friction forces which were approximated with a dynamical approach.



MOORING OF THE
 „DORDRECHT”
 MEASURING PERIOD 41
 FROM 30.09.1978 / 2030
 TO 03.10.1978 / 2300

MOORING LINE No.	1	2	3	4	5	6	7	8	9	10	11	12	13	14	15	16	17
BOLLARD No.	D2	D2	D2	D2	P1	P2	P3	P3	P6	P5	P9	P9	D3	D4	D4	D4	D4
HAWSE No.	201	201	101	101	104	105	107	108	110	112	113	116	118	119	121	122	221
FIXING AT THE SHIP T = TENSION WINCH B = SHIP BOLLARD	B	B	B	B	B	B	B	B	B	B	B	B	B	B	B	B	B
MATERIAL PP = POLYPROPYLENE S = STEEL WIRE CIRCUMFERENCE [INS.] DIAMETER [mm]	PP	PP	PP	PP	PP	S	S	PP	PP	S	S	S	S	PP	PP	PP	PP
FORCE TRANSDUCER No.	7	7	7	7	7	26	26	26	7	26	26	26	26	7	7	7	7
	5	2	6	4	3	10	8	9	7	—	T	1	S	K	G	R	B

Fig. 4: Mooring line layout in measuring period 41

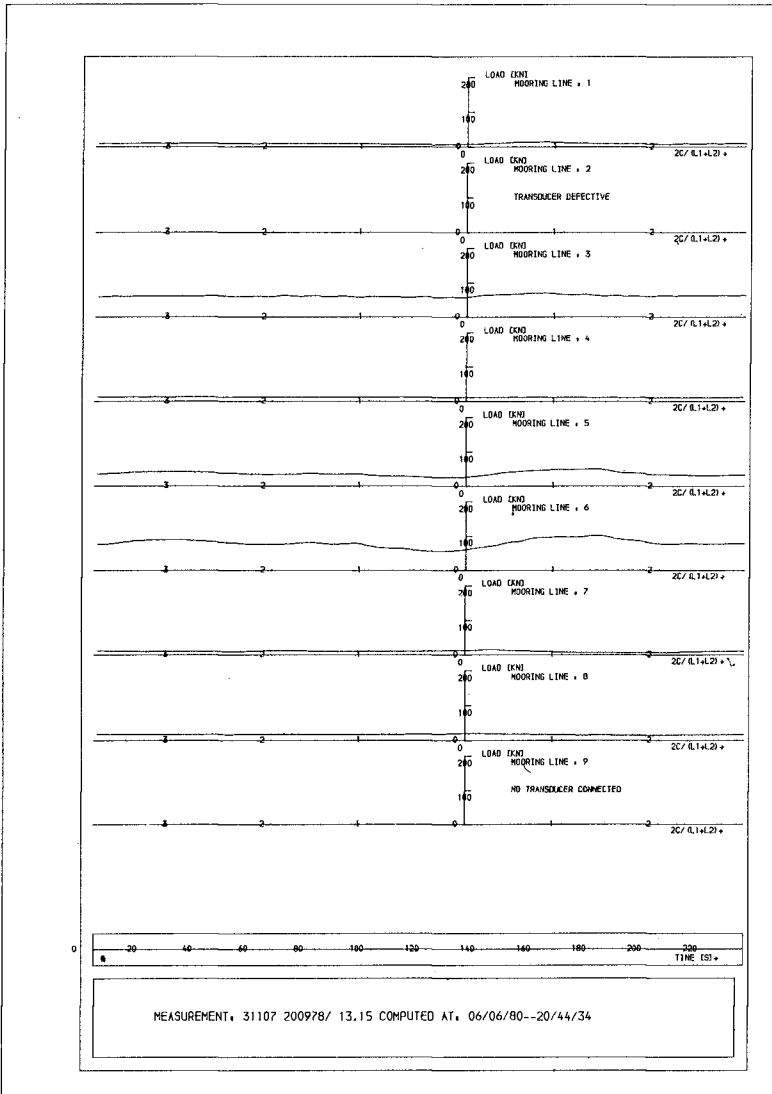


Fig. 5: Mooring forces - measurement No. 31107

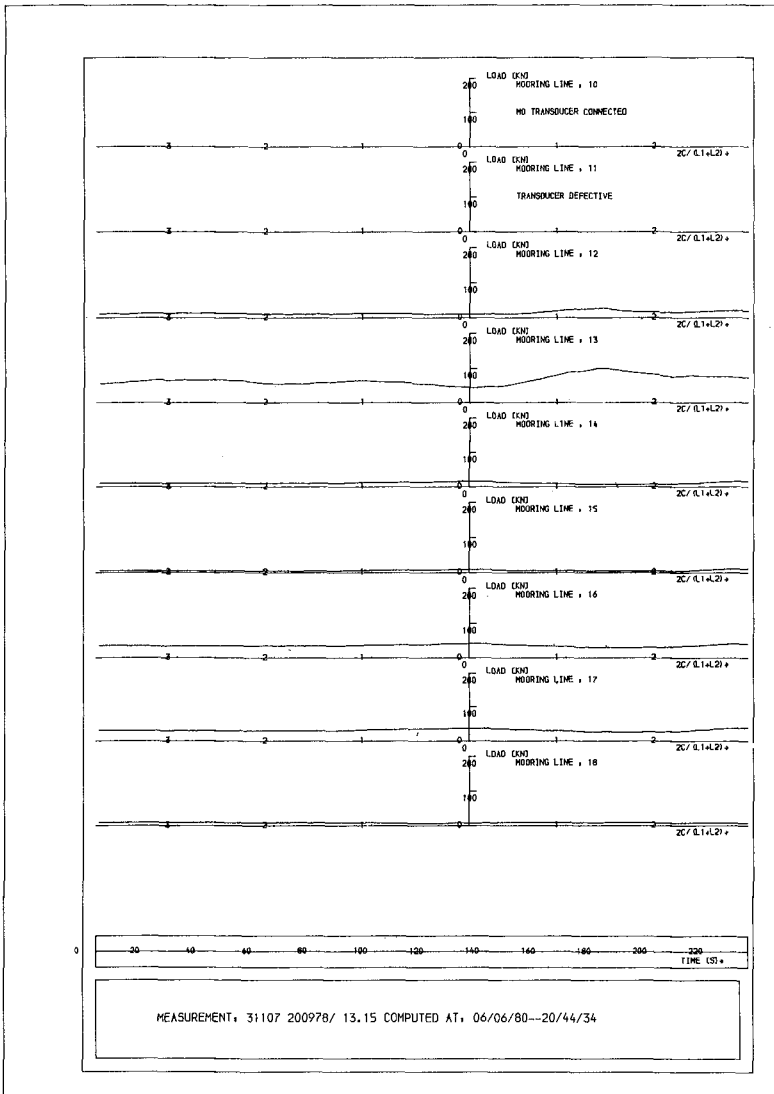


Fig. 6: Mooring forces - measurement No. 31107

For the determination of the forces due to passing ships only the data collection of Wang (1975) was used since these data provided the best approach with regard to the water depth - draught relation. In nearly all cases however it was also necessary here to extrapolate the data, since the given range of passing distances and water depths wasn't sufficient. The computations were performed for the overlapping position in which the force in sway reaches its maximum and the forces in surge and yaw become negligible. The wind and current forces were estimated with the data given by Remery and van Oortmerssen (1973).

The load-deflection curve of the installed tire fendering, a so called "Schweden Typ", which as well as the load-elongation characteristic of the mooring lines served as an input for the computations is shown in Figure 7. An other input of the computations was the initial static state of the mooring systems. This initial static state was estimated for each measuring period by some measurements at slack water and low wind velocities. Figure 8 and 12 give examples of such measurements.

4. RESULTS

As a result of the initial conditions, the fluctuating waterlevel and the varying draught and trim of the ships the pretension of the mooring systems differed widely between the measuring periods (see Figures 8 and 12) and within these periods between the various measurements too. In most cases the pretensions were moderate but in some however (periods 20, 21 and 22) they also reached considerable large values, corresponding to the magnitude of pretension fender friction forces gained importance.

During these measurements the spectrum of the passing ships was essentially determined by ships smaller than the moored ones; in most cases the velocities of the ships were in the upper part of the range characterising navigation in restricted waters. Due to the mostly large passing distances, which were not expected in this magnitude, however in most cases the response of the mooring systems was comparatively small.

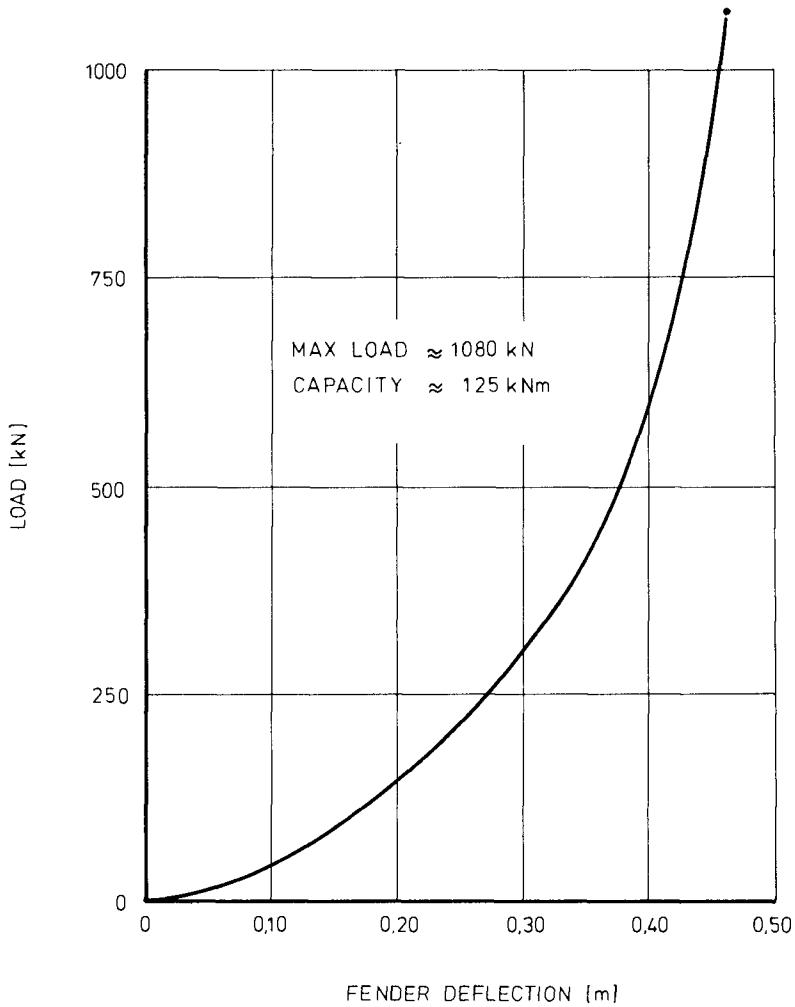


Fig. 7: load-deflection characteristic of the installed tire fendering

In figures 9, 10, 11 and 13 the results of some measurements are compared with computed data. These figures show, representative of all investigations: 1. that the mooring forces due to wind and current action computed with the fore mentioned data agree pretty well with the measured forces and 2. that the computed response due to passing ships determined with the data given by Wang differ widely from the measured forces at which in most cases the computed forces exceed the measured ones. The good agreement between measured and computed forces in those cases in which only wind and current forces appeared is certainly the result of the only small external loads but also shows that the applied static model is quite useful in this special case. The large difference between the measured and computed response in measurements with passing ships however seems in the main to be the result of an inaccurate estimation of those forces which were induced by passing ships. Consequently these investigations with their restrictions by the given range of passing vessels, velocities and passing distances can not verify the used data given by Wang.

Moreover these investigations showed the difficulties involved in handling, measuring and computation of soft mooring systems which like here in most cases are used at more protected sites such as jetties located at navigable waters and harbors.

5. REFERENCES

- | | | |
|--------------------------------|------|--|
| COLLATZ, G. | 1963 | Potentialtheoretische Untersuchung der hydrodynamischen Wechselwirkung zweier Schiffskörper,
Jahrbuch der Schiffbautechnischen Gesellschaft, 57. Band, 1963 |
| CUTHBERT, D.R.
SEIDL, L. H. | 1977 | Mathematical analysis of ship mooring systems and comparisons with hydraulic scale model investigations,
P. O. A. C., St. John's Newfoundland, 1977 |

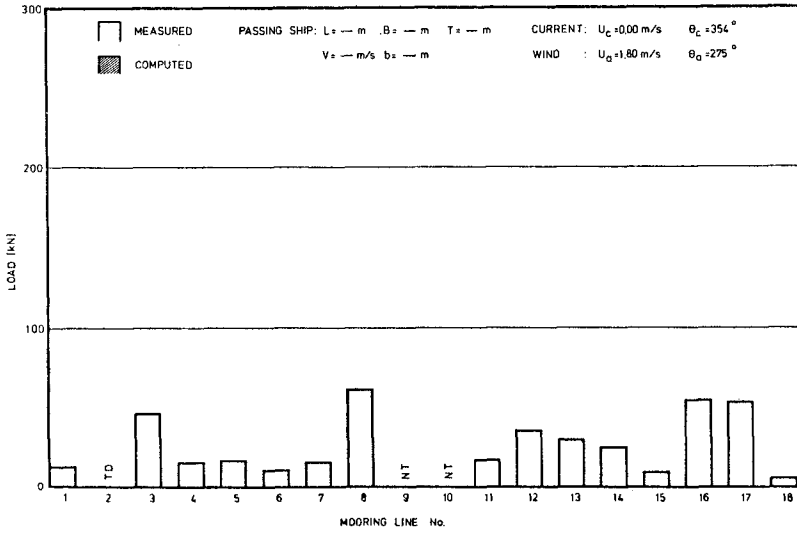


Fig. 8: Initial static state of the system - measurement No. 31116

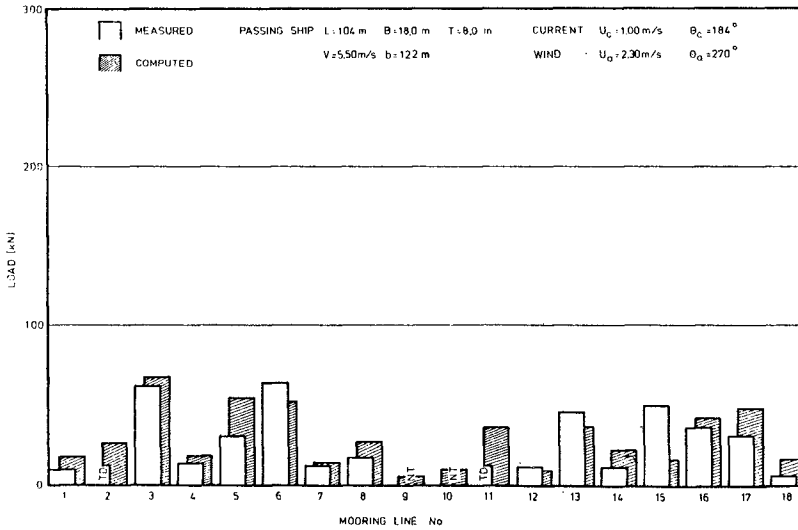


Fig. 9: Measured and computed forces - measurement No. 31106

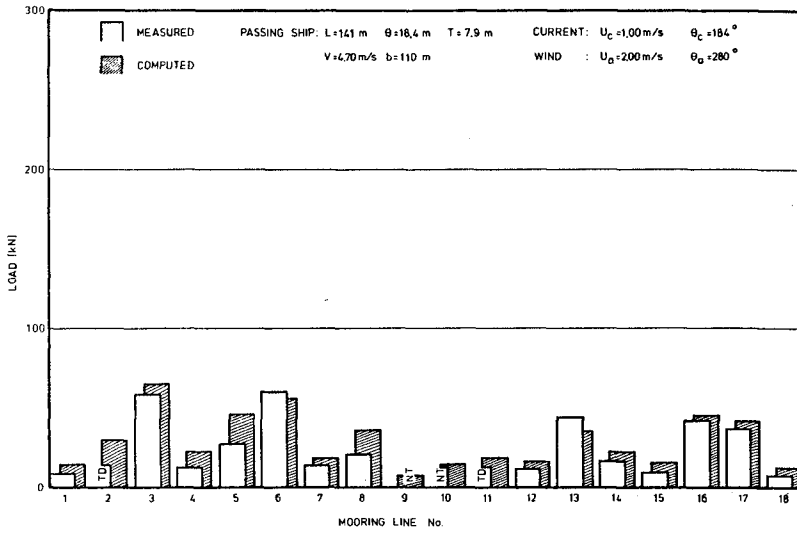


Fig. 10: Measured and computed forces - measurement No. 31107

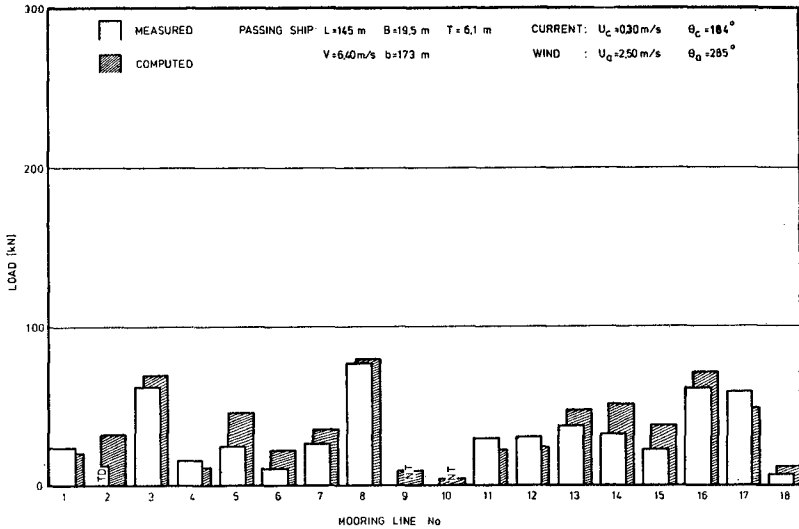


Fig. 11: Measured and computed forces - measurement No. 31115

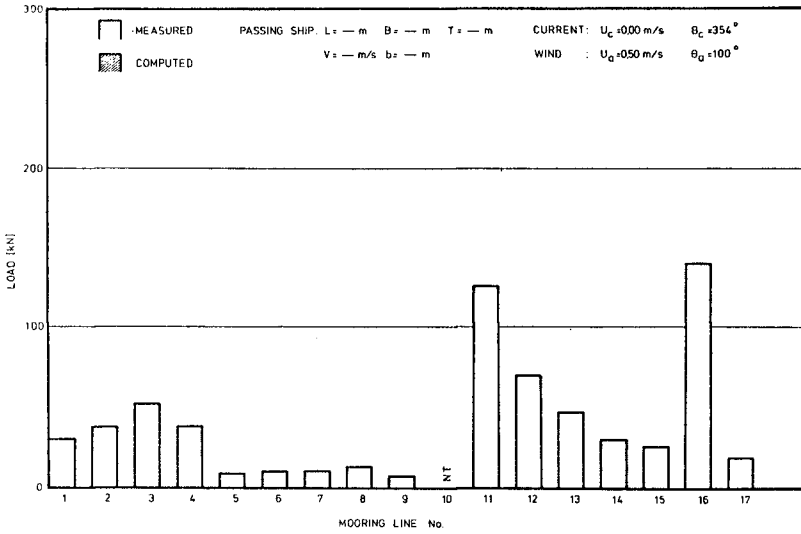


Fig. 12: Initial static state of the system - measurement No. 41206

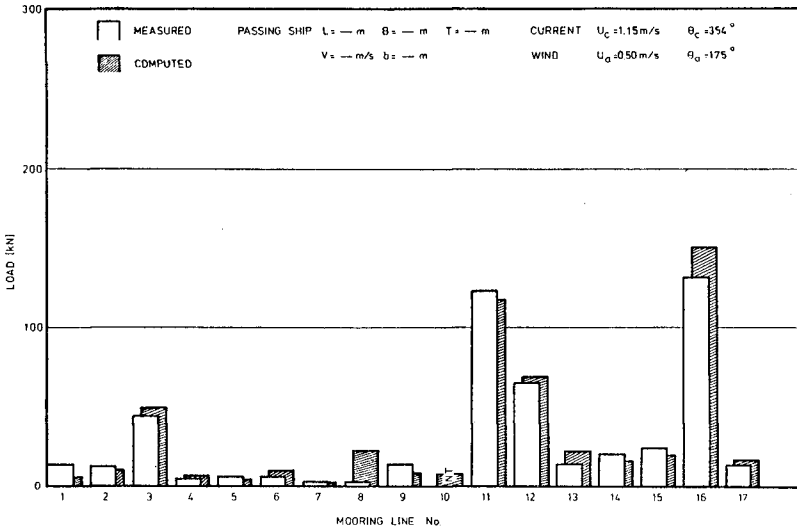


Fig. 13: Measured and computed forces - measurement No. 41209

- | | | |
|--|------|--|
| CUMMINS, W. E. | 1962 | The impulse response function and ship motions
Die Schiffstechnik, Band 9, Nr. 47 |
| GEMEENTEWERKEN
ROTTERDAM | 1972 | Troskrachtenmeting in prototype
Jan./Sept. 1972 (Report unpublished) |
| HAFFKE, K. | 1976 | Trossenkräfte infolge passierender Schiffe
- Messungen in der Natur -
Mitteilungen des Leichtweiß-Instituts der
TU Braunschweig, H. 50, 1976 |
| LAUCHT, H. | 1976 | Planungsprobleme im Seehafenbau
HANSA, 113. Jahrgang, Nr. 3, 1976 |
| MUGA, B. J.
FANG, S. | 1975 | Passing ship effects - from theory and
experiment,
Proc. Offshore Technology Conference,
paper No. OTC 2368, 1975 |
| OIL COMPANIES
INTERNATIONAL MARINE
FORUM | 1977 | Prediction of wind and current loads on
VLCC's,
London, Witherby and Co. Ltd., 1977 |
| OORTMERSSEN, G. van | 1976 | The motions of a moored ship in waves
N.S.M.B. publication No. 510, 1976 |
| REMMERY, G. F. M.,
OORTMERSSEN, G. van | 1973 | The mean wave wind and current forces on
offshore structures and their role in the
design of mooring systems,
Proc. Offshore Technology Conference,
paper No. OTC 1741, 1973 |
| REMMERY, G. F. M. | 1974 | Mooring forces induced by passing ships
Proc. Offshore Technology Conference,
paper No. OTC 2066, 1974 |

- WANG, S. 1975 Dynamic effects of ship passage on moored vessels,
Journal of the Waterways Harbors and Coastal Engineering Division, Aug. 1975, WW3
- WILSON, B. W. 1967 Elastic Characteristics of moorings,
Journal of the Waterways and Harbours Division, Nov. 1967, WW 4

ACKNOWLEDGEMENTS

The present investigation was supported by the German Science Foundation. The author wishes to thank the Wasser- und Schifffahrtsamt Bremerhaven and the Asbestos Corporation GmbH, Nordenham for their generous aid during the field measurements.

Numerical Modelling of Nearshore Circulation

by

Bruce A. Ebersole¹ and Robert A. Dalrymple², M.ASCEINTRODUCTION

Waves impinging on beaches induce mean flows, such as longshore and rip currents. This nearshore circulation is of fundamental importance in the study of the transport of nearshore contaminants as well as littoral materials. Analytic models of this nearshore flow (see, e.g. 4, 9, 11, 12) have been constrained to be linear (in the governing equations) and simplistic in the bottom topography. Only recently have numerical models been developed to examine more complex situations. Steady state, finite difference models (1, 14), as well as a finite element model (10), have been proposed. The numerical model, developed by Birkemeier and Dalrymple (1), allowed for time dependency. Yet, in all of these cases, the governing equations have not included the nonlinear convective accelerations or lateral mixing terms.

In this study, a nonlinear numerical model is presented based on a leapfrog finite difference scheme, which includes time dependency and eddy viscosity terms. Results are shown for a planar beach showing a comparison with the analytical longshore current models (with and without lateral mixing) of Longuet-Higgins (11, 12). The longshore current over a prismatic beach profile including an offshore bar is presented next, showing the effects of the bar on the velocity profile. The circulation set-up by a rip channel inset into a plane beach is then computed. A comparison is made to the linear model of Birkemeier and Dalrymple. Finally the model is applied to the case of synchronous intersecting wave trains (4). An interesting result occurs when the waves are of different amplitudes, which could provide an explanation of the formation of finger bars on a beach.

GOVERNING EQUATIONS

The numerical model is formulated using the usual time-averaged (over one wave period) and depth-averaged conservation equations of mass and momentum, written in terms of the mean horizontal velocities (U , V) and the mean free surface displacement η . These are

$$\frac{\partial \bar{\eta}}{\partial t} + \frac{\partial}{\partial x}(UD) + \frac{\partial}{\partial y}(VD) = 0 \quad (1)$$

$$\frac{\partial}{\partial t}(UD) + \frac{\partial}{\partial x}(U^2D) + \frac{\partial}{\partial y}(UVD) = -gD \frac{\partial \bar{\eta}}{\partial x} - \frac{1}{\rho} \left[\tau_{bx} + \frac{\partial S_{xx}}{\partial x} + \frac{\partial S_{xy}}{\partial y} + D \frac{\partial \tau_l}{\partial y} \right] \quad (2)$$

¹U. S. Army Waterways Experiment Station, Vicksburg, MS.

²Associate Professor, Department of Civil Engineering, University of Delaware, Newark, DE.

$$\frac{\partial}{\partial t}(\text{VD}) + \frac{\partial}{\partial x}(\text{UVD}) + \frac{\partial}{\partial y}(\text{V}^2\text{D}) = -gD \frac{\partial \bar{\eta}}{\partial y} - \frac{1}{\rho} \left[\tau_{b_x} + \frac{\partial s_{xy}}{\partial x} + \frac{\partial s_{yy}}{\partial y} + D \frac{\partial \tau_{\ell}}{\partial x} \right] \quad (3)$$

where $D = h + \bar{\eta}$, the total depth, h is the local still water depth, τ_{b_x} and τ_{b_y} are the bottom frictions in the x and y directions, τ_{ℓ} is the lateral shear stress due to turbulent velocity fluctuations, and ρ is the water density. The radiation stress terms, introduced by Longuet-Higgins and Stewart (see 13, 15), are specified throughout the region of interest in terms of the local wave energy and direction, θ . This information is supplied independently using a coupled wave refraction procedure modified from Noda et al. (14), which includes wave-current interaction, and wave breaking (based on a breaking index model for wave heights within the surf zone).

The bottom shear stress in each direction is found by numerically integrating over a wave period the nonlinear stresses

$$\left. \begin{aligned} \tau_{b_x} &= \frac{1}{T} \int_0^T \frac{\rho f}{8} \left| \bar{U} + \bar{U}_w \right| (U + U_m \cos \theta \cos \sigma t) dt \\ \tau_{b_y} &= \frac{1}{T} \int_0^T \frac{\rho f}{8} \left| \bar{U} + \bar{U}_w \right| (V + U_m \sin \theta \cos \sigma t) dt \end{aligned} \right\} \quad (4)$$

where the vertical bars denote absolute value (to ensure that the shear stress acts counter to the total velocity vector $\bar{U} = (U, V)$) and $\bar{U}_w = (U_m \cos \theta \bar{i} + U_m \sin \theta \bar{j}) \cos \sigma t$, which is the wave orbital velocity vector at the bottom. Through experimentation, 16 terms in a Simpson's rule integration yielded bottom stress results with sufficient accuracy.

FINITE DIFFERENCE FORMULATION AND SOLUTION TECHNIQUE

In order to use a finite difference technique, the region of interest must first be discretized into a grid system as shown in Figure 1, with x positive offshore and y in the longshore direction. All the variables of interest except the velocities are defined at the center of each grid (the centers being separated by distances of Δx and Δy in the x and y directions). The horizontal velocities, on the other hand, are defined at the grid boundaries and are positive if they enter a grid in the positive coordinate direction.

To numerically solve the governing equations, they were approximated by their finite differenced forms. Following the methods of Lilly (8) and Blumberg (3), certain differencing and averaging operators are defined:

$$\delta_x [F(x, y, t)] = \frac{1}{\Delta x} \left[F\left(x + \frac{\Delta x}{2}, y, t\right) - F\left(x - \frac{\Delta x}{2}, y, t\right) \right] \quad (5)$$

$$\delta_x [F(x, y, t)]^x = \frac{1}{2\Delta x} [F(x + \Delta x, y, t) - F(x - \Delta x, y, t)] \quad (6)$$

¹ U_m given by linear wave theory.

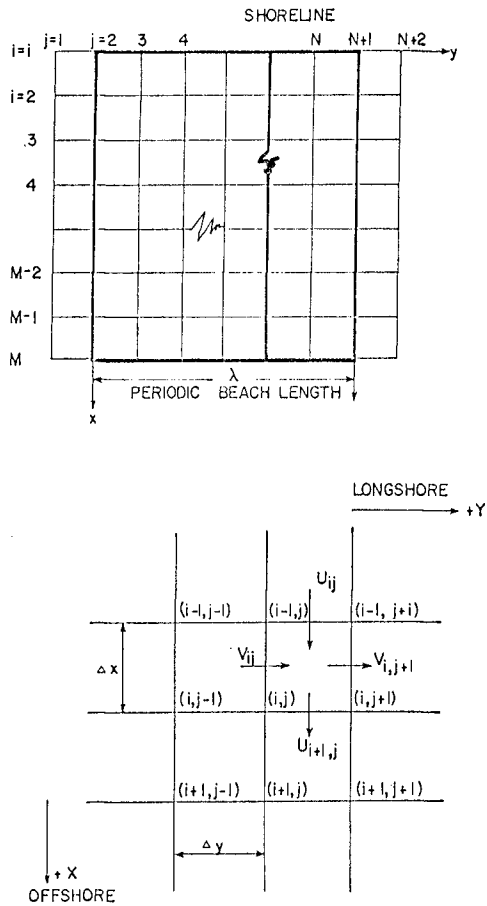


Figure 1. Discretization of Nearshore Region and Detail of Grid.

$$\overline{F(x,y,t)}^x \equiv \frac{1}{2} \left[F\left(x + \frac{\Delta x}{2}, y, t\right) + F\left(x - \frac{\Delta x}{2}, y, t\right) \right] \quad (7)$$

$$\overline{F(x,y,t)}^{xy} \equiv \overline{\overline{F(x,y,t)}^x}^y \quad (8)$$

The first two operators are essentially central finite differences about the point (x,y) over one spacial grid step, or two. Equations (7) and (8) are horizontal spacial averages in the x direction first then in both the x and y directions. Note that $F(x,y,t)$ may be any function that varies in space and time and that similar operators exist for the variables y and t .

Using these operators the governing equations can be written in their differenced forms as,

$$\text{CONTINUITY: } \delta_t(\overline{\eta}^t) + \delta_x(\overline{D^x U}) + \delta_y(\overline{D^y V}) = 0 \quad (9)$$

$$\begin{aligned} \text{x-MOMENTUM: } \delta_t(\overline{D^x U}) + \delta_x(\overline{D^x U} \overline{U^x}) + \delta_y(\overline{D^y V} \overline{U^y}) = \\ - g \overline{D^x} \delta_x(\eta) - \frac{1}{\rho} \left\{ \overline{\tau_{bx}^x} + \delta_y(\overline{S_{xy}^{xy}}) + \delta_x(\overline{S_{xx}^{xx}}) \right\} \\ + \overline{D^x} \delta_y[\varepsilon_y \delta_y(U)] + \overline{D^x} \delta_y[\varepsilon_x^{xy} \delta_x(V)] \end{aligned} \quad (10)$$

$$\begin{aligned} \text{y-MOMENTUM: } \delta_t(\overline{D^y V}) + \delta_x(\overline{D^x U} \overline{V^y}) + \delta_y(\overline{D^y V} \overline{V^y}) = \\ - g \overline{D^y} \delta_y(\eta) - \frac{1}{\rho} \left\{ \overline{\tau_{by}^y} + \delta_y(\overline{S_{yy}^{yy}}) + \delta_x(\overline{S_{xy}^{xy}}) \right\} \\ + \overline{D^y} \delta_x[\varepsilon_y \delta_y(U)] + \overline{D^y} \delta_x[\varepsilon_x^{xy} \delta_x(V)] \end{aligned} \quad (11)$$

In converting these differenced equations into the i, j notation of Figure 1 it is important to note that the x, y coordinate is defined at the location where the variable of interest, to be solved for in a particular equation, is defined. For example, the x -momentum equation is used to solve for the horizontal velocity, U , so the x, y coordinate is defined to be at the grid edge where $U_{i,j}$ is defined. Also in the above equations the bottom friction and lateral mixing terms were lagged one step in time to increase the computational stability, (3) and (6).

Before the problem can be solved numerically, initial and boundary conditions must be specified. In all applications of the model the initial conditions were assumed to be the state of rest. The mean

velocity and mean free surface displacement fields were set to zero, a still water depth matrix was specified, and the wave characteristics were determined using the procedures of Noda *et al.* The boundary conditions are as follows: at the first dry grid row and at the offshore grid row, M, no flow conditions were imposed by setting the velocity components equal to zero. This choice of boundary condition essentially simulates a wall at the onshore and offshore extremities of the area of interest. The onshore condition provides that there is no flow into the beach while the offshore condition is valid if, as the model approaches a steady state, the circulation due to longshore and offshore flows is negligible at row M-1. In the y-direction periodic boundary conditions were invoked. Referring again to Figure 1 periodicity requires that, for a quantity Q,

$$\left. \begin{aligned} Q(i,1) &= Q(i,N) \\ Q(i,2) &= Q(i,N+1) \\ Q(i,3) &= Q(i,N+2) \end{aligned} \right\} \quad (12)$$

and so forth. Periodicity in the longshore direction was chosen because circulation patterns in nature are oftentimes periodic. Also if a particular stretch of beach, lacking periodicity, is being investigated, the boundaries in the model may be placed far enough away from this area of interest so that it does not affect the flow in this region, making the choice of periodic boundary conditions valid.

The differenced equations, (9) through (11), were derived using a central difference in time, for the time dependent terms, in which case they can be written as

$$\eta_{i,j}^{n+1} = \eta_{i,j}^{n-1} + 2\Delta t F_1^{n,n-1} \quad (13)$$

$$U_{i,j}^{n+1} = AU_{i,j}^{n-1} + 2\Delta t F_2^{n,n-1} \quad (14)$$

$$V_{i,j}^{n+1} = BV_{i,j}^{n-1} + 2\Delta t F_3^{n,n-1} \quad (15)$$

where A and B are functions of depth alone, F_1 , F_2 and F_3 are functions of all the variables in the problem, and $n+1$, $n-1$, and n denote time levels. These equations represent the leapfrog technique used to solve the problem in which updated values of η , U , and V are calculated using quantities defined at the previous two time levels. Everytime updated values of these three variables are computed, they are used to solve for the wave parameters at the same time level. In order to initiate the leapfrog scheme a forward difference in time using the initial conditions was implemented to establish variables defined at time levels 2 and 1. The leapfrog procedure was used for the duration of the computational steps. However, as the model approached a steady state, the solution diverged into two disjoint solutions, one following the even times steps and the other the odd. In order to correct this time-splitting problem, an Euler backward correction scheme (7) was used

every tenth iteration to "tie" the solutions back together. The following two equations describe the backward corrector,

$$h^* = h^{n-1} + 2\Delta t G \quad (16)$$

$$h^{n+1} = h^n + \Delta t G^* \quad (17)$$

Equation (16) is essentially any one of Equations (9) through (11) where "*" denotes the updated value of the variable of interest whether it be η , U or V . The function G is then computed using the new variable values and the new value at this time $n+1$, is computed. Equation (17) is a backward difference to the time step n from $n+1$. This correction scheme was chosen because it selectively damps the artificial computational mode of the solution, which can occur, while leaving the physical mode relatively unaffected. With the usage of this correction scheme the solution proceeded to reach a steady state with no further instability.

Due to the nonlinearities of the problem, an exact stability criterion for the choice of the time step, Δt , could not be established. Therefore, in applications of the model the time step was chosen to be significantly lower than the two-dimensional Courant stability criterion given by

$$\Delta t \leq \frac{\sqrt{(\Delta x)^2 + (\Delta y)^2}}{\sqrt{gh}_{\max}}$$

RESULTS

Prismatic Beaches--The model was first applied to the case of a single progressive wave train approaching a planar beach (slope of 0.025) at some angle to the beach normal. The following input data was used. The deep water wave characteristics were: (1) a period of 8.0 seconds; (2) an angle of 30.0 degrees; and (3) a height of 2.0 meters built up over 200 ($\Delta t = 0.5$ second) iterations to avoid "shock" loading the system. The region of interest was broken into a 6 x 30 grid mesh with spacings of 10.0 and 15.0 meters in the x and y directions, respectively. The bottom friction factor, f , was chosen to be 0.08 and the mixing coefficients N and ϵ_y were chosen to be 0.01 and 0.5 meters²/sec. The model was run for 1200 iterations which was nearly steady state.

The steady longshore current distributions both with and without mixing included are shown in Figure 2 along with the analytical results of Longuet-Higgins for the same input data. The major differences between the two profiles that exclude mixing are the sharpness of the discontinuity at the breaker line, and the difference in peak velocities. The numerical model shows less of a discontinuity in the breaker zone due to the fact that velocities just outside the surf zone are calculated using those from within the surf zone in the differenced form of the y-momentum equation, which results in a numerical "mixing". Also due to the use of a discrete grid size in the x-direction the exact location

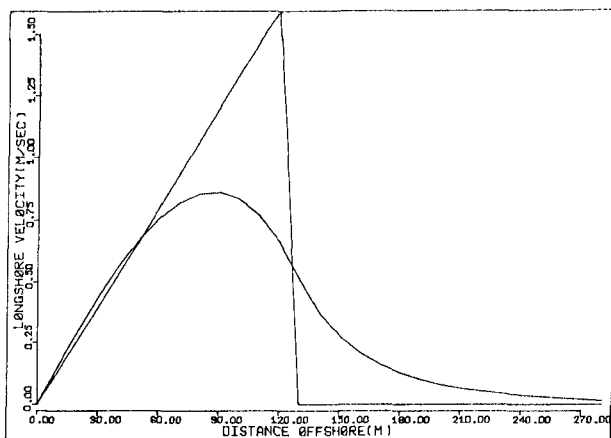


Figure 2a. Analytical Models of Longshore Current, With and Without Mixing [Longuet-Higgins (11, 12)].

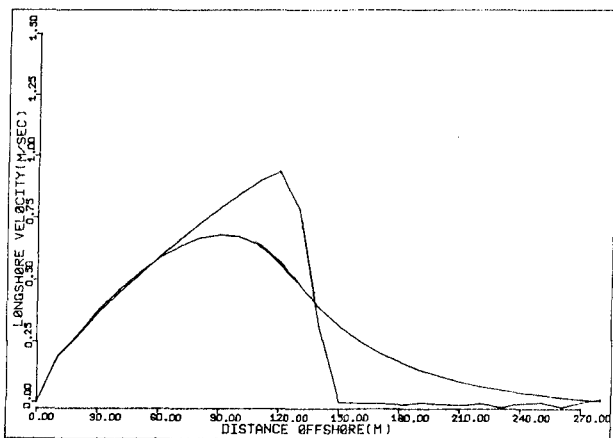


Figure 2b. Numerical Model Results for Longshore Current, With and Without Mixing.

of the breaker line is not adequately determined, resulting in a breaker line smoothing. As the grid size is decreased the location of the breaker line becomes better defined, making the discontinuity sharper as well as increasing the peak velocity. It must be noted that the peak velocities predicted by the model should not equal those resulting from Longuet-Higgins' theory due to the bottom friction formulation used in the model which was shown by Liu and Dalrymple (9) to decrease the analytical result by about 20% for the breaker angle and bottom slope found in this case.

In reality this strong discontinuity doesn't exist, and longshore current distributions tend to exhibit the properties shown by both the model and Longuet-Higgins results including mixing. These properties include: (1) a slight increase in velocities in the inner one-half of the surf zone; (2) a shift of the peak velocity from the breaker line shoreward; and (3) a slow decrease in the current to zero some distance beyond the breaker line.

Since in nature beach topographies often include longshore bars, the model was run on a bottom with an infinitely long longshore bar whose cross section is shown in Figure 3 in relation to a plane beach with slope 0.025. The remaining input into the model was identical to that used in the plane beach runs. The results for the model not including mixing are also shown in Figure 3. Notice the two distinct regions where a longshore current distribution exists. The velocity "spike" offshore is due to the waves breaking on the bar. As the wave height decreases, as a result of breaking, an onshore-offshore gradient of y-momentum flux is created which drives a longshore current. In the trough, however, the wave height starts to reform (no more breaking) resulting in the absence of a longshore current in this region. In reality a longshore current does exist in the trough, Allender et al. (1), due to the mechanisms of turbulent dissipation during breaking within a bore, lateral mixing which has been included in the model, and a set-up of water within the trough, Dalrymple (5). Figure 3b shows the velocity profile for the run including mixing. Note the reduction in current amplitude of the offshore "spike" and the smoothing of discontinuities resulting in the existence of a longshore current in the bar trough. Had the turbulent energy dissipation mechanism been included in the model the results would probably have approached those found in nature.

Periodic Bottom Topography Application--The model was next applied to the periodic bottom topography developed by Noda et al. (14) which is essentially a channel at some angle to the beach normal. The formulation for this bottom configuration is given in Appendix A. The model, including the effects of mixing, was compared to the linear model of Birkemeier and Dalrymple. The following wave characteristics were used in both instances: (1) deep water wave height of 1.0 meters; (2) wave period of 4.0 seconds; and (3) a deep water wave angle of 30.0 degrees to the beach normal. The bottom friction factor, f , was chosen to be 0.08, and the mixing coefficients, N and ϵ_y , were chosen to be 0.005 and 0.5 meters²/sec., respectively. In both runs the wave height was built up to its deep water value over 100 seconds.

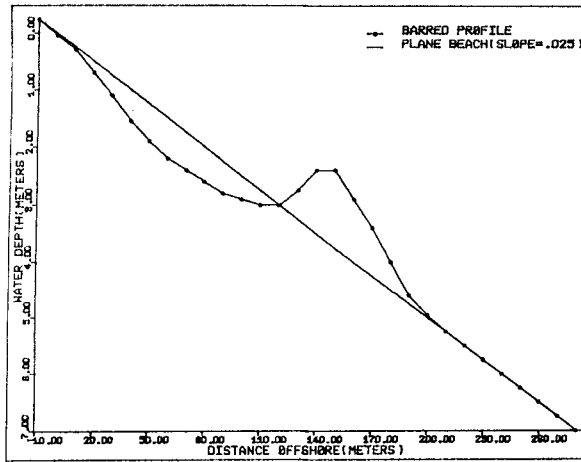


Figure 3a. Beach Profile for Planar and Barred Beach.

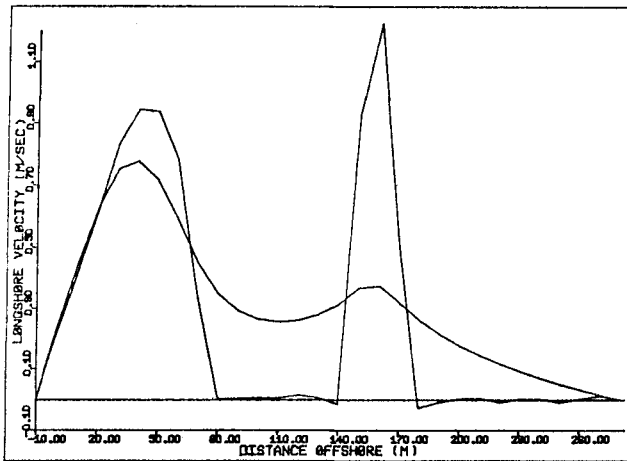


Figure 3b. Longshore Current Profiles on Barred Beaches, With and Without Mixing.

Both models were run until they reached approximately a steady state, about 500 seconds. The wave-current interaction process was halted in the linear model after 150 seconds because the offshore velocity components grew too large for the refraction routines to handle (i.e. wave breaking occurred in the rip channel). In the nonlinear model, however, the wave-current interaction process was included for the duration of the run time. The circulation patterns after 500 seconds are shown in Figure 4 and 5.

Note the strength of the rip and its offshore extent in the linear model compared to the nonlinear model. The peak velocity in the linear model run is about 3.0 meters per second whereas in the nonlinear model it is about 0.8 meters per second. This large discrepancy is due to the inclusion of mixing in the nonlinear model. The mixing tends to spread the rip out and decrease its offshore velocity components thus causing the rip to turn more in the longshore direction as shown in Figure 5. The effects of the convective acceleration terms are not clearly visible because it seems as though the form of the rip itself is governed primarily by horizontal mixing in this case. It is reasonable to expect, however, that in nature the lateral mixing in the rip current is far less than used here.

Synchronous Intersecting Waves--The final application of the model was to the case of intersecting wave trains of a common frequency on a plane beach which Dalrymple (4) showed could generate rip currents. The purpose here was to show the effect of the convective acceleration terms in the model. Certain changes were made to the model, namely: (1) the refraction routines of Noda *et al.* were replaced with those using Snells' law without wave-current interaction; (2) lateral mixing was excluded; (3) the "exact" bottom friction formulation was made to include two waves; (4) the radiation stresses due to both intersecting wave trains were calculated analytically for use in the momentum equations.

The waves were of equal heights (0.25 meters) and of equal deep water angles on either side of the beach normal (30.0 degrees). The period was chosen to be 7.1594 seconds which resulted in periodic rip currents with a spacing of 80.0 meters. The plane beach (slope 0.025) was broken into a platform area of 25 grids in the x-direction with a Δx spacing of 5.0 meters, and 21 grids in the y-direction with a Δy spacing of 4.0 meters. The time step was chosen to be 0.2 seconds and the wave was built up for 500 of the 1500 iterations run. The friction factor, f , was selected as 0.12 to allow the system to reach steady state faster and to decrease the magnitude of the resultant currents.

The total free surface described by these two wave trains is in essence a normally incident wave with a periodically modulated height. This is the driving mechanism which produces the rip currents shown in Figure 6. Note the constricted width of the rip current in relation to the width of the inflow region. This is a result of the convective acceleration terms. Also note the weak rip head where the currents diverge from the rip axis and return towards shore.

When one wave is of greater height than the other, all other variables remain the same, then a longshore current is superimposed over the cellular circulation, Figure 7.

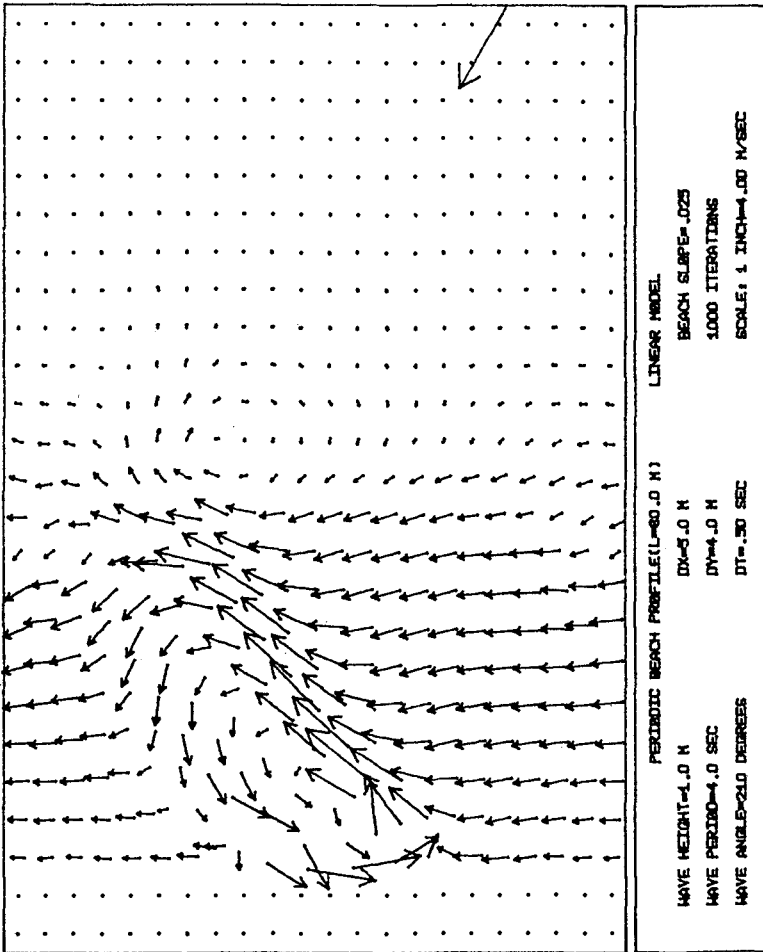


Figure 4. Current Vector Plot for the Model of Birkemeier and Dalrymple Run on the Periodic Bottom Topography.

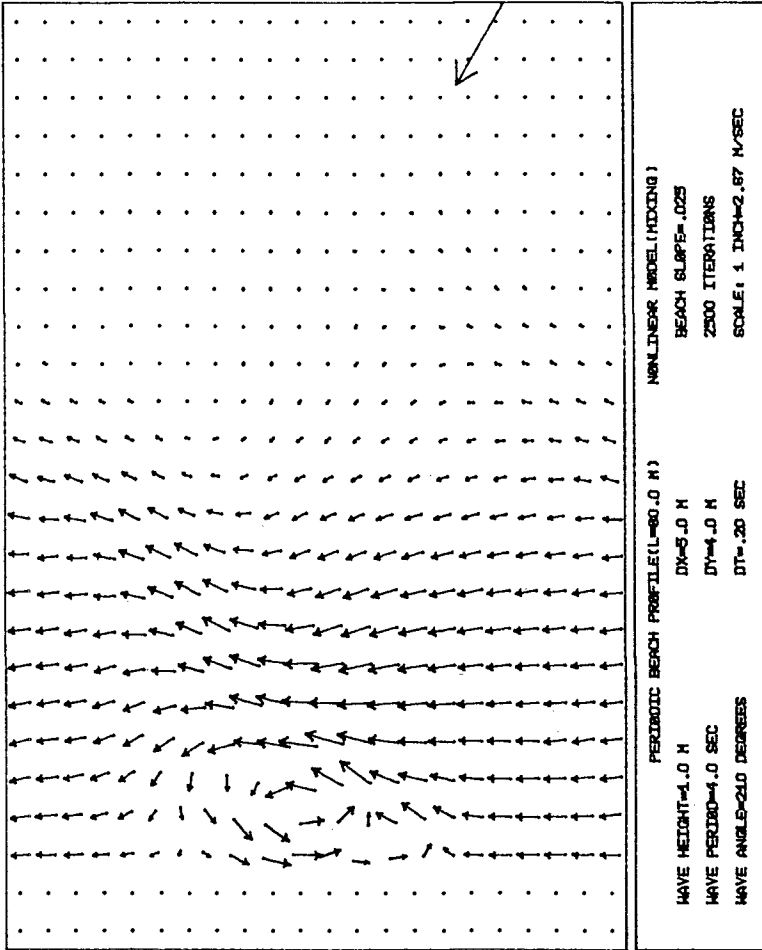


Figure 5. Current Vector Plot for the Present Model Including Mixing Run on the Periodic Bottom Topography. The Arbitrary Longshore Mixing Coefficient Probably Chosen as Too Large.

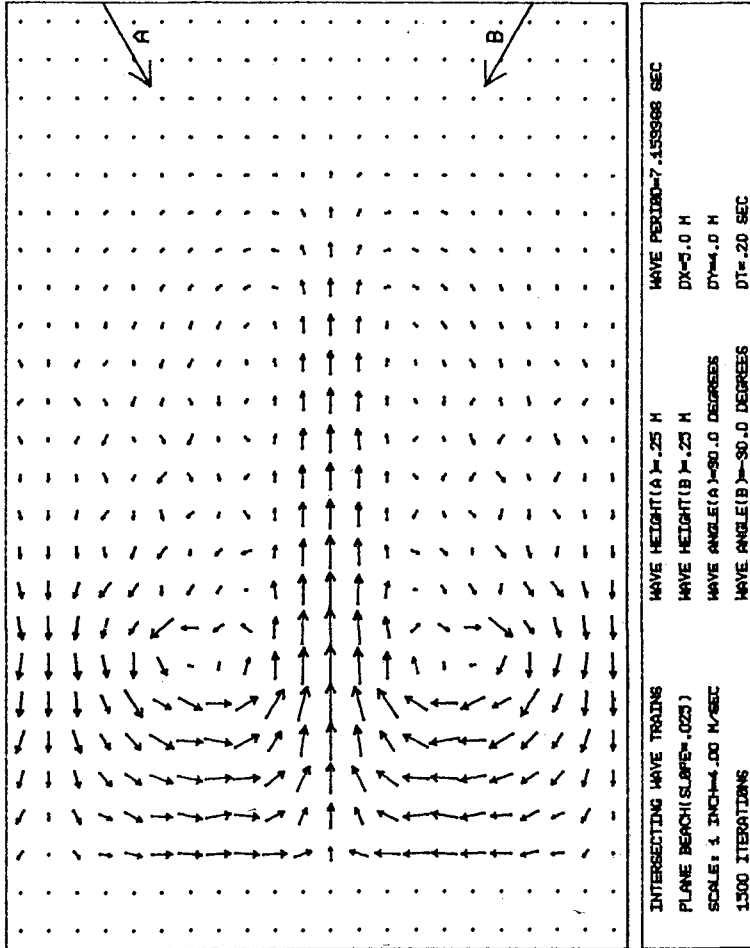


Figure 6. Current Vector Plot for a Rip Current Perpendicular to the Shoreline.

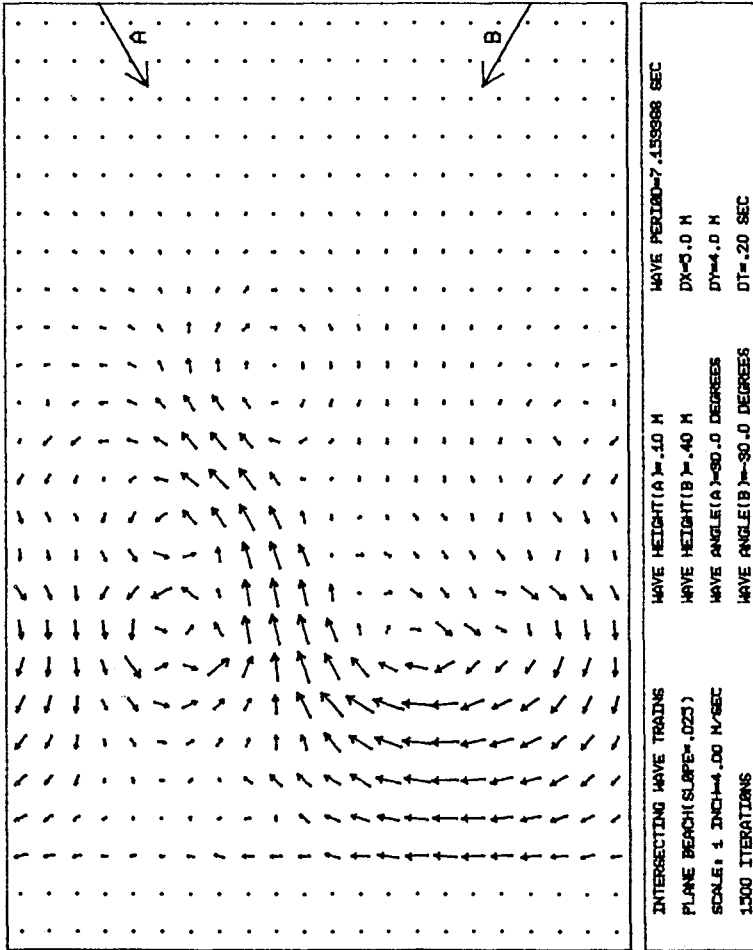


Figure 7, Current Vector Plot for the Meandering Circulation Pattern.

CONCLUSIONS

A model that can accurately predict currents and wave transformations in the nearshore zone is a necessary step in attempting to predict actual changes to our coastlines. From the results shown here it appears that the inclusion of the convective acceleration terms and lateral mixing terms in the horizontal momentum equations have important effects which must be included in models used to predict nearshore circulation. The terms become especially significant in attempts to model circulation over irregular bottom topographies which include bars and channels.

APPENDIX A - PERIODIC BOTTOM TOPOGRAPHY

The periodic bottom profile used in the model was developed by Noda et al. (14). The depths are given by

$$h = mx \left\{ 1 + A \exp \left[-3 \left(\frac{x}{20} \right)^{1/3} \right] \sin^{10} \frac{\pi}{\lambda} (y - x \tan \beta) \right\}$$

where m = beach slope = .025.

x, y are the coordinates of the depth location.

λ = length of periodic beach = 80 meters.

A = amplitude of bottom variation = 20.

β = angle of rip channel to beach normal = 30 degrees.

The grid spacing was chosen to be 5.0 and 4.0 meters in the x and y directions, respectively. There were 25 and 21 grids in the x and y directions. The last grid row and the "dry" grid rows were made planar with the slope being .025.

REFERENCES

1. Allender, J. H., Ditmars, J. D., Harrison, W. and Paddock, R. A., "Comparison of Model and Observed Nearshore Circulation," Proceedings of the 16th International Conference on Coastal Engineering, Hamburg, 1978.
2. Birkemeier, W. A. and Dalrymple, R. A., "Nearshore Water Circulation Induced by Wind and Waves," Proceedings of the Symposium on Modeling Technique, ASCE, 1975, pp. 1062-1081. Also, "Numerical Models for the Prediction of Wave Set-Up and Nearshore Circulation", ONR Tech. Rept. No. 1 and Ocean Eng. Rept. No. 3, Dept. of Civil Eng., Univ. of Del., Jan. 1976.
3. Blumberg, A. F., "Numerical Tidal Model of Chesapeake Bay," Journal of the Hydraulics Division, ASCE, Vol. 103, No. HY1, January, 1977, pp. 1-9.
4. Dalrymple, R. A., "A Mechanism for Rip Current Generation on an Open Coast," Journal of Geophysical Research, Vol. 80, 1975, pp. 3485-3487.
5. Dalrymple, R. A., "Rip Currents and Their Genesis," Proceedings of the 16th International Conference on Coastal Engineering, Hamburg, 1978.

6. Holland, W. R. and Lin, L. B., "On the Generation of Mesoscale Eddies and Their Contribution to the Oceanic General Circulation. I. A Preliminary Numerical Experiment," Journal of Physical Oceanography, Vol. 5, October, 1975, pp. 642-657.
7. Kurihara, Y., "On the Use of Implicit and Iterative Methods for Time Integration of the Wave Equation," Monthly Weather Review, Vol. 93, No. 1, January, 1965, pp. 33-46.
8. Lilly, D. K., "On the Computational Stability of Numerical Solutions of Time-Dependent Non-Linear Geophysical Fluid Problems," Monthly Weather Review, Vol. 93, No. 1, January 1965.
9. Liu, P. L.-F. and Dalrymple, R. A., "Bottom Frictional Stresses and Longshore Currents Due to Waves with Large Angles of Incidence," Sears Foundation: Journal of Marine Research, Vol. 36, No. 2, May, 1978, pp. 357-375.
10. Liu, P. L.-F., and Lennon, G. P., "Finite Element Modeling of Nearshore Currents," Journal of the Waterway, Port, Coastal and Ocean Division, ASCE, Vol. 104, No. WW2, May, 1978, pp. 175-189.
11. Longuet-Higgins, M. S., "Longshore Currents Generated by Obliquely Incident Sea Waves, 1," Journal of Geophysical Research, Vol. 75, No. 33, November, 1970, pp. 6778-6789.
12. Longuet-Higgins, M. S., "Longshore Currents Generated by Obliquely Incident Sea Waves, 2," Journal of Geophysical Research, Vol. 75, No. 33, November, 1970, pp. 6790-6801.
13. Longuet-Higgins, M. S. and Stewart, R. W., "Radiation Stress and Mass Transport in Gravity Waves with Application to Surf Beat," Journal of Fluid Mechanics, Vol. 13, 1962, pp. 481-504.
14. Noda, E. K., Sonu, C. J., Rupert, V. C. and Collins, J. I., "Near-shore Circulations Under Sea Breeze Conditions and Wave-Current Interactions in the Surf Zone," Tetra Tech Report TC-149-4, February, 1974.
15. Phillips, O. M., The Dynamics of the Upper Ocean, Cambridge University Press, 1969, pp. 45-48.

ACKNOWLEDGEMENTS

This study was supported by the Office of Naval Research, Geography Programs, Arlington, VA. Alan F. Blumberg was very helpful in the early stages of this study.

CHAPTER 164

MODELLING OF PLANFORM INFLUENCE ON CIRCULATION IN HARBOURS

by

ROGER A. FALCONER*

ABSTRACT

A two dimensional numerical model has been developed which is capable of predicting the tidal water elevations, depth averaged velocity components and horizontal concentration distributions in narrow entranced harbours and marinas. Particular attention has been paid to the numerical treatment of the convective accelerations where, as a result of narrow harbour entrances and the general nature of planform geometries, the resulting highly non-uniform flow fields can readily lead to non-linear instabilities and unstable numerical solutions.

In order to check the validity of the numerical results, a comprehensive study was carried out to compare, with scaled laboratory model studies, the predicted tidal velocity fields and flushing characteristics for a number of rectangular harbours of constant planform area but different length to breadth ratios. The experimentally measured average per cycle exchange coefficients and the observed mean water level pathlines agreed reasonably well with the corresponding numerically predicted exchange coefficients and depth averaged velocity fields.

The results of both the numerical and laboratory model studies confirmed conclusively that the maximum gross flushing characteristics occurred within a rectangular harbour when the length to breadth ratio was close to unity. Also, further tests showed that the insertion of impermeable barriers as a possible means of increasing the flushing efficiency proved to be unsatisfactory.

INTRODUCTION

In the past, harbours and marinas of various shapes and sizes have often been known to possess poor water quality characteristics, caused chiefly by internal stagnant regions known to dominate within the harbour. Historically though, the quality of water within harbours and marinas has been assumed, in part, to be dependent upon the basin's flushing rates and human activity on or adjacent to the basin. The natural engineering solution to this water quality problem is either to design the harbour initially such that the planform geometry produces a maximum flushing efficiency or, if the harbour has already been constructed, to alter the planform geometry favourably by modifying the boundary shape or inserting shear walls where appropriate.

Although a number of laboratory model studies have been carried

* Lecturer in Civil Engineering, University of Birmingham, Birmingham, England.

out for particular harbours and marinas (e.g. Nece and Richey (1,2)), where the main objective has been to determine the ideal boundary shape tending to produce a maximum overall flushing efficiency in the model, little use of numerical models appears to have been made in this type of analysis. This is possibly due to the generally complex nature of the velocity fields resulting from narrow entrances associated with harbours and marinas. The complexity of the velocity fields occurs in the form of separation streamlines around harbour entrances, and the resulting non-uniform properties of the flow, particularly on the incoming tide. This paper describes such a numerical model which has been specifically developed to predict the depth averaged velocities and concentrations in narrow entranced harbours and marinas.

The time dependent equations of mass, momentum and solute transport have been expressed in a two time level alternating direction implicit finite difference form, with the effects of bottom roughness and turbulent momentum transfer being included. The stability problems generally associated with the non-linear convective accelerative terms, particularly for the type of velocity fields being considered, have been overcome by time centring these terms with respect to the remaining velocity derivatives (3). The apparent favourable numerical properties of this difference scheme have been partially confirmed by applying the Fourier series stability method to a quasi-linearised one-dimensional form of the appropriate equations (4).

The numerical model has been applied to an idealised prototype rectangular harbour with an asymmetric entrance, a constant planform area and varying length to breadth ratios. The geometric dimensions of this harbour, together with the mean depth and tidal wave properties, were assumed to be similar to many existing and proposed basins in Puget Sound of the State of Washington. The resulting depth averaged velocity fields and mean concentration distributions, determined for each length to breadth ratio, were then compared to the corresponding observed path-lines and measured exchange coefficients for two independent hydraulic model studies (5,6). Also numerical and laboratory model tests and comparisons were carried out to determine the influence on the flushing efficiency of the insertion of impermeable barriers at selected locations within the harbour geometries considered.

GOVERNING DIFFERENTIAL EQUATIONS

The appropriate two-dimensional differential equations governing the tide induced fluid and concentration movements within harbours and marinas can be derived by integrating, over the depth, the standard equations of continuity, momentum and mass transport. For an incompressible turbulent fluid on a rotating earth, the depth averaged equations of horizontal motion can be expressed in Cartesian co-ordinate form as:

$$\frac{\partial U}{\partial t} + \frac{\alpha}{(h+\eta)} \left[\frac{\partial U^2(h+\eta)}{\partial x} + \frac{\partial UV(h+\eta)}{\partial y} \right] - fV + g \frac{\partial \eta}{\partial x} + \frac{gU\sqrt{U^2 + V^2}}{(h+\eta)C^2} - \epsilon \left[\frac{\partial^2 U}{\partial x^2} + \frac{\partial^2 U}{\partial y^2} \right] = 0 \quad \dots\dots\dots (1)$$

$$\frac{\partial V}{\partial t} + \frac{\alpha}{(h+\eta)} \left[\frac{\partial VU(h+\eta)}{\partial x} + \frac{\partial V^2(h+\eta)}{\partial y} \right] + fU + g \frac{\partial \eta}{\partial y} + \frac{gV \sqrt{U^2 + V^2}}{(h+\eta)C^2} - \epsilon \left[\frac{\partial^2 V}{\partial x^2} + \frac{\partial^2 V}{\partial y^2} \right] = 0 \quad \dots\dots\dots (2)$$

where U, V = depth average velocities in x, y directions respectively, α = velocity correction factor = 1.016 for seventh power law velocity distribution, h = mean depth, η = water surface elevation above or below mean depth, f = Coriolis parameter, g = gravitational acceleration, C = Chezy roughness coefficient and ϵ = depth mean eddy viscosity = $1.154 g(h+\eta) \sqrt{U^2 + V^2}/C^2$ for seventh power law velocity distribution. Similarly, the equations of continuity and mass transport can be written as, respectively:

$$\frac{\partial \eta}{\partial t} + \frac{\partial U(h+\eta)}{\partial x} + \frac{\partial V(h+\eta)}{\partial y} = 0 \quad \dots\dots\dots (3)$$

$$\frac{\partial S(h+\eta)}{\partial t} + \frac{\partial S(h+\eta)}{\partial x} + \frac{\partial S(h+\eta)}{\partial y} = \frac{\partial}{\partial x} \left[D_x(h+\eta) \frac{\partial S}{\partial x} \right] + \frac{\partial}{\partial y} \left[D_y(h+\eta) \frac{\partial S}{\partial y} \right] \quad \dots\dots\dots (4)$$

in which S = depth mean mass concentration and D_x, D_y = depth mean dispersion coefficients where, from Elder (7), it is assumed that $D_x = (5.93|U| + 0.23|V|) \sqrt{g(h+\eta)}/C$, and similarly for D_y where the U and V velocities are interchanged.

In addition to these differential equations, various boundary conditions had to be included in the numerical model. For the closed boundaries it was assumed that the normal velocity components and the advective and diffusive transport of concentrations were all zero. Likewise, for the open boundary conditions, it was assumed that the incoming tidal wave was sinusoidal in form, whereby:

$$\eta = a \cos(\omega t + \theta) \quad \dots\dots\dots (5)$$

with a = wave amplitude, ω = wave frequency, t = time and θ = phase lag; and that the velocity components at the harbour entrance, were given by the simplified form of the continuity equation:

$$U = A \frac{d\eta}{dt} / W(h+\eta) \quad \dots\dots\dots (6)$$

where A = harbour planform area and W = harbour entrance width. For the concentration values at the harbour entrance, these were assumed to be the same as those for the open sea on the incoming tide, whilst on the outgoing tide values were determined from those predicted within the harbour by linear interpolation.

FINITE DIFFERENCE EQUATIONS

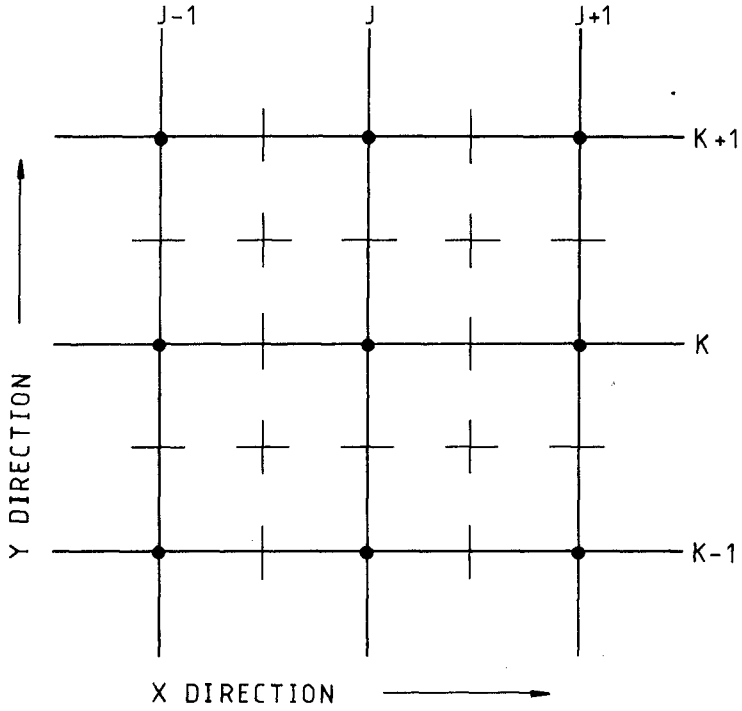
The differential equations (1) - (4) were expressed in an alternating direction implicit finite difference form, with all terms being fully centred in both space and time, except for the pressure gradients in the momentum equations. Using the space staggered grid scheme shown in Fig. 1, then for the first half time-step η , U and S were implicitly solved for using the following finite difference forms of the continuity, x-direction momentum and mass transport equations respectively:

$$\eta_{j,k}^{n+\frac{1}{2}} = \eta_{j,k}^n - \frac{\Delta t}{2\Delta x} \left[(h+n)U \left|_{j+\frac{1}{2},k}^{n+\frac{1}{2}} - (h+n)U \left|_{j-\frac{1}{2},k}^{n+\frac{1}{2}} + (h+n)V \left|_{j,k+\frac{1}{2}}^{n-1} - (h+n)V \left|_{j,k-\frac{1}{2}}^{n-1} \right. \right] \dots\dots\dots (7)$$

$$U_{j+\frac{1}{2},k}^{n+\frac{1}{2}} = U_{j+\frac{1}{2},k}^{n-3/2} - \frac{2\alpha\Delta t}{\Delta x} \left[U^2 \left|_{j+1,k}^{n-\frac{1}{2}} - U^2 \left|_{j,k}^{n-\frac{1}{2}} + UV \left|_{j+\frac{1}{2},k+\frac{1}{2}}^{n-\frac{1}{2}} - UV \left|_{j+\frac{1}{2},k-\frac{1}{2}}^{n-\frac{1}{2}} \right. \right] - \frac{2\Delta t g}{\Delta x} \left(\eta_{j+1,k}^{n+\frac{1}{2}} - \eta_{j,k}^{n+\frac{1}{2}} \right) - \frac{\Delta t g (U^{n+\frac{1}{2}} + U^{n+3/2}) \sqrt{U^2 + V^2}}{(h+n)C^2} \left|_{j+\frac{1}{2},k}^{n-\frac{1}{2}} + \frac{2\epsilon\Delta t}{\Delta x^2} \left[U_{j+3/2,k}^{n-\frac{1}{2}} + U_{j+\frac{1}{2},k+\frac{1}{2}}^{n-\frac{1}{2}} - 2 \left(U_{j+\frac{1}{2},k}^{n+\frac{1}{2}} + U_{j+\frac{1}{2},k}^{n-3/2} \right) + U_{j+\frac{1}{2},k-\frac{1}{2}}^{n-\frac{1}{2}} + U_{j-\frac{1}{2},k}^{n-\frac{1}{2}} \right] \dots\dots\dots (8)$$

$$[S(h+n)]_{j,k}^{n+\frac{1}{2}} = [S(h+n)]_{j,k}^n - \frac{\Delta t}{2\Delta x} \left[S(h+n)U \left|_{j+\frac{1}{2},k}^{n+\frac{1}{2}} - S(h+n)U \left|_{j-\frac{1}{2},k}^{n+\frac{1}{2}} + S(h+n)V \left|_{j,k+\frac{1}{2}}^n - S(h+n)V \left|_{j,k-\frac{1}{2}}^n \right. \right] - \frac{\Delta t}{2\Delta x^2} \left[(S_{j+1,k} - S_{j,k})(h+n)D_x \left|_{j+\frac{1}{2},k}^{n+\frac{1}{2}} - (S_{j,k} - S_{j-1,k})(h+n)D_x \left|_{j-\frac{1}{2},k}^{n+\frac{1}{2}} + (S_{j,k+1} - S_{j,k})(h+n)D_y \left|_{j,k+\frac{1}{2}}^n - (S_{j,k} - S_{j,k-1})(h+n)D_y \left|_{j,k-\frac{1}{2}}^n \right. \right] \dots\dots\dots (9)$$

where j,k = finite difference grid co-ordinates in x,y directions respectively, and n = time-step level. For the second half time-step, from level $n+\frac{1}{2}$ to $n+1$, similar equations were formulated with η,V and S written and solved for in an implicit form, whilst terms involving U



Symbols

•	η
—	V
	U
+	$h \& C$

Fig. 1 The Finite Difference Grid

were expressed explicitly.

This finite difference representation of the original differential equations has a truncation error of order $\Delta t, \Delta x^2$ and with the only stability constraint being introduced by the convective accelerative terms (4) as:

$$\frac{\alpha \Delta t}{\Delta x} |u_{\max}| \leq 1 \quad \dots\dots\dots (10)$$

For the type of velocity fields being considered, where the maximum velocity u_{\max} is relatively small, this stability constraint poses little restriction on the numerical model, particularly in comparison to the accuracy requirements suggested by Vreugdenhil and Voogt (8) as:

$$\frac{\Delta t}{\Delta x} \sqrt{gh} \leq 5 \quad \dots\dots\dots (11)$$

The finite difference equations were solved using the method of Gaussian elimination and back substitution and were found to give numerically stable results for all harbour configurations considered.

APPLICATION OF MODEL

In an attempt to check the reliability of the numerical model, comparisons were made with the results obtained from two laboratory model studies (5,6), carried out prior to the final development of the numerical model. In both of these experimental studies the main objectives were to compare the flushing characteristics and velocity fields for a number of different model rectangular harbour shapes. Each harbour shape had a different length to breadth ratio, but in all cases the harbour planform area remained constant. By comparing the flushing characteristics for the different shapes, it was possible to conclude which shape induced the maximum tidal flushing efficiency and hence, in general, resulted in the best overall water quality characteristics. Tests were also carried out to study the effects of inserting impermeable barriers at various locations within the different harbours, to investigate whether or not the flushing characteristics could be improved by altering the planform geometry accordingly.

The laboratory studies were treated as model studies of idealized harbour shapes, typical of many existing and proposed harbours and marinas in Puget Sound of the State of Washington. In the latter of the two laboratory studies in particular, where the experimental results were more directly comparable with the numerical model results, the prototype harbour was assumed to have a planform area of $4.0 \times 10^5 \text{ m}^2$, a mean depth of 6.0 m an asymmetric entrance of width 128.0 m. Also the prototype semi-diurnal tides, of period 12.4 hr., were assumed to be sinusoidal with an amplitude of 1.5 m. In the laboratory model the horizontal and vertical length scales were 1:1000 and 1:50 respectively, giving a vertical distortion of 20:1, with a Froude law scaling relationship being used to model the tidal period. The resulting physical model had a planform area of 0.4 m^2 , a mean depth of 120 mm, an entrance width

of 128 mm, a wave amplitude of 20 mm and a period of 10.52 min, see Fig. 2. The variable length to breadth ratios (L/B) considered ranged from 0.33 to 3.00, where the length L was defined as the harbour width in the plane of the entrance and the breadth B as the width perpendicular to the entrance plane.

Although vertically distorted hydraulic models do not properly scale diffusion and dispersion processes (9), the assumption was made that the dominant mode of water exchange was by convective, rather than diffusive or dispersive, transport. This allowed tracer dyes to be used in the model and for this purpose rhodamine B was used.

For the laboratory tests the harbour model, with adjustable side-walls, was inserted into a tidal tank in which an oscillating weir reproduced the required model tides (Fig. 2). With the harbour sidewalls set at the required length to breadth ratio, the tank and harbour were filled to the low tide water level and the harbour entrance temporarily sealed. Using a hypodermic syringe, 75 ml of rhodamine B (concentration 7.5 mg/l) was then thoroughly mixed with the harbour water and the average initial concentration recorded using a fluorimeter. The temporary entrance barrier was then removed and the tidal generator run for a period of three complete tidal cycles, at the end of which the harbour entrance was re-sealed. The fluid enclosed within the harbour was again thoroughly mixed and the average final concentration recorded as before. Knowing both the initial and final spatially averaged concentrations within the harbour, and the number of tidal cycles, then the average per cycle exchange coefficient was determined from the relationship given by Nece and Richey (2):

$$E = 1 - (C_i/C_0)^{1/i} \quad \dots\dots\dots (12)$$

where E = average per cycle exchange coefficient, C_0 = initial concentration and C_i = final concentration after i tidal cycles. The experimentally measured exchange coefficients for the various L/B ratios considered are given in Fig. 3, where it can be seen that the maximum value, resulting in the maximum flushing efficiency, occurs for an L/B ratio of unity i.e. a square harbour.

After measuring the exchange coefficient for each L/B ratio, the tide induced circulation patterns were determined using weighted drinking straws as drogues. The tidal generator was first run for two complete tidal cycles and on the third cycle the drogues were carefully inserted at fixed points, one minute before the flood and ebb mean tide water levels, and were then tracked for two minutes. The resulting pathlines were plotted to scale giving an indication of the corresponding velocity fields. Two sample results are shown for L/B ratios of 1.0 and 1.8 respectively, see Figs. 4 and 5.

In a similar procedure to that adopted for the laboratory model studies, the numerical model was applied to the prototype harbour with the planform area, mean depth and entrance width being as before, i.e. $4.0 \times 10^5 \text{ m}^2$, 6.0 m and 128.0 m respectively. Likewise the semi-diurnal sinusoidal tides had a period of 12.4 hr and an amplitude of 1.5 m. The model was started from the low water level, with an initial state of

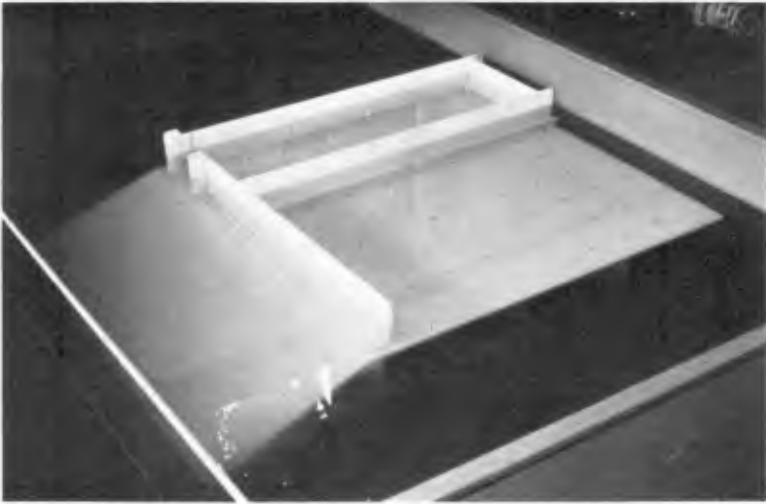


Fig. 2 General View of the Laboratory Model

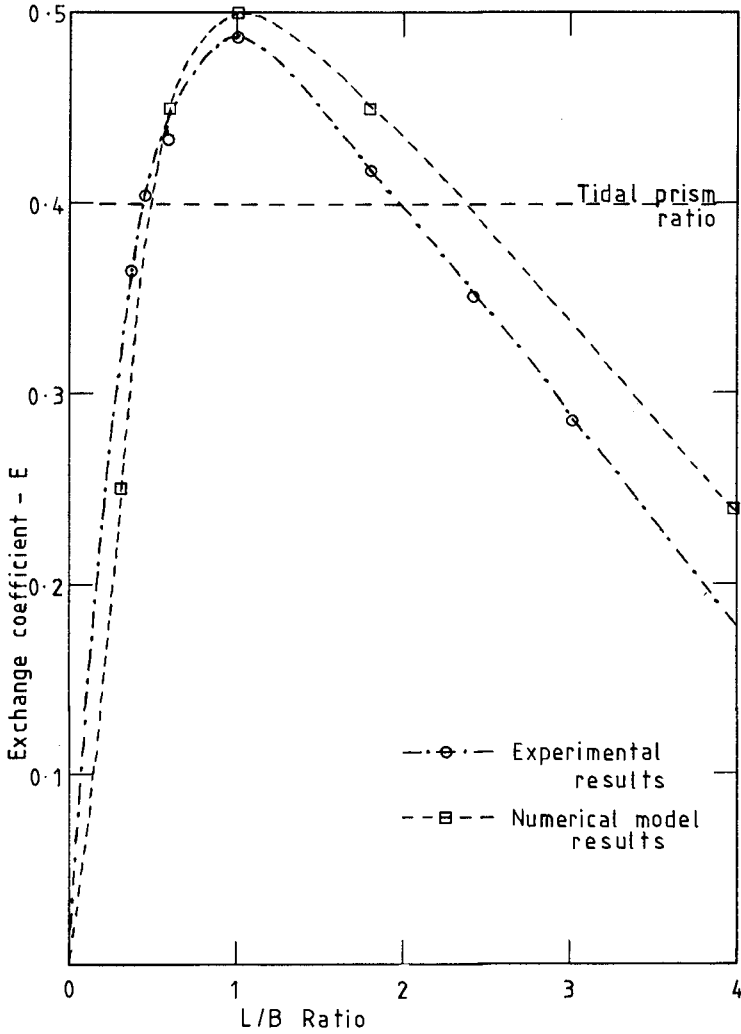
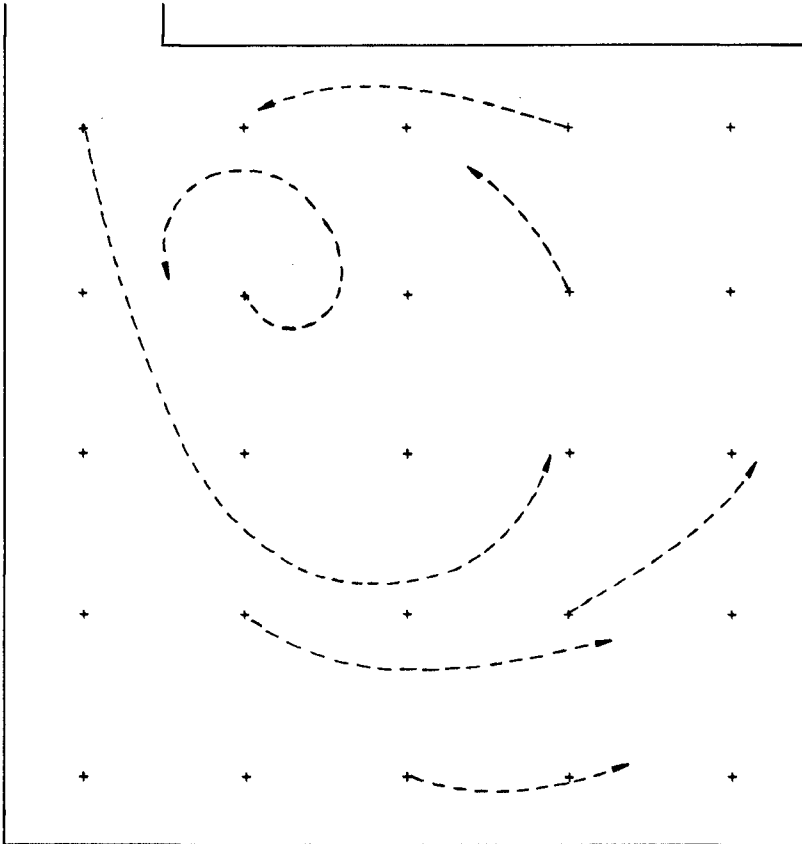
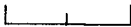


Fig. 3 Variation of Exchange Coefficient E with L/B Ratio

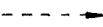
EXPERIMENTAL RESULTS

At MWL




 Scale : 100 mm

L/B = 1.0

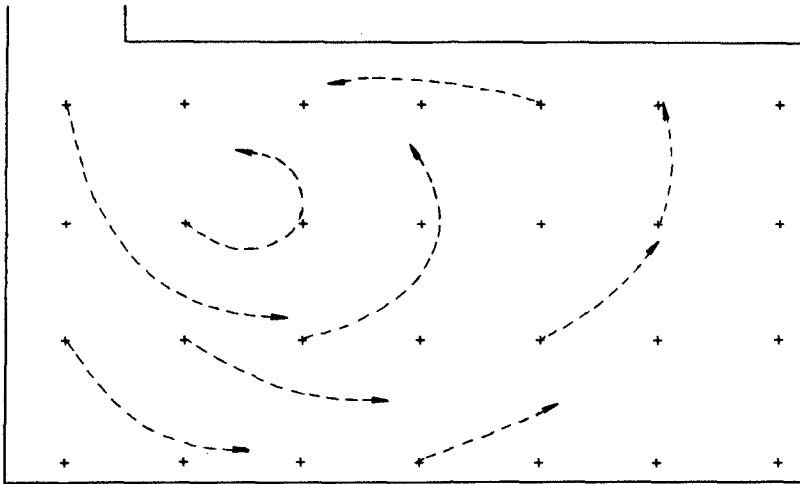
 Observed pathlines

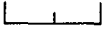
Mean depth = 120 mm

Fig. 4 Experimentally Observed Pathlines
for L/B Ratio of 1.0

EXPERIMENTAL RESULTS

At MWL




Scale : 100 mm
L/B = 1.8

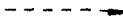
 Observed pathlines
Mean depth = 120 mm

Fig. 5 Experimentally Observed Pathlines
for L/B Ratio of 1.8

rest being assumed within the harbour. Also at the start of the model, the initial concentration (C_0) at each grid point within the domain was assumed to be 50 ppm. As for laboratory model studies, varying L/B ratios were considered ranging from 0.25 to 4.0; the range of values being larger in this study since no restraints were imposed by physical space requirements.

For all the L/B ratios considered the numerical model was run for three tidal cycles with the spatially averaged concentration (C_i) being calculated at the end of this period. As for the experimental results, the average per cycle exchange coefficient was evaluated using Eq. (12), with the results being given in Fig. 3. The agreement between the numerical and experimental results is encouraging, with the general trends of the relationship between the exchange coefficient and the L/B ratio being almost identical. In both cases the maximum exchange coefficient occurs for a square harbour, indicating as before that this shape induces the best flushing characteristics.

Graphical representations of the numerically predicted velocity fields were reproduced at the mean flood and ebb tides, thus allowing a direct comparison with the experimental results for the third tidal cycle. Again the agreement between the numerical and experimental results proved encouraging, with the general features of the tide induced circulation being satisfactorily reproduced. As an example of the numerical model results, the velocity fields are shown for L/B ratios of 1.0 and 1.8 respectively, see Figs. 6 and 7. These examples correspond directly to the experimental results of Figs. 4 and 5.

A further feature of the numerical model was that the variation of concentration across the planform area of the harbour was determined at particular time levels. By evaluating the standard deviation of concentration, and dividing by the average concentration, the corresponding coefficient of concentration variation was obtained. The results determined for the various L/B ratios, with and without the inclusion of barriers in the model, can be seen in Fig. 8. The results have again confirmed that an L/B ratio of unity provides the best mixing characteristics. For this case the lowest coefficient of variation was obtained, which meant that the concentration was more uniformly mixed within the harbour than for the other L/B ratios.

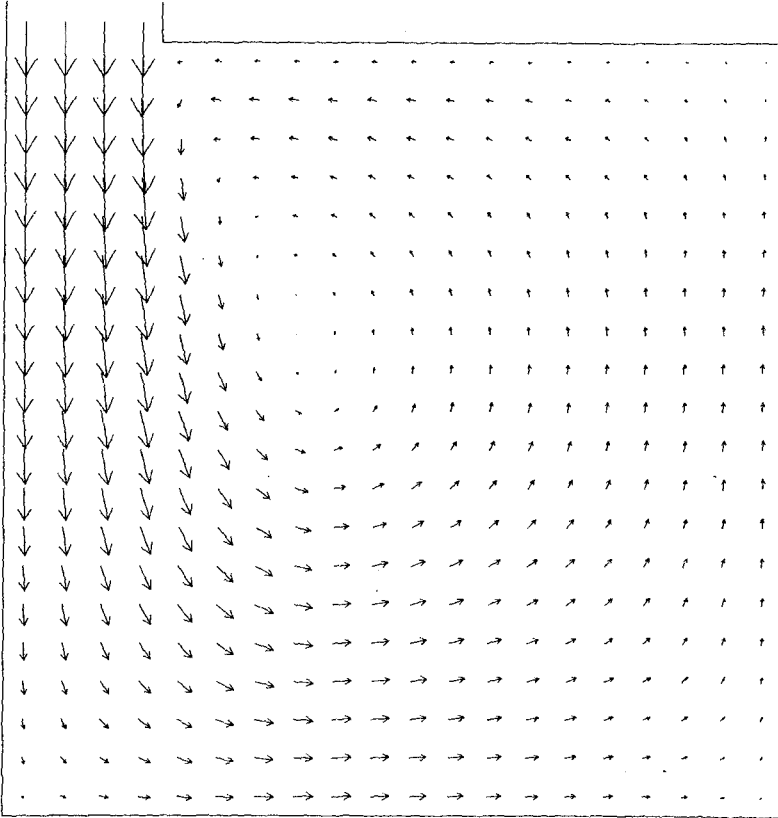
Further tests were carried out, both for the laboratory and numerical models, to study the effects on the gross flushing characteristics of inserting impermeable barriers at various positions within the harbours. Although the results are not reproduced here, it has been confirmed from both the experimental and numerical results that barriers do not in any way improve the flushing characteristics. In fact, the results recorded clearly showed that the barriers had a detrimental effect on the flushing efficiency.

CONCLUSIONS

It has been shown that by representing the differential equations of continuity, momentum and mass transport in the finite difference form described, numerically stable solutions can be obtained for the

TIDAL CIRCULATION IN A HARBOUR

TIME = 27.9 HRS



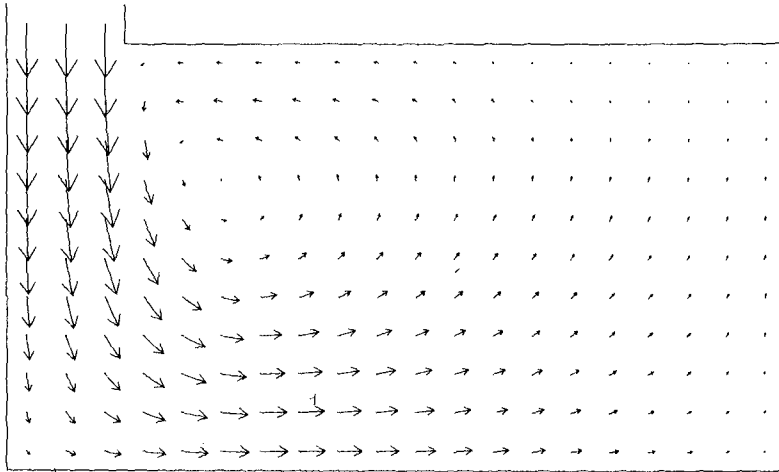
LENGTH SCALE — 32. M
 AVERAGE DEPTH = 5.99 M
 WAVE AMPLITUDE = 1.50 M
 AVERAGE CONC = 10.6 PPM

VELOCITY → .08 M/S
 MANNING NUMBER = .030
 WAVE PERIOD = 12.4 HRS
 STANDARD DEV = 7.2 PPM

Fig. 6 Computed Velocity Field and Concentration Parameters
 for L/B Ratio of 1.0

TIDAL CIRCULATION IN A HARBOUR

TIME = 27.9 HRS



LENGTH SCALE ——— 43. M
 AVERAGE DEPTH = 5.99 M
 WAVE AMPLITUDE = 1.50 M
 AVERAGE CONC = 12.5 PPM

VELOCITY ———→ .08 M/S
 MANNING NUMBER = .030
 WAVE PERIOD = 12.4 HRS
 STANDARD DEV = 12.4 PPM

Fig. 7 Computed Velocity Field and Concentration Parameters for L/B Ratio of 1.3

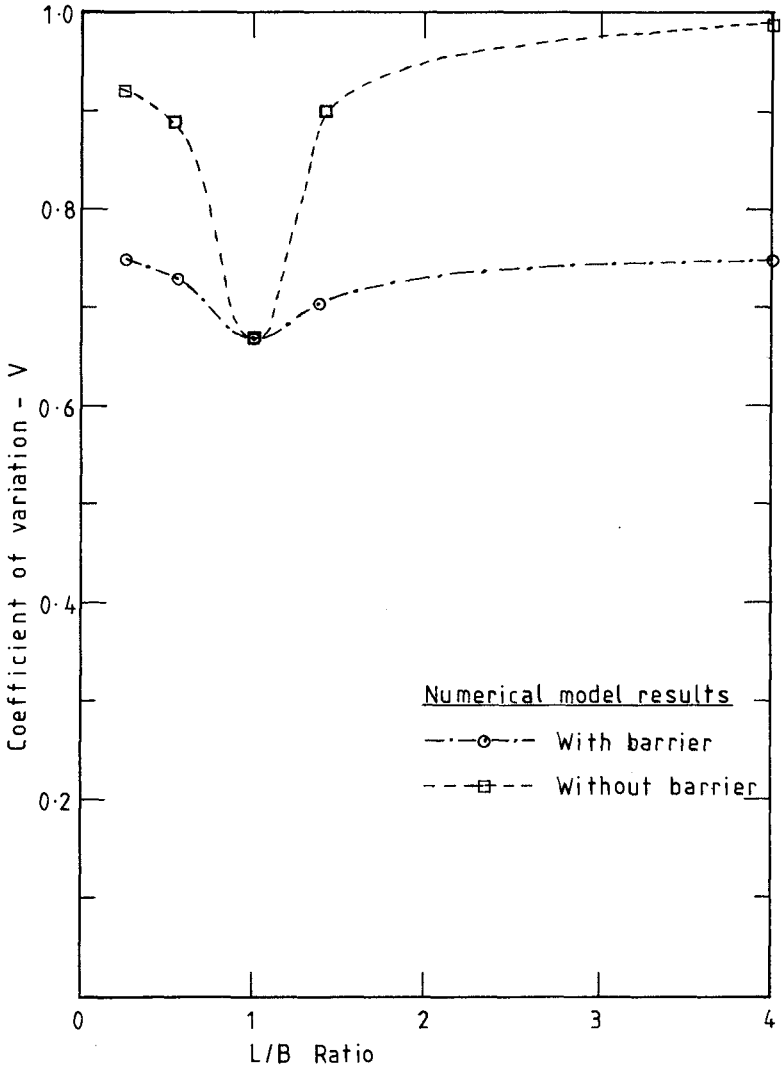
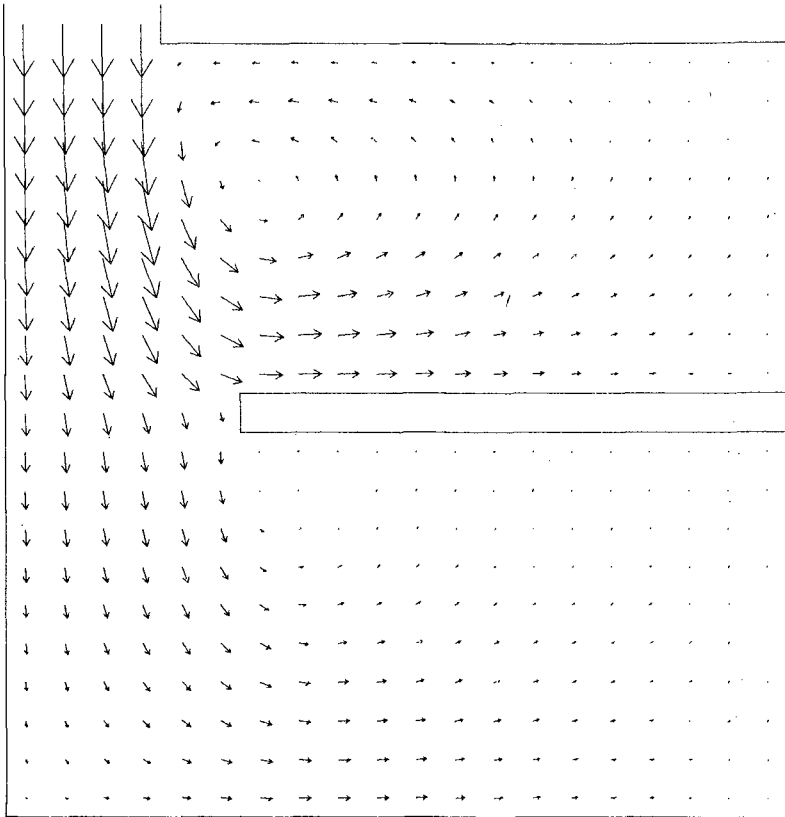


Fig. 8 Variation of Concentration Distribution with L/B Ratio

TIDAL CIRCULATION IN A HARBOUR

TIME = 27.9 HRS



LENGTH SCALE — 32. M
 AVERAGE DEPTH = 5.95 M
 WAVE AMPLITUDE = 1.50 M
 AVERAGE CONC = 22.1 PPM

VELOCITY → .08 M/S
 MANNING NUMBER = .030
 WAVE PERIOD = 12.4 HRS
 STANDARD DEV = 14.8 PPM

Fig. 9 Computed Velocity Field and Concentration Parameters for L/B of 1.0 with Barrier Included

relatively complex flow fields considered. This representation includes time centring of the convective accelerations, a technique which appears to have overcome the problems generally associated with non-linear instabilities. In all of the comparisons made between the numerical model velocity field predictions and the experimentally observed path-lines, the results have agreed reasonably well with the essential characteristics of the flowfields having been adequately reproduced.

By determining the spatially averaged concentrations at the beginning and end of three tidal cycles, it has been possible to ascertain the average per cycle exchange coefficient for various L/B ratios in the laboratory and numerical models. Comparisons of the results again showed good agreement, with the peak exchange coefficient occurring for an L/B ratio of unity; thus indicating that a square harbour gives the maximum flushing efficiency for a constant planform area.

For the numerical model studies only, results were obtained for the concentration distributions across the harbour planform area. As before these results indicated that for a square harbour the plan variation of the concentration distribution was a minimum, thereby confirming that for this case the concentrate was more uniformly mixed within the basin.

Finally, velocity field predictions and exchange coefficients for both the laboratory and numerical model results, showed that the insertion of impermeable barriers within the harbours was detrimental to the improvement of the basin's flushing efficiency and overall water quality characteristics.

REFERENCES

1. Nece, R.E. and Richey, E.P., "Flushing Characteristics of Small-Boat Marinas", Proceedings of the Thirteenth Coastal Engineering Conference, Vancouver, Canada, July 1972, pp 2499-2512.
2. Nece, R.E. and Richey, E.P., "Application of Physical Tidal Models in Harbor and Marina Design", Proceedings of the Symposium on Modeling Techniques, ASCE, San Francisco, California, September 1975, pp 783-801.
3. Falconer, R.A., "Numerical Modelling of Tidal Circulation in Harbours", Journ. of the Waterway, Port, Coastal and Ocean Division, ASCE, Vol. 106, No. WW1, February 1980, pp 31-48.
4. Falconer, R.A., "Mathematical Modelling of Jet-Forced Circulation in Reservoirs and Harbours", Ph.D. Thesis, University of London, London, England, 1976, 237 pp (unpublished).
5. Falconer, R.A., "Tidal Circulation Effects in Rectangular Harbours", MSCE Thesis, University of Washington, Seattle, Washington, 1974, 97pp (unpublished).
6. Roberts, K. and Withycombe, S.I., "Tidal Flushing Characteristics of Rectangular Harbours", B.Sc. Thesis, University of Birmingham, Birmingham, England, 1980, 56 pp (unpublished).
7. Elder, J.W., "The Dispersion of Marked Fluid in Turbulent Shear Flow", Journ. of Fluid Mechanics, Vol. 5, Part 4, 1959, pp 544-560.
8. Vreugdenhil, C.B. and Voogt, J., "Hydrodynamic Transport Phenomena in Estuaries and Coastal Waters", Proceedings of the Symposium on Modeling Techniques, ASCE, San Francisco, California, September 1975, pp 690-708.
9. Harleman, D.R.F., "Pollution in Estuaries", Chapter 14 in Estuary and Coastline Hydrodynamics (A.T. Ippen, Ed.), McGraw-Hill, 1966.

NOTATION

a	=	wave amplitude
A	=	planform area of harbour
B, L	=	breadth and length of harbour respectively
C	=	Chezy coefficient
C_0, C_i	=	initial and final concentrations in harbour respectively
D_x, D_y	=	depth mean dispersion coefficients in x,y directions respectively
E	=	exchange coefficient
f	=	Coriolis parameter
g	=	acceleration due to gravity
h	=	mean depth
i	=	number of tidal cycles
j, k	=	finite difference co-ordinates in x,y directions respectively
n	=	time-step level
S	=	depth mean mass concentration
U, V	=	depth mean velocities in x,y directions respectively
W	=	entrance width of harbour
x, y	=	longitudinal and lateral co-ordinates respectively
α	=	vertical velocity variation correction factor
Δt	=	time step
Δx	=	grid size in x,y directions
ϵ	=	depth mean eddy viscosity
θ	=	phase lag
ω	=	wave frequency

HYDRAULIC CIRCULATION PERFORMANCE
OF A CURVILINEAR MARINABY JEFFREY A. LAYTON, M.ASCE¹

INTRODUCTION

An innovative coastal engineering concept has been developed to maximize the hydraulic circulation and water quality of dredged backshore harbors and boat basins. The concept represents a radical departure from the hydraulic design of existing artificial boat basins in that the basin geometry and entrance channel are primarily sized for hydraulic purposes rather than navigational access. Specific elements of the concept are described below.

CONCEPT

Past design practice of backshore-dredged harbors, basins, and marinas has concentrated primarily on optimizing the dredged geometry to develop maximum maneuvering space and moorage area. Typically, little or no thought was given to water circulation and water quality within the artificial harbor. However, recent environmental studies have shown that rectangular dredged basins can have limited water circulation and flushing, resulting in the formation of stagnant zones throughout the harbor (Nece and Kroll, 1974, and Nece et al., 1976). Limited water circulation, in turn, can result in poor water quality levels in the harbor. Typically, water temperatures rise and dissolved oxygen levels decrease in basins with poor circulation. These changes can have profound effects on the flora and fauna inhabiting the harbor.

To overcome the above problems associated with limited hydraulic circulation, a new design concept was developed by the author in conjunction with Professors E. P. Richey and R. E. Nece of the University of Washington, Seattle.

The concept revolves around the use of a properly sized offset entrance coupled with a rounded basin shape. The curvilinear geometry allows "new" water entering the marina to move freely around the entire basin perimeter and mix with "old" basin water without forming isolated dead spots. Similarly, during ebb tide, the basin's shape minimizes restrictions to the potential flow field, eliminating stagnant zones. Specific elements of the concept are as follows:

- Conventional rectangular geometry of backshore-dredged basins is replaced with curvilinear

¹Principal, Layton and Associates, Consulting Coastal Engineers, 1611 - 116th Avenue NE, Bellevue, Washington 98004; formerly Senior Coastal Engineer, CH2M HILL NORTHWEST, Inc., Bellevue, Washington 98004.

geometry. Rounded corners of the basin reduce sideslope friction and eliminate stagnant zones common to sharp-edged rectangular corners.

- The rounded basin geometry is coupled with a single narrow entrance channel. This channel is hydraulically designed to produce a flooding tidal jet that possesses sufficient momentum to create large-scale rotating vortex systems within the curvilinear basin.

Through the above process a strong tidally driven basin circulation current system can be created. This current system is capable of maintaining water quality levels within enclosed harbors at near-ambient open water levels. Physical hydraulic model testing and post-construction prototype monitoring have verified the concept (discussed below).

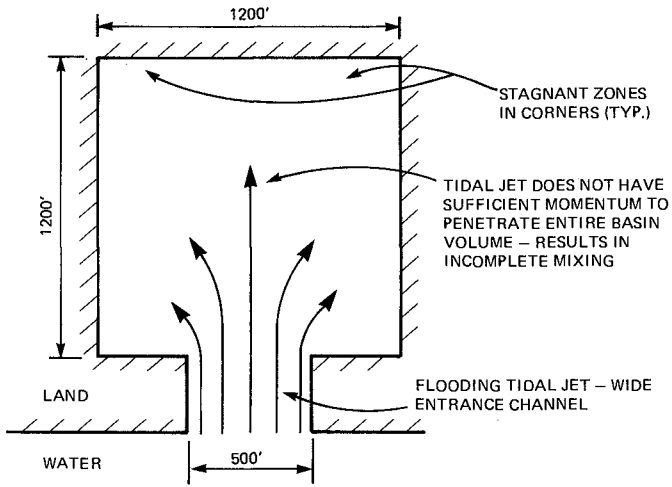
THEORY

Figure 1 illustrates a plan view of a typical small-craft harbor. The principal elements of the harbor's geometry consist of a wide entrance channel coupled to a large square or rectangular moorage basin. The efficiency at which the interior "old" basin water mixes with "new" incoming offshore water is directly affected by the velocity of the flooding tidal jet as it flows through the harbor entrance. For weak entrance channel currents, which are characteristic of wide channels, the flooding tidal jet may not possess sufficient momentum to allow the incoming water to penetrate to the farthest reaches of the basin. This can result in the formation of hydraulically stagnant zones in the harbor. For harbors with linear geometry, the stagnant zones commonly form in corner areas. This poor mixing action of tidal water can result in degradation of water quality as previously described.

To improve the circulation and mixing action of a harbor, two basic approaches are available:

1. Induce artificial circulation in stagnant zones with mechanical devices such as pumps or ducted propellers (Dunham, and Finn, 1974).
2. Redesign the geometry of the harbor basin and entrance channel to allow natural tidal action to improve hydraulic circulation and mixing.

The first method described above is a remedial solution. Reliance on mechanical devices (and the human personnel required to operate them) to work continually in a marine environment is questionable at best. Typically, mechanical systems corrode, become biofouled, and experience general electrical and mechanical problems such that they cannot be relied upon 100 percent. As an example, if a mechanical system used to induce circulation in a harbor fails at a critical period, such as during a prolonged hot spell in the summer season, solar heating of the stagnant basin water



**FIGURE 1
CONVENTIONAL
RECTANGULAR BASIN**

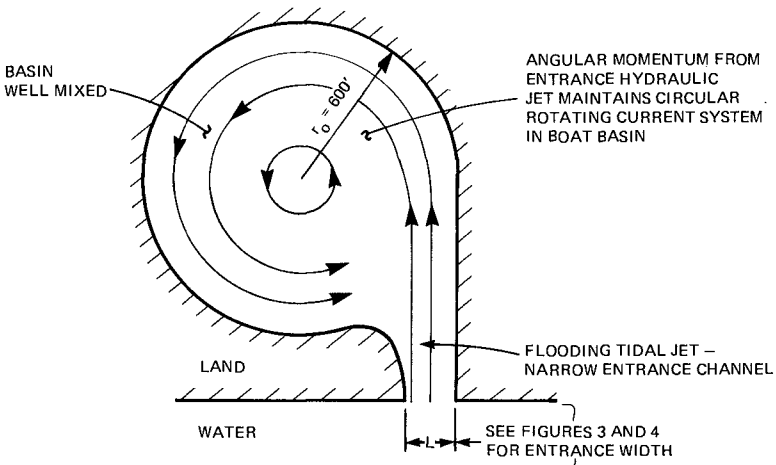


**FIGURE 2
CURVILINEAR BASIN**

could increase ambient temperatures to levels that are lethal to resident and migratory fish populations.

Because of poor reliability of mechanical systems, most governmental agencies responsible for issuing permits related to marine water quality are extremely reluctant to approve artificial circulation devices. The agencies prefer natural systems that do not require constant monitoring and maintenance. Thus, the use of artificial circulation systems in harbors to maintain water quality is generally not an acceptable solution.

As an alternative to mechanical systems, harbor geometry can be modified to allow nature, through the action of the tides, to produce sufficient hydraulic circulation to eliminate or minimize potential water quality problems. Such a modification of a conventional harbor is shown in Figure 2. The linear geometry of the square basin of Figure 1 has been replaced with curvilinear geometry to eliminate sharp corner areas. In addition, the entrance channel has been reduced in size and offset along one side of the basin. These simple changes in geometry result in the formation of a strong flooding tidal jet that now possesses sufficient angular momentum to carry new incoming offshore water throughout the entire volume of the basin. This naturally induced momentum results in excellent internal circulation and mixing within the harbor. To illustrate the angular momentum concept, an example problem is provided below.

DESIGN EXAMPLE

It is desired to dredge a small-boat harbor and entrance channel in a low-lying area landward of an existing shoreline (see Figure 2). To be economically justifiable, the basin must have sufficient area for 1,000 moorage berths, and the entrance channel should be wide enough to safely allow two-way boat traffic. Also, property boundary constraints require the entrance to be positioned to the right side of the basin. Environmental restrictions placed on the site to protect migrating salmon fry limit increases in basin water temperature to no more than 1-1/2 degrees C above ambient offshore waters. Also, the use of artificial circulation devices is prohibited. The mean tide range is 6 feet, and the mean tide level is 6 feet above mean lower low water (MLLW = 0). Size the basin and entrance channel to meet the above conditions.

Basin Size

Through the use of standard marina berth layout parameters (Dunham and Finn, 1974) and the use of a curvilinear boat basin geometry (Figure 2), it is determined that a circular basin with a radius of 600 feet will provide sufficient space for 1,000 small craft. Similarly, calculations of solar-heated basin water mixing with ambient offshore water over a tidal cycle show that basin temperatures will not exceed the 1-1/2 degrees C increase limit if the boat basin is well mixed. A complete rotation of the entire basin's water mass

over the flooding cycle is calculated to provide the necessary mixing. The problem now becomes to size the entrance channel such that the flooding tidal jet will produce the desired rotation of the basin water.

Entrance Channel Size

To size the entrance channel, consider the water within the circular basin of Figure 2 as a cylinder. Allow this water body to be given sufficient angular momentum to move with "solid-body" rotation, overcoming frictional resistance of the basin's bottom and sides. From the discussion above, assume that one complete revolution of the water body during a flooding tide period (approximately 6 hours) is sufficient to induce the necessary circulation. To produce this rotation, the entrance channel must be sized to transmit sufficient tidal jet momentum to the basin waters. The following describes procedures to calculate the required tidal jet energy.

Treat the basin as a cylindrical body with a 600-foot radius. Assume a uniform friction coefficient of 0.005 for all boundaries (Nece and Richey, 1975). The problem now becomes one of estimating the required torque of the solid-body water mass to overcome the bottom and sidewall frictional resistance of the basin. To calculate the resisting frictional torque exerted on the rotating water mass by the bottom, Nece and Richey (1975) suggest the following:

$$T_b = \int_0^{r_0} c_{f \frac{\rho}{2}} (\omega r)^2 2 \pi r r d_r \quad (1)$$

$$= c_{f \frac{\rho}{2}} \omega^2 2 \pi r_0^5 \frac{1}{5} \quad (2)$$

where T_b = bottom torque (ft-lb)

c_f = friction coefficient = 0.005

ρ = mass density (2 slugs/ft³ for seawater)

ω = angular velocity for one rotation
of boat basin water during one-half tidal
cycle

$$= \frac{2 \pi}{(6.2)(3600)} \quad \frac{\text{radians}}{\text{sec}}$$

r_0 = radius of basin = 600 feet

For the example problem a friction bottom torque of 38,600 foot-pounds is calculated.

For the sidewall torque, Nece and Richey (1975) suggest treating the basin perimeter as a cylindrical surface of revolution. The resulting peripheral torque is calculated as follows:

$$T_p = c_f \frac{\rho}{2} (\omega r_o)^2 2\pi r_o h r_o \quad (3)$$

where T_p = peripheral torque (ft-lb)

h = water depth corresponding to distance from mean tidal level to basin bottom. (For example, basin dredged to -10 with mean tide of 6 feet, $h = 16$ feet)

For the example problem a peripheral torque of 5,150 foot-pounds is calculated.

Combining the bottom and peripheral torque results in a net torque to be overcome by the entrance jet of approximately 43,750 foot-pounds. Startup, or inertial, effects have been neglected and are considered minor because of long tidal periods. Also, the current deflecting effects of the Coriolis force have been neglected because of the overriding influence of basin geometry on current direction. (It should be noted, however, that, if harbor geometry allows placement of the entrance channel on either side of the basin, it is preferable to place the entrance on the left side in the Northern Hemisphere. This will allow the Coriolis force to help augment the resulting clockwise circulation. For the Southern Hemisphere, a right-hand entrance is preferred.)

Assuming that all of the torque to overcome the net frictional torque of 43,750 foot-pounds is provided by an entrance channel hydraulic jet offset a distance of r_o to the side of the boat basin, the required entrance momentum can be calculated as follows:

$$QVr_o = T_b + T_p \quad (4)$$

where the entrance channel provides a volumetric flow rate of Q (ft³/sec) with a jet velocity of V (ft/sec).

For the example problem, a momentum flow of $QV = 36.5$ is required. To determine both Q and V , the following procedure is used:

$$\text{Average } Q = \frac{\text{basin tidal prism volume for mean tide level}}{\text{half-tidal cycle time period}} \quad (5)$$

$$= \frac{(6.0)(\pi)(600)^2}{(6.2)(3600)}$$

$$= 304 \text{ cubic feet per second}$$

The required average velocity of the entrance jet can then be calculated as follows:

$$v = \frac{36.5}{Q} = \frac{36.5}{304} = 0.12 \text{ foot per second} \quad (6)$$

Thus, the entrance channel must be designed to provide an average flooding entrance channel velocity of 0.12 foot per second. It should be noted that the actual entrance channel velocity will vary as a function of time and tidal height

such that peak velocities are two to four times higher than the average velocity and minimum velocities approach zero. However, the average velocity of 0.12 foot per second represents the same net momentum input to the basin when peak and minimum velocities are combined.

To estimate the required cross-sectional area of the channel, the continuity equation is employed:

$$Q = VA \quad (7)$$

where V = average tidal velocity (feet per second)

A = average area of entrance channel (square feet)

$$\text{Therefore, } A = \frac{Q}{V} = \frac{304}{0.12} = 2,500 \text{ square feet}$$

Thus, for the example problem, the entrance channel must have a cross-sectional area less than or equal to about 2,500 square feet.

Figures 3 and 4 illustrate two entrance channel configurations that are sized to produce an average tidal jet velocity of 0.12 foot per second. Both channel types are sufficiently wide to allow two-way vessel traffic into and out of the harbor.

Factor of Safety

To account for possible inaccuracies in the procedures described above (e.g., selection of friction coefficient, neglecting inertial forces), it is recommended that for design purposes the calculated minimum entrance channel velocity be increased by at least a factor of 1.35. This results in a reduction of the required entrance channel area by about 25 percent.

HYDRODYNAMIC ASYMMETRY

Angular momentum within a harbor basin will persist for some time after flooding stops and ebbing tide begins. This sets up a flow condition where rotating basin eddies encounter the potential flow regime of the ebbing tide. Thus, two different flow conditions occur at the same instance, producing hydrodynamic asymmetry. This is advantageous because it helps to further increase mixing action within the basin.

PROTOTYPE EXAMPLE

The concept described above was developed as a result of the design of a large marina located in northern Puget Sound at Point Roberts, Washington. Analytical studies, field measurements, and physical modeling efforts were all utilized in the hydraulic design of the marina's basin and entrance channel. Calculations presented in the example problem were based, in part, on the design of the marina. A brief description of the marina is provided below.

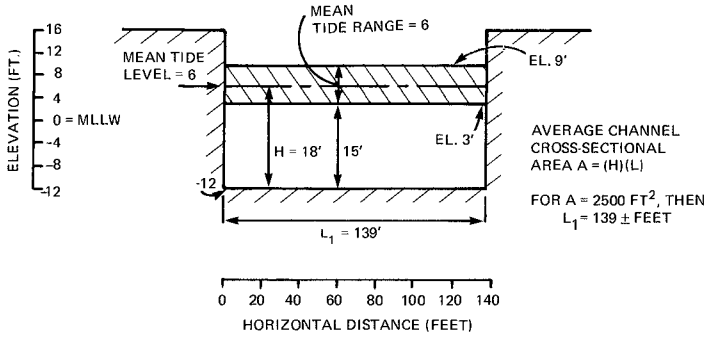


FIGURE 3
RECTANGULAR
ENTRANCE CHANNEL

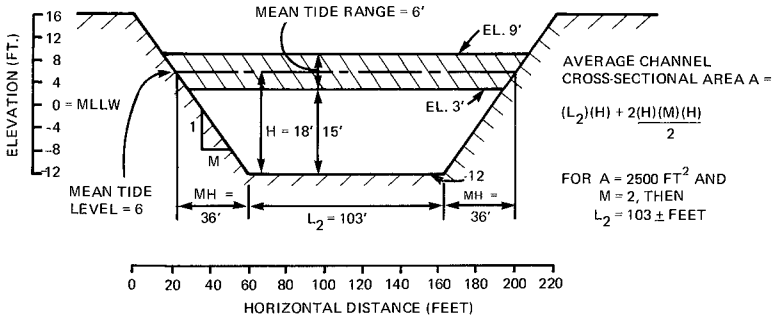


FIGURE 4
TRAPEZOIDAL
ENTRANCE CHANNEL

Point Roberts Marina

The 1,000-berth Point Roberts Marina is one of the largest privately owned coastal engineering developments on the Pacific coast of the United States. Construction of the marine portions of the \$6 million marina began in November 1976 and were completed in August 1978. The marina is located on the south shore of Point Roberts, a small peninsula politically part of the State of Washington, USA, but physically connected to British Columbia, Canada. The marina site encompasses approximately 140 acres and includes nearly 8,000 linear feet of marine shoreline (Layton, 1979).

Figures 5 and 6 present aerial views of the completed marina showing the relationship of the entrance channel to the back-shore curvilinear boat basin. This configuration was found to maximize hydraulic circulation within the marina's 40-acre boat basin, which in turn resulted in acceptable water quality levels. Construction of this marina represents the first application of the above-described concept and is representative of the state of the art in marina and harbor basin hydraulic design.

Hydraulic Model Study

Prior to construction of Point Roberts Marina, a hydraulic model of the proposed marina was constructed and a series of tracer dye tests conducted to predict the circulation performance (CH2M HILL, 1976, and Nece, 1976). Results showed that the marina would have excellent internal hydraulic circulation. A large counterclockwise rotating vortex system was found to occur in the boat basin during all ranges of flood tides. No stagnant zones were observed and the basin was found to be well mixed. Figures 7 and 8 illustrate typical circulation patterns of the boat basin and offshore waters during ebb and flood tide conditions.

Prototype Studies

After construction of the marina, several hydraulic and water quality studies have been conducted to determine the overall performance of the design concept. Figure 9 illustrates the results of one test where a drogue was used to trace the path of water mass movement in the basin during a typical flood tide. Of importance to note is that the drogue traveled from the entrance channel over 2,000 feet to the head of the boat basin. This verified the hydraulic model tests and demonstrated that the concept of curvilinear boat basin geometry coupled with a hydraulically designed entrance channel is effective in producing strong internal circulation.

Remote aerial sensing studies conducted by the U.S. Environmental Protection Agency in June 1978 also showed that the Point Roberts Marina basin has excellent thermal mixing. Comparison of thermal imagery of other conventional rectangular marina basins in Puget Sound clearly illustrated the superior mixing action of the curvilinear basin.



FIGURE 5
OBLIQUE AERIAL VIEW
OF POINT ROBERTS MARINA



FIGURE 6
PLAN VIEW OF POINT ROBERTS MARINA



FIGURE 7A
MOVEMENT OF DYE FROM ENTRANCE
CHANNEL TO BASIN DURING FLOOD TIDE



FIGURE 7B
DISTRIBUTION OF DYE IN BOAT
BASIN AT END OF FLOOD TIDE

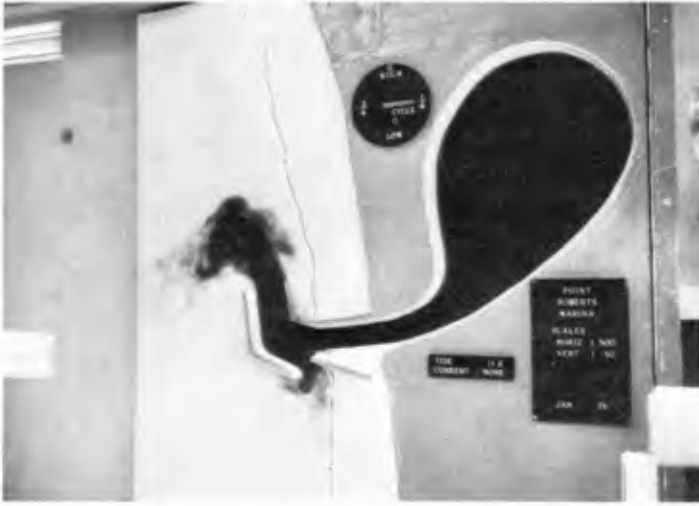


FIGURE 8A
DISCHARGE OF DYE FROM MARINA
DURING EBB FLOW (NO LONGSHORE CURRENT)



FIGURE 8B
DISTRIBUTION OF DYE AT END
OF EBB TIDE (NO LONGSHORE CURRENT)

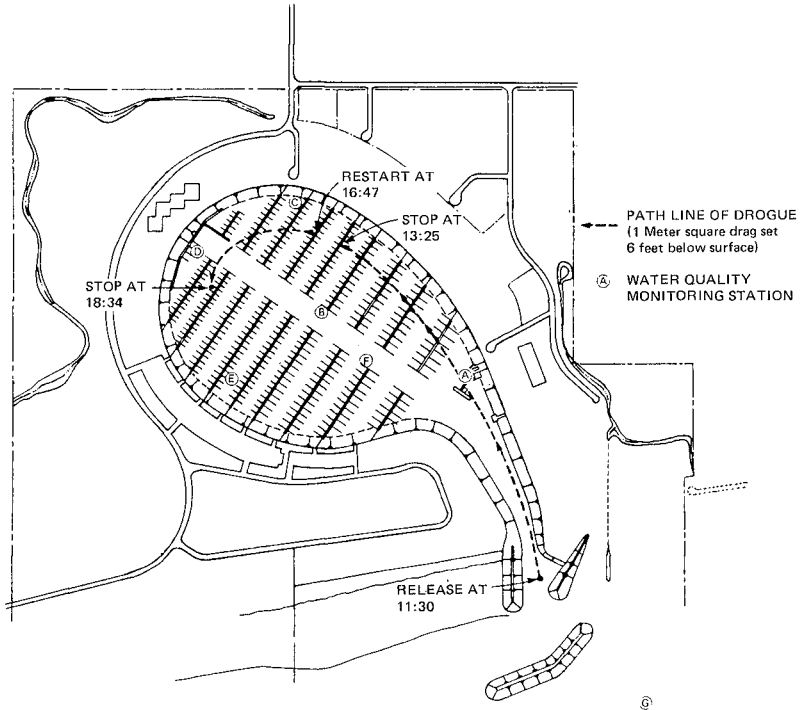


FIGURE 9
TYPICAL PATHLINE OF DROGUE RELEASE
ON OCTOBER 13, 1978

In addition to the above prototype studies, a water quality monitoring program was conducted at the marina during 1978. Table 1 presents a typical set of water temperature measurements recorded in the constructed boat basin. The results indicate that the interior of the boat basin has a fairly uniform temperature distribution with basically very little variation from ambient water temperature conditions in the Strait of Georgia.

Table 1
WATER TEMPERATURE MEASUREMENTS IN
POINT ROBERTS MARINA, October 12, 1978

Station*	Time	Depth (meters)					
		0	1	2	3	4	5
		Temperature °C					
A	1540	12.5	12.2	11.8	11.6	11.5	11.5
B	1600	12.4	12.1	11.8	11.5	11.2	11.2
C	1703	12.4	12.0	11.7	11.5	11.4	11.3
D	1728	11.9	11.8	11.6	11.4	11.4	11.3
E	1752	12.2	12.0	11.6	11.5	11.4	11.4
F	1815	12.1	12.0	11.6	11.4	11.2	11.2
G	1403	12.2	12.2	12.0	11.8	11.7	11.5

* See Figure 9 for station locations.

CONCLUSIONS

A new concept in the design of dredged backshore basins for maximizing hydraulic circulation and water quality has been described. The concept employs the use of curvilinear basin geometry coupled with a single offset entrance channel. This combination produces a flooding tidal jet that can have sufficient momentum to penetrate all portions of the basin, producing a well-mixed, stagnant-free water mass. The concept was employed in the design of a large marina, and subsequent post-construction monitoring has verified the concept.

ACKNOWLEDGEMENT

The author wishes to thank Mr. Roger Lindquist of CH2M HILL, Corvallis, Oregon, for presenting this paper for the author at the 17th International Conference on Coastal Engineering.

REFERENCES

1. CH2M HILL. Final Environmental Impact Statement: Point Roberts Marina--Parts 1 and 2. Prepared for Whatcom County Board of County Commissioners, Whatcom County Courthouse, Bellingham, Washington. July 6, 1976.
2. Dunham, J. W., and A. A. Finn. Small-Craft Harbors. Design, Construction, and Operation, Special Report No. 24, U.S. Army Corps of Engineers, Coastal Engineering Research Center, Fort Belvoir, Virginia. December 1974..
3. Layton, J. A. "Design and Construction of a Curvilinear Marina." Proceedings of the Coastal Structures '79 Conference of the Waterway, Port, Coastal, and Ocean Division of ASCE, Alexandria, Virginia. March 1979.
4. Nece, R. E., and C. R. Knoll. Flushing and Water Quality Characteristics of Small-Boat Marinas. Tech. Report No. 40. Charles W. Harris Hydraulics Laboratory. University of Washington, Seattle. 1974.
5. Nece R. E. Hydraulic Model Study: Point Roberts Marina. Prepared for CH2M HILL, Bellevue, Washington, by Harris Hydraulics Laboratory, University of Washington, Seattle. 1976.
6. Nece, R. E., R. A. Falconer, and Toshio Tsutsumi. "Planform Influence on Flushing and Circulation in Small Harbors." Proceedings of the Fifteenth Coastal Engineering Conference, ASCE, Honolulu, Hawaii, July 11 through 17, 1976. Volume IV, pp. 3471-3486.
7. Nece, R. E., and E. P. Richey. Hydraulic Model Study of a Proposed Marina Basin in the Northwest Corner of Penn Cove, Whidbey Island, Washington. Charles W. Harris Hydraulics Laboratory, University of Washington, Seattle. January 1975.

THE EFFECT OF BREAKING WAVES ON THE MIXING
OF LIQUID POLLUTANTS INTO THE SEA.

by

Dr.ing. Arvid Naess,
The Norwegian Hydrodynamic Laboratories,
Trondheim, Norway.

ABSTRACT.

Experience gathered during the last few years shows that a serious problem when fighting oil spills out in open waters, is the mixing of the oil into the sea by breaking waves. In this paper we propose a theoretical model that we believe represent a fruitful approach to the problem of determining the amount of oil mixed into the sea by breaking waves. Our model is based primarily on probabilistic methods, but with experimental observations and data as an essential foundation.

1. INTRODUCTION.

We shall in this paper consider the mixing of an oil spill into the sea caused by breaking waves, and the main topic will be a stochastic model for estimating the oil distribution with depth caused by this mixing. The answer to the question - How much oil can you expect to have left on the sea surface in a given sea state? - is rather crucial to planning and organizing oil pollution control. The reason is that oil being mixed into the sea is very difficult to recover.

The phenomenon that is the primary cause of dispersion is turbulence in the upper layers of the ocean. Now, the sea states of most immediate concern to us, are characterized by rather strong wind and breaking waves, which we shortly describe as rough seas. Under conditions as these, there are two mechanisms that completely dominate the generation of turbulence in the surface layers. One is breaking waves, the other is wind induced shear currents.

It is only in recent years that people have really begun to study breaking waves and their role in generating turbulence in the ocean. Of special interest to us would be a connection between sea state and turbulence level together with the penetration depth of the turbulent layer

beneath a breaking wave. However, in the literature there are no available data or analyses of a connection between sea state on the one hand and turbulence level and penetration depth on the other. In passing let me mention that some simple experiments we have done, indicated that the maximum penetration depth of the turbulence beneath a breaking wave is of the same order of magnitude as the wave height.

During conditions of rough seas, the strong down-welling turbulent water masses beneath breaking waves will constitute the main driving mechanism behind the dispersion of an oil slick into the sea. Generally speaking, we may say that breaking waves are two orders of magnitude more effective in dispersing surface oil than turbulence due to wind induced shear currents. This conclusion has also been drawn by other workers in this field, see reference 1.

However, it is not legitimate to conclude that turbulence due to dynamically instable shear currents in the surface region have little or no effect on dispersion when breaking waves dominate. While the turbulence generated by breaking waves is characterized by being highly non-stationary, i.e. the energy in the turbulence beneath a breaking wave dissipates rather quickly, we may with some confidence assert that the turbulence generated by wind induced shear currents has an approximately stationary character. This means that when the strong turbulence beneath the breaking waves dies out, a certain turbulence level is still present. How this turbulence will affect oil already being dispersed, is not well known. However, there is strong reason to believe that the residence time of an oil globule within the water column will depend significantly on this turbulence level.

When a breaking wave hits an oil slick, it will tear up part of it and drive a cloud of oil globules down into the sea. As long as the turbulent water motions beneath the breaker continues, the positions of the globules are mainly determined by this. But as soon as the turbulence has lost its energy, the buoyancy of the globules will drive them towards the surface. The rise velocity will certainly depend on globule size, but also probably on the background level of turbulence in the surface layers as we just mentioned.

How fast the amount of oil being mixed into the water will rise towards the surface again depend on how the amount of oil is distributed over different globule sizes, or more precisely, over different rise velocities and on how deep down into the water the oil globules are mixed. Every serious effort to estimate the dispersion of oil in open waters will consequently have to find estimates of rise velocity distribution and mixing depth due to breaking waves. And for this information to be of practical use, it has to be related to sea states by some suitable method.

In the first part of our paper we will describe the method or model chosen as a starting point in dealing with this problem. In the latter part a description of experiments and analyses we have done in order to estimate rise velocity distribution and mixing depth will be given.

However, before we enter the details of our paper, we shall list some excellent reports and papers dealing with the dispersion of oil. In reference 1 is presented a mathematical model of dispersion. In reference 2, detailed discussions of most of the phenomena playing a part in the dispersion of oil are given, and theoretical models for some of these are presented. This report is a highly valuable addition to the literature. A short presentation of some of the work contained in reference 2 is given in reference 3. Reports on work having a strong bearing on the experimental part of this paper are given in references 4 and 5.

2. THEORETICAL MODEL.

2.1 Basic assumptions.

In order to construct a manageable theoretical model to estimate the vertical distribution of oil in the sea due to the mixing induced by breaking waves, it is obvious that quite a few simplifying assumptions have to be made.

The basic assumptions on which we build our model, are as follows: Firstly, we shall assume that the time points when breaking waves pass a fixed location on the sea surface are randomly distributed according to some probability law that may, in principle, be determined for each environmental condition.

Assume then that initially we have an oil slick of surface density σ at our fixed location. With each passing of a breaking wave, a mixing of the oil into the sea will occur. In agreement with experimental observations, we will assume this mixing process to be instantaneous, i.e. relative to the time intervals between passing breakers. Further, we assume that with each breaking wave we may associate a quantity, called the "mixing depth", which gives a measure of the depth to which oil is carried by the mixing created by the breaking wave, and that this quantity is a random variable whose probability distribution may, in principle, be determined for each environmental condition. From our experimental observations, we may conclude that the "mixing depth" is largely determined by the depth to which the more or less turbulent water motion created by the breaking wave extends, and much less on the type of oil present. We shall, accordingly, assume that the probability distribution of "mixing depth" is independent of the particular type of oil present.

A few more simplifying assumptions are needed to avoid an intractable model.

To be precise, we neglect the horizontal motion of the oil due to waves and current, so that the vertical distribution of the oil always adds up to σ at our fixed point. If on the average the oil slick is moving with a uniform velocity, we may introduce a reference frame moving with the same velocity and relate our analyses to this. The probability distribution must then, of course, be determined relative to this frame. The next simplification is to neglect the variation of the vertical distance between specific water particles caused by the wave motion.

We shall also neglect the influence of the oil on the breaking waves. Now it is a fact that oil under some conditions does have an influence on breaking waves, but what limitations that put on our model is hard to say at present. For instance, observations in connection with the blow-out on the Ixtoc 1 field in the Gulf of Mexico, seem to indicate that strongly emulgated oil have no or very little effect on breaking waves. The main reason for neglecting this effect is, however, that the state of knowledge in this field is such as to allow no quantitative conclusion.

2.2 Probabilistic model.

With the simplifying assumptions made above in mind, we shall now construct our theoretical model. Starting with the occurrence of breaking waves, we then have a sequence of random time points

$$\dots, T_1, T_2, T_3, \dots, T_n, \dots$$

describing each passing of a breaking wave past a fixed location. With each T_k there is associated a random variable D_k , called the "mixing depth", and we assume that all the D_k 's are mutually independent and identically distributed with probability density f_D . The D_k 's are also assumed to be independent of the timepoints T_k . The last assumption is not essential.

Due to the mixing process, the oil will be broken up into droplets of different sizes, which we characterize by the parameter u equal to the terminal rise velocity of a droplet through calm water, cfr. section 4. For the present discussion, we will neglect the influence on the vertical distribution of oil of all but the last breaking wave. More precisely, we assume that the vertical distribution at an arbitrary time is determined by the last breaking wave to pass before that time. This approximation seems satisfactory if the ratio of "mixing depth" to the time interval between breakers is "small enough". It is clear that when this ratio increases the need to include the effect of earlier breakers will sooner or later become mandatory. Now, there is nothing in our model that prevents us from taking into consideration the effect of any number of preceding breakers, the only limitation being the unwieldiness of the expressions obtained.

To get on with our present model, assume that the density of droplets with rise velocity u as a function of depth z immediately after a breaker has passed, i.e. at time T_k for some k , is given by the function $\phi(D_k, z; u)$. For each definite value of the random variable D_k , this is an ordinary function of the real variable z . Letting $C(t; z, u)$ denote the density of droplets with rise velocity u at depth z at an arbitrary time t , we may write

$$C(T_k; z, u) = \phi(D_k, z; u) \text{ for every } k \dots\dots\dots(1)$$

and

$$C(t; z, u) = \phi(D_k, z + u(t - T_k); u); T_k \leq t < T_{k+1} \dots\dots\dots(2)$$

for every k.

We now want to determine the probability density of $C(t; z, u)$ for an arbitrary fixed time t . To this effect, let f_W denote the probability density function of the time interval W between t and the time of the last preceding breaker. Having fixed t, z and u , we suppress the variables from $C(t; z, u)$ and write simply C . We now have

$$C = \phi(D, z + uW; u) \dots\dots\dots(3)$$

As the next step, we shall exploit our experimental observations which indicate that the mixing created by the breaking wave gives a nearly uniform distribution down to a rather well defined depth, which we have called the "mixing depth". Accordingly, we shall assume that we may write

$$\phi(D, z; u) = \frac{p(u)}{D}, \text{ for } 0 \leq z \leq D \text{ (= 0 elsewhere)} \dots\dots\dots(4)$$

Here $p(u)$ denotes the fraction of droplets with rise velocity u , cfr. section 4. For simplicity, we shall assume $\sigma = 1$ so that

$$\int_0^{u_{\max}} p(u) du = 1 \dots\dots\dots(5)$$

From the above we may proceed to calculate the probability distribution function F_C of the random $C = C(t; z, u)$. Instead of entering the details of this calculation, we refer the interested reader to reference 6 where the details may be found. Here we shall just give the final answer, which is:

$$F_C(c) = \int_0^Z f_D(x) dx + \int_Z^\infty \int_{\frac{x-Z}{u}}^\infty f_W(w) f_D(x) dw dx + \int_0^\infty \int_0^{\frac{x-Z}{u}} f_W(w) f_D(x) dw dx \dots\dots\dots(6)$$

for $0 \leq c \leq \frac{p(u)}{Z}$ (the singular point $c = 0$ causes no difficulty here) while for c outside this interval:

$$F_C(c) = 0 \dots\dots\dots(7)$$

Before we continue to make specific assumptions about the probability laws, a few words on the probability density function f_W are appropriate. Now, it is obvious that to determine the probability law of W directly from observations of passing breakers is a rather cumbersome process. In trying to connect W to a random variable more easily determined, it is natural to investigate the connection between

W and the time intervals between passing breakers. Define, then, the random variables $Y_k = T_k - T_{k-1}$, which we assume to be identically distributed with probability density f_Y . It turns out that for most practical purposes we have the following connection between f_W and f_Y .

$$f_W(w) = \frac{1}{E(Y)} \int_w^\infty f_Y(y) dy; w \geq 0 \quad (=0; w < 0) \dots\dots\dots(8)$$

Consequently, an estimate of f_Y , which we may obtain directly from the observational data (with the proper assumptions), allow us quite easily to estimate f_W .

From our experimental data, we are able to give estimates of $p(u)$ as a function of u , cfr. section 4. By taking this into consideration, we see from (6) that the remaining unknown factors are the probability density functions f_W and f_D . At present, however, there is no information available regarding these probability laws. In passing we mention that we intend to carry out research aiming at providing this necessary information.

Using (6) and (7) and writing $C = C(z, u)$ since the probability structure of C is independent of t , as it should be, we shall have

$$E(C(z, u)) = \int_0^{p(u)/z} \{1 - F_C(c)\} dc \dots\dots\dots(9)$$

(9) gives the expected density at depth z of droplets with rise velocity u . To find the expected density of oil at depth z , we just integrate (11) over u (expectation commutes with integration) to find

$$E(C(z)) = \int_0^{u_{max}} E(C(z, u)) du \dots\dots\dots(10)$$

where $C(z)$ denotes the density of oil at depth z .

Denoting by $M(z)$ the amount of oil below the depth z , we find that

$$E(M(z)) = \int_z^\infty E(C(x)) dx \dots\dots\dots(11)$$

If, initially, the surface density is σ , then we just multiply (12) and (13) by σ to obtain the appropriate answers.

A quantity of special interest for oil recovery operations is the mean amount of oil left on the sea surface under given weather conditions. Expressed in per cent of total amount, we denote it by P_S . It is now easy to see that P_S will be given as follows:

$$P_S = 100 \cdot \{1 - E(M(0))\} \dots\dots\dots(12)$$

3. EXPERIMENTS.

This section is an adaption of the work reported in reference 7.

3.1 Test conditions and instrumentation.

In order to analyze the break-up and turbulent mixing into the sea of an oil slick on the surface caused by a spilling breaker passing the slick, a series of experiments were carried out in a towing tank of main dimensions 25 x 2.5 x 1.5 meters (length x width x depth). The principal aims were to find an estimate of the droplet size distribution, which is caused by the break-up of the oil slick, and to determine the "mixing depth" produced by each breaker.

After some preliminary experimentation, it was decided to apply the following testing procedure:

To produce the breaking waves, the technique of impulse waves was applied. An impulse wave is brought about by the dispersive properties of deep water waves. By decelerating the wave maker in a proper manner a wave train is produced that will converge at a preassigned location in the test tank. For details, see for instance reference 8. Using this technique, it was possible to produce a rather well defined spilling breaker in a given region in the middle of an oil slick with a thickness of about 5-7 mm. The height of the breaking impulse wave was varied by changing the amplitude of the wave maker. During the test programme, a wave height of approximately 0.4 metres was used.

To get a measure of the amount of oil at different depths as a function of time after the breaker had passed, an apparatus as sketched in Fig. 1 was used. (Tables and figures are placed at the end of the paper). It consisted of six thin glass tubes of different length, each inserted into a larger reservoir pipe, as shown in Fig. 1. The six reservoir pipes ended in a common suction chamber, which was connected to a vacuum tank by a flexible suction hose. A manually operated magnetic valve was used to open and close this connection. The suction chamber with its six protruding glass tubes was secured to an aluminium frame on the top of two light float elements in such a manner that the length of the submerged part of the glass tubes were 2, 4, 7, 10, 15 and 20 cm, respectively, when the assembled rig was floating on calm water. With this floating rig it was desired to take a sample of the oil/water mixture at the depths given above and at different times after the breaker had passed. In order to obtain this, it is obvious that the wave riding properties of the rig had to be very good. By trial and error, float elements were found that gave a wave rider that followed the wave forms nicely. The rig was kept in an upright vertical position by long nylon strings, as shown in Fig. 2. The strings were made sufficiently long to ensure unhampered vertical motion of the rig.

The sample of the oil/water mixture was taken by opening the connection between the suction chamber and the vacuum tank for a few tenths of a second. By allowing the oil to settle in each reservoir pipe, the fraction of oil in the sampled mixture could be measured, as illustrated in Fig. 1.

The tests were performed with a pure mineral oil both in fresh and emulgated state, i.e. oil that had been on the water for several weeks. In the non-emulgated state, the oil has properties similar to those of fresh crude oil from the Norwegian Continental Shelf. The properties of the oil in the two states are given in Table 1. As we mentioned above, during all the tests there was a mean oil film thickness of about 5 - 7 mm in the test tank.

The test programme we refer to in this report is detailed in Table 2. Explanatory comments to the tests are given in the table.

3.2 Presentation of results.

We shall present the experimental results in the form of diagrams giving the arithmetical mean and standard deviation of the measurements for each condition.

Fig. 3 to 7 show the percentage of emulgated oil in the sample as a function of time after the breaker had passed the rig. During these tests the wave started to break about 1.5 meters ahead of the rig.

Fig. 8 to 11 show the percentage of fresh oil in the sample as a function of time after the breaker had passed the rig. The wave started to break about 1.5 meters ahead of the rig.

3.3 Discussion of results.

In order to assess the errors we may commit in using the described sampling procedure to estimate the "mixing depth" and distribution of the oil, we need to consider what happens when a breaking wave hits the oil slick. During the first second after the breaker has passed, there is a mixing of the oil into the water which gradually reaches its maximum depth. Then, immediately, the oil droplets will start to rise towards the surface and, for instance, during three tenths of a second the fastest droplets may have risen as much as 4 cm. From this it is clear that sampling at time intervals of one second leads to the following conclusion: The deeper the sample is taken, the more we are in error when using the sample to estimate the initial density of oil. Consequently, the applied sampling procedure will not allow a proper estimate of the "mixing depth". However, the measured evolution with time of the density at the different sampling depths will be approximately correct, except for the first second after the breaker has passed. Therefore, if by some other means we are able to give a reasonably correct estimate of the initial distribution with depth of the density of oil, we shall also be able to estimate the droplet size distribution.

To obtain an estimate of the density distribution, we shall exploit the visual observations made of the mixing process. These observations did indicate a rather well-defined depth to which the mixing of oil extends and also a nearly uniform distribution of oil droplets with depth. The corresponding assumption of a uniform distribution down to a well-defined depth, called the "mixing depth", has already been used in section 2 in constructing our theoretical model. We shall also apply it in the next section in order to determine the droplet size distribution. From both visual observations and later experiments (cfr. reference 9) we have estimated the "mixing depth" to be approximately 0.2 meters.

4. DROPLET SIZE DISTRIBUTION.

Exploiting the experimental data given in section 3 and with the assumptions of section 2 still effective, we now want to find an estimate for the distribution of droplet sizes $p(u)$ characterized by the parameter u , which is the terminal rise velocity of a droplet through calm water. According to the assumptions we made in section 2, each passing breaker produce the same distribution $p(u)$ and a uniform depth distribution from the sea surface down to the "mixing depth". Assuming a unit surface density and letting $K_D(t, z; u)$ denote the density of droplets with rise velocity u at depth z as a function of time t after the breaker has passed, given the associated "mixing depth" D , we then have

$$K_D(0, z; u) = \frac{p(u)}{D}; D < z \leq D \dots\dots\dots(13)$$

Under the given conditions there will be an upper bound to the rise velocities. We shall consequently assume a fixed upper limit u_{max} to the rise velocities u , so that $p(u) = 0$ for $u > u_{max}$. u_{max} will generally depend on the type of oil present. A more detailed discussion of u_{max} is deferred to the end of this section.

We define $K_D(t, z)$ by

$$K_D(t, z) = \int_0^{u_{max}} K_D(t, z; u) du; 0 < z \leq D \dots\dots\dots(14)$$

$K_D(t, z)$ is then the density of oil at depth z at time t after the breaker has passed. From (13) and (14) we get

$$K_D(D, z) = \int_0^{u_{max}} K_D(D, z; u) du = \frac{1}{D}; D < z \leq D \dots\dots\dots(15)$$

At a time t after the breaker has passed, all droplets with a rise velocity $u > (D-z)/t$ will have passed the depth z on their way to the

surface. This, of course, presupposes that $t \geq (D-z)/u_{\max}$. Accordingly, we shall have

$$K_D(t,z) = K_D(0,z), \quad 0 \leq t < \frac{D-z}{u_{\max}}, \dots\dots\dots(16)$$

$$K_D(t,z) = \int_0^{\frac{D-z}{t}} \frac{p(u)}{D} du ; \quad t \geq \frac{D-z}{u_{\max}} \dots\dots\dots(17)$$

The experimental results for $K_D(t, z)$ show an exponential decrease with time. In agreement with our assumptions, we therefore expect to find that

$$K_D(t,z) = \frac{1}{D} e^{-\kappa(D,z)(t-t_{\min})} ; \quad t \geq t_{\min} \dots\dots\dots(18)$$

where $t_{\min} = (D-z)/u_{\max}$ and $\kappa(D,z)$ is constant for each D and z . To determine the dependence of κ on D and z , we apply the following one-to-one correspondence between the rise velocity and time

$$u = \frac{D-z}{t} ; \quad t \geq t_{\min} \dots\dots\dots(19)$$

Differentiating (17) and (18) with respect to time, by direct comparison we obtain, using (19):

$$p(u) = \kappa(D,z)(D-z)u^{-2} e^{-\kappa(D,z)(D-z)\left(\frac{1}{u} - \frac{1}{u_{\max}}\right)} \dots\dots\dots(20)$$

Our assumptions imply that $p(u)$ should not exhibit any dependence on D and z , which lead to the following equality

$$\kappa(D, z) = \frac{\kappa}{D-z} \dots\dots\dots(21)$$

where κ should depend only on the properties of the oil. Substituting (21) into (18) we obtain

$$K_D(t,z) = \frac{1}{D} e^{-\frac{\kappa}{D-z}(t-t_{\min})} ; \quad t \geq t_{\min} \dots\dots\dots(22)$$

Inserting (21) into (20) we get

$$p(u) = \kappa u^{-2} e^{-\kappa \left(\frac{1}{u} - \frac{1}{u_{\max}} \right)}, \quad 0 < u \leq u_{\max} \dots\dots\dots(23)$$

In order to test out the relations we have obtained on the basis of our assumptions, we plotted $K_D(t, z)$ taken from Fig. 4 -7 and 9 - 11. As mentioned at the end of the previous section, the "mixing depth" was estimated to be approximately 0.2 m. For fresh oil we found $\kappa = 0.17$ from Fig. 9, $\kappa = 0.20$ from Fig. 10 and $\kappa = 0.22$ from Fig. 11. This supports our assumptions rather well, and by putting $\kappa = 0.2$ in (22) we shall find that this expression fits the experimental results nicely. Similarly, we find that (22) with $\kappa = 0.02$ agrees tolerably well with the experimental results for the emulgated oil.

The distribution $p(u)$ that we have determined above is the result of one breaking wave. In reality, however, it is clear that the appropriate rise velocity distribution induced by a passing breaker is not determined solely by that wave, but also by preceding breakers. The reason for this is that the smaller oil globules may not have resurfaced when the next breaker comes along. The "equilibrium" rise velocity distribution will therefore contain a larger portion of small rise velocities than the $p(u)$ determined previously. In order to obtain a better approximation to the correct distribution, we shall assume a constant frequency of passing breakers and a constant mixing depth. It is natural to choose the corresponding mean values \bar{Y} and \bar{D} , respectively. We then have a limit velocity $u_1 = \bar{D}/\bar{Y}$, because all the oil with rise velocity greater than u_1 will have resurfaced before the next breaker comes. However, in many cases u_{\max} is smaller than u_1 , and as this simplifies the analysis below, we shall assume this to be the case.

Let us now study the effect of a sequence of breaking waves, equidistant in time, passing a fixed location with an initial surface density of oil $\sigma_0 = 1$. The rise velocity distribution induced by the first passing breaker we have already determined to be given by $p(u)$ as in (23).

With the assumption $u_{\max} \leq u_1$ in mind, we find that the amount of oil of rise velocity u having surfaced when the second breaker passes, i.e. after a time \bar{Y} , is given by

$$\sigma_1(u) = p(u) \frac{u}{u_1}; \quad 0 < u \leq u_{\max} \dots\dots\dots(24)$$

The surface density at that instant is given by

$$\sigma_1 = \int_0^{u_{\max}} \sigma_1(u) du \dots\dots\dots(25)$$

The distribution over rise velocity due to surface oil induced by the second breaker is $\sigma_1 p(u)$. The distribution due to oil being

in the water column will be $p(u) - \sigma_1(u)$. The rise velocity distribution, $p_1(u)$, due to the second breaker will then be given by

$$p_1(u) = (1 + \sigma_1) p(u) - \sigma_1(u) \text{ or } (\sigma_0 + \sigma_1)p(u) - \sigma_1(u) \dots\dots\dots(26)$$

We have, of course, tacitly assumed a uniform distribution with depth, as implied by the considerations of section 2.

The amount of oil of rise velocity u having surfaced when the third breaker passes, is given by

$$\sigma_2(u) = p_1(u) \frac{u}{u_1} = [(\sigma_0 + \sigma_1)p(u) - \sigma_1(u)] \frac{u}{u_1} \dots\dots\dots(27)$$

The corresponding surface density is

$$\sigma_2 = \int_0^{u_{\max}} \sigma_2(u) du \dots\dots\dots(28)$$

Similarly as above, we find that the rise velocity distribution $p_2(u)$, due to the third breaker is given by

$$\begin{aligned} p_2(u) &= \sigma_2 p(u) + p_1(u) - \sigma_2(u) \\ &= (\sigma_0 + \sigma_1 + \sigma_2)p(u) - (\sigma_1(u) + \sigma_2(u)) \dots\dots\dots(29) \end{aligned}$$

Continuing this process, we shall find generally for every $n = 1, 2, 3, \dots$

$$\sigma_n(u) = \left[\sum_{i=0}^{n-1} \sigma_i p(u) - \sum_{i=1}^{n-1} \sigma_i(u) \right] \frac{u}{u_1} \dots\dots\dots(30)$$

$$\sigma_n = \int_0^{u_{\max}} \sigma_n(u) du \dots\dots\dots(31)$$

$$p_n(u) = \sum_{i=0}^n \sigma_i p(u) - \sum_{i=0}^n \sigma_i(u) \dots\dots\dots(32)$$

Here $\sigma_n(u)$ denotes the surface density of oil of rise velocity u having surfaced just prior to the $(n+1)$ th breaker, σ_n is the total density of surfaced oil at that instant and $p_n(u)$ is the rise velocity distribution induced by the $(n+1)$ th breaker.

From (30) we easily establish the following recursion relation valid for every $n = 1, 2, \dots$

$$\sigma_{n+1}(u) = \sigma_n p(u) \frac{u}{u_1} + \left(1 - \frac{u}{u_1}\right) \sigma_n(u) \dots\dots\dots(33)$$

Using this recursion relation, we find that for $n = 1, 2, \dots$

$$\sigma_{n+1}(u) = p(u) \frac{u}{u_1} \sum_{i=0}^n \sigma_{n-i} \left(1 - \frac{u}{u_1}\right)^i \dots\dots\dots(34)$$

We have for every $n = 1, 2, \dots$

$$\sigma_{n+1}(u) = p_n(u) \frac{u}{u_1} \dots\dots\dots(35)$$

Combining (34) and (35), we get

$$p_n(u) = p(u) \sum_{i=0}^n \sigma_{n-i} \left(1 - \frac{u}{u_1}\right)^i \dots\dots\dots(36)$$

The appropriate rise velocity distribution to use in the model developed in section 2 would be $\lim_{n \rightarrow \infty} p_n(u)$ provided, of course, that

this limit exists. It turns out that with $p(u)$ as given by (23), $p_n(u)$ converges very fast for all relevant values on u_1 , and we may assume a stationary situation after just a few waves (~ 10).

To know $p(u)$ we see that we also need to know u_{max} . Unfortunately, we are not able to estimate u_{max} from our experiments, as is easily realized by recollecting the discussion in section 3.3. According to reference 10, the maximum rise velocity through calm water for oil droplets of fresh crude oil with properties similar to our mineral oil is approximately 0.1 m/sec. This corresponds to droplets with diameter about 2 - 3 mm. A further increase of the diameter leads to a decrease of the rise velocity. As we have nothing else to rely on at the present, we shall assume $u_{max} = 0.1$ m/sec. in the next section, where we try to illustrate our theory by some numerical examples. The value of u_{max} that enters the distribution $p(u)$ cannot be expected constant for each type of oil. For instance, u_{max} will most certainly depend on the surface density σ and the intensity of the mixing process. The assumptions $u_{max} = 0.1$ m/sec. may therefore prove to be a rather crude one.

For the sake of completeness we mention that some simple experiments we performed did corroborate a maximum rise velocity of the mineral oil of about 0.1 m/sec. More precisely, we found a maximum rise velocity of 0.13 - 0.15 m/sec, and there was no significant difference between fresh and emulgated oil.

Regarding the maximum rise velocity for emulgated oil, it turns out not to be easily accessible. This is due to the fact that the interfacial tension between the water phase and the emulgated phase is a key parameter in the mechanism that determines the maximum rise velocity, and this interfacial tension is almost impossible to measure.

5. CONCLUDING REMARKS.

In this paper we have constructed a theoretical framework which we believe will enable us to determine with reasonable accuracy the vertical distribution of oil in the sea under given environmental conditions. But this, of course, depends on the availability of sufficiently accurate input data. These, however, do not exist today.

At the Ship and Ocean Laboratory in Trondheim we are at present engaged in research aiming at developing suitable experimental methods that will allow us to establish the correct input data to our model by full scale measurements out at sea. Especially, we want to establish the statistical laws of breaking frequency and "mixing depth" which are the two most important inputs to the model.

The importance to pollution control of the problem we have considered in this paper should warrant a considerable effort towards the establishing of a reasonably correct solution.

ACKNOWLEDGEMENTS.

The author would like to express his appreciation of the many helpful discussions with Prof. E. Huse of the Ship and Ocean Laboratory. I also stress my debt to Mr. S. Eggen and Mr. E.G. Kringeland for supplying the experimental data given in this paper.

7. NOMENCLATURE.

- t - arbitrary, fixed time point
- T_k - random time points of passing breakers
- Y_k - $Y_k \stackrel{\text{def.}}{=} T_k - T_{k-1}$
- f_Y - probability density function of the random variables Y_k
- W - random variable equal to the time interval between t and time of the last preceding breaker
- f_W - probability density function of the random variable W (W_1)
- D_k, D - random "mixing depth" as induced by passing breakers
- f_D - probability density function of the random variables D_k and D
- u - rise velocity of an oil droplet
- $p(u)$ - fraction of droplets with rise velocity u
- $p_n(u)$ - fraction of droplets with rise velocity u just prior to (n+1)th breaker (section 4)

- $\sigma_n(u)$ - Surface density due to oil of rise velocity u just prior to $(n + 1)$ th breaker (section 4)
- δ_n - Surface density of oil just prior to $(n + 1)$ th breaker (section 4)
- z - Depth below the water surface
- $\phi(D,z;u)$ - Density of droplets with rise velocity u as a function of depth z immediately after a breaker inducing a "mixing depth" D has passed
- $C(t;z,u)$ - Density of droplets with rise velocity u at depth z at an arbitrary time t
- F_C - Probability distribution function of the random variables $C(t;z,u)$
- $M(z)$ - Amount of oil below depth z
- $K_D(t,z;u)$ - Density of droplets with rise velocity u at depth z as a function of time t after the breaking impulse wave has passed (section 4)
- $K_D(t, z)$ - Density of oil at depth z at time t after the breaking impulse wave has passed (section 4)
- P_S - Defined by $P_S = 100(1-E(M(D)))$, i.e. $P_S\%$ of the oil is expected on the surface
- κ - Parameter entering $p(u)$

8. REFERENCES.

1. Mackay, D. and Leinonen, P.J.: "Mathematical model of the behaviour of oil spills on water with natural and chemical dispersion". Report EPS 3-EC-77-19. Environmental Protection Service, Ottawa, Canada.
2. Raj, Phni P.K.: "Theoretical Study to Determine the Sea State Limit for the Survival of Oil Slicks on the Ocean". NTIS No. AD-A049-794. Arthur D. Little, Inc. report to USCG 1977.
3. Raj, P.K. and Griffiths, R.A.: "The Survival of Oil Slick on the Ocean as a function of Sea State Limit". Proceedings 1979 Oil Spill Conference, Los Angeles.
4. Lin, J.-T., Gad-el-Hak, M. and Liu, H.-T: "A Study to Conduct Experiments Concerning Turbulent Dispersion of Oil Slicks". Report No. CG-61688-A. U.S. Coast Guard, 1978.

5. Lin, J.-T. and Liu, H.-T.: "Effects of an Oil Slick on Wind Waves". Proceedings 1979 Oil Spill Conference, Los Angeles.
6. Naess, A: "The effect of breaking waves on the mixing of oil spills into the sea". NSFI Report R-74.78. The Ship Research Institute of Norway.
7. Eggen, S. og Kringeland, E.G.: "En oljes neddriving og fordeling i brytende bølger". NSFI Arbeidsnotat A.N.SMT 05.08.77.
8. Longuet-Higgins, M.S.: "Breaking waves - in deep or shallow water". Proc. 10th Conf. on Naval Hydrodynamics MIT June 1974.
9. Naess, A.: "The relation between wave induced turbulence and mixing depth of oil pollutants". NSFI Report (to be published).
10. Hu.S. and Kintner, R.C.: "The fall of single liquid drops through water". AIChE Journal, Vol. 1. 1955.

TABLE 1

Type of oil	Kinematic viscosity cSt (20 °C)	Density kg/m ³
Fresh mineral oil	2.75	795
Emulgated mineral oil	21.00	829

TABLE 2

Type of oil	Wave height of breaker (m)	Comments
Emulgated mineral oil	0.4	Samples taken at different points of time after the breaker had passed the rig. The rig was placed approx. 1.5 m downstream from where the wave started to break. 4 samples were taken for each condition. Fig. 3 - 7.
Fresh mineral oil	0.4	Same comments as above. 7 samples taken for each condition. Fig. 8 - 11.

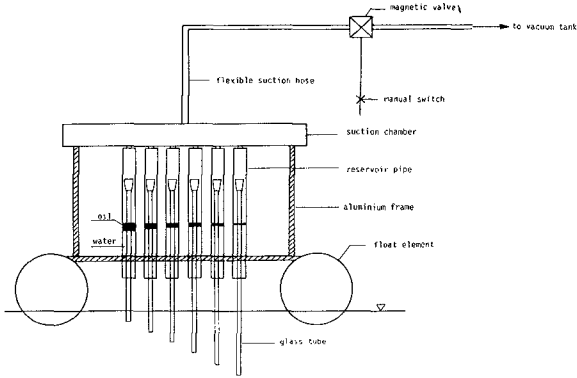


Fig. 1 - Rig for sampling the oil/water mixture.

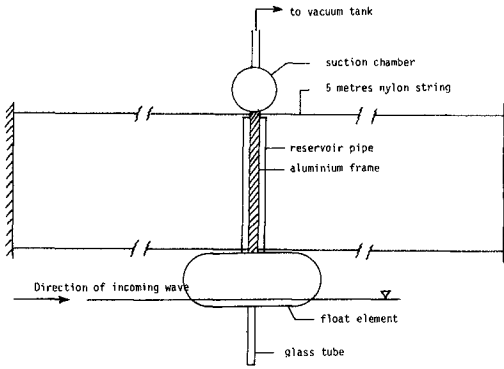


Fig. 2 - Side-view of rig showing crawl-foot arrangement to keep rig in vertical position.

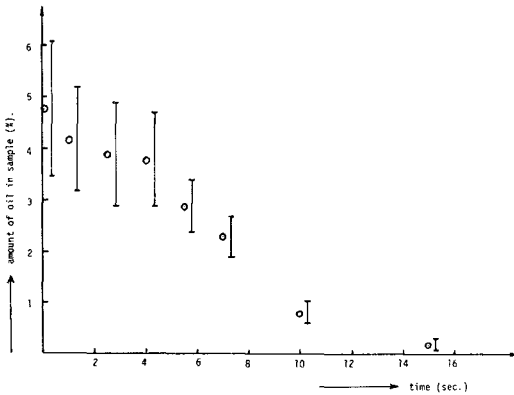


Fig. 3 - Sample taken at depth 2 cm. Emulgated oil.

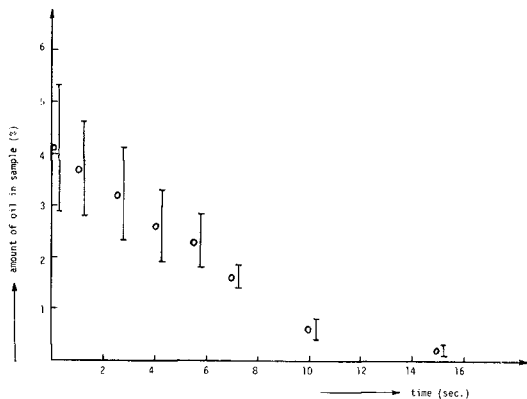


Fig. 4 - Sample taken at depth 4 cm. Emulgated oil.

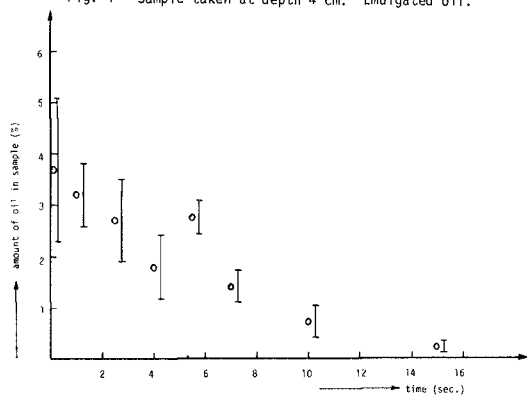


Fig. 5 - Sample taken at depth 7 cm. Emulgated oil.

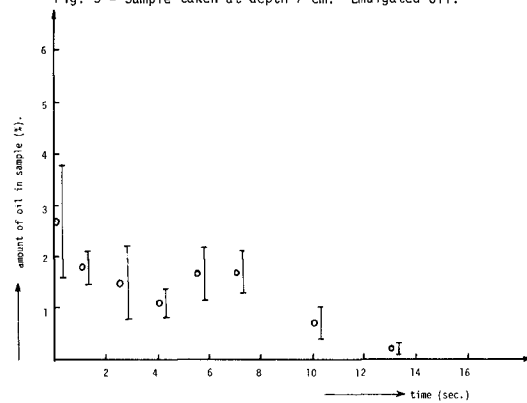


Fig. 6 - Sample taken at depth 10 cm. Emulgated oil.

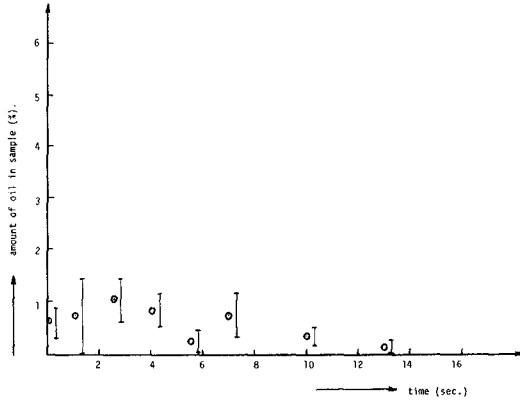


Fig. 7 - Sample taken at depth 15 cm. Emulgated oil.

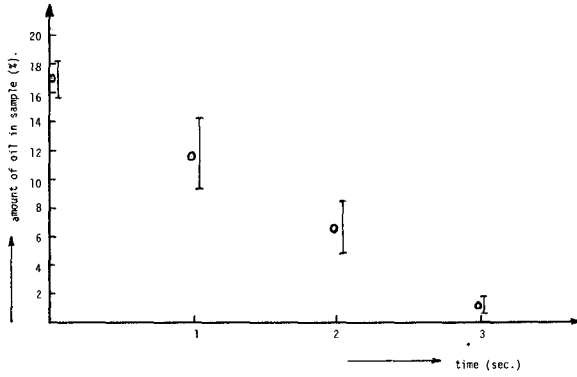


Fig. 8 - Sample taken at depth 2 cm. Fresh oil.

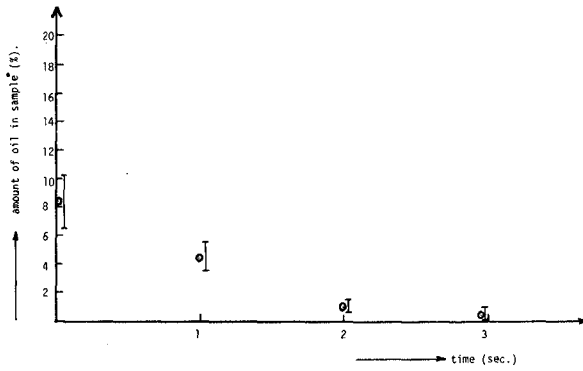


Fig. 9 - Sample taken at depth 4 cm. Fresh oil.

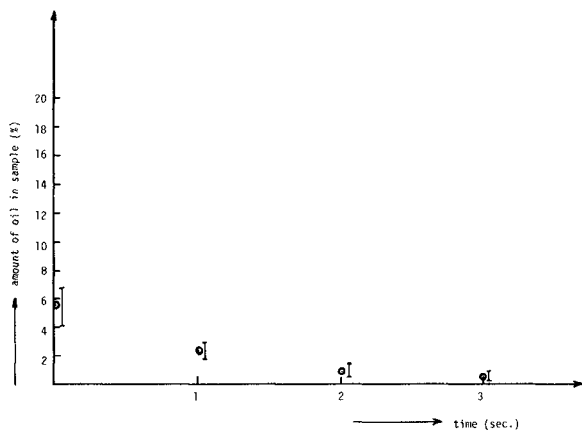


Fig. 10 - Sample taken at depth 7 cm. Fresh oil.

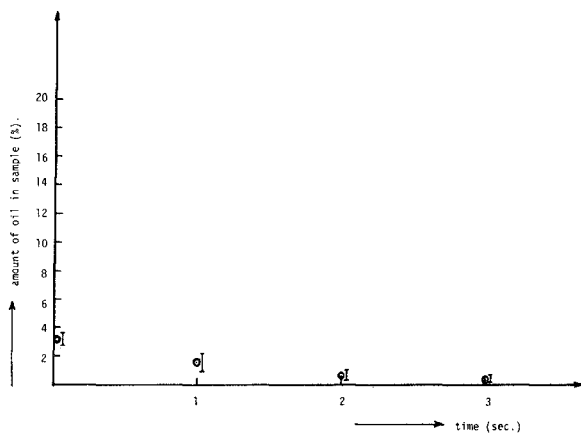


Fig. 11 - Sample taken at depth 10 cm. Fresh oil.

ON A ROLE OF THE INTERFACIAL FROUDE NUMBER

by

Masakazu Kashiwamura*

ABSTRACT

As already stated in the previous conference, the fresh-water flow which passes through a river mouth horizontally into the sea, exhibits a special characteristic due to the effect of buoyancy. Its dynamics belongs, essentially to the same category with the transonic flow in aerodynamics. The interfacial Froude number plays a dominant role in this case, as well as the Mach number does in the transonic gas flow. The supercritical zone, in which the interfacial Froude number exceeds unity, occupies the sea surface with some area, in response to a degree of the discharge amount of the fresh water. This zone begins at the river mouth and stretches in the offshore directions over the sea, accompanied with a lateral growth.

As is well known, on the other hand, supersonic zones are sometimes formed partially along an airfoil, or in a tube with a varying cross-section, if they are placed in a subsonic gas flow. Those two different phenomena have been proved to be identical dynamically with each other [KASHIWAMURA and YOSHIDA 1978], [KASHIWAMURA 1979]. There have been a great number of researches in order to obtain an analytical solution of the transonic flow, in the past several decades, but there seem still many difficulties to attain a complete solution, except some particular cases such as a stream-lined approximation of immersed bodies being possible.

Considering such circumstances, it may also be difficult for the present problem to be solved completely, although it has not been decided yet to be impossible. The present author describes the process of his efforts for obtaining an analytical solution and its results, from a view point of the inspection on an applicability of the hodograph method, and its modification to this problem. In spite of incompleteness, they provide us several findings which are useful to understand the dynamics of the outflow of the fresh water. In addition to those, a few examples of field data concerning the horizontal distribution of the interfacial Froude number around a river mouth, and some experimental results are presented.

* Professor of Engineering Science, Dr. Sc.
Faculty of Engineering, Hokkaido University, Sapporo, 060, JAPAN.

INTRODUCTION

Not only a river water, which flows into the sea, but also other types of flow, such as a thermal discharge of cooling water from a power plant, a drainage of waste water from human lives, etc. are dynamically in the same category of the density current. Studies on those topics seem to have been extensively carried on, all over the world, nowadays, based on an enhancement of the environmental assessment. A vast quantity of papers have been issued concerning those problems every year. However, in the opinion of the present author, studies related to the mixing mechanism have been too much highly weighted, judging from the trend of issued papers, compared with the buoyancy effect which is the essential origin of the density current.

The inertia of a fluid mass accelerated by the buoyant force, sometimes, causes unstable circumstances along the interface, which frequently lead to the occurrence of internal waves, interfacial unstable vortices, and their breaking and finally mixing. Although studies on mixing are surely very important from a view point of the dilution of water temperature and waste water, the essential solution of those problems seems not to be possible, unless the basic buoyancy effects are evaluated correctly.

Based on this conception, the present author started a series of theoretical studies on an idealized density current without mixing. Such a situation corresponds to the treatment of the transonic gas flow without viscosity effects and thermodynamical changes accompanied with a heat loss. The first thing to be dealt with, along this line, was an inspection of the fundamental equations related to the idealized two-layered flow. As a result, a certain type of equation was derived, with regard to the velocity potential, under the assumption of a steady, irrotational, inviscid and immiscible flow. This equation coincides in form with that of the transonic gas flow, except one point that the Mach number is replaced by the interfacial Froude number [KASHIWAMURA and YOSHIDA 1978].

Such a coincidence implies that the river water has a flow pattern which is dynamically similar to the transonic flow. As is well known, supersonic zones are sometimes formed in part around an airfoil which is placed in a uniform subsonic flow. The same trend can also be seen in a pipe flow with a varying cross-section. Those instances predict the existence of a supercritical zone in which the interfacial Froude number exceeds unity, over the sea surface, around a river mouth. The prediction was proved quite right from field observations which were already shown in the previous conference.

Since the above-mentioned equation is a mixed type of a partial differential equation of the second order, it is difficult to obtain an analytical solution with usual methods. The author shows developed processes of an analytical approach in this problem mainly with the hodograph method, although they are incomplete yet.

FUNDAMENTAL EQUATIONS AND THEIR TRANSFORMATION

Extremely idealized equations of motion will be followed, in regard to the two-layered flow, under the assumption of steadiness, inviscidity and immiscibility. Since it means that there is no entrainment from the sea water below, the fresh water maintains its density to be unchanged, and the lower sea water should be stagnant. Therefore, only the fresh-water flow may be taken into consideration, as follows.

$$u \frac{\partial u}{\partial x} + v \frac{\partial u}{\partial y} + \epsilon g \frac{\partial h}{\partial x} = 0 \quad (1)$$

$$u \frac{\partial v}{\partial x} + v \frac{\partial v}{\partial y} + \epsilon g \frac{\partial h}{\partial y} = 0 \quad (2)$$

$$\frac{\partial}{\partial x} (hu) + \frac{\partial}{\partial y} (hv) = 0 \quad (3)$$

Eqs. (1) and (2) are equations of motion, and Eq. (3) is a continuity equation. All symbols employed here, are listed in the last section.

As the fresh water is considered to have a uniform velocity at a distance sufficiently upstream from the river mouth, the flow may be regarded to be irrotational everywhere. Then,

$$\frac{\partial v}{\partial x} = \frac{\partial u}{\partial y} \quad (4)$$

and this is satisfied by

$$u = \frac{\partial \phi}{\partial x}, \quad v = \frac{\partial \phi}{\partial y} \quad (5)$$

Thus, the velocity potential ϕ exists. Combination of Eqs. (1), (2) and (3) produces the following equation, which was already presented in the previous conference.

$$\left(1 - \frac{u^2}{\epsilon gh} \right) \frac{\partial^2 \phi}{\partial x^2} - 2 \frac{uv}{\epsilon gh} \frac{\partial^2 \phi}{\partial x \partial y} + \left(1 - \frac{v^2}{\epsilon gh} \right) \frac{\partial^2 \phi}{\partial y^2} = 0 \quad (6)$$

Eq. (6) is of much significance, because of its mathematical form, showing that the fresh-water flow is dynamically the same with the transonic gas flow.

If the term $\sqrt{\epsilon gh}$ is replaced by the local sound velocity, Eq. (6) coincides with a two-dimensional equation of the transonic flow with a velocity potential. But this type of equation is extremely difficult to obtain a solution due to not only its non-linear form but also its mixed type with elliptic, parabolic and hyperbolic characters in response to numerical values of the dominant parameter, such as the Mach number, or the interfacial Froude number.

In the subsonic flow, however, immersed bodies are usually thin and stream-lined in shape, that some approximations have been adoptable to obtain a practically useful solution. On the other hand, in the present case, any river extends its width discontinuously from finite to infinite at its mouth, and the surrounding boundary cannot be changed into any convenient shape which is regarded as stream-lined.

Considering such a difference of both circumstances, the fresh-water flow seems to be more difficult than the transonic flow, in order to obtain a solution around a river mouth. Nevertheless, it will not be meaningless, to try to solve it, even with those methods already adopted in the transonic flow, since it may bring us something useful to understand this phenomenon deeply.

First, an attempt to transform the fundamental equations will be described. The stream function of some kind can be defined from Eq. (4), as follows.

$$hu = \frac{\partial \psi}{\partial y}, \quad hv = -\frac{\partial \psi}{\partial x} \quad (7)$$

Thus, Eqs. (1) and (2) are transformed into,

$$u \frac{\partial u}{\partial x} + v \frac{\partial v}{\partial x} - v \left(\frac{\partial v}{\partial x} - \frac{\partial u}{\partial y} \right) + \epsilon g \frac{\partial h}{\partial x} = 0 \quad (8)$$

$$u \frac{\partial u}{\partial y} + v \frac{\partial v}{\partial y} + u \left(\frac{\partial v}{\partial x} - \frac{\partial u}{\partial y} \right) + \epsilon g \frac{\partial h}{\partial y} = 0 \quad (9)$$

Those equations are rearranged by substituting Eq. (7), as follows.

$$\frac{\partial}{\partial x} \left(\frac{1}{2} q^2 + \epsilon gh \right) + \frac{\Gamma}{h} \frac{\partial \psi}{\partial x} = 0 \quad (10)$$

$$\frac{\partial}{\partial y} \left(\frac{1}{2} q^2 + \epsilon gh \right) + \frac{\Gamma}{h} \frac{\partial \psi}{\partial y} = 0 \quad (11)$$

where,

$$\Gamma = \frac{\partial v}{\partial x} - \frac{\partial u}{\partial y} = - \left\{ \frac{\partial}{\partial x} \left(\frac{1}{h} \frac{\partial \psi}{\partial x} \right) + \frac{\partial}{\partial y} \left(\frac{1}{h} \frac{\partial \psi}{\partial y} \right) \right\} \quad (12)$$

Therefore, the following form is derivable.

$$\frac{1}{2} q^2 + \epsilon gh + \int \frac{\Gamma}{h} d\psi = C \quad (13)$$

where C is an integral constant. Differentiation of Eq. (13) with regard to ψ , leads to,

$$\frac{dH}{d\psi} + \frac{\Gamma}{h} = 0 \quad (14)$$

or

$$\frac{1}{h} \left\{ \frac{\partial}{\partial x} \left(\frac{1}{h} \frac{\partial \psi}{\partial x} \right) + \frac{\partial}{\partial y} \left(\frac{1}{h} \frac{\partial \psi}{\partial y} \right) \right\} = \frac{dH}{d\psi} \quad (15)$$

where $H = q^2/2 + \epsilon gh$, which is a modified Bernoulli's term.

When the flow is assumed to be irrotational, Eqs. (4) and (5) can be employed, and Eq. (15) is divided into two parts.

$$H = \frac{1}{2} q^2 + \epsilon gh = \text{const.} \quad (16)$$

$$\frac{\partial}{\partial x} \left(\frac{1}{h} \frac{\partial \psi}{\partial x} \right) + \frac{\partial}{\partial y} \left(\frac{1}{h} \frac{\partial \psi}{\partial y} \right) = 0 \quad (17)$$

Eq. (17) is another expression of Eq. (4).

HODOGRAPH METHOD

It seems so difficult to eliminate h from both equations (16) and (17), that a derivation of the equation concerning ψ only may be hopeless. Then it is necessary to seek another approach. In such a case, the hodograph method has been sometimes effective, as is well known of some examples in aerodynamics. The following set arises from Eqs. (5) and (7).

$$u = \frac{\partial \phi}{\partial x} = \frac{1}{h} \frac{\partial \psi}{\partial y} \quad (18)$$

$$v = \frac{\partial \phi}{\partial y} = -\frac{1}{h} \frac{\partial \psi}{\partial x} \quad (19)$$

The existence of h makes it impossible to apply the conformal representation, since the Cauchy-Riemann's equation is not realized, though there is a little resemblance, in form, between them.

From both equations, the followings are derived.

$$d\phi = u dx + v dy \quad (20)$$

$$\frac{1}{h} d\psi = -v dx + u dy \quad (21)$$

Combining those two, with the latter being multiplied by the imaginary unit i , the complex equation can be formed as follows.

$$d\phi + i \frac{1}{h} d\psi = (u - iv)(dx + idy) = q e^{-i\theta} dz \quad (22)$$

Therefore,

$$\frac{\partial z}{\partial q} = q^{-1} e^{i\theta} \frac{\partial \phi}{\partial q} + i \frac{1}{hq} e^{i\theta} \frac{\partial \psi}{\partial q} \quad (23)$$

$$\frac{\partial z}{\partial \theta} = q^{-1} e^{i\theta} \frac{\partial \phi}{\partial \theta} + i \frac{1}{hq} e^{i\theta} \frac{\partial \psi}{\partial \theta} \quad (24)$$

are obtained. Differentiating the upper with respect to θ and the lower q , and putting them to be equal, two equations are obtainable from the real part and the imaginary part respectively, as follows.

$$\frac{\partial \phi}{\partial q} = q \frac{\partial}{\partial q} \left(\frac{1}{hq} \right) \frac{\partial \psi}{\partial \theta} \quad (25)$$

$$\frac{\partial \phi}{\partial \theta} = \frac{q}{h} \frac{\partial \psi}{\partial q} \quad (26)$$

Now, the transformation is made in the following manner.

$$t = \int \frac{h}{q} dq \quad (27)$$

Eqs. (25) and (26) are rearranged with respect to t and θ , by taking Eq. (16), which represents a conservation of the modified Bernoulli's term, into consideration, as follows.

$$\frac{\partial \phi}{\partial t} = - \Lambda \frac{\partial \psi}{\partial \theta} \tag{28}$$

$$\frac{\partial \phi}{\partial \theta} = \frac{\partial \psi}{\partial t} \tag{29}$$

where Λ is defined by,

$$\Lambda = \frac{1}{h^2} \left(1 - \frac{q^2}{\epsilon gh} \right) = \frac{1}{h^2} \left(1 - F_1^2 \right) \tag{30}$$

Eliminating ϕ from Eqs. (28) and (29), the following equation is obtained.

$$\frac{\partial^2 \psi}{\partial t^2} + \Lambda \frac{\partial^2 \psi}{\partial \theta^2} = 0 \tag{31}$$

Since the symbol Λ includes F_1 in itself, this equation shouldn't be linear in a strict sense, but if Λ can be replaced by any adequate function with respect to t and θ , this equation is regarded as a linear one, and there may be a possibility of obtaining an approximate solution.

The parameter Λ changes from positive to negative, while F_1 grows from a value smaller than unity to a value which exceeds unity. This means that Eq. (31) is also a partial differential equation of the mixed type. Therefore, it is the most important, in this case, to find a function which has a good agreement to the characteristic of Λ . Such a situation has already been experienced else, in the past, with several proposals of functional forms in the field of the two-dimensional transonic flow.

ANOTHER APPROACH

A great interest is centered on a knowledge of the interfacial Froude number, in particular, how it to distribute horizontally over the sea off a river mouth. It may be effective for this purpose, to employ the interfacial Froude number F_1 , as an independent variable in the governing equation of the fresh-water flow. It may be considered also as one of the modified hodograph methods. Let F be a newly defined variable, as $F = F_1^2$, that is,

$$F = F_1^2 = q^2 / \epsilon gh \tag{32}$$

If Eq. (16), that is, $(1/2)q^2 + \epsilon gh = C$, is employed simultaneously, the followings are obtainable.

$$h = 2C / \epsilon g (F + 2) \tag{33}$$

$$q = \sqrt{ 2CF / (F + 2) } \tag{34}$$

By the use of those two relationships, Eqs. (25) and (26) can be transformed into,

$$\frac{\partial \psi}{\partial F} = \frac{2C}{\epsilon_g F(F+2)^2} \frac{\partial \phi}{\partial \theta} \quad (35)$$

$$\frac{\partial \psi}{\partial \theta} = \frac{2CF}{\epsilon_g (F-1)} \frac{\partial \phi}{\partial F} \quad (36)$$

Cross-differentiation of both equations with respect to F and θ , leads to,

$$\frac{\partial^2 \psi}{\partial F^2} + \frac{3F+2}{F(F+2)} \frac{\partial \psi}{\partial F} + \frac{1-F}{F^2(F+2)^2} \frac{\partial^2 \psi}{\partial \theta^2} = 0 \quad (37)$$

$$\frac{\partial^2 \phi}{\partial F^2} + \frac{1}{F(1-F)} \frac{\partial \phi}{\partial F} + \frac{1-F}{F^2(F+2)^2} \frac{\partial^2 \phi}{\partial \theta^2} = 0 \quad (38)$$

Those are both linear partial differential equations of the second order, and it may be possible to obtain each solution, although there is a difficulty in transforming boundary conditions from the physical plane to the hodograph plane.

Let Eq. (37) only be treated with here. The solution is assumed to be in the form of

$$\psi = \int_{-\infty}^{\infty} f(F, n) e^{in\theta} dn \quad (39)$$

By substituting Eq. (39) into Eq. (37), an ordinary differential equation of the second order, with respect to the new function f , is obtained, as follows.

$$\frac{d^2 f}{dF^2} + \frac{3F+2}{F(F+2)} \frac{df}{dF} - n^2 \frac{1-F}{F^2(F+2)^2} f = 0 \quad (40)$$

This is the equation of the Fuchs' type, in which three regular singular points exist, at $F = 0$, $F = -2$ and $F = \infty$. From the indicial equation at each point, two roots, viz., the exponents can be obtained as follows, respectively.

$$\lambda_1 = \frac{n}{2}, \quad \lambda_2 = -\frac{n}{2} \quad \text{for } F = 0 \quad (41)$$

$$\mu_1 = \frac{1}{2}(-1 + \sqrt{1+3n^2}), \quad \mu_2 = \frac{1}{2}(-1 - \sqrt{1+3n^2}) \quad \text{for } F = -2 \quad (42)$$

$$\nu_1 = 2, \quad \nu_2 = 0 \quad \text{for } F = \infty \quad (43)$$

Therefore, the function f can be determined with the Riemann's P-function, as shown in the followings.

$$f = P \left\{ \begin{array}{ccc|c} 0 & -2 & \infty & \\ \frac{n}{2} & \frac{-1 + \sqrt{1+3n^2}}{2} & 2 & F \\ -\frac{n}{2} & \frac{-1 - \sqrt{1+3n^2}}{2} & 0 & \end{array} \right\} \quad (44)$$

Since the P-function is not concrete in a mathematical form, for a practical application, it is possible to transform the expression into a hypergeometric series with regard to the regular singular

points, if necessary. Thus, anyhow, the general solution of Eq. (37) can be obtained in the form;

$$\psi = \int_{-\infty}^{\infty} C(n) P \begin{pmatrix} 0 & -2 & \infty \\ \frac{n}{2} & \frac{-1+\sqrt{1+3n^2}}{2} & 2 \\ -\frac{n}{2} & \frac{-1-\sqrt{1+3n^2}}{2} & 0 \end{pmatrix} F e^{in\theta} dn \quad (45)$$

where $C(n)$ denotes a function of n , which must be determined by the boundary conditions.

On this stage, the determination of a functional form of $C(n)$ comes up to be a troublesome task in order to satisfy the boundary conditions. At the present, it prevents a further development for obtaining a satisfactory solution which is applicable for practical use. Although, unfortunately unsuccessful yet it is, those two kinds of mathematical approach strongly impress us again, that the outflow dynamics of the fresh-water flow belongs to a category which is quite the same with that of the transonic flow, from both dynamical and mathematical view points.

Numerical computations are in progress, in parallel with such analytical approaches, but they need a little more time to overcome the singularity which appears at a river mouth, where the equation changes its characteristic from elliptic to hyperbolic.

The present author has continued a series of studies on the density current which appears in the neighborhood of a river mouth, for more than twenty years, and has, just recently, reached a finding of this interesting problem. Since he has little knowledge about the progress at the present situation in aerodynamics, he desires earnestly to receive any advices and comments, kindly offered by those who have much experience in the field of the two-dimensional transonic flow.

FIELD EXAMPLES AND DISCUSSIONS

A supercritical zone, in which the interfacial Froude number F_i exceeds unity, extends over the sea surface, from a river mouth into offshore directions, as well as a supersonic zone in which the Mach number M exceeds unity, is formed partially along an airfoil which is placed in a subsonic flow. It has already become a common understanding that the interfacial Froude number must be unity at the river mouth, if a salt wedge lies along the river bed, beneath the fresh water. This condition is very important, in particular, to calculate a shape of the salt wedge. It is also widely accepted that the interfacial Froude number decreases its numerical value smaller and smaller with the distance upstream from the mouth. Outside the mouth, in contrast with it, the number grows larger than unity, as has been revealed in the field measurements made by the author and his collaborators [KASHIWAMURA and YOSHIDA 1978].

The trend of such a longitudinal change of the interfacial Froude number was, hitherto, sometimes treated by some researchers but usually only one-dimensionally, along the stream line. According to the present author, however, it must be considered horizontally. This paper neglects mixing from the fundamental equations intentionally, because of an attempt to put emphasis on the buoyancy characteristic of the fresh-water flow. However, needless to say, this type of flow is always accompanied with mixing, and therefore, some differences between theoretical and practical are expected at some points, for instance, a figure and a size of the supercritical zone, or a spatial distribution of the interfacial Froude number.

It is well known that the mixing grows intensively with an increase of the numerical value of the interfacial Froude number. Accordingly, the upper fresh water and the lower sea water must be mixed violently with each other, within the supercritical zone. This fact has also been examined in field measurements, in which salinity concentration in the fresh water abruptly grows in this zone. The mixing mechanism of this kind has been studied with a very careful observation in laboratory experiments, by Dr. Yoshida [YOSHIDA 1980].

Figs. 1, 2 and 3 show three field examples of the supercritical zone and a horizontal distribution of the interfacial Froude number, in the vicinity of the mouth of the Ishikari River, which flows by Sapporo City. The amount of the river discharge, in Fig. 1, is the greatest among three cases, and in Fig. 3, smallest. In every case, the salt wedge stretched inward, beneath the fresh water along the river, though its length differed. Judging from those figures, the area occupied by the supercritical zone seems to depend on the amount of the river discharge. From a theoretical view point, the numerical value of the interfacial Froude number at the front of the salt wedge should be a dominant parameter for determining the whole area occupied by the supercritical zone.

We can find a small zone in which $F_i > 3$, in Fig. 1, but on the other hand, the maximum of F_i doesn't reach 2, in Fig. 3. Thus, the area of the supercritical zone is also dependent on the maximum value of F_i itself within it. The inshore end of the zone is always located approximately at the river mouth in each case, and it must correspond to the control condition which has been believed to hold true that $F_i = 1$ at the river mouth. Another small supercritical zone is found locally at the end of the left sand spit in Figs. 2 and 3. It may perhaps be caused by a rapid flow based on a potential flow.

Fig. 4 shows a longitudinal change of the interfacial Froude number F_i along the main stream of the fresh-water flow, where F_i grows rapidly in the vicinity of the river mouth and exceeds unity. In this figure, since the distance is limited within 600 m offshore, the further trend of F_i cannot be seen, but it decays down again at some point beyond 600 m, undoubtedly, as shown in Fig. 3. The symbol E denotes a coefficient of entrainment which takes place from the lower sea water into the upper fresh water. Numerical values of E are obtainable from an equation which has been proposed, as Eq. (5), in

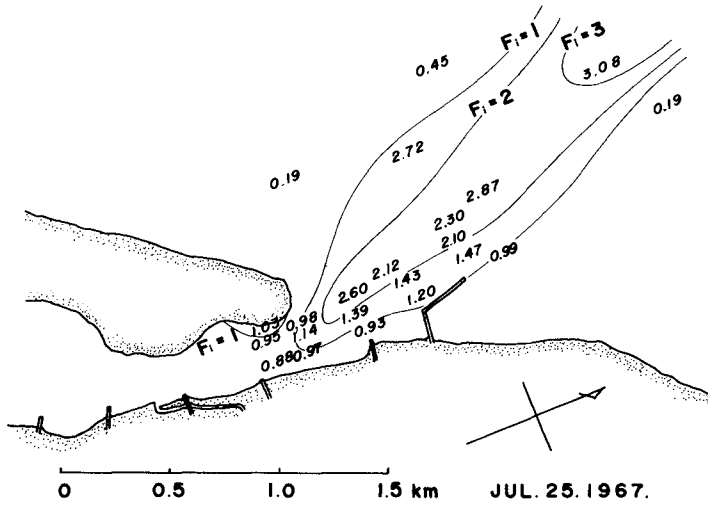


Fig. 1 The supercritical zone formed in the neighborhood of the mouth of the Ishikari River.

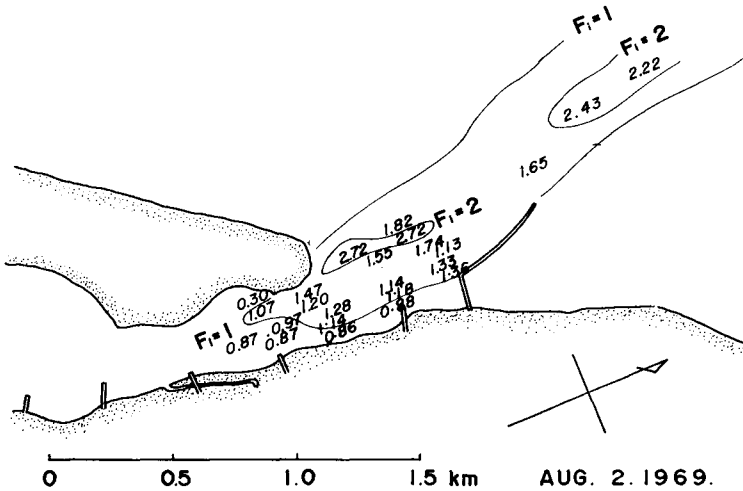


Fig. 2 Another example of the supercritical zone at the Ishikari River

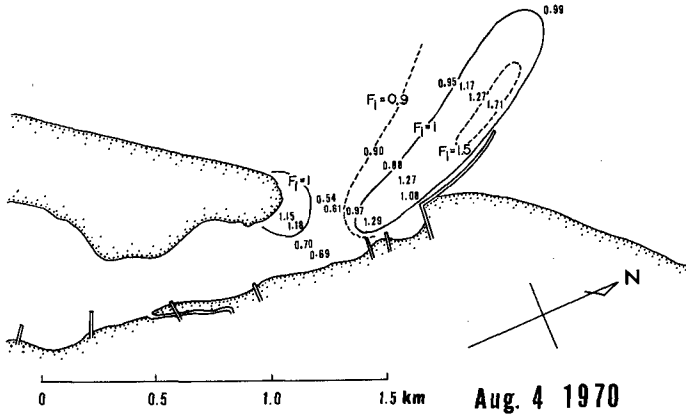


Fig. 3 The third example of the supercritical zone at the Ishikari River.

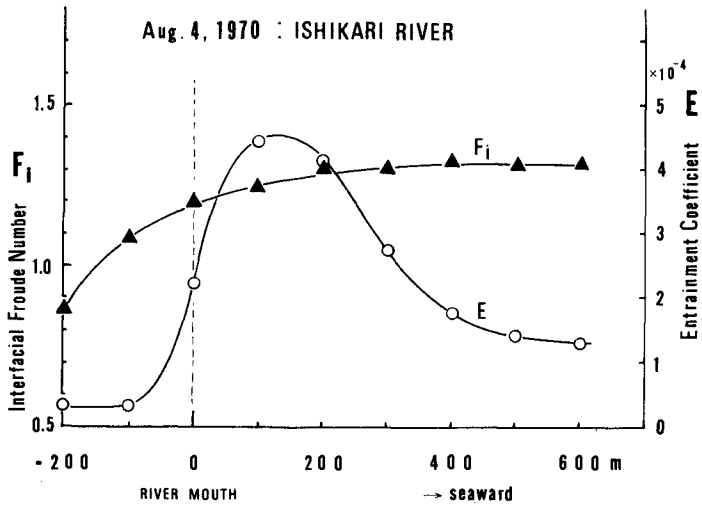


Fig. 4 Longitudinal change of the interfacial Froude number F_i and the entrainment coefficient E .

the previous proceedings. The entrainment coefficient E grows rapidly with an increase of F_i , but it is interesting that E decays soon much earlier than F_i . The relationship between E and F_i should be a theme which is necessary to reveal in the near future.

Figs. 5 and 6 show another field examples which have been obtained in the neighborhood of the mouth of the Teshio River, which is situated on the north-western district of Hokkaido. Since the observed points are much less than the previous examples at the Ishikari River, the extension of the supercritical zone cannot be determined in shape exactly, but the zone evidently exists just from the river mouth to offshore directions, as well as in each case of the Ishikari River. In both cases, in Figs. 5 and 6, the salt wedge was formed over a distance more than 10 km along the river bed. The longitudinal change of F_i is also shown in Fig. 7, whose data are based on the observation shown in Fig. 5. The trend resembles that of the Ishikari River, but it shows that there is a decaying stage after the distance of 200 m off the mouth. The symbol \bar{u}_1 is a velocity of the fresh-water flow, and its highest value is found at a little distance off from the mouth. This phenomenon has usually been believed to be peculiar to the two-layered flow at a river mouth, as has already been published by the present author [KASHIWAMURA 1972]. In this manner, the field examples have confirmed an existence of the supercritical zone, as already predicted by the theory.

If the discharge amount of the river water grows up beyond a certain limit, the salt wedge is pushed out from the river mouth into the sea, as is frequently experienced in a flood season. In such a case, as the interfacial Froude number F_i exceeds unity even inside the river, the dynamical situation is similar to a flow around an airfoil which is placed in a supersonic flow, and then, the supercritical zone may occupy a much larger area over the sea. A thermal discharge of cooling water from a power plant is also belonging to the same category with those cases.

As is well known, shock waves and thermodynamical changes are accompanying to the formation of the supersonic zone in aerodynamics. In our cases, the mixing between the fresh water and the sea water may correspond to those phenomena. Studies on a fine mechanism of the mixing seem to be very important from this view point.

Finally, an example in model experiments is shown in Fig. 8. This is one of the recent works which have been done by Mr. Nishida, graduate student of our laboratory. This shows a horizontal distribution of F_i and the supercritical zone which extends from the outlet of the channel into offshore directions, and it gives approximately the same trend with the field examples. Thus, the laboratory experiment and the field measurements have proved together, the existence of the supercritical zone, as the present author predicted from the theoretical consideration.

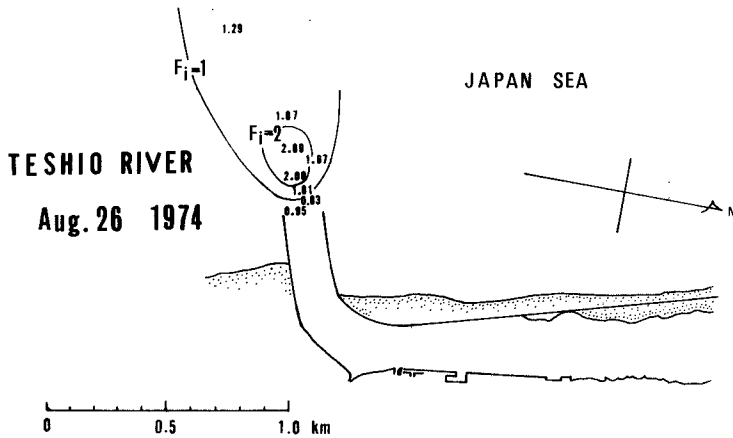


Fig. 5 The supercritical zone formed over the sea, in the neighborhood of the mouth of the Teshio River.

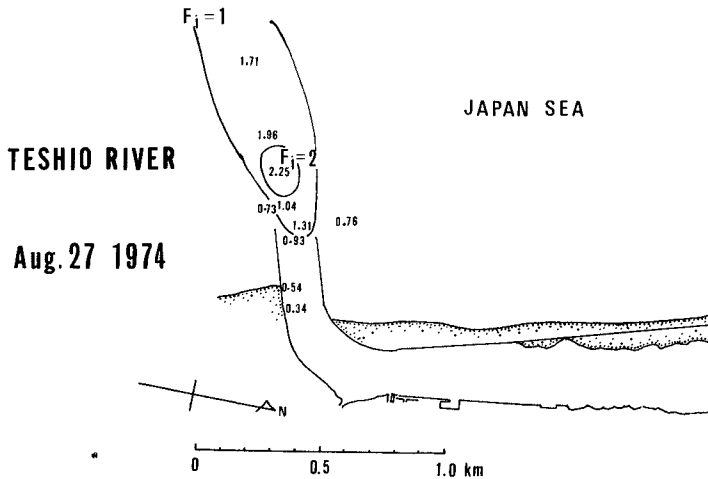


Fig. 6 Another example of the supercritical zone at the Teshio River.

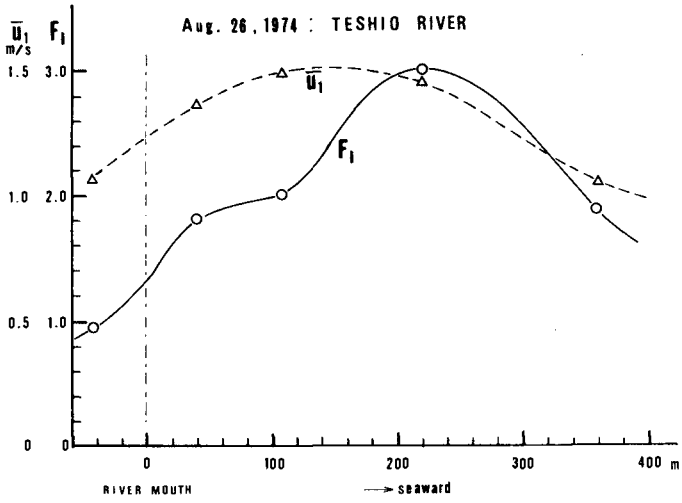


Fig. 7 Longitudinal change of F_i and the surface velocity \bar{u}_1 .

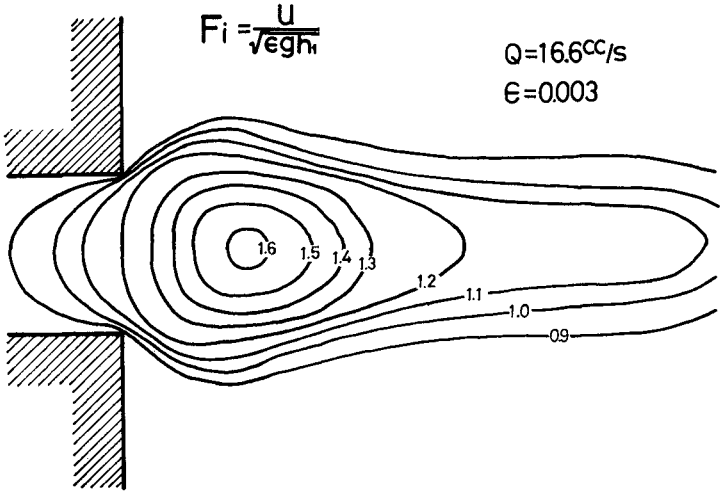


Fig. 8 The supercritical zone formed in the laboratory experiment. [After Mr. Nishida].

CONCLUSION

First, the equation of motion was treated, with regard to the fresh-water flow, which flows out from a river mouth, horizontally into the sea. Emphasis was placed on the buoyancy only, and then viscosity and mixing were neglected. As the result, the dominant equation agreed, in form, with the equation of a transonic gas flow. The interfacial Froude number plays a dominant part, in the place of the Mach number, which is dominant in the transonic flow.

Next, the governing equation was studied, with the hodograph method and its modification, in order to obtain a solution. Although unsuccessful yet they were, the coincidence between the fresh-water flow and the transonic flow, was still more confirmed, in dynamical and mathematical meanings. As the present author had predicted an existence of the supercritical zone outside a river mouth, by analogy of the existence of a supersonic zone in the transonic flow, several examples of the field observation were illustrated, in order to prove that the prediction was correct. Mixing takes place intensively in the supercritical zone, since the interfacial Froude number exceeds unity there.

Throughout the description, the author has put emphasis on the importance of the buoyancy effect of the fresh-water flow, so as to attract attentions to the singular characteristic of the two-layered density current, which resembles the transonic flow, and also to a significant role of the interfacial Froude number which dominates the entire flow characteristics even including the mixing between the fresh water and the salt water.

The author expresses his sincere thanks to all the collaborators in his laboratory for their helps of many kinds, in particular, to Mr. Nishida, who kindly offered an unpublished experimental result, for the present paper.

NOTATIONS

- x, y: Longitudinal and lateral coordinates.
- u, v: Velocity components referred to x and y.
- q: Absolute value of velocity, $q = \sqrt{u^2 + v^2}$.
- ϕ : Velocity potential.
- ψ : Modified stream function.
- F_1 : Interfacial Froude number, $F_1 = q/\sqrt{\epsilon gh}$.
- F: $F = F_1^2$.
- ϵ : Parameter of density difference, $\epsilon = 1 - (\rho_1/\rho_2)$.
- ρ_1, ρ_2 : Densities of fresh water and salt water.
- g: Gravitational acceleration.
- h: Depth of fresh water.
- M: Mach number.
- z: Complex number, $z = x + iy$.
- θ : Argument of velocity vector.
- Γ : $\Gamma = (\partial v/\partial x) - (\partial u/\partial y)$.

H: Modified Bernoulli's term, $H = (1/2)q^2 + \epsilon gh$.
t: $t = \int (h/q) dq$
 $\Lambda: \Lambda = (1 - F_1^2)/h^2$.
n: Arbitrary variable defined within $-\infty < n < \infty$.

REFERENCES

- Kashiwamura, M. and Yoshida, S. [1972], International Symposium on Stratified Flows, NOVOSIBIRSK, "Flow Pattern at a River Mouth", pp. 587-592.
- Kashiwamura, M. and Yoshida, S. [1978], Proceedings of the 16th Coastal Engineering Conference, HAMBURG, "Outflow Dynamics at a River Mouth", pp. 2925-2944.
- Kashiwamura, M. [1979], Memoirs of Faculty of Engineering, Hokkaido University, Vol. XV, No. 1 (No. 66), "Dynamical Singularities of Two-Layered Flow at the Outlet of an Open Channel", pp. 93-99.
- Yoshida, S. [1980], The 2nd International Symposium on Stratified Flows, TRONDHEIM, "Mixing Mechanism of Density Current System at a River Mouth", (to be published).

DISPERSION OF COOLING WATER FROM A COASTAL LNG PLANT.

P. ACKERS,* J.D. PITT,* G.THOMPSON,* AND K.G. RIPPIN+

ABSTRACT

The object of this case study was to predict the likely degree of pollution resulting from the discharge of heated water from a proposed LNG plant into the sea (Figure 1). The expected thermal loading was 40 m³/s at a temperature of 10°C above the natural ambient sea water temperature. The investigation was required to provide data for an ecological study to determine the possible impact of the plant on the coastal and marine environment.

Information on tide levels, tidal currents, salinity, sea temperature, wind strength and direction was obtained in a general survey programme which had already been commissioned. These data provided vital information on seasonal variations in marine conditions and further local information was obtained from short intensive hydrographic surveys. The data were analysed to yield a simplified description of the tidal and wind induced currents and suitable values of mixing parameters for use in two numerical models. The first dealt with the "near field" processes of the spread of a buoyant layer of heated water under the convecting influence of the tidal currents. The second model simulated the "far field" processes which give rise to a general increase in the temperature of the sea in the region.

*Binnie and Partners, London.

+Binnie International, Hong Kong and Australia.

1. INTRODUCTION

Objectives

1.1 The main object of the study was to obtain approximate indications of the extent of the spread of heated effluent from the proposed LNG plant, together with the probable range of temperature increase at locations which were environmentally sensitive. The methods used relate equally well to other conservative and non-conservative pollutants, and so an ancillary purpose of the work was to assess the spread and concentration of chemical pollutants, for example anti-fouling additives, that might be present at significant concentrations in the plant effluent. However, only the temperature aspects are described here. This information was required for a range of tidal and seasonal weather patterns, to enable other specialists to assess the impact of thermal and other pollution on the marine and coastal ecology. To this end, liaison between the ecologists and hydraulicians was necessary to identify sensitive areas requiring particular scrutiny.

1.2 In the time scale available and within the budget that appeared reasonable for an environmental study, physical modelling was inappropriate. In any case, there are severe limitations in making scale models of the relevant processes. Consequently the chosen method of study was by computer simulation. Within the time and budget constraints many approximations and simplifications were needed but it is believed that the predictions made were of appropriate detail and accuracy for the purposes of an environmental impact appraisal.

1.3 Two numerical models were used, one of which dealt with the "near field" processes of the spread of a buoyant layer of heated water under the convecting influence of the tidal currents. The second model simulated the "far field" processes which give rise to a general increase in the temperature of the sea in the region. In each case, output was presented as the increase above ambient temperature so absolute temperatures were derived by super-position of output data on existing conditions.

The Proposed Scheme

1.4 Woodside Petroleum Development Pty Ltd. are proposing to abstract natural gas from the North Rankin gas field located some 130 km offshore from Dampier in 125 m depth of water. The gas will be brought ashore through a single pipeline to the onshore terminal at Withnell Bay, approximately 12 km north-east of the town of Dampier (Figure 1). Here some of the gas will be piped directly to local markets and to the city of Perth through a proposed 1,500 km long gas pipeline, and some will be liquified to be exported in LNG tankers. It is expected that something like half of the total output from the North Rankin field will be liquified, for export, at Withnell Bay.

1.5 The proposed facilities at Withnell Bay include a gas inlet station, LNG loading jetty, service jetty, LNG storage tanks, offices, and the gas liquifaction plant. It is envisaged that the liquifaction plant will be divided into three equal sized modules (trains), each with a capacity of about 11 mill. m³ per day. To liquify gas it must be cooled

down to -160°C . This is achieved by compressing the gas in large steam driven compressors, typically of 20,000 hp or more each. The enormous amount of heat given off during the liquifaction process is dissipated through heat exchangers into the cooling water system, the heat load being of similar order of magnitude to a nuclear power station.

The Cooling Water System

1.6 Neither fresh water cooling nor air cooling is possible in the hot arid climate of the north-west. The only cooling medium readily available to the site is sea water. Optimisation studies carried out on the LNG complex as a whole indicated an optimum rise in the cooling water temperature of about 10°C , corresponding to a once-through sea water requirement of about $150,000\text{ m}^3$ per hour, i.e. $40\text{ m}^3/\text{s}$ approximately.

1.7 It is proposed that the water will be drawn from near the sea bed several hundred metres off the coast north of the plant site. The heated water will be discharged into a watercourse known as "No Name Creek" south of the plant site. From here the hot water will travel down the watercourse into "No Name Bay" and thence to the open sea. The proposed arrangement for the cooling water system is shown in Figure 2.

2. METHODOLOGY

Physical principles

2.1 The prediction of thermal pollution relies upon a detailed understanding of the mechanism by which the heat from the discharge will spread through the receiving body of water and overlying air. The heat absorbed by the seabed adjacent to hot water outfalls has been shown to be negligible in similar situations elsewhere (1) and so was not considered further.

2.2 As the heated water travels down No Name Creek a distance of 750 m, it will lose a small amount of heat by evaporation and radiation. On entering No Name Bay the heated water will mix with the relatively small body of water in the bay and it may form a surface layer in the deeper part of the bay, depending upon the tidal conditions. The total heat losses in the creek and bay were calculated to give a maximum temperature reduction of less than 1°C . Therefore in the rest of the analysis it was assumed that the nominal 10°C temperature rise through the plant applied at the outfall from No Name Bay into Mermaid Sound.

2.3 At the exit from No Name Bay, the heated water will spread out over the surface of the sea under the influence of buoyancy, momentum and shear stresses between the two layers. In this "near field", the water will be vertically stratified with the hot water forming a plume on the surface of the cooler sea water. This plume will be convected up and down the coast by the currents whilst being gradually dispersed by vertical and horizontal mixing. The temperature concentration will thus reduce and the edge of the plume will become indistinct. The degree of mixing occurring will be a function of the variability of the velocity, which in turn will depend upon tidal and wind conditions as well as local sea bed topography.

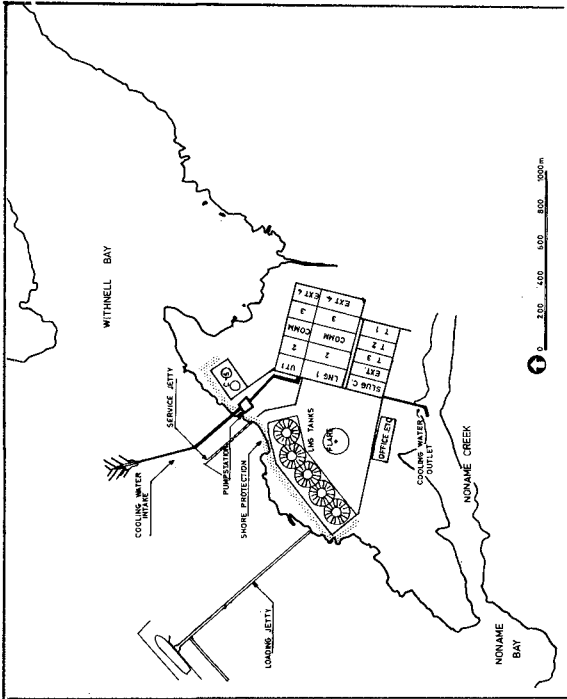


FIGURE 2 COOLING WATER OUTFALL ARRANGEMENT

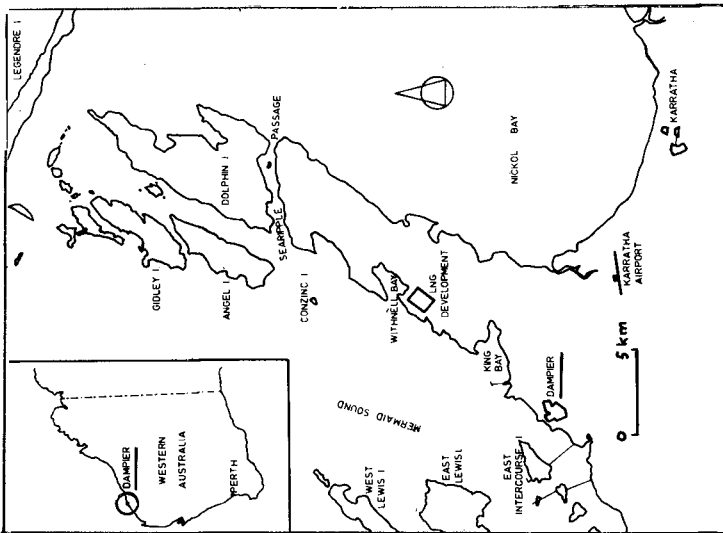


FIGURE 1 GENERAL LOCATION MAP

2.4 The hot water discharge can travel up to one tidal excursion from No Name Bay in the first tidal period after release; however, to travel further, it must rely upon net tidal and wind induced drifts and mixing. These are slower processes than inter-tidal convection. Outside a range of one tidal excursion from No Name Bay, the maximum temperature rise caused by the hot water discharge will be much reduced. The vertical stratification will also diminish progressively until mixing over the water depth is complete.

2.5 The continuous release of heat through No Name Bay will raise the general water temperatures above their natural levels over a large area of Mermaid Sound. The new temperature distribution will depend upon:

- the heat input by the LNG plant.
- the distribution of the cooling water by tidal drift and wind induced currents.
- the mixing of the cooling water with the water in the sound in both horizontal and vertical directions.
- the heat losses through the water surface into the atmosphere.

2.6 The computer programs which model the two main phases of cooling water dispersal are based on different assumptions. The "near field" model indicates the conditions in the intertidal zone close to the outlet at No Name Bay, in the surface layer generated by thermal stratification. The "far field" model looks at a much larger sea area beyond the zone of strong stratification assuming the heat to be distributed through the water depth and to be dissipated by surface cooling and spread by drift currents induced by wind and tides. In practice the "near field" and "far field" processes merge but they are commonly considered separately for simplicity.

Near field model

2.7 The "near field" model considers the initial spread of a buoyant plume entering Mermaid Sound via No Name Bay. It traces the change in shape of the plume and derives the temperature rise at various points within the plume for a variety of wind and tidal conditions.

2.8 The plan shape of the plume was determined by monitoring the movement of discrete labelled patches of hot water in a calculated velocity field over two or more tidal cycles. The velocity of a labelled patch in the surface layer was obtained as the vector addition of the ambient time-varying water velocity and the imposed velocity due to the source (2). The source has significant width compared to the tidal excursion, and was therefore treated as the summation of a large number of closely spaced point sources. The imposed velocity is then given by:-

$$U_x = \frac{Q}{4 \pi Da} \log \left\{ \frac{y^2 + (x+a)^2}{y^2 + (x-a)^2} \right\}$$

$$U_y = \frac{Q}{2 \pi Da} \left\{ \tan^{-1} \left(\frac{x+a}{y} \right) - \tan^{-1} \left(\frac{x-a}{y} \right) \right\} \quad \text{Equ.1.}$$

where a = half width of the line source.
 D = assumed depth of surface layer
 x,y = co-ordinates of the point relative to the centre of the line source.
 Q = volumetric discharge rate
 U_x, U_y = velocities in the x and y directions.

2.9 Random eddy motions and the non-uniformity of current patterns are inevitable components of any turbulent flow. Such motions will mix the cooling water discharge with the ambient water, and can be described by using a Fickian analogy in writing a steady-state two-dimensional diffusion convection equation. Taking into account a simple description of surface cooling based on temperature increment above an ambient equilibrium condition, the full cooling expression becomes:-

$$\frac{\partial}{\partial y} \left\{ -D_y \frac{\partial T}{\partial y} \right\} + U \cdot \frac{\partial T}{\partial x} + \frac{kT}{h} = 0 \quad \text{Equ. 2}$$

where T = temperature
 x,y = the local plan co-ordinates within the plume
 U = water velocity in the plume in the x direction
 D_y = instantaneous lateral dispersion coefficient
 k = surface heat loss coefficient
 h = plume depth

In the above, the dispersive flux in the direction of water movement has been ignored because it is generally much less than the convective flux due to the velocity U.

2.10 The solution of equation 2 has been treated by Brooks (3). Although his analysis was restricted to an unidirectional current, it is informative in that it gives an estimate of the likely dilution during either the ebb or flood tide and is therefore appropriate to the early life of the plume. In the equation, the mixing of the plume and the local water is described by a lateral dispersion coefficient which has to be assessed. It is a function of many physical phenomenon, including vertical density gradients, wind effects, tidal currents and local topography, but field and laboratory work has shown that a reasonable first estimate of the dispersive processes is given by:-

$$D_y = 0.01 L^{4/3} \quad (\text{in CGS units}) \quad \text{Equ. 3}$$

where L = plume width
 D_y = lateral dispersion coefficient.

Substituting into equation 2 and solving gives the centreline temperature of the plume (3) as:-

$$N_d = T/T_o = \exp \left\{ \frac{-kt}{h} \right\} \operatorname{erf} \left\{ \frac{3/2}{(L/b)^2 - 1} \right\}^{1/2} \quad \text{Equ. 4}$$

where b = initial plume width
 L = instantaneous plume width, where

$$L = b \left\{ 1 + \frac{2}{3} \beta \frac{x}{b} \right\}^{3/2} \quad \text{Equ. 5}$$

$$\beta = \frac{12 D_0}{U b} \quad \text{or} \quad \frac{12 D_0 t}{b x} \quad \text{Equ. 6}$$

D_0	=	initial dispersion coefficient
N_d	=	dilution at centreline
t	=	time since particle was released at source
x	=	distance travelled by particle since leaving the source
T	=	temperature of cooling water discharge
T_0	=	initial temperature of cooling water discharge

The initial plume width, b , was assessed from the spread of the plume during its first hour out of No Name Bay and this value was used to derive an initial dispersion coefficient from equation 3. Equation 4 was then used to derive the temperatures at various points in the plume.

The Far Field (background) Model

2.11 Cooling water from the LNG plant will be transported away from No Name Bay by tidal and wind induced currents. Turbulent mixing and dispersion will act to spread the heat horizontally and vertically, so that after the first one or two tidal cycles, the hot water from the LNG plant will have mixed with ambient water over the full depth. Eventually the heat content of the cooling water discharge is lost to the atmosphere by exchange across the water surface at a rate proportioned to the difference between the water temperature and the equilibrium temperature. The actual water temperatures change diurnally and seasonally, and strive to follow the changes in the instantaneous values of the equilibrium temperature, by heat transfer across the water surface. The LNG plant will increase the actual temperature and hence increase surface losses close to the outfall. The far field model calculates the distribution of this increase in the vertically averaged water temperature.

2.12 No Name Bay is situated on a relatively straight coastline. Therefore in order to maintain continuity of mass, the depth average current, in the nearshore zone, must be parallel to the coast. These currents were assumed to be made up of two parts; a steady predominantly wind induced longshore drift, and a periodic current with a tidal average value of zero. During the tide, water moves back and forth along the coast and hence the cooling water passes from No Name Bay into an oscillating tidal plug of water, of length equal to one tidal excursion along the shoreline.

2.13 The time scale associated with significant cooling by surface heat exchange can be shown to be at least an order of magnitude greater than a tidal period. Therefore the temperature distribution which results from this surface exchange can be represented by the tidal averaged equation:-

$$U \frac{\partial T'}{\partial x} - D_x \frac{\partial^2 T'}{\partial x^2} - D_y \frac{\partial^2 T'}{\partial y^2} + \frac{K}{h} T' = 0 \quad \text{Equ. 7}$$

where T' = vertically averaged temperature rise
 x, y = horizontal co-ordinates on the moving axis
 within the tidal plug.
 U = longshore drift velocity
 D_x, D_y = Tidal average dispersion coefficients in the
 x and y directions.
 h = water depth
 K = surface heat loss coefficient.

2.14 The solution to equation 7 for a shore-based outfall into a body of water of constant depth was derived from work by Atkins and Diver (4) to be:-

$$T'(x, y) = \frac{q T_o}{\pi h \sqrt{D_x D_y}} \exp\left(\frac{xU}{2D_x}\right) Ko(z) \quad \text{Equ. 8}$$

where $z = \left\{ \left(\frac{x^2}{D_x} + \frac{y^2}{D_y} \right) \left(\frac{u^2}{4D_x} + \frac{K}{h} \right) \right\}^{1/2}$

$T'(x, y)$ = the temperature at point, x, y
 T_o = the temperature at the outfall, above ambient
 q = the outfall discharge
 $Ko()$ = is the modified Bessels function of the second
 kind of order zero.

2.15 Equation 8 represents the solution for one point source at the origin, i.e. staying at the centre of the moving tidal plug. The solution in the present case must represent the movement of the plug past the outfall during each tide. In the tidal average solution this was done by considering the heat distributed over a length of the coastline equal to one tidal excursion centred on No Name Bay. The source was therefore divided into several point sources distributed over the tidal excursion. The solution is linear and therefore the temperature rises due to each of these sources were added directly to give the final solution.

2.16 As a point of interest, equation 8 was compared with a similar solution given by McQueen (5), and was found to agree well at all points except close to the source, where the assumptions on which the two solutions were based differed slightly.

2.17 Equation 8 indicates that the temperature distribution is dependent upon the tidal average dispersion coefficients which are themselves highly variable. The coefficients represent the overall effect of many physical phenomenon including local seabed topography, the variability of wind and tidal currents in time, the variability of velocities over depth and in plan, and the buoyancy of the cooling water itself. According to Talbot (6), a realistic value of the longitudinal dispersion coefficient is given by:-

$$D_x = 3.6 U_{\max} H \quad \text{Equ. 9}$$

where U_{\max} = the maximum tidal velocity
 H = mean tidal depth.

2.18 For effective temperature reduction, the heated water should dis-

perse offshore to mix with the main body of water in Mermaid Sound. It is generally found that such lateral dispersion is less than longitudinal dispersion. 0.1 is a typical ratio for the lateral to longitudinal dispersion coefficients, although this value could increase markedly with onshore/offshore wind activity. In modelling the seasonal changes of water temperature, the 14 day average drift velocity was used with typical dispersion coefficients of $D_x = 5.0 \text{ m}^2/\text{s}$ and $D_y = 0.26 \text{ m}^2/\text{s}$. The basic lateral dispersion coefficient was multiplied by a factor of between 1 and 20 depending on the onshore/offshore wind conditions in the preceding 14 days.

2.20 The loss of heat to the atmosphere is a much slower process than the convective and dispersive processes and is therefore not dominant in determining the plan distribution of the excess heat. In general a coefficient of 6 cm/hr was used. This value is typical of that used in recent similar studies (7,8,9). Sensitivity tests with the loss coefficient varying from 3 to 30 cm/hr did change the temperatures noticeably, but did not significantly change the general results. A greater change in the results could be obtained by relatively small changes in dispersion coefficients or drift velocities.

Data Synthesis

2.21 The data required for the models outlined above relate mainly to two basic parameters: the current pattern which determines overall movement, and dispersion coefficients which determine the degree of mixing. However both of these are dependent on many factors and a general understanding of the marine environment is required before suitable input data can be formulated. In particular the influence of winds and tides must be understood to define conditions appropriate to different seasonal or tidal conditions. Furthermore uncommon conditions, and the probability of their occurrence, must be considered.

2.22 As already explained dispersion coefficients were based on values obtained from relevant references adjusted by the application of appropriate empirical rules. Dye tests or similar field work to estimate dispersion coefficients in the Mermaid Sound area were not considered appropriate for this broad-brush study. A large number of tests in a variety of weather and sea conditions would have been necessary and neither funds nor time were available for such detailed work. Having assessed what were considered appropriate values, the sensitivity of the analysis to changes in dispersion coefficient was tested.

2.23 The distribution (spatial and temporal) of currents was required in two forms. For the near field and far field models respectively these were:

As variations over a tidal cycle for surface water in the nearshore zone. These data were required to predict the movement of the surface plume of recently released hot water and therefore could be restricted to a zone close to No Name Bay, about 6 km long and within 2 km of the shore.

As vertically-integrated residual velocities over a tidal cycle, so that the long term exchange of hot water with

the surrounding sea water could be evaluated. The area of interest is dependent on the smallest temperature rise considered significant, which was considered here to be 20 km by 10 km.

2.24 The following approach was adopted in formulating input data on currents for the models:-

- A general appreciation of tidal currents in Mermaid Sound and identification of principle flow patterns in spring and neap tides.
- Analysis of the effect of wind on surface currents and on depth integrated currents and hence the deduction of empirical relations between wind speed and current speed. A comparison was also made between observed data and available theory. (10,11).
- Analysis of long term wind records to deduce typical seasonal wind patterns and the duration of particular events, in particular calm periods which may be critical in the dispersion of cooling water.
- Formulation of alternative current patterns both nearshore e.g. tidal excursion etc. and in the far field zone e.g. residual drift, for use in the heat dispersion models.
- Sensitivity tests to determine where critical values of input data occur and where necessary to refine these.

2.25 Results of these analyses are presented in the following section.

3. MARINE ENVIRONMENT (Refs 12-20)

Available data

3.1 The main source of data used in the study were long-term recordings collected by E.G. & G, the principal survey contractor engaged on the project. An extensive programme had been organised to provide criteria for design of pipeline, the harbour, jetties and other coastal facilities: instrumentation to record data on wind, waves, tides, currents, salinity and temperature was installed over a wide area. However, many of the instruments were located offshore and were beyond the zone of interest so far as cooling water dispersion was concerned. It was therefore necessary to supplement the main programme with subsidiary data collection exercises specifically aimed at obtaining data on near shore conditions. Three exercises were mounted by Binnie International, in the periods 23-24 November 1978, 16-19 December 1978 and 16-22 January 1979.

Winds

3.2 Winds have a significant effect on the marine environment through the generation of waves, which increase mixing, and through the creation of currents, which change the pattern of advection. Two dominant wind patterns are evident (Figure 3):

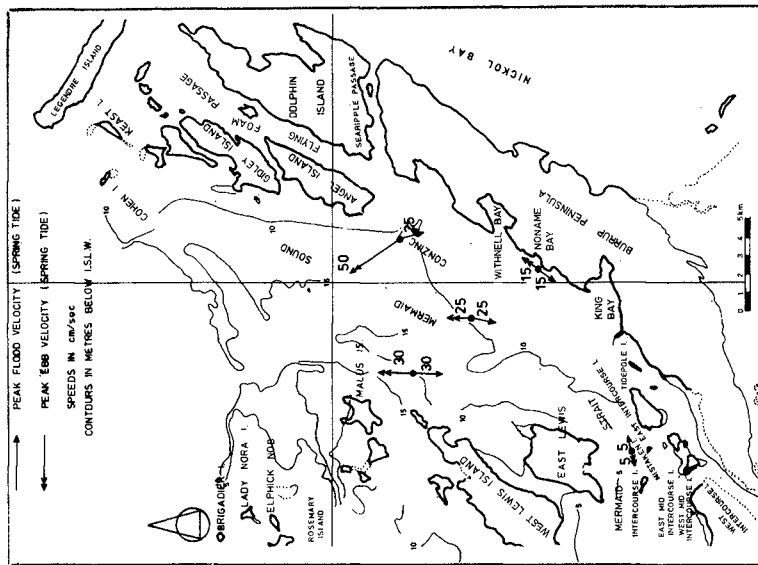


FIGURE 4 MERMAID SOUND

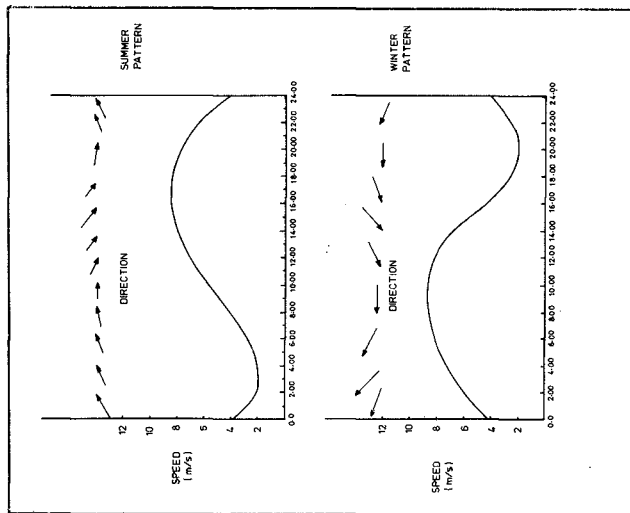


FIGURE 3 TYPICAL SUMMER AND WINTER WIND PATTERNS

- The summer pattern consists of a prevailing westerly wind, acted upon by the night and early morning south-easterly land breeze and by the afternoon north-westerly sea breeze.
- The winter pattern consists of a prevailing easterly wind, again acted upon by the night and early morning south-easterly land breeze and by the afternoon north-westerly sea breeze.

3.3 Cyclones can occur in the summer months between November and March, accompanied by sea surges and by severe wave action: however so far as the study of cooling water dispersion is concerned these are of little importance since they can only improve the mixing. Of greater concern are the possible calm periods in which there is relatively little mixing by wave action and significantly less convection in the absence of wind induced currents.

Currents

3.4 Tidal streams are summarised in Figure 4 and are given as depth averaged values deduced from the long-term current observations. The pattern is similar to that of a closed bay, with very little tidal flow near East Intercourse Island. The main flood flow is towards the south but is directed southwest along the coastline in the area near Withnell Bay. Ebb currents are generally of comparable magnitude and flow in the opposite direction. An exception to this is in the area southwest of Angel Island where water flowing through Boat Passage creates an ebb dominant flow with nett movement to the North West.

3.5 Tidal velocities along the shoreline between Phillip Point and Withnell Bay are significantly lower than those in the centre of Mermaid Sound and reach a maximum of only 15 cm/s. The tidal excursions corresponding to spring and neap tides in this area are 2.0 km and 0.6 km respectively, and it follows that tidal mixing is significantly less than in many other regions where tidal excursions may be in the range 15 to 25 km.

3.6 Whilst observed data are broadly consistent with the above pattern, the majority of cases are affected by winds. The vertical velocity profiles are complex, particularly where the local topography is irregular and when wind induced currents are generated at an angle to the tidal component. A further complication arises from the duration dependence of the velocity profile. The depth affected by wind stress increases with time. Surface currents were observed to respond within about an hour of changes in wind conditions and the whole depth was affected within 12 hours. However steady state conditions did not appear to be established for considerably longer.

3.7 A simple approach to generating input conditions for the near field model was provided by the observation that surface currents were about 1.5% of the wind speed (recorded 10 m above sea level) and were in line with the wind. This result is consistent with previously published data relating to open sea conditions, although in such cases the Coriolis effect is often significant, causing currents to deviate to the left of

the wind direction (to the right in the Northern hemisphere). It follows that the typical daily wind patterns (Fig. 3) can be used to derive surface currents, typical values being in the range 3-12 cm/s. Wind induced currents and tidal components were superimposed to formulate conditions under different tide and seasonal wind patterns.

3.8 Current data for the far field model was derived by relating residual movement of water in Mermaid Sound to longer term wind patterns, the tidal residual movement being small in comparison. Residual drift velocities induced by winds are governed partly by the direct action of the wind and partly by larger scale effects which control water movement outside Mermaid Sound. Typical net movements of water in summer and winter are shown in Figure 5. The summer pattern is governed by dominant westerly winds which force water through Mermaid Strait and then North-East into the Sound. In the winter months, South-Easterly winds cause high water levels along the North-West boundary of Nickol Bay and result in strong currents flowing Westwards through Boat Passage, which induce South-Westerly currents along the shoreline near Withnell Bay. It is the longshore residual drift which is of importance in the far field model and depends mainly on the longshore component of wind velocity. In addition the offshore component of wind velocity induces south westerly longshore currents. A simple model was proposed in which

$$u = 0.015 U - 0.010 V \quad (V > 0)$$

$$u = 0.015 U \quad (V < 0)$$

where u is the longshore drift current (north east)
 U is the longshore component of wind velocity (north east)
 V is the offshore component of wind velocity (north west).

Values of u ranged from -10 to +10 cm/s.

Temperature

3.9 Water temperatures were available from the long term records obtained from E.G. & G. They are fairly uniform over the area of Mermaid Sound and show an annual variation from 19°C in July or August to 32°C in February or March (Figure 6). Variation over the vertical is generally small though anomalies may occur giving temperature differences of about 2°C or more.

3.10 Variation through the tide is only significant in the area south-west of Angel Island, and results from warmer water in Nickol Bay passing through Boat Passage on the ebb tide: here temperature fluctuations of 1-2°C are common over the tidal cycle. Elsewhere the variation is less than 0.5°C over a tide but the effect is detected in variations over the two-week cycle between spring and neap tides. The greater quantity of warm water exchanged during spring tides increases general ambient temperatures by 1-3°C over the whole of Mermaid Sound. This effect is not always apparent when seasonal changes of temperature during the same spring/neap cycle are large.

3.11 Temperature variations in the shallow water of the bays along the coast are sometimes quite pronounced, and diurnal fluctuations of 5°C or more have been reported.

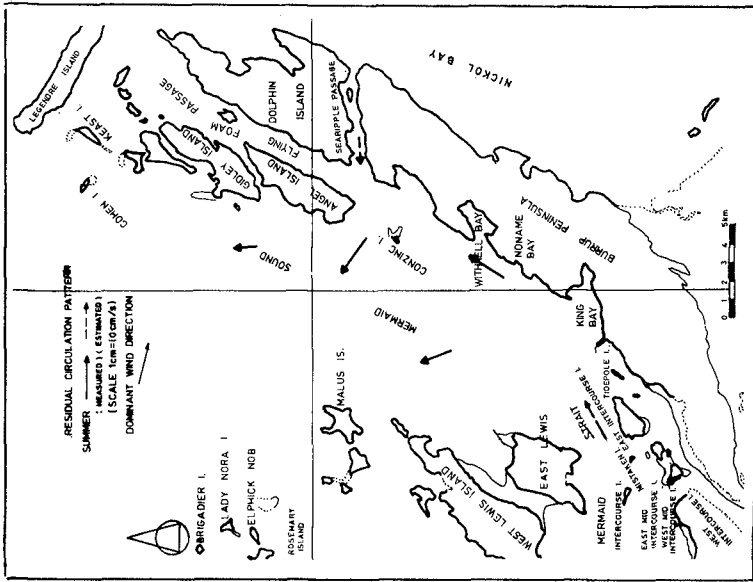


FIGURE 5b RESIDUAL CIRCULATION PATTERN (SUMMER)

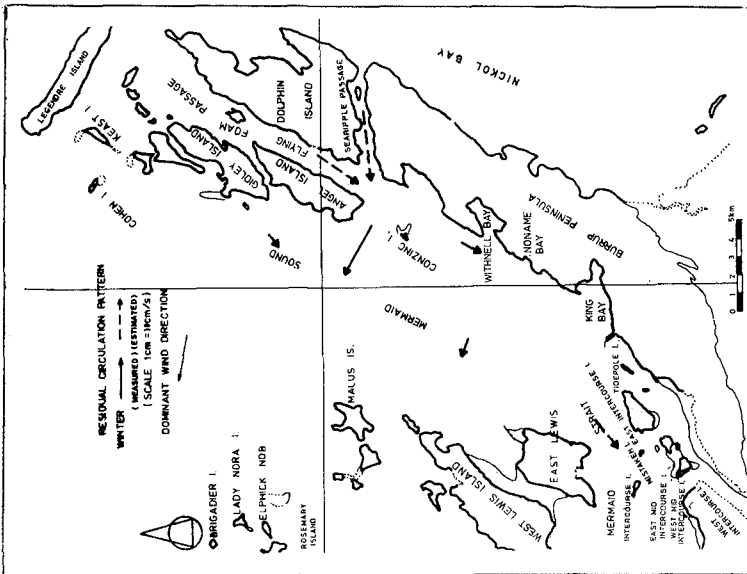


FIGURE 5a RESIDUAL CIRCULATION PATTERN (WINTER)

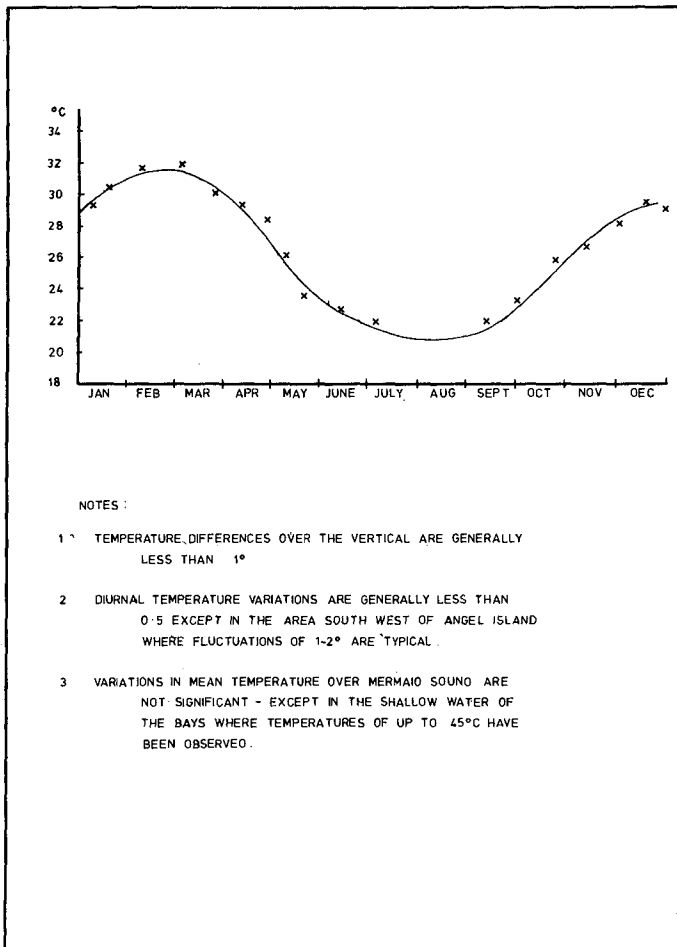


FIGURE 6 ANNUAL VARIATION OF SEAWATER TEMPERATURE IN MERMAID SOUND

4. RESULTS

The buoyant plume

4.1 Output of the near field model is in the form of age-contours and for each of these a temperature dilution factor can be estimated based on the turbulent mixing of the plume with its surroundings, with a minor additional effect due to surface cooling. Typical "plume" shapes are shown on Figure 7. By considering the plume movement over a period of 24 hours, envelopes of areas which reach specified temperature rises at any stage in that time can be plotted. Figure 8 shows conditions for a typical winter day when winds are offshore. In this case, shoreline temperature rises are negligible but in summer conditions when winds are onshore, temperature rises of up to 5°C were shown to occur near the entrance to Withnell Bay.

Background temperatures

4.2 The simulation used the weather pattern of 1978-1979 as 14-day averages to deduce the background temperature field on a tide average basis. The results were related to the environmental issues by extracting the variation of average background temperature at Withnell Bay, 3 km north-east of the cooling water outfall, and at Kings Bay, 4 km south-west of the outfall (Figure 9). Typical isotherm plots are presented in Figure 10.

4.3 The background temperature field has been considered by assuming the water to be fully mixed in the vertical. In practice, there is much overlap between the area swept by the buoyant plume and the background (far field) model. The background temperature results may be considered as applying to the main body of sea water underlying the buoyant surface layer.

4.4 Wherever there is an elevated background temperature beneath the surface plume, the plume temperatures quoted will be increased by a varying proportion of the background rise. There is no available method of combining plume temperature results with background temperature results. The problem is complicated by time and space variation and interaction between the models but for present purposes an adjusted surface temperature may be calculated from:

$$T_{\text{adjusted}} = T_{\text{plume}} + \left(\frac{1 - T_{\text{plume}}}{10} \right) \times T_{\text{background}}$$

This represents a rough upper limit, and is based on application of the estimated plume dilution factor with a warmed dilutant.

CONCLUSIONS

The framework of this study was the need to provide ecologists and environmental scientists with approximate forecasts of the temperature rises to be expected in the area and an indication of the extent of the main thermal impact, so that they could assess the effect on the marine environment should the project proceed.

In the time scale available and within the budget that appeared

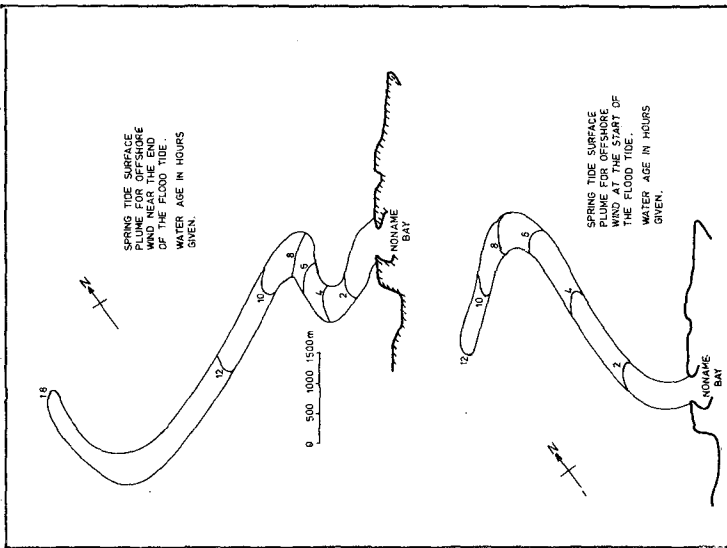


FIGURE 7 TYPICAL PLUME PATTERNS FOR OFFSHORE WIND

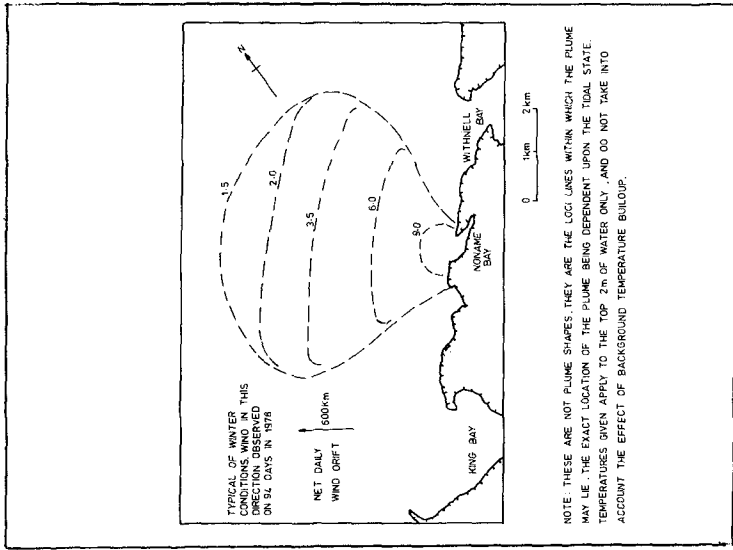


FIGURE 8 ENVELOPE OF MAXIMUM INSTANTANEOUS SURFACE TEMPERATURE RISES

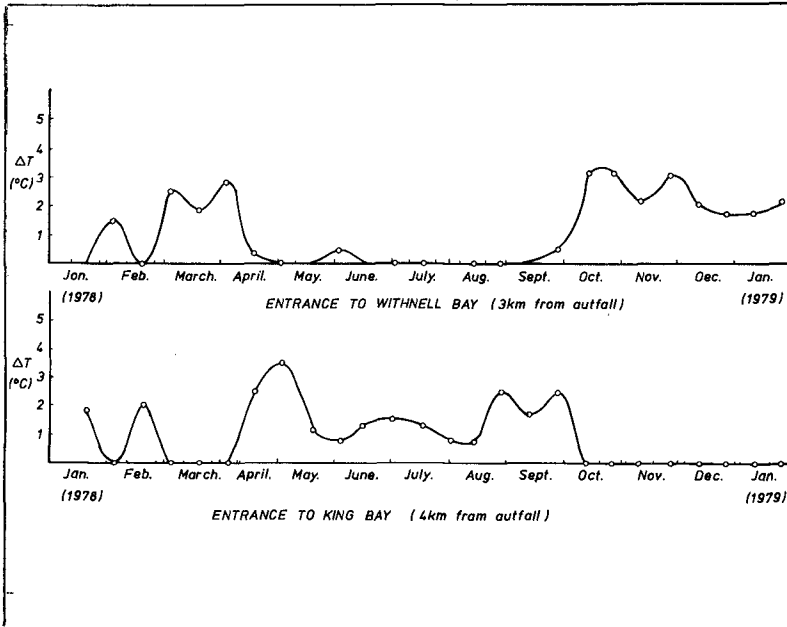


FIGURE 9 ANNUAL VARIATION IN TEMPERATURE RISE AT WITHNELL AND KING BAYS

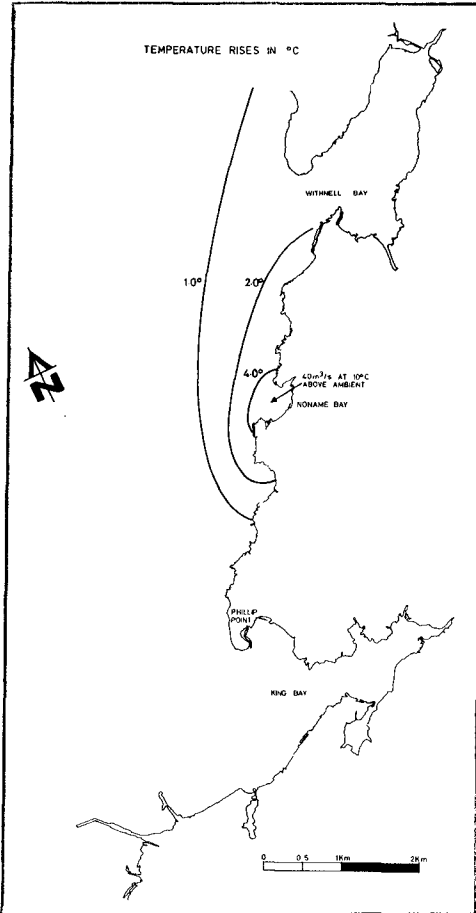


FIGURE 10 TIDAL AVERAGE TEMPERATURE RISE
LATE DECEMBER 1978

reasonable for an environmental study, physical modelling was inappropriate. In any case, there are severe limitations in making scale models of the relevant processes. Consequently the chosen method of study was by computer simulation.

Two numerical models were used, one of which dealt with the "near field" processes of the spread of a buoyant layer of heated water under the convecting influence of the tidal currents. The second model simulated the "far field" processes which gives rise to a general increase in the temperature of the sea in the region.

The simulations of the spread of pollutants, mainly hot water, from the outfall of the cooling water system provided indications of the likely range of temperatures and the extent of the spread of effluent in the environmentally sensitive coastal zone either side of No Name Bay.

The pattern of spread is strongly seasonal, being much influenced by wind induced drift of the tidal waters. The careful analysis of weather patterns and their effect on water movements is an essential part of any investigation of the spread of effluents. The study established the range of likely patterns and indicated the likely persistence at various points along the coast and elsewhere of temperature rises of several degrees Celsius.

ACKNOWLEDGEMENTS

This study was carried out in association with Maunsells (Perth) on behalf of Woodside Petroleum Limited, operator for the North West Shelf Joint Venture. Participants in the Venture are Woodside Petroleum Limited 50%, and North West Shelf Development Pty. Ltd., B.P. Petroleum Development Australia Pty. Ltd., and California Asiatic Oil Company, each with 16.2/3%. The authors are grateful to them, and also to E.G. and G Ltd. and to staff of HRS, Wallingford, for their ready co-operation and guidance. Development work on computer programs was carried out by M.C. Allen of Binnie and Partners London.

REFERENCES.

1. H.E. Jobson, "Bed Conduction Computation for Thermal Models". Discussion by G.H. Jirka, ASCE HY8, August 1978.
2. Burnett, J.M., McMillan, W., McQueen, J.F., Moore, D.J., Shephard, J.C. "Cooling of power stations". Ninth World Energy Conference, Detroit, 1974.
3. Brooks, N.H. "Diffusion of sewage effluent in an ocean current". Proc. 1st Int. Conference Waste Disposal Marine Environment, University of California, Pergamon Press, New York, 1960.
4. Atkins, R. and Diver, C.F.M. "Mathematical modelling of heated discharges in tidal flow, - plume development and dispersion". HRS report no. INT 147, 1975.
5. McQueen, J.F. "Background temperatures and power station discharges". Advances in Water Resources, vol. 1, no. 4, 1978.

6. Talbot, J.W. "Diffusion data". FRTR no.28, MAFF Lowestoft,1976.
7. HRS. "Sizewell power station,Mathematical modelling of primary and secondary recirculation". Report no. EX 645,1969.
8. HRS. "Orfordness power station, mathematical modelling of recirculation of heat". Report no. EX 685, 1975.
9. "A numerical model of thermal plume and river discharge". Proceedings of 17th Conference on Great Lakes Reservoir Research, Hamilton, Ontario, 1974.
10. Wu, J. "Prediction of near surface drift currents from wind velocity". Proc. ASCE, vol. 99, no. HY9, September 1973.
11. Rance, P.J. "Investigation of wind induced currents and their effect on the performance of sea outfalls". Proc. ICE, vol. 33, February 1966.
12. ERA, Perth. "Hydrological investigations - Dampier archipelago, 29 November-19 December 1972". Report prepared for BOC of Australia Ltd.
13. Glenn, A.H. and Associates, New Orleans, USA. "Meteorological and oceanographic conditions affecting planning and design of pipeline and marine terminal facilities: Dampier area, offshore N-W Australia". Report prepared for BOC of Australia Ltd. April, 1973.
14. Bureau of Meteorology, Melbourne. "Design winds and waves off Dampier, WA". Report prepared for BOC of Australia Ltd,undated.
15. ERA, Perth. "North West Shelf feasibility study environmental report vol. VII, book 16". Report prepared for BOCAL, October 1973.
16. Glenn, A.H. and Associates, New Orleans, USA. "Meteorological conditions affecting offshore petroleum operation in N-W Australia". Report prepared for BOC of Australia Ltd. August 1966.
17. ERA, Perth. "Introductory hydrological and climatological investigations of the NW Shelf of Australia, vol. 1, text: vol. 2, Figures". Report prepared for BOC of Australia Ltd, November, 1971.
18. Delft Hydraulics Laboratory. "Legendre port study - oceanographic conditions around Legendre island". Report prepared for Hammersley Iron Pty. Ltd. 1973.
19. Woodside Petroleum Development Pty. Ltd. "Technical note, wind statistics - Dampier area, WA". August 1977.
20. Oceanographic Services Inc., Santa Barabara, California. "North West Shelf hindcast study, phase 11 and phase 111". Report prepared for Chevron Oil Field Co. May 1974.

EXPERIMENTAL STUDY OF THE BUOYANT SURFACE JET
WITH THE PRESENCE OF BOTTOM BOUNDARY
AND CROSS CURRENT.

B. SAFAIE, Ph.D., A.M. ASCE
KUWAIT INSTITUTE FOR SCIENTIFIC RESEARCH

I. INTRODUCTION:

The problem of buoyant surface jet (BSJ) is relevant from the practical standpoint to the discharge of cooling water of power plants into the receiving water bodies. The buoyant surface jet has extensively been studied by numerous investigators both theoretically and experimentally. Most studies have been concerned with the problems of BSJ discharged horizontally into a surface of a deep ambient water with or without cross current.

From a practical standpoint, however, the design engineers are often confronted with the design of thermal outfalls in the coastal regions which are frequently shallow and have the boundary effects. Few investigators have studied the problem of BSJ discharged horizontally over slopping bottom into quiescent receiving water (1), (2), (4), (5), (6), and (7). However, no information on the foregoing problem with moving ambient water is available. The purpose of this paper is (a) to present the experimental results of BSJ which is discharged over slopping bottom into moving ambient water, and (b) to see the degree of error which is introduced by applying the deep water integral models to the case of a buoyant surface jet with a bottom boundary.

II. DIMENSIONAL ANALYSIS:

The BSJ is characterized by the following source parameters

1. Volume flux, $Q_o = U_o A_o (L^3 T^{-1})$;
2. Momentum flux, $M_o = U_o^2 A_o (L^4 T^{-2})$;
3. Buoyancy or kinematic mass deficiency. flux
 $B_o = \frac{\Delta \rho_o}{\rho_a} g U_o A_o (L^4 T^{-3})$;
4. Aspect ratio, $A_s = h_o/b_o$;

The subscript -o refers to source parameters and the subscript -a to ambient conditions (receiving water); U is velocity, A is area, h_o is discharge height, b is width, ρ is density, $\Delta \rho$ is $\rho_a - \rho$, and g is gravitational acceleration.

The bottom boundary is characterized by the bottom slope and the bottom friction. However, only the effect of bottom slope is considered in the present investigation.

In the present study, the direction of ambient current is assumed to be parallel to the shore line. Therefore the ambient current is characterized by current speed U_a .

By dimensional analysis one can show that the independent dimensionless numbers are

1. Source Densimetric Froude number,

$$F_o (A) = \frac{M_o^{5/4}}{B_o^{1/2} Q_o} = \frac{U_o}{(g'_o A_o^{1/2})^{1/2}}$$

where $g'_o = (\Delta\rho/\rho_a) g$

2. Discharge Aspect Ratio, $A_s = h_o/b_o$
3. Bottom slope, S
4. Current ratio, $U_r = U_a/U_o$

In this experimental study the range of values of the abovementioned dimensionless numbers have been chosen to be close to the typical range of values commonly encountered in the design of outfalls.

The range of the variation of the above dimensionless parameters in this experimental study are as follows:

1. $2 < F_o (A) < 13$
2. $A_s = 1.5$
3. $0 < S < 0.04$
4. $0.2 < U_r < 0.7$

It should be noted that in developing the foregoing dimensionless parameters, it is assumed implicitly that the Reynolds number is high enough so that viscous effects are negligible, the heat loss to the atmosphere is insignificant, and since we are mainly concerned with the near field the effect of ambient turbulence is negligible.

III. EXPERIMENTAL ARRANGEMENT:

The experimental arrangement is designed in such a way that the preceding dimensionless parameters could be varied systematically and their effect on temperature field could be studied. The main feature of the experimental arrangement is shown in figures 1 and 2.

The experimental set up consisted of three major systems:

1. Receiving water system;
2. Warm water discharge system;
3. Data acquisition system.

These are described briefly in the following:

III.1 The Receiving Water System:

The main components of the receiving water system consisted of (a) a wind wave tank, 45.7m x 2.4m x 1.5m. In the middle section of this tank there was a 3.6m x 1.2m glass window on one of the side walls. Thus the flow pattern could be visualized from the side as well as from the top. (b) A circulating pipe and pump, which could generate a maximum current of 15cm/sec., was used to simulate the off-shore currents. (c) The bottom boundary consisted of a plywood "beach" 2.4m x 4.6 m with a supporting frame. The "beach" slope and the direction of the slope was adjustable. The direction of the "beach" slope was adjusted so that the ambient current was parallel to the shore. It should be noted that since the "beach" was installed in the tank in such a way that there was minimum obstruction to the ambient current, an excellent uniform and parallel ambient current could be obtained. In other words the "beach" was acting as a "flat plat" in the uniform flow field.

III.2 The Warm Water Discharge System:

The main components of this system consisted of (a) the main insulated tank with the dimensions 1.2m x 0.91m X 0.91m. This tank was insulated and was used to mix the warm and cold water to obtain the desired temperature of the Warm water discharge in the main tank. During the mixing process and during the experimental run a stirrer was used to assure temperature homogeneity of the water in the main tank. During the mixing of warm and cold water, water was continuously pumped through a bypass to the drain. By this procedure it was possible to warm the pipeline to the temperature of the warm water to be discharged. Also, using a continuous discharge, the water temperature could be monitored by the use of a digital thermometer which was placed in the line. Thus, proper adjustments could be made of the flow rate of the warm and cold water supply to expedite

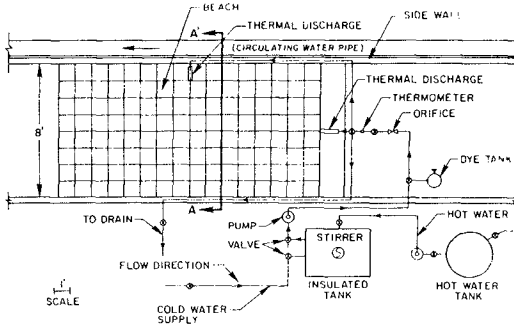


Fig.1 Schematic of the experimental set-up (Plan View)

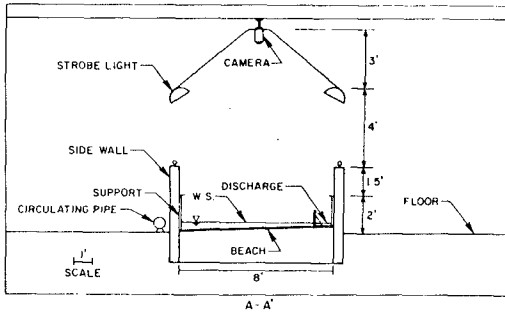


Fig.2 Schematic of the experimental set-up (Side View)
3a

achievement of the desired temperature.

b) The line from the main insulated tank to the discharge point: this "pipeline", most of which was a flexible hose, had an orifice meter installed in it which was used to measure the flow rate. It also had a dye injection assembly installed in it, which was used for the injection of dye into the discharge. Warm water was discharged from the side using a flexible hose (see figures 1 and 2).

c) Dye injection assembly: this consisted of a stainless steel tank for the dye supply in which dye could be stored and be kept under constant pressure. A needle valve was used to give the desired dye flow rate.

III.3 Data Acquisition System:

The data acquisition system can be divided into two main subsystems as follows:

III.3.1 The photographic system: consisted of a remotely controlled camera and four stroke lights which were mounted on a four adjustable arms. The camera and floodlight assembly were mounted under a moveable base which in turn was mounted on a rail, located just under the roof. The rail was above the longitudinal centerline of the tank (see figure 2).

III.3.2 The temperature measuring system: consisted of a number of thermistor probes, a moving carriage on which thermistor probes were mounted, electronic boxes for the thermistor probes, shielded cables, five channels of digital to analog (DA) for control and operation of experiments and 256 channels of analog to digital (AD) convertors, a 16K Nova mini-computer, 2 floppy disk systems, an acoustic coupler for data transfer to the computer of UCB, and ± 15 volt power supply.

A more detailed descriptions of the experimental arrangements, the experimental procedure, and the methodology for data analysis are given in Ref. (4).

IV. AN OVERVIEW OF THE FLOW AND CIRCULATION PATTERN:

Figures 3 to 10 show the photographs of a typical flow pattern generated by the discharge of a BSJ over a slopping bottom into an ambient water with cross current. In these photographs the squares are 30.48cm x 30.48cm and are on the the beach. Figure 3 shows the start of the discharge. Note that the nucleus of a circulating cell is forming at the tips. Figure 4 shows the flow pattern

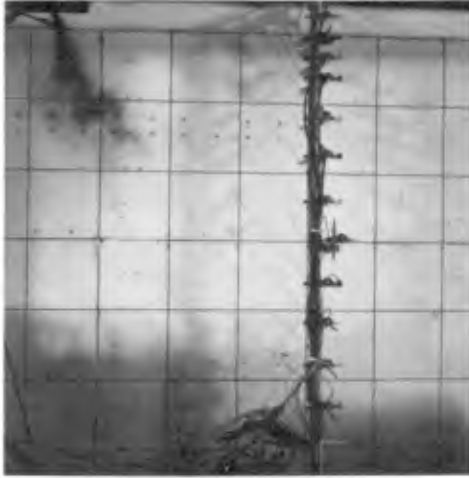


Fig.3 Photo of the Flow Pattern



Fig.4 Photo of the Flow Pattern

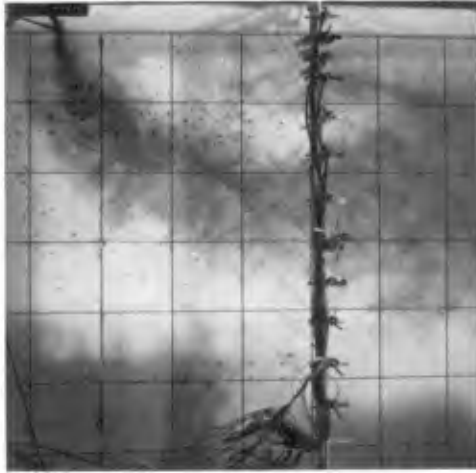


Fig.5 Photo of the Flow Pattern

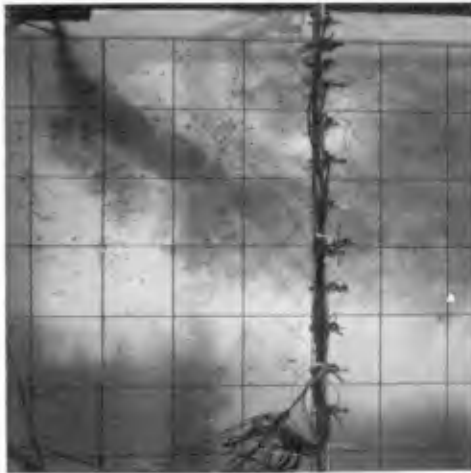


Fig.6 Photo of the Flow Pattern



Fig.7 Photo of the Flow Pattern



Fig.8 Photo of the Flow Pattern



Fig.9 Photo of the Flow Pattern



Fig.10 Photo Of the Flow Pattern

at a later time. As can be seen the BSJ is bent due to the cross current (parallel to the shore line). The circulating cell is still under development and have moved approximately 0.5m from the shore line. Figures 5 and 6 indicate that the circulating cell is reaching the equilibrium condition and has initiated the reentrainment of the warm water. Note the dye streaks from dye crystals is developing and showing the bottom flow pattern.

Figures 7 and 8 clearly show the recirculation pattern. As can be seen from these photographs the circulating cell has a two-dimensional character. Also to be noticed in these photographs is the interesting deflection pattern of the ambient current which was parallel to the shore line before discharging the BSJ. Figures 9 and 10 show the final equilibrium stage at which the reentrained warm water has completely filled the area between shore line and the BSJ. The bottom current pattern is also clearly shown by the developed dye streaks. Again note the interesting deflection pattern of the ambient current and the circulating cell in these photographs.

Based on these observations the flow field can be schematized as shown in figure 11. It was found that the location of the center of the circulating cell is mainly a function of the source Densimetric Froude number and the ambient current ratio.

V. PRESENTATION OF EXPERIMENTAL DATA:

The effect of the systematic variations of the independent dimensionless numbers on the centerline temperature and the jet trajectory is investigated experimentally. In this section the experimental results are presented.

Figure 12 shows the effect of the variation of the source Densimetric Froude number on the centerline temperature decay other parameters being constant. In this figure normalized centerline temperature, $\Delta T_m / \Delta T_0$ is plotted Vs. normalized distance, $S_c / \sqrt{A_0}$, for different values of the source Densimetric Froude number. Here $\Delta T_m = T_m - T_a$, $\Delta T_0 = T_0 - T_a$, T_m is maximum temperature at a given section, T_a is ambient temperature and T_0 is source temperature along the curvilinear co-ordinate as shown in figure 11. As can be seen for all practical purposes, within the experimental range, the centerline temperature decay does not vary with the source Densimetric Froude number.

The effect of the ambient current ratio on the centerline temperature can be seen in figure 13. The other parameters being constant, an increase in the cross-current

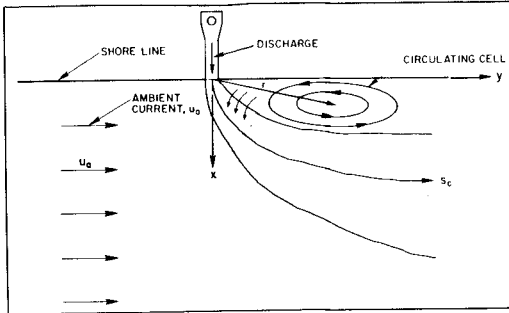


Fig.11 Schematic of the Flow Pattern

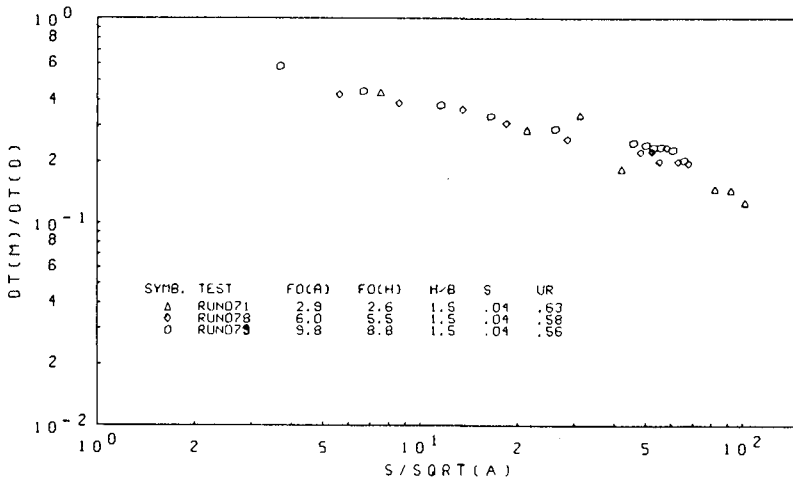


Fig.12 Normalized Centerline Temperature vs Normalized Curvilinear Distance (effect of F_0)

ratio will cause the centerline temperature to increase. The normalized centerline temperature is 26% higher for high ambient current ratio as compared to the one for low ambient current ratio, for $S_C/\sqrt{A_0} > 40$. The reason for this trend may be attributed to the increased recirculation, on the shore side, due to increase in the ambient current ratio, as well as the characteristics of the circulating cell which causes the warmer water to reentrain at a farther distance from the source. Shown in figure 14 is the effect of bottom slope on the centerline temperature decay. As can be seen increasing the bottom slope causes a decrease in the centerline temperature.

The effect of the important parameters on the centerline trajectory of a BSJ (i.e., the locus of the centerline temperature in the x-y plane) is depicted in figures 15 to 17. Figure 15 indicates that other parameters being constant an increase in the source Densimetric Froude number will cause a decrease in the radius of curvature of the jet trajectory. In other words the higher the Densimetric Froude number the closer is the jet trajectory to the shore line. This may be attributed to the high ambient pressure drag force at high Densimetric Froude numbers due to the jet attachment and the blockage of the ambient current. Figure 16 indicates that the higher the ambient current ratio the closer is the jet trajectory to the shore line. Finally figure 17 shows that, surprisingly, the reduction in bottom slope will cause the jet trajectory to move offshore, i.e., the jet trajectory assumes larger radius of curvature.

Realizing the unavailability of satisfactory numerical model for buoyant surface jet over slopping bottom with ambient cross current, it is desirable for practical purposes to know the degree of error in predicting the centerline temperature and the trajectory of a buoyant surface jet discharged over slopping bottom into moving ambient flow, by applying the simple integral models which have been developed for BSJs discharged into deep water. For this purpose, the Prych's model (3) was selected. An example of the results is shown in Figures 18 and 19. As can be seen from Figure 18, Prych's model overestimated the centerline temperature. Such overestimation was generally observed for other conditions as well. It was observed that in general Prych's model overestimates the centerline temperature by 10 to 36 percent. However, the predicted jet trajectory shows considerably less deflection than the observed jet trajectory. This can be seen in Figure 19. The comparison for additional conditions is reported in Ref. (4). In general, based on these results, one may conclude that the application of the simple integral models for the prediction of the characteristics of the

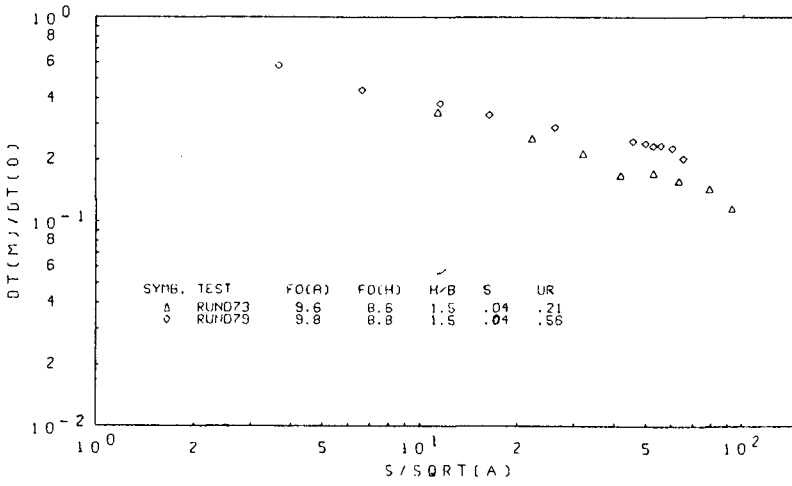


Fig.13 Normalized Centerline Temperature vs Normalized Curvilinear Distance (effect of U_r)

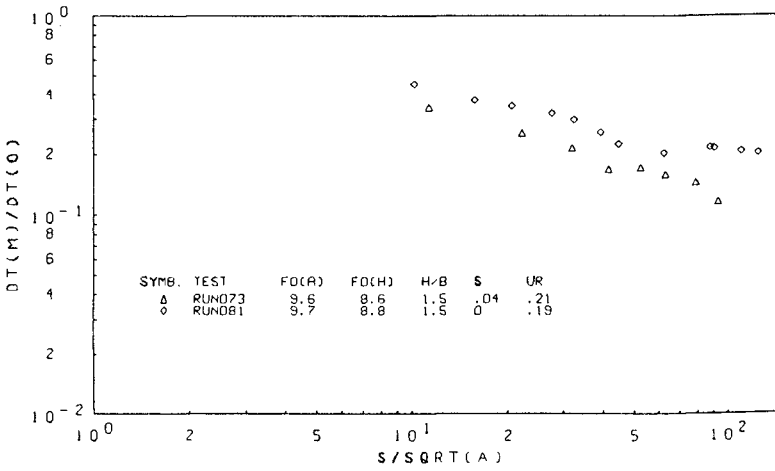


Fig.14 Normalized Centerline Temperature vs Normalized Curvilinear Distance (effect of bottom slope)

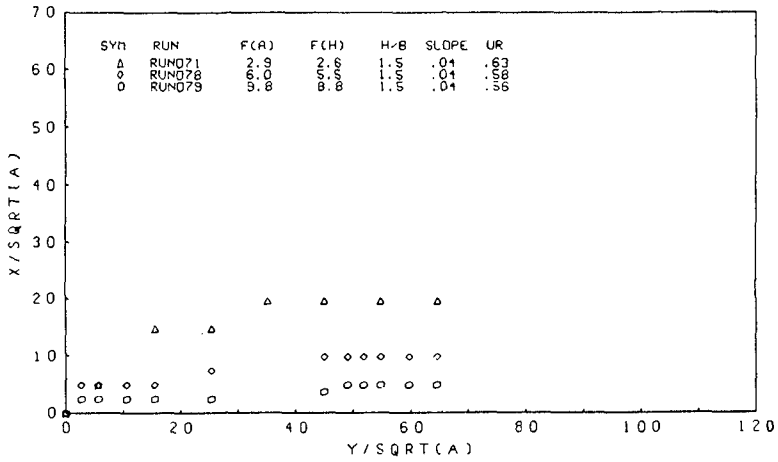


Fig.15 Normalized Jet Trajectory (effect of F_0)

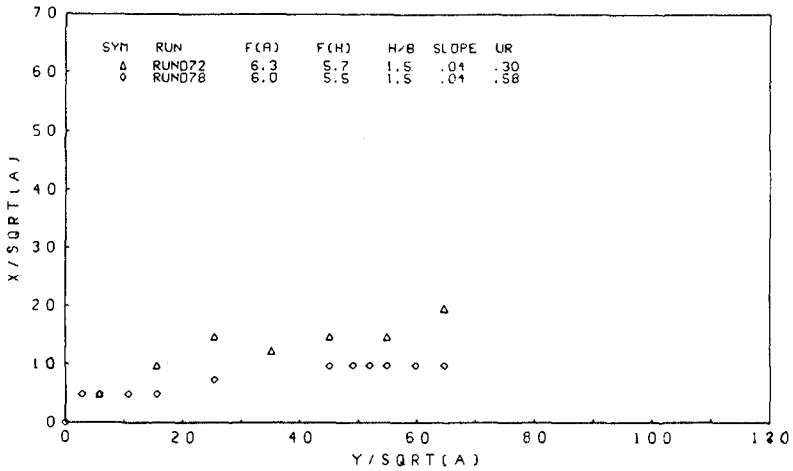


Fig.16 Normalized Jet Trajectory (effect of U_r)

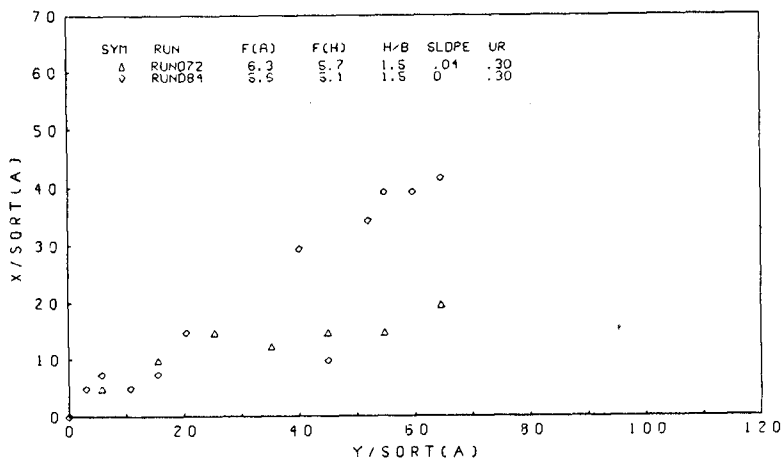


Fig.17 Normalized Jet Trajectory
(effect of Bottom Slope)

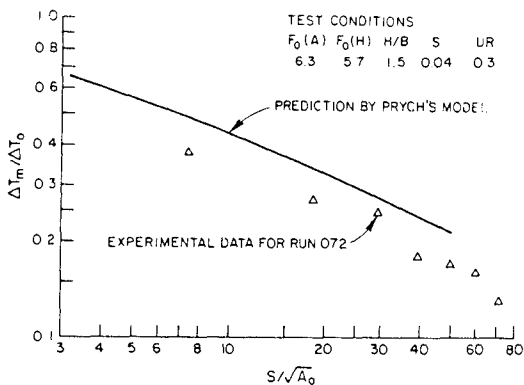


Fig.18 Comparison of the Experimental and Theoretical results for Centerline Temp.

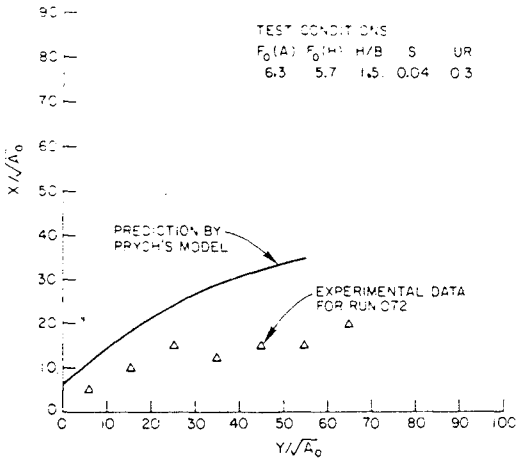


Fig.19 Comparison of the Experimental and Theoretical Results for Jet Trajectory

BSJ discharged over slopping bottom into moving ambient water, will result in conservative estimates.

VI. SUMMARY AND CONCLUSIONS:

The effect of important dimensionless parameters on the characteristics of a BSJ discharged over a slopping bottom into moving ambient water is investigated experimentally. The main results are presented in Figures 12 to 17 and are summarized in Table 1.

TABLE 1. Summary of the Experimental Results.

Increase in →	F_o	S	U_R
Centerline Temperature	No effect	Decrease	Increase
Jet Trajectory	Deflect further	Deflect further	Deflect further

The obtained results are expected to be helpful as general guidelines in the design of thermal outfall in the coastal regions.

The comparison between the experimental results and the predictions by Prych's model reveals that the integral models for BSJs discharged into deep water, generally overestimate the centerline temperature and jet trajectory of a BSJ discharged over slopping bottom into moving ambient water.

VII. LIST OF SYMBOLS:

A_o	Discharge Area
A_s	Discharge Aspect ratio, $A_s = h_o/b_o$
B_o	Discharge Buoyancy flux, $B_o = g'_o Q_o$
$F_o(A)$	Source Densimetric Froude number based on area
	$F_o(A) = M_o^{5/4} / B_o^{1/2} Q_o$
M_o	Kinematic momentum flux, $M_o = U_o^2 A_o$
Q_o	Volume flux, $Q_o = U_o A_o$
S	Bottom slope
S_c	Curvilinear co-ordinate (along trajectory)
S_n	Normalized curvilinear co-ordinate, $S_n = S_c / \sqrt{A_o}$
T	Fluid temperature in °C.
U_o	Magnitude of discharge velocity
U_a	Magnitude of ambient cross current
U_r	Dimensionless velocity ratio for ambient current,
	$U_r = U_a / U_o$
b_o	Discharge width
g	gravitational acceleration
g'_o	Modified gravitational acceleration, $g'_o = (\Delta\rho_o/\rho_a)g$
h_o	Discharge depth
x	Longitudinal cartesian co-ordinate axis
y	Transverse cartesian co-ordinate axis
ΔT	Excess temperature, $\Delta T = T - T_a$
$\Delta\rho$	Water density defficiency, $\Delta\rho = \rho_a - \rho$
ρ	Fluid density

VIII. REFERENCES:

1. Adams, E.E., Stolzenbach, K.D., and Harleman, D.R.F., "Near and far field analysis of buoyant surface discharges into large bodies of water," Report No. 205, Ralph M. Parsons Laboratory for Water Resources and Hydrodynamics, Massachusetts Institute of Technology, Cambridge, Massachusetts, August 1975.
2. Hansen, N.E.O., "The surface jet in shallow water," Progress Report No. 29, Institute of Hydrodynamics and Hydraulic Engineering, Technical University of Denmark, Denmark, August 1979, pp. 29-38.
3. Prych, E.A., "A warm water effluent analysis as a buoyant surface jet," Report No. 21, Notiser Och Preliminara Rapportes, Serie Hydrologi, Sveriges Meteorologiska och Hydrologiska Institute, Stockholm, Sweden, 1972.
4. Safaie, B., "Mixing of horizontal buoyant surface jet over sloping bottom," Report No. HEL-27-4, Hydraulic Engineering Laboratory, University of California at Berkeley, Berkeley, California, 1978, pp. 1-198.
5. Safaie, B., "Mixing of buoyant surface jet over sloping bottom," Journal of the Water Ways, Harbours, and Coastal Engineering Division, ASCE, Vol. 105, No. ww4, Proc. paper 14954, November, 1979, pp.357-373
6. Wiegel, R.L., Mobarek, I., and Jen, Y., "Discharge of warm water jet over sloping bottom," Proceedings of the Golden Jubilee Symposia on the Modern Trends in Hydraulic Engineering Research, Government of India, Vol. 2, January 1966.
7. Wiuff, R., and Wriksen, P.B., "Warm surface jet in shallow water," Progress Report No.37, Institute of Hydrodynamics and Hydraulic Engineering, Technical University of Denmark, Denmark, December 1975, pp. 25-30.

SUBSCRIPTS:

- o The value of a parameter at the discharge.
- a The value of a parameter for the receiving water.
- m The value of parameter at the centerline of the surface buoyant jet.

DESIGN OF AN INTERMITTENTLY
OPERATED OUTFALL

By Roger W. Lindquist, M.ASCE¹
and George J. Murphy, F.ASCE²

INTRODUCTION

The City of San Francisco, California, has a combined sewer system that presently overflows into the bay or ocean when it rains. Under the current wastewater management program being implemented, this combined flow of storm and sanitary wastes will be treated and discharged into the Pacific Ocean through a three-pipe outfall system. The system will dispose of the treated sanitary wastewater (dry weather flow) through a 2740-millimetre-(mm)-diameter, 6-kilometre (km) ocean outfall, and the mixture of sanitary wastewater and storm-water (wet weather flow) will be disposed of through two 2740-mm-diameter outfalls, 4 km long. The depth of the dry weather diffuser is approximately 24 m and the depth of the wet weather diffuser is approximately 17 m. The wet weather outfall will operate only when the rain exceeds 0.5 mm per hour. Rain exceeds this intensity about 4 percent of the time, or 350 hours per year. The peak wet weather flow is approximately 1800 megalitres per day (Ml/day)³. The average dry weather flow is 400 Ml/day and the peak dry weather flow is approximately 700 Ml/day.

This paper reviews the unique problems of an intermittently operated outfall located in an area of shallow water with loose bottom sediments on a coast subjected to high wave energy. The circulation of seawater through the dormant diffuser and the resulting reduction in hydraulic capacity by sediment intrusion and biofouling are identified as the most severe problems for the intermittently operated outfall. The features incorporated to reduce these problems are bottom-exiting risers, diffuser ports elevated above the seabed, four ports per riser with a dual valve system, and use of antifouling materials and a flushing system.

¹Project Engineer, CH2M HILL, INC., Corvallis, Oregon

²Project Manager, PBQ&D, INC., San Francisco, California

³1 Ml/day = 1,000 cubic metres per/day (m³/day) = 11.6 litres per second (lps)

BACKGROUND

San Francisco is undertaking an extensive wastewater management program to upgrade treatment and reduce the volume and frequency with which untreated effluent is discharged into both San Francisco Bay and the Pacific Ocean. This program involves construction of two secondary treatment plants for dry weather flow, and one chemically assisted primary treatment plant for the wet weather flow, several large storage and transmission facilities, and an ocean outfall system consisting of one dry weather and two wet weather outfall pipes. Figure 1 shows the basic configuration of the major elements of the wastewater treatment and disposal system.

The storage and transmission facilities will have the capacity to store excess combined sewage during most storms, thus limiting the number of overflows onto the beaches of the San Francisco peninsula. The chemically assisted primary plant will treat combined sewage in excess of that receiving secondary treatment. The combined sewage in storage will be processed as the storm flows subside. Once the transport and storage system is empty, the wet weather outfalls will be dormant until the next storm.

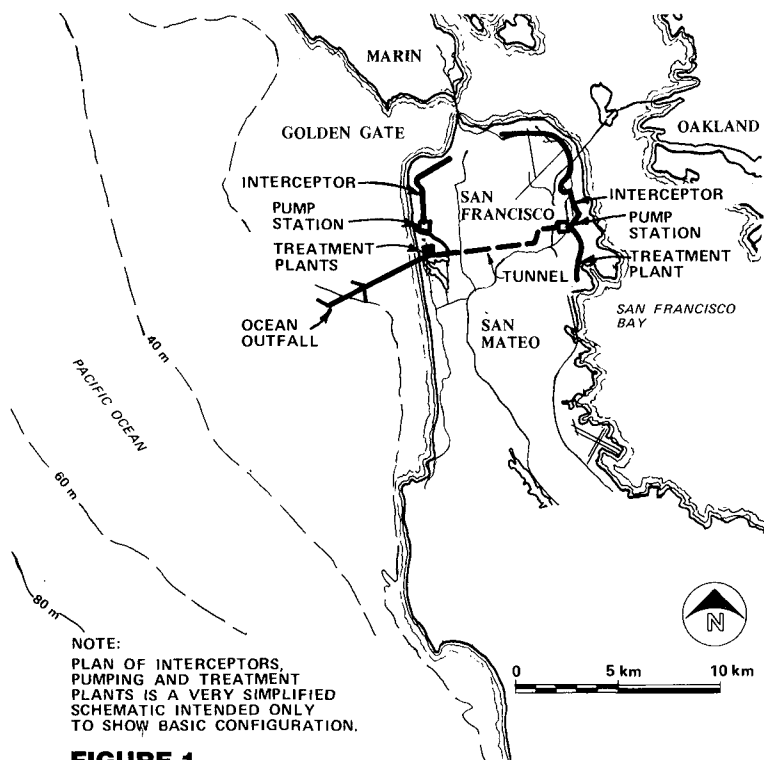
CONSTRAINTS

San Francisco's operating and site conditions make the design of the wet weather outfall considerably different from continuously flowing deep ocean outfalls. These constraints are reviewed below.

Dilution Requirements

The ocean outfall system must meet the requirements of the amended California Ocean Plan, which contains discharge regulations set by the California State Water Resources Control Board. These regulations do not contain specific requirements for dilution nor effluent criteria for biochemical oxygen demand (BOD) or coliform levels. The major provisions of the Ocean Plan include:

- Establish limits of receiving water quality, which the discharge does not violate
- Require that waste systems that discharge to the ocean will maintain the indigenous marine life
- Establish requirements for wastes that are discharged to the ocean



NOTE:
 PLAN OF INTERCEPTORS,
 PUMPING AND TREATMENT
 PLANTS IS A VERY SIMPLIFIED
 SCHEMATIC INTENDED ONLY
 TO SHOW BASIC CONFIGURATION.

FIGURE 1
SAN FRANCISCO
WASTEWATER PROGRAM MASTER PLAN

The limitations on wastewater characteristics include 75-percent removal of suspended solids and limits on discharge of grease and oil, settleable solids, turbidity, pH, toxicity concentration, and toxic materials. There are receiving water limits on heavy metals, floating particulates, organics, dissolved oxygen, and radioactive and toxic substances. Maximum coliform concentrations are specified for beach and shellfish areas.

The discharge requirements for effluent concentration include a 6-month median as well as a daily maximum and an instantaneous maximum limit. Thus, by using the 6-month median, the wet weather dilution requirements are considerably less than the dry weather dilution. The target established for the dry weather diffuser is for better than 100:1 average initial dilution at least 80 percent of the time. The target for the wet weather diffuser is for greater than 25:1 average initial dilution at peak discharges. The relatively low target dilution for the wet weather discharge can be obtained in shallow water.

Operation Constraints

The wet weather outfall will operate about 350 hours per year during the wet season (December through April) and remain dormant during the rest of the year. Both dry weather and wet weather outfalls will operate at their maximum design flows several times each year. Whenever the wet weather outfall is not discharging, wave pumping through the diffuser ports will occur. Wave pumping, as used here, is the circulation of seawater through the diffuser with water entering the ports under the wave crest and exiting through the wave trough. If allowed to occur, this circulating seawater will introduce fouling organisms and sediment into the diffuser.

Site Constraints

The ocean floor, in the vicinity of the outfall, has a relatively flat slope for over 45 km from shore. Thus, no significant advantage can be gained by extending the outfall beyond the minimum depth required to obtain the dilution. The location of the outfall, 8 km south of the Golden Gate, is subject to intense winter storms as well as continuous wave action throughout most of the year. The ocean floor in the outfall area consists of loose sediments to a depth of up to 3 m; also an abundance of fine-grained sediment is discharged through the Golden Gate from the Sacramento and San Joaquin Rivers. The shallow water and the high wave energy cause sediments to be suspended except during the calmest days.

Over the life of the project, the elevation of the sea floor is predicted to vary from approximately 1 m above to 2 m below the present floor.

The low elevation of the onshore treatment site limits the head available for gravity flow to 7 m during high tide and high flow conditions.

Structural Constraints

The outfall is designed to account for wave and seismic forces and soil liquefaction. To protect it, the outfall will be buried in a trench, with approximately 3 m of backfill materials and armor cover over the pipes. Along the San Andreas Fault, which the outfall crosses approximately 3 km from shore, movement perpendicular to the pipe of up to 20 feet is possible. Special joints that provide for some movement and are easily replaced were designed for the fault zone.

ANALYSIS

The analysis and design of the outfall required close coordination between many engineering and scientific disciplines. No single solution was completely satisfactory to each discipline; judgment and compromises were required to fully develop the design. The analysis of several major elements is described below.

Dilution

The results of the dilution analysis indicated that the wet weather diffusers should each be approximately 420 m long, have 96 ports with a nominal diameter of 200 mm, and discharge with approximately 15 m of water above the port. Figures 2, 3, and 4 show the configuration of the outfall, diffuser, and risers.

Wave Pumping

Various methods of analysis and levels of refinement were made to estimate the volume of water that would enter the ports due to wave pumping. It was determined that large volumes of water would enter each riser under each wave crest. For instance, by using a simple orifice equation and an average head of the wave crest over the still water level, it can be found that over 1 cubic metre (m^3) of water will enter a riser under a relatively small wave.

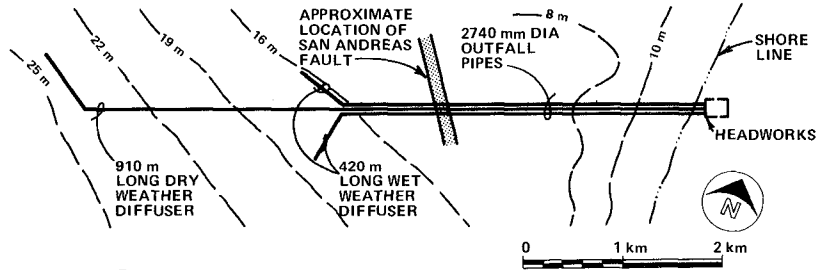
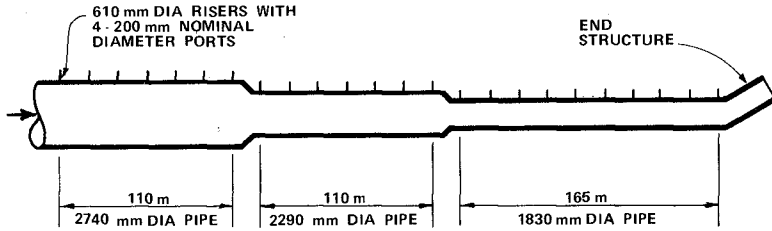


FIGURE 2
SCHEMATIC OUTFALL CONFIGURATION



TOTAL NUMBER OF PORTS = 96

FIGURE 3
WET WEATHER DIFFUSER CONFIGURATION

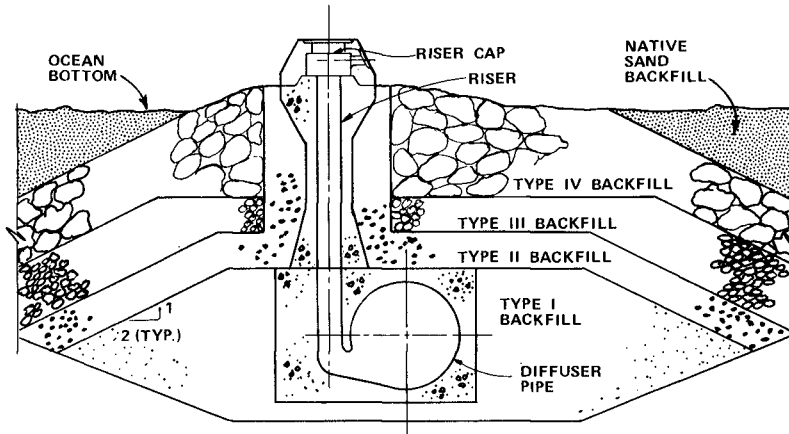


FIGURE 4
TYPICAL SECTION OF WET WEATHER RISER

Sediment Intrusion

The volume of sediment that enters the diffuser depends upon the concentration of sediment in suspension. This concentration in turn depends upon the bottom currents, the wave conditions, and the height of the port above the seabed. The trapping efficiency of the port and riser also affect the volume of sediment entering the diffuser. The trapping efficiency is defined as the percent of sediment entering the ports that is deposited in the diffuser. Various assumptions on concentration were made using sediment trap and water sample data. With the high trapping efficiency it was found that the diffuser could fill with sediment during a single storm.

Biofouling

Biofouling organisms were identified and methods of controlling them were examined. It was concluded that the diffuser would be an ideal habitat for certain organisms if seawater circulated through the diffuser. Unless circulation of seawater could be eliminated, fouling growth several inches thick could be expected inside the outfall. Other methods of control that were investigated included washing the newly settled, but poorly attached, fouling organisms off the structures with high velocity flushing water, use of antifouling materials, or discharge of small quantities of freshwater in the diffuser. None of these methods appeared satisfactory on close examination.

Various types of antifouling materials, including NOFOUL¹ rubber, various copper-nickel alloys, and aluminum bronze alloys were studied. Coupons of these materials were placed in the seawater at Monterey Bay, in bay water in the San Francisco Bay, and alternated between bay water and treated sewage effluent. These test coupons provided information on the rate of leaching of these compounds when alternately exposed to treated sewage effluent and seawater.

Flushing

Removal of sediments from the diffuser by flushing was analyzed. The diameter and length of the outfalls require a large volume of water for minimum flushing. There is no source of freshwater for flushing other than secondary treated sewage effluent. Various storage facilities were examined for storing the treated effluent flushing water,

¹ Manufactured by B.F. Goodrich, Akron, Ohio

including the tunnel storage system, the primary sedimentation basins at the wet weather treatment plantsite, and a separate storage reservoir built above the plantsite. The use of the sedimentation basins in the primary treatment system located near the headworks provides the most economical storage for flushing water. Samples of sediments, in suspension in the water column, were trapped in a nest of sediment traps, located near the wet weather diffuser. The sediments in suspension are a nonplastic silty fine sand with a mean diameter of 0.16 mm. This material is finer than the fine sand on the seafloor.

For the sediment flushing system to be effective, the flushing water must have sufficient velocity and volume to erode and transport the deposited sediment. Very little information is available that is applicable to large diameter outfalls and diffusers. A relationship of shear intensity parameters and transport parameters based on conduit data, flume data, and river data presented by Graf-Acaroglu(1) was used as a guide in developing a method of predicting the amount of sediment that could be flushed from the diffuser pipe. Using parameters for the outfall pipe diameter and Manning's flow equation, the Graf-Acaroglu relationship reduces to:

$$C = 1.03 \times 10^{-5} d^{-1.02} D^{-1.84} v^{4.04}$$

Where D = the diameter of the diffuser pipe in feet
 d = the grain size in millimetres
 V = velocity in the diffuser pipe in feet per second
 C = sediment concentration by volume

This equation was used to estimate the flushing characteristics in the outfall diffusers as a function of the sediment grain size and the effluent velocity through the diffusers. The analysis and computations are complicated because of the continually changing effluent velocity as it is discharged through the diffuser ports and it is transported through the tapered sections of the diffuser. A computer program was written to perform the calculations for flushing the diffuser and record the mathematical calculations.

This analysis indicates the upstream end of each tapered section would be the first to scour clean. Part of the sediment removed from these upstream sections would be discharged out of the first riser pipe, and part of it would be deposited in the downstream sections. After the upstream section was clean, the cleaning process would progress downstream. A very simple hydraulic model was used to

verify the concepts developed from the Graf-Acaroglu relationship. The results of this model study gave reasonable verification to this method of predicting the success of the flushing process.

Flushing with the end gate open and end gate closed were analyzed with the computerized hydraulic model. With the end gate open, a 90-minute flushing period will remove 0.6 m^3 of sediment per metre of diffuser, or approximately 240 m^3 . With the end gate closed, a 90-minute flushing period will remove less than half of this amount of sediment from the diffusers. With the end gate closed, the first sections of diffuser will be cleaned out, but the remainder of the sediment will be transported to the end of the diffuser, plugging the last few sections.

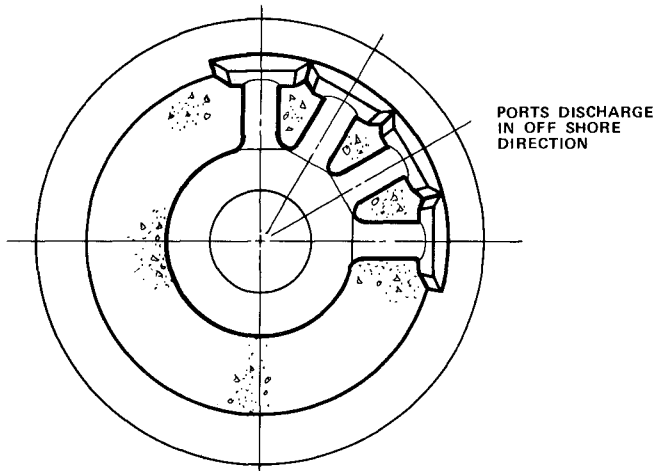
DESIGN FEATURES

The design features that were incorporated into the diffuser to protect it from the seawater circulation problems caused by wave pumping are discussed below. A double check valve system is considered the primary defense against seawater circulation. However, because of the severe site and operating conditions, the diffuser was designed with several safety features in case the check valve system does not work properly.

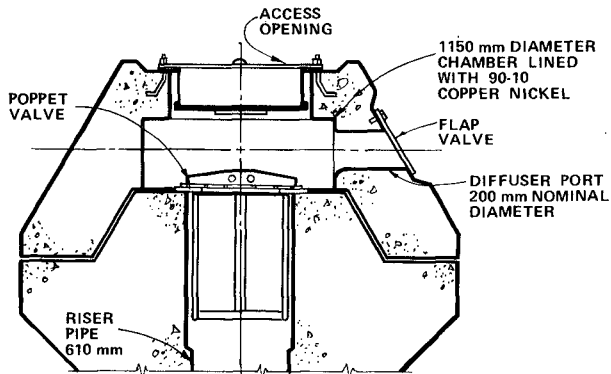
Double Valve System

After it was concluded that some sort of valve system was necessary to reduce wave pumping, many ideas were evaluated. These ideas varied from using manufacturers' standard check valves to complicated, remote-controlled valves that could be opened when the wet weather flow began and closed when it stopped. Because of the harsh environment, it was decided that the valve should be as simple as possible with few moving parts.

The final system consisted of a "poppet" valve over the riser and rubber flap valves over the ports, as shown on Figures 5 and 6. The poppet valve consists of a flat copper nickel plate, centered over the riser pipe with four guide legs. This plate rises when the outfall is flowing and closes under its own weight when the flow has stopped. It is provided with rubber gate seats. Each port is covered with a heavy rubber flap valve that is reinforced with a metal plate, which opens under flow and closes when the flow stops.



HORIZONTAL SECTION AT CENTERLINE OF PORTS



VERTICAL SECTION AT CENTERLINE OF RISER

FIGURE 5
WET WEATHER RISER CAP AND VALVES

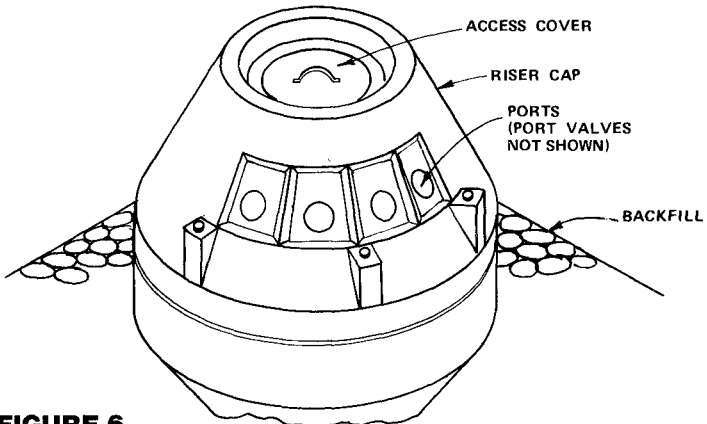


FIGURE 6
ISOMETRIC DETAIL OF WET WEATHER RISER CAP

Four hydraulic models were used as tools to develop and refine the design. The wave tank facilities at Oregon State University, Corvallis, Oregon, were used to study a 4:1 scale model of the riser cap and valves under wave action. While the combination of the flap and poppet valve greatly reduces the flow of seawater into the riser, waves cause some fluttering of the valve, which may allow some backflow of seawater. This fluttering is caused by wave forces, orbital velocities, and differential pressure on each flap valve. The fluttering can be reduced or eliminated by adding weights to the flap valves, but this increases the headloss across the valves. The headloss across the riser cap and valve system was 0.9 m under the maximum design flow of 1800 Ml/day.

Bottom-Exiting Risers

The wet weather risers are designed to exit from the invert of the diffuser pipe as shown on Figure 4. The main purpose of this configuration is to improve the effectiveness of flushing to remove sediments.

Multiport Riser

Normally, the diffuser ports are simply holes located in the sides of the diffuser pipe. However, with the buried diffuser, a riser pipe had to be used to bring the effluent from the buried pipe to about 1500 mm above the sea floor. Since the risers are exposed to damage by wave forces, anchors, and fishing gear, they must be structurally designed to resist these forces. The structural requirements control the external shape and size of each riser, regardless of the riser diameter. Such a riser is expensive and difficult to construct. In order to reduce the number of risers, two, three, and four ports per riser were studied and tested. In the final design, four ports were designed for each riser as shown on Figure 4.

Hydraulic modeling of the plume behavior was performed at the California Institute of Technology, Pasadena, California. Modeling consisted of comparisons of two, three, four, or eight ports per riser. Confirming tests were performed on the four-port-per-riser system, as finally designed. The four ports are located close together, in one quadrant, and positioned to discharge offshore, as shown in Figure 5.

Antifouling Materials

To reduce fouling, the riser cap was lined with copper nickel; the metal parts of the valves are copper nickel. The rubber valve seals, gaskets, and valve hinge are NOFOUL rubber. NOFOUL rubber is a chloroprene rubber impregnated with tributyltin oxide.

Height Above the Seabed

The highest concentration of suspended sediments occurs near the bottom. In order to reduce the concentration of sediment in suspension around the ports and to provide some protection from port burial caused by the fluctuating elevation of the seabed, the ports were located approximately 1500 mm above the seabed.

Flushing System

The sedimentation tanks for the proposed primary treatment system furnish storage for approximately 72,000 m³ of effluent for flushing the outfall. These tanks will be filled with secondary treated effluent and then discharged through the outfall. To be effective, the velocity of the flushing water must be at least 2 metres per second. It is estimated that this water, when flushed through the diffuser with the end gate open, will remove approximately 240 m³ of sediment.

ACKNOWLEDGEMENTS

The work on which this paper is based was performed for the City and County of San Francisco. PBQ&D, Inc. is the prime consultant on the Southwest Ocean Outfall Project (SWOOP). Woodward-Clyde Consultants is the principal subconsultant for oceanographic and geotechnical study. CH2M HILL is the principal subconsultant for the hydraulic and sanitary design of the project.

REFERENCES

1. Graf, W.H. and Acaroglu, E.R. "Sediment Transport in Conveyance Systems," Bulletin of the International Association of Scientific Hydrology, Vol. XIII, No. 2, 1968.

EXPERIMENTAL EVALUATION OF HEAT EXCHANGE
BETWEEN WATER SURFACE AND ATMOSPHERE

by

Günther BARG¹⁾, Horst SCHWARZE²⁾ and Gerhard VISSCHER³⁾

- 1) Dr.-Ing., Research Engineer, Franzius-Institut of the University of Hannover, Germany
- 2) Dr.-Ing., Chief Engineer, Franzius-Institut of the University of Hannover, Germany
- 3) Dipl.-Ing., Research Assistant, Franzius-Institut of the University of Hannover, Germany

ABSTRACT

The heat balance of a water body mainly depends upon the heat exchange processes at the water surface. An experimental method has been developed for determining the heat exchange, the exchange coefficient and the equilibrium temperature. The measuring equipment consists of two similar, well insulated pools which are exposed to the meteorological conditions of the Lower Weser River, Germany. The water temperature of the first pool (T_1) is artificially adjusted to the actual river temperature either by cooling or heating. The temperature of the second pool (T_2) is held constant above the temperature T_1 . The difference in power inputs required $W_2 - W_1$ is equivalent to the net rate of heat exchange due to the increase of temperature to ΔT above the river temperature.

1. INTRODUCTION

In order to protect the ecological system of a river the thermal load caused by heat discharge of power plants must be predicted and controlled. In many cases there is a mutual influence and superposition of several heat discharges.

In brackish zones of tidal rivers the ecology is especially sensitive. Therefore the permissible heating range in German tidal rivers is limited to 2°K. This limitation is relevant during periods with little heat exchange.

After the heated effluent is completely mixed with the receiving water, the decrease of water temperature mainly depends upon heat exchange processes between the water surface and atmosphere. Especially in tidal rivers, where a body of water repeatedly receives artificial heat and remains inside the region of discharge influence for a long time, the knowl-

edge of the heat exchange at the water surface is fundamental for determining the cooling rate.

In a previous comprehensive study Kuhn (1972) established a heat exchange coefficient which is proportional to the cooling rate and computed as a function of water temperature and meteorological variables. But past experience has demonstrated that the computation of heat exchange coefficients on the basis of meteorological variables becomes efficient only when extensive and very exact measurements of these parameters are available. Therefore an experimental method has been developed by the Franzius-Institut measuring the rate of heat exchange directly.

2. BASIC THEORY

The net rate of heat exchange at the water surface consists of the following components (Kuhn, 1972):

$$H = H_W + H_G + H_S + H_V + H_K + H_N \quad (1)$$

in which

H_W = net rate of heat exchange due to back radiation from the water to the atmosphere

H_G = net rate of heat exchange due to absorbed atmospheric radiation

H_S = net rate of heat exchange due to absorbed solar radiation

H_V = net rate of heat exchange due to evaporation and condensation at the water surface

H_K = net rate of heat exchange due to conduction at the water surface

H_N = net rate of heat exchange due to rainfall

Under the assumption that a body of water is well mixed the variation of temperature with time is determined by

$$\frac{dT}{dt} = \frac{H}{H \cdot \rho \cdot c} \quad (2)$$

in which

h = water depths

ρ = water density

c = specific heat of water

Neglecting heat exchange due to rainfall, only the terms H_W , H_V and H_K are changing due to heating up by artificial heat. The atmospheric radiation and the solar radiation are not influenced by increasing water temperatures.

If the net heat flux directed into the water body is defined to be positive, an increase of water temperatures due to artificial heat will cause a decreasing net heat flux at

the water surface, because back radiation from the water body and evaporation are increasing with higher temperature.

If there is a positive heat flux at a starting point, the temperature of the water will increase until the heat flux is equal to zero. This water temperature is defined as equilibrium temperature T^+ . The equilibrium temperature is that temperature, a body of water exposed to a constant set of meteorological conditions would approach.

The equilibrium temperature only depends on meteorological conditions, not on water depth. A change in meteorological conditions leads to another curve, describing the relationship between heat flux and temperature. Kuhn established a heat exchange coefficient A , which is the derivation of that curve in the point of non heat flux. The coefficient is proportional to the cooling rate and can be calculated as a function of water temperature and wind velocity. Kuhn expressed the net rate of heat exchange at the water surface as

$$H = \frac{\partial H}{\partial T} \cdot (T - T^+) = A (T^+ - T) \quad (3)$$

in which A = total heat exchange coefficient
 T^+ = equilibrium temperature
 T = water surface temperature

This equation shows, that the net rate of heat exchange is equal to the product of the heat exchange coefficient and the difference between the equilibrium temperature and the water surface temperature.

Combining Equation 2 and 3 gives

$$\frac{dT}{dt} = - \frac{A}{h \cdot \rho \cdot c} (T - T^+) \quad (4)$$

Assuming constant meteorological conditions, this equation is soluble and the solution shows the wellknown exponential course of temperature until reaching the equilibrium temperature.

$$T - T^+ = (T_0 - T^+) \cdot \exp \left(- \frac{A}{g \cdot \rho \cdot c} t \right) \quad (5)$$

Besides the heat exchange coefficient, water depth is the essential parameter of the range of temperature variation with time. For example, in case of wind velocity of 2 m/s and water depths of 5 m the half-life-period amounts to 8 days. Normally constant meteorological conditions can not be expected throughout such long periods.

Furthermore an applicable computation of heat exchange coefficients is only possible, if wellknown data about evaporation and condensation are available. This is one diffi-

culty when using the exchange coefficient for computation of heat exchange between water surface and the atmosphere.

Another problem is the determination of the equilibrium temperature, because generally the actual water temperature is not equal to the equilibrium temperature. There may occur large differences between actual temperatures and equilibrium temperatures with time of a day or under consideration of daily averaged values all the year round.

Considering a period of one day, normally the maximum of the equilibrium temperature will occur at noon due to solar radiation and the minimum at night. The temperature T_w of a water body will follow the variation of the equilibrium temperature T^* with a phase lag.

Considering the variation of temperature throughout a year there are similar curves with maximum in summer and minimum in winter. In spring and early summer the actual water temperatures are normally lower than the equilibrium temperatures, whereas in autumn and winter the relation is contrary.

If the equilibrium temperature is higher than the temperature of a water body including already artificial heat water temperature will continue to increase and the artificial heat will even remain in the water body.

The application of the heat exchange coefficient under the assumption that water temperature without any artificial heat is equal to the equilibrium temperature leads to an easy calculation. This assumption, however, will only casually agree with real conditions. Therefore it was thought desirable to determine the heat exchange between water surface and atmosphere by experimental evaluations.

3. EXPERIMENTAL PROCEDURE

3.1 Measuring Equipment

The measuring equipment consists of two similar plastic pools with a free water surface, 2.00 m in diameter and 30 cm deep. They are well insulated on the sides and bottom and generally filled to the same depths to within 3 cm of the top of the pool sides. Water loss by evaporation is refilled automatically. Identical stirring devices placed in each pool keep the water well mixed.

The pools are placed on a platform above the water surface of the river. They are directly exposed to the climate of the river region investigated.

The measuring equipment further consists of thermo-couples for temperature sensing, water level gauges, a flowmeter, electrical heating elements, a refrigerator, heat exchangers and a 12-point recorder. The arrangement of the measuring equipment is shown in Fig. 1.

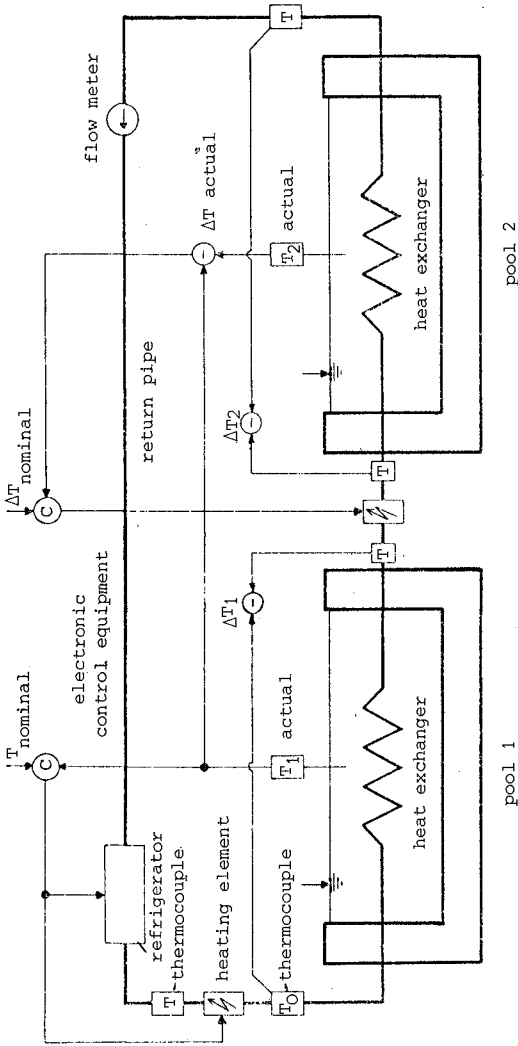


Fig. 1
Scheme of the Measuring Equipment

Additionally all relevant meteorological data are registered on the platform and recorded.

The principle of the measuring equipment is that both pools have equal dimensions and that they are exposed to the same meteorological conditions.

By means of an electronic control unit the water of the first pool is cooled or heated corresponding to the actual river temperature T_1 . The water of the second pool is also cooled or heated, but is controlled by a constant difference of temperature $\Delta T = 2.00^\circ\text{C}$ above the temperature of the first pool (tolerance 0.01°C). Water temperatures T_1 , T_2 , and the difference of temperatures ΔT are measured and recorded. The power inputs W_1 and W_2 are determined by measurements of initial and return temperatures at the heat exchangers and quantity of flow.

The difference of input $W_2 - W_1$, which is necessary to maintain the range of $\Delta T = 2.00^\circ\text{C}$ is equivalent to the net rate of the heat exchange between the water surface of a river artificially heated by 2.00°C and the atmosphere.

In analogy to Kuhn the heat flux can be expressed as the difference between equilibrium temperature and water temperature multiplied with the heat exchange coefficient, now called α , because it is evaluated experimentally.

$$H_1 = \alpha_1 (T^+ - T_1) + W_1 \quad H_2 = \alpha_2 (T^+ - T_2) + W_2 \quad (6)$$

in which

W_1 = power input to pool 1
 W_2 = power input to pool 2) (heating +, cooling -)
 α_1, α_2 = experimental heat exchange coefficient
 T^+ = equilibrium temperature

The constant difference of temperature implies, that the variation of temperature in pool 1 is equal to that of pool 2

$$\frac{dT_1}{dt} = \frac{dT_2}{dt} \quad (7)$$

and it follows, that the heat flux of pool 1 is equal to that of pool 2.

Assuming that for a low difference of temperature $\Delta T = 2.00^\circ\text{C}$ $\alpha_1 \approx \alpha_2 = \alpha$ Equation 6 produces

$$W_2 - W_1 = \alpha (T_2 - T_1) \quad (8)$$

and the heat exchange coefficient is

$$\alpha = \frac{W_2 - W_1}{T_2 - T_1} = \frac{W_2 - W_1}{\Delta T} \quad (9)$$

The equilibrium temperature can be determined by Equation 2 and 6:

$$H_1 = h \cdot \rho \cdot c \cdot \frac{dT_1}{dt} \stackrel{!}{=} \alpha (T^+ - T_1) + W_1 \quad (10)$$

$$T^+ = \frac{1}{\alpha} (h \cdot \rho \cdot c \cdot \frac{dT_1}{dt} - W_1) + T_1 \quad (11)$$

So the complex processes of heat exchange between water surface and atmosphere can be determined by measurements of temperature and power input.

3.3 Results of Measurements

The prototype of the measuring equipment described was installed on a platform above the water surface of the Lower Weser River, Germany, near by a nuclear power plant. The equipment was put into operation in April 1979 in connection with an already existing system of control points for water temperature in order to determine the cooling rate of river water artificially heated up by the discharge of cooling water.

Results of measurements are shown in Fig. 2 and 3, demonstrating the operation method of the measuring equipment. The water temperature of the first pool was controlled on the level of 18.30°C corresponding to the actual river temperature. For that purpose it was necessary to heat the pools during the night and to cool it in the day-time.

The net rate of heat flux can be determined separately for each of the pools by the difference between the temperatures of forward and return flow (ΔT_1 , ΔT_2) and quantity of flow in the heat exchanges. Furthermore the distance between the curves of ΔT_1 and ΔT_2 is proportional to the heat exchange coefficient α . Fig. 3 shows important meteorological data.

The results of the measurements have been compared with results of heat exchange computations which are conducted on the basis of meteorological measurements. This comparison yielded differences of a certain tendency, which requires further research. For example, measurements conducted during the night obtained better correspondence to the computations than those conducted in the day time.

4. CONCLUSIONS

The surface heat coefficient and equilibrium temperature can be evaluated using the experimental method described here. An advantage of this method consists in determining the complex processes of heat exchange at the water surface by simple measurements of temperature and power input.

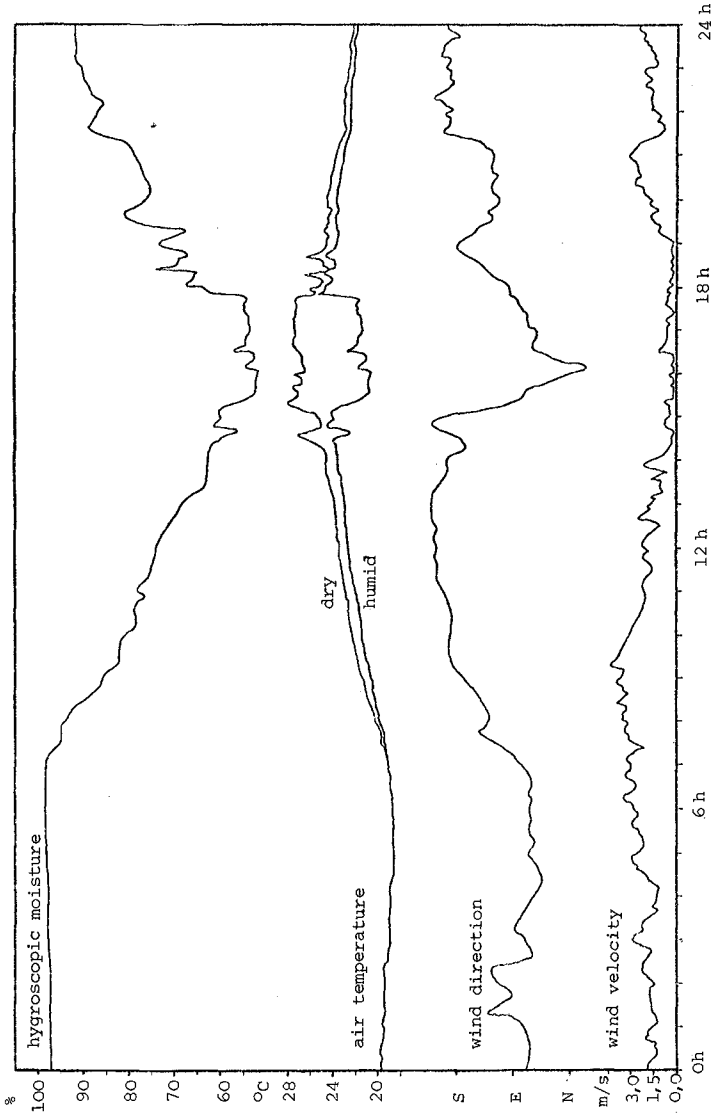


Fig. 2
Meteorological Measurements on 28.7.1979

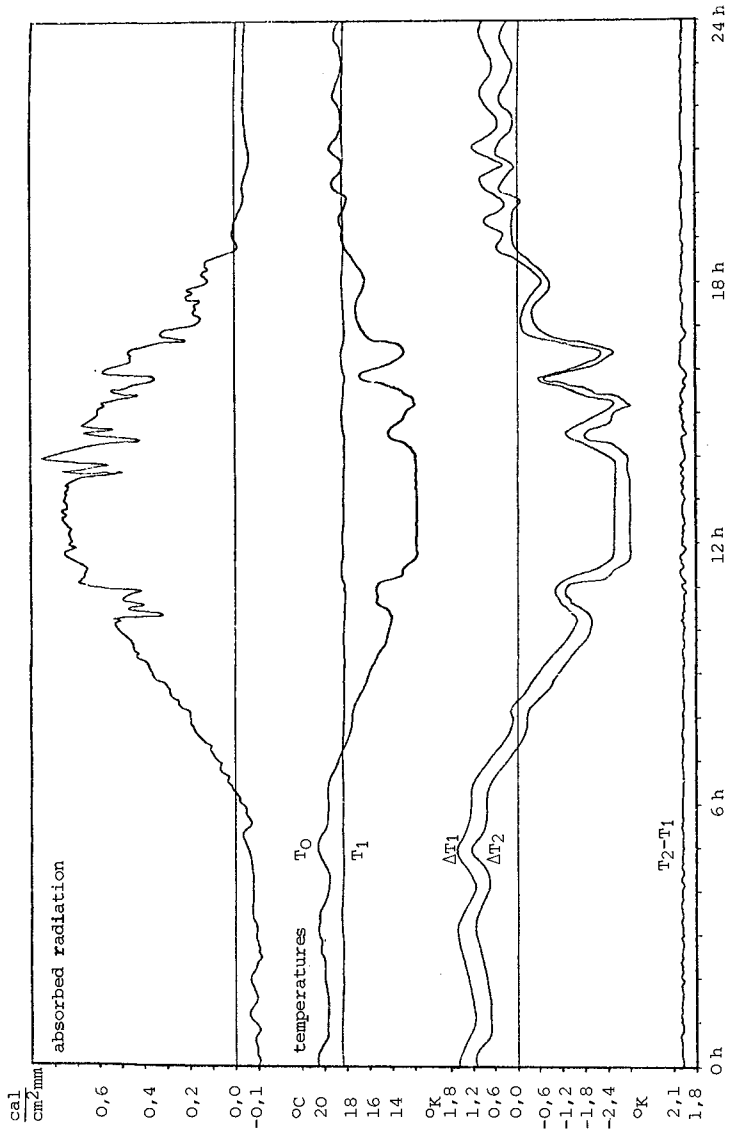


Fig. 3
Measurements of Heat Exchange on 28.7.1979

Because the physical actions of heat exchange at the pools are in principle similar to those at the river surface, different results are only imaginable as a consequence of different boundary conditions (wind,waves). Thus it is important to expose the pools as near the water surface of the river as possible.

Finally, a functional relation has to be found which allows to apply the results of pool measurements to the actual exchange at the river water surface.

5. REFERENCES

- KUHN, W. (1972). Physical and Meteorological Considerations on the Use of Waters for Cooling Purposes. Arch. Met. Geoph. Biokl., Switzerland, Ser. A, 21, pp. 95 - 122

DYNAMICS OF SILT IN ESTUARY, RESIDUAL CURRENT

OR FLOCCULATION WHICH PREVAILS ?

by
J.P. LEPETIT and M. DAVESNE¹

ABSTRACT

The transport of fine suspended sediment in a partly-mixed estuary has been simulated on a physical model of a schematic estuary reproducing the main geometrical and hydrodynamical characteristics of the Gironde Estuary (France). The natural sediment consisting of silt and clay is simulated using a light and fine material, gilsonite, and the flocculation processes in salt water and under turbulence induced by tidal currents have been reproduced by adding in salt water a flocculating salt solution (sodium pyrophosphate). Then the formation of the turbidity maximum surveyed in the field and its upstream-downstream migration in response to varying river discharge have been successfully simulated and the results of different series of tests lead to the following conclusions :

- flocculation processes - which are responsible of the variation of the settling velocity with salinity and turbulence-have to be reproduced to explain the formation of the turbidity maximum ;
- after high river discharges the convergence of bottom residual currents (null point) due to the salinity intrusion creates a trap for suspended sediments supplied by the river flood which accumulate in the form of the turbidity maximum. Without salinity intrusion, a large amount of sediment would escape out of the estuary to the sea ;
- during low river flows, a part of the suspended sediment migrates upstream but the amplitude of this migration is small compared with the displacement of the upstream limit of the salinity intrusion ;
- the upstream migration of the turbidity maximum is increased when a transverse bottom morphology (existence of a deeper navigation channel) is represented.

1. INTRODUCTION

Transport of fine suspended sediment in partly-mixed estuaries is generally characterised by the existence of an accumulation zone with high turbidities migrating with the season ; this maximum of concentrations occurs in the lower part of the estuary after high river flows and part of it progressively migrates upstream during low river flows. This mechanism has been attributed to various processes,

¹ Division Hydraulique Maritime. Laboratoire National d'Hydraulique. Electricité de France. Chatou. France.

e.g. flocculation, tidal resuspension of bottom sediment, convergence of bottom residual currents depending on the salt intrusion, river flow and estuary geometry. The contrasting results from different estuaries indicate that the question of defining the process controlling the transport has no general solution at the present stage of progress.

In order to study these phenomena in laboratory, a fixed-bed small scale model of a schematic estuary has been developed. The beginning of the study consisted in reproducing salinity intrusion for different tidal amplitudes and river flows, and extracting residual currents from flow velocity measurements with an optic fiber laser anemometer.

Then the simulation of suspended sediment transport has been undertaken ; the extreme complexity of the factors involved in suspended transport and their simulation on a very small scale model raised many difficulties but interesting results have been obtained which are presented in this report.

2. DESCRIPTION OF THE SCHEMATIC ESTUARY MOEEL

The geometrical and hydrodynamical characteristics of the schematic estuary are those of the Gironde estuary, France. This estuary has been chosen because of the smooth and monotonic longitudinal variation rate of both its width and cross sections and also because of the availability of numerous field measurements although most of them are located in the navigation deep channel.

The Gironde estuary (cf fig. 1) is formed by the junction of the Garonne and Oordogne rivers. The navigation channel is about 7 m deep (below LWL) upstream PK 80 (distance in kilometers from Bordeaux) where a break in slope occurs. Downstream the depths increase and reach 30 m at the mouth. The north channel is wider and shallower (3-5 m) and is also marked by a slope break at PK 80 with increasing depths downstream ; the two channels merge in the mouth. The upper estuary, extending from the Bec d'Ambès to about PK 50, is characterized by numerous banks, shoals and islands. The lower estuary exhibits a simpler morphology consisting of two channel systems separated by a succession of sandy banks.

The monthly averaged river discharge varies from 200 m³/s in summer to 1 500 m³/s in winter with a mean of 800 m³/s. During river floods the instantaneous discharge can often exceed 3 000 m³/s. The tidal amplitudes in the inlet vary from 2 m during neap tides to 5 m during spring tides. In spring tides, the tidally averaged ebb or flood discharges vary from 12 000 m³/s (15 times larger than the annual averaged river discharge) at the Bec d'Ambès to 100 000 m³/s (125 times larger than the mean river discharge) at the mouth. These figures show that the velocities of the tidal currents are not significantly influenced by the river discharge in the lower part of the estuary.

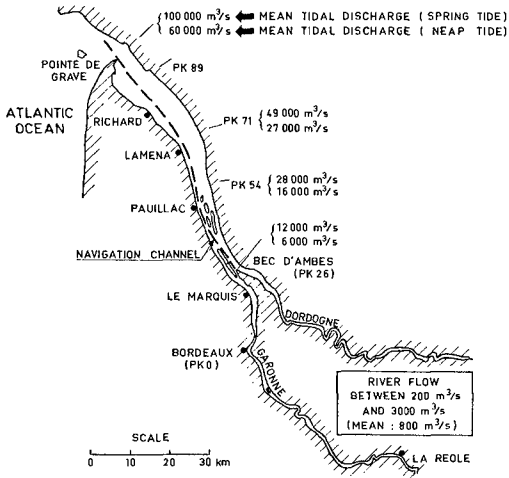


Fig. 1 : THE GIRONDE ESTUARY (France)

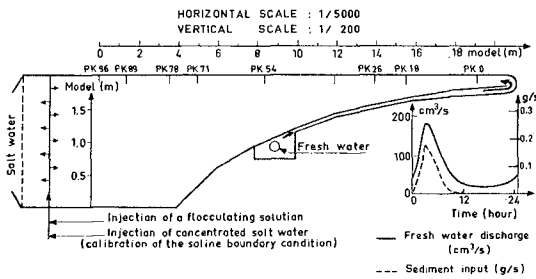


Fig. 2 : DESCRIPTION OF THE SCHEMATIC ESTUARY MOEEL

The silt and clay presently accumulating in the estuary are mainly supplied by the rivers. This influx of suspended sediment has been evaluated at about 2×10^6 tons/year.

The schematic estuary model presented in figure 2 reproduces the entire tidal part of the Gironde estuary.

It is a fixed-bed, distorted scale model with length scales of 1/200 vertically and 1/5000 horizontally with rectangular cross sections ; the longitudinal rate of variation of cross sections of the Gironde estuary is fitted by an exponential law.

The variation rate of its width is also exponential except near the mouth where the width is supposed to be constant between PK 76 and PK 96. The depth is constant transversely and equal to the cross sectional area divided by the width.

The experimental equipment allows to reproduce the following mechanisms :

- fortnightly variation of the tidal amplitude at the sea boundary ;
- annual variation of the river flow, as shown in figure 2 ;
- annual variation of sediment input introduced at river source with a turbidity proportional to the river flow ; in the experiments suspended sediments are supposed to be supplied only by the river ;
- variation of salinity intrusion with the tidal amplitude and river flow ;
- flocculation of sediment in salt water.

The natural sediment is simulated using a light and fine material, gilsonite, with a density of 1.035, an average grain size of 45 μm and a mean settling velocity of 0.04 mm/s in freshwater. The flocculation processes in salt water have been reproduced by adding in salt water a flocculating salt solution (sodium pyrophosphate). The flocculating solution induces formation of large flocks which entrap gilsonite particles (cf fig. 3).

This mechanism seems to be mainly linked with the value of the PH of the solution. So, the settling velocities of gilsonite flocks depend on both salinity and concentrations of pyrophosphate as shown in figure 4.

The concentrations of flocculating salt solution influence the characteristics of flocks - size and shear strength and consequently those of deposits - especially the critical shear stress of resuspension.



Fig. 3 : FLOCCULATION OF GILSONITE

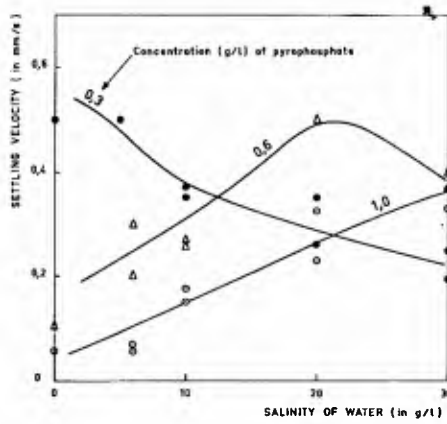


Fig. 4 : SETTLING VELOCITIES OF GILSONITE FLOCKS IN STILL WATER (initial concentration of gilsonite : 2 g/l)

This condition has been respected using a concentration of pyrophosphate of about 0,6 g/l for the salinity 20 ‰. If we suppose that the longitudinal gradients of salinities and pyrophosphate concentrations are identical in the model, the settling velocity of gilsonite flocks varies from about 0,3 mm/s to 0,5 mm/s (ten times more than the settling velocity of gilsonite without flocculation) when the salinity increases from 5 ‰ to 20 ‰. But in the model the size of flocks depends on turbulence ; so the settling velocity is a function of the flow velocity.

Gilsonite flocks represent the behavior of natural silt and clay much better than individual particles of constant size. Nevertheless it is doubtful that the extreme complexity of depositional and erosional behavior of cohesive sediments is reproduced in detail. For example the rates of deposition, which probably depend on the distributions of flocks shear strengths and the value of bed shear stress, have not precisely compared to their values in nature. So the experimental results must be considered as more qualitative than quantitative.

3. SALT INTRUSION AND RESIDUAL CURRENTS

In a first part of the study the model has been calibrated to reproduce water surface elevations, current velocities along the estuary and the mixing of salt and freshwater for different tidal ranges at the mouth of the estuary and different river discharges. Then the vertical profiles of residual currents¹ have been extracted from flow velocity measurements with an optic fiber laser anemometer. These results presented in detail in [1] lead to the following conclusions :

- salinity intrusion creates a zone of upstream bottom residual currents in the lower part of the estuary ;
- the point of convergence of the bottom residual currents (null point) depends on the tidal range (cf fig. 5) ;
- the migration of the null point with the river discharge is small in the range 500-2 500 m³/s for a fixed mean tidal amplitude, as shown in figure 6. So the zone of convergence of bottom residual flow does not follow the migration of the upstream limit of the salinity intrusion.

In nature the bottom residual flow field measured in the navigation channel is more complicated due to the influence of bottom topography, which creates successive zones of convergence and divergence (fig. 9). Nevertheless the measurements show the same influence of the tidal elevation as is pointed out by the results of the physical model : the residual velocities in spring tides are directed seaward for any river flow except at PK 89 near the bottom.

¹ It is the Eulerian residual velocity equal to the time average of the flow velocity within a tidal period calculated at a fixed point.

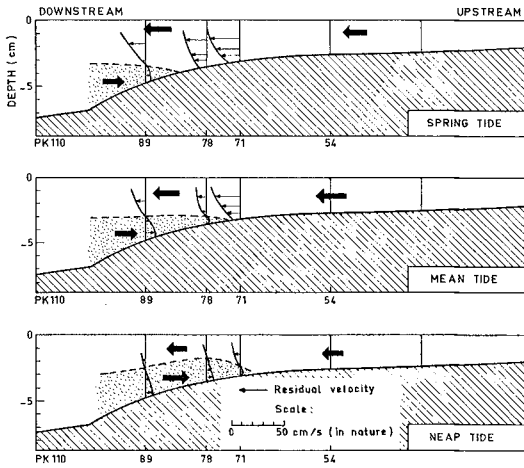


Fig. 5 : RESIDUAL VELOCITIES MEASURED IN THE MDEL (results for a mean river flow)

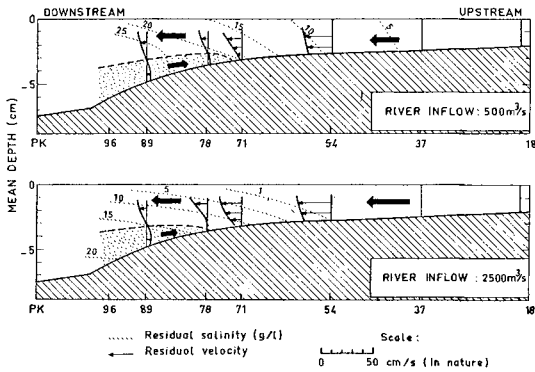


Fig. 6 : RESIDUAL VELOCITIES AND SALINITIES MEASURED IN THE MDEL (results for a mean tidal amplitude)

4. SUSPENDED TRANSPORT TESTS

4.1. Description of tests

At the beginning of a test, the model is operated with low river discharge until salinity concentrations throughout the model has become stabilized. Once stability has been obtained without sediment injection, the river discharge and suspended sediment influx cycles, as shown in figure 2, are initiated. The annual cycle is about one day long on the model. Salinity and suspended sediment concentration measurements are made continuously during the following cycle using an electro-optical system based on colorimetry method (colorimeter) and recorded on a magnetic tape.

Three series of experiments have been conducted : the first without reproducing flocculation processes. In this case the settling velocity of gilsonite particles is equal to 0,04 mm/s in fresh water and diminishes a little when moving from the fresh water to the salt water areas (for a salinity of 20 ‰ the settling velocity is about 0,02 mm/s). The following tests have been made with reproduction of flocculation. In that case the settling velocity increases from 0,04 mm/s to a maximum of about 0,5 mm/s when moving from the fresh water to the salt water areas. Other tests have been made in the same conditions but without upstream bottom residual currents (no salt but the flocculating zone is reproduced).

4.2. Principal results of tests

4.2.1. Without flocculation

The results show that the tidally-averaged concentration of suspended sediment diminishes seaward by dilution and settling out and there is no formation of a turbidity maximum. In the lower part of the estuary, a large amount of suspended material escapes out of the estuary by downstream advection. In the upper part of the estuary there are deposits of coarser gilsonite which are badly resuspended during spring tides.

4.2.2. With flocculation

The results obtained through the experiments taking into account flocculation processes can be summarized as follows :

- the tidal amplitude has a very important influence on the gilsonite flocks transport : after neap tides, the flocks deposit on the bottom and the turbidity decreases whereas after spring tides the deposits are resuspended and the turbidity increases ;

- the tidally averaged concentrations measured in spring tides depend on the river flow according to the following sequence described in figure 8 : at the maximum of flood the sediment input is large and the turbidity is high in the whole estuary ; when the river flow decreases, the development of a turbidity maximum is observed in the lower part of the estuary and the maximum is located near PK 85 at the end of the flood. During low river flows, the maximum diminishes and shifts upstream but the amplitude of this migration is small, the maximum being located near PK 71 at the end of low river flows ;
- different deposits can be observed : in the upper part of the estuary there are deposits of coarse non flocculated gilsonite which are badly resuspended during spring tides ; in the same way in the lower part of the estuary near the sea boundary there is an accumulation of flocculated gilsonite on the bottom ; except these two particular zones, the formation of deposits, only after neap tides, is linked to the turbidity maximum ; the upstream limit of the flocculated deposits is located near PK 75 after flood and near PK 54 after low river flow but several small deposits can be observed up to PK 30 ;
- the location of turbidity maximum seems to be linked to the convergence of bottom residual currents and not to the upstream limit of flocculating zone.

4.2.3. Without residual currents

The preceding conclusion has been confirmed by other tests carried out without residual circulation ; the results of these tests have shown no formation of turbidity maximum in spite of the reproduction of flocculation.

5. EFFECT OF TRANSVERSE BOTTOM MORPHOLOGY

In a last serie of experiments, the rectangular cross sections of the schematic estuary have been modified in order to study the influence of a deep navigation channel ; this channel was reproduced with the same depths as in nature without changing the cross sectional areas ; of course the lateral curvatures of the Gironde estuary are not still simulated. The measurements of tidally-averaged suspended sediment concentrations in spring tides and in the deep channel (fig. 8) show that the turbidities are higher in the channel than in the preceding tests with rectangular cross sections and that the upstream migration of the turbidity maximum is more important during low river flows.

So the transverse topography plays an important complementary role ; this influence is probably due to an enhanced density generated flow in the deeper channel but the results of velocities measurements are not yet available to confirm this hypothesis.

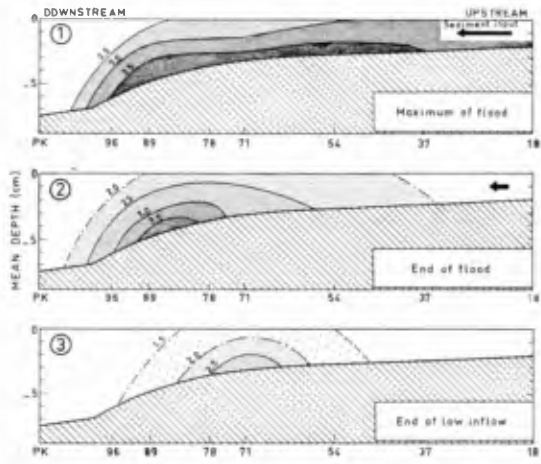


Fig. 7 : RESIDUAL SUSPENDED SEDIMENT CONCENTRATION (IN g/L) MEASURED IN SPRING TIDE (MODEL WITH RECTANGULAR CROSS SECTIONS)

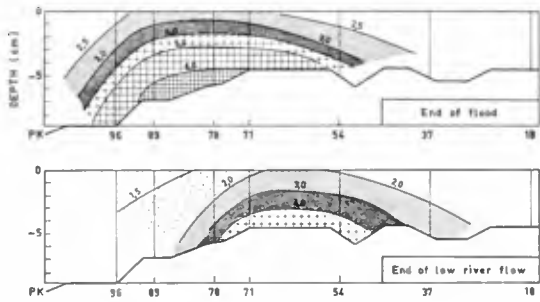


Fig. 8 : RESIDUAL SUSPENDED SEDIMENT CONCENTRATION (IN g/L) MEASURED IN THE CHANNEL (SPRING TIDE) (MODEL WITH TRANSVERSE GEOMETRY)

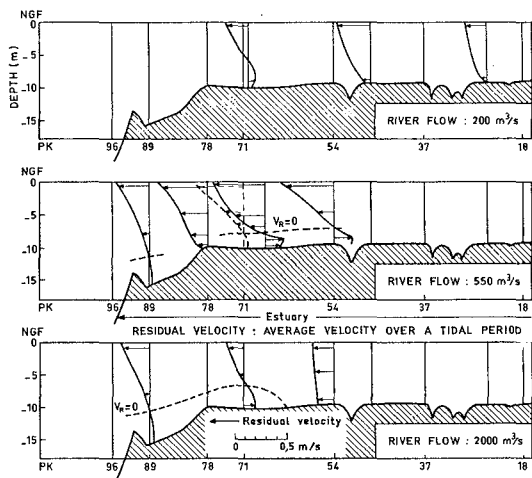


Fig. 9 : RESIDUAL VELOCITIES MEASURED IN THE MAIN CHANNEL OF THE GIRDNE ESTUARY (MEAN TIDAL RANGE)

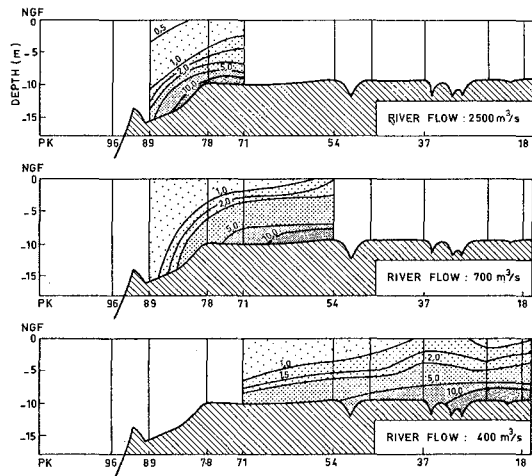


Fig. 10 : SUSPENDED SEDIMENT RESIDUAL CONCENTRATIONS MEASURED IN THE MAIN CHANNEL OF THE GIRDNE ESTUARY (SPRING TIDE)

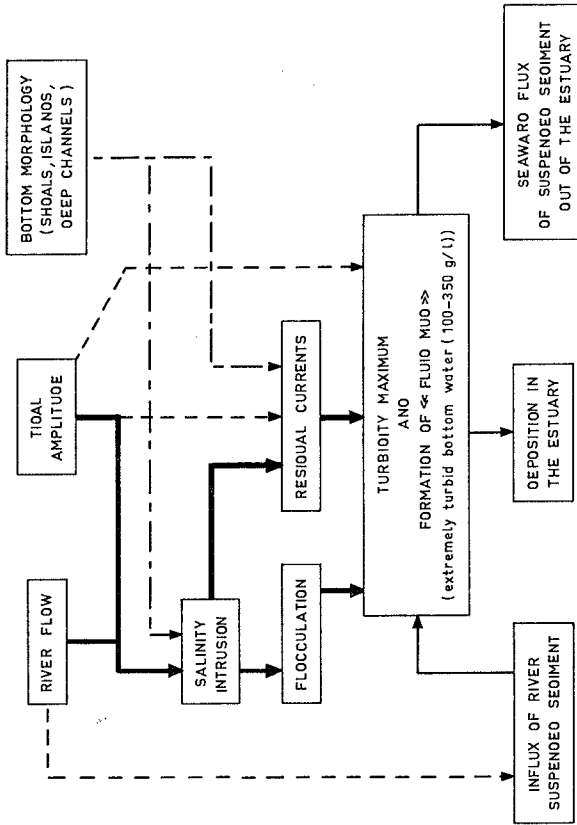


Fig. 11 : PRINCIPAL PHENOMENAE INVOLVED IN SUSPENDED SEDIMENT TRANSPORT IN ESTUARIES

6. CONCLUSION

The figure 11 summarizes the principal mechanisms involved in transport of fine sediments in estuaries. All these mechanisms or part of them have been simulated on a schematic physical model of the Gironde estuary. The formation of the turbidity maximum surveyed in the field has been successfully simulated by reproducing both the density generated residual currents and the flocculation processes when fresh water mixes with salt water. Gilsonite (density : 1.035, mean grain diameter : 45 μm) has been used for simulating natural sediment consisting of silt and clay and the addition of sodium pyrophosphate in salt water allows the reproduction of flocculation processes. The concentrations of sodium pyrophosphate have been adjusted to have a satisfactory reproduction of the fortnightly erosion-deposition cycle of the sediment in response to varying tidal amplitudes at the mouth of the estuary. With these concentrations the gilsonite flocks have a settling velocity of about 0,4 mm/s in still water (ten times more than the settling velocity of gilsonite without flocculation) but the observation of gilsonite flocks behavior in the model shows clearly that the settling velocity depends on the tidal current velocities.

In spite of some scale effects and the fact that the experimental approach is more qualitative than quantitative the results obtained on the schematic estuary show a sufficient likeness to field measurements (cf fig. 10) to let us suppose that the mechanisms reproduced in the model (flocculation and residual currents) are those which play an important role in the Gironde estuary. So we may conclude that residual velocities and flocculation are both responsible for the development of high turbidity zones in a partly-mixed estuary with hydrodynamical characteristics near those of the Gironde estuary.

The lateral geometry (effect of a deep channel) plays also an important role in the behavior of the turbidity maximum.

REFERENCE

- [1] M. DAVESNE. Intrusion saline et vitesses résiduelles dans un estuaire. Proceedings AIRH 1977 Vol. 3, pp 15-22.

FOR DISPOSAL: 10 M.cu.m. OF CALCIUM CARBONATE SLURRY

by

L. SUMMERS B.Sc. F.I.C.E.

C.A. FLEMING Ph.D. M.I.C.E.

Director

Engineer

Halcrow International Partnership, Dubai.

Abstract

Construction of the Jebel Ali Port complex, 35 km southwest of Dubai, in the United Arab Emirates, has included the disposal of 110 Million cubic metres of excavated spoil.

Disposal of dredged carbonaceous breccia raised particular problems due to the high proportion of fines generated and which, unless properly controlled, could cause wide scale environmental damage in the coastal zone. At the same time it was necessary that acceptable reclamation should be created. An extensive data collection exercise was carried out in order to monitor the geotechnical, hydraulic, meteorological, marine climate and marine biology aspects of the operation.

Introduction

The new port of Jebel Ali, situated on the Emirates coast 35 km south west of Dubai, consists of two very large basins constructed inland of the line of coastal dunes. These basins are connected to deep water in the Arabian Gulf by a dredged navigation channel 17 km in length with a bottom width of 235 m at 16 m below LAT. The inner basin is 3750 m long and 420 m wide, excavated to a depth of 11.5 m below LAT. The outer basin is 2500 m long and 600 m wide, excavated to a depth of 14 m below LAT. The basic layout, shown in Figure 1, provides 17 berths approximately 300 m long and 49 berths approximately 200 m long. In addition the harbour entrance channel is flanked by a tanker berth, with 15 m of water depth, and 2200 m of wharfage dredged to 5.5 m below LAT.

The Excavations involved in construction of the port were:

- Inner Basin : 31 million cu.m. of dry excavation from which the spoil was used to raise ground levels in the proposed industrial area to the south of the port.
- Outer Basin and Harbour Channel : 58 million cu.m. of dredging, the spoil being used to raise the levels and reclaim a total area of 700 hectares as indicated on Figure 1.
- Approach Channel : 21 million cu.m. of dredging, the spoil being mostly conveyed in barges to an offshore dump area.

Ground Conditions and Excavation

Ground Conditions

At the beginning of the project soils investigations revealed the presence of a variety of carbonate breccias overlain by sand and sandstone across the entire site. Sand in dunes just behind the original shoreline was up to 10 m thick, but this reduced rapidly to a thin layer at two to three hundred metres offshore. Underlying this sand was a layer of caprock varying in thickness up to 2 m. The four basic material types can be described as follows:-

- (i) Loose sand.
- (ii) Caprock, described as bioclastic limestone, containing numerous small solution features up to gravel size.
- (iii) Sandstone, fine to medium grained, occasionally laminated, with point load indeces averaging 2 MN/m^2 .
- (iv) Breccia, classified into five main types, the poorest of which consisted primarily of carbonate limestone containing attapulgate clay.

Samples taken from large diameter boreholes showed that, whilst the breccia would not present difficulties when excavated dry, when wetted a large portion tended to disintegrate into very finely divided material forming a soft slurry. This indicated that problems could arise in disposal of such material contained in a considerable volume of water after excavation by cutter suction dredgers. Even when cutting more uniform soils the process of disposal from a dredger pipeline inevitably involves fine material remaining in suspension when the excess water runs off.

With the exception of the Approach Channel and part of the Entrance Channel, the bulk of the excavation lay inland of the original shoreline and this presented the possibility of reducing the disposal problem by adopting dry excavation methods using conventional plant. The decision as to how much, if any, should be carried out in this way was dependent on a number of factors as follows:-

- (i) The availability of different types of plant required to carry out excavations entirely in the wet or partly in the dry.
- (ii) The method of construction of the blockwork quay walls.
- (iii) The phasing requirements for utilisation of completed parts of the port at the earliest possible opportunity.
- (iv) The suitability of the excavated material for backfilling, ground level raising and general reclamation.
- (v) The extent of dewatering required for such large excavations in the dry.
- (vi) The relative economics of each method of excavation.
- (vii) The quality and quantity of material resulting from each type of excavation.

Considering all of these factors it was decided that the combination of both dry excavation and dredging in the proportions given in the Introduction would satisfy the majority of the requirements.

Dry Excavation

The material in the areas scheduled for dry excavation comprised primarily sand and breccia. Excavation of the former was carried out with scrapers whilst the breccia in its dry state was quite hard and required blasting for removal by hydraulic excavators.

Wet Excavation

In the Entrance Channel and Outer Basin all the major dredging was to be carried out using four large cutter suction dredgers (2000 h.p. at the cutter head) and two smaller dredgers (1200 h.p. at the cutter head) together with booster pumps as required. All of the spoil was to be used for reclamation or was to be pumped to stockpiles for use as fill behind quay walls etc.

In the Approach Channel material was initially dredged using one cutter suction dredger and two dipper dredgers. The fleet was later supplemented by the worlds first self elevating cutter suction dredger (2). The majority of this material was loaded directly into barges for disposal offshore.

Disposal Methods

Disposal at Sea

The 21 million cubic metres of caprock and sandstone excavated from the Approach Channel was to be barge loaded and dumped offshore. Initially the disposal site was 21 km offshore in over 20 m depth of water. However, this was found to be unmanagable and the dump area was moved closer inshore, to an area in approximately 10 m of water as shown in Figure 2. This area is 5 km by 5 km so that the average depth of dumped material would be about one metre, although there were no rigorous controls on the dumping pattern. Barge loading was generally limited to between 50 and 75% of the theoretical full capacity in order to reduce overflow losses and re-sedimentation, while maintaining a high level of operational efficiency.

Disposal to raise existing land levels

Some areas of subkah flats around the port basins were low lying, much of it no higher than highest tide level. The area to the SE in particular required up to 4 m of fill to achieve an acceptable level for the proposed industrial development. This was achieved with spoil from dry excavations in the inner basin, and did not involve problems of fines disposal.

However, to the SW and NE of the port it was necessary to use considerable volumes of spoil arising from dredging the entrance channel and outer basin to fill the low areas (See Figure 1).

Discharge from the cutter suction dredger to be used would contain particles of all sizes from cobbles down to fine clays in view of the extent of breccia in these areas. A typical grading curve of actual discharge is given in Figure 3. This shows 30% silt and fines and immediately raised the questions, firstly, of how the fines were to be incorporated into the fill so as to provide land in an acceptable condition and secondly, how to control the flow into the sea of the calcareous fines suspended in the run-off water.

The initial wet filling was on the SW side of the port and it was anticipated that up to three of the large cutter suction dredgers could be discharging at any one time. Return of the potentially large quantity of water to the sea required a substantial channel excavated through the coastal dunes as shown on Figure 1.

In a second area to the north west of Quay 1 (See Figure 1) filling had to be done early in the Contract to provide areas for contractors depots and construction offices. Dry fill together with dredged sandstone was generally used for this. The eastern half of this area was also used for stockpiling dredged sandstone for re-use as selected fill behind quay walls etc.

Although not a serious problem, the run-off water from the area contained some calcareous fines arising from breakdown of the cementing material in the sandstone. The discharge was initially into the very large lagoon formed by the East Breakwater and the East Reclamation Bund shown in Figure 1.

A third area of land to be raised in level was to the east of Quay 2, and it was planned to fill this with spoil arising from dredging the east end of the outer basin. This was commenced late in the programme and the same procedure was adopted as that for the western area. In this case the water was returned to the sea via a long drainage channel down the east side of the site to discharge at the root of the East Breakwater.

Disposal to Reclamation

As originally planned in 1976 the east breakwater followed a conventional form on the lea side, being normal to the coast out to the harbour entrance. However, the problem of disposal of the carbonate breccias was appreciated immediately the results of the preliminary investigation began to come in. As a consequence, the breakwater was realigned to enclose together with the East Reclamation Bund a much larger area of approximately 320 hectares, so as to provide a disposal lagoon, as shown in Figure 1, in which the fines could be allowed to settle.

It was intended that this should be an area into which would be dumped material not suitable either for immediate use for raising land levels or stockpiling for use as backfill, and especially material in which the fines remaining in suspension would create environmental hazards if discharged directly into the sea. It was looked upon as a disposal area in which the ground conditions would improve over a long period and the land would be available for use in the later stages of port development. However, even before filling commenced proposals were being made for the land use for industry and consequently efforts had to be made to achieve the best ground conditions economically possible.

Disposal Problems

While it was anticipated that disposal from dry excavations would not present problems, the main concern in disposal of the breccias from wet excavations was the large amount of fines which were likely to remain in suspension. Little was known about the hydraulic disposal of carbonate breccia of the type to be encountered and literature on the subject, e.g. slurring for the cement industry, was of little assistance. There were no fixed guidelines to the quantity of carrier water to be expected due to the number of variables involved in the dredging process, but the ratio of water to solid matter pumped was expected to be about 10:1.

Without special care it was obvious that environmental problems could arise if the large proportion of fines that was anticipated remained in suspension when the discharge water returned to the sea. To indicate the scale of the problem, the quantity of water to be returned would be of the order of 450 million cu.m. which could contain up to 3.6 million tonnes of carbonate fines (i.e. equivalent to 2.3 million cubic metres of in situ rock at a dry density of 1.54).

Following early field trials the major problems could be identified:

- (i) It would be difficult to provide conditions in which an acceptable proportion of the fine material could settle out of suspension within a manageable retention period for the water. The bulking factors for breccia fines could remain very high for long periods of time before consolidation and meanwhile the fines would be sensitive to resuspension.
- (ii) When settled in the reclamation areas the fine material could create poor ground conditions.
- (iii) Disposal of the fines remaining in suspension in the vast quantities of overflow water which must eventually go into the Arabian Gulf, could damage the existing environment.
- (iv) Evaporation rates were not high enough to consider pumping all the material inland. In any case the distances involved would incur unacceptable costs and still involve environmental problems.

Of all the problems listed above the possibility of wide scale environmental damage was considered to be the most serious. If no special precautions were taken an average of 1500 cu.m. of soil would enter the sea in suspension each day for three years, with uncertain characteristics for settling in the turbulent open sea conditions. The cost of treating this amount of material, contained in about 100 times its volume of carrier water, was not economically feasible either by use of extracting equipment, such as cyclones or filters, or by flocculation.

Early experiments indicated that initial settlement of sediment from a fully mixed column of water achieved 50% clear water in a 2 m column within 24 hours, while further settlement was very slow indeed. It was hoped that this initial rate of settlement could be utilised in the field in a series of settling lagoons, the capacity of each lagoon being sufficient to take the 24 hour discharge from one of the larger dredgers. For example, there was sufficient area to provide six rows of four lagoons and to allocate two rows to each of three dredgers. The head lagoon could be filled and drained into the second one and similarly into the third lagoon and so on. The initially decanted water could contain fairly high concentrations of sediment, but this would reduce as the discharge progressed down the lagoons before eventually being allowed to seep through the breakwater into the sea. As the head lagoon filled the bunds, could be raised until filling reached the final level plus an allowance for settlement and the second lagoon would become the head lagoon.

This appeared to be a very attractive solution, but a number of problems were foreseen:

- (i) Bund building would have to be with dry material, otherwise material from a dredger discharge would flow out and considerably reduce the lagoon capacities. This would be an expensive operation and use material needed for fill elsewhere.
- (ii) Wet bund building would also produce its own problems with fines disposal.
- (iii) The fines might be so easily disturbed that it was quite possible that even the turbulence caused by bed shear as the flow crossed the lagoons to the decanting outlets would bring it back into suspension, especially as the discharge tends to form erosion channels through the fill.
- (iv) The front of coarser fill materials, as it progressed over the settled fine material would push it forward and upward against the opposite bund, but it was not known whether it would then dry out sufficiently to be rehandled or to incorporate it in the bunds once it rose above water level. Rehandling could be very expensive.

It was decided to obtain further information on behaviour of the fines by forming experimental lagoons, firstly to the west of the port to determine the settling and drying characteristics of the fines and secondly, when construction had progressed sufficiently to achieve protection from the breakwaters, in the coastal disposal area. The results of these experiments are given later

Experimental Lagoons

Preliminary Lagoon Studies

Before the four specially built, large cutter suction dredgers arrived on the site, it was decided to do test dredging of breccia with the discharge into an experimental lagoon on the west side of the site, (See Figure 1), where future development had a low priority. The aims of these tests were to determine:

- (i) The percentage of the breccia which would become fines in suspension when pumped through a representative length of pipe line.
- (ii) The settling characteristics of the total solids discharged into the lagoon.
- (iii) Quantities remaining in suspension when the carrier water was returned to the sea and diffusion characteristics of the suspended solids.
- (iv) Guidance as to areas likely to be affected by abnormal settlement of fine material and how soon the concentration of solids would reach acceptable levels.

The lagoon was divided into three sections.

Section 1 into which the pump mixture was discharged.

Section 2 into which the carrier water would overflow and where settlement of some of the fine material would take place.

Section 3 to take the discharge of sandstone and gravel when the dredger encountered these as they represented better fill material outside interest in carbonate fines.

Excess water from the two latter sections discharged through water boxes into the main discharge channel leading to the beach.

The lagoon bunds were raised as necessary to maintain a 2 m depth of water, with overflow water box having an initial invert level of 3.5 m above LAT. At the discharge end of the lagoon the ground was brought up to + 6.5 m and allowed to advance at this level. Silt was carried away towards the water box. The settled silt was so soft that it appeared to be entirely moved forward by the advancing face. However,

the characteristics changed once it heaved above water level and the advancing fill spilled over it. When this happened a fairly well mixed material could be achieved.

Based on resources available to undertake data collection within the short time available, a testing programme was devised, aimed at determining the best method to utilise this ability to trap the breccia fines and the effect this would have on early ground conditions.

The programme included:

- (a) Permeability tests on breccia fines situated above water level.
- (b) Durability tests on samples of each type of in situ breccia by agitating them in vessels containing sea water so as to simulate pumping and pipeline conditions.
- (c) Permeability tests on the rock fill breakwaters to determine their ability to filter out the fines from dredger discharge water.
- (d) Flocculation tests using polymer flocculants.
- (e) Analyses of particle size and shape of the material remaining in the lagoons.
- (f) Degree of trapping of fines beneath advancing coarse material.
- (g) Determination of bulking factors.
- (h) Determination of bearing capacity and consolidation characteristics of reclamation.

A complete review was also made of the location of breccia deposits in the areas to be dredged and the most likely areas to which they would be pumped.

To increase the retention of fines, stub bunds were built within the lagoon in order to increase the path of the discharge water while still controlling the flow to a low velocity on its way to the water-box.

Even so the discharge into the sea contained about 0.5% carbonate solids. It was of interest to note, however, that the flow, on entering the sea, hugged the coast towards the main west breakwater and most of the material in suspension was initially deposited near the beaches. Further, as sand was moved shorewards in calm to moderate seas, the beaches acquired a layered condition of silts and sand and, as this is an area of accretion, some of the fines were stabilised.

The deposition and accretion of the sediment in the lagoon was complex, but from the testing programme it appeared that the optimum settlement must be related not only to the percentage of clay size particles in the discharge, but also to time needed by the discharge to produce a suspended sediment concentration above an equilibrium value. The tests

using polymer flocculants which had indicated an initial improvement in settlement characteristics were not pursued as after about two hours in still water this advantage was lost and no difference in rate of settlement could subsequently be detected.

It was soon established that fairly substantial quantities of fine carbonate cementing material was released when the sandstone was broken down by dredger cutting and pumping operations.

By the time the large cutter suction dredgers arrived on site, (late 1977 early 1978) the evidence collected tended to indicate that small lagoons were unlikely to be satisfactory and three further experimental lagoons were established in the coastal disposal area as shown in Figure 4.

Trial Area No 1

The first of the experimental lagoons had an area of only some $1\frac{3}{4}$ hectares, and pumping was continuous with height of fill carried up from a bed level of about 3 m above LAT to about 7.5 m above LAT in six days. This meant that as the front advanced, time for discharge water to reach the fixed overflow was reduced and the concentration of fines carried into the main lagoon gradually increased. Over 50% of the fines were lost in this way and the lagoon size and method of filling were obviously inadequate.

The volume of material dredged was 50,000 cu.m. comprising primarily breccia with approximately 15% sandstone. The trial was monitored by sampling the dredger discharge and overflow water to determine quantities of fines entering and leaving the trial area. In addition pre and post fill surveys were carried out to determine the quantity of material retained in the area.

The scale of the trial was too small to create any significant pockets of silt, but it did enable sampling techniques to be tried out and confirmed the degree to which breccia would break down to form slurry.

Trial Area No.2.

The second experimental lagoon had a larger area and in this case pumping was intermittent over a period of six weeks. This produced a layered effect of coarser and finer fractions of the fines with a total thickness of about 3 to 4 m. and topped by 2 to 3 m of coarse material which had been dozed ahead over the finer material as filling proceeded. On completion of fill the lagoon contained entirely soft silty sand ahead of the final front of coarse material, overlying up to 1 m of very fine soft silt.

Float tracking showed that flow across a lagoon varies in a random manner, depending upon erosion channels leaving the point of discharge. However, loss of fines in the overflow water was found to be reasonably steady until the water in the lagoon was reduced to a critical depth.

From that point the velocity of flow was sufficient to carry most of the fines over the overflow and filling was stopped. It was possible to draw the immediate conclusions that:

- (a) Even using intermittent discharge the larger the lagoon the greater percentage of fines would be retained;
- (b) It would be possible to raise the overflow level by using coarse material to increase bund height and to have a water box in which the weir level could be raised to maintain sufficient depth of water for optimum settlement of fines in the lagoon;
- (c) The original proposals to create twenty four small settling lagoons within the coastal reclamation area would not be very efficient in trapping the fines.

A final survey of the lagoon and the dredged areas indicated that 390,000 cu.m. of in-situ material had been pumped to the lagoon. The volume of bulked material retained was 278,000 cu.m. indicating a considerable loss of material from a lagoon with an area of only 50,000 sq.m.

On completion of filling trial pits were excavated and boreholes sunk to examine and collect samples of the various strata within the reclaimed ground. Settlement pads and piezometers were installed and surveys were carried out before, during and after the filling. Samples of slurry which had settled in the lagoon were collected and analysed for bulk density, moisture content, grading, Atterberg limits and specific gravity of solids.

As a result of these trials it was decided to use large settling lagoons by dividing the coastal reclamation area into four quadrants and a programme for monitoring these was established.

Trial Area No.3.

This consisted of monitoring the reclamation in the SW quadrant of the Coastal Reclamation Area from September 1978 to April 1979 and included a soils investigation of the completed reclamation as for Trial Area No.2. The results in general supported those from Trial Area No.2. and as anticipated, the percentage of fines deposited increased with size and depth of the lagoon.

A summary of silt losses for the three trial areas is given in Table 1.

Trial Area No	1	2	3
Area (m ²)	17,000	60,000	390,000
Av.Depth (m)	1.0	3.0	4.0
% Silt loss	60%	33%	18%

Table 1 Summary of Lagoon Disposal Trials

Study of Marine Conditions

Hydrographic studies

A parallel programme of studies being undertaken on the project was the comprehensive collection and analysis of data on the marine climate, in order to predict sediment transport and hence maintenance dredging potential, as well as local coastline disruption that may be caused by the port works. This included standard meteorological data, regular hydrographic and topographic surveys, two wave height recording instruments, two wave direction recording instruments, float tracking, five automatic recording current meters, and extensive water/sediment sampling. The location of these instruments and limits of surveys are shown in Figure 2. The data gave good coverage of long term trends with respect to waves, currents and existing background suspended sediment concentrations.

Before it became necessary for any outflow of dredge run-off water from the coastal reclamation area to be discharged into the sea, an uncontained breccia disposal trial was carried out. This involved discharging a limited quantity of dredged breccia directly into the sea over the outer arm of the East Breakwater. The progress of the plume so produced was monitored by float tracking and pumped suspended sediment sampling. Contrary to expectations the breccia laden plume displayed relatively little mixing and was observed to run close to the breakwater, in an easterly direction, until it reached the knuckle of the breakwater and there separated.

Aerial photographs were also taken during the exercise and on two occasions after completion. The latter covered a 60 km length of coastline during both rough and calm conditions and the photos were processed so as to enhance underwater features. The photographs taken under rough sea conditions enabled an assessment of the general levels of turbidity along the adjacent shorelines to be made and any increases in the Jebel Ali area noted. The photographs taken under calm sea conditions enabled the areas of deposition of breccia fines to be broadly identified.

The photographic survey was intended also to monitor the behaviour of sediment already released into the sea from the offshore dredging in the Approach Channel and the first trial lagoon. The extent, nature and thickness of these, and subsequent, silt deposits were regularly estimated by diving surveys. Although a dual frequency echo sounder was used for the hydrographic survey work capable of giving broad indications of soft and hard deposits, it was found that there was no satisfactory way of calibrating the instrument to detect the interface between the original seabed and the overlying silt. However, successive silt surveys by diver, together with measurements of bulk densities allowed estimates to be made of volumes of material accumulating on the sea bed. Once all the dredger water discharge points were being monitored it was then possible to record concentrations of suspended material in the outflows and compare these with the volumes deposited in the survey areas.

Further records included regular chemical analyses of the dredge run-off water, the water in the lagoons and the sea water, close to and far from the port to determine whether there were any changes in the salinity levels or chemical changes in the sea due to disposal practices.

Marine Biology Study

The enclosed waters of the Arabian gulf are poor in marine organisms compared to the Red Sea and Indian Ocean. This is probably due to a combination of low nutrient levels, high salinities, (up to 40%) and high temperatures (30°C). As a result there are fewer species of coral forming reefs and less associated marine life where these conditions approach the limits of their tolerance.

In the Jebel Ali area the most abundant of the corals is *Acropora* (Staghorn coral) a genus with high salinity and temperature tolerance, but very sensitive to sediment in the water column. Other types of coral which are found to be less sensitive are *Seriatopora* (antler horn coral) *Meandrina* (Brain Coral), *Goniopora* and others. The approximate ratios by species are 50%, 10%, 20% and 20%. *Acropora* and *Seriatopora*, of all the corals, provide the biggest area of shelter with their flat table top and overhang effect. The largest of the fish associated with these corals were Groupers, Parrotfish, Perch, Angel Fish, Captain's Daughter, Sergeant Major, Clown Fish, Damsel Fish, Pampano, Sauge and Wrasse. These fish are not apparently seasonal. Demersal fish, however, appear to be seasonal and include Barracuda, Garfish, Spanish Mackerel, Yellow Tail Tuna, Yellow Jack and Sardines.

It is important to ascertain what damage the suspended fines might cause to various types of marine organisms. Marine life is dependent on the phytoplankton - microscopic floating green plants - which is marginally seasonal in tropical waters.

Zooplankton consists of minute animals both mature and larval forms living directly off the phytoplankton and serving in their turn as food for larger predators. This continuous dependence forms the food chain of the marine ecosystem. Fisheries are an important local industry and are vulnerable to changes in the environment especially if they are persistent over a long period.

Early in 1977 a fisheries expert was engaged to study the effect of the breccia fines in the sea and advise on the possible consequences of pollution.

Laboratory tests were performed to assess the chemical and physical tolerance to the fines by a range of marine organisms. These included microscopic plankton and larger organisms representing stages in the interdependent food chains.

The conclusions were that toxicity of the fines in suspension was negligible. This was confirmed quite dramatically in Nov.1978 when the last lagoon of the series of 4 had been relatively undisturbed for about 4 months. The lagoon had about 1.5 metre depth of water over about 1 metre of settled sediment. At this period a survey was carried out and it was found that the lagoon had developed into a clearly balanced environment with fish and young fry evidently hatched there. The breccia had been flocculated by the combined activity of microorganisms, bacteria and algae and considerable invertebrate fauna was present.

The physical laboratory tests showed, however, that some zooplankton species were vulnerable to sediment concentrations of more than 500 ppm. This figure provided the key to the control needed at the sea outfalls and also to the consequent problem should the fines remain in suspension or become disturbed by storm waves. If a cloud of suspended material covered a large area of the Gulf, the reduction in zooplankton would cause extensive damage to the pelagic fishing industry.

The two limiting factors then were the effect of concentration of suspended breccia on the microscopic fauna and the direct effect of settled sediment on the major coral species *Acropora*. Both of these could affect the fishing, the former especially the pelagic and the latter especially the coral fish, the former being the most important commercially.

The control of the outfall was established and continuous monitoring was maintained at fixed points on the coral reefs. Regular sampling of the plankton also was carried out.

Results

Offshore Reclamation Area

It is not the intention of this paper to rigorously discuss the geotechnical aspects of the completed reclamation. The proportions of fines trapped for different lagoon sizes are given in Table 1 and a typical grading envelope for spoil at the discharge point is shown in Figure 3. Figures 5, 6 and 7 show typical grading envelopes for material sampled as trapped fines, untrapped slurry in the lagoon and that material which found its way onto the sea bed. It can be seen that as the material progressed and was deposited through the system the proportion of very fine material increased, the coarser end of the grading having been retained.

Comparison of grading of the dredge discharge, concentration of suspended sediment in the lagoon, and the lagoon water level showed that the correlation between these three aspects was generally weak. There was a notable drop in concentrations when the lagoon water level was raised, but generally peak concentration levels appeared to correspond more with strong winds which maintained the material in suspension by way of the turbulence generated. It was also found that once the material had a chance to settle and form attractive bonds during a cessation in the dredge discharge it took a considerable flow to resuspend material below the water level. Table 3 gives a chronological account of the values of

material dredged, volumes lost in suspension, volumes of trapped fines and respective bulking factors. All volumes are expressed in millions of cubic metres and the volumes of discharge water include run-off from stockpiles of sandstone provided outside the reclamation area.

Date	Vol. of dredging to date	Vol. of discharge water direct to sea	Vol. of reclamation to date	Vol. of soil lost in suspension	Vol. of un-trapped slurry	Average bulking factor of slurry	Vol. of trapped fines	Average bulking factor
Nov 78	11	20	15.4	0.07	5.2	3.1	Small	-
Feb 79	13	20	17.8	0.20	5.9	3.1	Small	1.35
May 79	16	58	21.7	0.28	7.7	3.0	0.9	1.35
Sept 79	20	108	25.1	0.46	6.8	2.9	2.7	1.34
Jan 80	21	147	27.4	0.66	8.9	2.6	2.9	1.33
July 80*	26	187	29.9	1.32	3.5	2.3	8.0	1.3
Sept 80*	27	200	30.7	1.54	nil	-	10.2	1.3

*These quantities are predicted

Table 2: Chronological Summary of Dredged and Trapped Fines

The surveys of the offshore reclamation area showed that actual quantities compared well with predicted quantities as shown typically in Table 3. The predictions for Feb.1979 were based on borehole data from the early experimental lagoons, whereas the Jan.1980 predictions were based on all the information available in March 1979.

	Predicted		Actual from survey	
	Feb 79	Jan 80	Feb 79	Jan 80
Total volume dredged soil	12.5	21.3	13.2	21.3
Total volume of fill	18.4	28.6	17.8	27.4
Overall bulking factor	1.47	1.38	1.35	1.33
Volume of coarse fill	11.2	16.7	11.9	15.5
Volume of soft slurry	7.2	11.8	5.7	11.9
Percentage of soil as coarse fill	75	85	86	82
Percentage of soil as slurry	25	11	14	14
Percentage silt lost (Balance)	Trace	4	Trace	4

Table 3. Comparison between Predicted and Measured Quantities.

It can be seen that the actual volumes compare very well with the predicted volumes particularly with respect to silt losses.

Seabed Deposits

The unconfined breccia disposal trial did not lead to any firm conclusions with respect to levels of fines remaining in suspension near the discharge point. It did lead to the general conclusion that the plume of heavily concentrated sediment was very localised indicating that the majority of material found its way rapidly to the sea bed in the form of a density current. However, as a result of this trial it was decided that the reclamation area outfall should be a little way inshore of the knuckle on the East Breakwater as shown in Figure 1. on the grounds that the majority of the material would tend to deposit in this relatively sheltered area.

The development of the silt bank each side of the port was monitored as previously described. Figure 8 shows the extent of the area over which 100% coverage by silt occurred at various stages in time. It would appear that on the east side of the port the silt bank reached a sensibly stable limit beyond which further migration was extremely slow. On the west side of the port the silt bank was very much more spread out and was relatively more mobile. In fact, after an initial period of discharge from the western drainage outfall there was a long period over which there was no discharge. During this period it was noted that large areas of seabed naturally cleared and benthic communities began to re-establish themselves.

Tests on undisturbed core samples from the silt bank next to the East Breakwater revealed a sensibly linear relationship between bulk density and depth below surface, at least for the upper layers. It appeared that at the early stages of deposition bulking factors can be as high as 5 or more. Continual sampling of sediment concentrations and the dimensions of the silt bank enabled estimates of volume of fines which remained on the seabed in the immediate vicinity of the port and that which dispersed elsewhere to be made. This confirmed that most of the fines carried into the sea in suspension remained in the silt bank. Also the deposits on the east side were relatively stable, whilst those on the west side had a greater tendency to migrate, due to the higher degree of turbulence on the weather side of the port entrance breakwater. Without carrying out tracer studies it is difficult to be definitive as to the exact patterns of sediment movement. However, the extensive current measurements from the self recording current meters and float tracking enabled qualitative estimates of general movement to be made. From these it was evident that the material from the west silt bank migrated both to the west and around the breakwaters to the east to supplement the east silt bank. Migration from the east silt bank was limited and predominantly in a northerly direction.

Marine Life

The Plankton samples were collected for more than a year on a fortnightly basis. These did not reveal any particular seasonal trends and hence did not indicate that dredge run-off should be curtailed during any potentially sensitive periods.

Careful long term observations of specific monitoring areas close to and remote from the run-off discharge points were made. It was found that the sea bed in the immediate vicinity of the outfalls and over which there was complete coverage by silt, became completely sterile as predicted. The bank on the east side were more stable than anticipated partly due to the formation of an algae carpet over the surface of the bank. This helped to prevent the movement of the upper layers of fluid mud which might otherwise have occurred.

In January 1980 the situation was as shown in Figure 8. This shows an area outside the silt banks in which there was up to 10% mortality of *Goniopora* and *Meandrina* type corals. Further out as shown pollution resulted in 15% mortality of *Acropora* type corals, but no deterioration of the hardier species. These zones were not extensive and the area was soon reached where young corals were found re-colonising where the silt lay only sparsely in troughs and deterioration of coral was reduced to background levels in response to normal prevailing conditions.

Conclusions

The problems involved in dredged spoil disposal have attracted an increasing amount of attention during recent years particularly with respect to achieving acceptable reclamation with difficult spoil³, optimising disposal area dimensions and outfall arrangements^{4,5} and avoiding environmental problems^{6,7}. In the situation described in this paper the disposal area was under water so that assisted drainage techniques such as trenching etc, could not be employed. Pumping distances were too great to contemplate drying by evaporation and in any case the quantities involved were too large.

An ongoing monitoring and testing programme enabled timely measures to be taken so that silt losses to the sea were reduced to a minimum and an acceptable reclamation area was created within the economic constraints of the project. It was estimated that if no measures had been taken between 10 and 15% of the fines would have entered the marine environment. By optimising lagoon size, bund levels and water box controls it is predicted that this will be reduced to between 2 and 5%, a quantity that could be and was retained within an acceptably small area adjacent to the breakwater.

It appears that the major bank of silt created in the port area will remain quite stable due to the combination of shadow effects of the breakwater, high cohesion and consolidation of the sediment, the intermittent formation of an algal carpet and the damping effects on waves passing over a fluid mud bottom. Further the concentrations of suspended sediments measured in the sea never seriously exceeded the harmful levels established from laboratory experiments.

It was found that the corals, especially the more sensitive species, were excellent monitoring agents. Deterioration, initially identifiable by the bleached appearance at the centre of the branches was not a rapid process. Since *Acropora* are already living outside their temperature and salinity optima, further stress due to siltation of the fine coral polyps,

removal of adequate substrate for larval settlement and higher light attenuation due to silt turbidity could be readily detected.

In order to replace the reefs, in the immediate area of the port that have been unavoidably destroyed an experimental programme of installing artificial tyre reefs has been initiated. Several different pilot schemes have been implemented according to past practices. but it is too early to report whether these will be effective.

Acknowledgements

The authors gratefully acknowledge the contribution to the project of Mr M M Deas, who enthusiastically carried out all of the underwater survey and monitoring work. Also, to Mrs A J Summers for her contribution on marine biology.

References

- 1 Hayward R K, Moon J G & Palmer D J, "The Selection of Plant and Contract Arrangements for a Very Large Negotiated Dredging Contract in the Middle East", Proc. 3rd Int. Symp. on Dredging Technology, Bordeaux March 1980, pp 13-27.
- 2 Gaasterlaand D A "Concept, Design and Construction of the World's First Self Elevating Offshore Heavy Duty Cutter Suction Dredger: Al Wassl Bay", Proc. 3rd Int. Symp. on Dredging Technology, Bordeaux, March 1980, pp 79-88.
- 3 Haliburton T A and Willoughby R E, "Engineering Considerations in Dewatering and Reclamation of Fine Grained Dredged Material", Proc. 2nd Int. Symp. on Dredging Technology, Texas A & M University, 1977, Vol.1, pp G2.25 - G2.40.
- 4 Walski T M & Schroeder P R "Weir Design to Maintain Effluent Quality from Dredged Material Containment Areas", U.S. Army Engineer Waterways Experimental Station, Vicksburg, Mississippi, Report No. AD-A056 062, May 1978.
- 5 Dredged Material Research Program. "Investigation of Containment Area Design to Maximise Hydraulic Efficiency", U.S. Army Engineer Waterways Experimental Station, Vicksburg, Mississippi, Tech-Rep No. D-78-12, May 1978.
- 6 Dredged Material Research Program "Aquatic Disposal Field Investigations Duwamish Waterway Disposal Site Paget Sound Washington, Appendix A", U.S. Army Engineer Waterways Exp.Stn., Vicksburg, Mississippi, Tech Rep. D-79-24, May 1978.
- 7 SPADONI R H "Reef Monitoring of the Delray Beach Erosion Project". Shore and Beach, July 1979, pp 12-16.

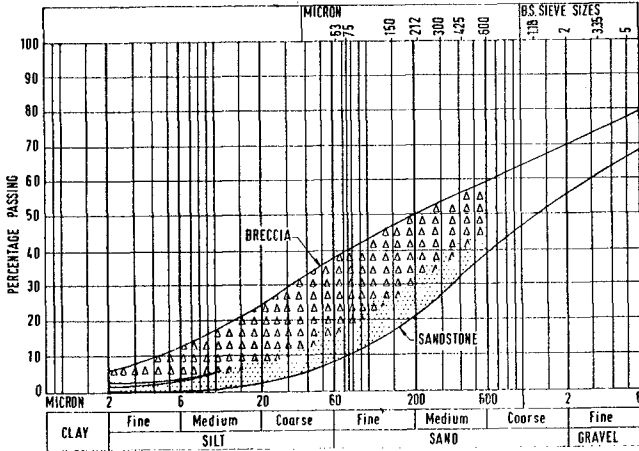


Figure 3. Particle Size Grading Envelope for Dredger Discharge

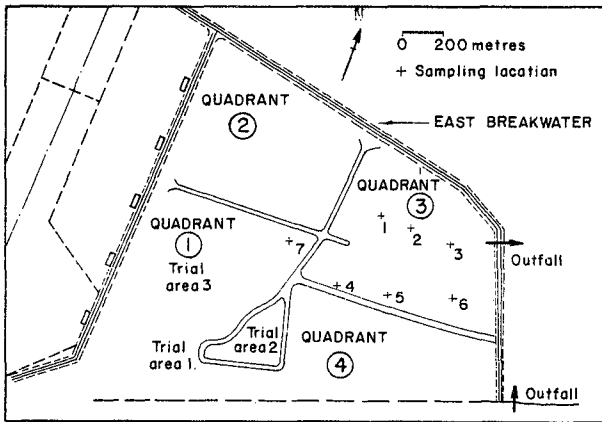


Figure 4. Location of Trial Areas

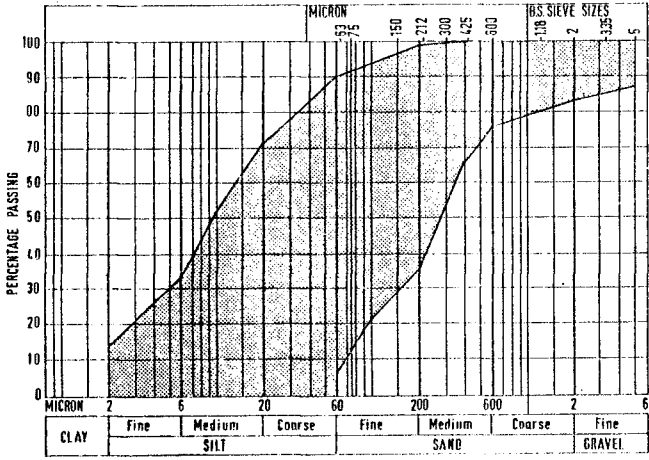


Figure 5. Particle Size Grading Envelope for Trapped Fines

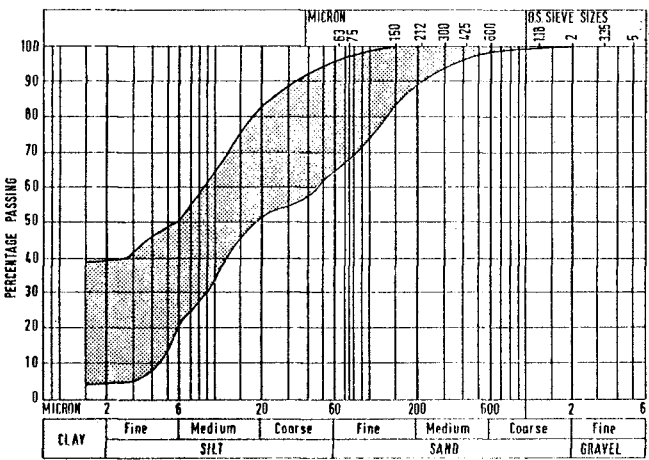


Figure 6. Particle Size Grading Envelope for Untrapped Fines

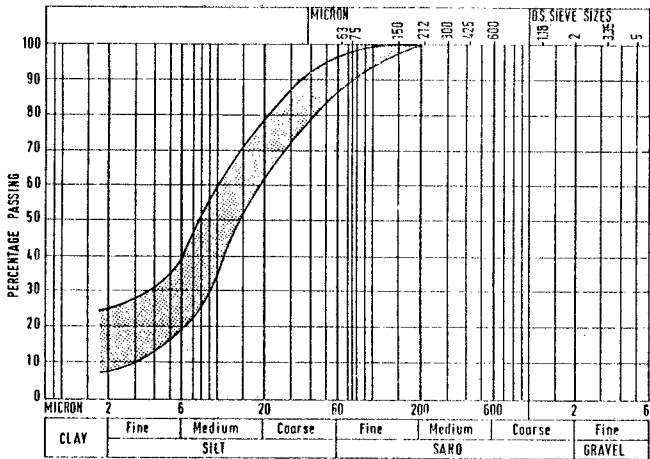


Figure 7. Particle Size Grading Envelope for Seabed Deposits

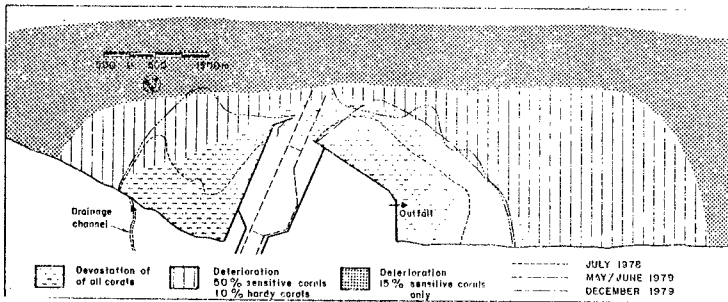


Figure 8. Development of Silt Bank and Areas of Coral Deterioration

CHAPTER 174

An Experiment on Clay Suspension under Water Waves

by

Prida Thimakorn

Associate Research Professor, Asian Institute of Technology

Bangkok, Thailand

SUMMARY

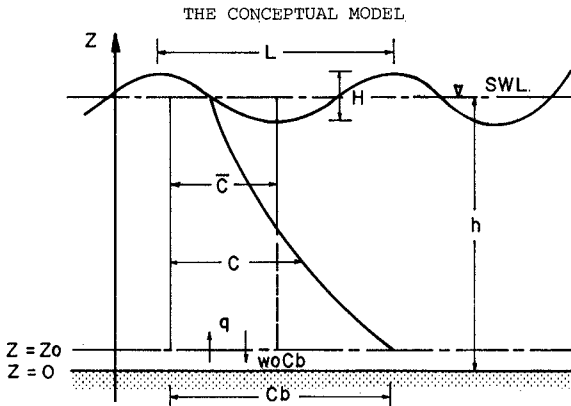
The physical behaviour of water waves upon the suspension of fine cohesive clay was explored experimentally in a wave channel. Results obtained from the experiment show that equilibrium concentration is reached in the wave field some time about five hours after the initiation of waves. The ratio between the mean bottom concentration and the vertical average is constant and yields almost the same value within the range 1.17 and 1.34 at equilibrium and the bottom concentration at equilibrium is linearly proportioning to the maximum bottom velocity of waves. The dimensionless transient concentration possesses a relationship also with the bottom velocity and the bottom shear stress can be related to the maximum value of the ratio between the bottom concentration and the vertical average value found within a short time after the initiation of waves.

INTRODUCTION

Tidal current, river flow, waves, longshore current and wind drifted current are those dynamic factors affecting sediment transport in a coastal region. Two kinds of the sediment; sand and clay exposed themselves to those forces differently. The loosened particles and larger densities of sand show its transport as bed load, suspended bed material load and suspended load while the cohesive property of clay and small density besides its chemical interactions shows its transport only in the form of suspension. Within the complex physico-chemical system in a coastal region various investigations were carried out under field conditions to quantify the coastal transport and relate it with the acting forces and the sediment properties.

In order to understand in particular the behaviour of waves on coastal sediment, studies were and are actively conducted also in the laboratories and theories are being developed. However, the majority of the works are concentrated on the behaviour of granular materials and sand, MONOHAR (1955) set up on oscillating plate with sand on top to investigate the vertical motion of sand under simulated water waves. Flume experiments were carried out by many investigators for example HOMMA and HORIKAWA (1963), HORIKAWA and WATANABE (1970), HATTORI (1971) and others to examine the behavior of waves on sand con-

centration. Emphasis have been made with respect to formation of ripples and evaluation of the diffusion coefficient affected by ripple dimensions. Researches on transportation of cohesive clay are mainly carried out under the two forces namely; the current and the settling. In the current system KRONE (1963) introduced a flume study to demonstrate the rheological properties of clay in the transport process METHA and PARTHENIADES (1974) clarified the physico-chemical properties of clay and the resisting shear stress in a rotating annular channel. LEE (1974) obtained the depositional characteristics of clay in different salinities. WATANABE et al (1979) showed that clay transport by tidal current can be simulated in a simplified experiment. Settling studies of clay were done for example by MALIK (1974). Information about the effect of waves upon clay were mentioned by ALLERSMA et al (1965). It is the objective of this study to determine the interaction between waves and the cohesive materials by means of an experiment



The concentration field under wave motion is shown in Fig.1. From the figure a level $z = z_0$ is defined as an active layer where the sediments at rest in the bottom, $z = 0$, are disturbed and entrain at the rate q into the upper layer, C_b is the concentration at this level. C is the concentration profile and \bar{C} is the vertical average concentration. The wave field possesses the depth at still water level (SWL) equals to h having the wave height H with the wave length L and the period T . The settling velocity of the sediment is w_0 ,

By definition, the average concentration is:

$$\bar{C} = \frac{1}{h} \int_0^h C dz \quad (1)$$

The total concentration is:

$$\hat{C} = \int_0^h C dz \quad (2)$$

Introducing a parameter β , the dimensionless concentration as:

$$\beta = \frac{C_b}{C} \quad (3)$$

THE EXPERIMENT

The experiment was carried out in a glass walled wave channel of 40 cm wide 60 cm deep and 45 m long. It has the horizontal steel bottom. A paddle type wave generator with hinge at the bottom is incorporated at the upper end of the channel. At the lower end, the perforated sloping wave absorber is located. To minimize the under current due to rise of water level at the stagnant lee end, a 15 cm diameter pipe connected the fore bay and the far bay of the channel. Waves were measured by a capacitance type wave gauge. Samples of clay water mixture were extracted through the mine siphons of 2 mm hole. The concentration of each sample was obtained from a calibrated photo-transistor sediment meter. Fig.2 shows the definition sketch of the general set-up of the experiment.

Clay sample taken from the Samut Sakhon river mouth, an estuary in central Thailand was used in the experiment. The sizes of the particles obtained from the hydrometer analysis are between 0.001 mm and 1.0 mm with the apparent densities of 1.21-1.64 kg/lit. Prior to placing the clay into the flume, the sample was washed through the U.S. standard sieve No.200 having the opening of 0.074 mm to ensure the uniformity of the particles and to eliminate the small fraction of the non-cohesive materials. The sample was rinsed through fresh water to remove the original high saline content of the clay so that effect of flocculation is reduced. The mixture was evenly filled over the length of the channel so that after two weeks settling it showed an approximate 2.5 cm clay layer above the steel bottom with a low concentration mixture of 30 cm depth above.

Waves in the experiment are confined within the intermediate range having $1/2 > h/L > 1/20$. The reason is that effect of turbulence due to breaking waves and the strong fluctuating shear stress within a wave period are not encountered. Twenty two runs were conducted and within each test run samples were siphoned and analysed simultaneously as shown in the time steps below.

Time Step	0	1	2	3	4	5	6	7	8	9
Time Interval (min)	0	5	5	10	20	30	30	60	60	120
Elapse Time (min)	0	5	10	20	40	70	100	160	220	340

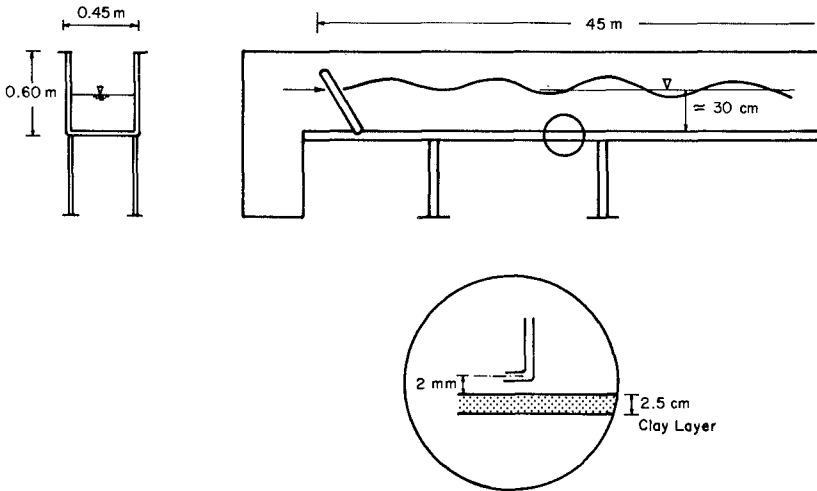


Fig. 2 The Wave Channel

Fig.3 shows the flow diagram of the experimental procedure.

THE RESULTS

The results obtained from the experiment are presented in the following manners:

i) Concentration Profiles Fig.4 shows an example of the concentration profiles which demonstrates the vertical exchanges of clay at successive time steps. It shows that there is a significant increase of the bottom concentration some time after waves were generated while the concentration in the upper layer remains unchanged. This means that the bottom clay are disturbed and entrain into the near bottom layer. At longer time concentration in the upper layer increases which shows that the sediment from the near bottom layer diffuses into the wave field.

ii) Equilibrium Concentration Time variation of the total concentration is shown in Fig.5. It shows some fluctuations at the early stages and becomes asymptote with time at a longer time period. Hence equilibrium condition is existed.

iii) The Normalized Concentration Fig.6 shows some plots of the normalized concentration, β , against time, t . Interpretation of this parameter is similar to (ii), however, with more physical emphasis. It shows the effect of bottom entrainment during the rising limb of β until it reaches the maxima (β). Follows by the diffusion process as shown by the gradual fall of β and consequently equilibrium when β is asymptotic with t . It also shows that at equilibrium β is nearly constant for all cases.

iv) Transient Concentration The characteristics of changes in the concentration can be obtained from the integrated diffusion equation which is derived from the mass conservation in the concentration field as:

$$(h - z_o) \frac{d\bar{C}}{dt} = -w_o C_b + q \quad (4)$$

and the boundary conditions at $t = 0$ when:

$$\beta_{eq} = \frac{(C_b)_{eq}}{\bar{C}} = \text{constant};$$

$$\bar{C} = \bar{C}_{(eq)}; \text{ and } \frac{d\bar{C}}{dt} = 0$$

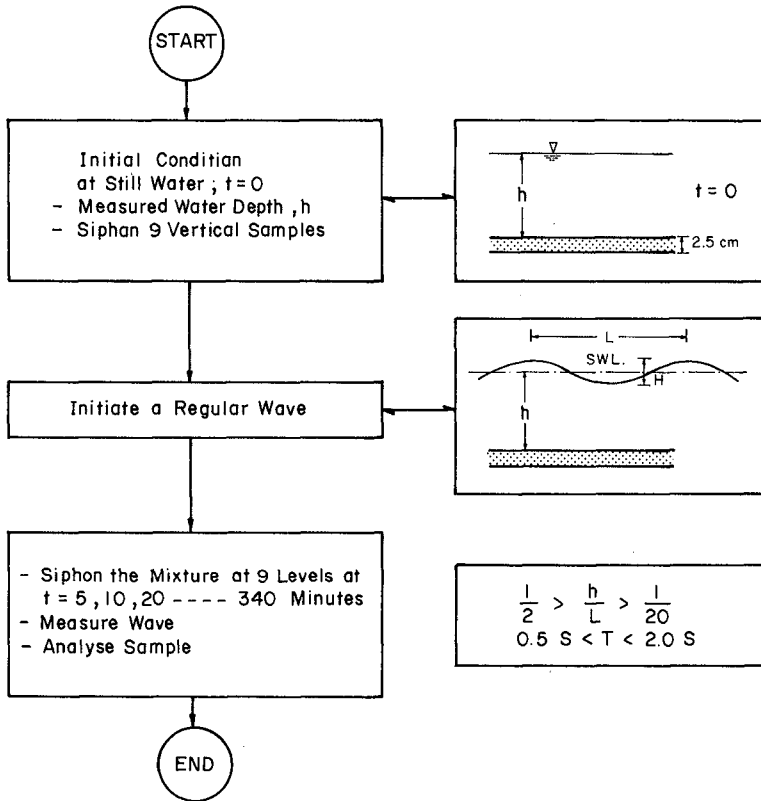


Fig. 3 Flow Diagram Showing the Procedure of the Experiment

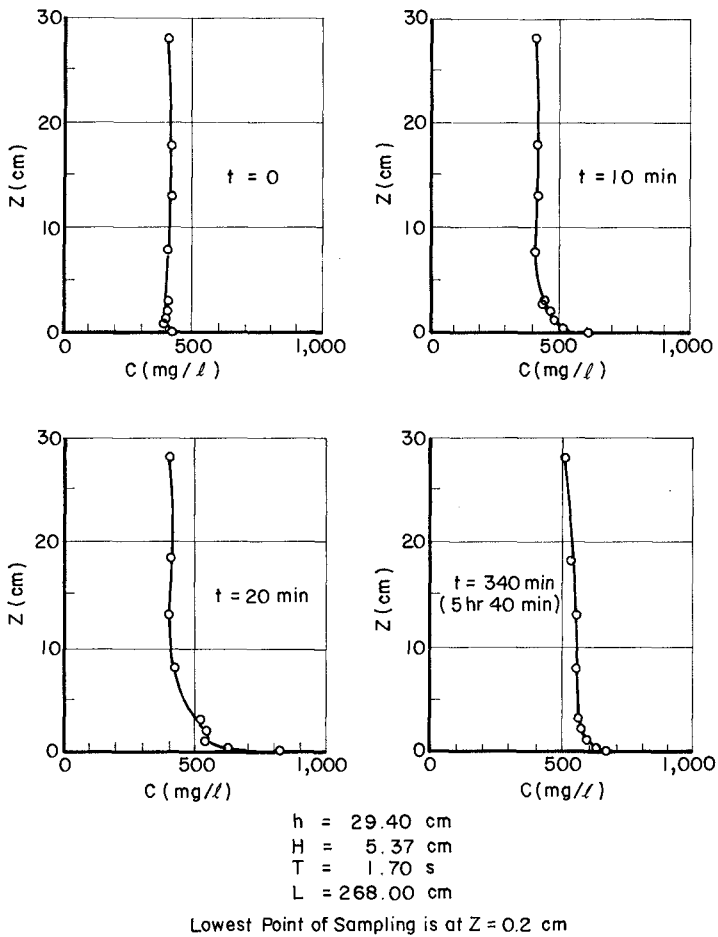


Fig. 4 An Example of Concentration Profiles

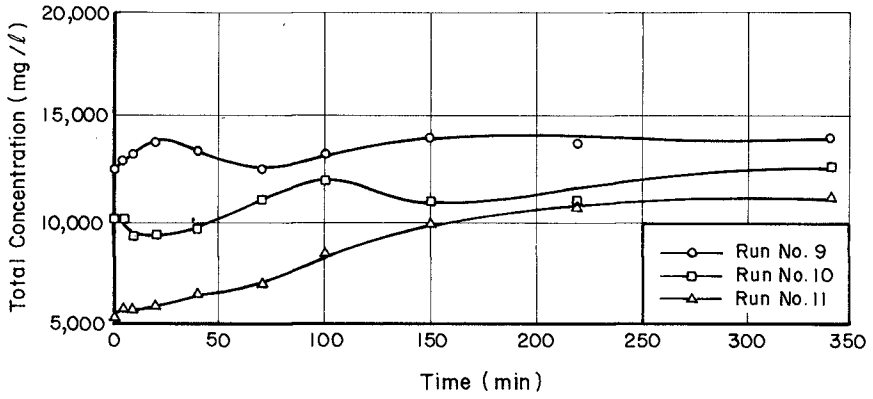


Fig. 5 Time Variation of Total Concentration

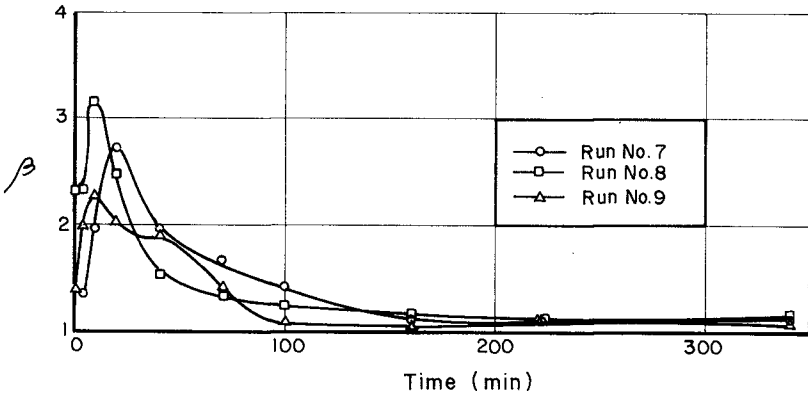


Fig. 6 The Normalized Concentration, β

At $t = 0$; $\bar{c} = \bar{c}_0$

The solution is:

$$\frac{\bar{c}_{(eq)} - \bar{c}_i}{\bar{c}_{(eq)} - \bar{c}_0} = e^{-\beta' t} \quad (5)$$

when $\beta' = \frac{\beta w_0}{h-z_0}$ (6)

Plotting $\frac{\bar{c}_{(eq)} - \bar{c}_i}{\bar{c}_{(eq)} - \bar{c}_0}$ with t the slope β' can be evaluated from the

known value of β of each run the average value of the terminal fall velocity, w_0 , is obtained which is equal to 2.15 mm/s.

v) Wave Effect on the Concentration This effect can be demonstrated by the maximum bottom velocity, \hat{U} , from:

$$\hat{U} = \frac{\pi H/T}{\sinh 2\pi h/L} \quad (7)$$

of the small amplitude wave theory and the bottom concentration at equilibrium, $C_{b(eq)}$. It was found that the two parameters give a relationship:

$$C_{b(eq)} = 191 + 47\hat{U} \quad (8)$$

Fig.7 shows the graphical relationship plotted from the data. The value 191 at the intercept is the bias concentration.

The effect of the bottom velocity can be demonstrated also by correlating it with the parameter $-\beta'$ which characterizes the transient concentration. Fig.8 shows the relationship between $-\beta'$ and \hat{U} as:

$$-\beta' = 3.59(10)^{-3} \hat{U}^{-0.12} \quad (9)$$

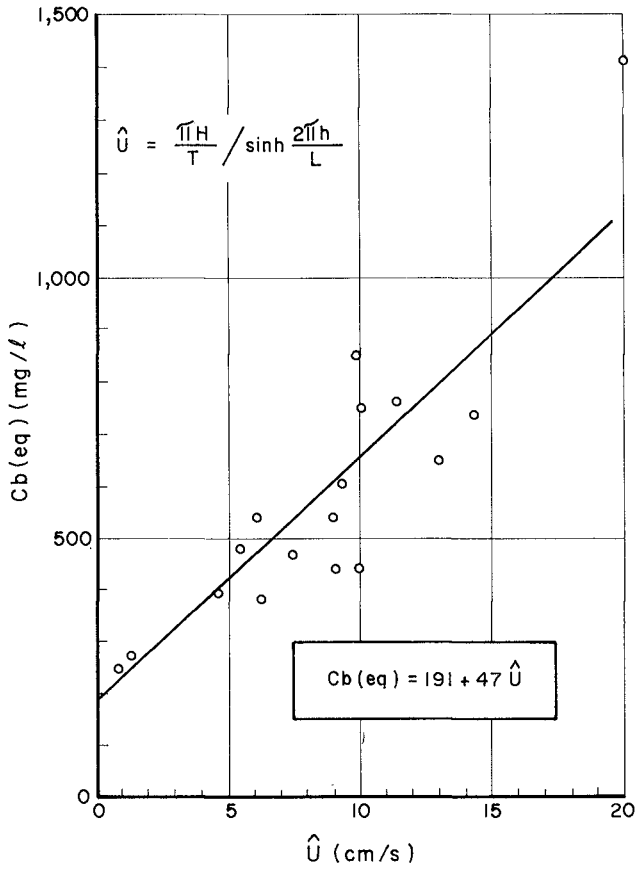


Fig. 7 Effect of Bottom Velocity, \hat{U} , upon the Equilibrium Concentration at Bed, $C_b(\text{eq})$

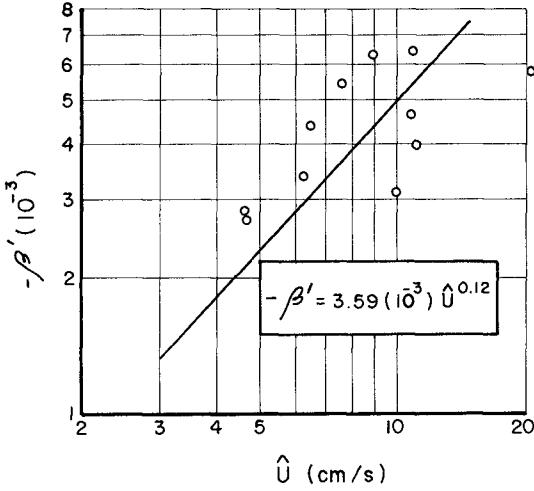


Fig. 8 Variation of Transient Concentration Parameter β' and the Bottom Velocity, \hat{U}

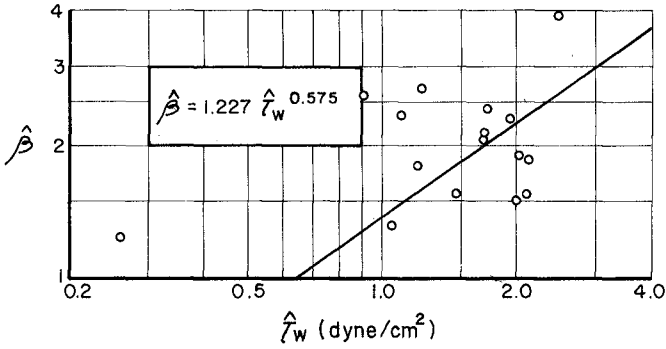


Fig. 9 Relationship between the Bottom Shear Stress $\hat{\tau}_w$, and the Maximum Normalized Concentration, $\hat{\beta}$

vi) Effect of the Bottom Shear Stress The bottom shear stress under intermediate waves is calculated using:

$$\hat{\tau}_w = f_w \frac{1}{2} \rho \hat{U}^2 \quad (10)$$

where $\hat{\tau}_w$ is the maximum bottom shear stress, f_w is the fiction factor, ρ is the water density and \hat{U} is the maximum oscillating velocity. It was found that the bottom shear stress can be correlated with the maximum value of the normalized concentration, $\hat{\beta}$, which indicates then the effect of shear force in disturbing the bottom clay into the active layer near the bottom. Fig.9 shows that:

$$\hat{\beta} = 1.227 \hat{\tau}_w^{0.575} \quad (11)$$

CONCLUSIONS

This experiment was conducted as a preliminary stage of the investigation to determine the effect of waves on the concentration of cohesive clay. The main part of the knowledge is to identify the parameters of the acting forces, eg velocity and shear stress effecting the concentration field. Physical natures of the two regions; one in the immediate vicinity of the bed and the other in the upper region of the wave field in the disturbing process are identified. Field application cannot yet be recommended until further theoretical back up with, if possible confirmation by field data will be made.

ACKNOWLEDGEMENT

The Asian Institute of Technology, Water Resources Engineering Division provide the facilities and assisting staff for the author to conduct the study, they are acknowledged.

REFERENCES

- ALLERSMA, E., HOEKSTRA, A.J., and BLIJKER, E.W. (1966), "Transport Pattern in the Chao Phraya Estuary" Proc. 10th Int. Conf. on Coastal Engineering - Tokyo, Japan.
- HATTORI, M. (1971), "A Further Investigation of the Distribution of Suspended Sediment Concentration due to Standing Waves", Coastal Engineering in Japan Vol.14.
- HOMMA, M. and HORIKAWA, H. (1963), "A Laboratory Study on Suspended Sediment due to Wave Action", Proc. 10th Congress IAHR.

- HORIKAWA, M. and WATANABE, A. (1970), "Turbulence and Sediment Concentration due to Waves", Coastal Engineering in Japan, Vol.13.
- KRONE, R.B. (1963), "A Study of Rheological Properties of Estuarial Sediments" Hydraulic Engineering Laboratory and Sanitary Engineering Research Laboratory, University of California, Berkeley, U.S.A.
- LEE, P.T. (1974), "Deposition and Scour of Clay Particles Due to Current" Thesis No.650, Asian Institute of Technology, Bangkok, Thailand.
- MALIK, M.A. (1974), "Flocculation of Silt and Clay" Thesis No.658, Asian Institute of Technology, Bangkok, Thailand.
- METHA, A.D. and PARTUENADES, E. (1974), "Effect of Physico Chemical Properties of Fine Suspended Sediment on the Degree of Deposition" Proc. IAHR Int. Conf. on River Mechanics, Bangkok, Thailand.
- MONOHAR, M. (1955), "Mechanics of Bottom Sediment due to Wave Action" U.S. Army Beach Erosion Board Tech. Memo. No.75.
- WATANABE, A., THIMAKORN, P. and DAS GUPTA, A., "Concentration of Suspended Clay in Periodic Flow", Proc. 16th Int. Conf. on Coastal Engineering, Hamburg, FDR Germany.

CONSIDERATIONS IN THE DESIGN OF AN
OFFSHORE DATA COLLECTION PROGRAMCortis Cooper¹ and Germán Febres²

1. INTRODUCTION

In-situ data collection in the ocean is costly and unpredictable even when the program is relatively well planned and executed. Despite these inherent difficulties, designers of a data collection program will find little guidance in the literature to assist them in the planning and organizational stages. Some papers have been published discussing particular aspects of a program such as instrumentation, and others have described some of the general experiences of various programs. However, there has been no attempt to conceptualize the process of design of an offshore data collection program and this is one of the purposes of the discussion which follows. The various steps involved in design are identified, ordered, and discussed in some detail. Specific examples are drawn from the authors' experiences with several offshore monitoring programs.

The work presented is most applicable to the collection of oceanographic and meteorological (O/M) data since the authors' experience is essentially restricted to this particular type of data collection. However, it is suspected that a significant portion of the aspects considered would apply to offshore programs involving the collection of other types of data such as geotechnical.

Many of the ideas presented originate from experience with two large O/M programs conducted by Instituto Tecnológico Venezolano del Petróleo (INTEVEP). One of the studies extended over the Orinoco Delta region of Venezuela with an area of roughly 150 x 150 kms. The program began in late 1977 and ended in the spring of 1979. O/M data were taken at nine stations in the region. Figure 1 shows the region and the location of the stations involved in the study.

The second INTEVEP program was started in the summer of 1979 and covers the contiguous coastline of Venezuela, approximately 1200 x 100 kms. O/M data are being taken at nine stations during the three year life of the program. Figure 2 shows the coast of Venezuela and the station locations.

¹ AM, ASCE, Research Engineer, New England Coastal Engineers, Inc., Penobscot Plaza, Bangor, ME 04401, USA.

² Research Engineer, INTEVEP, Los Teques, Venezuela

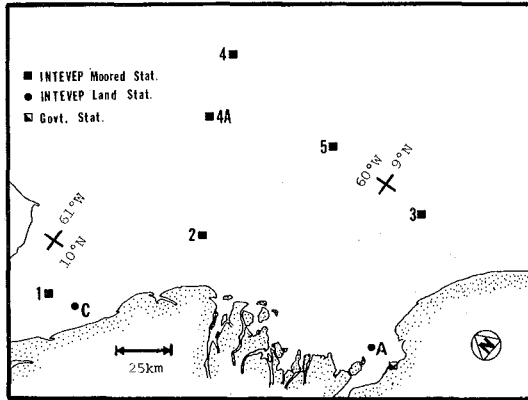


Figure 1: Locations of the oceanographic and meteorological stations in the Orinoco Delta region of Venezuela.

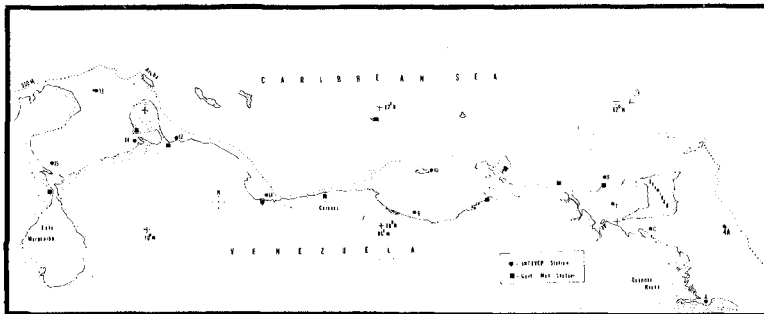


Figure 2: Locations of the oceanographic and meteorologic stations in the Integral Program along the coast of Venezuela.

The primary objective of these studies is to gather the information needed for design and operation of offshore petroleum facilities. The Orinoco program cost approximately \$3 million (U.S.) and the Integral Program is expected to cost about \$5 million (U.S.). Justification for these expenditures was based on the absence of historical data in the region and the high likelihood of petroleum deposits and subsequent development.

2. MAJOR STEPS IN DESIGN AND IMPLEMENTATION

An offshore data collection program can be conceptualized into six major steps: (1) identification of the objectives of the program; (2) identification of the data which must be obtained; (3) detailed design of the program including selection of the resolution of the monitoring network, instruments, quality control methods, navigation methods, logistics, and program duration; (4) implementation and execution of the program including modifications which become necessary during the life of the program; (5) data processing; and (6) data analysis.

Figure 3 summarizes these steps in the form of a flow chart. The first three fall within the planning stage and the latter three within the execution stage of the program.

The flow chart in Figure 3 implies a downward progression which is somewhat idealized. In fact there is likely to be a good deal of iteration during the first three steps as the designer faces the inevitable tradeoffs imposed by financial and technical constraints.

The discussion which follows will focus primarily on Steps 2 and 3. A fairly thorough discussion will be presented on parts 1 and 2 of Step 3, Program Design. The remaining parts of Step 3 are addressed only briefly primarily because of space limitations. Discussion of Step 1 is not included, but this should not be taken to imply that determination of the objectives of an O/M program is a trivial task. Rather, the usual processes of determining objectives is often influenced by political and financial considerations and is difficult to address in a general sense. It is simply assumed in the discussion which follows that the designers have (1) identified a set of reasonable objectives, (2) identified any financial constraints that may exist, and (3) defined the region or area to be monitored.

3. DATA IDENTIFICATION

There are two major questions which must be resolved at this stage. The first concerns identification of the data needed to satisfy the objectives of the program. The second is to determine what historical data is available for the region.

In programs primarily concerned with ecological impacts, the first question is a bit difficult to address in general terms. However, for programs whose results will be used primarily for design and operation

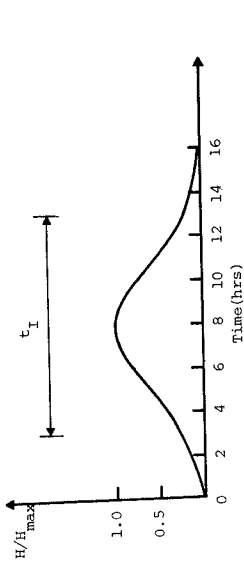


Figure 4: Time history of water level changes during a tropical storm.

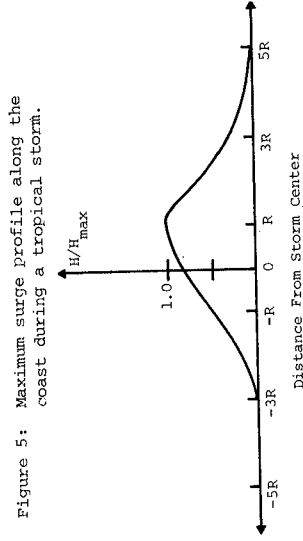


Figure 5: Maximum surge profile along the coast during a tropical storm.

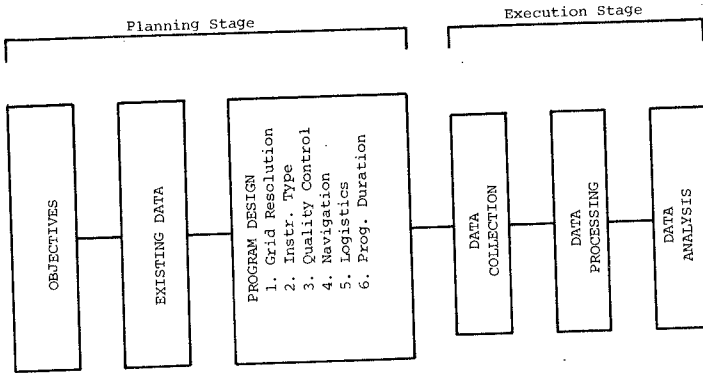


Figure 3: Steps in design & implementation of an O/M data collection Program.

of offshore structures, the questions are more easily addressed. The data of primary interest will include: (1) surface waves with 2 to 20 second period; (2) currents with periods of several minutes and longer; (3) winds, both gusts and sustained; and (4) tides, both astronomical and storm-induced. Some other parameters would probably be of secondary interest and these would include water conductivity, water temperature, air temperature and air pressure. The marginal cost of acquiring these secondary parameters for specific sites is relatively small.

The Data Identification stage should also include an assessment of historical data. This is important for several reasons. First, previous studies can give considerable insight into the nature of the processes which dominate in the region of interest. This information is particularly helpful in the selection of grid resolution, instrumentation, etc.. Second, existing data bases can sometimes be used to effectively extend the time span of a monitoring program. This is important since most data collection programs have a duration on the order of a year and calculation of extreme events with long recurrence intervals will be severely limited if other data sources are not available or are not used. Third, the historical data may satisfy some of the objectives of the program, thus making some data collection unnecessary.

4. DETAILED DESIGN

As indicated in Figure 3, Detailed Design involves six topics. An attempt has been made to place these topics in the order in which they should be addressed. However, all six are strongly interrelated, and initial choices limit options for later decisions. For instance, in specifying the resolution of the monitoring network, the designer must select the time increment between samples. If the designer chooses a relatively small interval between samples, this will often affect the instrument servicing interval, which in turn affects servicing vessel logistics, which in turn affect project costs, and project duration. This requires the designer to iterate many times in order to arrive at an optimal detailed design.

4.1 Resolution of the Monitoring Network

4.1.1 Characteristic Length and Time Scales. In designing the monitoring network, there are two main parameters which must be specified: T_I , the time increment between record samples of process I, and X_I , the distance between instruments which monitor process I. The term T_I refers to the time period between individual samples on the recording media. This, of course, implies a digital sampling method. For analog instruments such as the Datawell Waverider with a Wavrep receiver, the discussion of T_I which follows is not relevant, but comments regarding X_I remain valid.

One of the primary goals governing the choice of T_I and X_I is that both be small enough to adequately describe the process to be monitored. Determining the largest value of T_I and X_I which achieve sufficient

resolution is of considerable interest from the standpoint of minimizing program cost. Larger sampling intervals allow the use of fewer instruments which allow increased servicing intervals and reduced boat time. These optimizations can ultimately lead to substantial reductions in program costs.

As an illustration of how the maximum T_I can be estimated, consider the temporal variation of a process I . The process has a finite duration in which most of the energy associated with the process is concentrated. This duration will be referred to as t_I . To take the illustration a step further, assume the process to be the storm surge created by the passage of a hurricane or tropical storm. Figure 4 shows the time history of the normalized storm surge, H/H_{\max} , where H is the time history of the storm surge at the site of interest, and H_{\max} is the maximum observed surge at the site. Astronomical tides have been removed. The characteristic time scale (t_I) for a storm surge is on the order of 10 hours. Thus it follows that the sampling interval for a hurricane induced storm surge should be less than 10 hours, otherwise a definite risk exists that the event would go completely unrecorded.

In more general terms, the above example implies that the largest T_I which should be used for a monitoring network is slightly less than t_I . If such an interval is chosen, then some form of interpolation will be necessary in order to derive the extreme or peak at the site. On the other hand, if one wishes to eventually extrapolate the collected data to longer intervals, then many points must be taken within the storm period, t_I , so that the peak value (or near it) is recorded. For some processes it is possible to get these additional points with no substantial increase in program cost. Storm surges tend to be one of these processes. However, other processes, such as hurricane generated waves, can be costly to monitor frequently. If wave data is stored internally in a moored wave device, then storage space may become limiting long before the instrument might otherwise need servicing. This requires more frequent and costly retrieval and so the marginal cost of additional data points may be high. For such processes it is often more economical to apply mathematical models or statistical means to extrapolate and interpolate the data. In this mode, the data serves mainly to tune and verify the simulation method.

The determination of a maximum X_I can be approached in a manner similar to that used for determining the maximum T_I . Returning to the previous example of storm surge, it should be fairly evident that the largest X_I for storm surges should be less than the maximum distance x_I affected by the storm. Figure 5 indicates a typical spatial variation of the maximum surge associated with a tropical storm approaching a fairly straight coastline. In this figure, H is the maximum surge which occurred during the passage of the storm at locations along the coast and R is the radius to maximum winds. As indicated in the figure, the characteristic length scale of storm surges (x_I) is on the order of $8R$ and it follows that the largest X_I which could be used in a monitoring network is somewhat less than $8R$.

The characteristic length and time scales (i.e. x_L and t_L) can be identified for other processes besides surge and this is done in Figure 6. This figure is a modification of one appearing in Stolzenbach et al. (1977). Atmospheric disturbances are indicated by the lined regions and two current processes (tidal and geostrophic) are indicated in the clear regions. Other types of currents not shown are generated by local atmospheric disturbances and thus would occupy roughly the same region in the figure as the atmospheric disturbance which is responsible. For example, currents generated during a hurricane would tend to have the same characteristic length and time scales as the winds which create them. Similar observations can be made regarding surge and local wind-generated waves. Examples of processes contained in each region in the figure are: (1) weather system fluctuations - extratropical storms, tradewinds, and tropical storms; (2) mesoscale wind fluctuations - thermal and orographic types of air flow such as land-sea breezes and thunderstorms; (3) atmospheric boundary layer fluctuations - vortex shedding and natural convection near the sea surface; and (4) geostrophic currents - permanent currents such as the Gulf Stream and the gyres and eddies associated with them.

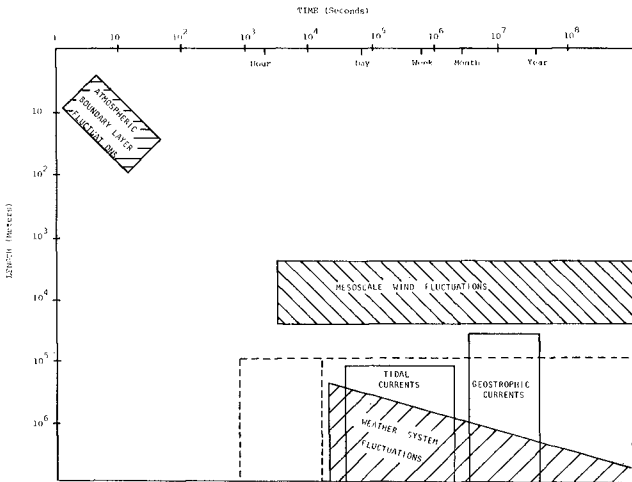


Figure 6: Typical length and time scales associated with winds (& the waves & currents associated with them) & currents in open areas.

It should be pointed out that the length scales shown in the figure apply primarily to open coastal regions. Complex coastlines or bathymetry tend to shorten the length scales of several of the processes such as currents and waves.

With the use of Figure 6, one can estimate the sampling intervals needed to describe various processes. In general, the maximum spatial distance (X_T) and time increment (T_T) needed to monitor a process will be given by the length and time scales associated with the upper left-hand corner of the appropriate region in Figure 6. For example, in order to monitor mesoscale wind fluctuations, the figure indicates that $X_T < 20$ km and $T_T < 1$ hour.

For most programs, one would not be interested in monitoring all the processes included in Figure 6 and this is indeed fortunate because doing so would be expensive, at least for programs covering any significant area. This is true because of the small sampling intervals which would be necessary to describe some of the processes shown in the figure, most notably atmospheric boundary layer fluctuations. Monitoring larger scale processes such as mesoscale wind fluctuations may be desirable from the standpoint of achieving certain objectives in the program. However, the cost of obtaining the data may be prohibitive if the region to be covered is large.

The comments on length scales made thus far have focused on horizontal spatial variations. A figure similar to Figure 6 can be constructed to show the vertical variations as well. This is of particular interest when deciding on the number of current meters to string in a given location.

4.1.2 Auxiliary Stations*. Losses of data and instruments are common and should be considered inevitable. It is interesting to examine data loss rates from a few O/M programs.

In the Orinoco Project, about 30% of potentially recoverable data was lost due to mooring failures, instrument malfunction or loss of instruments. The Integral Program has fared somewhat worse. Approximately 30, 65, 45, and 53% of the potentially recoverable data of waves, currents, tides and winds, respectively, has been lost, primarily due to outside interference.

One of the more extreme and recent cases of high data loss was the NEOCSPO program (EG&G, 1978), a study of the physical oceanography of New England outer continental shelf, including Georges Banks. In one region of the study, current meters were deployed for 8 months and of the 21 system-months of data potentially available, only 2 usable system-months were obtained. This translates to approximately a 10% recovery rate. A major factor in this poor showing was the use of unconventional instrumentation.

It should be evident from the above examples that significant data losses can be expected for O/M programs. If the monitoring network is

*The term "station" refers to a complete instrument package, e.g. current meter string, a meteorological buoy and mooring, etc.

designed such that $X_I \sim x_I$ and/or $T_I \sim t_I$ then loss of data may mean an inadequate description of the process. In the case of an O/M program oriented towards design of offshore structures, some loss of data during normal conditions would probably not meaningfully impair the overall success of the program. However, loss during significant storm events could be crucial.

There are several ways to minimize data losses. One way is to keep the instruments and moorings well maintained. Another is to use only instruments, moorings, and deployment techniques which are well proven in the ocean environment. Even with these precautions, some data losses are inevitable. Therefore, it may be wise to include some auxiliary stations to minimize the impact of those data losses.

A less expensive alternative to providing auxiliary stations would be the addition of more instruments at a station, e.g. the addition of an extra current meter on a string or the addition of extra anemometers to a meteorological buoy. In some situations, the marginal cost of the added instrumentation is relatively small and the method does improve the odds against loss due to instrument malfunction. Furthermore, the extra instrumentation can provide valuable data on the vertical variations of the process being monitored.

If it is decided to include auxiliary stations, the instrument capitalization costs can be minimal in some situations. For instance, if the storm patterns are highly seasonal, as they are on the coast of Venezuela (see Figure 7), then temporary stations can be established during the stormy seasons. In the case of Venezuela, temporary stations could be established during the months of August and September when about 85% of all major storm events occur. Since the temporary stations would only be deployed for 2 months per year, labor and capital expenses could be kept to a minimum. The additional instruments could be provided in a number of ways. Some of the spare instruments normally kept on hand in any large program could be temporarily utilized. Other instruments could be obtained by leasing. The typical rental rate for a two month lease would be about one-third of the retail price of the instrument. A further benefit of leasing is that it would not overburden servicing facilities since most leasing firms provide all servicing.

There are two primary schools of thought in positioning auxiliary stations. One may choose to place auxiliary instruments near primary stations. This was the method used for the BOMP and GAWWMP programs reported by McLeod (1979) in which the wave instruments were placed in clusters of three. This method has the advantage of minimizing retrieval-deployment time and giving a convenient means of calibration or inter-comparison. Clustering of instruments increases the visibility of the station and this is an advantage if the local outsiders are amicable towards the program, since they can more easily identify the station locations and avoid them. Needless to say the approach also offers considerable opportunity to outsiders with mischievous or larcenous intent.

The other school of thought is to place auxiliary stations at some distance between primary stations, possibly equidistant. The advantages include: (1) a decrease of the likelihood of multiple failures when such failures are caused by accidental interference by outsiders or by extreme

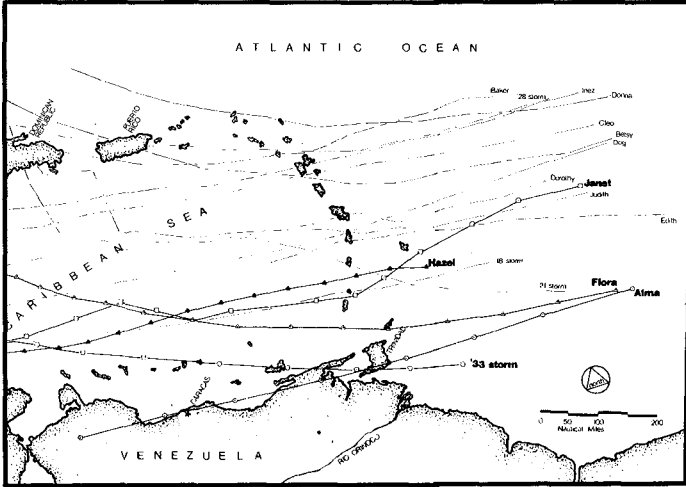


Figure 8: The paths of tropical storms in the southern Caribbean during the past 75 years of record.

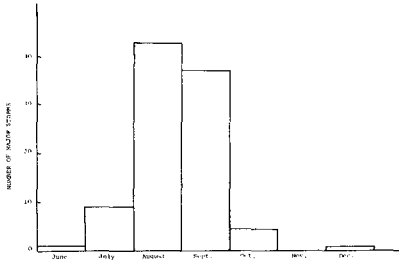


Figure 7: Monthly histogram of storms for the Orinoco Delta (75 yrs of record).

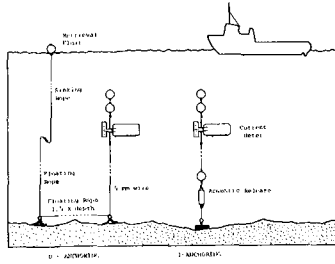


Figure 9: Two mooring configurations (from Aanderaa Brochure).

local environmental conditions, and (2) if failures do not occur, horizontal spatial information can be gained which will lessen the need for interpolation during the data analysis step.

4.1.3 Other Siting Considerations. The two major considerations presented above should ideally be of foremost importance in design. But other factors will clearly influence the final positioning of stations. The more important of these are briefly discussed below.

Interference from people outside the program often claims more instruments than Mother Nature or mistakes by program personnel. Mcleod (1979) attributed roughly 50% of all mooring failures to outside interference. In the ocean, certain neighborhoods, as it were, should be avoided - shipping lanes constituting a prime example. Other areas are also undesirable, such as heavily fished regions, although avoiding these often large areas is not always possible.

A second consideration in siting stations is that deployment in deeper waters may require costly special equipment. This cost may not be justified, particularly if the location is near the continental break and a small shift in position would eliminate the problem.

The navigation method to be used should also be considered. In general, the further one gets from shore the more difficult and costly it is to navigate precisely.

A fourth consideration is the method of data retrieval. For instance, the distance between instrument and shore-based receiving stations for VHF telemetry must be less than 50 km for most standard instrument packages.

Boundary effects should be considered in the placement of stations as well. The method described in Section 4.1.1 applies to open coastal areas and does not include the complicating effects caused by coastlines, such as shear currents and land induced fetch limitations. If information within these areas is desired it may be necessary to decrease the spatial distance between instruments.

Finally, servicing logistics should be taken into account. The servicing interval may vary from a few weeks to many months depending on the instrument and measurement interval. The cost of a large servicing vessel dedicated solely to an O/M program can constitute a significant portion of the budget for a typical O/M program. In the Orinoco Program, roughly 50% of the total budget was spent on the servicing vessel and crew. Thus, significant cost savings can be achieved by establishing stations on or near a coastline, an island, a fixed platform, or a semi-permanent ship, hence minimizing the use of a large vessel. However, data from stations on or near land can be seriously distorted by the land forms to the extent that the data are not representative of the open ocean. Fixed offshore platforms are generally the most favorable sites since they offer: (1) minimum interference with O/M processes; (2) a fixed, relatively dry environment; (3) some protection from outside interference (e.g. fishing); and (4) improved reliability since damaged or missing instruments can often be spotted and replaced more quickly.

4.1.4 Illustration-Integral Program. Figure 2 indicates that the typical distance between stations in the Integral Program is on the order of 100 km. In the case of winds and tides there are also some additional stations maintained by the Venezuelan Government which can be used to augment the stations in the Integral Program.

The time sampling intervals used in the program are 10 minutes for currents and winds and 15 minutes for tides. For waves, 1 sample is recorded each second for 20 minutes. This is repeated every 4 hours. These space and time intervals are indicated on Figure 6 by the three dotted lines and it is apparent that the network should describe weather system fluctuations, tidal currents and most characteristics of geostrophic currents.

Note that no attempt was made to monitor mesoscale wind fluctuations primarily because the cost was prohibitive. But peak winds along the Venezuelan coast are dominated by convective storms (thunderstorms) which fall within the range of mesoscale wind fluctuations. Fortunately, even though thunderstorms control the maximum design winds, they do not govern design waves or currents, the two more important factors in most aspects of design. Furthermore, the wind data collected in the program can be supplemented by comparatively plentiful wind data recorded at government installations.

There are several other aspects of the Integral Network which should be of general interest. For instance currents, winds, tides and waves are all recorded at each station, this despite the fact that each process has a different X_I as discussed previously. Stations were centralized for two main reasons. First, Figure 6 implies that X_I is roughly equivalent for the three processes of primary interest (i.e. tidal currents, weather system fluctuations and geostrophic currents) justifying a constant X_I . Second, servicing logistics and retrieval-deployment are significantly simplified.

The space and time intervals used in the Integral Program are quite close to the X_I and t_I of the respective processes and, hence, there may be an insufficient number of data points to adequately resolve the process using data alone. In these cases, mathematical or statistical modeling will be necessary to extrapolate and interpolate the data. Examples of these processes include tropical storm induced waves, currents and winds. Mathematical modeling of these particular processes has been fairly successful. See, for example, Forristall et al. (1977) and Ross and Cardone (1977).

Essentially no auxiliary stations were included in the program. This was due to financial reasons, but it can also be argued that because of the unique storm patterns along the coast, the network already has some inherent redundancy. Figure 8 shows the paths of tropical storms which passed near the Venezuelan coast in the past 75 years of record. As one can see, the storms tend to parallel the coast. Returning to Figure 2, it can easily be seen that if a station does fail during a tropical storm, it is likely that the storm will pass another station further along the coast.

4.2 Instrument Selection

The data of primary interest in O/M data collection programs would generally include one or more of the following: currents, winds, waves and/or water level. The sections below will focus on the considerations involved in selecting instruments for collecting these four types of data.

Remote sensing via airplane, land based radar and satellites are not presented here. The first two have considerable problems, including accuracy. The last option also is somewhat limited by accuracy and in addition it is not a technique readily available to non-governmental groups. All three techniques, however, deserve considerable attention since they may ultimately become technically competitive and they already offer some significant cost advantages over in-situ monitoring.

4.2.1 Siting Requirements. Some instrument types have inherent deployment limitations. Three helpful publications by NOS (1977, 1978, & 1979) give information concerning these limitations as well as other valuable information.

Wind sensors can be deployed on a buoy, ship, fixed platform, or land. Land stations have the advantage of being easy to service and relatively inexpensive to construct. However, as Hsu (1978) and others note, the effects of land can seriously distort the wind field so that it is not representative of the open ocean. Additional analysis is usually necessary in order to at least partially correct for the influence of land. Buoys avoid this major disadvantage of land stations but usually at a significant cost in terms of increased initial capital expenditure, long term maintenance and increased likelihood of loss. A site on a semi-permanent ship or platform is perhaps the best location for wind measurements. Some of the advantages of these two sites were given in Section 4.1.3.

It is not uncommon to place the instrument recorder in a comparatively dry, fixed site such as a platform and to moor the instrument sensor. The sensor and recorder can be linked via cable or telemetry. Rose et al. (1979) and Howell (1980) report examples of this approach. The major advantages of separating the two are that the recorder can be placed in a location which can be conveniently accessed and the likelihood of total loss of the instrumentation is usually lessened. Servicing of the recording component can be performed regularly and the sensor need only be retrieved when it shows signs of deterioration.

It is interesting to note that in the field of wave measurement, the instrument types capable of measuring wave direction are limited primarily to wave staffs. It is likely that measurement of wave direction will become more important, particularly in light of some recent results reported by Forristall et al. (1978) which indicate that wave direction is an important consideration in wave force calculations. Several manufacturers including Datawell and ENDECO are planning to manufacture buoys which will monitor both wave direction and vertical displacement.

4.2.2 Data Storage Technique. Once the data is measured by the instrument sensor, some preprocessing is usually performed and the data is stored. Existing methods of data storage include: (1) internal recording

on magnetic tape or strip charts; (2) telemetry of data to the shore, a platform or a ship where data is received and recorded on magnetic tape or strip chart; and (3) transmitting of data to a land station via satellite.

There have been several successful applications of satellites in transmitting oceanographic data including one by the U.S. Bureau of Land Management (1978). The major limitation as of mid 1978 appeared to be data volume. For instance the American Electronic Lab transmitter in conjunction with the GOES satellite used by the Bureau allows hourly transmissions of 192 bits. Such a rate would not allow actual time series data to be transmitted for most parameters. Data transmission rates for the ARGOS satellite are somewhat higher for some locations on the globe. The status of satellite transmission will no doubt change, and given many of the advantages of telemetry the topic certainly deserves close attention in the future.

Telemetry of data from the instrument sensor to a conveniently located recorder has many advantages. First the method minimizes the costly boat time required to retrieve and deploy internal recording instruments. Second, the recording station can usually be checked frequently at minimal cost and malfunctioning or lost equipment can be quickly identified. Third, once the sensor is in place it is often not necessary to remove it for extended periods of time unless the signal shows deterioration. This is a significant advantage since the deployment-retrieval process is costly and often damages instruments.

There are, however, several problems with existing, non-satellite, methods of telemetry. Most off-the-shelf O/M equipment with telemetry uses very high frequency (VHF) signals and the range is restricted to line of sight, or about 50 km under ideal conditions. Interference from sources such as citizens band radio can also be a problem.

The most popular recording media are magnetic tape (usually cassettes) and paper strip charts. The latter medium is a left-over from older technology and should be avoided for larger programs. Though the initial cost of the magnetic tape unit is somewhat higher than for a strip chart recorder, the labor saved during data processing usually more than justifies the additional expense in most data collection programs involving more than a few stations. Tapes can be processed quickly and accurately with computers and most manufacturers offer some form of data processing to the user who prefers not to purchase a reader and set up his own break-out facility.

Several recent developments in digital electronics will soon have some significant effects on recording techniques. For instance, it appears likely that solid state recording media such as bubble memory will soon become economically competitive with magnetic tape. This development should significantly enhance instrument reliability, increase storage capacity and lessen overall instrument size and weight.

The other area of significant progress is in the field of microprocessors. Several O/M instruments such as the EG&G current meter, already include internal microprocessors. Microprocessors have not yet

been incorporated extensively into other types of instruments. It is likely that this will change in the next few years, particularly for wave measurement devices where microprocessors appear to offer many advantages.

4.2.3 Servicing Frequency. Instruments must be routinely retrieved and serviced for one or more of the following reasons: (1) replacement of the instrument recording media; (2) replacement of the instrument batteries; (3) cleaning of sensors made necessary by fouling; (4) maintenance of mooring systems; and (5) replacement of deteriorated components. Not all of these reasons would apply to all types of instruments.

For instruments which record internally, retrieval is usually the only way of determining if the instrument was lost or functioned improperly. Thus there is a strong incentive to service these types of instruments frequently in order to minimize data gaps. This is particularly true if relatively few auxiliary stations have been incorporated into the program, making data gaps more difficult to fill. If an instrument is lost while on station, frequent servicing will probably increase the likelihood of recovery.

The cost of retrieving and deploying moored instruments can be high, since a large, well equipped servicing vessel is often needed. The cost of routine servicing is significantly less for instruments which have the recording unit on land or on a platform or ship. In these cases, servicing of the recording portion of the instrument should probably be done fairly frequently (i.e. on the order of a week) since the cost is small and benefits are substantial. The choice of a servicing interval for moored instruments with internal recorders is not nearly so simple. One must ultimately trade off the cost of servicing against the increased possibility of lost instruments and data.

4.2.4 Maintenance. The cost of maintaining instruments can vary substantially from one model to the next and thus should be considered when choosing instrumentation. Maintenance costs will clearly be affected by: (1) the technical sophistication of the instrumentation, (2) the quality of the components and the design, (3) calibration requirements and (4) availability and cost of replacement parts. Unfortunately, the NOS documents cited earlier give little information regarding these aspects, no doubt due to their subjective nature. Information on maintenance is best gathered from past experience, detailed instrument evaluations by independent sources (see NOS documents) or discussions with frequent users of the instruments being considered.

4.2.5 Reliability. The term is probably best defined as "an instrument's resistance to failure during conditions in which it will normally be used in the program". Some instrument models will experience more failure for a given usage than others. This may occur because of: (1) design, (2) quality of materials and workmanship, or (3) routine servicing which is not up to the manufacturer's specifications. Unfortunately it seems that little independent work has been done in evaluating the dependability of various instruments under similar conditions. Like the situation with maintenance, information on reliability is probably best gained from past experience, detailed instrument evaluations or discussions with others who have extensively used the instrument models being considered.

4.2.6 Cost. Equipment purchases normally constitute a significant portion of the overall program costs: roughly 25% in the case of the Integral and Orinoco Programs. Thus, significant cost savings could conceivably be made by careful shopping. Prices of instruments vary by an order of magnitude within each of the four groups (i.e. waves, currents, etc.). However, in many cases it is unfair to compare the price of one instrument model to another. For instance two instruments may have different capabilities, despite the fact that they both fall within the same group. When comparing purchase prices one should also keep in mind other long term costs associated with the instruments such as servicing. One model may initially cost somewhat more than another but the servicing costs of the less expensive instrument may outweigh the initial advantage.

Another complication to consider is that the life of O/M instruments is often quite short. In the Venezuelan Integral Program twenty instruments from a total of thirty-eight deployments were lost within 6 months. Losses were attributed to outside interference, particularly from fishermen. Since the life expectancy of O/M instruments is usually low, there is a definite incentive to use the least expensive equipment so as to minimize the financial loss of missing equipment.

4.2.7 Accuracy. The error incorporated into the instrument reading can be conveniently conceptualized into two categories: the error registered by the instrument when used under ideal conditions and the error registered under the actual conditions which will prevail in the field. Instrument manufacturers only list the first type of error and these are given in the NOS publications. For most O/M studies the first source of error is negligible when compared to the error from the second source. The Aanderaa RCM4 current meter is a classic example. The manufacturer lists the indicated speed to be accurate to $\pm 2\%$. However, if the instrument is used in the field in the presence of large wave-induced velocities then the error of the speed measurements is more on the order of 50% (Halpern and Pillsbury, 1976)¹.

Most O/M instruments available on the market are limited and the accuracy listed by the manufacturer will hardly ever be obtainable in the field. When considering an instrument model, the designer should examine all independent evaluations of the model in order to determine the instrument limitations and whether those limitations will be a problem in the study.

4.2.8 Instrument Standardization. A large portion of O/M programs monitor more than one parameter (e.g. waves, currents, etc.). In this case it can be advantageous to have instruments from the same manufacturer. This is no doubt one of the reasons Aanderaa Instruments have been popular. The manufacturer offers current meters, tide gauges, and meteorology stations, all using the same data logger (recorder). The advantages of the standardizing are: servicing personnel can be highly specialized, which probably results in more timely, high quality service; spare parts inventories can be minimized; only one reader for data processing of magnetic tape equipped instruments is needed; and data processing software is

¹ Aanderaa Instruments now recommends the RCM4 not be used in the wave zone.

simplified. Though the benefits seem significant it is somewhat difficult in practice to standardize instrumentation for several reasons. To begin with, there are only a few manufacturers which produce a line of instruments which measure more than one parameter. In addition, it is not likely that standardization can be achieved without some sacrifice in terms of the other important factors to be considered when selecting instruments (e.g. accuracy, reliability, purchase price, etc.).

4.2.9 Mooring Configuration. If it is not possible to provide a fixed platform at the station site then it will be necessary to moor the instruments. The term mooring is loosely defined here to include anchor, mooring line, connectors, acoustic release (if used) and buoyancy units (if used). Though deceptively simple in concept, moorings allow a multitude of problems. In many studies including the Venezuelan Orinoco Study and GAWWMP Study reported by Mcleod, mooring failures were the primary cause of instrument loss.

In designing a mooring one must consider the following points: (1) deployment and retrieval techniques; (2) environmental loads at the site; (3) deployment and retrieval loads; (4) strength requirements of the connectors and mooring line; (5) buoyancy and anchoring requirements; (6) long term maintenance including considerations of fatigue, corrosion and deterioration due to marine life.

Many instrument manufacturers can suggest mooring configurations which have been used successfully in the past. An example is shown in Figure 9. The I-anchoring system shown in the figure incorporates an acoustic release device and this configuration seems to be the most popular. Its popularity arises from the fact that the system is invisible from the surface and hence less susceptible to outside interference. The system is, however, obviously dependent upon the ability of the ship to get within range of the release in order to activate it. Also if the release should fail it may be difficult and time consuming to recover not only the release but the other instrument on the line. Finally, the cost of the release is often significant, varying from \$3,000 to \$10,000. Add to this the cost of the surface activation unit which is on the order of \$10,000.

4.3 Quality Control

The larger the O/M program the more quality control of the data will be a problem. The volume of data which must be processed from a large program can become staggering. Consider the Orinoco program as an example. During that program, approximately 2×10^7 words of data were collected and most were eventually processed. The likelihood for error even with the aid of extensive computerization should be obvious.

Errors can be incorporated into the data in a variety of ways. Calibration errors or instrument malfunctions are of major concern and a routine calibration schedule should be established and rigorously followed. An instrument log should be established and records kept of servicing and calibration for each instrument. Each instrument and station location should have unique numbers assigned to them.

Errors also occur in handling and processing the data. Each tape (or chart) must be properly labeled with essential information such as: instru-

ment type (i.e. currents, waves, etc.), instrument number, station number, time of start-up, time of deployment, time of retrieval and time of shut down. In the case where magnetic tapes are used as the instrument recording medium, the tapes should be quickly processed by computer into a form which expedites rapid scanning by program personnel. The quick break-out of data will assist in identifying problems and rectifying them quickly. This latter point is particularly advantageous if the error originates from an instrument malfunction which might otherwise go undetected.

4.4 Navigation

Whenever moored instruments are used, some form of navigation, however rudimentary, will be necessary. If the stations are within a few kilometers of the coastline then a compass or sextant will suffice. Locations further from the coast will require more sophisticated equipment. In the latter case, issues such as accuracy, cost, availability and reliability of the various alternatives should be thoroughly investigated.

4.5 Logistics

Issues involved here include: procurement of instrumentation and parts; scheduling of the servicing ship(s); and management of personnel.

It should be kept in mind that when procuring instruments, the manufacturer will often require several months delivery time. This means that in most cases spare instruments should be purchased in advance. Extra instruments should also be purchased if moored instruments are used in the program. This is necessary because most instruments can not be adequately serviced on the ship when they are retrieved but should usually be returned to a land-based servicing center. This of course means that replacement instruments must be on board the servicing ship so that at the time the old instruments are retrieved, the replacements can be deployed.

If servicing vessels are used then scheduling of the ships will be necessary. Suitable allowances should be made for contingencies such as poor weather or breakdown of the ship. A centralized servicing center should also be established and should be equipped with appropriate repair facilities and spare parts and staffed with competent personnel.

4.6 Program Duration

Most O/M programs last between 1 and 2 years, perhaps somewhat less in the case of environmental impact studies. In the case of design studies, this relatively short duration can present some problems when one attempts to derive design parameters for long recurrence intervals (i.e. on the order of 50 years). Resio (1975) suggests that the data itself should not be extrapolated in time for periods longer than 5 times the duration of the data. That would imply that data from a 2 year program should not be extrapolated past about 10 years.

The problem can be further aggravated if the recurrence interval of major storm events is large as is the case for Venezuela. Recall from Figure 8, the average recurrence interval for tropical storms along the

Venezuelan coast is about 8 years. Hence the probability of measuring a significant storm during a program of 2 year duration is small. As yet a significant tropical storm has not been recorded in either the Orinoco or Integral Programs.

Because data collection programs are costly it is usually not feasible to maintain the program for the time period needed to derive design information from data. Of course, the results from the program are usually needed long before a program of more desirable duration could be completed. Modeling, therefore, must play an important role in the derivation of design criteria. The data in effect serves primarily to calibrate and check the models, at least as the data pertains to deriving design criteria.

5. SUMMARY

The various steps involved in the planning and execution of an offshore data collection program have been outlined. The aspects that have been presented are most relevant to large programs involving the collection of oceanographic and meteorologic (O/M) data to be used ultimately in the design and operation of offshore oil production facilities. Many examples are taken from two large O/M programs off the coast of Venezuela in which the authors have been deeply involved. Although these are specific examples, the discussion is presented in fairly general terms and should be useful to planners and designers of other types of offshore data collection programs.

The discussion focuses on the steps in program design including selection of the resolution of the monitoring network, instruments, quality control methods, navigation methods, logistics, and program duration. Given the complexity of each topic and the space constraints, it is not feasible to discuss all the topics at a detailed level. A fairly detailed discussion of the monitoring network and instrument selection is given and a brief review of the major points involved in the other topics is presented.

AKNOWLEDGEMENTS

Thanks is expressed to Dr. Laurence Draper for several of his helpful comments. Mr. Bruce Fidler and Dr. Bryan Pearce are also acknowledged for their comments and assistance in preparing the final paper.

REFERENCES

- EG&G (1978), "Recommendations for the Continuation of the N.E. Outer Continental Shelf Physical Oceanography Program", Waltham, MA.
- Forristall, G. Z. et al. (1977), "Continental Shelf Currents in Tropical Storm Delia: Observation and Theory", J.P.O., 1, 532-546.
- Forristall, G. Z. et al. (1978), "Storm Wave Kinematics", O.T.C. Paper 3227.
- Halpern, D. and R. O. Pillsbury (1976), "Influence of Surface Waves on Sub-surface Current Measurements in Shallow Water", Limnology & Oceanography.
- Howell, G. L. (1980), "Florida Coastal Data Network", Proc. 17th Intern. Conf. on Coastal Engr., Sydney, March.
- Hsu, S. A. (1980), "On the Correction of Land-Based Wind Measurements for Oceanographic Applications", Proc. 17th Inter. Conf. on Coastal Engr., March, Sydney.
- McLeod, W. R. (1979), "Ocean Wave Measurement Experiences in Hostile Environments", O.T.C., Paper No. 3375.
- NOS (1977), "Current Measurement Subsystem Technology Survey" compiled by G. F. Appell and D. R. Crump, Nat. Ocean Survey Test & Evaluation Lab.
- NOS (1978), "Wave Sensor Technology Assessment", by R. L. Ribe, Nat. Ocean Survey Test & Evaluation Lab.
- NOS (1979), "Water Level Measurement System Technology Survey", by T. N. Mero and Alfred Zulueta, Nat. Ocean Survey Test & Evaluation Lab.
- Resio, D. T. (1975), "Extreme Wave Heights for Cleveland Harbor", Proc. from C.E. in the Oceans III, ASCE.
- Rose, F. W., et al. (1979), "The U.S. East Rig Instrumentation Program", O.T.C., Paper No. 3373.
- Ross, D. and V. J. Cardone (1977), "A Comparison of Parametric and Spectral Hurricane Wave Prediction Products", Proc. of NATO Symp. on Turb. Fluxes Through the Sea Surface, Wave Dynamics & Pred., Marseille, France, Sept.
- Stolzenbach, K. D., et al. (1977), "A Review and Evaluation of Basic Techniques for Predicting the Behavior of Oil Slicks", R. M. Parsons Lab, M.I.T., T.R. 222.
- U.S. Bureau of Land Management (1978), O.T.C., Paper No. 3178.

THE GERMAN "MORAN" PROJECT

by

Winfried Siefert^{*)} and
Volker Barthel^{**)}

Abstract

The project "MORAN" (Morphological Analyses of the North-Sea-Coast) is an extensive program in order to try and combine all knowledge of the morphologic behaviour of a transitional zone of 5 to 7 km width with weather, tide, current and wave data. The area to be considered is about 9000 km² size. The program started in 1979 and will probably continue until 1984.

*) Head, Coastal Engineering Research Group "Neuwerk", Cuxhaven, Fed. Rep. of Germany

***) Federal Waterways Administration, Wasser- und Schifffahrtsamt Bremerhaven, Fed. Rep. of Germany

Introduction

One of the supporters of the 16th ICCE was the "German Coastal Engineering Board" (KFKI). This committee is a board which is responsible for the administration of hydraulic engineering tasks on the North Sea coast and which has interested itself in encouraging practical applied research in the coastal area.

Though the German North Sea Coast is relatively short (370 km), its shape varies strongly with estuaries, extended tidal flats, partly protected by sandy islands with deep tidal gullies between them, sometimes with small unprotected islands etc. (fig. 1).

In order to gain more detailed informations and sufficient knowledge about variety and variations in this region, the KFKI (Kuratorium für Forschung im Küsteningenieurwesen) has initiated, supported and coordinated a number of extended projects. One of those was a synoptic survey program of the entire German North Sea Coast in 1974/75, covering an area of about 9.000 km². Moreover, the Board has inspired and promoted a lot of programs in order to sample data and learn about waves, currents, sediments etc. Now the amount of data and knowledge seems to be sufficient to start a demanding and extensive program, i.e. "MORAN".

"MORAN" means "Morphological Analyses of the North-Sea-Coast". The concern and the problems behind this project are manifold. A team of scientists and engineers coming from all German Coastal Engineering Authorities tries to find a way to the roots of morphological changes at the coast. Fundamentals for these investigations are:

- the first quasi-synoptical survey of coastal areas in 1974/75
- a second quasi-synoptical survey of this area in 1979/80
- charts of the changes between both states
- outline of tidal and wind-effected currents
- outline of wave climate
- outline of sediments and geology.

Of course this was already done, for small limited areas, in different parts of the world as case histories, but it will be the first time that this shall be done for an extended, complicated tidal area by synoptical data.

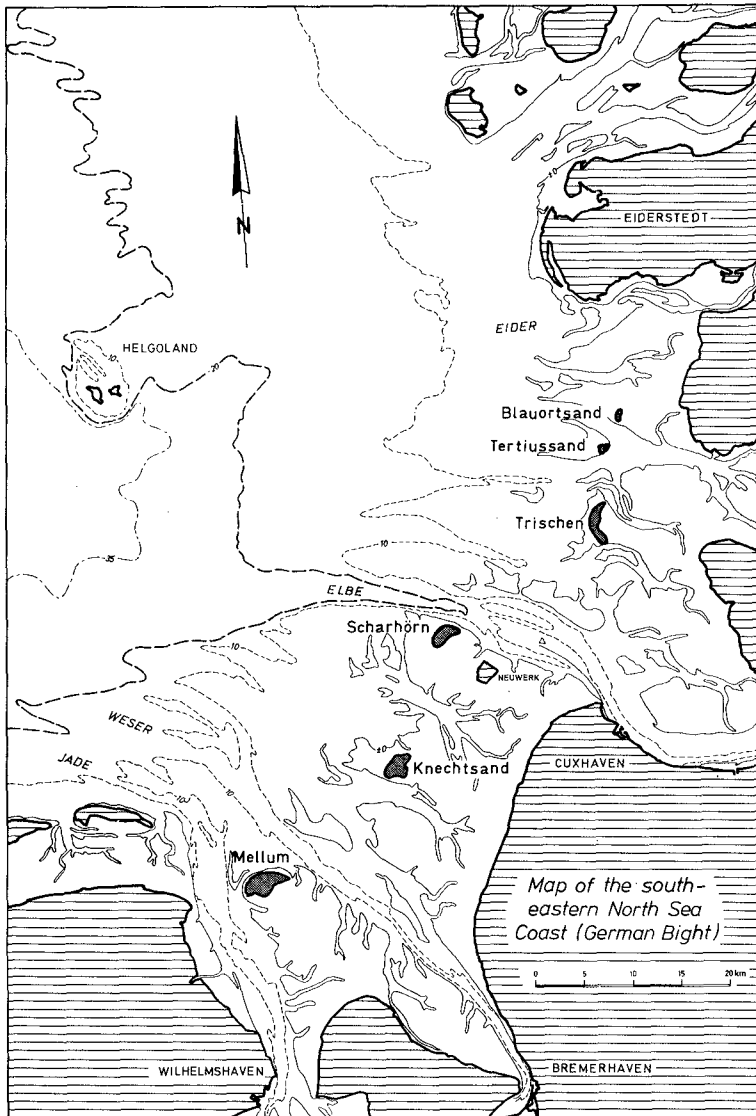


Fig. 1

General Review

The tidal flats and marshes form a transitional zone of an average width of 5 to 7 km in which various tidal flat facies interlock with lagoonal and limnic deposits and peat. These sediments lie on top of an old surface. In the high-lying Pleistocene areas, fluvial erosion and wind-born accretion have formed a rounded wavy relief cut through by separate channels. In the river valleys of the Ems, Weser and Elbe the base of the Holocene has a level surface gently dipping seawards. It corresponds there to the surface of the fluvial Weichselian low Terrace.

The Holocene marine transgression advanced first into these river valleys and channels. At these places there is sometimes a continuous from semi-terrestrial limnic facies to the brackish marine environment, and at other evidence of considerable processes of erosion, reworking and redeposition.

With further rises in sea level the marine influence spread laterally over the low lying regions. In the transitional zone of 5 to 7 km width fine sandy silty tidal flat sediments, mostly rich in lime, were deposited in the seaward part, or silty clayey brackish water deposits with varying lime content. To the landward follow clayey, mainly lime-free sediments with high organic components, and then muds and semi-terrestrial peats. The point of time when marine influenced sedimentation began varies from place to place, according both to its level and how exposed the deposition area was to the sea.

The tides are semidiurnal. The spring tide range lies around 2.6 m with a maximum of 4.1 m. Neap tide range is 1.8 m with a 3.1 m maximum. Mean tidal range in the inner German Bight is about 3 m with possible surges in winter of more than 3 m additional height.

The tidal currents over the flats reach velocities of 30 to 50 cm/s, with a maximum (at storm surges) of 150 cm/s. In smaller channels the current velocities are about 100 cm/s and in large channels sometimes up to 250 cm/s.

Wave movement is a very important factor. Waves procede from various directions and with changing strength. Nevertheless, the predominant movement is from the western sector. The wave movement over the tidal flats is the major factor influencing the distribution of sediments as well as erosion and sedimentation.

Tidal currents and wave movement combine to transport large quantities of suspended load over the tidal flats. Measurements in the Neuwerk flat gave concentrations of sus-

pension of 30 mg/l for a calm tide, and 300 mg/l was reached on a storm flood tide. If account is also taken of the shifting direction and volume with which the tide flows over the flats the transport of sediments during storm surges rises by two to three orders of magnitude.

The water temperature of the body of water which inundates the flats fluctuates greatly and is related to fluctuations in air temperature. In the same way the salt content in the large marine bays also varies, so that in dry summer weather the salt content can rise higher than that in the open sea. In winter the flats cool very much, so that the first ice forms here. When there are strong winds blowing in a landward direction there can be ice pressures which can endanger engineering structures.

Actual Situation

Prototype investigations were intensified during the last two decades. New survey programs have been carried out in the different areas, especially in the mouths of the large estuaries. In the early 1960s current and wave analyses started with concentrations in the areas round the island Norderney and in the Neuwerk/Scharhörn tidal flat complex. Later on a special KFKI project brought intense current investigations along the North Frisian coast, and wave climate measurements were carried out in front of the island Sylt and in the Jade-Weser estuary. Sedimentary and geologic knowledge was gained all over the coastal area with special stress on the region between Weser and Elbe mouths.

All investigations in Germany up to now were not synoptic, but most of them allow general conclusions and can improve our knowledge about the dynamic processes. But till now no attempt was made to include all these in a general survey for the 9.000 km² area in front of the coast.

Of course, we have a lot of examples from all over the world about what is now being done in this MORAN project. Here may be mentioned three of them, standing for others, also from the German coast, that will be incorporated in the actual program:

- One of the tidal channels - the Weser estuary - was presented by Barthel (1977). He investigated the migration of channels and sand banks in the outer Weser estuary from 1910 to 1973. The tendencies are tried to be explained by the predominant current situation.

- Göhren (1975) compared the movement of sand banks in the Elbe estuary (fig. 2), their grain size distributions and their cross sections with recorded currents during storm surges in these exposed tidal flats.
- Stability studies of natural tidal basin systems demand a regime-oriented analysis and a characteristic quantification of the morphological values. Hence Renger (1979) created relative form parameterization dependent on the location by means of a twodimensional system of natural coordinates (elevation and length). The relations derived may prove to be useful in the planning of future constructions and even in understanding and influencing the disadvantageous changes in running systems.

Performance of Project MORAN

Final results will not be available until the second survey will have been evaluated. Because of the vast amount of data this will probably last some years. To get first ideas of how to handle the data most efficiently and how to correlate morphology, topography, hydrology, meteorology and sedimentology, the managing KFKI group decided to select three test regions for a first-step evaluation under the following additional conditions:

- (1) earlier survey results available that can be used as a time series
- (2) no special dredging and depositing areas
- (3) current measurements, wave measurements, and surface sediment investigations during the last decade.

The 3 selected areas are (fig. 3):

- The gully system south of Norderney in a wadden sea area that is protected by an island;
- The unprotected tidal flat of Knechtsand with neighbouring gully systems;
- The wadden sea area west of Büsum, protected only by small islands and sands, in front of a new dike line.

In this first step the choice was influenced by the knowledge that the correlation of morphologic, hydrologic and sedimentologic data surely is simpler there than is in breaker areas or in deep estuaries.

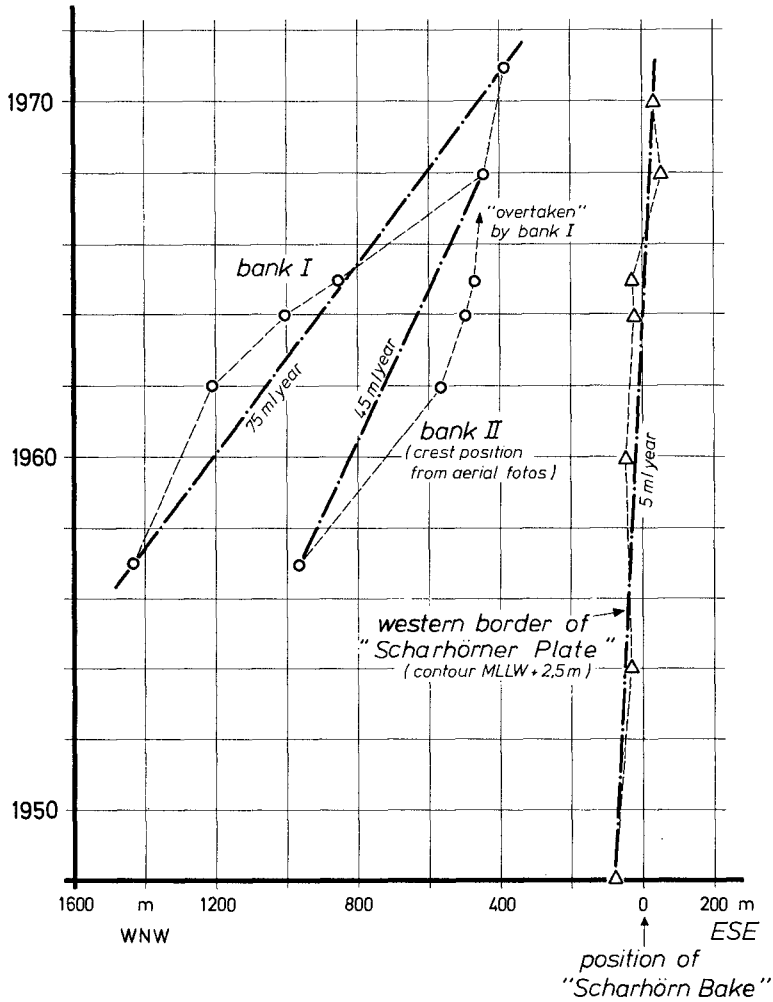


Fig. 2
 Movement of sand banks in the Elbe estuary
 (GÖHREN, 1975)

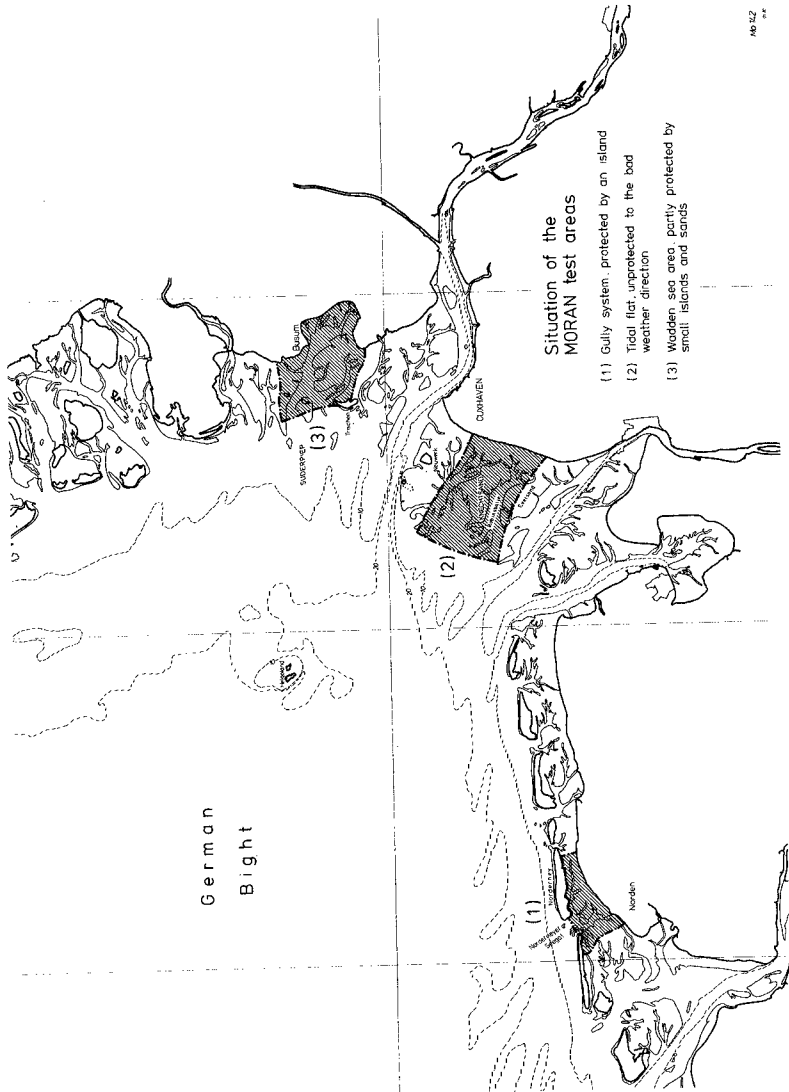


Fig. 3
Southeastern North Sea coast with MORAN test areas

KNECHTSAND AREA

MORPHOLOGIC CHANGES 1974 TO 1979 IN DECIMETERS

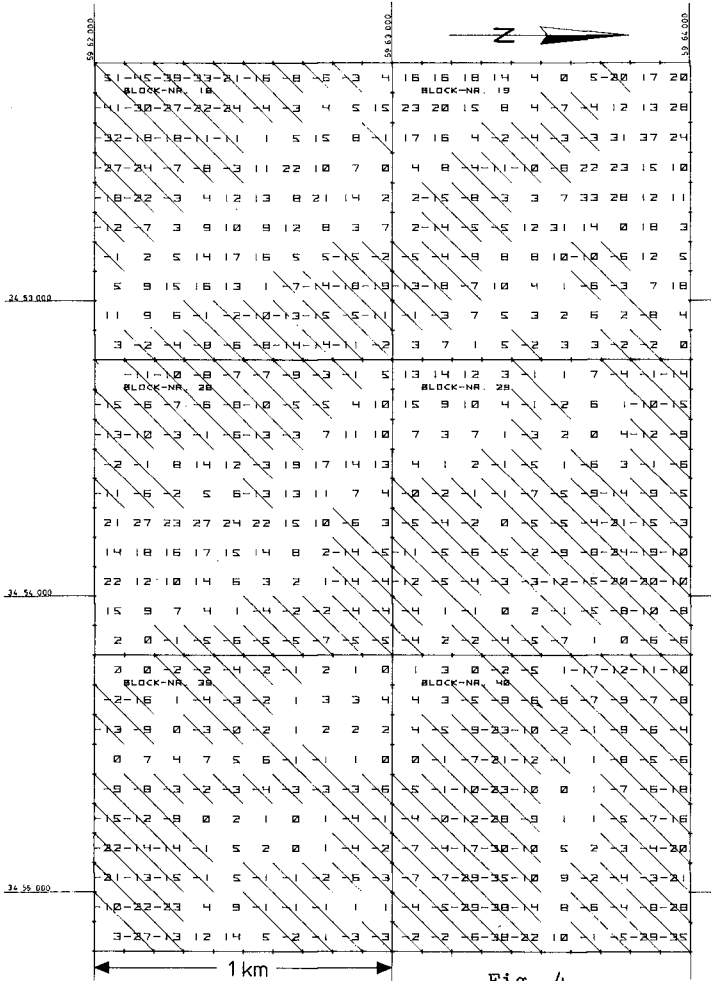


Fig. 4

The MORAN Project

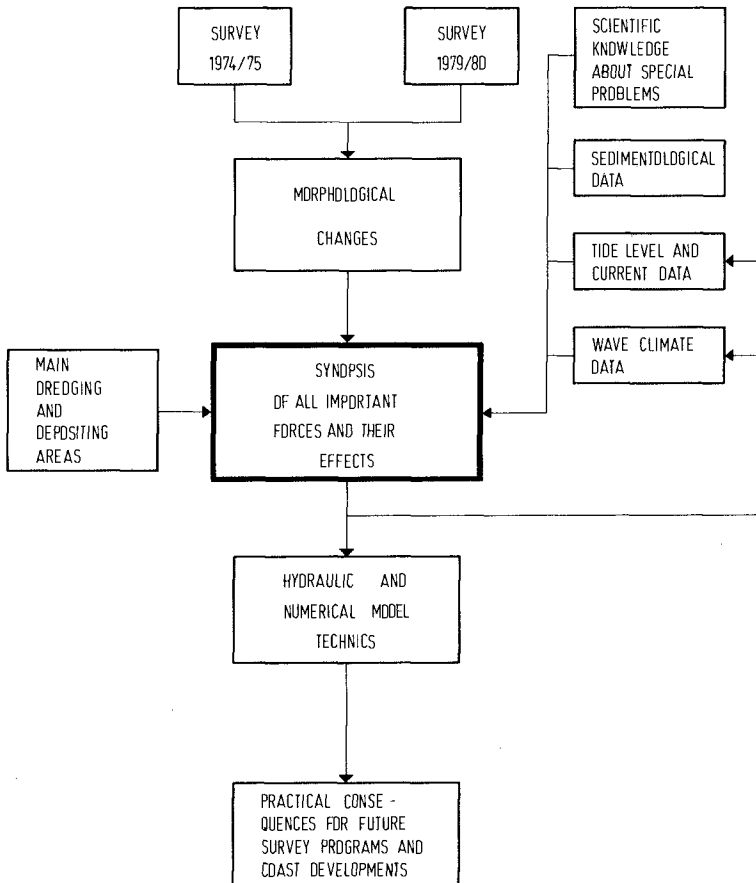


Fig. 5

Pilot Study

The test field is the Knechtsand area. About 1/3 of the survey data of 1974/75 are available in a digitized form. The rest of the data is now being transformed from conventional into digitized form, as is the data of 1979.

We had long discussions about how to evaluate the morphological changes. The result is that we now automatically evaluate mean heights of squares 100 x 100 m out of maps 1:10.000. The grid will be the same for all surveys. The net difference is then evaluated by a computer program and plotted afterwards. First results are shown fig. 4 with max. depth variations in the magnitude of 50 dm within 5 years.

Our Aim

Our aim is to demonstrate in these 3 test fields a synopsis of all available morphologic, hydrologic, sedimentologic and meteorologic informations (fig. 5) in order to find areas of similar morphologic behaviour and by that be able to predict morphological changes during the next decade.

References

- Barthel, V.: Stability of Tidal Channels Dependent on River Improvement. Proc. 15th ICCE, ASCE, New York N.Y. 1977
- Göhren, H.: Dynamics and Morphology of Sand Banks in the Surf Zone of Outer Tidal Flats. Proc. 14th ICCE, ASCE, New York N.Y. 1975
- Harten, H., Vollmers, H.: The Estuaries of the German North Sea Coast. Die Küste, Vol. 32, 1978
- Luck, G.: Islands in Front of the Southern North Sea Coast. Die Küste, Vol. 32, 1978
- Petersen, M.: Islands along the Eastern North Sea Coast. Die Küste, Vol. 32, 1978
- Reineck, H.-E.: The Tidal Flats on the German North Sea Coast. Die Küste, Vol. 32, 1978
- Renger, E.: Two-Dimensional Stability Analysis of Tidal Basins and Tidal Flats of Larger Extent. Proc. 16th ICCE, ASCE, New York N.Y. 1979

ENVIRONMENTAL ASPECTS OF OIL AND GAS
PIPELINE LANDFALLS IN NORTHEAST SCOTLAND

William Ritchie

Professor of Physical Geography,
 University of Aberdeen, Scotland.

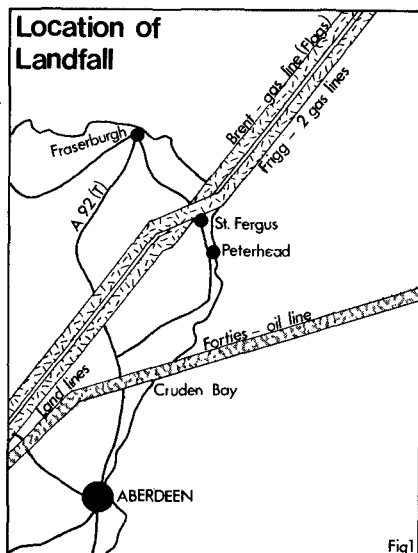
Abstract

Oil and gas pipelines from the North Sea have reached the northeast coast of Scotland from offshore production platforms. The pipelines date from 1973 to 1976. The environmental effects of these pipelines are compared as are the relationships between engineering work, environmental impact assessment and planning procedures. There is also a discussion of methods used to protect and restore these three landfall areas.

Introduction and Setting

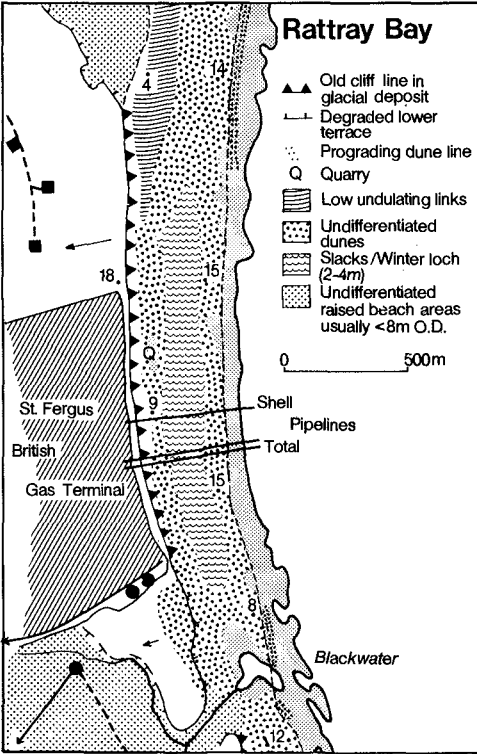
Three oil and gas pipelines make their landfall on the northeast coast of Scotland (Figure 1.). The first pipeline, from the Forties Field, was pulled ashore at Cruden Bay in 1973. Later, pipelines bringing natural gas from the Frigg Field reached the coastline further north at St. Fergus in 1975, to be followed in 1976 by a pipeline (known as the Flags pipeline) from the Brent Field. All three pipelines have very long offshore sections, running up to several hundred kilometres from the production fields. On land, the Forties pipeline goes to a nearby pumping station from which the crude oil is pushed southwards to the refinery at Grangemouth.

In contrast, the gas pipelines at St. Fergus lead a short distance across an area of dunes and links to the St. Fergus Gas Terminal, operated by British Gas (Figure 2). This massive terminal consists of two elements; the larger operational British Gas/Total Oil Marine (U.K.) Ltd.



complex from which the gas is fed via land pipelines into the national gas grid, and a northern extension, which is not yet complete, being developed by Shell to receive and process gas from the Brent Field.

Although separated by 20 km, the landfalls at Cruden Bay and St. Fergus share the common characteristics of the North Sea coastal environment. In particular, the three elements that are



significant relate to tides, waves and near shore sediment movements. The tidal range is approximately 3.0 m but more significant, exceptional tides can elevate the water surface in excess of 4 or 5 metres. These elevations are related to North Sea surges and occur with various periodicities. The maximum increase in height might occur once every hundred or even thousand years but smaller surges of less than a metre have been detected within any given year (Stove, 1978).

Accordingly, the design of coastline structures must be related to these somewhat unpredictable factors.

Fig 2 Sketch Block Diagram Near Pipeline Landfalls

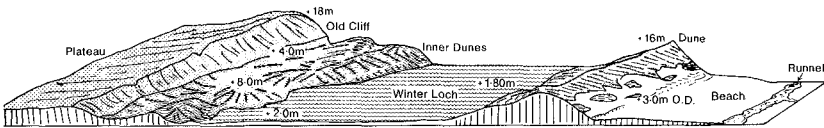




Photo 1. Pipeline Pulling of the Flags Gasline at St. Fergus.



Photo 2. A general view of the St. Fergus terminal and adjacent coastline at an early stage of site work.

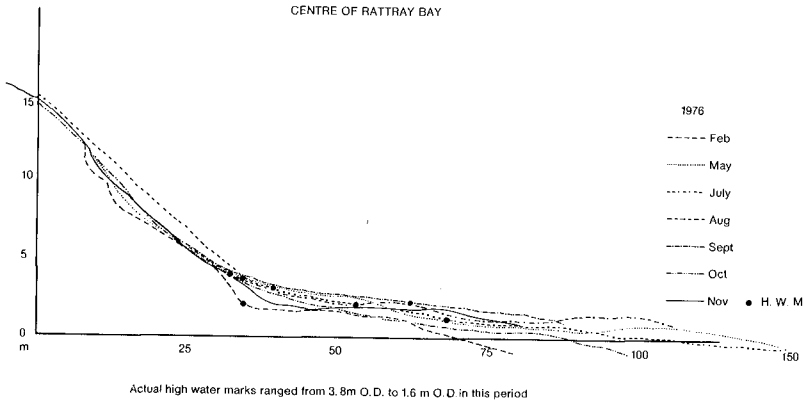
Wave conditions tend to consist of relatively low, short period waves typical of the North Sea basin. Elevations greater than 2 metres are unusual, and the period is normally of the order of 6 to 7 seconds (Buchan 1976, Weatherill 1980). Again, exceptionally high waves can occur when fetch and storm directions coincide, especially from the northeast and easterly directions. Inspection of available meteorological statistics for and local experiences of the North Sea Coast indicate the need to consider the possibility of single highly destructive periods of wave attack. Nearshore sedimentary cover and movement is another variable which is difficult to predict. On the whole, most of the inshore ground is covered by sand or other loose deposits.

Fig 3

1976 SELECTED BEACH PROFILES

(upper and mid- beach)

CENTRE OF RATTRAY BAY



Cruden Bay, for example, being a bayhead structure, appears to have abundant nearshore sediment but offshore surveys show that bedrock is never far from the surface and, in places, outcrops as reefs and shoal areas. Boulder clay on top of rock is particularly common in the St. Fergus area where sand deposits have a patchy distribution and normally occupy the lower areas in the rock platform. The wide sandy beaches are thus somewhat deceptive and although there are migrating sand bars at

and just below low water mark, bedrock outcrops normally lie only a few scores of metres to seaward. The sand bars also appear to be rhythmic and rip cells are common. In fact, the approach of the St. Fergus pipelines to the coast uses an exceptional area of unconsolidated sediments that runs across the rock platform and provides a tract for pipeline burial. In so far as the prediction of sand movements is concerned it is probably correct to state that little is known about nearshore dynamics in both Cruden Bay and St. Fergus. Sediment movements have to be deduced from morphological evidence. Beach profiling revealed that the beach at St. Fergus varied considerably in thickness (Figure 3.). On the basis of these profiles the lowest profile was defined and used as the level below which the pipeline had to be buried under 2m of sand.

Engineering Techniques for Pipe-pulling

For the three landfall areas the engineering technique of pulling strings of large diameter (c. 1m.) coated pipes ashore was essentially the same. Broadly, a trench was cut through the dunes and adjacent surfaces, and maintained by sheet piling. A pulling wire, attached to a powerful winch to the landward, was fixed to the welded pipe strings which were pulled into the sea off a laybarge. (Photograph 1. shows the pipepulling operation for the Flags pipeline at St. Fergus.) This vessel was anchored a few hundred metres offshore and once the landfall was made, the barge gradually worked seawards, laying the pipeline, towards the production platform. After pipe testing and other related work, the onshore end of the sea pipeline was connected to a land pipeline going either a short distance into the Terminal at St. Fergus or for a further 190 kilometres southwards to Grangemouth from the Cruden Bay landfall. Although the same engineering technique was used in both areas the nature of the terrain caused several minor changes to be adopted. Firstly, at Cruden Bay the presence of a high former coastline about a hundred metres inland made the location of the pulling block a difficult one, in so far as the winch was placed on top of this 30m high boulder clay cliff. The actual landfall was made through a beach and dune environment. The dunes at Cruden Bay were only 3m high and relatively protected. The beach was not particularly dynamic and the coastal edge was rarely subjected to wave attack. In short, this was a relatively sheltered landfall and the low sand dune relief provided a relatively simple site for excavation and restoration (Ritchie, 1975). In contrast, the St. Fergus area was much more dynamic and exposed. The dune face was subjected to more frequent wave and tidal contact. The beach was demonstrably more variable in plan and profile (Figure 3). In addition, the dune ridge was up to 14 metres high and retreating in the form of an undercut sand cliff at an estimated rate of up to

half a metre a year. Equally important, there was a long, flat, low, easily flooded strip of land termed the Winter Loch in the lee of the maturely vegetated dune backslope (Photograph 2 and Figure 2). This surface lay beneath the level of high water mark and flooded to a depth of over 30 centimetres from October to April every year. In addition it was recorded as being environmentally sensitive. There is, for example an area of relatively rare vegetation to the north of the landfall and the entire Winter Loch is an important roosting and feeding area for migrant birds. Landwards of this low surface there is a low degraded cliffline cut into glacial deposits. This inner slope leads to a plateau upon which the Gas Terminal was built. For both landfalls at St. Fergus the engineering technique was again that of cutting of a trench down through the dunes and Winter Loch surface to enable wires to run from the lay-barge to the pulling winch on top of the landward plateau some 500m from the beach (Photograph 1). The cutting and sheet piling operations were much more massive than at Cruden Bay. There was also the problem of waterlogging, and the surfaces being crossed were very soft and liable to be damaged easily by the passage of even the lightest vehicle. Moreover, the trench levels at the coast were substantially lower than the beach and the seaward end of the trench required protection from the possibility of flooding and wave damage. As at Cruden Bay there was no question of digging the trench through the inter-tidal beach until a short time before the actual pipe pulling operation.

The first pipe pulling operation, for Total Oil Marine (U.K.) Ltd., required two pipes to be pulled and the trench had to be cut and sheet piled completely across the Winter Loch. Storing sand for back-filling was necessary as it was impossible to take sand from the beach for restoration of the dune ridge. A storage area was therefore required, so that sand excavated during trenching could be used later to replace and restore the dune and adjacent surfaces. The area damaged by the storing operation was equal to that affected by the actual cut. No attempt was made to preserve the turf layer as Marram grass (*Ammophila Arenaria*) tussocks cannot be handled in this way. Later, the Shell pipeline (the Flags Gasline) used a slightly different technique in that the cutting and sheet piling only extended to the limit of the backslope of the coastal dune (Photograph 1). Nevertheless this was also a massive excavation. After excavation however the sand from the cut through the dune was dumped to form an inclined ramp leading, at a gentle gradient, up to the landward plateau where the pulling winch was sited. This ramp provided an access ridge to the cut in the dune. This sand ramp was covered by a nylon sheet upon which was placed crushed rock to form a road bed. The nylon sheet and superimposed road bed were rolled-back after the pipe was pulled and the sand used to backfill the trench and dune breach. As will be demonstrated below, the

the evolution in techniques which were developed successively for the three pipelines was partly the result of experience gained from the earlier operation and partly modified by the nature of the terrain.

Planning Framework

The timing of the three landfalls, 1973, 1975 and 1976 offers an opportunity to compare the evolution of planning processes in relation to industrial developments and related engineering work. Planning approval is normally required for engineering and similar work everywhere in Scotland. Application for permission is made at the District level and major applications are normally also referred to the Regional Authority*. If there are sufficient objections, then the procedure of public inquiry can be instituted. The proposal to develop must satisfy various national and local government acts and statutes. It is not mandatory for an environmental impact statement to be submitted. Unlike current practice in U.S.A. there is no formal procedure for such a submission (for a fuller discussion of issues related to environmental assessment see Chapman, 1981). Nevertheless, over the last few years it has become exceptional for a major developer not to submit some form of environmental impact assessment and/or statement. One of the effects of this flexible situation is that it encourages considerable pre-application discussion. It promotes contact between the developer, the planning authority personnel and interested parties and may lead to a useful interchange of information. In relation to the pipeline landfalls it is probably correct to state that planning for the Cruden Bay landfall took place before the practice of submitting any form of environmental assessment was established. That was not to say that the developer or the contracting engineer did not consider environmental issues, in fact, B.P. Ltd. prepared a massive in-house environmental assessment. In addition, at an early stage, an established environmental scientist was approached to act as consultant with the responsibility for environmental management during site work and to produce proposals for restoration.

For the two developments at St. Fergus environmental

*In Scotland there are three tiers of government, Districts which combine to form a Region. There is also a national dimension in the form of the Secretary of State who is a Cabinet Minister and has the power to call-in any planning application if it is deemed to be in the national interest to do so. The three island regions, Western Isles, Orkneys and Shetland are single tier all-purpose authorities.

assessment procedures and documentation were followed. Nevertheless there was an appreciable difference in the level of assessment, in that the second proposal required fuller statements particularly with regard to ancillary developments. The three pipeline landfalls thus embrace a period of time when planning was evolving to a stage where environmental impact procedures were becoming more widely accepted. Coincidentally it was also the time of local government reform. There was also some changes in the operation of planning functions developed from the Local Government Act of 1972 and Local Government (Scotland) Act of 1973. By 1976 developers and local government agencies had gained experience in these new procedures and a guidance manual was available from the Department of the Environment (Clark, et al., 1976). Although the transitional period is over the stage of rigid statutory procedures has not been reached.

A crucial figure in the linkages between the developer and planning authorities is the environmental scientist. It is difficult to express succinctly how he operates but he is essentially involved in a series of discussions which begin with preliminary proposals that gradually harden into specifications for engineering work. At the same time operational conditions remain of great importance with the need for future restoration being kept continually in mind. It is also useful for the same individual to be involved in monitoring conditions after restoration. That is not to say that he would necessarily produce the full environmental impact statement but would confine himself to those issues that are essentially concerned with the physical environment calling, if need be, on the assistance of other scientists and specialists.

In Scotland, applications for development are submitted to the planning authority which circulates them to three groups; statutory, advisory and informal parties who are invited to comment on the proposal. Since these parties are known there is no objection to prior consultation taking place before the document is submitted. In the long run this saves time and, assuming a constructive approach is taken, leads to a much better environmental statement as well as better planning constraints and conditions. In general there has been little complaint at St. Fergus with the operation of the planning procedures in relation to the pipeline landfalls. In the opinion of the writer much of the success is due to the inherent flexibility of the present planning system.

Inevitably the discussion revolves around different issues for a specific site. At an early stage the construction of an environmental impact matrix allows both developer and planning authority to identify those issues that require further

analysis and information. For example, at Cruden Bay there was little scientific or wildlife interest and even the agricultural interest in the area was minimal. There was some informal beach recreation nearby but the main factor was the presence of a championship golf course only a few metres to the north of the site. At St. Fergus, in addition to the difficult geomorphological situation, particularly that relating to the interface between beach and dune, there was the sensitive and ecologically important environment of the Winter Loch area with important botanical and ornithological interests. At St. Fergus there was little recreational use and the area was not considered as being scenically attractive. This contrasts with Cruden Bay which is undoubtedly a scenic area. There was, therefore, greater interest shown by such bodies as the Scottish Wildlife Trust, The Royal Society for the Protection of Birds, the Nature Conservancy Council and other bodies and individuals in the St. Fergus area. Moreover the scale of development, particularly as the pipeline landfall was only part of the total terminal complex, inevitably produced more local and even national interest. It therefore followed that the exercise of assessing the environmental conditions and the consequence of the operations at St. Fergus became a much larger and more comprehensive exercise.

Nature of Environmental Assessments for Cruden Bay and St. Fergus

The Cruden Bay development did not require an environmental impact statement although as stated previously a comprehensive assessment was prepared internally by B.P. Ltd. During the course of site work written comments were prepared for the developer and the site engineer, relating site work to such environmental issues as prevention of erosion and sand deposition. Implicit in many of these guidance notes were arrangements that looked ahead to the stage of reinstatement. After the pipe was pulled and tested the ground was restored to specifications drawn up by the environmental consultant with the approval of the local planning authority.

At St. Fergus environmental impact assessments were prepared. Essentially the approach consisted of balancing three sets of information. Firstly, it was necessary to understand the construction and operational techniques that would be employed by the developer and his agents. Secondly, the attitude of the planning agencies had to be ascertained. Normally this consists of determining the types of questions that the planning authority and possible objectors would ask of the developer (see Clark et al, 1976). The third factor to be considered was the specific attributes of the landfall area. The environmental impact assessment took the form of a matrix which divided the different parts of the landscape into separate elements, as for

example, drainage, vegetation, surface stability and so on. The remainder of the table consisted of the three phases of work; that is, the construction phase (to cut the pipeline trench), the operational phase and the restoration phase. The matrix approach proved to be an acceptable method of presentation and analysis particularly as each impact was assessed on a simple scale of low, moderate, high, and in the case of a "high" assessment, the issue was discussed at length in a complementary text. The whole document was prefaced by a description of such general factors as weather conditions and physiographic setting.

Having completed this exercise for the three landfill sites it is possible to indicate some of the problems that arise in such work. On the one hand there is the need to collate existing information on the area. This may vary greatly in quality and quantity. There are gaps in basic environmental information. Accordingly, if time is available, it is necessary to obtain information by conducting surveys or commissioning particular studies. For some environmental variables this is not possible and it is necessary to make assessments that are based on theoretical knowledge and/or from indirect evidence. Experience also shows that should objections arise they often revolve around what can only be described as vague issues and terminology. One may contrast, for example, an environmental impact such as produced by sound or heat radiation, (these impacts are calculable and can be compared against statutory limits and regulations), with issues that derive from the opinion of an observer. The word environment itself is vague. Similarly, how does one assess a criticism that cites "disturbance to wildlife" or, how does one evaluate the effect on the scenic appearance of an area? There is no easy way to resolve these arguments other than by discussion with the parties involved so that some consensus of opinion can be obtained. In the end these issues have to be considered against relative rather than absolute standards. Another issue which is worth stressing is the need for all parties to recognise that there will always be gaps in the environmental knowledge for any given area, and that these gaps cannot be filled in the time available, if at all. For example at St. Fergus an important issue is the movement of sediment in the nearshore area. Anyone with a basic knowledge of coastal geomorphology will recognise that this fundamental question is incredibly difficult to answer and would require considerable instrumentation and time to establish a measure of the amount and direction of potential sediment movement. Environmental restoration is also a difficult problem. At St. Fergus, and to a lesser extent at Cruden Bay, it was also made clear from the outset that full environmental restoration was impossible. This was particularly true at St. Fergus where the eroding coastal dune and the maturity of the vegetation on the backslope and Winter Loch area created insurmountable difficulties for full and complete

restoration programmes. The argument was presented that restoration should aim to produce a surface that was compatible and similar to adjacent areas. It was thought that in the fullness of time natural forces would probably achieve an ecological situation that was increasingly similar to adjacent areas. It would be wrong for the writer of an environmental impact statement and the developer who contracts such a survey to claim that an exact replacement of a complex habitat and environment such as that pertaining to a changeable open beach and eroding, mature sand dunes would be attainable. Equally it is unreasonable for a planning authority to expect such replication. In dealing with an environmental impact statement for a natural landscape area such as a dynamic coastline a truly scientific and comprehensive evaluation of the physical and biological environment is not possible. One should look for a more general statement, backed up as far as possible by all available scientific evidence, to which one should add knowledge gained from comparative experience augmented by whatever site and local surveys are feasible. It is important that the developer and the planning authorities accept the limitations of such an approach. Nevertheless, the environmental assessment and statement are major advances in the functional relationship between planning and industrial development. They provide an invaluable common basis for worthwhile discussion which should lead to sound engineering practice and good environmental management. The experience of the North Sea pipelines would show that this approach is successful but one would not recommend that the environmental impact assessment process should become more structurally defined and rigid. The success of the projects at Cruden Bay and St. Fergus can, at least partially, be related to the use of environmental assessment statements and similar documents but just as important has been the flexibility and exchange of information that has been involved in producing, interpreting and discussing these documents.

Environmental Restoration - Case Studies

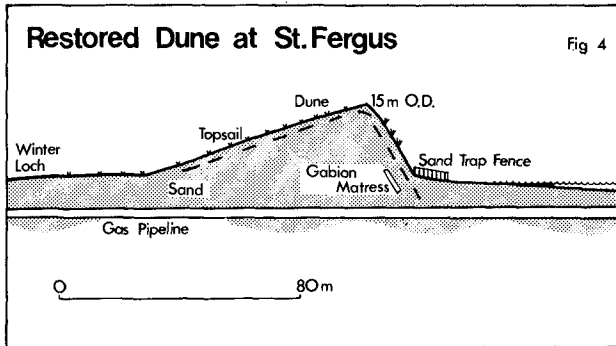
The Cruden Bay site was developed by B.P. Ltd. and they had selected what is arguably the best landfall site on the coast (Figure 1). It is a low energy, protected environment with little ecological or recreational interests. The only problem was the championship golf course nearby. The methods used to restore the surface were straightforward and largely adapted from the experience gained by workers in Holland on similar dune restoration problems. (For a useful summary see Brooks, 1979 or Quinn, 1977.) One of the important methods was the use of brushwood cuttings from local coniferous plantations. These branches were used to construct sand trapping fences and, later, they were used to clad the seaward face of the reconstructed dune. It should be stressed that the area involved in restoration was very small. The dune frontage was about 40 metres and the pipeline

trench and associated areas was of the order of 120 metres long. It is of interest that approximately the same area was affected by the need to store sand for back filling. The surface was restored in two stages since the landward end of the pipe had to remain open for several months for pipe testing procedures. Accordingly the access road was the last feature to be restored. Essentially the original profile was restored, but the dune face was set back and lowered slightly. The surface was then covered by a thin layer of top soil and seeded using a mixture determined by a local grassland expert. The alternative of leaving a bare surface and allowing natural recolonisation by plants was eschewed since sand might have blown onto the adjacent golf course. The crest was protected by a fence, designed to trap sand, but having an equally important function in preventing pedestrian access. The dune face was covered in brushwood and held down by netting. Dune grasses, Marram and Sea Lyme, were hand planted through this cover. Excess sand was deposited on the beach nearby. The remaining material that was used with great success was a water based bitumen compound called Crelawn, which not only held the surface stable but also promoted early and vigorous plant growth (Ritchie, 1975).

The success of this operation was obvious from the outset. Vegetation growth was rapid and the signs of engineering work disappeared within a year. At this stage it was possible to remove fences and other small structures. The beach surface was restored naturally by wave action within a few days. The situation now about seven years later is that the site is indistinguishable from adjacent areas. A botanical survey has shown that some of the early exotic species have been replaced by more local vegetation types. The dune face has built up, aided by the transfer of the excess sand from the beach. There is little sign of any brushwood or other devices used to promote restoration. Although one is tempted to suggest that this restoration was a product of good techniques, it is also important to stress that this was a particularly favourable location.

In contrast the sites at St. Fergus were recognised from the outset as being much more difficult. The scale of operation was larger and the coastline more open and changeable. Early discussions with the first developer, Total Oil Marine (U.K.) Ltd., emphasized that it would probably be impossible to provide complete restoration. The aim was to produce a surface that was similar to adjacent areas and to produce a series of landforms that effectively produced the same degree of stability and protection to the important Winter Loch zone to the landwards. At the St. Fergus site the same working procedures were involved as had been used at Cruden Bay but the area was much greater. There were also substantial delays in the timetable of sitework and pipe pulling,

related largely to the difficult progress of the offshore programme. Accordingly the period of storage of sand for backfilling was very long. There was also a protracted period of vehicle movements in all seasons across the various surfaces. The main access track required a surface bed of broken granite. The delay, a long storage period and considerable vehicle traffic across an artificial road bed combined to add to the problems of final restoration. The sequence of restoration consisted of replacing the sand in such a way as to restore the original profile. After considerable discussion it was agreed that a useful "insurance" should be pro-



vided by inserting a toe protection of gabions, buried at the base of the dune on the seaward face (Figure 4). The arguments of such emplacement concerned the need to protect the dune face in the interim period between restoration and the achievement of natural stability. The fear was that in this critical period the dune might be attacked by an exceptionally high water level with destructive waves. In the event, this did not happen and the gabion wall remains as a fail-safe device beneath about 1.5 metres of surface sand. The same device, for the same reasons, was used on the Shell pipeline landfall a hundred metres to the north. Once the profile was restored it was held in place by stretching old fishing nets from the toe of the dune over the crest and down the back-slope. A further 30 centimetres of sand was added, and the crest and back-slope were covered by a layer of topsoil. (Unfortunately in this particular area the topsoil proved to be of very low quality, with a high clay content, and this has led to some minor problems which had to be rectified at a later date.) The seaward face, crest and

backslope were then replanted. The backslope was planted by standard agricultural techniques using a carefully selected mixture of agricultural grasses. A small proportion of "wild" flower and grass species were also used; the species being selected from the list of plants that was compiled before site work commenced. A similar procedure was used for the Winter Loch surface. An open pattern of Marram grass was replanted by hand on the backslope although it was realised that it would have little chance of vigorous growth, as there was little sand accretion in the lee of the dune crest. The seaward face was hand planted exclusively with Marram grass.

Since the work was completed in 1976 it has been possible to assess the success of the various procedures. The best feature, and the feature that satisfies the prime need of protection, is that of the seaward face. There has been vigorous growth and ample sand accretion. This was certainly aided by constructing sand trapping fences at intervals along the toe of the dune. The backslope has been the least successful area for although growth was initially good this seems to have been aided more by the application of fertilizer than by any natural factors. It should be added that immediately after planting the weather for the next two years was exceptionally bad. There being periods of heavy rain followed by a summer of near-drought conditions. The situation was further exacerbated by the clay content of the top soil which is relatively impervious and caused surface runoff problems. The problem of compaction and the difficulty of removing all the crushed stone from the Winter Loch area also proved to be a problem and it is fortunate that the developer agreed to a second phase of restoration work so that this problem could be solved by a second period of surface clearing and reseeded. There were also minor drainage problems to the landward which were quite unforeseen and related to wider drainage changes brought about by the construction of the main terminal site. These highly localised problems were also solved but they emphasize the need for some form of monitoring programme for up to five years after site work is finished. Further north the same landform zones were breached by the trench for the Shell pipeline and with the experience of the B.P. Landfall at Cruden Bay and the Total Oil Marine (U.K.) Ltd. site a hundred metres or so to the south it was possible to anticipate some of the problems and refine environmental and restoration advice accordingly. It is possible to highlight these although one must stress that the techniques used were, in the main, the same as had proved successful on the two previous sites. One of the advantages was the greater lead-time which made it possible to complete a more thorough survey of the area before site work, this included a careful topographic survey. It was also possible to confine the working area by fencing before any vehicle reached the site area. Corridors

were established beyond which the areas were regarded as inaccessible. Since the storage of sand had proved to damage rather large areas, excavated sand was used to produce a ridge which descended at a low gradient to the dunes and became the bed for the access track and pulling wires (Photograph 1). This greatly reduced the area of surface damage. The sand ridge also had engineering advantages and these have already been described. After pipe pulling the sand ridge was used to fill the gap in the dunes, and the Winter Loch and adjacent surfaces were then carefully lowered to their previous elevation and slope. Exactly the same procedures were used for the dune face, the back-slope and Winter Loch surfaces as had been used previously with the significant difference that good quality top soil was imported to cover the backslope and Winter Loch surfaces. Another minor difference was that the seed mixture was cross-drilled rather than surface spread. This gave better establishment. In all other respects the methods and the progress has been similar to that of the other pipelines.

It is too early to judge the success of both St. Fergus operations but it is possible to state that the initial objectives have been satisfied in that environmental damage and disturbance was minimal and there were few if any side effects on adjacent areas and surfaces. The dune ridge is undoubtedly stable and providing a barrier which is equal if not superior to the original dune ridge. The hydrology of the Winter Loch surface has been restored and there are already signs that the vegetation is changing to that of its previous condition and the ecology, particularly the use of the area by birds, is little different from what it was before the onset of engineering work. It would be untrue to claim that the area is now indistinguishable from adjacent areas. Unlike Cruden Bay it was never felt that this was possible. The areas which give rise to least satisfaction are the backslope zones. It is doubtful if they will ever have their former Marram dominated, mature, tussocky appearance. Their pre-existing state was a sensitive combination of soil and micro-climatic conditions sustained by a precise input of blown sand escaping from the eroding front of the dune. By stabilizing the dune face and promoting vigorous vegetation growth the escape of sand to the backslope has been prevented. Since Marram grass requires an input of fresh sand for growth the situation is obviously one where a definite decision had to be taken. To achieve vigorous Marram growth one would have to have left large areas of dune face and back-slope bare of vegetation to enable sand to move freely across the dune crest. To do this would obviously have raised the possibility of severe sand erosion which could have disrupted the entire restoration programme; not only by creating blow-outs on the dune ridge but by transferring excessive amounts of sand to the fragile Winter Loch environment inland. Since priority was

given to physical stability it was obviously unacceptable to leave any areas bare of vegetation for any length of time.

Summary

Restoration and environmental work at Cruden Bay and St. Fergus has demonstrated the reciprocal advantages of environmental assessment and impact statements to the developer, the engineer and planner. It has also shown the value of early and informative discussions between the developer, site engineer, planning agencies and environmental consultants. It has also suggested the need for careful specific site selection in that some areas are manifestly easier to manage and restore than others. In this respect it is possible to recommend that an environmental consultant should be used before the precise site is chosen. No new techniques have been developed as a result of these three operational situations, although the policy of pre-determining access and working areas has been a useful innovation. Otherwise, the actual programme consisted of using techniques and methods developed elsewhere; they have simply been modified to suit particular local conditions. It has also been demonstrated that after restoration there is a need for a continuing monitoring programme to last at least 5 years. It has also shown that the developer needs to accept a commitment to review the progress of restoration work particularly in such dynamic and potentially fragile environments as the coastal zone. Management does not end when the pipelines come ashore. The input of capital and personnel for such monitoring is not great, amounting to little more than a few visits each year but this small provision will provide considerable benefits. It will also serve to improve or consolidate the relationships between the local community, the planning authority and the developing agent. At St. Fergus this has gone one stage further and the area including the restored ground has now assumed that status of Local Nature Reserve, with a Management Committee consisting of representatives of conservational interests and the pipeline and terminal operators.

Acknowledgements

The author wishes to record his gratitude to B.P. Ltd., Total Oil Marine (U.K.) Ltd. and Shell (Exploration and Production) Ltd. for financial assistance and permission to use the above information and data. Thanks are also expressed to Land and Marine Engineering Ltd. for technical advice and the use of Photograph 1. Dr. K. Chapman also provided valuable advice on matters relating to environmental impact assessment.

REFERENCES

- BROOKS, A. 1979 Coastlands. British Trust for Conservation Volunteers. London.
- BUCHAN, G.M. 1976 Dynamics of a river-mouth spit and related processes in Aberdeen Bay, Scotland. Unpublished Ph.D. thesis. University of Aberdeen.
- CHAPMAN, K. 1981 Issues in environmental impact assessment. Progress in Human Geography (in press). London.
- CLARK, B.D.,
CHAPMAN, K.,
BISSET, R. and
WATHERN, P. 1976 Assessment of major industrial applications: a manual. Department of the Environment Research Report 13., London.
- QUINN, A. 1977 Sand Dunes: Formation, Erosion and Management An Foras Forbatha. Dublin.
- RITCHIE, W. 1975 Environmental problems associated with a pipeline landfall in coastal dunes at Cruden Bay. Coastal Engineering. 3, American Soc. of Civil Engineers, pp. 2568-2581.
- STOVE, G.C. 1978 The hydrography, circulation and sediment movements of the Ythan Estuary. Unpublished Ph.D. thesis. University of Aberdeen.
- WEATHERILL, P.J. 1980 Personal communication.

STATISTICAL PROPERTIES OF RANDOM WAVE GROUPS

AKIRA KIMURA^{*}

ABSTRACT

This study deals with the statistical properties of the group formation of random waves determined by the zero-up-cross method. Probability distributions about

- (1) the run of high waves
- (2) the total run
- (3) the run of resonant wave period

are derived theoretically providing that the time series of wave height and wave period form the Markov chain. Transition probabilities are given by the 2-dimensional Rayleigh distribution for the wave height train and the 2-dimensional Weibull distribution for the wave period train. And very good agreements between data and the theoretical distributions have been obtained. Then the paper discusses those parameters which affect the statistical properties of the runs and shows that the spectrum peakedness parameter for the run of wave height and the spectrum width parameter for the run of wave period are the most predominant.

INTRODUCTION

It is often observed in the field observations that a large wave makes a group with another large waves. This characteristic of sea waves makes significant effects on several coastal engineering problems such as slow drift oscillation of vessel, stability of rubble mound, drainage of overtopping discharge and some other problems.

Arranging order of random waves is usually analyzed with a concept of the run. There have been two kinds of theoretical studies on the run of random sea waves. One is done by Goda(1) and the other is done by Ewing(2) and Nolte-Hsu(3). Goda derived the probability distribution providing the randomness of waves. On the other hand Ewing, Nolte-Hsu derived the probability distributions providing the narrow band spectrum. As the result of this assumption, succeeding several waves correlate each other. However several authors pointed that consecutive wave heights correlate each other, but the correlation of alternative wave heights diminishes nearly zero.(4),(5),(6) Then random wave height train seems to have a intermediate characteristics between these two theoretical assumptions.

Sawhny(7) examined the time series of crest-to-trough wave height by means of the Markov chain and found that consecutive three half waves

* Assistant Professor of Department of Civil Engineering, Faculty of Engineering, Tottori University, Tottori, Japan

correlate each other. Recently the author(8) showed that time series of zero-up-crossing wave height and wave period have properties very close to those of the Markov chain and that their transition probabilities may well be approximated with the 2-dimensional Rayleigh distribution and the 2-dimensional Weibull distribution respectively.

RUN OF WAVE HEIGHT

Transition equation of the Markov chain is given as:

$$p_n = p_0 P^n \tag{1}$$

where p_0 is a initial distribution, p_n is a distribution after n time transitions and P is a transition probability matrix. If wave height train h_j ($j=1,2,3, \dots$) are classified into the following states with reference to the standard wave height h_* :

$$\left. \begin{aligned} \text{State 1 : } & 0 < h_j \leq h_* \\ \text{State 2 : } & h_* < h_j \leq 2h_* \\ \dots\dots\dots & \dots\dots\dots \\ \text{State i : } & (i-1)h_* < h_j \leq ih_* \\ \dots\dots\dots & \dots\dots\dots \end{aligned} \right\} \tag{2}$$

$\dots\dots\dots (j=1,2,3, \dots)$,

then transition probability matrix is given by the following equations.

$$P = \begin{pmatrix} P_{11} & P_{12} & P_{13} \dots \\ P_{21} & P_{22} & P_{23} \dots \\ P_{31} & P_{32} & P_{33} \dots \\ \dots\dots\dots \end{pmatrix} \tag{3}$$

where

$$P_{ij} = \int_{(j-1)h_*}^{jh_*} \int_{(i-1)h_*}^{ih_*} p(h_1, h_2) dh_1 dh_2 / \int_{(i-1)h_*}^{ih_*} Q(h_1) dh_1 \tag{4}$$

$(i,j=1,2,3, \dots)$,

in which:

$$p(h_1, h_2) = \frac{4h_1 h_2}{(1-4\rho^2)h_r^4} \exp\left[-\frac{1}{1-4\rho^2} \left(\frac{h_1^2 + h_2^2}{h_r^2}\right)\right] I_0\left[\frac{4h_1 h_2 \rho}{(1-4\rho^2)h_r^2}\right] \tag{5}$$

$$Q(h_1) = \frac{2h_1}{h_r^2} \exp\left[-\frac{h_1^2}{h_r^2}\right] \tag{6}$$

h_r is the rms wave height, ρ the correlation parameter, I_0 the modified Bessel function of the 0-th order. Eq.(5) is the 2-dimensional Rayleigh distribution and eq.(6) the Rayleigh distribution. Correlation coefficient of consecutive wave height h_1 and h_2 is:

$$\gamma_h = \frac{E(2\rho) - 1/2(1-4\rho^2)K(2\rho) - \pi/4}{1 - \pi/4} \tag{7}$$

in which K and E are the complete elliptic integrals of the first and second kind respectively. In fig.1 the curve(n=2) shows the relation between γ_h and ρ . It follows that p_{ij} in eq.(3) can be determined from the correlation coefficient of consecutive wave heights by using eqs.(4), (5),(6) and (7).

ESTIMATION OF THE SUCCEEDING WAVE HEIGHT

The problem to estimate the succeeding wave height h_2 from the present wave height h_1 is treated as follows:

If the present wave height h_1 falls in the State i, p_0 is given as:

$$p_0 = (0, 0, \dots, 1, \dots) \tag{8}$$

Substituting eq.(8) into eq.(1), distribution p_1 becomes

$$p_1 = (p_{i1}, p_{i2}, \dots) \tag{9}$$

Element p_{ij} (j=1,2, ...) is given by eq.(4). If h_* in eq.(4) is sufficiently small, expectation of h_2 is:

$$\begin{aligned} \bar{h}_2 &= \int_0^\infty h_2 p(h_2|h_1) dh_2 \\ &= \int_0^\infty \frac{2h_2^2}{(1-4\rho^2)h_r^2} \exp\left[-\frac{(h_1^2 + h_2^2)}{(1-4\rho^2)h_r^2} + \frac{h_1^2}{h_r^2}\right] I_0\left[\frac{4h_1h_2\rho}{(1-4\rho^2)h_r^2}\right] dh_2 \end{aligned} \tag{10}$$

where $p(h_2|h_1)$ is the conditional Rayleigh distribution. Fig.2 shows the relation of \bar{h}_2/h_r and h_1/h_r . It shows that according to the increase of γ_h , \bar{h}_2 approaches h_1 . But when γ_h equals 0, \bar{h}_2/h_r is always $\sqrt{2}/2$.

RUN OF HIGH WAVES

The run of high waves which exceed the standard wave height h_* is one of our greatest concern. In this problem, time series of wave height:

$$\dots, h_{i-1}, h_i, h_{i+1}, h_{i+2}, \dots \tag{a}$$

are classified into two states. One is $h < h_*$ and the other is $h \geq h_*$. If these states are distinguished with suffixes 1 and 2 respectively, eq.(3) is reduced to:

$$p = \begin{pmatrix} P_{11} & P_{12} \\ P_{21} & P_{22} \end{pmatrix} \tag{11}$$

where

$$p_{11} = \int_0^{h_*} \int_0^{h_*} p(h_1, h_2) dh_1 dh_2 / \int_0^{h_*} Q(h_1) dh_1$$

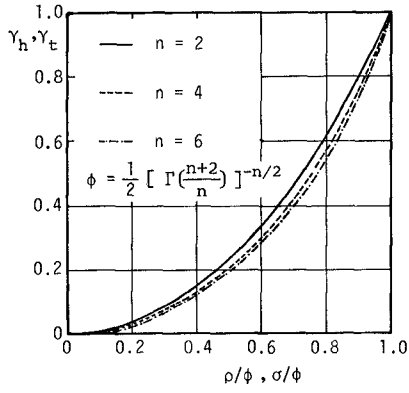


Fig.1 $\gamma_h \sim \rho/\phi$, $\gamma_t \sim \sigma/\phi$

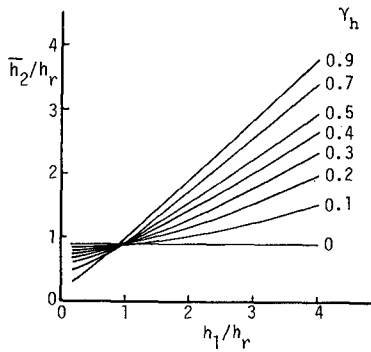


Fig.2 $\bar{h}_2/h_r \sim h_1/h_r$

$$\begin{aligned}
 p_{12} &= \int_{h_*}^{\infty} \int_0^{h_*} p(h_1, h_2) dh_1 dh_2 / \int_0^{h_*} Q(h_1) dh_1 \\
 p_{21} &= \int_0^{h_*} \int_{h_*}^{\infty} p(h_1, h_2) dh_1 dh_2 / \int_{h_*}^{\infty} Q(h_1) dh_1 \\
 p_{22} &= \int_{h_*}^{\infty} \int_{h_*}^{\infty} p(h_1, h_2) dh_1 dh_2 / \int_{h_*}^{\infty} Q(h_1) dh_1 ,
 \end{aligned}
 \tag{12}$$

in which $p(h_1, h_2)$ and $Q(h_1)$ are given by eqs.(5) and (6).

The run of high waves starts when a wave height exceeds h_* initially. Suppose $h_{i-1} < h_*$ and $h_i \geq h_*$, in the wave height train (a). The run starts from h_i . The initial distribution p_0 is (0,1). Substitution of p_0 and eq.(11) into eq.(1) gives:

$$\begin{aligned}
 p_1 &= (p_{21}, p_{22}) \quad \dots (n=1) \\
 p_2 &= (p_{21}p_{11} + p_{22}p_{21}, p_{21}p_{12} + p_{22}^2) \quad \dots (n=2) \\
 &\dots \dots \dots
 \end{aligned}$$

p_{21} is the probability that $h_i \geq h_*$ and $h_{i+1} < h_*$. Then the first element of p_1 gives the probability that the length of run is 1. But the first element of p_2 does not give the probability that the length of run is 2. That is, since $p_{21}p_{11}$ is the probability that $h_i \geq h_*$, $h_{i+1} < h_*$ and $h_{i+2} < h_*$, only $p_{22}p_{21}$ gives the probability that the length of run is 2. The elements which give the transition probability from State 1 should be precluded since they have no relation to the run of high waves. Finally transition probability matrix becomes:

$$P = \begin{pmatrix} 0 & 0 \\ p_{21} & p_{22} \end{pmatrix} \tag{13}$$

By substituting initial distribution and eq.(13) into eq.(1),

$$\begin{aligned}
 p_1 &= (p_{21}, p_{22}) \\
 p_2 &= (p_{22}p_{21}, p_{22}^2) \\
 &\dots \dots \dots \\
 p_\ell &= (p_{22}^{(\ell-1)} p_{21}, p_{22}^\ell) \\
 &\dots \dots \dots
 \end{aligned}
 \tag{14}$$

By simple induction, probability distribution of the run of high waves is represented by:

$$p_1(\ell) = p_{22}^{(\ell-1)} p_{21} = p_{22}^{(\ell-1)} (1-p_{22}) , \tag{15}$$

where ℓ is the length of the run. Mean length of the run is defined as:

$$\bar{\ell} = 1/(1-p_{22}) \quad (16)$$

Fig.3 (a), (b) and (c) show the probability distribution of the run of high waves for (a) $h_* = h_{\text{mean}}$, (b) $h_* = h_{1/3}$ and (c) $h_* = h_{1/10}$ respectively. When γ_h equals 0 in each figure, the theoretical distribution corresponds to the Goda's theory.

By analogy, the probability distribution of the run of low waves which fall below h_* consecutively can be given as:

$$p_2(\ell) = p_{11}^{(\ell-1)} p_{12} = p_{11}^{(\ell-1)} (1-p_{11}), \quad (17)$$

where ℓ is the length of the run of low waves. p_{11} is given by eq.(12).

Fig.4 shows the mean length of the run of low waves for $h_* = h_{\text{mean}}$ (solid line), $h_* = h_{1/3}$ (dotted line) and $h_* = h_{1/10}$ (chain line). Mean duration in which high waves do not take place can be estimated from this figure.

TOTAL RUN (1)

From eqs.(15) and (17) the probability distribution of the total run can be introduced.

$$p_3(\ell_0) = \frac{(1-p_{11})(1-p_{22})}{p_{11} - p_{22}} (p_{11}^{\ell_0-1} - p_{22}^{\ell_0-1}), \quad (18)$$

where ℓ_0 is the length of the total run. Mean length of ℓ_0 is:

$$\bar{\ell}_0 = 1/(1-p_{11}) + 1/(1-p_{22}), \quad (19)$$

in which p_{11} and p_{22} are given by eq.(12). Fig.5(a) and (b) show the probability distribution of the total run for (a) $h_* = h_{\text{mean}}$ and (b) $h_* = h_{1/3}$.

Equations (15) to (19) are determined from γ_h or ρ with eqs(5), (6) and (12). Figs.6 and 7 show the theoretical relations of $p_{11} \sim \gamma_h$ and of $p_{22} \sim \gamma_h$ respectively, providing that $h_* = h_{\text{mean}}$ (real line), $h_* = h_{1/3}$ (broken line) and $h_* = h_{1/10}$ (chain line).

VERIFICATION OF THE THEORETICAL PROBABILITY DISTRIBUTIONS

It is very difficult to obtain random sea waves which are long enough and statistically stationary to examine the properties of run. Therefore some numerical simulation techniques (9) have been used to generate random wave trains. Fig.8 shows the target spectra of five cases used in the numerical simulations. Slope of the spectrum changes from minus 4th to 8th power of frequency in the high frequency region. 5000 waves have been generated in each case.

Figs.9 (a) ~ (e) show the comparison between data and the theoretic-

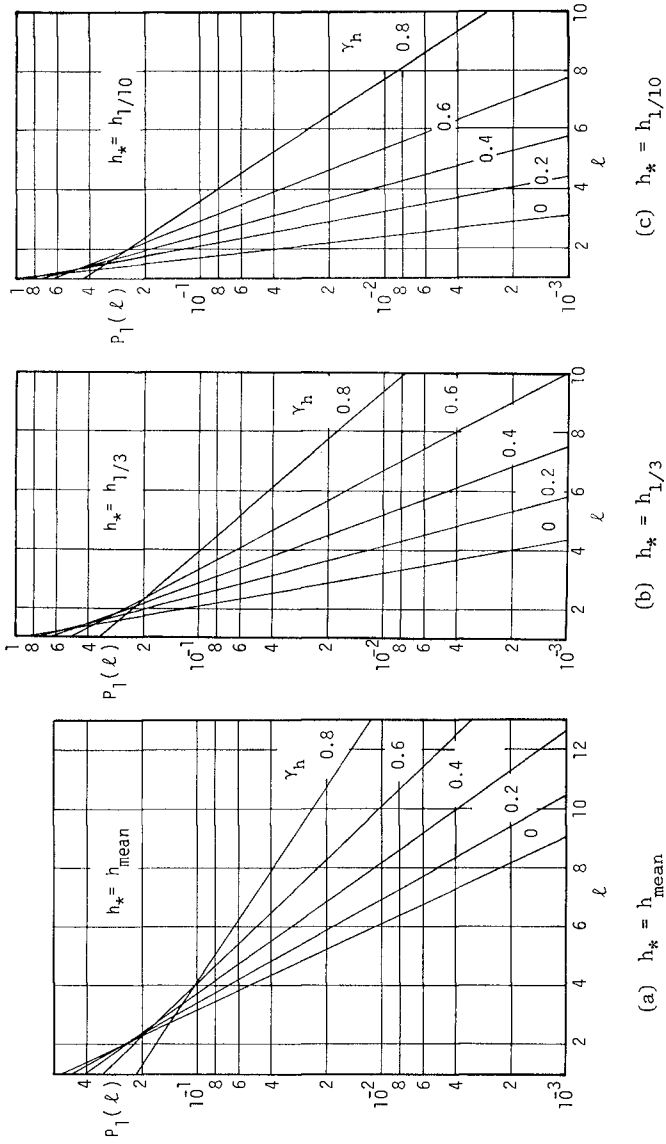


Fig. 3 Probability distribution of the run of high waves

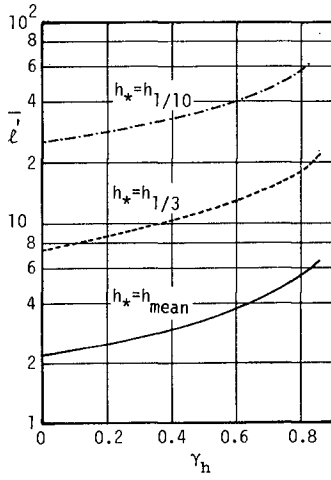


Fig. 4 Mean length of the run of low waves

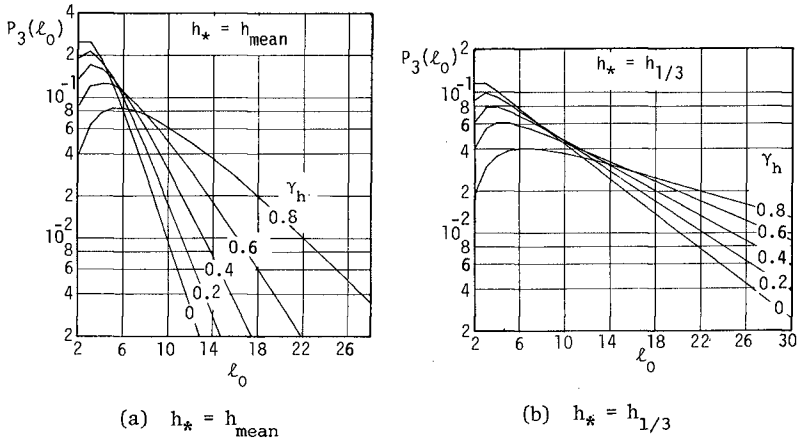


Fig. 5 Probability distribution of the total run

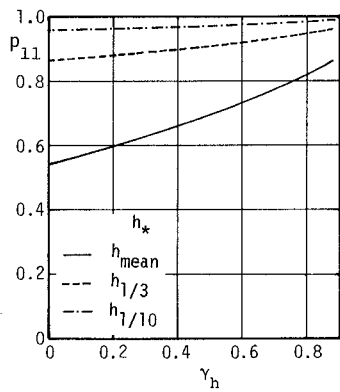


Fig.6 $P_{11} \sim \gamma_h$

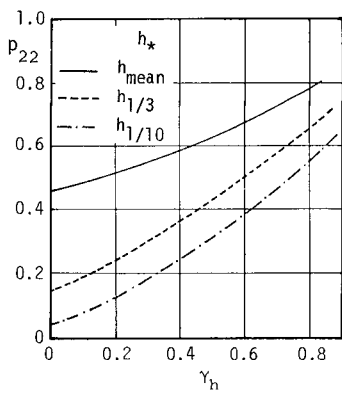


Fig.7 $P_{11} \sim \gamma_t$

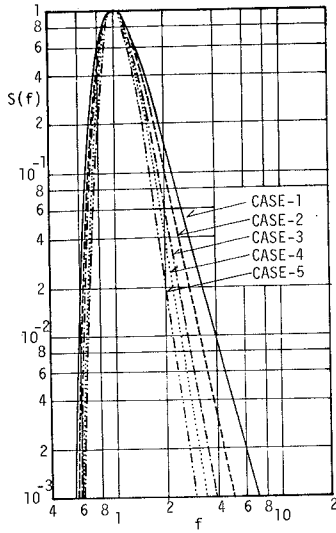
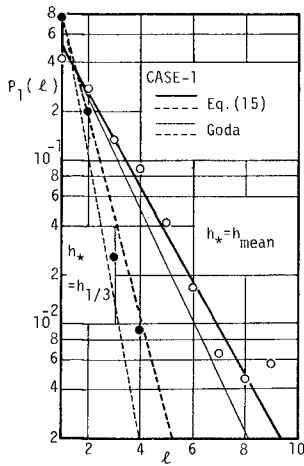
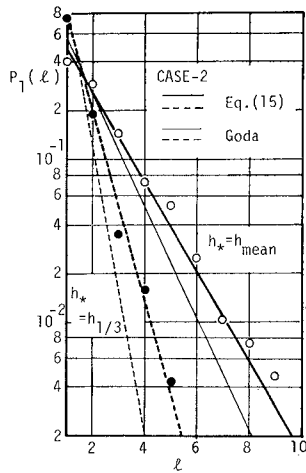


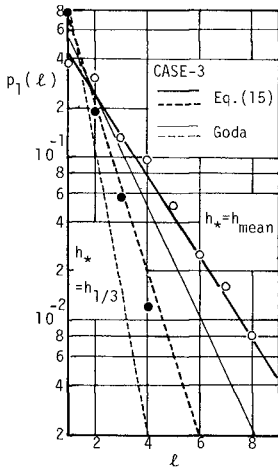
Fig. 8 Target spectra



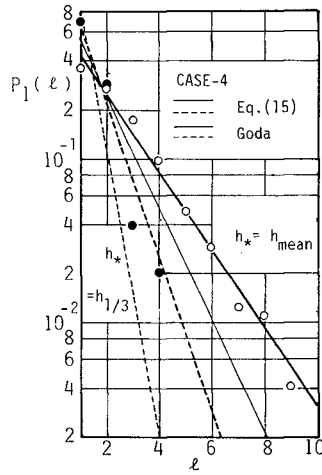
(a) CASE-1



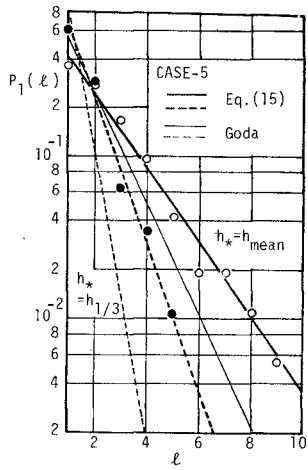
(b) CASE-2



(c) CASE-3



(d) CASE-4



(e) CASE-5

Fig.9 Distribution of the run of high waves

cal distribution of the run of high waves. The thick lines are the distributions from the theory developed here and the thin lines are those from the Goda's theory for $h_* = h_{\text{mean}}$ (solid line) and $h_* = h_{1/3}$ (dotted line). It can be seen that the plotted data agree very well with eq.(15). Figs.10 (a) ~ (e) show the comparison of data and the theoretical distribution of the total run providing $h_* = h_{\text{mean}}$. The solid curve shows eq.(18) and dotted curve is the theoretical distribution from Goda's theory. Good agreements between data and eq.(18) have been obtained. Tables 1 and 2 show the comparisons of the mean length of the run of high waves and the total run between data and theories. With the increase of the correlation coefficient γ_h , mean length of data becomes longer while the Goda's theory gives the constant value which is considerably small. And the theory by Nolte-Hsu gives also small values compared with data. Estimations with the theory presented here give reasonable values in each case.

RUN OF WAVE PERIOD

Time series of random wave period determined by the zero-up-cross method forms the Markov chain approximately(8). Then almost same analysis is available for the run of wave period with that of wave height. However in such a problem as a resonant oscillation of structure, it is more useful to analyze the run of wave periods which fall in the specified wave period band consecutively. For this purpose time series of wave period

$$\dots, t_{i-1}, t_i, t_{i+1}, t_{i+2}, \dots \tag{b}$$

may well be classified into these three states:

$$\begin{aligned} \text{State 1 :} & \quad t_j < t_{*1} \\ \text{State 2 :} & \quad t_{*1} \leq t_j \leq t_{*2} \\ \text{State 3 :} & \quad t_j < t_{*2} \end{aligned} \tag{20}$$

(j=1,2,3, ...),

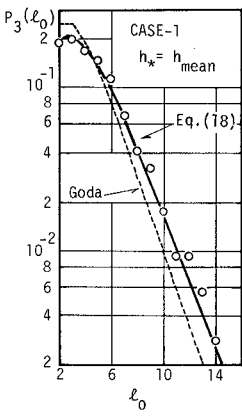
in which t_{*1} and t_{*2} are the low and high limit of the resonant period band of the oscillation system. The transition probability matrix reduces to the matrix of order 3: (p_{ij}) (i,j=1,2,3). With the same discussion, the first and third row of the matrix, p_{1j}, p_{3j} (j=1,2,3) should be precluded to introduce the run of resonant wave period. Finally P becomes

$$P = \begin{pmatrix} 0 & 0 & 0 \\ p_{21} & p_{22} & p_{23} \\ 0 & 0 & 0 \end{pmatrix} \tag{21}$$

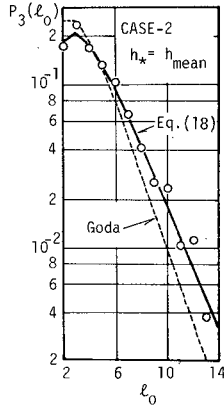
The run starts when a wave period falls in State 2 first; then initial distribution is (0,1,0) and the lth transition distribution is given as:

$$P_l = (p_{22}^{(l-1)} p_{21}^l, p_{22}^l, p_{22}^{(l-1)} p_{23}) \tag{22}$$

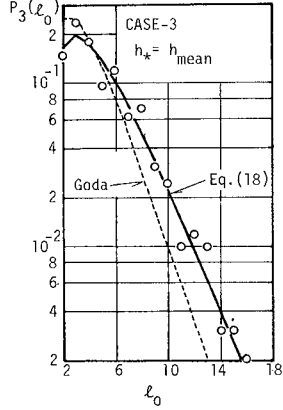
$p_{22}^{(l-1)} p_{21}^l$ and $p_{22}^{(l-1)} p_{23}$ are probability that consecutive l waves fall in State 2, but l+1th wave falls in State 1 or 3 respectively. Then the



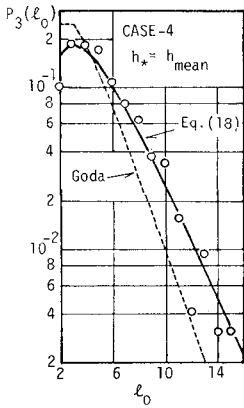
(a) CASE-1



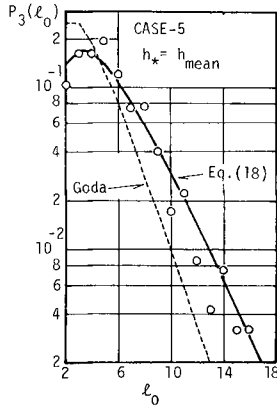
(b) CASE-2



(c) CASE-3



(d) CASE-4



(e) CASE-5

Fig.10 Distribution of the total run

Table-1 Mean length of the run of high waves

Case	γ_h	$h_* = h_{\text{mean}}$				$h_* = h_{1/3}$			
		data	Eq. (16)	Goda	Nolte-Hsu	data	Eq. (16)	Goda	Nolte-Hsu
1	0.19	2.20	2.08	1.84	1.33	1.28	1.33	1.15	1.12
2	0.23	2.29	2.15	"	1.47	1.29	1.37	"	1.19
3	0.29	2.34	2.28	"	1.64	1.29	1.44	"	1.28
4	0.33	2.42	2.37	"	1.78	1.37	1.50	"	1.36
5	0.38	2.45	2.46	"	1.92	1.53	1.57	"	1.44

Table-2 Mean length of the total run

Case	γ_h	$h_* = h_{\text{mean}}$			$h_* = h_{1/3}$		
		data	Eq. (19)	Goda	data	Eq. (19)	Goda
1	0.19	4.66	4.55	4.03	9.33	9.87	8.61
2	0.23	4.67	4.67	"	9.47	10.12	"
3	0.29	4.94	4.90	"	10.00	10.63	"
4	0.33	5.17	5.10	"	9.95	11.07	"
5	0.38	5.36	5.32	"	10.71	11.57	"

probability that the length of the run becomes ℓ is given by the sum of these probabilities.

$$P_4(\ell) = p_{22}^{(\ell-1)} p_{21} + p_{22}^{(\ell-1)} p_{23} = p_{22}^{(\ell-1)} (1-p_{22}), \quad (23)$$

$$\bar{\ell} = 1/(1-p_{22}). \quad (24)$$

Transition probability of the time series of wave period may well be approximated with the 2-dimensional Weibull distribution (8),(10). Then p_{22} is given by:

$$p_{22} = \int_{t_{*1}}^{t_{*2}} \int_{t_{*1}}^{t_{*2}} f(t_1, t_2) dt_1 dt_2 / \int_{t_{*1}}^{t_{*2}} R(t_1) dt_1 \quad (25)$$

where

$$f(t_1, t_2) = \frac{n^2 (t_1 t_2)^{n-1}}{4A t_r^{2n}} \exp\left[-\frac{\phi}{2A} \frac{(t_1^n + t_2^n)}{t_r^n}\right] I_0\left[\frac{\sigma}{A} \frac{(t_1 t_2)^{n/2}}{t_r^n}\right], \quad (26)$$

$$R(t_1) = \frac{n}{2\phi} \frac{t_1^{n-1}}{t_r^n} \exp\left[-\frac{1}{2\phi} \frac{t_1^n}{t_r^n}\right], \quad (27)$$

$$A = \phi^2 - \sigma^2, \quad \phi = \frac{1}{2} [\Gamma(\frac{n+2}{n})]^{-n/2},$$

in which $f(t_1, t_2)$ is the 2-dimensional Weibull distribution and $R(t_1)$ the Weibull distribution, σ the correlation parameter, n the shape parameter, t_r the rms wave period, Γ the Gamma function. Correlation coefficient of consecutive wave period t_1 and t_2 is:

$$\gamma_t = \frac{[\Gamma(\frac{n+1}{n})]^2 \{F[-\frac{1}{n}, -\frac{1}{n}; 1; (\frac{\sigma}{\phi})^2] - 1\}}{\Gamma(\frac{n+2}{n}) - [\Gamma(\frac{n+1}{n})]^2}, \quad (28)$$

in which F is the hypergeometric function. It follows that p_{22} can be determined from the correlation coefficient of consecutive wave period and the shape parameter with equations (25) to (28). But both parameters are closely correlated with each other as shown in Fig.11. Plotted data are obtained from the numerical simulations. Then p_{22} can be determined by either of these parameters using the average relation between them. Fig.12 shows the relation between p_{22} and γ_t for $t_{*1} = 0.4t_{\text{mean}}$, $t_{*2} = 0.6t_{\text{mean}}$ (solid line), $t_{*1} = 0.9t_{\text{mean}}$, $t_{*2} = 1.1t_{\text{mean}}$ (dotted line) and $t_{*1} = 1.4t_{\text{mean}}$, $t_{*2} = 1.6t_{\text{mean}}$ (chain line) for example.

Fig.13 shows the theoretical distribution of the resonant wave period providing $t_{*1} = 0.7t_{\text{mean}}$ and $t_{*2} = 1.2t_{\text{mean}}$. This is the period band in which dynamic response of a spring is greater than twice the static loading providing that the resonant period of the spring equals t_{mean} . Figs.14 (a) ~ (e) show the comparison of data and the theoretical distribution. The agreement of data and the distribution is very well.

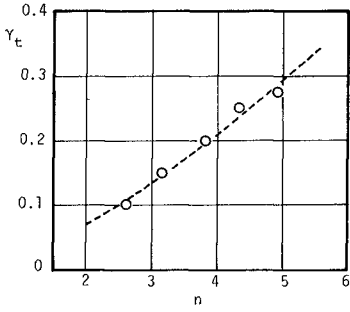


Fig. 11 $\gamma_t \sim n$

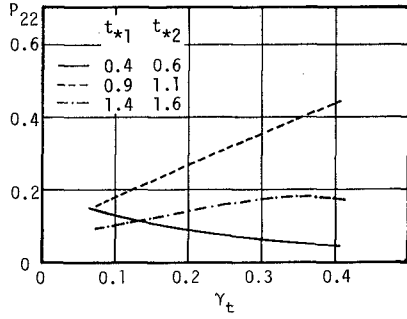


Fig. 12 $p_{22} \sim \gamma_t$

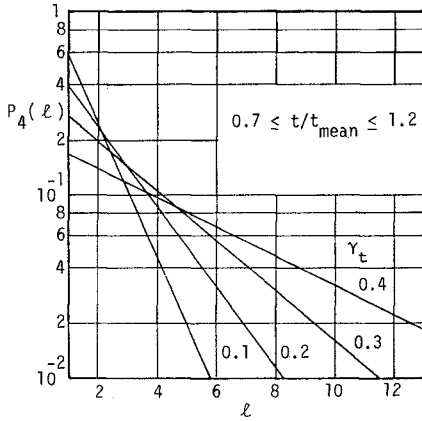
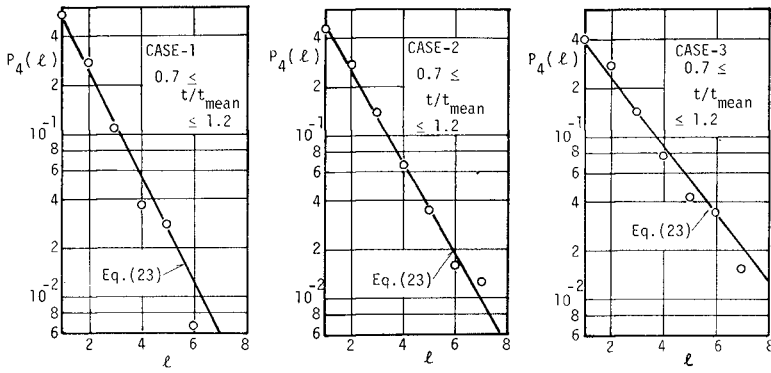


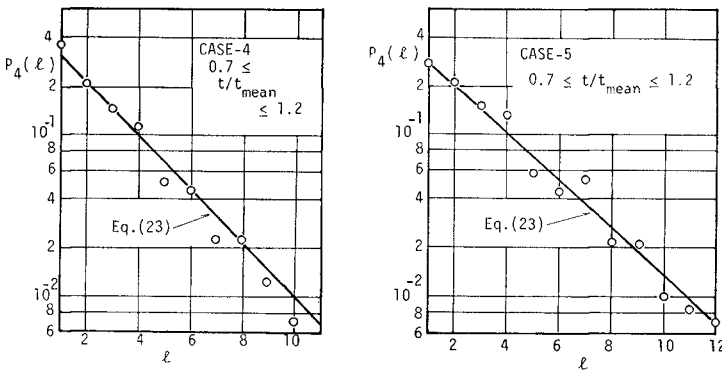
Fig. 13 Probability distribution of the run of low waves



(a) CASE-1

(b) CASE-2

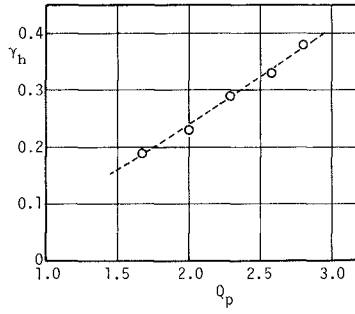
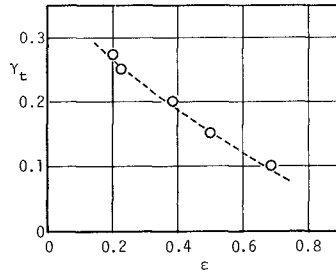
(c) CASE-3



(d) CASE-4

(e) CASE-5

Fig.14 Distribution of the resonant wave periods

Fig.15 $\gamma_h \sim Q_p$ Fig.16 $\gamma_t \sim \epsilon$

ESTIMATION OF PARAMETERS

Statistical properties of the run of wave height can be determined from the correlation coefficient of consecutive wave height γ_h . But γ_h changes with the width of the power spectrum. Fig.15 shows the relation between γ_h and wave peakedness parameter Q_p proposed by Goda(1). Plotted data are obtained from the numerical simulations. It is known from this figure that since γ_h can be approximated from Q_p , statistical properties of the run of wave height can be estimated from Q_p .

On the other hand in determining the run of wave period, n and γ_t are needed. But since both parameters are mutually correlated, statistical properties of the run can be determined by knowing either of them. Fig.16 shows the relation between γ_t and the spectrum width parameter ϵ . γ_t has close correlation with ϵ .

From Figs.15,16 it can be concluded that if the power spectrum of random waves is known, statistical properties of the run of wave height and wave period can be estimated.

REFERENCES

- (1) Goda, Y. : Numerical experiments on wave statistics with spectral simulation, Rept. Port and Harbour Res. Inst., Vol.9, No.3, 1970, pp.3-75.
- (2) Ewing, J. A. : Mean length of runs of high waves, Jour. Geophys. Res., Vol.78, No.12, 1973, pp.1933-1936.
- (3) Nolte, K. G. and F. H. Hsu : Statistics of ocean wave groups, Prepr. 4th OTC, No.1688, 1973, pp.139-146.
- (4) Wilson, J. R. and W. F. Baird : A discussion of some measured wave data, Proc. 13th Conf. Coastal Engineering, 1972, pp.113-130.
- (5) Rye, H. : Wave group formation among storm waves, Proc. 14th Conf. Coastal Engineering, 1974, pp.164-183.
- (6) Siefert, W. : Wave investigation in shallow water, Proc. 14th Conf. Coastal Engineering, 1974, pp.151-178.
- (7) Sawhney, M. D. : A study of ocean wave amplitudes in terms of the theory of runs and a Markov chain process, Tech. Rept. of New York Univ., 1962, 29p.
- (8) Kimura, A. : Statistical properties of the run of random wave heights and periods, Rept. Faculty of Engineering Tottori Univ., Vol.10, No.1, 1979, pp.310-324.
- (9) Kimura, A. and Y. Iwagaki : Random wave simulation in a laboratory wave tank, Proc. 15th Conf. Coastal Engineering, 1976, pp.368-386.
- (10) Kimura, A. : Combined distribution of wave heights and periods of random sea waves, Proc. JSCE, No.286, pp.53-64.

On the Synthesis of Realistic Sea States

by

E.R. Funke* and E.P.D. Mansard**

1.0 INTRODUCTION

Recent investigations by some researchers (Johnson et al, 1978; Burchart, 1979; Gravesen and Sorensen, 1977) have indicated that it is no longer sufficient to match the variance spectral density of a simulated sea state to that of the prototype. When testing models of various fixed and floating structures, it appears to be most important to simulate the wave grouping phenomenon as well. Some researchers also believe that the wave steepness, the particular sequencing of high and low waves (Burchart, 1979) and the ratio of the maximum to the significant wave height within a wave train are also of significance.

Methods for the generation of 'random' waves throughout the world vary greatly. One may, however, categorize these in terms of two substantially different approaches. These may be referred to as "probabilistic" on the one hand and "deterministic" on the other.

In the former, a random or pseudo-random noise source is used which will never repeat or which has a very long repetition period. The assumption is then made that, in the course of the long testing period, all possible outcomes of wave heights, wave periods and wave groups will occur. The only constraint, which is usually placed on the synthesis, is the shape of the variance spectral density and its zeroth moment. The "deterministic" approach, on the other hand, attempts to create very specific and typically extreme conditions. Subsequent analysis of structural response to these conditions must, of course, be related to the likelihood of these conditions occurring in the prevailing climate. The old standby method of testing with monochromatic waves is a typical example of this category. However, other techniques such as Funke and Mansard (1979a) and the reproduction of prototype wave trains as favoured by several laboratories (Gravesen and Sorensen, 1977) may also be described as deterministic.

* Senior Research Officer and **Assistant Research Officer, Hydraulics Laboratory, National Research Council of Canada, Ottawa, Canada.

This paper describes a method which can synthesize a wave train with a well defined grouping characteristic. Although, in principle, the wave train could be made arbitrarily long, for practical reasons it will normally be limited to a recycling period of 5 or 10 minutes in the laboratory. The method, which may also be identified as "deterministic", can synthesize a wave train with well defined grouping characteristics and, at the same time, with a good approximation to a specified continuous variance spectral density. Although these two features may not be sufficient for a completely realistic simulation of a natural sea state, the method is believed to be a step in the right direction.

The method produces a time series which describes the wave train as it is to be monitored at a prespecified location in a wave flume or basin and in the absence of reflections. It is therefore assumed that there exists a real time signal generator, such as an on-line digital computer (Funke, Crookshank and Wingham, 1980) which is capable of converting a number sequence (after suitable amplitude and phase compensation) into a smooth driving signal to a servo-controlled wavemaking machine. The method described here addresses itself only to the synthetic creation of the time series. Its conversion into a train of water waves at a specified location in the flume is the subject of other publications (Funke and Mansard, 1979a; Funke and Mansard, 1980).

As an input to the procedure, it is necessary to specify:

- a) the variance spectral density $S(f)$ of the desired water surface displacement (this includes, by implication, the characteristic wave height),
- b) the groupiness factor, GF ,
- c) the SIWEH spectral density, $\epsilon(f)$, and
- d) the desired repetition (or recycling) period of the wave train, T_n .

Both the SIWEH and the groupiness factor are concepts which had to be developed as descriptors for the sea state in order to realize a systematic procedure for synthesis. Whereas this paper addresses itself to the subject of how wave group activity may be defined and how this definition can be used to synthesize a wave train, it remains to be determined how important these parameters are in describing a wave climate and in causing severe and damaging structural response.

2.0 THE SIWEH

SIWEH is an abbreviation for Smoothed Intermediate Wave Energy History (Funke and Mansard, 1979b). It is a function of time which describes the distribution of energy along the time axis. This somewhat awkward name is proposed (with apologies) in order to distinguish this energy function of time from the more commonly used energy function of frequency and it is believed that the word history does suggest a time function.

The SIWEH is proposed as an alternative to 'envelope functions' for the purpose of describing group activity within a wave train. Fig. 1 illustrates a typical wave train and two envelope functions. The 'half-wave rectified' envelope has been constructed by joining all peaks of the wave record whereas the 'full-wave rectified' envelope requires first a folding of all negative values about the mean before the peaks are joined. The former does not properly account for wave troughs and the latter is always affected by the presence of non-linear waves which have sharp peaks and flat troughs. Therefore, the concept of computing the average wave energy over the period of the dominant wave appeals intuitively. If $\eta(t)$ is the water surface displacement with zero mean value, then the smoothed instantaneous wave energy history may be defined initially as:

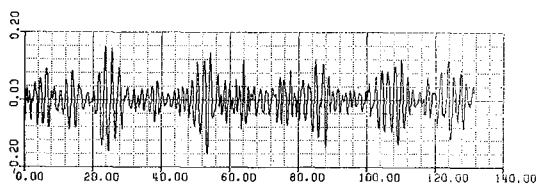
$$E^*(t) = \frac{1}{T_p} \int_{\tau=-T_p/2}^{T_p/2} \eta^2(t+\tau) \cdot d\tau \quad (1.1)$$

This function provides a uniform, running average of the squared water surface displacement over the interval $T_p = 1/f_p$, where f_p is the frequency at which the variance spectral density of $\eta(t)$ is a maximum. The operation defined by equation 1.1 may be considered convolution of a rectangular data window, Q_0 , with the function $\eta^2(t)$, i.e.

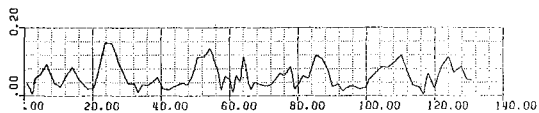
$$E^*(t) = \frac{1}{T_p} \int_{-\infty}^{\infty} \eta^2(t+\tau) \cdot Q_0(\tau) \cdot d\tau \quad (1.2)$$

Another window function is the Bartlett window, Q_1 , which has a triangular shape with a base of $2 \cdot T_p$. The result of this smoothing operation is also included in Fig. 1.

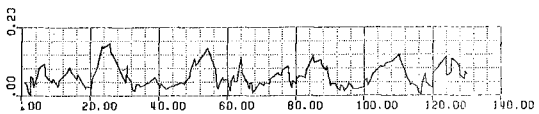
From Fig. 1 it may be observed that the SIWEH provides superior identification of groups and that the Bartlett window achieves better smoothing without an apparent loss of contrast.



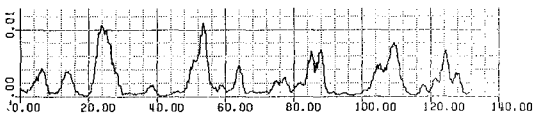
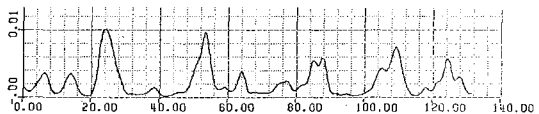
A WAVE RECORD



THE HALF-WAVE RECTIFIED ENVELOPE



THE FULL-WAVE RECTIFIED ENVELOPE

THE SMOOTHED INSTANTANEOUS WAVE ENERGY HISTORY
USING RECTANGULAR SMOOTHINGTHE SMOOTHED INSTANTANEOUS WAVE ENERGY HISTORY
USING BARTLETT SMOOTHINGFIG. 1 COMPARISON BETWEEN FUNCTIONS FOR WAVE GROUP
IDENTIFICATION

3.0 SPECTRAL CONSIDERATION TO SMOOTHING OF THE SIWEH

Convolution between two functions in the time domain is equivalent to multiplication between their respective Fourier transforms in the frequency domain. For this reason it is instructive to consider the Fourier transform of the smoothing windows, which were used for Fig. 1. Fig. 2 shows these frequency functions as a function of nor-

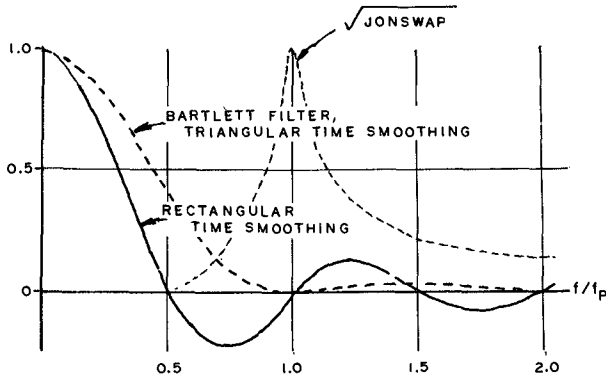


FIG. 2 FREQUENCY CHARACTERISTICS OF SMOOTHING FUNCTIONS

malized frequency f/f_p where f_p is the frequency at which the variance spectral density is a maximum. For comparison purposes the square root of a JONSWAP spectrum is also included. It should be noted that the rectangular window has a frequency response which is quite oscillatory. The consequence of using this function as a digital filter is leakage of energy from outside its nominal pass band. The Bartlett window, on the other hand, has smaller side-band leakage but suffers from reduced contrast in the pass band.

As the filters are applied to the square of the water surface displacement, it is essential to assess them in terms of the spectrum of $\eta^2(t)$. Fig. 3 illustrates first the function $\eta(t)$ and then its square after removal of the mean value $\bar{\eta}^2$. The SIWEH function, which was smoothed using the Bartlett window, is also shown with its mean value removed.

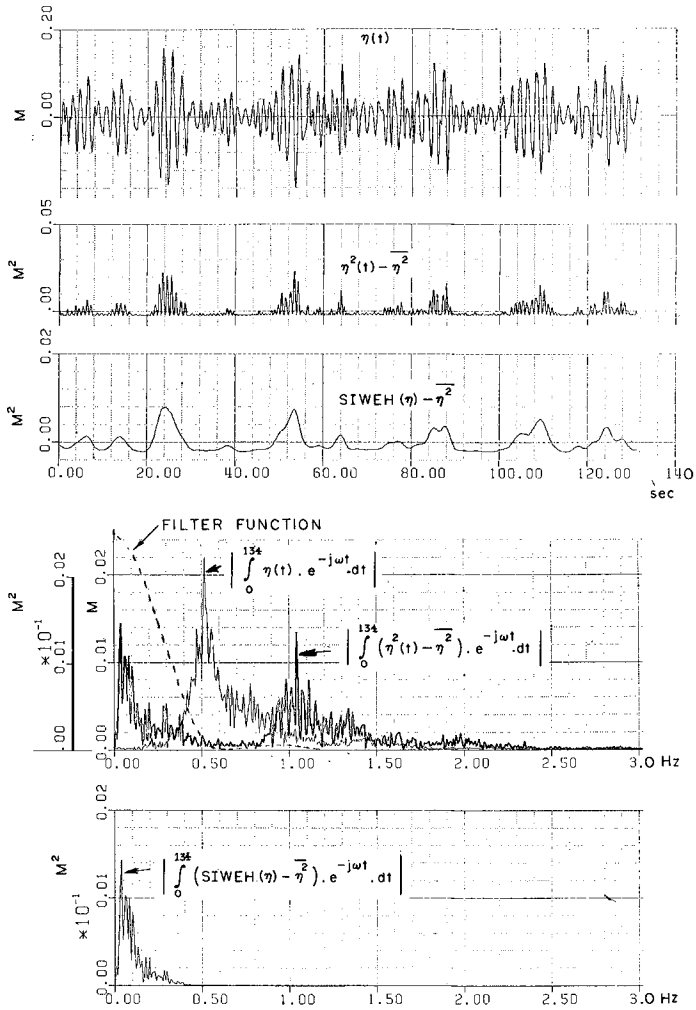


FIG. 3 SPECTRUM OF SQUARED WATER SURFACE ELEVATION

The fourth function in Fig. 3 gives the absolute values of the Fourier transforms of both $\eta(t)$ and $(\eta^2(t) - \bar{\eta}^2)$. The frequency response of the Bartlett filter function is also shown. The most surprising observation is the redistribution of energy in the frequency domain as a result of squaring in the time domain. It appears that energy is moved both above as well as below the band that was previously occupied by the variance spectral density of $\eta(t)$ with a notable absence of energy remaining in this latter band. The Bartlett smoothing filter which was selected intuitively does appear to be quite effective in separating the low-frequency from the high frequency part of the spectrum, although as can be seen, with some attenuation in accordance with its filter characteristics.

These frequency considerations suggest that convolution with a Bartlett window is superior to rectangular smoothing. Therefore, the following formulation for the computation of the SIWEH is proposed,

$$E'(t) = \frac{1}{T_p} \int_{\tau=-T_p}^{T_p} \eta^2(t+\tau) \cdot Q_1(\tau) \cdot d\tau \quad \text{for } T_p \leq t \leq T_n - T_p \quad (3.1)$$

and for the beginning and the tail end of the record:

$$E'(t) = \frac{2}{T_p+t} \int_{\tau=-t}^{T_p} \eta^2(t+\tau) \cdot Q_1(\tau) \cdot d\tau \quad \text{for } 0 \leq t \leq T_p \quad (3.2)$$

$$E'(t) = \frac{2}{T_p+T_n-t} \int_{\tau=-T_p}^{T_n-t} \eta^2(t+\tau) \cdot Q_1(\tau) \cdot d\tau \quad \text{for } T_n - T_p \leq t \leq T_n \quad (3.3)$$

where

$$Q_1(\tau) = 1 - |\tau|/T_p \quad \text{for } -T_p \leq \tau \leq T_p \\ = 0 \quad \text{everywhere else.}$$

4.0 AN ALTERNATE WAY OF DEFINING AND COMPUTING THE SIWEH

If the wave record of length T_n is given as a Fourier series expansion, i.e.

$$\eta(t) = \sum_{i=1}^N c_i \cdot \cos(\omega_i \cdot t + \phi_i) \quad (4.1)$$

with $\omega = 2\pi \cdot i \cdot t/T$ and

c_i being the Fourier coefficients, then $\eta^2(t)$ may be shown to contain four distinctly different groups of terms (Naes, 1978) namely:

- a) a group involving c_i^2 ,

- b) a group including the frequencies $2\omega_i$,
- c) another group with frequencies $\omega_j + \omega_i$, and
- d) finally, the fourth group with frequencies $\omega_j - \omega_i$.

The first and fourth group together make up the SIWEH of $\eta(t)$ which may thus be defined for the interval $0 \leq t \leq T$, SIWEH($\eta(t)$) = $E(t)$ =

$$\frac{1}{2} \sum_{i=1}^N c_i + \sum_{i,j} c_i \cdot c_j \cdot \cos[(\omega_j - \omega_i) + (\omega_j - \omega_i)] \quad 1 \leq i \leq j \leq N \quad (4.2)$$

The first term of this expansion is evidently the mean square value of $\eta(t)$ and must therefore be equal to the area under the variance spectral density of $\eta(t)$. In other words:

$$\overline{E(t)} = \mu_0$$

Although the authors are not, at the time of writing, applying equation 4.2 for the computation of the SIWEH, it is believed that it will prove superior to equations 3.1 to 3.3 as it is not dependent on smoothing windows in the time domain or the treatment of start-up and end transitions in the associated convolution operation.

5.0 THE SIWEH SPECTRUM

The unsmoothed SIWEH variance spectral density may also be computed in two possible ways. By application of the Fourier transform to the SIWEH one obtains:

$$e^*(f) = \frac{1}{2\Delta f} \left| \frac{2}{T_n} \int_0^{T_n} (E(t) - \bar{E}) \cdot e^{-j\omega t} \cdot dt \right|^2 \quad (5.1)$$

$$= \frac{2}{T_n} \left| \int_0^{T_n} (E(t) - \bar{E}) \cdot e^{-j\omega t} \cdot dt \right|^2 \quad (5.2)$$

where $\Delta f = 1/T_n$.

The second method may be derived from equation 4.2 by re-ordering the difference frequencies so that all terms with the same difference frequency are grouped together. Therefore, letting $j=i+k$ with $k=1,2,\dots,N-1$, equation 4.2 may

be written thus,

$$E(t) = \frac{1}{2} \sum_{i=1}^N c_i^2 + \sum_{k=1}^{N-1} \sum_{i=1}^{N-k} c_i \cdot c_{i+k} \cdot \cos(k \cdot \Delta\omega \cdot t + \theta_{i,k}) \quad (5.3)$$

where $\Delta\omega = \omega_{i+1} - \omega_i = 2\pi/T_n$

and $\theta_{i,k} = \phi_{i+k} - \phi_i$

Equation 5.3 may be abbreviated as:

$$E(t) = \frac{1}{2} \sum_{i=1}^N c_i^2 + \sum_{k=1}^{N-1} A_k \cdot \cos(k \cdot \Delta\omega \cdot t + \gamma_k) \quad (5.4)$$

where

$$A_k = \sqrt{\left(\sum_{i=1}^{N-k} (c_{i+k} \cdot c_i \cdot \cos \theta_{i,k}) \right)^2 + \left(\sum_{i=1}^{N-k} (c_{i+k} \cdot c_i \cdot \sin \theta_{i,k}) \right)^2} \quad (5.5)$$

and

$$\gamma_k = \text{atan} \left(\frac{\sum_{i=1}^{N-k} c_{i+k} \cdot c_i \cdot \sin \theta_{i,k}}{\sum_{i=1}^{N-k} c_{i+k} \cdot c_i \cdot \cos \theta_{i,k}} \right) \quad (5.6)$$

The unsmoothed SIWEH variance spectral density may then be obtained from equation 5.5 as follows:

$$\epsilon(f) = [A(k \cdot \Delta f)]^2 / (2 \cdot \Delta f) \quad (5.7)$$

It is of particular interest to note that the SIWEH spectral density is completely defined in terms of the Fourier coefficients and Fourier phases of the water surface displacement $\eta(t)$. The term

$$\sum_{i=1}^{N-k} c_{i+k} \cdot c_i \quad (5.8)$$

in equation 5.5 is reminiscent of the auto-covariance of the spectrum defined by c_i . It has been suggested by Nolte and Hsu (1972) that the spectrum of the envelope function is related to:

$$H(f) = \int_0^{\infty} S(x) \cdot S(x+f) \cdot dx / \int_0^{\infty} S^2(x) \cdot dx \quad (5.9)$$

where $S(f)$ is the variance spectral density of $\eta(t)$. This proposition is, however, challenged on the grounds that according to equation 5.9

$$H(0) > H(f)$$

It is known from observations that this does not describe reality because highly periodic wave group phenomena lead to a peak in the SIWEH spectral density at non-zero frequencies and this cannot be reproduced with equation 5.9.

On the other hand, equation 5.5 indicates that the SIWEH spectral density is also affected by the phase differences between adjacent frequency components. This suggests for the first time how the phase spectrum of wave trains may be related to the grouping phenomenon.

Smoothing of SIWEH variance spectral densities may be implemented by the usual statistical techniques.

6.0 THE GROUPINESS FACTOR

The SIWEH or its spectral density may be used to describe the degree of group activity. The groupiness factor is defined as

$$GF = \left(\sqrt{\int_0^T \eta (E(t) - \bar{E})^2 \cdot dt} \right) / \bar{E} \quad (6.1)$$

which gives the standard deviation of the SIWEH about its mean value \bar{E} .

Since the variance of $E(t)$ about its mean must equal the area under the variance spectral density, the groupiness factor may also be given as

$$GF = \sqrt{m_{c_0} / m_0} \quad (6.2)$$

where m_{c_0} is the zeroth moment of the SIWEH spectral density.

Groupiness factors for prototype wave data so far observed at one location over a period of six months (Sea of Japan, N38 44'33", E139 39'48") fall in the range $0.46 \leq GF \leq 0.94$.

7.0 A POSSIBLE MODEL FOR THE SIWEH SPECTRUM

It is expected that analysis of prototype wave data will reveal that SIWEH spectral densities will, occasionally exhibit a more or less pronounced peak indicating a periodicity of groups. However, the majority of SIWEH spectral densities, particularly for low wave heights, will decay almost exponentially with increasing frequencies. The

broadness of the SIWEH spectral densities are expected to be inversely related to the width of the average wave groups.

A model which may provide enough control over the spectral shape has been borrowed from linear system analysis and is given by

$$\epsilon(\lambda) = \frac{1}{\sqrt{(1-\lambda^2)^2 + 4 \cdot \zeta^2 \cdot \lambda^2}} \cdot \frac{\lambda}{\sqrt{1 + \lambda^2}}$$

This function is shown in Fig. 4 for $\lambda = 0.1$, $\zeta = 0.1, 0.3$ and 1 and the area under the function has been adjusted so that the groupiness factor according to the definition of equation 6.2 is 0.95.

8.0 SYNTHESIS OF A SIWEH FROM ITS SPECTRAL DENSITY

As it is expected that, in future, a sea state may be specified both in terms of its variance spectral density as well as its SIWEH spectral density, it must be determined if one can synthesize a SIWEH from the SIWEH spectral density. It is evident from inspection of a SIWEH that this function is highly non-Gaussian. This fact imposes a severe problem on the ability to synthesize such a function through inverse Fourier transformation as may be seen from the following argument.

When applying the inverse Fourier transform to an amplitude spectrum, some arbitrary phase spectrum must first be assumed. It is common practice to create such a phase spectrum by selecting phases for each of the constituent frequencies from a random number generator which has a uniform distribution of random numbers over the interval $-\pi$ to π . As a consequence of such a phase spectrum, the function resulting from inverse Fourier transformation can be shown to have a Gaussian amplitude probability density and non-Gaussian functions cannot be generated in this way.

The technique which has been used here to overcome this difficulty is an iterative procedure (see Funke and Mansard, 1979b). After the first inverse Fourier transform following a random phase selection, the resulting time function is then clipped below $-\alpha \cdot m_0$ so that the resultant time signal now looks highly distorted with all troughs being flat at $-\alpha \cdot m_0$. A subsequent forward Fourier transform of this clipped function will produce a new amplitude and phase spectrum. Evidently the new amplitude spectrum is wrong but the new phase spectrum is a better approximation of the unknown phase spectrum than the first guess. One therefore pairs up this new phase spectrum with the original amplitude spectrum and repeats the inverse Fourier transform. The resultant time function will now be non-Gaussian, however, there will still be exceedances below the $-\alpha \cdot m_0$ level. It

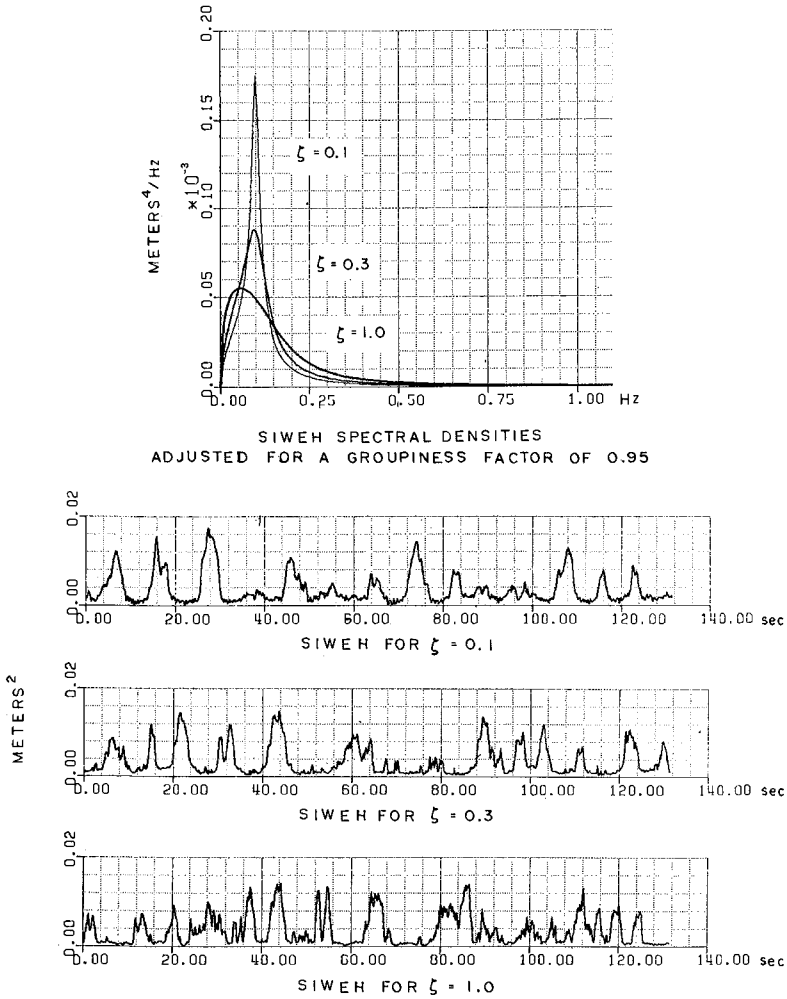


FIG. 4 THE SYNTHESIS OF A SIWEH

is therefore necessary to repeat this operation of clipping and transforming until these exceedances no longer occur.

Different values of α have been tried which appear to work equally well. For $\alpha = 0.6$ it was found that 20 iterations were required.

Fig. 4 gives three different SIWEHs which were synthesized from the three spectral densities also given in this figure. The SIWEH for $\zeta = 0.1$ is the one which has the most pronounced periodicity of groups.

9.0 THE SYNTHESIS OF A GROUPED WAVE

Fig. 5 illustrates the procedure which is now followed in order to create a wave train which not only has a given variance spectral density, but also has wave grouping as specified by a SIWEH, which may have been synthesized by the method described in section 8.0.

With reference to Fig. 5 one will recognize the desired variance spectral density and the desired SIWEH. From the latter a phase modulating function is created which is also shown in Fig. 5. It may be noticed that this phase modulator has large values when the SIWEH is small and vice versa. It is being used to phase modulate a constant amplitude sinusoid with a dominant frequency of 0.5 Hz, which is the peak frequency of the desired variance spectral density. Closer observation will reveal that the dominant frequency has been preserved in those intervals where the SIWEH has large values while everywhere else the frequency is increased. The reasoning behind this is that each wave group should have a dominance of energy in the peak frequency band if one wishes to match the desired variance spectral density by this initial approximation.

After this, the phase modulated carrier is also amplitude modulated by using the square root of the SIWEH as the modulating function. The result of these manipulations is a rough approximation of the synthesized wave train. Fourier transformation, as shown in Fig. 5, does in fact show that the amplitude spectrum approximates quite well the desired amplitude spectrum (which has been obtained by square-rooting the spectral density). The phase spectrum, which has been obtained from the Fourier transform of the rough approximator, is now paired with the desired amplitude spectrum. Subsequent inverse Fourier transformation will then produce the desired wave train or at least something which comes very close to the ideal.

By computing the SIWEH for this wave train, $E_2(t)$ and comparing it to the originally specified SIWEH, $E_1(t)$, a correcting function $C(t)$ may be computed which is

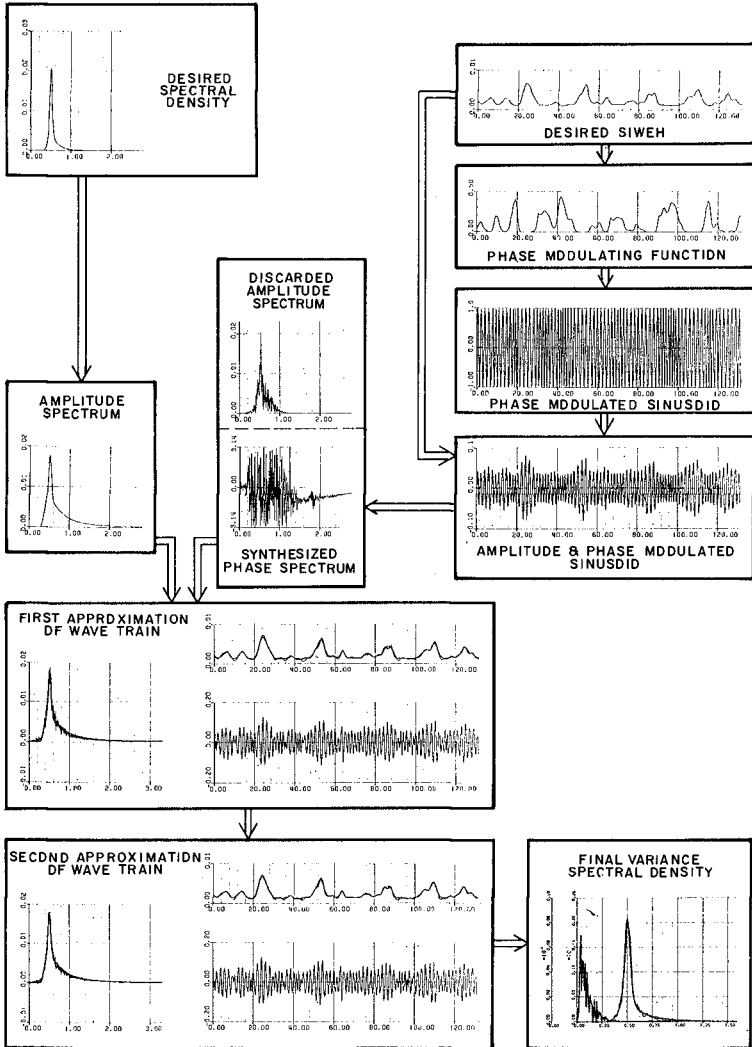


FIG. 5 THE SYNTHESIS OF A GROUPED WAVE

$$C(t) = \sqrt{E_1(t)/E_2(t)}$$

The first wave train is now multiplied by $C(t)$ and the product is also Fourier transformed. Again one obtains an amplitude and a phase spectrum. The new phase spectrum is then paired with the original amplitude spectrum and an inverse Fourier transform will then provide the second approximation of the desired wave train. This may be repeated a few times which occasionally leads to further improvements. Fig. 6 shows some other synthesized wave trains. Attention is drawn to the difference between the actual and the desired variance spectral density. It may be noticed that there are some differences, particularly in the higher frequency tail of the spectrum.

Beside this, Fig. 6 illustrates how one may generate any number of grouped wave trains from the same input specifications. In all three cases the same SIWEH spectral density and the same variance spectral densities were used. However, for the purpose of synthesizing the SIWEHs, three different random number sequences were generated.

10.0 SPECTRAL BROADNESS FACTOR AND GROUPINESS

With the availability of the synthesis tool described here, one may address oneself to the question of how the spectral broadness factor is related to wave groupiness. It has been generally accepted that waves with a narrow variance spectral density also have a more pronounced groupiness than broad-banded waves. It may, in fact be true that there is a strong correlation between these two which is a characteristic of natural gravity waves. This could be explained if strong grouping occurs after waves have travelled over long distances and, as is well known, waves due to swell do have narrow band spectra.

However, it should be noted that there is no necessary relationship between a spectral width parameter and groupiness. Fig. 7 illustrates three synthesized wave trains. Each of these were synthesized from the same SIWEH spectral density with the only difference that the area under the SIWEH spectral densities was rescaled according to equation 6.2 so that the groupiness factor could be varied from $GF = 0.95$ to 0.2 . In all three cases the variance spectral densities are more or less the same. Whereas the wave train for $GF = 0.95$ shows very pronounced grouping, the wave train for $GF = 0.2$ is almost of constant amplitude.

It may, perhaps, appear unbelievable that this latter wave record can have the variance spectral density which is shown. It must, however, be remembered that the record shown is not a pure sinusoid and that there is an appreciable amount of phase modulation which causes the

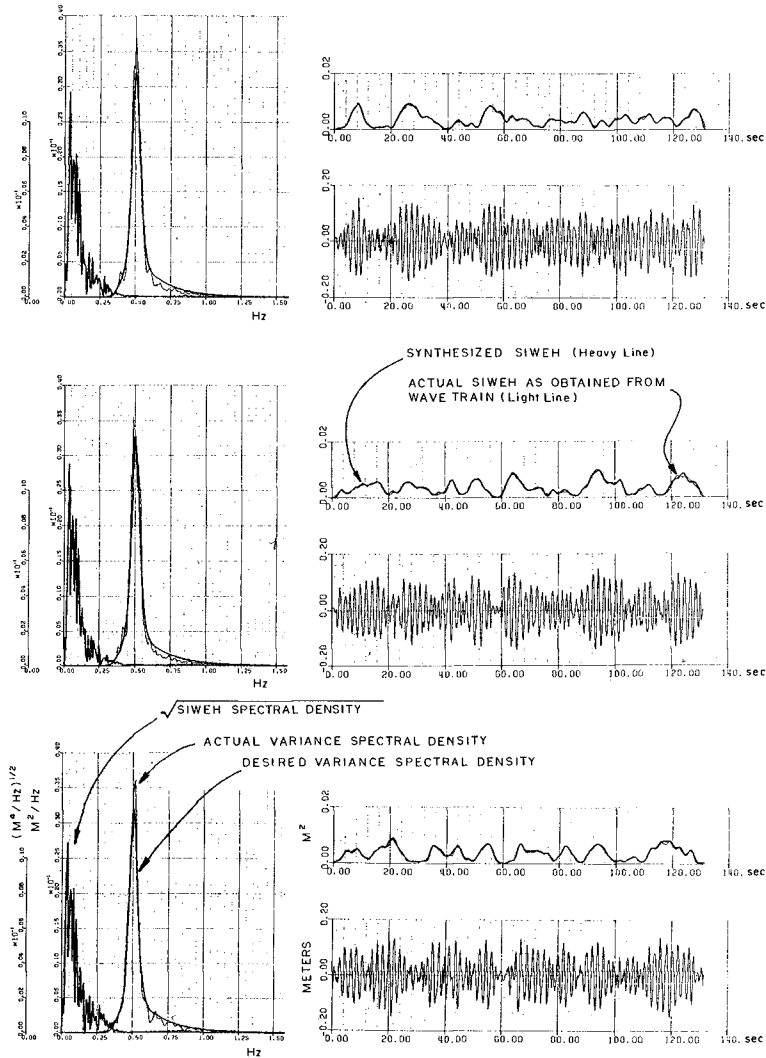


FIG. 6 THE SYNTHESIS OF GROUPED WAVES FROM COMMON SIWEH SPECTRAL DENSITIES

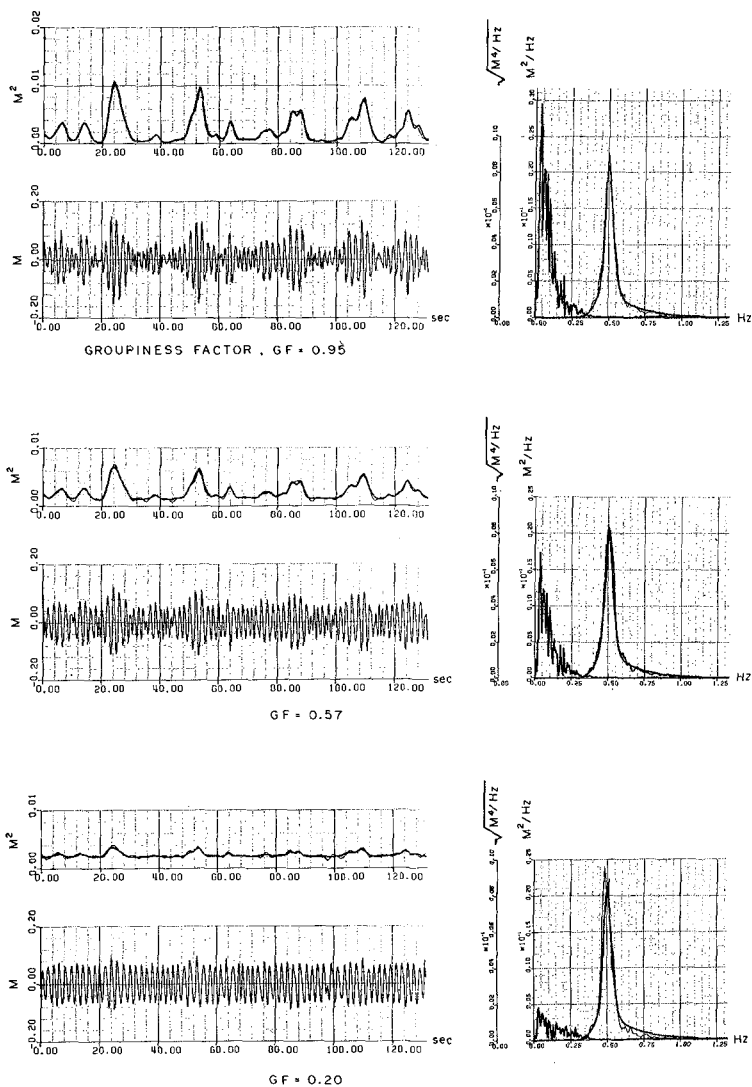


FIG. 7 SYNTHESIS OF GROUPED WAVE TRAINS FROM THE SAME SIWEH BUT WITH DIFFERENT GROUPINESS FACTORS

spectrum to be non-monochromatic. The authors have not attempted to reproduce this latter wave train in a wave flume, and it is therefore not known if this particular wave train is physically realizable.

11.0 REFERENCES

- Burcharth, H.F. (1979), "The Effect of Wave Grouping on On-Shore Structures", Coastal Engineering, Vol. 2, pp. 189-199.
- Funke, E.R. and E.P.D. Mansard (1979a), "SPLSH--A Program for the Synthesis of Episodic Waves in a Flume", Hydraulics Laboratory Technical Report LTR-HY-65, National Research Council of Canada.
- Funke, E.R. and E.P.D. Mansard (1979b), "On the Synthesis of Realistic Sea States", Hydraulics Laboratory Technical Report LTR-HY-66, National Research Council of Canada.
- Funke, E.R. and E.P.D. Mansard (1980), "Reproduction of Prototype Random Wave Trains in a Laboratory Flume", Hydraulics Laboratory Technical Report LTR-HY-64, National Research Council of Canada (to be published).
- Funke, E.R., N.L. Crookshank and M. Wingham (1980), "An Introduction to GEDAP - An Integrated Software System for Experiment Control, Data Acquisition and Data Analysis", Proc. 26th International Instrumentation Symposium. (Also available as NRC Hydraulics Laboratory Technical Report LTR-HY-75.)
- Gravesen, H. and T. Sorensen (1977), "Stability of Rubble Mound Breakwaters", Proc. 23rd PIANC Conference, Leningrad.
- Johnson, R.R., J. Ploeg and E.P.D. Mansard (1978), "Effects of Wave Grouping on Breakwater Stability", Proc. 16th Coastal Engineering Conf., Hamburg.
- Naess, Arvid (1978), "On Experimental Prediction of Low-Frequency Oscillations of Moored Offshore Structures", Norwegian Marine Research No. 3, pp. 30-37.
- Nolte, K.G. and P.M. Hsu (1972), "Statistics of Ocean Wave Groups", Offshore Technology Conference, Houston, Texas, Paper no. OTC 1688.

A COMPARISON OF NATURE WAVES AND MODEL WAVES
WITH SPECIAL REFERENCE TO WAVE GROUPING

by

Hans F. Burcharth**

1. ABSTRACT

This paper represents a comparative analysis of the occurrence of wave grouping in field storm waves and laboratory waves with similar power spectra and wave height distribution.

Two wave patterns - runs of waves and jumps in wave heights - which have significant influence on the impact on coastal structures were included in the analysis of storm wave records off the coasts of Cornwall, U.K. and Jutland, Denmark. Two different laboratory wave generator systems, based on random phase distribution of component waves, were used. Within the limitations given by the relatively small number of analysed records it is shown that wave group statistics can be satisfactorily reproduced by random phase generators that are not based on a limited number of component waves, but for example based on filtering of white noise. It is also shown that the statistics of large waves and wave groups containing large waves depend on whether the waves are defined from zero-upcrossings or zero-downcrossings. Although very similar seas were chosen for the analysis it was found that significant differences in the wave group statistics from the two locations existed. Also a considerable scatter in the wave group statistics throughout the storms was found.

** Prof. of Marine Civil Engineering, Aalborg University, Denmark.

2. INTRODUCTION

Very few quantitative data are available on the differences in stochastic nature of wave groups in model and prototype wave records. This in spite of the fact that it has been shown by authors like Johnson et al (1978) and Burcharth (1977), that certain sequences of waves - or wave groups - are important to the impact of waves on structures. For example, the stability of rubble mound breakwaters and also run-up are affected by wave grouping. It is therefore important that the statistics of wave grouping in model waves are the same as those in nature.

It may be argued that a safe method in model testing is a direct reproduction of recorded natural wave trains, but accepting this statement we are left with the problem of selecting the typical or say critical records, especially when the number of available records is limited. This is so because very often there is a considerable scatter in the wave group statistics throughout storms on a given location. Also, it is not possible to make a statistical analysis of any impact from waves if the model waves are reproduced - and maybe repeated - from a time limited wave record. This problem can, however, be overcome if the phase spectrum can be found and the model waves reproduced accordingly, for example as done by Funke et al. (1980). But to get it right, we need a good deal of knowledge and understanding of the variation of the phase spectrum - which we normally do not have. If, however, we are so lucky that a further analysis shows that the phase spectra do not vary too much during storms on a given location the method may be useful.

Another problem is that very few laboratories have facilities for a direct reproduction of natural wave trains or a reproduction based on a given phase spectrum. Most laboratories use wave generators which can reproduce waves in accordance with the shape of any power spectrum, but with phases of component waves more or less equally distributed.

The question is, therefore, can these random phase wave generators be used without introducing too big errors in the many cases where wave grouping has a significant influence on the impact from waves?

In order to answer this question a comparative study of wave groups in field waves and laboratory waves was performed.

3. METHOD

3.1 Wave Patterns

A relevant comparison between wave patterns in field waves and laboratory waves must be related to large waves if we are thinking in terms of wave impact on fixed structures and if we are not dealing with fatigue problems. Runs of large waves were included in the study because it has been demonstrated by Johnson et al. (1978) that such wave groups are dangerous to armour layer block stability. The definition of a run, which is shown in Fig. 1, is the same as previously used by Goda (1970) and Rye (1974). Only runs of waves bigger than or equal to the significant wave height were considered.

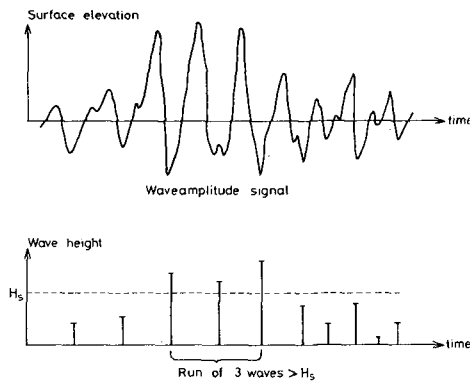


Fig. 1. Definition of runs.

Besides runs of large waves, another dangerous wave pattern in form of big jumps in wave height between successive waves was investigated. The definition of the jump is shown in Fig. 2. It consists of a small wave with the height a constant C times the mean wave height, followed by a large wave with a height bigger than or equal to the significant wave height. Only sizes of jumps corresponding to values of C of 0.5, 0.75 and 1 were considered.

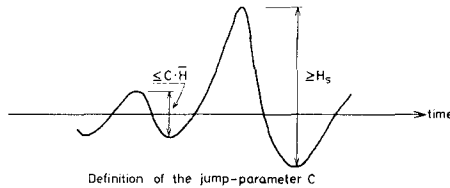


Fig. 2. Definition of jumps.

The jump pattern was included in the analysis because Burcharth (1977) found, from a series of experiments, that of the three wave patterns shown in Fig. 3 (regular waves, runs of waves, and jumps - all containing the same max. waveheight) the jump was the most dangerous to rubble mound breakwater stability and caused the highest run-up on slopes.

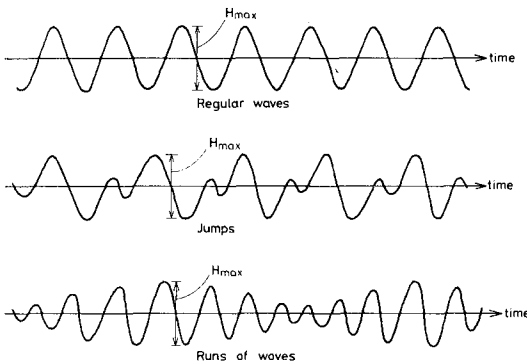


Fig. 3. Wave patterns.

Besides the physical relevance of the two described wave patterns it is important to mention that by including two different patterns in the comparative analysis a very strong proof of identity of the statistics of wave patterns in general is obtained.

3.2. Field Waves

The basic principle of the study was to analyse the statistics of runs and jumps in real sea and in laboratory waves, both with the same power spectra. The field data were collected from Waverider buoys at two rather exposed locations, see Fig. 4.

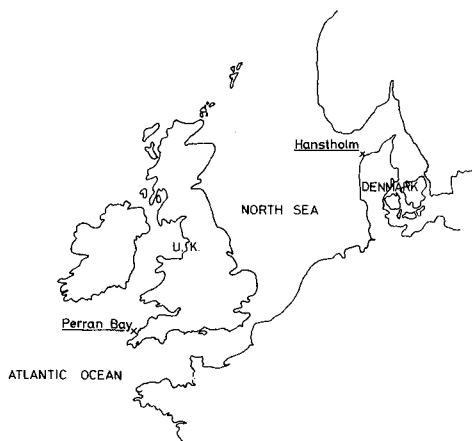


Fig. 4. Location of wave recording sites.

The one is Perran Bay on the north west coast of Cornwall in U.K., which is exposed to Atlantic waves. The other is Hanstholm, the north west corner of Denmark, which is exposed to North Sea waves. The Water depth at the Perran Bay buoy is approximately 22 m and at the Hanstholm buoy 20 m.

Two storms from Perran Bay and one from Hanstholm were analysed. Situations, where no or very little swell was present, were deliberately chosen in order to avoid the complicated

mixture of swell and storm waves. A total of 20 records was analysed. In both places waves were recorded during 20 minutes every 3 or 4 hours. The number of waves in each record varied from 115 to 300.

The variation in significant wave height during the storms is shown in Fig. 5. It is not extreme storm situations, but rather rough sea situations, which set in a couple of times every year.

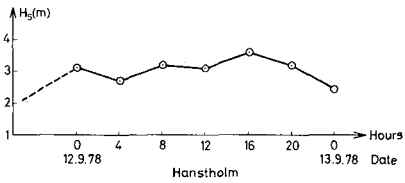
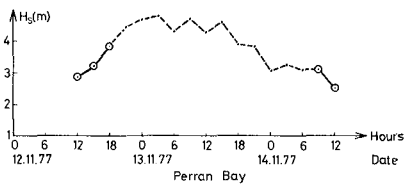
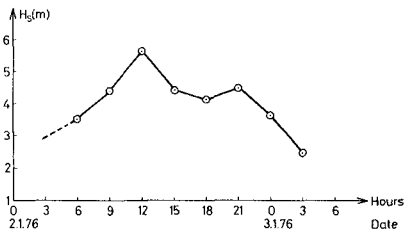


Fig. 5. Histories of analysed storms.

Fig. 6 shows some typical power spectra from two of the storms. It is seen that the spectra vary from fairly wide-band spectra to fairly narrow-band spectra.

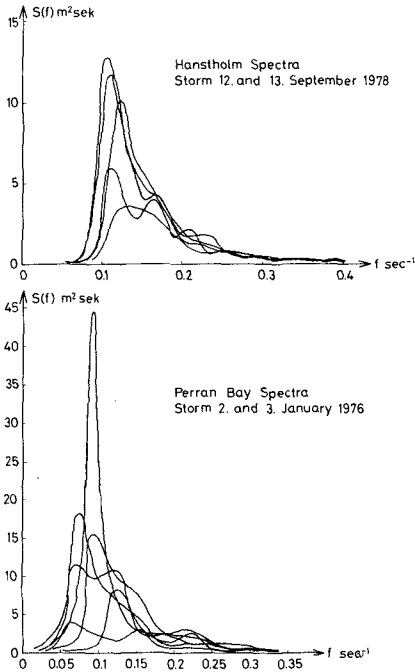


Fig. 6. Typical power spectra from analysed storms.

The wave height distribution in the field records was found to be fairly close to the Rayleigh distribution although the distributions showed a dependence on the applied wave height definition, see chapter 4.1. The waves on the most energy containing frequencies correspond to waves in the transition between deep-water waves and shallow-water waves.

3.3 Laboratory Waves

Modelwaves with the same power spectra as for the real sea records were generated in two laboratories.

The Perran Bay waves were generated at the Hydraulics Research Station, Wallingford, in a waveflume at a length scale of 1 in 25. The paddle was a hydraulic operated piston type controlled by a synthesizer, which operated on the basis of equally distributed phase angles. The synthesizer which is described in detail in a paper by Fryer et al. (1973) works on the principle of filtering white noise by means of a digital method.

The Hanstholm waves were generated at the Hydraulics Laboratory, Aalborg University, Denmark, in a small wave basin at a length scale of 1 in 70. Also this paddle was a hydraulic operated piston type, which could be controlled in different ways, but for this study the most simple way of generating irregular sea, namely that of adding sinewaves of different frequencies and amplitudes, was deliberately chosen. In order to make it as rough as possible, only 10 different frequencies were used. The phases of the component waves were random and different in each test.

For each field wave record batches of 4 or 5 records were generated in the laboratories. Each laboratory record contained approximately the same number of waves as the corresponding field record. It was found that the wave heights in the lab. waves were Rayleigh distributed and it was checked that the lab. wave spectra corresponded to the field wave spectra.

4. ANALYSIS AND RESULTS

4.1 Influence of Wave Height Definition

In the analysis two different definitions of waves were used, the zero-upcrossing definition and the zero-downcrossing definition, both of which are shown in Fig.7. The zero-downcrossing analysis uses the wave trough and the proceeding wave crest in the definition of a single wave and defines the wave height as the difference between these water levels.

The conventional zero-upcrossing analysis defines the wave height from a wave crest and the following wave trough. Generally it is difficult to say which of the two definitions gives the best representation of the physical conditions, but in cases where - for example - impact from breaking or almost breaking waves is important, the zero-downcrossing definition must be the most relevant.

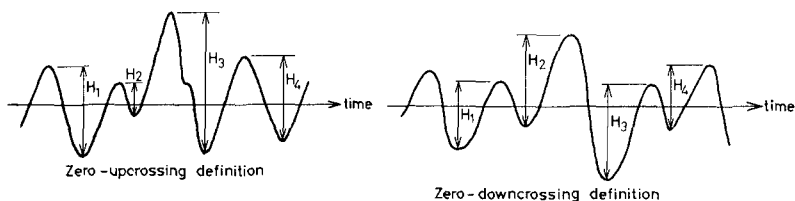


Fig. 7. Definitions of wave height.

The first interesting result that appeared from the analysis was that in the field wave records a zero-upcrossing definition gave significantly more high waves than a zero-downcrossing definition. In the Perran Bay records the upcrossing definition gave on an average 13% more waves bigger than significant wave height, and in the Hanstholm records it was 12%. Fig. 8 shows as an example the wave height distributions in some of the Perran Bay records.

In the lab. wave records no such difference was found. Eight Perran Bay records of typical swell situations were also analysed, and here again there was no difference. So it was only in the field storm wave records that the phenomenon was found, which then might be explained by the asymmetry of the waves caused by the wind. Fig. 9 shows the sort of asymmetry that would lead to differences in wave heights.

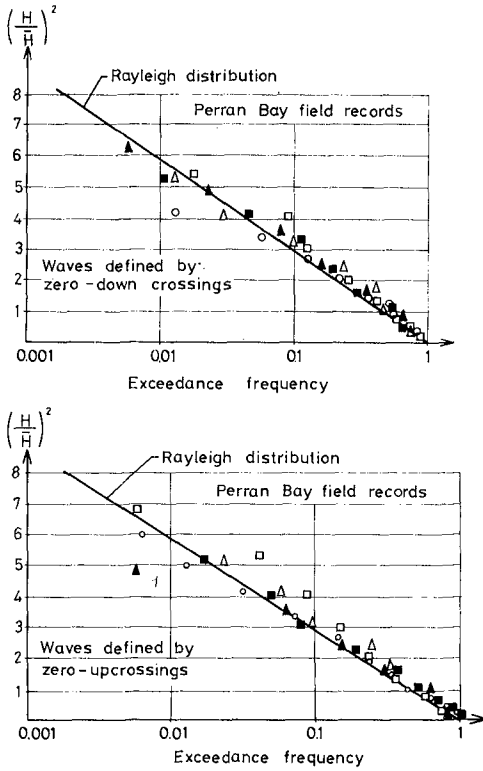


Fig. 8. Example of the influence of wave height definition on the wave height distribution in natural waves.

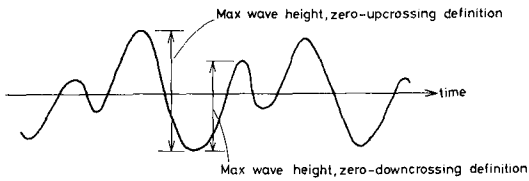


Fig. 9. Influence of zero-crossing definition on wave heights.

Field wave records from other near-shore areas than the two included in this project should be analysed in order to see if the wave definition influences the number of big waves. If it be so, a standard definition must be agreed.

4.2. Wave Grouping Analysis

The results from the comparative analysis of the occurrence of wave grouping in field waves and laboratory waves are shown in Fig. 10 and Fig. 11.

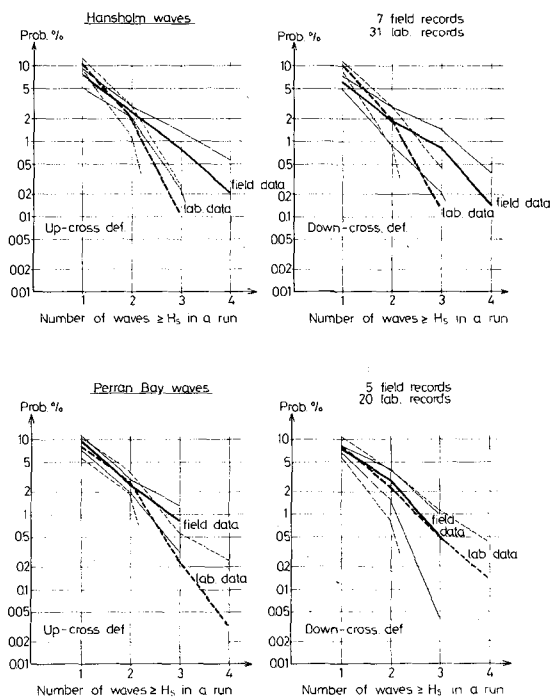


Fig. 10. Probability of runs in field storm wave records and laboratory records with the same power spectra. Graphs are mean values \pm standard deviation.

The vertical axes are the absolute probability of the wave patterns, which means that the events are related to the total number of analysed waves in the record. The graphs represent the mean values plus minus the standard deviation.

Fig. 10 shows the probabilities of the formation of runs of different lengths. Hanstholm data and Perran Bay data based on both zero-upcrossing and zero-downcrossing wave definition are represented. It is seen that in the case of the Perran Bay waves there is a good agreement between the field wave graphs and the lab. wave graphs if the zero-downcrossing definition is applied.

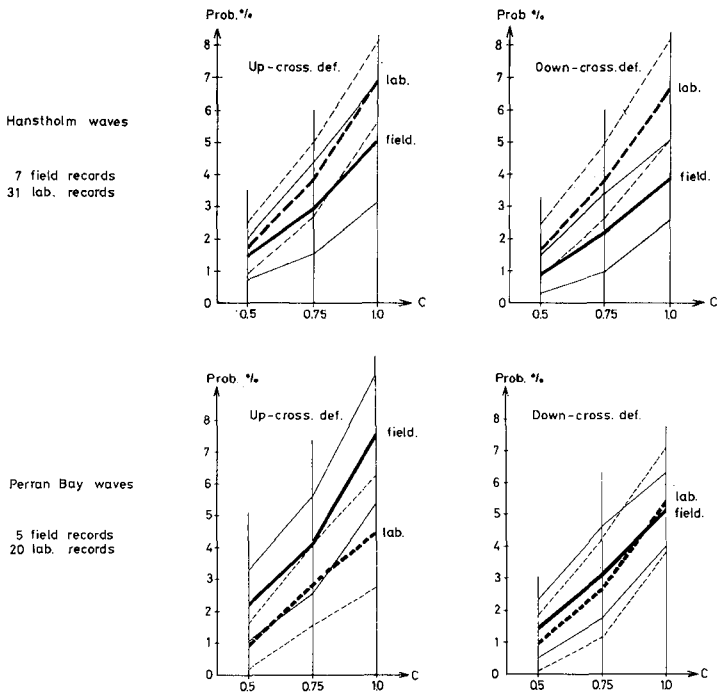


Fig.11. Probability of jumps in field storm wave records and laboratory records with the same power spectra. Graphs are mean values \pm standard deviation.

For the Hanstholm waves there is considerable discrepancy between field waves and lab. waves. The number of long runs in the lab. waves is much too small.

Fig. 11 shows the probabilities of the formation of jumps defined by the jump parameter C , see Fig. 2. Small values of C correspond to big jumps in successive wave heights. For the Hanstholm waves there is actually no acceptable agreement between the lab. and the field data results. For the Perran Bay waves, however, it is seen that the agreement is very good if, again, the downcrossing definition is used.

From Fig. 10 and Fig. 11 it is seen that in the Hanstholm case the lab. simulations of both runs and jumps are so bad that it can be concluded - as also expected - that the very simple wave generator used in this case is far from satisfactory, whereas the much more sophisticated generator or synthesizer, used for the Perran Bay waves, seems to be good if the downcrossing definition is applied. The last part of this conclusion must be regarded as a preliminary conclusion since the wave group statistics for the Perran Bay waves and the Hanstholm waves are different (see chapter 4.3) and a reproduction of the Hanstholm waves by means of the more complicated generator has not been tried.

4.3 Variations in The Wave Group Statistics

From the field data graphs in Figures 10 and 11 it is seen that the Perran Bay records contain considerable more jumps and fewer long runs than the Hanstholm records. So the wave-group statistics are different for the two sets of records.

If the group statistics for a single field wave record are compared with the group statistics for the corresponding batch of lab. wave records the agreement is generally not very good. Only approximately half of the field wave results will be well inside mean plus minus standard deviation for lab. wave results.

This is understandable since the group statistics for the field records vary considerably, and since each of the records contains a very limited number of waves. Because of this scatter in the field wave group statistics one has to be very careful if a model test procedure based on a direct reproduction of natural waves is applied. The selection of the wave records is difficult and can only be done properly if based on the analysis of many field records.

4.4 Comparison with Random Theory

From the field wave records it was found, as also reported by Wilson et al. (1972) and Rye (1974), that the formation of runs of big waves is more pronounced than would be expected from a random distribution of the wave height successions. Corresponding to this, fewer jumps than given by random theory were recorded. This is illustrated in Fig. 12 where graphs representing the theoretical distribution for jumps and runs are shown. The graphs are based on the assumption of independence between successive waves and Rayleigh distributed wave heights.

The theoretical expression for the graph representing runs is,

$$P(n) = (1 - P [H > H_s]) P [H > H_s]^{n-1}, \quad (1)$$

where $P(n)$ is the relative probability of the occurrence of a run of n waves that are bigger than H_s , and $P [H > H_s]$ is the probability of occurrence of a wave bigger than H_s , which, in the case of a Rayleigh distribution, is $\exp(-2)$.

The expression for the graph representing jumps is,

$$P = P [H > H_s] P [H < \bar{C}H], \quad (2)$$

where P is the absolute probability of the occurrence of a jump from a wave height smaller than or equal to C times the mean wave height to a wave height bigger than H_s .

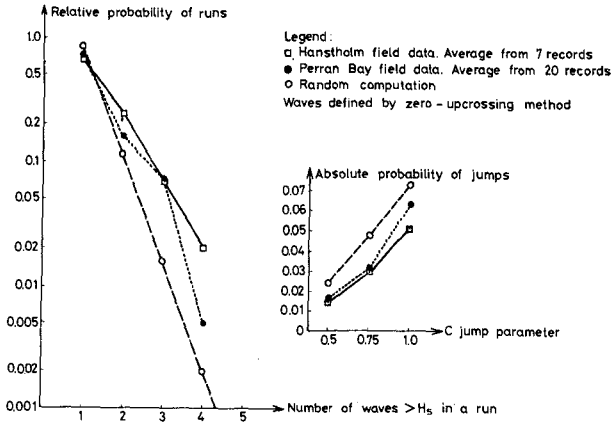


Fig. 12. Comparison of wave group formation with random theory.

Fig. 12 confirms that a correlation between successive wave heights exists. The lab. waves are not shown in the figure, but this conclusion also holds for the Perran Bay model waves.

4.5 Comparison with other Field Wave Records

The statistics of runs in the field waves have been compared with the results presented by Rye (1974). Rye's results are based on 60 storm wave records from a Waverider buoy outside Utsira on the west coast of Norway, where the water depth is approximately 100 m. In Fig. 13 the two sets of results, which both represent the average from many records, are compared. It is seen that the agreement between these averaged data is good.

Rye and other authors found that the formation of runs of large waves tends to be more pronounced for a growing sea than for a decaying sea and that growing seas have more sharply peaked spectra than decaying seas.

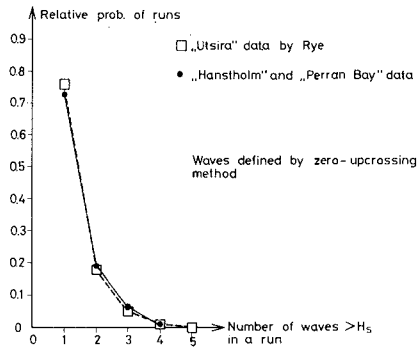


Fig. 13. The average probability of occurrence of runs of waves for field data from Utsira and from Hansthholm and Perran Bay

However in the Perran Bay and the Hansthholm data no significant correlation was found between the sea state and the occurrences of runs and jumps. But as to the spectral peakedness it was found - but only for the Hansthholm records - that there was a correlation between spectral width and sea state, as Rye also did. Many more records are needed, especially from near-shore areas, before a conclusion about the correlation between sea state and groupiness can be made.

5. CONCLUSIONS AND RECOMMENDATIONS

The main conclusion of this study is that if only pure storm waves in near-shore areas are considered, it seems possible to generate laboratory waves with a fairly good reproduction of nature wave trains by using random phase wave generators, but the very simple type of generators based on a limited number of pre-set sine components can not be used. It is important to stress that since the number of analysed records is little, much more work has to be done before a general

conclusion on the generation of wave patterns by means of random phase generators can be made.

It was found that the wave group statistics in the field records from the two locations are different. Further analysis from other near-shore areas could clarify if a general correlation between wave grouping and location exists.

The analysis of field wave records from a given location shows a considerable scatter in the wave group statistics. A model test procedure based on a direct reproduction of natural wave records might therefore imply unsafe results if not based on knowledge about the variations in the wave grouping.

The statistics of high waves in the field records were found to be influenced by the wave height definition. A zero-up-crossing definition gave significantly more high waves than a zero-downcrossing definition. If this holds for other near-shore areas a standard definition must be agreed. But in any case, the zero-downcrossing definition seems to be the most relevant if impacts on structures are considered.

In this study only wave grouping with respect to wave heights has been considered. However, since the dynamics of the waves are very important the wave period or the wave steepness should also be included in the wave grouping analysis. Work in this field has already been done by Cavanie et al. (1976), Ezraty et al. (1977) and Arhan et al. (1978) but more work has to be done before an applicable method is obtained.

6. ACKNOWLEDGEMENTS

Most of the work on which this paper is based was done during the author's stay at the Hydraulics Research Station, Wallingford in 1977 - 78. I would like to thank the Director and his staff for their kind assistance.

7. REFERENCES

- Arhan, M., Ezraty, R. Statistical relations between successive wave heights. *Oceanologica Acta* 1978. Vol. 1, No. 2
- Burcharth, H.F. The effect of wave grouping on on-shore structures. Annual Report 1977, Hydraulics Research Station, Wallingford, England and Coastal Engineering, 2 (1979), pp. 189 - 199.
- Cavanie, A., Arhan, M., Ezraty, R.A. Statistical relationship between individual heights and periods of storm waves. Proc. Boss'76 Conference, Trondheim, Norway. Vol. II pp. 354 - 360.
- Ezraty, R. et al. Comparison with observation at sea of period or height dependent sea state parameters from a theoretical model. Proc. OTC Conference, Houston 1977, Paper No. 2744.
- Fryer, D.K., Gilbert, G., Wilkie, M.J. A wave spectrum synthesizer. *Journal of Hydraulics Research*, 11 (3), 1973.
- Funke, E.R., Mansard, E.P.D. On the synthesis of realistic sea states. Proc. Int. Coastal Eng. Conf., 17th, 1980.
- Goda, Y. Numerical experiments on wave statistics with spectral simulation. Report of the Port and Harbour Research Institute, Vol. 9, No. 3, 1970, Japan.
- Goda, Y. On wave groups. Proc. Boss'76, Trondheim, Norway. Vol. I, pp. 115 - 128.
- Johnson, R.R., Ploeg, J. Effects of wave grouping on break-water stability. Proc. Int. Coastal Eng. Conf., 16th, 1978, Pap. No. 175.
- Rye, H. Wave Group formation among storm waves. Proc. Int. Coastal Eng. Conf., 14th, 1974, pp. 164 - 183.
- Wilson, J.R., Baird, W.F. A discussion of some measured wave data. Proc. Int. Coastal Eng. Conf., 13th, 1972, pp. 113 - 130.

WATER MOVEMENT STUDIES REQUIRED FOR PORT PLANNING

by

Graeme C. Dandy¹

Desmond A. Mills²

and Jon B. Hinwood³

1 INTRODUCTION

Some of the factors involved in the design of a programme of measurement and analysis of current, temperature and salinity data, required for the environmental assessment of an estuarine port, are considered in the context of a study carried out in the Port of Melbourne, Australia. The study was undertaken as part of the Port of Melbourne Environmental Study, 6 Webb Dock Marine Study which was aimed at assessing the present regime and the effects on the marine and coastal environments resulting from the construction of Berth 6, Webb Dock in Hobsons Bay (Figure 1). To this end, integrated investigations of water movement, water quality, coastal processes and marine ecology were conducted.

Although the results presented in this paper are specific to Hobsons Bay, the approach taken is of general applicability to the environmental assessment of proposed physical changes in complex estuaries and embayments. In such cases, the prediction of changed patterns of currents and density structure is a key element in assessing likely changes in other environmental factors such as water quality and the biota.

In general, an environmental study of water movement in an estuary will involve some measurements of the existing conditions of current, temperature and salinity, followed by appropriate analyses of these data to enable the likely changes to be predicted.

1 Lecturer, Department of Civil Engineering, University of Adelaide, Adelaide, Australia.

2 Research Fellow, Centre for Environmental Studies, University of Melbourne, Melbourne, Australia.

3 Senior Lecturer, Department of Mechanical Engineering, Monash University, Melbourne and Senior Associate, Centre for Environmental Studies, University of Melbourne, Melbourne, Australia.

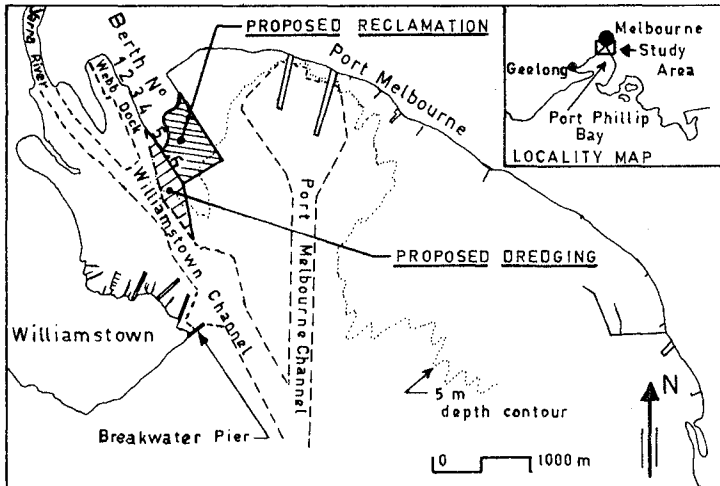


Figure 1. Hobsons Bay

The principal factors which must be considered in undertaking a study of water movement in a complex estuary are:

- (i) The major forcing functions and their relative influence on currents (i.e. tide, wind, freshwater inflow, etc.)
- (ii) The variability which exists in the processes under study, including time scales, range of variation and spatial scale.
- (iii) The choice of instrumentation and methods of data analysis which could be used in the study.
- (iv) The accuracy required in the predicted changes in flow regime.
- (v) The methods which could be used to predict likely changes in the estuary as a result of proposed development works (e.g. are mathematical or physical models appropriate?)

The consideration of these factors in relation to the Port of Melbourne Study is described in this paper.

2 DESCRIPTION OF STUDY AREA

Hobsons Bay, at the northern end of Port Phillip Bay, is a tidal embayment containing the delta and outer estuary of the Yarra River (see Figure 1). It is bounded to the west by the Williamstown promontory, and to the east by the north-east Port Phillip Bay coastline. The bay is of varying depth, being typically 6 m deep but with shipping channels dredged to approximately 12 m.

The bay is subject to a tide with a dominant M_2 constituent of 0.46 m range and spring tides of over 1 m range. Freshwater inflow from the Yarra River is received throughout the year. The minimum mean monthly flow occurs during March ($6.35 \text{ m}^3/\text{s}$) and the maximum occurs in October ($47.8 \text{ m}^3/\text{s}$). This water reaches the bay via an estuarine section of the river system. The dilution of the sea water creates a density stratified system of varying character.

The bay is subject to direct meteorological influence, principally from the action of wind and barometric pressure. Winds are predominantly from the north in winter, whereas southerly winds tend to predominate in summer.

Hobsons Bay is a complex embayment, both because of its irregular geometry and because of the fact that the currents are quite weak and may be influenced at various times by tide, wind and/or fresh water inflow from the Yarra River. The significant influence of meteorological factors, principally wind, means that the current regime is highly variable in time, in depth and in location in the bay.

3 FIELD PROGRAMME

Because of the complex flow regime known to exist in Hobsons Bay and time limitations on the study, the possible use of physical or mathematical models was not considered to be practicable. Instead, considerable effort was concentrated on the collection of a comprehensive set of field data which would form the basis for predicted changes in the physical regime.

The major forcing functions could not be identified *a priori* so the measurement programme had to embrace time scales appropriate to meteorological, hydrological and tidal phenomena. This was achieved by combining several intensive field exercises of short duration with continuous monitoring at a few locations over a 12 month period in order to cover as wide a range of conditions as possible.

The intensive field exercises provided detailed spatial resolution for relatively short periods, thus enabling overall flow patterns to be identified. The continuous monitoring, on the other hand, provided detailed time series information of currents at particular locations and thereby enabled statistical correlations of currents with external forcing factors to be carried out.

Current speeds were expected to be small, in general, hence current meters with a low threshold were required. The variability of the currents meant that net circulation had to be obtained by integrating over long periods of time. This variability also imposed severe demands on the accuracy of measurement.

The current meters selected had threshold speeds of 2.0 to 2.5 cm/s and were chosen on grounds of anticipated reliability, immediate availability and cost. To improve the measurement of net circulation, continuous recording current meters were used as described below. No special problems relating to salinity and temperature measurement were anticipated, however frequent calibration was necessary due to fouling of electrodes.

In essence, the field programme comprised the following activities:

- (i) Four intensive field exercises, each of three days duration conducted over the whole of Hobsons Bay
- (ii) Additional one day field exercises concentrated in areas of particular interest, namely Webb Dock and the Lower Yarra Estuary
- (iii) Long term continuous recording of currents, temperature, salinity and water levels at selected locations.

The four intensive field exercises were held in June, August and December 1977 and in February 1978 in order to obtain a range of external influences and flow conditions in the bay. During each exercise, monitoring was carried out over a full tidal cycle on each of three consecutive days. Direct profile measurements of current speed and direction, temperature and salinity were made from five boats each anchored at a fixed location in the bay or alternating between two stations. In general, readings were taken at 0.5 m intervals to 2 m depth and then at 1 m intervals to the bottom. Complete profiles were repeated at approximately half hour intervals.

In conjunction with the profiling, direct Lagrangian measurements of the current field were conducted on six of the monitored tidal cycles. Methods used included tracing the movements of free drogues and of dye releases. The drogues were suspended at selected depths and were connected to surface buoys and targets. Up to 20 drogues were tracked at any one time from a field radar station. On selected

days, dye was introduced into the near-surface waters and the movement and rate of spread of dye patches were monitored using radar fixes and aerial photography.

The one day field exercises conducted in Webb-Dock and the Lower Yarra Estuary were conducted in a similar manner to the bay-wide exercises but had a finer spatial focus. Two exercises were conducted in each of these locations.

To supplement the limited range of conditions which were covered in the intensive exercises, four automatic current recording instruments were deployed at selected locations in the bay. The meters used were Alexseev instruments which record current speed and direction at pre-set time intervals on paper tape. Each meter was deployed for a period ranging from one to six months at a particular location using a 15 minute recording interval. To record near-bottom currents, the meters were suspended from tripods which rested on the bay floor. Near-surface currents were recorded by suspending the meters from several floats which were free to move vertically with the rise and fall of the water level. In total, about 1166 days of useful data were recorded in this way.

Data from continuous temperature recorders at 8 locations in the bay were collected during the period of the field investigations. These had been installed by the State Electricity Commission of Victoria and provided records of three-hourly temperature readings dating back several years.

To provide information on the penetration of river water into the existing Webb Dock area, a continuous temperature/salinity recorder was installed in the dock for a period of two months.

The above field programme was complemented by the acquisition of suitable data by other agencies. These data included:

- (i) Meteorological measurements such as wind speed and direction, barometric pressure, rainfall and air temperature
- (ii) Freshwater inflow from the Yarra River System.
- (iii) Water level data at Breakwater Pier, Williamstown.

4 DATA ANALYSIS AND RESULTS

4.1 Velocity and Salinity Data

The field data were edited and adjusted for calibration errors before being entered on to computer files. These, together with data obtained from other agencies, formed a comprehensive data base for analysis. A variety of analyses were carried out using computer programs written specifically for the purpose.

The data from intensive field exercises were processed to produce

line printer plots of depth profiles at all stations. Density layers were defined by the occurrence of steep vertical density gradients in the profile. It was found that the bay was density stratified in most conditions. Vertical temperature gradients in the bay were found to be rather small, with most of the density variation being due to salinity differences between the fresher river water and the deeper bay water.

Usually two and sometimes three distinct density layers could be identified in water deeper than 4 metres, although the depth of the upper layer varied significantly in time and space. On occasions more complex layering occurred. Kinematic layers were identified by noting the change in the directional component of profiled current data.

The continuous current records were analysed to determine the relative importance of the various factors which influence currents in the bay. The current records were analysed using a tidal harmonic analysis to identify the tidal component. It was found that the M_2 tidal constituent accounted for about 25% of the variance in currents at each location. The non-tidal components of current were correlated with riverflow, wind speed, barometric pressure and rainfall in order to determine the relevant influence of these factors. It was found that wind, and principally its north-south component, had a major influence on currents in the bay. Riverflow had a significant effect on the currents at some locations and other parameters were of lesser importance. These results were substantiated by detailed examination of the results from the intensive field investigations.

4.2 Time Scales in Response to Wind Stress

There appear to be two time scales involved in the hydrodynamic response of Hobsons Bay to a change in the wind stress field. The first depends upon the rate of downward transport of the momentum imparted by the wind stress. The second relates to the time for establishment of flows driven by horizontal pressure gradients which arise due to the wind-induced set up (down) of water level near coastlines.

Neglecting the influence of lateral boundaries and in the absence of stratification, it is possible to make a rough estimate of the first time scale. It is assumed that, from an initial state of rest, a wind stress is imposed uniformly over the surface of the water. Empirical relationships allow an estimate of the surface shear stress, τ_w , and the surface wind drift speed, u_d (Spillane, Robinson and Hess, 1978). Application of the boundary layer momentum integral equation leads to an expression for the momentum thickness, θ , as a function of τ_w , u_d , ρ , the density of water, and t , the time elapsed:

$$\theta = \frac{\tau_w}{\rho u_d} t \dots\dots\dots (1)$$

Assuming a wind speed of 5 m/s, we obtain $u_d \approx 0.03$ $u_w = .15$ m/s and $\tau_w = \rho k u_w^2 = .03$ N/m². For $\theta = 1$ m, $t = 1.5$ hours; for $\theta = 2.5$ m, $t = 3.8$ hours.

Assuming a wind speed of 10 m/s, we obtain, for $\theta = 1$ m, $t = 0.6$ hours; for $\theta = 2.5$ m, $t = 1.6$ hours.

Drogues located from 0.5 - 2.5 m below the water surface were used to track upper layer water movement. It was possible to examine the response of drogue trajectories to sudden changes in wind direction. The response times varied between 45 minutes to approximately 3 hours. For example, on 23 February 1978, between 1200 and 1400 hours, drogue velocity vectors rotated about 45° in an anticlockwise direction. This appears to have been in response to the wind field which swung from west to south between 1000 and 1100 hours, while maintaining a low speed of 2 m/s, and then, maintaining direction, intensified to a speed of about 5 m/s during the period 1200-1400. A response time of about 3 hours seems in reasonable agreement with the above calculations.

Flows driven by pressure gradients become established as the pressure gradients become established. The latter require times in the order of L/\sqrt{gy} , where L is the fetch and y the depth. For $L = 4$ km and $y = 10$ m, the time is in the order of 7 minutes. If we say 5 to 30 minutes allowing for the approximate nature of the analysis, this is still less than the first time scale which then becomes the effective one.

5 TYPICAL FLOW PATTERNS

Information on the kinematic and density stratification of the bay was used to choose the most appropriate way of classifying and presenting the current field. In most cases, the movements of near-surface (0 - 2.5 m), mid (3 - 5 m) and deep (6 - 8 m) waters provided a useful division. Within each of these divisions, current vectors representative of each two hour period from all data sources were plotted on a single map; the two hour period being approximately equal to the response time of the bay to wind stress. The data sources included current profiles, drogue trajectories, dye patch trajectories, and recording current meters. Bay-wide plots of near-surface salinities were obtained for the same two hour periods. Temperature differences across the bay were small and had little influence on the flow patterns.

Typical current and salinity fields are shown in Figures 2 and 3. A detailed examination of these quasi-steady velocity and salinity fields indicated that certain flow patterns could be identified on the basis of wind speed and direction and river flow, with tidal influence being of minor importance.

Figure 2 shows the surface current and salinity fields on February 23, 1978, at 0800 to 1000 hours. During this time, the wind was from the north-west at 2 m/s, the river flow was 4.5 m³/s (low) and the tide was falling.

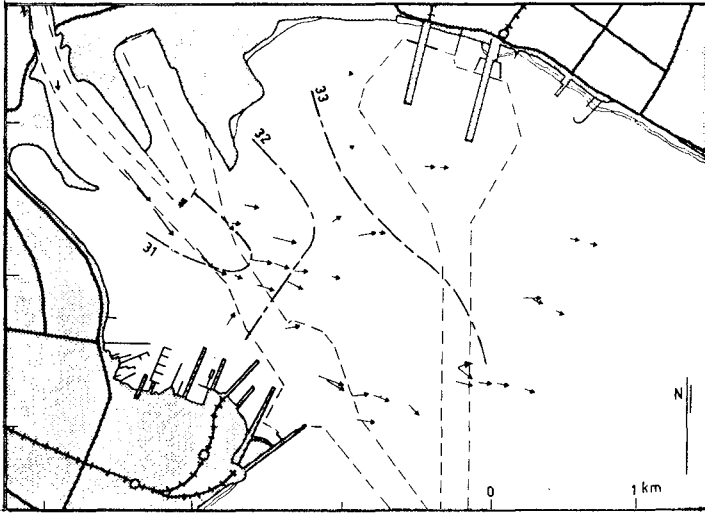


Figure 2. Surface Current and Salinity Fields on Feb. 23, 1978;
at 0800-1000 hours

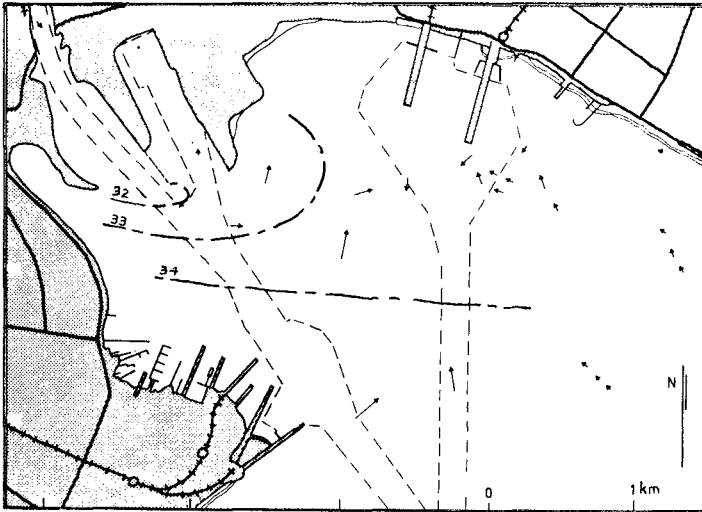


Figure 3. Surface Current and Salinity Fields on Feb. 23, 1978,
at 1800-2000 hours

It can be seen from Figure 2 that the near-surface water adjacent to the Yarra mouth exhibits a generally south-easterly movement with speeds in the range of 0.1 to 0.2 m/s. Once beyond the line of the proposed Webb Dock 6 extension, the surface water spread to the north-east and then re-aligned itself with the south-east trending coastline.

Water movement at mid-depth was quite sluggish, particularly in locations of large total water depth. Its direction of movement tended not to differ significantly from that of near-surface water except where it was deflected by the direct effect of the bay's bathymetry. Deeper water appeared to flow northward in the vicinity of both shipping channels with maximum speeds of about 0.1 m/s. Much of this deep water flux must have been induced in order to compensate for the net efflux of near-surface waters southward out of Hobsons Bay.

The surface salinities recorded at this time are in the range 30-34 g/l (Figure 2). They indicate the existence of a plume of river water moving towards the south-east in response to the currents in that direction. The depth of the maximum salinity gradient was about 0.7 m for locations near the central axis of the plume and about 2 m for the more marginal stations.

A different set of conditions are illustrated in Figure 3 which shows the near-surface current field and surface salinity distribution observed on February 23, 1978, at 1800 to 2000 hours. During this period, the wind speed averaged 7 m/s from the south-south-east, the river flow as 4.5 m³/s (low) and the tide was falling.

At this time, the near-surface currents throughout most of Hobsons Bay (except near the mouth of the Yarra River) exhibited a significant northward velocity component. Near-surface water on the east side of the Port Melbourne Channel moved to the north-west in conformity both with the direction of the wind and the coastal alignment. Water to the west of the channel moved north-north-east to north-east. There was a noticeable convergence of surface waters in the vicinity of the swinging basin located at the head of the Port Melbourne Channel.

The pattern of mid to deeper water movement was not well defined, with mid-depth water being essentially stagnant. The most unmistakable feature was a deeper-water movement to the south in the vicinity of the Port Melbourne Channel. Mass balance calculations indicated that this deep water flux to the south essentially balanced the near-surface flux to the north and the mass deficit due to the falling water level.

The near-surface salinity field (Figure 3) indicated a weak plume of less saline water extending into Hobsons Bay in an easterly direction from the Yarra mouth.

6 CLASSIFICATION OF FLOW PATTERNS

The detailed analysis of flow patterns in Hobsons Bay enabled the classification of these patterns into a limited number of representa-

tive conditions. Seven representative patterns were identified, each resulting from a different combination of high or low river flow and wind direction as shown in Table 1. It was found that tide made little difference to the basic flow patterns. The choice of $50 \text{ m}^3/\text{s}$ as a dividing point between high and low river flow was based on the measurements taken in the Lower Yarra Estuary which indicated the formation of a salt wedge for discharges greater than this figure. Below $50 \text{ m}^3/\text{s}$ the estuary was partially mixed.

The near-surface flow fields for two of the flow patterns are shown in Figures 4 and 5. Pattern A (Figure 4) corresponds to north to north-west winds and low river flow, while Pattern C (Figure 5) corresponds to south to south-east winds and low river flow. The tendency for the near-surface waters to converge in the vicinity of Station and Princes Piers under conditions of south to south-east winds should be noted.

The frequency of occurrence of each flow pattern was determined by analysing historical records of wind and river flow and determining the relative frequency of occurrence of each combination of these. These relative frequencies are included in Table 1 expressed in the form of the average number of days per year for which a particular pattern is expected to occur.

7. USE OF OBJECTIVE CLASSIFICATION SCHEMES

Attempts were made to put this descriptive classification into dynamic terms. Dynamic classification schemes relate the external forces or fluxes of energy which determine the water movement. The most complete of these schemes, that of Hansen and Rattray (1966), was applied successfully to the Lower Yarra estuary. However in the case of Hobsons Bay gross parameters used by Hansen and Rattray could not be measured with sufficient accuracy while the theoretical parameters contained products and ratios of diffusion parameters, which could only be inferred indirectly and then only for certain of the flow conditions.

Of the various energy ratio schemes, that of Ippen and Harleman (1961) is typical and has been well correlated with flow patterns through their model studies. Their scheme is based on the ratio of two parameters, one representing the rate of tidal energy dissipation per unit mass of water and the other the rate of gain of potential energy per unit mass of water. This scheme may be extended by considering also the energy input by the wind acting on the water surface and the inflow of kinetic energy to the bay from the river. A difficulty with all of these parameters is that the detailed information necessary to obtain exact numerical values is not available, so gross physical variables are used instead. Hence the quantities calculated are likely to suffer from errors ranging from perhaps 25% in the case of tidal and wind energy to perhaps 50% for the other two quantities (the potential energy term used is that of Ippen and Harleman (1961) and is not an actual energy change but it is a quantity indicative of the relative magnitude of the potential energy change as the river flow passes through an estuary).

TABLE 1. Flow Patterns in Hobsons Bay

Pattern	Occurrence (days/year)	River Flow (m ³ /s)	Wind Direction at Breakwater Pier	Flow Pattern
A	95.8	Low (< 50)	NW & N	Surface: SSE; mid and deep water: N and up channel at 0.1 m/s
B	54.9	Low	NE & E	Surface: S, SE; mid-depth: weak but similar; deep: up channel
C	96.5	Low	SE & S	Surface: generally NE, Yarra outflow swings E, inflow to N along Williamstown shore, convergence near Station Pier; mid: similar; deep: S in Pt. Melbourne Channel
D	83.0	Low	SW & W	Surface: generally NE, Yarra outflow swings E to NE, inflow to N along Williamstown shore; mid: similar to weak; deep: weak
E	5.2	High (> 50)	W	Surface: ESE with strong river plume extending into bay, N near Breakwater Pier; mid and deep: N to NW
F	13.8	High	NW to E	Surface: strong river plume following Williamstown Channel; deep: up channel
G	14.0	High	SE to SW	Surface: Strong river plume flowing S to Breakwater Pier then ESE; deep: up channel



Figure 4. Flow Pattern A

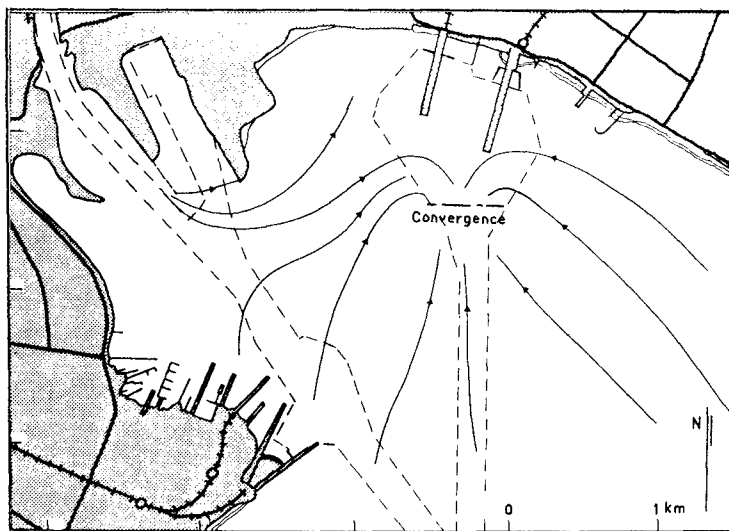


Figure 5. Flow Pattern C

The energy terms, calculated for an area of 8 km² of the bay for typical and high winds, for typical and high tidal currents and for typical and flood river flows, are given in Table 2. The most obvious feature of these results is the high energy input by the wind, and the small input by the tides. From this it may be inferred that mixing is primarily caused by the wind and hence in the absence of winds the bay is likely to be stratified, while wind is likely to be less important under high flow conditions. Both these features have been observed.

Under flood conditions, for the wind to impart sufficient power to negate the potential energy input of the river plume would require a very strong wind or a large area of bay surface. Thus the plume should persist as an identifiable feature for some distance. Using data from the flood of February 1973, a river plume with a well defined boundary covered an area of 3.6 km² on 7 February. The wind was relatively steady with a speed of 9 m/s and the river flow over the preceding 24 hours averaged 120 m³/s. For these conditions, the power input to the plume from the wind was 197 kw and that from the river was 240 kw. This agreement, which is surprisingly close in view of the usually low efficiency of the mixing process, can possibly be accounted for by the fact that mixing is only partially complete just outside the plume, and weakly stratified water extends over tens of square kilometres.

TABLE 2. Rates of Energy Dissipation in Hobsons Bay.

Wind Speed (m/s)	5		10	
Power Input by wind over 8 km ² (kw)	75		600	
Tidal Velocity (m/s)	0.02	0.02	0.05	0.05
Depth (m)	10	6	10	6
Tidal Power dissipated over 8 km ² (kw)	0.15	0.18	2.33	2.77
River Flow (m ³ /s)	5		150	
Rate of Potential Energy Change (kw)	1.50		300	

8 USE OF LONG-TERM CHANGES FOR ENVIRONMENTAL PREDICTION

Predictions of changes in the long term average currents, salinities and water quality variables (nutrients and dissolved oxygen)

TABLE 3. Projected Changes in Salinity and Current Speed Following Construction of Berth No. 6.

Pattern	Maximum Changes following Construction of Berth No. 6 1				
	Existing Dock	Berth No. 6	Within 300m E of No.6	Williamstown	Other
A	Nil	V+	Nil	Nil	(Bottom V+)
B	Nil	Nil	Nil	Nil	S - 0.2 at Parsons
C	Top layer 0.3m thicker	Plume impinge on No. 6	V-, S+1	S+0.4 to 1 maximum V-	Flotsam South of No. 6
D	S - 0.5	Plume impinge on No. 6	V-, S+0.5	Nil	Flotsam South of No. 6
E	S - 5	Nil	S+2,V+	Nil	Nil
F	Nil	Nil	Nil	Nil	Nil
G	Top S - 2.5, V+ Mid S ± 2	Top S - 2.5, V+ Mid S ± 2	Top S - 2.5 Mid S ± 1	Nil	River Entrance: Mid S ± 1

1. Changes given are maxima in all cases and unless specified apply only to the top 1.5 m; + indicates an increase, - a fall. Changes of less than 0.05 g/l in salinity and 3 cm/s in current speed have not been given a numerical estimate. Changes in salinity (S) are in g/l and in current speed (V) are in cm/s.

TABLE 4. Estimated Changes in Long-Term Average Velocities and Salinities

Location	Maximum change in average current speed (m/s)	Standard deviation of measured current speed (m/s)	Maximum change in average salinity of upper 1.5 m (g/l)	Standard deviation of measured salinity (g/l)
Existing Dock	Negligible	Not applicable	-0.3	4.0
Berth 6 Webb Dock	+ .01	.027	-0.1	3.9
Within 300m to the east of Berth 6	Negligible	Not applicable	+0.4 OR -0.1	4.0
Williamstown Foreshore	- .01	.04	+0.3	6.0
Other Locations	Less than .01	.03 to .04	Less than 0.05	3.0 to 6.0

resulting from dock construction were required in order to assess the likely effects on the biota in the bay. Predictions of changes in the physical variables to an accuracy of one significant figure was deemed adequate for the subsequent biological assessment. It was decided therefore to use relatively simple methods for predicting these physical changes.

The expected change in each flow pattern was determined by a close examination of the streamlines and by applying judgement to assess the way in which these would change following dock construction. The equations of continuity and conservation of salt were then applied to determine the expected changes in the velocities and salinities resulting from the displacement of the streamlines. The predicted changes are given in Table 3. The expected changes are, in general, relatively small except for infrequent combinations of external factors, e.g. high river flow and westerly wind which is expected to occur only about 5 days per year on average.

The long term average changes in velocities and salinities were computed by combining the changes expected in each flow pattern with the relative frequency of occurrence of that pattern. These are shown in Table 4 together with estimated standard deviations of the parameters due to natural variability. In general, it was found that the expected long term average changes in currents and salinity were much less than the natural variability which occurs in these parameters.

9 CONCLUSIONS

- (i) The investigation of water movement was central in assessing the environmental effects of port development works by enabling prediction of future water movements and environmental parameters. It was found that the proposed berth would not have a major effect on currents or salinity (or on other parameters) in Hobsons Bay.
- (ii) Current patterns in Hobsons Bay are influenced by salinity stratification at all times and are determined principally by river flow and wind, with tide having a minor influence. Currents take up to two to three hours to respond to changes in the wind.
- (iii) Published estuary classification schemes were not useful, but consideration of gross energy inputs by the different forcing processes provides a basis for understanding flow patterns.

ACKNOWLEDGEMENTS

This work arose out of a study commissioned by the Port of Melbourne Authority whose support is gratefully acknowledged.

REFERENCES

- (1) Hansen, D.V. and Rattray, M. Jnr., "New Dimensions in Estuary Classification". *Limnol, Oceanogr.*, Vol. 11, 1966, pp. 319-329.
- (2) Hinwood, J.B., Watson, J.E., Mills, D.A., Dandy, G.C. and Burrage, D.M., "Port of Melbourne Environmental Study. Marine Study - 6 Webb Dock". Centre for Environmental Studies, University of Melbourne, August, 1979.
- (3) Ippen, A.T. and Harleman, D.R.F., "One-dimensional Analysis of Salinity Intrusion in Estuaries". Technical Bulletin 5, Committee of Tidal Hydraulics, Corps Engineers, U.S. Army, 1961.
- (4) Mills, D.A., Colman, R. and Dandy, G.C., "Water Movement in a Complex Estuarine Embayment - A Methodology for Data Collection and Analysis". Proceedings Fourth Australian Conference on Coastal and Ocean Eng., Adelaide, Australia, Nov. 1978, pp. 153-159.
- (5) Spillane, K.T., Robinson, R.M. and Hess, G.C., "Surface Wind and Drift on Surface-Residing Materials on Westernport Bay". Div. of Atmospheric Physics Technical Paper No. 30, CSIRO, Australia, 1978.

CHAPTER 182

INTEGRATION AND COMPUTATION IN AN ENVIRONMENTAL STUDY

by

J.B. Hinwood¹, J.E. Watson² and D.M. Burrage³

ABSTRACT

A high level of integration of disciplines and use of a centralised computer data base and programming system were seen to offer advantages in a study of the marine and coastal environment of the Port Melbourne Authority. These goals were only partially attained but the effort was well worthwhile.

1. INTRODUCTION

For an environmental study to achieve an overview of the wide range of variables, processes and interactions in a given region, the results of work in many disciplines must be integrated. The integration of the different disciplines depends critically upon flows of information. These in turn depend upon the use of the computer to store, process and display information.

This paper describes the integration of disciplines and the centralised computer data base and programming system used in the Port of Melbourne Environmental Study. The purpose and results of the study are outlined first to provide the context.

2. THE PORT OF MELBOURNE ENVIRONMENTAL STUDY

2.1 Purpose

The Port of Melbourne Environmental Study was divided into firstly a study of the sociological implications of the possible expansion of Webb Dock with some emphasis on land transport serving the dock and secondly the Marine Study of 6 Webb Dock. The Marine Study was aimed at assessing the effects on the marine and coastal environment of reclamation and dredging activities associated with the construction of Berth 6 Webb Dock. The site of the proposed construction is in Hobsons Bay, close to the mouth of the Yarra River. The study involved investigations of water movement, water quality, coastal processes and the ecology of the Bay.

¹ Department of Mechanical Engineering, Monash University and Centre for Environmental Studies, University of Melbourne.

² Marine Science and Ecology, Melbourne.

³ Centre for Environmental Studies, University of Melbourne.

The Port of Melbourne has been developed over the last 150 years along the lower Yarra River and around its mouth, in an indentation of Port Phillip Bay known as Hobsons Bay. The Webb Dock container terminal is in Hobsons Bay immediately to the east of the mouth of the Yarra River (Fig. 1). Hobsons Bay forms the southern boundary to Melbourne, and hence is of importance to the city as a recreational area for boating, fishing, for swimming, and for the aesthetic enjoyment of water and its shoreline. The value of Hobsons Bay would be lowered if the water quality were to be reduced, if the ecosystem of the bay were to be disturbed or if the beaches were severely eroded. Severe changes in the regime of the bay could adversely affect commercial fishing within Port Phillip or could conceivably interfere with port operations. Proper management can avoid these problems, but management requires reliable baseline information on the present state of the bay, an understanding of the processes which are important and, based upon both of these, strategies for predicting changes to the ecosystem of the bay following construction or other activities. The study provided the baseline data on water circulation, water quality, beaches and sediments and marine ecology, an understanding of the important processes and specific predictions for the changes which would result following construction of Berth 6 Webb Dock.

2.2 Method

The Port of Melbourne Authority commissioned the Centre for Environmental Studies, University of Melbourne, to carry out a study to provide baseline information and to assess the consequences of construction of a new berth — No.6 — in Webb Dock. This study was commenced in 1977 and the final report was presented in August 1979. Following a three months planning period, twelve months of measurement were carried out within Hobsons Bay and the lower Yarra River. In addition to the data obtained specifically by the study, historical data and data collected on a continuing basis by government authorities were used.

Water movement was determined by direct current metering, continuous current metering, drogue tracking and from temperature and salinity data (Mills et al 1978, Dandy et al 1980). Wave records, tidal data, long-term meteorological data for the Melbourne Regional Station and wind data for periods of interest at Breakwater Pier were obtained from government departments. Water quality parameters measured were temperature, salinity, dissolved oxygen, light transmission, turbidity, nitrogen, phosphorus, *E. coli* and *Salmonella* bacteria and inflows from minor drains.

For the study of the beaches and sediments, beach profiling and lead-lining were carried out, sediment samples were collected and analysed, a sand tracer test was conducted and waves, winds and currents were measured. Other data used were air photos, records of construction, dredging and shipping movements.

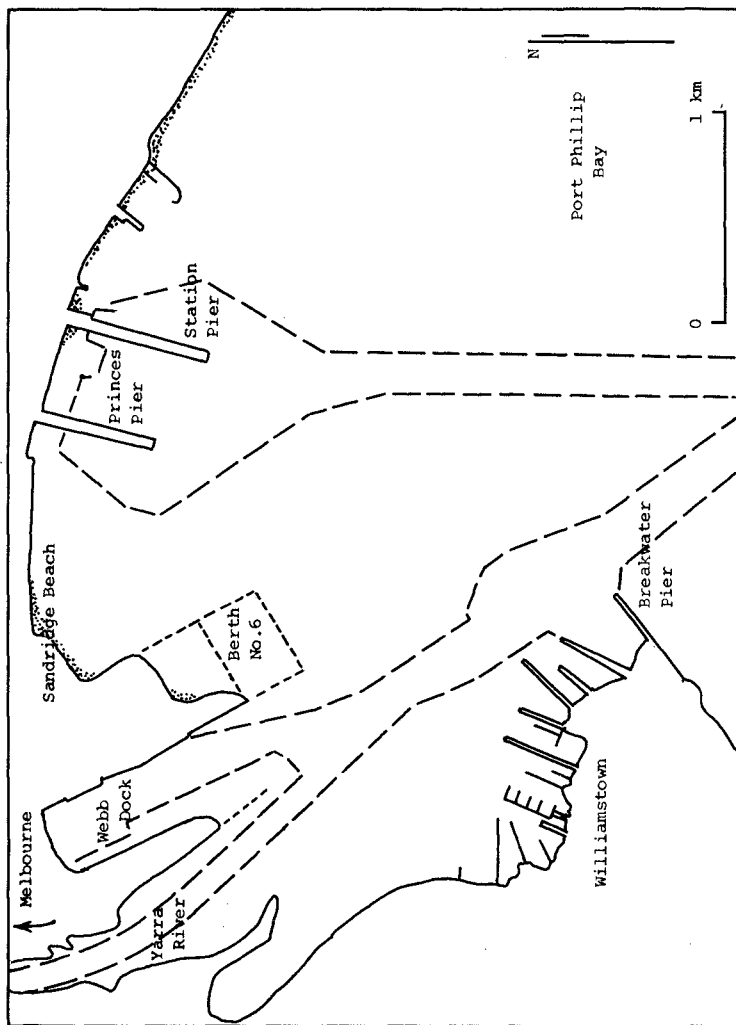


Fig. 1 Hobsons Bay, Melbourne

The ecological studies concentrated on sampling the intertidal and subtidal epibiota (algae and fauna) on port structures, and the benthic infauna of the bed and intertidal margins of the bay. Fish populations were sampled by seining in shallow water. A survey of recreational fishing in Hobsons Bay was conducted.

2.3 Results

The principal findings were:

- The water circulation in Hobsons Bay is primarily wind driven, but the effects of Yarra River flow and stratification must be taken into account and tides may be important in some circumstances.
- Except in the surface plume of water from the Yarra River, the water of Hobsons Bay is predominantly derived from Port Phillip Bay. Within the Yarra River and river plume, bacterial and nutrient levels are high and dissolved oxygen concentrations are below desirable levels. Elsewhere the water quality meets EPA objectives.
- Sand is found on and just offshore of the beaches. Sediment movement on Sandridge Beach, to the east of Webb Dock, is highly variable but is predominantly to the west. The silt bed of Hobsons Bay may be resuspended by wave action but is not undergoing significant net movement.
- Both the hard and soft substrates of Hobsons Bay and Webb Dock support a diverse and productive biota, and there are significant populations of fish. Productivity is lower in Webb Dock than in Hobsons Bay, but it is still high by general standards. The biological communities are well adapted to the existing environmental conditions and can withstand the disturbances imposed by shipping and the natural stresses of variable temperature and salinity.

All variables were related to water movement and water quality, hence predicted changes in flow patterns enabled the changes following construction of Berth 6 to be predicted.

3. COMPUTATION

3.1 Purpose

The extensive use of a computer data base and centralised programming system was anticipated to provide economical and fast data reduction and presentation and ready access to all data by all participants in the study. The advantages of centralisation are that by examining the needs of all groups together, uniformity of recording is obtained where possible, the number of data handling programs and the computational effort are reduced and ease of access and ease of inter-comparison of different types of variables are increased.

3.2 Method

The e.d.p. work was placed under the control of one staff member possessing both a broad knowledge of disciplines involved in environmental studies plus expert knowledge of computing, assisted by junior programmers and data entry personnel. The use of a purely computer oriented specialist was not seen to provide the proper liaison which this position required, but we recognise that we were very fortunate in obtaining the services of a man expert in both areas.

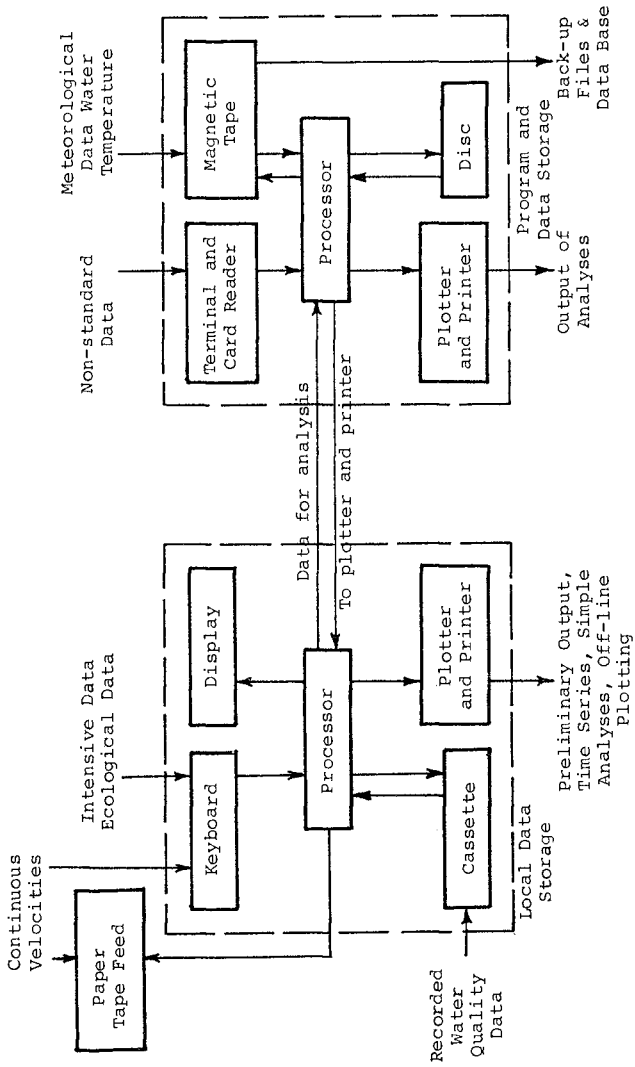
The e.d.p. specialist developed a general strategy for data entry and error checking, data file structure, frequently used data manipulation and reduction programs, and frequently used tabular and graphical presentations of data. He collaborated with other senior staff in development of these and specialised analysis programs required, supervised junior staff in preparing programs and using them, and trained all staff in the use of the system as it was developed.

Available funds permitted minor improvements to be made to the existing computer hardware. The existing system, shown schematically in Fig. 2, consisted of a Hewlett Packard model 9830 programmable calculator, with 8-K words memory, programmable in BASIC, with extended string and matrix handling capabilities. An internal cassette drive permitted storage of data with the capacity of 32-K words per cassette. The calculator was usable as stand-alone machine or as an intelligent terminal for data transmission to and from the University's Central Computer — a CDC Cyber. A small plotter was connected to the 9830 and other plotters were available at the University Computer Centre. This system serviced the Centre for Environmental Studies, and could not be wholly dedicated to this study, hence the decision was taken to provide an additional direct line to the University Computer and to provide an auxiliary cassette drive for the 9830.

The software required may be divided into four groups. Data entry and error checking routines were specially prepared for the study. Data manipulation, reformatting and editing routines were also specially written, to enable correction of data files, combination of files for use in calculations and to enable stranger tapes written in other computer installations to be read by the Cyber. Data preparation routines, including those used in smoothing raw data, for changing time base intervals, resolving vectors and so on, were again specially written although they utilised well known algorithms. Finally, the more substantial programs for tasks such as time series analysis or statistical analysis were obtained from other installations wherever possible. Because of its great convenience the SPSS package was utilised for all basic statistics operations, despite its inefficiency for some types of calculations.

3.3 Results

Approximately 300,000 data values were entered to form the main



CYBER

HP9830

Fig. 2 Computer configuration used for data entry archiving and processing

data base, while tapes obtained from government agencies contributed a further 200,000 data values, primarily meteorological data. The centralised programming facility provided approximately 80 programs, most of them in the area of data manipulation, reformatting and editing. Approximately 80 additional programs or variations of programs were prepared outside the central system, mostly in the areas of data analysis and presentation. Averaged over the course of the study, the computer specialist devoted between one and two days of each week to the job. Junior programmers contributed approximately one man year of work and data entry personnel approximately three man years. Other project staff contributed approximately half a man year to the programming and about the same to the data entry.

The forms of data input, principal computer files created and the source of the principal computer programs used are shown in Table 1 for the water quality and water movement data; the first six columns represent over 98% of the data. The table shows that a wide variety of input forms were used, most data were put onto local cassette for limited local computations and onto the central data base, and processed on the central computer programs. The similar tables for the sediment data again showed the same features with nearly all computation done centrally. The tables for the ecological and human activity data showed that most data were keyed in and entered into local cassette files and the central data base, but most computation was done locally or on programmable calculators.

The use of this system resulted in an excellent data base, achieved economically.

The anticipated benefits of rapidly available data and rapid presentation of simple analyses were not realised for three reasons. Firstly, at the conclusion of the year of data collection a bottleneck developed because of the excessive amount of data entry simultaneously with development and utilisation of the analysis programs. Computer specialists and hardware were both overloaded for several months and remained under pressure for a considerable time. Secondly, some members of the team possessed programming skills and chose to exercise them rather than await the development of programs by the hard-pressed computer specialist. This practical but necessary decision resulted in some duplication of efforts and reduced the future utility of the sets of programs developed, through use of different formats and less complete documentation.

Finally, the proper development of the analysis programs had to await the development of an understanding of the Hobsons Bay systems. For example, the spatial and temporal variability of currents in Hobsons Bay was greater than anticipated, so that the drogue movements — with their built in averaging — provided a better picture of water movements than did the current metering. The unexpectedly large populations of subtidal epibiota also lead to changes in methods of analysis.

TABLE 1 Use of Computer System for Water Quality Data

Date Type	Melb. wind, water Rain	Break-wind	River Flow	Cts. Current	Temp. Record	Intensive Data ³	Drain Data ⁴	Salinity Record	Droque Tracks	Bacteria Data ⁵
Input Form	T	K	K	KR	T (P,K,C)	K	P	K(C)	P	K
Local Cassette File	- ²	X	X	X	-	X	-	X	-	X
Central File (Data Box)	X	X	X	X	X	X	-	-	-	X
Local Computation	- ²	X	- ²	(X)	-	-	-	X	-	X
Central Computer Individual Programs	-	-	-	-	-	X	-	-	-	-
Central Computer Central Programs	X	X	X	X	X	(X)	-	-	-	-

T = Externally written tape

K = Keyed in

KR = Keyed in from record on paper tape

P = Paper copy only

C = Internally written cassette

() = Limited use only

X = Principal facility used

1 Calibration corrections only.

2 Limited data set used with bacteria data.

3 Current, temp., salinity, nutrients.

4 Discharge, temp., salinity, nutrients.

5 E. coli, temp., salinity, tide.

The appendix contains a description of one of the data entry programs and illustrates the passage of data from input to analysis.

4. INTEGRATION OF DISCIPLINES

4.1 Purposes of Integration of Disciplines

Direct collaboration between specialists in different disciplines is required for two principal reasons: firstly because of the need to utilise information obtained by one discipline to explain and extend the results obtained within another. For example, biomass and populations of the biota were found to depend upon the physical and chemical variables of temperature, salinity, turbidity, water velocity and location with respect to the river plume. Analysis and interpretation of these data required collaboration of sedimentologists, marine chemists, engineers and biologists.

Secondly, unless all factors are favourable, the making of a recommendation on proposed works requires that unlike quantities be compared or unlike measures be combined — for example a loss of water suitable for swimming might be offset by an increase in waters available for fish nursery areas.

4.2 Methods of Integration of Disciplines

Integration of the different disciplines required that the individuals perceive the benefits of close cooperation and that the facility for this cooperation be provided. As has been pointed out by many others, it is necessary to put effort into such collaborative work for it to succeed. Even the gaining of working knowledge of the jargon of the other disciplines requires effort, but is an essential pre-requisite to collaboration.

In the planning of this environmental study, as with most others, the tasks were distributed according to the specialised backgrounds of the different workers, so that one of the team was responsible for the ecological studies, another for the sediment studies, and so on. Such a division of labour seems to be unavoidable if high technical standards within each area of the study are to be achieved. The initial division then had to be overcome by conscious effort, by planning for the different parts of the study to interlock and by arranging for the offices of the different specialists to be in close proximity and for them to work together as much as possible.

Total integration was clearly not essential or even desirable. Determination of the hydrodynamic patterns required hour by hour measurements while determination of the typical populations of barnacles at a site required seasonal measurements and even the actual days of measurement did not have to coincide for the one series to provide support to the other. By not striving for needless synchronisation,

better use was made of boats, instruments and support personnel.

The flows of information are illustrated in Figs. 3, 4 and 5. Each figure shows the flows from left to right of raw data, reduced data and basic statistics, combined and correlated results of several types of data, culminating in the predicted change in a selected variable following construction. The flows of all levels of data to the data base have not been shown for clarity. Similar figures could be presented for other variables such as turbidity, epibiota, bacteria, algae, etc.

Both the correlated results, which describe the present regime of the bay, and the predictions are useful outputs from the study as are the raw data and basic statistics which provide a baseline against which future states may be compared.

4.3 Results of Integration of Disciplines

Despite an appreciation of the need for integration, the different specialist tasks diverged very early and some of the field measurements were carried out with inadequate regard to integration of the disciplines.

However, at the stage of analysis and reporting of results, a high degree of integration was achieved, in large measure by the channelling of all data through the e.d.p. specialist and by one of the senior staff making some contribution to the writing of all of the component parts of the report. The pressures of meeting deadlines within the specific tasks discouraged the other members of the team to become involved outside their own speciality except upon direct request. This is a very common experience with inter-group cooperation, where the willingness of the various individuals is not a sufficient stimulus in the face of the more clearly perceived pressures within their own specialist task, and since the collaboration between groups frequently depends on one or two individuals it may break down completely under such stress.

5. CONCLUSIONS

The interdependence of all parts of the study, at the level of interpretation and prediction has been shown. The water movement investigation and the water quality investigation proved so interdependent that they were completely merged early in the study. All parts of the study depended on the results of the water quality and water movement investigations with the latter playing the major role in the prediction of changes following construction. In this study, the predicted changes in all variables were very small and so application of multi-objective planning techniques was not necessary.

Integration was encouraged by joint planning, by working in close proximity, and by joint writing of each major section of the report.

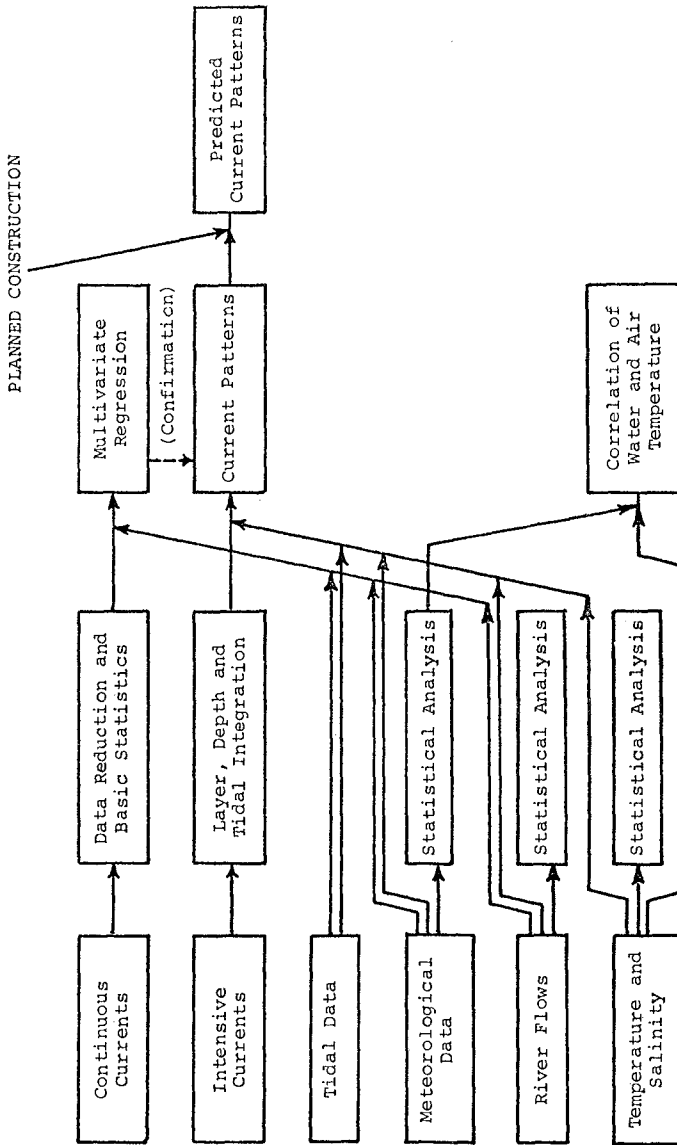


Fig. 3 Flows of information used to analyse currents and water temperatures

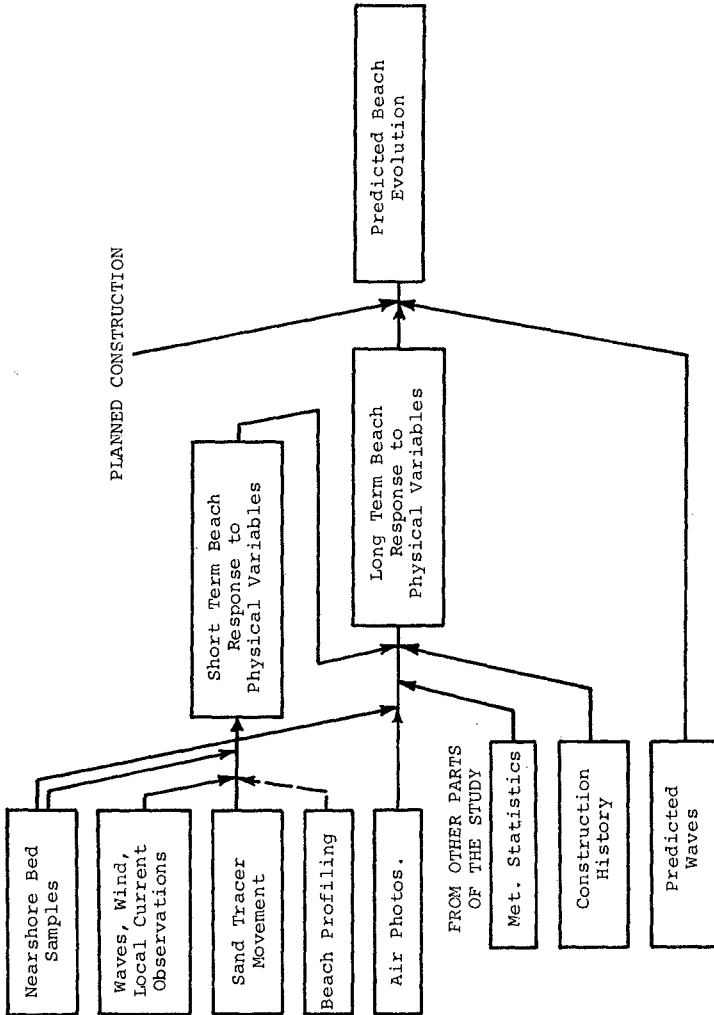


Fig. 4 Flows of information used to analyse beach dynamics

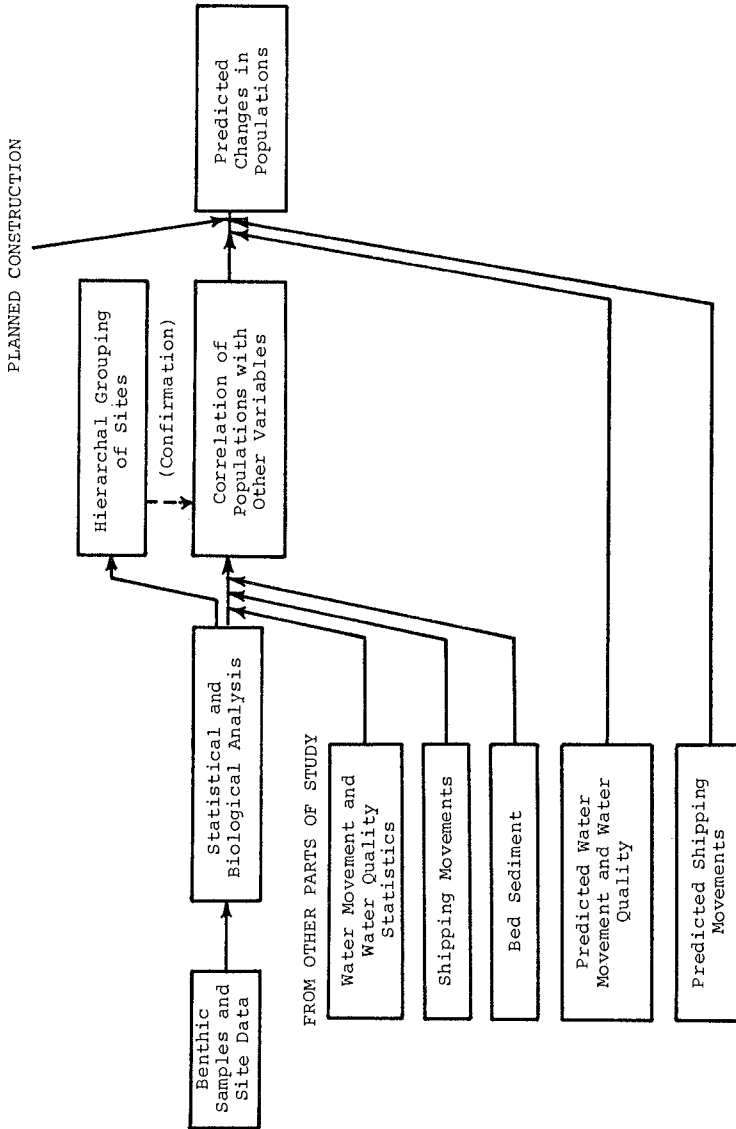


Fig. 5 Flows of information used to analyse benthic biota

However, full integration was not obtained because of the need to meet deadlines and the need to utilise specialists in each area to ensure high technical standards

The objective of a centralised computing service for the study was not wholly successful but was worthwhile by making available documented programs and data files, with common formats. The success achieved was largely due to having a person skilled in both computing and the disciplines involved in the study. Periods of high demand lead to delays, and to individually written programs which met the study objectives but are not of general use.

6. ACKNOWLEDGEMENT

The study was funded by the Port of Melbourne Authority, whose staff were of great assistance.

7. APPENDIX: DATA ENTRY, EDITING AND STORAGE

A suite of programs for use on the Hewlett Packard Model 9830 calculator was developed to facilitate data entry, error checking and transfer for the purposes of the study. Data collected during the intensive field exercise were recorded on special field sheets. These were hand edited in the office to correct for calibration and instrument errors prior to entry on the computer. Data were entered from the edited field sheets, or from printed paper tapes produced by the current meters, by specially trained operators, through the keyboard of the 9830, were stored on cassettes and were later transferred to the Cyber computer. Once stored in the Cyber, the data files could be corrected, data could be transformed, files could be joined or merged and listings or plots of data prepared.

As an example the sequence of steps for the continuously recording current meters will be described. These instruments printed the speed and direction on a paper tape at pre-determined intervals, normally five or fifteen minutes. For data entry the tapes were mounted in a specially constructed transport, mounted on the 9830. The operator, after mounting the tape and cassette, generated a header file on the cassette, specifying the maximum record length, number of data fields per record and the number of characters in each field. He then entered specifications of the parameters, comprising parameter name, measuring unit, alphanumeric or numeric, scalar or vector, precision, maximum and minimum expected values, time or position sequence of data, coordinate location of data point and time index.

The operator then commenced the actual entry of data entering a number for current speed and one for current direction. The following tests were automatically performed and if any succeeded, an error condition was signalled:

- Incorrect field length (number of characters).
- Illegal alpha characters.
- Number of decimal places does not correspond to specified precision.
- Decimal place omission.
- Presence of more than one decimal point.
- Presence of decimal point in integer field.
- Data out of range specified.

These errors had to be corrected by the operators before the data were stored on cassette. They could arise due to discrepancy between the raw data and the value entered or as a result of an anomalous value appearing in the data field resulting from instrumental or recording errors. Other errors were usually detected using basic statistical and time series functions, following data entry. The simplest check was to prepare a time series plot of the velocity magnitude and direction, or of the orthogonal components and to examine this plot for anomalous values. Basic statistics were obtained at the same time and gave an indication if the nature of the record differed from previous records.

The cassette prepared on the 9830 was then batched with various others to the Cyber as a raw data file. Errors detected through the time series plot and other means were then corrected using the file editing capability of the Cyber. Missing data were indicated by an asterisk or a sequence of 9s, but were not replaced. The raw data files then prepared form part of the data base.

Before the continuously recorded velocities could be used for analysis, files of 30 days of data had to be prepared. First the data were manipulated, to obtain values at constant time intervals throughout the files to be combined. This step was necessary as the starting time of one file might not be at an integral number of time steps after the end of the previous file, the time steps might not be equal in the two files, or the time step might be shorter than that needed for the analysis so that alternate data only might be required in the combined file. The two files were then combined, with the gap between them treated as any other missing data. If the sequences of missing data were short, they were filled by interpolation but if long they were filled manually utilising the best estimates after considering all of the available data. The resultant 30 day files were then stored as part of the data base and were utilised in data analysis.

Analyses performed using the 30 day files of current data included the preparation of velocity scattergrams, analysis of tidal harmonics, correlation of velocity data with wind and with atmospheric pressure, and correlation with velocity data obtained at other sites. From these analyses the physical factors responsible for the currents were ascertained, the likely velocities under particular sets of physical circumstances were predicted for periods of interest, and annual averages were estimated. In addition to time series plots and scattergrams, hodographs, cumulative vector plots and other pictorial representations were used to display the information on the velocity field. This work is presented by Dandy, Mills and Hinwood (1980). Tapes from

the instruments which were recorded in a computer compatible form were handled in the same fashion as 9830 raw data cassettes.

8. REFERENCES

DANDY, G.C., MILLS, D.A. and HINWOOD, J.B. (1980), Water movement studies required for port planning, 17 ICCE, Sydney, March 1980.

MILLS, D.A., COLMAN, R.S. and DANDY, G.C. (1978), Water movement in a complex estuarine embayment — a methodology for data collection and analysis, Proc. 4th Aust. Conf. on Coastal and Ocean Eng., Adelaide, Nov. 1978, Institution of Engineers, Aust., Canberra.

SOME RECENT RESULTS FOR WAVE INDUCED MOTIONS
OF A SHIP IN SHALLOW WATER

P. Å. Madsen* I. A. Svendsen* C. Michaelsen*

ABSTRACT

The paper describes an analytical approach to the problem of wave induced oscillations of a long ship in water with a depth which is only slightly larger than the draught of the ship. The problem is linearized (i.e. small amplitude motions and waves) and the water flow induced by the incident waves, and by the motion of the ship is determined. This also yields results for the forces in the equations of motion for the ship. These equations can be solved analytically, but the paper concentrates on giving numerical results for the solutions. Results are also given for the hydrodynamic masses and movements of inertia, and for the damping due to radiation of wave energy.

1. INTRODUCTION

The problem of ship motions in water of limited depth has been approached by several authors previously. The difficulty is the presence of the sea bed. Wilson (1958) represented this by empirically increasing the hydrodynamic mass and the damping of the ship, and Wendel (1950) determined the hydrodynamic mass of a hull section theoretically by conformal mapping. More successful is the integral equation method which consists in transforming the boundary value problem of the flow equations into an integral equation assuming the waves to be small amplitude sinusoidal (see e.g. Bai and Yeung (1974) and van Oortmerssen (1976)). Whereas this method works well for deep water conditions, the numerical computations require an increasingly large number of integration points as the depth decreases towards the draught of the ship. Yet van Oortmerssen is able to present results for hydrodynamic masses at a draught to depth ratio as large as 0.95.

Recently Andersen (1979) used a finite element technique to solve the problem numerically, but in principle had the same difficulties in describing the flow close to and underneath the ship when the draught of the ship is close to the depth of water. The largest value of the draught to depth ratio for which results are given is 0.67. Both van Oortmerssen and Andersen, however, can treat the full three-dimensional problem. The same does in principle Tuck (1970) who uses a slender body approach for which he gives results for added mass and damping coefficients.

*Inst. of Hydrodyn. and Hydraulic Engrg. (ISVA), Tech. Univ. Denmark, Build. 115, DK-2800 Lyngby. — Mail should be sent to: I. A. Svendsen.

The method presented in this paper is based on an approximation which makes it well suited to treat exactly the cases of very small underkeel clearance. In fact, the smaller the underkeel clearance, the better is the approximation. It is, however, essentially based on the assumptions of two-dimensional motion and hence restricted to application to a long ship and the heave, roll and sway motion of such a ship. Actually we will see that as the sway motion for a ship in very shallow water is strongly influenced by three-dimensional effects (the water can flow around the ends of the ship as well as beneath it) the results for sway are the least accurate. This is further discussed in § 5. The paper formulates the problem which originates from the above mentioned idea (§ 2). The equations are linearized, and the solution for the water flow is then determined by dividing the problem into subproblems which are described briefly, and examples of the solutions are given (§ 3). In § 4 we discuss the wave induced heave motion and in § 5 the roll and sway motions. Finally, the results for hydrodynamic masses and moments of inertia are given in § 6 and results for the wave generation (i.e. the damping coefficients) are presented in § 7.

2. BASIC ASSUMPTIONS AND EQUATIONS FOR THE WATER MOTION

The motion of the ship is caused by the pressure forces generated by the water motion. To determine this we consider the two-dimensional situation of a ship in beam seas. The hull is approximated by a rectangular shape (Fig. 1, which also shows the notation) and the basic assumptions are then

- (i) In the clearance $R \ll h$ the flow velocity is entirely horizontal (i.e. $w \ll u$) and uniform over R . This is assumed to apply at sections 1-1 and 2-2, and it implies static pressure variation under the ship.
- (ii) The motion under the ship is considered separately and matched directly to the flow outside the gap by requiring continuity in pressure (averaged over R) at 1-1 and 2-2.

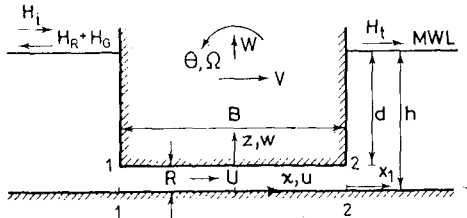


Fig. 1 Definition sketch.

a. The water motion beneath the hull

With reference to (i) the continuity equation for the flow beneath the hull is written

$$\frac{\partial Q}{\partial x} = - \frac{\partial R}{\partial t} \quad \text{with} \quad Q \equiv \int_0^R u dz = uR \quad (1)$$

Since

$$R = R_0 + z_0(t) + \theta(t) x \quad (2)$$

where R_0 represents the equilibrium position, z_0 and θ the heave and roll motions, respectively, we get

$$\frac{\partial R}{\partial t} = z_{0t} + \theta_t x \equiv W(t) + \Omega(t) x \quad (3)$$

where $W(t)$ and $\Omega(t)$ represent the velocity of the heave motion and the angular velocity of the roll, respectively, of the ship. Substituting (3) into (1) and integrating yields Q and hence U as a function of W and Ω

$$U(x,t) = -\frac{1}{R} \left\{ Wx + \Omega \frac{x^2}{2} + A(t) \right\} \quad (4)$$

where the arbitrary function $A(t)$ represents the net flux through the gap caused by different (wave) pressures at the two sides of the hull.

The horizontal component of the equation of momentum becomes

$$\frac{\partial U}{\partial t} + U \frac{\partial U}{\partial x} = -\frac{1}{\rho} \frac{\partial p}{\partial x} \quad (5)$$

The pressure $p^+(x,z,t)$ generated by the wave and ship motion is extracted from p by the definition

$$p(x,z,t) = p^+(x,t) + \rho g(h-z) \quad (6)$$

where p^+ according to (i) is independent of z .

Substitution of (4) and (6) into (5) then yields (after integration) the following relation between the pressure p^+ in the gap beneath the hull and the roll and heave motion described by Ω and W

$$\begin{aligned} -\frac{1}{\rho} p^+(x,t) = & \frac{1}{R^2} \left\{ \frac{\Omega^2}{8} x^4 + \frac{1}{2} W \Omega x^3 + \frac{1}{2} (W^2 + \Omega A) x^2 + W A x + \frac{1}{2} A^2 \right\} \\ & + \frac{1}{2} \Omega^2 \int x^3/R^2 dx + \frac{3}{2} W \Omega \int x^2/R^2 dx + (W^2 + \Omega A) \int x/R^2 dx \\ & + W A \int R^{-2} dx - W_t \int x/R dx - \frac{1}{2} \Omega_t \int x^2/R dx - A_t \int R^{-1} dx \\ & - p_0^+(t)/\rho \quad \quad \quad -\frac{B}{2} \leq x \leq \frac{B}{2} \quad (7) \end{aligned}$$

where the arbitrary function $p_0(t)$ represents the pressure $x=0$, and the integrals may be evaluated by substituting (2) for R .

Eq. (7) is the general result for the pressure beneath the hull, expressed in terms of the heave and roll motions of the ship, and $A(t)$ and p_0^+ . We can find $A(t)$ and p_0^+ and determine the water pressures on the side of the hull and then substitute this into the equations of motion for the hull we get three simultaneous, ordinary (but non-linear) second order differential equations for the heave, roll and sway motions. These equations can in principle be solved by straightforward numerical procedures.

To obtain analytical solutions, however, we will here assume that the vertical component of the ship motion causes only small changes in R (which will be true for most situations in practice anyway). Then

(7) in the first approximation can be shown to reduce to the far simpler

$$\frac{1}{\rho} p^+(x,t) = \omega_t \frac{x^2}{2R} + \Omega_t \frac{x^3}{6R} - \frac{A_t}{R} x + p_0^+(t)/\rho \tag{8}$$

The only real problem left is then to determine the pressure p_0^+ , the function A and the pressures on the side of the hull. All these quantities are closely related to the water motion at the side of the hull (i.e. $|x| \geq B/2$).

b. The water motion at the side of the hull

This water motion is caused by a combination of the incoming waves, their reflection from the hull and transmission through the gap beneath the ship hull to the other side, and by the waves generated by the heave, roll and sway motion of the ship.

The following additional assumptions are used:

- (iii) We neglect all energy dissipation and boundary layer effects and assume potential flow everywhere.
- (iv) Both incoming and generated waves are assumed of small amplitude.

Thus the problem of wave motion at the side of the ship is linear too and we may consider the different components separately. Introducing the velocity potential ϕ (with $\vec{v} = (u,w) = -\nabla\phi$) the problem is to solve the Laplace equation

$$\nabla^2 \phi = 0 \tag{9}$$

at each side of the ship satisfying the following boundary conditions (here formulated for the right hand side of the ship)

$$\phi_{tt} + g \phi_z = 0 \quad \text{at } z = h \quad 0 < x_1 < \infty \tag{10}$$

(with $x_1 = x - B/2$, see Fig. 1)

$$\phi_z = 0 \quad \text{at } z = 0 \quad 0 < x_1 < \infty \tag{11}$$

$$\phi_x = \begin{cases} -U_2 \\ \Omega(t)(z-m) - V \end{cases} \quad \left. \begin{matrix} 0 < z < R \\ R < z < h \end{matrix} \right\} x_1 = 0 \tag{12}$$

where $U_2 = U(x=B/2,t)$ in (4), and V is the velocity of the sway motion of the ship. m is the height of the point of rotation above the sea bed.

Finally at $x_1 \rightarrow \infty$ a radiation condition applies. This boundary value problem for the flow at $|x| > B/2$ is illustrated in Fig. 2.

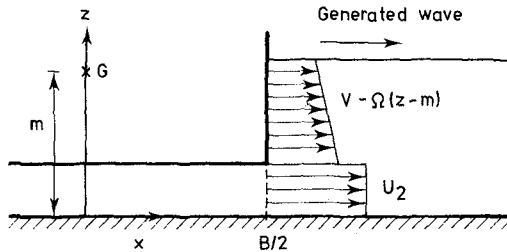


Fig. 2
Boundary value problem for flow at the side of the hull.

The total motion in the linear problem then consists of the following components:

1. The standing wave composed of the incoming plus a (formally) fully reflected wave. This motion occurs only at one side of the hull (assumed to be the left side in Fig. 1). (ϕ_W, H_W, p_W^+ etc.)
2. The motion generated under a fixed ship by the above mentioned standing wave. On the right hand side this represents the waves transmitted through the opening beneath the hull. On the left hand side it represents the reduction in reflection due to the transmission. (ϕ_G, H_G, p_G^+ etc.)
3. The waves generated by the sway motion of the ship. (ϕ_S, H_S, p_S^+ etc.)
4. The waves generated by the heave motion of the ship. (ϕ_H, H_H, p_H^+ etc.)
5. The waves generated by the roll motion of the ship. (ϕ_R, H_R, p_R^+ etc.) where we have

$$\phi = \phi_W + \phi_G + \phi_S + \phi_H + \phi_R; \text{ etc.} \quad (13)$$

It should be mentioned that it is not strictly necessary for a solution to split the problem into the components described above. The solution may, of course, well be obtained by solving the complete boundary value problem described by (9) - (12). The splitting is convenient, however, since the results are rather complicated and since the effect of the individual components of the total motion has to be separated anyway later on in the equations of motion for ship.

3. DESCRIPTION OF FLOW COMPONENTS AND RESULTS

In the following we give some results for the pressures induced on the ship in each of the flow situations mentioned above. As the calculations are rather tedious it will be impossible at the space available to bring details of the derivations.

A more detailed description of the solution for the heave generated flow was given by Svendsen (1968) (who in fact considered the case of large amplitudes). For roll (point 5 in the list above) the flow problem was analysed by Svendsen et al. (1977 a), and the reflection-transmission problem (points 1 and 2) was discussed in Svendsen et al. (1977 c).

The method of solution is to write the velocity potential at $|x| \geq B/2$ for each of the flow components

$$\phi_i = e^{i(\omega t + \psi_i)} \sum_n X_{in}(x) Z_{in}(z) \quad (14)$$

and assume that in (4) and (12) U_2, W, Ω and V vary as $e^{i(\omega t + \gamma_i)}$.

a. The reflection-transmission problem

The water flow around a fixed ship in waves is sketched in Fig. 3. The wave pattern consists of the standing wave which yields the pressure

$$p_W^+ = \rho g H_i \frac{\cosh kz}{\cosh kh} \cos \omega t \quad \text{at} \quad x = -B/2 \quad (15)$$

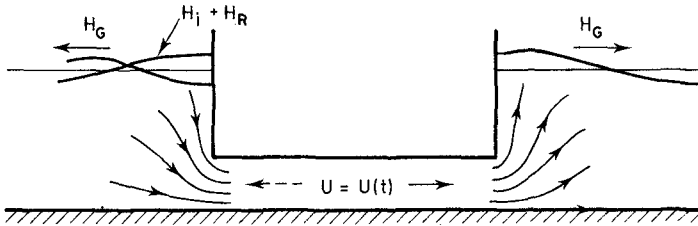


Fig. 3 Description of wave induced flow around a fixed ship.

and the waves generated by the water flow under the hull. This flow is induced by a combination of the standing wave pressure given by (15) and the pressure from the waves generated by the flow itself. Therefore the solution to the problem involves determination of the velocity U_G beneath the hull, and since the body of water has a certain inertia (finite width of the ship) U_G is not in phase with p_W^+ and neither are the waves generated.

To illustrate the nature of the results we find for U_G

$$U_G = \frac{H_i \omega}{a^2 + b^2} e^{(b \cos \omega t + a \sin \omega t)} \quad (16)$$

where

$$e = \frac{g}{\omega^2 B} \frac{\sinh kR}{kR \cosh kh} \quad (17)$$

$$a = 1 + 8h B_W/B; \quad b = 8h A_W/B \quad (18)$$

and

$$A_W = \frac{\sinh^2 kR}{(kR)^2 (\sinh 2kh + 2kh)} \frac{R}{h} \quad (19)$$

$$B_W = \sum_n \frac{\sin^2 \sqrt{\lambda_n} R}{(\sqrt{\lambda_n} R)^2 (\sin 2\sqrt{\lambda_n} h + 2\sqrt{\lambda_n} h)} \frac{R}{h} \quad (20)$$

The parameter k is the wave number which in general satisfies the dispersion relation

$$\omega^2 - gk \tanh kh = 0 \quad (21)$$

where ω is the frequency of the incident and the generated waves, and $\sqrt{\lambda_n}$ similarly satisfies the equation

$$\omega^2 + g\sqrt{\lambda_n} \tan \sqrt{\lambda_n} h = 0 \quad (22)$$

Eq. (21) has one root whereas (22) has infinitely many roots.

The total pressures p_{WG} under the hull corresponding to the combination of the standing wave and the generated waves may then be written

$$p_{WG}^+(x, t) = 8\rho\omega h \left\{ A_W U + B_W U_G/\omega \right\} \frac{x}{B} + \rho g H_i \frac{\sinh kR}{kR \cosh kh} \cos \omega t \left(\frac{1}{2} - \frac{x}{B} \right) \quad -\frac{B}{2} \leq x \leq \frac{B}{2} \quad (23)$$

and along the sides of the hull ($x = \pm B/2$) we get (in addition to p_W in (15))

$$\begin{aligned}
 p_G^+(\frac{B}{2}, z, t) &= - p_G^+(-\frac{B}{2}, z, t) \\
 &= 4 \rho \omega h \left\{ A U \cosh kz + \sum b_n \frac{U_t}{\omega} \cos \sqrt{\lambda_n} z \right\}
 \end{aligned}
 \tag{24}$$

where

$$A = \frac{\sinh kR}{kR(\sinh 2kh + 2kh)}
 \tag{25}$$

$$b_n = \frac{\sin \sqrt{\lambda_n} R}{\sqrt{\lambda_n} R (\sin 2 \sqrt{\lambda_n} h + 2 \sqrt{\lambda_n} h)}
 \tag{26}$$

Notice that in this case where U is independent of x we find (in accordance with (the linearized version of) (5)) that p^+ varies linearly with x in the gap underneath the ship ($- B/2 < x < B/2$). It should also be mentioned that since the pressure due to (24) varies with z , which p^+ under the ship by assumption does not (see (6)), the continuity in pressures at 1-1 and 2-2 (Fig. 1), has been imposed on the mean values over R .

Figs. 4 and 5 show the variation of the pressures given by (23) (at $x = B/2$) and (24), respectively. We see that for most situations the assumption of p^+ constant over k , which led to averaging p^+ over R for the flow outside the gap, is actually quite reasonable, in particular for long waves.

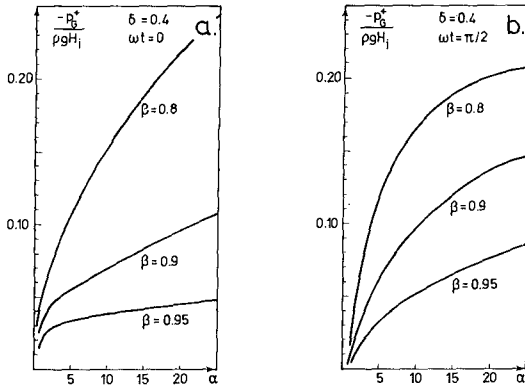


Fig. 4 Pressure variation at 2-2 versus $\alpha = g/\omega^2 h$ and $\beta = d/h$ for a fixed ship

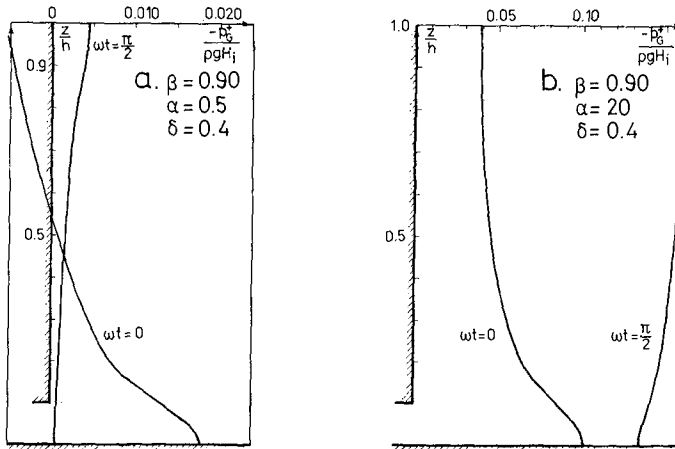


Fig. 5 Pressure variation along the side of a fixed ship.

b. Flow and pressures induced by sway

The instantaneous flow pattern generated by a forced sway motion is shown in Fig. 6. Qualitatively this flow resembles the motion generated by the standing wave system described above, but quantitatively the problem is closer related to the flow around a piston type wave generator with a large leak at the bottom. The difference is that in our problem the width of the ship is significant which (as mentioned above) makes the inertia of the water volume beneath the hull an important factor. It causes both a change in amplitude of the waves generated, and a phase shift relative to the motion of the ship.

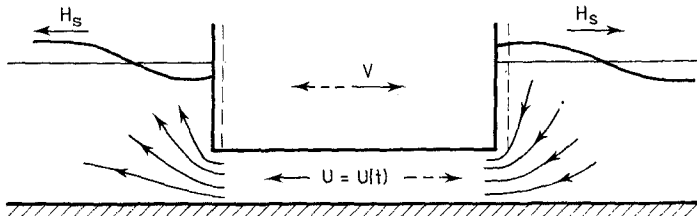


Fig. 6 Description of flow induced by a sway motion.

In the end the pressures on the hull corresponding to the flow will be integrated to forces which enter the equations of motion, and in principle we may envisage both horizontal and vertical forces, and moments about the center of gravity to originate from each component of motion considered. Since each of these forces or movements represents

the reaction on the ship from the surrounding water due to the motion in question and hence depends on that motion (e.g. the sway), it is crucial for the solution of the equations for the motion of the ship to express the magnitude of the above mentioned forces and moments in terms of the velocity and acceleration associated with the component of motion in question. Thus for sway the solution for the pressures on the hull is written

$$P_S^+ = f_1 \left(g/\omega^2 h, \frac{d}{h}, \frac{d}{B}, x \right) V + f_2 \left(g/\omega^2 h, \frac{d}{h}, \frac{d}{B}, x \right) V_t/\omega \quad -\frac{B}{2} \leq x \leq \frac{B}{2} \quad (27)$$

where V and V_t are instantaneous velocities and accelerations, respectively, in the sway motion.

Both Ω and W are zero for pure sway, so we see from (8) that for sway the pressure under the ship must vary linearly with x . The variation at $x = B/2$ (sect. 2-2) is shown in Fig. 7. The pressures are shown at two different times, namely at the time when $V_t = 0$ (Fig. 7 a) and at the time when $V = 0$ (Fig. 7 b). Thus the two figures give the coefficients of each of the two terms in (27). Along the side the pressure variation is a cosh kz superimposed by the classical $\cos \sqrt{\lambda_n} z$ terms also present in (24), and the same averaging of the pressures over R has again been applied in the matching procedure.

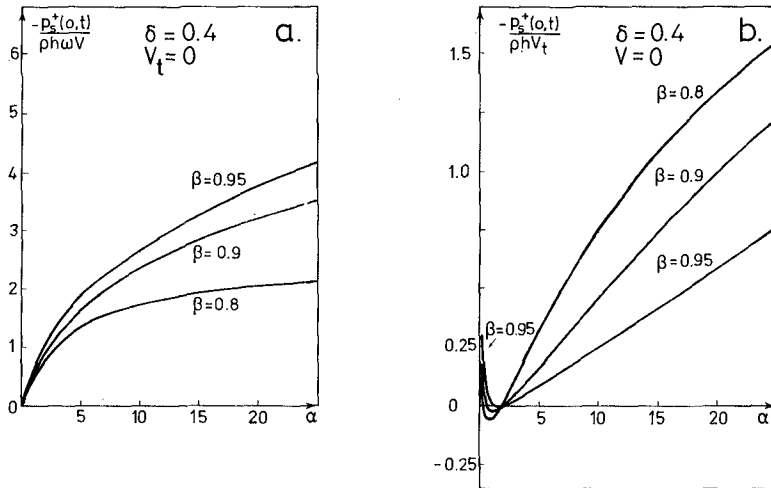


Fig. 7 Pressure variation at 2-2 versus $\alpha = g/\omega^2 h$ and $\beta = d/h$ for sway induced flow.

c. Flow and pressures induced by heave

The results for this case can be derived directly from Svendsen (1968) by linearizing with respect to W , the velocity in the heave motion. The flow is described in Fig. 8.

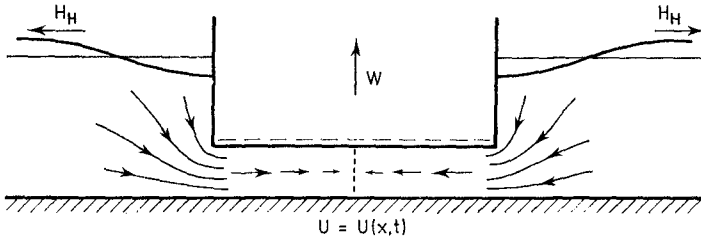


Fig. 8 Description of flow induced by a heave motion.

As can also be inferred from (8) the pressure under the ship varies as x^2 , because for symmetry reasons we must have $A(t) = 0$. Here we show figures with the pressure variation with x under the ship (Fig. 9) and the variation at sect. 2-2 (Fig. 10), in both cases at two different times, namely when $\dot{W}_t = 0$ (Fig. 10 a) and when $W = 0$ (Fig. 10 b). Writing again the pressures as

$$p_H^+ = g_1 W + g_2 \dot{W}_t / \omega \tag{28}$$

this means that Fig. 10 shows the two coefficients in (28) at sect. 2-2.

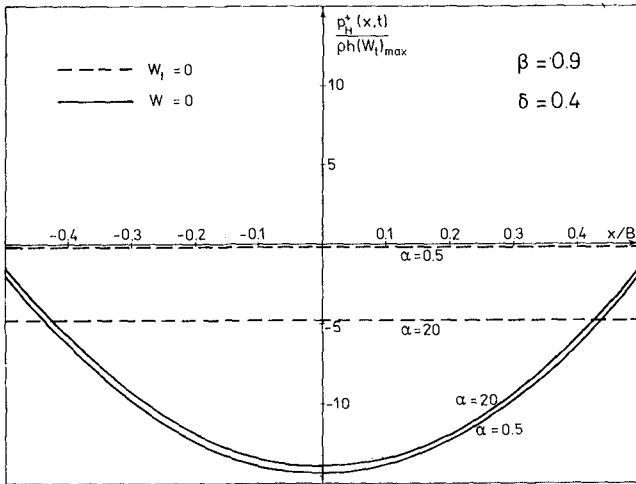


Fig. 9 Pressure variation under the ship induced by a heave motion.

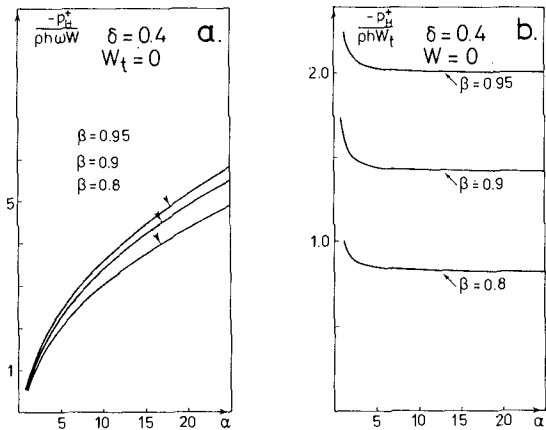


Fig. 10 Variation of pressure at 2-2 for heave induced flow.

d. Flow and pressures induced by roll

This represents by far the most complicated flow conditions. The situation is shown in Fig. 11. Whereas the flow outside the gap is more or less the same as in the previous cases we see that under the ship the direction of the flow changes at two points. The flow is illustrated quantitatively in Fig. 12 where the discharge Q is shown versus x for different phases. Two cases are shown: a typical deep water situation (Fig. 12 a) and a long wave situation (Fig. 12 b). Since $Q = UR$ we see from (4) that Q varies as x^2 . The situation is somewhat more complicated, however, because the waves generated are in antiphase which causes $A(t)$ to be non-zero which again means there is a phase difference between U and the angular velocity Ω of the roll motion (as for sway). This is particularly clear in Fig. 12 b where $U \neq 0$ when $\Omega = 0$ and the points of zero velocity are changing with time.

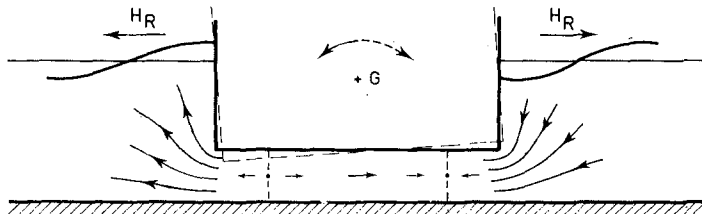


Fig. 11 Description of flow induced by a roll motion.

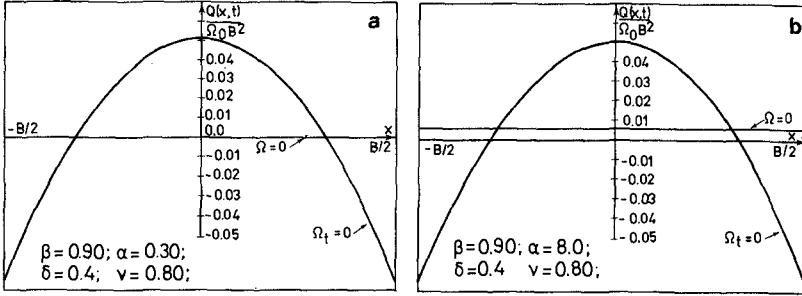


Fig. 12 Discharge Q under the ship induced by a roll motion.

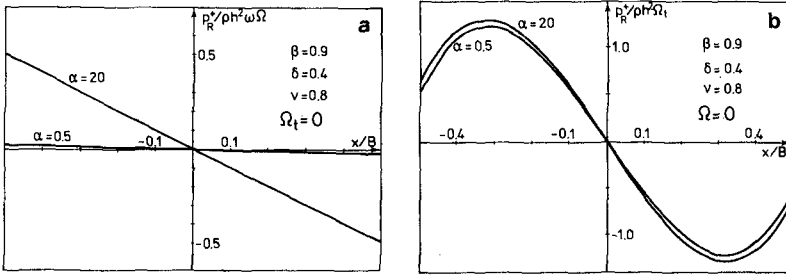


Fig. 13 Pressure variation under the ship induced by a roll motion.

Fig. 13 shows the corresponding pressures which according to (8) vary as x^3 with an x component due to $A(t)$.

As in the previous cases the result for the pressure along the side of the ship contains one term varying as $\cosh kz$ and an infinite number of terms varying as $\cos \sqrt{\lambda_n} z$ (where $\sqrt{\lambda_n}$ are the solutions to (22)) which are necessary to satisfy the boundary conditions for the flow at $|x| = B/2$. All the results for roll are rather complicated and we shall omit them here.

4. WAVE INDUCED HEAVE MOTION

The equations of motion for the ship are the three components of Newton's second law corresponding to horizontal and vertical projection, and moment about an axis perpendicular to the x - z -plane through the center of gravity G .

It turns out that neither roll nor sway produce total pressure forces on the ship which has vertical components. Similarly heave does not produce net horizontal forces or forces that have a moment about G . Consequently the equation for heave (vertical projection) does not contain terms proportional to V , V_t , Ω or Ω_t and the other two equations have no terms with W or W_t . This means that heave is not coupled to

the other two degrees of freedom, and the equation for wave induced heave may be solved independently of the equations for roll and sway. This problem of wave induced heave was described in some detail by Svendsen et al. (1977 b).

When the forces are integrated as mentioned previously we find for the heave motion $z_0(t)$ the equation

$$M_H \frac{d^2 z_0}{dt^2} + S_H \frac{dz_0}{dt} + g z_0/d = g \frac{H_i}{2d} \frac{\sinh kR}{kR \cosh kh} \cos \omega t \quad (29)$$

where

$$M_H = 1 + \frac{2B}{d} B_w + \frac{B^2}{12Rd} \quad (30)$$

$$S_H = \frac{2B}{d} A_w \omega \quad (31)$$

In (30) the first term (1) represents the mass of the ship. The other two terms in (30) originate from the components of the water pressures which are proportional to W_t . Hence these two terms represent the hydrodynamical mass for the heave motion.

The coefficient S_H represents the damping of the oscillation which is linear, i.e. proportional to W . The energy dissipation described by this W -term is physically caused by the generated waves which carry energy away from the ship.

Even though the problem has been linearized it still contains the leading or dominating effect of the presence of the bottom. From (29) we can deduce that this effect emerges as a quite significant change in the resonance frequency, relative to the value we would have in deep water. The reason is that the hydrodynamic mass increases rapidly when the underkeel clearance decreases (as we shall see later).

In Fig. 14 is shown the resonance or natural frequency ω_e (undamped) nondimensionalized as $g/(\omega_e^2 h \beta)$. The deep water value for ω_e shown in the figure has been determined using the results for the hydrodynamic mass in deep water given by Andersen (1978).

The equation (29) may be solved analytically, and the result becomes

$$\left. \begin{aligned} \frac{z_0(t)}{H_i} &= \frac{\alpha(\alpha - \beta M_H)}{2(\beta^2 S_H^2 + (\alpha - \beta M_H)^2)} \frac{\sinh kR}{kR \cosh kh} \frac{\cos(\omega t + \phi)}{\cos \phi} \\ \text{where} \quad \phi &= \arctan \left(\frac{-\beta S_H}{\alpha - \beta M_H} \right) \\ \text{and} \quad \alpha &\equiv g/\omega^2 h \quad \beta = d/h \end{aligned} \right\} (32)$$

Numerical results for the amplitude of (32) are shown in Fig. 15 for three different values of β . We notice that somewhat unexpected perhaps the amplitudes generally increase as the underkeel clearance decreases.

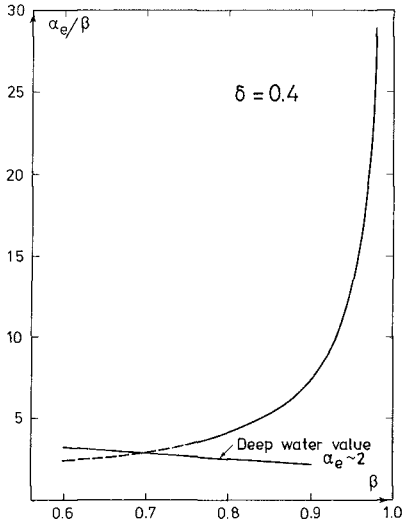


Fig. 14 The resonance frequency ω_e for heave versus $\beta = d/h$

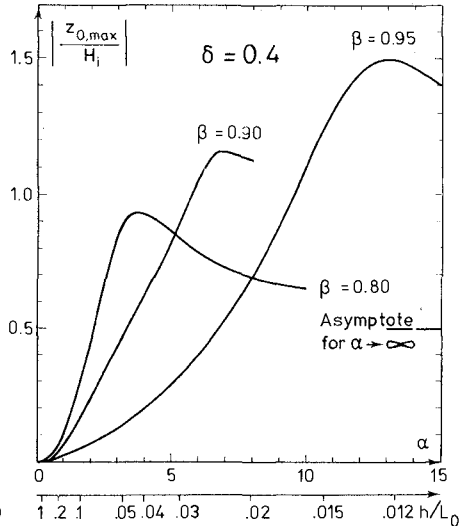


Fig. 15 The amplitudes of wave generated heave motion versus $\alpha = g/\omega^2 h$

5. WAVE INDUCED ROLL AND SWAY MOTION

In contrast to heave the presence of a sway motion will automatically generate a roll motion and vice versa. These two motions are even in this simple model coupled, and the corresponding two equations of motion consequently contain terms with both independent variables (simultaneous differential equations). This naturally complicates matters a great deal, but since the equations for a given incident wave are ordinary second order differential equations with constant coefficients an analytical solution is in principle straightforward. The algebra and the results are just rather complicated, so we only present the equations and numerical results for the solution. The equations may be written

$$a_1 \frac{d^2 \xi}{dt^2} + a_2 \frac{d\xi}{dt} + a_3 \xi = a_4 \frac{d^2 \theta}{dt^2} + a_5 \frac{d\theta}{dt} + a_6 \theta + a_7 \cos \omega t + a_8 \sin \omega t \quad (33)$$

$$b_1 \frac{d^2 \theta}{dt^2} + b_2 \frac{d\theta}{dt} + b_3 \theta = b_4 \frac{d^2 \xi}{dt^2} + b_5 \frac{d\xi}{dt} + b_6 \xi + b_7 \cos \omega t + b_8 \sin \omega t \quad (34)$$

where $\xi(t)$ represents the sway motion and $\theta(t)$ the roll.

The coefficients (a_i, b_i) are here functions of the parameters of the problem. Of those we have already mentioned $\delta = d/B$, $\beta = d/h$ and $\alpha = g/\omega^2 h$.

However, other parameters enter the problem too. Firstly, the coefficient a_3 which represents the restoring force in the sway motion can

only be nonzero if we introduce e.g. mooring lines. This brings two new parameters into the problem: $k_F/\rho gh$, the nondimensional stiffness of the moorings (pr. m length of the ship), and l/h the nondimensional height of the mooring point above the center of gravity (see Fig. 16). These parameters actually occur in a_3, b_3, a_6 and b_6 .

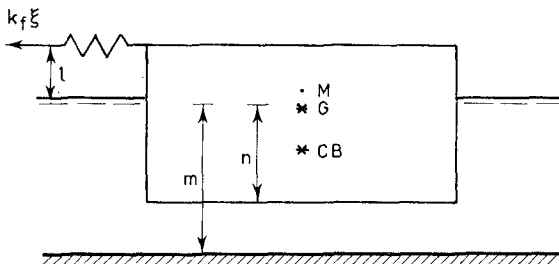


Fig. 16 The geometry of moorings and ship's stability.

Secondly, the roll motion of course depends on the stability of the ship, i.e. on the height n of the center of gravity above the bottom of the ship (Fig. 16). In the presentation of the numerical results n is nondimensionalized as $v = n/d$.

Quite obviously it is not possible numerically to map the variation of the results with all these parameters. We have therefore chosen to show the variation with what we consider the most interesting two, namely α and β , and in doing so we keep the other parameters fixed at chosen values.

Thus from stability considerations (ships usually have a metacentric height of a few metres) we have chosen $\gamma = 0.8$. For $k_F/\rho gh$ it may be shown that even a set of the stiffest steel wires cannot bring $k_F/\rho gh$ above about 0.1, and we will see that the stiffest moorings are the most interesting for our conclusions. So we show results for $k_F/\rho gh = 0.1$ only. Further we use (a little unrealistically) $l = 0$, but it may be inferred from the results that this is not so important. Finally we choose $\delta = 0.4$ which is a realistic value particularly for bulky ships as tankers or bulk carriers.

Fig. 17 then shows results for the resonance periods at different β . Since there are two degrees of freedom there are also two resonance frequencies. Each of these represents a free oscillation in which both roll and sway occur but locked together phasewise and with a fixed ratio between their amplitudes.

We notice that one of the resonance frequencies is much smaller than the other. The associated mode of resonant oscillation consists predominantly of sway. This shows that even for the stiffest moorings we can think of ($k_F/\rho gh = 0.1$) the resonance period for the sway-type mode of oscillations corresponding to very long period waves. In storm waves such waves merely occur as subharmonics. The phenomenon is quite well-known, as in harbours or model experiments with harbours particularly sway (and surge) motions often occur at a subharmonic frequency.

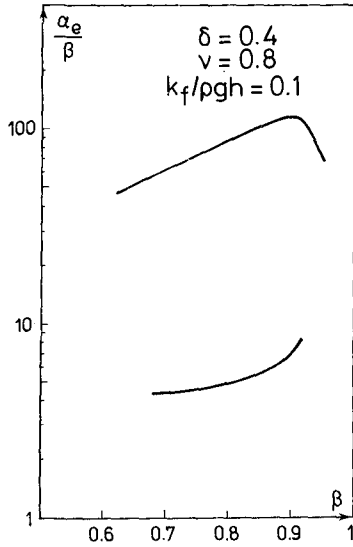


Fig. 17 Resonance frequencies for coupled roll and sway.

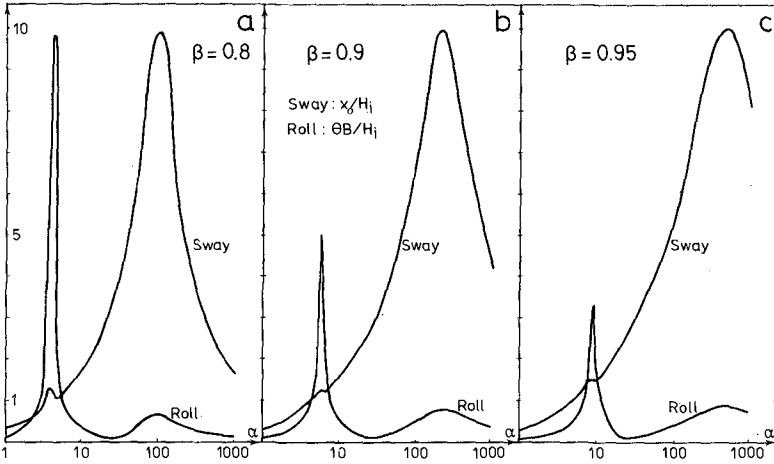


Fig. 18 The amplitudes of wave generated roll and sway.

It should be added, however, that in particular for sway the three-dimensional effects may be quite important. In a three-dimensional model the water can escape both beneath the ship and around the ends. The latter possibility is not included in our two-dimensional model, and in particular for a small underkeel clearance this will yield too large values of the hydrodynamical mass and consequently too large values of the resonance period.

Results for the wave induced amplitudes are given in Fig. 18 versus α for three different values of β .

6. HYDRODYNAMIC MASSES AND MOMENTS OF INERTIA

As was already indicated in the description of wave induced heave, one of the by-products of the solution for the water flow is the hydrodynamic masses for heave and sway and the hydrodynamic moment of inertia for roll.

These quantities represent that part of the pressure forces which is proportional to the acceleration in the motion considered. Numerical results are given in Fig. 19. The values given are relative to the ships mass or moment of inertia.

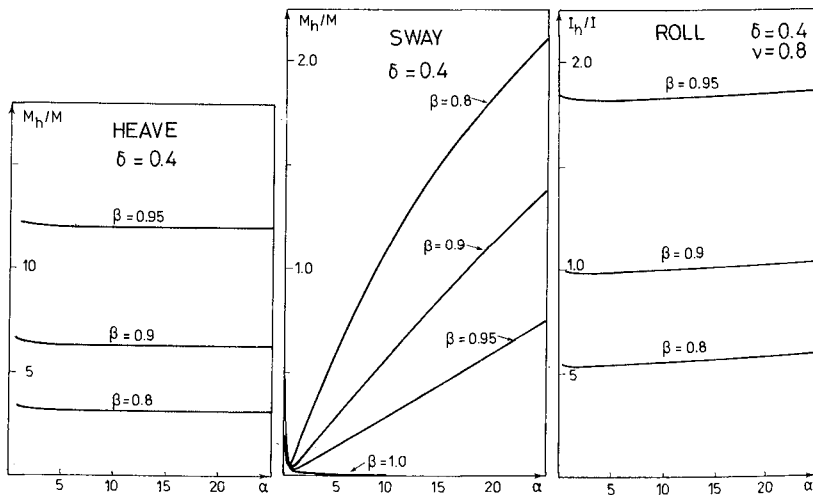


Fig. 19 Hydrodynamic masses for heave and sway, and moment of inertia for roll.

We see that in particular the hydrodynamic mass of heave (Fig. 19 a) is many times the ship's own mass and depends strongly on β , the relative draught of the ship.

The hydrodynamic moment of inertia found for roll is small — of the same order of magnitude as the ships own moment of inertia. Yet the result depends very much on β .

Both for heave and roll the results are virtually independent of α , the nondimensional wave period. This indicates that the major contribution in these cases comes from the flow underneath the ship which is consistent with the fact that when these two motions occur water is necessarily squeezed in and out of the gap.

This is not the case with sway (Fig. 19 c) where the water motion in the gap is driven entirely by the pressure from the waves generated which means that the hydrodynamic mass results from a combination of the e^{-x} -terms in the wave solution and the phase shift in that solution caused by the flow under the ship.

7. RESULTS FOR THE WAVE GENERATION

The oscillating ship acts as a wave generator, and the radiation of energy due to the waves represents the damping in the oscillations. It is therefore of interest to look at the height of the waves generated.

Fig. 20 shows numerical results for these waves for each of the three motions in question. In each of the translatory cases the wave height has been related to the amplitude of the motion, for roll to twice the amplitude $\theta_0 B$ at $x = B/2$.

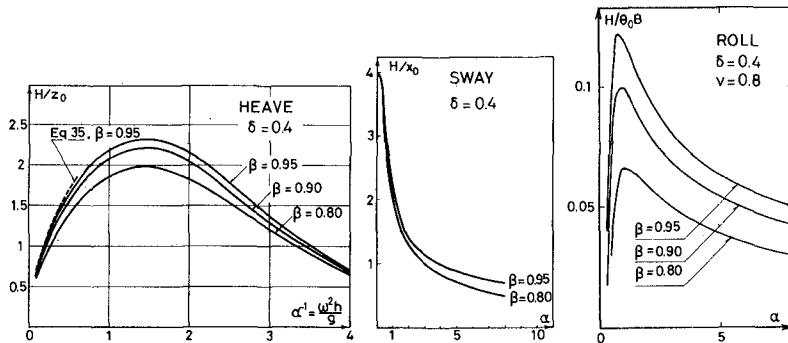


Fig. 20 Height of the generated waves.

We see that in particular at a sway motion the ship is a very efficient wave generator. We also notice that the difference in wave height at sway for different values of $\beta = d/h$ indicates the influence of the flow beneath the ship (i.e. the 'leakage' in the wave generator problem).

In contrast to the less frequency dependent damping at sway, both heave and roll show a maximum damping at intermediate frequencies. The reason is that in these two cases the waves are generated almost entirely by the water flow in and out of the gap. In the case of deep water waves (small α) this is a very inefficient way of generating waves, hence the small heights. For very long waves (large α) the height of the waves will decrease to the limit given by a purely 'hydraulic' model which e.g. for heave yields

$$\frac{H}{z_0} = \alpha^{-1/2} \frac{B}{h} \quad (35)$$

This result is also shown in Fig. 20 for $\beta = 0.95$.

It should be added that of course energy is conserved also in the case of a fixed ship even though it seems as if a standing wave (to the left in Fig. 1) — which yields no net energy flux towards the ship — causes generation of progressive waves which on both sides of the ship represents an energy flux away from the ship. The reason for this paradox is that the sum of the standing wave and the wave propagating towards the left at $x < -B/2$ actually has an energy flux towards the right which is exactly the energy transmitted through the gap and away from the ship through the wave at $x > B/2$.

8. CONCLUDING REMARKS

As mentioned in § 2 the method presented in this paper is based on a number of assumptions. The validity of some of these were already discussed by Svendsen (1968) who showed by comparison with experiments for heave that the pressure underneath the hull is quite accurately described by the present model. He also found that for a certain phase interval of each wave period the pressure close to 1-1 and 2-2 may (for β close to one) be influenced by the separation of the outgoing flow from the hull of the ship (jet-like flow). However, this deviation from the assumption (iii) will only have a minor effect on the total forces. Finally the results in Fig. 5 show that the patching of the average of the pressures at 1-1 and 2-2 will be a very good approximation except perhaps for quite short wave periods.

Thus in general we must expect that the model will yield rather accurate results for the two-dimensional situations it covers.

9. REFERENCES

- Andersen, P. (1978) Wave induced motions of and loads on a ship in restricted water (in Danish). Inst. Ocean Engrg., Tech. Univ. Denmark, Ph.D. thesis, 122 pp.
- Andersen, P. (1979) Ship motions and sea loads in restricted water depth. Ocean Engrg., 6, pp. 557-569.
- Bai, K.J. and R.W. Yeung (1974) Numerical solutions to free surface flow problems. Proc. 10th ONR Symposium.
- Oortmerssen, G. van (1976) The motion of a ship in shallow water. Ocean Engrg., 3, pp. 221-255.
- Svendsen, I.A. (1968) On the forces induced on a rectangular cylinder by a forced heave motion with draught-depth ratio close to unity. J. Hydr. Res., 6, 4, pp. 335-360.
- Svendsen, I.A., P. Madsen and C. Michaelsen (1977 a) The rolling of a ship in shallow water. Inst. Hydrodyn. and Hydr. Engrg., Tech. Univ. Denmark, Prog. Rep. 42, pp. 21-28.
- Svendsen, I.A., P. Madsen and C. Michaelsen (1977 b) Wave induced heave motion of a ship in shallow water. Inst. Hydrodyn. and Hydr. Engrg., Tech. Univ. Denmark, Prog. Rep. 43, pp. 23-30.

- Svendsen, I.A., P.Å. Madsen and C. Michaelsen (1977 c) Wave reflection and transmission from a ship in shallow water. Inst. Hydrodyn. and Hydr. Engrg., Tech. Univ. Denmark, Prog. Rep. 44, pp. 27-34.
- Tuck, E.O. (1970) Ship motions in shallow water. J. Ship Res., 14, pp. 317-327.
- Wendel, K. (1950) Hydrodynamische Massen und hydrodynamische Massenträgheitsmoment. Jahrbuch der Schiffbautechnischen Gesellschaft, 44.
- Wilson, B.W. (1958) The energy problem in the mooring of ships exposed to waves. Proc. Princeton Conf. on Berthing and Cargo Handling at Exposed Locations, Princeton Univ., New Jersey.

REPORT ON THE DAMAGES TO THE
SINES BREAKWATER, PORTUGAL

by

William F. Baird¹, M.ASCE,
Joseph M. Caldwell², F.ASCE,
Billy L. Edge³, M.ASCE,
Orville T. Magoon⁴, M. ASCE,
and
Donald D. Treadwell⁵, M.ASCE

ABSTRACT

Possible contributing factors to the 1978 failure of the massive main breakwater at Sines, Portugal are presented in a selective summary of the report of the Port Sines Investigating Panel. A failure scenario involving the impact breakage of unreinforced concrete armor units is developed.

INTRODUCTION

The final report of the Port Sines Investigating Panel is summarized in this paper. The objective of the Panel, which was funded in part by the U.S. National Science Foundation, was to collect data concerning and to evaluate possible causes of the failure on February 26, 1978, of the massive rubble mound breakwater at Port Sines, on the Atlantic coast of Portugal.

¹Managing Director, Hydrotechnology Ltd., Ottawa, Ontario, Canada

²Consulting Engineer, Arlington, Virginia, U.S.A.

³Professor of Civil Engineering, Clemson University, Clemson, South Carolina, U.S.A.

⁴Chief, Coastal Engineering Branch, U.S. Army Engineer Division, South Pacific, San Francisco, California, U.S.A.

⁵Senior Project Engineer, Woodward-Clyde Consultants, San Francisco, California, U.S.A.

The breakwater at Port Sines is among the largest in the world. Further, it is situated in a previously untried combination of unusually deep water (about 50 meters at the seaward terminus) and a high-energy marine setting (the 100-year return period significant wave height was estimated to be 11 meters). Construction was nearly complete when critical damage was sustained in storm waves thought by most to be below the 11 meter significant wave height for which the structure was designed. The damage consisted of the loss of about two-thirds of the armor layer of 42 metric tons dolos units. At a few locations, the concrete superstructure was severely damaged as a result of undermining and of wave impact on the front face where loss of the dolos has occurred. Figures 1 and 2 illustrate some of the damage to the breakwater.

The structure has sustained further damage since the February 1978 storm. In December 1978 and in February 1979, storm action removed all armor protection, including some temporary remedial works placed in the fall of 1978, from the seaward 1.5 km of the breakwater. Much of the concrete superstructure has been lost.

The scope of the Panel's study, as delineated in the proposal to the National Science Foundation for the Sines investigation, covered four simplified failure possibilities: (1) that design criteria were exceeded by the February 1978 storm; (2) that the breakwater construction was faulty; (3) that the materials used for breakwater construction were sub-standard; (4) that the procedures followed during the design of the breakwater were incomplete or incorrect for this specific set of environmental conditions.

The investigation undertaken by the Panel was based on two site visits and on discussions with responsible Portuguese authorities, the design engineers, the engineers of the Portuguese hydraulic laboratory (LNEC), and the officials of the construction company. The objective of the investigation was to report on possible problems, omissions, and errors that could have contributed to the failure of the Sines breakwater. It is the hope of the Panel that engineers will be able to benefit from the experience at Sines in the design of future breakwaters.

PROJECT DESCRIPTION

The Sines breakwater is the most critical single component of a vast industrial complex planned by the Portuguese government. The Atlantic deepwater port and extensive landside facilities depend on the efficient, safe operation of the port, which in turn depends on the breakwater. Port Sines, about 100 km south of Lishon on the Atlantic coast, lies along the present international routes for crude oil and iron ore carriers. The site has the steep ocean falloff needed for a supertanker port; required depths for an oil terminal occur within 0.5 to 1.5 km of the shore.

Development of a major port at Sines involved the construction of the main breakwater in depths of up to 50 meters. A layout of the port



Figure 1 Damage to the seawall and dolos, taken immediately after the February 1978 storm (photo from GAS)



Figure 2 Dolos removed from the front of the seawall and broken dolos and superstructure
(photo from GAS)

facility is given in Figure 3. Design was begun in 1972 by a consortium (BCL) of Bertlin and Partners of the United Kingdom and Consulmar and Lusotechna, both of Lisbon; the contractor chosen was Societa Italiana per Condotte d'Acqua of Italy. Construction began in mid-1973.

The breakwater is a dual-purpose structure, supporting oil pipelines as well as providing shelter from the Atlantic for the port. A quarry fill core is armored with heavier-cut stone, and on the seaward side that "selected" stone is blanketed with 42 metric concrete dolos. A concrete superstructure includes a wave wall, an inner (portside) roadway, and support for the oil pipelines. The latter are intended to serve the three harbor-side berths, built on caissons and connected to the breakwater. The three berths, beginning with the closest to shore, are intended to accommodate 100,000, 350,000 and 500,000 DWT tankers, respectively. A cross-section of the final breakwater design is shown on Figure 4.

About 160 square miles of inland facilities also depend on the port. These included an oil refinery, a steel mill, a pyrite plant, a petrochemical complex, and other industry, both heavy and light. Yet another aspect of the master plan is a "new town", for which a population of about 100,000 has been projected. Over 5,000 dwellings are complete, and the construction of schools, recreation centers, shopping facilities and related infrastructure are all underway.

The Gabinete da Area de Sines (GAS) has been the responsible Government agency for the entire Sines development since the project inception over a decade ago. At the time of the failure in February 1978, the Portuguese government is reported to have spent \$176,000,000 on the breakwater alone.

PANEL REPORT

The report prepared by the Panel includes discussions of the project, the physical setting and environment, the design and construction of the breakwater, the storm of February 1978, the status of the breakwater after the storm, studies performed after the failure, and considerations in evaluation of the failure. The report also includes appendices containing official replies to investigative inquiries, photographs of the damaged sections, records of dolos placement, summaries of wave climate during construction, and the like. The report is currently in final review by the Coastal Engineering Research Council of the American Society of Civil Engineers and should be available to practicing engineers and other interested parties in the near future.

No attempt has been made in this paper to completely summarize the report. Rather, the following sections present factors which may have contributed to the failure of the breakwater and a failure scenario which appears to fit the available evidence. It is recommended that the report and other published information be studied carefully by coastal engineers charged with the design and construction of future major shore protection structures.

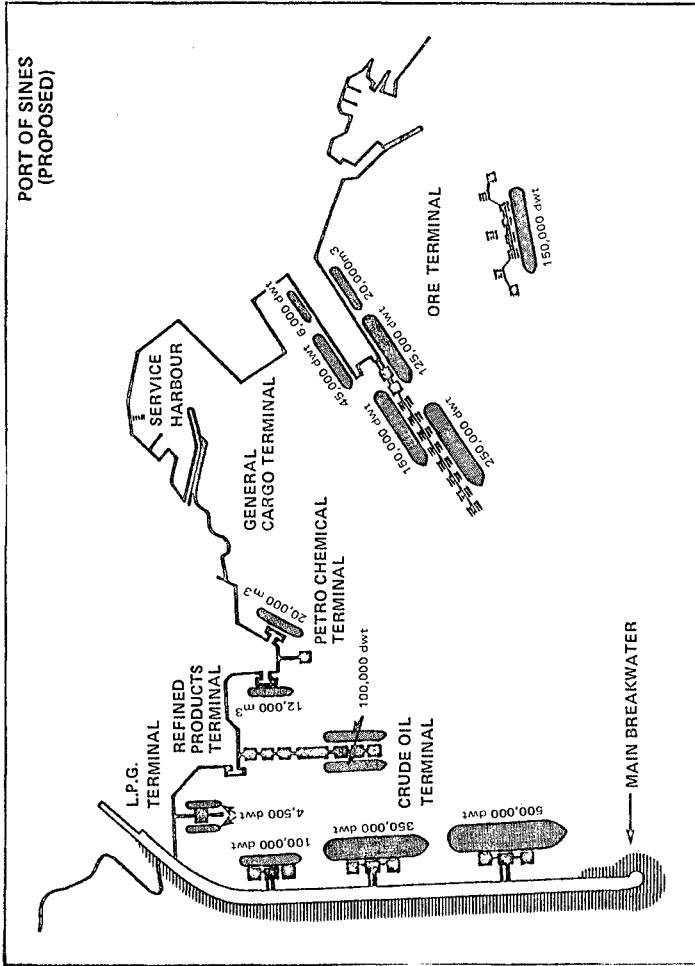


FIGURE 3 Proposed layout of the Port of Sines

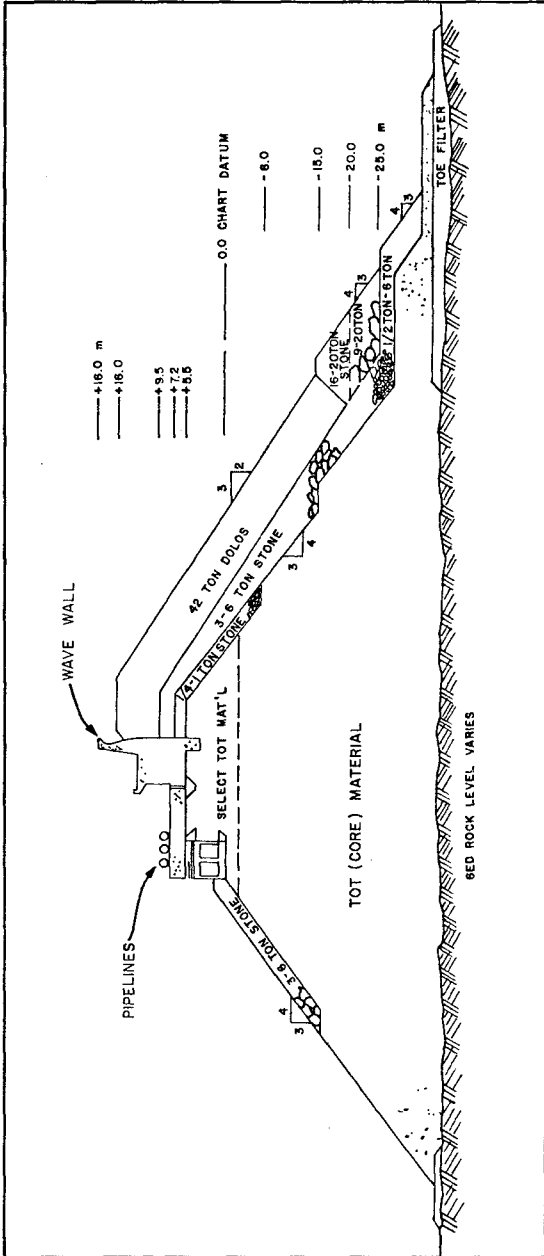


Figure 4 Cross-section of the final design

POSSIBLE FACTORS CONTRIBUTING TO FAILURE

In a project this complex, there are many possibilities for uncertainties in design and construction. What follows is a compilation of possible contributing factors mentioned to or observed by the Panel. Some appear to be difficulties inherent in any large construction project; others are more specifically related to the Sines project. They are all a legitimate part of the Sines data and should be taken into account when additional study of the Sines failure is in order and when future projects of this sort are considered. It is stressed that the list of factors should not be interpreted as identifying the cause(s) of failure.

Owner-Designer-Contractor Relationships

The designer (BCL) felt the primary area of concern was that they had no control over the execution of their plans during construction. In many cases, the designer is retained for inspection purposes or is the technical agent dealing with the contractor for the client. In the case of Sines, the Gabinete da Area de Sines (GAS) retained all inspection and technical supervision of the project. It may also be important to note that all official communication was in Portuguese. This may have contributed to difficulties in communication among the English design firm, the Italian contractor, and the Portuguese authorities.

Selection of Design Waves

Wave data available for the initial design of the Sines breakwater were sparse. Even by the end of the design process only a minimal amount of wave data were available. Thus it was difficult to estimate the design wave conditions with a high level of statistical reliability. The 100-year storm design wave belongs to a different statistical population than the non-storm design wave commonly measured along the Atlantic coast of Portugal. Moreover, it is commonly accepted that the extrapolation of extreme value events should not extend more than two or three times the total length of record. Nevertheless, project demands do at times dictate that insufficient data be used. Under these conditions, the designer's recourse is to perform a detailed error or confidence analysis of the data.

The effects of refraction and wave groupings were not considered in the selection of the design wave. Zwamborn (1979) says that:

"it appears that no tests were done on the final design,... using irregular waves of sufficient duration (say 6 to 12 hours prototype) with a significant wave height equal to or exceeding the design wave height of 11 m."

Furthermore, Zwamborn cites studies done by the French hydraulic laboratory (LCHF) after the failure:

"recent tests carried out by the LCHF showed that for wave periods between 16 to 18 s and wave heights in excess of 11 m, the vertical

upward water velocity near the still water line could be the same order of magnitude as the terminal settling velocity of 42-t dolosse in still water. As a result, groups of dolosse could be lifted from the slope by these long and high waves, a phenomenon frequently observed in model tests."

Three particular items that escaped consideration in the design wave selection were: (1) climatic analysis, an overall review that would show protection of the Portuguese coast by the Azores high and show the dependency of the results of a climatic analysis on the phenomenon; (2) error analysis, identification of the accuracy of the design wave; and (3) shallow water effects on the available recorded wave data and on the waves approaching the Sines area.

Storm of February 26, 1978

As indicated in the Panel's report, it is extremely difficult to identify the size of the waves that occurred on February 26 and those that preceded that day. The data measured at Cabo da Roca indicate waves with a significant height of 8 to 9 m. Refraction analyses by LCHF indicate significantly larger waves may have occurred at the structure. Because the wave recorder was not working, an indisputable definition of the wave field will never be available.

Breakwater Design

Although the breakwater was designed using available methods, the design still may not have been sufficient to resist the forces exerted by the February 1978 storm; this is not a criticism of the design but of the available references for design. The design for this very deep site which is exposed to deep ocean waves was predicated on an extension of the procedures which were well-understood for small breakwaters in shallow water conditions. Another aspect of the design that causes some concern is the complexity of the breakwater cross-section; the section would be difficult to inspect, as well as to construct, in these extreme water depths.

Dolos Placement

One item of concern is the ability of the floating cranes to adequately place the dolos above and below the water in characteristically rough conditions. The dolos were not placed by location but by density (instead of a coordinate for a particular dolos, a certain number were to be placed in a given area). Underwater inspection of dolos placement was infrequent because of the heavy seas during most of the year. Zwamborn (1979) reports that between 3.5 and 16.8 percent of the dolos in a sampled section were broken by August 1977 as a result of placement, settlement of the structure, and/or previous storms. Arrangement of the dolos was generally random (not with 60 percent having the vertical leg seaward as specified in the design, although the significance of this criteria has been discounted).

Dolos Reinforcement

The dolos were not reinforced. Subsequent to the February 1978 storm, some reinforced units were used as a test for the outer layer of dolos, to prepare the breakwater for the coming winter; both reinforced and unreinforced units sustained extreme damage in the 1978-1979 winter. This application of reinforced armor units (of both types) should not be considered a true test of the response of the original structure to storm waves.

Model Studies

The official model studies were done by Laboratorio Nacional de Engenharia Civil (LNEC) for CAS and not for the designer. Therefore, indirect communication resulted. The results of the irregular wave tests were not available to the designer before the design was complete. The model tests did not account for the effect of wave grouping that occurs in the wave data recorded at Sines. Refraction was also not analyzed or considered in the model studies. The model tests were not designed to simulate structural properties of the dolos armor units.

Permeability of the Core

The permeability of the quarry run (TOT) material in the core may have been significantly less in some sectors than that used in the model tests and specified in the contract. This difference may have resulted in added wave run-up on the face of the breakwater; and this, in turn, may have had an adverse effect on the stability of the armor layer. It is important to recognize that the stability of the armor layer might be jeopardized by the increased wave run-up that would result from a lack of permeability of the core. The volume of both wave uprush and the return flow down the face of the breakwater would impose a greater force on the individual breakwater armor units and could cause their dislodgment from the protective layer.

OFFICIAL STATEMENTS OF CAUSE

Several investigations have been conducted, at various levels of effort, to understand and identify the causes of failure. One of the first assessments was made by a team of Dutch engineers. They concluded that a likely cause of failure was the removal of the 16 to 20 t stone from the toe by the larger waves; subsequent to the removal of these stones the dolos layer shifted and was damaged.

The National Research Institute for Oceanography, South Africa, noted the cause of failure as follows:

"...the main causes of the damage and part failure of the Sines main breakwater during the February 1978 storm are the particularly damaging effect of the large waves in the spectrum which, because of the great water depth in front of the breakwater, could reach the structure without being reduced by prior breaking.

With a probable incident significant wave height during the peak of the storm of 9.5 to 10 m, maximum incident wave heights of at least 14 to 17 m must have occurred which, although infrequent, caused excessive movements of dolosse, probably resulting in breakages, particularly at and just below the still water level, thereby weakening the armor. In addition, the wave heights of the longer waves (peak periods at the height of the storm were 18 to 20 s) were locally increased due to wave refraction causing both the significant and the maximum wave heights in the failure areas to increase by, on average, 20 percent, that is to about 12 m and 17 to 20 m, respectively. These waves resulted in the removal and further breakage of the dolosse causing the collapse of the superstructure in the failure areas." (Zwamborn, 1979).

The official comments from the design team (BCL) have been included in the Panel's report. In these comments the problem is focused on project management, supervision, and construction. Mr. Peter Mornement of Bertlin & Partners, in an interview with the New Civil Engineer, said "we are sure inaccurate placing of the dolos and the supporting toe were the main causes of failure."

The official Portuguese investigation team filed their report with the Government in April 1979. Some of their conclusions are presented below:

- o Structural fragility of the dolos was the primary cause of failure.
- o There were serious shortcomings in the design wave selection.
- o The design of the breakwater was "theoretical" and difficult to build.
- o Consideration was not given to refraction of wave energy.
- o The LNEC was not exhaustive enough in its testing program.
- o The reliability of the dolos should have been questioned.
- o Gabinete da Area de Sines did not have the capability to plan and execute a marine project of such magnitude.
- o There were shortcomings in the management and supervision of the project by CAS.
- o LNEC should have had a more active role in the design phase.

A FAILURE SCENARIO

The causes of failure and the sequence of events leading to the failed armor layer during the storm of February 26, 1978 will never be

completely defined. This is because of the scarcity of information concerning the exact state of the structure prior to the storm, the wave conditions at the breakwater during the storm, and the condition of the breakwater during the storm. Many explanations of the cause of failure have been proposed, and the state of the breakwater following the storm was such that any number of events might have caused or contributed to the failure.

A description of the probable pattern of events leading to the destruction of the armor layer is proposed by the authors. The critical observations leading to the failure scenario are those on the extensive breakage of the dolos, the profile of the damaged breakwater, the model tests with irregular waves which showed rocking of dolos, the model tests with the artificially weakened dolos, and personal experiences with other breakwaters. It is the Panel's opinion that this description is plausible in that it fits with the available evidence. It is recognized that other failure scenarios can be proposed from the available data.

In the early stages of the storm, when the significant wave height reached 6 m, some dolos units began to move in the vicinity of the mean water level. These units were the ones which had been placed in a relatively unstable position and had little support from the adjacent units. (It is practically impossible to place dolos so that every unit is in a stable position.) The initial movements occurred when a larger wave ran up through the armor layer.

As the wave height and period increased, the movements became more severe and the units were accelerated to the velocity of the uprushing wave. The following impact with adjacent units produced stresses in the units that exceeded the strength of concrete. This resulted in breakage, and frequently the pieces were carried away by the uprushing or downrushing wave. During this process, the pieces themselves collided with other units, in some cases causing additional breakage.

At the peak of the storm, when the significant wave height exceeded 8 m, a large number of units located just below the water level broke. As the pieces were carried away, adjacent units were free to move and a rapid disintegration of the armor layer occurred. Initially the greatest damage occurred immediately below the mean water level. The broken pieces were moved by water motion and gravity from the armor layer to the lower part of the mound. The slope of the seaward side of the breakwater below the water level then became flatter.

During the final stages of the storm the armor layer was completely removed at some locations. The broken dolos pieces were displaced to the base of the armor layer and the underlying stone layers were exposed. Wave action then moved these exposed stones over the broken dolos pieces. Continuing wave action eroded the core material and began to undermine the superstructure.

As the concrete superstructure was undermined it tilted forward. In some instances, the structure broke in the base (where the pipelines carrying petroleum from the berths to shore would be located) and at some of these locations the wave wall at the top of the structure was snapped off and thrown back as a result of wave impact.

The reasoning leading to the above scenario of the failure of the Sines breakwater suggests the following:

- o The dolos units rocked, broke and moved in the armor layer under the wave conditions that existed during the storm of February 26, 1978.
- o The dolos units were of sufficient strength to withstand the forces of wave action except when they moved. In movement, however, they were unable to resist the impact stresses produced.

Support for the argument that the damage occurred as a result of breakage of dolos units is provided by model studies, prototype testing of dolos strength, and observation of damage to the Sines and other breakwaters.

CONCLUSIONS

In recent years, coastal and nearshore rubble mound structures (both proposed and constructed) have become much more massive and have been sited in deeper water than ever before. Examples of this sort of structure include breakwaters for petroleum terminals and offshore power plants and artificial islands for petroleum exploration and production facilities.

For critical facilities such as these, many traditional assumptions of rubble mound design and construction are being reexamined in response to environmental and safety concerns and the harsh economic consequences which accompany disruptions in energy supplies. One example of the design profession's recognition of these concerns is the recent emphasis on the evaluation of extreme wave conditions and their potential effect on the integrity of the structure, especially in cases where concrete armor units are utilized; another is the renewed interest in the management of design, construction, and inspection services.

The case history of the failure of the main breakwater at Port Sines is believed to be an important addition to coastal engineering knowledge. The members of the Panel hope that engineers will be able to benefit from the Sines experience in the design and construction of future breakwaters.

ACKNOWLEDGEMENTS

The efforts of the Port Sines Investigating Panel were made possible by the U.S. National Science Foundation under NSF Grant No. OP A78-18769;

special appreciation is given to those NSF staff members who expedited the normal review procedures. The Coastal Engineering Research Council of the American Society of Civil Engineers, represented by chairman M.P. O'Brien and vice-chairman R.L. Wiegel, recognized the need for the study and identified sources of support for the Panel. The efforts of Virginia Fairweather of ASCE also deserve special mention.

The cooperation of the following firms and organizations in sharing information and the results of special studies is gratefully acknowledged: Department of Public Works, Canada; National Research Council, Canada; Bertlin & Partners, U.K.; Institute of Oceanographic Sciences, U.K.; Gabinete da Area de Sines, Lisbon; Portuguese Investigating Commission, Lisbon; Societa Italiana per Condotte d'Acqua, Rome; Laboratorio Nacional de Engenharia Civil, Lisbon; Laboratoire Central d'Hydraulique de France; Consulmar, Lisbon; and the United States Nuclear Regulatory Commission.

Significant support in terms of staff time and other services was provided by: the American Society of Civil Engineers, New York; Woodward-Clyde Consultants, San Francisco; Clemson University, Clemson, South Carolina; Dames & Moore, Washington, D.C. and the U.S. Army Corps of Engineers, San Francisco.

SELECTED BIBLIOGRAPHY

- Anon., "Sines: Who is to take the blame?" New Civil Engineer International, London, June (1979).
- Barcelo, J.P., "Caracteristiques de l'agitation maritime dans la cote ouest due Portugal metropolitan," Proceedings, 9th Coastal Engineering Conference, ASCE, Lisbon (1964).
- Castanho, J.P., Carvalho, and Vera-Cruz, "Estudo da agitacao maritima no futuro porto de Sines," a report prepared for GAS Lisbon (1972).
- CERC, Shore Protection Manual, U.S. Army Corps of Engineers, Stock No. 008-022-003113-1, U.S. Government Printing Office (1975).
- Dames & Moore, "Marine Site Investigation, Breakwater and Berthing Facilities for Proposed Port of Sines, Portugal," report to Gabinete da Area de Sines (1974).
- Desai, H.C., "Volume and Strength of a Dolos," Journal Waterways, Harbors, Coastal and Ocean Engineering, ASCE, February (1976) and discussions by H. Bomze, O.T. Magoon, Y. Ouellet, and L.G. Hulman and E.G. Hawkins, September (1977).
- Hudson, R.Y., "Laboratory investigation of rubble mound breakwaters," Journal of the Waterways and Harbors Divisions, ASCE, Sept. (1959).

- Langlais, C. and C. Orgeron, "Port de Sines: Caracteristiques an large dela tempete du 26 Fevrier 1978, LCGH Report no. 1, Maison-Alfort, August (1978).
- Langlais, C. and C. Orgeron, "Conditions de propogation de la houle entre le large et la dique: Estude sur modele physique," LCHF Report no. 5, Maison-Alfort, November (1978).
- Magoon, O.T., and N. Shimuzu, "Use of Dolos Armor Units in Rubble Mound Structures," Proceedings 1st POAC Conference, Trondheim (1971).
- Magoon, O.T., and W.F. Baird, "Breakage of Breakwater Armor Units," Proceedings of Conference on Breakwater Stability, Isle of Wight (1977) (in press).
- Mansard, E.P.D., and J. Ploeg, "Model Tests of Sines Breakwater," Hydraulics Laboratory, National Research Council of Canada, Report No. LTR-HY-67, Ottawa, October (1978).
- Morais, C.C., "Irregular wave attack on a dolos breakwater," Proceedings, 14th Coastal Engineering Conference, Copenhagen, June (1974).
- Mettam, J.D., "Design of Main Breakwater at Sines Harbour," Proceedings, 15th Coastal Engineering Conference, Honolulu (1976).
- Paolella, C., and R. Agostini, "Impiego dei Dolos per il porto oceanico di Sines in Portogallo," L'Industria Italiana del Cemento, Anno XLVIII, February (1978).
- Vera-Cruz, D., "Model tests of Sines breakwater," Proceedings, 13th Coastal Engineering Conference, ASCE, Vancouver (1972).
- Zwamborn, J.A., "Analysis of causes of damage to Sines breakwater," Proceedings, Coastal Structures 79, Vol. 1, ASCE, Alexandria, Virginia, March (1979).
- Zwamborn, J.A., and Beute, "Stability of dolos armor units," ECOR Symposium, Stellenbosch, South Africa (1972).

DISCRETE-TIME MODELLING OF DISPERSION IN ESTUARIES

T. WOOD

Senior Lecturer, Department of Chemical Engineering,
The University of Sydney, N.S.W. 2006 Australia.

1 INTRODUCTION

This paper aims to put forward a case in favour of a simple discrete-time model describing mixing in an estuary. The model derives from the remarkably simple concepts developed by Ketchum (1951 a,b) which describe mixing in terms of tidal prism exchanges between segments. The author's view is that Ketchum's ideas were abandoned before they were fully explored. A major factor was the advent of the high-speed computer which opened up the possibility of using an approach based on the space-time formulation of the problem in terms of the partial differential equations of transport theory.

Intrinsically this approach, based on a continuum description, is more attractive than a gross description based on relatively large segments: one obvious reason is the possibility of providing a comprehensive space-time prediction of the spread of a pollutant. In practice, though, significant problems arise in its use: in particular, the following can be mentioned -

- a) substantial computing costs relating to computer program development and machine time
- b) specification of transport parameters inherent in the partial differential equations of transport: for example, dispersion coefficients
- c) model validation and state/parameter estimation.

The last of these is the primary concern of this paper. It is probably true to say that, to date, too little attention has been given to these topics, in the context of estuarine modelling. The point to be made is that there is small justification in using a sophisticated description of a system if the resulting predictions of the model cannot be effectively validated.

The ideas used in this paper stem from those put forward by Beck and Young (1975) in studies on non-tidal river pollution. The subsequent discussion suggests an extension to estuarine systems.

2 BASIS OF THE PROPOSED MODEL

A complete description of the proposed model can be found in the published paper by Wood (1979). Only the essentials relevant to the subsequent discussion in this paper are presented here, namely, the segmentation procedure and the exchanges between segments.

2.1 Segmentation

The estuary is segmented sequentially from the fresh water end. Segment (1) is always fresh; thereafter a progressive increase in salinity takes place through segments (2), (3), ..., (n). The high tide volumes H_i , and the low-tide volumes L_i , are determined from the fresh water input R per tidal cycle (assumed known) and the hydrography of the estuary, as follows -

$$L_i = R \quad (1a)$$

$$L_i = H_{i-1} \quad (1b)$$

Thus, except for segment (1), the low-tide volume of any segment is equal to the high-tide volume of its upstream neighbour.

2.2 Exchanges Between Segments

As a consequence of the chosen segmentation procedure, water is exchanged over a tidal cycle between a segment and its nearest neighbours. Thus the high-tide volume, H_i , of segment (i) is distributed over a tidal cycle, as follows -

$v_{i-1,i}$: the volume transferred to segment (i-1) from segment (i)

$v_{i,i}$: the volume returned to segment (i)

$v_{i+1,i}$: the volume transferred to segment (i+1) from segment (i)

Each volume of water carries with it the salinity, s_i , of its origin. Therefore, from one high-tide to the next, the discrete-time model describing salinity distribution changes is as follows -

$$H_i s_i(k) = v_{i,i-1} s_{i-1}(k-1) + v_{i,i} s_i(k-1) + v_{i,i+1} s_{i+1}(k-1) \quad (2)$$

where $i = 2$ to $n - 1$

and k is a time index based on a tidal cycle.

3 STATE/PARAMETER ESTIMATION

The principal point to be made in this paper is that the discrete-time model proposed in the previous section is directly amenable to the techniques of state and parameter estimation formulated by Kalman (1960). The mathematical background is too extensive to be discussed here and, indeed, the main purpose is to demonstrate what can be achieved by using these techniques, rather than to put forward an exposition of the mathematics per se. Excellent accounts are available in texts by Eykhoff (1974) and Jazwinski (1970).

3.1 The Defining Equations

The following equations describe the change in the state vector of salinity, \underline{s} , at discrete-time intervals and the relationship between the vector of salinity measurements, \underline{z} , and the salinity vector -

$$\text{Model Equation: } \underline{s}(k+1) = T.\underline{s}(k) + \underline{n}(k) \quad (3a)$$

$$\text{Measurement Equation: } \underline{z}(k) = M.\underline{s}(k) + \underline{e}(k) \quad (3b)$$

\underline{s} : (nx1) vector describing salinity distribution
 T : (nxn) matrix describing exchanges between segments
 \underline{n} : (nx1) vector of model error (Gaussian)
 \underline{z} : (mx1) vector of measured salinities
 M : (mxn) matrix relating measurement to salinity
 \underline{e} : (mx1) vector of measurement error (Gaussian)
 k : an index of discrete-time

3.2 The Kalman Filter: State Estimation

The Kalman Filter provides an estimate of the salinity vector at each time interval, based upon the measurements received up to that time. The procedure is recursive in that an updated estimate can readily be made each time new measurement information is received, based on the previous estimate and the new information. This scheme of sequential updating of estimates is particularly well suited to a system which is monitored in a regular way.

Kalman's solution to the problem of recursive state estimation assumes that the statistical properties of the vectors $\underline{n}(k)$ and $\underline{e}(k)$, representing system and measurement noise respectively, are known and described by -

$$\begin{aligned} E[\underline{n}(k)] &= E[\underline{e}(k)] = 0 \\ E[\underline{n}(k) \underline{n}(j)] &= Q \delta_{kj} \\ E[\underline{e}(k) \underline{e}(j)] &= R \delta_{kj} \\ E[\underline{n}(k) \underline{e}(j)] &= 0 \text{ for all } k, j \end{aligned} \quad (3c)$$

The following two-stage filter estimation algorithm can now be deduced -

Stage 1 - Prediction

$$\begin{aligned} \hat{\underline{s}}(k, k-1) &= T \hat{\underline{s}}(k) \\ P(k, k-1) &= T P(k-1) T + Q \end{aligned}$$

Stage 2 - Correction

$$\begin{aligned} \hat{\underline{s}}(k) &= \hat{\underline{s}}(k, k-1) + P(k, k-1) \begin{matrix} 1 \\ M \end{matrix} [M P(k, k-1) \begin{matrix} 1 \\ M + R \end{matrix}]^{-1} [\underline{z}(k) - M \hat{\underline{s}}(k, k-1)] \\ P(k) &= P(k, k-1) - P(k, k-1) \begin{matrix} 1 \\ M \end{matrix} [M P(k, k-1) \begin{matrix} 1 \\ M + R \end{matrix}]^{-1} M P(k, k-1) \end{aligned} \quad (3c)$$

where $\hat{\underline{s}}(k, k-1)$ is the first-stage estimate of the salinity distribution, previous estimate $\hat{\underline{s}}(k-1)$

$P(k, k-1)$ is the covariance matrix of the estimation error with $\hat{\underline{s}}(k, k-1)$

$\hat{\underline{s}}(k)$ is the second-stage estimate, based on the first-stage estimate $\hat{\underline{s}}(k, k-1)$ and the latest measurement information $\underline{z}(k)$

$P(k)$ is the covariance matrix of the estimation error associated with $\hat{\underline{s}}(k)$

The second-stage estimates $\hat{\underline{s}}(k)$, $P(k)$ for the k th time instant are therefore based on the complete data set collected between instants 1 and k .

3.3 The Extended Kalman Filter: State-Parameter Estimation

In many practical problems, the matrix appearing in the model equation cannot be specified because some of its elements are unknown. In the context of the dispersion model, the T matrix describing the exchanges between segments contains unknowns which have to be estimated from salinity measurements. The estimation problem then extends to the unknown parameters of the T matrix as well as the state vector of salinities mentioned in the previous section. The approach adopted essentially involves reformulating the defining equations (3a) and (3b) in terms of an augmented vector which contains as its elements the salinity vector elements and the unknown parameters. A simple example in the next section demonstrates the principle but for a comprehensive account of the technique the reader should consult the references previously mentioned, Eykhoff (1974) and Jazwinski (1970).

4 SIMPLE EXAMPLE OF THE APPLICATION OF STATE/PARAMETER ESTIMATION

A simple 4-segment example is used to demonstrate the use of the proposed discrete-time model and the application of the Kalman filter. Segment (1) is completely fresh at all times and segment (4) is completely saline at all times ($s_1 = 0$, $s_4 = 1$ all values of k). The transition matrix, T , in equation (3a) is -

$$\begin{bmatrix} 1 & 0 & 0 & 0 \\ t_{21} & t_{22} & t_{23} & 0 \\ 0 & t_{32} & t_{33} & t_{34} \\ 0 & 0 & 0 & 1 \end{bmatrix}$$

where $t_{ij} = v_{ij}/H_i$

Various categories of problem can be analysed, as described below.

4.1 State Estimation Only (all elements of T known).

4.1.1 Segments (2) and (3) monitored.

The Kalman filter provides estimates $\hat{s}_2(k)$, $\hat{s}_3(k)$ of the salinities in segments (2) and (3) from a sequence of monitored salinities $z_2(p)$, $z_3(p)$, for $p = 1$ to k . The measurement matrix, M, is

$$\begin{bmatrix} 0 & 0 & 0 & 0 \\ 0 & 1 & 0 & 0 \\ 0 & 0 & 1 & 0 \\ 0 & 0 & 0 & 0 \end{bmatrix}$$

4.1.2 Either segment (2) or segment (3) monitored.

The Kalman filter provides estimates $\hat{s}_2(k)$, $\hat{s}_3(k)$ from a sequence of monitored salinities: either $z_2(p)$ or $z_3(p)$, for $p = 1$ to k . The measurement matrix, M, is -

$$\text{either } \begin{bmatrix} 0 & 0 & 0 & 0 \\ 0 & 1 & 0 & 0 \\ 0 & 0 & 0 & 0 \\ 0 & 0 & 0 & 0 \end{bmatrix} \quad \text{or} \quad \begin{bmatrix} 0 & 0 & 0 & 0 \\ 0 & 0 & 0 & 0 \\ 0 & 0 & 1 & 0 \\ 0 & 0 & 0 & 0 \end{bmatrix}$$

Segment (2) monitored

Segment (3) monitored

4.1.3 A numerical example of state estimation

Consider a system with a T matrix specified as -

$$T = \begin{vmatrix} 1 & 0 & 0 & 0 \\ 0.5 & 0.3 & 0.2 & 0 \\ 0 & 0.35 & 0.45 & 0.2 \\ 0 & 0 & 0 & 1 \end{vmatrix}$$

Let the covariance matrices Q, R representing the system noise and the measurement noise, respectively, be -

$$Q = R = \begin{vmatrix} 0 & 0 & 0 & 0 \\ 0 & 4 \times 10^{-4} & 0 & 0 \\ 0 & 0 & 4 \times 10^{-4} & 0 \\ 0 & 0 & 0 & 0 \end{vmatrix}$$

Then, given a set of monitored salinities at successive sampling instants $k = 1, 2, \dots, 10$, for segments (2) and (3), the recursive estimates for the true salinities s_2, s_3 can be obtained using the Kalman Filter algorithm. Table 1 summarizes the results.

TABLE 1

k	z_2	\hat{s}_2	$P_{22} \times 10^3$	z_3	\hat{s}_3	$P_{33} \times 10^3$
1	0.526	0.499	3.94	1.02	1.02	0.398
2	0.358	0.326	0.626	0.753	0.775	0.289
3	0.254	0.252	0.470	0.660	0.661	0.237
4	0.197	0.209	0.451	0.594	0.590	0.226
5	0.225	0.183	0.448	0.561	0.551	0.225
6	0.179	0.162	0.447	0.480	0.494	0.224
7	0.162	0.150	0.447	0.504	0.493	0.224
8	0.134	0.146	0.447	0.503	0.491	0.224
9	0.073	0.138	0.447	0.426	0.446	0.224
10	0.130	0.134	0.447	0.476	0.470	0.224

k is the discrete sampling time index, based on an interval of a tidal cycle

z_2, z_3 are the monitored salinities in segments (2), (3) (relative to sea water as unity).

\hat{s}_2, \hat{s}_3 are the filtered estimates of the relative salinities in segments (2), (3).

P_{22}, P_{33} are the variances associated with the filtered estimates.

4.2 State/Parameter Estimation (some elements of T unknown)

4.2.1 Dimension of the problem

Although it would appear that there are six nonzero elements to be specified in the T matrix, only two need, in fact, to be estimated. The element t_{21} is fixed by the fresh water flow from segment (1) to segment (2). Also the following relationship for the exchanges between neighbouring segments leaves only two elements unknown -

$$H_i = v_{i,i-1} + v_{i,i} + v_{i,i+1} = v_{i-1,i} + v_{i,i} + v_{i+1,i} \quad (4)$$

where $i = 2$ to $n - 1$

Therefore in the 4-segment example there are two states and two parameters to be estimated: $\hat{s}_2, \hat{s}_3, \hat{t}_{22}, \hat{t}_{33}$.

4.2.2 The augmented state vector

The state vector $(0 \ s_1 \ s_2 \ 1)^T$ is augmented with the two unknown parameters t_{22}, t_{33} to yield $(0 \ s_1 \ s_2 \ 1 \ t_{22} \ t_{33})^T$. Let the augmented vector be designated \underline{x} . The defining equations can then be reformulated as follows -

$$\text{Model Equation:} \quad \underline{x}(k+1) = T\underline{x}(k) + \underline{n}'(k) \quad (5a)$$

$$\text{Measurement Equation:} \quad \underline{z}(k) = C\underline{x}(k) + \underline{e}'(k) \quad (5b)$$

The problem now becomes non-linear because some of the elements of T' contain elements of the augmented vector \underline{x} . After each estimate of the augmented vector $\hat{\underline{x}}$ the matrix T' is accordingly updated. Apart from this the Extended Kalman Filter follows the same algorithms as before, so that monitored salinities in segment (2) and/or segment (3) can provide recursive estimates of $\hat{s}_2, \hat{s}_3, \hat{t}_{22}$ and \hat{t}_{33} .

4.2.3 A numerical example of state/parameter estimation

As explained above, the T matrix contains effectively two unknown elements, and these are to be estimated in addition to the salinity values in segments (2),(3). The T matrix itself must therefore be updated at the beginning of each cycle of the Kalman Filtering process, using the best available estimates for $\hat{t}_{22}, \hat{t}_{33}$. At the beginning of the calculation, the initial values for the elements of the augmented vector \underline{x} and its associated error covariance matrix P must be guessed.

Consider a system with noise covariance matrices Q, R (for the model and measurements respectively), as follows -

$$Q \text{ Matrix (diagonal terms): } 0 \quad 9 \times 10^{-4} \quad 9 \times 10^{-4} \quad 0 \quad 0 \quad 0$$

$$R \text{ Matrix (diagonal terms): } 0 \quad 4 \times 10^{-4} \quad 4 \times 10^{-4} \quad 0 \quad 0 \quad 0$$

(all off-diagonal terms are zero).

Let the initial guesses for the augmented vector \underline{x} and its associated error covariance matrix P , be as follows -

$$\begin{array}{l} \underline{x}(0): \quad 0 \quad 0.5 \quad 0.5 \quad 1 \quad 0.5 \quad 0.5 \\ P(0): \quad 0 \quad 10 \quad 10 \quad 0 \quad 10 \quad 10 \end{array}$$

(diagonal terms only; off-diagonal terms zero)

Table 2 summarizes the filtered estimates from a sequence of monitored salinity values z_2, z_3 in segments (2), (3).

TABLE 2

k	z_2	\hat{s}_2	\hat{t}_{22}	z_3	\hat{s}_3	\hat{t}_{33}
1	0.483	0.483	0.316	0.961	0.961	0.368
2	0.376	0.375	0.226	0.831	0.830	-0.287
3	0.274	0.278	0.273	0.671	0.672	0.631
4	0.188	0.199	0.292	0.609	0.603	0.495
5	0.185	0.186	0.290	0.554	0.550	0.450
6	0.166	0.168	0.290	0.567	0.557	0.401
7	0.174	0.172	0.287	0.525	0.526	0.400
8	0.190	0.183	0.278	0.518	0.518	0.393
9	0.096	0.114	0.295	0.457	0.472	0.436
10	0.142	0.139	0.292	0.458	0.457	0.432

5 DISCUSSION

The potential advantage to be gained from using a discrete-time modelling approach to dispersion studies in estuaries would appear to lie in the area of model validation, and in particular in state/parameter estimation. The principal disadvantage is the trade-off of model accuracy, whereby the less rigorous, spatially segmented, discrete-time description is adopted in place of a continuum model in continuous time, in favour of a well-proven approach to system identification in the form of Kalman filtering. Clearly, the issue is far from proven either way, and only a series of thorough assessments based on actual case studies will indicate which is the more fruitful approach.

The principal merits of the discrete-time model are related to the principal features of the Kalman Filter, as follows -

- a) The procedure is recursive whereby the latest estimates are obtained from the most recent estimates and the latest available measurement information.

- b) The Kalman Filter algorithms incorporate measures of the uncertainties inherent in the model equations and the measured data.
- c) The method can be applied to a partially monitored system which is an important factor when resources of manpower and money are limited.
- d) The method provides a continuous updating of estimates and the errors associated with the estimates.
- e) The method offers a consistent approach to parameter estimation which is undoubtedly the key problem in modelling studies.

5 REFERENCES

- BECK, M.B. and YOUNG, P.C. (1975). A dynamic model for DO-BOD relationships in a non-tidal stream. Water Research, Vol. 9, pp. 769-776.
- EYKHOFF, P. (1974). System Identification. New York, Wiley.
- JAZWINSKI, A.H. (1970). Stochastic Processes and Filtering Theory. New York, Academic Press.
- KALMAN, R.E. (1960). A new approach to linear filtering and prediction problems. Trans. A.S.M.E., Series D. Journal of Basic Engineering, Vol. 82, pp. 35-46.
- KETCHUM, B.H. (1951a). The exchanges of fresh and salt water in tidal estuaries. Journal of Marine Research, Vol. 10, pp. 18-38.
- WOOD, T. (1979). A modification of existing simple segmented tidal prism models of mixing in estuaries. Estuarine and Coastal Marine Science. Vol. 8, pp. 339-348.

MEASUREMENTS OF OSCILLATORY DRAG ON SAND RIPPLES

Karl E. B. Lofquist
National Bureau of Standards
Washington, D.C.

ABSTRACT

Measurements have been made of drag on naturally rippled sand beds in an oscillatory-flow water tunnel. A partition splits the tunnel into two parallel channels with equal cross sections and volume rates of flow, one with a smooth flat rigid bottom and the other containing the sand bed. Roughly, the difference in the two bottom drags, the one known, is equal to the difference in the net pressure forces on the water in the two channels, which is obtained from measurements of pressure differences across the partition at each end of the sand bed. Each experiment provides the drag, or average bottom stress, on the rippled sand bed as a function of the phase, θ , of the sinusoidal flow. From a first set of thirteen experiments with a medium sand, a stress coefficient, $f(\theta)$, is presented in three families of curves which explore the additional effects of flow velocity, ripple length, and deviations of the ripple profile from normal equilibrium. Average rates of energy dissipation are calculated. Results show f to be a complicated function of θ and other parameters. In particular, the instantaneous stress is not simply related to the instantaneous velocity. Some salient features of $f(\theta)$ are described, qualitatively, by a simple model.

I. INTRODUCTION

1. General

Water waves on the sea surface and sand ripples on the sea bed interact by processes of drag. Surface waves provide an oscillatory flow above the bed which produces and maintains bed forms by local movements of sand. The sand is scoured from the bed by tangential stresses under flows which include separation and vortex formation and which largely are shaped by the pressure field around the bed form. This field produces a distribution of normal stress over the surface of the bed. The horizontal force of these tangential and normal stresses on a large area of the bed, divided by that area, defines the average bottom stress. This is a function of time which becomes periodic as the bed forms become stable. When the bed form is two dimensional and periodic in space, the bottom stress is obtained by an average over a single ripple length. The reverse effect of the ripples on the surface waves is less direct and relatively minor, but is significant. The bottom stress combines with the oscillatory flow above the bed to dissipate energy. Ultimately, this energy is supplied by the surface waves which decay in the process. Also, the bottom stress is a factor in the refraction of surface waves. This paper describes laboratory measurements of bottom stress on naturally rippled sand beds as function of time.

2. Definition of Terms

Terms introduced in the preceding paragraph with others to be used in this study are defined by a few equations. Above the bed and beyond its effects the velocity of flow is

$$u_{\infty} = \left(\frac{2\pi a}{T} \right) \sin \left(\frac{2\pi t}{T} \right) = U \sin \theta \quad (1)$$

where t is the time, T is the period and $2a$ is the orbital diameter of the water motion. Equation (1) defines the maximum velocity, U , and the phase, θ . The bed surface profile, assumed two dimensional and periodic with length λ , has elevation $h(x, \theta)$, where x is the horizontal coordinate. The average bottom stress is then defined by

$$\bar{\tau}(\theta) = \frac{1}{\lambda} \int_0^{\lambda} \left[\tau_h + (p_h - p_{\infty}) \frac{\partial h}{\partial x} \right] dx \quad (2)$$

where τ_h is the local tangential stress on the bed, and $(p_h - p_{\infty})$ is the difference between pressures at the bed surface and at any fixed elevation beyond the influence of the bed. Separate integrals for the two terms in the integrand would resolve $\bar{\tau}(\theta)$ into components expressing the effects of tangential and normal stresses, the latter being a form drag. However, such a separation is generally impossible. A stress coefficient,

$$f(\theta) = \frac{2 \bar{\tau}(\theta)}{\rho U^2} \quad (3)$$

where ρ is the density of the water, has been made dimensionless by dividing by ρU^2 , rather than by $\rho u_{\infty}^2(\theta)$, in order to keep $f(\theta)$ proportional to $\bar{\tau}(\theta)$ throughout the cycle. The maximum of $f(\theta)$ is denoted f_m . The energy dissipated per unit area of bed per period, or twice that per half period, is given by

$$\Delta E = 2 \int_0^{T/2} \bar{\tau} u_{\infty} dt \quad (4)$$

Then, inserting equations (1) and (3) into equation (4) and defining the average coefficient,

$$\bar{f}_1 = \frac{1}{\pi} \int_0^{\pi} f(\theta) \sin \theta d\theta \quad (5)$$

produces,

$$\frac{\Delta E}{T} = \rho \frac{U^3}{2} \bar{f}_1 \quad (6)$$

Thus, the rate of energy dissipation is proportional to \bar{f}_1 .

3. Past Work

In the past, $f(\theta)$, f_m and \bar{f}_1 have been measured or estimated by various methods. These methods are here divided into two groups according to whether the surface of the bed was (1) artificially rigid or (2) naturally rippled.

(1) With rigid surfaces: Bagnold (1946) calculated \bar{f}_1 by the work needed to oscillate a metal cusp-shaped profile in still water. Kalkanis (1964) oscillated roughened plates in still water and observed flows which could be analyzed to provide $f(\theta)$. Using oscillatory-flow water tunnels, Jonsson and Carlsen (1976), in two experiments, measured velocity profiles over a flat roughened bed to obtain $f(\theta)$, while Kamphuis (1975) obtained f_m on a roughened shear plate in terms of relative grain roughness and a Reynolds number.

(2) With naturally rippled beds, \bar{f}_1 only has been obtained. By observation of the decay of surface waves, \bar{f}_1 has been calculated, in wave tanks, by Savage (1953) and by Inman and Bowen (1962) and, in field studies, by Bretschneider (1954) and by Iwagaki and Kakinuma (1967). Values of \bar{f}_1 from these field studies are summarized by Vitale (1979) and vary widely. Carstens, Neilson and Altinbilek (1969) measured the energy input required to maintain flows over sand beds in an oscillatory-flow tunnel restricted to a single period of 3.56 seconds and, within this limitation, presented \bar{f}_1 as function of grain size, D , and of a/D . Vitale (1979) has further analyzed and interpreted their results.

In sum, except with rigid flat roughened beds, measurements of bottom drag remain fragmentary. In particular, no previous measurements of $f(\theta)$ with naturally rippled beds have been reported.

4. Scope of the Present Study

To help fill this gap, the present study measures $f(\theta)$ in laboratory experiments with naturally rippled sand beds. Experiments are still in progress, but results from thirteen of them are presented, and preliminary conclusions are drawn. Values of \bar{f}_1 are calculated, and some features of $f(\theta)$ are discussed in terms of a simple model.

II. EQUIPMENT AND PROCEDURES

1. The Tunnel and its Modifications

The experiments are carried out in an oscillatory-flow water tunnel described by Lofquist (1977). Briefly, it is of U-tube design, and two tight fitting pistons in cylinders, side by side at one end, moving sinusoidally in unison, drive water back and forth through a horizontal test section and into and out of two reservoirs open to the air at the other end. The test section is 255 cm long, 21 cm wide, and has a mean depth of flow of 30 cm. The orbital diameter, $2a$, and the period, T , can be selected arbitrarily below 250 cm and above, approximately, 1.5 seconds. Ranges in the present experiments are: $34.8 \text{ cm} < 2a < 76.6 \text{ cm}$, and $2.70 \text{ s} < T < 5.93 \text{ s}$.

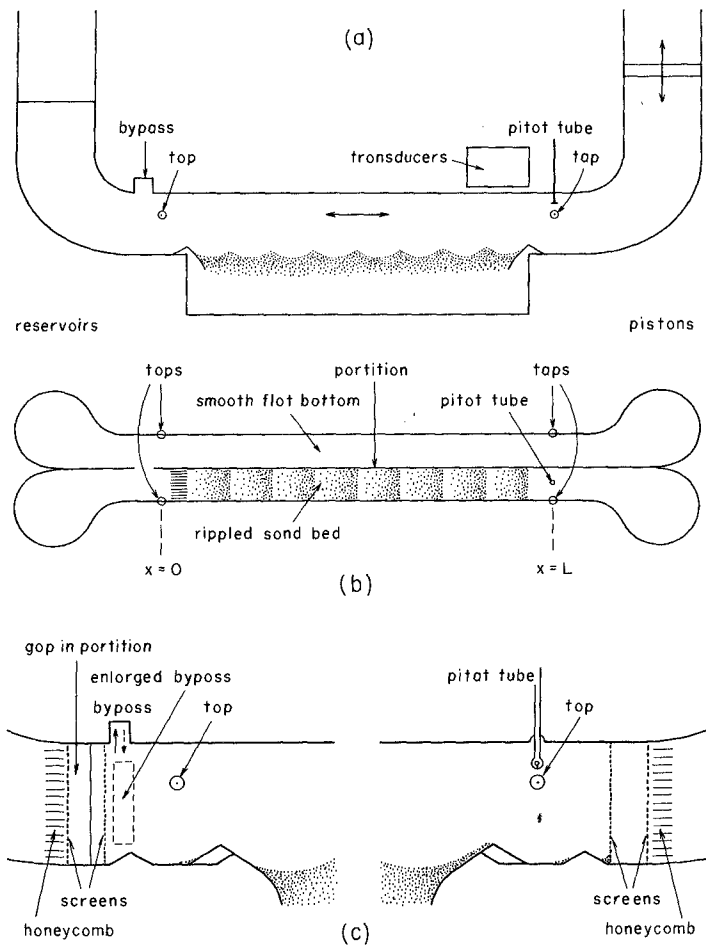


Figure 1. Schematic drawings of the tunnel and test section, (a) side view, (b) top view, (c) details of the two ends.

The tunnel has been modified for the present study as shown in the three schematic drawings of Figure 1(a),(b),(c). Of these, only (c) is drawn to scale. The channel has been split into two channels, each 10.1 cm wide, by a vertical partition (Fig.1,b). This partition separates each side from the other all the way from the pistons, at the right, to a point beyond the left end of the test section where the partition ends at a screen and there is a bypass over the channel top (Fig.1,c). (A screened bypass enlargement was cut in the partition just before the last three experiments.) One channel has a flat smooth metal bottom, while the other contains the rippled sand bed (Fig.1,b). In both channels, beyond the test section at either end, pressure taps have been mounted in the channel walls. These are indicated in all the drawings. A pitot tube has also been mounted which can be raised and lowered and which, with oppositely directed openings at its tip serving alternately as static and dynamic holes, can measure continuously the velocity of the reversing flow. The pressure taps in the walls and the pitot tube openings are connected to two differential pressure transducers which are located as indicated in Figure 1,(a). The connecting conduits are not shown. The purpose of these modifications will appear in the derivation of the stress measurement in section II,3 below.

2. End Conditions, Natural and Strained Profiles

The analysis in section II,3 requires that the areas of the four cross sections at the pressure taps be equal, so that migrations of the sand profiles into the conduits must be prevented. Therefore, rigid crest-shaped objects have been mounted at each end of the sand bed and, also, just before the first screens in order to stabilize the profiles and to keep the floor below the taps free of sand. These objects are shown in Figure 1,(c). The rigid crests at the ends of the bed are either of two sizes, selected best to match the sand crests between them. These rigid end crests condition the profiles since the number of sand ripple crests between them is some integer, M , and the fixed distance between them must equal $\lambda(M+1)$. Studies have shown (Lofquist, 1978, Fig. 22 and, more fully, Brebner, elsewhere in these proceedings) that an unconstrained two-dimensional profile adjusts λ/a to a natural value $(\lambda/a)_n$ which is a function of the degree of sand agitation and grain size but for low and moderate agitation is approximately equal to 1.33. Thus, in the tunnel, with λ and a selected such that $\lambda/a = (\lambda/a)_n$, the rigid end crests create minimum distortion of the sand profile between them.

With λ fixed by a selected number of sand ripple crests between the fixed end crests, it is possible, by varying a , deliberately to force λ/a away from $(\lambda/a)_n$ and so to produce a "strained" profile. Such profiles are described by Lofquist (1978), V,5. Briefly, as λ/a is reduced below 1.33, crests steepen and the profile appears "compressed" until at around $\lambda/a = 1.1$ somewhere a crest shrinks and disappears, and λ abruptly increases. As λ/a is increased above 1.33, crests flatten and the profile appears "extended", with low humps forming in the troughs, until at around $\lambda/a = 1.6$ one of these humps rises to become a new crest, and λ abruptly decreases. The deliberate variation of λ/a permits an investigation of the effect of profile strain on $f(\theta)$ and whether a natural profile gives $f(\theta)$ any special character.

3. Derivation of the Measurement of Stress

A simple analysis provides the average stress on the sand bed in terms of the pressures at the four taps and the velocity profiles measured by the pitot tube. Symbols used in the analysis are identified as applying either to the channel with the sand bed or with the smooth bottom by a subscript "s" or "o" respectively. These symbols are: L, H and b, the length, depth and width of the channels (the same for each); p(0) and p(L), the pressures at the taps at x = 0 and L; $\bar{\tau}$ and $\bar{\tau}_p$, the average stresses on the bottom and on the smooth perimeter of the walls and top; Q, the volume rate of flow; \bar{u}^2 , the average of u^2 over a cross section, where u is the local velocity.

Then, by momentum balance in each of the channels,

$$bH [p(0)-p(L)]_s - bL \bar{\tau}_s - L(2H+b) \bar{\tau}_{ps} = \rho L \dot{Q}_s + \rho bH [\bar{u}^2(L) - \bar{u}^2(0)]_s \quad (7)$$

and

$$bH [p(0)-p(L)]_o - bL \bar{\tau}_o - L(2H+b) \bar{\tau}_{po} = \rho L \dot{Q}_o + \rho bH [\bar{u}^2(L) - \bar{u}^2(0)]_o \quad (8)$$

where a dot denotes a derivative with respect to time. Since \dot{Q}_s is known and $\bar{\tau}_{ps}$ can be estimated, $\bar{\tau}_s$ can, in principle, be determined by equation (7). This approach was attempted before the channel was divided. But each side of equation (7) is dominated by its first term, and $L\bar{\tau}_s$ is easily obscured by noise and scatter in measurements of $H[p(0)-p(L)]_s$. Instead, equation (7) is subtracted from equation (8). In doing so, $\dot{Q}_o - \dot{Q}_s$ vanishes, since Q_o and Q_s are made equal by construction of the tunnel with two pistons of equal area. Also, $\bar{\tau}_{ps} - \bar{\tau}_{po}$ can be discarded, since the terms are of nearly equal magnitude and each, as estimated by laminar theory, is small compared with $\bar{\tau}_s$ as eventually determined. Finally, since the development of the velocity profile over the smooth bottom is relatively small, the last term in equation (8) can be discarded. The subtraction then provides,

$$\bar{\tau}_s - \bar{\tau}_o = \frac{H}{L} [(p_o - p_s)_L - (p_o - p_s)_0] - \frac{\rho H}{L} [\bar{u}_s^2(L) - \bar{u}_s^2(0)] \quad (9)$$

where the pressure differences are between pairs of taps at x = L, 0.

With $\bar{\tau}_o$ calculated by laminar theory, results of the experiments eventually show that $\bar{\tau}_s$ dominates the left side of equation (9) and that the right side is dominated by the first pressure difference, with the second kept relatively small by the action of the by-pass. The last term, which, like $\bar{\tau}_o$, proves to be small compared with $\bar{\tau}_s$, is provided by the single pitot tube at x=L with the assumption that, with z the vertical coordinate, $u_s(x, z, \theta)$ satisfies the condition of symmetry,

$$u_s(0, z, \theta) = -u_s(L, z, \theta + \pi) \quad (10)$$

4. Pressure Measurement

A differential pressure transducer mounted over the test section near the taps at $x = L$ (Fig.1,a) is alternately connected with the two pairs of taps at $x = 0, L$ by suitable conduits and valves (not shown in the drawings). Next to it is mounted a second pressure transducer connected with the pitot tube. Signals from the transducers are recorded on paper tape as functions of time. Pen deflections, in mm, are translated into pressure units by a calibration in which, immediately following an experiment, a simple device provides selected hydrostatic pressure differences to a transducer while the recorder runs with the same amplification as before.

Filters are required to reduce noise in the transducer output signals. These filters consist of six sand-filled glass loops one of which is included in each of the conduits between the transducers and the four pressure taps and the two pitot tube openings. This filtering reduces the amplitude and slows the response of the output signal. These distortions must be removed by calibration of another type. With the pressure at one tap, or pitot opening, fixed by draining the water in the tank to the level of an open hatch, the other is connected by a flexible tube to a vessel which is filled with water to this same level. The vessel is then oscillated vertically in simple harmonic motion with selected amplitude, h_c , and period, T_c , to supply a known (non hydrostatic) sinusoidal pressure difference to the transducer. Denoting, for given h_c , the ratio of the amplitude of the output signal as $T_c \rightarrow \infty$ to that at T_c by F_1 , and the phase lag by ϕ , calibrations are obtained in the form,

$$T_c^2 (\phi^2 - 1) = F_1(T_c) \quad (11)$$

and

$$T_c \tan \phi = F_2(T_c) \quad (12)$$

where F_1 and F_2 are independent of h_c and are slowly varying functions of T_c or constant. Although subject to T_c adjustments and slight drift over long periods of time, representative constant average values for both pairs of taps are, $F_1 \approx 4.3 \text{ sec}^2$, $F_2 \approx 2.5 \text{ sec}$, and for the pitot tube, $F_1 \approx 9.7 \text{ sec}^2$, $F_2 \approx 4.3 \text{ sec}$.

5. Processing the Data

As the first term on the right side of equation (9) has been found to dominate the last term, the processing of records from the pressure taps has differed from that of records from the pitot tube and will be considered first. The primary records from the pairs of taps at $x = 0, L$ are the pen deflections, in mm, which are denoted $P(0, \theta)$ and $P(L, \theta)$ respectively. Figure 2 shows $P(L, \theta)$ and $P(0, \theta)$ for a typical experiment (no. 2 in Table 1 below). In each case residual noise has been averaged out to produce a smoother curve. The deflections of $P(0, \theta)$ are kept relatively small by the action of the by-pass. The phase is marked for $\theta = 0, \pi, 2\pi$. A digitizing pad, or table, reads the analog tape records at each

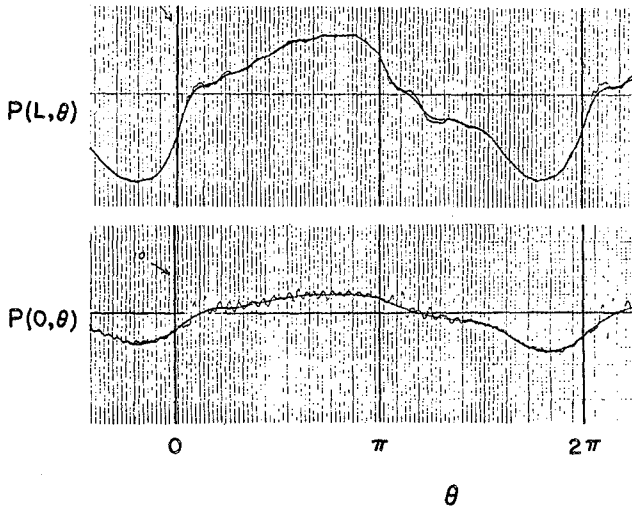


Figure 2. A typical record of transducer output from the two pairs of pressure taps.

10 degrees of phase and stores the data in a microcomputer. The computer then processes the data in the following steps:

(1) As required in equation (9), the difference in the records is taken to form

$$D(\theta) = P(L, \theta) - P(0, \theta) \quad (13)$$

(2) Ideally, the stress at any time should be the negative of that a half cycle earlier or later in the opposite direction, so that $D(\theta)$ should equal $-D(\theta + \pi)$. This condition is only approximately realized. Therefore, $D(\theta)$ is averaged with $-D(\theta + \pi)$ to produce the function

$$\bar{D}(\theta) = \frac{1}{2} [D(\theta) - D(\theta + \pi)] \quad (14)$$

which changes only in sign when advanced a half cycle. In Figure 3 below, for each of the thirteen experiments, points giving $\bar{D}(\theta)$ and $-D(\theta + \pi)$ are plotted at each 10 degrees of phase, and $\bar{D}(\theta)$ is shown.

(3) $\bar{D}(\theta)$ is resolved into a sum of sinusoidal components by Fourier analysis. Both sine and cosine terms are present with arguments $n\theta$, where n , an integer, is the number of the harmonic, but since $\bar{D}(\theta) = -\bar{D}(\theta + \pi)$, even harmonics are absent, and n is odd.

(4) Successively taking $T_c = T/n$, the calibration corrections for the filter distortions given by equations (11), (12) are applied to each component, and

(5) The series is reassembled to provide a corrected $\bar{D}(\theta)$. This reassembly has included terms as far as the 7th harmonic while checking that the increment from the 9th harmonic is insignificant.

(6) By use of the hydrostatic pressure calibrations, $\bar{D}(\theta)$ is expressed in pressure units to provide the first term on the right side of equation (9).

The records from the pitot tube, also contained on the paper tapes, have been processed manually, without computer or Fourier analysis. The last term in equation (9) has been approximated using overall filter corrections, those provided by equations (11) and (12) for $n = 1$. Errors associated with this approximation cannot be serious, since this term has been found to be small, its range less than 8%, and typically less than 5%, of the main term.

The remaining unknown term in equation (9), $\bar{\tau}_o$, is calculated by the theory for laminar oscillatory flow over a plane surface. Its range has proven to be less than 3% of that of $\bar{\tau}_s$.

IV. RESULTS

1. Summary of Experiments

The major results of this paper are curves of f as function of θ and of the parameters U , λ , λ/a from the thirteen experiments analyzed so far. In Table 1 these experiments are identified by number, in chronological sequence, and by values of their parameters M , λ , a , U , and including the redundant $T = 2\pi a/U$. The trough to crest ripple height, η , has also been added (except where the record remains on undeveloped film). M is the number of sand crests between the fixed end crests and determines λ , as described in section II,2. Experiments for which λ/a differs from $(\lambda/a)_p$, that is, those with strained profiles (sec. II,2), are denoted by asterisks. Experiment "C" is a composite of nos. 2 and 26 as described in section IV,2. All thirteen experiments have used quartz sand with $D_{50} = 0.55$ mm.

Table 1. Parameters for the Thirteen Experiments

$$D_{50} = 0.55 \text{ mm}$$

Exp. no.	M	λ , cm	a, cm	U, cm/s	T, s	η , cm
1	7	31.8	23.9	27.0	5.57	7.3
2	7	31.8	23.9	40.6	3.71	6.9
3	7	31.8	23.9	33.1	4.55	7.8
4*	7	31.8	25.5	33.3	4.83	7.2
5*	7	31.8	21.9	33.1	4.16	6.7
6*	7	31.8	20.6	33.15	3.90	5.7
7*	7	31.8	27.7	33.2	5.25	7.6
13	10	23.1	17.4	40.5	2.70	4.8
18	5	43.5	31.9	40.6	4.94	9.3
24	4	52.5	38.3	40.6	5.93	11.9
26	7	31.8	23.9	40.5	3.72	-
27	7	31.8	25.9	52.1	3.13	-
28	7	31.8	28.9	63.6	2.86	-
C	7	31.8	23.9	40.5	3.71	-

*With strained profiles, $\lambda/a \neq (\lambda/a)_n$

2. Reliability

Interpretation of the results to follow requires some assessment of their reliability. The most convenient measure of reliability is the extent to which the stress, and related measurements, change only in sign as θ is increased by π , that is, the agreement between $D(\theta)$ and $-D(\theta + \pi)$ defined in sec.II,5 and by equation (13). In Figure 3, $D(\theta)$, $-D(\theta + \pi)$ and their average $D(\theta)$ (eq. 14) are shown for each experiment, identified by its number in Table 1. The scales of $D(\theta)$ and $-D(\theta + \pi)$, are in tape units before calibration and are of no interest beyond the indicated zero marks. Discrepancies between $D(\theta)$ and $-D(\theta + \pi)$ remain within 10% for the most part but are occasionally considerably larger. Their cause is unknown. They are most plausibly associated with pressure buildups behind the screens and resulting

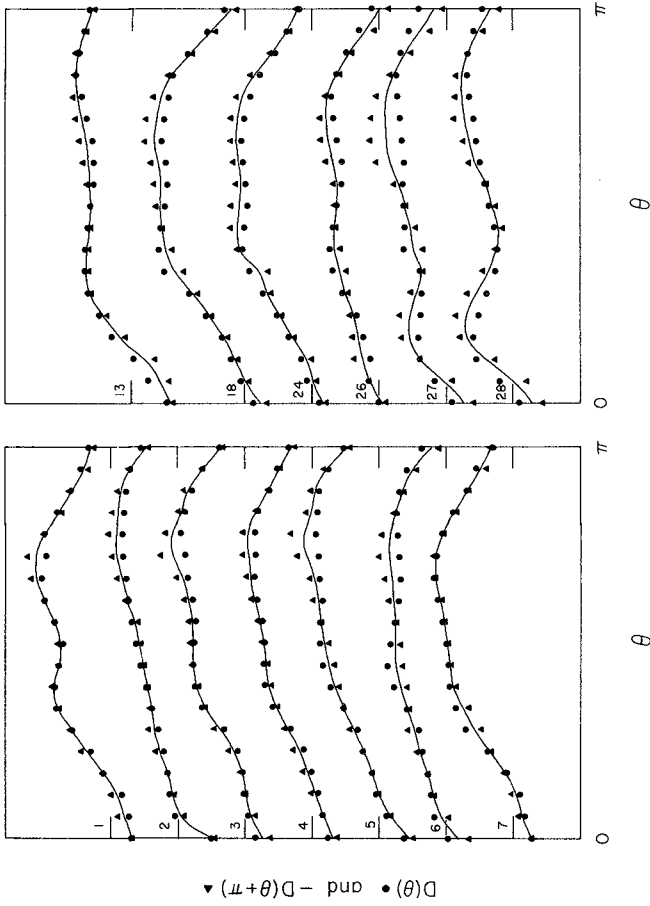


Figure 3. Applying the condition of symmetry between flows left to right, $D(\theta)$, and right to left, $-D(\theta+\pi)$. Experiments are numbered as in Table I.

flows through the by-pass. Pressure buildups are caused especially by sand in suspension being carried to and accumulating against a screen during a part of the cycle and become large enough to require limitations on U in order to forestall damage to the screens. The discrepancies may, in part, also derive from slight asymmetries in the sand profiles from one end of the bed to the other, particularly near the fixed end crests. Whatever their cause, such discrepancies reduce confidence in an experiment and if too large may cause it to be discarded.

Three of the experiments, nos. 26, 27, 28, were performed (after the oral presentation) following an enlargement of the by-pass to reduce the pressure difference $(p_o - p_s)_0$ (eq. 9) especially at higher values of U . Except for this enlargement, expts. 2 and 26 are ostensibly the same, and have been combined into a composite experiment numbered "C". Figure 4 shows $f(\theta)$ for expts. 2, 26, and "C". These curves agree reasonably well over most of the range but diverge substantially near times of flow reversal. Exps. 27 and 28 replace two experiments, included in the oral presentation, which had the same values of U , but had $\lambda/a = 1.33$, rather than $(\lambda/a)_n$ as in exps. 27 and 28. At these high values of U , $(\lambda/a)_n$ is significantly less than 1.33. In these two earlier experiments, ranges of $P(0, \theta)$ exceeded one half those of $P(L, \theta)$ and discrepancies between $D(\theta)$ and $-D(\theta + \pi)$ were substantially larger than in exps. 27 and 28, and, perhaps in consequence, their curves of $f(\theta)$ were quite different.

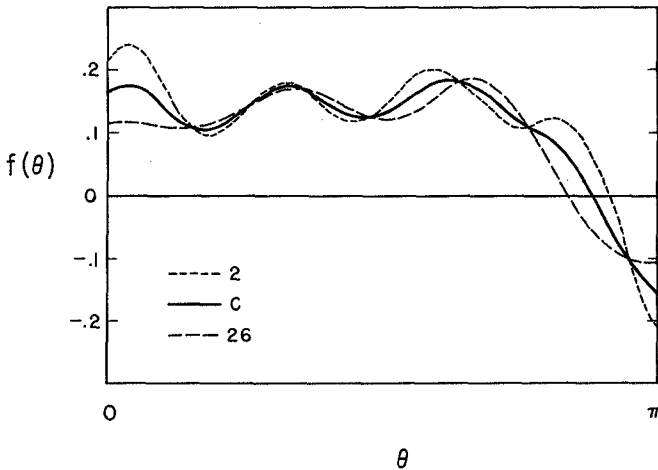


Figure 4. $f(\theta)$ for experiments 2 and 26 and their composite "C".

3. The Curves of $f(\theta)$

The curves of $f(\theta)$ from the twelve experiments (after combining nos. 2 and 26), for selected parameters, are shown in Figures 5,6,7. In Figures 5 and 6 the profiles are natural, with $\lambda/a = (\lambda/a)_n$, and in Figure 7 they are strained. $(\lambda/a)_n = 1.33$ in all experiments except nos. 27 and 28, in Figure 5, where it is reduced by the large values of U. In each figure, or family, the curves are identified at their left by their numbers in Table 1 and are arranged in order of monotonic increase or decrease in the defining parameter. In Figures 5 and 6 this parameter is U and λ , respectively, and in Figure 7 it is λ/a . The numerical value of the varying parameter is given at the right of each curve, and conditions and values of parameters held constant are shown above each family or figure. Although $f(\theta)$ is determined by its behavior over the restricted range $0 < \theta < \pi$, since $f(\theta + \pi) = -f(\theta)$, it is here presented over the entire cycle $-\pi/2 < \theta < 3\pi/2$ so that features of $f(\theta)$, such as maxima and minima, can more easily be followed from one curve to the next as the parameter is varied.

4. Values of \bar{f}_1 and f_m

With equation (5), values of \bar{f}_1 , the measure of energy dissipation, have been calculated from the twelve curves of $f(\theta)$ already presented. Table 2 lists these values in the same order as the curves in Figures 5, 6,7. For comparison, maximum values of $f(\theta)$, f_m , have been included.

Table 2. Values of \bar{f}_1 , proportional to the rate of energy dissipation, and f_m for the curves in Figures 5,6,7.

Natural profiles						Strained profiles		
$\lambda = 31.8 \text{ cm}$			$U \approx 40.6 \text{ cm/s}$			$\lambda = 31.8 \text{ cm}$ $U \approx 33.2 \text{ cm/s}$		
U, cm/s	\bar{f}_1	f_m	λ, cm	\bar{f}_1	f_m	λ/a	\bar{f}_1	f_m
27.0	.122	.299	52.2	.129	.282	1.15	.113	.253
33.1	.102	.236	43.5	.115	.259	1.25	.105	.228
40.5	.083	.180	31.8	.083	.180	1.33	.102	.236
52.1	.075	.218	23.1	.115	.452	1.45	.107	.228
63.6	.072	.348				1.54	.086	.227

The combination $U = 40.6 \text{ cm/s}$ and $a = 23.0 \text{ cm}$ occurs in the observations of Carstens, Neilson and Altinbilek (1969) where $T = 3.56\text{s}$. At this value of a and with $D = 0.585 \text{ mm}$, curves in their Figures 11 and 23 give $\lambda \approx 27.0 \text{ cm}$ and $\bar{f}_1 \approx .111$ (with their \bar{f} replaced by $3\pi\bar{f}_1$).

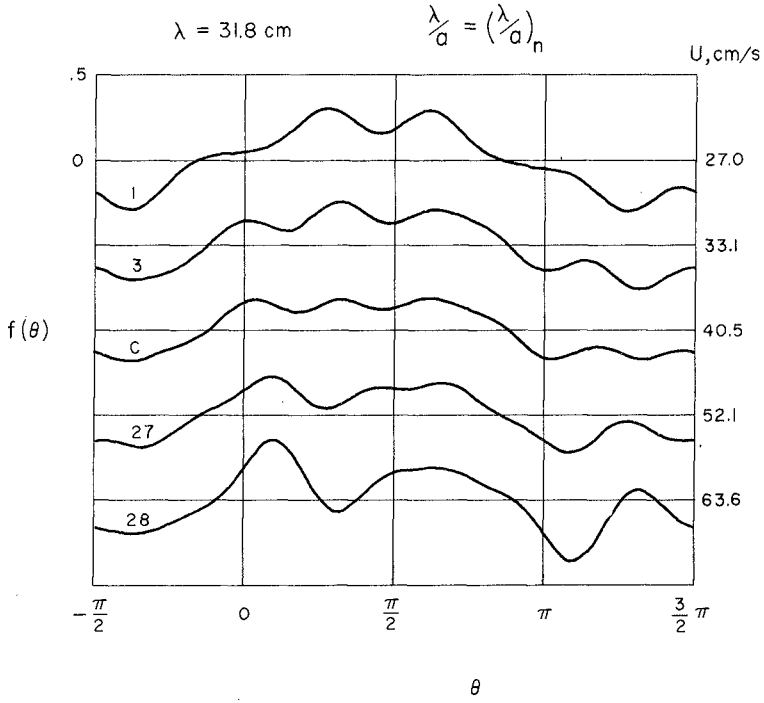


Figure 5. Stress coefficient f as function of phase θ and velocity U , for natural profiles.

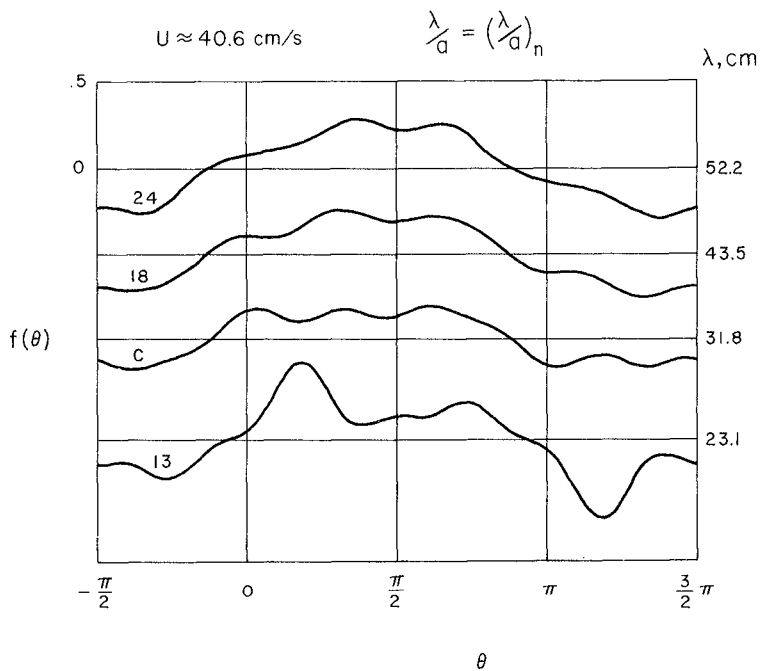


Figure 6. Stress coefficient f as function of phase θ and ripple length λ , for natural profiles.

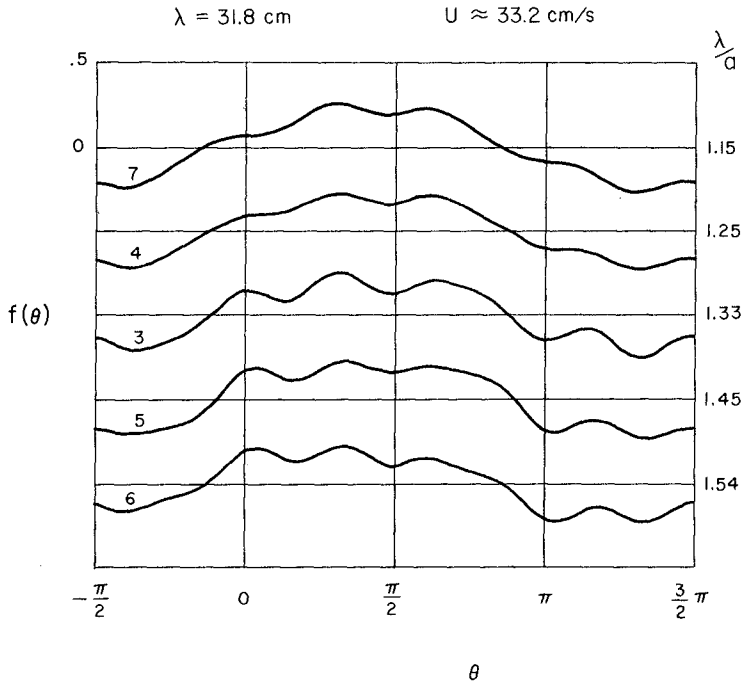


Figure 7. Stress coefficient f as function of phase θ and λ/a , for strained profiles.

IV. DISCUSSION

1. Conclusions Regarding $f(\theta)$ and \bar{f}_1 .

Defined by the magnitude, shape and phase of their peaks and valleys, the character of the curves in Figures 5,6,7 is found to progress continuously from one to the next as, within each family, U , λ and λ/a take on successive values. This continuity supports the reliability of the curves at hand, some of which will be repeated for further confirmation. Although restricted in the ranges of their parameters, the curves obtained permit some preliminary conclusions to be drawn. It is to be remembered that $u_{\infty}(\theta) = U \sin \theta$, as in equation (1).

The shapes of the functions $f(\theta)$ in Figures 5,6,7 differ markedly for different values of the parameters. Therefore, there can exist no "universal" function $f(\theta)$ to which all curves can be reduced by a selection of scale. In particular, in no case has $f(\theta)$ been found to be proportional to $\sin^2 \theta$. Thus, the instantaneous stress is not, in general, proportional to the square of the instantaneous velocity.

The values of \bar{f}_1 listed in Table 2 are found to vary smoothly with their parameters and, so far, to be fairly constant. In contrast, f_m , which is also listed, varies more abruptly and does not remain proportional to \bar{f}_1 . Thus, f_m does not provide a reliable measure of the rate of energy dissipation.^m

2. No Effect of Strain

It might be supposed that as a developing profile approaches equilibrium, or as a strained profile approaches an unstrained "natural" condition, the stress would take on some special stationary character, expressing, in some form, the principle of least action. However, the curves of $f(\theta)$ in Figure 7 and the values of \bar{f}_1 in Table 2 vary continuously with λ/a , with no discernible special character or extremum at $\lambda/a = 1.33$ where the profile is unstrained or natural. The ripple profiles of Figure 7, though strained, are stable, and these experiments have not examined the stress on unstable profiles during times of growth or change.

3. A Simple Model

Certain features common to all the curves of $f(\theta)$ in Figures 5,6,7 suggest a general, though limited, interpretation in terms of a simplified physical model. These features are three: (1) a positive stress at $\theta = 0$, (2) one or two peaks in $f(\theta)$ in the range $0 \leq \theta < \pi/2$, and (3) a single peak in $f(\theta)$ in the range $\pi/2 < \theta < \pi$. It is first recalled that the stress on a rigid flat bed precedes $u_{\infty}(\theta)$ by a shift in phase which is a maximum, $\pi/4$, for a smooth bed with laminar flow and stress and decreases as the bed becomes more rough and the stress more turbulent. Thus, with $u_{\infty}(\theta) = U \sin \theta$ such a stress would have a maximum in the range $\pi/4 < \theta < \pi/2$. The model simply combines such a "flat-bed stress" on the upstream face of the ripple crest with the stresses of vortex action, which is essential to ripple equilibrium.

The process of vortex formation and action adopted by the model is familiar. Following flow reversal, tangential stress on the upstream ripple face generates a boundary-vorticity layer and sets sand into motion, skewing the crest to end abruptly in a steep lee slope and sliding and spilling into the trough. The sharp curvature of the crest enhances separation of flow, and, as it is carried past, the boundary layer, with its vorticity, detaches and rolls into a vortex, still spilling sand into the trough. The center of the vortex is slowed and then held over the trough by reduced pressure on the lee slope of the crest, creating a form drag. Around the time of the succeeding flow reversal, the spinning vortex sweeps sand out of the trough and back up or over the crest, thus maintaining the profile.

Returning to $\theta = 0$, the spin of the vortex formed during the preceding half cycle and centered over the trough contributes a positive stress, while pressures needed to hold the vortex in position vanish at about this time. Thus, $f(0) > 0$. Following flow reversal, the vortex, decaying but still spinning, is carried up the ripple face where its spin hastens and increases the stress. Spin decay and the rapid drop off in spin stress as the vortex passes the ripple crest can account for an early maximum of the spin stress, slightly before or after $\theta = 0$, and preceding the maximum of the flat-bed stress. Thus, depending upon the relative strengths of these two maxima and their separation in time, $f(\theta)$ can display one or two peaks in the range $0 < \theta < \pi/2$. The deceleration of the forming vortex (or, more accurately, of several small vortices which later amalgamate) by reduced pressure on the lee slope begins with flow separation soon after flow reversal, but the associated form drag reaches a single peak as the vortex approaches full development sometime in the range $\pi/2 < \theta < \pi$, when the flat-bed stress is in decline. A negative back-flow stress on the lee ripple slope and under the vortex accompanies this form drag, and develops to make $f(\pi) < 0$ as the form drag vanishes.

The value of \bar{f}_1 from Carstens, Neilson and Altinbilek (1969), noted in section III, 4 above, fits well with values listed in Table 2. However, in Figures 5,6,7 the peaks in $f(\theta)$ preceding and nearest $\theta = \pi/2$, which the model associates with the flat-bed stress, are an order of magnitude larger than values of f_m obtained by Kamphuis (1975) at the same values of a/D and aU/ν . At least to some extent, this large increase may be a result of the movement of sand grains on the ripple face (cf. Lofquist in discussion of Vitale, 1979). Similarly, the peaks in $f(\theta)$ following $\theta = \pi/2$, which the model associates with form drag and vortex formation, suggest a form drag contribution to \bar{f}_1 of, roughly, one third. This is several times the seven percent which Tunstall and Inman (1975) have estimated for the ratio of vortex energy to the total energy dissipated in a half cycle. Their estimate was based upon a study of vortex formation behind rounded rigid (lithified) ripple crests. Possibly, the relative sharpness of a naturally skewing crest substantially enhances flow separation and vortex formation, or, the vortex energy is only a part of the form drag contribution to \bar{f}_1 .

4. Limitations and a Correction

Whatever its merits, the model is severely limited. Processes which interact cannot simply be added as flat-bed and vortex stresses. Concentration of all the vorticity generated on the upstream face of a crest into a single vortex formed in its lee is not a universal mechanism. In particular, at higher rates of flow, and scour, the ripple crests become lower and closer and unable to form and hold vortices large enough to contain all the detached boundary layer, and flow patterns modify. Such appeared to be the case with exp. 28.

When large quantities of sand are set in motion, $f(\theta)$ as calculated by equation (9) itself loses precision and requires the addition of a correction, $\Delta f(\theta)$. If, at any θ , the sand in motion lowers the mean surface by Δh (a positive quantity) and has a momentum \dot{m}_s per unit area of the bed, and with $Q_s = bHu \sin \theta$, a rederivation of $f(\theta)$ produces the correction term

$$\Delta f(\theta) = \frac{2\Delta h}{a} \cos \theta - \frac{2}{\rho U^2} \dot{m}_s \quad (15)$$

In experiment 28, Figure 5 shows $f(\theta)$, surprisingly, to be negative in the neighborhood of $\theta = \pi/3$. Here, $\Delta h \cos \theta$ is positive while \dot{m}_s is presumably negative, as sand scoured from the bed during the preceding peak in $f(\theta)$ falls back to impact the bed and lose its momentum. Thus, $\Delta f(\theta)$ is presumably positive and, while its magnitude can only be guessed at, it could suffice to keep the corrected $f(\theta)$ positive.

5. Future Work

The experiments described here are part of a larger program interrupted by the timing of the conference. As noted above, future experiments will investigate the repeatability of present results, and will extend the ranges and the number of combinations of the parameters. One or two finer sands will be included. Future more complete analyses will more consistently combine parameters into dimensionless ratios. A completed study is scheduled for publication in 1981 by the Coastal Engineering Research Center, Ft. Belvoir, Virginia.

ACKNOWLEDGEMENT

The results presented in this paper are based on research conducted at the National Bureau of Standards. This research is wholly supported by the Coastal Engineering Research Center under the Beach Behavior and Restoration Research Program of the U.S. Army Corps of Engineers. The findings reported here are not to be construed as an official Department of the Army position unless so designated by other authorized documents. Permission to publish this information is appreciated.

REFERENCES

- BAGNOLD, R.A., "Motion of Waves in Shallow Water, Interaction Between Waves and Sand Bottoms," Proc. Roy. Soc. London, Ser. A, Vol. 187, 1946, pp. 1-18.
- BRETSCHNEIDER, C.L., "Field Investigation of Wave Energy Loss of Shallow Water Ocean Waves," TM-46, U.S. Army Corps of Eng., BEB, Sept. 1954.
- CARSTENS, M.R., NEILSON, F.M., and ALTINBILEK, H.D., "Bed Forms Generated in the Laboratory Under and Oscillatory Flow: Analytical and Experimental Study," TM-28, U.S. Army Corps of Eng., CERC, June 1969.
- INMAN, D.L., and BOWEN, A.J., "Flume Experiments on Sand Transport by Waves and Currents," Proc. Eighth Coastal Eng. Conf., 1962, pp. 137-150.
- IWAGAKI, Y., and KAKINUMA, T., "On the Bottom Friction Factors Off Five Japanese Coasts," Coastal Eng. in Japan, Vol. 10, 1967, pp. 13-22.
- JONSSON, I.G., and CARLSEN, N.A., "Experimental and Theoretical Investigations in an Oscillatory Turbulent Boundary Layer," Journal Hyd. Res. Vol. 14, No. 1, (1976), pp. 45-60.
- KALKANIS, G., "Transportation of Bed Material Due to Wave Action," TM-2, U.S. Army Corps of Eng., CERC, Feb. 1964.
- KAMPHUIS, J.W., "Friction Factors Under Oscillatory Waves," Jour. Waterways, Harbors and Coastal Eng. Div., ASCE, Vol. 101, No. WW2, May 1974, pp. 135-144.
- LOFQUIST, K.E.B., "A Positive Displacement Oscillatory Water Tunnel," MR 77-1, U.S. Army Corps of Eng., CERC, Feb. 1977.
- LOFQUIST, K.E.B., "Sand Ripple Growth in an Oscillatory-Flow Water Tunnel," TP 78-5, U.S. Army Corps of Eng., CERC, Aug. 1978.
- SAVAGE, R.P., "Laboratory Study of Wave Energy Losses by Bottom Friction and Percolation," TM-31, U.S. Army Corps of Eng., BEB, Feb. 1953.
- TUNSTALL, E.B., and INMAN, D.L., "Vortex Generation by Oscillatory Flow Over Rippled Surfaces," Journal of Geophysical Research, Vol. 80, No. 24, Aug. 1975, pp. 3475-3484.
- VITALE, P., "Sand Bed Friction Factors for Oscillatory Flows," Journal of the Waterway, Port, Coastal and Ocean Div., Proc. ASCE, Vol. 105, No. WW3, Aug. 1979, pp. 229-245.

Contribution to the Discussion During Session C,
Coastal Processes, Friday, March 28, 2:00 p.m.

by

M. S. Longuet-Higgins
Institute of Oceanographic Sciences
Wormley, Surrey, England

Professor Brebner suggested that the profile of sand ripples should be approximated by a conformal transformation into a hexagon, as has been done for steep surface waves (Longuet-Higgins, 1973). In fact the ripple profile is often steeper than this, the angle at the crest being closer to 108° (the interior angle of a pentagon) than to 120° . See, for example, the experimental data summarized by Nielsen (1979), Figures 5.7 to 5.11. For the pentagon approximation, the ratio of ripple height to ripple wavelength would be

$$\frac{H}{L} = \frac{1n \sec \pi/5}{2\pi/5} = 0.169 .$$

In fact polygons with any number P of sides may be used, and we may extend the analysis to all rational values $P = N/M$ by considering polygons enclosing their centre M times.

The great advantage of the polygon approximation is that the flow outside the polygon (i.e., above the ripple) may be quite simply mapped onto the interior of a circle. Irrotational flow over the ripple is represented by a simple vortex at the center of the circle. Any other vorticity shed by boundary layers at the crests can be represented by point-vortices and their images in the circle.

Calculations using these ideas are at present in hand (Longuet-Higgins, 1980 a,b). It has already been shown that they yield drag coefficients in excellent agreement with those measured by Bagnold (1946) and by Carstens, et al. (1969).

References

- Bagnold, R.A. 1946 Proc. R. Soc. Lond. A 187, 1-15.
- Carstens, M.R. Nielson, F.M. and Altenbilek, H.D. 1969. C.E.R.C. Tech. Mem. No. 28, 78 pp.
- Longuet-Higgins, M.S. 1973. Proc. R. Soc. Lond. A 331, 445-465.
- Longuet-Higgins, M.S. 1980a. "Polygon transformations in fluid mechanics." Proc. 7th Int. Conf. on Numerical Methods in Fluid Mechanics, Stanford, California, June 1980.
- Longuet-Higgins, M.S. 1980 b "Oscillating flow over steep sand ripples." Submitted to J. Fluid Mech.
- Nielsen, P. 1979. I.S.V.A., Tech. Univ. of Denmark, Lyngby, Series Pap. No. 20, 160 pp.

Subject Index

- Acceleration; Breaking energy; Fluid mechanics; Water waves; Wavelength; Wave velocity**
The Fluid Mechanics of Waves Approaching Breaking, D. H. Peregrine, E. D. Cokelet and P. Melver, 512
- Accretion (geomorphology); Australia; Beach erosion; Coastal engineering; Field work; Wave action**
Beach Erosion-Accretion at Two Time Scales, B. G. Thom and G. M. Bowman, 934
- Airport construction; Australia; Estuaries; Inlets (waterways); Land reclamation; Littoral drift; Tidal effects; Tides**
Inlets/Estuaries Discharging into Sheltered Waters, H. P. Riedel and M. R. Gourlay, 2548
- Alaska; Cliffs; Coastal Processes; Erosion; Sea ice; Sediment transport; Tundra; Wave energy**
Sediment Transport Processes and Coastal Variability on the Alaskan North Slope, E. H. Owens, J. R. Harper and D. Nummendaal, 1343
- Alluvial deposits; Australia; Beach erosion; Beach sands; Deltas; Flood protection; Rivers; Sediment transport**
Barron River Delta Investigation, D. A. Robinson, D. J. Cook and J. G. Barff, 885
- Analogies; Electromagnetic radiation; Gravity waves; Microwaves; Seiches; Water waves**
An Electromagnetic Analogy For Long Water Waves, G. W. Jackson and D. L. Wilkinson, 801
- Analysis; Australia; Coastal engineering; Dredging; Ocean waves; Ports; Real time operations; Wave action; Wave height**
Realtime Wave Analysis, Newcastle, Australia, N. V. Lawson and P. H. Youll, 412
- Analysis; Submarine trenches; Water waves; Wave period; Wave propagation; Wave reflection**
Interactions of Waves With Submarine Trenches, Jjin-Jen Lee, Robert M. Ayer and Wen-Li Chiang, 812
- Anemometers; Friction factor; Hawaii; Tsunamis; Turbulent flow; Wind profiles; Wind velocity**
Tsunami Prone Friction Factors From Wind Measurements, Charles L. Bretschneider, 672
- Antifouling materials; California; Coasts; Design; Outfall sewers; San Francisco; Sediment deposits; Shallow water; Wastewater (pollution); Water pollution; Wave energy**
Design of an Intermittently Operated Outfall, Roger W. Lindquist and George J. Murphy, 2834
- Australia; Beach erosion; Beaches; Beach nourishment; Coastal engineering; Dunes; Shore protection**
The Beach Improvement Programme: New South Wales, Neale A. Philip and Philip H. White, 1668
- Australia; Beach erosion; Beaches; Beach nourishment; Coastal engineering; Dunes; Sand pumps**
Noosa Beach Restoration Scheme, R. J. Lloyd, 1618
- Australia; Beach erosion; Beaches; Coastal engineering; Shore protection**
Capricorn Coast Beaches, D. C. Patterson and L. R. Ford, 1648
- Australia; Beach erosion; Beaches; Field tests; Stability; Surf; Topography; Wave action**
Beach Cut in Relation to Surf Zone Morphodynamics, L. D. Wright, 978
- Australia; Beach erosion; Beach sands; Deltas; Flood protection; Rivers; Sediment transport; Alluvial deposits**
Barron River Delta Investigation, D. A. Robinson, D. J. Cook and J. G. Barff, 885
- Australia; Beach erosion; Coastal engineering; Field work; Wave action; Accretion (geomorphology)**
Beach Erosion-Accretion at Two Time Scales, B. G. Thom and G. M. Bowman, 934
- Australia; Beach erosion; Dunes; Dune sands; Revegetation; Sand control; Shore protection**
Research in Southern Queensland into the Management of Coastal Sand Dunes, James B. McKenzie and David A. Barr, 1547
- Australia; Beaches; Beach nourishment; Coastal engineering; Coasts; Morphology; Prisms; Wave action**
The Dynamic Swept Prism, David M. Chapman and A. W. Smith, 1036
- Australia; Beaches; Beach nourishment; Coastal engineering; Management methods; Sand; Topography**
Beach Nourishment as a Management Technique, David M. Chapman, 1635
- Australia; Beaches; Computer applications; Construction; Docks; Dredging; Environmental surveys; Ports; Water flow; Water quality**
Integration and Computation in an Environmental Study, J. B. Hinwood, J. E. Watson and D. M. Burrage, 3024
- Australia; Beach nourishment; Bed forms; Dredging; Estuaries; Rivers; Sand; Sediment transport; Tidal hydraulics**
Estuarine Response to Dredging in the Tweed River, Australia, Bruce M. Drury, 1598
- Australia; Breakwaters; Coastal engineering; Construction; Design; Model tests; Overtopping; Ports**
Design of an Overtopping Breakwater, P. D. Treloar and B. Nagle, 1910
- Australia; Breakwaters; Coastal structures; Design; Harbors; Shore protection; Storms; Storm surges; Wind forces**
The Design Concept of Dual Breakwaters and its Application to Townsville, Australia, W. Bremner, D. N. Foster, C. A. Miller and B. C. Wallace, 1899
- Australia; Budgeting; Coastal engineering; Coastal Processes; Model tests; Sediments**
An Approach to Understanding Coastal Processes, A. D. Gordon and D. B. Lord, 1234

- Australia; Coastal engineering; Coastal Processes; Coasts; Geologic control; Marine geology; Sediment transport; Wave action; Wave energy**
Geological Controls on Process-Response, SE Australia, P. S. Roy and A. W. Stephens, 913
- Australia; Coastal engineering; Coasts; Estuaries; Inlets (waterways); Tidal effects**
A Coastal Inlet with Fixed Bed and Mobile Sides, R. C. Nelson and A. J. Keats, 2532
- Australia; Coastal engineering; Dredging; Ocean waves; Ports; Real time operations; Wave action; Wave height; Analysis**
Realtime Wave Analysis, Newcastle, Australia, N. V. Lawson and P. H. Youll, 412
- Australia; Coastal engineering; Environmental impact statements; Estuaries; Planning; Ports; Water flow**
Water Movement Studies Required for Port Planning, Graeme C. Dandy, Desmond A. Mills and John B. Hinwood, 3007
- Australia; Coastal engineering; Resonance; Sea level changes; Subsonic flow; Waves**
Resonances of Coastal Waters Between Perth and Geraldton, H. Allison, A. Grassia and R. Litchfield, 290
- Australia; Coastal Processes; Estuaries; Floods; Inlets (waterways); Lakes; Littoral drift; Stability criteria; Tidal effects; Tidal waters**
Tidal Inlet Behavioural Analysis, A. F. Nielsen and A. D. Gordon, 2459
- Australia; Continental shelf; Currents (water); Field tests; Models; Predictions; Sediment transport; Wave height; Wind speed**
Sediment Dispersal on the NSW Continental Shelf, Ron Boyd, 1363
- Australia; Dunes; Sand control; Sediment transport; Shore protection; Wind action geology**
Wind and Sediment Movement in Coastal Dune Areas, John R. Hails and John Bennett, 1564
- Australia; Estuaries; Field investigations; Floods; Mathematical models; Ports; Sediment transport; Shoaling; Silting**
Port of Brisbane Siltation Study, N. V.M. Odd and T. Baxter, 2375
- Australia; Estuaries; Inlets (waterways); Land reclamation; Littoral drift; Tidal effects; Tides; Airport construction**
Inlets/Estuaries Discharging into Sheltered Waters, H. P. Riedel and M. R. Gourlay, 2548
- Australia; Jetties; Models; Morphology; Rivers; Rubble mounds; Sediment transport**
Mechanisms Operating at a Jettied River Entrance, Bruce M. Drury and Alexander F. Nielsen, 2605
- Australia; Ocean waves; Offshore drilling; Offshore platforms; Oil and gas fields; Wave measurement; Wind; Wind speed**
Wave Hindcasts and Measurements Bass Strait, M. N. Silbert, T. P. Barnett, D. J.H. Peters and R. C. Hamilton, 384
- Barriers; Basins; Channels (waterways); Dams; Estuaries; Inlets (waterways); Sedimentation; Tidal currents; West Germany**
Sedimentation Processes in Tidal Channels and Tidal Basins Caused by Artificial Constructions, E. Renger and H. W. Partenscky, 2479
- Barriers; Coastal engineering; Estuaries; Hydraulic tests; Netherlands; Storm surges**
Hydraulic Research in the Oosterschelde Estuary, A. W. Walther, 2358
- Basins; Channels (waterways); Dams; Estuaries; Inlets (waterways); Sedimentation; Tidal currents; West Germany; Barriers**
Sedimentation Processes in Tidal Channels and Tidal Basins Caused by Artificial Constructions, E. Renger and H. W. Partenscky, 2479
- Bathymetry; Coasts; Inlets (waterways); Landsat; Littoral drift; Remote sensing; Sandbars; Satellite Mapping**
Satellite Applications on a Coastal Inlet Stability Study, Yu-Hwa Wang, 2579
- Bathymetry; Currents (water); Models; Sediment transport; Shoaling; Shores; Topography; Waves**
Inshore-Nearshore Morphodynamics - A Predictive Model, John Chappell, 963
- Bays (topographic features); Beach erosion; Beaches; Littoral drift; Shore protection; Wave action**
Zeta Bays, Pocket Beaches and Headland Control, R. Silvester, Y. Tsuchiya and Y. Shibano, 1305
- Bays (topographic features); Coastal engineering; Currents (water); Estuaries; Maine; Models; Three-dimensional; Water pollution control; Water quality**
A 3-D Model for Penobscot Bay, Maine, Bryan R. Pearce, Bruce R. Fidler and Adrian C. Humphreys, 2395
- Bays (topographic features); Inlets (waterways); Tidal effects; Tide gages; Tides**
Tidal Prism-Inlet Area Relations for Small Tidal Inlets, R. J. Byrne, R. A. Gammisch and G. R. Thomas, 2515
- Bays (topographic features); Japan; Numerical calculations; Tsunamis; Wave equations; Wave runup**
Run-Up of Tsunamis by Linear and Nonlinear Theories, Chiaki Goto and Nobuo Shuto, 695
- Beach erosion; Beaches; Beach nourishment; Coastal engineering; Dunes; Sand pumps; Australia**
Noosa Beach Restoration Scheme, R. J. Lloyd, 1618
- Beach erosion; Beaches; Beach nourishment; Coastal engineering; Dunes; Shore protection; Australia**
The Beach Improvement Programme, New South Wales, Neale A. Philip and Philip H. Waite, 1666
- Beach erosion; Beaches; Beach nourishment; Morphology; Sand; Sediment transport; Wave energy; Wave height; Waves**
Beach Response to Variations in Breaker Height, A. D. Short, 1016
- Beach erosion; Beaches; California; Sediment transport; Topographic features; Wave action; Wave period**
Beach Cusps at Point Reyes and Drakes Bay Beaches, California, R. G. Dean and E. M. Maurmeyer, 863
- Beach erosion; Beaches; Coastal engineering; Shore protection; Australia**
Capricorn Coast Beaches, D. C. Patterson and L. R. Ford, 1648

- Beach erosion; Beaches; Field tests; Stability; Surf; Topography; Wave action; Australia**
Beach Cut in Relation to Surf Zone Morphodynamics, L. D. Wright, 978
- Beach erosion; Beaches; Littoral drift; Shore protection; Wave action; Bays (topographic features)**
Zeta Bays, Pocket Beaches and Headland Control, R. Silvester, Y. Tsuchiya and Y. Shibano, 1305
- Beach erosion; Beach sands; Deltas; Flood protection; Rivers; Sediment transport; Alluvial deposits; Australia**
Barron River Delta Investigation, D. A. Robinson, D. J. Cook and J. G. Barff, 885
- Beach erosion; Breakwaters; Coastal engineering; Dredging; Field investigations; Islands; Shore protection; South Carolina; Wave action**
Soft Designs for Coastal Protection at Seabrook Island, S.C., Miles O. Hayes, Timothy W. Kana and John H. Barwis, 897
- Beach erosion; Breakwaters; Design practices; Lakes; Lake shores; Lake waves; Ohio; Shore protection; Storms**
A Detached Breakwater System for Beach Protection, James R. Walker, Denton Clark and Joan Pope, 1969
- Beach erosion; Coastal engineering; Field investigations; Flood control; Inlets (waterways); Research projects; Tidal waters; U.S. Corps of Engineers**
The Corps of Engineer's General Investigation of Tidal Inlets, Robert M. Sorensen, 2563
- Beach erosion; Coastal engineering; Field work; Wave action; Accretion (geomorphology); Australia**
Beach Erosion-Accretion at Two Time Scales, B. G. Thom and G. M. Bowman, 934
- Beach erosion; Coastal Processes; Louisiana; Sedimentation; Shore protection; Wave energy**
Fluid Mud Dynamics and Shoreline Stabilization: Louisiana Chenier Plain, John T. Wells and Harry H. Roberts, 1381
- Beach erosion; Dunes; Dune sands; Revegetation; Sand control; Shore protection; Australia**
Research in Southern Queensland into the Management of Coastal Sand Dunes, James B. McKenzie and David A. Barr, 1547
- Beach erosion; Laboratory tests; Models; Sand; Sediment transport; Shallow water; Wave action**
A Laboratory Study of Offshore Transport of Sediment and a Model for Eroding Beaches, Tsuguo Sunamura, 1051
- Beaches; Beach nourishment; Coastal engineering; Coasts; Morphology; Prisms; Wave action; Australia**
The Dynamic Swept Prism, David M. Chapman and A. W. Smith, 1036
- Beaches; Beach nourishment; Coastal engineering; Dunes; Sand pumps; Australia; Beach erosion**
Noosa Beach Restoration Scheme, R. J. Lloyd, 1618
- Beaches; Beach nourishment; Coastal engineering; Dunes; Shore protection; Australia; Beach erosion**
The Beach Improvement Programme: New South Wales, Neale A. Philip and Philip H. White, 1668
- Beaches; Beach nourishment; Coastal engineering; Management methods; Sand; Topography; Australia**
Beach Nourishment as a Management Technique, David M. Chapman, 1635
- Beaches; Beach nourishment; Morphology; Sand; Sediment transport; Wave energy; Wave height; Waves; Beach erosion**
Beach Response to Variations in Breaker Height, A. D. Short, 1016
- Beaches; Beach sands; Coastal Processes; Hydraulics; Laboratory tests; Permeability (soils); Profiles; Surf; Waves**
Beaches: Profiles, Processes and Permeability, Michael R. Gourlay, 1319
- Beaches; Breaking energy; Phase shift; Wave action; Wave height; Waves; Wave velocity**
Breaker Type and Phase Shifts on Natural Beaches, Peter J. Cowell, 997
- Beaches; Breakwaters; Coastal engineering; Groins (structures); Japan; Shore protection**
Artificial Resort Beach Protected by Offshore Breakwaters and Groins, Shoji Sato and Norio Tanaka, 2004
- Beaches; California; Sediment transport; Topographic features; Wave action; Wave period; Beach erosion**
Beach Cusps at Point Reyes and Drakes Bay Beaches, California, R. G. Dean and E. M. Maurmeyer, 863
- Beaches; Coastal engineering; Currents (water); Flow; Waveguides; Waves**
Longshore Current Flows in a Wave Basin, P. J. Visser, 462
- Beaches; Coastal engineering; Currents (water); Japan; Littoral current; Power plant location; Wave action; Wave energy**
Nearshore Currents on a Partially Rocky Shore, T. O. Sasaki, H. Igarashi and S. Harikai, 1071
- Beaches; Coastal engineering; Experimental data; Wave action; Wave energy; Waves; Wave velocity**
Experimental Investigations of Periodic Wave Near Breaking, J. Buir Hansen, 260
- Beaches; Coastal engineering; Fluid mechanics; Similarities; Surf; Wave energy; Waves**
A Similarity Model in the Surf Zone, Hsiang Wang and Wei-Chong Yang, 529
- Beaches; Coastal engineering; Heuristic methods; Surf; Wave energy; Wave height; Waves**
An Heuristic Model of Wave Height Distribution in Surf Zone, Masaru Mizuguchi, 278
- Beaches; Coastal engineering; Littoral deposits; Littoral drift; Sediment transport; Shear stress; Wave action**
Beach Profiles and On-Offshore Sediment Transport, Akira Watanabe, Yoshihiko Riho and Kiyoshi Horikawa, 1106
- Beaches; Coastal engineering; Shore protection; Australia; Beach erosion**
Capricorn Coast Beaches, D. C. Patterson and L. R. Ford, 1648
- Beaches; Coastal Processes; Littoral drift; Sandbars; Shores; Topography; Wave action**
Migration of Longshore Bars, Hans H. Dette, 1475

- Beaches; Coasts; Littoral materials; Mathematical models; Water circulation; Water pollution; Water waves; Wave action**
Numerical Modelling of Nearshore Circulation, Bruce A. Ebersole and Robert A. Dalrymple, 2708
- Beaches; Computer applications; Construction; Docks; Dredging; Environmental surveys; Ports; Water flow; Water quality; Australia**
Integration and Computation in an Environmental Study, J. B. Hinwood, J. E. Watson and D. M. Burrage, 3024
- Beaches; Currents (water); Groundwater elevation; Slopes; Surf; Wave action; Wave energy**
Wave Forcing of Beach Groundwater, Evans Waddell, 1435
- Beaches; Currents (water); Littoral current; Surf; Topography; Wave energy; Wave height; Wave runup**
Topographic Control of Run-Up Variability, Mark P. Bradshaw, 1091
- Beaches; Deep water; Sediment transport; Stability analysis; Wave energy; Waves**
Criterion for Stability of Shoreline Platform, John D. Wang and Bernard Le Mehaute, 1994
- Beaches; Deformation; Littoral deposits; Littoral drift; Models; Sediment transport; Surf**
On-Offshore Sediment Transport Rate in the Surf Zone, Toru Sawaragi and Ichiro Deguchi, 1194
- Beaches; Disturbances; Experimentation; Flumes; Predictions; Wave equations; Waves**
Long Period Disturbances Due to Wave Groups, E. C. Bowers, 610
- Beaches; Field investigations; Japan; Littoral drift; Littoral materials; Ports; Sand**
Littoral Drift on Sand Near Port of Oarai, Kazumasa Mizumura, 2157
- Beaches; Field tests; Stability; Surf; Topography; Wave action; Australia; Beach erosion**
Beach Cut in Relation to Surf Zone Morphodynamics, L. D. Wright, 978
- Beaches; Hydraulics; Littoral drift; Sand; Sediment transport; Wave energy**
Secondary Sand Transport Mechanisms, A. W. Smith and A. D. Gordon, 1122
- Beaches; Littoral deposits; Littoral drift; Models; Sand; Sediment transport; Surf; Waves**
Onshore-Offshore Transport and Beach Profile Change, Masataro Hattori and Ryoichi Kawamata, 1178
- Beaches; Littoral drift; Shore protection; Wave action; Bays (topographic features); Beach erosion**
Zeta Bays, Pocket Beaches and Headland Control, R. Silverster, Y. Tsuchiya and Y. Shibano, 1305
- Beach nourishment; Bed forms; Dredging; Estuaries; Rivers; Sand; Sediment transport; Tidal hydraulics; Australia**
Estuarine Response to Dredging in the Tweed River, Australia, Bruce M. Druery, 1598
- Beach nourishment; Coastal engineering; Coasts; Morphology; Prisms; Wave action; Australia; Beaches**
The Dynamic Swept Prism, David M. Chapman and A. W. Smith, 1036
- Beach nourishment; Coastal engineering; Dunes; Sand pumps; Australia; Beach erosion; Beaches**
Noosa Beach Restoration Scheme, R. J. Lloyd, 1618
- Beach nourishment; Coastal engineering; Dunes; Shore protection; Australia; Beach erosion; Beaches**
The Beach Improvement Programme: New South Wales, Neale A. Philip and Philip H. Whaite, 1668
- Beach nourishment; Coastal engineering; Management methods; Sand; Topography; Australia; Beaches**
Beach Nourishment as a Management Technique, David M. Chapman, 1635
- Beach nourishment; Morphology; Sand; Sediment transport; Wave energy; Wave height; Waves; Beach erosion; Beaches**
Beach Response to Variations in Breaker Height, A. D. Short, 1016
- Beach sands; Coastal Processes; Hydraulics; Laboratory tests; Permeability (soils); Profiles; Surf; Waves; Beaches**
Beaches: Profiles, Processes and Permeability, Michael R. Gourlay, 1319
- Beach sands; Deltas; Flood protection; Rivers; Sediment transport; Alluvial deposits; Australia; Beach erosion**
Barron River Delta Investigation, D. A. Robinson, D. J. Cook and J. G. Barff, 885
- Bed forms; Drag; Experimentation; Measurement; Sands; Sand waves; Water tunnels; Water waves**
Measurements of Oscillatory Drag on Sand Ripples, Karl E. B. Lofquist, 3104
- Bed forms; Dredging; Estuaries; Rivers; Sand; Sediment transport; Tidal hydraulics; Australia; Beach nourishment**
Estuarine Response to Dredging in the Tweed River, Australia, Bruce M. Druery, 1598
- Bed forms; Dunes; Dynamic geology; Erosion; Models; Numerical calculations; Sediment transport**
A Numerical Model for Dune Dynamics, J. Sundermann, H.-J. Vollmers and W. Puls, 1583
- Bed forms; Motion studies; Oscillation; Sand; Water tunnels (testing); Wave action**
Sand Bed-Form Lengths Under Oscillatory Motion, Arthur Brebner, 1339
- Beds under water; Estimates; Sediment distribution; Sediment transport; Topographic features; Wave height; Wave period**
Longshore Water and Sediment Movement, D. H. Swart and C. A. Fleming, 1274
- Berths; Caissons; China; Concrete construction; Design; Mooring; Petroleum transportation; Piers (docks); Ports; Tanker ships**
The Design and Construction of the New Oil Port in Dalian, CPR, Zhu-zhuang Xin and Yu-cheng Li, 2081
- Bitumens; Breakwaters; Coastal engineering; Rubble-mound breakwaters; Sand; Shore protection**
Breakwater with a Sand Bitumen Core, E. Loewy, K. G. Witthaus, R. J. Maddrell and J. P. Wood, 2192

- Bottom sediments; Coastal engineering; Flumes; Sand; Sediment transport; Wave action; Waves**
Sand Transport by Waves, Jan van de Graaff and Wiel M.K. Tilmans, 1140
- Boundary conditions; Downstream; Inlets (waterways); North Carolina; Tidal waters; Water flow**
Boundary Conditions for Analysis of Flow in Tidal Inlets, T. C. Gopalakrishnan and J. L. Machemehl, 2593
- Boundary layer flow; Hydrofoils; Turbulent flow; Wakes; Waves; Wave velocity**
Velocity Field in a Steady Breaker, J. A. Battjes and T. Sakai, 499
- Breaking energy; Coastal engineering; Coasts; Littoral drift; Taiwan; Wave energy; Wave measurement**
Relationship Between Alongshore Wave Energy and Littoral Drift in the Mid West Coast at Taiwan, Ho-Shong Hou, Chung-Pan Lee and Lung-Hui Lin, 1254
- Breaking energy; Fluid mechanics; Water waves; Wavelength; Wave velocity; Acceleration**
The Fluid Mechanics of Waves Approaching Breaking, D. H. Peregrine, E. D. Cokelet and P. McIver, 512
- Breaking energy; Phase shift; Wave action; Wave height; Waves; Wave velocity; Beaches**
Breaker Type and Phase Shifts on Natural Beaches, Peter J. Cowell, 997
- Breakwaters; Caissons; Composite structures; Design; Impact loads; Laboratory tests; Wave action**
Wave Impact Pressures on Composite Breakwaters, G. R. Mogridge and W. W. Jamieson, 1830
- Breakwaters; Caissons; Concrete construction; Design; Islands; Shore protection; Terminals**
The Effects of Construction Techniques & Bulk Terminal Operational Requirements on the Design Criteria for Island Breakwaters, A. G. F. Eddle, J. D. Lawson, H. R. Graze and B. K. Dean, 2061
- Breakwaters; California; Coastal engineering; Field tests; Harbors; Sand traps; Sediment transport; Wave measurement**
Longshore Transport Evaluations at a Detached Breakwater, R. O. Bruno, R. G. Dean and C. G. Gable, 1452
- Breakwaters; Case reports; Deep water; Design criteria; Energy transfer; Harbors; Truncation errors; West Germany**
Energy Transmission Over Break Water - A Design Criterion?, P. Bade and H. Kaldenhoff, 1886
- Breakwaters; Coastal engineering; Coastal structures; Concrete structures failure; Damages; Portugal; Rubble-mound breakwaters**
Report on the Damages to the Sines Breakwater, Portugal, William F. Baird, Joseph M. Caldwell, Billy L. Edge and Orville T. Magoon, 3060
- Breakwaters; Coastal engineering; Concrete construction; Design; Model tests; Rubble-mound breakwaters**
Can We Develop New Breakwater Formulas, John Dorrington Mettam, 2302
- Breakwaters; Coastal engineering; Construction; Design; Model tests; Overtopping; Ports; Australia**
Design of an Overtopping Breakwater, P. D. Treloar and B. Nagle, 1910
- Breakwaters; Coastal engineering; Dredging; Field investigations; Islands; Shore protection; South Carolina; Wave action; Beach erosion**
Soft Designs for Coastal Protection at Seabrook Island, S.C., Miles O. Hayes, Timothy W. Kana and John H. Barwis, 897
- Breakwaters; Coastal engineering; Field tests; Numerical calculations; Wave height; Waves**
Wave Height Distribution Around Permeable Breakwaters, Shintaro Hotta, 221
- Breakwaters; Coastal engineering; Groins (structures); Japan; Shore protection; Beaches**
Artificial Resort Beach Protected by Offshore Breakwaters and Groins, Shoji Sato and Norio Tanaka, 2004
- Breakwaters; Coastal engineering; Marinas; Porous materials; Wave action; Wave propagation; Waves; Wind**
Wind Waves Transmission Through Porous Breakwater, Stanislaw R. Massel and Piotr Butowski, 333
- Breakwaters; Coastal engineering; Rubble-mound breakwaters; Sand; Shore protection; Bitumens**
Breakwater with a Sand Bitumen Core, E. Loeuwy, K. G. Withaus, R. J. Maddrell and J. P. Wood, 2192
- Breakwaters; Coastal structures; Concrete structures; Damage; Ports; Rubble-mound breakwaters**
Doibssc Past, Present, Future?, J. A. Zwamborn, D. E. Bosman and J. Moes, 1949
- Breakwaters; Coastal structures; Design; Harbors; Shore protection; Storms; Storm surges; Wind forces; Australia**
The Design Concept of Dual Breakwaters and its Application to Townsville, Australia, W. Bremner, D. N. Foster, C. A. Miller and B. C. Wallace, 1899
- Breakwaters; Cost comparisons; Floating bodies; Mooring; Wave energy; Waves; Wave tanks**
Floating Breakwater Performance Comparison, Volker W. Harms, 2135
- Breakwaters; Design practices; Lakes; Lake shores; Lake waves; Ohio; Shore protection; Storms; Beach erosion**
A Detached Breakwater System for Beach Protection, James R. Walker, Denton Clark and Joan Pope, 1969
- Breakwaters; Dikes; Docks; Fabrics; Filters; Filter tests; Groins (structures); Shore-line cover; Synthetic textiles**
Long-Term Experience with the use of Synthetic Filter Fabrics in Coastal Engineering, Georg Heerten, 2172
- Breccia; Carbonaceous rocks; Coastal engineering; Construction; Disposal; Dredge spoil; Dredging; Environmental effects; Ports**
For Disposal: 10 M.c.u.m. of Calcium Carbonate Slurry, L. Summers and C. A. Fleming, 2871

- Bridges (piers); Buffers; Protective structures; Ship piers; Ships; Tidal currents**
Ship-Bridge-Pier Protective Systems, Akira Iwai, Hitoshi Nagasawa, Kazuki Oda and Kuniaki Shoji, 2259
- Budgeting; Coastal engineering; Coastal Processes; Model tests; Sediments; Australia**
An Approach to Understanding Coastal Processes, A. D. Gordon and D. B. Lord, 1234
- Buffers; Protective structures; Ship piers; Ships; Tidal currents; Bridges (piers)**
Ship-Bridge-Pier Protective Systems, Akira Iwai, Hitoshi Nagasawa, Kazuki Oda and Kuniaki Shoji, 2259
- Bulk cargo; Currents (water); Jetties; Mathematical models; Mooring; Ships; Wind forces**
Mooring Forces Induced by Passing Ships - Measurements in Prototype, K. Haffke, 2689
- Caissons; China; Concrete construction; Design; Mooring; Petroleum transportation; Piers (docks); Ports; Tanker ships; Berths**
The Design and Construction of the New Oil Port in Dalian, CPR, Zhu-zhuang Xin and Yucheng Li, 2081
- Caissons; Composite structures; Design; Impact loads; Laboratory tests; Wave action; Breakwaters**
Wave Impact Pressures on Composite Breakwaters, G. R. Mogridge and W. W. Jamieson, 1830
- Caissons; Concrete construction; Deep water; Design; Japan; Overtopping; Sea walls; Waves**
Seawalls in Deep Seas, Shoshichiro Nagai and Shohachi Kakuno, 2024
- Caissons; Concrete construction; Design; Islands; Shore protection; Terminals; Breakwaters**
The Effects of Construction Techniques & Bulk Terminal Operational Requirements on the Design Criteria for Island Breakwaters, A. G. F. Eddie, J. D. Lawson, H. R. Graze and B. K. Dean, 2061
- Calculations; Coastal engineering; Design; Ocean waves; Stokes law; Water depth; Wave energy; Wave height; Wave period; Waves**
Some Implications of Recent Advances in Wave Theories, J. R. Chaplin and K. Anastasiou, 31
- Calculations; Coastal engineering; Gravity waves; Predictions; Shoaling; Two-dimensional; Wave height**
Wave Shoaling Calculated From Cokelet's Theory, T. Sakai and J. A. Battjes, 121
- Calculations; Coastal Processes; Fluid mechanics; Sand; Sand waves**
Contribution to the Discussion During Session C, Coastal Processes, Friday, March 28, 2:00 P.M., M. S. Longuet-Higgins, 3107
- Calculations; Cylinders; Ocean bottom; Offshore structures; Sand; Seepage; Water waves; Wave action**
Wave-Induced Seepage Effects on a Vertical Cylinder, Thomas J.P. Durand and Peter L. Monkmeier, 1782
- Calculations; Cylindrical bodies; Piles; Predictions; Wave action**
Wave Forces on an Inclined Circular Cylindrical Pile, Toshiyuki Shigemura, 1762
- Calibration; Coastal engineering; Estuaries; Mathematical models; Models; Rivers; Tidal waters; Tides; Waves; West Germany**
Automatic Calibration of Numerical Tidal Models, K.-P. Holz and U. Januszewski, 2448
- California; Channel improvements; Coastal Processes; Dredging; Harbors; Shoaling**
A Phased-Dredging Program for Santa Cruz Harbor, James R. Walker and Peter J. Williams, 1492
- California; Coastal engineering; Coastal Processes; Currents (water); Models; Predictions; Sediment transport; Waves**
Nearshore Sediment Transport Study Experiments, R. J. Seymour and C. G. Gable, 1401
- California; Coastal engineering; Field tests; Harbors; Sand traps; Sediment transport; Wave measurement; Breakwaters**
Longshore Transport Evaluations at a Detached Breakwater, R. O. Bruno, R. G. Dean and C. G. Gable, 1452
- California; Coastal engineering; Gages; Littoral zone; Visual surveillance; Wave height; Wave measurement; Waves**
Visually Observed Wave Data at PT. Mugu, Calif., Christine Schneider and J. Richard Weggel, 381
- California; Coasts; Design; Outfall sewers; San Francisco; Sediment deposits; Shallow water; Wastewater (pollution); Water pollution; Wave energy; Antifouling materials**
Design of an Intermittently Operated Outfall, Roger W. Lindquist and George J. Murphy, 2834
- California; Experimentation; Harbors; Littoral drift; Sand; Sediment control; Sediment transport**
A Sediment Trapping Experiment at Santa Cruz, CA, R. J. Seymour, G. W. Domurat and D. M. Pirie, 1415.
- California; Islands; Wave energy; Wave measurement; Waves; Wave spectra**
An Investigation of Wave Sheltering by Islands, S. V. Hsiao, J. F. Vesecky and O. H. Shemdin, 840
- California; Sediment transport; Topographic features; Wave action; Wave period; Beach erosion; Beaches**
Beach Cusps at Point Reyes and Drakes Bay Beaches, California, R. G. Dean and E. M. Maurmeyer, 863
- Carbonaceous rocks; Coastal engineering; Construction; Disposal; Dredge spoil; Dredging; Environmental effects; Ports; Breccia**
For Disposal: 10 M.c.u.m. of Calcium Carbonate Slurry, L. Summers and C. A. Fleming, 2871
- Case reports; Deep water; Design criteria; Energy transfer; Harbors; Truncation errors; West Germany; Breakwaters**
Energy Transmission Over Break Water - A Design Criterion?, P. Bade and H. Kaldenhoff, 1886
- Case reports; Inlets (waterways); Littoral deposits; Littoral materials; Migration; North Carolina; Shoals; Tidal effects**
Barden Inlet, NC a Case Study of Inlet Migration, Limberios Vallianos, 2638

- Catalogs; Coastal engineering; Oceanographic data; Wave measurement; Waves**
Sources of Measured Wave Data, Laurence Draper, 372
- Channel improvements; Coastal Processes; Dredging; Harbors; Shoaling; California**
A Phased-Dredging Program for Santa Cruz Harbor, James R. Walker and Peter J. Williams, 1492
- Channels (waterways); Coastal engineering; Sedimentation; Sediment transport; Suspended load; Trenches; Wave action**
Sedimentation in Channels and Trenches, E. W. Bijker, 1707
- Channels (waterways); Dams; Estuaries; Inlets (waterways); Sedimentation; Tidal currents; West Germany; Barriers; Basins**
Sedimentation Processes in Tidal Channels and Tidal Basins Caused by Artificial Constructions, E. Renger and H. W. Partenscky, 2479
- Channels (waterways); Dredging; Field work; Harbors; Nigeria; Sedimentation; Sediment transport**
Sedimentation in Dredged Navigation Channels, Lars Mikkelsen, Preben Mortensen and Torben Sorensen, 1718
- China; Coastal engineering; Estuaries; Harbors; Research; Sediment transport; Shore protection**
Some Aspects of Coastal Engineering Research Works in China, Yen Kai, 1734
- China; Concrete construction; Design; Mooring; Petroleum transportation; Piers (docks); Ports; Tanker ships; Berths; Caissons**
The Design and Construction of the New Oil Port in Dalian, CPR, Zhu-zhuang Xin and Yu-cheng Li, 2081
- Clay suspensions; Experimentation; Sediment concentration; Water waves; Wave action**
An Experiment on Clay Suspension Under Water Waves, Prida Thimakorn, 2891
- Cliffs; Coastal Processes; Erosion; Sea ice; Sediment transport; Tundra; Wave energy; Alaska**
Sediment Transport Processes and Coastal Variability on the Alaskan North Slope, E. H. Owens, J. R. Harper and D. Nummendam, 1343
- Coastal engineering; Coastal engineering; Engineering evaluation; Nuclear power plants; Oceanography; Philippines; Tsunamis**
Tsunamis Along West Coast of Luzon, Philippines, R. L. Wiegel, 652
- Coastal engineering; Coastal Processes; Coasts; Geologic control; Marine geology; Sediment transport; Wave action; Wave energy; Australia**
Geological Controls on Process-Response, SE Australia, P. S. Roy and A. W. Stephens, 913
- Coastal engineering; Coastal Processes; Coasts; Model studies; Reclamation; Singapore**
Major Reclamation Scheme for Marina City, Singapore, S. Y. Chew and J. Wei, 2243
- Coastal engineering; Coastal Processes; Currents (water); Models; Predictions; Sediment transport; Waves; California**
Nearshore Sediment Transport Study Experiments, R. J. Seymour and C. G. Gable, 1401
- Coastal engineering; Coastal Processes; Model tests; Sediments; Australia; Budgeting**
An Approach to Understanding Coastal Processes, A. D. Gordon and D. B. Lord, 1234
- Coastal engineering; Coastal structures; Concrete construction; Model tests; Outfall sewers; Storm water**
Construction and Model Investigation of Stormwater Outfall, K. A. Heathcote and G. W. Britton, 1850
- Coastal engineering; Coastal structures; Concrete structures failure; Damages; Portugal; Rubble-mound breakwaters; Breakwaters**
Report on the Damages to the Sines Breakwater, Portugal, William F. Baird, Joseph M. Caldwell, Billy L. Edge and Orville T. Magoon, 3060
- Coastal engineering; Coastal structures; Design; Hawaii; Mathematical models; Reefs; Wave attenuation**
Wave Attenuation and Wave Set-Up on a Coastal Reef, Francisus Gerritsen, 444
- Coastal engineering; Coastal structures; Rubble-mound breakwaters; Sea walls; Water waves; Wave reflection; Wave spectra**
Method of Analysis of Random Wave Experiments with Reflecting Coastal Structures, Pierre Gaillard, Michael Gauthier and Forrest Holly, 204
- Coastal engineering; Coasts; Currents (water); Shore protection; Union of Soviet Socialist Republics; Wave action**
Coast Protection Against the Action of Waves and Currents, Leren P. Mikhailov and Sergei M. Uspenskii, 2120
- Coastal engineering; Coasts; Dredging; Field tests; Morphology; Projects; Sedimentology; Tides; West Germany**
The German "Moran" Project, Winfried Siefert and Volker Barthel, 2924
- Coastal engineering; Coasts; Estuaries; Inlets (waterways); Tidal effects; Australia**
A Coastal Inlet with Fixed Bed and Mobile Sides, R. C. Nelson and A. J. Keats, 2532
- Coastal engineering; Coasts; Littoral drift; Taiwan; Wave energy; Wave measurement; Breaking energy**
Relationship Between Alongshore Wave Energy and Littoral Drift in the Mid West Coast at Taiwan, Ho-Shong Hou, Chung-Pan Lee and Lung-Hui Lin, 1254
- Coastal engineering; Coasts; Morphology; Prisms; Wave action; Australia; Beaches; Beach nourishment**
The Dynamic Swept Prism, David M. Chapman and A. W. Smith, 1036
- Coastal engineering; Computer applications; Flumes; Hydraulic models; Wave generation; Waves; Wave tanks**
A Survey of "Random" Wave Generation Techniques, J. Ploeg and E. R. Funke, 135
- Coastal engineering; Computerized simulation; Fourier transformation; Ocean waves; Wave velocity**
Conditional Simulations of Ocean Wave Properties, Leon R. Borgman, 318

- Coastal engineering; Concrete construction; Design; Model tests; Rubble-mound breakwaters; Breakwaters**
Can We Develop New Breakwater Formulas.
John Dorrington Mettam, 2302
- Coastal engineering; Construction; Design; Model tests; Overtopping; Ports; Australia; Breakwaters**
Design of an Overtopping Breakwater, P. D. Treloar and B. Nagle, 1910
- Coastal engineering; Construction; Disposal; Dredge spoil; Dredging; Environmental effects; Ports; Breccia; Carbonaceous rocks**
For Disposal: 10 M.c.u.m. of Calcium Carbonate Slurry, L. Summers and C. A. Fleming, 2871
- Coastal engineering; Cooling water; Currents (water); Discharge (water); Experimentation; Jets; Powerplants; Thermal pollution**
Experimental Study of the Buoyant Surface Jet with the Presence of Bottom Boundary and Cross Current, B. Safaie, 2814
- Coastal engineering; Cost estimates; Flooding; Harbors; Mathematical models; Sedimentation; Sedimentation tanks; Suspended sediments; Tidal effects**
Design of Enclosed Harbors to Reduce Sedimentation, Craig H. Everts, 1511
- Coastal engineering; Currents (water); Estuaries; Maine; Models; Three-dimensional; Water pollution control; Water quality; Bays (topographic features)**
A 3-D Model for Penobscot Bay, Maine, Bryan R. Pearce, Bruce R. Fidler and Adrian C. Humphreys, 2395
- Coastal engineering; Currents (water); Flow; Waveguides; Waves; Beaches**
Longshore Current Flows in a Wave Basin, P. J. Visser, 462
- Coastal engineering; Currents (water); Japan; Littoral current; Power plant location; Wave action; Wave energy; Beaches**
Nearshore Currents on a Partially Rocky Shore, T. O. Sasaki, H. Igarashi and S. Harikai, 1071
- Coastal engineering; Data analysis; Florida; Spectral analysis; Tides; Wave measurement**
Florida Coastal Data Network, Gary Howell, 421
- Coastal engineering; Data processing; Dynaqs; Estuaries; Models; Numerical calculations; Tidal effects; Tides**
The Use of Array Processors for Numerical Modeling of Tidal Estuary Dynamics, D. Prandle, E. R. Funke, N. Crookshank and R. Renner, 2411
- Coastal engineering; Design; Dikes; Dunes; Netherlands; Probability; Shore protection; Storm surges**
Probabilistic Design of Sea Defences, W. T. Bakker and J. K. Vrijling, 2041
- Coastal engineering; Design; Ocean waves; Stokes law; Water depth; Wave energy; Wave height; Wave period; Waves; Calculations**
Some Implications of Recent Advances in Wave Theories, J. R. Chaplin and K. Anastasiou, 31
- Coastal engineering; Design criteria; Docks; Islands; Piers (docks); Site investigation; Site selection**
Siting and Design Criteria of Dock Structures in the Marshall Islands, R. M. Noble, K. C. Leslie and D. O'Day, 2106
- Coastal engineering; Design criteria; Numerical calculations; Solitary waves; Walls; Wave energy; Wave reflection**
Accurate Numerical Solutions for Nonlinear Waves, J. D. Fenton and M. M. Rienecker, 50
- Coastal engineering; Dissipation; Fluid dynamics; Gravity waves; Mathematical studies; Turbulence; Water waves; Wave energy; Waves**
The Unsolved Problem of Breaking Waves, M. S. Longuet-Higgins, 1
- Coastal engineering; Dredging; Field investigations; Islands; Shore protection; South Carolina; Wave action; Beach erosion; Breakwaters**
Soft Designs for Coastal Protection at Seabrook Island, S.C., Miles O. Hayes, Timothy W. Kana and John H. Barwis, 897
- Coastal engineering; Dredging; Ocean waves; Ports; Real time operations; Wave action; Wave height; Analysis; Australia**
Realtime Wave Analysis, Newcastle, Australia, N. V. Lawson and P. H. Youll, 412
- Coastal engineering; Dunes; Sand pumps; Australia; Beach erosion; Beaches; Beach nourishment**
Noosa Beach Restoration Scheme, R. J. Lloyd, 1618
- Coastal engineering; Dunes; Shore protection; Australia; Beach erosion; Beaches; Beach nourishment**
The Beach Improvement Programme: New South Wales, Neale A. Philip and Philip H. White, 1668
- Coastal engineering; Dynamic characteristics; Shores; Surf; Wave action; Waves**
Dynamic Characteristics in the Nearshore Area, Kiyoshi Horikawa and Masahiko Isobe, 480
- Coastal engineering; Engineering evaluation; Nuclear power plants; Oceanography; Philippines; Tsunamis; Coastal engineering**
Tsunamis Along West Coast of Luzon, Philippines, R. L. Wiegell, 652
- Coastal engineering; Environmental effects; Estuaries; Estuarine environment; Models; Salinity**
Separation of Climatic Fluctuations and Impacts of Engineering Activities in Estuaries, G. Krause, 2323
- Coastal engineering; Environmental impact statements; Estuaries; Planning; Ports; Water flow; Australia**
Water Movement Studies Required for Port Planning, Graeme C. Dandy, Desmond A. Mills and John B. Hinwood, 3007
- Coastal engineering; Environmental impact statements; Gas pipelines; Petroleum pipelines; Scotland; Shore protection; Submarine pipelines**
Environmental Aspects of Oil and Gas Pipeline Landfalls in Northeast Scotland, William Ritchie, 2935
- Coastal engineering; Estuaries; Harbors; Research; Sediment transport; Shore protection; China**
Some Aspects of Coastal Engineering Research Works in China, Yen Kai, 1734

- Coastal engineering; Estuaries; Hydraulic tests; Netherlands; Storm surges; Barriers**
Hydraulic Research in the Oosterschelde Estuary.
A. W. Walther, 2358
- Coastal engineering; Estuaries; Mathematical models; Models; Rivers; Tidal waters; Tides; Waves; West Germany; Calibration**
Automatic Calibration of Numerical Tidal Models, K.-P. Holz and U. Januszewski, 2448
- Coastal engineering; Estuaries; Models; Physical tests; Storm surges; Tides**
Artificial Roughness in Physical Models of Estuaries for Storm Surge Investigations, D. Berndt, E. Giese, H. Schwarze and H.-J. Vollmers, 2493
- Coastal engineering; Experimental data; Wave action; Wave energy; Waves; Wave velocity; Beaches**
Experimental Investigations of Periodic Wave Near Breaking, J. Buhr Hansen, 260
- Coastal engineering; Field Investigations; Flood control; Inlets (waterways); Research projects; Tidal waters; U.S. Corps of Engineers; Beach erosion**
The Corps of Engineer's General Investigation of Tidal Inlets, Robert M. Sorensen, 2563
- Coastal engineering; Field tests; Harbors; Sand traps; Sediment transport; Wave measurement; Breakwaters; California**
Longshore Transport Evaluations at a Detached Breakwater, R. O. Bruno, R. G. Dean and C. G. Gable, 1452
- Coastal engineering; Field tests; Numerical calculations; Wave height; Waves; Breakwaters**
Wave Height Distribution Around Permeable Breakwaters, Shintaro Hotta, 221
- Coastal engineering; Field work; Wave action; Accretion (geomorphology); Australia; Beach erosion**
Beach Erosion-Accretion at Two Time Scales, B. G. Thom and G. M. Bowman, 934
- Coastal engineering; Finite difference method; Islands; Shallow water; Tsunamis; Wave equations**
Transient Finite-Difference Tsunami Calculations, Ove Skovgaard and Ivar G. Jonsson, 823
- Coastal engineering; Flowmeters; Laboratory tests; Velocity measurement; Velocity meters; Waves; Wave velocity**
Orbital Velocities in Irregular Waves, F. C. Vis, 173
- Coastal engineering; Fluid mechanics; Similarities; Surf; Wave energy; Waves; Beaches**
A Similarity Model in the Surf Zone, Hsiang Wang and Wei-Chong Yang, 529
- Coastal engineering; Flumes; Sand; Sediment transport; Wave action; Waves; Bottom sediments**
Sand Transport by Waves, Jan van de Graaff and Wiel M.K. Tilmans, 1140
- Coastal engineering; Froude number; Mixing; Outflows; Rivers; Saline water-freshwater interfaces; Water flow**
On a Role of the Interfacial Froude Number, Masakazu Kashiwamura, 2778
- Coastal engineering; Gages; Littoral zone; Visual surveillance; Wave height; Wave measurement; Waves; California**
Visually Observed Wave Data at PT. Mugu, Calif., Christine Schneider and J. Richard Weggel, 381
- Coastal engineering; Gravity waves; Ocean engineering; Oceanography; Water waves; Wave period; Wave reflection; Wave refraction; Waves**
Ray Curvature and Refraction of Wave Packets, J. Ernest Breeding, Jr., 82
- Coastal engineering; Gravity waves; Predictions; Shoaling; Two-dimensional; Wave height; Calculations**
Wave Shoaling Calculated From Cokerlet's Theory, T. Sakai and J. A. Battjes, 121
- Coastal engineering; Groins (structures); Japan; Shore protection; Beaches; Breakwaters**
Artificial Resort Beach Protected by Offshore Breakwaters and Groins, Shoji Sato and Norio Tanaka, 2004
- Coastal engineering; Harbors; Hydraulic design; Marinas; Water circulation; Water quality**
Hydraulic Circulation Performance of a Curvilinear Marina, Jeffrey A. Layton, 2743
- Coastal engineering; Harbors; Marinas; Model studies; Water waves; Wave action; Wave energy; Waves**
Non-Resonant Wave Agitation in Small Craft Harbours, J. W. Kamphuis and D. A.Y. Smith, 241
- Coastal engineering; Heuristic methods; Surf; Wave energy; Wave height; Waves; Beaches**
An Heuristic Model of Wave Height Distribution in Surf Zone, Masaru Mizuguchi, 278
- Coastal engineering; Hydraulic test tunnels; Sediment transport; Wave action; Waves; Wave velocity**
A Closely Responding, Versatile Wave Tunnel, C. H. Hulsbergen and J. J. Bosman, 310
- Coastal engineering; Littoral deposits; Littoral drift; Sediment transport; Shear stress; Wave action; Beaches**
Beach Profiles and On-Offshore Sediment Transport, Akira Watanabe, Yoshihiko Riho and Kiyoshi Horikawa, 1106
- Coastal engineering; Management methods; Sand; Topography; Australia; Beaches; Beach nourishment**
Beach Nourishment as a Management Technique, David M. Chapman, 1635
- Coastal engineering; Marinas; Porous materials; Wave action; Wave propagation; Waves; Wind; Breakwaters**
Wind Waves Transmission Through Porous Breakwater, Stanislaw R. Massel and Piotr Butowski, 333
- Coastal engineering; Mass transfer; Shallow water; Velocity; Water waves; Wave propagation; Waves; Wave tanks**
Mass Transport in Progressive Waves of Permanent Type, Yoshito Tsuchiya, Takashi Yasuda and Takao Yamashita, 70

- Coastal engineering; Measurement; Oceanography; Wind; Wind profiles; Wind speed**
On the Correction of Land-Based Wind Measurements for Oceanographic Applications, S. A. Hsu, 708
- Coastal engineering; Modets; Wave energy; Wave height; Wave refraction; Waves; Wind**
Verification of a Wave Refraction Model Utilizing Recorded and Observed Wave Data, G. Henderson and N. B. Webber, 101
- Coastal engineering; Oceanographic data; Wave measurement; Waves; Catalogs**
Sources of Measured Wave Data, Laurence Draper, 372
- Coastal engineering; Resonance; Sea level changes; Subsonic flow; Waves; Australia**
Resonances of Coastal Waters Between Perth and Geraldton, H. Allison, A. Grassia and R. Litchfield, 290
- Coastal engineering; Rubble-mound breakwaters; Sand; Shore protection; Bitumens; Breakwaters**
Breakwater with a Sand Bitumen Core, E. Loewy, K. G. Witthaus, R. J. Maddrell and J. P. Wood, 2192
- Coastal engineering; Sedimentation; Sediment transport; Suspended load; Trenches; Wave action; Channels (waterways)**
Sedimentation in Channels and Trenches, E. W. Bijker, 1707
- Coastal engineering; Shore protection; Australia; Beach erosion; Beaches**
Capricorn Coast Beaches, D. C. Patterson and L. R. Ford, 1648
- Coastal engineering; Spilling; Surf; Water waves; Wave measurement; Wave pressure; Waves; Wave velocity**
Velocity and Pressure Field of Spilling Breakers, M. J.F. Stive, 547
- Coastal Processes; Coasts; Geologic control; Marine geology; Sediment transport; Wave action; Wave energy; Australia; Coastal engineering**
Geological Controls on Process-Response, SE Australia, P. S. Roy and A. W. Stephens, 913
- Coastal Processes; Coasts; Model studies; Reclamation; Singapore; Coastal engineering**
Major Reclamation Scheme for Marina City, Singapore, S. Y. Chew and J. Wei, 2243
- Coastal Processes; Currents (water); Models; Predictions; Sediment transport; Waves; California; Coastal engineering**
Nearshore Sediment Transport Study Experiments, R. J. Seymour and C. G. Gable, 1401
- Coastal Processes; Dredging; Harbors; Shoaling; California; Channel improvements**
A Phased-Dredging Program for Santa Cruz Harbor, James R. Walker and Peter J. Williams, 1492
- Coastal Processes; Erosion; Sea-ice; Sediment transport; Tundra; Wave energy; Alaska; Cliffs**
Sediment Transport Processes and Coastal Variability on the Alaskan North Slope, E. H. Owens, J. R. Harper and D. Nummndal, 1343
- Coastal Processes; Estuaries; Floods; Inlets (waterways); Lakes; Littoral drift; Stability criteria; Tidal effects; Tidal waters; Australia**
Tidal Inlet Behavioural Analysis, A. F. Nielsen and A. D. Gordon, 2459
- Coastal Processes; Fluid mechanics; Sand; Sand waves; Calculations**
Contribution to the Discussion During Session C, Coastal Processes, Friday, March 28, 2:00 P.M., M. S. Longuet-Higgins, 3107
- Coastal Processes; Hydraulics; Laboratory tests; Permeability (soils); Profiles; Surf; Waves; Beaches; Beach sands**
Beaches: Profiles, Processes and Permeability, Michael R. Gourlay, 1319
- Coastal Processes; Littoral drift; Sandbars; Shores; Topography; Wave action; Beaches**
Migration of Longshore Bars, Hans H. Dette, 1475
- Coastal Processes; Louisiana; Sedimentation; Shore protection; Wave energy; Beach erosion**
Fluid Mud Dynamics and Shoreline Stabilization: Louisiana Chenier Plain, John T. Wells and Harry H. Roberts, 1381
- Coastal Processes; Model tests; Sediments; Australia; Budgeting; Coastal engineering**
An Approach to Understanding Coastal Processes, A. D. Gordon and D. B. Lord, 1234
- Coastal structures; Concrete construction; Model tests; Outfall sewers; Storm water; Coastal engineering**
Construction and Model Investigation of Stormwater Outfall, K. A. Heathcote and G. W. Britton, 1850
- Coastal structures; Concrete structures; Damage; Ports; Rubble-mound breakwaters; Breakwaters**
Dolosse Past, Present, Future?, J. A. Zwamborn, D. E. Bosman and J. Moes, 1949
- Coastal structures; Concrete structures failure; Damages; Portugal; Rubble-mound breakwaters; Breakwaters; Coastal engineering**
Report on the Damages to the Sines Breakwater, Portugal, William F. Baird, Joseph M. Caldwell, Billy L. Edge and Orville T. Magoon, 3060
- Coastal structures; Design; Harbors; Shore protection; Storms; Storm surges; Wind forces; Australia; Breakwaters**
The Design Concept of Dual Breakwaters and its Application to Townsville, Australia, W. Bremner, D. N. Foster, C. A. Miller and B. C. Wallace, 1899
- Coastal structures; Design; Hawaii; Mathematical models; Reefs; Wave attenuation; Coastal engineering**
Wave Attenuation and Wave Set-Up on a Coastal Reef, Francisus Gerritsen, 444
- Coastal structures; Design; Offshore structures; Predictions; Sea states; Statistical data; Wave height**
Prediction of the Severest Significant Wave Height, Michel K. Ochi and Joseph E. Whalen, 587

- Coastal structures; Model studies; Statistics; Storms; Wave generation; Wave height; Waves**
A Comparison of Nature Waves and Model Waves with Special Reference to Wave Grouping, Hans F. Burcharth, 2989
- Coastal structures; Rubble-mound breakwaters; Sea walls; Water waves; Wave reflection; Wave spectra; Coastal engineering**
Method of Analysis of Random Wave Experiments with Reflecting Coastal Structures, Pierre Gaillard, Michael Gauthier and Forrest Holly, 204
- Coasts; Currents (water); Shore protection; Union of Soviet Socialist Republics; Wave action; Coastal engineering**
Coast Protection Against the Action of Waves and Currents, Leren P. Mikhailov and Sergei M. Uspenskiĭ, 2120
- Coasts; Design; Outfall sewers; San Francisco; Sediment deposits; Shallow water; Wastewater (pollution); Water pollution; Wave energy; Antifouling materials; California**
Design of an Intermittently Operated Outfall, Roger W. Lindquist and George J. Murphy, 2834
- Coasts; Dredging; Field tests; Morphology; Projects; Sedimentology; Tides; West Germany; Coastal engineering**
The German "Moran" Project, Winfried Siefert and Volker Barthel, 2924
- Coasts; Estuaries; Inlets (waterways); Tidal effects; Australia; Coastal engineering**
A Coastal Inlet with Fixed Bed and Mobile Sides, R. C. Nelson and A. J. Keats, 2532
- Coasts; Field investigations; Sand; Sand control; Sediment transport; West Germany; Wind action geology; Wind speed**
Sand Transport Under the Action of Wind, Ulrich Zanke, 1575
- Coasts; Floods; Inlets (waterways); Sand; Sandy soils; Storms; Tidal effects; Tidal hydraulics; Wave action**
Comments on Tidal Entrances on Sandy Coasts, Morrrough P. O'Brien, 2502
- Coasts; Geologic control; Marine geology; Sediment transport; Wave action; Wave energy; Australia; Coastal engineering; Coastal Processes**
Geological Controls on Process-Response, SE Australia, P. S. Roy and A. W. Stephens, 913
- Coasts; Inlets (waterways); Landsat; Littoral drift; Remote sensing; Sandbars; Satellite Mapping; Bathymetry**
Satellite Applications on a Coastal Inlet Stability Study, Yu-Hwa Wang, 2579
- Coasts; Littoral drift; Taiwan; Wave energy; Wave measurement; Breaking energy; Coastal engineering**
Relationship Between Alongshore Wave Energy and Littoral Drift in the Mid West Coast at Taiwan, Ho-Shong Hou, Chung-Pan Lee and Lung-Hui Lin, 1254
- Coasts; Littoral materials; Mathematical models; Water circulation; Water pollution; Water waves; Wave action; Beaches**
Numerical Modelling of Nearshore Circulation, Bruce A. Ebersole and Robert A. Dalrymple, 2708
- Coasts; Model studies; Reclamation; Singapore; Coastal engineering; Coastal Processes**
Major Reclamation Scheme for Marina City, Singapore, S. Y. Chew and J. Wei, 2243
- Coasts; Morphology; Prisms; Wave action; Australia; Beaches; Beach nourishment; Coastal engineering**
The Dynamic Swept Prism, David M. Chapman and A. W. Smith, 1036
- Composite structures; Design; Impact loads; Laboratory tests; Wave action; Breakwaters; Caissons**
Wave Impact Pressures on Composite Breakwaters, G. R. Mogridge and W. W. Jamieson, 1830
- Computer applications; Construction; Docks; Dredging; Environmental surveys; Ports; Water flow; Water quality; Australia; Beaches**
Integration and Computation in an Environmental Study, J. B. Hinwood, J. E. Watson and D. M. Burrage, 3024
- Computer applications; Design; France; Harbors; Hydraulic tests; Models; Sedimentology; Wave diffraction; Wave refraction**
Harbour Design Including Sedimentological Problems Using Mainly Numerical Technics, B. Latteux, 2211
- Computer applications; Flumes; Hydraulic models; Wave generation; Waves; Wave tanks; Coastal engineering**
A Survey of "Random" Wave Generation Techniques, J. Ploeg and E. R. Funke, 135
- Computerized simulation; Fourier transformation; Ocean waves; Wave velocity; Coastal engineering**
Conditional Simulations of Ocean Wave Properties, Leon R. Borgman, 318
- Concrete construction; Deep water; Design; Japan; Overtopping; Sea walls; Waves; Caissons**
Seawalls in Deep Seas, Shoshichiro Nagai and Shohachi Kakuno, 2024
- Concrete construction; Design; Islands; Shore protection; Terminals; Breakwaters; Caissons**
The Effects of Construction Techniques & Bulk Terminal Operational Requirements on the Design Criteria for Island Breakwaters, A. G.F. Eddie, J. D. Lawson, H. R. Graze and B. K. Dean, 2061
- Concrete construction; Design; Model tests; Rubble-mound breakwaters; Breakwaters; Coastal engineering**
Can We Develop New Breakwater Formulae, John Dorrington Mettam, 2302
- Concrete construction; Design; Mooring; Petroleum transportation; Piers (docks); Ports; Tanker ships; Berths; Caissons; China**
The Design and Construction of the New Oil Port in Dalian, CPR, Zhu-zhuang Xin and Yu-cheng Li, 2081
- Concrete construction; Model tests; Outfall sewers; Storm water; Coastal engineering; Coastal structures**
Construction and Model Investigation of Stormwater Outfall, K. A. Heathcote and G. W. Britton, 1850

- Concrete structures; Damage; Ports; Rubble-mound breakwaters; Breakwaters; Coastal structures**
Dolosse Past, Present, Future?, J. A Zwamborn, D. E. Bosman and J. Moes, 1949
- Concrete structures; Destructive tests; Dynamic loads; Hydraulic tests; Model tests; Reinforced concrete; Rubble-mound breakwaters**
Full Scale Trails of Dolosse to Destruction, Hans F. Burcharth, 1929
- Concrete structures failure; Damages; Portugal; Rubble-mound breakwaters; Breakwaters; Coastal engineering; Coastal structures**
Report on the Damages to the Sines Breakwater, Portugal, William F. Baird, Joseph M. Caldwell, Billy L. Edge and Orville T. Magoon, 3060
- Connecticut; Dredging; Estuaries; Rivers; Sediment transport; Storms; Suspended load; Suspended sediments**
A Comparison Between Dredge Induced Sediment Resuspension and that Produced by Natural Storm Events, W. Frank Bohlen, 1699
- Construction; Design; Model tests; Overtopping; Ports; Australia; Breakwaters; Coastal engineering**
Design of an Overtopping Breakwater, P. D. Treloar and B. Nagle, 1910
- Construction; Disposal; Dredge spoil; Dredging; Environmental effects; Ports; Breccia; Carbonaceous rocks; Coastal engineering**
For Disposal: 10 M.c.u.m. of Calcium Carbonate Slurry, L. Summers and C. A. Fleming, 2871
- Construction; Docks; Dredging; Environmental surveys; Ports; Water flow; Water quality; Australia; Beaches; Computer applications**
Integration and Computation in an Environmental Study, J. B. Hinwood, J. E. Watson and D. M. Burrage, 3024
- Continental shelf; Currents (water); Field tests; Models; Predictions; Sediment transport; Wave height; Wind speed; Australia**
Sediment Dispersal on the NSW Continental Shelf, Ron Boyd, 1363
- Cooling water; Currents (water); Discharge (water); Experimentation; Jets; Powerplants; Thermal pollution; Coastal engineering**
Experimental Study of the Buoyant Surface Jet with the Presence of Bottom Boundary and Cross Current, B. Safaie, 2814
- Cooling water; Discharge (water); Heated water; Industrial plants; Liquefied natural gas; Refractometers; Temperature rise; Water pollution control**
Dispersion of Cooling Water from a Coastal LNG Plant, P. Ackers, J. D. Pitt, G. Thompson and K. G. Rippin, 2794
- Cost comparisons; Floating bodies; Mooring; Wave energy; Waves; Wave tanks; Breakwaters**
Floating Breakwater Performance Comparison, Volker W. Harms, 2135
- Cost estimates; Flooding; Harbors; Mathematical models; Sedimentation; Sedimentation tanks; Suspended sediments; Tidal effects; Coastal engineering**
Design of Enclosed Harbors to Reduce Sedimentation, Craig H. Everts, 1511
- Currents (water); Deep water; Field data; Shoaling; Transient waves; Wave height; Waves**
Wave-Wave Interactions, Current-Wave Interactions and Resulting Extreme Waves and Breaking Waves, Soren Peter Kjeldsen and Dag Myrhaug, 2275
- Currents (water); Discharge (water); Experimentation; Jets; Powerplants; Thermal pollution; Coastal engineering; Cooling water**
Experimental Study of the Buoyant Surface Jet with the Presence of Bottom Boundary and Cross Current, B. Safaie, 2814
- Currents (water); Eddy currents; Egypt; Erosion; Nile River Valley; Rivers; Sand; Sediment transport**
Eddy Currents and Sediment Transport Off the Damietta Nile, S. P. Murray, J. M. Coleman, H. H. Roberts and M. Salama, 1679
- Currents (water); Estuaries; Maine; Models; Three-dimensional; Water pollution control; Water quality; Bays (topographic features); Coastal engineering**
A 3-D Model for Penobscot Bay, Maine, Bryan R. Pearce, Bruce R. Fidler and Adrian C. Humphreys, 2395
- Currents (water); Field investigations; Motion; Sand; Sediment transport; Surf; Suspended load; Wave measurement; Wind**
Field Measurements of Sand Motion in the Surf Zone, Douglas L. Inman, James A. Zampol, Thomas E. White, Daniel M. Hanes, B. Walton Waldorf and Kim A. Kastens, 1214
- Currents (water); Field tests; Models; Predictions; Sediment transport; Wave height; Wind speed; Australia; Continental shelf**
Sediment Dispersal on the NSW Continental Shelf, Ron Boyd, 1363
- Currents (water); Flow; Waveguides; Waves; Beaches; Coastal engineering**
Longshore Current Flows in a Wave Basin, P. J. Visser, 462
- Currents (water); Groundwater elevation; Slopes; Surf; Wave action; Wave energy; Beaches**
Wave Forcing of Beach Groundwater, Evans Waddell, 1435
- Currents (water); Japan; Littoral current; Power plant location; Wave action; Wave energy; Beaches; Coastal engineering**
Nearshore Currents on a Partially Rocky Shore, T. O. Sasaki, H. Igarashi and S. Harikai, 1071
- Currents (water); Jetties; Mathematical models; Mooring; Ships; Wind forces; Bulk cargo**
Mooring Forces Induced by Passing Ships - Measurements in Prototype, K. Hafke, 2689
- Currents (water); Lagoons (ponds); Morphology; Reefs; Sediment transport; Wave action; Waves**
Physical Processes and Sediment Flux Through Reef-Lagoon Systems, Harry H. Roberts, 946
- Currents (water); Littoral current; Surf; Topography; Wave energy; Wave height; Wave runup; Beaches**
Topographic Control of Run-Up Variability, Mark P. Bradshaw, 1091

- Currents (water); Models; Predictions; Sediment transport; Waves; California; Coastal engineering; Coastal Processes**
Nearshore Sediment Transport Study Experiments, R. J. Seymour and C. G. Gable, 1401
- Currents (water); Models; Sediment transport; Shoaling; Shores; Topography; Waves; Bathymetry**
Inshore-Nearshore Morphodynamics - A Predictive Model, John Chappell, 963
- Currents (water); Shore protection; Union of Soviet Socialist Republics; Wave action; Coastal engineering; Coasts**
Coast Protection Against the Action of Waves and Currents, Leren P. Mikhailov and Sergei M. Uspenskii, 2120
- Cylinders; Ocean bottom; Offshore structures; Sand; Seepage; Water waves; Wave action; Calculations**
Wave-Induced Seepage Effects on a Vertical Cylinder, Thomas J.P. Durand and Peter L. Monkmeier, 1782
- Cylindrical bodies; Kinematics; Ocean waves; Structural members; Tidal currents; Tubes; Wave action; Wave velocity**
Full Scale Near Surface Water Particle Velocities and Pressure Acting on an Inclined Tubular Member, Fritz Busching and Eckehard Martini, 1870
- Cylindrical bodies; Piles; Predictions; Wave action; Calculations**
Wave Forces on an Inclined Circular Cylindrical Pile, Toshiyuki Shigemura, 1762
- Damage; Ports; Rubble-mound breakwaters; Breakwaters; Coastal structures; Concrete structures**
Dolosse Past, Present, Future?, J. A. Zwamborn, D. E. Bosman and J. Moes, 1949
- Damage; Rubble-mound breakwaters; Stability; Tests; Wave action; Wave height; Wave period**
Stability of Rubble Mound Breakwater, J. Feuillet and M. Sabaton, 1989
- Damages; Portugal; Rubble-mound breakwaters; Breakwaters; Coastal engineering; Coastal structures; Concrete structures failure**
Report on the Damages to the Sines Breakwater, Portugal, William F. Baird, Joseph M. Caldwell, Billy L. Edge and Orville T. Magoon, 3060
- Damping; Motion studies; Shallow water; Ships; Water flow; Wave action; Wave energy; Wave generation**
Some Recent Results for Wave Induced Motions of a Ship in Shallow Water, P. A. Madsen, I. A. Svendsen and C. Michaelsen, 3040
- Dams; Estuaries; Inlets (waterways); Sedimentation; Tidal currents; West Germany; Barriers; Basins; Channels (waterways)**
Sedimentation Processes in Tidal Channels and Tidal Basins Caused by Artificial Constructions, E. Renger and H. W. Partenscky, 2479
- Data analysis; Florida; Spectral analysis; Tides; Wave measurement; Coastal engineering**
Florida Coastal Data Network, Gary Howell, 421
- Data analysis; Lake waves; Michigan; Wave generation; Wave measurement; Waves; Wave spectra; Wind**
A Measurement of Slope, Curvature, and Directional Spectra of Wind Waves in Lake Michigan, Paul C. Liu, 432
- Data collection; Design; Meteorological data; Oceanographic data; Offshore structures; Oil and gas fields; Programs**
Considerations in the Design of an Offshore Data Collection Program, Cortis Cooper and German Febres, 2904
- Data processing; Dynamics; Estuaries; Models; Numerical calculations; Tidal effects; Tides; Coastal engineering**
The Use of Array Processors for Numerical Modeling of Tidal Estuary Dynamics, D. Prandle, E. R. Funke, N. Crookshank and R. Renner, 2411
- Deep water; Design; Japan; Overtopping; Sea walls; Waves; Caissons; Concrete construction**
Seawalls in Deep Seas, Shoshichiro Nagai and Shohachi Kakuno, 2024
- Deep water; Design criteria; Energy transfer; Harbors; Truncation errors; West Germany; Breakwaters; Case reports**
Energy Transmission Over Break Water - A Design Criterion?, P. Bade and H. Kaldenhoff, 1886
- Deep water; Estuaries; Field investigations; Wave energy; Wave spectra; West Germany**
Wave Energy Distribution in an Estuary Volker Barthel, 2338
- Deep water; Field data; Shoaling; Transient waves; Wave height; Waves; Currents (water); Wave-Wave Interactions, Current-Wave Interactions and Resulting Extreme Waves and Breaking Waves, Soren Peter Kjeldsen and Dag Myrhaug, 2275**
- Deep water; Sediment transport; Stability analysis; Wave energy; Waves; Beaches**
Criterion for Stability of Shoreline Planform, John D. Wang and Bernard Le Mehaute, 1994
- Deformation; Littoral deposits; Littoral drift; Models; Sediment transport; Surf; Beaches**
On-Offshore Sediment Transport Rate in the Surf Zone, Toru Sawaragi and Ichiro Deguchi, 1194
- Deltaic deposits; Deltas; Estuaries; Netherlands; Rivers; Sediment deposits; Stability**
Stability of Estuary Mouths in the Rhine-Meuse Delta, J. van de Kreeke and Jac Haring, 2625
- Deltas; Estuaries; Netherlands; Rivers; Sediment deposits; Stability; Deltaic deposits**
Stability of Estuary Mouths in the Rhine-Meuse Delta, J. van de Kreeke and Jac Haring, 2625
- Deltas; Flood protection; Rivers; Sediment transport; Alluvial deposits; Australia; Beach erosion; Beach sands**
Barron River Delta Investigation, D. A. Robinson, D. J. Cook and J. G. Barff, 885
- Design; Dikes; Dunes; Netherlands; Probability; Shore protection; Storm surges; Coastal engineering**
Probabilistic Design of Sea Defences, W. T. Bakker and J. K. Vrijling, 2041

- Design; France; Harbors; Hydraulic tests; Models; Sedimentology; Wave diffraction; Wave refraction; Computer applications**
Harbour Design Including Sedimentological Problems Using Mainly Numerical Technics, B. Latteux, 2211
- Design; Harbors; Shore protection; Storms; Storm surges; Wind forces; Australia; Breakwaters; Coastal structures**
The Design Concept of Dual Breakwaters and its Application to Townsville, Australia, W. Bremner, D. N. Foster, C. A. Miller and B. C. Wallace, 1899
- Design; Hawaii; Mathematical models; Reefs; Wave attenuation; Coastal engineering; Coastal structures**
Wave Attenuation and Wave Set-Up on a Coastal Reef, Franciscus Gerritsen, 444
- Design; Impact loads; Laboratory tests; Wave action; Breakwaters; Caissons; Composite structures**
Wave Impact Pressures on Composite Breakwaters, G. R. Morigridge and W. W. Jamieson, 1830
- Design; Islands; Shore protection; Terminals; Breakwaters; Caissons; Concrete construction**
The Effects of Construction Techniques & Bulk Terminal Operational Requirements on the Design Criteria for Island Breakwaters, A. G.F. Eddie, J. D. Lawson, H. R. Graze and B. K. Dean, 2061
- Design; Japan; Overtopping; Sea walls; Waves; Caissons; Concrete construction; Deep water**
Seawalls in Deep Seas, Shoshichiro Nagai and Shohachi Kakuno, 2024
- Design; Meteorological data; Oceanographic data; Offshore structures; Oil and gas fields; Programs; Data collection**
Considerations in the Design of an Offshore Data Collection Program, Cortis Cooper and German Febres, 2904
- Design; Model tests; Overtopping; Ports; Australia; Breakwaters; Coastal engineering; Construction**
Design of an Overtopping Breakwater, P. D. Treloar and B. Nagle, 1910
- Design; Model tests; Rubble-mound breakwaters; Breakwaters; Coastal engineering; Concrete construction**
Can We Develop New Breakwater Formulae, John Dorrington Mettam, 2302
- Design; Mooring; Petroleum transportation; Piers (docks); Ports; Tanker ships; Berths; Caissons; China; Concrete construction**
The Design and Construction of the New Oil Port in Dalian, CPR, Zhu-zhuang Xin and Yu-cheng Li, 2081
- Design; Ocean waves; Stokes law; Water depth; Wave energy; Wave height; Wave period; Waves; Calculations; Coastal engineering**
Some Implications of Recent Advances in Wave Theories, J. R. Chaplin and K. Anastasiou, 31
- Design; Offshore structures; Predictions; Sea states; Statistical data; Wave height; Coastal structures**
Prediction of the Severe Significant Wave Height, Michel K. Ochi and Joseph E. Whalen, 587
- Design; Outfall sewers; San Francisco; Sediment deposits; Shallow water; Wastewater (pollution); Water pollution; Wave energy; Antifouling materials; California; Coasts**
Design of an Intermittently Operated Outfall, Roger W. Lindquist and George J. Murphy, 2834
- Design criteria; Docks; Islands; Piers (docks); Site investigation; Site selection; Coastal engineering**
Siting and Design Criteria of Dock Structures in the Marshall Islands, R. M. Noble, K. C. Leslie and D. O'Day, 2106
- Design criteria; Energy transfer; Harbors; Truncation errors; West Germany; Breakwaters; Case reports; Deep water**
Energy Transmission Over Break Water - A Design Criterion?, P. Bade and H. Kaldenhoff, 1886
- Design criteria; Numerical calculations; Solitary waves; Walls; Wave energy; Wave reflection; Coastal engineering**
Accurate Numerical Solutions for Nonlinear Waves, J. D. Fenton and M. M. Rienecker, 50
- Design practices; Lakes; Lake shores; Lake waves; Ohio; Shore protection; Storms; Beach erosion; Breakwaters**
A Detached Breakwater System for Beach Protection, James R. Walker, Denton Clark and Joan Pope, 1969
- Destructive tests; Dynamic loads; Hydraulic tests; Model tests; Reinforced concretes; Rubble-mound breakwaters; Concrete structures**
Full Scale Trails of Dolosse to Destruction, Hans F. Burcharth, 1929
- Dikes; Docks; Fabrics; Filters; Filter tests; Groins (structures); Shore-line cover; Synthetic textiles; Breakwaters**
Long-Term Experience with the use of Synthetic Filter Fabrics in Coastal Engineering, Georg Heerten, 2172
- Dikes; Dunes; Netherlands; Probability; Shore protection; Storm surges; Coastal engineering; Design**
Probabilistic Design of Sea Defences, W. T. Bakker and J. K. Vrijling, 2041
- Discharge (water); Energy conversion; Environmental effects; Field investigations; Mathematical models; Ocean engineering; Ocean water; Thermal energy; Thermal power plants**
Dynamic Similarity of Transport Phenomena, M. S. Yalin and F. Gerritsen, 2669
- Discharge (water); Experimentation; Jets; Powerplants; Thermal pollution; Coastal engineering; Cooling water; Currents (water)**
Experimental Study of the Buoyant Surface Jet with the Presence of Bottom Boundary and Cross Current, B. Safaie, 2814
- Discharge (water); Heated water; Industrial plants; Liquefied natural gas; Refractometers; Temperature rise; Water pollution control; Cooling water**
Dispersion of Cooling Water from a Coastal LNG Plant, P. Ackers, J. D. Pitt, G. Thompson and K. G. Rippin, 2794

- Disposal; Dredge spoil; Dredging; Environmental effects; Ports; Breccia; Carbonaceous rocks; Coastal engineering; Construction**
For Disposal: 10 M.c.u.m. of Calcium Carbonate Slurry, L. Summers and C. A. Fleming, 2871
- Dissipation; Fluid dynamics; Gravity waves; Mathematical studies; Turbulence; Water waves; Wave energy; Waves; Coastal engineering**
The Unsolved Problem of Breaking Waves, M. S. Longuet-Higgins, 1
- Disturbances; Experimentation; Flumes; Predictions; Wave equations; Waves; Beaches**
Long Period Disturbances Due to Wave Groups, E. C. Bowers, 610
- Docks; Dredging; Environmental surveys; Ports; Water flow; Water quality; Australia; Beaches; Computer applications; Construction**
Integration and Computation in an Environmental Study, J. B. Hinwood, J. E. Watson and D. M. Burrage, 3024
- Docks; Fabricis; Filters; Filter tests; Groins (structures); Shore-line cover; Synthetic textiles; Breakwaters; Dikes**
Long-Term Experience with the use of Synthetic Filter Fabricis in Coastal Engineering, Georg Heerten, 2172
- Docks; Islands; Piers (docks); Site investigation; Site selection; Coastal engineering; Design criteria**
Siting and Design Criteria of Dock Structures in the Marshall Islands, R. M. Noble, K. C. Leslie and D. O'Day, 2106
- Downstream; Inlets (waterways); North Carolina; Tidal waters; Water flow; Boundary conditions**
Boundary Conditions for Analysis of Flow in Tidal Inlets, T. C. Gopalakrishnan and J. L. Machemehl, 2593
- Drag; Experimentation; Measurement; Sands; Sand waves; Water tunnels; Water waves; Bed forms**
Measurements of Oscillatory Drag on Sand Ripples, Karl E. B. Lofquist, 3104
- Dredge spoil; Dredging; Environmental effects; Ports; Breccia; Carbonaceous rocks; Coastal engineering; Construction; Disposal**
For Disposal: 10 M.c.u.m. of Calcium Carbonate Slurry, L. Summers and C. A. Fleming, 2871
- Dredging; Environmental effects; Ports; Breccia; Carbonaceous rocks; Coastal engineering; Construction; Disposal; Dredge spoil**
For Disposal: 10 M.c.u.m. of Calcium Carbonate Slurry, L. Summers and C. A. Fleming, 2871
- Dredging; Environmental surveys; Ports; Water flow; Water quality; Australia; Beaches; Computer applications; Construction; Docks**
Integration and Computation in an Environmental Study, J. B. Hinwood, J. E. Watson and D. M. Burrage, 3024
- Dredging; Estuaries; Rivers; Sand; Sediment transport; Tidal hydraulics; Australia; Beach nourishment; Bed forms**
Estuarine Response to Dredging in the Tweed River, Australia, Bruce M. Drucry, 1598
- Dredging; Estuaries; Rivers; Sediment transport; Storms; Suspended load; Suspended sediments; Connecticut**
A Comparison Between Dredge Induced Sediment Resuspension and that Produced by Natural Storm Events, W. Frank Bohlen, 1699
- Dredging; Field investigations; Islands; Shore protection; South Carolina; Wave action; Beach erosion; Breakwaters; Coastal engineering**
Soft Designs for Coastal Protection at Seabrook Island, S.C., Miles O. Hayes; Timothy W. Kana and John H. Barwis, 897
- Dredging; Field tests; Morphology; Projects; Sedimentology; Tides; West Germany; Coastal engineering; Coasts**
The German "Moran" Project, Winfried Siefert and Volker Barthel, 2924
- Dredging; Field work; Harbors; Nigeria; Sedimentation; Sediment transport; Channels (waterways)**
Sedimentation in Dredged Navigation Channels, Lars Mikkelsen, Preben Mortensen and Torben Sorensen, 1718
- Dredging; Fishing; Harbors; Jetties; Littoral drift; Shoaling; Taiwan**
New Jetties for Tung-Kang Fishing Harbor, Taiwan, Chi-Fu Su, 2928
- Dredging; Harbors; Shoaling; California; Channel improvements; Coastal Processes**
A Phased-Dredging Program for Santa Cruz Harbor, James R. Walker and Peter J. Williams, 1492
- Dredging; Ocean waves; Ports; Real time operations; Wave action; Wave height; Analysis; Australia; Coastal engineering**
Realtime Wave Analysis, Newcastle, Australia, N. V. Lawson and P. H. Youll, 412
- Dunes; Dune sands; Revegetation; Sand control; Shore protection; Australia; Beach erosion**
Research in Southern Queensland into the Management of Coastal Sand Dunes, James B. McKenzie and David A. Barr, 1547
- Dunes; Dynamic geology; Erosion; Models; Numerical calculations; Sediment transport; Bed forms**
A Numerical Model for Dune Dynamics, J. Sundermann, H.-J. Vollmers and W. Puls, 1583
- Dunes; Netherlands; Probability; Shore protection; Storm surges; Coastal engineering; Design; Dikes**
Probabilistic Design of Sea Defences, W. T. Bakker and J. K. Vrijling, 2041
- Dunes; Sand control; Sediment transport; Shore protection; Wind action geology; Australia**
Wind and Sediment Movement in Coastal Dune Areas, John R. Hails and John Bennett, 1564
- Dunes; Sand pumps; Australia; Beach erosion; Beaches; Beach nourishment; Coastal engineering**
Noosa Beach Restoration Scheme, R. J. Lloyd, 1618
- Dunes; Shore protection; Australia; Beach erosion; Beaches; Beach nourishment; Coastal engineering**
The Beach Improvement Programme: New South Wales, Neale A. Philip and Philip H. White, 1668

- Dune sands; Revegetation; Sand control; Shore protection; Australia; Beach erosion; Dunes**
Research in Southern Queensland into the Management of Coastal Sand Dunes, James B. McKenzie and David A. Barr, 1547
- Dynamic characteristics; Shores; Surf; Wave action; Waves; Coastal engineering**
Dynamic Characteristics in the Nearshore Area. Kiyoshi Horikawa and Masahiko Isobe, 480
- Dynamic geology; Erosion; Models; Numerical calculations; Sediment transport; Bed forms; Dunes**
A Numerical Model for Dune Dynamics, J. Sundermann, H.-J. Vollmers and W. Puls, 1583
- Dynamic loads; Hydraulic tests; Model tests; Reinforced concretes; Rubble-mound breakwaters; Concrete structures; Destructive tests**
Full Scale Trails of Dolosse to Destruction, Hans F. Burcharth, 1929
- Dynamics; Estuaries; France; Laboratory tests; Saline water intrusion; Sediment transport; Silts; Suspended sediments**
Dynamics of Silt in Estuary, Residual Current or Flocculation Which Prevails?, J. P. Lepetit and M. Davesne, 2858
- Dynamics; Estuaries; Models; Numerical calculations; Tidal effects; Tides; Coastal engineering; Data processing**
The Use of Array Processors for Numerical Modeling of Tidal Estuary Dynamics, D. Prandle, E. R. Funke, N. Crookshank and R. Renner, 2411
- Earth atmosphere; Experimentation; Heat balance; Powerplants; Rivers; Thermal pollution; Wastewater (pollution); Water surface**
Experimental Evaluation of Heat Exchange Between Water Surface and Atmosphere, Gunther Barg, Horst Schwarze and Gerhard Visscher, 2848
- Earthquakes; Ocean bottom; Time studies; Tsunamis; Water waves; Wave generation**
Long Waves Generated by Complex Bottom Motions, J. L. Hammack and E. Raichlen, 639
- Eddy currents; Egypt; Erosion; Nile River Valley; Rivers; Sand; Sediment transport; Currents (water)**
Eddy Currents and Sediment Transport Off the Damietta Nile, S. P. Murray, J. M. Coleman, H. H. Roberts and M. Salama, 1679
- Egypt; Erosion; Nile River Valley; Rivers; Sand; Sediment transport; Currents (water); Eddy currents**
Eddy Currents and Sediment Transport Off the Damietta Nile, S. P. Murray, J. M. Coleman, H. H. Roberts and M. Salama, 1679
- Electromagnetic radiation; Gravity waves; Microwaves; Seiches; Water waves; Analogies**
An Electromagnetic Analogy For Long Water Waves, G. W. Jackson and D. L. Wilkinson, 801
- Energy conversion; Environmental effects; Field investigations; Mathematical models; Ocean engineering; Ocean water; Thermal energy; Thermal power plants; Discharge (water)**
Dynamic Similarity of Transport Phenomena, M. S. Yalin and F. Gerritsen, 2669
- Energy dissipation; Laboratory tests; Turbulence; Wave damping; Wave energy**
The Dissipation of Wave Energy by Turbulence, Yu Kuang-ming, 850
- Energy transfer; Harbors; Truncation errors; West Germany; Breakwaters; Case reports; Deep water; Design criteria**
Energy Transmission Over Break Water - A Design Criterion?, P. Bade and H. Kaldenhoff, 1886
- Engineering evaluation; Nuclear power plants; Oceanography; Philippines; Tsunamis; Coastal engineering; Coastal engineering**
Tsunamis Along West Coast of Luzon, Philippines, R. L. Wiegel, 652
- Environmental effects; Estuaries; Estuarine environment; Models; Salinity; Coastal engineering**
Separation of Climatic Fluctuations and Impacts of Engineering Activities in Estuaries, G. Krause, 2323
- Environmental effects; Field investigations; Mathematical models; Ocean engineering; Ocean water; Thermal energy; Thermal power plants; Discharge (water); Energy conversion**
Dynamic Similarity of Transport Phenomena, M. S. Yalin and F. Gerritsen, 2669
- Environmental effects; Ports; Breccia; Carbonaceous rocks; Coastal engineering; Construction; Disposal; Dredge spoil; Dredging**
For Disposal: 10 M.c.u.m. of Calcium Carbonate Slurry, L. Summers and C. A. Fleming, 2871
- Environmental impact statements; Estuaries; Planning; Ports; Water flow; Australia; Coastal engineering**
Water Movement Studies Required for Port Planning, Graeme C. Dandy, Desmond A. Mills and John B. Hinwood, 3007
- Environmental impact statements; Gas pipelines; Petroleum pipelines; Scotland; Shore protection; Submarine pipelines; Coastal engineering**
Environmental Aspects of Oil and Gas Pipeline Landfalls in Northeast Scotland, William Ritchie, 2935
- Environmental surveys; Ports; Water flow; Water quality; Australia; Beaches; Computer applications; Construction; Docks; Dredging**
Integration and Computation in an Environmental Study, J. B. Hinwood, J. E. Watson and D. M. Burrage, 3024
- Erosion; Models; Numerical calculations; Sediment transport; Bed forms; Dunes; Dynamic geology**
A Numerical Model for Dune Dynamics, J. Sundermann, H.-J. Vollmers and W. Puls, 1583
- Erosion; Nile River Valley; Rivers; Sand; Sediment transport; Currents (water); Eddy currents; Egypt**
Eddy Currents and Sediment Transport Off the Damietta Nile, S. P. Murray, J. M. Coleman, H. H. Roberts and M. Salama, 1679
- Erosion; Sea ice; Sediment transport; Tundra; Wave energy; Alaska; Cliffs; Coastal Processes**
Sediment Transport Processes and Coastal Variability on the Alaskan North Slope, E. H. Owens, J. R. Harper and D. Nummendaal, 1343

- Estimates; Sediment distribution; Sediment transport; Topographic features; Wave height; Wave period; Beds under water**
Longshore Water and Sediment Movement, D. H. Swart and C. A. Fleming, 1274
- Estuaries; Estuarine environment; Hydraulic models; Identification; Mathematical models; Parameters; Salinity**
Parameter Identification in Estuarine Modeling, Wen-Sen Chu and William W-G. Yeh, 2431
- Estuaries; Estuarine environment; Models; Salinity; Coastal engineering; Environmental effects**
Separation of Climatic Fluctuations and Impacts of Engineering Activities in Estuaries, G. Krause, 2323
- Estuaries; Field investigations; Floods; Mathematical models; Ports; Sediment transport; Shoaling; Silting; Australia**
Port of Brisbane Siltation Study, N. V.M. Odd and T. Baxter, 2375
- Estuaries; Field investigations; Lagoon deposits; Sedimentation; Sediment control; Tidal waters**
Opening and Maintaining Tidal Lagoons & Estuaries, Scott A. Jenkins, Douglas L. Inman and James A. Bailard, 1527
- Estuaries; Field investigations; Wave energy; Wave spectra; West Germany; Deep water**
Wave Energy Distribution in an Estuary, Volker Barthel, 2338
- Estuaries; Floods; Inlets (waterways); Lakes; Littoral drift; Stability criteria; Tidal effects; Tidal waters; Australia; Coastal Processes**
Tidal Inlet Behavioural Analysis, A. F. Nielsen and A. D. Gordon, 2459
- Estuaries; France; Laboratory tests; Saline water intrusion; Sediment transport; Silts; Suspended sediments; Dynamics**
Dynamics of Silt in Estuary. Residual Current or Flocculation Which Prevails?, J. P. Lepetit and M. Davesne, 2858
- Estuaries; Harbors; Research; Sediment transport; Shore protection; China; Coastal engineering**
Some Aspects of Coastal Engineering Research Works in China, Yen Kai, 1734
- Estuaries; Hydraulic tests; Netherlands; Storm surges; Barriers; Coastal engineering**
Hydraulic Research in the Oosterschelde Estuary, A. W. Walther, 2358
- Estuaries; Inlets (waterways); Land reclamation; Littoral drift; Tidal effects; Tides; Airport construction; Australia**
Inlets/Estuaries Discharging into Sheltered Waters, H. P. Riedel and M. R. Gourlay, 2548
- Estuaries; Inlets (waterways); Sedimentation; Tidal currents; West Germany; Barriers; Basins; Channels (waterways); Dams**
Sedimentation Processes in Tidal Channels and Tidal Basins Caused by Artificial Constructions, E. Renger and H. W. Partensky, 2479
- Estuaries; Inlets (waterways); Tidal effects; Australia; Coastal engineering; Coasts**
A Coastal Inlet with Fixed Bed and Mobile Sides, R. C. Nelson and A. J. Keats, 2532
- Estuaries; Maine; Models; Three-dimensional; Water pollution control; Water quality; Bays (topographic features); Coastal engineering; Currents (water)**
A 3-D Model for Penobscot Bay, Maine, Bryan R. Pearce, Bruce R. Fidler and Adrian C. Humphreys, 2395
- Estuaries; Mathematical models; Models; Rivers; Tidal waters; Tides; Waves; West Germany; Calibration; Coastal engineering**
Automatic Calibration of Numerical Tidal Models, K.-P. Holz and U. Januszewski, 2448
- Estuaries; Mixing; Models; Saline water-freshwater interfaces; Saline water intrusion**
Discrete-Time Modelling of Dispersion in Estuaries, T. Wood, 3075
- Estuaries; Models; Numerical calculations; Tidal effects; Tides; Coastal engineering; Data processing; Dynamics**
The Use of Array Processors for Numerical Modeling of Tidal Estuary Dynamics, D. Prandle, E. R. Funke, N. Crookshank and R. Renner, 2411
- Estuaries; Models; Physical tests; Storm surges; Tides; Coastal engineering**
Artificial Roughness in Physical Models of Estuaries for Storm Surge Investigations, D. Berndt, E. Giese, H. Schwarze and H.-J. Vollmers, 2493
- Estuaries; Netherlands; Rivers; Sediment deposits; Stability; Deltaic deposits; Deltas**
Stability of Estuary Mouths in the Rhine-Meuse Delta, J. van de Kreeke and Jac Haring, 2625
- Estuaries; Planning; Ports; Water flow; Australia; Coastal engineering; Environmental impact statements**
Water Movement Studies Required for Port Planning, Graeme C. Dandy, Desmond A. Mills and John B. Hinwood, 3007
- Estuaries; Rivers; Sand; Sediment transport; Tidal hydraulics; Australia; Beach nourishment; Bed forms; Dredging**
Estuarine Response to Dredging in the Tweed River, Australia, Bruce M. Druery, 1598
- Estuaries; Rivers; Sediment transport; Storms; Suspended load; Suspended sediments; Connecticut; Dredging**
A Comparison Between Dredge Induced Sediment Resuspension and that Produced by Natural Storm Events, W. Frank Bohlen, 1699
- Estuarine environment; Hydraulic models; Identification; Mathematical models; Parameters; Salinity; Estuaries**
Parameter Identification in Estuarine Modeling, Wen-Sen Chu and William W-G. Yeh, 2431
- Estuarine environment; Models; Salinity; Coastal engineering; Environmental effects; Estuaries**
Separation of Climatic Fluctuations and Impacts of Engineering Activities in Estuaries, G. Krause, 2323
- Experimental data; Wave action; Wave energy; Waves; Wave velocity; Beaches; Coastal engineering**
Experimental Investigations of Periodic Wave Near Breaking, J. Buhr Hansen, 260

- Experimentation; Flumes; Least squares method; Wave measurement; Wave propagation; Waves**
The Measurement of Incident and Reflected Spectra Using a Least Squares Method, E. P.D. Mansard and E. R. Funke, 154
- Experimentation; Flumes; Predictions; Wave equations; Waves; Beaches; Disturbances**
Long Period Disturbances Due to Wave Groups, E. C. Bowers, 610
- Experimentation; Harbors; Littoral drift; Sand; Sediment control; Sediment transport; California**
A Sediment Trapping Experiment at Santa Cruz, CA, R. J. Scymour, G. W. Domurat and D. M. Pirie, 1415
- Experimentation; Heat balance; Powerplants; Rivers; Thermal pollution; Wastewater (pollution); Water surface; Earth atmosphere**
Experimental Evaluation of Heat Exchange Between Water Surface and Atmosphere, Gunther Barg, Horst Schwarze and Gerhard Visscher, 2848
- Experimentation; Jets; Powerplants; Thermal pollution; Coastal engineering; Cooling water; Currents (water); Discharge (water)**
Experimental Study of the Buoyant Surface Jet with the Presence of Bottom Boundary and Cross Current, B. Safaie, 2814
- Experimentation; Measurement; Sands; Sand waves; Water tunnels; Water waves; Bed forms; Drag**
Measurements of Oscillatory Drag on Sand Ripples, Karl E. B. Lofquist, 3104
- Experimentation; Primary waves; Shoaling; Standing waves; Surf; Surface waves; Wave measurement; Wave velocity**
Two-Dimensional Surf Beat, Reinhard E. Flick, Douglas L. Inman and Robert T. Gaza, 624
- Experimentation; Sediment concentration; Water waves; Wave action; Clay suspensions**
An Experiment on Clay Suspension Under Water Waves, Prida Thimakorn, 2891
- Fabrics; Filters; Filter tests; Groins (structures); Shore-line cover; Synthetic textiles; Breakwaters; Dikes; Docks**
Long-Term Experience with the use of Synthetic Filter Fabrics in Coastal Engineering, Georg Heerten, 2172
- Field data; Shoaling; Transient waves; Wave height; Waves; Currents (water); Deep water**
Wave-Wave Interactions, Current-Wave Interactions and Resulting Extreme Waves and Breaking Waves, Soren Peter Kjeldsen and Dag Myrhaug, 2275
- Field investigations; Flood control; Inlets (waterways); Research projects; Tidal waters; U.S. Corps of Engineers; Beach erosion; Coastal engineering**
The Corps of Engineer's General Investigation of Tidal Inlets, Robert M. Sorensen, 2563
- Field investigations; Floods; Mathematical models; Ports; Sediment transport; Shoaling; Silting; Australia; Estuaries**
Port of Brisbane Situation Study, N. V.M. Odd and T. Baxter, 2375
- Field investigations; Islands; Shore protection; South Carolina; Wave action; Beach erosion; Breakwaters; Coastal engineering; Dredging**
Soft Designs for Coastal Protection at Seabrook Island, S.C., Miles O. Hayes, Timothy W. Kana and John H. Barwis, 897
- Field investigations; Japan; Littoral drift; Littoral materials; Ports; Sand; Beaches**
Littoral Drift on Sand Near Port of Oarai, Kazumasa Mizumura, 2157
- Field investigations; Lagoon deposits; Sedimentation; Sediment control; Tidal waters; Estuaries**
Opening and Maintaining Tidal Lagoons & Estuaries, Scott A. Jenkins, Douglas L. Inman and James A. Bailard, 1527
- Field investigations; Mathematical models; Ocean engineering; Ocean water; Thermal energy; Thermal power plants; Discharge (water); Energy conversion; Environmental effects**
Dynamic Similarity of Transport Phenomena, M. S. Yalin and F. Gerritsen, 2669
- Field investigations; Motion; Sand; Sediment transport; Surf; Suspended load; Wave measurement; Wind; Currents (water)**
Field Measurements of Sand Motion in the Surf Zone, Douglas L. Inman, James A. Zampol, Thomas E. White, Daniel M. Hanes, B. Walton Waldorf and Kim A. Kastens, 1214
- Field investigations; Sand; Sand control; Sediment transport; West Germany; Wind action geology; Wind speed; Coasts**
Sand Transport Under the Action of Wind, Ulrich Zanke, 1575
- Field investigations; Wave energy; Wave spectra; West Germany; Deep water; Estuaries**
Wave Energy Distribution in an Estuary, Volker Barthel, 2338
- Field tests; Harbors; Sand traps; Sediment transport; Wave measurement; Breakwaters; California; Coastal engineering**
Longshore Transport Evaluations at a Detached Breakwater, R. O. Bruno, R. G. Dean and C. G. Gable, 1452
- Field tests; Models; Predictions; Sediment transport; Wave height; Wind speed; Australia; Continental shelf; Currents (water)**
Sediment Dispersal on the NSW Continental Shelf, Ron Boyd, 1363
- Field tests; Morphology; Projects; Sedimentology; Tides; West Germany; Coastal engineering; Coasts; Dredging**
The German "Moran" Project, Winfried Siefert and Volker Barthel, 2924
- Field tests; Numerical calculations; Wave height; Waves; Breakwaters; Coastal engineering**
Wave Height Distribution Around Permeable Breakwaters, Shintaro Hotta, 221
- Field tests; Stability; Surf; Topography; Wave action; Australia; Beach erosion; Beaches**
Beach Cut in Relation to Surf Zone Morphodynamics, L. D. Wright, 978

- Field work; Harbors; Nigeria; Sedimentation; Sediment transport; Channels (waterways); Dredging**
Sedimentation in Dredged Navigation Channels, Lars Mikkelsen, Preben Mortensen and Torben Sorensen, 1718
- Field work; Littoral deposits; Littoral drift; Sediment transport; Storms; Suspended sediments; Wave energy**
Nearshore Suspended Sediment Load During Storm and Post-Storm Conditions, Timothy W. Kana and Larry G. Ward, 1158
- Field work; Wave action; Accretion (geomorphology); Australia; Beach erosion; Coastal engineering**
Beach Erosion-Accretion at Two Time Scales, B. G. Thom and G. M. Bowman, 934
- Filters; Filter tests; Groins (structures); Shore-line cover; Synthetic textiles; Breakwaters; Dikes; Docks; Fabric**
Long-Term Experience with the use of Synthetic Filter Fabrics in Coastal Engineering, Georg Heerten, 2172
- Filter tests; Groins (structures); Shore-line cover; Synthetic textiles; Breakwaters; Dikes; Docks; Fabric; Filters**
Long-Term Experience with the use of Synthetic Filter Fabrics in Coastal Engineering, Georg Heerten, 2172
- Finite difference method; Islands; Shallow water; Tsunamis; Wave equations; Coastal engineering**
Transient Finite-Difference Tsunami Calculations, Ove Skovgaard and Ivar G. Jonsson, 823
- Fishing; Harbors; Jetties; Littoral drift; Shoaling; Taiwan; Dredging**
New Jetties for Tung-Kang Fishing Harbor, Taiwan, Chi-Fu Su, 2228
- Fixed structures; Flumes; Model tests; Sea states; Synthesis; Time series analysis; Water waves; Wave generation; Waves**
On the Synthesis of Realistic Sea States, E. R. Funke and E. P.D. Mansard, 2971
- Floating bodies; Mooring; Wave energy; Waves; Wave tanks; Breakwaters; Cost comparisons**
Floating Breakwater Performance Comparison, Volker W. Harms, 2135
- Flood control; Inlets (waterways); Research projects; Tidal waters; U.S. Corps of Engineers; Beach erosion; Coastal engineering; Field Investigations**
The Corps of Engineer's General Investigation of Tidal Inlets, Robert M. Sorensen, 2563
- Flooding; Harbors; Mathematical models; Sedimentation; Sedimentation tanks; Suspended sediments; Tidal effects; Coastal engineering; Cost estimates**
Design of Enclosed Harbors to Reduce Sedimentation, Craig H. Everts, 1511
- Flood protection; Rivers; Sediment transport; Alluvial deposits; Australia; Beach erosion; Beach sands; Deltas**
Barron River Delta Investigation, D. A. Robinson, D. J. Cook and J. G. Barff, 885
- Floods; Inlets (waterways); Lakes; Littoral drift; Stability criteria; Tidal effects; Tidal waters; Australia; Coastal Processes; Estuaries**
Tidal Inlet Behaviour Analysis, A. F. Nielsen and A. D. Gordon, 2459
- Floods; Inlets (waterways); Sand; Sandy soils; Storms; Tidal effects; Tidal hydraulics; Wave action; Coasts**
Comments on Tidal Entrances on Sandy Coasts, Morrough P. O'Brien, 2502
- Floods; Mathematical models; Ports; Sediment transport; Shoaling; Silting; Australia; Estuaries; Field investigations**
Port of Brisbane Siltation Study, N. V.M. Odd and T. Baxter, 2375
- Florida; Spectral analysis; Tides; Wave measurement; Coastal engineering; Data analysis**
Florida Coastal Data Network, Gary Howell, 421
- Flow; Waveguides; Waves; Beaches; Coastal engineering; Currents (water)**
Longshore Current Flows in a Wave Basin, P. J. Visser, 462
- Flowmeters; Laboratory tests; Velocity measurement; Velocity meters; Waves; Wave velocity; Coastal engineering**
Orbital Velocities in Irregular Waves, F. C. Vis, 173
- Fluid dynamics; Gravity waves; Mathematical studies; Turbulence; Water waves; Wave energy; Waves; Coastal engineering; Dissipation**
The Unsolved Problem of Breaking Waves, M. S. Longuet-Higgins, 1
- Fluid mechanics; Sand; Sand waves; Calculations; Coastal Processes**
Contribution to the Discussion During Session C, Coastal Processes, Friday, March 28, 2:00 P.M., M. S. Longuet-Higgins, 3107
- Fluid mechanics; Similarities; Surf; Wave energy; Waves; Beaches; Coastal engineering**
A Similarity Model in the Surf Zone, Hsiang Wang and Wei-Chong Yang, 529
- Fluid mechanics; Water waves; Wavelength; Wave velocity; Acceleration; Breaking energy**
The Fluid Mechanics of Waves Approaching Breaking, D. H. Peregrine, E. D. Cokelet and P. Melver, 512
- Flumes; Hydraulic models; Wave generation; Waves; Wave tanks; Coastal engineering; Computer applications**
A Survey of "Random" Wave Generation Techniques, J. Ploeg and E. R. Funke, 135
- Flumes; Least squares method; Wave measurement; Wave propagation; Waves; Experimentation**
The Measurement of Incident and Reflected Spectra Using a Least Squares Method, E. P.D. Mansard and E. R. Funke, 154
- Flumes; Model tests; Sea states; Synthesis; Time series analysis; Water waves; Wave generation; Waves; Fixed structures**
On the Synthesis of Realistic Sea States, E. R. Funke and E. P.D. Mansard, 2971
- Flumes; Predictions; Wave equations; Waves; Beaches; Disturbances; Experimentation**
Long Period Disturbances Due to Wave Groups, E. C. Bowers, 610

- Flumes; Sand; Sediment transport; Wave action; Waves; Bottom sediments; Coastal engineering**
Sand Transport by Waves, Jan van de Graaff and Wiel M.K. Tilmans, 1140
- Foundations; Foundation stability analysis; Ocean bottom; Ocean engineering; Ocean waves; Storms**
Stability Analysis of Seafloor Foundations, Tokuo Yamamoto and Yasumasa Suzuki, 1800
- Foundation stability analysis; Ocean bottom; Ocean engineering; Ocean waves; Storms; Foundations**
Stability Analysis of Seafloor Foundations, Tokuo Yamamoto and Yasumasa Suzuki, 1800
- Fourier transformation; Ocean waves; Wave velocity; Coastal engineering; Computerized simulation**
Conditional Simulations of Ocean Wave Properties, Leon R. Borgman, 318
- France; Harbors; Hydraulic tests; Models; Sedimentology; Wave diffraction; Wave refraction; Computer applications; Design**
Harbour Design Including Sedimentological Problems Using Mainly Numerical Technics, B. Latteux, 2211
- France; Laboratory tests; Saline water intrusion; Sediment transport; Silts; Suspended sediments; Dynamics; Estuaries**
Dynamics of Silt in Estuary, Residual Current or Flocculation Which Prevails?, J. P. Lepetit and M. Davesne, 2858
- Friction factor; Hawaii; Tsunamis; Turbulent flow; Wind profiles; Wind velocity; Anemometers**
Tsunami Prone Friction Factors From Wind Measurements, Charles L. Bretschneider, 672
- Froude number; Mixing; Outflows; Rivers; Saline water-freshwater interfaces; Water flow; Coastal engineering**
On a Role of the Interfacial Froude Number, Masakazu Kashiwamura, 2778
- Gages; Littoral zone; Visual surveillance; Wave height; Wave measurement; Waves; California; Coastal engineering**
Visually Observed Wave Data at PT, Mugu, Calif., Christine Schneider and J. Richard Weggel, 381
- Gas pipelines; Hydrodynamics; Ocean bottom; Ocean engineering; Petroleum pipelines; Submarine pipelines; Wave action**
Waves Forces on Offshore Pipelines, N. Jothishankar and V. Sundar, 1820
- Gas pipelines; Petroleum pipelines; Scotland; Shore protection; Submarine pipelines; Coastal engineering; Environmental impact statements**
Environmental Aspects of Oil and Gas Pipeline Landfalls in Northeast Scotland, William Ritchie, 2935
- Geologic control; Marine geology; Sediment transport; Wave action; Wave energy; Australia; Coastal engineering; Coastal Processes; Coasts**
Geological Controls on Process-Response, SE Australia, P. S. Roy and A. W. Stephens, 913
- Gravity waves; Mathematical studies; Turbulence; Water waves; Wave energy; Waves; Coastal engineering; Dissipation; Fluid dynamics**
The Unsolved Problem of Breaking Waves, M. S. Longuet-Higgins, 1
- Gravity waves; Microwaves; Seiches; Water waves; Analogies; Electromagnetic radiation**
An Electromagnetic Analogy For Long Water Waves, G. W. Jackson and D. L. Wilkinson, 801
- Gravity waves; Ocean engineering; Oceanography; Water waves; Wave period; Wave reflection; Wave refraction; Waves; Coastal engineering**
Ray Curvature and Refraction of Wave Packets, J. Ernest Breeding, Jr., 82
- Gravity waves; Predictions; Shoaling; Two-dimensional; Wave height; Calculations; Coastal engineering**
Wave Shoaling Calculated From Cokerlet's Theory, T. Sakai and J. A. Battjes, 121
- Groins (structures); Japan; Shore protection; Beaches; Breakwaters; Coastal engineering**
Artificial Resort Beach Protected by Offshore Breakwaters and Groins, Shoji Sato and Norio Tanaka, 2004
- Groins (structures); Shore-line cover; Synthetic textiles; Breakwaters; Dikes; Docks; Fabrics; Filters; Filter tests**
Long-Term Experience with the use of Synthetic Filter Fabrics in Coastal Engineering, Georg Heerten, 2172
- Groundwater elevation; Slopes; Surf; Wave action; Wave energy; Beaches; Currents (water)**
Wave Forcing of Beach Groundwater, Evans Waddell, 1435
- Harbors; Hydraulic design; Marinas; Water circulation; Water quality; Coastal engineering**
Hydraulic Circulation Performance of a Curvilinear Marina, Jeffrey A. Layton, 2743
- Harbors; Hydraulic tests; Models; Sedimentology; Wave diffraction; Wave refraction; Computer applications; Design; France**
Harbour Design Including Sedimentological Problems Using Mainly Numerical Technics, B. Latteux, 2211
- Harbors; Jetties; Littoral drift; Shoaling; Taiwan; Dredging; Fishing**
New Jetties for Tung-Kang Fishing Harbor, Taiwan, Chi-Fu Su, 2228
- Harbors; Littoral drift; Sand; Sediment control; Sediment transport; California; Experimentation**
A Sediment Trapping Experiment at Santa Cruz, CA, R. J. Seymour, G. W. Domurat and D. M. Pirie, 1415
- Harbors; Marinas; Models; Tidal waters; Water circulation; Water quality**
Modelling of Planform Influence on Circulation in Harbours, Roger A. Falconer, 2724
- Harbors; Marinas; Model studies; Water waves; Wave action; Wave energy; Waves; Coastal engineering**
Non-Resonant Wave Agitation in Small Craft Harbours, J. W. Kamphuis and D. A. Y. Smith, 241
- Harbors; Mathematical models; Sedimentation; Sedimentation tanks; Suspended sediments; Tidal effects; Coastal engineering; Cost estimates; Flooding**
Design of Enclosed Harbors to Reduce Sedimentation, Craig H. Everts, 1511

- Harbors; Models; Numerical calculations; Shallow water; Storms; Storm water; Waves**
A Numerical Model of Storm Waves in Shallow Water, A. Hauguel, 746
- Harbors; Nigeria; Sedimentation; Sediment transport; Channels (waterways); Dredging; Field work**
Sedimentation in Dredged Navigation Channels, Lars Mikkelsen, Preben Mortensen and Torben Sorensen, 1718
- Harbors; Research; Sediment transport; Shore protection; China; Coastal engineering; Estuaries**
Some Aspects of Coastal Engineering Research Works in China, Yen Kai, 1734
- Harbors; Sand traps; Sediment transport; Wave measurement; Breakwaters; California; Coastal engineering; Field tests**
Longshore Transport Evaluations at a Detached Breakwater, R. O. Bruno, R. G. Dean and C. G. Gable, 1452
- Harbors; Shoaling; California; Channel improvements; Coastal Processes; Dredging**
A Phased-Dredging Program for Santa Cruz Harbor, James R. Walker and Peter J. Williams, 1492
- Harbors; Shore protection; Storms; Storm surges; Wind forces; Australia; Breakwaters; Coastal structures; Design**
The Design Concept of Dual Breakwaters and its Application to Townsville, Australia, W. Bremner, D. N. Foster, C. A. Miller and B. C. Wallace, 1899
- Harbors; Truncation errors; West Germany; Breakwaters; Case reports; Deep water; Design criteria; Energy transfer**
Energy Transmission Over Break Water - A Design Criterion?, P. Bade and H. Kaldenhoff, 1886
- Hawaii; Mathematical models; Reefs; Wave attenuation; Coastal engineering; Coastal structures; Design**
Wave Attenuation and Wave Set-Up on a Coastal Reef, Francisus Gerritsen, 444
- Hawaii; Tsunamis; Turbulent flow; Wind profiles; Wind velocity; Anemometers; Friction factor**
Tsunami Prone Friction Factors From Wind Measurements, Charles L. Bretschneider, 672
- Heat balance; Powerplants; Rivers; Thermal pollution; Wastewater (pollution); Water surface; Earth atmosphere; Experimentation**
Experimental Evaluation of Heat Exchange Between Water Surface and Atmosphere, Gunther Barg, Horst Schwarze and Gerhard Visscher, 2848
- Heated water; Industrial plants; Liquefied natural gas; Refractometers; Temperature rise; Water pollution control; Cooling water; Discharge (water)**
Dispersion of Cooling Water from a Coastal LNG Plant, P. Ackers, J. D. Pitt, G. Thompson and K. G. Rippin, 2794
- Heuristic methods; Surf; Wave energy; Wave height; Waves; Beaches; Coastal engineering**
An Heuristic Model of Wave Height Distribution in Surf Zone, Masaru Mizuguchi, 278
- High frequency; Meteorological data; Oceanographic data; Ocean waves; Radar mapping; Wave measurement; Wave spectra; Wind**
HF Radar Mapping of Extensive Ocean Windfields, P. E. Dexter and R. C. Casey, 363
- Hurricanes; Hydrodynamics; Models; Numerical calculations; Storms; Storm surges; Tropical cyclones**
Numerical Modelling of Tropical Cyclone Storm Surge, Rodney J. Sobey, Bruce A. Harper and George M. Mitchell, 725
- Hurricanes; Kinematics; Wave action; Wave measurement; Wave spectra; Wave velocity**
Directional Wave Spectra and Wave Kinematics in Hurricanes Carmen and Eloise, G. Z. Forristall, E. G. Ward and V. J. Cardone, 567
- Hurricanes; Predictions; Wave energy; Wave generation; Wave height; Waves; Wind direction**
Prediction of Dominant Wave Properties Ahead of Hurricanes, Omar H. Shemdin, 600
- Hydraulic design; Marinas; Water circulation; Water quality; Coastal engineering; Harbors**
Hydraulic Circulation Performance of a Curvilinear Marina, Jeffrey A. Layton, 2743
- Hydraulic models; Identification; Mathematical models; Parameters; Salinity; Estuaries; Estuarine environment**
Parameter Identification in Estuarine Modeling, Wen-Sen Chu and William W.-G. Yeh, 2431
- Hydraulic models; Japan; Landsat; Remote sensing; Saline water-freshwater interfaces; Sea water intrusion; Straits; Tidal currents; Vortices**
Study on Vortex Current in Strait with Remote-Sensing, Sotoaki Omishi and Tsukasa Nishimura, 2653
- Hydraulic models; Simulation; Wave generation; Wave pressure; Waves; Wave velocity**
Investigations on Irregular Waves in Hydraulic Models, Karl-Friedrich Daemrich, Wolf-Dietrich Eggert and Soren Kohlhasse, 186
- Hydraulic models; Wave generation; Waves; Wave tanks; Coastal engineering; Computer applications; Flumes**
A Survey of "Random" Wave Generation Techniques, J. Ploeg and E. R. Funke, 135
- Hydraulics; Laboratory tests; Permeability (soils); Profiles; Surf; Waves; Beaches; Beach sands; Coastal Processes**
Beaches: Profiles, Processes and Permeability, Michael R. Gourlay, 1319
- Hydraulics; Littoral drift; Sand; Sediment transport; Wave energy; Beaches**
Secondary Sand Transport Mechanisms, A. W. Smith and A. D. Gordon, 1122
- Hydraulic tests; Models; Sedimentology; Wave diffraction; Wave refraction; Computer applications; Design; France; Harbors**
Harbour Design Including Sedimentological Problems Using Mainly Numerical Technics, B. Latteux, 2211
- Hydraulic tests; Model tests; Reinforced concretes; Rubble-mound breakwaters; Concrete structures; Destructive tests; Dynamic loads**
Full Scale Trails of Dolosse to Destruction, Hans F. Burcharth, 1929

- Hydraulic tests; Netherlands; Storm surges; Barriers; Coastal engineering; Estuaries**
Hydraulic Research in the Oosterschelde Estuary, A. W. Walther, 2358
- Hydraulic test tunnels; Sediment transport; Wave action; Waves; Wave velocity; Coastal engineering**
A Closely Responding, Versatile Wave Tunnel, C. H. Hulsbergen and J. J. Bosman, 310
- Hydrodynamics; Models; Numerical calculations; Storms; Storm surges; Tropical cyclones; Hurricanes**
Numerical Modelling of Tropical Cyclone Storm Surge, Rodney J. Sobey, Bruce A. Harper and George M. Mitchell, 725
- Hydrodynamics; Ocean bottom; Ocean engineering; Petroleum pipelines; Submarine pipelines; Wave action; Gas pipelines**
Waves Forces on Offshore Pipelines, N. Jothishankar and V. Sundar, 1820
- Hydrofoils; Turbulent flow; Wakes; Waves; Wave velocity; Boundary layer flow**
Velocity Field in a Steady Breaker, J. A. Battjes and T. Sakai, 499
- Identification; Mathematical models; Parameters; Salinity; Estuaries; Estuarine environment; Hydraulic models**
Parameter Identification in Estuarine Modeling, Wen-Sen Chu and William W.-G. Yeh, 2431
- Impact loads; Laboratory tests; Wave action; Breakwaters; Caissons; Composite structures; Design**
Wave Impact Pressures on Composite Breakwaters, G. R. Mogridge and W. W. Jamieson, 1830
- Industrial plants; Liquefied natural gas; Refractometers; Temperature rise; Water pollution control; Cooling water; Discharge (water); Heated water**
Dispersion of Cooling Water from a Coastal LNG Plant, P. Ackers, J. D. Pitt, G. Thompson and K. G. Rippin, 2794
- Inlets (waterways); Lakes; Littoral drift; Stability criteria; Tidal effects; Tidal waters; Australia; Coastal Processes; Estuaries; Floods**
Tidal Inlet Behavioural Analysis, A. F. Nielsen and A. D. Gordon, 2459
- Inlets (waterways); Land reclamation; Littoral drift; Tidal effects; Tides; Airport construction; Australia; Estuaries**
Inlets/Estuaries Discharging into Sheltered Waters, H. P. Riedel and M. R. Gourlay, 2548
- Inlets (waterways); Landsat; Littoral drift; Remote sensing; Sandbars; Satellite Mapping; Bathymetry; Coasts**
Satellite Applications on a Coastal Inlet Stability Study, Yu-Hwa Wang, 2579
- Inlets (waterways); Littoral deposits; Littoral materials; Migration; North Carolina; Shoals; Tidal effects; Case reports**
Barden Inlet, NC a Case Study of Inlet Migration, Limberios Vallianos, 2638
- Inlets (waterways); North Carolina; Tidal waters; Water flow; Boundary conditions; Downstream Boundary Conditions for Analysis of Flow in Tidal Inlets, T. C. Gopalakrishnan and J. L. Machemehl, 2593**
- Inlets (waterways); Research projects; Tidal waters; U.S. Corps of Engineers; Beach erosion; Coastal engineering; Field investigations; Flood control**
The Corps of Engineer's General Investigation of Tidal Inlets, Robert M. Sorensen, 2563
- Inlets (waterways); Sand; Sandy soils; Storms; Tidal effects; Tidal hydraulics; Wave action; Coasts; Floods**
Comments on Tidal Entrances on Sandy Coasts, Morrough P. O'Brien, 2502
- Inlets (waterways); Sedimentation; Tidal currents; West Germany; Barriers; Basins; Channels (waterways); Dams; Estuaries**
Sedimentation Processes in Tidal Channels and Tidal Basins Caused by Artificial Constructions, E. Renger and H. W. Partensky, 2479
- Inlets (waterways); Tidal effects; Australia; Coastal engineering; Coasts; Estuaries**
A Coastal Inlet with Fixed Bed and Mobile Sides, R. C. Nelson and A. J. Keats, 2532
- Inlets (waterways); Tidal effects; Tide gages; Tides; Bays (topographic features)**
Tidal Prism-Inlet Area Relations for Small Tidal Inlets, R. J. Byrne, R. A. Gammisch and G. R. Thomas, 2515
- Islands; Piers (docks); Site investigation; Site selection; Coastal engineering; Design criteria; Docks**
Siting and Design Criteria of Dock Structures in the Marshall Islands, R. M. Noble, K. C. Leslie and D. O'Day, 2106
- Islands; Shallow water; Tsunamis; Wave equations; Coastal engineering; Finite difference method**
Transient Finite-Difference Tsunami Calculations, Ove Skovgaard and Ivar G. Jonsson, 823
- Islands; Shore protection; South Carolina; Wave action; Beach erosion; Breakwaters; Coastal engineering; Dredging; Field investigations**
Soft Designs for Coastal Protection at Seabrook Island, S.C., Miles O. Hayes, Timothy W. Kana and John H. Barwis, 897
- Islands; Shore protection; Terminals; Breakwaters; Caissons; Concrete construction; Design**
The Effects of Construction Techniques & Bulk Terminal Operational Requirements on the Design Criteria for Island Breakwaters, A. G.F. Eddie, J. D. Lawson, H. R. Graze and B. K. Dean, 2061
- Islands; Wave energy; Wave measurement; Waves; Wave spectra; California**
An Investigation of Wave Sheltering by Islands, S. V. Hsiao, J. F. Vesecky and O. H. Shemdin, 840
- Japan; Landsat; Remote sensing; Saline water-freshwater interfaces; Sea water intrusion; Straits; Tidal currents; Vortices; Hydraulic models**
Study on Vortex Current in Strait with Remote-Sensing, Sotoaki Onishi and Tsukasa Nishimura, 2653
- Japan; Littoral current; Power plant location; Wave action; Wave energy; Beaches; Coastal engineering; Currents (water)**
Nearshore Currents on a Partially Rocky Shore, T. O. Sasaki, H. Igarashi and S. Harikai, 1071

- Japan; Littoral drift; Littoral materials; Ports; Sand; Beaches; Field investigations**
Littoral Drift on Sand Near Port of Oarai, Kazumasa Mizumura, 2157
- Japan; Numerical calculations; Tsunamis; Wave equations; Wave runup; Bays (topographic features)**
Run-Up of Tsunamis by Linear and Nonlinear Theories, Chiaki Goto and Nobuo Shuto, 695
- Japan; Overtopping; Sea walls; Waves; Calssons; Concrete construction; Deep water; Design**
Seawalls in Deep Seas, Shoshichiro Nagai and Shohachi Kakuno, 2024
- Japan; Shore protection; Beaches; Breakwaters; Coastal engineering; Groins (structures)**
Artificial Resort Beach Protected by Offshore Breakwaters and Groins, Shoji Sato and Norio Tanaka, 2004
- Jets; Powerplants; Thermal pollution; Coastal engineering; Cooling water; Currents (water); Discharge (water); Experimentation**
Experimental Study of the Buoyant Surface Jet with the Presence of Bottom Boundary and Cross Current, B. Safaie, 2814
- Jetties; Littoral drift; Shoaling; Taiwan; Dredging; Fishing; Harbors**
New Jetties for Tung-Kang Fishing Harbor, Taiwan, Chi-Fu Su, 2228
- Jetties; Mathematical models; Mooring; Ships; Wind forces; Bulk cargo; Currents (water)**
Mooring Forces Induced by Passing Ships Measurements in Prototype, K. Haffke, 2689
- Jetties; Models; Morphology; Rivers; Rubble mounds; Sediment transport; Australia**
Mechanisms Operating at a Jettied River Entrance, Bruce M. Drury and Alexander F. Nielsen, 2605
- Kinematics; Ocean waves; Offshore platforms; Statistics; Wave measurement; Wave velocity; Wind**
Field Measurements of Wind Wave Kinematics, J. A. Battjes and J. van Heteren, 347
- Kinematics; Ocean waves; Structural members; Tidal currents; Tubes; Wave action; Wave velocity; Cylindrical bodies**
Full Scale Near Surface Water Particle Velocities and Pressure Acting on an Inclined Tubular Member, Fritz Busching and Eckehard Martini, 1870
- Kinematics; Wave action; Wave measurement; Wave spectra; Wave velocity; Hurricanes**
Directional Wave Spectra and Wave Kinematics in Hurricanes Carmen and Eloise, G. Z. Forristall, E. G. Ward and V. J. Cardone, 567
- Laboratory tests; Models; Sand; Sediment transport; Shallow water; Wave action; Beach erosion**
A Laboratory Study of Offshore Transport of Sediment and a Model for Eroding Beaches, Tsuguo Sunamura, 1051
- Laboratory tests; Permeability (soils); Profiles; Surf; Waves; Beaches; Beach sands; Coastal Processes; Hydraulics**
Beaches: Profiles, Processes and Permeability, Michael R. Gourlay, 1319
- Laboratory tests; Saline water intrusion; Sediment transport; Silts; Suspended sediments; Dynamics; Estuaries; France**
Dynamics of Silt in Estuary, Residual Current or Flocculation Which Prevails?, J. P. Lepetit and M. Davesne, 2858
- Laboratory tests; Shallow water; Wave generation; Waves; Wave velocity**
The Generation of Long Waves in the Laboratory, Derek Goring and Fredric Raichlen, 763
- Laboratory tests; Turbulence; Wave damping; Wave energy; Energy dissipation**
The Dissipation of Wave Energy by Turbulence, Yu Kuang-ming, 850
- Laboratory tests; Velocity measurement; Velocity meters; Waves; Wave velocity; Coastal engineering; Flowmeters**
Orbital Velocities in Irregular Waves, F. C. Vis, 173
- Laboratory tests; Wave action; Breakwaters; Caissons; Composite structures; Design; Impact loads**
Wave Impact Pressures on Composite Breakwaters, G. R. Mogridge and W. W. Jamieson, 1830
- Lagoon deposits; Sedimentation; Sediment control; Tidal waters; Estuaries; Field investigations**
Opening and Maintaining Tidal Lagoons & Estuaries, Scott A. Jenkins, Douglas L. Inman and James A. Bailard, 1527
- Lagoons (ponds); Morphology; Reefs; Sediment transport; Wave action; Waves; Currents (water)**
Physical Processes and Sediment Flux Through Reef-Lagoon Systems, Harry H. Roberts, 946
- Lakes; Lake shores; Lake waves; Ohio; Shore protection; Storms; Beach erosion; Breakwaters; Design practices**
A Detached Breakwater System for Beach Protection, James R. Walker, Denton Clark and Joan Pope, 1969
- Lakes; Littoral drift; Stability criteria; Tidal effects; Tidal waters; Australia; Coastal Processes; Estuaries; Floods; Inlets (waterways)**
Tidal Inlet Behavioural Analysis, A. F. Nielsen and A. D. Gordon, 2459
- Lake shores; Lake waves; Ohio; Shore protection; Storms; Beach erosion; Breakwaters; Design practices; Lakes**
A Detached Breakwater System for Beach Protection, James R. Walker, Denton Clark and Joan Pope, 1969
- Lake waves; Michigan; Wave generation; Wave measurement; Waves; Wave spectra; Wind; Data analysis**
A Measurement of Slope, Curvature, and Directional Spectra of Wind Waves in Lake Michigan, Paul C. Liu, 432
- Lake waves; Ohio; Shore protection; Storms; Beach erosion; Breakwaters; Design practices; Lakes; Lake shores**
A Detached Breakwater System for Beach Protection, James R. Walker, Denton Clark and Joan Pope, 1969

- Land reclamation; Littoral drift; Tidal effects; Tides; Airport construction; Australia; Estuaries; Inlets (waterways)**
Inlets/Estuaries Discharging into Sheltered Waters, H. P. Riedel and M. R. Gourlay, 2548
- Landsat; Littoral drift; Remote sensing; Sandbars; Satellite Mapping; Bathymetry; Coasts; Inlets (waterways)**
Satellite Applications on a Coastal Inlet Stability Study, Yu-Hwa Wang, 2579
- Landsat; Remote sensing; Saline water-freshwater interfaces; Sea water intrusion; Straits; Tidal currents; Vortices; Hydraulic models; Japan**
Study on Vortex Current in Strait with Remote-Sensing, Sotoaki Onishi and Tsukasa Nishimura, 2653
- Least squares method; Wave measurement; Wave propagation; Waves; Experimentation; Flumes**
The Measurement of Incident and Reflected Spectra Using a Least Squares Method, E. P. D. Mansard and E. R. Funke, 154
- Liquefied natural gas; Refractometers; Temperature rise; Water pollution control; Cooling water; Discharge (water); Heated water; Industrial plants**
Dispersion of Cooling Water from a Coastal LNG Plant, P. Ackers, J. D. Pitt, G. Thompson and K. G. Rippin, 2794
- Littoral current; Power plant location; Wave action; Wave energy; Beaches; Coastal engineering; Currents (water); Japan**
Nearshore Currents on a Partially Rocky Shore, T. O. Sasaki, H. Igarashi and S. Harikai, 1071
- Littoral current; Surf; Topography; Wave energy; Wave height; Wave runup; Beaches; Currents (water)**
Topographic Control of Run-Up Variability, Mark P. Bradshaw, 1091
- Littoral deposits; Littoral drift; Models; Sand; Sediment transport; Surf; Waves; Beaches**
Onshore-Offshore Transport and Beach Profile Change, Masataro Hattori and Ryoichi Kawamata, 1178
- Littoral deposits; Littoral drift; Models; Sediment transport; Surf; Beaches; Deformation**
On-Offshore Sediment Transport Rate in the Surf Zone, Toru Sawaragi and Ichiro Deguchi, 1194
- Littoral deposits; Littoral drift; Sediment transport; Shear stress; Wave action; Beaches; Coastal engineering**
Beach Profiles and On-Offshore Sediment Transport, Akira Watanabe, Yoshihiko Riho and Kiyoshi Horikawa, 1106
- Littoral deposits; Littoral drift; Sediment transport; Storms; Suspended sediments; Wave energy; Field work**
Nearshore Suspended Sediment Load During Storm and Post-Storm Conditions, Timothy W. Kana and Larry G. Ward, 1158
- Littoral deposits; Littoral materials; Migration; North Carolina; Shoals; Tidal effects; Case reports; Inlets (waterways)**
Barden Inlet, NC a Case Study of Inlet Migration, Limberios Vallianos, 2638
- Littoral drift; Littoral materials; Ports; Sand; Beaches; Field investigations; Japan**
Littoral Drift on Sand Near Port of Oarai, Kazumasa Mizumura, 2157
- Littoral drift; Models; Sand; Sediment transport; Surf; Waves; Beaches; Littoral deposits**
Onshore-Offshore Transport and Beach Profile Change, Masataro Hattori and Ryoichi Kawamata, 1178
- Littoral drift; Models; Sediment transport; Surf; Beaches; Deformation; Littoral deposits**
On-Offshore Sediment Transport Rate in the Surf Zone, Toru Sawaragi and Ichiro Deguchi, 1194
- Littoral drift; Remote sensing; Sandbars; Satellite Mapping; Bathymetry; Coasts; Inlets (waterways); Landsat**
Satellite Applications on a Coastal Inlet Stability Study, Yu-Hwa Wang, 2579
- Littoral drift; Sand; Sediment control; Sediment transport; California; Experimentation; Harbors**
A Sediment Trapping Experiment at Santa Cruz, CA, R. J. Seymour, G. W. Domurat and D. M. Pirie, 1415
- Littoral drift; Sand; Sediment transport; Wave energy; Beaches; Hydraulics**
Secondary Sand Transport Mechanisms, A. W. Smith and A. D. Gordon, 1122
- Littoral drift; Sandbars; Shores; Topography; Wave action; Beaches; Coastal Processes**
Migration of Longshore Bars, Hans H. Dette, 1475
- Littoral drift; Sediment transport; Shear stress; Wave action; Beaches; Coastal engineering; Littoral deposits**
Beach Profiles and On-Offshore Sediment Transport, Akira Watanabe, Yoshihiko Riho and Kiyoshi Horikawa, 1106
- Littoral drift; Sediment transport; Storms; Suspended sediments; Wave energy; Field work; Littoral deposits**
Nearshore Suspended Sediment Load During Storm and Post-Storm Conditions, Timothy W. Kana and Larry G. Ward, 1158
- Littoral drift; Shoaling; Taiwan; Dredging; Fishing; Harbors; Jetties**
New Jetties for Tung-Kang Fishing Harbor, Taiwan, Chi-Fu Su, 2228
- Littoral drift; Shore protection; Wave action; Bays (topographic features); Beach erosion; Beaches**
Zeta Bays, Pocket Beaches and Headland Control, R. Silvester, Y. Tsuchiya and Y. Shibano, 1305
- Littoral drift; Stability criteria; Tidal effects; Tidal waters; Australia; Coastal Processes; Estuaries; Floods; Inlets (waterways); Lakes**
Tidal Inlet Behavioural Analysis, A. F. Nielsen and A. D. Gordon, 2459
- Littoral drift; Taiwan; Wave energy; Wave measurement; Breaking energy; Coastal engineering; Coasts**
Relationship Between Alongshore Wave Energy and Littoral Drift in the Mid West Coast at Taiwan, Ho-Shong Hou, Chung-Pan Lee and Lung-Hui Lin, 1254

- Littoral drift; Tidal effects; Tides; Airport construction; Australia; Estuaries; Inlets (waterways); Land reclamation**
Inlets/Estuaries Discharging into Sheltered Waters, H. P. Riedel and M. R. Gourlay, 2548
- Littoral materials; Mathematical models; Water circulation; Water pollution; Water waves; Wave action; Beaches; Coasts**
Numerical Modelling of Nearshore Circulation, Bruce A. Ebersole and Robert A. Dalrymple, 2708
- Littoral materials; Migration; North Carolina; Shoals; Tidal effects; Case reports; Inlets (waterways); Littoral deposits**
Barden Inlet, NC a Case Study of Inlet Migration, Limberios Vallianos, 2638
- Littoral materials; Ports; Sand; Beaches; Field investigations; Japan; Littoral drift**
Littoral Drift on Sand Near Port of Oarai, Kazumasa Mizumura, 2157
- Littoral zone; Visual surveillance; Wave height; Wave measurement; Waves; California; Coastal engineering; Gages**
Visually Observed Wave Data at PT. Mugu, Calif., Christine Schneider and J. Richard Weggel, 381
- Louisiana; Sedimentation; Shore protection; Wave energy; Beach erosion; Coastal Processes**
Fluid Mud Dynamics and Shoreline Stabilization: Louisiana Chenier Plain, John T. Wells and Harry H. Roberts, 1381
- Maine; Models; Three-dimensional; Water pollution control; Water quality; Bays (topographic features); Coastal engineering; Currents (water); Estuaries**
A 3-D Model for Penobscot Bay, Maine, Bryan R. Pearce, Bruce R. Fidler and Adrian C. Humphreys, 2395
- Management methods; Sand; Topography; Australia; Beaches; Beach nourishment; Coastal engineering**
Beach Nourishment as a Management Technique, David M. Chapman, 1635
- Marinas; Models; Tidal waters; Water circulation; Water quality; Harbors**
Modelling of Planform Influence on Circulation in Harbours, Roger A. Falconer, 2724
- Marinas; Model studies; Water waves; Wave action; Wave energy; Waves; Coastal engineering; Harbors**
Non-Resonant Wave Agitation in Small Craft Harbours, J. W. Kamphuis and D. A.Y. Smith, 241
- Marinas; Porous materials; Wave action; Wave propagation; Waves; Wind; Breakwaters; Coastal engineering**
Wind Waves Transmission Through Porous Breakwater, Stanislaw R. Massel and Piotr Butowski, 333
- Marinas; Water circulation; Water quality; Coastal engineering; Harbors; Hydraulic design**
Hydraulic Circulation Performance of a Curvilinear Marina, Jeffrey A. Layton, 2743
- Marine geology; Sediment transport; Wave action; Wave energy; Australia; Coastal engineering; Coastal Processes; Coasts; Geologic control**
Geological Controls on Process-Response, SE Australia, P. S. Roy and A. W. Stephens, 913
- Mass transfer; Shallow water; Velocity; Water waves; Wave propagation; Waves; Wave tanks; Coastal engineering**
Mass Transport in Progressive Waves of Permanent Type, Yoshito Tsuchiya, Takashi Yasuda and Takao Yamashita, 70
- Mathematical models; Mixing; Ocean waves; Oil spills; Oil-water interfaces; Water pollution control**
The Effect of Breaking Waves on the Mixing of Liquid Pollutants into the Sea, Arvid Naees, 2758
- Mathematical models; Models; Rivers; Tidal waters; Tides; Waves; West Germany; Calibration; Coastal engineering; Estuaries**
Automatic Calibration of Numerical Tidal Models, K.-P. Holz and U. Januszewski, 2448
- Mathematical models; Mooring; Ships; Wind forces; Bulk cargo; Currents (water); Jetties**
Mooring Forces Induced by Passing Ships - Measurements in Prototype, K. Haffke, 2689
- Mathematical models; Ocean engineering; Ocean water; Thermal energy; Thermal power plants; Discharge (water); Energy conversion; Environmental effects; Field investigations**
Dynamic Similarity of Transport Phenomena, M. S. Yalin and F. Gerritsen, 2669
- Mathematical models; Parameters; Salinity; Estuaries; Estuarine environment; Hydraulic models; Identification**
Parameter Identification in Estuarine Modeling, Wen-Sen Chu and William W.-G. Yeh, 2431
- Mathematical models; Ports; Sediment transport; Shoaling; Silting; Australia; Estuaries; Field investigations; Floods**
Port of Brisbane Siltation Study, N. V.M. Odd and T. Baxter, 2375
- Mathematical models; Reefs; Wave attenuation; Coastal engineering; Coastal structures; Design; Hawaii**
Wave Attenuation and Wave Set-Up on a Coastal Reef, Francisus Gerritsen, 444
- Mathematical models; Sedimentation; Sedimentation tanks; Suspended sediments; Tidal effects; Coastal engineering; Cost estimates; Flooding; Harbors**
Design of Enclosed Harbors to Reduce Sedimentation, Craig H. Everts, 1511
- Mathematical models; Water circulation; Water pollution; Water waves; Wave action; Beaches; Coasts; Littoral materials**
Numerical Modelling of Nearshore Circulation, Bruce A. Ebersole and Robert A. Dalrymple, 2708
- Mathematical studies; Turbulence; Water waves; Wave energy; Waves; Coastal engineering; Dissipation; Fluid dynamics; Gravity waves**
The Unsolved Problem of Breaking Waves, M. S. Longuet-Higgins, 1
- Measurement; Oceanography; Wind; Wind profiles; Wind speed; Coastal engineering**
On the Correction of Land-Based Wind Measurements for Oceanographic Applications, S. A. Hsu, 708
- Measurement; Sands; Sand waves; Water tunnels; Water waves; Bed forms; Drag; Experimentation**
Measurements of Oscillatory Drag on Sand Ripples, Karl E. B. Lofquist, 3104

- Meteorological data; Oceanographic data; Ocean waves; Radar mapping; Wave measurement; Wave spectra; Wind; High frequency**
HF Radar Mapping of Extensive Ocean
Windfields, P. E. Dexter and R. C. Casey, 363
- Meteorological data; Oceanographic data; Offshore structures; Oil and gas fields; Programs; Data collection; Design**
Considerations in the Design of an Offshore Data Collection Program, Cortis Cooper and German Febres, 2904
- Michigan; Wave generation; Wave measurement; Lakes; Wave spectra; Wind; Data analysis; Lake waves**
A Measurement of Slope, Curvature, and Directional Spectra of Wind Waves in Lake Michigan, Paul C. Liu, 432
- Microwaves; Seiches; Water waves; Analogies; Electromagnetic radiation; Gravity waves**
An Electromagnetic Analogy For Long Water Waves, G. W. Jackson and D. L. Wilkinson, 801
- Migration; North Carolina; Shoals; Tidal effects; Case reports; Inlets (waterways); Littoral deposits; Littoral materials**
Barden Inlet, NC a Case Study of Inlet Migration, Limberios Vallianos, 2638
- Mixing; Models; Saline water-freshwater interfaces; Saline water intrusion; Estuaries**
Discrete-Time Modelling of Dispersion in Estuaries, T. Wood, 3075
- Mixing; Ocean waves; Oil spills; Oil-water interfaces; Water pollution control; Mathematical models**
The Effect of Breaking Waves on the Mixing of Liquid Pollutants into the Sea, Arvid Naces, 2758
- Mixing; Outflows; Rivers; Saline water-freshwater interfaces; Water flow; Coastal engineering; Froude number**
On a Role of the Interfacial Froude Number, Masakazu Kashiwamura, 2778
- Models; Morphology; Rivers; Rubble mounds; Sediment transport; Australia; Jetties**
Mechanisms Operating at a Jettied River Entrance, Bruce M. Druery and Alexander F. Nielsen, 2605
- Models; Numerical calculations; Sediment transport; Bed forms; Dunes; Dynamic geology; Erosion**
A Numerical Model for Dune Dynamics, J. Sundermann, H.-J. Vollmers and W. Puls, 1583
- Models; Numerical calculations; Shallow water; Storms; Storm water; Waves; Harbors**
A Numerical Model of Storm Waves in Shallow Water, A. Hauguel, 746
- Models; Numerical calculations; Storms; Storm surges; Tropical cyclones; Hurricanes; Hydrodynamics**
Numerical Modelling of Tropical Cyclone Storm Surge, Rodney J. Sobey, Bruce A. Harper and George M. Mitchell, 725
- Models; Numerical calculations; Tidal effects; Tides; Coastal engineering; Data processing; Dynamics; Estuaries**
The Use of Array Processors for Numerical Modeling of Tidal Estuary Dynamics, D. Prandle, E. R. Funke, N. Crookshank and R. Renner, 2411
- Models; Physical tests; Storm surges; Tides; Coastal engineering; Estuaries**
Artificial Roughness in Physical Models of Estuaries for Storm Surge Investigations, D. Berndt, E. Giese, H. Schwarze and H.-J. Vollmers, 2493
- Models; Predictions; Sediment transport; Wave height; Wind speed; Australia; Continental shelf; Currents (water); Field tests**
Sediment Dispersal on the NSW Continental Shelf, Ron Boyd, 1363
- Models; Predictions; Sediment transport; Waves; California; Coastal engineering; Coastal Processes; Currents (water)**
Nearshore Sediment Transport Study Experiments, R. J. Seymour and C. G. Gable, 1401
- Models; Rivers; Tidal waters; Tides; Waves; West Germany; Calibration; Coastal engineering; Estuaries; Mathematical models**
Automatic Calibration of Numerical Tidal Models, K.-P. Holz and U. Januszewski, 2448
- Models; Saline water-freshwater interfaces; Saline water intrusion; Estuaries; Mixing**
Discrete-Time Modelling of Dispersion in Estuaries, T. Wood, 3075
- Models; Salinity; Coastal engineering; Environmental effects; Estuaries; Estuarine environment**
Separation of Climatic Fluctuations and Impacts of Engineering Activities in Estuaries, G. Krause, 2323
- Models; Sand; Sediment transport; Shallow water; Wave action; Beach erosion; Laboratory tests**
A Laboratory Study of Offshore Transport of Sediment and a Model for Eroding Beaches, Tsuguo Sunamura, 1051
- Models; Sand; Sediment transport; Surf; Waves; Beaches; Littoral deposits; Littoral drift**
Onshore-Offshore Transport and Beach Profile Change, Masataro Hattori and Ryoichi Kawamata, 1178
- Models; Sedimentology; Wave diffraction; Wave refraction; Computer applications; Design; France; Harbors; Hydraulic tests**
Harbour Design Including Sedimentological Problems Using Mainly Numerical Technics, B. Latteux, 2211
- Models; Sediment transport; Shoaling; Shores; Topography; Waves; Bathymetry; Currents (water)**
Inshore-Nearshore Morphodynamics - A Predictive Model, John Chappell, 963
- Models; Sediment transport; Surf; Beaches; Deformation; Littoral deposits; Littoral drift**
On-Offshore Sediment Transport Rate in the Surf Zone, Toru Sawaragi and Ichiro Deguchi, 1194

- Models; Shoaling; Water waves; Waveform generators; Wave generation; Wave period**
Correct Reproduction of Group-Induced Long Waves, N.-E. Ottesen Hansen, Stig E. Sand, H. Lundgren, Torben Sorensen and H. Gravesen, 784
- Models; Three-dimensional; Water pollution control; Water quality; Bays (topographic features); Coastal engineering; Currents (water); Estuaries; Maine**
A 3-D Model for Penobscot Bay, Maine, Bryan R. Pearce, Bruce R. Fidler and Adrian C. Humphreys, 2395
- Models; Tidal waters; Water circulation; Water quality; Harbors; Marinas**
Modelling of Planform Influence on Circulation in Harbours, Roger A. Falconer, 2724
- Models; Wave energy; Wave height; Wave refraction; Waves; Wind; Coastal engineering**
Verification of a Wave Refraction Model Utilizing Recorded and Observed Wave Data, G. Henderson and N. B. Webber, 101
- Model studies; Reclamation; Singapore; Coastal engineering; Coastal Processes; Coasts**
Major Reclamation Scheme for Marina City, Singapore, S. Y. Chew and J. Wei, 2243
- Model studies; Statistics; Storms; Wave generation; Wave height; Waves; Coastal structures**
A Comparison of Nature Waves and Model Waves with Special Reference to Wave Grouping, Hans F. Burcharth, 2989
- Model studies; Water waves; Wave action; Wave energy; Waves; Coastal engineering; Harbors; Marinas**
Non-Resonant Wave Agitation in Small Craft Harbours, J. W. Kamphuis and D. A.Y. Smith, 241
- Model tests; Outfall sewers; Storm water; Coastal engineering; Coastal structures; Concrete construction**
Construction and Model Investigation of Stormwater Outfall, K. A. Heathcote and G. W. Britton, 1850
- Model tests; Overtopping; Ports; Australia; Breakwaters; Coastal engineering; Construction; Design**
Design of an Overtopping Breakwater, P. D. Treloar and B. Nagle, 1910
- Model tests; Reinforced concretes; Rubble-mound breakwaters; Concrete structures; Destructive tests; Dynamic loads; Hydraulic tests**
Full Scale Trails of Dolosse to Destruction, Hans F. Burcharth, 1929
- Model tests; Rubble-mound breakwaters; Breakwaters; Coastal engineering; Concrete construction; Design**
Can We Develop New Breakwater Formulas, John Dorrington Mettam, 2302
- Model tests; Sea states; Synthesis; Time series analysis; Water waves; Wave generation; Waves; Fixed structures; Flumes**
On the Synthesis of Realistic Sea States, E. R. Funke and E. P.D. Mansard, 2971
- Model tests; Sediments; Australia; Budgeting; Coastal engineering; Coastal Processes**
An Approach to Understanding Coastal Processes, A. D. Gordon and D. B. Lord, 1234
- Mooring; Petroleum transportation; Piers (docks); Ports; Tanker ships; Berths; Caissons; China; Concrete construction; Design**
The Design and Construction of the New Oil Port in Dalian, CPR, Zhu-zhuang Xin and Yu-cheng Li, 2081
- Mooring; Ships; Wind forces; Bulk cargo; Currents (water); Jetties; Mathematical models**
Mooring Forces Induced by Passing Ships - Measurements in Prototype, K. Haifke, 2689
- Mooring; Wave energy; Waves; Wave tanks; Breakwaters; Cost comparisons; Floating bodies**
Floating Breakwater Performance Comparison, Volker W. Harms, 2135
- Morphology; Prisms; Wave action; Australia; Beaches; Beach nourishment; Coastal engineering; Coasts**
The Dynamic Swept Prism, David M. Chapman and A. W. Smith, 1036
- Morphology; Projects; Sedimentology; Tides; West Germany; Coastal engineering; Coasts; Dredging; Field tests**
The German "Moran" Project, Winfried Siefert and Volker Barthel, 2924
- Morphology; Reefs; Sediment transport; Wave action; Waves; Currents (water); Lagoons (ponds)**
Physical Processes and Sediment Flux Through Reef-Lagoon Systems, Harry H. Roberts, 946
- Morphology; Rivers; Rubble mounds; Sediment transport; Australia; Jetties; Models**
Mechanisms Operating at a Jettied River Entrance, Bruce M. Drucry and Alexander F. Nielsen, 2605
- Morphology; Sand; Sediment transport; Wave energy; Wave height; Waves; Beach erosion; Beaches; Beach nourishment**
Beach Response to Variations in Breaker Height, A. D. Short, 1016
- Motion; Sand; Sediment transport; Surf; Suspended load; Wave measurement; Wind; Currents (water); Field investigations**
Field Measurements of Sand Motion in the Surf Zone, Douglas L. Inman, James A. Zampol, Thomas E. White, Daniel M. Hanes, B. Walton Waldorf and Kim A. Kastens, 1214
- Motion studies; Oscillation; Sand; Water tunnels (testing); Wave action; Bed forms**
Sand Bed-Form Lengths Under Oscillatory Motion, Arthur Brebner, 1339
- Motion studies; Shallow water; Ships; Water flow; Wave action; Wave energy; Wave generation; Damping**
Some Recent Results for Wave Induced Motions of a Ship in Shallow Water, P. A. Madsen, I. A. Svendsen and C. Michaelsen, 3040
- Netherlands; Probability; Shore protection; Storm surges; Coastal engineering; Design; Dikes; Dunes**
Probabilistic Design of Sea Defences, W. T. Bakker and J. K. Vrijling, 2041

- Netherlands; Rivers; Sediment deposits; Stability; Deltaic deposits; Deltas; Estuaries**
Stability of Estuary Mouths in the Rhine-Meuse Delta, J. van de Kreeke and Jac Haring, 2625
- Netherlands; Storm surges; Barriers; Coastal engineering; Estuaries; Hydraulic tests**
Hydraulic Research in the Oosterschelde Estuary, A. W. Walther, 2358
- Nigeria; Sedimentation; Sediment transport; Channels (waterways); Dredging; Field work; Harbors**
Sedimentation in Dredged Navigation Channels, Lars Mikkelsen, Preben Mortensen and Torben Sorensen, 1718
- Nile River Valley; Rivers; Sand; Sediment transport; Currents (water); Eddy currents; Egypt; Erosion**
Eddy Currents and Sediment Transport Off the Damietta Nile, S. P. Murray, J. M. Coleman, H. H. Roberts and M. Salama, 1679
- North Carolina; Shoals; Tidal effects; Case reports; Inlets (waterways); Littoral deposits; Littoral materials; Migration**
Barden Inlet, NC a Case Study of Inlet Migration, Limberios Vallianos, 2638
- North Carolina; Tidal waters; Water flow; Boundary conditions; Downstream; Inlets (waterways)**
Boundary Conditions for Analysis of Flow in Tidal Inlets, T. C. Gopalakrishnan and J. L. Machemehl, 2593
- Nuclear power plants; Oceanography; Philippines; Tsunamis; Coastal engineering; Coastal engineering; Engineering evaluation**
Tsunamis Along West Coast of Luzon, Philippines, R. L. Wiegel, 652
- Numerical calculations; Sediment transport; Bed forms; Dunes; Dynamic geology; Erosion; Models**
A Numerical Model for Dune Dynamics, J. Sundermann, H.-J. Vollmers and W. Puls, 1583
- Numerical calculations; Shallow water; Storms; Storm water; Waves; Harbors; Models**
A Numerical Model of Storm Waves in Shallow Water, A. Hauguel, 746
- Numerical calculations; Solitary waves; Walls; Wave energy; Wave reflection; Coastal engineering; Design criteria**
Accurate Numerical Solutions for Nonlinear Waves, J. D. Fenton and M. M. Rienecker, 50
- Numerical calculations; Storms; Storm surges; Tropical cyclones; Hurricanes; Hydrodynamics; Models**
Numerical Modelling of Tropical Cyclone Storm Surge, Rodney J. Sobey, Bruce A. Harper and George M. Mitchell, 725
- Numerical calculations; Tidal effects; Tides; Coastal engineering; Data processing; Dynamics; Estuaries; Models**
The Use of Array Processors for Numerical Modeling of Tidal Estuary Dynamics, D. Prandle, E. R. Funke, N. Crookshank and R. Renner, 2411
- Numerical calculations; Tsunamis; Wave equations; Wave runup; Bays (topographic features); Japan**
Run-Up of Tsunamis by Linear and Nonlinear Theories, Chiaki Goto and Nobuo Shuto, 695
- Numerical calculations; Wave height; Waves; Breakwaters; Coastal engineering; Field tests**
Wave Height Distribution Around Permeable Breakwaters, Shintaro Hotta, 221
- Ocean bottom; Ocean engineering; Ocean waves; Storms; Foundations; Foundation stability analysis**
Stability Analysis of Seafloor Foundations, Tokuo Yamamoto and Yasumasa Suzuki, 1800
- Ocean bottom; Ocean engineering; Petroleum pipelines; Submarine pipelines; Wave action; Gas pipelines; Hydrodynamics**
Waves Forces on Offshore Pipelines, N. Jothishankar and V. Sundar, 1820
- Ocean bottom; Offshore structures; Sand; Seepage; Water waves; Wave action; Calculations; Cylinders**
Wave-Induced Seepage Effects on a Vertical Cylinder, Thomas J.P. Durand and Peter L. Monkmeier, 1782
- Ocean bottom; Time studies; Tsunamis; Water waves; Wave generation; Earthquakes**
Long Waves Generated by Complex Bottom Motions, J. L. Hammack and E. Raichlen, 639
- Ocean currents; Ocean engineering; Offshore structures; Pipe design; Pipelines; Submarine pipelines; Wave action**
Simultaneous Waves and Current Forces on a Pipeline, David A. Knoll and John B. Herbich, 1743
- Ocean engineering; Oceanography; Water waves; Wave period; Wave reflection; Wave refraction; Waves; Coastal engineering; Gravity waves**
Ray Curvature and Refraction of Wave Packets, J. Ernest Breeding, Jr., 82
- Ocean engineering; Ocean water; Thermal energy; Thermal power plants; Discharge (water); Energy conversion; Environmental effects; Field investigations; Mathematical models**
Dynamic Similarity of Transport Phenomena, M. S. Yalin and F. Gerritsen, 2669
- Ocean engineering; Ocean waves; Storms; Foundations; Foundation stability analysis; Ocean bottom**
Stability Analysis of Seafloor Foundations, Tokuo Yamamoto and Yasumasa Suzuki, 1800
- Ocean engineering; Offshore structures; Pipe design; Pipelines; Submarine pipelines; Wave action; Ocean currents**
Simultaneous Waves and Current Forces on a Pipeline, David A. Knoll and John B. Herbich, 1743
- Ocean engineering; Petroleum pipelines; Submarine pipelines; Wave action; Gas pipelines; Hydrodynamics; Ocean bottom**
Waves Forces on Offshore Pipelines, N. Jothishankar and V. Sundar, 1820
- Oceanographic data; Ocean waves; Radar mapping; Wave measurement; Wave spectra; Wind; High frequency; Meteorological data**
HF Radar Mapping of Extensive Ocean Windfields, P. E. Dexter and R. C. Casey, 363
- Oceanographic data; Offshore structures; Oil and gas fields; Programs; Data collection; Design; Meteorological data**
Considerations in the Design of an Offshore Data Collection Program Program, Cortis Cooper and German Febres, 2904

- Oceanographic data; Wave measurement; Waves; Catalogs; Coastal engineering**
Sources of Measured Wave Data, Laurence Draper, 372
- Oceanography; Philippines; Tsunamis; Coastal engineering; Coastal engineering; Engineering evaluation; Nuclear power plants**
Tsunamis Along West Coast of Luzon, Philippines, R. L. Wiegel, 652
- Oceanography; Water waves; Wave period; Wave reflection; Wave refraction; Waves; Coastal engineering; Gravity waves; Ocean engineering**
Ray Curvature and Refraction of Wave Packets, J. Ernest Breeding, Jr., 82
- Oceanography; Wind; Wind profiles; Wind speed; Coastal engineering; Measurement**
On the Correction of Land-Based Wind Measurements for Oceanographic Applications, S. A. Hsu, 708
- Ocean water; Thermal energy; Thermal power plants; Discharge (water); Energy conversion; Environmental effects; Field investigations; Mathematical models; Ocean engineering**
Dynamic Similarity of Transport Phenomena, M. S. Yalin and F. Gerritsen, 2669
- Ocean waves; Offshore drilling; Offshore platforms; Oil and gas fields; Wave measurement; Wind; Wind speed; Australia**
Wave Hindcasts and Measurements Bass Strait, M. N. Silbert, T. P. Barnett, D. J.H. Peters and R. C. Hamilton, 384
- Ocean waves; Offshore platforms; Statistics; Wave measurement; Wave velocity; Wind; Kinematics**
Field Measurements of Wind Wave Kinematics, J. A. Battjes and J. van Heteren, 347
- Ocean waves; Oil spills; Oil-water interfaces; Water pollution control; Mathematical models; Mixing**
The Effect of Breaking Waves on the Mixing of Liquid Pollutants into the Sea, Arvid Naces, 2758
- Ocean waves; Ports; Real time operations; Wave action; Wave height; Analysis; Australia; Coastal engineering; Dredging**
Realtime Wave Analysis, Newcastle, Australia, N. V. Lawson and P. H. Youll, 412
- Ocean waves; Radar mapping; Wave measurement; Wave spectra; Wind; High frequency; Meteorological data; Oceanographic data**
HF Radar Mapping of Extensive Ocean Windfields, P. E. Dexter and R. C. Casey, 363
- Ocean waves; Statistical data; Wave height; Wave period; Waves; Wave spectrum**
Statistical Properties of Random Wave Groups, Akira Kimura, 2952
- Ocean waves; Stokes law; Water depth; Wave energy; Wave height; Wave period; Waves; Calculations; Coastal engineering; Design**
Some Implications of Recent Advances in Wave Theories, J. R. Chaplin and K. Anastasiou, 31
- Ocean waves; Storms; Foundations; Foundation stability analysis; Ocean bottom; Ocean engineering**
Stability Analysis of Seafloor Foundations, Tokuo Yamamoto and Yasumasa Suzuki, 1800
- Ocean waves; Structural members; Tidal currents; Tubes; Wave action; Wave velocity; Cylindrical bodies; Kinematics**
Full Scale Near Surface Water Particle Velocities and Pressure Acting on an Inclined Tubular Member, Fritz Busching and Eckehard Martini, 1870
- Ocean waves; Wave velocity; Coastal engineering; Computerized simulation; Fourier transformation**
Conditional Simulations of Ocean Wave Properties, Leon R. Borgman, 318
- Offshore drilling; Offshore platforms; Oil and gas fields; Wave measurement; Wind; Wind speed; Australia; Ocean waves**
Wave Hindcasts and Measurements Bass Strait, M. N. Silbert, T. P. Barnett, D. J.H. Peters and R. C. Hamilton, 384
- Offshore platforms; Oil and gas fields; Wave measurement; Wind; Wind speed; Australia; Ocean waves; Offshore drilling**
Wave Hindcasts and Measurements Bass Strait, M. N. Silbert, T. P. Barnett, D. J.H. Peters and R. C. Hamilton, 384
- Offshore platforms; Statistics; Wave measurement; Wave velocity; Wind; Kinematics; Ocean waves**
Field Measurements of Wind Wave Kinematics, J. A. Battjes and J. van Heteren, 347
- Offshore structures; Oil and gas fields; Programs; Data collection; Design; Meteorological data; Oceanographic data**
Considerations in the Design of an Offshore Data Collection Program, Cortis Cooper and German Febres, 2904
- Offshore structures; Pipe design; Pipelines; Submarine pipelines; Wave action; Ocean currents; Ocean engineering**
Simultaneous Waves and Current Forces on a Pipeline, David A. Knoll and John B. Herbich, 1743
- Offshore structures; Predictions; Sea states; Statistical data; Wave height; Coastal structures; Design**
Prediction of the Severest Significant Wave Height, Michel K. Ochi and Joseph E. Whalen, 587
- Offshore structures; Sand; Seepage; Water waves; Wave action; Calculations; Cylinders; Ocean bottom**
Wave-Induced Seepage Effects on a Vertical Cylinder, Thomas J.P. Durand and Peter L. Monkmeyer, 1782
- Ohio; Shore protection; Storms; Beach erosion; Breakwaters; Design practices; Lakes; Lake shores; Lake waves**
A Detached Breakwater System for Beach Protection, James R. Walker, Denton Clark and Joan Pope, 1969
- Oil and gas fields; Programs; Data collection; Design; Meteorological data; Oceanographic data; Offshore structures**
Considerations in the Design of an Offshore Data Collection Program, Cortis Cooper and German Febres, 2904

- Oil and gas fields; Wave measurement; Wind; Wind speed; Australia; Ocean waves; Offshore drilling; Offshore platforms**
Wave Hindcasts and Measurements Bass Strait, M. N. Silbert, T. P. Barnett, D. J.H. Peters and R. C. Hamilton, 384
- Oil spills; Oil-water interfaces; Water pollution control; Mathematical models; Mixing; Ocean waves**
The Effect of Breaking Waves on the Mixing of Liquid Pollutants into the Sea, Arvid Naees, 2758
- Oil-water interfaces; Water pollution control; Mathematical models; Mixing; Ocean waves; Oil spills**
The Effect of Breaking Waves on the Mixing of Liquid Pollutants into the Sea, Arvid Naees, 2758
- Oscillation; Sand; Water tunnels (testing); Wave action; Bed forms; Motion studies**
Sand Bed-Form Lengths Under Oscillatory Motion, Arthur Brebner, 1339
- Outfall sewers; San Francisco; Sediment deposits; Shallow water; Wastewater (pollution); Water pollution; Wave energy; Antifouling materials; California; Coasts; Design**
Design of an Intermittently Operated Outfall, Roger W. Lindquist and George J. Murphy, 2834
- Outfall sewers; Storm water; Coastal engineering; Coastal structures; Concrete construction; Model tests**
Construction and Model Investigation of Stormwater Outfall, K. A. Heathcote and G. W. Britton, 1850
- Outflows; Rivers; Saline water-freshwater interfaces; Water flow; Coastal engineering; Froude number; Mixing**
On a Role of the Interfacial Froude Number, Masakazu Kashiwamura, 2778
- Overtopping; Ports; Australia; Breakwaters; Coastal engineering; Construction; Design; Model tests**
Design of an Overtopping Breakwater, P. D. Treloar and B. Nagle, 1910
- Overtopping; Sea walls; Waves; Caissons; Concrete construction; Deep water; Design; Japan**
Seawalls in Deep Seas, Shoshichiro Nagai and Shohachi Kakuno, 2024
- Parameters; Salinity; Estuaries; Estuarine environment; Hydraulic models; Identification; Mathematical models**
Parameter Identification in Estuarine Modeling, Wen-Sen Chu and William W-G. Yeh, 2431
- Permeability (soils); Profiles; Surf; Waves; Beaches; Beach sands; Coastal Processes; Hydraulics; Laboratory tests**
Beaches: Profiles, Processes and Permeability, Michael R. Gourlay, 1319
- Petroleum pipelines; Scotland; Shore protection; Submarine pipelines; Coastal engineering; Environmental impact statements; Gas pipelines**
Environmental Aspects of Oil and Gas Pipeline Landfalls in Northeast Scotland, William Ritchie, 2935
- Petroleum pipelines; Submarine pipelines; Wave action; Gas pipelines; Hydrodynamics; Ocean bottom; Ocean engineering**
Waves Forces on Offshore Pipelines, N. Jothishankar and V. Sundar, 1820
- Petroleum transportation; Piers (docks); Ports; Tanker ships; Berths; Caissons; China; Concrete construction; Design; Mooring**
The Design and Construction of the New Oil Port in Dalian, CPR, Zhu-zhuang Xin and Yucheng Li, 2081
- Phase shift; Wave action; Wave height; Waves; Wave velocity; Beaches; Breaking energy**
Breaker Type and Phase Shifts on Natural Beaches, Peter J. Cowell, 997
- Philippines; Tsunamis; Coastal engineering; Coastal engineering; Engineering evaluation; Nuclear power plants; Oceanography**
Tsunamis Along West Coast of Luzon, Philippines, R. L. Wiegell, 652
- Physical tests; Storm surges; Tides; Coastal engineering; Estuaries; Models**
Artificial Roughness in Physical Models of Estuaries for Storm Surge Investigations, D. Berndt, E. Giese, H. Schwarze and H.-J. Vollmers, 2493
- Piers (docks); Ports; Tanker ships; Berths; Caissons; China; Concrete construction; Design; Mooring; Petroleum transportation**
The Design and Construction of the New Oil Port in Dalian, CPR, Zhu-zhuang Xin and Yucheng Li, 2081
- Piers (docks); Site investigation; Site selection; Coastal engineering; Design criteria; Docks; Islands**
Siting and Design Criteria of Dock Structures in the Marshall Islands, R. M. Noble, K. C. Leslie and D. O'Day, 2106
- Piles; Predictions; Wave action; Calculations; Cylindrical bodies**
Wave Forces on an Inclined Circular Cylindrical Pile, Toshiyuki Shigemura, 1762
- Pipe design; Pipelines; Submarine pipelines; Wave action; Ocean currents; Ocean engineering; Offshore structures**
Simultaneous Waves and Current Forces on a Pipeline, David A. Knoll and John B. Herbich, 1743
- Pipelines; Submarine pipelines; Wave action; Ocean currents; Ocean engineering; Offshore structures; Pipe design**
Simultaneous Waves and Current Forces on a Pipeline, David A. Knoll and John B. Herbich, 1743
- Planning; Ports; Water flow; Australia; Coastal engineering; Environmental impact statements; Estuaries**
Water Movement Studies Required for Port Planning, Graeme C. Dandy, Desmond A. Mills and John B. Hinwood, 3007
- Porous materials; Wave action; Wave propagation; Waves; Wind; Breakwaters; Coastal engineering; Marinas**
Wind Waves Transmission Through Porous Breakwater, Stanislaw R. Massel and Piotr Butowski, 333

- Ports; Australia; Breakwaters; Coastal engineering; Construction; Design; Model tests; Overtopping**
Design of an Overtopping Breakwater, P. D. Treloar and B. Nagle, 1910
- Ports; Breccia; Carbonaceous rocks; Coastal engineering; Construction; Disposal; Dredge spoil; Dredging; Environmental effects**
For Disposal: 10 M.c.u.m. of Calcium Carbonate Slurry, L. Summers and C. A. Fleming, 2871
- Ports; Real time operations; Wave action; Wave height; Analysis; Australia; Coastal engineering; Dredging; Ocean waves**
Realtime Wave Analysis, Newcastle, Australia, N. V. Lawson and P. H. Youll, 412
- Ports; Rubble-mound breakwaters; Breakwaters; Coastal structures; Concrete structures; Damage**
Dolosse Past, Present, Future?, J. A. Zwamborn, D. E. Bosman and J. Moes, 1949
- Ports; Sand; Beaches; Field investigations; Japan; Littoral drift; Littoral materials**
Littoral Drift on Sand Near Port of Oarai, Kazumasa Mizumura, 2157
- Ports; Sediment transport; Shoaling; Silting; Australia; Estuaries; Field investigations; Floods; Mathematical models**
Port of Brisbane Siltation Study, N. V.M. Odd and T. Baxter, 2375
- Ports; Tanker ships; Berths; Caissons; China; Concrete construction; Design; Mooring; Petroleum transportation; Piers (docks)**
The Design and Construction of the New Oil Port in Dalian, CPR, Zhu-zhuang Xin and Yucheng Li, 2081
- Ports; Water flow; Australia; Coastal engineering; Environmental impact statements; Estuaries; Planning**
Water Movement Studies Required for Port Planning, Graeme C. Dandy, Desmond A. Mills and John B. Hinwood, 3007
- Ports; Water flow; Water quality; Australia; Beaches; Computer applications; Construction; Docks; Dredging; Environmental surveys**
Integration and Computation in an Environmental Study, J. B. Hinwood, J. E. Watson and D. M. Burrage, 3024
- Portugal; Rubble-mound breakwaters; Breakwaters; Coastal engineering; Coastal structures; Concrete structures failure; Damages**
Report on the Damages to the Sines Breakwater, Portugal, William F. Baird, Joseph M. Caldwell, Billy L. Edge and Orville T. Magoon, 3060
- Power plant location; Wave action; Wave energy; Beaches; Coastal engineering; Currents (water); Japan; Littoral current**
Nearshore Currents on a Partially Rocky Shore, T. O. Sasaki, H. Igarashi and S. Harikai, 1071
- Powerplants; Rivers; Thermal pollution; Wastewater (pollution); Water surface; Earth atmosphere; Experimentation; Heat balance**
Experimental Evaluation of Heat Exchange Between Water Surface and Atmosphere, Gunther Barg, Horst Schwarze and Gerhard Visscher, 2848
- Powerplants; Thermal pollution; Coastal engineering; Cooling water; Currents (water); Discharge (water); Experimentation; Jets**
Experimental Study of the Buoyant Surface Jet with the Presence of Bottom Boundary and Cross Current, B. Safaie, 2814
- Predictions; Sea states; Statistical data; Wave height; Coastal structures; Design; Offshore structures**
Prediction of the Severest Significant Wave Height, Michel K. Ochi and Joseph E. Whalen, 587
- Predictions; Sediment transport; Wave height; Wind speed; Australia; Continental shelf; Currents (water); Field tests; Models**
Sediment Dispersal on the NSW Continental Shelf, Ron Boyd, 1363
- Predictions; Sediment transport; Waves; California; Coastal engineering; Coastal Processes; Currents (water); Models**
Nearshore Sediment Transport Study Experiments, R. J. Seymour and C. G. Gable, 1401
- Predictions; Shoaling; Two-dimensional; Wave height; Calculations; Coastal engineering; Gravity waves**
Wave Shoaling Calculated From Cokelet's Theory, T. Sakai and J. A. Battjes, 121
- Predictions; Wave action; Calculations; Cylindrical bodies; Piles**
Wave Forces on an Inclined Circular Cylindrical Pile, Toshiyuki Shigemura, 1762
- Predictions; Wave energy; Wave generation; Wave height; Waves; Wind direction; Hurricanes**
Prediction of Dominant Wave Properties Ahead of Hurricanes, Omar H. Shemdin, 600
- Predictions; Wave equations; Waves; Beaches; Disturbances; Experimentation; Flumes**
Long Period Disturbances Due to Wave Groups, E. C. Bowers, 610
- Primary waves; Shoaling; Standing waves; Surf; Surface waves; Wave measurement; Wave velocity; Experimentation**
Two-Dimensional Surf Beat, Reinhard E. Flick, Douglas L. Inman and Robert T. Gaza, 624
- Prisms; Wave action; Australia; Beaches; Beach nourishment; Coastal engineering; Coasts; Morphology**
The Dynamic Swept Prism, David M. Chapman and A. W. Smith, 1036
- Probability; Shore protection; Storm surges; Coastal engineering; Design; Dikes; Dunes; Netherlands**
Probabistic Design of Sea Defences, W. T. Bakker and J. K. Vrijling, 2041
- Profiles; Surf; Waves; Beaches; Beach sands; Coastal Processes; Hydraulics; Laboratory tests; Permeability (soils)**
Beaches: Profiles, Processes and Pqrmability, Michael R. Gourlay, 1319
- Programs; Data collection; Design; Meteorological data; Oceanographic data; Offshore structures; Oil and gas fields**
Considerations in the Design of an Offshore Data Collection Program, Cortis Cooper and German Febres, 2904

- Projects; Sedimentology; Tides; West Germany; Coastal engineering; Coasts; Dredging; Field tests; Morphology**
The German "Moran" Project, Winfried Siefert and Volker Barthel, 2924
- Protective structures; Ship piers; Ships; Tidal currents; Bridges (piers); Buffers**
Ship-Bridge-Pier Protective Systems, Akira Iwai, Hitoshi Nagasawa, Kazuki Oda and Kuniaki Shoji, 2259
- Radar mapping; Wave measurement; Wave spectra; Wind; High frequency; Meteorological data; Oceanographic data; Ocean waves**
HF Radar Mapping of Extensive Ocean Windfields, P. E. Dexter and R. C. Casey, 363
- Real time operations; Wave action; Wave height; Analysis; Australia; Coastal engineering; Dredging; Ocean waves; Ports**
Realtime Wave Analysis, Newcastle, Australia, N. V. Lawson and P. H. Youll, 412
- Reclamation; Singapore; Coastal engineering; Coastal Processes; Coasts; Model studies**
Major Reclamation Scheme for Marina City, Singapore, S. Y. Chew and J. Wei, 2243
- Reefs; Sediment transport; Wave action; Waves; Currents (water); Lagoons (ponds); Morphology**
Physical Processes and Sediment Flux Through Reef-Lagoon Systems, Harry H. Roberts, 946
- Reefs; Wave attenuation; Coastal engineering; Coastal structures; Design; Hawaii; Mathematical models**
Wave Attenuation and Wave Set-Up on a Coastal Reef, Franciscus Gerritsen, 444
- Refractometers; Temperature rise; Water pollution control; Cooling water; Discharge (water); Heated water; Industrial plants; Liquefied natural gas**
Dispersion of Cooling Water from a Coastal LNG Plant, P. Ackers, J. D. Pitt, G. Thompson and K. G. Rippin, 2794
- Reinforced concretes; Rubble-mound breakwaters; Concrete structures; Destructive tests; Dynamic loads; Hydraulic tests; Model tests**
Full Scale Trails of Dolosse to Destruction, Hans F. Burcharth, 1929
- Remote sensing; Saline water-freshwater interfaces; Sea water intrusion; Straits; Tidal currents; Vortices; Hydraulic models; Japan; Landsat**
Study on Vortex Current in Strait with Remote-Sensing, Sotoaki Onishi and Tsukasa Nishimura, 2653
- Remote sensing; Sandbars; Satellite Mapping; Bathymetry; Coasts; Inlets (waterways); Landsat; Littoral drift**
Satellite Applications on a Coastal Inlet Stability Study, Yu-Hwa Wang, 2579
- Research; Sediment transport; Shore protection; China; Coastal engineering; Estuaries; Harbors**
Some Aspects of Coastal Engineering Research Works in China, Yen Kai, 1734
- Research projects; Tidal waters; U.S. Corps of Engineers; Beach erosion; Coastal engineering; Field investigations; Flood control; Inlets (waterways)**
The Corps of Engineer's General Investigation of Tidal Inlets, Robert M. Sorensen, 2563
- Resonance; Sea level changes; Subsonic flow; Waves; Australia; Coastal engineering**
Resonances of Coastal Waters Between Perth and Geraldton, H. Allison, A. Grassia and R. Litchfield, 290
- Revegetation; Sand control; Shore protection; Australia; Beach erosion; Dunes; Dune sands**
Research in Southern Queensland into the Management of Coastal Sand Dunes, James B. McKenzie and David A. Barr, 1547
- Rivers; Rubble mounds; Sediment transport; Australia; Jetties; Models; Morphology**
Mechanisms Operating at a Jettied River Entrance, Bruce M. Drury and Alexander F. Nielsen, 2605
- Rivers; Saline water-freshwater interfaces; Water flow; Coastal engineering; Froude number; Mixing; Outflows**
On a Role of the Interfacial Froude Number, Masakazu Kashiwamura, 2778
- Rivers; Sand; Sediment transport; Currents (water); Eddy currents; Egypt; Erosion; Nile River Valley**
Eddy Currents and Sediment Transport Off the Damietta Nile, S. P. Murray, J. M. Coleman, H. H. Roberts and M. Salama, 1679
- Rivers; Sand; Sediment transport; Tidal hydraulics; Australia; Beach nourishment; Bed forms; Dredging; Estuaries**
Estuarine Response to Dredging in the Tweed River, Australia, Bruce M. Drury, 1598
- Rivers; Sediment deposits; Stability; Deltaic deposits; Deltas; Estuaries; Netherlands**
Stability of Estuary Mouths in the Rhine-Meuse Delta, J. van de Kreeke and Jac Haring, 2625
- Rivers; Sediment transport; Alluvial deposits; Australia; Beach erosion; Beach sands; Deltas; Flood protection**
Barron River Delta Investigation, D. A. Robinson, D. J. Cook and J. G. Barff, 885
- Rivers; Sediment transport; Storms; Suspended load; Suspended sediments; Connecticut; Dredging; Estuaries**
A Comparison Between Dredge Induced Sediment Resuspension and that Produced by Natural Storm Events, W. Frank Bohlen, 1699
- Rivers; Thermal pollution; Wastewater (pollution); Water surface; Earth atmosphere; Experimentation; Heat balance; Powerplants**
Experimental Evaluation of Heat Exchange Between Water Surface and Atmosphere, Gunther Barg, Horst Schwarze and Gerhard Visscher, 2848
- Rivers; Tidal waters; Tides; Waves; West Germany; Calibration; Coastal engineering; Estuaries; Mathematical models; Models**
Automatic Calibration of Numerical Tidal Models, K.-P. Holz and U. Januszewski, 2448
- Rubble-mound breakwaters; Breakwaters; Coastal engineering; Coastal structures; Concrete structures failure; Damages; Portugal**
Report on the Damages to the Sines Breakwater, Portugal, William F. Baird, Joseph M. Caldwell, Billy L. Edge and Orville T. Magoon, 3060

- Rubble-mound breakwaters; Breakwaters; Coastal engineering; Concrete construction; Design; Model tests**
Can We Develop New Breakwater Formulas, John Dorrington Mettam, 2302
- Rubble-mound breakwaters; Breakwaters; Coastal structures; Concrete structures; Damage; Ports**
Dolosse Past, Present, Future?, J. A. Zwamborn, D. E. Bosman and J. Moes, 1949
- Rubble-mound breakwaters; Concrete structures; Destructive tests; Dynamic loads; Hydraulic tests; Model tests; Reinforced concretes**
Full Scale Trails of Dolosse to Destruction, Hans F. Burcharth, 1929
- Rubble-mound breakwaters; Sand; Shore protection; Bitumens; Breakwaters; Coastal engineering**
Breakwater with a Sand Bitumen Core, E. Loewy, K. G. Witthaus, R. J. Maddrell and J. P. Wood, 2192
- Rubble-mound breakwaters; Sea walls; Water waves; Wave reflection; Wave spectra; Coastal engineering; Coastal structures**
Method of Analysis of Random Wave Experiments with Reflecting Coastal Structures, Pierre Gaillard, Michael Gauthier and Forrest Holly, 204
- Rubble-mound breakwaters; Stability; Tests; Wave action; Wave height; Wave period; Damage**
Stability of Rubble Mound Breakwater, J. Feuillet and M. Sabaton, 1989
- Rubble mounds; Sediment transport; Australia; Jetties; Models; Morphology; Rivers**
Mechanisms Operating at a Jettied River Entrance, Bruce M. Druery and Alexander F. Nielsen, 2605
- Saline water-freshwater interfaces; Saline water intrusion; Estuaries; Mixing; Models**
Discrete-Time Modelling of Dispersion in Estuaries, T. Wood, 3075
- Saline water-freshwater interfaces; Sea water intrusion; Stralts; Tidal currents; Vortices; Hydraulic models; Japan; Landsat; Remote sensing**
Study on Vortex Current in Strait with Remote-Sensing, Sotoaki Onishi and Tsukasa Nishimura, 2653
- Saline water-freshwater interfaces; Water flow; Coastal engineering; Froude number; Mixing; Outflows; Rivers**
On a Role of the Interfacial Froude Number, Masakazu Kashiwamura, 2778
- Saline water intrusion; Estuaries; Mixing; Models; Saline water-freshwater interfaces**
Discrete-Time Modelling of Dispersion in Estuaries, T. Wood, 3075
- Saline water intrusion; Sediment transport; Silts; Suspended sediments; Dynamics; Estuaries; France; Laboratory tests**
Dynamics of Silt in Estuary, Residual Current or Flocculation Which Prevails?, J. P. Lepetit and M. Davesne, 2858
- Salinity; Coastal engineering; Environmental effects; Estuaries; Estuarine environment; Models**
Separation of Climatic Fluctuations and Impacts of Engineering Activities in Estuaries, G. Krause, 2323
- Salinity; Estuaries; Estuarine environment; Hydraulic models; Identification; Mathematical models; Parameters**
Parameter Identification in Estuarine Modeling, Wen-Sen Chu and William W.-G. Yeh, 2431
- Sand; Beaches; Field investigations; Japan; Littoral drift; Littoral materials; Ports**
Littoral Drift on Sand Near Port of Oarai, Kazumasa Mizumura, 2157
- Sand; Sand control; Sediment transport; West Germany; Wind action geology; Wind speed; Coasts; Field investigations**
Sand Transport Under the Action of Wind, Ulrich Zanke, 1575
- Sand; Sand waves; Calculations; Coastal Processes; Fluid mechanics**
Contribution to the Discussion During Session C, Coastal Processes, Friday, March 28, 2:00 P.M., M. S. Longuet-Higgins, 3107
- Sand; Sandy soils; Storms; Tidal effects; Tidal hydraulics; Wave action; Coasts; Floods; Inlets (waterways)**
Comments on Tidal Entrances on Sandy Coasts, Morrough P. O'Brien, 2502
- Sand; Sediment control; Sediment transport; California; Experimentation; Harbors; Littoral drift**
A Sediment Trapping Experiment at Santa Cruz, CA, R. J. Seymour, G. W. Dumurat and D. M. Pirie, 1415
- Sand; Sediment transport; Currents (water); Eddy currents; Egypt; Erosion; Nile River Valley; Rivers**
Eddy Currents and Sediment Transport Off the Damietta Nile, S. P. Murray, J. M. Coleman, H. H. Roberts and M. Salama, 1679
- Sand; Sediment transport; Shallow water; Wave action; Beach erosion; Laboratory tests; Models**
A Laboratory Study of Offshore Transport of Sediment and a Model for Eroding Beaches, Tsuguo Sunamura, 1051
- Sand; Sediment transport; Surf; Suspended load; Wave measurement; Wind; Currents (water); Field investigations; Motion**
Field Measurements of Sand Motion in the Surf Zone, Douglas L. Inman, James A. Zampol, Thomas E. White, Daniel M. Hanes, B. Walton Waldorf and Kim A. Kastens, 1214
- Sand; Sediment transport; Surf; Waves; Beaches; Littoral deposits; Littoral drift; Models**
Onshore-Offshore Transport and Beach Profile Change, Masataro Hattori and Ryoichi Kawamata, 1178
- Sand; Sediment transport; Tidal hydraulics; Australia; Beach nourishment; Bed forms; Dredging; Estuaries; Rivers**
Estuarine Response to Dredging in the Tweed River, Australia, Bruce M. Druery, 1598
- Sand; Sediment transport; Wave action; Waves; Bottom sediments; Coastal engineering; Flumes**
Sand Transport by Waves, Jan van de Graaff and Wiel M.K. Tilmans, 1140
- Sand; Sediment transport; Wave energy; Beaches; Hydraulics; Littoral drift**
Secondary Sand Transport Mechanisms, A. W. Smith and A. D. Gordon, 1122

- Sand; Sediment transport; Wave energy; Wave height; Waves; Beach erosion; Beaches; Beach nourishment; Morphology**
Beach Response to Variations in Breaker Height, A. D. Short, 1016
- Sand; Seepage; Water waves; Wave action; Calculations; Cylinders; Ocean bottom; Offshore structures**
Wave-Induced Seepage Effects on a Vertical Cylinder, Thomas J.P. Durand and Peter L. Monkmeier, 1782
- Sand; Shore protection; Bitumens; Breakwaters; Coastal engineering; Rubble-mound breakwaters**
Breakwater with a Sand Bitumen Core, E. Loewy, K. G. Witthaus, R. J. Maddrell and J. P. Wood, 2192
- Sand; Topography; Australia; Beaches; Beach nourishment; Coastal engineering; Management methods**
Beach Nourishment as a Management Technique, David M. Chapman, 1635
- Sand; Water tunnels (testing); Wave action; Bed forms; Motion studies; Oscillation**
Sand Bed-Form Lengths Under Oscillatory Motion, Arthur Brebner, 1339
- Sandbars; Satellite Mapping; Bathymetry; Coasts; Inlets (waterways); Landsat; Littoral drift; Remote sensing**
Satellite Applications on a Coastal Inlet Stability Study, Yu-Hwa Wang, 2579
- Sandbars; Shores; Topography; Wave action; Beaches; Coastal Processes; Littoral drift**
Migration of Longshore Bars, Hans H. Dette, 1475
- Sand control; Sediment transport; Shore protection; Wind action geology; Australia; Dunes**
Wind and Sediment Movement in Coastal Dune Areas, John R. Hails and John Bennett, 1564
- Sand control; Sediment transport; West Germany; Wind action geology; Wind speed; Coasts; Field investigations; Sand**
Sand Transport Under the Action of Wind, Ulrich Zanke, 1575
- Sand control; Shore protection; Australia; Beach erosion; Dunes; Dune sands; Revegetation**
Research in Southern Queensland into the Management of Coastal Sand Dunes, James B. McKenzie and David A. Barr, 1547
- Sand pumps; Australia; Beach erosion; Beaches; Beach nourishment; Coastal engineering; Dunes**
Noosa Beach Restoration Scheme, R. J. Lloyd, 1618
- Sands; Sand waves; Water tunnels; Water waves; Bed forms; Drag; Experimentation; Measurement**
Measurements of Oscillatory Drag on Sand Ripples, Karl E. B. Lofquist, 3104
- Sand traps; Sediment transport; Wave measurement; Breakwaters; California; Coastal engineering; Field tests; Harbors**
Longshore Transport Evaluations at a Detached Breakwater, R. O. Bruno, R. G. Dean and C. G. Gable, 1452
- Sand waves; Calculations; Coastal Processes; Fluid mechanics; Sand**
Contribution to the Discussion During Session C, Coastal Processes, Friday, March 28, 2:00 P.M., M. S. Longuet-Higgins, 3107
- Sand waves; Water tunnels; Water waves; Bed forms; Drag; Experimentation; Measurement; Sands**
Measurements of Oscillatory Drag on Sand Ripples, Karl E. B. Lofquist, 3104
- Sandy soils; Storms; Tidal effects; Tidal hydraulics; Wave action; Coasts; Floods; Inlets (waterways); Sand**
Comments on Tidal Entrances on Sandy Coasts, Morrough P. O'Brien, 2502
- San Francisco; Sediment deposits; Shallow water; Wastewater (pollution); Water pollution; Wave energy; Antifouling materials; California; Coasts; Design; Outfall sewers**
Design of an Intermittently Operated Outfall, Roger W. Lindquist and George J. Murphy, 2834
- Satellite Mapping; Bathymetry; Coasts; Inlets (waterways); Landsat; Littoral drift; Remote sensing; Sandbars**
Satellite Applications on a Coastal Inlet Stability Study, Yu-Hwa Wang, 2579
- Scotland; Shore protection; Submarine pipelines; Coastal engineering; Environmental impact statements; Gas pipelines; Petroleum pipelines**
Environmental Aspects of Oil and Gas Pipeline Landfalls in Northeast Scotland, William Ritchie, 2935
- Sea ice; Sediment transport; Tundra; Wave energy; Alaska; Cliffs; Coastal Processes; Erosion**
Sediment Transport Processes and Coastal Variability on the Alaskan North Slope, E. H. Owens, J. R. Harper and D. Nummedal, 1343
- Sea level changes; Subsonic flow; Waves; Australia; Coastal engineering; Resonance**
Resonances of Coastal Waters Between Perth and Geraldton, H. Allison, A. Grassia and R. Litchfield, 290
- Sea states; Statistical data; Wave height; Coastal structures; Design; Offshore structures; Predictions**
Prediction of the Severest Significant Wave Height, Michel K. Ochi and Joseph E. Whalen, 587
- Sea states; Synthesis; Time series analysis; Water waves; Wave generation; Waves; Fixed structures; Flumes; Model tests**
On the Synthesis of Realistic Sea States, E. R. Funke and E. P.D. Mansard, 2971
- Sea walls; Water waves; Wave reflection; Wave spectra; Coastal engineering; Coastal structures; Rubble-mound breakwaters**
Method of Analysis of Random Wave Experiments with Reflecting Coastal Structures, Pierre Gaillard, Michael Gauthier and Forrest Holly, 204
- Sea walls; Waves; Caissons; Concrete construction; Deep water; Design; Japan; Overtopping**
Seawalls in Deep Seas, Shoshichiro Nagai and Shohachi Kakuno, 2024

- Sea water intrusion; Straits; Tidal currents; Vortices; Hydraulic models; Japan; Landsat; Remote sensing; Saline water-freshwater interfaces**
Study on Vortex Current in Strait with Remote-Sensing, Sotoaki Onishi and Tsukasa Nishimura, 2653
- Sedimentation; Sedimentation tanks; Suspended sediments; Tidal effects; Coastal engineering; Cost estimates; Flooding; Harbors; Mathematical models**
Design of Enclosed Harbors to Reduce Sedimentation, Craig H. Everts, 1511
- Sedimentation; Sediment control; Tidal waters; Estuaries; Field investigations; Lagoon deposits**
Opening and Maintaining Tidal Lagoons & Estuaries, Scott A. Jenkins, Douglas L. Inman and James A. Bailard, 1527
- Sedimentation; Sediment transport; Channels (waterways); Dredging; Field work; Harbors; Nigeria**
Sedimentation in Dredged Navigation Channels, Lars Mikkelsen, Preben Mortensen and Torben Sorensen, 1718
- Sedimentation; Sediment transport; Suspended load; Trenches; Wave action; Channels (waterways); Coastal engineering**
Sedimentation in Channels and Trenches, E. W. Bijker, 1707
- Sedimentation; Shore protection; Wave energy; Beach erosion; Coastal Processes; Louisiana**
Fluid Mud Dynamics and Shoreline Stabilization: Louisiana Chenier Plain, John T. Wells and Harry H. Roberts, 1381
- Sedimentation; Tidal currents; West Germany; Barriers; Basins; Channels (waterways); Dams; Estuaries; Inlets (waterways)**
Sedimentation Processes in Tidal Channels and Tidal Basins Caused by Artificial Constructions, E. Renger and H. W. Partenscky, 2479
- Sedimentation tanks; Suspended sediments; Tidal effects; Coastal engineering; Cost estimates; Flooding; Harbors; Mathematical models; Sedimentation**
Design of Enclosed Harbors to Reduce Sedimentation, Craig H. Everts, 1511
- Sediment concentration; Water waves; Wave action; Clay suspensions; Experimentation**
An Experiment on Clay Suspension Under Water Waves, Prida Thimakorn, 2891
- Sediment control; Sediment transport; California; Experimentation; Harbors; Littoral drift; Sand**
A Sediment Trapping Experiment at Santa Cruz, CA, R. J. Seymour, G. W. Domurat and D. M. Pirie, 1415
- Sediment control; Tidal waters; Estuaries; Field investigations; Lagoon deposits; Sedimentation**
Opening and Maintaining Tidal Lagoons & Estuaries, Scott A. Jenkins, Douglas L. Inman and James A. Bailard, 1527
- Sediment deposits; Shallow water; Wastewater (pollution); Water pollution; Wave energy; Antifouling materials; California; Coasts; Design; Outfall sewers; San Francisco**
Design of an Intermittently Operated Outfall, Roger W. Lindquist and George J. Murphy, 2834
- Sediment deposits; Stability; Deltaic deposits; Deltas; Estuaries; Netherlands; Rivers**
Stability of Estuary Mouths in the Rhine-Meuse Delta, J. van de Kreeke and Jac Haring, 2625
- Sediment distribution; Sediment transport; Topographic features; Wave height; Wave period; Beds under water; Estimates**
Longshore Water and Sediment Movement, D. H. Swart and C. A. Fleming, 1274
- Sedimentology; Tides; West Germany; Coastal engineering; Coasts; Dredging; Field tests; Morphology; Projects**
The German "Moran" Project, Winfried Siefert and Volker Barthel, 2924
- Sedimentology; Wave diffraction; Wave refraction; Computer applications; Design; France; Harbors; Hydraulic tests; Models**
Harbour Design Including Sedimentological Problems Using Mainly Numerical Technics, B. Latteux, 2211
- Sediments; Australia; Budgeting; Coastal engineering; Coastal Processes; Model tests**
An Approach to Understanding Coastal Processes, A. D. Gordon and D. B. Lord, 1234
- Sediment transport; Alluvial deposits; Australia; Beach erosion; Beach sands; Deltas; Flood protection; Rivers**
Barron River Delta Investigation, D. A. Robinson, D. J. Cook and J. G. Barff, 885
- Sediment transport; Australia; Jetties; Models; Morphology; Rivers; Rubble mounds**
Mechanisms Operating at a Jettied River Entrance, Bruce M. Druery and Alexander F. Nielsen, 2605
- Sediment transport; Bed forms; Dunes; Dynamic geology; Erosion; Models; Numerical calculations**
A Numerical Model for Dune Dynamics, J. Sundermann, H.-J. Vollmers and W. Puls, 1583
- Sediment transport; California; Experimentation; Harbors; Littoral drift; Sand; Sediment control**
A Sediment Trapping Experiment at Santa Cruz, CA, R. J. Seymour, G. W. Domurat and D. M. Pirie, 1415
- Sediment transport; Channels (waterways); Dredging; Field work; Harbors; Nigeria; Sedimentation**
Sedimentation in Dredged Navigation Channels, Lars Mikkelsen, Preben Mortensen and Torben Sorensen, 1718
- Sediment transport; Currents (water); Eddy currents; Egypt; Erosion; Nile River Valley; Rivers; Sand**
Eddy Currents and Sediment Transport Off the Damietta Nile, S. P. Murray, J. M. Coleman, H. H. Roberts and M. Salama, 1679
- Sediment transport; Shallow water; Wave action; Beach erosion; Laboratory tests; Models; Sand**
A Laboratory Study of Offshore Transport of Sediment and a Model for Eroding Beaches, Tsuguo Sunamura, 1051
- Sediment transport; Shear stress; Wave action; Beaches; Coastal engineering; Littoral deposits; Littoral drift**
Beach Profiles and On-Offshore Sediment Transport, Akira Watanabe, Yoshihiko Riho and Kiyoshi Horikawa, 1106

- Sediment transport; Shoaling; Shores; Topography; Waves; Bathymetry; Currents (water); Models**
Inshore-Nearshore Morphodynamics - A Predictive Model, John Chappell, 963
- Sediment transport; Shoaling; Silting; Australia; Estuaries; Field investigations; Floods; Mathematical models; Ports**
Port of Brisbane Siltation Study, N. V.M. Odd and T. Baxter, 2375
- Sediment transport; Shore protection; China; Coastal engineering; Estuaries; Harbors; Research**
Some Aspects of Coastal Engineering Research Works in China, Yen Kai, 1734
- Sediment transport; Shore protection; Wind action geology; Australia; Dunes; Sand control**
Wind and Sediment Movement in Coastal Dune Areas, John R. Halls and John Bennett, 1564
- Sediment transport; Silts; Suspended sediments; Dynamics; Estuaries; France; Laboratory tests; Saline water intrusion**
Dynamics of Silt in Estuary, Residual Current or Flocculation Which Prevails?, J. P. Lepetit and M. Davesne, 2858
- Sediment transport; Stability analysis; Wave energy; Waves; Beaches; Deep water**
Criterion for Stability of Shoreline Platform, John D. Wang and Bernard Le Mehaute, 1994
- Sediment transport; Storms; Suspended load; Suspended sediments; Connecticut; Dredging; Estuaries; Rivers**
A Comparison Between Dredge Induced Sediment Resuspension and that Produced by Natural Storm Events, W. Frank Bohlen, 1699
- Sediment transport; Storms; Suspended sediments; Wave energy; Field work; Littoral deposits; Littoral drift**
Nearshore Suspended Sediment Load During Storm and Post-Storm Conditions, Timothy W. Kana and Larry G. Ward, 1158
- Sediment transport; Surf; Beaches; Deformation; Littoral deposits; Littoral drift; Models**
On-Offshore Sediment Transport Rate in the Surf Zone, Toru Sawaragi and Ichiro Deguchi, 1194
- Sediment transport; Surf; Suspended load; Wave measurement; Wind; Currents (water); Field investigations; Motion; Sand**
Field Measurements of Sand Motion in the Surf Zone, Douglas L. Inman, James A. Zampol, Thomas E. White, Daniel M. Hanes, B. Walton Waldorf and Kim A. Kastens, 1214
- Sediment transport; Surf; Waves; Beaches; Littoral deposits; Littoral drift; Models; Sand**
Onshore-Offshore Transport and Beach Profile Change, Masataro Hattori and Ryoichi Kawamata, 1178
- Sediment transport; Suspended load; Trenches; Wave action; Channels (waterways); Coastal engineering; Sedimentation**
Sedimentation in Channels and Trenches, E. W. Bijker, 1707
- Sediment transport; Tidal hydraulics; Australia; Beach nourishment; Bed forms; Dredging; Estuaries; Rivers; Sand**
Estuarine Response to Dredging in the Tweed River, Australia, Bruce M. Drury, 1598
- Sediment transport; Topographic features; Wave action; Wave period; Beach erosion; Beaches; California**
Beach Cusps at Point Reyes and Drakes Bay Beaches, California, R. G. Dean and E. M. Maurmeyer, 863
- Sediment transport; Topographic features; Wave height; Wave period; Beds under water; Estimates; Sediment distribution**
Longshore Water and Sediment Movement, D. H. Swart and C. A. Fleming, 1274
- Sediment transport; Tundra; Wave energy; Alaska; Cliffs; Coastal Processes; Erosion; Sea ice**
Sediment Transport Processes and Coastal Variability on the Alaskan North Slope, E. H. Owens, J. R. Harper and D. Nummedal, 1343
- Sediment transport; Wave action; Wave energy; Australia; Coastal engineering; Coastal Processes; Coasts; Geologic control; Marine geology**
Geological Controls on Process-Response, SE Australia, P. S. Roy and A. W. Stephens, 913
- Sediment transport; Wave action; Waves; Bottom sediments; Coastal engineering; Flumes; Sand**
Sand Transport by Waves, Jan van de Graaff and Wiel M.K. Tilmans, 1140
- Sediment transport; Wave action; Waves; Currents (water); Lagoons (ponds); Morphology; Reefs**
Physical Processes and Sediment Flux Through Reef-Lagoon Systems, Harry H. Roberts, 946
- Sediment transport; Wave action; Waves; Wave velocity; Coastal engineering; Hydraulic test tunnels**
A Closely Responding, Versatile Wave Tunnel, C. H. Hulsbergen and J. J. Bosman, 310
- Sediment transport; Wave energy; Beaches; Hydraulics; Littoral drift; Sand**
Secondary Sand Transport Mechanisms, A. W. Smith and A. D. Gordon, 1122
- Sediment transport; Wave energy; Wave height; Waves; Beach erosion; Beaches; Beach nourishment; Morphology; Sand**
Beach Response to Variations in Breaker Height, A. D. Short, 1016
- Sediment transport; Wave height; Wind speed; Australia; Continental shelf; Currents (water); Field tests; Models; Predictions**
Sediment Dispersal on the NSW Continental Shelf, Ron Boyd, 1363
- Sediment transport; Wave measurement; Breakwaters; California; Coastal engineering; Field tests; Harbors; Sand traps**
Longshore Transport Evaluations at a Detached Breakwater, R. O. Bruno, R. G. Dean and C. G. Gable, 1452
- Sediment transport; Waves; California; Coastal engineering; Coastal Processes; Currents (water); Models; Predictions**
Nearshore Sediment Transport Study Experiments, R. J. Seymour and C. G. Gable, 1401
- Sediment transport; West Germany; Wind action geology; Wind speed; Coasts; Field investigations; Sand; Sand control**
Sand Transport Under the Action of Wind, Ulrich Zanke, 1575

- Seepage; Water waves; Wave action; Calculations; Cylinders; Ocean bottom; Offshore structures; Sand**
Wave-Induced Seepage Effects on a Vertical Cylinder, Thomas J.P. Durand and Peter L. Monkmeier, 1782
- Seiches; Water waves; Analogies; Electromagnetic radiation; Gravity waves; Microwaves**
An Electromagnetic Analogy For Long Water Waves, G. W. Jackson and D. L. Wilkinson, 801
- Shallow water; Ships; Water flow; Wave action; Wave energy; Wave generation; Damping; Motion studies**
Some Recent Results for Wave Induced Motions of a Ship in Shallow Water, P. A. Madsen, I. A. Svendsen and C. Michaelsen, 3040
- Shallow water; Storms; Storm water; Waves; Harbors; Models; Numerical calculations**
A Numerical Model of Storm Waves in Shallow Water, A. Hauguel, 746
- Shallow water; Tsunamis; Wave equations; Coastal engineering; Finite difference method; Islands**
Transient Finite-Difference Tsunami Calculations, Ove Skovgaard and Ivar G. Jonsson, 823
- Shallow water; Velocity; Water waves; Wave propagation; Waves; Wave tanks; Coastal engineering; Mass transfer**
Mass Transport in Progressive Waves of Permanent Type, Yoshio Tsuchiya, Takashi Yasuda and Takao Yamashita, 70
- Shallow water; Wastewater (pollution); Water pollution; Wave energy; Antifouling materials; California; Coasts; Design; Outfall sewers; San Francisco; Sediment deposits**
Design of an Intermittently Operated Outfall, Roger W. Lindquist and George J. Murphy, 2834
- Shallow water; Wave action; Beach erosion; Laboratory tests; Models; Sand; Sediment transport**
A Laboratory Study of Offshore Transport of Sediment and a Model for Eroding Beaches, Tsuguo Sunamura, 1051
- Shallow water; Wave generation; Waves; Wave velocity; Laboratory tests**
The Generation of Long Waves in the Laboratory, Derek Goring and Fredric Raichlen, 763
- Shear stress; Wave action; Beaches; Coastal engineering; Littoral deposits; Littoral drift; Sediment transport**
Beach Profiles and On-Offshore Sediment Transport, Akira Watanabe, Yoshihiko Riho and Kiyoshi Horikawa, 1106
- Ship piers; Ships; Tidal currents; Bridges (piers); Buffers; Protective structures**
Ship-Bridge-Pier Protective Systems, Akira Iwai, Hitoshi Nagasawa, Kazuki Oda and Kuniaki Shoji, 2259
- Ships; Tidal currents; Bridges (piers); Buffers; Protective structures; Ship piers**
Ship-Bridge-Pier Protective Systems, Akira Iwai, Hitoshi Nagasawa, Kazuki Oda and Kuniaki Shoji, 2259
- Ships; Water flow; Wave action; Wave energy; Wave generation; Damping; Motion studies; Shallow water**
Some Recent Results for Wave Induced Motions of a Ship in Shallow Water, P. A. Madsen, I. A. Svendsen and C. Michaelsen, 3040
- Ships; Wind forces; Bulk cargo; Currents (water); Jetties; Mathematical models; Mooring**
Mooring Forces Induced by Passing Ships - Measurements in Prototype, K. Hafke, 2689
- Shoaling; California; Channel improvements; Coastal Processes; Dredging; Harbors**
A Phased-Dredging Program for Santa Cruz Harbor, James R. Walker and Peter J. Williams, 1492
- Shoaling; Shores; Topography; Waves; Bathymetry; Currents (water); Models; Sediment transport**
Inshore-Nearshore Morphodynamics - A Predictive Model, John Chappell, 963
- Shoaling; Silting; Australia; Estuaries; Field investigations; Floods; Mathematical models; Piers; Sediment transport**
Port of Brisbane Siltation Study, N. V.M. Odd and T. Baxter, 2375
- Shoaling; Sliding waves; Surf; Surface waves; Wave measurement; Wave velocity; Experimentation; Primary waves**
Two-Dimensional Surf Beat, Reinhard E. Flick, Douglas L. Inman and Robert T. Gaza, 624
- Shoaling; Taiwan; Dredging; Fishing; Harbors; Jetties; Littoral drift**
New Jetties for Tung-Kang Fishing Harbor, Taiwan, Chi-Fu Su, 2228
- Shoaling; Transient waves; Wave height; Waves; Currents (water); Deep water; Field data**
Wave-Wave Interactions, Current-Wave Interactions and Resulting Extreme Waves and Breaking Waves, Soren Peter Kjeldsen and Dag Myrhaug, 2275
- Shoaling; Two-dimensional; Wave height; Calculations; Coastal engineering; Gravity waves; Predictions**
Wave Shoaling Calculated From Cokerlet's Theory, T. Sakai and J. A. Battjes, 121
- Shoaling; Water waves; Waveform generators; Wave generation; Wave period; Models**
Correct Reproduction of Group-Induced Long Waves, N.-E. Ottesen Hansen, Stig E. Sand, H. Lundgren, Torben Sorensen and H. Gravesen, 784
- Shoals; Tidal effects; Case reports; Inlets (waterways); Littoral deposits; Littoral materials; Migration; North Carolina**
Barden Inlet, NC a Case Study of Inlet Migration, Limberios Vallianos, 2638
- Shore-line cover; Synthetic textiles; Breakwaters; Dikes; Docks; Fabrics; Filters; Filter tests; Groins (structures)**
Long-Term Experience with the use of Synthetic Filter Fabrics in Coastal Engineering, Georg Heerten, 2172
- Shore protection; Australia; Beach erosion; Beaches; Beach nourishment; Coastal engineering; Dunes**
The Beach Improvement Programme: New South Wales, Neale A. Philip and Philip H. White, 1668

- Shore protection; Australia; Beach erosion; Beaches; Coastal engineering**
Capricorn Coast Beaches, D. C. Patterson and L. R. Ford, 1648
- Shore protection; Australia; Beach erosion; Dunes; Dune sands; Revegetation; Sand control**
Research in Southern Queensland into the Management of Coastal Sand Dunes, James B. McKenzie and David A. Barr, 1547
- Shore protection; Beaches; Breakwaters; Coastal engineering; Groins (structures); Japan**
Artificial Resort Beach Protected by Offshore Breakwaters and Groins, Shoji Sato and Norio Tanaka, 2004
- Shore protection; Bitumens; Breakwaters; Coastal engineering; Rubble-mound breakwaters; Sand**
Breakwater with a Sand Bitumen Core, E. Loewy, K. G. Witthaus, R. J. Maddrell and J. P. Wood, 2192
- Shore protection; China; Coastal engineering; Estuaries; Harbors; Research; Sediment transport**
Some Aspects of Coastal Engineering Research Works in China, Yen Kai, 1734
- Shore protection; South Carolina; Wave action; Beach erosion; Breakwaters; Coastal engineering; Dredging; Field investigations; Islands**
Soft Designs for Coastal Protection at Seabrook Island, S.C., Miles O. Hayes, Timothy W. Kana and John H. Barwis, 897
- Shore protection; Storms; Beach erosion; Breakwaters; Design practices; Lakes; Lake shores; Lake waves; Ohio**
A Detached Breakwater System for Beach Protection, James R. Walker, Denton Clark and Joan Pope, 1969
- Shore protection; Storms; Storm surges; Wind forces; Australia; Breakwaters; Coastal structures; Design; Harbors**
The Design Concept of Dual Breakwaters and its Application to Townsville, Australia, W. Brenner, D. N. Foster, C. A. Miller and B. C. Wallace, 1899
- Shore protection; Storm surges; Coastal engineering; Design; Dikes; Dunes; Netherlands; Probability**
Probabilistic Design of Sea Defences, W. T. Bakker and J. K. Vrijling, 2041
- Shore protection; Submarine pipelines; Coastal engineering; Environmental impact statements; Gas pipelines; Petroleum pipelines; Scotland**
Environmental Aspects of Oil and Gas Pipeline Landfalls in Northeast Scotland, William Ritchie, 2935
- Shore protection; Terminals; Breakwaters; Caissons; Concrete construction; Design; Islands**
The Effects of Construction Techniques & Bulk Terminal Operational Requirements on the Design Criteria for Island Breakwaters, A. G. F. Eddie, J. D. Lawson, H. R. Graze and B. K. Dean, 2061
- Shore protection; Union of Soviet Socialist Republics; Wave action; Coastal engineering; Coasts; Currents (water)**
Coast Protection Against the Action of Waves and Currents, Leren P. Mikhailov and Sergei M. Uspenskii, 2120
- Shore protection; Wave action; Bays (topographic features); Beach erosion; Beaches; Littoral drift**
Zeta Bays, Pocket Beaches and Headland Control, R. Silvester, Y. Tsuchiya and Y. Shibano, 1305
- Shore protection; Wave energy; Beach erosion; Coastal Processes; Louisiana; Sedimentation**
Fluid Mud Dynamics and Shoreline Stabilization: Louisiana Chenier Plain, John T. Wells and Harry H. Roberts, 1381
- Shore protection; Wind action geology; Australia; Dunes; Sand control; Sediment transport**
Wind and Sediment Movement in Coastal Dune Areas, John R. Hails and John Bennett, 1564
- Shores; Surf; Wave action; Waves; Coastal engineering; Dynamic characteristics**
Dynamic Characteristics in the Nearshore Area, Kiyoshi Horikawa and Masahiko Isobe, 480
- Shores; Topography; Wave action; Beaches; Coastal Processes; Littoral drift; Sandbars**
Migration of Longshore Bars, Hans H. Detté, 1475
- Shores; Topography; Waves; Bathymetry; Currents (water); Models; Sediment transport; Shoaling**
Inshore-Nearshore Morphodynamics - A Predictive Model, John Chappell, 963
- Silting; Australia; Estuaries; Field investigations; Floods; Mathematical models; Ports; Sediment transport; Shoaling**
Port of Brisbane Siltation Study, N. V.M. Odd and T. Baxter, 2375
- Silts; Suspended sediments; Dynamics; Estuaries; France; Laboratory tests; Saline water intrusion; Sediment transport**
Dynamics of Silt in Estuary, Residual Current or Flocculation Which Prevails?, J. P. Lepetit and M. Davesne, 2858
- Similarities; Surf; Wave energy; Waves; Beaches; Coastal engineering; Fluid mechanics**
A Similarity Model in the Surf Zone, Hsiang Wang and Wei-Chong Yang, 529
- Simulation; Wave generation; Wave pressure; Waves; Wave velocity; Hydraulic models**
Investigations on Irregular Waves in Hydraulic Models, Karl-Friedrich Daemrich, Wolf-Dietrich Eggert and Soren Kohlhase, 186
- Singapore; Coastal engineering; Coastal Processes; Coasts; Model studies; Reclamation**
Major Reclamation Scheme for Marina City, Singapore, S. Y. Chew and J. Wei, 2243
- Site investigation; Site selection; Coastal engineering; Design criteria; Docks; Islands; Piers (docks)**
Siting and Design Criteria of Dock Structures in the Marshall Islands, R. M. Noble, K. C. Leslie and D. O'Day, 2106
- Site selection; Coastal engineering; Design criteria; Docks; Islands; Piers (docks); Site investigation**
Siting and Design Criteria of Dock Structures in the Marshall Islands, R. M. Noble, K. C. Leslie and D. O'Day, 2106
- Slopes; Surf; Wave action; Wave energy; Beaches; Currents (water); Groundwater elevation**
Wave Forcing of Beach Groundwater, Evans Waddell, 1435

- Solitary waves; Walls; Wave energy; Wave reflection; Coastal engineering; Design criteria; Numerical calculations**
Accurate Numerical Solutions for Nonlinear Waves, J. D. Fenton and M. M. Rienecker, 50
- South Carolina; Wave action; Beach erosion; Breakwaters; Coastal engineering; Dredging; Field investigations; Islands; Shore protection**
Soft Designs for Coastal Protection at Seabrook Island, S.C., Miles O. Hayes, Timothy W. Kana and John H. Barwis, 897
- Spectral analysis; Tides; Wave measurement; Coastal engineering; Data analysis; Florida**
Florida Coastal Data Network, Gary Howell, 421
- Spilling; Surf; Water waves; Wave measurement; Wave pressure; Waves; Wave velocity; Coastal engineering**
Velocity and Pressure Field of Spilling Breakers, M. J.F. Stive, 547
- Stability; Deltaic deposits; Deltas; Estuaries; Netherlands; Rivers; Sediment deposits**
Stability of Estuary Mouths in the Rhine-Meuse Delta, J. van de Kreeke and Jac Haring, 2625
- Stability; Surf; Topography; Wave action; Australia; Beach erosion; Beaches; Field tests**
Beach Cut in Relation to Surf Zone Morphodynamics, L. D. Wright, 978
- Stability; Tests; Wave action; Wave height; Wave period; Damage; Rubble-mound breakwaters**
Stability of Rubble Mound Breakwater, J. Feuillet and M. Sabaton, 1989
- Stability analysis; Wave energy; Waves; Beaches; Deep water; Sediment transport**
Criterion for Stability of Shoreline Platform, John D. Wang and Bernard Le Mehaute, 1994
- Stability criteria; Tidal effects; Tidal waters; Australia; Coastal Processes; Estuaries; Floods; Inlets (waterways); Lakes; Littoral drift**
Tidal Inlet Behavioural Analysis, A. F. Nielsen and A. D. Gordon, 2459
- Standing waves; Surf; Surface waves; Wave measurement; Wave velocity; Experimentation; Primary waves; Shoaling**
Two-Dimensional Surf Beat, Reinhard E. Flick, Douglas L. Inman and Robert T. Gaza, 624
- Statistical data; Wave height; Coastal structures; Design; Offshore structures; Predictions; Sea states**
Prediction of the Severest Significant Wave Height, Michel K. Ochi and Joseph E. Whalen, 587
- Statistical data; Wave height; Wave period; Waves; Wave spectrum; Ocean waves**
Statistical Properties of Random Wave Groups, Akira Kimura, 2952
- Statistics; Storms; Wave generation; Wave height; Waves; Coastal structures; Model studies**
A Comparison of Nature Waves and Model Waves with Special Reference to Wave Grouping, Hans F. Burcharth, 2989
- Statistics; Wave measurement; Wave velocity; Wind; Kinematics; Ocean waves; Offshore platforms**
Field Measurements of Wind Wave Kinematics, J. A. Battjes and J. van Heteren, 347
- Stokes law; Water depth; Wave energy; Wave height; Wave period; Waves; Calculations; Coastal engineering; Design; Ocean waves**
Some Implications of Recent Advances in Wave Theories, J. R. Chaplin and K. Anastasiou, 31
- Storms; Beach erosion; Breakwaters; Design practices; Lakes; Lake shores; Lake waves; Ohio; Shore protection**
A Detached Breakwater System for Beach Protection, James R. Walker, Denton Clark and Joan Pope, 1969
- Storms; Foundations; Foundation stability analysis; Ocean bottom; Ocean engineering; Ocean waves**
Stability Analysis of Seafloor Foundations, Tokuo Yamamoto and Yasumasa Suzuki, 1800
- Storms; Storm surges; Tropical cyclones; Hurricanes; Hydrodynamics; Models; Numerical calculations**
Numerical Modelling of Tropical Cyclone Storm Surge, Rodney J. Sobey, Bruce A. Harper and George M. Mitchell, 725
- Storms; Storm surges; Wind forces; Australia; Breakwaters; Coastal structures; Design; Harbors; Shore protection**
The Design Concept of Dual Breakwaters and its Application to Townsville, Australia, W. Bremner, D. N. Foster, C. A. Miller and B. C. Wallace, 1899
- Storms; Storm water; Waves; Harbors; Models; Numerical calculations; Shallow water**
A Numerical Model of Storm Waves in Shallow Water, A. Hauguel, 746
- Storms; Suspended load; Suspended sediments; Connecticut; Dredging; Estuaries; Rivers; Sediment transport**
A Comparison Between Dredge Induced Sediment Resuspension and that Produced by Natural Storm Events, W. Frank Bohlen, 1699
- Storms; Suspended sediments; Wave energy; Field work; Littoral deposits; Littoral drift; Sediment transport**
Nearshore Suspended Sediment Load During Storm and Post-Storm Conditions, Timothy W. Kana and Larry G. Ward, 1158
- Storms; Tidal effects; Tidal hydraulics; Wave action; Coasts; Floods; Inlets (waterways); Sand; Sandy soils**
Comments on Tidal Entrances on Sandy Coasts, Morrrough P. O'Brien, 2502
- Storms; Wave generation; Wave height; Waves; Coastal structures; Model studies; Statistics**
A Comparison of Nature Waves and Model Waves with Special Reference to Wave Grouping, Hans F. Burcharth, 2989
- Storm surges; Barriers; Coastal engineering; Estuaries; Hydraulic tests; Netherlands**
Hydraulic Research in the Oosterschelde Estuary, A. W. Walther, 2358
- Storm surges; Coastal engineering; Design; Dikes; Dunes; Netherlands; Probability; Shore protection**
Probabilistic Design of Sea Defences, W. T. Bakker and J. K. Vrijling, 2041

- Storm surges; Tides; Coastal engineering; Estuaries; Models; Physical tests**
Artificial Roughness in Physical Models of Estuaries for Storm Surge Investigations, D. Berndt, E. Giese, H. Schwarze and H.-J. Vollmers, 2493
- Storm surges; Tropical cyclones; Hurricanes; Hydrodynamics; Models; Numerical calculations; Storms**
Numerical Modelling of Tropical Cyclone Storm Surge, Rodney J. Sobey, Bruce A. Harper and George M. Mitchell, 725
- Storm surges; Wind forces; Australia; Breakwaters; Coastal structures; Design; Harbors; Shore protection; Storms**
The Design Concept of Dual Breakwaters and its Application to Townsville, Australia, W. Bremner, D. N. Foster, C. A. Miller and B. C. Wallace, 1899
- Storm water; Coastal engineering; Coastal structures; Concrete construction; Model tests; Outfall sewers**
Construction and Model Investigation of Stormwater Outfall, K. A. Heathcote and G. W. Britton, 1850
- Storm water; Waves; Harbors; Models; Numerical calculations; Shallow water; Storms**
A Numerical Model of Storm Waves in Shallow Water, A. Hauguel, 746
- Straits; Tidal currents; Vortices; Hydraulic models; Japan; Landsat; Remote sensing; Saline water-freshwater interfaces; Sea water intrusion**
Study on Vortex Current in Strait with Remote-Sensing, Sotoaki Onishi and Tsukasa Nishimura, 2653
- Structural members; Tidal currents; Tubes; Wave action; Wave velocity; Cylindrical bodies; Kinematics; Ocean waves**
Full Scale Near Surface Water Particle Velocities and Pressure Acting on an Inclined Tubular Member, Fritz Busching and Eckehard Martini, 1870
- Submarine pipelines; Coastal engineering; Environmental impact statements; Gas pipelines; Petroleum pipelines; Scotland; Shore protection**
Environmental Aspects of Oil and Gas Pipeline Landfalls in Northeast Scotland, William Ritchie, 2935
- Submarine pipelines; Wave action; Gas pipelines; Hydrodynamics; Ocean bottom; Ocean engineering; Petroleum pipelines**
Waves Forces on Offshore Pipelines, N. Jothishankar and V. Sundar, 1820
- Submarine pipelines; Wave action; Ocean currents; Ocean engineering; Offshore structures; Pipe design; Pipelines**
Simultaneous Waves and Current Forces on a Pipeline, David A. Knoll and John B. Herbich, 1743
- Submarine trenches; Water waves; Wave period; Wave propagation; Wave reflection; Analysis**
Interactions of Waves With Submarine Trenches, Jiin-Jen Lee, Robert M. Ayer and Wen-Li Chiang, 812
- Subsonic flow; Waves; Australia; Coastal engineering; Resonance; Sea level changes**
Resonances of Coastal Waters Between Perth and Geraldton, H. Allison, A. Grassia and R. Litchfield, 290
- Surf; Beaches; Deformation; Littoral deposits; Littoral drift; Models; Sediment transport**
On-Offshore Sediment Transport Rate in the Surf Zone, Toru Sawaragi and Ichiro Deguchi, 1194
- Surf; Surface waves; Wave measurement; Wave velocity; Experimentation; Primary waves; Shoaling; Standing waves**
Two-Dimensional Surf Beat, Reinhard E. Flick, Douglas L. Inman and Robert T. Gaza, 624
- Surf; Suspended load; Wave measurement; Wind; Currents (water); Field investigations; Motion; Sand; Sediment transport**
Field Measurements of Sand Motion in the Surf Zone, Douglas L. Inman, James A. Zampol, Thomas E. White, Daniel M. Hanes, B. Walton Waldorf and Kim A. Kastens, 1214
- Surf; Topography; Wave action; Australia; Beach erosion; Beaches; Field tests; Stability**
Beach Cut in Relation to Surf Zone Morphodynamics, L. D. Wright, 978
- Surf; Topography; Wave energy; Wave height; Wave runup; Beaches; Currents (water); Littoral current**
Topographic Control of Run-Up Variability, Mark P. Bradshaw, 1091
- Surf; Water waves; Wave measurement; Wave pressure; Waves; Wave velocity; Coastal engineering; Spilling**
Velocity and Pressure Field of Spilling Breakers, M. J.F. Stive, 547
- Surf; Wave action; Wave energy; Beaches; Currents (water); Groundwater elevation; Slopes**
Wave Forcing of Beach Groundwater, Evans Waddell, 1435
- Surf; Wave action; Waves; Coastal engineering; Dynamic characteristics; Shores**
Dynamic Characteristics in the Nearshore Area, Kiyoshi Horikawa and Masahiko Isobe, 480
- Surf; Wave energy; Wave height; Waves; Beaches; Coastal engineering; Heuristic methods**
An Heuristic Model of Wave Height Distribution in Surf Zone, Masaru Mizuguchi, 278
- Surf; Wave energy; Waves; Beaches; Coastal engineering; Fluid mechanics; Similarities**
A Similarity Model in the Surf Zone, Hsiang Wang and Wei-Chong Yang, 529
- Surf; Waves; Beaches; Beach sands; Coastal Processes; Hydraulics; Laboratory tests; Permeability (soils); Profiles**
Beaches: Profiles, Processes and Permeability, Michael R. Gourlay, 1319
- Surf; Waves; Beaches; Littoral deposits; Littoral drift; Models; Sand; Sediment transport**
Onshore-Offshore Transport and Beach Profile Change, Masataro Hattori and Ryoichi Kawamata, 1178
- Surface waves; Wave measurement; Wave velocity; Experimentation; Primary waves; Shoaling; Standing waves; Surf**
Two-Dimensional Surf Beat, Reinhard E. Flick, Douglas L. Inman and Robert T. Gaza, 624

- Suspended load; Suspended sediments; Connecticut; Dredging; Estuaries; Rivers; Sediment transport; Storms**
A Comparison Between Dredge Induced Sediment Resuspension and that Produced by Natural Storm Events, W. Frank Bohlen, 1699
- Suspended load; Trenches; Wave action; Channels (waterways); Coastal engineering; Sedimentation; Sediment transport**
Sedimentation in Channels and Trenches, E. W. Bijker, 1707
- Suspended load; Wave measurement; Wind; Currents (water); Field investigations; Motion; Sand; Sediment transport; Surf**
Field Measurements of Sand Motion in the Surf Zone, Douglas L. Inman, James A. Zampol, Thomas E. White, Daniel M. Hanes, B. Walton Waldorf and Kim A. Kastens, 1214
- Suspended sediments; Connecticut; Dredging; Estuaries; Rivers; Sediment transport; Storms; Suspended load**
A Comparison Between Dredge Induced Sediment Resuspension and that Produced by Natural Storm Events, W. Frank Bohlen, 1699
- Suspended sediments; Dynamics; Estuaries; France; Laboratory tests; Saline water intrusion; Sediment transport; Silts**
Dynamics of Silt in Estuary, Residual Current or Flocculation Which Prevails?, J. P. Lepetit and M. Davesne, 2858
- Suspended sediments; Tidal effects; Coastal engineering; Cost estimates; Flooding; Harbors; Mathematical models; Sedimentation; Sedimentation tanks**
Design of Enclosed Harbors to Reduce Sedimentation, Craig H. Everts, 1511
- Suspended sediments; Wave energy; Field work; Littoral deposits; Littoral drift; Sediment transport; Storms**
Nearshore Suspended Sediment Load During Storm and Post-Storm Conditions, Timothy W. Kana and Larry G. Ward, 1158
- Synthesis; Time series analysis; Water waves; Wave generation; Waves; Fixed structures; Flumes; Model tests; Sea states**
On the Synthesis of Realistic Sea States, E. R. Funke and E. P.D. Mansard, 2971
- Synthetic textiles; Breakwaters; Dikes; Docks; Fabrics; Filters; Filter tests; Groins (structures); Shore-line cover**
Long-Term Experience with the use of Synthetic Filter Fabrics in Coastal Engineering, Georg Heerten, 2172
- Taiwan; Dredging; Fishing; Harbors; Jetties; Littoral drift; Shoaling**
New Jetties for Tung-Kang Fishing Harbor, Taiwan, Chi-Fu Su, 2228
- Taiwan; Wave energy; Wave measurement; Breaking energy; Coastal engineering; Coasts; Littoral drift**
Relationship Between Alongshore Wave Energy and Littoral Drift in the Mid West Coast at Taiwan, Ho-Shong Hou, Chung-Pan Lee and Lung-Hui Lin, 1254
- Tanker ships; Berths; Caissons; China; Concrete construction; Design; Mooring; Petroleum transportation; Piers (docks); Ports**
The Design and Construction of the New Oil Port in Dalian, CPR, Zhu-zhuang Xin and Yu-cheng Li, 2081
- Temperature rise; Water pollution control; Cooling water; Discharge (water); Heated water; Industrial plants; Liquefied natural gas; Refractometers**
Dispersion of Cooling Water from a Coastal LNG Plant, P. Ackers, J. D. Pitt, G. Thompson and K. G. Rippin, 2794
- Terminals; Breakwaters; Caissons; Concrete construction; Design; Islands; Shore protection**
The Effects of Construction Techniques & Bulk Terminal Operational Requirements on the Design Criteria for Island Breakwaters, A. G.F. Eddie, J. D. Lawson, H. R. Graze and B. K. Dean, 2061
- Tests; Wave action; Wave height; Wave period; Damage; Rubble-mound breakwaters; Stability**
Stability of Rubble Mound Breakwater, J. Feuillet and M. Sabaton, 1989
- Thermal energy; Thermal power plants; Discharge (water); Energy conversion; Environmental effects; Field investigations; Mathematical models; Ocean engineering; Ocean water**
Dynamic Similarity of Transport Phenomena, M. S. Yalin and F. Gerritsen, 2669
- Thermal pollution; Coastal engineering; Cooling water; Currents (water); Discharge (water); Experimentation; Jets; Powerplants**
Experimental Study of the Buoyant Surface Jet with the Presence of Bottom Boundary and Cross Current, B. Safaie, 2814
- Thermal pollution; Wastewater (pollution); Water surface; Earth atmosphere; Experimentation; Heat balance; Powerplants; Rivers**
Experimental Evaluation of Heat Exchange Between Water Surface and Atmosphere, Gunther Barg, Horst Schwarze and Gerhard Visscher, 2848
- Thermal power plants; Discharge (water); Energy conversion; Environmental effects; Field investigations; Mathematical models; Ocean engineering; Ocean water; Thermal energy**
Dynamic Similarity of Transport Phenomena, M. S. Yalin and F. Gerritsen, 2669
- Three-dimensional; Water pollution control; Water quality; Bays (topographic features); Coastal engineering; Currents (water); Estuaries; Maine; Models**
A 3-D Model for Penobscot Bay, Maine, Bryan R. Pearce, Bruce R. Fidler and Adrian C. Humphreys, 2395
- Tidal currents; Bridges (piers); Buffers; Protective structures; Ship piers; Ships**
Ship-Bridge-Pier Protective Systems, Akira Iwai, Hitoshi Nagasawa, Kazuki Oda and Kuniaki Shoji, 2259
- Tidal currents; Tubes; Wave action; Wave velocity; Cylindrical bodies; Kinematics; Ocean waves; Structural members**
Full Scale Near Surface Water Particle Velocities and Pressure Acting on an Inclined Tubular Member, Fritz Busching and Eckehard Martini, 1870

- Tidal currents; Vortices; Hydraulic models; Japan; Landsat; Remote sensing; Saline water-freshwater interfaces; Sea water intrusion; Straits**
Study on Vortex Current in Strait with Remote-Sensing, Sotoaki Onishi and Tsukasa Nishimura, 2653
- Tidal currents; West Germany; Barriers; Basins; Channels (waterways); Dams; Estuaries; Inlets (waterways); Sedimentation**
Sedimentation Processes in Tidal Channels and Tidal Basins Caused by Artificial Constructions, E. Renger and H. W. Partenscky, 2479
- Tidal effects; Australia; Coastal engineering; Coasts; Estuaries; Inlets (waterways)**
A Coastal Inlet with Fixed Bed and Mobile Sides, R. C. Nelson and A. J. Keats, 2532
- Tidal effects; Case reports; Inlets (waterways); Littoral deposits; Littoral materials; Migration; North Carolina; Shoals**
Barden Inlet, NC a Case Study of Inlet Migration, Limberios Valianios, 2638
- Tidal effects; Coastal engineering; Cost estimates; Flooding; Harbors; Mathematical models; Sedimentation; Sedimentation tanks; Suspended sediments**
Design of Enclosed Harbors to Reduce Sedimentation, Craig H. Everts, 1511
- Tidal effects; Tidal hydraulics; Wave action; Coasts; Floods; Inlets (waterways); Sand; Sandy soils; Storms**
Comments on Tidal Entrances on Sandy Coasts, Morrough P. O'Brien, 2502
- Tidal effects; Tidal waters; Australia; Coastal Processes; Estuaries; Floods; Inlets (waterways); Lakes; Littoral drift; Stability criteria**
Tidal Inlet Behavioural Analysis, A. F. Nielsen and A. D. Gordon, 2459
- Tidal effects; Tide gages; Tides; Bays (topographic features); Inlets (waterways)**
Tidal Prism-Inlet Area Relations for Small Tidal Inlets, R. J. Byrne, R. A. Gammisch and G. R. Thomas, 2515
- Tidal effects; Tides; Airport construction; Australia; Estuaries; Inlets (waterways); Land reclamation; Littoral drift**
Inlets/Estuaries Discharging into Sheltered Waters, H. P. Riedel and M. R. Gourlay, 2548
- Tidal effects; Tides; Coastal engineering; Data processing; Dynamics; Estuaries; Models; Numerical calculations**
The Use of Array Processors for Numerical Modeling of Tidal Estuary Dynamics, D. Prandle, E. R. Funke, N. Crookshank and R. Renner, 2411
- Tidal hydraulics; Australia; Beach nourishment; Bed forms; Dredging; Estuaries; Rivers; Sand; Sediment transport**
Estuarine Response to Dredging in the Tweed River, Australia, Bruce M. Drucry, 1598
- Tidal hydraulics; Wave action; Coasts; Floods; Inlets (waterways); Sand; Sandy soils; Storms; Tidal effects**
Comments on Tidal Entrances on Sandy Coasts, Morrough P. O'Brien, 2502
- Tidal waters; Australia; Coastal Processes; Estuaries; Floods; Inlets (waterways); Lakes; Littoral drift; Stability criteria; Tidal effects**
Tidal Inlet Behavioural Analysis, A. F. Nielsen and A. D. Gordon, 2459
- Tidal waters; Estuaries; Field investigations; Lagoon deposits; Sedimentation; Sediment control**
Opening and Maintaining Tidal Lagoons & Estuaries, Scott A. Jenkins, Douglas L. Inman and James A. Bailard, 1527
- Tidal waters; Tides; Waves; West Germany; Calibration; Coastal engineering; Estuaries; Mathematical models; Models; Rivers**
Automatic Calibration of Numerical Tidal Models, K.-P. Holz and U. Januszewski, 2448
- Tidal waters; U.S. Corps of Engineers; Beach erosion; Coastal engineering; Field investigations; Flood control; Inlets (waterways); Research projects**
The Corps of Engineer's General Investigation of Tidal Inlets, Robert M. Sorensen, 2563
- Tidal waters; Water circulation; Water quality; Harbors; Marinas; Models**
Modelling of Planform Influence on Circulation in Harbours, Roger A. Falconer, 2724
- Tidal waters; Water flow; Boundary conditions; Downstream; Inlets (waterways); North Carolina**
Boundary Conditions for Analysis of Flow in Tidal Inlets, T. C. Gopalakrishnan and J. L. Machemehl, 2593
- Tide gages; Tides; Bays (topographic features); Inlets (waterways); Tidal effects**
Tidal Prism-Inlet Area Relations for Small Tidal Inlets, R. J. Byrne, R. A. Gammisch and G. R. Thomas, 2515
- Tides; Airport construction; Australia; Estuaries; Inlets (waterways); Land reclamation; Littoral drift; Tidal effects**
Inlets/Estuaries Discharging into Sheltered Waters, H. P. Riedel and M. R. Gourlay, 2548
- Tides; Bays (topographic features); Inlets (waterways); Tidal effects; Tide gages**
Tidal Prism-Inlet Area Relations for Small Tidal Inlets, R. J. Byrne, R. A. Gammisch and G. R. Thomas, 2515
- Tides; Coastal engineering; Data processing; Dynamics; Estuaries; Models; Numerical calculations; Tidal effects**
The Use of Array Processors for Numerical Modeling of Tidal Estuary Dynamics, D. Prandle, E. R. Funke, N. Crookshank and R. Renner, 2411
- Tides; Coastal engineering; Estuaries; Models; Physical tests; Storm surges**
Artificial Roughness in Physical Models of Estuaries for Storm Surge Investigations, D. Berndt, E. Giese, H. Schwarze and H.-J. Vollmers, 2493
- Tides; Wave measurement; Coastal engineering; Data analysis; Florida; Spectral analysis**
Florida Coastal Data Network, Gary Howell, 421
- Tides; Waves; West Germany; Calibration; Coastal engineering; Estuaries; Mathematical models; Models; Rivers; Tidal waters**
Automatic Calibration of Numerical Tidal Models, K.-P. Holz and U. Januszewski, 2448

- Tides; West Germany; Coastal engineering; Coasts; Dredging; Field tests; Morphology; Projects; Sedimentology**
The German "Moran" Project, Winfried Siefert and Volker Barthel, 2924
- Time series analysis; Water waves; Wave generation; Waves; Fixed structures; Flumes; Model tests; Sea states; Synthesis**
On the Synthesis of Realistic Sea States, E. R. Funke and E. P.D. Mansard, 2971
- Time studies; Tsunamis; Water waves; Wave generation; Earthquakes; Ocean bottom**
Long Waves Generated by Complex Bottom Motions, J. L. Hammack and E. Raichlen, 639
- Topographic features; Wave action; Wave period; Beach erosion; Beaches; California; Sediment transport**
Beach Cusps at Point Reyes and Drakes Bay Beaches, California, R. G. Dean and E. M. Maurmeyer, 863
- Topographic features; Wave height; Wave period; Beds under water; Estimates; Sediment distribution; Sediment transport**
Longshore Water and Sediment Movement, D. H. Swart and C. A. Fleming, 1274
- Topography; Australia; Beaches; Beach nourishment; Coastal engineering; Management methods; Sand**
Beach Nourishment as a Management Technique, David M. Chapman, 1635
- Topography; Wave action; Australia; Beach erosion; Beaches; Field tests; Stability; Surf**
Beach Cut in Relation to Surf Zone Morphodynamics, L. D. Wright, 978
- Topography; Wave action; Beaches; Coastal Processes; Littoral drift; Sandbars; Shores**
Migration of Longshore Bars, Hans H. Dette, 1475
- Topography; Wave energy; Wave height; Wave runup; Beaches; Currents (water); Littoral current; Surf**
Topographic Control of Run-Up Variability, Mark P. Bradshaw, 1091
- Topography; Waves; Bathymetry; Currents (water); Models; Sediment transport; Shoaling; Shores**
Inshore-Nearshore Morphodynamics - A Predictive Model, John Chappell, 963
- Transient waves; Wave height; Waves; Currents (water); Deep water; Field data; Shoaling**
Wave-Wave Interactions, Current-Wave Interactions and Resulting Extreme Waves and Breaking Waves, Soren Peter Kjeldsen and Dag Myrhaug, 2275
- Trenches; Wave action; Channels (waterways); Coastal engineering; Sedimentation; Sediment transport; Suspended load**
Sedimentation in Channels and Trenches, E. W. Bijker, 1707
- Tropical cyclones; Hurricanes; Hydrodynamics; Models; Numerical calculations; Storms; Storm surges**
Numerical Modelling of Tropical Cyclone Storm Surge, Rodney J. Sobey, Bruce A. Harper and George M. Mitchell, 725
- Truncation errors; West Germany; Breakwaters; Case reports; Deep water; Design criteria; Energy transfer; Harbors**
Energy Transmission Over Break Water - A Design Criterion?, P. Bade and H. Kaldenhoff, 1886
- Tsunamis; Coastal engineering; Coastal engineering; Engineering evaluation; Nuclear power plants; Oceanography; Philippines**
Tsunami Along West Coast of Luzon, Philippines, R. L. Wiegel, 652
- Tsunamis; Turbulent flow; Wind profiles; Wind velocity; Anemometers; Friction factor; Hawaii**
Tsunami Prone Friction Factors From Wind Measurements, Charles L. Bretschneider, 672
- Tsunamis; Water waves; Wave generation; Earthquakes; Ocean bottom; Time studies**
Long Waves Generated by Complex Bottom Motions, J. L. Hammack and E. Raichlen, 639
- Tsunamis; Wave equations; Coastal engineering; Finite difference method; Islands; Shallow water**
Transient Finite-Difference Tsunami Calculations, Ove Skovgaard and Ivar G. Jonsson, 823
- Tsunamis; Wave equations; Wave runup; Bays (topographic features); Japan; Numerical calculations**
Run-Up of Tsunamis by Linear and Nonlinear Theories, Chiaki Goto and Nobuo Shuto, 695
- Tubes; Wave action; Wave velocity; Cylindrical bodies; Kinematics; Ocean waves; Structural members; Tidal currents**
Full Scale Near Surface Water Particle Velocities and Pressure Acting on an Inclined Tubular Member, Fritz Busching and Eckehard Martini, 1870
- Tundra; Wave energy; Alaska; Cliffs; Coastal Processes; Erosion; Sea ice; Sediment transport**
Sediment Transport Processes and Coastal Variability on the Alaskan North Slope, E. H. Owens, J. R. Harper and D. Nummendaal, 1343
- Turbulence; Water waves; Wave energy; Waves; Coastal engineering; Dissipation; Fluid dynamics; Gravity waves; Mathematical studies**
The Unsolved Problem of Breaking Waves, M. S. Longuet-Higgins, 1
- Turbulence; Wave damping; Wave energy; Energy dissipation; Laboratory tests**
The Dissipation of Wave Energy by Turbulence, Yu Kuang-ming, 850
- Turbulent flow; Wakes; Waves; Wave velocity; Boundary layer flow; Hydrofoils**
Velocity Field in a Steady Breaker, J. A. Battjes and T. Sakai, 499
- Turbulent flow; Wind profiles; Wind velocity; Anemometers; Friction factor; Hawaii; Tsunamis**
Tsunami Prone Friction Factors From Wind Measurements, Charles L. Bretschneider, 672
- Two-dimensional; Wave height; Calculations; Coastal engineering; Gravity waves; Predictions; Shoaling**
Wave Shoaling Calculated From Cokerlet's Theory, T. Sakai and J. A. Battjes, 121

- Union of Soviet Socialist Republics; Wave action; Coastal engineering; Coasts; Currents (water); Shore protection**
Coast Protection Against the Action of Waves and Currents, Leren P. Mikhailov and Sergei M. Uspenskii, 2120
- U.S. Corps of Engineers; Beach erosion; Coastal engineering; Field investigations; Flood control; Inlets (waterways); Research projects; Tidal waters**
The Corps of Engineer's General Investigation of Tidal Inlets, Robert M. Sorensen, 2563
- Velocity; Water waves; Wave propagation; Waves; Wave tanks; Coastal engineering; Mass transfer; Shallow water**
Mass Transport in Progressive Waves of Permanent Type, Yoshito Tsuchiya, Takashi Yasuda and Takao Yamashita, 70
- Velocity measurement; Velocity meters; Waves; Wave velocity; Coastal engineering; Flowmeters; Laboratory tests**
Orbital Velocities in Irregular Waves, F. C. Vis, 173
- Velocity meters; Waves; Wave velocity; Coastal engineering; Flowmeters; Laboratory tests; Velocity measurement**
Orbital Velocities in Irregular Waves, F. C. Vis, 173
- Visual surveillance; Wave height; Wave measurement; Waves; California; Coastal engineering; Gages; Littoral zone**
Visually Observed Wave Data at PT. Mugu, Calif., Christine Schneider and J. Richard Weggel, 381
- Vortices; Hydraulic models; Japan; Landsat; Remote sensing; Saline water-freshwater interfaces; Sea water intrusion; Straits; Tidal currents**
Study on Vortex Current in Strait with Remote-Sensing, Sotoaki Onishi and Tsukasa Nishimura, 2653
- Wakes; Waves; Wave velocity; Boundary layer flow; Hydrofoils; Turbulent flow**
Velocity Field in a Steady Breaker, J. A. Battjes and T. Sakai, 499
- Walls; Wave energy; Wave reflection; Coastal engineering; Design criteria; Numerical calculations; Solitary waves**
Accurate Numerical Solutions for Nonlinear Waves, J. D. Fenton and M. M. Rienecker, 50
- Wastewater (pollution); Water pollution; Wave energy; Antifouling materials; California; Coasts; Design; Outfall sewers; San Francisco; Sediment deposits; Shallow water**
Design of an Intermittently Operated Outfall, Roger W. Lindquist and George J. Murphy, 2834
- Wastewater (pollution); Water surface; Earth atmosphere; Experimentation; Heat balance; Powerplants; Rivers; Thermal pollution**
Experimental Evaluation of Heat Exchange Between Water Surface and Atmosphere, Gunther Barg, Horst Schwarze and Gerhard Visscher, 2848
- Water circulation; Water pollution; Water waves; Wave action; Beaches; Coasts; Littoral materials; Mathematical models**
Numerical Modelling of Nearshore Circulation, Bruce A. Ebersole and Robert A. Dalrymple, 2708
- Water circulation; Water quality; Coastal engineering; Harbors; Hydraulic design; Marinas**
Hydraulic Circulation Performance of a Curvilinear Marina, Jeffrey A. Layton, 2743
- Water circulation; Water quality; Harbors; Marinas; Models; Tidal waters**
Modelling of Planform Influence on Circulation in Harbours, Roger A. Falconer, 2724
- Water depth; Wave energy; Wave height; Wave period; Waves; Calculations; Coastal engineering; Design; Ocean waves; Stokes law**
Some Implications of Recent Advances in Wave Theories, J. R. Chaplin and K. Anastasiou, 31
- Water flow; Australia; Coastal engineering; Environmental impact statements; Estuaries; Planning; Ports**
Water Movement Studies Required for Port Planning, Graeme C. Dandy, Desmond A. Mills and John B. Hinwood, 3007
- Water flow; Boundary conditions; Downstream; Inlets (waterways); North Carolina; Tidal waters**
Boundary Conditions for Analysis of Flow in Tidal Inlets, T. C. Gopalakrishnan and J. L. Machemehl, 2593
- Water flow; Coastal engineering; Froude number; Mixing; Outflows; Rivers; Saline water-freshwater interfaces**
On a Role of the Interfacial Froude Number, Masakazu Kashiwamura, 2778
- Water flow; Water quality; Australia; Beaches; Computer applications; Construction; Docks; Dredging; Environmental surveys; Ports**
Integration and Computation in an Environmental Study, J. B. Hinwood, J. E. Watson and D. M. Burrage, 3024
- Water flow; Wave action; Wave energy; Wave generation; Damping; Motion studies; Shallow water; Ships**
Some Recent Results for Wave Induced Motions of a Ship in Shallow Water, P. A. Madsen, I. A. Svendsen and C. Michaelsen, 3040
- Water pollution; Water waves; Wave action; Beaches; Coasts; Littoral materials; Mathematical models; Water circulation**
Numerical Modelling of Nearshore Circulation, Bruce A. Ebersole and Robert A. Dalrymple, 2708
- Water pollution; Wave energy; Antifouling materials; California; Coasts; Design; Outfall sewers; San Francisco; Sediment deposits; Shallow water; Wastewater (pollution)**
Design of an Intermittently Operated Outfall, Roger W. Lindquist and George J. Murphy, 2834
- Water pollution control; Cooling water; Discharge (water); Heated water; Industrial plants; Liquefied natural gas; Refractometers; Temperature rise**
Dispersion of Cooling Water from a Coastal LNG Plant, P. Ackers, J. D. Pitt, G. Thompson and K. G. Rippin, 2794

- Water pollution control; Mathematical models; Mixing; Ocean waves; Oil spills; Oil-water interfaces**
The Effect of Breaking Waves on the Mixing of Liquid Pollutants into the Sea, Arvid Naces, 2758
- Water pollution control; Water quality; Bays (topographic features); Coastal engineering; Currents (water); Estuaries; Maine; Models; Three-dimensional**
A 3-D Model for Penobscot Bay, Maine, Bryan R. Pearce, Bruce R. Fidler and Adrian C. Humphreys, 2395
- Water quality; Australia; Beaches; Computer applications; Construction; Docks; Dredging; Environmental surveys; Ports; Water flow**
Integration and Computation in an Environmental Study, J. B. Hinwood, J. E. Watson and D. M. Babbage, 3024
- Water quality; Bays (topographic features); Coastal engineering; Currents (water); Estuaries; Maine; Models; Three-dimensional; Water pollution control**
A 3-D Model for Penobscot Bay, Maine, Bryan R. Pearce, Bruce R. Fidler and Adrian C. Humphreys, 2395
- Water quality; Coastal engineering; Harbors; Hydraulic design; Marinas; Water circulation**
Hydraulic Circulation Performance of a Curvilinear Marina, Jeffrey A. Layton, 2743
- Water quality; Harbors; Marinas; Models; Tidal waters; Water circulation**
Modelling of Planform Influence on Circulation in Harbours, Roger A. Falconer, 2724
- Water surface; Earth atmosphere; Experimentation; Heat balance; Powerplants; Rivers; Thermal pollution; Wastewater (pollution)**
Experimental Evaluation of Heat Exchange Between Water Surface and Atmosphere, Gunther Barg, Horst Schwarze and Gerhard Visscher, 2848
- Water tunnels; Water waves; Bed forms; Drag; Experimentation; Measurement; Sands; Sand waves**
Measurements of Oscillatory Drag on Sand Ripples, Karl E. B. Lofquist, 3104
- Water tunnels (testing); Wave action; Bed forms; Motion studies; Oscillation; Sand**
Sand Bed-Form Lengths Under Oscillatory Motion, Arthur Brebner, 1339
- Water waves; Analogies; Electromagnetic radiation; Gravity waves; Microwaves; Seiches**
An Electromagnetic Analogy For Long Water Waves, G. W. Jackson and D. L. Wilkinson, 801
- Water waves; Bed forms; Drag; Experimentation; Measurement; Sands; Sand waves; Water tunnels**
Measurements of Oscillatory Drag on Sand Ripples, Karl E. B. Lofquist, 3104
- Water waves; Wave action; Beaches; Coasts; Littoral materials; Mathematical models; Water circulation; Water pollution**
Numerical Modelling of Nearshore Circulation, Bruce A. Ebersole and Robert A. Dalrymple, 2708
- Water waves; Wave action; Calculations; Cylinders; Ocean bottom; Offshore structures; Sand; Seepage**
Wave-Induced Seepage Effects on a Vertical Cylinder, Thomas J.P. Durand and Peter L. Monkmeier, 1782
- Water waves; Wave action; Clay suspensions; Experimentation; Sediment concentration**
An Experiment on Clay Suspension Under Water Waves, Prida Thimakorn, 2891
- Water waves; Wave action; Wave energy; Waves; Coastal engineering; Harbors; Marinas; Model studies**
Non-Resonant Wave Agitation in Small Craft Harbours, J. W. Kamphuis and D. A.Y. Smith, 241
- Water waves; Wave energy; Waves; Coastal engineering; Dissipation; Fluid dynamics; Gravity waves; Mathematical studies; Turbulence**
The Unsolved Problem of Breaking Waves, M. S. Longuet-Higgins, 1
- Water waves; Waveform generators; Wave generation; Wave period; Models; Shoaling**
Correct Reproduction of Group-Induced Long Waves, N.-E. Ottesen Hansen, Stig E. Sand, H. Lundgren, Torben Sorensen and H. Gravesen, 784
- Water waves; Wave generation; Earthquakes; Ocean bottom; Time studies; Tsunamis**
Long Waves Generated by Complex Bottom Motions, J. L. Hammack and E. Raichlen, 639
- Water waves; Wave generation; Waves; Fixed structures; Flumes; Model tests; Sea states; Synthesis; Time series analysis**
On the Synthesis of Realistic Sea States, E. R. Funke and E. P.D. Mansard, 2971
- Water waves; Wavelength; Wave velocity; Acceleration; Breaking energy; Fluid mechanics**
The Fluid Mechanics of Waves Approaching Breaking, D. H. Peregrine, E. D. Cokelet and P. McIver, 512
- Water waves; Wave measurement; Wave pressure; Waves; Wave velocity; Coastal engineering; Spilling; Surf**
Velocity and Pressure Field of Spilling Breakers, M. J.F. Stive, 547
- Water waves; Wave period; Wave propagation; Wave reflection; Analysis; Submarine trenches**
Interactions of Waves With Submarine Trenches, Jjin-Jen Lee, Robert M. Ayer and Wen-Li Chiang, 812
- Water waves; Wave period; Wave reflection; Wave refraction; Waves; Coastal engineering; Gravity waves; Ocean engineering; Oceanography**
Ray Curvature and Refraction of Wave Packets, J. Ernest Breeding, Jr., 82
- Water waves; Wave propagation; Waves; Wave tanks; Coastal engineering; Mass transfer; Shallow water; Velocity**
Mass Transport in Progressive Waves of Permanent Type, Yoshito Tsuchiya, Takashi Yasuda and Takao Yamashita, 70

- Water waves; Wave reflection; Wave spectra; Coastal engineering; Coastal structures; Rubble-mound breakwaters; Sea walls**
Method of Analysis of Random Wave Experiments with Reflecting Coastal Structures, Pierre Gaillard, Michael Gauthier and Forrest Holly, 204
- Wave action; Accretion (geomorphology); Australia; Beach erosion; Coastal engineering; Field work**
Beach Erosion-Accretion at Two Time Scales, B. G. Thom and G. M. Bowman, 934
- Wave action; Australia; Beach erosion; Beaches; Field tests; Stability; Surf; Topography**
Beach Cut in Relation to Surf Zone Morphodynamics, L. D. Wright, 978
- Wave action; Australia; Beaches; Beach nourishment; Coastal engineering; Coasts; Morphology; Prisms**
The Dynamic Swept Prism, David M. Chapman and A. W. Smith, 1036
- Wave action; Bays (topographic features); Beach erosion; Beaches; Littoral drift; Shore protection**
Zeta Bays, Pocket Beaches and Headland Control, R. Silvester, Y. Tsuchiya and Y. Shibano, 1305
- Wave action; Beach erosion; Breakwaters; Coastal engineering; Dredging; Field investigations; Islands; Shore protection; South Carolina**
Soft Designs for Coastal Protection at Seabrook Island, S.C., Miles O. Hayes, Timothy W. Kana and John H. Barwis, 897
- Wave action; Beach erosion; Laboratory tests; Models; Sand; Sediment transport; Shallow water**
A Laboratory Study of Offshore Transport of Sediment and a Model for Eroding Beaches, Tsuguo Sunamura, 1051
- Wave action; Beaches; Coastal engineering; Littoral deposits; Littoral drift; Sediment transport; Shear stress**
Beach Profiles and On-Offshore Sediment Transport, Akira Watanabe, Yoshihiko Riho and Kiyoshi Horikawa, 1106
- Wave action; Beaches; Coastal Processes; Littoral drift; Sandbars; Shores; Topography**
Migration of Longshore Bars, Hans H. Dette, 1475
- Wave action; Beaches; Coasts; Littoral materials; Mathematical models; Water circulation; Water pollution; Water waves**
Numerical Modelling of Nearshore Circulation, Bruce A. Ebersole and Robert A. Dalrymple, 2708
- Wave action; Bed forms; Motion studies; Oscillation; Sand; Water tunnels (testing)**
Sand Bed-Form Lengths Under Oscillatory Motion, Arthur Brebner, 1339
- Wave action; Breakwaters; Caissons; Composite structures; Design; Impact loads; Laboratory tests**
Wave Impact Pressures on Composite Breakwaters, G. R. Mogridge and W. W. Jamieson, 1830
- Wave action; Calculations; Cylinders; Ocean bottom; Offshore structures; Sand; Seepage; Water waves**
Wave-Induced Seepage Effects on a Vertical Cylinder, Thomas J.P. Durand and Peter L. Monkmeier, 1782
- Wave action; Calculations; Cylindrical bodies; Piles; Predictions**
Wave Forces on an Inclined Circular Cylindrical Pile, Toshiyuki Shigemura, 1762
- Wave action; Channels (waterways); Coastal engineering; Sedimentation; Sediment transport; Suspended load; Trenches**
Sedimentation in Channels and Trenches, E. W. Bijker, 1707
- Wave action; Clay suspensions; Experimentation; Sediment concentration; Water waves**
An Experiment on Clay Suspension Under Water Waves, Prida Thimakorn, 2891
- Wave action; Coastal engineering; Coasts; Currents (water); Shore protection; Union of Soviet Socialist Republics**
Coast Protection Against the Action of Waves and Currents, Leren P. Mikhailov and Sergei M. Uspenskii, 2120
- Wave action; Coasts; Floods; Inlets (waterways); Sand; Sandy soils; Storms; Tidal effects; Tidal hydraulics**
Comments on Tidal Entrances on Sandy Coasts, Morrough P. O'Brien, 2502
- Wave action; Gas pipelines; Hydrodynamics; Ocean bottom; Ocean engineering; Petroleum pipelines; Submarine pipelines**
Wave Forces on Offshore Pipelines, N. Jothishankar and V. Sundar, 1820
- Wave action; Ocean currents; Ocean engineering; Offshore structures; Pipe design; Pipelines; Submarine pipelines**
Simultaneous Waves and Current Forces on a Pipeline, David A. Knoll and John B. Herbich, 1743
- Wave action; Wave energy; Australia; Coastal engineering; Coastal Processes; Coasts; Geologic control; Marine geology; Sediment transport**
Geological Controls on Process-Response, SE Australia, P. S. Roy and A. W. Stephens, 913
- Wave action; Wave energy; Beaches; Coastal engineering; Currents (water); Japan; Littoral current; Power plant location**
Nearshore Currents on a Partially Rocky Shore, T. O. Sasaki, H. Igarashi and S. Harikai, 1071
- Wave action; Wave energy; Beaches; Currents (water); Groundwater elevation; Slopes; Surf**
Wave Forcing of Beach Groundwater, Evans Waddell, 1435
- Wave action; Wave energy; Wave generation; Damping; Motion studies; Shallow water; Ships; Water flow**
Some Recent Results for Wave Induced Motions of a Ship in Shallow Water, P. A. Madsen, I. A. Svendsen and C. Michaelsen, 3040
- Wave action; Wave energy; Waves; Coastal engineering; Harbors; Marinas; Model studies; Water waves**
Non-Resonant Wave Agitation in Small Craft Harbours, J. W. Kamphuis and D. A.Y. Smith, 241
- Wave action; Wave energy; Waves; Wave velocity; Beaches; Coastal engineering; Experimental data**
Experimental Investigations of Periodic Wave Near Breaking, J. Buhr Hansen, 260

- Wave action; Wave height; Analysis; Australia; Coastal engineering; Dredging; Ocean waves; Ports; Real time operations**
 Realtime Wave Analysis, Newcastle, Australia, N. V. Youll and P. H. Youll, 412
- Wave action; Wave height; Wave period; Damage; Rubble-mound breakwaters; Stability; Tests**
 Stability of Rubble Mound Breakwater, J. Feuillet and M. Sabaton, 1989
- Wave action; Wave height; Waves; Wave velocity; Beaches; Breaking energy; Phase shift**
 Breaker Type and Phase Shifts on Natural Beaches, Peter J. Cowell, 997
- Wave action; Wave measurement; Wave spectra; Wave velocity; Hurricanes; Kinematics**
 Directional Wave Spectra and Wave Kinematics in Hurricanes Carmen and Eloise, G. Z. Forristall, E. G. Ward and V. J. Cardone, 567
- Wave action; Wave period; Beach erosion; Beaches; California; Sediment transport; Topographic features**
 Beach Cusps at Point Reyes and Drakes Bay Beaches, California, R. G. Dean and E. M. Maurmeyer, 863
- Wave action; Wave propagation; Waves; Wind; Breakwaters; Coastal engineering; Marinas; Porous materials**
 Wind Waves Transmission Through Porous Breakwater, Stanislaw R. Massel and Piotr Butowski, 333
- Wave action; Waves; Bottom sediments; Coastal engineering; Flumes; Sand; Sediment transport**
 Sand Transport by Waves, Jan van de Graaff and Wiel M.K. Tilmans, 1140
- Wave action; Waves; Coastal engineering; Dynamic characteristics; Shores; Surf**
 Dynamic Characteristics in the Nearshore Area, Kiyoshi Horikawa and Masahiko Isobe, 480
- Wave action; Waves; Currents (water); Lagoons (ponds); Morphology; Reefs; Sediment transport**
 Physical Processes and Sediment Flux Through Reef-Lagoon Systems, Harry H. Roberts, 946
- Wave action; Waves; Wave velocity; Coastal engineering; Hydraulic test tunnels; Sediment transport**
 A Closely Responding, Versatile Wave Tunnel, C. H. Hulsbergen and J. J. Bosman, 310
- Wave action; Wave velocity; Cylindrical bodies; Kinematics; Ocean waves; Structural members; Tidal currents; Tubes**
 Full Scale Near Surface Water Particle Velocities and Pressure Acting on an Inclined Tubular Member, Fritz Busching and Eckehard Martini, 1870
- Wave attenuation; Coastal engineering; Coastal structures; Design; Hawaii; Mathematical models; Reefs**
 Wave Attenuation and Wave Set-Up on a Coastal Reef, Francisus Gerritsen, 444
- Wave damping; Wave energy; Energy dissipation; Laboratory tests; Turbulence**
 The Dissipation of Wave Energy by Turbulence, Yu Kuang-ming, 850
- Wave diffraction; Wave refraction; Computer applications; Design; France; Harbors; Hydraulic tests; Models; Sedimentology**
 Harbour Design Including Sedimentological Problems Using Mainly Numerical Technics, B. Latteux, 2211
- Wave energy; Alaska; Cliffs; Coastal Processes; Erosion; Sea ice; Sediment transport; Tundra**
 Sediment Transport Processes and Coastal Variability on the Alaskan North Slope, E. H. Owens, J. R. Harper and D. Nummendal, 1343
- Wave energy; Antifouling materials; California; Coasts; Design; Outfall sewers; San Francisco; Sediment deposits; Shallow water; Wastewater (pollution); Water pollution**
 Design of an Intermittently Operated Outfall, Roger W. Lindquist and George J. Murphy, 2834
- Wave energy; Australia; Coastal engineering; Coastal Processes; Coasts; Geologic control; Marine geology; Sediment transport; Wave action**
 Geological Controls on Process-Response, SE Australia, P. S. Roy and A. W. Stephens, 913
- Wave energy; Beach erosion; Coastal Processes; Louisiana; Sedimentation; Shore protection**
 Fluid Mud Dynamics and Shoreline Stabilization: Louisiana Chenier Plain, John T. Wells and Harry H. Roberts, 1381
- Wave energy; Beaches; Coastal engineering; Currents (water); Japan; Littoral current; Power plant location; Wave action**
 Nearshore Currents on a Partially Rocky Shore, T. O. Sasaki, H. Igarashi and S. Harikai, 1071
- Wave energy; Beaches; Currents (water); Groundwater elevation; Slopes; Surf; Wave action**
 Wave Forcing of Beach Groundwater, Evans Waddell, 1435
- Wave energy; Beaches; Hydraulics; Littoral drift; Sand; Sediment transport**
 Secondary Sand Transport Mechanisms, A. W. Smith and A. D. Gordon, 1122
- Wave energy; Energy dissipation; Laboratory tests; Turbulence; Wave damping**
 The Dissipation of Wave Energy by Turbulence, Yu Kuang-ming, 850
- Wave energy; Field work; Littoral deposits; Littoral drift; Sediment transport; Storms; Suspended sediments**
 Nearshore Suspended Sediment Load During Storm and Post-Storm Conditions, Timothy W. Kana and Larry G. Ward, 1158
- Wave energy; Wave generation; Damping; Motion studies; Shallow water; Ships; Water flow; Wave action**
 Some Recent Results for Wave Induced Motions of a Ship in Shallow Water, P. A. Madsen, I. A. Svendsen and C. Michaelsen, 3040
- Wave energy; Wave generation; Wave height; Waves; Wind direction; Hurricanes; Predictions**
 Prediction of Dominant Wave Properties Ahead of Hurricanes, Omar H. Shemdin, 600
- Wave energy; Wave height; Wave period; Waves; Calculations; Coastal engineering; Design; Ocean waves; Stokes law; Water depth**
 Some Implications of Recent Advances in Wave Theories, J. R. Chaplin and K. Anastasiou, 31

- Wave energy; Wave height; Wave refraction; Waves; Wind; Coastal engineering; Models**
Verification of a Wave Refraction Model Utilizing Recorded and Observed Wave Data, G. Henderson and N. B. Webber, 101
- Wave energy; Wave height; Wave runup; Beaches; Currents (water); Littoral current; Surf; Topography**
Topographic Control of Run-Up Variability, Mark P. Bradshaw, 1091
- Wave energy; Wave height; Waves; Beach erosion; Beaches; Beach nourishment; Morphology; Sand; Sediment transport**
Beach Response to Variations in Breaker Height, A. D. Short, 1016
- Wave energy; Wave height; Waves; Beaches; Coastal engineering; Heuristic methods; Surf**
An Heuristic Model of Wave Height Distribution in Surf Zone, Masaru Mizuguchi, 278
- Wave energy; Wave measurement; Breaking energy; Coastal engineering; Coasts; Littoral drift; Taiwan**
Relationship Between Alongshore Wave Energy and Littoral Drift in the Mid West Coast at Taiwan, Ho-Shong Hou, Chung-Pan Lee and Lung-Hui Lin, 1254
- Wave energy; Wave measurement; Waves; Wave spectra; California; Islands**
An Investigation of Wave Sheltering by Islands, S. V. Hsiao, J. F. Vesecky and O. H. Shemdin, 840
- Wave energy; Wave reflection; Coastal engineering; Design criteria; Numerical calculations; Solitary waves; Walls**
Accurate Numerical Solutions for Nonlinear Waves, J. D. Fenton and M. M. Rienecker, 50
- Wave energy; Waves; Beaches; Coastal engineering; Fluid mechanics; Similarities; Surf**
A Similarity Model in the Surf Zone, Hsiang Wang and Wei-Chong Yang, 529
- Wave energy; Waves; Beaches; Deep water; Sediment transport; Stability analysis**
Criterion for Stability of Shoreline Platform, John D. Wang and Bernard Le Mehaute, 1994
- Wave energy; Waves; Coastal engineering; Dissipation; Fluid dynamics; Gravity waves; Mathematical studies; Turbulence; Water waves**
The Unsolved Problem of Breaking Waves, M. S. Longuet-Higgins, 1
- Wave energy; Waves; Coastal engineering; Harbors; Marinas; Model studies; Water waves; Wave action**
Non-Resonant Wave Agitation in Small Craft Harbours, J. W. Kamphuis and D. A.Y. Smith, 241
- Wave energy; Waves; Wave tanks; Breakwaters; Cost comparisons; Floating bodies; Mooring**
Floating Breakwater Performance Comparison, Volker W. Harms, 2135
- Wave energy; Waves; Wave velocity; Beaches; Coastal engineering; Experimental data; Wave action**
Experimental Investigations of Periodic Wave Near Breaking, J. Buhr Hansen, 260
- Wave energy; Wave spectra; West Germany; Deep water; Estuaries; Field investigations**
Wave Energy Distribution in an Estuary, Volker Barthel, 2338
- Wave equations; Coastal engineering; Finite difference method; Islands; Shallow water; Tsunamis**
Transient Finite-Difference Tsunami Calculations, Ove Skovgaard and Ivar G. Jonsson, 823
- Wave equations; Wave runup; Bays (topographic features); Japan; Numerical calculations; Tsunamis**
Run-Up of Tsunamis by Linear and Nonlinear Theories, Chiaki Goto and Nobuo Shuto, 695
- Wave equations; Waves; Beaches; Disturbances; Experimentation; Flumes; Predictions**
Long Period Disturbances Due to Wave Groups, E. C. Bowers, 610
- Waveform generators; Wave generation; Wave period; Models; Shoaling; Water waves**
Correct Reproduction of Group-Induced Long Waves, N.-E. Ottesen Hansen, Stig E. Sand, H. Lundgren, Torben Sorensen and H. Gravesen, 784
- Wave generation; Damping; Motion studies; Shallow water; Ships; Water flow; Wave action; Wave energy**
Some Recent Results for Wave Induced Motions of a Ship in Shallow Water, P. A. Madsen, I. A. Svendsen and C. Michaelsen, 3040
- Wave generation; Earthquakes; Ocean bottom; Time studies; Tsunamis; Water waves**
Long Waves Generated by Complex Bottom Motions, J. L. Hammack and E. Raichlen, 639
- Wave generation; Wave height; Waves; Coastal structures; Model studies; Statistics; Storms**
A Comparison of Nature Waves and Model Waves with Special Reference to Wave Grouping, Hans F. Burchard, 2989
- Wave generation; Wave height; Waves; Wind direction; Hurricanes; Predictions; Wave energy**
Prediction of Dominant Wave Properties Ahead of Hurricanes, Omar H. Shemdin, 600
- Wave generation; Wave measurement; Waves; Wave spectra; Wind; Data analysis; Lake waves; Michigan**
A Measurement of Slope, Curvature, and Directional Spectra of Wind Waves in Lake Michigan, Paul C. Liu, 432
- Wave generation; Wave period; Models; Shoaling; Water waves; Waveform generators**
Correct Reproduction of Group-Induced Long Waves, N.-E. Ottesen Hansen, Stig E. Sand, H. Lundgren, Torben Sorensen and H. Gravesen, 784
- Wave generation; Wave pressure; Waves; Wave velocity; Hydraulic models; Simulation**
Investigations on Irregular Waves in Hydraulic Models, Karl-Friedrich Daemrich, Wolf-Dietrich Eggert and Soren Kohlhasse, 186
- Wave generation; Waves; Fixed structures; Flumes; Model tests; Sea states; Synthesis; Time series analysis; Water waves**
On the Synthesis of Realistic Sea States, E. R. Funke and E. P.D. Mansard, 2971

- Wave generation; Waves; Wave tanks; Coastal engineering; Computer applications; Flumes; Hydraulic models**
A Survey of "Random" Wave Generation Techniques, J. Ploeg and E. R. Funke, 135
- Wave generation; Waves; Wave velocity; Laboratory tests; Shallow water**
The Generation of Long Waves in the Laboratory, Derek Goring and Fredric Raichlen, 763
- Waveguides; Waves; Beaches; Coastal engineering; Currents (water); Flow**
Longshore Current Flows in a Wave Basin, P. J. Visser, 462
- Wave height; Analysis; Australia; Coastal engineering; Dredging; Ocean waves; Ports; Real-time operations; Wave action**
Realtime Wave Analysis, Newcastle, Australia, N. V. Lawson and P. H. Youll, 412
- Wave height; Calculations; Coastal engineering; Gravity waves; Predictions; Shoaling; Two-dimensional**
Wave Shoaling Calculated From Cokerlet's Theory, T. Sakai and J. A. Battjes, 121
- Wave height; Coastal structures; Design; Offshore engineering; Predictions; Sea states; Statistical data**
Prediction of the Severest Significant Wave Height, Michel K. Ochi and Joseph E. Whalen, 587
- Wave height; Wave measurement; Waves; California; Coastal engineering; Gages; Littoral zone; Visual surveillance**
Visually Observed Wave Data at PT. Mugu, Calif., Christine Schneider and J. Richard Weggel, 381
- Wave height; Wave period; Beds under water; Estimates; Sediment distribution; Sediment transport; Topographic features**
Longshore Water and Sediment Movement, D. H. Swart and C. A. Fleming, 1274
- Wave height; Wave period; Damage; Rubble-mound breakwaters; Stability; Tests; Wave action**
Stability of Rubble Mound Breakwater, J. Feuillet and M. Sabaton, 1989
- Wave height; Wave period; Waves; Calculations; Coastal engineering; Design; Ocean waves; Stokes law; Water depth; Wave energy**
Some Implications of Recent Advances in Wave Theories, J. R. Chaplin and K. Anastasiou, 31
- Wave height; Wave period; Waves; Wave spectrum; Ocean waves; Statistical data**
Statistical Properties of Random Wave Groups, Akira Kimura, 2952
- Wave height; Wave refraction; Waves; Wind; Coastal engineering; Models; Wave energy**
Verification of a Wave Refraction Model Utilizing Recorded and Observed Wave Data, G. Henderson and N. B. Webber, 101
- Wave height; Wave runoff; Beaches; Currents (water); Littoral current; Surf; Topography; Wave energy**
Topographic Control of Run-Up Variability, Mark P. Bradshaw, 1091
- Wave height; Waves; Beach erosion; Beaches; Beach nourishment; Morphology; Sand; Sediment transport; Wave energy**
Beach Response to Variations in Breaker Height, A. D. Short, 1016
- Wave height; Waves; Beaches; Coastal engineering; Heuristic methods; Surf; Wave energy**
An Heuristic Model of Wave Height Distribution in Surf Zone, Masaru Mizuguchi, 278
- Wave height; Waves; Breakwaters; Coastal engineering; Field tests; Numerical calculations**
Wave Height Distribution Around Permeable Breakwaters, Shintaro Hotta, 221
- Wave height; Waves; Coastal structures; Model studies; Statistics; Storms; Wave generation**
A Comparison of Nature Waves and Model Waves with Special Reference to Wave Grouping, Hans F. Burcharth, 2989
- Wave height; Waves; Currents (water); Deep water; Field data; Shoaling; Transient waves**
Wave-Wave Interactions, Current-Wave Interactions and Resulting Extreme Waves and Breaking Waves, Soren Peter Kjeldsen and Dag Myrhaug, 2275
- Wave height; Waves; Wave velocity; Beaches; Breaking energy; Phase shift; Wave action**
Breaker Type and Phase Shifts on Natural Beaches, Peter J. Cowell, 997
- Wave height; Waves; Wind direction; Hurricanes; Predictions; Wave energy; Wave generation**
Prediction of Dominant Wave Properties Ahead of Hurricanes, Omar H. Shemdin, 600
- Wave height; Wind speed; Australia; Continental shelf; Currents (water); Field tests; Models; Predictions; Sediment transport**
Sediment Dispersal on the NSW Continental Shelf, Ron Boyd, 1563
- Wavelength; Wave velocity; Acceleration; Breaking energy; Fluid mechanics; Water waves**
The Fluid Mechanics of Waves Approaching Breaking, D. H. Peregrine, E. D. Cokelet and P. McIver, 512
- Wave measurement; Breaking energy; Coastal engineering; Coasts; Littoral drift; Taiwan; Wave energy**
Relationship Between Alongshore Wave Energy and Littoral Drift in the Mid West Coast at Taiwan, Ho-Shong Hou, Chung-Pan Lee and Lung-Hui Lin, 1254
- Wave measurement; Breakwaters; California; Coastal engineering; Field tests; Harbors; Sand traps; Sediment transport**
Longshore Transport Evaluations at a Detached Breakwater, R. O. Bruno, R. G. Dean and C. G. Gable, 1452
- Wave measurement; Coastal engineering; Data analysis; Florida; Spectral analysis; Tides**
Florida Coastal Data Network, Gary Howell, 421
- Wave measurement; Wave pressure; Waves; Wave velocity; Coastal engineering; Spilling; Surf; Water waves**
Velocity and Pressure Field of Spilling Breakers, M. J.F. Stive, 547

- Wave measurement; Waves; Wave propagation; Waves; Experimentation; Flumes; Least squares method**
The Measurement of Incident and Reflected Spectra Using a Least Squares Method, E. P.D. Mansard and E. R. Funke, 154
- Wave measurement; Waves; California; Coastal engineering; Gages; Littoral zone; Visual surveillance; Wave height**
Visually Observed Wave Data at PT. Mugu, Calif., Christine Schneider and J. Richard Weggel, 381
- Wave measurement; Waves; Catalogs; Coastal engineering; Oceanographic data**
Sources of Measured Wave Data, Laurence Draper, 372
- Wave measurement; Waves; Wave spectra; California; Islands; Wave energy**
An Investigation of Wave Sheltering by Islands, S. V. Hsiao, J. F. Vesecky and O. H. Shemdin, 840
- Wave measurement; Waves; Wave spectra; Wind; Data analysis; Lake waves; Michigan; Wave generation**
A Measurement of Slope, Curvature, and Directional Spectra of Wind Waves in Lake Michigan, Paul C. Liu, 432
- Wave measurement; Wave spectra; Wave velocity; Hurricanes; Kinematics; Wave action**
Directional Wave Spectra and Wave Kinematics in Hurricanes Carmen and Eloise, G. Z. Forristall, E. G. Ward and V. J. Cardone, 567
- Wave measurement; Wave spectra; Wind; High frequency; Meteorological data; Oceanographic data; Ocean waves; Radar mapping**
HF Radar Mapping of Extensive Ocean Windfields, P. E. Dexter and R. C. Casey, 363
- Wave measurement; Wave velocity; Experimentation; Primary waves; Shoaling; Standing waves; Surf; Surface waves**
Two-Dimensional Surf Beat, Reinhard E. Flick, Douglas L. Inman and Robert T. Gaza, 624
- Wave measurement; Wave velocity; Wind; Kinematics; Ocean waves; Offshore platforms; Statistics**
Field Measurements of Wind Wave Kinematics, J. A. Battjes and J. van Heteren, 347
- Wave measurement; Wind; Currents (water); Field investigations; Motion; Sand; Sediment transport; Surf; Suspended load**
Field Measurements of Sand Motion in the Surf Zone, Douglas L. Inman, James A. Zampol, Thomas E. White, Daniel M. Hanes, B. Walton Waldorf and Kim A. Kastens, 1214
- Wave measurement; Wind; Wind speed; Australia; Ocean waves; Offshore drilling; Offshore platforms; Oil and gas fields**
Wave Hindcasts and Measurements Bass Strait, M. N. Silbert, T. P. Barnett, D. J.H. Peters and R. C. Hamilton, 384
- Wave period; Beach erosion; Beaches; California; Sediment transport; Topographic features; Wave action**
Beach Cusps at Point Reyes and Drakes Bay Beaches, California, R. G. Dean and E. M. Maurmeyer, 863
- Wave period; Beds under water; Estimates; Sediment distribution; Sediment transport; Topographic features; Wave height**
Longshore Water and Sediment Movement, D. H. Swart and C. A. Fleming, 1274
- Wave period; Damage; Rubble-mound breakwaters; Stability; Tests; Wave action; Wave height**
Stability of Rubble Mound Breakwater, J. Feuillet and M. Sabaton, 1989
- Wave period; Models; Shoaling; Water waves; Waveform generators; Wave generation**
Correct Reproduction of Group-Induced Long Waves, N.-E. Ottesen Hansen, Stig E. Sand, H. Lundgren, Torben Sorensen and H. Gravesen, 784
- Wave period; Wave propagation; Wave reflection; Analysis; Submarine trenches; Wave waves**
Interactions of Waves With Submarine Trenches, Jii-Jen Lee, Robert M. Ayer and Wen-Li Chiang, 812
- Wave period; Wave reflection; Wave refraction; Waves; Coastal engineering; Gravity waves; Ocean engineering; Oceanography; Water waves**
Ray Curvature and Refraction of Wave Packets, J. Ernest Breeding, Jr., 82
- Wave period; Waves; Calculations; Coastal engineering; Design; Ocean waves; Stokes law; Water depth; Wave energy; Wave height**
Some Implications of Recent Advances in Wave Theories, J. R. Chaplin and K. Anastasiou, 31
- Wave period; Waves; Wave spectrum; Ocean waves; Statistical data; Wave height**
Statistical Properties of Random Wave Groups, Akira Kimura, 2952
- Wave pressure; Waves; Wave velocity; Coastal engineering; Spilling; Surf; Water waves; Wave measurement**
Velocity and Pressure Field of Spilling Breakers, M. J.F. Stive, 547
- Wave pressure; Waves; Wave velocity; Hydraulic models; Simulation; Wave generation**
Investigations on Irregular Waves in Hydraulic Models, Karl-Friedrich Daemrich, Wolf-Dietrich Eggert and Soren Kohlhasse, 186
- Wave propagation; Wave reflection; Analysis; Submarine trenches; Water waves; Wave period**
Interactions of Waves With Submarine Trenches, Jii-Jen Lee, Robert M. Ayer and Wen-Li Chiang, 812
- Wave propagation; Waves; Experimentation; Flumes; Least squares method; Wave measurement**
The Measurement of Incident and Reflected Spectra Using a Least Squares Method, E. P.D. Mansard and E. R. Funke, 154
- Wave propagation; Waves; Wave tanks; Coastal engineering; Mass transfer; Shallow water; Velocity; Water waves**
Mass Transport in Progressive Waves of Permanent Type, Yoshito Tsuchiya, Takashi Yasuda and Takao Yamashita, 70
- Wave propagation; Waves; Wind; Breakwaters; Coastal engineering; Marinas; Porous materials; Wave action**
Wind Waves Transmission Through Porous Breakwater, Stanislaw R. Massel and Piotr Butowski, 333

- Wave reflection; Analysis; Submarine trenches; Water waves; Wave period; Wave propagation**
Interactions of Waves With Submarine Trenches, Jjin-Jen Lee, Robert M. Ayer and Wen-Li Chiang, 812
- Wave reflection; Coastal engineering; Design criteria; Numerical calculations; Solitary waves; Walls; Wave energy**
Accurate Numerical Solutions for Nonlinear Waves, J. D. Fenton and M. M. Rienecker, 50
- Wave reflection; Wave refraction; Waves; Coastal engineering; Gravity waves; Ocean engineering; Oceanography; Water waves; Wave period**
Ray Curvature and Refraction of Wave Packets, J. Ernest Breeding, Jr., 82
- Wave reflection; Wave spectra; Coastal engineering; Coastal structures; Rubble-mound breakwaters; Sea walls; Water waves**
Method of Analysis of Random Wave Experiments with Reflecting Coastal Structures, Pierre Gaillard, Michael Gauthier and Forrest Holly, 204
- Wave refraction; Computer applications; Design; France; Harbors; Hydraulic tests; Models; Sedimentology; Wave diffraction**
Harbour Design Including Sedimentological Problems Using Mainly Numerical Technics, B. Latteux, 2211
- Wave refraction; Waves; Coastal engineering; Gravity waves; Ocean engineering; Oceanography; Water waves; Wave period; Wave reflection**
Ray Curvature and Refraction of Wave Packets, J. Ernest Breeding, Jr., 82
- Wave refraction; Waves; Wind; Coastal engineering; Models; Wave energy; Wave height**
Verification of a Wave Refraction Model Utilizing Recorded and Observed Wave Data, G. Henderson and N. B. Webber, 101
- Wave runup; Bays (topographic features); Japan; Numerical calculations; Tsunamis; Wave equations**
Run-Up of Tsunamis by Linear and Nonlinear Theories, Chiaki Goto and Nobuo Shuto, 695
- Wave runup; Beaches; Currents (water); Littoral current; Surf; Topography; Wave energy; Wave height**
Topographic Control of Run-Up Variability, Mark P. Bradshaw, 1091
- Waves; Australia; Coastal engineering; Resonance; Sea level changes; Subsonic flow**
Resonances of Coastal Waters Between Perth and Geraldton, H. Allison, A. Grassia and R. Litchfield, 290
- Waves; Bathymetry; Currents (water); Models; Sediment transport; Shoaling; Shores; Topography**
Inshore-Nearshore Morphodynamics - A Predictive Model, John Chappell, 963
- Waves; Beach erosion; Beaches; Beach nourishment; Morphology; Sand; Sediment transport; Wave energy; Wave height**
Beach Response to Variations in Breaker Height, A. D. Short, 1016
- Waves; Beaches; Beach sands; Coastal Processes; Hydraulics; Laboratory tests; Permeability (soils); Profiles; Surf**
Beaches: Profiles, Processes and Permeability, Michael R. Gourlay, 1319
- Waves; Beaches; Coastal engineering; Currents (water); Flow; Waveguides**
Longshore Current Flows in a Wave Basin, P. J. Visser, 462
- Waves; Beaches; Coastal engineering; Fluid mechanics; Similarities; Surf; Wave energy**
A Similarity Model in the Surf Zone, Hsiang Wang and Wei-Chong Yang, 529
- Waves; Beaches; Coastal engineering; Heuristic methods; Surf; Wave energy; Wave height**
An Heuristic Model of Wave Height Distribution in Surf Zone, Masaru Mizuguchi, 278
- Waves; Beaches; Deep water; Sediment transport; Stability analysis; Wave energy**
Criterion for Stability of Shoreline Planform, John D. Wang and Bernard Le Mehaute, 1994
- Waves; Beaches; Disturbances; Experimentation; Flumes; Predictions; Wave equations**
Long Period Disturbances Due to Wave Groups, E. C. Bowers, 610
- Waves; Beaches; Littoral deposits; Littoral drift; Models; Sand; Sediment transport; Surf**
Onshore-Offshore Transport and Beach Profile Change, Masataro Hattori and Ryoichi Kawamata, 1178
- Waves; Bottom sediments; Coastal engineering; Flumes; Sand; Sediment transport; Wave action**
Sand Transport by Waves, Jan van de Graaff and Wiel M.K. Tilmans, 1140
- Waves; Breakwaters; Coastal engineering; Field tests; Numerical calculations; Wave height**
Wave Height Distribution Around Permeable Breakwaters, Shintaro Hotta, 221
- Waves; Caissons; Concrete construction; Deep water; Design; Japan; Overtopping; Sea walls**
Seawalls in Deep Seas, Shoshichiro Nagai and Shohachi Kakuno, 2024
- Waves; Calculations; Coastal engineering; Design; Ocean waves; Stokes law; Water depth; Wave energy; Wave height; Wave period**
Some Implications of Recent Advances in Wave Theories, J. R. Chaplin and K. Anastasiou, 31
- Waves; California; Coastal engineering; Coastal Processes; Currents (water); Models; Predictions; Sediment transport**
Nearshore Sediment Transport Study Experiments, R. J. Seymour and C. G. Gable, 1401
- Waves; California; Coastal engineering; Gages; Littoral zone; Visual surveillance; Wave height; Wave measurement**
Visually Observed Wave Data at PT. Mugu, Calif., Christine Schneider and J. Richard Weggel, 381
- Waves; Catalogs; Coastal engineering; Oceanographic data; Wave measurement**
Sources of Measured Wave Data, Laurence Draper, 372
- Waves; Coastal engineering; Dissipation; Fluid dynamics; Gravity waves; Mathematical studies; Turbulence; Water waves; Wave energy**
The Unsolved Problem of Breaking Waves, M. S. Longuet-Higgins, 1

- Waves; Coastal engineering; Dynamic characteristics; Shores; Surf; Wave action**
Dynamic Characteristics in the Nearshore Area, Kiyoshi Horikawa and Masahiko Isobe, 480
- Waves; Coastal engineering; Gravity waves; Ocean engineering; Oceanography; Water waves; Wave period; Wave reflection; Wave refraction**
Ray Curvature and Refraction of Wave Packets, J. Ernest Breeding, Jr., 82
- Waves; Coastal engineering; Harbors; Marinas; Model studies; Water waves; Wave action; Wave energy**
Non-Resonant Wave Agitation in Small Craft Harbours, J. W. Kamphuis and D. A. Y. Smith, 241
- Waves; Coastal structures; Model studies; Statistics; Storms; Wave generation; Wave height**
A Comparison of Nature Waves and Model Waves with Special Reference to Wave Grouping, Hans F. Burcharth, 2989
- Waves; Currents (water); Deep water; Field data; Shoaling; Transient waves; Wave height**
Wave-Wave Interactions, Current-Wave Interactions and Resulting Extreme Waves and Breaking Waves, Soren Peter Kjeldsen and Dag Myrhaug, 2275
- Waves; Currents (water); Lagoons (ponds); Morphology; Reefs; Sediment transport; Wave action**
Physical Processes and Sediment Flux Through Reef-Lagoon Systems, Harry H. Roberts, 946
- Waves; Experimentation; Flumes; Least squares method; Wave measurement; Wave propagation**
The Measurement of Incident and Reflected Spectra Using a Least Squares Method, E. P. D. Mansard and E. R. Funke, 154
- Waves; Fixed structures; Flumes; Model tests; Sea states; Synthesis; Time series analysis; Water waves; Wave generation**
On the Synthesis of Realistic Sea States, E. R. Funke and E. P. D. Mansard, 2971
- Waves; Harbors; Models; Numerical calculations; Shallow water; Storms; Storm water**
A Numerical Model of Storm Waves in Shallow Water, A. Hauguel, 746
- Waves; Wave spectra; California; Islands; Wave energy; Wave measurement**
An Investigation of Wave Sheltering by Islands, S. V. Hsiao, J. F. Vesecky and O. H. Shemdin, 840
- Waves; Wave spectra; Wind; Data analysis; Lake waves; Michigan; Wave generation; Wave measurement**
A Measurement of Slope, Curvature, and Directional Spectra of Wind Waves in Lake Michigan, Paul C. Liu, 432
- Waves; Wave spectrum; Ocean waves; Statistical data; Wave height; Wave period**
Statistical Properties of Random Wave Groups, Akira Kimura, 2952
- Waves; Wave tanks; Breakwaters; Cost comparisons; Floating bodies; Mooring; Wave energy**
Floating Breakwater Performance Comparison, Volker W. Harms, 2135
- Waves; Wave tanks; Coastal engineering; Computer applications; Flumes; Hydraulic models; Wave generation**
A Survey of "Random" Wave Generation Techniques, J. Ploeg and E. R. Funke, 135
- Waves; Wave tanks; Coastal engineering; Mass transfer; Shallow water; Velocity; Water waves; Wave propagation**
Mass Transport in Progressive Waves of Permanent Type, Yoshito Tsuchiya, Takashi Yasuda and Takao Yamashita, 70
- Waves; Wave velocity; Beaches; Breaking energy; Phase shift; Wave action; Wave height**
Breaker Type and Phase Shifts on Natural Beaches, Peter J. Cowell, 997
- Waves; Wave velocity; Beaches; Coastal engineering; Experimental data; Wave action; Wave energy**
Experimental Investigations of Periodic Wave Near Breaking, J. Bühr Hansen, 260
- Waves; Wave velocity; Boundary layer flow; Hydrofoils; Turbulent flow; Waves**
Velocity Field in a Steady Breaker, J. A. Battjes and T. Sakai, 499
- Waves; Wave velocity; Coastal engineering; Flowmeters; Laboratory tests; Velocity measurement; Velocity meters**
Orbital Velocities in Irregular Waves, F. C. Vis, 173
- Waves; Wave velocity; Coastal engineering; Hydraulic test tunnels; Sediment transport; Wave action**
A Closely Responding, Versatile Wave Tunnel, C. H. Hulsbergen and J. J. Bosman, 310
- Waves; Wave velocity; Coastal engineering; Spilling; Surf; Water waves; Wave measurement; Wave pressure**
Velocity and Pressure Field of Spilling Breakers, M. J. F. Stive, 547
- Waves; Wave velocity; Hydraulic models; Simulation; Wave generation; Wave pressure**
Investigations on Irregular Waves in Hydraulic Models, Karl-Friedrich Daemrich, Wolf-Dietrich Eggert and Soren Kohlhase, 186
- Waves; Wave velocity; Laboratory tests; Shallow water; Wave generation**
The Generation of Long Waves in the Laboratory, Derek Goring and Fredric Raichlen, 763
- Waves; West Germany; Calibration; Coastal engineering; Estuaries; Mathematical models; Models; Rivers; Tidal waters; Tides**
Automatic Calibration of Numerical Tidal Models, K.-P. Holz and U. Januszewski, 2448
- Waves; Wind; Breakwaters; Coastal engineering; Marinas; Porous materials; Wave action; Wave propagation**
Wind Waves Transmission Through Porous Breakwater, Stanislaw R. Massel and Piotr Butowski, 333
- Waves; Wind; Coastal engineering; Models; Wave energy; Wave height; Wave refraction**
Verification of a Wave Refraction Model Utilizing Recorded and Observed Wave Data, G. Henderson and N. B. Webber, 101

- Waves; Wind direction; Hurricanes; Predictions; Wave energy; Wave generation; Wave height**
Prediction of Dominant Wave Properties Ahead of Hurricanes, Omar H. Shemdin, 600
- Wave spectra; California; Islands; Wave energy; Wave measurement; Waves**
An Investigation of Wave Sheltering by Islands, S. V. Hsiao, J. F. Vesecky and O. H. Shemdin, 840
- Wave spectra; Coastal engineering; Coastal structures; Rubble-mound breakwaters; Sea walls; Water waves; Wave reflection**
Method of Analysis of Random Wave Experiments with Reflecting Coastal Structures, Pierre Gaillard, Michael Gauthier and Forrest Holly, 204
- Wave spectra; Wave velocity; Hurricanes; Kinematics; Wave action; Wave measurement**
Directional Wave Spectra and Wave Kinematics in Hurricanes Carmen and Eloise, G. Z. Forristall, E. G. Ward and V. J. Cardone, 567
- Wave spectra; West Germany; Deep water; Estuaries; Field investigations; Wave energy**
Wave Energy Distribution in an Estuary, Volker Barthel, 2338
- Wave spectra; Wind; Data analysis; Lake waves; Michigan; Wave generation; Wave measurement; Waves**
A Measurement of Slope, Curvature, and Directional Spectra of Wind Waves in Lake Michigan, Paul C. Liu, 432
- Wave spectra; Wind; High frequency; Meteorological data; Oceanographic data; Ocean waves; Radar mapping; Wave measurement**
HF Radar Mapping of Extensive Ocean Windfields, P. E. Dexter and R. C. Casey, 363
- Wave spectrum; Ocean waves; Statistical data; Wave height; Wave period; Waves**
Statistical Properties of Random Wave Groups, Akira Kimura, 2952
- Wave tanks; Breakwaters; Cost comparisons; Floating bodies; Mooring; Wave energy; Waves**
Floating Breakwater Performance Comparison, Volker W. Harms, 2135
- Wave tanks; Coastal engineering; Computer applications; Flumes; Hydraulic models; Wave generation; Waves**
A Survey of "Random" Wave Generation Techniques, J. Ploeg and E. R. Funke, 135
- Wave tanks; Coastal engineering; Mass transfer; Shallow water; Velocity; Water waves; Wave propagation; Waves**
Mass Transport in Progressive Waves of Permanent Type, Yoshito Tsuchiya, Takashi Yasuda and Takao Yamashita, 70
- Wave velocity; Acceleration; Breaking energy; Fluid mechanics; Water waves; Wavelength**
The Fluid Mechanics of Waves Approaching Breaking, D. H. Peregrine, E. D. Cokelet and P. McIver, 512
- Wave velocity; Beaches; Breaking energy; Phase shift; Wave action; Wave height; Waves**
Breaker Type and Phase Shifts on Natural Beaches, Peter J. Cowell, 997
- Wave velocity; Beaches; Coastal engineering; Experimental data; Wave action; Wave energy; Waves**
Experimental Investigations of Periodic Wave Near Breaking, J. Buhr Hansen, 260
- Wave velocity; Boundary layer flow; Hydrofoils; Turbulent flow; Wakes; Waves**
Velocity Field in a Steady Breaker, J. A. Battjes and T. Sakai, 499
- Wave velocity; Coastal engineering; Computerized simulation; Fourier transformation; Ocean waves**
Conditional Simulations of Ocean Wave Properties, Leon R. Borgman, 318
- Wave velocity; Coastal engineering; Flowmeters; Laboratory tests; Velocity measurement; Velocity meters; Waves**
Orbital Velocities in Irregular Waves, F. C. Vis, 173
- Wave velocity; Coastal engineering; Hydraulic test tunnels; Sediment transport; Wave action; Waves**
A Closely Responding, Versatile Wave Tunnel, C. H. Hulsbergen and J. J. Bosman, 310
- Wave velocity; Coastal engineering; Spilling; Surf; Water waves; Wave measurement; Wave pressure; Waves**
Velocity and Pressure Field of Spilling Breakers, M. J.F. Stive, 547
- Wave velocity; Cylindrical bodies; Kinematics; Ocean waves; Structural members; Tidal currents; Tubes; Wave action**
Full Scale Near Surface Water Particle Velocities and Pressure Acting on an Inclined Tubular Member, Fritz Busching and Eckhard Martini, 1870
- Wave velocity; Experimentation; Primary waves; Shoaling; Standing waves; Surf; Surface waves; Wave measurement**
Two-Dimensional Surf Beat, Reinhard E. Flick, Douglas L. Inman and Robert T. Gaza, 624
- Wave velocity; Hurricanes; Kinematics; Wave action; Wave measurement; Wave spectra**
Directional Wave Spectra and Wave Kinematics in Hurricanes Carmen and Eloise, G. Z. Forristall, E. G. Ward and V. J. Cardone, 567
- Wave velocity; Hydraulic models; Simulation; Wave generation; Wave pressure; Waves**
Investigations on Irregular Waves in Hydraulic Models, Karl-Friedrich Daemrich, Wolf-Dietrich Eggert and Soren Kohlhasse, 186
- Wave velocity; Laboratory tests; Shallow water; Wave generation; Waves**
The Generation of Long Waves in the Laboratory, Derek Goring and Fredric Raichlen, 763
- Wave velocity; Wind; Kinematics; Ocean waves; Offshore platforms; Statistics; Wave measurement**
Field Measurements of Wind Wave Kinematics, J. A. Battjes and J. van Heteren, 347
- West Germany; Barriers; Basins; Channels (waterways); Dams; Estuaries; Inlets (waterways); Sedimentation; Tidal currents**
Sedimentation Processes in Tidal Channels and Tidal Basins Caused by Artificial Constructions, E. Renger and H. W. Partenscky, 2479

- West Germany; Breakwaters; Case reports; Deep water; Design criteria; Energy transfer; Harbors; Truncation errors**
Energy Transmission Over Break Water - A Design Criterion?, P. Bade and H. Kaldenhoff, 1886
- West Germany; Calibration; Coastal engineering; Estuaries; Mathematical models; Models; Rivers; Tidal waters; Tides; Waves**
Automatic Calibration of Numerical Tidal Models, K.-P. Holz and U. Januszewski, 2448
- West Germany; Coastal engineering; Coasts; Dredging; Field tests; Morphology; Projects; Sedimentology; Tides**
The German "Moran" Project, Winfried Stiefert and Volker Barthel, 2924
- West Germany; Deep water; Estuaries; Field investigations; Wave energy; Wave spectra**
Wave Energy Distribution in an Estuary, Volker Barthel, 2338
- West Germany; Wind action geology; Wind speed; Coasts; Field investigations; Sand; Sand control; Sediment transport**
Sand Transport Under the Action of Wind, Ulrich Zanke, 1575
- Wind; Breakwaters; Coastal engineering; Marinas; Porous materials; Wave action; Wave propagation; Waves**
Wind Waves Transmission Through Porous Breakwater, Stanislaw R. Massel and Piotr Butowski, 333
- Wind; Coastal engineering; Models; Wave energy; Wave height; Wave refraction; Waves**
Verification of a Wave Refraction Model Utilizing Recorded and Observed Wave Data, G. Henderson and N. B. Webber, 101
- Wind; Currents (water); Field investigations; Motion; Sand; Sediment transport; Surf; Suspended load; Wave measurement**
Field Measurements of Sand Motion in the Surf Zone, Douglas L. Inman, James A. Zampol, Thomas E. White, Daniel M. Hanes, B. Walton Waldorf and Kim A. Kastens, 1214
- Wind; Data analysis; Lake waves; Michigan; Wave generation; Wave measurement; Waves; Wave spectra**
A Measurement of Slope, Curvature, and Directional Spectra of Wind Waves in Lake Michigan, Paul C. Liu, 432
- Wind; High frequency; Meteorological data; Oceanographic data; Ocean waves; Radar mapping; Wave measurement; Wave spectra**
HF Radar Mapping of Extensive Ocean Windfields, P. E. Dexter and R. C. Casey, 363
- Wind; Kinematics; Ocean waves; Offshore platforms; Statistics; Wave measurement; Wave velocity**
Field Measurements of Wind Wave Kinematics, J. A. Battjes and J. van Heteren, 347
- Wind; Wind profiles; Wind speed; Coastal engineering; Measurement; Oceanography**
On the Correction of Land-Based Wind Measurements for Oceanographic Applications, S. A. Hsu, 708
- Wind; Wind speed; Australia; Ocean waves; Offshore drilling; Offshore platforms; Oil and gas fields; Wave measurement**
Wave Hindcasts and Measurements Bass Strait, M. N. Silbert, T. P. Barnett, D. J.H. Peters and R. C. Hamilton, 384
- Wind action geology; Australia; Dunes; Sand control; Sediment transport; Shore protection**
Wind and Sediment Movement in Coastal Dune Areas, John R. Hails and John Bennett, 1564
- Wind action geology; Wind speed; Coasts; Field investigations; Sand; Sand control; Sediment transport; West Germany**
Sand Transport Under the Action of Wind, Ulrich Zanke, 1575
- Wind direction; Hurricanes; Predictions; Wave energy; Wave generation; Wave height; Waves**
Prediction of Dominant Wave Properties Ahead of Hurricanes, Omar H. Shemdin, 600
- Wind forces; Australia; Breakwaters; Coastal structures; Design; Harbors; Shore protection; Storms; Storm surges**
The Design Concept of Dual Breakwaters and its Application to Townsville, Australia, W. Bremner, D. N. Foster, C. A. Miller and B. C. Wallace, 1899
- Wind forces; Bulk cargo; Currents (water); Jetties; Mathematical models; Mooring; Ships**
Mooring Forces Induced by Passing Ships - Measurements in Prototype, K. Haffke, 2689
- Wind profiles; Wind speed; Coastal engineering; Measurement; Oceanography; Wind**
On the Correction of Land-Based Wind Measurements for Oceanographic Applications, S. A. Hsu, 708
- Wind profiles; Wind velocity; Anemometers; Friction factor; Hawaii; Tsunamis; Turbulent flow**
Tsunami Prone Friction Factors From Wind Measurements, Charles L. Bretschneider, 672
- Wind speed; Australia; Continental shelf; Currents (water); Field tests; Models; Predictions; Sediment transport; Wave height**
Sediment Dispersal on the NSW Continental Shelf, Ron Boyd, 1363
- Wind speed; Australia; Ocean waves; Offshore drilling; Offshore platforms; Oil and gas fields; Wave measurement; Wind**
Wave Hindcasts and Measurements Bass Strait, M. N. Silbert, T. P. Barnett, D. J.H. Peters and R. C. Hamilton, 384
- Wind speed; Coastal engineering; Measurement; Oceanography; Wind; Wind profiles**
On the Correction of Land-Based Wind Measurements for Oceanographic Applications, S. A. Hsu, 708
- Wind speed; Coasts; Field investigations; Sand; Sand control; Sediment transport; West Germany; Wind action geology**
Sand Transport Under the Action of Wind, Ulrich Zanke, 1575
- Wind velocity; Anemometers; Friction factor; Hawaii; Tsunamis; Turbulent flow; Wind profiles**
Tsunami Prone Friction Factors From Wind Measurements, Charles L. Bretschneider, 672

Author Index

- Ackers, P.**
Dispersion of Cooling Water from a Coastal LNG Plant, with J. D. Pitt, G. Thompson and K. G. Rippin, 2794
- Allison, H.**
Resonances of Coastal Waters Between Perth and Geraldton, with A. Grassia and R. Litchfield, 290
- Anastasiou, K.**
See J. R. Chaplin, 31
- Ayer, Robert M.**
See Jiin-Jen Lee, 812
- Bade, P.**
Energy Transmission Over Break Water - A Design Criterion?, with H. Kaldenhoff, 1886
- Bailard, James A.**
See Scott A. Jenkins, 1527
- Baird, William F.**
Report on the Damages to the Sines Breakwater, Portugal, with Joseph M. Caldwell, Billy L. Edge and Orville T. Magoon, 3060
- Bakker, W. T.**
Probabilistic Design of Sea Defences, with J. K. Vrijling, 2041
- Barff, J. G.**
See D. A. Robinson, 885
- Barg, Gunther**
Experimental Evaluation of Heat Exchange Between Water Surface and Atmosphere, with Horst Schwarze and Gerhard Visscher, 2848
- Barnett, T. P.**
See M. N. Silbert, 384
- Barr, David A.**
See James B. McKenzie, 1547
- Barthel, Volker**
Wave Energy Distribution in an Estuary, 2338
See Winfried Siefert, 2924
- Barwis, John H.**
See Miles O. Hayes, 897
- Battjes, J. A.**
Field Measurements of Wind Wave Kinematics, with J. van Heteren, 347
Velocity Field in a Steady Breaker, with T. Sakai, 499
See T. Sakai, 121
- Baxter, T.**
See N. V.M. Odd, 2375
- Bennett, John**
See John R. Hails, 1564
- Berndt, D.**
Artificial Roughness in Physical Models of Estuaries for Storm Surge Investigations, with E. Giese, H. Schwarze and H.-J. Vollmers, 2493
- Bijker, E. W.**
Sedimentation in Channels and Trenches, 1707
- Bohlen, W. Frank**
A Comparison Between Dredge Induced Sediment Resuspension and that Produced by Natural Storm Events, 1699
- Borgman, Leon R.**
Conditional Simulations of Ocean Wave Properties, 318
- Bosman, D. E.**
See J. A. Zwamborn, 1949
- Bosman, J. J.**
See C. H. Hulsbergen, 310
- Bowers, E. C.**
Long Period Disturbances Due to Wave Groups, 610
- Bowman, G. M.**
See B. G. Thom, 934
- Boyd, Ron**
Sediment Dispersal on the NSW Continental Shelf, 1363
- Bradshaw, Mark P.**
Topographic Control of Run-Up Variability, 1091
- Brebner, Arthur**
Sand Bed-Form Lengths Under Oscillatory Motion, 1339
- Breeding, J. Ernest, Jr.**
Ray Curvature and Refraction of Wave Packets, 82
- Bremner, W.**
The Design Concept of Dual Breakwaters and its Application to Townsville, Australia, with D. N. Foster, C. A. Miller and B. C. Wallace, 1899
- Bretschneider, Charles L.**
Tsunami Prone Friction Factors From Wind Measurements, 672
- Britton, G. W.**
See K. A. Heathcote, 1850
- Bruno, R. O.**
Longshore Transport Evaluations at a Detached Breakwater, with R. G. Dean and C. G. Gable, 1452
- Burcharth, Hans F.**
A Comparison of Nature Waves and Model Waves with Special Reference to Wave Grouping, 2989
Full Scale Trails of Dolosse to Destruction, 1929
- Burrage, D. M.**
See J. B. Hinwood, 3024
- Busching, Fritz**
Full Scale Near Surface Water Particle Velocities and Pressure Acting on an Inclined Tubular Member, with Eckehard Martini, 1870
- Butowski, Piotr**
See Stanislaw R. Massel, 333
- Byrne, R. J.**
Tidal Prism-Inlet Area Relations for Small Tidal Inlets, with R. A. Gammisch and G. R. Thomas, 2515

- Caldwell, Joseph M.**
See William F. Baird, 3060
- Cardone, V. J.**
See G. Z. Forristall, 567
- Casey, R. C.**
See P. E. Dexter, 363
- Chaplin, J. R.**
Some Implications of Recent Advances in Wave Theories, with K. Anastasiou, 31
- Chapman, David M.**
Beach Nourishment as a Management Technique, 1635
The Dynamic Swept Prism, with A. W. Smith, 1036
- Chappell, John**
Inshore-Nearshore Morphodynamics - A Predictive Model, 963
- Chew, S. Y.**
Major Reclamation Scheme for Marina City, Singapore, with J. Wei, 2243
- Chiang, Wen-Li**
See Jiin-Jen Lee, 812
- Chu, Wen-Sen**
Parameter Identification in Estuarine Modeling, with William W.-G. Yeh, 2431
- Clark, Denton**
See James R. Walker, 1969
- Cokelet, E. D.**
See D. H. Peregrine, 512
- Coleman, J. M.**
See S. P. Murray, 1679
- Cook, D. J.**
See D. A. Robinson, 885
- Cooper, Curtis**
Considerations in the Design of an Offshore Data Collection Program Program, with German Febres, 2904
- Cowell, Peter J.**
Breaker Type and Phase Shifts on Natural Beaches, 997
- Crookshank, N.**
See D. Prandle, 2411
- Daemrich, Karl-Friedrich**
Investigations on Irregular Waves in Hydraulic Models, with Wolf-Dietrich Eggert and Soren Kohlhase, 186
- Dalrymple, Robert A.**
See Bruce A. Ebersole, 2708
- Dandy, Graeme C.**
Water Movement Studies Required for Port Planning, with Desmond A. Mills and John B. Hinwood, 3007
- Davesne, M.**
See J. P. Lepetit, 2858
- Dean, B. K.**
See A. G.F. Eddie, 2061
- Dean, R. G.**
Beach Cusps at Point Reyes and Drakes Bay Beaches, California, with E. M. Maumey, 863
See R. O. Bruno, 1452
- Deguchi, Ichiro**
See Toru Sawaragi, 1194
- Detle, Hans H.**
Migration of Longshore Bars, 1475
- Dexter, P. E.**
HF Radar Mapping of Extensive Ocean Windfields, with R. C. Casey, 363
- Domurat, G. W.**
See R. J. Seymour, 1415
- Draper, Laurence**
Sources of Measured Wave Data, 372
- Druery, Bruce M.**
Estuarine Response to Dredging in the Tweed River, Australia, 1598
Mechanisms Operating at a Jettied River Entrance, with Alexander F. Nielsen, 2605
- Durand, Thomas J.P.**
Wave-Induced Seepage Effects on a Vertical Cylinder, with Peter L. Monkneyer, 1782
- Ebersole, Bruce A.**
Numerical Modelling of Nearshore Circulation, with Robert A. Dalrymple, 2708
- Eddie, A. G.F.**
The Effects of Construction Techniques & Bulk Terminal Operational Requirements on the Design Criteria for Island Breakwaters, with J. D. Lawson, H. R. Graze and B. K. Dean, 2061
- Edge, Billy L.**
See William F. Baird, 3060
- Eggert, Wolf-Dietrich**
See Karl-Friedrich Daemrich, 186
- Everts, Craig H.**
Design of Enclosed Harbors to Reduce Sedimentation, 1511
- Falconer, Roger A.**
Modelling of Planform Influence on Circulation in Harbours, 2724
- Febres, German**
See Curtis Cooper, 2904
- Fenton, J. D.**
Accurate Numerical Solutions for Nonlinear Waves, with M. M. Rienecker, 50
- Feuillet, J.**
Stability of Rubble Mound Breakwater, with M. Sabaton, 1989
- Fidler, Bruce R.**
See Bryan R. Pearce, 2395
- Fleming, C. A.**
See D. H. Swart, 1274
See L. Summers, 2871
- Flick, Reinhard E.**
Two-Dimensional Surf Beat, with Douglas L. Inman and Robert T. Gaza, 624

- Ford, L. R.**
See D. C. Patterson, 1648
- Forristall, G. Z.**
Directional Wave Spectra and Wave Kinematics in Hurricanes Carmen and Eloise, with E. G. Ward and V. J. Cardone, 567
- Foster, D. N.**
See W. Bremner, 1899
- Funke, E. R.**
On the Synthesis of Realistic Sea States, with E. P.D. Mansard, 2971
See J. Ploeg, 135
See E. P.D. Mansard, 154
See D. Prandle, 2411
- Gable, C. G.**
See R. J. Seymour, 1401
See R. O. Bruno, 1452
- Gaillard, Pierre**
Method of Analysis of Random Wave Experiments with Reflecting Coastal Structures, with Michael Gauthier and Forrest Holly, 204
- Gammisch, R. A.**
See R. J. Byrne, 2515
- Gauthier, Michael**
See Pierre Gaillard, 204
- Gaza, Robert T.**
See Reinhard E. Flick, 624
- Gerritsen, F.**
See M. S. Yalin, 2669
- Gerritsen, Franciscus**
Wave Attenuation and Wave Set-Up on a Coastal Reef, 444
- Giese, E.**
See D. Berndt, 2493
- Gopalakrishnan, T. C.**
Boundary Conditions for Analysis of Flow in Tidal Inlets, with J. L. Machemehl, 2593
- Gordon, A. D.**
An Approach to Understanding Coastal Processes, with D. B. Lord, 1234
See A. W. Smith, 1122
See A. F. Nielsen, 2459
- Goring, Derek**
The Generation of Long Waves in the Laboratory, with Fredric Raichlen, 763
- Goto, Chiaki**
Run-Up of Tsunamis by Linear and Nonlinear Theories, with Nobuo Shuto, 695
- Gourlay, M. R.**
See H. P. Riedel, 2548
- Gourlay, Michael R.**
Beaches: Profiles, Processes and Permeability, 1319
- Grassia, A.**
See H. Allison, 290
- Gravesen, H.**
See N.-E. Ottesen Hansen, 784
- Graze, H. R.**
See A. G.F. Eddie, 2061
- Haffke, K.**
Mooring Forces Induced by Passing Ships - Measurements in Prototype, 2689
- Hails, John R.**
Wind and Sediment Movement in Coastal Dune Areas, with John Bennett, 1564
- Hamilton, R. C.**
See M. N. Silbert, 384
- Hammack, J. L.**
Long Waves Generated by Complex Bottom Motions, with E. Raichlen, 639
- Hanes, Daniel M.**
See Douglas L. Inman, 1214
- Hansen, J. Buhr**
Experimental Investigations of Periodic Wave Near Breaking, 260
- Hansen, N.-E. Ottesen**
Correct Reproduction of Group-Induced Long Waves, with Stig E. Sand, H. Lundgren, Torben Sorensen and H. Gravesen, 784
- Harikai, S.**
See T. O. Sasaki, 1071
- Haring, Jac**
See J. van de Kreeke, 2625
- Harms, Volker W.**
Floating Breakwater Performance Comparison, 2135
- Harper, Bruce A.**
See Rodney J. Sobey, 725
- Harper, J. R.**
See E. H. Owens, 1343
- Hattori, Masataro**
Onshore-Offshore Transport and Beach Profile Change, with Ryoichi Kawamata, 1178
- Hauguel, A.**
A Numerical Model of Storm Waves in Shallow Water, 746
- Hayes, Miles O.**
Soft Designs for Coastal Protection at Seabrook Island, S.C., with Timothy W. Kana and John H. Barwis, 897
- Heathcote, K. A.**
Construction and Model Investigation of Stormwater Outfall, with G. W. Britton, 1850
- Heerten, Georg**
Long-Term Experience with the use of Synthetic Filter Fabrics in Coastal Engineering, 2172
- Henderson, G.**
Verification of a Wave Refraction Model Utilizing Recorded and Observed Wave Data, with N. B. Webber, 101
- Herbich, John B.**
See David A. Knoll, 1743
- Hinwood, J. B.**
Integration and Computation in an Environmental Study, with J. E. Watson and D. M. Burrage, 3024

- Hinwood, John B.**
See Graeme C. Dandy, 3007
- Holly, Forrest**
See Pierre Gaillard, 204
- Holz, K.-P.**
Automatic Calibration of Numerical Tidal Models,
with U. Januszewski, 2448
- Horikawa, Kiyoshi**
Dynamic Characteristics in the Nearshore Area, with
Masahiko Isobe, 480
See Akira Watanabe, 1106
- Hotta, Shintaro**
Wave Height Distribution Around Permeable
Breakwaters, 221
- Hou, Ho-Shong**
Relationship Between Alongshore Wave Energy and
Littoral Drift in the Mid West Coast at Taiwan,
with Chung-Pan Lee and Lung-Hui Lin, 1254
- Howell, Gary**
Florida Coastal Data Network, 421
- Hsiao, S. V.**
An Investigation of Wave Sheltering by Islands, with
J. F. Vesecky and O. H. Shemdin, 840
- Hsu, S. A.**
On the Correction of Land-Based Wind
Measurements for Oceanographic Applications, 708
- Hulsbergen, C. H.**
A Closely Responding, Versatile Wave Tunnel, with
J. J. Bosman, 310
- Humphreys, Adrian C.**
See Bryan R. Pearce, 2395
- Igarashi, H.**
See T. O. Sasaki, 1071
- Inman, Douglas L.**
Field Measurements of Sand Motion in the Surf
Zone, with James A. Zampol, Thomas E. White,
Daniel M. Hanes, B. Walton Waldorf and Kim A.
Kastens, 1214
See Reinhard E. Flick, 624
See Scott A. Jenkins, 1527
- Isobe, Masahiko**
See Kiyoshi Horikawa, 480
- Iwai, Akira**
Ship-Bridge-Pier Protective Systems, with Hitoshi
Nagasawa, Kazuki Oda and Kuniaki Shoji, 2259
- Jackson, G. W.**
An Electromagnetic Analogy For Long Water
Waves, with D. L. Wilkinson, 801
- Jamieson, W. W.**
See G. R. Mogridge, 1830
- Januszewski, U.**
See K.-P. Holz, 2448
- Jenkins, Scott A.**
Opening and Maintaining Tidal Lagoons & Estuaries,
with Douglas L. Inman and James A. Bailard, 127
- Jonsson, Ivar G.**
See Ove Skovgaard, 823
- Jothishankar, N.**
Waves Forces on Offshore Pipelines, with V. Sundar,
1820
- Kai, Yen**
Some Aspects of Coastal Engineering Research
Works in China, 1734
- Kakuno, Shohachi**
See Shoshichiro Nagai, 2024
- Kaldenhoff, H.**
See P. Bade, 1886
- Kamphuis, J. W.**
Non-Resonant Wave Agitation in Small Craft
Harbours, with D. A.Y. Smith, 241
- Kana, Timothy W.**
Nearshore Suspended Sediment Load During Storm
and Post-Storm Conditions, with Larry G. Ward,
1158
See Miles O. Hayes, 897
- Kashiwamura, Masakazu**
On a Role of the Interfacial Froude Number, 2778
- Kastens, Kim A.**
See Douglas L. Inman, 1214
- Kawamata, Ryoichi**
See Masataro Hattori, 1178
- Keats, A. J.**
See R. C. Nelson, 2532
- Kimura, Akira**
Statistical Properties of Random Wave Groups, 2952
- Kjeldsen, Soren Peter**
Wave-Wave Interactions, Current-Wave Interactions
and Resulting Extreme Waves and Breaking Waves,
with Dag Myrhaug, 2275
- Knoll, David A.**
Simultaneous Waves and Current Forces on a
Pipeline, with John B. Herbich, 1743
- Kohlhase, Soren**
See Karl-Friedrich Daemrich, 186
- Krause, G.**
Separation of Climatic Fluctuations and Impacts of
Engineering Activities in Estuaries, 2323
- Kuang-ming, Yu**
The Dissipation of Wave Energy by Turbulence, 850
- Latteux, B.**
Harbour Design Including Sedimentological Problems
Using Mainly Numerical Technics, 2211
- Lawson, J. D.**
See A. G.F. Eddie, 2061
- Lawson, N. V.**
Realtime Wave Analysis, Newcastle, Australia, with
P. H. Youil, 412
- Layton, Jeffrey A.**
Hydraulic Circulation Performance of a Curvilinear
Marina, 2743
- Lee, Chung-Pan**
See Ho-Shong Hou, 1254

- Lee, Jiin-Jen**
Interactions of Waves With Submarine Trenches,
with Robert M. Ayer and Wen-Li Chiang, 812
- Le Mehaute, Bernard**
See John D. Wang, 1994
- Lepetit, J. P.**
Dynamics of Silt in Estuary. Residual Current or
Flocculation Which Prevails?, with M. Davesne,
2858
- Leslie, K. C.**
See R. M. Noble, 2106
- Li, Yu-cheng**
See Zhu-zhuang Xin, 2081
- Lin, Lung-Hui**
See Ho-Shong Hou, 1254
- Lindquist, Roger W.**
Design of an Intermittently Operated Outfall, with
George J. Murphy, 2834
- Litchfield, R.**
See H. Allison, 290
- Liu, Paul C.**
A Measurement of Slope, Curvature, and Directional
Spectra of Wind Waves in Lake Michigan, 432
- Lloyd, R. J.**
Noosa Beach Restoration Scheme, 1618
- Loewy, E.**
Breakwater with a Sand Bitumen Core, with K. G.
Whitthaus, R. J. Maddrell and J. P. Wood, 2192
- Lofquist, Karl E. B.**
Measurements of Oscillatory Drag on Sand Ripples,
3104
- Longuet-Higgins, M. S.**
Contribution to the Discussion During Session C,
Coastal Processes, Friday, March 28, 2:00 P.M.,
3107
The Unsolved Problem of Breaking Waves, 1
- Lord, D. B.**
See A. D. Gordon, 1234
- Lundgren, H.**
See N.-E. Ottesen Hansen, 784
- Machemehl, J. L.**
See T. C. Gopalakrishnan, 2593
- Maddrell, R. J.**
See E. Loewy, 2192
- Madsen, P. A.**
Some Recent Results for Wave Induced Motions of a
Ship in Shallow Water, with I. A. Svendsen and C.
Michaelsen, 3040
- Magoon, Orville T.**
See William F. Baird, 3060
- Mansard, E. P.D.**
The Measurement of Incident and Reflected Spectra
Using a Least Squares Method, with E. R. Funke,
154
See E. R. Funke, 2971
- Martini, Eckehard**
See Fritz Busching, 1870
- Massel, Stanislaw R.**
Wind Waves Transmission Through Porous
Breakwater, with Piotr Butowski, 333
- Maurmeyer, E. M.**
See R. G. Dean, 863
- McIver, P.**
See D. H. Peregrine, 512
- McKenzie, James B.**
Research in Southern Queensland into the
Management of Coastal Sand Dunes, with David
A. Barr, 1547
- Mettam, John Dorrington**
Can We Develop New Breakwater Formulae, 2302
- Michaelsen, C.**
See P. A. Madsen, 3040
- Mikhailov, Leren P.**
Coast Protection Against the Action of Waves and
Currents, with Sergei M. Uspenskii, 2120
- Mikkelsen, Lars**
Sedimentation in Dredged Navigation Channels, with
Preben Mortensen and Torben Sorensen, 1718
- Miller, C. A.**
See W. Bremner, 1899
- Mills, Desmond A.**
See Graeme C. Dandy, 3007
- Mitchell, George M.**
See Rodney J. Sobey, 725
- Mizuguchi, Masaru**
An Heuristic Model of Wave Height Distribution in
Surf Zone, 278
- Mizumura, Kazumasa**
Littoral Drift on Sand Near Port of Oarai, 2157
- Moes, J.**
See J. A. Zwamborn, 1949
- Mogridge, G. R.**
Wave Impact Pressures on Composite Breakwaters,
with W. W. Jamieson, 1830
- Monkmeyer, Peter L.**
See Thomas J.P. Durand, 1782
- Mortensen, Preben**
See Lars Mikkelsen, 1718
- Murphy, George J.**
See Roger W. Lindquist, 2834
- Murray, S. P.**
Eddy Currents and Sediment Transport Off the
Damietta Nile, with J. M. Coleman, H. H. Roberts
and M. Salama, 1679
- Myrhaug, Dag**
See Soren Peter Kjeldsen, 2275
- Naaes, Arvid**
The Effect of Breaking Waves on the Mixing of
Liquid Pollutants into the Sea, 2758
- Nagai, Shoshichiro**
Seawalls in Deep Seas, with Shohachi Kakuno, 2024

- Nagasawa, Hitoshi**
See Akira Iwai, 2259
- Nagle, B.**
See P. D. Treloar, 1910
- Nelson, R. C.**
A Coastal Inlet with Fixed Bed and Mobile Sides,
with A. J. Keats, 2532
- Nielsen, A. F.**
Tidal Inlet Behavioural Analysis, with A. D. Gordon,
2459
- Nielsen, Alexander F.**
See Bruce M. Drury, 2605
- Nishimura, Tsukasa**
See Sotoaki Onishi, 2653
- Noble, R. M.**
Siting and Design Criteria of Dock Structures in the
Marshall Islands, with K. C. Leslie and D. O'Day,
2106
- Nummendal, D.**
See E. H. Owens, 1343
- O'Brien, Morrrough P.**
Comments on Tidal Entrances on Sandy Coasts,
2502
- Ochi, Michel K.**
Prediction of the Severest Significant Wave Height,
with Joseph E. Whalen, 587
- Oda, Kazuki**
See Akira Iwai, 2259
- O'Day, D.**
See R. M. Noble, 2106
- Odd, N. V.M.**
Port of Brisbane Siltation Study, with T. Baxter, 2375
- Onishi, Sotoaki**
Study on Vortex Current in Strait with Remote-
Sensing, with Tsukasa Nishimura, 2653
- Owens, E. H.**
Sediment Transport Processes and Coastal Variability
on the Alaskan North Slope, with J. R. Harper and
D. Nummendal, 1343
- Partenscky, H. W.**
See E. Renger, 2479
- Patterson, D. C.**
Capricorn Coast Beaches, with L. R. Ford, 1648
- Pearce, Bryan R.**
A 3-D Model for Penobscot Bay, Maine, with Bruce
R. Fidler and Adrian C. Humphreys, 2395
- Peregrine, D. H.**
The Fluid Mechanics of Waves Approaching
Breaking, with E. D. Cokelet and P. McIver, 512
- Peters, D. J.H.**
See M. N. Silbert, 384
- Philip, Neale A.**
The Beach Improvement Programme: New South
Wales, with Philip H. Whaite, 1668
- Pirie, D. M.**
See R. J. Seymour, 1415
- Pitt, J. D.**
See P. Ackers, 2794
- Ploeg, J.**
A Survey of "Random" Wave Generation
Techniques, with E. R. Funke, 135
- Pope, Joan**
See James R. Walker, 1969
- Prandle, D.**
The Use of Array Processors for Numerical Modeling
of Tidal Estuary Dynamics, with E. R. Funke, N.
Crookshank and R. Renner, 2411
- Puls, W.**
See J. Sundermann, 1583
- Raichlen, E.**
See J. L. Hammack, 639
- Raichlen, Fredric**
See Derek Goring, 763
- Renger, E.**
Sedimentation Processes in Tidal Channels and Tidal
Basins Caused by Artificial Constructions, with H.
W. Partenscky, 2479
- Renner, R.**
See D. Prandle, 2411
- Riedel, H. P.**
Inlets/Estuaries Discharging into Sheltered Waters,
with M. R. Gourlay, 2548
- Rienecker, M. M.**
See J. D. Fenton, 50
- Riho, Yoshihiko**
See Akira Watanabe, 1106
- Rippin, K. G.**
See P. Ackers, 2794
- Ritchie, William**
Environmental Aspects of Oil and Gas Pipeline
Landfalls in Northeast Scotland, 2935
- Roberts, H. H.**
See S. P. Murray, 1679
- Roberts, Harry H.**
Physical Processes and Sediment Flux Through Reef-
Lagoon Systems, 946
See John T. Wells, 1381
- Robinson, D. A.**
Barron River Delta Investigation, with D. J. Cook
and J. G. Barff, 885
- Roy, P. S.**
Geological Controls on Process-Response, SE
Australia, with A. W. Stephens, 913
- Sabatón, M.**
See J. Feuillet, 1989
- Safaie, B.**
Experimental Study of the Buoyant Surface Jet with
the Presence of Bottom Boundary and Cross
Current, 2814
- Sakai, T.**
Wave Shoaling Calculated From Cokelet's Theory,
with J. A. Battjes, 121
See J. A. Battjes, 499

- Salama, M.**
See S. P. Murray, 1679
- Sand, Stig E.**
See N.-E. Ottesen Hansen, 784
- Sasaki, T. O.**
Nearshore Currents on a Partially Rocky Shore, with H. Igarashi and S. Harikai, 1071
- Sato, Shoji**
Artificial Resort Beach Protected by Offshore Breakwaters and Groins, with Norio Tanaka, 2004
- Sawaragi, Toru**
On-Offshore Sediment Transport Rate in the Surf Zone, with Ichiro Deguchi, 1194
- Schneider, Christine**
Visually Observed Wave Data at PT. Mugu, Calif., with J. Richard Weggel, 381
- Schwarze, H.**
See D. Berndt, 2493
- Schwarze, Horst**
See Gunther Barg, 2848
- Seymour, R. J.**
Nearshore Sediment Transport Study Experiments, with C. G. Gable, 1401
A Sediment Trapping Experiment at Santa Cruz, CA, with G. W. Domurat and D. M. Pirie, 1415
- Shemdin, O. H.**
See S. V. Hsiao, 840
- Shemdin, Omar H.**
Prediction of Dominant Wave Properties Ahead of Hurricanes, 600
- Shibano, Y.**
See R. Silvester, 1305
- Shigemura, Toshiyuki**
Wave Forces on an Inclined Circular Cylindrical Pile, 1762
- Shoji, Kuniaki**
See Akira Iwai, 2259
- Short, A. D.**
Beach Response to Variations in Breaker Height, 1016
- Shuto, Nobuo**
See Chiaki Goto, 695
- Siefert, Winfried**
The German "Moran" Project, with Volker Barthel, 2924
- Silbert, M. J. N.**
Wave Hindcasts and Measurements Bass Strait, with T. P. Barnett, D. J.H. Peters and R. C. Hamilton, 384
- Silvester, R.**
Zeta Bays, Pocket Beaches and Headland Control, with Y. Tsuchiya and Y. Shibano, 1305
- Skovgaard, Ove**
Transient Finite-Difference Tsunami Calculations, with Ivar G. Jonsson, 823
- Smith, A. W.**
Secondary Sand Transport Mechanisms, with A. D. Gordon, 1122
See David M. Chapman, 1036
- Smith, D. A.Y.**
See J. W. Kamphuis, 241
- Sobey, Rodney J.**
Numerical Modelling of Tropical Cyclone Storm Surge, with Bruce A. Harper and George M. Mitchell, 725
- Sorensen, Robert M.**
The Corps of Engineer's General Investigation of Tidal Inlets, 2563
- Sorensen, Torben**
See N.-E. Ottesen Hansen, 784
See Lars Mikkelsen, 1718
- Stephens, A. W.**
See P. S. Roy, 913
- Stive, M. J.F.**
Velocity and Pressure Field of Spilling Breakers, 547
- Su, Chi-Fu**
New Jetties for Tung-Kang Fishing Harbor, Taiwan, 2228
- Summers, L.**
For Disposal: 10 M.c.u.m. of Calcium Carbonate Slurry, with C. A. Fleming, 2871
- Sunamura, Tsuguo**
A Laboratory Study of Offshore Transport of Sediment and a Model for Eroding Beaches, 1051
- Sundar, V.**
See N. Jothishankar, 1820
- Sundermann, J.**
A Numerical Model for Dune Dynamics, with H.-J. Vollmers and W. Puls, 1583
- Suzuki, Yasumasa**
See Tokuo Yamamoto, 1800
- Svendsen, I. A.**
See P. A. Madsen, 3040
- Swart, D. H.**
Longshore Water and Sediment Movement, with C. A. Fleming, 1274
- Tanaka, Norio**
See Shoji Sato, 2004
- Thimakorn, Prida**
An Experiment on Clay Suspension Under Water Waves, 2891
- Thom, B. G.**
Beach Erosion-Accretion at Two Time Scales, with G. M. Bowman, 934
- Thomas, G. R.**
See R. J. Byrne, 2515
- Thompson, G.**
See P. Ackers, 2794
- Tilmans, Wiel M.K.**
See Jan van de Graaff, 1140

- Treloar, P. D.**
Design of an Overtopping Breakwater, with B. Nagle, 1910
- Tsuchiya, Y.**
See R. Silvester, 1305
- Tsuchiya, Yoshito**
Mass Transport in Progressive Waves of Permanent Type, with Takashi Yasuda and Takao Yamashita, 70
- Uspenskii, Sergei M.**
See Leren P. Mikhailov, 2120
- Vallianos, Limberios**
Barden Inlet, NC a Case Study of Inlet Migration, 2638
- van de Graaff, Jan**
Sand Transport by Waves, with Wiel M.K. Tilmans, 1140
- van de Kreeke, J.**
Stability of Estuary Mouths in the Rhine-Meuse Delta, with Jac Haring, 2625
- van Heteren, J.**
See J. A. Battjes, 347
- Vesecy, J. F.**
See S. V. Hsiao, 840
- Vis, F. C.**
Orbital Velocities in Irregular Waves, 173
- Visscher, Gerhard**
See Gunther Barg, 2848
- Visser, P. J.**
Longshore Current Flows in a Wave Basin, 462
- Vollmers, H.-J.**
See J. Sundermann, 1583
See D. Berndt, 2493
- Vrijling, J. K.**
See W. T. Bakker, 2041
- Waddell, Evans**
Wave Forcing of Beach Groundwater, 1435
- Waldorf, B. Walton**
See Douglas L. Inman, 1214
- Walker, James R.**
A Detached Breakwater System for Beach Protection, with Denton Clark and Joan Pope, 1969
A Phased-Dredging Program for Santa Cruz Harbor, with Peter J. Williams, 1492
- Wallace, B. C.**
See W. Bremner, 1899
- Walther, A. W.**
Hydraulic Research in the Oosterschelde Estuary, 2358
- Wang, Hsiang**
A Similarity Model in the Surf Zone, with Wei-Chong Yang, 529
- Wang, John D.**
Criterion for Stability of Shoreline Planform, with Bernard Le Mehaute, 1994
- Wang, Yu-Hwa**
Satellite Applications on a Coastal Inlet Stability Study, 2579
- Ward, E. G.**
See G. Z. Forristall, 567
- Ward, Larry G.**
See Timothy W. Kana, 1158
- Watanabe, Akira**
Beach Profiles and On-Offshore Sediment Transport, with Yoshihiko Riho and Kiyoshi Horikawa, 1106
- Watson, J. E.**
See J. B. Hinwood, 3024
- Webber, N. B.**
See G. Henderson, 101
- Weggel, J. Richard**
See Christine Schneider, 381
- Wei, J.**
See S. Y. Chew, 2243
- Wells, John T.**
Fluid Mud Dynamics and Shoreline Stabilization: Louisiana Chenier Plain, with Harry H. Roberts, 1381
- Whaite, Philip H.**
See Neale A. Philip, 1668
- Whalen, Joseph E.**
See Michel K. Ochi, 587
- White, Thomas E.**
See Douglas L. Inman, 1214
- Wiegel, R. L.**
Tsunamis Along West Coast of Luzon, Philippines, 652
- Wilkinson, D. L.**
See G. W. Jackson, 801
- Williams, Peter J.**
See James R. Walker, 1492
- Witthaus, K. G.**
See E. Loewy, 2192
- Wood, J. P.**
See E. Loewy, 2192
- Wood, T.**
Discrete-Time Modelling of Dispersion in Estuaries, 3075
- Wright, L. D.**
Beach Cut in Relation to Surf Zone Morphodynamics, 978
- Xin, Zhu-zhuang**
The Design and Construction of the New Oil Port in Dalian, CPR, with Yu-cheng Li, 2081
- Yalin, M. S.**
Dynamic Similarity of Transport Phenomena, with F. Gerritsen, 2669
- Yamamoto, Tokuo**
Stability Analysis of Seafloor Foundations, with Yasumasa Suzuki, 1800

Yamashita, Takao
See Yoshito Tsuchiya, 70

Yang, Wei-Chong
See Hsiang Wang, 529

Yasuda, Takashi
See Yoshito Tsuchiya, 70

Yeh, William W-G.
See Wen-Sen Chu, 2431

Youll, P. H.
See N. V. Lawson, 412

Zampol, James A.
See Douglas L. Inman, 1214

Zanke, Ulrich
Sand Transport Under the Action of Wind, 1575

Zwamborn, J. A.
Dolosse Past, Present, Future?, with D. E. Bosman
and J. Moes, 1949